



A Statistical Study of Sources of Variation in Primary Battery Testing

K. Y. Cheung,* W. S. Lindsay, and D. J. Friedland*

Allied Corporation, Buffalo Research Laboratory, Buffalo, New York 14210

ABSTRACT

An analysis of variance (mixed model) experimental design was employed to quantify sources of variation in primary battery testing procedures for lithium/fluorinated carbon (CF_x) systems. Factors investigated were mix repeatability, mix uniformity, electrode fabrication method, and cell assembly and testing. Parameters measured were percent utilization and closed-circuit voltage (CCV) at various depths of discharge (DOD). The standard deviations (for a random cell from a random blend on a random day) for percent utilization and CCV at 50% DOD were 4.2 percentage points (0.49 relative standard deviation) and 16 mV (0.006 relative standard deviation), respectively, indicating that the test method was adequate for evaluation of the performance of different CF_x samples. No significant difference due to electrode fabrication method in any of the measured parameters was observed. The CCV at 50% DOD was identified as the representative quantity of the performance of a CF_x sample. Improvements have been made in the areas of variability identified by this study, leading to more consistent test results.

Extensive study of nonaqueous lithium batteries incorporating fluorinated carbon (CF_x) as a cathode has resulted in commercialization of lithium/carbon monofluoride battery (1-6). The system offers a very stable high discharge voltage (about 2.6V on 1 k Ω load) during 85% of its discharge life, excellent shelf life, and a wide range of operating temperatures. It is used as a backup power supply for volatile computer memory and is a primary power supply in the disk camera, digital watches, and other electronic devices where a portable energy source is required.

We have found large variations in the performance of CF_x samples from different manufacturers and batches. Because no physical or chemical property can reliably predict electrical performance, a battery testing procedure has been developed to evaluate the performance of CF_x prepared from different carbon starting materials under various process conditions.

Any test procedure will be subject to a number of variations other than the intrinsic characteristics of the material of interest. It is very important to separate these variables from the intrinsic properties, so that differences of materials can be investigated. To differentiate a good sample from a bad one, it is necessary to know the precision (standard deviation) of the test method; this allows one to assess the difference that the method is able to detect. We have applied components of variance analysis to our test procedure in order to determine the precision of the test and the contribution of each factor to the overall variation. We also intend to determine in this study a representative quantity of the battery performance of CF_x samples for comparison purposes. In this paper, the results of the statistical study are presented.

Statistical Background

In many scientific test procedures, it is often desirable not only to know the major sources of variation in the experimental data, but to quantify the effect of each factor. The components-of-variance method allows a quantitative analysis. Having identified the major sources of variation, one can improve the test by reducing the contribu-

tions of these major sources. This section explains briefly how the experimental design was set up and discusses some of the terms used in analysis of variance studies.

Proper planning is very important for a meaningful analysis of variance design. Practical experience of the researcher is very helpful in determining what factors should be investigated. Four factors were selected for the analysis of variance design in our study: preparation of the cathode mixture (blend), electrode fabrication methods (method), between-run repeatability (day), and within-run repeatability (cell). The interactions between method and blend, and between method and day, were also investigated. Six cathode mixtures were prepared using one single batch of CF_x , and each mixture was used on two separate days for a total of 12 days. The experimental procedures for a given mixture on a given day consisted of preparing two electrodes for each of the electrode fabrication methods and discharging these electrodes in laboratory test cells with a constant load. A schematic diagram of the design is given in Fig. 1. In the model below, the cell effect, or within-run repeatability, is referred to as either the random experimental error or the noise effect. Although it is true that experimental error is always present in an experiment, it is considered a selected factor here because we made the choice to run a statistical design in which this experimental error could be separated from the other effects by making repeat runs.

Once the factors (potential sources of variation) were identified, the following mathematical model was postulated

$$X_{ijk} = \bar{X}' + M'_i + B'_j + (MB)'_{ij} + D'_{k(j)} + (MD)'_{1k(j)} + E'_{eijk}$$

where

- X_{ijk} = an observation on method i , blend j , day k
- \bar{X}' = average effect
- M'_i = method effect $i = 1, 2$ (fixed effect)
- B'_j = blend effect $j = 1, 2, 3, 4, 5, 6$ (random effect)
- $(MB)'_{ij}$ = method-blend interaction effect (assumed to be a random effect)
- $D'_{k(j)}$ = day effect $k = 1, 2$ (random effect)

* Electrochemical Society Active Member.

Factor in the Design

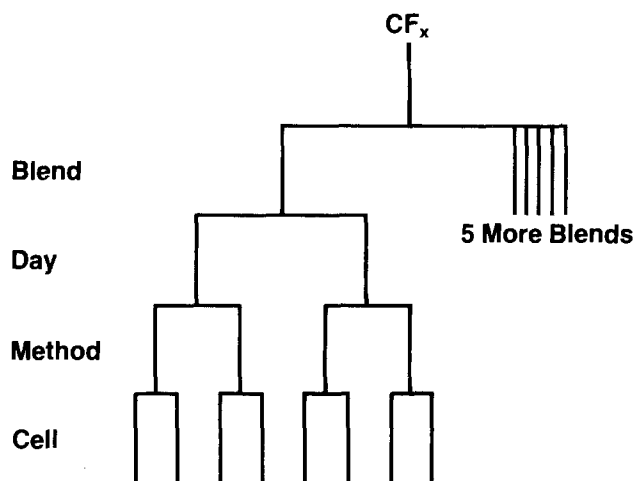


Fig. 1. The statistical design

$(MD)'_{(ikj)}$ = method-day interaction effect (assumed to be a random effect)

$E'_{e(ijk)}$ = random error, cell effect, noise, repeat effect, $e = 1, 2$ (random effect)

This model, in analysis of variance terminology, is a mixed model due to the inclusion of random and fixed effects.

After the model was expressed and the levels of all the factors had been decided, an important mathematical expression known as the expected mean square (EMS) was derived for each factor (Table I). The EMS is the mean square to be expected if the model is correct. Each factor's variance component was determined from the appropriate EMS expression, using a computer program. The EMS expressions were also used to determine which mean squares should be compared in order to test for the statistical significance of effects. For example, in order to determine if the variance component due to "blend" is significantly different from zero, it must be compared to the variance component due to "days." This comparison of ratios is known as the F-test. The resulting F-ratio is compared with published values in statistical F-tables using the proper degrees of freedom associated with the numerator and denominator for each F-ratio. If the observed F-ratio exceeds the tabulated value at some predetermined confidence level, then statistical significance is concluded at that level of confidence. A derivation of an EMS expression is involved, and a simple algorithm (7) has been developed to formulate the EMS expression for each factor in an analysis of variance design. The algorithm makes use of the specified model, whether the factors are fixed or random, and of the levels of each factor. The EMS expressions can be formulated manually, or analysis of variance programs (such as BMDP8V) from the BMDP statistical software package (8) can be used.

There are inseparable subsources of variation contained in the factors selected for this study. The results of this study will reveal the collective contribution of these subfactors to the overall variance. The "blend" factor con-

tains the uniformity of CF_x , the variation of composition in other components, and the repeatability of the mixing method. When a cathode mix is divided into two portions, each run on separate days, the uniformity of the mix is the primary source of variation in the "day" factor. Two electrode fabrication methods are studied: forming a large pellet using all the cathode mix and cutting out electrode pieces for tests (method A); and sampling material from the cathode mix to form electrodes and use as formed (method B). The subfactors included in "method," therefore, are the difference in sampling from both the large pellet and the mix, the pressures of forming the pellets, and the geometric areas. The "cell" factor is similar to the repeatability of a test, consisting of the variation in cell assembly, the environmental factors such as temperature, and the inherent error of the test method. Table II lists the summary of these components in the investigated factors. Results will be discussed in terms of the components which are believed to be the most important (underlined in Table II).

The situation of the interacting factors is more complicated because the numbers of subfactors and interactions are increased. The two interactions (method \times blend and method \times day) considered in this study contain primarily the compounding effects of different fabrication methods and the uniformity of cathode mix. For example, different pelletizing pressures may have enhanced the difference in composition of electrodes, leading to different morphologies in the resultant electrode species. Due to their random nature in contributing to the test results, and in order to evaluate the individual effect of method and uniformity of the mix, we have considered these interactions as a part of the "cell" factor in the discussion of results.

Experimental Section

Preparation of cathode blends.—Six blends containing, by weight, 1 part CF_x (Ozark Mahoning, Lot RT-11-4A), 0.2 parts carbon (Electrodag[®] 230, obtained from Acheson Colloids), and 0.2 parts PTFE (Fluon[®] AD1, obtained from ICI Americas) were prepared in the same way. Electrodag (1.05g) was added to about 20 ml of isopropyl alcohol in a 150 ml beaker and was dispersed by placing the beaker in an ultrasonic bath for about 3 min. CF_x (1.2g) was then added and dispersed in the same way. The pH of the dispersion was adjusted to 10 by dropwise addition of 7.4N NH_4OH , and 0.29 ml of the PTFE dispersion was added with stirring. Once again, the beaker was placed in the ultrasonic bath to assure homogeneity. Finally, solvent was removed by heating on a hot plate, causing coagulation of the dispersion.

Fabrication of electrodes.—Half of each mixture was used to form two 9.5 mm diam pellets at 6.2×10^7 Pa and one 28.6 mm diam pellet at 4.8×10^7 Pa. The three pellets were then heat-treated at 250°C under vacuum for 3h. Two 7×7 mm² electrode pieces were cut from the 28.6 mm pellet. The two 9.5 mm pellets (geometric area 71.3 mm²) and the two cut pieces (geometric area 49 mm²) were tested for battery performance.

Test cell assembly.—The electrolyte used in our tests was 1M $LiBF_4$ in an equal volume mixture of propylene carbonate (PC) and 1,2-dimethoxyethane (DME). The lith-

Table I. Analysis of variance table

Source	Degrees of freedom	Expected mean square
1. Method	1	$24 \sigma_1^2 + 4 \sigma_4^2 + 2 \sigma_5^2 + \sigma_6^2$
2. Blend	5	$8 \sigma_2^2 + 4 \sigma_3^2 + \sigma_6^2$
3. Days (blend)	6	$4 \sigma_3^2 + \sigma_6^2$
4. Method \times blend	5	$4 \sigma_4^2 + 2 \sigma_5^2 + \sigma_6^2$
5. Method \times day (blend)	6	$2 \sigma_5^2 + \sigma_6^2$
6. Runs (method, blend, day)	24	σ_6^2

Table II. Some confounding components in the investigated factors

Blend:	Uniformity of the CF_x sample <u>Mix repeatability</u> — Uniformity of the dispersions — Variations in the mixing processes
Day:	Cathode <u>mix uniformity</u>
Method:	Uniformity of the divided mix — Differences in the sampling procedures — Variations in fabricating the electrodes Difference in geometric area of electrodes
Cell:	Variations of <u>cell assembly and testing</u> — Cell assembly — Environmental factors — Noise

ium salt was obtained from Ozark-Mahoning and dried at 100°C under vacuum. The solvents, purchased from Burdick and Jackson, and Aldrich, respectively, were dried by refluxing with CaH_2 , followed by distillation under reduced pressure for PC and under argon atmosphere for DME. The dried components were transferred into a Vacuum-Atmosphere dry box, and the salt was dissolved in the mixed solvent. The electrolyte was further purified by electrolysis at 2.5V between two lithium electrodes, filtered, and stored over 3A molecular sieves in the dry box.

Test cells, employing a 12.7 mm diam drilled-through PTFE Swagelok® union (Fig. 2), were assembled entirely in the dry box. The CF_x cathode and the lithium anode were separated by a nonwoven polypropylene absorber (Permion® A-1260 supplied by RAI Research Corporation) soaked with the electrolyte. The sandwich was placed between two 304 stainless steel pistons, through which the electrical contact was made.

Data acquisition and analysis.—The assembled test cell was removed from the dry box and discharged across a 10 k Ω resistor. The discharge voltage was recorded every 2h using a HP-3497 multiplexor/voltmeter (measurement precision = 0.3 mV) controlled by a HP-85 computer. The typical discharge curves for this CF_x material are shown in Fig. 3. Because of the sloping nature of these curves, it is not apparent which closed-circuit voltage (CCV) is most representative of the discharge characteristics of the material. Three of the quantities used in this study as measures of battery performance are noted on this figure: discharge voltage at 50% DOD (V_1), 66.7% DOD (V_2), and at 2/3 of the time to the cutoff voltage (V_3). The MINITAB (9) subsystem installed on a Hewlett-Packard Model 3000 computer was used to extract these values from the discharge data. The time to a 2V cutoff was determined by applying the linear regression capabilities of the MINITAB package to the last five ex-

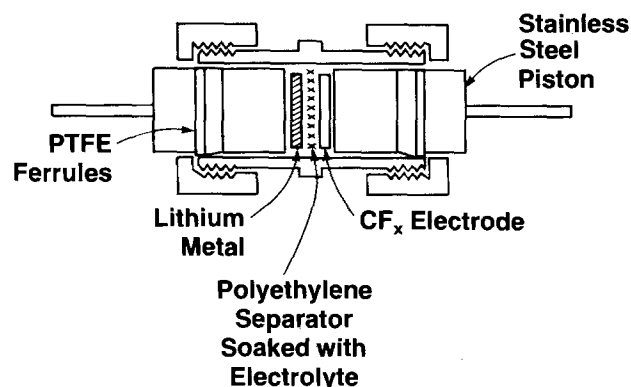


Fig. 2. The demountable test cell made from a drilled-through 1/2 in. PTFE Swagelok union.

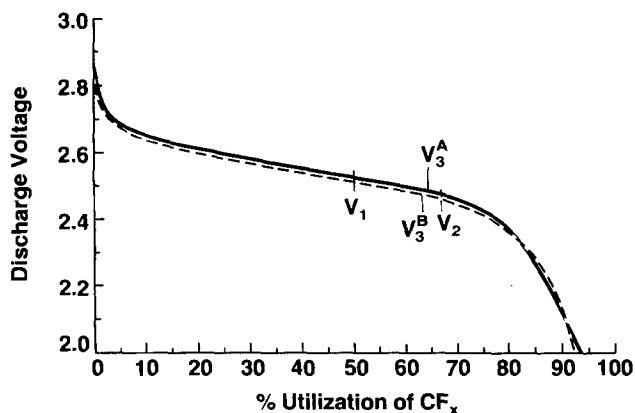


Fig. 3. Typical discharge performance of CF_x electrodes. (—) fabricated using method A; (---) fabricated using method B.

perimental data points, including the first one below 2V. The discharge voltages at 50 and 66.7% DOD were determined by applying the linear regression method to the five data points closest to the desired depth of discharge. The time needed to reach the CCV values differs from cell to cell due to the different weight of electrodes. The average discharge time of 6 typical cells to V_1 , V_2 , V_3 , and cut off voltage is 68, 92, 80, and 119h, respectively.

The fourth measure of battery performance, percent utilization of CF_x , is calculated from the theoretical energy and the energy actually delivered to a 2V cutoff. The theoretical energy is calculated from the weight and fluorine content of the CF_x in the cathode. The delivered energy is determined by integration of the discharge curve prior to the 2V cutoff, using the trapezoid method. Graphical analysis (10) of the data was performed (Fig. 4-7) to identify any outliers which would unduly influence the analysis. An example of an outlier is seen in Fig. 4 for blend 3, method A, day 2. Also, the cell prepared from blend 2 using method B and tested on day 1 is an obvious outlier, as shown in Fig. 5-7. In Fig. 6, the result for blend 4, method B, day 1 also appears to be an outlier. These suspected outliers were verified using statistical methods (Nair's statistic) (11). For every outlier, a value equal to the average of the other values from the mix was assigned before the variance components were calculated. By doing so, the requirement of the analysis of variance program for an equal number of observations per blend was met. Also, the statistical significance of the analysis was not changed any more than that introduced

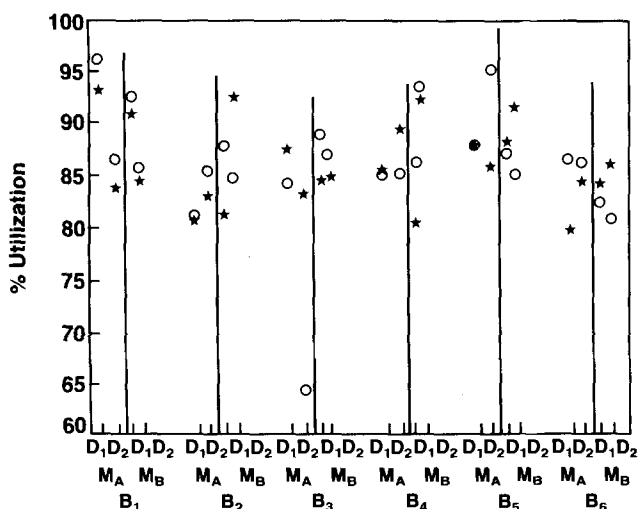


Fig. 4. Graphical analysis of the experimental data for percent utilization. (★) run 1, (○) run 2; M = method, D = day, B = blend.

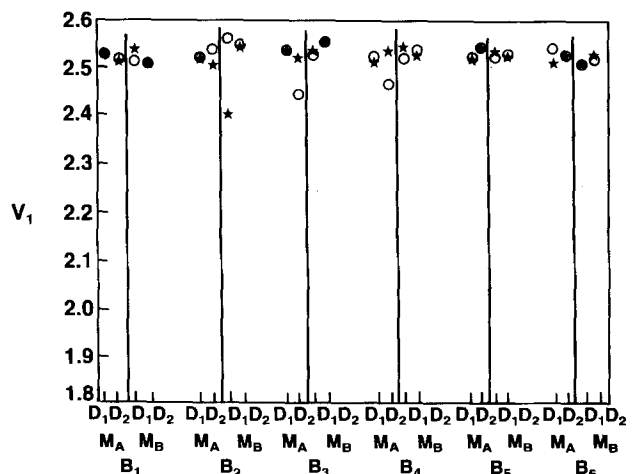


Fig. 5. Graphical analysis of the experimental data for CCV at 50% DOD. (★) run 1, (○) run 2; M = method, D = day, B = blend.

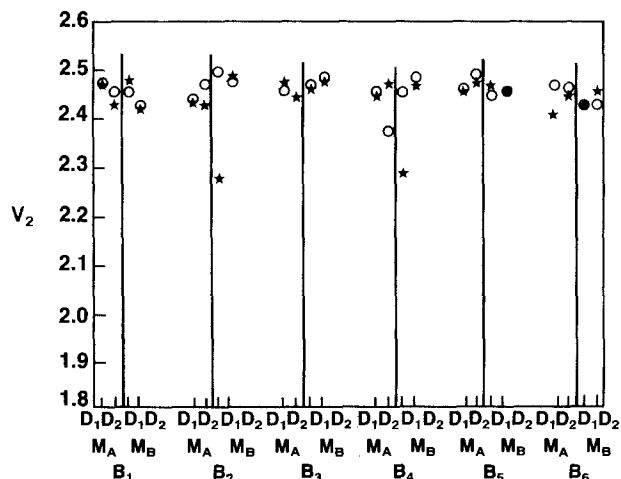


Fig. 6. Graphical analysis of the experimental data for CCV at 67.7% DOD. (★) run 1, (o) run 2; M = method, D = day, B = blend.

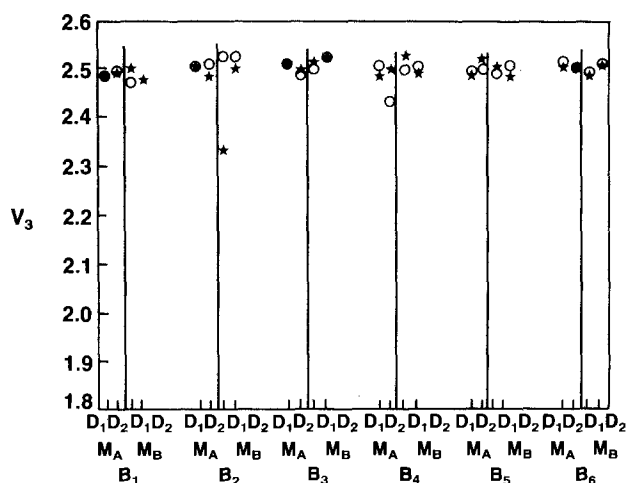


Fig. 7. Graphical analysis of the experimental data for CCV at 2/3 time to cutoff voltage. (★) run 1, (o) run 2; M = method, D = day, B = blend.

by discarding the outliers. The total variance in the measured parameters was separated into the components due to the sources investigated using an analysis of variance program (BMDP8V) from the BMDP statistical software package (8). The computational aspects of analysis of variance will not be discussed here, but many textbooks (12) and journal articles (13) are available which provide the necessary details.

Results and Discussion

The results of the statistical analysis are given in Table III. The standard deviation, as determined by the square root of the total variance of the significant random effects, of percent utilization is 4.2 percentage points (0.49 relative standard deviation). In other words, the precision of the percent utilization determined by our test method is ≈ 4.2 . For the CCV at 50% DOD (V_1) and at 2/3 the time to the cutoff voltage (V_3), the precision is ≈ 16 mV (0.006 relative standard deviation). For the CCV at 66.7% DOD (V_2), the precision is ≈ 38 mV (0.015 relative standard deviation). The CCV precisions are very meaningful quantities when compared to an instrument precision of 0.3 mV. These figures are very close to the acceptable range generally employed in the battery manufacturing industry. This signifies that our test method is adequate for evaluating the battery performance of the fluorinated carbon material.

If a single CCV value had to be chosen as representative of the discharge characteristics of a CF_x sample, V_1 would be a suitable choice. It can be determined precisely, as the standard deviation suggests. Examination of the dis-

Table III. Distribution of variance by sources

	% Utilization	CCV at 50% U (V_1)	CCV at 66.7% U (V_2)	CCV at 2/3 the time to cutoff (V_3)
Standard deviation	4.2	0.016	0.038	0.016
Source	% of total variance			
Mix repeatability	NS	16	3	33
Mix uniformity	44	8	2	NS
Method	NS	NS	NS	NS
Cell assembly and testing	56	76	95	67

NS = not significant.

charge curve (Fig. 3) shows that V_1 is situated at the flat region of the curve and is therefore less susceptible to the variations in the test. V_2 is located nearest the vicinity where the discharge voltage begins to drop. The value of V_2 is therefore sensitive to small variations in battery testings. The choice of V_3 as one of the measured CCV values is rather arbitrary, and it is measured at different DOD for different cells. It is located in the region just before the CCV starts to drop and is therefore a more precise value than V_2 .

Examining the contribution of variance by source, no significant difference due to electrode fabrication method was observed in any of the measured parameters. This indicates that the different pressures used in forming the pellets and the different sampling procedures did not contribute any significant variation to the quantities measured in this study. It also indicates that the different geometric areas of the two types of electrodes in the test did not have any significant effect on the battery performance. The nominal discharge current density (2.6V on 10 k Ω) is 5.31×10^{-1} mA/cm 2 for 49 mm 2 electrodes and is 3.65×10^{-1} mA/cm 2 for 71.3 mm 2 electrodes. We did observe a detrimental effect on battery performances when the geometric area of the electrode was reduced to 36 mm 2 in tests outside of this statistical study. These data suggest that the electrodes formulated and fabricated in the way described can sustain the discharge current densities in the range of our study; when a higher current density is drawn from the cell, the battery performance could be more susceptible to small variations in the electrode formulation, leading to premature failure.

The variance in percent utilization is due to the "mix uniformity" and the "cell assembly and testing," the latter being the more important factor. "Cell assembly and testing" is the major component of variance in CCV values. Mix repeatability is also significant, particularly for V_3 . "Mix uniformity" for CCV values is insignificant compared with the effect it has on percent utilization.

The sample size required to detect a difference in performance between two cells depends on several criteria. The size of the difference to be detected, as well as the desired significance level, must be determined. As shown in Table III, the estimated standard deviation in V_1 for one random cell from a random blend on a random day is 16 mV. Two standard deviations is 32 mV. Therefore, the 95% confidence interval for V_1 would be $V_1 \pm 32$ mV. The largest variance component for V_1 is cell assembly and testing. Thus, the estimated standard deviation of V_1 is decreased by running additional cells. If four cells are tested for a given blend on a given day, the estimated standard deviation of V_1 is reduced to 10 mV, and the 95% confidence interval for V_1 is $V_1 \pm 20$ mV.

Conclusions

The test method described here is adequate for evaluating CF_x samples for nonaqueous lithium battery applications. The CCV at 50% DOD (V_1) is recommended as a representative quantity to measure the performance of a CF_x sample, due to the high precision of this quan-

tity. Fabrication and sampling methods have no significant effect on any of the performance parameters measured. The geometric area of an electrode also shows a null effect. However, if the area is excessively reduced, a detrimental effect will result. Based on our results, mix repeatability, mix uniformity, and cell assembly are the areas in which improvements can be made for more consistent test results. Factors like uniformities of CF_x , cathode mix and electrode in both composition and morphology, good electrical contact in the cell, and thorough wetting of the electrode would likely yield a significant improvement. Indeed, we have made progress along these lines and have now been able to reduce the standard deviation of V_1 to below 10 mV.

Acknowledgments

The authors thank Acheson Colloid and RAI Research Corporation for their respective gifts, the Electrodog® and the initial Permion® A-1260 separator.

Manuscript submitted July 5, 1984; revised manuscript received Sept. 11, 1984. This was Paper 3 presented at the San Francisco, California, Meeting of the Society, May 8-13, 1983.

Allied Corporation assisted in meeting the publication costs of this article.

REFERENCES

1. N. Watanabe and M. Fukuda, U.S. Pat. 3,536,532 (1970).
2. H. F. Hunter and G. J. Heymach, *This Journal*, **120**, 1161 (1973).
3. R. G. Hunter, in "Power Sources 5," D. H. Collins, Editor, p. 729 (1975).
4. A. Morita, T. Iijima, T. Fujii, and H. Ogawa, *J. Power Sources*, **5**, 111 (1980).
5. N. Watanabe, M. Endo, and K. Ueno, *Solid State Ionics*, **1**, 501 (1980).
6. M. Fukuda and T. Iijima, 12th Symposium on Batteries, Japan (1971).
7. C. A. Hicks, *Ind. Quality Control*, **12**, 1 (1956).
8. W. J. Dixon, Editor, "BMDP Statistical Software," University of California Press (1981).
9. T. A. Ryan, B. L. Joiner, and B. F. Ryan, "MINITAB Reference Manual," (1982).
10. R. D. Snee, *J. Quality Technol.*, **15**, 76 (1983).
11. F. E. Grubbs, *Technometrics*, **11**, 1 (1969).
12. G. E. P. Box, W. G. Hunter, and J. S. Hunter, "Statistics For Experimenters," John Wiley & Sons, New York (1978).
13. P. I. Feder, *J. Quality Technol.*, **6**, 98 (1974).

A General Energy Balance for Battery Systems

D. Bernardi,** E. Pawlikowski,* and J. Newman*

Department of Chemical Engineering, University of California, Berkeley, California 94720

ABSTRACT

A general energy balance for battery systems has been developed. This equation is useful for estimating cell thermal characteristics. Reliable predictions of cell temperature and heat-generation rate are required for the design and thermal management of battery systems. The temperature of a cell changes as a result of electrochemical reactions, phase changes, mixing effects, and joule heating. The equation developed incorporates these effects in a complete and general manner. Simplifications and special cases are discussed. The results of applying the energy balance to a mathematical model of the LiAl/FeS cell discharged through two different reaction mechanisms are given as examples. The examples illustrate how the energy equation may be applied to a specific system to examine the relative contributions corresponding to the terms in the equation. The examples show that the processes involved in cell heat generation may be complex and that the application of a sufficiently general energy equation is advantageous.

Energy balance calculations are required for the design and thermal management of battery systems. A proper cell energy balance will give reliable predictions of thermal characteristics such as heat generation and temperature-time profiles. In this work, we present a general energy-balance equation for battery systems. This equation includes energy contributions from mixing, phase changes, and simultaneous electrochemical reactions with composition-dependent open-circuit potentials. Such a thorough treatment has not appeared in the literature.

The problem of determining heat effects with simultaneous electrochemical reactions was first addressed by Sherfey and Brenner in 1958 (1). They presented an equation for the rate of thermal energy generation in terms of the current fraction, the entropy change, and the overpotential for each reaction. Later, Gross (2) presented essentially the same equation, but introduced a quantity called the enthalpy voltage for each reaction. The enthalpy voltage is the enthalpy of reaction per coulomb of charge, and it may be derived from the overpotential and the entropy change terms in Sherfey and Brenner's equation. These treatments are restricted in their application to cell reactions in which every reactant is present in a single, pure phase. Gibbard (3) discussed the calculation of thermodynamic properties of battery systems when some of the reactants are dissolved in solution; however, his treatment of the energy balance considers the case of a single reaction without mixing effects.

Numerous researchers (1, 2, 4-8) have adopted experimental approaches and used calorimetry to determine heat output directly. Dibrov and Bykov (5) used calorimetric data and enthalpy voltages to determine current fractions of the reactions of cadmium-silver-oxide and zinc-silver-oxide cells.

The formulation of a general energy balance is useful in developing a fundamental understanding of the processes involved in cell heat generation. However, in its most rigorous form, the energy balance presented is difficult to apply without a detailed mathematical model because instantaneous composition profiles and current fractions are required. For example, Tiedemann and Newman (9) have developed such a model for the lead-acid cell. A model for the lithium-aluminum iron-sulfide battery was presented by Pollard and Newman. (10, 11) These models do provide the necessary information needed to calculate the thermal characteristics from an energy balance such as the one presented in this work; however, these works utilize a relatively simple energy equation in which mixing effects are ignored and a single cell reaction occurs. Pollard's model calculates current fractions of the two simultaneously occurring reactions, but the fractions are not utilized in the energy balance. In practice, it is difficult to obtain concentration profiles and to predict the partitioning of current among possible reactions. However, applying an energy equation that includes the effects of simultaneous reactions to experimental measurements will allow the calculation of the current fractions. In this work, simplifications and special cases of the general energy equation are discussed. The results of

*Electrochemical Society Active Member.

**Electrochemical Society Student Member.

applying the energy balance to a mathematical model of the LiAl/LiCl-KCl/FeS cell are given as examples. The relative contributions corresponding to the terms in the equation are examined.

The Energy Balance

In this section, the general energy balance for a battery system will be derived. The temperature of the battery is assumed to be uniform throughout and changes with time to be determined by the following processes

- (1) reactions
- (2) changes in the heat capacity of the system
- (3) phase changes
- (4) mixing
- (5) electrical work
- (6) heat transfer with the surroundings

A battery may be thought of as a composite of many discrete phases that are changing in energy content. It is assumed that these phases are interacting by way of electrochemical reactions, phase changes, and mixing processes. The first law of thermodynamics may be written as

$$\frac{dH_{\text{tot}}}{dt} = q - IV \quad [1]$$

where H_{tot} is the sum of the enthalpies of the phases expressed as

$$H_{\text{tot}} = \sum_i \int_{v_j} \left[\sum_i c_{i,j} \bar{H}_{i,j} \right] dv_j \quad [2]$$

and i and j denote the individual species and phase, respectively. The term q represents the rate of heat transfer with the surroundings, and IV is the electrical work. It is convenient to define an average composition for each of these phases and write dH_{tot}/dt as

$$\frac{dH_{\text{tot}}}{dt} = \frac{d}{dt} \sum_j \sum_i \left[n_{i,j} \bar{H}_{i,j}^{\text{avg}} + \int_{v_j} c_{i,j} (\bar{H}_{i,j} - \bar{H}_{i,j}^{\text{avg}}) dv_j \right] \quad [3]$$

The first term on the right side of Eq. [3] represents the rate of change of the enthalpy of the cell when all species are present at their average composition. The second term is a correction accounting for composition variations. In the development that follows, the first term in Eq. [3] will be split into three separate terms. Applying the product rule for differentiation and recalling that

$$\left(\frac{\partial \bar{H}_{i,j}^{\text{avg}}}{\partial T} \right)_p = \bar{C}_{p,i,j}^{\text{avg}} \quad [4]$$

we obtain

$$\sum_j \sum_i \frac{d}{dt} (n_{i,j} \bar{H}_{i,j}^{\text{avg}}) = \sum_j \sum_i \left[n_{i,j} \bar{C}_{p,i,j}^{\text{avg}} \frac{dT}{dt} + \bar{H}_{i,j}^{\text{avg}} \frac{dn_{i,j}}{dt} \right] \quad [5]$$

for the first term in Eq. [3].

It is assumed that there are several simultaneous electrode reactions of the form

$$\sum_i s_{i,l} M_i^{z_i} = n_l e^- \quad [6]$$

occurring within the battery. The reactions are written so that species i is always in phase m , having a certain secondary reference state. For example, in a LiCl-KCl molten salt cell, all the electrode reactions are written so that the ionic lithium species is always present in the molten electrolyte phase and so that any precipitation of LiCl is accounted for separately.

A species balance may be written as

$$\frac{dn_{i,m}}{dt} = \sum_i \frac{s_{i,l} I_l}{n_i F} - \sum_{j,j \neq m} \frac{dn_{i,j}}{dt} \quad [7]$$

The first term on the right side of Eq. [7] represents the amount of i that is produced or consumed by electrode reactions. The partial current, I_l , is positive for a cathodic

reaction and negative for an anodic reaction. The second term accounts for phase changes such as the LiCl precipitation mentioned above. Integration of Eq. [7] yields

$$n_{i,m} = n_{i,m}^0 - \sum_{j,j \neq m} (n_{i,j} - n_{i,j}^0) + \sum_l \frac{s_{i,l}}{n_i F} \int_0^t I_l dt \quad [8]$$

We may express partial molar enthalpies in the form

$$\bar{H}_{i,m}^{\text{avg}} = H_{i,m}^0 - RT^2 \frac{d}{dT} \ln (a_{i,m}^{\text{avg}}) \quad [9]$$

The theoretical open-circuit potential for reaction l at the average composition, relative to a reference electrode of a given kind, is given by

$$U_{i,\text{avg}} = U_l^0 - U_{\text{RE}}^0 + \frac{RT}{n_{\text{RE}} F} \sum_i s_{i,\text{RE}} \ln (a_{i,\text{RE}}) - \frac{RT}{n_l F} \sum_i s_{i,l} \ln (a_{i,m}^{\text{avg}}) \quad [10]$$

By utilizing the Gibbs-Helmholtz relation for each reaction, we may write the standard reaction enthalpy in terms of the standard cell potential

$$\sum_i \frac{s_{i,l}}{n_l F} H_{i,m}^0 = T^2 \frac{d}{dT} \left(\frac{U_l^0}{T} \right) \quad [11]$$

Looking at Eq. [5] and [7], we can see that the contribution to the rate of enthalpy change associated with the electrode reactions may be written as

$$\sum_m \sum_i \bar{H}_{i,m}^{\text{avg}} \sum_l \frac{s_{i,l} I_l}{n_l F} = \sum_m \sum_l \frac{I_l}{n_l F} \sum_i \bar{H}_{i,m}^{\text{avg}} s_{i,l} \quad [12]$$

Using Eq. [9] and [11], we may write this contribution in terms of the electrode reaction potentials

$$\sum_m \sum_l \frac{I_l}{n_l F} \sum_i \bar{H}_{i,m}^{\text{avg}} s_{i,l} = \sum_l I_l \left[T^2 \frac{d}{dT} \left(\frac{U_l^0}{T} \right) - \frac{RT^2}{n_l F} \sum_i \frac{d}{dT} \ln (a_{i,m}^{\text{avg}})^{s_{i,l}} \right] \quad [13]$$

Using Eq. [10], we may write Eq. [13] in terms of the theoretical open-circuit potentials relative to a reference electrode of a given kind as

$$\sum_l I_l \sum_m \sum_i \frac{\bar{H}_{i,m}^{\text{avg}} s_{i,l}}{n_l F} = \sum_l I_l \left[T^2 \frac{d}{dT} \left(\frac{U_{l,\text{avg}}}{T} \right) \right] \quad [14]$$

The quantity multiplying I_l on the right and left sides of Eq. [14] is sometimes termed the enthalpy voltage of reaction l .

Substitution of Eq. [7], [8], and [14] into Eq. [5] and placing this result into Eq. [3] results in the final form for dH_{tot}/dt . Equating this to $q - IV$ (Eq. [1]) gives the following form for the energy-balance equation

Table I. Model discharge mechanisms in the FeS electrode

Reaction	a_l^0 [V]	$b_l \times 10^3$ [V/K]
Mechanism 1 (X-phase intermediate)		
1) $2\text{FeS} + 2\text{Li} + 2e^- \rightarrow \text{Li}_2\text{FeS}_2 + \text{Fe}$ (X-phase)	1.367	-0.022
2) $\text{Li}_2\text{FeS}_2 + 2\text{Li}^+ + 2e^- \rightarrow 2\text{Li}_2\text{S} + \text{Fe}$	1.454	-0.178
Mechanism 2 (J-phase intermediate)		
3) $26\text{FeS} + \text{Li}^+ + \text{Cl}^- + 6\text{K}^+ + 6e^- \rightarrow \text{LiK}_6\text{Fe}_{26}\text{S}_{26}\text{Cl} + 2\text{Fe}$ (J-phase)	1.955	-0.680
4) $\text{J} + 51\text{Li}^+ + 46e^- \rightarrow 26\text{Li}_2\text{S} + 24\text{Fe} + 6\text{K}^+ + \text{Cl}^-$	1.440	-0.024

^a a_l and b_l were obtained from Ref. (13).

$$q - IV =$$

$$\begin{aligned} & \sum_I \left[I_1 T^2 \frac{d \frac{U_{1,avg}}{T}}{dT} \right] \text{enthalpy-of-reaction} \\ & - \sum_j \frac{d}{dt} \left[\int_{v_j} \sum_i c_{i,j} R T^2 \frac{\partial}{\partial T} \ln \left(\frac{\gamma_{i,j}}{\gamma_{i,j}^{avg}} \right) dv_j \right] \text{enthalpy-of-mixing} \\ & - \sum_{i,j \neq m} \sum_i \left[\left(\Delta H_{i,j \rightarrow m}^0 - R T^2 \frac{d}{dT} \ln \frac{\gamma_{i,m}^{avg}}{\gamma_{i,j}^{avg}} \right) \frac{dn_{i,j}}{dt} \right] \text{phase-change} \\ & + \frac{dT}{dt} \left[\sum_j \sum_i n_{i,j}^0 \bar{C}_{p,i,j}^{avg} + \sum_i \int_0^t \frac{I_1 dt}{n_i F} \Delta C_{p,i} \right] \text{heat-capacity} \\ & + \sum_{i,j \neq m} \sum_i \left(\bar{C}_{p,i,j}^{avg} - \bar{C}_{p,i,m}^{avg} \right) (n_{i,j} - n_{i,j}^0) \end{aligned} \quad [15]$$

where

$$\Delta C_{p,i} \equiv \sum_i s_{i,i} \bar{C}_{p,i,m}^{avg} \quad [16]$$

and

$$\Delta H_{i,j \rightarrow m}^0 \equiv H_{i,m}^0 - H_{i,j}^0 \quad [17]$$

It should be recognized that all the composition dependence of Eq. [15] may be expressed in terms of activity coefficients ($a_{i,j} = x_{i,j} \gamma_{i,j}$). This is a reflection of the fact that the composition dependence of any thermodynamic quantity is completely determined if the activity coefficient behavior of the species is known. This analysis does not include enthalpy changes associated with nonfaradaic reactions. However, reactions such as self-discharge or corrosion may be divided into anodic and cathodic components and included in the enthalpy-of-reaction term (other reactions must be accounted for and included as an additional term). Also, the heat capacities of the battery support materials should be understood to be included in Eq. [15]. Actually, in most practical applications, the heat capacity of a battery module does not change substantially during operation. In such cases, the heat-capacity term may be replaced by some average value. Also, the rate of heat transfer q between the battery and surroundings may be expressed as

$$q = -hA(T - T_A) \quad [18]$$

where the heat-transfer coefficient h is based on separator area and is estimated from the heat losses for a battery module.

As an example of how Eq. [15] may be used, let us apply it to the LiAl/LiCl-KCl/FeS battery. We shall assume that any number of reactions may be occurring and that all the reacting phases are pure except the electrolyte. The molten LiCl-KCl electrolyte phase is considered to be a solution of varying composition throughout the battery. The species present are the Li^+ , K^+ , and Cl^- in the electrolyte and those corresponding to the pure reacting phases. The open-circuit-potential data are considered to be given at the eutectic composition of the electrolyte as a reference condition and to be of the form $U_{1,eut} = a_1 + b_1 T$. All the electrode reaction potentials are given relative to the two-phase (α , β) LiAl-alloy reference electrode. It is convenient that this is also the negative electrode material. We may relate $U_{1,eut}$ to $U_{1,avg}$ by

$$U_{1,avg} = U_{1,eut} - \frac{RT}{F} \ln \left[\left[\frac{a_{\text{LiCl}}^{avg}}{a_{\text{LiCl}}^{eut}} \right]^{\frac{S_{\text{Li}^+, \text{Li}}}{n_1}} \left[\frac{a_{\text{LiCl}}^{avg}}{a_{\text{LiCl}}^{eut}} \right]^{-\frac{S_{\text{Li}^+, \text{RE}}}{n_{\text{RE}}}} \left[\frac{a_{\text{KCl}}^{avg}}{a_{\text{KCl}}^{eut}} \right]^{\frac{S_{\text{K}^+, \text{Li}}}{n_1}} \right] \quad [19]$$

The resulting equation will allow for precipitation of pure LiCl and pure KCl solid phases. With the above considerations, Eq. [15] becomes

$$\begin{aligned} MC_p^m \frac{dT}{dt} &= -hA(T - T_A) - IV \\ &+ \sum_I I_1 \left[a_1 + \frac{RT^2}{F} \frac{d}{dT} \ln \left[\left(\frac{\gamma_{\text{LiCl}}^{avg}}{\gamma_{\text{LiCl}}^{eut}} \right)^{\frac{S_{\text{Li}^+, \text{Li}}}{n_1}} \left(\frac{\gamma_{\text{LiCl}}^{avg}}{\gamma_{\text{LiCl}}^{eut}} \right)^{-\frac{S_{\text{Li}^+, \text{RE}}}{n_{\text{RE}}}} \left(\frac{\gamma_{\text{KCl}}^{avg}}{\gamma_{\text{KCl}}^{eut}} \right)^{\frac{S_{\text{K}^+, \text{Li}}}{n_1}} \right] \right] \\ &+ \frac{d}{dt} \int_v \epsilon R T^2 \left[c_{\text{LiCl}} \frac{\partial}{\partial T} \ln \left(\frac{\gamma_{\text{LiCl}}}{\gamma_{\text{LiCl}}^{avg}} \right) + c_{\text{KCl}} \frac{\partial}{\partial T} \ln \left(\frac{\gamma_{\text{KCl}}}{\gamma_{\text{KCl}}^{avg}} \right) \right] dv - \frac{dn_{\text{LiCl}_s}}{dt} \left[\Delta H_{\text{LiCl}_s}^0 + R T^2 \frac{d \ln \gamma_{\text{LiCl}}^{avg}}{dT} \right] - \frac{dn_{\text{KCl}_s}}{dt} \left[\Delta H_{\text{KCl}_s}^0 + R T^2 \frac{d \ln \gamma_{\text{KCl}}^{avg}}{dT} \right] \end{aligned} \quad [20]$$

where dn_{LiCl_s}/dt and dn_{KCl_s}/dt are the crystallization rates of solid LiCl and KCl phases, respectively. There is a considerable amount of simplification involved in going from Eq. [15] to Eq. [20]. For example, the ionic activity coefficients, ionic concentrations, and ionic partial molar enthalpies have been combined into neutral combinations that refer to undissociated LiCl and KCl. If the electrolytes were considered to be completely dissociated, then Eq. [15] could be rearranged to contain mean ionic activity coefficients (neutral combinations of individual ionic activity coefficients).

In the next section, each of the terms in Eq. [15] will be discussed. Afterwards, Eq. [20] will be applied more specifically to the LiAl/FeS cell.

Discussion of Terms

Enthalpy-of-reaction.—If we use an average heat capacity and do not consider enthalpy-of-mixing and phase-change terms, then Eq. [15] may be written as

$$q = IV + \sum_I I_1 \left[T^2 d \frac{U_{1,avg}}{dT} \right] + MC_p^m \frac{dT}{dt} \quad [21]$$

During discharge, the chemical energy of the cell is directly converted into work in the form of electricity. The work that the cell delivers is maximum when the cell op-

erates reversibly. This reversible work, expressed as a rate, can be written as

$$IV_{\text{rev}} = \sum_i I_i [U_{i,\text{avg}}] \quad [22]$$

and is tucked into the enthalpy-of-reaction term. The difference between V_{rev} and V is the cell overpotential. The overpotential is indicative of irreversibilities such as ohmic losses, charge-transfer overpotentials, and mass-transfer limitations. The overpotential multiplied by the current is termed the polarization heat and is composed of the joule heating within the battery, as well as the energy dissipated in electrode overpotentials.

Also housed in this enthalpy-of-reaction term is the entropic-heat

$$q_{\text{rev}} = - \sum_i I_i \left[T \frac{d(U_{i,\text{avg}})}{dT} \right] \quad [23]$$

Equations [22] and [23] represent the power and the heat generation that accompany reversible isothermal cell operation, respectively. The reversible work is related to the change in Gibbs function of the cell's contents. The entropic-heat is related to the entropy change. We may write Eq. [21] in terms of these contributions as

$$q = \left[IV - \sum_i I_i U_{i,\text{avg}} \right] + \sum_i I_i T d \frac{U_{i,\text{avg}}}{dT} + MC_p^m \frac{dT}{dt} \quad [24]$$

Equations [22] and [23] have allowed the enthalpy-of-reaction and electrical work terms in Eq. [21] to be combined and restated as irreversible and reversible heat effects. This form is most convenient when dealing with reversible conditions because the polarization heat, $IV - \sum_i I_i [U_{i,\text{avg}}]$ is zero in that case. Furthermore, Eq. [24] is the form of the energy balance that is most commonly encountered in the literature. The composition dependence of the open-circuit potential is contained in $U_{i,\text{avg}}$ (see Eq. [10]). The original form (Eq. [21]) has an advantage in that a strong composition dependence of the two terms separately may partially cancel in the enthalpy voltage. Also, if the open-circuit potentials $U_{i,\text{avg}}$ are independent of composition and linearly related to temperature, then the enthalpy-of-reaction term becomes

$$- \sum_i I_i a_i \quad [25]$$

Notice that the temperature coefficients, b_i , are not needed and that the enthalpy voltage of reaction l is $-a_l$.

Enthalpy-of-mixing.—The enthalpy-of-mixing term represents the heat effects associated with generation or relaxation of concentration profiles. For example, if we do not consider phase-change terms, then this term represents the rate of heat generation after current interruption of cell operation. First, the definition of the average composition will be discussed. Later, an estimate of the adiabatic temperature rise due to relaxation of concentration profiles in a lead-acid cell after full discharge will be made.

The enthalpy-of-mixing term is the only term in Eq. [15] that is dependent on the spatial variation of composition. This term may be thought of as a correction because the other terms depend only on the average composition. The term is difficult to treat because it involves integrations of concentration profiles. Consequently, it is instructive to discuss the conditions under which it may be neglected. The definition of the average composition of species i is arbitrary. Therefore, if mixing effects are to be neglected, then the average composition should be chosen such that the value of this neglected term is minimized. For a binary phase, with components 1 and 2, it

can be shown that the integral in the mixing term may be minimized if the average concentration is defined as

$$c_1^{\text{avg}} = \frac{\int_v c_1 dv}{\int_v dv} \text{ or } x_1^{\text{avg}} = \frac{\int_v c x_1 dv}{\int_v c dv} \quad [26]$$

where

$$c = c_1 + c_2$$

This will be shown as follows. For a binary system, the integral in the mixing term in Eq. [15] may be written as

$$\int_v c [H - (x_1 \bar{H}_1^{\text{avg}} + x_2 \bar{H}_2^{\text{avg}})] dv \quad [27]$$

where the molar enthalpy is defined as

$$H = x_1 \bar{H}_1 + x_2 \bar{H}_2$$

and \bar{H}_i^{avg} is the partial molar enthalpy of species i at the average composition. It should be recognized that in this development it is assumed that the spatial variation of composition is fixed and that Eq. [27] is only a function of x_1^{avg} . By writing the mixing integral in this form, we may obtain a clearer interpretation of the mixing term. The sum subtracted from H is the tangent line to the enthalpy-*vs.*-composition ($H - x_1$) plot at the average composition. The integral may be considered to be a measure of the ability to approximate the H curve with a tangent, in the range of composition variation throughout the cell. Therefore, if the enthalpy curve is linear in this range, then \bar{H}_1 and \bar{H}_2 are independent of composition, and the integral is zero regardless of the value of x_1^{avg} . Also, if the activity coefficients are independent of temperature (see Eq. [9]), then mixing effects can be ignored. Different choices of the tangent, corresponding to different values of the average composition may give better or worse approximations of the enthalpy curve. Equation [27] may be minimized with respect to the average composition by solving the following equation for x_1^{avg}

$$\frac{d}{dx_1^{\text{avg}}} \left[\int_v c(x_1 \bar{H}_1^{\text{avg}} + x_2 \bar{H}_2^{\text{avg}}) dv \right] = 0 \quad [28]$$

In formulating Eq. [28], it was recognized that the composition profiles and enthalpy curve are independent of the choice of x_1^{avg} . We may further simplify Eq. [28] and write

$$\int_v c_1 dv \frac{d\bar{H}_1^{\text{avg}}}{dx_1^{\text{avg}}} + \int_v c_2 dv \frac{d\bar{H}_2^{\text{avg}}}{dx_1^{\text{avg}}} = 0 \quad [29]$$

The Gibbs-Duhem equation

$$x_1^{\text{avg}} \frac{d\bar{H}_1^{\text{avg}}}{dx_1^{\text{avg}}} + x_2^{\text{avg}} \frac{d\bar{H}_2^{\text{avg}}}{dx_1^{\text{avg}}} = 0 \quad [30]$$

may be applied, and Eq. [29] may be solved for x_1^{avg} as given in Eq. [26]. The corresponding development for multicomponent mixtures is given in Appendix A. Equation [26] is guaranteed to be the choice of the average composition that will minimize Eq. [27] only if the integral has simple behavior. The behavior is said to be simple if the second derivative of the integral is nonzero for all possible values of x_1^{avg} (in range of concentration variation throughout the cell). For example, if the integral has a point of inflection such that its value may be either positive or negative depending upon x_1^{avg} , then x_1^{avg} may be chosen so that the integral is zero. In this case, the best choice of the x_1^{avg} is not necessarily defined by Eq. [26]. Regardless of the behavior of the integral, Eq. [26] is the most convenient definition of the average composition. It has physical significance, and it is usually a simple function of state-of-charge. It is the final uniform composition of a concentration profile that is allowed to relax, and the energy effect associated with this process, in this case, is

proportional to the value of the integral for the initial profile.

It is useful to examine further the sign of the integral. The sign of Eq. [27] will indicate such things as whether mixing effects will tend to heat or cool a cell during operation. It is convenient now to look at Eq. [27] as a function of the mixing behavior and assume that the average composition in it is fixed. Equation [27] will be positive if

$$H > (x_1 \bar{H}_1^{\text{avg}} + x_2 \bar{H}_2^{\text{avg}}) \quad [31]$$

The right side of Eq. [31] is linear in x_1 . If Eq. [31] is differentiated twice with respect to x_1 , we obtain

$$\frac{d^2 H}{dx_1^2} > 0 \quad [32]$$

In other words, if in the range of concentration variation throughout the cell the enthalpy curve is always concave upward, then the integral will be positive. Conversely, the integral will be negative if the enthalpy curve is everywhere concave downward. For example, in the lead-acid cell, the sulfuric acid-water system has an enthalpy curve that is always concave upward. Consequently, the temperature of a well-insulated lead-acid cell will always increase after current interruption during operation due to relaxation of concentration profiles. To illustrate this, in Appendix A, Eq. [15] is used to estimate this temperature rise. The temperature rise, after full discharge, is approximately 1.6 K. It is also important to investigate the consequence of neglecting mixing effects in thermal calculations. For the lead-acid cell, the temperature during operation (generation of concentration profiles) is overestimated if calculations are made by neglecting the mixing term. The situation is reversed for a high-temperature cell employing LiCl-KCl electrolyte. In the range of concentration variation throughout this cell, the enthalpy curve is always concave downward and the cell temperature will decrease due to mixing effects after current interruption. Calculations that neglect mixing will give underestimations of temperature when concentration profiles are being generated (during cell operation). This will be investigated in greater detail later.

If the enthalpy curve, in the range of composition variation, may be concave upward or concave downward, then the sign of the integral depends on the choice of the average composition. Certain associated systems, such as ethanol and water, exhibit inflection points in their enthalpy curves.

Phase-change terms.—In the enthalpy-of-reaction term of Eq. [15], all the reactions have species i in the same phase m . For example, in Eq. [20], LiCl is always present as a molten LiCl-KCl solution phase in all reactions. However, one of the phases present in the cell during operation may be pure solid LiCl. The purpose of the phase-change terms is to account for the enthalpy change due to crystallization of this solid phase. For example, ice crystals form during low temperature operation of aqueous batteries, and an energy balance such as Eq. [23] would not correctly predict cell temperatures. If the m phase types in the enthalpy-of-reaction contribution (Eq. [15]) are the only phases present in the cell during operation, then the phase-change terms are zero.

Heat-capacity.—The quantities to the right of dT/dt in the heat-capacity term of Eq. [15] represent the heat capacity of the cell. This heat capacity changes with time because the composition of the cell changes due to electrochemical reactions and phase changes. The first part of this heat capacity represents the initial heat capacity of the cell's reactive material. The heat capacity of the cell's inert supporting material should be included in this part. The second and third parts account for changes in the initial heat capacity as a result of electrochemical reactions and phase changes, respectively.

As mentioned earlier, the total heat capacity of a typical cell (including supporting material) is approximately constant so that this term usually reduces to a simple expression.

Description of Examples

The results of applying Eq. [15] to the existing model of the LiAl/LiCl, KCl/FeS cell will be given. The purpose of these examples is to illustrate how the energy-balance equation may be applied to a specific system and to examine the relative contributions corresponding to the terms in this equation. The use of Eq. [15] is best illustrated by application to a mathematical model of a battery in which concentration profiles can be used to calculate energy contributions from mixing, and current fractions can be used to calculate energy contributions from simultaneous reactions. This model was originally developed by Pollard and Newman in 1981, and the details of the theoretical analysis are given in their publications (10, 11). The model gives the galvanostatic discharge behavior of a one-dimensional cell sandwich consisting of a porous LiAl negative electrode, porous FeS positive electrode, electrolyte reservoir, and separator. The model simulates the discharge processes in the positive by the two simultaneously occurring reactions given as mechanism 1 in Table I. Pawlikowski (12) in 1982 developed a model of the cell with mechanism 2 as the positive electrode discharge reactions. Mechanisms 1 and 2 yield the same overall reaction and differ mainly in the intermediate phase (X-phase or J-phase).

The electrochemistry of the FeS electrode is reasonably well understood. The actual discharge processes are complicated and are more like a mixture of the two proposed mechanisms along with simultaneously occurring chemical reactions. There is evidence, however, for the simple 2-reaction mechanisms under certain operating conditions (13). In practice, batteries are operated between 400° and 500°C. Higher operating temperatures and LiCl concentrations tend to favor mechanism 1. Lower temperatures and LiCl concentrations favor mechanism 2. Discharge through the X-phase intermediate is preferred because of the poor reversibility of the J-phase reactions. For purposes of comparison, the simulations of the two mechanisms will use the same initial temperature and electrolyte composition.

The model discharges are meant to simulate a well-insulated (but not adiabatic) battery operating in an ambient temperature environment with no external heating. The relevant input data and energy equation specific to each mechanism are given in Appendix B.

Results

Figure 1 gives the cell temperature as a function of utilization for both mechanisms. The dashed lines show the temperature profile for adiabatic and reversible discharge. Under these conditions the two mechanisms yield the same temperature at 100% depth of discharge because the overall reaction is the same. In both cases, the reactions are exothermic, so that the cell temperature increases throughout discharge. Though the adiabatic-reversible profile of mechanism 1 appears linear, there is actually a slight amount of curvature, due to the logarithmic dependence of the cell temperature. The composition dependencies associated with the J-phase reactions result in the more discernible curvature of each portion of the adiabatic-reversible profile of mechanism 2. The criterion of reversibility allows the stoichiometry of the reactions to yield the discontinuities in slope located at 50% and 12% for mechanism 1 and mechanism 2, respectively. For example, with mechanism 1 up to 50% utilization, only reaction 1 occurs, and after this point reaction 2 occurs. The dashed curve in Fig. 2 is the heat generation rate for reaction 1. It is approximately constant because the temperature is not changing substantially, and this is responsible for the apparent linearity in Fig. 1. With the J-phase reactions, the stoichiometry dictates that the transition from reaction 3 to reaction 4 occurs at 12% utilization.

It is interesting to compare these results to the results of the more realistic simulations. The solid lines in Fig. 1 are the results of the mathematical models. The relevant input data and energy equation specific to each mecha-

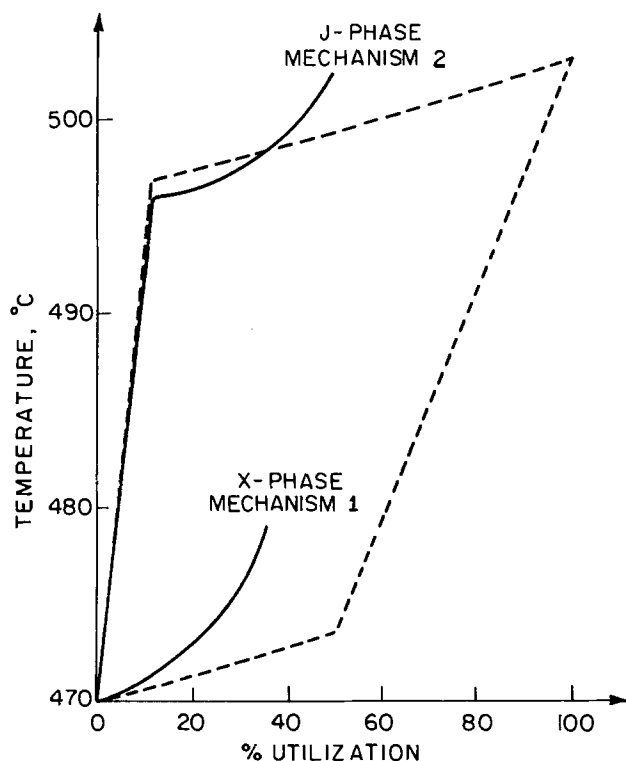


Fig. 1. Cell temperature as a function of utilization for mechanisms 1 and 2. The dashed lines are for adiabatic-reversible discharge. The solid lines are the results of the mathematical model simulations. Cutoff voltages of 1.2 and 1.0V were used for mechanisms 1 and 2, respectively.

nism are given in Appendix B. In these simulations, the irreversibilities associated with ohmic losses, migration effects, mass-transfer, and charge-transfer overpotentials cause electrode polarization. The onset of the second reaction of each mechanism may occur before the prediction based on reversibility, because of the resulting potential distribution in the porous, positive electrode. Compared to the values of 50% and 12% utilization, the second reaction begins at 30% and 11% utilization for mechanisms 1 and 2, respectively. At these operating conditions, the reaction potential difference $U_{3,avg} - U_{4,avg}$ for the J-phase mechanism is always about four times larger than the difference $U_{1,avg} - U_{2,avg}$ for the X-phase mechanism. We see that the onset of the second reaction occurs closer to the reversible prediction in the case of the J-phase mechanism because a larger positive electrode polarization is required to promote the onset of the second reaction as compared with the X-phase mechanism.

The solid lines in Fig. 2 are plots of the terms in Eq. [B-1] as functions of utilization for the X-phase mechanism up to 30% utilization. The dashed line in Fig. 2 is called the entropic-heat and has the value of $-i_1 b_1 T$. It would be the only term on the right side of Eq. [B-1] if the equation were written for the adiabatic-reversible case. The polarization heat, $i_1(U_{1,avg} - V)$, and the entropic heat add up to the enthalpy-of-reaction and electrical-work term. The heat-loss contribution does not change markedly because the cell is well insulated and the overall cell temperature does not change substantially. The profile for the X-phase mechanism in Fig. 1 follows the adiabatic-reversible profile up to about 5% utilization because the heat-loss contribution tends to cancel the polarization heat. The polarization heat is mainly responsible for the increasing departure of the cell temperature from the reversible case throughout discharge. With increasing utilization, the polarization heat increases because the open-circuit potential ($U_{1,avg}$) is approximately constant and the cell voltage drops.

These results can be contrasted to the results with the J-phase mechanism from 0% to 11% utilization. The average LiCl concentration increases, and the composition de-

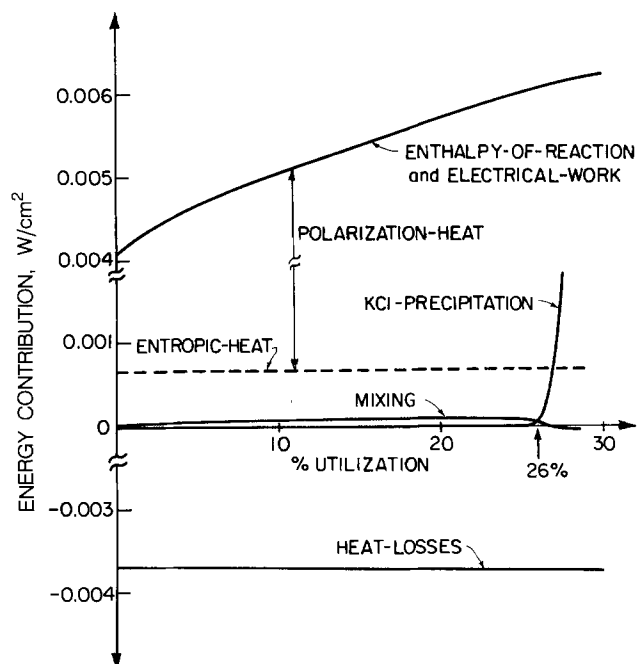


Fig. 2. Terms comprising the energy balance for a LiAl/FeS cell [Eq. B-1] as a function of utilization.

pendent $U_{3,avg}$ decreases accordingly (Eq. [19]). Actually, $U_{3,avg}$ decreases at about the same rate as the cell voltage, so that the polarization heat remains relatively constant. Up to about 5% utilization, the heat-loss term approximately cancels the polarization heat, and the temperature profile follows the adiabatic-reversible case. The cell temperature increases enough from 5% to 11% utilization so that the heat-loss term dominates, and the temperature remains below the adiabatic-reversible case. After 12% utilization, the heat losses and $U_{4,avg}$ stay approximately constant, so that the polarization heat dominates; by the time of 36% utilization, the profile lies above the adiabatic-reversible case.

Although the mixing term offers a negligible contribution to the energy balance, it is interesting to investigate the processes that determine its behavior. As we mentioned earlier, for the molten LiCl-KCl system, the value of the integral in Eq. [B-1] is always negative. Therefore, if the heat losses are made negligible, the cell temperature will decrease after current interruption. Prior to the onset of precipitation, this is entirely a mixing effect. At 25% utilization in Fig. 2, this temperature decline is only about 0.2 K. Before precipitation, the concentration of LiCl steadily decreases in the positive electrode and increases in the negative electrode, and the average composition, $x_{LiCl}^{avg} = 0.58$ (defined by Eq. [26]), is constant. The mixing term (the time derivative of the integral) also increases, and the cell temperature would be slightly underestimated if mixing effects were ignored. The concentration throughout the separator and reservoir volumes remains close to the average composition, so that their contributions to the integral are two orders of magnitude smaller than the contributions from integration through the electrodes. Figure 2 shows that the integral increases in magnitude to the point where the mixing term is zero (26.5% utilization). After this point, the mixing term is slightly negative, corresponding to a decrease in the magnitude of the integral with time. The mixing term decreases when KCl precipitates because, in the region of precipitation, the electrolyte composition is approximately constant at its saturation value. Following the onset of precipitation, the adiabatic temperature decline after current interruption is determined by the more complex processes of simultaneous melting of KCl and electrolyte mixing. We present the breakdown of contributions only up to 30% utilization, because when the second reaction begins simultaneously, reaction heat effects and

precipitation effects cause oscillatory behavior. The description and discussion of this phenomenon will be treated in a subsequent publication.

Conclusions

The examples presented help to illustrate that the processes involved in cell heat generation may be complex and that the application of a sufficiently general energy equation is advantageous. Equation [23], written for a single cell reaction, is the energy equation most commonly used in battery applications. The use of this form of an energy balance is justified only if phase-change effects, mixing effects, and simultaneous reactions are not important. An energy equation including the effects mentioned above is, of course, most easily applied to modeling studies. However, applying an energy equation that includes the effects of simultaneous reactions to experimental measurements may help elucidate reaction mechanisms. For example, if heat generation rates and cell voltage measurements are made on LiAl/FeS cells under isothermal operating conditions, an energy equation may be fit to the experimental data to determine the current fractions of simultaneously occurring reactions. The experiments performed under truly isothermal conditions have the advantage that an estimate of the mean cell heat capacity is not required. However, if experimental cells are not kept isothermal, then heat capacity effects or the effects of nonuniform temperature may obscure the relationship of the experimental results to the energy balance.

The reversible-isothermal model is relatively easy to construct from knowledge of the stoichiometry of the probable cell reactions and the temperature dependence of their open-circuit potentials. The comparison of such a model with experimental results may also aid in the understanding of the system, just as the adiabatic-reversible model was used to aid in the interpretation of the simulation of the well-insulated cell in the examples. Regardless of the application, understanding the fundamental processes involved in cell heat generation will aid our ability to design and develop more efficient and reliable battery systems.

Acknowledgment

This work was supported by the Assistant Secretary for Conservation and Renewable Energy, Office of Energy Systems Research, Energy Storage Division of the U. S. Department of Energy, under Contract no. DE-AC03-76SF00098.

Manuscript submitted May 4, 1984; revised manuscript received Sept. 4, 1984.

University of California assisted in meeting the publication costs of this article.

APPENDIX A

Choice of the Average Composition for a Multicomponent System

For a multicomponent phase, the integral in Eq. [15] may be written as

$$\int_{\nu} \sum_i c x_i (\bar{H}_i - \bar{H}_i^{avg}) dv \quad [A-1]$$

In this development, it will be assumed that Eq. [A-1] is only a function of the average composition and that the spatial variation of composition is fixed. If the molar enthalpy is defined as

$$H = \sum_i x_i \bar{H}_i \quad [A-2]$$

Eq. [A-1] may be written as

$$\int_{\nu} c [H - \sum_i x_i \bar{H}_i^{avg}] dv \quad [A-3]$$

In certain cases, Eq. [A-1] is minimized with respect to the average composition by equating the total differential

to zero. Recognizing that the enthalpy is independent of the choice of the average composition, we may write

$$\begin{aligned} d \left[\sum_i \int_{\nu} \bar{H}_i^{avg} c x_i dv \right] \\ = \sum_i \left(\int_{\nu} c x_i dv \right) d \bar{H}_i^{avg} = 0 \end{aligned} \quad [A-4]$$

If we multiply and divide each term in Eq. [A-4] by x_i^{avg}

$$\sum_i \left[\frac{\int_{\nu} c x_i dv}{x_i^{avg}} \right] x_i^{avg} d \bar{H}_i^{avg} = 0 \quad [A-5]$$

and compare this to the Gibbs-Duhem equation

$$\sum_i x_i^{avg} d \bar{H}_i^{avg} = 0 \quad [A-6]$$

we see that the bracketed quantity in Eq. [A-5] must be equal to a constant. This constant

$$K = \frac{\int_{\nu} c x_i dv}{x_i^{avg}} \quad [A-7]$$

must be independent of x_i^{avg} in order to satisfy the Gibbs-Duhem equation. If we apply a mole fraction balance

$$\sum_i x_{i,avg} = \frac{\sum_i \int_{\nu} c x_i dv}{K} = 1 \quad [A-8]$$

we may solve for this constant

$$K = \int_{\nu} c dv \quad [A-9]$$

Substituting this into Eq. [A-7], we obtain the final form for the average composition

$$x_i^{avg} = \frac{\int_{\nu} c x_i dv}{\int_{\nu} c dv} \quad [A-10]$$

Equation [A-10] is guaranteed to be the average composition that minimizes Eq. [A-1] only if its second total differential is positive for all possible values of x_i^{avg} .

Estimate of the Temperature Rise in a Lead-Acid Cell Following Current Interruption

Prior to discharge, the cell is assumed to have a uniform composition of 5 molal sulfuric acid. It is assumed that one-third of the electrolyte is contained in the cathode and anode spaces and that one-third is in the space between the electrodes. It is also assumed that during discharge the concentration of acid in the intermediate space remains unchanged and that the acid concentrations throughout the electrode compartments are uniform. Basing the discharge on two Faradays (1 mol PbO₂) and a transference number of 0.74 for hydrogen ion, we may calculate that the concentration in the cathode space and anode space drops to 1.04 and 2.79 molal, respectively (14). If we regard the cell as well-insulated, and if there are no phase changes (such as formation of ice crystals), Eq. [15] may be written as

$$\begin{aligned} 1.15 \frac{dT}{dt} (n_{\text{PbSO}_4} C_{\text{PbSO}_4} + n_1 \bar{C}_{p_1}^{avg} + n_2 \bar{C}_{p_2}^{avg}) = \\ - \frac{d}{dt} \int_{\nu} c [H - (x_1 \bar{H}_1^{avg} + x_2 \bar{H}_2^{avg})] dv \end{aligned} \quad [A-11]$$

In writing this equation, it is assumed that the heat capacity of the battery support material is 15% of the heat capacity of the reactive material. The integral on the right side is easy to evaluate in this case because the concentration is uniform and the volume is the same in each compartment. The average composition of acid, defined by Eq. [26], is 2.95 molal. As mentioned earlier, this is the

final uniform concentration after relaxation, and the temperature rise is proportional to the value of the integral when the current is interrupted (8630J or 6.5 J/g of electrolyte). Using the data available in Ref. (14) (for 298 K), we calculate the temperature rise to be about 1.6 K (if we allow 1.25 mol of PbO₂ for discharge, the concentrations in the cathode and anode space drop to 0.05 and 2.23 molal, respectively, and the temperature rise is 2.9 K). We recognize that the assumed concentration jumps at the interfaces are artificial and that, realistically, diffusion tends to equalize the concentrations. The estimated temperature rise would be slightly lower if the above effect were taken into account. We must also, however, recognize the effects of nonuniform reaction distribution in porous electrodes and that this will tend to make the concentration distribution nonuniform. Reference (9) gives spatial distributions of concentration and reaction for a one-dimensional model of a lead-acid cell.

APPENDIX B

Energy Equations for Model Studies

Mechanism 1 (the number subscripts refer to the reactions in Table I)

$$\frac{M}{A} C_p^m \frac{dT}{dt} = -h(T - T_A) \quad \text{heat-losses}$$

$$+ (i_1 a_1 + i_2 a_2) - V(i_1 + i_2) \quad \text{enthalpy-of-reaction and electrical-work}$$

$$+ \frac{d}{dt} \int_0^L \epsilon R \left[c_{\text{LiCl}} T \ln \left(\frac{\gamma_{\text{LiCl}}}{\gamma_{\text{LiCl}}^{\text{avg}}} \right) \right]$$

$$+ c_{\text{KCl}} T \ln \left(\frac{\gamma_{\text{KCl}}}{\gamma_{\text{KCl}}^{\text{avg}}} \right) dy \quad \text{mixing}$$

$$+ \frac{1}{A} \frac{dn_{\text{KCl}_3}}{dt} [\Delta H_{\text{KCl}_3}^{\circ} + RT \ln \gamma_{\text{KCl}}^{\text{avg}}] \quad \text{KCl-precipitation} \quad [\text{B-1}]$$

Mechanism 2

The energy equation for mechanism 2 differs only in the enthalpy-of-reaction and electrical-work term, which may be written as

$$+ (i_3 a_3 + i_4 a_4) - V(i_3 + i_4)$$

$$- i_3 \frac{RT}{F} \ln \left(\left(\frac{\gamma_{\text{LiCl}}^{\text{avg}}}{\gamma_{\text{LiCl}}^{\text{eut}}} \right)^{5/6} \left(\frac{\gamma_{\text{KCl}}^{\text{avg}}}{\gamma_{\text{KCl}}^{\text{eut}}} \right)^{-1} \right)$$

$$- i_4 \frac{RT}{F} \ln \left(\left(\frac{\gamma_{\text{LiCl}}^{\text{avg}}}{\gamma_{\text{LiCl}}^{\text{eut}}} \right)^{-5/46} \left(\frac{\gamma_{\text{KCl}}^{\text{avg}}}{\gamma_{\text{KCl}}^{\text{eut}}} \right)^{-3/23} \right) \quad [\text{B-2}]$$

Relevant Input Data

Quantity	Value	Quantity	Value
x_{LiCl}°	0.58 (eutectic)	MC_p^m/A	1.89 J/cm ² -K
$\Delta H_{\text{KCl}_3}^{\circ}$	26,530 J/mol	i	0.0416 A/cm ²
h	$8.25 \cdot 10^{-6}$ W/cm ² -K	T_A	273.15 K
Capacity	835.27 C/cm ²	$\epsilon_{\text{FeS}}^{\circ}$	0.555

$$T \ln \gamma_{\text{LiCl}} = 723.15 (0.52628 x_{\text{KCl}} - 1.2738 x_{\text{KCl}}^2 - 2.9783 x_{\text{KCl}}^3)$$

$$T \ln \gamma_{\text{KCl}} = 723.15 (-0.52628 x_{\text{LiCl}} - 5.7413 x_{\text{LiCl}}^2 + 2.9783 x_{\text{LiCl}}^3 - 0.52628 \ln x_{\text{KCl}})$$

LIST OF SYMBOLS

$a_{i,j}$	activity of species i in phase j
a_{RE}	activity of species i in the reference electrode
A	separator area, cm ²
a_1	constant in the expression for the open-circuit potential of reaction 1, V
b_1	temperature coefficient in the expression for the open-circuit potential of reaction 1, V/K
$c_{i,j}$	concentration of species i in phase j , mol/cm ³
C_p^m	mean heat capacity at constant pressure, J/g-K
$C_{p,i,j}$	partial molar constant pressure heat capacity of species i in phase j , J/mol-K
dv_j	differential volume element of phase j , cm ³
e^-	symbol for an electron

F	Faraday's constant, 96,487 C/eq
h	heat transfer coefficient, W/cm ² -K
H_{tot}	enthalpy, J
H	molar enthalpy, J/mol
$H_{i,m}^{\circ}$	molar enthalpy of species i in the secondary reference state corresponding to phase m , J/mol
$\bar{H}_{i,j}$	partial molar enthalpy of species i in phase j , J/mol
i_l	partial current density of electrode reaction l , A/cm ²
I	cell current, A
I_l	partial current of electrode reaction l , A
K	constant in Eq. [A-7], mol
L	length of cell, cm
M	mass of the cell, g
M_i	symbol for the chemical formula of species i
n_1	number of electrons involved in reaction 1
n_{RE}	number of electrons involved in the reference electrode reaction
$n_{i,j}$	moles of species i in phase j , moles
q	heat-transfer rate, W
R	universal gas constant, 8.3143 J/mol-K
$s_{i,l}$	stoichiometric coefficient of species i in reaction l
t	time, s
T	absolute temperature, K
$U_{l,\text{avg}}$	theoretical open-circuit potential for reaction l at the average composition relative to a reference electrode of a given kind, V
U_l°	standard electrode potential for reaction l , V
U_{RE}°	standard electrode potential for the reference electrode reaction, V
v_j	see dv_j
V	cell potential, V
$x_{i,j}$	mole fraction of species i in phase j
y	distance from electrode, cm
z_i	charge number of species i

Greek

ϵ	porosity
$\gamma_{i,j}$	activity coefficient of species i in phase j

Subscripts

A	ambient
f	heat of fusion
i	refers to a species
j,m	refer to phases
l	refers to a reaction
rev	reversible
RE	reference electrode reaction
tot	total

Superscripts

avg	average
eut	eutectic composition
m	mean
o	refers to secondary reference state or initial
RE	reference electrode composition

REFERENCES

- J. M. Sherfey and A. Brenner, *This Journal*, **105**, 665 (1958).
- S. Gross, *Energy Convers.*, **9**, 55 (1969).
- H. F. Gibbard, *This Journal*, **125**, 353 (1978).
- I. A. Dibrov and V. A. Bykov, *Sov. Electrochem.*, **13**, 298 (1977).
- I. A. Dibrov and V. A. Bykov, *J. Appl. Chem.*, **49**, 2025 (1977).
- L. D. Hansen and R. M. Hart, *This Journal*, **125**, 842 (1978).
- F. B. Tudron, *ibid.*, **128**, 516 (1981).
- D. M. Chen and H. F. Gibbard, *ibid.*, **130**, 1975 (1983).
- W. H. Tiedemann and J. Newman, in "Battery Design and Optimization," S. Gross, Editor, pp. 23-38, The Electrochemical Society Softbound Proceedings Series, Princeton, NJ (1979).
- Richard Pollard and John Newman, *This Journal*, **128**, 491 (1981).
- Richard Pollard and John Newman, *ibid.*, **128**, 502 (1981).
- E. Pawlikowski, Postdoctoral research, unpublished, Department of Chemical Engineering, University of California, Berkeley, CA (1982).
- Z. Tomczuk, S. K. Preto, and M. F. Roche, *This Journal*, **128**, 760 (1981).
- Hans Bode, "Lead-Acid Batteries," R. J. Brodd and K. V. Kordes, Translators, Wiley-Interscience, New York (1977).

New Electrochemical Process for Making Ni/Ni Hydroxide Battery Electrodes

C. K. Dyer*,¹

AT&T Bell Laboratories, Murray Hill, New Jersey 07974

ABSTRACT

Ni positive electrodes with coulombic capacities suitable for battery electrode use have been made using ac and dilute aqueous solutions of KCl and KBr. The process is simpler and offers several potential cost and performance benefits compared with the conventional electrochemical impregnation process.

Reported methods to produce thin hydroxide or "active" films directly from Ni, by conversion rather than by electrodeposition are: (i) anodize at constant current in KOH or neutral borate solutions (1), (ii) periodically reverse the current through a Ni electrode immersed in an aqueous KOH solution (2). The mechanism of film growth by these techniques has not been widely investigated or reported. Growth is presumably a result of Ni dissolution then immediate precipitation from the high pH solution in both methods rather than by the high field ion transport mechanism of film growth on valve metals where surface films have, essentially, no electronic conductivity. The amount of active material generated in these procedures (1-100 mC/cm²) is obviously insufficient to yield a practical battery electrode. But for this serious limitation there could be considerable cost and performance advantages compared with existing methods of manufacture of Ni electrodes for batteries, which involve chemical or cathodic electrochemical deposition of nickel hydroxide from a solution of a Ni salt (e.g., nitrate) into a porous Ni sinter substrate or "plaque." The preferred but costly electrochemical method requires very careful control of concentrations, pH, and temperature of the deposition electrolyte to obtain a "loading" of Ni(OH)₂ with a controlled amount of voidage, while the product of the chemical impregnation method (precipitation of hydroxide by alternately dipping, first, into Ni nitrate and, then, into NaOH) suffers from overloading and subsequent plaque expansion during battery cycling.

It is well known that breakdown of passivity and dissolution of many metals is enhanced in the presence of so-called "aggressive" anions, such as chloride. So, addition of chloride to the KOH solution during anodic polarization of a bare Ni surface might be expected to increase the amount of Ni oxidation to hydroxide under the otherwise usual constant current or pulsed conditions. Indeed, it would not be necessary to operate in alkaline solutions at all if the current is reversed, since the dominant hydrogen evolution reaction (HER) might raise the surface pH enough (3) to precipitate local Ni cations in the form of hydroxide (minimum equilibrium solubility of Ni(OH)₂ is 10⁻⁸ mol/liter at pH 10.2). On subsequent cycles, the hydroxide should still be stable: in neutral solutions the solubility rises but to only ~10⁻³ mol/liter. However, these are equilibrium solubilities and the kinetics of dissolution of hydroxides could be very slow. Previous work on another metal, Al, has shown (3) that a thin stable surface hydroxide can form by application of an alternating current even in acid solutions despite the high solubility of Al hydroxides in acid. It is particularly interesting and relevant to note that in that work, incorporation of chloride in the hydroxide was absent, an important consideration in the capacitor industry where this process finds application and any corrosion would be catastrophic. So, the possibility of using ac to form a pure (chloride-free) hydroxide product on Ni in aqueous halide solutions was thought to be possible.

The concept was tested, and the results confirmed that indeed uniformly thick, halide-free layers of hydroxide can be produced rapidly on Ni in neutral KCl, KBr, and other solutions using ac. Considerable cost benefits in production as well as improved electrode quality are anticipated to result from this process.

Experimental

Two Ni substrates were used in this work: pure Ni sheet, masked with epoxy resin to expose ~1 cm², and Ni sinter supported on a wire mesh (made by Eagle Picher Industries, Incorporated) with an overall thickness of 0.030 in. and a projected area of 1 cm². A 1 mm Ni wire lead was spot-welded to a coined edge of the sinter, to allow immersion in the cell. The average porosity of the sinter was 77.5% with mean pore size 12.7 μm.

A Model 371 EG&G potentiostat was programmed to give various controlled-current waveforms. Most of the work to date has been with square wave shapes.

After cycling, the electrodes with their transparent film deposits were washed in distilled water and charged and then discharged in 30% KOH at 2 mA/cm² (foil electrodes) or 250 mA/cm² (sinter); capacities were calculated from discharges to ~0.0V(NHE). The reference electrode was a cathodically charged Pd/PdH_x wire or a standard calomel electrode. Counterelectrodes were either graphite or a large area of Ni foil.

Results and Interpretations

Foil.—Table I shows the results with Ni foil. In pure 1M KOH, positive or positive then negative current pulses produce small amounts of hydroxide, as indicated by the low discharge capacities (*D*) and as expected from previous work (1, 2). The effect of negative pulses only was unexpected and indicates that corrosion might have taken place during the zero-current half of each cycle. The last column of Table I indicates the coulombic efficiency (2*D*/*C*₊) of conversion of Ni to Ni(OH)₂. It is in all cases less than 0.5%. The low return on power consumed makes it a poor candidate for a manufacturing process!

Film growth in 1M KCl solution was, in several cases, an order of magnitude greater and was accompanied by a similar improvement in efficiency. In some experiments, intermediate capacities were measured for the same specimen and showed an increasing discharge capacity (roughly proportional to "film thickness") with number of cycles applied [indicated by (1), (2), (3), etc., in Table I] without decline in efficiency. The highest discharge capacities resulted from asymmetric current (*i*) cycling such that *i*₊ > *i*₋. There was also an effect of frequency (while maintaining similar charge (*q*) during each half cycle, i.e., *q*₊ = *q*₋). The discharge capacity decreased with increase in frequency from 0.5 to 10 Hz, as did the efficiency, and, unlike at lower frequencies (0.5 Hz), efficiency did not stay nearly constant with cycling, but decreased; this can be seen in Table I at 1, 2, and 20 Hz. Reduction in KCl concentration to 0.2M at 10 Hz, however, raised *D*. At lower pH (in 1M HCl) the capacity, as expected, was low.

The efficiency of conversion to useful hydroxide in KCl solutions, although much higher than in KOH alone,

* Electrochemical Society Active Member.

¹ Present address: Bell Communications Research, Inc., Murray Hill, New Jersey 07974.

Table I. Pure Ni foil, area $\sim 1 \text{ cm}^2$, square wave current

Solution	Freq. (Hz)	Peak (mA)	Total cycles	Discharge capacity (D)* (C)	Total anodic half-cycle charge (C^+) (C)	Conversion efficiency ($2D/C^+$) (%)
1M KOH	0.5	± 100	1000	0.230	100	0.46
1M KOH	0.5	± 100	1600	0.300	160	0.38
1M KOH	0.5	± 100	3100	0.225	310	0.14
1M KOH	0.5	+100	2100	0.340	210	0.32
1M KOH	0.5	-100	2600	0.340	(-)260	0.26
1M KCl	0.5	± 100	1000	1.075	100	2.14
1M KCl	0.5	± 100	(1) 130	0.350	13	5.38
1M KCl	0.5	± 100	(2) 250	0.600	25	4.80
1M KCl	0.5	± 100	(3) 375	1.050	37.5	5.60
1M KCl	0.5	± 100	(4) 500	1.550	50	6.20
1M KCl	0.5	± 100	(5) 625	1.800	62.5	5.76
1M KCl	1.0	± 200	(1) 350	0.800	35	4.56
1M KCl	1.0	± 200	(2) 700	1.435	70	4.10
1M KCl	1.0	± 200	(3)1050	1.600	105	3.04
1M KCl	1.0	+200 -100	500	3.400	50	13.60
1M KCl	1.0	+160 - 80	500	2.900	40	14.50
1M KCl	1.0	+240 -100	750	2.600	90	5.78
0.2M KCl	1.0	± 200	1000	1.600	100	3.20
1M KCl	2.0	± 100	(1) 625	0.600	15.6	7.70
			(2)1250	0.850	31.2	5.44
			(3)1900	1.050	47.5	4.42
1M KCl	10.0	± 1000	7500	0.500	375	0.26
0.2M KCl	10.0	± 1000	7500	1.200	375	0.64
1M KCl	20.0	± 100	6000	0.225	15	3.00
1M KCl	20.0	± 100	21000	0.245	52.5	0.94
1M KCl	20.0	± 300	6000	0.240	45	1.06
0.2M KCl	20.0	± 1000	7500	0.400	187	0.42
1M HCl	0.5	± 100	750	0.100	75	0.26

* In 30% KOH at 2.0 mA/cm².

was considered to be unattractive for a commercial process to make battery plates from Ni in the form of foil. The low efficiency was believed to be due to considerable loss of precipitated hydroxide to the electrolyte, since large accumulations were observed in the bottom of the cell during this work. A better substrate from this point of view was considered to be the porous sinter in which a higher $[\text{Ni}^{2+}]$ should be encountered internally with gradients in concentration of Ni^{2+} and OH^- from the Ni sur-

faces such that the solubility product would be exceeded closer to the Ni surface to cause more adhesion and less loss of hydroxide.

Sinter.—The results with sintered electrodes are shown in Table II and Fig. 1 and 2. As a reference point, 1 cm² of electrodes loaded by the conventional electrochemical impregnation or deposition process (4, 5) ("ED") gave discharge capacities of 62-78 C/cm², measured under the same conditions as electrodes in Table II.

Table II. Ni sinter, projected area $\sim 1 \text{ cm}^2$, square wave current

Freq. (Hz)	Peak (mA)	Total cycles	Discharge capacity (D)* (C)	Total anodic half-cycle charge (C^+) (C)	Conversion efficiency ($2D/C^+$) (%)
1. Asymmetric					
1M KCl					
1.0	+500 -250	500	16.5	125	26.4
1.0	+500 -250	1000	19.0	250	15.2
1.0	+500 -175	500	7.5	125	12.0
1.0	+500 -325	500	24.5	125	39.2
1.0	+500 -500	500	33	125	52.8
1.0	+500 -600	500	26	125	41.8
1.0	+650 -325	1000	22.5	325	13.8
1.0	+750 -375	500	21.0	187	22.4
1.0	+300 -200	1600	37	250	29.6

Continued on next page

Table II. Continued

	Freq. (Hz)	Peak (mA)	Total cycles	Discharge capacity (D)* (C)	Total anodic half-cycle charge (C+) (C)	Conversion efficiency (2D/C+) (%)
2. Symmetric						
			1M KCl			
	1.0	±225	1111	31.0	125	49.6
	1.0	±300	833	34.5	125	55.2
	1.0	±375	667	33.0	125	52.8
	1.0	±425	588	33.5	125	53.6
	1.0	±575	434	29.5	125	47.2
	1.0	±300	1600	49	250	39.2
	1.0	±300	2400	64.5	375	34.4
	1.0	±300	3200	69	500	27.6
	1.0	±225	4400	68	500	27.2
	1.0	±400	2500	69	500	27.6
	1.0	±400	1400	61	280	43.6
	1.0	±400	1600	61	320	38.2
	1.0	±500	1000	57	250	45.6
	1.0	±500	1200	62	300	41.4
	1.0	±500	1400	63	350	50.4
	0.5	±150	1200	51.5	180	57.2
	0.5	±150	1400	58	210	55.2
	0.5	±150	1600	64	240	53.4
	0.5	±150	1600	67	240	55.8
	0.5	±150	1800	75	270	55.6
	0.5	±150	2000	70.5	300	47.0
	0.5	±150	2000	76	300	50.6
	0.5	±150	3200	72.5	480	30.2
[0.2M KCl]	[0.5]	[±150]	[2000]	[37]	[300]	[24.6]
	0.5	±100	2000	54	200	54.0
	0.5	±100	2500	64	250	51.2
	0.5	±100	3000	68	300	45.4
	0.5	±200	800	50	160	62.4
	0.5	±200	975	55	195	56.4
	0.5	±200	1000	59	200	59.0
	0.5	±200	1200	75.5	240	62.8
	0.5	±200	1400	70	280	50.0
	0.5	±200	1600	78	320	48.8
	0.5	±250	700	52	175	59.4
	0.5	±250	800	60	200	60.0
	0.5	±250	900	67	225	59.6
	0.5	±250	1000	71	250	56.8
	0.5	±250	1000	65	250	52.0
	0.25	±75	1600	66.5	240	55.4
	0.25	±75	3200	82.5	680	34.4
	0.25	±100	1600	83.5	320	52.2
	0.25	±125	800	62.5	200	62.4
	0.25	±125	1000	72	250	57.6
	0.25	±125	1200	81	300	54.0
	0.25	±125	1600	13	400	6.4
	0.25	±150	700	62.5	210	59.6
	0.25	±150	800	72	240	60.0
	0.25	±150	900	30	270	22.2
	0.25	±175	600	67	210	63.8
	0.25	±200	400	51	160	63.8
{ Asymmetric }	{ 0.25	{ +100 0	1600	0.5	320	0.2
	{ 0.25	{ -100 0	1600	0	—	0
			1M NiCl ₂			
	0.5	±150	2000	2	300	1.4
	0.5	±300	1500	48	450	21.4
	0.5	±300	2000	72.5	600	24.2
	0.5	±300	2000	34	600	11.4
	0.5	±300	4000	Corroded	1200	0
	1.0	±600	2000	27.5	600	9.2
	5.0	±3000	1500	22	450	9.8
	5.0	±3000	3000	19	900	4.2
	5.0	±3000	12000	13	3600	0.8
	10.0	±3000	7800	23	1170	3.8
			1M KBr			
	0.25	±125	1000	49	250	39.2
	0.25	±125	1400	55	350	31.4
	0.25	±175	1200	80	420	38.0
	0.25	±225	600	60	270	44.4
	0.25	±225	800	78	360	43.4
	0.25	±225	1000	76	450	33.8
	0.25	±275	600	73	330	44.2
	0.5	±200	1600	38	320	23.8
	0.5	±250	1000	65	250	52.0

* In 30% KOH at 250 mA/cm².

Initially, asymmetric waveforms were used since for foil this was more effective. However, for the sinter, symmetric shapes gave the highest discharge capacities (part 2 of Table II). Discharge capacities comparable or higher

than conventional ED electrodes were obtained. Also, efficiencies were much higher than with foil. The higher capacities were achieved at the lowest frequencies used in this work of 0.25 Hz and at low apparent current densi-

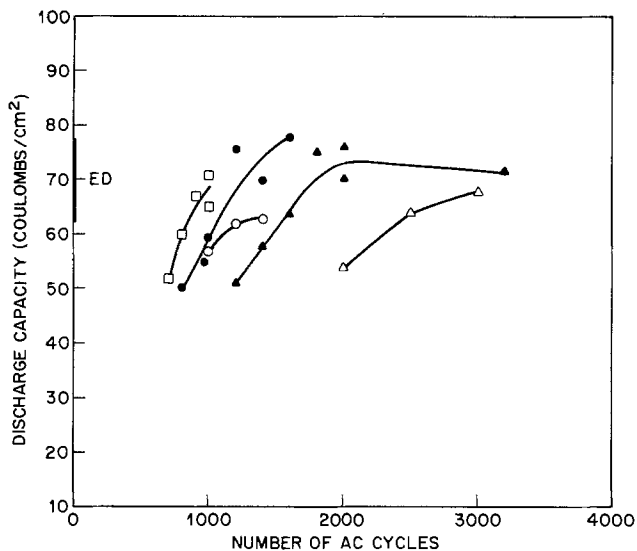


Fig. 1. Discharge capacities of 1 cm^2 (projected) Ni sinter after cycling at 0.5 Hz in 1M KCl with the following apparent current densities (mA/cm^2): ± 100 (Δ); ± 150 (\blacktriangle); ± 200 (\bullet); ± 250 (\square); and ± 500 at 1.0 Hz (\circ).

ties. The requirement for a combination of both positive and negative half-cycle currents contrasts with the process in KOH where either a succession of anodic or of cathodic current pulses were as effective as a combination. This indicates a different mechanism but similar to that proposed for Al dissolution during anodic then precipitation during cathodic half cycles (3). Overcycling results in a capacity plateau or a slight capacity loss as can be seen in Fig. 1 under several conditions at 0.5 Hz. At 0.25 Hz, where the highest discharge capacities were recorded, overcycling led to more dramatic drops (at ± 125 and $\pm 150 \text{ mA}/\text{cm}^2$) (Fig. 2).

Using 1M NiCl_2 , more cycling than 1M KCl was required to yield comparable discharge capacities, and so efficiencies were generally lower and some Ni plating may have occurred.

After cycling in 1M KBr, electrodes yielded similar capacities to those from 1M KCl solutions, but with slightly lower efficiencies under comparable conditions.

Optical micrographs of cross sections of epoxy-mounted electrodes were taken using a new technique to reveal the distribution of active material (6, 7) and are shown in Fig. 3 and 4 for a sintered Ni electrode which

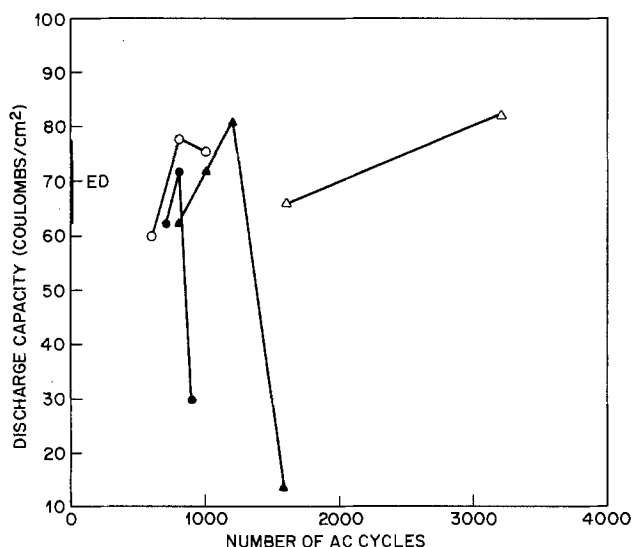


Fig. 2. Discharge capacities of 1 cm^2 (projected) Ni sinter after cycling at 0.25 Hz in 1M KCl with the following apparent current densities (mA/cm^2): ± 75 (Δ); ± 125 (\blacktriangle); ± 150 (\bullet); and as above but in 1M KBr with $\pm 225 \text{ mA}/\text{cm}^2$ (\circ).

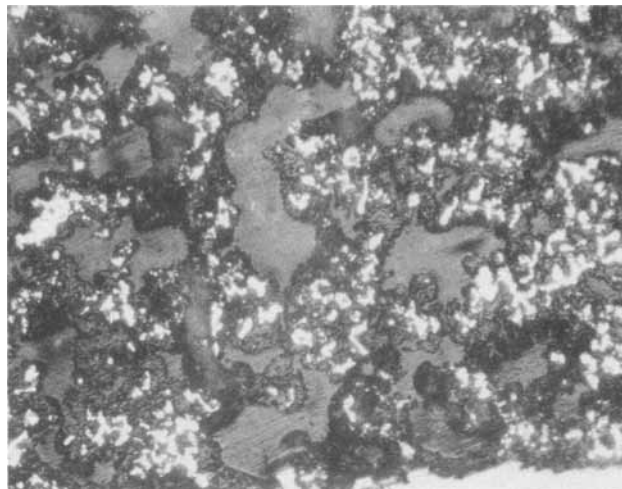


Fig. 3. Cross section of sintered Ni electrode made in 1M KCl at 0.5 Hz, $\pm 150 \text{ mA}/\text{cm}^2$, after 1600 cycles. Capacity: $64 \text{ C}/\text{cm}^2$. Ni: white. Ni hydroxide: dark gray (striated). Epoxy mount: light gray (from center). Magnification: 680X.

gave $64 \text{ C}/\text{cm}^2$ (0.5 Hz, $\pm 150 \text{ mA}/\text{cm}^2$, 1600 cycles in 1M KCl). The distribution of active material over Ni particles in the sinter (white) appears fairly uniform and from the surface to the center of the electrode, there were unblocked electrolyte channels in between prior to filling with epoxy. Such a structure should have an operational advantage over that produced by the ED process. Figure 5, taken at the same magnification, is a cross section of a conventional electrochemically impregnated electrode (4, 5) and shows a rather nonuniform distribution of active material, some only in poor contact (apparently) with Ni particles. Heavier loading of voids near the electrode surface and depletion of hydroxide in the electrode interior is a common and unwanted characteristic of some ED electrodes. Previous work (6, 7) showed that large particles of active material such as the one in the center of Fig. 5, oxidized (or charged) with difficulty when there were few or no electron sinks (Ni) within the particle [see Fig. 2 of Ref. (6)] and was more susceptible to electrical isolation on discharge [Fig. 3 of Ref. (6)]. Thus, a fraction of Ni hydroxide deposited in the ED process probably does not participate in charge storage and so leads to lower actual (or usable) electrode energy density in a battery. There may be other operational disadvantages associated with the heavier surface loadings of ED electrodes such as electrolyte blockage and outward migration of hydroxide.

Comparison of Fig. 3 and 4 with Fig. 5 shows that a considerable amount of Ni is converted by the ac process, and this must be at the expense of the mechanical sup-

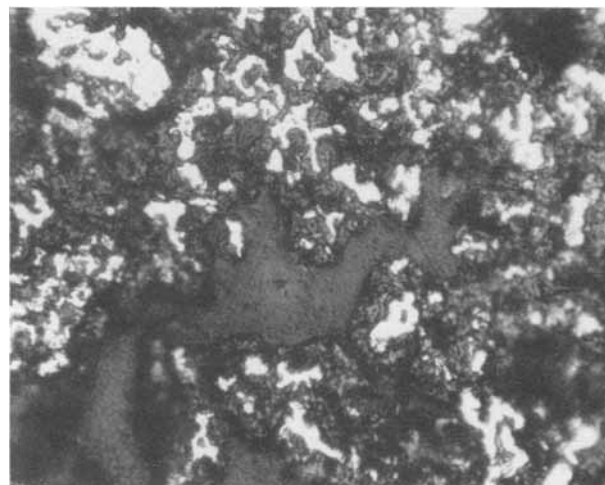


Fig. 4. Same as Fig. 3

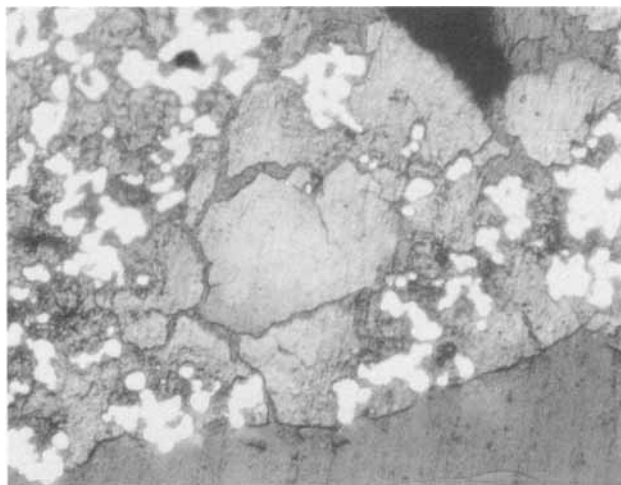


Fig. 5. Cross section of conventional electrochemically impregnated sinter electrode. Capacity: 60-70 C/cm². Ni: white. Ni hydroxide: light gray. Epoxy mount: dark gray (from lower right). Magnification: 680X.

port function and so a stronger/thicker sinter will probably be required in making practical electrodes.

Examination by Auger electron spectroscopy did not reveal halides in the surface of ac deposited hydroxide that had been charged and discharged in KOH. After *in situ* ion milling for several thousand angstroms, no response from halide ions appeared above the detection limit of 0.1 atomic percent (a/o).

Discussion

The experimental work has demonstrated that the capacities of sintered Ni electrodes made by the very simple and easily controllable ac process are comparable with those of electrodes made by the conventional electrochemical-impregnation technique (4, 5) and that the uniformity of film thickness produced has operational advantages. In addition, the technique could be of general application where thick and uniform conversion layers of electrochemically active oxides or hydroxides of other metals are required, since anodic dissolution of many metals can be activated by the presence of "aggressive" halide ions and an increase in pH on current reversal can cause the solubility product of their hydroxides to be exceeded. Pourbaix (8) shows that a large number of metal hydroxides have minimum solubility even at low to neutral pH, while the metal can anodically dissolve at lower pH. Cycling the pH in this "window" at a suitable potential should, therefore, produce films of hydroxide in contact with substrate metal. The process could be generally accelerated by alternating anodic then cathodic potential excursions and by addition of suitable anions to break down passivating films. It is likely that anions other than chloride and bromide, for instance, iodide, oxyanions, etc., could promote conversion of metals to their hydroxides by ac. There are probably other waveshapes and frequencies and current densities which could be equally effective.

A detailed model of the unusual kinetics involved in ac deposition of Al hydroxide films on Al has been proposed (3) and with some modifications can also explain film growth by ac on Ni. In that work, scanning electron microscopy (SEM) supported by calculations of ion concentrations near the metal surface showed the formation of a thin cathodically deposited Al hydroxide film on application of ac to Al, in HCl. A cubic etch-pit formed during the anodic half cycle of applied ac, and then, on current reversal, the walls of the pit became covered and partially protected by a thin dense layer of Al hydroxide, as they became cathodic, and the local pH rose. Imperfections in this dense but thin layer then led to further local attack to form another cubic pit during the subsequent anodic half cycle, and so on. Eventually the Al developed a "cellular" structure with walls of Al covered by thin hy-

droxide deposits despite the low pH electrolyte, in which Al hydroxide solubility is normally high. In the case of Ni, the transparent hydroxide films formed are much thicker and less dense and the mechanism involves, during the anodic half cycle, probably more general dissolution activated by the halide ions, since the SEM microstructure does not show a metal/hydroxide cubic morphology similar to Al, but shows strands of Ni within low density hydroxide films (9).

During the cathodic half cycle immediately following an anodic half cycle on Ni, the generally high concentration of Ni²⁺, [Ni²⁺], within the pores of the Ni sinter would be lowered at the surfaces of Ni particles by precipitation if the pH was locally sufficiently high. The minimum solubility of Ni(OH)₂ occurs at pH 10.2 (8), although even at pH 8 its solubility is ~10⁻³ M/liter. So, near-neutral aqueous salt solutions are already close to these precipitation conditions. In addition to the high [Ni²⁺] present, steepening of the pH gradient near the metal surface is likely as the hydrogen evolution reaction (HER) occurs, this would cause precipitation close to and at the metal surface and so provide good contact between hydroxide and metal. While the limited internal electrolyte volume in pores may help increase [Ni²⁺], rapid diffusion of protons by mechanisms such as Grotthus hopping towards the surface may limit the pH rise (3). However, it is possible that, as in the Al case, protonic diffusion is slow under conditions prevailing in the pores and particularly slow near the surfaces of the Ni particles because of a high local [Ni²⁺] produced there by the end of the anodic half cycle, which might hinder rotation of water molecules. Measurements of the diffusion coefficient of H⁺ ions, D_{H⁺}, in aqueous chloride solutions measured polarographically (10) show that D_{H⁺} decreases with increase in salt concentration and depends upon the cation. It falls from 9 · 3 × 10⁻⁵ to 5 · 3 × 10⁻⁵ cm²/s from 0 to 2M Li⁺ solutions, while it only drops to 7 · 5 × 10⁻⁵ cm²/s for the equivalent concentration change in K⁺ solutions. It is likely that the dependence on the cation is related to its hydration number or the effective number of water molecules attached to the ion in its hydration sheath and partially "immobilized." The inability of these water molecules to orient in an electric field causes a decrement in the static dielectric constant of water containing metal ions which is larger for solutions of small, highly charged cations, where the interaction is greater. Hydration numbers can be calculated from the effect on the dielectric constant and show that, while K⁺ and Rb⁺ have hydration numbers ~1, for small ions, such as Li⁺, it is ~3, while for small but highly charged cations, such as Al³⁺, the hydration number is as high as 16 (11), which effectively immobilizes ~30% of the water molecules in 1M AlCl₃. For a divalent ion such as Ni²⁺, the hydration number is less, but only by about one-third, i.e., ~11, from several determinations (12, 13) which is sufficient to immobilize a larger number of water molecules, particularly near the metal surface, where the [Ni²⁺] gradient turns upward prior to the beginning of the cathodic half cycle. H⁺ ion transport would then be by conventional diffusion with D_{H⁺} ~ 2 × 10⁻⁵ cm²/s, comparable with D_{Ni²⁺}, so that a fairly steep upward gradient in [OH⁻] could prevail at the metal surface during HER and facilitate precipitation very close to the metal surface.

The physical and other properties of films will largely depend on the steepness of the pH gradient that can be developed at the metal/electrolyte interface, since this will affect the density of the deposit. The observed thick, low density Ni hydroxide films formed on Ni by ac (9) could be a consequence of a lower cathodic half-cycle pH gradient than at an Al/Al³⁺ interface, owing to less water immobilization. Factors other than the pH gradient might also affect the density and thickness of deposits. The pH dependence of Al hydroxide solubility is an order of magnitude greater than for Ni hydroxide (8), so that shorter pH excursions could result in precipitation. This, together with the lower pH for minimum solubility (by 5 pH units), could have contributed to-

wards the denser film precipitation on Al. However, equilibrium solubility data may not be appropriate in the discussion of a large ac perturbation! Indeed, it was the rate of surface pH adjustment that was calculated, in the case of Al hydroxide deposition, to be critical, and not the time needed for precipitation which was much faster.

The form of the deposit will also be affected by the frequency used. The much lower frequencies needed to build up thick Ni hydroxide films at high efficiency may be related not only to pH effects but to the need to build up a high $[\text{Ni}^{2+}]$ within electrolyte-filled voids in the Ni sinter, so that on current reversal, a precipitation front can move from the metal interface for some distance into the Ni^{2+} -rich electrolyte. The difference in conversion efficiency between foil and sinter could be explained in this way. This, together with the pH gradient at the Ni/Ni^{2+} interface, might explain the rather good adhesion between the hydroxide and Ni surface which is better than that produced by the ED process. SEM examination of ac-processed electrodes (9) did not reveal Ni particles of the sinter clearly separated from hydroxide in specimen fracture zones, as is commonly observed in ED electrode fractures. The frequency and shape of the cathodic half cycle is also important in determining the pH gradient and hence the film density.

The inefficiency of conversion presumably reflects coulombic losses to such processes as Ni hydroxide shedding, Ni plating, and possibly gaseous oxidation products, but conversion efficiencies as high as 60% for the sintered Ni electrodes makes the process highly competitive, in terms of power consumption, with conventional dc electrochemical impregnation. A fuller explanation of the general mechanism and understanding of the dependence on a low ac frequency as well as the requirement for symmetrical ac (in contrast to the foil experiments) requires further experimental investigation. However, it is already clear that, by whatever mechanism, a new commercial process for making Ni battery electrodes is feasible. Full commercialization might involve Co^{++} additive to the electrolyte if it is shown that increased utilization (14) and mechanical stabilization of the active material (15) are still required in the highly energy-efficient ac formed electrode. Also, a stronger sinter support-structure may be needed.

Several operational advantages in production are likely in addition to the low direct costs, anticipated, for this simpler process. It exhibits a high effective "throwing power" because the process involves local generation of Ni^{2+} followed by precipitation, so the latter is not limited by diffusion of Ni^{2+} from the bulk solution as in the ED process. Also, chloride ions are not consumed, but are, rather, recycled and hydroxyl ions are made available locally by the reaction: $\text{H}_2\text{O} + e^- \rightarrow 1/2 \text{H}_2 + \text{OH}^-$. This translates into uniform thickness of deposited layers throughout the Ni sinter. Uniformity in thickness of the electrochemically active hydroxide will reduce electrical isolation (6, 7) and so ensure high utilization, improve chargeability and dischargeability, and allow thicker Ni sinter to be uniformly "loaded." Each of these will increase the electrode energy-density. Also, sinter considered too poor for the ED process because of wide void size distribution can be used. So, the feature of high throwing power will provide an indirect cost advantage commercially.

Aspects of the process which lead directly to low anticipated commercial costs are as follows. There is no prepassivation necessary as in the electrochemical impregnation process. The electrolyte cost is low, as are

operating costs because of the room temperature operation, and there is no need for close pH control. Costs will also be reduced if the process is made contact-less which is easier for an ac process than for dc. Because of the high throwing power, sinters with a smaller mean pore size than usual for making electrochemically deposited electrodes can be used, which will allow higher energy density electrodes to be made and also help increase electrode strength. Finally, there is no "bath aging" phenomenon, which is characteristic of the ED process, where electrode loading decreases with time in a very complex manner (16), requiring eventually costly replacement of the ED solution.

Conclusions

Implementation of this ac method should offer the following advantages over the conventional dc electrochemical method: (i) cheap chemicals (NaCl , KCl , etc.); (ii) simpler control (wide operational "windows," for pH, temperature, etc.), (iii) a room temperature process, (iv) no prepassivation would be required, (v) more uniform distribution of active material, (vi) insensitivity to large void distribution in the sinter, (vii) the possibility of a contact-less process, (viii) thicker sinter of similar porosity could be deeply loaded, e.g., using higher current density or more ac cycles (than in Fig. 1 and 2) to raise electrode energy density, (ix) higher inherent energy density using less porous Ni sinter (because of conversion of Ni to hydroxide rather than addition of hydroxide to Ni), (x) better electrode performance (a more uniform distribution of active material will improve chargeability, reduce internal polarization, and reduce electrical isolation on discharge), (xi) high coulombic efficiency of conversion of Ni to $\text{Ni}(\text{OH})_2$, and (xii) no "bath aging" phenomenon.

Manuscript submitted April 2, 1984; revised manuscript reviewed Aug. 4, 1984.

AT&T Bell Laboratories assisted in meeting the publication costs of this article.

REFERENCES

1. B. MacDougall and M. J. Graham, *This Journal*, **128**, 2321 (1981).
2. S. H. Glarum and J. H. Marshall, *ibid.*, **129**, 535 (1982).
3. C. K. Dyer and R. S. Alwitt, *ibid.*, **128**, 300 (1981).
4. R. L. Beauchamp, U.S. Pat. 3,653,967.
5. L. Kandler, U.S. Pat. 3,214,355 (1965).
6. C. K. Dyer, in "The Nickel Electrode," R. G. Gunther and S. Gross, Editors, p. 118, *The Electrochemical Society Softbound Proceedings Series*, Pennington, NJ (1982).
7. C. K. Dyer, in "Proceedings of the NASA/Goddard Battery Workshop 1981," G. Halpert, Editor, p. 459, Conference Publication 2217, NASA, Washington, DC (1982).
8. M. Pourbaix, "Atlas of Electrochemical Equilibria in Aqueous Solutions," NACE, Houston, TX (1974).
9. C. K. Dyer, To be published.
10. M. Stastny and F. Strafelda, *Coll. Czech. Chem. Commun.*, **34**, 168 (1969).
11. J. B. Hasted, "Aqueous Dielectrics," pp. 145 ff., Chapman and Hall, London (1973).
12. J. O'Bockris and B. E. Conway, "Modern Aspects of Electrochemistry," Vol. 1, p. 62, Academic Press, New York (1954).
13. J. Burgess, "Metal Ions in Solution," Ellis Norwood Ltd., Chichester, England (1978).
14. S. U. Falk and A. K. Salkind, "Alkaline Storage Batteries," John Wiley and Sons, New York (1969).
15. D. M. Fritts, *This Journal*, **129**, 118 (1982).
16. M. W. Earl and T. F. Noble, *J. Power Sources*, **12**, 277 (1984).

Effect of Antimony on Lead-Acid Battery Negative

B. K. Mahato,* J. L. Strebe,* D. F. Wilkinson,* and K. R. Bullock*

Johnson Controls, Incorporated, Electrochemical Research, Milwaukee, Wisconsin 53201

ABSTRACT

The role of antimony on the lead-acid battery negative in terms of its effect on charge efficiency, its effect on gassing overpotential, its interactive influence with lignin expander in controlling the charge efficiency, and its retentive behavior or purging characteristics as SbH_3 in the overcharge gas stream was investigated. Linear potential sweep (LPS) cycling of Planté-type lead electrodes was used to determine the effect of antimony and/or lignin expander on charge efficiency. Pasted-type lead electrodes were used to determine the effect of antimony on gassing overpotential and to monitor its concentration either in the active material or the exit gas stream. Results showed a significant contribution of antimony in decreasing charge efficiency and an overwhelming role of lignin expander in suppressing the effect of antimony on charge efficiency. The critical lead-electrode potential for purging antimony from the electrode is close to -1275 mV (*vs.* $\text{Hg}/\text{Hg}_2\text{SO}_4$).

Antimony in a lead-acid battery negative electrode comes primarily from two sources: (i) oxide raw material prepared from battery scrap secondary lead, and (ii) the antimonial positive grid alloy. During normal battery operation, the antimonial positive grid corrodes and releases antimony as oxidized species. This antimony slowly migrates through the positive active material and the electrolyte and deposits at the lead electrode, initiating a performance degradation of the battery. Adverse effects include: (i) increased self-discharge, (ii) excessive water loss or increased maintenance, (iii) decreased charge efficiency, and (iv) formation of toxic stibine (SbH_3) environment around the battery.

The detrimental influence of antimony on the lead electrode performance is well known (1, 2). The use of expander, particularly the lignin constituent of expander, in the lead electrode in improving its overall performance has also been common in the state of the art (1-4). However, the information related to the effect of antimony on the lead electrode performance is still qualitative. There is no reference dealing with the possible interaction of expander and antimony that may influence the lead-acid battery negative electrode performance. The objectives of the present investigation have been (i) to estimate quantitatively the effect of antimony on the lead electrode charge efficiency, (ii) to evaluate the interaction of antimony and expander-lignin on the lead electrode charge efficiency, and (iii) to determine the antimony retention within or purging out the lead electrode during charging.

Experimental

Table I shows our experimental plan. For charge efficiency, we used linear potential sweep (LPS) cycling of Planté-type lead electrodes between 100 mV anodic and 200 mV cathodic to open-circuit potential. We calculated the charge efficiency as percent ratio of anodic to cathodic charge. For gassing behavior, we used the cathodic LPS of a pasted lead electrode from -980 mV to hydrogen evolution potential. To define the antimony purging behavior from or the retention within the plate, we used constant potential charging of pasted and Planté-type electrodes.

The LPS cycling equipment has previously been described (4). The test cell had a 2 cm long, 2 mm diam test electrode, an oversized counterelectrode, and a reference electrode, all immersed in sulfuric acid electrolyte. Both test and counterelectrodes were made out of 99.999% pure lead (Cominco). The reference electrode was $\text{Hg}/\text{Hg}_2\text{SO}_4/m\text{H}_2\text{SO}_4$, where m is the acid concentration in the reference electrode reservoir. The conversion of the electrode to a Planté-type, moderately high surface area electrode was carried out in two stages. In the first stage, the electrode capacity was developed by LPS cycling in 1.050 sp gr H_2SO_4 between -860 and -1160 mV (*vs.* reference) for 48h at 0.5 mV/s scan rate. The second stage was

the stabilization in 1.250 sp gr H_2SO_4 by identical cycling treatment for an additional 48h. The steady-state electrode charge efficiencies were monitored during development and stabilization cycles. This was followed by the determination of the effect of 20 ppm Sb, 20 ppm lignin-expander, and their combination in the cell electrolyte on the lead electrode charge efficiency. The antimony used in this series of experiments was the atomic absorption quality reference solution (1 $\mu\text{g}/\text{ml}$) obtained from Anderson Laboratory (Fort Worth, Texas). The lignin-expander was Maracell-XC obtained from American Can Company (Rothschild, Wisconsin).

The influence of antimony on the lead electrode gassing behavior was determined by the cathodic LPS between -980 mV (*vs.* reference) to free gassing potential at 0.5 mV/s scan rate. The electrode (type A) was commercially obtained $4.30 \times 5.00 \times 0.155$ cm dry charge negative with 10.5g active material. It was tested against two counter positive electrodes having the same dimensions in a three-plate-element cell with or without antimony in the electrolyte. The influence of constant potential overcharge on the antimony content in the lead electrode was carried out by testing a pasted lead electrode containing antimony. This electrode (type B) was $12.0 \times 14.0 \times 0.155$ cm with reagent-grade Sb_2O_3 fines (Fisher Scientific) in the paste. It was formed in a three-plate-element cell with two counter positives in 1.050 sp gr H_2SO_4 at -1125 mV (*vs.* reference) constant potential with total amount of charge equivalent to twice the theoretical amount needed to form the plate. The -1125 mV (*vs.* reference) charging potential was used to avoid the "antimony loss" from the plate during formation. The formed electrode was then tested for its antimony retention characteristics under potentiostatic overcharge with or without step input. The antimony retention in the plate was analyzed by neutron activation at the University of Wisconsin, Madison, facility. In one case, the testing was carried out in a sealed container in which the overcharged gas was continuously purged by 20 cm^3/min argon gas stream to two stibine gas absorbing solution columns in series. The solution used for stibine absorption was prepared according to Varma *et al.* (5). The antimony content in the absorbing solution was determined colorimetrically (5).

Results and Discussion

Effect of antimony and/or lignin expander on charge efficiency.—The steady-state capacity of Planté-type electrodes at the end of development and stabilization cycles are shown in Table II. Q_a , Q_c , and E are anodic charge, cathodic charge, and charge efficiency, respectively. The data show that the Planté-type electrodes prepared by LPS cycling have excellent reproducibility, charge efficiency in excess of 98% in 1.050 and 1.250 sp gr H_2SO_4 , and a greater anodic charge in 1.050 sp gr H_2SO_4 than in 1.250 sp gr. The four stabilized electrodes given in Table II were used to determine the effect of antimony, lignin-expander, and their combination on the charge ef-

* Electrochemical Society Active Member.

Table I. Experimental scheme

Objective	Electrode type	Technique	Measurements
Charge efficiency	Planté	LPS-cycling, -1160 to -860 mV at 0.5 mV/s	$Q_a/Q_c \times 100$
Hydrogen over-potential	Pasted	Cathodic LPS from -980 mV	E_{H_2} from i-E curve
Antimony purging potential	Pasted Planté	Constant potential charge Constant potential charge	Sb in paste Sb in exit gas stream E_{H_2} from i-E curve

Table II. Capacity and charge efficiency of Planté-type lead electrodes after development and stabilization cycles

Test electrodes	Charge at the end of development cycles (C)			Charge at the end of stabilization cycles (C)		
	Q_a	Q_c	E	Q_a	Q_c	E
I	1.0640	1.0790	98.6	0.7664	0.7776	98.6
II	1.0950	1.1040	99.2	0.8263	0.8349	99.0
III	1.0510	1.0720	98.0	0.7742	0.7868	98.4
IV	1.1900	1.2040	98.8	0.8996	0.9110	98.8

Q_a = anodic charge; Q_c = cathodic charge; $E = Q_a/Q_c \times 100$.

iciency. Electrode 1, which was used as a control, underwent continued cycling in 1.250 s g H_2SO_4 ; electrode 2 was cycled in acid with 20 ppm lignin expander; electrode 3 was cycled in acid with 20 ppm antimony; and electrode 4 was cycled with 20 ppm lignin-expander plus 20 ppm antimony. All four electrodes were cycled for 290 cycles, i.e., for 4 days. Their steady-state charge/discharge characteristics were noted at the end of the test.

Table III summarizes the steady-state characteristics of the control and test electrodes LPS cycled with antimony and/or lignin-expander in the solution. The results indicate (i) that the charge efficiency of the control electrode was maintained close to 100%, (ii) that presence of expander did not affect the charge efficiency and helped to build up the steady-state capacity close to three times that of the control, (iii) that the antimony in the solution decreased the charge efficiency to 13.5% and capacity to about 75% of the control, and (iv) that inclusion of lignin-expander in antimony containing solution suppressed the adverse effect of antimony on charge efficiency and increased it to 80.6% level. Moreover the lignin-expander in antimony containing solution increased the test electrode anodic capacity to almost 3.5 times that of the control. These observations suggest the ability of lignin-expander in suppressing the effect of antimony on the lead electrode charge efficiency. These data also show a synergistic influence of lignin-expander and antimony on the lead electrode performance. The efficacy of the electrode in developing and maintaining its capacity during cycling was better in solution with lignin-expander and antimony than with lignin-expander alone.

The mechanistic understanding of the interaction of antimony and lignin-expander on the lead electrode performance is not clear from this series of experiments. However, the cyclic voltammograms (Fig. 1) and SEM micrographs (Fig. 2) of the electrodes taken at the end of the

Table III. Effect of lignin-expander and/or antimony on Planté lead electrode charge efficiency in 1.250 sp gr H_2SO_4

Electrolyte additive	Charge (C)		Efficiency (E)
	Q_a	Q_c	
No additive (control)	0.9587	0.9619	99.7
20 ppm lignin expander	2.9230	2.9380	99.5
20 ppm antimony	0.7200	5.3500	13.5
20 ppm lignin expander and 20 ppm antimony	3.388	4.206	80.6

Q_a = anodic charge; Q_c = cathodic charge; $E = Q_a/Q_c \times 100$.

test do help, at least qualitatively, to show the interaction of these two important components on the lead electrode behavior. The voltammogram in Fig. 1a is typical of the lead electrode in pure sulfuric acid solution (4). The low current acceptance at the end region of anodic and cathodic LPS indicates completion of the anodic ($Pb \rightarrow Pb^{2+} + 2e$) and cathodic ($Pb^{2+} + 2e \rightarrow Pb$) processes during cycling. Figures 1a-1d show that a change in the electrolyte composition does affect the cathodic portion of the electrode voltammograms more profoundly than their anodic counterparts. In presence of lignin-expander in the test solution (Fig. 1b), the cathodic voltammogram is characterized by a suppressed peak intensity and broadening of peak area, resulting in a significant increase in net cathodic charge. This increased cathodic charge is subsequently reflected in a greater anodic capacity. The decrease or suppressed cathodic peak intensity is due to restricted reaction surface or deposition sites caused by the surface adsorption of the lignin-expander. This observation agrees well with the previously reported findings (4). Figure 1c shows the dramatic influence of antimony in solution in changing the lead electrode cathodic voltammogram. It causes the onset of gassing at the electrode at 80 mV cathodic to open-circuit potential, a loss in anodic charge, and a significant decrease in charge efficiency. The decreased charge efficiency is primarily due to loss of its hydrogen overpotential, which, in turn, causes excessive gassing and possibly a deficiency in the $PbSO_4 \rightarrow Pb$ conversion process.

The cathodic voltammogram (Fig. 1d) shows the influence of lignin-expander in modifying the effect of antimony on the lead electrode cathodic process given in Fig. 1c. Figure 1d has two cathodic peaks and a noticeably high current acceptance at the end region of the cathodic LPS. We observed very little gassing on the electrode surface compared to what we observed with antimony in the solution (Fig. 1c) during the cycling. This partially explains the greater capacity development and maintenance of the lead electrode cycled in solution with antimony and lignin-expander (Table III). Out of two cathodic peaks observed in Fig. 1d, the first one is similar to the influence of lignin-expander on the lead electrode in absence of antimony in the test solution (Fig. 1b). The

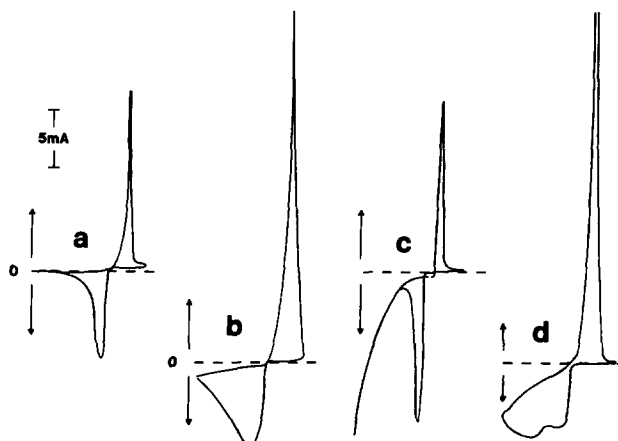


Fig. 1. Steady-state lead electrode cyclic voltammograms between -1160 and -860 mV (vs. Hg/Hg_2SO_4) in 1.250 s g H_2SO_4 with (a) no additive, (b) 20 ppm lignin expander, (c) 20 ppm antimony, and (d) 20 ppm antimony plus 20 ppm lignin expander.

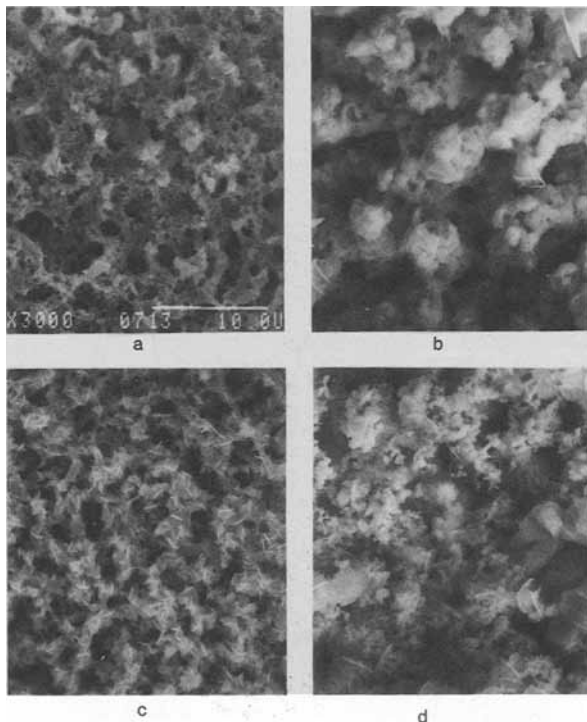


Fig. 2. Planté-type lead electrode surface morphology at the end of the test in 1.250 sp gr H₂SO₄ with (a) no additives, (b) 20 ppm antimony, (c) 20 ppm lignin expander, and (d) 20 ppm lignin expander plus 20 ppm antimony.

comparison of the cathodic voltammogram in Fig. 1b, 1c, and 1d suggests that the second cathodic peak in Fig. 1d must relate the interaction between the antimony and lignin expander on the lead electrode cathodic process. This change in the cathodic process may have resulted from the opposing effect of antimony and lignin-expander on the lead electrode hydrogen overpotential, preferential adsorption of lignin on freshly deposited antimony, and possibly the occurrence of a complexation reaction between Sb³⁺ and liginosulfonate anion at the reaction interface. More work is definitely needed to explain the interactive influence of antimony and lignin expander on the lead electrode charging process.

Another indication of the interactive influence of lignin and antimony on the lead electrode is apparent from the comparison of anodic capacities of lead electrodes developed in expander containing electrolyte with and without antimony. The anodic capacity of the lead electrode in the test solution with expander and antimony is about 16% greater than in the test solution with expander only (Table III). This suggests that trace antimony in the sys-

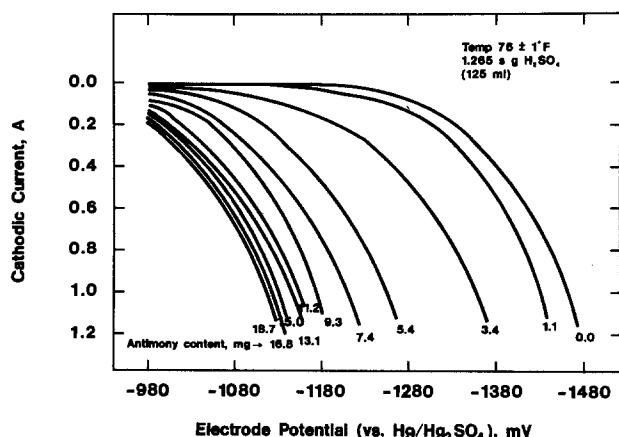


Fig. 3. Cathodic LPS behavior of pasted-type lead electrode as function of antimony content in the electrolyte.

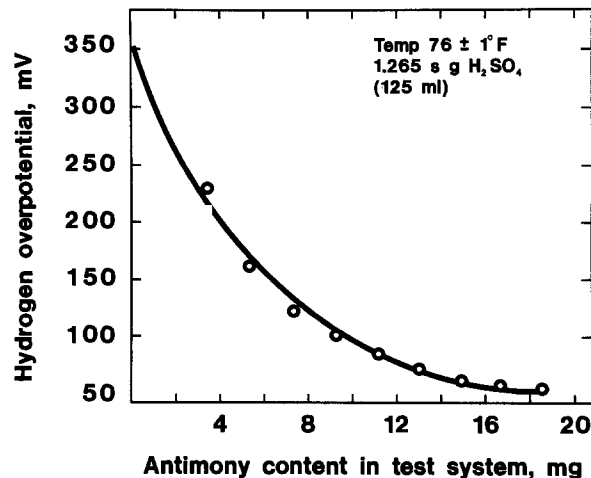


Fig. 4. Replotted data from Fig. 3 showing the hydrogen overpotential behavior of the test electrode as function of antimony content in the test system.

tem in the presence of expander may favor the formation of high surface area negative active material. The effect of expander and/or antimony on the lead electrode morphology is shown in Fig. 2. The low surface area of the lead electrode with or without antimony in the test solution (Fig. 2a and 2b) is apparent. Greater depth of the porous matrix, seen in Fig. 2b, may have resulted from the role of antimony in inducing the self-discharge or the lead oxidation process. A significant fineness in surface texture is evident for the electrode in the presence of expander (Fig. 2c). The very fine structure with interspersed lead sulfate is noticeable for the electrode with expander and antimony in the test system. This extrafine structure at least qualitatively explains the greater anodic capacity of this electrode compared to the electrode cycled in expander containing solution.

Effect of antimony on hydrogen evolution potential.—The effect of antimony on the hydrogen evolution overpotential of a pasted-type lead electrode (type A) was carried out in a three-plate element test cell with 125 ml 1.265 sp gr H₂SO₄ solution at 76° ± 1°F. The three-plate-element had one test electrode and two counter positives of identical dimension with microporous polypropylene separator in between. The fully charged test electrode was subjected to linear potential sweep at 0.5 mV/s from -980 mV (vs. Hg/Hg₂SO₄) to a cathodic potential of profuse hydrogen evolution. The experiment was repeated with continued addition of antimony to the electrolyte. The maximum concentration of antimony used in this study was

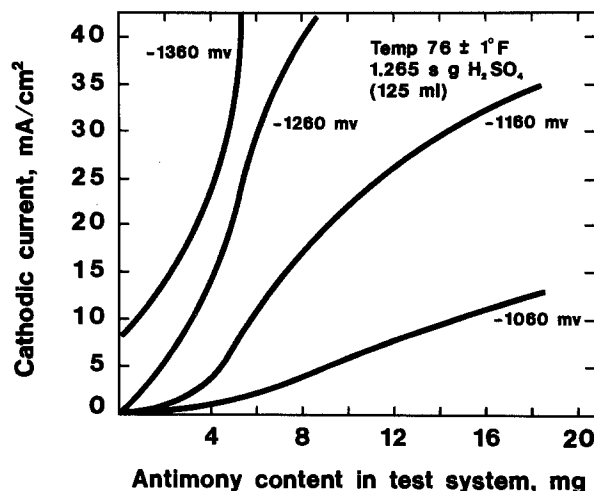


Fig. 5. Replotted data from Fig. 3 showing the isopotential cathodic current behavior of the test electrode as function of antimony content in the test system.

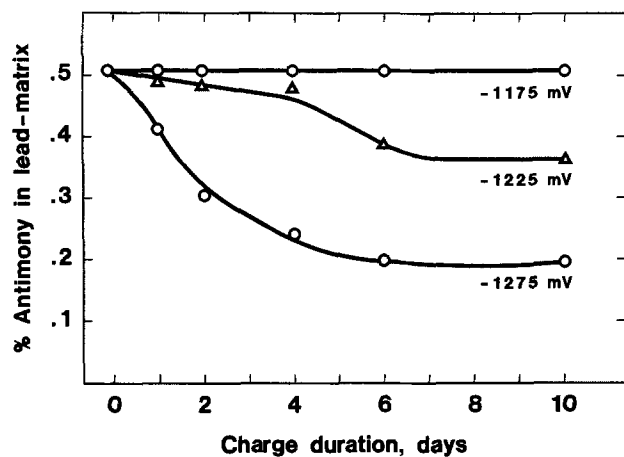


Fig. 6. Antimony purging behavior of pasted-type lead electrodes with antimony in the formed active material under constant potential charging.

close to 0.18%, based on the weight of negative active mass used in the test electrode.

The cathodic LPS data of the type A electrodes are shown in Fig. 3. The figure shows a continuous decrease in lead electrode gassing potential with increasing antimony content in the system. This study suggests that continuing accumulation of antimony at the lead electrode could decrease the lead electrode charging potential to less than -1100 mV *vs.* $\text{Hg}/\text{Hg}_2\text{SO}_4$, and could lead to a situation in which, under constant potential charging, excessive gassing, incomplete charging of negative, and rampant positive grid corrosion may occur.

Figures 4 and 5 are replotted from the data given in Fig. 3 to show the dependence of the lead electrode hydrogen overpotential and current acceptance on the antimony concentration in the test system. The hydrogen evolution

potential of the lead electrode is arbitrarily defined as the intersection of the base current of the lead electrode at -980 mV *vs.* $\text{Hg}/\text{Hg}_2\text{SO}_4$, and the tangent of the LPS curve at 0.5 A current acceptance. The lead electrode hydrogen overpotential is obtained by subtracting the hydrogen evolution potential from the open-circuit potential of the test lead electrode. Figure 4 shows the asymptotic decrease of hydrogen overpotential with increasing antimony content in the test system. The isopotential current acceptance characteristics of the lead electrode as function of antimony concentration are shown in Fig. 5. These isopotential lines show the approximate critical concentration of antimony for an electrode with 10.5 g lead active material and the possibility that antimony can be purged from the lead electrode at potentials close to -1260 mV *vs.* $\text{Hg}/\text{Hg}_2\text{SO}_4$.

Critical potential to purge antimony from the lead electrode.—Figure 6 shows the antimony retention behavior of type B electrode with 0.5% Sb in the formed active material during constant potential charging at 1175 , 1225 and 1275 mV *vs.* reference for a 10 day duration. We note that the steady-state antimony content in the lead matrix is overcharge potential dependent; no release of antimony at -1175 mV *vs.* reference) overcharge and steady-state "Sb" concentration of 0.340 and 0.182 weight percent (w/o) in lead matrix for overcharge potentials of -1225 and -1275 mV *vs.* reference), respectively. Overcharging the test electrode at potentials more cathodic than -1275 mV *vs.* reference) was not possible because of a 10 A current limitation in our potentiostat.

Figure 7 shows the antimony retention characteristics of antimony containing type B plates during constant potential step charging from -1175 to 1375 mV *vs.* reference) at 50 mV step using two approaches. In the first approach 1, we analyzed the conventionally washed and dried plate samples for antimony content after each step of overcharge. In the second approach, we analyzed the stibine absorbing solution after each step of overcharge.

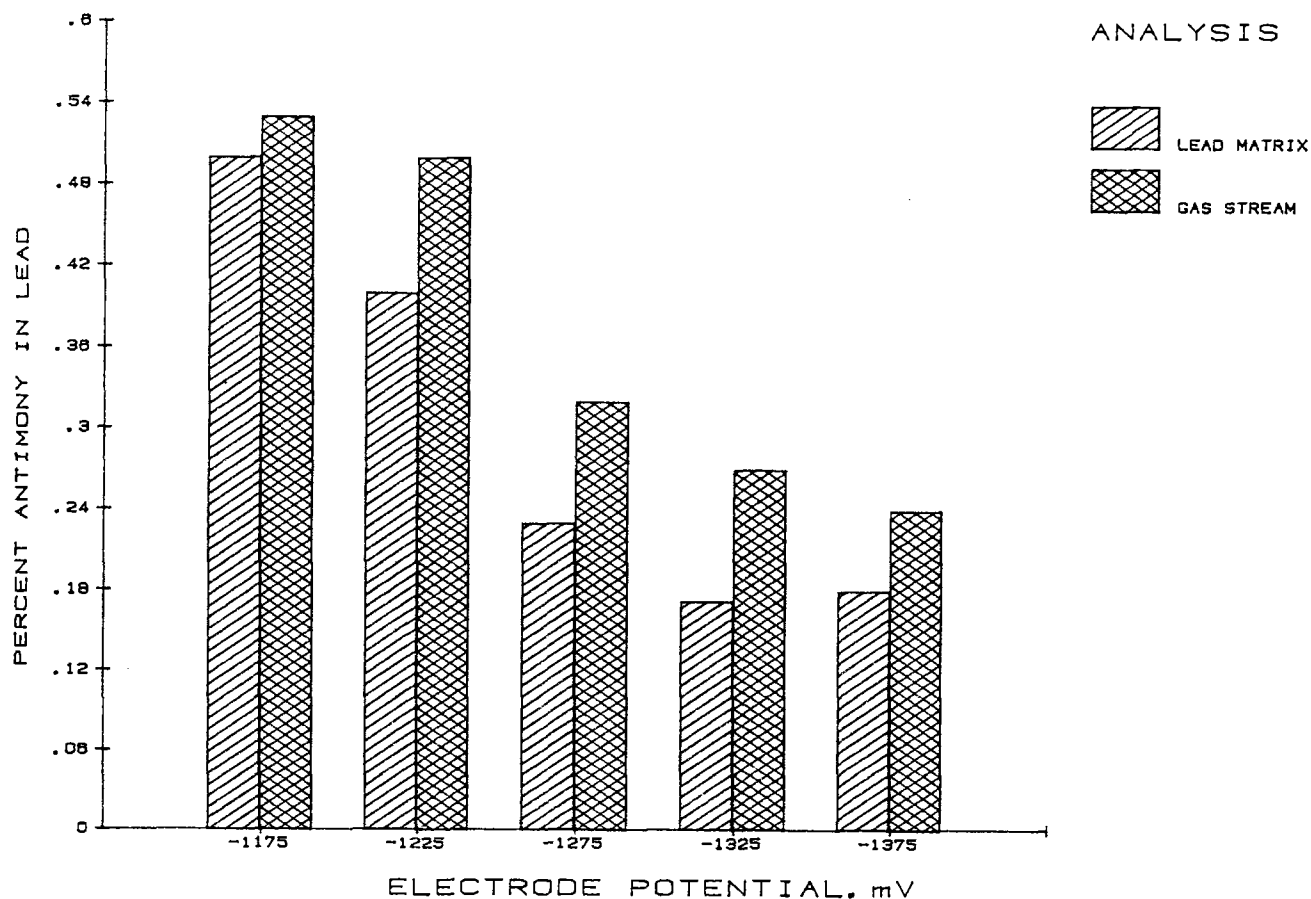


Fig. 7. Antimony purging behavior of the pasted-type electrode under increasing constant potential step charging.

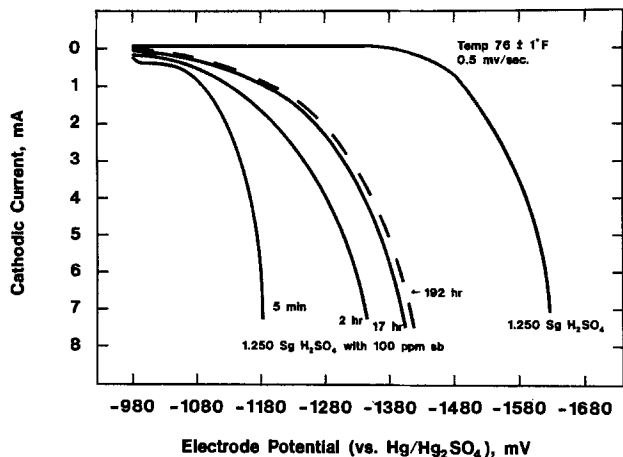


Fig. 8. Cathodic LPS of 2 mm diam and 2 cm long lead electrode in 100 ppm antimony containing 1.250 sp gr H_2SO_4 as function of -1270 mV vs. Hg/Hg_2SO_4 constant potential charge duration. Lead electrode cathodic LPS in 1.250 sp gr is included for comparison.

The residual antimony in the plate in the second approach was determined by difference. We used test plates with two levels of initial antimony content, one with 0.5% and the other with 0.53%, in these two experiments, as evident from Fig. 7. The amount of overcharge at each potential step was 4.63 Ah/(gram negative paste), equivalent to 20.5 times the theoretical capacity. The data for antimony retention in the plate using these two approaches are very consistent (Fig. 7). The slightly low value of antimony content obtained from the plate matrix analysis could be considered due to some material loss during washing and drying of plate samples. The data presented in Fig. 6 and 7 suggest that a significant amount of antimony, when present in the negative, may come out of the plate at potentials close to -1275 mV (*vs.* reference) and the complete removal of antimony from the lead electrode by constant potential charging may not be possible. These results further show that antimony, once it has migrated to the lead electrode, may become electrochemically inseparable. This is substantiated by a side experiment in which the lead electrode cathodic LPS was monitored as a function of constant potential overcharge at -1270 mV (*vs.* reference) in presence of 100 ppm antimony in the test solution. The results are shown in Fig. 8. It shows a dramatic decrease in lead electrode hydrogen overpotential after addition of antimony in the test solu-

tion. Upon continuous charging at -1270 mV *vs.* Hg/Hg_2SO_4 , the gas evolution potential shifted cathodically and recovered about 150 mV after 17h charge. However, even after extensive charging to the extent of an additional 175h, no further cathodic shift in gassing potential was observed. This, again, indicates that the lead electrode experiences an irreversible change in the presence of antimony.

Conclusions

1. The lead-acid battery negative electrode has a charge efficiency in excess of 98% and remains unaffected by the presence of lignin-expander.
2. Antimony in the negative electrode reduces its charge efficiency and hydrogen overpotential.
3. Lignin-expander suppresses the adverse effect of antimony on lead electrode charge efficiency.
4. The critical antimony purging potential for the negative electrode is close to -1275 mV (*vs.* reference).
5. Antimony causes an irreversible anodic shift in the lead electrode hydrogen overpotential.

Acknowledgments

This work was supported in part by Argonne National Laboratory under Contract no. 31-109-38-4205. We gratefully acknowledge the encouragement and support of W. Tiedemann for this work.

Manuscript submitted May 14, 1984; revised manuscript received Sept. 1, 1984. This was Paper 80 presented at the Washington, DC, Meeting of the Society, Oct. 9-14, 1983.

Johnson Controls, Incorporated, assisted in meeting the publication costs of this article.

REFERENCES

1. H. Bode, "Lead-Acid Batteries," pp. 238-242, John Wiley and Sons, New York (1977).
2. F. Burbank, A. C. Simon, and E. Willihnganz, in "Advances in Electrochemistry and Electrochemical Engineering," Vol. 8, P. Delahay and C. W. Tobias, Editors, pp. 229-245, John Wiley and Sons, New York (1970).
3. J. R. Pierson, P. J. Gurlusky, A. C. Simon, and S. M. Caulder, *This Journal*, **11**, 1463 (1970); A. C. Simon, S. M. Caulder, P. J. Gurlusky, and J. R. Pierson, *ibid.*, **121**, 463 (1974); A. C. Simon, S. M. Caulder, P. J. Gurlusky, and J. R. Pierson, *Electrochim. Acta*, **19**, 739 (1974).
4. B. K. Mahato, *This Journal*, **127**, 1679 (1980); *ibid.*, **128**, 1416 (1981).
5. R. Varma, G. M. Cook, and N. P. Yao, Argonne National Laboratory Report ANL/OEPM-78-4 (1979).

An Optical Study of the Iron Electrode in Alkaline Electrolyte

Z. Q. Huang¹ and J. L. Ord*

Department of Physics, University of Waterloo, Waterloo, Ontario, Canada N2L 3G1

ABSTRACT

Ellipsometric measurements made as an iron electrode is cycled galvanostatically in unstirred 0.05M NaOH show that a low density outer layer builds up progressively over an inner compact oxide layer. The inner layer reaches a maximum thickness of approximately 38Å at oxygen evolution and is removed by cathodic reduction, whereas the outer layer thickens by over 100Å on each cycle. The outer layer is made up of partially dissolved reaction products which are alternately oxidized and reduced on each cycle, but there is no evidence that the inner layer (of Fe₃O₄) undergoes solid-phase oxidation or reduction under galvanostatic cycling. Under anodic conditions, the inner layer acts as a barrier layer for field-limited ionic transport, and when it is reduced on a cathodic cycle it provides the iron which enables the outer layer to grow on the subsequent anodic cycle.

Much of the recent work on the anodic oxidation of iron, particularly work involving ellipsometric measurements, has been carried out in the deaerated neutral borate electrolyte initially selected by Cohen and co-workers (1) for cathodic reduction studies. This electrolyte has features which make it ideal for studies of the passivity of iron, but boron is involved in the electrochemical processes, and quite different results are obtained in other electrolytes of the same pH. The feature convenient for ellipsometric work is the ability to reduce the surface back to its initial optical state without significant surface roughening or buildup of a layer of reaction products. In our initial optical study of the passivity of iron (2), we used both neutral borate and sulfuric acid electrolytes, but we found that a reaction-product layer built up rapidly in acid electrolyte and made it difficult to study the underlying passive layer optically.

A variety of models for the passive film on iron can be found in the literature. These range from single-phase films of FeOOH or Fe₂O₃ to two-phase films of FeOOH on top of Fe₂O₃ or Fe₃O₄ on top of Fe₃O₄. Although work on the system continues unabated, in our opinion (3, 4), it is unlikely that a consensus will emerge as long as workers in the field hold widely differing views of the fundamental processes involved. Our work on the system (5, 6) culminated in a model in which high field ionic transport controls the growth of a two-phase film composed of a layer of Fe₂O₃ adjacent to the electrolyte and a layer of Fe₃O₄ adjacent to the iron substrate. This model differs from the model proposed earlier by Sato and Cohen (7, 8) in the kinetics of film growth, but not in the structure of the two-phase film. In our model, the field in the inner Fe₃O₄ layer limits film growth, and passivity is conferred by the outer Fe₂O₃ layer.

Nonequilibrium transport-limited models have long been used to describe the growth kinetics in valve-metal systems where the potentials are too high to have thermodynamic significance, but it is not surprising that such models encounter considerable resistance when they are applied to the iron system, where potential clearly has thermodynamic significance in the two-wave cathodic reduction process. Our model of the anodic oxidation of iron is definitely a nonequilibrium model; the Fe₃O₄ film continues to grow in the passive region at potentials where Fe₂O₃ is thermodynamically favored. This feature of the model is in accord with our experimental findings; we find no evidence of solid-phase oxidation or reduction processes converting films of Fe₃O₄ to or from films of Fe₂O₃ in deaerated neutral borate electrolyte.

In this paper, we report the results of an ellipsometric study of the oxidation and reduction processes which occur when an iron electrode is cycled galvanostatically in air-saturated alkaline electrolyte. The objectives of this study are (i) to look for evidence of solid-phase oxidation or reduction processes involving films of Fe₂O₃ or Fe₃O₄,

(ii) to see whether ellipsometry can identify processes involving dissolved intermediates, and (iii) to see whether ellipsometry is better able to deal with the buildup of by-product layers in alkaline electrolyte than it is in acid electrolyte. One recent study (9) details a complex series of sequential and parallel oxidation and reduction processes many of which involve dissolved phase intermediates. This study describes Fe₃O₄ as a second-stage oxidation product which is subsequently further oxidized, whereas others claim that the subsequent reaction is the production of Fe₂O₃ by direct oxidation of metallic iron (10). Still others regard Fe₃O₄ as a byproduct layer produced after 3-5 reduction cycles in lithiated electrolyte (11), or by aging of Fe₂O₃ · H₂O (12). Recently Dunnwald *et al.* (13) studied iron in alkaline electrolyte using Raman spectroscopy and concluded that a primary passivating layer of Fe₃O₄ is covered by a nearly nonadhesive low density outer layer of alpha-FeOOH.

Experimental

Our preliminary measurements in alkaline electrolyte were carried out in 1M NaOH, but the results reported here were all obtained in air-saturated 0.05M NaOH at 22°C. The cell holds 60 ml of electrolyte, which is free of reaction products at the beginning of an experiment. The iron electrode is a cylindrical single crystal with a flat on one side for optical measurements. It is clamped between Teflon washers in a glass electrode holder which exposes a vertical area of 1.145 cm² to the electrolyte when mounted in the cell. The cell also contained a mercury/mercurous sulfate electrode, to which all potential measurements are referenced, and a platinum counterelectrode, but no gas-dispersion tube, and the electrolyte was not stirred.

The self-nulling ellipsometer uses quadrature Faraday modulation decoded by a two-phase lock-in amplifier and fed back to ministepping drives through voltage-to-frequency converters. Under typical operating conditions, the instrument has a response time of a few tenths of a second and a resolution of a few thousandths of a degree. The angle of incidence is set at 60°C to accommodate the equilateral prism used as a cell, and refractive index values quoted here are for a wavelength of 6328Å, the wavelength of the helium-neon laser used as a light source.

A process-control computer operates the circuitry used with the cell and records current and potential along with the polarizer and analyzer settings at specified time intervals. Potentials are digitized by a 16-bit analog-to-digital converter with a 25-μs conversion time. The operation of the ellipsometer is monitored on a four-trace oscilloscope, and progress of the experiment is followed on two storage displays and an X-Y plotter which are updated by the computer.

Results

In situ measurements with a null ellipsometer are best performed under galvanostatic conditions, where the re-

*Electrochemical Society Active Member.

¹Permanent address: Department of Chemistry, Chongqing University, Chongqing, Sichuan, China.

quired null-tracking rate can be controlled. Rotating analyzer instruments operate in a somewhat different manner, but they also require time to achieve accuracy, and perform best when the rate of the process being studied is controlled directly. Linear potential sweeps are also useful for ellipsometric studies, but processes which involve significant charge transfer over a narrow potential range require slow sweep rates if the tracking speed of the ellipsometer is not to be exceeded. Linear sweeps are popular because peaks on the current-potential plot identify most of the electrochemical processes involved, but care must be taken not to ignore processes such as field-limited film growth which only shift the base line.

We use galvanostatic cycles for all of the measurements we report here. Using our recorded data we can compute values of dQ/dV to plot *vs.* potential if we wish to generate a plot analogous to a linear potential sweep *i-V* plot. (In a linear sweep, V is proportional to t , and, hence, the current, dQ/dt , is proportional to dQ/dV .) A variety of techniques can be used to carry out the numerical differentiation, but there is no very satisfactory way of dealing with the overshoot which can occur under galvanostatic conditions.

The first series of figures shows the results of an experiment in which an iron electrode is cycled repetitively at $87 \mu\text{A}/\text{cm}^2$ between oxygen and hydrogen evolution in 0.05M NaOH. Figure 1 shows the results obtained on the first cycle after a freshly polished iron electrode is inserted into a cell filled with air-saturated electrolyte which is free of reaction products, and Fig. 2 shows the results obtained on the ninth cycle. Corresponding points (chosen to identify the fully developed features observed on the ninth cycle) bear the same labels in the two figures. The initial cathodic cycle used to reduce the oxide film left after chemical polishing is not shown in Fig. 1. In deaerated borate electrolyte the initial reduction leaves the surface free of any film, but we cannot assume that this is true in air-saturated alkaline electrolyte. The first anodic cycle shows some structure between A and D, but the pronounced arrest between B and C which characterizes later cycles does not show up on the first cycle. Beyond point D, the potential exhibits the linear increase with time which we attributed to field-limited passive-state film growth in our work in neutral borate electrolyte. Oxygen evolution begins at E and continues to the beginning of the cathodic cycle at F. The first cathodic cycle exhibits two major arrests, F-G and H-I, but not the arrest between G and H seen on the ninth cycle. Close examination of the arrest between H and I shows that it is actually composed of two arrests at closely

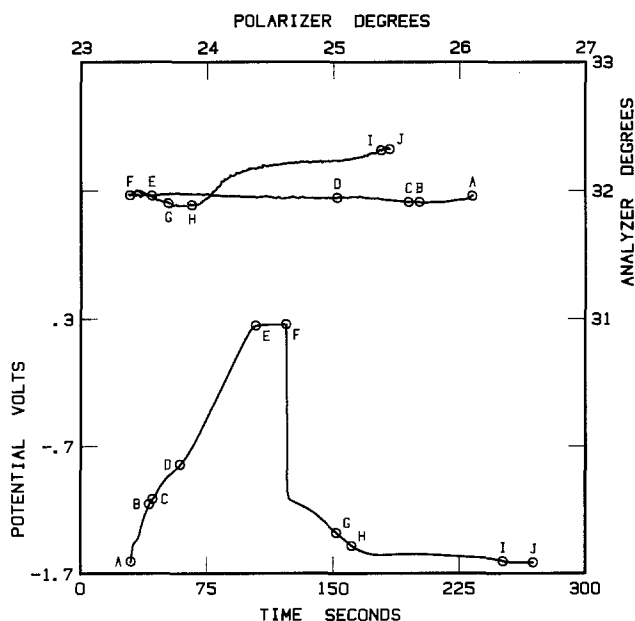


Fig. 1. First galvanostatic cycle at $87 \mu\text{A}/\text{cm}^2$ in 0.05M NaOH

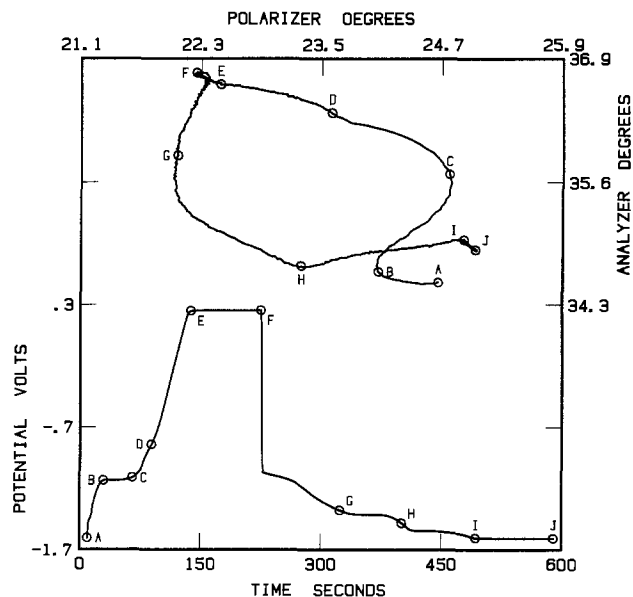


Fig. 2. Ninth galvanostatic cycle at $87 \mu\text{A}/\text{cm}^2$ in 0.05M NaOH

spaced potentials. Hydrogen evolution begins at I and continues to the end of the cathodic cycle at J.

The curves traced out by the null settings of the ellipsometer during the first and ninth galvanostatic cycles are shown in the upper portions Fig. 1 and 2 in the form of plots of polarizer null setting *vs.* analyzer null setting. The optical data exhibit a complex structure which correlates strongly with the structure in the *V-t* curves, but the ninth cycle appears very different from the first cycle, and the reason for the difference is not apparent in Fig. 1 and 2.

The optical data do, however, have a definite pattern, and this pattern can be seen in Fig. 3 where we plot the data from all 18 cycles. A1-F1-J1 identify the first-cycle end points from Fig. 1, and A9-F9-J9 identify the ninth-cycle end points from Fig. 2. (The initial cathodic segment, omitted from Fig. 1, is shown in Fig. 3.) The dominant features of the pattern in Fig. 3 are the "loops" traced out by the cycle end points, and it is these loops which are the starting point for the optical analysis described in the next section.

There are two other ways of plotting the data in Fig. 2 which aid in their interpretation. In Fig. 4, we show the derived dQ/dV *vs.* potential plot we discussed at the beginning of this section. Three anodic processes, O1, O2, and O3, have peaks associated with them, and O4, passive-

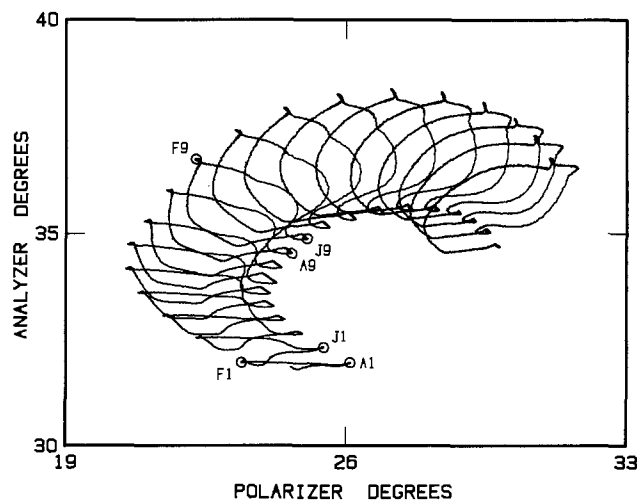


Fig. 3. Optical data from 18 galvanostatic cycles at $87 \mu\text{A}/\text{cm}^2$ in 0.05M NaOH. End points of the first and ninth cycles, points A, F, and J in Fig. 1 and 2, have corresponding labels.

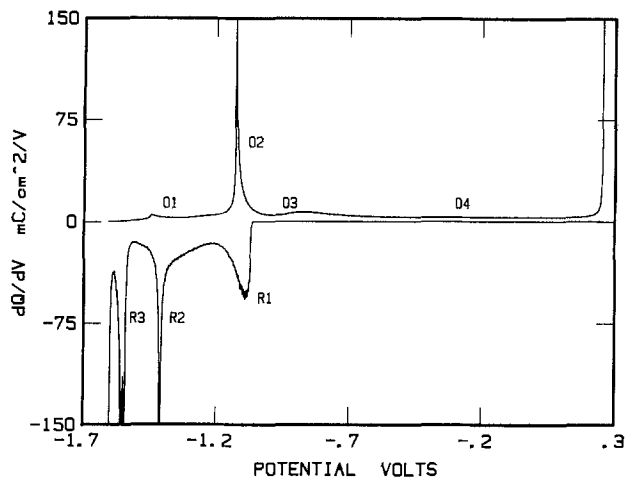


Fig. 4. Plot of dQ/dV vs. potential derived from the potential-time plot in Fig. 2. Four oxidation peaks and three reduction peaks can be identified in the figure.

state oxidation, shows up as an offset in the base line. Cathodic processes R1 and R2 have single peaks associated with them, but R3 is really two processes (which we will refer to as R3a and R3b) with closely spaced peaks which are just resolved on the scale in Fig. 4. Figure 4 contains really no information beyond what appears in Fig. 2, but it puts the information in a form which is more closely comparable to a linear sweep plot.

Figure 5, however, contains time-rate-of-change information about the optical data which is not present in the P-A plot in Fig. 2. The "optical tracking rate" plotted vs. time in the figure is the rate at which the null setting of the ellipsometer tracks along the P-A locus on the ninth galvanostatic cycle. Figure 5 uses the same time scale as the potential-time plot in Fig. 2, and corresponding points bear the same labels. Under galvanostatic conditions, film growth by substrate oxidation and removal by cathodic reduction produce optical changes which proceed at a steady controlled rate, whereas a process such as dissolution-precipitation produces changes which start slowly and then build rapidly to a peak before slowing down as the reaction products are consumed. Neither hydrogen nor oxygen evolution produces significant optical changes.

Cycles with restricted anodic or cathodic end points can help a great deal in the interpretation of both optical and electrochemical data. Figure 6 shows the results of a galvanostatic cycling experiment at $87 \mu\text{A}/\text{cm}^2$, in which the cathodic segment of the eighth cycle is terminated at the end of process R2 (point O in the figure). The cathodic segment of the preceding cycle is shown for

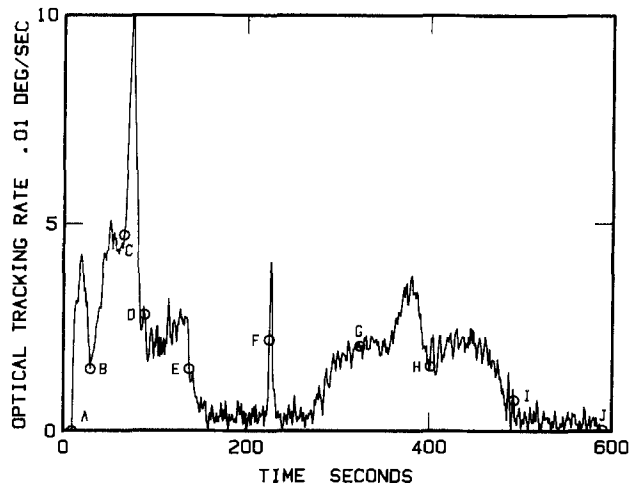


Fig. 5. Plot of optical tracking rate vs. time for the ninth cycle data. The time scale and the labeling are the same as in Fig. 2.

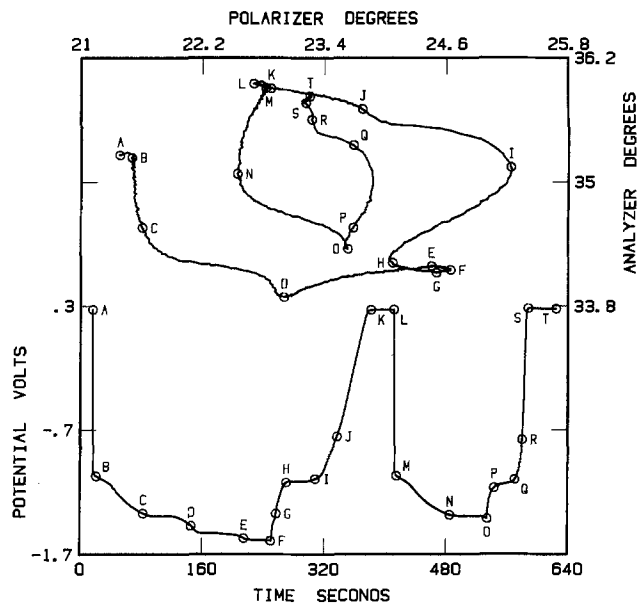


Fig. 6. Galvanostatic cycles at $87 \mu\text{A}/\text{cm}^2$ in 0.05M NaOH showing the effect of stopping the cathodic cycle at point O.

comparison purposes (points A through F), and the anodic segment of the subsequent cycle is plotted from O through T. The experiment was continued by applying three additional cycles with the same cathodic end point, then a complete cycle to gas evolution at each end, and finally a series of cycles with restricted anodic end points. The first cycle with a restricted anodic end point is shown in Fig. 7, along with the cathodic segment of the preceding complete cycle. The anodic cycle is terminated at the end of process O2 at point I, and the subsequent cathodic segment continues to point L.

Discussion

The loops traced out by the cycle end points in Fig. 3 act as the starting point for the optical analysis. An ellipsometer measures the change in polarization resulting from interference between light reflected at the electrolyte-film and film-substrate interfaces, and loops of this type are produced by the growth of a film which does not absorb light very strongly. If the refractive index of the film is only slightly higher than that of the electrolyte, the amplitude of the light reflected at the film-

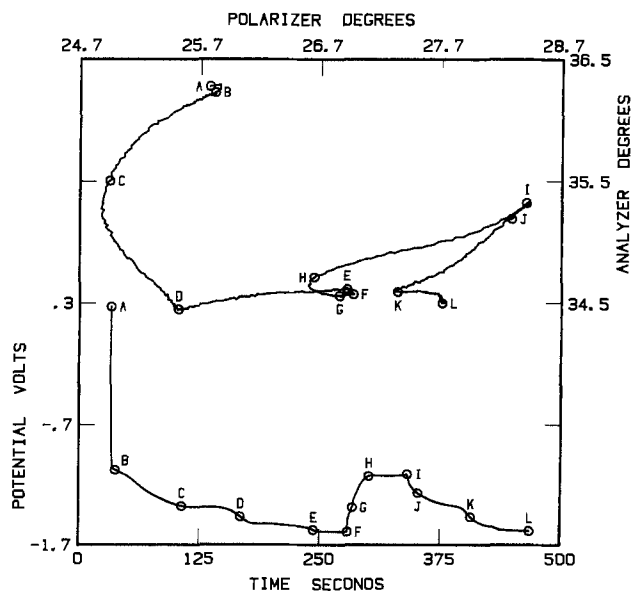


Fig. 7. Galvanostatic cycles at $87 \mu\text{A}/\text{cm}^2$ in 0.05M NaOH showing the effect of stopping the anodic cycle at point I.

electrolyte interface is much smaller than the amplitude of the light reflected at the film-substrate interface, and hence interference does not greatly change the polarization of the reflected light, and the null settings of the instrument trace out a relatively small loop as the film grows. Loop closure will occur when the product of the film thickness, and the cosine of the angle of refraction is equal to half the wavelength of light in the film; hence, the lower the film index, the greater the thickness at which closure occurs.

These considerations enable us to deduce a great deal from the optical data in Fig. 3 without detailed analysis. First, the film grows progressively and is not removed from the surface by cathodic reduction. Second, the film has a very low index (about 1.4), much lower than that of a solid-phase oxide film. Third, the difference in size of the end-point loops shows that the oxidized form of the film must have a higher index than the reduced form. Fourth, the film reaches a considerable thickness (well over 1000Å) after 18 cycles.

We conclude, therefore, that the film which grows progressively on iron in alkaline electrolyte is best thought of either as a very porous film containing considerable electrolyte, or as a film of electrolyte containing partially dissolved reaction products. The cyclic change in film index shows that the the oxidation state of the film is raised and lowered each cycle, and the processes by which this occurs account for the structure in the $V-t$ curves which is enhanced by cycling. We chose to use an unstirred electrolyte in these experiments so that we could study the growth and change in oxidation state of a film which does not adhere strongly to the surface, and we chose 18 cycles to get a thickness range wide enough for unambiguous optical analysis.

We know that an underlying compact oxide must also be present on the iron electrode at the end of an anodic cycle, and we next turn to the problem of how we distinguish its optical effects from those due to the outer layer. The problem is relatively easy to solve because the two layers have greatly different refractive indexes. The scales in Fig. 3 can accommodate only a small segment of the growth loop of a compact oxide and, over the thickness range found in neutral electrolyte, the growth segment appears essentially linear. In Fig. 8, we replot the optical data from Fig. 3, showing only the segments associated with processes O2 and R3b. The loops traced out by the end points of the segments are still an important feature of the figure, but now it is readily apparent that the optical changes associated with process R3b trace out a sequence of parallel linear segments of approximately the same length, whereas those associated with process O2 are of variable length and have changes in slope which reflect the change in the slope of the loop. From this, we

conclude that process O2 involves the progressively growing outer layer, and process R3b involves the underlying oxide layer. The O2 optical data initially parallel the growth curve for the lower oxidation state of the outer layer, then swing rapidly outward toward the curve for its higher oxidation state. From this, we conclude that O2 involves both growth and oxidation of the outer layer. R3b, however, appears to involve only the removal of the compact inner layer by cathodic reduction.

If we use this approach to classify the other processes, we conclude that formation of the compact oxide is begun by process O1 and continued to limiting thickness by process O4. O3 is more difficult to classify, because the rapid optical changes associated the O2 end just as O3 is reached, and the optical effects which can be identified with O3 appear little different from those associated with O4. R1 and R2 appear to be reduction processes involving primarily the outer layer, whereas R3a appears to involve reduction of the inner compact layer as well as continued reduction of the outer layer. The inflection point which divides R3 into R3a and R3b appears to mark the point at which reduction of the outer layer ceases.

The results of a quantitative analysis of the optical data based on the procedure described above for distinguishing between layers are plotted in Fig. 9. The data used in the analysis were taken from a sequence of eight standard cycles followed by the short cycle plotted in Fig. 6. The end-point data, offset slightly in P from the data in Fig. 3 because of a difference in surface roughness, are shown in Fig. 9 identified by cycle number. The short cycle points labeled A, F, L, and O in Fig. 6 are labeled O7, R8, O8, and P9, respectively, in Fig. 9. The bare surface point, point B, was chosen to provide the most consistent fit to the cathodic end-point data. They were found to fit a curve for the growth of a transparent film of index 1.381, and this curve is shown in the figure for growth to a thickness of 1400Å. The point corresponding to an inner layer of maximum thickness on a bare iron surface, point C, was similarly chosen to give a consistent fit to the anodic end-point data. If a value of 2.0 is assumed for N of the inner layer, a value of 0.25 is found for K, and the maximum thickness reached by the layer at point B is 38Å. The anodic end-point data fit a curve through B representing the growth of a transparent film of index 1.411, and this curve is shown in the figure for growth to a thickness of 1400Å. Also passing through B is a curve for growth of the 1.381 index film to a maximum thickness of 1400Å, this time on top of the 38Å inner layer. Points, such as P9, which fall on this locus are reached at the end of the outer-layer reduction processes R1 and R2. The outer layer can be treated as having some optical absorption, but the K values determined in the analysis are com-

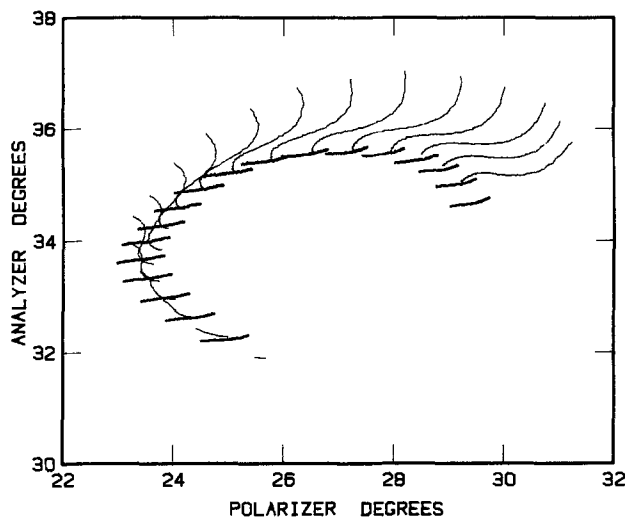


Fig. 8. Replot of the optical data in Fig. 3 showing only the O2 (fine line) and R3b (bold line) segments.

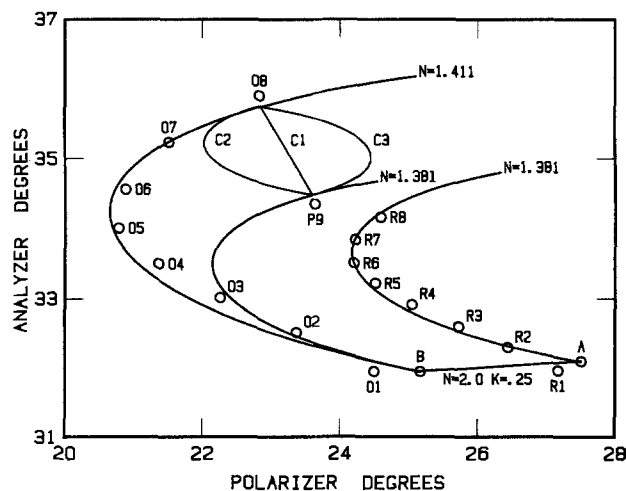


Fig. 9. Theoretical analysis of eight complete galvanostatic cycles (reduction end points R1-R8, oxidation end points O1-O8) followed by the short cycle in Fig. 6 (in Fig. 6 L is O8, O is P9).

parable with the estimated error in K; hence, we prefer to treat the layer as transparent.

Figure 9 also shows theoretical curves for models of an outer-layer conversion process with end points at O8 and P9 (actually on the 1.411 index curve at 1192Å and on the 1.381 index curve at 1251Å). In model C1, the conversion takes place by homogeneous proportionate changes in index and thickness, and the corresponding P-A locus is roughly a straight line between the end points. In models C2 and C3, the conversion sweeps across the film from one interface to the other. In model C2, the outer layer has index 1.381, and in model C3 it has index 1.411. All three models can describe oxidation as well as reduction, but the theoretical curves are all drawn for a process which takes place on top of a 38Å inner layer, and these conditions pertain on an anodic cycle only for the short cycle shown in Fig. 6. The phase boundary between the components of the low index film is probably not as sharply defined as the models require, but the counter-clockwise looping of the optical data shows that oxidation generally follows model C3 and reduction follows model C2. This means that both oxidation and reduction sweep inward across the layer from the electrolyte interface. We cannot determine layer composition from our optical measurements, but we see no reason to dispute the identification of the oxidized form of the outer layer as α -FeOOH (13), which converts to ferrous hydroxide on reduction.

We agree also with the identification of the primary passivating layer as Fe_3O_4 (13) rather than Fe_2O_3 , and we regard the evidence in support of this identification to be equally as strong as it is in neutral electrolyte. The short cycle in Fig. 6 presents this evidence most clearly. Reduction is carried to a point where it is universally agreed that any Fe_2O_3 present will be reduced to Fe_3O_4 , then the anodic current is reapplied, and the anodic cycle shows no sign of a process which could possibly correspond to the oxidation of Fe_3O_4 back to Fe_2O_3 . Process O4 is completely absent, and the potential rises rapidly between R and S, in accordance with the predictions of a model in which the current is limited by the electric field in the Fe_3O_4 film. We do expect the outer surface of the Fe_3O_4 to be oxidized to Fe_2O_3 on an anodic cycle, and this likely occurs when the oxidation wave sweeping through the outer layer reaches the oxide surface. (This, finally, is our identification of process O3).

The short cycles are also useful for studying layer growth processes. The short cycle in Fig. 6 shows that outer-layer growth does not occur on an anodic cycle unless the inner layer is reduced on the previous cathodic

cycle, and it shows how process O2 is modified when oxidation takes place without layer growth. The short cycle in Fig. 7 shows that the outer-layer growth is complete and its oxidation is well advanced by the end of O2, and inner-layer growth has the overpotential proportionality expected of a field-limited process. If we trace the path of the iron which ends up in the outer layer, we see that it is removed from the substrate by the field in the inner layer on an anodic cycle, then delivered to the outer layer as dissolved ferrous ions on the next cathodic cycle, and finally incorporated into the outer layer as ferrous hydroxide which is oxidized to FeOOH by the oxidation wave sweeping in from the electrolyte interface.

Acknowledgment

This work received partial support from the Natural Sciences and Engineering Research Council of Canada under Grant no. A-1151.

Manuscript submitted April 18, 1984; revised manuscript received July 3, 1984. This was Paper 12 presented at the Washington, DC, Meeting of the Society, Oct. 9-14, 1983.

The University of Waterloo assisted in meeting the publication costs of this article.

REFERENCES

1. M. Nagayama and M. Cohen, *This Journal*, **109**, 781 (1962).
2. J. L. Ord and D. J. DeSmet, *ibid.*, **113**, 1258 (1966).
3. J. L. Ord, in "Passivity of Metals," R. P. Frankenthal and J. Kruger, Editors, pp. 273-284, The Electrochemical Society Monographs Series, Princeton, NJ (1978).
4. J. L. Ord, "Passivity of Metals and Semiconductors," M. Froment, Editor, pp. 95-100, Elsevier, New York (1983).
5. F. C. Ho and J. L. Ord, *This Journal*, **119**, 139 (1972).
6. J. L. Ord and D. J. DeSmet, *ibid.*, **123**, 1876 (1976).
7. N. Sato and M. Cohen, *ibid.*, **111**, 512 (1964).
8. N. Sato and M. Cohen, *ibid.*, **111**, 519 (1964).
9. M. C. H. McKubre and M. J. Madou, Abstract 53, p. 81, The Electrochemical Society Extended Abstracts, Vol. 83-1, San Francisco, CA, May 8-13, 1983.
10. D. D. Macdonald and D. Owen, *This Journal*, **120**, 317 (1973).
11. Y. Geronov, T. Tomov, and S. Georgiev, *J. Appl. Electrochem.*, **5**, 351 (1975).
12. R. S. Schreiber Guzman, J. R. Vilche, and A. J. Arvia, *Electrochim. Acta*, **24**, 395 (1979).
13. J. Dunnwald, R. Lossy, and A. Otto, "Passivity of Metals and Semiconductors," M. Froment, Editor, pp. 107-112, Elsevier, New York (1983).

Resistance of Titanium to Phosphidation and the Reaction Mechanism

Y. Sasaki and Y. Kabuto¹

Department of Synthetic Chemistry, Chiba University, Yayoi-cho, Chiba 260, Japan

ABSTRACT

A study was undertaken concerning the resistance of titanium to phosphidation at 650°-950°C in phosphorus vapor at 1 atm by a sealed-tube method. X-ray diffraction patterns and an electron microprobe analysis of the product films showed that the phosphide layer structure was $\text{TiP}_{1+x}/\text{TiP}/\text{Ti}_3\text{P}_2/\text{Ti}$. All the phosphidation reactions obeyed a parabolic rate law; hence, the rate-determining step was apparently a diffusion process. The parabolic rate constant was given as a function of the absolute temperature by the following expression.

$$K_p = 1.34 \exp(-34.5 \times 10^3/RT) \text{ g}^2\text{cm}^{-4}\text{h}^{-1}, (1 \text{ atm}, 923\text{-}1223 \text{ K})$$

A marker experiment indicated that the component which diffused was not phosphorus, but was titanium. Titanium metal was appreciably superior to iron, nickel, and chromium, which are the main constituent metals of stainless steel, with respect to phosphidation resistance.

Metallic materials such as stainless steel, Hastelloy, and Monel have been widely utilized because they have a corrosion-resistant property. One of the authors has reported previously on the kinetics and mechanism of the phosphidation reactions of iron (1), nickel (2, 3), chromium (4), and copper (5), which are the main constituents of these materials and also of Fe-Ni (6), Ni-Cr (7), and Fe-Cr (8) alloys.

As part of a series of studies on the phosphidation of metals, this study has been undertaken to develop a phosphorus resisting metallic material and to synthesize titanium phosphides; information is provided concerning the layer structure of phosphide films, the relationship between the products and reaction conditions, kinetics, and diffusing species.

Experimental

Materials.—A titanium sheet 0.5 mm thick with a purity of 99.7 mass % was cut into rectangles of approximately 6 mm × 25 mm. According to an analysis by the manufacturer, the impurity level of this sheet was as follows: O, 0.12 mass %; Fe, 0.05; C, 0.02; N, 0.02; H, 0.008. These coupons were abraded through 0/6-0/9 emery papers, then washed with refined toluene. They were chemically polished for 20s at room temperature in a solution consisting of 45 parts by volume 62% HNO_3 , 10 parts 46% HF , and 45 parts distilled water. These polished specimens were then rinsed in distilled water. Their geometric surface areas and weights were measured.

Red phosphorus was treated with a boiling 10% aqueous solution of sodium hydroxide for 5h, then with dilute hydrochloric acid. After being washed with distilled water, the refined red phosphorus was preserved in a desiccator with phosphorus pentoxide.

Apparatus and procedures.—The evacuated- and sealed-tube method (2, 5) was employed for the phosphidation. A sample sheet and an excess of red phosphorus were each placed at an end of the silica tube; this tube was sealed under vacuum. It seems reasonable that red phosphorus with various crystal structures will not give stable pressures of phosphorus vapor. Therefore, a conversion from red to liquid phosphorus is necessary to secure the stable pressures of phosphorus vapor in the closed system. In this study, the phosphorus vapor that evolved by heating the red phosphorus in the sealed tube was condensed by water cooling into liquid phosphorus.

The reaction apparatus consisted of a porcelain tube maintained in two temperature zones, the first zone being used to heat the sample sheet in a sealed silica tube and the second zone being used to control the vapor pressure of phosphorus in this tube. A vapor pressure of phos-

phorus was governed by the minimum temperature in the closed system. A temperature of 280°C gave 1 atm for the phosphorus vapor pressure (9) and was employed for all the phosphidation reactions. The apparatus and experimental methods employed in this study have been described in detail in previous papers (2, 5).

Results and Discussion

Metallic titanium was phosphidized at temperatures of 650°, 750°, 800°, 850°, 900°, and 950°C in phosphorus vapor at 1 atm. Because the sheet of titanium was used as a sample in this study, all the products of the phosphidation were films.

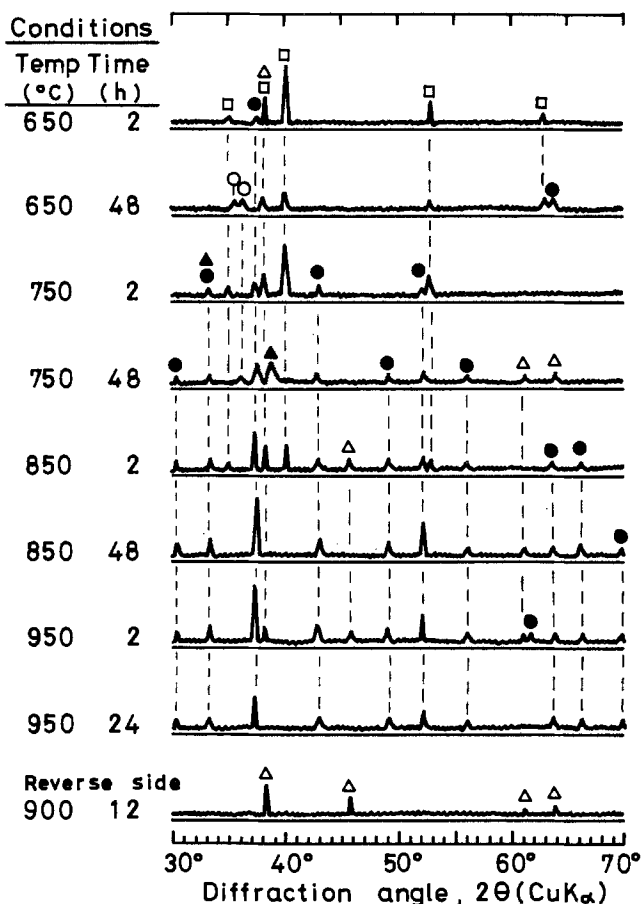


Fig. 1. X-ray diffraction patterns of the surface and reverse side of phosphide films formed on titanium sheets in phosphorus vapor at 1 atm. Effect of temperature and of reaction time: ○ TiP_2 ; ● TiP ; △ Ti_3P_2 ; ▲ Ti_5P_3 ; □ $\alpha\text{-Ti}$.

¹ Present address: Fuji Heavy Industries, Ltd., Nishi-shinjuku 1-7-2, Shinjuku-ku, Tokyo 160, Japan.

Compositions of phosphide layers.—Figure 1 illustrates the x-ray diffraction patterns of the surfaces of the phosphide films formed at 650°, 750°, 850°, and 950°C, employing nickel-filtered copper radiation. Also shown is the x-ray pattern of the reverse side of the film formed at 900°C. The diffraction peaks are identified by comparison with the literature values of diffraction angles of Ti (10), Ti_3P_3 (10), Ti_4P_3 (10), TiP (11), and TiP_2 (12).

Figure 1 shows that the composition of the products changes gradually with the reaction temperature. The reaction starting temperature seems to be somewhat less than 650°C because, in the diffraction patterns at 650°C-reaction for 2h, the diffraction angle $2\theta(CuK\alpha) = 37.6^\circ$ belongs alone to TiP, whereas all the other peaks are due to Ti. In the reaction for 48h at the same temperature, the diffraction peaks belonging to both TiP and the higher phosphide TiP_2 are found, as are those belonging to unaltered Ti. At the elevated temperature of 750°C for 2h, three new diffraction peaks belonging to TiP are observed. In the reaction for 48h at the same temperature, the peaks of Ti disappear completely. This phosphide film was composed of the mixture of mainly TiP and small amounts of Ti_3P_3 , Ti_4P_3 , and TiP_2 . At 850°C-reactions for 2 and 48h, the higher phosphide TiP_2 was not formed, but almost all the peaks were for TiP. Because no data for the equilibrium $TiP_2(s) \rightleftharpoons TiP(s) + 1/4 P_4(g)$ are reported, it is impossible to discuss what is expected to be formed under certain fixed reaction conditions. The pattern of 950°C-24h reveals the product to be TiP alone.

The diffraction pattern of the reverse side of the phosphide film formed at 900°C is in close agreement with that of Ti_4P_3 ; this is the same behavior found at other temperatures. It is worth noting that at the phosphide/titanium interface, the formation of Ti_4P_3 takes place. Lower phosphides Ti_2P (13) and Ti_3P (13) cannot be detected from x-ray diffraction at each temperature.

Composition variations through the phosphide film formed at an advanced stage of reaction were examined by EPMA. The specimens phosphidized at 850°C-48h and 950°C-24h were embedded in a polyester resin, the cross sections were polished with finely divided chromium (III) oxide powder, and the concentration distributions of phosphorus were then examined. These results are shown in Fig. 2.

It is clear from Fig. 2 that at the surfaces of both of the specimens, the concentrations of phosphorus reach about

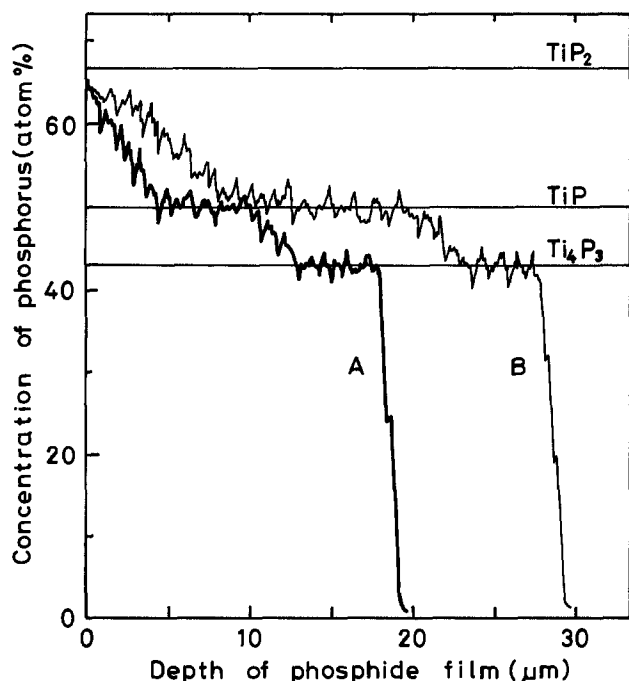


Fig. 2. Distribution of phosphorus in the titanium phosphide film: A—850°C, 1 atm, 48h; B—950°C, 1 atm, 24h.

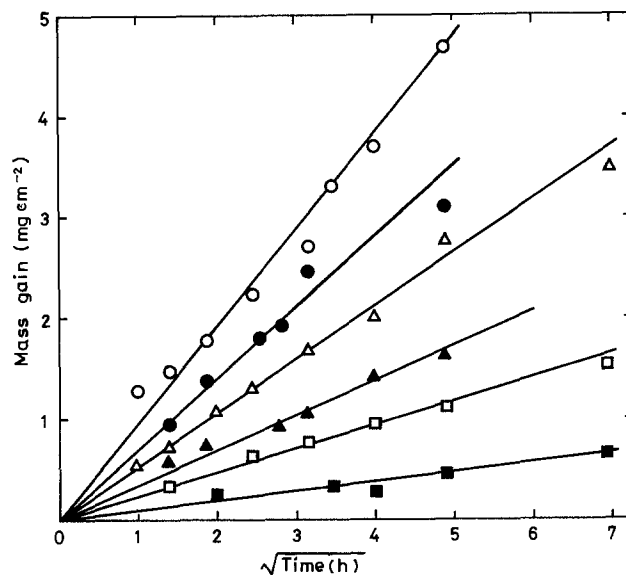


Fig. 3. Phosphidation of titanium in phosphorus vapor at 1 atm: ○ 950°C; ● 900°C; △ 850°C; ▲ 800°C; □ 750°C; ■ 650°C.

65 atom percent (a/o) and decrease toward the inner scale layers. It must be noted that two plateaus having constant phosphorus contents of 50 ± 2 and 42 ± 2 a/o are present in the bulk phosphide. The composition of the first plateau should correspond to TiP, and the second plateau adjacent to unchanged titanium should correspond to Ti_4P_3 from the x-ray diffraction patterns. The higher concentration of phosphorus observed at the surface is assumed to represent a dissolution of phosphorus in the TiP matrix. If this layer is tentatively termed TiP_{1+x} , the layer structure of the phosphide scaling film becomes approximately $TiP_{1+x}/TiP/Ti_4P_3/Ti$.

Kinetics and temperature dependence.—Plots of the mass gain per unit area vs. $\sqrt{\text{time}}$ are shown in Fig. 3. The small scatter of the data points is attributed to the fact that each point represents phosphidation of separate specimens.

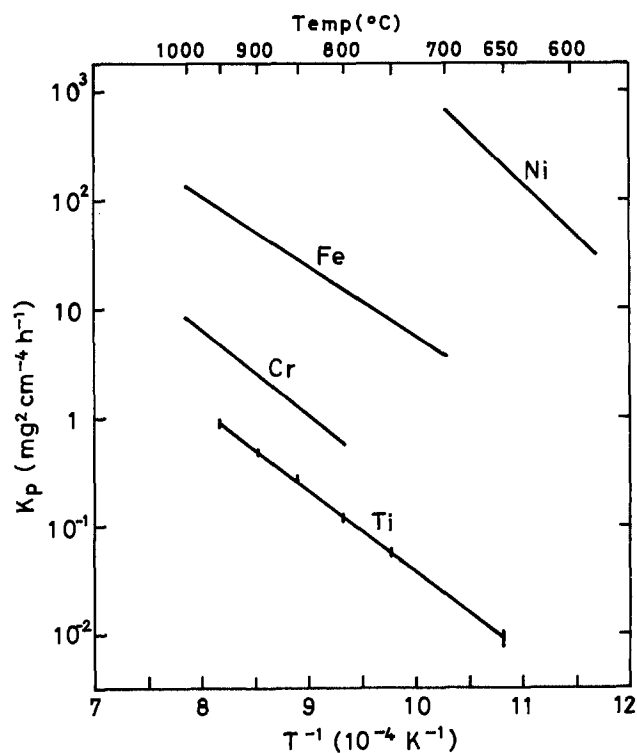


Fig. 4. Comparison of K_p of Ti with values for Ni, Fe, and Cr (phosphorus pressure: 1 atm).

Table I. Parabolic rate constants for phosphidation of titanium in phosphorus vapor at 1 atm

Temp, °C	K_p , $\text{mg}^2\text{cm}^{-4}\text{h}^{-1}$
650	0.0093 ± 0.0015
750	0.0570 ± 0.0050
800	0.1200 ± 0.0100
850	0.2800 ± 0.0200
900	0.4900 ± 0.0400
950	0.9200 ± 0.0600

All the plots yield approximately straight lines, showing that the phosphidation proceeds according to a parabolic rate law; hence, the rate-determining step is apparently a diffusion or a transport process of titanium or phosphorus. Values of the parabolic rate constants, K_p , obtained from the slopes of these straight lines, are summarized in Table I.

A semilogarithmic plot of K_p vs. the reciprocal of the absolute temperature is shown in Fig. 4. This relationship gives a straight line, which may be approximately expressed as follows

$$K_p = 1.34 \exp(-34.5 \times 10^3/RT) \text{ g}^2\text{cm}^{-4}\text{h}^{-1},$$

(1 atm, 923-1223 K)

There is no effect of the conversion of α -Ti into β -Ti, which occurs at 882°C, on these kinetics. For comparison, the parabolic rate constants of phosphidation of iron (1, 6, 8), nickel (2, 6, 7), and chromium (4, 7, 8), which are the main constituent metals of stainless steel, are included in the same figure. As shown, the K_p of titanium is considerably smaller. Therefore, titanium metal should be superior to these metals with respect to phosphidation resistance.

Determination of diffusing species.—A marker experiment relating to the diffusion process was carried out for the phosphidation of titanium, with the use of alumina powder as a marker. Figure 5A shows a cross section of the specimen phosphidized at 950°C for 24h and the position of the alumina marker; this is confirmed in the SEM by AlK α radiation and is shown in Fig. 5B. Since the marker is situated at the phosphide/metal interface, the reaction is regarded as limited by diffusion of titanium through the phosphide layer. It has been reported previously that metal has diffused in the phosphidation of iron (6), chromium (4), nickel (7), and zinc (14) as in this study.

Acknowledgments

The authors wish to acknowledge the financial support of this work by the Asahi Glass Foundation for Industrial Technology, Tokyo. The authors wish to thank Dr. M. Hirohashi for the EPMA measurements.

Manuscript submitted March 27, 1984; revised manuscript received Aug. 27, 1984.

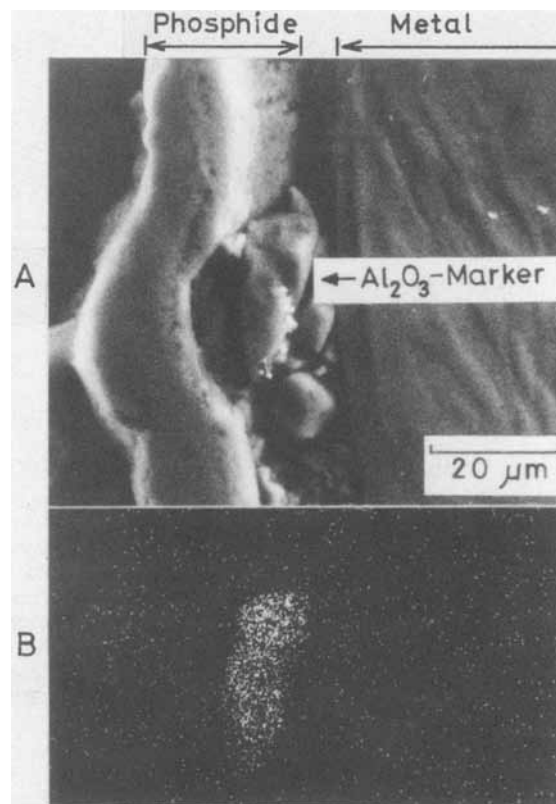


Fig. 5. Cross section of titanium phosphide scale formed at 950°C for 24h in phosphorus vapor at 1 atm and position of alumina marker: A—Secondary electron image; B—AlK α image.

Chiba University assisted in meeting the publication costs of this article.

REFERENCES

1. Y. Sasaki and S. Ueda, *Denki Kagaku*, **40**, 865 (1972).
2. Y. Sasaki, A. Kato, and S. Ueda, *This Journal*, **118**, 101 (1971).
3. Y. Sasaki and S. Ueda, *ibid.*, **119**, 1771 (1972).
4. Y. Sasaki and S. Ueda, *Nippon Kagaku Kaishi*, 956 (1978).
5. Y. Sasaki and S. Ueda, *Bull. Chem. Soc. Jpn.*, **45**, 2977 (1972).
6. Y. Sasaki, Y. Iida, A. Yokoo, and S. Ueda, *Z. Anorg. Allg. Chem.*, **487**, 232 (1982).
7. Y. Sasaki, Y. Iida, and S. Ueda, *This Journal*, **126**, 1948 (1979).
8. Y. Sasaki, *Z. Anorg. Allg. Chem.*, **489**, 227 (1982).
9. D. R. Stull, *Ind. Eng. Chem.*, **39**, 540 (1947).
10. ASTM X-Ray Powder Data File. α -Ti; card 5-0682. Ti_5P_3 ; card 22-945. Ti_4P_3 ; card 22-944.
11. P.-O. Snell, *Acta Chem. Scand.*, **21**, 1773 (1967).
12. P.-O. Snell, *ibid.*, **22**, 1942 (1968).
13. T. Lundström and P.-O. Snell, *ibid.*, **21**, 1343 (1967).
14. Y. Sasaki and S. Ueda, *This Journal*, **124**, 305 (1977).

Impedance Relaxation Spectrum Analysis of Oxidized Silver Electrodes

Maria Hepel* and Micha Tomkiewicz*

Department of Physics, Brooklyn College of The City University of New York, Brooklyn, New York 11210

ABSTRACT

The real and imaginary parts of the impedance of the oxidized silver electrode in 1M KOH solutions have been measured in a frequency range of $1-1.3 \times 10^7$ Hz. When the electrode is oxidized at a potential when only Ag_2O is formed, we were able to isolate three passive elements: the high frequency capacitance and the high and low frequency resistances. On further oxidation, at a potential in which AgO can be formed, we were able to isolate five passive elements: two capacitive and three resistive. Two of these elements were identified as originating from the Ag_2O layer. The functional dependence of all these elements on the amount of charge that is used for oxidation reveals that the Ag_2O layer can be analyzed in terms of a single dielectricum in a parallel-plate capacitor. Parameters such as thickness of the layer, resistivity of the material, and roughness factor could be evaluated. We have found that at the potential in which AgO is formed, a significant fraction of the charge is used for the formation of Ag_2O .

The electrochemical behavior of silver-silver oxide electrode has been extensively studied (1-7) because of the importance of electrochemical storage systems such as silver-zinc, silver-cadmium, silver-iron, and silver-hydrogen batteries. It is known (17) that in alkaline solutions, silver is oxidized in two steps. During first stages of oxidation, silver undergoes dissolution with formation of $\text{Ag}(\text{OH})_2^-$ complexes (18), and Ag_2O is formed, which can be further oxidized to AgO . Impedance measurements (3, 19), in addition to more conventional electrochemical methods, were used extensively to characterize the chemical and morphological mechanism of the oxidation process (20). The technique of relaxation spectrum analysis, in which the impedance is monitored over a wide frequency range and the results are portrayed in terms of a set of parallel, frequency independent, R-C elements, was used in the past to describe the potential distribution at the semiconductor electrolyte interface (21). Recently, the technique was extended to characterize the interface of metallic single-crystal RuO_2 with aqueous electrolytes (22).

The principal condition under which one can apply this mode of interpretation to the frequency dispersion of the impedance of the interface is that the faradaic components will be negligible during the impedance measurements. Thus, if this condition is satisfied, the impedance measurements are used to monitor static characteristics of the interface and changes in these characteristics due to perturbation of the system prior to the impedance measurements. The correlation between the changes in the static characteristics and the perturbations which give rise to them provide the tools for understanding certain aspects of the dynamics of the system. The generalized equivalent circuit, which is based on a network of parallel RC elements and was so useful for the simple interfaces, is clearly not appropriate for the study of the oxidation of the silver electrode.

Ag_2O is a small bandgap [1.2 eV at 293 K (23)] semiconductor which is insulating with resistivities of the order at $10^6-10^8 \Omega \text{ cm}$ at room temperature (24). Although its electronic properties are not as well characterized as those of the better-known semiconductors, and not even as well as the properties of its structural analog, Cu_2O , there is no known method of doping this material to reduce its resistivity to the region in which its semiconducting properties will dominate.

Our knowledge of the solid-state properties of AgO are even less complete than that of Ag_2O . X-ray and neutron diffraction studies (25-27) suggest that AgO has a monoclinic structure, with two different Ag-O distances (2.18 and 2.03Å, approximately) corresponding to the distances Ag(I)-O and Ag(III)-O. AgO was characterized as an n type semiconductor, with a bandgap of ~ 2 eV (28). Unlike

Ag_2O , its resistivity can be reduced considerably to a level of $\sim 10 \Omega \text{ cm}$ (29-31). Since these two oxides vary so much in their transport properties, it is natural that the interpretation of the impedance data should assume their separate contributions to the transport properties to be in series with each other. This simplified assumption should result in two possible RC elements connected in series. If, however, AgO is formed not by direct oxidation of Ag_2O at the oxide electrolyte interface, but is instead through nucleation, then a random distribution of the two oxides may be expected. Such a random distribution cannot be analyzed in terms of well-defined, dielectric materials connected in series, but rather as a changing dielectric constant of a random composite that can be analyzed by utilizing effective medium theories (32). These theories can calculate the frequency dispersion of the dielectric constant of the composite as a function of its changing composition.

In this paper, we present evidence that, under certain experimental conditions, the evolution of the two oxides can be separately monitored. We present evidence that at least Ag_2O behaves as a pure dielectricum with a frequency-independent dielectric constant, and we follow the growth of Ag_2O as it is further oxidized to AgO .

Experimental

Apparatus.—The experimental setup for impedance measurements was similar to the one described elsewhere (11). It consisted of a Hewlett-Packard 3320-B frequency synthesizer, 3575-A gain-phase meter, and dc-bias supply. The system control and data acquisition were performed by a Hewlett-Packard Model 9830A microcomputer. The experimental data, relative magnitude M and phase shift Φ between the two input signals (derived from the impedance of the reference circuit and total impedance), were processed and analyzed by a computer interactive program. The electronic equipment used allowed for measurements up to a frequency of 13 MHz, a limit unsuitable in practice for potentiostatic systems.

Special precautions concerning the electrochemical cell design (as in the case of bridge methods) had to be undertaken. Although balancing the reference impedance and the cell impedance is not required for the method used, a comparable value of the reference impedance was always maintained in order to achieve the best accuracy of readings. The parasitic inductance of leads has been diagnosed, and all the results presented here are corrected for the high frequency inductance effects.

Electrochemical cell and materials.—The electrochemical cell used for measurements was a standard two-compartment plexiglass cell with a capacity of 100 cm^3 . The counterelectrode was made from a large graphite cylinder. A double-junction saturated (KCl) silver/silver chloride electrode with 1M KNO_3 external solution was used

*Electrochemical Society Active Member.

as a reference electrode. A high purity silver rod substrate (Johnson-Matthews, 99.99%) with an exposed surface area 0.385 cm^2 was used as a working electrode. The oxide films were prepared on this substrate according to a procedure described below.

All chemicals used were of analytical-grade purity. Deionized water ($18 \text{ M}\Omega$) was obtained using Mili-Q purification system.

Procedure.—The polycrystalline silver substrate electrodes were polished to a mirror-like surface using $0.05 \mu\text{m}$ alumina. The surface was subsequently degreased in acetone and propyl alcohol, etched in dilute HNO_3 solution, rinsed with deionized water, and dried in air. The bilayer electrodes were prepared in two steps. During the first step, a Ag_2O film was deposited in 1 mol/dm^3 KOH solution at constant potential $E = +300 \text{ mV}$ (vs. Ag/AgCl double-junction reference electrode) using standard electrochemical equipment (an EG&G Model 173 potentiostat, equipped with a Model 179 digital coulometer and Model 175 universal programmer). The deposition was carried out for several hours and was interrupted after a given charge had been passed through the cell. Then the electrode potential was increased to $+600 \text{ mV}$, which is in the region of the AgO formation. The deposition was carried out for different times in order to grow oxide films of different thicknesses. The anodic charge consumed in the second step was from 0.47 to 15.1 C . The electrodes obtained in this way were then subsequently used in the impedance measurements with the network analyzer setup described above.

All the solutions used were deoxygenated by passing argon through the cell. During the experiments an argon purge was maintained.

Results and Discussion

Figure 1 shows the cyclic voltamogram of the oxidation and reduction of the silver/silver oxide electrode with the arrows indicating at which potentials the films were oxidized and the potentials at which the impedance of the system was measured. Figure 2 shows the impedance spectrum of the system when only Ag_2O is deposited, and Fig. 3 shows the impedance spectrum with 0.44 C used for Ag_2O deposition, followed by further oxidation to form AgO . Similar data were taken for different amounts of deposition charge. Next, a generalized way of analyzing these results will be presented, followed by a detailed account of the $\text{Ag/Ag}_2\text{O}$ and $\text{Ag/Ag}_2\text{O/AgO}$ systems.

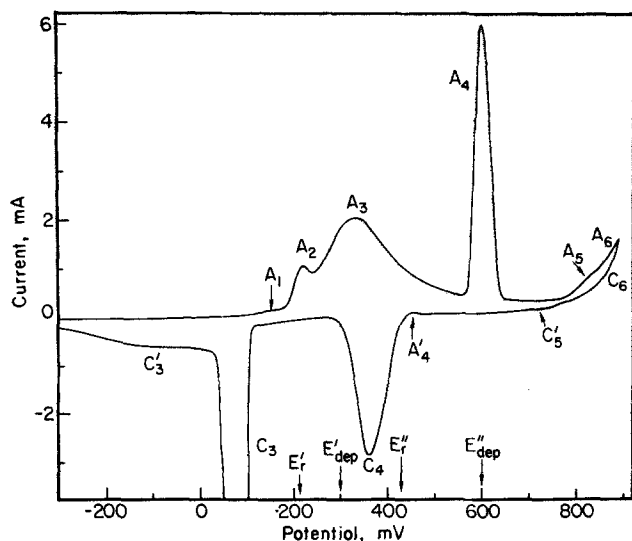


Fig. 1. The CV characteristic for the polycrystalline silver electrode (geometric area $A = 0.385 \text{ cm}^2$) in 1 mol dm^{-3} KOH solution at 22°C . $V = 10 \text{ mV/s}$. E_{dep}' and E_{dep}'' are potentials of deposition of Ag_2O and AgO , respectively (used in further deposition experiments). E_r' and E_r'' are the rest potentials at which impedance spectra were measured.

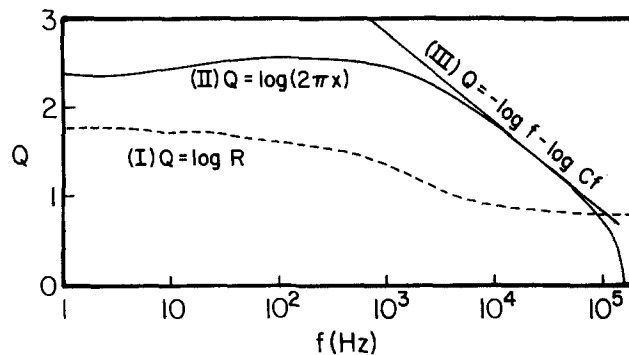


Fig. 2. Impedance spectrum for a polycrystalline silver electrode covered by a thin film of Ag_2O deposited at $E = +300 \text{ mV}$ (vs. Ag/AgCl). (I) $Z = \log R$, (II) $Q = \log(2\pi X)$, (III) $Q = -\log f - \log C_f$. Solution: 1 mol dm^{-3} KOH.

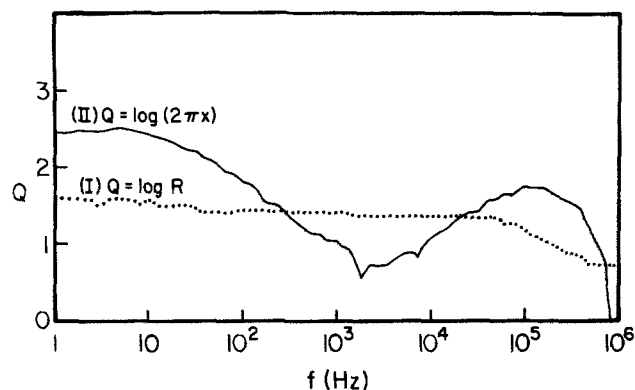


Fig. 3. Impedance spectrum for a bilayer $\text{Ag/Ag}_2\text{O/AgO}$ electrode in 1 mol dm^{-3} KOH. Total deposition charge: 2.9 C/cm^2 . (I) $Q = \log R$, (II) $Q = \log(2\pi X)$.

Relaxation spectrum analysis in a series presentation.—The generalized equivalent circuit of the system is presented as a series of passive R-C elements, as shown in Fig. 4(a), where R_s is the series resistance due to the electrolyte, r_s^i the series resistance of phase i , and C_p^i and R_p^i the capacitance and shunt resistance, respectively, of phase i . If phase i behaves like an insulator, then $r_s^i = 0$ and C_p^i and R_p^i will relate, through the geometry of the system and the frequency, to the real and imaginary parts of the dielectric constant. If, on the other hand, phase i behaves like a semiconductor with a space-charge layer which is small compared to the thickness of the material, then only r_s^i relates to the resistivity of the system and C_p^i and R_p^i will relate to the charge distribution at the space-charge layer and will vary with the potential drop across phase i . The impedance of such an equivalent circuit is given by

$$Z = R + jX = R_s + \sum_i Z^i \quad [1]$$

where R and X are the real and imaginary components of the impedance.

$$Z^i = r_s^i + \frac{R_p^i}{1 + j\omega\tau^i} = r_s^i + \frac{R_p^i}{1 + (\omega\tau^i)^2} - j \frac{\omega R_p^i \tau^i}{1 + (\omega\tau^i)^2} \quad [2]$$

where ω is the angular frequency and $\tau^i = R_p^i C_p^i$ is the relaxation time characteristic of phase i . Substituting Eq. [2] into Eq. [1], we will obtain the following expressions for the real and imaginary parts of the total impedance

$$R = R_s + \sum_i r_s^i + \sum_i \frac{R_p^i}{1 + (\omega\tau^i)^2} \quad [3]$$

$$X = -\omega \sum_i \frac{R_p \tau_i^i}{1 + (\omega \tau_i)^2} \quad [4]$$

Thus, as in the parallel case, a function can be formulated, in this case, simply by the imaginary part of the impedance, in which one obtains a line shape which is a superimposition of lorentzian-type peaks. If the various contributions can be resolved, then the number of peaks will indicate the number of components i . Each peak will be centered at $\omega = 1/\tau_i$, and X at the maximum will be equal to $R_p/2$, from which one can readily evaluate C_p^i and R_p^i .

From the high frequency components of the real part, one can evaluate $R_s + \sum_i \tau_s^i$. The individual τ_s^i cannot be evaluated by this technique.

Figure 3 shows the impedance spectra, when both Ag_2O and AgO are present. The imaginary part of the impedance, even in the logarithmic scale, shows clearly two main peaks. It remains to be established whether either of these peaks is due to a single relaxing, passive, RC element, but clearly the procedure that was established here offers the best starting point.

Figure 2 shows the impedance spectra when only Ag_2O is present; it does not show any resolvable peaks in the imaginary part. The behavior here resembles the one observed with single phase interfaces and was analyzed (11) in terms of a network of parallel RC elements as shown in Fig. 4b. We will not attempt a full analysis of the network here and will concentrate only on the fastest relaxing RC element and the shunt resistance $R(O)$.

It should be emphasized that the analysis of the data in terms of parallel or series networks is not unique and is a matter of convenience only. It serves primarily to isolate charge accumulation modes according to their relaxation times.

Ag/Ag₂O system.—Under the conditions in which relaxation spectrum analysis on a parallel network can be performed, there exists a frequency region in which the equivalent circuit can be reduced to a single RC element (11). In this frequency range, the impedance is given by

$$Z_{\text{HF}} = R - \frac{j}{\omega C_f} \quad [5]$$

In this region

$$\log(2\pi X) = -\log f - \log C_f \quad [6]$$

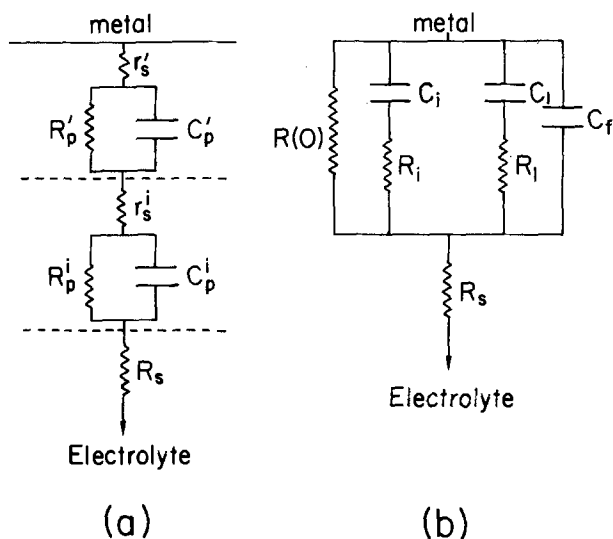


Fig. 4. Generalized equivalent circuit for series (a) and parallel (b) configurations of the passive elements. R_p and C_p are the parallel resistance and capacitance, respectively, for the inner film (prime) and the interface (i); τ_s 's stand for the respective time constants; R_s is the ohmic resistance mainly due to the electrolyte; $R(O)$ is the low frequency resistance; C_f is the film capacitance; and C_i, R_i are the series time constants.

and $\log(2\pi X)$ should be linear with $\log f$ with a slope of -1 and an intercept from which C_f can be extracted. The real part is frequency independent and equal to R_s , the series resistance of the system which is due to the electrolyte. From Fig. 2, the frequency range of 8,000-800,000 Hz satisfies these criteria (curve III in Fig. 2). The exact frequency domain in which these criteria are met varies from experiment to experiment. For each experiment, the entire frequency dispersion of the impedance was measured, the frequency domain with the fastest relaxing RC element identified, and the resistance and capacitance values measured. The variations of these parameters with the amount of charge that was passed to oxidize silver to Ag_2O will be discussed in this section. The oxidation was done at a constant potential of 0.3V vs. Ag/AgCl with different oxidation times, and the measurements were taken at the rest potential which changed little between the limits 0.19-0.24V vs. Ag/AgCl with increasing film thickness. For each experiment, the electrode was freshly polished.

Figure 5 shows the results of the dependence of $1/C_f$ on the oxidation charge Q . Figure 6 shows the dependence of R_s on Q which was taken from the high frequency component of R . The same figure also shows the dependence on Q of $R(l)$, the real part of the impedance at low frequency. The spread in the data is considerable; nevertheless, a few qualitative conclusions can be drawn: (i) R_s is independent of Q and can be shown to be dominated by the resistance of the electrolyte, and (ii) C_f decreases as Q increases, while $R(l)$ remains approximately constant within the large spread of the data. If we attempt to treat the system as a parallel-plate capacitor in which Ag_2O serves as the dielectricum and further assume a unit faradaic efficiency for formation of Ag_2O , then

$$Q = \frac{2Fd\gamma Al}{M} \quad [7]$$

where F is the Faraday constant, d is the density, A the geometric area, l the thickness of the capacitor, γ the roughness factor, and M the molecular weight of Ag_2O . The capacitance will be given by

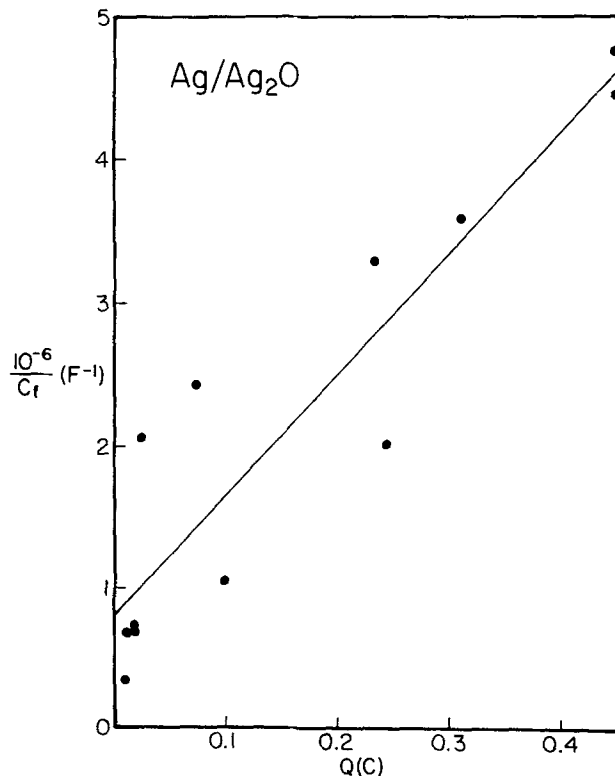


Fig. 5. Dependence of the reciprocal of the Ag_2O film capacitance $1/C_f$ determined from the impedance relaxation spectra upon the oxidation-charge Q . Coefficients of the linear fit to the experimental points are given.

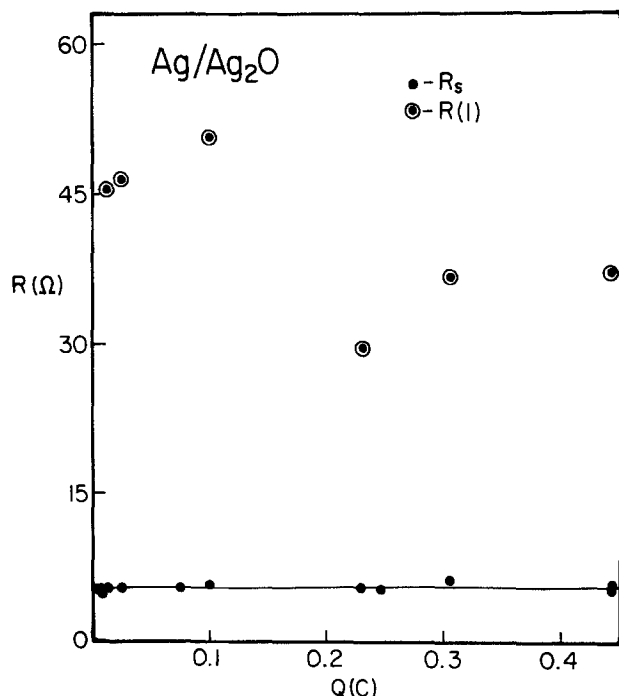


Fig. 6. Plot of the experimental data R_s and $R(l)$ vs. deposition charge Q for the $\text{Ag}/\text{Ag}_2\text{O}$ electrode in 1 mol dm^{-3} KOH solution.

$$C = \frac{\epsilon_0 \epsilon \gamma A}{l} \quad [8]$$

where ϵ is the dielectric constant and ϵ_0 is the permittivity of free space. The resistance, R_T , which is associated with this dielectricum is given by

$$R_T = \frac{\rho l}{\gamma A} \quad [9]$$

where ρ is the resistivity of Ag_2O . Substituting l from Eq. [7] into Eq. [8] and [9], one gets

$$\frac{1}{C_T} = \frac{MQ}{2Fd\epsilon\epsilon_0 A^2 \gamma^2} \quad [10]$$

$$R_T = \frac{\rho MQ}{2FdA^2 \gamma^2} \quad [11]$$

These equations predict linear behavior of $1/C_T$ and R_T with respect to Q , and they predict also that $\tau = R_T C_T = \rho \epsilon \epsilon_0$ is independent of the geometric factor involved. The data from Fig. 5 can be analyzed in terms of Eq. [10] after correcting for C_e , the capacitive element on the electrolyte side of the interface, such that

$$\frac{1}{C_f} = \frac{1}{C_T} + \frac{1}{C_e} \quad [12]$$

Analysis of Fig. 5 in terms of Eq. [10] and [12] yields an intercept of $8 \times 10^5 \text{ F}^{-1}$, a slope of $8.5 \times 10^6 \text{ C}^{-1} \text{ F}^{-1}$, with a correlation coefficient of 0.92.

The dielectric constant of Ag_2O is not reported in the literature, but the variations in similar solids (oxides and nonoxides) are all within the range of 5-10. If we take the dielectric constant of Ag_2O to be similar to that of Cu_2O , which is its structural analog, then $\epsilon \approx 7$. Taking $d = 7.44 \text{ g/cm}^3$, $M = 232$, and $A = 0.385 \text{ cm}^2$, one can calculate from the slope of Fig. 5 and from Eq. [10] that $\gamma = 14$. From the intercept, we obtain $C_e = 3.2 \times 10^{-6} \text{ F/cm}^2$ (geometric area), and if one takes into account the roughness factor, $C_e = 2.3 \times 10^{-7} \text{ F/cm}^2$. These values are on the low side of the capacitance of the Helmholtz layer, but the quality of the data and the assumptions in the model make further speculation unwarranted.

If, at least qualitatively, the data in Fig. 5 could be analyzed in terms of Eq. [10], it is obvious that the data in Fig.

6 cannot be analyzed in terms of Eq. [11]. $R(l)$ does not represent R_T . We will return to the possible characterization of $R(l)$ in the next section. At this stage, since we do not possess, as yet, information about the resistive component across the oxide, we cannot evaluate the relaxation time of the material. Hence, we cannot evaluate its resistivity.

Ag/Ag₂O/AgO system.—For this set of experiments, the amount of charge used for Ag_2O formation was kept constant at 0.44C. Following Ag_2O formation, we increased the potential to $E = 0.600 \text{ V vs. Ag/AgCl}$, where AgO formation takes place (see Fig. 1). We have measured the impedance at the rest potential of $\text{Ag}_2\text{O}/\text{AgO}$, which is $0.450 \text{ V vs. Ag/AgCl}$. We have measured the impedance as a function of the amount of charge that was used for deposition of AgO . Figure 3 shows a typical result of such a measurement. As mentioned above, even on a logarithmic scale, two peaks, one at high frequency and the other at low frequency, can be seen. The procedure developed above will be used as a basis for interpreting the results. The first step in this process is to establish whether either of these peaks is due to a single relaxing, passive, RC element. Examination of the low frequency peak in Fig. 3 clearly shows that the peak is too broad for a single lorentzian. Figure 7 shows the change of the frequency dispersion of the imaginary part of the impedance with the amount of charge that was used to form the oxide. The amplitude of the high frequency peak increases in direct proportion to the deposition charge, while the high frequency tail of the low frequency peak is little affected by the deposition. Figure 8 shows the numerical fit of the high frequency peak to a normalized single lorentzian. Except at the tail ends of the peak, where an inductance dominates on the high side and low frequency contributions affect the low side, the fit is very good; the peak will be treated as a single lorentzian.

As was mentioned before, the low frequency peak is much too broad for a single lorentzian. We do not want to speculate here about the various processes that might contribute to this peak. Figure 7 shows that the high frequency tail of this peak remains constant with deposition charge. It will be useful to determine whether this high frequency tail corresponds to a single passive RC element. From Eq. [4], the contributions of a single lorentzian to the imaginary part of the impedance is given by

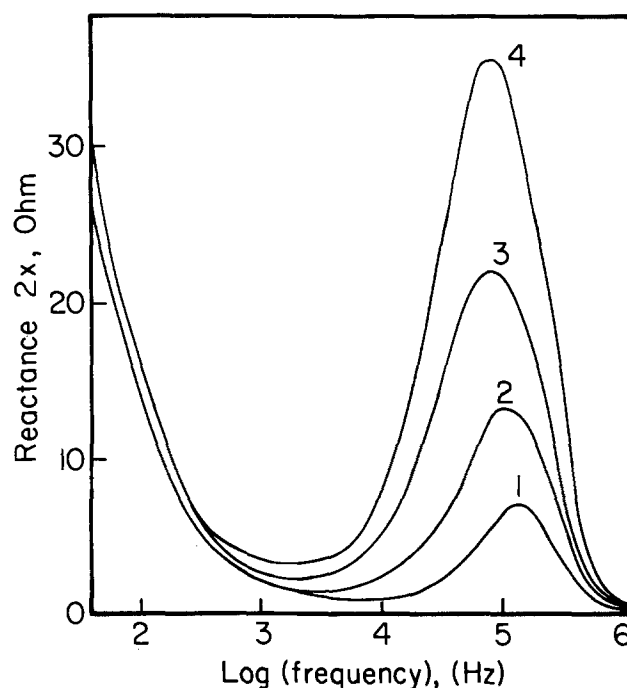


Fig. 7. Frequency dispersion of the imaginary part of the impedance of the bilayer $\text{Ag}/\text{Ag}_2\text{O}/\text{AgO}$ electrode in 1 mol dm^{-3} KOH at various AgO deposition charges [C]: (1) 0.91, (2) 1.05, (3) 1.19, (4) 1.48.

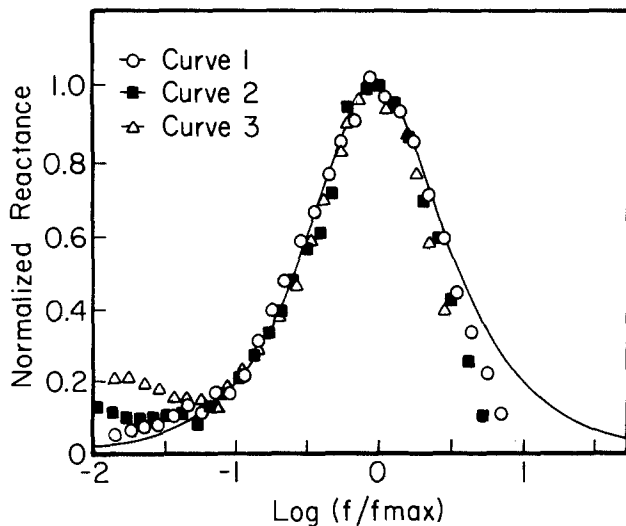


Fig. 8. Computer fit of the high frequency reactance peak to a single lorentzian for different AgO deposition charges [C]: (1) 0.91, (2) 1.05, (3) 1.19.

$$X^i = - \frac{\omega R_p \tau^i}{1 + (\omega \tau)^2} \quad [13]$$

The high frequency tail of this peak is defined for $\omega \tau^i \gg 1$. Under these conditions

$$X^i = -1/\omega C_p^i \quad [14]$$

and the analysis will be similar to that for the high frequency component of the parallel case which was used above.

Figure 9 shows the fit between the experimental points on the high frequency tail of the low frequency peak and Eq. [14]. The fit is good over nearly two orders of magnitude of frequencies. From the intercept of this curve

$$C_p = 4.10^{-5} \text{ F} \approx 1.0 \times 10^{-4} \text{ F/cm}^2$$

based on the geometric area of the electrode.

Based on the absolute value of C_p and particularly the observation that it is nearly independent of the amount of AgO deposition or Ag_2O growth during the deposition of AgO, it is reasonable to associate this capacitive element with the junction between AgO and the electrolyte. It can be dominated by the capacitance of the Helmholtz layer, or by that of the space-charge layer in the conductive oxide or by combination of the two. As long as the width of the space-charge layer is smaller than the thickness of the

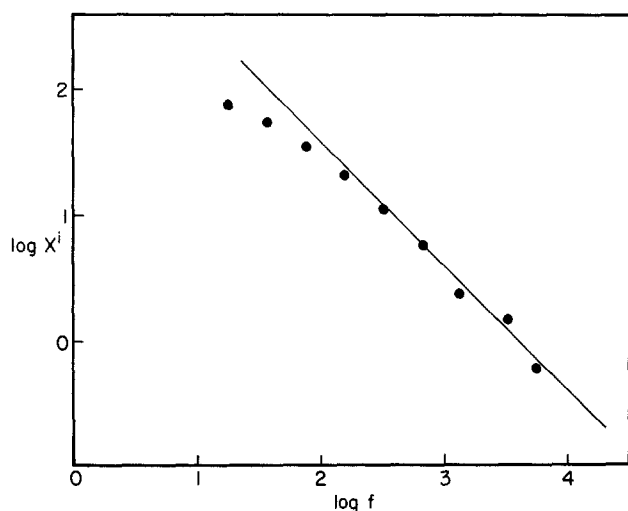


Fig. 9. Fit of the high frequency tail of the low frequency peak to a single lorentzian for the bilayer Ag/Ag₂O/AgO electrode.

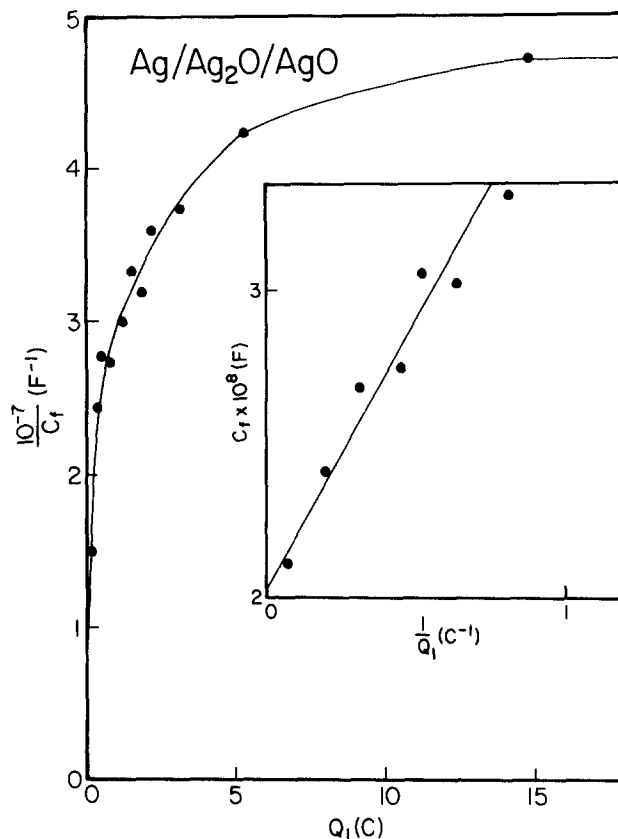


Fig. 10. Dependence of the reciprocal of the inner film capacitance $1/C_f$ for the bilayer Ag/Ag₂O/AgO electrode in 1 mol dm⁻³ KOH upon the oxide deposition charge Q_1 .

oxide, the value of the capacitance will be independent of charge.

Let us now turn our attention to the fastest relaxing RC element. Figures 10 and 11 show the variation of $1/C_f$ and R_f with the amount of charge Q_1 associated with deposition at 0.6V on top of 0.44C associated with Ag_2O that was deposited at 0.3V vs. Ag/AgCl. Figures 10 and 11 show that both R_f and $1/C_f$ increase with Q_1 , where Q_1 is the total amount of charge deposited at 0.6V vs. Ag/AgCl. They then both saturate at $Q_1 > 5\text{C}$. If we neglect the low coverage (up to 0.5C) where nucleation is known to take place, the functional dependence can be represented by

$$\frac{1}{C_f} = \frac{5.6 \times 10^7 Q_1}{1 + 1.1 Q_1} \quad [15]$$

$$R_f = \frac{187 Q_1}{1 + 0.67 Q_1} \quad [16]$$

The inserts in both figures show the dependence of C_f and $1/R_f$ on $1/Q_1$, from which the constants in Eq. [15] and [16] were evaluated. If we take the saturation in both R_f and C_f to indicate saturation in the formation of the dielectric material that is responsible for the high frequency peak, then, within the parallel-plate approximation

$$\tau = (R_f C_f)_{\text{sat}} \approx 5.10^{-6} \text{ s} = \rho \epsilon \epsilon_0 \quad [17]$$

Taking again, as in Eq. [2] $\epsilon = 7$, we obtain $\rho \approx 8.2 \times 10^6 \Omega \text{ cm}$.

The high resistivity can only be due to Ag_2O . We arrive at the conclusion that at the potential at which we form AgO, the characteristics of the Ag_2O layer changes as well. If AgO is being formed by oxidation of Ag_2O whose thickness does not increase, the expected changes would have been the exact opposite to those actually observed. One can observe a decrease in the thickness of the Ag_2O layer when nucleation of AgO proceeds. This case corresponds to consumed charges for oxidation much less than 0.5C. In our experiments, we were in the region of

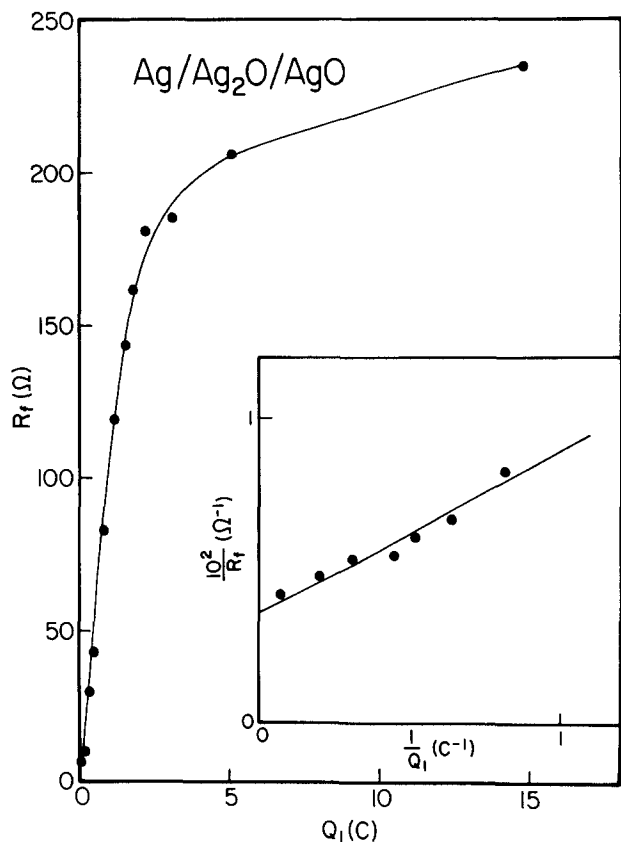


Fig. 11. Plot of the reciprocal of the inner film resistance R_f vs. Q_1 for the Ag/Ag₂O/AgO layered electrode in 1 mol dm⁻³ KOH.

charges used for oxidation far behind the nucleation process. In this set of experiments, the electrode was oxidized at $E = +600$ mV vs. Ag/AgCl with charge consumption up to 15C. The observed results in Fig. 10 and 11 can be interpreted that at this potential both oxides Ag₂O and AgO grow simultaneously.

Assuming, as a result, that Fig. 10 and 11 indicate continuous deposition of Ag₂O while Ag₂O is being further oxidized to AgO, we will try to analyze the correlation between R_f and $1/C_f$ with Q in a manner similar to that in the previous section. Let us assume that fraction of the charge, Q_1 , was used for the oxidation of Ag₂O to AgO and that the remaining charge was used for the oxidation of Ag to Ag₂O. The net amount of charge used for deposition of new Ag₂O is given by

$$Q_{\text{net}} = (1 - 2\alpha) Q_1 \quad [18]$$

Following the arguments that led to Eq. [10] and [11] in the previous section, the capacitance and resistance of the newly formed Ag₂O layer will be given by

$$\frac{1}{C_f} = \frac{n(1 - 2\alpha)Q_1}{2Fd\epsilon\epsilon_0 A^2 \gamma^2} + \frac{1}{C_f^0} \quad [19]$$

$$R_f = \frac{\rho M(1 - \alpha)Q_1}{2FdA^2 \gamma^2} + R_f^0 \quad [20]$$

where C_f^0 and R_f^0 are the values for $Q_1 = 0$.

Comparing Eq. [15] and [16] with Eq. [19] and [20] prior to saturation one can evaluate $\gamma/\sqrt{1 - 2\alpha}$. This implies that, if we can evaluate the roughness factor in an independent experiment, then the ratio between the two oxidation reactions can be evaluated. From Eq. [19] and [15], one can calculate that $\gamma/\sqrt{1 - 2\alpha} = 15.3$.

Up to now, we have evaluated all the data that we could extract from the frequency dispersion of the imaginary part of the impedance. From Fig. 3, one can observe that at both ends of the frequency spectrum, the real part of the impedance is frequency independent. Figure 12 shows the dependence of the high frequency component,

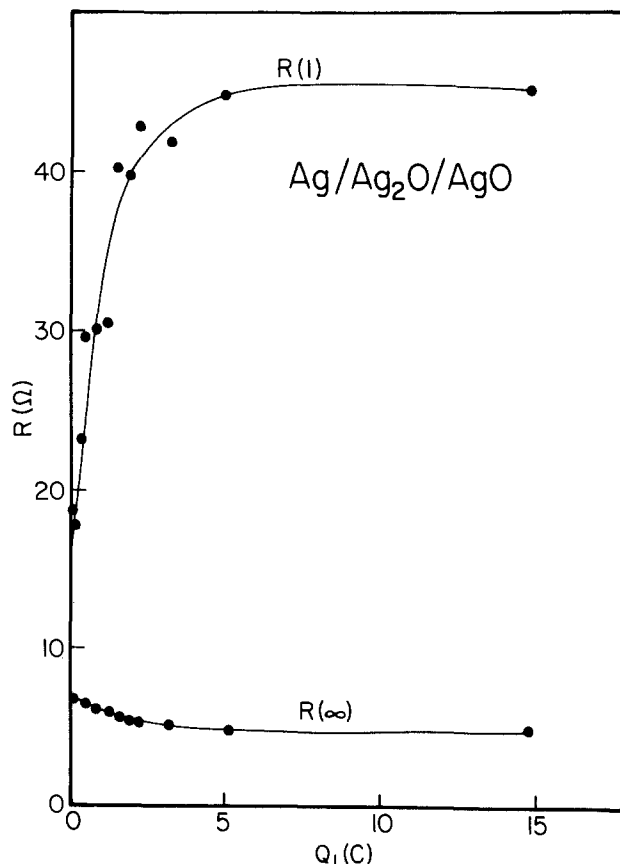


Fig. 12. Dependence of $R(\infty)$ and $R(1)$ upon the oxide deposition charge Q_1 for the bilayer Ag/Ag₂O/AgO electrode in 1 mol dm⁻³ KOH.

$R(\infty)$ and the low frequency component, $R(1)$, as a function of deposition charge. The high frequency component exhibits the behavior that was shown in Fig. 6, when only Ag₂O was present and is consistent with the interpretation that $R(\infty)$ is due to the series resistance, R_s , which is due to the electrolyte. $R(1)$, on the other hand, increases with deposition charge in a manner which resembles R_f in Fig. 11. However, the absolute values are considerably smaller than the R_f values. This is in sharp contradiction with Eq. [2], which demands that

$$R(O) = \lim_{\omega \rightarrow 0} R = R_s + \sum r_s^i + \sum R_p^i \quad [21]$$

Since R_f is one component of this sum, Eq. [21] requires that $R(O) > R_f$. Since the low frequency part of the imaginary part of the impedance was shown to result from multiplicity of unresolved processes, we do not feel secure in proposing a definite explanation for this fact. More work is needed before some conclusion about the low frequency regime can be reached.

Conclusions

It was shown that impedance measurements can be used to gain information about the chemical and topological changes that take place during oxidation of the silver electrode. The distinction between perturbation and detection was the key in enabling us to interpret the results using the simplest possible model and to correlate the measurements with the perturbation in a straightforward way.

The technique of relaxation spectrum analysis separates the charge accumulation modes at simple interfaces, according to their relaxation times, expressed in terms of simple, frequency-independent, RC elements. This technique can be extended to systems in which to first approximation, the charge accumulation modes are in series with each other. Under conditions when only Ag₂O is deposited, the impedance spectra behaved similarly to that

of a single interface. Three well-behaved, passive elements were extracted: the high frequency capacitance, the high frequency resistance, and the low frequency resistance. The physical origin of these elements was identified by monitoring their dependence on the amount of charge that was used to oxidize the electrode. The resistive element was found to be independent of charge, while the reciprocal of the capacitive element increased linearly with the amount of charge. The functional dependence of the capacitive element on the amount of charge was consistent with a simple model of a parallel-plate capacitor in which Ag_2O serves as the dielectric material. Based on this model, an "average" roughness factor, which is independent of the thickness of the layer was calculated and found to be ~ 14 . Based on this model, it was determined that, at least for the conditions that were investigated here, Ag_2O behaves as an insulator in which the electric field is distributed across the entire sample and does not concentrate at the interface. The high frequency resistance was associated with the resistivity of the electrolyte, while the low frequency resistance was associated with kinetic effects. At the potential in which the silver can be oxidized to AgO , five well-behaved, passive elements were extracted, and their variation with the amount of deposited charge was monitored. The capacitive and resistive elements of a single dielectricum were isolated. In terms of a parallel-plate model, these two parameters relate to the real and imaginary parts of the dielectric constant of the material through the geometric factor of the capacitor. The relaxation time of this material was found to be $\sim 5 \cdot 10^{-6}$ s from which a resistivity of $\sim 8 \times 10^6 \Omega \text{ cm}$ was evaluated. The high resistivity clearly demonstrates that the material is still Ag_2O . The conclusion was that, at the potential where silver can be oxidized to AgO , a significant fraction of the charge is used to increase the thickness of the Ag_2O layer. For an amount of charge in excess of $\sim 15 \text{ C/cm}^2$, the capacitive and resistive elements which are associated with the Ag_2O saturate, and a steady state is achieved between formation of Ag_2O and oxidation of Ag_2O to AgO .

Acknowledgments

This work was supported by the Office of Naval Research. The authors wish to thank Dr. Benedict Aurian-Blajeni for his helpful discussions.

Manuscript submitted Feb. 13, 1984; revised manuscript received Sept. 24, 1984.

Brooklyn College assisted in meeting the publication costs of this article.

REFERENCES

- S. U. Falk and A. J. Salkind, "Alkaline Storage Batteries," John Wiley and Sons, New York (1969).
- J. M. M. Droog and F. Huisman, *J. Electroanal. Chem.*, **115**, 211 (1980).
- B. W. Tilak, R. S. Perkins, H. A. Kozłowska, and B. E. Conway, *Electrochim. Acta*, **17**, 1447 (1972).
- R. S. Perkins, B. V. Tilak, B. E. Conway, and H. A. Kozłowska, *ibid.*, **17**, 1471 (1972).
- R. Memming, F. Mollers, and G. Neumann, *This Journal*, **117**, 451 (1970).
- M. L. Teijelo, Y. R. Vilche, and A. J. Arvia, *J. Electroanal. Chem.*, **131**, 331 (1982).
- M. Fleischmann, D. J. Lax, and H. R. Thirsk, *Trans. Faraday Soc.*, **64**, 3128, 3137 (1968).
- P. Stonehart and F. P. Portante, *Electrochim. Acta*, **13**, 1805 (1968).
- B. D. Cahan, Y. B. Ockerman, R. F. Amlie, and P. Ruetschi, *This Journal*, **107**, 725 (1960).
- Y. A. McMillan, *Chem. Rev.*, **62**, 65 (1962).
- M. J. Dignam, H. M. Barnett, and C. D. Nagy, *Can. J. Chem.*, **471**, 4253 (1969).
- D. B. Gibbs, B. Rao, R. A. Griffen, and M. J. Dignam, *This Journal*, **122**, 1167 (1975).
- M. J. Dignam, in "Comprehensive Treatise of Electrochemistry," Vol. 4, J. O'M. Bockris, B. E. Conway, E. Yeager, and R. E. White, Editors, Chap. 5, pp. 247-306, Plenum Publishing Co., New York (1981).
- B. G. Pound, D. D. MacDonald, and Y. W. Tomlinson, *Electrochim. Acta*, **24**, 929 (1979).
- B. G. Pound, D. D. MacDonald, and Y. W. Tomlinson, *ibid.*, **25**, 563 (1980).
- B. G. Pound, D. D. MacDonald, and Y. W. Tomlinson, *ibid.*, **25**, 1293 (1980).
- C. P. Wales and J. Burbank, *This Journal*, **106**, 885 (1959); *ibid.*, **111**, 1002 (1964).
- B. Miller, *ibid.*, **117**, 491 (1970).
- B. G. Pound, D. D. MacDonald, and J. W. Tomlinson, *Electrochim. Acta*, **27**, 1489 (1982).
- T. P. Hoar and C. K. Dyer, *ibid.*, **17**, 1563 (1972).
- M. Tomkiewicz, *This Journal*, **126**, 2220 (1979).
- M. Tomkiewicz, Y. S. Huang, and F. H. Pollak, *ibid.*, **130**, 1514 (1983).
- A. Goltzené and C. Schwab, "Landolt-Börnstein," New Series, Vol. 17, O. Madelung, Editor, p. 155, Springer-Verlag, Berlin (1983).
- E. Fortin and F. L. Weichman, *Phys. Status Solidi*, **5**, 515 (1964).
- I. A. McMillan, *J. Inorg. Nucl. Chem.*, **13**, 28 (1960); *Nature*, **195**, 594 (1962); *Acta Crystallogr.*, **7**, 640 (1954).
- W. S. Graft and N. N. Stadelmaier, *This Journal*, **105**, 446 (1958).
- V. Scatturin, P. Bellon, and A. Salkind, *Ric. Sci.*, **30**, 1034 (1960).
- E. Farhat and S. Robin-Kandare, *Thin Solid Films*, **23**, 315 (1974).
- A. Tvarusko, *This Journal*, **115**, 1105 (1968).
- M. Le Blanc and H. Sachse, *Z. Phys.*, **32**, 887 (1931).
- A. B. Naïding and J. A. Kazarnovskii, *Dokl. Akad. Nauk SSSR*, **78**, 713 (1951).
- D. E. Aspnes, *Am. J. Phys.*, **50**, 704 (1982).

Nucleation of Pb Electrodeposits on Ag and Cu

Joseph C. Farmer and Rolf H. Muller*

Materials and Molecular Research Division, Lawrence Berkeley Laboratory and Department of Chemical Engineering, University of California, Berkeley, California 94720

ABSTRACT

Initial stages in the electrocrystallization of Pb (up to 200Å thick) from 1M NaClO₄, 0.5 and 5 mM Pb(NO₃)₂, pH 3, on Ag(111) and Cu(111) have been investigated by ellipsometry and light scattering during cyclic voltammetry. Optical constants, thickness, valence, and free energy of adsorption of the underpotential deposit have been determined. An optical model which agrees with experimental data for fractional coverage by the underpotential deposit is based on the two-dimensional spreading of islands of monolayer thickness. The bulk deposit immediately following formation of the underpotential monolayer involves three-dimensional growth from nucleation centers, even at the 20Å level of deposit thickness, and results in a particulate, porous film on top of the underpotential deposit.

Two separate steps can often be identified in the early stages of the electrocrystallization of a metal on a dissimilar substrate: the formation of an underpotential deposit (UPD) and that of a bulk deposit (1-3). The properties of these layers are expected to be an important factor for determining the properties of subsequently formed deposits of practical interest with macroscopic thicknesses. This work was undertaken to investigate the transition from the underpotential deposit (the first monolayer) to the bulk deposit and the micromorphology of the two deposits by *in situ* optical techniques. Fast automatic ellipsometry and light scattering during cyclic voltammetry made it possible to separate optical changes due to formation of the first monolayer from those associated with subsequent formation of the bulk deposit. The system chosen for study was the deposition of Pb on Ag and Cu because of the well-known formation of the underpotential layers (4). There are also significant differences in the optical constants of Pb and the substrates, making detection of small amounts of Pb on the electrode surface by ellipsometry possible (5-7).

Schmidt and Gyax (3) have determined the Gibbs free energy of adsorption for Pb electrosorption on polycrystalline Ag and Cu by integrating the cathodic UPD peak in the cyclic voltammogram and deriving coverage as a function of potential. Here, adsorption isotherms for the Pb underpotential deposit have been determined similarly on single-crystal Ag and Cu surfaces. In addition, thickness and optical constants of the underpotential deposit were derived from ellipsometer measurements and a knowledge of surface coverage determined electrochemically. Unusual optical properties of the bulk deposit have been attributed to its morphology.

Experimental Procedure

Experiments were conducted potentiodynamically while simultaneous ellipsometer and light scattering measurements of the electrode surface were performed. A bipotentiostat (Pine RDE 3) was used to drive the electrochemical cell. The potential was swept from 200 to -800 mV (*vs.* Ag/AgCl) at sweep rates varying from 0.1 to 1.5 V/min.

A self-nulling ellipsometer (8) was operated at an angle of incidence of 75° with a stabilized 75W xenon short-arc light source (Oriol C-72-20) and an interference filter for 515 nm (bandwidth 9 nm, transmission 43%). An acrylic electrolytic cell used in an earlier investigation of anodic silver oxidation (9) was employed. The cell had two quartz windows for ellipsometry with an angle of incidence of 75°, a volume of approximately 250 ml, and ports for introduction and draining of electrolyte, for a nitrogen purge stream, and for a reference electrode capillary. A Pt counterelectrode was used and positioned so as not to interfere with the observation of the working electrode.

Ag(111) and Cu(111) working electrodes were used. The single-crystal surfaces were approximately 1.20 × 2.85 cm (3.42 cm²), and were mounted in epoxy. The electrodes

were polished mechanically, ultimately using 0.05 μm aluminum oxide powder suspended in water. The polishing was followed by ultrasonic cleaning, chemical polishing for Ag surfaces (9, 10), a period of soaking in the acidic electrolyte, and pre-electrolysis. Any oxides formed on the electrode surface during transfer to the cell were unstable at the pH and potential used for the experiments and removed during pre-electrolysis at a potential anodic to that for Pb deposition (11, 12). No significant electrochemical or ellipsometric differences were observed between Ag electrodes polished mechanically and chemically and those polished only mechanically, although a smoother surface, important for light scattering measurements, was expected to result from chemical polishing. The chemical polishing step was omitted after scattering measurements were completed.

The reference electrode used was a double-junction Ag/AgCl electrode (Dow-Corning 476067). The inner compartment, containing the electrode, was filled with 4M KCl saturated with AgCl, the outer compartment with 1M KNO₃.

A second cell was used for light scattering studies, and has been described elsewhere (9). This cell used high purity, polycrystalline Ag sheets rather than single crystals. The electrode was 0.5 × 5.0 × 0.2 cm and was 60% immersed in electrolyte. It was located in a cylindrical glass cell of 4 cm diam and illuminated with the beam from an argon laser (515 nm line) at an angle of incidence of 75°.

All experiments used a supporting electrolyte of 1M NaClO₄ at pH 3. Pb²⁺ ion was introduced into the electrolyte as a nitrate at concentrations of either 0.5 or 5.0 mM. The pH was adjusted to the desired level by adding small amounts of dilute HClO₄, and measured with a digital pH meter (Corning 130).

Experimental Results

Potential ramp and cyclic voltammogram data for the deposition of Pb on Ag(111) from a 0.5 mM solution at a sweep rate of 0.1 V/min are shown in Fig. 1 and 2.

Ellipsometer measurements (psi and delta) during two potential cycles for deposition on silver are shown in Fig. 3 and 4 together with the current trace. The separate formation of underpotential and bulk deposits is clearly shown by the relative amplitude parameter psi (Fig. 3). During the anodic part of the potential cycle, the two layers are dissolved in reverse order and the process is repeated in the next cycle. Reversibility and reproducibility are also seen in the relative phase parameter delta (Fig. 4). The response of that measurement to the underpotential deposit is representative of a metal-like layer, while dielectric-like properties are indicated for the bulk deposit. These unexpected optical results for delta are caused by the micromorphology of the deposits: the cathodic UPD peaks have been interpreted as the formation of a complete monolayer of Pb on the substrate; the bulk deposit is shown to be of a particulate, porous nature. Similar results were obtained for potentiodynamic deposition of Pb on Cu(111) at concentrations of 0.5 and 5.0 mM and a sweep rate of 1.5 V/min.

*Electrochemical Society Active Member.

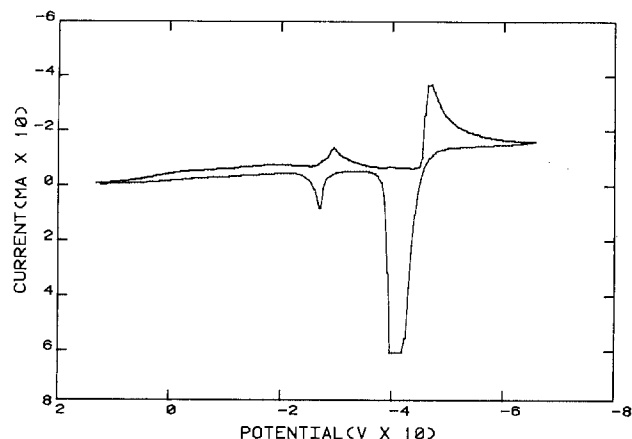


Fig. 1. Cyclic voltammogram for Pb deposition on Ag(111) (3.42 cm^2) from 1 M NaClO_4 , $0.5 \text{ mM Pb(NO}_3)_2$, $\text{pH } 3$, first sweep. Potential relative to Ag/AgCl reference. Pt counterelectrode, acrylic cell.

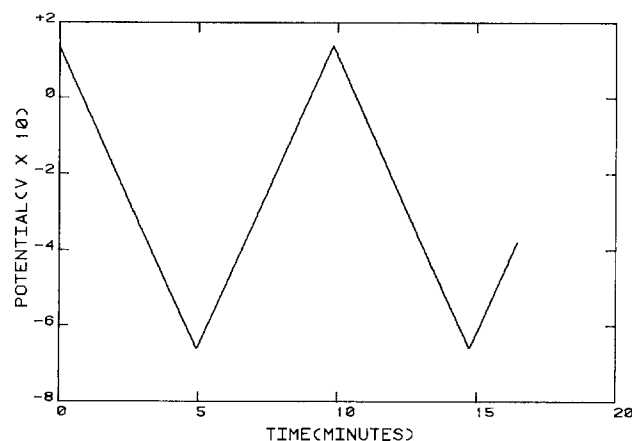


Fig. 2. Potential ramp corresponding to Fig. 1 from $+150$ to -660 mV . Sweep rate: 0.15 V/min .

Light scattering measurements from the electrode surface during cyclic voltammetry are shown in Fig. 5. An argon-ion laser (Lexel 75.2) tuned to 514.5 nm , served as light source (30 mW , 75° angle of incidence). Scattered light was collected 15° from the specular direction with a fiber-optic probe (1° acceptance) and measured with a photomultiplier (RCA R136). The lower oscillogram traces in Fig. 5 represent the current passed through the cell, with cathodic peaks shown negative, anodic peaks positive. The poor cathodic peak waveform is due to the electrode geometry in the scattering cell, which results in nonuniform current distribution. The upper traces represent the photomultiplier current. Figure 5a shows the in-

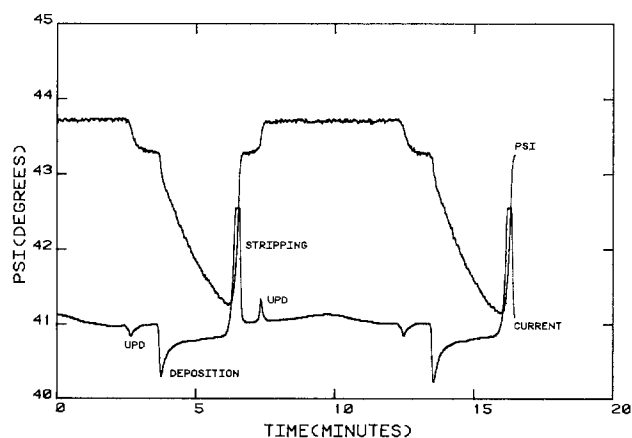


Fig. 3. Response of current and ellipsometer parameter ψ to potential ramp shown in Fig. 2. Wavelength of light 515 nm , angle of incidence 75° , other conditions as in Fig. 1.

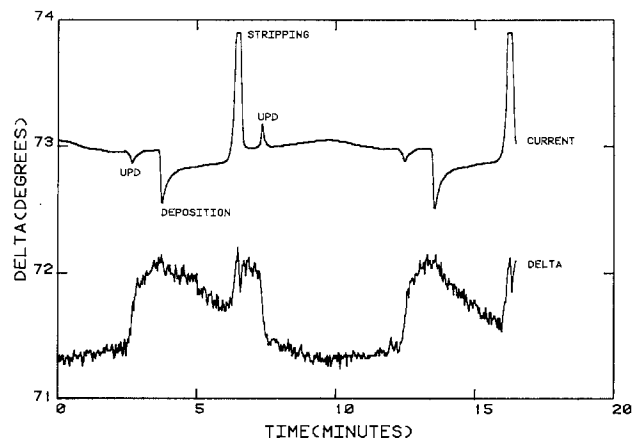


Fig. 4. Response of current and ellipsometer parameter δ , conditions as in Fig. 3.

crease in scattered light intensity with the onset of bulk deposition and its return to the initial level upon stripping the deposit. A particle diameter of 16 \AA , derived from ellipsometer measurements, has been associated with a significant increase in light scattering. No increase in scattering light intensity is observed during formation of the underpotential deposit layer. Light scattering, like the ellipsometer measurements, are reversible and repeatable during potential cycling. Increased light scattering is indicative of the formation of very small three-dimensional nuclei appearing on top of the Pb monolayer which completely covers the substrate. This interpretation agrees with that found for the ellipsometer measurements.

Optical Model of the Initial Stage of Deposit Formation

The general theory for submonolayer ellipsometry has been reviewed by Bootsma (13, 14). Other authors who have written on this topic have paid particular attention to the anisotropic nature of the adsorbate layer (15-17).

As discussed elsewhere (18), it has been found that the ellipsometer measurements of the formation of the underpotential deposit can best be interpreted with a coherent superposition (island) model; the Bruggeman model failed to explain the data. In this model, it is assumed that the surface is partially bare and partially covered with patches or islands of a thin film (19). With the islands having a smaller diameter than the spatial coherence of the incident light, the state of polarization of the reflected light is determined by the coherent superposition of polarization states resulting from reflection on bare and film-covered surface elements.

Application of this island concept to the underpotential deposit implies that (i) metal adatoms adsorbed to the surface, as two-dimensional clusters or individually, can be treated as equivalent thin film islands of some apparent thickness and complex refractive index, (ii) the optical constants and thickness of individual islands are the same as those of the complete monolayer, (iii) the overall reflectance of the surface is due to a coherent superposition of beams reflected from island-covered portions of the electrode and bare portions of the electrode, and (iv) the optical constants of the individual islands and the substrate are potential and coverage independent. Predictions derived from this model agree well with experimental data for the development of the underpotential deposit monolayer as the potential is ramped (Fig. 6). Assumption (i) above requires elaboration. As will be shown in the discussion that follows, the Pb UPD obeys a Langmuirian adsorption isotherm, which indicates that there is minimal lateral interaction between adsorbed Pb atoms, while clustering would require strong attraction. Based upon the isotherm alone, one would expect the Bruggeman optical model for a layer of randomly distributed atoms to fit the data. This dilemma will have to be resolved by future work.

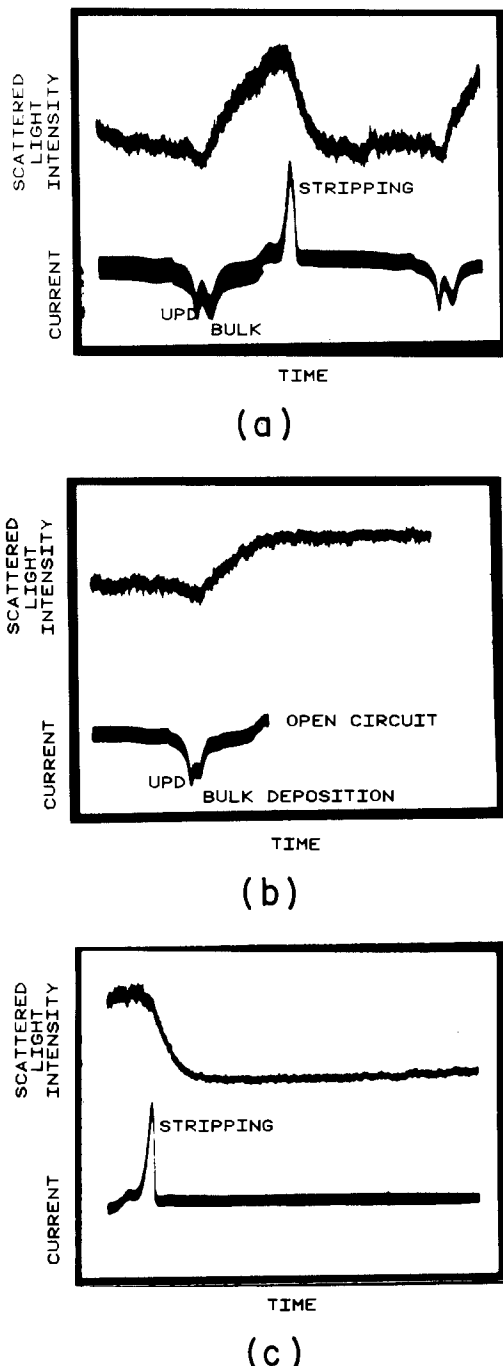


Fig. 5. Light scattering data at conditions similar to those of Fig. 1, except that the experiments were conducted on polycrystalline Ag in a light scattering cell. Top traces, scattered light intensity (increasing in the positive direction); bottom traces, current response to the potential ramp (cathodic peaks negative). The first cathodic peak is UPD deposition; the second is bulk deposition. Light source argon ion laser at 515 nm. (a) Increase of light scattering with onset of bulk deposition, (b) stability of deposit on open circuit, and (c) removal of deposit after open-circuit stand.

An investigation of different optical models to interpret the present *in situ* ellipsometer measurements of the bulk deposit has been reported elsewhere (20). This layer was found to form on top of the first monolayer of Pb adatoms and to be of a granular, porous form. The optical properties of this layer are intermediate between those of metallic Pb and electrolyte and have been determined by use of the Bruggeman theory (21). This approach is analogous to that used by representing microrough surfaces as equivalent films (21-23).

Other investigators have suggested that three-dimensional nucleation occurs on a completely formed monolayer, on the basis of *ex situ* experiments using Auger

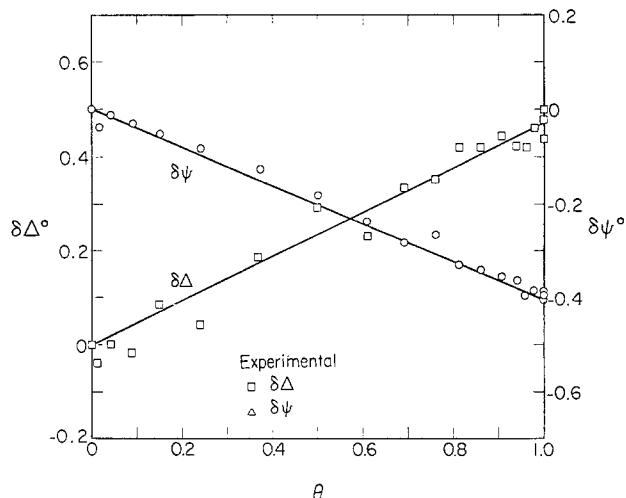


Fig. 6. Prediction by optimized coherent superposition model (solid line) and measurement of changes in ellipsometer parameters ψ and δ due to progressive deposition of an underpotential layer of Pb on Ag(111). Properties of the underpotential deposit derived from the optimized data fit given in Table I.

spectroscopy (24), x-ray fluorescence (25), and scanning electron microscopy (26).

To model both the UPD monolayer and the bulk deposit collectively, a two-film model is used, analogous to the approach of Smith and Müller (19, 27). First, one calculates a value of the complex reflection coefficient ratio due to the UPD layer on the electrode. Then, using this ratio, an apparent refractive index is calculated, which includes both the effects of the substrate and the UPD monolayer. The optical effect (δ and ψ) of the porous bulk deposit is then determined on the apparent substrate. The Bruggeman theory is used to compute the effective refractive index of the porous film material.

By minimizing the sum-of-squares error between the model predictions and the measurement of δ and ψ , one determines optimum values of the adjustable model parameters (28, 29). Parameters to be fitted are (i) complex refractive index of the UPD, (ii) apparent thickness of the UPD, (iii) porosity of the bulk deposit, and (iv) thickness of the bulk deposit. Fine tuning of the metal optical constants is done initially to compensate for uncertainty in the optical constants found in the literature or determined experimentally. Equation [1] defines the sum-of-squares error for the model.

$$S_{\Delta, \psi} = \sum_{i=1}^N (\Delta_{M,i} - \Delta_{C,i})^2 + \sum_{i=1}^N (\psi_{M,i} - \psi_{C,i})^2 \quad [1]$$

The parameter variance is then defined by

$$SE(p) = \frac{\sigma^2}{\frac{1}{2} \frac{\partial^2 S_{\Delta, \psi}}{\partial p^2}} \quad [2]$$

Parameter confidence intervals (Eq. [3]) are calculated from this variance and the student-t statistic for $2N-P$ degrees of freedom, where N is the number of δ - ψ measurements and P is the number of adjustable model parameters

$$\delta(p) = t(2N - P, 1 - 2\alpha)[SE(p)]^{1/2} \quad [3]$$

Both the parameter variance and the model variance are required, and are estimated numerically by use of Eq. [4] and [5], respectively

$$\sigma^2 \sim S_{\text{MIN}}/df = S_{\text{MIN}}/(2N - P) \quad [4]$$

$$\frac{1}{2} \frac{\partial^2 S_{\Delta, \psi}}{\partial p^2} \sim \frac{S_{(+)} + S_{(-)} - 2S_{\text{MIN}}}{2(\Delta p)^2} \quad [5]$$

Separate optimizations are performed to determine UPD and bulk optical properties. This is possible since

Table I. Optical properties of the Pb underpotential deposit (UPD) at complete coverage ($\theta = 1$). Wavelength: 514.5 nm. Electrolyte: 0.5 and 5.0 mM Pb^{2+} , 1M NaClO_4 , pH 3. Errors given for 95% level of confidence

Substrates	Ag(111)	Cu(111)	Cu(111)
Pb concentration (mM)	0.5	0.5	5
UPD refractive index	$n_{\text{UPD}} = 1.285 \pm 0.007$	1.225 ± 0.066	0.952 ± 0.417
UPD extinction coefficient	$k_{\text{UPD}} = 4.080 \pm 0.040$	3.520 ± 0.041	3.898 ± 0.021
UPD thickness (\AA)	$d_{\text{UPD}} = 5.149 \pm 0.026$	4.030 ± 0.178	4.777 ± 1.101

potential ramping separates formation of the two layers in time. As the UPD was formed, 19 values of current, delta, and psi were logged by computer during formation of the Pb UPD on Ag; these measurements were used collectively to determine the three parameters needed for the characterization of the UPD (complex refractive index and thickness). These values can be determined from data for a single cathodic sweep with a high degree of accuracy. Optical constants and thicknesses determined thus for the Pb UPD layer on Ag(111) and Cu(111) for a wavelength of 515 nm are given in Table I (18). The error limits are given for a 95% level of confidence, based upon 37° of freedom. The thickness of the layer of 4-5Å compares well with an atomic diameter of about 3.5Å.

Estimates of the parameters for the bulk deposit are more uncertain. Confidence intervals for these parameters can only be derived by averaging comparable values of delta and psi from replicate experiments (or multiple sweeps). Modeling results for the bulk Pb deposit are presented in Table II for different substrates, electrolytes, and potential cycles. From these results, it was concluded that the bulk deposit formed in the experiments conducted with 0.5 mM was approximately 30% porous and about 10Å thick; the bulk deposit formed with 5.0 mM was approximately 40% porous and 200Å thick.

Adsorption Isotherm

Conway *et al.* present general theories of adsorption at liquid-solid interfaces and the proper selection of standard states (30). Conway and Kozłowska also discuss the effects of sweep rate, etc., on the UPD peak in voltammetry (31). Ross has shown that the Langmuir isotherm can be applied to hydrogen adsorption on Pt single crystals with data taken from cyclic voltammograms (32). Swathirajan *et al.* have presented a detailed thermodynamic model for Ag and Pb underpotential deposition on polycrystalline Au, and determined that both of these UPD layers involved electroadsorbed species having valences equivalent to those of their respective dissolved

ions (33). If one assumed that the valence of the electroadsorbed Pb species on Ag(111) and Cu(111) is equivalent to that of Pb^{2+} , the term $RT/F(1/\gamma_{\text{UPD}} - 1/z) \ln a_{\text{M}^{2+}}$ in Eq. [12] of Ref. (33) becomes zero, and the adsorption behavior is therefore independent of the solution activity of Pb^{2+} . The terms γ_{UPD} , z , and $a_{\text{M}^{2+}}$ correspond to the terms z , z_{pb} , and α , respectively, in this paper. By assuming that both the Frumkin and Temkin parameters are zero, and by taking the reference potential $U_{1/2}$, to be that giving $\theta = 0.5$, Eq. [12] of Ref. (33) reduces to the Langmuir isotherm, Eq. [6], which is linear in potential

$$\ln \left(\frac{\theta}{1 - \theta} \right) = - \frac{zF}{RT} (U - U_{1/2}) \quad [6]$$

The Gibbs free energy of adsorption is related to the underpotential at half-monolayer coverage ($U_{1/2}$) through Eq. [7]

$$\Delta G_{\text{ADS}}^{\circ} = -zFU_{1/2} \quad [7]$$

Since Eq. [6] is linear in potential (underpotential scale), it can be applied to experimental data easily by using regression analysis (34). Equation [8] is used for data reduction; the slope m and intercept b are then related to the Gibbs free energy of adsorption

$$\ln \left(\frac{\theta}{1 - \theta} \right) = mU + b \quad [8]$$

$$G_{\text{ADS}}^{\circ} = -bRT \quad [9]$$

The underpotential at half-coverage and the apparent valence are given by Eq. [10] and [11], respectively

$$U_{1/2} = -b/m \quad [10]$$

$$z = -mRT/F \quad [11]$$

Rigorous analysis relates the error in these physical quantities (Eq. [12]-[14]) to the uncertainties in the slope and intercept of the regression line (Eq. [15] and [16]), and to the model variance (Eq. [17])

$$\delta(\Delta G_{\text{ADS}}^{\circ}) = F[(U_{1/2} \cdot \delta z)^2 + (z \cdot \delta U_{1/2})^2]^{1/2} \quad [12]$$

$$\delta(U_{1/2}) = U_{1/2} \left[\left(\frac{\delta b}{b} \right)^2 + \left(\frac{\delta m}{m} \right)^2 \right]^{1/2} \quad [13]$$

$$\delta(z) = \frac{RT}{F} |\delta m| \quad (\text{also written as } \delta z) \quad [14]$$

$$\delta m = S \cdot t(N - 2, 1 - 2\alpha) \left[\sum_{i=1}^N (U_i - \bar{U})^2 \right]^{-1/2} \quad [15]$$

$$\delta b = S \cdot t(N - 2, 1 - 2\alpha) \left[\left(\sum_{i=1}^N U_i^2 \right) / \left(N \sum_{i=1}^N (U_i - \bar{U})^2 \right) \right]^{1/2} \quad [16]$$

Table II. Optical properties of bulk Pb deposits from 1M NaClO_4 supporting electrolyte at pH 3. Electrode area: 3.42 cm^2 . Underpotential deposit indicated by *.

t (s)	E (mV)	Q (mC)	$d_q(\text{\AA})$	Δ_M	ψ_M	Δ_C	ψ_C	$d(\text{\AA})$	θ_{pb}	n_{pb}	k_{pb}
Ag(111), 0.5 mM Pb^{2+} , 0.1 V/min											
219*	-443	1.55	3.52	72.06	43.27	72.06	43.27	5.53	1	1.30	4.27
300	-490	12.93	29	71.90	41.85	71.58	41.97	16	0.75	2.05	4.27
413	-663	18.35	42	71.62	41.13	71.30	41.18	26	0.75	2.10	4.27
Cu(111), 0.5 mM Pb^{2+} , 0.5 V/min											
18*	-452	1.58	3.52	60.31	38.44	60.32	38.43	5.05	1	1.35	4.03
24	-592	2.20	5	60.56	38.22	60.52	38.13	6	0.71	1.95	4.27
30	-746	3.14	7	60.61	38.11	60.61	38.11	6	0.71	1.95	4.27
46	-476			60.61	37.90	60.51	38.14	6	0.71	1.95	4.27
48	-438	4.47	10	60.83	37.84	60.82	37.80	12	0.73	1.98	4.24
Cu(111), 5.0 mM Pb^{2+} , 1.5 V/min											
17*	-422	2	3.52	59.34	38.04	59.32	37.97	4.79	1	0.95	3.99
23	-576	28	49	56.59	36.17	56.52	36.09	76	0.56	1.90	4.30
40	-606	80	141	58.00	33.95	58.01	34.03	170	0.60	1.94	4.26
45	-478	91	160	58.55	33.56	58.63	33.16	194	0.61	1.99	4.28

Table III. Linear regression analysis of adsorption isotherm data

Quantity	Units	Ag(111)	Cu(111)	Ag(111) + Cu(111)
$\Delta G_{\text{ADS}}^{\circ}$	kcal/mol	-8.75	-7.75	-7.90
$U_{1/2}$	mV	151	156	155
z		2.52	2.15	2.21
m	mV^{-1}	-0.09826	-0.083678	-0.086188
b		14.783091	13.090754	13.339047
$\delta(\Delta G_{\text{ADS}}^{\circ})$	kcal/mol	1.23	0.87	0.88
$\delta(U_{1/2})$	mV	17	13	15
$\delta(z)$		0.21	0.12	0.12
$\delta(m)$	mV^{-1}	0.008001	0.004746	0.004523
$\delta(b)$		1.134927	0.800944	0.706471
S		0.485484	0.437346	0.572739
r		-0.989448	-0.992104	-0.986668

Note: $N - 2 = 17$, $1 - \alpha/2 = 0.95$, and $t(17, 0.95) \sim 2.11$. $N - 2 = 36$, $1 - \alpha/2 = 0.95$, and $t(36, 0.95) \sim 2.02$.

$$S = \left[\sum_{i=1}^N \left(\ln \left(\frac{\theta_i}{1 - \theta_i} \right) - \ln \left(\frac{\theta_u}{1 - \theta_u} \right) \right)^2 \frac{1}{N - 2} \right]^{1/2} \quad [17]$$

Results of the linear regression and error analysis are presented in Table III. The data for the Pb UPD on Ag(111) and Cu(111) were first analyzed separately, then together. The noninteger values of the electroadsorption valence could imply that Frumkin and Temkin parameters should be included in the adsorption isotherm model; however, it is believed that these unusual values are attributable to integration errors at low coverage and have no physical significance. The coverage, which is determined by integration of the cathodic UPD peak, cannot be determined accurately at low values since the current is of the same order as the background noise.

Inspection of the experimental data plotted in Fig. 7 shows that the underpotential at half-coverage is about 155 mV for both substrates, which corresponds to a Gibbs free energy of adsorption of 7.14 kcal/mol for an assumed electroadsorption valence of $z = 2$ (35). Note that a value of 5 kcal/mol has been reported for polycrystalline substrates (3). Theoretical predictions of coverage at different poten-

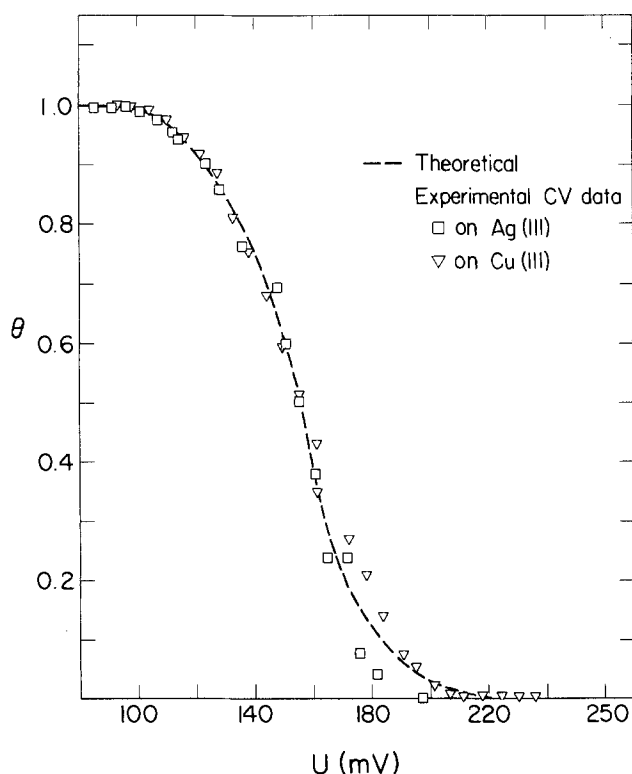


Fig. 7. Electroadsorption isotherm for Pb UPD on Ag(111) and Cu(111), model predictions for a free energy of adsorption of 7 kcal/mol and a valence of 2 (broken line) and experimental data from cyclic voltammetry. Coverage computed from charge.

Table IV. Comparison of amount of Pb deposit d_a based on charge passed with amount $\theta_{\text{Pb}}d$ derived from ellipsometer measurement

Substrate	Pb ⁺⁺ (mM)	t(s)	$d_a(\text{\AA})$	θ_{Pb} (vol. fract.)	$d(\text{\AA})$	$\frac{\theta_{\text{Pb}} \cdot d}{d_a}$
Ag(111)	0.5	300	29	0.75	16	0.41
		413	42	0.75	26	0.46
Cu(111)	0.5	24	5	0.71	6	0.85
		30	7	0.71	6	0.61
		46	9	0.71	6	0.47
		48	10	0.73	12	0.88
Cu(111)	5.0	23	49	0.56	76	0.87
		40	141	0.60	170	0.72
		45	160	0.61	194	0.74

tials can be made by substituting these values into the adsorption isotherm equation. These predictions are represented by the broken line in Fig. 7, which agrees well with experimental data except at very low coverages. Continuous adsorption isotherms have been reported for different Ag faces (36).

Double layer charging currents were subtracted by base-line extrapolation across the base of the UPD peak, assuming the *a priori* separability of charging currents. This method can lead to errors in coverage estimation, but the error for the Pb UPD on Ag and Cu may be small if the points of zero charge (pzc's) of the two materials are nearly equal (37). The concept of partial discharge associated with electroadsorption bonds (38) in the underpotential deposit is not supported by this work.

Charge Balance

Equation [18] was used to calculate the charge passed to the working electrode during deposition

$$Q = \int_0^t i(t) \hat{A} dt = \frac{(xyd_a)\rho_{\text{Pb}}}{MW_{\text{Pb}}} z_{\text{Pb}} e N_{\text{avg}} \quad [18]$$

This charge was used to calculate the coverage of Pb adatoms on the electrode surface. The actual charge required for a complete UPD agreed with that expected for a monolayer with a roughness factor of 1.25.

The thickness of the bulk deposit and the volume fraction of Pb in it, determined from ellipsometer measurements, were used to compute the total amount of Pb on the electrode surface. This quantity was then compared to the amount expected on the basis of charge passed. The ellipsometer measurements consistently predict less Pb on the surface than the charge balance (a discrepancy ranging from 10% to 50%, Table IV). This difference might be due to uneven current distribution on the electrode, with more Pb being deposited around the edge of the electrode, while the ellipsometer measurement was performed at the center.

Conclusions

The initial stages of electrodeposition (0-200 \AA) can be elucidated by the simultaneous use of ellipsometry, cyclic voltammetry, and light scattering measurements. The application of a potential ramp allows one to separate underpotential and bulk deposits in time and thus investigate them separately.

An optical model which fits the data very well involves the two-dimensional growth of monolayer islands during UPD formation and the three-dimensional nucleation and growth of a microporous bulk deposit on top of it. Thickness, optical constants, Gibbs free energy of adsorption, and apparent valence for the Pb UPD on Ag(111) and Cu(111) have been determined.

Acknowledgments

This work was supported by the Director, Office of Energy Research, Office of Basic Energy Sciences, Materials Science Division of the U.S. Department of Energy

under Contract no. DE-AC-03-76SF00098. We wish to thank W. J. Plieth for use of the light scattering cell.

Manuscript submitted May 10, 1983; revised manuscript received Sept. 18, 1984. This was Paper 823 presented at the San Francisco, California, Meeting of the Society, May 8-13, 1983.

The University of California assisted in meeting the publication costs of this article.

LIST OF SYMBOLS

\hat{A}	electrode area (cm ²)
\hat{A}, \hat{B}	complex parameters for quadratic equation
a	activity of Pb ²⁺ in solution
b	linear regression intercept
C	concentration
d	thickness of bulk deposit derived from ellipsometer measurement
d_{UPD}	thickness of underpotential deposit
df	degrees of freedom ($2N - P$)
d_q	deposit thickness based on change (\AA)
e	electronic charge (1.602×10^{-19} C)
E	electrode potential vs. Ag/AgCl (V)
F	Faraday's constant (96,487 C/eq)
g	interaction parameter
$u(t)$	time varying current density during cyclic voltammetry (A/cm ²)
k_{UPD}	extinction coefficient of underpotential deposit
k_{Pb}	extinction coefficient of bulk Pb
m	slope of linear regression (V ⁻¹)
MW_{Pb}	atomic weight of Pb (207.2 g/mol)
n_{Pb}	refractive index of bulk Pb
n_{UPD}	refractive index of underpotential deposit
N	number of data points defining experimental electroadsorption isotherm and number of pairs of Δ and ψ measurements
N_{AVG}	Avogadro's number (6.02×10^{23} at./mol)
N_i	atomic number density of component i in the effective medium
p	arbitrary model parameter to be fitted
P	number of model parameters to be fitted
Q	total charge passed to working electrode (C)
r	regression coefficient (Table III)
RT	constant (0.592 kcal/mol)
S	variance between experimental data and prediction of electroadsorption model
$S(\)$	error of quantity in parentheses (except for $\delta\Delta$ and $\delta\psi$)
$SE(p)$	variance of parameter p
$S_{\Delta,\psi}$	sum-of-squares error between theoretical ellipsometer parameters and those measured experimentally
S_{MIN}	minimum value of $S_{\Delta,\psi}$ corresponding to a selection of optimum "p" values
$S_{(+)}$	value of $S_{\Delta,\psi}$ computed at a parameter value of $p + \Delta p$
$S_{(-)}$	value of $S_{\Delta,\psi}$ computed at a parameter value of $p - \Delta p$
t	time
$t(2N - P, 1 - 2\alpha)$	the t-statistic for "2N - P" degrees of freedom at a "1 - 2 α " level of confidence
U	underpotential relative to Nernst potential $E^0(V)$
U_i	measured value of U (controlled) at the i th coverage; the i th data point
$U_{1/2}$	underpotential corresponding to $\theta = 0.5(V)$
\bar{U}	mean underpotential (V)
V	electrode potential (V)
x	electrode dimension (cm)
y	electrode dimension (cm)
z	apparent valence of metal adatom after electroadsorption
z_{Pb}	valence of lead ion in solution (2)
α	level of confidence ($1 - 2\alpha$)
$\delta(p)$	error in parameter "p" at a "1 - 2 α " level of confidence
$\delta\Delta$	change in ellipsometer parameter delta due to underpotential deposit (deg.)
$\delta\psi$	change in ellipsometer parameter psi due to underpotential deposit (deg.)
Δ or delta	ellipsometer parameter, phase difference between p and s electric field components after reflection, relative to the incident (deg.)
Δ_C	calculated value of Δ for bulk deposit
$\Delta_{C,i}$	calculated value of Δ corresponding to $\Delta_{M,i}$
Δ_M	measured value of delta for bulk deposit (deg.)

$\Delta_{M,i}$	the i th measured value of Δ for the UPD at the i th coverage; the i th data point
ΔG_{ADS}^0	Gibbs free energy of adsorption for UPD monolayer (kcal/mol)
θ	fractional coverage of electrode surface by UPD monolayer
θ_f	fraction of surface covered by film of refractive index \hat{n}_f
θ_i	UPD monolayer coverage measured at underpotential U_i
θ_{Pb}	volume fraction of Pb in composite thin film deposit
θ_u	monolayer coverage predicted by electroadsorption model for underpotential U_i
ρ_{Pb}	density of Pb (11.34 g/cm ³)
σ^2	variance of the model predictions for Δ and ψ
ψ or psi	ellipsometer parameter, amplitude ratio of p and s electric field components after reflection (tan ψ), relative to the incident (deg.)
ψ_C	calculated value of ψ for bulk deposit
$\psi_{C,i}$	calculated value of ψ corresponding to $\psi_{M,i}$
$\psi_{M,i}$	measured value of ψ for the UPD at the i th coverage; the i th data point
ψ_M	measured value of psi for bulk deposit (deg.)

REFERENCES

1. D. M. Kolb, in "Advances in Electrochemistry and Electrochemical Engineering," Vol. 11, H. Gerischer and C. W. Tobias, Editors, pp. 125-271, John Wiley and Sons, New York (1978).
2. J. A. Harrison and H. R. Thirsk, in "Electroanalytical Chemistry," Vol. 5, A. J. Bard, Editor, p. 64, Dekker, New York (1971).
3. E. Schmidt and H. R. Gygas, *J. Electroanal. Chem.*, **12**, 300 (1966).
4. K. Jüttner and W. J. Lorenz, *Z. Phys. Chem. NF*, **122**, 163 (1980).
5. G. Hass and L. Hadley, in "American Institute of Physics Handbook," 2nd ed., D. E. Gray, Editor, pp. 6-133, McGraw-Hill, New York (1963).
6. P. B. Johnson and R. W. Christy, *Phys. Rev. B*, **6**, 4370 (1972).
7. R. Adzic, E. Yeager, and B. D. Cahan, *This Journal*, **121**, 474 (1974).
8. H. J. Mathieu, D. E. McClure, and R. H. Muller, *Rev. Sci. Instrum.*, **45**, 798 (1974).
9. R. H. Muller, W. J. Plieth, and J. C. Farmer, Lawrence Berkeley Laboratory Report, LBL-12965, Berkeley, CA (1981).
10. G. Petzow, "Metallographic Etching, Metallographic and Ceramographic Methods for Revealing Microstructure," pp. 37, 38 ASM, Metals Park, OH (1978).
11. P. Delahay, M. Pourbaix, and P. Van Rysselberghe, *This Journal*, **98**, 65 (1951).
12. M. Pourbaix, "Atlas of Electrochemical Equilibria in Aqueous Solutions," p. 384, Pergamon Press, New York (1966).
13. G. A. Bootsma and F. Meyer, *Surf. Sci.*, **14**, 52 (1969).
14. G. A. Bootsma, L. J. Hanekamp, and O. L. J. Gijzeman, in "Proceedings of the 5th Summer Institute for Surface Science," R. Howe and R. Vanselow, Editors, p. 77, Springer, Berlin (1982).
15. A. M. Brodski and M. I. Urbakh, *Sov. Electrochem.*, **38**, 1553 (1979).
16. W. Plieth, H. Bruckner, and H.-J. Hensel, *Surf. Sci.*, **101**, 261 (1980).
17. K. Takamura, F. Watanabe, and T. Takamura, *Electrochim. Acta*, **26**, 979 (1981).
18. R. H. Muller and J. C. Farmer, *Surf. Sci.*, **135**, 521 (1983).
19. R. H. Muller and C. G. Smith, *ibid.*, **96**, 375 (1980).
20. R. H. Muller and J. C. Farmer, *J. Phys.*, **44**, C10-57 (1983).
21. D. E. Aspnes, J. B. Theeten, and F. Hottier, *Phys. Rev. B*, **20**, 3292 (1979).
22. K. Brudzewski, *Thin Solid Films*, **61**, 183 (1979).
23. T. Smith, P. Smith, and F. Mansfeld, *This Journal*, **126**, 799 (1979).
24. K. Takayanagi, D. M. Kolb, K. Kambe, and G. Lehmpfuhl, *Surf. Sci.*, **100**, 407 (1982).
25. B. H. Vassos and H. B. Mark, Jr., *J. Electroanal. Chem.*, **13**, 1 (1967).
26. V. V. Povetkin and I. M. Kovenskii, *Sov. Electrochem.*, **17**, 1461 (1981).
27. C. G. Smith, Ph.D. Thesis, University of California, Berkeley, CA (1978).
28. C. Hendrix, "An R/D Technical Education Course in Recent Advances in Statistics, Lecture No. 2," Union

- Carbide Technical Center, So. Charleston., WV, April 18, 1978.
29. G. E. P. Box and G. A. Coutie, *Proc. Inst. Electr. Engrs.*, **102**, Part B, Suppl. 1, 100 (1956).
 30. B. E. Conway, H. Angerstein-Kozłowska, and H. P. Dhar, *Electrochim. Acta*, **19**, 455 (1974).
 31. B. E. Conway and H. Angerstein-Kozłowska, *J. Electroanal. Chem.*, **113**, 63 (1980).
 32. P. N. Ross, Jr., in "Proceedings of the 5th International Summer Institute for Surface Sciences," R. Howe and R. Vanselow, Editors, p. 173, Springer, Berlin (1982).
 33. S. Swathirajan, H. Mizota, and S. Bruckenstein, *J. Phys. Chem.*, **86**, 2480 (1982).
 34. W. J. Dixon and F. J. Massey, Jr., "Introduction to Statistical Analysis," p. 195, McGraw-Hill, New York (1969).
 35. H. Bort, K. Jüttner, and W. T. Lorenz, *J. Electroanal. Chem.*, **90**, 413 (1978).
 36. W. J. Lorenz, E. Schmidt, G. Staikov, and H. Bort, *Faraday Discuss. Chem. Soc.*, **12**, 14 (1978).
 37. S. Swathirajan and S. Bruckenstein, *J. Electroanal. Chem.*, **146**, 137 (1983).
 38. E. E. Mola, *Electrochim. Acta*, **26**, 1253 (1983).

Band-Edge Shift and Surface Charges at Illuminated n-GaAs/Aqueous Electrolyte Junctions

Surface-State Analysis and Simulation of Their Occupation Rate

P. Allongue and H. Cachet

Laboratoire "Physique des Liquides et Electrochimie" du CNRS associé à l'Université Pierre et Marie Curie, 75230 Paris Cedex 05, France

ABSTRACT

Mott-Schottky plots for n-GaAs/aqueous electrolyte junctions under various illuminations show that the semiconductor bandedges are shifted with respect to their position in the dark, the magnitude of the shift increasing with increasing light intensity. Correlatively, the surface-state capacitance $C_{ss}(V)$ presents a sharp peak; its height increases with illumination. A model for the electron occupation rate of a surface-state distribution is described in order to interpret these experimental facts. It is shown that such a kinetic model explains only impedance $C_{ss}(V)$ results; chemical modifications at the surface have to be invoked to account for the flatband-potential shift at the illuminated electrode. The surface-state capture cross sections are pulled from impedance analysis through the relaxation time $R_{ss} \cdot C_{ss} = \tau_{ss}$.

In several papers, it has been reported that in semiconductor liquid junctions, bandedges are shifted under illumination (1-4). For n-type (p-type) semiconductors, the shift is positive (negative) of the flatband potential V_{FB} in the dark; in our case, this shift is experimentally evidenced by impedance measurements under illumination. In a recent model for the photoresponse of the n-GaAs/(Se²⁻/Se₂²⁻) junction, we accounted for this shift by taking a pseudo flatband potential V_{FB}^* as the reference for the band bending $V_b = V - V_{FB}^*$, where V is the external applied voltage (3). We pointed out that impedance measurements under illumination are absolutely necessary to avoid wrong interpretations and reach the real charge-transfer kinetics. A surface-state capacitance distribution on n-GaAs was experimentally determined and surface charges were invoked to interpret the band-edge shift.

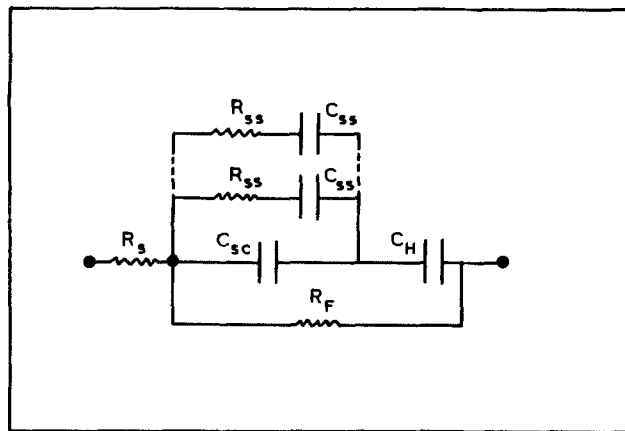
In this paper, we intend to specify by using impedance measurements the fundamental role played by the surface states. Experimental results show an increase in the flatband-potential shift and the peak in surface-state capacitance $C_{ss}(V)$, when light intensity increases. A question arises: are these evidenced states responsible for the band-edge shift? In order to answer this question, we present a kinetic model for the filling process of the surface states. It is similar to the model presented by Kelly and Memming, who developed their model to explain the large delay of the photocurrent onset potential with respect to the flatband potential in the dark, at p-GaAs electrodes (1). They performed extensive simulations. A similar model was also developed for metal-GaAs Schottky barriers, to reach the real surface-state distribution from capacitance measurements in the dark (5). And Chazalviel described the impedance and current behaviors of n-Si/acetonitrile junctions by using a very simple model which assumed that the only current pathway was a surface-state distribution over the whole gap (6).

In our model, the surface states may exchange charges with their three surrounding charge reservoirs, which are the conduction and valence bands of the semiconductor and the solution. We do not perform simulations. This

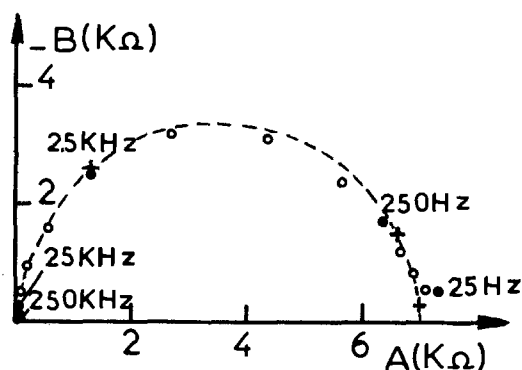
work is based upon experimental data such as surface-state capacitance $C_{ss}(V)$, surface-charge relaxation time $\tau_{ss}(V)$, Mott-Schottky plots, and I-V characteristics. The adjustable parameters are found to be very few, compared to the number of conditions to be satisfied. The aim is to use our theoretical model, for the occupation rate of the surface-state distribution, to fit the calculated $C_{ss}(V)$ and $\tau_{ss}(V)$ curves to the experimental ones for various light intensities. It is shown that a narrow, constant surface-state distribution is sufficient to explain our results and that the surface-charge variation associated with this distribution cannot account for the difference between the Mott-Schottky plots in the dark and these under illumination. The distribution always empties, more or less even in the dark. The way the distribution empties is photon-flux dependent through the minority carrier (hole) surface concentration. Finally, the flatband-potential shift with illumination is discussed in terms of chemical modifications at the surface.

Experimental

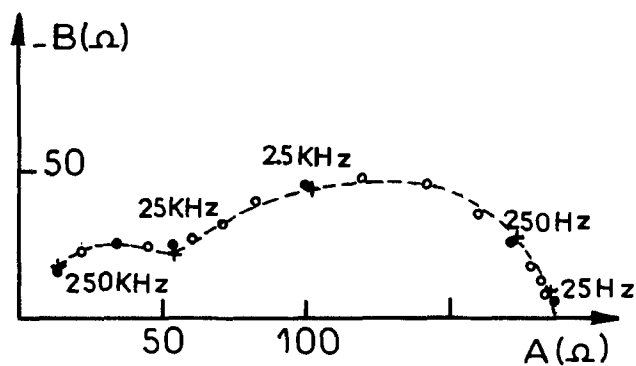
Undoped n-type ($2.3 \times 10^{16} \text{ cm}^{-3}$, <100> orientation) GaAs single crystals are purchased from MCP Limited. After polishing, semiconductor electrodes are etched with H₂SO₄:H₂O₂:H₂O, 2:1:1 mixture. All measurements are made in a classical three-electrode electrochemical cell. All potentials are referred to a saturated calomel reference (SCE). Selenide electrolytes 1M KOH + 1M Se²⁻/Se₂²⁻ are prepared by electrochemical reduction of selenium on a mercury cathode (7). A 100W quartz halogen lamp is used for illumination, and light intensity is changed with neutral filters and measured with a MACAM TR 3010 radiometer. Stationary I-V curves and impedance measurements are performed under potentiostatic conditions. At each potential, impedance $Z(\omega, V)$ is determined in the frequency range of 1 Hz-250 kHz by using a 1174 Solartron connected to a data management system. Every $Z(\omega, V)$ diagram is analyzed by means of a nonlinear least squares method, in accordance with the classical electrical equivalent circuit (Fig. 1a). We want to



(a)



(b)



(c)

Fig. 1. (a) Electrical equivalent circuit of a semiconductor-electrolyte junction used in Ref. (3). C_{sc} is the space-charge capacitance in the semiconductor, C_H the Helmholtz capacitance, R_F and R_s the faradic and series resistances. The series $R_{ss}C_{ss}$ circuit accounts for a charge relaxation in surface states. At some potential, a second $R'_{ss}C'_{ss}$ circuit is necessary to fit our impedance spectra. (b) and (c) Impedance spectra of the n-GaAs/selenide junction under 22 mW/cm² illumination at different potentials (electrode area = 0.34 cm²). (○) experimental data. (---) calculated spectrum according to the scheme in (a). The calculated (+) and experimental (●) points correspond to the same frequency indexation. (b) $V = -0.60$ V/SCE; $C_{sc} = 15.1$ nF; $R_f = 7020$ Ω; $R_{ss} = 664$ Ω; $C_{ss} = 4.2$ nF; $R_s = 5.7$ Ω; $C_H = 1$ μF. (c) $V = -1.575$ V/SCE; $C_{sc} = 36.2$ nF; $R_f = 176$ Ω; $R_{ss} = 106$ Ω; $C_{ss} = 181$ nF; $R'_{ss} = 211$ Ω; $C'_{ss} = 1800$ nF; $R_s = 7.9$ Ω; $C_H = 1$ μF.

emphasize that each component of this scheme is not frequency-dependent. Because the series resistance is $R_s \approx 2$ Ωcm², the IR drop is negligible ($I < 10$ mA/cm²) and cannot account for the flatband-potential shift. It is worth pointing out that to obtain a good fit of the impedance diagrams at some potentials, several time constants,

$R_{ss}C_{ss}$, have to be considered. This indicates that a surface-state distribution exists in the bandgap, as is further confirmed by calculations. However, to limit the number of parameters in impedance analysis, we take only two time constants, $R_{ss}C_{ss}$. This is found to be sufficient in most cases. In the following, the surface-state capacitance $C_{ss}(V)$ at a given potential is defined as the sum of the two elementary C_{ss} to account for the whole surface-charge variation (8, 9). In the same way, a mean relaxation time $\tau_{ss}(V)$ is defined as the weighted mean of the two time constants $\tau_{ss} = R_{ss}C_{ss}$, with respect to their associated C_{ss} . It appears that the slower τ_{ss} always corresponds to the greater C_{ss} and then refers to the main surface-charge variation.

Finally, C_H has to be estimated. Because this is not possible using the impedance analysis alone, we use an indirect method. It appears, judging by the equivalent scheme (Fig. 1a), that when $C_{ss} \ll C_{sc}$, the fixed value of C_H does not influence the analysis ($C_H \gg C_{sc}$), and that when $C_{ss} \gg C_{sc}$ (see Fig. 4), the series combination of C_H and C_{ss} is measured. Hence, in the latter case, at a given potential, a value of C_{ss} (or $C_{ss} + C'_{ss}$) corresponds to a fixed C_H . Consequently, the $C_{ss}(V)$ curve is C_H -dependent; the $C_{sc}^{-2}(V)$ is not. Knowing all the capacitances of the circuit, the actual band bending $V_b(V)$ can be calculated at any bias (10). Introducing it into our model for the photoresponse (3), we compare the experimental and theoretical I-V characteristics, especially in the photocurrent-rise region. In fact, the band bending variations deeply influence the calculated slope of the I-V curve at these potentials. The best fits lead to $C_H = 2.8$ μF/cm² in the case of the n-GaAs/selenide junction. It is noted also that C_H represents the series combination of Helmholtz and oxide capacitances if there is an oxide layer.

Results

In the following, the presented results are those of the n-GaAs/selenide junction. However, these results seem to be characteristic of n-GaAs/aqueous electrolyte interfaces because the same behavior has been found for n-GaAs dipped in 1M KOH, 1M KOH + 1M S²⁻/S_n²⁻, and 0.1M Fe^{2+/3+} (citrate) buffered at pH = 9.4 Figure 1b and 1c show two impedance diagrams of the junction in two extreme cases (these are Nyquist plots with the convention of electrochemistry). In the photocurrent plateau region, the only required (R_{ss}, C_{ss}) circuit indicates small ($C_{ss} < C_{sc}$) surface charge variations. The diagram is almost a semi-circular loop (Fig. 1b). However, a second loop appears if the contribution of the surface states is important (Fig. 1c). Here, two time constants are required and $C_{ss} + C'_{ss} \gg C_{sc}$. The latter happens in the photocurrent-rise region. Figure 2 illustrates the I-V characteristics of the junction and their corresponding Mott-Schottky plots under various illuminations. These latter curves are almost straight and parallel over more than 1V and are shifted toward more positive potentials as light intensity is increased. In the dark, $V_{FB} = -2.06$ V/SCE. In the potential region corresponding to the photocurrent existence ($V > -1.55$ V/SCE), the band bending can be defined with respect to a pseudo flatband potential V_{FB}^* . It is the intercept of the $C_{sc}^{-2} - V$ straight line with the potential axis. For potential near V_{FB}^* , all the curves seem to tend toward the "dark" curve. Figure 3 illustrates the shift $\Delta V_{FB} = V_{FB}^* - V_{FB}$ of the flatband potential as a function of the saturation current density. It appears that this shift presents an asymptotic value of ~ 0.370 V for strong illumination.

It is tempting to connect the above result to the change in the surface charge revealed by the surface-state capacitance $C_{ss}(V)$ curves under illumination. Figure 4 presents the "slow" and the "fast" C_{ss} , associated with a long and a short relaxation time constant, respectively (Fig. 5). As stated above, two time constants are required to fit the impedance spectra for potentials close to -1.6 V/SCE. This corresponds to the sharp peak region of the "slow" C_{ss} and indicates a great surface-charge variation for these potentials. For polarizations cathodic of -1.7 V/SCE, the

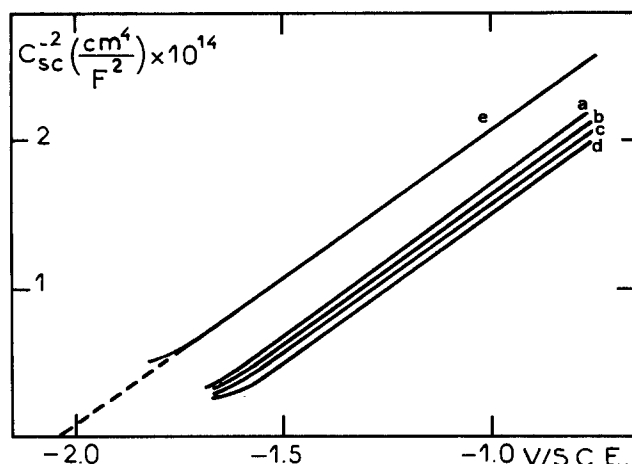
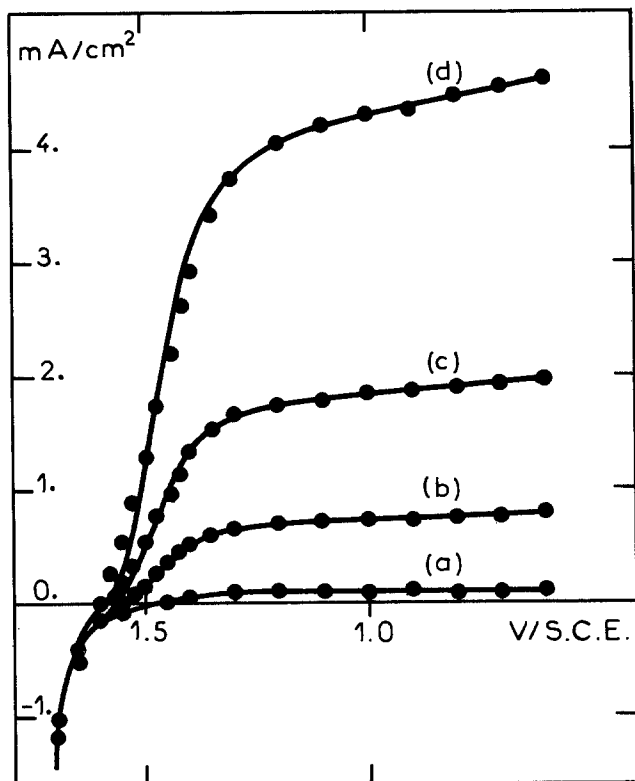


Fig. 2. (top) I-V curves of the n-GaAs/selenide junction under (a) 1.5 mW/cm², (b) 9 mW/cm², (c) 22 mW/cm², and (d) 50 mW/cm² illumination. (●) experimental data and (—) theoretical curve according to the model in Ref. (3) completed with the present model. Parameters are: $\alpha = 26,000 \text{ cm}^{-1}$; $L = 0.2 \mu\text{m}$; $\tau = 1.45 \times 10^{-10} \text{ s}$; $N_D = 2.3 \times 10^{16} \text{ cm}^{-3}$; $V_{FB} = -2.06 \text{ V/SCE}$; $V_{redox} = -0.96 \text{ V/SCE}$; $\lambda = 1 \text{ eV}$. The surface-state distribution characteristics are those of Fig. 11 at a given light intensity. (bottom) Mott-Schottky plots (a), (b), (c), and (d) correspond to the I-V curves (a), (b), (c), and (d), respectively. In the dark, $V_{FB} = -2.06 \text{ V/SCE}$.

high electron current associated with H₂ evolution might be responsible for the C_{ss} rise. Because measurements in this region are difficult, they are not yet interpreted, and, in the following, the main point we discuss is the peak which is reproducible. For anodic potentials, it is not possible to distinguish two time constants because their associated C_{ss} are very small compared to C_{sc} (the space-charge capacitance) and their determinations become less accurate. That is why we have only evidence of the "fast" C_{ss}. Figure 6 shows the evolution under various illuminations of the C_{ss}(V) curves, as defined in the experimental section. This recalls the admittance peak recently observed at n-GaAs and n-GaP electrodes (11). The peak height increases with light intensity, but it does not exist anymore in the dark. Its location remains almost constant

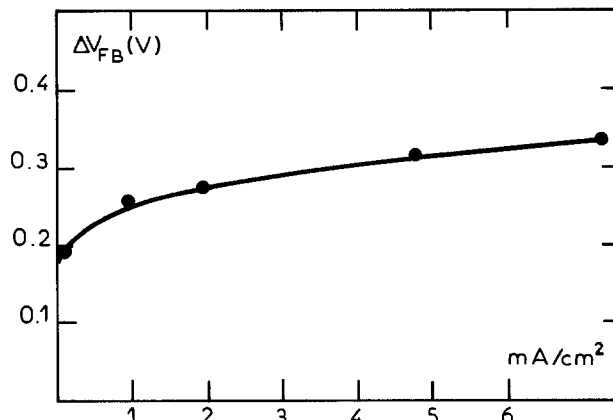


Fig. 3. Variations of $\Delta V_{FB} = V_{FB}^* - V_{FB}$ vs. saturation current density of an n-GaAs/selenide junction. Light intensity varies from 1.5 to 76 mW/cm².

for the illumination range we use. However, the mean relaxation time $\tau_{ss}(V)$ remains almost independent of the photon flux: it always presents the same abrupt variations around -1.6 V/SCE in correspondence with the C_{ss}(V) peak (Fig. 7). Finally, Fig. 8 shows the polarization resistance of the photocurrent characteristics R_p vs. the applied voltage. R_p becomes smaller when illumination is increased at a given potential.

Model

In a previous paper, we dealt with the direct charge-transfer kinetics between the valence band and the occupied states in solution. A model was presented for the photoresponse of the junction, thanks to the Marcus-Gerischer theory (3). In this section, we intend to explain the increasing peak in C_{ss}(V) and its associated band-edge

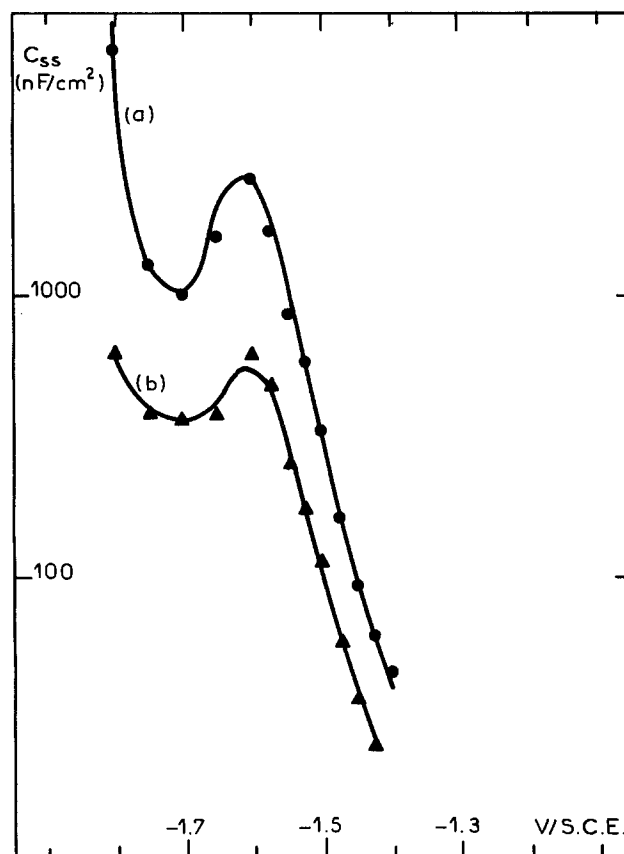


Fig. 4. Surface-state capacitances C_{ss} of an n-GaAs/selenide junction vs. applied voltage. (a) "slow" and (b) "fast" capacitances under 22 mW/cm² illumination.

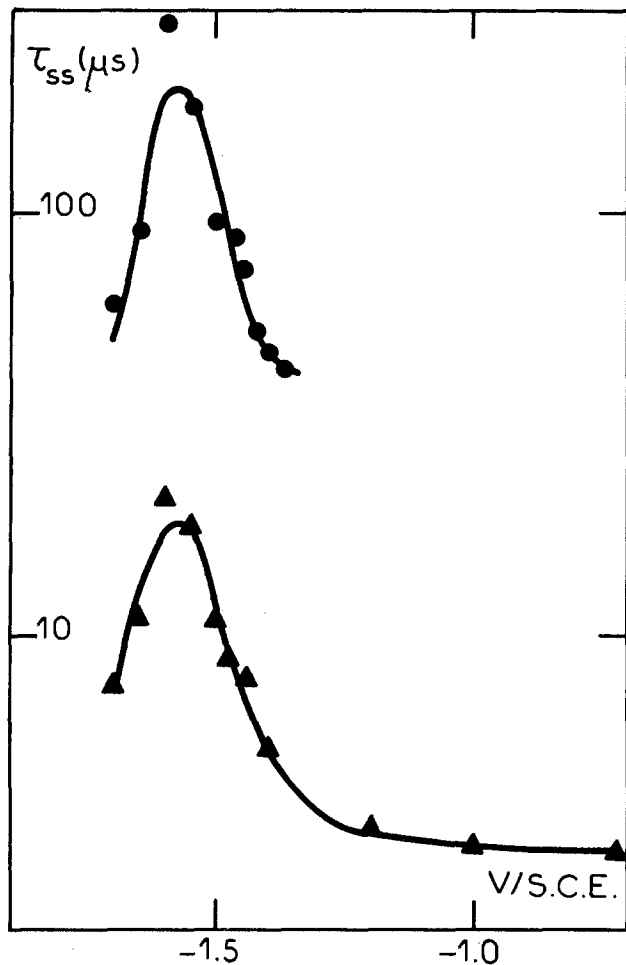


Fig. 5. Relaxation times τ_{ss} vs. potential under 22 mW/cm² illumination. Experimental data for slow (●) and fast (▲) τ_{ss} for an n-GaAs/selenide junction.

shift ΔV_{ss} with increasing light intensity. The contribution in the flatband-potential shift ΔV_{FB} of the surface states giving rise to a $C_{ss}(V)$ will be discussed in the following. In the case of a single surface state, ΔV_{ss} and $C_{ss}(V)$ are defined by

$$\Delta V_{ss} = qN_{ss}\Delta f/C_H \quad [1]$$

$$C_{ss}(V) = -qN_{ss}df/dV_b \quad [2]$$

where V_b is the band bending of the semiconductor, f the electron occupancy of the single surface state with a density N_{ss} , and Δf the total variation of f with potential.

The occupancy f depends on charge exchanges between the surface state, the valence (VB) and the conduc-

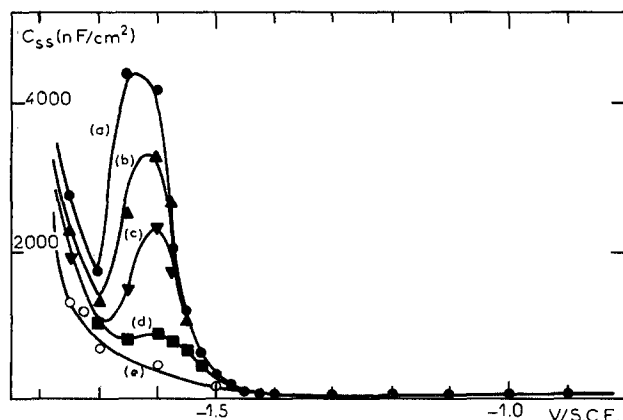


Fig. 6. Surface-state capacitance $C_{ss}(V)$ curves of an n-GaAs/selenide junction, under (a) 50 mW/cm² illumination, (b) 22 mW/cm², (c) 9 mW/cm², (d) 1.5 mW/cm², and (e) in the dark.

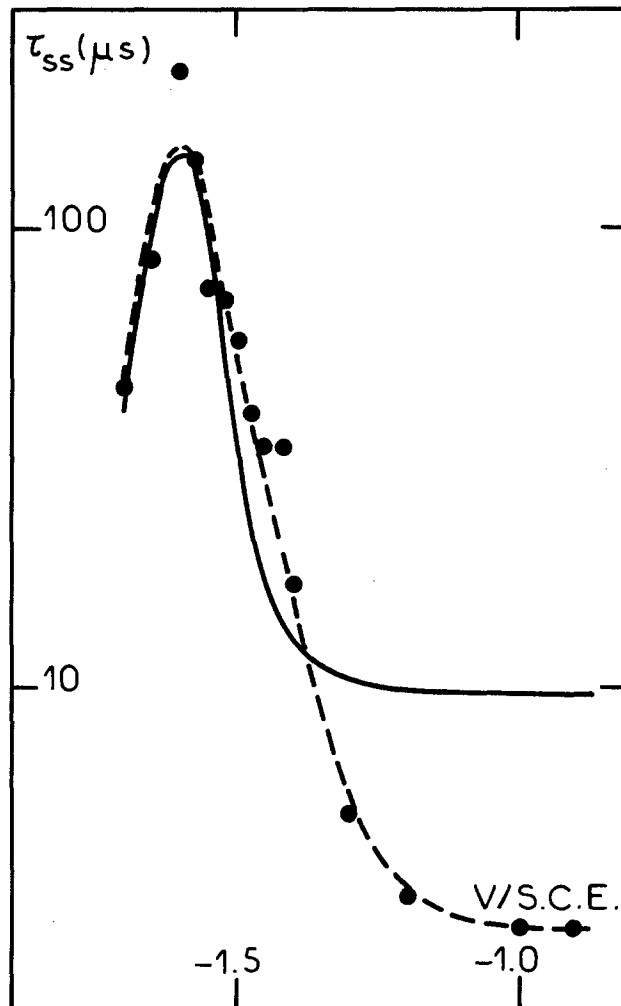


Fig. 7. Mean relaxation time $\tau_{ss}(V)$ curve of an n-GaAs/selenide junction under 22 mW/cm² illumination. (●) experimental data according to the definition given in the experimental section. (—) theoretical $\tau_{ss}(V)$ according to the model. Parameters are $V_{FB} = -2.06$ V/SCE, $C_H = 2.8$ μ F/cm², and $V_{FB}^* = -1.79$ V/SCE. The surface-state distribution extends between $E_c - 0.2$ eV and $E_c - 0.4$ eV with a constant density $N_{ss} = 1.05 \times 10^{13}$ cm⁻² eV⁻¹, $\sigma_n = 3.10^{-17}$ cm², $\sigma_p = 4.10^{-16}$ cm², $\sigma_s = 10^{-15}$ cm².

tion (CB) bands, and charges on the redox species in solution. For CB and VB exchanges, the Shockley-Read-Hall statistics hold. The conduction (valence) band exchange rate $R_c(R_v)$ expresses

$$R_c = k_c n_s N_{ss}(1-f) - k_c n_1 N_{ss} f \quad [3]$$

$$R_v = k_v p_s N_{ss} f - k_v p_1 N_{ss}(1-f) \quad [4]$$

and a similar equation can be written for the capture rate R_s of a hole, trapped in the surface state, by a reduced species in solution

$$R_s = k_s c_{red} N_{ss}(1-f) - k_s^{-1} c_{ox} N_{ss} f \quad [5]$$

where the k 's are constants as defined in Fig. 9, n_s and p_s are the electron and hole surface concentrations, and $c_{red}(c_{ox})$ are the reduced (oxidized) species concentrations. n_1 and p_1 are given by

$$n_1 = N_c \exp \frac{E_{ss} - E_c}{kT}$$

$$p_1 = N_v \exp - \frac{E_v - E_{ss}}{kT}$$

where E_{ss} is the energy level of the surface state. The capture of an electron by an oxidized species is very unlikely in our case because of coulombic repulsion, the oxidized species being Se_2^{2-} . Thus, in Eq. [5], the second term is

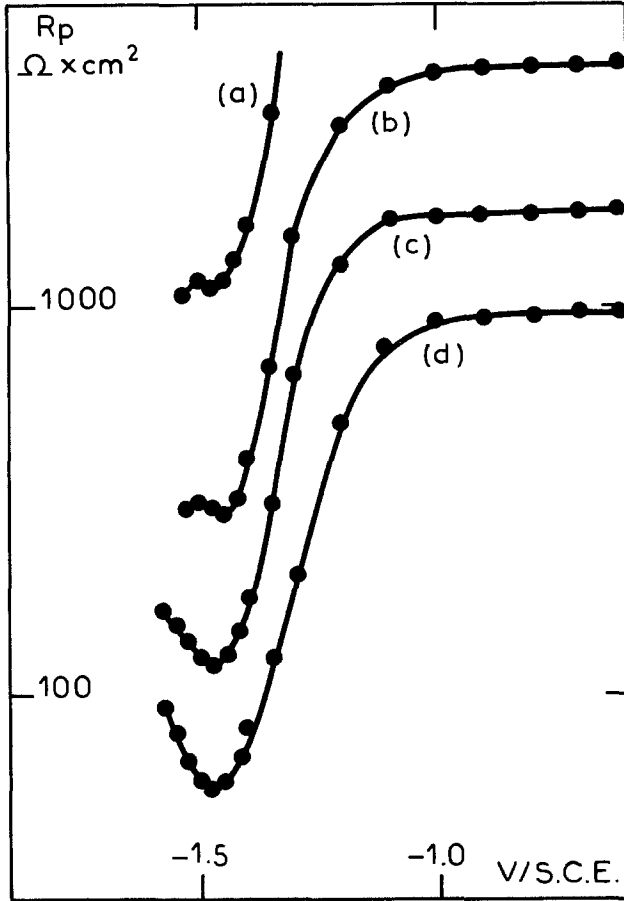


Fig. 8. Polarization resistance R_p vs. potential under various illuminations of an n-GaAs/selenide junction. (a) 1.5 mW/cm², (b) 9 mW/cm², (c) 22 mW/cm², and (d) 50 mW/cm².

neglected. df/dt is given by

$$\frac{df}{dt} = R_c - R_v + R_s \quad [6]$$

From stationary conditions, $df/dt = 0$, one gets f and its derivative df/dV_b

$$f = \frac{k_s c_{\text{red}} + k_c n_s + k_v p_1}{k_s c_{\text{red}} + k_c (n_s + n_1) + k_v (p_s + p_1)} \quad [7]$$

$$\frac{df}{dV_b} = \frac{-k_v f (dp_s/dV_b) + k_c (1-f) (dn_s/dV_b)}{k_c (n_s + n_1) + k_v (p_s + p_1) + k_s c_{\text{red}}} \quad [8]$$

$p_s(V)$ and $n_s(V)$ are provided by I-V analysis, as pre-

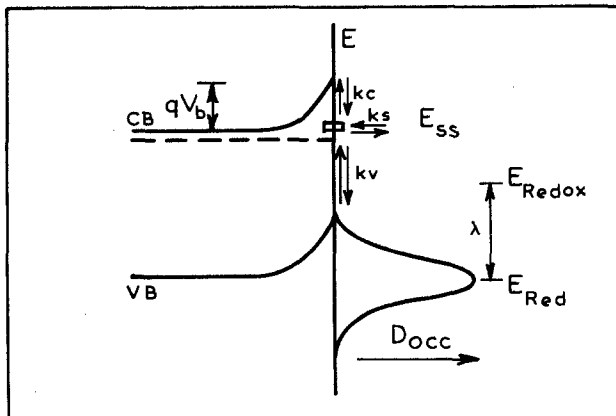


Fig. 9. Energy diagram of an n-type semiconductor/electrolyte interface and the various types of charge exchange mechanisms between a single state at E_{ss} with the conduction band (k_c), the valence band (k_v), and the solution (k_s). The density of the only occupied state in solution is represented for clarification.

sented elsewhere (3). On the other hand, k_s is supposed to follow the Marcus-Gerischer law

$$k_s = \sigma_s v (kT/\pi\lambda)^{1/2} \exp[-(E_{ss} - E_{\text{red}})^2/4\lambda kT] \quad [9]$$

where v is the thermal velocity for holes, and σ_s is the capture cross section of a hole trapped in the surface state by a reduced species. σ_s will be estimated later. Note that $k_s c_{\text{red}}$ remains constant with potential only if the band-edges of the semiconductor are fixed; otherwise the overlap $E_{ss} - E_{\text{red}}$ varies with potential. This possibility is accounted for in the following. Equation [6] allows defining a relaxation time τ_{ss} for f

$$\tau_{ss}(V) = [k_c(n_s + n_1) + k_s c_{\text{red}} + k_v(p_s + p_1)]^{-1} \quad [10]$$

Equations [7], [8], and [10] show that f , df/dV_b , and τ_{ss} are (i) functions of the state localization through p_1 and n_1 , (ii) functions of the applied potential through n_s and p_s , and (iii) functions of light intensity through p_s .

Knowing $k_v = \sigma_p v$ and $k_c = \sigma_n v$ ($v = 1.7 \times 10^7$ cm/s is the thermal velocity for holes and electrons), it is possible to estimate σ_p , σ_n , the capture cross sections for holes and electrons, and σ_s , from the measured relaxation time $\tau_{ss}(V)$. For small band bending, CB exchanges are predominant and τ_{ss} gives information about σ_n . However, at larger band bending, $n_s \ll p_s$ under illumination and $k_v p_s$ dominates in Eq. (10).

As a preliminary remark, assuming that illumination is not responsible for the surface state, it is obvious that if $k_s c_{\text{red}} \gg$ both $k_c n_s$ and $k_v p_s$, f remains equal to 1 at any bias (Eq. [7]). For such states, $C_{ss}(V) = 0$. This is the case if E_{ss} is taken close to E_v , the top of the valence band at the surface, because of a better overlap with the occupied states in solution. However, if E_{ss} is close to E_c , the bottom of the conduction band at the surface, the occupation rate f follows a kind of Fermi statistics; consequently, the surface state empties for sufficiently large bias, leading to a flatband-potential shift ΔV_{ss} independent of light intensity. Finally, if under illumination $k_s c_{\text{red}}$ is of the order of magnitude of $k_v p_s$, our results can be explained. For large enough band bending, f decreases with light intensity because p_s becomes larger; Δf and the associated band-edge shift ΔV_{ss} increase. Equation [8] shows that $C_{ss}(V)$ depends on dp_s/dV_b and dn_s/dV_b . By the hole-transfer current expression, one gets (3)

$$dp_s/dV_b = (dp_s/dV) (dV/dV_b) = (1/R_p^p) (p_s^0/J_p^0) (dV/dV_b) \quad [11]$$

with dV/dV_b given by Eq. [10]

$$dV/dV_b = (C_H + C_{sc} + C_{ss})/C_H \quad [12]$$

R_p^p is the polarization resistance associated with the only photocurrent; J_p^0 and p_s^0 are defined in Ref. (3). In Eq. [12], C_{sc} can be neglected ($C_{sc} \ll C_H$). Using $n_s = N_D \exp(-qV_b/kT)$, its differential, and combining Eq. [8]-[10], [12], and [2], $C_{ss}(V)$ reads

$$C_{ss} = qN_{ss}\tau_{ss} \frac{[k_v f (dp_s/dV) - k_c (1-f) (dn_s/dV_b)]}{1 - qN_{ss}\tau_{ss} k_v f (dp_s/dV_b)/C_H} \quad [13]$$

As a first approximation when $C_{ss} \ll C_H$, $dV/dV_b = 1$ and $C_{ss}(V)$ reduces to the numerator of Eq. [13], and it can be seen that $C_{ss}(V)$ is strongly correlated to $1/R_p^p$. Note that if the electron current may be neglected, $R_p^p = R_p$, the polarization resistance of the junction. Moreover, if the band bending is sufficient, $dn_s/dV_b \ll dp_s/dV$ and $C_{ss}(V)$ is proportional to R_p^{-1} . This fact partly explains the shape of the $C_{ss}(V)$ curves and their evolution with light intensity because it is well known that R_p decreases with increasing photon flux (Fig. 8). When C_{ss} and C_H have the same order of magnitude, the correlation $R_p^{-1} - C_{ss}$ is less evident. The denominator tends approximately to enhance the peak of C_{ss} for given parameters.

As a first conclusion from this model, it appears that the behavior of a single surface state, for given capture cross sections, depends on its location in the gap. This

also shows that only one relation time τ_{ss} at any bias corresponds to a single state.

If a surface-state distribution is considered, Eq. [1-5] have to be integrated vs. E_{ss} , Eq. [6-10] describing the behavior of an elementary state located at E_{ss} with a density $N_{ss}(E_{ss})dE_{ss}$. Each elementary state gives rise to an elementary surface-state capacitance $dC_{ss}(V, E_{ss})$ that has to be integrated to get the whole capacitance $C_{ss}(V)$ associated with the whole distribution (8, 9). Moreover, at a given potential, it becomes obvious that each elementary state has its own time constant $\tau_{ss}(V, E_{ss})$. This shows that in such a case, several time constants, $R_{ss}C_{ss}$ have to be found by impedance measurements. As stated in the experimental section, the calculated $\tau_{ss}(V)$ is defined as the weighted mean of elementary $\tau_{ss}(V, E_{ss})$, with respect to their associated $dC_{ss}(V, E_{ss})$.

Discussion

Surface-state capacitance $C_{ss}(V)$ results allow us to calculate the effective band bending of the semiconductor at any potential, for a given C_H . It appears that the $C_{ss}(V)$ data only cover the region $E_c - 0.1$ eV to $E_c - 1.3$ eV and that the surface-charge variation associated with the $C_{ss}(V)$ peak is too small to yield a band-edge shift ΔV_{ss} of the order of ΔV_{FB} , ΔV_{ss} being calculated by means of Eq. [12].

Analysis of the I-V characteristics gives $p_s(V)$ (3). Then we calculate $C_{ss}(V)$, $\tau_{ss}(V)$, and $f(V)$, thanks to our model, and we compare them to the experimental data. The only adjustable parameters are k_c , k_v , and σ_s ; all the others are determined through experiments. These three simultaneous constraints allow one to obtain reasonable values for the k constants and σ_s . In the case of a single surface state, calculations, show that σ_s has a greater effect upon Δf than upon C_{ss} ; the opposite is true for k_c and k_v . At first, relative values of k_c , k_v , and k_s are obtained by fitting $C_{ss}(V)$ and ΔV_{ss} . Then, to obtain their final values, it is sufficient to adjust $\tau_{ss}(V)$ by multiplying the three parameters by the same factor (Eq. [10]). By doing this, $f(V)$ and $C_{ss}(V)$ are not changed (Eq. [7] and [13]). The following discussion is based upon results concerning the n-GaAs/selenide junction, but the same model would apply to other experimental results with different aqueous electrolytes.

Single surface-state hypothesis.—Simulations based on such a simple hypothesis show that it is possible to fit our experimental results, but without obvious physical significance. If we try to obtain the best agreement for each illumination, it appears that, with increasing light intensity, (i) the state moves up in the gap from $E_c - 0.3$ to $E_c - 0.15$ eV, (ii) the state empties completely for even large $\sigma_s(10^{-14} \text{ cm}^{-2})$, and (iii) the density N_{ss} increases from 7.10^{10} to $2.6 \times 10^{12} \text{ cm}^{-2}$, whereas the capture cross sections σ_n , σ_p , σ_s remain unchanged ($\sim 5 \times 10^{-17} \text{ cm}^2$).

However, these simulations are interesting evidence of the influence of some parameters. It is confirmed that for given cross sections, a state empties less and less as it goes down in the gap, and correlatively, the $C_{ss}(V)$ peak vanishes (Fig. 10a). Moreover, the relaxation time τ_{ss} depends on the electron occupancy. The unusual experimental peak in τ_{ss} vs. V (Fig. 10b) can be explained as follows. For potentials cathodic of -1.60 V/SCE, τ_{ss} increases with the applied potential because of decreasing $n_s = N_D \exp -qV_b/kT$ ($n_s \gg p_s$ in Eq. [10] in such a case). Under illumination, p_s and n_s have the same order of magnitude as soon as $V = -1.60$ V/SCE, and then $p_s \gg n_s$ for more positive potentials. Consequently τ_{ss} begins to decrease if $V > -1.60$ V/SCE (Eq. [10]). Figure 10b also shows that τ_{ss} is much smaller when f remains constant than when f undergoes variations. A factor of ~ 50 exists between the two situations. The latter point means physically that the smaller the surface-charge variation, the shorter the rearrangement. If the state is sufficiently high in the bandgap, it is empty ($f = 0$) at equilibrium. So, even in the dark, when the band bending becomes small enough, the state is fully or partly occupied by electrons. This could explain the slight deviation of the Mott-Schottky plot in

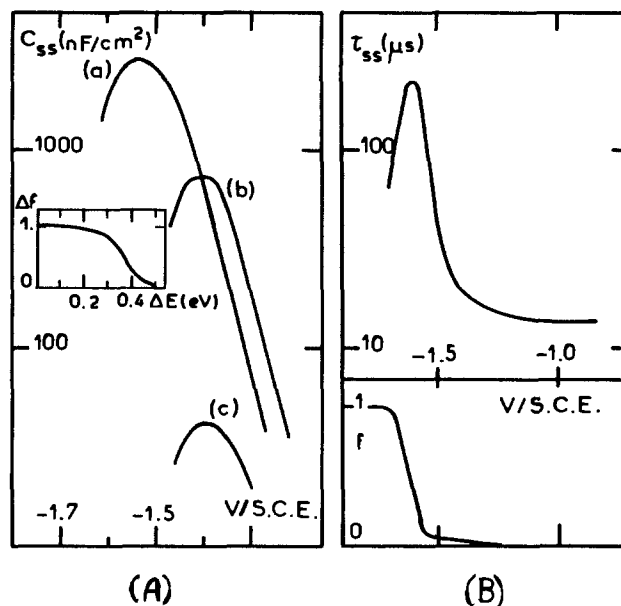


Fig. 10. (A) Evolution of the calculated $C_{ss}(V)$ curve associated with a single surface state, when E_{ss} moves down in the gap: $\Delta E = E_c - E_{ss} = 0.3$ eV (a), 0.4 eV (b), and 0.5 eV (c). In the insert, the corresponding Δf is figured (Δf is the maximum variation of f for a large potential excursion). (B) Calculated $\tau_{ss}(V)$ and $f(V)$ associated with the curve (a) of (A).

the dark for cathodic potentials (Fig. 2b, curve e). Thus, in that case, the shift ΔV_{FB} between illumination and dark conditions cannot be accounted for, even partially, by such a mechanism. On the other hand, if the surface state is close to the valence band, it never empties except for $\sigma_s = 0$. Only in this case could ΔV_{FB} be explained.

Case of a surface-state distribution.—It seems that a single state is too simple an assumption to account for all our capacitance results and, particularly, the light intensity dependence of the peak height. A better description is possible if a surface-state distribution is considered. In this case, each elementary state [density $N_{ss}(E_{ss})dE_{ss}$, energy E_{ss}] of the distribution behaves as a single state, with the same density and energy. This behavior has been discussed above. The increase of N_{ss} with light intensity is physically understood as a surface-state distribution which empties more and more. When the photon flux becomes larger, states located higher in the gap empty earlier. This simply means that for a given surface hole concentration p_s , the required band bending is smaller for a greater light intensity. In this way we explain the increase in the area of the peak in C_{ss} capacitance, which represents the associated surface-charge variation. In the same way, the sharp increase of the surface hole concentration, for potentials close to -1.6 V/SCE, promotes a strong surface-charge variation responsible for the peak existence. Moreover, the greater the illumination, the greater dp_s/dV_b and, correlatively, the peak height increases. In the dark, these states also empty for large enough band bending. However, the much slower variation of p_s in such conditions does not allow observing a peak (Fig. 6). At last, although the peak moves in the bandgap, it remains at almost the same potential in the SCE scale because of the band-edge shift.

The peak magnitude accounts then for the way the surface-state distribution loses its negative charges or traps holes. It does not account for the flatband-potential shift ΔV_{FB} under illumination as it would have been expected to. As a final remark about these simulations, it is worth noting that the solution is not unique. Quite different constant surface-state distributions (N_{ss} density, ΔE width) may give the same result for a given illumination, provided σ_s is changed. However, the simulations we present are performed for a distribution with a constant density $N_{ss} = 1.05 \times 10^{13} \text{ cm}^{-2} \text{ eV}^{-1}$ which extends between $E_c - 0.2$ eV and $E_c - 0.4$ eV. This distribution is

found to be one of the best choices for keeping σ_n , σ_p , and σ_s almost constant when illumination is changed (Fig. 11). Values of $\sim 3.10^{-16}$ cm and 5.10^{-17} cm² are found for σ_p and σ_n , while σ_s can take values in the range of 10^{-16} to 10^{-15} cm² (Fig. 7 and 11). Such values lead to negligible currents through this state distribution. The deviation of the theoretical $\tau_{ss}(V)$ curve from the experimental one for anodic potentials may come from a rough C_{ss} determination in this region (Fig. 7). C_{ss} is very small compared to C_{sc} for potential $V > -1.3$ V/SCE ($C_{ss} < 0.1 C_{sc}$).

Flatband potential shift.—As a consequence of our model, it appears that the band-edge shift under illumination cannot be accounted for by the mechanism we discussed above. This shift has to be related to other mechanisms, such as chemical surface reactions involving surface intermediates. It is the case for the dependence of the flatband potential on pH (12, 13) and on redox concentration (14, 15). Surface modification may also be the result of oxide or hydroxide intermediate formation (2), such as As_2O_3 on n-GaAs (16, 17). If we consider a surface reaction involving surface agent and holes, our experimental result concerning ΔV_{FB} might be explained. In the dark, this chemical equilibrium presents stationary conditions which are fixed by the small surface hole concentration. As soon as the electrode is illuminated, the large

amount of photogenerated holes disturbs this “equilibrium,” leading to new stationary conditions. One can imagine, for example, a transient modification of the surface at the very time when the electrode is illuminated. At the same time, electrical charges may be transferred from the surface to solution or be trapped at the surface, leading to a light dependent change of the Helmholtz potential drop. In fact, there exists a non-negligible time constant (a few seconds) for obtaining a stationary photocurrent when illumination is put on. The variations of ΔV_{FB} with the photon flux show that this modification becomes effective for low light intensities (~ 1.2 mW/cm²). Because the band-edge shift is positive, the surface-charge variation must be positive. For example, the surface may gain holes. Furthermore, as mentioned earlier (3), this shift is reversible. This means that the flatband potential returns to its initial value in the dark, when light is cut off. This fact indicates that the surface reaction is reversible and that *in situ* experiments have to be performed to identify these surface modifications. Note that a shift of $\Delta V_{FB} = 0.20$ V is promoted by only trapping 3.5×10^{12} cm⁻² charges at the surface ($C_H = 2.8$ μ F/cm²). This means that one surface atom out of about three hundred is involved in such a mechanism. We know that the n-GaAs/selenide PEC cell is almost completely stabilized (18), but it is not unreasonable to think that the shift ΔV_{FB} is linked to steps of the photocorrosion process as it was described by Tsubomura *et al.* (2). Similar results exist in various aqueous electrolytes, especially in 1M KOH (19).

Conclusion

From simultaneous I-V and impedance experiments upon n-GaAs/aqueous electrolyte junctions, we proposed a model for mechanisms that take place at the interface. Particularly, impedance measurements showed that two types of surface states have to be considered (i) slow surface states which promote surface-charge variations independent of the potential and due to chemical transformations of the surface because of photogenerated holes. These states are responsible for the flatband-potential shift ΔV_{FB} . (ii) fast surface states which exchange charges with the semiconductor bands and the solution. These charge variations account for the differential capacitance $C_{ss}(V)$ and modify the potential distribution through the junction in the photocurrent rise region.

According to our analysis, the band-edge shift under illumination cannot be induced by surface-charge variations of the second type. This result differs from the one of Kelly and Memming, who attributed the whole shift to the charge variation in a single state close to the midgap region. We believe that the strong variation of the surface charge with potential, according to the mechanism they considered, would completely block the band bending for potential close to -1.6 V/SCE. In that case, a plateau in the photocurrent rise would appear. This is not experimentally observed. Finally, the surface-state distribution we find reinforces the assumption of a direct hole-transfer current to solution via the valence band, as it was assumed by others (20). It appears that the working conditions of the illuminated junction are the consequences of one or several surface modification processes via holes.

Acknowledgments

The authors thank Dr. J. N. Chazalviel (Laboratoire PMC, Ecole Polytechnique, 91128 Palaiseau, France) for very useful discussions. This work was supported by the GRECO 130061 of CNRS.

Manuscript submitted Dec. 29, 1983; revised manuscript received Aug. 14, 1984.

CNRS assisted in meeting the publication costs of this article.

REFERENCES

1. J. J. Kelly and R. Memming, *This Journal*, **129**, 730 (1982).

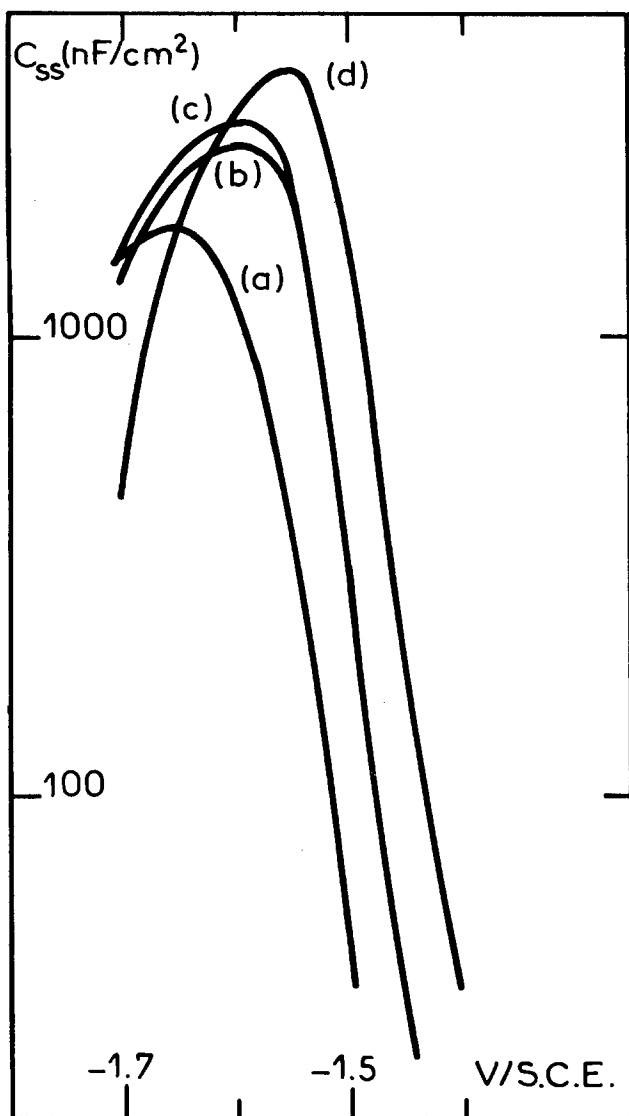


Fig. 11. Calculated $C_{ss}(V)$ curves under various illuminations. The surface-state distribution has a density $N_{ss} = 1.05 \times 10^{13}$ cm⁻² eV⁻¹ between $E_c - 0.2$ eV and $E_c - 0.4$ eV. $\sigma_s = 10^{-15}$ cm². (a) 1.5 mW/cm²; $\sigma_n = 1.5 \cdot 10^{-16}$ cm²; $\sigma_p = 3.10^{-16}$ cm². (b) 9 mW/cm²; $\sigma_n = 6.10^{-17}$ cm²; $\sigma_p = 3.10^{-16}$ cm². (c) 22 mW/cm²; $\sigma_n = 3.10^{-17}$ cm²; $\sigma_p = 4.10^{-16}$ cm². (d) 50 mW/cm²; $\sigma_n = 3.10^{-17}$ cm²; $\sigma_p = 3.10^{-16}$ cm².

2. Y. Nakato, A. Tsumura, and H. Tsubomura, *ibid.*, **127**, 1502 (1980).
3. P. Allongue, H. Cachet, and G. Horowitz, *ibid.*, **130**, 2352 (1983).
4. K. W. Frese, Jr., *ibid.*, **130**, 28 (1983).
5. C. Barret, Thesis, University of Paris-Sud, Orsay (1981); C. Barret and J. Massies, *J. Vac. Sci. Technol.*, **1**, 819 (1983).
6. J. N. Chazalviel, *This Journal*, **129**, 963 (1982).
7. A. Bourrasse, H. Cachet, G. Horowitz, and S. Le Crom, *Rev. Phys. Appl.*, **17**, 801 (1982).
8. E. H. Nicollian and A. Goetzberger, *Bell Syst. Tech. J.*, **46**, 1055 (1967).
9. L. M. Terman, *Solid-State Electron.*, **5**, 285 (1965).
10. K. W. Frese, Jr., and S. Roy Morrison, *This Journal*, **126**, 1235 (1979).
11. B. Wolf and W. Lorenz, *Electrochim. Acta*, **28**, 699 (1983).
12. H. Gerischer, in "Physical Chemistry," Vol. IXA, H. Eyring, D. Henderson, and W. Jost, Editors, Chap. 5, Academic Press, New York (1970).
13. W. P. Gomes and F. Cardon, in "Semiconductor Liquid Junction Solar Cells," A. Heller, Editor, p. 120, The Electrochemical Society Softbound Proceedings Series, Princeton, NJ (1977).
14. R. H. Wilson, *This Journal*, **126**, 1187 (1979).
15. L. F. Schneemeyer and B. Miller, *ibid.*, **129**, 1977 (1982).
16. H. Cachet, R. Calsou, M. Froment, and H. Mathlouthi, *J. Microsc. Spectrosc. Electron.*, **7**, 9 (1982).
17. P. Allongue, H. Cachet, and M. Froment, p. 719, Extended Abstracts of the 34th Meeting of the I.S.E., Erlangen, (RFA) (1983).
18. A. Heller and B. Miller, *Electrochim. Acta*, **25**, 29 (1980).
19. P. Allongue and H. Cachet, *This Journal*, **131**, 2861 (1984).
20. K. W. Frese, Jr., M. J. Madou, and S. R. Morrison, *J. Phys. Chem.*, **84**, 3172 (1980); *This Journal*, **128**, 1527 (1981).

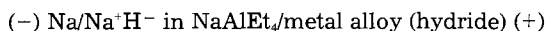
Electrochemical Investigation of Hydrogen Storage in Metal Hydrides

C. M. Luedecke, G. Deublein, and R. A. Huggins

Department of Materials Science and Engineering, Stanford University, Stanford, California 94305

ABSTRACT

A new technique has been developed to study and control hydrogen storage in solid metal hydrides. The formation of metal hydrides and their thermodynamic and kinetic properties have been investigated by electrochemical methods employing a low temperature molten salt galvanic cell of the type



The choice of the electrolyte is of great importance in this method. Besides having to be thermodynamically stable when in contact with the electrodes, it must conduct charge by transport of hydrogen containing species. For this purpose, the low temperature organometallic salt NaAlEt₄ (melting point 128°C) has been synthesized. It is saturated with NaH, the hydride ions of which act as hydrogen transmitters. This electrolyte has the additional advantage that its oxygen activity is extremely low, so that no oxide layers form which could block hydrogen reaction with the alloy and thus reduce its apparent capacity. It even cleans the surface of oxide layers which may have been present initially. This technique allows easier investigation of metal hydrides than the conventional pressure-temperature experiments and, in addition, avoids the main problems involved in using aqueous solution electrolytes, *i. e.*, the corrosion of the metal alloys and, especially, the formation of oxide or hydroxide layers. With the aid of this cell, charge/discharge experiments have been carried out and hydrogen has been added to and deleted from the hydride forming metal alloy systems Mg-Ni, Mg-Cu, and Mg-Al at 142° and 170°C. Equilibrium open-circuit voltage measurements provide information about the thermodynamic properties as a function of the overall composition of the electrode material. Thermodynamic data for the different metal hydride systems have been determined as a function of hydrogen content and interpreted in terms of the corresponding ternary phase diagrams (Mg-Ni-H, Mg-Cu-H, and Mg-Al-H, respectively). The Gibbs free energies corresponding to the various reactions of hydrogen with the binary metal alloys measured in this way have been found to be in good agreement with data determined by conventional pressure-temperature experiments. For the Gibbs free energy of formation of MgH₂, for instance, we find $\Delta G_f = -4.8$ kcal/mol at 142°C, whereas the data reported in literature range from -4.2 to -5.0 kcal/mol. The results are also in accordance with a model in which these systems are treated as ternaries rather than as pseudo-binary reactions. Using this new approach, the relevant three-phase triangles and two-phase tie lines of the ternary phase diagrams can be calculated from the Gibbs formation energies of the phases present in these systems. The hydrogen capacities in these several metal alloy systems are also readily interpreted in terms of the phase boundaries of the corresponding three-phase equilibria.

Hydrogen is being looked upon as an ideal energy carrier: it is nonpolluting, light weight, relatively inexpensive, and readily available because it can be produced from water. However, there are a number of problems to be solved, one of them being the storage of hydrogen.

One approach to this is the use of solid metal hydrides, in which the density of hydrogen per unit volume can be greater than in either liquid or gaseous hydrogen, even under quite high pressures. Therefore, metal hydrides are often discussed as potentially useful hydrogen storage media (1-4). They are mostly intermetallic compounds which are generally thought to reversibly absorb hydrogen at convenient temperatures and pressures according to a reaction of the type



where Me is the metal or alloy and MeH_x is its hydride.

Many investigations concerning the formation of metal hydrides have been done by absorption experiments in which hydrogen from the gas phase reacts with solid alloys (1, 2, 5-7). Pressure and temperature are generally the controlling parameters. However, another possible way to investigate metal hydrides is by means of electrochemical methods. According to the Nernst equation, the hydrogen activity or pressure p_{H_2} at the interface between the electrolyte and the solid hydride electrode can be controlled by the electrochemical potential if a suitable electrolyte and cell configuration can be found. Thus, control of the cell voltage E should cause the metal hydride to either absorb or desorb hydrogen.

$$\Delta E = RT/zF \ln p_{\text{H}_2}$$

(R = gas constant, F = Faraday's constant). Therefore, measurements can be done under isothermal conditions

by applying an electrical potential, rather than changing the pressure and/or the temperature.

There are several advantages the electrochemical technique has over the traditional methods. First, as there is no temperature change necessary for adsorption or desorption, the hydrogen activity at the surface of the metal hydride can be changed very rapidly. Second, large variations in hydrogen activity can be attained by relatively small differences in the cell voltage so that the effective pressure can be changed easily over several orders of magnitude, a feature that is not normally possible using the conventional pressure-temperature methods.

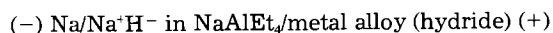
However, in spite of these potential advantages, only a few electrochemical investigations of hydride systems have been done thus far (8-10). The reason for this seems to be that aqueous electrolytes have been used. These electrolytes poison the metal hydrides by forming oxide layers on the surface and give rise to a loss of capacity and poor cycling properties. This drawback can be avoided by using nonaqueous electrolytes. In this work, NaH dissolved in a low temperature molten salt is used as the electrolyte. The hydrogen transmitting species in this case are not H^+ ions, but H^- ions.

In addition to this new experimental method, we propose a new theoretical approach to the interpretation of the formation of hydrides from binary metallic alloys, namely, treating them as ternary systems instead of as pseudobinary reactions, as is generally done in the literature, and describing them by means of ternary thermodynamics and phase diagrams. The plateau voltages, or hydrogen pressures, thus correspond to regimes of three-phase equilibria, and the widths of these regions correspond to the lengths of the plateaus and, therefore, the hydrogen capacity of different alloys.

This experimental method and theoretical approach have been applied to three systems: Mg-Ni-H, Mg-Cu-H, and Mg-Al-H. They serve as models to simultaneously test the experimental technique and theoretical interpretation. They are also possible reversible hydrogen storage materials themselves.

Experiments

The electrochemical investigations of the ternary Mg-based alloys were carried out using galvanic cells of the type



The experiments were performed at 142° and 170°C under high purity helium gas in a controlled atmosphere glove box.

An important feature of this cell is the use of a hydride ion conducting nonaqueous electrolyte. The low temperature organometallic salt $NaAlEt_4$ was used as a solvent and saturated with NaH. The $NaAlEt_4$ was synthesized by direct reaction of $AlEt_3$ with Na at 130°-140°C in a glove box.

Elemental sodium is stable in $NaAlEt_4$ and can be used as the reference/counterelectrode (11). This solvent is also stable in the presence of up to 1 atm H_2 . NaH, which has a dissociation voltage of 246 mV at 142°C (12), is soluble in it, and the hydride ions serve as hydrogen carriers.

The sample to be hydrided was used as the working electrode. Several metal alloys were investigated: $Mg_{2.35}Ni$ (99.9 weight percent [w/o], Hy-Stor Alloy 301, Ergenics); $Mg_{2.08}Cu$ (99.6 w/o, Hy-Stor Alloy 302, Ergenics); and Mg-Al alloys of the nominal concentrations Mg_3Al , $MgAl$, and $MgAl_4$. The Mg-Al alloys were prepared by melting the metals in the proper amounts in a small molybdenum bucket. The hydride forming alloys were crushed and ground to fine powder in a porcelain mortar and pestle. The powder was then cold pressed into thin pellets. These were held and electrically connected by means of ribbons of molybdenum which do not show any solubility for hydrogen (13, 14). This whole process was done in a high purity He atmosphere.

This type of hydride electrode proved to be very successful. It provided a high surface area, and while extensive studies of cycling behavior were not undertaken, such electrodes did not show any obvious degradation as a result of a number of hydriding/dehydriding experiments. The thermodynamic results remained consistent during repeated cycling.

The counter and reference electrodes consisted of commercially pure Na. At the temperatures present, it was liquid and was therefore kept in a U-shaped quartz tube. The electrical contact to the Na was provided by a ribbon of molybdenum, which shows good compatibility with Na under these conditions.

The electrochemical experiments involved passing constant currents of about 100 μA through the cell. By this means, hydrogen was added to, as well as deleted from, the hydride forming alloys. Potentials, currents, and charges were measured and controlled by means of a potentiostat/galvanostat (PAR, Model 173) and a digital coulometer (PAR, Model 179). A multimeter and a chart recorder helped with monitoring the data.

Results

With the galvanic cell described above, electrochemical measurements have been done on $Mg_{2.35}Ni$, $Mg_{2.08}Cu$, and three Mg-Al alloys of nominal concentrations Mg_3Al , $MgAl$, and $MgAl_4$ at 142° and 170°C. According to the binary phase diagrams (13-15), these alloys are mixtures of the phases Mg and Mg_2Ni , Mg and Mg_2Cu , Mg and Mg_5Al_4 , Mg_3Al_4 and Mg_2Al_3 , and Mg_2Al_3 and Al, respectively.

Because the potentials are measured with respect to the reference electrode, the EMF of which is determined by the Na/NaH equilibrium, the dissociation voltage of NaH has to be taken into account to convert the cell voltage to the voltage vs. 1 atm H_2 . This is done using the tabulated data (12).

As mentioned above, the starting alloys consist of two phases. By adding hydrogen, a three-phase equilibrium is established so that, according to the Gibbs phase rule, the hydriding reactions should give constant cell voltages. Only if a two-phase tie line is crossed and another triangle entered will the voltage change to a new fixed value. The electrical potentials which have been measured in three-phase equilibria are listed in Table I. They are given vs. Na/NaH and vs. 1 atm H_2 . The hydrogen activities and Gibbs free energies of the reactions calculated from these data are included in the table as well. The EMF spans

Table I. Electrochemical data for various three-phase reactions in the ternary magnesium alloy hydride systems Mg-Ni-H, Mg-Cu-H, and Mg-Al-H, as measured at 142°C. E = equilibrium open-circuit cell voltage; a_{H_2} = hydrogen activity = hydrogen pressure (atm); ΔG = Gibbs free energy of the corresponding reaction

System	Three-phase equilibrium	E [mV] vs. Na/NaH	E [mV] vs. 1 atm H_2	a_{H_2}	ΔG [kcal/mol H_2]
Mg-Ni-H	Mg_2Ni -Mg- MgH_2	140	107	2.4×10^{-3}	-4.9
	Mg_2Ni - MgH_2 - Mg_2NiH_4	168	79	1.1×10^{-2}	-3.7
Mg-Cu-H	Mg_2Cu -Mg- MgH_2	145	102	3.2×10^{-3}	-4.7
	Mg_2Cu - $MgCu_2$ - MgH_2	181	66	2.4×10^{-2}	-3.1
Mg-Al-H	Mg_3Al_4 -Mg- MgH_2	142	105	2.7×10^{-3}	-4.8
	Mg_2Al_3 - Mg_3Al_4 - MgH_2	166	81	1.1×10^{-2}	-3.7
	Al- Mg_2Al_3 - MgH_2	180	67	2.3×10^{-2}	-3.1

from about 140 to 181 mV vs. Na/NaH or from about 107 to 67 mV vs. 1 atm H_2 . Accordingly, the hydrogen activity or pressure changed by about one order of magnitude, from 2.4×10^{-3} to 2.3×10^{-2} . The lower values in all three cases correspond to the formation of MgH_2 , which these systems have in common.

These data can be interpreted in terms of Gibbs triangles. Figures 1-3 show the isothermal sections of the corresponding ternary phase diagrams valid for temperatures in the range 140° to 170°C. The initial compositions of the various alloys are marked by arrows, and the paths of overall concentrations during the addition or deletion of hydrogen are indicated by dotted lines.

Whereas Mg_2Ni forms a stable ternary hydride, namely, Mg_2NiH_4 , the phase diagrams of the systems Mg-Cu-H and Mg-Al-H do not exhibit any ternary hydride compounds. Instead, these alloys react during the uptake of hydrogen to form MgH_2 and an intermetallic compound less rich in Mg than the initial alloys. However, in all three systems, the addition of hydrogen to the magnesium-rich two-phase alloy causes MgH_2 to be formed until

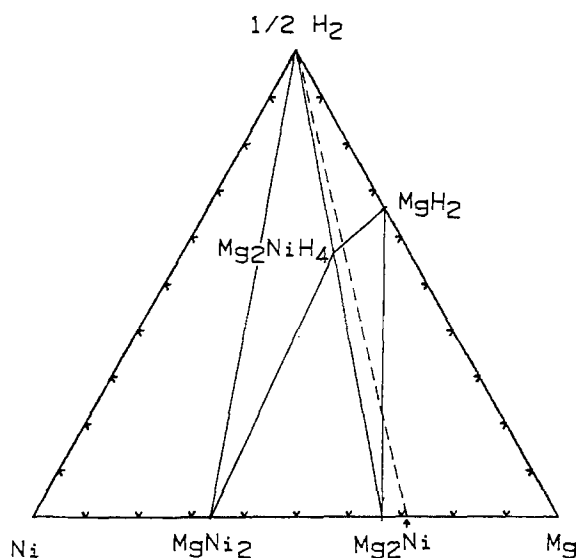


Fig. 1. Ternary phase diagram of Mg-Ni-H valid for the temperature range 140°-170°C. The arrow shows the initial concentration of the alloy, and the dotted line shows the concentration change during the hydriding experiment.

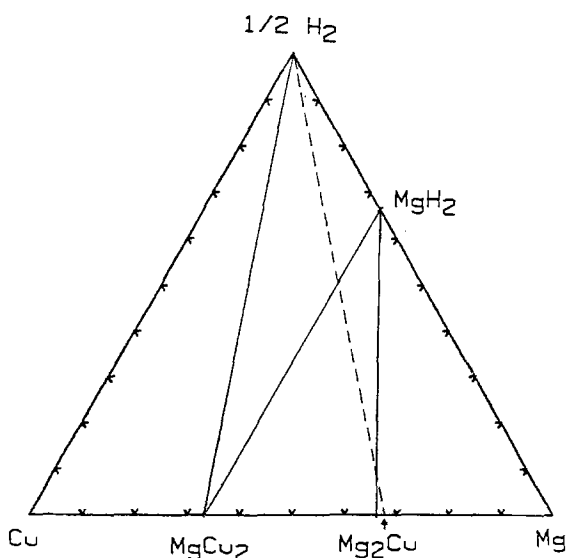


Fig. 2. Ternary phase diagram of Mg-Cu-H valid for the temperature range 140°-170°C. The arrow shows the initial concentration of the alloy, and the dotted line shows the concentration change during the hydriding experiment.

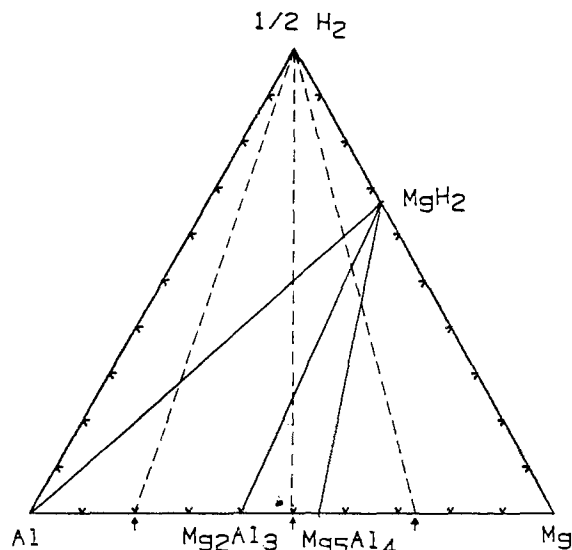


Fig. 3. Ternary phase diagram of Mg-Al-H valid for the temperature range 140°-170°C. The arrows show the initial concentrations of the alloys, and the dotted lines show the concentration changes during the hydriding experiments.

the boundary of the neighboring three-phase equilibrium is reached.

For $Mg_{2.35}Ni$ and $Mg_{2.08}Cu$, the voltages of the second plateaus neighboring the triangle in which MgH_2 is formed have been measured at both 142° and 170°C. The results are given in Table II, which also includes data from the literature (16-18) for comparison. It is seen that these values, as well as their small temperature dependence, are in good agreement.

Discussion

The reaction of hydrogen with binary alloys Mg-Ni, Mg-Cu, and Mg-Al has been studied by use of electrochemical techniques. The results of this approach will be compared to data (available in the literature) obtained by conventional pressure-temperature experiments. They will also be related to thermodynamic calculations based on the corresponding binary phase diagrams.

As the ternary phase diagrams (Fig. 1-3) show, the magnesium-rich two-phase alloys of all three systems will first form MgH_2 during hydrogenation. The plateau voltage and Gibbs free energy change of these reactions correspond to the formation of MgH_2 from elemental Mg according to $Mg + H_2 \rightarrow MgH_2$ [1]. The values obtained are -4.9, -4.7, and -4.8 kcal/mol, from measurements on the Mg-Ni-H, Mg-Cu-H, and Mg-Al-H systems, respectively, at 140°C. The differences between these values are well within experimental error.

The literature contains a number of values for the thermodynamic parameters of this reaction, obtained from experiments performed by the use of conventional methods. These are shown in Table III. It is seen that the enthalpy of formation is about -18 kcal/mol H_2 , and the entropy change is about -33 cal/K mol H_2 (corresponding to the disappearance of 1 mol of gas). The values of the Gibbs free energy of formation of MgH_2 at 140°C range from -4.2 to -5.0 kcal/mol, with an average of -4.6

Table II. Equilibrium potentials in the systems Mg-Ni-H and Mg-Cu-H at 142° and 170°C. The voltages are given vs. the Na/NaH reference electrode. They are compared to data reported in the literature (16-18)

Temperature	Three-phase equilibrium			
	Mg ₂ Ni-MgH ₂ -Mg ₂ NiH ₄ Measured (mV)	Mg ₂ NiH ₄ -Mg ₂ Ni Literature (mV)	Mg ₂ Cu-MgCu ₂ -MgH ₂ Measured (mV)	MgH ₂ -Mg Literature (mV)
142°C	168	177	181	175
170°C	165	171	176	172

Table III. Thermodynamic data for the formation of MgH₂ obtained by the use of conventional methods (T = 142°C)

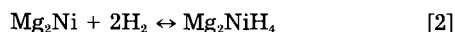
ΔH [kcal/mol H ₂]	ΔS [cal/K mol H ₂]	ΔG [kcal/mol H ₂]	Ref.
-18.7	-34.9	-4.2	19
-16.7	-30.1	-4.2	20, 21
-18.7	—	—	22
-17.5	—	—	23
-18.4	—	—	24
-18.6	-32.7	-5.0	12
-18.5	-33.0	-4.8	16
-18.7	-33.4	-4.8	18
-17.8	-32.3	-4.4	25

kcal/mol. We see that the values obtained from the experiments reported here fall well inside this range.

Discussion of the results of each of the three ternary systems follows.

Mg-Ni-H.—Interpreting the hydrogenation of binary alloys in terms of ternary phase diagrams makes possible calculating the thermodynamic data related to various ternary equilibria from data on the corresponding binary systems (13-15), in this case Mg-H, Mg-Ni, and Ni-H. Mg has a very small solubility for hydrogen [< 0.1 atom percent (a/o)] and forms only one binary compound, MgH₂, the Gibbs free energy of formation of which is about -4.6 kcal/mol at 140°C (cf. Table III). Ni and Mg have a very small solubility for each other as well (< 0.1 a/o) and form two intermediate phases, MgNi₂ and Mg₂Ni, both having narrow ranges of stoichiometry (13-15). Their Gibbs free energies of formation at 140°C are about -13 kcal/mol and -10 kcal/mol, respectively (12, 26). Ni has only negligible solubility for hydrogen ($\leq 10^{-4}$ a/o) (13), and the binary compounds are either not confirmed (NiH₄ and NiH₂) or they decompose (NiH) (15). Mg, Ni, and H form only one ternary phase, Mg₂NiH₄. Its Gibbs free energy of formation is -16.6 kcal/mol at 140°C (27). Calculations based on these data confirm the ternary phase diagram presented in Fig. 1.

From the phase diagram in Fig. 1, we can see that hydrogenation of an alloy with initial composition Mg_{2.35}Ni causes MgH₂ to form (the amount of Mg will decrease) until the overall concentration crosses the MgH₂-Mg₂Ni tie line. Thereafter, the intermetallic compound Mg₂NiH₄ begins to form, and the Mg₂Ni gradually disappears. The equilibrium voltage steps from one plateau to another. The first plateau represents the Mg-Mg₂Ni-MgH₂ triangle, which has the same thermodynamic properties as the equilibria along its edges. One of these is the Mg-MgH₂ equilibrium, which can be related to the Gibbs free energy of formation of MgH₂ from Mg and H₂. The second plateau corresponds to the Mg₂Ni-MgH₂-Mg₂NiH₄ triangle, whose thermodynamic properties correspond to the reaction



because both Mg₂Ni and Mg₂NiH₄ are at its corners. These two plateau voltages give the Gibbs free energies of the corresponding reactions to be -4.9 and -3.7 kcal/mol H₂. These results are in good agreement with data gained by conventional methods mentioned earlier for Reaction [1], as well as those listed in Table IV for Reaction [2]. The effect of temperature on the thermodynamic data of Reaction [2] is very small and is in accordance with the literature as well, as is shown in Table II.

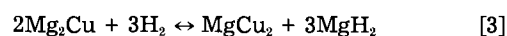
Mg-Cu-H.—The thermodynamic parameters of this system have been determined from the data of the corresponding binary phase diagrams.

Mg and Cu have a negligibly small solubility in each other. They form two intermetallic compounds, MgCu₂ and Mg₂Cu; MgCu₂ has compositional ranges of the order of 1 a/o, whereas Mg₂Cu has a very narrow range of stoichiometry (13). Their Gibbs free energies of formation are either -8.2 and -6.3 kcal/mol (26) or -8.49 and -6.75 kcal/mol (28). The solubility of hydrogen in Cu is less than 10^{-4} a/o, and no hydride phases are formed (13-15).

Table IV. Thermodynamic data for the formation of Mg₂NiH₄ measured with conventional methods (T = 142°C)

ΔH [kcal/mol H ₂]	ΔS [cal/K mol H ₂]	ΔG [kcal/mol H ₂]	Ref.
-15.2	—	—	22
-15.0	—	—	29
-15.0	-28.5	-3.2	17
-15.4	-29.2	-3.3	16

From the information on the three binary systems and the assumption that no ternary phases exist (the literature does not indicate the existence of any, and it will be seen later that this assumption is confirmed by measurements), the ternary phase diagram has been determined. It is shown in Fig. 2. The phase diagram shows that during the hydrogenation of an alloy with initial composition Mg_{2.08}Cu, two tie triangles are crossed by the overall composition. The first one represents the formation of MgH₂ according to Reaction [1]; the second one corresponds to the reaction of Mg₂Cu with hydrogen according to

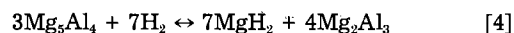


The Gibbs free energies of these reactions have been found from the electrochemical experiments to be -4.7 and -3.1 kcal/mol H₂, respectively.

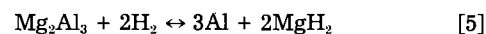
These data are in very good agreement with data measured by use of *p-T* methods, being -4.6 kcal/mol H₂ in the first case, as mentioned earlier, and -3.3 kcal/mol H₂ ($\Delta H = -17.4$ kcal/mol H₂; $\Delta S = -34.0$ kcal/mol H₂) (18) for the second, respectively. The measured change of the Gibbs free energy of reaction [3] with temperature is again small, in accordance with the literature (Table II).

For reaction [3], the thermodynamic data of the binary compounds available in the literature lead to -3.1 kcal/mol H₂ (26) and -3.9 kcal/mol H₂ (28), which are also in good agreement with the experiments.

Mg-Al-H.—The literature does not give precise enough data, for the Gibbs free energies of formation of the binary Mg-Al alloys, to allow the accurate calculation of the Gibbs free energies of the three-phase reactions in the resulting ternary diagram. However, the phase diagrams of the binary systems are known, so the ternary phase diagram can be mapped out. Mg and Al are both soluble up to 2 a/o in each other and form two intermetallic compounds, Mg₂Al₃ (38-40 a/o Mg) and Mg₅Al₄ (53-60 a/o Mg). Al does not form any hydride phase stable at the temperatures present (12), and it dissolves less than 10^{-6} a/o hydrogen (13, 14). The resulting ternary phase diagram is shown in Fig. 3. This diagram exhibits three triangles which do not contain elemental hydrogen. The thermodynamic parameters of the first, whose corners are at Mg₅Al₄, Mg, and MgH₂, correspond to the formation of MgH₂. The second and third involve the reactions



and



The Gibbs free energy changes resulting from all three reactions have been found from the electrochemical measurements reported here to be

$$-4.8 \text{ kcal/mol H}_2 \text{ for Reaction [1]}$$

$$-3.7 \text{ kcal/mol H}_2 \text{ for Reaction [4]}$$

$$-3.1 \text{ kcal/mol H}_2 \text{ for Reaction [5]}$$

The value for Reaction [1], which corresponds to the Gibbs free energy of formation of MgH₂, is in good accordance with values in the literature for this reaction, as mentioned earlier. There are no available data for Reaction [4]. In the case of Reaction [5], $\Delta H = -16.4$ kcal/mol

Table V. Gibbs free energy of various three-phase reactions in the ternary magnesium alloy hydride systems Mg-Ni-H, Mg-Cu-H, and Mg-Al-H at $T = 142^\circ\text{C}$. Comparison between data measured electrochemically (this work) and data measured with conventional pressure-temperature experiments (taken from literature)

System	Three-phase equilibrium	ΔG [kcal/mol] H_2		
		Electrochemical	p - T methods	Ref.
Mg-Ni-H	$\text{Mg}_2\text{Ni-Mg-MgH}_2$	-4.9	-4.6	^a
	$\text{Mg}_2\text{Ni-MgH}_2\text{-Mg}_2\text{NiH}_4$	-3.7	-3.3	(16, 17)
Mg-Cu-H	$\text{Mg}_2\text{Cu-Mg-MgH}_2$	-4.7	-4.6	^a
	$\text{Mg}_2\text{Cu-MgCu}_2\text{-MgH}_2$	-3.1	-3.3	(18, 27)
Mg-Al-H	$\text{Mg}_2\text{Al}_7\text{-Mg-MgH}_2$	-4.8	-4.6	^a
	$\text{Mg}_2\text{Al}_7\text{-Mg}_5\text{Al}_7\text{-MgH}_2$	-3.7	—	—
	$\text{Al-Mg}_2\text{Al}_3\text{-MgH}_2$	-3.1	-3.1	(2)

^a Weighted average of various measurements; discussion in text.

H_2 and $\Delta S = -31.9$ cal/K mol H_2 have been found (2), which gives ΔG $142^\circ\text{C} = -3.1$ kcal/mol H_2 , in excellent agreement with our own measurements.

Conclusions

An electrochemical technique has been developed to investigate metal hydrides. As has been pointed out, the choice of the electrolyte is important. In order to avoid the formation of oxides and hydroxides, a low melting organometallic salt of high ionic conductivity has been used, rather than an aqueous solution. In this case, the hydrogen containing species is the hydride anion, H^- . This method has several advantages over the use of the traditional pressure-temperature variables to control the formation of the various possible phases in these systems. Because the hydrogen activity is established by electrochemical means, it can be controlled with ease and high precision over wide ranges. For example, if a solution of NaH is used as the electrolyte, the range can be extended from well over 1 atm down to less than 10^{-5} atm. This span includes several metal alloy systems which are of interest for application as hydrogen storage materials.

In addition to this new experimental technique, a theoretical approach has been presented which interprets the formation of ternary metal hydrides in terms of ternary phase equilibria, rather than as pseudobinary reactions. This has been found to be very useful in explaining observed hydrogenation reactions, as well as in providing a framework for predicting them. In this interpretation, plateaus in traditional pressure-temperature experiments correspond to regimes of three-phase equilibria. The pressures of these plateaus can be directly calculated from the thermodynamic data of the phases present, by consideration of the ternary reactions predicted from the phase diagram. Furthermore, the compositional limits of the observed plateaus correspond to the compositions at which the overall composition crosses a two-phase tie line. Thus, the hydrogen capacity of the metal alloy can readily be read from the phase diagram, and the reactions taking place can readily be seen.

This experimental technique and this theoretical approach have until now been applied to the hydrogen storage alloy systems Mg-Ni, Mg-Cu, and Mg-Al. The measurements are in good agreement with the calculations and with the results of conventional pressure-temperature methods (Table V). With this concept, experimental as well as theoretical, it is possible to investigate several families of new potential hydrogen storage alloys and to design materials with appreciable capacities at desirable temperatures and hydrogen activities.

Acknowledgments

C. M. Luedecke gratefully acknowledges a grant from the Deutsche Akademische Austauschdienst (DAAD)

through a NATO scholarship, as well as assistance from the Fulbright Commission. Preliminary work was undertaken by R. A. Huggins while supported by Alexander von Humboldt Stiftung. A grant from INCO also provided partial financing. This program is now being supported under Contract no. 126597-S with the Brookhaven National Laboratory.

Manuscript submitted Jan. 13, 1984; revised manuscript received June 28, 1984.

Stanford University assisted in meeting the publication costs of this article.

REFERENCES

- J. J. Reilly, *Z. Phys. Chem.*, **117**, 155 (1979).
- R. Wiswall, "Topics in Applied Physics," Vol. 29, Chap. 5, p. 201, Springer Verlag, Berlin (1978).
- P. S. Rudman and G. D. Sandrock, in "Annual Review of Materials Science," Vol. 12, R. A. Huggins, Editor, p. 271, Annual Reviews, Inc., Palo Alto, CA (1982).
- H. Buchner, "Proceedings of the International Symposium on Hydrides for Energy Storage," Geilo, Norway, A. F. Andresen and A. J. Maeland, Editors, p. 569, Pergamon Press, London (1978).
- G. G. Libowitz, "The Solid State Chemistry of Binary Metal Hydrides," W. A. Benjamin, New York (1965).
- E. L. Huston and G. D. Sandrock, *J. Less-Common Met.*, **14**, 435 (1980).
- H. van Mal, K. H. J. Buschow, and A. R. Miedema, *ibid.*, **35**, 65 (1974).
- H. Ewe, E. W. Justi, and K. Stephan, *Energy Convers.*, **13**, 109 (1973).
- G. Bronoel, J. Sarradin, M. Bonnemay, A. Percheron, A. C. Achard, and L. Schlappbach, *Int. J. of Hydrogen Energy*, **1**, 251 (1976).
- H. F. Bittner and C. C. Badcock, *This Journal*, **130**, 193C (1983).
- G. Deublein and R. A. Huggins, In press.
- I. Barin, O. Knacke, and O. Kubaschewski, "Thermochemical Properties of Inorganic Substances," Springer Verlag, Berlin (1973, 77).
- M. Hansen and K. Anderko, "Constitution of Binary Alloys," McGraw-Hill, New York (1958).
- R. P. Elliott, "Constitution of Binary Alloys, First Supplement," McGraw-Hill, New York (1965).
- F. A. Shunk, "Constitution of Binary Alloys, Second Supplement," McGraw-Hill, New York (1969).
- J. J. Reilly and R. H. Wiswall, *Inorg. Chem.*, **7**, 2254 (1968).
- M. M. Lutz and O. DePous, *Proc. 2nd Int. Congr. on Hydrogen in Met.*, **1F5**, 1 (1978).
- J. J. Reilly and R. H. Wiswall, *Inorg. Chem.*, **6**, 2220 (1967).
- J. M. Boulet and N. Gerard, *J. Less-Common Met.*, **89**, 151 (1983).
- A. S. Pedersen, J. Kjoeller, B. Larsen, and B. Vigeholm, *Int. J. of Hydrogen Energy*, **8**, 205 (1983).
- B. Vigeholm, J. Kjoeller, B. Larsen, and A. S. Pedersen, *J. Less-Common Met.*, **89**, 135 (1983).
- E. Akiba, K. Nomura, S. Ono, and Y. Mizuor, *ibid.*, **83**, L43 (1982).
- H. Hbika, Ph.D. Thesis, Bordeaux, France (1979).
- B. Tanguy, J. L. Soubeyroux, M. Pezat, J. Portier, and P. Hagenmueller, *Mater. Res. Bull.*, **11**, 1441 (1976).
- J. F. Stampfer, C. E. Holley, and J. F. Suttle, *J. Am. Chem. Soc.*, **82**, 3504 (1960).
- R. Hultgren, R. L. Orr, P. D. Anderson, and K. K. Kelly, "Selected Values of Thermodynamic Properties of Metals and Alloys," John Wiley and Sons, New York (1963).
- J. J. Reilly, "Proceedings of the International Symposium on Hydrides for Energy Storage," Geilo, Norway, A. F. Andresen and A. J. Maeland, Editors, p. 301, Pergamon Press, London (1978).
- M. Arita, Y. Ichinose, and M. Someno, "Chemical Metallurgy," N. A. Gokcen, Editor, Metallurgical Society of AIME, Warrendale, PA (1981).
- E. Akiba, K. Nomura, S. Ono, and S. Suda, *Int. J. of Hydrogen Energy*, **7**, 787 (1982).

Molten Carbonate Fuel Cell Electrolyte Structure Fabrication Using Electrophoretic Deposition

Charles E. Baumgartner,* Vincent J. DeCarlo, Paul G. Glugla¹ and John J. Grimaldi²

General Electric Company, Corporate Research and Development, Schenectady, New York 12301

ABSTRACT

Electrophoretic deposition has been evaluated as a technique for preparing porous LiAlO₂ matrices suitable for use as molten carbonate fuel cell electrolyte structures. Although both the technique and the deposited product initially appeared to be well suited for the application, structural fracture resulted during impregnation with the alkali carbonate electrolyte necessary for fuel cell operation. Data are presented comparing and contrasting the physical properties of electrophoretically fabricated and hot-pressed electrolyte structures.

The electrolyte structure of a molten carbonate fuel cell (MCFC) is comprised of a porous ceramic matrix whose interstitial volume is filled with alkali carbonates. This structure plays a pivotal role in determining overall fuel cell performance as it serves both as the carbonate ion conduction path required for cell operation and also as a barrier to prevent gas-phase mixing of the fuel and oxidant. Satisfying both criteria requires the electrolyte structure to remain essentially carbonate filled during its operation, *i.e.*, free of cracks and interconnected voids.

Conventional electrolyte structure fabrication entails hot-pressing an intimate mixture of the ceramic (LiAlO₂) and the electrolyte (typically 62 mole percent [m/o] Li₂CO₃:38 m/o K₂CO₃) at a temperature just below the carbonate's 763 K liquidus to yield a brittle structure of greater than 95% theoretical density (1). The prepressed mixture is obtained by either dry mixing the respective components (2) or preferably from a precursor mixture of an aqueous solution/slurry containing all components (3, 4). Hot-pressed structures suffer from several disadvantages: first, carbonate agglomerates, formed in the mixture prior to pressing, drain into the porous electrodes during cell operation leaving voids in the structure which can act as centers for crack initiation. In addition, owing to the fragile nature of the final compact, structures are typically 0.125 cm or more thick. As the specific conductance of a 0.18 cm thick hot-pressed electrolyte structure is ~ 0.3 ($\Omega\text{-cm}$)⁻¹ at 923 K (5) the electrolyte related voltage drop for a fuel cell operating at a current density of 0.16 A/cm² is, therefore, given by

$$E_{\text{drop}} \text{ (V)} \approx 0.533t \quad [1]$$

where t is the electrolyte structure thickness in centimeters. A fuel cell possessing a 0.025 cm thick electrolyte structure would operate at a potential 82 mV higher than an identical cell possessing a 0.178 cm thick structure, owing to the decrease in required carbonate conduction length. Therefore, electrolyte structures thinner than those readily prepared by hot-pressing are desired. Finally, the economics associated with hot-pressing at temperatures approaching 750 K add greatly to the cost of the final fuel cell package.

Various methods have been suggested as alternative fabrication techniques including tape casting (6), vacuum casting (7), and electrophoretic deposition (ED) (8, 9). Of these, tape casting and ED are especially attractive as they are commercial processes for fabricating thin structures. This communication details our work on ED as a technique for preparing porous LiAlO₂ matrices for use as MCFC electrolyte support structures.

Method

Particle electrophoresis has been known for over a century and has been utilized as a fabrication technique by

*Electrochemical Society Active Member.

¹Present address: Department of Chemistry, University of Colorado, Boulder, Colorado 80309.

²Present address: Michelin, Greenville, South Carolina 29610.

the ceramics industry for several years (10, 11, 16-18). The technique can be separated into the two stages of suspension preparation and electric-field-induced deposition.

Particles suspended in an "inert" vehicle are categorizable, in broad terms, as being either stable or flocculating. In flocculating suspensions, particle-particle collision resulting from Brownian motion leads to permanent contact and thus a decrease in the number and an increase in the size of suspended particles. Particle concentrations have been shown both theoretically and experimentally to decrease at a second-order rate which is dependent upon factors such as particle diameter, vehicle viscosity, and temperature (12, 13). Conversely, in stable suspensions particles exhibit repulsive surface charges resulting from one or more of a variety of mechanisms, such as site-specific solvent adsorption or selective ion dissolution. These repulsive interactions slow particle flocculation rates by reducing the degree of attractive interaction upon collision.

The preparation of stable suspensions is important in electrophoretic fabrication for the following reason. The external electric field in an ED process simply serves to draw particles together onto the mandrel surface. Flocculating suspensions, which already possess an affinity to coalesce, form only a few contact locations during deposition, resulting in a very weak structure. However, deposits from stable suspensions lead to a more idealized, close-packed structure characterized by a higher density and improved strength. The deposit's microstructure and morphology are therefore stringently dependent upon the suspension characteristics. The choice of suspension vehicle and the use of binders or deflocculants are known to affect the suspension stability and electrophoretic mobility, which, in turn, affects the deposit quality.

Experimental

Powder and suspension preparation.—LiAlO₂ powders were prepared by either a molten-salt-mediated synthesis or a high temperature synthetic reaction. The molten salt synthesis (14) reacts high surface area Al₂O₃ (Alcoa) with LiOH in a molten NaCl/KCl solvent. The reaction is carried out at 1073-1273 K in air for 4-8h, depending upon the particle size of the desired product. Following cooling, the alkali chloride solvent is dissolved in water and the γ -LiAlO₂ collected by filtration using a Millipore 0.22 μm filter (Millipore Corporation). The synthesis yields a uniform particle-sized LiAlO₂ with a BET surface area between 6 and 8 m²/g. Lower surface area powders were prepared by reacting Al₂O₃ (Alcoa) with Li₂CO₃ at 1473 K in air for 24h. This reaction yields a highly aggregated γ -LiAlO₂ which must be comminuted to the desired surface area.

Ten solvents (reagent-grade alcohols and ketones) ranging in dielectric constant from 13.1 to 25.7, were evaluated as deposition vehicles. Of these, 2-propanol yielded the best results and was used for the majority of the sample preparations reported here. The deposition behavior in

other vehicles will be detailed later. Suspensions were typically prepared by combining 200g of LiAlO_2 , 540 ml of 2-propanol previously dewatered by passing over molecular sieves, and 400g of dense $\alpha\text{-Al}_2\text{O}_3$ grinding media in a 1 liter plastic bottle. Just prior to this step the LiAlO_2 was heated to 1275 K in air for 1h to remove adsorbed moisture. A vibratory milling (Sweco, Incorporated) of 4-24h yielded an acceptably stable suspension exhibiting less than 5% settling in 10 min.

Deposition and postdeposition.—Flat LiAlO_2 structures were deposited electrophoretically by applying a dc voltage of between 125 and 800V across the suspension. The deposit accumulated on a prepared mandrel (charged negatively for 2-propanol suspensions), the counter-electrode being either the stainless steel container or an additional stainless steel insert. A millisecond timer (Minarik Electric Company) controlled the duration of the applied potential (Sorensen Power Supply, Raytheon Company) (Fig. 1). For example, deposit thicknesses of 0.025 and 0.178 cm were obtained using deposition times of 4.0 and 60.0s, respectively, at 400V from a 2-propanol suspension. Various materials were evaluated as deposition mandrels including graphite, stainless steel, and nickel, and various deposition time/voltage conditions were evaluated.

Following deposition, the mandrel containing the deposit was removed from the suspension for drying. Drying procedures to yield crack-free deposits ranged from air drying for thin (0.013-0.038 cm thick) deposits to controlled 2-propanol vapor pressure conditions for thicker (0.127-0.178 cm thick) structures.

Electrolyte addition.—Following the fabrication of a dried, porous LiAlO_2 layer, the pore volume must be impregnated with alkali carbonates to yield a MCFC electrolyte structure. Electrolyte additions (62 m/o Li_2CO_3 :38 m/o K_2CO_3) were accomplished by heating the deposit containing premelted and ground carbonate on its surface above the 763 K carbonate liquidus. As the carbonates melted, it was drawn into the porous deposit by capillarity. Various impregnation conditions were evaluated.

Sample evaluation.—Following electrolyte filling, structures were examined for fractures by optical microscopy (10-70 \times); crack-free structures were stored in a dry atmosphere. The sample's hermeticity as a function of differential gas pressure (pressure capacity) was measured at 923 K and compared with that of hot-pressed structures (15). The apparatus employed consists of two 304 stainless steel canisters, the faces of which contain a series of 1/16 or 1/8 in. holes arrayed within a 1 in. diam circle (Fig. 2). The sample itself (> 1 in. diam) was held between two pieces of perforated gold foil. A piece of 40 mesh screen was utilized as a bottom support. Alignment of the top and bottom canister was aided by locating pins and assembly within a cradle; the cradle was then placed

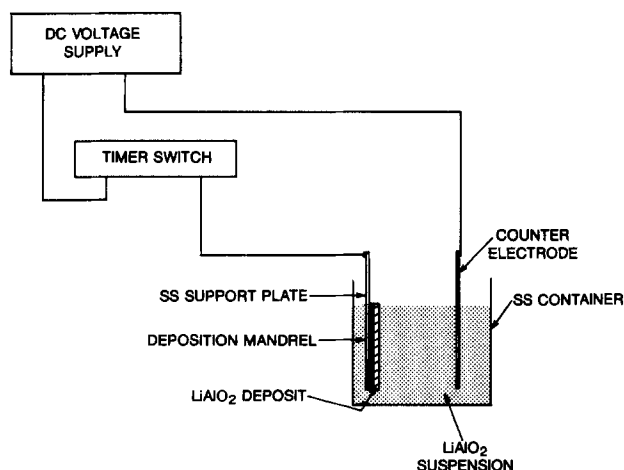


Fig. 1. Electrophoretic deposition apparatus

BUBBLE PRESSURE TEST APPARATUS

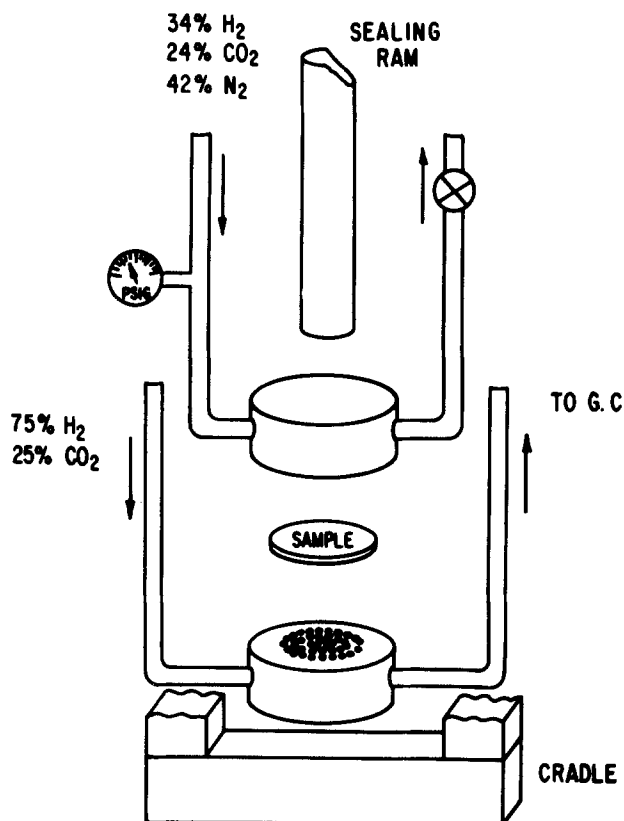


Fig. 2. Pressure capacity test apparatus. For clarity, the gold foil and expanded metal mesh are not shown.

inside a N_2 -purged box furnace. A hydraulic ram was used to apply sealing pressure, making a gastight seal between the sample and canister halves.

Each canister half contained both a gas inlet and outlet. The top canister was coupled to a pressure gauge and micrometer valve (cf. Fig. 2). This canister was pressurized, relative to the bottom half, using a N_2 containing gas such as 34% H_2 , 24% CO_2 , and 42% N_2 . The N_2 -free gas (75% H_2 , 25% CO_2) used in the bottom canister exited to a Carle series S analytical gas chromatograph equipped with two thermal conductivity detectors and a Shimadzu C-RIA chromatopac. The pressure capacity of the sample was taken to be the pressure differential at which a N_2 level in excess of background was first detected in the exit gas from the bottom canister. Both the sample's initial pressure capacity and its capacity following thermal cycling below the electrolyte liquidus were measured using this equipment.

In addition, the thermal expansion behavior of both hot-pressed and free standing ED structures was evaluated using a high sensitivity dilatometer. The samples, $2.0 \times 0.33 \times 0.15$ - 0.18 cm, were suspended lengthwise within an Al_2O_3 tube between two gold-foil sheets and held in place by a 10g holding force applied horizontally between one end of the sample and the tube's end. Specimens were heated at $3.3^\circ\text{C}/\text{min}$ from ambient to 973 K for three cycles under a CO_2 atmosphere. A LVTD continuously provided data on the sample's expansion/contraction during each heating and cooling cycle.

Results and Discussion

Matrix fabrication.—The importance of vehicle dielectric constant on suspension preparation and the quality of electrophoretically deposited sodium beta-alumina samples was shown previously by Powers (16). Ten solvents were evaluated here as LiAlO_2 deposition vehicles

ranging in dielectric constant from 13.1 to 25.7. Deposition occurred from all suspensions following a several-hour vibratory milling. The milling step was found to be essential to the preparation of stable suspensions. Milling fractures larger particles and particle agglomerates to yield newly exposed surfaces thereby promoting solvent adsorption and stable suspension formation. For the vehicles examined here, the resulting deposit quality was found not to depend upon vehicle dielectric constant, but rather to be strongly dependent upon the solvent type (Table I). Suspensions prepared with ketones settled significantly more rapidly than those from alcohols indicating more flocculating conditions. As a result, deposits from ketone vehicles were less dense and, on several occasions, slid from the mandrel following deposition. Those that were retrieved successfully invariably cracked upon drying. Alcohols as vehicles gave significantly stronger deposits but the deposits were plagued by extensive bubble-hole formation, *i.e.*, physical holes in the deposit which result from gases evolved as the solvent heats and eventually decomposes at the solvent/electrode interface. This effect was particularly prevalent for primary alcohols and somewhat less apparent for 2-propanol.

Deposition occurred on the negatively charged mandrel for all vehicles investigated with the exception of 3-pentanone. The general mechanism responsible for suspension formation here is believed to be solvent-specific adsorption as shown in reactions [2] and [3] below for a protonated solvent. The ceramic-solvent association is assumed to be dipole in nature (19).



Reaction [3], which possesses an adsorbed solvent sheath with a ceramic-directed negative dipole, is inferred to be predominant in most of the vehicles investigated here since deposition occurred on the negatively charged mandrel. Deposition from ketone-prepared suspensions also occurred on the negatively charged electrode, with the exception of 3-pentanone, in which a reversal in charging mechanism occurred. This charge reversal also occurred in acetone + 1-pentanol mixtures, where deposition obtained on the negatively charged mandrel for either pure solvent, but on the positively charged mandrel for solvent mixtures from 10-90% acetone. The specifics of the mechanism have not been confirmed experimentally.

The structures reported above were all deposited on polished stainless steel mandrels. In addition, mandrels of carbon, polished nickel, and porous nickel were evaluated. Whereas neither deposits on carbon nor polished nickel showed any significant differences from those made on stainless steel, the porous nickel mandrel (Gould Corporation porous nickel, > 60% porosity, 6 μm median pore size) was found to considerably reduce the occurrence of bubble holes within the deposit. The porous mandrel also aided in reducing the frequency of cracked deposits during drying by increasing drying uniformity.

Table I. Solvents investigated as ED vehicles

Material	Resulting structure
Ketones	
2-Pentanone (15.4) ^a	Cracked
3-Pentanone (17.0)	Cracked
2-Butanone (18.5)	Cracked
Acetone (20.7)	Cracked
2,4-Pentadione (25.7)	Cracked
Alcohols	
Benzyl alcohol (13.1)	Extensive bubble holes
1-Pentanol (13.90)	Extensive bubble holes
2-Propanol (18.3)	Some bubble holes
1-Propanol (20.1)	Extensive bubble holes
Ethanol (24.3)	Some bubble holes, cracked

^a The number in parenthesis is the solvent dielectric constant.

All results reported subsequently utilized 2-propanol suspensions deposited on negatively charged, porous nickel mandrels.

Deposition voltages exceeding ~125V were satisfactory for LiAlO₂ deposition, with about 6.0s at 125V or 4.0s at 400V required to produce a 0.025 cm thick matrix, and 60.0s at 400V to produce a 0.18 cm thick deposit. In suspension, each LiAlO₂ particle is surrounded by a solvent sheath or double layer. During deposition, this double layer is retained, in effect separating the individual ceramic particles by one or more monolayers of solvent. Following deposition, this solvent must be removed from the structure; accompanying solvent removal the structure shrinks, owing to a collapse of the solvent occupied volume. Structures on the order of 0.025 cm thick were readily dried in air for 24h followed by vacuum at ~373 K. Thicker structures, *e.g.*, > 0.050 cm thick, however required slower drying under a 2-propanol partial pressure to prevent cracking, because the outer surface of the deposit physically contracted prior to the center. This was accomplished by drying the deposits in a loosely covered container over a 2-propanol soaked towel. The resulting structures, in both cases, were extremely fragile, causing all deposits to be difficult to remove from the deposition mandrel without fracture. Deposits thicker than ~0.05 cm were removable, however, by careful horizontal pressure applied along one edge following complete deposit drying. Examination of density, pore-size distribution, and pore morphology showed these properties to be independent of deposit thickness for identically prepared samples. Therefore, thicker structures, removed from the deposition mandrel, were used in future evaluation when possible to remove influences associated with the porous nickel backing. For studies involving thinner deposits which incorporated the porous mandrel, a MCFC porous Ni anode was used as the deposition mandrel. Such a deposition technique would be necessary for the preparation of thin ED layers for MCFC applications.

Figure 3 displays mercury porosimetry curves for material deposited at 400V for 4s. As the LiAlO₂ surface area increased from 6.8 to 0.3 m²/g, the median pore size increased from ~0.3 to 1.8 μm and the pore diameter distribution broadened. Interestingly, the porosity showed no clear surface area dependence, varying between 55 and 61%. The deposit's pore-size distribution is important in determining its use as a MCFC electrolyte matrix. During fuel cell operation, the electrolyte structure is in intimate contact with both porous electrodes. Although the carbonate electrolyte is initially present within the electrolyte structure matrix, it will redistribute from the matrix to the electrodes, in accordance with the respective pore diameters and wetting characteristics of the individual components. The median pore diameter of the electrodes is between 2 and 6 μm . Since the electrolyte structure must retain sufficient electrolyte within its matrix during cell testing to prevent gas crossover, the electrolyte struc-

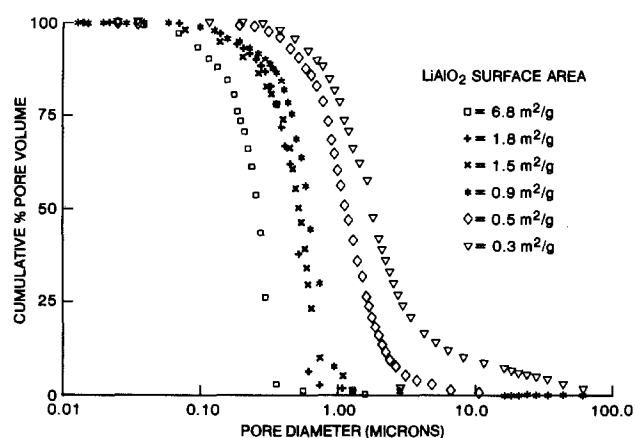


Fig. 3. Mercury intrusion porosimetry curves of ED LiAlO₂ layers deposited from various surface area LiAlO₂ powders.

ture's median pore diameter must not overlap excessively with that of the electrodes. The degree of optimum pore overlap has not been quantified; however, as the median pore diameter obtained on the deposit fabricated using $0.3 \text{ m}^2/\text{g}$ LiAlO_2 powder is approaching $2 \mu\text{m}$, it is assumed that this represents a lower limit in surface area for usable LiAlO_2 powders.

Electrolyte addition.—Electrolyte impregnation of deposited matrices was accomplished for both thick ($> 0.05 \text{ cm}$) deposits removed from the deposition mandrel and for thinner deposits (0.025 cm) still retained on the porous substrate by spreading the electrolyte, as a powder, over the matrix surface and heating above the electrolyte's liquidus. Once molten, the electrolyte was drawn into the pores by capillarity. The quantity of electrolyte to be added was determined prior to impregnation from mercury intrusion porosimetry results obtained on a separate, identically fabricated matrix. The influences of heating rates, gas atmospheres, and volume percent electrolyte fills on the propensity for matrix fracture during electrolyte addition were evaluated. A variety of gas atmospheres were chosen, including O_2 , CO_2 , H_2 , N_2 , their combinations, and vacuum, with CO_2 atmosphere-impregnated structures showing the least propensity towards cracking. Although the exact reason for this gas atmosphere influence has not been determined, it is possibly due to alkali carbonate decomposition in non- CO_2 containing environments (20). The incidence of structure fracture during impregnation was also found to decrease with decreasing electrolyte-fill fraction, decreasing heating/cooling rates, and decreasing LiAlO_2 surface area with the surface area influence being the most pronounced of these three (Table II).

Visual observation of 0.18 cm thick, $4 \times 4 \text{ cm}$ free standing ED matrices during electrolyte impregnation revealed at least two different fracture mechanisms to be operating. The specimens were placed on an Al_2O_3 pedestal within a quartz plate covered box furnace under a flowing CO_2 atmosphere. Samples were monitored visually during heating and cooling cycles. Immediately after the carbonate liquidus temperature was exceeded and the molten carbonate was absorbed into the LiAlO_2 matrix, LiAlO_2 particle rearrangement occurred driven by strong capillary forces (several hundred psi). This resulted in an overall structure shrinkage of approximately 1%. Structures which were unable to contract uniformly developed cracks at this time. These cracks were primarily manifest as peripheral wedge-shaped openings, if matrix edge-flaws were present, and otherwise as isolated microfractures covering the entire structure. A photograph showing severe microcracking in a sample impregnated with carbonate under a CO_2 atmosphere is presented in Fig. 4. These fractures, only barely detectable without magnification, extend completely through the thickness of the impregnated matrix imparting a translucency to the otherwise opaque structure.

Table II. Parameter influence on fracture of impregnated ED structures

Parameter	Results
Gas environment (O_2 , CO_2 , H_2 , N_2 , vacuum)	Crack-free structure yield slight better in CO_2 , worst in vacuum.
Impregnation temperature (773-973 K)	Little effect.
Structure cooling rate (60° to $5^\circ\text{C}/\text{h}$)	Slower cool rate moderately improved crack-free yield.
Electrolyte-filled void volume (50% to 100%)	Reducing electrolyte loading improved crack-free yield.
Initial LiAlO_2 surface area (6.8 to $0.3 \text{ m}^2/\text{g}$)	Lower surface area LiAlO_2 greatly increased crack-free yield.
Electrophoretic deposition voltage (175-800V)	Little effect.
Deposited LiAlO_2 thickness (0.178-0.013 cm)	Thinner structures increased crack-free yield.

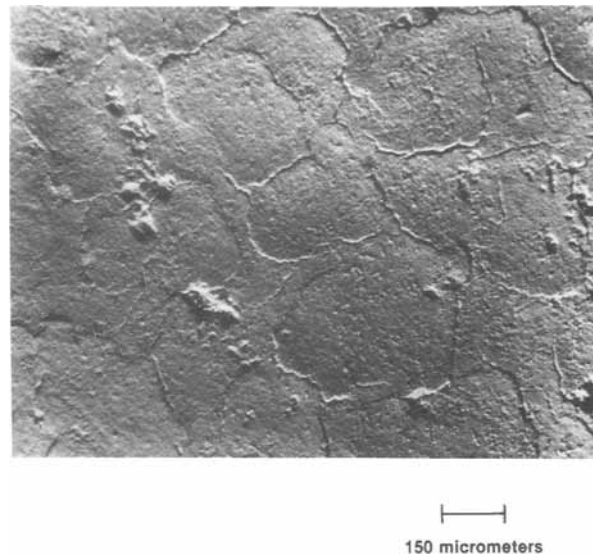


Fig. 4. SEM micrograph showing microcracking of electrolyte-impregnated, $6.8 \text{ m}^2/\text{g}$ LiAlO_2 ED sample.

The severity and incidence of microcracks formed during electrolyte addition could be lessened by either lightly sintering the LiAlO_2 matrix prior to electrolyte addition or by decreasing the LiAlO_2 surface area. As the fractures result from physical particle rearrangement, lightly sintering the particle microstructure is obviously advantageous. Heat-treatments of at least 1000°C for 1h in air were found to be necessary to fuse the LiAlO_2 particle bridges sufficiently to produce a factor of 2 or 3 reduction in microcrack density. The alternate technique of increasing fracture resistance by decreasing the LiAlO_2 surface area was helpful but less effective. The larger particle size LiAlO_2 is not only more difficult to rearrange, owing to its increased mass, but also generates larger pores, thereby reducing the capillary drawing forces for structural rearrangement. Therefore, fractures associated with electrolyte addition could be partially eliminated by depositing LiAlO_2 powders with a surface area of $< 1 \text{ m}^2/\text{g}$.

No fractures were directly observed in the furnace during cooling through the carbonate solidification region; however, a second fracture mechanism was evident upon examination of cooled electrolyte filled structure. These fractures were concluded to be due to thermal stresses introduced into the now composite structure (electrolyte + LiAlO_2). ED-prepared porous LiAlO_2 structures were measured to possess a linear thermal expansion coefficient of $11.3 \times 10^{-6} \text{ in./in. } ^\circ\text{C}$ in this temperature region (see below). In contrast, the carbonate electrolyte undergoes a 5% volume contraction upon solidification at 763 K and exhibits a 373-673 K linear thermal expansion coefficient of $35.7 \text{ in./in. } ^\circ\text{C}$ (21), more than three times that of the ceramic matrix. The significant stresses generated by this thermal expansion mismatch leads to fractures ranging from long major cracks, several centimeters long, to crazing, similar to glazes placed under tension. Whereas lightly sintering the matrix was found to be beneficial in eliminating particle rearrangement-related fractures, such heat-treatments appear to have little or no impact on thermal stress related fractures. Instead, the microstructure of the porous ceramic layer, as dictated by the LiAlO_2 particle size and morphology, appeared to be the dominating influence. As before, matrices deposited using larger particle size LiAlO_2 powders showed a decreased propensity towards fracture. However, even matrices prepared using $0.3 \text{ m}^2/\text{g}$ LiAlO_2 commonly fractured during electrolyte impregnation. The final "optimized" impregnation procedure, therefore, involves a multistep impregnation whereby approximately 1/2 of the matrix's pore volume is electrolyte filled in each of two steps. Both steps are carried out under a CO_2 atmosphere with a controlled heating/cooling cycle of $\sim 0.75 \text{ K}/\text{min}$ to 873 K.

Using this procedure, approximately one-third of the 3×3 cm samples fabricated using LiAlO_2 powder with a surface area below $1 \text{ m}^2/\text{g}$ could be successfully impregnated to a crack-free status.

Evaluation and comparison to hot-pressed structures.—Electrolyte-impregnated structures were evaluated to determine their compatibility with fuel cell requirements. One of these requirements is that the structure must remain crack-free in the event that the cell undergoes a thermal cycle between the 923 K operating temperature and some temperature below the electrolyte liquidus, for example, 573 K. Structures which were electrolyte impregnated following the "optimized procedure" stated above were microscopically examined for fractures at 70X. Crack-free structures were then evaluated for their ability to prevent gas crossover as a function of differential pressure. This test is a sensitive technique for microcrack detection, and it simulates the fuel cell condition where a differential pressure could arise between the anode and cathode owing to a pressure malfunction on one side of the cell. In the event this occurs, the capillarity of the electrolyte structure alone prevents reactant gas mixing.

The pressure resistance or pressure capacity arises from the capillary force exerted by the electrolyte-filled pores, the relationship between capillary pressure capacity (P) and pore radius (r) is given by Eq. [4]

$$P = \frac{2\gamma_{1,v} \cos \theta}{r} \quad [4]$$

Janz (22) measured a value of 200 dyne/cm for $\gamma_{1,v}$ for molten Li/K carbonate, and contact angle measurements (23) have shown $\cos \theta$ for molten carbonates on most oxides to be equal to 1. Therefore, the theoretical pressure capacity of a molten carbonate-filled LiAlO_2 pore with a radius of $1.0 \mu\text{m}$ would be equal to 58 psi.

Pressure capacity measurements on hot-pressed and ED electrolyte structures were conducted at 923 K, using the apparatus shown in Fig. 2 and described elsewhere (15). Prior to sample heating, gas flow at a few inches of water was initiated through the canister halves to protect the sample. The temperature was increased from ambient to ~ 475 K and held constant for ~ 12 h; temperature was monitored with a Chromel-Alumel thermocouple located adjacent to the apparatus. Following this "drying period" the temperature was raised to 793 K. In general, a 1-1.5 K/min heating rate was maintained from ~ 733 to 793 K so that melting of the eutectic occurred uniformly. At ~ 793 K, the entire "sandwich" was hydraulically sealed from the top with 3-6 psi. Seal quality and background N_2 concentration were determined by monitoring the bottom canister's gas environment with no differential pressure across the sample. The temperature was then elevated to ~ 923 K. Throughout each pressure capacity measurement, the external sealing pressure was maintained greater than the pressure differential between the top and bottom canister. Background N_2 concentration was determined and found to be independent of applied sealing pressure.

Hot-pressed samples (containing 67 volume percent [v/o] electrolyte) successfully withstood a ΔP up to 36 psi, the limit of the apparatus employed. This indicates that the samples neither cracked during heat-up nor possessed sufficient large pores ($\approx 3.2 \mu\text{m}$ diam) to allow blow through at these pressures. A hypothetical hot-pressed structure median pore diameter of $0.3 \mu\text{m}$ calculated from the LiAlO_2 powder surface area and carbonate volume fraction is predicted to possess a pressure capacity in excess of 350 psi based on Eq. [4]. Moreover, these structures were shown to be fracture resistant following thermal cycling below the electrolyte liquidus, as evidenced by a sustained pressure capacity upon reheating. In contrast, the majority of ED structures examined, whether removed from the deposition mandrel or impregnated as a composite on the porous Ni plaque, fractured either prior to or during heat-up in the test apparatus. All

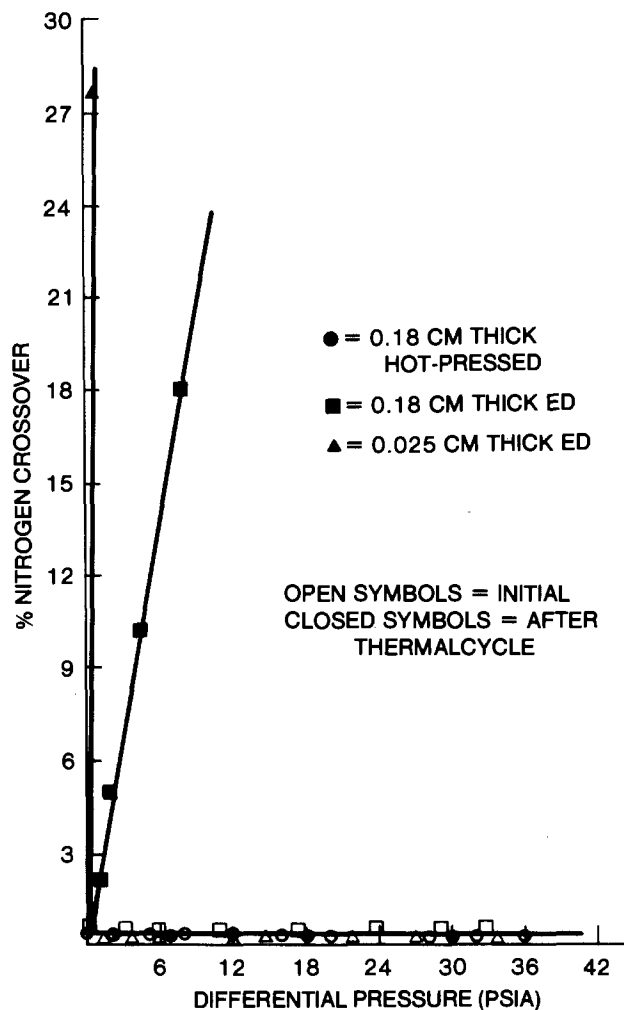


Fig. 5. Percent nitrogen crossover as a function of differential pressure at 923 K for a 0.18 cm thick hot-pressed, a 0.18 cm thick ED, and a 0.025 cm thick ED electrolyte structure. The open and filled symbols represent the initial and post-thermal cycle data, respectively.

samples were examined microscopically prior to testing to insure they were crack-free; however, microcracks were extremely difficult to detect, especially in thinner deposits. Therefore, some of the fractures may have been present prior to testing. Figure 5 shows the N_2 crossover recorded at 923 K for three samples prior to and following one thermal cycle from 923 K to below 623 K. Both ED structures were fully impregnated prior to testing. Whereas the hot-pressed structure retained its resiliency towards gas crossover following the thermal cycle, both ED structures fractured, as evidenced by a substantial N_2 crossover as 1 psi ΔP upon reheating to 923 K. The hot-pressed structure continued to survive a second thermal cycle and exhibited only a slight crossover following the third.

The difference in fracture propensity between ED and hot-pressed structures was further examined by comparing their thermal expansion behavior under a CO_2 atmosphere (Fig. 6-8). The hot-pressed structure, 0.18 cm thick and containing 67 v/o electrolyte, contracted $\sim 1.5\%$ during the initial pass through the electrolyte liquidus (Fig. 6). This contraction is due both to LiAlO_2 particle rearrangement as the structure melts and to the collapse of residual voids entrapped during pressing. Subsequent thermal cycles showed only two regions of fairly linear thermal expansion, the change in slope occurring at ~ 773 K during heating, owing to electrolyte melting, and at ~ 733 K during cooling upon electrolyte solidification. The separation of liquidus and solidus temperatures is explained by the observation of Janz and Lorenz (24) that unless the carbonate is seeded to initiate crystallization, it

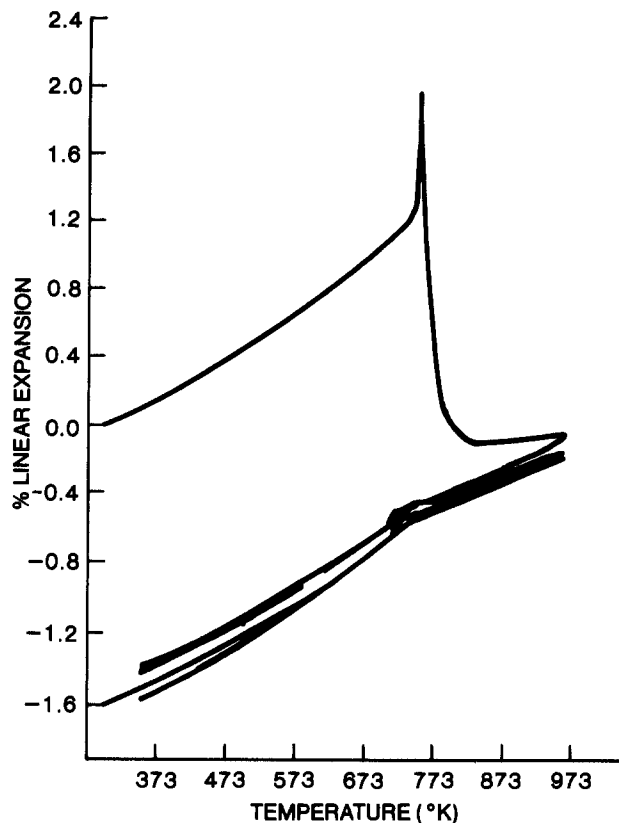


Fig. 6. Thermal expansion curve for 67 v/o electrolyte, hot-pressed structure between 373 and 973 K under a CO_2 atmosphere.

supercools to a eutectic liquidus of ~ 733 K. Linear thermal expansion coefficients, derived from these curves at temperatures above and below the liquidus (Table III), are in good agreement with previously reported data on similar systems (21).

The thermal expansion behavior of a nonimpregnated ED structure was linear between 373 and 973 K with a thermal expansion coefficient of 11.3×10^{-6} in./in. $^\circ\text{C}$ (Fig. 7 and Table III). This value is less than one-third the thermal expansion coefficient of 35.7×10^{-6} in./in. $^\circ\text{C}$ published for the free carbonate electrolyte (21). The stresses generated during thermal cycle as a result of the significant differences in thermal expansion behavior of the two materials is likely responsible for the fracture mechanism observed previously during structure cooling following impregnation. This was clearly evident when an

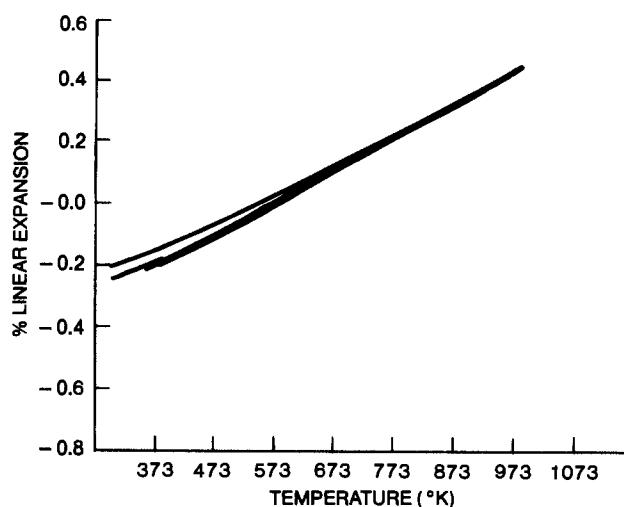


Fig. 7. Thermal expansion curve for a nonimpregnated LiAlO_2 layer between 373 and 973 K under a CO_2 atmosphere. Prepared using $1.8 \text{ m}^2/\text{g}$ LiAlO_2 powder.

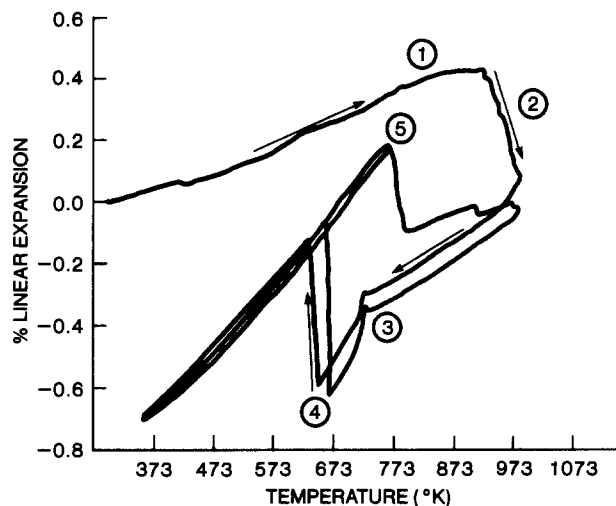


Fig. 8. Thermal expansion curve for an ED LiAlO_2 matrix electrolyte filled within the dilatometer during the initial heating cycle between 373 and 973 K under a CO_2 atmosphere. Prepared using $1.8 \text{ m}^2/\text{g}$ LiAlO_2 powder.

ED structure was electrolyte filled within the dilatometer (Fig. 8). Upon initially passing through the liquidus (region 1 in Fig. 8), approximately 0.5h was required for the electrolyte to melt and be absorbed into the porous structure. At that time, the structure shrank approximately 0.4% (region 2) owing to LiAlO_2 rearrangement. This is in agreement with the observation of the first fracture mechanism (microcracking) discussed previously. Cooling from 973 K to the electrolyte liquidus gave an initial contraction very similar to that observed for the nonimpregnated matrix, indicating that the electrolyte did not contribute significantly to the expansion characteristics while in the molten state. A small perturbation was seen as the electrolyte solidified (region 3), accompanied by a change in thermal expansion slope, showing that the electrolyte now dominated the expansion characteristics. At approximately 663 K, an abrupt 0.5% expansion resulted from thermally induced stresses (region 4). This is consistent with the second fracture mechanism identified earlier. A second thermal cycle yielded almost identical results, with the exception that the fracture which opened during the initial cooling cycle closed as the temperature exceeded the electrolyte liquidus (region 5). Microscopic examination of the sample following testing showed branched fractures, similar to those observed previously during cooling of electrolyte-filled structures.

At first glance, hot-pressed and electrolyte-filled ED structures appear similar in that both are ceramic/alkali carbonate composites of roughly the same volume proportions. The above comparison of the structure's thermal behavior, however, clearly illustrates that significant differences exist between these two structures; these dif-

Table III. Linear thermal expansion coefficient of hot-pressed and electrophoretically deposited electrolyte structures

Matrix	Linear thermal expansion coefficient ($\times 10^6$ in./in. $^\circ\text{C}$)	
	373-673 K	773-923 K
Hot-pressed		
62 v/o electrolyte	22.5	16.0
67 v/o electrolyte	22.0	16.5
ED		
No electrolyte	11.3	11.3
65 v/o electrolyte filled	18.5	13.7
80 v/o electrolyte filled	16.0-25.5 ^a	12.0
100 v/o electrolyte filled	16.5-25.0 ^a	13.3

^a Nonreproducible curves due to structural fracture on cooling led to a range of calculated expansion coefficients.

ferences are associated with the fundamental differences in their fabrication routes. A hot-pressed structure, fabricated in an integral step, is analogous to a particle reinforced body in which at temperatures above the electrolyte liquidus, the LiAlO_2 particles are surrounded by liquid. In contrast, impregnated ED samples, fabricated in a two-step process, are typified as a porous ceramic exhibiting particle-particle contact and whose interstitial volume is electrolyte filled. As the exact microstructure of either sample is unknown, precise fracture modeling of either system is impossible. However, it is well known that the thermal properties of a composite structure are a complex function of each material's thermal expansion characteristics and bulk modulus, as well as the extent that each phase is continuous. ED and hot-pressed structures differ considerably in this last category, *i.e.*, hot-pressed structures are assumed to be continuous only in the carbonate phase, whereas ED structures are continuous in both the carbonate and LiAlO_2 phases. It is believed that this difference is responsible for the poor thermal expansion resiliency found here for carbonate-filled ED structures. Following electrolyte filling, high tensile stresses develop in the cooling matrix as the lower thermal expansion LiAlO_2 framework prevents the electrolyte from contracting. As was seen in the thermal expansion curves, these stresses are apparently sufficient to fracture not only the brittle, solidified carbonate but the weak ceramic matrix as well.

Conclusions

High quality porous LiAlO_2 layers are easily deposited electrophoretically from 2-propanol suspensions. The deposited layers are approximately 60% porous exhibiting a uniform thickness with a median pore diameter and pore size distribution which can be tailored by varying the initial powder's surface area.

Comparison of ED fabrication to hot-pressing for MCFC use shows ED to be considerably easier, faster, and more economical. In addition, thin ED LiAlO_2 layers are easily deposited allowing thinner electrolyte structure fabrication and, therefore, lower in-cell ohmic losses associated with the electrolyte. However, the application of these layers for use in MCFCs relies on their successful impregnation with Li/K carbonate electrolyte. The difficulties associated with crack-free impregnation of these structures has been demonstrated. In addition, the results of the pressure capacity and thermal expansion evaluations reported here clearly show the fragility of impregnated ED LiAlO_2 layers. This fragility leads one to seriously question the utility of this fabrication technique for MCFC usage.

Acknowledgments

The authors wish to acknowledge the assistance of many colleagues, in particular Dr. R. H. Arendt for the molten salt synthesized LiAlO_2 , Dr. B. R. Karas for collaboration on the pressure capacity measurements, and Dr. R. W. Powers for discussions on this work. The Electric Power Research Institute is acknowledged for its funding of this work under Contracts RP-1085-1 and RP 1085-8. Dr. A. J. Appleby, EPRI Program Manager, is thanked for his direction and interest.

Manuscript submitted Nov. 30, 1983; revised manuscript received Aug. 23, 1984. Parts of this work were pre-

sented as Paper 138 at the Hollywood, Florida, Meeting of the Society, Oct. 5-10, 1980, and as Paper 371 at the Montreal, Quebec, Canada, Meeting of the Society, May 9-14, 1984.

General Electric Company assisted in meeting the publication costs of this article.

REFERENCES

1. H. A. Liebafsky and E. J. Cairns, "Fuel Cells and Fuel Batteries," Chap. 2, John Wiley and Sons, New York (1968).
2. D. M. Mason, *et al.* U.S. Pat. 3,998,939 (1976).
3. K. Kinoshita, *et al.*, U.S. Pat. 4,115,632 (1978).
4. "Fuel Cell Research on Second Generation Molten Carbonate Systems," Technical Progress Report for 1 April-30 June 1978, Institute of Gas Technology for U.S. Department of Energy, SAN-1735-3, July 1978.
5. P. G. Glugla and V. J. DeCarlo, *This Journal*, **129**, 1745 (1982).
6. United Technologies Corp., "Development of Molten Carbonate Fuel Cell Power Plant Tech.," DOE Contract DE-AC01-79ET15440, Quarterly Report no. 4, July-Sept. 1980.
7. General Electric Co., "Development of Molten Carbonate Fuel Cell Power Plant," DOE Contract DE-AC02-80ET17019, Quarterly Report no. 3, Aug.-Oct. 1980.
8. J. J. Grimaldi, V. J. DeCarlo, and P. G. Glugla, Abstract 138, p. 375, The Electrochemical Society Extended Abstracts, Vol. 80-2, Hollywood, FL, Oct. 5-10, 1980.
9. H. C. Maru, A. Pigeaud, and L. Paetsch, Abstracts 133-136, "National Fuel Cell Seminar Abstracts," Norfolk, VA, Meeting, June 1981.
10. *Ceram. Ind.*, **5**, 30 (1980).
11. E. Patai and Z. Tomaschek, *Koll. Z.*, **74**, 253 (1936).
12. G. D. Parfitt and J. Peacock, in "Surface and Colloid Science," Vol. 10, E. Matijevic, Editor, p. 163, Plenum Press, New York (1980).
13. Z. Krut, *Physik. Chem.*, **100**, 250 (1922).
14. R. H. Arendt and M. J. Curran, *This Journal*, **127**, 1660 (1980).
15. B. R. Karas, C. E. Baumgartner, and C. D. Iacovangelo, in "Molten Carbonate Fuel Cells," J. R. Selman, Editor, The Electrochemical Society Softbound Proceedings Series, Pennington, NJ (to be published).
16. R. W. Powers, *This Journal*, **122**, 490 (1975).
17. J. H. Kennedy and A. A. Foissy, *ibid.*, **122**, 482 (1975).
18. A. A. Foissy and G. Robert, *Am. Ceram. Soc. Bull.*, **61**, 251 (1982).
19. J. H. Kennedy and A. A. Foissy, *J. Am. Ceram. Soc.*, **60**, 33 (1977).
20. P. K. Lorenz and G. J. Janz, *Electrochim. Acta*, **15**, 2001 (1970).
21. "Fuel Cell Research on Second-Generation Molten Carbonate Systems," Technical Progress Report to Dept. of Energy under Contract no. EM-78-C-03-1735, Institute of Gas Technology, Oct. 1, 1978-June 30, 1979.
22. G. J. Janz, "Physical Properties Data Compilations Relevant to Energy Storage," NBS Publication no. NSRDS-NBS61, Part II, p. 374, NBS, Washington, DC (1979).
23. P. Lessing and M. Johnston, Montana Energy and MHD Research and Development Institute, Department of Energy Quarterly Progress Report for the Period December 1, 1980 to March 31, 1981. DOE Contract DE-AC03-77ET11321 modification no. A004.
24. G. J. Janz and M. R. Lorenz, *J. Chem. Eng. Data*, **6**, 321 (1961).

Improved Nickel Anodes for Industrial Water Electrolyzers

C. K. Dyer*¹

AT&T Bell Laboratories, Murray Hill, New Jersey 07974

ABSTRACT

A method of increasing the energy efficiency of hydrogen production by alkaline water electrolysis is described. An ac activation of sintered Ni anodes leads to reductions in the oxygen evolution overpotential of ~230 mV at 100-250 mA/cm². The resulting reduction in cell voltage yields an increased energy efficiency and a significantly lowered cost of hydrogen production. Compared with other processes to raise anode efficiency, ac activation provides a fourfold improvement.

Hydrogen production by water electrolysis is already a well-established industrial process. To meet increasing demands for hydrogen (1-4), it is widely recognized that improved energy efficiencies and reduced capital costs are necessary. A major goal in developing advanced electrolyzer technology for high purity hydrogen is to reduce the cell voltage at a given current density (5). Electrical energy accounts for 78% of the cost of producing electrolytic hydrogen (based on 30 mil/kWh). Nickel and its alloys are the preferred anode materials in alkaline electrolysis owing to their high corrosion resistance at anodic potentials in alkaline electrolyte (up to 30 weight percent [w/o] KOH) and their low cost. However, the overpotential for oxygen evolution on Ni is higher than several expensive alternatives. There is evidence that a thin initial surface coating of Ni(OH)₂ on a porous Ni electrode lowers the oxygen overpotential at 200 mA/cm² by 40-60 mV in 30 w/o KOH at 80°C (6). At high loadings of Ni(OH)₂, the overpotential increases due to the plugging of pores in the porous electrode during the electrochemical impregnation.

A new method of producing a very uniform layer of active Ni(OH)₂ within a porous Ni structure without pore plugging was described recently (7). This method should be very suitable for activating oxygen electrodes for the hydrogen production industry. A highly uniform film, free of blockage of electrolyte channels within the electrode, was demonstrated in that work (7).

Experimental

Sintered Ni electrodes having an average porosity of 77.5% and mean pore size of 12.7 μm were supported on a Ni wire mesh. The projected area was 1 cm². The test electrodes were subject to "activation" pretreatments using ± 125 mA (p-p) ac current (square wave) at 0.25 Hz in a 1M KCl aqueous solution. This was one of several ac treatments which has yielded conversions of Ni to electrochemically active material [Ni(OH)₂] with relatively high coulombic efficiency (~ 60%). The details of the technique and other ac conditions which are expected to yield comparable results are reported elsewhere (7).

After different amounts of activation, consisting of 25, 50, 100, 200, or 300 ac cycles, electrodes were washed in distilled water, then charged and discharged at 250 mA/cm² in 30 w/o KOH to determine their coulombic capacity and hence the loading level of active Ni(OH)₂. Each electrode was recharged to oxygen evolution potentials in 30 w/o KOH at a given constant current in the range of 25-250 mA/cm² at 25° or 80°C, and the electrode potential was measured at its surface by means of a Luggin capillary probe with a Hg/HgO reference electrode [+0.926V (RHE)]. The position of the probe tip on the electrode surface was changed, and a new set of readings was taken in order to average out potential measurement errors due to different distances between the probe tip and the surface, nonuniformity in current flow especially near edges, etc. Counterelectrodes on either side of the porous Ni electrode were made of a sintered Teflon®

* Electrochemical Society Active Member.

¹ Present address: Bell Communications Research, Inc., Murray Hill, New Jersey 07974.

and Pt powder mixture supported on a Ni screen, of area ~50 cm², and similar to electrodes used to generate H₂ in the Ni/H₂ secondary cell. The cell was a closed Pyrex® beaker; recombination of evolved oxygen and hydrogen occurred within the cell nonexplosively above the electrolyte level, on the exposed portion of the Pt counterelectrodes. Thus, the KOH concentration was maintained over long periods (6h) of testings at 200 mA/cm². Temperature was held at 80° ± 1°C using a temperature-controlled hot plate.

Results

Reduction of the oxygen evolution potential on Ni (at 25°C).—The discharge capacities in coulombs per square centimeter (C/cm²) are proportional to the number of cycles of activation applied to the different electrodes (Fig. 1) and indicate the amount of electrochemically active Ni(OH)₂ produced ("loading level") on the surfaces of the sintered Ni particles comprising the electrode.

During oxygen evolution at a given current density, the variation of electrode potential from point to point on the exterior surface of a particular electrode is relatively small compared with the overall effect of an increase in loading level. Table I shows the average electrode potential for six probe positions at each current density at 25°C after 0, 25, 50, 100, 200, or 300 cycles of the ac square-wave current activation. The data are not corrected for the iR drop between the probe tip and the electrode surface. This is very small [Hall (8) estimates 10-20 mV] and potentials are generally constant to less than ± 10 mV (Table I). The average electrode potentials for anodic current densities of 100, 200, and 250 mA/cm² are shown in Fig. 2 as a function of the number of ac cycles applied. Reductions of ~200 mV were achieved for the oxygen evolution reaction (OER) after a 200 cycle (800s) pretreatment, while even 25 cycles (100s) gave a substantial improvement of ~125 mV.

Stability of the lowered oxygen evolution potentials (at 25°C).—Increasing cell voltage with time is a problem in

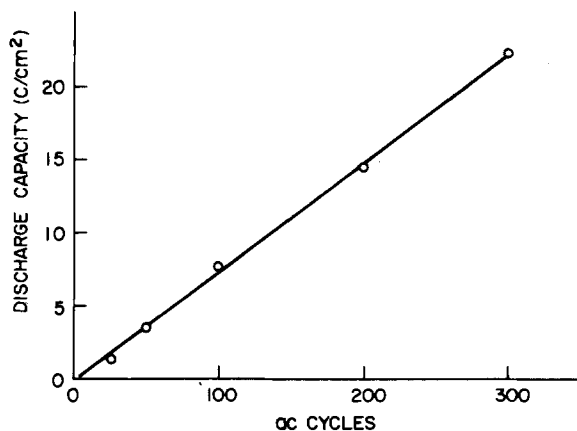


Fig. 1. Discharge capacities of ac activated electrodes in 30 w/o KOH at 250 mA/cm² after charging at 250 mA/cm² to oxygen evolution. Dependence on activation pretreatment is shown as the number of ac cycles at 0.25 Hz, ± 125 mA/cm² in 1M KCl.

Table I. Average electrode potentials and their standard deviations for up to six probe positions (mV vs. Hg/HgO) for oxygen evolution on sintered Ni electrodes before and after ac activation (in 30 w/o KOH at 25°C)

Current density (mA/cm ²)	25	50	100	150	200	250
No ac treatment	740 ± 5	774 ± 6	809 ± 7	832 ± 9	852 ± 11	868 ± 14
After 25 cycles	615 ± 7	642 ± 7	679 ± 9	706 ± 12	729 ± 14	748 ± 18
After 50 cycles	585 ± 2	612 ± 2	644 ± 2	667 ± 2	685 ± 2	701 ± 1
After 100 cycles	586	607 ± 1	636 ± 2	655 ± 3	669 ± 5	681 ± 4
After 200 cycles	—	585 ± 3	614 ± 4	636 ± 6	653 ± 8	669 ± 10
After 300 cycles	552 ± 2	575 ± 1	606 ± 3	626 ± 4	644 ± 6	659 ± 9

Table II. Effect of 1h of oxygen evolution at 100 mA/cm² on Ni electrode potentials at 25°C in 30 w/o KOH

Electrode	Electrode potential [V(Hg/HgO)] at various current densities (mA/cm ²)					
	25	50	100	150	200	250
Unactivated Ni	0.729	0.765	0.801	0.823	0.842	0.857
Unactivated Ni after 1h	0.769	0.803	0.839	0.860	0.878	0.894
Change in potential	+0.040	+0.038	+0.038	+0.037	+0.036	+0.037
After 20 min O.C.*	0.760	0.794	0.831	0.853	0.872	0.888
Ni with 25 cycles ac	0.623	0.651	0.688	0.717	0.742	0.763
Ni with 25 cycles after 1h	0.636	0.670	0.708	0.736	0.757	0.779
Change in potential	+0.013	+0.019	+0.020	+0.019	+0.015	+0.016
After 20 min O.C.*	0.629	0.657	0.694	0.721	0.745	0.766
Ni with 300 cycles ac	0.552	0.575	0.603	0.622	0.637	0.650
Ni with 300 cycles after 1h	0.558	0.582	0.609	0.627	0.642	0.655
Change in potential	+0.006	+0.007	+0.006	+0.005	+0.005	+0.005

* O.C. = Open circuit in 30 w/o KOH.

present hydrogen production (1). Table II shows that there is a trend towards higher electrode potentials at all current densities after prolonged gassing, but that this is also a function of the electrode pretreatment. An unactivated Ni sintered electrode showed as much as a 40 mV increase after 1h of gassing at 100 mA/cm², although at higher loading levels there was a smaller increase with time and so the electrode potential was more stable. This phenomenon was partially reversible on open circuiting: e.g., the 25 cycle electrode showed only ~6 mV increase in potential after 20 min on open circuit, previous to which there had been an average 17 mV increase at all current levels. The recovery after open circuiting unactivated Ni was also ~10 mV (Table II).

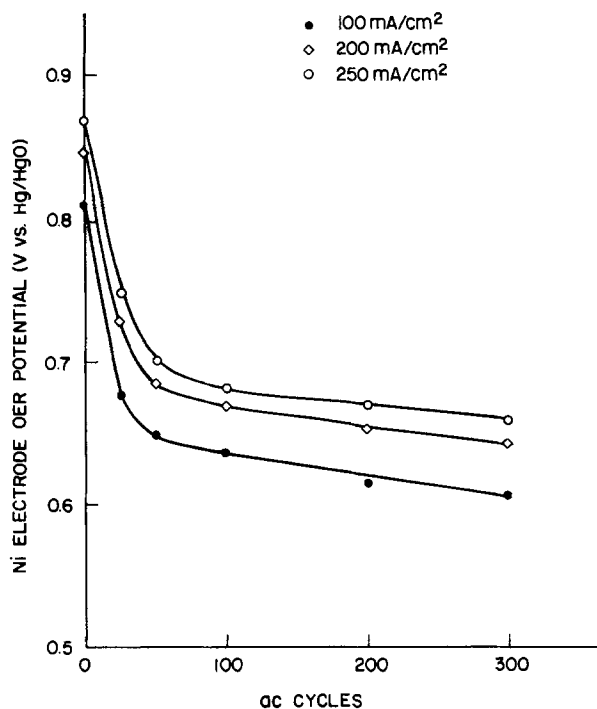


Fig. 2. OER potentials (V vs. Hg/HgO) in 30 w/o KOH at 25°C of Ni electrodes with different amounts of activation. ●: 100 mA/cm². ◇: 200 mA/cm². ○: 250 mA/cm².

Oxygen evolution potentials at 80°C.—In order to obtain a comparison with previously published work under commercial electrolyzer conditions (6), results were obtained at 80°C in 30% KOH for the ac activated electrodes over a 6h period of gassing at 200 mA/cm².

The data after 5h at 200 mA/cm² are shown in Fig. 3 and 4. As expected, the higher temperature initially produced lower OER potentials for all electrodes at each current density (compare Fig. 3 with Fig. 2) and the potentials of activated electrodes rose by no more than ~5 mV/h at any current density over the 6h test period of continuous gas-

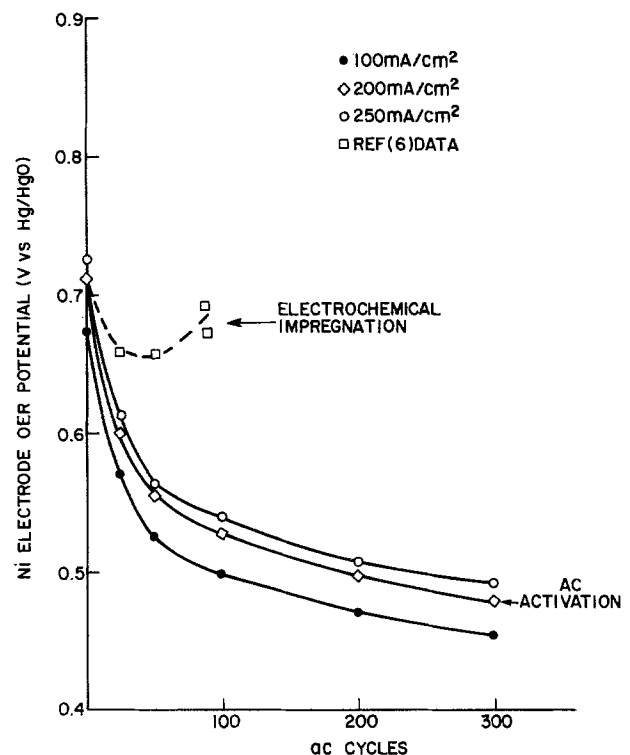


Fig. 3. OER potentials (V vs. Hg/HgO) in 30 w/o KOH at 80°C after 5h at 200 mA/cm² (at 80°C). Symbols as in Fig. 2. □: Data from Ref. (6) at 80°C after 6h at 200 mA/cm² (electrochemically impregnated electrodes).

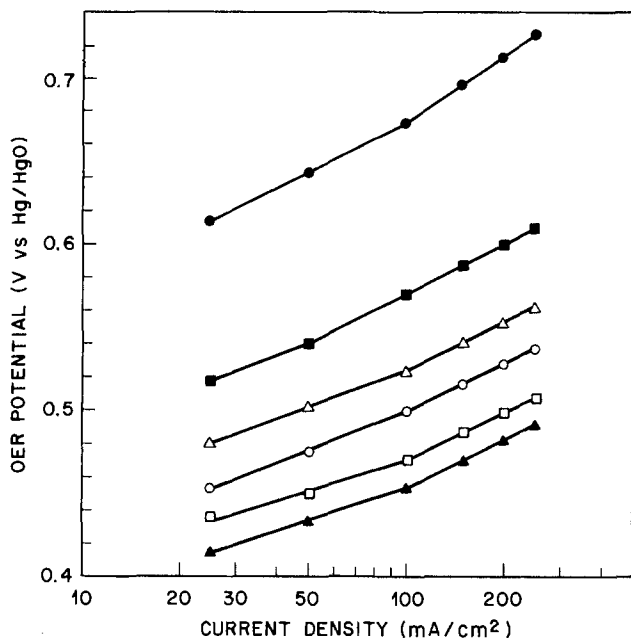


Fig. 4. Tafel plots after 5h at 200 mA/cm² in 30 w/o KOH at 80°C for Ni sinter which was unactivated (●), or activated with: 25 (■), 50 (△), 100 (○), 200 (□), or 300 (▲) ac cycles.

sing (Table III) and therefore generally rose less than during the first hour at 25°C and 100 mA/cm² (Table II). The largest reduction in potential, ~230 mV, was again shown by the 300 ac cycle electrode and is about 20 mV larger than the improvement at 25°C.

These reductions in electrode potential at 80°C are significantly larger than the 40-60 mV reductions previously reported (6) for other activation procedures, which were by impregnation of Ni(OH)₂ using either the chemical (9) or electrochemical technique (10) to similar loading levels (namely, 1.6-6 mg/cm², which would have an equivalent discharge capacity of ~1.6-6 C/cm²).

Discussion

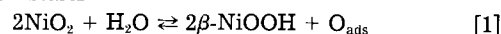
Methods of producing the nickel hydroxide catalyst on Ni surfaces have either been by prolonged anodic pretreatment in KOH (11) or, more recently, by electrochemical impregnation (6). Neither of these two methods seems to have produced the degree of improvement demonstrated by the ac activation. Hall (6) found that loadings of Ni(OH)₂ in the range 1.6-6.1 mg/cm² (projected area) gave the minimum OER potentials for 50% porous Ni electrodes impregnated electrochemically (10). Higher loading levels gave higher OER potentials, owing to "pore plugging." The loading levels of 1.6-6.1 mg/cm² correspond to discharge capacities of 1.7-6.3 C/cm² (based on 0.289 Ah/g Ni(OH)₂). The actual initial surface areas of Hall's electrodes were 140-180 cm² per cm² (projected), which were higher than the 120-140 cm² per cm² electrodes used in the present work. Note that both estimates are based on BET measurements. For direct comparison with ac activation, Hall's data, which were taken after 6h of gassing at 200 mA/cm² in 30% KOH at 80°C, are plotted on Fig. 3 at ac cycle numbers corresponding to the coulombic capacities of ac activated electrodes from Fig. 1, with the unactivated data superimposed to compensate for the iR corrections in Hall's work.

A much larger drop in OER potential results from equivalent Ni(OH)₂ loadings by ac activation. Also, no "blockage" effects appear at high loading levels up to 21.4 mg/cm², partly owing to the higher level of porosity (80%) of electrodes used in this work, but mostly to the uniform "nonblocking" nature of ac conversion of Ni to Ni(OH)₂ and the high surface area of the film produced (7). Higher sinter porosity does not account for the fourfold greater reduction in OER potentials compared with 50% porous structures (6). A uniform film thickness produced by ac

Table III. Maximum rate of electrode potential change (m V/h), after the first hour, of activated sintered electrodes during 6h of oxygen evolution at 200 mA/cm² in 30 w/o KOH at 80°C. Data at different current densities were taken every hour with the reference electrode probe in the same position

Electrode treatment (ac cycles)	Current density (mA/cm ²)					
	25	50	100	150	200	250
25	+2	+3	+3	+3	+3	+2
50	+3	+4	+3	+3	+5	+5
100	+3	+3	+2	+3	+2	+2
200	+2	+2	+2	+3	+3	+2
300	0	0	0	+1	0	+1

activation should allow most of the surface of the hydroxide film to participate in the OER. However, Appleby *et al.* (12) demonstrated that there was little difference in overpotentials for the OER on smooth, woven, or sintered Ni, so that the present results might be due to the smaller percentage of the total hydroxide film surface surrounding unblocked passages towards and at the outside of the activated sinter. It is these outer regions of the sinter that are particularly susceptible to blockage during electrochemical and chemical impregnation but are not blocked during the ac process (7). Experimental Tafel slopes for the 80°C data decreased with increase in the amount of ac activation from 100 to 65 mV per decade below 100 mA/cm² and from 135 to 95 mV per decade above 100 mA/cm² (Fig. 4). At 25°C, Tafel slopes were higher but also decreased with increase in ac activation, from 120 to 90 mV per decade below 100 mA/cm² and from 160 to 105 mV per decade above 100 mA/cm². Exchange current density determinations were not made. The OER mechanism is thought to involve Ni⁴⁺ in the surface of the oxyhydroxide (11, 13), to which Ni(OH)₂ has converted before the OER starts



So, in addition to the effect of a larger or more available surface area in lowering the true current density, the observed lower potentials of the OER on ac activated electrodes would promote more efficient reduction of Ni⁴⁺ to Ni³⁺ and hence oxygen evolution.

The rise of the OER potentials after 1h of gassing at 25°C (Table II) was greater for unactivated Ni sinter electrodes at all current densities than for activated electrodes. This, apparently, is related to the thickness or amount of the active Ni(OH)₂, originally deposited, since the 21.4 mg/cm² electrode (300 ac cycles) only gave a ~5 mV rise in OER potential after 1h, compared with ~17 mV for the 1.4 mg/cm² electrode (25 ac cycles). Since the rise in potential is partially reversible on open circuiting, a surface area decrease of the hydroxide films in these electrodes is unlikely. The effect could be due a rising Ni⁴⁺:Ni³⁺ ratio, which would inhibit the OER by converting active Ni³⁺ sites to inactive Ni⁴⁺ sites (11). It seems reasonable that a higher ratio of Ni⁴⁺ to Ni³⁺ would be more rapidly attained in the thinner films since, on average, the ions experience a higher field.

At 80°C, the rates of rise of OER potentials during the first hour at all current densities and for all electrodes was lower than at 25°C. For the unactivated electrode the rate was +6 to +10 mV/h during the first hour at all c.d.'s, while for the activated electrodes the rate was +2 to +6 mV/h. Table III shows the maximum increases in OER potentials after the first hour up to 6h of continuous gassing. The rates of rise were generally lower than during the first hour. These rates at 80°C for the activated electrodes are lower than for commercial electrodes during 5h of operation. An unactivated Ni-plated steel anode in 28% KOH at 70°C gave initial rates of increase in the OER potential of ~12 mV/h after 2h at 135 mA/cm², which fell to ~2 mV/h after 6h (1).

The generally lower rates of OER potential rise at 80°C even for unactivated Ni may be due to a rapid initial at-

tainment of a stable and higher surface activity (higher $\text{Ni}^{3+}:\text{Ni}^{4+}$) at the higher temperature.

Finally, a large part of the overall improvement in performance compared with electrochemically impregnated electrodes is due to the characteristic uniformity of thickness of films produced by the ac process (7), which ensures uniform film conductance. This uniformity of film thickness is due to a high effective "throwing power" caused also by the local nature of the dissolution/precipitation process. Dissolution of Ni is enhanced by adsorption of Cl^- ions from solution during the anodic half-cycle, causing Ni to dissolve rapidly then reprecipitate as hydroxide during the cathodic half-cycle (7) as the pH of the surface rises (14). This process also removes the risk of pore blockage endemic with electrochemical deposition of Ni hydroxide, where throwing power is much lower because deposition is dependent upon diffusion of Ni^{2+} ions within the highly tortuous pore structure to internal deposition sites.

Chloride ions were not detected in the ac produced films at levels above the detection limit of 0.1 atomic percent using Auger-electron spectroscopy and ion milling (7). Backscattered electron images from scanning electron microscopy showed a significant change in atomic-number contrast towards the ac produced film surfaces, indicating a very low density of Ni. The surfaces of the films are therefore probably highly porous with a high true surface area, allowing a lower $\text{Ni}^{4+}:\text{Ni}^{3+}$.

Application of ac activation to other types of Ni anode should be a straightforward extension of the technique. The high throwing power and small amount of Ni converted to catalytic oxyhydroxide would ensure the structural integrity of nickel substrates.

Further improvements in anode efficiency and life might be attainable through the presence of other components, such as cobalt ions, in the active $\text{Ni}(\text{OH})_2$ film. NiCo_2O_4 has been shown to be a good catalyst for the OER (15) and 1-10% of cobalt hydroxide codeposited with $\text{Ni}(\text{OH})_2$ has been shown to reduce film stress in battery plates (16). Other cations can be introduced into $\text{Ni}(\text{OH})_2$ films made by ac activation through additions to the electrolyte. Deposition, as the pH rises during the cathodic half-cycle, would include nickel ions dissolved during the preceding anodic half-cycle together with cations from the bulk solution.

Practical application of ac activation will probably make use of low voltage power-FET technology which, in the near future, should be able to provide the low frequency (< 1 Hz), large alternating currents needed, with high efficiency (17).

Conclusions

Ac activation is a simple and most effective method of raising energy efficiencies of Ni anodes for electrolytic hydrogen production. AC activated sintered Ni electrodes have demonstrated a 230 mV reduction in OER potential at normal operating current densities of a commercial water electrolyzer.

This reduction in cell voltage would translate into a considerably lowered cost of electrolytic hydrogen production, where 80% of the cost arises from electrical energy consumption within the cell.

Manuscript submitted March 8, 1984; revised manuscript received July 7, 1984.

AT&T Bell Laboratories assisted in meeting the publication costs of this article.

REFERENCES

1. R. L. LeRoy, M. B. I. Janjua, R. Renaud, and U. Leuenberger, *This Journal*, **126**, 1674 (1979).
2. R. L. LeRoy and A. K. Stuart, "Hydrogen Energy System," T. N. Veziroglu and W. Seifritz, Editors, Pergamon Press, Oxford, England (1978).
3. A. J. Konopka and D. P. Gregory, in "Proceedings of 10th Inter-Society Energy Conversion and Engineering Conference," p. 1184, IEEE, Newark, DE (1975).
4. G. Kissel, P. W. T. Lu, M. H. Miles, and S. Srinivasan, in "Proceedings of the 10th Inter-Society Energy Conversion and Engineering Conference," p. 1194 (1975).
5. K. E. Cox and K. D. Williamson, "Hydrogen: Its Technology and Implications," Vol. 1, CRC Press, Inc., Boca Raton, FL (1977).
6. D. E. Hall, *This Journal*, **130**, 317 (1983).
7. C. K. Dyer, *ibid.*, **132**, 13 (1985).
8. D. E. Hall, *ibid.*, **128**, 740 (1981).
9. A. J. Salkind and U. Falk, "Alkaline Storage Batteries," John Wiley and Sons, Inc., New York (1969).
10. E. J. McHenry, *Electrochem. Technol.*, **5**, 275 (1967).
11. P. W. T. Lu and S. Srinivasan, *This Journal*, **125**, 1416 (1978).
12. A. J. Appleby, G. Crepy, and J. Jacquelin, *Int. J. Hydrogen Energy*, **3**, 21 (1978).
13. J. Labat, *Ann. Chem.*, **9**, 399 (1964).
14. C. K. Dyer and R. S. Alwitt, *This Journal*, **128**, 300 (1981).
15. A. C. C. Tseung and S. Jasem, *Electrochim. Acta*, **22**, 31 (1977).
16. D. H. Fritts, *This Journal*, **129**, 118 (1982).
17. K. P. Lisiak and J. Berger, *IEEE Trans. Electron Devices*, **ed-25**, 1229 (1978); S. Waaben, in "Proceedings of INTELEC 1981," Institute of Electrical Engineers publication no. 196, p. 250, IEE, London (1981).

Electrochemical Properties of Silver-Nylon Fabrics

Andrew A. Marino, Visit Malakanok, and James A. Albright

Department of Orthopaedic Surgery, Louisiana State University Medical School, Shreveport, Louisiana 71130-3932

Edwin A. Deitch

Department of Surgery, Louisiana State University Medical School, Shreveport, Louisiana 71130-3932

Robert D. Specian

Department of Anatomy, Louisiana State University Medical School, Shreveport, Louisiana 71130-3932

ABSTRACT

Composites consisting of inert fiber substrates coated with metallic silver were shown to be potentially useful as a source of silver ions for infection control. Using an *in vitro* system, the ability of six silver-coated nylon fabrics to support an electric current was studied, and the resulting silver levels up to 23h after initiation of the current were measured. In four fabrics, $1.7 \mu\text{A}/\text{cm}^2$ for 16h produced fabric corrosion that prevented further current flow. Comparable changes in two other fabrics did not occur until $16 \mu\text{A}/\text{cm}^2$. At fixed current densities, the fabrics produced differing solution silver concentrations. For one fabric, the measured silver concentrations approached the theoretically predicted level. The results indicated that silver-nylon fabrics could produce antimicrobially significant silver levels at relatively low currents and voltages, and that the rate of ion production can be predicted on the basis of electrochemical considerations.

Silver compounds are used in clinical medicine because of their antiseptic properties (1). The prophylaxis of ocular infections and prevention and treatment of burn-wound sepsis are two examples. Beginning in the late 19th century, metallic silver in the form of sutures and foils was used to produce bacteriostatic effects via the passive disassociation of silver from the metallic phase into tissue (2). Metallic silver continued to be used clinically until the systemic antibiotics were introduced in the 1930's.

Interest in the possible use of metallic silver as a topical antimicrobial agent developed again in the 1970's, when a series of studies showed that electrically generated silver ions inhibited the growth of bacteria and fungi (3-8). The first attempt at clinical application of this concept involved the treatment of osteomyelitis (9). To increase the area of tissue actually exposed to silver ions, silver-coated nylon fabric as well as thin silver wire were used.

The concept of applying an antiseptic agent by passing a current through a metallized fabric has clinical appeal: (i) the dose can be regulated by controlling the current; (ii) the textile characteristics of the substrate can be chosen to produce an occlusive or nonocclusive dressing, as needed; (iii) since a typical wound dressing would contain only a few milligrams of silver, the cost of the dressing would be low.

To pursue this idea, the *in vitro* electrical properties of a commercially available class of silver-coated nylon fabrics were studied. Our aim was to elucidate the electrochemical response of the fabrics under conditions that simulated actual clinical use.

Methods

Six fabrics (Swift Textile Metalizing Corporation, Hartford, Connecticut) were studied. The fabric designations and some of their physical properties are listed in Table I. The fabrics consisted of woven or knitted nylon fibers, 20-50 μm diam, that had been uniformly coated with pure silver to a calculated average thickness of 0.02-0.4 μm , depending on the fabric. The coating process did not affect the handling characteristics or mechanical strength of the fabrics.

For dc studies, the fabrics were prepared as annular electrodes with tabs to permit introduction of the current (Fig. 1A). The fabrics were not treated prior to use except for a brief rinse in distilled water. In most experiments, the tabs were coated with an insulating material (Paraplast, Lancer, St. Louis, Missouri) to prevent wick action.

The Paraplast was applied to the tabs at 56°C and allowed to harden at room temperature; it did not affect the pertinent physical properties of the fabrics. In some cases, to increase the current per unit area of the fabric, part of the annular ring was removed (Fig. 1A). The fabrics were operated as anodes against silver-wire cathodes (23 cm of 0.5 mm diam silver wire) in the configuration shown in Fig. 1B. The cathode material and configuration were chosen for convenience, and they had no specific effect on events within the anodic chambers which did not vary when stainless steel, copper, or silver-nylon fabrics (surface area 0.16-60 cm^2) were used.

Silver measurements were made by atomic absorption spectroscopy using standard methods (10). Briefly, aliquots of the solution under study, after dilution if needed, were directly aspirated into an air-acetylene flame. Silver concentrations were determined by absorbance measurements (Perkin-Elmer 306, with a silver hollow-cathode lamp) with the use of standard curves generated by adding known concentrations of silver to the same medium as the test solution. The 328.0 nm resonance line of silver was used, and all measurements were made in triplicate and the results averaged.

Current was applied using a variable power supply (EICO 10645) and measured with an electrometer (Keithley, 610C) or a digital multimeter (Beckman 3020) (see Fig. 1). A second such multimeter was used for resistance

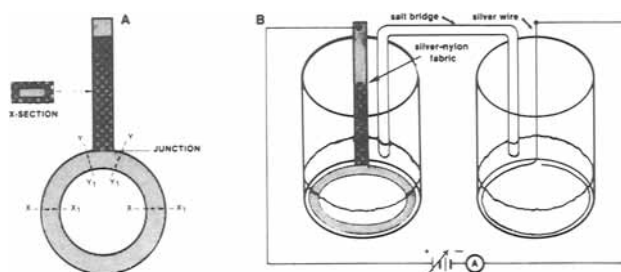


Fig. 1. The experimental system. (A) Geometry of the annular electrode. Two additional electrode geometries were used in some measurements. The semi-annular electrode produced by cutting the fabric at X-X₁ (and discarding the distal portion); the tab electrode produced by cutting the fabric at Y-Y₁. The surface areas were, respectively, 19, 9.5, 1 cm^2 . (B) For passage of current, the portion of the electrode distal to the junction was immersed in 50 ml of medium—either saline or tryptic soy broth—contained in 400 ml beakers. Electrical connection to the cathodal beaker was made via a tryptic-agar bridge.

Table I. Properties of silver-nylon fabrics

Fabric style	HRS	LRS	SN	R	4H	IT
Pattern	Weave	Weave	Knit	Knit	Knit	Knit
Cell shape	Square	Square	Square	Diamond	Hexagonal	Hexagonal
Cell size (mm)	Closed	Closed	Closed	4.8	2.5	0.76
Weight (g/m ²)	84.6	37.2	111.7	67.7	13.5	10.2
Silver content (μg/cm ²)	2545	783	4364	2371	500	371

Table II. Electrical resistance of silver-nylon fabrics as a function of immersion time in saline at 20° (upper) and 37°C (lower). Average and one standard deviation (*n* = 1 weighting) of triplicate determinations. NM: not measured

Fabric style	Resistance (Ω/□)				
	Nonimmersed	1h	4h	24h	96h
HRS	1.0 ± 0.2	1.4 ± 0.5 199.7 ± 182.2	3.5 ± 2.6 558.1 ± 552.6	>20 MΩ >20 MΩ	NM >20 MΩ
LRS	1.6 ± 0.8	2.1 ± 0.5 1.8 ± 1.8	3.0 ± 0.3 1.6 ± 1.1	2.0 ± 0.7 2.0 ± 2.0	NM 2.8 ± 0.5
SN	1.2 ± 0.2	1.3 ± 0.1 1.3 ± 0.1	1.3 ± 0.1 1.6 ± 0.1	3.4 ± 0.7 >20 MΩ	NM >20 MΩ
R	0.6 ± 0.1	1.1 ± 0.1 1.0 ± 0.1	0.9 ± 0.1 1.0 ± 0.1	1.0 ± 0.1 1.0 ± 0.1	NM 1.1 ± 0.1
4H	2.5 ± 0.5	3.7 ± 0.1 4.9 ± 1.3	3.6 ± 0.3 5.2 ± 0.8	6.1 ± 1.7 10.3 ± 3.0	NM 65.1 ± 60.2
IT	1.3 ± 0.1	1.9 ± 0.1 2.2 ± 0.5	1.8 ± 0.1 2.1 ± 0.1	2.2 ± 0.2 5.2 ± 0.3	NM 1300 ± 1900

measurements. The voltages reported were the potential differences applied between the chambers; they were monitored with a high impedance voltmeter (RCA WV 510-A). For scanning electron microscopy (SEM), 1 cm squares of fabric were cut out and adhered to aluminum scanning stubs with copper-impregnated tape. The specimens were examined and photographed in an AMR 1200 scanning electron microscope at an accelerating voltage of 25 kV.

The unmetallized fabrics did not undergo detectable changes in resistance when subjected to the conditions of immersion employed in this study. The electrical changes observed are, therefore, attributed to changes in the silver coating, and not the nylon itself.

Results

The fabrics exhibited changes in surface resistance following immersion in saline (Table II). A typical current *vs.* time curve for fabric HRS is shown in Fig. 2. At 1V after 9-10h, the current dropped precipitously. When the average current density was increased using a semi-annular or tab anode (the total current was unchanged), the current drop-off occurred at proportionately earlier times (Table III).

For immersion times greater than 24h, the resistance between any two points on the annular portion of the

HRS anode (or between any two points, one of which was in the annular portion) was essentially infinite regardless of whether it had been used to pass current or not. But for immersion times sufficiently short that the passive disassociation of silver from the fabric did not affect the total system current, the pattern of resistance measurements was related to the current density passed through the fabric and, more particularly, to the occurrence of the drop-off phenomenon. Before the drop-off, all resistance measurements, including those having a path across the junction, were on the order of 1Ω. Immediately after the drop-off, however, only resistance paths that did not cross the junction yielded low values; all paths through the junction showed essentially infinite resistance.

The sequence of measurements was repeated with IT which, unlike HRS, underwent negligible changes in resistance due to immersion in saline (Table II), and again the current drop-off was observed (Table III). Before the current drop-off occurred, all resistance measurements were on the order of 1Ω; after the drop-off, essentially infinite resistance across the junction was again measured.

The extent of the region at the junction manifesting the electrolytic effects on surface resistance depended on

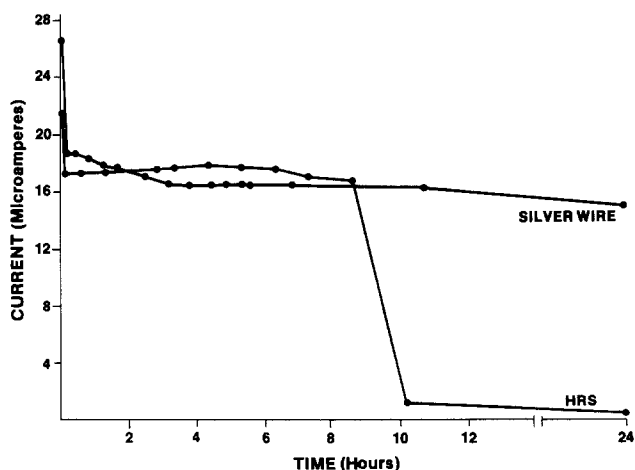


Fig. 2. Total current through HRS and silver-wire onodes: 1V, 20°C, in saline.

Table III. Maximum duration of current flow as a function of average current density. All measurements were made at 1V, 20°C, in saline

Fabric style	Electrode geometry	Current density (μA/cm ²)	Time to current drop-off (h)
HRS	Annular	0.85	10
	Semi-annular	1.70	5
	Tab	16	3
LRS	Annular	0.85	24
	Semi-annular	1.70	8-16
	Tab	16	2
SN	Annular	0.85	>24
	Semi-annular	1.70	>24
	Tab	16	17-23
R	Annular	0.85	>24
	Semi-annular	1.70	>24
	Tab	16	10-14
4H	Annular	0.85	21
	Semi-annular	1.70	10-14
	Tab	16	3
IT	Annular	0.85	17
	Semi-annular	1.70	10
	Tab	16	3

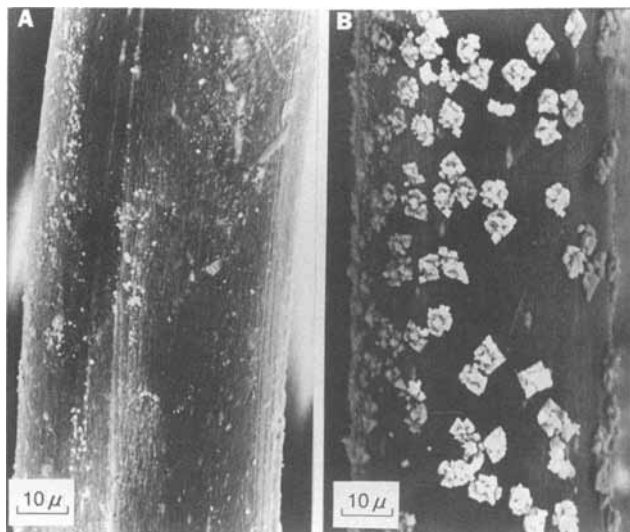


Fig. 3. Scanning electron micrograph of the junction region of IT. A: Control. B: after passage of current for 23h, 1V, 20°C, in saline.

electrode geometry and voltage. Generally, it was 1-3 cm², which corresponded to 10-100% of the electrode surface actually exposed to the solution.

4H and LRS exhibited behavior qualitatively similar to that of IT; they were stable (Table II) and exhibited both a current drop-off (Table III) and a corresponding high resistance in the neighborhood of the junction. R and SN were also stable, but were able to support a current for 24h for all but the highest current density (Table III).

SEM showed that the formation of surface-adhering crystals — presumed to be silver chloride — accompanied the passage of current. Figure 3, which depicts the crystal formation in the junction region of IT, is typical of the observed surface corrosion. By SEM, the density of crystal formation appeared to be greater in the junctional region compared to that in the opposite portion of the electrode (Fig. 4), but actual measurements were not performed. Al-

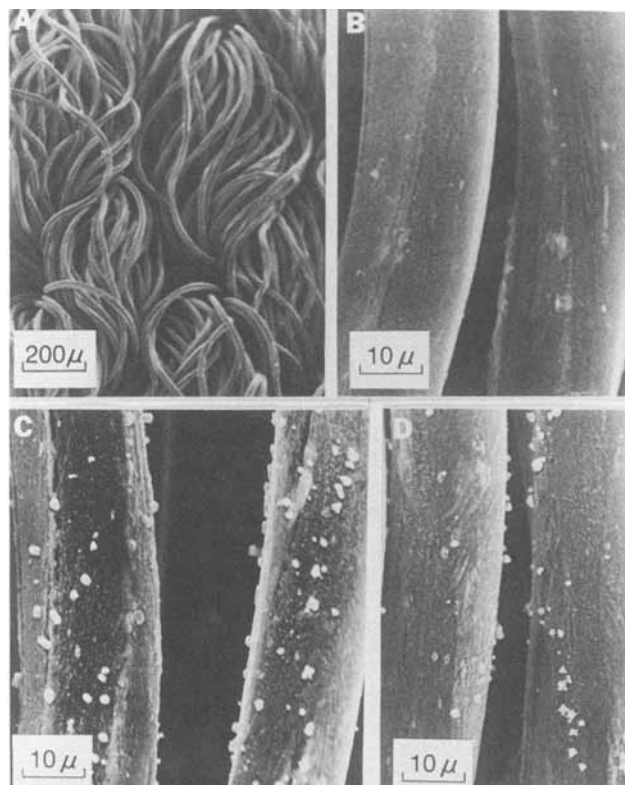


Fig. 4. Scanning electron micrograph of SN. A and B: control. C and D: after 1V, 20°C, in saline. C: region near the junction. D: region in the most distal portion of the electrode.

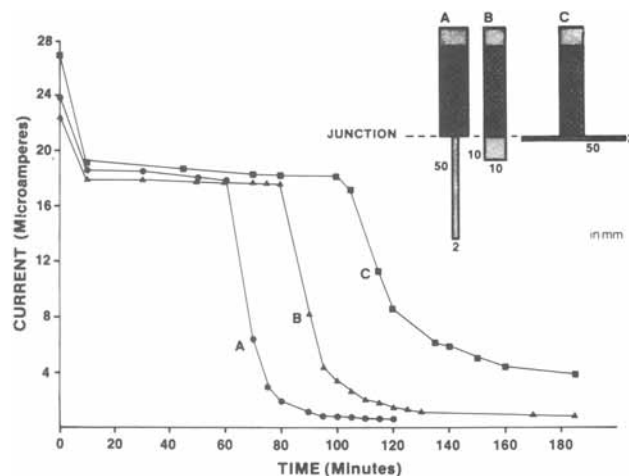


Fig. 5. Total current through HRS anodes having the same areas but differing in junction geometries. In saline, 20°C, 1V.

though the effect of the passage of current through the fabrics could be readily detected by SEM, there were no corresponding macroscopic changes in any of the fabrics.

To explore the role of the geometry of the junction itself when the average current density was held constant, we prepared electrodes having the same surface area but widely different junction geometries (Fig. 5). The narrowest junction exhibited both the most rapid onset of the current drop-off, and lowest base-line current. The 50 mm junction exhibited a diffuse current drop-off with the longest onset and highest base-line level. The 10 mm junction was intermediate with respect to both characteristics.

Knowledge of the electrical characteristics of the silver-nylon fabrics is important with regard to their contemplated clinical uses for infection control. Data regarding the fabrics' silver-ion releasing properties is also needed, because clinical efficacy requires tissue silver levels of 5-20 $\mu\text{g/ml}$ (6). We therefore measured the silver concentrations in tryptic soy broth (a standard medium that supports microbial growth).

The fabrics themselves did not undergo significant changes in resistance following immersion in the medium (Table IV). The silver measurements were made using annular anodes. At 1V, the total system current was approximately 22 μA (average current density: 1.2 $\mu\text{A/cm}^2$ of fabric). The silver levels released into solution by both passive disassociation and electrolysis (1 and 2V) up to 23h are shown in Table V.

Discussion

Previous work showed that HRS can be effective against micro-organisms (11); silver dissolved from the fabric's surface diffused through the medium and inhibited growth. This movement of silver has been confirmed indirectly by the present measurements of fabric resistances, which rise with immersion time, suggesting that silver ions are being liberated. It has also been confirmed by the direct measurement of silver in solution. After 23h, HRS liberated 2.6 $\mu\text{g/ml}$ of silver, which is essentially the same concentration deduced in the earlier study (11).

Table IV. Electrical resistance of silver-nylon fabrics after immersion in tryptic soy broth for 24h at 37°C. Average and one standard deviation ($n = 1$ weighting) of triplicate measurements

Fabric style	Resistance (Ω/\square) 24h
HRS	1.8 \pm 0.2
LRS	2.9 \pm 0.1
SN	1.7 \pm 0.1
R	1.0 \pm 0.1
4H	5.3 \pm 0.6
IT	2.4 \pm 0.1

Table V. Silver levels in tryptic soy broth (50 ml) at 37°C. Average and one standard deviation ($n = 1$ weighting) of triplicate measurements at (from top to bottom in each data group) 0 (control), 1, and 2V. NM: not measured

Fabric style	Silver concentration ($\mu\text{g/ml}$)				
	1h	2h	4h	7h	23h
Silver wire	<0.01	<0.01	<0.01	<0.01	<0.01
	1.1 ± 0.1 1.6 ± 0.3	2.1 ± 0.1 3.2 ± 0.4	4.4 ± 0.2 6.5 ± 2.0	7.0 ± 0.5 9.4 ± 1.9	21.3 ± 0.7 26.6 ± 6.4
HRS	0.8 ± 0.3	1.0 ± 0.3	1.4 ± 0.3	1.8 ± 0.3	2.6 ± 1.0
	1.4 ± 0.3	2.2 ± 0.5	3.9 ± 0.7	7.3 ± 0.6	14.0 ± 0.4
	3.1 ± 0.1	5.3 ± 0.6	10.2 ± 0.6	13.2 ± 0.1	$20.9 \pm 1.3^*$
LRS	0.4 ± 0.1	0.5 ± 0.1	0.7 ± 0.1	1.1 ± 0.1	1.1 ± 0.4
	1.6 ± 0.4	2.8 ± 0.1	6.0 ± 0.1	10.2 ± 0.4	$21.8 \pm 0.6^*$
	NM	NM	NM	NM	NM
SN	2.3 ± 0.2	3.0 ± 0.2	4.4 ± 0.4	5.8 ± 0.6	11.5 ± 1.2
	3.2 ± 0.2	4.7 ± 0.2	8.3 ± 0.2	12.1 ± 0.4	21.3 ± 1.7
	3.4 ± 0.3	6.4 ± 0.6	11.2 ± 0.7	15.2 ± 0.9	25.0 ± 5.2
R	1.4 ± 0.2	1.9 ± 0.2	3.0 ± 0.3	4.0 ± 0.4	8.0 ± 0.6
	2.3 ± 0.1	3.5 ± 0.2	7.2 ± 0.2	10.6 ± 0.6	23.4 ± 1.0
	4.2 ± 0.2	7.9 ± 1.6	15.4 ± 1.2	20.7 ± 2.1	29.6 ± 2.5
4H	0.7 ± 0.1	0.9 ± 0.1	1.4 ± 0.1	1.9 ± 0.2	3.0 ± 0.9
	2.5 ± 0.6	4.3 ± 0.6	7.9 ± 1.2	11.8 ± 1.7	$31.6 \pm 1.7^*$
	4.6 ± 0.4	8.6 ± 0.2	17.6 ± 0.3	$23.6 \pm 0.8^*$	NM
1T	0.5 ± 0.1	0.6 ± 0.1	1.0 ± 0.1	1.4 ± 0.1	2.6 ± 0.6
	2.6 ± 0.7	4.4 ± 0.7	7.9 ± 0.9	12.9 ± 0.6	$33.2 \pm 1.6^*$
	4.8 ± 0.2	9.4 ± 0.1	19.3 ± 0.2	$24.5 \pm 1.3^*$	NM

* Current drop-off observed.

All the fabrics produced silver when immersed in the medium, and the resulting silver levels varied by about a factor of 6 during the first 8h; at 23h, the range was greater than a factor of 10 (LRS compared to SN). Silver levels produced by silver wire under identical experimental conditions were below the level of detection (0.01 $\mu\text{g/ml}$). The surface area of the silver-wire anode was 3.6 cm^2 . The geometric surface of the fabrics was 19 cm^2 , but the actual surface area varied depending on the particular fabric. Based on the fabric properties listed in Table I, and assuming a fiber diameter of 20 μm (50 μm for 1T), it can be shown the actual surface area, depending on the fabric, was 0.8-22 times as great as the corresponding geometric area. Thus the fabric anodes had 4-116 times the surface area of the silver anodes. Consider SN, which is the most extreme case. It had a calculated actual surface area 22 times that of its geometric area. The area of the SN anode was, therefore, $22 \times 19/3.6 \approx 116$ times that of the silver-wire anode. Although there was a difference of two orders of magnitude in the surface areas, there was a difference of at least three orders of magnitude in the corresponding silver levels produced by passive disassociation (Table V). This indicated that the metallic silver coating on SN was significantly more labile than silver wire. Similar calculations for the other fabrics lead to the same conclusion.

The passage of current through the fabrics resulted in increased silver levels. When the silver levels at 1 and 2V were corrected for the base-line levels, the materials ranked as follows in decreasing order of relative electrolytic efficiency with regard to liberating silver: 1T, 4H, LRS, silver wire, R, SN, HRS, at 1V up to 7h; 1T, 4H, R, HRS, SN, silver wire, at 2V up to 4h. Faraday's law gives as the upper limit for silver production 4 $\mu\text{g}/\mu\text{A}\cdot\text{h}$. In Fig. 6, the range of measured silver levels produced by the fabrics and silver wire is compared to the theoretical level. 1T was the most faradaic of the materials in that it produced silver levels close to the predicted values.

It is the total silver concentration that determines whether microbial growth will be inhibited. Under the conditions we employed, the threshold of such an effect (approximately 5 $\mu\text{g/ml}$) occurred after 2h at 1V and after 1h at 2V. Under different but realistic experimental conditions, this threshold could probably be achieved even more quickly.

1T was one of the most interesting of the fabrics studied. Even though it was the lightest and least-silvered fab-

ric (Table I), it produced high silver concentrations (Table V). Its major drawback was that it was among the fabrics most prone to exhibit the current drop-off (Table III).

The current drop-off phenomenon apparently arises from the preferential liberation of silver ions at the junction zone. We know of no theoretical reason to expect that the current density would be greater near the junction, but such an occurrence would explain both the high resistance region found at the junction and the SEM observations of increased corrosion at that location.

We have shown that the fabrics will electrolytically liberate silver ions into solution, producing silver levels that would be expected to inhibit the growth of micro-organisms. Studies to be published elsewhere have established this activity against gram-positive and gram-negative bacteria and fungus (12). Clinical application of the silver-nylon fabrics will require attention to both the design of the electrode and its geometric relationship to the treatment site. The current drop-off phenomenon exhibited by the fabrics will probably not impede their development for clinical use.

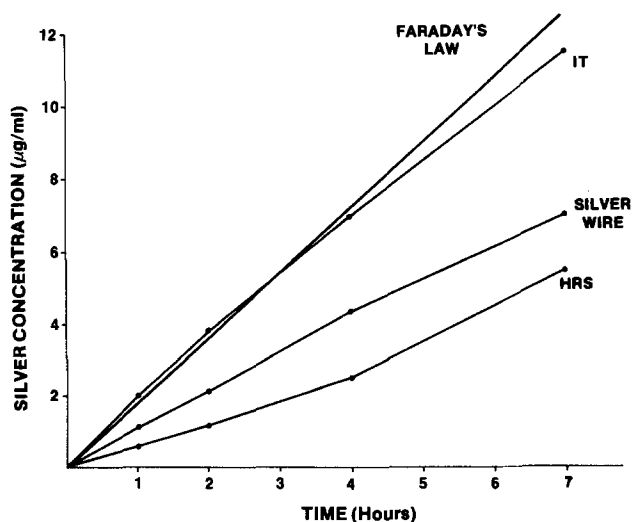


Fig. 6. Electrically produced silver concentrations (corrected for base-line levels) compared to theoretical maximum concentrations. In tryptic soy broth, 1V, 37°C.

Manuscript submitted July 9, 1984; revised manuscript received Aug. 21, 1984.

REFERENCES

1. A. G. Goodman, L. S. Goodman, and A. Gilman, "Goodman and Gilman's Pharmacological Basis of Therapeutics," 6th ed., p. 976, MacMillan Publishing Co., New York (1980).
2. W. S. Halsted, *J. Am. Med. Assoc.*, **60**, 1119 (1913).
3. S. D. Barranco, J. A. Spadaro, T. J. Berger, and R. O. Becker, *Clin. Orthop.*, **100**, 250 (1974).
4. V. W. Golubovich and I. L. Rabotnova, *Microbiology*, **43**, 948 (1974).
5. J. A. Spadaro, T. J. Berger, S. D. Barranco, S. E. Chapin, and R. O. Becker, *Antimicrob. Agents Chemother.*, **6**, 637 (1974).
6. T. J. Berger, J. A. Spadaro, S. E. Chapin, and R. O. Becker, *ibid.*, **9**, 357 (1976).
7. T. J. Berger, J. A. Spadaro, R. Bierman, S. E. Chapin, and R. O. Becker, *ibid.*, **10**, 856 (1976).
8. E. A. Thibodeau, S. L. Handelman, and R. E. Marquis, *J. Dent. Res.*, **57**, 922 (1978).
9. R. O. Becker and J. A. Spadaro, *J. Bone Joint Surg.*, **60A**, 871 (1978).
10. D. G. Van Ormer, in "CRC Handbook of Spectrophotometric Data of Drugs," I. Sunshine, Editor, p. 349, CRC Press, Boca Raton, FL (1980).
11. E. A. Deitch, A. A. Marino, T. E. Gillespie, and J. A. Albright, *Antimicrob. Agents Chemother.*, **23**, 356 (1983).
12. A. A. Marino, E. A. Deitch, V. Malakanok, J. A. Albright, and R. E. Specian, *J. Biol. Phys.*, To be published.

Current Efficiency Losses in Indirect Electrochemical Processing

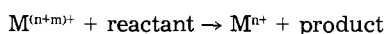
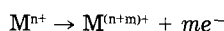
Ch. Comninellis, Ch. Griessen, and E. Plattner

Institut de génie chimique, Ecole Polytechnique Fédérale de Lausanne, CH-1015 Lausanne, Switzerland

ABSTRACT

The loss of current efficiency in the indirect two-stage electrochemical process using the Mn^{2+}/Mn^{3+} system is due to the oxidation of organics present in the recycled electrolyte. There is no evidence of electrode poisoning under the experimental conditions studied (88% H_2SO_4 ; Pt anode, 85°C).

At the present time, there is considerable industrial interest in the indirect two-stage electrochemical process ("ex-cell" process) for the synthesis of organic compounds. In this process, a carrier (M^{n+}) is electrochemically oxidized (or reduced) and then allowed to react with the organic compound in a separate vessel. When reaction is complete, a separation of product takes place and the spent liquor is returned back to the electrochemical cell, where the carrier is regenerated



This method and its advantages have been described in a number of publications (1, 2), but its application on an industrial scale is limited. One reason why this process has not become common is the loss in current efficiency observed in working process due to organic matter present in the recycled electrolyte (3, 4). In this paper, the reason for current efficiency losses in the indirect two-stage process using the Mn^{2+}/Mn^{3+} system has been studied by cyclic voltammetry and by preparative electrolysis.

Mechanisms of Current Efficiency Losses

Current efficiency losses observed in the indirect two-stage electrochemical process can occur by two main mechanisms: oxidation of the organic compound carried over with the recycled electrolyte (mechanism I), and electrode poisoning (mechanism II).

Current efficiency losses due to oxidation of the organic compound.—In this mechanism, the only reason for current efficiency loss is the oxidation of the organic compound (mainly to CO_2) at the anode and/or with the carrier $M^{(n+m)+}$ formed electrochemically. The loss of coulometric charge is defined as the charge of induction period [Q_{ind}] and can be estimated from the charge needed for complete combustion of the organic compound [Q_{comb}] from the relation

$$[Q_{ind}] = K[Q_{comb}] \quad [1]$$

The constant K in this relation is equal to 1 if the organic compound is completely oxidized to CO_2 and is smaller than one if the oxidation is not complete (formation of CO, fatty acids, and others). This type of inefficiency can

be characterized as reversible because after the partial or complete oxidation of the organic compound, the electrochemical regeneration of M^{n+} is carried out as in the absence of organics.

Current efficiency losses due to electrode poisoning.—In this mechanism, the organic compound forms a film at the anode, modifying its electrochemical properties; it may change the standard rate constant (k_s) for the couple $M^{n+}/M^{(n+m)+}$ and/or influence the overpotential for oxygen evolution. For example, if k_s for the couple $M^{n+}/M^{(n+m)+}$ is strongly decreased and the overpotential for oxygen evolution is not changed, the oxidation of water competes with the oxidation of M^{n+} producing a large amount of oxygen. In this type of inefficiency, it is difficult to establish a quantitative relationship to estimate the loss of charge due to oxygen generation. This type of inefficiency can be characterized as irreversible if the poison is electrochemically inactive and as reversible if it can be oxidized.

Both of these mechanisms have already been discussed by Kuhn (3), who has studied the electrochemical regeneration of Cr^{6+} in the oxidation of o-toluene sulfonamide to saccharin. He has shown that two main reasons contribute to current efficiency losses: namely oxidation of organics (mechanism I), and oxygen evolution due to the formation of a film at the anode (mechanism II). Lin-Cai and Pletcher (5) have studied the influence of organics (benzyl alcohol) in the electrochemical oxidation of Cr^{3+} using cyclic voltammetry. They concluded that an organic film was formed at the electrode which increases the current due to oxygen evolution (mechanism II).

In preliminary work (6), the volume of gas evolved during the anodic oxidation of Mn^{2+} in the presence of organics (bibenzanthrone) was measured and a partial analysis of CO_2 was made. We assumed that the remainder was oxygen. In this paper, the reason for current efficiency losses in the indirect two-stage process using Mn^{2+}/Mn^{3+} has been studied using cyclic voltammetry and analyzing the gas evolved during electrolysis by gas chromatography.

Experimental

Preparative electrolysis was carried out in an electrolytic cell of 150 ml capacity. The anode was made of a

Table I. Classification of organic compounds according to their action on the selectivity of Mn(II) oxidation

Class of compounds	Studied compounds	Group
Paraffins	Octane	A
Cycloparaffins	Cyclohexane	A
Fatty acids ^a	Acetic acid	A
Aliphatic diacids	Oxalic	B
	Malonic	
	Tartaric ^b	
Ketones	Acetone	B
Cycloketones	Cyclohexanone	B
Aromatic	Benzoic acid	B
	Benzenesulfonic acid	
	Benzaldehyde	
	Phenol	
	4,4 Bibenzanthrone	

^a An exception is formic acid, which belongs to group B.

^b Tartaric acid is also decomposed in hot concentrated H₂SO₄.

platinum sheet (10 cm² area), and the cathode was a platinum spiral enclosed in a 10 ml porous porcelain pot (ABS); the anolyte was a slurry of MnSO₄ · H₂O (0.66 mol dm⁻³ suspension) and Ag₂SO₄ (6 × 10⁻³ mol dm⁻³) in 88% w/w H₂SO₄; the catholyte was H₂SO₄ 88% w/w. The electrolysis was carried out at constant current density (100 mA cm⁻²) and temperature (85°C). The amount of Mn³⁺ formed in the anolyte was determined by potentiometric titration with Fe²⁺. Gas evolved during electrolysis was stripped from the electrolyte with helium, and analyzed by gas chromatography with a TC detector at regular intervals by automatic injection in a column separating O₂, N₂, CO₂, and CO.

The voltammetric experiments were performed in a conventional three-electrode cell. A platinum wire (0.55 cm² area) was used as working electrode, and a platinum sheet (10 cm² area) as counterelectrode. Hg/Hg₂SO₄ · sat K₂SO₄ [0.656V (NHE) at 25°C] was used as reference electrode. All potentials in this paper are quoted against this electrode. A Tacussel potentiostat and a PAR 175 signal generator were used for the experiments, and voltammograms were recorded either on a Honeywell X-Y recorder or a Tektronic X-Y memory oscilloscope. All voltammetric experiments have been carried out in 88% w/w H₂SO₄ at 85°C. The concentration of MnSO₄ was 2 × 10⁻² mol dm⁻³ when present and concentrations of or-

ganic compounds were varied between 1 × 10⁻³ and 5 × 10⁻² mol dm⁻³ when present.

Results and Discussion

Preparative electrolysis. — In order to study the influence of organics on the selectivity of Mn²⁺ oxidation (in presence of Ag⁺ as catalyst), the electrochemical oxidation of Mn²⁺ to Mn³⁺ was carried out in the presence of different organic compounds. It was found that the behavior of organics toward the selectivity of Mn²⁺ oxidation can be related to the stability of the organic toward oxidation. Thus, compounds which are stable toward oxidation in the potential range of Mn³⁺ do not influence the selectivity of Mn²⁺ oxidation (group A compounds in Table I), as opposed to compounds which are easily oxidized and which influence very strongly the selectivity of the reaction, decreasing the current efficiency of Mn³⁺ formation (group B compounds in Table I). In order to study the mechanism of current efficiency losses, benzoic acid was chosen as model aromatic compound (group B).

The electrochemical oxidation of Mn²⁺ to Mn³⁺ in the presence of benzoic acid has an induction period (Fig. 1a), which means that some time is required before the maximum rate of Mn³⁺ formation occurs. The loss of charge observed in the induction period [Q_{ind}] is proportional to the benzoic acid concentration (Fig. 1b) and increases the applied current density (Fig. 2). The increase of [Q_{ind}] with the applied current density is due to oxygen evolution, which is favored at high current density even in the absence of organics. The constant K in the relation [1] is smaller than 1, indicating a partial oxidation of benzoic acid.

Figure 3 shows the composition of gases obtained during the electrochemical oxidation of Mn²⁺ in the presence of benzoic acid. Three regions can be distinguished.

Region I.—In this region, the charge is mainly consumed for the oxidation of benzoic acid (to CO and CO₂) at the anode and/or with Mn³⁺ (and/or Ag²⁺) formed electrochemically.

Region II.—The oxidation of Mn²⁺ to Mn³⁺ occurs with the same instantaneous yield as in the absence of organics.

Region III.—The conversion of Mn²⁺ to Mn³⁺ is complete and oxygen evolution is the main reaction.

The fact that in region I the amount of oxygen formed is the same or less as that obtained in absence of organics and that there is a good agreement between the loss of

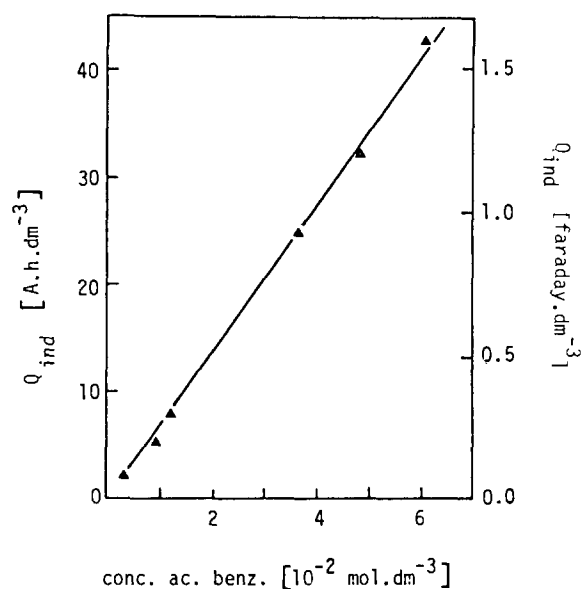
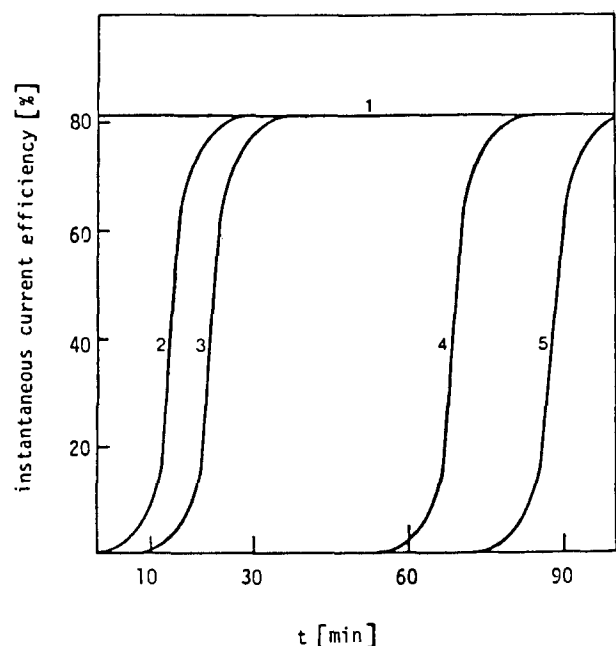


Fig. 1. a(left): Variation of induction periods for different concentrations of benzoic acid. Volume of electrolyte: 135 ml; T : 85 °C; current density: 300 mA cm⁻²; 88% H₂SO₄; Ag₂SO₄ 5 × 10⁻³ mol dm⁻³; MnSO₄ 0.66 mol dm⁻³; benzoic acid: 0, 1.23 × 10⁻³, 1.64 × 10⁻³, 4.92 × 10⁻³, and 6.56 × 10⁻³ mol for curves 1-5, respectively. **b(left):** Reported values of [Q_{ind}] as a function of concentration of benzoic acid.

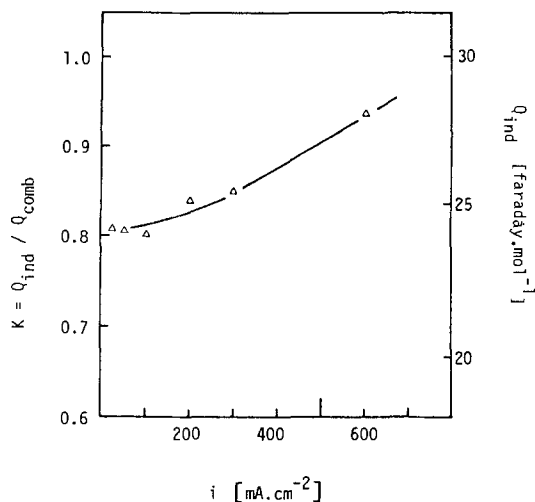


Fig. 2. Influence of current density on $K = [Q_{ind}/Q_{comb}]$ for benzoic acid $2.43 \times 10^{-2} \text{ mol dm}^{-3}$, in a solution of MnSO_4 0.66 mol dm^{-3} in $88\% \text{ H}_2\text{SO}_4$, at 85°C .

charge and the charges for the oxidation of benzoic acid to CO and CO_2 (Table II) indicates that the losses in current efficiency are due to an oxidation mechanism (mechanism I).

Reaction of organics with Mn^{3+} .—The chemical reaction of Mn^{3+} in excess with organic compounds has been studied by measuring the concentration of Mn^{3+} and by analyzing the gas evolved during the reaction. It has been found that only organics of group B react with Mn^{3+} , producing mainly CO_2 and CO . Figure 4 shows the rate of oxidation of benzoic acid (taken as model aromatic compound) by means of disappearance of Mn^{3+} .

Electrochemical measurements.—Figure 5a shows typical cyclic voltammograms (at different sweep rates) for the $\text{Mn}^{2+}/\text{Mn}^{3+}$ couple in presence of organics of group A, while Fig. 5b shows reported values of i_p vs. the square root of sweep rate ($v^{1/2}$). The diffusion coefficient of Mn^{2+} can be calculated from the linear dependence of $i_p - v^{1/2}$ using the relation (Randles-Sevcik equation)

$$i_p = kn^{3/2}D^{1/2}cv^{1/2}$$

where $k = 2.45 \times 10^5$ for the experimental conditions.

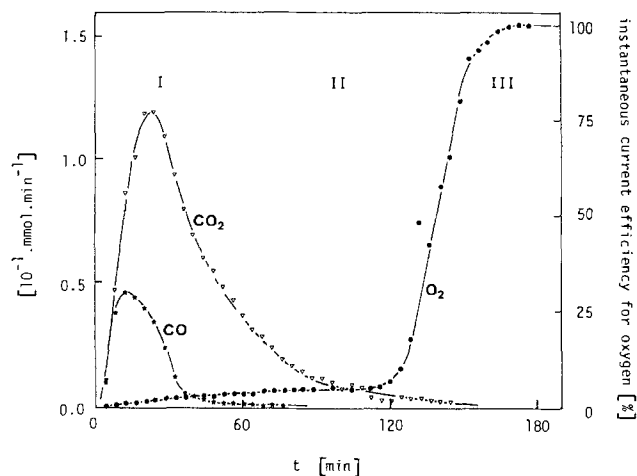
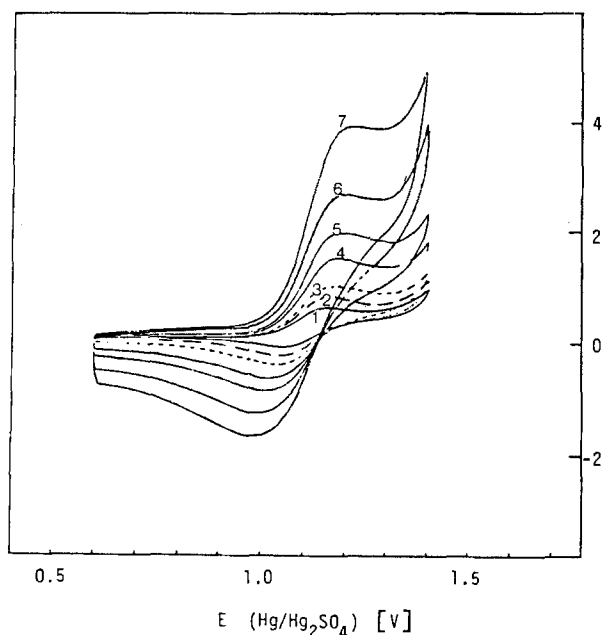


Fig. 3. Evolved gases during electrolysis of Mn^{2+} to Mn^{3+} in presence of benzoic acid. Volume of electrolyte: 135 ml ; $T: 85^\circ\text{C}$; MnSO_4 0.44 mol dm^{-3} ; benzoic acid $1 \times 10^{-3} \text{ mol}$; current density: 100 mA cm^{-2} .

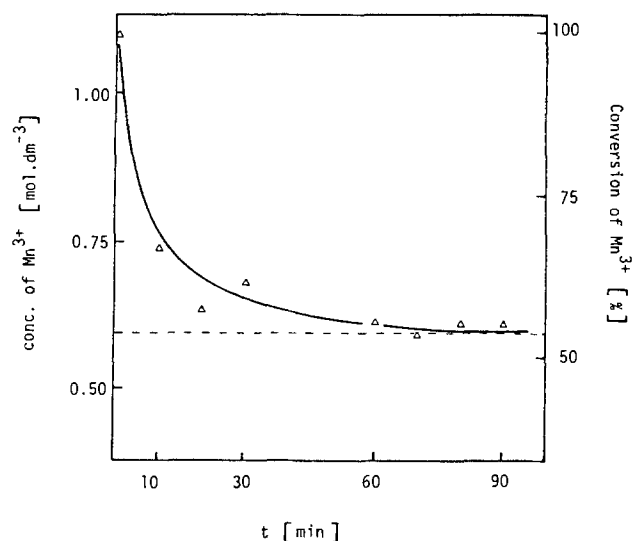


Fig. 4. Conversion of Mn^{3+} in excess with benzoic acid. Volume of solution: 135 ml ; $T: 85^\circ\text{C}$; benzoic acid $2.43 \times 10^{-2} \text{ mol dm}^{-3}$.

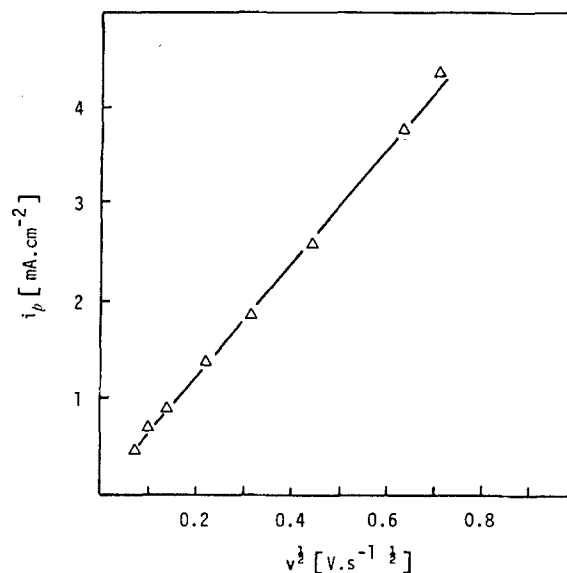


Fig. 5. a(left): Cyclic voltammograms of $\text{Mn}^{2+}/\text{Mn}^{3+}$ couple, in presence of acetic acid, at different sweep rates. $88\% \text{ H}_2\text{SO}_4$; $T: 85^\circ\text{C}$; MnSO_4 $2 \times 10^{-2} \text{ mol dm}^{-3}$; acetic acid $1 \times 10^{-2} \text{ mol dm}^{-3}$; scan rate: 5, 10, 20, 50, 100, 200, and 400 mV s^{-1} for curves 1-7, respectively, b(right): Reported values of peak current as a function of $v^{1/2}$.

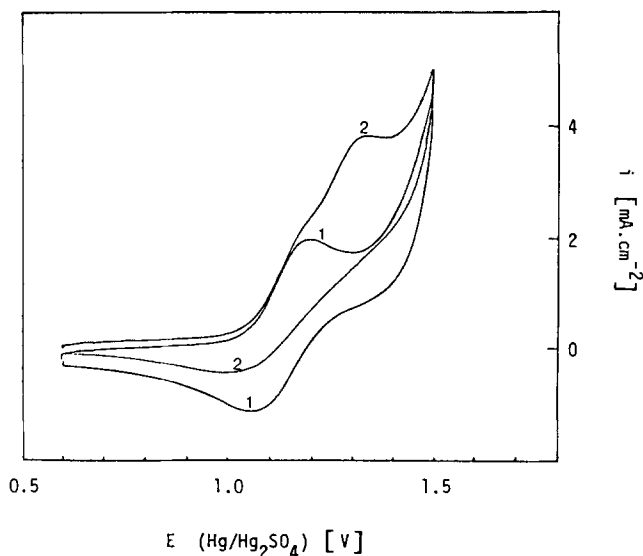


Fig. 6. Cyclic voltammogram of $\text{Mn}^{2+}/\text{Mn}^{3+}$. 88% H_2SO_4 ; T : 85°C; MnSO_4 2×10^{-2} mol dm^{-3} . (1): In absence of benzoic acid. (2): In presence of benzoic acid $\sim 1 \times 10^{-3}$ mol dm^{-3} .

The calculated value ($1.4 \pm 0.3 \times 10^{-6}$ $\text{cm}^2 \text{s}^{-1}$) agrees well with that given from Mn^{2+} in absence of organics (7).

From the separation of anodic and cathodic peak potential (ΔE_p), the constant (k_s) for the $\text{Mn}^{2+}/\text{Mn}^{3+}$ couple (in the presence of organics of group A) can be calculated using the relation proposed by Nicholson (8)

$$\psi = \gamma^{\alpha} k_s / \sqrt{\pi a D_0}$$

where $a = nFv/RT$, and $\gamma = (D_0/D_R)^{1/2}$ is approximately 1. Voltammograms obtained in Fig. 5a show a $\Delta E_p = 140$ mV at 100 mV s^{-1} ; thus, the value for k_s obtained in the presence of organics of group A is

$$k_s = 1.0 \pm 0.3 \times 10^{-3} \text{ cm s}^{-1}$$

This value of k_s for the $\text{Mn}^{2+}/\text{Mn}^{3+}$ couple is almost the same as that obtained in absence of organics ($1.2 \pm 0.3 \times 10^{-3}$ cm s^{-1}).

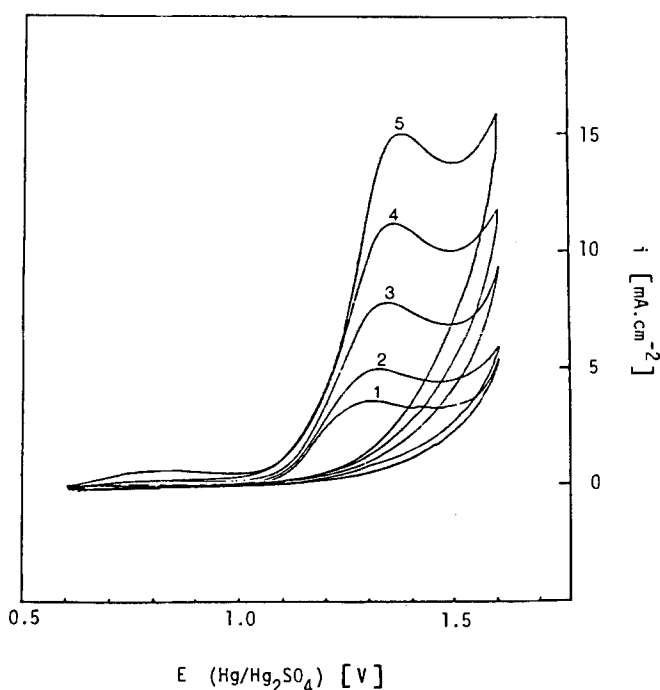


Fig. 7. a(left): Cyclic voltammograms of $\text{Mn}^{2+}/\text{Mn}^{3+}$ in presence of benzoic acid at different sweep rates. 88% H_2SO_4 ; T : 85°C; MnSO_4 2×10^{-2} mol dm^{-3} ; benzoic acid 1×10^{-2} mol dm^{-3} ; scan rate 10, 20, 50, 100, and 200 mV s^{-1} for curves 1-5, respectively. b(right): Reported values of peak current as a function of $v^{1/2}$. (1): MnSO_4 2×10^{-2} mol dm^{-3} + benzoic acid 1×10^{-2} mol dm^{-3} . (2): MnSO_4 2×10^{-2} mol dm^{-3} .

Table II. Comparison of losses (caulometric charge or oxidant charge) for electrochemical and chemical reaction

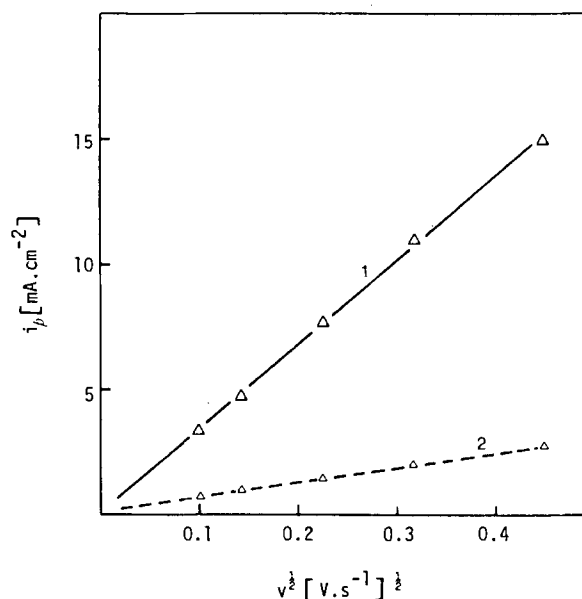
	Q_{ind} ($\text{F} \cdot \text{mol}^{-1}$)	Q_{CO_2} ($\text{F} \cdot \text{mol}^{-1}$)	Q_{CO} ($\text{F} \cdot \text{mol}^{-1}$)	Q_{O_2} ($\text{F} \cdot \text{mol}^{-1}$)
Benzoic acid				
Electrochemistry	24 ± 2	18.0	2.3	1
Chemistry	21 ± 2	15.4	1.8	0

Organic compounds of group B are electrochemically active. Figure 6 shows cyclic voltammogram for the oxidation of Mn^{2+} in presence of benzoic acid (curve 2), in reference to the oxidation of Mn^{2+} without an organic (curve 1). The peak of reduction is affected by the presence of benzoic acid, that being the result of the chemical reaction, and the value of ΔE_p for $\text{Mn}^{2+}/\text{Mn}^{3+}$ is slightly increased. The standard rate constant for $\text{Mn}^{2+}/\text{Mn}^{3+}$ couple is approximately identical to the k_s obtained in presence of an organic of group A.

For a larger concentration of benzoic acid (in presence of Mn^{2+}) the reduction peak of Mn^{3+} is completely absent, as shown in Fig. 7a, and the anodic peak for the oxidation of Mn^{2+} is no longer visible, but Mn^{2+} is still active: the diffusion coefficient for Mn^{2+} calculated from the slope of $i_p - c_{\text{Mn}^{2+}}$ has been found to be the same as in the absence of benzoic acid. In Fig. 7b are reported values of $i_p - v^{1/2}$ for the oxidation of benzoic acid in presence of Mn^{2+} , showing that the oxidation of organic compound is effected in a diffusion-controlled process. Values of $i_p - v^{1/2}$ for the oxidation of Mn^{2+} are reported for comparison.

Conclusions

It has been shown that, under the experimental conditions studied, the current losses were due to oxidation of the organic compound at the anode or with Mn^{3+} . Evolved oxygen is never greater than that obtained in absence of organics during the electrolysis, and is never present during chemical reactions. Compounds which are stable in presence of Mn^{3+} are electrochemically inactive at the studied potentials (group A); compounds which are unstable in presence of Mn^{3+} are electrochemically active (group B). Oxidized products of group B, resulting from electrochemical or chemical reaction, are approximately



the same. The standard rate constant for the oxidation of Mn^{2+} (k_s) is slightly affected by the presence of the organics of both groups A and B, but there is no poisoning of the electrode to permit oxygen evolution.

Manuscript submitted Feb. 23, 1984; revised manuscript received Sept. 3, 1984.

Ecole Polytechnique Fédérale de Lausanne assisted in meeting the publication costs of this article.

LIST OF SYMBOLS

c	concentration of electroactive species (mol cm^{-3})
i	current density (A cm^{-2})
i_{pa} , i_{pc}	current density of anodic and cathodic peaks
k	Randles and Sevcik constant
k_s	standard rate constant (cm s^{-1})
n	number of electrons exchanged
v	potential sweep rate (V s^{-1})
w/w	weight/weight
ABS	porous porcelain diaphragm
D_o , D_R	diffusion coefficient of the oxidized and reduced species ($\text{cm}^2 \text{s}^{-1}$)
E	potential (V)
ΔE_p	separation between E_{pa} and E_{pc}
F	Faraday's constant
K	Q_{ind}/Q_{comb}
M^{n+}	charge carrier at the reduced state
$M^{(n+m)+}$	charge carrier at the oxidized state
NHE	normal hydrogen electrode

Q	electrical charge (F) (here reported to 1 mol or 1 dm^{-3})
Q_{ind}	charge passed to destruct the active organic compound
Q_{comb}	charge for complete combustion of the organic compound
R	gas constant ($8.31 \text{ J mol}^{-1} \text{ K}^{-1}$)
T	temperature ($^{\circ}\text{C}$)
TC	thermal conductivity

Greek symbols

α	charge transfer coefficient
γ	$(D_o/D_R)^{1/2}$
ψ	charge transfer parameter

REFERENCES

1. R. Ramaswamy, M. S. Venkatachalapathy, and H. V. K. Udupa, *This Journal*, **110**, 202 (1963).
2. Ch. Comninellis, E. Plattner, and Ph. Javet, *J. Appl. Electrochem.*, **9**, 753 (1979).
3. A. T. Kuhn and M. Birkett, *ibid.*, **9**, 777 (1979).
4. Ch. Comninellis and E. Plattner, *ibid.*, **14**, 533 (1984).
5. G. Lin-Cai and D. Pletcher, *J. Electroanal. Chem.*, **152**, 157 (1983).
6. Ch. Comninellis and E. Plattner, Paper 592 presented at the Montreal, Que., Canada, Meeting of the Society, May 9-14, 1982.
7. Ch. Comninellis, Ch. Griessen, and E. Plattner, *This Journal*, To be published.
8. R. S. Nicholson, *Anal. Chem.*, **37**, 1351 (1965).

Some Aspects of Large Frequency Dispersion of Mott-Schottky Plots in TiO_2 Electrodes

Gyoichi Nogami

Department of Electrical Engineering, Kyushu Institute of Technology, Tobata-ku, Kitakyushu 804, Japan

ABSTRACT

The origin of large frequency dispersion in Mott-Schottky plots was studied for TiO_2 electrodes, the surface structure of which was analyzed by x-ray photoelectron spectroscopy (XPS) and impedance measurements. XPS spectra revealed that the atomic composition at the surface was different from that in the bulk. Impedance measurements showed that a Bode plot had a slope of $-1/2$. The results were analyzed in terms of a thick interfacial layer, in which interface states distribute in the forbidden gap. A new model was proposed in order to explain above results: the interface states were in quasi-equilibrium with the Fermi levels of the semiconductor and electrolyte. Charging and discharging of the interface states by ions in the electrolyte causes a large frequency dispersion in Mott-Schottky plots.

The primary method to characterize a semiconductor electrode is based on capacitance-voltage measurements (1-7). A Mott-Schottky relationship gives a theoretical background. However, it has not been rigorously confirmed that the Mott-Schottky theory could be applicable to an electrolyte-semiconductor contact. Does the electrolyte play the same role as the metal electrode in a metal-semiconductor contact?

With capacitance-voltage characteristics, a large Helmholtz layer capacitance (C_H), which is in series with a depletion layer capacitance (C_D), is generally neglected in evaluating a total capacitance. The large Helmholtz layer capacity is partly owed to a rapid "dielectric" relaxation by solvent molecules such as H_2O molecules in an aqueous electrolyte.

With current-voltage characteristics, on the other hand, it is generally accepted that the surface state plays a decisive role in electrode reaction and is a key parameter in determining cell performance. The presence of the surface state enables a rapid charge transfer between the semiconductor and electrolyte, mainly because charge transfer can take place equienergetically. It is assumed that charge exchange between the surface state and the electrolyte occurs quite easily. However, one says that the surface states are in equilibrium with the Fermi level of

the semiconductor bulk in the interpretation of the C-V characteristics. Nonlinear Mott-Schottky plots have been ascribed to the surface state. The Fermi level scans the surface state in accordance with an applied bias, which gives information about the energy level of the surface state. If this is the case, a large energy difference between the Fermi level of the electrolyte and the top of the filled surface state will result under a large anodic bias; charge transfer from an ion in the electrolyte to the surface state might easily occur in an anodic bias. Surface state charging will occur, and potential drops across the Helmholtz layer will change. In other words, the surface states are pinned to the redox energy level in the electrolyte. In this case, a frequency dispersion due to surface states could not be observed if the energy level of the surface states (E_A) is deep because the charge-transfer process can be characterized by the Boltzmann factor of $\exp(E_A/kT)$. The electrolyte plays quite the same role as the metal electrode.

What is the cause of large frequency dispersion frequently observed in oxide semiconductors such as TiO_2 and Fe_2O_3 ? Dutoit *et al.* (6, 7) have developed an empirical theory to explain a dispersive Mott-Schottky plot, the physical origin of which has not been clarified. The dispersive Mott-Schottky plots are not unusual in a semicon-

ductor-electrolyte contact (6-13). Especially in a TiO₂ electrode, it is an important problem to obtain the electrode which shows less dispersive C-V characteristics (5).

The present author has explained a nonlinear Mott-Schottky plot in terms of a thick interfacial layer (14-16). There must be a relatively thick interfacial layer of ~0.1 μm, which contains the interface states, probably because the semiconducting property of the oxide semiconductors is obtained by defect doping. The model does not include the frequency dispersion of the Mott-Schottky plots.

The objective of the present study is to elucidate the origin of the frequency dispersion of Mott-Schottky plots in a semiconductor electrode.

Two types of experiments were performed: XPS and impedance measurements. XPS study revealed that there existed a relatively thick interfacial layer, the atomic composition of which is certainly different from that in the bulk. Impedance measurements showed that the Bode plots had the slope of -1/2, the cause of which could not be ascribed to the semiconductor only. The slope of -1/2 in Bode plots is characteristics for a Warburg impedance: a diffusion impedance of the electrolyte. Combining these results, a band model for the electrolyte-semiconductor interface was proposed.

Experimental

Sample preparation.—A single crystal of TiO₂ was purchased from Fujititan. C-cut wafers were mechanically polished and then etched in NaOH at 500°C for 1h. NaOH was removed with boiling distilled water and then HCl. Two samples as a pair were reduced under the same conditions: reducing conditions were varied from pair to pair, typically $2 \sim 10 \times 10^{-5}$ torr, 800° ~ 900°C, and 6 ~ 10h; one of the pair was for the impedance measurements and the other for the XPS measurements. Many pairs (more than ten pairs) were prepared.

XPS and impedance measurements.—A Shimadzu-Pont Model 650B was used in the XPS measurements.

Energy in our system was calibrated by setting Cu 2P_{3/2} at 932.0 eV and Au 4f_{7/2} at 84.0 eV. Al Kα radiation was used. The scan rate was 0.05 eV/s. Depth profiles of XPS spectra were obtained by an Ar ion etching technique. Unfortunately, the precise ion etching rate is quite difficult to determine in our system and could not be ascertained. A dual phase lock-in amplifier (PAR Model 5204) was used in the impedance measurements. The electrolyte used was 1M KOH solution. The quantities measured were the equivalent series capacitance C and resistance R, which were determined by measuring the out-of- and in-phase components of the complex impedance.

Results

X-ray photoelectron spectroscopy.—Figure 1a and 1b show the XPS spectra for the paired sample reduced under the same conditions as the sample which gave the most favorable data in interpreting the present result unambiguously: namely, the slope of the Bode plot was -1/2 (see Fig. 3 and 4). However, nearly the same XPS spectra were observed for another sample; no appreciable difference could be found between two measurements. The peaks at 465.0 and 459.5 eV are due to 2P_{1/2} and 2P_{3/2}, respectively, while the peak at 531.0 eV is due to O 1s. The binding energy difference of the O 1s and Ti 2p_{3/2} bands is 71.5 eV, the value of which agrees with that reported elsewhere (17, 18). The peak at 459.5 eV suggests the formation of TiO₂. With increasing ion etching time, a shoulder at 457 eV appears. Usually, the peak due to TiO appears at ~455 eV. Therefore, the shoulder may be a sign of coexistence of Ti³⁺. The peak heights for 2P_{1/2} (465.0 eV) and 2P_{3/2} (459.5 eV) are plotted as a function of ion etching time in Fig. 2, where the background intensity is subtracted. It is clearly seen that the peak intensity shows a gradual increase as a function of ion etching time. This fact implies that the atomic composition at the surface is certainly different from that in the bulk: Ti content at the surface is smaller than that in the bulk, probably owing to the reduction process. Some Ti atoms might be evaporated.

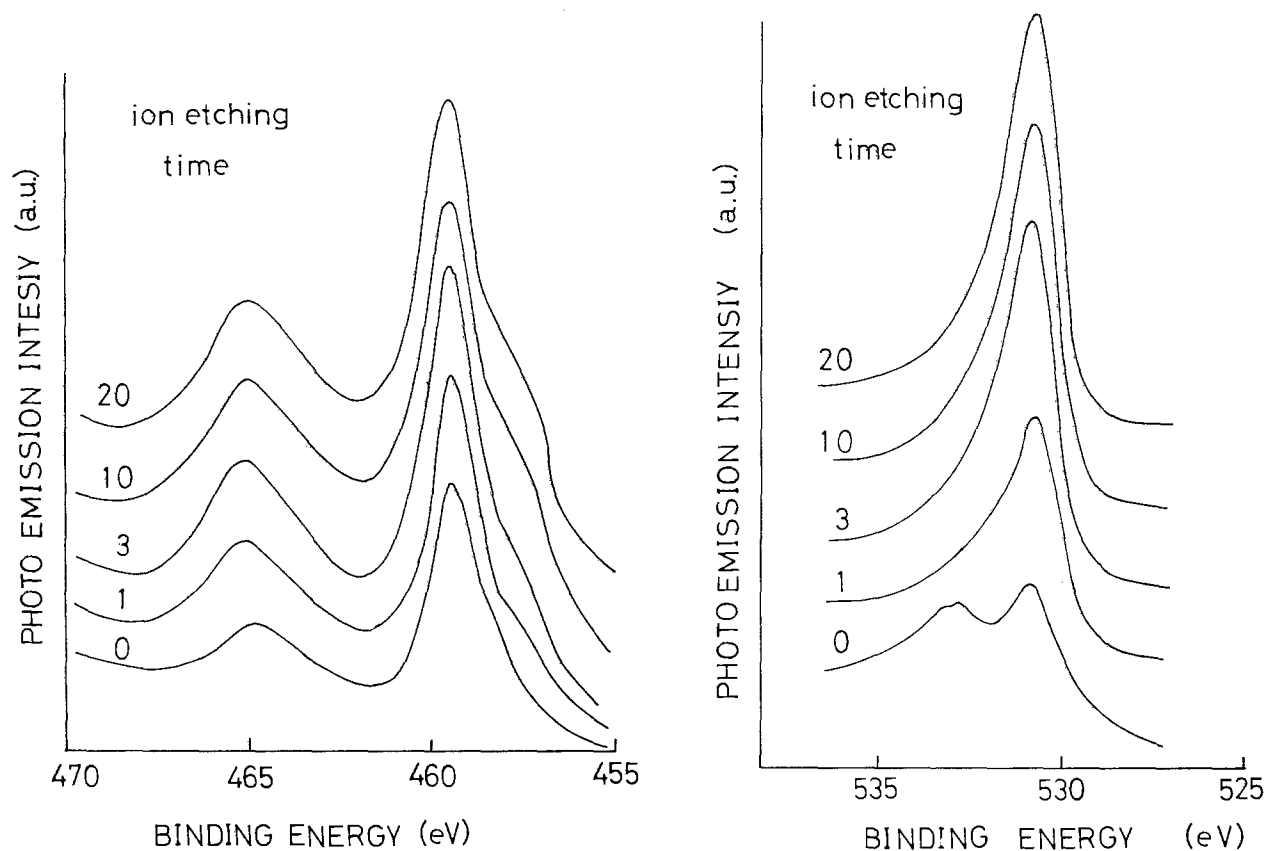


Fig. 1. a(left): The XPS spectra of Ti 2p region. The peaks at 465.0 and 459.5 eV are due to 2p_{1/2} and 2p_{3/2} of Ti, respectively. b(right): The XPS spectra of O 1s region.

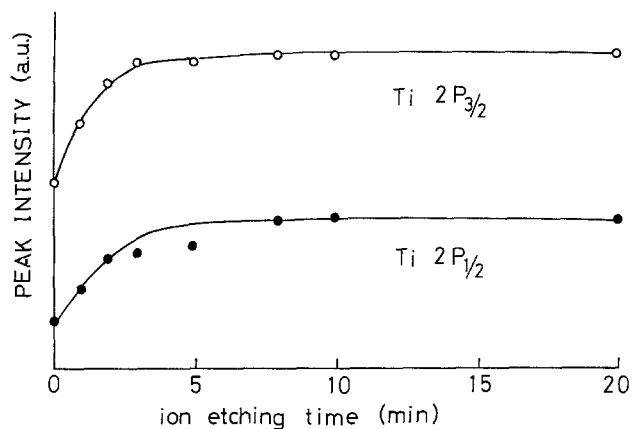


Fig. 2. Depth profiles of $2P_{3/2}$ and $2P_{1/2}$. It is clearly seen that the atomic composition at the surface is different from that in the bulk. Based on this figure, the existence of the thick interfacial layer is assumed.

Impedance measurements.—Impedance measurements were made for every pair prepared. All the samples studied showed more or less a large frequency dispersion in Mott-Schottky plots. A typical example is shown in Fig. 3. Nonlinear Mott-Schottky plots like Fig. 3 are not unusual in a TiO_2 electrode. Nearly the same result has been also shown by Wilson *et al.* (19, 20), although they have not shown the frequency dependence. Dutoit *et al.* (7) have obtained a linear Mott-Schottky plot for a TiO_2 electrode. However, they have only shown the C^{-2} -V plots under large anodic biases, far from the flatband potential [Fig. 1 and 2 in Ref. (7)]. Nonlinear Mott-Schottky plots are, in the author's opinion, to be observed near the flatband potential (19, 20). In the course of a variety of attempts, we observed a linear Mott-Schottky plot for the sample

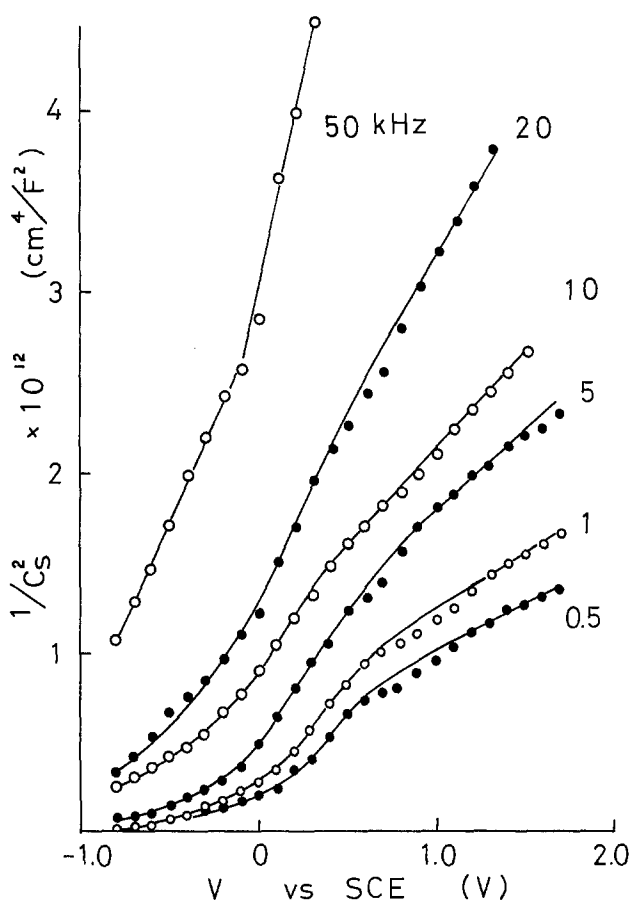


Fig. 3. Mott-Schottky plots for a TiO_2 electrode. Large frequency dispersion is observed.

which was merely mechanically polished and not chemically etched by NaOH. In this case, too, a large frequency dispersion was observed. These results may suggest, as was pointed out by Cooper *et al.* (5), that a linear Mott-Schottky plot without any dispersion might be obtained after removing the damaged surface layer. Even in that case, some dispersion may be observed if the electrolyte concentration is low enough (5).

A Bode plot, a log-log plot of the impedance $|Z|$ vs. frequency, showed complicated behavior. Some samples showed an ideal Bode plot at low frequencies (below ~ 1 kHz), where a slope precisely equals -1 . At higher frequencies, however, the slope deviated from -1 , where the Mott-Schottky plot showed a large frequency dispersion, such as appears in Fig. 3. Other samples gave more complicated Bode plots. Under cathodic biases with larger capacity, a slope typically approaches $-1/2$ and deviated from $-1/2$ with increasing anodic biases, as shown in Fig. 4. The sample shown in Fig. 3 and 4 was reduced in vacuum of 5×10^{-5} torr at $850^\circ C$ for 8h. However, the same preparation conditions did not necessarily give the same result. The electrode was quite sensitive to its history. Figure 4 shows that each plot can be represented as a straight line with a slope of about $-1/2$, which is characteristic for a Warburg impedance. If the rate-determining step is a diffusion, the impedance of the system is characterized by the Warburg impedance. Therefore, some sort of a diffusion process might be the cause of large frequency dispersion in Mott-Schottky plots. The equivalent series resistance R is also plotted against frequency in Fig. 4. A slope of $\log R$ vs. $\log f$ is precisely equal to $-1/2$. As our total system is regarded as a series connection of R and C , a resistance component of our system can be characterized by a diffusion resistance of the electrolyte. The value of R observed seems to be too large to be regarded as the diffusion resistance of $1M$ KOH solution used. We feel, therefore, that electroactive species may penetrate into the defective interface layer and their effective concentration may be reduced as a result of charge rearrangement when the electrolyte and semiconductor are brought into contact. The defective interface layer may also serve as a resistive layer for diffusion. Cooper *et al.* (5) have found that even the sample which shows the ideal Mott-Schottky relation begins to show a large frequency dispersion if the electrolyte concentration is reduced below $0.25M$. They ascribed this phenomenon to dielectric relaxation in a disturbed surface layer.

Discussion

One way to realize a dispersive Mott-Schottky relation with an equivalent circuit diagram is to consider a relaxa-

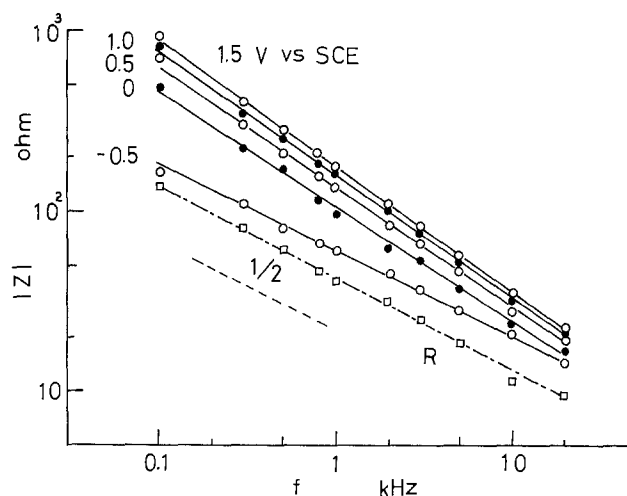


Fig. 4. Bode plots with an external dc bias as a parameter. The slope of Bode plots is nearly equal to $-1/2$ and approaches closer and closer to $-1/2$ with decreasing anodic bias. The equivalent series resistance R is also plotted. The slope of $\log R$ vs. $\log f$ plot is equal to $-1/2$.

tion impedance of a series connection of R_s and C_s , which is in parallel with the depletion layer capacitance. C_s is so called surface-state capacitance. The product of $C_s R_s$ performs the relaxation time. This configuration has a crucial defect because their relaxation time is characterized by the Boltzmann factor typically expressed as $\tau = \tau_0 \exp(E/kT)$. If we assume that the surface states equilibrate with the semiconductor, τ increases exponentially and then drastically with increasing anodic bias. Frequency dispersion could not be observed at large anodic biases (21). Experimental results show, however, that the large frequency dispersion is observed over the potential range examined.

Another way to explain the large frequency dispersion is to consider dielectric relaxation in a disturbed surface layer (5). Observed frequency dispersion seems to be too large, in the author's opinion, to be ascribed to the dielectric relaxation of the surface layer.

We consider here the interaction between the thick interfacial layer and the electrolyte.

An equivalent circuit analysis.—We consider here the equivalent circuit and the energy band diagram as shown in Fig. 5(a) and 5(b), respectively. The basic ideas proposed here are as follows: (i) The interface states are principally in thermal equilibrium with the Fermi level of the semiconductor bulk E_F . (ii) With increasing anodic bias, electrons which lie above E_F must transfer from the interface state to the conduction band by thermal excitation. This process proceeds quite slowly because the interface state is deep. (iii) The interface states which emitted electrons into the conduction band are rather "quickly" filled by the electrons transferred from the electrolyte. The interface states are always occupied by electrons. (iv) Consequently, the interface states in the l region of Fig. 5(b) lie below the quasi-Fermi level E_{Fn} which is extended horizontally from the redox level of the electrolyte E_{FE} across the l region. (v) Electrons injected from the interface state into the conduction band of the semiconductor pass through the external circuit and appear at the counter-

electrode, where cathodic reaction takes place. In this situation, reaction products such as H₂ and O₂ may be produced. As a result, charge neutrality condition is maintained in the electrolyte: potential drop across the Helmholtz double layer remains unchanged. (vi) Even in this case, an appreciable reaction current might not be observed because a rate-determining step is assumed to be the thermal excitation of electrons from the interface state to the conduction band, the rate of which is assumed to be quite slow. (vii) Under a low amplitude ac excitation, the interface state exchanges charges with the electrolyte. With increasing frequencies, a relaxation phenomenon takes place. The relaxation phenomenon is characterized by the relaxation time τ , which is equivalent to the product $C_s R_s$ in an equivalent circuit diagram. (viii) At low frequencies, a capacitance in the l region, C_l , is shunted by the impedance of C_s and R_s in series. Then, the total capacitance is given by that in an L region, C_l , if C_s is sufficiently large. At high frequencies, however, the charge transfer (diffusion) cannot respond to an external excitation so that C_l contributes to the total capacitance. (ix) Pure "dielectric response" is characterized here by the series connection of C_l , C_1 , and C_H (C_H is the Helmholtz layer capacitance). The charge transfer process is characterized by the series connection of C_s , R_s , C_w , and R_w , where C_w and R_w are the capacitance and resistance components of the Warburg impedance.

We make here additional assumptions that $C_w \gg C_s$, $C_H \gg C_l$, and $R_w \gg R_s$. The impedance is then expressed as

$$Z = \frac{1}{j\omega C_L} + \frac{1 + j\omega\tau_{sw}}{j\omega(C_s + C_l)(1 + j\omega\tau_{mw})} \quad [1]$$

$$\frac{1}{C} = \frac{1}{C_L} + \frac{1}{C_s + C_l} \cdot \frac{1 + \omega^2\tau_{mw}\tau_{sw}}{1 + \omega^2\tau_{mw}^2} \quad [2]$$

$$R = \frac{\tau_{sm} - \tau_{mw}}{(C_s + C_l)(1 + \omega^2\tau_{mw}^2)} \quad [3]$$

where $\tau_{sw} = C_s R_w$ and $\tau_{mw} = C_l R_w / (C_s + C_l) < \tau_{sw}$. If $\omega\tau_{sw} \gg 1 \gg \omega\tau_{mw}$, then $|Z|$ is given by

$$|Z| = \sqrt{R_w^2 + \frac{1}{\omega^2 C_L^2}} \quad [4]$$

Therefore, a Bode plot will be characterized by the diffusion resistance R_w in a frequency range where $R_w > 1/\omega C_L$, as is exemplified in Fig. 4. C_L becomes larger, and then $1/\omega C_L$ becomes smaller with increasing cathodic biases, so that above condition $R_w > 1/\omega C_L$ is well satisfied under cathodic biases, as is also exemplified in Fig. 4, where $|Z|$ approaches R , and the slope to $-1/2$ with increasing cathodic bias. If R_w is always small enough to be $R_w \ll 1/\omega C_L$, then the resultant Bode plot may have a slope of -1 , as usually observed. Even in this case, a large frequency dispersion in Mott-Schottky plots can be explained, as shown later. Moreover, in the potential range where $R_w \sim 1/\omega C_L$, a slope may range from $-1/2$ to -1 , and is typically about -0.7 , as shown in Fig. 4: R_w and $1/\omega C_L$ depend on $\omega^{-1/2}$ and ω^{-1} , respectively. One may ascertain a slope of ~ -0.7 for two decades if he plots Eq. [4] in the frequency range of $R_w \sim 1/\omega C_L$. It is noteworthy here that a slope of $-1/2$ in a Bode plot may be observed only when $R_w \gg 1/\omega C_L$, while a large frequency dispersion in a Mott-Schottky plot can be observed even when $R_w \ll 1/\omega C_L$, if C_s is sufficiently large, in an equivalent circuit diagram. C_l is shunted by the surface-state capacitance C_s at low frequencies, while C_s is not effective at high frequencies, owing to a relaxation effect.

Model calculation.—Our system is quite complicated. The purpose of the present study is not to explain the observed C^{-2} -V characteristics in detail but to elucidate the origin of large frequency dispersion in Mott-Schottky plots. Therefore, we make here simplified assumptions in order to derive analytical expressions for dispersive

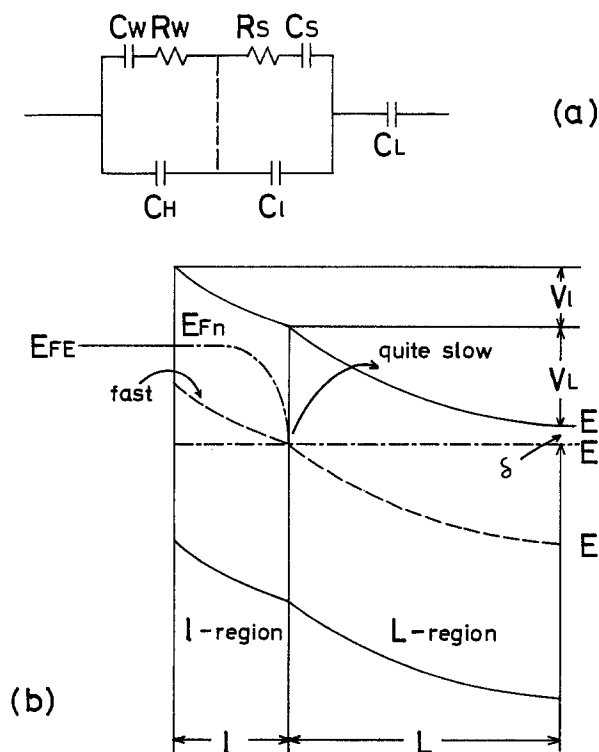


Fig. 5. (a): An equivalent circuit for an electrolyte-semiconductor contact with a thick interfacial layer. A series connect of C_L and C_1 , and C_H represents the dielectric response, while that of C_s , R_s , C_w , and R_w represents the usual relaxation of charges. (b): Assumed energy band diagram. The interface state is assumed to lie below E_{FE} and to be occupied by an electron.

Mott-Schottky plots. The interface states are assumed to distribute rather deep into the semiconductor bulk with the concentration of N_s , while the shallow impurities distribute uniformly throughout the electrode with the concentration of N . Figure 5(b) shows the energy band diagram for an electrode anodically biased by V from its flatband condition. If the expressions must be expressed in terms of a flatband potential V_{FB} , then V or V_D in the following expressions must be replaced by $(V - V_{FB} - kT/q)$. Potential drop across the L and l layers, V_L and V_l , are given, respectively, by

$$V_L = \frac{qN_c}{2\epsilon} L^2 \quad [5]$$

$$V_l = \frac{qN_c}{2\epsilon} \{(l^2 + 2lL) - \alpha l^2\} \quad [6]$$

where $N_c = N - N_s$ and $\alpha = N_s/N_c$. N_c denotes the net charge density in the depletion layer. These situations are quite the same as the preceding result (21). The potential drop across the depletion layer V is given by

$$V = V_L + V_l = \frac{qN_c}{2\epsilon} \{(L + l)^2 - \alpha l^2\} \quad [7]$$

Derivation of the admittance of the electrode is now straightforward. Hereafter, we denote the dc and ac component by subscripts D and A, respectively. Applying the same procedure as the preceding study, the ac components of l_{AO} , l_A , and L_A are given by

$$l_{AO} = \frac{1}{L_D + (1 - \alpha)l_D} \cdot \frac{\epsilon}{qN_c} V_A \quad [8]$$

$$l_A = \frac{1}{1 + j\omega\tau} l_{AO} \quad [9]$$

$$L_A = \frac{L_D + (1 - \alpha)l_D}{L_D + l_D} \cdot \frac{j\omega\tau}{1 + j\omega\tau} l_{AO} \quad [10]$$

where subscript o denotes the quasi-static value.

Then, the small signal ac admittance Y_A can be expressed by the following relation

$$I_A = Y_A V_A = \frac{dQ_{sc}}{dt} = j\omega q N_c (L_A + l_A) \quad [11]$$

Combining Eq. [11] with Eq. [8], [9], and [10] leads to

$$Y_A = \frac{j\omega}{1 + j\omega\tau} \cdot [C_o + C_\infty j\omega\tau] \quad [12]$$

where

$$C_o = \frac{\epsilon}{L_D + (1 - \alpha)l_D} \quad [13]$$

$$C_\infty = \frac{\epsilon}{L_D + l_D} \quad [14]$$

An equivalent length of the l region reduces by a factor of $(1 - \alpha)$. If the interface state density N_s is large enough to be $\alpha = 1$, then the capacitance at a low frequency limit is determined only by the thickness of the L region, L_D . The capacitance C and the conductance G are given by

$$C = \frac{C_o + C_\infty \omega^2 \tau^2}{1 + \omega^2 \tau^2} \quad [15]$$

$$G = \frac{\omega^2 \tau (C_o - C_\infty)}{1 + \omega^2 \tau^2} \quad [16]$$

where C_o and C_∞ are the capacitance at the low and high frequency limit, respectively. In order to obtain a Mott-Schottky relation, C must be expressed as a function of a dc bias V_D . The dc component of Eq. [7] is expressed as

$$(1 - \alpha)l_D^2 + 2l_D L_D - \frac{\epsilon}{qN_c} (V_D - V_o) = 0 \quad [17]$$

where

$$L_D^2 = \frac{2\epsilon}{qN_c} V_D = \frac{2\epsilon}{qN_c} (E_A - \delta) \quad [18]$$

Combining Eq. [17] and [18] with Eq. [13] and [14] leads to

$$\frac{1}{C_o^2} = \frac{2(1 - \alpha)}{qN\epsilon} \left\{ V_D + \frac{\alpha}{1 - \alpha} V_o \right\} \quad [19]$$

$$\frac{1}{C_\infty} = \frac{1}{1 - \alpha} \cdot \frac{1}{C_o} - \frac{\alpha}{1 - \alpha} \sqrt{\frac{2}{qN\epsilon}} V_o \quad [20]$$

where the relation $N = N_c(1 + \alpha)$ is used.

Equations [19] and [20] show that a slope of a Mott-Schottky plot at the low and high frequency limit gives $2(1 - \alpha)/qN\epsilon$ and $2/(1 - \alpha)qN\epsilon$, respectively. Large frequency dispersion of a Mott-Schottky plot is characterized by a factor of $1/(1 - \alpha)^2$. If $\alpha = 0.5$, then the slopes differ by a factor of 4. The model calculation in this chapter indicates that the origin of a large frequency dispersion in the Mott-Schottky plots does not necessarily depend on a Warburg impedance. The main origin of a dispersive Mott-Schottky plot is ascribed to the interface or surface state, as was conventionally accepted. However, the role played by the interface state is considered here to be somewhat different from that usually accepted: the interface state is also in equilibrium with the electrolyte. A lot of C-V measurements enabled us to observe some characteristic Bode plots: a slope of $-1/2$ could not be ascribed to the semiconductor alone.

Conclusions

A dispersive Mott-Schottky plot frequently observed in an electrolyte-semiconductor contact has been explained in terms of the interface states, which distribute rather deep into the electrode. The interface states could exchange charges with the electrolyte. The relaxation phenomenon of charge transfer between the interface state and the electrolyte can be characterized by a single relaxation time because charge transfer could take place energetically: the relaxation time is independent of a Boltzmann factor.

In other words, the relaxation time is considered to be constant and independent of an applied dc bias. This is one of the most important conclusions drawn here. The assumption that the energy level which lies above the Fermi level of the semiconductor bulk is occupied by an electron may offer a new concept in the interpretation of the Mott-Schottky plot.

In a usual metal-semiconductor contact, rather "clean," well-defined semiconductors and metals are used; the thick interfacial layer considered here may be absent. However, in an electrolyte-semiconductor contact, both the semiconductor and electrolyte are quite complicated; semiconductors used are generally "reduced" oxides such as TiO_2 and $SrTiO_3$, which are structure sensitive or processing dependent. Large frequency dispersion in Mott-Schottky plots frequently observed in these semiconductors could not be explained because the electrolyte has been regarded as playing the same role as the metal electrode. The large Helmholtz layer capacitance which is in series with the small depletion layer capacitance can be surely neglected in so far as we consider the dielectric response, *i.e.*, dielectric relaxation. However, if we are forced to consider the interface state, the energy level of which lies below the redox energy level of the electrolyte, an additional relaxation effect such as a Warburg impedance must be taken into consideration because charge exchange between the interface state and the electrolyte is possible. Charges are supplied to or taken out from the interface states by the bulk of the electrolyte, where a motion of charge carriers is controlled by diffusion.

Acknowledgments

The author wishes his sincere thanks to Professor T. Ohshige for his continuous encouragement in carrying out this work. He is also grateful to Professor W. P. Gomes and Professor W. H. Laflere for their stimulating discussions. He wishes to thank Dr. T. Nakamura and Mr. H. Ito for their help in XPS measurements as well as stimulating discussions. This work was supported in part by Meisenkai 80 Fund.

Manuscript submitted March 5, 1984; revised manuscript received Aug. 27, 1984.

Kyushu Institute of Technology assisted in meeting the publication costs of this article.

REFERENCES

1. F. Cardon and W. P. Gomes, *J. Phys. D.*, **11**, L63 (1978).
2. R. De Gryse, W. P. Gomes, F. Cardon, and V. Vennik, *This Journal*, **125**, 711 (1975).
3. M. Tomkiewicz, *ibid.*, **129**, 1505 (1979).
4. M. Tomkiewicz, *ibid.*, **129**, 2220 (1979).
5. G. Cooper, J. A. Turner, and A. J. Nozik, *ibid.*, **129**, 1973 (1982).
6. E. C. Dutoit, R. L. Van Meirhaeghe, F. Cardon, and W. P. Gomes, *Ber. Bunsenges. Phys. Chem.*, **79**, 1206 (1975).
7. E. C. Dutoit, F. Cardon, and W. P. Gomes, *ibid.*, **80**, 475 (1980).
8. H. O. Finklea and R. W. Murray, *J. Phys. Chem.*, **83**, 353 (1979).
9. B. D. Cahan and C.-T. Chen, *This Journal*, **129**, 474 (1982).
10. J. F. McCann and J. Pezy, *ibid.*, **128**, 1735 (1981).
11. G. Nagasbramanian, A. S. Gioda, and A. J. Bard, *ibid.*, **128**, 2158 (1981).
12. P. Salvador and C. Gutierrez, *ibid.*, **131**, 326 (1984).
13. K. S. Yun, S. M. Wilhelm, S. Kapusta, and N. Hackerman, *ibid.*, **127**, 85 (1980).
14. G. Nogami, *Denki Kagaku*, **48**, 628 (1980).
15. G. Nogami, *ibid.*, **49**, 56 (1981).
16. G. Nogami, *Bull. Kyushu Inst. Technol.*, **43**, 27 (1981).
17. C. N. Sayers and N. R. Armstrong, *Surf. Sci.*, **77**, 301 (1978).
18. D. R. Robinson and R. W. Murray, *This Journal*, **131**, 337 (1984).
19. R. H. Wilson, L. A. Harris, and M. E. Gerstner, *ibid.*, **126**, 844 (1979).
20. L. A. Harris, M. E. Gerstner, and R. H. Wilson, *ibid.*, **126**, 850 (1979).
21. G. Nogami, *This Journal*, **129**, 2219 (1982).

The Power Conversion Efficiency of the Thionine Photoelectrochemical Cell Containing Uncoated and Thionine Coated Photoelectrodes

T. I. Quickenden and I. R. Harrison

Department of Physical and Inorganic Chemistry, The University of Western Australia, Nedlands, Western Australia, 6009, Australia

ABSTRACT

The power conversion efficiencies, voltage efficiencies, and current efficiencies of thionine cells containing various combinations of thionine coated and uncoated gold and SnO₂ electrodes have been determined. Cyclic voltammetry was used to determine coating thicknesses and to ascertain whether the thionine/leucothionine couple or the Fe³⁺/Fe²⁺ couple was reversible on the various electrodes. The power conversion efficiency of the thionine cell containing two uncoated gold electrodes was $(4.1 \pm 0.9) \times 10^{-4}\%$, and contrary to previous predictions, when the photoelectrode was coated with thionine, the efficiency did not increase, but was reduced by a factor of 19. Larger decreases in efficiency were observed when SnO₂ photoelectrodes were coated with thionine. Previous electrochemical studies have suggested that the thionine coating suppresses the Fe³⁺/Fe²⁺ couple and is reversible towards the thionine/leucothionine couple in solution, these being the requirements for optimal power output. This study has shown that both solution couples are substantially suppressed, the reported reversibility toward the thionine couple arising from facile oxidation and reduction of thionine in the dye coating, the latter producing negligible photoelectrochemical activity.

The thionine photoelectrochemical cell has often been suggested as a possible transducer of solar energy to electricity (1-4). This cell usually comprises two identical inert electrodes which are immersed in a solution containing a ferric/ferrous couple and a light-sensitive thionine/leucothionine couple. In normal use, only one electrode is illuminated; at that electrode, leucothionine is oxidized to thionine. At the dark electrode, ferric ion is reduced to ferrous ion. The detailed mechanism of the processes which occur at the electrodes and in the bulk of the electrolyte solution has been discussed elsewhere (5).

The power conversion efficiency, ϕ_p , of a photoelectrochemical cell is the ratio of the photoelectric output power to the optical input power, and it can be expressed as

$$\phi_p = \phi_v \cdot \phi_q \cdot f \quad [1]$$

where f is the fill factor, ϕ_v is the open-circuit voltage conversion efficiency, and ϕ_q is the quantum efficiency of current production in the short-circuit condition. The voltage conversion efficiency is effectively the ratio of the mean energy per photoelectron to the energy per inci-

dent photon, and it is given by

$$\phi_v = \frac{V_{oc}F}{N_a} \left/ \frac{hc}{\lambda} \right. \quad [2]$$

where V_{oc} is the open-circuit photovoltage, F is the Faraday constant, N_a is Avogadro's number, h is Planck's constant, c is the velocity of light, and λ is the wavelength of the incident light (6).

The quantum efficiency of current production in the short-circuit condition is given by

$$\phi_q = \frac{dn_e/dt}{dn_p/dt} \quad [3]$$

where dn_p/dt is the number of incident photons per unit time and dn_e/dt is the number of electrons fed to the external circuit per unit time by the light-induced cell reaction when the cell is short circuited. The fill factor is unity in a cell with rectangular photovoltage-photocurrent characteristics (6), but in practice it is usually fractional, due to the various types of overvoltage which lead

to deviation from the rectangular cell characteristics (7). The fill factor can be expressed as

$$f = \frac{V_p I_p}{V_{oc} I_{sc}} \quad [4]$$

where I_{sc} is the short-circuit current delivered by the cell, and V_p and I_p are the cell voltage and current, respectively, at the point of maximum power on the voltage-current characteristic curve of the cell (6). If the latter curve is linear, then $f = 0.25$.

Although over 45 papers have been published on the thionine photoelectrochemical cell, only six of these papers (2, 4, 8-10, 14) present explicit determinations of the cell's power conversion efficiency. The other papers lack one or another of the quantities (*e. g.*, irradiance, current-voltage characteristics, fill-factor) necessary for the determination of power conversion efficiency. However, in four of these cases (12, 14, 15, 17) it has been possible to estimate power conversion efficiencies from the published data by assuming a fill-factor of 0.25. The values obtained are included with the six direct determinations in Table I. The fill-factor of 0.25 is probably a reasonable estimate. As indicated previously, it arises from linear V - I characteristic curves and is not greatly different from the practical values of 0.25, 0.22-0.33, and 0.33 which have been observed in various photoelectrochemical systems (6, 9, 10, 16).

The performance data aggregated into Table I provide a useful profile of the thionine cell. In particular, the data placed in perspective some of the more optimistic claims regarding the cell's efficiency. Such claims probably stem from the prediction by Rabinowitch (1) that the cell may be capable of reaching a power conversion efficiency of 1%. Table I shows that no practical determination for incident light comes anywhere near this value: most power conversion efficiencies lie within the 10^{-4} - $10^{-3}\%$ range, and the only system reaching into the $10^{-2}\%$ region is the nonaqueous solvent cell of Hall *et al.* (9, 10). Some workers have presented efficiencies with respect to absorbed light, and these are naturally higher than those for incident light because the photoelectrochemically active region near the photoelectrode is much thinner

than the path length of the absorbed light (18). However, power conversion efficiencies determined with respect to absorbed light are of little practical value because they do not represent the practical performance of the device and because they can be inflated at will by reducing the cell thickness (because the absorption path length of the electrolyte is usually greater than the thickness of the region of photoelectrochemical activity). The practical efficiency of the device with respect to the light incident upon it is, of course, unchanged by such mathematical manipulations, and the absorbed efficiency has practical significance only if cells are to be stacked optically in series, as done by Hall *et al.* (9).

Some variation in efficiency may result from variations in the spectral distribution of the "white light" used by the various workers in Table I. Ideally, the spectral distribution should be defined; otherwise, monochromatic light should be used. In either of these cases, efficiencies with respect to sunlight can be precisely calculated if desired.

The power conversion efficiencies in Table I have been accompanied by values for ϕ_v , the open-circuit voltage conversion efficiency, and ϕ_a , the quantum efficiency of production of the short-circuit current by following the procedure adopted by Potter and Thaller (2). These quantities have been defined in Eq. [2] and [3]. ϕ_v would assume a value of unity if all the energy of the absorbed photon were transferred to the relevant photoelectron, but in practice, energy is lost in the various photochemical and electrochemical steps that intervene between absorption of light and electrodic electron transfer. The value of ϕ_v is mediated by the efficiencies of the photochemical steps and by activation polarization, but not by ohmic considerations or mass transport limitations. However, the value of ϕ_a does depend on the latter two quantities, and it is normally dominated by the rate of mass transport because ohmic limitations can usually be minimized easily in any optimal cell design.

Table I shows that the ϕ_v values for the thionine cell are relatively high and are surprisingly similar from worker to worker, despite the wide variety of cell designs. Thus, if the value of the photovoltaic-assisted cell from Mountz and Tien (14) is excluded, all the ϕ_v values lie between 4%

Table I. Published power conversion efficiencies of the thionine photoelectrochemical cell with respect to incident white light

Ref.	Electrodes (photo/dark)	Electrode separ./mm	[Electrolyte]/(10^{-3} mol dm $^{-3}$):				Solvent	Voltage eff., ϕ_v /%	Current eff., ϕ_a /%	Power conv. eff., ϕ_p /%
			Thionine	Fe $^{2+}$	Fe $^{3+}$	H $^+$				
(2)	Pt/Pt or Au/Au	1	0.015	10	0.05	3.0	H $_2$ O, N $_2$	8.2	0.0015 ^b	3×10^{-5} (3×10^{-4}) ^a
(4)	Pt/Pt	large	0.4	10	0.5	10.0	H $_2$ O, N $_2$	11.0	0.031 ^b	8.4×10^{-4} (3×10^{-3}) ^a
(8)	SnO $_2$ /Pt	0.1	0.01-1.0	10	0.01-1.0	1-100	H $_2$ O	9.7	0.041 ^b	1.5×10^{-3} ^c (1.5) ^{a,c}
(9)	SnO $_2$ /Pt	0.08	1.0	10	0.5	10.0	50% H $_2$ O/ CH $_3$ CN	6.6	1.0	2.2×10^{-2} ^d
(10)	SnO $_2$ /Pt	0.08	0.2-1.0	10	0.5	10.0	50% H $_2$ O/ CH $_3$ CN, N $_2$	7.2	3.0 ^e	6.3×10^{-2} ^{d,e} 2.9×10^{-2}
(11)	Pt/Pt	large	0.05	5 ^f	0.1-0.5 ^f	10.0	H $_2$ O	7.8	0.11 ^b	2.1×10^{-3} ^d
(12)	SnO $_2$ /Pt or Pt/Pt	2.0-3.5	0.043	4.3	0.00022	10.0	H $_2$ O, N $_2$	5.6	0.17	(0.15-2.4) $\times 10^{-4}$ ^{d,g}
(13)	Pt/Pt	large	0.05	5	0.1	10.0	H $_2$ O	8.2	0.0073 ^b	1.5×10^{-4} ^d
(14)	Pt/Pt or Pt + tetraphenylporphyrin/Pt	large	0.1	10	0.1	0.032	H $_2$ O	8.1 18 ^h	0.12 0.15 ^b	2.4×10^{-3} ^{d,g} 6.8×10^{-3} ^g
(15)	SnO $_2$ /Pt	0.2-2.0	0.5	100	0.005	10.0	H $_2$ O, N $_2$ + gels	6.2	0.046	(2.1-7.2) $\times 10^{-4}$ ^{d,g}
(16)	(Au+Nb)/Pt		0.05	25	0.1-0.5		H $_2$ O, N $_2$	4.6	0.021	(1.9-2.1) $\times 10^{-4}$ ^d
(17)	Pt/Pt, Pt/SnO $_2$, Pt/C, SnO $_2$ /SnO $_2$, polypyrrole on some	various	0.05	50		10.0	H $_2$ O, N $_2$	6.7	0.15	(4.8-26) $\times 10^{-4}$ ^{d,g}

^a Efficiency calculated with respect to absorbed light.

^b I_{sc} was not presented. ϕ_a was calculated from ϕ_p , assuming a fill-factor of 0.25.

^c 578 nm light was used instead of white light.

^d ϕ_a was not given by the author, but was calculated from data in the paper.

^e Obtained for a multilayer cell.

^f In dark compartment, [Fe $^{2+}$] = 0.001 mol dm $^{-3}$ and [Fe $^{3+}$] = 0.1 mol dm $^{-3}$.

^g A fill-factor of 0.25 was assumed.

^h Includes a photovoltaic component.

and 11%. On the other hand, the ϕ_a values are much more dependent on cell design, and they vary between 0.0015% and 3%, most of the values lying in the 10^{-2} - 10^{-10} % range. The highest value obtained for ϕ_a in a single thionine cell is that of about 1% from the work of Hall *et al.* (9, 10). The high quantum efficiency may result from the presence of acetonitrile (50% by volume) in the aqueous electrolyte because this solvent enables the thionine concentration to be raised to 10^{-3} mol dm $^{-3}$, thus facilitating the absorption of light close to the photoelectrode. Shigehara *et al.* (15) have suggested that some of the high photocurrents observed to be coming from the thionine cell may be short-lived transients which have little relevance to long-term energy output; the authors suggest that this may explain their lack of success in replicating the high currents reported by Clark and Eckert (8). It is also possible that the semiconductive characteristics of the SnO $_2$ electrodes vary considerably from worker to worker and are responsible for such variations.

It should be noted that two basic types of thionine cell are listed in Table I. The first type (2, 4, 11, 13, 16, 17) employs well separated dark and light electrodes. In the other type (8-10, 12, 14, 15, 17), both electrodes are illuminated, but each electrode is preferentially reversible to a different redox couple in the electrolyte solution. In general, the latter type of cell possesses the higher efficiencies shown in Table I and has been developed from the experiments of Clark and Eckert (8) and the theory of Albery and Archer (3).

Albery and Archer (18-20) have discussed extensively the electrochemical processes which occur in the thionine cell and have shown that a major electrochemical condition for optimal power output is a large difference between reversibilities of the light sensitive and non-light sensitive redox couples in the cell. Albery *et al.* (21-23) have further argued that the Fe $^{3+}$ /Fe $^{2+}$ couple can be rendered irreversible, without greatly affecting the reversibility of the thionine/leucothionine couple, by anodically coating the photoelectrode with a layer of thionine. They have argued that this should enhance the power conversion efficiency, but they have not determined whether this is truly the case, though they have confirmed that the reversibilities are affected in the required manner by the surface coating.

The aim of this study is to determine whether as predicted by Albery *et al.* (21-23), the power conversion efficiency of the thionine cell is enhanced by anodically coating the photoelectrode with thionine. This work follows a previous study by Quickenden and Bassett (25) which shows that the power conversion efficiency of the rhodamine B photoelectrochemical cell is enhanced by as much as 14 times following anodic deposition of dye on to the gold photoelectrode.

Experimental

Chemicals.—All reagents used in the present study were of analytical reagent grade, except for SbCl $_5$, which was of reagent grade, and thionine, which was of biological grade (Gurr). Thionine purity was checked by paper chromatography and by thin layer chromatography on a silica substrate. Only one chromatographic spot was observed under both visible and ultraviolet illumination after four effluents of differing polarities had been used to develop the chromatograms. Further purification was thus considered unnecessary, apart from filtration to remove insoluble impurities.

The cell electrolyte used for photoelectrochemical measurements was prepared by adding to water the calculated amounts of solutes required to give 0.0100 mol dm $^{-3}$ FeSO $_4$, 0.010 mol dm $^{-3}$ H $_2$ SO $_4$, and 2.1×10^{-4} mol dm $^{-3}$ thionine (80% of saturation at 298 K). As is usual Fe $^{3+}$ ion was provided by the impurity level (about 5×10^{-4} mol dm $^{-3}$) present in the FeSO $_4$ (9, 10). When necessary, the electrolyte was deoxygenated by bubbling with high purity N $_2$ which had been presaturated with water vapor. FeSO $_4$ was always stored as a deoxygenated solution to avoid significant oxidation by atmospheric oxygen. All

solutions used in this study were prepared with water which had been redistilled once after distillation from alkaline permanganate.

Cell construction.—Figure 1 shows the array of photoelectrochemical cells designed to facilitate rapid determination of the power conversion efficiency and to enable extensive reproducibility checks of the latter to be carried out. This type of cell construction also permits dye layers to be electrochemically deposited on the photoelectrode and provides a convenient arrangement for carrying out cyclic voltammetry on the photoelectrode.

The photoelectrode was either a semitransparent layer of gold or transparent SnO $_2$ glass doped with Sb. In the first case, high purity (>99.99%) gold was vacuum deposited on one face of a sheet of Perspex (8.5 cm \times 5.0 cm \times 0.15 cm). The thickness of the gold was kept in the range of 25-35 nm to avoid layers which were too thin (< ca. 5 nm) to ensure electrical continuity but not so thick as to prevent a substantial portion (ca. 40%) of the incident light reaching the gold/electrolyte interface (24). The Perspex-backed layer of gold acted as a semitransparent photoelectrode which was common to all 20 cells in the array (Fig. 1) and acted as their base. Five uncoated strips of Perspex (5.0 cm \times 1.5 cm \times 0.2 cm), each bored with 4 holes of diameter 0.63 cm, were then attached to the gold-coated Perspex base with an acrylic resin glue (Acrifix 92, Röhm). Extensive cyclic voltammetric studies using the Fe $^{3+}$ /Fe $^{2+}$ couple showed that cells manufactured with this glue exhibited identical behavior to those constructed without the glue.

When conducting SnO $_2$ glass was used as the photoelectrode material, the same mode of construction was adopted, except that a previously used (6, 25, 26) vinyl-acrylic mixed resin glue (Selley's Plastic Glue) replaced

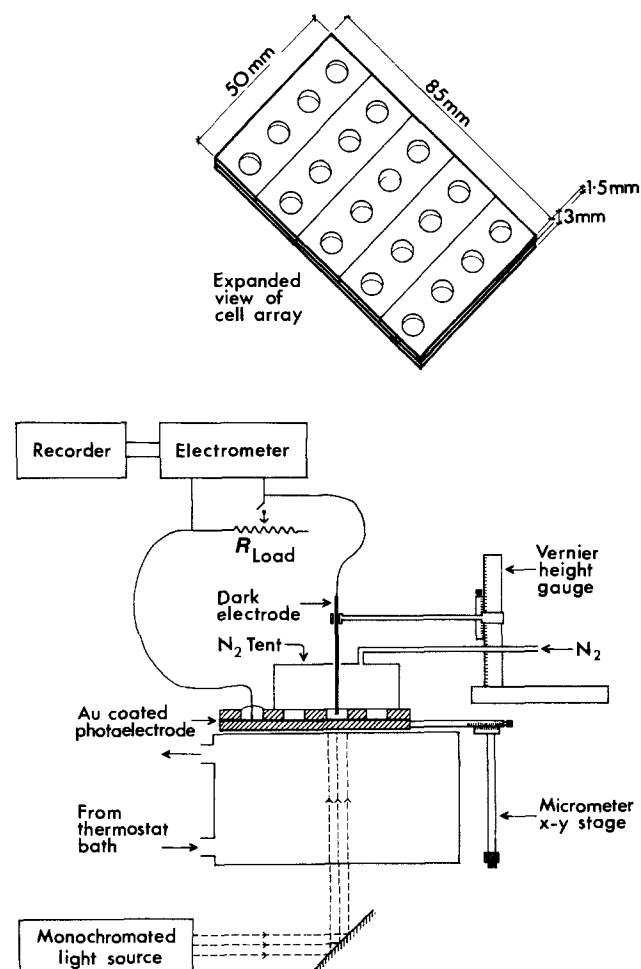


Fig. 1. Schematic diagram (not to scale) of the array of photoelectrochemical cells and associated optical and electrical equipment.

the acrylic resin glue, and the gold-coated Perspex was replaced by a sheet of SnO₂ glass (5.0 cm × 8.0 cm × 0.50 cm). The latter was prepared by spraying (5) the surface of borosilicate glass, heated to a temperature of 933 K, with a solution made by mixing 10 cm³ of SnCl₄ with 0.60 cm³ of SbCl₃ and 20 cm³ of ethyl acetate. A moist atmosphere was necessary for the production of satisfactory SnO₂ glass which had a conductivity of about 70 Ω cm⁻¹.

Electrical connection was made to the SnO₂ glass or gold photoelectrode by attaching a wire to the surface with an electrically conducting glue (Silver Dag, Acheson) mechanically strengthened by a superficial layer of epoxy resin glue (Araldite). Each cell in the array of 20 cells contained 80 mm³ of electrolyte solution, which was introduced with a micrometer controlled syringe. Each cell and its solution was thermostated at 298 ± 0.5 K during measurements by placing the cell array on the surface of a large transparent tank through which thermostating water was passed. When required, a cell in the array could be maintained in an oxygen-free atmosphere by covering it with a small plastic "tent" equipped with a thin tube to pass N₂ over the surface of the electrolyte solution. The array of cells and the associated equipment were contained in a light-proof enclosure.

Photoelectrochemical measurements.—The dark electrode used in photoelectrochemical measurements comprised a 0.70 mm diameter wire of 99.99% purity gold or a thin SnO₂-coated rod of similar dimensions. The dark electrode dipped vertically into the electrolyte solution with its lower end accurately located 1.00 ± 0.01 mm from the photoelectrode by means of a precision height gauge (Mitutoyo 506-201). It was shown that the small amount of light transmitted by the solution to the dark electrode produced a negligible photovoltage.

During photoelectrochemical work, an individual cell was illuminated from below (Fig. 1) by light from a voltage-stabilized tungsten lamp (Bausch and Lomb, 33-86-39-01) which had been monochromated by passage through a Bausch and Lomb High Intensity Monochromator equipped with a UV-visible grating (33-86-02). The incident light was focused by a lens system to provide uniform illumination of the base of the cell. The absolute irradiance of the light incident on the base of the cell and of the light incident on the gold/electrolyte interface was measured with a calibrated photometer (United Detector Technology, 181). The lamp intensity was adjusted in each case to ensure a constant irradiance of 6.4 × 10⁻⁴ W m⁻² at the gold/electrolyte interface.

The voltages and currents developed by the cells across various resistive loads (Jay-Jay 0.1% precision resistance box) were measured with a calibrated electrometer (Keithley 610C) connected to a chart recorder. Photovoltages and photocurrents were separated from dark voltages and dark currents by the graphical procedure described previously (26). The maximum output power from the photoelectrochemical cell was obtained from the rectangle of greatest area (6) under the voltage-current characteristic curve.

Cyclic voltammetry and chronopotentiometry.—Cyclic voltammograms were produced on an X-Y recorder (Houston 2000) using a ramp generator (H. B. Thompson DRG 16) and a potentiostat (H. B. Thompson "Ministat"). The cell arrangement was the one used for the photoelectrochemical measurements, except that the cell was not illuminated and the straight wire dark electrode was replaced by a small Ag/AgCl reference electrode (Microelectrodes MI 401) around which was wrapped the counterelectrode in the form of a coil containing 20 cm of 0.25 mm diameter gold wire (purity > 99.99%). The surface area of the counterelectrode (1.57 cm²) was about five times greater than that of the working electrode deposited on the base of the cell. The reference electrode housing contained a liquid junction separator comprised of a single fiber asbestos frit, which prevented thionine dye from entering the Ag/AgCl compartment. When necessary, the counterelectrode was cleaned separately in boil-

ing concentrated nitric acid. The reference electrode/counterelectrode assembly was accurately located in the electrolyte by the height gauge described in the previous section. IR compensation was not necessary during cyclic voltammetry measurements because of the slow sweep rates, small electrode separation, and relatively high H⁺ concentration.

Chronopotentiometry was carried out with the same cells and electrodes used for cyclic voltammetry, but with the potentiostat operated in the galvanostatic mode. The potential was recorded as a function of time on a chart recorder. All chronopotentiometry and cyclic voltammetry was carried out with the cell inside the darkened enclosure, at a temperature of 298 ± 0.5 K.

UV-visible spectrophotometry.—Transmittances of solutions and of gold layers were determined with a Hewlett Packard HP 8450 spectrophotometer at a temperature of 298 ± 0.3 K.

Results and Discussion

Dye layer deposition.—Previous workers (21-23, 25) have deposited dye layers on metal electrodes by maintaining the electrode at some empirically selected potential while it was immersed in a solution of the dye. This method is inconvenient if a number of different dyes are to be deposited because each must be separately investigated in order to determine the optimum deposition potential. The present method of depositing dye layers by repetitive cycling has been developed¹ in order to overcome this difficulty and has been tested on several different dyes. It possesses another advantage too, in that the thickness of the coating can be monitored from the progressive expansion of the cyclic voltammograms obtained during the deposition process.

Figures 2 and 3 show the cyclic voltammograms (CV's) obtained during the deposition of thionine on Au and

¹Since submitting this work for publication, we have received a copy of a recent paper (in *Electrochim. Acta*, 28, 1515 (1983)) which also describes the electrochemical deposition of thionine layers by repetitive cycling and speculates that the layers are held together by covalent bonds formed in a polymerization mechanism.

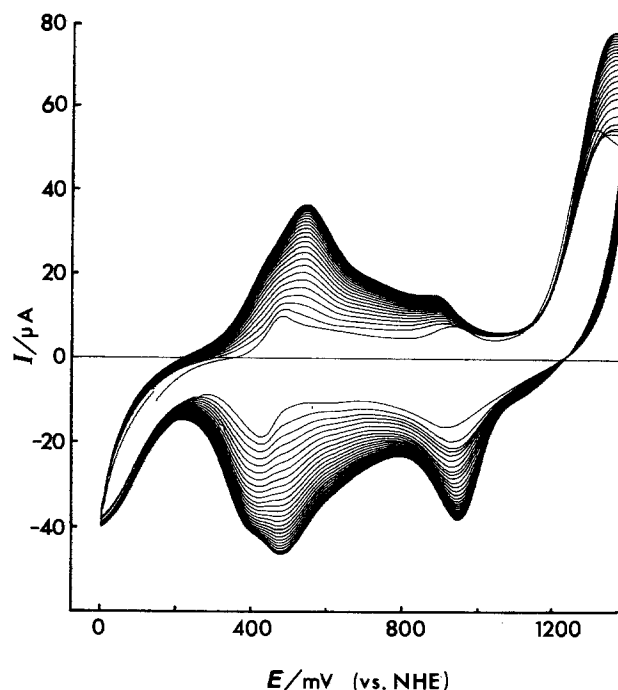


Fig. 2. Cyclic voltammogram of applied potential, E , vs. current, I , showing the process of thionine deposition on Au during successive potential cycles. Oxidative (anodic) currents are shown as positive. Every second trace has been recorded. Sweep rate = 100 mV s⁻¹, area of working electrode = 0.31 cm², temperature = 298 ± 0.5 K [thionine] = 6 × 10⁻⁵ mol dm⁻³, and [H₂SO₄] = 0.050 mol dm⁻³ in water. The leucothionine oxidation peak occurs at 540 mV, and the thionine reduction peak occurs at 490 mV (vs. NHE).

SnO₂ electrodes, together with the CV's obtained from the same electrodes after the thionine solutions used for depositions are removed and replaced by background electrolyte after washing 5 times in 0.050 mol dm⁻³ H₂SO₄. The depositions are carried out in the same cells (Fig. 1) used for the power conversion measurements, but the electrolyte comprises 80 mm³ of aqueous 6 × 10⁻⁵ mol dm⁻³ thionine containing 0.050 mol dm⁻³ H₂SO₄. The voltage limits of 0.05-1.40V (NHE) shown in Fig. 2 and 3 are chosen so as to stay between the reductive region of hydrogen production and the region (> 1.6V) where oxidative destruction of the thin gold electrodes becomes important.

The heights of the characteristic thionine oxidation and reduction peaks in Fig. 2 and 3 increase with the number of cycles to asymptotic limits after about 70 cycles, in the case of a gold electrode, and after about 500 cycles, in the case of SnO₂. The areas within the CV's similarly reach plateau values. Because the areas ($\int Idt$) are also independent of cycling speed, it can be concluded that complete oxidation and reduction of the electroactive species occurs during each cycle, thus validating the use of areas under peaks for determining layer thicknesses.

Determinations of dye layer thickness.—Dye layers deposited on the gold electrodes are not discernible to the eye, apart from the appearance of a slight scoring on the electrode surface. The measured optical absorption of the layers is also negligible, thus indicating that the layer thickness is less than 1-2 nm if the molar decadic absorption coefficient of solid thionine is 2.6 × 10³ m² mol⁻¹.² This thickness corresponds to less than 3-6 monolayers if the molecules lie flat on the surface and have a thickness of 0.325 nm (27).

The layers deposited on the SnO₂ electrode are visible to the eye and give a broad absorption around 475-640 nm (cf. 598 nm for an aqueous thionine solution). The weak absorption indicates a layer thickness somewhat greater than 6 monolayers.

The CV's in Fig. 2-4 permit a more accurate determination of thickness to be carried out, via Eq. [5]

$$c_s = \int Idt / (2nFA) \quad [5]$$

where c_s is the surface concentration in mol m⁻², n is the number of electrons transferred in the redox process [= 2 in the present case (21)], F is the Faraday constant, and A is the electrode area in m². $\int Idt$ is the total charge, in coulombs, contained under the relevant oxidation and reduction peaks after the background charge (determined with the background electrolyte only) has been subtracted.

Table II shows the layer thicknesses obtained from Eq. [5] and from the charge deposited in chronopotentiometric reduction of the layer. It is seen that the thicknesses determined by these two methods agree well and are consistent with the thickness limits established by absorption spectrophotometry. Table II also shows that the thicknesses of the layers deposited by the static potential method and the cycling potential method are similar. The layer thicknesses determined by CV and chronopotentiometry require that the thionine molecules lie flat on the electrode surface and that the cross-sectional area of a molecule is 1.08 nm² and that its thickness is 0.325 nm (27).

Analysis of voltammogram peaks.—During the cyclic deposition process on Au (Fig. 2), the thionine reduction and leucothionine oxidation peaks which are originally at 430 and 490 mV, respectively, shift in turn to 490 and 540 mV, and a small shoulder appears at about 430 mV. How-

²The value of 2.6 × 10³ m² mol⁻¹ for the molar decadic absorption coefficient of solid thionine is obtained (21) by halving the value measured for an aqueous solution. This approach assumes that if the thionine in the deposited layers is polymerized (see footnote 1), its absorption coefficient is not substantially altered from that given by the above procedure. Corresponding electrochemical assumptions apply to the thicknesses determined by cyclic voltammetry and chronopotentiometry. It is noted that the optical and electrochemical methods yield similar values for the layer thickness.

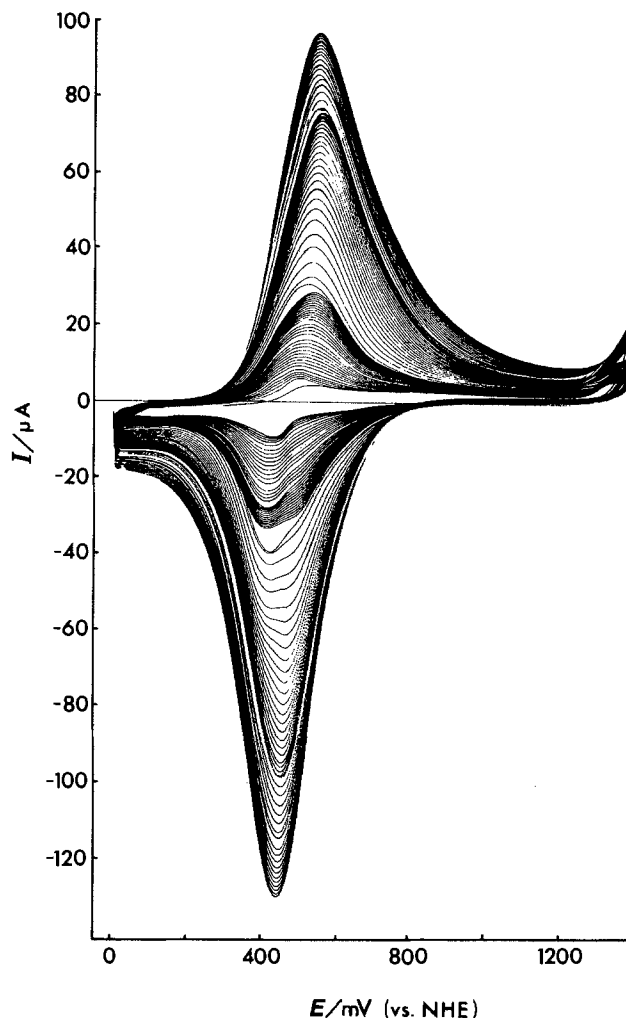


Fig. 3. Cyclic voltammogram showing thionine deposition on SnO₂. Same conditions as in Fig. 2, except that the trace was recorded at 56s intervals for 20 min and at 5 min intervals thereafter. The electrolyte solution was replenished twice during this deposition. Leucothionine oxidation: 535 mV. Thionine reduction: 435 mV.

ever, during the deposition on SnO₂, the thionine reduction peak at 435 mV does not shift. But the oxidation peak moves from 535 to 550 mV, and the shoulder on the reduction peak appears only temporarily during the middle stages of the deposition.

It is clear from a comparison of the CV's obtained when the thionine-coated electrodes are immersed in background and thionine containing electrolytes (Fig. 4 and 5) that the thionine and leucothionine peaks observed with the coated electrodes originate almost entirely from the dye coating, rather than from any thionine in solution. Furthermore, the peak current separation observed for the thionine-coated Au and SnO₂ electrodes in Fig. 4 and 5 increases linearly with sweep rate, as is expected for surface bound species (28). This result means that it is difficult to ascertain the reversibility of dissolved thionine/leucothionine at a thionine-coated electrode because of the swamping of the solution couple by the couple in the deposited layer. Previous reports (5, 21) of the reversibility of the solution couple on thionine-coated electrodes thus need to be viewed with some caution. This observation also has implications in photoelectrochemical studies, as photovoltage generation in the thionine system arises mainly from the photochemical reactions of dissolved thionine, rather than from adsorbed thionine, because of the small amount of light absorbed in the dye layer. This matter is discussed further in the section on power conversion efficiencies.

Albery *et al.* (21) have reported that the Fe³⁺/Fe²⁺ couple is suppressed on thionine-coated Pt and SnO₂. Figure 7 confirms this result for the thionine-coated SnO₂ elec-

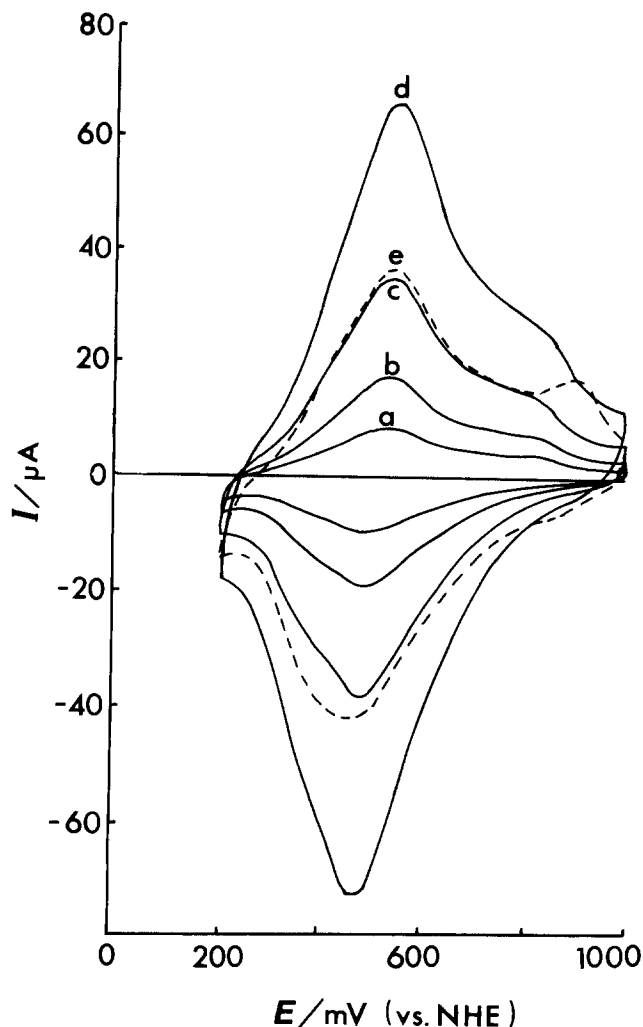


Fig. 4. Cyclic voltammograms of the thionine-coated gold electrode from Fig. 2 in aqueous $0.050 \text{ mol dm}^{-3} \text{ H}_2\text{SO}_4$ (no thionine). (a), (b), (c), and (d) are traces at sweep rates of 25, 50, 100, and 200 mV s^{-1} , respectively. (e) is a trace recorded in $6 \times 10^{-5} \text{ mol dm}^{-3}$ thionine and $0.050 \text{ mol dm}^{-3}$ aqueous H_2SO_4 at 100 mV s^{-1} . Other conditions are as in Fig. 2.

trode, but Fig. 6 shows that the situation is more complicated on the thionine-coated gold electrode. In the latter case (Fig. 6), though the $\text{Fe}^{3+}/\text{Fe}^{2+}$ peaks are absent from their usual positions, the height of the thionine reduction peak is substantially increased by the presence of the $\text{Fe}^{3+}/\text{Fe}^{2+}$ couple and the leucothionine oxidation peak is substantially decreased. This surprising result may arise from a shift (rather than suppression) of the Fe^{3+} reduction peak into the region of thionine reduction, thus augmenting the thionine peak.

Measured power conversion efficiencies.—Table III shows the power conversion efficiencies obtained for the thionine cells used in the present investigation and lists the measured voltage conversion efficiencies and quantum efficiencies of current production. Each value in Table III is the mean of a number of replicate determinations on different cells, and the error ranges represent 50% confidence intervals in these means.

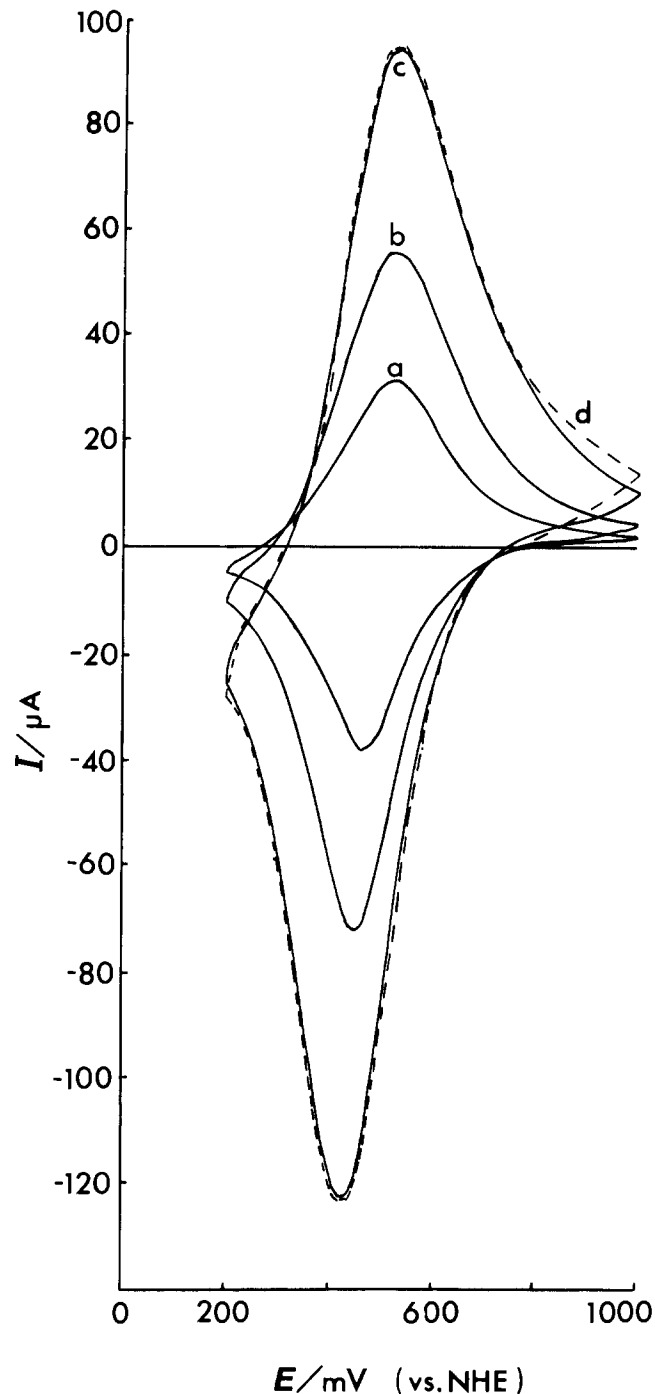


Fig. 5. Cyclic voltammograms of the thionine-coated SnO_2 electrode from Fig. 3 carried out in aqueous $0.050 \text{ mol dm}^{-3} \text{ H}_2\text{SO}_4$ (no thionine). (a), (b), and (c) are traces run at sweep rates of 25, 50, and 100 mV s^{-1} . (d) is a trace of the same electrode when 6×10^{-5} thionine is also present and the sweep rate is 100 mV s^{-1} . Other conditions are as in Fig. 2.

Deoxygenation of the cell electrolyte results in a three-fold increase in the power conversion efficiency, due mostly to an increase in the voltage efficiency and probably arising from decreased oxidation of leucothionine or semithionine in the electrolyte solution. All the subse-

Table II. Measured thicknesses of thionine coatings on gold and SnO_2 electrodes

Electrode	Method of layer deposition	Method of thickness determination	Surface concentration/ ($10^{-6} \text{ mol m}^{-2}$)	Thickness/ nm	Number of monolayers
Au	Static potential	Cyclic voltammetry	9.8 ± 0.5	2.5 ± 0.1	7.7 ± 0.4
Au	Cycled potential	Cyclic voltammetry	8.6 ± 0.4	2.2 ± 0.1	6.7 ± 0.3
Au	Cycled potential	Chronopotentiometry	9.6 ± 2.6	2.4 ± 0.6	7.5 ± 2
SnO_2	Cycled potential	Cyclic voltammetry	50.1 ± 0.3	12.7 ± 0.1	39.1 ± 0.2

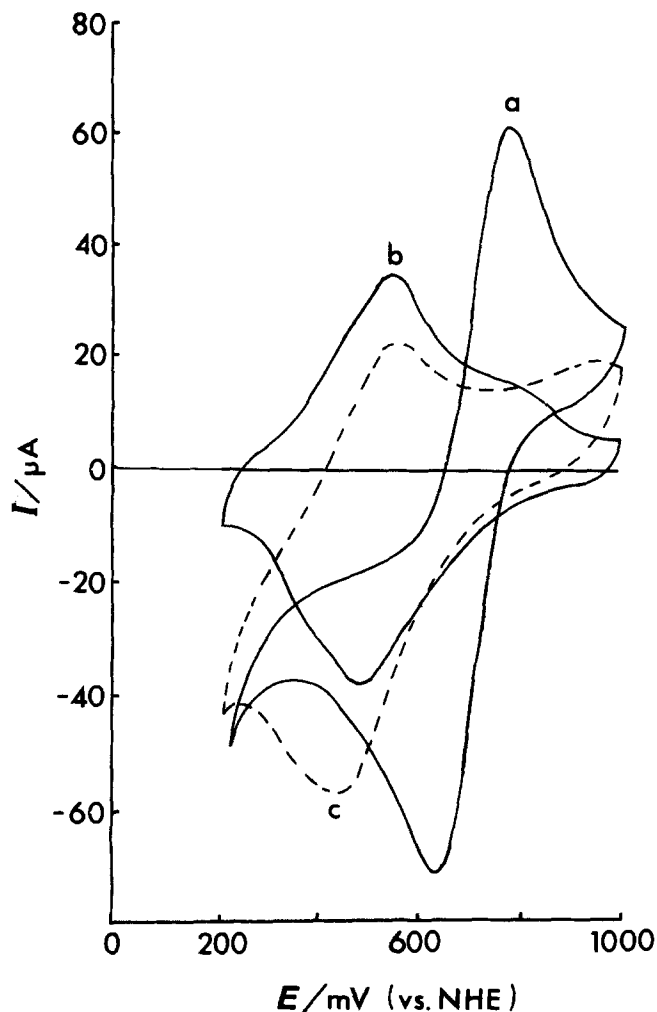


Fig. 6. Cyclic voltammograms of Fe^{3+} on gold electrodes in aqueous $0.050 \text{ mol dm}^{-3} \text{ H}_2\text{SO}_4$ at a sweep rate of 100 mV s^{-1} . (a): $1.00 \times 10^{-3} \text{ mol dm}^{-3} \text{ Fe}^{3+}$ on an uncoated gold electrode. (c): $1.00 \times 10^{-3} \text{ mol dm}^{-3} \text{ Fe}^{3+}$ on a thionine-coated electrode. (b): Thionine-coated electrode in H_2SO_4 only. All other conditions are as in Fig. 2.

quent measurements in Table III are performed under a N_2 atmosphere. The light intensity transmitted to the dark electrode by the solution is about 8% of that incident on the gold-electrolyte interface of the photoelectrode, but is shown to have negligible effect on the cell photocurrent and photovoltage by an experiment in which the dark electrode is located in a shadowed configuration. This result is not surprising because only about 5% of the dark electrode (the end of the wire) receives even this small illumination.

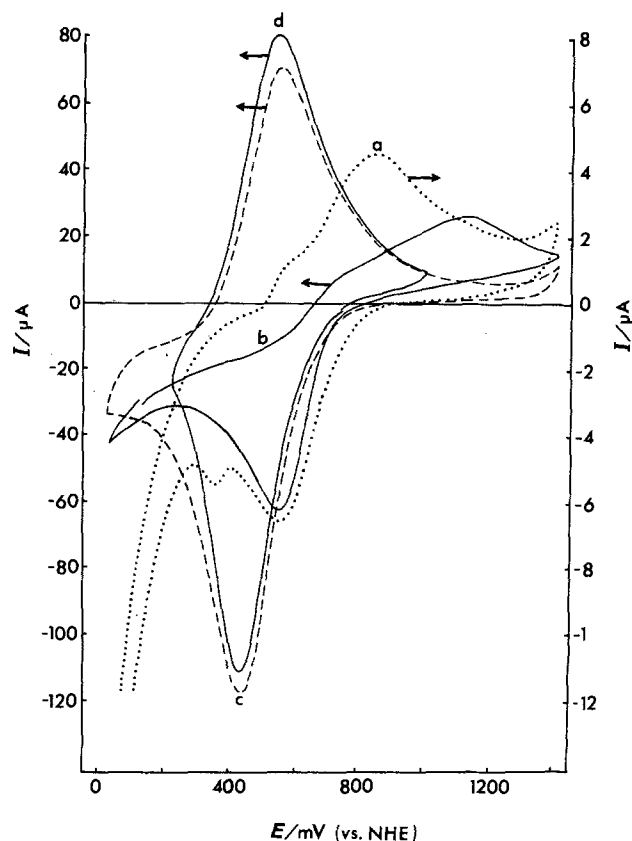


Fig. 7. Cyclic voltammograms of Fe^{3+} on SnO_2 electrodes in aqueous $0.050 \text{ mol dm}^{-3} \text{ H}_2\text{SO}_4$ at a sweep rate of 100 mV s^{-1} . (a): $1.00 \times 10^{-4} \text{ mol dm}^{-3} \text{ Fe}^{3+}$ on an uncoated SnO_2 electrode. (b): $1.00 \times 10^{-3} \text{ mol dm}^{-3} \text{ Fe}^{3+}$ on an uncoated SnO_2 electrode. (c): $1.00 \times 10^{-3} \text{ mol dm}^{-3} \text{ Fe}^{3+}$ on a thionine-coated electrode. (d): Thionine-coated electrode in H_2SO_4 .

The efficiencies in Table III are determined with monochromatic ($598 \pm 5 \text{ nm}$) light whose irradiance is measured at the gold-electrolyte interface after passage through the semitransparent gold photoelectrode. The use of the interface irradiance in the calculation of the power conversion efficiency represents a departure from the previous policy (6, 25) followed by this laboratory in calculating efficiencies relative to irradiances incident on the outside of semitransparent gold electrodes. The new procedure is more comparable with the procedures used in the literature determinations reported in Table I for the thionine cell.

The data in Table III serves the prime purpose of this study—testing the prediction of Albery *et al.* (21-23) that on electrochemical grounds, the deposition of a thionine

Table III. Measured power conversion efficiencies of various types of thionine cell containing thionine-coated and uncoated photoelectrodes. Each value is the mean of several determinations on replicate cells

Electrodes (light/dark)	Number of cells	Electrode treatment	Electrolyte ^a	Open-circuit voltage/mV	Short-circuit current/(10^{-3}A)	Conversion efficiencies/%		
						Voltage, ϕ_v	Current, ϕ_c	Power, ϕ_p
Au/Au	8	Uncoated	Thionine/ N_2	68.3 ± 4.5	153 ± 24	3.3 ± 0.2	$(4.9 \pm 0.8) \times 10^{-2}$	$(4.1 \pm 0.9) \times 10^{-4}$
Au/Au	4	Uncoated	Thionine/air	35.2 ± 3.0	105 ± 11	1.7 ± 0.1	$(3.4 \pm 0.3) \times 10^{-2}$	$(1.4 \pm 0.3) \times 10^{-4}$
SnO_2/Au	3	Uncoated	Thionine/ N_2	6.2 ± 0.4	56 ± 6	0.3 ± 0.02	$(1.8 \pm 0.2) \times 10^{-2}$	$(1.4 \pm 0.2) \times 10^{-5}$
Au/SnO_2	3	Uncoated	Thionine/ N_2	97 ± 10	451 ± 37	4.7 ± 0.5	$(1.5 \pm 0.1) \times 10^{-1}$	$(1.7 \pm 0.3) \times 10^{-3}$
Au/Au	3	Coated by cycling	N_2	0.4 ± 0.2^b	2.6 ± 1.2	0.019 ± 0.01	$(8.4 \pm 3.9) \times 10^{-4}$	$(4.1 \pm 3.9) \times 10^{-8}$
Au/Au	3	Coated by cycling	Thionine/ N_2	23 ± 3.6^b	24 ± 1.2	1.1 ± 0.2	$(7.7 \pm 0.4) \times 10^{-3}$	$(2.1 \pm 0.4) \times 10^{-5}$
Au/Au	3	Coated at fixed ptl.	Thionine/ N_2	13 ± 7^b	20 ± 2	0.63 ± 0.3	$(6.6 \pm 0.6) \times 10^{-3}$	$(1.0 \pm 0.6) \times 10^{-5}$
SnO_2/Au	2	Coated by cycling	Thionine/ N_2	0.30 ± 0.05	7.0 ± 0.7	0.015 ± 0.002	$(2.2 \pm 0.2) \times 10^{-3}$	$(8.3 \pm 2.2) \times 10^{-8}$

^a [Thionine] = $2.1 \times 10^{-4} \text{ mol dm}^{-3}$ (when present). All cell electrolytes also contain H_2O $0.010 \text{ mol dm}^{-3} \text{ H}_2\text{SO}_4$, $0.0100 \text{ mol dm}^{-3} \text{ FeSO}_4$, and about $5 \times 10^{-4} \text{ mol dm}^{-3} \text{ Fe}^{3+}$. Cell temperature = $298 \pm 0.5 \text{ K}$; irradiance = $6.4 \times 10^{-4} \text{ W m}^{-2}$.

^b Direction of cell EMF reversed.

layer on the photoelectrode of the thionine cell should significantly increase the power conversion efficiency of the thionine cell. It is clear from Table III that whether the photoelectrode is coated with thionine by the fixed potential or cycling potential methods, the prediction is not supported because the efficiencies fall substantially, rather than increase, when the dye layers are deposited. In the case of the Au photoelectrode, the efficiency drops by about 19 times, and in the case of the SnO₂ photoelectrode, the somewhat thicker thionine layer drops the efficiency by about 200 times.³

It is important to note that the thionine coating reverses the direction of the electron flow, which is originally from the photo- to the dark electrode in the external circuit of the cell containing gold electrodes. This observation suggests that the coated gold electrode is preferentially selective (18-20) toward the Fe³⁺/Fe²⁺ couple, rather than the dye couple, and that the small electron flow obtained is due to the residual amount of light striking the uncoated dark electrode. This order of reversibility is opposite to the condition predicted by the electrochemical measurements of Albery and Archer (18-20) and considered by them desirable for optimal power output.

The reason that Albery and Archer's (18-20) electrochemical predictions are not borne out in terms of photoelectrochemical performance is that whereas CV or similar measurements show facile thionine reactivity in thionine-coated electrodes, these redox processes arise almost entirely from the thionine in the coating and not from thionine in solution, as shown in the previous section. However, the main photoelectrochemical activity does not occur within the thionine coating, but occurs mainly in the bulk of the solution, as shown by the negligible power conversion efficiency in Table III for thionine-coated gold electrodes immersed in background electrolyte containing no thionine.

Other points of interest also arise from the data in Table III. The power conversion efficiency of the thionine cell equipped with an uncoated SnO₂ photoelectrode and a gold dark electrode is about one thirtieth of that for a cell containing uncoated gold electrodes. Most of this difference arises from the low voltage efficiency of the SnO₂/Au cell, which suggests that the voltage difference between the two redox couples may be less on an SnO₂ electrode than on a gold electrode. When the electrode arrangement is reversed so that SnO₂ becomes the dark electrode and gold becomes the photoelectrode (the gold wire dark electrode is replaced by a SnO₂-coated glass rod of similar dimensions), the power conversion efficiency is increased by about four times. This result presumably indicates that the SnO₂ electrode is more selective toward the Fe³⁺/Fe²⁺ couple than the gold electrode and is thus more suitable for use as a dark electrode.

Table III also indicates that the power conversion efficiencies of thionine cells containing thionine-coated SnO₂ photoelectrodes are very low indeed, being about 0.6% of the value for an uncoated SnO₂/Au cell and an Au/Au cell with a coated photoelectrode. The dye coating on the SnO₂ is much thicker than on the gold electrode, and Fig. 5 and 7 show that this thick layer effectively suppresses the Fe³⁺/Fe²⁺ and thionine/leucothionine couples in solution, thereby decreasing the power conversion efficiency, though the thionine/leucothionine couple in the dye layer is electrochemically active.

Acknowledgments

We are grateful to Dr. J. M. Austin of the Department of Chemistry of the University of Canterbury for providing samples of SnO₂-coated glass and for a number of helpful discussions. I. R. H. gratefully acknowledges receipt of a Commonwealth of Australia Postgraduate Research Award during the course of this work.

Manuscript submitted Jan. 16, 1984; revised manuscript received July 28, 1984.

³Thinner layers are also briefly examined, but they similarly produce an efficiency decrease.

List of Symbols

A	Electrode area
c	Velocity of light in a vacuum
c _s	Surface concentration
E	Electrical potential applied to a system
f	Fill-factor
F	Faraday constant
h	Planck's constant
I	Current
I _{sc}	Short-circuit current
I _p	Current delivered at maximum power point
n	Number of electrons
N _a	Avogadro's number
n _e	Number of photoelectrons
NHE	Normal hydrogen electrode
n _p	Number of photons
R	Resistance
t	Time
T	Absolute temperature
V _{oc}	Open-circuit voltage produced by a cell
V _p	Cell voltage at maximum power point
λ	Wavelength of light
φ _p	Power conversion efficiency
φ _q	Quantum efficiency of short-circuit current production
φ _v	Open-circuit voltage conversion efficiency

REFERENCES

1. E. Rabinowitch, in "Solar Energy Research," F. Daniels and J. A. Duffie, Editors, pp. 193-202, University of Wisconsin Press, Madison, WI (1955).
2. A. E. Potter, Jr. and L. H. Thaller, *Solar Energy*, **3**, 1 (1959).
3. W. J. Albery and M. D. Archer, *Electrochim. Acta*, **21**, 1155 (1976).
4. L. J. Miller, "A Feasibility Study of a Thionine Photogalvanic Power Generation System," Final Report, Contract no. AF33(616)-7911, Sunstrand Aviation, ASTIA Document no. 282878 (1962).
5. W. J. Albery, A. W. Foulds, K. J. Hall, and A. R. Hillman, *This Journal*, **127**, 654 (1980).
6. T. I. Quickenden and G. K. Yim, *Solar Energy*, **19**, 283 (1977).
7. J. O'M. Bockris and S. Srinivasan, "Fuel Cells: Their Electrochemistry," Chap. 4, McGraw-Hill, New York (1969).
8. W. D. K. Clark and J. A. Eckert, *Solar Energy*, **17**, 147 (1975).
9. D. E. Hall, J. A. Eckert, N. N. Lichtin, and P. D. Wildes, *This Journal*, **123**, 1705 (1976).
10. D. E. Hall, W. D. Clark, J. A. Eckert, N. N. Lichtin, and P. D. Wildes, *Ceramic Bull.*, **56**, 408 (1977).
11. P. V. Kamat, M. D. Karkhanavala, and P. N. Moorthy, *Indian J. Chem.*, **15A**, 342 (1977).
12. K. Shigehara, M. Nishimura, and E. Tsuchida, *Bull. Chem. Soc. Jpn.*, **50**, 3397 (1977).
13. P. V. Kamat, M. D. Karkhanavala, and P. N. Moorthy, *Solar Energy*, **20**, 171 (1978).
14. J. M. Mountz and H. T. Tien, *ibid.*, **21**, 291 (1978).
15. K. Shigehara, M. Nishimura, and E. Tsuchida, *Electrochim. Acta*, **23**, 855 (1978).
16. M. S. De Groot, P. A. J. M. Hendriks, and J. C. M. Brokken-Zijp, *Chem. Phys. Lett.*, **97**, 521 (1983).
17. A. S. N. Murthy and K. S. Reddy, *Electrochim. Acta*, **28**, 473 (1983).
18. W. J. Albery and M. D. Archer, *This Journal*, **124**, 688 (1977).
19. W. J. Albery and M. D. Archer, *J. Electroanal. Chem.*, **86**, 1 (1978).
20. W. J. Albery and M. D. Archer, *ibid.*, **86**, 19 (1978).
21. W. J. Albery, W. R. Bowen, F. S. Fisher, A. W. Foulds, K. J. Hall, A. R. Hillman, R. G. Egdell, and A. F. Orchard, *ibid.*, **107**, 37 (1980).
22. W. J. Albery, M. G. Boutelle, P. J. Colby, and A. R. Hillman, *ibid.*, **133**, 135 (1982).
23. W. R. Bowen, *Acta Chem. Scandinavia*, **A34**, 437 (1980).
24. O. S. Heavens, "Optical Properties of Thin Solid Films," Chap. 6, Butterworth, London (1955).
25. T. I. Quickenden and R. L. Bassett, *J. Phys. Chem.*, **85**, 2232 (1981).
26. T. I. Quickenden and G. K. Yim, *ibid.*, **84**, 670 (1980).
27. J. J. Kipling and R. B. Wilson, *J. Appl. Chem.*, **18**, 203 (1970).
28. A. J. Bard and L. R. Faulkner, "Electrochemical Methods: Fundamentals and Applications," p. 552, John Wiley, New York (1982).

Water Absorption and Conductivity in Poly(Ethylene Oxide)-Lithium Tetrafluoroborate Films

M. M. Nicholson*

Rockwell International Science Center, Anaheim, California 92803

T. P. Weismuller

Rockwell International Corporation, Defense Electronics Operations, Anaheim, California 92803

ABSTRACT

Water-vapor absorption and conductivity in spin-cast poly(ethylene oxide)-lithium tetrafluoroborate films were investigated near 21°C by *in situ* near-infrared spectroscopy and ac conductance measurements. The film conductivity was $\leq 2 \times 10^{-5} \Omega^{-1} \text{cm}^{-1}$ until the water content exceeded that corresponding to $\text{LiBF}_4 \cdot 3\text{H}_2\text{O}$. It increased with additional water, reaching $3 \times 10^{-3} \Omega^{-1} \text{cm}^{-1}$ at the composition equivalent to $\text{LiBF}_4 \cdot 20\text{H}_2\text{O}$. Most of the water above the trihydrate level was unstably absorbed, however, and began to escape from the film within a few minutes. This syneresis was attributed to spontaneous restructuring or crystallization of the polymer. The conductivity data were interpreted on the basis of a two-phase model, in which one portion of the salt remained in a nonconductive solid region, while the other portion dissolved in a more fluid conductive polymer-water region.

Complexes of salts with aliphatic poly-ethers are a relatively new class of solid electrolytes (1, 2). Some of these materials can attain conductivities of the order of $10^{-5} \Omega^{-1} \text{cm}^{-1}$ at room temperature, and the conduction is known to increase greatly on absorption of water. Because of their potential importance for lithium battery electrolytes, most research on such complexes has been done with carefully dried preparations. For other types of batteries and electrochemical devices, however, some water is acceptable, or even required, and the higher conductivity is advantageous. The influence of water on these solids is, in any case, a point of scientific interest which has received only cursory treatment in previous studies.

This paper describes results of conductance measurements near 21°C on thin solid films of poly(ethylene oxide) (PEO) complexed with lithium tetrafluoroborate, and containing various amounts of water. The water content of the films was monitored *in situ* by near-infrared absorption spectroscopy, while the ac conductance at 1000 Hz was determined on an impedance bridge. This thin film technique permitted much faster acquisition of data than conventional bulk methods for investigation of polymers. Both the water content and the conductance showed a peculiar but repeatable time dependence, which probably was caused by spontaneous restructuring of the polymer.

Experimental

The PEO preparation, with an average molecular weight of 4,000,000, was from Polysciences, Incorporated. The LiBF_4 was from Ozark-Mahoning. Electrolyte films of the order of 1 μm thick were prepared on single-crystal sapphire plates by spin casting from a viscous aqueous solution containing 4.5 polymer repeating units per molecule of LiBF_4 . These plates had, near one edge, a pair of narrow-line electrodes formed from conductive silver paste, with an interelectrode spacing of 0.4 mm. Margins around the film were defined by masking tape, which was removed after the casting process.

The films were dried under vacuum at room temperature for 24h and transferred, without air exposure, to a helium-atmosphere glove box, where they were mounted in the double cell shown in Fig. 1. For the measurements of conductance and water absorption, the cell was placed in a Beckman DK-2A spectrophotometer, with the electrical leads connected to a Fluke Model 710B impedance bridge. Nitrogen containing known partial pressures of water was passed into the optical reference compartment of the cell and out through the sample compartment. The water pressure was controlled at known levels by passing

the nitrogen through water in a cooled, thermostated gas washing bottle. The moist nitrogen then traveled through a long copper tube to reach room temperature, near 21°C, before entering the cell.

Resistances and near-infrared (IR) spectra of the films were determined at various times up to 2h and, in some instances, the transmittance at the characteristic wavelength of the OH stretching band near 2.9 μm was recorded continuously as a function of time. The amount of water present per unit film area during an experiment was found by comparing the IR absorbance of the film with that of a known thickness of liquid water retained between two glass slides. Following a systematic run, the cell could be placed, open, in the vacuum chamber to redry the film in preparation for the next set of measurements.

Two methods were used to determine the original thickness of the PEO- LiBF_4 film after completion of the conductance measurements. The polymer electrolyte was too soft for measurement with a profilometer. For a rough thickness estimate ($\pm 40\%$), the used film was redried, then dissolved in water, and the resulting weight loss noted. For a more accurate evaluation, the lithium content of the dissolved film was determined by atomic absorption. The density of the anhydrous PEO- LiBF_4 preparation was found to be 1.23 g/cm^3 by weighing a known volume of the bulk solid packed into a glass tube.

Results and Discussion

The system PEO-LiBF₄-H₂O.—The PEO- LiBF_4 system at the 4.5:1 mole ratio was selected for investigation primarily because the anhydrous complex of this composition was known to have the comparatively high conductivity

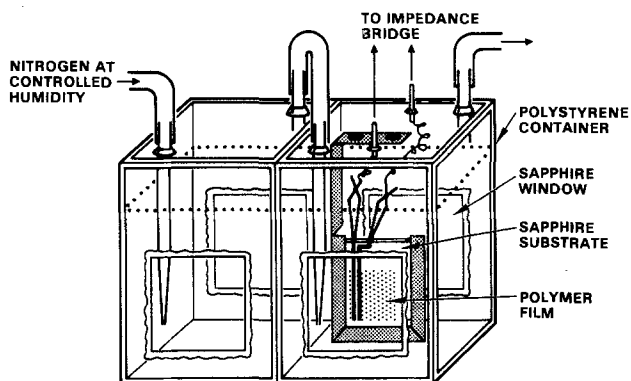


Fig. 1. Experimental cell

*Electrochemical Society Active Member.

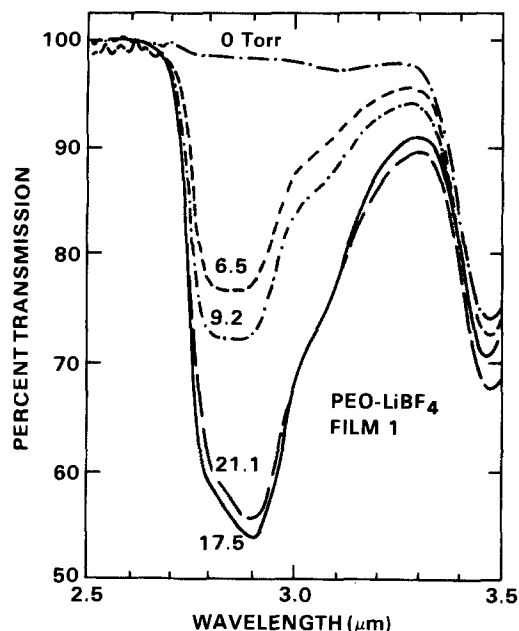


Fig. 2. Infrared spectra of PEO-LiBF₄-H₂O film recorded 30 min after changes of ambient water vapor pressure.

of $10^{-5} \Omega^{-1} \text{cm}^{-1}$ at 20°C (1). This suggests a tendency toward amorphous behavior which could be conducive to the incorporation of water in the organic phase.

The PEO-LiBF₄-H₂O films were colorless and highly transparent. As expected, water was readily absorbed from the vapor phase with an immediate increase in conductivity. Figure 2 shows a typical set of near-infrared spectra recorded after 30 min exposures to each of the indicated partial pressures of water. The maximum absorption due to OH stretching occurred at 2.90 μm in pure liquid water. This band acquired a doublet character in the PEO-LiBF₄-H₂O films, with increased absorption near 2.85 μm , which was more evident at the lower water levels. The shift to the shorter wavelength apparently was due to binding of water with the lithium ion, since it did not occur with PEO in the absence of the salt.

Conductances ($1/R$) of two PEO-LiBF₄ films are plotted as functions of the water absorbance in Fig. 3 and 4. The symbol R represents the measured resistance of the film specimen. The anhydrous film thickness was roughly 1.8 μm for film 1 and, more accurately, 0.88 μm for film 2. The circles and other symbols represent different runs which covered a wide range of water pressures and standing times, as well as different predrying conditions. It is noteworthy that the data for each film can be adequately represented by a single line, even though many non-equilibrium points are included. The significance of the slopes of these lines is discussed later. The absorbance in-

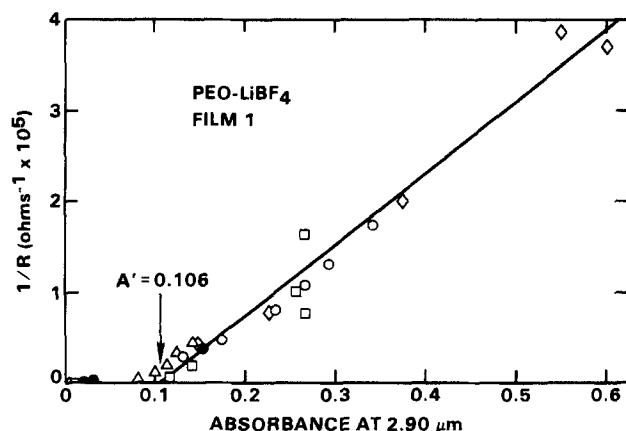


Fig. 3. Dependence of measured conductance on IR absorbance due to water in film 1.

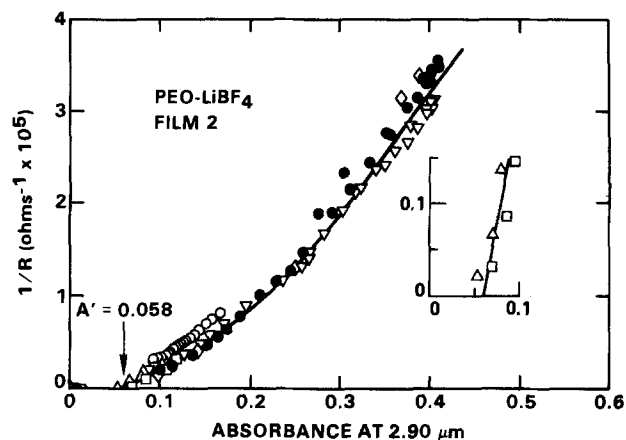


Fig. 4. Dependence of measured conductance on IR absorbance due to water in film 2. Inset shows the extrapolation in detail.

tercept for film 2 in Fig. 4 corresponds to the composition LiBF₄ · 2.9H₂O. The approximate composition LiBF₄ · 2.5H₂O was found in a similar way for film 1 in Fig. 3. Two hydrates of LiBF₄ have been characterized in the literature (3, 4). LiBF₄ · H₂O is stable above 23°C in the presence of an aqueous solution of the salt, while LiBF₄ · 3H₂O crystallizes below 23°C. In the present study, near 21°C, the measured film conductances dropped abruptly to $< 10^{-7} \Omega^{-1}$ as the water content fell below the trihydrate composition. It is thus apparent that the initial portion of the absorbed water was utilized primarily in hydration of the salt. The "free" water above the trihydrate level was responsible for the higher magnitude of conductivity discussed in this paper.

The absorption of water by the PEO-LiBF₄ films displayed an unusual time dependence. Figure 5 illustrates this behavior in the IR absorbance recorded under a constant water vapor pressure of 18.7 torr. After 24h of predrying under vacuum, the film added water rapidly at first. The absorbance then reached a maximum in 7-10 min, after which it gradually decayed toward the level corresponding to LiBF₄ · 3H₂O. This behavior was repeatable with thorough drying between runs. Less extensive drying produced a related, but distinctly different, result shown by the lower curve in Fig. 5. With a vacuum drying time of 0.5h the initial absorbance again was essentially zero. The water uptake also was quite rapid at first, but the loss set in after only 1 min, and the IR absorbance approached the asymptotic value much earlier than it did with 24h of drying.

The change of conductance with time closely paralleled that of the water content, as one can infer from Fig. 3 and 4. This is shown explicitly by Fig. 6 for the same runs that are represented in Fig. 5.

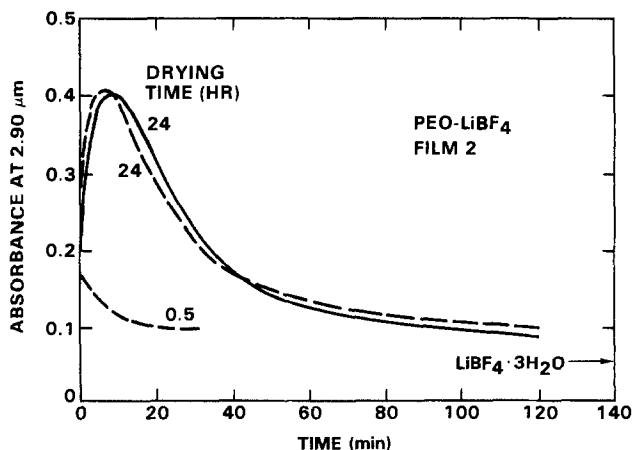


Fig. 5. Time dependence of water absorbance in PEO-LiBF₄-H₂O film recorded continuously under water pressure of 18.7 torr after different predrying times. All curves start at zero absorbance.

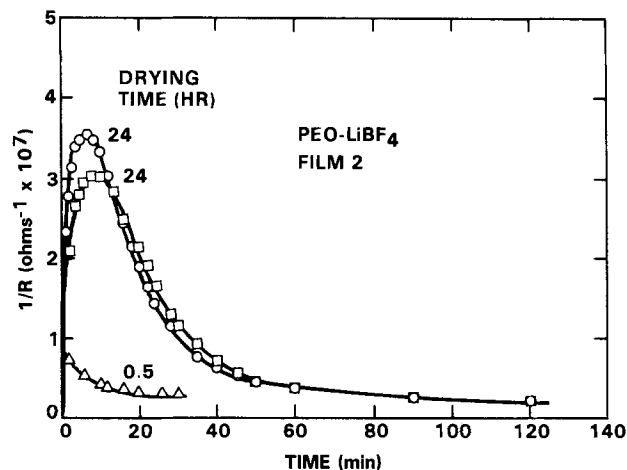


Fig. 6. Time dependence of conductance of PEO-LiBF₄-H₂O film under conditions of Fig. 5. All curves start at zero conductance on this scale.

The system PEO-H₂O.—It was of great interest to know whether the spontaneous water loss was a property of the salt or the polymer. A spin-cast film of PEO without the salt was prepared for this purpose and dried under vacuum 24h. Its infrared absorption under 18.7 torr of water vapor was then examined.

Infrared spectra recorded at various exposure times under constant water pressures are shown in Fig. 7. This group of spectra differs in several ways from the PEO-LiBF₄-H₂O spectra of Fig. 2. The salt-free film was visually cloudy, and infrared light scattering is evident in the lower transmission range of the spectra. Although the absorption maximum shifted slightly with water content, any doublet character of the OH band is not obvious. Finally, the salt-free spectra showed isosbestic points at 2.76 and 3.21 μm . Such points are characteristic of a fixed stoichiometry between initial and final species in a chemical process. They were not observed with the non-scattering films containing LiBF₄. Figure 8 indicates a time-dependent gain and subsequent loss of water by the PEO which is very similar to that for PEO-LiBF₄ in Fig. 5. The final water absorbance was relatively closer to zero, however, in the salt-free film.

Although the scattering effect prevented an absolute determination of water in the PEO, it is clear that the major time dependence was associated with the polymer. A comparable syneresis, or loss of solvent component, was reported by Weiss and Lenz for water in phosphonate esters derived from PEO oligomers (5). Those authors deter-

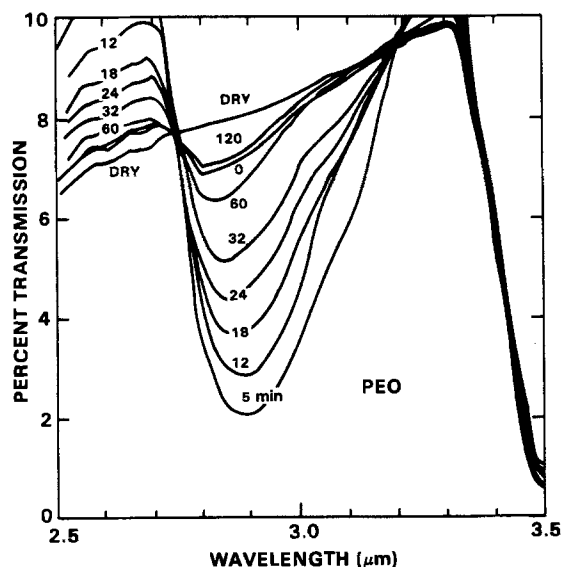


Fig. 7. Infrared spectra of PEO-H₂O film recorded at different times under water pressure of 18.7 torr.

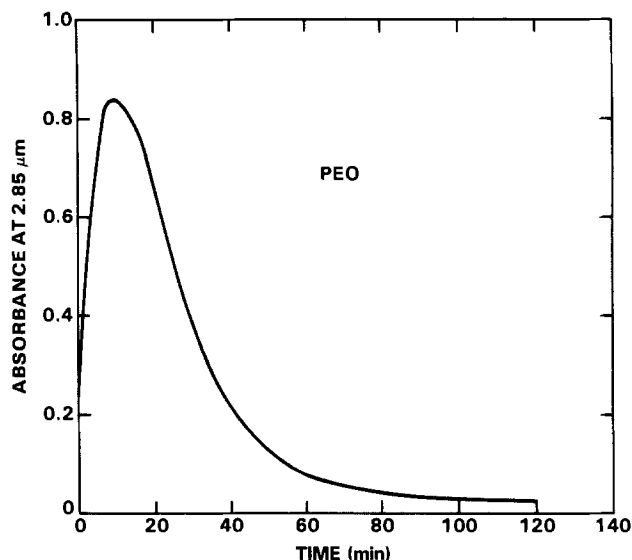


Fig. 8. Time dependence of water absorbance in PEO-H₂O film recorded continuously under water pressure of 18.7 torr after predrying 24h.

mined the absorbed water gravimetrically on bulk samples in experiments lasting several days. With the thin film technique used here, the time dependence could be detected in a few minutes and well characterized in about an hour. An apparently related heat-induced syneresis in cross-linked PEO-H₂O gels was attributed by Graham *et al.* to increased ordering of the polymer, with some water still attached (6).

Further correlations.—Conductivity relationships in the PEO-LiBF₄-H₂O system can be examined in greater detail by means of Fig. 9, in which the total thickness of the swollen film is considered, and Fig. 10, which treats the free water, with its incremental thickness, as a separate region supporting of all the observed conduction.

For calculating the bulk conductivity σ plotted in Fig. 9, the total film thickness was taken, as a first approximation, to be the sum of the dry PEO-LiBF₄ thickness, based on bulk density, and the liquid water thickness equivalent to the IR absorbance of the film. This estimated total thickness ranged from 0.88 μm in the dry state to 2.26 μm for the swollen film at a ratio of 21 mol of H₂O per mole of LiBF₄. All of the smoothed data points for film 2 fell close to a straight line intersecting the mole-ratio axis at 3.1. The corresponding plot for film 1 was a slightly curved line with a similar intercept; it is not shown because of uncertainty in the dry-film thickness.

The cause of the linear relationship in Fig. 9 is not obvious. In a very simple model for the system, it could be en-

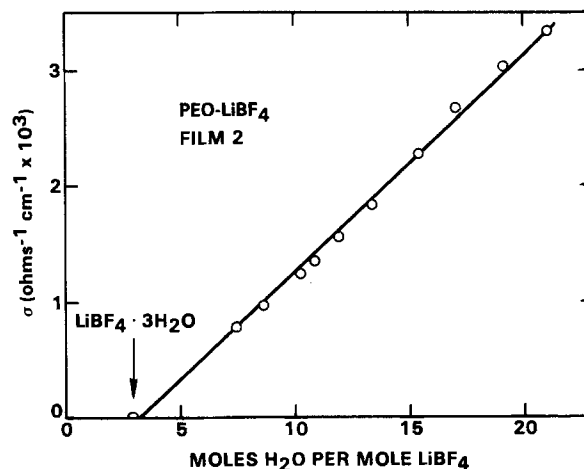


Fig. 9. Conductivity of swollen PEO-LiBF₄-H₂O film as a function of the mole ratio of H₂O to LiBF₄. Points are smoothed data from Fig. 4.

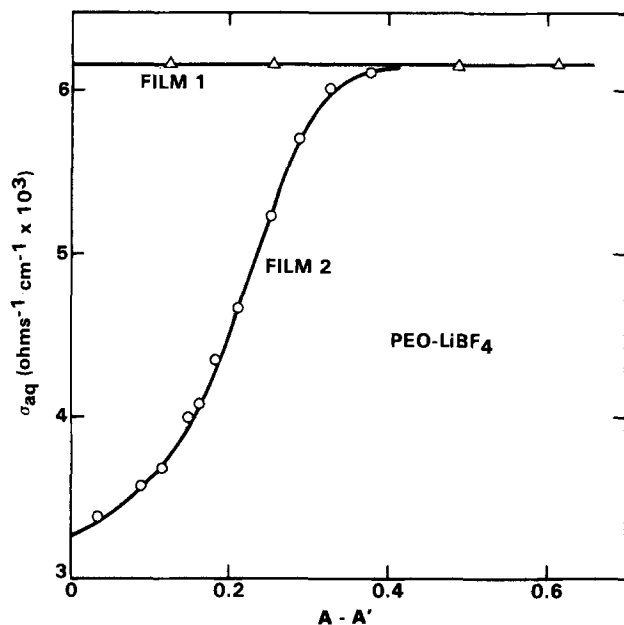


Fig. 10. Conductivity based on incremental thickness equivalent to free water in PEO-LiBF₄-H₂O films as function of free-water absorbance. Points are smoothed data from Fig. 3 and 4.

visioned that all of the salt dissolves in a homogeneous conductive phase, with water acting only as a diluent. The conductivity would then decrease with increasing water content. Factors opposing this effect could be the dissociation of ion pairs and the lowering of viscosity on addition of water. However, those trends, superimposed on the dilution, would not account for the straight line in Fig. 9. The actual behavior was more consistent with a system of two microphases, one a conductive fluid or amorphous region containing dissolved salt, and the other a nonconductive solid including the remainder of the LiBF₄ · 3H₂O. The linear relationship could then occur if the dissolved-salt concentration in the film as a whole were proportional to the free-water content and the mobilities of Li⁺ and BF₄⁻ remained constant. This model treats the conductive microphase as an aqueous region saturated with both PEO and LiBF₄ and disregards effects of porosity or tortuosity created by the solid PEO-salt matrix.

A lower limit for the apparent equivalent conductance of LiBF₄ can be estimated as follows from the plot in Fig. 9. At the mole ratio of 20, the concentration *c* of LiBF₄ dissolved in the entire film had to be ≤ 1.65*M*. With the corresponding experimental conductivity σ of $3.1 \times 10^{-3} \Omega^{-1} \text{cm}^{-1}$, the equivalent conductance Λ_{LiBF_4} , expressed as $1000 \sigma/c$, would have been $\geq 1.9 \Omega^{-1} \text{cm}^2 \text{mol}^{-1}$. It may be noted from the work of Radchenko and Ryss that LiBF₄ completely dissolves in pure water at a ratio as low as 5.35

mol of water per mole of salt (7). In the presence of PEO, however, the salt probably is much less soluble. The lower limit of $1.9 \Omega^{-1} \text{cm}^2 \text{mol}^{-1}$ for Λ_{LiBF_4} is two orders of magnitude less than typical equivalent conductances of salts in water, but it is not inconsistent with their behavior in viscous polymer-water mixtures. For example, a paper by Isono *et al.* indicates an equivalent conductance of $7.9 \Omega^{-1} \text{cm}^2 \text{mol}^{-1}$ for NaCl in a concentrated poly(ethylene glycol)-water mixture at 25°C (8).

Figure 10 accentuates the contrast between the two types of film behavior encountered in this study. An incremental conductivity σ_{aq} was calculated by taking the effective film thickness as that equivalent to the free water. This incremental thickness was found from the IR absorbance term $A-A'$, where A is the measured absorbance and A' is the intercept from Fig. 3 or 4. These are nonequilibrium data. The pronounced difference between the plots in Fig. 10 may reflect a difference in the rates of syneresis for the two films: the polymer apparently rearranged readily in film 1 to an ordered, or crystalline, phase, forming an aqueous region with a constant conductivity σ_{aq} of $6.2 \times 10^{-3} \Omega^{-1} \text{cm}^{-1}$. This water was subsequently lost by evaporation. With slower crystallization in film 2, the data included some intermediate stages, where σ_{aq} was lower due to more polymer in solution. The same limiting level was eventually reached by film 2, however, and water loss occurred, as represented in Fig. 5.

Further research is planned to characterize related polymer-salt-solvent electrolyte systems.

Acknowledgment

This work was supported in part by the Office of Naval Research.

Manuscript submitted March 13, 1984; revised manuscript received Aug. 30, 1984.

Rockwell International Science Center assisted in meeting the publication costs of this article.

REFERENCES

1. M. B. Armand, J. M. Chabagno, and M. J. Duclot, in "Fast Ion Transport in Solids," P. Vashishta, J. N. Mundy, and G. K. Shenoy, Editors, p. 131, Elsevier North Holland, Amsterdam (1979).
2. D. F. Shriver, B. L. Papke, M. A. Ratner, R. Dupon, T. Wong, and M. Brodwin, *Solid State Ionics*, **5**, 83 (1981).
3. C. D. West, *Z. Kristallogr.*, **91**, 480 (1935).
4. K. C. Moss, D. R. Russell, and D. W. A. Sharp, *Acta Crystallogr.*, **14**, 330 (1961).
5. R. A. Weiss and R. W. Lenz, *J. Appl. Polymer Sci.*, **23**, 2443 (1979).
6. N. B. Graham, N. E. Nwachuku, and D. J. Walsh, *Polymer*, **23**, 1345 (1982).
7. I. V. Radchenko and A. I. Ryss, *J. Struct. Chem. USSR*, **6**, 171 (1965).
8. T. Isono, K. Takahashi, and R. Tamamushi, *Bull. Chem. Soc. Jpn.*, **54**, 2183 (1981).

The Application of Linear Sweep Voltammetry to a Rotating Disk Electrode with a Catalytic Process

S. L. Lanny Ng*¹ and H. Y. Cheh*

Department of Chemical Engineering and Applied Chemistry, Columbia University, New York, New York 10027

ABSTRACT

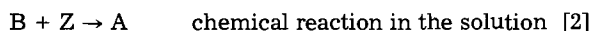
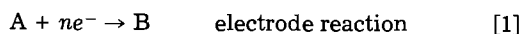
The current response of a catalytic process to a linear sweep of the potential on a rotating disk electrode is analyzed with the aid of a Nernst diffusion model. Special solutions for a fast chemical reaction are obtained for reversible, quasi-reversible, and irreversible electrode reactions. Results for the reversible case are compared with experimental data.

Theoretical and experimental studies concerning the application of linear sweep voltammetry (LSV) to a rotating disk electrode (RDE) for simple charge-transfer reactions have been reported recently (1-6). Natural convection is diminished by using a RDE. By applying a LSV to the RDE system, it is expected that both kinetic and mechanistic information on the electrode process can be attained in a relatively simple and fast experiment. Furthermore, it permits an extension in the range of rate constants to be measured. Kinetic and catalytic processes in electrochemistry have been studied in stagnant systems by a wide variety of electrochemical techniques, such as chronopotentiometry and ac polarography. The initial investigation of catalytic systems was carried out by Bricka and Wiesner (7) in polarography. Reviews on this subject are available in several monographs (8-10) and in an article by Nicholson and Shain (11).

This paper reports our investigation on the application of LSV to a RDE for an electron charge-transfer reaction coupled to an irreversible and homogeneous chemical reaction in which the product of the electrode reaction reacts with an electroinactive species to regenerate the initial species. This type of reactive system is often called a catalytic process in the electroanalytical literature, and the resulting current is called a catalytic current (12). Theoretical calculations were conducted by using a Nernst diffusion model, in which the concentration change occurs within a diffusion layer of thickness δ . The same model was used by Andricacos and Cheh (3). An experimental investigation was carried out for the case of a reversible electrode reaction. A similar problem has been studied by Saveant and Vianello (13) in a stagnant system.

Theoretical

Consider the following catalytic mechanism



in which A is reduced to B at the electrode surface and B undergoes a catalytic, homogeneous chemical reaction with an electroinactive species Z to regenerate A. The limiting current density for species A is increased by the presence of species Z, and its magnitude depends on the kinetics of the chemical reaction and mass transport of all the species. In general, the chemical reaction is of the second order. However, it is assumed that the amount of the species Z exists in large quantity. The second-order reaction degenerates to a pseudo-first-order reaction.

By assuming a Nernst diffusion model in the absence of double-layer and adsorption effects, and equal diffusion coefficients for A and B, the governing partial differential equations and the boundary conditions are as follows

$$\frac{\partial c_A}{\partial t} = D \frac{\partial^2 c_A}{\partial x^2} + kc_B \quad [3]$$

$$\frac{\partial c_B}{\partial t} = D \frac{\partial^2 c_B}{\partial x^2} - kc_B \quad [4]$$

$$c_A = c_A^0, c_B = c_B^0 \approx 0 \text{ at } t = 0, x \geq 0 \quad [5]$$

$$c_A = c_A^0, c_B = c_B^0 \approx 0 \text{ at } t > 0, x \geq \delta \quad [6]$$

$$\frac{\partial c_A}{\partial x} = -\frac{\partial c_B}{\partial x} = \frac{i}{nFD} \text{ at } t > 0, x = 0 \quad [7]$$

with

$$\frac{i}{nF} = k^0 \left\{ c_A(0, t) \exp \left[-\frac{\alpha nF}{RT} (E(t) - E_0) \right] - c_B(0, t) \exp \left[\left(1 - \alpha\right) \frac{nF}{RT} (E(t) - E_0) \right] \right\} \quad [8]$$

and

$$E(t) = E_i - vt \quad [9]$$

where c_A and c_B are the concentrations of species A and B, c_A^0 and c_B^0 are the bulk concentrations, D is the diffusion coefficient, k is the rate constant of the catalytic chemical reaction, i is the current density, x is the distance from the electrode surface, t is the time, k^0 is the standard rate constant of the heterogeneous electrode reaction, n is the number of electrons involved in the electrode reaction, v is the sweep rate, α is the transfer coefficient, E is the electrode potential, E_i is the initial potential at which polarization of the electrode begins, and E_0 is the standard electrode potential. R , T , and F have their usual significance.

Let us introduce the following dimensionless parameters

$$C_A = c_A/c_A^0 \quad [10]$$

$$C_B = c_B/c_A^0 \quad [11]$$

$$\theta = Dt/\delta^2 \quad [12]$$

$$X = x/\delta \quad [13]$$

$$z = k\delta^2/D \quad [14]$$

$$\phi = i/i_1 \quad [15]$$

$$s = nFv\delta^2/RTD \quad [16]$$

$$u = (E_i - E_0)nF/RT \quad [17]$$

$$p = k^0\delta/D \quad [18]$$

where i_1 is the limiting current density. According to Levich (14), i_1 and δ for a RDE system can be calculated by

$$i_1 = nFDc_A^0/\delta \quad [19]$$

$$\delta = 1.61D^{1/3}\nu^{1/6}\omega^{-1/2} \quad [20]$$

where ν is the kinematic viscosity and ω is the rotation speed of the RDE. Equations [3]-[7] can now be rewritten as

*Electrochemical Society Active Member.

¹Present address: AT&T Technologies, Engineering Research Center, Princeton, New Jersey 08540.

$$\frac{\partial C_A}{\partial \theta} = \frac{\partial^2 C_A}{\partial X^2} + zC_B \quad [21]$$

$$\frac{\partial C_B}{\partial \theta} = \frac{\partial^2 C_B}{\partial X^2} - zC_B \quad [22]$$

$$C_A = 1, C_B = 0 \text{ at } \theta = 0, X \geq 0 \quad [23]$$

$$C_A = 1, C_B = 0 \text{ at } \theta > 0, x \geq 1 \quad [24]$$

$$\phi(0) = \frac{\partial C_A}{\partial X} = -\frac{\partial C_B}{\partial X} \text{ at } \theta > 0, X = 0 \quad [25]$$

The above equations are solved by Laplace transform (15), and the solution is

$$\frac{\psi(\xi)}{[\Lambda \exp(\alpha\xi)][1 + \exp(-\xi)]} = \frac{1}{1 + \exp(-\xi)} - \frac{2}{\sqrt{s}} \int_{-u}^{\xi} \psi(\xi) \exp[-\lambda(\xi - \eta)] \times \sum_{n=1}^{\infty} \exp\left[\frac{-(2n-1)^2\pi^2(\xi - \eta)}{4s}\right] d\eta \quad [26]$$

where

$$\psi = \phi/s^{1/2} \quad [27]$$

$$\xi = s\theta - u \quad [28]$$

$$\Lambda = p/s^{1/2} \quad [29]$$

$$\lambda = z/s \quad [30]$$

For sufficiently large values of u ($u > 10$), the lower limit of the integral can be replaced by negative infinity. The current-potential behavior no longer depends on u . This situation can be arrived at in practice by allowing the initial potential to be 300 mV more anodic than the half-wave potential, $E_{1/2}$.

Note that when $\xi \rightarrow \infty$

$$\phi \rightarrow \sqrt{z} \coth \sqrt{z} \quad [31]$$

At $\sqrt{z} > 3$, Eq. [31] further reduces to

$$\phi \rightarrow \sqrt{z} \quad [32]$$

Therefore, when the potential is highly cathodic, i/i_1 is independent of both the potential sweep rate and the electrode kinetics but is a function of the catalytic reaction-rate constant and the bulk concentrations of species A and Z. Equation [32] thus provides a simple method to determine the rate constant for the catalytic reaction. Unfortunately, the application is limited due to the interference of side reactions at large values of the overpotential.

For reversible electrode reactions ($\Lambda \rightarrow \infty$, or $k^0 \rightarrow \infty$), Nernstian behavior is obtained. Equation [26] reduces to

$$\frac{1}{1 + \exp(-\xi)} = \int_{-u}^{\xi} \frac{2}{s} \phi(\eta) \exp[-\lambda(\xi - \eta)] \times \sum_{n=1}^{\infty} \exp\left[\frac{-(2n-1)^2\pi^2(\xi - \eta)}{4s}\right] d\eta \quad [33]$$

Alternately, the following expression for the dimensionless current function can be derived explicitly by using the Duhamel theorem (15)

$$\frac{\phi(\xi)}{\sqrt{s}} = \int_{-u}^{\xi} \frac{[1 + \lambda + \lambda \exp(\eta)]}{4 \cosh^2(\eta/2)} \exp[-\lambda(\xi - \eta)] \times \frac{\left\{1 + 2 \sum_{n=1}^{\infty} \exp[-n^2s/(\xi - \eta)]\right\}}{\sqrt{\pi(\xi - \eta)}} d\eta \quad [34]$$

The integral can be calculated by cautious adaptive Romberg extrapolation (16). Figures 1 and 2 illustrate the results at $s = 100$ and $s = 1$, respectively. At high sweep rates ($s > 10$), current peaks are observed for $\lambda \leq 0.3$. How-

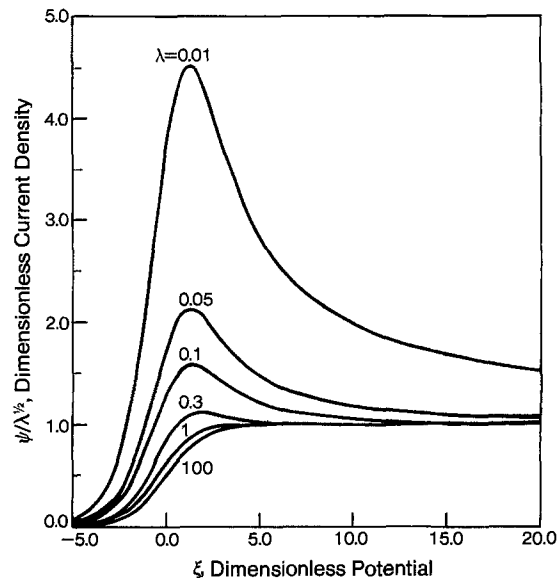


Fig. 1. Current-potential behavior for a reversible electrode reaction at $s = 100$.

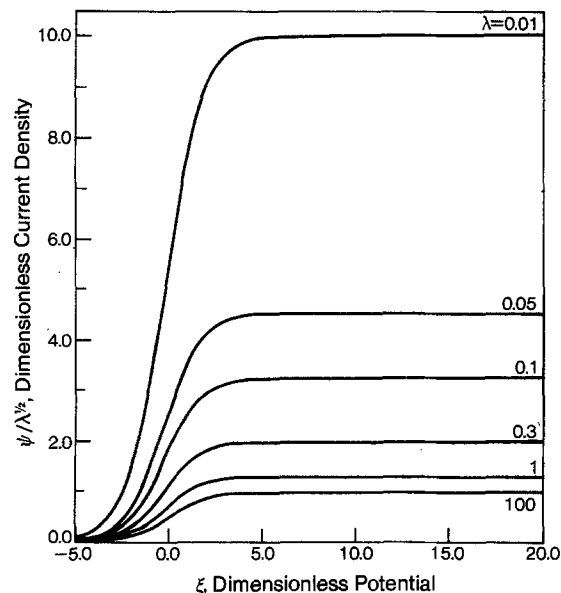


Fig. 2. Current-potential behavior for a reversible electrode reaction at $s = 1$.

ever, i - E curves resemble polarographic waves at large values of the catalytic rate constant and at low sweep rates. From the characteristics of the peak current and the wave height, it is possible to describe the dependence of the peak current on $\lambda^{1/2}$. The results are shown in Fig. 3. The rate constant of the catalytic reaction can be obtained by applying these results to experimental measurements. The half-wave potential² can also be deduced from the i - E curves and be related to the chemical rate constant, as shown in Fig. 4.

In the case of an irreversible electron charge-transfer reaction ($k^0 \rightarrow 0$), Eq. [26] reduces to

$$1 - \psi^*(\xi^*) \exp(-\xi^*) = \int_{\ln H}^{\xi^*} \frac{2\psi^*(\eta)}{\sqrt{s^*}} \exp[-\lambda^*(\xi^* - \eta)] \times \sum_{n=1}^{\infty} \exp\left[\frac{-(2n-1)^2\pi^2(\xi^* - \eta)}{4s^*}\right] d\eta \quad [35]$$

²For the case where a current peak exists, the half-wave potential is defined to be the potential at which the corresponding current density is half the peak current density.

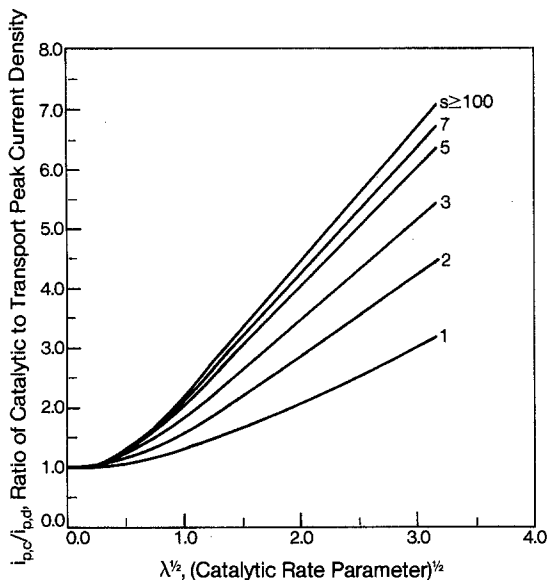


Fig. 3. Dependence of the catalytic peak current density on the catalytic rate parameter.

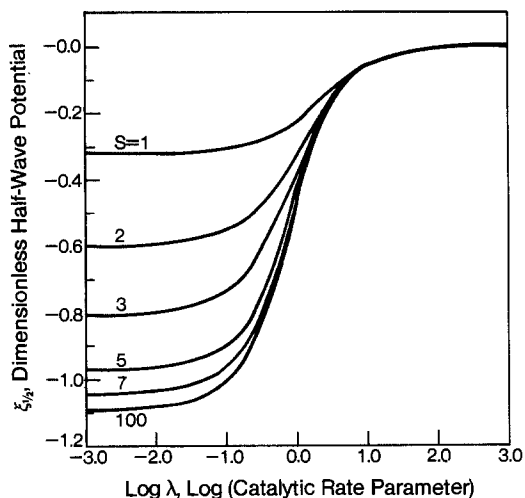


Fig. 4. Dependence of the half-wave potential on the catalytic rate parameter.

where

$$\psi^* = \psi/\alpha^{1/2} \tag{36}$$

$$\xi^* = s^*\theta + \ln H \tag{37}$$

$$s^* = \alpha s \tag{38}$$

$$H = p(s^*)^{-1/2} \exp [-(E_1 - E_0)\alpha nF/RT] \tag{39}$$

$$\lambda^* = \lambda/\alpha \tag{40}$$

The dimensionless current is a complicated function of the kinetic parameters for the irreversible electrode reaction and the dimensionless sweep rate. The integral can be calculated numerically. Figures 5 and 6 show the i - E characteristics at $s = 100$ and $s = 1$, respectively.

Theoretical investigation of polarographic waves for simple charge-transfer processes in the absence of chemical reaction was studied in detail by Matsuda and Ayabe (17). These authors classified the electrode reactions into three cases: reversible, quasireversible, and irreversible reactions. The homogeneous chemical reaction can be ignored when $\lambda \rightarrow 0$. The application of LSV to a RDE in this case has been reported in detail by Andricacos and Cheh (3-5), and by Quintana *et al.* (6). However, when $\lambda \rightarrow \infty$, the rate of the chemical reaction is fast relative to the sweep rate, and the resulting current is called the catalytic current.

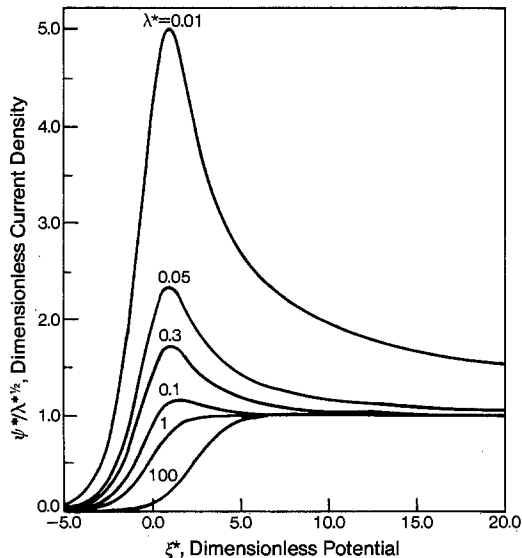


Fig. 5. Current-potential behavior for an irreversible electrode reaction at $s^* = 100$.

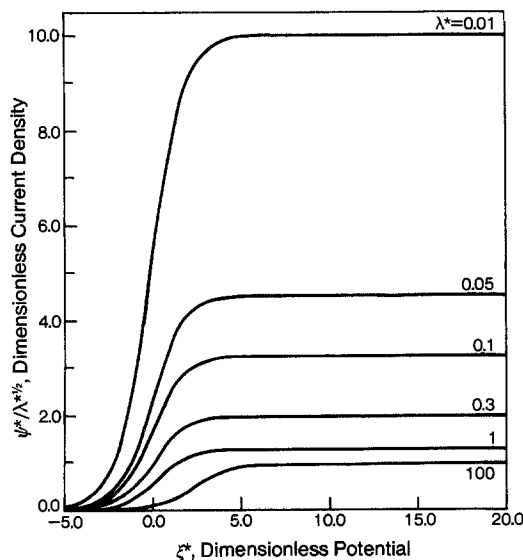


Fig. 6. Current-potential behavior for an irreversible electrode reaction at $s^* = 1$.

In the case of a reversible electrode reaction, there is no current peak and the dimensionless current is derived from Eq. [34]

$$\phi(\xi) = \frac{\sqrt{z} \coth \sqrt{z}}{1 + \exp [-\xi]} \tag{41}$$

The current is independent of s , with the ratio of the catalytic to the mass transport current density i_d (4) (in the absence of the chemical reaction) given by

$$\frac{i}{i_d} = \sqrt{z} \coth \sqrt{z} \tag{42}$$

For a quasireversible electrode reaction, with $\xi \rightarrow \infty$ and large values of λ , Eq. [26] reduces to

$$\phi(\xi) = \frac{1}{[1 + \exp (-\xi)] \frac{\tanh \sqrt{z}}{\sqrt{z}} + \frac{\exp (-\alpha\xi)}{p}} \tag{43}$$

The dimensionless current $\phi(\xi)$ and the dimensionless half-wave potential are both controlled by the rates of the electrode and the chemical kinetics, but not by s . At highly cathodic potential, Eq. [43] reduces to Eq. [31].

If the electrode reaction is an irreversible one, Eq. [35] simplifies to

$$\phi(\xi) = \frac{1}{\frac{\tanh \sqrt{z}}{\sqrt{z}} + \frac{\exp(-\alpha\xi)}{p}} \quad [44]$$

To summarize, one may conclude that when $\lambda^{1/2} < 0.5$, the process is controlled by mass transport with $i_{p,c}/i_{p,d} \approx 1$, where $i_{p,c}/i_{p,d}$ is the ratio of the catalytic peak current to the mass transport peak current. The effect of the catalytic reaction is negligible. On the other hand, when $\lambda^{1/2} > 1$, the system is dominated by the catalytic reaction with

$$i_{p,c}/i_{p,d} \approx z^{1/2} \text{ at } 1 < s \leq 5 \quad [45]$$

and

$$i_{p,c}/i_{p,d} \approx 2.2z^{1/2} \text{ at } s \geq 7 \quad [46]$$

The system is under mixed reaction and transport control at $1.0 > \lambda^{1/2} > 0.5$.

Experimental

Experiments were conducted for the case of a reversible electrode reaction with a catalytic and irreversible chemical reaction on a Au RDE (area = 0.461 cm²). The system Fe⁺⁺⁺/Fe⁺⁺/H₂O₂ was chosen to apply the theory for the determination of the catalytic rate constant. The experimental setup was similar to that reported by Andriacos and Choh (3) except that a function generator (Tacussel, GSTP2) connected to a potentiostat (ECO) instead of the potential scanner (Pine Instrument, RDE3) was used. The electrolyte consisted of 0.75 mM Fe⁺⁺⁺ from FeCl₃ in a 0.5M KCl solution. The pH of the electrolyte was adjusted to 2 by adding HCl. Nitrogen gas was passed through the electrolyte for at least 15 min prior to the experiment and was kept above the solution during measurements.

Initially, a blank solution of 0.5M KCl with a pH of 2 was run at several sweep rates ranging from 1 to 0.005 V/s and at rotation speeds ranging from 0 to 2550 rpm. The initial voltage was set at 600 mV vs. SCE, and the sweep potential range was 500 mV. The stock solution with 0.75 mM Fe⁺⁺⁺ in 0.5M KCl was run at corresponding sweep rates and rotation speeds. A small amount of H₂O₂ was added to the fresh stock solution, and the measurements were repeated. The concentration of H₂O₂ in the Fe⁺⁺⁺ stock solution was determined by titration with 6×10^{-3} N KMnO₄.

Before each experiment, the electrode was polished, cleaned, and cycled for a few times using LSV in the Fe⁺⁺⁺ solution to assure the reproducibility of the results.

Results and Discussion

A significant amount of residual current was observed at high sweep rates ($v > 10$ V/s) in the blank solution. The magnitude of the residual current decreased exponentially as the sweep rate was decreased. The addition of a small amount of H₂O₂ and the variation of the rotation speed did not affect significantly the magnitude of the residual current in the voltage range studied in this work. All currents reported here are net currents, i.e., the observed minus the residual current.

The limiting current density for the reduction of ferric ion to ferrous ion was plotted against the square root of the rotation speed, and the result obeyed satisfactorily the Levich equation, as shown in Fig. 7 for $c_{\text{H}_2\text{O}_2} = 0$. The diffusion coefficient of 4.6×10^{-6} cm²/s was taken from the literature (18), and the kinematic viscosity was calculated to be 8.5×10^{-3} cm²/s which is in agreement with literature values.

The reversibility of the system Fe⁺⁺⁺/Fe⁺⁺ was tested by applying the method of LSV to a RDE. The quantity i_p/i_l was measured at several values of s , where i_l is the limiting current density corresponding to the s value at which i_p was measured for the electrode reduction of Fe⁺⁺⁺. Current-potential curves showed current peaks at $s > 3$ and plateaus at $s < 3$. The peak current-sweep rate dependence is shown in Fig. 8, which shows the theoretical line with a slope of 0.447 and the experimental data for the re-

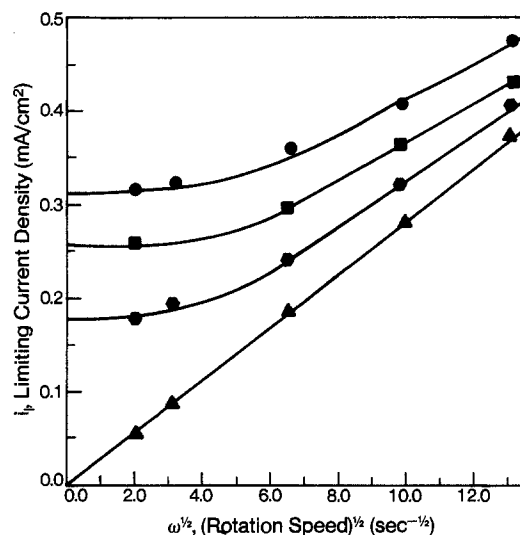


Fig. 7. Dependence of limiting current density on rotation speeds at a voltage sweep rate of 0.01 V/s and at various concentrations of hydrogen peroxide. $c_{\text{H}_2\text{O}_2}$ (M): $\blacktriangle = 0$, $\bullet = 0.0167$, $\blacksquare = 0.036$, $\blacklozenge = 0.052$.

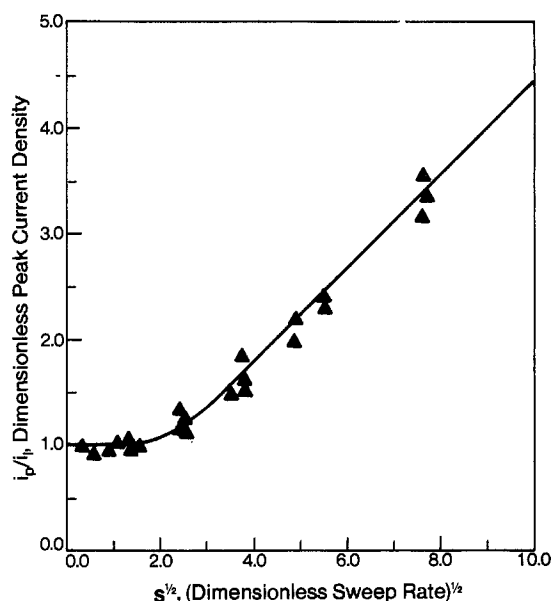
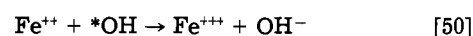
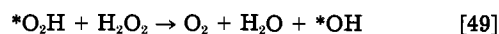
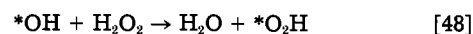
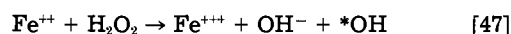


Fig. 8. Dependence of the dimensionless peak current density on dimensionless sweep rates for Fe⁺⁺⁺/Fe⁺⁺ system. \blacktriangle : Experimental data.

versible electrode reaction. One may therefore conclude that the Fe⁺⁺⁺/Fe⁺⁺ system satisfies the requirement of reversibility in the potential scan range examined.

With the addition of hydrogen peroxide into the solution, a catalytic reaction occurs. The peroxide reacts with ferrous ion and regenerates ferric ion. The following mechanism was proposed by Haber and Weiss (19)



The first step is the rate-determining step, and the reaction rate can be expressed by

$$\text{rate} = k'c_{\text{H}_2\text{O}_2}c_{\text{Fe}^{++}} \quad [51]$$

where k' is the rate constant for reaction [47]. All experiments were carried out with a relatively large excess of H₂O₂. The rate constant measured is therefore $k'c_{\text{H}_2\text{O}_2}$.

When H₂O₂ is present, the catalytic current does not increase at high sweep rates, and $i_{p,c}/i_{p,d} = 1$. The result is close to that for the case without a coupled chemical reac-

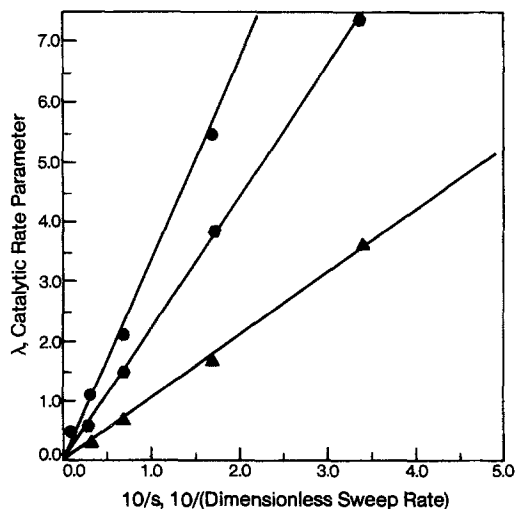


Fig. 9. Dependence of the catalytic rate parameter on voltage sweep rates at various concentrations of hydrogen peroxide. $c_{\text{H}_2\text{O}_2}$ (M): ● = 0.052, ■ = 0.036, ▲ = 0.0167.

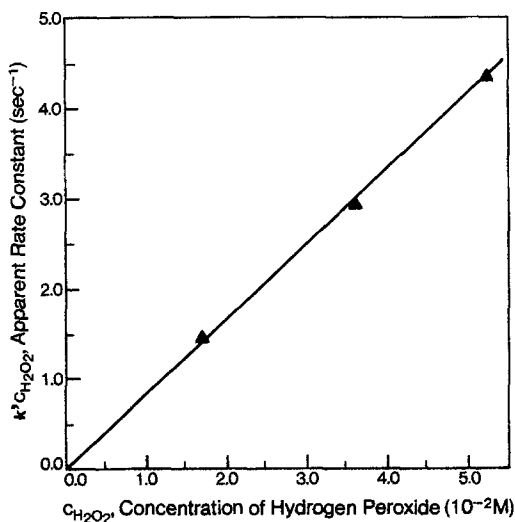


Fig. 10. Rate of the catalytic reaction

tion. When s is decreased, polarographic waves are formed and $i_{p,c}/i_{p,d}$ is increased. Eventually, the current is dominated by the chemical reaction kinetics. The half-wave potential was observed to shift to a more positive direction. This can be shown by considering the Nernst equation

$$E = E_0 - \frac{RT}{nF} \ln \frac{c_B}{c_A} \quad [52]$$

As B is converted to A by the catalytic reaction, c_B/c_A decreases, leading to a more positive potential.

By applying the theoretical results presented in Fig. 3 to the experimental data, values of λ at different experimental conditions are determined. A plot of λ vs. $1/s$ with different concentrations of H_2O_2 is presented in Fig. 9. Values of the dimensionless parameter z are then calculated from the slope. Knowing the rotation speed and the physical properties of the solution, the rate constant can then be determined. Figure 10 shows the dependence of $k'c_{\text{H}_2\text{O}_2}$ on the concentration of H_2O_2 . The slope gives k' a value of 83.2 liter/mol-s.

At sufficiently large values of λ or low sweep rates, Eq. [42] is applicable. This condition implies that a quasi-steady state is established within the diffusion layer. This equation has been derived by Haberland and Landsberg (20) to a RDE at a steady-state condition. At $v = 0.01$ V/s, this steady state is established. The experimental results lead to a linear relationship between $z^{1/2}$ and $\omega^{-1/2}$. From a plot of $k'c_{\text{H}_2\text{O}_2}$ vs. $c_{\text{H}_2\text{O}_2}$, shown in Fig. 11, the slope gives a

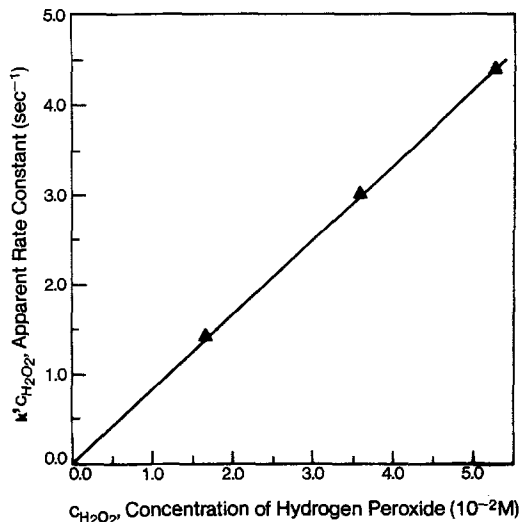


Fig. 11. Rate of the catalytic reaction

rate constant of 83.6 liter/mol-s. Table I summarizes the literature values of the rate constant measured by different methods and under different conditions for the system $\text{Fe}^{3+}/\text{Fe}^{2+}/\text{H}_2\text{O}_2$.

It is unfortunate that literature results on the rate of the ferrous ion-hydrogen peroxide reaction are all based on different electrodes as well as electrolytes. This makes a quantitative comparison difficult. Our results are close to those by Aoki *et al.* (18), and are self-consistent between transient and steady-state measurements.

Conclusions

An analysis of the transient LSV-RDE using the Nernst diffusion model has been developed for an electrode reaction followed by a catalytic, homogeneous chemical reaction. An experimental system involving $\text{Fe}^{3+}/\text{Fe}^{2+}/\text{H}_2\text{O}_2$ was used to demonstrate the applicability of the theoretical results.

Manuscript submitted March 5, 1984; revised manuscript received July 9, 1984.

AT&T Technologies assisted in meeting the publication costs of this article.

Table I. Rate constant for the $\text{Fe}^{3+}/\text{Fe}^{2+}/\text{H}_2\text{SO}_4$ system

Method	Experimental system	Rate constant liter/mol-s
LSV-RDE (Au) (this work)	$7.5 \times 10^{-4}\text{M Fe}^{3+}$	83.2
	0.5M KCl $1.5 \times 10^{-2}\text{M H}_2\text{O}_2$	83.6 ^a
Flow with a channel electrode (Au) (18)	$7 \times 10^{-4}\text{M Fe}^{3+}$ 0.5M H_2SO_4	80
	0.02-0.1M H_2O_2	
Flow with a tubular electrode (Au) (21)	$2 \times 10^{-4}\text{M Fe}^{3+}$ 0.25M H_2SO_4	86
	$3-8 \times 10^{-3}\text{M H}_2\text{O}_2$	
RDE (Pd) (22)	$10^{-3}-10^{-4}\text{M Fe}^{3+}$ in $\text{Cl}^-/\text{O}_4^{-2}$ solution	76.4 ^a 91.7 ^b
	0.1N H_2O_2	
Rotating ring-disk electrode (23) carbon paste	$6.4 \times 10^{-3}\text{M Fe}^{3+}$ 2M HCl	105
	$6.4 \times 10^{-3}\text{M H}_2\text{O}_2$	
RDE (Au) (20)	10^{-3}M Fe^{3+} 1M KCl	145 ^a
	$1.6-3.4 \times 10^{-2}\text{M H}_2\text{O}_2$	
Polarography (Hg) (24)	$2.5 \times 10^{-4}\text{M Fe}^{3+}$ 0.25M H_2SO_4	78
	0.0355M H_2O_2	
Polarography (Hg) (25)	$4 \times 10^{-4}\text{M Fe}^{3+}$ 0.5M KCl	155
	$1.27 \times 10^{-2}\text{M H}_2\text{O}_2$	

^a RDE at steady state.

^b Method of moment.

LIST OF SYMBOLS

A, B, Z	symbols for chemical species
c_A, c_B, c_Z	concentrations of species A, B, and Z
c_A^0, c_B^0, c_Z^0	concentrations of species A, B, and Z in the bulk solution
C_A, C_B	dimensionless concentrations of species A and B
$c_{Fe^{++}}, c_{H_2O_2}$	concentrations of Fe^{++} and H_2O_2
D	diffusion coefficient
E	electrode potential
E_i, E_0	initial and standard electrode potential
$E_{1/2}$	half-wave potential
F	Faraday's constant
H	dimensionless parameter, defined in Eq. [39]
i	current density
i_d	current density controlled by mass transport
i_l	limiting current density
$i_{p,d}, i_{p,c}$	peak transport current density, and peak catalytic current density
k'	rate constant for the catalytic reaction in Eq. [47]
k	pseudo-first-order rate constant for the catalytic reaction
k^0	standard rate constant for the electrode reaction
n	number of electrons transferred in an electrode reaction
p	dimensionless rate constant for the electrode reaction, defined in Eq. [18]
R	universal gas constant
s	dimensionless sweep rate, defined in Eq. [16]
s^*	dimensionless sweep rate, defined in Eq. [38]
t	time
T	temperature
u	dimensionless initial potential, defined in Eq. [17]
v	voltage sweep rate
x	axial distance from the RDE
X	dimensionless axial distance, defined in Eq. [13]
z	dimensionless catalytic reaction rate constant, defined in Eq. [14]
α	transfer coefficient of an electrode reaction
δ	thickness of the Nernst diffusion layer
η	a dummy variable
θ	dimensionless time, defined in Eq. [12]
λ	dimensionless catalytic rate parameter, defined in Eq. [30]
λ^*	dimensionless catalytic rate parameter, defined in Eq. [40]
Λ	dimensionless rate parameter for an electrode reaction, defined in Eq. [29]
ν	kinematic viscosity of an electrolyte
ξ	dimensionless time, or potential, defined in Eq. [28]
ξ^*	dimensionless time, or potential, defined in Eq. [37]
$\xi_{1/2}$	dimensionless half-wave potential
ϕ	dimensionless current density, defined in Eq. [15]
ψ	dimensionless current density, defined in Eq. [27]

ψ^*	dimensionless current density, defined in Eq. [36]
ω	rotation speed

REFERENCES

- G. P. Girina, V. Yu. Filinovskii, and L. G. Feoktistov, *Sov. Electrochem.*, **3**, 831 (1967).
- I. Fried and P. J. Elving, *Anal. Chem.*, **37**, 464 (1965).
- P. C. Andricacos and H. Y. Cheh, *This Journal*, **127**, 2153 (1980).
- P. C. Andricacos and H. Y. Cheh, *ibid.*, **127**, 2385 (1980).
- P. C. Andricacos and H. Y. Cheh, *J. Electroanal. Chem.*, **124**, 95 (1981).
- G. C. Quintana, P. C. Andricacos, and H. Y. Cheh, *ibid.*, **144**, 77 (1983).
- R. Bricka and K. Wiesner, *Coll. Czech. Chem. Commun.*, **12**, 39 (1947).
- D. D. MacDonald, "Transient Technique in Electrochemistry," p. 213, Plenum Press, New York (1977).
- J. Heyrovsky, "Principles of Polarography," p. 380, Academic Press, New York (1966).
- I. M. Kolthoff and J. J. Lingane, "Polarography," Vol. 1, 2nd ed., p. 268, Interscience Publishers, New York (1952).
- R. S. Nicholson and I. Shain, *Anal. Chem.*, **36**, 706 (1964).
- P. Delahay, "New Instrumental Methods in Electrochemistry," p. 100, Interscience Publishers, New York (1954).
- J. M. Saveant and E. Vianello, *Electrochim. Acta*, **10**, 905 (1965).
- G. V. Levich, "Physicochemical Hydrodynamics," p. 60, Prentice-Hall, Englewood Cliffs, NJ (1963).
- H. S. Carslaw and J. C. Jaeger, "Operational Methods in Applied Mathematics," p. 88, Dover Publications, New York (1963).
- C. de Boor, "CADRE: An Algorithm for Numerical Quadrature," Mathematical Software, John R. Rice, Editor, Academic Press, New York (1971).
- H. Matsuda and Y. Ayabe, *Z. Elektrochem.*, **59**, 494 (1955).
- K. Aoki, K. Tokuda, and H. Matsuda, *J. Electroanal. Chem.*, **76**, 217 (1977).
- F. Haber and J. Weiss, *Proc. R. Soc. (London)*, **A147**, 332 (1934).
- D. Haberland and R. Landsberg, *Ber. Bunsenges. Phys. Chem.*, **70**, 724 (1966).
- L. N. Klatt and W. J. Blaedel, *Anal. Chem.*, **40**, 512 (1968).
- F. Opekar and P. Beran, *J. Electroanal. Chem.*, **32**, 49 (1971).
- K. B. Prater and A. J. Bard, *This Journal*, **117**, 1517 (1970).
- P. Delahay and G. L. Stiehl, *J. Am. Chem. Soc.*, **74**, 3500 (1952).
- Z. Pospisil, *Coll. Czech. Chem. Commun.*, **18**, 337 (1953).

The Application of Linear Sweep Voltammetry to a Rotating Disk Electrode with a Kinetic Process

S. L. Lanny Ng*¹ and H. Y. Cheh*

Department of Chemical Engineering and Applied Chemistry, Columbia University, New York, New York 10027

ABSTRACT

The current response of a kinetic process to a linear sweep of the potential on a rotating disk electrode is analyzed with the aid of a Nernst diffusion model. An experimental study involving the reaction of oxidized, N,N-dimethyl-p-phenylenediamines with hydroxide ion is used to test the applicability of the theoretical results.

Recently, Ng and Cheh (1) reported a detailed study on the application of linear sweep voltammetry (LSV) to a rotating disk electrode (RDE) for a catalytic process in which the electrode reaction is followed by a homogeneous chemical reaction to regenerate the reacting species. The present paper is concerned with a similar study ex-

cept that the chemical reaction generates a new product. The resulting current which is influenced by the chemical reaction is known as a kinetic current (2). Nicholson and Shain (3) and Saveant and Vianello (4) studied the application of LSV to the same problem in stagnant systems. In flow systems, this problem was studied by Galus and Adams (5) and by Kir'yanov and Filinovskii (6), based on the concept of a reaction layer. Tong *et al.* (7) applied the Nernst diffusion layer model to a RDE to study

*Electrochemical Society Active Member.

¹Present address: AT&T Technologies, Engineering Research Center, Princeton, New Jersey 08540.

rapid and irreversible reactions of oxidized *N,N*-dialkyl-*p*-phenylenediamines with hydroxide ion and with phenolates. In the present paper, theoretical calculations based on the application of linear sweep voltammetry to a rotating disk electrode are conducted and an experimental investigation is reported for the case of a reversible electrode reaction using *N,N*-dimethyl-*p*-phenylenediamines as an example.

Theoretical

Consider an electrode reaction which is followed by a homogeneous chemical reaction



where A is the only electroactive species in the potential range of interest. B, which is produced by the electrode reaction, is transformed to C by a homogeneous chemical reaction.

When the chemical reaction is slow, the effect of chemical polarization is negligible and the current-potential behavior resembles that of a single electrode reaction. However, the effect of the chemical reaction is predominant when the chemical reaction is fast and irreversible and the electrode reaction is reversible.

By adopting the Nernst diffusion model and by assuming that the diffusion coefficients of all ions are equal, the governing differential equations and the boundary conditions are as follows

$$\frac{\partial c_A}{\partial t} = D \frac{\partial^2 c_A}{\partial x^2} \quad [3]$$

$$\frac{\partial c_B}{\partial t} = D \frac{\partial^2 c_B}{\partial x^2} - kc_B \quad [4]$$

$$\frac{\partial c_C}{\partial t} = D \frac{\partial^2 c_C}{\partial x^2} + kc_B \quad [5]$$

$$c_A = c_A^0, c_B = 0, c_C = 0 \text{ at } t = 0, x \geq 0 \quad [6]$$

$$c_A = c_A^0, c_B = 0, c_C = 0 \text{ at } t > 0, x \geq \delta \quad [7]$$

$$\frac{\partial c_A}{\partial x} = -\frac{\partial c_B}{\partial x}, \frac{\partial c_C}{\partial x} = 0 \text{ at } t > 0, x = 0 \quad [8], [9]$$

with

$$\frac{i}{nF} = k^0 \left\{ c_A(0, t) \exp \left[-\frac{\alpha nF}{RT} (E(t) - E_0) \right] - c_B(0, t) \exp \left[(1 - \alpha) \frac{nF}{RT} (E(t) - E_0) \right] \right\} \quad [10]$$

and

$$E(t) = E_i - vt \quad [11]$$

where c_A , c_B , and c_C are the concentrations of species A, B and C, respectively, c_A^0 and c_B^0 are bulk concentrations, D is the diffusion coefficient, k is the first-order rate constant of the homogeneous chemical reaction, δ is the thickness of the Nernst diffusion layer, i is the current density, x is the distance from the electrode surface, t is time, k^0 is the standard rate constant of the electrode reaction, α is the transfer coefficient, v is the sweep rate, E is the electrode potential, E_i and E_0 are the initial and standard electrode potentials, respectively, and R , T , and F have their usual significance.

By introducing the following dimensionless parameters

$$C_A = c_A/c_A^0 \quad [12]$$

$$C_B = c_B/c_A^0 \quad [13]$$

$$\theta = Dt/\delta^2 \quad [14]$$

$$X = x/\delta \quad [15]$$

$$z = k\delta/D \quad [16]$$

$$\phi = i/i_1 \quad [17]$$

$$s = nFv\delta^2/RTD \quad [18]$$

$$u = (E_i - E_0)nF/RT \quad [19]$$

and

$$p = k^0\delta/D \quad [20]$$

Equations [3]-[11] can be recast into a dimensionless form, and the following solution can be obtained by using Laplace transform

$$\frac{\psi(\xi)}{\Lambda \exp(\alpha\xi)} = 1 - \int_{-u}^{\xi} \psi(\eta) \{1 + \exp(-\xi) \exp[-\lambda(\xi - \eta)]\} \times \frac{\left\{1 + 2 \sum_{n=1}^{\infty} (-1)^n \exp[-n^2s/(\xi - \eta)]\right\}}{\sqrt{\pi(\xi - \eta)}} d\eta \quad [21]$$

where

$$\psi = \phi/s^{1/2} \quad [22]$$

$$\xi = s\theta - u \quad [23]$$

$$\Lambda = p/s^{1/2} \quad [24]$$

$$\lambda = z/s \quad [25]$$

and i_1 is the limiting current density.

For a RDE, i_1 and δ can be calculated by (8)

$$i_1 = nFDc_A^0/\delta \quad [26]$$

and

$$\delta = 1.61D^{1/3}\nu^{1/6}\omega^{-1/2} \quad [27]$$

where ν is the kinematic viscosity of the solution and ω is the rotation speed of the RDE.

For a reversible electron transfer reaction ($\Lambda \rightarrow \infty$), Eq. [21] reduces to

$$1 = \int_{-u}^{\xi} \psi(\eta) \{1 + \exp(-\xi) \exp[-\lambda(\xi - \eta)]\} \times \frac{\left\{1 + 2 \sum_{n=1}^{\infty} (-1)^n \exp[-n^2s/(\xi - \eta)]\right\}}{\sqrt{\pi(\xi - \eta)}} d\eta \quad [28]$$

The integral equation was solved numerically. Figures 1-3 are the current-potential curves for various values of λ and s . Similar to results reported previously (1, 9, 10), current peaks are observed for $s \geq 3$.

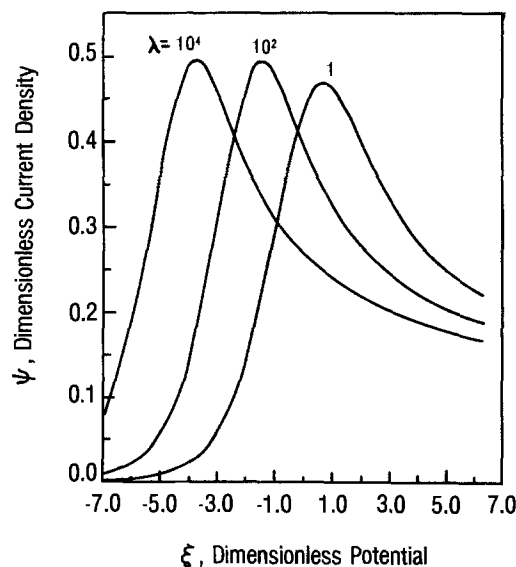


Fig. 1. Current-potential behavior for a reversible electrode reaction at $s = 100$.

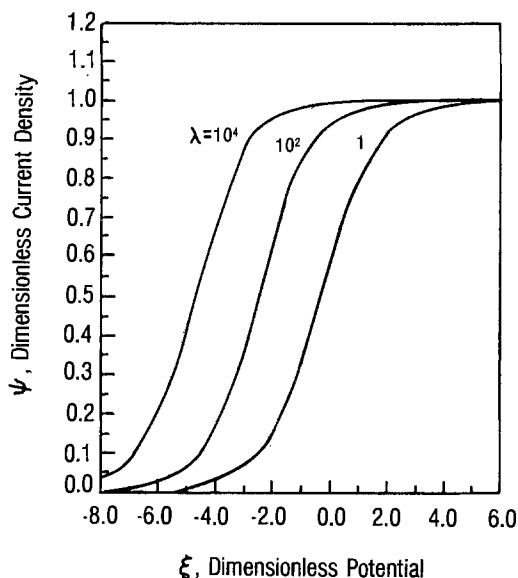


Fig. 2. Current-potential behavior for a reversible electrode reaction at $s = 1$.

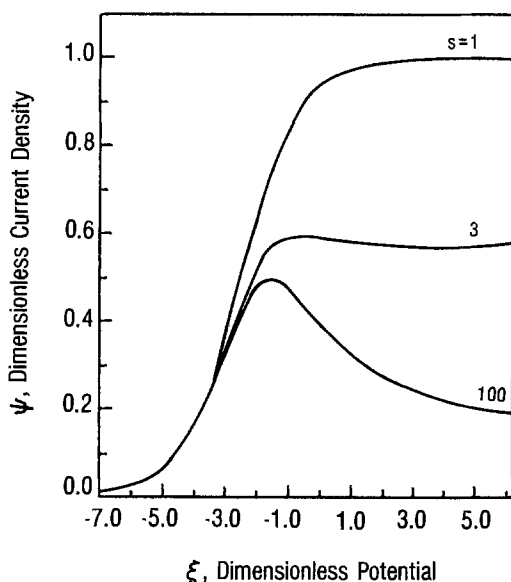


Fig. 3. Current-potential behavior for a reversible electrode reaction at $\lambda = 100$.

When $\lambda \rightarrow 0$, Eq. [28] simplifies to

$$\frac{1}{1 + \exp(-\xi)} = \int_{-\infty}^{\xi} \psi(\eta) \frac{\left\{ 1 + 2 \sum_{n=1}^{\infty} (-1)^n \exp[-n^2 s / (\xi - \eta)] \right\}}{\sqrt{\pi(\xi - \eta)}} d\eta \quad [29]$$

which is identical to the result presented by Andricacos and Cheh (10) for the case of a reversible electrode reaction without a following chemical reaction.

When $\lambda \rightarrow \infty$, Eq. [28] simplifies to

$$\phi(\xi) = \frac{1}{1 + \frac{\tanh \sqrt{z} \exp(-\xi)}{\sqrt{z}}} \quad [30]$$

with the half-wave potential², $E_{1/2}$, given by

$$E_{1/2} = E_0 + \frac{RT}{nF} \ln(\sqrt{z} \coth \sqrt{z}) \quad [31]$$

²For the case where a current peak exists, the half-wave potential is defined to be the potential at which the corresponding current density is half the peak current density.

For large values of z , $\coth \sqrt{z}$ approaches unity (e.g., at $\sqrt{z} = 3$, $\coth \sqrt{z} = 1.005$), Eq. [31] further reduces to

$$E_{1/2} = E_0 + \frac{RT}{nF} \ln \sqrt{z} \quad [32]$$

Tong (7) obtained a similar result without assuming equal diffusion coefficients for species A and B. The expression is

$$E_{1/2} = E_0 + \frac{RT}{nF} \ln \frac{D_A}{D_B} + \ln(\sqrt{z} \coth \sqrt{z}) \quad [33]$$

where D_A and D_B are the diffusion coefficients for species A and B, respectively.

Figure 1 shows the current-potential behavior for a reversible electrode reaction at various values of λ . As $\lambda \rightarrow 0$, the i - E characteristics approach that for a simple reversible electrode reaction. As λ increases, the peak as well as the half-wave potentials shift to more anodic values with little change in the peak current density. A plot of $\xi_{1/2}$ vs. $\log \lambda$ at various s values, shown in Fig. 4, allows one to determine the rate constant for the homogeneous chemical reaction. The same figure can also be used to define several regimes of interest. For instance, it is reasonable to consider the process to be controlled by mass transfer for $\lambda < 0.1$, and the process controlled by chemical kinetics at $\lambda > 1$. Furthermore, at $\lambda > 3$, one may derive the following equations

$$\xi_{1/2} = -1.148 \log \lambda - 1.088, \quad s > 10 \quad [34]$$

$$\xi_{1/2} = -1.15 \log \lambda - 1.044, \quad s = 7 \quad [35]$$

$$\xi_{1/2} = -1.15 \log \lambda - 0.859, \quad s = 3 \quad [36]$$

$$\xi_{1/2} = -1.15 \log \lambda - 0.160, \quad s = 1 \quad [37]$$

Finally, for $s > 10$, the current-potential curve approaches that of a stagnant system.

Experimental

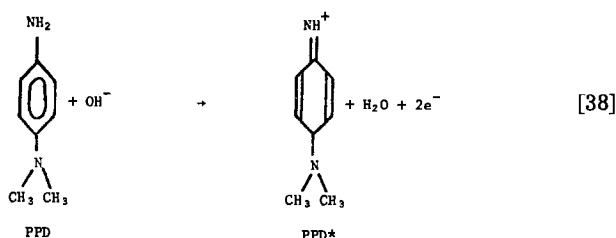
Experiments were conducted for the rapid and irreversible reaction of oxidized *N,N*-dimethyl-*p*-phenylenediamines (PPD) with hydroxide ion at 23°C. The experimental setup and procedure were similar to those described earlier (1, 10). At Pt-RDE (area = 0.461 cm²) was used. The electrolyte contained 10⁻⁴M PPD in a 0.188M dipotassium hydrogen phosphate buffer solution which was adjusted to a pH of 11.2 by adding NaOH. The buffer solution was saturated with N₂ before the addition of PPD. The viscosity of the solution was determined by a Canon-Fenske viscometer to be 0.0103 cm²/s. The diffusion coefficient of PPD and PPD radical were found from the literature to be 0.678 × 10⁻⁵ and 0.567 × 10⁻⁵ cm²/s, respectively (7).

LSV at different scan rates was performed at rotation speeds ranging from 0 to 191 rpm. The half-wave potentials were determined from the current-potential curves. The accuracy of measurements decreased at scan rates greater than 0.1 V/s.

Results and Discussion

The kinetics of deamination of PPD have been studied by Tong spectrometrically (11) and by Tong *et al.* electrochemically on a RDE (7).

The reaction mechanism is as follows



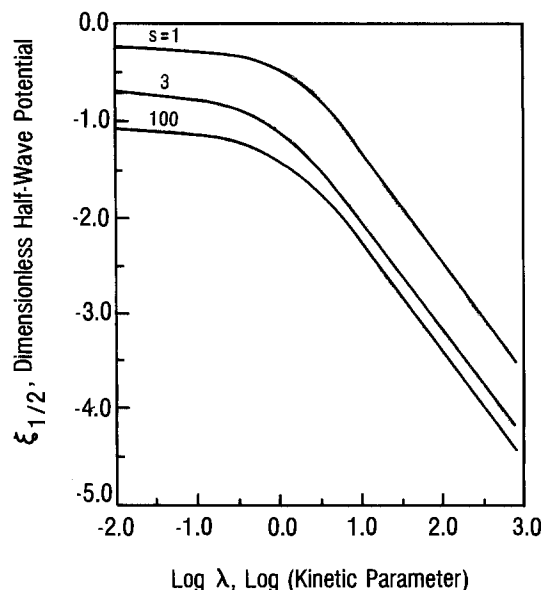
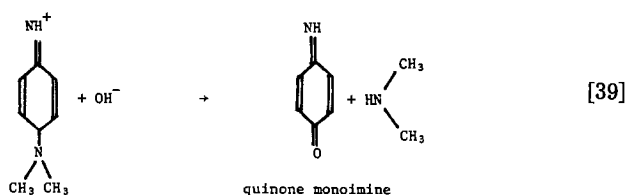


Fig. 4. Dependence of the half-wave potential on the kinetic parameter



In the presence of an excess of OH⁻, the redox potential for the electrode reaction is

$$E = E_o + \frac{RT}{nF} \ln \left\{ \frac{[PPD^*]}{[PPD][OH^-]} \right\} \quad [40]$$

$$= E_o' + \frac{RT}{2F} \ln \left\{ \frac{[PPD^*]}{[PPD]} \right\} \quad [41]$$

where

$$E_o' = E_o - \frac{RT}{2F} \ln [OH^-] \quad [42]$$

and

$$E_o = -0.063V \text{ vs. SCE (7)} \quad [43]$$

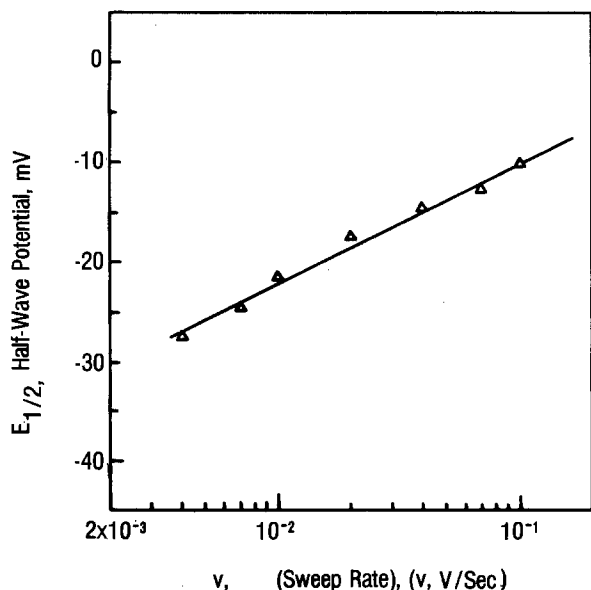


Fig. 5. Experimental results on the dependence of the half-wave potential vs. SCE on the sweep rate.

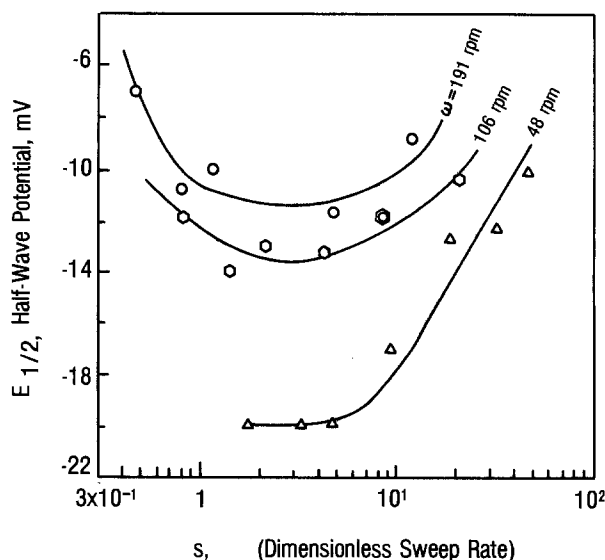


Fig. 6. Experimental results on the dependence of the half-wave potential vs. SCE on the dimensionless sweep rate.

At $\omega = 0$, the system is stagnant, the measured current decreases, and the half-wave potential is shifted cathodically as the scan rate decreases. The half-wave potential $E_{1/2}$ is plotted against $\log v$, as shown in Fig. 5. A linear relationship is obtained with a slope of 12.31 mV as compared to the theoretical value of 14.79 mV. The average rate constant obtained by applying Eq. [34] is 70.9 s^{-1} .

By applying LSV to the RDE, the current decreases and the half-wave potential is shifted first cathodically and then anodically as s is decreased. A plot of the half-wave potentials vs. $\log s$ is shown in Fig. 6. Since the pH of the solution and E_o are known, Fig. 4 can be used to determine λ . A plot of λ vs. $1/s$ at different rotation speeds is illustrated in Fig. 7. The average rate constant is found to be 44.9 s^{-1} .

At $s < 1$ (i.e., at very slow scan rate and fast rotation speed), the experimental half-wave potential is shifted anodically as the rotation speed is increased. A plot of $E_{1/2}$ vs. $\log \omega^{1/2}$ is shown in Fig. 8. The slope is 32.8 mV, as compared with the theoretical value of 29.6 mV. The average rate constant calculated by using Eq. [33] is found to be 70.4 s^{-1} .

A quantitative determination of the rate constant requires a high degree of accuracy in the experimental data. A 1 mV error in the half-wave potential leads to an error of the rate constant of about 15%. This is the reason for the difference in the measured rate values.

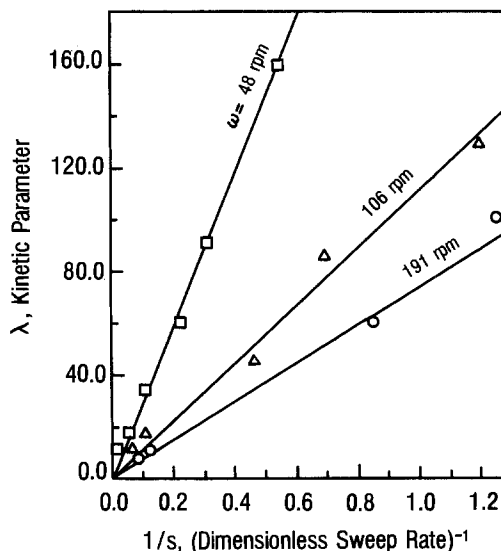


Fig. 7. Experimental results on the dependence of the kinetic parameter on the dimensionless sweep rate.

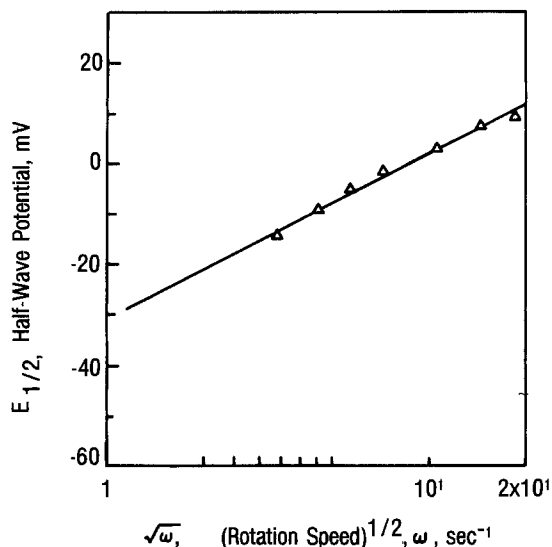


Fig. 8. Experimental results on the dependence of the half-wave potential vs. SCE on the rotation speed at a sweep rate of 7 mV/s.

Conclusions

An analysis of the transient LSV-RDE by using the Nernst diffusion model was developed for an electrode reaction followed by an irreversible and homogeneous chemical reaction. Mathematical expressions were derived to relate the kinetic current to system parameters. An experimental study of the deamination of N,N-dimethyl-p-phenylenediamines was conducted to test the applicability of the theoretical results. It was found that minor experimental error could lead to a considerable variation in the rate constants. Nevertheless, the application of LSV to RDE is useful in estimating the order of magnitude of the chemical rate constant and in the analysis of reaction mechanisms.

Manuscript submitted March 29, 1984; revised manuscript received July 10, 1984.

AT&T Technologies, Incorporated, assisted in meeting the publication costs of this article.

LIST OF SYMBOLS

A, B, C symbols for chemical species
 c_A, c_B, c_C concentrations of species A, B, and C
 c_A^0, c_B^0 concentrations of species A and B in the bulk solution
 C_A, C_B dimensionless concentrations of species A and B
 D diffusion coefficient
 D_A, D_B diffusion coefficients of species A and B
 E_i, E_0 initial and standard electrode potentials

E_0' potential defined in Eq. [43]
 $E_{1/2}$ half-wave potential
 F Faraday's constant
 i, i_1 current density and limiting current density
 k pseudo-first-order rate constant for the electrode reaction
 k^0 standard rate constant for the electrode reaction
 n number of electrons transferred in an electrode reaction
 p dimensionless rate constant for the electrode reaction, defined in Eq. [20]
 R universal gas constant
 s dimensionless sweep rate, defined in Eq. [18]
 t time
 T temperature
 u dimensionless initial potential, defined in Eq. [19]
 v voltage sweep rate
 x axial distance from the RDE
 X dimensionless axial distance, defined in Eq. [15]
 z dimensionless kinetic rate constant, defined in Eq. [16]
 α transfer coefficient of an electrode reaction
 δ thickness of the Nernst diffusion layer
 η a dummy variable
 θ dimensionless time, defined in Eq. [14]
 λ dimensionless kinetic rate parameter, defined in Eq. [25]
 Λ dimensionless rate parameter for an electrode reaction, defined in Eq. [24]
 ν kinematic viscosity of an electrolyte
 ξ dimensionless potential, defined in Eq. [23]
 $\xi_{1/2}$ dimensionless half-wave potential
 ϕ dimensionless current density, defined in Eq. [17]
 ψ dimensionless current density, defined in Eq. [22]
 ω rotation speed

REFERENCES

1. S.-L. L. Ng and H. Y. Cheh, *This Journal*, **132**, 93 (1985).
2. P. Dehalay, "New Instrumental Methods in Electrochemistry," p. 87, Interscience Publishers, New York (1954).
3. R. S. Nicholson and I. Shain, *Anal. Chem.*, **36**, 706 (1964).
4. J. M. Saveant and E. Vianello, *Electrochim. Acta*, **12**, 629 (1967).
5. Z. Galus and R. N. Adams, *J. Electroanal. Chem.*, **4**, 248 (1962).
6. V. A. Kir'yanov and V. Yu. Filinovskii, *Rus. J. Phys. Chem.*, **37**, 1150 (1963).
7. L. K. J. Tong, K. Liang, and W. R. Ruby, *J. Electroanal. Chem.*, **13**, 245 (1967).
8. V. G. Levich, "Physicochemical Hydrodynamics," p. 60, Prentice-Hall, Englewood Cliffs, NJ (1963).
9. P. C. Andricacos and H. Y. Cheh, *J. Electroanal. Chem.*, **124**, 95 (1981).
10. P. C. Andricacos and H. Y. Cheh, *This Journal*, **127**, 2385 (1981).
11. L. K. J. Tong, *J. Phys. Chem.*, **58**, 1090 (1954).

Oxygen Evolution and Corrosion on Ruthenium-Iridium Alloys

R. Kötz and S. Stucki

Brown Boveri Research Center, CH-5405 Baden, Switzerland

ABSTRACT

The initial stages of O_2 evolution and anodic corrosion on ruthenium-iridium alloys have been investigated in 1N H_2SO_4 using voltammetry and x-ray photoelectron spectroscopy (XPS). The alloys were prepared by mixed RF sputtering onto glass substrates. Cyclic voltammetry shows that the corrosion of the Ru component is significantly reduced with increasing Ir content. Simultaneously, the activity for O_2 evolution decreases as a consequence of increased Tafel slope and overpotential. The XPS studies show that the reduced corrosion of Ru is paralleled by an increased tendency to oxide formation of the Ir component. The stabilization of Ru by admixtures of Ir is assigned to the formation of a protective oxide layer with increased Ir content. In addition, a shift of redox potentials for oxide formation is observed.

The excellent catalytic properties of RuO_2 for O_2 evolution are well known and have initiated a series of studies on the electrochemical behavior of metallic oxide electrodes (1, 2). In acidic electrolytes, however, RuO_2 suffers from heavy corrosion during anodic polarization. As a consequence, many efforts were undertaken to stabilize the ruthenium dioxide without losing too much of its catalytic performance.

In the authors' laboratory, mixed oxides of ruthenium and iridium have turned out to be the best catalysts for O_2 evolution in Membrel electrolyzer cells, where a proton conducting membrane serves as the electrolyte (3, 4). While admixtures of iridium significantly increase the stability of the catalyst, only a minor increase in overpotential was observed (3-6). Although, for catalytic application, the mixed oxides are of higher interest than the alloys, we believe that, in a first approximation, the behavior of the alloys is qualitatively comparable to that of the mixed oxides. The stabilizing effect of Ir on Ru has been observed for the oxides (3-6) as well as for the metal alloys (7, 8). This similarity can be understood as a consequence of oxide formation on the metals preceding O_2 evolution (9-11).

There are, however, significant differences between Ru-Ir alloys and the mixed oxide catalysts. Firstly, the anodic oxides formed on the metals are hydrous and most probably amorphous. Secondly, the mixed oxides form a solid solution over the entire composition range, while the phase diagram of Ru-Ir alloys shows a two-phase region, between 43% and 54% Ru and two solid solutions with face-centered cubic structure for low Ru content and hexagonal structure for low Ir content (12). These differences have to be considered before transferring the results, obtained on the alloys, to mixed oxides because the importance of structural parameters for catalysis is well known.

In order to understand the mechanisms leading to a stabilization of Ru by Ir, it is inevitable to know the processes governing the anodic O_2 evolution and corrosion on the single components. This has been the subject of recent investigations (10, 11, 13). In the present paper, we report on the anodic performance of Ru-Ir alloys in an acidic electrolyte. The investigation was limited to the initial stages of O_2 evolution and corrosion. Within these limits, significant changes in surface roughness and morphology can be neglected and the electrode surface remains relatively well defined. Long-term stabilities and time dependences of O_2 evolution and corrosion are beyond the scope of this paper. In view of our results, we shall address the question of whether replacement of the high cost Ir component by other low cost metals is advisable.

Experimental

The metal electrodes were prepared by RF sputtering onto glass substrates in a Balzers Sputron II chamber. In order to produce films with different Ru-Ir compositions, the disk-shaped sputtering target was divided into two half-circles, one made of Ru the other made of Ir. By placing a circular stop excentrically in front of the target

the ratio of effective Ru to Ir target area could be varied continuously. The thickness of the films was about 2000Å. In agreement with known phase diagrams for Ru_xIr_{1-x} alloys (12), the x-ray diffraction patterns exhibited the hexagonal structure for $x = 0.86$ and $x = 0.45$. The face-centered cubic structure of Ir was observed for $x = 0.15$.

All electrochemical measurements were performed in 1N H_2SO_4 using the standard three-electrode potentiostatic arrangement, with the saturated calomel electrode serving as the reference electrode and a platinum wire as counterelectrode. The sputtered working electrodes were used shortly after preparation without further cleaning procedure. All electrochemical measurements were performed at room temperature.

XPS measurements were performed in a Kratos ES 300 photoelectron spectrometer using nonmonochromized Mg $K\alpha$ radiation. Binding energies were calibrated with respect to the Au $4f_{7/2}$ line at 84.0 eV.

After electrochemical treatment, the electrodes were rinsed with triply distilled water and dried in a nitrogen gas stream. Transfer from the electrochemical cell to the UHV chamber of the spectrometer was achieved within 1 min through the fast insertion lock. Experiments performed with the electrochemical preparation chamber, described previously (14), under controlled argon atmosphere showed identical XP-spectra of the metal core levels.

Results

Voltammetry.—In a recent investigation (15), we demonstrated that the species formed during anodic corrosion of Ru is reduced in the cathodic scan of the cyclic voltammogram. The reduction peak, observable in unstirred electrolytes, corresponds to the reduction of RuO_4 being the only corrosion product (15). Figure 1 shows the cyclic voltammogram of pure iridium and the corresponding cathodic scans for three different alloys Ru_xIr_{1-x} and pure ruthenium. The anodic scan limit was $1.3 V_{SCE}$. The curves shown in Fig. 1 correspond to the first scans up to $1.3 V_{SCE}$ after five cycles of the electrodes between $-0.25 V_{SCE}$ and different anodic scan limits (below $1.3 V_{SCE}$) during a window opening experiment. The pronounced reduction peak of 0.75V for the ruthenium electrode ($x = 1$) is strongly diminished with decreasing x . The major decrease of the reduction peak occurs for $Ru_{0.86}Ir_{0.14}$. Further increase of the iridium content has only minor influence. Taking the height of the reduction peak as a measure for the amount of RuO_4 formed, it is obvious that, already, small admixtures of iridium to ruthenium inhibit the corrosion of ruthenium, i.e., formation of RuO_4 in solution, significantly. This effect becomes especially pronounced if the anodic scan limit is shifted to more anodic values.

Unfortunately, the reduced corrosion of Ru is coupled with a reduced activity of the alloy for O_2 evolution. The O_2 evolution current drops considerably with the admixture of iridium to ruthenium. For the alloy $Ru_{0.86}Ir_{0.14}$, the current for oxygen evolution at $1.25 V_{SCE}$ is already reduced to one-fifth of the current measured for pure Ru.

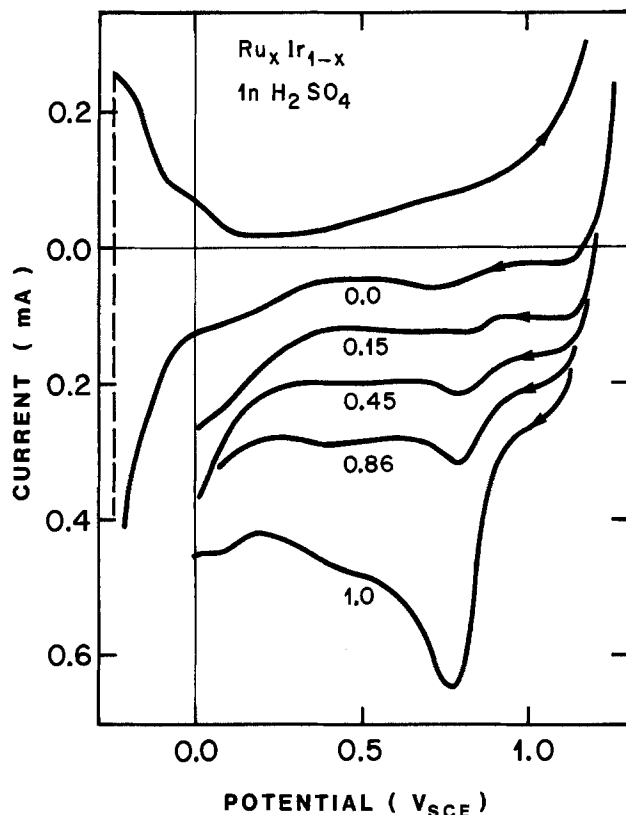


Fig. 1. Cyclic voltammogram of an iridium electrode ($x = 0.0$) and cathodic scans for different alloys $Ru_x Ir_{1-x}$. x is given at the respective curve. Anodic scan limit: $1.3 V_{SCE}$; scan rate: 100 mV/s . No electrolyte stirring. The cathodic scans are displaced by -0.05 mA each.

Again, increasing the amount of iridium above 50% has only negligible influence on the activity for O_2 evolution.

In order to obtain more information about the anodic O_2 evolution on Ru-Ir alloys, we measured the Tafel slope as a function of alloy composition. The results are plotted in Fig. 2. For the alloys $Ru_x Ir_{1-x}$ with $x < 0.5$, the measured Tafel slope of $\sim 50 \text{ mV}$ corresponds to that of pure iridium. The transition from the Tafel slope of 37 mV for Ru to 50 mV occurs for $1 > x > 0.5$.

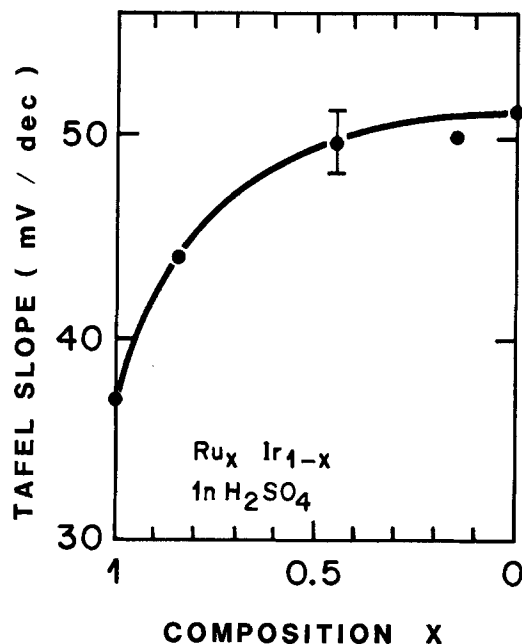


Fig. 2. Anodic Tafel slopes as a function of alloy composition, scan rate: 2 mV/s , first scan up to $1.4V$.

The catalytic activity of an O_2 evolution catalyst is mainly determined by the onset potential for the O_2 evolution reaction. This potential can be determined from the measured Tafel curves at low current densities. The O_2 evolution potential at 0.1 mA cm^{-2} is shown in Fig. 3 as a function of composition. There appears to be a linear correlation between the O_2 evolution potential and the alloy composition. Thus, the reduced O_2 evolution activity is a consequence of an increased potential for the onset of the O_2 evolution reaction. At higher current densities, the increased Tafel slope reduces the activity (O_2 evolution current at a certain potential) even further.

The data of Fig. 2 and 3 were taken from the first anodic scan for a fresh electrode up to $1.4 V_{SCE}$ (2 mV/s). During this procedure, oxide growth is limited and the changes in surface composition are relatively small, as will be shown below.

X-ray photoelectron spectroscopy.—Before drawing any conclusions from the macroscopic, electrochemical parameters, it is important to know the actual state of the electrode surface. For this purpose, we have applied x-ray photoelectron spectroscopy (XPS). The spectra of the Ru3d and Ir4f levels after O_2 evolution at $1.7 V_{SCE}$ (i.e., current densities of $50\text{--}100 \text{ mA cm}^{-2}$) for 5 min are shown in Fig. 4 for different alloy compositions. On pure ruthenium, the formation of a thick oxide layer gives rise to a shift in binding energy of the Ru3d_{5/2} level to 281.0 eV (10). This shift is strongly reduced for the alloy with the composition $Ru_{0.86}Ir_{0.14}$ ($E_B = 280.2 \text{ eV}$). No shift of the Ru level could be observed for $Ru_{0.45}Ir_{0.55}$ and $Ru_{0.15}Ir_{0.85}$. For the latter alloys the position of the Ru3d level corresponds to that of the metal. Thus, the formation of the thick anodic oxide on ruthenium is inhibited by the presence of iridium.

However, oxide formation on Ir is enhanced. While on pure iridium only a thin oxide layer is formed during O_2 evolution, which could only be detected by deconvolution of the spectra recorded at a low electron emission angle ($\theta = 20^\circ$) (11), the presence of Ru leads to a distinct shift of the Ir4f_{7/2} level to higher binding energies. For Ru mole fractions $x = 0.45$ and $x = 0.86$, the Ir4f_{7/2} binding energies were determined to be 61.5 and 61.9 eV , respectively, which have to be compared to a binding energy of 60.9 eV for the metal (11, 16). Oxide formation on Ru is inhibited at the expense of an increased tendency to oxide formation on Ir.

The actual surface composition of the electrodes can deviate significantly from that of the bulk, especially at

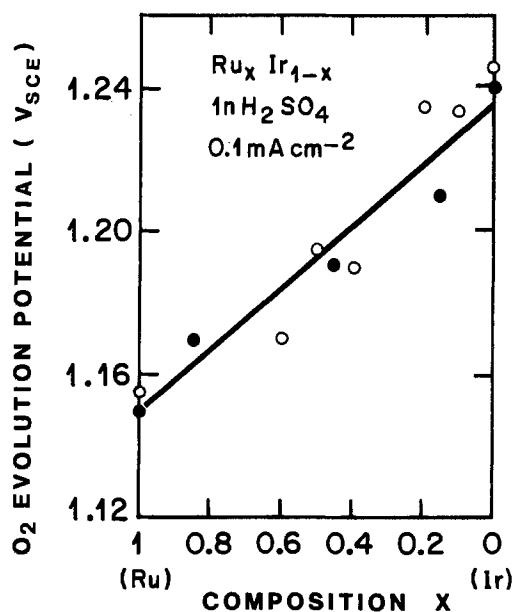


Fig. 3. O_2 evolution potential at 0.1 mA cm^{-2} as a function of alloy composition. Open circles are taken from Ref. (6).

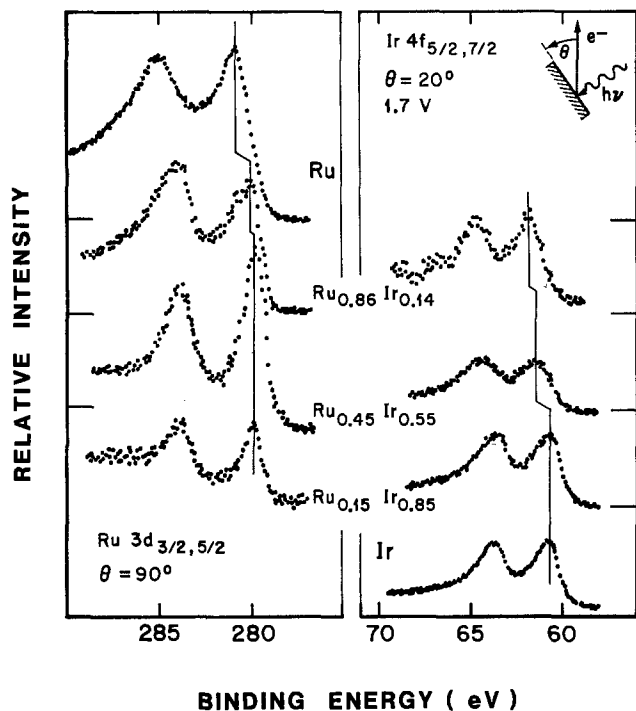


Fig. 4. XP-spectra of the Ru3d and Ir4f level for the pure metals and three different alloys after O_2 evolution at 1.7V for 5 min.

potentials where O_2 evolution and corrosion occurs. We therefore determined the surface composition by use of XPS. The surface sensitivity of XPS, which is a consequence of the limited mean free path of the electrons in the solid, can be increased further by lowering the electron emission angle θ (see Fig. 4). In Fig. 5, the surface composition of the three alloy electrodes is shown as a function of the electrode potential for electron emission angles $\theta = 90^\circ$ and $\theta = 20^\circ$. The results in Fig. 5 were independent of whether a fresh electrode was used for each data point or one electrode was used for a sequence of

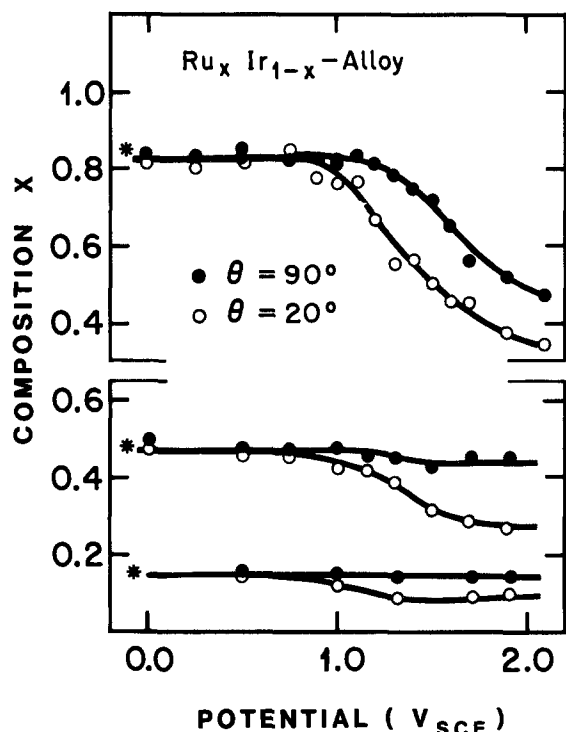


Fig. 5. Surface composition x of Ru_xIr_{1-x} alloys after electrochemical treatment at various electrode potentials after 5 min. The asterisk indicates the bulk composition of the alloy.

measurements with anodically increasing potentials. For the three alloys, a change in surface composition in favor of a higher Ir content can be observed for potentials anodic of 0.9V vs. SCE. While the increase in Ir surface concentration is evident for $\theta = 90^\circ$ and $\theta = 20^\circ$ in the $Ru_{0.86}Ir_{0.14}$ alloy, the change in surface composition for the alloys with higher Ir content is detected only with $\theta = 20^\circ$. This indicates that the surface layer on the latter samples is very thin.

The thickness of a surface layer on a substrate can be calculated from the relative intensities of the photoelectron emission from the surface layer and the substrate under certain assumptions using Eq. [3] of Ref. (16). We assume that a homogeneous oxide layer covers the metal substrate and there is no metallic Ir or Ru within the oxide layer. The electron mean free path was assumed to be 20Å, and the ratio of metal to oxide density was 1.7. In Fig. 6, the measured relative intensity of oxidized Ru plus Ir over metallic Ru plus Ir is plotted as a function of the electrode potential. The data were obtained by deconvolution and integration of the metals' 3d and 4f levels. Also given is the calculated thickness, which should be regarded as qualitative only, owing to the uncertainty of the above assumptions. It turns out that the thickness of the oxide layer, formed during O_2 evolution, is strongly dependent on the alloy composition. For the alloy with the highest Ir content, the oxide thickness ($\sim 4\text{Å}$) is close to that on pure Ir (11). As the Ir content of the bulk material decreases, the oxide thickness increases. For $Ru_{0.45}Ir_{0.55}$, a limiting oxide thickness of $\sim 8\text{Å}$ is reached at 1.8V, while for $Ru_{0.86}Ir_{0.14}$, the oxide thickness increases with anodic polarization up to 2.2 V_{SCE} .

From Fig. 6, it is also obvious that oxide formation starts at electrode potentials cathodic of the O_2 evolution potential. This is in agreement with the results obtained on Ir (9, 11) and compares well with the results of Fig. 5, where the initial changes in surface composition occur at a potential of about 0.9 V_{SCE} , far below the O_2 evolution potential.

Discussion

The results presented above demonstrate clearly that the corrosion of ruthenium is considerably inhibited after alloying with iridium. The major inhibition effect occurs for rather low iridium admixtures. Similar observations were made before by Miles *et al.* (7) and Gottesfeld *et al.* (8). These authors, however, analyzed the alloy's stability just by the coloration of the electrolyte after heavy O_2 evolution. After alloying Ru with Ir, the lack of electrolyte coloration due to RuO_4 indicated higher stability. The method used in the present study allows the detection of RuO_4 formation at low current densities during the initial stages of corrosion (15).

The decrease in Ru corrosion of the metal electrode is achieved, however, at the expense of activity for O_2 evolution. Apparently both the corrosion rate as well as the O_2 evolution activity drop in the same qualitative manner with increasing iridium content. The loss in activity for O_2 evolution is a consequence of increasing Tafel slope and increasing overpotential. Taking the Tafel slope as an indicator for the reaction mechanism, one has to conclude (see Fig. 2) that O_2 evolution on Ru_xIr_{1-x} alloys with $x < 0.5$ proceeds via the mechanism assumed for Ir anodes and no longer via that for Ru (1).

The simultaneous inhibition of ruthenium corrosion and O_2 evolution is not too surprising because it has been shown that both processes have a common reaction intermediate (5, 17, 18). If the formation of this intermediate—most probably RuO_4 (15)—is inhibited, both the O_2 evolution rate and corrosion rate will be diminished. The question, however, remains of how the formation of RuO_4 is suppressed.

On the basis of our XPS results, we conclude that segregation and preferential corrosion of ruthenium leads to a surface layer with considerably increased iridium content. Whether the topmost layer is only iridium oxide or still a mixture of ruthenium and iridium oxide cannot be

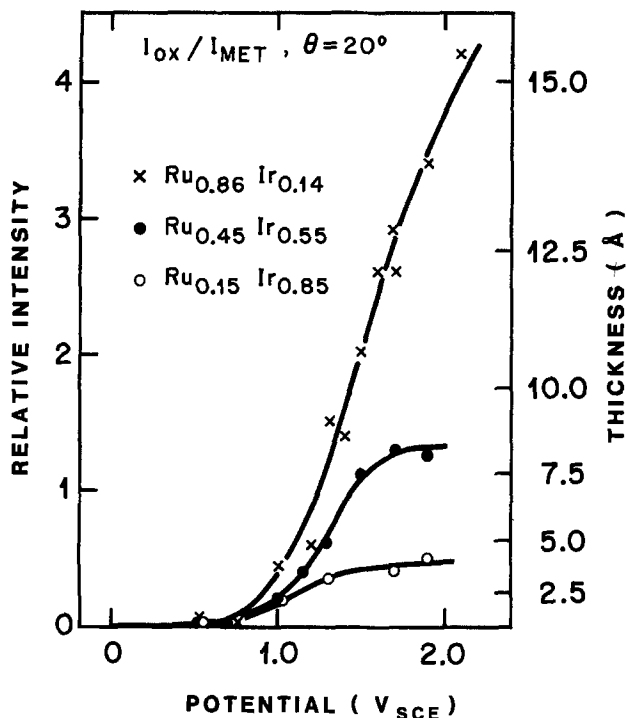


Fig. 6. Relative integrated intensity of the surface oxide and substrate metal contributing to the Ir4f and Ru3d spectra measured for $\theta = 20^\circ$ as a function of the electrode potential. For estimation of the corresponding oxide thickness, refer to the text.

distinguished on the basis of our results. It is clear, however, that the electrochemical performance of the alloys shifts towards that of iridium as a consequence of a change in surface composition. With respect to the measured Tafel slopes, one could assume that for alloys with $x < 0.5$ the topmost layer is pure iridium oxide.

The growth of this surface layer is rationalized as follows. Oxide formation on both metals occurs at potentials far below the O_2 evolution potential. This is evidenced in Fig. 6 where the oxide layer on the alloys has a measurable thickness already at 0.9V. As can be seen in Fig. 5, the oxide formation, preceding the O_2 evolution, leads to some segregation at the surface in favor of a higher Ir content. At more anodic potentials, where O_2 evolution and corrosion set in, the surface composition changes even further, now being a consequence of preferential corrosion of the Ru component. The thickness, as well as the surface composition, reaches a limiting value for the Ru_xIr_{1-x} alloys with $x = 0.15$ and $x = 0.45$, indicating that film formation and corrosion are equilibrated and that Ru no longer corrodes preferentially. This situation is different for the alloy with $x = 0.86$, where no limiting film thickness is reached within the potential range under investigation. In all three cases, the electrochemically formed overlayer is enriched in iridium and, therefore, the electrochemical performance is much closer to that of pure iridium than would be expected on the basis of the bulk composition. However, ruthenium is removed from the interface, and its contribution to the overall electrochemical reaction becomes negligible.

Upon inspection of Fig. 2 and 3, it becomes evident that the O_2 evolution reaction on the alloys with high iridium content ($x = 0.45$, $x = 0.15$) is not totally identical to the reaction on pure iridium with respect to macroscopic electrochemical parameters. While the Tafel slope is equal to that measured on Ir, the O_2 evolution onset potential is shifted to more cathodic values. In addition, the oxides formed on the alloys are thicker than those formed on pure iridium during O_2 evolution. In order to be sure that the decrease of the onset potential for O_2 evolution is a real effect and not just due to an increase in real surface area we have measured the charge enhancement factor (CEF) (19) for the $Ru_{0.45}Ir_{0.55}$ alloy after O_2 evolution at po-

tentials up to $2.0 V_{SCE}$. The CEF was about 1.5 and too small to explain the observed shift with the increased surface area.

On the basis of the results obtained by Stucki and Müller (6) in combination with the present results, we assume that a general shift of the oxidation potentials of iridium, due to the presence of ruthenium, is responsible for the observed shift in O_2 evolution potential. These authors investigated the electrochemical behavior of thick anodic oxide films grown on Ru-Ir alloys. They found a shift of the highly reversible redox reaction at $0.7 V_{SCE}$, which can be assigned to a change in Ir-valence state from III to IV, as well as a shift of the O_2 evolution potential as a function of alloy composition. As is evident from Fig. 3, the results obtained in the previous study (6) are in complete agreement with those of the present investigation obtained on "thin" oxide layers. Most probably, the addition of ruthenium makes the iridium oxide less noble and shifts the redox potential of the surface oxides.

A shift of the redox potential for the initial stages of oxidation [$M \rightarrow M_x(OH) \rightarrow M_{x-n}(OH)$ in Ref. (9)], which are rather reversible on Ru and Ir, is also observed on the metal alloys. In Fig. 7, the cyclic voltammograms of Ru, Ir, and $Ru_{0.45}Ir_{0.55}$ are compared for anodic scan limits below $0.8 V_{SCE}$. The most interesting result is that the alloy shows only one reduction feature at a potential between those of pure metals. It is clear that the voltammogram of the alloy is not a superposition of the two compounds but it represents a homogeneous phase with a shifted redox potential. This result strongly supports the idea of shifted redox potentials due to alloying in the case of Ru and Ir. The shift of the O_2 evolution onset can be rationalized along these lines, if the O_2 evolution process is under-

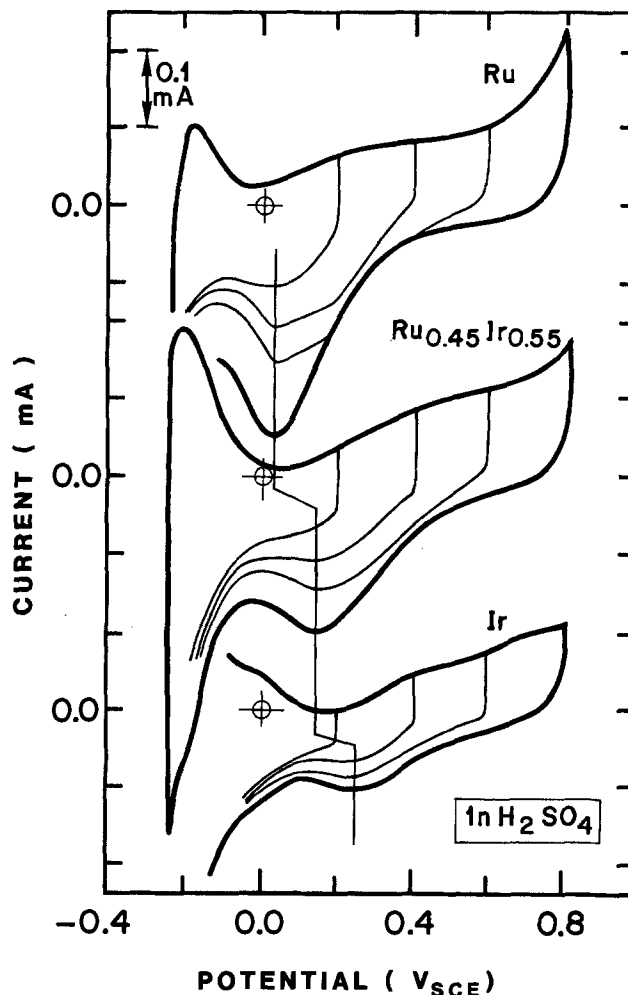


Fig. 7. Cyclic voltammograms of Ru, $Ru_{0.45}Ir_{0.55}$, and Ir for a cathodic potential limit $-0.25V$ and different anodic potential limits below $+0.8 V_{SCE}$. $1N H_2SO_4$, scan rate: $100 mV/s$.

stood as the formation and decomposition of "higher oxides" (6, 7, 10, 11). Our results are in good agreement with observations made on alloys like Pd-Au or Pt-Rh (20). Different results have been observed for Pt-Au alloys which, however, do not form solid solutions (21). Most probably, the formation of a solid solution is a prerequisite for the observation of shifted redox potentials in alloys. In the case of O₂ evolution, it is not clear whether the metal substrate or the oxides, from which O₂ is released, or both have to form solid solutions in order to show a shifted O₂ evolution potential. For the system under investigation, however, both the metals as well as the oxides do form solid solutions.

The observed shift in redox potentials is assumed to be a consequence of charge transfer or band mixing of the metal's d band (22) as well as the d derived t_{2g} band of the surface oxides (23). The correlation between the number of valence electrons and the O₂ evolution potential by Miles and Thomason (24) might be fortuitous but may well play an important role in determining the O₂ evolution potential in mixed systems assuming the rigid band model to be applicable (20). Another way of explaining the shift in redox potentials might be the assumption of coadsorption and exchange lateral interaction between surface dipoles (25).

The question whether the iridium component can be replaced by some other low cost component is of importance for industrial application of O₂ evolution catalysts. In view of the present results replacement of Ir does not appear to be advisable. The iridium component does not only stabilize the ruthenium component, while O₂ evolution still proceeds on Ru, but it becomes also the O₂ evolving component. The idea of keeping the advantageous properties of both metals, i.e., the catalytic activity of Ru and the relative stability of Ir, by alloying did not come true.

In order to determine the minimum amount of Ir in the alloy, necessary for a reasonable stabilization effect, more data are needed. The present investigation, however, shows that an iridium content of about 30% may be sufficient.

Application of the results obtained on metal alloys to powder catalysts made of mixed Ru-Ir oxides may appear premature. Investigations in our laboratory, however, indicate a similar behavior of metal alloys and Ru-Ir mixed oxides with respect to O₂ evolution potential in practical cells and Tafel slope as a function of the composition. While surface segregation effects during O₂ evolution on the mixed oxides seem to be negligible, the shift in redox potentials is still observed (23).

Conclusions

The catalytic properties of Ru-Ir alloys for anodic O₂ evolution are determined by two effects (i) surface segregation and (ii) redox potential shifts.

Surface segregation in favor of a higher iridium content starts at potentials cathodic of the O₂ evolution potential. The thickness of the oxide layer formed during O₂ evolution increases with decreasing Ir content of the alloy.

The potentials for O₂ evolution and for the initial steps in oxide formation on the alloys shift to more cathodic values with increasing Ru content of the alloys. This result is in complete agreement with previous investigations (6) showing a similar shift of the potential for O₂ evolution and the reversible oxidation state change on thick anodic oxide films formed on the alloys by potential cycling.

As a consequence of both effects the corrosion of and O₂ evolution on ruthenium is significantly inhibited by alloying with iridium. For alloys with a composition of 50% and more iridium, anodic O₂ evolution proceeds with

a Tafel slope equal to that of pure iridium but with a reduced overpotential

Acknowledgment

The excellent technical assistance of R. Weder is gratefully acknowledged. We thank K. Müller for many helpful discussions. This work was supported by the Nationaler Energie-Forschungs-Fond.

Manuscript submitted May 4, 1984; revised manuscript received Aug. 27, 1984.

Brown, Boveri & Company assisted in meeting the publication costs of this article.

REFERENCES

1. S. Trasatti and G. Lodi, in "Electrodes of Conductive Metallic Oxides," S. Trasatti, Editor, p. 521, Elsevier, Amsterdam (1980), and references therein.
2. S. Trasatti and W. E. O'Grady, in "Advances in Electrochemistry and Electrochemical Engineering," Vol. 12, H. Gerischer and C. W. Tobias, Editors, p. 177, Interscience, New York (1981).
3. R. Hutchings, K. Müller, R. Kötz, and S. Stucki, *J. Mater. Sci.*, In press.
4. K. Müller, G. Scherer, and S. Stucki, in "Extended Abstracts of 32nd ISE Meeting," Vol. I, p. 28 Dubrovnik, Yugoslavia (1981).
5. R. S. Yeo, J. Orehotsky, W. Visscher, and S. Srinivasan, *This Journal*, **128**, 1900 (1981).
6. S. Stucki and R. Müller, Abstract 651, p. 1653, The Electrochemical Society Extended Abstracts, Vol. 79-2, Los Angeles, CA, Oct. 14-19, 1979.
7. M. H. Miles, E. A. Klaus, B. P. Gunn, J. R. Locker, W. E. Serafin, and S. Srinivasan, *Electrochim. Acta*, **23**, 521 (1978).
8. S. Gottesfeld, S. Rishpon, and S. Srinivasan, in "Electrolysis," W. E. O'Grady, P. N. Ross, and F. G. Will, Editors, p. 155, The Electrochemical Society Softbound Proceedings Series, Pennington, NJ (1982).
9. H. Angerstein-Kozłowska, B. E. Conway, B. Barnett, and J. Mozota, *J. Electroanal. Chem.*, **100**, 417 (1979).
10. R. Kötz, H. J. Lewerenz, and S. Stucki, *This Journal*, **130**, 825 (1983).
11. R. Kötz, H. J. Lewerenz, P. Brüesch, and S. Stucki, *J. Electroanal. Chem.*, **150**, 209 (1983).
12. E. Raub, *J. Less Common Metals*, **1**, 3 (1959).
13. R. Kötz, H. Neff, and S. Stucki, *This Journal*, **131**, 72 (1984).
14. H. Neff, W. Foditsch, and R. Kötz, *J. Electron Spectrosc. Relat. Phenom.*, **33**, 171 (1984).
15. R. Kötz, S. Stucki, D. Scherson, and D. M. Kolb, *J. Electroanal. Chem.*, **172**, 211 (1984).
16. K. S. Kim, W. E. Baitinger, J. W. Amy, and N. Winograd, *J. Electron Spectrosc. Relat. Phenom.*, **5**, 351 (1974).
17. M. M. Pecherskii, V. V. Gorodetskii, V. M. Pulina, and V. V. Losev, *Elektrokhimiya*, **12**, 1445 (1976).
18. L. D. Burke and T. O. O'Meara, *J. Chem. Soc. Faraday Trans. 1*, **68**, 839 (1972).
19. B. E. Conway and J. Mozota, *Electrochim. Acta*, **28**, 9 (1983).
20. D. A. J. Rand and R. Woods, in "Electrocatalysis," M. W. Breiter, Editor, p. 140, The Electrochemical Society Softbound Proceeding Series, Princeton, NJ (1974).
21. M. W. Breiter, *J. Phys. Chem.*, **69**, 901 (1965).
22. M. O. Robbins and L. M. Falicov, *Phys. Rev. B.*, **29**, 1333 (1984).
23. R. Kötz and S. Stucki, *Electrochim. Acta*, To be published.
24. M. H. Miles and M. A. Thomason, *This Journal*, **123**, 1459 (1976).
25. T. Hepel, Abstract 580, p. 1266, The Electrochemical Society Extended Abstracts, Vol. 83-1, San Francisco, CA, May 8-13, 1983.

Adsorption at the Solid/Solution Interface

An FTIR Study of Phosphoric Acid on Platinum and Gold

M. A. Habib* and J. O'M. Bockris*

Department of Chemistry, Texas A&M University, College Station, Texas 77843

ABSTRACT

The paper represents an FTIR study of the adsorption from aqueous solutions of phosphoric acid onto Pt and Au electrodes at various concentrations and potentials. The experimental method utilizes parallel polarized light; the light path through the solution is around 10^{-4} cm. The signal-to-noise ratio was made acceptable by subtracting spectra obtained in regions in which H_3PO_4 was known from radiotracer measurements not to be adsorbed from the spectra at potentials at which adsorption occurs. It was found that there is one main peak at 1074 cm^{-1} which varies parabolically with potential. Values of the electrode coverage, θ , were obtained by calibrating the peak heights against the results of parallel radiotracer measurements. Plots of θ against $\log C$ are linear. The adsorption maximum on Au was *ca.* 300 mV more positive than that on Pt. The validity of the measurements is supported by the rational trends of the data obtained, in particular, the relation to the spectroscopic data separately obtained for H_3PO_4 in solution. H_3PO_4 in solution is 99% molecular and 1% ionic. It is shown that the coverage data can be evaluated in such a way (solvation of H_3PO_4) that $0.2 < \theta < 0.6$, so that a Temkin isotherm may be applicable. The difference in results on Au and Pt may not be interpreted unambiguously in terms of displacement by oxide: accounting for water bonding appears necessary. The method offers an alternative to SERS.

One of the current approaches to improve fuel cell performance is the use of phosphoric acid as an electrolyte. These cells employ 85%-100% (aqueous) phosphoric acid at a temperature of 175° - 200°C (1). The mechanism of the cell is not understood. It may be that the main reason for the good performance is an $e^{+E/RT}$ effect: the acid makes possible the use of elevated temperatures. Cathodic polarization limits the performance.

Although the Arrhenius factor contributes to an increase in efficiency, other factors must be taken into account.

The dissociation constants of H_3PO_4 at 25° , 100° , and 200°C are $10^{-2.15}$, $10^{-2.6}$, and $10^{-3.5}$, respectively (2). The corresponding degrees of ionization for more than 85% concentrated H_3PO_4 ($>14.7\text{ mol dm}^{-3}$), are 0.02, 0.01, and 0.005. Hence, H_3PO_4 electrolyte under fuel cell condition remains 99% molecular. The occupancy of reaction sites by adsorbed acid molecules may be high. If this is the case, O_2 reduction would, in fact, actually be impeded, compared with an electrolyte at the same temperature, which is ionic and which would be expected to occupy only a small fraction of the electrode surface owing to anion repulsion.

If this view is applicable, the high efficiency of fuel cells using H_3PO_4 would indeed be due to the Arrhenius factor but still better results (*e.g.*, higher electrochemical rate constants) might be obtained with an acid equally refractory as H_3PO_4 , but existing predominantly as ions so that a greater degree of surface is left unblocked.

Other factors affecting the oxygen reduction rate may be associated with a change of environment. For example, it may be possible that another acid may increase the activity of protons at a given concentration and thereby increase the rate of O_2 reduction. Alternatively adsorbed layers of some species on the electrode surface may give rise to improved resonance tunneling (3) of electrons at the electrode/solution interface. Similarly, the solubility of O_2 may be increased in certain aqueous solutions, and this would give rise to higher exchange current densities and limiting currents and, hence, increased performance in energy conversion.

Recently, trifluoromethane sulfonic acid (TFMSA) (CF_3SO_3H), which is completely dissociated in aqueous solution (4), and its homologs have been introduced as fuel cell electrolytes (5). These acids produce remarkable results. The exchange current density for the oxygen reduction reaction at 1 atm pressure and ordinary temperature is 3 orders of magnitude greater than that in 85% orthophosphoric acid (5); this leads to a reduction of the

overvoltage by 0.25V and an increase of fuel cell efficiency by 35%. Thus, in the trifluoromethane sulfonic acid fuel cells, fuel cell efficiencies close to 80% would be possible.

Yeager *et al.* (6) investigated the effects of additions of CF_3SO_3H and CF_3SO_3K to H_3PO_4 . From a comparison of limiting currents, they concluded that, while addition of CF_3SO_3H increases O_2 transport to the electrode, the simultaneous addition of $CF_3SO_3K + CF_3SO_3H$ results in only a small increase. Hence, the O_2 reduction kinetics do not appear to be dependent on the proton activity in the H_3PO_4 electrolyte (6). Ross *et al.* (7) found a dramatic decrease of O_2 reduction rate in TFMSA solution by the addition of H_3PO_4 and inferred that, in addition to geometric blocking, a small increase in activation energy may be responsible. Although infrared reflectance spectroscopy has been used to detect organic radicals and carbon containing species as electrochemical reaction products in nonaqueous solvents (8-12), because of high IR absorption by water, the applicability of this method for the study of electrochemical phenomena in aqueous solutions remains limited (13-18). However, a fast Fourier transform infrared (FTIR) spectrometer with higher energy throughput, in combination with a highly polished electrode surface having a thin film of solution between the electrode surface and IR transparent window, brings new promise to the field of electrochemical adsorption studies (8, 10, 19). We report here the electrochemical adsorption of phosphoric acid on platinum and gold electrodes from an aqueous solution, as measured with an FTIR spectrometer system.

Experimental

The working electrode used was a highly polished Pt or Au disk of 0.6 cm diam and 1 mm thick attached to a copper rod clad with heat shrinkable Teflon tube supplied by Small Parts, Incorporated (Miami, Florida). The electrode surface was polished with $0.05\text{ }\mu\text{m}$ alumina. Owing to the necessity of having an optically flat surface, the electrode surface was kept parallel to the polishing surface by mounting it in a vertical aluminum cylinder of 3.1 cm od and 1 cm id (see Fig. 1). The aluminum cylinder with the mounted electrode was then attached to the lever of a Buehler Minimet polisher (Fig. 1), and the electrode was polished until a mirror finish was obtained. The polished electrode was cleaned with conc. HNO_3 , and rinsed thoroughly with tridistilled water. Any traces of aluminum from the holder was found to be removed by conc. HNO_3 cleaning, since the voltammograms of the clean Pt or Au were the same as those previously taken with pure Au or Pt wire electrodes in clean acid solution.

*Electrochemical Society Active Member.

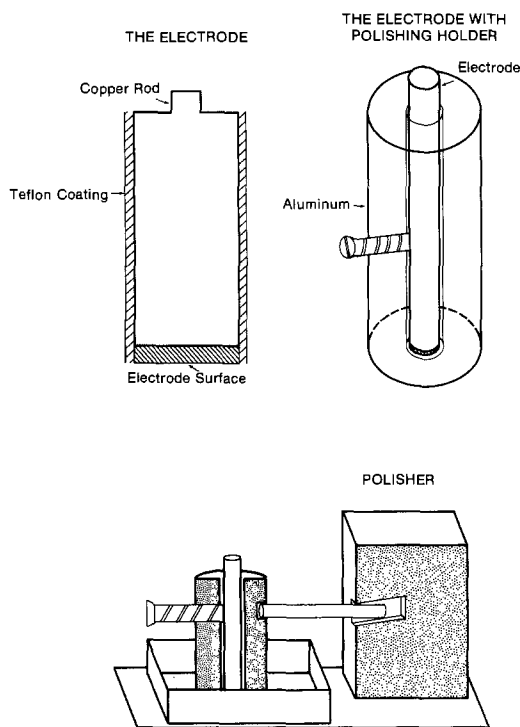


Fig. 1. The electrode polisher

The polished electrode was positioned in the cell very close to the IR-transparent ZnSe cell window, leaving only a very thin film of solution in front of it (Fig. 2) (8). The ZnSe window, supplied by Foxboro (North Haven, Connecticut), was 3 mm thick and of 25 mm diam. The cell window was cleaned with toluene, dried thoroughly, and rinsed with tridistilled water. A Pt counterelectrode and a saturated calomel reference electrode were used. All potentials mentioned in this paper are referred to the normal hydrogen electrode (NHE).

The phosphoric acid, supplied by MCB, was purified by refluxing with 10% v/v of 30% H_2O_2 . Excess water was removed by distillation. Phosphoric acid electrolyte of the desired concentration was then made by addition to a 1 mol dm^{-3} solution of $HClO_4$ in tridistilled water. The electrode was subjected to a fast potentiodynamic cycling of 1 V s^{-1} for 5 min. A voltammogram was taken at 100 mV s^{-1} to determine the surface area of the electrode from the charge due to hydrogen reduction. The cell was then placed in the FTIR spectrometer, so that the electrode surface was in the optical path of the IR beam (Fig. 3). Boil-off of liquid nitrogen was used for purging the system. N_2 gas from a cylinder was used for deaerating the solution.

A HI-TEK potentiostat (Model DT2101) and HI-TEK waveform generator (Model PPR1) were used for controlling the electrode potential. The electrode surface was irradiated with the incident IR beam in the sample com-

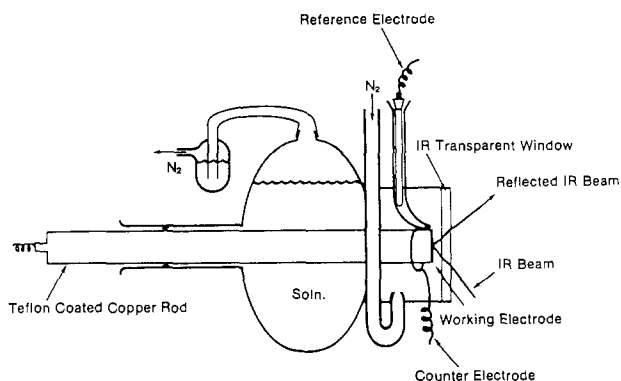


Fig. 2. The electrochemical cell

partment of a Digilab FTS-20E FTIR spectrometer system equipped with a Data General Nova 4 computer. A versatile reflection attachment (Harrick Model VRA S5D) with retromirror accessory (RMA-4DG) was used to guide the incident IR beam to the electrode surface and the reflected beam back to the detector. The angle of incidence was $\approx 67^\circ$. The optical configuration is shown in Fig. 3. A Moletron IGP228 gold grid polarizer was used to plane polarize the beam.

The stability of the infrared source (glowbar) is extremely important for the reproduction of the peak intensities. The voltage corresponding to the current passing through the glowbar during experimentation must be stable within ± 1 mV. The power supply for the glowbar showed the voltage to be 1.000V. The fluctuation of this voltage, which corresponds to the variation of the source signal, was monitored by a digital voltmeter and an X-t recorder. When the glowbar voltage fluctuation was more than 1 mV from its adjusted value of 1.000V, then the variations of peak heights for the same experiments were more than 5%; in such cases, the results were rejected.

Constancy of the spectral intensity also depended on the constancy of the flow of nitrogen for purging the spectrometer system. It was noticed that when the flow rate of purging N_2 was changed, the glowbar voltage also changed by about 5 mV and thus affected the spectral intensity. Therefore, the flow rate of N_2 was always kept constant during any given experiment. A gas flowmeter, Gilmont Model F1500, was used, and a flow rate of 30 liter/min was maintained during the experiment.

The electrode was polarized potentiostatically in the range of 0.0 V (NHE) to 1.2V (NHE) for Pt and 0.0 V-1.6V (NHE) for Au, at intervals of 200 mV. A total of 1000 scans were collected at each potential. All spectra at each potential were added together and signal averaged to improve the signal-to-noise (S/N) ratio. Synchronization between the application of the potential step and the beginning of data collection was made by tapping a TTL signal accompanying the beginning of data collection at the Digilab A/D converter and applying the signal to trigger the appropriate potential step at the potentiostat (HI-TEK DT2101). The spectra reported here represent the difference between the spectra at a given anodic potential and that at 0.0 V, where no adsorption of H_3PO_4 molecule is detected by FTIR¹ or in the corresponding radiotracer measurements (20, 21).

All spectra were measured with parallel polarized IR radiation, because the perpendicular polarized light is not absorbed by the adsorbed layer on a reflecting surface and hence does not carry information from the adsorbed layer (22, 23). The calculated spectra are thus termed p-polarized differential spectra, which give information about the adsorbed layer, provided no new species in solution is formed.

Results

Results before subtraction of solution spectra.—In Fig. 4a and 4b, the p-polarized spectra at 800 mV and 0.0 V for Pt, before the subtraction of the spectra at 0.0 V, are shown. Because these broad bands include information from the solution, the two spectra appear to be very much the same. However, when the spectrum at 0.0 V is subtracted from the spectra at 800 mV, the resultant differential spectrum of Fig. 5a is obtained.

Influence of light polarization.—When the IR light was polarized parallel to the plane of incidence, the spectra were taken at 0.0 V and at 800 mV, and the former was subtracted from the latter, the resultant spectrum, as shown in Fig. 5a, distinctly shows the peak due to a P-O

¹Since $(\Delta R/R_{ref}) \ll 1$, the spectra reported here are in the absorbance mode which is equivalent to $-(\Delta R/R_{ref}) = -(R - R_{ref})/R_{ref}$, where R is the reflected intensity at a desired potential and R_{ref} is that at a reference potential. Absorbance = $-\log(R/R_{ref}) = -\log[(R_{ref} + R - R_{ref})/R_{ref}] = -\log(1 + \Delta R/R_{ref}) = -\Delta R/R_{ref}$.

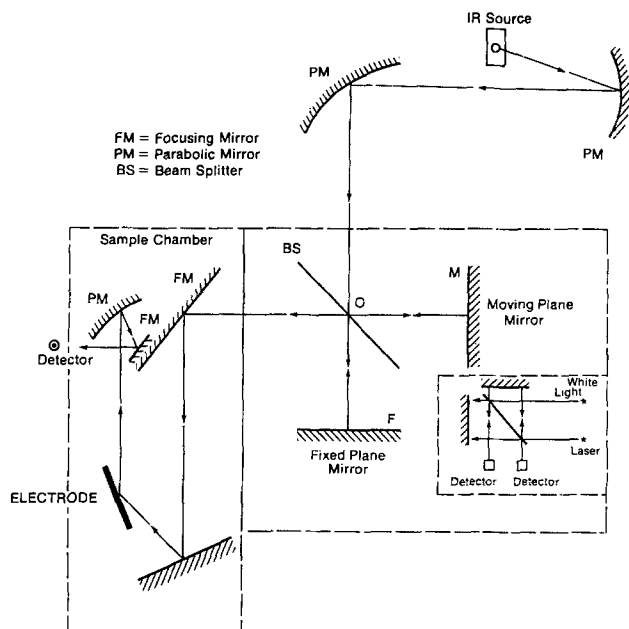


Fig. 3. Optical arrangements for the FTIR spectrometer with the reflection attachments for the electrochemical experiments.

vibration, the area and height of which changes with potential (Fig. 6). With perpendicular polarization, no such peak was observed (Fig. 5b). Hence, when the plane of po-



Fig. 4. *In situ* IR spectra of Pt surface in $1 \text{ mol dm}^{-3} \text{ HClO}_4 \text{ (aq.)} + 6.6 \times 10^{-3} \text{ mol dm}^{-3} \text{ H}_3\text{PO}_4 \text{ (aq.)}$ at (b) 0.0V and (a) 800 mV, before the subtraction of the solution spectrum.

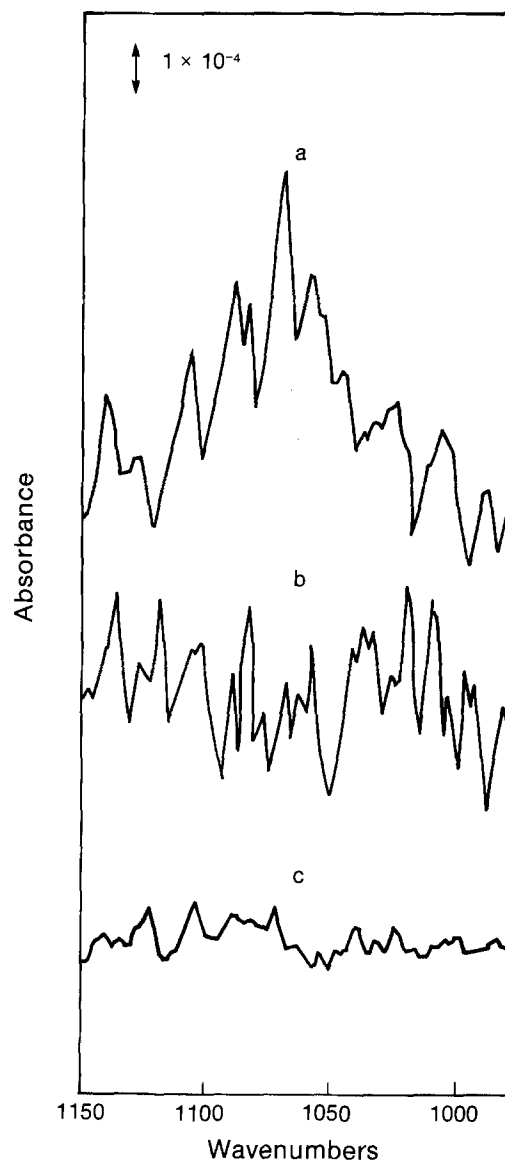


Fig. 5. Differential spectra of the electrode surface at 800 mV with (a) parallel and (b) perpendicular polarization of the IR beam with respect to 0.0 V [solution = $1 \text{ mol dm}^{-3} \text{ HClO}_4 + 6.6 \times 10^{-3} \text{ mol dm}^{-3} \text{ H}_3\text{PO}_4 \text{ (aq.)}$] and (c) spectra in the absence of H_3PO_4 .

larization of the IR light was oriented parallel to the plane of incidence, the spectra recorded were then indeed the spectra of H_3PO_4 adsorbed on the electrode as a function of potential.

Adsorption as a function of potential.—In Fig. 6, the p-polarized differential spectra of the Pt electrode surface at 200, 600, 800, 1000, and 1200 mV (NHE) are shown. The absorbance peak at 1074 cm^{-1} is hardly visible at 200 mV, but increases with increasing anodic potential, and reaches a maximum at 800 mV. With further increase of anodic potential, this peak decreases. This peak was not detectable when H_3PO_4 was absent from the solution (Fig. 5c) and, hence, must originate from H_3PO_4 ; the observed peaks are in the characteristic group frequency range of the P-O stretching vibrations in H_3PO_4 (24). The adsorption peak areas as a function of potential are plotted and compared with coverages measured by the radiotracer method (21) in Fig. 7. Some smaller peaks seem to appear at 1110, 1090, and 1025 cm^{-1} and seem to vary with potential (Fig. 6) but the magnitude of these peaks is really comparable to the noise level as discussed in the Discussion section.

Adsorption as a function of concentration.—In Fig. 8, the absorption peak at 1074 cm^{-1} as a function of the logarithm of H_3PO_4 concentration in solution with the electrode at 800 mV are shown. The peak heights correspond-

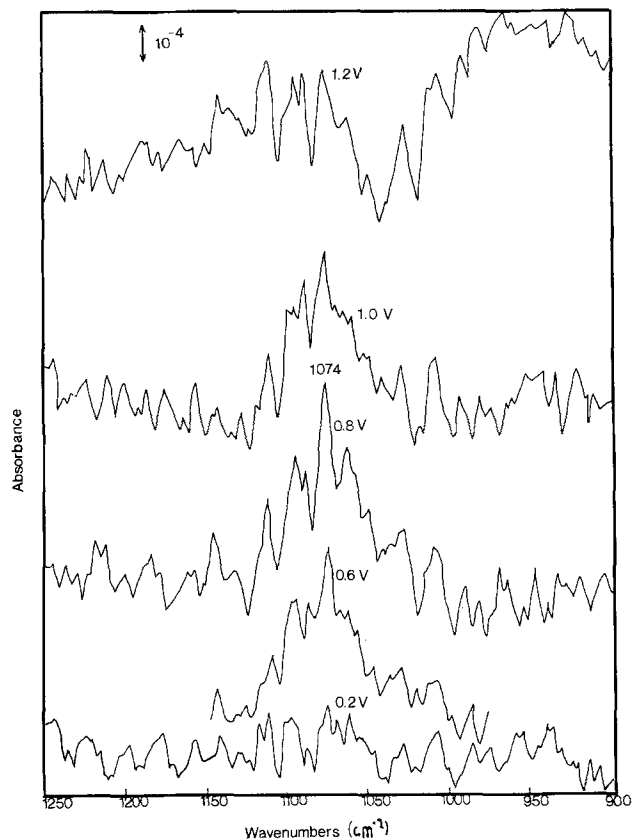


Fig. 6. *In situ* differential IR spectra of H_3PO_4 species adsorbed on Pt at different potentials [solution = $1 \text{ mol dm}^{-3} \text{ HClO}_4 + 6.6 \times 10^{-3} \text{ mol dm}^{-3} \text{ H}_3\text{PO}_4$ (aq.)].

ing to surface concentrations are found to vary linearly with $\log C$.

During the experiment, the change of concentration was carried out in the following way: first, the cell was filled with the most dilute concentration of H_3PO_4 solution ($10^{-4} \text{ mol dm}^{-3}$), and the spectra were recorded in the way described in the previous section. Since it is impor-

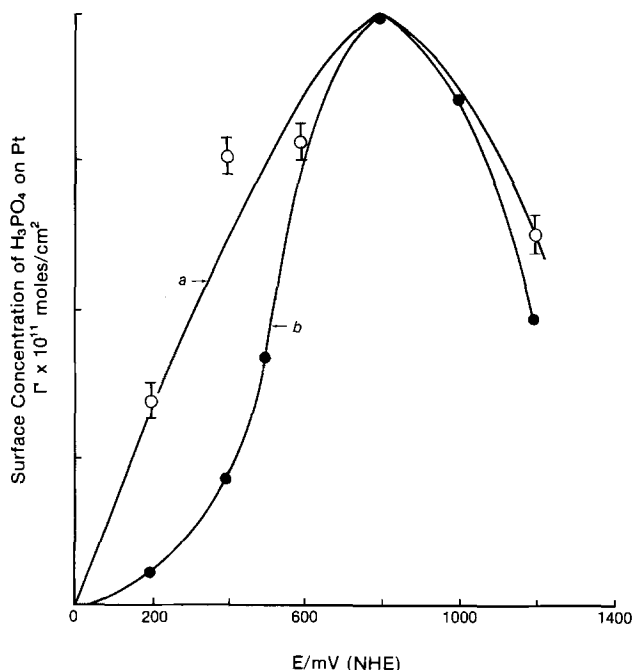


Fig. 7. Surface concentration, Γ , of H_3PO_4 on Pt as a function of potential. (a): Γ as normalized area of IR peak at 1074 cm^{-1} . The highest peak area is assumed to be the highest surface concentration, as obtained from (b), the radiotracer measurements. The scoring on the Y-axis is in units of 5. Solution as in Fig. 6.

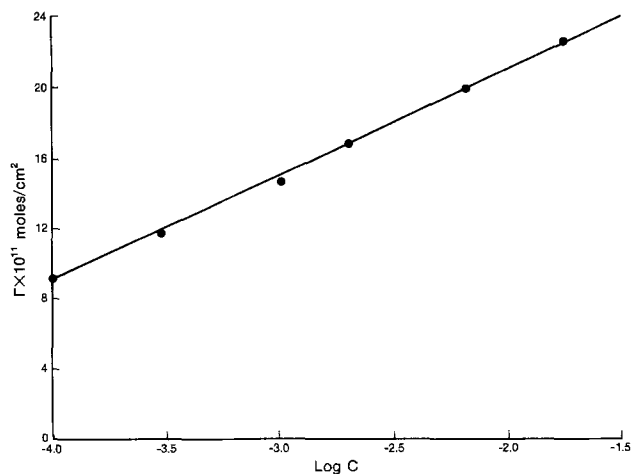


Fig. 8. Variation of the surface concentration of H_3PO_4 on Pt with logarithm of the concentration of H_3PO_4 in solution.

tant not to disturb the position of the electrode or the cell, so that comparison of different spectra can be made, the solution concentration was changed by adding a defined amount of a 25% (aq.) solution of H_3PO_4 to the existing solution in the cell, with the help of a Hamilton microsyringe. Since sufficient diffusion time is needed² for the entire solution to attain a uniform desired concentration, the next set of data collection was started at least 1.5h after the addition of H_3PO_4 to the solution.

Adsorption on gold.—The p-polarized differential spectra of adsorbed H_3PO_4 on Au at various potentials are shown in Fig. 9. The H_3PO_4 peak at 1074 cm^{-1} , due to P-O vibrations, is distinctly visible (Fig. 9).

In Fig. 10, the H_3PO_4 adsorption peaks are shown as a function of potential. The adsorption increases up to 1.2V and then decreases upon further increase of potential.

Discussion

Significance of signal relative to noise.—The amplitude of the signal of interest from the adsorbed layer being extremely small relative to the total light energy hitting the detector, there may be a considerable noise level associated with the main signal from the adsorbed layer. It is, therefore, desirable to determine the noise level before one may ascribe any apparent peak to molecular vibrations. When the incident IR beam was polarized perpendicularly, the main peak at 1074 cm^{-1} was not observed, but there appeared to be several smaller peaks (Fig. 5b). Since the perpendicularly polarized light does not carry information from the surface layer, the extent of these peaks is then only to be associated with the noise level. The magnitude of the noise level is thus 2×10^{-4} (Fig. 5b), and, therefore, any peaks in $\Delta R/R$ smaller than or equal to 2×10^{-4} may not be ascribed to any molecular bond vibration. In Fig. 5 and 6, thus, only one peak, that at 1074 cm^{-1} , may be safely identified. Some peaks, however, appear periodically, but these are smaller than the noise level and hence are assumed to originate in some experimental artifacts. Experiments giving rise to these results were repeated at least twice.

Spectra such as that shown in Fig. 6 are obtained by subtracting the intensities obtained at 0.0 V from those obtained at the potential shown, the light being parallel polarized. The absorbance peak height or area increased with anodic potential first, reached a maximum at 800 mV, and then decreased with further increase of poten-

²The time required for the diffusion of material for the newly concentrated H_3PO_4 into the space between the electrode and the window may be obtained by applying the equation (25)

$$C_1 = \frac{C_0}{(\pi Dt)^{1/2}} \exp\left(\frac{-x^2}{4Dt}\right) \quad [1]$$

where x is the radius of the electrode, with $x = 0.25 \text{ cm}$ and $D = 10^{-5}$, it is easy to see that C_0/C_1 would be 1 in less than 1h.

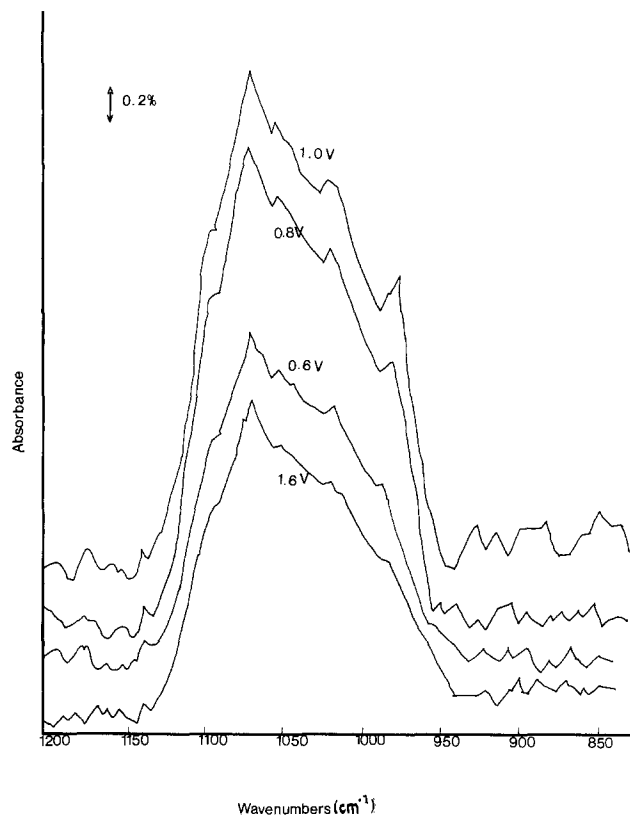


Fig. 9. *In situ* differential IR spectrum of adsorbed H_3PO_4 on Au electrode at various potentials.

tial, as shown in Fig. 7. This behavior could not be due to species in solution, and, hence, what we are looking at is the adsorbed layer, as is also supported by the linear variation of the peak height with $\log C$ (Fig. 8). The absorbance peak at 1074 cm^{-1} is due to the P-O vibration in the H_3PO_4 molecule, as discussed in the "Assignment of peaks" section below.

Intensities of IR light reflected from the electrode surface are taken here as a measure of the amount of adsorbed species on the electrode. From gas-phase measurements (26, 30), it is known that the intensity is linearly proportional to the surface concentration, up to a surface coverage of 0.5 for most compounds studied. In the present case of H_3PO_4 adsorption, independent measurements by the radiotracer method in this laboratory (20) show

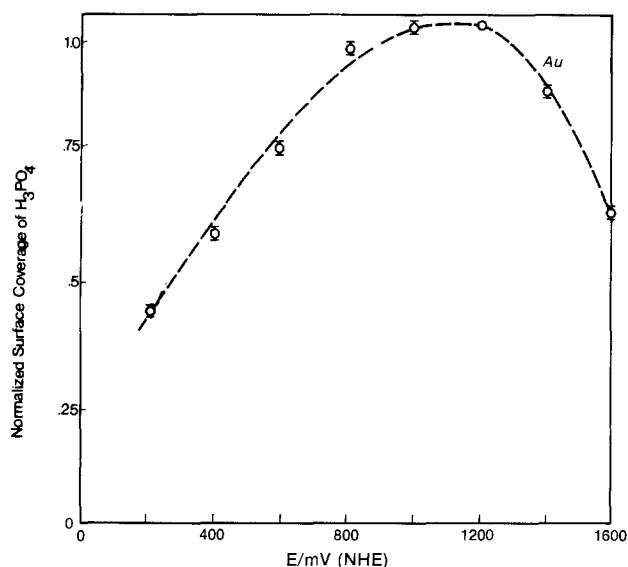
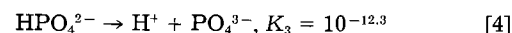
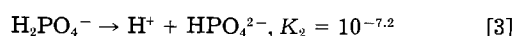
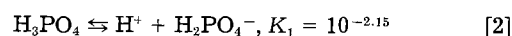


Fig. 10. Areas of IR peaks at 1074 cm^{-1} on Au normalized to 1 at maximum as a function of the electrode potential.

that in the concentration range studied, the fraction of the surrounding coverage is well below 0.5, and, therefore, the spectral intensities here can be assumed to be linearly proportional to the surface coverage.

Spectral intensities may be used for quantitative determination (30), provided that the extinction coefficient of the IR absorbing species is known. For IR measurements in electrochemistry, the extinction coefficients as a function of surface coverage are unknown. Owing to the difference in refractive indexes in the IR window, in the aqueous solution layer, and in the adsorbed layer, the determination of the extinction coefficient is difficult. However, if the maximum intensity is normalized with respect to the maximum coverage determined independently, *e.g.*, by the radiotracer method (20, 21), then the variation with respect to potential or concentration may be obtained (Fig. 7 and 8).

State of H_3PO_4 in solution.—The possible states of phosphoric acid in aqueous solution are molecular H_3PO_4 and H_2PO_4^- , HPO_4^{2-} , and PO_4^{3-} ions, according to the following dissociation reactions (2)



where K_1 , K_2 , and K_3 are the respective dissociation constants at room temperature. Since the second and third dissociation constants are very low, it may be assumed that the presence of HPO_4^{2-} and PO_4^{3-} in solution is negligible. Owing to the presence of an excess of H^+ ions in solution from the base electrolyte 1M HClO_4 , about 1% of the dissolved H_3PO_4 will dissociate to give $\text{H}_2\text{PO}_4^{2-}$ ions at room temperature. Thus, in solution, there are 99% H_3PO_4 molecules and 1% H_2PO_4^- ions which are to be considered for adsorption.

Assignment of peaks.—According to spectral data, H_3PO_4 has a spectral band at $900\text{--}1100\text{ cm}^{-1}$ due to the P-O stretching vibration (24). The differential spectra of the platinum electrode surface at different potentials with H_3PO_4 in solution are shown in Fig. 6. A major peak appears at 1074 cm^{-1} , which is in the region of P-O stretching frequency. First, confirmation that the peaks originate in H_3PO_4 was obtained by carrying out the same set of experiments without H_3PO_4 in solution. None of the peaks in Fig. 6 appeared (Fig. 5c). Lower noise level in Fig. 5c than Fig. 5a and 5b may be due to reflected light intensity loss due to absorption by H_3PO_4 in the bulk electrolyte.

The major peak at 1074 cm^{-1} first increases with increase of anodic potential, reaches a maximum, and then decreases with further increase of potential (Fig. 7), and, thus, this peak is assigned to the P-O vibrations in molecular H_3PO_4 . If it were due to the P-O vibrations in the H_2PO_4^- ion, then the decrease of this peak with further increase of anodic potential would be difficult to justify.

Horanyi *et al.* (27), in their earlier work on the adsorption of H_3PO_4 on Pt by the radiotracer method, mentioned H_2PO_4^- as the adsorbed species, while, in their later paper (21), the adsorbed species was said to be H_3PO_4 . Since during the radiotracer measurements the P atom was tagged, the amount of adsorption detected by the counter gives the total amount, including both the ionic and molecular species containing P^{32} , and no distinction could be made. However, measurement on gold shows that the IR peak at 1074 cm^{-1} starts decreasing at potential higher than that on Pt: namely, above about 1.1V (Fig. 10), at which oxide formation is significant, and hence the decrease in coverage of the H_3PO_4 species due to the displacement by the oxide layer is consistent. Reasonable symmetry of the curve is suggestive of displacement by the adsorbed water molecules. Although the main spectral peak on Pt and Au appear at the same frequency, namely, at 1074 cm^{-1} , the noise level in spectra on Pt (Fig. 6) is far higher than on Au (Fig. 10). This may be due to a greater degree of adsorption of H_3PO_4 on Au than on Pt.

Calibrating radiotracer measurement was only done on Pt, but not on Au, so that this observation remains without confirmation.

Precise calculation of the relative displacement of molecular and ionic species in any reasonable way is impeded by the absence of dipole moment data on H_3PO_4 [cf. Ref. (31)]. The necessary dipole moment to fit the result is 2.5 D (cf. $\mu_{\text{HNO}_3} = 2.16$ D) (31). With respect to the ionic model, the same number of water molecules have to be replaced. A rough calculation (neglecting lateral repulsion and imaging) of the electrostatic bond for ions at 0.8V (i.e., ca. 0.5V positive to the pzc) would be $E_{\text{FI}} = (4\pi qe_0 r_i)/\epsilon$, where q , e_0 , r_i , and ϵ represent electrode charge, charge of an electron, radius of the ion, and dielectric constant at the interphase, respectively. With $\epsilon = 6$, $r_i = 3\text{\AA}$, $q = 10 \mu\text{C cm}^{-2}$, the field ion interaction energy is $E_{\text{FI}} = 9 \times 10^{-13}$ erg. The field dipole interaction is $E_{\text{FD}} = 4\pi\mu q/\epsilon \approx 1.6 \times 10^{-13}$ erg, i.e., about 6 times less than the ion field interaction. Thus, the ions will be preferentially attracted to the electrode. But the number of H_2PO_4^- ions is about 6.6×10^{-5} mol/liter, while that of H_3PO_4 molecules is 6.6×10^{-3} mol/liter. From the radiotracer measurement, the coverage at 0.8V is 2×10^{-10} mol/cm², which corresponds to 1.2×10^{14} phosphorous containing species per centimeter squared. But the ionic H_2PO_4^- present in solution at a concentration of 6.6×10^{-5} mol/liter corresponds to 1.13×10^8 ion/cm², which seems negligibly small compared to the surface concentration. However, ions may diffuse into the double layer from the solution, and from Eq. [1], and with $x = 10\text{\AA}$, one may see that H_2PO_4^- diffusion will take ca. 25 min to diffuse into the diffuse layer to correspond to the amount of the observed amount of adsorption. While this is plausible, the adsorption of molecular H_3PO_4 which was present at 2 orders of magnitude higher concentration seems favorable, and the experimental results fit reasonably well with the theoretical adsorption model (29) based on the molecular nature of the adsorbing species (cf. next section).

The adsorption isotherm.—As shown in Fig. 8, the surface concentration of H_3PO_4 varies linearly with the logarithm of concentration of H_3PO_4 in solution at constant potential. A Temkin isotherm may be applicable. Thus

$$f(\theta) = A \log KC$$

where A is a constant, θ is the fraction of the surface covered, C is the concentration of H_3PO_4 in solution, and K is the adsorption equilibrium constant.

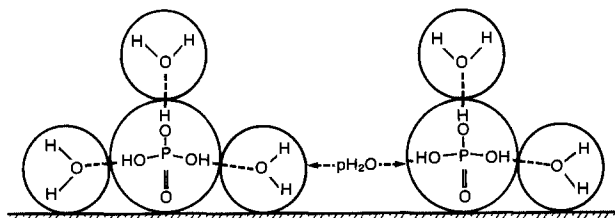
At 800 mV, the surface concentration is 20×10^{-11} mol/cm², and if the area occupied by a single H_3PO_4 molecule is 12\AA^2 based on the molecular dimension of the H_3PO_4 molecule, then the maximum fraction of the surface covered is only 0.15 and then the validity of the application of the Temkin isotherm becomes questionable. But molecular adsorbed species may be laid down on second nearest neighbor platinum sites (28) with water molecules in between (Fig. 11); then the area occupied by each H_3PO_4 molecule would be closer to 35\AA^2 , so that the surface coverage would really be ~ 0.42 in 6.6×10^{-3} mol dm⁻³ H_3PO_4 solution with the electrode at 800 mV. This is within the Temkin-type isotherm range. Surface heterogeneity also contributes to the Temkin-type behavior.

Decrease of surface coverage at potentials higher than 800 mV may be caused by two factors: (i) displacement by the oxide layer on Pt, and (ii) displacement by the water.

Pt-O starts forming from 800 mV, and, if the oxide layer were responsible for the decrease of θ , then the near symmetry of the θ -V curve around θ_{max} seems unexpected; the coverage should decrease more rapidly with the increase of the oxide layer.

However, measurement on gold shows that θ starts decreasing from a higher potential (Fig. 10) of about 1.1V, the potential of gold oxide formation. This is consistent with the suggestion that the adsorbed species are being displaced by the strongly adsorbed O species. However, the symmetry of the θ -V curve still remains and suggests that molecular H_3PO_4 continues to adsorb on the oxide

POSITIVE TO P.Z.C.:



NEGATIVE TO P.Z.C.:

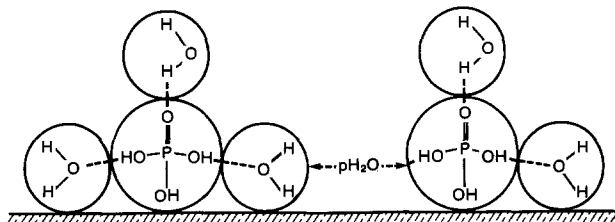


Fig. 11. Schematic model of adsorbed phosphoric acid molecules separated from each other by the adsorbed water molecules.

layer and that the gradual decrease of θ occurs by the displacement of H_3PO_4 by the adsorbed water molecules. The adsorption isotherm may, thus, be represented by

$$\ln \frac{\theta}{e^{n-1}(1-\theta)^n} - r\theta = \frac{X_{\text{H}_3\text{PO}_4} K_{\text{H}_3\text{PO}_4}}{X_{\text{H}_2\text{O}}^n K_{\text{H}_2\text{O}}^n} \quad [5]$$

where the logarithmic term is the configurational term given by Dhar *et al.* (28) for the process of adsorption by water displacement, r is the Temkin factor representing lateral interactions between the adsorbed H_3PO_4 mole-

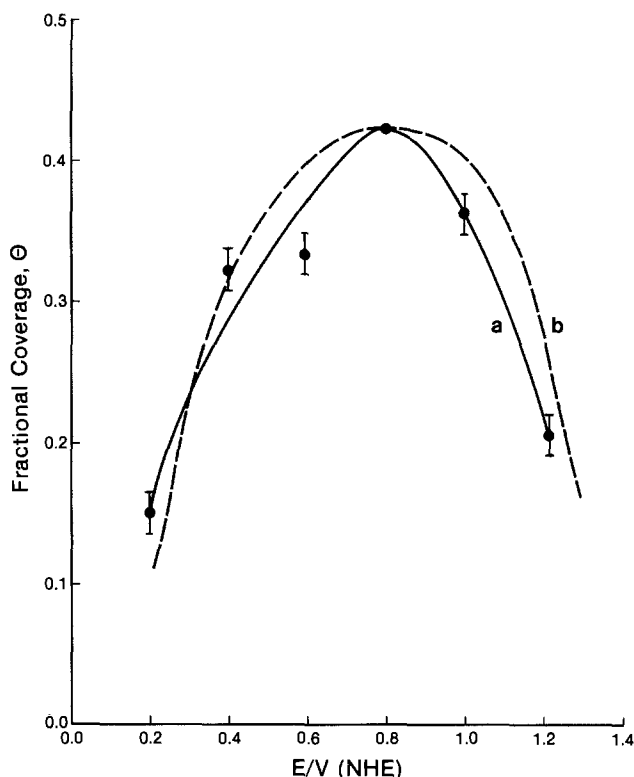


Fig. 12. Fraction of the surface covered, $\theta = \Gamma/\Gamma_{\text{max}}$, where Γ_{max} is the maximum surface concentration obtained on the basis of 35\AA^2 area occupied by one H_3PO_4 molecule as a function of potential. a: Experimental data obtained from the normalized IR peak at 1074 cm^{-1} . b: θ obtained from Eq. [5] with adsorption equilibrium constants obtained from the water displacement theory of Bockris *et al.* (29) with $En/RT = 2$, $\Delta\Delta G_s = 2RT$, and $r = 1$, where E is the lateral interaction energy between the adsorbed water molecules and $\Delta\Delta G_s$ is the difference in the free energies of adsorption for the solvent molecules having different orientation at the pzc.

cules, n is the number of water molecules displaced by one phosphoric acid molecule, X is the mole fractions, and K is the adsorption equilibrium constant.

The ratio of the equilibrium constants was calculated from the "adsorption with competition with water" theory of Bockris *et al.* (29). Equation [5] was used to obtain the surface coverage, θ , and is represented in Fig. 12. The nature of adsorption of H_3PO_4 regarding its variation with potential is thus explainable in terms of the molecular theory based on water displacement.

Conclusions

1. The combination of radiotracer and FTIR measurements allows quantitative determination of adsorption of IR absorbing species in aqueous solution on electrodes.

2. H_3PO_4 adsorbs on Pt, giving IR peaks from the P-O vibrational mode.

3. The potential dependence of the adsorption depends at least partly on water desorption, although an influence from oxide film formation at anodic potentials would be consistent with the results.

4. The concentration dependence of $\theta_{H_3PO_4}$ is temkinian.

Acknowledgments

The authors are grateful to Dr. S. Pons for his introduction to them of the principles of the FTIR method in electrochemical systems, and for several discussions. Discussions with Dr. John Appleby in respect to H_3PO_4 orientation and modeling has proved fruitful. Dr. Kunimatsu's comments on the experimental setup are acknowledged. Thanks are also due to Mr. J. Carbajal for the radiotracer measurements. Financial support for this work from the Electrical Power Research Institute and the National Foundation for Cancer Research is acknowledged. This work would not have been possible without the continued interest of Dr. Hampton Robinson, Jr., in scientific work associated with improvement in environmental quality and the corresponding financial support in the purchase of equipment.

Manuscript submitted Feb. 23, 1984; revised manuscript received Aug. 15, 1984.

REFERENCES

1. C. J. Warde, R. J. Ruka, and A. O. Osenburg, "Fuel Cells, Energy Conversion Alternatives Study," Vol. XII, Westinghouse Phase I, Final Report, NASA CR-134941 (1976).
2. D. D. Perrin, "Ionization Constants of Inorganic Acids and Bases in Aqueous Solution," 2nd ed. IUPAC Chemical Data Series No. 29, Pergamon Press, New York (1982).
3. W. Schmickler, *J. Electroanal. Chem.*, **83**, 387 (1977).
4. R. D. Howells and J. D. McCown, *Chem. Rev.*, **77**, 69 (1977).
5. A. J. Appleby and B. S. Baker, *This Journal*, **125**, 404 (1978).
6. E. Yeager, EPR/CWRU Contract RP 1200-7, Report XV, March 1981.
7. P. N. Ross and P. C. Andricacos, *J. Electroanal. Chem.*, **154**, 205 (1983).
8. S. Pons, *J. Electroanal. Chem.*, **150**, 495 (1983).
9. A. Bewick, *ibid.*, **150**, 481 (1983).
10. B. A-Blajeni, M. A. Habib, I. Taniguchi, and J. O'M. Bockris, *ibid.*, **157**, 399 (1983).
11. J. Russell, J. Overend, K. Scanlon, M. W. Severson, and A. Bewick, *J. Phys. Chem.*, **86**, 3066 (1982).
12. T. Davidson, S. Pons, A. Bewick, and P. P. Schmidt, *J. Electroanal. Chem.*, **125**, 237 (1981).
13. A. Bewick, K. Kunimatsu, J. Robinson, and J. Russell, *ibid.*, **119**, 175 (1981).
14. A. Bewick and K. Kunimatsu, *Surf. Sci.*, **101**, 31 (1980).
15. A. Bewick, K. Kunimatsu, and B. S. Pons, *Electrochim. Acta*, **25**, 465 (1980).
16. K. Kunimatsu, *J. Electroanal. Chem.*, **145**, 219 (1983).
17. H. Neff, P. Lange, D. K. Roe, and J. K. Sass, *ibid.*, **150**, 513 (1983).
18. B. Beden, A. Bewick, and C. Lamy, *ibid.*, **150**, 505 (1983).
19. R. N. Dominey, *This Journal*, **129**, 300C (1982).
20. J. O'M. Bockris, M. A. Habib, and J. Carbajal, *ibid.*, To be submitted.
21. G. Horanyi, E. M. Rizmayer, and G. Inzelt, *J. Electroanal. Chem.*, **93**, 183 (1978).
22. R. G. Greenler, *J. Chem. Phys.*, **44**, 310 (1966).
23. A. E. Dowrey and C. Marcott, *Appl. Spectrosc.*, **36**, 414 (1982).
24. K. Nakamoto, "Infrared and Raman Spectra of Inorganic and Co-ordination Compounds," 3rd ed., p. 172, John Wiley and Sons, New York (1978).
25. J. O'M. Bockris and A. K. N. Reddy, "Modern Electrochemistry," Vol. 1, Plenum Rosetta Edition, p. 331, Plenum Press, New York (1977).
26. K. Kunimatsu, Private communication (1983).
27. G. Horanyi and E. M. Rizmayer, *J. Electroanal. Chem.*, **36**, 496 (1972).
28. H. P. Dhar, B. E. Conway, and K. M. Joshi, *Electrochim. Acta*, **18**, 789 (1973).
29. J. O'M. Bockris, E. Gileadi, and K. Muller, *ibid.*, **12**, 1301 (1967).
30. J. D. E. McIntyre, in "Advances in Electrochemistry and Electrochemical Engineering," Vol. 9, P. Delahay and C. W. Tobias, Editors, John Wiley and Sons, New York (1973).
31. A. L. McClellan, "Experimental Dipole Moments," Vol. 2, Rahara Enterprises, El Cerrito, CA (1974).

Electrochemical Behavior of Organic Compounds at the (SN)_x Paste Electrode

Graham Cheek* and Pamela A. Horine

Naval Research Laboratory, Surface Chemistry Branch, Chemistry Division, Washington, DC 20375

ABSTRACT

The electrochemical characteristics of several types of organic compounds have been investigated at the (SN)_x paste electrode in acetonitrile/TEAP solution. The current density for reduction of benzoquinone in the presence of protons, formed either by hydroquinone oxidation or by addition of HClO₄ to benzoquinone, was found to be considerably less than that for this process at platinum or vitreous carbon. A similar effect was observed for proton reduction at (SN)_x paste, indicating, as for (SN)_x single-crystal electrodes, a high hydrogen overpotential for the electrode surface. Comparative experiments investigating the redox behavior of the benzoquinone/hydroquinone system in aqueous media at (SN)_x paste indicate that slow protonation kinetics are involved in the voltammetric behavior observed for this system. Electrochemical oxidation of representative aromatic amines and hydrocarbons (including phenothiazine, N,N-dimethyl-o-phenylenediamine, N,N-dimethylaniline, 2,3-diphenylindole, 2,3-benzanthracene, and perylene) involved behavior similar to that observed at platinum, showing that the oxidized species produced, both stable and unstable, undergo no specific interaction with the electrode surface. Oxidation of pyrrole occurs at the anodic background limit of (SN)_x paste, producing a black film on the electrode surface which has voltammetric properties similar to those of polypyrrole films formed at other electrodes. Although the heterocyclic compounds pyridine, quinoline, and acridine are not themselves oxidizable in the (SN)_x paste potential range, addition of these compounds caused the appearance of an oxidation process at a potential approximately 100 mV negative of the (SN)_x anodic background oxidation. The dependence of the current observed for the process upon heterocycle concentration indicates that the process corresponds to a shift of the (SN)_x oxidation caused by a nucleophilic interaction of the heterocycles with the (SN)_x as it undergoes oxidation. Further negative shifts in the potential for (SN)_x oxidation were observed in the presence of several alkylpyridines having greater nucleophilicities than that of pyridine itself. Addition of the less nucleophilic compound thiazole did not produce this effect. These results indicate that the oxidation of (SN)_x itself leads to the formation of rather reactive products, while the (SN)_x surface behaves essentially as a noninteracting, metallic electrode in the potential region between +0.95 and -0.40V vs. SCE, over which (SN)_x is electrochemically stable in acetonitrile.

Polythiazyl, or (SN)_x, has been studied extensively over the past several years and has been found to possess very interesting physical and chemical properties (1, 2). The high conductivity of this substance allows its use as an electrode material, and several reports have appeared describing electrochemical investigations at (SN)_x single-crystal electrodes (3-5). These studies have involved characterization of the electrodes in aqueous media by establishing potential limits for anodic and cathodic background processes (3, 4), studying the effect of alkali metal cations on these potentials (4), surface modification by metal cations (5), and observation of the electrochemical behavior of both inorganic (Pb, Ru systems) and organic species (hydroquinone) in solution (4). Recently, a more convenient electrode system has been devised in which the (SN)_x fibrils are thoroughly mixed with Apiezon M grease (6). The background potential limits for this (SN)_x paste electrode are similar to those of the (SN)_x single-crystal electrode, although the background currents are much lower at the (SN)_x paste electrode (6). Initial work on this system has shown that the cathodic background process involves the depolymerization of (SN)_x, while the anodic background process involves the oxidation of (SN)_x to as yet undetermined products (6).

It was decided to study the electrochemical behavior of a wide range of organic compounds at the (SN)_x paste electrode in order to compare the results to those obtained at other electrodes, including the (SN)_x single-crystal electrodes. It is evident from the available potential range at (SN)_x paste [+0.95 to -0.40V vs. SCE in AN/TEAP (6)] that certain classes of organic compounds which are difficult to oxidize or reduce, such as ketones, halogen-substituted compounds, conjugated π systems, etc. (7, 8), cannot be studied at this electrode. However, several classes of organic compounds, electrochemical studies of which abound, can be investigated, including aromatic amines, quinones, and certain heterocyclic systems (7, 8). Of particular interest in this study is the possibility of specific interactions between the (SN)_x paste and the organic compounds or their redox products and the corresponding effect on their electrochemical behavior. The results of these investigations are reported herein.

Experimental

Cyclic voltammetric experiments were carried out using a PAR 173 Potentiostat/Galvanostat with Model 179 Digital Coulometer (affording iR compensation), a Model 175 Universal Programmer, and a Houston 2000 X-Y recorder. Some experiments utilized a Bioanalytical Systems CV-1B electrochemical instrument and produced the same results. A PAR Model 174A Polarographic Analyzer was used for normal pulse and differential pulse voltammetric experiments. Potentials in this work are reported with respect to a NaCl SCE reference electrode.

Pyridine (99+%, Gold Label), thiazole, perylene (99+%), and 2,3-benzanthracene (tetracene) were used as received from Aldrich Chemical Company. Phenothiazine, acridine, chloranil, p-benzoquinone, and hydroquinone were recrystallized from absolute ethanol or ethanol/petroleum ether mixture. N,N-dimethylaniline and quinoline were purified by reduced-pressure distillation. 2,3-Diphenylindole was prepared and purified as described previously (9).

Acetonitrile (Burdick and Jackson) was dried over 4Å molecular sieves prior to use. Tetraethylammonium perchlorate (Southwestern Analytical Chemicals) was dried under vacuum at 70°C and stored in a desiccator over calcium sulfate.

Polythiazyl, (SN)_x, was synthesized as described previously (10). Owing to the explosion hazard associated with the S₄N₄ intermediate involved in this preparation (11), appropriate safety procedures should be followed (12). (SN)_x paste electrodes were prepared by mixing a 2:1 ratio of (SN)_x to Apiezon M grease, a composition previously found to produce optimum results (6). The paste was then packed into disposable pipettes, electrical contact being made with a platinum wire.

Results and Discussion

Quinones.—As seen in Fig. 1, the electrochemical behavior of hydroquinone (H₂Q) at the (SN)_x paste electrode is in many ways similar to that observed at platinum (13). Both curves show the oxidation of H₂Q, followed by a process on the return sweep for reduction of BQ in the presence of protons liberated upon H₂Q oxidation. In pre-

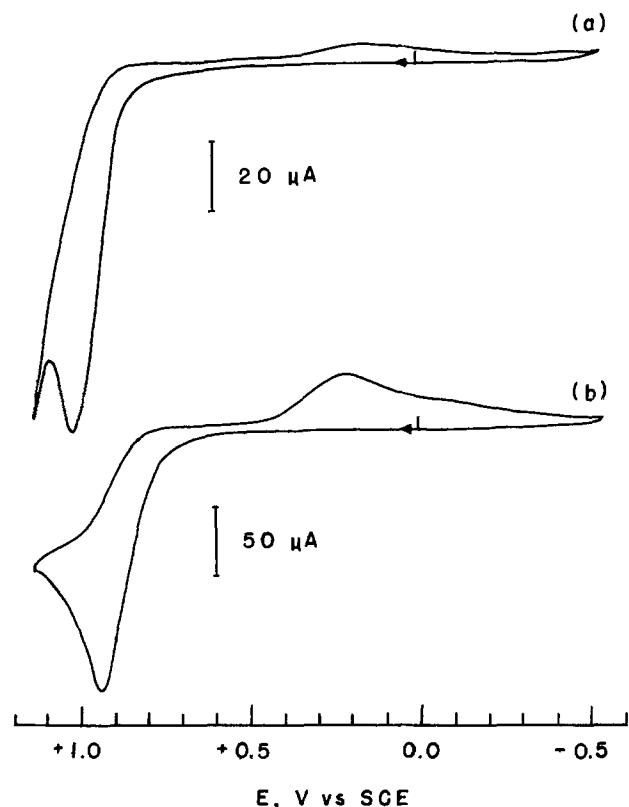


Fig. 1. Cyclic voltammograms of hydroquinone in AN at (a) $(\text{SN})_x$ paste and (b) platinum. $\text{H}_2\text{Q} = 3.0 \text{ mM}$; scan rate = 100 mV/s .

vious work at platinum (13), this reduction process was described as a "Q/H⁺ wave," indicating that the existence of protonated BQ as the predominant species in solution is in doubt. Since the same general situation is presumably involved at $(\text{SN})_x$ paste, this description of the reduction process will also be used in this work. As at platinum and vitreous carbon, the H_2Q oxidation process was found to be diffusion controlled at $(\text{SN})_x$ paste, a plot of i_p vs. $v^{1/2}$ being linear over the range $10\text{--}350 \text{ mV/s}$. In comparison to the behavior seen at platinum, however, the current response for the reduction process at $(\text{SN})_x$ paste is greatly diminished relative to that for the oxidation process. This phenomenon was also observed using reverse normal pulse voltammetry, scanning toward more negative potentials from an initial potential corresponding to E_p for H_2Q oxidation. Further experiments were carried out in order to determine the cause of the rather low current observed for the Q/H⁺ reduction process.

The proximity of the H_2Q oxidation process to the anodic background limit suggested the possible interaction of $(\text{SN})_x$ oxidation products with the oxidized quinone, thereby lowering the amount of quinone (oxidized form) available for reduction and giving rise to the above effect. In order to determine whether any of the various possible H_2Q oxidation products were involved in such an interaction, an $(\text{SN})_x$ paste electrode was cycled (100 mV/s) several times in a 2.0 mM H_2Q solution between the H_2Q redox processes. No new peaks appeared during these scans, and it was noted that the oxidation peak current on the second and successive sweeps were only slightly lower than that seen on the first sweeps. After cycling, the electrode was transferred to a fresh AN/TEAP solution. A voltammogram taken in this solution, while having a somewhat higher background current than that usually observed at a freshly prepared electrode, did not reveal any well-defined processes, the observation of which would indicate the presence of electroactive surface-bound species (14). These results indicate that a decrease in the amount of quinone at the electrode surface, caused by interaction with anodic breakdown products, does not seem to be the cause of the low current observed for Q/H⁺ reduction.

This reduction process was further investigated in both acetonitrile (AN) and aqueous media, adding 0.1 M HClO_4 as a proton source to benzoquinone (BQ) solutions. In AN, the effects of HClO_4 addition were followed at vitreous carbon and platinum electrodes and were similar to those found by previous workers (15). After addition of a 2:1 molar ratio of HClO_4 :BQ, only the Q/H⁺ process was observed at vitreous carbon and platinum. At $(\text{SN})_x$ paste, a very ill-defined reduction wave, corresponding to that seen on the return sweep in Fig. 1, was seen, the current density of which was smaller by a factor of 7 compared to that at vitreous carbon and platinum. In this study, it was assumed that the geometrical and electrochemical areas of the $(\text{SN})_x$ paste electrodes were essentially the same (6); addition of hydroquinone (H_2Q) to the solution and observation of the relative peak currents for H_2Q oxidation at the various electrodes supported this assumption. Considering the results observed at single-crystal $(\text{SN})_x$ electrodes in aqueous solutions, at which well-defined reduction processes for the protonated quinone were seen (4), it is clear that either the medium involved or the presence of the hydrocarbon (Apiezon M) in the $(\text{SN})_x$ paste has profoundly affected the reduction of the protonated quinone. It was deemed necessary to carry out further experiments in order to differentiate between these factors.

Voltammetric experiments of the $\text{H}_2\text{Q}/\text{Q}$ system at $(\text{SN})_x$ paste electrodes were also performed in aqueous media, both to allow comparison with results at $(\text{SN})_x$ single crystals (4) and to more clearly define the effect of solvent in reduction of the protonated quinone. In 1.0 M acetate buffer (pH 5) at $(\text{SN})_x$ paste, the cyclic voltammogram for the H_2Q system in Fig. 2 shows that the peak current ratio of Q/H⁺ reduction to H_2Q oxidation is similar to that for the H_2Q system at $(\text{SN})_x$ single-crystal electrodes (pH 5 acetate buffer) (4), and is much greater than that observed at $(\text{SN})_x$ paste in AN/TEAP.

Other experiments involved quinone reduction in aqueous 0.1 M KClO_4 solutions with variation of solution acidity by addition of 0.1 M HClO_4 . Cyclic voltammograms of BQ reduction at vitreous carbon (Fig. 3a), as well as at platinum, revealed a 105 mV peak separation for the reduction and oxidation processes, behavior which has been noted at platinum (16) and at carbon paste electrodes (17, 18). At $(\text{SN})_x$ paste, the voltammogram in Fig. 3b shows that the quinone reduction process is somewhat broader than that seen at vitreous carbon or platinum, while the following oxidation process is very poorly defined. It appears, however, that oxidation back to the quinone occurs very gradually during the passage through this region, since the height of the quinone reduction peak observed in the second sweep is only slightly less than that observed in the first sweep. This behavior is thought to be due to slow deprotonation kinetics at the $(\text{SN})_x$ paste electrode surface, since the corresponding results at vitreous carbon and platinum are rather uncomplicated (Fig. 3a).

Addition of 0.1 M HClO_4 to the above solution (1:1 HClO_4 :BQ) caused a shift of the reduction process at vit-

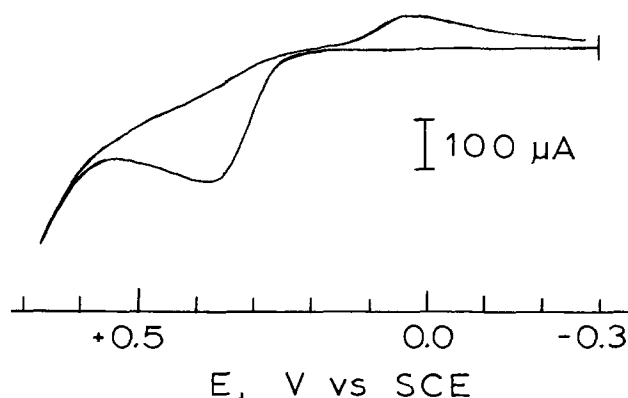


Fig. 2. Cyclic voltammogram of hydroquinone in pH 5 acetate buffer at $(\text{SN})_x$ paste. $\text{H}_2\text{Q} = 92 \text{ mM}$; scan rate = 20 mV/s .

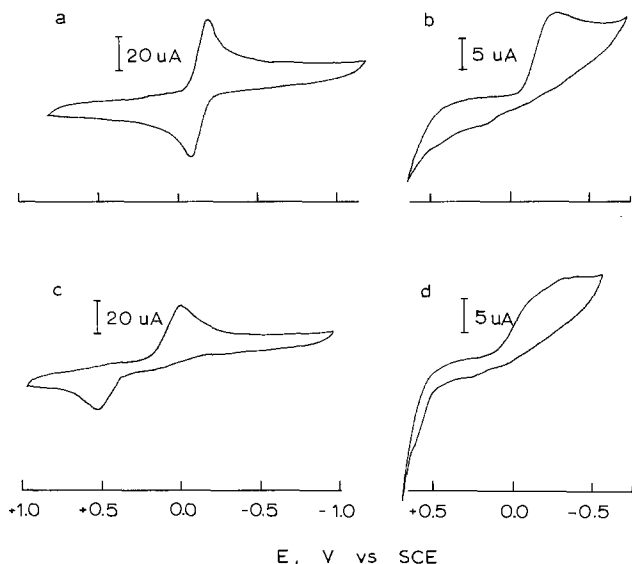


Fig. 3. Cyclic voltammograms of benzoquinone in aqueous 0.1M KClO_4 . Scans taken at: (a) vitreous carbon; (b) $(\text{SN})_x$ paste; (c) vitreous carbon, 1:1 HClO_4 :BQ; (d) $(\text{SN})_x$ paste, 1:1 HClO_4 :BQ. BQ = 1.6 mM; scan rate = 100 mV/s.

reous carbon to a more positive potential, as seen in Fig. 3c. The rather large potential separation for the redox processes indicates considerable irreversibility in the associated protonation equilibria. Voltammetry at $(\text{SN})_x$ paste (Fig. 3d) shows a very gradual reduction process, the current density for which is much higher than that seen for the Q/H^+ process at $(\text{SN})_x$ paste in AN. The reduction process consists of a broad peak, the potential of which corresponds to that for Q/H^+ reduction at vitreous carbon. Oxidation of H_2Q formed in the reduction occurs immediately before the anodic background limit, resulting in nearly identical behavior in the second cathodic sweep to that seen in the first sweep. Further addition of acid (2:1 HClO_4 :BQ) did not improve the resolution or change the relative sizes of the redox processes.

Comparison of the results found in different media provides some insight into the nature of the Q/H^+ process at $(\text{SN})_x$ paste. An important observation is that Q/H^+ reduction proceeds easily both at platinum in AN and at $(\text{SN})_x$ paste in aqueous media. It appears, then, that neither the presence of the nonpolar grease (Apiezon) used in the $(\text{SN})_x$ paste nor the relatively nonpolar AN medium can account entirely for the diminished current observed for the Q/H^+ reduction at $(\text{SN})_x$ paste in AN. The most likely explanation for this behavior is that the effects of the lower dipole moment of AN and the nonpolar character of the Apiezon grease combine to create a situation (*i.e.*, a general nonpolar environment) in which the protonation kinetics in the Q/H^+ system are slow at the electrode surface. Unfortunately, the amount of quinone not involved in the Q/H^+ process at $(\text{SN})_x$ paste could not be determined since its reduction potential (observed at vitreous carbon and platinum) is negative of the $(\text{SN})_x$ paste cathodic background limit. Further investigation in AN/ NaClO_4 solutions produced results which are similar to those in AN/TEAP, indicating that the nature of the supporting electrolyte cation is not critically involved in this effect. It is also possible that the electrode kinetics for Q/H^+ reduction are slow, as observed at platinum (13). The fact that reduction of other positively charged species (*e.g.*, *N,N*-dimethyl-*p*-phenylenediamine cation radical) at $(\text{SN})_x$ paste occurs readily, however, favors the involvement of slow protonation kinetics in the benzoquinone system.

p-Chloranil was chosen as another example in this study, since the reduction of the quinone to its anion radical is observable within the $(\text{SN})_x$ paste potential range (19). Cyclic voltammetric investigations of chloranil at $(\text{SN})_x$ paste showed reversible behavior ($\Delta E_p = 60$ mV) for the first reduction process of this system.

Aromatic amines.—In view of the wide variety of aromatic amines which have been studied at other electrodes (7, 20), a survey was also undertaken of several of these systems at $(\text{SN})_x$ paste. These systems were chosen on the basis of stability of their cation radicals, examples of both stable and unstable species being included.

Two reversible one-electron systems were observed for *N,N*-dimethyl-*p*-phenylenediamine at $(\text{SN})_x$ paste, the potentials for which were similar to those observed at Pt (Table I) (21). This result indicates that the oxidized species involved do not undergo chemical reaction with the $(\text{SN})_x$ paste surface in the potential range studied; in other words, the surface is acting as a metallic conductor with no particular affinity for the radicals produced during oxidation of this compound.

The electrochemical behavior of *N,N*-dimethylaniline (DMA) at $(\text{SN})_x$ paste was found to be very similar to that previously observed at platinum (22). The principal aspects of this oxidative pathway involve the initial production of the cation radical by oxidation, followed by a rapid coupling reaction to form benzidine, which is itself oxidized at the potential for *N,N*-dimethylaniline oxidation. At both $(\text{SN})_x$ paste and Pt electrodes, this behavior is manifested by a large DMA oxidation process, with two one-electron reversible systems at slightly less positive potentials, corresponding to benzidine redox processes. Although the peak currents for the benzidine processes at $(\text{SN})_x$ paste were slightly lower in relation to that for the primary oxidation than is the case at platinum, it is again apparent that the $(\text{SN})_x$ paste surface itself does not dramatically alter the electrochemical oxidation pathway for this system.

Heterocyclic aromatic systems.—For this class of compounds, it was found that the electrochemical behavior of those compounds electroactive within the potential range of $(\text{SN})_x$ paste was usually similar to that observed at other electrodes. Phenothiazine (Table I), for instance, was oxidized in two reversible one-electron steps at potentials close to those found at platinum (23). 2,3-Diphenylindole, the cation radical of which undergoes a rapid coupling reaction at platinum (9), was also found to be irreversibly oxidized at $(\text{SN})_x$ paste, although the product oxidation process [+1.2V at Pt (9)] could not be observed at $(\text{SN})_x$ paste.

Pyrrrole oxidation was observed at a potential corresponding to the anodic potential limit and, while no clear oxidation process was seen, led to the formation of a black deposit on the $(\text{SN})_x$ paste electrode surface. It has long been known that electrochemical oxidation of pyrrole at other electrodes produces a polymeric film on the electrodes (24), and recent work by Diaz *et al.* (25, 26) has demonstrated the formation of a conducting polypyrrole film under these conditions.

Investigation of this system on platinum by cyclic voltammetry has shown fairly well-defined processes for the redox behavior of the polypyrrole (26). The cyclic voltammetric behavior of the film on $(\text{SN})_x$ paste was found to be qualitatively similar to these previous results, the redox processes being much broader and less well-

Table I. Redox potentials for compounds studied

Compound	$E_{(\text{SN})_x}$ (V)	E_{Pt} (V)	Ref.
Hydroquinone	+0.93	+0.87	
Chloranil ^a	-0.03	-0.03	
Phenothiazine ^a	+0.60, 0.94	+0.60, 0.92	
2,3-Diphenylindole	+0.90	+0.97	(9)
<i>N,N</i> -dimethylaniline	+0.73	+0.71	(22)
<i>N,N</i> -dimethyl- <i>p</i> -phenylenediamine ^a	+0.24, 0.81	+0.16, 0.74	(21)
2,3-Benzanthracene	+0.82	+0.81	
Perylene ^b	+0.98	+0.95	

^a Denotes reversible system, for which $E = (E_{p,a} + E_{p,c})/2$. $E_{p/2}$ values are given for other systems. Potentials in this work were obtained at 100 mV/s.

^b Quasireversible system.

defined in the present case. Other characteristics of the film, such as its physical adherence and stability upon exposure to air, were similar to those of the film formed at platinum. One interesting possibility in the present work is that the concurrent oxidation of $(\text{SN})_x$ and pyrrole may have some effect on the nature of the film produced, possibly explaining the broader redox processes for the polypyrrole film formed on $(\text{SN})_x$ as compared to that at platinum.

Other heterocyclic systems, the electrochemical behavior of which were not directly observable in the $(\text{SN})_x$ paste potential range, were nevertheless found to produce an interesting effect on the anodic background process. For heterocycles such as pyridine, quinoline, and acridine, addition of these compounds to AN/TEAP solution caused the appearance of an oxidation process approximately 100 mV negative of the usual anodic potential limit. Cyclic voltammetric responses for this process were poorly resolved from the background oxidation; however, better resolution was obtained using differential pulse voltammetry (Fig. 4), the peak currents increasing linearly with increasing concentration of the heterocycles. Since the potentials ($E_{p/2}$) for quinoline and acridine oxidation at platinum occur at +1.97 and +1.58V vs. SCE (27), respectively, while pyridine gives rise to a very poorly defined oxidation process at these potentials (28), it seems likely that the observed responses at $(\text{SN})_x$ paste are not due to the oxidation of the heterocycles themselves, but are due to a lowering of the potential necessary for $(\text{SN})_x$ oxidation, caused by some sort of interaction between the $(\text{SN})_x$ and the added heterocycles. The most likely form of this interaction involves a nucleophilic attack of the heterocycle on the oxidized $(\text{SN})_x$ species, which would be positively charged. This phenomenon is analogous to the oxidation of mercury in the presence of various anions and chelating agents (29-31). This sort of "complexation" should cause the $(\text{SN})_x$ to be more easily oxidized, the extent of this effect being proportional to the amount of the heterocycle at the surface, accounting for the concentration dependence of the current observed for the process. This phenomenon was further investigated by observing the oxidation processes caused by individual pyridines in a series of alkylpyridine derivatives having various nucleophilicities. The compounds chosen for study are given in Table II, along with differential pulse voltammetric peak potentials for $(\text{SN})_x$ oxidation in the presence of these pyridines. Figure 4 illustrates the effect of these pyridines on the $(\text{SN})_x$ oxidation process. As in the case of pyridine itself, the peak heights for the processes depend linearly on concentration in the range 1-20 mM. None of these pyridines was found to be itself electrochemically active at platinum or vitreous carbon in the potential region of interest. The negative shift in peak potential for $(\text{SN})_x$ oxidation in the presence of 4-methylpyridine compared to that in the presence of pyridine itself is apparently due to the greater nucleophilicity of 4-methylpyridine with respect to that of pyridine, as has been observed in other reactions (32-33). An even larger decrease in the potential for $(\text{SN})_x$ oxidation is observed in the presence of 2,4,6-trimethylpyridine, which is expected if the trend in nucleophilicity follows that in basicity (32) [$pK_a = 5.21$ for pyridine and 7.51 for 2,4,6-trimethylpyridine in water (34)]. The potential value in the case of 2,6-dimethylpyridine seems somewhat anomalous in this

Table II. Differential pulse voltammetric peak potentials for $(\text{SN})_x$ oxidation. Effect of pyridine addition

Compound	E_p (V vs. SEC)
Pyridine	+0.99
4-Methylpyridine	+0.93
2,6-Dimethylpyridine	+0.93
2,4,6-Trimethylpyridine	+0.82

Differential pulse voltammetric conditions are as described for Fig. 4.

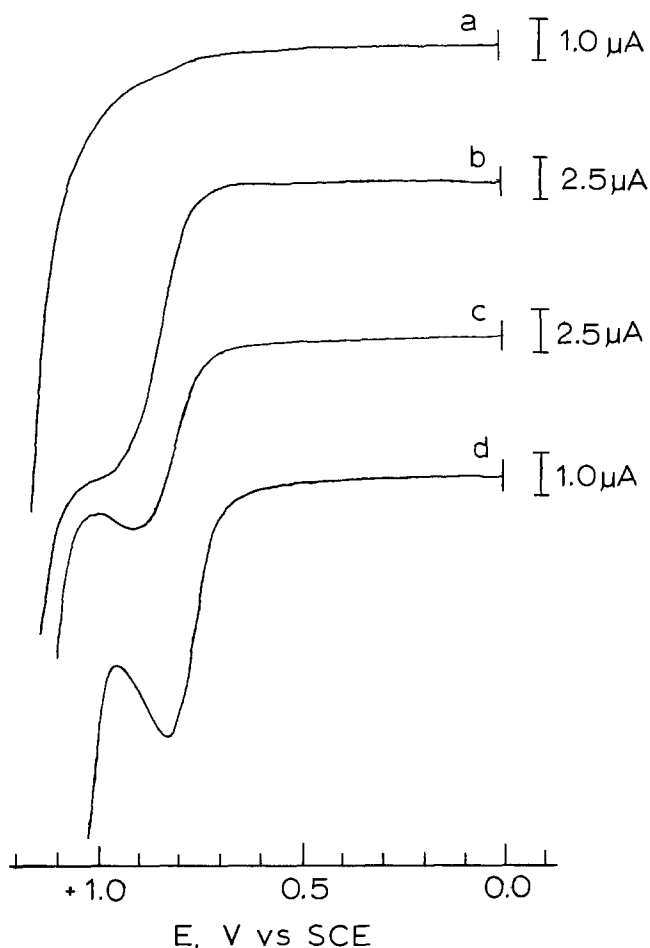


Fig. 4. Electrochemical behavior of $(\text{SN})_x$ paste in AN containing various pyridines. Differential pulse voltammograms at $(\text{SN})_x$ paste containing (a) no added pyridine (background curve), (b) 0.62 mM pyridine, (c) 0.51 mM 4-methylpyridine, and (d) 0.38 mM 2,4,6-trimethylpyridine. Scan rate = 5 mV/s; modulation = 25 mV; drop time = 0.5s.

series [$pK_a = 6.65$ in water (34)] and may reflect the predominance of steric effects for this molecule (33). The fact that addition of thiazole [$E_{1/2} = +2.2\text{V}$ at platinum (35)], a weaker nucleophile than those studied above (36), produced only a slight negative shift in the anodic potential limit (i.e., with no discernible peak) supports the above explanation that the observed shifts in potential are due to an interaction between the nucleophiles and the oxidized $(\text{SN})_x$.

Aromatic hydrocarbons.—The potentials for oxidation of aromatic hydrocarbons in nonaqueous media generally are greater than +1.0V vs. SCE (37), greatly restricting those amenable to study at $(\text{SN})_x$ electrodes. It was found, however, that oxidation of both perylene and 2,3-benzanthracene (tetracene) could be observed at +0.98 and +0.82V vs. SCE, respectively, at $(\text{SN})_x$ paste, in fairly good agreement with results obtained in the same medium at platinum electrodes (38) (Table I).

The reversible nature of the one-electron oxidation of perylene, observed in this work at platinum and vitreous carbon and in nitrobenzene by others (39), was also evident at $(\text{SN})_x$ paste, although measurements of relative anodic and cathodic peak currents could not be made, owing to the proximity of the process to the anodic potential limit. Under the present conditions, oxidation of 2,3-benzanthracene was found to be irreversible at $(\text{SN})_x$ paste as well as at platinum and vitreous carbon.

Conclusions

From the preceding discussion, it is evident that, for the $(\text{SN})_x$ paste electrode, there is no apparent interaction between the $(\text{SN})_x$ in the electrode and the oxidized or reduced solute species studied, regardless of the stability of

the initially generated species. Specific effects are observed, however, upon oxidation of the (SN)_x itself, as seen with the interaction between nitrogen heterocycles and the (SN)_x oxidation product. The low reduction current for protonated benzoquinone at (SN)_x paste in acetonitrile is thought to be due primarily to a medium effect, while the high overpotential observed for proton reduction seems to be a more general characteristic of (SN)_x since it is also observed at single-crystal (SN)_x electrodes.

Manuscript submitted Dec. 27, 1982; revised manuscript received July 30, 1984.

Naval Research Laboratory assisted in meeting the publication costs of this article.

REFERENCES

- G. B. Street and W. D. Grill, in "Molecular Metals," W. E. Hatfield, Editor, pp. 301-326, Plenum Press, New York (1979).
- F. E. Saalfeld, J. J. DeCorpo, and J. R. Wyatt, in "Extended Linear Chain Compounds," Vol. 1, J. S. Miller, Editor, pp. 50-58, Plenum Press, New York (1982).
- R. J. Nowak, H. B. Mark, Jr., A. G. MacDiarmid, and D. Weber, *J. Chem. Soc. Chem. Commun.*, 9 (1977).
- R. J. Nowak, W. Kutner, H. B. Mark, Jr., and A. G. MacDiarmid, *This Journal*, **125**, 232 (1978).
- R. J. Nowak, W. Kutner, J. F. Rubinson, A. Voulgaropoulos, and H. B. Mark, Jr., *ibid.*, **128**, 1927 (1981).
- R. J. Nowak, C. L. Joyal, and D. C. Weber, *J. Electroanal. Chem.*, **143**, 413 (1983).
- M. R. Rifi, in "Technique of Electroorganic Synthesis," N. L. Weinberg, Editor, Chap. 8, Part II, Vol. V, "Techniques of Chemistry," A. Weissberger, Series Editor, John Wiley and Sons, New York (1975).
- L. Meites and P. Zuman *et al.*, "CRC Handbook Series in Organic Electrochemistry," CRC Press, Inc., Cleveland, OH (1978).
- G. T. Cheek and R. F. Nelson, *J. Org. Chem.*, **43**, 1230 (1978).
- C. M. Mikulski, P. J. Russo, M. S. Saran, A. G. MacDiarmid, A. F. Garito, and A. J. Heeger, *J. Am. Chem. Soc.*, **97**, 6358 (1975).
- H. B. Mark, Jr., and K. J. Mulligan, *Chem. Eng. News*, **62** (5), 4 (1984).
- A. J. Banister, *Inorg. Synthesis*, **57**, 197 (1977).
- B. R. Eggers and J. Q. Chambers, *This Journal*, **117**, 186 (1970).
- R. W. Murray, *Acc. Chem. Res.*, **13**, 135 (1980).
- L. Jeftic and G. Manning, *J. Electroanal. Chem.*, **26**, 195 (1970).
- I. M. Kolthoff and J. J. Lingane, "Polarography," Vol. 1, Chap. XIX, Interscience, New York (1952).
- R. N. Adams, "Electrochemistry at Solid Electrodes," p. 366, Marcel Dekker, New York (1969).
- J. Lindquist, *J. Electroanal. Chem.*, **52**, 37 (1974).
- M. E. Peover, *J. Chem. Soc.*, 4540 (1962).
- R. N. Adams, "Electrochemistry at Solid Electrodes," Chap. 10, Marcel Dekker, New York (1969).
- R. F. Nelson, in "Techniques of Electroorganic Synthesis," N. L. Weinberg, Editor, Chap. V, p. 709, Part II, Vol. V, "Techniques of Chemistry," A. Weissberger, Series Editor, John Wiley and Sons, New York (1975).
- E. T. Seo, R. F. Nelson, J. M. Fritsch, L. S. Marcoux, D. W. Leedy, and R. N. Adams, *J. Am. Chem. Soc.*, **88**, 3498 (1966).
- J. P. Billon, *Bull. Soc. Chim. Fr.*, 1923 (1961).
- J. W. Loveland and G. G. Dimeler, *Anal. Chem.*, **33**, 1196 (1961).
- K. K. Kanazawa, A. F. Diaz, R. H. Geiss, W. D. Grill, J. F. Kwak, J. A. Logan, J. F. Rabolt, and G. B. Street, *J. Chem. Soc. Chem. Commun.*, 854 (1979).
- A. F. Diaz and J. I. Castillo, *ibid.*, 397 (1980).
- L. Marcoux and R. N. Adams, *J. Electroanal. Chem.*, **49**, 111 (1974).
- H. Lund, in "Organic Electrochemistry," M. Baizer and H. Lund, Editors, p. 553, Marcel Dekker, New York (1983).
- M. Wojciechowski and J. Osteryoung, *Anal. Chem.*, **54**, 1713 (1982).
- W. F. Smyth, G. Svehla, and P. Zuman, *Anal. Chim. Acta*, **52**, 129 (1970).
- K. Niki, K. Suzuki, G. P. Sato, and N. Mori, *J. Electroanal. Chem.*, **49**, 27 (1974).
- J. A. Zoltewicz and H. L. Jacobson, *Tetrahedron Lett.*, 189 (1972).
- H. C. Brown and A. Cahn, *J. Am. Chem. Soc.*, **77**, 1715 (1955).
- D. L. Perrin, "Dissociation Constants of Organic Bases in Aqueous Solutions," Butterworths, London (1965).
- J. Bonnier, P. Arnaud, and M. Maurey-Mey, *C. R. Acad. Sci. Ser. C*, **267**, 10 (1968).
- F. Filippini and R. F. Hudson, *J. Chem. Soc. Chem. Commun.*, 522 (1972).
- H. Siegeman, "Techniques of Electroorganic Synthesis," N. L. Weissberger, Editor, Appendix, p. 690, John Wiley and Sons, New York (1975).
- E. S. Pysh and N. C. Yang, *J. Am. Chem. Soc.*, **85**, 2124 (1963).
- L. S. Marcoux, J. M. Fritsch, and R. N. Adams, *ibid.*, **89**, 5766 (1967).

Characterization of Chloroclosoborane Acids as Electrolytes for Acid Fuel Cells

M. W. Rupich,* J. S. Foos,* and S. B. Brummer*

EIC Laboratories, Incorporated, Norwood, Massachusetts 02062

ABSTRACT

The perchloroclosoborane acids, H₂B₁₂Cl₁₂ and H₂B₁₀Cl₁₀, were prepared in high purity and investigated as alternative electrolytes to H₃PO₄ in moderate temperature acid fuel cells. Procedures were developed for the purification of the acids prepared from commercially available salts. The purified acids were characterized by infrared, electronic, NMR, and mass spectroscopy. Concentrated aqueous solutions of the acids were found to have low ionic conductivity and a moderate water vapor pressure. The mono anions, B₁₂Cl₁₂⁻ and B₁₀Cl₁₀⁻, formed from reactions of concentrated aqueous solutions or the solid hydrates of the acids. The B₁₂Cl₁₂²⁻ and B₁₀Cl₁₀²⁻ anions were also found to adsorb on electrocatalytic Pt surfaces.

One approach to improving fuel cell performance is to find an electrolyte which is superior to H₃PO₄. In particular, it would be advantageous to find an electrolyte which would allow for more efficient oxidation of H₂/dirty H₂ and more efficient reduction of O₂. This would result in superior fuel cell performance and expand the range of

* Electrochemical Society Active Member.

acceptable fuels. In addition, any electrolyte which replaces H₃PO₄ in an acid fuel cell must meet the following requirements: good ionic conductivity, thermal stability in solution to ≥200°C, electrochemical stability between 0.0 and 1.0V (RHE), low vapor pressure and high viscosity, and preferably compatibility with existing fuel cell components.

Two materials we have evaluated as alternative electrolytes are the inorganic acids $H_2B_{12}Cl_{12}$ and $H_2B_{10}Cl_{10}$. The chloroclosoborane anions, $B_{12}Cl_{12}^{2-}$ and $B_{10}Cl_{10}^{2-}$, are two examples of a unique class of inorganic compounds characterized by their exceptional stability. The structure of the anions consists of clusters of borons each attached to a terminal Cl^- , as shown in Fig. 1. The reported properties of the chloroclosoboranes include exceptional thermal stability (some alkali metal salts are stable to $>600^\circ C$), good chemical and electrochemical stability, and high solution conductivities (1-7). The acids, $H_2B_{12}Cl_{12}$ and $H_2B_{10}Cl_{10}$, have been characterized as stronger than H_2SO_4 (1). The reported properties of these chloroclosoborane anions suggested that their acids may be useful as electrolytes in acid fuel cells. In this paper, we report on the preparation, purification, and characterization of $H_2B_{12}Cl_{12}$ and $H_2B_{10}Cl_{10}$.

Experimental

Synthesis and purification of $H_2B_{12}Cl_{12}$.— $H_2B_{12}Cl_{12}$ was prepared from $Li_2B_{12}Cl_{12}$ purchased from Callery Chemical Company. Analyses of two lots of as-received $Li_2B_{12}Cl_{12}$ found B-to-Cl stoichiometries of $B_{12}Cl_{11.6}$ and $B_{12}Cl_{9.4}$, indicating incomplete chlorination of the B_{12} cage. The samples also contained varying amounts of organics, which were predominantly decomposition products of triethylamine used in the synthesis of $Li_2B_{12}Cl_{12}$ (8).

$Li_2B_{12}Cl_{12}$ was purified and converted to the acid as follows: an aqueous solution of $Li_2B_{12}Cl_{12}$ was passed over neutral alumina resulting in the removal of the organic contaminants. The resulting solution was then converted to the acid by passage over an acidic Dowex 50W-X8 cation exchange resin ($<30\%$ of the column capacity was utilized) or by electrolysis across a Nafion 125 membrane (du Pont). Chlorine gas was then passed through the aqueous acid solution at $85^\circ-90^\circ C$ for 6h, resulting in complete chlorination of the B_{12} cage. Excess Cl_2 was removed by purging the solution with N_2 at $85^\circ C$. The H_2O and HCl were removed under vacuum at $\leq 80^\circ C$, leaving a white, hygroscopic solid. Elemental analysis of the white solid established a B-to-Cl stoichiometry of 1.0. A potentiometric titration and gravimetric analysis established the overall composition of $H_2B_{12}Cl_{12} \cdot 8H_2O$. (Infrared (cm^{-1}): 3620(S), 3440(M), 1610(M), 1220(W), 1030(S), 850(M), 730(W), 650(W), and 540(S). ^{11}B NMR (CD_3CN): $\delta + 12.9$).

Synthesis and purification of $H_2B_{10}Cl_{10}$.— $H_2B_{10}Cl_{10}$ was prepared from $Li_2B_{10}Cl_{10}$ (Callery Chemical Company) using the same procedure as described for $H_2B_{12}Cl_{12}$. The chlorination step was not necessary with the $Li_2B_{10}Cl_{10}$. The composition of the final product was $H_2B_{10}Cl_{10} \cdot 7.5H_2O$. (Infrared (cm^{-1}): 3620(S), 3420(M), 1610(M), 1160(M); sh. at 1190), 1010(S), 855(M), and 535(S). ^{11}B NMR (CD_3CN): $\delta + 5.3$ and 10.6 with a ratio of 1:4.)

Vapor pressure and conductance measurements.—The water vapor pressure-saturation concentration relationship and conductance measurements of aqueous solutions of $H_2B_{12}Cl_{12}$ were obtained at temperatures between 110° and $150^\circ C$. During an experiment, $N_2(g)$ was saturated with a specified H_2O vapor pressure, and then bubbled through a solution of the acid contained in a sealed cell thermostated at a set temperature. The $N_2(g)$ finally

passed through a trap, where any volatile acidic species were trapped. A capillary conductance cell (cell constant of 220 cm^{-1}) built into the flask allowed *in situ* measurement of the ionic conductivity of the $H_2B_{12}Cl_{12}$ solution. Standardization measurements with H_3PO_4 were in excellent agreement with literature values.

Instrumental analysis.—Infrared spectra were recorded on a Beckman Acculab II spectrophotometer. Solid samples were analyzed in KBr disks or Nujol mulls. Mass spectral data were obtained with a Nuclide 1290G mass spectrophotometer at Biomeasure, Incorporated (Hopkinton, Massachusetts). NMR spectra were acquired with a Joel FX-90Q spectrophotometer in either D_2O or CD_3CN (also at Biomeasure). Chemical shifts were referenced to TMS (1H and ^{13}C spectra) or external $^{11}BF_3 \cdot O(C_2H_5)_2$ (^{11}B spectra). Conductivity data were recorded on a YSI Model 30 conductivity bridge at 1000 Hz. Electronic spectra were recorded on a Cary 14 or Shimadzu 210 spectrophotometer in 1 cm matched quartz cells.

Cyclic voltammetry experiments were performed with a PAR Model 173 potentiostat and a PAR Model 175 universal programmer. Data were recorded on a Bascom-Turner Model 4120 electronic recorder. The electrochemical cell consisted of a three-neck flask with a volume of approximately 15 ml. The working electrode was a Pt wire, and the counterelectrode was a Pt loop. The reference electrode was a H_2 gas electrode.

Chemical analyses.—The concentration of $H_2B_{12}Cl_{12}(aq)$ and $H_2B_{10}Cl_{10}(aq)$ was determined by potentiometric titration with standard 0.1N NaOH. The $B_{12}Cl_{12}^{2-}$ ion was also determined gravimetrically as $[(C_2H_5)_4N]_2B_{12}Cl_{12}$. Chloride (to ~ 0.1 ppm) was detected by precipitation as $AgCl$ in alcoholic solution. Elemental analyses were performed by Galbraith Laboratories, Incorporated, Knoxville, Tennessee. All water used was doubly distilled from Barnstead tin stills, then distilled from alkaline permanganate in an all glass system and stored under N_2 .

Results and Discussion

Characterization of $H_2B_{12}Cl_{12}$ and $H_2B_{10}Cl_{10}$.—The purity of the acids was established by chemical and spectral methods. The infrared spectrum of $H_2B_{12}Cl_{12} \cdot 8H_2O$ is shown in Fig. 2. The absence of a B-H absorption in the 2400 cm^{-1} region and the sharpness of the absorption at 540 cm^{-1} confirm the complete chlorination of the B_{12} cage (1, 5). The ^{11}B NMR spectrum of $H_2B_{12}Cl_{12}$ displays only the absorption at 12.9 ppm reported in the literature for $B_{12}Cl_{12}^{2-}$ (1, 9). 1H and ^{13}C NMR spectra of concentrated solutions of $H_2B_{12}Cl_{12} \cdot 8H_2O$ in CD_3CN indicated the level of organics was $<0.01\%$. The electronic spectrum of $H_2B_{12}Cl_{12}(aq)$ prepared with the described procedure, has a weak absorption at 224 nm ($\epsilon < 200\text{ M}^{-1}\text{ cm}^{-1}$).

The complete chlorination of the B_{10} cage was confirmed by the absence of any absorption due to B-H in the infrared spectrum of $H_2B_{10}Cl_{10} \cdot 7.5H_2O$ (1, 5) and by the absence of any B-H resonance in its ^{11}B NMR spectrum (1, 9). The electronic spectrum of $H_2B_{10}Cl_{10}(aq)$ has a maximum at 224 nm ($\epsilon 10,900\text{ M}^{-1}\text{ cm}^{-1}$).

Conductivity and vapor pressure measurements.—Water vapor pressure-saturation-concentration relationships and conductivity measurements were obtained on aqueous solutions of $H_2B_{12}Cl_{12}$ at temperatures between 110° and $150^\circ C$ and water vapor pressures of 250-600 torr. The results are presented in Table I. At $140^\circ C$ and a water vapor pressure of <600 torr, the solution was very viscous. At temperatures $>145^\circ C$, the solution solidified.

No volatile, acidic species were detected coming from the solution during the measurements below $145^\circ C$. During the measurements, the initially colorless solution darkened. The solution, at the end of the measurements, had the electronic spectrum shown in Fig. 3. Gel permeation chromatography (Bio-Beads S-X8 resin) of the aqueous solution did not indicate multiple components. Chemical tests for Cl^- were negative. The infrared spectrum of the solid, after removal of the excess H_2O , is virtually identical to that of the starting material.

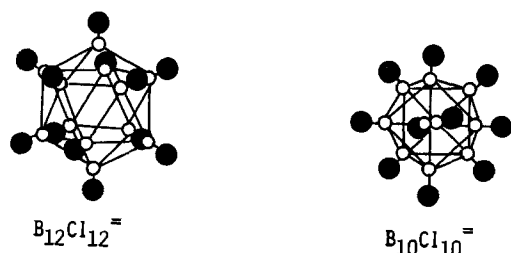


Fig. 1. Structures of the $B_{12}Cl_{12}^{2-}$ and $B_{10}Cl_{10}^{2-}$ anions

Fig. 2. Infrared spectrum of $\text{H}_2\text{B}_{12}\text{Cl}_{12} \cdot 8\text{H}_2\text{O}$ in KBr

After extended measurements at $>150^\circ\text{C}$ a water-insoluble, black material formed along with free Cl^- . The infrared spectrum of the insoluble, black material contains absorptions at 1030 cm^{-1} , indicating retention of the B_{12} cage structure (1, 3). In addition, the infrared spectrum shows absorptions characteristic of B—O bonds at $\sim 1450\text{ cm}^{-1}$. The material was not characterized further, but is probably a polymeric oxygen bridged species such as $(-\text{B}_{12}\text{Cl}_{10}\text{O})_n$ (3, 7).

Chemical and thermal stability.—The solid hydrates and concentrated solutions of both $\text{H}_2\text{B}_{12}\text{Cl}_{12}$ and $\text{H}_2\text{B}_{10}\text{Cl}_{10}$ partially decompose when heated above 100°C . $\text{H}_2\text{B}_{12}\text{Cl}_{12} \cdot 8\text{H}_2\text{O}$, which is initially colorless, turns tan within 1-2h, then progressively darkens when heated to 150°C under vacuum. No infrared detectable gases form during this process. The resulting brown, hygroscopic solid analyzes as the tetrahydrate $\text{H}_2\text{B}_{12}\text{Cl}_{12} \cdot 4\text{H}_2\text{O}$. The infrared spectrum of $\text{H}_2\text{B}_{12}\text{Cl}_{12} \cdot 4\text{H}_2\text{O}$ is virtually identical to that of $\text{H}_2\text{B}_{12}\text{Cl}_{12} \cdot 8\text{H}_2\text{O}$, except for the O—H bands in the $3400\text{--}3600\text{ cm}^{-1}$ region. The ^1H and ^{11}B NMR spectra of the tetrahydrate are indistinguishable from those of $\text{H}_2\text{B}_{12}\text{Cl}_{12} \cdot 8\text{H}_2\text{O}$.

When $\text{H}_2\text{B}_{12}\text{Cl}_{12} \cdot 4\text{H}_2\text{O}$ is dissolved in H_2O , the initially brown solution turns violet over a 24h period. The UV spectrum of the tetrahydrate has a maximum at 224 nm , with an intensity that varies from sample to sample.

$\text{H}_2\text{B}_{10}\text{Cl}_{10} \cdot 7.5\text{H}_2\text{O}$ behaves similarly. Heating of $\text{H}_2\text{B}_{10}\text{Cl}_{10} \cdot 7.5\text{H}_2\text{O}$ to between 100° and 160°C results in a violet solid that analyzes as the tetrahydrate, $\text{H}_2\text{B}_{10}\text{Cl}_{10} \cdot 4\text{H}_2\text{O}$. The infrared spectrum of the tetrahydrate is virtually identical to that of $\text{H}_2\text{B}_{10}\text{Cl}_{10} \cdot 7.5\text{H}_2\text{O}$.

The violet color of the tetrahydrate rapidly disappears upon dissolution in H_2O or exposure to air. However, the color remains for 5-10 min in acetonitrile. The violet solution has maxima at 596 and 421 nm , in a ratio of 2.1 to 1, and at 224 nm . This is the same as that of the monoanion, $\text{B}_{10}\text{Cl}_{10}^-$ which can be prepared by the $1e^-$ oxidation of $\text{Li}_2\text{B}_{10}\text{Cl}_{10}$ in acetonitrile (4).

Table I. Specific conductivity ($1/\Omega\text{-cm}$) of $\text{H}_2\text{B}_{12}\text{Cl}_{12}$ and H_2O vapor pressure (mm Hg) over $\text{H}_2\text{B}_{12}\text{Cl}_{12}$

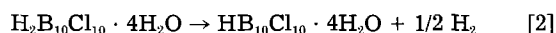
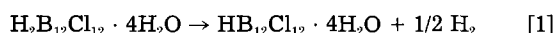
110°C			133°C		
Vapor pressure	w/o $\text{H}_2\text{B}_{12}\text{Cl}_{12}$	Specific conductivity	Vapor pressure	w/o $\text{H}_2\text{B}_{12}\text{Cl}_{12}$	Specific conductivity
250	51.9	0.160	500	52.4	0.206
500	47.5	0.360	600	51.3	0.239
600	47.0	0.373			

We believe the changes in $\text{H}_2\text{B}_{12}\text{Cl}_{12}$ and $\text{H}_2\text{B}_{10}\text{Cl}_{10}$ during heating result from dehydration of the acids. To verify this, solutions of $\text{H}_2\text{B}_{10}\text{Cl}_{10} \cdot 7.5\text{H}_2\text{O}$ and $\text{H}_2\text{B}_{12}\text{Cl}_{12} \cdot 8\text{H}_2\text{O}$ in acetonitrile were dried by passage over 4 \AA molecular sieves. The spectra of the resulting pale violet solutions were that of the $\text{B}_{10}\text{Cl}_{10}^-$ and presumably the $\text{B}_{12}\text{Cl}_{12}^-$ monoanions, respectively.

$\text{H}_2\text{B}_{12}\text{Cl}_{12} \cdot 8\text{H}_2\text{O}$ and $\text{H}_2\text{B}_{10}\text{Cl}_{10} \cdot 7.5\text{H}_2\text{O}$ can also be dehydrated to the tetrahydrates at room temperature by storing them over P_2O_5 under vacuum. Over a 1-2 week period, the solids obtain the violet color of the monoanions. The violet color rapidly fades upon exposure to the atmosphere.

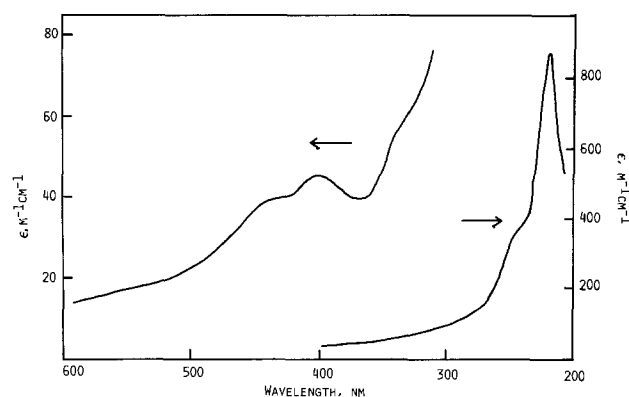
In contrast, dilute ($0.2M$) aqueous solutions of $\text{H}_2\text{B}_{12}\text{Cl}_{12}$ are indefinitely stable when stored in sealed tubes at 110°C .

The intensities of the visible absorptions of the monoanions indicate that $\text{H}_2\text{B}_{12}\text{Cl}_{12} \cdot 4\text{H}_2\text{O}$ and $\text{H}_2\text{B}_{10}\text{Cl}_{10} \cdot 4\text{H}_2\text{O}$ are not quantitatively converted to the monoanions under any of the above conditions. The formation of the monoanions can be explained by the disproportionation reactions



Reactions that may involve similar mechanisms have been reported with the hydrides, $\text{H}_2\text{B}_{12}\text{H}_{12}$ and $\text{H}_2\text{B}_{10}\text{H}_{10}$ (10).

The insoluble precipitate observed in the conductivity-vapor pressure measurements of $\text{H}_2\text{B}_{12}\text{Cl}_{12}(\text{aq})$ likely

Fig. 3. Electronic spectrum of an aqueous solution of $\text{H}_2\text{B}_{12}\text{Cl}_{12}$ after conductivity and water vapor pressure measurements at temperatures between 110° and 140°C .

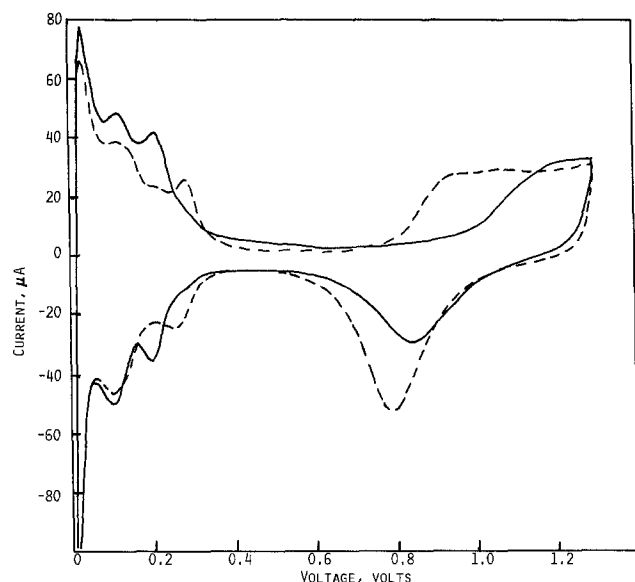
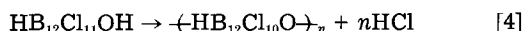


Fig. 4. Cyclic voltammograms of 50 mM $\text{H}_2\text{B}_{12}\text{Cl}_{12}$ in 0.5M H_2SO_4 (—) and 0.5M H_2SO_4 (---) on a Pt wire electrode at a scan rate of 20 mV/s vs. RHE.

formed from reactions of the monoanion such as (6, 10, 11)



The differences in the reaction of $\text{HB}_{12}\text{Cl}_{12}$ and $\text{HB}_{10}\text{Cl}_{10}$ with water and the resultant products reflect the differences in the electronic properties of the B_{12} and B_{10} structures which have been found with the hydrides (1, 10, 11). The final products of these reactions, which depend on the experimental conditions, were not investigated.

The formation of the violet color upon dehydration of $\text{H}_2\text{B}_{10}\text{Cl}_{10} \cdot 7.5\text{H}_2\text{O}$ to the tetrahydrate has been reported previously, but was attributed to unknown impurities in the material (12, 13).

Solid-probe mass spectral analysis of $\text{H}_2\text{B}_{12}\text{Cl}_{12} \cdot 8\text{H}_2\text{O}$ and $\text{H}_2\text{B}_{10}\text{Cl}_{10} \cdot 7.5\text{H}_2\text{O}$ shows that both decompose below 200°C. The most intense mass ion peaks in the $\text{H}_2\text{B}_{12}\text{Cl}_{12}$ spectrum correspond to HCl (m/e of 36) and B_8Cl_6 (m/e of 298). The major mass ion peaks from $\text{H}_2\text{B}_{10}\text{Cl}_{10}$ correspond to HCl (m/e of 36), BCl_2 (m/e of 81), and B_9Cl_7 (m/e of 344). Both compounds show other mass peaks which can be assigned to various B_xCl_y fragments. It should be noted that the experimental setup prohibited measurement of m/e values of <20 . Thus the formation of H_2 , as suggested in Eq. [1] and [2], was not verified.

Electrochemical characterization of $\text{H}_2\text{B}_{12}\text{Cl}_{12}$ and $\text{H}_2\text{B}_{10}\text{Cl}_{10}$.—A cyclic voltammogram of a solution of 50 mM $\text{H}_2\text{B}_{12}\text{Cl}_{12}$ and 0.5M H_2SO_4 on a Pt electrode is shown in Fig. 4, along with a cyclic voltammogram of 0.5M H_2SO_4 . The suppression of the formation of the oxide layer on the Pt and the shift in the potential of the hydrogen reduction and oxidation peaks is characteristic of anionic absorption on the Pt surface.

The electrochemical behavior of solutions of $\text{H}_2\text{B}_{10}\text{Cl}_{10}$ is similar to that of $\text{H}_2\text{B}_{12}\text{Cl}_{12}$. The $\text{B}_{10}\text{Cl}_{10}^{2-}$ anion can be oxidized at very anodic potentials in aqueous media on a Pt electrode. The oxidation product is the violet monoanion $\text{B}_{10}\text{Cl}_{10}^-$, which rapidly decomposes in aqueous media.

Conclusions

The low decomposition temperature of the acids is in contrast to that of the alkali metal salts which are stable to $>200^\circ\text{C}$ (1) and to previous reports on the thermal stability of the acids (7, 13). The greater stability of the alkali metal salts is the result of the cations which are not easily reducible (10). Thus the analogous reactions [1] and [2] do not occur at $<200^\circ\text{C}$, even with the anhydrous salts. However, with H^+ as the cation, these reactions become favorable as the water of hydration is removed. It can also be expected that similar reactions may occur with alkali metal salts when used in reducible, nonaqueous solvents such as $\text{SO}_2(\text{l})$ under the proper conditions (14).

In conclusion, it appears that $\text{H}_2\text{B}_{12}\text{Cl}_{12}$ and $\text{H}_2\text{B}_{10}\text{Cl}_{10}$ are not attractive for use as alternative electrolytes to H_3PO_4 in acid fuel cells.

Acknowledgment

The authors wish to thank the Electric Power Research Institute for their support of the research reported in this paper.

Manuscript submitted April 2, 1984; revised manuscript received July 27, 1984. This was Paper 401 presented at the Washington, DC, Meeting of the Society, Oct. 9-14, 1983.

REFERENCES

- W. H. Knoth, H. C. Miller, J. C. Sauer, J. H. Balthis, Y. T. Chia, and E. L. Muettterties, *Inorg. Chem.*, **3**, 159 (1964).
- R. L. Middaugh, in "Boron Hydride Chemistry," E. L. Muettterties, Editor, Chap. 8, Academic Press, New York (1975).
- N. T. Kuznetsov, L. N. Kulikova, and V. I. Faerman, *Acad. Nauk SSSR Neorg. Mater.*, **12**, 1212 (1976).
- W. Bowden, *This Journal*, **129**, 1249 (1982).
- J. W. Johnson and J. F. Brody, *ibid.*, **129**, 2213 (1982).
- S. Trofimenko, *J. Am. Chem. Soc.*, **88**, 1899 (1966).
- L. N. Kulikova, N. T. Kuznetsov, I. V. Lappo, and S. T. Zhukov, *Russ. J. Inorg. Chem.*, **21**, 509 (1976).
- C. R. Schlaikjer, in "Proceedings of the 28th Power Sources Symposium," Atlantic City, NJ, June 12-15, 1978, The Electrochemical Society, Inc., p. 241 (1979).
- G. R. Eaton and W. N. Lipscomb, "NMR Studies of Boron Hydrides and Related Compounds," Editors, pp. 241-267, W. A. Benjamin, Inc., New York (1969).
- E. L. Muettterties, J. H. Balthis, Y. T. Chia, W. H. Knoth, and H. C. Miller, *Inorg. Chem.*, **3**, 444 (1964).
- W. H. Knoth, J. C. Sauer, D. C. England, W. R. Hertler, and E. L. Muettterties, *J. Am. Chem. Soc.*, **86**, 3973 (1964).
- J. A. Forstner, T. E. Haas, and E. L. Muettterties, *Inorg. Chem.*, **3**, 155 (1964).
- D. A. Saulys, N. A. Kutz, and J. A. Morrison, *ibid.*, **22**, 1821 (1983).
- K. M. Abraham and L. Pitts, Final Report on NSW Contract N60921-82-C-0178 (1983).

Electrical Conduction in AgI-Al₂O₃ Composites

P. Chowdhary, V. B. Tare, and J. B. Wagner, Jr.*

Center for Solid State Science, Departments of Chemistry, Mechanical, and Aerospace Engineering and Physics, Arizona State University, Tempe, Arizona 85287

A dispersion of submicron size γ -Al₂O₃ particles in the matrix of an ionic solid is known to enhance the electrical conductivity of such a matrix by several orders of magnitude (1, 2). Although the importance of surface area of the dispersoid has been realized, the precise mechanism of enhancement of conduction has not yet been established. Recently, Khandkar and Wagner (3) suggested that the enhanced condition in AgCl-Al₂O₃ composites is possibly due to the presence of additional silver ion vacancies at the AgCl-Al₂O₃ interface because of the space-charge layer. The effect of the dispersion of γ -Al₂O₃ in AgI on the electrical conductivity of the composite has been investigated by Shahi and Wagner (4). The work reported in the present paper is an extension of that work and involves measurement of ac electrical conductivity as a function of temperature and concentration of Al₂O₃ of 0.06 and 0.3 μ m diam, with an emphasis on the changes in the transformation temperature of β -AgI to α -AgI during heating and cooling cycles for various AgI-Al₂O₃ compositions.

AgI, 99.999% pure, was purchased from Aldrich Chemicals. Agglomerate-free γ -Al₂O₃, 0.06 and 0.3 μ m diam and 99.8% pure, was obtained from Adolf Meller Company. The surface area of this alumina was determined independently by the BET method and was 80 and 22 m²/g for 0.06 and 0.3 μ m diam alumina, respectively. The sample preparation technique and the cell assembly used for conductivity measurements were the same as reported in Ref. (4), except that in the present study all the Al₂O₃ was used in the as-received condition, *i.e.*, not dried. The Al₂O₃ contains about 3 weight percent (w/o) moisture. Before starting measurements the pellets were annealed under argon in the cell at 160°C for 24h. For the measurements, the temperature was varied at random while cooling as well as while heating. The conductivity was measured at each temperature after allowing at least one hour after the previous change in temperature. Measurements were found to be reproducible with respect to several heating and cooling cycles for the same pellet in the temperature range 25°-200°C. Similarly, the conductivity was measured on at least two pellets of the same composition.

Figure 1 shows the variation of $\ln \sigma T$ (σ is the conductivity, and T the temperature in K) of pure AgI and AgI containing 10 and 20 mole percent (m/o) (0.06 and 0.3 μ m) as a function of reciprocal temperature in the temperature range 25°-200°C. The arrows indicate the heating and cooling cycles. Although the conductivity data for a large number of AgI-Al₂O₃ compositions with concentration of Al₂O₃ varying from 0 to 40 m/o have been obtained, data for only two compositions are shown in Fig. 1 for clarity. The sudden change in conductivity at \sim 148°C is due to the transformation of β -AgI to α -AgI. Log σ of (β -AgI + Al₂O₃) at 25°C as well as (α -AgI + Al₂O₃) at 200°C is shown in Fig. 2 as a function of mole percent as well as volume percent Al₂O₃ of 0.06 and 0.3 μ m particle sizes. As expected, the dispersion of Al₂O₃ increases the conductivity of the composite at 25°C with a maximum in conductivity at 30 m/o Al₂O₃. For a given amount of Al₂O₃ added, enhanced conduction is larger for composites containing

0.06 μ m particles than for the 0.3 μ m particles. At 200°C, where only α -AgI is stable, the dispersion of Al₂O₃ decreases the conductivity. The absolute magnitude of the decrease in conductivity is, however, much smaller than the corresponding increase in conductivity of β -AgI at 25°C under similar conditions. Similarly, this decrease appears larger than can be accounted for by the decrease in the volume fraction of AgI as a result of dispersion of Al₂O₃. The conductivities of all the composites are less than that of pure α -AgI. However, the conductivities are of the order of 1 Ω^{-1} cm⁻¹ so small experimental errors and resistances of lead wires contribute significantly. Consequently, two of the decreases for α -AgI(Al₂O₃) are not in the same order as the increases for β -AgI(Al₂O₃) (see Fig. 1). The temperature of transformation of β -AgI as noted from the sudden change in conductivity remains unchanged at 148°C during the heating cycle for pure AgI as well as the AgI-Al₂O₃ composites. During cooling, however, this temperature is found to be lower than 148°C for the composites. The difference in the transformation temperature obtained from heating and cooling cycles, ΔT , increases linearly with increase in mole percent of Al₂O₃ (see Fig. 3). For the same concentration of Al₂O₃, ΔT is smaller for samples containing 0.3 μ m Al₂O₃ than for samples containing 0.06 μ m Al₂O₃. Figure 4 shows the variation of ΔT with the surface area of Al₂O₃ per gram of AgI for samples containing 0.06 μ m as well as 0.3 μ m Al₂O₃. The linear change in ΔT indicates that, irrespective of the particle size, the ΔT is same for same surface area of the

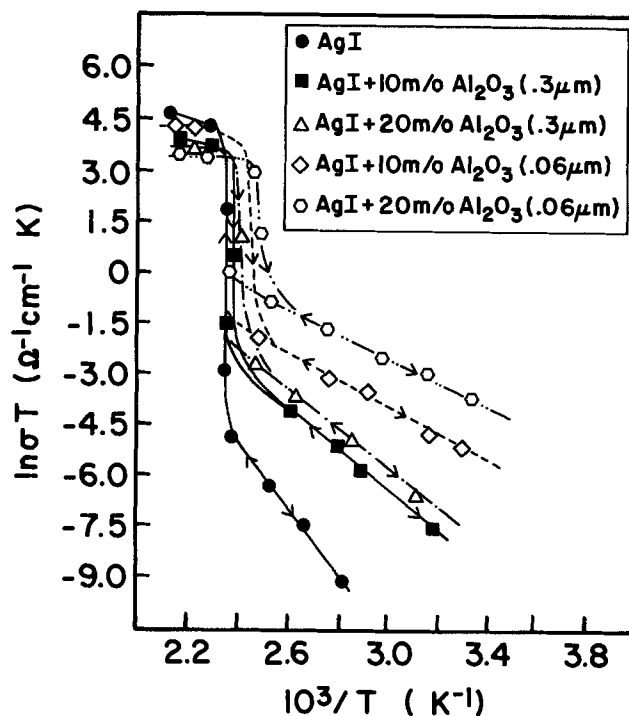


Fig. 1. $\ln \sigma T$ vs. $10^3/T$ for AgI-Al₂O₃ system

*Electrochemical Society Active Member.

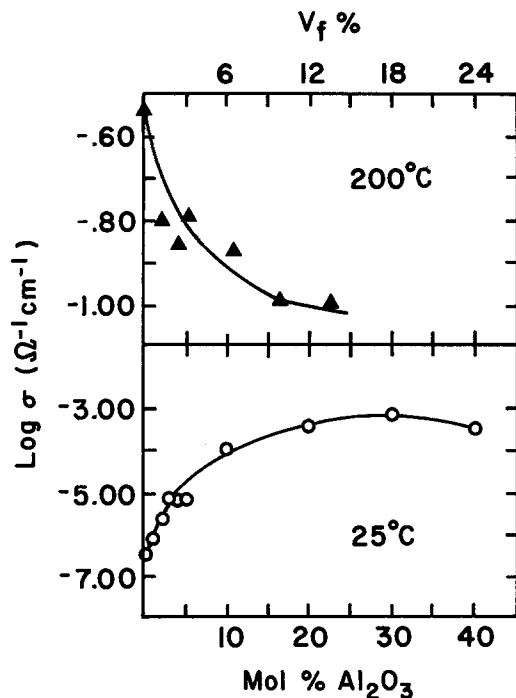


Fig. 2. Log σ vs. v/o and m/o Al_2O_3 ($0.06 \mu\text{m}$)

dispersoid. The role of interfacial area in two-phase mixtures in explaining the enhancement in conduction has been realized by earlier investigators. Khandkar and Wagner (3) suggested that additional silver ion vacancies are generated at the $\text{AgCl}/\text{Al}_2\text{O}_3$ interface and these contribute significantly to the enhancement in conduction. Thermoelectric measurements on $\text{AgI}-\text{Al}_2\text{O}_3$ composites reported by Shahi and Wagner (4) also suggest that at lower temperatures ($\sim 25^\circ\text{C}$) enhancement in conduction is predominantly due to the presence of silver ion vacancies.

Rice *et al.* (5) suggested that the interaction of the cation interstitials with the strain field associated with the volume change was the principal factor responsible for the phase transition. Consequently, a critical concentration of silver ion interstitials is essential to drive the transition from α - AgI to β - AgI , or conversely.

AgI exhibits a Frenkel disorder. We assume that the dispersion of Al_2O_3 in AgI is associated with additional cation vacancies at the $\text{AgI}/\text{Al}_2\text{O}_3$ interface for both the α - and the β - AgI . At high temperatures, α - AgI has the so-

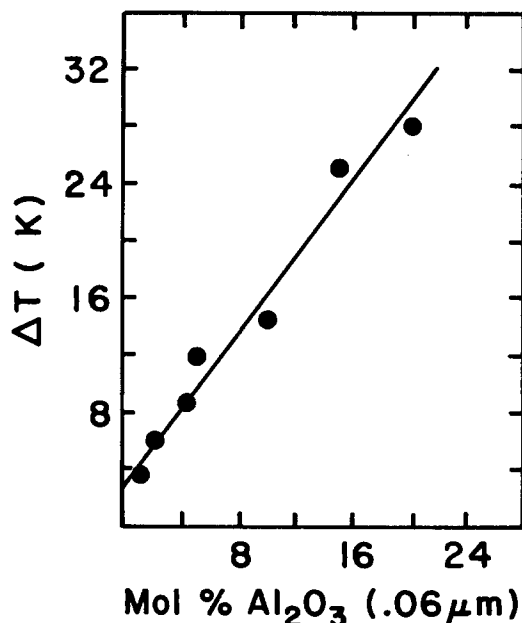


Fig. 3. ΔT as a function of m/o Al_2O_3

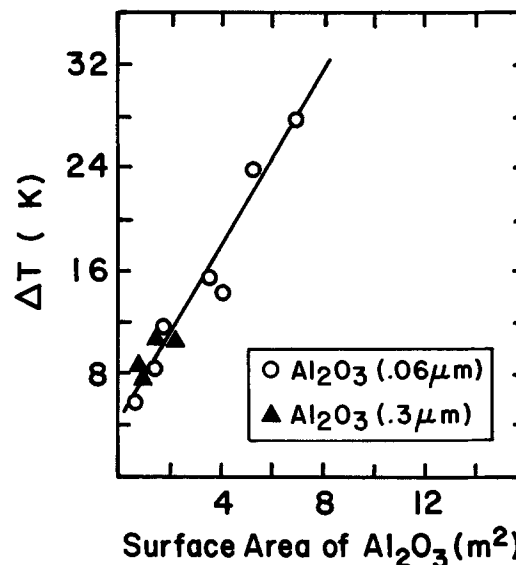


Fig. 4. ΔT as a function of surface area of Al_2O_3 per gram of AgI .

called "average structure," in which all the silver ions are moving in between relatively immobile iodine ions in a bcc arrangement. The silver ion mobility in this phase is so high that equilibrium between various defects is readily attained. Consequently, when Al_2O_3 is introduced into α - AgI , the cation vacancies generated at the interface act as sinks for some of the mobile silver ions and hence, the conductivity decreases. On cooling the composite from above 148°C , the smaller concentration of interstitials in the composite relative to the α - AgI without Al_2O_3 results in a lowered phase-transformation temperature because of the requirement of critical concentration of interstitials to drive the transition. However, at lower temperatures the increased conductivity in β - $\text{AgI}-\text{Al}_2\text{O}_3$ composites is due to the increased vacancy concentration. These vacancies are localized at or near the Al_2O_3 interface and do not affect chemical equilibrium in the bulk matrix. The concentration of vacancies in the bulk matrix is given by the square root of the Frenkel constant at each temperature, so the bulk phase transformation β to α occurs at 148°C , the same as for AgI without Al_2O_3 dispersoids.

Because the decrease in the number of interstitials is dependent on the number of additional vacancies at the $\text{AgI}/\text{Al}_2\text{O}_3$ interface and these in turn depend on the interfacial area or the mole percent Al_2O_3 added, the decrease in transformation temperature is expected to be proportional to the concentration of Al_2O_3 , as is observed.

Electroneutrality must be preserved. At present, we do not know what compensates the suggested presence of the additional cation vacancies. The mechanism suggested above is a working hypothesis which is consistent with the observed experimental data, but further study is required to test this suggestion.

Acknowledgment

This research was supported by The Basic Energy Sciences Division of DOE under Contract DEACO2-82ER 11091 and by a grant from the Center for Solid State Science.

Manuscript submitted March 26, 1984; revised manuscript received Aug. 13, 1984. This was paper 468 presented at the Washington, DC, Meeting of the Society, Oct. 9-14, 1983.

Arizona State University assisted in meeting the publication costs of this article.

REFERENCES

1. J. B. Wagner, Jr., *Mater. Res. Bull.*, **15**, 1691 (1980).
2. C. Liang, *This Journal*, **120**, 1289 (1973).
3. A. Khandkar and J. B. Wagner, Jr., Paper 833 presented at the Electrochemical Society Meeting, San Francisco, May 8-13, 1983.
4. K. Shahi and J. B. Wagner, Jr., *This Journal*, **128**, 6 (1981).
5. M. J. Rice, S. Strassler, and G. A. Toombs, *Phys. Rev. Lett.*, **32**, 596 (1974).

Galvanic Action Between MnO₂-Metal Couples and Its Effect on the Discharge of Li/MnO₂ Cells

Niles A. Fleischer^{*,1} and Ronald J. Ekers*

RAYOVAC Corporation, Madison, Wisconsin 53711

The Li/MnO₂ primary battery system delivers energy via a reaction where lithium ions are inserted into the host MnO₂ cathode (1). This insertion reaction has been argued to be responsible for the voltage profile during discharge. After a relatively fast drop from the open-circuit value, the voltage decreases slowly but continuously during a significant fraction of the useful life of the battery. At the end-of-life, the cell voltage drops precipitously. In addition, the conductivity of the MnO₂ decreases so that the cell impedance slowly but continuously increases during discharge, with a rapid increase occurring near the end of cell life. However, we conclude from laboratory experiments and testing of actual cells that a corrosive interaction between the MnO₂ cathode and metal cell case exists and contributes to the declining cell voltage and increasing internal cell resistance during discharge. The magnitude of this corrosive contribution is a function of the composition of the metal cell case.

Galvanic activity between beta MnO₂ and various metal case materials was measured with a galvanic couple current test (GCCT) (2). MnO₂ cathodes (3), 1.48 cm diameter, were initially saturated with an organic electrolyte of LiClO₄-propylene carbonate/dimethoxyethane. These cathodes were installed in the fixture of Fig. 1 along with the metal coupon, and the fixture was filled with 1.0M LiClO₄-PC/DME with initial water content of less than 50 ppm. The MnO₂ and the metal coupon were connected externally with a 300 kΩ resistor.

The metals and alloys studied are shown in Table I, where the galvanic corrosion current at $t = 0$ and $t = 8$ h were recorded at room temperature. The coupons were degreased and dried but otherwise used as received in order to compare the results with later cell tests.

The data in Table I indicate that the stainless steels most resistant to galvanic action with MnO₂ under these conditions generally have a chromium content above 18%, 1-4% molybdenum, and no nickel. Cold rolled steel (CRS) with a surprisingly low GCC, and 29-4 were exceptions to this trend. The 29-4 is differentiated from the more resistant 29-4-C by its lack of a titanium stabilizer. Perhaps, the poorer than expected performance of 29-4 can be explained by the apparent improved protection provided by titanium stabilizers (T-439 vs. 430 and 29-4-C vs. 29-4). Molybdenum was found to be necessary as a minor component; its complete absence increased the GCC (444 vs. T-439). The Ni-Cr alloy Inconel 600 was more resistant to galvanic action than the Ni 200.

Some of the materials in Table I were fabricated into CR2016 coin cells. Open-circuit voltage and impedance were measured after 21-25 days (Table II). These cells were then discharged on 15 kΩ at room temperature. The time

* Electrochemical Society Active Member.

¹ Permanent address: TADIRAN, Lithium Battery Plant, Rehovot 76 100, Israel.

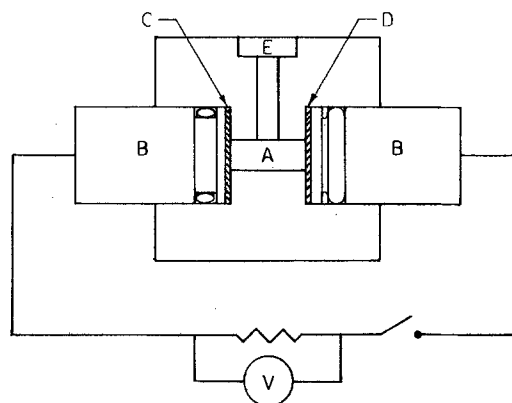


Fig. 1. Experimental apparatus for measuring the galvanic couple current with: A, electrolyte reservoir; B, contact pistons; C, MnO₂ cathode; D, coupon of can material; and E, stopper for the electrolyte fill tube of the Teflon block.

required to reach a 2.4V cutoff voltage and a 50Ω impedance level were recorded.

There was good correlation between galvanic activity and the hours to 2.4V, delivered capacity and open-circuit impedance. That is, case materials with higher galvanic currents delivered less energy than materials with lower galvanic currents. Additionally, the internal impedance of these cells increased at a more rapid rate than did the other cells. Similar correlation between open-circuit voltage and galvanic activity was not apparent. The galvanic activity is

Table I. Galvanic couple currents for various stainless steel and nickel alloys vs. MnO₂ in LiClO₄-PC/DME electrolyte at room temperature. Average values of two measurements. Where appropriate, the remainder of the composition is iron

Material	Composition				GCC, $\mu\text{A}/\text{cm}^2$	
	% Cr	% Mo	% Ni	Stabilizer	$t = 0$	$t = 8$ h
SHOMAC 30-2	30	2	—	—	0.25	0.00
CRS	—	—	—	—	0.28	0.12
Inconel 600	15.5	—	76	—	0.37	0.19
E-Brite	26	1	—	Nb	1.90	0.00
Ni 200	—	—	99.0 min	—	2.10	0.00
29-4-C	29	4	—	Ti	3.87	0.04
444	18	2	—	Nb, Ti	5.87	0.05
304L	18-20	—	8-12	—	9.45	0.31
316L	16-18	2-3	10-14	—	11.10	0.40
T-439	18	—	—	Ti	11.97	0.20
430	14-18	—	—	—	13.40	2.15
29-4-2	29	4	2	—	13.93	0.42
29-4	29	4	—	—	15.62	0.38

Table II. Open-circuit and 15 kΩ discharge data for cell lots built with different can materials ranked according to the MnO₂-can galvanic activity. The data represent an average of three CR2016 cells/lot. The capacity data consist of the mean \pm the standard deviation. Cells were stored three weeks at room temperature prior to the measurements

Lot	Can material	OCV (V)	Open-circuit impedance (Ω)	Hours to 50Ω	Hours to 2.4V	mAh to 2.4V	$\overline{\text{GCC}}$ ($\mu\text{A}/\text{cm}^2$)
006	Shomac 30-2	3.313	15	288	362	67 \pm 1.0	0.13
707	E-Brite	3.243	22	204	337	63 \pm 1.0	0.95
704	316L	3.22	23	192	323	60 \pm 2.3	5.75
706	430	3.254	25	156	333	62 \pm 1.2	7.78

taken as the time averaged GCC using the readings at $t = 0$ and $t = 8$ h from Table I.

Corrosion of the case material seems to be the most likely cause of the galvanic activity measured in these experiments. Changes of the inner surface of the case due to the accumulation of corrosion products might interfere with contact to the MnO_2 , which could account for the higher predischARGE impedance levels for case materials with larger GCC. The simplest explanation is that the additional impedance contributed to the cell by the corrosion process is additive with the increase in impedance due to the lithium insertion process. Thus, cells built with materials exhibiting a high GCC reach the 50Ω impedance cutoff sooner than cells built with corrosion resistant case materials, e.g., Shomac 30-2. High cell impedance and the degraded con-

tact between the MnO_2 and the case can also be used to explain the lower discharge capacity generally found in cells built with materials having high levels of GCC (Table II). The lower capacity is due to slope of the discharge curve which shortens the discharge time.

Manuscript submitted July 31, 1984; revised manuscript received Aug. 16, 1984.

REFERENCES

1. M. Voinov, *Electrochim. Acta*, **26**, 1373 (1981).
2. C. H. Sample, in "Corrosion Handbook," H. H. Uhlig, Editor, p. 1002, John Wiley and Sons, New York (1948).
3. D. P. Johnson, in "Proceedings of the 29th Power Sources Conference," Atlantic City, NJ, June 9-12, 1980, The Electrochemical Society, Inc., p. 89 (1981).

Cycling Characteristics of Secondary Li Electrode in LiBF_4 /Mixed Ether Electrolytes

Ken-ichi Takata, Masayuki Morita, and Yoshiharu Matsuda*

Department of Industrial Chemistry, Faculty of Engineering, Yamaguchi University, Tokiwa-dai, Ube, Yamaguchi, Japan

Kanenobu Matsui

Ube Industries, Limited, Kogushi, Ube, Yamaguchi, Japan

In the course of the development of ambient temperature Li secondary cells, it has been pointed out that the choice of an electrolyte system is of special importance in the efficient cycling characteristics of the Li electrode (1, 2). It is generally agreed that suitable solvents for the Li secondary electrode are 1,3-dioxolane (DOL) and 2-methyltetrahydrofuran (2Me-THF) (3). As electrolytic salts, LiClO_4 and LiAsF_6 have been used for DOL and 2Me-THF, respectively. The Li cycling efficiencies are sufficiently high in these solvent-salt systems, but some problems are still left. For instance, it has been shown that DOL/ LiClO_4 solutions are susceptible to detonation (4), and the solubility of LiAsF_6 in 2Me-THF is at most $1.5M$ (mol dm^{-3}), which leads the relatively low conductivity ($\sim 4.0 \times 10^{-3} \text{ S cm}^{-2}$) of the solution (5, 6). Therefore, various solvent-salt combinations are now under investigation (3).

Previously, the authors proposed the use of the mixed DOL-THF (1:1 vol)/ LiBF_4 system as an electrolytic solution for Li secondary cells (7). The principal advantages of the mixed solution are its high conductance, compared with DOL/ LiBF_4 and THF/ LiBF_4 (7, 8), and a slight potential change of the Li electrode during the charge-discharge cycle (7). In the present paper, influences of the charge-discharge current densities and the electrolyte concentration on the Li cycling efficiency were investigated in DOL-THF/ LiBF_4 solutions. Furthermore, 2-substituted-1,3-dioxolanes such as 2-methyl-1,3-dioxolane (2Me-DOL) and 2,2-dimethyl-1,3-dioxolane (2,2Me₂-DOL) were examined as a cosolvent with THF instead of DOL, which was subject to polymerize at high LiBF_4 concentration (3, 8).

Experimental

The purification of DOL (Tokyo Kasei Kogyo) and THF (Toyo Soda Manufacturing), and preparation of LiBF_4 (Morita Chemical Industries) solutions were carried out as described previously (7, 8). 2Me-DOL and 2,2Me₂-DOL were synthesized at the Central Research Laboratory, Ube Industries, and were purified in a similar manner as DOL.

Li cycle efficiency was measured by Koch's method (9). A beaker-type glass cell (volume = 100 cm^3) was used for the measurement. The test substrate was a Ni sheet mounted on a Teflon holder. Apparent surface area of the Ni substrate exposed to the solution was 0.95 cm^2 . The counterelectrode was a Li sheet with a Ni mesh ($2.5 \times 3 \text{ cm}$). A Li fragment on the tip of Ni wire was used as the reference electrode, which was connected to the test electrode

through a Luggin capillary. The plating and stripping current densities (i_p, i_s) were normally 2 mA/cm^2 , and the plated charge (Q_p) was 0.2 C/cm^2 . The cycle efficiency was evaluated by $Q_s/Q_p \times 100$ (%), where Q_s is stripped charge.

The current-potential curves of the Li electrode were also measured by using the same apparatus as described above, except for the Li test electrode. A Li foil disk (Kyokuto Metal Industries; $1.33 \text{ cm}^2 \times 0.02 \text{ cm}$) was used as the test electrode. The disk was mounted on a Teflon holder and was kept in contact with a Ni current collector. Current-potential curves were potentiostatically measured, where the electrode potential was stepwise changed at first from the reversible potential to anodic (discharging) ones and then changed to cathodic (charging) potentials. These experiments were carried out in a dry Ar atmosphere at room temperature (18 - 20°C). The electrolytic conductivity of the solution and the relative permittivity and the viscosity of the solvent were measured by usual methods (8) at 30°C .

Results and Discussion

In the previous work (7), it was proved that the Li cycle efficiency in mixed DOL-THF (1:1 vol)/ LiBF_4 was initially lower than that in THF/ LiBF_4 , but that the efficiency variation with cycle number in the mixed solution was rather small. The efficiency in DOL/ LiBF_4 was much lower than that in THF/ LiBF_4 or DOL-THF/ LiBF_4 . Figure 1 shows the variation of the efficiencies in DOL-THF/ LiBF_4 (1M) for different i_p ($= i_s$), where Q_p was kept constant at 0.2 C/cm^2 . Average efficiency during the first ten cycles decreased with decreasing the current densities. This was probably related to the film formation on deposited Li in the solution containing THF (10, 11). The lower i_p and i_s were, the longer the deposited Li contacted with the solution, as Q_p was kept constant. This would lead to the result that the Li deposited under low i_p is not effectively utilized owing to the inert film on Li. Conversely, in fact, decreasing Q_p tended to increase the efficiency, under the conditions of constant i_p and i_s . The efficiency at 4 mA/cm^2 was initially the highest, but it decreased gradually with increasing the cycle. When the plating is made at such high current density, the polarization of the electrode becomes high ($\sim 0.5 \text{ V}$), and then some side reaction (e.g. cathodic reduction of the solvents) would occur during the charge (plating) at the Li electrode. This results in the efficiency loss with repeating the cycle.

The efficiency variation with LiBF_4 concentration in the DOL-THF solution is shown in Fig. 2. The electrolytic conductivity of the solution increased with an increase in LiBF_4 concentration (8), and the overvoltage at the Li elec-

* Electrochemical Society Active Member.

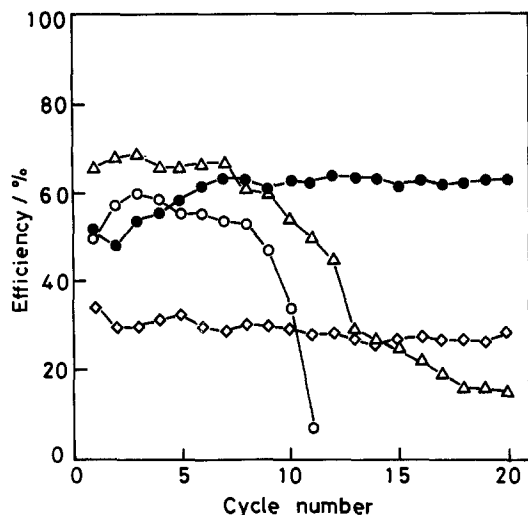


Fig. 1. Variation of efficiency with cycle number in DOL-THF/LiBF₄ (1M), $Q_p = 0.2 \text{ C/cm}^2$. Δ : 4 mA/cm²; \bullet : 2 mA/cm²; \circ : 1 mA/cm²; \diamond : 0.5 mA/cm².

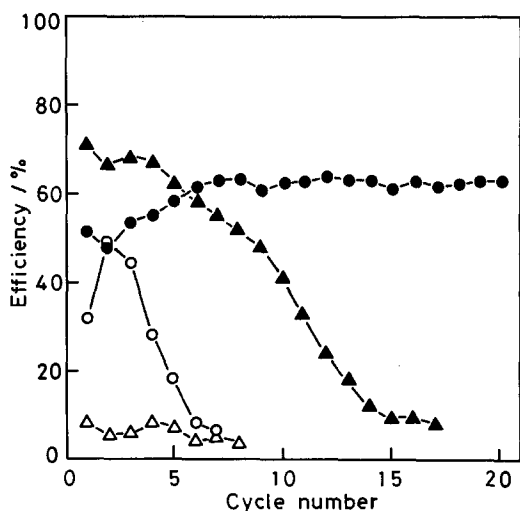


Fig. 2. Variation of efficiency with cycle number in DOL-THF/LiBF₄, $Q_p = 0.2 \text{ C/cm}^2$, $i_p = i_s = 2 \text{ mA/cm}^2$. Δ : 2M. \circ : 1.5M. \bullet : 1M. \blacktriangle : 0.5M LiBF₄.

trode decreased with LiBF₄ concentration at constant current density. In spite of these conditions, the cycle efficiency tended to decrease with an increase in LiBF₄ concentration. The efficiency in 0.5M LiBF₄ was relatively high during the initial cycles, but it decreased with repeating the cycle, probably owing to high overvoltage in such a low LiBF₄ concentration solution. However, the low efficiencies in the high concentration solutions were possibly caused by degradation of the electrolytic solution. Viscosity of the solutions containing high concentration of LiBF₄ increased after the cycling experiments. DOL is polymerized by Lewis acid catalysts (12). Since the salt, LiBF₄, usually contains a small amount of the Lewis acid, BF₃, as an impurity, the polymerization would take place at high LiBF₄ concentration, even in the mixed DOL-THF solution. These results suggested that the maximum cycling efficiency in the DOL-based electrolytes would be gained only under the restricted conditions and it would be at most 70%. The cycling characteristics in the DOL-THF system might be improved by minor modifications of the solvents, such as the substitution of THF for 2Me-THF.

Introduction of alkyl groups to DOL at the 2 position generally reduces the rate of polymerization (13). Thus, the modification of DOL was examined in the present work. Table I shows the electrolytic conductivity of the LiBF₄ solutions. The conductivity of the mixed DOL-THF/LiBF₄ was higher than that of each parent solution, DOL/LiBF₄ or

Table I. Electrolytic conductivity (κ) of the LiBF₄ solutions at 30°C

Solvent	Concentration of LiBF ₄ (M)	$\kappa \times 10^3$ (S cm ⁻¹)
DOL	1.0	1.54
	2.0	2.25
THF	1.0	1.80
	3.0	4.30
DOL-THF(1:1)	1.0	2.33
	3.0	6.06
2Me-DOL-THF(1:1)	1.0	1.32
2,2Me ₂ -DOL-THF(1:1)	1.0	0.96

Table II. Relative permittivity (ϵ_r) and viscosity (η) of the solvents at 30°C

Solvent	ϵ_r	$\eta \times 10^3$ (kg ⁻¹ s ⁻¹)
THF	7.51	0.45
DOL	6.74	0.57
2Me-DOL(1:1)	4.39	0.54
2,2Me ₂ -DOL(1:1)	3.35	0.62

THF/LiBF₄ (8). However, the solutions consisting of DOL derivatives, 2Me-DOL-THF/LiBF₄ and 2,2Me₂-DOL-THF/LiBF₄, had rather lower conductance. This decrease in the conductivity with the substitution of DOL for 2Me-DOL or 2,2Me₂-DOL is probably due to changes in the relative permittivity and the viscosity of the solvent, which are listed in Table II. High viscosity or low permittivity of the solvent generally leads to low conductance of the electrolytic solutions (14, 15). This is also the case for the present mixed systems.

Figure 3 shows the current-potential relations at the Li electrode in the mixed ether solutions. Overvoltages at given current densities (so-called polarization) in DOL-THF were lower than those in DOL or in THF (7). In 2Me-DOL-THF and 2,2Me₂-DOL-THF, however, relatively high overvoltages were observed. The Li electrode reactions in those solutions are mostly controlled by mass transfer process, if the potential is somewhat far from the reversible potential. As the current densities were dependent on solution stirring, the process was mainly controlled by Li⁺ ion diffusion in the solution (7). The results shown in Fig. 3 suggest that the diffusion rates in 2Me-DOL-THF and 2,2Me₂-DOL-THF are lower than that in DOL-THF. This is consistent with the result of the solution conductivity shown in Table I, because diffusion rate of ion is related to electrolytic con-

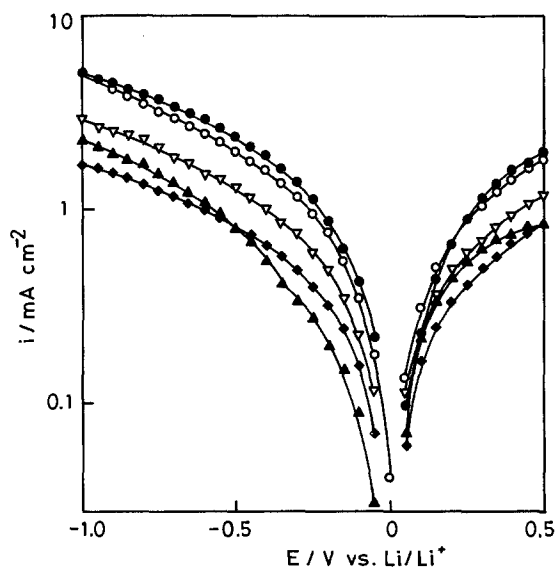


Fig. 3. Current-potential curves of the Li electrode in 1M LiBF₄ solutions. ∇ : DOL. \circ : THF. \bullet : DOL-THF. \blacktriangle : 2Me-DOL-THF. \blacklozenge : 2,2Me₂-DOL-THF.

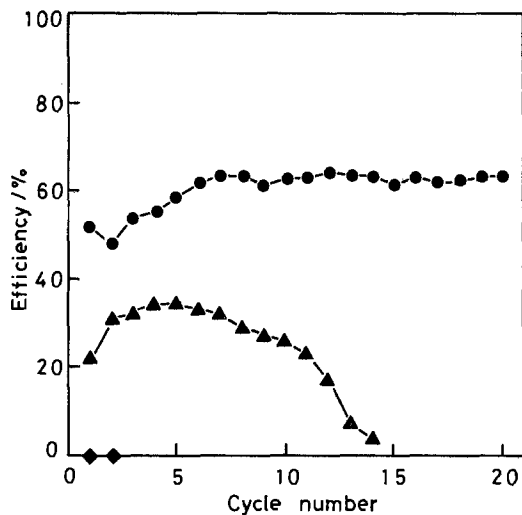
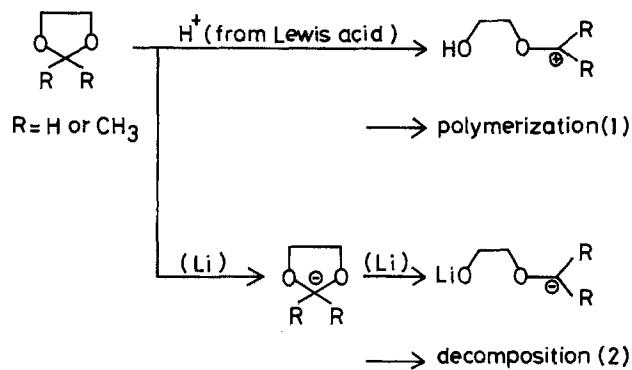


Fig. 4. Variation of efficiency with cycle number in 1M LiBF₄ solutions, $Q_D = 0.2$ C/cm², $i_p = i_s = 2$ mA/cm². ●: DOL-THF. ▲: 2Me-DOL-THF. ◆: 2,2Me₂-DOL-THF.

ductivity through ionic mobility. Consequently, a lowering of the solution conductivity by introducing 2Me- or 2,2Me₂-DOL causes not only an increase in the voltage loss in the electrolytic solution during the charge-discharge cycles, but also an increase in the overvoltage for the electrode reaction itself.

The Li cycle efficiencies in 2Me-DOL-THF and 2,2-Me₂-DOL-THF were shown in Fig. 4, compared with that in DOL-THF. Substitution of DOL to 2Me-DOL reduced the efficiency, and the discharge capacity in 2,2-Me₂-DOL-THF was practically null. The reason for this efficiency reduction was not clear, but the following interpretations might be possible. As the overvoltage for the Li electrode reaction is considerably higher in 2Me-DOL-THF and 2,2Me₂-DOL-THF, some side reactions such as electrochemical decomposition of the solvents are more likely to occur during the cycle. However, methyl substituents at the 2-position of DOL contributed to depressing polymerization, but enhanced the reactivity of DOL with metallic Li. These two effects would result from stabilization of ring-opened products of DOL with methyl substituents (13). The detail of the ring-opened products was not clear, but some examples for the reactions would be presented as shown Scheme I, where Eq. [2] is analogous to that of THF (11). Both the high overvoltage for the electrode reaction and the high reactivity of the solvents with Li would reduce the Li cycle efficiency in the solutions consisting of the modified DOL. That is, the effect of methyl group introduction to DOL was a negative one for the cycling characteristics of the Li electrode, in spite of the depression of DOL polymerization in the LiBF₄ solutions.

In conclusion, however, these results suggest a possibility that high performance electrolytes can be developed by appropriate modification of common solvents.



Scheme I

Acknowledgments

We are grateful to Ube Industries, Limited for financial support. Thanks are also due to the Central Research Laboratory, Ube Industries, Limited for supplying dioxolane derivatives.

Manuscript submitted Aug. 6, 1984; revised manuscript received Sept. 6, 1984.

Yamaguchi University assisted in meeting the publication costs of this article.

REFERENCES

1. J. O. Besenhard and G. Eichinger, *J. Electroanal. Chem.*, **68**, 1 (1976).
2. V. R. Koch, *J. Power Sources*, **6**, 357 (1981).
3. K. M. Abraham and S. B. Brummer, in "Lithium Batteries," J. P. Gabano, Editor, p. 371, Academic Press, London (1983).
4. G. H. Newman, R. W. Francis, L. H. Gaines, and B. M. L. Rao, *This Journal*, **127**, 2025 (1980).
5. V. R. Koch and J. H. Young, *Science*, **204**, 499 (1979).
6. J. L. Goldman, R. M. Mank, J. H. Young, and V. R. Koch, *This Journal*, **127**, 1461 (1980).
7. Y. Matsuda, M. Morita, and K. Takata, *ibid.*, **131**, 1991 (1984).
8. Y. Matsuda, M. Morita, and T. Yamashita, *ibid.*, **131**, 282 (1984).
9. V. R. Koch and S. B. Brummer, *Electrochim. Acta*, **23**, 55 (1978).
10. V. R. Koch and J. H. Young, *This Journal*, **125**, 1371 (1978).
11. V. R. Koch, *ibid.*, **126**, 181 (1979).
12. Y. Yamashita, M. Okada, and M. Hirota, *Agnew. Makromol. Chem.*, **9**, 136 (1969).
13. M. Okada, Y. Yamashita, and Y. Ishii, *Makromol. Chem.*, **80**, 196 (1964).
14. R. Jasinski, in "Advances in Electrochemistry and Electrochemical Engineering," Vol. 8, P. Delahay and C. W. Tobias, Editors, p. 253, John Wiley and Sons, New York (1971).
15. Y. Matsuda, M. Morita, and K. Kosaka, *This Journal*, **130**, 101 (1983).

Electrolytic Corrosion of Gold and the Formation of $\text{Au}_2(\text{SO}_4)_3$ in Concentrated Sulfuric Acid

Frank E. Senffle and Donald B. Wright¹

U.S. Geological Survey, Reston, Virginia 22092

Because metallic gold is relatively stable in concentrated and dilute sulfuric acid, the formation of $\text{Au}_2(\text{SO}_4)_3$ is not simply a matter of dissolution of the metal in the acid. Jirsa and Jelinck (1) prepared auric sulfate by first preparing $\text{Au}(\text{OH})_3$ by anodic oxidation of gold in dilute H_2SO_4 (0.1N) and subsequently dissolving the $\text{Au}(\text{OH})_3$ in hot concentrated H_2SO_4 to form $\text{Au}_2(\text{SO}_4)_3$. From the information in the literature, it appears that $\text{Au}_2(\text{SO}_4)_3$ is stable only in concentrated H_2SO_4 ; no isolation of a solid of this composition has been reported (2).

Although anodic oxidation of gold in dilute sulfuric acid (3, 4) has been studied, there are very few similar investigations for concentrated H_2SO_4 . Spiller (5), many years ago, reported what appears to be the formation of $\text{Au}_2(\text{SO}_4)_3$ by electrolysis of gold in concentrated H_2SO_4 . Although his work concerning the corrosion of gold has been amply verified (6), the equations describing the mechanism of formation of auric sulfate have not been well established. We have examined the direct anodic oxidation of gold in concentrated H_2SO_4 to more fully understand the chemical reactions. $\text{Au}_2(\text{SO}_4)_3$ is unstable and cannot be isolated for chemical analysis, but our experiments are consistent with the formation of $\text{Au}_2(\text{SO}_4)_3$ in concentrated H_2SO_4 , in which it is stable. Equations describing chemical reactions which are compatible with the experimental data are presented.

Concentrated H_2SO_4 (96-98%, AR grade) with a density of 1.84 was used for all the experiments, except where specifically mentioned otherwise. The electrolysis was carried out with two gold wire electrodes (99.99% pure, 1.3 mm diam) either (i) in a U-tube partially filled with glass beads to separate the anolyte and catholyte or (ii) in a beaker fitted with inverted burettes over the electrodes to collect the gases evolved. Each electrode was soldered to an insulated copper wire and, with the exception of about 2.5 cm of exposed gold wire, the electrode was encased in paraffin so that electrolysis took place only along the approximately 2.5 cm exposed section. Most of the experiments were run either at constant voltage or at constant current. A potential of about 15V and a current density close to 0.35 A/dm² was used for most of the experiments. A few experiments were run at voltages as low as 4V and as high as 21V.

In all the experiments, the results were about the same. About a minute after initiating electrolysis, we observed a yellow color about the anode, indicating the dissolution of gold. Although the anode showed a significant loss of weight during the electrolysis, the fact that no change in weight of the cathode was observed even after 10-15h of electrolysis indicated that no gold was plated out during electrolysis. After several minutes of electrolysis, a cloud of very fine white powder, subsequently analyzed as elemental sulfur, was observed at the cathode. When the yellow anolyte is allowed to mix with the catholyte containing the elemental sulfur, a black precipitate, presumably a form of gold sulfide, is immediately precipitated. Gas chromatographic analysis of the evolved electrode gases showed only hydrogen at the cathode and oxygen at the anode. However, the gas evolved at the anode initially had a distinct odor of ozone, and was undoubtedly the precursor of the oxygen formed. It is worthy of note that at ambient temperatures Hoffman (7) also observed ozone at the platinum anode and S at the cathode in an electrolysis cell using a concentrated H_2SO_4 electro-

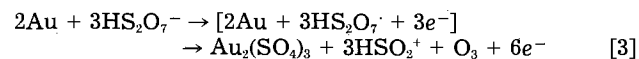
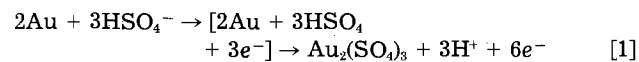
lyte. We found no significant (< 10 ppm) SO_2 at either electrode.

More than ten electrolysis experiments were made using concentrated H_2SO_4 as an electrolyte to measure the hydrogen-to-oxygen volume ratio. In each experiment, about 6-12 measurements of the gas volume of each burette were made successively, the current being turned off between each measurement so that bubbles of gas in the solution had time to rise in the burettes. It should be noted that incremental changes in volume rather than total change in volume over the time of the experiment was measured. In these experiments, the initial ratio of the volume of hydrogen to oxygen was close to 3, but gradually dropped on successive readings to a final value of 2. At first, this was thought to be experimental error, but by using different burettes, checking for leaks, etc., we concluded that the decrease in the ratio was real. The curve in Fig. 1 is typical for these experiments. The general pattern of change in the ratio of hydrogen to oxygen volumes evolved is as follows: During stage A, an initial ratio of about 3 decreased very slowly for the first 2 min of electrolysis. The ratio gradually dropped to and remained about 2.5 for about 10 min (stage B), and then dropped to 2 (stage C), where it remained throughout the balance of the run.

Because the electric potentials used are well above the threshold for any electrode reaction, and because essentially the same results were obtained in constant-potential experiments at different potentials, one must conclude that the change in gas volume ratio with time of electrolysis is not potential-related. However, it is reasonable to assume that the observed results are related to a change in chemistry with time of electrolysis. After exploring the various possible chemical reactions, only one set of reactions was found to give results compatible with the observations.

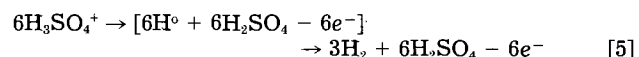
In the concentrated sulfuric acid prior to electrolysis, autoprotolysis produces the major ions H_3SO_4^+ and HSO_4^- , and a lesser ionic concentration of H_3O^+ and HS_2O_7^- (about 20-10% of the ionization, respectively) (8). As gold is relatively inert in concentrated H_2SO_4 , it is reasonable to assume that during electrolysis the cause of the dissolution of gold is the highly reactive free radicals formed by the discharge of the negative ions in the concentrated sulfuric acid.

The anode reactions are given by Eq. [1]-[4]



O_3 is the only gas formed at the anode, as was inferred from the experiments.

The three hydrogen ions from reaction [1] protonate the undissociated H_2SO_4 molecules in the acid to form three H_3SO_4^+ ions (Eq. [2]). These ions together with three H_3SO_4^+ ions initially in equilibrium with the three HSO_4^- ions in Eq. [1] acquire electrons at the cathode to form hydrogen. Thus, at the cathode, the following reaction takes place



¹Permanent address: Howard University, Washington, DC 20059.

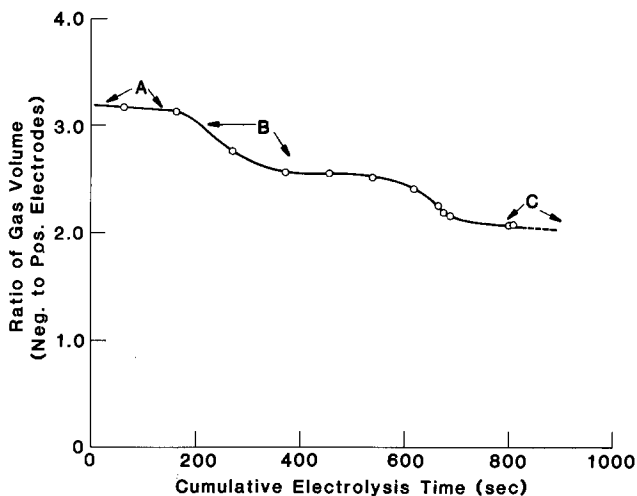
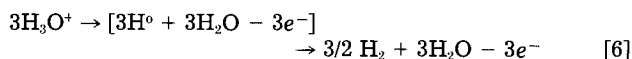


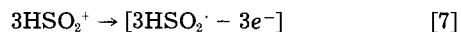
Fig. 1. Ratio of the incremental change in gas volume at the cathode to the gas volume change at the anode as a function of time of electrolysis.

In addition, the three H_3O^+ ions, initially in equilibrium with the three HSO_2^+ ions shown in Eq. [3], are also neutralized at the cathode

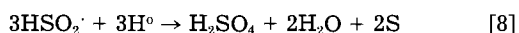


and yields 1.5 molecular volume of hydrogen. The total yield of hydrogen at the cathode from Eq. [5] and [6] is thus 4.5 mol, the required amount of hydrogen to give the initial hydrogen-to-oxygen ratio of 3 that was observed experimentally (stage A, Fig. 1).

To maintain a conservation of charge, an additional reaction takes place at the cathode. The HSO_2^+ ions formed at the anode (Eq. [3]) migrate to the cathode, gain one electron, and for a short time exist as free radicals. Thus



At the cathode surface, atomic hydrogen is also being formed (Eq. [5] and [6]), and is available to react with the HSO_2^\cdot formed at the same site. Thus



The consumption of the 3H° radicals thus reduces the hydrogen output from 4.5 to 3 mol, and the hydrogen-to-oxygen ratio decreases to 2. At the same time, elemental sulfur is formed. On initiation of electrolysis the reactions [1]-[6] take place immediately because H_3SO_4^+ and H_3O^+ ions exist throughout the bulk of the electrolyte. Thus, the hydrogen-to-oxygen gas volume ratio is initially about 3 (stage A). However, the HSO_2^+ ions form at the anode surface and must migrate to the cathode. As the HSO_2^+ ions begin to arrive at the cathode, the rate of hydrogen production decreases because of reaction [8], causing the hydrogen-to-oxygen ratio to decrease to a value of 2. If the gas volumes could be measured without interrupting the current, the transition of the ratio from 3 to 2 would undoubtedly be monotonically decreasing. During stage B in Fig. 1, the essentially flat section of the curve probably reflects the current shut-off periods during which the

volume measurements were made. Because of the bubbles clinging to the sides of the burette, a current shut-off period was necessary to obtain good volume measurements.

The above reactions take place only in concentrated H_2SO_4 . To determine the degree of concentration required, a series of experiments was made with increasingly diluted H_2SO_4 . It was found that the same electrode reactions took place until the concentration of H_2SO_4 was reduced to 16.3N. At this concentration, a dark brown precipitate was observed at the anode which was probably auric oxide, as observed by Jeffery (9), or $\text{Au}(\text{OH})_3$, as reported by Jirsa and Jelinck (1) in dilute sulfuric acid. The dark brown precipitate persisted for all dilute sulfuric acid electrolytes with concentrations between 16.3 and 6.3N. Below 6.3N, both gold electrodes were inert, and electrolysis was essentially that of water.

The above experiments and electrode reactions help to explain the formation of S at the cathode, and of $\text{Au}_2(\text{SO}_4)_3$ and O_3 at the anode. One can write equations to yield other gold compounds or ion complexes, but, invariably, one or another of the experimental results is left unexplained. For example, one can assume that monovalent rather than trivalent gold is dissolved during electrolysis, but it is easily shown that the hydrogen-to-oxygen ratio obtained is not that which is observed experimentally. While the above model uniquely fits the experimental data, it should be retained as an hypothesis.

Additional work must be done to prove all the steps. We tentatively conclude that trivalent gold formed by electrolytic corrosion in the concentrated sulfuric acid is in the form of $\text{Au}_2(\text{SO}_4)_3$.

Acknowledgments

The authors are grateful to their colleagues, Dr. Frederick Simon for his helpful comments and to Robert Johnson for x-ray fluorescence analysis of the sulfur formed during the electrolysis. Donald Wright also thanks Dr. J. Morris of Howard University for making it possible for him to take part in the research program at the U.S. Geological Survey.

Manuscript submitted June 11, 1984; revised manuscript received Aug. 24, 1984.

The U.S. Department of the Interior assisted in meeting the publication costs of this article.

REFERENCES

1. F. Jirsa and H. Jelinck, *Z. Elektrochem.*, **30**, 286 (1924); see also *Chem. List*, **18**, 104 (1924).
2. M. C. Sneed, J. L. Maynard, and R. C. Brasted, "Comprehensive Inorganic Chemistry," Vol. 2, J. W. Laist, Editor, p. 230, Van Nostrand, New York (1954).
3. R. P. Frankenthal and D. E. Thompson, *This Journal*, **123**, 799 (1976).
4. A. T. Kuhn and M. Byrne, *Electrochim. Acta*, **16**, 391 (1971).
5. J. Spiller, *Chem. News*, **10**, 173 (1964).
6. V. Lenker, *J. Am. Chem. Soc.*, **26**, 550 (1904).
7. H. Hoffmann, *Z. Elektrochem.*, **27**, 442 (1921).
8. R. J. Gillespie and E. A. Robinson, in "Advances in Inorganic Chemistry and Radiochemistry," Vol. 1, H. Emeleus and A. Sharpe, Editors, pp. 385-423, Academic Press, New York (1959).
9. F. H. Jeffrey, *Trans. Faraday Soc.*, **11**, 172 (1916).

On Depositing Conductors from Solution with a Laser

A. Auerbach

General Electric Company, Corporate Research and Development, Schenectady, New York 12301

The integration of lasers into a variety of technologies is presently occurring. In no area is this more apparent than microelectronic processing (1, 2). Among the features making this possible is the ability of the laser to function as a

highly localized photon and/or heat source, and the fact that it can be used in a hands-off manner to effect processing. To date, most work has involved gaseous systems; this is because they offer the least interference to the laser radiation.

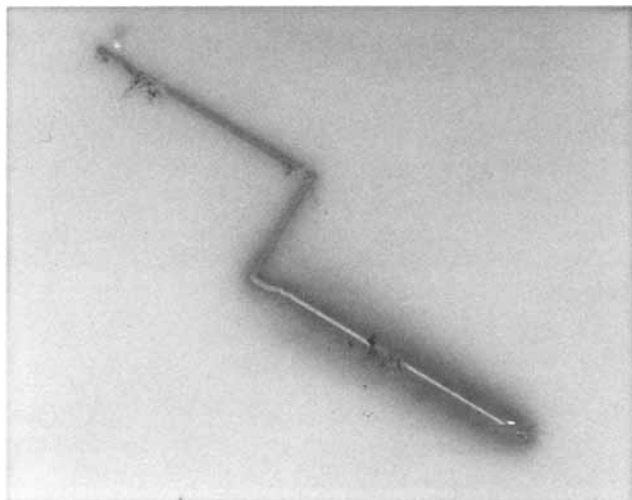


Fig. 1. Silver conductor reduced from solution onto alumina substrate. Thin portion was written using 100 mW. Thicker region was written using 500 mW. Scan rate was 300 $\mu\text{m/s}$. Laser radiation was focused through 10 \times objective.

A variety of metals have been deposited from the gas phase. Deutsch *et al.* (3) used a UV laser to deposit silicon nitride (Si_3N_4) from gaseous reactants. Refractory metals such as iron, chromium, and tungsten have also been deposited (4, 5). Recently, Solanki *et al.* deposited aluminum oxide and aluminum thin films from gaseous reactants using a UV laser (6).

Liquid systems have also been investigated. von Gutfeld *et al.* (7) used an argon-ion laser to provide localized heating to rapidly electroplate gold onto a nickel-plated beryllium

substrate without adversely affecting the quality of the deposit. The gold electroplate was crack-free, dense, and had excellent adhesion to the substrate material. Karlicek *et al.* (8) used a pulsed dye laser to electrolessly plate gold or platinum from an aqueous solution of chloroplatinic or chloroauric acid. The focused laser output heats the substrate material to promote reaction between the substrate and dissolved metal salt.

In this communication, we describe an alternative system which has been used to electrolessly deposit continuous silver conductors from solution onto an aluminum substrate. A laser is used to provide local heating of the substrate. The heat promotes a novel redox reaction between the solvent and dissolved salt to deposit silver. Since the redox reaction occurs at a moderate temperature ($< 250^\circ\text{C}$), a relatively low laser power is required to deposit silver on the alumina substrate. Substrates having higher thermal conductivities require higher laser powers so that an adequate average temperature is maintained during the scan.

The solution is formulated by dissolving 50% by weight silver nitrate (Metron, Incorporated) into N-methyl pyrrolidone (Aldrich). The salt is dissolved with mild heat and stirring. The resulting solution is colorless since the loose complex formed between the silver ion and amide group does not absorb in the visible.¹ This is significant because it is desirable that the laser energy be absorbed by the substrate and not the solution.

The apparatus consists of a quartz cell with liquid input and exit ports. The substrate is mounted in the cell with its surface 2 mm from the window. The output from an argon-ion laser is focused, through a 10 \times objective, onto the sub-

¹ A charge transfer complex to the silver ion results when the amide group contains an electron-rich side chain (e.g., N-vinyl pyrrolidone). The solution is then colored, since the charge transfer complex absorbs in the visible.

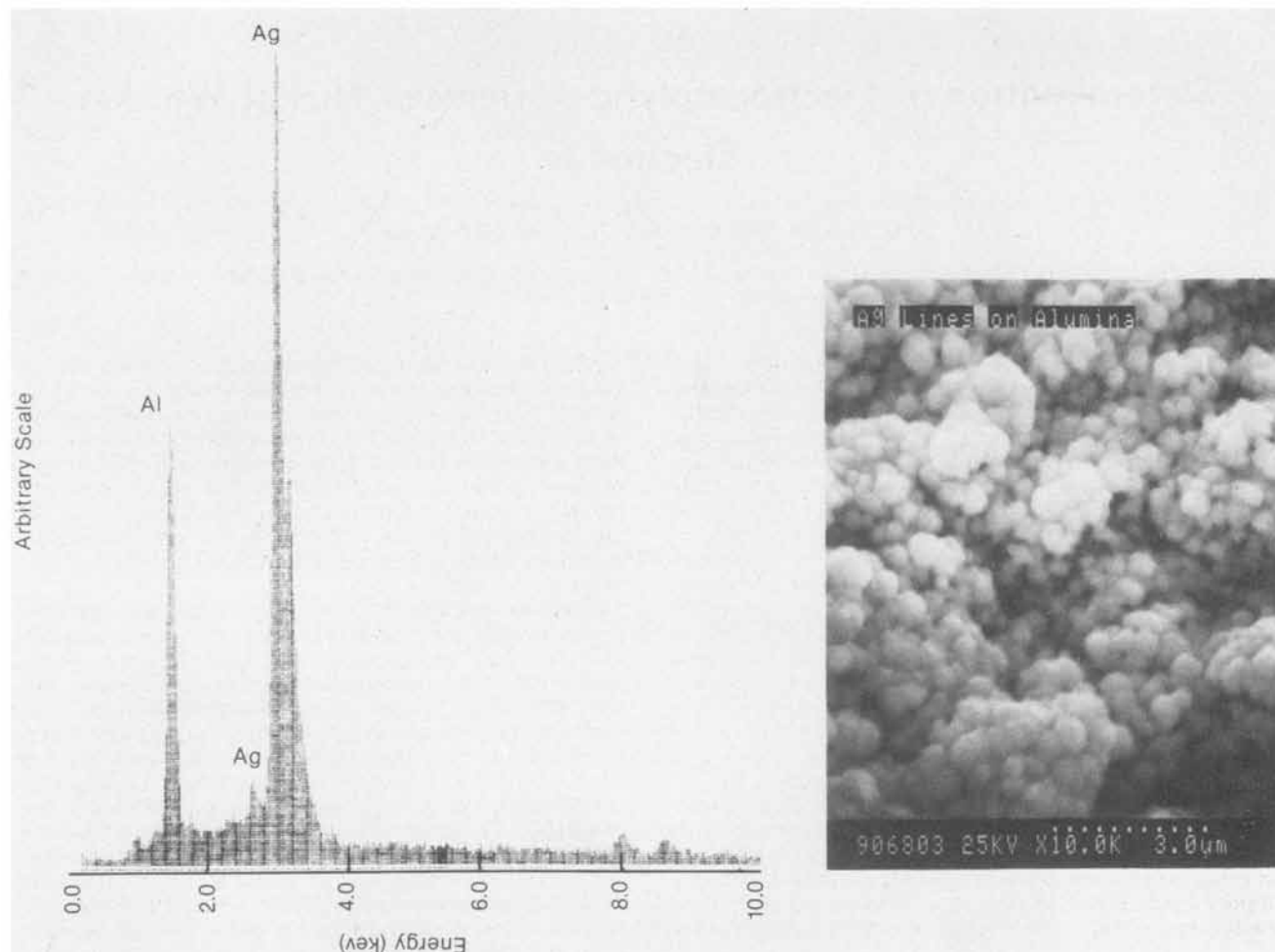


Fig. 2. 10K magnification SEM of conductor region. X-ray analysis also shown.

strate. The work area is simultaneously viewed by a video camera and displayed. The cell is translated relative to the laser using a programmable X-Y translator stage (Anorad, Incorporated).

Figure 1 shows one such silver conductor deposited onto an alumina substrate from the above solution. The wider conductor section was written using a laser power of 500 mW and translation speed of 300 $\mu\text{m/s}$. The thinner section was written using only 100 mW of power. The measured resistance of a 0.5 cm length of thicker conductor was $\sim 5\Omega$. This is close to the calculated value for pure silver of comparable dimensions (75 $\mu\text{m} \times 0.1 \mu\text{m} \times 0.5 \text{cm}$). Figure 2 shows an SEM plate at 10,000 \times of the conductor region. The silver grains (about 1000 \AA across) are obvious. Similar grain structure was previously observed for laser-assisted reduction of silver ions in a polymer matrix (9). We suspect, therefore, that the silver is incorporated in a matrix of oxidized solvent. In agreement with this, the conductivity of the silver deposit decreases with exposure to ambient atmosphere and humidity. Also shown in the figure is the x-ray spectrum of a grain showing the predominant silver peak and the background aluminum peak resulting from the substrate. Although various translation speeds and laser powers were investigated, lowest resistance values were achieved using speeds between 200-600 $\mu\text{m/s}$ and output power between 0.1 and 1W.

The advantage of this method for depositing metals is that the materials used require no special handling and are not toxic. Also, since the metal deposits in the immediate vicinity at the localized heat, little waste occurs. Since a very high density of silver ions is available in the reduction volume, conductors are formed in a single, relatively fast ($\sim 500 \mu\text{m/s}$) scan of the focused laser beam.

An important consideration is careful choice of the solvent. The solvent must be a good electron donor, but have a high boiling point. This is so that reduction can be accomplished without solvent boiling. We have found that amide

bearing solvents (e.g., N-methylpyrrolidone, N-vinylpyrrolidone, N-N-dimethyl formamide, etc.) work well.

In summary, we have demonstrated one system which was used to write silver conductors directly from solution. In the future, we will investigate gold and copper forming systems. Such systems are possible since both copper and gold ions contained in a polymer matrix have been reduced with a laser (10).

Manuscript submitted May 14, 1984; revised manuscript received Sept. 5, 1984.

General Electric Company assisted in meeting the publication costs of this article.

REFERENCES

1. D. J. Ehrlich, T. F. Deutsch, R. M. Osgood, Jr., and D. J. Silversmith, *Jpn. J. Appl. Phys.*, Suppl., 161 (1982).
2. D. J. Ehrlich, R. M. Osgood, and T. F. Deutsch, *IEEE J. Quantum Electron.*, **qe-16**, 1233 (1980).
3. T. F. Deutsch, D. J. Silversmith, and R. W. Mountain, in "Proceedings of a Symposium on Laser Diagnostics and Photochemical Processing for Semiconductor Devices," (Boston, MA, Nov. 1982) p. 129, North Holland, New York (1983).
4. D. J. Ehrlich, R. M. Osgood, and T. F. Deutsch, *This Journal*, **128**, 2039 (1981).
5. S. D. Allen, A. B. Trigubo, and R. Y. Jan, in "Proceedings of a Symposium on Laser Diagnostics and Photochemical Processing for Semiconductor Devices," (Boston, MA, Nov. 1982) p. 207, North Holland, New York (1983).
6. R. Solanki, W. H. Ritchie, and G. J. Collins, *Appl. Phys. Lett.*, **43**, 454 (1983).
7. R. J. von Gutfeld, M. H. Gelchinski, L. T. Ronankin, and D. R. Vigliotti, *Appl. Phys. Lett.*, **43**, 876 (1983).
8. R. F. Karlicek, V. M. Donnelly, and G. J. Collins, *J. Appl. Phys.*, **53**, 1084 (1982).
9. A. Auerbach, *This Journal*, To be submitted.
10. A. Auerbach and D. Haitko, Manuscript in preparation.

Determination of Electrocatalytic Activity of Nickel Whisker Electrodes

J. D. Hansen,* G. L. Cahen, Jr.,* and G. E. Stoner*

Applied Electrochemistry Laboratory, Department of Materials Science, University of Virginia, Charlottesville, Virginia 22901

An investigation of the effects of extremely small grained nickel electrodes on the rate of electrochemical hydrogen production was conducted. More specifically, the comparative evaluations of the electrocatalytic properties of conventional nickel 200 plate electrodes and nickel whisker electrodes for hydrogen evolution in alkaline solutions were performed. This work was stimulated by previous research performed at the University of Virginia which indicated an improvement in the energy efficiency of the hydrogen evolution reaction at porous nickel whisker electrodes as compared to nickel 200 screens on an apparent area basis (1, 2). However, it was not determined whether the energy gained by the use of sintered nickel whisker electrodes was due to their extremely high surface area or to some truly innate electrocatalytic property of the metal's composition and microstructure. The surface morphology of these whiskers is complex and is the result of their production by the chemical vapor deposition of nickel tetracarbonyl gas, $\text{Ni}(\text{CO})_4$. To separate the effects of this more complex surface condition from microstructural considerations such as grain boundaries, other types of defects, and possible impurity associated phases, it was necessary to expose the internal metal of these whiskers and use it as an elec-

trode. Thus, the fundamental question of specific electrocatalytic behavior of nickel whisker electrodes, independent of their high surface area, was the principal objective of this investigation, and no further attempt to identify effects caused by the naturally occurring whisker surface other than that previously identified (2) was made. As a result, standard quantitative comparative tests for electrocatalysis needed to be developed, and some basic questions concerning what determines an electrocatalyst were considered.

Scanning electron microscopy of nickel whisker electrodes reveals their high porosity (~ 85 volume percent) and their high surface to volume ratio (50,000 cm^2/cm^3). These characteristics created a very high surface area electrode which allows increased electrochemical reaction rate and, consequently, increased energy efficiency. In addition to their high surface area, the nickel whisker electrodes have a unique metallurgical microstructure which could result in some interesting electrocatalytic properties. The grain size of these whiskers was typically 200-400 \AA . Thus, each whisker was composed of many small grains creating a large grain boundary area. Enhanced electrocatalysis could have resulted from nucleation sites provided by the grain boundaries or possibly from the increased energy associated with these grain boundaries.

* Electrochemical Society Active Member.

Table I. Experimental data for typical nickel 200 Tafel plot

Current density	Voltage (V)	IR (mV)	Voltage corrected for IR	Experimental condition
10 μ A	-1.172	—	—	N ₂ purge, Teflon airtight cell, low [Fe] KOH, ½h equilibrium time, 1 cm ² electrode
30 μ A	-1.258	—	—	
100 μ A	-1.338	—	—	
300 μ A	-1.390	—	—	
1 mA	-1.445	—	—	
3 mA	-1.503	—	—	
10 mA	-1.585	7, 6, 7, 6	-1.579	
30 mA	-1.668	21, 21, 21, 19	-1.647	
100 mA	-1.797	77, 77, 74, 74	-1.722	
300 mA	-2.03	251, 250, 249, 254	-1.779	
800 mA	-2.51	704, 640, 700, 664	-1.833	

Linear regression calculations: fit (0-1) = 0.9990; Tafel slope = 132 mV/decade; exchange current density = 1.1×10^{-6} A/cm².

Electrocatalytic Activity of Nickel 200

Electrocatalytic activity should be determined on a true electrochemically active surface area basis so that current densities will be accurately known. Therefore, a comparison of the electrocatalytic activity between different electrodes requires a reproducible and consistent method of measuring effective surface area. Such a method, using low amplitude cyclic voltammetry, was carried out for this electrocatalytic comparison between nickel 200 and nickel whiskers (3). There was no problem in finding a nonfaradaic potential region for both the nickel 200 and the nickel whisker material. This provided both a confidence and reproducibility in the area calculations.

With the active electrochemical surface area of an electrode being known to an acceptable level of reproducibility by cyclic voltammetry, the electrocatalytic activity was determined by the generation of a Tafel plot. The Tafel slope and the exchange current density were the parameters used in determining electrocatalysis. Tafel plots obtained for nickel 200, determined galvanostatically from lower to higher values of current density, were quite reproducible. With proper IR (potential caused by the solution resistance) compensation, these plots were linear over five decades of current density as calculated by linear regression. A typical Tafel plot with its experimental data is shown in Fig. 1 and Table I, respectively. Table II shows that a series of Tafel experiments run on nickel 200 electrodes yielded an average Tafel slope of 135 mV/decade and an average exchange current density of 1.2×10^{-6} A/cm². These values of Tafel slope and i_0 agree favorably with those reported by Appleby *et al.* (4), who performed similar experiments and with data obtained from current industrial electrolyzers used by Teledyne Energy Systems (Baltimore, Maryland) (5).

Tafel experiments were conducted in an airtight Teflon beaker cell. Teflon was used because of its high resistivity to chemical degradation. The top of the cell provided three openings for the working, counter, and

reference electrodes. Nickel 200 plates embedded in epoxy and polished to a planar mirror finish were used as counterelectrodes as well as working electrodes in these Tafel experiments. The reference electrode was a standard calomel electrode with a minor adaptation which was necessary for IR compensation. The electrodes were supported by Teflon dowels, which extended through the openings and kept the electrode geometry relatively constant. The working electrode was approximately 3 cm from the reference electrode and 4 cm from the counterelectrode. Two additional openings were also provided for the nitrogen purge gas. All openings and fittings were sealed with O-rings. The cell was cylindrical shaped with a diameter of 7.5 cm and a height of 8 cm.

Experiments were performed at room temperature (23°C), which never varied more than a few degrees. The Teflon cell was purged prior to experiments with nitrogen gas for about 15 min to remove any dissolved gases in the electrolyte which could react at the electrodes. Purging continued throughout the experiments at a moderate rate. Reactive species were also removed by a thorough cleaning procedure, which consisted of washing the cell and electrodes in a soap solution and then rinsing with acetone, ethanol, distilled water, and electrolyte successively. The electrolyte was obtained from the stock utilized by Teledyne in their industrial electrolytic cells. It was a 25 weight percent potassium hydroxide (KOH) solution with a pH of 14.8.

Electrocatalytic Activity of Nickel Whiskers

Once surface area could be reproducibly measured and the electrocatalytic activity of conventional nickel 200 was determined with reasonable precision, a comparison with polycrystalline nickel whiskers was made. To eliminate gas masking problems and the high surface area of the porous nickel whisker electrodes, the whiskers were embedded in an inert epoxy resin. The epoxy resin filled the pores of the whisker electrode and enabled the electrode to be polished to a smooth planar surface. This allowed the nickel whisker electrode to be compared to a planar nickel 200 electrode for electrocatalytic activity on a true surface area basis, as determined by cyclic voltammetric surface area analysis. This also enabled a determination of electrocatalytic behavior based on metallurgical parameters such as microstructure and phase composi-

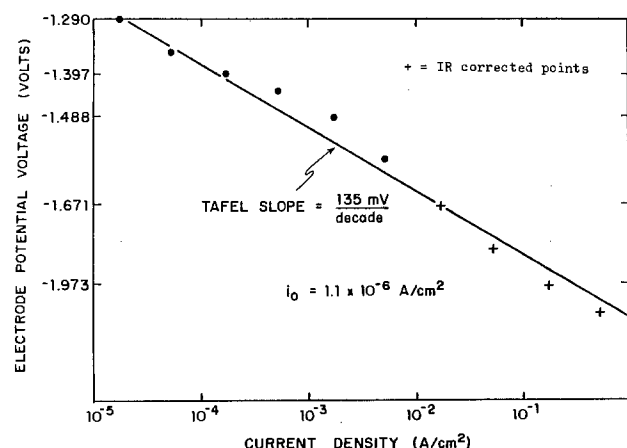


Fig. 1. Tafel plot for H₂ evolution on nickel 200 electrode in KOH.

Table II. Nickel 200 Tafel plots

Date	Tafel slope (mV/decade)	Exchange current density (A/cm ²)	Linear fit (0-1)	Experimental conditions
4/8	150	2.1×10^{-6}	0.9930	N ₂ purge, Teflon airtight cell, low [Fe] KOH, ½h equilibrium time, 1 cm ² electrode
4/9	139	1.4×10^{-6}	0.9974	
4/10	132	1.1×10^{-6}	0.9990	
4/12	135	1.3×10^{-6}	0.9753	
4/13	133	1.0×10^{-6}	0.9940	
5/29	138	1.2×10^{-6}	0.9957	

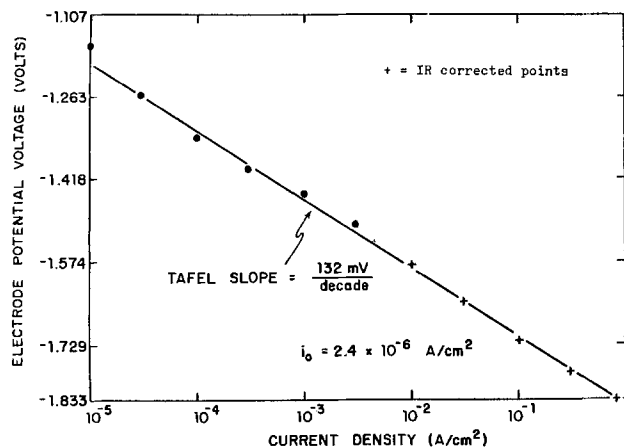


Fig. 2. Tafel plot for H_2 evolution on nickel whisker electrode in KOH.

tion. If such an innate property of the material caused increased electrochemical activity, it would now be identified and noted as an effect in addition to that normally attributed solely to the high surface area associated with these sintered whisker electrodes.

To embed the whiskers, both sintered and nonsintered assemblies, the atmosphere within the pores was removed, which allowed the epoxy to enter. The whiskers were placed on a copper current collector in a Teflon mold and held rigidly in place by a magnet. This assembly was then placed within a vacuum system. After the system was evacuated, a valve to an epoxy reservoir was opened, permitting epoxy to flow into the mold and embed the whiskers. The epoxy was outgassed in the vacuum for a short time and then cured in an oven at 80°C until completely hard. A slow curing, low viscosity epoxy consisting of Dow 331 resin, Jeffamine D-230 hardener, and Texaco accelerator 399 was used. Once cured, a Teflon-insulated wire was attached to the current collector, thereby providing electrical connection to the whiskers and making a usable electrode. The surface of the whisker electrode when polished consists of many small metal islands surrounded by an epoxy matrix.

These nickel whisker electrodes of approximately 1 cm^2 true surface area were evaluated for electrocatalytic activity under identical experimental conditions as the conventional nickel 200 specimens. A typical Tafel plot for nickel whiskers is shown in Fig. 2. The Tafel experiments resulted in an average exchange current density of $8.2 \times 10^{-7}\text{ A/cm}^2$, with an average Tafel slope of 133 mV/decade , as seen in Table III. Therefore, no significant difference in electrocatalytic activity between the two types of nickel was observed. Annealed nickel 200, which has considerably larger grains and less strain energy than non-heat-treated nickel 200, also exhibited essentially the same electrocatalytic properties as those already mentioned. It should be noted that none of the test electrodes were run for extended periods of time, and therefore, time effects were not observed nor studied.

Conclusions

From these evaluations of the electrocatalytic activity of extremely different types of microstructure, it must be concluded that the added energy of increased grain boundary area and/or any other microstructural oddity present in these whiskers does little to enhance their hydrogen evolving capabilities in KOH. However, current-voltage improvements in alkaline electrolysis using nickel electrodes are noticeably realized by increases in

Table III. Ni whisker Tafel plots

Date	Tafel slope (mV/decade)	Exchange current density (A/cm^2)	Linear fit (0 - 1)	Experimental conditions
Sintered whiskers				
6/15	125	8.4×10^{-7}	0.9945	N_2 purge, Teflon
6/22	130	9.3×10^{-7}	0.9963	airtight cell, low
6/10	135	1.2×10^{-6}	0.9921	[Fe] KOH, $\frac{1}{2}$ h equi-
6/4	132	1.3×10^{-7}	0.9955	librium time, 1 cm^2 electrode
Free whiskers				
7/1	141	1.2×10^{-6}	0.9932	
6/29	136	6.7×10^{-7}	0.9954	

electrode surface areas (1, 2). One possible consideration would have been to break up the whiskers prior to sintering into an electrode. Because the internal material of these whiskers does not show improved performance over the naturally occurring whisker surface, electrodes can be fabricated from the whiskers in their as-formed condition. Thus, they can be produced as small or as large as the condition of use might dictate. Since only a fraction of the surface area of porous electrodes is active under gas evolution, owing to gas masking conditions, efforts should be directed towards maximizing electrode flooding and active surface area. This could possibly be done by orienting the individual whiskers into some optimum configuration and/or by taking advantage of the porosity of whisker mat electrodes by using flow-through techniques.

Although the above conclusion is a negative result in this particular case, it should not be extended to imply that microstructure has no effect on electrocatalytic activity in other electrochemical systems. Under different conditions, microstructure may have a pronounced effect on electrochemical reaction rate. This is because electrocatalysis can be influenced by the solution, the specific electrochemical reaction, and the type of electrode material. Thus, it is possible nickel whiskers may have additionally enhanced electrocatalytic activity for hydrogen evolution over nickel 200 in solutions other than potassium hydroxide or for the oxygen evolution reaction in potassium hydroxide solutions.

Finally, the data in Tables II and III and in Fig. 1 and 2 show linearity for five decades of current, indicating a well-behaved activation-controlled reaction whose kinetics are well represented by these measurements. The linearity of these plots lends support to the argument that there is only one Tafel slope for hydrogen evolution on nickel 200 in KOH, as opposed to two slopes, resulting from a change in reaction mechanism at high values of current density.

Manuscript submitted Jan. 6, 1984; revised manuscript received Aug. 6, 1984.

The University of Virginia assisted in meeting the publication costs of this article.

REFERENCES

- P. J. Moran, Ph.D. Thesis, University of Virginia, Charlottesville, VA (1980).
- G. L. Cahen, Jr., P. J. Moran, L. L. Scribner, and G. E. Stoner, *This Journal*, **128**, 1877 (1981).
- J. D. Hansen, M. S. Thesis, University of Virginia, Charlottesville, VA (1982).
- A. J. Appleby, G. Crepy, and J. Jacquelin, *Int. J. Hydrogen Energy*, **3**, 21 (1978).
- J. N. Murray, Teledyne Energy Systems, Baltimore, MD, Personal communication (1981).



Ellipsometric Study of the Etch-Stop Mechanism in Heavily Doped Silicon

E. D. Palik, V. M. Bermudez, and O. J. Glebocki

Naval Research Laboratory, Washington, DC 20375

ABSTRACT

The etch-stop phenomenon which occurs in both p- and n-Si when the doping density exceeds 10^{19} cm^{-3} has been studied *in situ* with ellipsometry. Biasing the samples both anodically and cathodically from open-circuit potential causes layers to grow which can then be observed to etch back when the applied potential is released. We are lead to the conclusion that p-Si etch stops because of spontaneous passivation which produces a thin oxide-like layer, while n-Si shows a tendency to etch stop, probably owing to formation of a prepassive layer.

Aqueous solutions of KOH (1, 2) and ethylenediamine pyrocatechol (3) are widely used as orientation-dependent etches of Si, the etch rate of {100} surface being 1-2 orders of magnitude faster than that of the {111} surface. The etch rates are generally independent of free-carrier type and concentration (4, 5) up to 10^{19} cm^{-3} . Above this density, the etch rates on both surfaces are observed to slow down drastically (1-3 orders of magnitude) for both boron (p) and phosphorus (n) dopants, although the stopped etch rate is still angstroms per minute. This etch stop is used in the fabrication of various device configurations (6).

The mechanism for etching of boron-doped Si (B:Si) in pyrocatechol etchant (7) has been described as an oxidation-reduction process in which oxidation produces electrons in the Si surface (100Å layer) which, in turn, are used in the reduction process at the surface. When the hole doping density passes 10^{19} cm^{-3} , the electrons recombine with holes instead, thus stopping the reduction step. The etch-rate ratio (ERR) for this model varies as: $\text{ERR} \propto [1 + (p/p_c)^2]^{-4}$, where p is the doping density and $p_c = 5.5 \times 10^{19} \text{ cm}^{-3}$ is a fitting parameter related to recombination-theory parameters at high doping levels in the range 10^{19} - 10^{20} cm^{-3} . This model is not applicable to n-type Si. Another mechanism (5) suggests that B:Si and phosphorus-doped Si (P:Si) can spontaneously passivate in aqueous KOH to form a thin, protecting oxide layer. It is suggested that the tendency to grow an oxide is encouraged by the strain in the Si surface due to the high dopant density, and a borate or phosphate glass is formed.

We have made *in situ* ellipsometric studies of the formation and dissolution of surface layers as a function of applied potential bias (both cathodic and anodic) for boron- and phosphorus-doped silicon both below and above 10^{19} cm^{-3} . These studies indicate that at open-circuit potential (OCP) B:Si above 10^{19} cm^{-3} has a layer on the surface suggestive of the connective or transition layer between crystalline Si (c-Si) and amorphous SiO_2 (a-SiO₂). P:Si above 10^{19} cm^{-3} has a different layer on the surface. Similar layers are observed on lightly doped Si when the applied potential is made anodic (connective-layer formation) and cathodic (cathodic-layer formation), respectively. Consequently, we have attempted to understand the etch-stop layer formation in terms of band bending (or equivalently, a shift in OCP) and the numbers of holes or electrons needed at the surface to induce the appropriate chemical reaction to dominate, thus producing the anodic connective layer or the cathodic layer.

Experimental Approach

A spectroscopic polarization-modulation ellipsometer (8) has been adapted to measure ψ and Δ for a Si sample suspended in 2M KOH in a BK-7 glass (angle of incidence: 60.2°) or fused quartz (54.6°) hollow prism. The samples were approximately $1 \times 4 \times 0.03 \text{ cm}^3$ obtained by cleaving standard Si wafers polished on one side. Samples were immersed $\sim 2 \text{ cm}$ into the etchant. Leads were made with InGa eutectic and a pressure contact. Potential was measured with respect to a standard calomel reference electrode (SCE). Measurements were made at three wavelengths 800, 435.8, and 319 nm. Ambient temperature was $\sim 20^\circ\text{C}$. A microcomputer read and printed the pertinent parameters, such as applied potential V ; current I , photomultiplier high voltage (proportional to $\log R$, where R is the sample reflectance), and ellipsometric parameters ψ and Δ . Further details concerning the optical system will be given elsewhere (13).

We have modeled the surface layers (11) in terms of physical and chemical mixtures (9) of SiO_2 , anticipating that a connective layer will consist of such a material. A multilayer model is used to simulate gradation of optical constants across the interface.

Results

Lightly doped B:Si and P:Si.—Palik *et al.* (5) and Faust and Palik (10) measured the open-circuit potential and passivation potential (PP) for a large number of Si samples of different doping densities. Below 10^{19} cm^{-3} the OCP was nearly constant. They observed that above 10^{19} cm^{-3} the OCP for p-type samples tended to shift in the anodic direction by 0.2-0.6V, while the OCP for n-type samples shifted in the cathodic direction by about 0.1V. They also noted that the PP tended to approach the OCP at high doping levels for both n- and p-type Si, this separation being $\sim 0.5\text{V}$ below and nearing $\sim 0.1\text{V}$ above 10^{19} cm^{-3} . Certain samples were erratic, sometimes showing a peak in current just prior to passivation and sometimes not showing a peak. The data suggested that perhaps there is a prepassive layer which forms at a potential slightly cathodic of PP and forces the etch to stop when heavy doping shifts PP toward OCP.

Some of our results for light doping have been reported (11-13) along with a model to explain them. They are summarized in Fig. 1a, for p {111} Si with $1.8 \times 10^{15} \text{ cm}^{-3}$, for anodic and cathodic directions starting at OCP (solid dot). These are composite curves taken from different runs.

1985

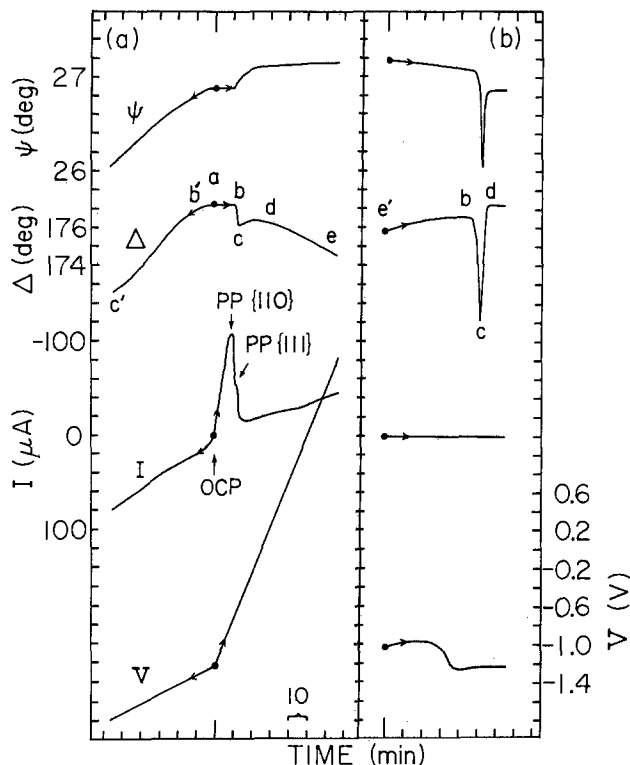


Fig. 1. (a): Changes in ψ , Δ , and I starting at the solid circle at OCP ($-1.2V$) as a function of applied potential V anodic and cathodic for p {111} Si boron doped with $1.8 \times 10^{15} \text{ cm}^{-3}$. The sweep rate is different for anodic and cathodic directions. Angle of incidence $\theta = 54.6^\circ$. (b): Once a thin anodic-oxide layer has grown to near point e, the applied potential is released and the changes in ψ , Δ , I , and OCPV are followed as a function of time.

Generally, n {111} Si gave similar results. Without going into the detail of the modeling, we can assign the various features of the curves. The current I shows a peak and a shoulder in the anodic direction for the nominal {111} plane. The first peak is due to passivation of the edges and back of the sample with their exposed fast etching {100}, {110}, etc., surfaces. Coating these surfaces with glycol thylate or arranging a cell in which only the wafer surface contacts the liquid removes this first peak. The shoulder is the true {111} passivation peak.

The sample is etching at the solid dot at a rate of $\sim 35 \text{ \AA/min}$. As etching progresses at OCP, there is a slight roughening of the surface, which over several hours results in decreases of several tenths of a degree in ψ and Δ . In contrast to the case for GaAs (14), there is no indication of a prepassive layer forming before PP (decrease in Δ , increase in ψ) as the applied potential is slowly swept anodic.

We model the surface at OCP as an equilibrium etching layer of 4 \AA of $\text{SiO}_{0.2}$ (essentially disordered Si). At point b, another layer begins to form and etching stops. We model the region b-c as the sudden appearance of a rudimentary connective layer modeled as $\text{SiO}_{0.4}$ which undergoes change (gradation) to point d with a- SiO_2 also growing on top. At point d the connective layer stabilizes and a- SiO_2 grows on top of the connective layer from point d to e. The experiment and fitting were done for three wavelengths, although we show experimental results only for $\lambda = 435.8 \text{ nm}$.

In the cathodic direction (starting at OCP) no changes in ψ and Δ occur for about a tenth of a volt; then a layer starts growing at point b' with both ψ and Δ decreasing. We term this a "slush" layer because it is assumed that the layer is composed of insoluble silicates, as discussed below (13). It has growth and etchback features suggesting that n and k vary as the layer grows or etches (where $\tilde{n} = n - ik$ is the complex index of refraction). Interestingly, this layer continues to grow when the potential sweep is halted at a cathodic bias at point c', even for days, al-

though slowing down. The layer takes on a tan-gray color. When the potential is released to OCP conditions, this slush layer disappears slowly over several hours with the ellipsometric parameters returning very nearly to their original OCP values, but not totally along the same path in ψ - Δ space as was followed during growth. A slight anodic potential speeds up this process. Some roughening of the surface occurs as indicated by the final values of ψ , Δ , and R . We have used an SiO_x model to account for this layer (12) by assuming an equilibrium etching layer of 4 \AA of $\text{SiO}_{0.2}$ and then allowing this layer to grow at point b' getting thicker and in the process changing to $\text{SiO}_{0.7}$. This amounts to a substantial decrease in the initial large values of n and k for $\text{SiO}_{0.2}$.

As has been observed by Glembocki *et al.* (15), the etch rate is bias dependent. For p-Si, the rate drops very little in the cathodic direction, while, for n-Si, the rate decreases drastically at a few tenths of a volt cathodic. This has been qualitatively explained in terms of an abundance of electrons in the surface accumulation layer for n-Si, which favors electrolysis rather than etching. Without going into details, we note only that experimentally the etching "stops" for cathodic potential for n-Si and continues for p-Si. In both cases, some slush layer grows; however, it grows much more rapidly on the n-Si surface. Presumably, the decrease in etch rate is due, in part, to incomplete etching with accumulation of incomplete silicates which stick to the surface forming the slush layer. The p-Si continues etching at only a slightly reduced rate, producing H_2 and mostly complete silicates in the form (16) of soluble $\text{SiO}_2(\text{OH})_2^-$, while only a little incomplete etching occurs, giving rise to a more slowly growing slush layer.

When a thin oxide is established at a potential $< 5V$ as at point e' and then the applied potential is released, the layer begins to etch back at a slow rate of $\sim 0.3 \text{ \AA/min}$, as shown in Fig. 1b. Very characteristic of all samples $< 10^{19} \text{ cm}^{-3}$ are small, rapid dips in ψ , Δ , V (and R) when the connective layer is reached at point b. This effect has been modeled previously (11) as the SiO_x connective layer becoming more dielectric-like (O/Si ratio increasing), so that its optical constants decrease drastically, and then dissolving prior to the onset of etching of c-Si. In any event, these features (b \rightarrow d) are the signature for the onset of Si etching. Oxides grown at less than 5V, we term "soft"; those grown at higher potentials are referred to as "hard" because of the similarity in etch-back behavior to that of device-quality thermal oxides.

For {111} surfaces (10, 11) etch back of soft anodic oxides produces small dips in ψ and Δ [~ 0.3 and $\sim 2^\circ$ with full width at half maximum (FWHM) values of 2-4 min, respectively] and small dip in R , but etch back of hard anodic oxides produces large dips in ψ and Δ ($\sim 5^\circ$ and $\sim 15^\circ$ with FWHM values of 6-15 min, respectively) and a large dip in R . The connective-layer model (11) explains the soft-oxide etch-back effects, while we are presently trying to develop a transient-roughness model to explain the hard-oxide effect. For the fast etching (lightly doped) {100} surface, etch back of a soft anodic oxide produces a large dip in ψ and Δ ($\sim 5^\circ$ and $\sim 15^\circ$ with FWHM values of 2-4 min, respectively) and a return of ψ and Δ nearly to their initial values; a large, steady decrease in R occurs. Then, ψ and Δ decrease, while R continues to decrease, indicating rapid roughening of the surface. Etch back of a hard anodic oxide produces large decreases in ψ and Δ ($\sim 10^\circ$ and $\sim 35^\circ$) which do not recover much along with a steady decrease in R . This is a permanent roughening of this fast etching surface (13). The roughening effects no doubt dominate the small connective-layer effects shown in Fig. 1b.

Heavily doped B:Si and P:Si.—For a p {100} Si sample with $2 \times 10^{20} \text{ cm}^{-3}$, the composite results are shown in Fig. 2a. The sample is HF cleaned first, washed in deionized water, and then allowed to remain in 2M KOH for several minutes before an anodic potential is applied (at the solid dot). No peak in passivation current is seen, as

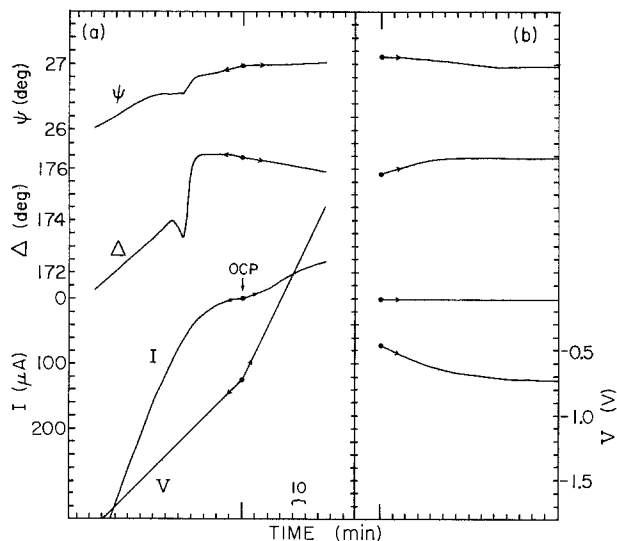


Fig. 2.(a): Changes in ψ , Δ , and I starting at the solid circle at OCP ($-0.7V$) as a function of applied potential V anodic and cathodic for p {100} Si boron doped with $2 \times 10^{20} \text{ cm}^{-3}$. The sweep rate is different for anodic and cathodic directions. Angle of incidence $\theta = 54.6^\circ$. (b): Once a thin anodic-oxide layer has grown, the applied potential is released and the changes in ψ , Δ , I , and OCPV are followed as a function of time. No dips in ψ , Δ , or V occur even for another 3h beyond the right edge of the graph, in contrast to results in Fig. 1(b).

though an oxide layer were already on the surface and merely thickened as an anodic potential was applied. It has previously been shown that a very thin oxide layer is sufficient to cause the disappearance of the passivation peak (5).

In the cathodic direction starting again (at the solid dot), very interesting dips in ψ and Δ occur, after which both ψ and Δ decrease in a manner similar to Fig. 1a, suggesting growth of a slush layer. The small dips in ψ and Δ in Fig. 2a for cathodic potential appear to be muted versions of what would be seen at OCP after etch back for the lightly doped p {100} surface, *i.e.*, large dips in ψ and Δ occurring over 2-4 min. The concurrent growth of slush layer also tends to skew the line shape. This suggests that cathodic potential allows the further etch back of the connective layer and then the start of etching of c-Si. Most of the results of Fig. 2 were also obtained for a {111} B:Si sample with $2.4 \times 10^{20} \text{ cm}^{-3}$. In the cathodic direction, however, there is little or no dip in ψ and Δ observed since these features are obscured by the larger effects of rapid slush layer growth.

After a definite anodic oxide has been grown and the applied potential released, the results of Fig. 2b are obtained. ψ and Δ decrease and increase, respectively, in a manner typical of an SiO_2 film getting thinner. Then, no dips in ψ and Δ are observed even after several hours. OCP stabilizes at $-0.7V$. We conclude that the surface has spontaneously grown a connective layer (or maintains a portion of the one anodically grown), so that the c-Si surface is never directly reached by the etchant.

To check this possibility in more detail, we prepared a p-Si {111} wafer of free-carrier density $N = 1.6 \times 10^{15} \text{ cm}^{-3}$ half implanted with $5 \times 10^{15} \text{ cm}^{-3}$ boron at 100 keV and then annealed at 1000°C for 1h. The peak free-carrier density was estimated to be $\sim 1 \times 10^{20} \text{ cm}^{-3}$, based on an implantation depth of $\sim 0.5 \mu\text{m}$ and a four-point probe measurement of resistivity $\rho = 0.00010 \Omega \text{ cm}$. Also, no H_2 bubbles were observed on the surface, indicating that the etch stop was in effect. After stripping of any oxides which may have formed, the sample was arranged with a smooth vertical motion of about 2 cm so that the top (T) of the sample (light doping) could be measured ellipsometrically; then the sample could be raised enough to illuminate the bottom (B) (heavy doping). The uncertainty in ψ and Δ was $\pm 0.1^\circ$ owing to the mechanical motion of the sample plane.

The differences in the ψ and Δ parameters for the T and B samples at OCP should be due to an additional layer on the B sample, a spontaneously grown connective layer. This difference was measured three times by anodizing both the T and B samples to 0 V and following the etch back of sample T at point d in Fig. 1b and then moving to sample B. The change from T at point d to B was made quickly, before many etching bubbles formed on the T surface. The scattering effect of macroscopic bubbles is to lower ψ and Δ slightly. The average experimental changes in ψ and Δ are given in Table I. We also measured $\delta\psi$ and $\delta\Delta$ when both surfaces had anodic oxides grown to 0 V. The average experimental changes in ψ and Δ are also given in Table I.

To fit these two sets of $\delta\psi$ and $\delta\Delta$, we have modeled the etching T surface as c-Si covered with 4\AA of $\text{SiO}_{0.2}$ equilibrium etching layer and the B surface as c-Si covered with 7\AA of $\text{SiO}_{0.4}$ connective layer. The equilibrium etching layer is included for self-consistency as it improves other modeling of the initial anodization process and the growth of the cathodic slush layer (12, 13). The anodized T and B surfaces are modeled as c-Si under 7\AA of $\text{SiO}_{0.4}$ connective layer under 10\AA of SiO_2 (identical oxides on both surface). For the T surface, we used the pure-Si optical constants $n = 4.88$ and $k = 0.14$ at 435.8 nm (18). For the B surface, we assumed the optical constants $n = 4.79$ (1.8% smaller) and $k = 0.16$ (14% larger) to fit the data. Such changes (n smaller, k larger) have been observed for heavily doped B:Si (19) and As:Si (20, 21). We assumed that both halves, T and B, are microscopically smooth and isotropic and that sample B is uniformly implanted to a depth greater than the penetration depth of light at 435.8 nm ($\sim 0.2 \mu\text{m}$).

The calculated changes in ψ and Δ from T to B upon etch back are given in Table I along with the calculated changes in ψ and Δ from T and B for identical oxides. We give differences because the absolute values of ψ and Δ [which have not been corrected for systematic errors in the ellipsometer (8)] are accurate only to few tenths of a degree, whereas changes in ψ and Δ can be measured with high precision ($\sim 0.01^\circ$) at a fixed wavelength. Considering the mechanical motion involved and the assumption of equal oxides on the T and B surfaces, the reasonable agreement suggests that there is a connective layer on the B etch-stopped surface compared to the etching T surface. The calculated $\delta\psi$ and $\delta\Delta$ are more sensitive to the substrate optical constants than to the exact values of x and thickness. However omission of any layer in the model can change the signs of $\delta\psi$ and $\delta\Delta$ or their magnitudes by a factor of two.

The results for lightly doped P:Si are similar to those for lightly doped B:Si except that, in the dark, owing to lack of holes, no additional oxide grows between points d and e in Fig. 1a. The results for an n {111} Si sample with $5 \times 10^{20} \text{ cm}^{-3}$ are shown in Fig. 3. In this case, we first start with the sample having a soft anodic oxide. Upon release of the applied potential, classical etch back of the layer begins. The usual dips in ψ and Δ for an n {111} surface occur, but then there is immediately rapid growth of what appears to be a slush layer (still at OCP = $-1.3V$). This slush layer grows indefinitely (we observed its growth for 6h without signs of termination and little change in OCP). Recall that we have previously identified the rapid slush layer growth on cathodically etch-stopped, lightly doped n-Si with the decrease in etch rate. During subsequent anodization, the optical effects of the growth of the

Table I. Experimental and calculated changes in ψ and Δ , $\delta\psi(\text{T-B})$ and $\delta\Delta(\text{T-B})$ for surfaces T and B with anodic oxides and after etch back of the anodic oxide

	Anodic oxide		Etch back	
	Exp.	Calc.	Exp.	Calc.
$\delta\psi(\text{T-B})$	-0.25	-0.32	-0.23	-0.31
$\delta\Delta(\text{T-B})$	-0.21	-0.22	-0.53	-0.83

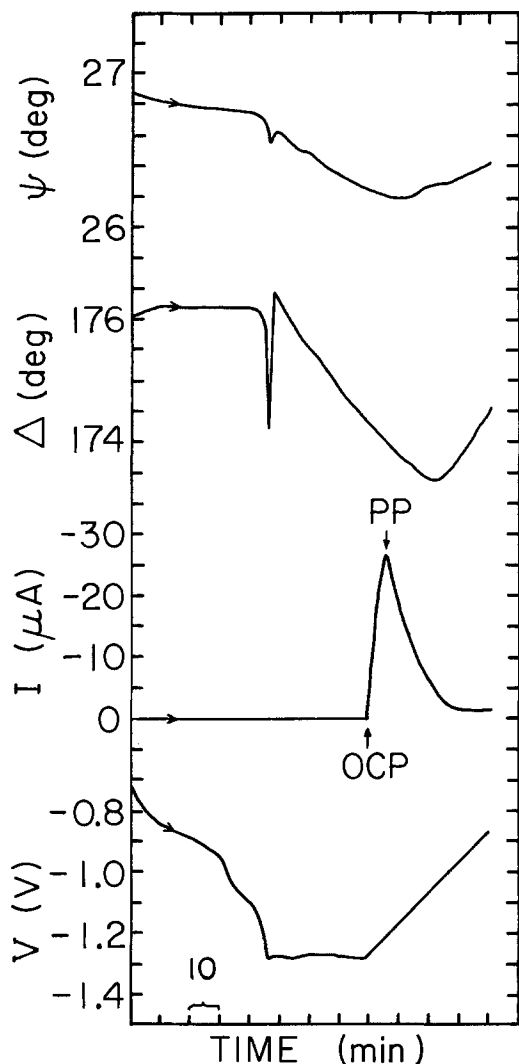


Fig. 3. Once a thin anodic-oxide layer has grown on n {111} Si phosphorous doped with $5 \times 10^{20} \text{ cm}^{-3}$, the applied potential is released and the changes in ψ , Δ , I , and OCP V are followed. When a steady-state OCP = -1.3 V is reached, a potential is applied which causes current to flow and passivation to occur (peak in I at the PP). The slush layer begins to disappear and masks formation of the connective layer and SiO_2 layer. Ultimately, the slush layer disappears and growing oxide layer can be seen (not shown). Angle of incidence $\theta = 54.6^\circ$.

connective layer on heavily doped P:Si are obscured by the dissolution of the slush layer. However, a PP is clearly seen with $\text{PP-OCP} < 0.1 \text{ V}$. Preliminary experiments with As:Si {111} with $7 \times 10^{19} \text{ cm}^{-3}$ gave results similar to Fig. 3.

Discussion

We will now proceed to a discussion and interpretation of the experimental results given above. The essential finding may be summarized as follows. Using ellipsometry, in conjunction with electrochemical measurements, we have detected a layer on the surface of etch-stopped (heavily B-doped) p-type Si at OCP which is similar to that observed on lightly doped material under anodic bias (for which the etch rate is drastically reduced). Likewise, for etch-stopped (heavily P-doped) n-type Si at OCP, we have observed a layer similar to that formed on lightly doped samples under cathodic bias (for which the etch rate is also greatly diminished). The implication is that the processes which occur for lightly doped Si at anodic or cathodic bias occur spontaneously at OCP for heavily doped material. What follows is a discussion of this idea in terms of both electrode potentials and energy levels at the Si/electrolyte interface. A detailed microscopic description of the relationship between changes in ψ and Δ and those in the surface films is deferred until a

later publication (13). For the present, the ellipsometric results are used simply as a basis for the above analogy between heavily doped Si at OCP and lightly doped Si under bias.

Electrode-potential considerations.—The applied potential divides between the Si space-charge layer and the liquid Helmholtz layer (electrode potential), the latter determining the chemical (or electrochemical) reactions that take place at the semiconductor surface. The nature of the semiconductor bands at the surface—depleted, accumulated, or pinned—will play a critical role in the effect that the applied bias has on the electrode potential. This, in turn, can have a profound influence on how H_2O and OH^- interact with Si-Si bonds. In fact, we have suggested that etching is the sequential attack of Si bonds by H_2O and then OH^- (11, 15).

For lightly doped n-Si at OCP, the conduction band is in electron accumulation and for p-Si the valence band is depleted of holes. In the case of n-Si, variations in the applied bias around OCP and especially cathodic will have a significant effect on the electrode potential and, therefore, on the chemical reactions which can occur. However, for p-Si changes in applied voltage, at least cathodically, do not significantly change the electrode potential.

It has been suggested that the rate-determining steps (RDS) for both etching and connective-layer growth are chemical (15). However, the nature of the RDS was shown to be a function of electrode potential. For example, at the passivation peaks of I-V curves the oxidation of n- or p-Si (connective-layer growth) dominates over the dissolution of the oxidized species and etching stops. With p-Si, further anodic shifts increase the hole concentration at the surface and induce thick oxide growth. However, the n-Si becomes depleted and further applied bias has little effect on the electrode potential or surface charge and no further oxide grows. We therefore observe that an anodic potential creates an anodic etch stop, as evidenced by the observation of the connective layer.

An analogous situation holds for n-Si under cathodic bias. As mentioned, the n-Si exhibits metallic behavior at the surface, owing to an accumulation of electrons at OCP. A cathodic bias changes the electrode potential in such a manner as to change the nature of the RDS. Current begins to flow, implying that the bias has changed the energetically favored reaction at the surface from etching, accompanied by hydrogen evolution and (possible) oxidation of OH^- ions to electrolysis of water accompanied by hydrogen evolution and production of current carrying OH^- ions. This can also be thought of in terms of energy levels, as discussed in the next section.

The effect of cathodic bias on p-Si is straightforward, since the surface is already depleted (maybe pinned). Increasing the applied potential cathodically has virtually no effect on the electrode potential, and, consequently, the current saturates and etching is affected very little.

Heavy doping of n- and p-Si (indicated as n^+ and p^+) can also induce metallic-like surface conditions. In the case of the p^+ -Si, a large number of holes at the surface causes spontaneous passivation and is accompanied by an anodic shift of the OCP. The OCP is now determined not by etching reactions (involving the conduction band) but by oxidation processes (involving the valence band). However, cathodic bias (which will change the electrode potential) begins to shift the surface reactions toward more balance between the cathodic and anodic reactions, and the oxide can be etched back. From these considerations, one might expect a resumption of etching at slight cathodic bias, as Fig. 2a suggests.

The case of the n^+ -Si etch stop is somewhat more difficult to understand. The analogy with the cathodic etch stop for lightly doped Si is attractive, since in each case the surface is metallic-like. But it is hard to imagine electrolysis dominating etching at OCP with no net current flow. We suggest another mechanism. We will make a note of important experimental observations: (i) the passivation potential for heavily doped n-Si shifts cathodically about 0.5 V and approaches the OCP, while OCP

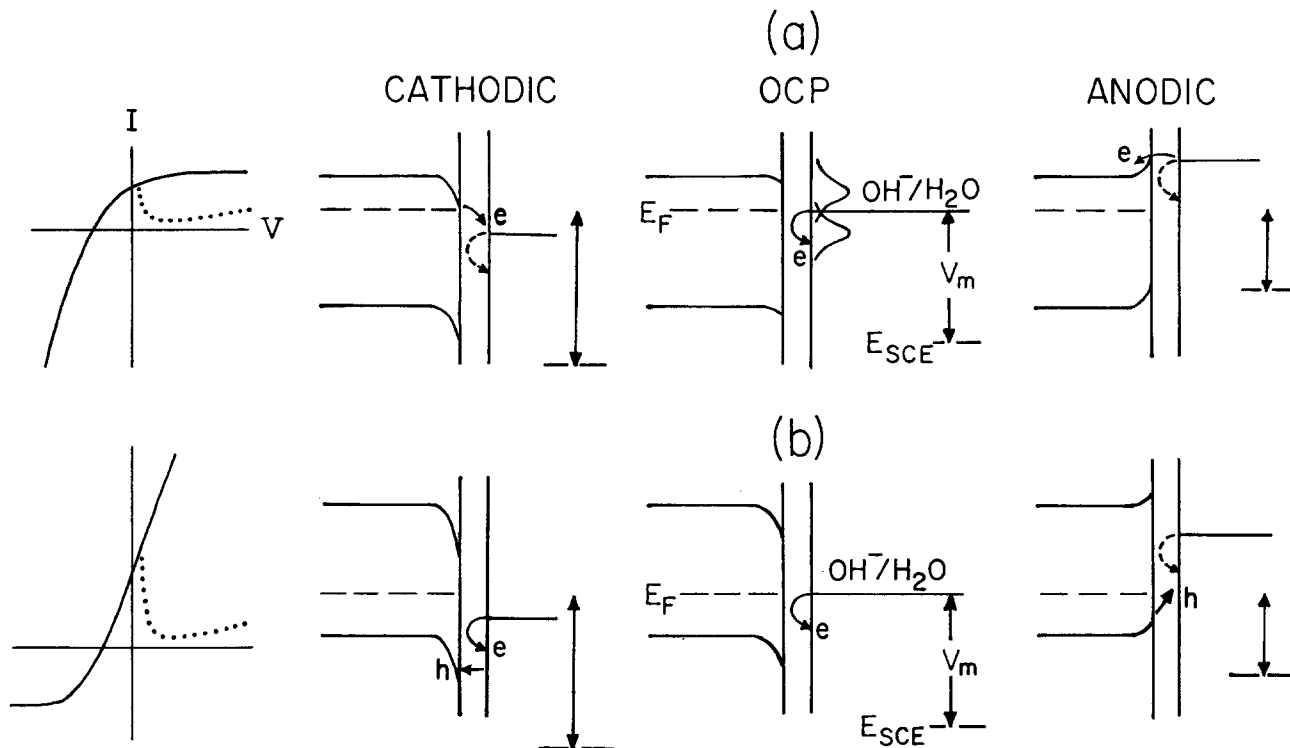


Fig. 4. (a): Schematic diagram of band bending and redox couple as a function of applied potential anodic and cathodic for n-Si. Fermi levels of bulk Si and SCE are indicated by dashed lines. The left inset shows large forward-bias current and reverse-bias saturation current with the onset of passivation (dotted line) masking saturation. (b): Schematic diagram of band bending and redox couple as a function of applied potentials anodic and cathodic for p-Si. The left inset shows reverse-bias saturation current and large forward-bias current with the onset of passivation (dotted line) masking current runaway.

shifts only 0.1V compared to lightly doped Si; (ii) Glembocki *et al.* (15) found that the etch rates for lightly doped n-Si were substantially reduced between the OCP and PP well before the PP was reached. In Ref. (15), the etch stop between OCP and PP was explained by a shift in the RDS toward connective-layer growth. For potentials between the PP and OCP, there were competitive processes, the oxidation of Si and the dissolution of the oxidized species, as well as dissolution of the crystalline substrate. In this case, as long as some oxidation occurred, the etching would be reduced and some thin layer of prepassive oxide would form only to be etched off and then regrown. In fact, the more rapid the oxidation, the lower the etch rate, until finally the connective layer was established. This suggests that at some narrow range of cathodic bias there might be a resumption of etching before the usual n-Si cathodic etch stop takes over. In the next section, we will consider the role of the band edge in this process.

Energy-level consideration.—We now give a complementary discussion of etching and etch stop based on an energy level approach. Such a band-energy-level picture can be useful, although the details are necessarily sketchy. These ideas are illustrated in Fig. 4 and 5 in terms of the Si conduction and valence bands, the redox couple level of $\text{OH}^-/\text{H}_2\text{O}$ and the Fermi levels. In Fig. 4, we assume a redox couple $\text{OH}^-/\text{H}_2\text{O}$ supplies the species for etching, electrolysis, and oxidation. We illustrate this reaction region as a thin layer between c-Si and the electrolyte. This can be the region where the surface states and the decomposition states (23) involved in the reactions are located, where initial layers begin to grow or where the Helmholtz layer forms. The $\text{OH}^-/\text{H}_2\text{O}$ couple with its Fermi level is shown at OCP, the lower lobe being the filled electron states due to OH^- and the upper lobe being the empty electron states to be associated with H_2O . This population distribution is omitted in other panels of Fig. 4. We do not include the decomposition states of $\text{SiO}_2(\text{OH})_2^-$ and SiO_2 or the surface states, since we do not know their locations or distributions in such a variety of complicated reactions (24). The SCE Fermi level is also

indicated, since all measured potentials V_m are between the Si bulk Fermi level and the SCE. The positions of the various levels are only approximately to scale, the $\text{OH}^-/\text{H}_2\text{O}$ couple being 1.1V above the SCE (24). The horizontal dimensions are not to scale. We assume that an applied potential moves the liquid levels in unison with the SCE level. Note, that in Fig. 4 we have chosen to keep the bulk Si bands constant from panel to panel rather than the SCE Fermi level.

At OCP (-1.2V), we show the bands bent down, since it has been determined that for n-Si flatband occurs near

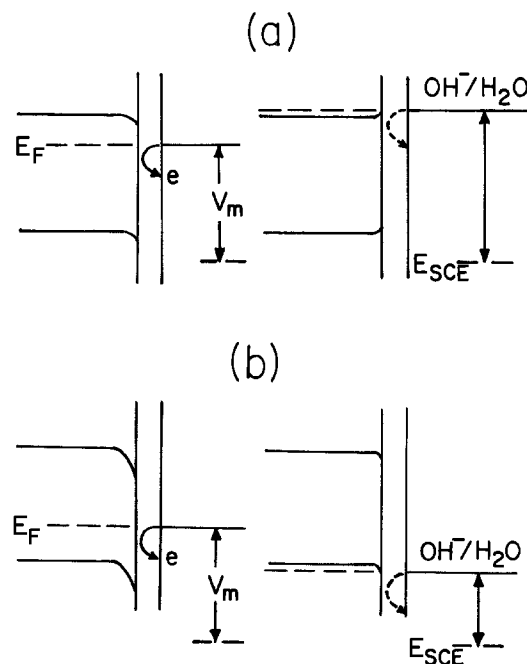


Fig. 5. (a): Schematic diagram of band bending and redox couple for lightly and heavily doped n-Si suggesting how OCP shifts cathodic. (b): Schematic diagram of band bending and redox couple for lightly and heavily doped p-Si suggesting how OCP shifts anodic.

-1.0V, while for p-Si it occurs near -0.2V (22). The etching reaction transfers an electron from the OH⁻ into the Si surface bond (or the conduction band at the surface) and then to the etch products (no net current flow), as the semicircular arrow indicates. This sequence of charge transfer must be maintained in order for etching to continue.

If the charge transfer sequence is broken, one expects the etching to stop. This may be accomplished in n-Si through a cathodic bias (15) when strong accumulation of electrons occurs in the conduction band. Then, electrons can flow from the Si electrode to solution via the OH⁻/H₂O couple. Water, which would normally participate in etching, is electrolyzed to produce H₂ and current carrying OH⁻ through the reaction $\text{Si} + 2\text{H}_2\text{O} + 2e^- \rightarrow \text{Si} + \text{H}_2 + 2\text{OH}^-$. This cathodic current is shown schematically in the I-V curve at the left side of Fig. 4a. Also, OH⁻ ions cannot easily discharge electrons into the accumulated conduction band, owing to the relative positions of the redox Fermi level and the conduction-band edge at the surface. Both mechanisms would decrease the etch rate, as the dashed semicircular arrow indicates.

Anodic potential applied to n-Si raises the OH⁻/H₂O level with respect to the conduction band, causing electron current to flow into the depleted conduction band of Si, presumably with some etching continuing. Eventually, the few thermal holes can fall into the filled redox state, causing some oxide to grow, stopping the etching, and drastically reducing the nearly saturated current at passivation. This is shown as a dotted line in the I-V curve. We observe that only the thin connective layer can be grown in the dark.

An etch stop with similarities to both the cathodic etch stop and the anodic etch stop (connective layer) occurs for n⁺ doping (Fig. 5). As the doping density is raised, the semiconductor Fermi level rises above the OH⁻/H₂O couple initially; then, as the Fermi levels equilibrate, electrons flow from Si to liquid. We note that the upward Fermi-energy shift of the semiconductor might produce a slight cathodic increase in the OCP as is observed (OCP = -1.3V). The space-charge region is shown narrow with a slight upward band bending. As Fig. 3 shows, while etching has stopped (slowed down drastically), a slush layer continues to grow. The appearance of this layer signals that, while water continues to attack Si-Si bonds, subsequent OH⁻ attack has been inhibited, so that mostly incomplete, nonsoluble silicates are formed which stick to the surface.

At equilibrium, no current flows (Fig. 5a). It is now somewhat difficult to understand the etch stop. We can only suggest two possibilities: (i) if there is a large upward band bending (not shown), this would form a barrier to electron transfer from OH⁻ to the conduction band, thus interrupting the etching charge transfer process, just as in the cathodic panel of Fig. 4a electrons are stopped from moving from the redox level to the conduction band; (ii) since the PP has shifted very close to OCP, oxide attempting to form consumes OH⁻, thus slowing the etch rate. This prepassive layer undergoes etch back and growth (perhaps as a monolayer). We have not clearly seen its presence by ellipsometry, since the slush layer dominates, and we have not seen it in lightly doped Si. Note, however, that as soon as an anodic potential is applied, the surface passivates within <0.1V in spite of the slush layer, implying that OH⁻ can penetrate it. We are tempted to compare the right panel of Fig. 5a with the right panel of Fig. 4a as regards transfer of electrons from OH⁻ to the conduction band, not to produce net current, but to form the prepassive connective layer. The few thermal holes available would be needed to start the oxidation of Si and keep the net current zero.

For lightly doped p-Si the Fermi level is much lower than the OH⁻/H₂O level before contact. A large band bending is induced when the semiconductor is brought into contact with the electrolyte at OCP (see Fig. 4b), since the OH⁻/H₂O couple discharges electrons into the

semiconductor surface to equilibrate the Fermi levels. The etching charge transfer process continues, however.

Cathodic bias drives the p-Si into depletion (Fig. 4b), and, therefore, the energy separation between the conduction band and the OH⁻/H₂O couple becomes almost constant and the current saturates. The little current that flows is shown schematically in the I-V curves and is due to a small number of holes in the H₂O redox states flowing into the valence band during electrolysis. The etching charge-transfer sequence is not interrupted since electrons from redox tail states can still reach the conduction band so etching continues.

With the application of an anodic potential (Fig. 4b), hole current initially flows from p-Si to the filled electron states of the OH⁻/H₂O couple. This increase in current is shown in the I-V curve of Fig. 4b. With further anodic bias, initial oxide (connective-layer) growth is induced. This stops the etch and produces a drastic drop in current, as the dotted portion of the I-V curve shows. A thick oxide can be grown since there are plenty of holes available.

Heavy doping of a p-Si sample at OCP to produce a p⁺-Si sample moves the bulk Fermi level toward the valence band (see Fig. 5b). These holes move to the electron-filled redox couple state, lowering its Fermi level as equilibrium is achieved. The OCP shifts in the anodic direction (OCP = -0.7V), a potential which favors initial growth of the connective layer, and etching stops. Conversely, note that one could argue that the etching charge transfer sequence is interrupted because the electron-filled redox states are too far below the conduction band. However, the ellipsometric observations of connective layer rule this out as the primary etch-stop mechanism.

Summary

Ellipsometry has been used to "tag" optically the events that occur during anodization and etching and, thus, to permit correlation among the various processes. The microscopic model relating changes in the different interfaces to observed variation in ψ and Δ is beyond the scope of the present work and will be presented elsewhere (13). Specifically, we have shown that etching through the connective layer on a lightly doped substrate is signaled by the appearance of dips (negative peaks) in ψ and Δ . The absence of such dips for a heavily doped B:Si substrate indicates that the connective layer is never penetrated (or else spontaneously regenerated). The persistence of the connective layer and the drop in etch rate are both related to the shift in OCP. Similarly, cathodic bias of a lightly doped n-type sample leads to rapid slush layer growth related to a decrease in etch rate (cathodic etch stop). For heavily doped P:Si, we observed the optical signature of rapid slush layer growth immediately upon etching through the connective layer at OCP. This is taken as an indication that what happens on the surface of lightly doped, cathodically etch-stopped n-Si may also happen spontaneously at (the shifted) OCP for heavily doped P:Si; alternately, a prepassive connective layer may begin to form with subsequent slow down of etch rate. Heavily doped As:Si behaves similarly. We assume that other dopants, such as Sb (n) and Al (p) would also etch stop if the doping density could be raised toward 10^{20} cm⁻³. Of special interest is the fact that the connective layer on p⁺-Si can be removed by slight cathodic bias so that the sample may start etching again. Also, there is the possibility of cathodically biasing n⁺-Si and encouraging etching. We have not yet measured the stopped and unstopped etch rates.

We assume that since orientation-dependent etching and the etch stop are seen for both aqueous KOH and ethylenediamine pyrocatechol, the present results would also be observed in the pyrocatechol etchant. Thus, the etch-stop mechanism of Raley *et al.* (7) for p⁺-Si is probably not valid; rather, p⁺-Si probably spontaneously passivates.

Acknowledgments

We thank H. B. Dietrich of NRL for the boron implantation and J. R. Ehrstein of the National Bureau of Standards for several heavily doped Si samples. We have had many fruitful discussions of possible etching and stopping mechanisms with J. W. Faust, Jr., of the University of South Carolina, and D. L. Kendall, of Instituto Nacional de Astrofisica, Optica y Electronica, Puebla, Mexico. O.J.C. is a NRC-NRS Research Associate.

Manuscript submitted June 4, 1984; revised manuscript received Aug. 20, 1984. This was Paper 362 presented at the Washington, DC, Meeting of the Society, Oct. 9-14, 1983.

The Naval Research Laboratory assisted in meeting the publication costs of this article.

REFERENCES

1. D. L. Kendall, *Ann. Rev. Mater. Sci.*, **9**, 373 (1979); *Appl. Phys. Lett.*, **26**, 195 (1975).
2. K. E. Beam, *IEEE Trans. Electron Devices*, **ed-25**, 1185 (1978).
3. A. Reisman, M. Berkenblit, S. A. Chan, F. B. Kaufman, and D. C. Green, *This Journal*, **126**, 1406 (1979).
4. J. B. Price, in "Semiconductor Silicon," H. R. Huff and R. R. Burgess, Editors, p. 339, The Electrochemical Society Softbound Proceedings Series, Princeton, NJ (1973).
5. E. D. Palik, J. W. Faust, Jr., H. F. Gray, and R. F. Greene, *This Journal*, **129**, 2051 (1982).
6. J. B. Angell, S. C. Terry, and P. W. Barth, *Sci. Amer.*, **44** (April 1983).
7. N. F. Raley, Y. Sugiyama, and T. Van Duzer, *This Journal*, **131**, 161 (1984).
8. V. M. Bermudez and V. H. Ritz, *Appl. Opt.*, **17**, 542 (1978).
9. D. E. Aspnes and J. B. Theeten, *This Journal*, **127**, 1359 (1980).
10. J. W. Faust, Jr., and E. D. Palik, *ibid.*, **130**, 1413 (1983).
11. E. D. Palik and V. M. Bermudez, *J. Phys. (Paris)*, **44**, C10-179 (1983).
12. E. D. Palik and V. M. Bermudez, Abstract 362, p. 578, The Electrochemical Society Extended Abstracts, Vol. 83-2, Washington, DC, Oct. 9-14, 1983.
13. E. D. Palik, V. M. Bermudez, and O. J. Glembocki, Submitted to *This Journal*.
14. W. W. Harvey and J. Kruger, *Electrochim. Acta*, **16**, 2017 (1971).
15. O. J. Glembocki and R. E. Stahlbush, Abstract 363, p. 579, The Electrochemical Society Extended Abstracts, Vol. 83-2, Washington, DC, Oct. 9-13, 1983; O. J. Glembocki, R. E. Stahlbush, and M. Tomkiewicz, *This Journal*, **132**, 145 (1985).
16. E. D. Palik, H. F. Gray, and P. B. Klein, *ibid.*, **130**, 956 (1982).
17. K. Watanabe, M. Miyao, I. Takemoto, and N. Hashimoto, *Appl. Phys. Lett.*, **34**, 518 (1979).
18. G. E. Jellison, Jr. and F. A. Modine, *J. Appl. Phys.*, **53**, 3745 (1982).
19. G. E. Jellison, Jr., F. A. Modine, C. W. White, R. F. Wood, and R. T. Young, *Phys. Rev. Lett.*, **46**, 1414 (1981).
20. L. Viña, C. Umback, M. Cardona, A. Compaan, and A. Axmann, *Solid-State Commun.*, **48**, 457 (1983).
21. D. E. Aspnes, A. A. Studna, and E. Kinsbron, *Phys. Rev. B*, **29**, 768 (1984).
22. O. J. Glembocki and E. D. Palik, *Bull. Am. Phys. Soc.*, **28**, 360 (1983).
23. S. R. Morrison, "Electrochemistry at Semiconductor and Oxidized Metal Electrodes," Chap. 7, Plenum, New York (1980).
24. H. Gerischer, *J. Vac. Sci. Technol.*, **15**, 1422 (1978).
25. R. W. Murray and C. N. Reilley, "Electroanalytical Principles," p. 2119, Interscience, New York (1963).

Deposition and Reflow of Phosphosilicate Glass

R. A. Bowling and G. B. Larrabee

Texas Instruments Incorporated, Materials Science Laboratory, Dallas, Texas 75265

ABSTRACT

The chemical vapor deposition (CVD) and reflow of phosphosilicate glass (PSG) have been reviewed. The CVD reaction from silane and phosphine has been simulated by SOLGAS thermochemical calculations. This equilibrium calculation method predicts stoichiometric conversion of silane and phosphine. In comparison to experimental determinations, the calculations underestimate the glass phosphorus content by about 1-3 weight percent. In addition, recent observations that the reflow of PSG is greatly enhanced by the presence of a steam ambient during heating have been examined. A possible mechanism of this reflow enhancement has been discussed. Experimental evidence, which support this mechanism, by electron microprobe, FTIR, and SIMS studies of PSG films, are presented.

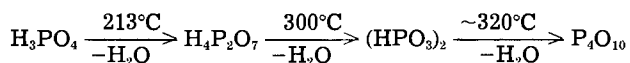
Phosphosilicate glass (PSG) is widely used throughout the semiconductor industry in the fabrication of bipolar and metal oxide semiconductor (MOS) devices. Many of the properties of PSG make it well suited for use as a solid-to-solid diffusion source, as a mask against other dopant diffusion, as a gettering agent for mobile alkali ions, as an interlayer dielectric and insulation for multilevel interconnections, or a passivation layer. The ability of PSG to stabilize devices against mobile ions such as sodium has been well known for over a decade (1-5). As an interlevel layer, the addition of phosphorus pentoxide to silica glass to form PSG significantly reduces the temperature needed to reflow the glass to provide smooth steps for metallization interconnection. Higher phosphorus contents give lower reflow temperatures, but high phosphorus concentrations can induce metal corrosion by reaction of phosphorus pentoxide with water to form phosphoric acid. This is particularly important in the production of low cost plastic-encapsulated devices as compared to the more expensive water-protected ceramic packages. Devices packaged in ceramic are sealed against water so that much higher phosphorus levels are tolera-

ble. This water-induced corrosion possibility can have a dramatically adverse effect on the long-term reliability of plastic-packaged devices, particularly since the rate of corrosion and thus the time to failure are dependent upon the temperature and humidity conditions of use for the device. As a passivation layer, thermally grown silicon dioxide has a limited thickness range over which it can be used because of thermal expansion mismatch with the substrate and high internal stresses which induce cracking. Alternatively, PSG is more dense and thus provides more contaminant protection. Its reduced intrinsic stress improves the layer's resistance to cracking (6-8). As the level of device integration increases, there is an increasing need for lower process temperatures of reflow in order to reduce undesired lateral diffusions. Therefore, it is imperative to control the phosphorus content of the PSG and the reflow conditions so that the optimum reflow is achieved at the lowest possible temperature, yet maintain phosphorus levels that do not induce metal corrosion. Understanding the processes of PSG formation and reflow is, then, of great importance in making decisions about present process control and process improvements

and about future plans to meet the needs of more highly integrated devices. This understanding could also play a significant role in the possible development of new glasses required for future device processing.

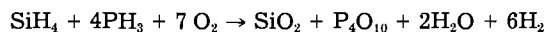
The phase diagram for the silicon dioxide-phosphorus pentoxide system is well characterized (9, 10). Since PSG is a glass and not a crystalline solid, it has no phase diagram, but some general implications may be taken from the phase diagram of the silicon dioxide-phosphorus pentoxide system. It can be seen from the phase diagram that a mixture of silicon dioxide and phosphorus pentoxide with a composition to the left of the eutectic which is cooled from liquid to solid will be composed of crystals of silicon dioxide as quartz in a solid of eutectic composition. This solid is water insoluble (11) and is inert to water attack, so that interaction with water will not occur to produce phosphoric acid. Metallization should not corrode in the presence of moisture when deposited on such a solid. Conversely, a mixture with composition to the right of the eutectic should form a material composed of crystals of $2\text{SiO}_2 \cdot \text{P}_2\text{O}_5$ in the solid eutectic composition. While the solid matrix is not water soluble, the crystals of $2\text{SiO}_2 \cdot \text{P}_2\text{O}_5$ are readily soluble. If the phase diagram were correct for PSG, glasses formed from compositions greater than about 0.2 mole fraction of phosphorus pentoxide or equivalently about 15.7 weight percent (w/o) phosphorus will contain water soluble crystals and metallization will corrode in the presence of moisture. It is not correct, and thus the maximum allowable amount of phosphorus before encountering metallization corrosion problems may be significantly less than 15.7 w/o. Particularly in a production situation, the maximum advisable phosphorus content is probably on the order of 10-12 w/o.

Another introductory topic which should be considered because of its relevance to phosphoric acid-induced metal corrosion and to the PSG reflow mechanism is the thermochemistry of phosphoric acid (H_3PO_4) and phosphorus pentoxide (P_4O_{10}). Phosphoric acid is the product of hydration of phosphorus pentoxide. Phosphoric acid undergoes a partial loss of water at 213°C and complete dehydration above ~320°C. The dehydration reaction can be written as follows



Thus, phosphoric acid is only stable at fairly low temperatures. Also, phosphorus pentoxide begins to sublime at about 300°C and is completely gaseous above approximately 600°C. The significance of this property will become apparent in the discussion section.

Presently, the most commonly used method for PSG deposition is chemical vapor deposition (CVD). The reaction of silane and phosphine with excess oxygen to form a PSG of silicon dioxide and phosphorus pentoxide is typically used. This reaction at 300°-500°C can be written as



Phosphorus pentoxide is correctly written as P_4O_{10} , but, in many cases, is referred to as P_2O_5 . They are most often used interchangeably to mean the same compound. Mass spectrometric evidence by Kern *et al.* (12, 13) showed that both hydrogen and water vapor are present as reaction products in the exhaust of a PSG deposition reactor. Excess hydrogen is present because phosphine is used as a mixture of phosphine, hydrogen, and argon. One major concern, with water vapor being present as a reaction product, is that water might become incorporated into the glass or that water will react with the phosphosilicate glass to form phosphoric acid. However, the instability of phosphoric acid above 320°C specifically excludes the possibility of acid formation during high temperature deposition. Infrared spectroscopic results by Kern *et al.* (12, 13) suggest that, even with the addition of excess amounts of water vapor into the reactant gas flow, there

is no evidence of incorporation of water into the glass during chemical vapor deposition. Their data further suggest, however, that water vapor is actually helpful to the deposition reaction, since they found empirically that it reduces the intrinsic stress of the deposited film. High phosphorus content glasses are a problem in the presence of moisture only at temperatures lower than about 320°C. This, however, does not preclude water incorporation into the glass at room temperature and thus does not rule out corrosion under normal device operation conditions. However, water should not pose any problems during deposition or reflow.

The technical literature contains several studies of the conditions of PSG chemical vapor deposition and the dependence of the glass deposition rate and phosphorus content upon various experimental parameters, including the reactant gas flow rates, substrate temperature, and several others (12-16). From a comparison of the experimental results of Kern *et al.* (12, 13) and Shibata *et al.* (14, 15), the PSG always contains more phosphorus than is predicted from stoichiometric conversion of silane and phosphine because the conversion of silane to silicon dioxide is generally believed to be inhibited by surface kinetics during co-oxidation with phosphine. This deviation from stoichiometry appears never to be more than about 2-4 w/o phosphorus. In most cases, it is on the order of 1-2 w/o phosphorus.

Phosphosilicate glass, as it is chemically vapor deposited, does not have a density as high as possible for the film. The film, however, can be annealed at temperatures ranging from about 450° to 800°C for periods of time ranging from 15 min to over 10h to produce densification of the film to a desired level (17). In other instances, the densification is achieved simultaneously with the higher temperature (950°-1050°C) reflow process which is designed to give a surface with smooth gradual steps on which to put metallization interconnections. A larger amount of phosphorus in the glass allows reflow at lower temperatures, but, as stated earlier, there is a limit to the amount of phosphorus before one encounters the probability of interaction with water to form phosphoric acid and the consequential corrosion of the metallization. One approach has been to deposit a PSG with a moderate level of phosphorus and then carry out the reflow while introducing POCl_3 gas into the reflow chamber. This introduces additional phosphorus into the outer layer of the PSG, allowing it to be reflowed more completely. The reflow is then followed by an anneal to remove the excess phosphorus, which was added for the reflow. This procedure of reflow with high surface phosphorus and then the removal of this excess phosphorus works because of the high vapor pressure of phosphorus pentoxide, as explained above, which can volatilize from the surface of the PSG, owing to the open porous structure of the glass.

Recently, it has also been observed that reflow is also greatly enhanced by the presence of a steam ambient during the reflow process, and that reflow is increased to a lesser extent by an oxygen ambient gas. These results are supported by several experimental reports in the chemical literature. Nauman and Boyd (18) found that the flow of PSG in wet nitrogen is greater than for dry nitrogen. Armstrong and Tolliver's SEM investigation (19) of PSG reflow showed the greatest flow for steam, and the least flow for dry nitrogen. Also, recently, Razouk and Lie (20) found that the high pressure-induced flowtime of PSG is reduced the most for a pyrogenic steam ambient. Steam-enhanced reflow of PSG may then be an important alternative for avoiding the use of high temperatures and high phosphorus contents to achieve the desired surface reflow.

Experimental

In an attempt to model the PSG system so that predictions of glass phosphorus content could be made, the reaction was simulated using a thermochemical calculation program called SOLGAS. It is a computer program for

the calculation of equilibrium compositions based upon minimization of the free energy of the system being considered. The method has been described in some detail by Eriksson (21). Calculations were performed for temperatures ranging from 300° to 450°C, for SiH_4/PH_3 molar ratios from 1 to 50, and for $\text{O}_2/(\text{PH}_3 + \text{SiH}_4)$ molar ratios of 1 to 50.

All thermodynamic heats of formation used by the program were taken from the JANAF thermochemical tables (22), except for PSG, which was estimated from the values of silicon dioxide and phosphorus pentoxide. The results of these calculations are discussed in the section on results.

To evaluate the effects of water vapor on the reflow of PSG film produced by the CVD reaction of silane and phosphine with oxygen at 430°C, films were studied using Fourier transform infrared spectroscopy (FTIR), secondary ion mass spectrometry (SIMS), electron microprobe analysis, and wet chemical colorimetric analysis.

For the purpose of these studies, silicon wafers with the deposited films of PSG in the 7-12 w/o phosphorus range were broken into four parts. One part was left unannealed for comparison as the as-deposited film. The other three parts were annealed one in each of the following gas ambients: dry nitrogen, dry oxygen, and steam. The steam was flowed into the annealing furnace using nitrogen and all anneals were carried out at 950°C for 15 min. The FTIR analyses were carried out on an IBM IR98-14 FTIR instrument. SIMS measurements were made on an ARL ion microprobe basing the quantitative results on phosphorus standards generated from neutron activation analysis. The electron microprobe results were obtained on a JEOL JSM-35 scanning electron microscope with Kevex x-ray detector. Its results were also based on the same neutron activation generated phosphorus standards. The wet chemical colorimetric determinations of phosphorus were based on weighed and dissolved phosphorus salt standards.

Results and Discussions

All SOLGAS calculations indicate a complete stoichiometric conversion of phosphine and silane to PSG. That is, thermodynamically, all the reactant silane and phosphine go to make a glass with the same silane to phosphine molar ratio as for the reactant gas mixture. This was true as long as there was excess oxygen, *i.e.*, sufficient oxygen to convert all silane to silicon dioxide and to convert all the phosphine to phosphorus pentoxide. The other predicted products of the deposition reaction were hydrogen and water vapor, consistent with the experimental findings of Kern *et al.* (12, 13). The stoichiometric conversion predicted by SOLGAS, though possibly a good first approximation of the reaction, does not take into account two important factors. First, CVD is not in an equilibrium situation as assumed by the SOLGAS program; second, SOLGAS bases its results upon thermodynamic consideration only, and does not include other factors, such as kinetic effects.

Enhanced reflow of PSG by the addition of steam as an ambient gas, although it greatly enhances the PSG reflow, should not be used as a process before considering its effects on the other aspects of semiconductor devices. Whether or not reflow in the presence of steam causes water to be trapped in the glass is of extreme importance to the long-term reliability of a semiconductor device. Recent FTIR results in this laboratory on samples which had been annealed in steam have shown no evidence of trapped water. In support of this finding, it is known that a temperature of about 400°C facilitates the removal of OH^- groups and condensed water molecules from a silica surface (23).

Many people in the semiconductor industry talk about the concept of steam leaching of phosphorus from the glass by phosphoric acid formation. They have noted that when the glass is reflowed in the presence of steam the final film has a lower phosphorus concentration than the

as-deposited film, and they are familiar with the reaction of phosphorus pentoxide and water to form phosphoric acid and the consequential metal corrosion that occurs at low temperatures. The two facts have been incorrectly pieced together to indicate that the water reacts with the phosphorus to facilitate its removal. What has not been considered is that the water may interact with the glass structure to allow the phosphorus pentoxide to escape from the sample because of its high vapor pressure. Another supporting fact is that phosphoric acid is not stable at these high temperatures. To further examine this phosphorus loss during annealing, a discussion of the interaction of water with silica glass structures is required. This is given below.

It is a very common practice for a ceramicist to add steam to any glass to reflow it at a lower temperature or reflow it more quickly at a given temperature (23, 24). Vitreous silica glass has a very high viscosity. The silica glass Si-O bonds are very strong, and the major cation (Si^{4+}) core has a rigid screening demand which requires four-fold coordination. Its network of O^{2-} ions in only two-fold coordination represents a very open, porous structure. The anion-to-major network forming cation ratio is by far the most important factor which determines the screening of the cation and the need of the cation to share anions, that is, to "polymerize" and form a glass. The addition of O^{2-} ions introduced by oxides such as phosphorus pentoxide or sodium oxide improves the screening of the major cation and decreases the need to polymerize, therefore lowering the viscosity of the glass. This is the reason that PSG, which contains phosphorus pentoxide in silica, has a much lower viscosity than pure silica and can consequently be reflowed at a much lower temperature than pure silica glass. Silica is also very sensitive to defects which cause any asymmetry, again because of the cation screening demand; a reduction in viscosity can also occur by this mechanism. Vitreous silica glass can contain OH^- groups or electron pairs in the place of O^{2-} ions. This fact is very important in explaining the reduction of viscosity by addition of water vapor or oxygen during reflow. The viscosity of silica can be reduced by an order of magnitude by the introduction of water because it participates in the structure of the glass as OH^- ions, displacing some of the bridging oxygen bonds, and thus increasing the number of anions. This not only increases the screening of the major cation, but also introduces an asymmetry, both of which act to reduce the glass viscosity. Oxygen can produce more limited viscosity reduction by accepting an electron transfer and participating in the structure as an electron pair substitution for an O^{2-} ion (24). By similarity, since PSG is primarily a silica glass with a relatively small percentage of added phosphorus pentoxide, water and oxygen are expected to produce similar viscosity reduction in PSG.

The reflow enhancement of steam by its participating in the glass structure as OH^- ions would give the necessary structural changes to bring about the observed loss of phosphorus during annealing in steam. This phenomenon of loss is much more than can be explained by surface volatilization alone. The glass changes to a less viscous substance which has a more open porous structure, thus allowing more phosphorus pentoxide to evaporate. Balk and Eldridge (1) first proposed this type of mechanism in 1969. The mechanism is also supported by a recent study of the densification and water absorption of PSG films chemical vapor deposited at 640°C using phosphine, tetraethyl orthosilicate, and oxygen (25). The following experimental observations were made by the present authors in an attempt to investigate the feasibility of this mechanism.

In Fig. 1 are shown the FTIR spectrum of an as-deposited PSG film and the spectra of the same film annealed in steam, oxygen, and nitrogen gas ambients. In the FTIR spectrum of PSG annealed in steam, the energy and shape of the Si-O stretch band most closely resembles the same band of the as-deposited PSG, thus indicating a structure which is more open and less dense as is

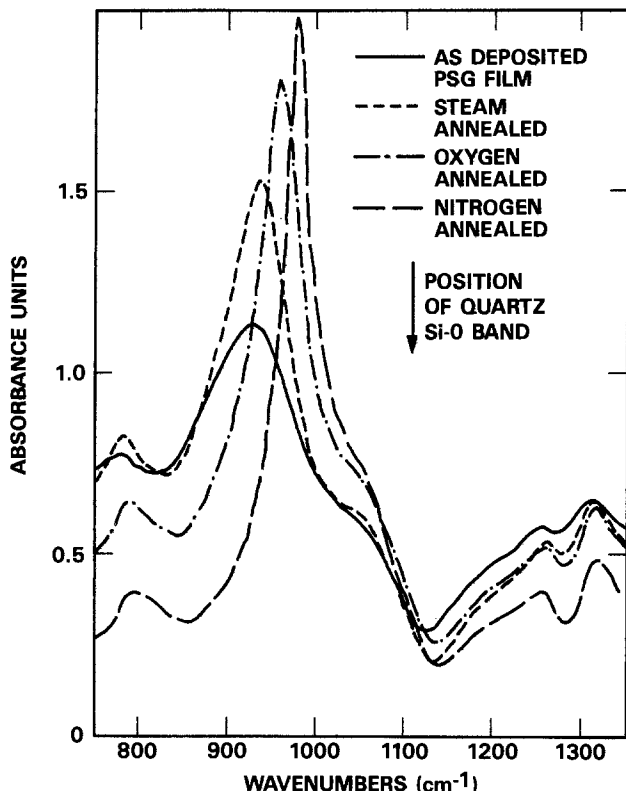


Fig. 1. FTIR spectra of PSG film annealed in different gas ambients

characteristic of the as-deposited film. However, the same band in the spectrum of PSG annealed in nitrogen is shifted to an energy much closer to the corresponding band of quartz, a much more closed densely packed structure. Oxygen shows an effect intermediate between the other two. Further information on FTIR studies of PSG films can be found in Ref. (26). Confirmation of the loss of phosphorus during annealing, the amount of which depends on the ambient and its effect on the structure, is shown in Fig. 2 and in Table I. Figure 2 shows the SIMS profiles of phosphorus in a PSG sample, pieces of which have been annealed separately in steam, nitrogen, and oxygen. The steam-annealed sample has significantly less phosphorus than the other two. Table I indicates the phosphorus contents obtained for similar samples *vs.* the as-deposited PSG from electron microprobe and wet chemical complexation colorimetric analysis. Both methods indicate the highest phosphorus content for the as-deposited film and the lowest for the steam-annealed samples. Nitrogen is closest to the as-deposited film in phosphorus content, and oxygen is intermediate, indicative of its more limited reduction of the glass viscosity. There is a large discrepancy between the

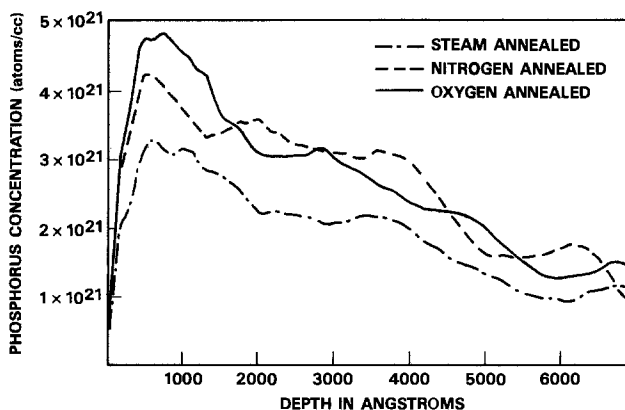


Fig. 2. SIMS profiles of phosphorus in PSG sample annealed in different gas ambients.

Table I. Annealed PSG phosphorus content as a function of gas ambient

Reflow gas ambient	Average PSG phosphorus content (w/o P) Electron microprobe	Wet chemical analysis
As-deposited PSG	7.6	11.4
Dry nitrogen	7.4	9.9
Dry oxygen	7.1	9.6
Steam	6.8	7.6

absolute magnitudes of the values obtained by the two techniques first because the analyses were performed on different samples which were only deposited under similar conditions and because of the use of different standards for the techniques as described in the experimental section. The ordering of phosphorus content which is the same for both is the more important observation. This combination of FTIR results showing most dense films for nitrogen anneal, and other results showing least remaining phosphorus for steam reflow, supports the mechanism described above but does not specifically exclude all other explanations.

In light of all these results, the addition of steam to reflow PSG films is feasible and poses no water-related problems to the device reliability during reflow. Addition of steam to enhance the reflow may then be a viable and safe procedure of PSG processing for semiconductor device manufacture (27).

Summary

The useful properties of PSG as applied to use as a semiconductor oxide layer have been discussed along with the problems that it can induce if not closely controlled. The simulation of the CVD reaction from silane and phosphine by SOLGAS thermochemical calculations was shown to predict stoichiometric conversion, this prediction always being about 1-3 w/o phosphorus less than actual experimental observations. The differences arise because CVD is not an equilibrium situation, as assumed by SOLGAS, and because SOLGAS neglects kinetic factors influencing the reaction. It was shown that PSG reflow enhancement by steam has been well documented by several authors. A mechanism for this reflow enhancement involving the participation of water in the glass structure as OH⁻ ions is described, and supporting evidence has been given.

Acknowledgments

The authors are very grateful to Julie Spicer, Eddie Breashears, and Doug Baker for their help in special sample preparation and processing. Special thanks are also extended to Tom Moore for electron microprobe investigations, to Joe Keenan for NAA results, to Steve Marks for FTIR studies, to Mark Anthony for SIMS data, and to Toni Queen for wet chemical analyses.

Manuscript submitted April 2, 1984; revised manuscript received Aug. 27, 1984. This was Paper 91 presented at the San Francisco, California, Meeting of the Society, May 8-13, 1983.

Texas Instruments, Incorporated, assisted in meeting the publication costs of this article.

REFERENCES

1. P. Balk and J. M. Eldridge, *Proc. IEEE*, **57**, 1558 (1969).
2. W. Kern, G. L. Schnable, and A. W. Fisher, *RCA Rev.*, **37**, 3 (1974).
3. W. M. Paulson and R. W. Kirk, in "Proceedings of the 12th Annual Conference on Reliability Physics," p. 172, IEEE, New York (1974).
4. W. Kern, *Solid State Technol.*, **18**, 25 (1975).
5. L. J. Gallace, *ibid.*, **23**, 102 (1980).
6. E. H. Snow and B. E. Deal, *This Journal*, **113**, 263 (1966).
7. H. Sunami, Y. Itoh, and K. Sato, *J. Appl. Phys.*, **41**, 5115 (1970).
8. R. S. Keen, R. A. Lathean, and G. L. Schnable, *IEEE Trans.*, **17**, 1077 (1969).
9. T.-Y. Tien and F. A. Hummel, *J. Am. Ceram. Soc.*, **45**, 38 (1962).
10. J. M. Eldridge and P. Balk, *Trans. Met. Soc. AIME*, **242**,

- 539 (1969).
11. N. Nagasima, H. Suzuki, K. Tanaka, and S. Nishida, *This Journal*, **121**, 434 (1974).
 12. W. Kern and R. S. Rosler, *J. Vac. Sci. Technol.*, **14**, 1082 (1977).
 13. W. Kern and V. S. Ban, in "Thin Film Processes," J. L. Vossen and W. Kern, Editors, pp. 302-309, Academic Press, New York (1978).
 14. M. Shibata and K. Sugawara, *This Journal*, **122**, 155 (1975).
 15. M. Shibata, T. Yoshimi, and K. Sugawara, *ibid.*, **122**, 157 (1975).
 16. J. Wong and M. Ghezzi, *ibid.*, **122**, 1268 (1975).
 17. W. Kern and R. Heim, *ibid.*, **117**, 568 (1970).
 18. A. Nauman and J. T. Boyd, *J. Vac. Sci. Technol.*, **17**, 529 (1980).
 19. W. E. Armstrong and D. L. Tolliver, *This Journal*, **121**, 307 (1974).
 20. R. R. Razouk and L. N. Lie, Abstract 85, p. 138, The Electrochemical Society Extended Abstracts, Vol. 82-1, Montreal, Que., Canada, May 9-14, 1982.
 21. G. Eriksson, *Acta Chem. Scand.*, **25**, 2651 (1971).
 22. D. R. Stull and H. Prophet, Project Directors, JANAF Thermochemical Tables, Second ed., NSRDS-NBS37, NBS, Washington, DC (1971).
 23. L. Holland, "The Properties of Glass Surfaces," pp. 194-253, John Wiley and Sons, New York (1964).
 24. W. A. Weyl and E. C. Marboe, "The Constitution of Glasses," Vol. II, pp. 438-722, Interscience, New York (1964).
 25. R. M. Levin, *This Journal*, **129**, 1765 (1982).
 26. A. S. Tenney and M. Ghezzi, *ibid.*, **120**, 1276 (1973).
 27. R. A. Bowling and G. B. Larrabee, Abstract 91, p. 140, The Electrochemical Society Extended Abstracts, Vol. 83-1, Washington, DC, May 8-13, 1983.

Bias-Dependent Etching of Silicon in Aqueous KOH

Orest J. Glembocki and Robert E. Stahlbush

Naval Research Laboratory, Washington, DC 20375

Micha Tomkiewicz*

Physics Department, Brooklyn College of CUNY, Brooklyn, New York 11210

ABSTRACT

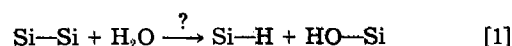
The current-voltage characteristics and the bias dependence of the etch rates of <100>- and <111>-oriented n- and p-type low doped Si samples in aqueous KOH have been studied. We find that voltages cathodic of the open-circuit potential have little effect on the p-type etch rates, while the n-type etching is stopped. Anodic of the open-circuit potential, both carrier types stop etching, owing to passivation of the surface. These results are used to characterize the rate-determining steps of the chemical or electrochemical reactions which take place at the semiconductor surface at various biases. A mechanism is proposed in which the rate-determining step shifts between among chemical, electrochemical, or diffusion limited. Also, a mechanism involving susceptibility to nucleophilic attack is proposed to explain the vastly different etching rates of <100> and <110> vs. <111> faces.

The etching of silicon in aqueous KOH is of both technological and fundamental interest. Its technological promise stems from two properties. First, the etching rate of the <111> face can be several orders of magnitude less than that of the <110>, <100>, and any other fast etching plane (1). Second, heavy phosphorous or boron doping ($>10^{19}$ cm⁻³) inhibits the etching (2). As a result of these phenomena, it is possible to fabricate microstructures using KOH etching in conjunction with standard semiconductor processing techniques. For example, V-grooves, pyramids, and high-aspect-ratio structures of micron dimensions are routinely constructed. For more information about these types of applications, the reader is referred to the work of Kendall (3) and Angell *et al.* (4).

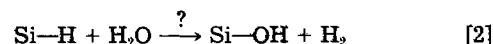
The fundamental interest in the etch-stop and orientation-dependent etching (ODE) of Si in KOH, as well as certain other basic solutions, dates back many years. Various studies such as current-voltage (1, 2, 5, 6), capacitance (6, 7), pH dependence of the etch rates (3, 8-11), illumination effects (6, 10), etc., have been performed. It is interesting to note that despite the volume of work on the problem, the mechanism of the corrosion processes that take place is still not understood. This state of events is not particularly surprising in view of our incomplete knowledge of the mechanism of corrosion reactions in simpler systems such as metals, in which passivation competes with corrosion. It is our objective, in this paper, to shed additional light on some of the most basic mechanistic questions concerning the etching of Si. In doing so, we hope to present a coherent picture of the current status of the field.

The most important question to consider is whether the rate-determining steps in the etching reactions are chemi-

cal or electrochemical in nature. The distinction between the two rests on the participation of free carriers in any rate-determining step (RDS). If the RDS is chemical, one might expect a simultaneous oxidation-reduction of the Si bond through a reaction sequence such as



followed by



The question marks in reactions [1] and [2] indicate the unknown nature of the catalysts (if any) that participate. In basic solutions, for example, OH⁻ is a good candidate to play this role. The question marks also imply that reactions [1] and [2] are not elementary steps, but are, rather, stoichiometric manifestations of an overall process which must be considered before any attempt at the understanding of the elementary steps can be contemplated. Equations [1] and [2] do not predict the final form of the etch by-products, as this will be greatly influenced by the pH of the solution. Therefore, the species leaving the surface could be different from those in solution.

If, however, the reaction is electrochemical in nature, then the most useful presentation on a level commensurate with Eq. [1] and [2] is given in terms of a short-circuit electrochemical cell. For a corrosion reaction to be represented as a short-circuit, energy producing cell, the potential difference across the interface should be between the equilibrium potential of the reduction reaction of the electrode and the equilibrium potential of the oxidation reaction of the electrode. Note that this implies that both reactions occur at the open-circuit potential (12). Electrochemical reactions can be complicated by the fact that

*Electrochemical Society Active Member.

the process can take place by short circuiting, physically separated reaction sites on the electrode or through the Wagner-Traud mechanism which does not require that the reaction sites be distinct in space and time; they can occur randomly over the surface of the electrode (12). Since our cell is energy producing, the presence of corrosion pits ("noise" in the etch profiles: see the experimental section) suggests some spatial separation in the oxidation and reduction sites. When an insoluble oxide forms at potentials anodic of the corrosion potential, as in the present case, the rate-determining step will change (for these biases) from being determined by the interfacial kinetics to diffusion through the passivating film.

The most useful tool to distinguish between the two mechanisms is to monitor the etch rate as a function of the electrode potential. For an electrochemical RDS, the etch rate should be proportional to the concentration of free carriers at the surface, which varies exponentially with the potential drop across the space-charge layer. If the mechanism is chemical, then the only dependence on the electric field across the interface is expected if the ionic diffusion across the passivating film is electric-field assisted. Even this simple criterion should be treated with caution. In the case of Fermi-level pinning, the concentration of free carriers will be unaffected by the electrode potential, and an electrochemical mechanism may behave like a chemical one.

In this paper, we present a study of the bias dependence of the etch rates of n- and p-type, lightly doped Si samples of $\langle 111 \rangle$ and $\langle 100 \rangle$ orientations. Hereafter, the notation n(111), etc., will be used in referring to n-type samples of $\langle 111 \rangle$ orientation, etc. We will compare the etch rates to linear-sweep voltammograms (I-V curves), taken under identical conditions. Waggener and Dalton (13) had previously studied the bias dependence of the etch rates for voltages anodic of the open-circuit potential (OCP), but did not consider potentials cathodic of the OCP, and thus their data are not adequate for our purposes. In the discussion section, we will utilize the rich harvest of prior experimental work, together with our own data and try to reach some conclusions as to the relative importance of the chemical and electrochemical mechanisms in the orientation-dependent etching of Si in KOH.

Experimental

The samples used in our experiments were commercial 2 in. diam wafers obtained from General Diode, Incorporated. The resistivities were typically 9-10 Ω -cm, and the orientation was within $\pm 1^\circ$ of the $\langle 111 \rangle$ or $\langle 100 \rangle$ planes. No special surface treatments were used. Two closely spaced contacts were made by first scratching the surface and then rubbing In-Ga amalgam into the damaged area. The two spots were subsequently tested on an I-V curve tracer. Finally, pressure contact was made to a copper wire.

In Fig. 1, we show a schematic representation of the experimental apparatus which was used for both the I-V measurements and the etching work. A PAR 173 potentiostat was used to bias the sample with respect to a standard calomel electrode (SCE). The sample cell was a beaker filled with KOH and was raised and lowered with respect to the electrodes with a scissor jack. Before etching, the wafers were masked with thermal oxide 0.6 μ m thick. Portions of the oxide were removed through standard lithographic techniques, leaving a grid pattern composed of squares of oxide, 0.8 mm on a side, separated by 0.4 mm wide streets and avenues of clean Si. The wafer was then cleaved into strips 3.6 mm wide. Figure 2 shows a schematic representation of a typical strip and the expected etch grooves. A negative oxide pattern was also tried, with no observable differences in the results.

The strip was submerged in 2M KOH at 20°C with the contact above solution. After removing the native oxide (signaled by bubbling and OCP stabilization), the KOH level was lowered by approximately 1 cm, and the sample was etched at the OCP. Typically, the level was lowered

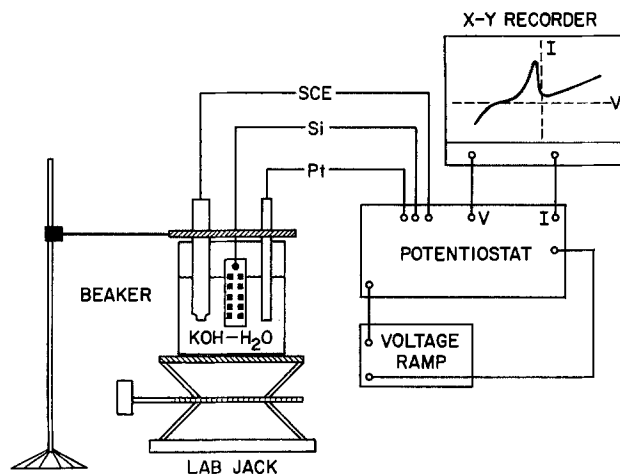


Fig. 1. The experimental arrangement for measuring current-voltage (I-V) characteristics and bias-dependent etch rates. The lab jack is used to lower the liquid level with respect to the sample. The voltage ramp is used only to obtain the I-V curve. All voltages are with respect to a standard calomel electrode (SCE).

several times and each time the sample was etched at a different bias. The etch times were 20 min for the fast etching $\langle 100 \rangle$ plane and 60 min for the $\langle 111 \rangle$ face. Key points as well as several random ones were rechecked using only three measurements per sample, i.e., native-oxide removal, OCP, and one bias.

The etch steps were measured by removing the oxide mask with HF and running a Dektak mechanical stylus down the length of the strip. This technique has a resolution of a few percent. In Fig. 3, we display a typical result from a stylus measurement (Dektak trace), which shows two nearly flat regions separated by a transition section of variable depth. The transition section is caused by etching due to a small amount of liquid creeping up the strip. The "noise" in the etched grooves is a result of nonuniform etching and was substantially reduced by stirring.

Results

In addition to the bias-dependent etch rates, we have also measured the current-voltage (I-V) characteristics of our samples. From these curves, we are able to determine

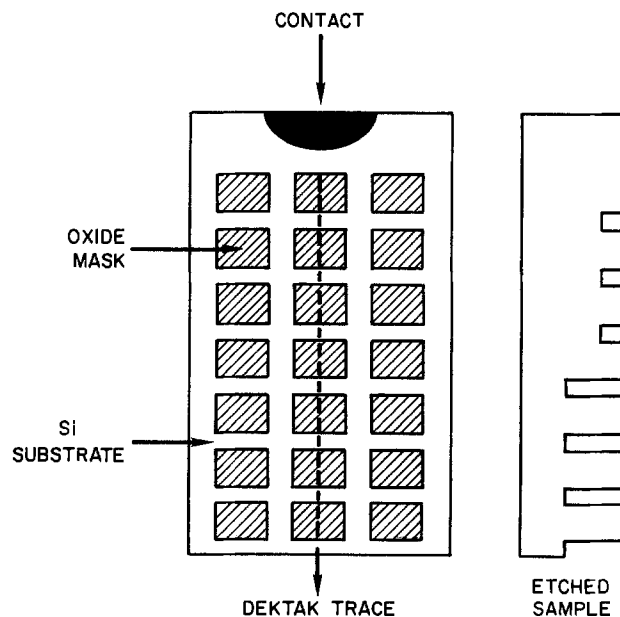


Fig. 2. A schematic representation of the oxide pattern used to protect portions of the sample during etching. The dashed line shows the direction of travel of the Dektak needle. To the right is a cross-sectional view of the expected etch grooves.

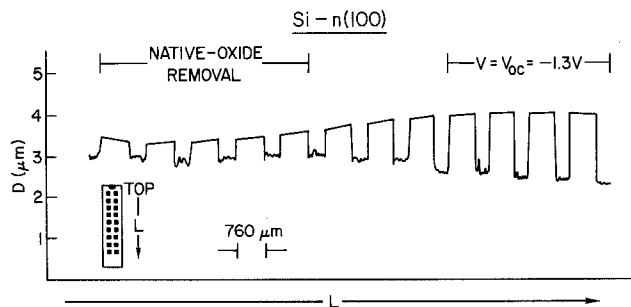


Fig. 3. A typical Dektak scan for an n(100) sample at the open-circuit potential (V_{oc}), which in the text is called the OCP. The trace is taken from left to right and corresponds to motion from the top of the sample toward the bottom. The unetched regions are $760 \mu\text{m}$ on a side.

both the open-circuit potential (OCP) and the passivation potential (PP). This information allows us to choose a range of voltages in which the sample has no oxide on the surface and is under etching conditions. Displayed in Fig. 4 and 5 are the linear-sweep voltammograms (taken at 0.02 V/min) for both n- and p-type Si samples of $\langle 100 \rangle$ and $\langle 111 \rangle$ orientations. The areas of all of the samples were approximately 1 cm^2 . There are two voltage regions of importance to us, and they are separated by the passivation potential. Just cathodic of the PP, the sample etches, while just anodic an oxide grows. For oxide-free surfaces, the OCP is always at more negative voltages than the PP.

The I-V curves of the $\langle 111 \rangle$ oriented samples show two peaks for both n- and p-type materials. Faust and Palik (1) have suggested that the more cathodic (left) peak is due to the passivation of the exposed edges, which correspond to $\langle 100 \rangle$ and $\langle 110 \rangle$ faces. Consequently, the true I-V curve of the $\langle 111 \rangle$ surface should be similar in shape to that of the $\langle 100 \rangle$ curves shown in Fig. 4. The major difference between the two orientations is the fact that the current densities at the passivation peak are almost an order of magnitude smaller on the $\langle 111 \rangle$ surface than on the $\langle 100 \rangle$ surface.

Another parameter which is very important in electrochemical reactions at semiconductor electrodes is the

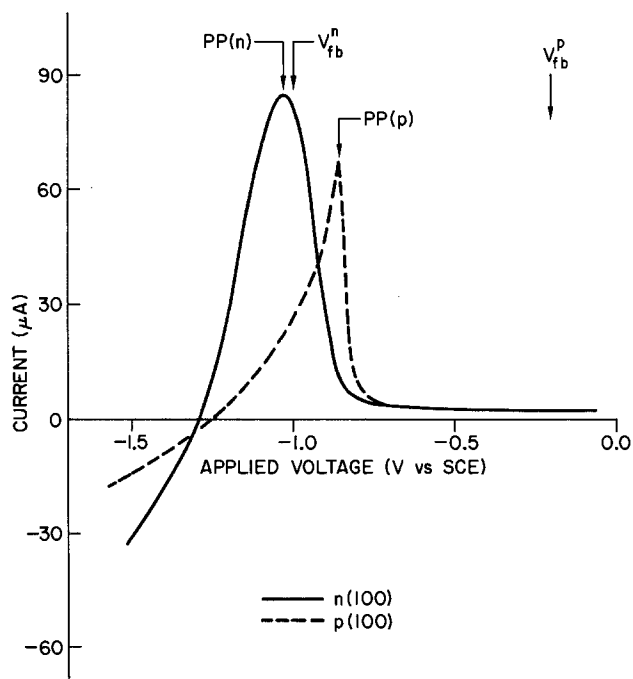


Fig. 4. The room-temperature (I-V curves) voltammograms for n-type (solid line) and p-type (dashed line) samples of $\langle 100 \rangle$ orientation, denoted by n(100) and p(100), respectively. Here PP(n) and PP(p) refer to the passivation potentials of the n- and p-type samples, respectively, while V_{fb} is the flatband potential. The areas of the samples were similar and approximately equal to 1 cm^2 .

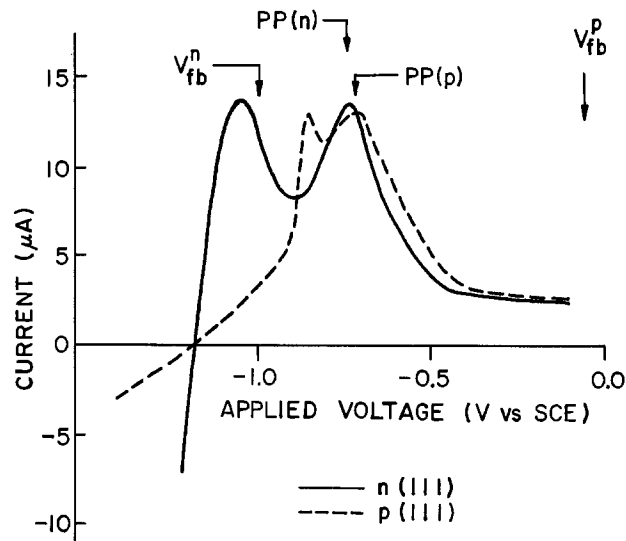


Fig. 5. The room-temperature (I-V curves) voltammograms for n-type (solid line) and p-type (dashed line) samples of $\langle 111 \rangle$ orientation. The notation for the passivation and flatband potentials is the same as in Fig. 4. The areas of the samples were similar and approximately equal to 1 cm^2 . The more negative peaks in both curves are spurious and caused by the passivation of exposed edges, which may have $\langle 110 \rangle$ or $\langle 100 \rangle$ orientations.

flatband potential. With previously unpublished electrolyte electroreflectance (14) and capacitance (15) measurements, the flatband potentials have been determined for Si in $2M \text{ KOH}$ and are $V_{FB} = -1.0V$ and $V_{FB} = -0.2V$ for n- and p-type samples, respectively. From these numbers, we find that the p-type sample was in depletion (hole) during both etching and oxide growth. However, since there is evidence for Fermi-level pinning in p-type Si, its value of flatband is somewhat questionable (16). For the n-type sample, the situation is different and the data clearly show that flatband occurs between the OCP and the passivation potential. Therefore, the n-type sample is in electron accumulation during etching and in depletion at oxide producing potentials.

A closer examination of the figure reveals that the OCP as well as the PP are not the same for n- and p-type Si; the values for the p-type samples are somewhat more cathodic than for the n-type. This information will be used in our discussion of the bias dependence of etching.

In Fig. 6, we display our results for the etch rates of n(111), n(100), p(111), and p(100) Si over the range of -2.0 to $-0.5V$. The measurements were taken at room temperature, and the resistivities of all of the samples were similar. Each point represents an average of several measurements, with a spread of $\pm 20\%$. The first thing to note is the fact that our OCP results for the $\langle 111 \rangle$ face (both carrier types) agree with the etch rates previously measured by weight loss (1), whereas our p(100) and n(100) values are somewhat larger. This may be attributable to the fact that the wafers used in the weight-loss experiments had roughened back surfaces, which probably exposed many $\langle 111 \rangle$ facets, having reduced etch rates. Under these conditions, the measured etch rate would be an average of the etch rates of the front and back faces. Since in our case, etch depths were measured, no such problem was encountered.

We also note that the etch rates for the $\langle 111 \rangle$ surface are about an order of magnitude smaller than for the $\langle 100 \rangle$ face. For "perfectly" oriented samples, Kendall (17) has shown that this factor is 400 and that the etching in misoriented materials is due to ledges formed by the intersection of the $\langle 111 \rangle$ surface with a faster etching plane, such as the $\langle 110 \rangle$ or $\langle 100 \rangle$ faces. Since the n(100) and p(100) etch rates are similar at the OCP, the factor of 3 difference between the n(111) and p(111) etch rates in the data of Faust and Palik (1) as well as this work may be a manifestation of the misorientation effect rather than a carrier-type effect.

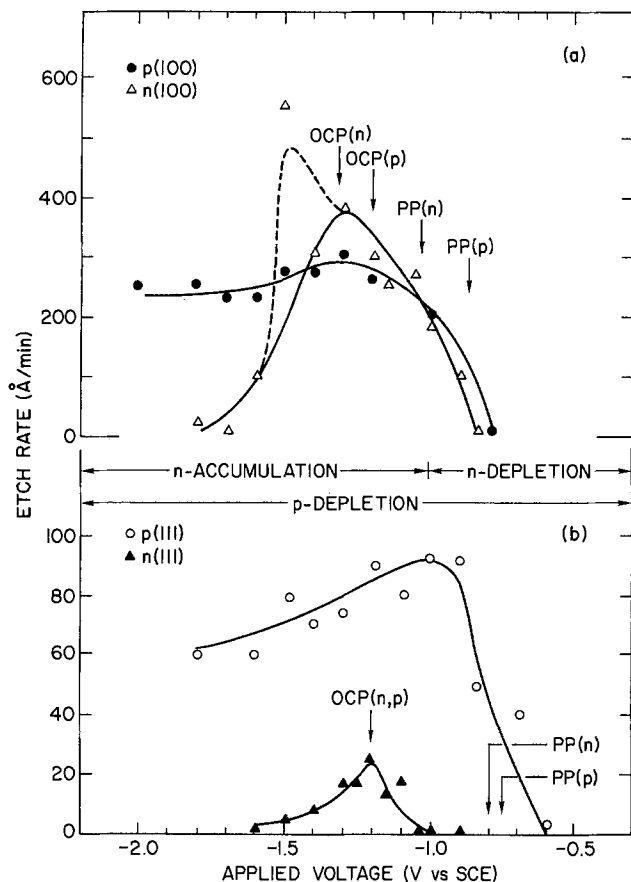


Fig. 6. The bias dependence of the etch rates for (a) p(100) and n(100), and (b) p(111) and n(111) low-doped Si. The data have an experimental spread of approximately $\pm 20\%$. The open-circuit (OCP) and passivation (PP) potentials are marked. Note that the OCP is the same for the n(111) and p(111) samples. Also shown are the approximate potential ranges in which the samples (of both orientations) are in accumulation and depletion modes. Even though we have depicted the p-type samples as in depletion, the experimental evidence strongly supports Fermi-level pinning at these biases.

Next, we see that all of the samples stopped etching at anodic biases, owing to passivation of the surface. The etch rates are finite near the passivation potential for all samples except n(111), because, even though oxidation begins to occur, etching of the substrate and newly formed oxide continues. For these biases, our results are similar to those of Waggener and Dalton (13).

At cathodic potentials, however, we see a substantial difference in the n- and p-type etch rates. The p-type samples continue to etch at a rate close to that of the OCP value, whereas the n-type Si exhibits etch-stop. We also note that for the n(100) sample there is an increase in etching for voltages between the OCP and the cathodic etch-stop bias. Furthermore, a point is seemingly out of place. However, this point and its immediate neighbors were checked several times and found to be reproducible, suggesting the possibility of structure in the curve in this voltage range. Since we currently have no reason to expect structure, we have chosen to draw two curves, which fit the data.

We also notice that not only is the etch rate for the $\langle 111 \rangle$ face much smaller than for the $\langle 100 \rangle$ plane, but that under bias the ratio of the $\langle 111 \rangle$ etch rate to the $\langle 100 \rangle$ etch rate is not a constant and, in particular for the p-type samples, it can be decreased by an order of magnitude. This fact presents us with the possibility of utilizing a bias to control the orientation-dependent effect. The fact that even low doped n-type samples stopped etching under cathodic bias suggests that p-n junctions could be used to make thin ($< 3 \mu\text{m}$) Si membranes of fairly low carrier density. This would be accomplished by a diffusion or implantation of donor atoms into one side of a

p-type wafer. The etching would then be performed at a bias (cathodic or anodic) which exhibits n-type etch stop. A similar idea was suggested by Waggener (18) for the case of anodic potentials at which the n-type material passivates and the p-type does not. But, to our knowledge, the cathodic etch-stop has not been previously observed. In the next section, we will attempt to understand the origins of the observed bias dependence of the etch rates.

Discussion

Chemical mechanism.—The most compelling argument in favor of a chemical mechanism for etching of Si in KOH is based on the results observed by Price (8) and by Palik *et al.* (2) that the etching is independent of carrier density, for both n- and p-type Si, up to a concentration of about $N \approx 10^{19} \text{ cm}^{-3}$. For $N > 10^{19} \text{ cm}^{-3}$, there is a dramatic decrease in the etch rate, i.e., the etch-stop mechanism. For fixed flatband and electrode potentials, the electric field, and free-carrier density at the surface depend upon the doping level (linear with $N^{1/2}$ for conditions within the Mott-Schottky approximation) (18). Therefore, one expects a strong variation of the concentration of free carriers at the surface with the doping level. Here again, if the Fermi level is pinned to surface states (even for the low doped materials), the conclusions that one draws from these experiments might have to be modified. As stated in the previous section, there is strong evidence for Fermi-level pinning in p-type Si in 2M KOH, and care must be taken in dealing with these data.

Since for n-type materials the OCP is slightly negative of the flatband potential, the system will be in an accumulation mode at the OCP. Glembocki and Palik (14) have observed in their electroreflectance work evidence for the onset of Fermi-level pinning (in n-type samples) for biases cathodic of -2V , but not in the range of voltages of interest to us. Thus, one is hard pressed to find a mechanism that will depend on the free-carrier density at the surface and yet be insensitive to five orders of magnitude variation in doping level for both n- and p-type materials. Another strong argument in favor of a chemical mechanism which is independent of free carriers is the observation that under open-circuit conditions there is very little difference between the etch rates of n- and p-type samples of the same orientation (1-3). These results point to a chemical RDS under open-circuit conditions.

Electrochemical mechanism.—In Fig. 6, we show the experimental etch rates for both orientations and carrier types over a broad potential range. At the OCP, where the etching is close to its maximum, the difference in the etch rates is small (at most a factor of 3 for the misoriented samples). But this difference increases substantially as one goes anodic and cathodic of the OCP.

This result might be addressed in relation to the differences found in the linear-sweep voltammograms (I-V curve) taken under identical conditions and shown in Fig. 4 and 5 for the $\langle 100 \rangle$ and $\langle 111 \rangle$ faces. It is seen here, confirming prior observations, that the current densities at the PP are almost the same for the n- and p-type samples. However, aside from this, very little else is identical. The passivation and rest (OCP) potentials are different for n- and p-type samples of a given orientation and cathodic to the PP, the current of the p-type material saturates (or passivates), while for the n-type the cathodic current (hydrogen evolution) grows. All of this seems to suggest that free carriers play a dominant role in these reactions. In the next section, we will try to relate the facts mentioned above to the nature of the RDS.

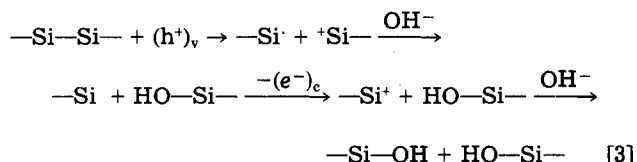
Characterization of the rate-determining steps.—Here, we will concentrate on the ramifications of our experimental results to the question of whether the RDS involves free carriers or is chemical in nature. As stated above, the evidence is strongly in favor of a chemical RDS at the open-circuit potential. However, all of our data indicate that this may not be the case at other applied voltages. The voltammogram itself is an electro-

chemical experiment which measures the flow of free carriers in some parts of the electrochemical cell. Since the contributions of ionic mobilities within the semiconductor are negligible, the similar current densities at the passivation peaks of the n- and p-samples (for both orientations) strongly support the contention that at least at these potentials the RDS is chemical. Faust and Palik (1) also found that the peak currents are independent of carrier density. Furthermore, Palik and Bermudez (20) have observed a thin connective layer ($\sim 7\text{-}10\text{\AA}$ thick) between the substrate and oxide on both n- and p-type samples. The transition region is oxygen deficient and can be characterized as $\text{Si}_{1-y}(\text{SiO}_2)_y$, with $y \approx 0.1$. The fact that the connective layer is the same for both carrier types favors a chemical RDS for its formation. This is in contrast to the growth (at more positive voltages) of an anodic oxide (SiO_2), which requires the presence of holes.

A chemical mechanism, similar to Eq. [1] and [2], for the oxidation of the first Si—Si bond, followed by faster electrochemical processes to oxidize subsequent bonds (of the same atom), offers a qualitative explanation for the similar current densities of the different carrier-type samples at the PP. Here, both the first and subsequent bonds lie below the oxidized (or hydrated) surface. It should be noted that the chemical reaction is the RDS for the connective layer growth (as well as the current production). This type of mechanism is similar to one proposed for the oxidation of GaAs in the presence of bromine (21).

The growth of the oxide comes as a result of a competition between the oxidation of Si at the interface and the dissolution of the oxidized products. If the dissolution of the oxidized species is faster than their formation, significant hydrogen evolution should take place. At potentials anodic to the PP, the electrochemical hydrogen-evolution will be quenched and the equilibrium will shift to the formation of the oxide. Here, the RDS will change from being determined by the charge-transfer reactions at the Si interface to being controlled by diffusion across the oxide (1). In the following discussion, we describe the various reactions as applied to the n- and p-type samples.

p-Type silicon.—We will first consider p-type materials, for which the majority carriers are holes. Anodic to the PP, the surface is in depletion and enough holes are available to oxidize the Si through an electrochemical mechanism such as



where v and c denote valence and conduction bands, respectively. This reaction involves current doubling (21, 22) and is similar to one proposed by Turner for Ge (23, 24) in F^- solutions. In our case, the oxide dissolution is much slower than its formation and a film grows. An oxide (SiO_2) can be formed by removing water from the final products in Eq. [3]. The electrons, which are injected into the conduction band, will either recombine with the majority carriers at the surface or reduce the electrolyte producing hydrogen. At potentials in which such a mechanism can take place, the diffusion of the electrolyte through the oxide will be the RDS.

If, after oxide growth, we go cathodic and approach the PP, the surface starts to be strongly depleted of holes and the chemical mechanism takes over. Dissolution of the oxidized species will compete with their synthesis. If the new applied potential is anodic of the PP, only a portion of the oxide will be removed, whereas for biases cathodic of the PP all of the oxide etches. Cathodic of the OCP, the current saturates, and the etch rate remains constant and near its OCP value. The be-

havior of the current can be understood from a band model of the semiconductor/electrolyte interface (22). In our case, depletion conditions will result in current saturation. Since in depletion, few free carriers are present, the position of the bandedges with respect to any redox couple in the liquid is independent of the applied voltage, and, therefore, any electrochemical reactions which may occur at the solid surface should be independent of bias. For p-type samples, the equilibrium between electrochemical hydrogen evolution due to the electrolysis of water (current-producing) and the chemical one resulting from Si etching will be independent of the applied bias. The large cathodic voltage range over which the current saturates and the etch rate is nearly constant probably results from Fermi-level pinning.

n-Type silicon.—The flatband potential of the n-type sample occurs at a voltage slightly cathodic of the PP. At the PP, the chemical oxidation process is the RDS and a connective layer is formed. In this sample, however, there is a lack of holes and reaction [3] cannot readily proceed. Consequently, even at large anodic biases (which result in thick films on the p-type material), no appreciable oxide is grown. This is consistent with ellipsometric measurements, which indicate that intense illumination is required to produce any substantial amount of oxide on an n-type sample (1).

Cathodic to the PP, the semiconductor is in accumulation and majority carriers become available at the surface for reducing the solvent. At the OCP, the etching reactions, accompanied by H_2 evolution, will dominate. However, more negative of the OCP, hydrogen evolution will proceed not through the hydrolysis of Si—Si bonds (etching) but rather through the reduction of the solvent (electrolysis). Etching will stop, and the hydrogen evolution will follow the conventional electric-field-mediated activation mechanism which is dominant on most metals and n-type semiconductors in an accumulation mode.

Illumination effects.—The nature of the RDS can also be probed by the introduction of free carriers. Even though the etching of Si under illumination has been studied by several workers, a clear picture of the effects of light on the OCP etch rates has not been developed. The weight-loss measurements of Repinskii and Pershkova (10) in NaOH showed that under illumination, the n-type Si etch rates were reduced, whereas Izidinov *et al.* (6) found that light had no effect on the hydrogen evolution of n-Si in KOH. We have performed preliminary weight-loss measurements which indicate that under illumination the n-type etch rates are decreased, while the p-type etching is unaffected. These results, along with those of the hydrogen-evolution experiments of Izidinov *et al.* (6), suggest that the introduction of free carriers has a different effect on the two carrier types. For the n-type material, the RDS seems to shift toward the electrochemical hydrogen-evolution reaction, while in the case of the p-type sample a large anodic shift in the OCP suggests the possibility that the Fermi level is unpinned without any change in etching. The reason for this phenomenon is not known. In general, the effects of light on the etching of Si are not understood and require further investigation.

Orientation dependence.—The orientation dependence of the OCP etch rates is the focus of the technological interest in this system. From Fig. 4, 5, and 6, one can see that qualitatively the $\langle 100 \rangle$ and $\langle 111 \rangle$ faces behave similarly as a function of the electrode potential. The mechanistic arguments that were explored in the previous section will apply equally to both orientations (or any other orientation). The only obvious difference that can be observed is in the magnitudes of the etch rates and current densities involved. Since our samples were probably misoriented by approximately 1° , the differences shown here may not reflect the actual differences between the $\langle 100 \rangle$ and $\langle 111 \rangle$ surfaces. Kendall (17) has

shown that the etch rate of a misoriented $\langle 111 \rangle$ sample is that of ledges formed from the intersection of the $\langle 111 \rangle$ plane and $\langle 100 \rangle$ or any other fast etching face.

Kendall also noted that the oxidation rates go in reverse order to the etch rates (3). He suggested that since the $\langle 111 \rangle$ plane oxidizes more rapidly, it is immediately covered with an oxide layer that slows further etching. Such a protective prepassive layer was reported to be observed on GaAs (25). However, the more recent ellipsometric results of Palik and Bermudez (20) found no such layer on Si. Epova *et al.* (9) proposed that the selectivity correlates with heat of adsorption of water, which according to Meyer and Moributo (26) is smaller for the $\langle 100 \rangle$ surface than for the $\langle 111 \rangle$ face. According to them the reaction requires simultaneous adsorption of OH^- and H_2O , in agreement with Eq. [1] and [2]. They showed that propyl alcohol, which can reduce the number of available adsorption sites for water, decreases the pre-exponential factor in the expression for the etch rate by as much as three orders of magnitude. This correlation can account for the observations and is fully consistent with the mechanism proposed in the previous section.

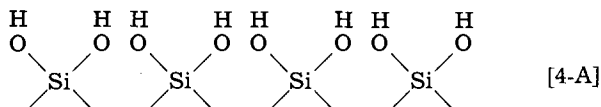
Price (8) has tried to correlate the etch rates to the bond densities on the two surfaces. However, these differ by no more than a factor of 2. A related argument that was advanced by Ligenza (27) to account for the orientation dependence of oxidation rate of Si by steam, is that bonds which are parallel to the surface are easier to oxidize than bonds at an angle with surface. On this basis, it was postulated that the activation energies for this reaction (oxidation) should increase in the following order: $\Delta E_{100} > \Delta E_{111} > \Delta E_{311} > \Delta E_{110}$.

Let us now introduce some "chemical" arguments into this picture and try to correlate them with the mechanistic considerations that we have previously discussed. The etch rate of a given surface can be written as (14)

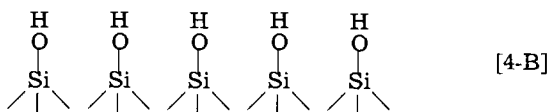
$$R(s) = R_0(s)e^{-\Delta E_s/kT} \quad [3]$$

where s denotes the surface orientation and can be 111, 100, etc. Here R_0 is a pre-exponential factor which may depend upon s , the free-carrier density, etc., ΔE_s is the activation energy of the chemical reaction, and T is the temperature.

If we neglect relaxation of the surface then on the average, the termination of the lattice for the $\langle 100 \rangle$ face can be represented as



and for the $\langle 111 \rangle$ surface as



where we have assumed that all of the dangling bonds are fully oxidized. Based on the electronegativity of the hydroxyl group, we expect the surface OH species to behave as an electron withdrawing group, making the Si susceptible to nucleophilic attack by OH^- (28). This effect should be stronger in the case of the $\langle 100 \rangle$ surface, which has two OH groups per surface atom. The difference in the susceptibility to nucleophilic attack would manifest itself through the activation energy and would have an exponential effect on the ratio of the etch rates of the $\langle 100 \rangle$ and $\langle 111 \rangle$ faces. It is interesting to note that the etch rates increase with the concentration of the base to a maximum near $4M$ and then slowly decrease. This effect may be related to the relative concentrations of water and OH^- .

The activation energies of the $\langle 100 \rangle$ and $\langle 111 \rangle$ faces have been measured, and little difference between the two was found (8, 29). This result is not surprising, because the samples were of commercial grade and probably oriented only to $\pm 1^\circ$. Based on Kendall's work, we conclude that the measured activation energy for the $\langle 111 \rangle$ surface was actually representative of the ledges, rather than the true $\langle 111 \rangle$ face.

The $\langle 110 \rangle$ face is somewhat more complex than the $\langle 100 \rangle$ and $\langle 111 \rangle$ surfaces (3). Each surface atom has one back bond to the lattice and one oxidized bond. The remaining two bonds are in the plane of the surface and connect adjacent surface atoms. This situation is different from that of the other faces, on which neighboring surface atoms do not share common bonds. We postulate that even though there is only one oxidized surface bond per atom, the OH group on its neighbor will also contribute to electron withdrawing from the common Si-Si bond. Therefore, the activation energy of the $\langle 110 \rangle$ face should be comparable to that of the $\langle 100 \rangle$ surface, and the difference in etch rates between the two attributable to the pre-exponential factor.

Until now, we have neglected the role of the pre-exponential factor, which is characteristic of the entropy of the reaction and is related to the crystal orientation. Since the etch rates depend linearly upon this parameter, it is difficult to imagine that it alone could account for a factor 400 in the etch rates. However, owing to the difference in bond orientations on any two faces, one does expect it to contribute. As mentioned above, its effect may be important in the difference in the etch rates of the $\langle 100 \rangle$ and $\langle 110 \rangle$ faces.

From the above discussion, we see that it is vital to accurately determine the relative contributions to the etch rates of R_0 and ΔE_s . The activation energy of the $\langle 111 \rangle$ surface must be measured on a perfectly oriented material. This might be accomplished through a technique similar to the one used by Kendall to obtain the true $\langle 111 \rangle$ etch rates.

Conclusions

We have presented experimental results for the bias-dependent etch rates and the current-voltage behavior of n- and p-type Si of $\langle 111 \rangle$ and $\langle 100 \rangle$ orientations. The data show that at voltages cathodic of the OCP, the n-type materials stops etching, while the p-type etch rate is unaffected. In order to account for these observations as well as the results of the considerable amount of prior work, we proposed a mechanism which involves an RDS that shifts between a chemical mechanism, an electrochemical mechanism which involves free carriers, and one limited by the diffusion of electrolyte through the oxide layer. At the OCP, the RDS participates in the chemical cleavage of the first Si-Si bond and is accompanied by hydrogen evolution. Anodic to the PP, the hydrogen-evolution reaction is quenched, and the forming oxide layer limits diffusion of the electrolyte. Cathodic to OCP, and RDS remains the same for the p-type material, while for the n-type material the reaction shifts to an electrochemical hydrogen-evolution reaction, resulting from the presence of majority carriers (electrons) at the surface.

We also proposed a mechanism which can account for the orientation dependence of the etch rates and is consistent with the overall scheme. The mechanism involves the difference in reactivity to nucleophilic attack of a Si sample which has two oxidized surface bonds (the $\langle 100 \rangle$ surface) compared with one that has only one oxidized bond ($\langle 111 \rangle$ face). This mechanism also accounts for the relative etch rate of the more complicated $\langle 110 \rangle$ face.

Owing to the complexity of the system, we have not concentrated upon the details of the reaction, but rather have developed an overview from which more detailed questions can be more systematically asked. In particular, we have attempted to clarify under which conditions the experimental results indicate participation by free-charge carriers and under which conditions spontaneous chemical reaction accounts for the rate-determining step.

Acknowledgments

We thank E. D. Palik and V. M. Bermudez for their continuing support, assistance, and useful discussions throughout various stages of this work. One of us (M.T.) would like to acknowledge the support of the Office of Naval Research. O.J.G. is a NRC-NRL Research Associate.

Manuscript submitted Feb. 6, 1984; revised manuscript received Aug. 11, 1984.

The Naval Research Laboratory assisted in meeting the publication costs of this article.

REFERENCES

- J. W. Faust, Jr., and E. D. Palik, *This Journal*, **130**, 1413 (1983), and references therein.
- E. D. Palik, J. W. Faust, Jr., H. F. Gray, and R. F. Greene, *ibid.*, **129**, 2051 (1982), and references therein.
- D. L. Kendall, *Ann. Rev. Mater. Sci.*, **9**, 373 (1979).
- J. B. Angell, S. C. Terry, and P. W. Barth, *Sci. Am.*, **44**, (April 1983).
- R. M. Hurd and P. T. Wrotenbery, *Ann. N.Y. Acad. Sci.*, **101**, 876 (1963).
- S. O. Izidinov, T. I. Borisova, and V. I. Veselovskii, *Russ. J. Phys. Chem.*, **36**, 659 (1962); *Zh. Fiz. Khim.*, **36**, 1246 (1962).
- A. Prologe, G. Kamarinos, and P. Gentil, *Proc. 4th Int. Conf. Solid Surf.*, **1**, 619 (1980); this work was for an oxide-covered electrode.
- J. B. Price, in "Semiconductor Silicon," H. R. Huff and R. R. Burgess, Editors, p. 339, The Electrochemical Society Softbound Proceedings Series, Princeton, NJ (1973).
- A. A. Epova, S. M. Repinskii, and T. P. Kirpichnikova, *Inorg. Mater. USSR*, **12**, 144 (1976); *Izv. Akad. Nauk SSSR Neorg. Mater.*, **12**, 166 (1976).
- S. M. Repinskii and S. V. Pershkova, *Russ. J. Phys. Chem.*, **46**, 519 (1972); *Zh. Fiz. Khim.*, **46**, 896 (1972).
- S. O. Izidinov, *J. Appl. Chem. USSR*, **44**, 1660 (1971); *Zh. Prik. Khim.*, **44**, 1642 (1971).
- See, for example, J. O'M. Bockris and A. K. N. Reddy, in "Modern Electrochemistry," Vol. 2, Chap. 11, Plenum Press, New York (1970).
- H. A. Waggner and J. V. Dalton, Abstract 183, p. 450, The Electrochemical Society Extended Abstracts, Vol. 70-2, Atlantic City, NJ, Oct. 4-8, 1970.
- O. J. Glembocki and E. D. Palik, To be published.
- O. J. Glembocki, M. Kramer, and M. Tomkiewicz, Unpublished results.
- O. J. Glembocki, *Proc. Int. Soc. Optical Eng. Conf.*, **452**, Cambridge, MA, Nov. 9-10, 1983, To be published.
- D. L. Kendall, *Appl. Phys. Lett.*, **26**, 195 (1975).
- H. A. Waggner, *Bell Syst. Tech. J.*, **49**, 473 (1970).
- See, for example, S. M. Sze, in "Physics of Semiconductor Devices," 2nd ed., Chap. 7, John Wiley and Sons, New York (1981).
- E. D. Palik and V. M. Bermudez, *J. Phys.*, To be published.
- H. Gerischer, *Surf. Sci.*, **18**, 97 (1969); H. Gerischer and W. Mindt, *Electrochim. Acta*, **13**, 1329 (1968).
- See, for example, S. R. Morrison in "Semiconductor and Oxidized Metal Electrodes," p. 75, Plenum Press, New York (1980).
- F. Beck and H. Gerischer, *Z. Electrochem.*, **63**, 500 (1959).
- D. R. Turner, *This Journal*, **103**, 252 (1956); *ibid.*, **107**, 810 (1960).
- W. W. Harvey and J. Kruger, *Electrochim. Acta*, **16**, 2017 (1971).
- F. Meyer and J. M. Moributo, *J. Phys. Chem.*, **75**, 2922 (1971).
- J. R. Ligenza, *J. Phys. Chem.*, **65**, 2011 (1961).
- See, for example, F. A. Cotton and G. Wilkinson, in "Advanced Inorganic Chemistry," Chap. 19, Interscience, New York (1962).
- J. W. Faust, Jr., in "The Surface Chemistry of Metals and Semiconductors," H. Gatos, J. W. Faust, Jr., and W. J. LaFeur, Editors, p. 151, John Wiley and Sons, New York (1960).

Comparison of Thin Thermal SiO₂ Grown Using HCl and 1,1,1 Trichloroethane (TCA)

Richard G. Cosway and Schyi-yi (C.-E.) Wu

Motorola, Incorporated, Process Technology Laboratory, SRDL, Phoenix, Arizona 85008

ABSTRACT

HCl and 1,1,1 trichloroethane (TCA) were used as chlorine sources for the growth of thin ($\leq 150\text{\AA}$) oxides. The resultant oxides were compared for ϕ_{ms} , breakdown voltage (both ac and dc), tertiary breakdown fractions, C-V shifts, and leakage current. The total C-V shift at flatband was more than twice as large for the TCA oxides as for the HCl oxides though ϕ_{ms} , the average breakdown voltage, tertiary breakdown fractions, and leakage current were comparable for the two chlorine sources. The breakdown and C-V shift distributions were tighter for the HCl oxides.

Several chlorine sources (HCl, Cl₂, 1,1,2 trichloroethene (TCE), 1,1,1 trichloroethane (TCA), and dichloroethane) can be used during oxidation to enhance the oxide growth rate, reduce defects, and improve the passivating ability of the resultant oxide. The role of chlorine in silicon oxidation was reviewed in more detail by Monkowski (1, 2). HCl has been widely used while TCA is emerging as an alternate chlorine source.

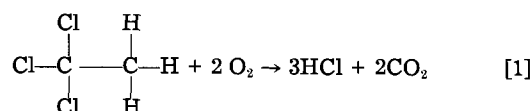
At room temperature, HCl is a gas and so is plumbed into a furnace in the same manner as the other gases except that special attention must be paid to ensure that the HCl stays as dry as possible. When dry, HCl is noncorrosive, but it can readily absorb water and become very corrosive even to stainless-steel fittings. Therefore, all fittings for HCl use must be kept tight to keep any air and its moisture from entering the lines.

TCA is a volatile liquid at room temperature with a boiling point of 74.1°C (3). At room temperature, TCA has a high enough vapor pressure to be carried to the tube in

significant amounts by a carrier gas passing through a bubbler containing the liquid. An inert gas (N₂ or Ar) must be used as the carrier because O₂ used as a carrier can cause the mixture to burn or explode (4).

TCA can be dangerous at elevated temperature even with small amounts of oxygen present, since it can react to form phosgene (COCl₂), an extremely poisonous gas (5). An excess of oxygen must be maintained to assure no phosgene formation in the lines or the tube. For this reason, as soon as possible after the TCA leaves the bubbler in an inert stream, it is mixed with a great excess of oxygen before it starts heating up near the tube entrance.

When in an oxygen excess at temperatures > 300°C, TCA reacts initially according to the reaction



These primary reaction products can then further react, depending on temperature, to compounds such as Cl_2 , H_2O , and, to a lesser extent, CO .

In this paper, the oxides grown using these two chlorine sources are compared for ϕ_{ms} , dielectric breakdown voltage, tertiary breakdown fraction, C-V stability, and current leakage.

Experimental

The wafers used were 75 mm Czochralski-grown of $\langle 100 \rangle$ orientation. All were phosphorus doped to 8.0-12.0 $\Omega\text{-cm}$ except for the p-type samples used in the ϕ_{ms} study. Those were boron doped to 14.0-22.0 $\Omega\text{-cm}$. All wafers were given a standard piranha clean immediately prior to being run.

The 160 mm id quartz tube and boat used for all oxidations were cleaned prior to every run at 1000°C for 1h, with either 10% HCl/90% N_2 for HCl oxidations or TCA to yield after pyrolysis 9.2, 6.1, 76.4, and 8.3% HCl, CO_2 , O_2 , and N_2 , respectively, for TCA oxidation.

The furnace that was used for all oxidations was equipped with a microprocessor which controlled the rate of the boat pusher/puller, the temperature of the tube, ramp temperature, and gases.

The wafers were pushed into the oxidation tube at low temperature, to prevent thermal stress-induced damage, and then ramped to 900°C in N_2 containing a small amount of oxygen to grow a thin layer of SiO_2 to protect the wafer surface from being thermally etched. Oxidation at 900°C consisted of a 20 min dry O_2 cycle followed by 22 min of O_2 + 3 volume percent (v/o) HCl equivalence. Thick enough oxide was grown in the 20 min dry O_2 oxidation to insure no surface etching by HCl in the subsequent oxidation cycle. The 3 v/o HCl equivalence is 3 v/o HCl or the amount of TCA necessary to yield, after pyrolysis, the same HCl flow rate. The concentration of HCl during a TCA oxidation was actually somewhat less than 3 v/o because the CO_2 and carrier gas present increased the total flow. A 60 min 900°C N_2 anneal followed the oxidation.

Following the oxidation, 4000Å of aluminum was deposited (dc magnetron) on the front of the wafers using a mask that gave circular dots with nominal areas of $7.5 \times 10^{-3} \text{ cm}^2$. The back oxide was then RF sputter etched for 3 min and 1000Å of Al was deposited all over to provide good back contact. Following this, the wafers were annealed at 450°C in forming gas (5 v/o H_2 /95 v/o N_2) for 30 min. This forming gas anneal gave the best C-V stability upon bias-temperature stressing among all conditions investigated (350°-550°C for 30 min and 450°C for 10-60 min).

Oxide thicknesses were measured using an automated spectrophotometer after the metal had been deposited and annealed.

C-V measurements were made on a computerized C-V plotter with the first trace being taken after unbiased (shorted) heating of the sample to 200°C, holding it there for 1 min, and then cooling it back to 25°C. The second trace was taken after biasing the sample at 3 MV/cm oxide while it was heated to 200°C, held at 200°C for 1 min, and cooled back to 25°C. The third trace was taken after biasing the sample at -3 MV/cm of oxide while it was heated to 200°C, held at 200°C for 1 min, and then cooled back to 25°C. The only flatband voltage shifts reported are the total shifts, i.e., the shift between the leftmost and rightmost trace at flatband.

Dielectric breakdown measurements were taken using a curve tracer with the collector output connected to a probe on the top of the aluminum dots. The base output was connected to the vacuum chuck holding the wafer. AC and dc breakdowns were taken in the same manner, with the collector voltage ramped manually (at about 5 V/s in accumulation mode), the only difference being the waveform used. In the case of the ac breakdown, it was a full-rectified (60 Hz) sine wave. As noted in the text, breakdowns are destructive or defined at $26 \mu\text{A cm}^{-2}$. The latter value corresponds to about 10 MV cm^{-1} , below which the breakdown field is independent of ramp rate (6).

Note that the spread in destructive breakdown voltage is partly due to variation in voltage ramp rate (6). In addition, ac destructive breakdown voltage is about 2V higher than the dc destructive breakdown. This is explained below.

Two charging processes can occur upon application of high enough field: (i) charging of pre-existent traps and (ii) creation of traps and trapped electrons. Charging may enhance local internal field. When a certain local internal field is exceeded, numerous Si-O bonds have been broken and the oxide breaks down (6). The charging processes continue uninterrupted in dc measurements since applied voltage continues to rise. But, the charging processes are constantly interrupted in ac measurements because the applied voltage oscillates up and down. That is, the average rate of charging is lower in ac measurements than in dc measurements at the same ramp rate. Thus, higher applied ac voltage is required to cause oxide breakdown than applied dc voltage.

Leakage current measurements were taken using a power supply/amplifier and a picoammeter connected to a shielded probe.

Results and Discussion

ϕ_{ms} and total oxide charge.—An oxide related parameter that is of particular importance to device characteristics is ϕ_{ms} , i.e., the metal-semiconductor work function difference. Previous investigations (7) have shown that ϕ_{ms} is process related and so, for an accurate value, it must be determined for each set of process conditions. One way to determine ϕ_{ms} from oxide C-V data is from the equation (8)

$$V_{\text{FB}} = \phi_{\text{ms}} - \frac{Q t_{\text{ox}}}{\epsilon_0} \quad [2]$$

By plotting V_{FB} (the voltage corresponding to the flatband capacitance of the initial unbiased trace) as a function of t_{ox} (the oxide thickness), a straight line should be obtained with a slope of $-Q/\epsilon_0$ (total charge divided by oxide permittivity) and an intercept at ϕ_{ms} .

Oxides were grown in both HCl and TCA and on both n- and p-type substrates in thicknesses of 100-300Å. The resultant V_{FB} 's are plotted as a function of t_{ox} in Fig. 1. The data follows a straight line well with each ambient and substrate. For each substrate type, little or no difference is seen between HCl and TCA oxides. The "total charge" is about $1 \times 10^{11} \text{ cm}^{-2}$ on n-type substrates and $5 \times 10^{10} \text{ cm}^{-2}$ on p-type substrates.

ϕ_{ms} is shown to be about +0.1V for the n-type and about -0.7V for the p-type substrate. Compare this with -0.3

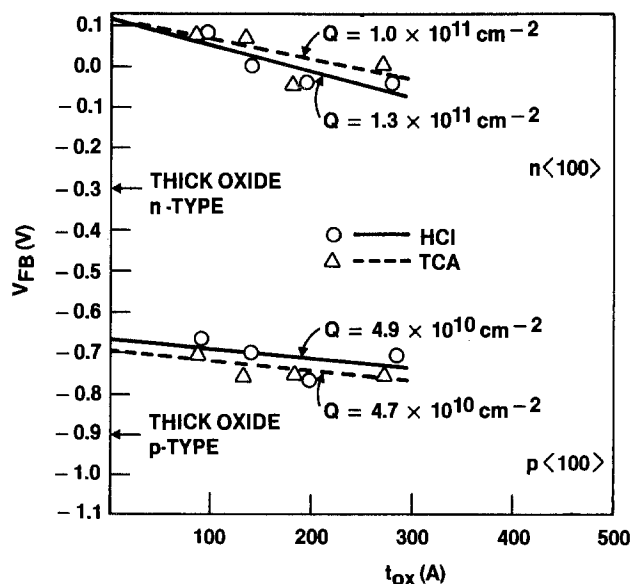


Fig. 1. V_{FB} as a function of t_{ox} for TCA and HCl oxides

and $-0.9V$, respectively, for thick oxides given in the literature (8).

Also implicit in Fig. 1 is a comparison of the rate of oxidation in HCl vs. TCA. Adjacent points, that is each circle with the corresponding triangle for HCl and TCA oxidations, respectively, were oxidized for the same time. It can be seen that, in all cases, TCA runs result in 5-10% thinner oxides than the comparable HCl runs. This is likely due to the lower concentration of O₂ and HCl in the TCA runs.

C-V stability.—For each kind of oxide, a total of 12 capacitors (6 wafers \times 2 capacitors/wafer) were measured for total flatband voltage shift. HCl oxide gave less shift than TCA oxide (14 ± 12 vs. 37 ± 20 mV) at the 90% confidence level. There was no apparent difference in the skewedness of the plots for the two chlorine sources, so no qualitative or quantitative statement about D_{it} differences can be made.

Current conduction.—The conduction of both HCl and TCA oxides followed the Fowler-Nordheim tunneling mechanism (9) in the high field regime, as evidenced by the linear relationship between $\log(J/E^2)$ vs. $1/E$. Leakage is <1 nA cm⁻² for voltages up to 7.5V for both kinds of oxides. The above conduction measurements were taken in dc mode at 1/2V increments with a 1 Vs⁻¹ ramp rate and a 4s delay between attaining the desired voltage and taking the reading.

Dielectric breakdown.—DC breakdown voltage (defined at $26 \mu A$ cm⁻²) histograms are shown in Fig. 2 for HCl oxide and Fig. 3 for TCA oxide. Each histogram was obtained from three oxidation runs (six wafers from one run and two wafers each of the other two runs). Ten capacitors per wafer were measured. The yields (those capacitors that failed at the highest voltage peak) were 85%, 85%, and 95% (14.5V) for HCl oxide and 90%, 100%, and 75% (14.0) for TCA oxide. Thus, the average yield by this definition is the same for both types of oxides (88.3%), but HCl oxide showed tighter distribution below the highest breakdown voltage peak.

CO₂ effect.—Since the amount of CO₂ generated during the pyrolysis of TCA is comparable to the amount of HCl formed, an investigation was undertaken to see what effect the presence of CO₂ had on the resultant oxides. Also, to give an idea of the process latitude with respect to CO₂, extreme amounts were used, even though when using TCA this concentration is fixed. The same flow sequence used for 150Å HCl oxides was used; however, the O₂/HCl cycle gas flows were changed. The HCl flow remained the same but the rest of the flow was made up of various combinations of CO₂ and O₂ (Table I). The CO₂ flow was about 2% in the standard TCA oxidation. Note that, as the CO₂ concentration increased, the HCl/O₂ ratio

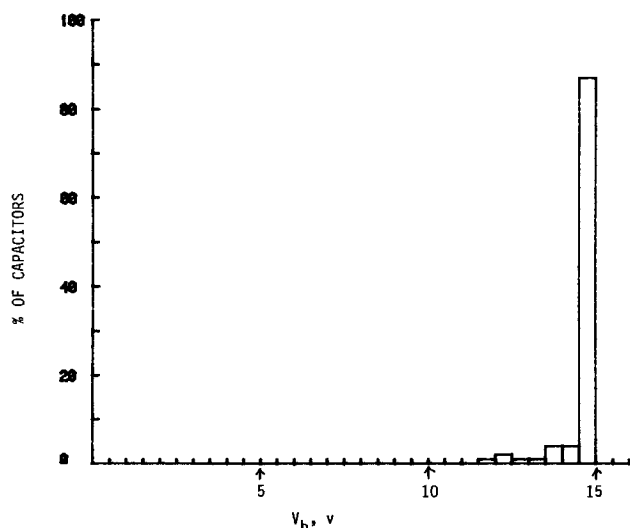


Fig. 2. Breakdown voltage (dc, $26 \mu A/cm^2$) histogram for 150Å HCl oxide.

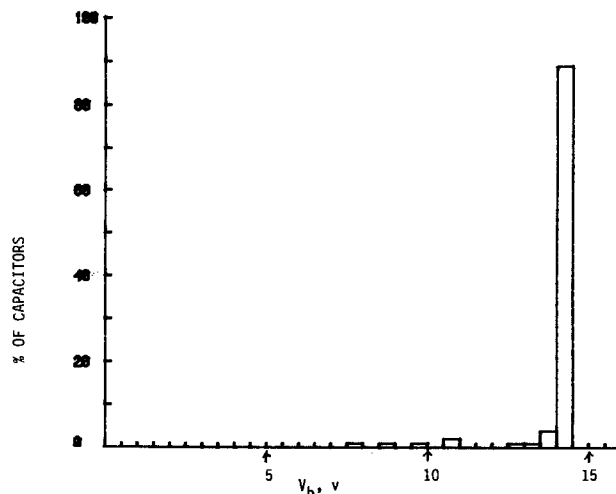


Fig. 3. Breakdown voltage (dc, $26 \mu A/cm^2$) histogram for 150Å TCA oxide.

increased and the O₂ concentration decreased. The last set of flow conditions means an ambient of only CO₂ and HCl and no O₂. In this case, the oxide is produced in dry O₂ and then "annealed" in a mixture of CO₂ and HCl before the N₂ anneal.

Oxide thickness is shown to monotonically decrease with increasing CO₂ concentration. This is due to the corresponding decrease in O₂ concentration. Previous experiments showed oxidation by CO₂ at 900°C for 1h to be insignificant.

No significant effect on tertiary breakdowns ($<1V$) is seen, at least up to a CO₂ concentration of 72.75%. (Note that no tertiary breakdowns were measured for 100Å oxide.) The higher fraction of tertiary breakdowns (10%) for the 90Å oxide could be due to thinner oxide rather than a CO₂ effect, since 100Å HCl oxide sometimes showed $>10\%$ tertiary breakdowns.

DC breakdown field (destructive) and the spread are not degraded by CO₂ in the concentration range studied. The same Fowler-Nordheim I-V characteristics were observed for CO₂ concentrations $\leq 48.5\%$. At 72.75%, the I-V characteristics deviate only slightly from those for lower CO₂ concentration. At 97%, I-V characteristics showed obvious departure from those for lower concentrations and a more gradual increase in current with voltage. This could be due to the thickness or HCl effect, since no O₂ is present at this CO₂ concentration and etching of the silicon and/or the SiO₂ by HCl is possible. Nevertheless, it appears possible to produce oxides as thin as 100Å with only a few low field breakdowns.

Total flatband C-V shift is seen to be small for all concentrations investigated. Even though the data show some scatter, because of the small magnitudes, all results are considered equivalent.

From this study then, it can be concluded that CO₂ present during oxidation using TCA produces insign-

Table I. CO₂ effect

[CO ₂] (%)	0.0	24.25	48.5	72.75	97.0
[O ₂] (%)	97.0	72.75	48.5	24.25	0.0
[HCl] (%)	3.0	3.0	3.0	3.0	3.0
t_{ox} (Å)	142	137 ^b	123 ^b	110 ^b	80-90 ^c
Tertiary breakdowns ^a (%)	5	0	0	0	10
\bar{E}_b^* (MV cm ⁻¹) (dc, destructive)	11.8	12.2	13.8	12.9	12.1-13.65
$2\sigma/\bar{E}_b^*$ (%)	33.6	8.36	14.1	13.8	22.4
ΔV_{FB} (mV)	14	22	16	12	11

^a Two wafers from each run, ten capacitors per wafer were measured.

^b Estimated from I-V characteristics, (i.e., the same current density should be obtained at the same field.)

^c Estimated from oxidation kinetics data.

Table II. Lag time effect on ac breakdown field of 150Å HCl and TCA oxides (MV/cm)

Premetal lag time	Postanneal lag time	1 day	1 week	2 weeks	1 month	2 months	3 months
		1 day	HCl TCA	14.0 11.9	13.7 14.0	14.3 15.3	14.6 14.0
1 week	HCl TCA	13.5 12.8	14.6 13.0	14.1 13.7	14.0 10.8	13.8 12.6	12.7 13.1
2 weeks	HCl TCA	15.3 13.5	— —	14.7 13.0	— —	14.3 13.8	14.0 13.5
1 month	HCl TCA	14.1 14.0	13.2 12.5	14.3 14.1	— —	14.3 13.6	15.4 14.3
2 months	HCl TCA	14.1 14.7	14.8 15.0	14.3 14.4	14.4 15.7	14.6 13.9	13.7 14.5
3 months	HCl TCA	14.4 15.9	— —	— —	15.3 15.9	15.2 16.0	14.2 13.8

nificant effects on tertiary breakdowns ($< 1V$), dc breakdown field (destructive), total flatband C-V shift, and oxide thickness.

Process lag times.—One concern, especially for thin oxides, is that the oxides may degrade upon storage. To examine this effect we chose two long lag times and ran a matrix with each lag time ranging from 1 day to 3 months. These two lag times were the premetalization lag time between oxidation and metal deposition and the postanneal lag time between metal anneal and breakdown measurement (ac destructive). Four wafers were prepared for each of the six metallization lag times, and five capacitors were measured on each wafer to arrive at an average breakdown field for each point in the premetalization and postanneal lag time matrix.

Results for both HCl and TCA oxides are shown in Table II, where it is apparent that storing has no effect on breakdown voltage in the chosen time span.

In this experiment, a total of 598 capacitors on 24 wafers for each kind of oxide were measured. The fraction of tertiary breakdowns ($< 1V$) is only 0.5% in each case. The means and standard deviations are 21.2 and 3.8V for the HCl oxide and 20.9 and 4.5V for the TCA oxide. T- and F-tests with a 95% confidence level show that the average ac breakdown voltages (destructive) can be considered

equal, but the HCl distribution is tighter than the TCA distribution.

Conclusions

Electrical characteristics of 150Å HCl and TCA oxides are summarized in Table III. Both HCl and TCA yield acceptable 150Å oxides with few tertiary breakdowns (0.5% $< 1V$), average breakdown strength of 14 MV/cm (ac, destructive), and low leakage current. However, HCl oxides have less C-V shift and a tighter breakdown distribution. The CO₂ present during TCA pyrolysis has been shown to have no significant effect on tertiary breakdowns ($< 1V$), average breakdown field and spread, and C-V shift.

Acknowledgments

The authors wish to thank Ginger Stapleton for providing all of our metal deposition, Dan McGuire for performing the I-V measurements, Craig Thornton for his valuable assistance in the design of the TCA transport system, and Glenn Shirley for helpful discussions.

Manuscript submitted Feb. 8, 1984; revised manuscript received Aug. 15, 1984. This was Paper 224 presented at the Washington, DC, Meeting of the Society, Oct. 9-14, 1983.

Motorola, Incorporated, assisted in meeting the publication costs of this article.

Table III. Electrical characteristics of 150Å oxides

	HCl	TCA
ϕ_{ms} (V)	0.1	0.1
ΣQ , (10^{11} cm ⁻²)	1.3	1.0
ΔV_{FB} (mV)	14 ± 12	37 ± 20
J up to 7.5V (nA cm ⁻²)	<1	<1
Lag time effect	None	None
Tertiary breakdowns (%)	0.5	0.5
Average breakdown field (ac, destructive) (MV cm ⁻¹)	14.1 ± 2.5	13.9 ± 3.0
Yield (%) (dc, 26 μA cm ⁻² , highest breakdown voltage peak)	88.3	88.3
Breakdown distribution spread	Smaller	Larger

REFERENCES

1. J. Monkowski, *Solid State Technol.*, 58 (July 1979).
2. J. Monkowski, *ibid.*, 113 (Aug. 1979).
3. "Perry's Chemical Engineers' Handbook," 4th Ed., Perry, Chilton, and Kirkpatrick, Editors, pp. 3-41, McGraw-Hill, New York (1963).
4. J. C. Schumacher Co. Product Application Note no. 2.
5. Apache Chemical sales information.
6. E. Harari, *Appl. Phys. Lett.*, 30, 601 (1977).
7. R. R. Razouk and B. E. Deal, *This Journal*, 129, 806 (1982).
8. W. N. Carr and J. P. Mize, "MOS/LSI Design and Application," p. 34, McGraw-Hill, New York (1972).
9. M. Lenzlinger and E. H. Snow, *J. Appl. Phys.*, 40, 278 (1969).

Thermal and Physical Properties and Etching Characteristics of PI Films

Atsushi Endo and Toshio Yada

Mitsubishi Electric Corporation, Materials and Electronic Devices, 1-1, Tsukaguchi Honmachi 8 Chome, Amagasaki, Hyogo 661, Japan

ABSTRACT

The thermal properties of spin-coated polyimide films and their etching characteristics are evaluated. The physical properties of polyimide films are presented, such as density, softening temperature, thickness, and wet etching characteristics which change with curing temperature. Wet etching characteristics, such as the etch rate and the pattern profile, are influenced not only by the imidization, but also by the molecular state of aggregation. When the crystallinity is chosen as the physical parameter, the wet etching characteristics closely correspond to the crystallinity. Desirable patterns of polyimide films can be obtained when the crystallinity is about 10%.

Polyimide (PI) films are finding wide acceptance in electronics industry as an interlayer dielectric material and for passivation and other applications. PI films provide excellent step coverage and can be coated in very thin layers. PI films remain pinhole and crack free, so they have excellent quality and good controllable metallic ion content. PI films can be precisely etched both by wet processes with organic amines and by dry processes with an O₂ plasma.

The published studies have discussed the patterning techniques, the application methods to devices, and the electric properties of PI films (1-4). There have only been a few reports published on the effect of the heat-treatment on the molecular structure and on the etching characteristics such as etch rate and pattern profile.

The purpose of this paper is to report the experimental results of the thermal and physical properties, the molecular structures, and the etching characteristics of PI films.

Experiments

Polyimide film.—SP 510 (Toray Industries, Japan) was used as a polyimide resin. The main solvent of PI materials was DMAc(N,N-dimethylacetamide). A prepolymer solution of 15.9% and 12 poise viscosity was spin coated onto silicon wafers and thermally cured for 1h in a N₂ atmosphere at various temperatures. The film thickness was typically 3 μm.

Etching.—The masks employed were negative photoresists, such as OMR83 (Tokyo Ohka Kogyo, Japan), which were spun onto the cured PI films and photoetched by the conventional technique (1-2). Wet etching was carried out 25°C with hydrazine hydrate containing 80% ethylene diamine. Dry etching was carried out in a parallel-plate plasma etcher. Pure dry oxygen was used as the etching gas.

Evaluation of the PI film properties.—The chemical structure and the imidization of the sample films were investigated by IR absorption spectra. The mass thermal analyses were carried out for characterizing the thermal properties, and chromium-polyimide-chromium structures were prepared on silicon wafers for measuring the dielectric properties. The various mixtures of ortho-xylene and carbon tetrachloride were prepared to obtain the film density. Samples were cut to 2 × 2 mm and then placed in the mixture. The measurement was carried out at 25°C with the pycnometer. The crystallinity of the films was calculated from the results of the density measurements (5)

$$X = \frac{d_c(d - d_a)}{d(d_c - d_a)} \quad [1]$$

Where X is the crystallinity of the films, d_c is the density of the crystalline phase 1.58 (6), d_a is the density of the amorphous phase 1.39 (7), and d is the density of the sample films. The softening temperature was determined

from the thermomechanical analysis in a N₂ atmosphere. The weight of the probe was 7.0g, and the thickness of the sample films was about 7 μm. The surface of the sample films was scratched to measure the film thickness with a surface roughness analyzer.

Results

IR spectral analysis.—PI materials used in this work were formed by imidization of polypyromellitic acid (PAA) as shown in Fig. 1. The IR spectra of the sample films are recorded to evaluate the change of the chemical structure with additional heating. Figure 2 shows the IR spectra of the films cured at 100°C (broken line) and 300°C (solid line) for 1h. The former film shows the absorption bands at 1650, 1540, and 1320 cm⁻¹ belonging to the amino groups (—NH—CO—). The latter film does not show these absorption bands, but does show the characteristic bands at 1785, 1375, and 723 cm⁻¹ corresponding to the imide groups (>N—CO—). However, two films show the unchanged absorption bands at 1495 and 880 cm⁻¹ for the phenyl groups (C₆H₅—). When the peak height of the absorption bands which changes with heating temperature is traced, the change of the chemical structure of the films can be known. Figure 3 shows the change of the chemical structure of the films with additional heating. The absorption bands for the phenyl groups are used for normalizing the characteristic absorption bands. The absorption ratio and the relative imidization were calculated from the absorption ratio change with additional heating. From the analysis of the IR spectra shown in Fig. 3, it is known that the sample films cured below 250°C show the

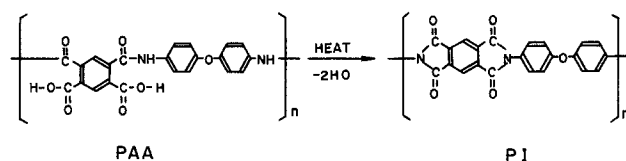


Fig. 1. Imidization reaction of PI materials

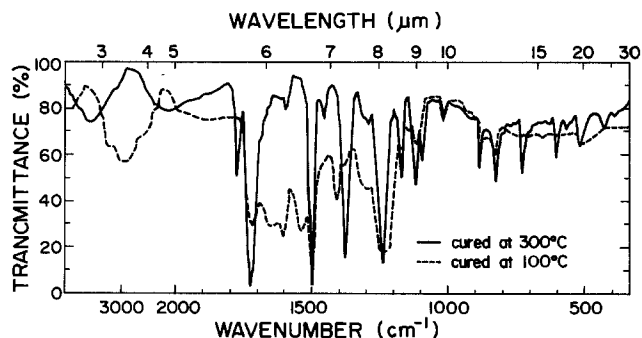


Fig. 2. IR absorption spectra of PI films cured at 100°C (broken line) and 300°C (solid line).

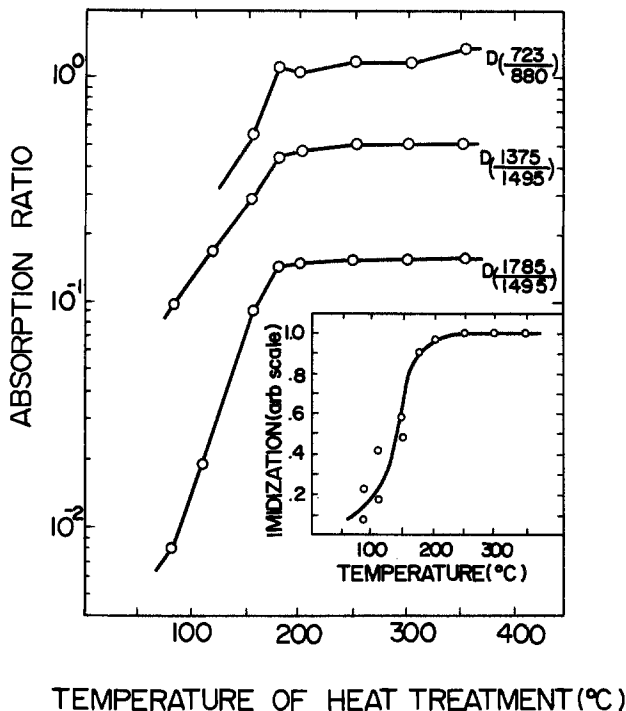


Fig. 3. Imidization of PI films obtained from the IR analysis. PI films were cured for 1h.

change of the chemical structure, and that those films cured above 250°C show no further detectable change in the IR spectra with additional heating.

Mass thermal analysis.—The sample film cured at 80°C for 1h generated H₂O and DMAc with additional heating. The peak heights of the fragments (H₂O: *m/e* = 18, DMAc:

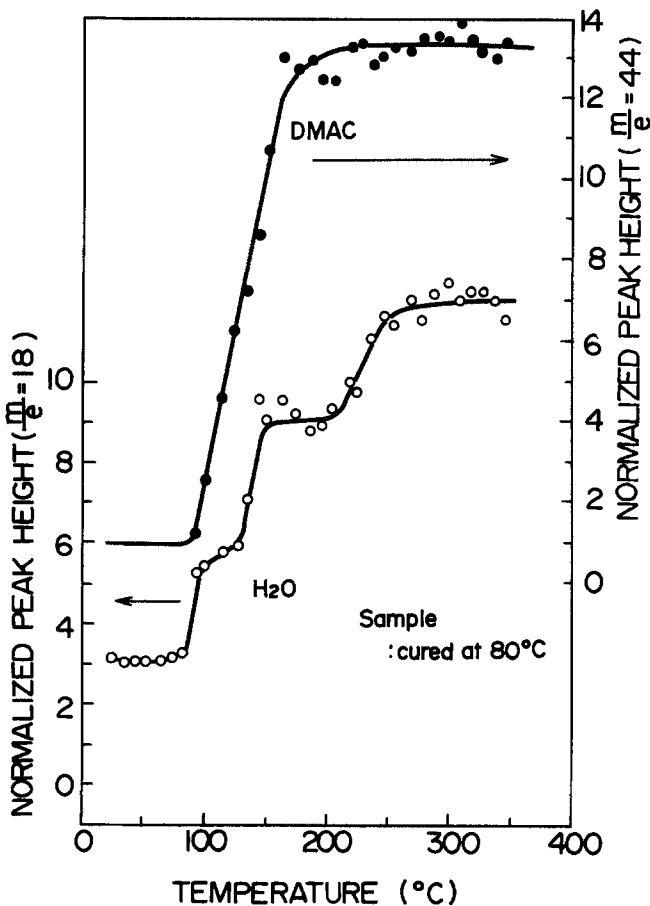


Fig. 4. Plots of the fragment peak height of H₂O (*m/e* = 18) and DMAc (*m/e* = 44) with additional heating.

Table I. Crystallinity and etch rate of PI films cured for 1h

	Temperature of heat-treatment (°C)					
	150	200	250	300	350	400
Crystallinity (%)	(0)	6.65	11.7	17.2	17.6	22.7
Wet etch rate ^a (μm/min)	10.0	2.0	0.65	0.35	0.22	0.20
Dry etch rate ^b (μm/min)	0.76	0.65	0.60	0.59	0.59	0.59

^a Etchant is hydrazine hydrate containing 80% ethylene diamine, and temperature is 25°C.

^b Oxygen flow rate is 20 sccm, power density is 0.49 W/cm², and pressure is 0.16 torr.

m/e = 44) were traced with the temperature. Figure 4 shows the plots of the fragment peak height of H₂O and DMAc. The generation of H₂O continues till 250°C, and that of DMAc continues till 180°C. Other gasses cannot be detected and traced above this temperature.

Dry etch rate and dielectric properties.—The dry etch rate varies with the cure temperature and shows the constant value about 0.59 μm/min above 300°C (Table I) (O₂ flow rate is 20 sccm, the power density is 0.49 W/cm², and the pressure is 0.16 torr). The etch rate shows little dependence on the O₂ flow rate and the power density. Figure 5 shows the dielectric properties such as the dielectric constant ε' and the dielectric loss factor tan δ. The dielectric properties vary with the cure temperature as well as the dry etch rate and reach a constant value (ε' is about 3.3, and tan δ is about 0.003). The PI films used in this work exhibit excellent electrical characteristics of an insulator.

These experimental results show that it is necessary to cure the film above 300°C in order to obtain a stable film. When the sample film is stabilized, the dry etch rate and the dielectric properties show a constant value. The reasons why the chemical structure in the IR spectra shows no further detectable change above 250°C and the dry etch rate and the dielectric properties show constant value above 300°C are not yet clear from these experiments.

Physical properties.—Figures 6 and 7 show the physical properties of PI films such as the density, the softening temperature, and the thickness. It is shown that the physical properties vary with the cure temperature even when the temperature is above 250°C. For example, the softening temperature depends on the cure temperature and shows almost the sample temperature as the cure temperature. The film thickness decreases with additional heating, and these results show no dependence on the initial thickness for the sample films. Figure 8 shows the visible absorption spectra of PI films. The films become colored upon additional heating. It is predicted that PI films prepared in this work undergo other reactions at a high

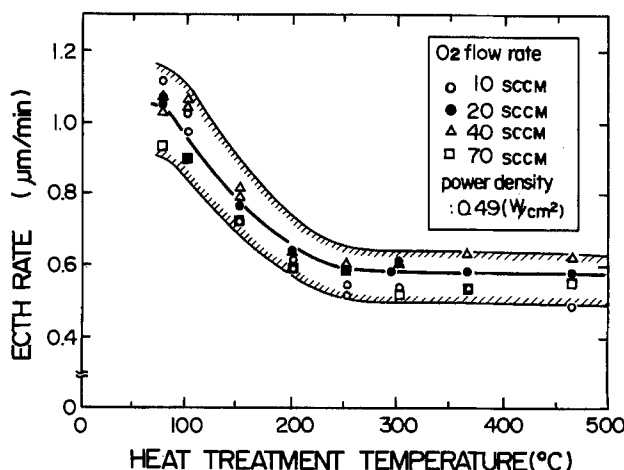


Fig. 5. Dielectric properties of PI films

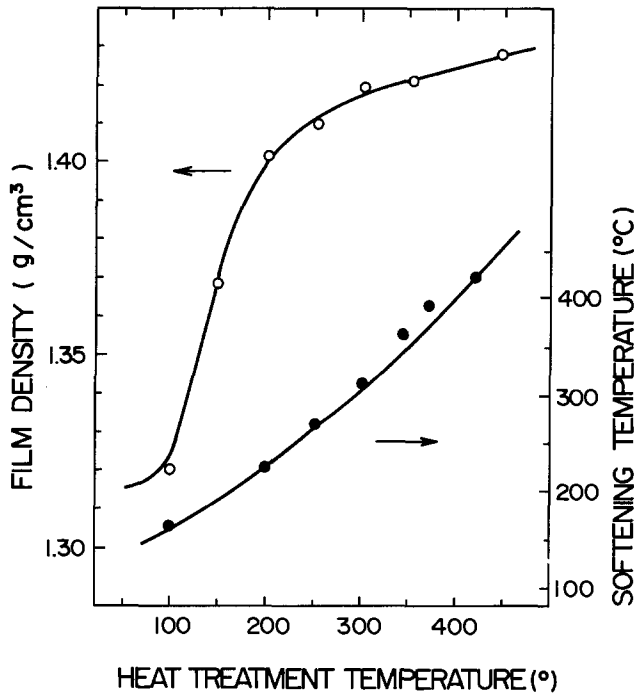


Fig. 6. Density and softening temperature vs. heat-treatment temperature. PI films were cured for 1h.

temperature because the imidizing reaction cannot describe clearly this result.

X-ray diffraction analysis.—Figure 9 shows the x-ray diffraction patterns of the sample films. There are differences in the diffraction patterns among the sample films cured at various temperatures. As the cure temperature increases, the diffraction peak becomes narrower and a new peak appears. The diffraction pattern of the sample films with the higher cure temperature becomes similar to that of du Pont Kapton film, which has been identified as crystalline material by the x-ray measurement method (8-9). The crystallinity of the sample films is calculated by Eq. [1] and is listed in Table I. The crystallinity increases with additional heating and goes up to about 23%.

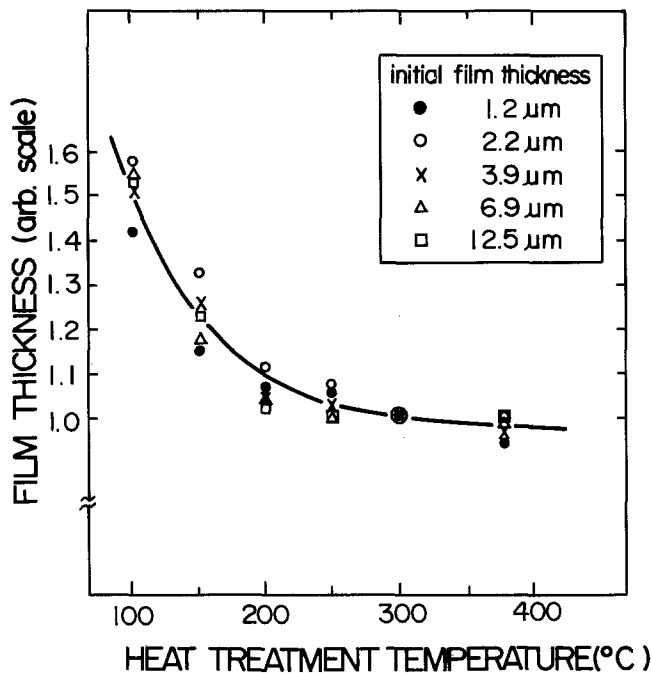


Fig. 7. Relation between the film thickness and the heat-treatment temperature. PI films were cured for 1h.

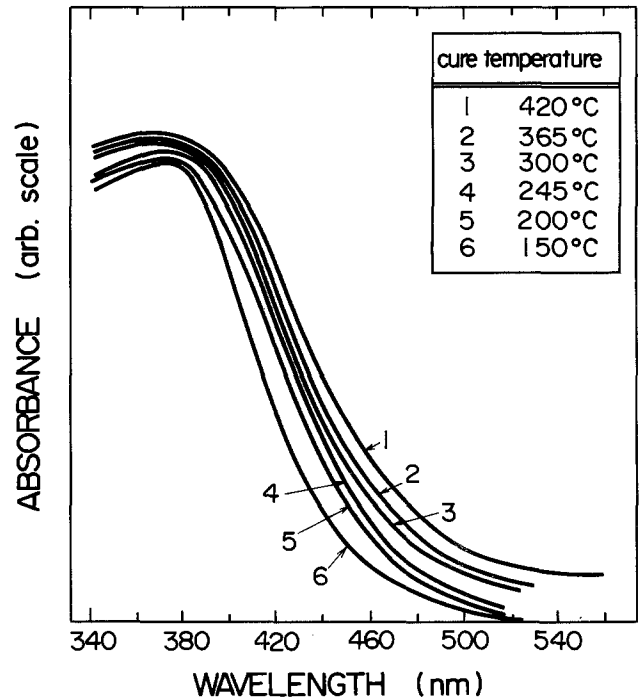


Fig. 8. Visible absorption spectra of PI films cured at various temperatures and cured for 1h.

Wet etching characteristics.—Wet etching characteristics such as the etch rate and the pattern profile are influenced by the cure temperature. The etch rate of the sample films varies from 0.2 to 10.0 μm/min, as shown in Table I, and the pattern profile of the sample films is changed with the cure temperature, as shown in Fig. 10.

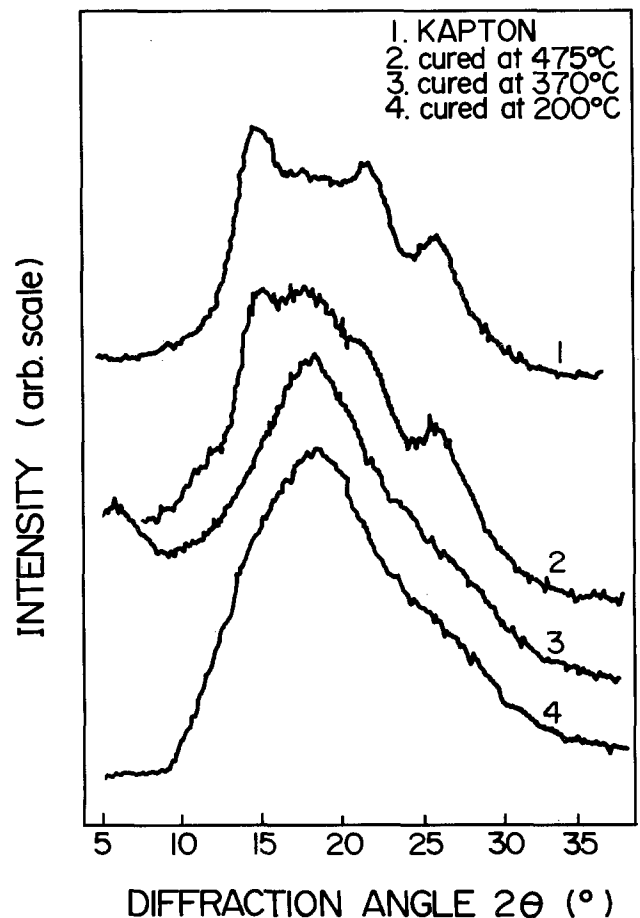


Fig. 9. X-ray diffraction patterns of PI films cured for 1h

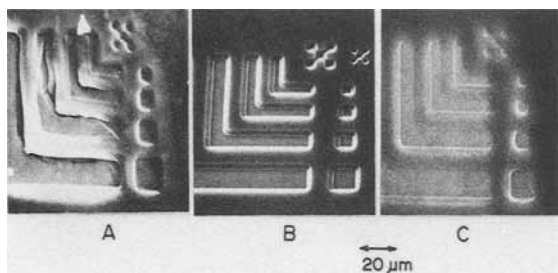


Fig. 10. Patterns of PI films cured at 150°C (A), 250°C (B), and 340°C (C). Cured for 1h.

Discussion

IR spectral analysis indicates that, when the cure temperature is below 250°C, the physical properties of the sample films correspond to the change of the primary chemical structure of the materials, but that, when the cure temperature is above 250°C, the physical properties of the sample films do not depend on the change of primary chemical structure of the materials. The x-ray diffraction analysis shows that the films prepared for this work have the crystalline phase during the cure process. So, the reason why the physical properties of the sample films cured above 250°C change as the cure temperature increases is predicted by the change of the molecular state of aggregation, especially the production of higher-ordered region in the sample films. From the result of the x-ray diffraction analysis, it is shown that the change of

physical properties of the sample films cured above 250°C is consistent with the degree of the molecular state of aggregation. The physical properties of the sample films change with the crystallinity. However, the relationship between the wet etching characteristics and the chemical structure was evaluated for PI films. Figure 11 shows the relationship between the etch rate and the degree of imidization obtained from the IR analysis and the crystallinity obtained from the film density. The imidization reaches the saturated value of 1.0 when the crystallinity varies from 0% to 23%. The etch rate does not saturate and varies from 0.2 to 2.0 $\mu\text{m}/\text{min}$. It is clear from these results that the etch rate depends not only on the degree of imidization but also on the crystallinity. The pattern profile is influenced by the molecular state of aggregation and the desirable pattern can be obtained when the cure temperature is 250°C. The crystallinity of the sample film cured at 250°C is about 10%.

Conclusions

The thermal properties and the etching characteristics have been evaluated for spin-coated polyimide films. Experimental results show that in order to obtain a stable PI film, it must be cured above 300°C. When a stable film is formed, the dry etch rate and the dielectric properties have a constant value.

The physical properties of PI films, such as density, softening temperature, thickness, and wet etching characteristics, are proportional to the cure temperature. Wet etching characteristics, such as the etch rate and the pattern profile, are influenced not only by the imidization, but also by the molecular state of aggregation. When the crystallinity is chosen as the physical parameter, the wet etching characteristics closely correspond to the crystallinity. Desirable patterns of polyimide films can be obtained when the crystallinity is about 10%.

Acknowledgments

The authors wish to thank Y. Onishi, T. Sugiura, T. Maejima, H. Ono, and T. Ando for useful discussions, T. Masumi, H. Koezuka, and S. Isoda for their help in evaluation of film properties, and D. Odaka for his help in x-ray diffractometry.

Manuscript submitted March 12, 1984; revised manuscript received Aug. 10, 1984.

Mitsubishi Electric Corporation assisted in meeting the publication costs of this article.

REFERENCES

1. K. Sato, S. Harada, A. Saeki, T. Kimura, T. Okubo, and K. Mukai, *IEEE Trans. Parts Hybrid Packag.*, **php-9**, 176 (1973).
2. Y. Harada and H. Fukuda, *IEEE Trans. Electron Devices*, **ed-26**, 1799 (1979).
3. J. H. Nevon and G. L. Sume, *Microelectron. Reliab.*, **21**, 669 (1981).
4. Y. Harada, F. Matsumoto, and T. Nakado, *This Journal*, **130**, 129 (1983).
5. Y. Wada, "Bussei Kogaku Koza," (Materials Engineering, in Japanese,) p. 144, Omusha, Tokyo (1976).
6. L. G. Kazaryan, D. Ya. Tsvankin, B. M. Gimzberg, Sh. Tuichiev, L. N. Korzhavin, and S. Ya. Frenkel, *Vysokomol. Soed.*, **A14**, 1199 (1972).
7. M. Kochi, H. Shimada, and H. Kanbe, *Polymer Prepr. Jpn.*, **29**, 2095 (1980).
8. H. Kambe, T. Kato, S. Kuga, and R. Yokota, *ZAIRYO, (Materials)*, **21**, 405 (1972).
9. S. Isoda, H. Shimada, M. Kochi, and H. Kambe, *J. Polym. Sci. Polym. Phys. Ed.*, **19**, 1293 (1981).

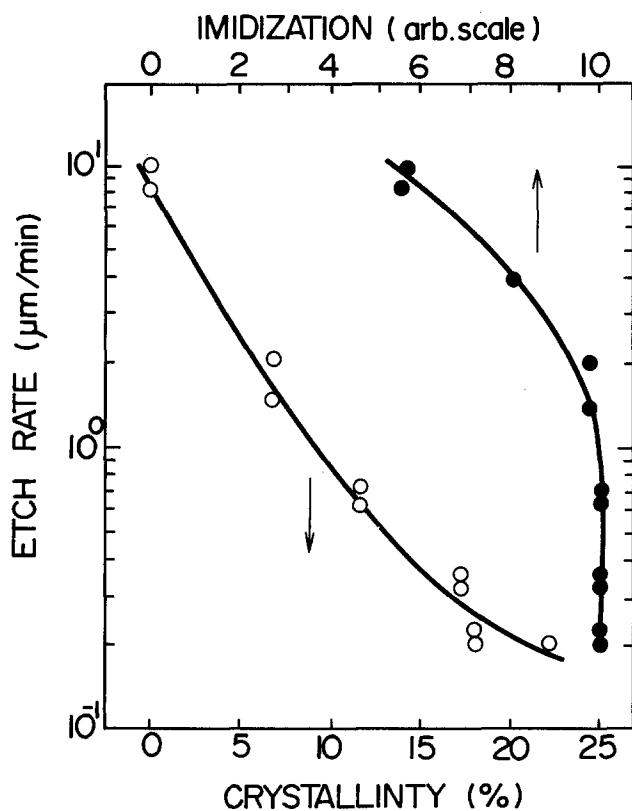


Fig. 11. Wet etching characteristics of PI films

In-Source Al-0.5%Cu Metallization for CMOS Devices

R. A. Levy,* L. C. Parrillo, L. J. Lecheler, R. V. Knoell

AT&T Bell Laboratories, Murray Hill, New Jersey 07974

ABSTRACT

This study examines the use of radiation-free RF induction-source evaporated (In-Source[®]) Al-0.5%Cu as a viable metallization scheme for CMOS devices. The fact that it is radiation free offers ways of optimizing the thermal cycle so as to achieve desirable device and electromigration characteristics. Wafers fabricated with 3.5 μm design rules have shown no threshold shifts or changes in the transistor gain at sintering temperatures up to 450°C, in either H₂ or N₂, for both N- and P-channel devices, confirming the absence of deposition-induced fixed interface charges. Wafers processed with 2.5 μm design rules have exhibited low and well-behaved values of contact resistance to N⁺ and P⁺ diffusions, at sintering temperatures in the range 300°-400°C in either H₂ or N₂, with no evidence of junction penetration. Electromigration measurements, gathered over a wide range of processing conditions, have yielded values of median time to failure (MTF) that were observed to improve with narrower linewidths, higher sintering temperatures, and in the presence of a plasma SiN passivation coating. In typical device operation conditions of 80°C and $1 \times 10^5 \text{A/cm}^2$, the extrapolated MTF value of $3.6 \times 10^7 \text{h}$, for 3.0 μm wide In-Source Al-0.5%Cu lines is found to exceed the value of $\sim 2 \times 10^6 \text{h}$ reported for E-Gun Al-0.5%Cu.

Aluminum and aluminum-silicon-copper alloy films are widely used for metallizing devices in IC processing. The silicon is generally introduced in concentrations of up to ~ 2 atom percent (a/o) to minimize the Al-Si interdiffusion at contact areas (1), while copper is added at concentrations of up to ~ 4 a/o to enhance the electromigration resistance of the metal (2, 3). The industry standard for aluminum deposition has, by far, been electron-beam evaporation (E-Gun[®]), although more recently high rate sputtering techniques have become more prominent. The major justification for using E-Gun aluminum has been its superior electromigration characteristics (4), while one of the major drawbacks in fine-line CMOS processing is the high temperature sintering required to anneal out radiation damage effects.

In this study, we examine the use of radiation-free RF induction-source evaporated (In-Source[®]) Al-0.5%Cu as a viable metallization technology for CMOS devices. Our primary thrust for investigating the use of In-Source Al-0.5%Cu was based on the premise that this deposition process induces no radiation damage. That in turn, affords ways of optimizing the thermal cycle so as to achieve low junction leakage currents as well as good contact resistance to both P⁺ and N⁺ areas. Historically, the selection of 0.5%Cu dates back to the period where the aluminum was patterned by wet chemical etching and the additional Cu was observed to improve linewidth uniformity. With the advent of dry etching techniques, this concentration level was observed not to adversely affect pattern definition and was consequently maintained for traditional reasons. Silicon was purposely excluded as an alloying element in the binary Al-0.5%Cu system in order to eliminate supersaturated precipitates of Al-doped Si at contact areas and minimize the contact resistance to the N⁺ source/drain regions. The results of this work will establish the viability of In-Source Al as a metallization technology by examining its effect on CMOS device performance and by evaluating its electromigration characteristics.

CMOS Device Performance

The effect of In-Source Al-0.5%Cu on device performance was evaluated by automatically probing the IGFET and contact resistance testers present across device wafers fabricated in accordance with the 3.5 and 2.5 μm Twin-Tub CMOS process (5, 6). Wafers processed with the 3.5 μm design rules (5) were targeted for investigation of the transistor characteristics because the thicker gate oxide used ($\sim 600\text{\AA}$) enhanced the sensitivity of the MOS structure to changes in the density of fixed interface charges. Wafers processed with the 2.5 μm design rules (with TaSi₂) were selected for examination of contact resistance and leakage currents due to junction spiking. All

device wafers were metallized with In-Source Al-0.5%Cu deposited at $\sim 220^\circ\text{C}$, patterned using single-level resist, dry etched, and sintered isochronally for 30 min in either a H₂ or N₂ ambient at temperatures of 200°, 300°, 350°, 400°, or 450°C. Results pertinent to device performance will now be considered.

Transistor characteristics.—The threshold voltage, V_T , and beta, β , were determined as a function of sintering temperature and ambient gas from probing various $75 \times 75 \mu\text{m}$ transistors. Both parameters were calculated from measurements of drain current, I_D , vs. gate voltage, V_G , at a constant drain voltage ($V_D = 0.1\text{V}$) using the relationship.

$$I_D = \beta(V_G - V_T)V_D \quad [1]$$

The test structure consisted of $\sim 6500\text{\AA}$ phosphorus-doped (PBr₃) polysilicon gate with a sheet resistance of $\sim 10 \Omega/\square$, a $\sim 0.060 \mu\text{m}$ thermally grown gate oxide, and a $\sim 1 \mu\text{m}$ In-Source Al-0.5%Cu metallization. The N⁺ and P⁺ source/drain areas were formed by ion implantation of P and B with subsequent diffusion during the phosphosilicate glass (P-glass) flow and reflow cycles yielding sheet resistance values of ~ 28 and $\sim 100 \Omega/\square$, respectively. In Fig. 1, the average values of threshold voltage and beta are plotted as a function of temperature for N- and P-channel devices sintered in H₂. For the N-channel devices, V_T is observed to exhibit, for the as-deposited Al films, a value of $0.89 \pm 0.02\text{V}$, which remains stable with sintering temperatures up to 450°C. A similar temperature-independent behavior is observed for the threshold voltage of the P-channel devices, which maintain through the various thermal cycles the as-deposited value of $-0.87 \pm 0.04\text{V}$. This lack of variation in the value of V_T with sintering temperature is a direct indication of the absence of radiation damage in the In-Source deposition process. If fixed interface charges were generated during deposition, they would be expected to anneal out with higher sintering temperatures, causing observable shifts in the threshold voltage of both N- and P-channel devices. The values of β_{\square} (i.e., the gain for transistors with $75 \times 75 \mu\text{m}$ square geometries) for both types of devices remain, as shown in Fig. 1, temperature independent but differ in magnitude by a factor of ~ 3 , reflecting the difference in the mobility of electrons and holes. Examination of devices sintered in N₂ were seen to exhibit similar transistor parameters as well as a similar temperature-dependent behavior to those sintered in H₂.

Contact resistance.—The contact resistance of aluminum to N⁺ and P⁺ source/drain areas was measured from testers present on device wafers processed in accordance with the 2.5 μm Twin-Tub CMOS process (6). The test pattern, shown in Fig. 2A, is comprised of three sections, where windows in the P-glass are opened to make contact to the gate material and to the N⁺ or P⁺ diffusions. These

*Electrochemical Society Active Member.

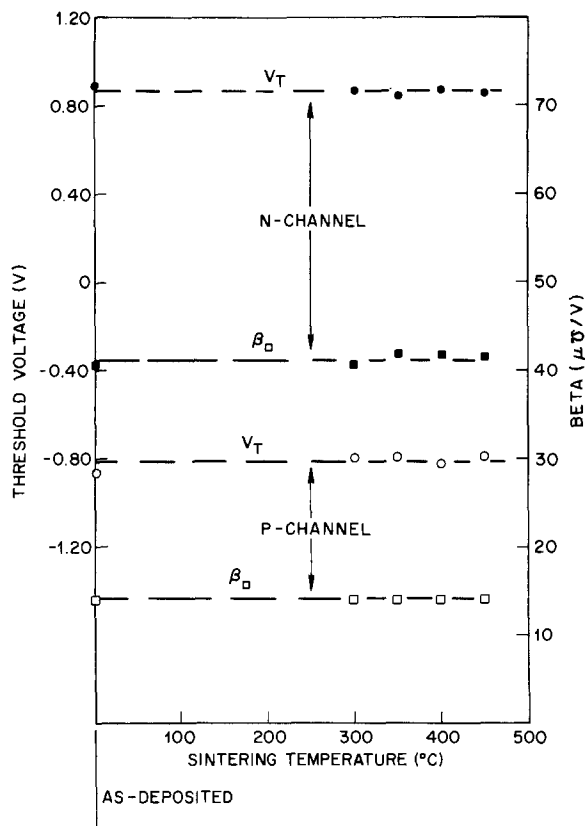


Fig. 1. Average values of threshold voltage and beta per square as a function of sintering temperature for both N- and P-channel square devices. Sintering time was 30 min; sintering ambient was H_2 .

were formed by ion implantation of P and B and a subsequent drive-in to yield sheet resistance values of ~ 30 and $\sim 115 \Omega/\square$, respectively, and junction depths of $\sim 0.9 \mu m$. Provisions are also provided on this tester to contact the N- and P-tub for leakage current measurements between source/drain regions and tubs. An expanded photograph of the active region is shown in Fig. 2B. It is designed to cover an area of $(190 \times 5 \mu m)$, ending within the center of $(20 \times 20 \mu m)$ pads on each side, and to include four variable size contact windows defined on the mask with dimensions of $(2 \times 2 \mu m)$, $(2.5 \times 2.5 \mu m)$, $(3 \times 3 \mu m)$ and $(4 \times 4 \mu m)$. The measurement is conducted by passing a current between two adjoining contact windows of different sizes and measuring the voltage drop between a common window site and another adjoining contact window of a different size. This measurement is based on a four-point probe technique with the contact resistance calculated from the ratio of the voltage drop at the "contact end" (i.e., the common window site) to that of the input current

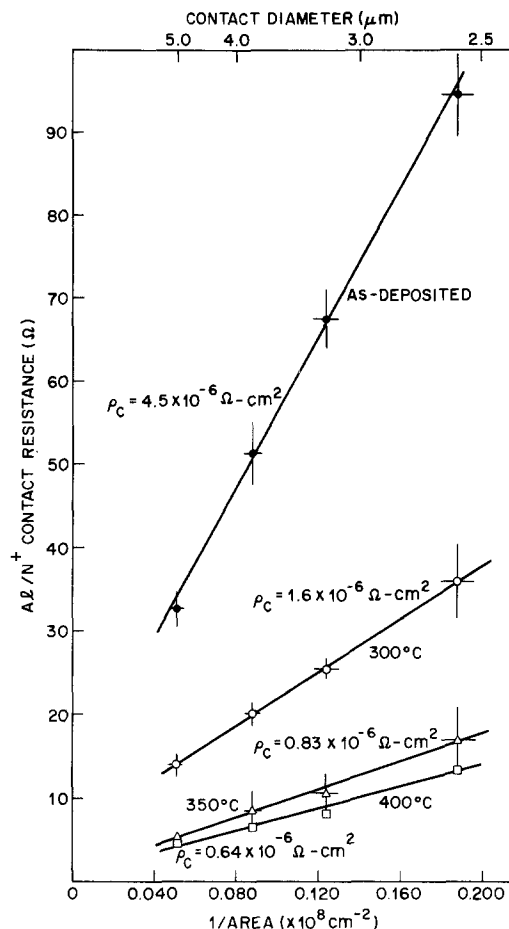


Fig. 3. Plot of Al/N⁺ contact resistance as a function of reciprocal area for as-deposited Al-0.5%Cu and Al-0.5%Cu sintered at 300°, 350°, and 400°C for 30 min in H_2 .

set in this case at 0.5 mA. In Fig. 3, the Al/N⁺ contact resistance is plotted as a function of reciprocal area for the as-deposited Al-0.5%Cu and after sintering at 300°, 350°, and 400°C in H_2 . The contact area was assumed not to be that specified by mask dimensions but was measured for each contact size directly from scanning electron micrographs. The Al/N⁺ contact resistance is seen, over the investigated range of contact sizes and sintering temperatures to scale linearly with reciprocal area. The contact resistivity, ρ_c , calculated from the slope of these linear curves, is observed to decrease significantly with higher sintering temperatures. For the as-deposited Al-0.5%Cu condition, $\rho_c = 4.5 \times 10^{-6} \Omega\text{-cm}^2$; for progressively higher sintering temperatures, the value of ρ_c decreases from $1.6 \times 10^{-6} \Omega\text{-cm}^2$ at 300°C to $0.83 \times 10^{-6} \Omega\text{-cm}^2$ at 350°C and

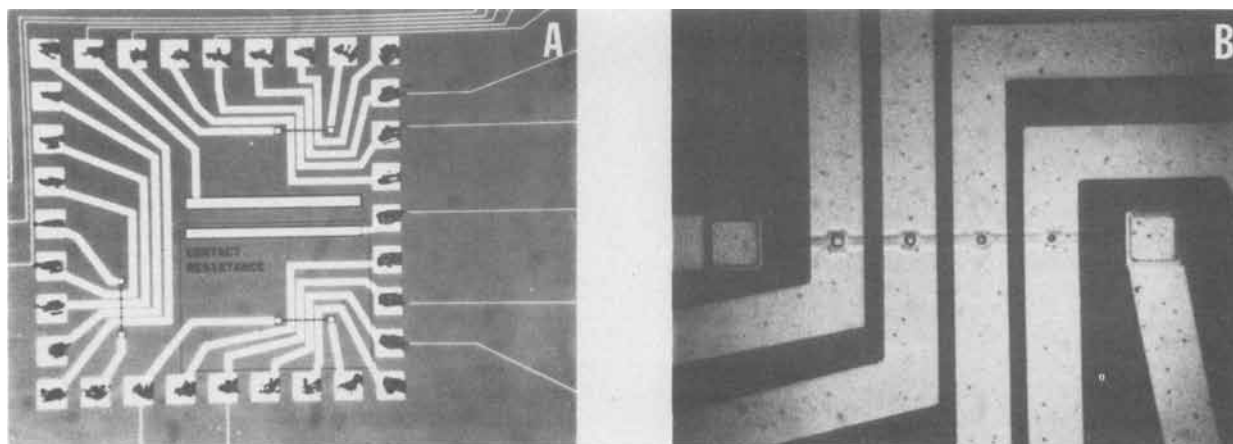


Fig. 2. (A) Optical photograph of contact resistance tester. (B) SEM micrograph of active region on contact resistance tester.

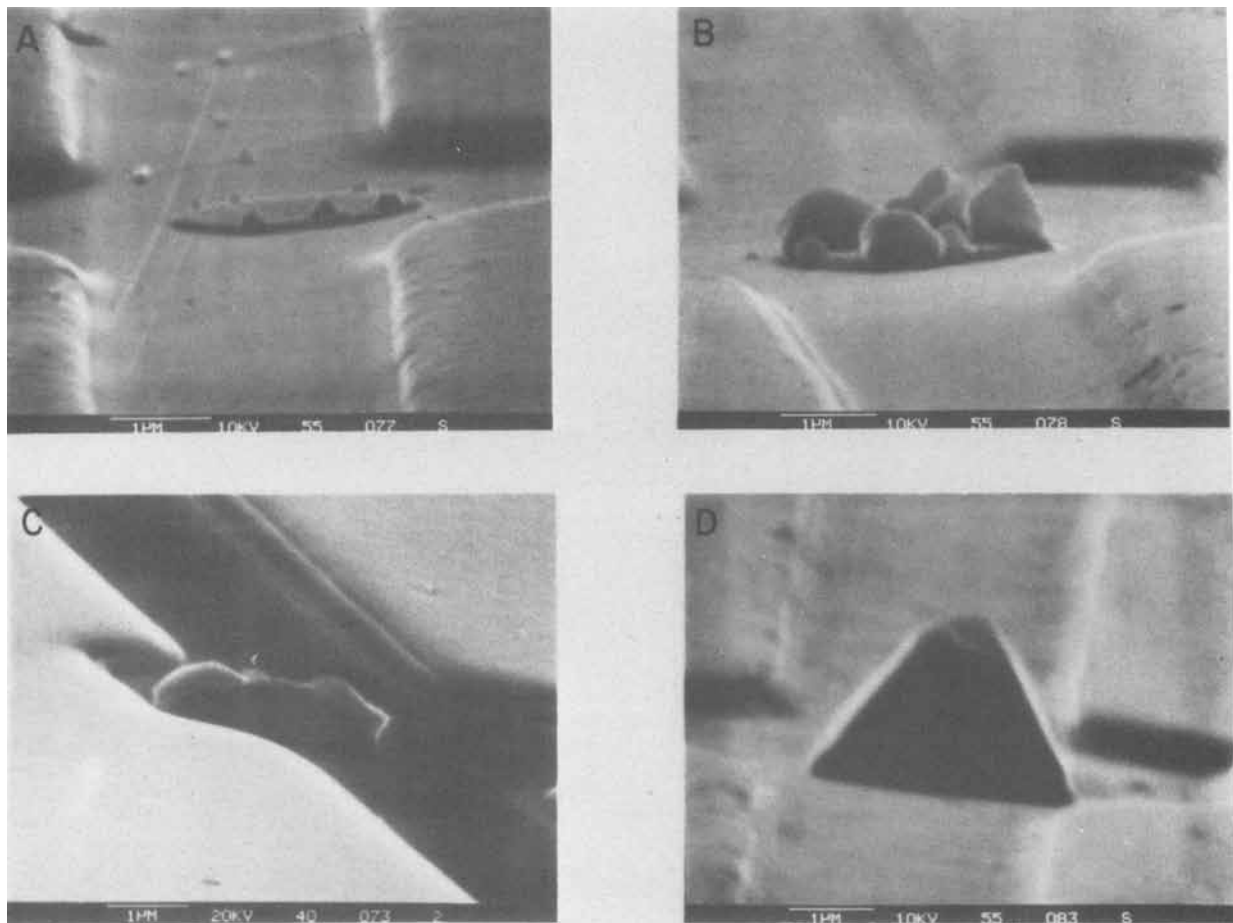


Fig. 4. SEM replicas of nominal ($2 \times 2 \mu\text{m}$) windows to Si on the contact resistance tester after sintering for 30 min in N_2 at temperatures of (A) 300°C , (B) 350°C , (C) 400°C , and (D) 450°C .

$0.64 \times 10^{-6} \Omega\text{-cm}^2$ at 400°C . We postulate that this variation in the Al/N^+ contact resistance is directly related to the degree of interdiffusion occurring through the native oxide at the Al-Si interface. In the presence of an imperfect native oxide, the interdiffusion, which is a thermally activated process, has been reported to proceed through pinholes in the oxide, causing, in the case of (100) silicon, preferential spiking along $\langle 111 \rangle$ crystallographic planes (7). The extent of the interdiffusion, as determined by the density and size of those spikes, provides an "effective" area, by which Al contacts N^+ silicon. In order to investigate the spike formation mechanism as a function of sintering temperature and contact area, polyimide replicas of the silicon surface were prepared and examined with the aid of a scanning electron microscope (SEM). Figure 4 represents a series of SEM replicas of the nominal ($2 \times 2 \mu\text{m}$) window on the contact resistance tester at progressively higher sintering temperatures. At 300°C (Fig. 4A), the spikes are observed to be sparsely concentrated at the conduit to the largest Al supply *i.e.*, at the periphery of the contact window, and to extend in height up to $\sim 0.20 \mu\text{m}$. At a sintering temperature of 350°C (Fig. 4B), spikes retain their individuality but grow significantly in size reaching, in some cases, peaks of $\sim 0.75 \mu\text{m}$. At 400°C (Fig. 4C), coalescence among spikes yield an almost continuous ring with little unreacted space and with a dimensional height of as much as $\sim 0.80 \mu\text{m}$. At 450°C (Fig. 4D), results of the interdiffusion achieve the extreme case in which a single pyramidal pit is now formed extending beyond the original contact area and exhibiting an apex at a height of $\sim 2 \mu\text{m}$. At the sintering temperature of 400°C , the extent of interdiffusion is revealed in Fig. 5 for the four available contact sizes. For a specific thermal cycle and given window geometry, a given amount of Si will be transported into the Al to satisfy the solubility limit. The smaller the cross-sectional area of that contact window,

the deeper will be the loss of Si required to achieve this transported volume. For the 450°C sinter, the Al/N^+ contact resistance, as seen in Fig. 6, ceases to scale with reciprocal area. That is believed to be due to the influence of lateral diffusion which, as shown in the series of micrographs of Fig. 7, is now causing uptake of silicon for aluminum from beyond the original contact boundaries. That has the effect of minimizing differences in the "effective" contact area of the various windows, which is in turn reflected in the lack of variation of the Al/N^+ contact resistance. As observed in the case of the transistor parameters, the values and temperature dependent behavior

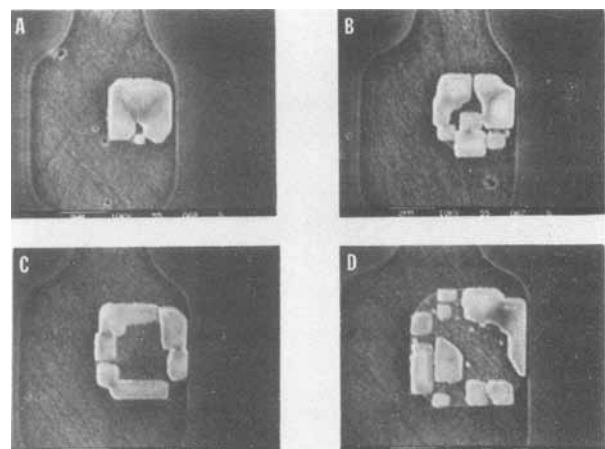


Fig. 5. Top view of SEM replicas of windows to Si on contact resistance tester after a $400^\circ\text{C}/30\text{min}/\text{N}_2$ sinter. Contact dimensions as defined on the mask were (A) $2 \times 2 \mu\text{m}$, (B) $2.5 \times 2.5 \mu\text{m}$, (C) $3 \times 3 \mu\text{m}$, and (D) $4 \times 4 \mu\text{m}$.

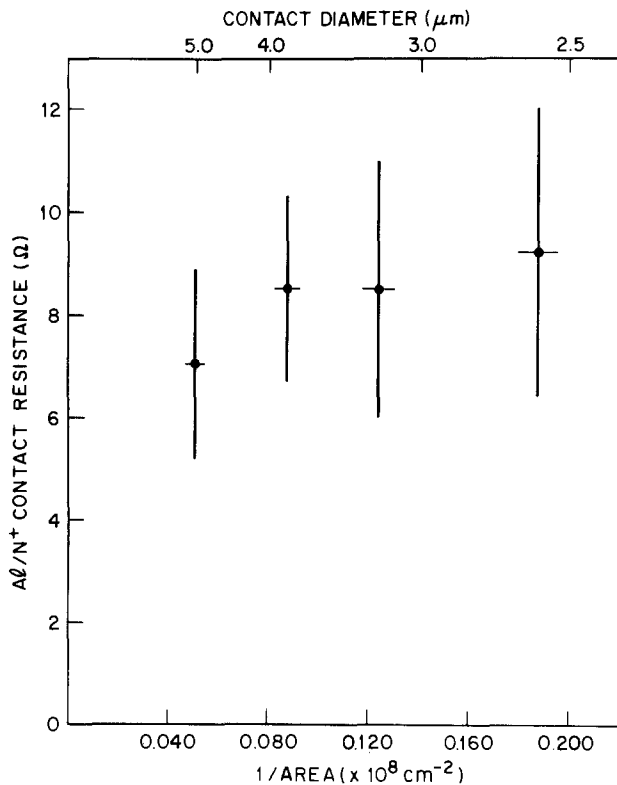


Fig. 6. Plot of Al/N⁺ contact resistance as a function of reciprocal area for In-Source Al-0.5%Cu sintered at 450°C/30min/H₂.

of Al/N⁺ contact resistivity for devices sintered in N₂ are similar to those sintered in H₂. At 200°C, the contact resis-

tivity is $3.5 \times 10^{-6} \Omega\text{-cm}^2$; at progressively higher sintering temperatures, the value of ρ_c decreases from $1.5 \times 10^{-6} \Omega\text{-cm}^2$ at 300°C to $0.77 \times 10^{-6} \Omega\text{-cm}^2$ at 350°C and $0.58 \times 10^{-6} \Omega\text{-cm}^2$ at 400°C.

The dependence of the Al/P⁺ contact resistance on contact dimensions and sintering temperature is revealed in Fig. 8. Values of contact resistance plotted against reciprocal area are observed to fall, generally, regardless of the sintering temperature, on a single line with a slope yielding a contact resistivity of $0.66 \times 10^{-6} \Omega\text{-cm}^2$. This temperature independent behavior of ρ_c suggests that the mechanism by which the Al/P⁺ contact is established is different than that for the Al/N⁺ contact and is based primarily on barrier height considerations. The barrier height for p-type silicon (8) is ~ 0.4 eV, a value significantly lower than that of ~ 0.7 eV reported for n-type silicon (8). The increase in the data scatter with decreasing contact dimensions reflects, in this case, secondary effects caused by the extent of the Al-Si interdiffusion.

Leakage current.—The contact resistance tester used to generate the results discussed in the previous section had also provisions for automatic determination of leakage current at five sites across the wafer. As a test of junction penetration due to Al-Si interdiffusion, the N⁺/P Tub leakage current was measured at a reverse bias of 1V on devices processed in accordance with the 2.5 μm Twin-Tub CMOS process (6) and sintered in H₂ or N₂ at 200°, 300°, 350°, 400°, and 450°C. Regardless of the sintering ambient, the leakage current is observed to exhibit a value of $\sim 10^{-10}$ A (low current limit of automatic test equipment) for the as-deposited Al-0.5%Cu condition. That value is observed to remain independent of sintering temperature up to 400°C. This falls within the range of temperatures in which the maximum observable spike height (Fig. 4C) was ~ 0.80 μm. However, that is still shallower than the

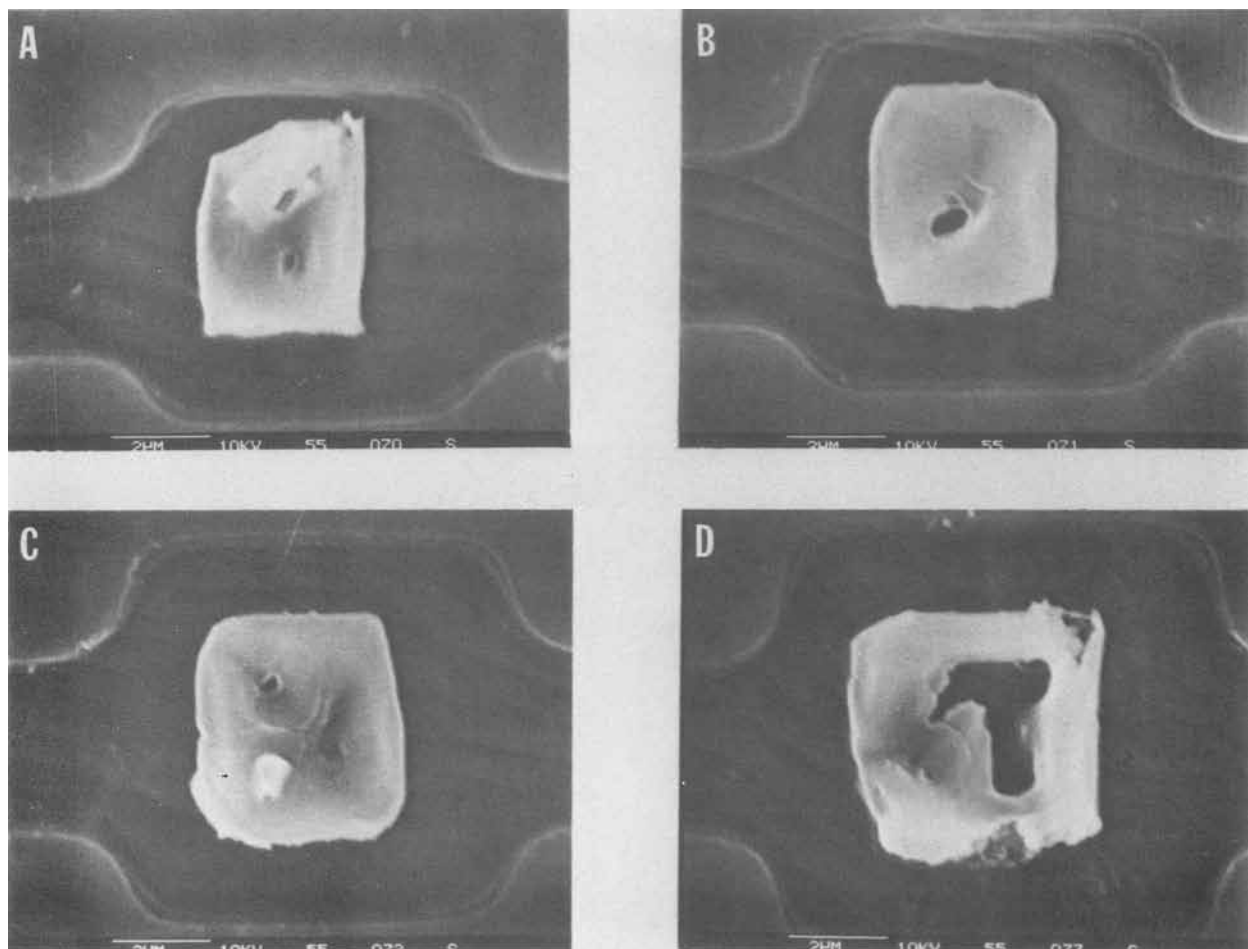


Fig. 7. Top view of SEM replicas of windows to Si on contact resistance tester after a 450°C/30min/N₂ sinter. Contact dimensions as defined on mask were (A) $2 \times 2 \mu\text{m}$, (B) $2.5 \times 2.5 \mu\text{m}$, (C) $3 \times 3 \mu\text{m}$, and (D) $4 \times 4 \mu\text{m}$.

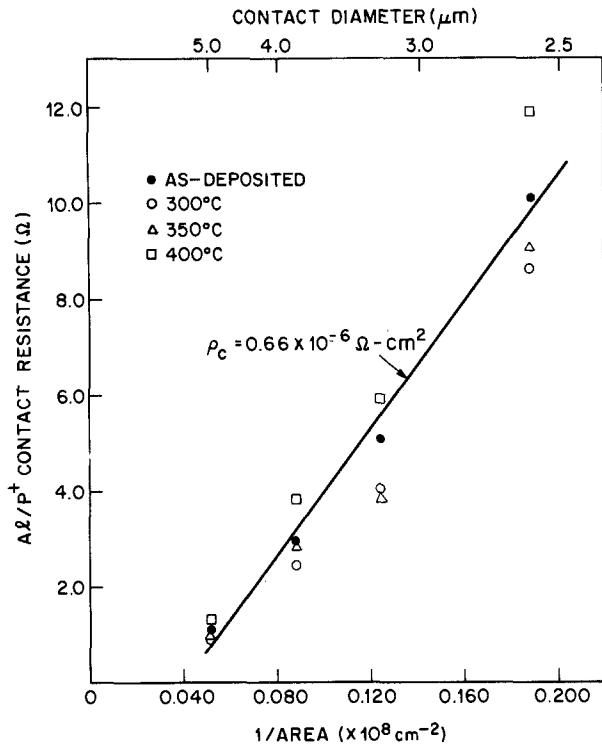


Fig. 8. Plot of Al/P contact resistance as a function of reciprocal area for as-deposited In-Source Al-0.5%Cu and Al-0.5%Cu sintered at 300°, 350°, and 400°C.

$\sim 0.9 \mu\text{m}$ N^+ junction depth characteristic of those devices and is therefore consistent with the present data. At the 450°C sintering temperature, the leakage current is observed to increase significantly with values as high as $\sim 10^{-6}\text{A}$, pointing to serious junction penetration. This is consistent, specifically, with the SEM replica of Fig. 4D which had shown a pyramidal pit, $\sim 2 \mu\text{m}$ high, for the smallest contact geometry. It is important to note that the present contact resistance tester represents a worst-case evaluation of the effect of junction spiking because the contact windows considered are small and are strapped individually by wide ($\sim 25 \mu\text{m}$) metal runners. Typically in device patterns, several contact windows share a common narrow ($\sim 5 \mu\text{m}$) metal strap, easing considerably the spiking situation.

Having evaluated the effect of In-Source Al-0.5%Cu on device properties, we wish now to focus on its electromigration characteristics.

Electromigration Characteristics

Electromigration is a major concern as a failure mode associated with the use of Al or Al alloys in VLSI devices (9-11). It is defined as the transport of matter caused by the passage of an electric current and is the result of momentum exchange between conduction electrons and diffusing metal atoms. Nonvanishing divergences of this atomic (or vacancy) flux, generated by structural inhomogeneities or temperature gradients, can lead to open-circuit failures because of depletion of matter.

The temperature and current density dependence of electromigration is generally expressed by the relationship (12)

$$\text{MTF} = \text{CJ}^{-n} \exp(Q/kT) \quad [2]$$

where MTF is the median time to failure, C a constant, J the current density, n the current density exponent, Q the activation energy, k Boltzmann's constant, and T the absolute temperature. For Al conductors the reported values of Q and n lie in the ranges of 0.3-1.2 eV and 1-7, respectively (13). The median time to failure has been observed to improve with increases in grain size, with decreases in grain size distribution, and with a higher degree of (111) texture in the Al film (4). Henceforth,

optimization of these parameters becomes a prerequisite in the present electromigration investigation of In-Source Al-0.5%Cu. Using transmission electron microscopy (TEM), horizontal cross-sectional micrographs depicting the grain size and grain size distribution were examined for In-Source Al-0.5%Cu deposited over a wide range of temperatures (135°-300°C) and rates (10-140 Å/s). A sample representation of this data is shown in Fig. 9. At a given background pressure of $\sim 2 \times 10^{-6}$ torr and a deposition temperature of $\sim 135^\circ\text{C}$, the grain size is seen to increase from an average value of $\sim 0.3 \mu\text{m}$ for Al films deposited at $\sim 30 \text{ Å/s}$ (Fig. 9A) to $\sim 0.7 \mu\text{m}$ for Al film deposited at $\sim 140 \text{ Å/s}$ (Fig. 9B); for a higher deposition temperature of $\sim 245^\circ\text{C}$, the grain size increases from $\sim 0.6 \mu\text{m}$ for Al films deposited at $\sim 30 \text{ Å/s}$ (Fig. 9C) to $\sim 1.3 \mu\text{m}$ for Al films deposited at $\sim 140 \text{ Å/s}$ (Fig. 9D). The distribution of grain sizes, characterized by the calculated standard deviation, was found typically to be of the order of $\pm 10\%$. The observed increase in grain size with higher deposition temperature and higher deposition rate provides, henceforth, the guideline necessary to optimize the deposition parameters and produce films with desirable electromigration characteristics.

The electromigration test structure used in the present investigation consisted of five meander patterns on a chip, each 1 cm long and all with nearly identical linewidths. An array of 116 chips was laid out for 75 mm size wafers so as to provide a wide selection of meanders with defined widths of 2, 2.5, 3, 4, and 5 μm . The combination of lines and spaces were designed on the meander pattern to add up, in all cases, to 15 μm . After separation, the chips were eutectically bonded, using Au-P preforms, onto 40-pin dual-in-line ceramic packages. In order to eliminate the possibility of Al-Au interdiffusion on the test pattern, Al-1% Mg wires, 25 μm thick, were wedge bonded ultrasonically at room temperature to aluminum pads on the chip side and gold pads on the package side. The electromigration tests were conducted typically on 24 packages heated in atmospheric ambient in an oven capable of providing temperatures up to 300°C and controlled within $\pm 1^\circ\text{C}$. Constant current sources were designed to power up to 96 meanders with adjustable outputs of 10-250 mA and a stability better than $\pm 1\%$. Chart recorders were used to monitor the voltage drop across summing resistors and to mark the failure time. One meander on each of the chips was dedicated to monitor the temperature through the testing period. The procedure consisted of passing a low current of typically 250 μA through that monitor meander at room temperature and measuring the voltage drop across it. The furnace was then brought up to test temperature and the procedure repeated. From the recorded change in temperature and voltage drop, the temperature dependent coefficient of resistivity, α , was calculated. One of the other four test meanders is then powered and from the known value of α , and from the change in voltage drop caused by the additional Joule heating, the average temperature of the monitor meander was established. A comparison between the temperature as measured on the monitor meander to that as measured directly on the other four test meanders using the above procedure revealed, within the considered range of current densities, insignificant differences. The test temperature referred to during the course of the present investigation represents the overall (i.e., ambient + Joule contribution) average of the experimental cell.

The In-Source Al-0.5%Cu films, typically 1 μm thick, were all deposited at $\sim 300^\circ\text{C}$ on thermally oxidized Si substrates. They were patterned using tri- or single-level resist and defined using reactive ion etching. The cross-sectional area, A, was calculated from the product of the average thickness and linewidth of the patterned Al lines which were measured using a Dektak stylus and a Nanospec interferometer, respectively.

The data were fitted to a log-normal distribution using a computer program which derived values of median time to failure and proceeded to produce a graphical display of the results. The dependence of median time to failure on

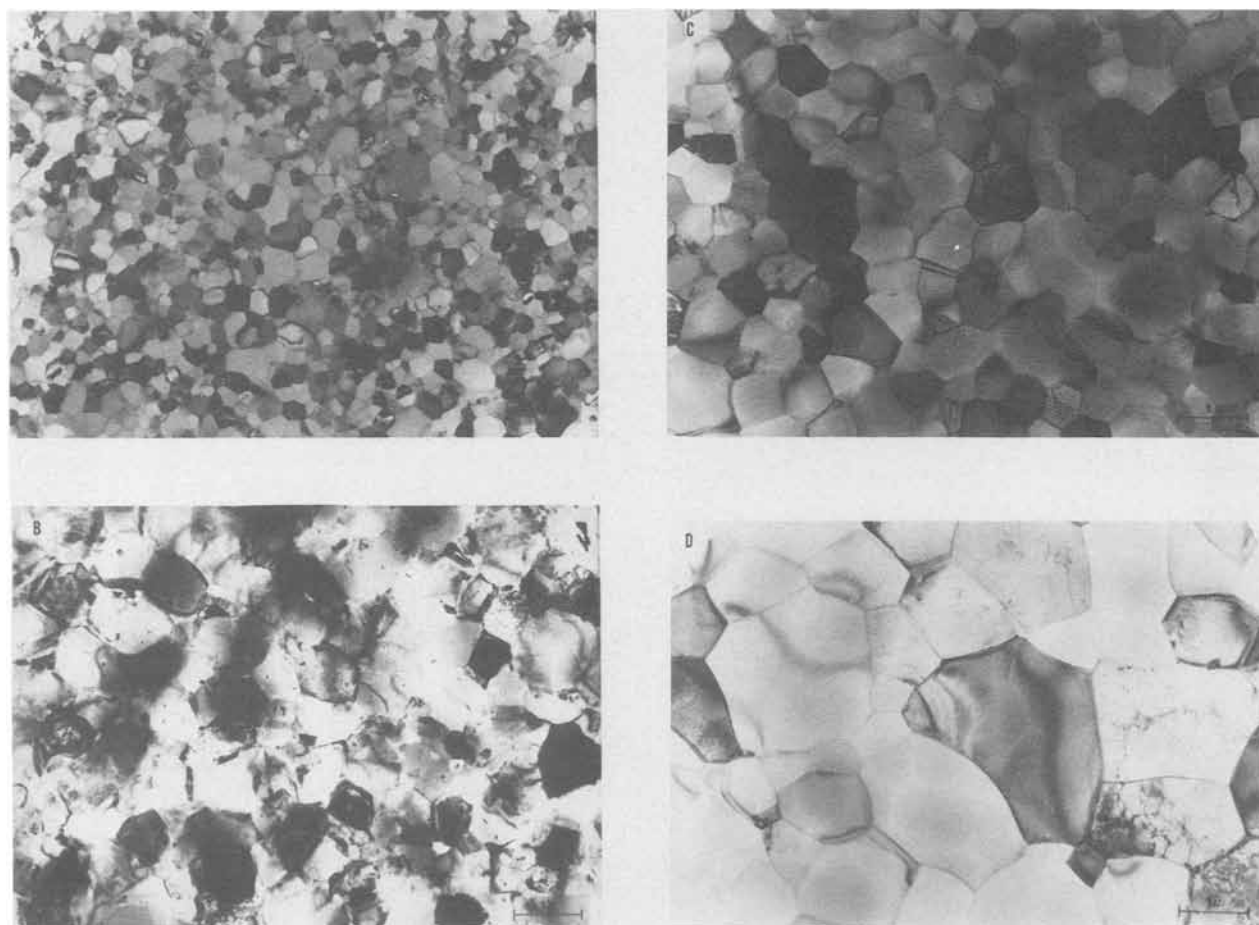


Fig. 9. TEM horizontal cross-sectional micrographs illustrating grain size and grain size distribution for In-Source Al-0.5%Cu films deposited at a temperature and rate of (A) 135°C, ~ 30 Å/s, (B) 135°C, 140 Å/s, (C) 245°C, ~ 30 Å/s, and (D) 245°C, ~ 140 Å/s.

sintering temperature, plasma SiN capping, linewidth, and current density acceleration will now be considered.

Effect of sintering temperature.—In order to investigate the effect of sintering temperature on the median time to failure, In-Source Al-0.5%Cu films were evaporated on thermally oxidized Si wafers under optimized conditions for deposition temperature ($\sim 300^\circ\text{C}$) and deposition rate (~ 140 Å/s). The films were then sintered for 30 min in H_2 at either 300° or 450°C . Meander lines with a 3.0 μm linewidth were selected for testing. For samples sintered at $300^\circ\text{C}/30$ min/ H_2 , the electromigration measurements were carried out at test temperatures of 209° and 264°C and at a current density of 2.1×10^6 A/cm 2 . The samples sintered at $450^\circ\text{C}/30$ min/ H_2 were tested, under accelerated conditions, at temperatures set at 232° , 258° , 289° , and 304°C and a current density set at 1.62×10^6 A/cm 2 . In Fig. 10, values of the median time to failure, normalized with the use of Eq. [2] and a value of $n = 2$ to $J = 1 \times 10^5$ A/cm 2 , are plotted on an exponential scale as a function of reciprocal temperature for the samples sintered at 300° and 450°C . A comparison between these two curves indicate, in the case of the higher sintering temperature, a factor of ~ 3 improvement in lifetime as well as an enhanced value of the activation energy (0.84 vs. 0.73 eV). These observations reflect the differences in the microstructure of the Al-0.5%Cu films. TEM cross-sectional micrographs, taken at a pad area on the electromigration tester, are seen to exhibit an average grain size of 2.9 μm for samples sintered at 450°C (Fig. 11C) as compared to 1.8 μm for samples sintered at 300°C (Fig. 11A). An increase in the ratio of grain size to strip width, as in the case of the higher sintering temperature, has been reported (14) to enhance the lifetime because of possible formation of single-crystal grains, across parts of the meander, blocking the mass transport. The larger grains are also expected (9) to

cause a reduction in the number of grain boundaries, with their associated low energy diffusion paths, accounting for the observed increase in activation energy. SEM examination of electromigration-induced defects reveals, as shown in the series of micrographs of Fig. 12, the presence of voids, cracks, and hillocks randomly distributed along the length of the stressed meanders. The depleted areas assumed a variety of sizes and shapes with the fatal openings generally observed to cross the meander width in a direction perpendicular to current flow. Evidence for the accumulation of materials was found in the vicinity of large voids or cracks always in the direction of positive bias (electron flow). Using the measured values of Q and the conventional value of $n = 2$, the median times to failure extrapolated to 80°C and 1×10^5 A/cm 2 were determined to be equal to 3.7×10^6 h and 3.6×10^7 h for samples sintered at 300° and 450°C , respectively. The value of 3.6×10^7 h is more than an order of magnitude higher than that of 12×10^6 h reported for E-Gun Al-0.5%Cu deposited and sintered under similar conditions (4). That demonstrates that In-Source Al-0.5%Cu processed under optimum conditions can, indeed, provide excellent resistance to electromigration failure.

Effect of plasma SiN capping.—In the final stages of IC processing, a scratch-resistant plasma SiN passivation coating is generally deposited to protect devices from mechanical damage. In order to investigate the effect of plasma SiN capping on median time to failure, one of the patterned wafers metallized with In-Source Al-0.5%Cu deposited at 300°C , at a rate of 140 Å/s, was sintered at 300°C for 30 min in H_2 and then capped with a 1.4 μm plasma SiN coating. The plasma SiN cap was deposited at 330°C for 105 min in a plasma-assisted CVD reactor known to produce tensile films. The wafer was patterned and plasma etched in a barrel reactor to expose the aluminum

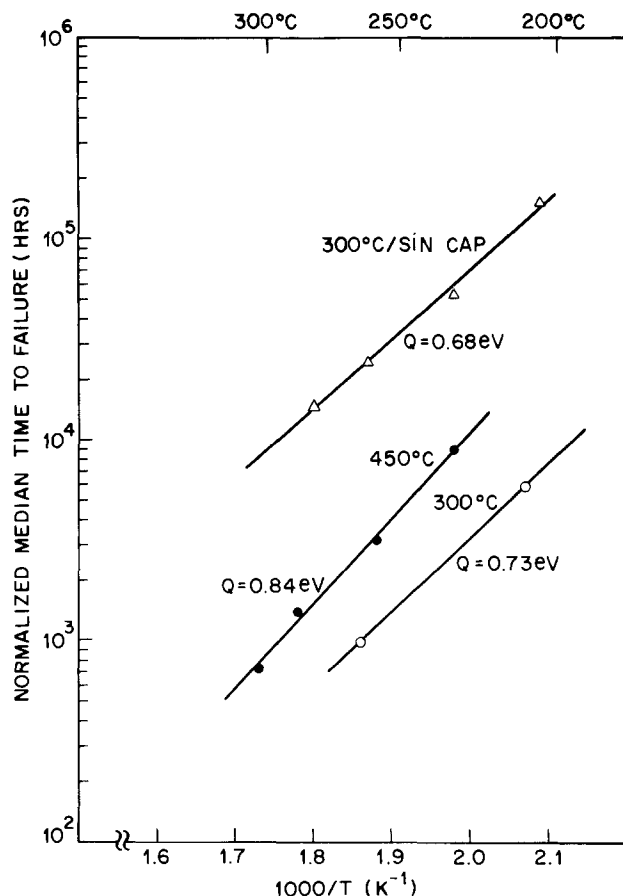


Fig. 10. Plot of normalized median time to failure as a function of reciprocal temperature for In-Source Al-0.5%Cu deposited at 300°C, at a rate of $\sim 140 \text{ \AA/s}$ and sintered under different conditions.

pads for wire bonding. Groups of typically 24 meanders with a $3.0 \mu\text{m}$ linewidth were tested, under accelerated conditions, at temperatures of 205°, 231°, 263°, and 283°C and at a current density of $1.82 \times 10^6 \text{ A/cm}^2$. A plot of normalized median time to failure vs. reciprocal temperature is shown in Fig. 10 for samples sintered at 300°C with plasma SiN caps and for those with no caps sintered isochronally at 300° and 450°C. It is evident from a comparison of the data that the presence of the passivation coating enhances the median time to failure by almost an order of magnitude, when compared to uncoated samples sintered at 450°C, and by a factor ~ 22 when compared to uncoated samples sintered at 300°C. SEM examination of the stressed meanders revealed significant reduction in the occurrence of macroscopic voids and in the degree of material accumulation below the plasma SiN layer. This is an indication that the electrotransport rate has, indeed, been slowed down, presumably by a consequence of reduced vacancy density. Vacancies are generally generated by inward diffusion from the surface or through formation of Schottky defects. In both cases, as reported by Learn and Shepherd (15), the addition of a strongly bonded impervious coating can reduce vacancy generation and movement. From the slope of the MTF vs. $1/T$ curve a value of $Q = 0.68 \text{ eV}$ was calculated for the samples capped with plasma SiN. This value for the activation energy is quite comparable to that of 0.73 eV, for samples similarly sintered at 300°C/30min/ H_2 but with no plasma SiN. Examination of TEM micrographs of samples with (Fig. 11B) and without (Fig. 11A) plasma SiN also reveal quite comparable dimensions in grain size, establishing the fact that the thermal cycle associated with the present plasma SiN deposition process has an insignificant effect on both grain growth and activation energy. Using the value of $Q = 0.68 \text{ eV}$ and the conventional value of $n = 2$, the extrapolated median time to failure (80°C , $1 \times 10^5 \text{ A/cm}^2$) for In-Source Al-0.5%Cu sintered at 300°C with plasma SiN was calculated to be



Fig. 11. TEM horizontal cross-sectional micrographs illustrating grain size and grain size distribution of In-Source Al-0.5%Cu deposited at 300°C at a rate of $\sim 140 \text{ \AA/s}$ and sintered at (A) 300°C/30 min/ H_2 , (B) 300°C/30 min/ H_2 with additional $1.4 \mu\text{m}$ plasma SiN cap, and (C) 450°C/30 min/ H_2 .

equal to $5.0 \times 10^7 \text{ h}$. The closing of the gap between the extrapolated MTF values of samples with the additional plasma SiN cap and those sintered at 300° and 450°C with no plasma SiN is a result of differences in the activation energy which owing to the exponential dependence, strongly affect the extrapolation procedure.

In order to evaluate the effect of lower deposition rates on the electromigration characteristics, In-Source Al-0.5%Cu was evaporated at $\sim 300^\circ\text{C}$, at a rate of $\sim 63 \text{ \AA/s}$ onto thermally oxidized Si monitors. Following patterning with single-level resist and a 300°C/30min/ H_2 sintering cycle, a $1 \mu\text{m}$ thick plasma SiN cap was deposited at 330°C for 145 min in a plasma-assisted CVD reactor known to produce compressive films. Packaged testers with $2.0 \mu\text{m}$ lines were selected for the present study. The testing proceeded at temperatures of 194°, 221°, 250°, and 274°C and at a current density of $1.9 \times 10^6 \text{ A/cm}^2$. From the slope of a plot of normalized median time to failure as a function of reciprocal temperature, an activation energy of $Q = 0.68 \text{ eV}$ was calculated. This value is identical to that calculated for In-Source Al-0.5%Cu at the higher rate of 140 \AA/s pointing to heat-treatment, i.e., sintering and plasma SiN deposition as the determining factor in the establishment of the final microstructure. Using the value of $Q = 0.68$ and the conventional value of $n = 2$, the

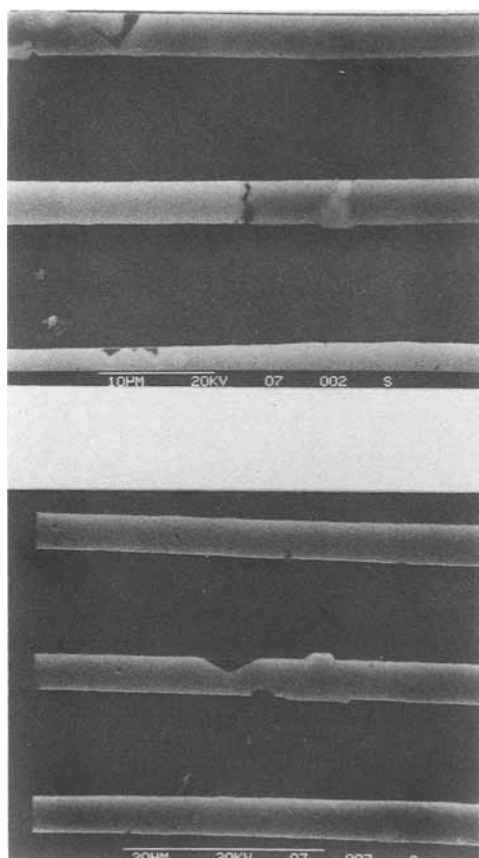


Fig. 12. SEM micrographs showing electromigration-induced defects such as voids, cracks, and hillocks for samples with In-Source Al-0.5% Cu deposited at 300°C at ~ 140 Å/s and sintered at 450°C/30min/ H_2 .

extrapolated median time to failure (80°C, 1×10^5 A/cm²) was calculated to be equal to 2.7×10^7 h. With the exception of using a thicker plasma SiN cap (1.4 vs. 1.0 μ m), a repeat of these measurements on lines with the identical 2.0 μ m linewidth patterned from samples deposited under identical conditions (300°C, ~ 63 Å/s) and also sintered at 300°C for 30 min in H_2 , yielded an extrapolated median time to failure (80°C, 1×10^5 A/cm²) equal to 3.5×10^8 h. The difference in these values of MTF is believed to be directly related to the plasma SiN cap thickness and not, as to be discussed in the following paragraphs, to the induced stress. With the thinner films, there is the distinct possibility of encountering a higher density of pinholes or microcracks which would form the source of vacancies and Schottky defects necessary to enhance the electrotransport mechanism. Similar results on the effect of a passivation coating on median time to failure have recently been reported by Lloyd and Smith (16) who observed that E-Gun Al-4%Cu stripes covered with 1.5 μ m of glass lasted as much as 18 times longer than those which were not covered. Furthermore, an increase in passivation film thickness from 1.5 to 4.0 and 8 μ m was reported to monotonically enhance the lifetime of the underlying thin film conductors from 636 to 909 and 1083h, respectively. Electromigration-induced compressive stresses were believed to be responsible for these observations.

A comparison of samples with similar linewidth (~ 3.0 μ m) deposited at different rates (~ 63 vs. ~ 140 Å/s) but otherwise identical in terms of deposition temperature (~ 300 °C), sintering cycle (300°C/30min/ H_2), and plasma SiN thickness (1.4 μ m) revealed, as shown in Fig. 13, similar values of median time to failure (4.5×10^7 vs. 5.0×10^7 h). That provides additional correlation and support for the reproducibility of our results. It is, however, interesting to note that in the case of Al films deposited at ~ 63 Å/s the plasma SiN process used was known to produce compressive films ($\sim -10^{10}$ dyne/cm²); in the case

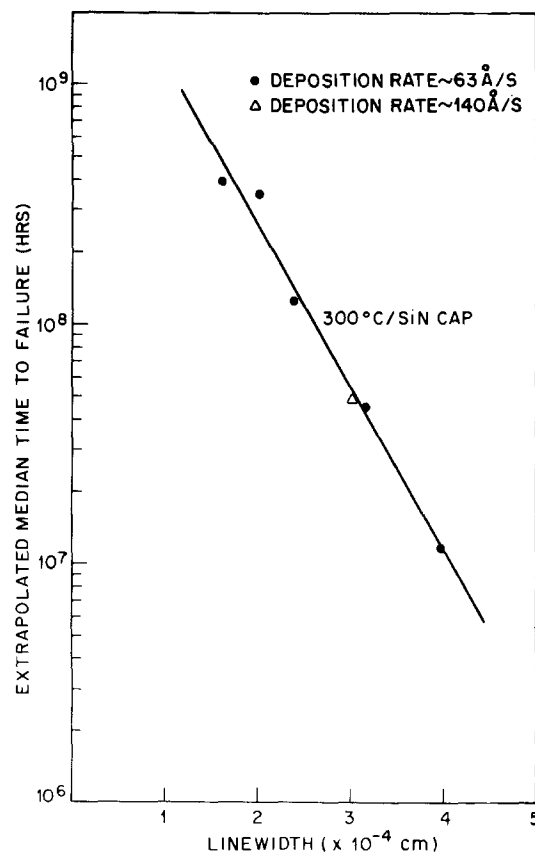


Fig. 13. Plot of extrapolated median time to failure (80°C, 1×10^5 A/cm²) as a function of linewidth for In-Source Al-0.5%Cu deposited at 300°C, at a rate of ~ 63 Å/s, sintered at 300°C/30min/ H_2 , and capped with 1.4 μ m plasma SiN.

of Al films deposited at ~ 140 Å/s, the plasma SiN process used was different and known to produce tensile films ($\sim +10^9$ dyne/cm²). Thus, the noted similarity in the electromigration results over such extreme stress conditions tends to undermine the role of stress in accounting for the lifetime enhancement observed in the presence of a passivation coating.

Effect of linewidth.—In order to determine the dependence of median time to failure on linewidth, films metallized with In-Source Al-0.5%Cu (300°C, ~ 63 Å/s), sintered at 300°C for 30 min in H_2 , and capped with 1.4 μ m plasma SiN (330°C, 145 min) were tested. The linewidth was varied to cover a range in values extending from 1.6 to 4.0 μ m. The electromigration measurements were carried out for all samples at test temperatures around 275°C and at a current density of 2.0×10^5 A/cm². Using values for $Q = 0.68$ eV and $n = 2$, the extrapolated median time to failure (80°C, 1×10^5 A/cm²) is plotted as a function of linewidth in Fig. 13. The results point to an exponential increase with narrower linewidth with values ranging from 1.1×10^7 h at 4.0 μ m to 3.9×10^8 h at 1.6 μ m. As previously discussed, a narrowing of linewidth enhances the likelihood that the meander cross section will be blocked at some points by single-crystal grains. That develops a configuration consisting of polycrystalline segments blocked at both ends by a single-crystal grain. Since electromigration is known to proceed primarily through grain boundary diffusion, mass transport from the cathode to anode end within a polycrystalline segment is expected to develop concentration gradients and compressive stresses at these ends which can create a reverse mass flow to that produced by electromigration. At progressively narrower linewidths the display of single-crystal grains across the stripe ought to become more prominent favoring, in the extreme case, formation of the "bamboo structure" (4). This model, first proposed by Blech (17), appears to be consistent with our experimental observations.

Effect of current density acceleration.—There is considerable disagreement over the value of the current density exponent, n in the J^{-n} dependence. Values of n in the published literature (18) range from 1 to 7. Early work predicted that n was a constant, with a value of 1 for failures at structural sites (19) and a value of 3 where temperature gradients were dominant (20). The work of Venables and Lye (21) and also of Sigsbee (22) has predicted that n is a function of current density and varies from a value of 1 at current densities below 1×10^5 A/cm² to greater than 3 at current densities exceeding 2×10^6 A/cm². The results of Blair *et al.* (23) yielded a value of $n = 5$ for current densities between 1×10^6 and 2×10^6 A/cm². In order to determine the value of n within our range of testing conditions, electromigration measurements were carried out at different current densities for the In-Source Al samples deposited at ~ 140 Å/s as well as those deposited at ~ 63 Å/s. A log-log plot of current density vs. normalized median time to failure is shown in Fig. 14 for the $3.0 \mu\text{m}$ wide In-Source Al-0.5%Cu samples deposited at a rate of 140 Å/s and sintered at 300° and 450°C . From the slope of these curves values of n equal to 3.2 and 3.8 were calculated, in the range of $\sim 5 \times 10^5$ to $\sim 2 \times 10^6$ A/cm², for samples sintered at 300° and 450°C , respectively. A similar plot is shown in Fig. 15 for In-Source Al-0.5%Cu samples with 3.2 and $4.0 \mu\text{m}$ linewidths deposited at a rate of ~ 63 Å/s, sintered at 300°C for 30 min in H_2 , and capped with a $1.4 \mu\text{m}$ film of plasma SiN. The results reveal over the investigated range of current densities ($1 \times 10^6 - 2 \times 10^6$ A/cm²) a value of n , also, close to 4.0 for both linewidths precluding the influence of sintering or plasma SiN addition. This calculated value of n is significantly higher than that of $n = 2$ used, throughout the present investigation, to extrapolate the median time to failure, showing the extrapolation procedures in this study to be quite conservative.

Effect of thermal annealing.—The possibility that the electromigration samples underwent thermal annealing during accelerated testing was addressed by searching for changes in the failure distribution, the failure mechanism, the temperature dependent behavior of MTF, and the metal structure. A likely occurrence for such an effect would expectedly be in the case of samples stressed at temperatures relatively high compared to the sintering temperature, and for long periods of time. Sim (18) has observed for as-deposited E-Gun Al samples, with an average grain size of $2 \mu\text{m}$, a change in failure distribution for meanders tested at 220°C between 100 and 5000h at current densities in the range of 2×10^4 A/cm², which was attributed to thermal annealing. Furthermore, these samples showed evidence of very local failure indicating that some potential failure sites (*i.e.*, dislocations) had

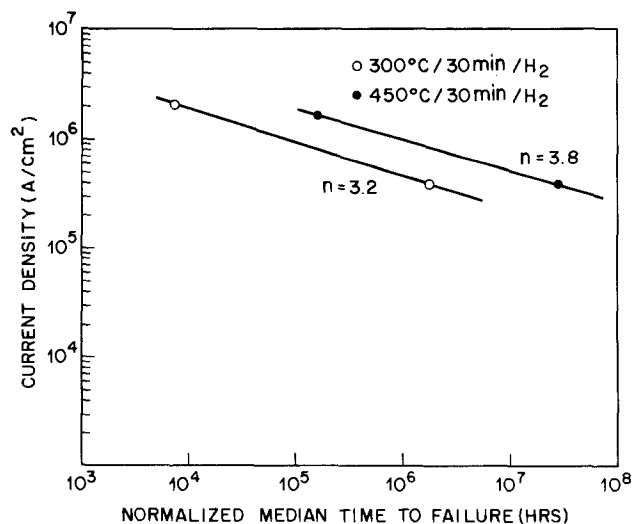


Fig. 14. Log-log plot of current density vs. normalized median time to failure for In-Source Al-0.5%Cu deposited at 300°C , at a rate of ~ 140 Å/s and sintered under different conditions.

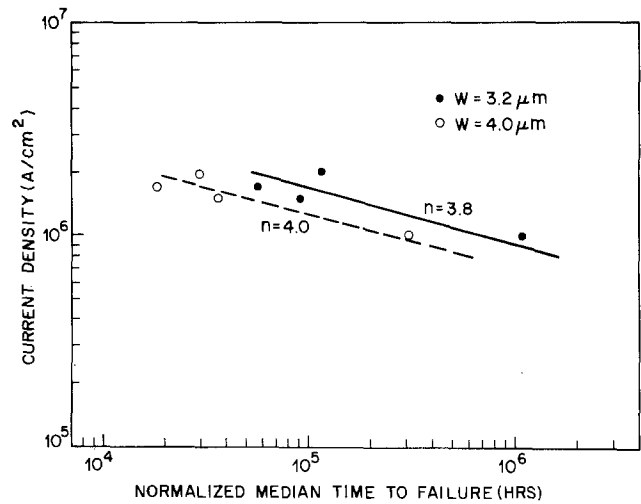


Fig. 15. Log-log plot of current density vs. normalized median time to failure for In-Source Al-0.5%Cu, of various linewidths, deposited at 300°C , at a rate of ~ 63 Å/s, sintered at $300^\circ\text{C}/30\text{min}/\text{H}_2$, and capped with $1.4 \mu\text{m}$ plasma SiN.

been annealed out. However, no obvious physical change in the metal structure, such as a change in grain size, could be found. The author remarks that other contributing factors, such as a redistribution of impurities in the aluminum, could have also accounted for those observations. Examination of our results on sintered In-Source Al-0.5%Cu revealed over the range of testing conditions, a unique failure distribution in all cases and, as shown, for instance, in Fig. 12, a random occurrence of voids along the meander length. Reproducibility measurements on sintered samples ($300^\circ\text{C}/30\text{min}/\text{H}_2$), with no passivation coating, stressed at 215°C after a prior 47h thermal exposure yielded a comparable value of median time to failure (13.40 ± 0.97 vs. $13.44 \pm 0.63\text{h}$) to that of the earlier test. In the course of determining the activation energy, a well-behaved linear fit of MTF to $1/T$ has been exhibited with no evidence of anomalous deviations in lifetime. Measurements of grain size before and after accelerated testing, on samples with no passivation coating, revealed no detectable differences. All these observations are consistent with the absence of significant thermal annealing effects in the course of present testing procedures.

Conclusions

Our results have established that In-Source Al-0.5%Cu is a viable metallization technology compatible with fine-line CMOS processing. The fact that it is radiation free has offered ways of optimizing the thermal cycle so as to achieve desirable device and electromigration characteristics. CMOS device wafers fabricated in accordance with the $3.5 \mu\text{m}$ Twin-Tub CMOS process have shown no threshold shifts or changes in the transistor grain at sintering temperatures up to 450°C , in either H_2 or N_2 , for both N- and P-channel devices, confirming the absence of deposition-induced fixed interface charges. CMOS device wafers fabricated in accordance with the $2.5 \mu\text{m}$ Twin-Tub CMOS process have exhibited low and well-behaved values of contact resistance to N^+ and P^+ diffusions, at sintering temperatures in the range of $300^\circ-400^\circ\text{C}$, in either H_2 or N_2 , with no evidence of junction penetration. Electromigration measurements, gathered over a wide range of processing conditions, have yielded values of median time to failure which were observed to improve with narrower linewidths, higher sintering temperatures, and in the presence of a plasma SiN passivation coating. In typical device operation conditions of 80°C and 1×10^5 A/cm², the calculated lifetime of $\sim 10^6\text{h}$ for the $2.5 \mu\text{m}$ wide passivated In-Source Al-0.5%Cu lines epitomizes the superior reliability of this metallization process.

Acknowledgments

The authors wish to thank R. S. Payne for suggesting this project, W. J. Valentine for deposition of the In-

Source Al-0.5%Cu films used in the electromigration evaluation, G. W. Reutlinger for assistance in the preparation of the polyimide replicas, T. E. McGahan for the scanning electron microscopy work, W. L. Brodsky for guidance in computer analysis of the data, A. W. Anderson and B. Moehring for wire bonding our testers, and J. T. Clemens as well as E. Kinsbron and D. B. Fraser for many fruitful discussions.

Manuscript submitted June 1, 1984; revised manuscript received Sept. 7, 1984. This was Paper 356 RNP presented at the Detroit, Michigan, Meeting of the Society, Oct. 17-21, 1982.

AT&T Bell Laboratories assisted in meeting the publication costs of this article.

REFERENCES

1. J. O. McCaldin and H. Sankur, *Appl. Phys. Lett.*, **19**, 524 (1971).
2. I. Ames, F. M. D'Heurle, and R. Horstmann, *IBM J. Res. Dev.*, **14**, 461 (1970).
3. B. N. Agarwala, B. Patnaik, and R. Schnitzel, *J. Appl. Phys.*, **43**, 1487 (1972).
4. S. Vaidya, D. B. Fraser, and A. K. Sinha, in "Proceedings of the 18th Reliability Physics Symposium of IEEE," p. 165, IEEE, New York (1980).
5. L. C. Parrillo, R. S. Payne, R. E. Davis, G. W. Reutlinger, and R. L. Field, *IEEE Tech. Dig., Int. Electron Device Meet.*, p. 752 (1980).
6. L. C. Parrillo, L. K. Wang, R. D. Swenumson, R. L. Field, R. C. Melin, and R. A. Levy, *ibid.*, 706, (1982).
7. H. M. Naguib and L. H. Hobbs, *This Journal*, **124**, 573 (1977).
8. H. C. Card, *IEEE Trans. Electron Devices*, **ed-23**, 538 (1976).
9. I. A. Blech and E. S. Meieran, *Appl. Phys. Lett.*, **11**, 263 (1967).
10. P. B. Ghate, *ibid.*, **11**, 14 (1967).
11. R. Rosenberg and L. Berenbaum, *ibid.*, **12**, 201 (1968).
12. J. R. Black, *IEEE Trans. Electron Devices*, **ed-16**, 338 (1969).
13. P. B. Ghate, J. C. Blair, and C. R. Fuller, *Thin Solid Films*, **45**, 69 (1977).
14. E. Kinsbron, *Appl. Phys. Lett.*, **36**, 968 (1980).
15. A. J. Learn and W. H. Shepperd, in "Proceedings of the 9th Reliability Physics Symposium of IEEE," p. 129, IEEE, New York (1971).
16. J. R. Lloyd and P. M. Smith, *J. Vac. Sci. Technol.*, **1**, 455 (1983).
17. I. A. Blech, *J. Appl. Phys.*, **47**, 1203 (1976).
18. S. P. Sim, *Microelectron. Reliab.*, **19**, 207 (1979).
19. H. B. Huntington and A. Grove, *J. Phys. Chem. Solids*, **20**, 76 (1961).
20. C. B. Oliver and D. E. Bower, in "Proceedings of the 8th Reliability Physics Symposium of IEEE," p. 116, IEEE, New York (1970).
21. J. D. Venables and R. W. Lye, in "Proceedings of the 10th Reliability Physics Symposium of IEEE," p. 159, IEEE, New York (1972).
22. R. A. Sigsbee, in "Proceedings of the 11th Reliability Physics Symposium of IEEE," p. 301, IEEE, New York (1973).
23. J. C. Blair, P. B. Ghate, and C. T. Haywood, *Appl. Phys. Lett.*, **17**, 281 (1970).

Approximating Spun-On, Thin Film Planarization Properties on Complex Topography

L. K. White

RCA Laboratories, David Sarnoff Research Center, Princeton, New Jersey 08540

ABSTRACT

A method for characterizing and estimating spun-on, thin film planarization properties is proposed. The spun-on film is considered to be a low pass frequency filter. Two adjustable parameters are used to weight the frequencies to experimental planarization data for isolated line features. Using these parameters, the planarization properties on more complex topographies having a nominal unity of step height can be accurately estimated. One fitting parameter, α , gives an indication of the planarization (flow) properties of the spun-on solution. The other fitting parameter, P_{\min} , represents the minimum period (maximum frequency) with a weighting factor equal to one. Planarization properties of two distinctly different spun-on solutions are simulated on complex topography to verify the approximation procedure. The stencil pattern used to obtain the experimental planarization data for isolated line features can also be used to obtain an unambiguous determination of the planarization properties independent of step height and the spun-on film thickness.

Detailed descriptions of the spun-on planarization properties of thin films are becoming increasingly important for integrated circuit processing. Resist dimensional control issues on topographical features are strongly influenced by resist thickness changes (1, 2). Dual-etch-back techniques for the planarization of passivation and isolation layers (3-5) also depend on the spun-on, thin film planarization properties. Our previous work (6, 7) and the work of others (5, 8-11) have provided insights into the planarization phenomena that occurs for spun-on films. All of these workers point out the complexity of these phenomena. One of the most complex aspects is the effect that the surrounding topography has on planarization. Changes in the position and size of topographical features can change the polymer film thickness on adjacent features. In this work, a method of characterizing and estimating the magnitude of these effects is proposed. Film shrinkage, thermal flow of films, and radial flow anomalies over different topography orientations can further complicate this situation. This work confines itself to situations where these effects do not play a prominent role.

To calculate polymer planarization properties from first principles is a difficult rheological problem. Poly-

mer solution viscous-elastic properties during the turbulent spun-on planarization process are not completely understood. Film deformations are frequently the same order of magnitude as the film thickness. Deformations of this magnitude do not follow the analytical procedures frequently used to model relatively small deformations. On complex topography even with a well-defined approach, the problem becomes exceedingly complex. In light of these considerations, we have chosen a semi-empirical approach to simulate spun-on film planarization properties. The spun-on film is considered to be a low-pass frequency filter for the topography. The data from isolated line features are fitted to a mathematical model with two adjustable parameters. These parameters can then be used to approximate the spun-on planarization properties for any complex topography having a unification of step heights.

Experimental

Substrates for the planarization characterization studies were prepared by growing thermal oxide on 3 in. silicon wafers to a thickness equivalent to the desired step height. The thermal oxide was patterned with positive resist and an anisotropic plasma etching procedure. These

topographical features were then coated with a LPCVD polysilicon film 0.5 μm thick. The patterned substrates contain isolated line features of various widths and lengths in excess of 500 μm . Typically, isolated line features with widths of 40, 30, 20, 15, 10, 5, 3, 2, 1.5, and 1.0 μm were used. The spacing between the isolated line features was 100 μm . Linewidths were determined with a flar eyepiece and step heights measured with a Tencor Alpha-Step Profilometer.

Two different spun-on solutions are analyzed here: OFPR 800 (30 Hz) positive resist and KTI polymethylmethacrylate, PMMA, at 9% solids. These two solutions were selected because of their substantially different planarization properties and their resistance to thermal flow during cures to harden the films for profilometric analysis. A static dispense, maximum acceleration to a spin speed of 6000 rpm and a spin time of 30s were used to coat the substrates. The OFPR 800 coating was cured at 110°C and the PMMA coating at 140°C. Thicknesses of the spun-on coating were measured with an instrument similar to a Rudolph Thin-Film Thickness Monitor at a refractive index setting of 1.60 on bare silicon substrates. Spun-on, thin film planarization properties were also determined with the Tencor Alpha-Step Profilometer operating at a 15 mg tracking force. A stylus radius of 3 μm was used to minimize the effects of the stylus tracking on the recorded profilometer trace. The accuracy of this step-height determination is nominally $\pm 100\text{\AA}$ on the 10 kÅ scale. All the profilometer traces were taken on grating and isolated lines that had the ends of the features oriented toward the wafer center.

Calculation Procedure

A number of investigators (5-11) have observed the strong dependence feature size (dimension) has on planarization phenomena. Figure 1 shows this dependence on the isolated line features for two different polymer films. The initial step heights were all 0.5 μm and both spun-on film thicknesses were nominally 0.9 μm . At feature sizes greater than 20 μm , the PMMA coating reduces the step height (planarizes better) than the OFPR coating. Below the 20 μm feature size, the OFPR coating shows significantly better planarization properties. Over a wide range of feature sizes, there is a linear correlation between the logarithm of the feature size and the step-height reduction. This type of planarization property dependence on feature size suggested to us that the periods or frequency components of the topography may contribute to the observed planarization phenomena.

If the topography can be described by a piecewise continuous function, the same topography can be described with a series of sine and cosine functions (12): for example, when a one dimensional function, $T(y)$, is represented by an even number of and a sequence of evenly spaced

points, N . Then $T(y)$ can be expressed as

$$T(y) = \sum_{n=0}^j a_n \cos \frac{2\pi ny}{N} + b_n \sin \frac{2\pi ny}{N}$$

where $j = N/2$. The cosine and sine coefficients, a_n and b_n , can be obtained from the fast Fourier transform (13) of $T(y)$.

When a spun-on coating is applied to the topography, $T(y)$, a deformed or smoothed topography results, $T_s(y)$. An approximation of the smoothed topography is obtained by weighting the a_n and b_n coefficients. Thus

$$T_s(y) \approx \sum_{n=0}^j a_n w_n \cos \frac{2\pi ny}{N} + b_n w_n \sin \frac{2\pi ny}{N}$$

where $1.0 > w_n > 0.0$ and $w_{n+1} \geq w_n$.

Several weighting schemes are possible, but Fig. 1 suggests a form that has worked reasonably well for us. The w_n 's are selected below a certain minimum period, as shown in Fig. 2, and are proportional to the logarithm of the period associated with the corresponding cosine and sine coefficient. The change in w_n with respect to the logarithm of the period is specified by the adjustable parameters, P_{\min} and a . P_{\min} is the minimum period with a w_n equal to one. a is the slope of the w_n curve or the change in the w_n value divided by the change in the logarithm of the period. This weighting procedure dampens high frequency or small period components on the surface topography. It results in approximating planarization properties as function of feature size, smooths sharp corners, and broadens the bottom of steps. Although the curves in Fig. 1 suggest the form of the weighting factors, the factors themselves cannot be obtained directly from Fig. 1. Isolated square-wave features are themselves an ensemble of sine and cosine functions. Nonetheless, a frequency weighting scheme can be obtained from a series of isolated square-wave features with various dimensions. Generally, the P_{\min} value is approximately 3-4 times the feature size denoted by the intercept of the planarization curve with original step height. The a parameter is usually 1.0-1.5 times the slope of planarization curve where the Y-axis units are expressed as the fraction of the original step height. The values of the adjustable parameters to fit the experimental data in Fig. 1 are 165 μm and 0.60 for the OFPR 800 coating and 300 μm and 0.28 for the PMMA coating. Figure 3 shows simulated computer traces of the OFPR 800 and HPR 204 materials on isolated line features ranging from 40-5 μm wide. Table I shows the comparison between the experimental and simulated step heights.

The selection of the proper interval between points and the number of points, N , are important to obtain the best simulation results. N should span a range at least twice the P_{\min} distance. The interval between points depends on

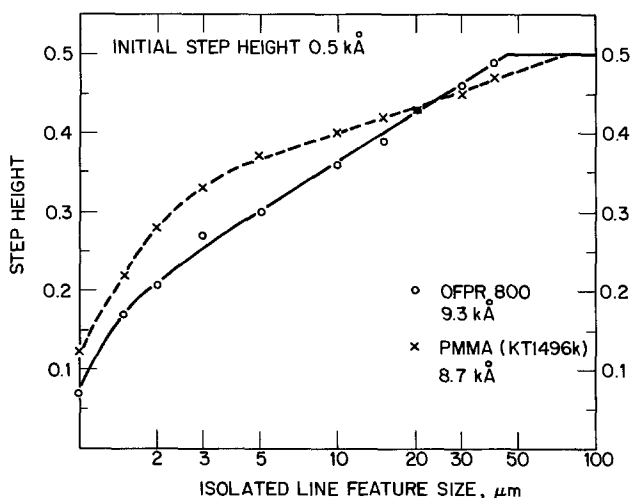


Fig. 1. Planarization properties of OFPR 800 and PMMA on 0.5 μm step heights.

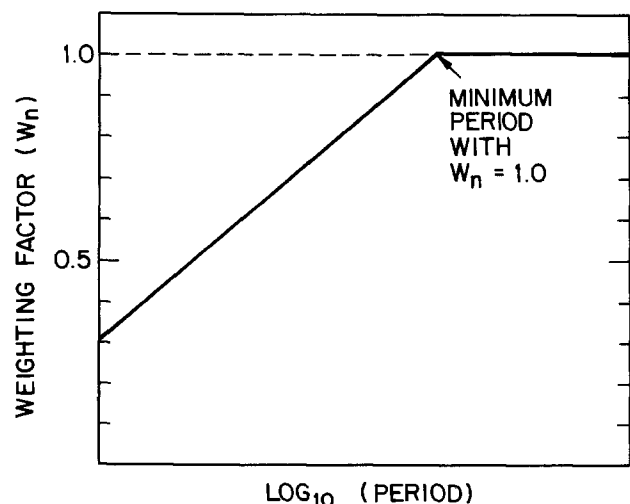


Fig. 2. Period weighting schematic for spun-on, thin film simulations

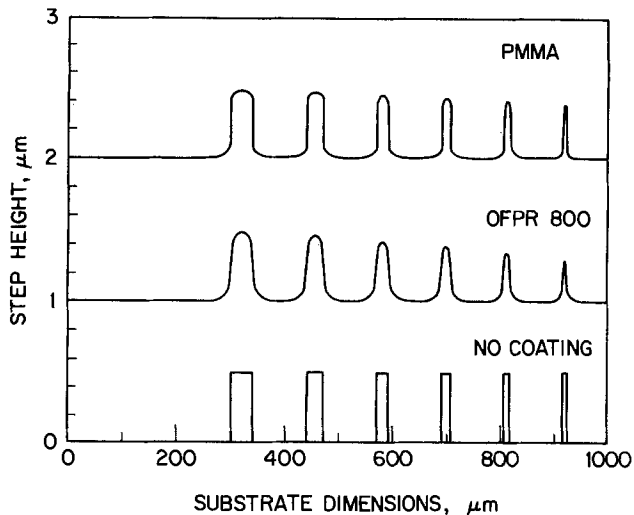


Fig. 3. Simulated planarization properties for isolated line features. Original step height is 0.5 μm. Top: PMMA 0.87 μm thick. Middle: OFPR 800 0.93 μm thick. Bottom: no coating.

the feature size dimension that needs to be simulated. Generally, the interval between points should be one-tenth that of the minimum feature size. For small deformations, (i. e., little planarization), this requirement can be relaxed to some degree. Our simulations typically span a distance of 1260 μm and use a 1 μm interval between points. The filtering of the high frequency components produces ripple effects in the simulated planarization curves. These effects are usually much smaller than the experimental error. Smoothing routines for the high frequency ripple can be used, if further refinements are required. The simulations presented here are set up for a minimum feature size of 10 μm.

Figure 1 shows that the step-height vs. logarithm of feature size curve is no longer linear in the small feature size range. Weighting the sine and cosine coefficients according to logarithm of the period over the 10-40 μm feature size range does produce simulated planarization curves that exhibit a similar nonlinear behavior at small feature sizes. The simulated nonlinear behavior in the small feature size range resembles that shown in the PMMA experimental curve of Fig. 1. In general, the simulated curves at small feature sizes predict a step height that is slightly lower than that observed experimentally. If a spun-on coating does not show this characteristic nonlinear behavior at small feature sizes, errors in simulated planarization properties are possible. These high frequency components not only influence small feature sizes, but also the wall profiles on relatively large feature sizes. More sophisticated frequency weighting procedures may be required to simulate the planarization properties of small feature sizes accurately. Thus far, we are pleased with the simulation results at the top and bottom of steps for large feature sizes (> 10 μm).

These weighting factors only apply to a specific spun-on coating thickness and step height. Figure 4 shows how the planarization properties change with the step height and the spun-on film thickness. Note that all the curves

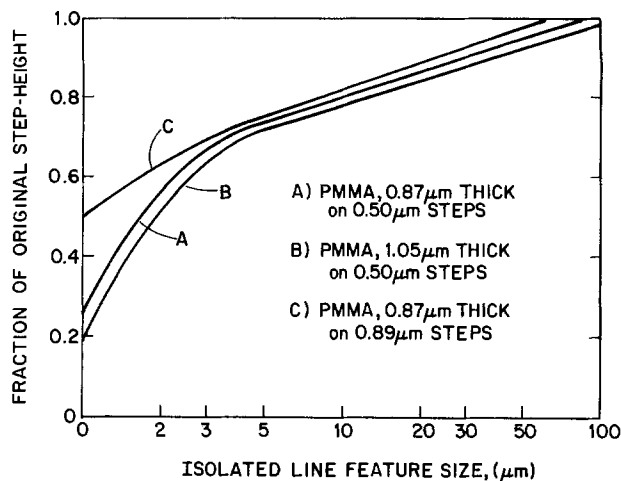


Fig. 4. Planarization properties of PMMA for different film thicknesses and step heights.

follow the same slope over the 5-40 μm feature size range. The intercept with the original step height and the behavior in the high frequency (small period) region changes. For an increased spun-on thickness, the intercept with original step height becomes larger, and for an increased step height the same intercept becomes smaller. Our frequency weighting parameters, α and P_{min} show the same behavior. Evidently, our α fitting parameter represents a characteristic planarization property of a specific spun-on polymer solution. P_{min} changes with film thickness and the step-height variations. Since P_{min} represents the first frequency component of the topography that is changed by the spun-on film, an estimation of the range of the feature-feature interaction is also implied. If this frequency weighting scheme is correct, the P_{min} values suggest that thicker spun-on coatings influence planarization properties over a wider range, while taller step heights appear to reduce the range of feature-feature interactions.

Simulation Results

After obtaining the frequency weighting parameters for the two spun-on coatings, planarization properties were simulated for other topographies. Figure 5 shows experimental profilometer traces for the two spun-on films on 10 × 10 μm gratings. A schematic of the relevant step

Table I. Measured and simulated step heights for isolated lines (μm)

Feature size (μm)	PMMA experimental results	$P_{min} = 300 \mu m$ $\alpha = 0.28$		$P_{min} = 165 \mu m$ $\alpha = 0.60$	
		experimental results	simulated results	experimental results	simulated results
40	0.47	0.465	0.48	0.478	
30	0.45	0.450	0.45	0.455	
20	0.43	0.431	0.42	0.417	
15	0.42	0.416	0.38	0.386	
10	0.40	0.393	0.35	0.343	
5	0.37	0.364	0.30	0.294	

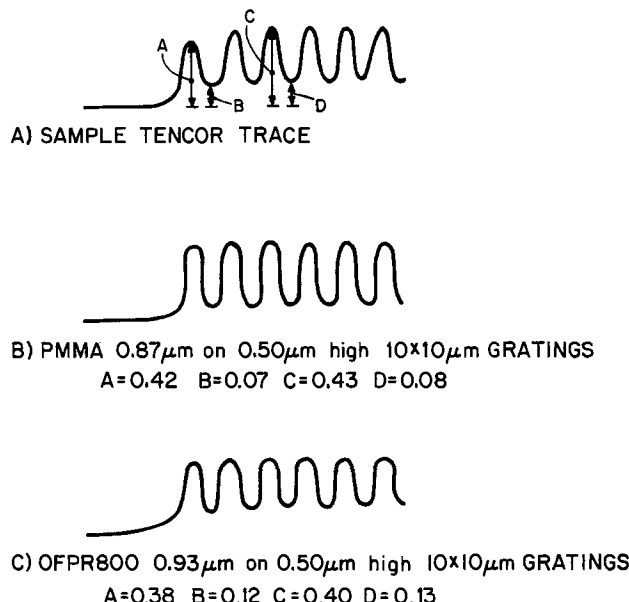


Fig. 5. Experimental profilometer traces for OFPR 800 and PMMA on 10 × 10 μm line-space gratings.

heights is also displayed. The grating is assumed to run infinitely to the right and flat expanse infinitely to the left. Planarization data obtained for an isolated $10\ \mu\text{m}$ feature cannot be used to predict the step height, A, at the edge 10×10 grating or the step heights within the $10 \times 10\ \mu\text{m}$ grating, B, C, and D. Simulated planarization curves are shown in Fig. 6, and a comparison of measured and simulated step heights in Table II.

The simulated step heights match the experimental step heights for both coatings. Even shapes of the simulated traces resemble those of the experimental traces. We have simulated the planarization properties of these polymer films on more complex topography with good success. The step heights were predicted accurately, and the general shapes of the computed traces were consistent with the experimental profilometer traces.

Limitations of Approximation Techniques

This approximation technique does not address some important aspects of spun-on, thin film planarization phenomena. Many topographies of interest do not exhibit a uniform step height. However, for some of these cases, this technique can give reasonable results. We have shown experimentally that the wall profile does not affect measured planarization properties at the top and bottom of steps (7). Narrow shelves at the edge of larger steps and tapered-wall features should not introduce major errors. The most difficult cases are those involving small features on top of the larger ones. Here, the prevailing step height should be used in the approximation procedure, although significant errors may be introduced in the vicinity of the smaller feature.

Planarization properties are not necessarily constant with respect to feature position relative to the center of the wafer. Different spun-on, planarization properties have been reported for PMMA-coated E-beam alignment marks (14). We have detected changes in the measured step height as a function of orientation with respect to the wafer center for several polymer films. These effects also produce asymmetries in the step profile for large feature sizes and higher step heights. Orientation effects become less prominent at the smaller features sizes. This simulation technique does not correct for these deviations, owing to radial flow anomalies during spinning. Care should be taken that the isolated line data are oriented so that the end of the lines are oriented toward the substrate center.

Shrinkage during the cures of the spun-on film increases the measured step heights. Films that shrink considerably (*i. e.*, greater than 20% of original thickness) and topography configurations that show the more reduced step heights are expected to show the most significant

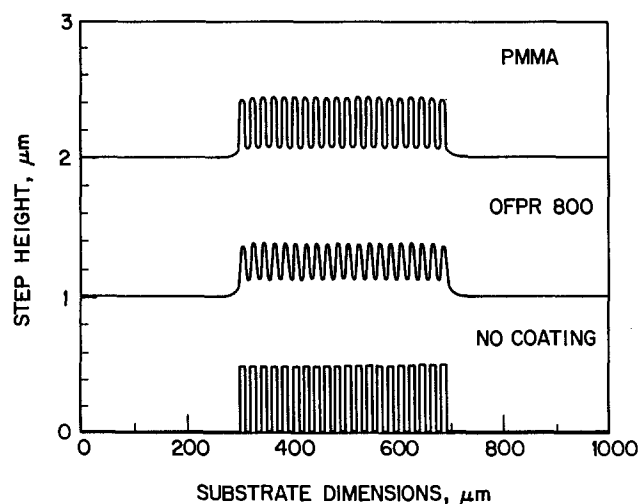


Fig. 6. Simulated planarization properties for $10 \times 10\ \mu\text{m}$ line-space gratings. Original step height is $0.5\ \mu\text{m}$. Top: PMMA ($0.87\ \mu\text{m}$ thick). Middle: OFPR 800 ($0.93\ \mu\text{m}$ thick). Bottom: No coating.

Table II. Measured and simulated step heights for 10×10 line space grating

	PMMA experimental results (μm)	$P_{\min} = 300\ \mu\text{m}$ $\alpha = 0.28$	OFPR 800 experimental results (μm)	$P_{\min} = 165\ \mu\text{m}$ $\alpha = 0.60$
A	0.42	0.418	0.38	0.374
B	0.07	0.072	0.13	0.132
C	0.43	0.435	0.40	0.397
D	0.08	0.083	0.14	0.137

discrepancies. Thermal flow of the film, however, tends to reduce the measured step heights.

The simulated and experimental results have thus far only considered single-dimensional feature sizes (*i. e.*, finite width and infinite length). On most device surfaces, both the width and length of a feature influence the planarization properties. For example, the data for isolated $10\ \mu\text{m}$ line features here only represent maximum possible step height for that feature size on a device structure. Features with lengths less than the range of feature-feature interaction can produce reduced step heights (*i. e.*, a more planar, less conformal coating). We believe that the same planarization frequency weighting (filtering) parameters for the single-dimensional feature sizes can be applied to features that have both finite width and length.

Concluding Remarks

In spite of the apparent limitations of this technique, the spun-on planarization properties of spun-on films can be estimated with reasonable accuracy under some conditions that are encountered in device processing. The experimentally determined fitting parameters appear to represent meaningful physical constants related to the nature of the spun-on, thin film planarization phenomena. It involves expressing the topographical features in frequency domain (*i. e.*, a Fourier transform) and weighting the frequency components to simulate the smoothed topographical features. Two adjustable parameters are used to fit experimental planarization data for isolated line features. The α fitting parameter gives an unambiguous indication of the planarization properties of the spun-on solution. The P_{\min} parameter represents the minimum period that does not require a weighting factor.

Although the frequency weighting procedure lacks theoretical and mathematical rigor, reasonable results have been obtained using a fairly simple low pass frequency filtering scheme. Conceivably, more accurate and justifiable filtering schemes may be devised in the future. These results show that useful approximation procedures are possible by treating topographical features in the frequency domain. To verify this approximation procedure, the planarization properties of two distinctly different spun-on solutions, OFPR 800 (30 Hz) and KTI 496K PMMA (9% solids) have been simulated on complex topography.

Acknowledgments

The author thanks Nancy Miszkowski and Metodi Popov for the technical assistance they provided.

Manuscript submitted March 6, 1984; revised manuscript received Aug. 17, 1984. This was Paper 96 presented at the Cincinnati, Ohio, Meeting of the Society, May 7-11, 1984.

RCA Laboratories assisted in meeting the publication costs of this article.

REFERENCES

1. D. W. Widmann and H. Binder, *IEEE Trans. Electron Devices*, **ed-22**, 467 (1975).
2. M. M. O'Toole, E. D. Lin, and M. S. Chang, *ibid.*, **ed-28**, 1405 (1981).
3. A. C. Adams, *Solid State Technol.*, **24**, 178 (April, 1981).
4. H. B. Pogge, G. A. Kaplita, and R. R. Wilbarg, Abstract 309, p. 805, The Electrochemical Society Extended Abstracts, Vol. 80-2, Hollywood, FL, Oct. 5-10, 1980.

5. A. C. Adams and C. D. Capio, *This Journal*, **128**, 423 (1981); *ibid.*, **126**, 1042 (1979).
6. L. K. White, *ibid.*, **130**, 1543 (1983).
7. L. K. White, *J. Vac. Sci. Technol.* **B1**, 1235 (1983).
8. L. B. Rothman, *This Journal*, **127**, 2216 (1980).
9. K. Hirata, Y. Ozaki, M. Oda, and M. Kimizuka, *IEEE Trans. Electron Devices*, **ed-28**, 1373 (1981).
10. E. Bassous, L. M. Ephraph, G. Pepper, and D. J. Mikalsen, *This Journal*, **130**, 478 (1983).
11. L. B. Rothman, *ibid.*, **130**, 1131 (1983).
12. E. Kreyszig, "Advanced Engineering Mathematics," pp. 434-439, 126-196, 2nd ed., John Wiley and Sons, New York (1967).
13. R. C. Singleton, *Commun. ACM*, **10**, 647 (1967).
14. Y. C. Lin, A. R. Neureuther, and W. G. Oldham, *This Journal*, **130**, 939 (1983).

Investigation of Melt Carry-Over during Liquid Phase Epitaxy

I. Growth of Indium Phosphide

R. B. Wilson,¹ P. Besomi,^{*2} and R. J. Nelson¹

AT&T Bell Laboratories, Murray Hill, New Jersey 07974

ABSTRACT

Melt carry-over characteristics as a function of melt height, wafer clearance, push speed, and wafer surface morphology during the liquid phase epitaxy growth of InP are described. It is found that a "critical clearance" exists, below which carry-over is minimized and nearly independent of clearance. For single layers of InP doped with zinc and grown on planar [100] oriented substrates, this critical clearance is about 75 μm . It is shown that deviations from nonplanarity of the substrate influence carry-over in this subcritical regime. A theory is developed to explain this behavior in terms of a flow model which is dependent upon the melt pressure head and surface tension effects. A new boat design is proposed to reduce melt carry-over effects.

Liquid phase epitaxy (LPE) has played an important role in the development of optoelectronic devices fabricated from III-V semiconductor materials (1). Although it has successfully competed with other growth technologies such as molecular beam epitaxy, vapor phase epitaxy, and metal-organic chemical vapor deposition, the LPE technique suffers from several disadvantages inherent in using the liquid phase. Because of the high density, viscosity, and surface tension of the liquid metal melts used for growth, hydrodynamic and surface effects can strongly modify local growth conditions, resulting in inhomogeneous growth over the surface of the wafer. One example of these effects is melt carry-over or dragover, which occurs when the substrate is moved from one growth melt to another. Because some clearance must be maintained between the bottom of the graphite melt holder and the top of the substrate to prevent scratching, indium can be trapped in this clearance volume above the wafer. As the wafer is moved underneath the next growth melt, this trapped solution can locally alter the composition of the melt, resulting in inhomogeneous and/or nonreproducible growth characteristics (2). This is particularly true in the case of double heterostructure (DH) growth, where very thin (0.2 μm), uniform active layers must be grown to achieve high yields of low threshold laser devices (3). For this reason, a detailed understanding of the carry-over phenomena is desirable, particularly with respect to how carry-over can be influenced by accessible growth variables such as clearance and push speed.

In Part I of this work (this paper), we have studied melt carry-over during LPE growth of InP as a function of wafer clearance, push speed, melt height, and wafer surface morphology under otherwise identical growth conditions. This has led to an improved understanding of the factors which govern the carryover phenomena and indicates that a region of critical clearance exists below which carry-over is minimized and nearly independent of clearance. In addition, it is shown that surface morphology can strongly influence carry-over in this critical regime. In Part II of this study (the following paper) (4), the practical implications of melt carry-over is reported for growth of InGaAsP double heterostructure wafers.

*Electrochemical Society Active Member.

¹Present address: Lytel, Incorporated, Bridgewater, New Jersey 08807.

²Present address: Lasertron, Incorporated, Burlington, Massachusetts 01803.

Experimental

An automated LPE growth system was used for these experiments. The temperature cycle, as well as the gas flows, were computer controlled in order to improve run-to-run repeatability as compared to manual LPE systems (5). Moreover, the push mechanism used to translate the InP substrate from melt was also computer controlled to a time accuracy of 50 ms. Single layers of InP doped with zinc ($p \sim 10^{18}/\text{cm}^3$) were grown on [100] InP substrates at 580°C using step cooling at a supersaturation of 6°C. The growth melt was prepared from InP and metallic indium weighed to an accuracy of $\pm 5 \mu\text{g}$. The substrates were 1.27 cm length \times 1.52 cm width \times 0.25 mm thickness. After measuring the substrate thickness to $\pm 3 \mu\text{m}$, graphite shims of known thickness were used to obtain the desired clearance for the growth run. The substrates were degreased in successive chloroform, acetone, and methanol rinses prior to a 10 min etch in 10:1:1 (H_2SO_4 : H_2O_2 : H_2O). This latter etch removes about 0.4 μm of surface from the wafer and leaves a flat, smooth, reproducible surface for growth. After the growth run, the used indium melt was weighed to $\pm 5 \mu\text{g}$ to determine the weight loss of the melt. The maximum weight loss of a melt due to P evaporation was determined to be less than 0.05 mg. The weight loss due to the thickness of the grown layer was 0.6-0.8 mg in all cases.

Theory

Flow model.—In order to understand the results presented in this paper, we first develop a model for melt carry-over based on the expected fluid flow characteristics. Shown in Fig. 1 is a schematic drawing of the graphite boat, growth melt, and substrate in an arbitrary position of the slider during the push from one melt to the next. We examine the flow of liquid melt from the melt bin into the narrow channel above the substrate and below the graphite boat bins block. This problem is similar to the flow of the melt out of the channel as the substrate is moved away from the melt. This channel has a height equal to the clearance (c) above the substrate and is typically 0.5-5 mil. The width of the channel is approximately equal to the width of the substrate (W), and the channel length, X_0 , is determined by the wall thickness between adjacent melts. The substrate length (L) is usually larger than the wall thickness, X_0 .

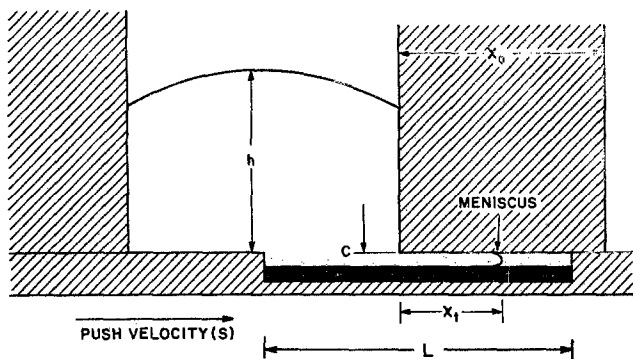


Fig. 1. Schematic diagram of indium carry-over in a typical graphite boat.

For a rectangular channel of this sort, the velocity distribution in the y direction is given by well-known expressions (6) for Couette flow between two parallel plates in which one is moving with speed S

$$V = \frac{1}{2\rho\nu} \frac{\partial P}{\partial X} (y^2 - cy) + \frac{Sy}{c} \quad [1]$$

In this expression, ρ and ν are the density and kinematic viscosity of the melt. By integrating this expression with respect to y and dividing it by c , an equation for the average fluid velocity into the channel is obtained (6)

$$\langle v \rangle = \left(-\frac{\partial P}{\partial X} \right) \frac{c^2}{12\rho\nu} + \frac{S}{2} \quad [2]$$

It should be pointed out that these expressions are steady-state expressions which are valid after a period of time on the order of $t \geq c^2/\nu$, which for the conditions of these experiments is $\sim 10^{-2}$ s. Since the duration of the push is 0.1s, this is considered to be an acceptable approximation. However, these expressions assume laminar flow conditions and do not take account of the possible discontinuous motion of the slider, which is driven by a stepper motor. Thus at high slider velocities, turbulence effects are expected to modify the $S/2$ dependence in Eq. [2]. Likewise, at low slider velocities, the $S/2$ term will not properly take account of the stepwise motion of the slider. In addition to these expected problems with the $S/2$ term, it has been found that inclusion of this term in the flow model theory results in expressions for melt carry-over which disagree significantly with experimental results. We therefore anticipate our experimental results in the remaining theoretical development and disregard the $S/2$ term for the reason mentioned above. Further experimental investigation may be required to ascertain why the $S/2$ term in Eq. [2] may be neglected without negative consequences on the validity of this model.

The quantity $(-\partial P/\partial X)$ in Eq. [2] is the pressure gradient across the melt flowing into the clearance channel shown in Fig. 1. Because the push speeds we consider here are much less than the velocity of sound and the melt fluid is considered to be incompressible, this gradient can be rewritten as

$$\left(\frac{\partial P}{\partial X} \right) = \frac{\Delta P}{X_1} \quad [3]$$

where ΔP is the pressure applied to the fluid at the mouth of the clearance channel, and X_1 is the distance from the mouth of the channel to the moving meniscus of the fluid in the channel. In the next two sections, we consider the origin of the pressure ΔP which drives fluid into the clearance channel.

Melt pressure head.—One contribution to the pressure which drives melt carry-over is gravitational force on the melt. At the base of the melt, this pressure is given by the weight of the melt divided by the wafer area

$$P_g = \frac{\rho L W h g}{L W} = \rho g h \quad [4]$$

where L is the length of the wafer, g is the gravitational constant, and h is the melt height. Because the top surface of the melt is curved due to surface tension, h is defined such that

$$h = \frac{\text{melt weight}}{L W \rho} \quad [5]$$

In these expressions, the melt density can be assumed to be very nearly equal to that of pure indium. At 580°C, the density is calculated by extrapolation of known data (7) to be 6.69 g/cm. This gravitational contribution to the melt carry-over driving pressure ΔP , then, is approximately equal to 3×10^3 dyn/cm² for a 6g melt. From Eq. [4] and [5], this pressure should vary linearly with melt height and melt weight.

Surface tension effects.—An additional contribution to ΔP comes from surface tension effects inside the clearance channel. The well-known principles of capillarity (8) arise because of a capillary pressure, P_c , which is most generally expressed for a rectangular channel by the equation (8)

$$P_c = \frac{2\gamma \cos \Theta}{r} \quad [6]$$

where r is the radius of curvature of the meniscus, Θ is the contact angle, and γ is the fluid surface tension. Pressure is defined such that a positive pressure causes fluid to flow into the channel. It is clear from this equation that the wetting properties of the materials forming the walls of the rectangular channel will strongly influence the magnitude of the capillary pressure P_c because of the dependence on contact angle.

In the case where the surfaces are not wetted by the melt, e.g., having two parallel graphite walls, $\Theta \approx 180^\circ$ and P_c is large and negative. In this case, the capillary pressure tends to force fluid out of the clearance channel unless the gravitational pressure P_g is greater. Using a value of $\gamma = 630$ dyn/cm (9) and $\Theta = 180$, the capillary pressure P_c is calculated to be approximately -1.3×10^5 dyn/cm for a 4 mil clearance. The absolute magnitude of this value is considerably larger than the value of P_g estimated in the previous section.

A second case occurs if both surfaces are wetted by the melt where $\Theta \approx 0$. In this situation, P_c is large and positive, and melt will be drawn into the clearance channel much in the same way that water is drawn into a glass capillary tube. This situation is partially realized in LPE growth when a sapphire bins block is used. It has been found (11) that the amount of melt carry-over is larger for sapphire boats than for equivalent graphite boats of similar clearance in the LPE growth of AlGaAs.

The third case is the more usual one in LPE growth in graphite boats where one surface is nonwetting (upper graphite bins block surface) and one is wetting (substrate). In this case, the meniscus curvature is not well-defined, and the resultant capillary pressure can be calculated only in certain symmetrical cases (11). However, it is intuitively clear that the resulting capillary pressure should be intermediate between the former two cases and be significantly smaller than the previously calculated value, and it should easily compare to the pressure which arises from gravitational effects, P_g . Furthermore, because the surface tension and contact angle are expected (12) to be strongly influenced by the composition of the melt and grown layer, P_c should be composition dependent.

In accordance with the foregoing discussion, we can write the pressure which drives melt carry-over, ΔP , as a sum of two terms

$$\Delta P = P_g + P_c = \rho g h + P_c \quad [7]$$

It is next asserted that the mass of melt carry-over is proportional to the total volume of melt which flows into the channel during the time elapsed for the push. This is given by the time integral

$$M_{\text{carry-over}} = \rho c W \int_0^{L/S} \langle v \rangle dt \quad [8]$$

where t_0 is equal to L/S . Combining Eq. [2]-[4], [7], and [8], we arrive at the expression

$$M_{\text{carry-over}} = \rho c W \int_0^{L/S} \left[\frac{c^2}{12\rho\nu} \frac{(\rho gh + P_c)}{X_t} \right] dt \quad [9]$$

Because the parameter X_t varies during the push, we replace this variable with an average value, X_{eff} , which remains as an adjustable constant to be determined by experiment. Integration with respect to time then yields the expression

$$M_{\text{carry-over}} = \frac{c^3 W}{12\nu X_{\text{eff}}} (\rho gh + P_c) \frac{L}{S} \quad [10]$$

In the next section, we experimentally establish the magnitudes of $\Delta P = \rho gh + P_c$ and of P_c by measuring the functional dependence of melt carry-over on melt height. This data, in conjunction with melt carry-over *vs.* clearance data, allows comparison with the theoretical model just developed.

Results and Discussion

Shown in Fig. 2 is a plot of experimentally obtained melt carry-over data *vs.* melt height as defined by Eq. [5]. These data were obtained using a constant clearance of $102 \pm 8 \mu\text{m}$ and a push speed of 12.7 cm/s. The linear behavior of these data strongly support the assertion that the experimental conditions are such that Eq. [10] of the theoretical model is applicable. Using known indium viscosity data (13), the slope obtained from a least squares fit to the data yields a value of $X_{\text{eff}} = 0.60 \text{ cm}$. This value is reasonable because the spacing between growth bins is 0.76 cm. From the y -intercept, P_c is calculated to be $-1.4 \times 10^3 \text{ dyn/cm}^2$, again in good agreement with the expectations previously discussed. The negative value of P_c indicates that the meniscus effects tend to keep melt out of the clearance space. This effect, however, is overcome by pressure head effects for melt heights greater than $\sim 0.25 \text{ cm}$. It is important to point out that the dependence of melt carry-over on melt height strongly suggests that confined melts (14) should significantly reduce melt carry-over, provided that a pressure head is not maintained on the confined melt by weights or other configurations such as a baffled solution holder. It is therefore desirable that boat configurations which minimize melt

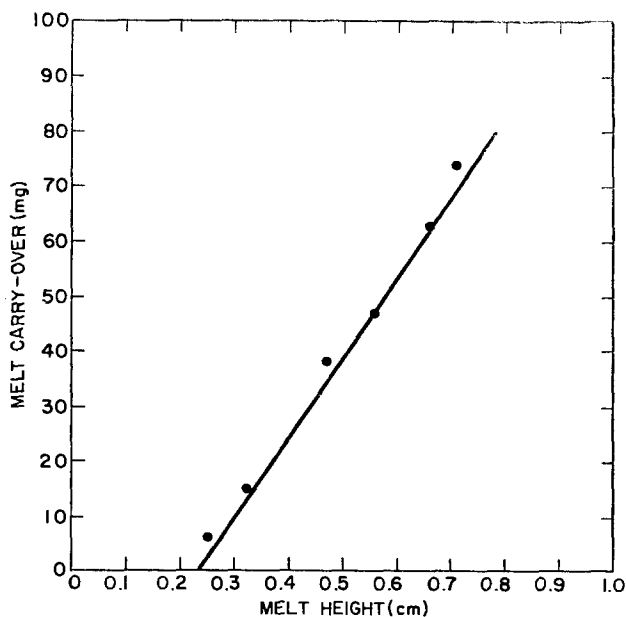


Fig. 2. Plot of melt carry-over *vs.* melt height. The solid line is a least squares fit to the experimental data, with slope of 146 mg/cm and y -intercept of -33.8 mg .

pressure head and, hence, carry-over be utilized in the LPE growth of InGaAsP.

In a second set of experiments, melt carry-over was measured as a function of clearance for a constant melt height of 0.47 cm (6g melt). These data are shown in Fig. 3, along with the theoretical prediction (solid curve) using the parameters just derived. Although the calculated curve is consistently too high by about 20%, the agreement is seen to be fair and could be improved using somewhat different values of the adjustable parameters X_{eff} and P_c . Of great practical importance is the predicted and experimentally observed minimization of melt carry-over for clearance values less than $\sim 75 \mu\text{m}$.

In order to further verify the cubic dependence of melt carry-over on clearance, the data of Fig. 3 was replotted on a log-log scale, shown in Fig. 4. The solid line is a least squares fit to the data and yields an exponent of 3.8. If the fit is performed setting the exponent to 3 and allowing only the pre-exponential factor to vary, the dashed curve is obtained. Although the scatter of the experimental points does not allow a clear determination of the exponent, the agreement with the theoretical model is fair. Furthermore, the value of P_c determined from the pre-exponential factor corresponding to the dashed line was calculated to be $-1.2 \times 10^3 \text{ dyn/cm}^2$, in reasonable agreement with the previous determination from melt height data.

Until now, the theoretical model and results presented have been for planar substrates such as those used for LPE growth of double heterostructure wafers. However, another important application of LPE is the regrowth step used in fabrication of buried heterostructure lasers (3). In this case, the substrate has nonplanar etched features (mesas) present on the substrate which can influence melt carry-over. Shown in Fig. 3 is a plot of melt carry-over *vs.* clearance data for $6 \mu\text{m}$ -high etched mesa substrates (triangles) compared to the previously presented planar substrate results. In addition, points corresponding to single epilayers which exhibited meniscus lines are also presented (squares). These data suggest that surface morphology can significantly increase the melt carry-over in the clearance region below $\sim 75 \mu\text{m}$. In terms of the theoretical model, this can be attributed to the effects of surface tension and surface wetting. Because

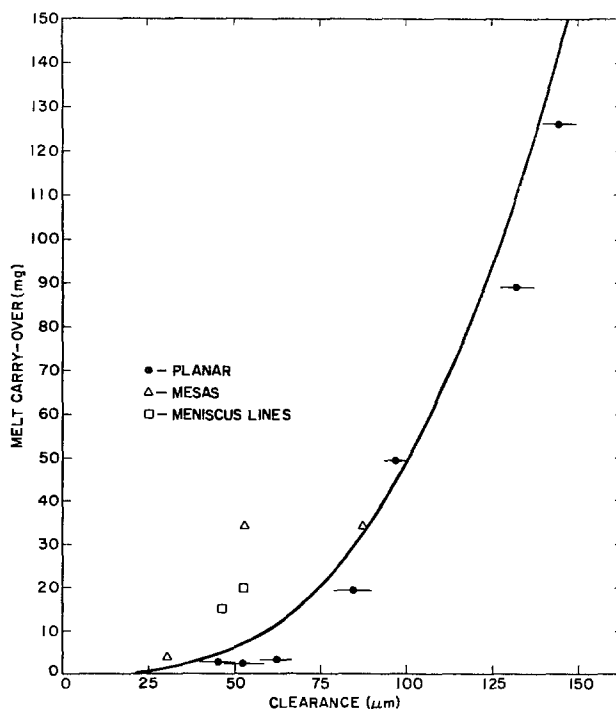


Fig. 3. Plot of melt carry-over *vs.* clearance for a single Zn-doped InP layer on planar and nonplanar [100] InP substrates. The solid line is the relationship predicted from Eq. 10 for planar substrates. The typical error bar on the clearance was $\pm 3 \mu\text{m}$ for these experiments.

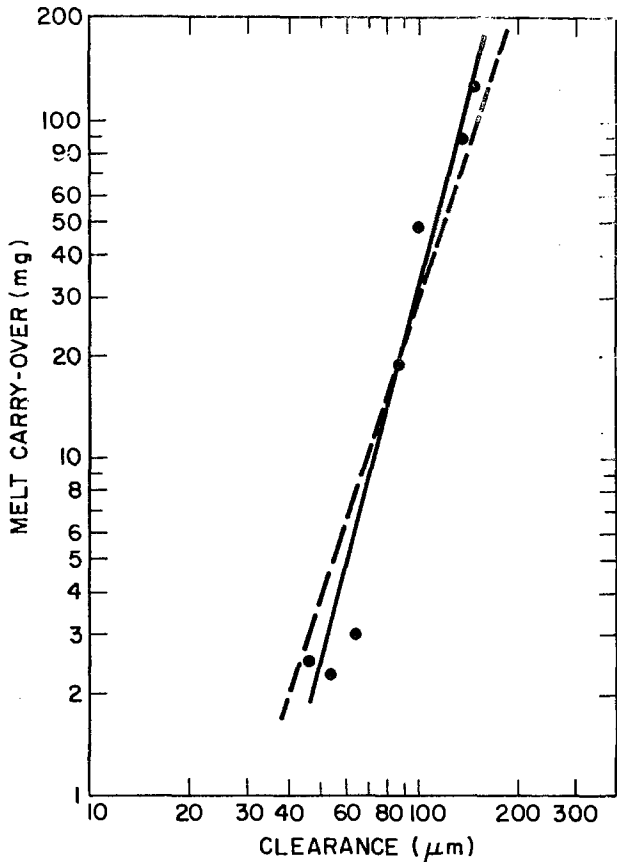


Fig. 4. Log-log plot of melt carry-over vs. clearance. Solid line is a least squares fit to the data allowing the exponent and pre-exponential factor to vary. The dashed line is a least squares fit with the exponent fixed at 3.0. The typical error bar on the clearance for these experiments was $\pm 3 \mu\text{m}$.

nonplanar surface features will in general enhance the surface wetting, $|P_c|$ will be reduced, resulting in more carry-over. This can also be interpreted as "edge-effects," where etched surface features act as excess edges on the surface of the wafer. It can also be expected that other perturbations of surface morphology, such as roughness created during meltback, might significantly enhance melt carry-over (2).

Because Eq. [10] predicts a variation in melt carry-over with push speed S , the influence of this parameter was also investigated experimentally, and the results for planar wafers are shown in Fig. 5 for a constant melt height of 0.47 cm and clearance of $51 \mu\text{m}$. A least squares fit to

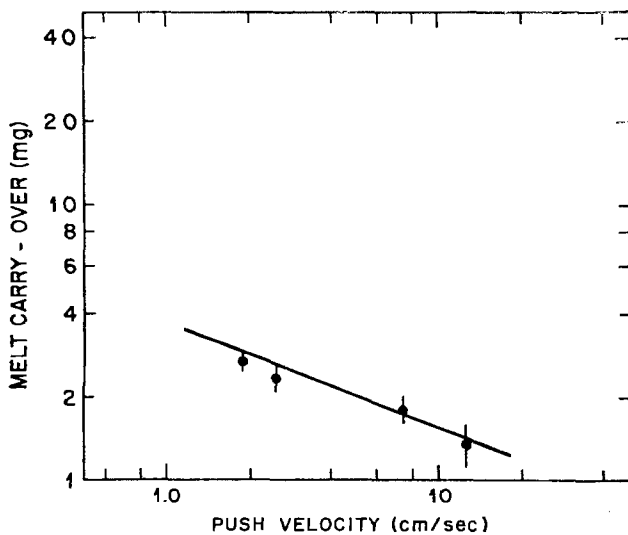


Fig. 5. Log-log plot of carry-over vs. push speed

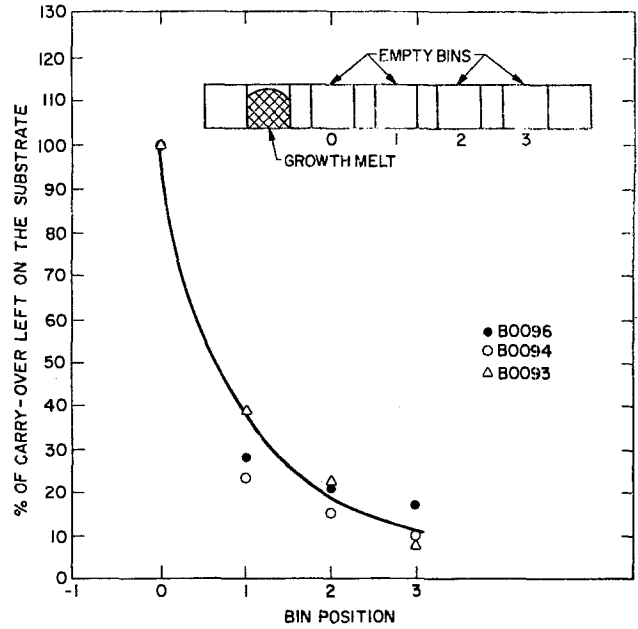


Fig. 6. Plot of relative decrease in carry-over left on the substrate vs. successive empty bin number for three different growth runs.

these data gives an exponent of -0.31 . Although this value is substantially different than the value of -1.0 predicted by Eq. [10], the trend of decreasing carry-over with increasing push speed is qualitatively in agreement. This discrepancy may be due to wafer edge effects, or possibly to dynamic surface wetting effects (13). In any case, the push duration time, determined by L/S , is an important variable in carry-over phenomena and should be taken into consideration when wafer area is "scaled up."

Another phenomenon, which we describe as a wipe-off effect, was noticed during the course of these experiments. It was found that for a given amount of melt carry-over left on the wafer after leaving the melt, this material was wiped off the surface as the wafer was pushed through empty melt bins at the push velocity. After the run, small quantities of residual wiped-off melt were found in these empty bins. These quantities were collected for each empty bin following the growth melt bin and were weighed. It was found that the amount left in each well decreased for successive empty bins away from the grown melt. These data are plotted in Fig. 6. The explanation for this wipe-off effect is that as the wafer leaves the growth melt, the carried-over melt, no longer constrained by the clearance space, collects into approximately hemispherical balls because of surface tension effects. As the wafer continues through the empty bin, these balls are sheared off at the opposing bin wall. This process is then repeated in successive empty bins. This suggests an effective melt carry-over removal scheme, which would be to have a series of slots on the underside of the graphite boat adjacent to the wafer, as shown in Fig. 7. Provided that the spacing and width of these slots

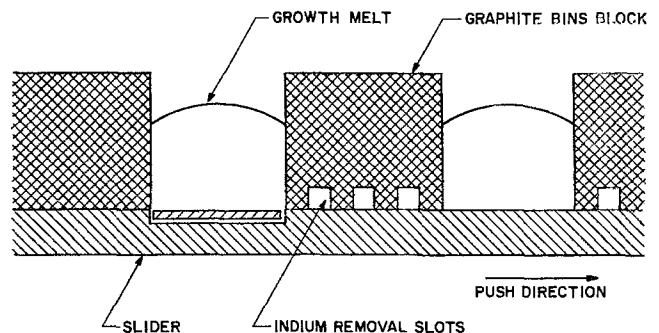


Fig. 7. Schematic diagram of proposed graphite boat designed to reduce melt carry-over.

is large enough to allow relaxation of the melt carry-over into balls, these slots will trap the residual melt and remove it from the wafer surface.

Conclusions

It has been shown that melt carry-over phenomena can be successfully modeled by a fluid flow mechanism which is driven predominantly by a pressure head originating from the growth melt. The degree of melt carry-over can be influenced by melt height, clearance, melt composition, push speed, and surface morphology. Because small values of melt height result in reduced carry-over, it is concluded that confined melts that do not maintain any additional pressure head should be effective in controlling carry-over. In addition, narrow clearances, fast push speeds, and smooth surface morphologies also result in reduced carry-over. Finally, a boat design has been proposed which should reduce carry-over effects via a geometrical shearing effect.

Acknowledgments

The authors acknowledge the excellent technical assistance of S. G. Napholtz and S. Maynard and acknowledge several informative discussions with S. Y. Leung, D. P. Wilt, and P. D. Wright.

Manuscript submitted March 12, 1984; revised manuscript received Aug. 15, 1984.

AT&T Bell Laboratories assisted in meeting the publication costs of this article.

REFERENCES

1. H. C. Casey, Jr., and M. B. Panish, "Heterostructure Lasers," Academic Press, New York (1978).
2. S. Mahajan, D. Brasen, M. A. DiGiuseppe, V. G. Keramidis, H. Temkin, C. L. Zipfel, W. A. Bonner, and G. P. Schwartz, *Appl. Phys. Lett.*, **41**, 266 (1982).
3. R. J. Nelson, R. B. Wilson, P. D. Wright, P. A. Barnes, and N. K. Dutta, *IEEE J. Quantum Electron.*, **17**, 202 (1981).
4. P. Besomi, R. B. Wilson, and R. J. Nelson, *This Journal*, **132**, 176 (1985).
5. P. Besomi, R. B. Wilson, J. Degani, and R. J. Nelson, Paper 332 presented at The Electrochemical Society Meeting, San Francisco, CA, May 8-13, 1983; P. Besomi, J. Degani, W. R. Wagner, N. K. Dutta, and R. J. Nelson, *J. Appl. Phys.*, (1984).
6. W. F. Hughes, "An Introduction to Viscous Flow," p. 20, Hemisphere Publishing Corp., Washington (1979).
7. "Reactor Handbook," 2nd ed., C. R. Tipton, Jr., Editor, p. 996, Interscience Publishers, New York (1960).
8. J. J. Bikerman, "Physical Surfaces," p. 20, Academic Press, New York (1970).
9. V. B. Lazarev, *Zh. Fiz. Khim.*, **38**, 325 (1964).
10. M. C. Tamargo Personal communication; C. L. Reynolds, Jr., and M. C. Tamargo, *J. Appl. Phys.*, **53**, 9217 (1982).
11. V. B. Lazarev, *Zh. Fiz. Khim.*, **38**, 39 (1964).
12. V. B. Lazarev, *ibid.*, **38**, Chap. II & VI (1964).
13. A. V. Grosse, *J. Inorg. Nucl. Chem.*, **23**, 333 (1961).
14. A. A. Bergh, R. H. Saul, and C. R. Paola, *This Journal*, **120**, 1558 (1973).

Investigation of Melt Carry-Over during Liquid Phase Epitaxy

II. Growth of Indium Gallium Arsenic Phosphide Double Heterostructure Material Lattice-Matched to Indium Phosphide

P. Besomi,^{*2} R. B. Wilson,¹ and R. J. Nelson¹

AT&T Bell Laboratories, Murray Hill, New Jersey 07974

ABSTRACT

The effects of indium melt carry-over were investigated during liquid phase epitaxy (LPE) growth of InGaAsP double heterostructure (DH) material lattice-matched to InP substrates. Compositional and thickness variations associated with melt carry-over were studied as a function of the clearance between the substrate and the graphite boat. Moreover, x-ray lattice-constant measurements, as well as photoluminescence spectrum analysis, showed that meltback of the substrate prior to growth may lead to enhanced indium melt carry-over. Finally, broad area lasers were fabricated, and it was shown that enhanced indium melt carry-over led to nonlasing devices. A study of secondary ion mass spectroscopy (SIMS) profiles for the major constituents of DH material showed that indium melt carry-over adversely affects interface abruptness and subsequent device performance.

A major problem encountered in liquid phase epitaxy (LPE) is the carrying of melt solution from one growth well to the next, induced by the movement of the substrate. This carry-over phenomenon can affect important material parameters such as epitaxial layer thickness, lattice mismatch, and layer composition. These effects are especially deleterious in the case of LPE growth of InGaAsP double heterostructure (DH) material closely lattice-matched to InP substrates, because binary InP melt carried over into adjacent quaternary or ternary solutions can modify such critically melt-composition-sensitive solutions. If not corrected, melt carry-over can potentially reduce LPE yield because of the reduced available wafer area having the desired material characteristics.

In Part I of this study (1), melt carry-over was investigated for the LPE growth of InP layers grown on InP substrates. For this binary material, a theoretical model was developed which adequately describes experimental data. The most significant feature of our model is its prediction of melt carry-over as a function of melt height,

melt composition, push speed, and clearance. In particular, melt carry-over is a cubic function of clearance, giving rise to a drastic increase in carry-over for clearances greater than $\sim 75 \mu\text{m}$. By utilizing this dependence on clearance, it is possible to vary melt carry-over in a well-defined manner and systematically investigate the influence of melt carry-over on critical DH material characteristics such as layer thickness, composition, and lattice mismatch. The purpose of this work is therefore to evaluate effects of clearance control upon DH material and device characteristics during LPE growth. It is shown that increasing clearance and, hence, increasing melt carry-over lead to variations in active layer wavelength, lattice mismatch, and increased broad-area threshold current densities, all of which have a negative effect on devices fabricated from this type of DH material. In addition, it will be shown that interface properties and dopant profiles are also adversely affected. Finally, practical solutions for reducing or eliminating melt carry-over will be discussed.

Experimental

In the experiments reported here, the LPE growth was carried out in a palladium-diffused hydrogen ambient. A multiwell graphite boat (see Fig. 1) held the various

*Electrochemical Society Active Member.

¹Present address: Lytel, Inc., Bridgewater, New Jersey 08807.

²Present address: Lasertron, Inc., Burlington, Massachusetts 01803.

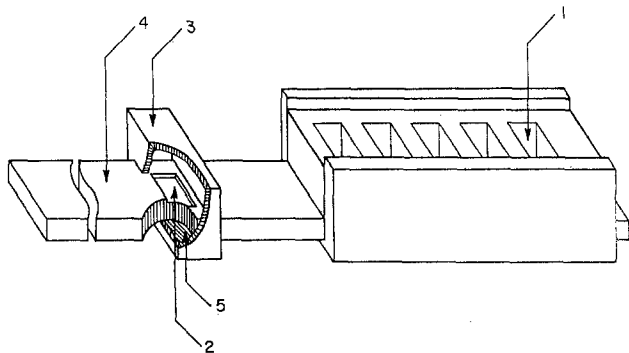


Fig. 1. Schematic of an LPE boat assembly. 1) indium melt well; 2) InP substrate; 3) graphite chambers; 4) graphite slider; 5) Sn-In-P solution.

growth solutions, and a graphite slider transported the InP substrate from one growth melt to the next. A combination of boat assembly clamping by recessed walls and graphite plugs, in addition to a tight machining tolerance, lead to no more than $\pm 25 \mu\text{m}$ clearance variation between the graphite slider and the graphite boat. This corresponded to an improvement of the boat design, compared to the design discussed in another work (2).

In order to eliminate the decomposition of the InP substrate before growth due to phosphorus evaporation, a graphite chamber (see Fig. 1) external to the LPE boat assembly and containing a Sn-In-P solution was used (3). The near-equilibrium LPE growth method developed by Nelson (4) was used: undoped InP, GaAs, and InAs pieces were weighed and were added to 99.9999% pure indium melts baked for at least 14h at 720°C in hydrogen. At the end of the typical growth procedure, the wafer was pushed under the end part of the graphite block until the boat was cooled to 300°C to limit thermal degradation of the epitaxial layers and then was pushed out of the boat.

The substrates used were sulfur-doped [100] InP having a dislocation etch-pit density less than 10^3 cm^{-2} . They were etched in a solution of $\text{H}_2\text{SO}_4:\text{H}_2\text{O}_2:\text{H}_2\text{O}$ (10:1:1 concentration) and thoroughly rinsed in deionized water prior to growth. The typical structures consisted of either a Sn-doped InP buffer layer ($3\text{--}4 \mu\text{m}$ thick, $n \sim 2 \times 10^{18} \text{ cm}^{-3}$) and an unintentionally doped InGaAsP layer ($E_g = 0.95 \text{ eV}$, $0.5 \mu\text{m}$ thick, $n \sim 5 \times 10^{16} \text{ cm}^{-3}$) or of a p-InP buffer layer ($2.5 \mu\text{m}$ thick, $p \sim 1 \times 10^{17} \text{ cm}^{-3}$) and a p^+ top-layer InGaAs ($E_g = 0.75 \text{ eV}$, $0.5 \mu\text{m}$ thick, $p \geq 3 \times 10^{19} \text{ cm}^{-3}$). The various layer thicknesses were determined using a scanning electron microscope (SEM), and the doping levels reported here were calculated from the atomic fraction of the dopants in the growth solutions (5), as well as from Hall measurements.

The photoluminescence (PL) measurements were performed using a CW YAG laser or an Argon laser for excitation and using a grating monochromator to resolve the PL spectrum (6). The mismatch of the epitaxial layers was determined by x-ray diffraction measurements of the wafer curvature, with $\bar{g} = \langle 511 \rangle$ or $\langle 422 \rangle$ as the operating reflection. Secondary ion mass spectroscopy (SIMS) analysis was performed to determine the interface profile of the major constituents and to detect the possibility of dopant diffusion (7).

Results and Discussion

The most obvious effect related to melt carry-over is certainly the presence of an indium-rich alloy, usually at the trailing edge of the wafer, after the run is completed. Shown in Fig. 2 is a plot of indium melt carry-over, as determined by the weight increase of the wafers after growth, vs. clearance. These results were corrected for the grown layers' weight contribution. The push speed used was approximately 5 cm/s , similar to the one used in Part I for the study on InP (1). The observed nonlinear increase in melt carry-over is similar to that previously described in Part I for InP (1). However, the ternary $\text{In}_{0.53}\text{Ga}_{0.47}\text{As}$ alloy exhibits a slightly stronger dependence on clearance than the $1.3 \mu\text{m}$ wavelength InGaAsP alloy,

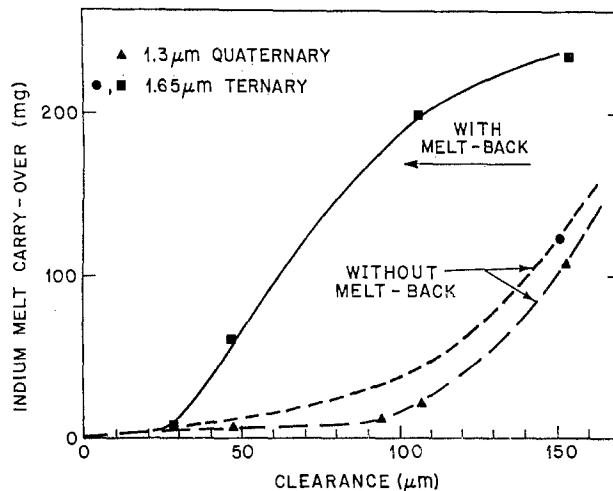


Fig. 2. Plot of the amount of indium melt carry-over vs. the clearance between the substrate and the graphite boat, for ternary (using meltback prior to growth) and quaternary (without meltback) epitaxial layers. The labeled point corresponds to ternary growth without a meltback.

as evidenced by the increased indium melt remaining on the wafer (dotted line in Fig. 2). Such composition dependence of melt carry-over is consistent with the model developed in Part I (1).

Another phenomenon which may affect melt carry-over is surface roughness. In fact, improper melt composition due to melt carry-over may also lead to surface roughness and thus enhance the melt carry-over itself. A common manifestation of excessive melt carry-over is the presence on the wafer of cross hatching dislocation patterns (8). Eliminating surface roughness is therefore an important consideration in LPE reproducibility. It has been observed that melt carry-over is reduced in the case of the ternary growth when meltback of the substrate prior to growth of the first layer is avoided (see Fig. 2). These results further demonstrate the advantages of eliminating substrate thermal degradation prior to growth and, thus, the meltback usually associated with improper substrate protection schemes (3). Along with the drastic increase in melt carry-over for large clearances, our study suggests that clearances of $50 \mu\text{m}$ or less should be used and that the commonly used meltback technique should be avoided.

Another effect related to melt carry-over is the control of epitaxial layer thickness. Layer thickness results are listed in Table I for a series of consecutive LPE runs in which clearance increased from 30 to $160 \mu\text{m}$. The thickness of the binary InP layers does not significantly vary. Such results are also compared in Table II with expected changes of melt supersaturation. Since the amount of phosphorus carried over to the next melt does not significantly modify the supersaturation of the following binary melt composition, no effect on layer thickness should be expected. Moreover, in the case of the $1.3 \mu\text{m}$ wavelength quaternary alloy, the thickness variation is not significant, although the melt supersaturation increases a few centigrade degrees because of InP melt carry-over (see Table II). Only for very large changes in melt composition will the layer thickness increase.

The effects of melt carry-over are more dramatic for the ternary layers. In the case of ternary growth it was observed that the trailing area of the wafers were covered by

Table I. Epitaxial layer thickness for increasing substrate clearance

Clearance (μm)	InP layer (μm)	InGaAsP layer (μm)	InGaAs layer (μm)	"Postgrowth" InGaAs layer (μm)
30	1.2	0.5	1.3	None
100	1.3	0.5	2.4	1.6
160	1.2	0.5	3.0	2.7

Table II. Change in LPE melts supersaturation for increasing substrate clearance

Melt	Indium mole fraction (%)	Phosphorus mole fraction (%)	Arsenic mole fraction (%)	Gallium mole fraction (%)
Binary InP melt, without melt carry-over	0.993906	0.006094	0.0	0.0
Binary InP melt with 60 mg InGaAsP melt carry-over	0.993198	0.006236	0.000486	0.000080

a second epitaxial layer much thicker than the original layer present on the whole wafer. This feature can again be explained by the presence of an indium melt thinly spread over the wafer during the cooling down phase, from which a "postgrowth" layer up to 3 μm thick grows after the scheduled run is over (9). By pushing the wafer out of the graphite boat, using a long graphite slider, immediately after completion of the growth, it was noted that the postgrowth ternary layer was eliminated, although In-rich droplets remained on the trailing edge of the wafer. Finally, similar questions may arise for the effects of melt carry-over from the 1.3 μm wavelength quaternary alloy into the InP binary melt. Table II indicates that the change of InP binary melt composition due to melt carry-over of 60 mg of InGaAsP melt has a negligible effect on melt composition. Only the phosphorus content increases, by almost 5%, corresponding to an increase of 0.2°C in the supersaturation of the melt.

These various layers were also characterized by photoluminescence. As shown in Fig. 3, the composition of 1.3 μm quaternary layers is not sensitive to the change of melt composition because of the indium melt carry-over (less than 1% change in the bandgap for a 160 μm clearance related to less than 3×10^{-4} change in arsenic mole fraction of the melt). However, the InGaAs ternary layers exhibit two features. First, the photoluminescence wavelength decreases from 1.665 to 1.623 μm , indicating a slow change in the alloy composition containing an increasingly large amount of phosphorus. Second, the postgrowth ternary layer grown over the original ternary layer during the cool-down phase has a much longer wavelength, 1.698-1.703 μm . This indicates that it is an InAs-rich ternary layer which grows during cool-down, because the bandgap of InAs is only 0.35 eV (9) smaller than the one of GaAs.

Figure 4 shows the plots of the lattice mismatch $\Delta a/a$ determined by x-ray diffractometric measurements for the quaternary and ternary layers. It is noted that the lattice mismatch remains small for the quaternary layer, even when the indium melt carry-over is large. However,

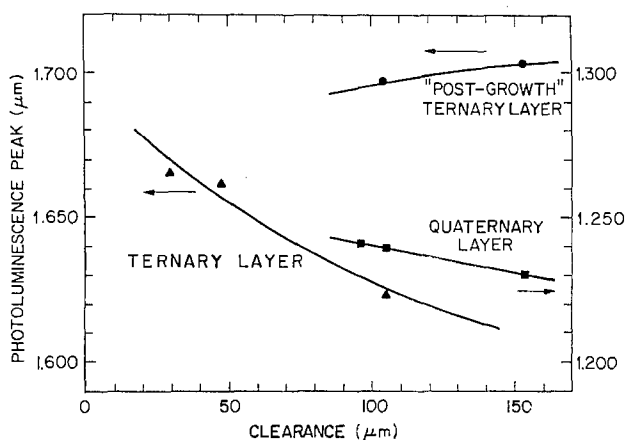


Fig. 3. Plot of the photoluminescence spectrum shift vs. substrate clearance for ternary and quaternary epitaxial layers.

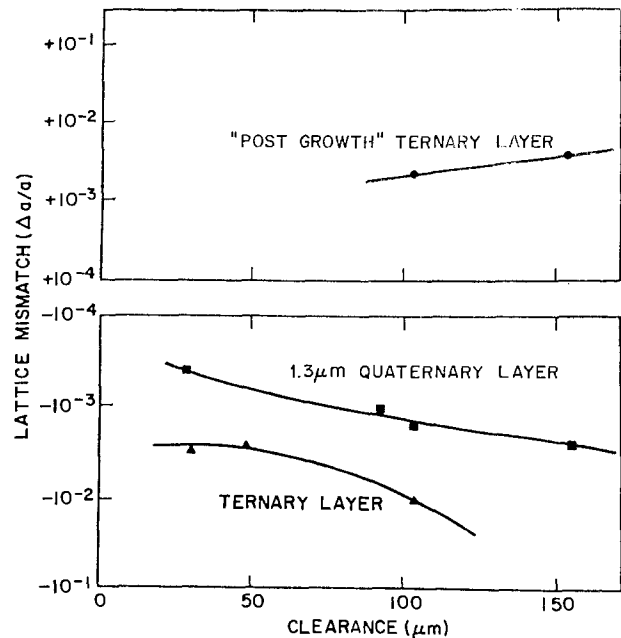


Fig. 4. Plot of the lattice mismatch $\Delta a/a$ vs. substrate clearance for ternary and quaternary epitaxial layers.

for a clearance larger than 50 μm , the mismatch $\Delta a/a$ is more than -5×10^{-4} , an upper limit for device applications (10). For the ternary layers, the mismatch of the original ternary layer increases to very large values (nearly $\sim 10^{-2}$, from Fig. 4) because of the addition of phosphorus to the melt, as pointed out earlier. Moreover, the trailing edge postgrowth layer is heavily mismatched by up to $+4.2 \times 10^{-2}$ with a lattice larger than the one of InP. This result again suggests that the postgrowth layer is InAs-rich, because the lattice of the InGaAs ternary increases when the alloy tends towards the InAs composition.

Finally, this study of the effects of indium melt carry-over during LPE growth was completed by analyzing its consequences on InP/InGaAsP DH lasers. The typical laser structure was described earlier (11), and the clearance used during DH growth was varied between 20 and 160 μm . The broad-area laser thresholds reported in Table III for devices with identical active layer thicknesses of 0.2 μm also indicate that large clearance should be avoided. The influence of melt carry-over on the active layer properties was further investigated in order to ascertain the sensitivity of the electrical properties of DH lasers on growth procedure, possible constituent segregation, or dopant diffusion. In Fig. 5a, the SIMS profile of phosphorus and arsenic shows a marked decrease in the interface abruptness of sample F1664, which did not lase and was grown with a wipe-off clearance of 160 μm , as compared to sample F1669 (1.3 kA/cm² threshold), grown with a wipe-off clearance of 25 μm . Similar results were obtained in Fig. 5b for gallium. Moreover, it is seen from Fig. 5b that zinc diffusion into the quaternary active layer from the p-InP cladding layer was more pronounced in the case of sample F1664. The enhanced zinc diffusion observed here for the sample grown with the 160 μm clearance is probably the result of a high concentration of interface defects in this poorly lattice-matched layer.

Table III. Broad-area threshold current density for increasing substrate clearance

Sample	Broad-area lasers threshold (kA/cm ²)	Clearance (μm)
F1662	2.0	50
F1663	1.8	50
F1664	Did not lase	160
F1667	1.5	20
F1668	1.4	25
F1669	1.3	25

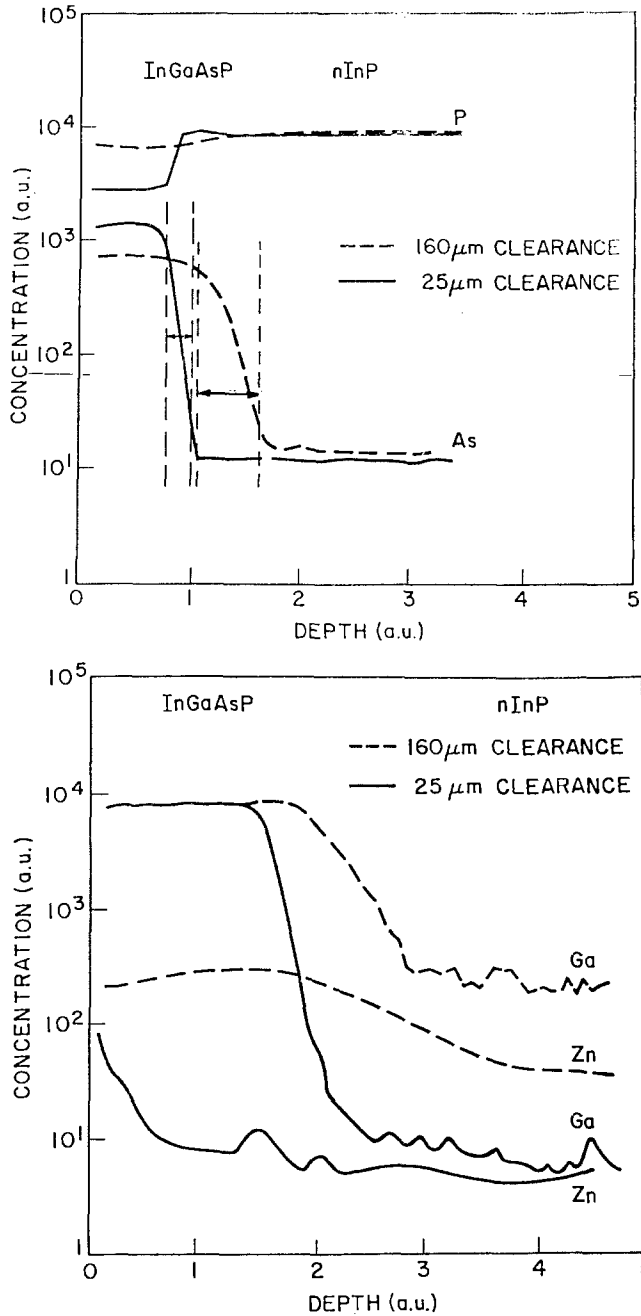


Fig. 5. SIMS profile of: a, top) phosphorus and arsenic; b, bottom) gallium and zinc dopant at the interface of InGaAsP/n-InP DH material. The dashed lines represent the interface widths as determined from these data.

Conclusions

It has been shown that indium melt carry-over during LPE growth of InP/InGaAsP DH material is enhanced by large clearances between the substrate and the graphite boat. Not only is the available wafer area reduced in size because of remaining indium melt, but layer thicknesses, compositions, and lattice mismatches are also adversely affected by melt carry-over. The results of this study therefore indicate that (i) indium melt carry-over usually increases as substrate clearance increases and as melt-back is used, and (ii) increased indium melt carry-over has a deleterious effect on InP/InGaAsP DH material lasing properties because important materials characteristics (such as lattice match, interface abruptness, and doping level) deteriorate.

This study suggests that the use of an improved boat design ensures that good control of clearance between substrates and graphite block can be maintained during LPE growth and that melt carry-over can be eliminated. And finally, the broad area threshold of DH lasers increases because melt carry-over leads to mismatched layers, less abrupt interfaces, and enhanced zinc diffusion into the active layer.

Acknowledgments

The authors thank S. G. Napholtz and R. G. Sobers for their technical assistance with the LPE growth, as well as W. R. Wagner and S. M. Woelfer for x-ray measurements.

Manuscript submitted March 12, 1984; revised manuscript received Aug. 15, 1984.

AT&T Bell Laboratories assisted in meeting the publication costs of this article.

REFERENCES

1. R. B. Wilson, P. Besomi, and R. J. Nelson, *This Journal*, **132**, 172 (1985).
2. P. Besomi, R. B. Wilson, J. Degani, and R. J. Nelson, Paper 332 presented at The Electrochemical Society Meeting, San Francisco, CA, May 8-13, 1983.
3. P. Besomi, R. B. Wilson, W. R. Wagner, and R. J. Nelson, *J. Appl. Phys.*, **54**, 535 (1983).
4. R. J. Nelson, *Appl. Phys. Lett.*, **35**, 654 (1979).
5. M. G. Astles, F. G. H. Smith, and E. W. Williams, *This Journal*, **120**, 1750 (1973).
6. J. Degani, P. Besomi, D. P. Wilt, R. J. Nelson, and R. B. Wilson, *J. Appl. Phys.*, **54**, 7114 (1983).
7. SIMS analysis performed by Charles Evans and Associates, San Mateo, CA 94402.
8. G. H. Olsen, *J. Cryst. Growth*, **31**, 223 (1975).
9. Y. Takeda, Y. Imamura, and A. Sasaki, *ibid.*, **46**, F5 (1978).
10. G. H. Olsen, C. J. Nuese, and M. Ettenberg, *IEEE J. Quantum Electron.*, **qe-15**, 688 (1979).
11. P. Besomi, J. Degani, W. R. Wagner, N. K. Dutta, and R. J. Nelson, *J. Appl. Phys.*, (1984).

Mechanism of Dry Etching of Silicon Dioxide

A Case of Direct Reactive Ion Etching

Ch. Steinbrüchel, H. W. Lehmann,* and K. Frick

Laboratories RCA Limited, CH-8048 Zürich, Switzerland

ABSTRACT

Reactive sputter etching of SiO₂ with CHF₃-O₂ plasmas has been investigated in a parallel-plate reactor by combining etch-rate measurements with concurrent determination of ion densities (using a Langmuir probe) and the composition of neutral plasma species (using a mass spectrometer), and by examining etched profiles in the SEM. The importance of geometrical variables, such as plate separation and plate area, and the electrical parameters appropriate for characterizing the discharge are discussed. Etch rates are found to follow the ion density and to be fairly independent of the plasma chemistry under most experimental conditions. Moreover, a comparison of reactive sputter etching and reactive ion beam etching of SiO₂ with CHF₃ and CF₄ shows that etch yields per incoming ion are essentially independent of the flux of neutral radicals to the substrate. This strongly suggests as the dominant etch mechanism for SiO₂ direct reactive ion etching, where ions themselves are the main reactants in the etch reaction. Measured etch yields are consistent with this picture. However, the plasma chemistry has a decisive influence on the etch rate of Si, and thus on the etch selectivity of SiO₂ with respect to Si, and also on the exact shape of profiles etched into SiO₂.

One of the many steps in the production of large-scale integrated devices involves delineating fine patterns in thin films of various materials by plasma processing. In silicon-based technology, two of the main materials of interest are Si, as the active medium, and SiO₂, as a compatible insulator. Thus, in order to control the manufacturing process properly one needs to address two key issues: how to etch profiles with a desired shape into the two materials, and how to etch them selectively with respect to each other.

As regards etching of SiO₂, we showed in our early investigations, using SEM micrographs, that it is quite possible to etch well-defined square wave profiles with submicron dimensions (1, 2). In another publication, it was demonstrated that the directionality of the incoming ions plays a crucial role in defining the actual etch profiles (3). In addition, etch rates were shown to be enhanced significantly by ion impact (4, 5, 30). Heinecke (6) and Ephrath (7) pointed out that maximum selectivity for SiO₂ with respect to Si could be obtained in fluorine-deficient plasmas. But it was also realized that, whenever the C/F ratio increased beyond a certain critical point (the polymer point), deposition of polymers occurred on chamber walls and even on SiO₂ surfaces (8). Thus one must work in a relatively limited regime in terms of gas composition and pressure in order to obtain maximum selectivity and a minimum of polymer deposition.

A large number of publications has appeared since, describing etch processes with a variety of gases (CHF₃, CF₄ + H₂, C₃F₈, etc.), reactors, and processing conditions. Whereas in general the reported etch rates are similar, the exact gas composition at which polymerization occurs, the selectivity, and the shape of etched profiles often differ slightly from paper to paper. In addition, a variety of contamination effects has been observed. Thus, although dry etching of SiO₂ is used in almost all IC manufacturing lines, its fundamentals are still rather poorly understood. This is quite in contrast to dry etching of Si, for which numerous studies have revealed many details about the relevant etch mechanisms [see e.g., Ref. (9, 10)].

It is the purpose of this paper to elucidate the mechanisms giving rise to anisotropic etching of SiO₂. To this end, we have investigated the relationships between reactor geometry, gas composition, and ion densities and energies in CHF₃-O₂ plasmas and how they affect etch rates, anisotropy, and selectivity. Our investigation is based on etch rate measurements with concurrent mass spectrometry, Langmuir probe measurements (to determine ion densities), and scanning electron microscopy of etched profiles.

Experimental Arrangement

The reactor used in this study is essentially the same as described before (11) but with a few modifications (Fig.

1). The vacuum chamber is made of stainless steel, 42 cm diam, and 24 cm height. The RF-driven copper cathode is of 20 cm diam and, except where noted otherwise, is covered with an SiO₂ plate. A copper tape around the vertical edge of the SiO₂ plate provides sufficient electrical contact between the plasma and the cathode to make possible reliable measurements of the RF-induced dc bias voltage. Opposite to the cathode, a movable grounded Al plate of equal diameter is mounted so that the reactor configuration can be changed continuously between a symmetrical parallel-plate and a so-called reactive-sputter-etch geometry (with the top plate removed). A differentially pumped mass spectrometer (UTI 100C) is connected to the side of the chamber. The background pressure in the mass spectrometer is about 1×10^{-7} torr (1.3×10^{-5} Pa), and during etching a pressure ratio of about 10^3 can be maintained between the plasma chamber and the mass spectrometer. Data acquisition is computer controlled and allows the rapid recording of either entire mass spectra or only selected mass peaks of neutral plasma species (12). With the movable Langmuir probe the dc current to the probe *vs.* the applied voltage is measured as a function of the probe position within the plasma. From such measurements spatially resolved ion densities and electron temperatures can be inferred, as described before (13). Etch rates are determined interferometrically *in situ*, using a He-Ne laser.

Results

With the results described below, we wish to address four issues important for the etching of SiO₂ in CHF₃, the goal being a better understanding of the factors determining etch rate, anisotropy, and selectivity. First, we study the effect of changing the reactor geometry, especially the separation of the parallel plates, on the discharge characteristics. We then examine etch rates in pure CHF₃ and CHF₃-O₂ mixtures, specifically in relationship to plasma ion densities and to changes in the composition of neutral plasma species. Finally, we show that on this basis one can understand slight variations in the shape of etched profiles and, in particular, the conditions for perfect anisotropic etching.

Geometrical effects.—It is generally recognized that the geometry of a reactor affects a discharge sustained therein, and thus the etching by that discharge, in rather unpredictable ways. We have investigated systematically one aspect of this problem, *i.e.*, the effect of the plate separation in a reactive sputter etch system with parallel-plate geometry (Fig. 1). Figure 2 shows the RF power P dissipated (really the forward power read on the RF power supply, with the system tuned well) as a function of the peak-to-peak voltage V_{RF} at various plate separations, while gas pressure and flow rate are being held constant. Clearly, P is always proportional to V_{RF} , but the

*Electrochemical Society Active Member.

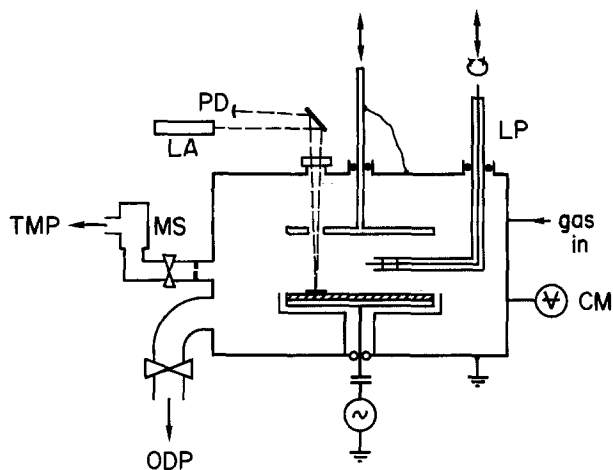


Fig. 1. Schematic diagram of parallel plate reactor. LP: Langmuir probe (movable vertically and horizontally). LA: He-Ne laser. PD: photo diode. MS: quadrupole mass spectrometer. TMP: turbo molecular pump. ODP: oil diffusion pump. CM: capacitance manometer.

proportionality factor depends on the plate separation. Thus it is not obvious whether P or V_{RF} is the relevant parameter in establishing equivalent plasma conditions. We have found that in general etch rates R_e (and ion densities N_i) correlate better with P than with V_{RF} if the plate separation is varied. The same applies if the cathode material is changed. However, for a mistuned system it is V_{RF} which determines R_e (and N_i) rather than P or the difference between forward and reflected power.

Figures 3 and 4 show the spatial variation of the ion density N_i and the electron temperature T_e between the plates, along a line perpendicular to the plates in the center of the plasma. (We assume, in accord with mass spectrometric results, that the major ion in a CHF₃ plasma is CHF₂⁺). N_i is very small near the cathode, but rises rapidly through the dark space to a maximum, then decreases gradually up to the counterelectrode. At 20 mtorr, for plate separations smaller than about 5 cm the maximum of N_i is reduced and shifted towards the cathode, whereas for plate separations larger than about 5 cm the region of maximum N_i is unaffected by the plate separation. We also note that varying the power P changes the magnitude of N_i , but not the shape of its spatial distribution. In the horizontal direction, at 2 cm within the plate edge N_i is reduced by 25% as compared to its value in the center of the plasma.

Etch rates and ion densities.—First, we point out that at constant RF power and constant pressure of CHF₃ the

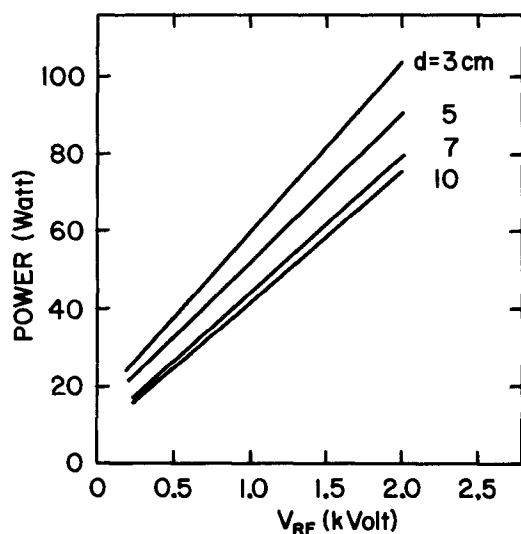


Fig. 2. RF power vs. peak-to-peak RF voltage for different plate separations. CHF₃ at 20 mtorr (flow rate = 30 sccm).

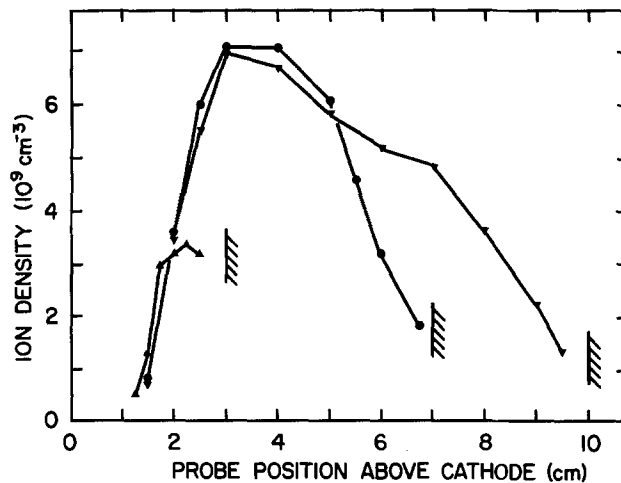


Fig. 3. Ion density vs. probe position in the center of a CHF₃ plasma for three different plate separations. $p = 20$ mtorr (flow rate = 30 sccm), RF power = 60W. Hatched symbols at the right end of the curves denote position of the upper plate.

etch rate of SiO₂ does not depend significantly on the plate separation as long as the plates are far enough apart to allow for a fully developed dark space (cf. Fig. 3). Hence, the results of this and the following sections were all obtained with the top plate removed.

Figure 5 shows etch rates R_e of SiO₂ vs. total pressure p in different CHF₃-O₂ mixtures. Here, the RF power and the flow rate of CHF₃ have been held constant. (At constant power V_{RF} decreases with increasing p). At low p , R_e increases with increasing p up to a maximum. The pressure at which R_e reaches its maximum is the higher the larger the O₂ content. The maximum value of R_e becomes smaller with larger O₂ content.

The ion density N_i in the plasma also varies with p , as shown for pure CHF₃ in Fig. 6. The maximum in N_i occurs closer to the cathode at higher p , which indicates a decreasing width of the dark space with increasing p (Fig. 6). The reason for this is, of course, the smaller mean free path for plasma collisions at higher p . The main point to note here is that the maximum value of N_i , $N_{i,max}$, follows closely R_e as a function of p (Fig. 7). For a CHF₃-O₂ mixture, $N_{i,max}$ and R_e also show qualitatively similar behavior vs. p , although the correspondence is not quite as good as with pure CHF₃ (Fig. 7).

Plasma chemistry.—In order to correlate the above results with changes in the composition of neutral plasma species, we tried two different methods of sampling the

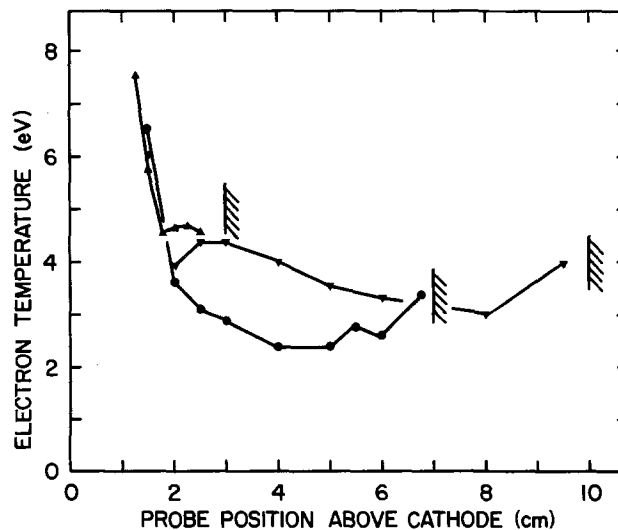


Fig. 4. Electron temperature vs. probe position. Same conditions as in Fig. 3. Hatched symbols at the right end of the curves denote position of the upper plate.

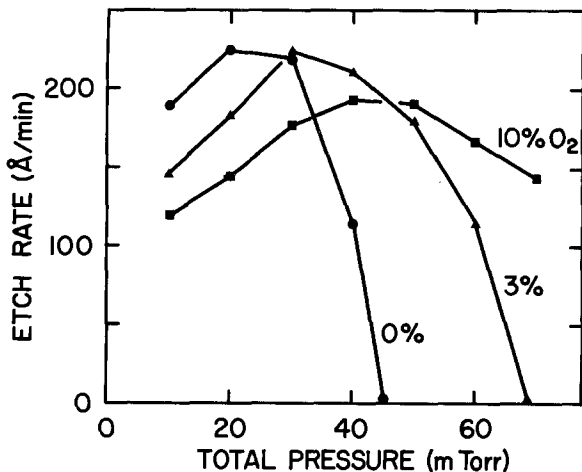


Fig. 5. Etch rate of SiO_2 vs. total pressure with three different CHF_3 - O_2 mixtures. CHF_3 flow rate = 30 sccm, RF power = 75W.

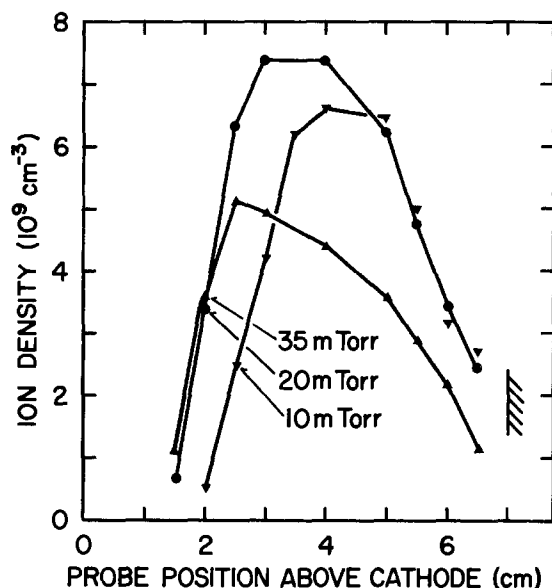


Fig. 6. Ion density vs. probe position in the center of a CHF_3 plasma for three different pressures. Flow rate = 30 sccm, RF power = 60W.

plasma: spatially resolved (in a direction perpendicular to the cathode) through a thin flexible tube, or spatially averaged through an orifice (Fig. 1), into the differentially pumped mass spectrometer chamber. However, in sampling with the tube we were unable to detect any spatial variations in the plasma composition of neutrals that would have paralleled those seen for the ions. Thus, the following remarks will refer to sampling through the orifice.

Figure 8 illustrates the behavior of some representative plasma species observed upon adding O_2 to a constant partial pressure of CHF_3 , at constant RF power. First we note that SiF_3^+ , as the main peak deriving from the reaction product SiF_4 , is easily detectable. With increasing O_2 content, both SiF_3^+ and the etch rate (cf. Fig. 5) decrease similarly, species arising from the parent molecule also decrease, whereas larger polymeric species are strongly suppressed. At the same time, oxygen bearing species increase continuously. A point of interest here is that the oxygen introduced into the plasma by etching the SiO_2 cathode with pure CHF_3 is equivalent, in our system, to the effect of adding about 1 sccm of O_2 in the gas phase. If the cathode material is Al, then no increase in the O bearing peaks results from turning on the plasma with pure CHF_3 , and the qualitative behavior of the various species upon addition of O_2 is the same as in Fig. 8.

Results for pure CHF_3 as a function of pressure (RF power constant) are given in Fig. 9, where differences in peak heights between the plasma-on and the plasma-off

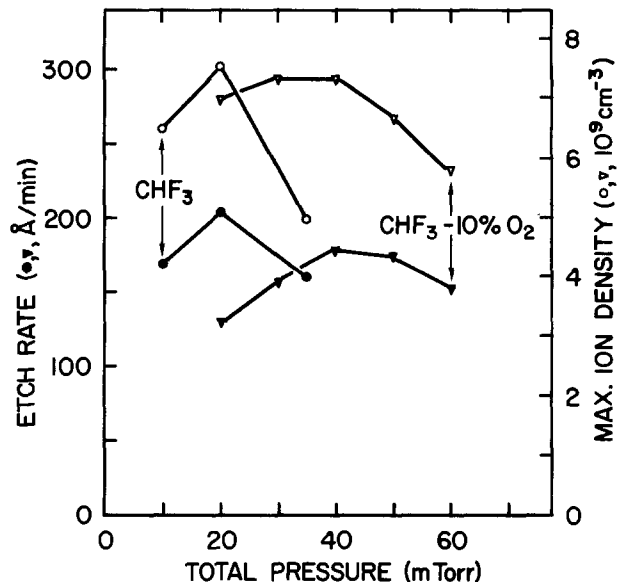


Fig. 7. Etch rate and maximum ion density vs. total pressure for CHF_3 and CHF_3 -10% O_2 plasmas. RF power = 60W.

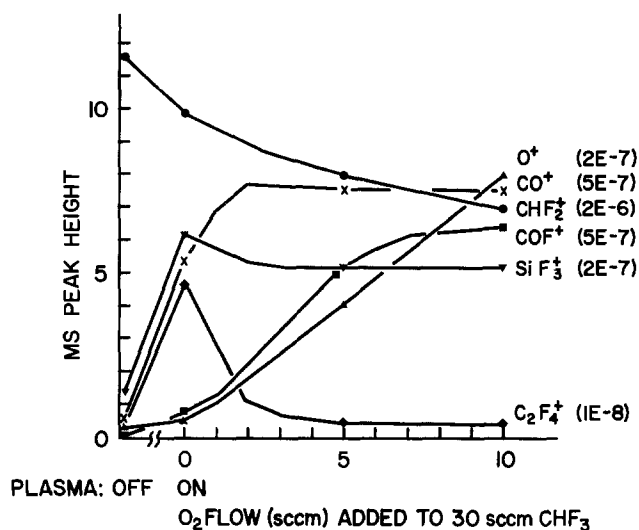


Fig. 8. Mass spectral data for neutral plasma species, ionized in the mass spectrometer, with O_2 added to CHF_3 . 10 units on the ordinate correspond to the full scale ion currents given in brackets. CO_2^+ (on the 2E-7 scale) and CO_3^+ (on the 5E-7 scale) show behavior identical to that of COF^+ . Larger polymers decrease more rapidly than C_2F_4^+ upon addition of O_2 . Partial pressure of CHF_3 is 20 mtorr. RF power = 75W.

condition are plotted. The dissociation of CHF_3 is clearly visible, amounting to 10% at 10 mtorr, and becomes somewhat more efficient as the pressure increases. Again, the SiF_3^+ peak height follows the same behavior as the etch rate R_e (cf. Fig. 5). So do the intensities of the CO^+ , CO_2^+ , COF^+ (or SiF^+), and COF_2^+ (or SiF_2^+) peaks. Beyond the point of maximum R_e (25 mtorr, cf. Fig. 5), a rapid increase of polymeric species (e.g., C_2F_4^+ , C_2HF_4^+ , etc.) is observed.

In CHF_3 - O_2 mixtures, generally similar results are obtained vs. total pressure, with the provision that etching proceeds to higher pressures as indicated by the SiF_3^+ peak (cf. Fig. 5), and that much larger amounts of such species as CO^+ , COF^+ , etc., are seen, presumably because of gas phase reactions between O atoms and CHF_3 -derived radicals (14) (see also Fig. 8).

With the etch rate of SiO_2 quite independent of minor variations in the plasma composition, the selectivity in etching SiO_2 over Si turns out to be largely a function of the Si etch rate. This is very sensitive to even minute amounts of O or Cl containing gaseous impurities, whether they are introduced directly with the etching gas or liberated by the plasma from the reactor walls or the

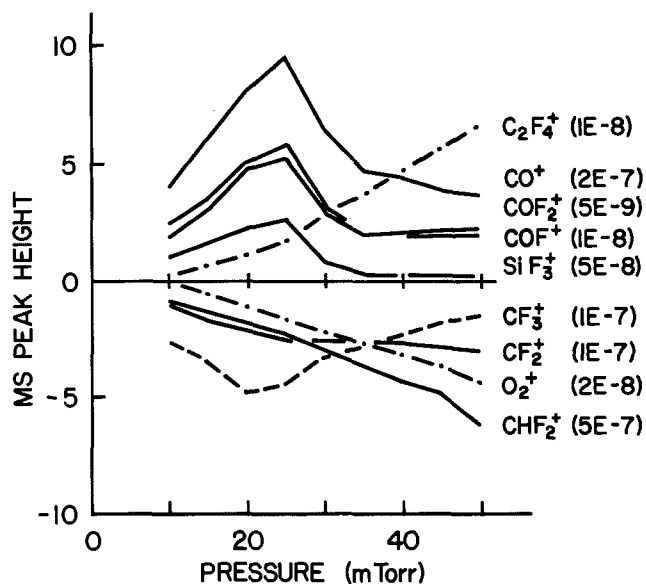


Fig. 9. Mass spectrum peak height differences between plasma-on and plasma-off condition vs. CHF_3 pressure. 10 units on the ordinate correspond to the full scale ion currents given in brackets. CO_2^+ (on the 2E-8 scale) shows behavior identical to that of COF^+ . RF power = 75W.

cathode. Such impurities invariably cause a significant increase in the etch rate of Si and thus a reduction in the selectivity.

Etched profiles.—In Fig. 10, we show a few profiles etched into SiO_2 under different conditions. The mask was a square wave grating of $3\ \mu\text{m}$ periodicity exposed and developed in a layer of HPR 206 photoresist about $1\ \mu\text{m}$ thick. In all experiments, the flow rate of CHF_3 was 30 sccm and the RF power was 65W, this being the maximum power still assuring the integrity of the photoresist in our reactor.

If one relates the etching conditions of Fig. 10a-10e to the results described above, it is apparent that careful control of the plasma chemistry is required for perfect anisotropic etching. This can be achieved either at low pressure in pure CHF_3 (Fig. 10a) or at much higher pressure with the addition of O_2 (Fig. 10b). However, O_2 in excess of the optimum at a given pressure leads to a slightly overetched profile (Fig. 10d). Conditions favoring polymerization give rise to nonvertical sidewalls, which are produced by the growth of a thin polymeric film extending from the top of the photoresist to the bottom of the etched trough (Fig. 10c and 10e). Everything else being the same, polymerization is enhanced at higher pressure (Fig. 10c) or by an oxygen consuming cathode (Fig. 10e), and also at lower flow rate or at lower RF power.

Discussion

We now wish to discuss our results, putting them in context with previous work, by focusing attention on two main themes: the truly important parameters and proper characterization of an etching discharge, and the physical and chemical mechanisms determining etch rates and etch anisotropy.

Plasma discharge parameters.—In reviewing the literature on dry etching, one is struck by the large number of processes (*i.e.*, combinations of reactor configuration, etch gas, and discharge operating conditions) in existence to etch any one of several materials of interest. The present work, together with previous results (13), allows us to give a fairly comprehensive description of the relevant discharge parameters for the etching of SiO_2 with CHF_3 and CF_4 . As variables, we have examined in detail plate separation (including the case of reactive sputter etching [RSE] with only one, RF-driven plate and the reactor chamber as counterelectrode) material of the RF-driven plate (or cathode), and, previously, size of the cathode (13)

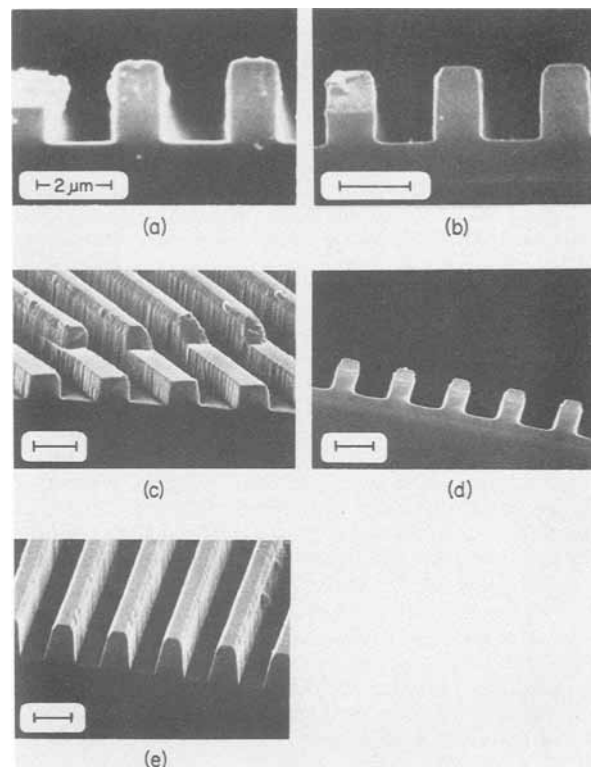


Fig. 10. SEM micrographs of profiles etched into SiO_2 under different conditions. Photoresist still present. RF power = 65W. (a): 15 mtorr CHF_3 . (b): 60 mtorr CHF_3 -4% O_2 . (c): 30 mtorr CHF_3 . (d): 30 mtorr CHF_3 -2% O_2 . (e): 30 mtorr of CHF_3 , graphite cathode. Bars indicate $2\ \mu\text{m}$ scale.

in a given reactor. We wish to characterize the conditions producing comparable etch discharges, as reflected by the etch rate R_e .

If at constant gas pressure the plate separation is varied, we find that R_e changes in accordance with the RF power P , and not with the peak-to-peak voltage V_{RF} or the induced dc bias voltage at the cathode, V_{dc} (see also Fig. 2). This agrees with behavior found for a rather different process: etching Si with SF_6 (15). If one changes the material covering the cathode from SiO_2 to Al or graphite, everything else being the same, again P correlates best with R_e , rather than V_{RF} or V_{dc} . (But note that the cathode material has a noticeable effect on the discharge chemistry.) However, if in the RSE mode the cathode size is changed, then it is V_{RF} which best parallels R_e rather than the power P , or the power density (*i.e.*, P divided by the cathode area), or V_{dc} [cf. Ref. (29)]. [In etching Si with SF_6 , V_{dc} was said to correlate best with R_e , but V_{RF} was not looked at (15)]. The same also holds if, with fixed geometry, the RF power is not properly matched to the reactor.

We emphasize that if one considers major changes in the reactor configuration, then none of the above externally accessible electrical variables are useful in a comparison with the parallel-plate geometry. Thus, for example, in a flexible diode reactor (16) it is not true, in general (17), that the state of the discharge as indicated by the ion density is independent of the division of power between the two driven electrodes as long as the total power is constant (16). Also, with a "hollow cathode" (18), V_{RF} is vastly different from that with a single cathode of the same size at a given power, so that it is not obvious why one should compare the two situations at constant V_{RF} .

Taking into account the different reactor configurations as described, we arrive at the remarkable conclusion that the operating conditions for a given etch rate R_e of SiO_2 all have one feature in common: the same ion density at the edge of the dark space. (We define this edge, somewhat loosely, as the point of maximum ion density

in a direction normal to the cathode; see Fig. 3.) The correlation between R_e and $N_{i,max}$ is excellent if at a fixed pressure the cathode size (13) or the plate separation are changed, or if with fixed geometry the pressure is changed (Fig. 7). The correlation between R_e and $N_{i,max}$ also holds with minor changes in plasma chemistry [e.g., addition of small amounts of O_2 or H_2 to CF_4 (13)] but breaks down with major changes in plasma chemistry (e.g. addition of O_2 to CHF_3 for p beyond the polymer point; see Fig. 7). This intimate connection between R_e and $N_{i,max}$ is of great significance for the etch mechanism, as we will show below.

Etch mechanisms.—Having recognized the important role of the ions, we now wish to elucidate the contribution of neutral species to the etching of SiO_2 . Our goal is to identify the main reactants and products and the processes relating them. In doing mass spectrometry of plasma species, we are aware of potential pitfalls, such as complications due to wall reactions, memory effects, etc. Still, we believe that our experimental setup, with excellent background pressure in the differentially pumped mass spectrometer chamber, allows us to monitor without difficulty stable neutral plasma species.

In order to identify such species, we rely on their characteristic cracking patterns as produced by electron impact in the mass spectrometer ionizer. We note, in agreement with Ref. (19), that for SiF_4 the major peak is SiF_3^+ at $M/e = 85$ and that the next most important peak, SiF^+ at $M/e = 47$, is down by almost two orders of magnitude. Two other potential etch products are COF_2 and SiF_2 , which, unfortunately, have the same mass. However, the cracking patterns of the two species are quite different. For COF_2 , the ratio of peak heights at $M/e = 66$ (COF_2^+), 47 (COF^+), 44 (CO_2^+), and 28 (CO^+) is roughly 1:2:2:1, whereas for SiF_2 the ratio of peak heights at $M/e = 66$ (SiF_2^+) and 47 (SiF^+) is about 2:1 [cf. also Ref. (8, 19)].

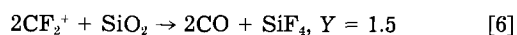
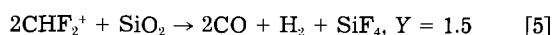
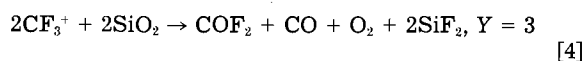
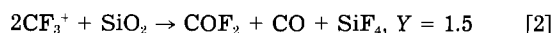
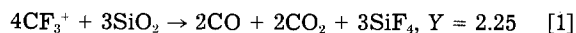
With these facts in mind, we conclude, from Fig. 9, that SiF_4 is the main Si bearing product in the etching of SiO_2 by a CHF_3 plasma. Indeed, the SiF_3^+ peak parallels nicely R_e vs. pressure p and also $N_{i,max}$ vs. p (cf. Fig. 5 and 7). At the same time, we observe substantial amounts of CO , CO_2 , and COF_2 as etch products, all showing the same behavior vs. p as does SiF_4 , with CO apparently the main O bearing product. Furthermore, O_2 is only present in the background in small amounts and is not produced by the etch reaction. Thus, our results are in agreement with those of Winters (19), who used XeF_2 as etchant and bombardment by Ar^+ or CF_3^+ ions, as far as the production of SiF_4 is concerned, but we observe far larger amounts of O bearing products and no O_2 . Comparing CHF_3^+ , CF_3^+ , and CF_2^+ peaks vs. p (Fig. 9) we note that beyond the polymer point their relative intensities do not correspond to those of the cracking pattern of CHF_3 anymore. At about 20 mtorr, a new source of CF_3^+ and CF_2^+ begins to appear, for which the most logical candidate is polymeric species resputtered from the SiO_2 surface. At much higher p , when etching of SiO_2 has virtually ceased, the additional production of CF_3^+ just about compensates for the reduction of CF_3^+ from the dissociation of CHF_3 in the discharge.

In CHF_3 - O_2 mixtures, qualitatively similar results are obtained vs. p . SiF_4 is again a major product and follows R_e vs. p . However, the production of CO , CO_2 , and COF_2 is greatly enhanced, probably because of efficient oxidation of polymeric species as well as CHF_3 in the gas phase (cf. also Fig. 8). Upon adding O_2 to a constant partial pressure of CHF_3 (Fig. 8), the correspondence between SiF_4 (i.e., SiF_3^+) and R_e is not quite as close, in that R_e decreases somewhat faster than SiF_3^+ with increasing O_2 .

So far, we have pointed out the parallel behavior of the etch rate R_e , the production of SiF_4 , and the ion density $N_{i,max}$ at not too large p (i.e., $p \approx 20$ mtorr), and also the rapidly increasing deposition of polymeric material on the substrate above the point of maximum R_e . Since we cannot detect neutral radicals, we cannot investigate directly potential neutral reactants although we can rule out

HF as one of them (3). The role of the radicals is clarified, however, if one compares etch yields per ion in reactive sputter etching (RSE) with those in reactive ion beam etching (RIBE), as shown in Table I. The etch yields in RSE were estimated as described before (13), based on the measured ion densities $N_{i,max}$ at the dark space edge. Most surprisingly, at a fixed ion energy, the etch yields turn out to be quite independent of the flux of radicals to the substrate, with the ratio of the radical flux to the ion flux varying over about four orders of magnitude.

All our results point to the conclusion that in the etching of SiO_2 by CHF_3 or CF_4 plasmas, ions are the main reactants. The following reactions, among others, can be visualized as being involved [the first one was suggested also by Harper *et al.* (20)], with the respective etch yields Y in atoms per ion (e.g., in reaction [1], three SiO_2 units are removed by four CF_3^+ ions, so that $Y = 3 \times 3/4$)



The figures for these etch yields should be interpreted as maximum yields possible which may only be attained by sufficiently energetic ions. The yields depend on the F/C ratio in the reactant ion (cf. reactions [1], [5], and [6]) and on the extent to which available F atoms are used to volatilize Si rather than O (cf. reactions [1] and [2] or [3] and [4]). Of course, reactions producing SiF_2 rather than SiF_4 have a higher etch yield (cf. reactions [1] and [3]). Furthermore, the production of SiF_2 seems to be tied to the production of O_2 (cf. reactions [3] and [4]). We note that the idea of ions as reactants is consistent with the picture advanced earlier (26) that energetic molecular ions dissociate completely upon impact on the substrate, thus creating highly reactive atoms.

Since several or all of these reactions may occur simultaneously, the measured etch yields (Table I) are in good agreement with those predicted. For example, for CF_3^+ at

Table I. Etch yields (at./ion) for SiO_2

Ion	E_i (keV)	j_{ion} (mA/cm ²)	Mode	Y (at./ion)	$\frac{f_{ion}}{f_{radical}}$	Ref.
CF_3^+	0.1	0.15	RSE	1	10^{-2}	(13)
		0.12		0.6		(13)
		0.1	RIBE	0.9-1.3	10^0	(20)
Ar^+	0.1	?		0.53		(21)
		0.1	Sputter	0.12	—	(20)
		?		0.09		(21)
		0.15		3	10^{-2}	(13)
CHF_3^+	0.5	0.15	RSE	2.5		(13)
		0.1	RIBE	2.5	10^0	(20)
		0.15		3		(22)
		0.4		1.5		(23)
		0.003	Sputter	3	10^2	(24)
		0.1	Sputter	0.7	—	(20)
		?		1		(21)
CF_3^+	1	0.8	RIBE	2.9	10^0	(25)
		0.8		3.2		(25)
		0.8		1.0		(25)
		0.8		1.0		(25)

E_i is the ion energy, j_{ion} the ion current density at the substrate, and $f_{ion}/f_{radical}$ the ratio of particle fluxes at the substrate.

With a reactive gas in the RIBE mode, the beam contains a mixture of ions, the one given in the table being the main ion except for the work of Ref. (23) and (25), where the main ion was more likely CF_2^+ (22, 26). The plasma potential in RSE turns out to be about 30V, regardless of the plate separation or the plasma pressure, so that to a good approximation E_i in RSE is equal to the induced dc bias voltage V_{dc} .

500 eV on SiO₂, the physical sputtering yield is estimated as 0.7 at./ion (26), so that the part of the total yield due to reactions [1]-[6] is 2.3 at./ion. Table I also indicates that etch yields saturate at high ion energies, as is expected from reactions [1]-[6]. At low ion energies, yields are considerably smaller but still independent of the neutral flux. This may be rationalized as arising from the lower dissociation probability of the impinging ions. Moreover, relative yields predicted for different ions CF_r⁺ compare favorably with those deduced by Mayer and Barker (22), who used an ion beam of well-characterized composition.

Let us add, however, that there is also evidence showing the non-negligible contribution of neutrals (radicals) to the etching of SiO₂. The composition of products depends on the nature of the neutrals present (compare this work with Ref. (19), where the neutrals were F atoms from XeF₂). Also, the measured etch yields for 500 eV ions may be slightly higher than predicted on the basis of reactions [1]-[6], in light of the fact that high yield reactions such as [3] and [4], leading to SiF₂ as a product, are evidently less probable than those leading to SiF₄, the main product [cf. Ref. (19)]. In addition, changes in the ion beam composition in RIBE cannot account for the entire change in the etch rate *vs.* pressure (22). It is clear, though, that, in the case of SiO₂, the nature of the ions is much more important, and the flux of radicals much less important, than in the case of Si. This conclusion receives additional support from the fact that loading effects are much smaller for SiO₂ than for Si (4).

Anisotropic etching.—We argued above that the overall ion-enhanced etch rate of SiO₂ is to a large extent due to direct etching by reactive ions, in competition at higher pressure with deposition (and resputtering) of polymeric species. The former mechanism leads naturally to anisotropic etching because the etch rate is only appreciable on surfaces exposed to ion bombardment. However, the shape of etched profiles also depends in a subtle way on the latter, surface inhibiting mechanism (9).

In order to achieve clean profiles with vertical sidewalls, one must operate somewhat below the polymer point, *i.e.*, somewhat below the point of maximum etch rate (cf. Fig. 5 and 10). At the polymer point, growth of a thin polymeric film has set in already on vertical surfaces, becoming more pronounced at higher pressure (Fig. 10c). This results in profiles with nonvertical sidewalls. Addition of O₂ in the gas phase counteracts the polymerizing tendency of the plasma (Fig. 10b and 10d), but O₂ in excess of the optimum attacks the photoresist and, thus, also leads to nonvertical sidewalls. In addition, excess O₂ degrades the selectivity with respect to Si.

Thus it is the plasma chemistry which determines the conditions for optimal anisotropic etching, and minor changes in that chemistry may have a major effect on the shape of the etched profiles. Given the large number of parameters affecting the plasma chemistry, such as gas composition, pressure, flow rate, cathode material, RF power applied, etc., it is not surprising that one can obtain acceptable results with a variety of combinations of these parameters. Proven processes for SiO₂ have been based on CHF₃ (1, 2), CF₄-H₂ (7), C₂F₈ (6), and CHF₃-H₂ (27) plasmas. We have been able to etch good profiles even with a C₂F₄-O₂ mixture, although with pure C₂F₄ there is no etching, only deposition, under any conditions.

Let us keep in mind that the plasma chemistry has a decisive influence not only on the etch anisotropy, but also on the etch selectivity of SiO₂ with respect to Si (see the "Plasma chemistry" section). In general, one may expect the conditions for maximum selectivity to yield slightly nonvertical sidewalls in SiO₂. Conversely, the best profile shape may only be obtainable at less than maximum selectivity. Thus, in a practical situation an optimal trade-off between the two requirements will have to be achieved.

Conclusion

Winters *et al.* (10) have discussed ion-enhanced etching in terms of three possible mechanisms. One is called

chemically enhanced physical sputtering, in which the role of the ions is to remove physically reaction products which are loosely held on the substrate surface. In the second mechanism, ion bombardment is visualized as creating a damaged surface with sites particularly suitable for reaction. The third mechanism, favored by Winters *et al.* (10), is called chemical sputtering and assumes that ion bombardment provides the energy required for certain exothermic reactions to occur in the near-surface region of the substrate which lead to products desorbing into the gas phase.

We contend that the dominant mechanism in the etching of SiO₂ is a fourth one, for which we propose the name "direct reactive ion etching." By this, we mean that energetic reactive ions serve as the main reactants in the overall etching reaction. Or, in other words, ions themselves do most of the etching, rather than radicals (9). This conclusion is based on the finding that etch yields per ion are largely independent of the flux of radicals to the substrate in a wide variety of situations. Only under rather polymerizing conditions do the radicals affect the etch yield significantly, by way of forming a polymeric layer on the substrate. However, small changes in the plasma chemistry of neutral species have large effects on the etch anisotropy and selectivity.

Of course, ion-enhanced etching in general may involve all four of these mechanisms contributing simultaneously to the overall etch rate. Indeed, etching of Si in a fluorine-based plasma appears to be due largely to chemical sputtering (10) and chemically enhanced physical sputtering (28), whereas the dominant mechanism in etching Si with a chlorine-based plasma is still to be determined.

The term "reactive ion etching" is often used to describe the general situation of ion-enhanced etching whereby the substrate is etched at low pressure on the RF-driven cathode and thus is exposed to ion bombardment (4, 7, 16). We propose, in light of our results, that the term "reactive ion etching" be reserved for the particular etch mechanism in which ions themselves react, and that the more general mode of etching mentioned above be referred to as "reactive sputter etching," *i.e.*, etching involving ion bombardment in a reactive environment.

Manuscript submitted May 15, 1984; revised manuscript received Sept. 10, 1984.

Laboratories RCA Limited assisted in meeting the publication costs of this article.

REFERENCES

1. H. W. Lehmann and R. Widmer, Paper presented at the International Conference on Microlithography, Paris, June 21-23, 1977.
2. H. W. Lehmann and R. Widmer, *Appl. Phys. Lett.*, **32**, 163 (1978).
3. H. W. Lehmann and R. Widmer, *J. Vac. Sci. Technol.*, **15**, 319 (1978).
4. M. J. Vasile, *J. Appl. Phys.*, **51**, 2510 (1980).
5. G. C. Schwartz, L. B. Rothman, and T. J. Schopen, *This Journal*, **126**, 464 (1979).
6. R. A. H. Heinecke, *Solid State Electron.*, **18**, 1146 (1975).
7. L. M. Ephrath, *This Journal*, **126**, 1419 (1979).
8. J. W. Coburn and E. Kay, *IBM J. Res. Dev.*, **23**, 33 (1979).
9. D. L. Flamm and V. M. Donnelly, *Plasma Chem. Plasma Process.*, **1**, 317 (1981).
10. H. F. Winters, J. W. Coburn, and T. J. Chuang, *J. Vac. Sci. Technol. B*, **1**, 469 (1983).
11. K. Knop, H. W. Lehmann, and R. Widmer, *J. Appl. Phys.*, **50**, 3841 (1979).
12. H. W. Lehmann, E. Heeb, and K. Frick, *Solid State Technol.*, **24** (10), 69 (1981).
13. Ch. Steinbrüchel, *This Journal*, **130**, 648 (1983).
14. I. C. Plumb and K. R. Ryan, in "Proceedings of the International Symposium on Plasma Chemistry," M. I. Boulos and R. J. Munz, Editors, p. 326, Montreal, July 24-28, 1983, Université de Sherbrooke, Montreal (1983).
15. Ph. Laporte and L. Peccoud, in "Proceedings of the International Symposium on Plasma Chemistry," B. Waldie and G. A. Farnell, Editors, p. 344, Edinburgh, August 10-14, 1981, Heriot-Watt University,

- Edinburgh (1981).
16. L. M. Ephrath, *This Journal*, **129**, 62C (1982).
 17. Ch. Steinbrüchel and B. J. Curtis, Unpublished results.
 18. C. M. Horwitz, *Appl. Phys. Lett.*, **43**, 977 (1983).
 19. H. F. Winters, *J. Vac. Sci. Technol. B*, **1**, 927 (1983).
 20. J. M. E. Harper, J. J. Cuomo, P. A. Leary, G. M. Summa, H. R. Kaufman, and F. J. Bresnock, *This Journal*, **128**, 1077 (1981).
 21. T. M. Mayer, R. A. Barker, and L. J. Whitman, *J. Vac. Sci. Technol.*, **18**, 349 (1981).
 22. T. M. Mayer and R. A. Barker, *This Journal*, **129**, 585 (1982).
 23. B. A. Heath, *ibid.*, **129**, 396 (1982).
 24. Y. Y. Tu, T. J. Chuang, and H. F. Winters, *Phys. Rev. B*, **23**, 823 (1981).
 25. B. Meusemann, *J. Vac. Sci. Technol.*, **16**, 1886 (1979).
 26. Ch. Steinbrüchel, *J. Vac. Sci. Technol. B*, **2**, 38 (1984).
 27. M. T. Duffy, J. F. Corboy, and R. A. Soltis, *RCA Rev.*, **44**, 157 (1983).
 28. R. A. Haring, A. Haring, F. W. Saris, and A. E. deVries, *Appl. Phys. Lett.*, **41**, 174 (1982).
 29. C. M. Horwitz and J. Melngailis, *J. Vac. Sci. Technol.*, **19**, 1408 (1981).
 30. H. Toyoda, H. Komiya, and H. Itakura, *J. Electron. Mater.*, **9**, 569 (1980).

Beryllium Ion-Implanted Junctions in GaAs with Submicron Lateral Diffusion

P. M. Campbell and B. J. Baliga

General Electric Company, Corporate Research and Development Center, Schenectady, New York 12345

ABSTRACT

Beryllium ion implants in GaAs annealed at 900°C for 30 min with a Si₃N₄ encapsulant have been shown to form p-n junctions with lateral diffusion between 0.5 and 1.0 μm, junction depth of 0.7 μm, and implant activation rate of ~ 100%. SiO₂ and phosphosilicate glass encapsulants yield similar values of lateral diffusion, junction depth, and activation rate, but are shown to induce near-surface degradation effects manifested by a reduced carrier concentration within 1.0 μm of the surface in unimplanted annealed material and to produce anomalously high breakdown voltages and high leakage currents in Be-implanted junctions.

One of the critical requirements for GaAs device technology is a reliable technique for the fabrication of high quality micron-size planar p-n junctions. For example, such junctions are required for the gate region of JFET's in high speed GaAs integrated circuits. Planar junctions have previously been fabricated using sealed-tube diffusions with both vapor and solid sources (1, 2). Although lateral diffusions equal to the depth were achieved in the sealed-tube process, these studies indicated that lateral diffusion of 100 times the vertical depth can be observed if the diffusion conditions are not carefully controlled. The fabrication of diffused JFET's with tolerable lateral diffusion using a metal-organic Zn source has been reported (3), but for integrated circuit fabrication, it would be preferable to use ion implantation followed by an open tube annealing cycle in order to obtain greater control and uniformity, as well as simplified processing. However, surface degradation during the high temperature annealing required to activate the implant remains a serious problem, requiring either an encapsulant or an arsenic overpressure to prevent dissociation of the GaAs. A comprehensive review of ion implantation techniques in GaAs is given in Ref. (4). It has been demonstrated that p-n junctions can be fabricated in GaAs with beryllium ion implantation (5). However, the lateral diffusion during high temperature annealing was measured by junction staining, which may not reveal surface diffusion between implant islands, which, for example, has been detected in Zn-diffused GaAsP using high sensitivity SEM techniques (6).

We have investigated the comparative suitability of silicon dioxide, phosphosilicate glass, and plasma-deposited silicon nitride as encapsulants for high temperature (900°C) annealing of Be implants in GaAs. These Be implants were performed in high purity ($n = 2.5 \times 10^{15}/\text{cm}^3$) liquid-phase epitaxial GaAs, which served as a sensitive medium for the detection of surface lateral diffusion and other degradation effects induced by high temperature annealing.

Sample Preparation

The bare GaAs samples were first cleaned in boiling solvents, then soaked in hot H₂O to form a thin oxide film which was then removed in hot HCl. The wafers were then coated front and back with a thin film of either SiO₂, phosphosilicate glass (PSG), or Si₃N₄.

The SiO₂ films were formed by the reaction of silane and oxygen at atmospheric pressure and a temperature of 400°C. The phosphosilicate glass films were deposited under the same conditions, but with the addition of flowing phosphine, yielding films with 8% phosphorous by weight. The rate of deposition for the SiO₂ and PSG films was 300 Å/min, with a thickness of 4000Å used for each film, as measured by ellipsometry. The refractive index of the SiO₂ and PSG films was 1.45.

The Si₃N₄ films were formed by the plasma-enhanced reaction of both silane and ammonia in an argon ambient at a pressure of 0.6 torr and a temperature of 450°C. The rate of deposition for this process was 150 Å/min. All Si₃N₄ layers were 900Å thick and had a refractive index between 1.95 and 1.98.

Following deposition, a pattern of closely spaced implant windows was opened in each film, using standard photolithographic techniques, with a thick (2 μm) layer of positive photoresist, which also served as a selective mask during the implantation. The opened implant windows varied in separation from 1 μm upwards in steps of 1 μm.

Next, Be ions of energy 100 keV and fluence $5 \times 10^{13}/\text{cm}^2$ were implanted in the open windows (Fig. 1). The wafers were then stripped of the remaining photoresist and coated with a second identical layer of either SiO₂ (4000Å), PSG (4000Å), or Si₃N₄ (900Å). Following this, the wafers were annealed in flowing nitrogen gas at a temperature of 900°C for 30 min. Finally, contact windows were opened to each implant island. If desired, a lift-off metallization was then deposited to improve the ohmic nature of the contacts.

Lateral Diffusion Measurement Technique

The lateral diffusion of the implanted and annealed Be was measured electrically by detecting the punch-through of the lateral diffusion between adjacent implant islands, which is clearly observable because the I-V characteristic of two P⁺ islands joined by diffusion (Fig. 2, top) will be ohmic, while that of two P⁺ islands separated by a thin N region (Fig. 2, bottom) will be rectifying. Since the implant islands varied in separation from 1 μm upward in steps of 1 μm, the lateral diffusion can be measured to within half the smallest distance, or 0.5 μm. This electrical measurement of lateral diffusion is of direct relevance to device and circuit fabrication because it measures directly the electrical isola-

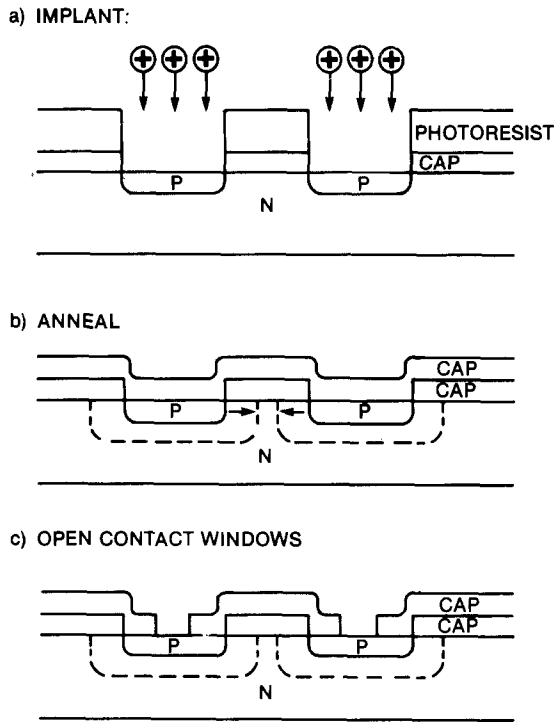


Fig. 1. Processing steps for lateral diffusion measurement

tion of the implanted regions, unlike the commonly used angle lapping/staining technique which may not, for example, detect the formation of thin diffused conductive surface channels under the encapsulant. This technique has the additional advantage of being compatible with nondestructive on-chip testing during processing, whereas the staining method in Ref. (5) and the SEM technique in Ref. (6) each require cleaving of the sample.

Lateral Diffusion Results

The lateral diffusion of the implanted Be after a 30 min anneal at 900°C was measured to be between 0.5 and 1.0 μm for each of the three encapsulants Si₃N₄, SiO₂, and PSG. This measurement technique is demonstrated in Fig. 3 for the case of Si₃N₄; a rectifying characteristic between two implant windows separated by 2 μm is shown, indicating a lateral diffusion of less than half the window separation, or 1.0 μm. A 1 μm window separation gives an ohmic charac-

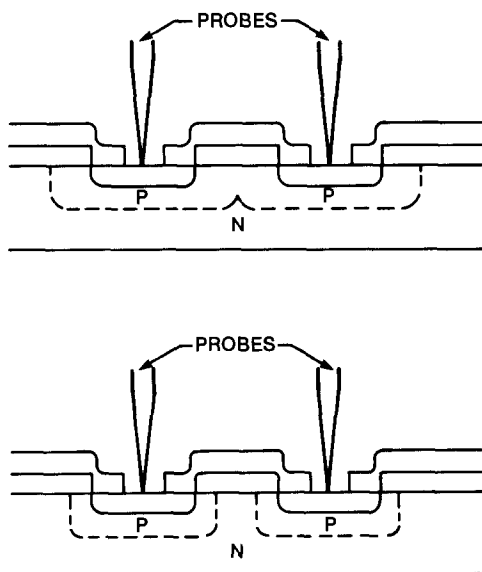


Fig. 2. Two P⁺ implant islands joined by diffusion (top) yield ohmic I-V characteristics, while two islands separated by N region (bottom) yield rectifying I-V characteristics.

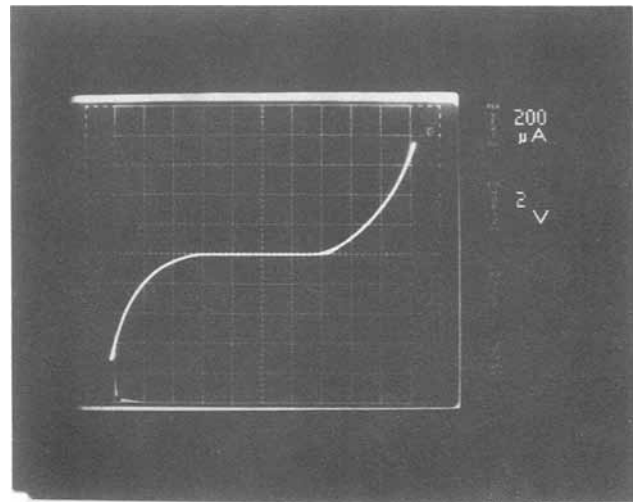


Fig. 3. I-V characteristic of two implant islands separated by 2 μm is rectifying, indicating a lateral diffusion of less than half the separation, or 1 μm.

teristic, indicating a lateral diffusion of at least 0.5 μm. In the rectifying case, no current flows until the two depletion regions touch; this occurs in Fig. 3 at a bias of 4V, and the characteristic is symmetric, as expected. The depletion width of each junction varies as $W = [2\epsilon(\psi - V)/qN]^{1/2}$, where ϵ is the permittivity, ψ = built-in potential of the junction, V = external bias across the junction, q = electronic charge, and N = doping of the base material. Hence, for greater window separation, a greater bias voltage is required for the depletion region of the reverse-biased junction to penetrate the additional distance and reach that of the forward-biased junction, causing the onset of conduction. Figure 4 shows a graph of this punch-through voltage as a function of implant window separation, with ohmic characteristics plotted as having a zero punch-through voltage. The data points with nonzero punch-through voltage in Fig. 4 follow a roughly parabolic form, as expected from the depletion width equation, and could in principle be used to solve the equation for a precise value of the lateral diffusion if N were accurately known. This is not simple in the case of GaAs because there exist near-surface compensation effects resulting from the high-temperature anneal which can affect the value of N , as shown in a later section.

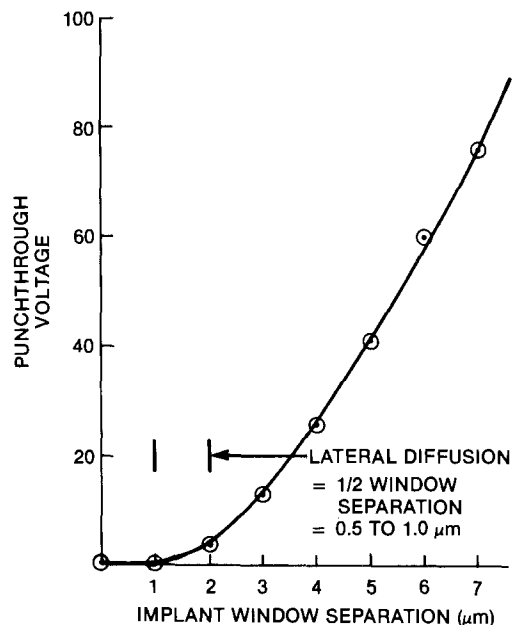


Fig. 4. Punch-through voltage vs. implant window separation for implant islands annealed with Si₃N₄ encapsulant.

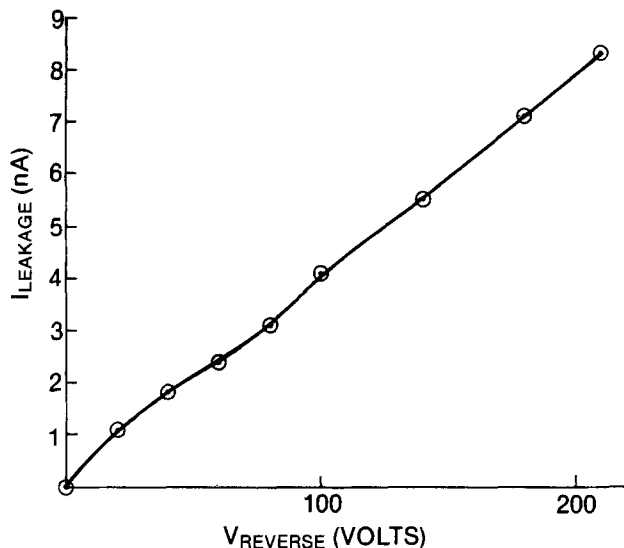


Fig. 5. Leakage current vs. reverse bias for implanted junction diode annealed with Si_3N_4 encapsulant.

Electrical Characterization

There exist significant differences in the electrical characteristics of diodes annealed with different encapsulants. Circular junction diodes (diameter = $250\ \mu\text{m}$), fabricated as above on $n = 2.5 \times 10^{15}/\text{cm}^3$ LPE GaAs and annealed at 900°C for 30 min using Si_3N_4 as the encapsulant, exhibit leakage currents as low as the 10^{-9}A range for reverse bias as high as 200V (Fig. 5), whereas those fabricated with SiO_2 or PSG caps show leakage currents in the 10^{-6}A range. In addition, the diodes annealed with a Si_3N_4 cap undergo avalanche breakdown at a reverse bias of $\sim 200\text{V}$, as predicted by Sze and Gibbons (7) for GaAs with $n = 2.5 \times 10^{15}/\text{cm}^3$. However, identical diodes annealed with SiO_2 or PSG as the encapsulant show anomalously high breakdown voltages of up to 450V. This suggests the existence of a near-surface compensation mechanism associated with the SiO_2 and PSG encapsulants, but not with the Si_3N_4 .

Annealing Damage Study

In order to investigate the effect of high temperature annealing with the various encapsulants on the near-surface carrier concentration independently of any ion implantation effects, adjacent pieces from the center of a single unimplanted wafer of boat-grown silicon-doped ($n = 1.4 \times 10^{18}/\text{cm}^3$) bulk GaAs were coated with either SiO_2 , PSG, or Si_3N_4 as above and annealed at 900°C for 30 min. The films were then removed with HF, and each sample was measured with a Polaron Semiconductor Profile Plotter (8), which performs a series of differential capacitance-voltage measurements in sequence with a series of photochemical step-etches and generates a plot of carrier concentration as a function of depth. Figure 6 shows the postanneal carrier profiles of the samples capped with SiO_2 , PSG, and Si_3N_4 , as well as a profile of unannealed material. In comparison with the unannealed material, which, as expected, has a flat profile, the SiO_2 -capped material shows a marked decrease in the carrier concentration within $1\ \mu\text{m}$ of the surface. The PSG-capped material shows a similar decrease that is almost as severe as the SiO_2 case, while the damage in the Si_3N_4 -capped material is confined to a region closer to the surface than in the other two cases. This postanneal decrease in the carrier concentration could account for the anomalously high breakdown voltages achieved with implanted junctions in material annealed with SiO_2 and PSG caps, provided the junction depth is shallower than the depth of the compensation. As will be seen in the next section, the junction depths are shallower than the damage with SiO_2 and PSG caps, but not shallower than that with Si_3N_4 . This compensation may be due to the out-diffusion of Ga and/or As through the films, creating vacancies which could be electrically active or serve as sites for the migration of active impurities. Such near-surface degradation

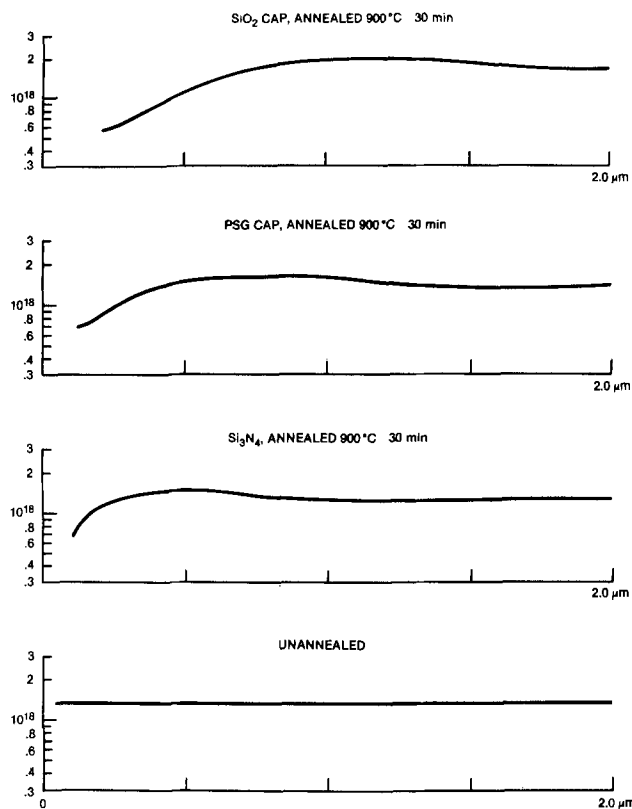


Fig. 6. Carrier concentration depth profiles of unimplanted boat-grown silicon-doped ($n = 1.4 \times 10^{18}/\text{cm}^3$) bulk GaAs annealed at 900°C for 30 min with: a) SiO_2 cap; b) PSG cap; c) Si_3N_4 cap; and d) unannealed material.

could also be responsible for the higher leakage currents observed with SiO_2 and PSG and may be related to the thermal conversion effects observed in the high temperature annealing of semi-insulating GaAs (9).

Implanted Junction Depth Profiles

In order to measure the depth profiles of the implanted junctions, unpatterned LPE GaAs was implanted with Be ($100\ \text{keV}$, $5 \times 10^{13}/\text{cm}^2$), capped with either SiO_2 , PSG, or Si_3N_4 as above, and annealed for 30 min at 900°C to duplicate the conditions of the lateral diffusion experiment. After removing the encapsulant, each sample was analyzed with the Polaron Profiler. The results are shown in Fig. 7.

The SiO_2 -capped sample (Fig. 7a) shows a peak carrier concentration of $2 \times 10^{18}/\text{cm}^3$ at a depth of $0.1\ \mu\text{m}$, with the CV characteristic indicating p-type material. The concentration decreases to a plateau value of $\sim 1.5 \times 10^{18}/\text{cm}^3$ in the range of 0.3 to $0.5\ \mu\text{m}$, then drops rapidly, with the junction occurring at a depth of $0.7\ \mu\text{m}$, as shown in Fig. 7a and also determined from a plot of the electrical phase of the capacitance-voltage data recorded automatically by the Polaron Profiler as a function of depth. The total integrated carrier density gives an implant activation rate of $\sim 100\%$.

The PSG-capped sample (Fig. 7b) shows a similar profile, but the peak value is only $1.3 \times 10^{18}/\text{cm}^3$ and the plateau is $\sim 7.5 \times 10^{17}/\text{cm}^3$. This profile yields an activation rate of $\sim 80\%$. The junction depth is $0.8\ \mu\text{m}$.

Figure 7c gives the profile of a PSG-capped sample annealed at 900°C for 60 min. This longer anneal raises the peak value to $2.5 \times 10^{18}/\text{cm}^3$ and the plateau value to $\sim 1.2 \times 10^{18}/\text{cm}^3$. This increases the activation rate to $\sim 100\%$, but does not change the junction depth.

Figure 7d shows the profile of the Si_3N_4 -capped sample annealed at 900°C for 30 min. In contrast to the three preceding cases, there is no near-surface peak. The carrier concentration has a constant value of $1.7 \times 10^{18}/\text{cm}^3$ to a depth of $0.2\ \mu\text{m}$, decreases slowly to $1.4 \times 10^{18}/\text{cm}^3$ at $0.4\ \mu\text{m}$, and then begins to drop more rapidly, with the junction occurring at a depth of $0.7\ \mu\text{m}$. The implant activation rate is $\sim 100\%$.

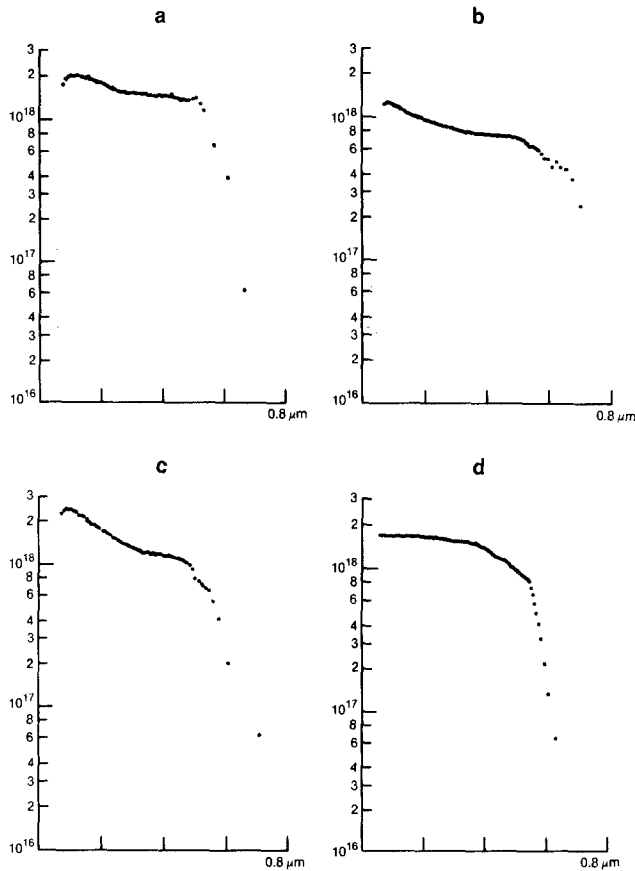


Fig. 7. Carrier concentration depth profile of implanted junction annealed at: a) 900°C for 30 min with SiO₂ cap; b) 900°C for 30 min with PSG cap; c) 900°C for 60 min with PSG cap; and d) 900°C for 30 min with Si₃N₄ cap.

The distinguishing characteristic of the Si₃N₄-capped profile is the lack of the near-surface peak evident in the SiO₂ and PSG cases. This peak occurs too near the surface (0.1 μm) to be a remnant of the preanneal implant profile because the LSS theory gives a projected range of 0.32 μm for 100 keV Be in GaAs. One possible explanation is that the near surface degradation shown to occur in both SiO₂ and PSG serves to getter the implanted Be. Because electrically active Be atoms would have preferentially occupied Ga sites, this suggests that the near-surface degradation may be the result of Ga vacancies created during the anneal. An-

other possibility is that the thermal damage of Fig. 6, acting as an acceptor in compensating n-type material, would in p-type material increase rather than decrease the carrier concentration. If this is the case, then the implant activation rates given above may be overestimated because some of the measured hole density may arise from these damage-induced acceptors, rather than from the implanted Be atoms.

Conclusion

Beryllium ion implants in GaAs annealed at 900°C for 30 min using either SiO₂, phosphosilicate glass (PSG), or Si₃N₄ encapsulants have been shown to form p-n junctions with lateral diffusion between 0.5 and 1.0 μm, junction depths of 0.7 (SiO₂ and Si₃N₄) to 0.8 μm (PSG), and implant activation rates of 80 (PSG) to 100% (SiO₂ and Si₃N₄). However, SiO₂ and PSG encapsulants induce more severe near-surface degradation effects manifested by a reduction carrier concentration within 1 μm of the surface in unimplanted annealed GaAs, and they induce anomalously high breakdown voltages and higher leakage currents in Be-implanted p-n junctions, as compared with similar material annealed with a Si₃N₄ encapsulant.

Acknowledgments

The authors wish to acknowledge R. S. Ehle for providing the liquid phase epitaxial GaAs and R. F. Reihl for performing the ion implantations.

Manuscript submitted Dec. 21, 1983; revised manuscript received Aug. 22, 1984.

General Electric Company assisted in meeting the publication costs of this article.

REFERENCES

1. B. J. Baliga and S. K. Ghandi, *IEEE Trans. Electron Devices*, **ed-21**, 410 (1974).
2. B. J. Baliga and S. K. Ghandi, *This Journal*, **126**, 135 (1979).
3. M. Dohsen, J. Kasahara, Y. Kato, and N. Watanabe, *IEEE Electron Device Letters*, **ed1-2**, 157 (1981).
4. D. V. Morgan, F. H. Eisen, and E. Ezis, *IEEE Proc.*, **128**, 109 (1981).
5. M. J. Helix, K. V. Vaidyanathan, and B. G. Streetman, *IEEE J. Solid-State Circuits*, **sc-13**, 426 (1978).
6. P. K. Chatterjee and B. G. Streetman, *Solid-State Electron.*, **20**, 305 (1977).
7. S. M. Sze and G. Gibbons, *Appl. Phys. Lett.*, **8**, 111 (1966).
8. T. Ambridge, J. L. Stevenson, and R. M. Redstall, *This Journal*, **127**, 222 (1980).
9. L. B. Ta, H. M. Hobgood, A. Rohatgi, and R. N. Thomas, *J. Appl. Phys.*, **53**, 5771 (1982).

Continuous Optical Measurement of the Dry Etching of Silicon Using the Diffraction of a Lamellar Grating

Geraldo F. Mendes, Lucila Cescato, and Jaime Frejlich

Laboratório de Óptica, Instituto de Física "Gleb Wataghin," Universidade Estadual de Campinas, 13100, Campinas, SP, Brazil

Edmundo S. Braga and Alaide P. Mammana

Laboratório de Eletrônica e Dispositivos, Faculdade de Engenharia de Campinas, Universidade Estadual de Campinas, 13100, Campinas, SP, Brazil

ABSTRACT

An optical method using the diffraction of a lamellar grating is described for continuously measuring the etching of a substrate through a masking layer. The finite selectivity of the process is accounted for. Automation and real-time measurement are possible. Some theoretical situations are analyzed, and the method is applied for the experimental plasma etching of silicon through a thermally grown silicon dioxide layer.

Dry etching plays an important role in the manufacture of semiconductor devices requiring high resolution lithography. Many times, not only the end point detection for the process is desirable but also the measurement of the depth of incompletely etched areas is desirable. This is the case with etching silicon substrates for isolation purposes, when the etched depth should be carefully controlled in real time if a precise control of thickness is required.

Kleinknecht and Meier (1) first proposed monitoring the plasma etching of dielectric films by measuring the diffraction of a lamellar grating adequately lithographed somewhere on the sample.

Recently, Sternheim and van Gelder (2) used an interferometric system for monitoring the etching of a patterned silicon substrate. A laser beam is diffracted by the pattern being etched onto the substrate, and the zero-order diffracted intensity is monitored. Its principal advantage is the fact that it uses the etched pattern itself for control purposes.

Mendes *et al.* (3-6) further developed a method using lamellar gratings for thickness measurement and etching monitoring which permits one to measure the point-by-point evolution of the depth of the layer being etched. In this paper, we shall profit from the previous developments, extending the method to monitor the etching of the substrate, and accounting for the selectivity of the process with respect to the mask layer. We illustrate its advantages in continuously measuring the evolution of the etched depth of a silicon substrate masked with silicon dioxide.

Description of the Method

The optical modulation of a lamellar grating recorded in the full depth of a layer may be used to monitor the etch rate of the layer by measuring the first-to-zero diffraction intensity orders ratio I_1/I_0 (4, 5). If a substrate is etched through a lamellar grating masking layer, the etched depth h may also be determined by measuring the I_1/I_0 ratio of the grating being formed in the process, as shown in Fig. 1. The I_1/I_0 ratio may be written as

$$I_1/I_0 = \frac{|r_a - r_b|^2 (a/d)^2 \sin^2 c^2(a/d)}{|r_b + (r_a - r_b) a/d|^2} \quad [1]$$

with $\sin c(x) \equiv \sin \pi x / (\pi x)$ and r_a and r_b being the complex amplitude reflectivities on bars and grooves of the grating, respectively. For normal laser beam incidence, it should be written (7)

$$\left. \begin{aligned} r_a &= \frac{r_1 + r_2 e^{i2\beta}}{1 + r_1 r_2 e^{i2\beta}} \\ r_b &= r_3 e^{i2\gamma} \end{aligned} \right\} \quad [2]$$

with

$$2\beta \equiv 4\pi T n_1 / \lambda$$

$$2\gamma \equiv 4\pi(T + h)n_0 / \lambda$$

and

$$\left. \begin{aligned} r_1 &= (n_0 - n_1)/(n_0 + n_1) \\ r_2 &= (n_1 - n_2)/(n_1 + n_2) \\ r_3 &= (n_0 - n_2)/(n_0 + n_2) \end{aligned} \right\} \quad [3]$$

where T is the thickness of the masking layer and h represents the etched depth of the substrate. In our experiment, we shall choose $a/d = 0.5$ for which value the I_1/I_0 ratio is less sensitive to a/d variations (4). In this case, Eq. [1] simplifies to

$$I_1/I_0 = \frac{|r_a - r_b|^2 \sin^2 c^2(a/d)}{|r_a + r_b|^2} \quad [4]$$

Substituting Eq. [2] into Eq. [4], we get the following terms contained in the latter equation

$$\left. \begin{aligned} \cos 2\beta &= \cos(4\pi T n_1 / \lambda) \\ \cos 2\gamma &= \cos([4\pi n_0 / \lambda]T + [4\pi n_0 / \lambda]h) \\ \cos(2\beta - 2\gamma) &= \cos(4\pi T[n_1 - n_0] / \lambda - [4\pi n_0 / \lambda]h) \end{aligned} \right\} \quad [5]$$

If we assume the plasma etching to be infinitely selective (which means that the film thickness T remains constant throughout the process), the I_1/I_0 ratio should be periodic in h with a spatial period $H = \lambda/(2n_0)$. It means that two successive extrema appearing in the I_1/I_0 measured ratio represent a variation in the substrate etched depth (h) of $\lambda/(4n_0)$. In this way, the measurement should be carried out in exactly the same way as for the reflectivity method (8) for thin transparent films. The layer of air lim-

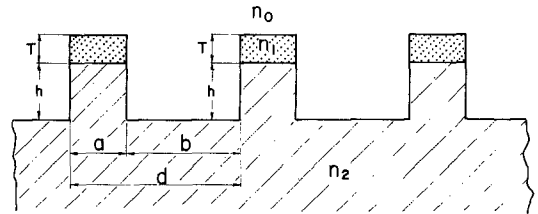


Fig. 1. A stage of the etching of a lamellar grating into a substrate. The substrate has been etched a depth h and a thin mask film of thickness T remains on the top of the structure. The period of the grating is d and the bar and groove sizes are a and b , respectively. The complex indexes of refraction of the mask and substrate are n_1 and n_2 , respectively.

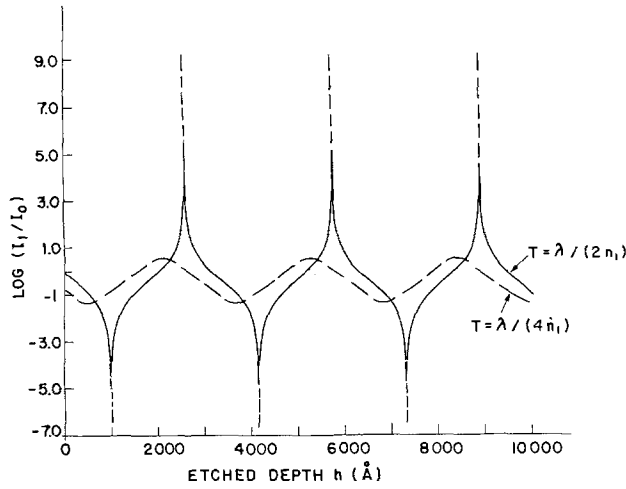


Fig. 2. Computed first-to-zero diffraction intensity orders ratio (I_1/I_0) as a function of the etched silicon depth (h) for two different thicknesses of SiO_2 film ($T = \lambda/(2n_1)$ and $T = \lambda/(4n_1)$), n_1 being the SiO_2 refractive index for the test wavelength $\lambda = 6328\text{Å}$. We assume the process to be infinitely selective, which means that T remains constant. Note that period of both curves is $\lambda/2$, but the amplitudes are widely different. We assumed $n_0 = 1$ (air).

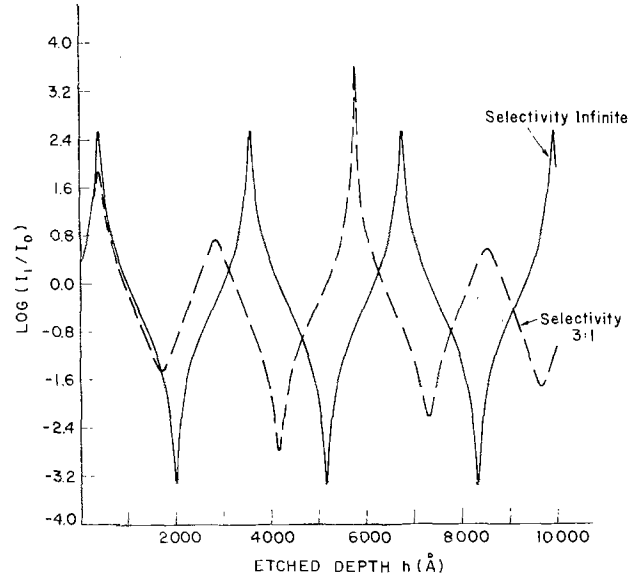


Fig. 4. Computed I_1/I_0 as a function of the etched Si depth (h) for a SiO_2 masking film with an initial film thickness $T_0 = 4000\text{Å}$, assuming infinite selectivity (continuous line) and a selectivity $S = 3$ (dashed line). The former example shows a periodic function (period of $\lambda/2$); the latter one is not apparently periodic and shows only relative extrema. $n_0 = 1$ in both cases.

ited by the upper and lower surfaces of the patterned structures plays the role of the transparent film in the reflectivity method. This is basically the method described by Sternheim, with the difference that we measure I_1/I_0 instead of I_0 , and use an auxiliary lamellar grating instead of the patterned structure itself.

The method we are proposing in this paper, however, presents two important advantages upon the Kleinknecht and Sternheim methods. First, during the etching process, we compare the measured temporal variation of the I_1/I_0 ratio with the computed I_1/I_0 vs. h curve, which permits describing the temporal evolution of h . In this way, we are continuously measuring the substrate etched depth so that we are not limited to monitoring thicknesses in intervals of quarter wavelength as with the methods referred to above. Second, infinitely selective processes are an idealized situation, and rather low selectivities are encountered in actual etching processes. This finite selectivity may be accounted for in Eq. [1]-[4].

These improvements arise from the fact that the well-defined grating structure that is used lends itself to accu-

rate description by the mathematical model represented by Eq. [1]-[4].

Temporal evolution of h for infinite selectivity processes.—This matter was already described in a recent paper concerning the real-time measurement of the etching of thin film samples (5). The approach here is similar, except that, in this case, the film thickness T is constant and the substrate etched depth h is the variable in Eq. [4]. As pointed out above, the I_1/I_0 curve is periodic in h with period $\lambda/(2n_0)$ and $\lambda/(4n_0)$ between successive extrema (3), no matter whether the mask is metallic or dielectric. It should be noted that the film thickness T affects the sensitivity of the method: the period remains unchanged, but the amplitude of the I_1/I_0 oscillations is very dependent on the parameter T . Figures 2 and 3 illustrate this effect for a SiO_2 mask [$n_1 = 1.46$ (9)] on a Si substrate [$n_2 = 3.85 + i0.02$ (9)] for a wavelength of 6328Å , showing that T may be adequately chosen for optimizing the sensitivity of the I_1/I_0 variations.

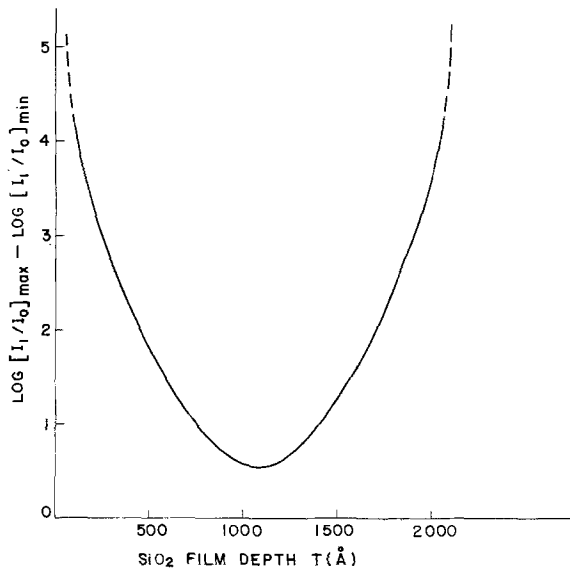


Fig. 3. Plotting of the amplitude of the I_1/I_0 vs. h curve as a function of the SiO_2 mask film thickness T (assuming $n_0 = 1$), showing that $T = \lambda/(4n_1) \sim 1100\text{Å}$ corresponds to the minimum. This curve is periodic in T , with period $\lambda/2n_1$.

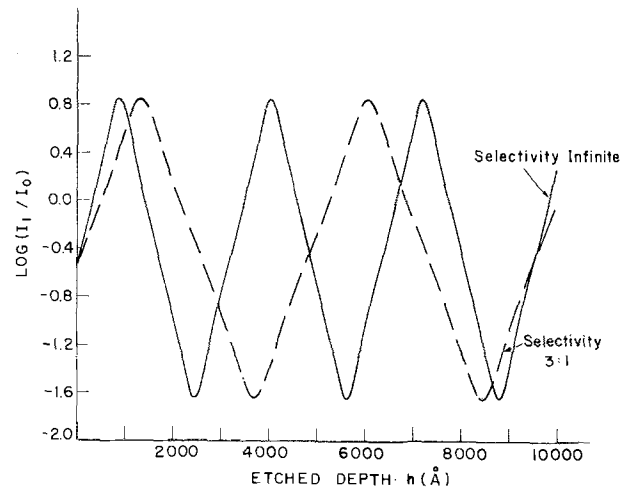


Fig. 5. This figure shows the same case as in Fig. 4, except that there is a 4000Å Al film on the Si instead of the SiO_2 film. Note that both curves corresponding to $S = \infty$ and $S = 3$ are periodic, but only the former has a period of $\lambda/2$. The dashed line ($S = 3$) has a period of $3\lambda/4$ as computed from Eq. [9].

Temporal evolution of h for finite selectivity processes.—A finite selectivity process means that T is somewhat modified from its initial value (T_0) as h increases from its initial zero value, so that

$$T = T_0 - \frac{h}{S} \quad [6]$$

where S should be defined as the selectivity of the process. The higher this value is, the more selective the process is.

Substituting Eq. [6] into Eq. [4] and assuming the sample in air ($n_0 = 1$), the terms in Eq. [5] turn into

$$\left. \begin{aligned} \cos 2\beta &= \cos(4\pi n_1 T_0/\lambda - 4\pi n_1 h/(S\lambda)) \\ \cos 2\gamma &= \cos(4\pi T_0/\lambda + 4\pi(1 - 1/S)h/\lambda) \\ \cos(2\beta - 2\gamma) &= \cos(4\pi T_0(n_1 - 1)/\lambda + 4\pi(1 - (n_1 - 1)/S)h/\lambda) \end{aligned} \right\} [7]$$

Through Eq. [7], it may be realized that all three cosine terms have different periods in h , which are

$$S \frac{\lambda}{2n_1}, S \frac{\lambda}{2(S - 1)}, \text{ and } \frac{2\lambda}{2(S - n_1 + 1)}$$

respectively.

If the selectivity S is finite, all three cosinoidal terms should have different periods so that the I_1/I_0 curve may not even be periodic. It may have relative extrema but in general they are not uniformly spaced from $\lambda/4$.

Figure 4 shows the computed I_1/I_0 vs. h for the case of a SiO_2 mask on a Si substrate having an initial thickness $T_0 = 4000\text{\AA}$, corresponding to a finite selectivity ($S = 3$) and to infinite selectivity for comparative purposes.

If a metallic mask is used instead of the SiO_2 , the three cosinusoidal terms in Eq. [5] turn into just one

$$\cos 2\gamma = \cos \left[\frac{4\pi T_0}{\lambda} + \frac{4\pi h}{\lambda} (1 - 1/S) \right] \quad [8]$$

which is periodic in h even considering a finite selectivity S , being the period H no longer $\lambda/2$ but

$$H = \frac{\lambda}{2(1 - 1/S)} \quad [9]$$

In Fig. 5, we have plotted the computed curves corresponding to an aluminum mask ($T_0 = 4000\text{\AA}$) on a Si substrate showing a period of $\lambda/2$ for infinite selectivity, and a period of $3\lambda/4$ (Eq. [9]) for finite selectivity ($S = 3$).

Note that for practical situations, the influence of the finite selectivity of the process cannot be neglected.

Experimental Setup and Results

The sample was a 2 in. silicon wafer in which a thin SiO_2 film was thermally grown. A lamellar grating with a period of $100\ \mu\text{m}$ and $a/d = 0.5$ was photolithographed in

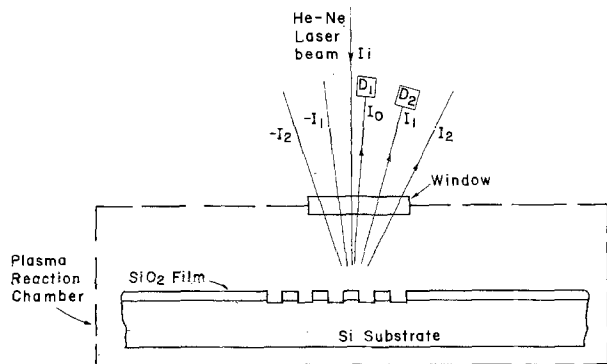


Fig. 6. Simplified schema of the plasma etching chamber and associated diffraction measurement setup.

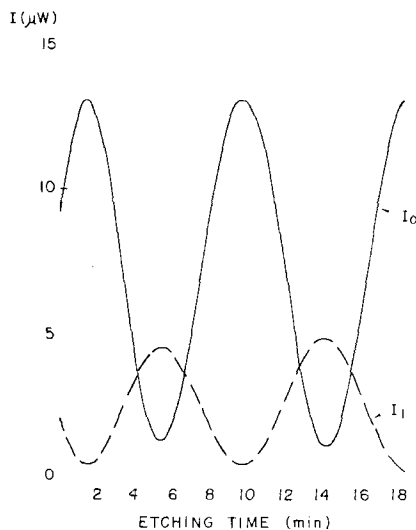


Fig. 7. The experimentally measured first and zero diffraction intensity orders as a function of the etching time for a lamellar grating being etched on a Si wafer through a thin SiO_2 mask, in air.

the SiO_2 film. The plasma etching of the silicon was carried out through the SiO_2 mask in a home-made planar reaction chamber of 8 in. diam with 20 mm distance between the electrodes. The reacting gas was CCl_4 . The plasma was excited by a 60W, 13.56 MHz RF generator. The pressure in the chamber was kept constant at 0.1 torr. A 1 mW commercial He-Ne laser ($\lambda = 6328\text{\AA}$) was directed near normal incidence onto the grating and the first and zero diffraction orders on reflection were measured and recorded with two photovoltaic silicon detectors D_1 and D_2 , as seen in the schematic setup in Fig. 6.

During the plasma etching process, the I_1 and I_0 orders were recorded as a function of the etching time (Fig. 7) in a Hewlett-Packard dual channel strip-chart recorder. From the above recorded data, we obtain the I_1/I_0 ratio evolution as a function of time, as seen in Fig. 8a. Note that the plot is not periodic (neither the amplitude nor the interval between successive extrema is constant), showing that the selectivity is not infinite and that it must be accounted for.

In Fig. 8b, we show the computed I_1/I_0 vs. h curve which best fits the experimental data in Fig. 8a. For doing that, a value for S was found that provided the best matching with the successive experimental I_1/I_0 vs. time extrema. For the present experiment, a slightly variable selectivity averaging $S = 30$ was found to suit the best, which value agrees in order of magnitude with previous independent tests performed on similar samples. Comparing the experimental and the fitted curve, a correlation between h and the etching time is obtained; it is plotted in Fig. 8c, which slope provides the evolution of the etching rate. For the present process it appears to be quite constant at $300\ \text{\AA}/\text{min}$.

Two pictures obtained with an interference microscope are shown in Fig. 9, where the shape and modulation of the sample grating may be appreciated before and after completion of the etching process.

Conclusions

The method we describe in this paper allows the continuous measurement of the etching depth, thus resulting in a very fine control over each individual sample. It is especially suited for small depths because it does not depend upon the presence of any singular point, such as the extrema in the reflectivity curve.

Furthermore, this method accounts for the presence of finite selectivities for the etching process and can even be used to calculate it if it is not known in advance with enough precision.

The method requires the etching of a lamellar grating, somewhere on the sample, to be carried out during the process that is being monitored.

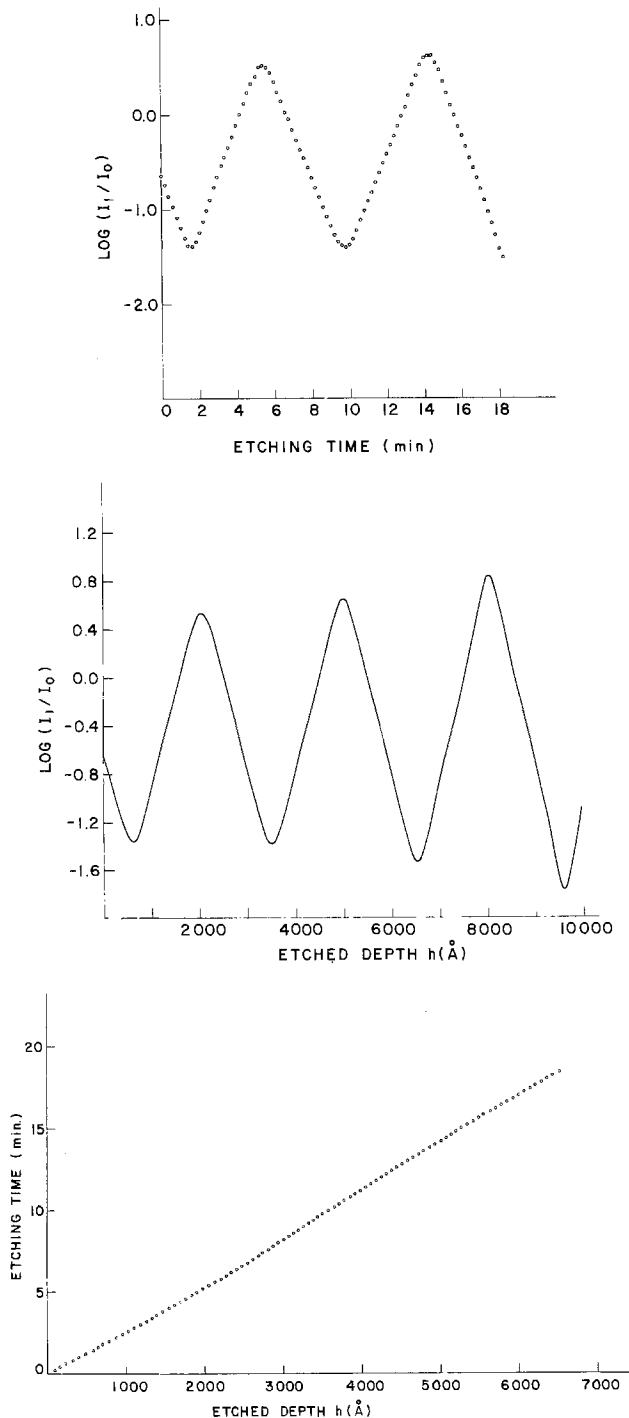


Fig. 8. The experimental data in Fig. 7 is rearranged in order to plot the I_1/I_0 ratio (a, top). A computed I_1/I_0 vs. h curve was plotted (b, middle) which best fits the experimental data. This fitting leads to a value of $S \approx 30$. Comparing the experimental and computed curves, the etched Si depth (h) vs. etching time is plotted in (c, bottom) which slope indicates etching rate of $\approx 300 \text{ \AA}/\text{min}$.

Some optical parameters of the sample must be known in order to provide the data required by the mathematical model of the lamellar grating (Eq. [2]-[3]).

Automation and real-time measurement are possible, depending upon the degree of complexity of the experimental situation and availability of computational resources.

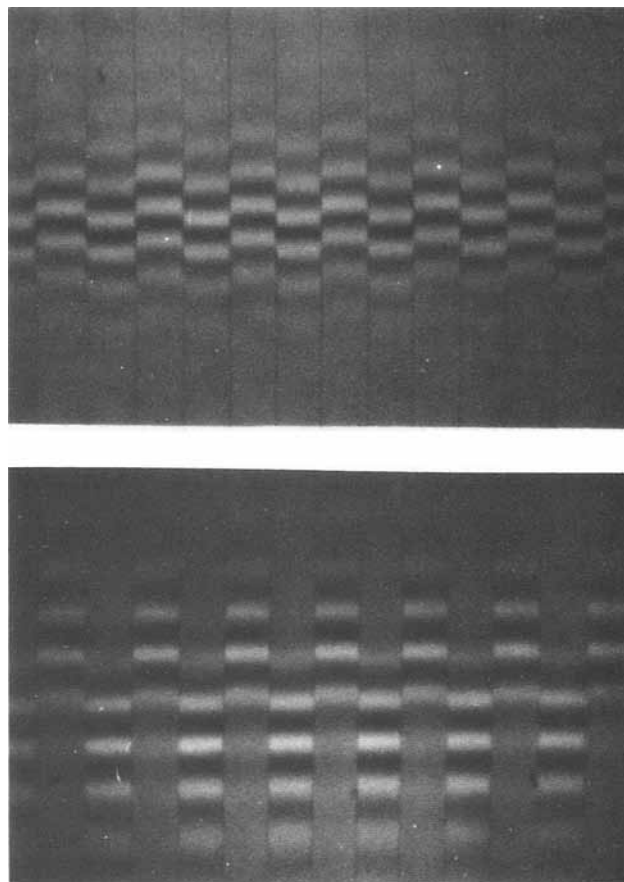


Fig. 9. Interferential microscope pictures showing the sample (a, top) before the plasma etching of Si and (b, bottom) after the plasma etching of Si and with the masking layer removed. $\lambda = 6000 \text{ \AA}$ is the average illumination on wavelength.

Acknowledgments

This work was supported by CNPq (Conselho Nacional de Desenvolvimento Científico e Tecnológico), FINEP (Financiadora de Estudos e Projetos), TELEBRÁS (Telecomunicações Brasileiras S/A), and FAPESP (Fundação de Amparo à Pesquisa do Estado de São Paulo). The authors would like to thank Mr. H. C. Carvalho and Mr. M. Barnett for technical assistance.

Manuscript submitted Feb. 27, 1984; revised manuscript received Aug. 22, 1984.

REFERENCES

1. H. P. Kleinknecht and H. Meier, *This Journal*, **125**, 798 (1978).
2. M. Sternheim and W. van Gelder, *ibid.*, **130**, 655 (1983).
3. G. F. Mendes, L. Cescato, and J. Frejlich, *Appl. Opt.*, **23**, 571 (1984).
4. G. F. Mendes, L. Cescato, and J. Frejlich, *ibid.*, **23**, 576 (1984).
5. G. F. Mendes, L. Cescato, E. S. Braga, J. Frejlich, and A. P. Mammana, *Thin Solid Films*, **117**, 107 (1984).
6. E. S. Braga, G. F. Mendes, J. Frejlich, and A. P. Mammana, *ibid.*, **109**, 363 (1983).
7. M. Born and E. Wolf, "Principles of Optics," 5th ed., pp. 61-62, Pergamon Press, Oxford, England (1975).
8. P. H. Berning, "Physics of Thin Films," Vol. 1, p. 69, Academic Press, New York (1963).
9. Ellipsometric Tables, Ellipsometer Model L-117, from Gaertner Scientific Corporation, Chicago, IL.

Dopant Activation and Redistribution in As⁺-Implanted Polycrystalline Si by Rapid Thermal Processing

R. A. Powell and R. Chow

Varian Associates, Incorporated, Corporate Solid State Laboratory, Palo Alto, California 94303

ABSTRACT

Dopant activation and redistribution in ⁷⁵As⁺-implanted (100 keV, 1×10^{15} - 1×10^{16} cm⁻²) polysilicon films following rapid thermal processing (RTP) are reported. For the annealing conditions used (10-30s exposure to a 1150°C graphite heater), significant arsenic redistribution was observed, unlike the case of comparably implanted and annealed single-crystal silicon. For uncapped films, surface loss of arsenic during RTP resulted in high sheet resistance; however, a thin oxide cap (600Å) prevented this arsenic loss. Sheet resistance comparable to furnace-annealed samples ($\sim 30 \Omega/\square$ for 1×10^{16} cm⁻² dose films) could then be obtained in ~ 15 s. The shape of carrier concentration and total dopant depth profiles following RTP was found to be dependent on both implant dose and time of annealing. These results can be qualitatively understood using recently proposed models for arsenic diffusion in furnace-annealed polysilicon films.

Doped polysilicon is employed for a variety of purposes in the fabrication of microelectronic devices, including interconnect lines and gate electrodes in MOS integrated circuits, emitters in bipolar transistors, and high-value load resistors in static random access memory circuits (1). For the latter two applications, the required doping can be accomplished with precise control by use of ion implantation (2, 3). For the fabrication of polycide structures (silicide/n⁺-polysilicon), it may also be advantageous to use ion implantation, since the high conductivity of the silicide allows reduced doping levels to be used in the underlying polysilicon (4). Following implantation, polysilicon films are in general subjected to a variety of high temperature cycles, and the effect of dopant redistribution must be considered. For example, unwanted lateral diffusion of arsenic in implanted-polysilicon load resistors can reduce resistor length and alter circuit electrical characteristics (3).

Over the last several years, rapid thermal processing (RTP) has been developed as an alternative to conventional furnace annealing, whereby high temperature steps are carried out in times so short that minimal dopant redistribution occurs (5). Particularly attractive is RTP performed in an isothermal mode, whereby the whole wafer volume is uniformly heated to temperature $\geq 800^\circ\text{C}$ in times on the order of 1-10s. Isothermal RTP has been successfully used to activate dopants and anneal out implant damage in single-crystal Si (6, 7) and, more recently, to rapidly sinter silicides (8-9) and Ti-polycides (10).

In actual device fabrication, such applications of RTP are likely to affect polysilicon layers as well. For example, when isothermal RTP is used to remove implant damage from the self-aligned source/drain regions of a MOSFET, the adjacent polysilicon gate will also be subjected to the same rapid high temperature anneal. For this reason, it is important to understand the effect of RTP on ion-implanted polysilicon. In cases where annealing of polysilicon is desired, e.g., for the activation of implanted species or for dopant drive-in into an underlying single-crystal substrate (11), it may be possible to precisely control dopant redistribution profiles by a proper choice of rapid annealing conditions.

In this paper, we report the effect of isothermal RTP on ⁷⁵As⁺-implanted polysilicon films, with particular attention to dopant activation and redistribution.

Experimental

Polysilicon films of thickness $0.41 \pm 0.10 \mu\text{m}$ were deposited by low pressure CVD onto oxidized Si substrates. Substrates were Czochralski-grown, 100 mm diam, n-type Si (100) wafers on which 800Å of thermal oxide was grown. The oxide was used to simulate a polysilicon gate MOS structure and served to isolate the polysilicon overlayer for subsequent sheet resistance measurements. Samples were implanted with either 1×10^{15} cm⁻² or 1×10^{16} cm⁻² As⁺ at 100 keV, which is a shallow implant with

respect to the polysilicon film thickness [experimentally measured range and standard deviation are $R_p = 500\text{Å}$ and $\Delta R = 235\text{Å}$, respectively (12)]. To investigate the effectiveness of a surface barrier in preventing arsenic outdiffusion, one-half of each wafer was capped with about 600Å of SiO₂, deposited by plasma-enhanced CVD. The low temperature (<200°C) of the plasma-deposition step prevented activation or diffusion of the implanted arsenic prior to rapid annealing.

All annealed samples were subsequently characterized by four-point probe measurement of sheet resistance. Selected samples were analyzed by secondary ion mass spectrometry (SIMS) to determine arsenic concentration depth profiles¹ and by spreading resistance probe measurements to determine electrically active dopant profiles.²

RTP was carried out using an automated, serial process rapid thermal processing system (Varian Model IA-200) (13). This same equipment has been used to successfully anneal and activate As⁺-implanted single-crystal Si with minimal dopant redistribution (7, 14-16). Wafers are exposed in vacuum of $\sim 2 \times 10^{-6}$ torr to the blackbody radiation of a resistively heated planar graphite heater which is continuously on during the annealing process. The time which a Mo shutter, located between heater and sample, is open determines exposure time and can be regulated to ± 0.15 s. Past experience with RTP of As⁺-implanted single-crystal Si (14-16) guided the choice of annealing conditions used in the present study of polysilicon; viz., heater temperature was set at 1150°-1300°C in 50°C intervals and exposure times ranged from 5 to 25s in 5s intervals. From measurements of the wafer's central area with a focused IR pyrometer, sample temperature was estimated to be $>900^\circ\text{C}$ after 10s and within $\sim 10^\circ\text{C}$ of the heater set-point temperature after 25s. Figure 1 plots the measured wafer temperature as a function of exposure time to the graphite heater (1150°-1300°C). As used in this paper, the terms "annealing temperature" and "annealing time" refer to heater temperature and total exposure time to the heater, respectively.

Results

Four-point probe data from As⁺-implanted polysilicon films annealed without an oxide cap is presented in Fig. 2. Sheet resistance, R_s , is plotted vs. exposure time for implant doses of 1×10^{15} cm⁻² and 1×10^{16} cm⁻² and heater temperatures of 1150°-1300°C. For comparison, data obtained by Wilson *et al.* on As⁺-implanted (100 keV, 1×10^{15} cm⁻²) single-crystal Si annealed in an identical RTP system is also shown (14). Arsenic doses in excess of 1×10^{15} cm⁻² are sufficient to amorphize the polysilicon surface region and increase its reflectivity. Films exposed to the

¹SIMS performed at Charles Evans & Associates, San Mateo, California.

²Spreading resistance probe measurements performed at Solcon Laboratories, Sunnyvale, California.

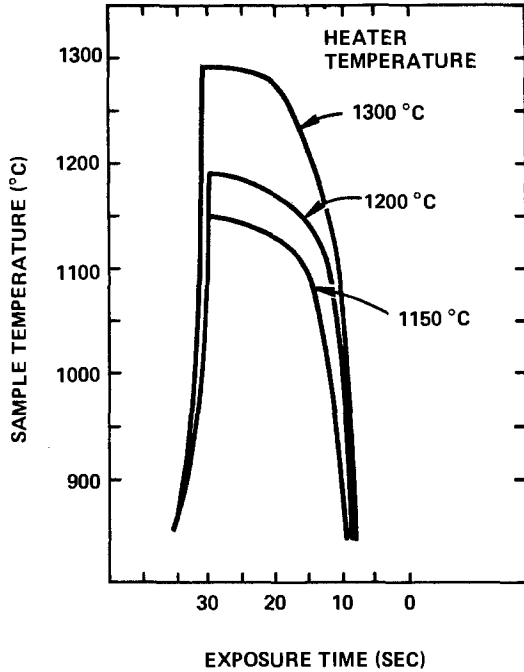


Fig. 1. Time-temperature profile of a Si (100) wafer exposed to a graphite heater for 30s with heater temperatures as shown. After 30s, the heater is shuttered off and the wafer cools by radiation.

heater for 5s or less maintained this higher reflectivity over their complete surface area. For exposures between 5 and 10s, incomplete annealing, as evidenced by gross

nonuniformity of both surface reflectivity and sheet resistance, was observed.

For exposures above 10s, the sheet resistance increases rapidly with time of RTP, this increase being more pronounced at higher annealing temperatures. For example, at 1300°C, depending on implant dose, R_s increases by 3-4 orders of magnitude as exposure time increases from 10-25s. The lowest values of R_s , obtained following 1150°C, 10s exposure, were ~ 220 and $\sim 1000 \Omega/\square$ for $1 \times 10^{16} \text{ cm}^{-2}$ and $1 \times 10^{15} \text{ cm}^{-2}$ As⁺ dose, respectively. By contrast, comparably implanted (100-keV, As⁺, $1 \times 10^{15} \text{ cm}^{-2}$) and annealed single-crystal Si has a sheet resistance which is 10-100 times lower than that of polysilicon (Fig. 2) and which is relatively insensitive to exposure time. For the single crystal, R_s reaches a minimum value of $\sim 90 \Omega/\square$ after 15s exposure at 1150°C and then increases to $\sim 110 \Omega/\square$ after 25s. Wilson *et al.* attribute this increase to loss of implanted arsenic from the uncapped single-crystal Si surface (14) and, for these RTP conditions, calculate an arsenic diffusivity of $\sim 9 \times 10^{-13} \text{ cm}^2/\text{s}$. It is well known that the diffusion coefficient of As in polysilicon is enhanced due to grain boundary diffusion and can be much greater than in single-crystal Si: 10^2 - 10^3 times greater at temperatures $\sim 1150^\circ\text{C}$ (2, 12, 17). Assuming this enhancement holds under RTP conditions as well, one expects effects observed in single-crystal Si and attributed to dopant outdiffusion to be far more pronounced in the case of polysilicon. This is seen to be the case in Fig. 2 for the $1 \times 10^{15} \text{ cm}^{-2}$ dose implants annealed at 1150°C. As exposure time varies from 15-25s, sheet resistance of the single crystal increases by about 20%, while that of the polysilicon film increases by more than an order of magnitude.

In the case of ³¹P⁺-implanted polysilicon ($1 \times 10^{16} \text{ cm}^{-2}$, 40-80 keV), surface loss of dopants during RTP has also contributed to high values of sheet resistance (18). Dopant depth profiles to be presented later support the conclusion that significant arsenic migration is occurring in our polysilicon films under RTP conditions which, in single-crystal Si, give rise to negligible redistribution.

One way of avoiding arsenic outdiffusion during furnace annealing of polysilicon is to employ an oxidizing ambient (2, 12) or Si₃N₄ cap (12). In the case of isothermal RTP, thin oxide capping layers ($\sim 500\text{\AA}$) have successfully prevented arsenic loss from single-crystal samples (14, 15), while thick capping layers ($\sim 3000\text{\AA}$) of phosphosilicate glass have prevented phosphorus outdiffusion (18). In Fig. 3, we present our results for polysilicon samples capped with a thin oxide. The implantation and the rapid annealing conditions are the same as in Fig. 2; the 600Å of plasma-deposited oxide was wet chemically stripped in BHF prior to sheet resistance measurement.

Comparison in Fig. 3 with data of Wilson *et al.* (15) show that the sheet resistance of identically implanted and rapidly annealed (1200°C) single and polycrystalline silicon samples exhibit qualitatively the same behavior, but values of R_s for the single-crystal case are several times lower. For example, after a 25s 1200°C anneal, R_s for implanted single-crystal Si ($1 \times 10^{16} \text{ cm}^{-2}$ dose) is $\approx 11 \Omega/\square$, while the corresponding value of polysilicon is $\approx 35 \Omega/\square$. This difference is more pronounced at $1 \times 10^{15} \text{ cm}^{-2}$ dose where values of $R_s = 80$ and $700 \Omega/\square$ are obtained for single-crystal and polysilicon, respectively.

Depth profiles of total dopant concentration (*i.e.*, both electrically active and inactive arsenic), measured by SIMS, and carrier concentration, measured by spreading resistance probe, are plotted in Fig. 4-6 for capped polysilicon films. Conditions of RTP were 1150°C and 15-25s. The atomic concentration scale is based on previous analysis of an As⁺ implant standard, while the depth scale is determined by direct profilometer measurement of the sputtered crater depth following SIMS. In the absence of direct mobility profile measurements on these films, spreading resistance data were converted to carrier concentration by using mobility values obtained by Wilson on similarly implanted and rapidly annealed LPCVD polysilicon films (18).

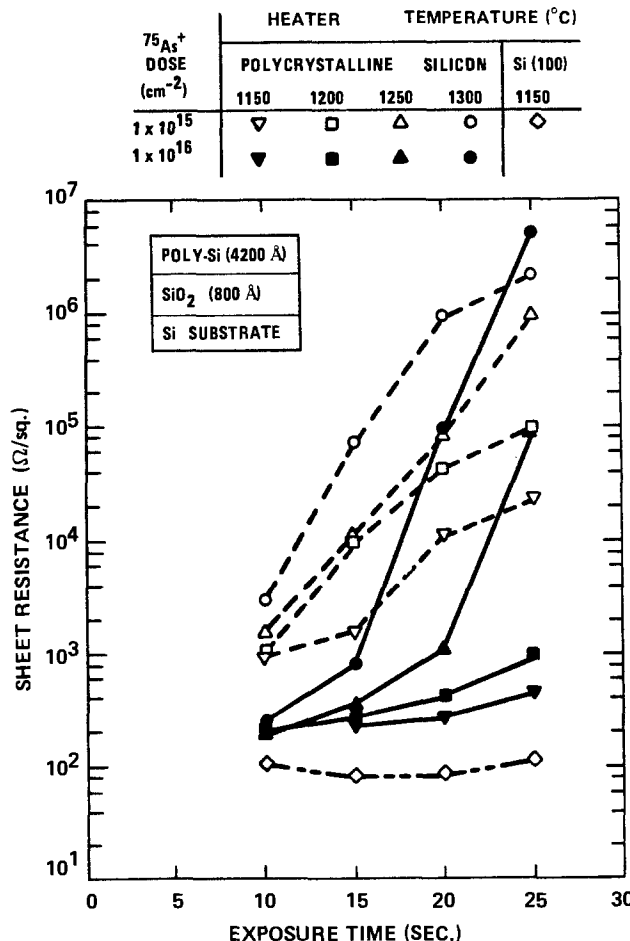


Fig. 2. Sheet resistance vs. exposure time to the graphite heater (1150°-1300°C) for As⁺-implanted polysilicon films. The films were uncapped and had either a $1 \times 10^{16} \text{ cm}^{-2}$ (solid line) or a $1 \times 10^{15} \text{ cm}^{-2}$ (dashed line) implant dose. Results of similarly processed single-crystal Si(100) wafers [Ref. (14)] are given for comparison (phantom line).

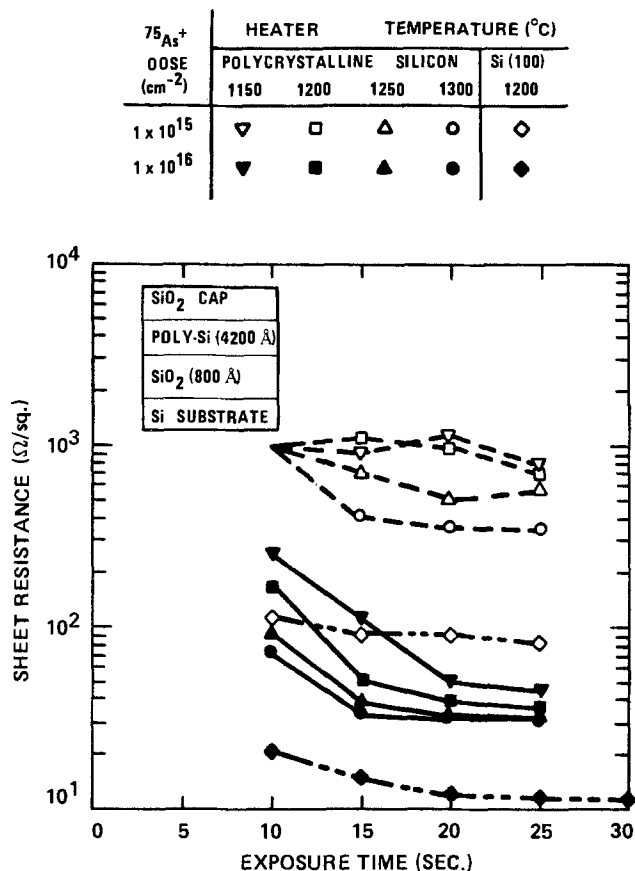


Fig. 3. Sheet resistance vs. exposure time to the graphite heater (1150° - 1300°C) for As^+ -implanted polysilicon films. The films were capped with 600\AA of SiO_2 prior to rapid anneal, and had either a $1 \times 10^{15} \text{ cm}^{-2}$ (solid line) or a $1 \times 10^{16} \text{ cm}^{-2}$ (dashed line) implant dose. The results of similarly processed single-crystal Si(100) wafers [Ref. (16)] are given for comparison (phantom line).

Figures 4 and 5 show data obtained from $1 \times 10^{15} \text{ cm}^{-2}$ dose implants annealed for 15 and 25s, respectively. In Fig. 4, the Gaussian as-implanted arsenic profile, taken from experimental result of Tsukamoto *et al.* (12) for 100-keV $^{75}\text{As}^+$ into polysilicon, is also shown. After 15s anneal, the atomic arsenic concentration still peaks at the range of the as-implanted profile, but at a value which is slightly less (about $1.2 \times 10^{20} \text{ cm}^{-3}$) than that before RTP (about $1.8 \times 10^{20} \text{ cm}^{-3}$). The concentration profile then gradually tails exponentially off with distance, reaching about $2 \times 10^{18} \text{ cm}^{-3}$ at the polysilicon-oxide interface, where it decreases abruptly.

By contrast, As^+ implants into single-crystal Si (100 keV, $1 \times 10^{15} \text{ cm}^{-2}$) show only slight dopant redistribution after identical rapid annealing conditions (14). Moreover, the polysilicon carrier concentration profile (dashed line) is dramatically different than the dopant profile (solid line) in that it does not exhibit a gradual tail. Instead, it decreases rapidly with depth, closely resembling the tail off of the Gaussian as-implanted profile. Comparison of carrier and dopant profiles show that at depths $\geq 0.2 \mu\text{m}$ arsenic is present in relatively high concentration ($\sim 10^{18}$ - 10^{19} cm^{-3}) but is almost completely inactive.

After 25s anneal (Fig. 5), however, the shape of carrier and atomic concentration profiles are seen to be similar. Namely, dopant redistribution is so great that relatively flat profiles are measured throughout the entire polysilicon film thickness. The sharp peak at the oxide interface is probably not arsenic pile-up, but an artifact of the SIMS technique caused by oxide charging and higher secondary ion yield from arsenic in the oxide matrix (20). Good agreement of the integrated area under the SIMS profile with the implanted dose shows that loss of arsenic from the capped films is negligible.

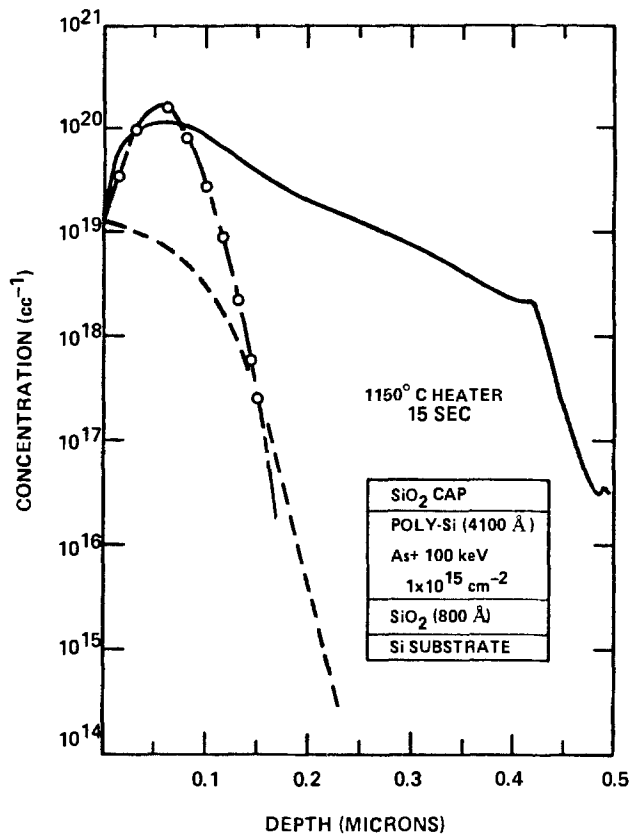


Fig. 4. Depth profiles of atomic dopant concentration (solid line) obtained by SIMS and carrier concentration (dashed line) determined from spreading resistance data for $1 \times 10^{15} \text{ cm}^{-2}$ dose implanted polysilicon films. The films were capped with 600\AA of SiO_2 and exposed to the heater at 1150°C for 15s. The as-implanted arsenic profile prior to RTP (dotted line) is taken from Ref. (12) for 100-keV, $1 \times 10^{15} \text{ cm}^{-2} \text{ As}^+$.

Discussion

The behavior observed in Fig. 4 and 5 can be qualitatively understood by a model for the thermal diffusion of implanted arsenic in polysilicon proposed by Swaminathan *et al.* (17). In this model, As atoms are electrically active when located within the crystalline grains, but inactive when located along the grain boundaries. In addition, arsenic diffuses much more rapidly along the grain boundaries than within the bulk of the grains (about four orders of magnitude faster). Before RTP, the implanted arsenic is mostly in the interior of the grains and is distributed within $\sim R_p + \Delta R \approx 0.1 \mu\text{m}$ of the surface. Upon rapid heating, implant damage begins to anneal out as As atoms begin to activate within the grains and to segregate out at the grain boundaries. Diffusion along the grain boundaries then rapidly transports electrically inactive arsenic deeper into the film, where it much more slowly diffuses back into the grain interiors and becomes electrically active. In light of this model, the gradual tail of the atomic concentration profile seen in Fig. 4 at depth $\geq 0.2 \mu\text{m}$ is taken to represent electrically inactive As atoms along the grain boundaries. The carrier concentration, similar in shape to the as-implanted profile, is taken to represent As atoms which have been activated but have not diffused far from their original positions within the grains. This interpretation is consistent with estimated diffusion lengths for As in single-crystal and polysilicon. Data of Swaminathan *et al.* (17) extrapolated to 1100°C gives a grain boundary diffusion coefficient of $D_1 \approx 2 \times 10^{10} \text{ cm}^2/\text{s}$. Data of Wilson *et al.* (14) give a diffusion coefficient of $D_2 \approx 9 \times 10^{-13} \text{ cm}^2/\text{s}$ for single-crystal silicon samples with implant and RTP conditions the same as the polycrystalline samples used in the present study. Assuming our wafers were close to 1100°C for $t \sim 5\text{s}$ (Fig. 1), leads to thermal diffusion of $\sqrt{2D_1 t} \sim 0.5 \mu\text{m}$ and $\sqrt{2D_2 t}$

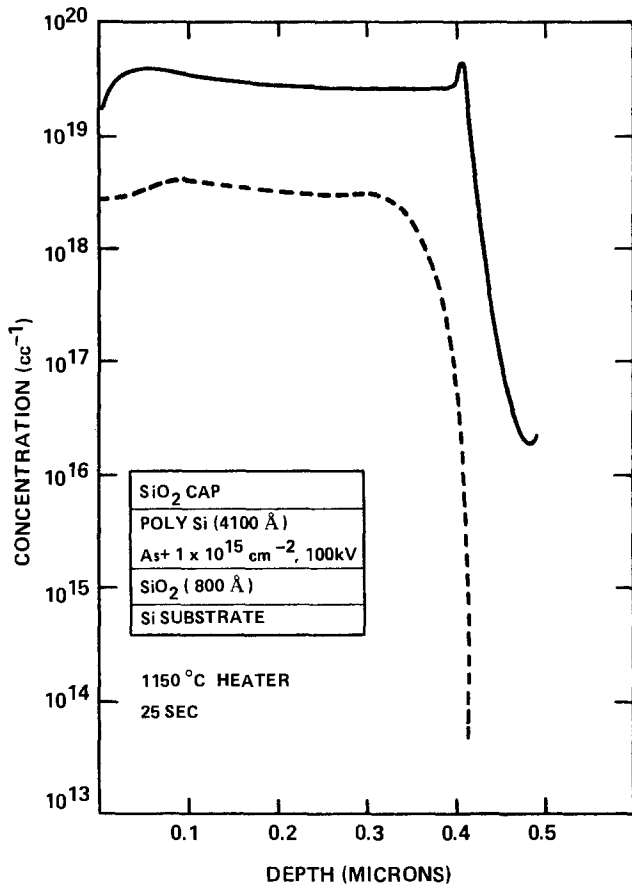


Fig. 5. Depth profiles of dopant (solid line) and carrier (dashed line) concentration for implanted and capped polysilicon films (As⁺, 100 keV, $1 \times 10^{15} \text{ cm}^{-2}$) which were exposed to the 1150°C heater for 25s.

$\sim 0.03 \mu\text{m}$. The former length is comparable to the polysilicon film thickness, while the latter is approximately the observed broadening of the carrier profile relative to that of the as-implanted dopants. As exposure time increases to 25s and wafer temperature to $\sim 1150^\circ\text{C}$, one expects diffusion lengths within the grains to be comparable to or greater than the average grain size [$\sim 600\text{\AA}$ as determined from TEM micrographs³ of these samples] and a larger fraction of the implanted arsenic can reach the grain boundaries. In addition, As atoms which have diffused into the film have had more time to diffuse back into deeper lying grains and be activated. The net effect is that after 25s exposure (Fig. 5), the shape of electrically active and total dopant profiles are brought into closer agreement.

Data for a polysilicon film implanted at $1 \times 10^{16} \text{ cm}^{-2}$ dose and annealed for 15s are shown in Fig. 6. Unlike the $1 \times 10^{15} \text{ cm}^{-2}$ dose data in Fig. 4, the carrier and atomic concentration curves in this case have a similar, flat profile throughout the film, more like the 25s anneals shown in Fig. 5. One possible explanation for this dose-dependent behavior is that the wafer with the higher dose implant may have more quickly reached thermal equilibrium with the heater, so that the effective time for arsenic diffusion at 1150°C was longer. Measurements of wafer temperature *vs.* exposure time made with an IR pyrometer do not support this explanation. Instead, we propose that dose-dependent differences in the arsenic profiles following RTP are due to the concentration-dependent diffusivity of arsenic in single-crystal silicon which is known to increase with carrier concentration (21).

Studies by Swaminathan *et al.* (17) of concentration profiles of As⁺-implanted polysilicon after furnace annealing (750°-950°C) indicate that the grain boundary diffusion coefficient is more or less independent of arsenic concentration or polysilicon grain size (0.2-0.5 μm grains),³ TEM analysis performed by Universal Energy Systems, Dayton, Ohio.

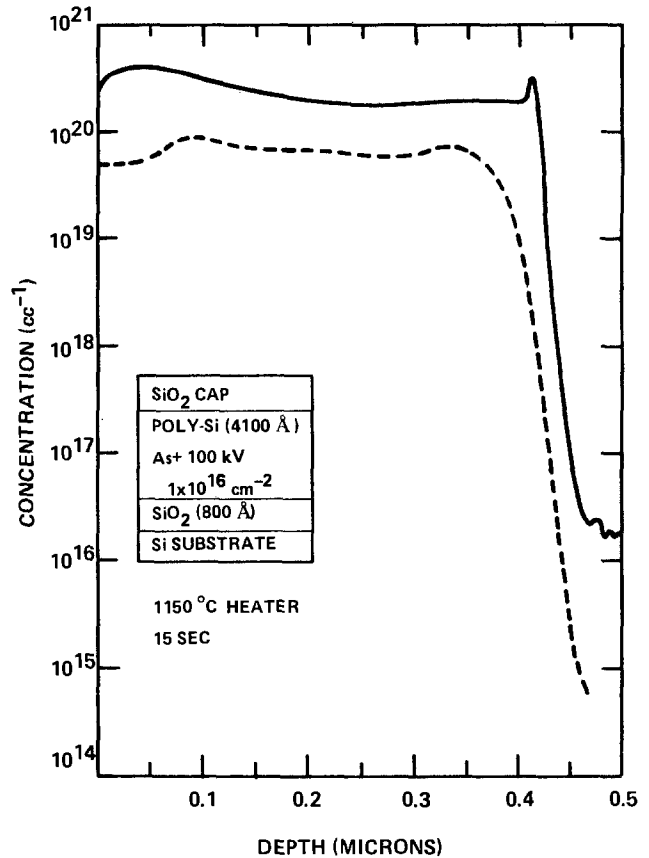


Fig. 6. Depth profiles of dopant (solid line) and carrier concentration (dashed line) for implanted (As⁺, 100 keV, $1 \times 10^{16} \text{ cm}^{-2}$) and capped polysilicon films which were exposed to the 1150°C heater for 15s.

while the diffusion coefficient within the grains is the same as in single-crystal Si. Using the model presented earlier in connection with Fig. 4 and 5, we qualitatively explain the difference between Fig. 4 and 6 as follows. Upon rapid annealing, As atoms diffuse from the bulk to segregate at the grain boundaries. Since the diffusivity of As in Si increases with concentration, we expect a greater percentage of implanted arsenic to reach the grain boundaries of the film with the higher, $1 \times 10^{16} \text{ cm}^{-2}$, dose. This greater source of dopant is then available for diffusion deeper into the film. Since diffusion back into the grain interiors is also expected to proceed more rapidly in the higher dose case, the activation profile can more closely track the dopant profile deeper in the film.

The $1 \times 10^{16} \text{ cm}^{-2}$ dose film annealed for 25s at 1150°C produced a relatively flat concentration profile averaging about $2.5 \times 10^{20} \text{ cm}^{-3}$ throughout the 0.41 μm thick polysilicon layer (Fig. 6) and exhibited a sheet resistance (Fig. 3) of $\sim 45 \Omega/\square$ ($\sim 1.8 \times 10^{-3} \Omega\text{-cm}$). Murota and Sawai (22) have reported the dependence of resistivity for annealed polysilicon films as a function of carrier concentration. Following 1150°C furnace anneal (N₂, 30 min), films with dopant concentrations the same as in Fig. 6 had resistivity about $1.6 \times 10^{-3} \Omega\text{-cm}$, comparable to that measured in this work under RTP conditions. Recently, Josquin *et al.* (11) reported sheet resistance of furnace-annealed 100-keV, $1 \times 10^{16} \text{ cm}^{-2}$, ⁷⁵As⁺-implanted, 0.5 μm polysilicon deposited onto field oxide. Following furnace anneal (1000°C, 95 min in N₂), a value of 65 Ω/\square was obtained, which again is similar to our result of $\sim 45 \Omega/\square$ for a 1150°C rapid anneal.

Summary

In conclusion, we have measured sheet resistance, dopant profiles, and carrier concentration profiles for As⁺-implanted polysilicon films. For the RTP conditions used, both $1 \times 10^{15} \text{ cm}^{-2}$ and $1 \times 10^{16} \text{ cm}^{-2}$ dose films exhibit significant dopant redistribution and, when uncapped, surface loss of arsenic after even 15s anneal,

unlike the case of comparably implanted and annealed single-crystal Si.

By use of a thin (600Å) oxide cap, however, arsenic outdiffusion could be completely prevented and stable sheet resistance of $\sim 30 \Omega/\square$ obtained for $1 \times 10^{16} \text{ cm}^{-2}$ films (25s, 1250°C). This value of sheet resistance is comparable to that of n⁺-polysilicon films produced by furnace annealing of identical As⁺ implants. The shape of the carrier concentration and total dopant profiles following RTP are dependent both on implant dose and annealing time. The behavior of these profiles can be qualitatively understood in terms of a model whereby (i) thermal diffusion of electrically active arsenic within the polysilicon grains and electrically inactive arsenic along the grain boundaries occur with significantly different rates, and (ii) where the former process is concentration dependent and the latter is not.

As a result of the rapid redistribution of dopants, thick ($\sim 0.4 \mu\text{m}$) polysilicon films could be uniformly doped in times on the order of 15s from a relatively shallow, high dose As⁺ implant (100 keV, $1 \times 10^{16} \text{ cm}^{-2}$). Under these same RTP conditions, comparably implanted and annealed single-crystal Si shows minimal dopant redistribution. It may be possible to use this fact to advantage when fabricating NMOS devices with self-aligned gates. In this case, a single, high dose As⁺-ion-implantation step could be used to dope source and drain regions as well as the surface of the polysilicon gate (capped by a thin oxide or Si₃N₄ layer). RTP could then be used to anneal implant damage and activate implanted dopants in the single-crystal source/drain regions with minimal dopant redistribution, preserving shallow n⁺-p junction depths. In the polysilicon layer, however, this same rapid anneal would produce significant arsenic redistribution resulting in a uniformly doped, low sheet resistance gate electrode. A second possibility suggested by the present study is to use heavily implanted polysilicon as a diffusion source and RTP as a means of rapidly driving arsenic from the polysilicon surface into a much deeper, underlying, single-crystal Si substrate. Fabrication of emitters and buried collectors for npn bipolar devices, for example, could then be carried out in the doped, damage-free single-crystal regions (11).

Finally, we note that the behavior of implanted arsenic observed under RTP in this work should not be assumed to hold, *a priori*, for other implanted species. For example, recent work on RTP of ¹¹B⁺-implanted polysilicon shows that successful activation can be achieved without having to cap the film surface (23).

Acknowledgments

Useful discussions with R. L. Bell are gratefully acknowledged, as is the technical support of M. Erickson, J.

Sonico, and H. Gilliland. N. Anderson prepared the manuscript.

Manuscript submitted Feb. 28, 1984; revised manuscript received Aug. 31, 1984.

Varian Associates, Incorporated, assisted in meeting the publication costs of this article.

REFERENCES

1. K. C. Saraswat, in "Grain Boundaries in Semiconductors," G. E. Pike, C. H. Seager, and H. J. Leamy, Editors, pp. 261-274, Elsevier, New York (1982).
2. H. Rysse, H. Iberl, M. Bleier, G. Prinke, K. Habberger, and H. Kranz, *Appl. Phys.*, **24**, 197 (1981).
3. N. Lewis, G. Gildenblat, M. Ghezzi, W. Katz, and G. A. Smith, *Appl. Phys. Lett.*, **42**, 171 (1983).
4. H. Norstrom, F. Runovc, R. Buchta, P. Wiklund, M. Ostling, and C. S. Petersson, *J. Vac. Sci. Technol. A*, **1**, 463 (1983).
5. T. O. Sedgwick, *This Journal*, **130**, 484 (1983), and references therein.
6. R. T. Fulks, C. J. Russo, P. R. Hanley, and T. I. Kamins, *Appl. Phys. Lett.*, **39**, 604 (1981).
7. D. F. Downey, C. J. Russo, and J. T. White, *Solid State Technol.*, **87**, (Sept., 1982).
8. R. T. Fulks, R. A. Powell, and W. T. Stacy, *IEEE Electron. Dev. Lett.*, **ed1-3**, 179 (1982).
9. R. A. Powell, R. Chow, C. Thridandam, R. T. Fulks, I. A. Blech, and J.-D. T. Pan, *ibid.*, **ed1-4**, 380 (1983).
10. C. B. Cooper III, R. A. Powell, and R. Chow, in "Energy Beam-Solid Interactions and Transient Thermal Processing," J. C. C. Fan and N. M. Johnson, Editors, p. 739, Elsevier, New York (1984).
11. W. J. M. J. Josquin, P. R. Boudewijn, and Y. Tamminga, *Appl. Phys. Lett.*, **43**, 960 (1983).
12. K. Tsukamoto, Y. Akasaka, and K. Horie, *J. Appl. Phys.*, **48**, 1815 (1977).
13. R. Iscoff, *Semicond. Intl.*, **69**, (Nov., 1981).
14. S. R. Wilson, R. B. Gregory, W. M. Paulson, A. H. Hamdi, and F. D. McDaniel, *Appl. Phys. Lett.*, **41**, 978 (1982).
15. S. R. Wilson, R. B. Gregory, W. M. Paulson, A. H. Hamdi, and F. D. McDaniel, in "Laser-Solid Interactions and Transient Thermal Processing of Materials," J. Narayan, W. L. Brown, and R. A. Lemons, Editors, p. 369, North-Holland, Amsterdam (1983).
16. S. R. Wilson, R. B. Gregory, W. M. Paulson, A. H. Hamdi, and F. D. McDaniel, *IEEE Trans. Nucl. Sci.*, **ns-30**, 1734 (1983).
17. B. Swaminathan, K. C. Saraswat, R. W. Dutton, and T. I. Kamins, *Appl. Phys. Lett.*, **40**, 795 (1982).
18. K. Takebayashi, T. Yokoyama, M. Yoshida, and M. Inoue, *This Journal*, **130**, 2271 (1983).
19. S. R. Wilson, Private communication.
20. C. Hopkins, Private communication.
21. M. Y. Tsai, F. F. Morehead, J. E. E. Baglin, and A. E. Michel, *J. Appl. Phys.*, **51**, 3230 (1980).
22. J. Murota and T. Sawai, *ibid.*, **53**, 3702 (1982).
23. R. Chow and R. A. Powell, Paper EMPWeA-05 presented at the 31st National Symposium of the American Vacuum Society, Reno, NV, Dec. 4-7, 1984.

Electrical Characteristics of Tantalum Pentoxide-Silicon Dioxide-Silicon Structures

S. Seki, T. Unagami, and B. Tsujiyama

Ibaraki Electrical Communication Laboratory, Nippon Telegraph and Telephone Public Corporation, Tokai, Ibaraki 319-11, Japan

ABSTRACT

Electrical characteristics for metal-tantalum pentoxide-silicon dioxide-silicon structures are described. The interface charge density and the surface-state density are measured to determine the interface properties. By optimizing each insulator thickness, the interface charge density can be reduced to as low as $6\text{--}12 \times 10^9 \text{ cm}^{-2}$ at flatband. The surface-state density of $3\text{--}4 \times 10^{10} \text{ cm}^{-2} \text{ eV}^{-1}$ can be obtained near the midgap by inserting a 25 nm thickness of SiO_2 . It is indicated that the interface charge density variation with each insulator thickness can be explained by the charge compensation mechanism between the positive charge at SiO_2/Si interface and the negative charge at $\text{Ta}_2\text{O}_5/\text{SiO}_2$ interface. It is found that the negative charge localized at $\text{Ta}_2\text{O}_5/\text{SiO}_2$ interface gradually decreases and that the dielectric constant for Ta_2O_5 deposited on SiO_2 monotonically increases with the underlying SiO_2 layer thickness.

In recent years, tantalum pentoxide (Ta_2O_5) film has been of interest for use as a storage capacitor in large-scale integrated-circuit memory cells (1, 2) and as a gate insulator for MOS devices (3, 4). The higher dielectric constant of Ta_2O_5 , compared with that of SiO_2 , makes it attractive as dielectric material for these devices. In our most recent paper, it was reported that a relatively good quality Ta_2O_5 gate insulator could be fabricated using RF-magnetron sputtering and that annealing in the hydrogen ambient had a great effect on removing damage produced during the sputtering process (4). Under optimum annealing conditions, the interface charge density could be reduced to as low as $-1.4 \times 10^{11} \text{ cm}^{-2}$ and the surface-state density of $1.5 \times 10^{11} \text{ cm}^{-2} \text{ eV}^{-1}$ could be obtained near the midgap. These were the lowest values in the $\text{Ta}_2\text{O}_5/\text{Si}$ interface to have been reported. However, in order to obtain high-quality MOS devices with high transconductance and low threshold voltage, it becomes increasingly important to reduce both the interface charge density and the surface-state density to much lower values.

In this work, the electrical characteristics of MTOS (metal-tantalum pentoxide-silicon dioxide-silicon) double-dielectric insulator structures have been studied. In this structure, a SiO_2 layer is inserted between the Ta_2O_5 layer and the silicon substrate in order to reduce damage induced during the Ta_2O_5 sputtering process. The interface charge density and the surface-state density are calculated from the high-frequency capacitance-voltage characteristics to investigate the interface behavior. This paper reports the results of these experiments and shows the effects of the inserted SiO_2 layer on the electrical properties of MTOS structures.

Experimental

$\text{Al}/\text{Ta}_2\text{O}_5/\text{SiO}_2/\text{Si}$ structures were used to investigate the interface behavior. All of the MTOS structures were fabricated on p-type, $\langle 100 \rangle$ -oriented, 10-20 $\Omega\text{-cm}$ silicon wafers. SiO_2 was thermally grown at 1100°C in dry oxygen atmosphere. The SiO_2 thickness was 86 nm. Immediately before being installed into the sputtering chamber, the wafer was etched by buffered HF solution to adjust the SiO_2 thickness. Sputtering was performed using an ULVAC SBH-2204 RS RF-magnetron sputtering system. Instead of the conventional oil diffusion pump, a cryogenic pump was used to eliminate oil contamination. The Ta_2O_5 target was 10 cm in diameter and 5 mm thick. The target-to-substrate distance was 5 cm. The sputtering gas consisted of mixtures of argon and oxygen (partial pressure ratio of $\text{Ar}/\text{O}_2 = 80/20$). The sputtering chamber was evacuated to less than 1×10^{-7} torr prior to sputtering and was then backfilled with the sputtering gas. The sputtering pressure was 5×10^{-3} torr. Typical deposition rate for Ta_2O_5 ranged from 2 to 6 nm/min. Aluminum dot electrodes 300 μm in diameter were electron-beam-deposited. To minimize the radiation damage, the wafers

were annealed at 450°C for 30 min in the hydrogen ambient.

After a final H_2 anneal, high-frequency capacitance-voltage characteristics were measured. In this measurement, capacitance meters (HP 4274A and HP 4275A) and a dc voltage source (HP 4140B) were automatically controlled by a microcomputer (APPLE II plus) through the General Purpose Interface Bus (GPIB). The interface charge density was calculated from the flatband voltage measured at 1 MHz, and the surface-state density distribution was obtained from the C-V characteristics measured at 1 mHz, using the Terman method (5). Frequency dispersion in the C-V characteristics was studied by varying the measurement frequencies in the range of 1 kHz to 1 MHz. These measurements were performed in the dark at room temperature.

Results and Discussion

Ta_2O_5 thickness dependence.—The interface charge density in the $\text{Al}/\text{Ta}_2\text{O}_5/\text{SiO}_2/\text{Si}$ structures has been studied for various Ta_2O_5 thicknesses. The SiO_2 thickness was adjusted to 22 nm by chemical etching, prior to the Ta_2O_5 sputtering deposition. After annealing in the hydrogen ambient, no apparent hysteresis and frequency dispersion were observed in their C-V curves.

Figure 1 shows the interface charge density variation with different Ta_2O_5 thicknesses. The interface charge density changes monotonically from positive to negative as the Ta_2O_5 thickness increases. The results shown in Fig. 1 indicate that the interface charge density can be controlled by adjusting the Ta_2O_5 thickness. This interface charge density variation can be explained by the charge compensation mechanism between the positive charge localized at the SiO_2/Si interface and the negative charge in the Ta_2O_5 layer. In our most recent paper, it was shown that the negative charge in the Ta_2O_5 layer was fully localized in the transition layer formed in the early stage of the Ta_2O_5 formation (4). Based upon this result, the negative charge in the Ta_2O_5 layer deposited on SiO_2 is assumed to be localized at the $\text{Ta}_2\text{O}_5/\text{SiO}_2$ interface. In this model, the interface charge density Q_{ss}/q can be given by

$$\begin{aligned} \frac{Q_{ss}}{q} &= \frac{1}{q} \int_0^{d_s} \frac{x}{d_{ox}} \rho_{ox}(x) dx \\ &= \frac{1}{q} \left\{ \frac{Kd_t}{d_s + Kd_t} (-Q_2) + Q_1 \right\} \quad K = \epsilon_s/\epsilon_t \quad [1] \end{aligned}$$

where d_s is the SiO_2 thickness, d_t is the Ta_2O_5 thickness, $\rho_{ox}(x)$ is the charge distribution function in the insulator, ϵ_s is the dielectric constant for SiO_2 , and ϵ_t is the dielectric constant for Ta_2O_5 . Q_1/q is the positive charge density at the SiO_2/Si interface and $-Q_2/q$ is the negative charge density at the $\text{Ta}_2\text{O}_5/\text{SiO}_2$ interface. Introducing

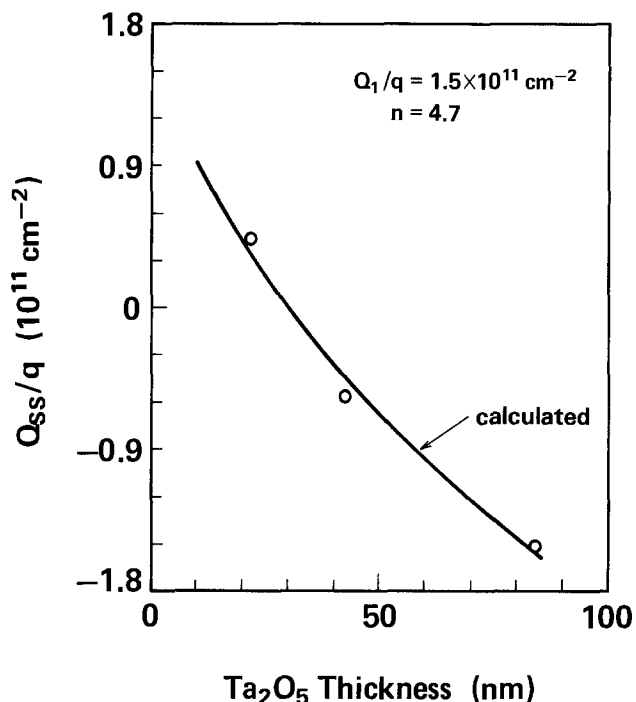


Fig. 1. The interface charge density variation with different Ta_2O_5 thickness. The SiO_2 thickness is adjusted to 22 nm. Calculated result of the interface charge density variation with Ta_2O_5 thickness is depicted by the solid line.

$$n = Q_2/Q_1 \quad [2]$$

Eq. [1] becomes

$$\frac{Q_{ss}}{q} = \frac{Q_1}{q} \left(1 - \frac{n}{1 + d_s/(Kd_i)} \right) \quad [3]$$

The interface charge density variations with Ta_2O_5 thickness were calculated for several sets of n and Q_1/q . Calculated results are given in Fig. 1. It is found that the best fit is obtained with $n = 4.7$ and $Q_1/q = 1.5 \times 10^{11} \text{ cm}^{-2}$.

SiO₂ thickness dependence.—Figure 2 shows the interface charge density variation with different SiO_2 thicknesses. The Ta_2O_5 thickness was kept within the range of 75–80 nm, and the SiO_2 thickness was varied within the

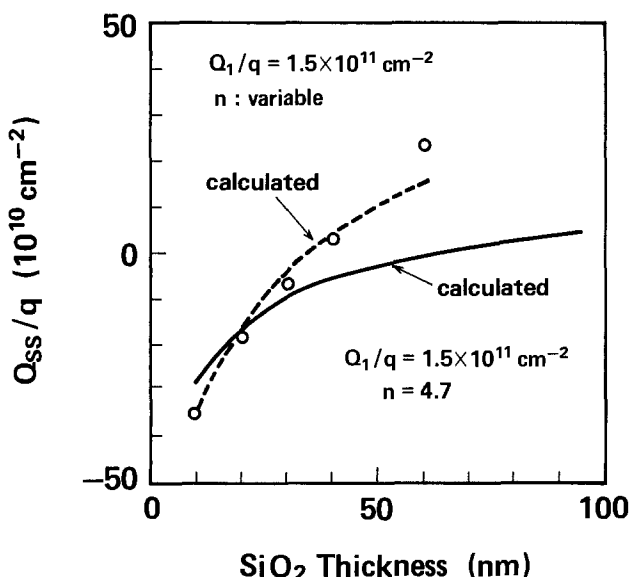


Fig. 2. The interface charge density variation with different SiO_2 thickness. The Ta_2O_5 thickness is kept within a range of 75–80 nm. Calculated results of the interface charge density variation with SiO_2 thickness are shown in the solid and dashed lines.

range of 10–60 nm by chemical etching. The interface charge density changes monotonically from negative to positive as the SiO_2 thickness increases. Results shown in Fig. 2 indicate that the interface charge density can be controlled by adjusting the SiO_2 thickness.

This interface charge density variation is based on the charge compensation mechanism described above. If Q_1 and Q_2 are assumed to be invariant with different SiO_2 thicknesses, the interface charge density variation can be expressed by Eq. [3] with $n = 4.7$ and $Q_1/q = 1.5 \times 10^{11} \text{ cm}^{-2}$. Calculated results based upon these values of n and Q_1/q are plotted in Fig. 2 (solid line). The experimental values do not coincide with the calculated result. This implies that the assumption mentioned above cannot be applied to the MTOS structure with different SiO_2 thicknesses, *i.e.*, charges in the insulator change with the underlying SiO_2 thickness. The positive charge localized at the SiO_2/Si interface is invariant throughout the whole SiO_2 thickness range studied. Therefore, results shown in Fig. 2 indicate that the negative charge at the $\text{Ta}_2\text{O}_5/\text{SiO}_2$ interface monotonically changes with the underlying SiO_2 thickness.

The variation of the negative charge with the underlying SiO_2 thickness is expressed by the simultaneous variation of the parameter n in Eq. [3]. Calculated results for the case that the parameter n is variable with the SiO_2 thickness are also shown in Fig. 2 (dashed line). In this case, the inversely proportional relationship between the parameter n and the SiO_2 thickness is considered as one example of variation manners of n ; the parameter n is assumed to decrease linearly from 5.5 to 0.5 as the SiO_2 thickness increases from 10 to 60 nm. The coincidence of the experimental data with calculated values is improved. Therefore, it is concluded that the negative charge at the $\text{Ta}_2\text{O}_5/\text{SiO}_2$ interface gradually decreases as the underlying SiO_2 thickness increases.

Based upon the results mentioned above, the MTOS structure with low interface charge density has been designed and fabricated. Figure 3 shows capacitance-voltage characteristics for the MTOS capacitor with the 25 nm-thick SiO_2 and the 38 nm-thick Ta_2O_5 . Measurement frequencies were varied in the range of 1 kHz to 1 MHz. As shown in Fig. 3, nearly ideal C-V curves were obtained, and no apparent hysteresis and frequency dispersion were observed. The interface charge density, calculated from the flatband voltage measured at 1 MHz, ranges from $6\text{--}12 \times 10^9 \text{ cm}^{-2}$. These are the lowest values to have been reported.

Surface-state density.—Figure 4 shows the surface-state density distributions near the valence band for $\text{Al}/\text{Ta}_2\text{O}_5/$

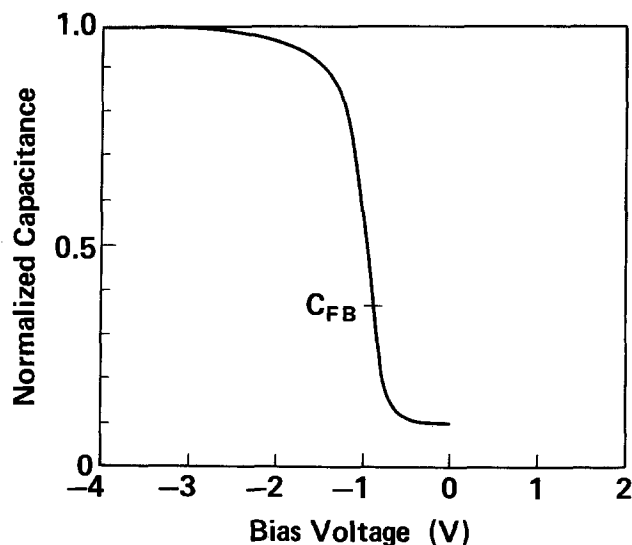


Fig. 3. Capacitance-voltage characteristics of the MTOS capacitor with optimum insulator thickness. The Ta_2O_5 thickness is adjusted to 38 nm; the SiO_2 thickness is adjusted to 25 nm.

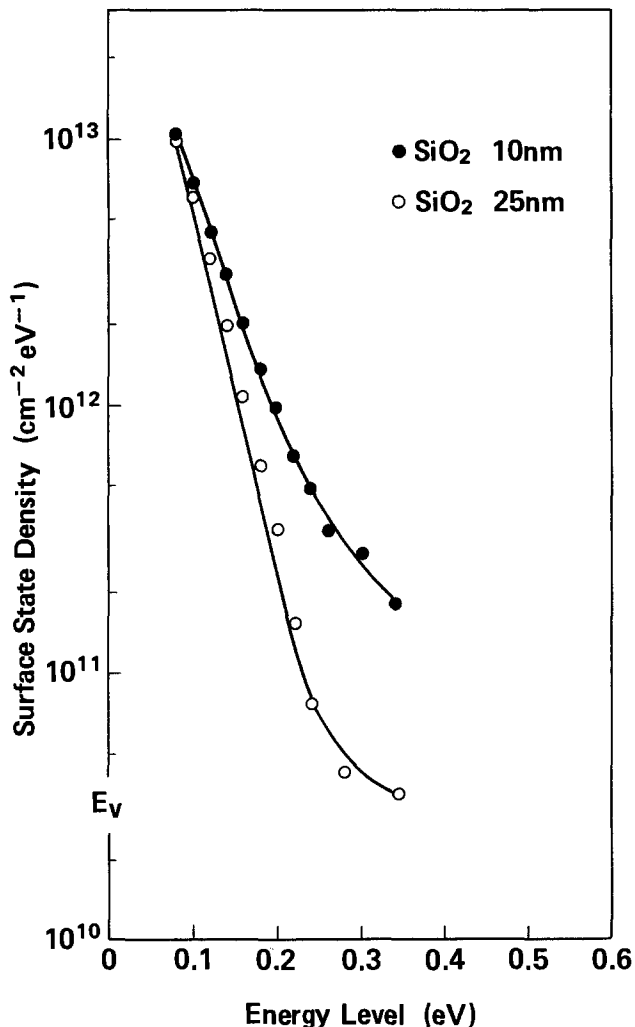


Fig. 4. The surface-state density distributions near the valence band are compared for two samples with different SiO₂ thicknesses. The SiO₂ thicknesses are 10 and 25 nm, respectively.

SiO₂/Si structures. The surface-state density distributions for two samples with different SiO₂ thicknesses are compared. The SiO₂ thicknesses are 10 and 25 nm, respectively. As shown in Fig. 4, lower surface-state density has been obtained for the sample with the thicker SiO₂ layer. The surface-state density has been able to be reduced to as low as $3.4 \times 10^{10} \text{ cm}^{-2} \text{ eV}^{-1}$ near the midgap. These are the lowest values in Al/Ta₂O₅/SiO₂/Si structure devices. Furthermore, the values obtained in this work are comparable to those for SiO₂/Si interface with an aluminum gate. Therefore, it is concluded that the SiO₂ layer, inserted between Ta₂O₅ and Si, has a great effect on the protection of the damage produced at the silicon surface during the Ta₂O₅ sputtering process.

Dielectric properties.—Dielectric properties of the Ta₂O₅ deposited on the SiO₂ layer have been studied. The dielectric constant of the Ta₂O₅ layer is calculated from the capacitance in the accumulated region of the C-V characteristics measured at 1 MHz, the Ta₂O₅ thickness, the SiO₂ thickness, the dielectric constant of SiO₂, and the electrode area. Figure 5 shows the dielectric constant variation for the Ta₂O₅ layer with changes in the underlying SiO₂ layer thickness. As shown in Fig. 5, the dielectric constant of the Ta₂O₅ layer monotonically increases as the SiO₂ layer thickness increases. The dielectric constant of Ta₂O₅ deposited on 10 nm-thick SiO₂ is 16.8, which is a smaller value than that for the bulk of Ta₂O₅. On the other hand, the dielectric constant of the Ta₂O₅ layer deposited on the 60 nm-thick SiO₂ reaches 23.8, which is very close to that for the bulk of Ta₂O₅.

It was reported in our most recent paper (4) that Ta₂O₅ deposited on single-crystalline silicon consisted of two re-

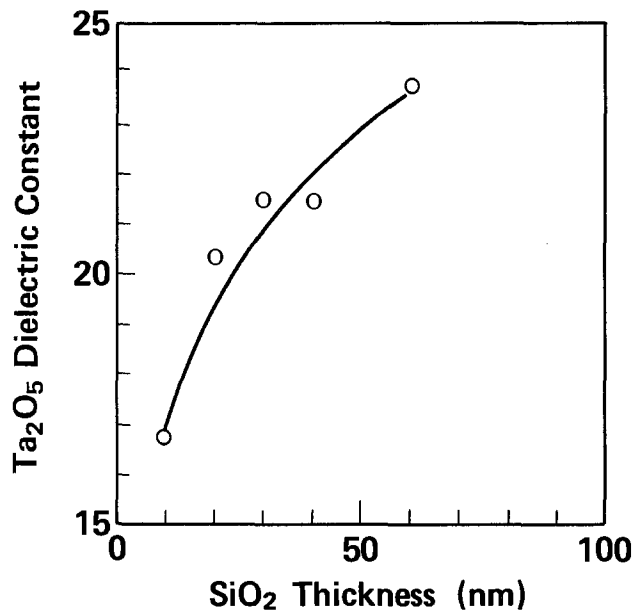


Fig. 5. The dielectric constant variation of Ta₂O₅ with the underlying SiO₂ thickness.

gions: a low dielectric-constant transition layer at the interface; and the following homogeneous layer, whose dielectric constant was close to that for the bulk of Ta₂O₅ (4). Applying this two-layer model to the Ta₂O₅ deposited on SiO₂, the dielectric constant variation shown in Fig. 5 can be explained by transition layer thickness changes: the low dielectric-constant transition layer thickness decreases as the underlying SiO₂ layer thickness increases. In this two-layer model, the negative charge is fully localized in the transition layer and it is assumed to change with the transition layer thickness variation. Under these assumptions, the dielectric constant variation with the underlying SiO₂ thickness is in coincidence with the gradual variation of the negative charge density localized at the Ta₂O₅/SiO₂ interface mentioned above.

Conclusions

Ta₂O₅ films were deposited onto thermally grown SiO₂ on the silicon substrate, using RF-magnetron sputtering. High-frequency capacitance-voltage characteristics were measured to determine the interface charge density and the surface-state density in the Al/Ta₂O₅/SiO₂/Si structures. The results indicate that the interface charge density can be controlled by adjusting the Ta₂O₅ and SiO₂ thickness. By optimizing each thickness, the interface charge density ranging from $6\text{--}12 \times 10^9 \text{ cm}^{-2}$ can be obtained. The surface-state density can be reduced to as low as $3.4 \times 10^{10} \text{ cm}^{-2} \text{ eV}^{-1}$ near the midgap by inserting 25 nm-thick SiO₂. These are the lowest values to have been reported.

It is also indicated that the interface charge density variation with Ta₂O₅ or SiO₂ thickness can be explained by the charge compensation mechanism between the positive charge at SiO₂/Si interface and the negative charge at Ta₂O₅/SiO₂ interface. In addition, it is found that the negative charge gradually decreases as the underlying SiO₂ thickness increases. The dielectric constant of the Ta₂O₅ layer deposited on the SiO₂ layer gradually increases with the underlying SiO₂ thickness. The negative charge variation and the dielectric constant variation with the underlying SiO₂ thickness can be explained by a two-layer model. A narrow transition layer exists at the interface, where the rest of the film is homogeneous.

Acknowledgment

The authors thank K. Murase for his encouragement during the course of this work.

Manuscript submitted Feb. 14, 1984; revised manuscript received June 7, 1984.

Nippon Telegraph and Telephone Public Corporation assisted in meeting the publication costs of this article.

REFERENCES

1. M. E. Elta, A. Chu, L. J. Mahoney, R. T. Cerretani, and W. E. Courteny, *IEEE Electron Device Lett.*, **ed1-3**, 127 (1982).
2. K. Ohta, K. Yamada, K. Shimizu, and Y. Tarui, *IEEE Trans. Electron Devices*, **ed-29**, 368 (1982).
3. D. J. Smith and L. Young, *ibid.*, **ed-28**, 22 (1981).
4. S. Seki, T. Unagami, and B. Tsujiyama, *This Journal*, **131**, 2621 (1984).
5. L. M. Terman, *Solid-State Electron.*, **5**, 285 (1962).

Surface Potential Profiling of HV Devices Using Scanning Auger Microscopy

D. M. Taylor¹, D. W. Tong, and W. R. VanDell²

General Electric Company Research & Development Center, Schenectady, New York 12345

ABSTRACT

The shift in Auger electron energies is used to measure the voltage profile on high voltage semiconductor devices. The scanning mode available on present-day Auger microscopes allows two-dimensional quantitative voltage-contrast imaging. This technique has been used to measure surface potentials on a high voltage npn transistor biased up to 1 kV. An accuracy of better than 10V and a spatial resolution of 8 μm are demonstrated.

Computer modeling is used extensively in the design of high voltage semiconductor devices. However, not many convenient techniques are available for testing the accuracy of the modeling, and often the breakdown voltage of the device is the only measurable parameter for comparison. Fine metal probes can be used for measuring the surface potential, but they have limited spatial resolution and may well be ineffective in the presence of passivation.

By measuring the energy shift of the secondary electrons, the scanning electron microscope (SEM) has been widely used as a noncontacting probe of submicron spatial resolution to measure voltages on integrated circuits (1-3). However, the low energy (5-10 eV) of the secondary electrons makes them unsuitable for probing high voltage devices where high lateral fields are present (4). For this reason, the use of Auger electrons of much higher energies was proposed over a decade ago for surface potential measurement of high voltage devices (5, 6). Surface potentials of $\pm 40\text{V}$ were successfully measured in this way. Since that time, Auger spectroscopy instrumentation has been considerably refined, and sophisticated signal processing has enhanced the capabilities of the method. Whereas the earlier instruments could only make point-by-point measurements, newer instruments provide a scanning mode so that two-dimensional potential contour images can be obtained. This work demonstrates, using a high voltage npn transistor, that surface potentials of up to 1 kV can be measured in this way.

It is known that a high energy beam penetrating an insulating film can render it locally conductive (7). This feature makes electron beam probing methods particularly suited to semiconductor devices having passivation layers, as demonstrated by the results of this work.

Experimental

The test devices used in the study were npn power transistors designed to operate up to 1 kV. Figure 1a is a schematic diagram of the cross section of the base-collector junction of such a device, and the surface of the device in this same region is shown in the SEM photograph in Fig. 1b. At the outer edge of the device and concentric with the base region are two p^+ field spreading rings. The outlines of the diffusion windows are clearly visible in the SEM image and serve as useful references for beam location. The devices were passivated with a 200 nm silicon nitride layer over a

450 nm semi-insulating polycrystalline silicon (SIPOS) layer.

All measurements were carried out in a PHI 590 SAM. Possible drift in the energies of the Auger lines, caused by charging of the insulating nitride layer, were minimized by using an accelerating voltage of 8 keV so that the beam easily penetrated through the nitride layer, thus rendering it conductive (7). During the measurements, the beam current was held constant at $\sim 1 \mu\text{A}$. The Auger spectrometer uses a lock-in amplifier (PAR Model 120) for the detection of the Auger signal. The modulation voltage of the amplifier can be varied from 1 to 20V, with the smaller values re-

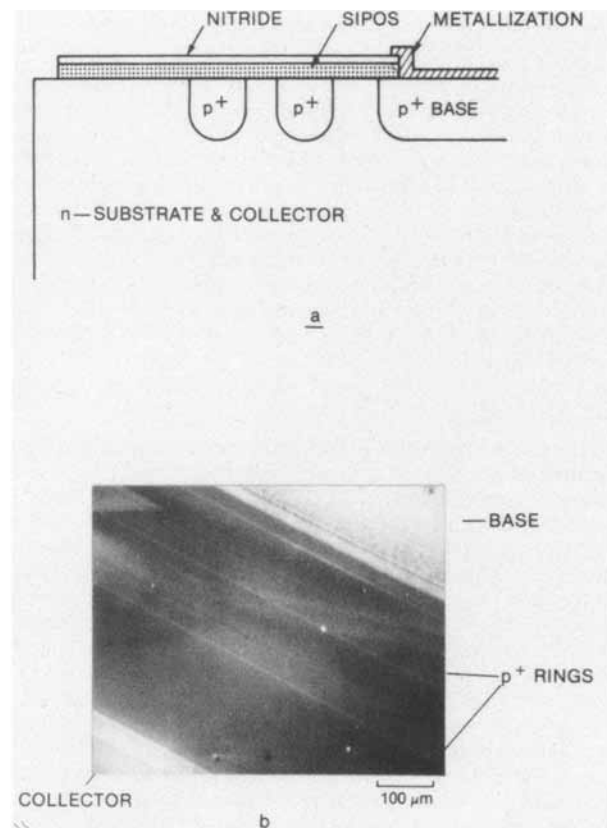


Fig. 1. (a) Cross-sectional diagram of the base collector junction in the test device; (b) a SEM photograph of the same area of the device.

¹ School of Electronic Engineering Science, University College of North Wales, Bangor, Gwynedd, Wales.

² General Electric Company, Discrete Semiconductor Device Center, Syracuse, New York 13221.

sulting in better voltage resolution, but poorer signal-to-noise ratio. For the results reported below, a modulation of 10V was used. Voltages for biasing the devices were provided by a Fluke Model 412B high voltage power supply.

Results

Curve (a) in Fig. 2 shows a typical Auger spectrum obtained from the test device when all terminals are grounded. In addition to the silicon and nitrogen lines expected from the Si_3N_4 passivation, lines due to carbon and oxygen contamination on the surface are also present. These extra lines do not detract from the measurement technique. Indeed, in many instances, the oxygen line can be used to advantage because of its high intensity, as will be demonstrated later. That all the lines in Fig. 2a occur at the expected energies (within $\pm 5\text{V}$) confirms that any charging effects in the nitride must be small. With the base biased to -200V , the spectrum from this same location (between the base and first p^+ ring) shifts to higher energies as shown by curve (b) in Fig. 2. A shift of 165 eV in the energy of each line indicates a local surface potential of -165V . The accuracy of the measurement can be demonstrated by following the calibration procedure described below.

Calibration.—Negative voltages of up to -1 kV are calibrated by locating the beam on the base of the device in an area close to the metallization and observing the shifts in the silicon (1620 eV) and oxygen (508 eV) lines when known voltages are applied to the base. The silicon line cannot be followed beyond -600V because of the 2300 eV upper limit of the electron energy analyzer. The oxygen line is followed over the whole voltage range.

Calibration of positive voltages is achieved by positioning the beam over the collector region, well away from any depletion edges, and using the shift in the silicon line which occurs when biasing the collector. For this part of the measurement, the base is grounded and the device is mounted on an insulating support to isolate the silicon substrate (collector) from the grounded header. Measurements above 500V are not possible because of the unexpectedly rapid reduction in signal strength as the bias increases. A similar effect sets in at much lower voltages for the oxygen line. It is believed that this loss of signal is caused by the fringing field pattern directing the Auger electrons away from the analyzer. However, in the range of -1 kV to $+500\text{V}$, excellent correlation is obtained between the applied voltage and the shift in the energy of the peaks, as demonstrated in Fig. 3.

The fringing field from the device bias also causes a deflection of the primary beam, as evidenced by a noticeable shift of the SEM image. Fringing fields far from the device surface will result in a uniform deflection of the beam over the image area. Provided the beam location is measured with respect to a known reference point on the sample surface, say, a metallization edge, a uniform deflection will not affect measurement accuracy. On the other hand, fringing fields close to the sample surface can

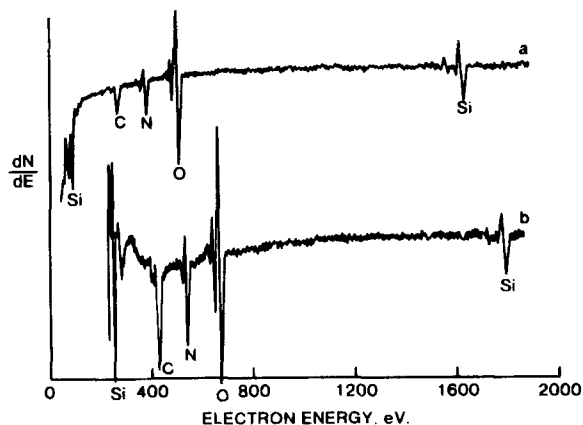


Fig. 2. Auger spectra from a location near the collector-base junction when (a) $V_{BC} = 0\text{ V}$ and (b) $V_{BC} = -200\text{V}$.

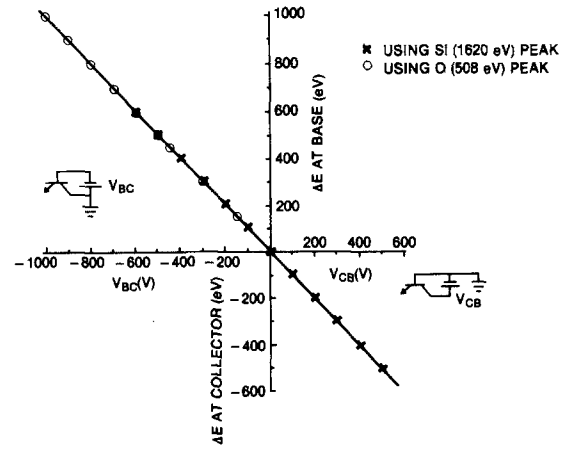


Fig. 3. Shifts in the energy of the silicon (X) and oxygen (O) lines for known voltages applied to the base or collector.

result in a nonuniform beam deflection and can lead to erroneous beam location. Visually, a nonuniform beam deflection will translate into an expansion or compression of the SEM image. The relative shift in beam position can be estimated by approximating a lateral field of V_b/W , where W is the width over which the bias voltage V_b is dropped. For a high voltage transistor, this corresponds to the collector-base depletion width. This lateral field acts upon the primary beam over a vertical distance of approximately W . From the vertical velocity of the primary electrons

$$v_v = \sqrt{2qV_p/m_e}$$

where V_p is the primary electron energy and m_e the electron mass, the transit time of the electrons through the lateral field zone is

$$\Delta t = W \sqrt{m_e/2qV_p}$$

In this period, the lateral displacement δ is approximately

$$\delta = qV_b \Delta t^2 / 2m_e W = V_b W / 4V_p$$

For a typical W of $100\ \mu\text{m}$ at 1 kV of bias, δ is about $2\ \mu\text{m}$, which is of the order of the spatial resolution of the beam. Thus, at the voltage levels of this work, the deflection of the primary beam is not considered significant. Indeed, while uniform image shifts can be detected in the measurements described, no significant distortion of the device image is apparent.

Resolution.—The linearity of Fig. 3 means that voltage resolution is in the range of a few volts and is determined by the accuracy of the analyzer ($\pm 1\text{V}$) and by the chosen modulation voltage. To obtain satisfactory signal strength, a modulation voltage of 10V was chosen for these experiments.

Positional information is currently being obtained from photographic records, and spatial resolution is estimated to be $\sim 8\ \mu\text{m}$. Improvements are obviously possible, but ultimately, resolution will be determined by the primary beam size. Again, there is a trade-off between signal strength and spatial resolution because a larger beam current results in a greater beam diameter.

Voltage profiles.—To determine the voltage distribution on the device, a spectrum similar to that in Fig. 2 is recorded at several locations along the surface. For example, Fig. 4 shows the energies of the silicon peak as the beam is moved from point to point along a line from the outer p^+ ring toward the edge of a device where $V_{BC} = -1\text{ kV}$ is applied. By matching the corresponding spatial positions for each spectrum to the secondary electron image taken at the same time (Fig. 4, inset), plots such as in Fig. 5 are obtained for different values of V_{BC} . These plots clearly show the isopotential bands formed by the two p^+ rings. Obviously, the voltage profiles can be better defined if more points are taken, but this is a slow process which, under certain cir-

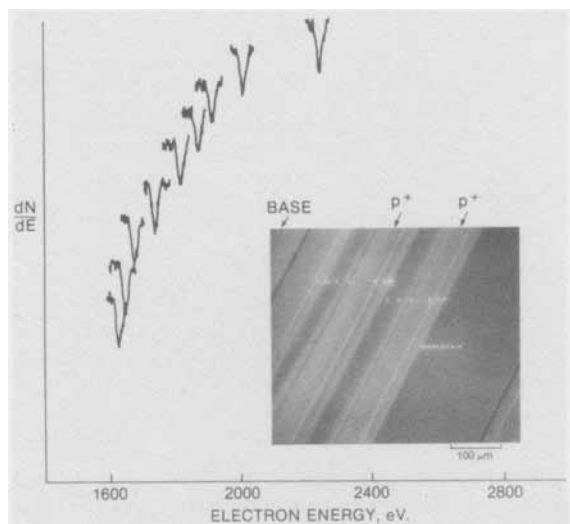


Fig. 4. Shifts in the silicon (1620 eV) line at the locations shown by the group of 9 dots right of center in the inset photograph. $V_{BC} = -1$ kV.

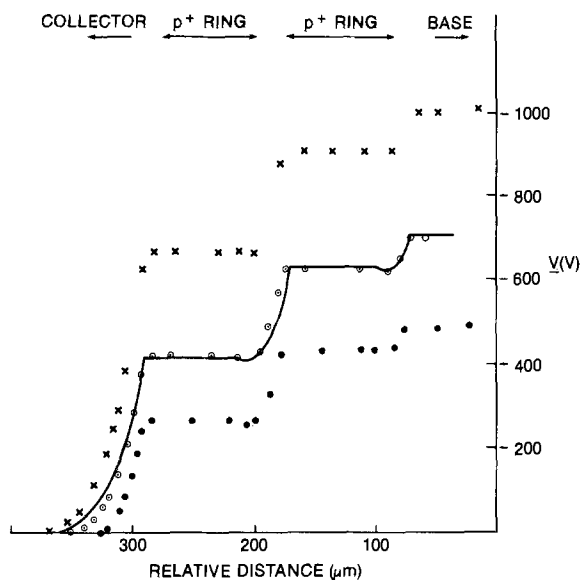


Fig. 5. Voltage profiles along the surface of a device when $V_{BC} = -1000$ V (X), $V_{BC} = -700$ V (O), and $V_{BC} = -500$ V (●). Solid line is the computer result for $V_{BC} = -700$ V.

cumstances, can be obviated by using the scanning facility of the SAM.

Two-dimensional surface mapping.—By setting the electron analyzer to detect electrons of one energy, e.g., setting the oxygen line at 508 eV and raster scanning the beam over the surface, a two-dimensional image corresponding to the oxygen distribution over the surface can be displayed on the video monitor. If the device is not biased, the distribution is essentially uniform. If the device is biased and the analyzer energy is changed to $508 + V$ (eV), then the only oxygen Auger electrons detected will be those emitted from that part of the device at a voltage of $-V$. Therefore, the image displayed will be an isopotential contour corresponding to $-V$ volts.

Using the oxygen line and the procedure outlined above, the images of Fig. 6a-6e are obtained for the various analyzer energies indicated. In this sequence of photographs, $V_{BC} = -200$ V. By use of multiple exposures, images corresponding to several analyzer settings can be superimposed on one photograph to analyze the data.

An alternative, more rapid method used to obtain the same information is to step the analyzer energy by known amounts during a scan. This method produces an image with a stepped appearance (Fig. 7) from which the potential distribution can be obtained. There is no observable differ-

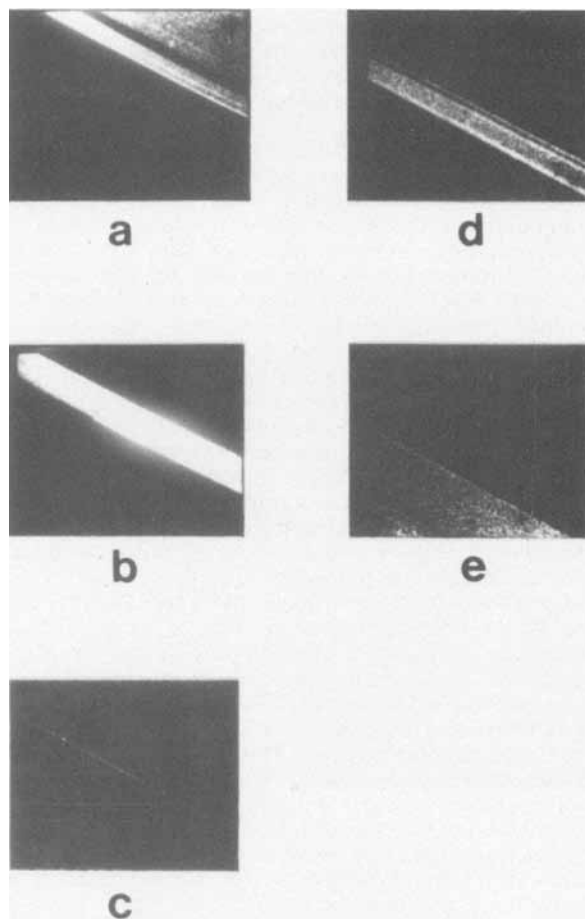


Fig. 6. SAM images of the oxygen (508) line from a device when the electron analyzer is set to (a) 706 eV, (b) 669 eV, (c) 657 eV, (d) 554 eV, and (e) 514 eV. The voltage corresponding to each isopotential = analyzer voltage - 508V. $V_{BC} = -200$ V.

ence between the voltage profiles obtained by the raster scanning or by the point-by-point method.

Discussion

After establishing that the SAM can be used to obtain voltage profiles on the surface of high voltage devices, the technique is used to compare the measured data with data obtained from a computer simulation of the test device, as illustrated in Fig. 5. The program used solves Poisson's equation in two dimensions using a finite difference formulation and successive over-relaxation (SOR), and it self-

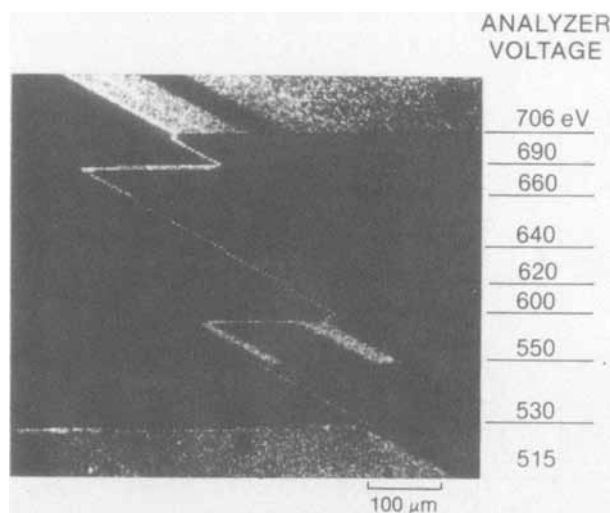


Fig. 7. SAM image obtained when the analyzer energy is changed in discrete steps while scanning the beam. $V_{BC} = -200$ V.

consistently calculates the potential at each point in the device (8). Although the solution shown ignores the presence of surface charges and the passivation layer, the model predicts the avalanche voltage with an accuracy of $\sim \pm 5\%$. Therefore, it is presumed that a high degree of confidence can be put in the theoretical voltage profiles. It is reassuring to obtain such good agreement between the theoretical and the measured values in Fig. 5. This agreement also indicates that for the particular sample tested, the passivation has insignificant influence on device behavior.

The Auger profiling technique has also proved particularly useful in troubleshooting devices and in evaluating the effects of various device process steps. For example, Fig. 8 shows the voltage profiles corresponding to $V_{BC} = -300V$ in devices subjected to three different process conditions. In (a), the process has resulted in a device which goes into avalanche well below the designed voltage of 1 kV. The voltage profiles reveal that the p^+ rings are not functioning correctly, their potentials differing only slightly from the base. Changing the process conditions results in a device which apparently meets the design performance, but the Auger measurement, (b), once again reveals incorrect functioning of the p^+ rings, suggesting possible early failure of the device in operation. With further modification of the process, the device functions correctly, as shown in (c).

Limitations of the technique.—The general limitation of the technique as currently used is the time required to extract the positional information from photographic records. Digital beam positioning now available in new SAM's will certainly improve the ease of making point-by-point scans.

A limitation of the raster scanning mode appears when the bias on the device exceeds $-500V$ or so, causing a rapid change in the collection efficiency of Auger electrons to occur as the beam scans the surface. Between the base and outer p^+ ring, the carbon, nitrogen, and oxygen peaks are large, but when the beam is just beyond this outer ring, the signals decrease rapidly, resulting in a loss of image. This shows up clearly in Fig. 9, in which the device is biased to $-800V$ and the carbon signal is used to measure the surface voltage. No isopotentials can be observed beyond the outer p^+ ring. Figure 9 also shows the reappearance of signals from the base and the inner p^+ ring as the analyzer energy is reduced. This is caused by an increase in the background noise in the measurement window for electron energies ≤ 150 eV.

In principle, these difficulties can be overcome by detecting the 1620 eV silicon line whose intensity remains almost unchanged over a wide range of voltage. Unfortunately, the intensity of this line is insufficient to produce good two-dimensional scans. Enhancement techniques, e.g., signal averaging, can conceivably be applied to facili-

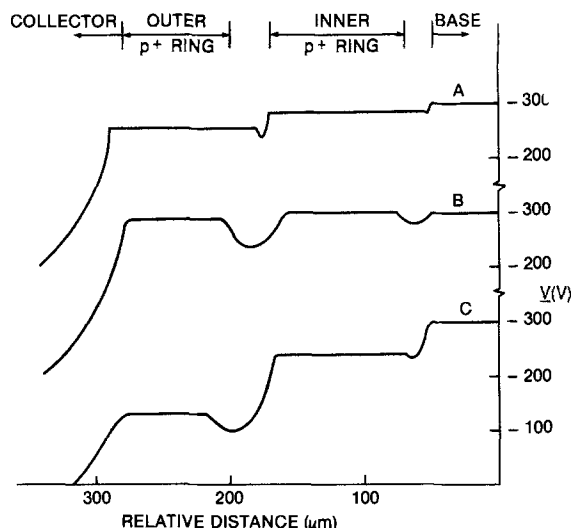


Fig. 8. Voltage profiles obtained using SAM from nominally identical test devices that have undergone different processing.

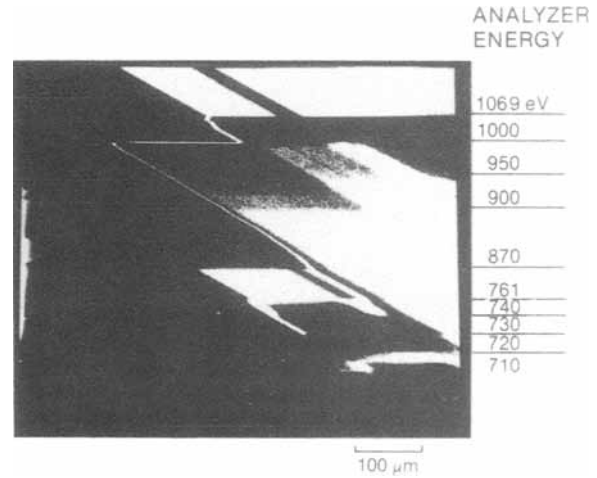


Fig. 9. Effect of high bias voltages on the SAM image. Here the carbon line has been used and the analyzer energy changed in discrete steps during the scan. $V_{BC} = -800V$.

tate such measurements (at the expense of longer measurement time).

The beam energy of 8 keV chosen for this work is sufficient to allow energetic electrons to penetrate the SIPOS layer and cause ionization in the silicon substrate. This can conceivably change the local potentials, and to check this possibility, the measurements are repeated with a 4 keV beam which cannot penetrate the silicon. The results obtained are almost identical, except for an apparent stretching out of the distribution near the depletion edge. Repeating the experiments with zero bias on the device shows that this effect is caused by the beam-induced resistive drop across the SIPOS film. In the vicinity of the outer p^+ ring, this voltage is about $-10V$, but between the ring and the edge of the device, it increases to about $-60V$. After correcting for this effect, the 4 and 8 keV data are in agreement, showing that no adverse effects result from using the higher beam energy.

An interesting effect noticed during this work is the appearance of apparently spurious noise peaks in the Auger spectrum when the device is biased. These tend to appear in groups of three, and their energies always coincide with the voltages on the base and the two p^+ rings. For example, with $-500V$ applied to the base, the p^+ rings float at -440 and $-240V$, and the extra lines induced in the Auger spectrum are seen at 505, 435, and 250 eV. The peaks are believed to arise from the elastic reflections of primary electrons from the device to the walls of the vacuum chamber and back to the device. Because of the large area of the base and field rings, a significant background current of secondary electrons will be emitted from these areas, and their energies will be within 5 or 10 eV of the voltages on these features, thus giving the extra lines observed. Occasionally, the line being used for the voltage measurement can be swamped by these extra lines in the spectrum.

The penetration of highly energetic electrons into the silicon can conceivably disturb the local silicon surface potential. This is certainly likely if, for example, the passivation is oxide and the oxide-trapped charges determine device behavior in some way. Hence, for each application, the effect of the beam probing itself on device behavior should be carefully assessed.

Conclusions

The scanning Auger microscope has been shown to be a powerful tool for measuring the voltage distribution on the surface of a high voltage transistor. This technique has been demonstrated on an npn transistor with biases of up to 1 kV. An accuracy of 10V and a spatial resolution of $8 \mu m$ or better can be readily achieved on commercially available instruments.

The method is suitable for unpassivated devices, as well as those having thin ($\leq 2 \mu m$) passivation layers. Even

highly insulating layers present no surface charging problems if the beam energy is high enough for the beam to penetrate into the conductive silicon. The method is not suitable for devices with thick passivation.

Acknowledgments

The authors are indebted to Dr. R. B. Bolon and Mr. M. D. McConnell for their assistance and expertise in operating the SAM.

Manuscript submitted Oct. 17, 1983; revised manuscript received March 29, 1984.

General Electric Corporation assisted in meeting the publication costs of this article.

The Dependence of Silicon Etching on an Applied DC Potential in $CF_4 + O_2$ Plasmas

H. Kawata, K. Murata, and K. Nagami

Department of Electronics, College of Engineering, University of Osaka Prefecture, Sakai, Osaka, Japan

ABSTRACT

A copper rod which is biased by a dc potential, V_s , is placed in $CF_4 + O_2$ plasmas. The etch rate of a (100) silicon wafer placed on the rod is measured as a function of V_s at various O_2 contents. At the 45% O_2 content, there are plenty of F and O atoms, and a relatively high value of V_s is necessary to enhance the etch rate. At the 10% O_2 content, the density of O atoms decreases remarkably, and the etch rate is enhanced with a low value of V_s . This difference can be interpreted by reference to the O atom adsorption on a silicon surface. The silicon etching by F atoms is enhanced effectively by incident ions with low energy, but incident ions with relatively high energy are necessary to remove adsorbed O atoms. At oxygen-free content with a silicon load on the anode, the numbers of F and O atoms are small, and the enhancement of the etch rate by incident ions is not large, even when V_s increases. This means that the physical sputtering rate is much lower than the chemical one. The etch rates on the cathode and the anode are discussed, based on these results.

Because the mobility of electrons is much higher than that of ions, an ion sheath is formed in front of any material exposed to a plasma, in order to satisfy the charge neutralization. Through this ion sheath, positive ions gain some amount of kinetic energy and hit the surface of the material (1, 2). The ion incidence with kinetic energy is very important in interpreting the etch rate, the etching selectivity, and the etching anisotropy. Recently, silicon etching has been performed with a reactive ion beam (3) and a source of F atoms (4), instead of a plasma environment, because it is almost impossible to control only a desirable plasma parameter. For the etching mechanism, a clear explanation has been made by these experiments. However, in practical use, the etching is performed under a plasma environment because both active and ionic species, which are easily formed in the plasma, seem to be necessary to obtain a satisfactory etch rate (5).

In this work, a copper rod is placed in the plasma produced by a parallel-plate-type reactor. The etch rate of silicon placed on the rod is measured by varying the dc bias voltage, V_s , which is applied between the rod and the anode. A change in V_s seems to have little effect on the plasma. The energy of incident ions on the rod must be smaller than eV_s . Our experiments are mainly performed under three conditions: with a large number of F and O atoms at the 45% O_2 content; with a small number of O atoms at the 10% O_2 content; and with a very small number of F and O atoms at the 0% O_2 content. It will be shown that the dependence of the etch rate on V_s can be characterized at each condition. Moreover, the etch rates on the cathode and on the anode are also discussed, based on the experimental results of the etch rate on the rod.

Experimental

A schematic view of the experimental apparatus is shown in Fig. 1. A copper rod is inserted between the cathode and anode electrodes in a conventional parallel-

REFERENCES

1. T. E. Everhart, O. C. Wells, and R. K. Matta, *This Journal*, **111**, 929 (1964).
2. W. J. Tee and A. Gopinath, *Rev. Sci. Instr.*, **8**, 350 (1977).
3. P. R. Thomas, K. G. Gopinathan, and A. Gopinath, "Microcircuit Engineering," pp. 479-499, C.U.P. (1980).
4. M. C. Driver, in "Proceedings of the 2nd Annual SEM Symposium," pp. 405-413, IIT Research Institute (1969).
5. N. C. MacDonald, *App. Phys. Lett.*, **16**, 76 (1970).
6. N. C. MacDonald, in "Proceedings of the 3rd Annual SEM Symposium," pp. 483-487, IIT Research Institute (1970).
7. D. M. Taylor, *J. Phys. D.*, **11**, 2443 (1978).
8. M. S. Adler, V. A. K. Temple, A. P. Ferro, and R. C. Rustay, *IEEE Trans. Electron Devices*, **ed-24**, 107 (1977).

plate-type reactor (6). The diameter of the rod is 15 mm, and one end of the rod is flattened to make it easy to set a sample. The center of the rod is set at distances of 21 and 14 mm from the cathode and the anode, respectively. The rod is cooled by cold water and is biased by applying a dc potential, V_s , between the rod and the anode. Because a large current can flow to the rod when a large area is exposed to a plasma, the plasma condition seems to change as V_s is varied. In order to suppress this effect, the copper rod is covered with a quartz tube, except at its end, where a silicon sample is mounted. The area of the rod directly exposed to the plasma is estimated to be about 6 cm². The temperature of the rod is measured by a thermocouple and found to be $10^\circ \pm 3^\circ\text{C}$. The thermocouple is set at the other end of the rod, outside the chamber, as shown in Fig. 1. The temperature of the rod inside the chamber can be different from the temperature observed outside the chamber. In order to check this difference, both temperatures are measured simultaneously with two thermocouples. The temperature of the rod end inside the chamber is $23^\circ \pm 3^\circ\text{C}$ after 10 min discharge, while the temperature

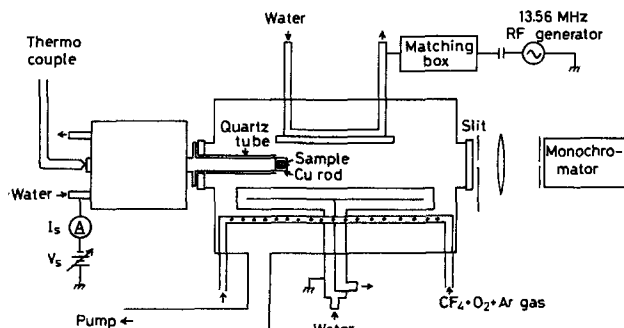


Fig. 1. The schematic view of the experimental apparatus

outside the chamber remains at 10°C. This temperature rise, however, is almost independent of discharge condition.

The flow rate of $\text{CF}_4 + \text{O}_2$ gas is maintained at 50 cm^3/min , even when the O_2 content is changed from 0% to 45%. In order to correct the optical emission intensity, Ar gas is added at a flow rate of 1 cm^3/min . The pressure is 0.3 torr, the RF power of 13.56 MHz is 100W, and the etching time is 10 min. The sample is a p-type single-crystal silicon wafer with (100) orientation. The area of the sample is 0.6–0.8 cm^2 . It is dipped into a 46% HF solution in order to remove a native oxide before mounting on the copper rod. The sample weight is measured before and after the etching; from the difference, the etch rate is obtained by dividing by both etching time and surface area. A silicon sample is also placed on the anode to check, by measuring the etch rate, the effect of V_s on the plasma.

At the center between the cathode and the anode, the optical emission intensities from F, O, and Ar atoms are measured at wavelengths of 703.7, 777.1, and 705.4 nm, respectively. An optical fiber, which is not shown in Fig. 1, is used in order to guide a light beam to a monochromator. The dc potential of the cathode is measured through a low-pass filter.

The etch rates on both the cathode and the anode are measured before the copper rod is introduced. In this case, the etch rate is measured by an interferometer by using a small silicon sample half-covered by an aluminum film. The etching time is 7 min. The CO emission intensity is also measured at 519.8 nm, as are the F, O, and Ar emission intensities.

In some experiments, additional silicon wafers are placed on either the anode or the cathode to examine the loading effect. The word "load" appearing in this paper means, unless otherwise specified, that three pieces of 2 in. Si wafer, whose total area is 60 cm^2 , are placed on the anode.

Results

The dependence of the rod current, I_s , on V_s is shown in Fig. 2. When net positive charges flow to the rod, I_s is defined to be positive. V_s is taken positive when the potential of the rod is negative relative to the anode. At $V_s = 0$ V, i.e., when the rod potential is equal to that of the anode, I_s is about -2 mA. This means that particles with negative charge, mostly electrons, dominantly flow to the rod. A floating potential, where $I_s = 0$ mA, is about 30V. Because the rod current is the sum of electron and ion currents under $V_s = 50$ V, it greatly depends on V_s . From $V_s = 50$ V to $V_s = 100$ V, I_s is almost independent of V_s . In this region, electrons are repelled completely. Only positive ions can reach the rod, and then I_s can be regarded as the ion-saturated current. When V_s increases further, I_s increases gradually in our experiments. The result is also shown in Fig. 2, when the rod end is covered by an Al foil at the 45% O_2 content. In this case, the ion-saturated current is not changed, but an increase in I_s beyond $V_s = 100$ V is larger than that without the Al foil. With increasing V_s , the length of the ion sheath increases, and I_s also increases, in spite of a constant electrode area, because of an increase in a capture area of positive ions. However, the increase in I_s at large values of V_s seems to be caused by secondary electrons emitted from the surface by incident ions, along with the effect of the ion sheath length, considering the dependence of I_s on the rod material. The energy of incident ions must be smaller than eV_s . However, the energy of incident ions will be proportional, though maybe not directly proportional, to eV_s , considering the increase in I_s .

The rod current and the Ar emission intensity are shown in Fig. 3 as a function of the O_2 content at $V_s = 100$ V. The rod current at $V_s = 100$ V is sufficiently saturated, as shown in Fig. 2. These values show a different dependence on the O_2 content. The F and O emission intensities are shown in Fig. 4 as a function of V_s . They are obtained by dividing the measured emission intensities by the Ar emission intensity (7). The data at $V_s = -25$ V, when the

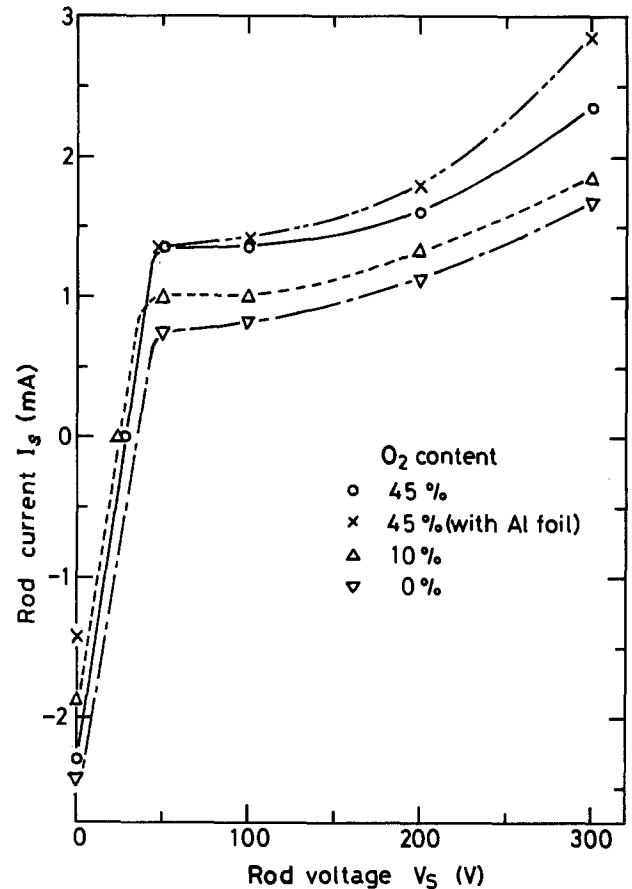


Fig. 2. The rod current as a function of V_s at various O_2 contents. There are Si loads on the anode at oxygen-free O_2 content, but no Si load at other O_2 contents. The rod current is also measured when a portion of the rod is covered with an Al foil at the 45% O_2 content.

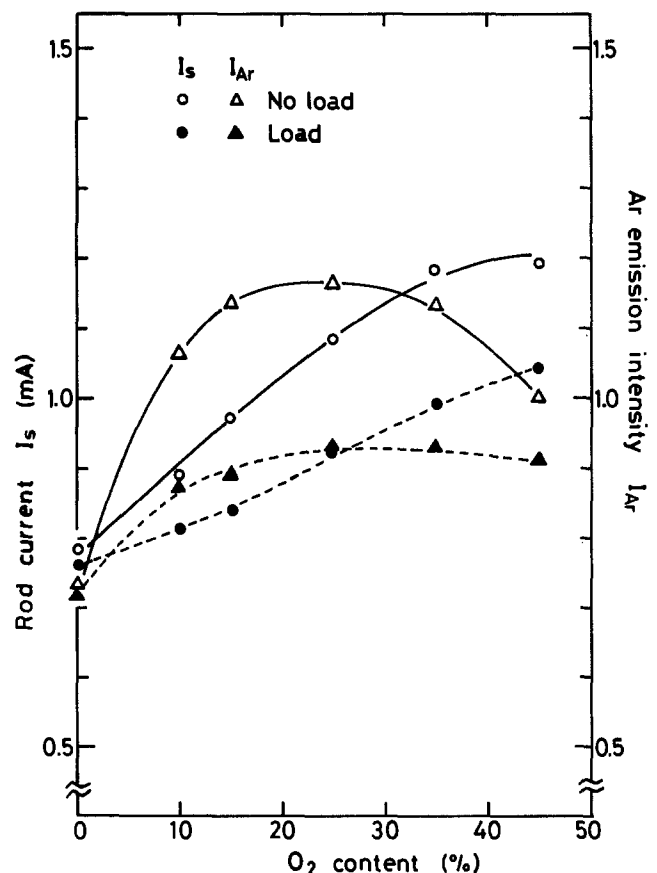


Fig. 3. The rod current, I_s , and the Ar emission intensity, I_{Ar} , as a function of the O_2 content. The solid lines show those without Si loads; the broken lines show those with Si loads on the anode.

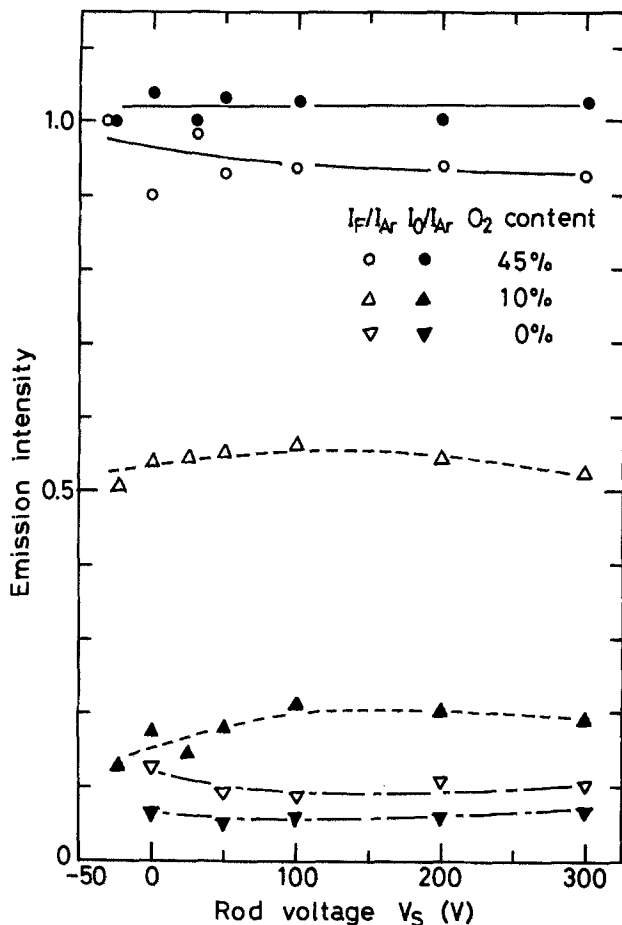


Fig. 4. The F and O emission intensities as a function of V_s in the same condition as the one in Fig. 2. At the 45% O_2 content, only the data are shown without an Al foil. The data near $V_s = -25V$ show those when the rod current is adjusted to -5 mA, and the ones near $V_s = 25V$ show those at the floating potential.

rod current is adjusted to -5 mA, are also shown in this figure. They are normalized to unity at the 45% O_2 content and the rod current of -5 mA. The F and O emission intensities are strong at the 45% O_2 content. At the 10% O_2 content, the F emission intensity decreases to about 55% of that at 45% O_2 content, while a decrease in the O emission intensity is much faster than that in the F emission intensity. At oxygen-free content with the Si load, there are only a small number of F and O atoms. According to the changes in these emission intensities, the etching condition at each O_2 content can be characterized as follows. Because there are enough F and O atoms in the plasma at the 45% O_2 content, O atoms adsorbed on a silicon surface prevent silicon etching by F atoms (8). Because there are plenty of F atoms in the plasma, but not plenty of O atoms at the 10% O_2 content, the effect of adsorbed O atoms is small. The number of active species for silicon etching is few at oxygen-free content. All of the emission intensities are almost independent of V_s . This shows that the incident fluxes of F and O atoms are not affected by V_s .

The etch rates on the anode and on the copper rod are shown in Fig. 5 and 6, respectively. The etch rate on the anode is almost independent of V_s . This shows that the plasma is not affected largely by a change in V_s . Probably, the potential of V_s is shielded by the ion sheath formed in front of the rod. In all cases in Fig. 6, the silicon etch rate on the copper rod increases as V_s increases beyond the floating potential. At the 45% O_2 content, the etch rate increases gradually below $V_s = 200V$, but increases rapidly above $V_s = 200V$. On the other hand, at the 10% O_2 content, the etch rate increases rapidly at low V_s and goes to saturation at high V_s . At oxygen-free content with the Si load, an increase in the etch rate is not remarkable.

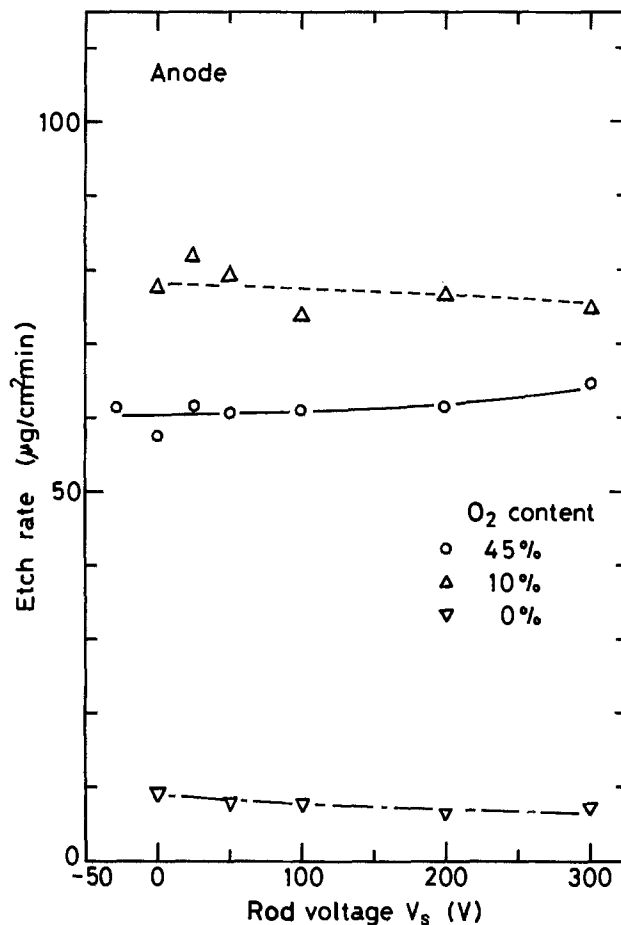


Fig. 5. The etch rates on the anode as a function of V_s in the same condition as the one in Fig. 4.

Figure 7 shows the etch rates on the cathode and on the anode without the rod as a function of the O_2 content. These are obtained from etched depth measurements. $100 \mu\text{g}/\text{cm}^2 \text{ min}$ in Fig. 5 and 6 corresponds to about $430 \text{ nm}/\text{min}$ in Fig. 7, assuming that the etching proceeds uniformly on the sample surface. The etch rate on the anode in this figure is somewhat different from that in Fig. 5. Probably, this is because the plasma condition is disturbed by the rod, and/or the etching uniformity is insufficient. There is an O_2 content where the etch rate is the largest. Obviously, these O_2 contents are different between the cathode and the anode.

Discussion

Optical emission intensity and rod current.—The Ar emission intensity, I_{Ar} , which is proportional to the Ar density at the excited level (9), is expressed as $k_e n_e n_{Ar}$, where k_e is the rate constant, n_e the electron density, n_{Ar} the Ar density. Because the flow rate of Ar gas is constant through our experiments, n_{Ar} is also constant. When a Maxwell distribution is assumed, I_{Ar} is directly proportional to $n_e \sqrt{T_e'} \exp(-E_i/kT_e')$ (10), where T_e' is the electron temperature and E_i is the excitation energy ($E_i = 13.5 \text{ eV}$ for the Ar emission line of 750.4 nm) (11). Because the electron temperature, T_e , which is not always equal to T_e' (as discussed later), for the bulk of electrons is much larger than the ion temperature, T_i (i.e., $T_e \gg T_i$), the ion current, I_i , is proportional to $n_i \sqrt{T_e/M_i}$, where n_i is the ion density and M_i is the ion mass (12). At $V_s = 100V$, electrons are repelled completely, and the rod current in Fig. 3 seems to be equal to I_i at each O_2 content. I_i increases monotonically as the O_2 content increases, but I_{Ar} has a maximum value at about 25% O_2 content. When the O_2 content is varied, the constituent of ions in the plasma is also changed. Coburn and Winters (13) have reported from the observation of mass spectra of positive ions that CF_3^+ is a main component with the powered electrode of

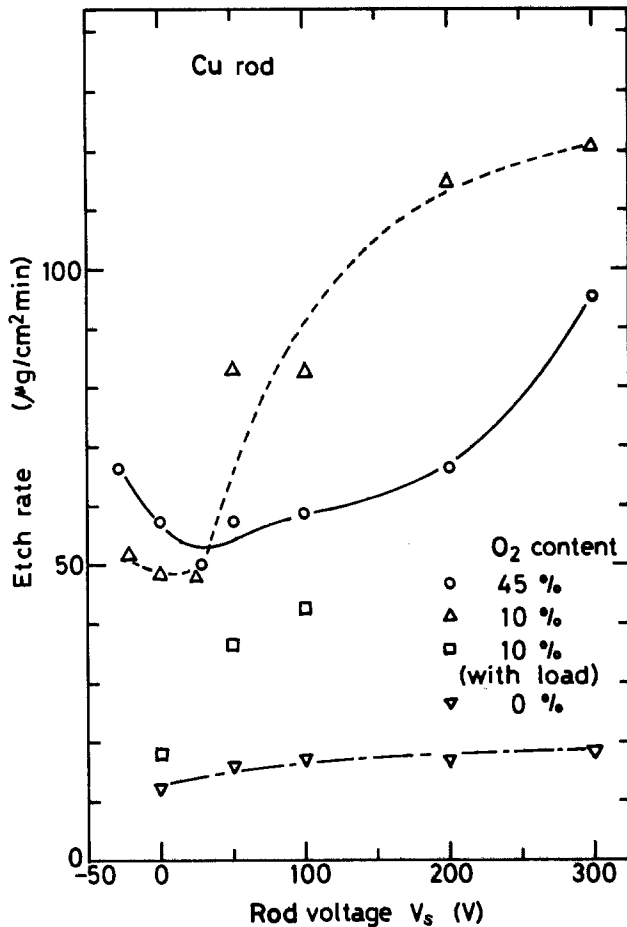


Fig. 6. The etch rates on the copper rod as a function of V_s in the same conditions as the one in Fig. 4. Some data are also shown when Si loads are placed on the anode at the 10% O_2 content.

Si, and CF_3^+ , COF^+ , and COF_2^+ are main components with the one of SiO_2 . O atoms are liberated from the SiO_2 powered electrode. From their results, CF_3^+ is a main component at oxygen-free content, but CF_3^+ , COF^+ , and COF_2^+ must be mixed when O_2 is added. Supposing that all ions are converted from CF_3^+ to COF^+ , and that n_i and T_e are not changed when O_2 is added, I_i increases by about 20%. Because an increase in I_i is more than 20%, as shown in Fig. 3, n_i and/or T_e seem to be increasing. This contradicts the fact that the Ar emission intensity decreases at the high O_2 content region. Ar atoms are excited only by electrons whose energy is greater than E_i . T_e' has to be the electron temperature for such electrons. Kushner (14) measures the electron energy distribution, $f(\epsilon)$, by the electrostatic probe method and shows that the maximum value of $f(\epsilon)$ appears in higher electron energies when the fraction of CF_4 is increased, because there are fewer inelastic processes to slow the electrons down. When inelastic collisions occur, the number of electrons with high energy decreases. Then, T_e' decreases, and T_e' is not equal to T_e (10). Considering this effect, it is possible that T_e' decreases while T_e is constant or increases and that I_{Ar} decreases while I_i increases when the O_2 content is changed. Because both I_i and I_{Ar} at oxygen-free content are smaller than those at the other O_2 contents, both the electron temperature and the plasma density seem to be small at oxygen-free content (12).

Etch rate on the copper rod.—We discuss the etch rate on the copper rod, as shown in Fig. 6, at each O_2 content.

0% O_2 content.—Because the F atom density is very low at oxygen-free content with the Si load, the etch-rate enhancement by incident ions seems to be caused mainly by the physical sputtering. This enhancement is not large, even though we take into consideration that I_s is relatively small at oxygen-free content.

10% O_2 content.—Because the O atom density is low, silicon etching by F atoms is enhanced by incident ions without effects of adsorbed O atoms. This enhancement is possible with a relatively low energy of incident ions. Some data are also shown in Fig. 6 at the 10% O_2 content with the Si load. If the etch-rate difference between $V_s = 0$ V and $V_s = 50$ V is assumed to be the etch-rate enhancement by incident ions at $V_s = 50$ V, this enhancement without the Si load is about 1.8 times as large as that with the Si load. The F emission intensity is about 2.7 times as large as that with the Si load. The two rod currents are almost equal with and without the Si load. Though the etch-rate enhancement is not directly proportional to the F emission intensity, it seems to depend strongly on the F emission intensity in our experimental condition. Tu *et al.* (15) have measured the silicon etch yield when XeF_2 gas and energetic ions are exposed simultaneously. They have shown that the yield has a large dependence on XeF_2 flux, but only a slight dependence on incident ion energy. Their results are in good agreement with ours at the 10% O_2 content.

45% O_2 content.—The F and O atom densities are high. In order to enhance the etch rate, incident ions have to remove O atoms adsorbed on a silicon surface. Probably, the energy of incident ions required to sputter the adsorbed O atoms is larger than that required to enhance silicon etching by F atoms. If a value of V_s larger than 300 V is applied in order to remove adsorbed O atoms sufficiently, the etch rate on the rod at the 45% O_2 content seems to become larger than that at the 10% O_2 content because the F atom density is higher than that at the 10% O_2 content. Paraszczak and Hatzakis (16) show that silicon can be etched in the vertical direction of the mask even when the lateral etch rate is zero at the high O_2 content. This shows that adsorbed O atoms are removed by incident ions in the vertical direction.

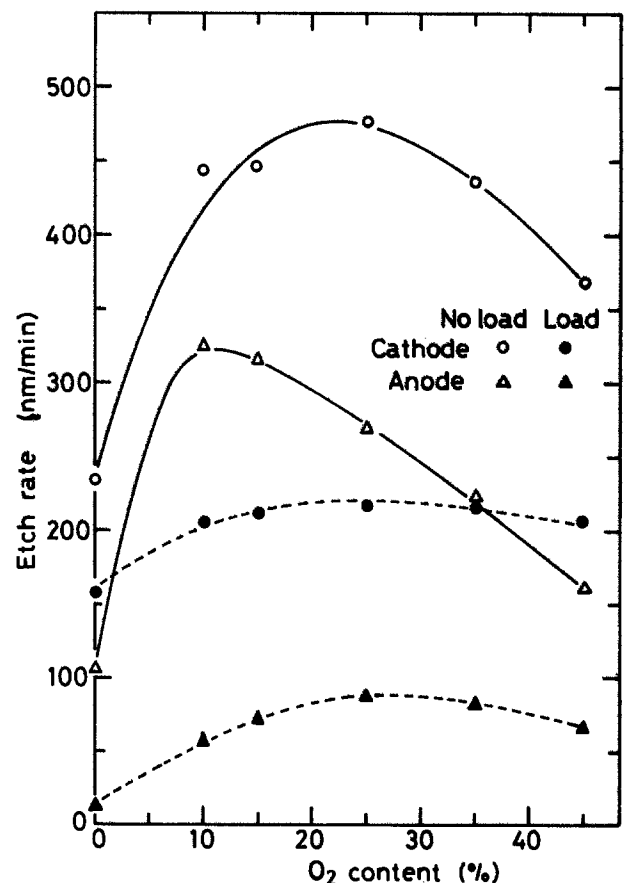


Fig. 7. The etch rates on the cathode and on the anode as a function of the O_2 content without the copper rod. About 430 nm/min of the etch rate in this figure are equal to 100 $\mu\text{g}/\text{cm}^2$ min (assuming uniform etching). The solid lines show those without Si loads; the broken lines show those with Si loads.

The following results are obtained: (i) the energy of incident ions needed to enhance silicon etching by F atoms is small; (ii) the physical sputtering is much weaker than the chemical sputtering, which indicates etch-rate enhancement by incident ions with the consumption of active species; and (iii) the etching is prevented by the adsorbed O atoms at even a relatively high energy of incident ions.

Lee and Chen (17) have shown that the etch-rate enhancement by incident ions is proportional to $V_{bi}^{5/2}$, where V_{bi} is a self-bias voltage. We define the etch-rate enhancement by incident ions, ΔE , as the difference between the etch rates at V_s and at $V_s = 0$ V and suppose the ΔE is proportional to V_s^α . An accurate value of α cannot be obtained, because ΔE becomes too small at low V_s to obtain reliable data. However, a value of 2.7 is obtained when data points at $V_s = 300$ V and $V_s = 200$ V are connected linearly at the 45% O₂ content. This is close to a value of 5/2. But at the 10% O₂ content, α is smaller than unity, as seen from the curve in Fig. 6. It is difficult to compare their results with ours due to different experimental conditions. However, when we discuss incident ion effects in a CF₄ + O₂ plasma, it is certainly important to take account of the O atom adsorption, along with the plasma density, pressure, and so on. Tachi *et al.* (18) show that the chemical sputtering yield is smaller than the physical one when silicon is etched by F⁺ ions with the incident energy larger than about 200 eV. Because one source of F atoms is only F⁺ ions in their experiment, the F atom density is insufficient and the chemical sputtering is suppressed.

Under the floating potential, the etch rate also increases. This increase is especially remarkable at the 45% O₂ content. The enhancement seems to be caused by an incidence of electrons or a change in the plasma condition. The latter is suspicious because a change in the Ar emission intensity at the 10% O₂ content is similar to that at the 45% O₂ content when V_s is changed, but the enhancement of the etch rate is hardly observed at the 10% O₂ content. SiO₂ is etched when it is exposed to XeF₂ gas and electrons simultaneously (19). Incident electrons seem to affect the adsorbed O atoms on a silicon surface, though we cannot confirm this at present.

Etch rates on the cathode and on the anode.—The etch rates on the cathode and on the anode are discussed, based on the experimental results. Because no copper rod is used in this experiment, the plasma condition seems to differ from that obtained above. The dc potential at the cathode without the Si load decreases monotonically from 300V at oxygen-free content to 210V at 45% O₂ content and is about 20V smaller than that with the Si load. This potential is considered as the cathode fall potential because the plasma potential seems to be small due to a smaller cathode area than that of the earthed area (20).

Let us consider that the O₂ contents where the etch rates are the largest on the cathode and on the anode are not consistent. Because the amount of adsorbed O atoms on the cathode is smaller than that on the anode by sputtering of O atoms, the O₂ content giving the maximum etch rate on the cathode becomes a little larger than that without the effects of incident ions. If the sample on the anode is not affected by incident ions, the difference between the etch rates on both electrodes shows the etch-rate enhancement by incident ions on the cathode. This difference is 120 nm/min at the 10% O₂ content and 130 nm/min at oxygen-free content without the Si load. Though this difference at the 10% O₂ content has to be larger than that at oxygen-free content according to the previous discussions, these two differences are almost identical. It is probably not assumed, strictly speaking, that the etch rate on the anode is the etch rate without the effects of incident ions. Because the etch rate is enhanced by incident ions with low energy at the 10% O₂ content, the etch rate on even the anode seems to be enhanced by incident ions with approximately the plasma-potential energy. Because the enhancement by incident ions with low energy is possible at the low O₂ content, the etch rate on

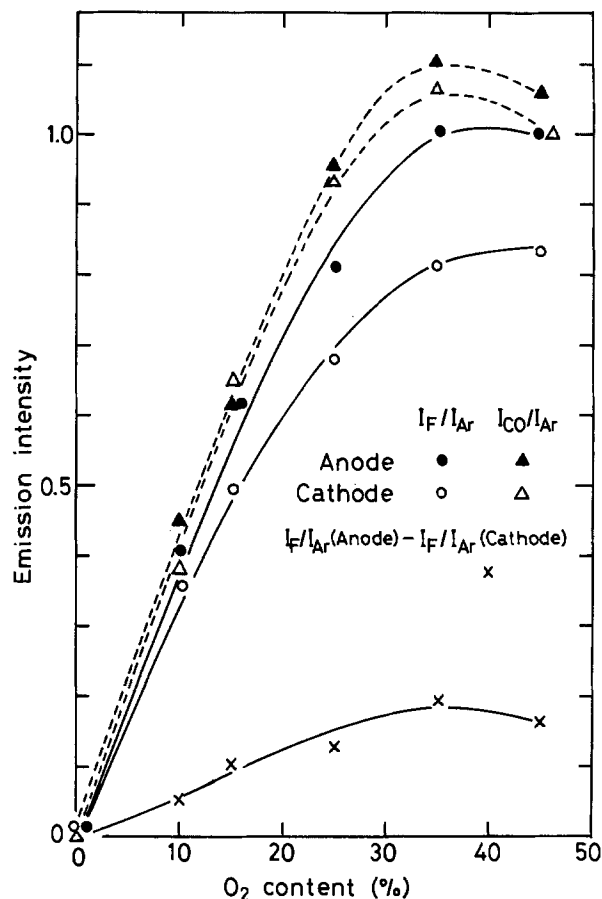


Fig. 8. The F and CO emission intensities as a function of the O₂ content when a 3 in. Si wafer is placed on either the cathode or the anode. The solid lines show the F emission intensity, and the broken lines show the CO emission intensity. The difference between the F emission intensities is also shown in this figure.

the anode can be increased by incident ions at the low O₂ content. These are the reasons why the O₂ contents where the etch rates are the largest are different. However, this enhancement on the anode seems not to be large because the dependence of E/I_F , which is the ratio of the etch rate to the F emission intensity, on I_O/I_F , which is the ratio of the O emission intensity to the F emission intensity, becomes linear (8) within an approximate 10% deviation (6).

The F and CO emission intensities are shown in Fig. 8 with a 3 in. Si wafer placed on the cathode or on the anode. The F emission intensity with the Si wafer on the cathode is weaker than that with the Si wafer on the anode. Lee and Chen (17) have measured the F emission intensities in both a plasma etching mode and a reactive ion etching mode when Si loads are etched. They have found that the F emission intensity in the reactive ion etching mode is weaker than that in the plasma etching mode. Our result in Fig. 8 is consistent with theirs. This shows that silicon on the cathode consumes more F atoms than that on the anode. As the enhancement of the etch rate by incident ions consumes F atoms, the chemical sputtering by energetic ions must be induced on the cathode.

Conclusion

The silicon etch rate on the copper rod is examined by changing the potential, V_s , applied to this rod. It is confirmed that a change in V_s hardly affects the plasma. The chemical sputtering can be induced by incident ions with relatively low energy. This chemical sputtering is reduced by adsorbed O atoms, which can be removed by the incidence of energetic ions. The ion energy needed for sputtering O atoms is higher than that needed to induce the chemical sputtering. The physical sputtering is much lower than the chemical sputtering. In our experimental condition, the etch-rate enhancement is limited by the F

atom density, rather than by the incident ion flux at the low O atom density.

At higher potentials than the floating potential, the electron flux is smaller than the ion flux on the rod. However, both fluxes are equal to the cathode and at the anode. If the electron flux influences the silicon etch rate seriously, it will be difficult to discuss the etch rates on both the electrodes from the results on the rod. Incident electrons seem to enhance the etch rate. However, this enhancement is not large, even when the rod current is -5 mA, which is about three times as large as the ion current. The enhancement must mainly be caused by the energetic ions.

Based on these results, the etch rates on the cathode and on the anode are investigated. It is important to consider the effects of adsorbed O atoms and their removal by energetic ions. The etch rate is enhanced even on the anode at the 10% O₂ content.

Manuscript submitted March 21, 1984; revised manuscript received Aug. 6, 1984.

REFERENCES

1. J. L. Vossen, *This Journal*, **126**, 319 (1979).
2. R. H. Bruce, *Solid State Technol.*, **24**, 64 (1981).
3. For example, K. Miyake, S. Tachi, K. Yagi, and T. Tokuyama, *J. Appl. Phys.*, **53**, 3214 (1982).
4. For example, H. F. Winters and J. W. Coburn, *Appl. Phys. Lett.*, **34**, 70 (1979), and M. J. Vasile and F. A. Stevie, *J. Appl. Phys.*, **53**, 3799 (1982).
5. J. W. Coburn, in "Proceedings of the Second Symposium on Dry Processes," p. 103, Institute of Electrical Engineers of Japan, Tokyo, Japan (1980).
6. H. Kawata, T. Shibano, K. Murata, and K. Nagami, *J. Appl. Phys.*, **54**, 2720 (1983).
7. J. W. Coburn and M. Chen, *ibid.*, **51**, 3134 (1980).
8. C. J. Mogab, A. C. Adams, and D. L. Flamm, *ibid.*, **49**, 3796 (1978).
9. R. d'Agostino, F. Cramarossa, S. De Benedictis, and G. Ferraro, *ibid.*, **52**, 1259 (1981).
10. L. Vriens, *ibid.*, **44**, 3980 (1973).
11. A. R. Striganov and N. S. Sventitskii, "Tables of Spectral Lines of Neutral and Ionized Atoms," IFI/Plenum, New York-Washington (1968).
12. Ch. Steinbrüchel, *This Journal*, **130**, 648 (1983).
13. J. W. Coburn and H. F. Winters, *J. Vac. Sci. Technol.*, **16**, 391 (1979).
14. M. J. Kushner, *J. Appl. Phys.*, **53**, 2939 (1982).
15. Y.-Yi Tu, T. J. Chuang, and H. F. Winters, *Phys. Rev.*, **B23**, 823 (1981).
16. J. Paraszczak and M. Hatzakis, *J. Vac. Sci. Technol.*, **19**, 1412 (1981).
17. Y. H. Lee and M.-M. Chen, *J. Appl. Phys.*, **54**, 5966 (1983).
18. S. Tachi, K. Miyake, and T. Tokuyama, *Jpn. J. Appl. Phys.*, **20**, L411 (1981).
19. J. W. Coburn and H. F. Winters, *J. Appl. Phys.*, **50**, 3189 (1979).
20. C. M. Horwitz, *J. Vac. Sci. Technol. A*, **1**, 60 (1983).

Dielectrically Isolated Thick Si Films by Lateral Epitaxy from the Melt

G. K. Celler,* McD. Robinson,*¹ and L. E. Trimble

AT&T Bell Laboratories, Murray Hill, New Jersey 07974

D. J. Lischner

AT&T Bell Laboratories, Allentown, Pennsylvania 18103

ABSTRACT

Dielectric isolation (DI) technology has been available for almost 20 years. It was first developed for low capacitance, high speed circuits, and was later adapted to radiation-hardened devices and for high voltage isolation. The conventional DI technology is expensive, and device yields are reduced by mechanical instability of the polycrystalline substrates. We review a novel approach to forming DI structures, based on recrystallization from the melt of thick Si films deposited over oxidized Si wafers, with a regular array of seeding windows opened in the isolation oxide. The recrystallized films are free of grain boundaries and subboundaries and contain few dislocations. Most important, the polycrystalline substrates and the associated wafer bow are eliminated.

Fabrication of single-crystalline thin Si films on SiO₂ has been attempted only in the last few years (1). In contrast, thick Si films on SiO₂ were first demonstrated about 20 years ago (2), and have been commercially produced for many years. The process of making dielectrically isolated (DI) wafers consists of several steps. First, (100) Si wafers are V-grooved to a depth of ~ 50 μm by anisotropic etching and oxidized to form a dielectric isolation layer. A very thick layer of ~ 500 μm of polysilicon is then deposited by a high temperature CVD process over the oxide to form a new mechanical support or "handle." Once this is accomplished, 80%-90% of the initial crystalline substrate is mechanically removed, as shown schematically in Fig. 1. Only small, device-size segments of the original single-crystalline wafer remain embedded in the polysilicon handle, electrically isolated from it and from each other. This procedure, developed and perfected over the years, is expensive and includes grinding

and lapping steps that are difficult to control and automate. Nevertheless, this is still the only proven technique for obtaining dielectrically isolated thick film structures and the only commercial process for fabricating crystalline Si films of any thickness on the SiO₂.

We have recently proposed an alternative to conventional DI technology that is potentially simpler and less expensive (3-5). This method of lateral epitaxial growth over oxide (LEGO) results in crystalline Si dielectrically isolated from a single-crystalline substrate. The process is based on controlled melting and recrystallization of 50-100 μm thick Si films in a special lamp furnace (6). The polysilicon handle is eliminated and with it the problem of wafer deformation caused by volume changes in polysilicon (7).

Below, we describe formation of planar crystalline films over the SiO₂, since this allowed us to prove the concept and examine in detail the kinetics of crystallization. Crystallization of Si over nonplanar structures provides simultaneously vertical and sidewall dielectric isolation necessary for high voltage devices. Formation of

*Electrochemical Society Active Member.

¹Present address: Epsilon Technology, Incorporated, Tempe, Arizona 85282.

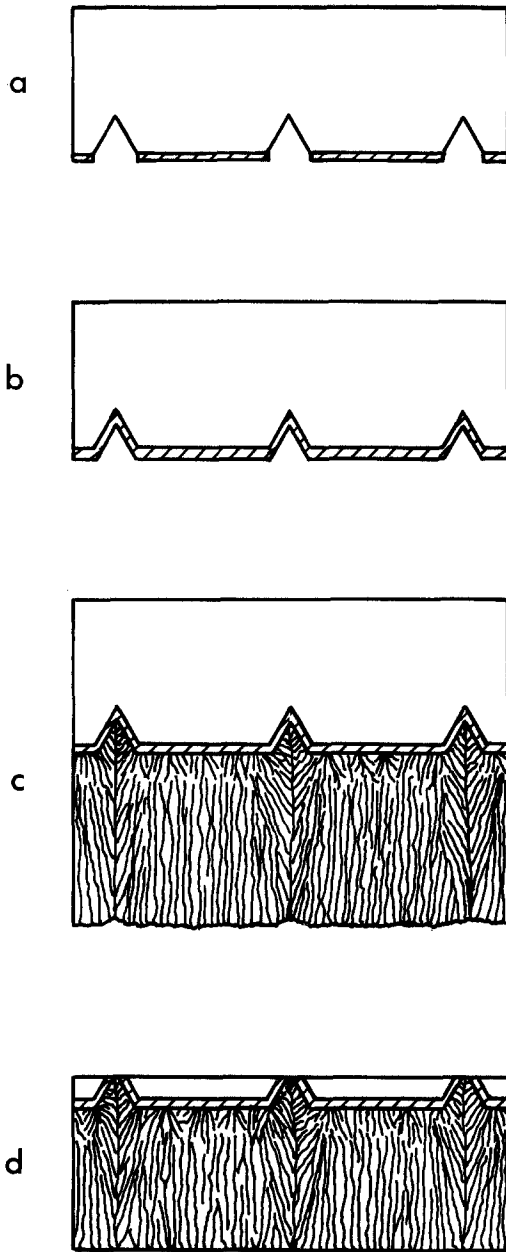


Fig. 1. Conventional DI processing sequence: (a) V-groove etching, (b) oxidation, (c) deposition of polysilicon handle, (d) grinding, lapping, and polishing to form isolated silicon tubs.

such structures and crystallization results are presented in the third section. The isolated crystalline regions have the same geometry as the conventional device tubs, assuring compatibility with the standard device designs.

Crystallization of Planar Films

Laser (8) and strip heater (9) recrystallization have been used by many groups to form device-quality thin Si films on oxidized Si wafers. In particular, seeded crystallization has been explored in many experimental configurations. In most cases, the molten zone was moved across the surface by the relative motion of the sample and the heat source. This way, if epitaxial growth occurred at the seed region, it propagated a certain distance with the trailing edge of the melt. Tamura *et al.* demonstrated that, in principle, the beam motion is not necessary since the thermal gradients alone can carry lateral recrystallization (10). In their experiments, "bridging epitaxy" was indeed demonstrated, but the lateral growth distance for a $0.5 \mu\text{m}$ film was $\sim 3\text{--}5 \mu\text{m}$. In an experiment with a stationary strip heater, crystallization over a distance of $\sim 10 \mu\text{m}$ was achieved by Fan *et al.* (9).

For recrystallization of thick Si films, heating with one localized source of energy is not acceptable because loss by lateral conduction from the heated spot necessitates a very high local power density, often leading to surface vaporization and always causing large thermal stresses. A high temperature thermal bias superimposed over a localized heat source, such as a laser beam or a scanned graphite filament, can reduce these problems.

Our approach has been to melt uniformly the entire polysilicon film. A regular array of windows cut in the buried oxide provides seeding necessary for epitaxial growth, and also imposes temperature gradients that are the driving force for lateral crystallization. Undercooling of the liquid Si can also play a role in preventing competitive nucleation, since molten Si is contained within amorphous silica walls.

The lamp furnace for large area melting and controlled recrystallization has been described before (6) and is shown schematically in Fig. 2. Briefly, it consists of two rectangular chambers, each 10×12.5 in. in lateral dimensions, positioned one above the other and separated by a quartz window. Air-cooled tungsten halogen lamps are suspended under a gold-plated reflector in the upper chamber. Wafers are placed on quartz pins ~ 0.5 in. above the water-cooled base of the lower chamber. Samples are heated uniformly from one side with a broad-band radiative flux emitted by the lamps. At typical settings required for melting, the spectrum is centered at $\sim 1 \mu\text{m}$ wavelength. Cooling is predominantly by black body radiation from both front and back side of the samples. The presence of the metal base held at a nearly constant temperature $< 100^\circ\text{C}$ assures reproducible cooling rates and a uniform gradient across the wafer thickness of $\sim 100^\circ\text{C}/\text{cm}$.

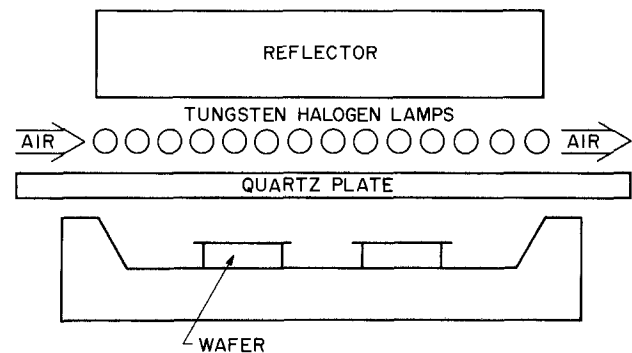


Fig. 2. Schematic view of the lamp furnace

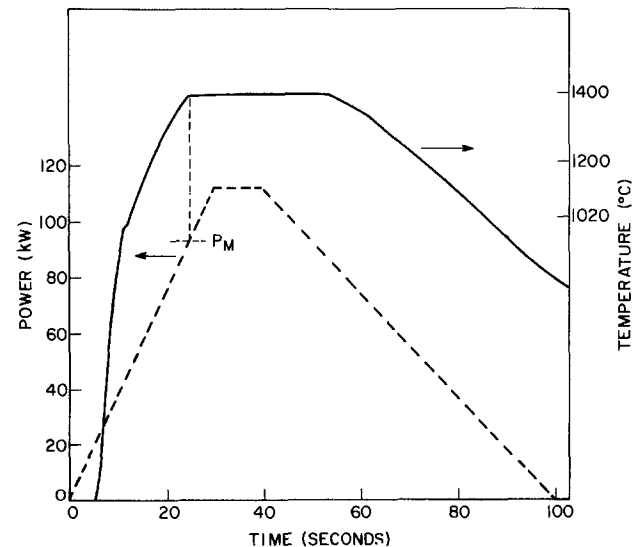


Fig. 3. Electrical power input and wafer temperature vs. time for a typical thermal cycle. P_M is the power threshold for melting.

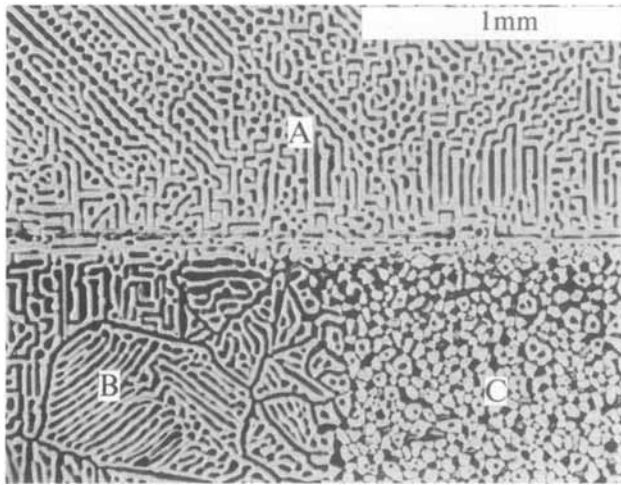


Fig. 4. Optical micrograph of surface ripples on solidified Si surface. In the single-crystalline region A, the ripples are caused by freezing that started at regularly spaced solid inclusions floating in the liquid. In regions B and C, an oxide film is buried under a thick Si layer. In C, the surface protrusions (black features) delineate grain boundaries which always are the last to freeze. In region B, large grains were formed by recrystallization, and this is reflected in the surface pattern.

To recrystallize a Si layer on an oxidized Si wafer, the lamps are ramped linearly over 10-30s to a predetermined power setting that exceeds the threshold power for melting, P_M , held at that value for 10-100s, and shut off by a linear reduction of electrical power, as shown in Fig. 3. The sample temperature is monitored with an optical pyrometer focused on the back side of the wafer. After a few seconds lag when the power is first applied, the sample temperature increases rapidly until it reaches the melting temperature T_M . This occurs at $\sim 100 \text{ W/cm}^2$. The onset of melting is easily determined from the pyrometer output even if the absolute temperatures are not known precisely because of some uncertainty in the value of emissivity. The temperature curve has a knee at the melting temperature, and its slope is essentially zero for the melt duration. All the absorbed power exceeding the threshold value is taken by the heat of fusion (for silicon $\sim 1800 \text{ J/g}$). Since all heating is radiative and the reflectivity of molten metallic Si is higher than that of the solid, elongated inclusions of superheated solid are present on the surface of the liquid. These inclusions have the same origin as those observed in laser melting experiments (11), and also as inferred from our experiments on melting of single-crystalline Si in the lamp furnace (12, 13). During solidification, the lamellar pattern of solid and liquid inclusions leaves a very characteristic imprint on the frozen surface, as shown in Fig. 4. The solid inclusions reduce

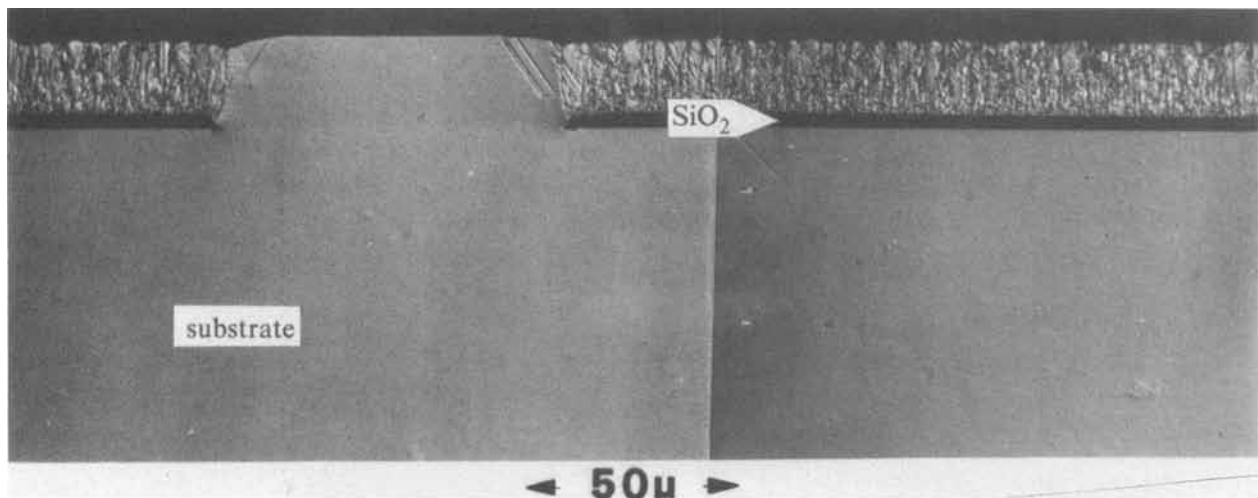


Fig. 5. Optical micrograph of as-deposited sample after cross sectioning and 10s Schimmel etching. The vertical line in this and two other figures is an edge of a photograph.

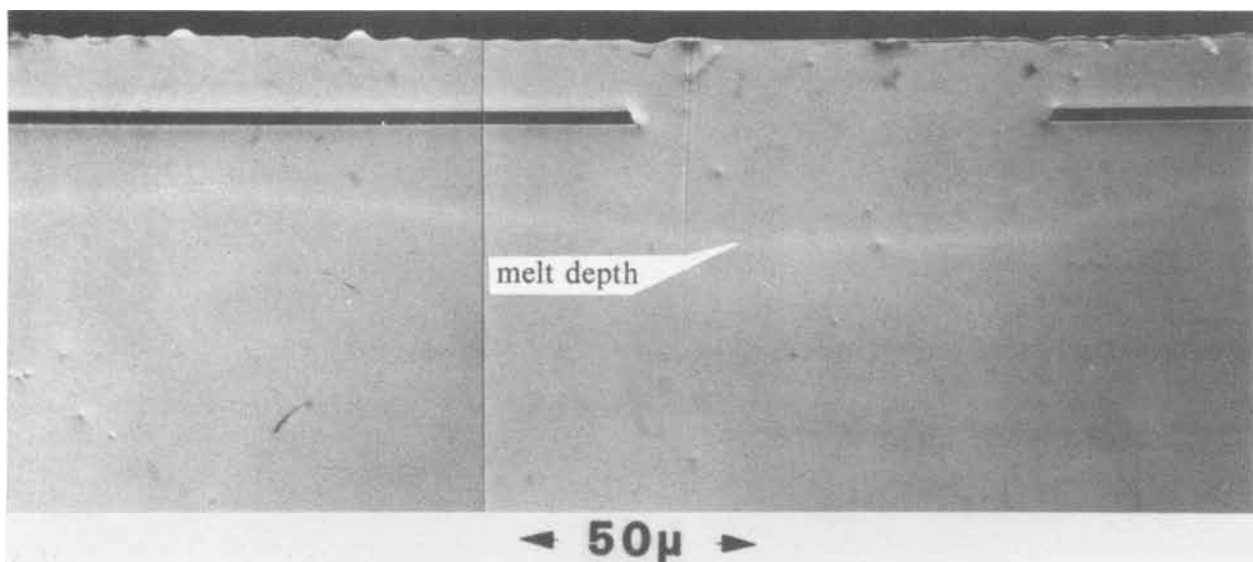


Fig. 6. Schimmel-etched cross section of a recrystallized sample

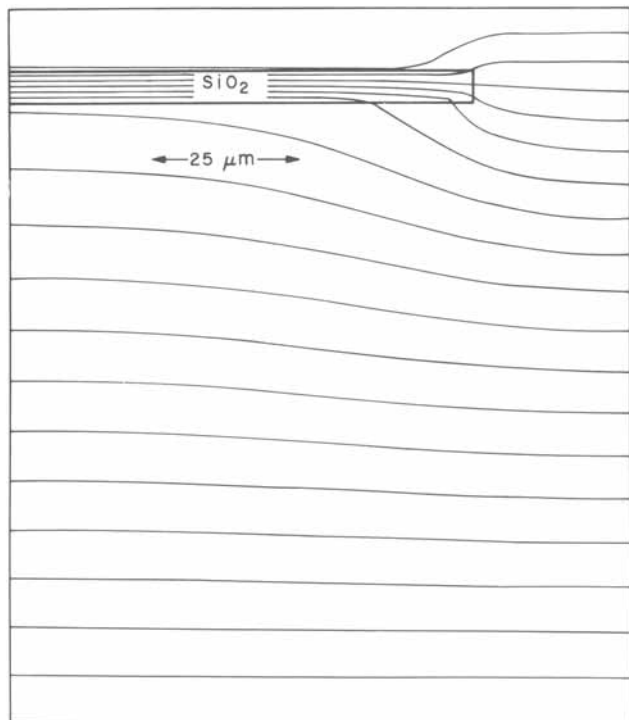


Fig. 7. Calculated isotherm distribution near a seeding window in oxide, before melting occurs. The image is symmetrical about the right vertical edge. [After Wilson (16).]

the surface-averaged reflectivity to a value permitting a steady-state heat flow over a wide range of input powers. Because of this, the melt depth is a complicated function of time and input power.

Samples for crystallization are prepared by oxidation, photolithography, and deposition of silicon and SiO_2 films. Silicon (100) starting wafers are cleaned and oxidized in a steam ambient to form the dielectric isolation barrier. The oxide is patterned by photolithography to obtain an array of seeding windows. CVD deposition of polysilicon is carried out at high temperatures in a conventional vertical epitaxial reactor (14, 15). To achieve epitaxial growth over the windows in oxide, samples are

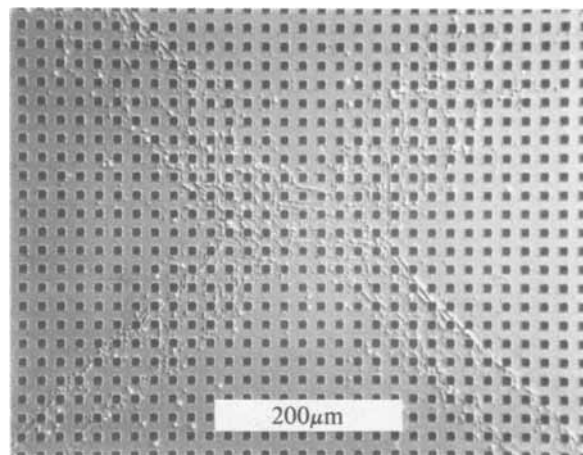


Fig. 9. The center part of a recrystallized island similar to that in Fig. 8, with edges of etch pits aligned over the entire area.

etched briefly with HCl vapor at 1050°C to remove the native oxide from the silicon surface. Deposition is often done in two steps: (i) nucleation and (ii) rapid growth. Uniform nucleation of Si over SiO_2 is achieved by decomposition of SiH_4 at 1050°C . After a continuous silicon layer has been formed, the temperature is increased to 1150°C and SiH_4 is replaced with SiHCl_3 for a higher, $>1 \mu\text{m}/\text{min}$, growth rate. The $10\text{-}100 \mu\text{m}$ thick films have columnar grain structure with an average grain diameter $>1 \mu\text{m}$ and with a surface roughness of $1\text{-}3 \mu\text{m}$. As a final step, the surface is capped with a $2 \mu\text{m}$ layer of LPCVD oxide that is needed to contain molten silicon. A cross section of a typical precursor structure is shown in Fig. 5, with the grain boundaries delineated by 10s Schimmel etching (15).

Crystallization of the molten Si starts in the seeding windows and proceeds laterally over the oxide. Upon recrystallization, the entire film is single crystalline, and it is free of grain boundaries or subboundaries. A cross section of the recrystallized film is shown in Fig. 6. The maximum depth of melt penetration is delineated by the doping dependent etching rate of the cross-sectional surface. The trace of the solid-liquid interface is not planar, but dips down in the seeding region. Preliminary results from a numerical analysis of heat flow (16) in a similar

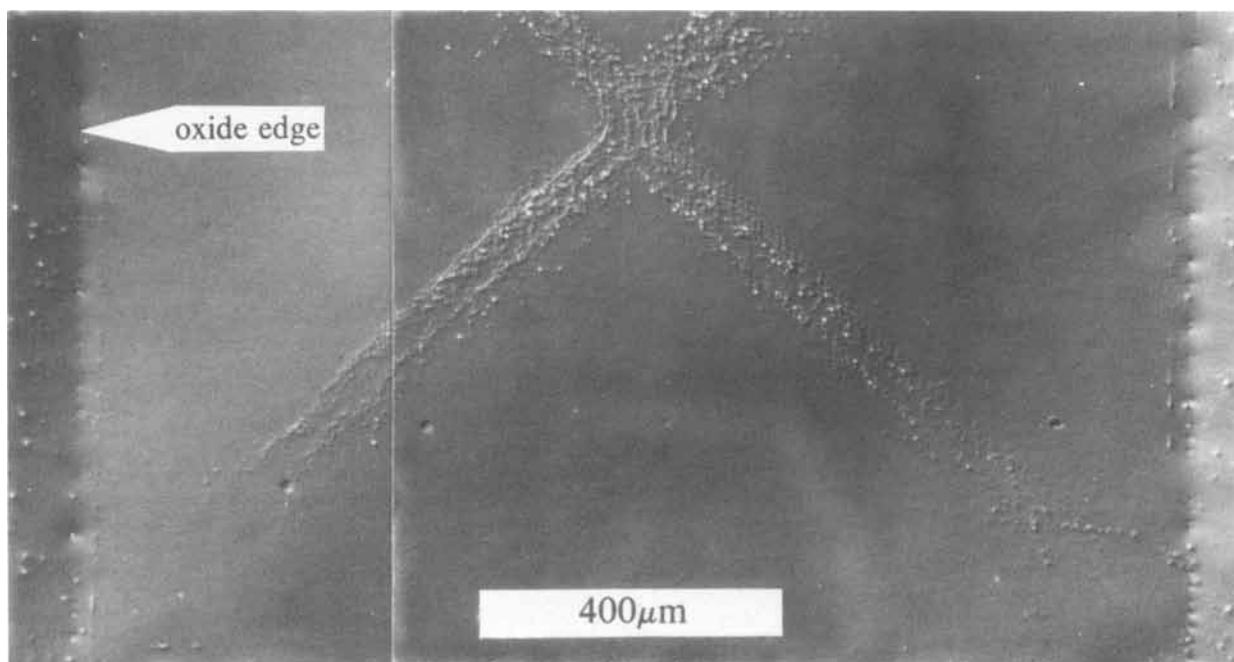


Fig. 8. Top view of lamp recrystallized $30 \mu\text{m}$ thick Si film over a buried square island of SiO_2 , 1.6 mm on each side

configuration agree with this observation. The calculated isotherms are shown in Fig. 7, for temperatures $T < T_M$. This computation does not fully reflect our experimental conditions, where the difference in conductivities of the solid and liquid Si and the heat of fusion have to be included. Still, there is no doubt that isotherms should crowd within the oxide, the thermal conductivity of which is ~ 10 times lower than that of the solid silicon.

A top view of recrystallized Si over a square region of SiO_2 , 1.6 mm on each side, is shown in Fig. 8. The surface was polished before Schimmel etching, since the capping layer preserves the roughness of the as-deposited surface through melting and recrystallization. There is a clear pattern of dislocation pits aligned with the diagonals of the square, indicating symmetrical solidification from all four sides and a collision of the solidification fronts along the diagonals. As expected, the highest dislocation density is right in the center of the square, where all four fronts meet. However, even there, the silicon is single crystalline and free of subboundaries. In Fig. 9, a magnified view of this center region is shown, with superimposed pattern of square pits formed by the grid-of-etch-pits (17) technique. The ridges of all the pits are aligned parallel to each other. In Fig. 10, RBS and channeling spectrum are shown for a sample similar to the one in Fig. 9. The He ion beam of ~ 0.6 mm diam probed a region not including the most defective spot in the center of the epitaxially recrystallized square. Any structural misalignment caused by twinning or subboundaries within the beam diameter would increase the scattering yield. The fact that χ_{\min} value is 3% and identical to the bulk Si, indicates lack of such extended defects over large areas of our films. In contrast, for a typical thin film recrystallized with a strip heater, χ_{\min} varies from 20% to 80% because of the subboundaries.

All crystallization processes are necessarily affected by surface tension effects. In order to control the shape of crystals grown by Czochralski, float-zone, and, in particu-

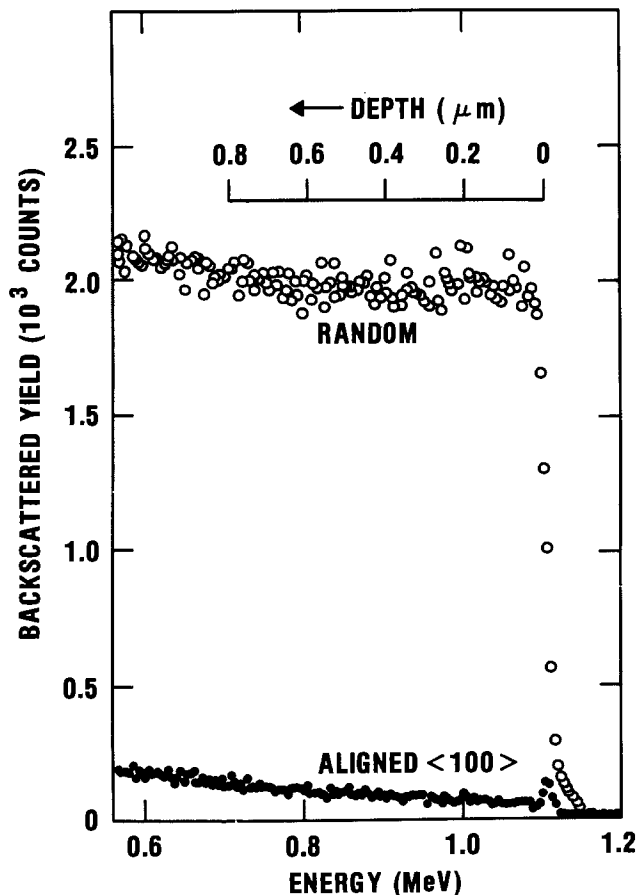


Fig. 10. RBS and ion channeling spectrum for a recrystallized 30 μm thick film. The aligned yield is the same as for the bulk Si.

lar, ribbon growth methods, the relationship between the meniscus angle and the growth direction should be known. The configuration in LEGO experiments is similar to the conditions examined in detail by Surek and Chalmers for the case of a Si wafer melted with an electron beam and recrystallized (18). The variables used in their analysis are defined in Fig. 11. The angle θ is measured between the crystal growth direction and the crystal-vapor interface. ϕ is the angle between the growth direction and the tangent to the meniscus at the growth interface. The relative angle between the free surfaces of the liquid and the solid is $\delta = \phi - \theta$. In their experiments, θ was initially negative, then crossed zero and became progressively more positive, reflecting the initial thinning of the growing crystal and considerable thickening in the last-to-freeze region. The meniscus angle also varied with time. After sectioning resolidified samples, Surek *et al.* measured instantaneous values of θ and derived corresponding values of ϕ from a geometrical analysis. They established that when the uniform thickness growth is momentarily reached in the radially freezing molten zone (*i.e.*, $\theta = 0$), the angle $\phi \sim 11^\circ$. Since $\phi > 0$, there is a pile-up of silicon ahead of the solidification front that leads to reduced crystal thickness at the beginning of crystallization and accumulation of mass at the later stage.

These observations of time-dependent shapes in solidifying bulk crystals also approximate well the behavior of freezing films. Films recrystallized by the LEGO process are thinner near the seeds and considerably thicker in the regions that freeze last, as shown in Fig. 12. This thick-

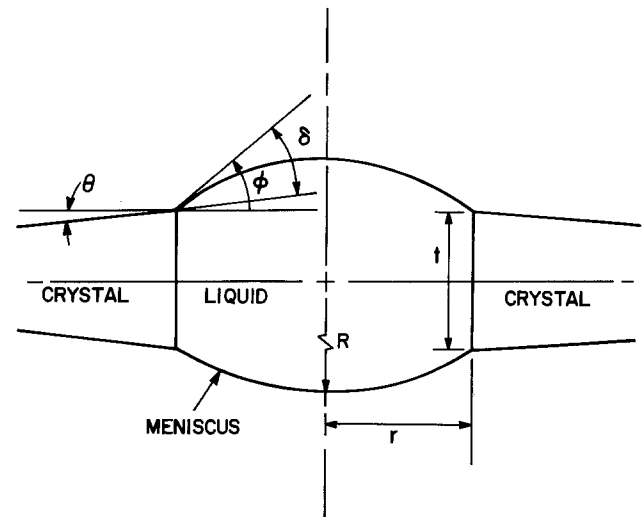


Fig. 11. Solid-vapor and liquid-vapor interfaces shown schematically for a radially freezing molten zone [After Surek and Chalmers (18).]

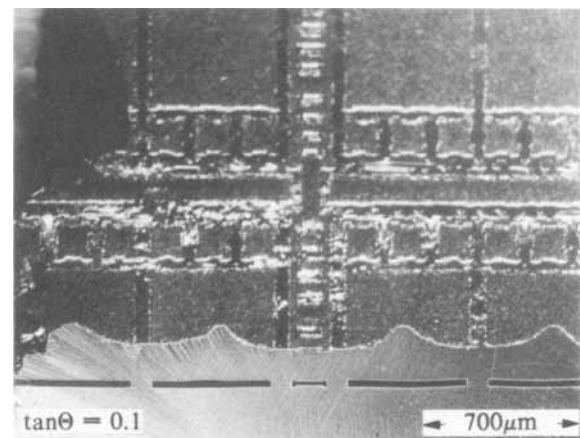


Fig. 12. Angle-lapped sample, showing redistribution of Si towards the center of each recrystallized zone.

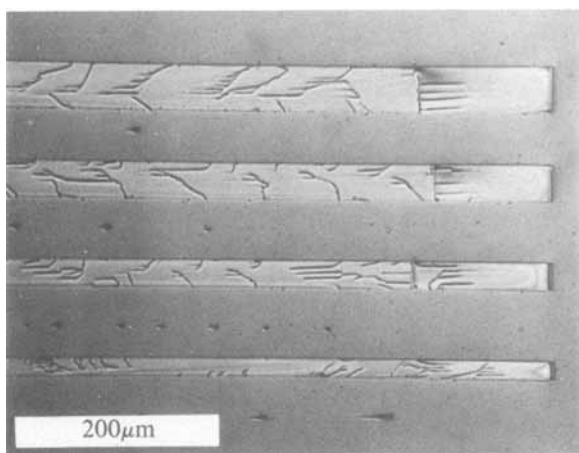


Fig. 13. Patterned thin film recrystallized in the lamp furnace. Seeding occurred through narrow openings in the oxide at both ends of each stripe (only one end is visible in the photograph).

ness variation is the main limitation in thin film crystallization with extended stationary heaters. Scanning of a narrow molten zone produced with a laser or a hot wire reduces redistribution effects, but does not eliminate them.

One important difference between our experimental configuration and that of Surek is the presence of the capping oxide. This cap reduces the meniscus angle ϕ from 11° to about 1.5° according to Yablonovitch (19). Smaller ϕ means less pile-up of Si and a more uniform film thickness than would be possible with a free surface.

Redistribution of Si through the snowplowing effect of the propagating interface limits the application of LEGO to relatively thick films, $> 10 \mu\text{m}$. Crystallization of thinner films with widely spaced seeding windows often leads to a discontinuous coverage of oxide with Si. This problem can be eliminated by patterning the Si film into sections. For example, Fig. 13 shows four stripes of $0.6 \mu\text{m}$ thick Si on $1 \mu\text{m}$ of oxide successfully recrystallized in the lamp furnace. Seeding occurred through narrow openings in the oxide at the ends of each stripe. This micrograph also shows the presence of subboundaries similar to those obtained by all the other methods of crystallization of thin films.

During high temperature processing of multilayer structures, there is always a risk of wafer bowing. In our configuration, the wafers are supported only at three points during the melting process, and the entire substrate is within a few degrees of melting. Nevertheless, the back surface of 3 in. wafers remains flat to within $10\text{-}50 \mu\text{m}$. The amount of bow is equal or lower than that caused by other processing steps such as growth of a thick isolation oxide or polysilicon deposition.

1. WIDE SIDE UP



2. WIDE SIDE DOWN



3. VERTICAL ISOLATION

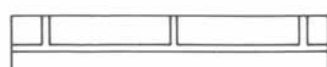


Fig. 14. Three possible configurations of DI silicon tubs

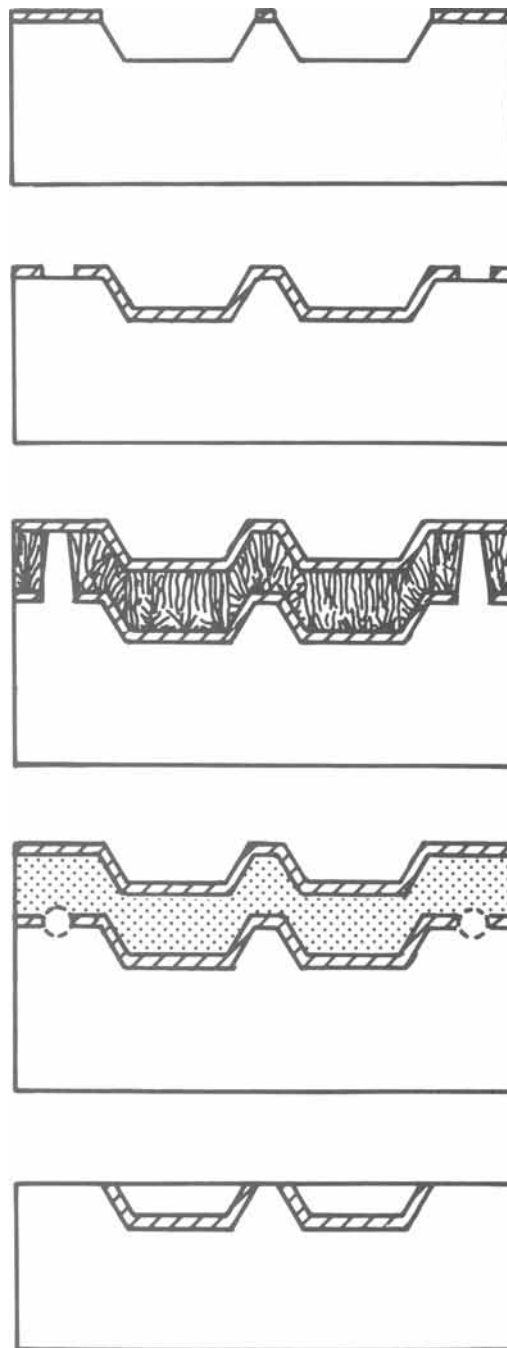


Fig. 15. LEGO processing sequence for complete dielectric isolation

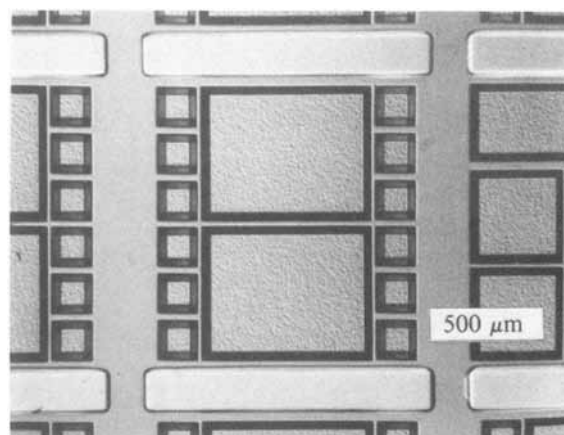


Fig. 16. Top view of etched tubs in Si substrate after oxidation and opening of seeding windows but before polysilicon deposition.

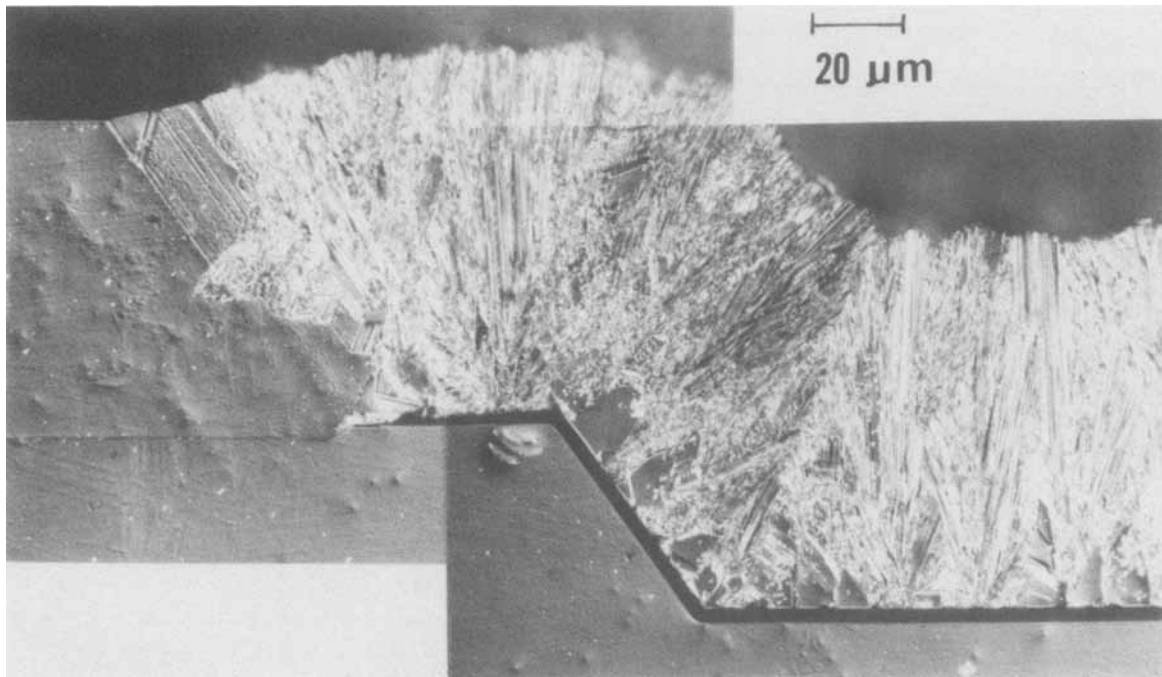


Fig. 17. Etched vertical section of polysilicon film deposited over oxidized nonplanar substrate

Strip heaters can also be used to recrystallize seeded thick films. In unseeded crystallization of thin films, (100) texture and in-plane alignment of the $\langle 100 \rangle$ axis with the growth direction is achieved and the crystalline quality is marred mainly by the presence of the subboundaries. For films thicker than $5 \mu\text{m}$, the preferential growth direction and texturing are lost (20). However, thick films were grown successfully from seeding windows (21). They were free of subboundaries just like the films crystallized in the lamp furnace. The main features distinguishing these results from the stationary heater experiments were a different mass transport and a higher density of dislocations. Since the solidification front propagated only in one direction, the film thickness increased somewhat along the scan. Dislocations tended to be concentrated in the center region of the films, away from the upper and lower Si-oxide interfaces.

Crystallization of Nonplanar Films

In the previous section, we showed that high crystalline quality films can be obtained by LEGO. This is not sufficient to obtain device-worthy structures. What is necessary is the means for achieving sidewall as well as vertical isolation.

In principle, three different approaches to sidewall isolation are possible, as shown in Fig. 14. Vertical walls can be formed by etching, oxidation, and backfilling. V-grooves can be formed by anisotropic etching. This process is the simplest for planar recrystallized films but it would cause loss of surface area for devices and would

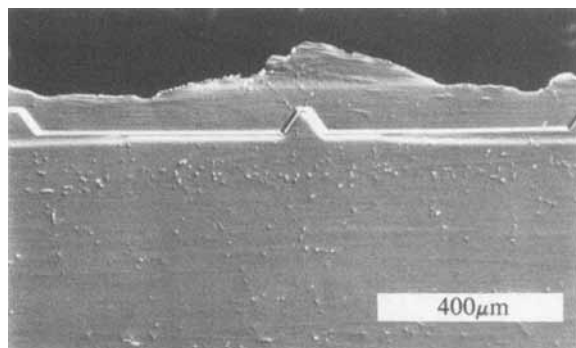


Fig. 18. Etched vertical section of recrystallized nonplanar film

limit the minimum device size. The “wide-side-up” structure showed in Fig. 14 is most compatible with device fabrication schemes.

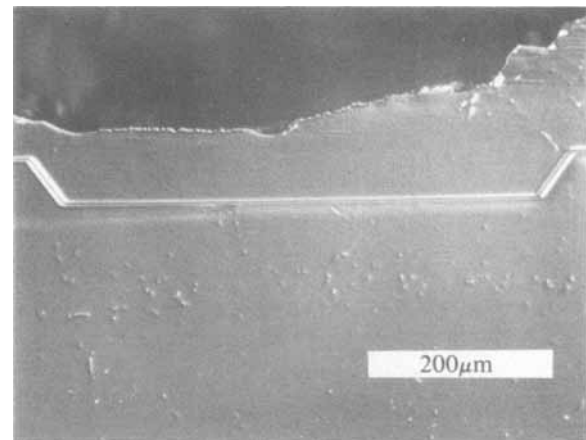


Fig. 19. Magnified view of the etched vertical section of recrystallized nonplanar film.

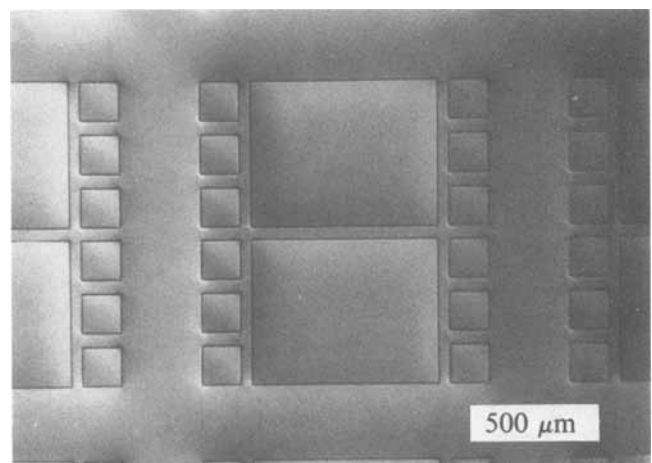


Fig. 20. Top view of recrystallized nonplanar film after isolation was completed by polishing. One small isolated Si tub and a part of a larger one are seen.

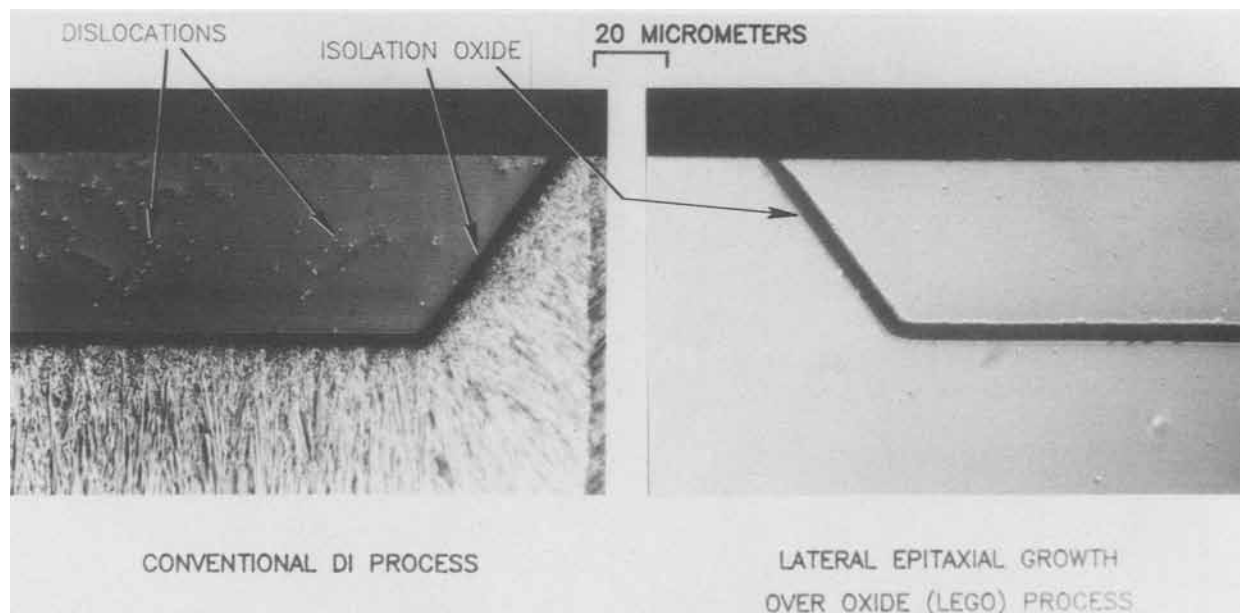


Fig. 21. Comparison of device tubs formed by the conventional DI process and by the LEGO process

To obtain such structures, the crystallization procedure was changed. The new sequence is shown in Fig. 15. It starts with formation of nonplanar substrates by KOH etching of rectangular tub-shaped depressions, followed by oxidation and opening of seeding windows in the oxide. A top view of the tubs and seeding windows in the SiO_2 is shown in Fig. 16. Notice that the tubs are truly rectangular with 90° corners, and that their shape is exactly that of the pattern in the mask. In contrast, in the conventional processing sequence the etched pattern is essentially a negative of that used in the LEGO process, and the geometry of etched areas requires corner compensation to achieve approximately rectangular device regions.

Defining seeding windows in the SiO_2 requires conformal coating of a nonplanar substrate with a photoresist. Conventional photoresist spinning does not provide complete surface coverage, especially at the sharp edges. Several approaches are being investigated, and the problem of reliably forming windows in oxide should be resolved soon.

A cross section of the structure after polysilicon deposition but before crystallization is shown in Fig. 17. Notice that epitaxial growth occurred over the window and that columnar crystallites are present over the oxide. The interface between the substrate and the epitaxially grown layer in the window area can be seen. This interface is recessed because of *in situ* surface etching with HCl immediately before the deposition.

After recrystallization, the film is single crystalline, with defect localized outside the potential device area, in the regions that froze last. Cross sections of a recrystallized sample are shown in Fig. 18 and 19. From these micrographs, it is clear that the density of dislocations in the substrate is higher than that in the recrystallized Si on SiO_2 . Although the defects below the buried oxide have no influence on the device performance, we examined the processing steps in detail to determine their origin. We found that oxidation needed to form the dielectric isolation layer introduced a high density of stacking faults that were transformed into dislocations during subsequent high temperature steps. The density of these dislocations was not increased during recrystallization. Any conventional method that prevents formation of the oxidation-induced stacking faults should eliminate most linear and planar defects in LEGO processed substrates.

After crystallization of Si over a nonplanar substrate, excess Si is removed by polishing to complete isolation of individual device tubs. A top view of a magnified segment of a polished wafer is shown in Fig. 20. Buried oxide

intersecting the surface delineates the boundaries between isolated regions and the substrate.

Summary

We have demonstrated that, by melting of large areas with a stationary heater, single-crystalline thick Si films can be formed. Such films are free of grain boundaries and subboundaries and have few dislocations. The thermal gradients necessary for lateral crystallization are defined by a pattern of windows in the buried oxide, and seeded growth can proceed from each window over a distance > 1 mm. The process works best for films thicker than $10 \mu\text{m}$. The continuity of thinner, unpatterned films can be disrupted by Si redistribution that is driven by the nonzero meniscus angle of the liquid Si during solidification. Patterned, seeded films as thin as $0.5 \mu\text{m}$ can be recrystallized, but with subboundaries similar to those formed by the scanning methods of crystallization.

Recrystallization of thick films over substrates with $\sim 50 \mu\text{m}$ deep depressions lends itself to formation of crystalline regions with complete dielectric isolation, sidewall as well as vertical. This should allow simplified fabrication of DI wafers. Moreover, the wafers formed by the LEGO process are entirely crystalline, without the polysilicon handle. Figure 21 illustrates the difference between the two approaches.

Much further effort is necessary to assure reproducible and uniform crystallization of Si over complete 4 in. wafers. The problems related to lithography on nonplanar wafers have to be resolved and the control of crystallization improved. Methods for introducing dopants to form buried layers inside the device tubs also need development. Assuming that these issues are successfully resolved, DI wafers formed by recrystallization will be less expensive to make and will contain fewer yield limiting structural defects.

Acknowledgments

The authors are grateful to L. O. Wilson for permission to use her unpublished data. We also acknowledge the technical assistance of R. L. MaSaitis and R. F. Benjamin.

Manuscript submitted June 18, 1984; revised manuscript received Aug. 31, 1984.

AT&T Bell Laboratories assisted in meeting the publication costs of this article.

REFERENCES

1. "Single-Crystal Silicon on Non-Single-Crystal Insulators," G. W. Cullen, Editor, *J. Cryst. Growth*, **63**, no. 3 (1983).
2. K. E. Bean and W. R. Runyan, *This Journal*, **124**, 5C (1977).
3. G. K. Celler, McD. Robinson, and D. J. Lischner, *Appl. Phys. Lett.*, **42**, 99 (1983).
4. G. K. Celler, McD. Robinson, D. J. Lischner, and T. T. Sheng, *Mater. Res. Soc. Symp. Proc.*, **13**, 575 (1983).
5. McD. Robinson, D. J. Lischner, and G. K. Celler, *J. Cryst. Growth*, **63**, 484 (1983).
6. D. J. Lischner and G. K. Celler, *Mater. Res. Soc. Symp. Proc.*, **4**, 759 (1982).
7. T. Suzuki, A. Mimura, and T. Ogawa, *This Journal*, **124**, 1776 (1977).
8. G. K. Celler, *J. Cryst. Growth*, **63**, 429 (1983).
9. J. C. C. Fan, B.-Y. Tsaur, and M. W. Geis, *ibid.*, **63**, 453 (1983).
10. M. Tamura, H. Tamura, M. Miyao, and T. Tokuyama, *Jpn. J. Appl. Phys.*, **20**, Suppl. 20-1, 43 (1981).
11. W. G. Hawkins and D. K. Biegelsen, *Appl. Phys. Lett.*, **42**, 358 (1983).
12. G. K. Celler, McD. Robinson, L. E. Trimble, and D. J. Lischner, *ibid.*, **43**, 868 (1983).
13. G. K. Celler, K. A. Jackson, McD. Robinson, L. E. Trimble, and D. J. Lischner, *Mater. Res. Soc. Symp. Proc.*, **23**, 409 (1984).
14. McD. Robinson, in "Impurity Doping Processes in Silicon," F. F. Wang, Editor, pp. 249-314, North Holland, New York (1981).
15. D. G. Schimmel, *This Journal*, **126**, 479 (1979).
16. L. O. Wilson, Unpublished data.
17. K. A. Bezjian, H. I. Smith, J. M. Carter, and M. W. Geis, *This Journal*, **129**, 1848 (1982).
18. T. Surek and B. Chalmers, *J. Cryst. Growth*, **29**, 1 (1975).
19. E. Yablonovitch, Unpublished data.
20. H. A. Atwater, H. I. Smith, C. V. Thompson, and M. W. Geis, *Mater. Lett.*, **2**, 269 (1984).
21. L. Pfeiffer, G. K. Celler, T. Kovacs, and McD. Robinson, *Appl. Phys. Lett.*, **43**, 1048 (1983).

Autodoping in Silicon Epitaxy

Hsueh-Rong Chang

General Electric Company, Corporate Research and Development Center, Schenectady, New York 12345

ABSTRACT

Vertical and lateral autodoping in silicon epitaxy deposited in a vertical pancake-type reactor were examined as a function of pre-epitaxial bake cycle, dopant type, source gas, and growth parameters. Boron, phosphorus, arsenic, and antimony were used as dopant elements to form a localized buried layer at the center of substrates. Silane, dichlorosilane, and silicon tetrachloride were used as the silicon source for epitaxial growth. The results show that higher prebaking temperature produces more lateral autodoping for boron and phosphorus, while the opposite holds for arsenic and antimony. Autodoping in both vertical and lateral directions decreases with increasing prebake time. A continual decrease in lateral autodoping is found with increasing growth rate for phosphorus; for arsenic, only a slight difference is noticed in the growth-rate range studied. Phosphorus and arsenic show a similar trend at the deposition temperature of lateral autodoping, *i.e.*, autodoping decreases at first, then increases with increasing temperature. For all the dopants studied, vertical and lateral autodoping decrease with increasing number of chlorine atoms in the source gases.

Silicon epitaxy is widely used in semiconductor devices, primarily for its ability to grow lightly doped epitaxial layers over heavily doped substrates in a controlled manner. A high quality epitaxial layer with an abrupt interface is required for high frequency, high efficiency, and high reliability operation of semiconductor devices. Emphasis has been placed on obtaining sharp transition regions between the epitaxial layer and the substrate and on minimizing the autodoping. Dopants can transfer from the substrate to the epitaxial layer by either solid-state diffusion or redeposition via the gas phase, *i.e.*, autodoping. A clear separation of the solid-state diffusion and gas-phase transport effects has been made possible by using high resistivity substrates with localized buried layers (1-6). Such structures are more typical of the processing involved in the fabrication of integrated circuits.

Numerous studies on autodoping in silicon epitaxy have appeared in the literature describing various aspects of this phenomenon. In most cases, RF-heated horizontal-type reactors have been used for epitaxial growth. In the horizontal reactor, the gas flow is straightforward, entering the reactor tube at one end and flowing along the susceptor surface. In this reactor system, the gas flow is typically in the laminar regime (7). Such a flow can be analyzed by established fluid-flow relationships and has been discussed in detail by Eversteijn *et al.* (8), Ban and Gilbert (9), and Berkman *et al.* (10). There is little published information on autodoping using vertical reactor for epitaxial growth (6, 11). The gas-flow pattern in the vertical reactor is very complex. The gases are introduced through the center of the susceptor; they impinge on the hemispherical upper portion of the bell jar and swirl down the sides of the bell jar and across the substrates. The gases recirculate over the substrates many times be-

fore they exit through the annulus between the susceptor and the bell jar. Since the gas-flow dynamics in the vertical reactor are very different from those of the horizontal reactor, they can have a significant influence on autodoping behavior. Previous studies on the growth-rate dependence of autodoping show conflicting results between these two reactor systems. Bozler (11) reports an increase in vertical autodoping with increasing growth rate, using a vertical-type reactor for epitaxial deposition; the opposite result is obtained by Tabe and Nakamura (12) using a horizontal reactor. However, Srinivasan (3, 5) finds that lateral autodoping increases with increasing growth rate using a horizontal reactor. In an attempt to clarify these contradictory results, experiments have been conducted to investigate the influence of growth parameters on vertical and lateral autodoping in a vertical reactor. The results are compared with previously published data.

Arsenic has been used as dopant in most of the autodoping studies. Relatively less work has been carried out on autodoping with boron, phosphorus, and antimony (6, 13-16). Boron and phosphorus have smaller atomic sizes and diffuse much faster in silicon than does arsenic (17). High temperature CVD epitaxial processes can result in different autodoping behavior for different dopants. It has been shown that the major portion of autodoping occurs during the pre-epitaxial bake cycle (5, 12, 13, 18). Many models have been proposed to describe autodoping phenomena. Joyce *et al.* (13) claims that autodoping is controlled by the out-diffusion from the back of the heavily-doped substrates. This model, however, cannot explain the occurrence of lateral autodoping with localized buried layer structures. Bozler (11) assumes that autodoping is dependent on the dopant concentration in the turbulent, well-mixed gas phase. Based on this as-

sumption, lateral autodoping should be independent of the distance from the buried layer, which contradicts experimental evidence (2, 5, 6). Srinivasan (3, 5), on the other hand, assumes that autodoping is directly proportional to the dopant concentration at the substrate surface on the buried layer region just before epitaxial growth. This study gives evidence contrary to this assumption, as will be discussed. Tabe and Nakamura (12) postulate that an adsorbed dopant layer formed during prebaking acts as a dominant reservoir for autodoping. In their derivation, time is used as the independent variable, whereas in practical applications, the epitaxial film thickness is generally used. If time is replaced by film thickness in their model, then it predicts that higher growth rate results in higher autodoping. This relationship is in fact contradicted by the accompanying data. In this study, the effect of pre-epitaxial bake temperature and time on autodoping for boron, phosphorus, arsenic, and antimony is investigated. The dopant concentration at the surface of the buried layer before and after prebake cycles is measured in an attempt to correlate autodoping with surface concentration of the buried layer.

It has been found that different source gases affect autodoping differently (5, 6, 19). Suzuki and Endo (19) report that if arsenic-doped substrate is used under identical growth condition, silane epitaxy gives lower autodoping than SiCl_4 . They attribute this result to the absence of chlorine, which is presumed to be the dopant carrier, in the silane system. However, a conflicting result is reported by Srinivasan (5), based on the use of arsenic-doped buried layer structures. Srinivasan claims that an *in situ* etching by HCl (or Cl_2) released by the H_2 reduction of SiCl_4 reduces the dopant incorporation in the epitaxial layer. A study of the effect of the source gas chlorine on autodoping is included as part of this work. New data are presented concerning the autodoping differences between epitaxial layers using silane, dichlorosilane, and silicon tetrachloride as source gases. A correlation between the number of chlorine atoms in the source gases and autodoping has been obtained.

Experimental

All the epitaxial layers examined in this study were grown in a vertical-type CVD reactor Model AMV 1200 made by Applied Materials, Incorporated. The cross section of the reactor chamber is shown in Fig. 1. The susceptor had a 30.48 cm diameter and was made of high purity graphite coated with a layer of silicon carbide. The gases were introduced from a 9.5 mm (od) injection tube through the center of the susceptor into the reactor chamber. During operation, the susceptor rotated continuously and a constant hydrogen carrier gas flow of 50 liters/min was used. Before loading the wafers for epitaxial growth, the susceptor was etched with hydrogen chloride at 1200°C , then coated with a fresh layer of undoped silicon having an impurity concentration less than $1 \times 10^{14} \text{ cm}^{-3}$.

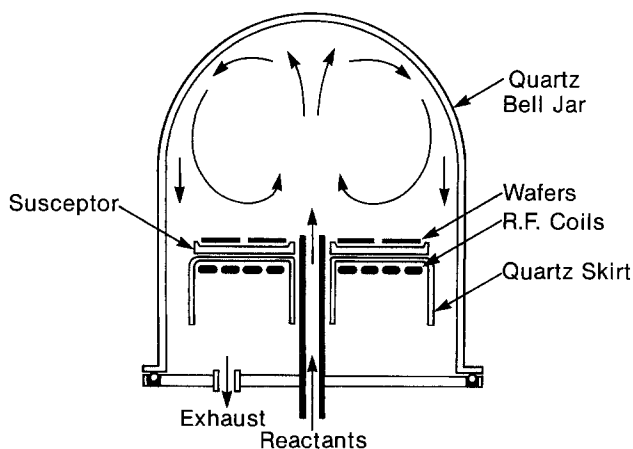


Fig. 1. Vertical silicon epitaxial reactor

Only one substrate was used per experiment. All the epitaxial deposits were $5 \mu\text{m}$ thick, with no external doping. The temperature of silicon wafers was measured with an optical pyrometer corrected for emissivity and wall transmission losses.

The substrates used in this study were lightly doped p-type and n-type silicon wafers having resistivities of $80\text{--}120 \Omega\text{-cm}$ and $\langle 100 \rangle$ orientation. Boron was implanted on n-type substrates, while phosphorus, arsenic, and antimony were implanted on p-type substrates, to form a 4 cm^2 buried layer at the center of 3 in. wafers. The surface concentrations of boron, phosphorus, arsenic, and antimony were $\sim 3 \times 10^{18} \text{ cm}^{-3}$, $8 \times 10^{19} \text{ cm}^{-3}$, $1.5 \times 10^{19} \text{ cm}^{-3}$, and $2 \times 10^{19} \text{ cm}^{-3}$, with corresponding junction depths of $\sim 3 \mu\text{m}$, $2 \mu\text{m}$, $1.3 \mu\text{m}$, and $1.5 \mu\text{m}$, respectively.

In the pre-epitaxial bake experiments, 1050° and 1150°C were the prebake temperatures, and the prebake time was varied from 10 to 70 min. Depositions were made at 1050°C , with a growth rate of $0.25 \mu\text{m}/\text{min}$, using silane, dichlorosilane, and silicon tetrachloride as the silicon source. In the growth-rate and deposition-temperature experiments, dichlorosilane was used for epitaxial growth. The dichlorosilane flow rate was varied from 60 to 250 cm^3/min , with the corresponding growth rate changing from 0.25 to $1.1 \mu\text{m}/\text{min}$. Deposition temperature ranged from 1050° to 1150°C .

The dopant profiles were measured by the spreading resistance technique using an instrument made by Solid State Measurements, Incorporated.

Results and Discussion

Autodoping from a substrate with a buried layer structure can be classified into two types. One is vertical autodoping, which is in the epitaxial layer over a buried

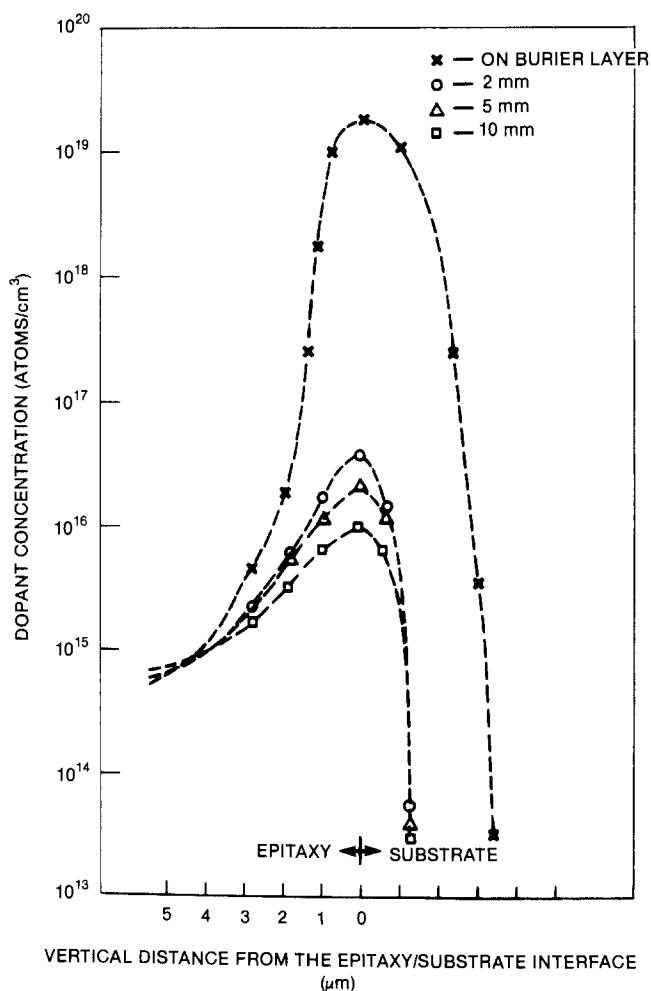


Fig. 2. Phosphorus profiles in an epitaxial layer on and off the buried layer region.

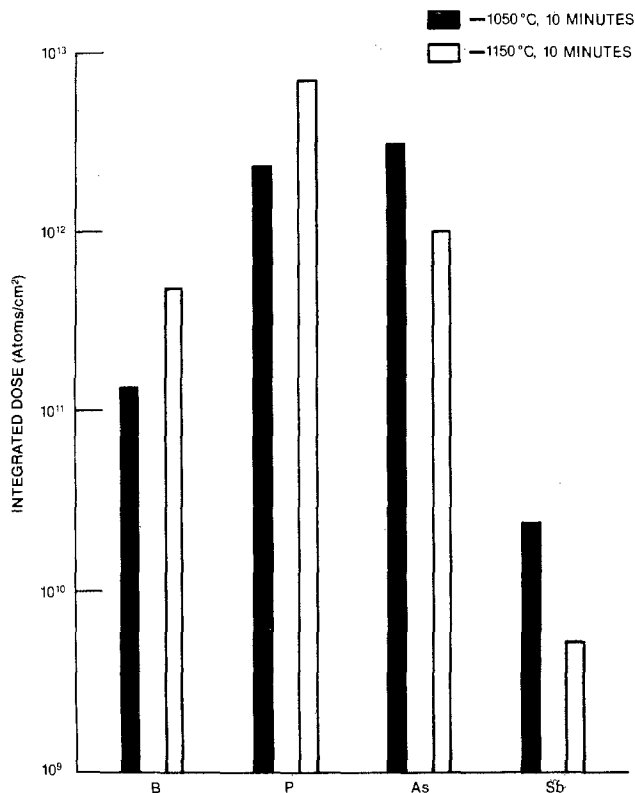


Fig. 3. Variation of lateral autodoping with prebaking temperature (2 mm from the edge of the buried layer region). Deposition temperature 1050°C; growth rate 0.25 $\mu\text{m}/\text{min}$.

layer region. The other is lateral autodoping, which is adjacent to the buried layer. Vertical autodoping contains out-diffusion of impurities from buried layers, in addition to autodoping from the vapor phase. In order to study autodoping (gas-phase), it is desirable to separate the out-diffusion effect by obtaining impurity profiles laterally away from the buried layer regions, i.e., lateral autodoping. Lateral autodoping has its maximum value at the epitaxy-substrate interface, as illustrated in Fig. 2. It is evident that the maximum dopant concentration decreases with the increase of the lateral distance from the edge of the buried layer. This is true regardless of dopant type. Lateral autodoping can be characterized by either the maximum dopant concentration at a chosen lateral position away from the buried layer or the integrated quantity under the vertical profile at that chosen position. The latter is used in the present study. The results in Fig. 2 indicate that the lateral autodoping is controlled by the evaporated dopant diffusing in a laminar flow regime just above the substrate surface, in which the lateral autodoping is predicted to decrease with increasing distance from the edge of the buried layer (20). The assumption of a well-mixed, turbulent gas flow in the vertical reactor proposed by Bozler (11) does not apply to the region very near the substrate surface. Similar behavior is also observed for arsenic autodoping using silane and SiCl_4 (2, 5) in a horizontal epitaxy reactor system where the gas flow is typically laminar (7).

Pre-epitaxial bake cycle.—Pre-epitaxial bake temperature has shown different effects on autodoping behavior for various dopants. As shown in Fig. 3, for boron and phosphorus, higher prebake temperature results in more autodoping, while the opposite holds for arsenic and antimony. The measurements are taken 2 mm away from the edge of the buried layer. This is true for all the source gases studied. Figure 4 shows the dopant profiles in the epitaxial layers for phosphorus and arsenic 2 mm away from the edge of the buried layer. Because the growth rate (0.25 $\mu\text{m}/\text{min}$) is much faster than the diffusivity at the deposition temperature of 1050°C, a Gaussian distri-

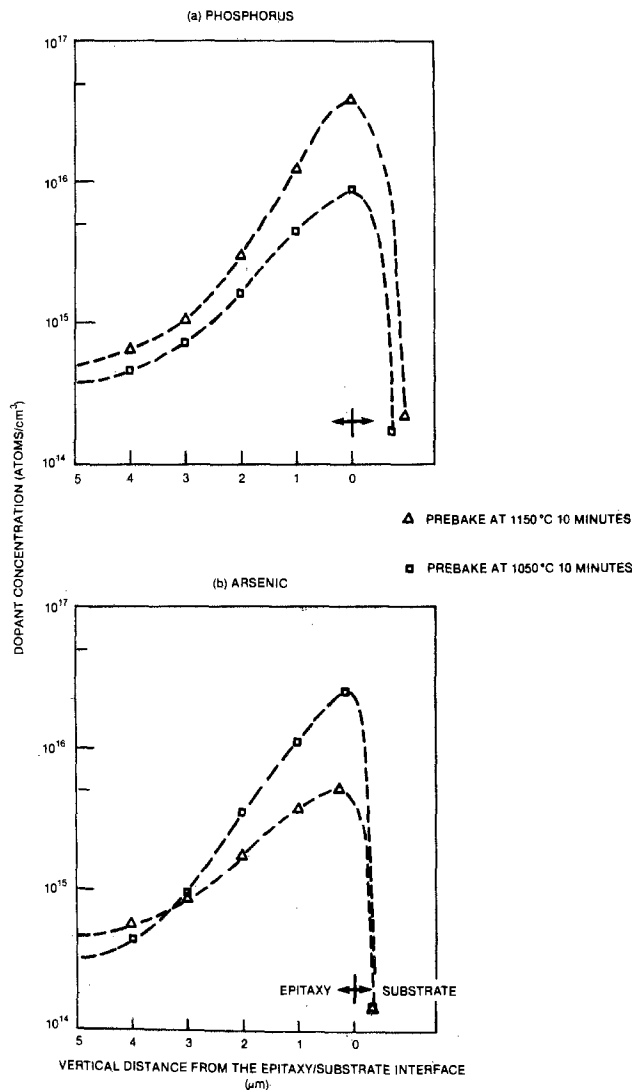


Fig. 4. Impurity concentration profiles in the epitaxial layers 2 mm laterally away from the buried layer regions: a) phosphorus; b) arsenic. Deposition temperature 1050°C; growth rate 0.25 $\mu\text{m}/\text{min}$.

bution centered at the original interface could be expected. These curves suggest that a continuous but slowly decreasing gas-phase source of dopant exists throughout the deposition cycle.

Srinivasan (3) reports that the lateral autodoping decreases with increasing prebake temperature and time when using arsenic as dopant. Based on his findings, Srinivasan proposes a model to describe the lateral autodoping as controlled by the impurity surface concentration over the buried layer region that exists just prior to epitaxial deposition. If this model were valid for all dopants, then the results of Fig. 3 would suggest an increasing surface impurity concentration with an increasing prebake temperature for boron and phosphorus. Experiments were carried out to obtain the surface concentration after the prebake cycle for all the dopants studied. It was found that higher prebake temperature produced lower surface concentration, as illustrated in Fig. 5. The impurity profiles of phosphorus- and arsenic-buried layers before and after the prebake cycles are shown in Fig. 6. Therefore, it is not necessarily true that higher surface concentration produces more autodoping. The dopant redistribution during epitaxial deposition cycle is not controlled only by the evaporation of the dopant from the buried layer; the size of dopant atoms or the adsorption/desorption of dopant at the growing surface can significantly affect autodoping behavior.

The variation of autodoping with pre-epitaxial bake time for phosphorus and arsenic is shown in Fig. 7 and 8.

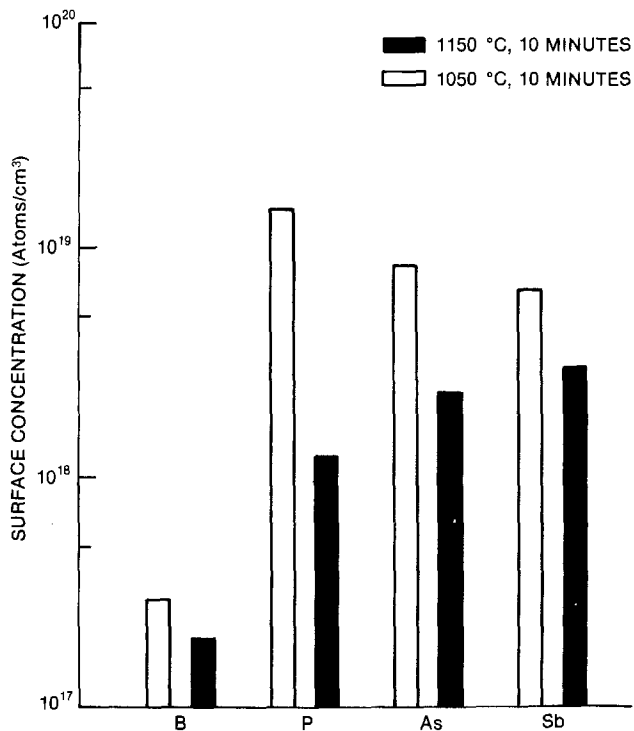


Fig. 5. Dopant surface concentrations on the buried layers after prebake cycles.

Vertical and lateral autodoping decrease with increasing prebake time. These results are consistent with previously published data on lateral autodoping using arsenic in SiCl_4 epitaxy with a horizontal reactor (3). As prebake time increases, dopant atoms continuously evaporate from the substrate and are carried away by the hydrogen gas. It is believed that the depletion of the buried layer region results in lower dopant concentration in the vapor phase and thus leads to less autodoping in the epitaxial layer.

Growth rate.—Autodoping in the epitaxial layers is a function of the epitaxial growth rate. Figure 9 shows the variation of lateral autodoping with growth rate for phosphorus and arsenic. These results indicate that for phosphorus, autodoping decreases with increasing growth rate, while only a slight change is obtained for arsenic. Similar results are obtained for the vertical autodoping.

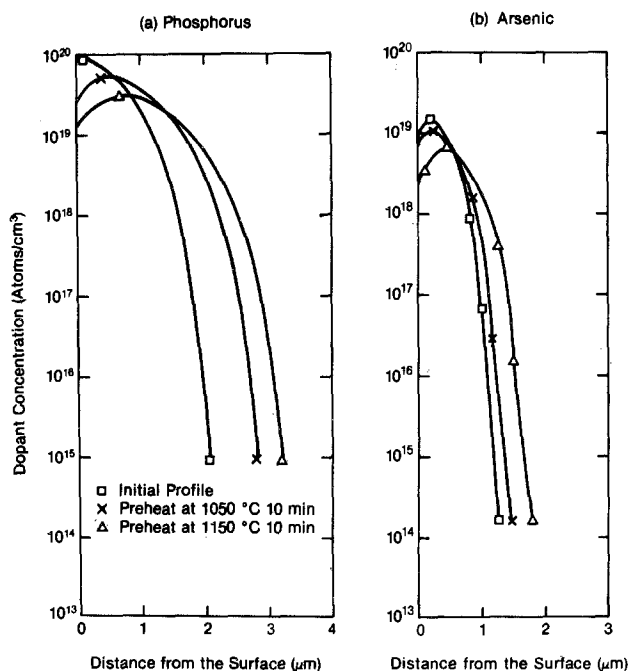


Fig. 6. Impurity concentration profiles of buried layers before and after prebake cycles: a) phosphorus; b) arsenic.

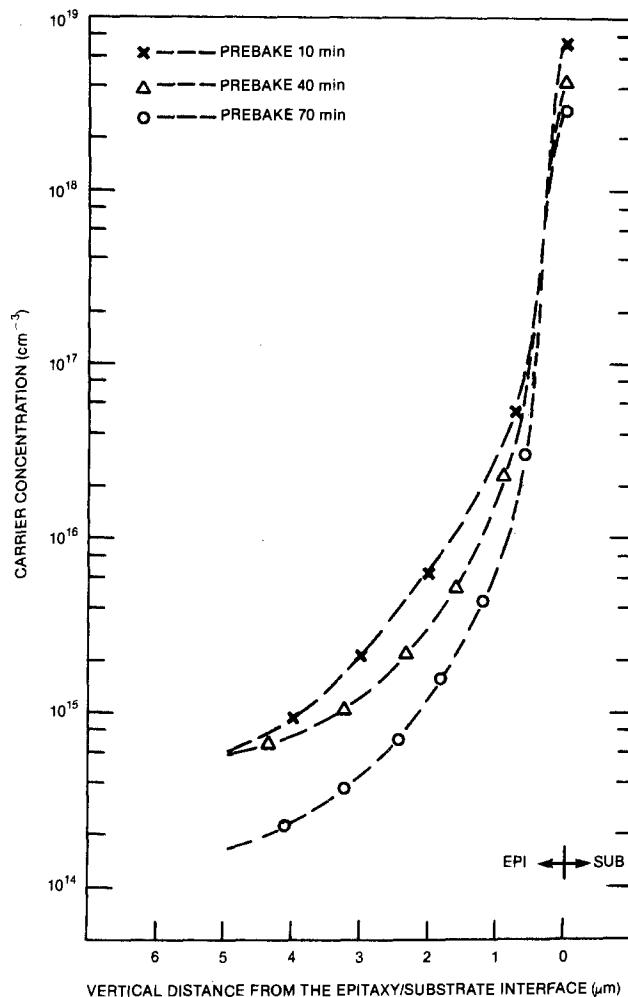


Fig. 7. Arsenic concentration profiles in the epitaxial layers on As-buried layer using SiH_2Cl_2 as the silicon source. Deposition temperature 1050°C ; growth rate $0.25 \mu\text{m}/\text{min}$.

phorus and arsenic. These results indicate that for phosphorus, autodoping decreases with increasing growth rate, while only a slight change is obtained for arsenic. Similar results are obtained for the vertical autodoping.

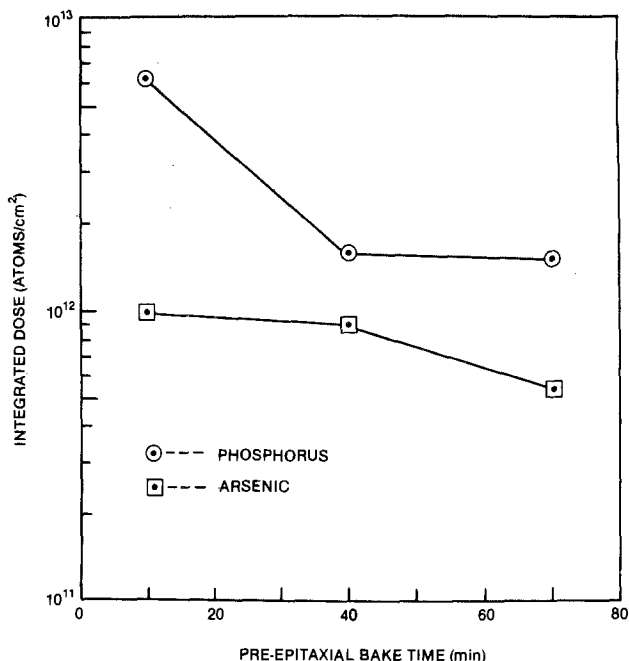


Fig. 8. Decrease in lateral autodoping for phosphorus and arsenic with increasing pre-epitaxial bake time.

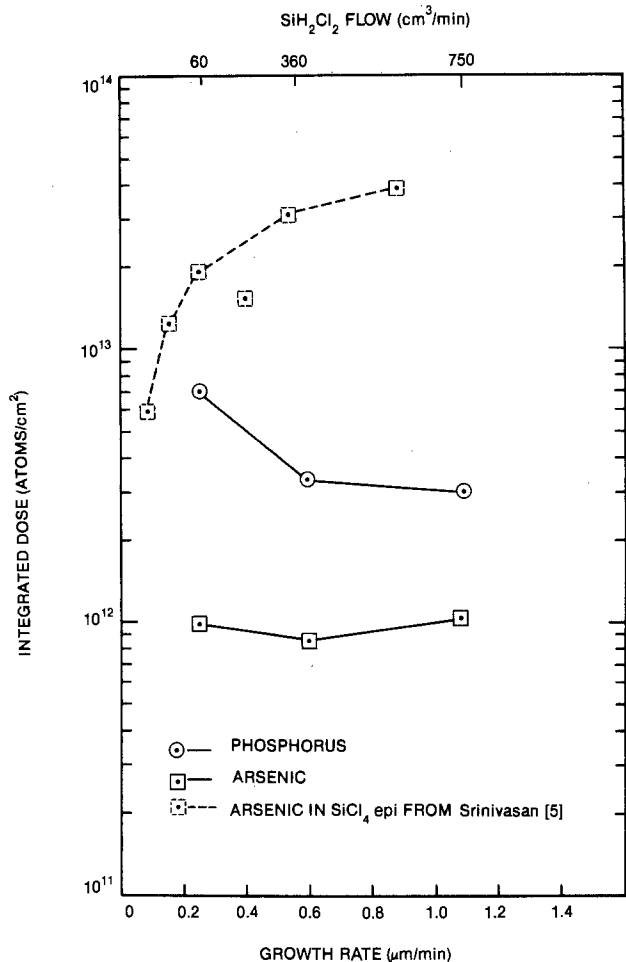


Fig. 9. Variation of lateral autodoping for phosphorus and arsenic with growth rate in SiH_2Cl_2 epitaxy. Prebaking cycle: 1150°C , 10 min; deposition temperature 1050°C .

This difference shows that arsenic autodoping behavior cannot be generally attributed to phosphorus. It is not clear why the growth rate has different effects on the autodoping behavior for phosphorus and arsenic. The adsorption/desorption of dopant at the growing surface and the incorporation into the epitaxial layer may play an important role on the growth rate dependence of autodoping. Alternatively, because phosphorus atoms are smaller and diffuse much faster than arsenic atoms in silicon, a high temperature process could enhance solid-phase redistribution of phosphorus and result in different autodoping behavior. Srinivasan (3, 5) reports that in SiCl_4 epitaxy with a horizontal reactor system, lateral autodoping of arsenic increases with increasing growth rate (0.08-1.0 $\mu\text{m}/\text{min}$), as shown in Fig. 9. The cause of this discrepancy is not clear at present, but it is presumably associated with the use of different reactor types.

Deposition temperature.—The effect of epitaxial deposition temperature on lateral autodoping is shown in Fig. 10. Both phosphorus and arsenic show similar autodoping variations with deposition temperature: autodoping first decreases with increasing temperature; further increase in temperature results in higher autodoping. Similar results are reported for silane and SiCl_4 epitaxy using arsenic as dopant (see Fig. 10), and a model is proposed which predicts the decreasing lateral autodoping with increasing deposition temperature (5). However, the model cannot explain the autodoping behavior for deposition temperatures above 1100°C .

Source gas.—Autodoping in the epitaxial layers has been found to be a function of the source gases. For all the dopants studied, both vertical and lateral autodoping decreases with increasing number of chlorine atoms in the source gases. Figure 11 shows the variation of vertical

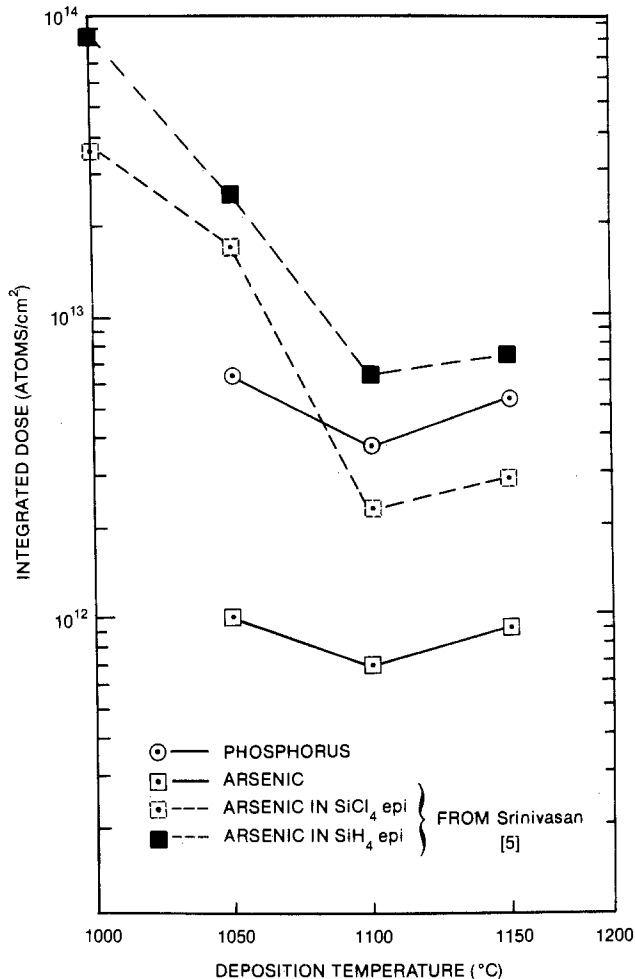


Fig. 10. Variation of lateral autodoping for phosphorus and arsenic with deposition temperature in SiH_2Cl_2 epitaxy. Prebaking cycle 1150°C , 10 min; growth rate $0.25 \mu\text{m}/\text{min}$.

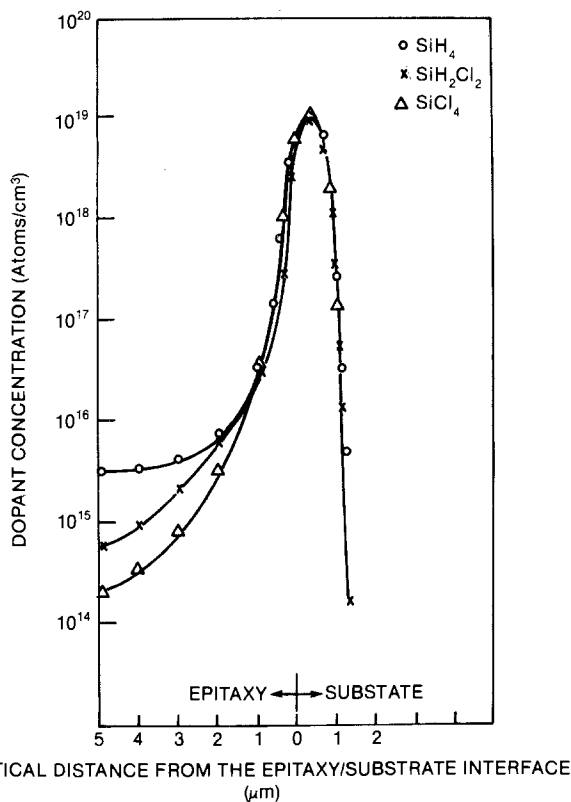


Fig. 11. Arsenic concentration profiles in the epitaxial layers on As-buried layers using SiH_4 , SiH_2Cl_2 , and SiCl_4 for epitaxial growth. Deposition temperature 1050°C ; growth rate $0.25 \mu\text{m}/\text{min}$.

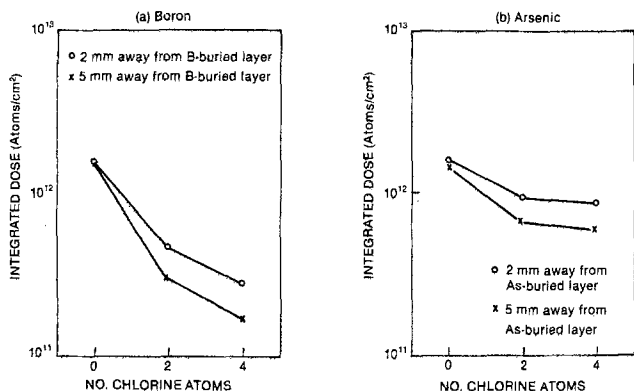


Fig. 12. Increasing lateral autodoping with increasing chlorine number in the source gases: a) boron; b) arsenic. Deposition temperature 1050°C; growth rate 0.25 $\mu\text{m}/\text{min}$.

autodoping with different source gases using arsenic as dopant. Figure 12 shows the variation of lateral autodoping for boron and arsenic. These results are consistent with those obtained by Srinivasan (5), who reports SiCl_4 epitaxy giving lower autodoping than silane, but are opposite to those reported by Suzuki and Endo (19). The HCl released by the reduction of chlorosilane could etch the growing epitaxial film at the impurity lattice sites and hence reduce the dopant incorporation, i.e., autodoping. It is likely that more chlorine atoms in the source gas will produce more HCl and therefore result in lower autodoping in the epitaxial layer. A correlation between autodoping and the number of chlorine atoms in the source gas has been achieved for the first time.

Summary

Intrinsic silicon epitaxial layers are grown on high resistivity substrates with heavily doped buried layers using boron, phosphorus, arsenic, and antimony as dopant elements. Impurity concentration profiles are measured by spreading resistance technique. The following results are obtained using a vertical epitaxial reactor with silane, dichlorosilane, and silicon tetrachloride.

1. Lateral autodoping decreases with increasing distance from the buried layer region. This indicates that the lateral autodoping is controlled by the evaporated dopant diffusing along the substrate surface in a laminar flow layer. The complex gas flow in the vertical reactor plays only a secondary role in determining lateral autodoping.

2. Pre-epitaxial bake temperature affects differently the autodoping behavior of the dopants tested. This is the first time such effects have been reported.

3. Vertical and lateral autodoping decrease with increasing prebake time.

4. Autodoping decreases with increasing growth rate for phosphorus, but only a slight change in autodoping is observed in the growth-rate range studied for arsenic.

5. Phosphorus and arsenic show similar changes in autodoping with epitaxial deposition temperature.

6. Vertical and lateral autodoping decrease with increasing number of chlorine atoms in the source gases. This correlation has been obtained for the first time.

Work is still being done to obtain better understanding of the autodoping mechanisms and to explain the differences between this study and previously reported results.

Manuscript submitted March 14, 1984; revised manuscript received Aug. 16, 1984.

General Electric Company assisted in meeting the publication costs of this article.

REFERENCES

- H. P. Pogge, D. W. Boss, and E. Ebert, in "Chemical Vapor Deposition," J. M. Blocher, Jr., and J. C. Withers, Editors, p. 767, The Electrochemical Society Softbound Proceedings Series, Princeton, NJ (1970).
- M. Ogirima, H. Saida, M. Suzuki, and M. Maki, *This Journal*, **124**, 903 (1977).
- G. R. Srinivasan, *ibid.*, **125**, 146 (1978).
- M. Ogirima, H. Saida, and M. Maki, Paper 218 presented at The Electrochemical Society Meeting, Pittsburgh, PA, Oct. 15-20, 1978.
- G. R. Srinivasan, *This Journal*, **127**, 1334 (1980).
- H-R. Chang, Papers 342 and 343 presented at The Electrochemical Society Meeting, Washington, DC, Oct. 9-14, 1983.
- L. J. Giling, *This Journal*, **129**, 634 (1982).
- F. C. Eversteijn, P. J. W. Severin, C. H. J. v. d. Brekel, and H. L. Peek, *ibid.*, **117**, 925 (1970).
- V. S. Ban and S. L. Gilbert, *J. Cryst. Growth*, **31**, 284 (1975).
- S. Berkman, V. S. Ban, and N. Goldsmith, "Heteroepitaxial Semiconductors for Electronic Devices," p. 264, Springer-Verlag, Berlin (1978).
- C. O. Bozler, *This Journal*, **122**, 1705 (1975).
- M. Tabe and H. Nakamura, *ibid.*, **126**, 822 (1979).
- B. A. Joyce, J. C. Weaver, and D. J. Maule, *ibid.*, **112**, 1100 (1965).
- P. Rai-Choudhury and E. I. Salkovitz, *J. Cryst. Growth*, **7**, 353 (1970).
- J. Bloem, *ibid.*, **13/14**, 302 (1972).
- P. H. Langer, *This Journal*, **124**, 591 (1977).
- S. M. Sze, "Physics of Semiconductor Devices," p. 68, John Wiley & Son, New York (1981).
- J. L. Deines and A. Spiro, Paper 62 presented at The Electrochemical Society Meeting, San Francisco, CA, May 12-17, 1974.
- K. Suzuki and M. Endo, Paper 96 presented at The Electrochemical Society Meeting, Los Angeles, CA, May 10-15, 1970.
- G. R. Srinivasan, *J. Appl. Phys.*, **51**, 4824 (1980).

Dual Diffusion of Gold and Platinum into Silicon

R. Saito, N. Momma, M. Naito

Hitachi Limited, Hitachi Research Laboratory, Hitachi, Ibaraki, Japan

ABSTRACT

Dual diffusion of gold (Au) and platinum (Pt) into silicon is examined. When Au and Pt coexist in silicon, two levels of Au, $E_c - 0.54$ eV and $E_v + 0.35$ eV, and two levels of Pt, $E_c - 0.22$ eV and $E_v + 0.30$ eV, are observed by deep level transient spectroscopy (DLTS). New levels arising from the interaction of Au and Pt are not found. In the case of sequential diffusion (first Pt, then Au diffusion, or vice versa), replacement of the first diffused atoms in substitutional sites by the second ones is found to occur in the lower temperature range of the second diffusion. Replacement does not occur below 600°C of the second diffusion temperature. With the second diffusion above 800°C, replacement is almost complete. In the second diffusion temperature range, between 600° and 800°C, partial replacement occurs, and the sum of substitutional Au and Pt atoms is constant, irrespective of the second diffusion temperature, and is equal to the number of substitutional atoms of the first diffusant. From these facts, it is considered that Au and Pt atoms occupy the same kinds of substitutional sites in silicon.

In the manufacturing of diodes, transistors, and thyristors, deep level impurities such as gold (Au) or platinum (Pt) have been widely used to control carrier lifetime to improve their switching properties. A large number of studies on Au (1, 2) and Pt (3) have been done concerning the mechanism of diffusion, energy levels, and gold and platinum's electrical properties as lifetime killers. It is well known that the diffusion of these impurities is very structure sensitive. Lattice defects in silicon, *e.g.*, dislocation loops, affect the diffusion of these impurities because they act as sources of vacancies (4). Reverse leakage current (I_R) of Au-doped diodes is much larger than that of Pt-doped diodes for the same value of reverse recovery time (t_r). On the other hand, forward voltage drop (FVD) of Au-doped diodes is smaller than that of Pt-doped diodes (5).

Although these impurities have been studied individually, interaction of these impurities has not been studied. Concerning dual diffusion of lifetime killers, Hayashi *et al.* (6) studied the dual diffusion of iron (Fe) and Au. They concluded that by use of Fe and Au dual diffusion, the lifetime was reproducibly controlled and weak temperature dependence of the FVD of the device was obtained. They referred to the diffusion of Fe and Au as an interaction of these atoms.

This paper discusses dual diffusion of Au and Pt into silicon to reveal the interaction of these lifetime killers. We fabricated p^+nn^+ diodes doped with Au and Pt in several conditions and studied their trap concentrations and trap energy levels.

Experimental

The silicon wafers used in this study were FZ grown, n -type, and $\langle 111 \rangle$ oriented, with a resistivity of 35 Ωcm . Phosphorus and boron were diffused into opposite sides of the wafers, resulting in p^+nn^+ diode structure. Experiments were done for the following three cases

- sequential diffusion (Pt \rightarrow Au)
- sequential diffusion (Au \rightarrow Pt)
- simultaneous diffusion of Au and Pt

In case (a), Pt was deposited on the p^+ side of alkali and $\text{HF} + \text{HNO}_3$ etched silicon wafers by sputtering and then was diffused for 40 min in nitrogen atmosphere at different temperatures. The velocity of loading and unloading to the diffusion furnace was more than 1000 mm/min. After Pt diffusion, the wafers were boiled in $\text{HCl}:\text{HNO}_3 = 3:1$ to eliminate the residual Pt on the surface. Then Au was deposited on the p^+ sides of the wafers and diffused in the same way. In case (b), all of the procedures were the same as those in case (a), except for the order of Au and Pt diffusion. In case (c), Pt and Au were diffused simultaneously. As control samples, Au or Pt was diffused individually at different temperatures. After the diffusion of Au and Pt, Al was deposited on both sides of the wafers. From these wafers 1.4 mm diam diodes were prepared.

By using these p^+nn^+ diodes, trap concentrations and trap energy levels of Au and Pt in the n regions of the diodes were measured by DLTS (7, 8).

Results

It is well known that Au or Pt in silicon occupy substitutional and interstitial lattice sites. Only the atoms in substitutional sites are electrically active; therefore, they act as lifetime killers. As is well established, Au in substitutional sites forms two energy levels, a donor level at $E_v + 0.35$ eV and an acceptor level at $E_c - 0.54$ eV. A greater variety of levels has been published for Pt trap levels than for Au. Among them, two levels, a donor level at $E_v + 0.30$ eV and an acceptor level at $E_c - 0.22$ eV, are confirmed by many authors. Our DLTS measurement also shows the presence of these two trap levels.

In the case of the samples in which Au and Pt coexist, no energy levels other than those mentioned above were detected in any diffusion conditions. This result shows that new energy levels are not formed by the interaction of Au and Pt.

Trap concentration was estimated from the DLTS signal peak height of the majority carrier trap in n -type silicon, *i. e.* $E_c - 0.54$ eV (Au) and $E_c - 0.22$ eV (Pt).

Sequential diffusion (Pt \rightarrow Au).—Au and Pt trap concentrations of various diffusion conditions in case (a) are shown in Fig. 1 and Fig. 2, respectively. In these figures,

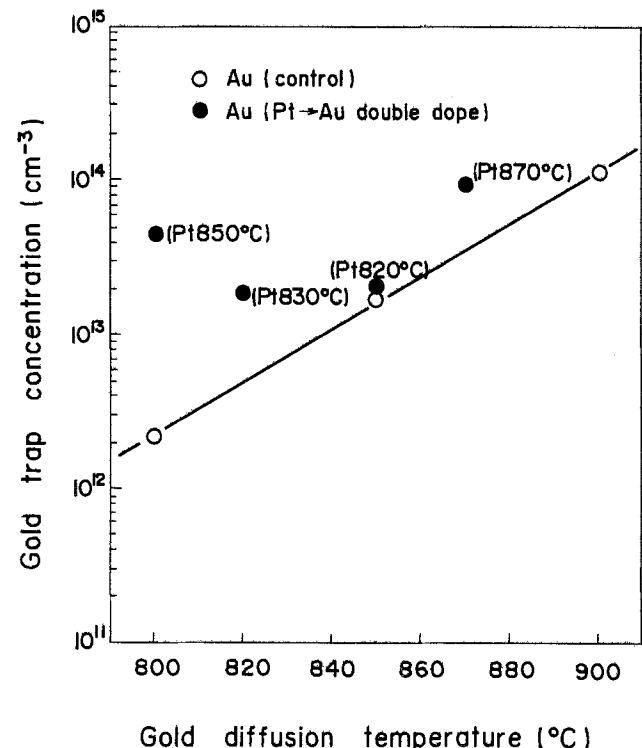


Fig. 1. Dependence of gold concentration on gold diffusion temperature.

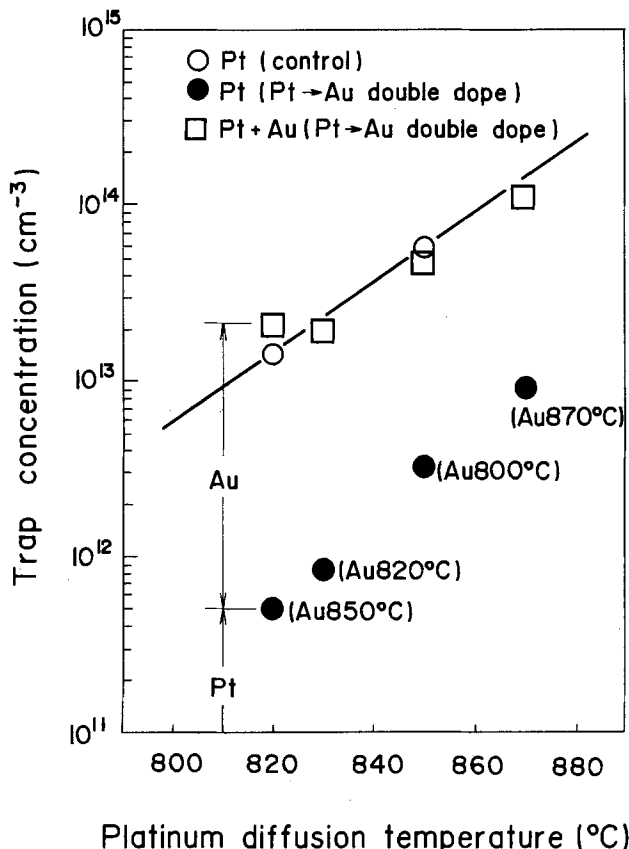


Fig. 2. Dependence of platinum or of sum of gold and platinum concentration on platinum diffusion temperature.

open circles show control samples (Au or Pt diffused singly), and solid circles show Au and Pt double-doped samples. In Fig. 1, Au trap concentrations (N_{Au}) are not simply related to Au diffusion temperatures. For example, N_{Au} of sample A (Pt 850°C → Au 800°C) is higher than that of sample B (Pt 830°C → Au 800°C) and of sample C (Pt 820°C → Au 850°C); Band C in Au is diffused at a higher temperature than in sample A. Also, the N_{Au} of sample A is 10 times higher than that of control samples in which Au is diffused at the same temperature.

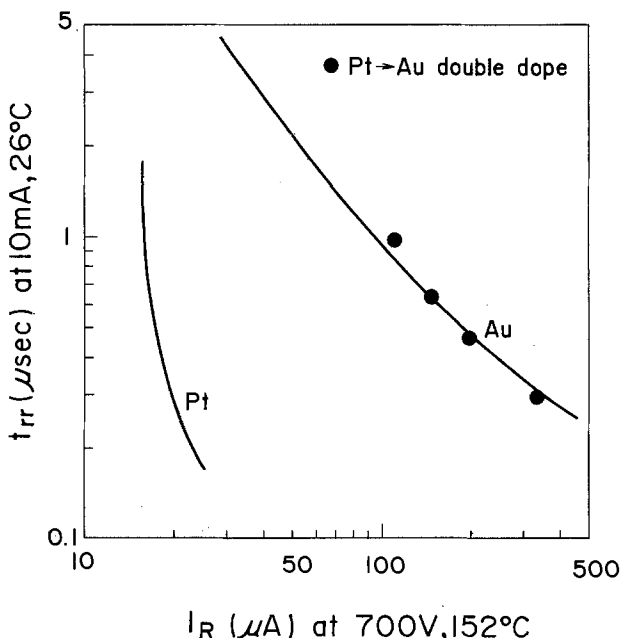


Fig. 3. Reverse leakage current (I_R) vs. reverse recovery time (t_{rr}). Solid lines: gold or platinum single doped. Solid circles: gold and platinum double doped.

In Fig. 2, Pt trap concentrations (N_{Pt}) of double-doped samples increases with Pt diffusion temperature, but these values are one order of magnitude less than the control samples. Figure 2 also shows the relation between the sum of N_{Au} and N_{Pt} and the Pt diffusion temperature. It is clear from this figure that the sum of N_{Au} and N_{Pt} is nearly equal to Pt concentration of the control sample. Before Au diffusion, N_{Pt} was the same as that of the control sample, but after Au diffusion, N_{Pt} decreased to less than 10% of the initial value, and the values of N_{Au} corresponded to the decrease in Pt concentration. This phenomenon obviously shows that Pt, which was diffused previously, is replaced by Au, which was diffused later.

This phenomenon is also confirmed by the measurement of the electrical properties of p^+nn^+ diodes. Figure 3 shows the relation between t_{rr} and I_R . In this figure, solid lines indicate the properties of Au single-doped diodes and Pt single-doped diodes; the solid circles indicate those of Au and Pt double-doped diodes.

It is clear that the properties of Au and Pt double-doped diodes are the same as those of Au single-doped diodes. Figure 4 shows the relation between t_{rr} and FVD. The properties of Au and Pt double-doped diodes are the same as those of Au single-doped diodes. These electrical measurements show again that Pt was replaced by Au when Pt and Au were diffused into silicon sequentially.

In order to reveal the replacement phenomenon more precisely, the effect of Au diffusion temperature on trap concentration was studied. Pt diffusion temperature was fixed at 850°C, and the following Au diffusions were performed in a temperature range of 600°-750°C. In Fig. 5, N_{Au} and N_{Pt} were plotted against Au diffusion temperature. As shown in this figure, N_{Au} increased and, correspondingly, N_{Pt} decreased with the increase of Au diffusion temperature. The sum of N_{Au} and N_{Pt} was constant and was equal to the initial Pt concentration before Au diffusion, irrespective of Au diffusion temperature. It is clear from Fig. 5 that the replacement does not occur at an Au diffusion temperature lower than 600°C. In the temperature range of 600°-770°C, replacement occurs partially, hence Au and Pt coexist. When Au was diffused at a temperature higher than 770°C, Pt was completely replaced by

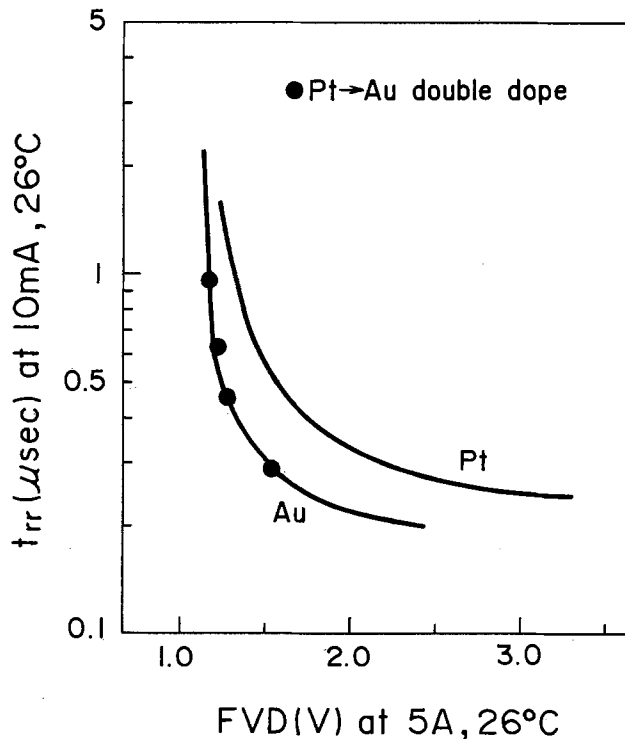


Fig. 4. Forward voltage drop (FVD) vs. reverse recovery time (t_{rr}). Solid lines: gold or platinum single doped. Solid circles: gold and platinum double doped.

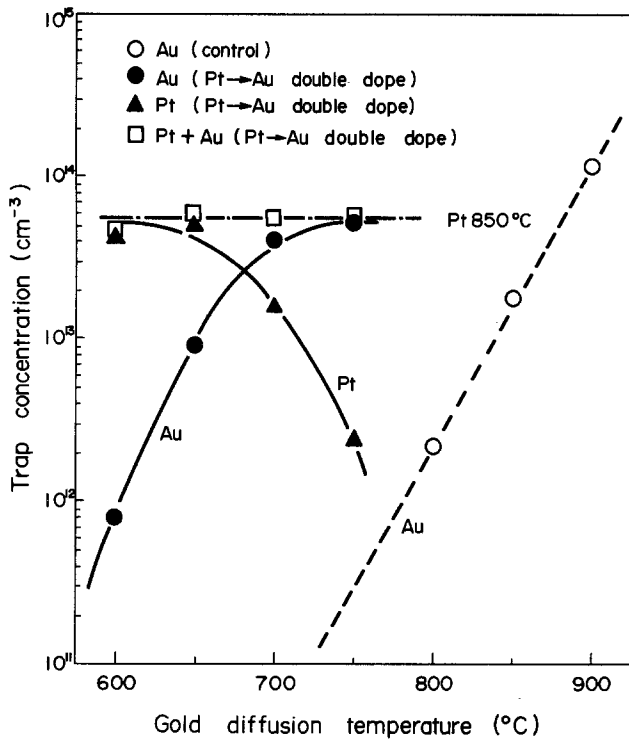


Fig. 5. Dependence of gold or platinum concentration or of sum of them on gold diffusion temperature.

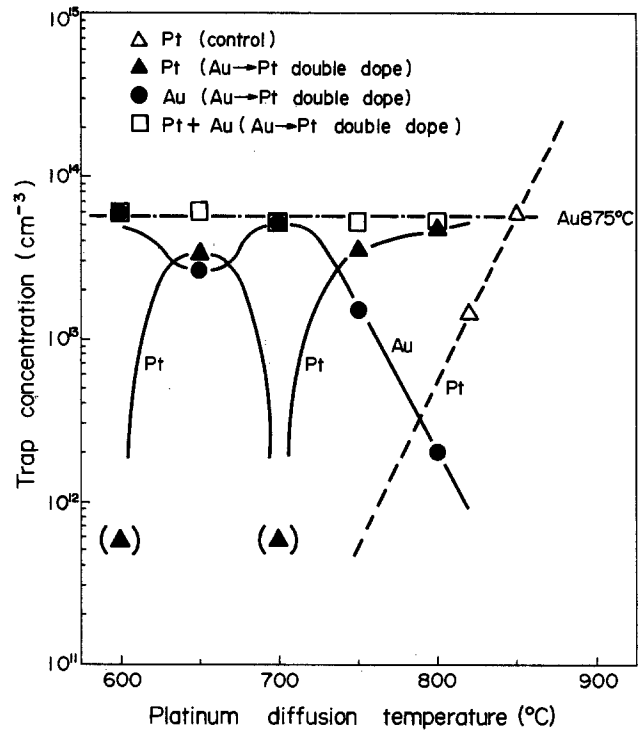


Fig. 7. Dependence of gold or platinum concentration or of sum of them on platinum diffusion temperature. Parentheses indicate the levels of the limiting concentration of DLTS measurement.

Au. Figure 6 shows the ratio (R) of N_{Au} to the sum of N_{Au} and N_{Pt} [$R = N_{Au}/(N_{Au} + N_{Pt})$] vs. Au diffusion temperature.

Sequential diffusion (Au → Pt).—In Fig. 7 N_{Au} and N_{Pt} are plotted against Pt diffusion temperatures in which Au diffusion was carried out at 875°C. In this case, a replacement phenomenon also occurred, but it was somewhat more complex than in case (a). Au was not replaced by Pt at temperatures lower than 600°C. The replacement occurred partially at around 650°C, but the replacement did not occur at around 700°C. When Pt was diffused at a higher temperature than 750°C, replacement occurred again. The sum of N_{Au} and N_{Pt} was almost constant, irrespective of Pt diffusion temperature and was equal to the initial Au concentration before Pt diffusion, as was the case for (a). Figure 8 shows R vs. Pt diffusion tempera-

ture. From these facts, it is considered that Au and Pt atoms occupy the same kinds of substitutional sites in silicon.

Simultaneous diffusion of Au and Pt.—Both Au and Pt were detected in case (c), where Au and Pt were diffused simultaneously, as shown in Fig. 9. In this case, N_{Au} and N_{Pt} were lower than the Au and Pt concentrations of the control samples (solid lines). The sum of N_{Au} and N_{Pt} was an intermediate value between the Au and Pt concentrations of the respective control samples.

Discussion

Experimental results can be interpreted qualitatively as follows:

Au and Pt occupy substitutional and interstitial lattice sites in silicon, with the former acting as lifetime killers. Diffusion of interstitial atoms is much larger than that of

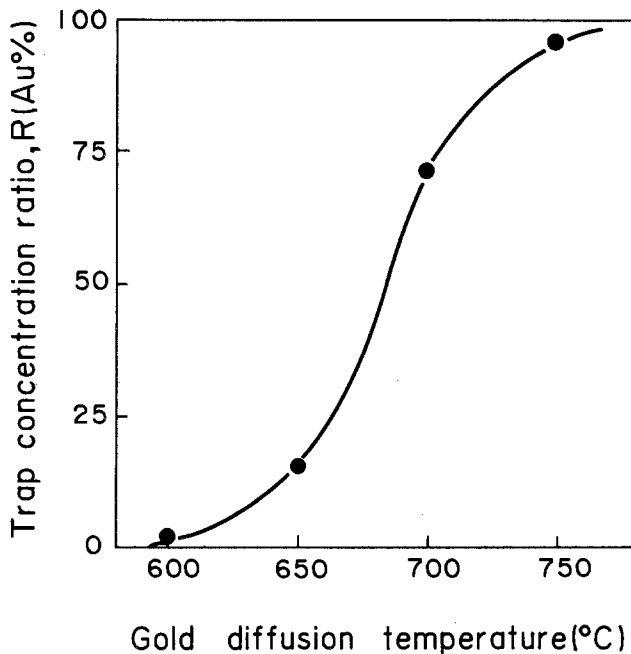


Fig. 6. Dependence of concentration ratio (R) on gold diffusion temperature.

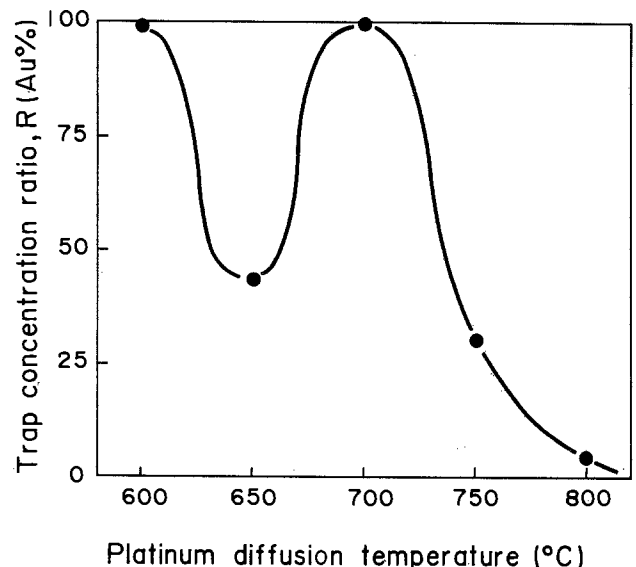


Fig. 8. Dependence of concentration ratio (R) on platinum diffusion temperature.

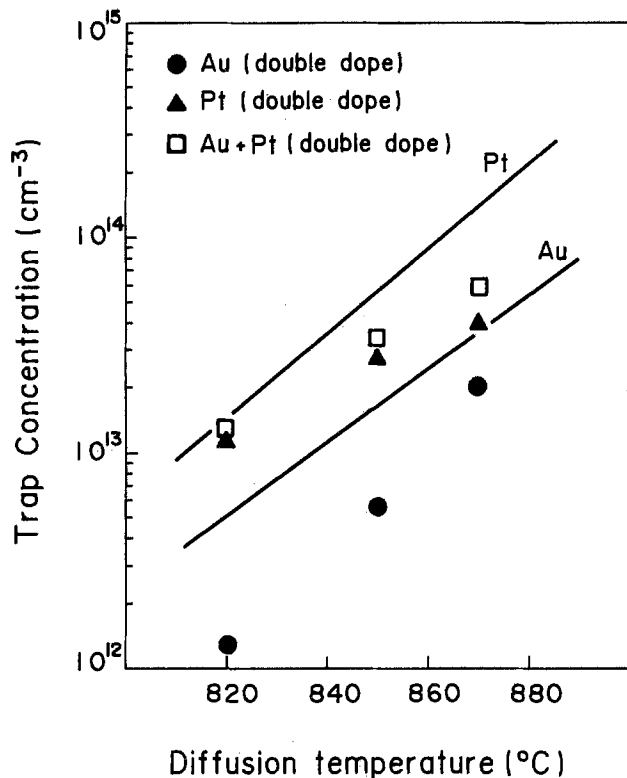
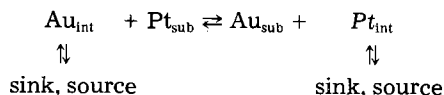


Fig. 9. Dependence of gold or platinum concentration or of sum of them on simultaneous diffusion temperature.

substitutional atoms. A dissociative diffusion mechanism (2, 9) and a kick-out mechanism (10) have been proposed for Au and Pt diffusion. In the dissociative diffusion mechanism, an interstitial metal atom and a vacancy are in thermal equilibrium with a substitutional metal atom. On the other hand, according to the kick-out mechanism, a substitutional metal atom and an interstitial silicon are in thermal equilibrium with an interstitial metal atom.

In the case of Au and Pt dual diffusion, we assume the following reaction



Sources of Au_{int} and Pt_{int} are Au and Pt deposited on the surface of the silicon. Sinks for Au_{int} and Pt_{int} should be dislocations at the surface, or some other kind of defect.

In addition to these sinks and sources, we should assume that other kinds of sinks and sources of Pt_{int} exist, because an instability in resistivity was detected in Pt-doped specimens on low temperature annealing. Figure 10 shows (a) the spreading resistance of Pt-diffused silicon wafer and (b) that of the wafer annealed at 730°C after Pt diffusion. As shown in Fig. 10a, the spreading resistance was almost constant inside the wafer (>50 μm depth). But when it was annealed at about 730°C, the spreading resistance increased and the distribution became irregular. This change of resistance was observed only when it was annealed at around 700°C. When this wafer was annealed again at high temperature, *e. g.*, 900°C, the resistance became constant again, as shown in 10c. The change in resistance occurs reversibly and indicates that some kind of complex state exists in silicon. This state is stable only around 700°C and has a trap level showing a compensating effect on the resistivity which results in the increase of the spreading resistance. This state can be assumed to be a complex compound. We designate this state as $\text{Pt}_{\text{complex}}$ and show the reaction again as follows

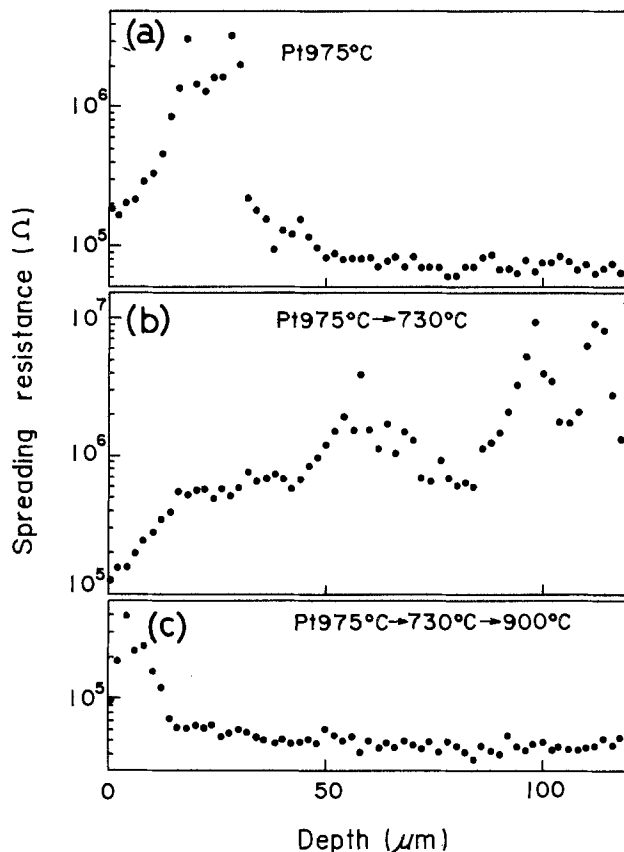
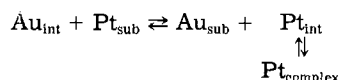


Fig. 10. Distribution of spreading resistance: (a) platinum diffused at 975°C; (b) platinum annealed at 730°C after platinum diffusion; (c) platinum annealed again at 900°C after platinum diffusion and 730°C annealing.

In this reaction, Pt_{int} changes $\text{Pt}_{\text{complex}}$ greatly only around 700°C.

In case (a), Au_{int} diffused into silicon with a large number of Pt_{sub} . Then Pt_{sub} was replaced by Au_{int} . Therefore, Au_{int} and Pt_{sub} decrease, while Au_{sub} and Pt_{int} increase by the replacement until they reach thermal equilibrium state. The increase in Au_{sub} is equal to the decrease in Pt_{sub} . When Au was diffused at a higher temperature, Au_{int} increased; hence, the replacement of Pt_{sub} by Au_{sub} increases with Au diffusion temperature. When Au diffusion is performed at nearly 700°C, Pt_{int} changes to $\text{Pt}_{\text{complex}}$, and the replacement of Pt_{sub} by Au_{sub} increases. At a temperature higher than 700°C, Pt_{int} does not change to $\text{Pt}_{\text{complex}}$. However, the replacement is not retarded because the number of Au_{int} is larger at these temperatures.

In case (b), the replacement of Pt_{sub} for Au_{sub} increases with the increase of Pt diffusion temperature. But when Pt diffusion is performed at around 700°C, Pt_{int} changes to $\text{Pt}_{\text{complex}}$, hence the replacement of Pt_{sub} for Au_{sub} is stopped. At higher temperatures than 700°C, Pt_{int} does not change to $\text{Pt}_{\text{complex}}$, hence the replacement of Au_{sub} to Pt_{sub} occurs again.

Summary

Dual diffusion of Au and Pt into silicon was examined. Measurement of trap energy levels and trap concentrations was performed by DLTS. Results obtained in this paper are summarized here.

1. When Au and Pt coexist in silicon, two levels of Au, $E_c - 0.54$ eV and $E_v + 0.35$ eV, and two levels of Pt, $E_c - 0.22$ eV, and $E_v + 0.30$ eV, are observed. New levels arising from the interaction of Au and Pt are not found.
2. In the case of sequential diffusion, replacement of the first diffusant atoms in substitutional sites by the second ones is found to occur in the lower temperature range of the second diffusion. (i) Replace-

ment does not occur below 600°C of the second diffusion temperature. (ii) Replacement is almost complete above 800°C of the second diffusion temperature. (iii) In the second diffusion temperature range between 600° and 800°C, replacement occurs partially, and the sum of substitutional Au and Pt atoms is constant, irrespective of the second diffusion temperatures, and equals the number of substitutional atoms of the first diffusant.

Acknowledgments

The authors are greatly indebted to Dr. T. Takasuna and Dr. M. Okamura and Mr. T. Hidaka and Mr. H. Toida for their helpful suggestions and encouragement to this study.

Manuscript submitted April 13, 1984; revised manuscript received Sept. 17, 1984.

Hitachi Limited assisted in meeting the publication costs of this article.

REFERENCES

- O. Engstrom and H. Grimmeiss, *J. Appl. Phys.*, **46**, 831 (1975).
- M. Yoshida and K. Saito, *Jpn. J. Appl. Phys.*, **9**, 1217 (1970).
- A. O. Ewvaraye and E. Sun, *J. Appl. Phys.*, **47**, 3172 (1976).
- T. Iizuka, *Jpn. J. Appl. Phys.*, **5**, 1018 (1966).
- S. D. Brotherton and P. Bradley, *Solid-State Electron.*, **25**, 119 (1982).
- H. Hayashi, T. Mamine, and T. Matsushita, *IEEE Trans. Electron Devices*, **ed-28**, 246 (1981).
- D. V. Lang, *J. Appl. Phys.*, **45**, 3023 (1974).
- Y. Tokumaru and H. Okushi, *Jpn. J. Appl. Phys.*, **19**, 2441 (1980).
- F. C. Frank and D. Turnbull, *Phys. Rev.*, **104**, 617 (1956).
- U. Gosele, W. Frank, and A. Seeger, *Appl. Phys.*, **23**, 361 (1980).

Vaporization Chemistry and Thermodynamics of the MnS-In₂S₃ System by the Simultaneous Knudsen and Torsion-Effusion Method

J. P. Botor¹ and J. G. Edwards*

Department of Chemistry, University of Toledo, Toledo, Ohio 43606

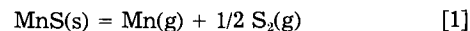
ABSTRACT

The MnS-In₂S₃ system was investigated in the temperature range of 1065-1246 K by measurements of vapor pressures with the computer-automated simultaneous Knudsen and dynamic torsion-effusion method. This study was the first investigation of vaporization chemistry and thermodynamics of the Mn-In-S system. Between compositions corresponding to In₂S₃ and MnIn₂S₄ the vaporization reaction was In₂S₃(s) = In₂S(g) + S₂(g). For this vaporization reaction, third-law analyses gave $\Delta H^\circ(298\text{ K}) = 617.9 \pm 0.9$ kJ/mol, in good agreement with the literature. Between compositions corresponding to MnIn₂S₄ and MnS, the vaporization reaction was MnIn₂S₄(s) = MnS(s) + In₂S(g) + S₂(g). Third-law analyses gave $\Delta H^\circ(298\text{ K}) = 633.0 \pm 1.0$ kJ/mol. Over the first vaporization reaction, the apparent molecular weight of the vapor was 184.7 ± 3.4 , and over the second, it was 178.3 ± 3.7 . The average molecular weight of In₂S(g) + S₂(g) is 181.5. The $\Delta H^\circ(298\text{ K})$ of combination of 1 mol of MnS(s) with 1 mol of In₂S₃(s) to give MnIn₂S₄(s) was -15.1 ± 2.0 kJ/mol. This value was justified by those for other ternary metal sulfides of the type M^{II}M₂^{III}S₄(s).

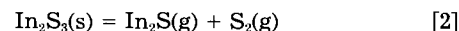
The sulfides of transition metals have been the subject of extensive investigation, with particular emphasis put upon the structures, phase equilibria, and electrical and magnetic properties of the solid phases. The compound MnIn₂S₄ was first reported by Hahn and Klingler (1) and later by several investigators, including Schlein and Wold (2) and Kanomata and Ido (3), who reported preparation, crystallographic studies, and electrical and magnetic properties of several indium thiospinels. MnIn₂S₄ has a mixed spinel structure with lattice constant $a = 10.69$ (1), 10.72 (2), or 10.71 Å (3). Electrical resistivity measurements at room temperature indicate that MnIn₂S₄(s) is a semiconductor with resistivity greater than $10^5 \Omega\text{ cm}^2$. It is paramagnetic down to 4.2 K. The magnetic interactions that occur in MnIn₂S₄ are primarily antiferromagnetic with negative Weiss constant at -78 K (2, 3). No information is available on the thermodynamics of the system MnS-In₂S₃, except at the binary extremes.

Considerable information about the thermodynamic properties of MnS and In₂S₃ is available, and much of it has been tabulated by Mills (4). The vapor pressure of MnS is much lower than that of In₂S₃; the vapor pressures are 1 Pa at 1616 K and 1090 K for MnS (8) and In₂S₃ (12), respectively. The vaporization of MnS(s) has been studied by several investigators (4), including Wiedemeier and Schäfer (5), who used the Knudsen effusion method, Colin *et al.* (6), who used mass spectrometry, Wiedemeier and Gilles (7), who also used mass spectrometry, and Viswanadham and Edwards (8), who used simultaneous

Knudsen and torsion effusion. The vaporization reaction was found to be



The vaporization of In₂S₃(s) has been investigated by Colin and Drowart (9) and Miller and Searcy (10, 11), who used mass spectrometry, and by Haque *et al.* (12), who used simultaneous Knudsen and torsion effusion. The vaporization reaction was congruent by



Standard enthalpies of vaporization at 298 K of reaction [2] were 602 ± 13 kJ/mol (9), 617 ± 13 kJ/mol (10), and 613.4 ± 3.0 kJ/mol (12), respectively.

The purposes of this investigation are to learn the vaporization reaction of MnIn₂S₄(s), to use the simultaneous Knudsen-effusion and torsion-effusion methods to measure the vapor pressures, and to calculate equilibrium constants of the vaporization reactions as functions of temperature and then calculate the thermodynamic properties of the vaporization reactions and the reactants and products therein.

Experimental

Samples.—Solid samples with compositions ranging from MnS to In₂S₃ in increments of 10 mole percent (m/o) on the basis of these formulas were prepared by heating the elements in evacuated, sealed, Vycor tubes. The samples were prepared by directly combining stoichiometric amounts of manganese metal powder (purity greater than 99.4%) (Fisher Scientific Company) with indium wire (Indium Corporation of America) and sulfur

*Electrochemical Society Active Member.

¹Present address: Institute of Non-Ferrous Metals, Gliwice, Poland.

(Johnson Matthey Chemicals Limited) (purities greater than 99.99%).

The samples were obtained as polycrystalline, single-phase products after three successive 48h heating periods at temperatures of 400°, 700°, and 1000°C. Each sample was quenched in water. The products were ground with an agate mortar and pestle and stored in a vial inside a desiccator over CaSO₄. Each sample was analyzed for phase content by x-ray powder diffractometry.

Preliminary effusion experiments.—To establish the vaporization reaction of MnIn₂S₄(s), two samples of compositions 10 and 50 m/o MnS were heated under vacuum of 10⁻⁶ torr in graphite effusion cells. Each experiment consisted of several successive heatings, with examination of the sample residue after each heating.

Each preliminary experiment involved the following steps, except as noted below. The Knudsen cell containing the sample was weighed and placed in the vacuum system, and the system was evacuated. The cell was heated for 10-25h (with one exception, when the time was 4h) at 1023 ± 10 K or 1123 ± 10 K. At the end of each heating, the power was switched off and the sample was allowed to cool by radiation. After several hours, when the sample was at room temperature, the system was brought to atmospheric pressure with nitrogen gas, and the cell was removed and weighed. The cell lid was removed, and samples for x-ray analysis were taken from the surface and from the bulk of the residue. The details of the procedure and results of these experiments can be found in Table I. The table's first column gives the sample designation. The second through eighth columns give, respectively, number of the successive heating, initial composition of the sample, mass of the sample, time, temperature, rate of mass-loss, and phases present after heating.

Apparatus.—The apparatus used for vapor-pressure measurements has been described (13, 14). It consists of a dynamically operated torsion-effusion pendulum suspended from one pan of an automatic vacuum semimicrobalance with paper strip-chart output. Data from the pendulum and the strip chart are acquired automatically by a laboratory computer.

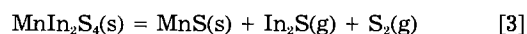
Two graphite torsion-effusion cells labeled "1" and "2" were used. The design of the cells has been described (12). Graphite cell 1 had diverging right-circular-conical orifices with semiapex angles of about 30° drilled with a conical tool. The two orifices in cell 2 were cylindrical. The cells were cleaned and then outgassed under vacuum in a radio-induction furnace at 1400 K for about 24h. Moment arms of the orifices and thicknesses of the walls in which orifices were drilled were measured with a traveling microscope. The transmission probability and recoil force factors of the orifices were calculated with computer programs using equations from Freeman and Edwards (15).

Temperatures were measured with a Pt, Pt-10%-Rh thermocouple in a dummy cell identical in design and materials to the torsion-effusion cell. The two cells were

placed symmetrically, the torsion cell above and the dummy cell below the center of the furnace and separated by about 2 mm. The thermocouple was calibrated by observing the temperature of the dummy cell with the thermocouple and a calibrated optical pyrometer. This procedure introduced uncertainties of ± 4 K into the temperature measurements.

The torsion constants, *k*, of the fibers were calibrated before and after each set of vapor pressure measurements by the usual method (12) of observing the period, *τ*, of a calibration pendulum suspended from the fiber.

Data collection and treatment.—On the basis of results from the preliminary heating experiments (Table I), the vaporization of the ternary compound MnIn₂S₄(s) was taken to be incongruent by the reaction



The vaporization reaction of In₂S₃(s) was assumed to be congruent by reaction [2].

Two sets of experiments were done, each with a different sample and effusion cell. The set of experiments with cell 1 will be called set Y and that with cell 2 will be called set Z. The composition region in which the vaporization reaction is given by Eq. [2], where In₂S₃(s) and MnIn₂S₄(s) are in equilibrium with the vapor, will be denoted as region I. The composition region in which the vaporization reaction is given by Eq. [3], where MnIn₂S₄(s) and MnS(s) are in equilibrium with the vapor, will be denoted as region II.

In set Y and set Z, 380 mg of sample were loaded into the effusion cell. In set Y, 190.2 mg of the sample were placed in the first chamber of the cell and 189.2 mg were placed in the second. In set Z, 190.0 mg of the sample were placed in each chamber of the cell. In set Y, the initial sample composition was 40.0 m/o MnS and 60.0 m/o In₂S₃; in set Z, it was 10.0 m/o MnS and 90.0 m/o In₂S₃. Experiments were done in region I and then, as the composition of the solid sample changed, in region II.

Data acquired in the course of each effusion experiment was taken from three types of measurements: (a), the temperature of the effusion cell; (b), the mass of the torsion-effusion pendulum and the time; and (c), the times at which the torsion-effusion pendulum was at a number of preset positions.

The torque, *Q_e*, caused by effusion of vapor from the effusion cell was obtained from the time vs. pendulum-position measurements by a least squares fit of the ideal-torsion-pendulum equation to the data, as previously described (13, 14, 16). The torsion pressure, *P_T*, was calculated (17) with the equation

$$P_T = 2Q_e / (d_1 F_1 A_1 + d_2 F_2 A_2) \quad [4]$$

where the subscripts 1 and 2 identify the effusion orifices, and *d* is the moment arm of the orifice, *A* its area, and *F* its recoil force correction factor (15).

The Knudsen vapor pressure, *P_K*, was calculated from the measured temperatures, *T*, and the rate of mass loss,

Table I. Results of preliminary effusion experiments

Sample	Successive heating	m/o MnS	Mass of sample/mg	Time (min)	T/K (± 10)	Rate of mass loss (mg/min)	Phases present after heating
0.5 MnS	1	50.0	1092.2	1120	1123	61.75 × 10 ⁻²	MnIn ₂ S ₄ + MnS
	+0.5 In ₂ S ₃	88.7	338.8	248	1123	50.97 × 10 ⁻²	
0.1 MnS	1	10.0	1007.2	1497	1023	8.94 × 10 ⁻²	In ₂ S ₃ + MnIn ₂ S ₄
	+0.9 In ₂ S ₃	11.4	821.4	1234	1023	8.89 × 10 ⁻²	
	3	13.0	711.7	1372	1023	8.77 × 10 ⁻²	
	4	15.4	581.4	1418	1023	8.87 × 10 ⁻²	In ₂ S ₃ + MnIn ₂ S ₄
	5	18.9	424.0	1273	1023	8.85 × 10 ⁻²	
	6	24.6	311.3	1286	1023	8.79 × 10 ⁻²	
	7	35.1	198.3	1242	1023	6.91 × 10 ⁻²	MnIn ₂ S ₄ + MnS
	8	51.8	112.5	721	1023	3.09 × 10 ⁻²	
	9	59.0	70.2	652	1023	3.14 × 10 ⁻²	
	10	70.7	49.7	729	1023	3.01 × 10 ⁻²	
	11	89.8	27.8	614	1023	1.35 × 10 ⁻²	

Table II. Gibbs-energy functions, $-[G^\circ(T) - H^\circ(298\text{ K})]/T$, in J/mol K

T/K	In ₂ S ₃ (s)	In ₂ S(g)	S ₂ (g)	MnS(s)	MnIn ₂ S ₄ (s)	Reaction [3]
1000	228.40	343.51	245.73	104.40	332.80	360.84
1100	237.73	347.27	248.15	108.00	345.73	357.69
1200	247.02	350.62	250.45	111.40	358.42	254.05
1300	255.94	354.20	252.62	114.70	370.64	350.88

dg/dt , with the Knudsen equation

$$P_K = (dg/dt)(2\pi RT/M^*)^{1/2}/(W_1A_1 + W_2A_2) \quad [5]$$

in which M^* is the assigned molecular weight of the effusing vapor and W is the transmission probability of the orifice (15).

Vapor pressures were converted to reaction quotients of reactions [2] and [3] with the equation

$$Q_P = P_{\text{In}_2\text{S}_3} P_{\text{S}_2} \quad [6]$$

$$= 0.221P^2 \quad [7]$$

The apparent molecular weight M of the effusing vapor was calculated (17) from

$$M = M^*(P_K/P_T)^2 \quad [8]$$

The assigned molecular weight can be any positive real number, but in order to produce accurate Knudsen pressures, M^* was set equal to the average molecular weight \bar{M} of In₂S₃ vapor effusing by either reaction [2] or reaction [3]. \bar{M} was calculated (17) from the equation

$$\bar{M} = \left(\sum_{j=1}^n m_j M_j^{-1/2} \right)^{-2} \quad [9]$$

where n is the number of species effusing, m_j is the mass fraction, and M_j is the molecular weight of species j in the effusing vapor. The result for In₂S₃ vapor was $\bar{M} = 181.5$.

Pressures were observed to vary as functions of orifice area in comparing results from sets Y and Z. The vapor pressures, P_i , in the effusion cell were related (18) to vapor pressures, P_o , at a given temperature in a hypothetical cell with orifice area of zero by

$$P_o = P_i (1 + WA/\alpha A_s)_i \quad [10]$$

where A is the orifice area, W is the transmission probability of the orifice, A_s is the vaporizing sample area, and α is the condensation coefficient of the vaporizing sample.

In each region, and for each type of measurement, *i.e.*, in four cases in each set, values of P_Y and P_Z were obtained from least squares fits of $\log P$ vs. $1/T$ at five equally spaced temperatures in the experimental range. Values of P_o at a given temperature were obtained by extrapolation of a straight line through the two points from sets Y and Z on a plot of P_i vs. $(PWA)_i$, with $i = Y$ and Z. The uncertainty of P_o was calculated from the standard deviations of P_Y and P_Z . In each case, average ratios of P_Y/P_o and P_Z/P_o were calculated from both torsion and Knudsen results. In each case, the resulting five values of P_o were substituted into Eq. [7], and the assumption was made that the resulting reaction quotient was the corresponding equilibrium constant, K_p .

The equilibrium pressures were calculated from the equation

$$P_{\text{eq}} = 0.942P_o \quad [11]$$

Least squares, straight-line fits were made to the equation

$$\log P_{\text{eq}} = -C/T + D \quad [12]$$

The uncertainty in $\log P_{\text{eq}}$ was calculated from the standard deviations in C and D from a fit of $\log P_m$ vs. $1/T$ and from the standard deviations in P_o/P_m in Table VI.

Third-law values of $\Delta H^\circ(298\text{ K})$ of the vaporization reactions were calculated from ratios of P/P_o , the measured vapor pressures and temperatures, and standard Gibbs energy functions $\Delta\phi^\circ(T)$

$$\phi^\circ(T) = -[G^\circ(T) - H^\circ(298\text{ K})]/T \quad [13]$$

with the equation [Ref. (19)]

$$\Delta H^\circ(298\text{ K}) = T\Delta\phi^\circ(T) - RT \ln(Q_P/P_a^2) + 2RT \ln(P/P_o) + 23.052RT \quad [14]$$

In Eq. [14], Q_P is the reaction quotient of the vaporization reaction from Eq. [7], the third term on the right corrects the results to zero orifice area, and the last term accounts for the fact that standard pressure is 1 atm (= 101,325 Pa).

The values of $\Delta H^\circ(298\text{ K})$ derived from a given type of measurement in each set were averaged. The uncertainty in the average $\Delta H^\circ(298\text{ K})$ was calculated from the standard deviation of the values and the standard deviations in each value resulting from the standard deviation of the ratio P/P_o in Eq. [14].

Second-law values of $\Delta H^\circ(298\text{ K})$ were obtained by a standard sigma treatment (20). Values of Gibbs energy functions for MnS(s), In₂S₃(s), In₂S(g), and S₂(g) were taken from Mills (4). The Gibbs energy functions of MnIn₂S₄(s) were estimated to be the sum of those for MnS(s) and In₂S₃(s). Values of Gibbs energy functions are given in Table II. The first column gives the temperatures, and subsequent columns give the Gibbs energy functions of In₂S₃(s), In₂S₃(g), S₂(g), MnS(s), MnIn₂S₄(s), and the vaporization reactions of In₂S₃(s) and MnIn₂S₄(s), respectively, at the temperatures in the first column.

Results

The torsion constant of the fiber used in set Y was $(3.017 \pm 0.016) \times 10^{-8}$ Nxm/rad, before and after set Y, and that used in set Z was $(3.029 \pm 0.012) \times 10^{-8}$ Nxm/rad, before and after set Z. The mensural properties of the effusion cells used in set Y and set Z are given in Table III. The first column gives the cell and orifice designation. The second through eighth columns give, respectively, the minimum orifice radius, the orifice length, the minimum orifice area, the semiapex angle, the moment arm, the transmission probability, and the recoil force correction factor.

Debye-Scherrer x-ray diffractograms of samples prepared at 10 m/o intervals and the results of the preliminary effusion experiments established that the only stable ternary compound in the MnS(s)/In₂S₃(s) system is MnIn₂S₄(s). In the composition range of 100-50 m/o In₂S₃ (region I), the solid contained In₂S₃(s) and MnIn₂S₄(s). In the range of 50-0 m/o In₂S₃ (region II), the solid contained MnIn₂S₄(s) and MnS(s). X-ray diffractograms gave no evidence of solid solution with concentration greater than 5 m/o in any of the three compounds.

Table III. Mensural properties of effusion cells

Effusion cell and orifice	$(r \pm 0.0006)/\text{cm}$	$(l \pm 0.001)/\text{cm}$	$10^3 A/\text{cm}^2$	$(\theta \pm 0.5)/\text{deg}$	$(d \pm 0.006)/\text{cm}$	$W \pm 0.004$	$F \pm 0.005$
1	1	0.0308	0.208	2.98	29.28	0.827	0.9010
	2	0.0328	0.208	3.34	28.78	0.827	0.8972
2	1	0.0305	0.126	2.92	0.0	0.811	0.3497
	2	0.0305	0.128	2.92	0.0	0.811	0.3446

Rates and amounts of mass loss between regions I and II and after region II as the solid became MnS were the best indicators of the extent of solid solutions. They showed that the solubilities of MnS in In_2S_3 and of In_2S_3 in MnIn_2S_4 , in region I, were less than 1 m/o and that the solubility of MnS in MnIn_2S_4 in region II was less than 1 m/o. However, the solubility of In_2S_3 in MnS in region II was 2.6 ± 1 m/o or 7.4 ± 3 equivalent percent. The latter numbers were surely dependent on temperature, but the method did not yield this dependence.

Figure 1 shows the results from the preliminary effusion experiments. The upper, dashed lines represent average rates of mass loss from the first experiment at 1123 K and with an initial sample composition of 50 m/o MnS. The lower, solid lines represent the same from the second experiment at 1023 K and with an initial sample composition of 10 m/o MnS. The dots represent the beginnings and ends of single heatings. The rate of mass loss decreased when the composition region changed and when the composition of pure MnS was reached. Intermediate decreases occurred when the composition during a single heating changed from one region to another.

In set Y, the vapor pressure was measured by both Knudsen effusion and torsion effusion at 22 temperatures in the range of 1065-1192 K in region I and at 56 temperatures in the range of 1091-1228 K in region II. In set Z, the vapor pressure was measured by both methods at 67 temperatures in the range of 1115-1233 K in region I and at 15 temperatures in the range of 1134-1246 K in region II.

Table IV gives results from region I, and Table V gives results from region II. In each table, columns 1, 2, 3, and 4 give the temperature of the measurements, torsion pressure, Knudsen pressure, and apparent molecular weight of the vapor, respectively. Columns 5 and 6 give third-law $\Delta H^\circ(298 \text{ K})$ values derived from torsion pressure and Knudsen pressure, respectively. Second-law results are given at the bottom of columns 5 and 6 in each table. The second-law results were not subsequently used.

Third-law $\Delta H^\circ(298 \text{ K})$ was plotted against temperature for each of the eight cases established by type of measurement, set, and region. The plots were highly scattered, but small trends were evident. Straight lines were fitted through the plots, and variations of $\Delta H^\circ(298 \text{ K})$ over the temperature range were taken from the lines. For a given set and region, the variations were always the same within 0.2 kJ/mol for the Knudsen and torsion measurements. The variations, $\Delta\Delta H^\circ(298 \text{ K})/(\text{kJ/mol})$, were: region I, set Y, -3.5 ± 4.0 , and set Z, $+1.0 \pm 4.0$; region II, set Y, -9.0 ± 4.0 , and set Z, -5.4 ± 4.0 .

Table VI gives ratios of pressures at orifice area of zero to measured pressures, as well as the condensation coefficients obtained from the estimated ratio $A/A_s = 0.01$

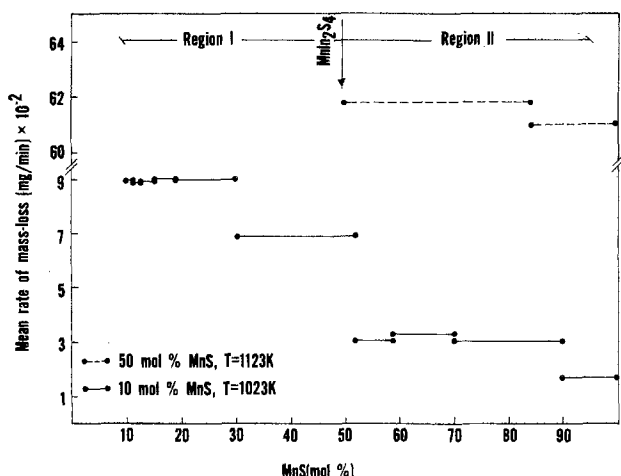


Fig. 1. Mean rate of mass-loss of In_2S_3 -MnS vs. the composition of MnS at 1023 and 1123 K. Evidence for two regions with two solid phases is shown.

Table IV. Vapor pressures and thermodynamics of reaction [2]:
 $\text{In}_2\text{S}_3(\text{s}) = \text{In}_2\text{S}(\text{g}) + \text{S}_2(\text{g})$

T/K	P_T/Pa	P_K/Pa	M	Third law $\Delta H^\circ(298 \text{ K})/(\text{kJ/mol})$	
				Torsion (± 0.4)	Knudsen (± 0.4)
Set Y					
1117	1.15	1.07	157.8	618.3	619.3
1128	1.63	1.62	181.3	618.3	617.2
1139	2.37	2.43	190.8	616.8	615.0
1103	0.75	0.73	171.0	619.3	619.1
1136	1.96	1.80	153.3	618.9	619.2
1188	8.34	8.40	184.1	616.3	614.9
1152	3.16	3.12	176.7	617.8	616.7
1120	1.26	1.27	183.7	619.0	617.6
1160	3.96	3.98	182.6	617.4	616.0
1136	2.04	2.03	179.2	618.1	617.0
1089	0.55	0.56	186.8	618.1	616.6
1180	6.28	6.15	173.9	618.1	617.2
1140	2.27	2.30	186.3	618.1	616.6
1084	0.45	0.46	194.7	619.0	617.4
1111	0.98	0.90	153.8	619.1	619.4
1192	8.71	8.74	182.8	617.4	616.0
1132	1.94	2.01	194.6	618.0	616.1
1146	2.79	2.66	165.6	617.2	616.8
1163	4.29	4.23	176.6	617.3	616.3
1170	5.04	5.00	178.6	617.6	616.4
1065	0.24	0.22	150.9	619.9	620.3
1101	0.77	0.75	172.6	618.3	617.6
Average:			176.5 ± 2.7	618.2 ± 0.2	617.3 ± 0.3
			Second law	(642.1 ± 4.6)	(648.7 ± 8.3)
Set Z					
				Torsion (± 0.4)	Knudsen (± 0.3)
1152	3.88	3.73	167.0	618.4	618.5
1174	6.59	6.91	199.6	618.5	617.0
1115	1.32	1.40	204.3	617.7	615.6
1175	7.01	7.38	200.9	618.9	617.4
1174	6.71	6.67	179.3	619.3	618.9
1121	1.48	1.51	189.9	618.7	617.4
1165	5.43	5.59	198.6	617.9	616.8
1216	19.33	19.41	183.1	618.5	618.0
1170	6.17	7.31	254.7	619.3	615.6
1208	15.97	15.94	180.8	618.9	618.5
1186	9.22	8.66	160.1	618.0	618.7
1117	1.42	1.44	187.0	618.0	616.7
1150	3.53	3.92	223.4	619.0	616.3
1196	11.68	11.74	183.5	618.6	617.9
1222	22.29	21.16	163.1	617.7	618.2
1188	9.64	9.75	185.6	618.6	617.8
1134	2.27	2.18	167.1	619.5	619.6
1145	3.13	3.11	179.0	618.1	617.5
1170	6.00	5.94	178.1	617.9	617.6
1212	17.58	18.30	196.6	620.6	619.3
1130	2.02	2.34	242.6	619.0	615.9
1158	4.46	4.72	203.5	618.7	617.2
1121	1.54	1.44	158.5	618.7	619.6
1158	4.48	4.88	215.5	617.7	615.5
1136	2.24	2.67	217.1	618.2	616.3
1209	16.31	17.52	209.3	617.8	615.8
1194	11.28	11.30	182.1	620.0	619.5
1147	3.40	3.39	180.1	618.1	617.5
1220	20.93	22.17	203.7	619.2	617.5
1121	1.68	1.60	165.5	617.2	618.0
1186	9.13	9.32	189.1	617.2	616.2
1230	27.02	25.80	165.5	619.3	618.7
1233	28.57	30.18	202.5	618.8	617.2
1211	17.00	17.95	202.3	618.2	616.5
1201	13.26	13.22	180.3	619.4	619.0
1180	7.67	7.71	183.5	618.9	618.2
1177	7.27	7.32	184.1	618.3	617.6
1204	14.48	14.48	181.6	618.8	618.2
1161	4.82	4.84	183.0	618.5	617.8
1156	4.13	4.18	185.7	618.5	618.0
1188	9.57	9.75	188.4	622.0	621.1
1171	6.08	6.28	193.4	619.0	617.9
1135	2.44	2.70	221.6	617.6	615.4
1148	3.28	3.21	173.6	617.9	618.1
1204	14.26	13.83	170.7	617.8	618.7
1232	27.96	28.90	160.1	617.0	617.0
1157	4.28	4.32	184.7	618.2	617.7
1193	10.86	10.56	171.5	619.5	619.5
1216	19.18	20.47	206.7	619.8	618.0
1189	9.78	9.91	186.4	618.5	617.7
1212	17.54	17.55	181.8	618.0	617.4
1170	6.02	6.06	184.0	619.2	618.5
1116	1.36	1.32	171.6	617.4	617.7
1150	3.55	3.60	186.7	618.6	617.8
1170	5.98	5.86	174.0	617.0	616.9

continued on next page

T/K	P _T /Pa	P _K /Pa	M	Third law ΔH° (298 K)/(kJ/mol)	
				Torsion (± 0.4)	Knudsen (± 0.4)
1184	8.67	8.75	184.7	617.8	617.0
1156	4.08	4.12	185.1	619.6	618.8
1205	14.63	14.19	170.8	619.5	619.6
1222	20.08	21.45	171.4	618.8	618.8
1233	28.95	25.90	145.3	618.6	620.4
1223	22.47	22.94	189.3	619.1	618.1
1152	3.59	3.92	215.9	618.7	616.5
1184	8.60	8.30	168.9	619.0	619.2
1145	2.96	3.05	193.1	618.4	617.5
1208	15.71	15.87	185.2	618.6	617.9
1127	1.88	1.84	173.2	618.0	618.1
1144	3.05	3.09	185.8	619.8	619.3
Average:			187.4 ± 2.3	618.4 ± 0.2	617.6 ± 0.2
Second law			(645.2 ± 3.6)	(639.5 ± 5.0)	

and slopes of plots of P₁ vs. (PWA)₁ (16). The first column gives the type of measurement, and the second column gives the region. The third through sixth columns give the ratios and the condensation coefficients in sets Y and Z, respectively. Average condensation coefficients of (2.8 ± 0.5) × 10⁻² and (3.2 ± 0.5) × 10⁻² in region I and region II, respectively, can be calculated. The pressures at orifice areas of zero were 33.5 ± 19.0% higher than pressures from set Y, and 11.0 ± 15.0% higher than pressures from set Z.

After application of Eq. [11] to the torsion results from sets Y and Z, equilibrium pressure in region I was represented by

$$\log(P_{eq}/\text{Pa}) = [-(1.5518 \pm 0.00460) \times 10^4 K/T] + (14.060 \pm 0.03957) \quad [15]$$

covariance (C,D) = -1.8209

After application of Eq. [11] to the Knudsen results, equilibrium pressure in region I was represented by

$$\log(P_{eq}/\text{Pa}) = [-(1.5469 \pm 0.00917) \times 10^4 K/T] + (14.037 \pm 0.07880) \quad [16]$$

covariance (C,D) = -7.2208

The equilibrium pressure from the torsion results in region II was represented by

$$\log(P_{eq}/\text{Pa}) = [-(1.6889 \pm 0.00653) \times 10^4 K/T] + (14.910 \pm 0.05644) \quad [17]$$

covariance (C,D) = -3.6826

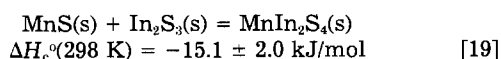
and the pressure from the Knudsen results was represented by

$$\log(P_{eq}/\text{Pa}) = [-(1.7009 \pm 0.01033) \times 10^4 K/T] + (15.025 \pm 0.08932) \quad [18]$$

covariance (C,D) = -9.2246

The average third-law values of ΔH°(298 K), of vaporization reactions [2] of In₂S₃(s), and of vaporization reactions [3] of MnIn₂S₄(s) are tabulated in Table VII. For vaporization reaction [2], ΔH°(298 K) is 618.3 ± 0.6 kJ/mol from torsion results and 617.5 ± 0.7 kJ/mol from Knudsen results, respectively. For vaporization reaction [3], ΔH°(298 K) is 633.2 ± 0.7 kJ/mol from torsion results and 632.8 ± 0.7 kJ/mol from Knudsen results, respectively. For vaporization reaction [2], ΔH°(298 K) = 617.9 ± 0.9 kJ/mol is selected; for vaporization reaction [3], ΔH°(298 K) = 633.0 ± 1.0 kJ/mol is selected.

From third-law selected data, the enthalpies of vaporization by reactions [2] and [3] yield the standard enthalpy, ΔH_c°(298 K), of the combination reaction



Equation [8] gives values from sets Y and Z for the apparent molecular weight of the effusing vapor of 184.7 ± 3.4 for region I and of 178.3 ± 3.7 for region II, which are in good agreement with the average molecular weight, 181.5, calculated from Eq. [9].

Table V. Vapor pressures and thermodynamics of reaction [3]:
MnIn₂S₄(s) = MnS(s) + In₂S(g) + S₂(g)

T/K	P _T /Pa	P _K /Pa	M	Third law ΔH° (298 K)/(kJ/mol)	
				Torsion (± 0.4)	Knudsen (± 0.3)
Set Y					
1114	0.47	0.48	192.0	634.8	633.7
1096	0.26	0.27	200.0	636.0	634.6
1098	0.28	0.29	208.9	635.8	634.4
1134	0.86	0.84	175.6	634.0	633.7
1164	2.23	2.24	176.3	631.0	630.2
1179	2.99	3.01	183.7	632.8	631.9
1186	3.97	4.04	188.0	630.7	629.5
1181	3.25	3.30	191.6	632.1	631.1
1136	0.86	0.81	160.7	635.0	635.4
1088	0.18	0.19	195.9	638.3	636.6
1104	0.37	0.35	162.5	633.9	634.2
1109	0.39	0.36	152.4	635.6	636.4
1124	0.64	0.63	178.7	634.3	633.9
1150	1.45	1.42	173.3	632.3	631.9
1164	2.19	2.23	188.4	631.4	630.3
1172	2.57	2.60	184.6	632.3	631.3
1102	0.32	0.30	153.4	635.5	636.0
1121	0.59	0.59	182.7	634.3	633.5
1147	1.29	1.30	185.2	633.0	632.1
1160	1.83	1.84	182.9	632.8	632.0
1170	2.66	2.59	172.9	630.6	630.4
1085	0.18	0.18	191.8	636.6	636.0
1106	0.37	0.33	145.8	634.9	636.4
1124	0.62	0.60	172.3	634.9	634.8
1142	1.09	1.05	168.4	633.6	633.6
1155	1.66	1.57	162.2	632.2	632.5
1165	2.17	2.07	164.9	632.1	632.2
1167	2.23	2.23	178.7	632.5	631.9
1179	3.06	3.11	187.5	632.3	631.2
1201	5.67	5.75	186.9	630.8	629.8
1105	0.36	0.32	140.3	634.9	636.4
1115	0.48	0.49	181.5	634.9	633.8
1128	0.72	0.68	161.0	634.2	634.5
1145	1.12	1.10	177.6	634.6	634.2
1153	1.50	1.52	186.9	633.1	632.1
1161	1.87	1.70	148.7	632.9	634.0
1165	2.12	2.30	213.4	632.5	630.2
1178	3.21	3.40	203.2	630.9	629.0
1183	3.70	3.71	182.4	630.6	629.7
1196	5.07	4.85	166.4	620.4	630.8
1190	4.01	3.85	167.4	632.4	633.4
1105	0.35	0.33	163.4	635.4	635.8
1108	0.37	0.35	165.2	636.0	636.3
1117	0.49	0.51	190.4	635.6	634.1
1129	0.76	0.69	149.6	633.7	634.8
1135	0.91	0.94	193.2	633.4	632.1
1143	1.07	1.09	189.7	634.5	633.4
1162	2.05	2.09	188.8	631.7	630.5
1168	2.29	2.25	174.8	632.5	632.1
1172	2.65	2.71	189.7	631.7	630.5
1190	4.01	3.85	167.4	632.4	633.4
1213	8.07	7.88	173.1	629.6	629.3
1220	9.94	9.88	179.1	628.7	628.0
1222	10.14	10.86	208.0	629.2	627.1
1155	1.75	1.66	163.0	631.2	631.5
1167	2.16	2.18	184.5	633.1	633.2
Average:			178.2 ± 2.2	633.3 ± 0.3	632.8 ± 0.3
Second law			(695.1 ± 3.4)	(701.3 ± 4.4)	
Set Z					
1134	0.99	0.89	146.5	635.1	635.9
1184	4.37	4.14	162.9	632.5	633.1
1233	15.82	15.89	183.0	631.7	631.0
1174	3.34	3.53	191.4	633.3	632.6
1161	2.19	2.18	180.6	634.7	634.2
1197	5.97	5.46	151.6	632.4	633.8
1226	13.24	12.51	162.1	631.8	632.5
1197	6.34	6.38	183.7	632.0	631.5
1149	1.70	1.74	190.9	635.2	633.9
1215	10.17	10.05	177.1	632.0	631.8
1237	17.78	17.46	176.0	629.6	629.2
1246	21.83	23.80	215.8	632.4	630.0
1217	10.78	10.74	180.2	632.6	632.1
1175	3.51	3.59	189.7	634.1	632.8
1180	3.75	3.83	189.2	633.8	632.9
Average:			178.7 ± 4.4	632.0 ± 0.4	632.5 ± 0.4
Second law			(715.1 ± 7.2)	(719.5 ± 7.9)	

Discussion

The vapor pressure over the system MnS(s) – In₂S₃(s) was measured by both the torsion-effusion and Knudsen-effusion methods in each of two separate experiments in

Table VI. Pressure at orifice area of zero relative to pressures measured and condensation coefficient in set Y and set Z

Measurement	Region	Set Y		Set Z	
		$P_o/P_m \pm (\text{std. dev.})$	$[\alpha \pm (\text{std. dev.})] \times 10^2$	$P_o/P_m \pm (\text{std. dev.})$	$[\alpha \pm (\text{std. dev.})] \times 10^2$
Knudsen	I	1.41 ± 0.21	2.19 ± 0.47	1.13 ± 0.14	2.67 ± 0.39
Torsion	I	1.32 ± 0.19	2.80 ± 0.40	1.10 ± 0.16	3.47 ± 0.51
Knudsen	II	1.33 ± 0.17	2.71 ± 0.46	1.12 ± 0.15	2.89 ± 0.43
Torsion	II	1.28 ± 0.18	3.20 ± 0.44	1.09 ± 0.14	3.86 ± 0.41

Table VII. Third-law ΔH° (298 K) from pressures extrapolated to zero orifice area

Vaporization reaction	Pressure	ΔH° (298 K)/(kJ/mol)	Average value ΔH° (298 K)/(kJ/mol)
$\text{In}_2\text{S}_3(\text{s}) = \text{In}_2\text{S}(\text{g}) + \text{S}_2(\text{g})$	Torsion	618.3 ± 0.6	617.9 ± 0.9
	Knudsen	617.5 ± 0.7	
$\text{MnIn}_2\text{S}_4(\text{s}) = \text{MnS}(\text{s}) + \text{In}_2\text{S}(\text{g}) + \text{S}_2(\text{g})$	Torsion	632.2 ± 0.7	633.0 ± 1.0
	Knudsen	632.8 ± 0.7	

the temperature range of 1065-1246 K. Manganese indium sulfide, MnIn_2S_4 , was found to vaporize incongruently by reaction [3] in the temperature range of 1115-1245 K. The compound MnIn_2S_4 was found in the residues from all sealed tube experiments and vaporization experiments in which the final overall compositions were between 10 m/o and 90 m/o MnS, inclusive.

Torsion-effusion equilibrium vapor pressures were given by Eq. [15] over $\text{In}_2\text{S}_3(\text{s})/\text{MnIn}_2\text{S}_4(\text{s})$ and by Eq. [17] over $\text{MnIn}_2\text{S}_4(\text{s})/\text{MnS}(\text{s})$. These values are in line with Knudsen-effusion results given by Eq. [16] and [18]. Pressures in region I in this work were 15% lower than those reported by Haque *et al.* (12) for indium sulfide which was a residue from sublimation of PbS from PbIn_2S_4 . They are only 50% lower than those measured by Miller and Searcy (10) for pure indium sulfide. In region I, $\text{In}_2\text{S}_3(\text{s})$ was in equilibrium with $\text{MnIn}_2\text{S}_4(\text{s})$. If the latter solid were significantly soluble in $\text{In}_2\text{S}_3(\text{s})$, the vapor pressure could have been lowered; however, the univariance of the vapor pressure in that region was a strong contradiction to any significant solid solution, and mass losses in the transition from region I to region II showed solid solution to be <1 m/o. An unknown ternary compound with a composition very near that of In_2S_3 might have caused the observed lower vapor pressures in our experiments. But such a compound would have to contain less than 10 m/o MnS because the initial composition of the sample in set Z was 10 m/o MnS, and it would have to exist only at high temperature because x-ray examination of samples with 10-50 m/o MnS revealed only $\text{In}_2\text{S}_3(\text{s})$ and $\text{MnIn}_2\text{S}_4(\text{s})$. The differences between our results and those of Miller and Searcy must be attributed to unknown factors.

Good agreement was found between the apparent molecular weight of the effusing vapor of 184.7 ± 3.4 for region I, 178.3 ± 3.7 for region II, and the calculated average molecular weight of 181.5. This result confirms that the vapor composition was that of In_2S_3 .

The second-law values of ΔH° (298 K) were significantly higher than those obtained by the third-law method. Differences between second- and third-law values of ΔH° (298 K) arise from temperature-dependent trends in temperature or equilibrium-constant measurements, or from wrong Gibbs-energy functions. Minor trends can produce large differences because of the temperature range involved in the second-law calculation. Trends in temperature measurements in this study were small, as indicated by the thermocouple calibration and by comparison between torsion and Knudsen results. There is little reason to suspect large temperature-dependent errors in the Gibbs-energy functions used. Small amounts of solid solution could have introduced temperature dependence into the equilibrium constant measurements, particularly in region II, where up to 7.4 ± 3 equivalent percent of In_2S_3 could have been dissolved in the MnS. A

combination of the factors above probably contributed to the differences between the two types of ΔH° (298 K). None of the factors would have a large effect on the third-law values and, thus, they were used in preference to the second-law values. For instance, the possible solid solution of In_2S_3 in MnS in region II, if ideal, would affect the third-law ΔH° (298 K) of reaction [3] by less than the ± 1 kJ/mol given for that reaction.

The standard enthalpy ΔH° (298 K) of vaporization of the ternary compound $\text{MnIn}_2\text{S}_4(\text{s})$ by reaction [3] was 633.0 ± 1.0 kJ/mol, and that of $\text{In}_2\text{S}_3(\text{s})$ by reaction [2] was 617.9 ± 0.9 kJ/mol. The ΔH° (298 K) of vaporization of $\text{In}_2\text{S}_3(\text{s})$ from this work is in good agreement with that from Haque *et al.* (12), 613.4 ± 3.0 kJ/mol, and is in reasonable agreement with the value 617 ± 13 kJ/mol calculated from the data of Miller and Searcy (10) and the Gibbs-energy functions in Table II. It is also in agreement with the value from Colin and Drowart (9), 602 ± 13 kJ/mol.

In Table VIII are compared enthalpies of combination ΔH_c° (298 K), of ternary metal sulfides of the type $\text{M}^{\text{II}}\text{M}^{\text{III}}\text{S}_4$, where $\text{M}^{\text{II}} = \text{Mn, Pb, Zn, and Cd}$, and $\text{M}^{\text{III}} = \text{Ga or In}$. The enthalpy of combination of $\text{MnIn}_2\text{S}_4(\text{s})$ from its constituent binary sulfides by reaction [19] was -15.1 ± 2.0 kJ/mol. This value is at the smaller end of the range of values for similar ternary sulfides and oxides, *i.e.*, -15 to -50 kJ/mol (16, 21-26), with the exception of $\text{CdIn}_2\text{S}_4(\text{s})$, which is a saturated ideal solid solution (26) with a normal spinel structure.

Table VIII shows that the enthalpies of combination of compounds where $\text{M}^{\text{III}} = \text{Ga}$ are higher than those of compounds where $\text{M}^{\text{III}} = \text{In}$, with the exception of ZnIn_2S_4 . The latter exception may be related to the fact that ZnIn_2S_4 has a unique structure among these compounds. It has a rhombohedral crystal structure in space group C_{3v}^5 (R3m) and may be thought of as a series of layers with strong In-S and Zn-S bonds in the layers and weak S-S bonds between the sulfur atoms belonging to different layers (27).

We cannot explain on the basis of a sound theory why the enthalpy of combination of $\text{MnIn}_2\text{S}_4(\text{s})$ is the lowest

Table VIII. Enthalpy of combination of some ternary metal sulfides, $\text{M}^{\text{II}}\text{M}^{\text{III}}\text{S}_4$

$\text{M}^{\text{II}} \backslash \text{M}^{\text{III}}$	$-\Delta H_c^\circ$ (298 K)/(kJ/mol)			
	Gallium	Ref.	Indium	Ref.
Manganese	39.0 ± 2.0	(2)	15.1 ± 2.0	^a
Lead	34.4 ± 3.0	(22)	23.0 ± 4.0	(12)
Zinc	38.0 ± 12.0	(15)	49.4 ± 1.4	(24)
Cadmium	22.6 ± 0.9	(23)	1.7 ± 1.2	(25)

^a This work.

among the listed ternary sulfide compounds. But we have observed that MnIn₂S₄(s) has a mixed spinel structure in which quenched samples have 65% of the Mn²⁺ ions in tetrahedral sites and have 35% in octahedral ones (3, 28). The paramagnetic moment of MnIn₂S₄(s) is 5.68 μB, which corresponds to 4.7 unpaired electrons on each Mn²⁺. MnIn₂S₄(s) is orange. The stable form of MnS(s) is green with the rock salt structure, which places the Mn²⁺ ions in octahedral coordination (30, 31). The paramagnetic moment of MnS(s) is 5.92 μB, which corresponds to 5 unpaired electrons on each Mn²⁺ (30, 31). Clearly, the state of Mn²⁺ in MnS(s) and MnIn₂S₄(s) is different. Indium ions, too, must accommodate a change from octahedral sites in the defect spinel, In₂S₃(s), to 17-18% tetrahedral sites in MnIn₂S₄(s). The energy promotions necessary to transform the states of the positive ions, particularly the Mn²⁺, no doubt are related to the low combination enthalpy.

It is worth noting here that in MnGa₂S₄(s), with a combination enthalpy of 39 ± 2 kJ/mol, Mn²⁺ appears to be in a state much like that in MnS(s), and Ga³⁺ appears to be in a state much like that in Ga₂S₃(s). MnS(s) is green and has a paramagnetic moment corresponding to Mn²⁺ in the high spin state (32). MnGa₂S₄(s) below 1258 K is green and has a monoclinic structure in which Mn²⁺ ions are in octahedral sites and Ga³⁺ ions are in tetrahedral sites (33). Ga₂S₃(s) has a wurtzite-like structure in which Ga³⁺ ions are in tetrahedral sites (33). The energy promotions necessary to transform the states of the positive ions in MnGa₂S₄(s) are probably lower than those for MnIn₂S₄(s). However, such qualitative observations, if valid, must also take into account the unique monoclinic structure of MnGa₂S₄(s).

Acknowledgments

This research was supported by the National Science Foundation under Grant no. CPE-8103676. Valuable discussions with Dr. H. Bradford Thompson are gratefully acknowledged.

Manuscript submitted Jan. 27, 1984; revised manuscript received July 23, 1984.

The University of Toledo assisted in meeting the publication costs of this article.

REFERENCES

- H. Hahn and W. Klingler, *Z. Anorg. Allg. Chem.*, **260**, 97 (1949).
- W. Schlein and A. Wold, *J. Solid State Chem.*, **4**, 286 (1972).
- T. Kanomata and H. Ido, *J. Phys. Soc. Jpn.*, **34**, 554 (1973).
- K. C. Mills, "Thermodynamic Data for Inorganic Sulfides, Selenides, and Tellurides," Butterworths, London (1974).
- H. Wiedemeier and H. Schäfer, *Z. Anorg. Allg. Chem.*, **326**, 230 (1964).
- R. Colin, P. Goldfinger, and M. Jeunehomme, *Nature (London)*, **194**, 282 (1962).
- W. Wiedemeier and P. W. Gilles, *J. Chem. Phys.*, **42**, 2766 (1965).
- P. Viswanadham and J. G. Edwards, *ibid.*, **62**, 3875 (1975).
- R. Colin and J. Drowart, *Trans. Faraday Soc.*, **64**, 2611 (1968).
- A. R. Miller and A. W. Searcy, *J. Phys. Chem.*, **67**, 2400 (1963).
- A. R. Miller and A. W. Searcy, *ibid.*, **69**, 3826 (1965).
- R. Haque, A. S. Gates, and J. G. Edwards, *J. Chem. Phys.*, **73**, 6301 (1980).
- J. G. Edwards, in "Characterization of High Temperature Vapors and Gases," J. Hastie, Editor, National Bureau of Standards, Special Publication 561, Washington, DC (1979).
- J. G. Edwards, M. K. Heckler, and H. B. Thompson, *Rev. Sci. Instrum.*, **50**, 274 (1979).
- R. D. Freeman and J. G. Edwards, in "Characterization of High Temperature Vapors," J. L. Margrave, Editor, Appendix C, Wiley, New York (1967).
- A. S. Gates and J. G. Edwards, *J. Phys. Chem.*, **82** 2789 (1978).
- R. D. Freeman, in "Characterization of High Temperature Vapors," J. L. Margrave, Editor, Chap. 7, Wiley, New York (1967).
- E. D. Cater, in "Techniques of Metals Research," R. A. Rapp, Editor, Vol. 4, Chap. 2A, Wiley, New York (1970).
- D. Cubicciotti, *J. Phys. Chem.*, **70**, 2410 (1966).
- G. N. Lewis, M. Randall, K. S. Pitzer, and L. Brewer, "Thermodynamics," 2nd ed., p. 175, McGraw-Hill, New York (1961).
- T. A. Kessler, Yu. D. Tretyakov, I. V. Gorolev, and V. A. Alferov, *J. Chem. Thermodyn.*, **8**, 101 (1976).
- A. S. Gates and J. G. Edwards, *J. Phys. Chem.*, **84**, 3263 (1980).
- M. Williamson, M. S. Thesis, University of Toledo (1984).
- J. G. Edwards and S. T. Kshirsagar, *Thermochim. Acta*, **59**, 81 (1982).
- J. G. Edwards, R. Haque, and A. H. Qusti, *ibid.*, **62**, 197 (1983).
- S. T. Kshirsagar, H. B. Thompson, and J. G. Edwards, *This Journal*, **129**, 1835 (1982).
- U. Giorianni, V. Grasso, G. Moudio, and G. Saitta, *Phys. Lett. A*, **68**, 247 (1978).
- F. A. Cotton and G. Wilkinson, "Advanced Inorganic Chemistry," Wiley, New York (1972).
- N. Menyuk, K. Dwight, and A. Wold, *J. Appl. Phys.*, **36**, 1088 (1965).
- F. Jellinek, in "Inorganic Sulphur Chemistry," G. Nickless, Editor, Elsevier, Amsterdam (1968).
- A. F. Wells, "Structural Inorganic Chemistry," Clarendon Press, Oxford (1975).
- P. Viswanadham and J. G. Edwards, *Mater. Res. Bull.*, **8**, 1079 (1973).
- M. P. Pardo, P. H. Fourcroy, and J. Flahaut, *ibid.*, **10**, 665 (1975).

Vaporization Behavior of Chromium Phosphides

The Solid Two-Phase Regions CrP-Cr₁₂P₇, Cr₁₂P₇-Cr₃P, and Cr₃P-Cr

C. E. Myers,* G. A. Kisacky, and J. K. Klingert

Department of Chemistry, State University of New York at Binghamton, Binghamton, New York 13901

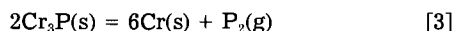
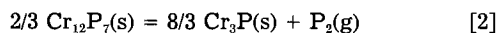
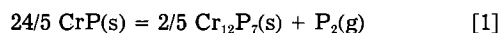
ABSTRACT

The vaporization reactions $24/5 \text{ CrP(s)} = 2/5 \text{ Cr}_{12}\text{P}_7\text{(s)} + \text{P}_2\text{(g)}$ (1194-1479 K), $2/3 \text{ Cr}_{12}\text{P}_7\text{(s)} = 8/3 \text{ Cr}_3\text{P(s)} + \text{P}_2\text{(g)}$ (1421-1541 K), and $2\text{Cr}_3\text{P(s)} = 6\text{Cr(s)} + \text{P}_2\text{(g)}$ (1543-1768 K) have been studied under mass-loss effusion in the temperature ranges indicated. The reactions are kinetically inhibited. Enthalpies of formation and atomization, respectively, are found to be in kK: for $1/2\text{CrP(s)}$, -5.69 ± 0.18 and 49.67 ± 0.2 ; for $1/19 \text{ Cr}_{12}\text{P}_7\text{(s)}$, -4.48 ± 0.32 and 49.47 ± 0.3 ; for $1/4 \text{ Cr}_3\text{P(s)}$, -3.18 ± 0.04 and 49.08 ± 0.04 . CrP is found to follow the trend in atomization enthalpy to valence state atoms established in the series MnP, FeP, CoP, and NiP.

The atomization enthalpy, $\Delta H_{\text{at}}^{\circ}$, of a solid compound may be used as a measure of its stability and of the strength of its chemical bonds. It has been shown (1), however, that the proper quantity is the atomization enthalpy to valence state atoms, $\Delta H_{\text{at}}^*/R$. The stability of compounds in a series should increase with the number of bonding electrons per atom. As shown in Fig. 1, $\Delta H_{\text{at}}^*/R$ (kK) exhibits a regular decrease in the series MnP (141.3), FeP (130.0), CoP (119.1), and NiP (104.4) as the number of bonding (unpaired) electrons per metal atom decreases from five in MnP to two in NiP for the presumed valence state $3d^{n-1}4s^1$, where n is the total number of valence electrons. Because Cr should have six bonding electrons in the valence state, one should expect $\Delta H_{\text{at}}^*/R$ for CrP to be proportionately larger; an extrapolation produces an estimate of about 150 kK. Trends in the enthalpies of sublimation of the metallic elements to valence state atoms, $\Delta H_{\text{at}}^*/R$, suggest an estimate of 147 kK. A mass-loss effusion study of chromium phosphides has been done to test the extrapolation.

The phase relations in the Cr-P system have been reviewed by Hansen (2), Elliott (3), and Shunk (4). Well-established compounds are Cr₃P, CrP, and CrP₂, which appear to have narrow ranges of homogeneity. Evidence for "Cr₂P" has been contradictory, but Baurecht and co-workers (5) have shown the composition to be Cr₁₂P₇ with a slight range of homogeneity.

It has been established, as shown below, that the vaporization reactions are



The enthalpy changes for these reactions, when combined with the enthalpy of formation (6) of P₂(g)



give the enthalpies of formation of the chromium phosphides

$$\Delta H_5 = \Delta H_{\text{f}}^{\circ}(\text{Cr}_3\text{P}) = 1/2 \Delta H_4^{\circ} - 1/2 \Delta H_6^{\circ} \quad [5]$$

$$\Delta H_6 = \Delta H_{\text{f}}^{\circ}(\text{Cr}_{12}\text{P}_7) = 3/2 \Delta H_4^{\circ} + 4\Delta H_5^{\circ} - 3/2 \Delta H_6^{\circ} \quad [6]$$

$$\Delta H_7 = \Delta H_{\text{f}}^{\circ}(\text{CrP}) = 5/24 \Delta H_4^{\circ} + 1/12 \Delta H_6^{\circ} - 5/24 \Delta H_6^{\circ} \quad [7]$$

Experimental

The samples used in this study were prepared in the manner described in Ref. (7), by direct combination of chromium powder (99.99%) obtained from SPEX Industries, Inc., and red phosphorus (99.9%) obtained from CERAC/Pure, Inc. The products, as well as residues from effusion runs, were characterized by x-ray powder diffraction; the observed patterns were compared with com-

puter-generated patterns (8) based on data from the literature (CrP (9, 10, 11), Cr₁₂P₇ (5), Cr₃P (9, 10, 12)). The channel-orifice effusion cells were machined from 1.59 cm graphite rod and were fitted with a tantalum liner to prevent the phosphide samples from coming into direct contact with the graphite. The effective orifice areas were measured with KCl as a vapor-pressure standard; data for KCl(g) and K₂Cl₂(g) were taken from Ref. (13). The effusion apparatus, with calibration and operation procedures, has been described previously (7, 14). It consists of a vacuum system, an induction heater, and a recording vacuum balance. For the experiments described here, the apparatus was fitted with an eddy current concentrator, and the temperatures were measured with a tungsten, 25% rhenium-tungsten, 3% rhenium thermocouple calibrated as described in Ref. (7).

Results and Discussion

The primary data¹ were temperature, corrected for thermocouple calibration, and the rate of mass loss determined from the readout of the recording vacuum balance. Individual experiments were of sufficient duration to keep the uncertainty in the slope of the mass vs. time plot less than 5%. Partial pressures of P₂(g) were calculated from the rate of mass loss (assuming that P₂ and P₄ were in equilibrium in the gas phase) with the modification of the effusion equation derived in Ref. (7)

$$P(\text{P}_2) = \frac{K}{2\sqrt{2}} \left\{ \left[1 + \frac{8m}{aK} \left(\frac{\pi RT}{M} \right)^{1/2} \right]^{1/2} - 1 \right\} \quad [8a]$$

$$= \frac{K}{2\sqrt{2}} \left\{ \left[1 + \frac{C'm}{aK} \left(\frac{T}{M} \right)^{1/2} \right]^{1/2} - 1 \right\} \quad [8b]$$

When $P(\text{P}_2)$ is obtained in atmospheres from m (the rate of mass loss) in mg/min, T in Kelvins, M (the molecular weight of P₂), and a (the effective orifice area) in cm², the constant is $C' = 2.127 \times 10^{-6}$. K is the equilibrium constant for $\text{P}_4\text{(g)} = 2\text{P}_2\text{(g)}$; this constant was calculated for each temperature from data given in Ref. (13).

Initial heating of two of the samples resulted in apparent univariant behavior at temperatures near 800 K. Further heating with loss of phosphorus developed univariant behavior in the range 1194-1479 K, and the residues from these latter experiments were shown by x-ray powder diffraction to be a mixture of CrP and Cr₁₂P₇. Further heating with additional loss of phosphorus developed both a third univariant condition (1421-1541 K) for which the residues were Cr₁₂P₇ and Cr₃P and a fourth univariant condition (1543-1768 K) for which the residues were Cr₃P and Cr. The first region was presumed to result from the decomposition of small amounts of CrP₂ from the initial preparation; this region was not studied further. The remaining three invariant regions were studied in detail, and the resulting data are shown in Fig. 2.

¹Thermochemical data in this paper are given in "rational" units; values in other units may be obtained by multiplying by the appropriate value of the gas constant, R .

*Electrochemical Society Active Member.

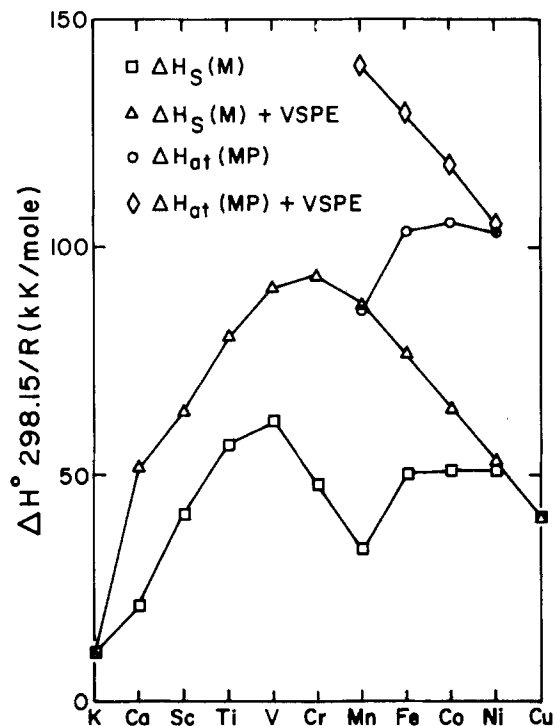


Fig. 1. Sublimation enthalpies of metals and atomization enthalpies (per mole) of some monophosphides to ground-state atoms and to valence-state atoms.

Data taken during the evolution of the samples from one region to another have been omitted. For these two-phase regions, effective orifice areas of $2.39 (\pm 0.06) \times 10^{-4} \text{ cm}^2$ and $8.91 (\pm 0.2) \times 10^{-5} \text{ cm}^2$ gave the same results in each region, within experimental uncertainty, and these runs were presumed to be at equilibrium. Larger orifices gave lower calculated pressures, presumably without achievement of equilibrium. The cross-sectional area of the sample was 1.76 cm^2 in all experiments. Only the equilibrium data from the three two-phase regions were used in

subsequent thermodynamic calculations. These data are presented in Tables I, II, and III, and the lines in Fig. 2 result from a least squares treatment of each set of data. For the $\text{CrP-Cr}_{12}\text{P}_7$ and $\text{Cr}_{12}\text{P}_7\text{-Cr}_3\text{P}$ regions, phosphorus was assumed to be the only volatile component, whereas in the $\text{Cr}_3\text{P-Cr}$ region, the rates of mass loss were corrected for the vapor pressure of elemental chromium.

There are neither entropy nor high-temperature heat-capacity data for chromium phosphides in the literature; hence, these were estimated. Entropy estimates were based (7) on data for chromium silicides (15, 16). Heat capacity estimates were based on data for manganese phosphides (17). These estimated values are given in Table IV. Second-law enthalpies, ΔH^{III} , were calculated for the temperature ranges of the measurements from the least squares slopes of $\log P(\text{P}_2)$ vs. $1/T$ and were corrected to 298.15 K by means of $\Delta(H^{\circ}_T - H^{\circ}_{298.15})$ evaluated from Cp. Third-law enthalpies of reaction, ΔH^{III} , were obtained by means of free-energy functions, $\Phi' \equiv -(G^{\circ}_T - H^{\circ}_{298.15})/T$, calculated from the entropy and heat-capacity data. Tables I, II, and III summarize calculations for reactions [1], [2], and [3], respectively. The agreement of respective second-law and third-law enthalpies is acceptable, partic-

Table I. Data for reaction $24/5 \text{ CrP(s)} = 2/5 \text{ Cr}_{12}\text{P}_7\text{(s)} + \text{P}_2\text{(g)}$

T (K)	$m \times 10^3$ (mg/min)	$P \times 10^5$ (atm)	$\Delta G^{\circ}/RT$	$\Delta \Phi'/R$	$\Delta H^{\circ}_{298.15}{}^{\text{III}}/R$ (kJ)
$(a_{\text{eff}} = 2.39 \times 10^{-4} \text{ cm}^2)$					
1380	33.1	24.5	8.31	22.27	42.21
1408	66.1	49.5	7.61	22.26	42.07
1377	33.2	24.6	8.31	22.27	42.11
1315	7.91	5.73	9.77	22.29	42.16
1365	25.0	18.4	8.60	22.28	42.15
1289	4.37	3.13	10.37	22.30	42.12
$(a_{\text{eff}} = 8.91 \times 10^{-5} \text{ cm}^2)$					
1479	118.0	242	6.02	22.25	41.81
1437	46.3	93.9	6.97	22.26	42.00
1398	20.8	41.6	7.79	22.27	42.01
1485	125.0	257.0	5.96	22.25	41.89
1355	8.21	16.2	8.73	22.28	42.02
1329	4.14	8.08	9.42	22.29	42.15

$\Delta H^{\circ}_{1382}{}^{\text{II}}/R = 43.5 \pm 1.4$
 $\Delta H^{\circ}_{298.15}{}^{\text{II}}/R = 44.1 \pm 1.5$
 Mean $\Delta H^{\circ}_{298.15}{}^{\text{III}}/R = 42.06 \pm 2.5$

Table II. Data for reaction $2/3 \text{ Cr}_{12}\text{P}_7\text{(s)} = 8/3 \text{ Cr}_3\text{P(s)} + \text{P}_2\text{(g)}$

T (K)	$m \times 10^3$ (mg/min)	$P \times 10^5$ (atm)	$\Delta G^{\circ}/RT$	$\Delta \Phi'/R$	$\Delta H^{\circ}_{298.15}{}^{\text{III}}/R$ (kJ)
$(a_{\text{eff}} = 2.39 \times 10^{-4} \text{ cm}^2)$					
1497	6.68	5.16	9.87	19.70	44.28
1512	9.29	7.22	9.54	19.70	44.21
1521	10.9	8.50	9.37	19.70	44.22
1506	8.75	6.79	9.60	19.70	44.13
1467	3.72	2.85	10.47	19.71	44.27
1488	5.66	4.36	10.04	19.71	44.26
1435	1.84	1.39	11.18	19.72	44.34
1508	7.90	6.13	9.70	19.70	44.34
1541	16.9	13.30	8.93	19.70	44.12
1512	8.33	6.48	9.65	19.70	44.37
1421	1.28	0.964	11.55	19.72	44.44
$(a_{\text{eff}} = 8.91 \times 10^{-5} \text{ cm}^2)$					
1513	3.46	7.22	9.54	19.70	44.24
1499	2.62	5.43	9.82	19.70	44.26
1516	3.68	7.68	9.48	19.70	44.23
1465	1.20	2.46	10.61	19.71	44.43
1530	4.61	9.67	9.25	19.70	44.29
1508	3.22	6.70	9.61	19.70	44.21
1539	5.70	12.0	9.03	19.70	44.21

$\Delta H^{\circ}_{1498}{}^{\text{II}}/R = 46.6 \pm 2.7$
 $\Delta H^{\circ}_{298.15}{}^{\text{II}}/R = 46.9 \pm 2.8$
 Mean $\Delta H^{\circ}_{298.15}{}^{\text{III}}/R = 44.29 \pm 4.0$

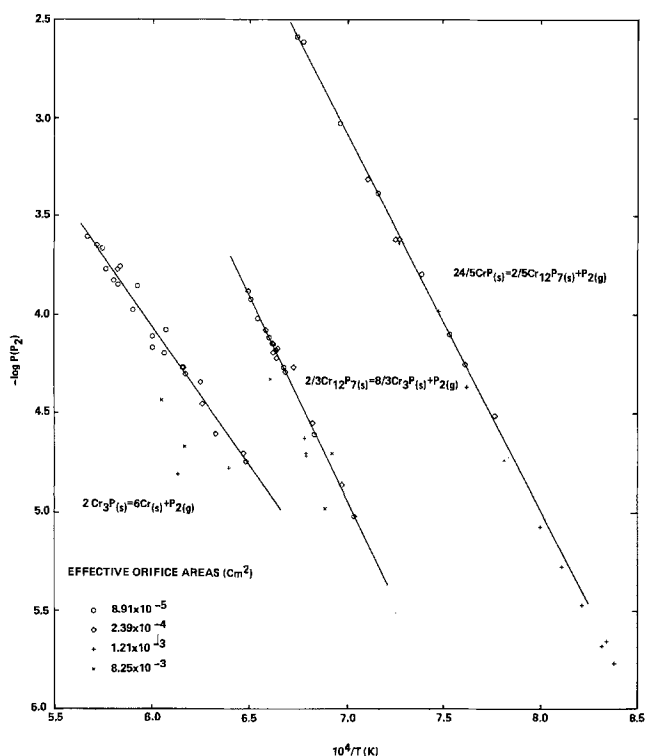


Fig. 2. Phosphorus dissociation pressures for chromium phosphides

Table III. Data for reaction $2\text{Cr}_3\text{P}(s) = 6\text{Cr}(s) + \text{P}_2(g)$

T (K)	$m \times 10^3$ (mg/min)	$P \times 10^6$ (atm)	$\Delta G^\circ/RT$	$\Delta\Phi'/R$	$\Delta H_{298.15}^\circ/R$ (kK)
$(\alpha_{\text{eff}} = 2.39 \times 10^{-4} \text{ cm}^2)$					
1543	2.32	1.82	10.92	19.10	46.31
1601	5.70	4.57	9.99	18.95	46.35
1546	2.55	2.00	10.82	19.09	46.24
1581	3.18	2.52	10.59	19.00	46.79
1624	6.76	5.46	9.82	18.89	46.62
1650	10.45	8.46	9.38	18.82	46.53
1621	6.28	5.05	9.90	18.90	46.68
1599	4.48	3.56	10.24	18.96	46.69
1720	20.60	17.1	8.68	18.65	47.00
1753	27.10	22.7	8.39	18.59	47.29
$(\alpha_{\text{eff}} = 8.91 \times 10^{-5} \text{ cm}^2)$					
1690	6.33	14.0	8.88	18.72	46.63
1716	7.19	17.6	8.65	18.66	46.86
1744	9.68	21.7	8.44	18.60	47.16
1669	3.57	7.8	9.46	18.77	47.12
1738	7.60	17.0	8.68	18.61	47.44
1720	6.37	14.2	8.86	18.65	47.32
1697	4.83	10.6	9.15	18.70	47.25
1726	6.75	15.0	8.81	18.64	47.37
1768	10.99	24.3	8.30	18.56	47.49
1626	2.53	5.47	9.82	18.89	46.67
1651	2.96	6.44	9.65	18.82	47.01
1668	3.14	6.87	9.59	18.77	47.31

$$\Delta H_{1498}^\circ/R = 32.0 \pm 2.7$$

$$\Delta H_{298.15}^\circ/R = 38.7 \pm 2.8$$

$$\text{Mean } \Delta H_{298.15}^\circ/R = 46.9 \pm 0.2$$

Table IV. Estimated thermochemical data for chromium phosphides

	$S_{298.15}^\circ/R$	A	$B \times 10^3$	$C \times 10^{-5}$
CrP	4.78	7.12	-0.06	-1.36
Cr_{12}P_7	50.33	60.67	12.42	-9.70
Cr_3P	10.57	11.45	5.08	-1.42

$$C_p/R = A + BT + CT^{-2}$$

Table V. Stability data for chromium phosphides at 298.15 K

	$-\Delta H_f/R$ (from red P) (kK)	$\Delta H_{\text{at}}/R$ (kK)
1/2 CrP(s)	5.69 ± 0.18	49.67 ± 0.2
1/19 Cr_{12}P_7 (s)	4.48 ± 0.32	49.47 ± 0.3
1/4 Cr_3P (s)	3.18 ± 0.04	49.08 ± 0.04
1/3 CrP_2 (s)	4.8 ± 0.7	47.5 ± 0.7

ularly in view of the limited temperature ranges imposed by the difficulty of obtaining equilibrium. Enthalpies of formation calculated from the third-law enthalpies by Eq. [5], [6], and [7] are given in Table V, together with enthalpies of atomization. Uncertainty limits were assigned in the manner described in Ref. (1). Also included in Table V are the enthalpies of formation and atomization of CrP_2 (s), based on the static vapor-pressure studies

of Faller and Blitz (19) and estimated free-energy functions.

The enthalpy of atomization of CrP to valence state atoms was obtained by adding the valence state preparation energy (18) of chromium (45.9 kK) to the ground-state atomization enthalpy. The resulting value, 145.3 kK, is in excellent agreement with the estimate, 147 kK, based on trends in $\Delta H^*/R$ of the metals. As is pointed out in Ref. (1), this result confirms a similarity in bond type in the series CrP, MnP, FeP, CoP, and NiP. The extrapolation to compounds such as ScP which have significant ionic character gives poor agreement with measured values.

Acknowledgments

The authors are pleased to acknowledge the support of the U.S. Office of Naval Research. Mr. Weldon Willard aided greatly in solving some practical technical problems.

Manuscript submitted May 29, 1984; revised manuscript received Sept. 10, 1984.

State University of New York at Binghamton assisted in meeting the publication costs of this article.

REFERENCES

- C. E. Myers, E. D. Jung, and E. L. Patterson, *Inorg. Chem.*, **19**, 532 (1980).
- M. Hansen, "Constitution of Binary Alloys," 2nd ed., pp. 548-549, McGraw-Hill, New York (1958).
- R. P. Elliott, "Constitution of Binary Alloys, First Supplement," p. 354, McGraw-Hill, New York (1965).
- F. A. Shunk, "Constitution of Binary Alloys, Second Supplement," p. 227, McGraw-Hill, New York (1969).
- H. E. Baurecht, H. Boller, and H. Nowotny, *Monatsh. Chem.*, **102**, 373 (1971).
- R. Hultgren, P. D. Desai, D. T. Hawkins, M. Gleiser, K. K. Kelley, and D. D. Wagman, "Selected Values of the Thermodynamic Properties of the Elements," American Society for Metals, Metals Park, Ohio (1973).
- C. E. Myers, *High Temp. Sci.*, **6**, 309 (1974).
- A. C. Larson, R. B. Roof, Jr., and D. T. Cromer, "An Integrated Series of Crystallographic Computer Programs. X. Anisotropic Structure Factor Calculation and Powder Pattern Generation," Report LA33335, Los Alamos Scientific Laboratory, Los Alamos, NM (1965).
- N. Schonberg, *Acta Chem. Scand.*, **8**, 226 (1954).
- S. Rundqvist, *Ark. Kemi.*, **20**, 67 (1962).
- S. Rundqvist and P. C. Nawapong, *Acta Chem. Scand.*, **19**, 1006 (1965).
- T. Lundstrom, *ibid.*, **16**, 149 (1962).
- D. R. Stull and H. Prophet, National Standard Reference Data Series, National Bureau of Standards, No. 37 (1971).
- M. H. Hannay and C. E. Myers, *J. Less-Common Met.*, **66**, 145 (1979).
- Y. M. Golutvin and C. Liang, *Russ. J. Phys. Chem. (Engl. Transl.)*, **35**, 62 (1961).
- G. I. Kalishevich, P. V. Gel'd, and R. P. Krentsis, *ibid.*, **39**, 1602 (1965).
- I. A. Makharadze, I. B. Baratashvili, D. S. Tsagareishvili, and G. G. Gvelesiani, *Inorg. Mater. (Engl. Transl.)*, **11**, 515 (1975).
- J. S. Griffith, *J. Inorg. Nucl. Chem.*, **3**, 15 (1956).
- F. E. Faller and W. Blitz, *Z. Anorg. Chem.*, **248**, 209 (1941).

Influence of Growth Temperature on the Physical Properties of Si Films on Yttria-Stabilized, Cubic Zirconia Substrates

Alice L. Lin* and Ilan Golecki*

Rockwell International, Microelectronics Research and Development Center, Defense Electronics Operations, Anaheim, California 92803

ABSTRACT

Epitaxial (100) Si films 0.4-0.5 μm thick were grown by the pyrolysis of silane in a hydrogen atmosphere on (100) yttria-stabilized, cubic zirconia (15 mole percent [m/o] Y_2O_3) at temperatures in the range 910°-1000°C and deposition rates of 0.06-0.58 $\mu\text{m}/\text{min}$. The heteroepitaxial Si films have been characterized by ultraviolet reflectance, Rutherford backscattering/channeling, and Hall effect measurements. It was found that the Si film quality depends strongly on substrate temperature. An optimum growth temperature range between 930° and 960°C was obtained and explained by two defect formation mechanisms: generation at growth temperature and that during cooling from growth temperature to room temperature. The best quality Si/YSZ films produced in this investigation had a value of surface channeling yield, χ_0 , equal to 0.048, as compared to 0.1 for Si/YSZ films reported previously, and 0.12 for typical commercial SOS films, respectively, at 1.5 MeV $^4\text{He}^+$ energy.

Single-crystal silicon films on insulating substrates (SOI) offer many advantages over bulk single-crystal silicon for use in fabricating high speed, very large scale integrated circuits (VLSI); these advantages include low parasitic capacitance, increased radiation hardness, and low power dissipation. The current state-of-the-art SOI material, available commercially in 3 and 4 in. diam wafers, is chemically vapor-deposited (CVD) (100) Si film on (01 $\bar{1}2$) sapphire (SOS), first developed at Rockwell International (1). Submicron-thick SOS films are routinely used in the electronics industry for fabricating high speed, radiation-hard VLSI.

Yttria-stabilized cubic zirconia, $(\text{Y}_2\text{O}_3)_m(\text{ZrO}_2)_{1-m}$, single crystal is potentially a better bulk insulator substrate for growing heteroepitaxial Si film, (Si/YSZ), than sapphire substrate, (SOS) (2). The lattice mismatch between Si and sapphire is about 10%, whereas between Si and YSZ it can be as low as 3.7% by properly adjusting the yttria content. Moreover, constituents of YSZ, such as zirconium and yttrium, do not form shallow levels in silicon. Zirconium, as a group IVB element, is electrically inactive in silicon (3). Yttrium has been known to create deep levels in Si (4). However, the reported concentration of these deep levels is very low, on the order of 10^{13} cm^{-3} (4). Sapphire, however, is well known to act as a source of Al shallow acceptors in Si during CVD and subsequent high temperature processing (5), although state-of-the-art, as-deposited SOS films contain less than $10^{15} \text{ Al}/\text{cm}^3$. Epitaxial Si/YSZ films have been achieved in our laboratory (6, 7). Film crystal quality is indeed found to be better than commercial SOS films in the thickness range 0.4-0.5 μm (6, 7).

One possible drawback of using YSZ material as a substrate for Si film deposition is the high thermal expansion coefficient of YSZ material. The average value between 25° and 1000°C is $11.4 \times 10^{-6}/^\circ\text{C}$ for YSZ with 9 mole percent (m/o) of Y_2O_3 (8, 9) as compared to $3.8 \times 10^{-6}/^\circ\text{C}$ for Si (10). In order to reduce the strain and the lattice defects created in Si film during cooling from growth temperature to room temperature, it is desirable to grow the Si film at a temperature as low as possible. The present work attempts to further improve the Si/YSZ film quality by investigating the optimum growth temperature. The heteroepitaxial Si films have been characterized by UV reflectance, Rutherford backscattering/channeling, and Hall effect measurements. We have obtained an optimum growth temperature ranging between 930° and 960°C. The Si/YSZ films produced in this temperature range have crystal quality better than that of commercial SOS films and Si/YSZ films reported previously (6, 7) of similar thickness.

Experimental Procedures

Single-crystal $(\text{Y}_2\text{O}_3)_m(\text{ZrO}_2)_{1-m}$ boules grown by the skull melting technique (11) at 2700°C in air were obtained

from Ceres Corporation (North Billerica, Massachusetts) and Singh Industries, Incorporated (Cedar Knolls, New Jersey). Nominal yttria mole fraction, m , in YSZ material used in this study was 0.15 and 0.21. The as-received boules were transparent, with an increasingly yellowish hue as the concentration of yttria increased. No gross defects were visible to the eye. The boules were oriented parallel to the $\langle 100 \rangle$ axis to within a few degrees by standard x-ray back-reflection Laue technique (12) and then mounted on an automatic, diamond-blade saw. An 18 mil thick slice was cut off. This was reoriented. The boule was realigned on the saw. The procedure was repeated to obtain a final orientation within less than 1° of the desired crystal axis. After the desired orientation had been obtained, wafers 18 mil thick were sliced from each boule. They were then lapped using mixtures of Al_2O_3 powders of progressively finer particle size in colloidal silica and chemically mechanically polished in a mixture of colloidal silica and phosphoric acid, at pH = 3-4, to obtain specular surface finish. The size of the wafers was larger than 10 cm^2 , but their shapes were irregular. After polishing, wafers were degreased in hot trichloroethane, acetone, and methanol and blown dry with nitrogen gas prior to being loaded in the CVD reactor.

The epitaxial reactor was a vertical, cold-wall quartz reactor containing a 57 mm diam, silicon-carbide-coated graphite susceptor, which was RF heated. The susceptor was rotated continuously during Si growth in order to minimize lateral thermal gradients. Silicon films were deposited through pyrolytic decomposition of silane, SiH_4 (5% in He) in Pd-purified H_2 at atmospheric pressure. Both gases passed through cold traps, acetone (218 K) and liquid nitrogen (78 K) for SiH_4 and H_2 , respectively, before being admitted into the reactor. Typical gas flow rates used were 10-100 cm^3/min and 3000 cm^3/min for SiH_4 and

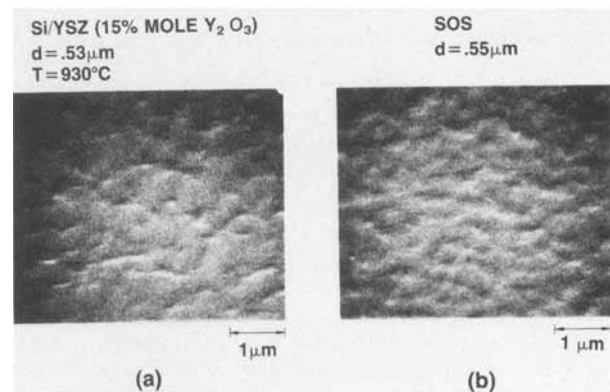


Fig. 1. SEM photographs of a Si/YSZ film (15 m/o Y_2O_3) 0.53 μm thick, grown at 930°C (a) and a commercial SOS film 0.55 μm thick (b).

H₂, respectively. Before each growth experiment, the quartz reactor was evacuated to at least 10⁻³ torr pressure, and then filled with purified flowing H₂ prior to heating the susceptor. Temperature was monitored on the side of the susceptor using an optical pyrometer. Values given here are uncorrected readings; previous calibrations (13) had shown that the actual wafer temperature on the top of the susceptor was 33°-50°C lower at 950°-1075°C, respectively. Before Si deposition at 910°-1000°C, substrates were annealed in H₂ at ≈ 1250°C for 30 min. As reported earlier (6, 7), this predeposition, high temperature annealing in H₂ resulted in a YSZ substrate with better crystalline perfection and an oxygen-deficient composition. It avoided the presence of oxygen near the substrate surface during Si deposition, which otherwise might have evolved out of the YSZ, reacted with the SiH₄ and H₂ to generate SiO₂ at the surface, and impeded epitaxy. Si films grown in this study were in the 0.4-0.5 μm thickness range. The growth rate was 0.06-0.58 μm/min.

The thickness of the heteroepitaxial Si films was measured routinely with the Nanospec spectrophotometric reflectometer (Nanometrics, Incorporated), using Rutherford backscattering spectroscopy (RBS) for calibration.

The Si surface quality was examined by optical microscopy with a Nomarski interference attachment and by scanning electron microscopy. It was also quantified by the value of ultraviolet reflectance (UVR) parameter, ΔR, which was measured by using an RCA UV reflectometer (14). This instrument measured the difference in reflected intensity from a well-polished, high quality Si wafer and from the sample, and normalized to the lamp intensity of wavelengths of 280 and 400 nm. The value of reflectance parameter, ΔR, was obtained by subtracting the signal level at 280 nm, R₂₈₀, from that at 400, R₄₀₀. It had been found that ΔR was related not only to the surface roughness of the Si films, but also to the crystalline quality, especially the microtwin density of certain SOS films (14).

Depth profiles of the concentration of crystallographic imperfections in the Si/YSZ films were measured by Rutherford backscattering and channeling spectrometry (RBS/C) using 1.5 MeV ⁴He⁺ ions. In particular, the technique of grazing-exit detection (15) of the backscattered ⁴He⁺ particles was shown to largely overcome the basic difficulties inherent in analyzing a low mass film on a heavy mass substrate by RBS.

Hall coefficient and conductivity were measured using six-contact, standard Hall bar by a low noise, high sensitivity, computer-controlled Hall apparatus. The system consisted of four unity-gain high input-impedance amplifiers for each of the four potential lines from the Hall bar, a HP 4140B PA meter/dc voltage source, a HP 3456A digital voltmeter, a Digital Equipment MINC-23 computer/controller, a Varian magnet with Model V2900 regulated power supply, and an Air Products displax closed-cycle refrigeration system. Prior to electrical measurement, samples were degreased, dipped into 10% HF solution for 10 min, rinsed in methanol, blown dry with N₂ gas, and then soldered with In contacts.

Results and Discussion

The thickness of the Si films deposited in this study was in the range of 0.4-0.5 μm, and its uniformity was found to be better than ±5%. The surfaces of the heteroepitaxial Si films grown in this study were specular. Under optical microscopy with a Nomarski interference attachment, Si films grown between 930° and 980°C in general, showed no gross features except a grainy appearance similar to that observed in SOS films. Figure 1 compares the surface morphology of a Si/YSZ film grown at 930°C to that of a commercial SOS film of similar thickness. Si/YSZ films grown at 910° and at 1000°C often showed hillocks on the surface. Results presented in this paper were mainly those of epitaxial (100) Si films grown on (100) YSZ (15 m/o Y₂O₃) substrates. Similar results were also obtained for (100) Si/YSZ (21 m/o Y₂O₃) films grown under the same conditions.

Growth rate.—The dependence of growth rate on substrate temperature is shown in Fig. 2 for gas flow rates of 10 and 3000 cm³/min for SiH₄ and H₂, respectively. The curve shown in Fig. 2 is found to be similar to that reported for homoepitaxial Si films grown on silicon substrate by the pyrolysis of silane (16, 17). Two temperature regions can be distinguished; from 930° to 1000°C; the growth rate is relatively temperature independent. This indicates that gas-phase diffusion of reactants controls the growth process (17). Below 930°C, the growth rate becomes strongly dependent on temperature, suggesting that a thermally activated surface reaction limits the growth process (17). The activation energy calculated from the line at curve of growth rate vs. the reciprocal temperature is ±51 kcal/mol, which is higher than 37 kcal/mol reported for growing homoepitaxial Si film at low temperature (16, 17). In growing Si/YSZ films at low temperature, it is not clear which surface reaction, such as absorption of silane, dehydrogenation of the absorbed silane, or surface diffusion and incorporation of Si adatoms into the lattice, is the rate-limiting step.

UV reflectance.—UVR was used routinely as a rapid tool for quantifying the Si surface quality. Figure 3 shows the growth temperature dependence of relative reflectance from Si films measured at 280 nm, R₂₈₀. Most of the Si films presented here were deposited at a rate of 0.11 ± 0.01 μm/min. At 945° and 910°C, growth rates of both 0.11 and 0.58 μm/min, and of both 0.11 and 0.06 μm/min, respectively, were studied.

It was found that, by varying the growth temperature from 910° to 1000°C, the value of R₂₈₀ started to decrease, reaching a minimum at growth temperature in the range of 930°-960°C, and then increasing at higher temperature. Varying growth rate between 0.06 and 0.58 μm/min showed no effect on surface quality of Si/YSZ films measured by UVR technique. At 1000°C, R₂₈₀ data were scattered, which may be caused by the scattering of light from those hillocks found on the surface. As mentioned earlier, R₂₈₀ corresponded to the difference in reflected intensity from a well-polished, high quality Si wafer and from the Si/YSZ films. Lower R₂₈₀ values indicated a surface quality of Si/YSZ films to be closer to the one of a well-polished, high quality Si wafer. Thus, the optimum growth temperature, as far as surface quality was concerned, was in the range of 930°-960°C. Values of R₂₈₀ for the Si/YSZ films grown in this temperature range were 10-15, as compared to 16-40 for commercial available SOS films of similar thickness, measured by the same UV reflectometer.

Figure 4 shows the dependence of reflectance parameter ΔR (R₂₈₀ - R₄₀₀) on the growth temperature. Again, an optimum growth temperature in the range of 930°-960°C was obtained. The best quality Si/YSZ films produced in

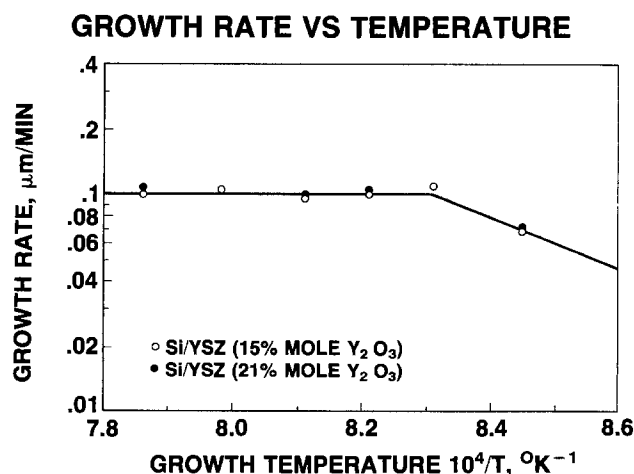


Fig. 2. Dependence of Si growth rate on substrate temperature for Si/YSZ films.

ULTRA-VIOLET REFLECTIVITY,
R (280 nm), OF 0.4 – 0.5 μm
(100) Si/(Y₂O₃)_{0.15}(ZrO₂)_{0.85} FILMS

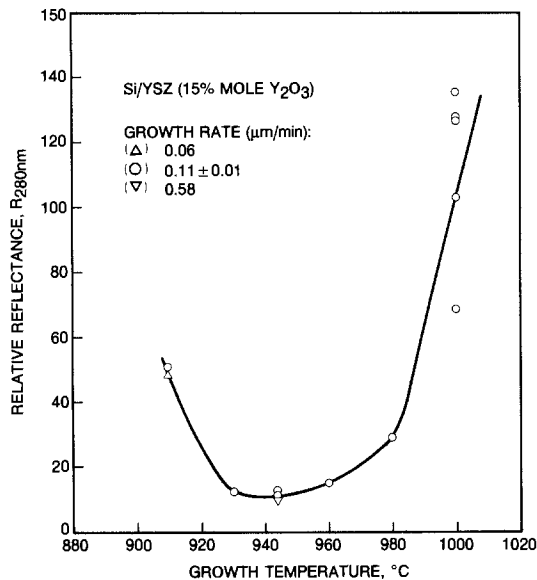


Fig. 3. Growth temperature dependence of ultraviolet reflectance (in arbitrary units) at $\lambda = 280 \text{ nm}$, R_{280} , measured with an RCA instrument on 0.4-0.5 μm thick Si/(Y₂O₃)_{0.15}(ZrO₂)_{0.85} films.

this study had values of ΔR close to -10 , as compared to 0-10 for standard commercial SOS films.

At growth temperatures from 930° to 1000°C, both Fig. 3 and 4, as well as Fig. 7 and 8 in the following sections, show that the surface quality of Si/YSZ films decreases with increasing substrate temperature. As discussed in the last section, the growth of Si/YSZ films in this temperature region is limited by the gas-phase diffusion of reactants towards the growing surface. It suggests that the majority of the defects in Si/YSZ films grown at this

ULTRA-VIOLET REFLECTIVITY,
 $\Delta R = R(280 \text{ nm}) - R(400 \text{ nm})$, OF 0.4 – 0.5 μm
(100) Si/(Y₂O₃)_{0.15}(ZrO₂)_{0.85} FILMS

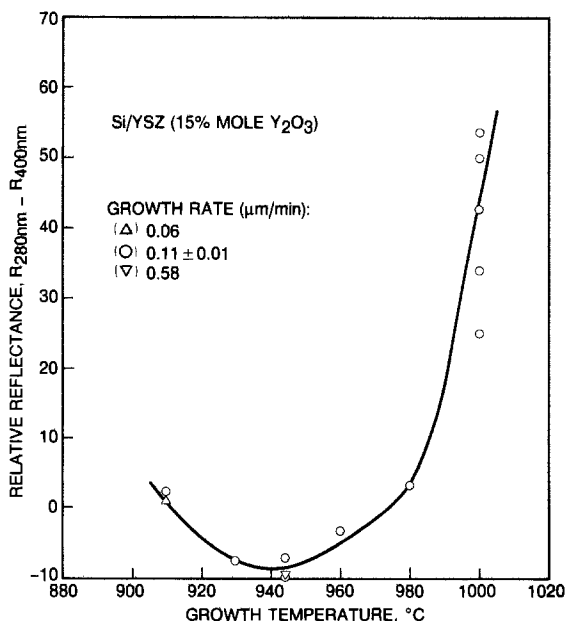


Fig. 4. Growth temperature dependence of reflectance parameter ΔR ($= R_{280} - R_{400}$) measured on the same Si/YSZ films as shown in Fig. 1.

temperature region are generated during cooling from growth temperature to room temperature, and are due to the differences in thermal expansion coefficients of Si and YSZ. In this temperature region, surface reactions, such as adsorption and desorption of gas species, surface diffusion, and incorporation of Si adatoms into the lattice, are relatively fast. The as-deposited Si films at growth temperature must have relatively good quality. As they cool from growth temperature to room temperature, those films grown at high temperature suffer larger thermal compression force, and thus result in larger defect formation.

The surface quality of Si/YSZ films grown below 930°C decreases with decreasing temperature. As discussed earlier, in this temperature region, growth of Si/YSZ films is limited by surface reaction. This suggests that increasing number of defects in Si/YSZ films grown in this temperature region is formed during deposition. As growth temperature is lowered, surface reaction of atoms decreases, leading to an increase in defect formation.

Rutherford backscattering/channeling.—Quantitative depth profiles of the crystalline perfection of selected Si/YSZ films were measured by RBS/C, using 1.5 MeV ⁴He⁺ ions, with a variable scattering-angle detection system. The Si films were first aligned and measured in the glancing exit mode (scattering angle $\theta = 95^\circ$ - 108°). This geometry enabled the top half of submicron-thick Si/YSZ films to be measured without the high intensity, interfering background from the heavy elements Y and Zr in the substrate, and with high depth resolution (15, 18). Figure 5 (curve Si/YSZ) illustrates the result of energy spectra of 1.5 MeV ⁴He⁺ ions, backscattered at 102.5° from a 0.45 μm thick, epitaxial (100) Si/YSZ films grown at 960°C and 0.09 $\mu\text{m}/\text{min}$. After the low scattering angle measurement, the surface-barrier detector was positioned at a larger scattering angle ($\theta = 150^\circ$ - 168°), and the channeling spectra were remeasured without the need to realign the sample with the ⁴He⁺ analyzing beam. This latter geometry provided useful information on the crystal quality of the Si films throughout their thickness, and especially near the Si/YSZ interface. Figure 6 illustrates the energy spectra of 1.5 MeV ⁴He⁺ ions, backscattered at 150° from the same Si/YSZ sample shown in Fig. 5. The concentration of the dechanneling defects present in the Si/YSZ films increased rapidly with depth, and was highest at the Si/YSZ interface, similar to the one found in SOS films.

The effect of growth temperature on surface channeling yield, χ_0 , of Si/YSZ films is shown in Fig. 7. Although four Si/YSZ samples were selected for characterization by the Rutherford backscattering channeling technique, the data shown in Fig. 7 confirm the results taken by the UVR technique shown in Fig. 3 and 4. The χ_0 vs. growth temperature curve can be characterized into two regions. At the lower growth temperature region, the surface quality of Si/YSZ films increases with increasing growth temperature. It then decreases with increasing temperature at high growth temperature. The optimum growth temperature found in Fig. 7 is roughly in the range of 940°-960°C. In this investigation, we have obtained Si/YSZ films in the 0.4-0.45 μm thickness range, with a value of χ_0 equal to 0.048, as compared to 0.1 and 0.12 for Si/YSZ films reported previously (6, 7) and for typical commercial SOS films, respectively.

Figure 5 compares the energy spectra of 1.5 MeV ⁴He⁺ ions, backscattered at 102.5° from a 0.45 μm thick, (100) Si/YSZ film grown at 960°C, a state-of-the-art, commercial (100) SOS film of similar thickness, and a (100) bulk Si. This particular Si/YSZ film was the highest quality (100)-oriented film of this thickness characterized by RBS/C under this program. A number of other (100) Si/YSZ films had similar crystal quality. The SOS sample selected for comparison was the best in this thickness range that we have measured out of a large number of commercial wafers, grown under various conditions in the last 5 yr. Surface channeling yields, χ_0 , and average

NEAR-SURFACE CRYSTALLINE QUALITY OF 0.45 μm Si/YSZ, SOS, AND BULK Si

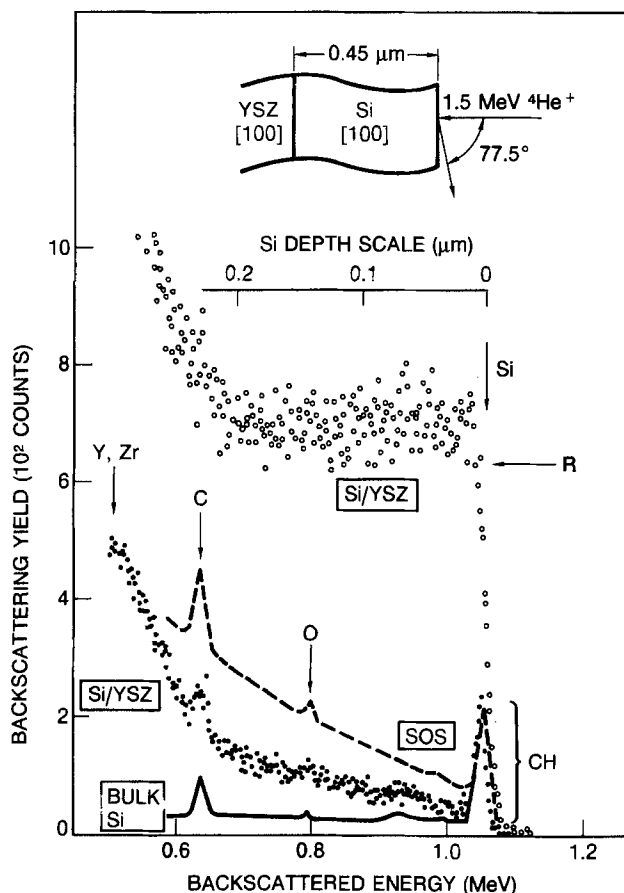


Fig. 5. Energy spectra of 1.5 MeV $^4\text{He}^+$ ions, backscattered at 102.5° from (top) a $0.45 \mu\text{m}$ thick, epitaxial (100) Si/(100) $(\text{Y}_2\text{O}_3)_{0.15}(\text{ZrO}_2)_{0.85}$ film grown at 960°C and $0.09 \mu\text{m}/\text{min}$, (middle) a state-of-the-art, commercial (100) Si/(0112) Al_2O_3 film of similar thickness, and (bottom) a (100), bulk Si single crystal. The small oxygen signal, marked O, is due to the native Si surface oxide; the carbon signal, marked C, is due to a slight contamination by the analyzing beam, and neither of these surface layers results in any measurable dechanneling. See Table I for χ_0 and $d\chi/dz$ values.

dechanneling rates, $d\chi/dz$, calculated for the samples shown in Fig. 5 are summarized in Table I. It is clear that the surface and near-surface crystal quality of the (100) Si/YSZ films grown in our laboratories are far superior to that of state-of-the-art, commercial CVD (100) SOS films of similar thickness. In fact, it is very close to that found in defect-free, (100) bulk Si, although this does not imply that no defects, such as dislocations, are present at the surface of the Si/YSZ films. For both Si/YSZ films and SOS films, the concentration of the dechanneling defects increases rapidly with depth, and is highest at the Si/insulator interface.

Conductivity and Hall mobility.—The undoped Si/YSZ films grown in this study were n-type, high resistivity

Table I. Surface channeling yields, χ_0 , and average dechanneling rates, $d\chi/dz$, for the best quality $0.45 \mu\text{m}$ thick (100) Si/(100) $(\text{Y}_2\text{O}_3)_{0.15}(\text{ZrO}_2)_{0.85}$ film, a commercial state-of-the-art CVD (100) Si/(0112) Al_2O_3 film of similar thickness, and bulk, defect-free (100) Si, measured with 1.5 MeV $^4\text{He}^+$ ions

Sample	χ_0	$d\chi/dz$ (μm^{-1})	
		0-0.2 μm	0-0.45 μm
Si/YSZ	0.048	0.7	1.1
SOS	0.12	1.1	1.3
Bulk Si	0.034	0.062	0.062

EPITAXIAL Si ON $(\text{Y}_2\text{O}_3)_{0.15}(\text{ZrO}_2)_{0.85}$

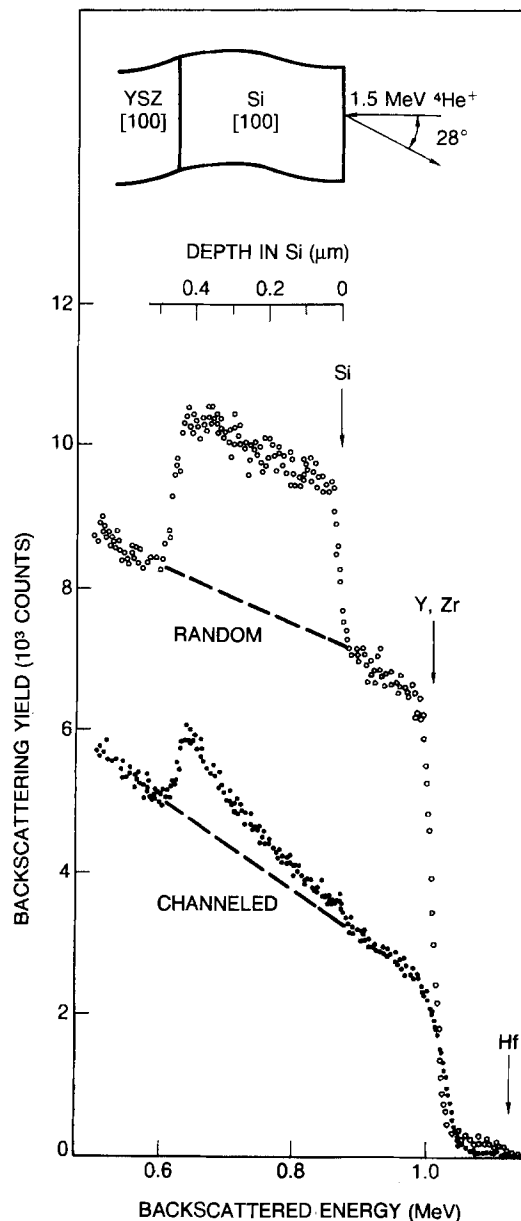


Fig. 6. Energy spectra of 1.5 MeV $^4\text{He}^+$ ions, backscattered at 150° from the same (100) Si/(100) $(\text{Y}_2\text{O}_3)_{0.15}(\text{ZrO}_2)_{0.85}$ sample as shown in Fig. 3. The dashed lines indicate the background, due to Y and Zr in the YSZ substrate, which must be subtracted in order to calculate the channeling yield in the Si film. See Table I for χ_0 and $d\chi/dz$ values.

material. The resistivity of Si/YSZ films increased with time after being exposed to ambient air. This increase in resistivity from air exposure was reduced after Si films were dipped into 10% HF solution. For the sake of comparison among Si/YSZ films grown at different temperatures, a Hall-effect measurement was made on the Hall bar sample right after it was dipped into 10% HF solution for 10 min. The Hall factor was assumed to be unity for data reduction. The average free electron concentrations of Si/YSZ films measured were found to be 2×10^{14} – 3×10^{15} carrier/cm 3 . The unintentional background doping level in our reactor was close to 3×10^{15} carrier/cm 3 (n-type). The effect of growth temperature on electron Hall mobility of Si/YSZ films is shown in Fig. 8. As growth temperature increases from 910° to 1000°C , electron Hall mobility increases first and then decreases at higher temperature. Again, an optimum growth temperature of 930° – 960°C is obtained, which is similar to that found either by UVR technique or by RBS/C technique.

Electron Hall mobility in undoped Si/YSZ films 0.4 – $0.5 \mu\text{m}$ thick grown at optimum temperature of 930° – 960°C

SURFACE CHANNELING YIELD, χ_0 , AT 1.5 MeV $^4\text{He}^+$, IN SOME OF THE 0.4 - 0.5 μm Si/YSZ FILMS MEASURED BY UVR

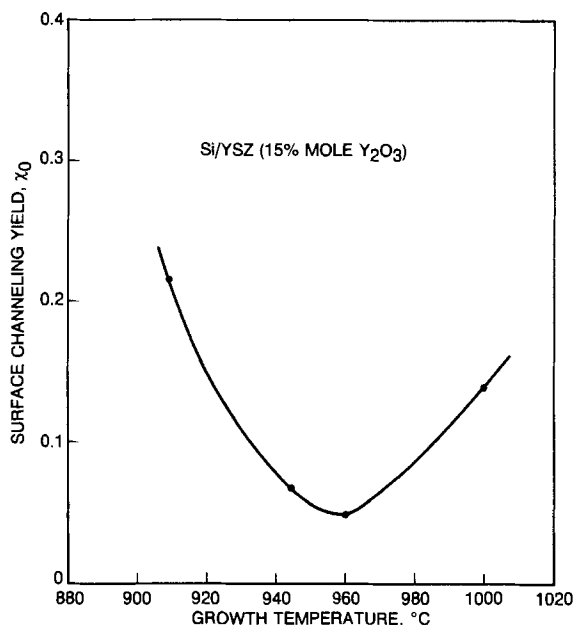


Fig. 7. Growth temperature dependence of Si surface channeling yield, χ_0 , measured at 1.5 MeV $^4\text{He}^+$ energy on Si/YSZ films.

were in the range of 200-270 $\text{cm}^2/\text{V}\cdot\text{s}$. These values are about 25% lower than those measured in n-type intentionally doped, CVD SOS films of similar thickness and carrier concentration. There are two possible reasons for this effect. First, at a doping level of $3 \times 10^{15} \text{ cm}^{-3}$ or lower in Si films, considerable surface depletion can occur (19). The current, during Hall effect measurement, is only flowing in the lower portion of Si films, which is close to the Si/YSZ interface. Results of RBS/C showed that, although both surface channeling yield, χ_0 , and average dechanneling rate, $d\chi/dz$, of Si/YSZ films are lower than that of state-of-the-art, commercial, CVD SOS films, opposite results are obtained in the lower portion of Si film near the Si/substrate interface. This suggests that the defect density is probably higher at the interface between Si and YSZ than at the interface between Si and Al_2O_3 . This could lead to a lower carrier mobility in Si/YSZ films when current flows only near Si/YSZ interface. For VLSI applications, using enhancement-mode MOSFET, the speed of the devices is determined only by the surface mobility. The lower mobility found in Si/YSZ films near the substrate area should not inhibit the use of Si/YSZ films for VLSI applications.

Another possible explanation for the lower electron mobility is the high in-plane compressive strain found in Si/YSZ films. Results of double-crystal x-ray diffractometry measurements showed that, at a thickness of $\approx 0.4 \mu\text{m}$, Si/YSZ films had a $\approx 32\%$ higher compressive strain than SOS films (6, 7, 20). This is due to the difference in thermal expansion coefficients between Si film and the substrate, which is higher for Si/YSZ than for Si/sapphire. In SOS films, because of the compressive strain, the electron Hall mobility is 30-40% lower than the drift mobility (21-23). The higher compressive strain in Si/YSZ films could lead to a lower electron Hall mobility, but does not necessarily mean that the drift mobility is lower too.

Conclusion

Epitaxial (100) Si films 0.4-0.5 μm thick were grown by the pyrolysis of silane in a hydrogen atmosphere on (100) YSZ (15% Y_2O_3) at temperatures in the range of 910°-1000°C and deposition rate of 0.06-0.58 $\mu\text{m}/\text{min}$. From 930° to 1000°C, growth rate is found to be limited by gas-phase

DEPTH - AVERAGED HALL MOBILITY IN SOME OF THE 0.4 - 0.5 μm Si/YSZ FILMS MEASURED BY UVR

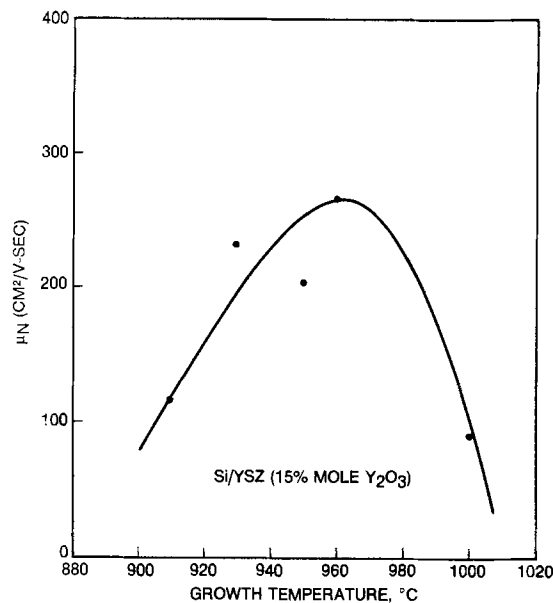


Fig. 8. Effect of growth temperature on electron Hall mobility of 0.4-0.5 μm thick, (100) Si/YSZ (15 m/o Y_2O_3) films.

diffusion of reactants. Below 930°C, the growth rate becomes surface reaction limited. The heteroepitaxial Si films have been characterized by UV reflectance, Rutherford backscattering/channeling, and Hall effect measurements.

Results of UV reflectance showed that by varying the growth temperature from 910° to 1000°C, the surface quality of Si films starts to improve, reaches the highest degree at an optimum growth temperature in the range of 930°-960°C, and then deteriorates at higher temperature. The best quality Si/YSZ films produced in our laboratory so far have values of ΔR close to -10.

Quantitative depth profiles of the crystalline perfection of Si/YSZ films were measured by Rutherford backscattering and channeling using 1.5 MeV $^4\text{He}^+$. Characteristic surface channeling yield, χ_0 , vs. growth temperature curves also indicate an optimum growth temperature ranging between 940° and 960°C. In this investigation, we have obtained Si/YSZ films with value of χ_0 equal to 0.048, as compared to 0.1 and 0.12 for Si/YSZ films reported previously and for typical commercial SOS films, respectively.

Si/YSZ films grown at different temperatures are all n-type and have high resistivity as measured by the Hall effect technique. Mobility measured on Si/YSZ films grown at temperatures between 930° and 960°C is found to be higher than those grown at either higher or lower temperatures.

The optimum growth temperature found around 930°-960°C is the result of two possible defect generation mechanisms: formation of defects (i) at growth temperature and (ii) during cooling of Si films after growth, which results from the difference in thermal expansion coefficient of Si and of YSZ substrates.

Acknowledgments

The authors are grateful to Dr. H. M. Manasevit for his significant technical assistance and many stimulating discussions. We also wish to thank A. Crouse for slicing the YSZ boules, D. Medellin for polishing, R. E. Johnson for SEM characterizations, Dr. H. L. Glass for x-ray measurements, and Dr. J. E. Mee for support. This research was funded by the Materials Laboratory, Electromagnetic Materials Division, AFWAL, Wright-Patterson Air Force

Base, Ohio 45433, under Contract no. F33615-81-C-5041
J. O. Crist and M. C. Ohmer).

Manuscript submitted June 15, 1984; revised manuscript received Aug. 13, 1984.

Rockwell International Science Center assisted in meeting the publication costs of this article.

REFERENCES

- H. M. Manasevit and W. I. Simpson, *J. Appl. Phys.*, **35**, 1349 (1964).
- Suggested to us by M. C. Ohmer and J. O. Crist, Electromagnetic Materials Division, Materials Laboratory, Wright-Patterson AFB, Ohio 45433.
- I. Golecki and I. Suni, in "Materials Research Society Symposia Proceedings," Vol. 14, S. Mahajan and J. W. Corbett, Editors, p. 541, North Holland, New York (1983).
- A. A. Lebedev, N. A. Sultanov, and P. Yusupov, *Sov. Phys. Semicond.*, **14**, 342 (1980).
- D. J. Dumin and P. H. Robinson, *This Journal*, **113**, 469 (1966).
- I. Golecki, H. M. Manasevit, L. A. Moudy, J. J. Yang, and J. E. Mee, *Appl. Phys. Lett.*, **42**, 501 (1983).
- H. M. Manasevit, I. Golecki, L. A. Moudy, J. J. Yang, and J. E. Mee, *This Journal*, **130**, 1752 (1983).
- T. H. Nielsen and M. H. Leipold, *J. Am. Ceram. Soc.*, **47**, 155 (1964).
- V. A. Osipova and V. A. Andrianova, *Tr. Mosk. Energ. Inst.*, **133**, 24 (1976).
- Y. S. Touloukian, "Thermophysical Properties of High-Temperature Solid Materials," Vol. 4, MacMillan, New York (1967).
- V. I. Aleksandrov, V. V. Osiko, A. M. Prokhorov, and V. M. Tatarintsev, in "Current Topics in Materials Science," Vol. 1, E. Kaldis, Editor, p. 421, North Holland, Amsterdam (1978).
- See, for example, B. D. Cullity, "Elements of X-Ray Diffraction," Addison-Wesley, Reading, MA (1956).
- W. I. Simpson, Unpublished data.
- M. T. Duffy, J. F. Corboy, G. W. Cullen, R. T. Smith, R. A. Soltis, G. Harbecke, J. R. Sandercock, and M. Blumenfeld, *J. Cryst. Growth*, **58**, 10 (1982).
- J. S. Williams, *Nucl. Instr. Meth.*, **126**, 205 (1975); J. S. Williams and W. Moller, *ibid.*, **157**, 213 (1978).
- B. A. Joyce and R. R. Bradley, *This Journal*, **110**, 1235 (1963).
- Jan Bloem, *Acta Electron.*, **21**, 3 (1978).
- I. Golecki, *Nucl. Instr. Meth. Phys. Res.*, **218**, 63 (1983).
- W. E. Ham, *Appl. Phys. Lett.*, **21**, 440 (1972).
- I. Golecki, "Alternate Substrate Materials: Si on Yttria-stabilized Cubic Zirconia (Si/YSZ)," Final Technical Report no. AFWAL-TR-83-4137 (1984).
- S. Onga, K. Hatanaka, K. Shinji, and Y. Yasuda, *Jpn. J. Appl. Phys.*, **17**, 413 (1978).
- J. H. Lee, S. Cristoloveanu, and A. Chovet, *Solid State Electron.*, **25**, 947 (1982).
- A. L. Lin, R. L. Maddox, and J. E. Mee, *Microelectron. J.*, **14**, 22 (1983).

Oxidation of Nickel Sulfides in Oxygen at 700°C

G. M. Mehrotra,* V. B. Tare, and J. B. Wagner, Jr.*

Center for Solid State Science, and Departments of Chemistry, Mechanical, and Aerospace Engineering and Physics, Arizona State University, Tempe, Arizona 85287

ABSTRACT

The kinetics of oxidation of $\text{Ni}_{3\pm r}\text{S}_2$ containing ~38, 39, 40, 41.4, and 42 atom percent (a/o) S and NiS were studied at $700^\circ \pm 5^\circ\text{C}$ in oxygen at 1 atm. The oxidation of $\text{Ni}_{3\pm r}\text{S}_2$ was strongly dependent on its composition. All compositions showed an initial increase followed by a slow decrease in weight. For compositions with 41.4 and 42 a/o S, however, the initial increase in weight was extremely small. Oxidation products of all the compositions were identified by x-ray diffraction as NiO. Oxidation of NiS showed a sharp initial decrease, followed by a slow increase in weight. The oxidation products were identified as Ni_3S_2 and NiO only. The morphology of the oxidized samples was studied using SEM. EDAX was used to identify phases. The possible mechanisms of oxidation are discussed.

Available literature on the phase diagram (1) of the nickel-sulfur system indicates that nickel forms three stable sulfides at 700°C , viz., NiS_2 , NiS, and Ni_3S_2 . Whereas NiS_2 is almost stoichiometric, NiS and Ni_3S_2 are known to deviate from stoichiometric composition to an appreciable extent. The composition of NiS has been reported to vary from NiS to $\text{NiS}_{1.06}$, while that of $\text{Ni}_{3\pm r}\text{S}_2$ from $\text{Ni}_{2.54}\text{S}_2$ to $\text{Ni}_{3.40}\text{S}_2$ in the temperature range $600^\circ\text{--}800^\circ\text{C}$ (1).

The Ni_3S_2 phase is often found as an intermediate corrosion product when nickel is oxidized in sulfur containing gaseous atmosphere (2). High corrosion rates in such atmospheres have been attributed to the presence of this sulfide. Oxidation rates of pure nickel sulfides were, however, not reported in the literature until after completion of the present study. Recently, one paper on this subject has been published by Asaki *et al.* (4). In the present paper, we report results of our studies on the kinetics of oxidation of $\text{Ni}_{3\pm r}\text{S}_2$ in pure oxygen at 700°C as a function of its composition. The oxidation of NiS has also been investigated under similar conditions.

Experimental

Five compositions of $\text{Ni}_{3\pm r}\text{S}_2$ containing ~38, 39, 40, 41.4, and 42 atom percent (a/o) sulfur were prepared from mixtures containing appropriate proportions of powders

of spectroscopic grade nickel, purchased from Johnson-Matthey, and 99.99% pure NiS, purchased from Ventron. These mixtures were sealed in evacuated quartz tubes and then heated at $\sim 700^\circ\text{C}$ for about three days and subsequently near ($\sim 20^\circ$ below) the melting point of the resulting composition for about 12-15h. The capsules were then air quenched to room temperature. The product was ground to a fine powder (~ 325 mesh) and characterized by x-ray diffraction. No phases other than $\text{Ni}_{3\pm r}\text{S}_2$ were detected. The sulfur content of the prepared compounds was confirmed, within ± 0.2 a/o, by hydrogen reduction. Cylindrical pellets of ~ 10 mm diam and 5 mm height were pressed from these powders in a steel die, sintered in evacuated, sealed quartz tubes at $\sim 750^\circ\text{C}$ for three days, and then air quenched to room temperature. The surfaces of these pellets were polished on 4/0 emery paper. Their apparent densities were determined from their dimensions and weights. The total porosity of the sintered pellets varied from $\sim 15\%$ to 25% .

NiS pellets were pressed from as-purchased NiS powder and sintered in evacuated, sealed quartz tubes at $\sim 900^\circ\text{C}$ for 60h. The porosity of these pellets was $\sim 25\text{--}30\%$. The sulfur content of NiS as determined by hydrogen reduction indicated the composition of NiS to be $\text{NiS}_{1.09}$.

Oxidation of $\text{Ni}_{3\pm r}\text{S}_2$ and NiS pellets was carried out in a flowing stream of oxygen (linear flow rate ~ 50 cm/min)

* Electrochemical Society Active Member.

at $700^\circ \pm 5^\circ\text{C}$. Prior to the beginning of oxidation, the $\text{Ni}_{3-x}\text{S}_2$ pellets were annealed at 700°C for at least 1h in a flowing stream of argon (oxygen content ~ 20 ppm) for homogenization. A small weight change (fractional weight change ~ 0.0005 - 0.003) was observed during this period. The kinetics of oxidation were followed by a 1000 Cahn electrobalance thermogravimetric setup. A chart recorder, connected to the electrobalance, continuously recorded the weight changes. These were replotted as the fractional weight changes calculated from the observed changes in weight and the initial weight of the sample. The weight changes observed during the annealing period were included in calculations. The time at which the argon gas flow was terminated and oxygen was started was taken as the starting time ($t = 0$).

Results

Figure 1 shows typical results from oxidation runs on $\text{Ni}_{3-x}\text{S}_2$ of five compositions. All the compositions showed an initial increase in weight, followed by a decrease in weight.

For compositions containing 41.4 and 42 a/o S, the initial increase was extremely small. For the 40.0 a/o S composition, the weight increased slowly for almost 6h, followed by a slow continuous decrease. The sample with 39 a/o S increased in weight within first hour after which the weight remained constant for several hours (~ 24 h). The samples with 38 a/o S showed an initial sharp increase in weight within the first half-hour, followed by an almost linear decrease in weight. Significant initial increase in weight is thus observed for compositions containing 38, 39, and 40 a/o sulfur. The rate of increase, however, decreased with increasing sulfur percentage. The rate of oxidation for composition containing 39 a/o S became negligibly small after 1h.

X-ray powder diffraction patterns of samples after the oxidation runs indicated the presence of NiO and Ni_3S_2 phases only. The pellets were also examined under SEM and analyzed by EDAX for morphological details and phase identification.

Figure 2(A) shows the surface of an oxidized sample of nickel sulfide containing 42 a/o S. The surface appears to be very nonuniform. A line scan for Ni and S across the surface of the sample shows the presence of discontinuous layer of NiO along with unoxidized or partially oxidized porous nickel sulfide. The cross-sectional view of an almost completely oxidized sample is shown in Fig. 2(B). A line scan across this sample shows a sudden drop

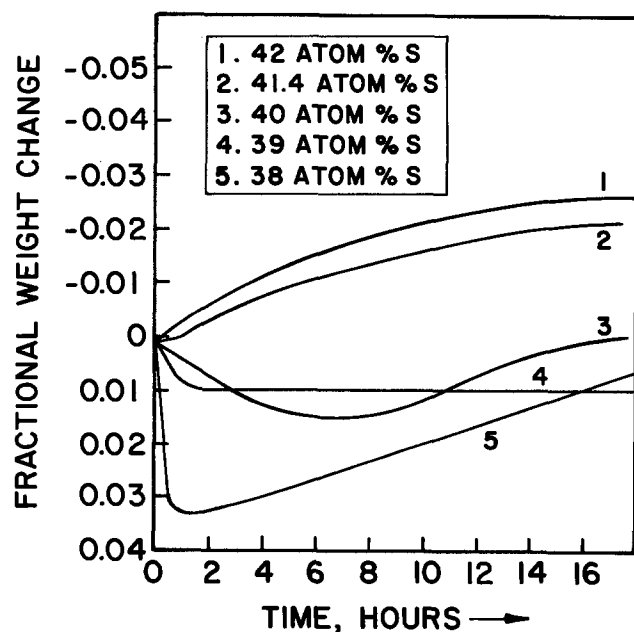


Fig. 1. Oxidation of Ni_3S_2 in oxygen at 700°C for various compositions.

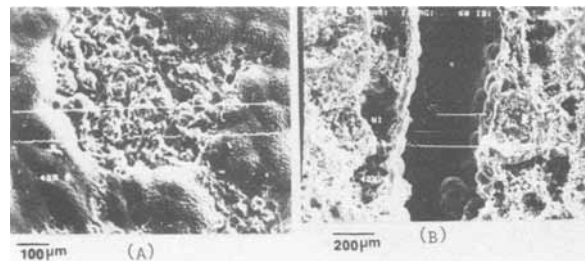


Fig. 2. SEM picture of nickel sulfide containing 42 a/o S. (A): Oxidized surface. (B): Cross section of the oxidized specimen.

in nickel concentration and absence of sulfur throughout the specimen, suggesting the presence of a cavity almost at the center of the pellet.

Figure 3(A) shows the cross section of an oxidized specimen containing 40 a/o S. A line scan for Ni and S across this is shown in Fig. 3(B). Two distinct regions identified as NiO and Ni_3S_2 are clearly seen in Fig. 3(A). The presence of occasional cracks in the NiO layer formed during oxidation is seen in Fig. 3(C).

Two distinct regions with nickel oxide at the surface and Ni_3S_2 underneath are also clearly identifiable in the cross-sectional view of the oxidized sample containing 39 a/o S [Fig. 4(A)]. The oxidized surface shown in Fig. 4(B) appears to be uniform and free from cracks.

A large number of cracks are found in the oxidized surface of samples with 38 a/o S [Fig. 5(C)]. Highly oxidized samples show the presence of isolated particles [Fig. 5(A)] identified by the line scan of nickel and sulfur [Fig. 5(B)] as nickel sulfide surrounded by nickel oxide.

Figure 6 shows the change in weight of NiS as a function of time during its oxidation in pure oxygen at 700°C . There is a very rapid, almost linear decrease in weight for the first 10 min, after which the weight slowly increases at a rate which decreases rapidly with time. The x-ray examination of the samples oxidized for 18h showed the presence of Ni_3S_2 and NiO phases only. The composition of Ni_3S_2 formed was not determined.

Discussion

The reaction of $\text{Ni}_{3-x}\text{S}_2$ with oxygen can be represented by the following equations

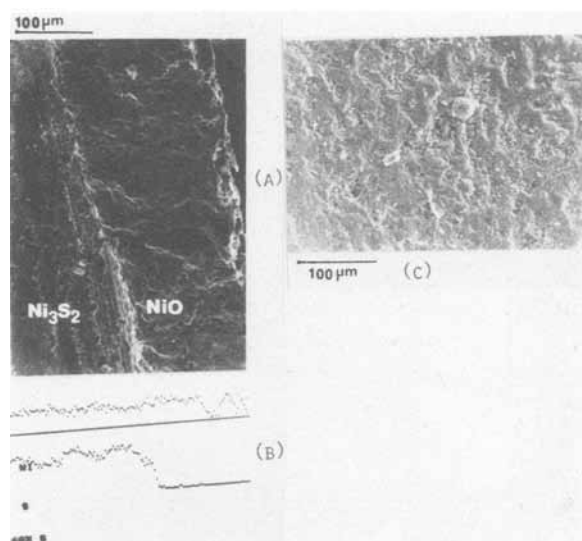
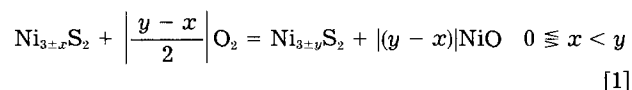


Fig. 3. SEM picture of nickel sulfide containing 40 a/o S. (A): Cross section of an oxidized specimen. (B): Line scan across the specimen. (C): Surface of an oxidized specimen.

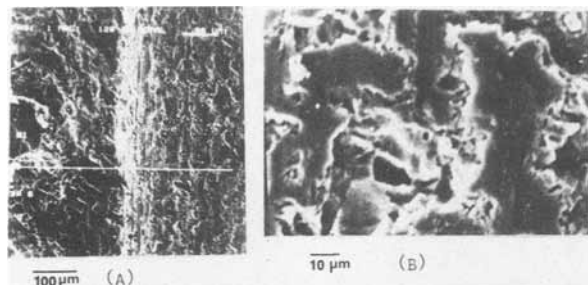


Fig. 4. SEM picture of nickel sulfide containing 39 a/o S. (A): Cross section of the oxidized specimen. (B): Surface of the oxidized specimen.

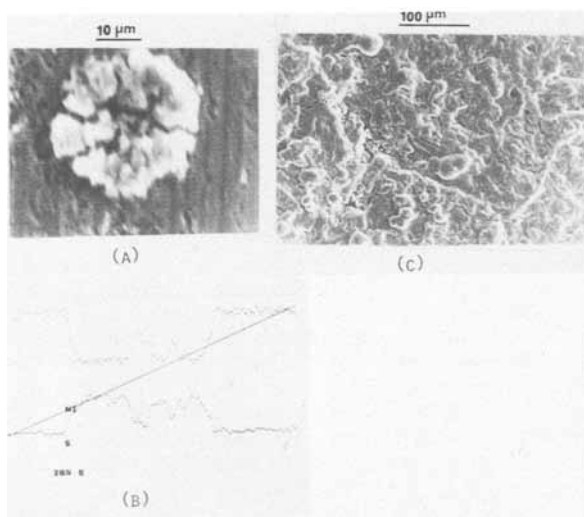
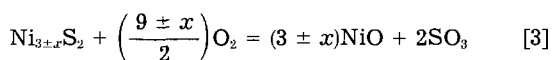
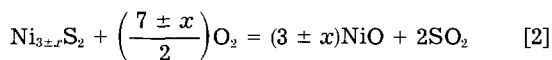


Fig. 5. SEM picture of nickel sulfide containing 38 a/o S. (A): Unoxidized Ni_3S_2 particle in the interior of the specimen. (B): Line scan across the above specimen. (C): Surface of the oxidized specimen.



Reaction [1] is characterized by the increase in weight of the sample due to oxidation without evolution of SO_2 , whereas reactions [2] and [3] are associated with the decrease in weight because of evolution of SO_2 and/or SO_3 as one of the reaction products. The initial weight increase observed during oxidation of $\text{Ni}_{3 \pm x}\text{S}_2$ is thus suggested to be due to the formation of NiO and simultaneous change in the stoichiometry of $\text{Ni}_{3 \pm x}\text{S}_2$, in accordance

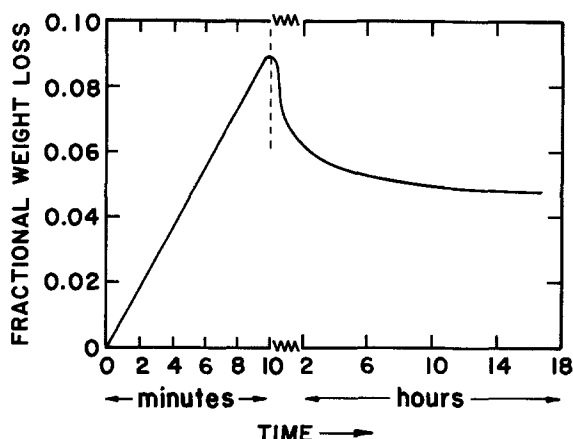


Fig. 6. Oxidation of NiS in oxygen at 700°C

with reaction [1]. This is followed by reaction [2] and/or [3], resulting in subsequent weight loss.

In the present studies, negligibly small increase in weight during the initial stages of oxidation of nickel sulfide containing 42 a/o sulfur indicates that this is probably close to the limiting composition which favors the formation of NiO directly by reaction [2] and/or [3]. Any composition of nickel sulfide which contains nickel in excess of this limiting composition would result in a weight gain owing to the oxidation of excess nickel to NiO. The fractional weight increase calculated assuming that all the excess nickel oxidizes to form NiO is shown in Table I along with experimentally observed fractional weight increase. The agreement between the calculated and experimentally observed values, except for the starting composition of 39 a/o sulfur, is extremely good.

It is interesting to note that similar results were obtained by Asaki *et al.*, who studied the oxidation of dense pellets of FeS (3) at 750°-850°C and $p_{\text{O}_2} \sim 0.01$ -0.2 atm, and of nickel sulfide ($X_s = 0.4$ -0.44) (4) at 650°-750°C and $p_{\text{O}_2} \sim 0.2$ atm. They analyzed the exit gases formed during oxidation by infrared gas analysis and found that during oxidation of stoichiometric FeS, a very small amount of SO_2 was evolved in the initial 5s, and then it stopped for several hours afterward. The initial weight increase was explained by them to be due to the formation of Fe_3O_4 with the simultaneous change in the stoichiometry of FeS. In the case of oxidation of nickel sulfide, their results show that there is a weight increase in the initial stages of oxidation and that the progress of oxidation is dependent on the composition of nickel sulfide and temperature of oxidation. They found that, in the oxidation runs in which an increase in weight occurred, a very small amount of SO_2 was evolved during the initial 30s, and the evolution was even less during the subsequent period of weight increase. This shows that during the initial stages of oxidation with a weight increase, the rate of oxidation due to reaction [2] and/or [3] is negligible. No increase in the weight of the sample containing 44 a/o sulfur was observed by them during its oxidation at 700°C. The results of Asaki *et al.* are thus qualitatively in agreement with our results.

During the initial stages, the rate at which nickel oxide is formed is expected to be higher on compositions containing higher concentrations of nickel because of the larger concentration gradients. The subsequent reaction rate will, however, depend upon the morphology of the nickel oxide formed. It is interesting to note that, except for the composition containing 39 a/o S, the rate of weight loss after the initial weight gain is approximately the same. This is consistent with the view that, irrespective of the starting composition, the compositions at the start of reaction [2] and/or [3] above are approximately the same.

Almost complete protection offered by the formation of NiO on composition containing 39 a/o S may be attributed to the slow formation and hence a compact layer of NiO. In the case of nickel sulfide containing 38 a/o S, the rate of formation of NiO is relatively high and hence the resultant NiO layer is full of cracks as observed experimentally. However, the large number of cracks observed in NiO formed on compositions containing 40, 41.4, and 42 a/o S are possibly due to the simultaneous occurrence of reactions [1], [2], and/or [3] above, leading to the formation of SO_2 .

Table I. Calculated and experimentally observed fractional weight increase during the initial stages of oxidation of various Ni_3S_2 compositions

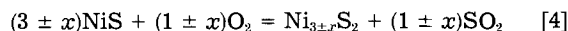
Initial a/o S in Ni_3S_2	Fractional weight calculated	Increase experimental
42	0.000	~0.000
41.4	0.007	0.005
40	0.015	0.015
39	0.023	0.010
38	0.031	0.030

Asaki *et al.* (3, 4) suggested that, during initial stages of oxidation of FeS or Ni₃S₂, diffusion through sulfide may control the overall rate of oxidation. Yagi and Wagner (5) studied the chemical diffusivity in Ni_{3±x}S₂ as a function of composition and showed that, although there is a small compositional dependence of diffusivity, the diffusivity values for all the compositions are very high. The concentration gradients in Ni₃S₂ throughout its oxidation may, therefore, be regarded as negligibly small.

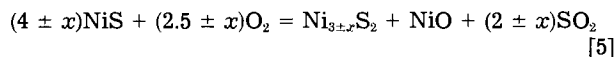
The oxidation reaction leading to the formation of SO₂ and NiO may take place either at NiO/O₂ interface or at Ni₃S₂/NiO interface. The former requires transport of nickel and sulfur through a compact NiO layer. This is extremely slow and may be the cause of the observed negligibly small rates of oxidation of nickel sulfide containing 39 a/o S. For all the other compositions, because of the presence of cracks in the nickel oxide layer formed, oxygen can migrate through the cracks and react with nickel sulfide at the NiO/Ni₃S₂ interface forming fresh NiO and SO₂, which is again carried away by the diffusion through cracks in NiO. The rate is thus governed by either the diffusion of O₂ or of SO₂ through cracks in NiO. It is surprising, however that even after 16h of oxidation only 25% of the reaction is complete. The rate after this period becomes extremely slow. This suggests that the number and/or size of cracks present in NiO are likely to be very small.

Unlike Ni₃S₂, the oxidation of NiS at 700°C in oxygen exhibits a very fast initial weight loss within the first 10 min, followed by a weight gain, the rate of which becomes so small that the oxide formed offers virtual protection against further oxidation. X-ray and EDAX indicated the presence of NiO and Ni₃S₂ phases only.

The initial oxidation of NiS may be represented by



or



Once the Ni_{3±x}S₂ is formed, subsequent oxidation takes place by the mechanisms discussed above. The subsequent slow rate of oxidation suggests that nickel sulfide with either 39 or 40 a/o S is probably formed as the intermediate oxidation product. However, from the observed fractional weight loss in the initial stage, it seems that nickel sulfide containing ~42.7 a/o sulfur is formed.

Acknowledgments

This research was supported by The Army Research Office under Contract no. DAAG29-81-K-0109 and a grant from the Center for Solid State Science.

Manuscript submitted March 26, 1984; revised manuscript received ca. Sept. 11, 1984. This was Paper 463 presented at the San Francisco, California, Meeting of the Society, May 8-13, 1983.

Arizona State University assisted in meeting the publication costs of this article.

REFERENCES

1. R. Y. Lin, D. C. Hu, and Y. A. Chang, *Metall. Trans.*, **9B**, 531 (1978).
2. K. L. Luthra and W. L. Worrell, *ibid.*, **9A**, 1055 (1978).
3. Z. Asaki, K. Matsumoto, T. Tanabe, and Y. Kondo, *ibid.*, **14B**, 109 (1983).
4. Z. Asaki, K. Hajika, T. Tanabe, and Y. Kondo, *ibid.*, **15B**, 127 (1984).
5. H. Yagi and J. B. Wagner, Jr., *Oxid. Met.*, **18**, 42 (1982).

The Standard Gibbs Energy of Formation of Ni_{3±x}S₂

G. M. Mehrotra,* V. B. Tare, and J. B. Wagner, Jr.*

Center for Solid State Science, Arizona State University, Tempe, Arizona 85287

ABSTRACT

The standard Gibbs energy of formation of Ni_{3±x}S₂ has been determined in the temperature range ~973-1173 K using galvanic cells of the configuration.

Pt, air/yttria-stabilized zirconia//NiO, Ni_{3±x}S₂, SO₂ (1 atm), Pt or Au

In the temperature range of the investigation, the open-circuit EMF of the cell, at any given temperature, was found to be independent of the starting composition of Ni_{3±x}S₂ within the experimental error limits. With the composition of Ni_{3±x}S₂ in equilibrium with NiO and SO₂ (1 atm) being Ni_{2.666}S₂, the results in calories per gram mole are

$$\Delta G^{\circ}_{\text{Ni}_{2.666}\text{S}_2}(\text{s}) = -68,670 + 27.257T \quad (973-1089 \text{ K})$$

$$\Delta G^{\circ}_{\text{Ni}_{2.666}\text{S}_2}(\text{l}) = -55,035 + 14.734T \quad (1089-1173 \text{ K})$$

The temperature and enthalpy of fusion of Ni_{2.666}S₂ are, therefore, 1089 K and 13,635 cal/mol, respectively. For the stoichiometric Ni₃S₂, we obtained

$$\Delta G^{\circ}_{\text{Ni}_3\text{S}_2}(\text{s}) = -74,740 + 31.007T \quad (973-1089)$$

$$\Delta G^{\circ}_{\text{Ni}_3\text{S}_2}(\text{l}) = -60,420 + 17.855T \quad (1089-1173)$$

The enthalpy of fusion of Ni₃S₂ is 14,320 cal/mol.

The thermodynamics of nickel sulfides has been the subject of several investigations. Rosenqvist (1) studied the NiS₂/H₂S/H₂ equilibria and reported thermodynamic data for solid Ni₃S₂, Ni₃S_{2±x}, Ni₇S₆, NiS_{1±x}, and NiS₂ compounds. Lin *et al.* have also studied the nickel-sulfur system, in the temperature range 823-1023 K, using a gas equilibration technique. More recently, Schaefer (3) has carried out electrochemical determination of the free energy of formation of solid Ni_{2.515}S₂ phase. Nagamori and Ingraham (4) have investigated the nickel-sulfur melts by

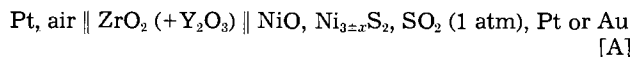
measuring the equilibrium weight of the melt in gas streams of H₂ and H₂S and have reported the standard Gibbs energy of formation of liquid Ni₃S₂ and liquid NiS. However, there appears to be no thermodynamic investigation over a wide temperature range covering both solid as well as liquid Ni_{3±x}S₂. Moreover, the data obtained by various investigators separately for solid and liquid Ni₃S₂ do not yield consistent values for temperature and enthalpy of fusion of Ni₃S₂. In the present work, the thermodynamics of solid and liquid Ni_{3±x}S₂ have been studied using solid electrolyte galvanic cells in the temperature range ~973-1173 K.

*Electrochemical Society Active Member.

Experimental Materials and Procedure

Four compositions of $Ni_{3\pm x}S_2$ containing 38, 40, 42, and 44 atom percent (a/o) sulfur were prepared from 99.999% pure nickel powder (Johnson-Matthey) and 99.99% pure NiS (Alfa/Ventron) or 99.999% pure sulfur. The mixtures, containing appropriate proportions of nickel and NiS powders, or of nickel and sulfur powders, were sealed in evacuated quartz tubes. The sealed ampules were held at ~ 970 K for ~ 72 h and subsequently at ~ 1020 - 1070 K for 24 h, after which they were air quenched. The product was then ground to a fine powder. The chemical compositions of the prepared compounds were verified by reducing them completely in hydrogen. These agreed within 0.3% of the expected sulfur content. Phase identification was done by x-ray diffraction.

Galvanic cells of the scheme



were used. One-end closed tubes of yttria-stabilized zirconia, ~ 7 mm id, purchased from Zirconium Corporation of America, served as the solid electrolyte. Moghadam and Stevenson (5) have reported that the conductivity of partially stabilized YSZ in a SO_2 atmosphere is greater than its conductivity in air and that its ionic transport number is decreased to 0.95-0.67 in the temperature range 773-1273 K by exposure to SO_2 . In separate experiments in our laboratory, we have measured the ac conductivity of 9 mole percent (m/o) yttria-stabilized zirconia in air and in flowing SO_2 (1 atm). In the temperature range 873-1273 K, no significant difference in the values of conductivity was observed for this composition of YSZ. This indicates that the electronic transport number of 9 m/o Y_2O_3 -ZrO₂ is negligible under our experimental conditions. This is in contrast to the results of Moghadam and Stevenson for yttria-stabilized zirconia containing 4.5 m/o Y_2O_3 .

In our experiments, SO_2 was passed over Drierite and P_2O_5 . Since, under our experimental conditions, the pressure of SO_3 in equilibrium with SO_2 and O_2 is negligible ($\sim 8 \times 10^{-7}$ - 3×10^{-6} atm), no correction for SO_3 has been applied and the pressure of SO_2 has been taken to be 1 atm. The open-circuit EMF of cells was measured in the temperature range ~ 973 - 1173 K using a Keithley high-impedance multimeter. The temperature of the cell was measured using a Pt-10%Rh/Pt thermocouple.

Results and Discussion

Figure 1 shows the open-circuit EMF as a function of temperature. The results shown are for cells with four different starting compositions of $Ni_{3\pm x}S_2$ and also with NiS. For each composition, the results were obtained from at least two cells. It can be seen that, irrespective of the starting composition of nickel sulfide, the values of EMF at any given temperature, in the range ~ 973 - 1173 K, are identical within the experimental error limits. This suggests that, at a given temperature, the composition of $Ni_{3\pm x}S_2$ in equilibrium with SO_2 (1 atm) and NiO is fixed and that any other $Ni_{3\pm x}S_2$ initial composition will convert

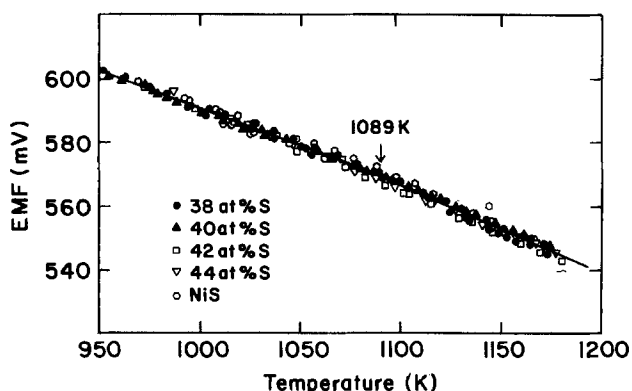


Fig. 1. Cell EMF as a function of temperature

to this composition. The value of EMF at any temperature remained steady for several hours and was reproducible within ± 1 mV during random heating and cooling of the cell, the measurements on which were carried out for a period of up to ten days, and within ± 2 mV between independent runs. However, in any run, when the cell was cooled from a temperature above the melting point of Ni_3S_2 to a temperature of ~ 1000 K or lower, the EMF values obtained were lower than the original values. The values of EMF at temperatures higher than 1000 K could be reproduced any number of times. The values of EMF at temperatures less than ~ 1000 K could be reproduced in heating and cooling cycles if the cell was not heated to a temperature above ~ 1073 K.

In order to determine the composition of $Ni_{3\pm x}S_2$ in equilibrium with SO_2 (1 atm) and NiO at various temperatures, two compositions of $Ni_{3\pm x}S_2$ containing 38 and 42 a/o sulfur were equilibrated, without NiO present, at ~ 973 , 1073, and 1173 K in a flowing stream of SO_2 . These were subsequently analyzed for sulfur using x-ray fluorescence and gravimetric chemical analysis. The results indicate that the average sulfur content of the $Ni_{3\pm x}S_2$ is ~ 42 a/o, although it must be mentioned that the accuracy of these methods for sulfur determination, in the presence of oxygen, was not optimum, the error limits being $\pm 2\%$ a/o sulfur. However, the fact that the EMF values fall on a straight line, in the temperature ranges 973-1089 K and 1089-1173 K, suggests that the variation in the composition of $Ni_{3\pm x}S_2$ with temperature, if any, is not appreciable. This composition is very close to $Ni_{2.666}S_2$ or Ni_4S_3 (i.e., 42.86 a/o sulfur) which has been suggested to be a stable phase (β_2 - Ni_4S_3), in the temperature range 845-1040 K, according to the Ni-S phase diagram reported by Lin *et al.* (2) (shown in Fig. 2). Schaefer (3) has, however, reported that the composition of $Ni_{3\pm x}S_2$ in equilibrium with NiO and SO_2 (1 atm) is $Ni_{2.515}S_2$ (i.e., 44.3 a/o sulfur). Moreover, he has reported no change in the composition of $Ni_{2.515}S_2$ with temperature in the temperature range (969-1054 K) of his investigation.

The EMF vs. temperature relationship has been found to be linear in the present studies. Linear regression analysis of our data in the temperature ranges 973-1053 K and 1083-1173 K yielded the following relationships

$$E = 827.24 - 0.23634T \quad (973-1089 \text{ K}) \quad [1]$$

and

$$E = 871.62 - 0.27707T \quad (1089-1173 \text{ K}) \quad [2]$$

where E is the EMF of cell [A] in mV and T is the temperature in degrees Kelvin.

The change in the slope of the E vs. T straight line at 1089 K corresponds to the melting temperature $Ni_{3\pm x}S_2$. This is in good agreement with that (1083 K) reported by Rosenqvist and is higher than that (1063 K) reported for Ni_3S_2 by Turkdogan (6), and by Kubaschewski and Alcock (7). However, it must be pointed out that the tem-

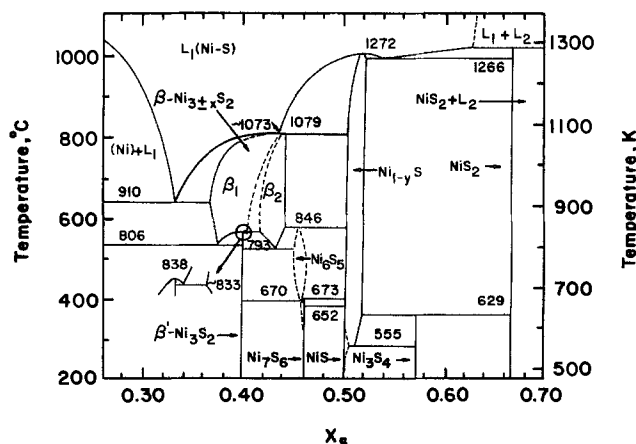
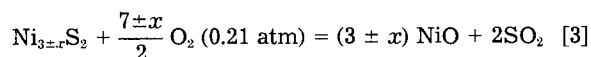


Fig. 2. Nickel-sulfur phase diagram, after Lin *et al.* (2).

perature at which the change in slope occurs is extremely sensitive to the terms which correspond to the entropy in the above equations, and hence the errors in the melting temperature are likely to be large. The EMF values obtained from Eq. [1] are in good agreement with those obtained by Schaefer (3) after correcting for the oxygen pressures of the reference electrodes. Our EMF data are also in agreement within ± 2 mV with those reported subsequently by Chang and Hsieh (8) for solid $\text{Ni}_{3\pm x}\text{S}_2$ in the temperature range 945-1070 K.

The virtual cell reaction for cell [A] is



Therefore

$$\Delta G^\circ_{\text{cell}} = 2\Delta G^\circ_{\text{SO}_2} + (3 \pm x) \Delta G^\circ_{\text{NiO}} - \Delta G^\circ_{\text{Ni}_{3\pm x}\text{S}_2} - \left(\frac{7 \pm x}{2}\right) RT \ln 0.21 \quad [4a]$$

or

$$\Delta G^\circ_{\text{Ni}_{3\pm x}\text{S}_2} = 2 \Delta G^\circ_{\text{SO}_2} + (3 \pm x) \Delta G^\circ_{\text{NiO}} + 2F(7 \pm x)(E + 0.03362T) \quad [4b]$$

where $\Delta G^\circ_{\text{Ni}_{3\pm x}\text{S}_2}$, $\Delta G^\circ_{\text{SO}_2}$, and $\Delta G^\circ_{\text{NiO}}$ are the standard Gibbs energies of formation of $\text{Ni}_{3\pm x}\text{S}_2$, and SO_2 , and NiO , respectively, and F is Faraday's constant.

Using the reported data for $\Delta G^\circ_{\text{NiO}}$ and $\Delta G^\circ_{\text{SO}_2}$, one obtains

$$\Delta G^\circ_{\text{Ni}_{3\pm x}\text{S}_2}(\text{s}) = 74,740 + 31.007T \pm x(-18,160 + 11.221T) \quad (973-1089 \text{ K}) \quad [5]$$

and

$$\Delta G^\circ_{\text{Ni}_{3\pm x}\text{S}_2}(\text{l}) = -60,420 + 17.855T \pm x(-16,110 + 9.343T) \quad (1089-1173 \text{ K}) \quad [6]$$

For the composition of the $\text{Ni}_{3\pm x}\text{S}_2$ in equilibrium with NiO and SO_2 (1 atm) to be $\text{Ni}_{2.666}\text{S}_2$ (42.86 a/o S), we obtain

$$\Delta G^\circ_{\text{Ni}_{2.666}\text{S}_2}(\text{s}) = -68,670 + 27.257T \quad (973-1089 \text{ K}) \quad [7]$$

and

$$\Delta G^\circ_{\text{Ni}_{2.666}\text{S}_2}(\text{l}) = -55,035 + 14.734T \quad (1089-1173 \text{ K}) \quad [8]$$

From Eq. [7] and [8], the enthalpy of fusion of $\text{Ni}_{2.666}\text{S}_2$ is found to be 13,635 cal/mol.

For the sake of comparison with the data reported in the literature, it is also possible to obtain the Gibbs energy of formation of stoichiometric Ni_3S_2 by assuming the composition in equilibrium with NiO and 1 atm SO_2 to be 40 a/o sulfur. One thus obtains from Eq. [5] and [6]

$$\Delta G^\circ_{\text{Ni}_3\text{S}_2}(\text{s}) = -74,740 + 31.007T \quad (973-1089 \text{ K}) \quad [9]$$

and

$$\Delta G^\circ_{\text{Ni}_3\text{S}_2}(\text{l}) = -60,420 + 17.855T \quad (1089-1173 \text{ K}) \quad [10]$$

The enthalpy of fusion of Ni_3S_2 , as obtained from Eq. [9] and [10], is 14,320 cal/mol. This is much higher than the estimated value of 5800 cal/mol reported by Kubaschewski and Alcock (7) and is comparable to 11,300 cal/mol reported by Nagamori and Ingraham(4).

Figure 3 shows $\Delta G^\circ_{\text{Ni}_{2.666}\text{S}_2}$ and $\Delta G^\circ_{\text{Ni}_3\text{S}_2}$, as obtained from Eq. [7]-[10], as functions of temperature. It also shows some of the data reported in the literature. The values of Gibbs energy of formation of solid and liquid Ni_3S_2 obtained from our Eq. [9] and [10] are in good agreement with those reported by Rosenqvist (1) for solid Ni_3S_2 and with those reported by Nagamori and Ingraham (4) for liquid Ni_3S_2 . The values of Gibbs energy of formation of solid $\text{Ni}_{2.666}\text{S}_2$ obtained from our Eq. [7] are also in good agreement with those calculated from Rosenqvist's data in the temperature range 918-1083 K. The enthalpy and entropy terms in our equations are, however, different from those reported by Rosenqvist and by Nagamori and

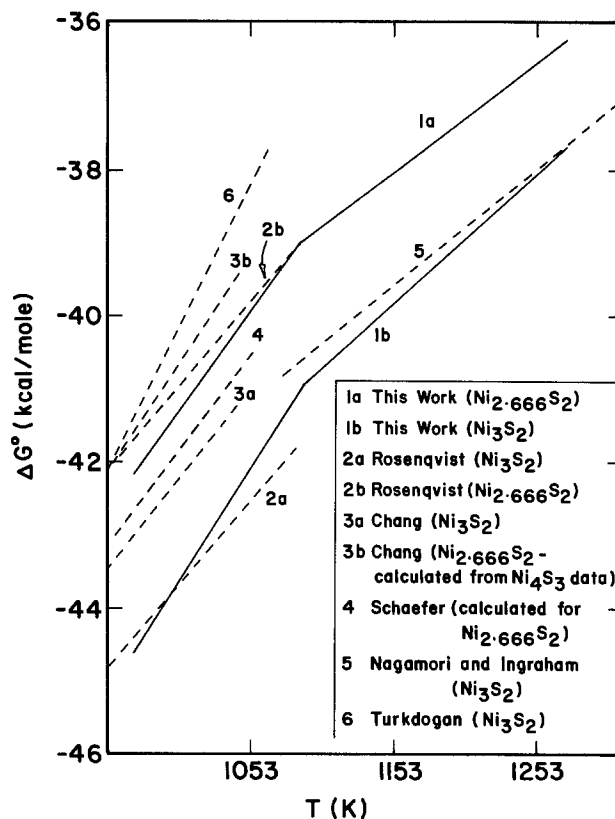


Fig. 3. Standard Gibbs energy of formation of Ni_3S_2 and $\text{Ni}_{2.666}\text{S}_2$

Ingraham. The agreement between our $\Delta G^\circ_{\text{Ni}_{2.666}\text{S}_2}$ values and those calculated for the same composition from Schaefer's EMF data is good. The values reported by Lin *et al.* (2) for $\beta_2\text{-Ni}_4\text{S}_3$ (or $\text{Ni}_{2.666}\text{S}_2$) phase are also in good agreement with those obtained from our Eq. [7]. However, their values for $\beta_1\text{-Ni}_3\text{S}_2$ (40 a/o sulfur) phase are higher than those obtained from our Eq. [9]. The values obtained from the equation for $\Delta G^\circ_{\text{Ni}_3\text{S}_2}$ (298-1063 K) in Turkdogan's (6) and Kubaschewski and Alcock's (7) compilations, which are actually Rosenqvist's data for the temperature range 673-808 K, are higher by 3-4 kcal/mol than the values obtained in the present work. Because of the very good reproducibility of cell EMF's over the entire temperature range (973-1173 K) and extended durations (4-10 days) of our experiments, and also because of the accuracy of the EMF method itself, the data obtained in the present work may be considered to be more reliable.

Combining the heat capacity data for nickel, sulfur, and Ni_3S_2 reported in literature (7, 9, 10) with the EMF data obtained in this work, one obtains, from the third law analysis, for the enthalpy of formation of Ni_3S_2 from the elements, ΔH°_{298} , a value of -47.9 ± 2.2 kcal/mol. This is in fair agreement with the value of -51.6 ± 2.5 kcal/mol reported by Kubaschewski and Alcock (7). The values of ΔH°_{298} calculated from our EMF data for various temperatures show a random variation and therefore are considered to be free from systematic experimental errors.

Acknowledgments

This research was supported by the Army Research Office under Contract no. DAAG-29-81-K0109 and a grant through the Center for Solid State Science.

Manuscript submitted April 20, 1984; revised manuscript received ca. Sept. 11, 1984. This was Paper 429 presented at the Washington, DC, Meeting of the Society, October 9-14, 1983.

Arizona State University assisted in meeting the publication costs of this article.

REFERENCES

1. T. Rosenqvist, *J. Iron Steel Inst.*, **176**, 37 (1954).
2. R. Y. Lin, D. C. Hu, and Y. A. Chang, *Metall. Trans.*, **9B**, 531 (1978).

3. S. C. Schaefer, U. S. Bureau of Mines RI 8588 (1981).
4. M. Nagamori and T. R. Ingraham, *Metall. Trans.*, **1**, 1821 (1970).
5. F. K. Moghadam and D. A. Stevenson, *J. Appl. Electrochem.*, **13**, 587 (1983).
6. E. T. Turkdogan, "Physical Chemistry of High Temperature Technology," pp. 17, 20, Academic Press, New York (1980).
7. O. Kubaschewski and C. B. Alcock, "Metallurgical Thermochemistry," 5th ed., pp. 300, 331, Pergamon Press, Oxford, England (1979).
8. Y. A. Chang and K. C. Hsieh, Private communication, March, 1984.
9. I. Barin and O. Knacke, "Thermochemical Properties of Inorganic Substances," pp. 579, 648, Springer-Verlag, Berlin (1973).
10. I. Barin, O. Knacke, and O. Kubaschewski, "Thermochemical Properties of Inorganic Substances," Supplement, pp. 460, 467, 600, Springer-Verlag, Berlin (1977).

A Study of Lapping and Polishing Damage in Single-Crystal CdTe

Donald F. Weirauch

Texas Instruments, Incorporated, Dallas, Texas 75265

ABSTRACT

The surfaces of single-crystal CdTe specimens subjected to lapping and polishing operations were studied. Optical microscopy was used to establish that lapping with an abrasive creates damage principally in the form of microcracks extending below the surface. The depth of damage was similar to that reported for single-crystal Si and was 50 μm from 240 grit (47 μm) SiC and 15 μm from 600 grit (28 μm) SiC. Polished surfaces were studied using a dislocation revealing etchant. Lapping-induced microcracks could be removed by sufficient polishing with an abrasive, but the specimen always possessed a surface layer of very high dislocation density, with the average depth of the dislocations being a function of abrasive particle size. The maximum dislocation depths were found to be 9 μm from a 5 μm Al_2O_3 polishing abrasive and 3 μm from 0.3 μm Al_2O_3 . The correlation of this surface layer of high dislocation density with the frequently reported "amorphous" or "Beilby" surface layer was demonstrated. It was shown that during the formation of this layer, small microcracks and surface defects could be covered and rendered invisible by a lateral movement of material along the specimen surface. A chemical polishing technique employing a bromine-methanol solution was shown to be capable of creating damage-free CdTe surfaces.

The quality of the polished surface is of critical importance to many materials' applications. The growth of an epitaxial film on a single-crystal substrate is an example where an improperly polished surface can seriously affect the quality and properties of the film or even cause it to grow with a randomly oriented or polycrystalline character. Ideally, the substrate surface should have the same crystallographic perfection as its interior. CdTe is a material which is useful as a substrate in the growth of epitaxial (Hg, Cd)Te. It is soft (2.75 on the Moh's hardness scale) and brittle, with a strong tendency to cleave along (110) planes. The purposes of this study are to investigate the nature of lapping and mechanical polishing damage associated with CdTe substrate preparation and to evaluate chemical polishing as a method of creating a damage-free surface.

The lapping and polishing of all brittle materials possess similarities which transcend the individual differences in the materials' physical properties (1-5). Thus, materials such as diamond, one of the hardest of materials, glass, an amorphous material of intermediate hardness, and gypsum, one of the softest materials, all exhibit the same phenomenological events during lapping and polishing; only the rates are significantly different. In contrast, though lapping and polishing operations appear to be nearly identical processes (as, for example, when a rotating wheel and an abrasive are employed), the effects of the two operations on the specimen surface are dramatically different, as described below.

The lapping process is a grinding operation in which an abrasive, a lapping surface, and suitable pressure are combined to create microcracks in the surface of the material being lapped. Microcracks propagating from the surface intersect within the material to release chips. The grinding action is the formation and removal of these chips from the surface. Finer abrasives result in shorter microcracks and finer chips. However, under normal lapping conditions, the grinding action ceases when the abrasive size decreases below approximately 4 μm . After the lapping operation, the surface will contain numerous microcracks. Associated with the microcracks will be strained material and dislocation arrays.

There are two types of polishing: chemical and mechanical. Chemical polishing relies on a chemical to dissolve the surface of the specimen so that a smooth polished surface results. A polishing pad might or might not be used in this process. Mechanical polishing bears a resemblance to lapping in that an abrasive and polishing surface are used in a manner similar to lapping. However, during polishing, microcracks are not created in the surface, as they are in lapping. Instead, material is displaced from the high spots, either to be transferred to valleys of the surface or to be removed totally. During the initial polishing with coarser polishing agents, fine scratches will be introduced into the material; associated with these scratches will be deformation of the material and dislocations. As the polishing process continues with finer polishing agents, the surface quality will continue to improve until no surface defects are visible — even under a microscope. This appearance can be misleading because x-ray or etching studies will often reveal considerable damage in the form of filled-in scratches, microcracks, and pits, as well as dislocation arrays concealed by the surface flow of the material being polished. The flow or smearing of the surface has been observed for several materials and has been referred to as the "Beilby layer" (1). Figure 1 is a cross-sectional representation of a partially polished crystalline specimen in which microcracks created during lapping are still present. At the surface is the "amorphous," or "Beilby," layer. This layer can totally conceal the underlying damage of pits, scratches, and microcracks. The zone of microcracks represents lapping damage which has not yet been removed by polishing. Dislocations arrays extend below the microcracks; beneath these arrays lie "good" material with a crystallographic perfection representative of the interior of the specimen.

Experimental Procedure

Both lapping and polishing damage were studied using $\langle 111 \rangle$ oriented CdTe single crystals. Lapping damage was investigated by lapping the specimen on a glass plate previously conditioned by thoroughly abrading the surface with the abrasive size under study. After lapping the

CdTe sufficiently to create a representative surface, the specimen was cleaved along the (110) plane, which was then examined microscopically. The abrasives studied were 240 grit (47 μm) and 600 grit (28 μm) SiC.

Both the mechanical and the chemical polishing studies were conducted using a Strasbaugh polishing machine¹ with Rodel² 600 polishing pads. "Mechanical" polishing refers to the polishing of CdTe using only an abrasive having no apparent chemical action on the specimens. For these studies, 5 μm and 0.3 μm polishing suspensions³ of Al_2O_3 were used. "Chemical" polishing refers to the polishing of CdTe using a reagent known to chemically react with the specimen. For this study, the reagent was 0.5 volume percent (v/o) bromine dissolved in methyl alcohol. During the polishing, the reagent was dripped onto the polishing pad at a rate sufficient to keep the pad saturated with the chemical. Prior to the chemical polishing, the specimens were mechanically polished with 5 μm , then 0.3 μm , Al_2O_3 .

To determine the extent of damage caused by the polishing, the specimens were coated with an organic wax which covered all of the specimen except for a small (0.25 cm^2) region that was to be directly exposed to chemical reagents. Two reagents were used in the polishing damage evaluation. One reagent (6), composed of 10 ml H_2O , 5 ml conc HNO_3 , and 2g $\text{K}_2\text{Cr}_2\text{O}_7$, was very effective in isotropically removing CdTe from the specimen surface. Because this chemical technique did not introduce dislocations into the specimen, it was possible to "chemically mill" into the specimen's surface and examine the dislocation etch-pit structure at selected locations. Dislocation etch pits were revealed by dipping the specimen for 20s in a reagent (7) composed of 29 v/o H_2O , 29 v/o H_2O_2 , and 42 v/o conc HF. This process created on the specimen surface a dark film which was removed by a 1s immersion in the $\text{K}_2\text{Cr}_2\text{O}_7$ reagent described above. When sufficient material had been chemically milled from the surface so that the dislocation etch-pit structure was characteristic of the underlying crystal, the etch mask was removed with a chemical solvent, and the step height between the chemically milled regions and the protected regions was measured microscopically.

To determine if CdTe could be displaced at the specimen surface during mechanical polishing to fill in pits and low spots, a scratch was made in a specimen surface with a diamond point. The specimen was then dipped for 15s in a saturated AuCl_3 solution which reacted slightly with the CdTe to effectively open up microcracks and coat all exposed surfaces with a layer of elemental gold. The specimen was lightly polished with 5.0 μm Al_2O_3 and, after a microscopic examination, was immersed for 2s in the $\text{K}_2\text{Cr}_2\text{O}_7$ solution diluted 4-to-1 with H_2O . The specimen was then examined with an optical microscope and an electron microprobe. Because the action of the diamond point across the CdTe surface was somewhat analogous to the action of an abrasive particle during the polishing operation, the associated surface deformation and dislocation generation in the specimen surface were studied in greater detail.

Results and Discussion

The most pronounced defects created during the lapping operations were a myriad of microcracks in the surface; dislocations were undoubtedly present also, but they were not examined. The microcrack damage to CdTe caused by lapping with 240 grit SiC is shown in Fig. 2 (top view) and Fig. 3 (cross-sectional view). The cross-sectional view revealed microcracks of irregular depth, but of an average of 50 μm depth. The surface lapped with 600 grit SiC was similar, but on a finer scale, with the average observed microcrack depth being 15 μm . These results were very similar to lapping damage reported for silicon (4).

¹Product of R. Howard Strasbaugh, Incorporated Huntington Beach, California.

²Product of Rodel Company, Scottsdale, Arizona.

³Product of Buehler Limited, Evanston, Illinois.

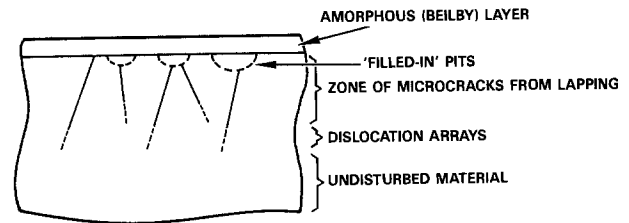


Fig. 1. Cross-sectional view of lapping and mechanical polishing defects.

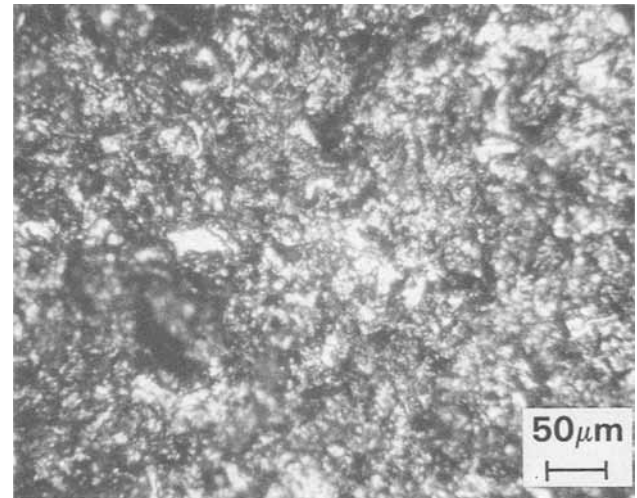


Fig. 2. Surface of CdTe after lapping

The damage created by mechanical polishing was primarily in the form of dislocations, and these were evaluated using chemical milling and an etchant. Figure 4 shows the surface of the specimen polished with 5 μm Al_2O_3 ; fine scratches were evident. Figure 5 shows the same area after being exposed to the dislocation revealing etchant. Most of the existing polishing scratches were enhanced (although some disappeared), and new ones appeared. For example, the prominent horizontal line in Fig. 5 was imperceptible in the original polished specimen. When 4 μm of the surface was chemically removed and then etched, the surface had the appearance seen in Fig. 6. Only the deepest polishing scratches were still visible (as dense linear arrays of etch pits), but etch pits delineating subgrain boundaries of the crystal were now present as a mosaic pattern. After chemically removing an additional 9 μm from the specimen, the etch pits associated with the polishing scratches were gone, although remnants of a smooth groove remained, as shown in Fig.

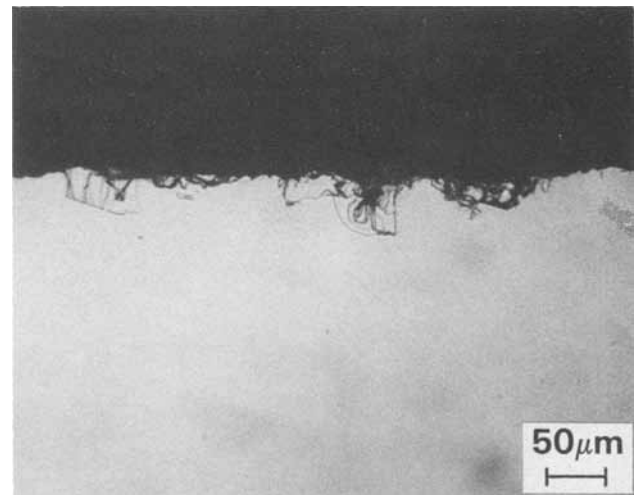


Fig. 3. Cross section of lapped CdTe specimen

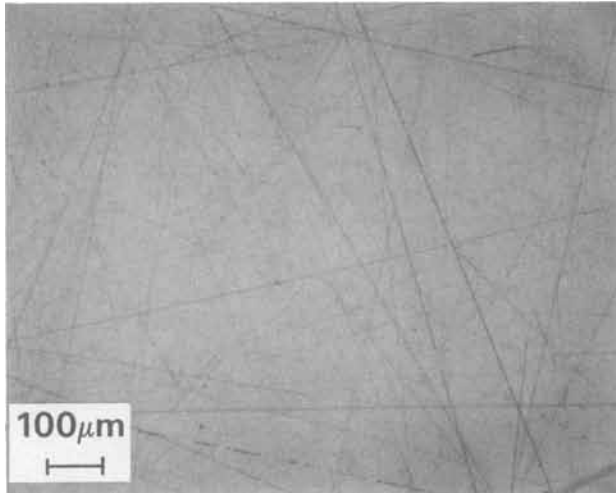


Fig. 4. Mechanically polished CdTe surface

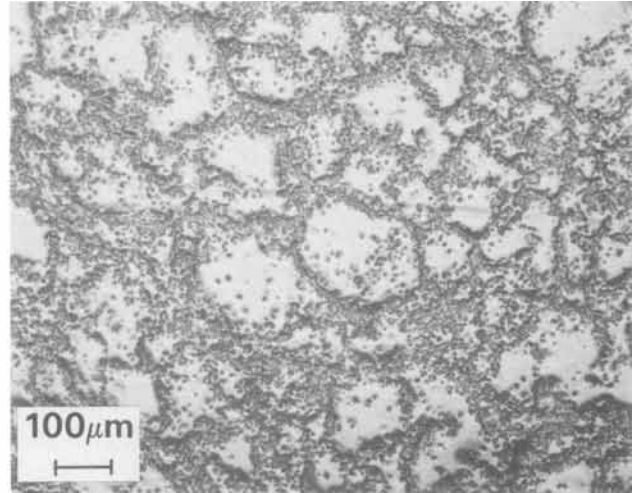


Fig. 7. Etch-pit structure 13 μm below the mechanically polished surface.

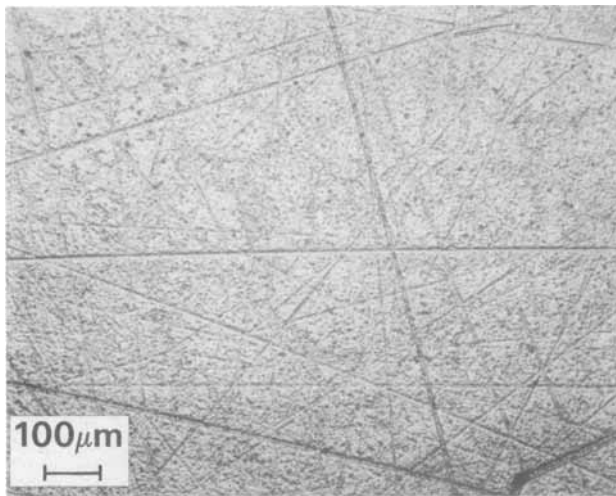


Fig. 5. Mechanically polished CdTe surface after chemical etching

7. The mosaic etch pit pattern was virtually unchanged from that observed in Fig. 6. Because the additional chemical milling and etching steps had revealed the same mosaic structure, it was evident that gross crystallographic changes caused by the polishing did not extend to even 4 μm below the surface. The major mechanical polishing damage found by this technique consisted of

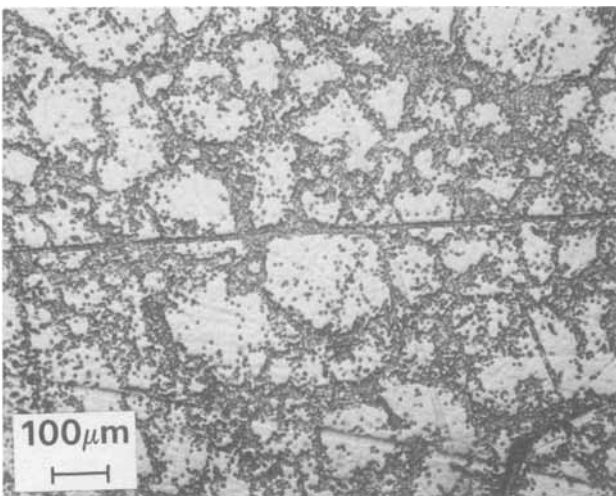


Fig. 6. Etch-pit structure 4 μm below the mechanically polished surface.

linear dislocation arrays created by individual abrasive particles. The maximum depths of damage were 9 μm from the 5 μm Al_2O_3 and 3 μm from the 0.3 μm Al_2O_3 .

The appearance of new polishing marks after exposure to a chemical etchant (Fig. 5) was strong evidence that scratches had been "filled in" during the polishing operation. Added support to this conclusion was obtained using CdTe specimens scratched with a diamond point. Figure 8 shows well-defined grooves created using light and moderate pressures. Slip lines (the parallel lines on each side of the groove) and microcracks (short, irregular lines visible primarily on one side of the groove) emanated from the deeper groove. When lightly polished, many of the microcracks vanished only to reappear when exposed to an etchant. To ensure that this was not simply a result of having polished to a region of the microcrack too thin to be seen optically, a similarly scratched specimen was immersed in a AuCl_3 solution to deposit a thin gold layer on all exposed surfaces, including the interior of microcracks. The specimen was then lightly polished with 5 μm Al_2O_3 such that many microcracks were no longer visible (see Fig. 9). Localized regions of smeared gold in otherwise featureless areas indicated the presence of the gold-coated microcracks, and this presence was confirmed using a very light etch which exposed previously-invisible microcracks (see Fig. 10). An examination with an electron microprobe revealed that the microcracks were coated with gold, which confirmed that they were the ones originally present and established that they had been of a sufficient size to be easily detect-

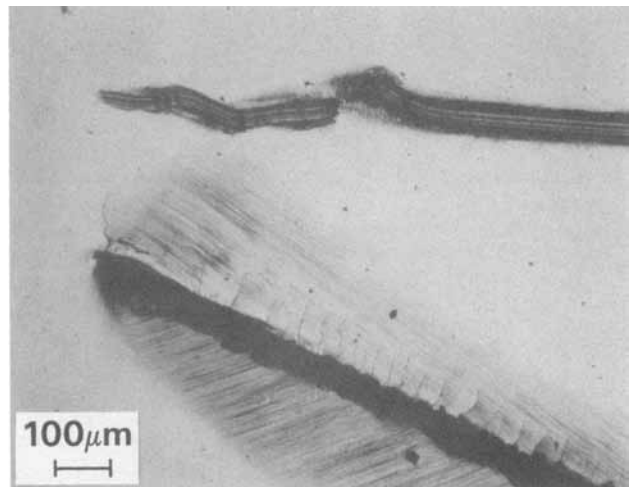


Fig. 8. Deep and shallow scratch marks in CdTe

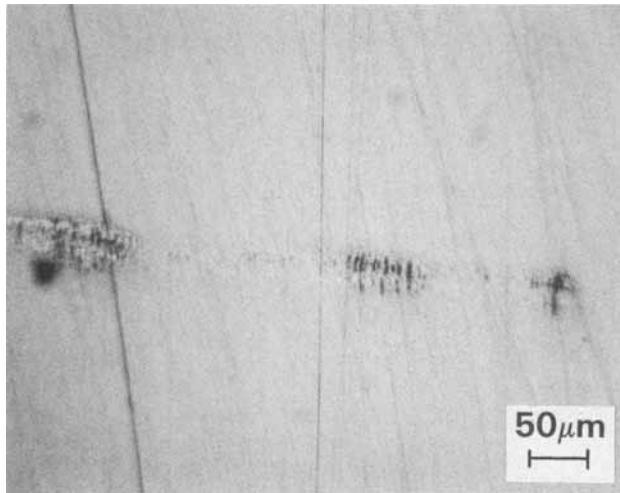


Fig. 9. Partially polished surface scratch

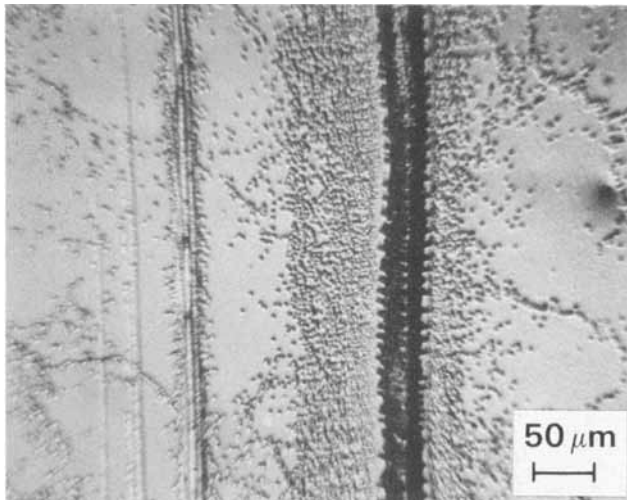


Fig. 10. Partially polished surface scratch after chemical etching

able with an optical microscope prior to the chemical etch. Therefore it was unambiguously established that during polishing, a "Beilby" layer had been created on the CdTe specimen surface.

Using a diamond point, a fresh groove was made in a specimen surface, and a thin glass sheet was placed over it. When illuminated by a monochromatic light source with a wavelength of $0.589 \mu\text{m}$, a series of interference fringes, as shown in Fig. 11, were generated in the air gap between the specimen surface and the transparent glass. These fringes revealed the topographical profile of the specimen surface and showed that the diamond point had created a furrow with edges extending above the specimen surface by at least $0.5 \mu\text{m}$. Thus, even though the CdTe was extremely brittle, it was possible for substantial deformation to occur without fracture. This was possible because of the generation of dislocations in the vicinity of the groove. Figure 12 shows dislocation arrays associated with a series of four parallel grooves of various depths made in CdTe by a single pass with an irregular diamond point. Also present were dislocations associated with the crystal's mosaic subgrain structure. The width of the dislocation bands on each side of a groove were related to the depth of the groove. The etch pits associated with the two shallowest grooves were indistinct, showing that the depth of those dislocations had been less than the amount of CdTe removed by the etchant (less than $1 \mu\text{m}$). The pressure of the diamond scribe had not been perpendicular to the specimen surface, and this is believed responsible for the fact that the bands of dislocations were not of equal width on each side of the grooves.

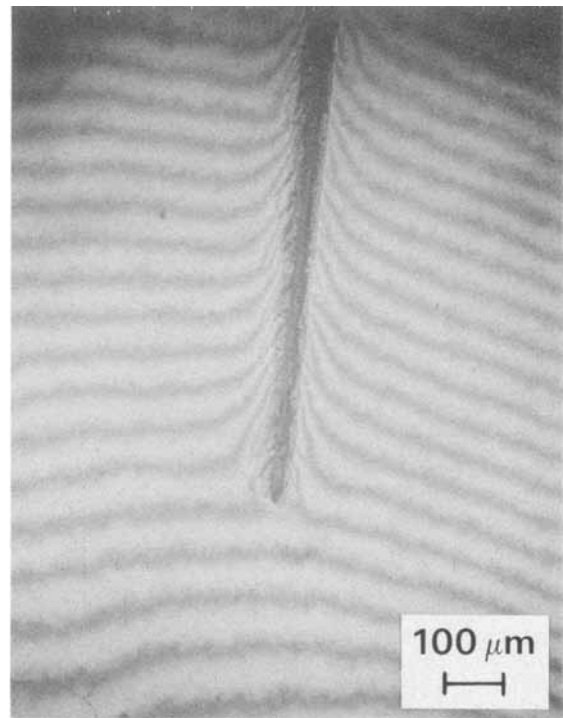


Fig. 11. Surface scratch topography

The results of these tests suggest that the origin of the amorphous Beilby layer, created during mechanical polishing, was from abrasive particles acting on the specimen in a manner similar to the diamond point to create grooves and dislocation arrays and to cause material deformation in the specimen surface. During this process, sufficient lateral movement of material occurred at the specimen surface to fill and seal the surface of microcracks and small surface pits (a cold welding type of mechanism is assumed). The surface layer, appearing completely continuous, then contained an extremely high dislocation density which was very similar to the "amorphous" or "Beilby" layer. The depth of this layer was dependent upon the abrasive particle size, but also was sometimes dependent upon the hardness of the polishing surface. During this process, of course, there also occurred the relatively slow removal of surface material normally associated with polishing.

No evidence of a Beilby layer was found on the specimen chemically polished in the bromine-methanol solution. The as-polished surface was featureless, with a very slight trace of an "orange peel" texture which could be

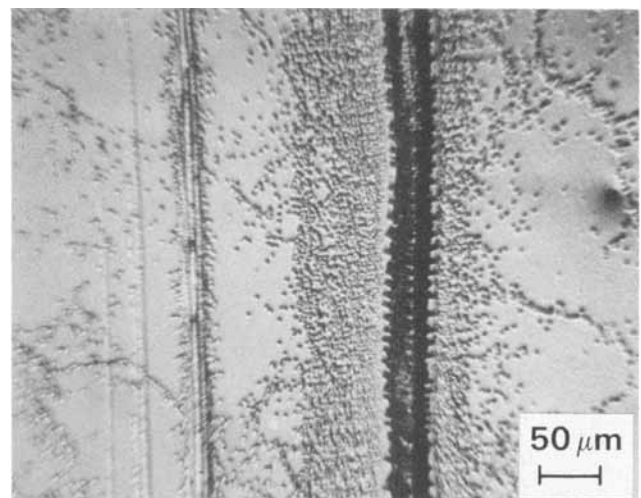


Fig. 12. Dislocation etch pits associated with surface deformation

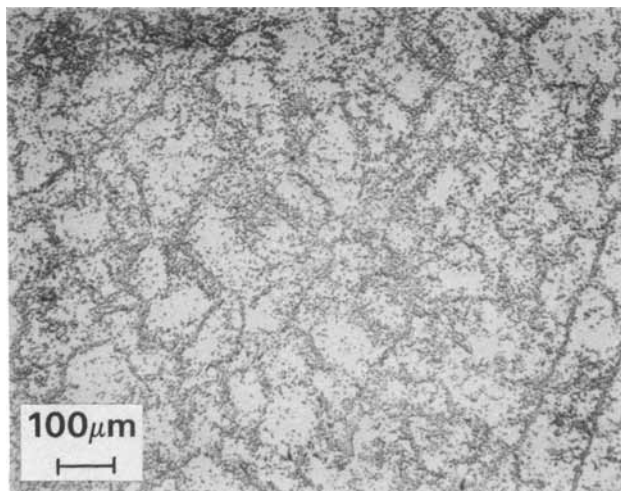


Fig. 13. Chemically polished surface after chemical etching

seen microscopically only with Nomarski interference contrast. When exposed to the dislocation revealing etchant which removed less than $1 \mu\text{m}$ of CdTe surface, only a mosaic pattern of etch pits was produced (see Fig. 13). No linear dislocation arrays characteristic of the mechanical polishing were seen. Chemically removing additional CdTe from this specimen did not appreciably change the mosaic etch-pit structure, which indicated that any polishing-induced damage did not extend more than $1 \mu\text{m}$ below the original surface. Thus, within the limits of resolution of this technique, the surface of the chemically polished specimen possessed a crystallographic perfection representative of the crystal interior. This result was substantially different from that obtained from the mechanically polished specimen, and it gave added evidence that the amorphous Beilby layer was a mechanically induced surface layer of high dislocation density. Because of the similarity in polishing behavior of most materials, these results are believed to be generally applicable and not limited to CdTe.

Conclusions

The "amorphous," or "Beilby," layer created during mechanical polishing was shown to be a surface layer of

very high dislocation density created by the abrasive particles during polishing. The creation of this layer was associated with sufficient material deformation to effectively cover and conceal microcracks, small surface pits, and other defects. The thickness of the surface layer was dependent upon the abrasive particle size used during polishing.

A chemical polishing technique employing a bromine-methanol solution was shown to be capable of creating a CdTe surface free of polishing damage. The mechanical polishing of CdTe with Al_2O_3 abrasive created damage in the form of shallow surface scratches and dislocation arrays penetrating into the material. The maximum observed depth of the dislocations ranged from $9 \mu\text{m}$ from a $5 \mu\text{m}$ Al_2O_3 polishing agent to $3 \mu\text{m}$ from a $0.3 \mu\text{m}$ Al_2O_3 polishing agent.

The lapping of CdTe with SiC created a surface zone of microcracks which averaged $50 \mu\text{m}$ depth from 240 grit abrasive and $15 \mu\text{m}$ depth from 600 grit abrasive.

Acknowledgments

The author wishes to acknowledge the capable technical assistance of J. G. Hurt in polishing and D. A. Schultz in the electron microprobe analysis.

Manuscript submitted Dec. 27, 1983; revised manuscript received Aug. 29, 1984.

Texas Instruments Incorporated assisted in meeting the publication costs of this article.

REFERENCES

1. G. Beilby, "Aggregation and Flow of Solids," Macmillan and Co. Ltd., London (1921).
2. F. Twyman, "Prism and Lens Making," Hilger and Watts Ltd., London (1957).
3. L. Motz, "On the Nature of a Polished Surface," *J. Opt. Soc. Am.*, **32**, 147 (1942).
4. E. N. Pugh and L. E. Samuels, "Damaged Layers in Abraded Silicon Surfaces," *This Journal*, **111**, 1429 (1964).
5. P. Rai-Choudhury, "Substrate Surface Preparation and Its Effect on Epitaxial Silicon," *ibid.*, **118**, 1183 (1971).
6. M. Inoue, I. Teramoto, and S. Takayanagi, "Etch Pits and Polarity in CdTe Crystals," *J. Appl. Phys.*, **33**, 2578 (1962).
7. K. Nakagawa, K. Maeda, and S. Takeuchi, "Observation of Dislocations in Cadmium Telluride by Cathodoluminescence Microscopy," *Appl. Phys. Lett.*, **34**, 574 (1979).



COMMENTS

Each issue of the **Journal** will have a section of "Comments." In this section, we provide a means via short pieces, *i.e.*, one column or less, to applaud, dispute, or otherwise discuss the papers published in the **Journal**. Space will be provided for one response by the paper's author(s) to each comment.

Since space available in each issue for the "Comments" section is limited; it is important to be concise.

Comments should be sent to the Editor, Dr. Norman Hackerman, President's Office, Rice University, P.O. Box 1892, Houston, TX 77251.

Norman Hackerman
Editor

Corrosion Study of a Carbon Steel in Neutral Chloride Solution by Impedance Techniques

A. Bonnel, F. Dabosi, C. Deslouis, M. Duprat, M. Keddou, and B. Tribollet

(pp. 753-761, Vol. 130, no. 4)

F. Mansfeld:¹ In their paper, Bonnel *et al.* investigate the electrochemical behavior of a C-Mn steel in 3% NaCl, using a rotating disk electrode. We have been carrying out similar studies of the important subject of corrosion in aerated neutral media and its inhibition²⁻⁴ and have noted some important discrepancies in the impedance spectra reported by Bonnel *et al.* and by ourselves. In the paper under discussion, two capacitive loops are shown in Nyquist plots obtained at the corrosion potential. In our previous studies of steel in 0.5M Na₂SO₄³ and in tapwater², only one capacitive semicircle was observed in experiments with rotating iron² or 4340 steel³ cylinder electrodes (RCE). Our unpublished data for steel RCE's in 0.5N NaCl have been repeated to extend the frequency range to 5 mHz. For frequencies between 10⁵ Hz and 0.1 Hz, a Solartron transfer function analyzer (TFA) (Model 1174) was used, while a fast fourier transform technique (FFT) was used between 0.5 Hz and 5 mHz. The software program for the FFT technique was provided by Princeton Applied Research Corporation. The results of this study show clearly that only one depressed capacitive semicircle occurs between 10⁵ and 5 × 10⁻³ Hz. The Bode plots in Fig. 1 show excellent

agreement between experimental data and a fit to a theoretical model of the impedance as

$$Z = R_{\Omega} + \frac{R_p}{1 + (j\omega CR_p)^{\alpha}} \quad [1]$$

where R_{Ω} is the ohmic electrolyte resistance, the capacitance C is calculated from the frequency ω_m of the maximum of the imaginary component Z'' ($C = (\omega_m R_p)^{-1}$), R_p is the polarization resistance, and α relates to the depression of the semicircle as discussed before⁵. R_p and R_{Ω} were calculated using the CIRFIT computer program⁵. The FFT data in Fig. 1 were taken 2h after the end of the TFA data. Due to the continuous increase of corrosion rates with time, the R_p value obtained from the FFT data is lower than that obtained from the dc limit of the TFA data. Nevertheless, it is obvious that a second time constant does not occur at the lowest frequencies. It should be noted that an accurate fit of the frequency dependence of the impedance $|Z|$ and the phase angle δ is a more severe test than a Nyquist plot of both types of data.

These experiments have also been conducted at other rotation speeds r . Table I summarizes the results of an analysis according to Eq. [1]. As expected, R_p decreases with increasing r , while E_{corr} becomes more noble. With increasing exposure time, R_p becomes smaller. After exposure for more than 24h, a thick rust layer has developed, which is reflected in the more than ten-fold increase of the capacitance C . The value of α does not change significantly with experimental conditions. The following additional comments need to be made.

1. It is not clear why the high-frequency loop depends on rotation speed in galvanostatic conditions but not in potentiostatic conditions (Fig. 9 and 10 of the paper under discussion). The caption for Fig. 10 seems to imply that the experiments for 600 and 2400 rpm were conducted at the same applied potential (the E_{corr} for 1000 rpm?).

2. An experiment with the TFA technique down to 5 mHz takes many hours, depending on the integration

⁵M. W. Kendig, E. M. Meyer, G. Lindberg, and F. Mansfeld, *Corros. Sci.*, **23**, 1007 (1983).

¹Rockwell International Science Center, Thousand Oaks, California 91360.

²F. Mansfeld, M. W. Kendig, and S. Tsai, *Corros. Sci.*, **22**, 455 (1982).

³F. Mansfeld and M. W. Kendig, *Werkst. Korros.*, **34**, 397 (1983).

⁴W. J. Lorenz and F. Mansfeld, in "Proceedings of the International Congress on Corrosion Inhibition," National Association of Corrosion Engineers, Dallas, Texas (1983).

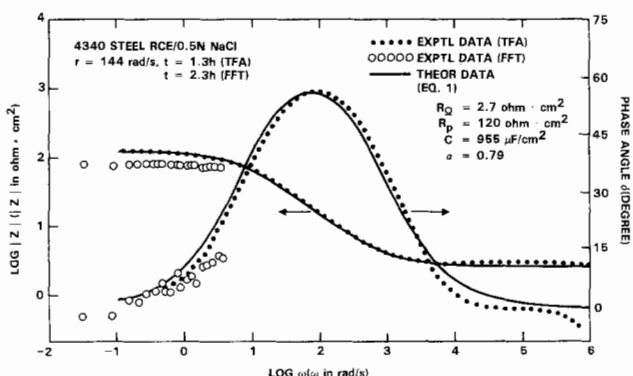


Fig. 1. Agreement between experimental data and a fit to a theoretical model of the impedance.

Table I. Impedance data for 4340 RCE in 0.5N NaCl

t (h)	r (rad/s)	E _{corr} (mV)	R _p (Ω · cm²)	C (μF/cm²)	α
1.3	144	-549	120	955	0.79
3.1	144	-544	96	685	0.77
4.5	16	-554	251	1,473	0.76
5.5	16	-627	297	1,337	0.79
6.0	324	-545	60	846	0.78
22.5	324	-580	143	11,100	0.71
24.0	144	-592	170	9,352	0.74
25.5	16	-615	245	6,490	0.74

time. Because E_{corr} and R_p vary with time, it is very likely that the data in Fig. 12 are strongly affected by this time dependence, especially for $t \sim 0$ and 30 min. What appear to be two capacitive loops could be due to these time effects.

3. The statement "the product $R_p I$ which remains close to 30 mV above 750 $\mu\text{A}/\text{cm}^2$ indicating a simultaneous transfer of the two electrons" is incorrect, because the Tafel slope is $b_a = 2.3 R_p I = 69$ mV, which is not consistent with anodic Tafel slopes derived for accepted mechanisms of iron dissolution. According to Bonnel *et al.*'s Table I, b_a increases continuously with applied anodic current from 27 to 79 mV, which suggests that no true Tafel slope exists in the current region studied.

A. Bonnel,⁶ F. Dabosi,⁶ C. Deslouis,⁷ M. Duprat,⁶ M. Keddad,⁷ and B. Tribollet:⁷ The introducing remarks of the discussion concern some divergences observed between the work of Mansfeld *et al.*⁸ and our work⁹. This is not so surprising, because the electrolyte, on one hand, and almost the metal, on the other hand, particularly concerning the contents of Ni, Cr, and Mn, are different.

The impedance diagrams reported by these authors displayed only one capacitive loop, rather than two, in our case. Nevertheless, it must be emphasized that the diameter of this single loop (R_p) is decreased with the rotation speed (Ω) (see Table I of the comments), thus indicating a probable influence of the mass transport process; in our case, the influence of this last process is clearly evidenced by the occurrence of a low frequency capacitive loop. The reason for the existence of two time constants has therefore been clearly explained as follows.

—The corrosion rate is controlled by the cathodic process, *i.e.*, oxygen reduction, and the role of mass transport was quantitatively established by plots (I_d , $\Omega^{1/2}$) and by EHD impedance measurements.

—Hence, the high-frequency (HF) loop corresponds to the charge-transfer process, whereas the low-frequency (LF) loop corresponds to mass transport.

The following answers can then be given to points 1-3 of the comments.

1. The influence of the rotation speed on the HF loop only observed in galvanostatic conditions results from the mixed nature of the corrosion potential.

—In potentiostatic conditions, the anodic process is obviously not modified, and there are no meaningful variations of the diameter of the HF loop. The decrease of the LF loop when Ω is increased is consistent with a mass transport process.

—When a galvanostatic control is applied, the change in Ω modifies the cathodic current I_d . Therefore, the anodic current I_A evolves so that the overall current $I_A + I_d$ remains constant, leading to a variation of the diameter of the HF loop.

2. We reported (Fig. 12) at time zero only one capacitive loop (flattened) which is in agreement with the conclusions of Mansfeld. However, a second loop is clearly evidenced at longer times ($t \geq 2$ h). Because a layer of corrosion products develops, it constitutes, as demonstrated in our paper, a hindrance to diffusion. With increasing elapsed time, the time constant due to diffusion becomes higher and, therefore, sufficiently different from that corresponding to charge transfer, and the two loops can be well separated. It is thus likely that these two time constants are not separated at time zero and exhibit only a frequency dispersion, as is probably the case for the experiments reported by Mansfeld.

⁶Equipe de Recherche Associée au CNRS, no. 263 "Laboratoire de Metallurgie Physique," Ecole Nationale Supérieure de Chimie, 31077 Toulouse Cedex, France.

⁷Groupe de Recherche du CNRS, no. 4 "Physique des Liquides et Electrochimie," Associé à l'Université Pierre et Marie Curie, 75230 Paris Cedex 05, France.

⁸M. W. Kendig, A. T. Allen, and F. Mansfeld, *This Journal*, **131**, 935 (1984).

⁹A. Bonnel, F. Dabosi, C. Deslouis, M. Duprat, M. Keddad, and B. Tribollet, *ibid.*, **130**, 753 (1983).

3. Concerning the anodic Tafel slope b_a for the iron dissolution, Mansfeld asserts that a value of 69 mV for b_a is incorrect as regards the "accepted mechanisms," but he does not mention any reference. In a recent paper of his¹⁰, he stated that anodic slopes b_a of 60 ± 5 mV can be clearly observed for the iron dissolution; this is consistent with our results. Somewhat earlier, a work by a member of our group¹¹ led to the same conclusion. In addition, the $R_p I$ values at low anodic currents must be disregarded, due to the significant contribution of the cathodic process in this potential range.

Formation of Salt Films during Anodic Dissolution in the Presence of Fluid Flow

Richard Alkire and Antonia Cangelari

(pp. 1252-1259, Vol. 130, no. 6)

M. Keddad¹² and R. Oltra:¹³ This very interesting paper, particularly its experimental part, has suggested to us the following remarks.

It is concluded from the data shown in Fig. 8 that repassivation can occur only when the intensity and mass-transfer conditions for precipitation of an iron sulfate layer are fulfilled.

Experiments are said to be performed by stepping the potential to 0.8, 1.0, and 1.2V, whereas experimental points in Fig. 8 are in the range 1.2-1.7V. If the data of Fig. 7 are added to Fig. 8, passivation is shown to occur well above the theoretical line for $f_{sc} = 1.3$. What about 0.8V?

It is clear that the model does not intend to account for the passivation process, because the surface overpotential is taken as a Tafel polarization. However, when discussing the experimental data, it must be kept in mind that even in the simplest view, the active-to-passive transition of a metal cannot take place when the electrode potential, corrected for ohmic drop, is lower than a critical passivation potential close to 0.8V/NHE for iron in 0.5M H_2SO_4 .

Using the data of Fig. 7 and $R_d = 1/4\kappa\tau_0$, it is easily shown that during the active part of the transient, the applied potential is pure ohmic drop in the solution; hence, the metal is not polarized in the passive range. This explains why the active current density is independent of R_e , a rather strange result for active iron. Also, it would be of interest to consider the dependence of the active current in Fig. 7 with respect to the applied potential. Therefore, the most important role of salt precipitation in passivation phenomenon must be related to its influence on ohmic drop.

It is not certain that iron/ H_2SO_4 is the most convenient system for testing simple views of the onset of passivity. It is known as a very complicated system at the active-passive transition (see our work and recent papers by J. Newman and co-workers).

R. Alkire¹⁴ and A. Cangelari:¹⁴ As indicated in the paper, potentials given in Fig. 7 (denoted ϕ_a) are with respect to NHE, whereas those in Fig. 8 (ϕ_A) are with respect to the rest potential of the system as defined by Eq. [1] on p. 1253. There is no inconsistency between data of which the same set appears in both figures; the potential of 0.8V in Fig. 7 corresponds to approximately 1.24V in Fig. 8.

Reference (7) of the publication cited previous work by Alkire, Ernsberger, and Beck on the topic of transient behavior during repassivation of iron in sulfuric acid. It was reported that, following sudden application

¹⁰Aksüt, W. Lorenz, and F. Mansfeld, *Corros. Sci.*, **22**, 611 (1982).

¹¹M. Keddad, O. Rosa Mattos, and H. Takenouti, *This Journal*, **128**, 257 (1981).

¹²Groupe de recherche no. 4 du C.N.R.S., "Physique des Liquides et Electrochimie" associé à l'Université, P. et M. Curie, 4, place Jussieu 75230 Cedex 05, Paris, France.

¹³L. A. C.N.R.S., Faculté des Sciences, BP 138, Dijon, France.

¹⁴Department of Chemical Engineering, and Materials Research Laboratory, University of Illinois, Urbana, IL 61801.

of an anodic potential in the passive range to a bare metal surface, the ensuing sequence of events includes: (a) rapid metal dissolution under IR-limited conditions, causing an increase in metal-salt concentration near the surface; (b) precipitation onto the surface of a metal-salt film; (c) formation on the surface of a passive-oxide film; and (d) dissolution of the metal-salt film, leaving only the passive-oxide film on the surface. Rapid metal dissolution under IR-limited conditions was also reported by Alkire and Perusich,¹⁵ who used focused ultrasound to cause localized cavitation damage to the passive film on Fe in H₂SO₄. Figure 6 of that work showed that the IR-limited dissolution rate varied linearly with applied potential and that the slope was given by the ohmic resistance of the solution, as computed from the primary current distribution.

Keddam and Oltra are correct in recognizing that the data in Fig. 7 of the paper under discussion also correspond to IR-limited conditions. It should not be surprising that an IR-limited current exhibits no dependence upon flow rate. The IR-limited current plateau shown in Fig. 7 depends only upon applied potential, solution conductivity, and electrode geometry.

It has been our experience that the Fe/H₂SO₄ system is a well-behaved model system for investigation of high-rate metal dissolution-precipitation phenomena. It is reproducible and convenient for study, and it exhibits stable behavior which is free of oscillations and which can be analyzed by basic principles of convective transport. We have found essentially identical results for single-crystal iron, for 99.99% polycrystalline iron, and for commercial cold-rolled steel. While other features of the Fe/H₂SO₄ passivation phenomena are undoubtedly complex, the dissolution and precipitation of metal-salt films in that system appears to be straightforward in comparison.

Preparation and Open-Circuit Potentials of Silver-Intercalated 2H-TaS₂ and 1T-TiS₂

G. A. Scholz and R. F. Frindt

(pp. 1763-1767, Vol. 131, no. 8)

B. Scrosati:¹⁶ The study of the silver-intercalated electrodes reported in this paper closely resembles that described in a paper that we published five years ago¹⁷. The only difference lies in the fact that we used a solid electrolyte cell in order to avoid all problems of self-intercalation and corrosion which the authors have faced with their liquid electrolyte cell.

Indeed, Scholz and Frindt have prepared their Ag_xTiS₂ samples in the same way we did, *i.e.*, both thermally and electrochemically, and the trend of their Ag_xTiS₂ EMF-composition curve is identical to ours¹⁷. The EMF values reported by Scholz and Frindt are slightly lower than ours and, in my opinion, this is due to the fact that the time allowed for the measurements (8h) was too short to reach equilibrium.

In fact, we¹⁷⁻¹⁹ and other authors²⁰ have found that the diffusion of silver in Ag_xTiS₂ and in Ag_xTaS₂ is very slow, so that long times are required for the equilibration of the intercalation electrodes.

It was also interesting to read that the authors were surprised to "discover" that the silver intercalation reac-

tions in TaS₂ and in TiS₂ are reversible, since we clearly demonstrated such reversible behavior some years ago¹⁸.

It is now well recognized that the kinetics of the intercalation processes are generally controlled by the diffusion of the guest species in the layer structure of the dichalcogenides. Therefore, the apparent lower reversibility that the authors observed for the intercalation process in TiS₂ with respect to that in TaS₂, is not at all unclear and unexpected, because silver diffuses much slower in the former ($D \sim 10^{-10} \div 10^{-12} \text{ cm}^2 \text{ s}^{-1}$)¹⁸ than in the latter ($D \sim 10^{-6} \div 10^{-9} \text{ cm}^2 \text{ s}^{-1}$)²⁰ dichalcogenide.

G. A. Scholz²¹ and R. F. Frindt:²¹ The work presented by us²² is a detailed discussion of the techniques used by us in preparing Ag_xTaS₂ and Ag_xTiS₂ intercalation compounds which we did not have the space to discuss in earlier publications.

We agree with B. Scrosati that our EMF *vs.* degree of intercalation (x) curve for Ag/Ag_xTiS₂ is very similar to their curve,²³ and we sincerely regret the oversight of not referencing their work. We were in fact familiar with their work and had referred to it in an earlier publication²⁴ in which we pointed out that the voltage drops observed for the Ag/Ag_xTiS₂ cell were due to staging. The slightly lower EMF values observed by us may be related to equilibration times to some extent, but other factors, such as the electrolytes, should also be considered, considering that neither of us reported standard EMF values.

We would also point out that we are aware of the diffusion constants for Ag in layered crystals. In fact, we measured the diffusion constants of Ag for single crystals using optical methods and reported the value of $\sim 10^{-10} \text{ cm}^2 \text{ sec}^{-1}$ for Ag in Ag_xTiS₂ and $\sim 10^{-8} \text{ cm}^2 \text{ sec}^{-1}$ for Ag in Ag_xTaS₂ at the Yamada Conference in 1980²⁴. In addition, we also reported at that time that the intercalation rate is strongly dependent on the crystal thickness, so in view of this finding, it would appear that measurements on dichalcogenide powders are actually somewhat ill-defined.

With respect to the reversible intercalation of Ag in Ag_xTiS₂ and Ag_xTaS₂, we are somewhat puzzled on three counts by B. Scrosati's comments.

1. The reversible behavior that he refers to was for silver in the range $0 < x < 0.06$ for Ag_xTaS₂²⁵ and in the range $0 < x < 0.03$ for Ag_xTiS₂²⁶. In our study,²² the intercalated mole fractions were over the much larger range of $0 \leq x \leq 2/3$ for Ag_xTaS₂ and of $0 \leq x \leq 0.42$ for Ag_xTiS₂.

2. Contrary to B. Scrosati's comments that we found the intercalation of Ag in TiS₂ reversible, we did not find this to be the case; we found only partially reversible behavior. Stage 1 ($1/5 \leq x \leq 2/5$) could be deintercalated, but stage 2 ($0 \leq x \leq 1/5$) could not. However, although the unsuccessful deintercalation of stage 2 may be a consequence of parasitic reactions caused by the electrolyte, we believe it is certainly not due to a low diffusion rate. Of course, it may certainly be the case that in the very low concentration range ($0 < x < 0.03$), intercalation occurs reversibly.

3. We were indeed surprised to discover the reversible intercalation behavior for Ag in Ag_xTaS₂ in the range $0 \leq x \leq 2/3$, in view of the gross stacking rearrangements that occur in the host layers for $x \approx 1/6, 1/3$, and $2/3$ ²⁷.

²¹Physics Department, Simon Fraser University, Burnaby, British Columbia, Canada V5A 1S6.

²²G. A. Scholz and R. F. Frindt, *This Journal*, **131**, 1763 (1984).

²³A. Bottini, M. Lazzari, G. Razzini, B. Rivolta, G. De Felici, M. A. Voso, and B. Scrosati, *J. Electroanal. Chem.*, **96**, 165 (1975).

²⁴G. A. Scholz, P. Joensen, J. M. Reyes, and R. F. Frindt, *Physica*, **105B**, 214 (1981).

²⁵F. Bonino, A. Lazzari, C. A. Vincent, and A. R. Wondless, *Solid State Ion.*, **1**, 311 (1980).

²⁶M. Patriarca, M. A. Voso, B. Scrosati, and F. Croce, *ibid.*, **9**, 10, 311 (1980).

²⁷G. A. Scholz and R. F. Frindt, *Mater. Res. Bull.*, **15**, 1703 (1980).

¹⁵R. C. Alkire and S. Perusich, *Corros. Sci.*, **23**, 1121 (1983).

¹⁶Dipartimento di Chimica, University of Rome, Italy.

¹⁷A. Bottini, M. Lazzari, G. Razzini, B. Rivolta, G. De Felici, M. A. Voso, and B. Scrosati, *J. Electroanal. Chem.*, **96**, 165 (1979).

¹⁸M. Patriarca, M. A. Voso, B. Scrosati, F. Bonino, and M. Lazzari, *Solid State Ion.*, **6**, 15 (1982).

¹⁹A. Padula, M. Patriarca, B. Scrosati, and F. Croce, *ibid.*, **9**, 10, 365 (1983).

²⁰F. Bonino, A. Lazzari, C. A. Vincent, and A. R. Wondless, *ibid.*, **1**, 311 (1980).

ERRATUM

In the paper "TEM Cross Section Sample Preparation Technique for III-V Compound Semiconductor Device Materials by Chemical Thinning" by S. N. G. Chu and T. T. Sheng [*This Journal*, 131, 2663 (1984)], the caption to Fig. 8 on page 2665 was inadvertently omitted. The figure, with caption, appears below.

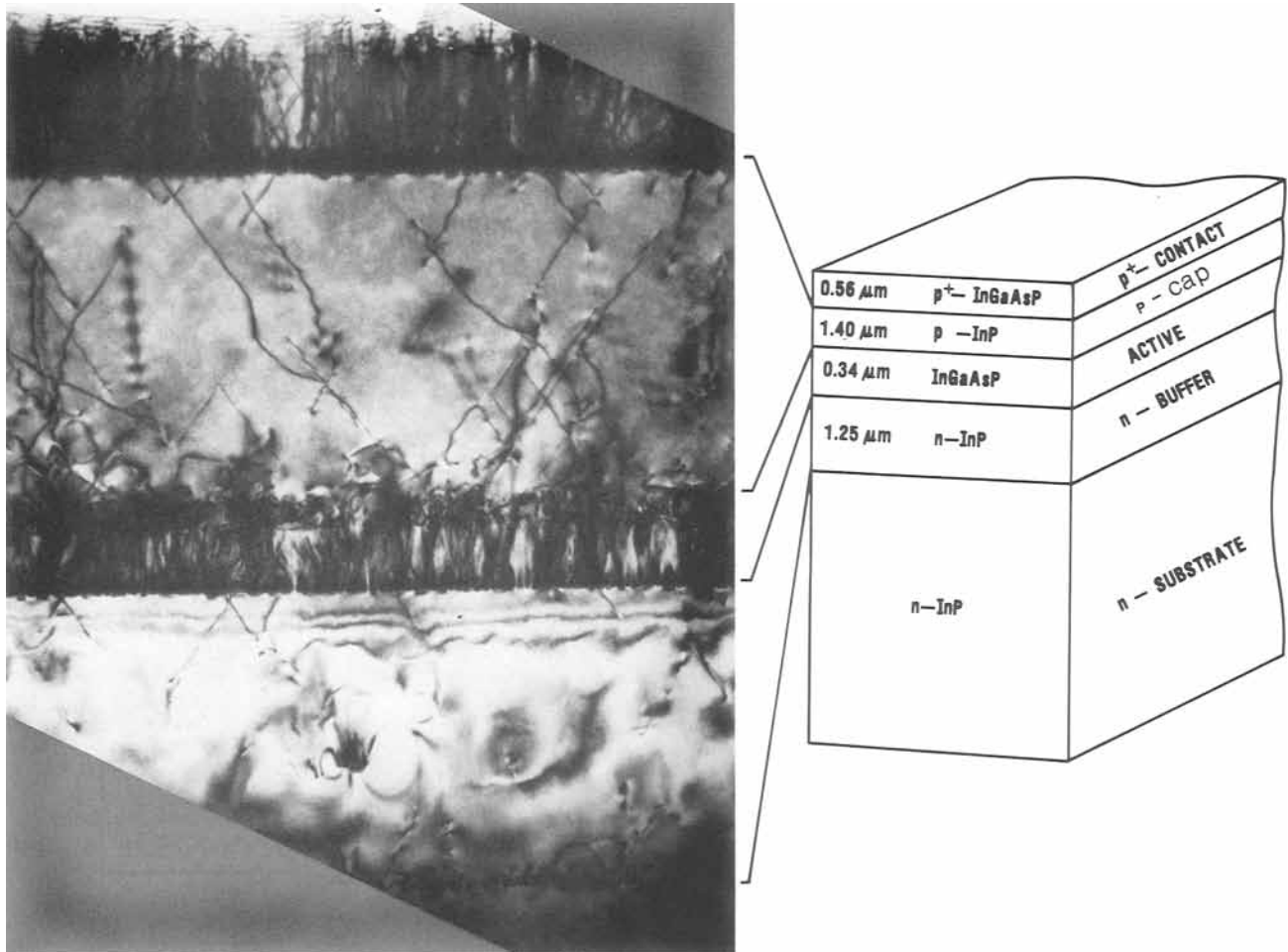


Fig. 8. XTEM of a four-layer InGaAsP/InP laser structure grown by VPE

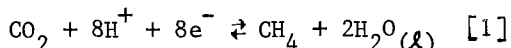


Electrochemical Reduction of Carbon Dioxide to Methane, Methanol, and CO on Ru Electrodes

K. W. Frese, Jr.,* and S. Leach*

SRI International, Menlo Park, California 94025

An important goal of research on CO_2 reduction is the synthesis of methane in an aqueous electrochemical process. Electrochemical reduction of CO_2 to CH_3OH with high faradaic efficiency has already been demonstrated (1,2). The standard electrode potential for the electrochemical half-cell



is only +0.17 V (SHE). Under standard conditions it is expected that reaction [1] should occur at potentials close to that for the hydrogen evolution reaction. Ruthenium was chosen because it is a known catalyst (3) for the gas phase conversion of CO_2 to CH_4 and is also known to be active at rather low temperatures, (3,4), e.g., $\sim 100^\circ\text{C}$.

EXPERIMENTAL

Both electroplated and teflon-supported Ru electrodes (geometrical area, 1-3 cm^2) were used for CO_2 electrolysis. The former were formed on spectroscopic pure carbon rods using a plating bath consisting of 0.0084 M $\text{Ru}(\text{NO})\text{Cl}_3$ and 0.4M reagent H_2SO_4 . The latter type of electrode was fabricated by pressing a mixture of 4-5 gm of Ru sponge (99.99%, Matthey-Bishop) with 5-12 weight % Halon TFE resin, type 6-80 onto a Cu mesh. The resulting pellets were contacted by a Cu wire and sealed in a glass tube with epoxy resin (Epoxy Patch). A 5 min. dip in conc. HCl was used to clean the Ru surfaces.

Electrolytes were prepared from reagent grade Na_2SO_4 or H_2SO_4 and purified, distilled H_2O (Milligard filtered). A Pine RDE-3 potentiostat was used for controlled potential electrolysis in a closed system that was described before (1,2). Current-time plots were obtained and manipulated by a laboratory microcomputer. Product analysis by gas chromatography was described earlier (1,2).

RESULTS

The faradaic efficiencies for CH_4 , CO, and CH_3OH are given in Table 1. These results were obtained with the electroplated electrodes in

CO_2 -saturated 0.2M Na_2SO_4 or 0.1M H_2SO_4 electrolytes. The average current obtained by dividing the integral charge (Column 5) by the total elapsed time is given in Column 3. The apparent increase in CH_4 yield with increasing temperature is not surprising in view of the expected kinetic complications for an 8e^- reduction. The efficiency for CO was always 1 to 5% with the exception of one datum. Rather high yields of CH_3OH were also found as shown in the last column of Table 1. A portion of the CO and CH_3OH may be due to CO_2 reduction by localized cathodic and anodic reactions at the Ru electrode (see below). Recent attempts of reaction [1] in 0.5M H_2SO_4 at -0.15 to -0.3 V(sce) ($55-60^\circ\text{C}$) gave faradaic efficiencies of 0.4%. Perhaps too high a coverage with H_{ad} is obtained in such strongly acidic solutions.

It was necessary to show that CH_4 could be produced in the absence of the carbon substrate because of the potential reactivity of carbon atoms adsorbed on the Ru surface (5). For this reason, teflon-supported Ru sponge electrodes were utilized. The results of two trials in 0.1N H_2SO_4 at 46°C were faradaic decimal efficiencies of 0.059 and 0.098 for CH_4 . The electrode potential was -0.37 to -0.39 V(sce) and the average current was 0.3 to 0.6 mA. Clearly the carbon substrate is not essential to the formation of CH_4 .

It was also shown that the Ru surface is active in CO_2 reduction under open circuit conditions in 0.2M Na_2SO_4 , pH 4-5. The data in Table 2 reveal that CO and small amounts of CH_3OH are produced by a localized cell reaction. The time of these open circuit experiments was equivalent to the 15-20 coulomb runs in Table 1. Note the similar pH change accompanying the CO_2 reduction. Importantly, no CH_4 was detected in these trials.

REFERENCES

- 1) D. Canfield and K. W. Frese, Jr., *Electrochem. Soc.* **130**, 1772 (1983).
- 2) K. W. Frese, Jr., and D. Canfield, *J. Electrochem. Soc.* **131**, No. 11 (1984).

- 3) F. Solymosi, A. Erdohelyi, and M. Kocsis, J. Catalysis 77, 1003 (1981).
 4) D. W. McKee, J. Catalysis 8, 240 (1967).
 5) H. Wise and J. McCarty, Surf. Sci. 133, 31 (1983).

Table 1
 FARADAIC EFFICIENCIES AS DECIMAL FOR CH₄, CO, AND CH₃OH ON
 ELECTROPLATED RUTHENIUM ELECTRODES IN CO₂-SATURATED ELECTROLYTES

pH range	T °C	$\langle i \rangle$ mA	V(sce)	Q coul	F _{CH₄}	F _{CO}	F _{CH₃OH}
0.2M Na ₂ SO ₄							
4.2-6.8	46	0.300	-0.65	98.5	0.046	0.025	0.029
4.2-4.8	50	1.6	-0.60	3.9	.086	.042	--
4.2-5.5 ^a	55	0.243	-0.56	15.4	0.045	0.048	0.094
3.5-5.5 ^b	60	0.387	-0.54	27.2	0.11	0.012	0.42
4.2-6.8	61	0.313	-0.55	19.8	0.30	0.45	0.25
4.2-5.9	67	0.270	-0.57	19.0	0.24	0.03	0.15
1.4 ^c	46	0.500	-0.35	114.0	0.088	0.024	trace

^aAlso contained 0.1M H₃BO₃ to slow pH increase.

^b0.1N H₂SO₄ added to lower pH range.

^cIn 0.1N H₂SO₄

Table 2
 MOLARITY OF CO AND CH₃OH PRODUCED UNDER OPEN-CIRCUIT CONDITIONS
 WITH TEFLON-SUPPORTED Ru ELECTRODES IN CO₂-SATURATED 0.2M Na₂SO₄^a

T °C	Time hrs.	pH _{initial}	pH _{final}	[CH ₄] _g	[CO] _g	[CH ₃ OH] _l
21	18	4.2	5.2	ND	6.0 x 10 ⁻⁶	ND
21	20	4.2	5.0	ND	6.1 x 10 ⁻⁶	< 10 ⁻⁴
46	16.5	4.2	5.2	ND	1.3 x 10 ⁻⁶	1 x 10 ⁻⁴
68 ^b	18.6	4.2	5.6	ND	2.3 x 10 ⁻⁶	5 x 10 ⁻⁴

^aCell vapor space, 1.3 liter; electrolyte volume, 0.025 l

^bUnknown small concentration of formaldehyde detected

ND = none detected

Acknowledgement: This research was supported by the Basic Research Division of the Gas Research Institute.

* Electrochemical Society Active Member.
 Manuscript submitted October 8, 1984.
 SRI International assisted in meeting the publication costs of this article.

Studies on Electrochemical Photovoltaic Cells Formed with Bi₂CdS₄ Film Electrodes

S. H. Pawar, S. P. Tamhankar, and C. D. Lokhande

Department of Physics, Shivaji University, Kolhapur 416004, India

CdS and Bi₂S₃ are promising semiconductors in the conversion of solar energy into electrical energy by means of electrochemical photovoltaic processes. However, the bandgaps of CdS ($E_g = 2.4$ eV) and Bi₂S₃ (1.4 eV) do not lie close to the solar energy spectrum maximum. Thus new solar energy materials need to be considered which satisfy desirable technical properties such as bandgap matching with the solar spectrum, high mobility and lifetime of the charge carriers and low cost (1). In this connection, we have reported a new material, Bi₂CdS₄, with a bandgap energy equal to 2 eV (2). The electrical and optical properties are reported in earlier communications (3,4).

In this communication, we report the electrochemical properties of Bi₂CdS₄ film electrodes. The experimental procedure for the deposition of Bi₂CdS₄ films by the spray pyrolysis technique is reported elsewhere (4). In short, aqueous solutions of Bismuth nitrate, cadmium chloride and thiourea were mixed in appropriate volumes in order to obtain Bi:Cd:S ratio as 2:1:4. The concentration of the solutions was 0.08 M. The substrate temperature was optimized as 250°C. The solution was sprayed at a rate of 3 cm³/min and total quantity sprayed was 200 C.C. Bi₂CdS₄ films with thicknesses of about 0.5 μm were deposited by spray pyrolysis technique. X-ray diffraction (XRD) pattern showed that the films were amorphous in nature. Compositional analysis of film based on energy dispersive analysis of x-rays (EDAX) showed that the films were deficient in cadmium and sulphur.

Key words: Bi₂CdS₄ films, spray pyrolysis technique, electrochemical photovoltaic cells

The electrochemical photovoltaic (ECPV) cells of the configuration, SnO₂:Bi₂CdS₄/1M NaOH - 1M Na₂S - 0.2 M S/C were formed. The electrical and optical properties of the cell were studied with the help of the Aplab nanoammeter, TFM 13 and PLA digital voltmeter DPM 10. A tungsten filament lamp (500 Watt) was employed for illuminating the cell. A water filter was interposed between the lamp and the ECPV cell in order to avoid heating of the cell. Spectral response of the cell was studied with the monochromator (Carl Zeiss Jena, Germany make) by noting variations of short circuit photocurrent, I_{sc} , with wavelength, λ . The capacitance-voltage (C-V) measurement was carried out with digital capacitance meter type VCM.13A.

To reveal the nature of the junction, current-voltage characteristics of the cells in dark were studied. In a electrode-electrolyte system the nature of the charge transfer reaction is given by Butler-Volmer equation as (5)

$$I = I_0 e^{(1-\beta)VF/RT} - e^{-\beta VF - RT} \quad 1$$

where I_0 is equilibrium exchange current density, β is the symmetry factor, V is the over voltage, R is the universal gas constant and F is the Faraday constant.

For voltage greater than 100 mV equation (1) reduces to

$$I = I_0 e^{(1-\beta)VF/RT} \quad 2$$

and when $\beta \neq 0.5$, the junction shows rectifying property. The magnitude of β was calculated by plotting $\log I$ versus V . The typical plot for the cell is shown in Fig.1. The magnitude of β was 0.6 which shows that the junction is rectifying in nature.

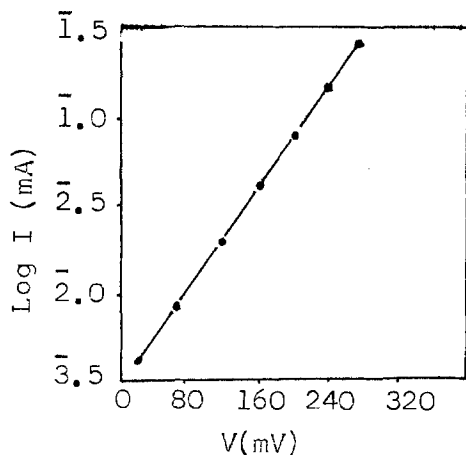


Fig. 1. Log I versus V plot for the ECPV cell formed with Bi_2CdS_4 film.

The films were etched in 50% dilute HCl for 5 seconds and heated in air at 150°C for 30 minutes before employing in the ECPV cells. A typical photovoltaic power output curve under illumination of $100 \text{ mW}/\text{cm}^2$ is shown in Fig. 2. The I_{SC} of the order of $0.2 \text{ mA}/\text{cm}^2$ and V_{OC} of the order of 260 mV were obtained under illumination. Recently, I_{SC} of the order of $0.2 \text{ mA}/\text{cm}^2$ and V_{OC} of the order of 100 mV with the ECPV cells formed with Bi_2S_3 films and polysulfide electrolyte were reported (6). The increased voltage for Bi_2CdS_4 films may be attributed to the increased bandgap of Bi_2CdS_4 films. The conversion efficiency η and fill factor, ff , were estimated as 0.03% and 40% respectively.

The spectral response of the cell was studied by noting variation of I_{SC} with wavelength, λ . Fig. 3 shows relative spectral response of the cell; I_{SC} peaks at 520 nm giving bandgap equal to 2.4 eV while the optical absorption studies of Bi_2CdS_4 films showed the cut off at 600 nm giving the bandgap equal to 2 eV . Such shifting of peak towards high energy side in the case of CdS ECPV cell is also reported (7). The lower photocurrent on the shorter wavelength side may be due to the absorption of light in the electrolyte and large amount of surface recombination of photogenerated minority carriers. Similarly lower photocurrent at the longer wavelength

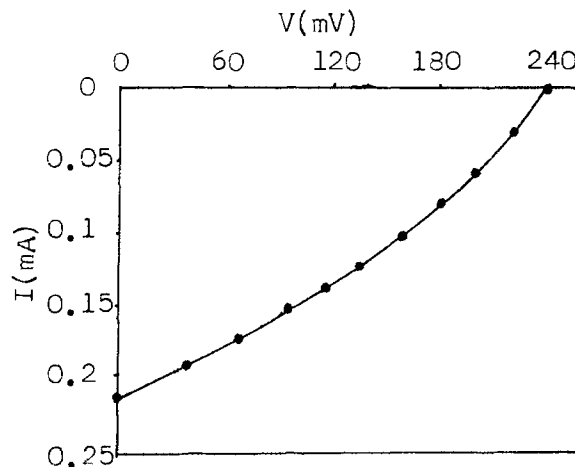


Fig. 2. A typical photovoltaic power output for the ECPV cell formed with Bi_2CdS_4 film; intensity of illumination was $100 \text{ mW}/\text{cm}^2$.

side is attributed to the lower absorption of light at the photoanode used (8).

The flat-band potential, V_{fb} , of $\text{Bi}_2\text{CdS}_5/\text{Polysulfide}$ redox electrolyte was estimated by carrying out C-V measurements. In fact, capacitance observed in this case corresponds to the semiconductor depletion region capacitance and hence amount of band bending of the semiconductor can be estimated from C-V measurements. The flat band potential, V_{fb} , is calculated using the relation as (9)

$$\frac{1}{C^2} = \frac{2}{q\epsilon_0\epsilon N_D} \left(V - V_{\text{fb}} - \frac{kT}{q} \right) \quad 3$$

where ϵ is dielectric constant; ϵ_0 is permittivity of vacuum, N_D is carrier concentration and V is applied voltage. Fig. 4 shows Mott-Schottky plots for Bi_2CdS_4 cell, in which two regions with different slopes are seen. This is attributed to the presence of defect and surface states in Bi_2CdS_4 films. The V_{fb} was determined as -1.1 V (SCE) .

ACKNOWLEDGEMENTS

Two of the authors (SHP & SPT) are grateful to Department of Non-Conventional Energy Sources, New Delhi, for financial support and one of the authors (CDL) is indebted to Council of Scientific and Industrial Research,

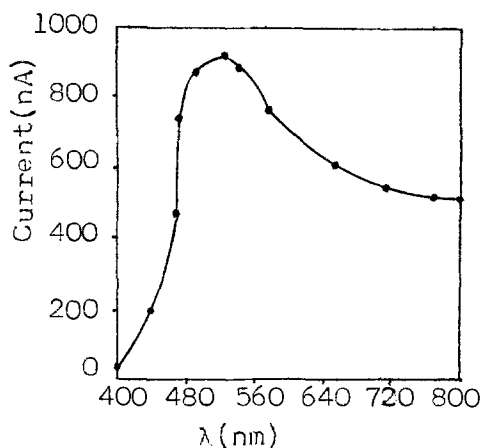


Fig. 3. Relative spectral response of the cell.

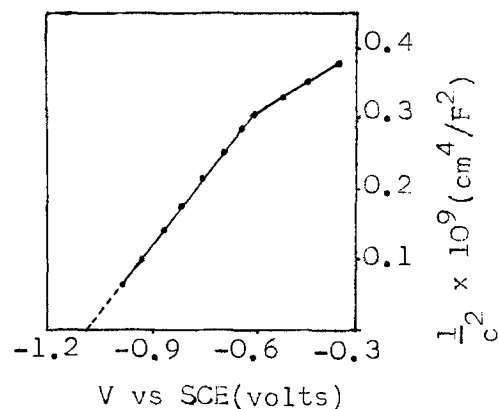


Fig. 4. $\frac{1}{C^2}$ versus voltage plot for the ECPV cell formed with Bi₂CdS₄ film.

New Delhi, for the award of Senior Research Fellowship.

Manuscript submitted March 21, 1984;
revised manuscript received August 23, 1984.

REFERENCES

1. M.Schoijet, Solar Energy Materials, 1, 43 (1979).
2. S.H.Pawar, Miss S.P.Tamhankar and C.D.Lokhande, Physica Status Solidi (a) (in press).
3. S.H.Pawar, Miss S.P.Tamhankar and C.D.Lokhande, J.Mat.Sci.lett. 3, 427 (1984).
4. S.H.Pawar, Miss S.P.Tamhankar and C.D.Lokhande, Proc.N.P. and S.S.P. Symposium, Mysore (1983).
5. Jo'm Bockris and A.K.N.Reddy, Modern Electrochemistry, Vol.2, A Plenum/Rosetta Edition, Chapter 8 (1973).
6. S.H.Pawar, Miss S.P.Tamhankar and C.D.Lokhande, Materials Chemistry and Physics (in press).
7. C.D.Lokhande and S.H.Pawar, Solid State Commun., 49, 765 (1983).
8. A.Heller, K.C.Chang and B.Miller, This Journal, 100, 684 (1978).
9. H.Gerischer, in Physical Chemistry- An Advanced Treatise, Vol.IX A.H. Eyring, Editor, Chap.5,p.473, Academic Press, New York, (1970).

Minority Carrier-Diffusion Length Measurement on p-CuInSe₂/Electrolyte Diodes

C. L. Johnson

Department of Chemistry, Princeton University, Princeton, New Jersey 08544

S. Wagner^{*,1}

Department of Electrical Engineering and Computer Science, Princeton University, Princeton, New Jersey 08544

K. J. Bachmann^{*}

Department of Chemistry, North Carolina State University, Raleigh, North Carolina 27650

The n-(Zn,Cd)S/p-CuInSe₂ heterodiode has elicited much interest as a candidate for an efficient (1-3) and stable (3) thin film solar cell. The cell is fabricated by deposition of the n-type window layer onto the CuInSe₂ substrate. In both the single crystal and thin film form, the CuInSe₂ has been observed to change during the deposition process. The net acceptor concentration near the interface declines in single crystal devices (4). For thin films, type conversion from n to p has been reported (3). It is therefore important to characterize the CuInSe₂ substrate before and after the growth of the window layer. The characterization technique must not alter the substrate. In this note we report the use of a temporary semiconductor/electrolyte barrier. We employed this barrier for a measurement of the diffusion length L_n of the photogenerated minority carrier (electron). For this measurement we used the constant surface photovoltage (SPV) technique (5). The same technique can be applied to the finished (Zn,Cd)S/CuInSe₂ diode, for a determination of L in CuInSe₂ after diode fabrication.

The SPV technique, adapted to semiconductor/electrolyte barriers (6) can be applied easily to direct gap semiconductors which have high optical absorption coefficients (7). The conditions for a straightforward application of the SPV technique pertain to the optical absorption length in the range of measuring wavelengths $1/\alpha$, the sample thickness d , the space charge width W of the collecting junction and the minority carrier diffusion length L . They are

- (1) $1/\alpha \ll d$,
- (2) $1/\alpha \gg W$,
- (3) $d \gg L$ and
- (4) $W \ll L$.

CuInSe₂ is noted for its high optical absorption coefficient (8). $\alpha(\lambda)$ lies in the vicinity of 10^5 cm^{-1} for photon energies above its band gap value of 1.0 eV. The SPV

measurements were carried out near the band gap energy with $0.34 \mu\text{m} < 1/\alpha < 0.76 \mu\text{m}$. C-V measurements on the electrolyte barrier showed that the semiconductor/electrolyte barrier had a depletion width of $\sim 0.01 \mu\text{m}$. Therefore, condition (2) was met. The measured diffusion length was $1.08 \mu\text{m}$. All four conditions were satisfied in our measurement.

Two values of L_n have been published earlier. One is a value of $L_n = 0.5 \mu\text{m}$, derived from photoelectromagnetic measurements on a single crystal (9). The other, $1.43 \mu\text{m} < L_n < 2.5 \mu\text{m}$, was determined from the electron beam induced current on a single crystal CdS/CuInSe₂ heterodiode (10).

The CuInSe₂ crystal studied here had been grown from the melt by the gradient freeze technique. The Se pressure was kept high to obtain a p-type crystal. At room temperature the Hall mobility of the holes was $16 \text{ cm}^2 \text{ V}^{-1} \text{ s}^{-1}$ and the hole density, $1.9 \times 10^{17} \text{ cm}^{-3}$. From a Mott-Schottky ($1/C^2$ vs. V) plot, we obtained an acceptor density in the depletion layer of $3 \times 10^{18} \text{ cm}^{-3}$, a value supported by the small width of the depletion layer. We tentatively ascribe the large difference between the densities of free holes in the bulk and of acceptors in the space charge to a high degree of compensation (11,12). Platelets were cut parallel to and including the free selenium ($\bar{1}\bar{1}\bar{2}$) surface of the crystal. The back was contacted with Ag epoxy and a Cu wire which was encased in a glass tube. The package, except for the front (electrolyte) face, was sealed with epoxy resin resistant to acetonitrile. After a 10 sec. etch in 2 vol.% Br_2/MeOH , the semiconductor electrode was inserted into the measuring cell. For routine measurements, the sample would be mounted at an opening in the cell with a temporary O-ring seal. A Pt wire served as the counterelectrode. The electrolyte was a solution of ~ 10 millimole of ferrocene and ferricenium (equal amounts by weight) as the

redox couple, and a supporting 1 molar concentration of tetrabutylammonium perchlorate in acetonitrile. The acetonitrile had been dried by distillation and was stored over a molecular sieve. The electrolyte was added to the N₂-purged cell by positive N₂ pressure. The cell was sealed from air. The measurement equipment includes a white light source, a mechanical chopper (22 to 175 Hz), a monochromator, and a split optical wave guide. Half of the beam was directed onto the sample, the other half onto a liquid-nitrogen cooled InSb detector for measurement of the photon flux. Both the sample and detector signals were processed through lock-in amplifiers.

During the SPV measurement, a value for the SPV is set by adjusting the photon flux $\Phi(\lambda)$ onto the sample. The wavelength λ is then varied and Φ is re-adjusted to restore the initial SPV. Assuming low-level injection and a constant sample reflectance, the following relation holds:

$$(5) \quad \Phi(\lambda) = \text{Const.} (L + 1/\alpha) \quad .$$

Extrapolation of the Φ vs. $1/\alpha$ data to $\Phi = 0$ therefore results in an intercept at $1/\alpha = -L$. A typical plot is shown in Fig. 1. The average L_n of a series of measurements was 1.08 μm . This value, reasonable in view of the earlier data, again underscores the high current collection efficiency of CuInSe₂-based solar cells.

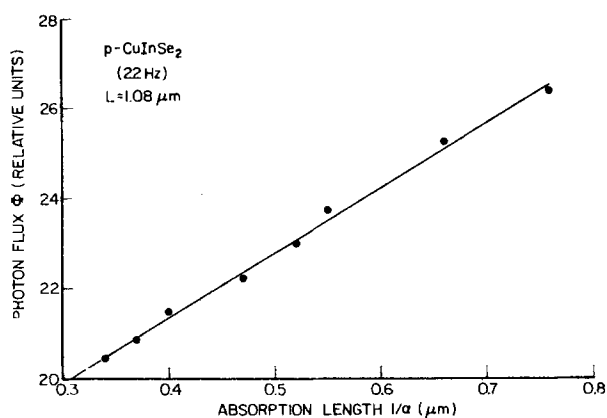


Figure 1. Plot of the intensity of the probing beam vs. absorption length. Note that the origin of the coordinates lies to the lower left, outside of the graph.

As mentioned above, we also carried out a series of C-V measurements to determine the net ionized acceptor density and the flatband voltage. These measurements equally demonstrate that CuInSe₂/electrolyte diodes are practicable for the electrical characterization of CuInSe₂ crystals.

This work was supported by the Solar Energy Research Institute under subcontract XL-2-02075-01.

REFERENCES

1. J.L. Shay, S. Wagner and H.M. Kasper, *Appl. Phys. Lett.* **27**, 89 (1975).
2. L.L. Kazmerski, F.R. White and G.K. Morgan, *Appl. Phys. Lett.* **29**, 268 (1976).
3. R.A. Mikkelsen and W.S. Chen, Record of the 16th IEEE Photovoltaic Specialists Conference, IEEE, New York, 1982, 781-785.
4. S. Wagner, J.L. Shay and H.M. Kasper, *J. de Physique* **36**, C3, 97 (1975).
5. A.M. Goodman, 1980 IEDM Tech. Digest, pp. 231-234, IEEE, New York, 1980.
6. A.R. Moore, *Appl. Phys. Lett.* **40**, 403 (1982).
7. C.-L. Chiang, S. Wagner and A.A. Ballman, *Materials Lett.* **1**, 145 (1983).
8. L.L. Kazmerski, M. Hallerdt, P.J. Ireland, R.A. Mikkelsen and W.S. Chen, *J. Vac. Sci. Technol.* **A1**, 395 (1983).
9. S. Mora and N. Romeo, *J. Appl. Phys.* **48**, 4826 (1977).
10. J. Piekozewski, L. Castaner, J.J. Loferski, J. Beall and W. Girit, *J. Appl. Phys.* **51**, 5375 (1980).
11. T. Irie, S. Endo and S. Kimura, *Japan. J. Appl. Phys.* **18**, 1303 (1979).
12. K.J. Bachmann, M. Fearheiley, Y.H. Shing and N. Tran, *Appl. Phys. Lett.* **44**, 407 (1984).

* Electrochemical Society Active Member.

¹ Author to whom correspondence should be addressed.

Manuscript submitted September 19, 1984; revised manuscript received October 16, 1984.

A Novel Effect. Changes in the Electrochemical Response of Polycrystalline Platinum Promoted by Very Fast Potential Perturbations

R. M. Cerviño, W. E. Triaca, and A. J. Arvia*

Instituto de Investigaciones Fisicoquímicas Teóricas y Aplicadas (INIFTA), Casilla de Correo 16, Sucursal 4, 1900 La Plata, Argentina

It is well established that the voltammogram of polycrystalline platinum in acid electrolyte in the potential range corresponding to the stability of bulk water depends on the electrochemical history including the type of perturbation applied to the electrode and on the electrolyte composition. Thus, the voltammogram obtained with polycrystalline platinum in 1 M sulphuric acid at 25°C under a repetitive triangular potential sweep at 0.1 V.s⁻¹, exhibits the conventional three regions, namely, the H- and O-adatoms electroadsorption/electrodesorption and the so-called double layer regions (Fig.1). The former region shows a multiplicity of reversible current peaks each pair of conjugated current peaks being generally associated with the electrochemical response of a determined type of single crystal face (1-8).

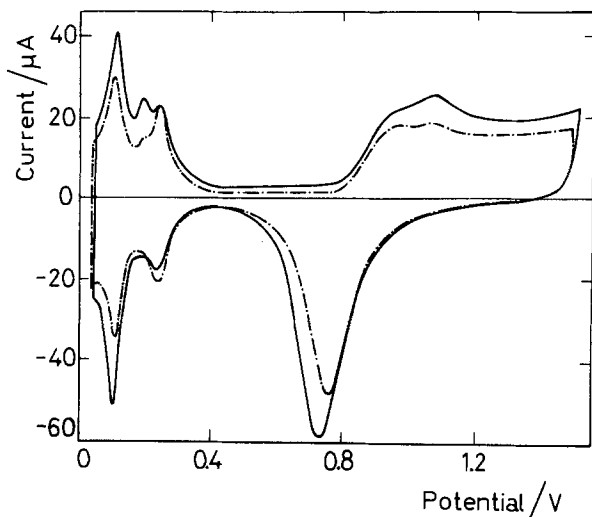


Figure 1 - Stabilized voltammograms (third cycle) run at 0.1 V.s⁻¹ in 1 M sulphuric acid at 25°C (—) after 5 s cycling at 2000 V.s⁻¹ between 0.4 and 1.6 V; (---) polycrystalline platinum electrode.

*Electrochemical Society Active Member.
Key words: platinum, oriented Pt surface, potential perturbation

When such an electrode is perturbed with a very fast repetitive triangular potential sweep at $v = 2000 \text{ V.s}^{-1}$ between $E_{\ell} = 0.4 \text{ V}$ and $E_u = 1.6 \text{ V}$ during 5 s, the voltammogram run immediately afterwards at 0.1 V.s⁻¹ is much more similar to that of a Pt(111) single crystal surface after it has been cycled at a relatively low v (e.g. 0.1 V.s⁻¹) a few times through the anodic oxide region (2,3,5-8) (Fig. 1).

On the other hand, when the potential perturbation conditions are changed to 10⁴ V.s⁻¹ in the 0.04 V to 1.5 V range during 5 min, the following voltammogram run at 0.1 V.s⁻¹ in the H-adatom potential range approaches closely the characteristics described in the literature for Pt(100) single crystal surface (1,3-5, 7,8) (Fig. 2). The electrochemical characteristics of the resulting platinum surface remain unchanged after 2 h cycling between 0.04 V and 1.5 V at 0.1 V.s⁻¹, except for a small surface reconstruction.

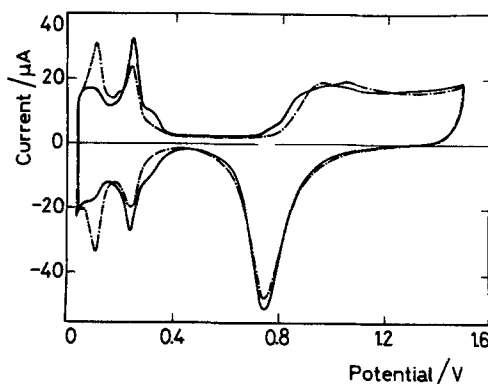


Figure 2 - Stabilized voltammograms (third cycle) run at 0.1 V.s⁻¹ in 1 M sulphuric acid at 25°C (—) after 5 min cycling at 10⁴ V.s⁻¹; (---) polycrystalline platinum electrode.

The surface structures achieved after the potential perturbation at high v are stable for at least four weeks by keeping the electrode in contact with distilled water. The poly-

crystalline structure is recovered after etching the electrode in aqua regia.

The above described experiments were made with a low resistance designed electrochemical cell consisting of a polycrystalline platinum wire working electrode (ca. 0.15 cm² geometric area) concentrically surrounded by a large area platinum counterelectrode (ca. 50 cm²). The potential of the working electrode was measured against a hydrogen reference electrode in the same acid electrolyte solution. The shape of the triangular potential signal was increasingly distorted accordingly to v and the shift from linearity at $(E_\ell + E_u)/2$ was ca. 10 percent at 10^4 V.s⁻¹.

The voltammograms run at 0.1 V.s⁻¹ imply no charge increase above that corresponding to the monolayer of adsorbed either H or O atoms, at least for the platinum surface obtained after cycling at 10^4 V.s⁻¹ during 5 min. However, for the surface resulting after cycling at 2000 V.s⁻¹ when the duration of the potential perturbation extends to 30 s, then a charge increase is noticed which is probably related to surface roughening.

The type of surface restructuring achieved during these experiments depends on E_ℓ , E_u and v . The results show that there is a frequency threshold for producing definite changes in the electrochemical response of polycrystalline platinum, which is ca. 0.5 kHz. This figure coincides with that of the repetitive square wave potential sweep which was able to produce a preferential orientation of grains at polycrystalline platinum electrodes (9) and its reciprocal was associated with the half life time of electroadsorbed OH species on platinum produced in the initial underpotential electrooxidation of water. Furthermore, similar changes in the electrochemical response of polycrystalline platinum as those described in the present communication were also achieved by applying to the electrode in acid electrolyte other very fast periodic potential perturbations such as either a repetitive square wave or a sinusoidal signal within the H- and O- adatom electroadsorption/electrodesorption potential range (10). Therefore, the metal surface modification promoted by the very fast potential perturbations should be related to the occurrence of the initial reversible underpotential electrooxidation of water. When the probable rate constants of the various stages involved in the O-electroadsorption are considered (11) it is concluded that at frequencies greater than 0.5 kHz, either (O)Pt electroformation or ageing effects of the O-adsorbed monolayer can be ignored. The latter processes are relevant when relatively slow repetitive triangular potential sweeps are applied to platinum electrodes in acid electro-

lyte into the region of oxide formation. In this case, when single crystal electrodes are used, it results in oriented but atomically stepped surfaces (12). Further studies on the optical and electrocatalytic properties of these electrodes as well as the mechanism involved in the modification of their electrochemical response are in progress.

Acknowledgement.-

INIFTA is sponsored by the University Nacional de La Plata, the Consejo Nacional de Investigaciones Científicas y Técnicas and the Comisión de Investigaciones Científicas (Provincia de Buenos Aires).

REFERENCES

1. F.G. Will, J. Electrochem. Soc., 112, 451 (1965).
2. P.N. Ross, Jr., J. Electroanal. Chem., 76, 139 (1977).
3. A.T. Hubbard, R.M. Ishikawa and J. Katakari, J. Electroanal. Chem., 86, 289 (1978).
4. E. Yeager, W.E. O'Grady, M.Y.C. Woo and P. Hagans, J. Electrochem. Soc., 125, 348 (1978).
5. K. Yamamoto, D.M. Kolb, R. Kotz and G. Lehmpfuhl, J. Electroanal. Chem., 96, 233 (1979).
6. J. Clavilier, R. Fauré, G. Guinet and R. Durand, J. Electroanal. Chem., 107, 205 (1980).
7. P.N. Ross, Jr., Surf. Sci., 102, 463 (1981).
8. F.E. Woodward, C.L. Scortichini and C.N. Reilly, J. Electroanal. Chem., 151, 109 (1983).
9. A.C. Chialvo, W.E. Triaca and A.J. Arvia, J. Electroanal. Chem., 146, 93 (1983).
10. J.C. Canullo, W.E. Triaca and A.J. Arvia, J. Electroanal. Chem., (in press).
11. J.O. Zerbino, N.R. de Tacconi, A.J. Calandra and A.J. Arvia, J. Electrochem. Soc., 124, 475 (1977).
12. F.T. Wagner and P.N. Ross, Jr., J. Electroanal. Chem., 150, 141 (1983).

Manuscript submitted January 1, 1984; revised manuscript received August 27, 1984.

INIFTA assisted in meeting the publication costs of this article.

The Influence of Thallium on the Redox Reaction $\text{Cr}^{3+}/\text{Cr}^{2+}$

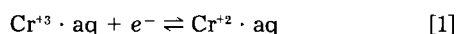
D. Sh. Cheng and E. Hollax

Fraunhofer-Institut für Solare Energiesysteme, D-7800 Freiburg, Germany

ABSTRACT

Investigations on the kinetics and electrocatalysis of the $\text{Cr}^{3+}/\text{Cr}^{2+}$ reaction were carried out. By means of cyclic voltammetry, it was discovered that the addition of thallium-I-chloride not only accelerates the $\text{Cr}^{3+}/\text{Cr}^{2+}$ reaction in HCl electrolytes catalytically, using graphite electrodes with small amounts of Au, but also raises the hydrogen overvoltage more than lead and bismuth, the heavy metal catalysts already tested in the practical redox cells. Investigations concerning the reaction rate, the influence of chrome ion concentrations, the electrolyte storage time, temperature, and the presence of iron are being conducted.

It has been shown that the course of the reaction [1] is slow



in both directions when carried out on carbon. This material is used in practical redox electrodes, because it is cheap and relatively durable in acidic as well as basic electrolytes (1, 2).

In addition, the hydrogen liberating reaction



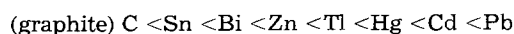
poses problems during the Cr^{3+} reduction, because the coulombic efficiency diminishes and the increasing number of cycles throws the system out of electrical balance. This reaction makes it difficult to use the redox couple in practical redox cells (3-6). The following is, therefore, necessary: (i) the acceleration of the reaction [1] with catalysts, and (ii) the shifting of reaction [2] to a more negative potential value (compared to the thermodynamic approachable standard potential) by increasing in the hydrogen overvoltage.

The standard potential for the $\text{Cr}^{3+}/\text{Cr}^{2+}$ redox reaction is approximately -0.401V vs. NHE , which corresponds to -0.645V vs. SCE . The hydrogen liberation on carbon begins at about -0.600V vs. SCE . It has been stated in the literature that traces of lead chloride or bismuth chloride, and gold, silver or copper are advantageous additions for the cathodic and anodic reactions, respectively (7-9).

Bonhoeffer (10) discovered that the larger the catalytic effectiveness of the surface is, regarding the gas reaction, the smaller the overvoltage will become. Considering the constant a in the Tafel equation

$$\eta = a + b \log j \quad [3]$$

(where η = average potential, j = current density, and a , b = values characteristics of the electrode), the following orders can be expected for the hydrogen overvoltage (11-19)



Investigations carried out regarding the influence of thallium on the kinetics of the $\text{Cr}^{3+}/\text{Cr}^{2+}$ reaction, and its suitability as catalyst in combination with gold for practical electrodes are described.

The high overvoltage of Tl compared to the cathodic hydrogen overvoltage had already been noted by Pietzsch and Josephy (20).

Experimental

Measurements were made at 25°C (unless indicated otherwise) with a Potentiostat POS73 (Bank), an X-Y recorder 2000 (Houston Instruments), and an electrolysis cell EA-875-10 (Methrom) with a working electrode, counterelectrode, and reference electrode. Figure 1 shows the working electrode with exchangeable measuring head

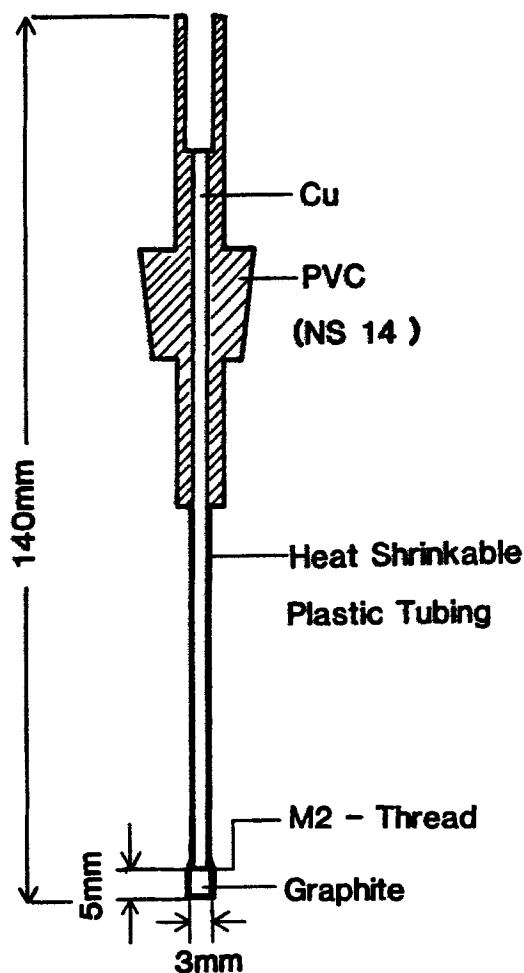
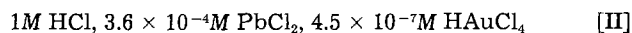
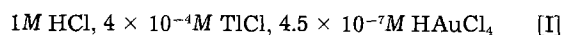
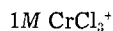


Fig. 1. Working electrode with exchangeable measuring head of high pressure graphite.

developed at the Fraunhofer-Institut für Solare Energiesysteme Freiburg.

The geometric surface area is 0.113 cm^2 , and the electrode material is high pressure graphite. A platinum electrode was the counterelectrode and a sat. KCl, Hg/Hg₂Cl₂ electrode (SCE) was the reference electrode. Before measuring, the solution was purged for 10-30 min with N₂. The SEM photos were made with a JEOL/35-LF scanning electron microscope.

All chemicals were analytical grade. Solutions were made using doubly distilled water. The following standard-(stock-) electrolytes were used when not otherwise stated

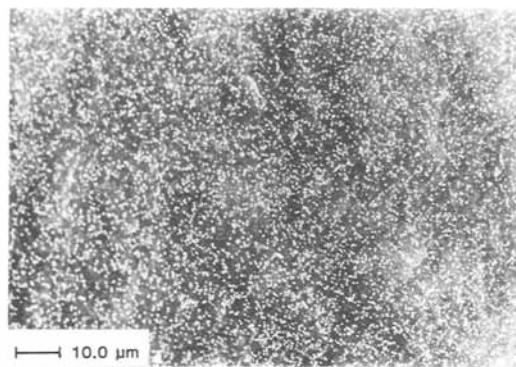


Results and Discussion

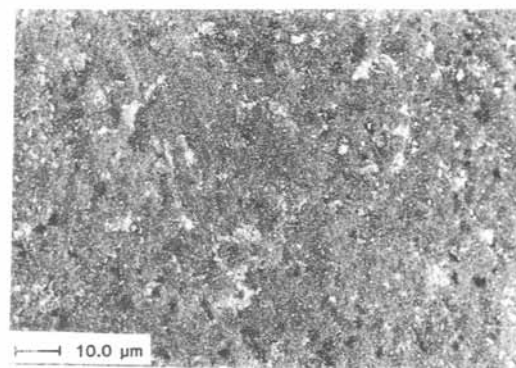
Electrode pretreatment.—The pretreatment of the graphite electrode has a substantial influence on the form of catalyst deposition and therefore on the catalytic activity. The pretreatment of the electrode surface by polishing with corundum paste (particle size: $1 \mu\text{m}$) did not result in a completely smooth surface, because, under these conditions, graphite tends to smear. The roughness was, however, reduced. This could be confirmed by our electron microscope photographs. From literature results (21-24), it was estimated that the roughness factor of polished electrodes should be smaller than 15. This value has been derived by double-layer capacitance measurements.

The measured double-layer capacitance for a smooth graphite electrode are $3 \mu\text{F cm}^{-2}$ for a basal plane and for an edge plane $60 \mu\text{F cm}^{-2}$ (23, 24).

It was found that the cathodic thallium deposition on the polished surface occurred evenly over the entire sur-



a



b

Fig. 2. SEM photographs after (a) cathodic thallium deposition and (b) anodic dissolution. Standard electrolyte I, 25°C.

face. This was established by SEM photographs and also by x-ray microprobe analysis (Fig. 2a).

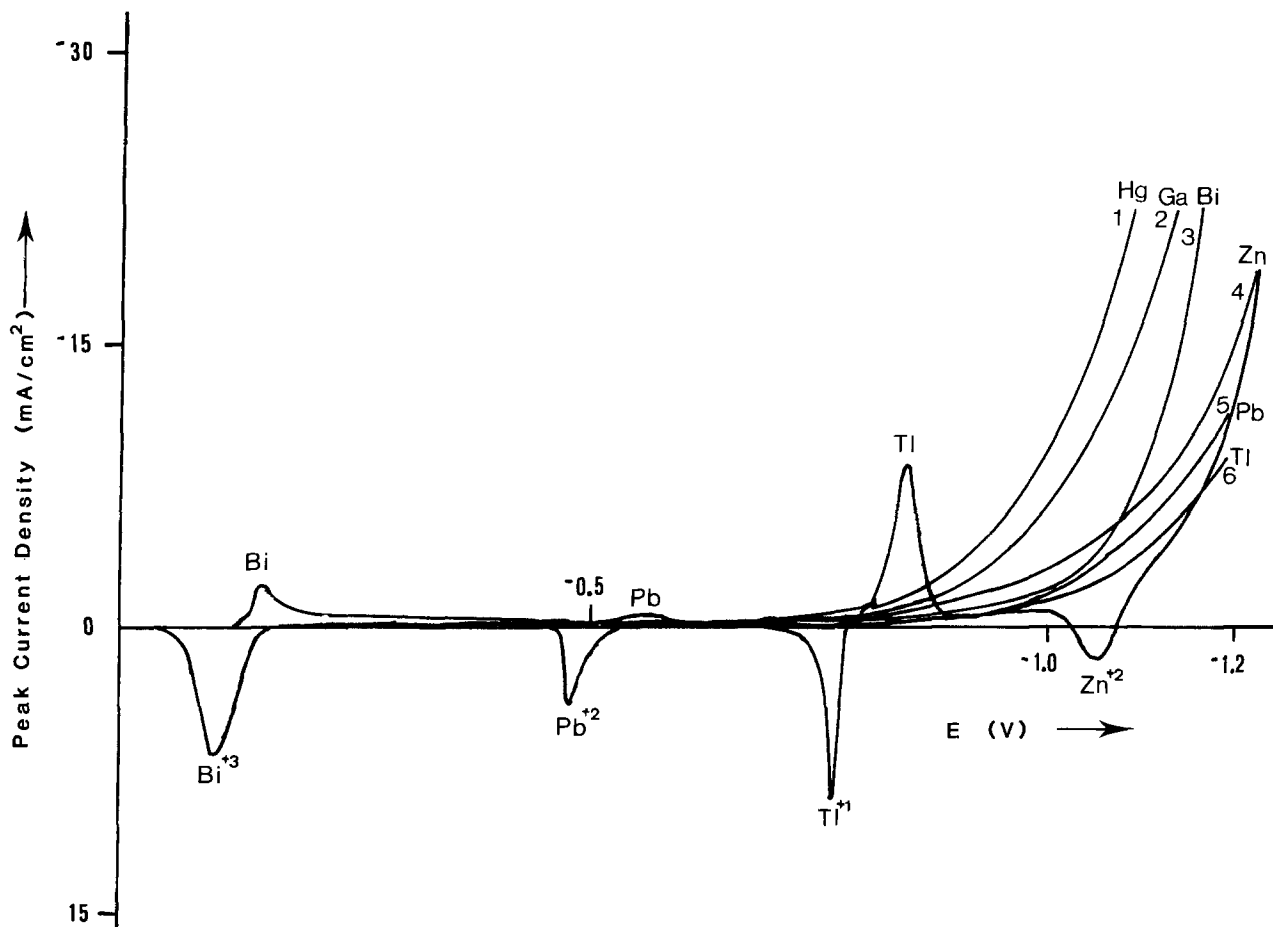


Fig. 3. Cyclic voltammogram of various heavy metals ($v = 100 \text{ mV/s}$, 25°C) $1M \text{ HgCl}_2$, $6.3 \times 10^{-4}M$ salt concentration. Curve 1, HgCl_2 ; curve 2, GaCl_3 ; curve 3, BiCl_3 ; curve 4, ZnCl_2 ; curve 5, PbCl_2 ; curve 6, TiCl_4 .

In addition, the thallium dissolves quantitatively when anodically loaded (Fig. 2b). Uneven catalyst deposition and dissolution were observed using an unpolished electrode.

Hydrogen overvoltage and catalytic activity.—In Fig. 3, the location of the deposition and dissolution peaks of HgCl_2 , GaCl_3 , BiCl_3 , ZnCl_2 , and TlCl in 1N HCl using a polished electrode are shown. The scan rate was 100 mV/s, and the concentration was $6.3 \times 10^{-4}\text{M}$. The result shows that thallium has a slightly higher hydrogen overvoltage than that of lead chloride, and, comparing the peak heights of PbCl_2 and TlCl , it can be seen that the latter has in addition a higher catalytic effectivity (Fig. 4).

Under these conditions, the optimal TlCl concentration was found to be $6.5 \times 10^{-4}\text{M}$ (Fig. 5). A stronger inhibition effect, which was found in the case of underpotential deposition of Pb on silver (21), has not been observed even at higher Tl^{1+} ion concentrations.

The mechanism of hydrogen liberation has been frequently investigated (11), and there are numerous mechanisms discussed in the literature: for example, the Volmer-Heyrovsky and Tafel reactions.

In the Tafel reaction, the rate-limiting step is the recombination of the hydrogen atoms



Until now, there has been no universally valid reaction mechanism. The dependency on electrode material, electrolyte solution, current density, and temperature complicated matters.

In reaction [4], it is expected that the overvoltage is dependent above all on electrode material because it is ac-

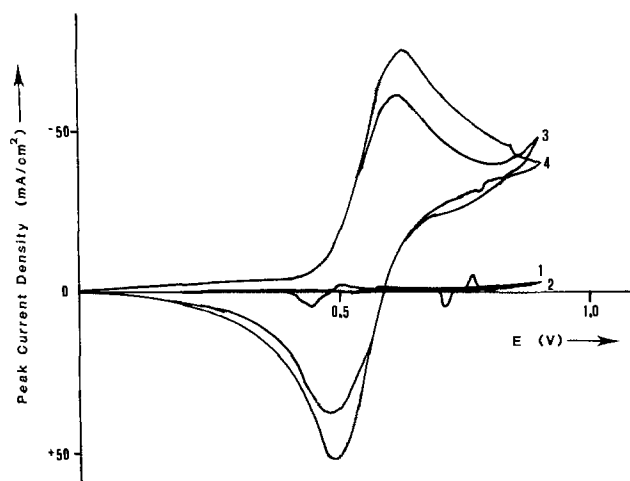


Fig. 4. Comparison of the influence of thallium and lead on the $\text{Cr}^{3+}/\text{Cr}^{2+}$ redox reaction and the hydrogen overvoltage (scan rate $v = 100$ mV/s, polished graphite surface, 25°C). Curves 1 and 2: without chromium ions; curve 3: stock electrolyte [I]; curve 4: stock electrolyte [II].

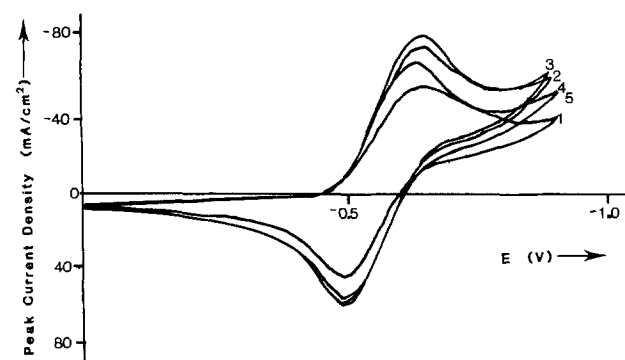


Fig. 5. Dependence of peak current density on thallium concentration ($v = 100$ mV/s, polished graphite surface, 25°C , 1M CrCl_3 , 1M HCl , $4.5 \times 10^{-7}\text{M HAuCl}_4$). Curve 1: $1 \times 10^{-5}\text{M TlCl}$. Curve 2: $1 \times 10^{-4}\text{M TlCl}$. Curve 3: $6.5 \times 10^{-4}\text{M TlCl}$. Curve 4: $1 \times 10^{-3}\text{M TlCl}$. Curve 5: $1 \times 10^{-2}\text{M TlCl}$.

celerated by the catalytic reaction. The large shift of the H_2 liberation to a negative potential in the presence of thallium chloride is only conceivable when there is an even Tl deposition as an inhibition of the active centers of the H_2 formation. We found that, as with Pb (3, 6, 7), very small amounts are sufficient to cover the deposited gold. There is not direct proof, but it can be assumed that there is an especially high reaction overvoltage of the reaction [4] in the presence of thallium in the temperature and current density regions of our measurements.

Reaction rate, reversibility.—Kinetic and thermodynamic data can be obtained with cyclic voltammetric measurements (25-30). It was observed that the peak potential difference, ΔE_p , for reversible reactions, that is, for processes that follow the Nernst relation, is approximately 58 mV. As the scan rate $v = dE/dt$ ($t = \text{time}$) increases, the peak current and the peak potential difference ΔE_p ($E_{pa} - E_{pc}$) also increase (25, 27, 31). This points to the onset of the heterogeneous electron-transfer rate. Through the variation of v and, therefore, ΔE_p , the rate constant k_s of heterogeneous reactions can be calculated with good approximation using a method developed by Matsuda and Ayabe (25) and Nicholson (27) and through the use of the kinetic parameter ψ introduced by Nicholson (26-28). This is portrayed in Eq. [5]

$$k_s = \psi \sqrt{\pi D a} \quad [5]$$

where $a = v(nF/RT)$, $v = \text{scan rate}$, $D = \text{diffusion coefficient}$, $\psi = \text{kinetic parameter for } \Delta E_p$ (32), and ΔE_p peak potential difference.

When $k_s \leq 10^{-5}$ cm/s, the reaction is irreversible, and if $10^{-5} \leq k_s \leq 1$ cm/s, according to Matsuda and Ayabe (25), the reaction is quasireversible. As shown in Table I, k_s has values of approximately 1.5×10^{-3} cm/s under the given conditions. This suggests that a quasireversible reaction proceeds.

For a Nernstian wave with stable product, the ratio of anodic and cathodic peak current density j_{pa}/j_{pc} is equal to 1.

This is true regardless of scan rate, switching potential E_s , and diffusion coefficients when j_{pa} is measured from the extrapolated decaying cathodic current. Because of the inaccuracy of this baseline determination, Nicholson (27) suggests that the ratio can be calculated from the uncorrected anodic peak current density $(j_{pa})_0$ with respect to the zero current baseline, the current density at switching potential $(j_{sp})_0$, and cathodic peak current density j_{pc} , with respect to the zero current baseline (Eq. [6])

$$\frac{j_{pa}}{j_{pc}} = \frac{(j_{pc})_0}{(j_{pc})} + \frac{0.485(j_{sp})_0}{j_{pc}} + 0.086 \quad [6]$$

The ratios are approximately equal to 1 (see Fig. 6).

Chromic ion concentration.—The peak current densities of reaction [1] increase linearly with the Cr^{3+} ion concentration as shown in Fig. 7. The concentration in the double layer is directly proportional to that in the solution.

Cycle numbers and electrolyte storage time.—It was determined that there is no strong decline of catalytic activity after up to 100 cycles measured after one another (Table II). The results are different, however, when the electrolyte storage time increases (Table III). A clear decline in activity resulted already after 25 days (25°C).

Table I. Heterogeneous rate reaction dependence on scan rate ($D_{\text{Cr}^{3+}} = 6 \times 10^{-6}$ cm²/s (22), 2M CrCl_3 , 2M HCl , $6.5 \times 10^{-4}\text{M TlCl}$, $4.5 \times 10^{-7}\text{M HAuCl}_4$, 25°C)

v (mV/s)	ΔE_p (mV)	ψ	k_s (cm/s)
20	115	0.394	1.5×10^{-3}
30	128	0.323	1.5×10^{-3}
40	135	0.269	1.46×10^{-3}
50	140	0.248	1.51×10^{-3}
60	150	0.212	1.41×10^{-3}

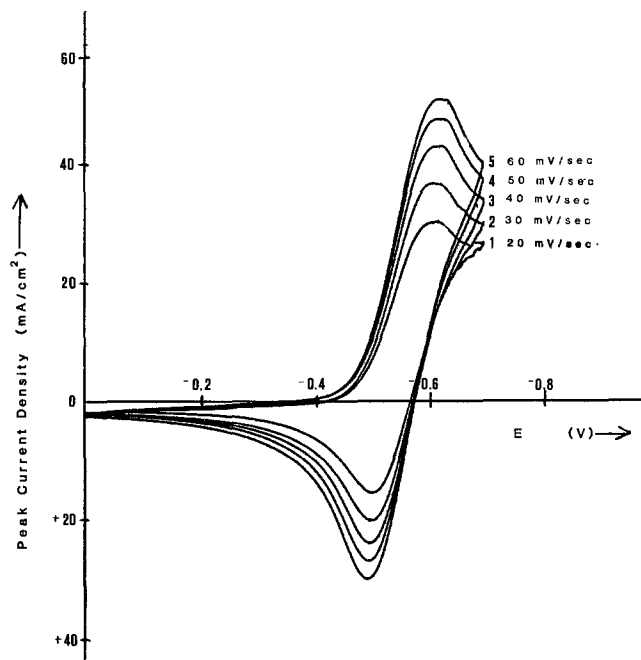


Fig. 6. Influence of scan rate on k_s ($2M CrCl_3$, $6.5 \times 10^{-4}M TiCl_4$, $4.5 \times 10^{-5}M HAuCl_4$, $2M HCl$, $25^\circ C$).

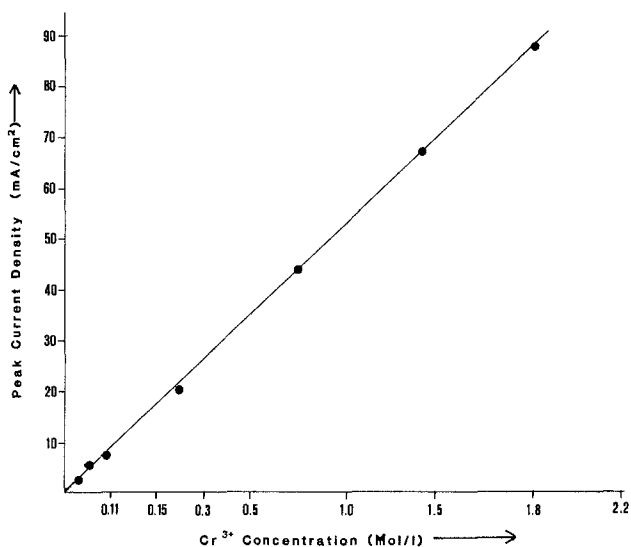


Fig. 7. Dependence of peak current density on Cr^{3+} ion concentration ($6.5 \times 10^{-4}M TiCl_4$, $4.5 \times 10^{-5}M HAuCl_4$, $2M HCl$).

This decline in activity is comparable to other catalysts (33, 34) which were also measured, and is the result of the so-called "aging effect" of the chromic-III-chloride solution

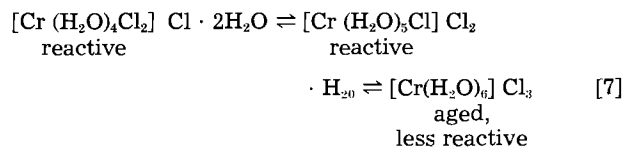


Table II. Cathodic peak current density (cpcd) dependence on cycle number (multisweep, graphite electrode, standard electrolyte I)

Cycle no.	cpcd (mA/cm ²) ($\pm 2.5\%$)
1	82
5	82
10	80
50	80
75	79
100	75

Table III. Cathodic peak current density (cpcd) dependence on the storage time t_s (electrolyte I, $25^\circ C$; scan rate: $100 mV/s$)

t_s (d)	cpcd (mA/cm ²)
0.1	82
1	80
5	68
25	42
75	19
200	10

It is known that chromium forms complexes very easily and, with a few exceptions, has a coordination number of 6. According to Eq. [7] chromium forms relatively stable hexaquo complexes where ligand substitution reactions proceed with half-lives on the order of an hour. We have shown that aged chromium-III-hexaquo complexes can be reactivated with N-alkylimines (33, 34).

Temperature.—The influence of the temperature was measured between 20° and $60^\circ C$ using the standard electrolytes I.

The cyclic voltammograms in Fig. 8 show the expected peak current density enhancement with increasing temperature. The increase of peak current density of $20 mA/cm^2$ between 20° and $60^\circ C$ corresponds to 40% enhancement. This result was to be expected because the transport process inside the Nernst diffusion layers ($<10^{-3} cm$), as well as the charge transfer, is accelerated by the rise in temperature. However, since ΔE_p changes only minimally, the result is actually due to the former effect.

Noteworthy is the hydrogen gas formation between 0.5 and 0.6V at $60^\circ C$. This is probably due to the extreme decline of the reaction overpotential of the Tafel reaction [4].

Conclusions

1. The use of Tl results in a higher catalytical activity for the Cr^{3+}/Cr^{2+} reaction and in a slightly higher hydrogen overvoltage than Pb.

2. The reaction rate declines quickly even in the presence of thallium as a result of the "aging effect" due to the hexaquo chrome-(III) complexes.

3. An observable peak current density can be increased through a temperature, but hydrogen formation also increases because of the decline in reaction overvoltage for the Tafel reaction. The increasing of the peak current density can be explained by the acceleration of transport phenomena.

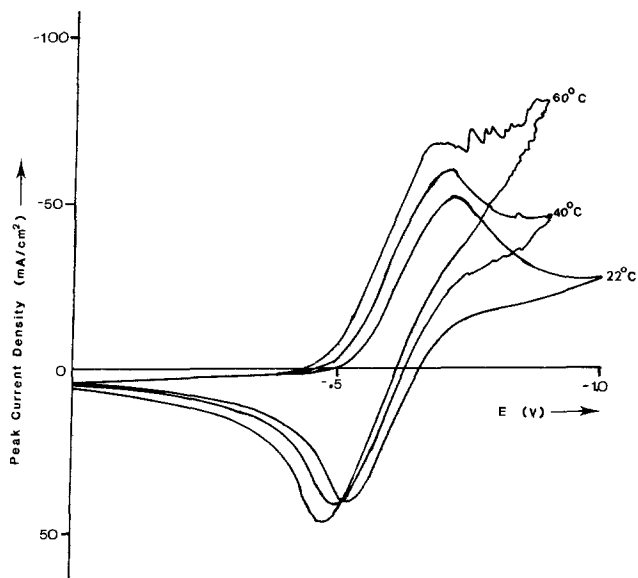


Fig. 8. Temperature dependence (stock electrolyte [I], $50 mV/s$)

Acknowledgments

We wish to thank the National Ministry for Research and Technology (Germany), the Academia Sinica and the Fraunhofer-Gesellschaft, especially Professor A. Goetzberger, director of the FhG-Institut für Solare Energiesysteme, for the support of Professor D. Sh. Cheng during his residence in Germany. We also wish to thank Dr. J. Heinze for the details discussion of the results, Dr. A. Hurre and G. Schätzle for the SEM photographs, H.-D. Gaa for construction of the hardware, and R. Kneusel for the figures and the English translation.

Manuscript submitted March 21, 1984; revised manuscript received Oct. 4, 1984.

Institut für Solare Energiesysteme assisted in meeting the publication costs of this article.

REFERENCES

1. J. E. Early and R. D. Cannon, *Trans. Met. Chem.*, **1**, 33 (1965).
2. M. J. Weaver and F. C. Anson, *Inorg. Chem.*, **15**, 1871 (1976).
3. L. Thaller, "Recent Advances in Redox Flow Cell Storage Systems," DOE/NASA/1002-79-4, National Aeronautics and Space Administration, Washington, D.C., NASA TM-79186 (1979).
4. K. Nozaki *et al.*, in Proceedings of the 22nd Battery Symposium in Japan," p. 93 (1981).
5. K. Nozaki and T. Ozawa, in "Proceedings of the 17th IECEC," p. 610 (1980).
6. N. H. Hagedorn, "NASA Redox Project Status Summary," DOE/NASA/12726-22, NASA TM-83401, NASA-Lewis Research Center, Cleveland, OH (1982).
7. J. Giner and K. J. Cahill, U.S. Pat. 4,192,910 (1980).
8. R. F. Gahn, N. H. Hagedorn, and J. S. Ling, "Single cell performance studies on the Fe/Cr Redox Energy storage system using mixed reactant solutions at elevated temperature," DOE/NASA/12726-21 NASA-Lewis Research Center, Cleveland, OH, TM-83385 (1983).
9. N. A. Reid, A. F. Gahn, J. S. Ling, and J. Charleston, DOE/NASA/12726-13, NASA TM-82702, NASA-Lewis Research Center, Cleveland, OH (1980).
10. K. F. Bonhoeffer, *Z. Phys. Chem. A*, **113**, 199 (1924).
11. K. J. Vetter, "Elektrochemische Kinetik," pp. 410-497, Monographie, Springer-Verlag, Berlin (1961).
12. S. Glasstone, *J. Chem. Soc.*, **125**, 250, 2414, 2646 (1924).
13. F. P. Bowden and K. E. Grew, *Discuss. Faraday Soc.*, **1**, 86 (1947).
14. A. Hickling and F. W. Salt, *Trans. Faraday Soc.*, **37**, 224, 319, 333, 450 (1941); *ibid.*, **38**, 474 (1942).
15. F. P. Bowden and E. K. Rideal, *Proc. R. Soc. Ser. A*, **120**, 59 (1928).
16. J. O.-M. Bockris and A. M. Azzam, *Trans. Faraday Soc.*, **48**, 145 (1952).
17. B. Kabanow and S. Jofa, *Acta Physicochim. USSR*, **10**, 617 (1939).
18. J. P. Hoare and S. Schuldiner, *J. Chem. Phys.*, **25**, 786 (1956).
19. K. Schwabe, "in Physikalische Chemie," Bd. 2, Elektrochemie, p. 305, Akademie-Verlag, Berlin (1975).
20. E. Pietzsch and E. Josephy, *Z. Elektrochem.*, **37**, 837 (1931).
21. S. S. Donovan and E. Yeager, Technical Report no. 24 Electrochemistry Research Lab., Case Western Reserve University, Cleveland, OH (1969).
22. J. P. Randin and E. Yeager, *This Journal*, **118**, 711 (1971).
23. J. P. Randin and E. Yeager, *ibid.*, **36**, 257 (1972).
24. J. P. Randin and E. Yeager, *ibid.*, **58**, 313 (1975).
25. H. Matsuda and Y. Ayabe, *Z. Elektrochem.*, **59**, 494 (1955).
26. R. S. Nicholson and J. Shain, *Anal. Chem.*, **36**, 706 (1969).
27. R. S. Nicholson *ibid.*, **37**, 1351 (1965).
28. R. S. Nicholson and J. Shain, *ibid.*, **37**, 178 (1965).
29. D. S. Polecyn and J. Shain, *ibid.*, **38**, 370 (1966).
30. A. J. Bard and L. R. Faulkner, "Electrochemical Methods," Chap. 6, John Wiley and Sons, New York (1980).
31. D. A. Johnson and M. A. Reid, Paper 252 presented at the Electrochemical Society Meeting, Detroit, MI, Oct. 17-22, 1982.
32. J. Heinze, *Ber. Bunsenges. Phys. Chem.*, **85**, 6-1103, Table 2 (1981).
33. D. Sh. Cheng, E. Hollax, and A. Reiner, Poster 0507, 34th Meeting of the International Society of Electrochemistry, Erlangen, Germany, Sept. 18-23, 1983; E. Hollax and D. Sh. Cheng, In preparation.
34. D. Sh. Cheng, A. Rainer, and E. Hollax, *J. Appl. Electrochem.*, To be published.

Investigation of Li/SO₂ Cell Chemistry and Hazards by Spectroscopy and Accelerating Rate Calorimetry

W. P. Kilroy*

Naval Surface Weapons Center, White Oak Laboratory, Silver Spring, Maryland 20903-5000

W. Ebner* and D. L. Chua*

Honeywell Power Sources Center, Horsham, Pennsylvania 19044

H. V. Venkatesetty*

Honeywell, Incorporated, Corporate Technology Center, Bloomington, Minnesota 55420

ABSTRACT

Accelerating rate calorimetry (ARC) has been used to define the thermal and pressure behavior of Li/SO₂ cells during overdischarge as a function of cell balance and operating temperature. Lithium-limited cells are shown to be intrinsically safe while cells containing excess lithium at end of life have been shown to be capable of undergoing thermal runaway through a series of coupled reactions. The most serious thermal hazards occurred upon overdischarge at low temperature. ARC analyses of cell components, *in situ* FTIR analyses, and mass spectroscopic analyses of discharged cathodes have been used to investigate the chemistry associated with the thermal behavior of Li/SO₂ cells. As expected, the lithium/acetonitrile reaction and the thermal decomposition of lithium dithionite contribute to the thermal runaway process observed in cells overdischarged at ambient temperature. In addition, however, two other reactions have been identified; one initiating at approximately 140°C involving lithium and the electrolyte solution and another initiating at approximately 190°C which is believed to involve lithium and the decomposition products of lithium dithionite. Further investigations are needed to elucidate the chemistry involved in the low temperature safety problems.

The high energy battery most widely used for military applications employs the Li/SO₂ electrochemical system. However, concern for the safety of personnel has precluded its widespread acceptance and full utilization. Although safety hazards occur from such abuse modes as shorting or charging, the problems encountered during normal operation are of particular concern. These include additional discharge of stored cells that have already been partially discharged, resistive overdischarge (when a resistive load is not removed at the end of cell life) and forced overdischarge, which occurs when a weak or prematurely depleted cell in a series of cells is overdischarged by the remaining cells. This paper focuses on the hazards resulting from overdischarge of Li/SO₂ cells.

Previous investigations on overdischarged Li/SO₂ cells have described cell behavior and some of the chemistry involved in the observed safety problems (1-5). In those studies, analyses were made on cell reaction products and gases recovered from vented cells, and it was shown that the materials balance in the cells plays a major role in the observed safety characteristics.

Based on those investigations, thermal runaway produced by exothermic chemical reactions is believed to be a primary cause of safety problems arising from overdischarge of Li/SO₂ cells. DTA studies have identified a number of exothermic chemical reactions that could contribute to a thermal runaway (6, 7). The most important are believed to involve the thermal decomposition of lithium dithionite, the major discharge product of Li/SO₂ cells, or the reaction of lithium or lithium/aluminum alloy with acetonitrile.

The objective of the present work, therefore, was to quantitatively define the thermal effects of exothermic reactions resulting from overdischarge of Li/SO₂ cells and to determine if thermal runaway was indeed the cause of the observed safety problems. Accelerating rate calorimetry (ARC) has been employed to study the thermal and pressure behavior of observed exothermic reactions. Component analyses involving both ARC and mass spectroscopy, along with *in situ* FTIR studies of cell electrolysis products, have been employed in an attempt

to identify the key reactions involved in cell exothermicity.

Experimental

Mass spectroscopic studies were performed employing a Finnigan Model 4000 GC chemical ionization electron impact mass spectrometer.

Infrared spectra of electrolysis products of Li/SO₂ cells were recorded *in situ* using a Digilab Model 14 FTIR spectrometer. Spectroelectrochemical cells were constructed with either AgCl or KBr windows separated by polyethylene spacers to permit insertion of electrodes. The cell assembly had a path length of <1.0 mm and was sealed with epoxy. The anode consisted of a nickel minigrad current collector, with or without lithium, located in the center of the cell in the direct path of the infrared radiation. The cathode collector was Shawinigan carbon black with Teflon pressed on an aluminum grid and located on the inside periphery of the cell. A lithium reference electrode was included. An external jacket was built to permit subambient operation (to -22°C) by circulating nitrogen cooled by dry ice and acetone. The cells were filled in a glove box with the electrolyte solution cooled to -10°C to prevent loss of SO₂.

The accelerating rate calorimeter was manufactured by Columbia Scientific Industries. The experimental 1/2 C-size Li/SO₂ cell used in the ARC studies was a spirally wound cell employing conventional components and housed in a 316L stainless steel case acting as the negative terminal. The primary electrolyte consisted of 6.4 weight percent (w/o) LiBr, 25.6 w/o acetonitrile (AN), and 68.0 w/o SO₂. One experiment employed propylene carbonate (PC) electrolyte with 6.4 w/o LiBr, 33.6 w/o PC, and 60.0 w/o SO₂. The PC was vacuum distilled prior to use.

In the ARC experiments, discharge and overdischarge at ambient temperature was carried out in the calorimeter but not under adiabatic conditions. Periodically, the testing was interrupted and the cells checked for exothermicity while on open circuit. Exotherms were monitored under adiabatic conditions to completion before electrical testing was continued. Force overdischarge tests were carried out for a minimum 200%, based on ini-

* Electrochemical Society Active Member.

Table I. Summary of Li/SO₂ cell descriptions, test conditions, and performance for ARC test cells

Cell no.	Li/SO ₂ ^a ratio	Test temperature	Overdischarge mode	Discharge to 2V cutoff			Overdischarge	
				Avg. current density (mA/cm ²)	Delivered capacity (Ah)	Final Li/SO ₂ ratio	Capacity removed (Ah)	Overdischarge (%)
1	0.52	Ambient	Resistive (5Ω)	4.6	0.77	0.12	0.17	9.93
2	0.36	Ambient	Resistive (5Ω)	5.0	0.65	0.05	0.16	8.15
3	0.50	Ambient	Resistive (5Ω)	4.8	0.93	0.14	0.09	3.92
4 ^b	0.00	Ambient	Forced (1 mA/cm ²)	N/A	N/A	N/A	7.63	375
5	1.48	Ambient	Forced (1 mA/cm ²)	1.0	1.32	5.26	3.63	244
6	1.46	Ambient	Resistive (5Ω)	5.5	1.08	2.32	0.38	22.7
7	1.54	Ambient	Resistive (5Ω)	5.8	1.07	2.56	0.39	23.7
8	1.54	Ambient	Resistive (5Ω)	5.5	1.03	2.16	0.40	20.8
9 ^c	1.50	Ambient	Forced (1 mA/cm ²)	1.0	0.89	1.97	4.28	234
10	0.98	-35	Forced (3 mA/cm ²)	3.0	0.60	0.98	3.96	220
11	1.00	-35	Forced (3 mA/cm ²)	3.0	0.61	1.00	Vent	Vent
12	1.00	-35	Forced (3 mA/cm ²)	3.0	0.57	1.00	4.46	246

^a Cells 1-4, lithium limited; cells 5-9, excess lithium; cells 10-12, coulombically balanced (based on theoretical Li/SO₂ capacities).

^b Cell 4 employed a bare nickel grid as an anode. No lithium was present. The percent overdischarge represents the quantity of charge passed through the cell in excess of the starting SO₂ capacity.

^c Cell 9 employed propylene carbonate as solvent in place of acetonitrile.

tial SO₂ capacity. Resistive overdischarge was continued until the cell potential dropped below 0.1V.

Results and Discussion

The ARC is a microprocessor-controlled adiabatic calorimeter that automatically searches for exothermic reactions by elevating the temperature of a sample or a complete cell by a fixed increment and then checking for a self-heating rate exceeding a preselected threshold. Once an exotherm is detected, the instrument maintains the sample in an adiabatic environment and continuously monitors its thermal and pressure behavior. In this way, the ARC can provide a complete hazard analysis for each exothermic reaction detailing the kinetics of the reaction, the rate and quantity of heat generated, and the rate and magnitude of pressure generated. Additional details concerning the theory and operation of the ARC can be found in the literature (8, 9).

Hazards associated with exothermic reactions occurring in Li/SO₂ cells during and following overdischarge have been characterized by six parameters relating to cell thermal and pressure behavior. They are (i) initiation temperature, (ii) total heat output, (iii) total pressure rise, (iv) maximum rate of temperature rise, (v) maximum rate of pressure generation, and (vi) maximum observed pressure. The ARC thermal data have been presented as a log temperature rate vs. temperature plot. The temperature data are plotted as 1/T K while the temperature axis is labeled in degrees centigrade for convenience. This is essentially an Arrhenius plot of the data which is very useful for interpreting the ARC results since each exothermic reaction occurring will show up as a separate peak. Discontinuity in the ARC thermal curves represents a heat/search mode of operation where self-heating was not observed in the sample.

A description of the ARC cells tested, the test conditions and cell performance are summarized in Table I. Three cell types have been investigated, each having a different coulombic Li/SO₂ ratio, as follows: lithium limited ≈ 0.5 , balanced ≈ 1.0 , and excess lithium ≈ 1.5 . These ratios were chosen so that the lithium would always be completely consumed in lithium-limited cells at end of life while lithium would always remain at end of life in excess-lithium cells, regardless of operating conditions. Balanced cells are balanced in theoretical terms only and may or may not have lithium remaining at end of life, depending on operating conditions. For example, operation at low temperatures or high rates of discharge can severely degrade cathode utilization efficiencies, causing a theoretically balanced cell to contain significant quantities of lithium at end of life.

All cells used in these studies incorporated a reverse wrap configuration in which the cathode is on the outside of the wrap. In this configuration, all lithium is electrochemically accessible, making the lithium-limited cells truly lithium limited. In contrast, most commercial cells employ a conventional wrap, with the lithium anode on the outside of the wrap. In these cells, part of the lithium on the last turn of the wrap assembly is not electrochemically accessible and will remain at end of life regardless of the initial materials balance in the cell or the operating conditions employed. Such cells are never truly lithium limited.

Ambient temperature tests.—Lithium-limited cells.—Table II summarizes the hazard analysis data for lithium-limited cells resistively overdischarged at ambient temperature. Typical thermal behavior is illustrated by cell no. 3 in Fig. 1. Initial exothermicity generally occurred near 104°C, the result of a low activation energy exotherm, as evidenced by the minimal acceleration of rate with increasing temperature. All the cells exhibited a second exotherm between 210° and 260°C. Two of the

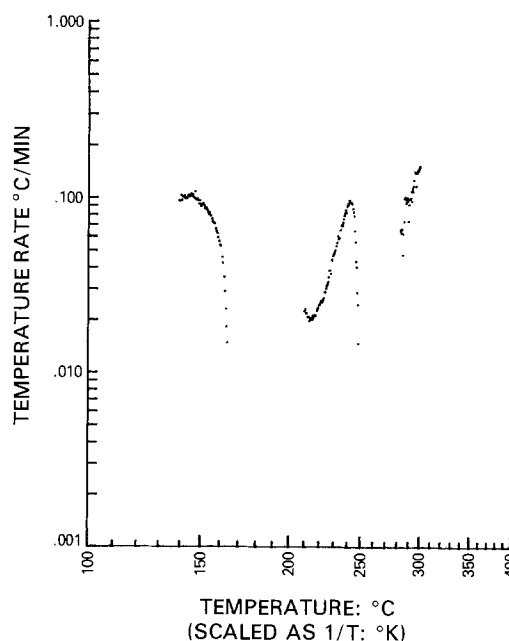


Fig. 1. ARC thermal behavior for lithium-limited cell no. 3 resistively overdischarged of ambient temperature.

cells exhibited a third exotherm initiating between 280° and 290°C. In the remaining cell, cell no. 1, the two high temperature exotherms appeared to be combined as a single exotherm. The reproducible innocuous thermal and pressure data appear to confirm the intrinsic safety of the lithium-limited design.

Forced overdischarge of a lithium-limited cell could cause oxidation of the electrolyte solution, anode grid material (if a grid is employed), and/or the cell case material, generating products that could significantly affect cell safety.

Conventional Li/SO₂ employs nickel-plated steel cases (10, 11), while some cells manufactured for special applications incorporate a nickel grid as an anode collector (12). Overall, nickel is used in virtually all Li/SO₂ cells and is a key material to consider when investigating the effects of overdischarge of lithium-limited cells. For this reason, our test cells incorporated nickel anode grids. FTIR analysis on electrolyte solutions stored 15 days with nickel confirmed the stability of this system.

In situ FTIR analysis during electrolysis of a lithium-limited cell, containing a bare nickel grid as an anode (Fig. 2A), showed distinct changes in the solution spectra when compared to the spectra of a cell containing a lithium anode (Fig. 2B). In the cell with the lithium anode, the IR spectra remains unchanged from that of the original electrolyte solution when electrolyzed to 23% of its SO₂ capacity, indicating the absence of any soluble discharge products. In the cell with the bare nickel grid, however, the water bands at 3460 and 1630 cm⁻¹ disappear and a band at 2665 cm⁻¹ decreases. Small bands appear at 980, 1060, and 1265 cm⁻¹. A 880 cm⁻¹ shoulder becomes a peak at 900 cm⁻¹ on continued electrolysis. A new band appears at 800 cm⁻¹.

Interestingly, several of these bands were also observed under some cell conditions involving a lithium anode. For example, if the partially discharged cell of Fig. 2B is stored at 25°C for 11 days, some IR bands split, major bands appear at 500, 560, 800, 880, 920, and 980 cm⁻¹, and some minor bands, indicative of sulfate (13), form at 445, 615, and 1100 cm⁻¹ (Fig. 2C). With the exception of the 800 and 880 cm⁻¹ bands, the other bands have been observed in the spectra of solid discharge products (14, 15). Also, when a fresh Li/SO₂ cell is charged at 25°C, major IR bands appear at 800, 880, 980, and 1260 cm⁻¹ (Fig. 2D).

The effects of solvation by SO₂ make *in situ* identification difficult. The bands near 1265, 1060, 980, and 660 cm⁻¹ generally grow or appear upon discharging a cell with no lithium or on charging a fresh Li/SO₂ cell. Similar bands have been identified with metabisulfite, S₂O₅²⁻ (16, 17). However, it is plausible these bands arise from redox reactions involving SO₂ to form an indistinguishable solvated sulfite, SO₃²⁻ · SO₂.

The 800 cm⁻¹ band is strongly IR active (18) and is attributed to an asymmetric stretching frequency of a —SOS— group (19). This band appears to be influenced by kinetic factors. It develops on storage (Fig. 2C), on charging, but only at current densities ≥0.5 mA/cm² (Fig. 2D) and upon loss of lithium in cells overdischarged at 25°C (Fig. 2A) but not at -22°C.

Presumably, this 800 cm⁻¹ band involves the interaction of the highly reactive [SO₂]⁻ ion with [SO₂]⁻, SO₂ or other sulfur oxy-anions. An ion pair, [Li⁺ · SO₂⁻] (20), and a charge transfer complex, S₂O₄⁻ formed between SO₂ and SO₂⁻ (21), have been reported. Also, a reactive form of dithionite [SO₂ · SO₂]²⁻ with —SOS— bonding (22) has been proposed to be the reactive intermediate in which metals, such as nickel, are oxidized by organic-SO₂ solvents to disulfates or sulfates (23, 24).

To determine if these oxidation products affect cell safety, a cell containing no lithium at all and employing a bare nickel grid as an anode was force discharged at 1 mA/cm² for 7.63 Ah, 3.75 times the initial SO₂ capacity. Occasionally, the discharge was interrupted and the cell was checked by ARC for exothermicity. No exotherms were detected. Next, the cell was subjected to a heat and search operation in the ARC; only one small exotherm

occurred at approximately 225°C. The self-heating rate was only 0.06°C/min with a pressure of 100 psig. Although

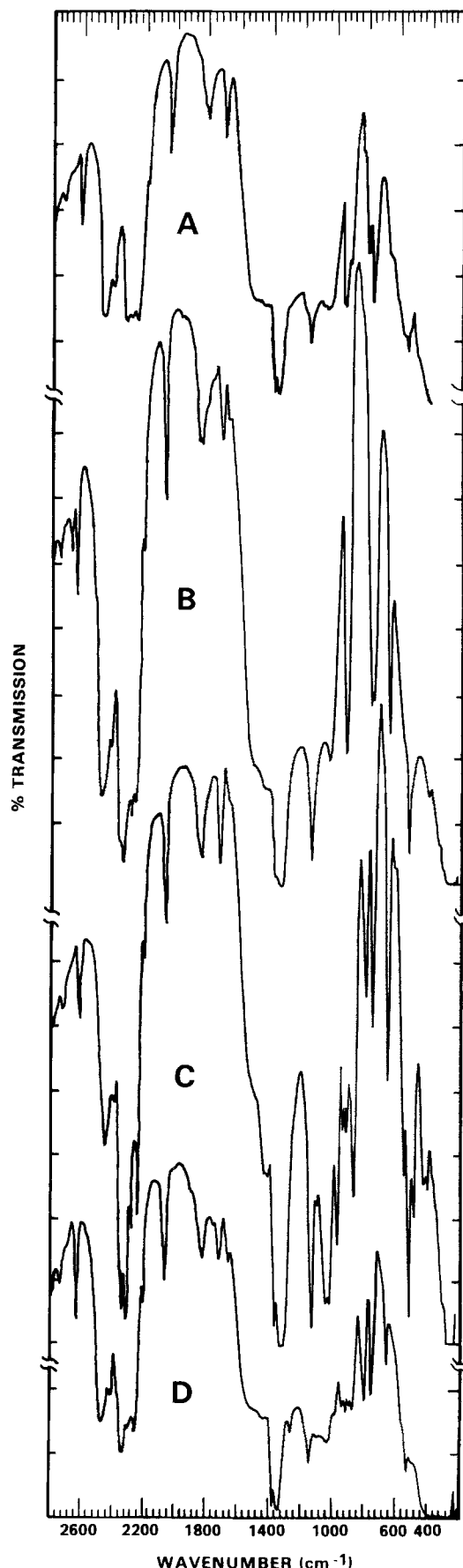


Fig. 2. *In situ* infrared spectra of a SO₂ cell. A: Cell containing a Ni anode, partially discharged at 0.56 mA/cm². B: Li/SO₂ cell, partially discharged at 0.56 mA/cm² at 25°C. C: Li/SO₂ cell partially discharged at 0.2 mA/cm² at 25°C and stored 11 days. D: Fresh Li/SO₂ cell charged at 2 mA/cm² at 25°C.

Table II. Hazard analysis of lithium-limited cells resistively overdischarged at ambient temperature

Cell no.	Minimum initiation temperature (°C)	Total heat evolved (cal)	Maximum temperature rate (°C/min)	Maximum pressure rate (psi/min)	Total ^a pressure rise (psig)	Maximum observed pressure (psig)
1	145	669	0.63	7.1	126	315
2	148	636	0.30	1.1	121	244
3	139	1178	0.15	0.8	163	273

^a Represents the maximum increases observed from the start of the first exotherm detected to the end of the last exotherm observed.

Table III. Hazard analysis of excess-lithium cells overdischarged at ambient temperature

Cell no.	Overdischarge mode	Minimum initiation temperature (°C)	Total heat evolved (cal)	Maximum temperature rate (°C/min)	Maximum pressure rate (psi/min)	Total ^a pressure rise (psig)	Maximum observed pressure (psig)
5	Forced (1 mA/cm ²)	40	2987	0.34	1.35	490	524
6	Resistive	29	3559	0.54	3.70	258	272
7	Resistive	36	3275	3.18	3.36	530	544
8	Resistive	29	3366	0.50	7.19	679	690

^a Represents the maximum increases observed from the start of the first exotherm detected to the end of the last exotherm observed.

oxidation products in the absence of lithium at the anode revealed no intrinsic safety problems, we have not ruled out hazards that may occur in "anode"-limited cells containing some electrochemically inactive lithium. This is more likely to occur in cells using a standard wrap configuration.

Excess lithium cells.—ARC analysis revealed very complex thermal behavior for Li/SO₂ cells containing excess lithium. The hazard analysis data for excess lithium cells overdischarged at ambient temperature are tabulated in Table III. Figure 3 illustrates ARC thermal data for cell no. 5 force overdischarged at 1 mA/cm². Both the thermal and pressure ARC curves are displayed in Fig. 4 for a similar cell, no. 7, which has been resistively overdischarged using a 5Ω load. All excess lithium cells, whether forced overdischarged or resistively overdischarged, exhibited initial exothermicity shortly after overdischarge began, often with the cells still near ambient temperatures. In addition, all the resistively overdischarged cells exhibited an exotherm, beginning at approximately 110°C. A similar peak was observed in the forced overdischarged cell at approximately 125°C. All the cells exhibited several addi-

tional exotherms in the temperature range 140°-200°C and displayed a common high temperature exotherm near 260°C.

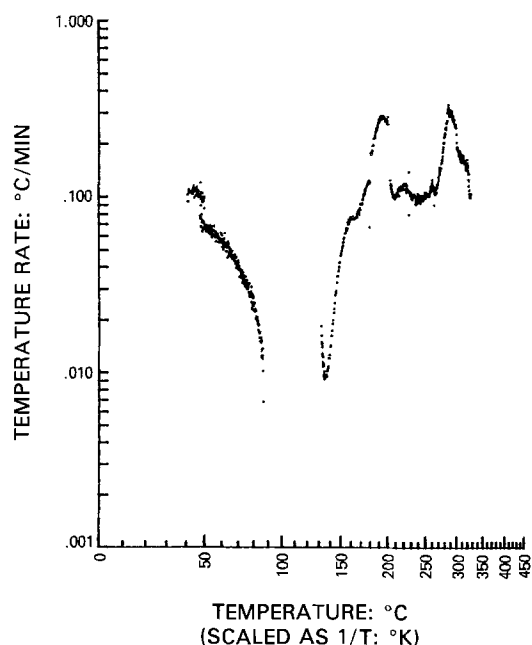


Fig. 3. ARC thermal behavior for excess lithium cell no. 5 forced overdischarged at 1 mA/cm² at ambient temperature.

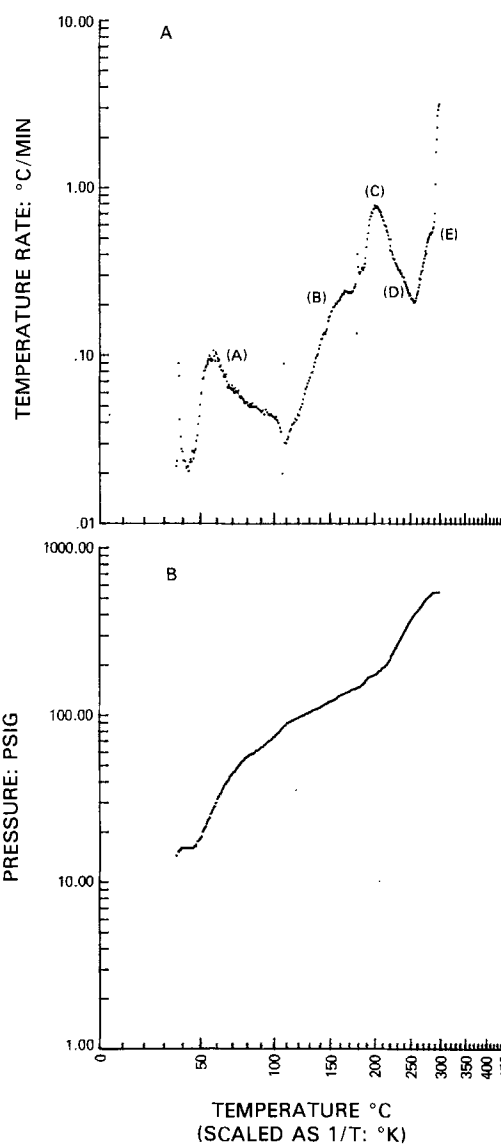


Fig. 4. A: ARC thermal behavior for excess lithium cell no. 7 resistively overdischarged at ambient temperature. B: ARC pressure behavior for cell no. 7.

In general, overdischarged excess lithium cells exhibited one continuous exotherm, resulting in self-heating to temperatures of 300°C or more. The ARC data indicate that several coupled reactions are responsible for the self-heating rather than one single reaction. Although thermal runaway did occur, the observed rates of heat and pressure generation were low, indicating the absence of explosion hazards but the magnitude of overall pressure generation was sufficient to cause venting in commercial cells.

Low temperature tests.—Significant safety hazards have been observed in Li/SO₂ cells force overdischarged at ~3 mA/cm² at low temperatures and allowed to warm to room temperature (25). To simulate these conditions, cells coulombically balanced at ambient temperature were force overdischarged at -35°C under a constant current of 3 mA/cm². Three replicate cells were tested. One cell, cell no. 11, vented during the overdischarge, generating an internal pressure of greater than the 2500 psig required to rupture the disk vent incorporated in the ARC hardware. The two remaining cells were successfully overdischarged but exhibited distinctly different thermal behavior. Cell no. 12 became exothermic at 35°C and continued self-heating to 182°C. This cell generated only a maximum pressure rate of 8.51 psi/min to a total of 160 psig. The exotherm at 32°C was similar to the reactions observed in the cells overdischarged at ambient temperature, attributed to reaction of lithium with acetonitrile. At 61°C, a second reaction occurred exhibiting a maximum temperature rate of only 1.84°C/min. The other cell, cell no. 10, did not become exothermic until 77°C, but, near 110°C, a very rapid reaction occurred producing heating rates of >180°C/min and pressure generation rates exceeding 1700 psi/min (Fig. 5). The maximum observed pressure was 881 psig.

The results obtained with cell no. 10 and 11 confirm that overdischarge of Li/SO₂ cells at low temperature can indeed produce explosion-type hazards. The fact that cell no. 11 vented while still at low temperature before being allowed to warm up raises even more concern.

Cell component study.—The near ambient temperature exotherms observed in the cells with excess lithium are attributed to the reaction of lithium and acetonitrile (AN) at the end of cell life. Since AN could also be involved in some of the elevated temperature reactions, an experiment was conducted to define the role of AN in the thermal runaway process. An excess lithium cell was activated with electrolyte solution containing propylene carbonate (PC) in place of AN. PC was selected because of its good stability with lithium (6, 26). The cell was discharged and force overdischarged at 1 mA/cm² beyond 234% of its original SO₂ capacity. No exothermic behavior was detected by the ARC during the discharge-overdischarge process. Following overdischarge, ARC analysis revealed an exotherm occurs on warming the cell to 45°C. A second exotherm occurs at 80°C, and continues to the 300°C cutoff temperature. The thermal and pressure behavior, illustrated in Fig. 6, reveals extremely high rates of heat generation (358°C/min for PC vs. 3.18°C/min for AN, cell no. 7, Table III) and pressure generation (13,000 psi/min for PC vs. 7.19 psi/min for AN, cell 8, Table III). The total pressure generated in this PC system was 2325 psig, compared to a maximum 690 psig for an AN system, (cell no. 8, Table III).

Contrary to expectations, the thermal runaway threat that can occur in overdischarged Li/SO₂ cells was not diminished when AN was replaced with PC. The near ambient temperature exotherm still occurs using PC. The overall rate of heat and pressure generation was significantly enhanced as a result of subsequent exotherms arising from coupled reactions. In view of the stability of lithium in PC, these results support the contention that either a Li-Al alloy (2) or an intercalated lithium-carbon black compound (27) may contribute to cell safety. Propylene carbonate is known to be reduced with high efficiency by lithium amalgam and lithium-

carbon compounds (27, 28). The reaction may be delayed by passivation from residual SO₂, similar to the observed SO₂ passivation of the Li-PC reaction (29). This may allow Li-Al or Li-C to accumulate to a greater degree than in AN, whereupon the reaction, beginning near 45°C, occurs with increased intensity.

On the assumption that reactions observed in the lithium-limited cells were due to cathode reaction products, ARC analyses were performed on various cathode samples from commercial Li/SO₂ 2/3 A and D-size cells discharged at constant current to a 2.0V cutoff.

The D cells were discharged at 10 mA/cm² at ambient temperature and at 71°C. The cathodes were removed from the cell hardware, rolled up with the grid intact, and while still wet with electrolyte were inserted into the ARC bomb under inert gas. The ambient temperature cathode displayed two uncoupled regions of exothermicity, one near 80°C and the other at 280°C. The cathode from the 71°C discharge displayed an exotherm peaking at 130°C and coupled exotherms initiating at 246° and 280°C. No significant thermal or pressure hazards were observed by ARC analysis of the cathodes from either D cell.

The 2/3 A cells were discharged at 1 mA/cm² to 2.0V at ambient temperature. Under an inert atmosphere, the cathodes were removed, subjected to vacuum for 1/2h to remove bulk SO₂, the grid removed, and the powdered cathode placed in the ARC bomb. Lithium dithionite has been reported to be the sole product formed after analysis of cathodes taken from identical cells discharged in a sim-

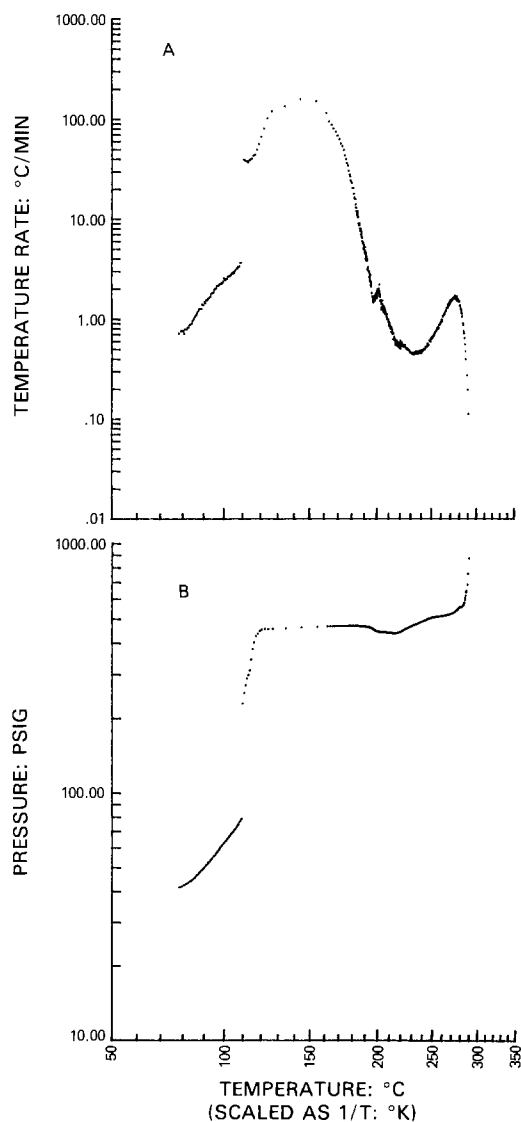


Fig. 5. A: ARC thermal behavior for coulombically balanced cell no. 10 forced overdischarged at 3 mA/cm² at -35°C. B: ARC pressure behavior for cell no. 10.

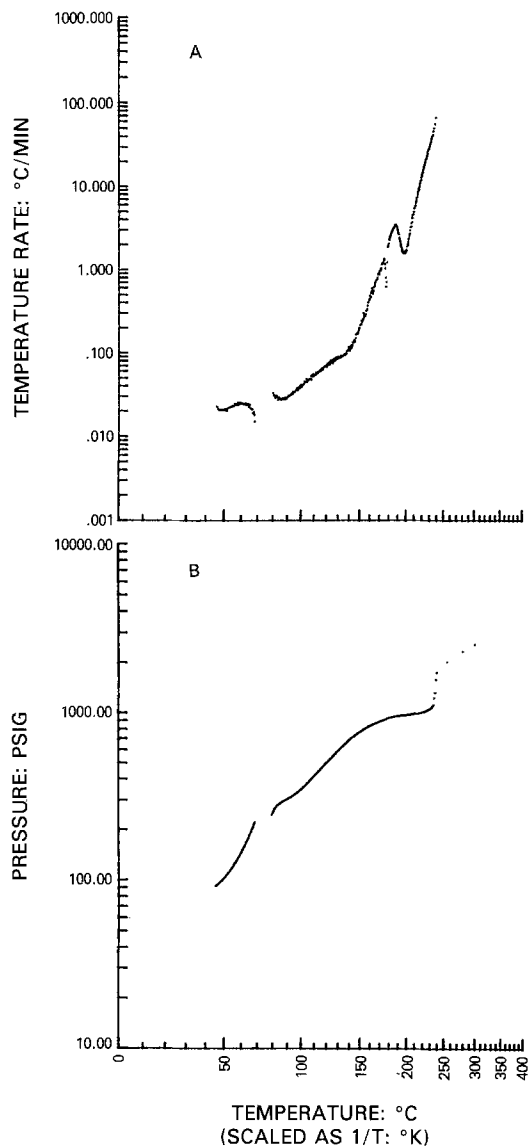


Fig. 6. A: ARC thermal behavior for excess lithium cell no. 9 with propylene carbonate electrolyte solution forced overdischarged at 1 mA/cm² at ambient temperature. B: ARC pressure behavior for cell no. 9.

ilar manner (30). Figure 7 shows reproducible ARC thermal data from this cathode, presumably representing a mixture of carbon, Teflon, Li₂S₂O₄, with some residual electrolyte. The first exotherm begins at 91°C and gives rise to a pressure of about 150 psig. The second exotherm beginning near 116°C and rising to near 200°C is very re-

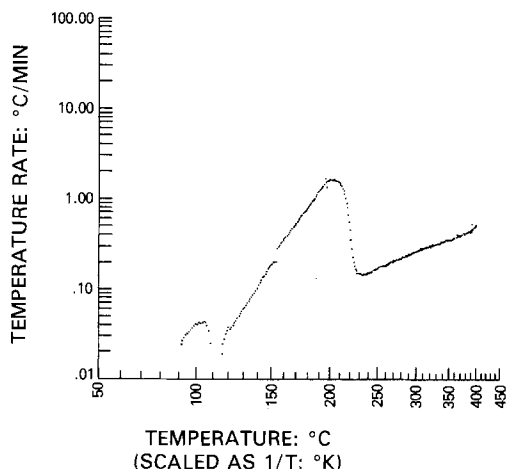


Fig. 7. ARC thermal behavior for a carbon cathode from a 2/3 A size Li/SO₂ cell discharged at 1 mA/cm² at 25°C to a 2.0V cutoff.

producible and is characterized by a rise near 155°C. The final exotherm begins near 230°C and generates gaseous pressure.

Both the 2/3 A- and D-size cathodes from cells discharged at ambient temperature displayed similar pressure and thermal behavior from reactions near 80°-90°C. These appear to be relatively low activation energy reactions, as evidenced by the absence of any significant increase in temperature rate with increasing temperature. However, unlike the D-cell cathodes which exhibited thermal and pressure behavior similar to lithium-limited cells, the 2/3 A-cell cathodes display an additional exotherm starting near 116°C, similar to those observed on all the resistively overdischarged excess-lithium cells (see Fig. 4, part B of curve A). The reason for this difference in behavior is not understood at this time, but may have to do with the amount of electrolyte solution present with the cathode sample. Another factor may be the amount of moisture contained in the cathode. Mass spectroscopy revealed that the D-cell cathodes contained significantly more moisture (as much as 15% of the volatiles exclusive of air) than the <1% moisture found in the 2/3 A cell cathodes.

In contrast to the thermal behavior observed in lithium-limited cells and discharged cathode samples, the excess lithium cells exhibited distinct peaks in the 100°-180°C region, indicating that reactions other than dithionite decomposition may be occurring. In overdischarged cells, likely candidates were either a lithium/electrolyte reaction or reaction between lithium and lithium dithionite. Both possibilities were investigated.

The results of an ARC analysis between 0.27g of lithium metal and 3.49g of commercial 68 w/o SO₂ electrolyte solution reveals a large exothermic reaction occurs at 140°C. Sulfur dioxide is completely inert toward lithium metal up to 320°C (31). Therefore, the observed lithium/electrolyte reaction probably represents the lithium/acetonitrile reaction pushed to higher temperatures by the inhibiting effects of SO₂. The initiation temperature of this reaction has been previously demonstrated to be sensitive to the SO₂ concentration of the electrolyte (7). Figure 8 shows the lithium/electrolyte ARC data compared with the ARC data obtained from an excess lithium cell resistively overdischarged (cell no. 8). The lithium/electrolyte reaction was found to coincide with one of the cell exotherms.

In order to examine the behavior of lithium metal with cell discharge products, a cathode from a D cell discharged to a 2.0V cutoff at 10 mA/cm² at ambient temper-

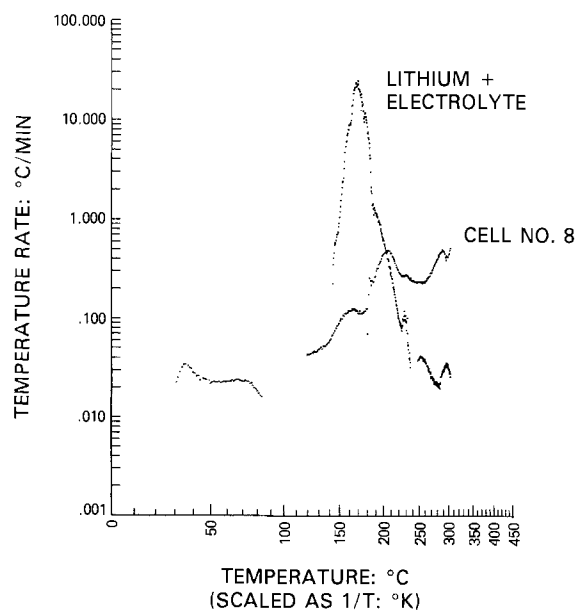


Fig. 8. Comparison of lithium + SO₂ electrolyte solution ARC behavior with excess lithium cell no. 8 resistively overdischarged at ambient temperature.

ature was sandwiched between two layers of lithium foil (0.68g) and subjected to ARC analysis. The cathode had the aluminum grid intact and contained some residual electrolyte solution. A very large exotherm was observed initiating at 190°C following the melting of lithium. Presumably, this was due to the reaction of lithium with decomposition products of lithium dithionite. Figure 9 compares this exothermic behavior between lithium and a discharged D cell cathode with ARC data for a resistively overdischarged excess lithium cell (cell no. 7). As the figure illustrates, the exotherm at 190°C coincides with a major exothermic reaction found in the cell.

Included in Fig. 9 is a mass spectroscopic temperature profile of the total ion intensity in relative units found on warming a carbon cathode from a similarly discharged D cell. The spectral profile shows that volatiles begin to appear near 100°C and peak at 150°C. Examination of the component gases shows the initial evolution is mostly due to masses 41 (CH_3CN) and 64 (SO_2), with the bulk evolution starting near 125°C. The profile for mass 256 (sulfur) exhibits identical behavior. Major evolution begins near 130°C and peaks at 152°C. This sulfur is attributed to the decomposition of dithionite.

A double peak appears in the 130°-150°C region of curve A, Fig. 9 (lithium and cathode). The first peak agrees well with the lithium-electrolyte reaction (Fig. 8), whereas the second peak coincides with the decomposition of dithionite.

The initiation temperature and kinetics of each of these exothermic reactions may be interdependent and could also be affected by the amount of electrolyte present. Decomposition of lithium dithionite will generate SO_2 , thereby affecting the lithium/electrolyte reaction, which has been shown to be dependent on SO_2 concentration. In turn, the thermal stability of lithium dithionite has not been fully explored. Its decomposition may be a function of its degree of wetness with electrolyte.

It has been postulated that one of the major causes of safety in the Li/SO_2 system is the reaction of lithium with molten sulfur formed from the thermal decomposition of lithium dithionite. Consequently, ARC analysis was performed to evaluate the role of the lithium/sulfur reaction in cell safety. A sample of 0.14g lithium was pressed onto the bottom of the sample bomb and an equal mass of sulfur was smeared onto its surface to maintain intimate contact. Electrolyte solution, 2.01g 68 w/o SO_2 , was added

last. ARC analysis revealed no low temperature exotherm due to the lithium/sulfur reaction, as previously reported to occur near 142°C if the molten sulfur "wets" the lithium (26). Presumably, the electrolyte inhibits this wetting by film formation. Conversely, the sulfur may have affected the lithium/electrolyte reaction. A much reduced lithium/electrolyte reaction was observed in this experiment. Additional exotherms were observed to start near 190° and 226°C. The 190°C exotherm was observed before, and exotherms between 220° and 240°C have been consistently observed. Depending on conditions, either exotherm could be from a lithium/sulfur reaction. The reaction at 226°C produced relatively low rate of heat generation. However, a substantial quantity of heat is liberated, which could propagate a thermal runaway.

Conclusions

ARC analysis reveal that resistively overdischarged lithium-limited cells exhibited simple thermal behavior. The exothermic reactions that occur are attributed to the thermal decomposition of dithionite and are characterized by slow self-heating rates and initiation temperatures above 100°C and are not coupled, thus eliminating the thermal runaway hazard. Forced overdischarging of lithium-limited cells produced no additional hazards.

In contrast, cells containing excess lithium at end of life have been found to be capable of undergoing thermal runaway when overdischarged at ambient temperature in either a resistive or forced mode. The rates of temperature rise and pressure generation occurring during thermal runaway, however, were found to be low, indicating the absence of any explosion hazard. The magnitude of overall pressure rise, however, was large enough to cause venting in commercial cells.

The thermal runaway process was found to be the result of a series of coupled, exothermic chemical reactions, as illustrated in Fig. 4A. Exotherm (A), which initiates at near ambient temperature (30°-50°C), is attributed to the low activation energy reaction of lithium and acetonitrile. This reaction did not initiate in any of the cells until the potential dropped below 2.0V implying that a triggering mechanism may be necessary. This could involve depletion of SO_2 , localized heating effects, or perhaps a reaction with freshly deposited lithium, Li-Al, or Li-C formed at the start of overdischarge.

The reactions occurring in the second temperature region (B) are critical to Li/SO_2 safety since they provide the pathway for the propagation of thermal runaway to the melting point of lithium. Exotherms in this region have been shown to involve the thermal decomposition of lithium dithionite and a reaction of lithium with the electrolyte solution.

The exotherm observed in region C upon the melting of lithium is believed to involve lithium with dithionite or a decomposition product of dithionite. Causes of exotherms produced in the high temperature regions at approximately 230°C and in regions D and E are speculative. Possible reactions include lithium with sulfur and lithium with the Teflon contained in the carbon cathode (26).

Replacing acetonitrile in the electrolyte solution with propylene carbonate did not eliminate the thermal runaway hazard in excess lithium cells. In addition, much higher rates of heat and pressure generation were observed indicating that PC-based cells would constitute a much more serious safety hazard than the standard AN-based cells.

Cells coulombically balanced at ambient temperature and force overdischarged at -35°C have been shown to lead to serious safety problems, potentially with explosion-type hazards. The results indicate that these cells can become hazardous during the overdischarge process, even before they are allowed to warm up.

The *in situ* IR study revealed kinetic parameters such as current density and storage time may be contributing factors in the observed low temperature or excess lithium cell safety problems. Additional studies are needed to elucidate this chemical, kinetic, and thermal relationship.

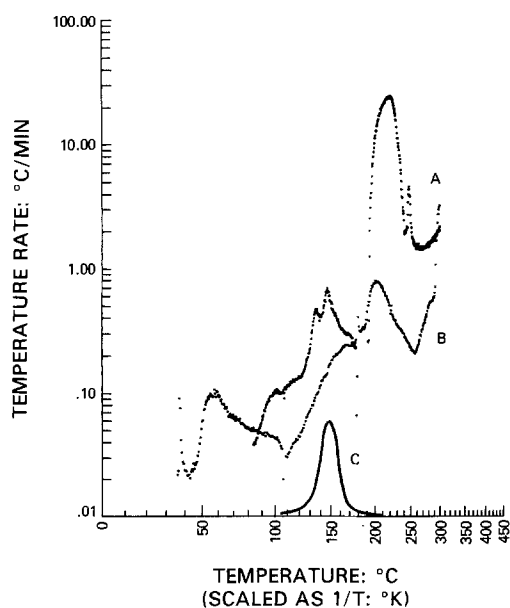


Fig. 9. A: ARC thermal behavior for lithium + cathode from D cell discharged at 10 mA/cm² to 2.0V at 25°C. B: ARC thermal behavior for cell no. 7 (excess lithium cell resistively overdischarged at ambient temperature). C: Mass spectra showing total ion intensity in arbitrary units from D cell carbon cathode. Peak intensity occurs at 150°C. Identical curve occurs for mass 256 (sulfur), presumably from dithionite decomposition.

Acknowledgments

This work was supported by the Independent Research Program of the Naval Surface Weapons Center and the Naval Sea Systems Command High Energy Batteries for Weapons Block Program.

Manuscript submitted March 19, 1984; revised manuscript received Sept. 17, 1984.

Naval Surface Weapons Center assisted in meeting the publication costs of this article.

REFERENCES

- G. J. DiMasi and J. A. Christopoulos, in "Proceedings of the 28th Power Sources Symposium," Atlantic City, NJ, June 12-15, 1978, The Electrochemical Society, Inc., p. 179 (1978).
- H. Taylor, W. Bowden, and J. Barrella, in "Proceedings of the 28th Power Sources Symposium," Atlantic City, NJ, June 12-15, 1978, The Electrochemical Society, Inc. p. 183 (1978).
- A. N. Dey, *This Journal*, **127**, 1886 (1980).
- M. W. Rupich, L. Pitts, and K. M. Abraham, *ibid.*, **129**, 1857 (1982).
- W. B. Ebner and D. W. Ernst, in "Proceedings of the 30th Power Sources Symposium," Atlantic City, NJ, June 7-10, 1982, The Electrochemical Society, Inc., p. 119 (1982).
- A. N. Dey and R. W. Holmes, *This Journal*, **126**, 1637 (1979).
- S. Dallek, S. D. James, and W. P. Kilroy, *ibid.*, **128**, 508 (1981).
- D. I. Townsend and J. C. Tou, *Thermochim. Acta*, **37**, 1 (1980).
- J. C. Tou and L. F. Whiting, *ibid.*, **48**, 21 (1981).
- J. N. Barrella and G. P. Klein, in "Proceedings of the 30th Power Sources Symposium," Atlantic City, NJ, June 7-10, 1982, The Electrochemical Society, Inc., p. 143 (1982).
- B. Jagid, T. Watson, and S. M. Chodosh, in "Power Sources for Biomedical Implantable Applications and Ambient Temperature Lithium Batteries," B. B. Owens and N. Margalit, Editors, p. 615, The Electrochemical Society Softbound Proceedings Series, Princeton, NJ (1980).
- J. T. Cutchen, A. R. Baldwin, and S. C. Levy, Abstract **42**, p. 90, 2nd International Meeting on Lithium Batteries, Paris, France, April 25-27, 1984.
- G. Nickless, Editor, "Inorganic Sulfur Chemistry," pp. 162-170, Elsevier, New York (1968).
- R. L. Ake, D. M. Oglesby, and W. P. Kilroy, *This Journal*, **131**, 968 (1984).
- W. L. Bowden, L. Chou, D. L. DeMuth, and R. W. Holmes, *ibid.*, **131**, 449 (1984).
- V. A. Simon, K. Waldman, and E. Steger, *Z. Anorg. Allg. Chem.*, **288**, 131 (1956).
- K. Buijs, *J. Inorg. Nucl. Chem.*, **24**, 229 (1962).
- R. J. Gillespie and E. A. Robinson, *Spectrochim. Acta*, **19**, 741 (1963).
- A. Simon and H. Wagner, *Z. Anorg. Chem.*, **311**, 102 (1961).
- W. D. Harrison, J. B. Gill, and D. C. Goodall, *J. Chem. Soc. Dalton Trans.*, 847 (1979).
- F. C. Laman, C. Gardner, and D. T. Fouchard, *J. Phys. Chem.*, **86**, 3130 (1982).
- R. G. Rinker and S. Lynn, *Ind. Eng. Chem.*, **8**, 338 (1969).
- W. D. Harrison, J. B. Gill, and D. C. Goodall, *J. Chem. Soc. Dalton Trans.*, 1431 (1978).
- N. K. Graham, J. B. Gill, and D. C. Goodall, *ibid.*, 1363 (1983).
- M. W. Rupich and K. M. Abraham, First Quarterly Report, NSWC Contract N60921-81-C-0084, May 1981.
- W. P. Kilroy and S. Dallek, *J. Power Sources*, **3**, 291 (1978).
- P. H. Smith, L. DeVries, J. N. Shih, S. D. James, and W. P. Kilroy, NSWC TR 83-30, May 1983.
- J. O. Besenhard and H. P. Fritz, *J. Electroanal. Chem. Interfacial Electrochem.*, **53**, 329 (1974).
- A. V. Losev, *Sov. Electrochem.*, **14**, 236 (1978).
- W. P. Kilroy and C. R. Anderson, *J. Power Sources*, **9**, 397 (1983).
- A. N. Dey and R. W. Holmes, Final Report DELET-TR-77-0472-F, Duracell, Inc., Nov. 1979.

Li/Li_{1+x}V₃O₈ Secondary Batteries

III. Further Characterization of the Mechanism of Li⁺ Insertion and of the Cycling Behavior

G. Pistoia

Centro di Studio per la Elettrochimica e la Chimica Fisica delle Interfasi, C. N. R., Via del Castro Laurenziano 7, Rome, Italy

M. Pasquali and M. Tocci

Dipartimento di Chimica, Facolta' di Ingegneria, Universita' di Roma, Rome, Italy

R. V. Moshtev and V. Maner

Central Laboratory of Electrochemical Power Sources, Bulgarian Academy of Sciences, Sofia, Bulgaria

ABSTRACT

The reduction mechanism of the bronze Li_{1.2}V₃O₈ in nonaqueous Li cells has been elucidated. Upon Li⁺ insertion, a solid solution is formed with an upper composition of Li_{1.3}V₃O₈. Within this composition range, Li⁺ progressively fills the tetrahedral sites available in the unit cell. Four such sites are supposed to be filled at the upper composition limit. Beyond this, a new phase is nucleated to accommodate excess Li⁺, this resulting in a constant cell's OCV. Li⁺ insertions not greater than 3.0 eq/mol are reversible, as shown by the cycling behavior and the x-ray patterns. Owing to the outstanding structure stability and to the high speed of Li⁺ diffusion in Li_{1.2}V₃O₈, extended cycling at high rates is achievable with cells based on this bronze. 445 cycles at discharge rates variable in the range of 2-10 mA/cm² have been obtained.

In previous communications (1, 2), we have reported data on the features of Li_{1+x}V₃O₈ as a reversible cathode for Li cells. This bronze, a layered compound whose layers are held together by Li⁺ ions (3), has proven to be able to insert Li⁺ in its structure with outstanding energy, power, and cycling capability.

Given the difficulties encountered with V₆O₁₃ (both stoichiometric and nonstoichiometric), which had shown

promise for successful use in rechargeable Li batteries (4-6), the search for new materials is even more justified. On the other hand, by directly comparing the characteristics of Li_{1+x}V₃O₈ with those of V₆O₁₃ (S) (2), we obtained evidence that the former could be estimated superior to the latter in such aspects as energy density, rate capability (power density), cycle life, and resistance to overdischarge. On this basis, this ternary oxide did seem worthy

of a further investigation aimed at assessment of the mechanism of Li^+ uptake/removal and at evaluation of those parameters which are relevant to practical rechargeable batteries.

The first commitment may perhaps be easier to fulfill, whereas the second requires a larger number of tests eventually oriented to batteries with practical characteristics. So, we feel that with our previous papers and the present one, the mechanistic aspects of the redox reactions occurring in $\text{Li}/\text{Li}_{1+x}\text{V}_3\text{O}_8$ cells have been sufficiently elucidated. On the other hand, as for the technological aspects, the contribution presented here is still partial and will be followed by a more substantial work.

Experimental

The relevant experimental procedure has already been reported (2). The bronze used in the present investigation was prepared by melting Li_2CO_3 and V_2O_5 (obtained by decomposing NH_4VO_3) in quartz vessels at 680°C in the air. Although this temperature is higher than that reported in the phase diagram for the existence of only $\text{Li}_{1+x}\text{V}_3\text{O}_8$ (7), we found that the sample so prepared has a satisfactory electrochemical behavior. However, a more complete evaluation of the influence of the preparation procedure on performance is now under way and will be reported in a forthcoming paper.

The composition of the sample so prepared was checked by both atomic absorption spectroscopy and chemical analysis (7). With the latter, the relative amounts of V^{+4} and V^{+5} were evaluated, and the former was found to be present as 7.45% of total V. From this value, an average oxidation number of 4.92 was derived for V, so that the composition of the bronze may be represented as $\text{Li}_{1.2}\text{V}_3\text{O}_8$. Compositions close to this have often been found when trying to prepare low-lithium $\text{Li}_{1+x}\text{V}_3\text{O}_8$ (7-9).

1M LiClO_4 in PC-DME was used as a solution because of its satisfactory chemical and electrochemical stability. The latter was checked in this work by galvanostatic and sweep voltammetry experiments.

The electrodes were mostly prepared by pressing at 800 kg/cm^2 on an expanded Ni net a mixture ($20\text{-}30\text{ mg/cm}^2$) of $\text{Li}_{1.2}\text{V}_3\text{O}_8$ (70%), acetylene black (20%), and Teflon (10%). For extended cycle tests, relatively thin electrodes were prepared by rolling a nonexpanded Ni net prior to and after applying about 10 mg/cm^2 of the above mixture on it.

For the cyclic voltammetry experiments, a cell of the type described by Shaw (10) was used with Li as both reference and counterelectrode. The working electrode was prepared as reported above.

Results and Discussion

The main features of the structure of $\text{Li}_{1+x}\text{V}_3\text{O}_8$ have been described by Wadsley (3) and summarized in a previous work of this series (2). It is sufficient to emphasize here that the basic structural elements of the bronze, *i.e.*, octahedra and trigonal bipyramids, are arranged to form puckered layers with the Li^+ ions arranged in between by occupying octahedral sites (Fig. 1). In the unit cell, dashed in the figure, there are two such sites to which six tetrahedral sites have to be added (1-6 in Fig. 1). The latter can be filled by excess Li^+ as supposed by Wadsley (3) and experimentally checked by us (2) and others (9) through the observation of a solid solution formation upon Li^+ uptake.

However, based on the evidence presented by the coulometric titration curve (Fig. 2), incomplete filling of the tetrahedral sites occurs. Indeed, the single-phase behavior typical of solid-solution formation (EMF decreasing with x) is only visible up to an x value of about 1.7. By adding to this figure excess Li^+ with respect to stoichiometric LiV_3O_8 (0.2 Li^+ ions per molecule), one obtains about 2 Li^+ ions added to each molecule. As the unit cell is based on 2 $\text{Li}_{1+x}\text{V}_3\text{O}_8$, up to 4 Li^+ may be accommodated

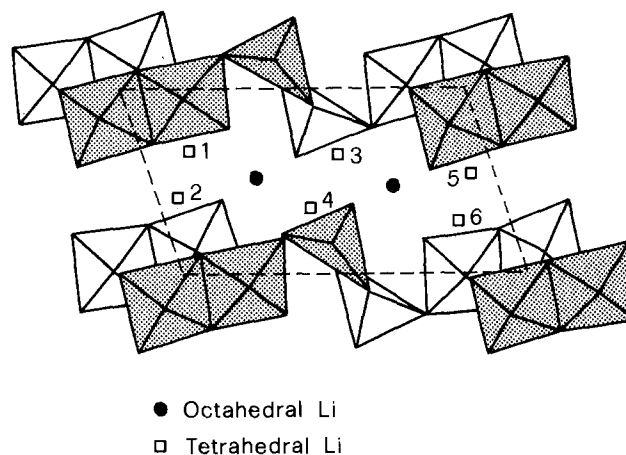


Fig. 1. Structure of $\text{Li}_{1+x}\text{V}_3\text{O}_8$, projected onto (010), showing both octahedra and trigonal bipyramids. The unit cell is dashed.

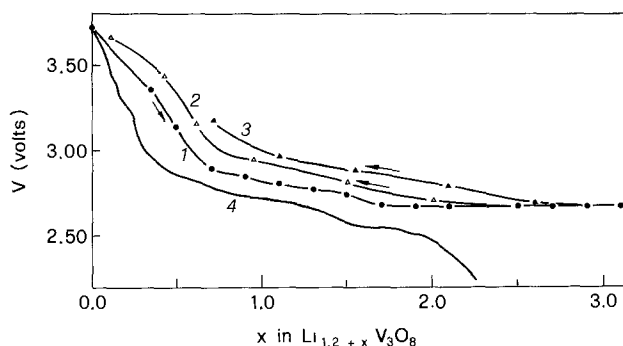


Fig. 2. 1: Compositional variation of OCV during the first discharge. 2: OCV after stopping at $x = 2.5$ and recharging. 3: OCV after stopping at $x = 3.0$ and recharging. 4: discharge curve at 0.2 mA/cm^2 .

in its tetrahedral sites. On the basis of the interatomic distances, they may for instance correspond to the numbers 1, 3, 4, and 6. Indeed, from the data reported by Wadsley (3), one may assign to sites 1-2 and 5-6 (close to the octahedra) a distance of about 1.7 \AA , whereas sites 3-4 (close to the bipyramids) have a distance of about 2.2 \AA . The latter value is exceeded by the distances between tetrahedral and octahedral Li^+ . Therefore, simultaneous occupation of the couples of sites 1-2 and 5-6 is less probable, owing to the repulsion forces between Li^+ ions ($r_{\text{Li}^+} = 0.7\text{ \AA}$).

Beyond a total Li^+ insertion greater than 2 eq/mol, further Li^+ may only be accommodated if a structural rearrangement occurs. The structure has to be partially distorted by excess Li^+ until a new phase is nucleated which is in equilibrium with that corresponding to the solid solution. A constant EMF is then observed (Fig. 2), as is typical of a two-phase region. Attempts to characterize the new phase were thwarted by the low number of its peaks.

In their preliminary investigation on the same phase, $\text{Li}_{1+x}\text{V}_3\text{O}_8$, Raistrick and Huggins (9) obtained a similar EMF/ x curve, although the single-phase region ends somewhat earlier in their work ($x = 1.5$).

The initially high and rapidly falling EMF's indicate a high value of the Li chemical potential and its sharp decrease after occupation of the first sites. We may define $\mu_{\text{Li}}^{\text{cathode}} - \mu_{\text{Li}}^{\text{anode}} = -FE$ as the variation of μ_{Li} in the cathode with respect to that in the anode. The latter may be assumed to be zero (11). As a consequence of the rapid decrease of μ_{Li} , the overall energy of intercalation, defined as $\Delta G_1 = -F \int_0^x E \cdot dx$, has a minor increase in this region. After this stage, E diminishes less rapidly with x . The flat final part of the E/x curve at $E = 2.62$ and the high x value observed allow for a high free energy of intercalation ΔG_1 to be calculated for the overall process. For $x = 3.1$ ($\text{Li}_{\text{tot}} = 4.3$) ΔG_1 is equal to -200 kcal/mol , a large value which is in turn related to the high energy capacity shown by this

compound. As a comparison, ΔG_1 for LiTiS₂ is -57.4 kcal/mol (11).

A value of 815 Wh/kg (cathode only) may be calculated for $x = 3.1$ and $\bar{E} = 2.83$ V. By considering the weight of Li consumed in the reaction, a value of 758 Wh/kg is obtained, which represents the maximum energy density of a Li/Li_{1.2}V₃O₈ cell. For comparison, the theoretical specific energies of V₆O₁₃ (NS), V₆O₁₃ (S), and TiS₂ are reported to be 890, 710, and 490 Wh/kg, respectively (5, 12).

The complex reduction mechanism of Li_{1+x}V₃O₈ is also reflected in the pattern of the linear sweep voltammograms. Figure 3 shows that, especially at low scan rates, all the features shown by the titration curve are present and even more evident. In particular, the 3 small peaks above ~3.15 V point to the inequivalence of the sites about 1 per unit cell; see titration curve) initially occupied by Li⁺. The large peak corresponding to the single-phase region with a lower slope is split to match the inflection noted at $E = \sim 2.8$. Finally, the last peak corresponds to the biphased region noted at $x > \sim 1.7$.

The x-ray diffractograms of Fig. 4 show the structure evolution following Li⁺ insertion. At $x = 1.6$, the pattern is very similar to the one initially observed, apart from a limited structure expansion testified by the shifting of the peaks to lower angles. In particular, the peak corresponding to the interlayer distance, at $2\nu = \sim 14.0^\circ$, is only shifted by about 0.1° , i.e., less than 1%. At $x = 2.7$, the

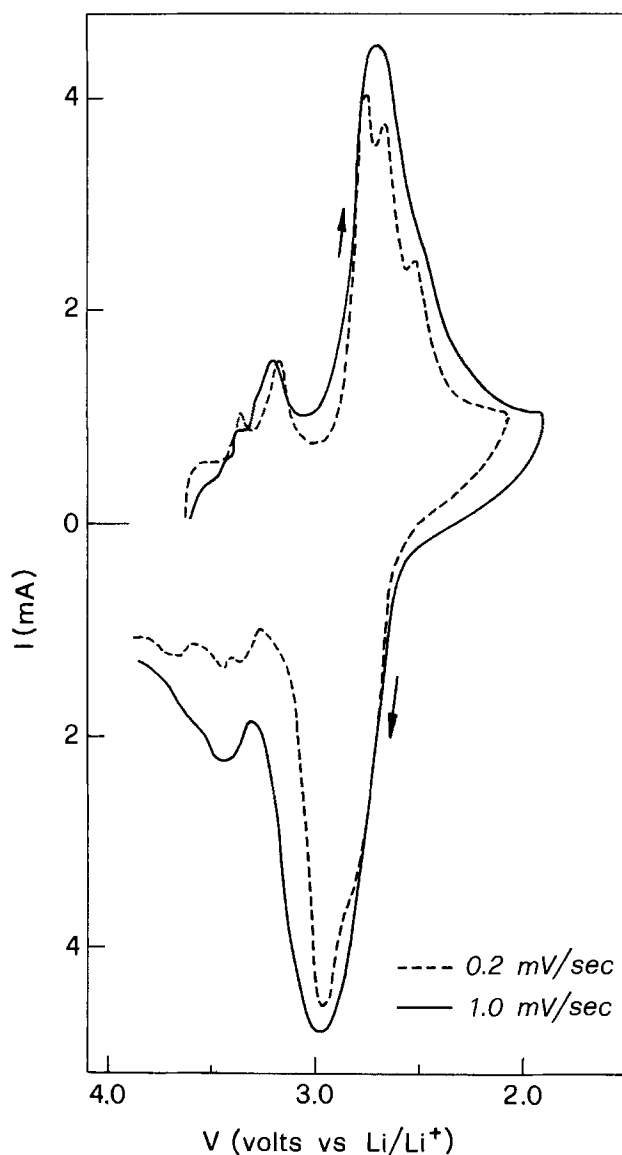


Fig. 3. Cyclic voltammety of a Li_{1.2}V₃O₈ electrode (30% Teflonized acetylene black) at a sweep rate of 0.2 mV/s (dashed curve) and 1.0 mV/s (continuous curve).

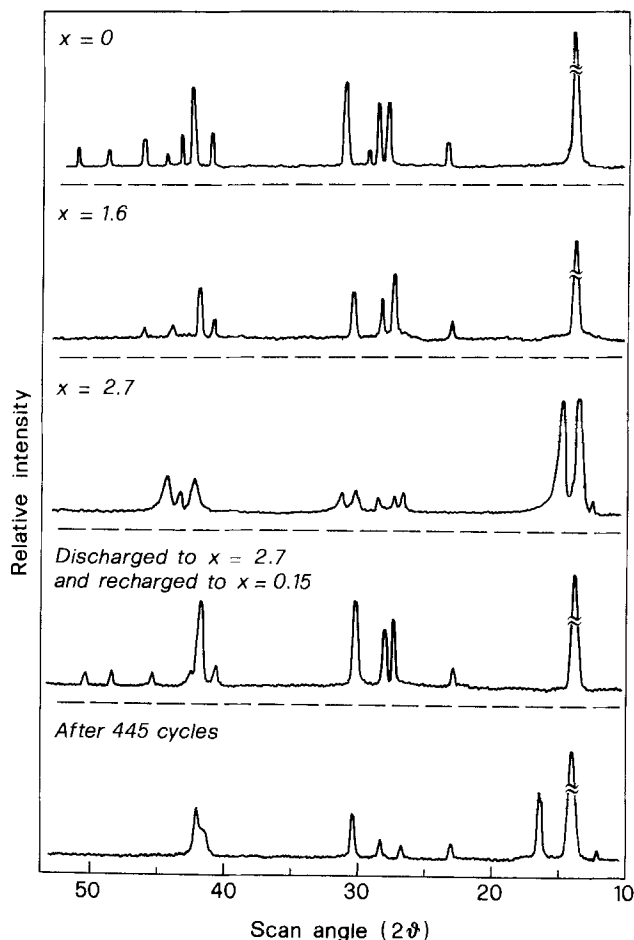


Fig. 4. X-ray diffractograms of Li_{1.2}V₃O₈ electrodes after discharge and cycling.

main peaks of the original structure are still present, but some new peaks (especially the one at $2\nu = \sim 14.7^\circ$) reveal the nucleation of a new phase.

The x-ray analysis also shows that the structural integrity is highly preserved even after injecting massive amounts of Li⁺, in spite of the observed nucleation of a new phase and of the hysteresis of the EMF/ x curve shown in Fig. 2. Indeed, the pattern after discharge to $x = 2.7$ and recharge to $x = 0.15$ (Fig. 4) is very similar to that of the undischarged material ($x = 0$). It can be noted that the peaks corresponding to the new phase have disappeared. The limited expansion of the structure, possibly

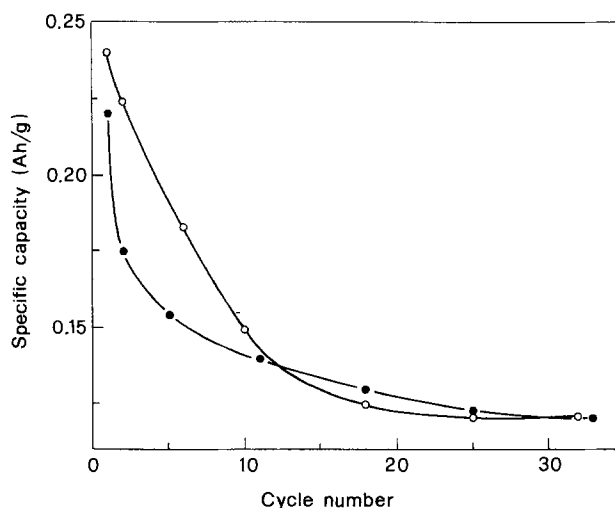


Fig. 5. Initial cycling of Li/Li_{1.2}V₃O₈ cells at 1 mA/cm². ○: discharge limit, 1.0V. ●: discharge limit, 1.8V.

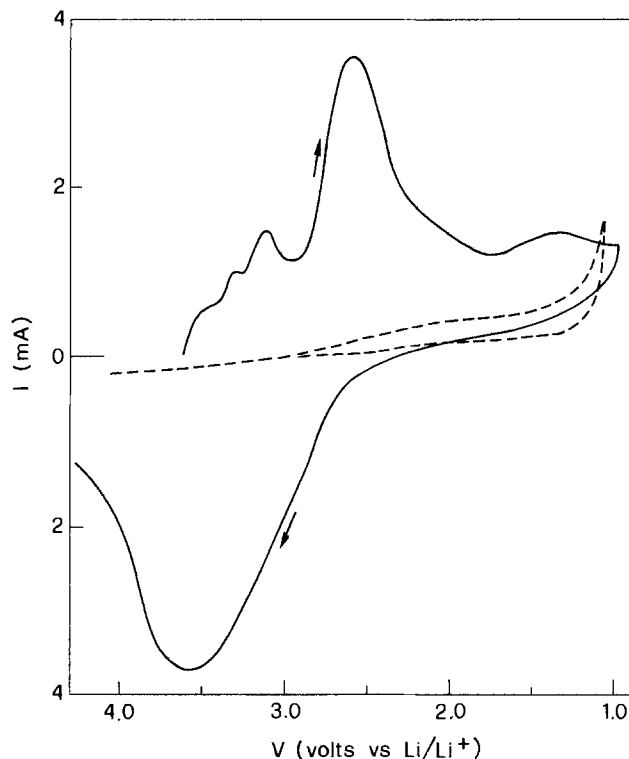


Fig. 6. Cyclic voltammetry of a $\text{Li}_{1.2}\text{V}_3\text{O}_8$ electrode with a cathodic limit of 1.0V. The dashed line refers to a blank electrode (Teflonized acetylene black on Ni) in $\text{LiClO}_4/\text{PC-DME}$. Sweep rate, 1 mV/s.

related to the pinning effect of Li^+ over the layers, is believed to be the main reason for this structural stability.

As for the hysteresis of the EMF/x curve, it was ascertained that its extent is a function of the depth of discharge. This phenomenon was observed even when the discharge was limited to the solid-solution range. We obtained evidence that the structural reorganization shown by the hysteresis is maintained after the first cycle. Indeed, the E 's measured during the second discharge lie substantially on the same curve obtained during charge. However, this is valid for x values not greater than about 3.

Another feature observed in the E/x curves (both under load and on OCV) is the absence of plateaus and steps on charging. The potential values smoothly increase up to about 3.0V where a change in slope is observed. Similar behavior has been reported for V_2O_5 (13).

This pattern is confirmed by the cyclic voltammetry at low rates (Fig. 3). During the anodic sweep, the 3 main peaks observed during discharge tend to merge into a single peak, and only a shoulder is still distinguishable. It looks like the Li^+ ions leave the structure randomly in an environment in which the site energies seem to have leveled off.

We have ascertained the effect on the cycle life of discharging a cell to a 1.0V cutoff on the charge efficiency (Fig. 5). At 1.0 mA/cm², 0.24 Ah/g were obtained during the first discharge, this corresponding to 2.6 eq Li^+ /mol (87% d.o.d. with respect to $x = 3$). The capacity decline over about 30 cycles (after which the cell was voluntarily stopped) was comparable to that of a cell cycled with a limit of 1.8V. In general, it was observed that cycling $\text{Li}/\text{Li}_{1+x}\text{V}_3\text{O}_8$ cells at such regimes limits the Li^+ uptake to about 3 eq/mol; repeated overdischarges had no adverse effects on the cycle life. The situation tends to change at lower discharge rates when greater amounts of Li^+ may be inserted. A cell cycled at 0.2 mA/cm² between 1.0 and 3.5V reached an x value of 3.1 during the first discharge, but showed a more rapid capacity decline. This behavior is also reflected by the cyclic voltammetry curve of Fig. 6, where the cathodic limit was set to 1.0V. The anodic peak is here highly shifted and merges with the 3 small peaks observed above 3V. This provides clear

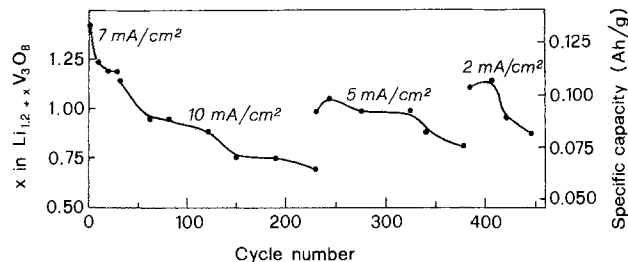


Fig. 7. Extended cycling at high c.d. of a $\text{Li}/\text{Li}_{1.2}\text{V}_3\text{O}_8$ cell in $\text{LiClO}_4/\text{PC-DME}$. Charge c.d. = 2 mA/cm² for all. Voltage limits: 1.6 and 3.5V.

evidence of major structural rearrangements for $x > 3$, rearrangements which were indeed confirmed by the x-ray analysis (new peaks were still present after recharge).

Finally, the ability of the structure to sustain a high number of cycles at high rates was checked by using a relatively thin cathode (10 mg/cm²) made with the rolling technique. The results are reported in Fig. 7. The average d.o.d. at 7, 10, 5, and 2 mA/cm² were 42, 30, 32, and 33%, respectively. During cycling, neither Li nor the solution were replaced. The performance shown in Fig. 7 is remarkable and has to be related at the same time to the high speed of Li^+ diffusion (2) (high rate) and to the ruggedness of the structure (high cycle number). The latter was confirmed by the pattern of Fig. 4, showing a substantial retention of the structure after cycling.

Conclusions

This further characterization of the bronze $\text{Li}_{1+x}\text{V}_3\text{O}_8$ has confirmed that it can act as a cathode capable of high energy, high rates, and outstanding reversibility in non-aqueous Li cells.

The Li^+ insertion, even though leading eventually to the nucleation of a new phase and to the onset of a permanent hysteresis in the E/x curve, is highly reversible even at high Li^+ contents (below about $x = 3.2$, being the initial Li^+ excess included in this figure).

From now on, this material will be mainly characterized from a technological point of view, which has led to a final assessment of its capability of being used in practical secondary Li batteries. In this respect, an investigation on several aspects of the bronze, cathode, and complete cells' preparation is under way, and a progressive scaling up to cells of practical characteristics has been planned.

Manuscript submitted March 27, 1984; revised manuscript received Sept. 26, 1984.

Consiglio Nazionale Delle Ricerche assisted in meeting the publication costs of this article.

REFERENCES

1. S. Panero, M. Pasquali, and G. Pistoia, *This Journal*, **130**, 1225 (1983).
2. G. Pistoia, S. Panero, M. Tocci, R. V. Moshtev, and V. Manev, *Solid State Ionics*, In press.
3. A. D. Wadsley, *Acta Crystallogr.*, **10**, 261 (1957).
4. K. M. Abraham, J. L. Goldman, and M. D. Dempsey, *This Journal*, **128**, 2493 (1981).
5. K. West, B. Zachau-Christiansen, and T. Jacobsen, *Electrochim. Acta*, **28**, 1829 (1983).
6. K. M. Abraham, P. B. Harris, and D. L. Natwig, *This Journal*, **130**, 2309 (1983).
7. D. G. Wickham, *J. Inorg. Nucl. Chem.*, **27**, 1939 (1965).
8. R. Schollhorn, F. Klein-Reesink, and R. Reimold, *J. Chem. Soc. Chem. Commun.*, 399 (1979).
9. I. D. Raistrick and R. A. Huggins, Paper 71 presented at The Electrochemical Society Meeting, Washington, DC, Oct. 9-14, 1983.
10. M. Shaw, O. A. Paez, and F. Ludwig, Contract Nas 3-8509, Final Report, January 1969.
11. A. S. Nagelberg and W. L. Worrell, *J. Solid State Chem.*, **29**, 345 (1979).
12. B. Zachau-Christiansen, K. West, and T. Jacobsen, *Solid State Ionics* **9 & 10**, 399 (1983).
13. B. Araki, C. Mailhe, N. Baffier, J. Livage, and J. Vedel, *ibid.*, 439.

Ellipsometer Studies of Surface Layers on Lithium

F. Schwager,¹ Y. Geronov,² and R. H. Muller*

Materials and Molecular Research Division, Lawrence Berkeley Laboratory, University of California, Berkeley, California 94720

ABSTRACT

The growth of surface layers on lithium in propylene carbonate solutions can be followed by ellipsometry, although the refractive indexes of many potential film materials are close to those of the electrolyte. Film thicknesses calculated from ellipsometer measurements increase over periods of several days at open circuit; they are several times larger than those derived from galvanostatic pulse measurements. Films are found to be inhomogeneous with properties continuously varying as a function of distance from the substrate; compact regions are located adjacent to the metal and porous regions are located adjacent to the solution. Electrode capacitance measurements are sensitive to the thin compact region, which can also be generated by reaction with water vapor. Ellipsometer measurements are primarily affected by the thicker, porous region, which may be formed by the precipitation of decomposition products of the solution.

Surface layers formed under open-circuit conditions on lithium in propylene carbonate (PC) solvent and its solutions of lithium perchlorate and lithium hexafluoroarsenate have been investigated by ellipsometry. The present study was conducted in conjunction with galvanostatic pulse measurements reported earlier (1), and the results obtained by the two techniques are compared.

Experimental

Ellipsometric and electrochemical measurements were conducted *in situ* in a hermetically sealed polypropylene cell consisting of an electrode compartment with two strain-free quartz windows arranged for 75° angle of incidence of the light beam, and a solution container located above the electrode compartment. The Fig. 1 configuration enables one to take measurements very soon after the electrode is brought in contact with the solution. The ellipsometer used was of the self-compensating type in the polarizer-quarter wave plate-sample-analyzer configuration (2). Corrections for component imperfections were derived from four-zone measurements. A mercury lamp (150W with interference filter for the wavelength of 5461Å) and an argon-ion laser (Lexel Model 75 at a wavelength of 5145Å) were used as light sources. The mercury lamp could be used only for smooth, well reflecting electrode surfaces.

Working and counterelectrodes consisted of high purity (Foote) lithium disks, of 25 mm diam and 3 mm thickness. The cross section of a freshly extruded lithium wire of 1 mm diam served as reference electrode. The working electrodes were prepared by scraping the lithium with a scalpel and pressing it with a polycarbonate sheet in a recirculating purified helium atmosphere (<0.5 ppm O₂, H₂O, 5 ppm N₂) as described previously (1). No significant difference between the native film of an electrode which was only cleaned and one which was also pressed was found by depth profiling Auger spectroscopy (PHI Model 590). Solutions of LiClO₄ or LiAsF₆ with and without added water were investigated; their preparation has also been described before (1). In the purified helium atmosphere, the electrodes were inserted in the electrode compartment, and the solution compartment was filled with electrolyte. The closed cell was then transferred to air for conducting the measurements. A delay of about 1 min after contact of the electrodes with solution was required to optically align the cell.

Film growth was followed simultaneously by ellipsometry and electrochemical pulse techniques. After the experiment, the working electrode was washed with pure propylene carbonate, then dried and transferred into an UHV-chamber for Auger spectroscopy and ellipsometry of the dry film.

*Electrochemical Society Active Member.

¹Present address: Mettler Instruments AG, CH-8606 Greifensee, Switzerland.

²Permanent address: Central Laboratory of Electrochemical Power Sources, Bulgarian Academy of Sciences, Sofia, Bulgaria.

Results

The ellipsometric results are presented as plots of the relative amplitude change ψ vs. the relative phase change Δ due to reflection. Figure 2 shows a plot obtained for film growth on lithium in propylene carbonate of low water content (~10 ppm) without salt and with 1M LiClO₄. The immersion time is indicated on both curves. The presence of the electrolyte has a great effect on the rate of film formation. Ellipsometer parameters ψ and Δ change

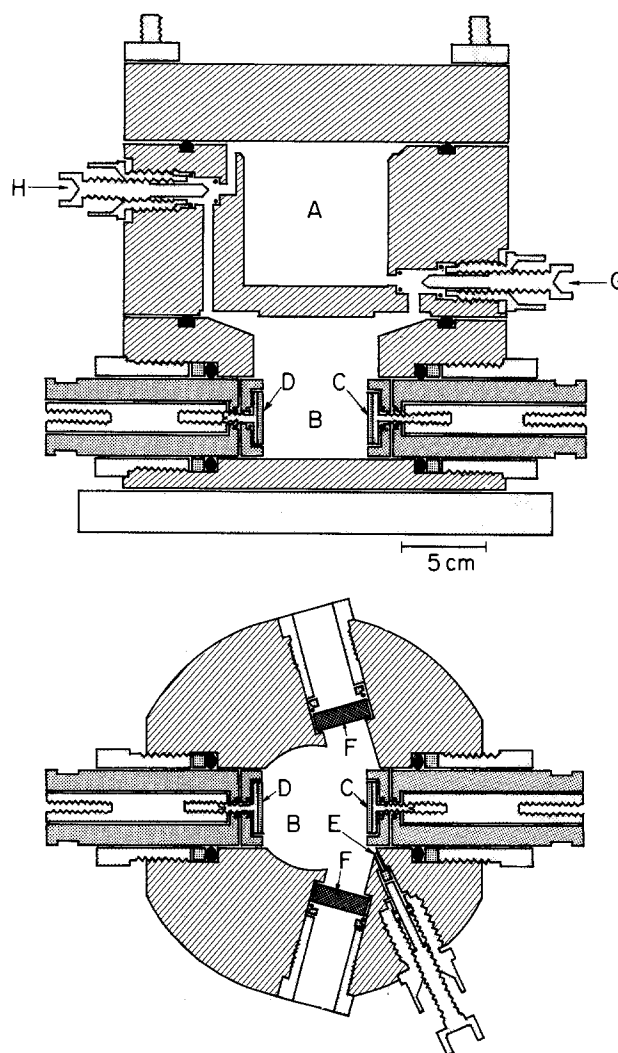


Fig. 1. Nonaqueous cell for ellipsometry and potential measurements on lithium electrodes immediately after contact with electrolyte—vertical and horizontal cross sections. A) reservoir, B) cell, C) working electrode, D) counterelectrode, E) reference electrode, F) windows, G) liquid valve, H) gas valve.

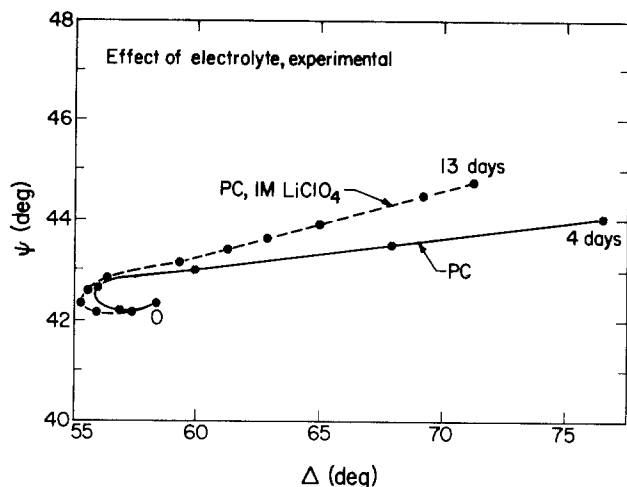


Fig. 2. Effect of the presence of electrolyte on film formation on lithium in propylene carbonate (PC). Measured ellipsometer parameters ψ and Δ . Pure solvent (PC) and 1M LiClO₄ in PC. Period of immersion in days given along the curves.

faster for lithium immersed in pure PC, indicating faster film growth. However, both electrochemical measurements at the end of the experiment (small amounts of salt were added to provide conductivity), as well as depth profiling with Auger spectroscopy, indicate the presence of a thin film, which shows a nonporous appearance in micrographs. Scanning electron micrographs have shown that film formation (by corrosion or precipitation) on lithium in PC with small amounts of added water is faster than in PC-LiClO₄ solutions with the same amount of added water (1). The difference between electrochemical and ellipsometric measurement for pure PC with no water added is, at present, difficult to explain. It may involve the formation of a poorly adhering, highly porous film and its loss during the rinsing and drying operations.

Ellipsometer measurements of film growth in solutions of 0.5 and 1.0M LiClO₄ in PC did not show much difference. Addition of water to LiClO₄ solutions seems to slow down the rate of film formation slightly (Fig. 3). This finding is in agreement with electrochemical measurements (1), where it was also found that films formed in these solutions are less conductive.

LiAsF₆ solutions form much thicker films in shorter time than LiClO₄ solutions (Fig. 4). This result emphasizes the importance of the anion for film formation and is in agreement with the findings from electrochemical measurements.

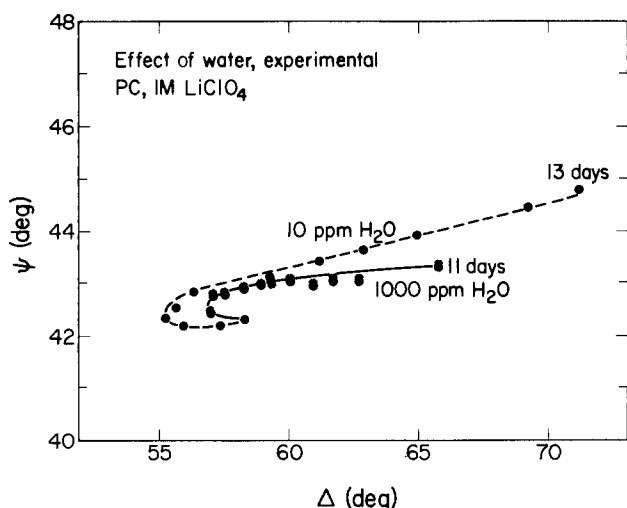


Fig. 3. Effect of water content of 1M LiClO₄ solution in PC on film formation. No water added (10 ppm) and 0.1% water added. Measured ellipsometer parameters.

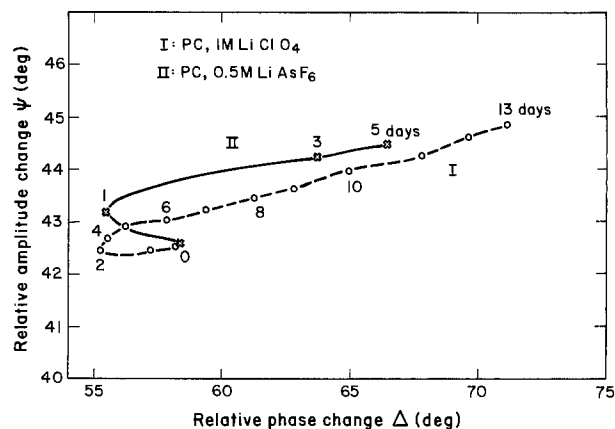


Fig. 4. Effect of the nature of electrolyte on film formation. I) 1M LiClO₄, II) 0.5M LiAsF₆ in PC, measured ellipsometer parameters. Period of immersion in days given along the curves.

Elemental film compositions were determined by Auger spectroscopy. Typical spectra are given in Fig. 5. The prominent peaks are those for carbon and oxygen. Films grown in LiClO₄ solution show a small chlorine content. No arsenic could be detected in films grown in LiAsF₆ solution. Depth profiles given in Fig. 6 indicate composition varying with depth. A positive secondary ion mass spectrum (SIMS) given in Fig. 7 shows a large number of peaks between masses of 2 and 50.

To investigate the precipitation of solution decomposition products as a possible mechanism for the formation of porous layers, a polished silver surface was used as an inert electrode in 1M LiClO₄ in PC. Ellipsometer measurements on this surface showed only small changes, which

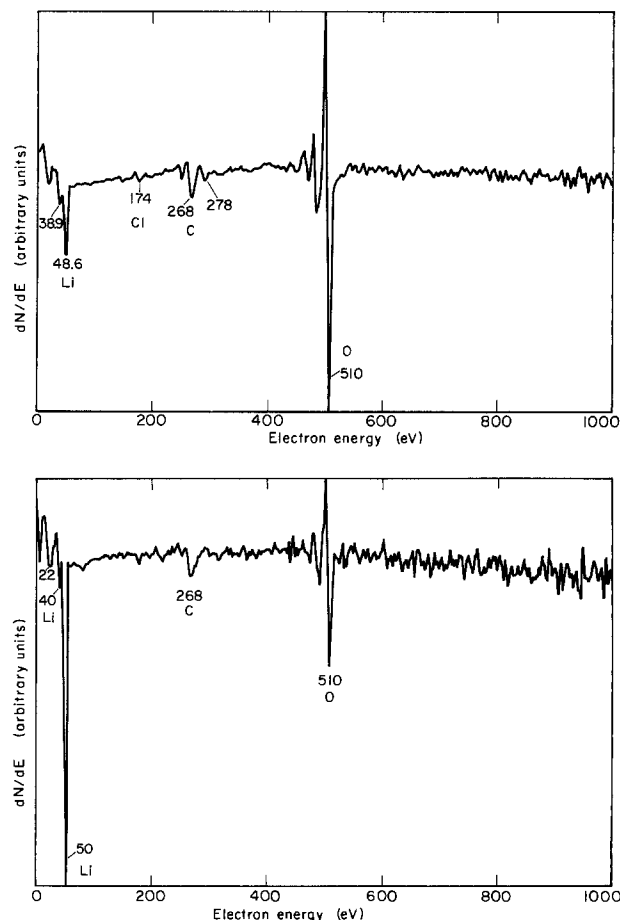


Fig. 5. Auger spectra of films formed after (top) 10 days in solutions of 1M LiClO₄ and (bottom) 7 days in 0.5M LiAsF₆. Spectra taken after 30s ion etching at 2 keV.

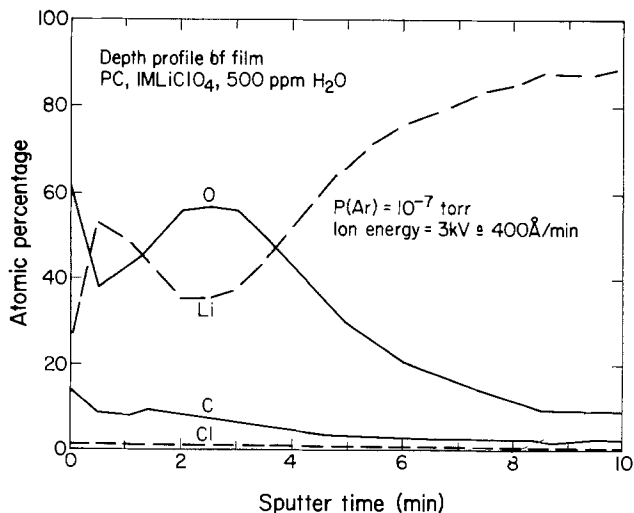


Fig. 6. Depth profile of film formed during 9 days in 1M LiClO₄ + 500 ppm H₂O. Ion etching with 3 keV, 15 nA argon beam (approximately 400Å/min).

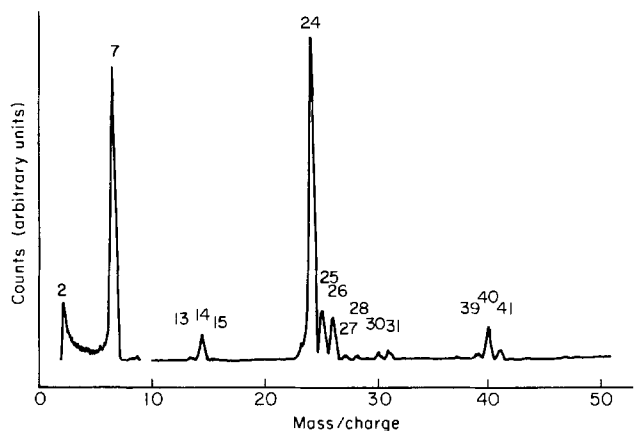


Fig. 7. Positive ion SIMS spectrum of film formed during 10 days in 1M LiClO₄, 1 kV argon ion beam, 17 nA, 14 min.

could be interpreted as the growth of a highly porous layer. SEM micrographs of the same surface showed discrete hillocks which were principally composed of C, O, and Cl, according to the Auger spectrum. Positive ion SIMS showed three principal mass peaks above 60, namely 63 (H₃CO₃⁺, not present in the film, Fig. 7), 73, and 81.

Discussion

Optical models.—Two features in the Δ/ψ plots of Fig. 2-4 are characteristic: the first one is a loop at the beginning of the experiment, the second is an almost-straight section with ever increasing ψ values at the later stages of the experiment. Calculations have shown that the real part of the refractive index of the film is primarily responsible for the size of the loop, the imaginary part for the slope of the straight part (Fig. 8). Refractive indexes for some possible film materials, solution, and substrate are listed in Table I. It was not possible to fit the experimental results satisfactorily with calculated values, assuming a homogeneous film with refractive indexes for any of the materials listed or their combination with solu-

Table I. Refractive index of potential film materials, solution, and substrate. 5461Å wavelength

LiOH	1.466
Li ₂ CO ₃	1.50
Li ₂ O	1.644
LiCl	1.662
PC, 1M LiClO ₄	1.429
Li	0.25-2.3i

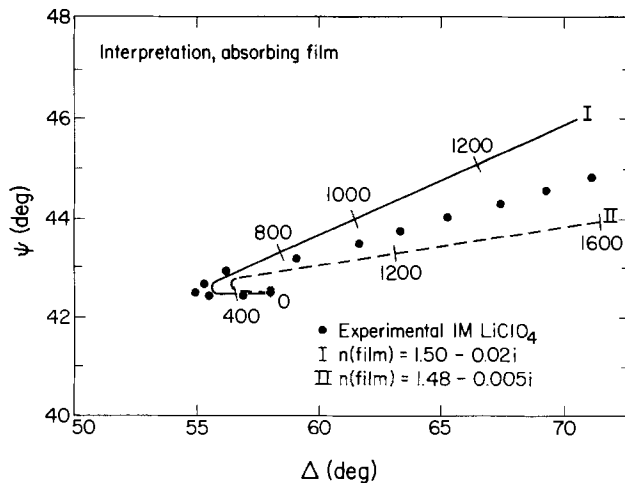


Fig. 8. Effect of real and imaginary parts of the film refractive index on ellipsometer parameters computed for homogeneous films. Film thickness (Å) given along computed curves.

tion in a uniformly porous film. Film thicknesses indicated along the theoretical curves of Fig. 8 are also much larger than those derived by capacitance measurements, which reach values of 200-400Å at the most. This discrepancy indicates a more complex film structure. Micrographs of a film grown in a 1M LiClO₄/PC solution for two weeks indeed show densely packed particles of approximately 2000-3000Å diam.

In an attempt to reconcile the results obtained by electrochemical transient techniques and those obtained by ellipsometry, a dual film model was investigated (Fig. 9, inset). In this model, both films are assumed to be homogeneous. The bottom film (film 2) is a thin (max 200-400Å) nonporous dielectric which is responsible for the electrode capacitance. The upper film (film 1) is thick and porous and is mainly responsible for the ellipsometer measurement.

The dual film model provides a means for explaining the discrepancy between ellipsometric and electrochemical results and gives improved, although not satisfactory, agreement between experimental and theoretical Δ/ψ plots. It was found that a rather high real part of the refractive index of the bottom films had to be assumed. Literature values for different lithium compounds (Table I) show that LiCl or Li₂O would have to be present in a mixture with low refractive index compounds to account for values of 1.55 and higher. Li₂CO₃, which had been proposed as the film material (3-5) shows too low a refractive

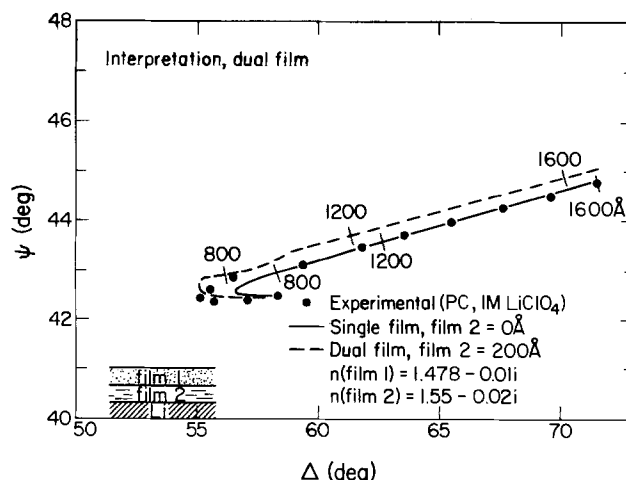


Fig. 9. Dual film model. Computed ellipsometer parameters for a dual film (broken curve) with compact, thin bottom layer (film 2) and a porous, growing top layer (film 1). Computation for growing single film shown by solid curve. Film thickness (Å) given along curves. Dual film model shown in inset.

index to be the primary constituent of the bottom (barrier) film. Polymerization products of the solvent, which had also been suggested as film material (6, 7), could make up the top film. Depth profiling by Auger spectroscopy showed that only small amounts (~2 atom percent [a/o]) of chlorine (for which Auger spectroscopy is very sensitive), but large amounts of oxygen (35-50 a/o), are present in the film. Lithium oxide is thermodynamically the favored product of a reaction between Li and water (or oxygen), which could be present in sufficient amounts in the solution. Keil *et al.* (8) found in gas phase experiments that oxygen reacts faster than water with Li. Auger peaks at 37 and 31 eV found in films are attributed (8) to Li in Li_2O . A dual-film structure of adsorbed oxygen and porous lithium carbonate has been proposed by Leif and Gilmour (9).

In order to improve agreement with ellipsometer measurements in the first stages of film growth, several inhomogeneous film models with continuously varying refractive index (Fig. 10) were investigated. The real and imaginary parts of the complex refractive index were assumed to decrease from the metal/film boundary to the film/solution boundary. Such an inhomogeneity could be due to variable porosity. It was found that predictions based on a linear profile of refractive index were in best agreement with the experimental results. Again, a rather high value of the real part of the refractive index had to be chosen for the part of the film close to the substrate; at the film/solution interface, the refractive index of the film was chosen to be equal to that of the solution.

Figure 11 illustrates the satisfactory agreement between experimental results and calculations based on a linear profile of the refractive index. The loop in the curve is determined by the high real part at the bottom of the film. The small imaginary part is introduced to adjust the slope of the curve at the later stages of growth and indicates a slightly absorbing film. Light absorption in the film could be due to nonstoichiometry or the presence of F-centers. F-centers have been extensively studied for

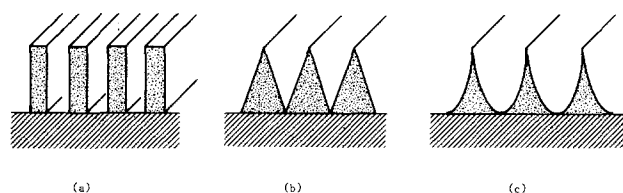


Fig. 10. Models of film porosity (or refractive index) profiles: (a) homogeneous; (b) inhomogeneous with linear profile; (c) inhomogeneous with parabolic profile.

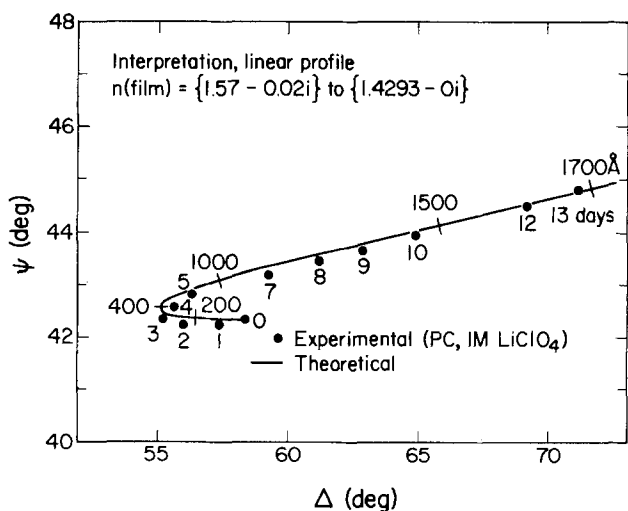


Fig. 11. Interpretation of ellipsometer measurements on Li in 1M LiClO_4 in PC with an inhomogeneous film of linear refractive index profile. Thickness of inhomogeneous film (\AA) given along computed curve. Period of immersion in days given with measured points.

Table II. Film thickness derived from ellipsometer measurements in solution and in vacuum for linear and parabolic refractive index profiles. Refractive index at bottom of film $1.57-0.02i$, at top 1.4293 in solution, 1.0 in vacuum. 1M LiClO_4 in PC, $1000\text{ ppm H}_2\text{O}$ added

Refractive index profile	Thickness	
	Solution	Vacuum
Linear	1500 \AA	1550 \AA
Parabolic	1950 \AA	2350 \AA

lithium halides. According to Hunderi (10), the F-center excitation energy for LiOH should be about the same as that for LiCl .

The model of a porous inhomogeneous film with continuously variable refractive index (or porosity) has been tested in a different way. By changing the refractive index of the immersion medium from a value of 1.43 for the solution to 1.0 for vacuum, one can change the effective refractive index of a film with fluid-filled pores drastically, as illustrated for a homogeneous porosity in Fig. 12. A realistic physical film model should produce the same film thickness for measurements in solution and in vacuum if the pore structure remains the same in the two immersion media. Table II shows a comparison of film thicknesses obtained from ellipsometer measurements in solution and in vacuum for a linear and a parabolic profile of the film refractive index with the same values at the inner and outer edge. The data support a refractive index (or porosity) varying linearly with thickness.

Film growth.—Film growth derived from ellipsometer and galvanostatic pulse measurement are presented in

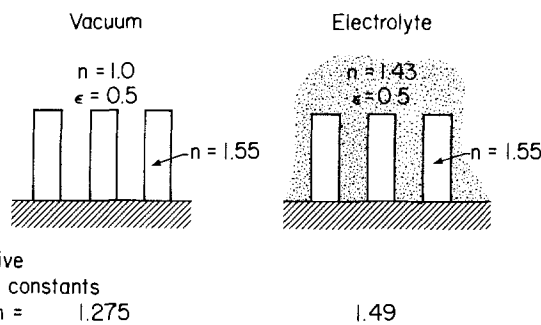


Fig. 12. Effect of immersion medium on the effective refractive index of a porous film illustrated with a homogeneous film of 50% porosity, pores evacuated or filled with electrolyte.

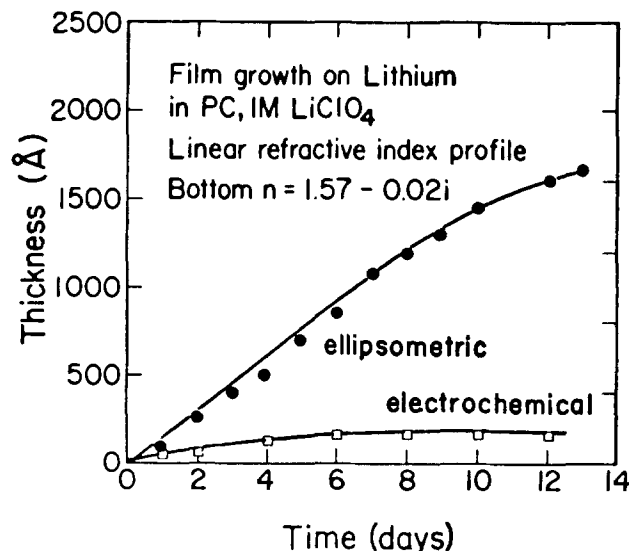


Fig. 13. Film growth on Li in 1M LiClO_4 in PC derived from ellipsometer measurements for a linear refractive index profile and film growth derived from galvanostatic pulse measurements ($\epsilon = 4.9$).

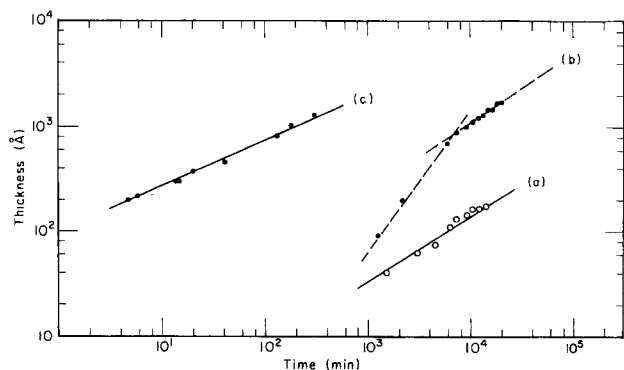


Fig. 14. Rate laws for film formation on Li; (a) capacitance measurements, 1M LiClO_4 in PC, $\epsilon = 4.9$; (b) ellipsometer measurements, 1M LiClO_4 in PC; (c) ellipsometer measurements, water vapor 1 ppm in He, thickness based on $n = 1.46$ (LiOH).

Fig. 13. An approximately parabolic rate law (exponent 1.6) holds for film growth derived from capacitance measurements (curve (a), Fig. 14, based on a dielectric constant $\epsilon = 4.9$ corresponding to Li_2CO_3). Film growth derived from ellipsometer measurements (curve (b), Fig. 14) follows a near-linear rate law initially (exponent 0.7), but approaches the parabolic law later (exponent 1.5). A parabolic rate law (exponent 2.2) has also been found to hold for film growth with water vapor [Fig. 14, curve (c)]. Figure 15 shows ellipsometer measurements and interpretation for the latter case. A homogeneous optical film model appeared to be satisfactory over most of the range of measurements if apparent optical constants of the substrate ($n = 0.35\text{--}2.14i$), indicative of a surface layer formed during electrode preparation in the glove box, were used. This simplification is responsible for the different origins of the computed and measured curves.

Conclusions

Ellipsometer measurements have shown that surface layers on lithium are inhomogeneous, with porosity increasing approximately linearly from a dense region facing the electrode to a highly porous region facing the liquid. The refractive index of the dense region is higher than that of Li_2CO_3 or LiOH and supports the presence of Li_2O . Ellipsometer measurements qualitatively agree with results obtained by electrochemical transient techniques (except for film growth in pure PC), because the dense region only is detected by electrical measurements.

Films are formed more rapidly in pure propylene carbonate than in the presence of electrolyte salts. LiClO_4 solutions form slower growing (more protective) films than LiAsF_6 solutions. Perchlorate also reduces the effect of water. Reaction with water is the most likely origin of the dense region, and its protective properties are confirmed by the parabolic rate law. A continuing growth of the porous region could indicate a different film origin, and precipitation of insoluble products resulting from the decomposition of the solution may be a contributing factor.

Acknowledgments

This work was supported by the Assistant Secretary for Conservation and Renewable Energy, Office of Ad-

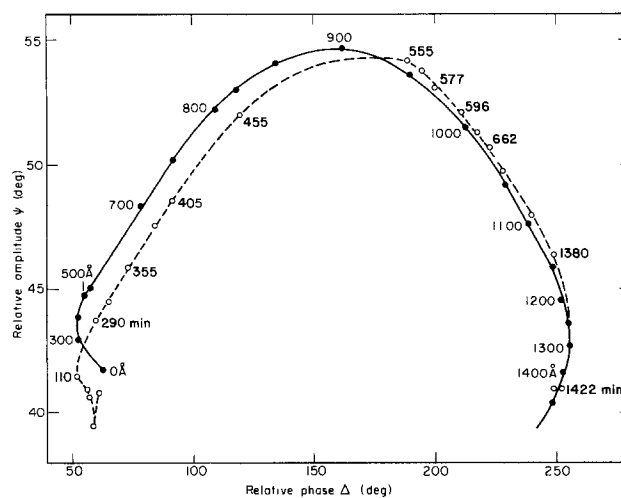


Fig. 15. Ellipsometer parameters for film growth on Li in He with 1 ppm water vapor. \circ : Measurements 110-1422 min. \bullet : Computation for homogeneous films, $n = 1.4664$, 0-1400 Å, substrate $n = 0.35\text{--}2.14i$.

vanced Conservation Technologies, Electrochemical Research Division of the U.S. Department of Energy under contract no. DE-AC03-76SF00098. We thank Mr. Kenneth A. Gaugler for taking the Auger and SIMS spectra and Mr. Water T. Giba for design and construction of the cell.

Manuscript submitted Nov. 28, 1983; revised manuscript received Oct. 8, 1984. This was Paper 37 presented at the Hollywood, Florida, Meeting of the Society, Oct. 5-10, 1980.

University of California assisted in meeting the publication costs of this article.

REFERENCES

1. Y. Geronov, F. Schwager, and R. H. Muller, *This Journal*, **129**, 1422 (1982).
2. H. J. Mathieu, D. E. McClure, and R. H. Muller, *Rev. Sci. Instrum.*, **45**, 798 (1974).
3. F. P. Dousek, J. Jansta, and J. Riha, *J. Electroanal. Chem.*, **46**, 281 (1973).
4. A. N. Dey, *Thin Solid Films*, **43**, 131 (1977).
5. A. N. Dey, in "Lithium Nonaqueous Battery Electrochemistry," E. B. Yeager, B. Schumm, Jr., G. Blomgren, D. R. Blankenship, V. Leger, and J. Akridge, Editors, p. 83, The Electrochemical Society Softbound Proceedings Series, Pennington, NJ (1980).
6. M. Garreau and J. Thevenin, *J. Microsc. Spectrosc. Electron.*, **3**, 27 (1978).
7. I. Epelboin, M. Froment, M. Garreau, J. Thevenin, and D. Warin, in "Power Sources for Biomedical Implantable Applications and Ambient Temperature Lithium Batteries," B. B. Owens and N. Margalit, Editors, p. 417, The Electrochemical Society Softbound Proceedings Series, Pennington, NJ (1980).
8. R. Keil, J. Hoenigman, W. Modeman, T. Wittenberg, and J. Peters, AFWAL-TR-80-2018, Interim Technical Report, University of Dayton Research Institute, Dayton, OH October 1979.
9. G. A. Leif and A. Gilmour, *J. Appl. Electrochem.*, **9**, 663 (1979).
10. O. Hunderi, *Surf. Sci.*, **57**, 451 (1976).

Corrosion Inhibition in Neutral, Aerated Media

F. Mansfeld* and M. W. Kendig*

Rockwell International Science Center, Thousand Oaks, California 91360

W. J. Lorenz*

University Karlsruhe, Karlsruhe, Germany

ABSTRACT

The concepts of interface and interphase inhibition as two different types of corrosion inhibition mechanisms are discussed briefly. Most of the studies reported in the literature have dealt with interface inhibition in acid media. Experimental results of interphase inhibition have been obtained for a 4340 steel rotating cylinder electrode (RCE) by impedance measurements during exposure over 48h in aerated, neutral 0.5M Na₂SO₄, 0.5M NaCl, tapwater and deionized water containing 10 mM NaNO₂, and mixtures of phosphonic acid/fatty amine or polyacrylic acid/fatty amine. An optimized approach for collecting impedance data for high R_p values and a low frequency limit between 0.4 mHz and 5 mHz has been applied in this study. A very good fit of the experimental data to a theoretical model is observed. For the phosphonic acid/fatty mixture, a second time constant occurs at high frequencies in Na₂SO₄ and NaCl, from which the porosity of the inhibitor layer can be calculated.

Generally, inhibition represents retardation of electrode reactions, especially of corrosion processes. Two types of inhibition can be distinguished: interface and interphase inhibition (1-4).

Interface inhibition presumes a strong interaction between the corroding substrate and the inhibitor (1-10). In this case, the inhibitor is potential-dependently adsorbed. The two-dimensional (2-D) adsorbate layer can affect the basic corrosion reactions in various ways which may be discussed in terms of the inhibition efficiency, ϵ , defined by

$$\epsilon = \frac{i - i_{inh}}{i} \quad [1]$$

where i and i_{inh} represent the current densities of the electrode reaction at constant potential in the absence of and presence of inhibitor, respectively. The three types of interface inhibition are

1. Geometrical blocking effect of the electrode surface by an indifferent adsorbate at a relatively high degree of coverage, θ_{inh} .

In this case, $(1 - \theta) i = i_{inh}$, and therefore

$$\epsilon = \theta \quad [2]$$

where $\theta = \Gamma/\Gamma_s$; Γ denotes the potential-dependent surface concentration of inhibitor, and Γ_s represents its saturation value.

2. Blocking of active surface sites by an indifferent adsorbate at a relatively low degree of coverage.

In this case, Eq. [2] holds again, if Γ_s is replaced by a surface concentration $\Gamma_{a,s}$ necessary for a complete blocking of all active surface sites.

3. The adsorbate is not indifferent, but reactive.

Two cases may be distinguished. The inhibitor acts as a positive or negative electrocatalyst on the corrosion reaction, or the adsorbate itself undergoes an electrochemical redox process. In the latter case, primary and/or secondary inhibition can occur, depending on the retardation effects caused by the original adsorbate and its reaction product, respectively.

In the case of a reactive coverage, ϵ will be a more complex function of θ than Eq. [2] and can also be negative

$$\begin{aligned} \text{Inhibition } 0 \leq \epsilon(\theta) \leq 1 \\ \text{Stimulation } \epsilon(\theta) < 0 \end{aligned} \quad [3]$$

These three types of interface inhibition are mostly observed in corrosion systems involving a bare metal surface in contact with the corrosive medium. This condition is often realized for the active metal dissolution in acid solutions.

*Electrochemical Society Active Member.

Interphase inhibition presumes a three-dimensional (3-D) layer between the corroding substrate and the electrolyte (3, 4, 11-13). Such 3-D layers generally consist of weakly soluble compounds of corrosion products and/or inhibitors. The inhibition efficiency depends strongly on the mechanical, structural, and chemical properties of the 3-D layers which are formed under the particular experimental conditions. This type of inhibition is mostly observed in corroding systems forming porous or nonporous protective layers. Porous 3-D layers are built up, for example, in neutral media in the absence of or presence of oxygen, whereas nonporous 3-D layers are formed in the passive metal state.

Maximum protection of such 3-D layers is obtained in passive systems without pitting corrosion. On the other hand, the density and distribution of pores will determine the inhibition efficiency in the case of porous 3-D layers, retarding mainly the transport-controlled corrosion processes. The inhibition efficiency can then be correlated with the rate of the mainly transport-controlled cathodic corrosion reaction taking place within the pores of the 3-D layers

$$\epsilon(t) = \frac{i_-(t) - i_{-,inh}(t)}{i_-(t)} \quad [4]$$

where $i_-(t)$ and $i_{-,inh}(t)$ denote the cathodic current densities at constant electrode potential and defined hydrodynamic conditions in the absence of and presence of the inhibitor, respectively. Since the cathodic current density depends on both the corrosion time and the hydrodynamic conditions, the protective properties of the 3-D layer are also a function of both variables.

Effective interphase inhibitors should not only be adsorbed at the metal/oxide and oxide/electrolyte interfaces, but should also be incorporated in the 3-D layers, leading to more homogeneous and more densely packed networks of less porosity and higher stability.

Most of the previous studies have dealt with interface inhibition in acid-deaerated systems. However, the corrosion mechanisms of non-noble transition metals in alkaline media and in neutral-aerated media, even in the absence of corrosion inhibitors, are strongly determined by the formation of 3-D oxidic layers, which are porous in the active, transition, and prepassive ranges.

Experimental results of interphase inhibition in neutral-aerated media have been collected as part of a program in which interphase inhibition will be evaluated for a number of different metal/environment/inhibitor systems. In this paper, the results of the corrosion behavior of steel in aerated neutral 0.5M Na₂SO₄, 0.5M NaCl, tapwater and deionized water containing NaNO₂, and mixtures of phosphonic acid/fatty amine or polyacrylic

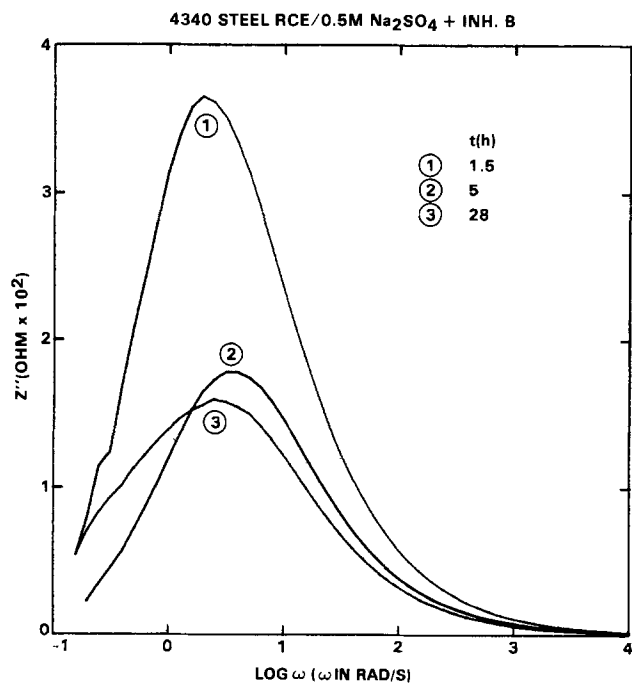


Fig. 1. Frequency dependence of the imaginary component Z'' . The integration method is used to determine R_p , Eq. [5] to determine C .

acid/fatty amine will be discussed. The corrosion behavior has been studied by determining the polarization resistance R_p from ac impedance measurements and from dc measurements in the case of 0.5M Na_2SO_4 . Only the ac impedance was measured for the remaining systems. A rotating cylinder electrode was used to ensure constant hydrodynamic conditions and adequate current distribution.

Experimental Approach

Rotating cylinder electrodes were prepared from 4340 steel, and experiments were carried out with a modified IBM EC 219 rotating disk electrode system at 144 rad/s in solutions which were open to air. A concentric Pt band or mesh served as the counterelectrode. Exposure time was usually 48h. Impedance measurements were carried out as discussed before (14-17), using a computerized system and a Solartron 1174 transfer function analyzer. The high impedance values of well-inhibited systems make it necessary to accurately measure impedance data over a large range of values between those of the solution resistance R_Ω and the polarization resistance R_p . Previously, this was accomplished by manually adjusting the gain of the current-measuring amplifier several times during a run to be within a factor of ten of the measured impedance. Additional experimental problems arise from the fact that corrosion systems usually have time-dependent kinetics and the fact that the measurements have to be extended to very low frequencies in the case of high inhibitor efficiencies. These problems have recently been solved to a large extent (18), using the autoranging capabilities of the PAR Model 276 interface and a low-pass filter. In this manner, the gain of the current amplifier interface is optimized and data sampling is reduced to one cycle with filtering at each frequency below 1 Hz, thereby improving both speed and signal-to-noise resolution for collection of the low frequency data. Impedance measurements have been extended to 0.4 mHz.

The solutions were prepared from reagent grade chemicals and deionized water. The inhibitor mixtures were made from polyacrylic acid (avg M.W. = 2000), phosphonic acid (tri-nitrilo-tris methylene phosphonic acid), and fatty amine (N-oleyl-1,3-propane diamine).

Data Analysis

R_p values from dc measurements at a scan rate of 0.2 mV/s have been determined as the slope of the current-

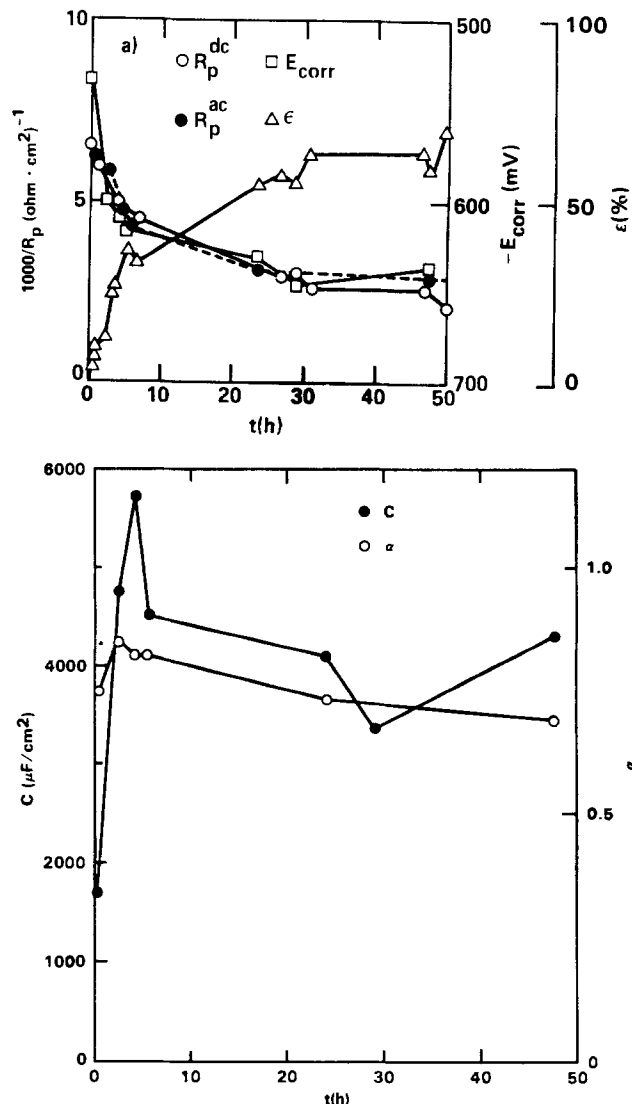


Fig. 2. Time dependence of R_p^{ac} , R_p^{dc} , E_{corr} , ϵ , C , and α for 4340 steel in neutral 0.5M Na_2SO_4 .

potential curve at the corrosion potential E_{corr} as a function of time and, in some instances, of rotation speed. Various methods for analysis of the impedance data, from which R_Ω , R_p , and the electrode capacitance C can be determined, have been discussed recently by the authors (14, 15, 17, 19, 20). Since in most cases a simple impedance diagram in the form of a depressed semicircle in a Nyquist plot is obtained, the CIRFIT-computer program (19) or the integration method (20) can be used to determine R_Ω , R_p , C , and α , where α is related to the deviation from ideal capacitive behavior ($0 \leq \alpha \leq 1$), which could be caused by surface inhomogeneity (21). The latter method has the advantage that the capacitance can be determined more accurately from the plot of the imaginary component Z'' of the impedance $|Z|$ as a function of $\log \omega$, where ω is the frequency f in rad/s ($\omega = 2\pi f$). C is calculated as

$$C = \frac{1}{\omega_m R_p} \quad [5]$$

where ω_m is the frequency of the maximum Z'' and R_p is determined by integration of the $Z'' \log \omega$ curve down to ω_m (20). The parameter α can be determined from the ratio $2Z''_m/R_p$. Figure 1 gives an example of this method in the case of 0.5M Na_2SO_4 and polyacrylic acid/fatty amine.

These methods of analysis are sufficient, since it has been found for all cases studied that the impedance spectra fit very well to a theoretical model of the impedance as

$$|Z| = R_\Omega + \frac{R_p}{1 + (j\omega CR_p)^\alpha} \quad [6]$$

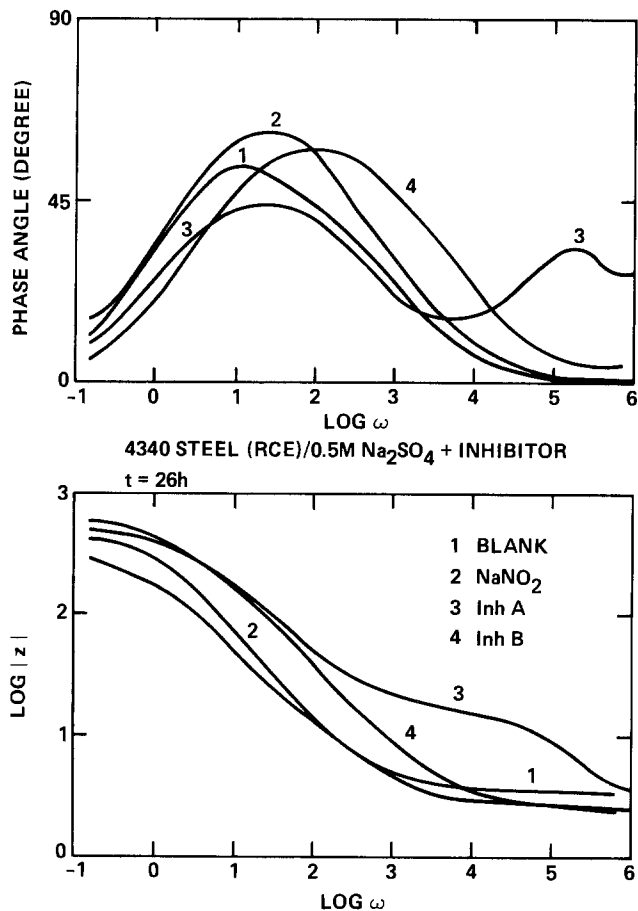


Fig. 3. Bode plots for 4340 steel RCE in 0.5M Na_2SO_4 containing inhibitors.

Experimental Results and Discussion

The experimental data for 4340 steel in 0.5M Na_2SO_4 with the three inhibitors have been analyzed. For NaCl, tapwater, and deionized water, examples of the experimental data will be given.

Na_2SO_4 .—In inhibitor-free Na_2SO_4 , corrosion rates (qualitatively expressed as R_p^{-1}) decrease with time in parallel with a shift of E_{corr} to more negative values (Fig. 2). This result suggests that the rate of the cathodic reaction decreases due to formation of 3-D layers of porous oxides. Excellent agreement was found between R_p^{ac} and R_p^{dc} . An inhibitor efficiency $\epsilon = (R_p - R_p^0)/R_p$ can be calculated, based on R_p^0 at $t \rightarrow 0$. It increases continuously during the 50h exposure time. The capacitance C has very high values, between 2000 and 6000 $\mu\text{F}/\text{cm}^2$, averaging about 4000 $\mu\text{F}/\text{cm}^2$ (Fig. 2) and not representing the double layer capacitance.

Figure 3 compares the impedance spectra in neutral 0.5M Na_2SO_4 containing NaNO_2 and mixtures of phosphonic acid and fatty amine (inhibitor A) or polyacrylic acid and fatty amine (inhibitor B). The impedance spectra for the inhibitor-free solution and for the presence of NaNO_2 or inhibitor B conform to the model in Eq. [6]. The effect of the inhibitors is seen in the increase of R_p (low frequency limit of the impedance $|Z|$) and a lowering of the capacitance. For inhibitor A, an additional time constant occurs at high frequencies, with a maximum of the phase angle at about 25 kHz. The impedance spectra are similar to those for polymer coatings such as polybutadiene on steel (22, 23). From the high frequency portion of the impedance, the pore resistance R_{p0} of the inhibitor film and its changes with exposure time can be calculated. The polarization resistance R_p^{ac} , which is the limit of the impedance for $\omega \rightarrow 0$, will be compared in the following with R_p^{dc} , which is determined from the linear sweep at E_{corr} .

In the presence of NaNO_2 , corrosion rates were reduced and E_{corr} was shifted to more noble values (Fig. 4), which

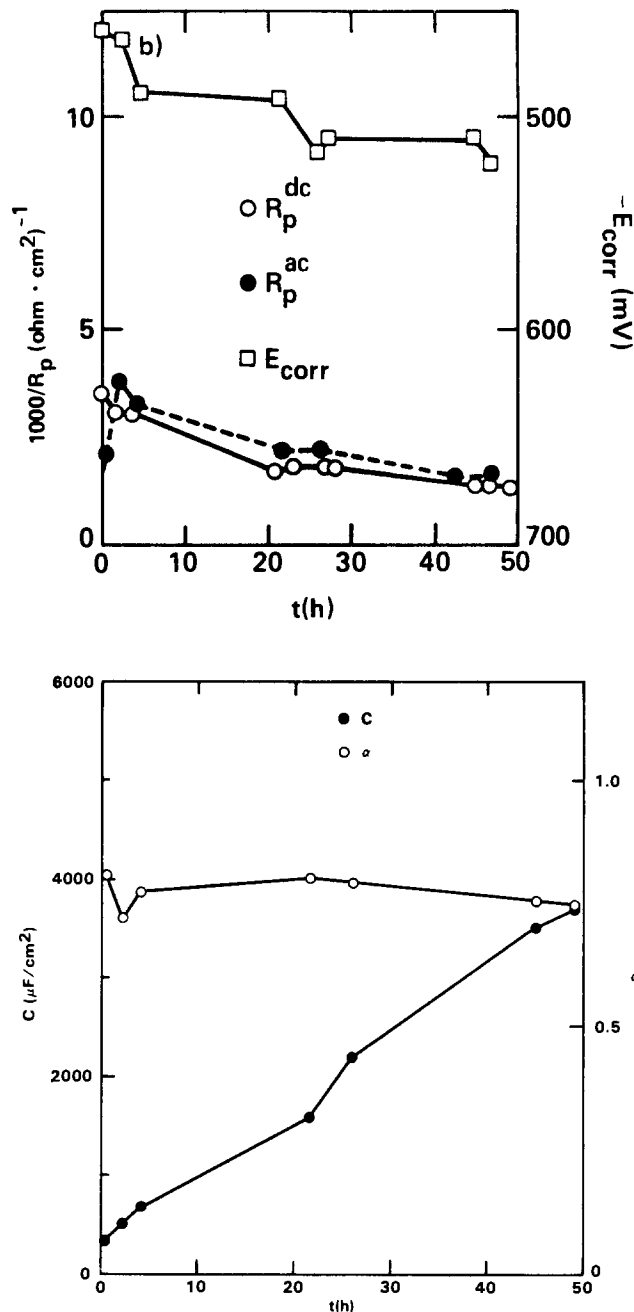


Fig. 4. Same as for Fig. 2, but in 0.5M Na_2SO_4 + 10 mM NaNO_2 .

suggests that the rate of the anodic reaction was decreased. Very little rusting was observed. Since the corrosion rate decreased by only about 60%, it is surprising that the capacitance increased by about a factor of ten in 50h. The value of α remained close to 0.8.

The corrosion rate in the presence of the phosphonic acid/fatty amine mixture (inhibitor A, Fig. 5) is similar to that observed in the presence of NaNO_2 and decreases only slightly with time. The porosity of the coating, R_{p0}^{-1} , decreases as the inhibitor layer is formed and then doubles to a more or less constant value for longer exposure times, without a corresponding change of the corrosion rate. As for the case of NaNO_2 , the capacitance C increases continuously with time. The capacitance C_p , which is associated with the reactions in the pores, is very small and decreases with time to about 1.2 $\mu\text{F}/\text{cm}^2$ based on the total geometrical surface area.

In the presence of the polyacrylic acid/fatty amine mixture (inhibitor B), corrosion rates were very low initially, but increased with time to values similar to those determined at longer exposure times in the presence of other inhibitors (Fig. 6). As for the other inhibitors, the capacitance increased continuously, but not as sharply as for

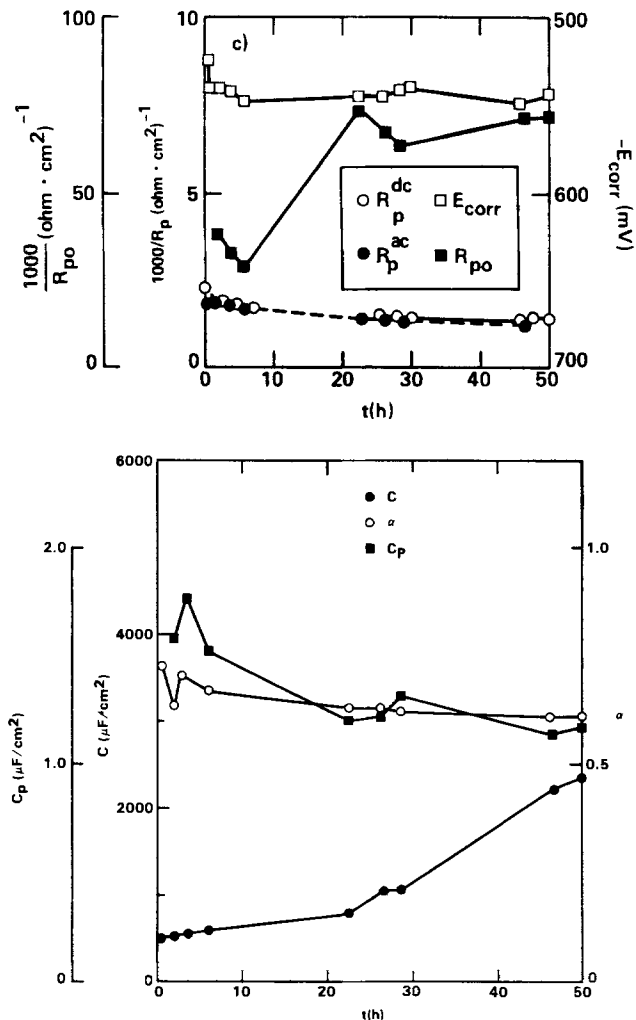


Fig. 5. Same as for Fig. 2, but in 0.5M Na₂SO₄ + inhibitor A; R_{p0} and C_p relate to the porous inhibitor layer.

NaNO₂ (Fig. 4) or inhibitor A (Fig. 5). The value of α stayed more or less constant at about 0.7.

The dependence of E_{corr} and $(R_p^{dc})^{-1}$ on rotation speed $\tau^{0.7}$ (turbulent flow) is shown in Fig. 7. Without an inhibitor, a pronounced effect of τ can be seen. This effect is much smaller in the presence of NaNO₂ and absent in the presence of inhibitor A, indicating that mass transport does not affect the corrosion kinetics in the presence of the porous inhibitor film.

NaCl.—Figure 8 gives an example of the impedance characteristics observed in 0.5M NaCl. Only one time constant is observed between 10⁵ Hz and 5 mHz. Excellent agreement is observed between the experimental results, as shown in Fig. 8 for 3.5h and for longer exposure times, and the model in Eq. [6]. These results cast some doubt on the experimental data and the model proposed by Bonnel *et al.* (24) and Duprat *et al.* (25), who reported the occurrence of a second time constant at low frequencies (<0.1 Hz) for a carbon steel rotating disk electrode in 3% NaCl. Since the measurement in Fig. 8 was performed in 76 min, and since corrosion rates did not change very much in the first hours of exposure, time effects do not affect the analysis of the impedance data according to Eq. [6].

The addition of 10 mM NaNO₂ increases the polarization resistance R_p^{ac} by about a factor of 10 at similar exposure times (Fig. 9). As in Na₂SO₄, R_p and C increase continuously with exposure time, but to a lesser extent. The agreement between the theoretical model and the experimental data in Fig. 9 is not as good as for the inhibitor-free solution in Fig. 8, which can be seen to be due to the lack of symmetry around the frequency of the maximum phase angle in Fig. 9.

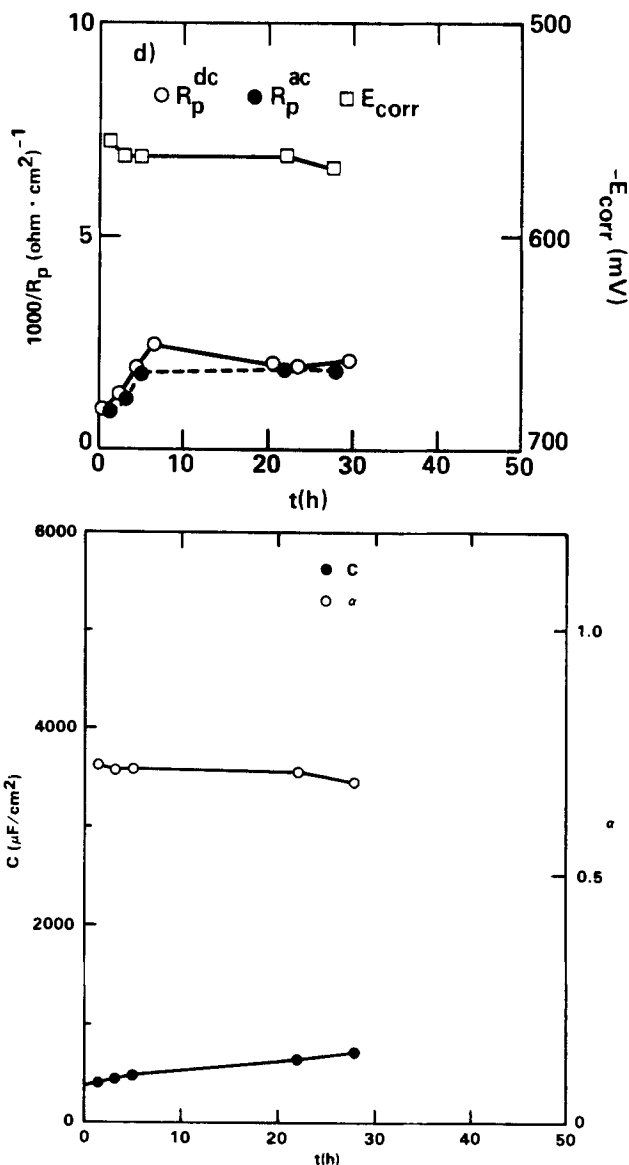


Fig. 6. Same as for Fig. 2, but in 0.5M Na₂SO₄ + inhibitor B.

As for Na₂SO₄ (Fig. 3), a second high frequency maximum occurred at about 100 kHz in the presence of inhibitor A. Similar effects have been observed by Duprat *et al.* (24). To obtain accurate data without excessive phase shift at these high frequencies, a gold wire connected to the saturated calomel reference electrode through a 0.1 μF capacitor is used as a reference electrode at high frequencies.

Tapwater.—Some experimental data have been reported for tapwater containing NaNO₂ (16). Data obtained with the optimized technique (18) are shown in Fig. 10 with a lower frequency limit of 0.4 mHz at 29h exposure, as compared to a lower frequency limit of 25 mHz in the earlier measurements. By curve-fitting according to Eq. [6], $R_p = 4.15 \times 10^6 \Omega$ ($2.78 \times 10^6 \Omega\text{cm}^2$) was determined for $t = 29\text{h}$. Very good agreement between the experimental data and the curve according to Eq. [6] with the parameters shown in Fig. 10 is found in the capacitive part of the Bode plot; however, some deviation occurs at the lower frequencies. The capacitance changed very little with time. The example in Fig. 10 shows clearly that in the case of very high R_p values, the impedance measurements must be extended to very low frequencies. The low-frequency breakpoint f_1 (14)

$$f_1 = \frac{1}{2\pi C (R_p + R_s)} \quad [7]$$

lies at 1.3 mHz for the parameters calculated for $t = 29\text{h}$. It

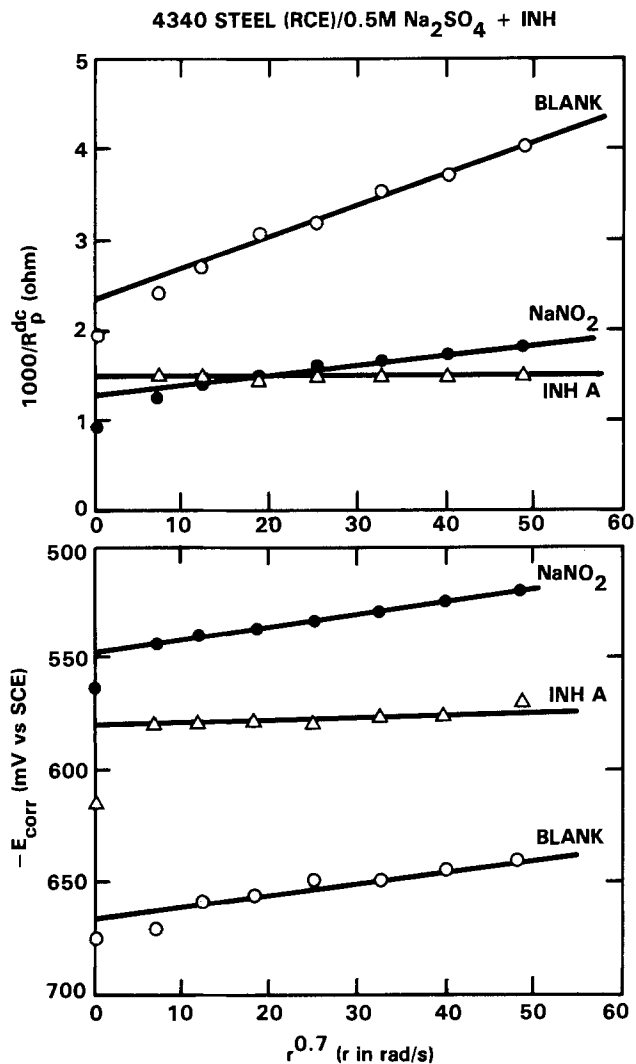


Fig. 7. Effect of rotation speed of the RCE on E_{corr} and R_p .

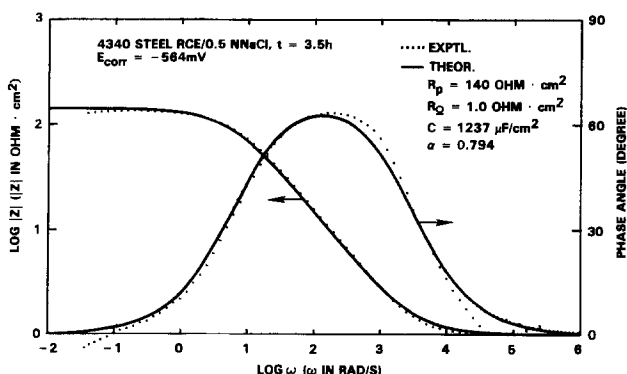


Fig. 8. Bode plot and fit to model in Eq. [6] for 4340 steel RCE in 0.5M NaCl.

should be noted that a dc measurement of R_p in this case had to be carried out with a scan rate of less than 4×10^{-3} mV/s or 14 mV/h (26). Many reported disagreements between electrochemical and weight-loss measurements can be traced to a choice of an excessively high scan rate, which leads to a R_p value which is too low.

For inhibitor A, the high-frequency time constant indicating presence of a porous inhibitor layer was not observed. Over a 48h exposure period, R_p increased slowly from about 1×10^5 to $4 \times 10^5 \Omega \text{ cm}^2$, with little change of the capacitance. Similar results were obtained for inhibitor B, which was less effective than inhibitor A (Fig. 11).

Deionized water.—The optimized method for obtaining accurate impedance data, which was developed for this study, also makes it possible to obtain impedance spectra in low-conductivity media such as deionized water. Data

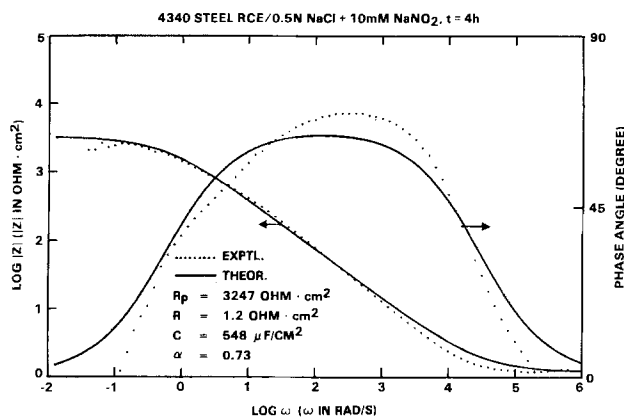


Fig. 9. Bode plots for 4340 steel RCE in 0.5M NaCl + 10mM NaNO_2 , $t = 4\text{h}$.

for short exposure times could not be analyzed, since $R_\Omega > R_p$. Figure 12 shows data for exposure times of 2.5h and a fit to the model in Eq. [6] and for 4.5h. The agreement between the model and the experimental data is remarkable, considering the difficulty of conducting this experiment.

Figure 13 shows the time dependence of the corrosion rate (expressed as R_p^{-1}), E_{corr} , and R_Ω . The increase of the corrosion rate with time is accompanied by a continuous decrease of the solution resistance R_Ω and a shift of E_{corr} to more negative values.

For deionized water containing 10 mM NaNO_2 (Fig. 14), two time constants can be resolved. The R_p value in-

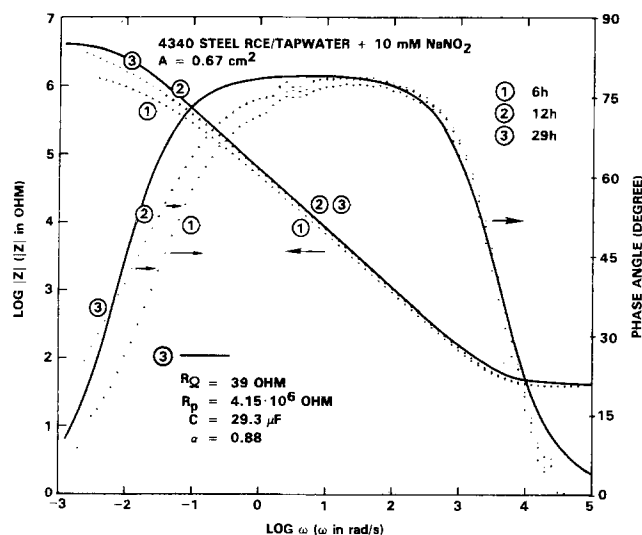


Fig. 10. Bode plots for 4340 RCE in tapwater + 10 mM NaNO_2 .

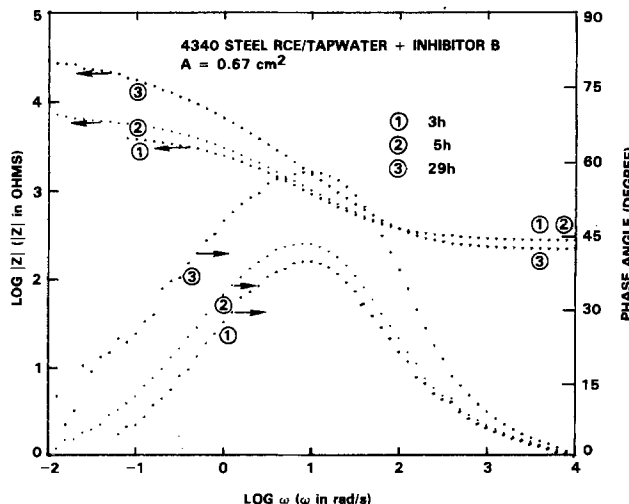


Fig. 11. Same as Fig. 10, but for inhibitor B.

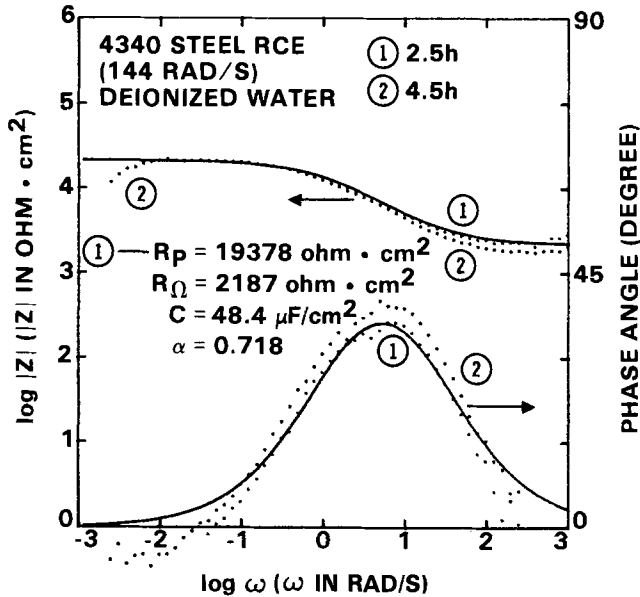


Fig. 12. Bode plots and fit to theoretical model in Eq. [6] for 4340 steel RCE in deionized water.

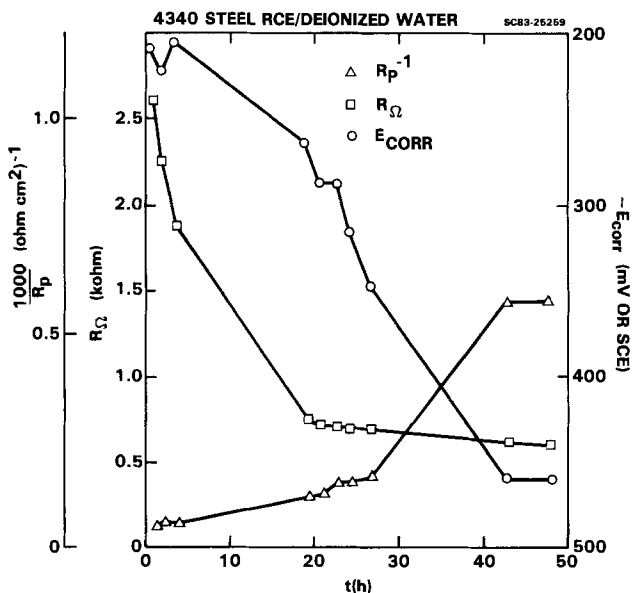


Fig. 13. Time dependence of R_p^{-1} , R_Ω , and E_{corr} for 4340 steel RCE in deionized water.

increases by more than a factor of 20 during the 48h exposure test. For the inhibitor B, a continuous decrease of R_p with time was observed, combined with a decrease of R_Ω , a shift to more negative values of E_{corr} , and an increase of the capacitance C (Fig. 15). A very good fit to the theoretical model (Eq. [6]) was observed for the parameters shown in Fig. 15 for $t = 7h$.

It will be noted that the experiments in deionized water allow the study of the effects of inhibiting ions without the presence of any other ions (except corrosion products), which could have synergistic effects. This question will be addressed when all data of this test series have been collected and analyzed.

Summary

The concepts of interface and interphase inhibition have been discussed briefly. Examples of interphase inhibition have been given for steel in a variety of neutral, aerated solutions containing corrosion inhibitors using ac impedance spectroscopy. For Na_2SO_4 solutions, the polarization resistance has been determined from the impedance spectra and from dc measurements, with good agreement between both data. The impedance data fit a theoretical model with deviations from ideal capacitive behavior which could be due to surface inhomogeneities.

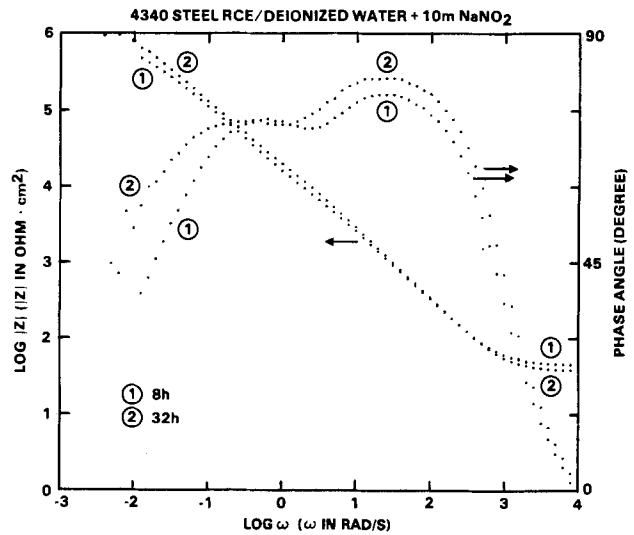


Fig. 14. Bode plots for 4340 steel RCE in deionized water + 10 mM $NaNO_2$.

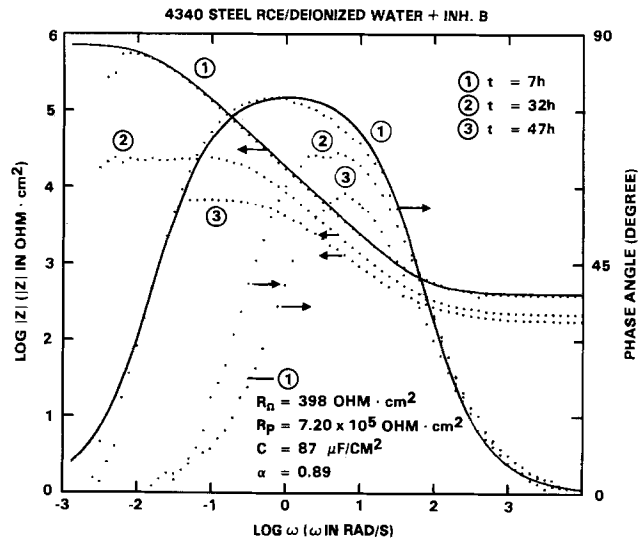


Fig. 15. Bode plots and fit to theoretical model (Eq. [6]) for 4340 steel RCE in deionized water and inhibitor B.

Porosity of inhibitor layers can result in an additional time constant at high frequencies.

Acknowledgments

The experimental portion of this project has been carried out under the Rockwell International R&D Program. S. Tsai and A. T. Allen collected the experimental data. One of us (W.J.L.) acknowledges financial support by the West German research program Corrosion and Corrosion Protection (FE-KKS).

Manuscript submitted April 20, 1984; revised manuscript received Sept. 28, 1984.

Rockwell Science International Center assisted in meeting the publication costs of this article.

REFERENCES

1. G. Trabaneli and V. Carrassiti, in "Advances in Corrosion Science and Technology," M. G. Fontana and R. W. Staehle, Editors, Vol. 1, p. 147, Plenum Press, New York-London (1970).
2. H. Fischer, *Werkst. Korros.*, **24**, 525, 575 (1973).
3. W. J. Lorenz and F. Mansfeld, in "Proceedings of the International Conference on Corrosion Inhibition," NACE, Dallas, Texas (1983).
4. W. J. Lorenz and F. Mansfeld, Paper 174 presented at The Electrochemical Society Meeting, Washington, DC, Oct. 9-14, 1983.
5. F. C. Raducanu and W. J. Lorenz, *Electrochim. Acta*, **16**, 995, 1143 (1971).

6. M. Erbil and W. J. Lorenz, *Werkst. Korros.*, **29**, 505 (1978).
7. W. J. Lorenz and F. Mansfeld, 31st ISE-Meeting, Venice (1980).
8. M. S. Abdelaal, A. A. El Miligy, G. Reinners, and W. J. Lorenz, *Electrochim. Acta*, **20**, 507 (1975).
9. W. J. Lorenz and F. Mansfeld, *Corros. Sci.*, **21**, 647 (1981).
10. A. A. Aksüt, W. J. Lorenz, and F. Mansfeld, *ibid.*, **22**, 611 (1982).
11. P. Lorbeer and W. J. Lorenz, *Electrochim. Acta*, **25**, 375 (1980).
12. M. A. Morsi, Y. A. Elewadi, P. Lorbeer, and W. J. Lorenz, *Werkst. Korros.*, **31**, 108 (1980).
13. P. Lorbeer and W. J. Lorenz, in "Proceedings of the 5th European Symposium on Corrosion Inhibitors," Vol. 1, p. 377, Ferrara (1980).
14. F. Mansfeld, *Corrosion*, **37**, 301 (1981).
15. F. Mansfeld, M. W. Kendig, and S. Tsai, *ibid.*, **38**, 570 (1982).
16. F. Mansfeld, M. W. Kendig, and S. Tsai, *Corros. Sci.*, **22**, 455 (1982).
17. F. Mansfeld and M. W. Kendig, *Werkst. Korros.*, **34**, 397 (1983).
18. M. W. Kendig, A. T. Allen, and F. Mansfeld, *This Journal*, **131**, 935 (1984).
19. M. W. Kendig, E. Meyer, G. Lindberg, and F. Mansfeld, *Corros. Sci.*, **23**, 317 (1983).
20. M. W. Kendig and F. Mansfeld, *Corrosion*, **39**, 466 (1983).
21. W. J. Lorenz, K. Jüttner, M. W. Kendig, and F. Mansfeld, Submitted.
22. F. Mansfeld, M. W. Kendig, and S. Tsai, *Corrosion*, **38**, 478 (1982).
23. F. Mansfeld and M. W. Kendig, in "Proceedings of the 9th International Congress on Metallic Corrosion," Vol. 3-74, Toronto, Canada, June 1984.
24. A. Bonnel, F. Dabosi, C. Deslouis, M. Duprat, M. Keddum, and B. Tribollet, *This Journal*, **130**, 753 (1983).
25. M. Duprat, F. Moran, and F. Dabosi, *Corros. Sci.*, **23**, 1047 (1983).
26. F. Mansfeld and M. W. Kendig, *Corrosion*, **37**, 545 (1981).

Recent Developments with High Temperature Stabilized-Zirconia pH Sensors

Mike J. Danielson* and Oscar H. Koski

Pacific Northwest Laboratory, Richland, Washington 99352

Jonathan Myers

Rockwell Hanford Operations, Richland, Washington 99352

ABSTRACT

The pH response of 8 weight percent yttria-stabilized zirconia sensors is examined over a temperature range of 373-573 K. Good pH response was found throughout the temperature range. The internal half-cell was discovered to be poisoned by oxygen, which permits some simplification in the calibration of the sensor. Activation energy measurements imply that the primary conduction process involves the oxide ion. An improved electrical/mechanical seal is also discussed.

pH is the most important variable in water chemistry. It is often overlooked today, but pH electrodes operating at 298 K lead to the determination of the thermodynamic properties of many aqueous species. The lack of a simple and reliable pH electrode for environments above 373 K has been a great impediment to assembling the thermodynamic data base to make aqueous chemistry at elevated temperatures a quantitative science.

Niedrach (1) was the first to publish the high temperature (558 K) pH response of yttria-stabilized zirconia closed-end tubes. pH response was shown to be independent of the redox state of the solution. This initial design used an aqueous internal buffer, but all later designs featured a solid-state Cu/Cu₂O internal cell. No doubt the change to a solid-state design was needed because (i) the sensors have an extremely high impedance at lower temperatures and the complicated electrical/pressure seal with an aqueous fill could result in a shunting of the internal cell, and (ii) the pH of the internal buffer can easily degrade with time resulting in a potential drift. Niedrach (2) was awarded a patent on pH sensors which are oxide-ion conductors. In later papers, (3, 4), his work was extended to lower temperatures and to the geothermal environment. The sensors have nearly perfect Nernstian response at 558 K and do not suffer degradation even after weeks at elevated temperature. However, their 368 K response has been less ideal, with reports that the probes become sluggish with duration of exposure (at 368 K) and that temperature cycling between 558 and 368 K results in a loss of pH response at the lower temperature. Very little work has been carried out at temperatures between 368

and 558 K. Niedrach has successfully used both 8 and 17 weight percent (w/o) yttria-stabilized zirconia sensors in his investigations. Until recently, all electrical/pressure seals were made at the open end of the tube using Conax (Buffalo, New York) fittings. Tube breakage, as well as solution leakage into the seal region (especially with temperature cycling), has been a problem which results in shunting out of the pH sensor. Niedrach and Stoddard (5) have recently replaced the Conax pressure fitting by brazing the sensor directly to a titanium fitting. In this latest paper, they show that the pH response at 368 K is free of sodium-ion error in alkaline solutions and is Nernstian throughout the entire pH range. However, the pH response becomes increasingly sluggish with time of exposure, and they suggest it is due to slow hydrolysis reactions at the grain boundaries where second phase materials exist. One recurring problem with Niedrach's pH measurements in his lack of success in using a high temperature reference electrode. Consequently, his potential data could not be placed on the Standard Hydrogen Electrode (SHE) scale.

Tsuruta and Macdonald (6) examined the pH response of one 17 w/o yttria-stabilized zirconia sensor at 373, 423, 573, 498, 523, and 548 K. Design details are sparse on the electrical/mechanical seal. The closed-end sensor tube penetrates into the autoclave and is in contact with the solution whose pH is to be measured. The inside of the sensor tube is filled with an aqueous buffer containing KCl. The Ag/AgCl portion of the electrode sits at ambient temperature (resulting in a thermal liquid junction potential), though the pressure on the inside of the tube is at the saturation pressure fixed by the highest temperature. Degradation of the internal buffer was a problem until it

* Electrochemical Society Active Member.

was replaced with 0.01M KOH. A hydrogen electrode was included within the autoclave so that the pH could be measured, and the pH response of the sensor was evaluated over a wide range of pH buffers (approximately 3-9). In general, they found a good Nernstian pH response at temperatures above 473 K, although there was a small deviation on the acid side (pH of 3-5). Large, unexplained deviations from Nernstian response were observed at 373 and 423 K. Niedrach *et al.* (5) do not observe with this brazed sensor any significant deviations from Nernstian response at 368 K throughout the entire pH range. Because Tsuruta *et al.* (6) observe their largest deviations in pH response at 373 and 423 K, where the impedance of the sensors is greatest, the most likely explanation for their results is electrical shunting of the Ag/AgCl termination by some lower impedance path made possible by aqueous solutions on both sides of the sensor.

In this paper, we will discuss some observations and improvements with yttria-stabilized zirconia pH sensors which will bring them closer to successful and convenient use in the laboratory and field.

Experimental

A total of 62 zirconia tubes of 8 w/o yttria were purchased from Coors (ZDY-4 composition; Golden, Colorado) and Corning (Solon, Ohio) in the standard dimensions of 0.64 cm od (0.25 in.) and 0.48 cm id (0.19 in.). They were mounted in standard Conax fittings (Buffalo, New York) and installed in a 3.8 liter Hastelloy-C autoclave. Four lid penetrations were used for zirconia pH sensors. Two other penetrations were used for the Ag/AgCl external reference electrode (7) (0.100 molal KCl) and a platinized-platinum hydrogen electrode. The hydrogen electrode was replatinized at the beginning of each experiment using the standard procedure (8). The hydrogen electrode was necessary because the buffers degrade with time, and it permitted the determination of the actual pH change with which to compare the response of the zirconia pH sensors. Buffers were stored in 208 liter (55 gal) polyethylene barrels in which high-purity hydrogen was continuously sparged. The hydrogen was passed through a catalyst (Deoxo; Engelhard, Union, New Jersey) to remove the final traces of oxygen before entering the tanks. A high-pressure pump recirculated the buffer solution through the autoclave at 2.6 l/h with a pressure of 10.1 MPa (1450 psig). Solution exited the autoclave through a cooler, the pressure relief valve, and back to the storage tank. Only two buffers were used in this study and were chosen to bracket the values expected in natural ground water. They were 0.01M B(OH)₃ and 0.01M B(OH)₃ + 0.01M NaOH. Table I shows the pH values at temperatures calculated using the data of Baes and Mesmer (9). Dimer formation of boric acid was taken into account, as well as activity coefficients, using the Debye-Huckel relation. A separate instrumentation-grade high input impedance preamplifier (>10¹¹Ω, Beckman Model 633100; Fullerton, California) was used for each of the five pH sensors, and all shared the common external reference electrode. Data was stored at 30 min intervals on a Model 2240B Fluke Datalogger (Seattle, Washington). pH response was studied in 50 K increments over a temperature range of 373-573 K. Duration of experiments varied from 5 to 30 days.

The electronic assembly illustrated in Fig. 1 was used to determine the resistive impedance. The sinusoidal frequency for the ac interrogation was 10⁻³ Hz with an am-

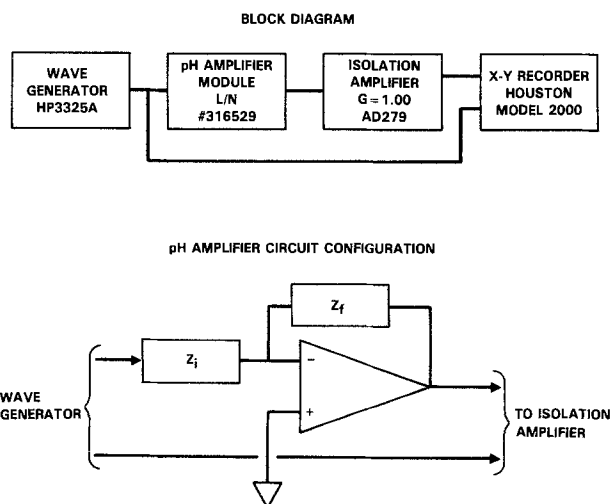


Fig. 1. AC measurement system

plitude of 1V peak to peak. The pH/reference electrode pair was used either in the input (Z_i) or feedback circuit (Z_f), whichever suited the following criteria: (a) the feedback impedance was lower than 10⁹Ω to ensure that the bandpass and bias offset currents of the amplifier made no contribution to the observed results; (b) the current level was insufficient to polarize the reference electrode; and (c) the output voltage of the amplifier was substantially below saturation. The resistive impedance changes approximately by a factor of 10 for each 50 K. The temperature range of the study was 373-573 K; therefore, four decades of resistance values were required to optimize the amplifier gain. Lissajous plots of the current vs. potential behavior were recorded on an X-Y recorder. From these plots, the impedance of the sensors was determined. At low temperatures, the pH response is a low frequency phenomenon. At 368 K, the ac response is independent of pH at frequencies above 10⁻² Hz.

Sensor Mounting

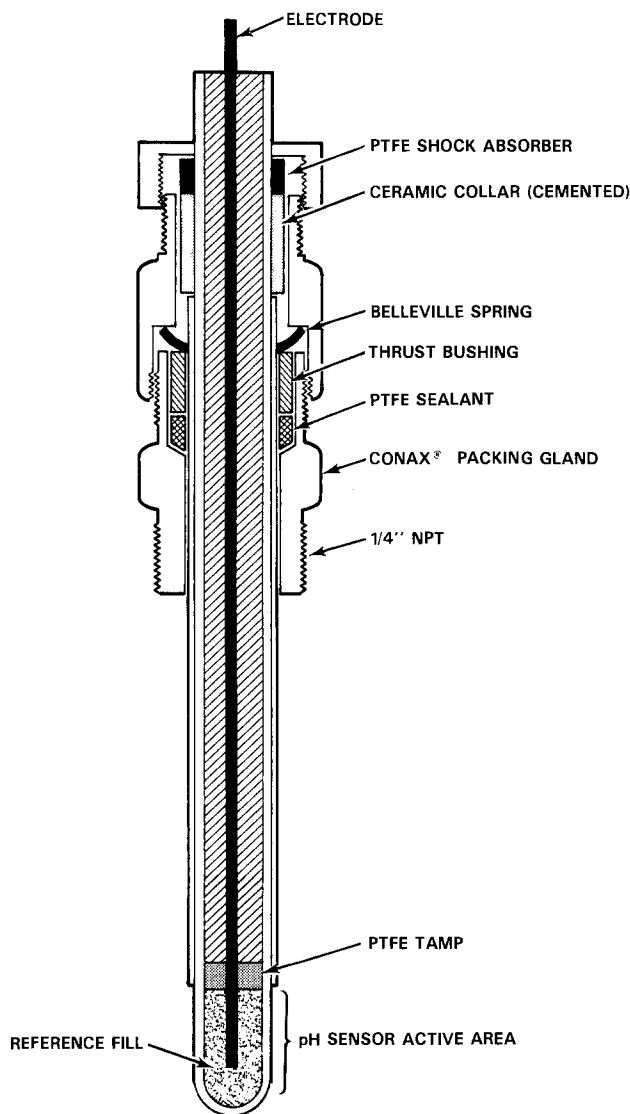
The two major problems with mounting the ceramic pH sensors are their fragility and high impedance. Polytetrafluorethylene (PTFE) is used as the pressure sealant in a Conax (Model PG2-250-B-T; Buffalo, New York) packing gland. This design is shown in Fig. 2. The soft sealant applies the compressive load in a uniform manner to minimize tube breakage. Unlike Niedrach's (1-4) early designs, the electrical termination region of the sensor was moved outside the PTFE pressure sealant region to ensure that any traces of moisture leaking out of the seal could not shunt the pH signal. A ceramic collar is cemented to the sensor barrel (Cotronics 940; Brooklyn, New York) to prevent the sensor from being extruded out of the pressure fitting. Belleville spring washers are used to spring load the PTFE sealant to improve the seal reliability during temperature cycling.

pH Response Amongst New Tubes

To understand how frequently natural pH response appears in 8 w/o yttria-stabilized zirconia sensor tubes, a total of 62 tubes were purchased from Coors and Corning and subjected to a rapid pH screening test at 358 K. The test protocol was to place the sensors in a National Bureau of Standards (NBS) pH 4 buffer thermostated at 358 K. 1M KCl with an Ag/AgCl electrode was used inside each tube, and the potential was measured against a 4.0M KCl, Ag/AgCl reference electrode at temperature. They were exposed to the pH 4 buffer for no more than 30 min before they were placed in a NBS thermostated pH 9.8 buffer, and the potential was recorded after 60 sec. This test was only for screening, not for steady-state pH response; however, 60 of the tubes responded with >80% Nernstian response. Two tubes had no response and were found to be cracked. This test demonstrated that pH response is a common phenomenon at least among these

Table I. pH buffer data

Temperature	0.01M B(OH) ₃ pH	0.01M B(OH) ₃ + 0.01M NaOH pH
298 K	5.57	10.56
373 K	5.41	9.51
423 K	5.39	9.14
473 K	5.42	8.94
523 K	5.48	8.91
573 K	5.56	9.04



TUBE YTTRIA STABILIZED ZIRCONIA
NOMINAL 1/4" OD x 8" LONG

Fig. 2. pH electrode and mount

batches of tubes. Unlike the glass pH electrode, long hydration times are not needed to develop pH response.

Activation Energy

The activation energy of the pH sensors was determined over a temperature range of 373-573 K by measuring the ac impedance at 10^{-3} Hz. AC methods are preferred because the pH sensors polarize when using dc methods. Four different types of internal electrodes were used

1. An Ag coat applied by brushing silver paint (Aremco no. 525; Ossining, New York) on the bottom of the tube to a height of about 2.5 cm; oven baking at 573 K to remove the organic binder; and electrical contact made with a copper wire.
2. 99.9% silver powder placed inside the tube to a depth of about 2.5 cm and contact made with a copper wire.
3. Graphite powder placed inside the tube to a depth of 2.5 cm with contact by a copper wire.
4. A Cu/Cu₂O (A. R. grade chemicals) made according to Niedrach's recipe (3) of 1:1::Cu powder:Cu₂O powder (by mass) to a depth of 2.5 cm; contact made with a copper wire.

A least squares fit of the impedance data as a function of temperature is shown in Fig. 3 for sensors in the basic buffer. Activation energies were lowest for the Cu/Cu₂O and Ag coat electrodes at 22.9 kcal. Data (12) on the high

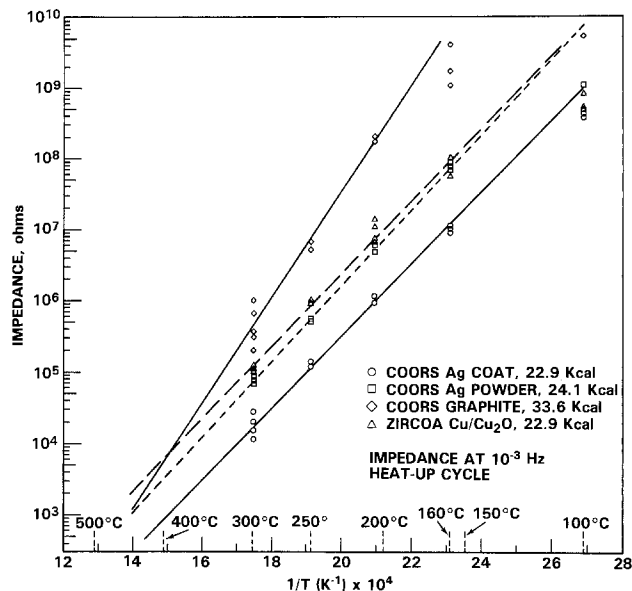


Fig. 3. Arrhenius plots of pH sensors

temperature (673-923 K) behavior of 8 w/o yttria-stabilized zirconia oxygen probes where the conduction mechanism is known to be due to the oxide ion reveals an activation energy for conduction of 23 kcal. Similarity in the activation energies indicates that the conduction mechanism with the pH sensors is most likely due to oxide-ion conduction.

The graphite fill had the highest activation energy (33.6 kcal), and this demonstrates that the internal electrode can dominate the conduction process. Measured potentials from this electrode were also several hundred mV more negative than the others, and its pH response was poor. Little further work was done with it.

Figure 3 data illustrate the impedance encountered with pH sensors. Values of 10^9 - $10^{10}\Omega$ at 373 K are common, though the values fall dramatically with increased temperature. It is at the lowest temperatures that other researchers have had the most trouble with the pH sensors, and we believe this is partially due to shunting of the high-impedance pH signal. Shunts could easily result from traces of moisture. The impedance of the electrodes which have an Ag fill are almost a factor of 10 lower than electrodes which use the Cu/Cu₂O fill, and for that reason most of our work has used Ag. An additional problem with the Cu/Cu₂O fill is that it continues to oxidize with time. The molar volume of the oxide is larger than that of the metal, and the tubes will ultimately be placed under tension. One tube with Cu/Cu₂O fill failed by cracking from the inside at the fill region.

The high impedance of the sensors increases the time constant of the system, which also places a low temperature limitation on their practical use because four time constants must pass before the measured voltage is 99.9% of the final value. For example, the Beckman instrumentation-grade preamplifiers require about 60 min to reach full response for a purely resistive $10^{11}\Omega$ load. Either pH sensors must be developed with a much lower resistance, or electrometers must be developed which have a lower input capacitance if zirconia pH sensors are to have a practical use below 373 K.

pH Response

The pH and potential data for a 20-day experiment is shown in Table II. All sensors were subjected to a 573 K "seasoning" (48h) before the autoclave was cooled to 373 K and the pH response was determined using the two buffers. The hydrogen electrode response to the buffer was used as the primary standard, with the response of the zirconia pH sensors compared to it. Standard deviations of the data are also shown. Temperatures were increased in 50 K increments to 573 K, whereupon the autoclave was again cooled to 373 K. The pH response of three

Table II. pH response

Sensor	Description	373 K		423 K	
		pH response	$E_{Zr} - E_{H_2}$ (mV)	pH response	$E_{Zr} - E_{H_2}$ (mV)
0	H ₂	100 ± 1%	—	100 ± 3%	—
1	Corning, Cu/Cu ₂ O ^a	89 ± 1%	1123 ± 1 1151 ± 3	92 ± 7%	1090 ± 3 1074 ± 14
2	Corning, Ag ^b	98 ± 1%	1109 ± 1 1113 ± 2	103 ± 6%	1090 ± 2 1097 ± 12
3	Corning, Ag ^c	46 ± 2%	1020 ± 3 1154 ± 4	43 ± 10%	1111 ± 6 990 ± 19
4	Corning, Ag ^b	100 ± 1%	1115 ± 2 1116 ± 2	106 ± 6%	1088 ± 1 1100 ± 12

Sensor	Description	473 K		523 K	
		pH response	$E_{Zr} - E_{H_2}$ (mV)	pH response	$E_{Zr} - E_{H_2}$ (mV)
0	H ₂	100 ± 1%	—	100 ± 1%	—
1	Corning, Cu/Cu ₂ O ^a	106 ± 4%	1047 ± 3 1033 ± 7	100 ± 4%	1013 ± 3 1014 ± 9
2	Corning, Ag ^b	102 ± 4%	1069 ± 4 1065 ± 6	97 ± 3%	1023 ± 2 1016 ± 8
3	Corning, Ag ^c	87 ± 4%	1049 ± 4 1079 ± 9	98 ± 3%	1040 ± 3 1034 ± 8
4	Corning, Ag ^b	102 ± 3%	1064 ± 4 1060 ± 6	100 ± 2%	1015 ± 1 1016 ± 6

Sensor	Description	573 K		373 K	
		pH response	$E_{Zr} - E_{H_2}$ (mV)	pH response	$E_{Zr} - E_{H_2}$ (mV)
0	H ₂	100 ± 2%	—	100 ± 2%	—
1	Corning, Cu/Cu ₂ O ^a	100 ± 4%	964 ± 10 963 ± 11	81 ± 6%	1166 ± 1 1124 ± 12
2	Corning, Ag ^b	100 ± 4%	970 ± 10 971 ± 11	102 ± 6%	1114 ± 1 1118 ± 12
3	Corning, Ag ^c	99 ± 4%	989 ± 9 992 ± 11	0%	1101 ± 4 854 ± 9
4	Corning, Ag ^b	100 ± 3%	962 ± 7 961 ± 9	103 ± 6%	1119 ± 0 1126 ± 12

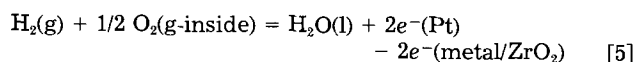
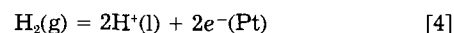
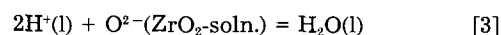
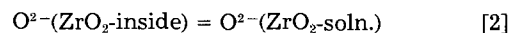
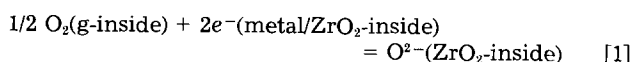
^a Sensor previously subjected to 17 days of autoclave testing ≥ 373 K.

^b New sensor.

^c Sensor previously subjected to 40 days of autoclave testing ≥ 373 K.

of the sensors is good, with two of them (no. 2 and no. 4) exceptional throughout the entire temperature range. Sensors no. 2 and no. 4 have since been subjected to over 45 days of autoclave testing with continued excellent results. One of the sensors (no. 3) is defective because its pH response at 373 and 423 K is less than 50% of theoretical. At ≥ 473 K, the pH response of this sensor (no. 3) is Nernstian, though it is completely unresponsive when returned to 373 K. All our tests show that excellent pH response is common to sensors at temperatures ≥ 473 K. This general observation has been confirmed by Niedrach (3, 4) and Tsuruta *et al.* (6). The low temperature failure of sensor no. 3 is not understood because the impedance has not decreased (which would indicate micro-cracking) and a replacement of the internal half-cell did not restore the performance. A large enough population of aged pH sensors has not been examined as yet to understand the failure modes at low temperature. It is not possible to state whether the behavior of sensor no. 3 is representative or anomalous.

The potentials for "seasoned" sensors in Table II are measured between the zirconia pH sensor and the hydrogen electrode in the autoclave. They are representative of the values measured in other experiments. Table III contains the calculated standard potentials (10) for the hydrogen-oxygen electrode, as well as the potentials expected for the system studied in the autoclave. As Niedrach (5) has pointed out in a consideration of the electrochemical equilibrium at each interface, only the fundamental pH-determining reactions show up in the final pH-potential expression. In this case, we consider those reactions to be



Oxygen in the air ($f_{O_2} = 0.2$) is assumed to control the oxygen fugacity on the inside of the zirconia sensor, and dissolved hydrogen in solution is assumed to control the hydrogen fugacity in the autoclave. The data in Table III show the theoretical potentials for the hydrogen-oxygen electrode under standard conditions (E°) and corrected for hydrogen fugacity temperature effects (E^*). Hydrogen is sparged into the buffer solutions at 298 K where f_{H_2} is defined as unity. Therefore, a Henry's law correction factor (11) is necessary to calculate the f_{H_2} and theoretical potential (E^*) at elevated temperatures. Equation [5] should not show any pH response. It is surprising to discover the good agreement between the measured potentials of Table II and the calculated thermodynamic potentials of Table III. This indicates that the internal half-cell of the zirconia sensors is "poised" by the oxygen electrode, even

Table III. Theoretical potentials for hydrogen-oxygen electrode

Temperature	E° (mV)	E^* (mV)
298 K	1229	—
373 K	1167	1158
423 K	1127	1112
473 K	1088	1062
523 K	1050	1009
573 K	1013	951

at temperatures as low as 373 K. Four different internal fills have been used: 1) graphite; 2) Cu/Cu₂O; 3) Ag; and 4) Ag/AgCl. Once they have been seasoned at 573 K, fills 2-4 all act as oxygen electrodes between 373 and 573 K. The potential of the graphite fill is several hundred millivolts more reducing.

A test was performed to determine if the internal fill is poised by gas-phase reactions. Hydrogen gas was introduced into the inside of the Ag fill sensors at 438 and 573 K. An almost instant change of potential in the reducing direction was noticed. Unfortunately, steady-state potentials measured during this test do not exactly correspond to the potential difference expected for the hydrogen fugacity difference between the inside of the autoclave and the inside of the sensor. The more negative potential seen with the graphite is apparently due to its tendency to create a reducing environment resulting in a low-oxygen fugacity. Hydrogen is apparently working in an analogous manner.

Between 523 and 573 K, newly made Cu/Cu₂O or Ag fill sensors suddenly jump several hundred millivolts in the oxidizing direction and become poised by oxygen. Once poised, they remain poised when returned to 373 K. Tests as long as two weeks at 373 K indicate that they are still poised. However, if a "seasoned" sensor (Cu/Cu₂O or Ag fill) is permitted to stand at ambient temperature for more than a couple of days and is retested at 373 K, it will no longer be poised to oxygen and suffers a significant loss of pH response. These sensors can be restored by autoclaving between 523 and 573 K or baking (in air) in a 623 K oven. An example of this behavior can be seen in Table IV, in which the sensors were kept at ambient conditions for a week before testing at 373 K. The optimum restoration procedure has not been investigated as yet. Silver oxide forms below 425 K when in equilibrium with the oxygen in air. It was hypothesized that the reformation of silver oxide at ambient conditions resulted in a loss of pH response. However, tests with hydrogen (which would reduce the silver oxide) at 438 K had no effect on poisoning the potential. We currently believe the problem is due to the absorption of moisture at the zirconia-metal (internal) interface which interferes with the kinetics of the electrochemical conversion of oxygen (gaseous) into oxide ion. If the reaction rate becomes sufficiently slow, even the small current demands of the electrometer can polarize the interface and result in an apparent loss of pH response. The result of the high temperature bakeout may be to dehydrate the surface. The oxygen electrode is so irreversible in aqueous solutions that the thermodynamic potential is never observed. Yet it is observed

when a ceramic oxide is used as the electrolyte connecting the aqueous side of the cell with the gaseous portion. It may be that water slows down the oxygen-oxide kinetics.

Compositional Differences

Theoretically, if all the interfaces are at equilibrium, the composition of the stabilized zirconia will not affect the potential. Two different manufacturers of 8 w/o yttria-stabilized zirconia were used in this study. The Coors material (ZDY-4 composition) is white and is found by x-ray diffraction to be cubic in structure (13). X-ray spectrophotometric analysis of the grain boundaries with a SEM (scanning electron microscope) revealed significant amounts of Ca, Al, and Si, implying that some second-phase glassy materials are present (possibly added to assist the sintering process of manufacture). Re-examination of the grain boundaries with a SEM after several days of autoclaving at 573 K revealed a significant widening, indicating that the second-phase materials were dissolving. A higher purity composition (ZDY-8) has not been evaluated.

The Corning material is yellow-colored. X-ray diffraction revealed both a cubic and tetragonal structure. SEM analysis indicated only small amounts of Ca at the grain boundaries, and the grain boundaries did not show significant widening after several days at 573 K. No iron was found.

The data will not be shown, for brevity, but for "seasoned" sensors, there was no significant difference in potentials between the Coors and Corning zirconia throughout the temperature range of study.

Calibration

A major deterrent to the use of high-temperature pH sensors is problems associated with their calibration at a given temperature. Now that we have recognized that poised (seasoned) sensors are acting in a thermodynamic manner to oxygen, it should be possible to calibrate them at a lower temperature and predict their pH-potential behavior at higher temperatures. We have not done this as yet, but in principle the following procedure could be carried out

1. Prepare new sensors and season them in a 623 K oven.
2. Verify their pH response and that the potentials are poised by oxygen at 368 K (open beaker) using NBS buffers.
3. Install pH electrodes in the high-temperature process.

4. pH-potential response can be interpreted by using a reference electrode whose potential is known with respect to the standard hydrogen electrode. The data in Table III can be used to convert the potential into pH using the Nernst equation.

The pH accuracy using this method would be estimated by considering the difference between the poised potential the sensor developed and the calculated thermodynamic value. Using the data of Table II for 573 K, if the measured potential was within ± 30 mV of the calculated thermodynamic value, the uncertainty in the measured pH would be $\pm 30 \text{ mV} / (114 \text{ mV/pH}) \approx \pm 0.3$ pH units. If greater pH accuracy is needed, then the sensor should be calibrated in an autoclave at the process temperature for later installation into the process. Another method in which the calibration plumbing is combined with installation in the high-temperature process has been discussed by Niedrach (4) for geothermal applications.

Discussion

There is no problem with using zirconia pH sensors above 473 K. Once they are poised, they appear to be stable with regard to potential and pH response over a period of at least 4-6 weeks. Longer term stability has not been pursued at this time. The principal deterrent for use above 473 K is difficulty with the calibration. Our discovery that the sensors are reversible to oxygen will assist in their calibration.

Table IV

Sensor	Description	373 K	
		pH response	$E_{Zr} - E_{H_2}$ (mV)
1	Corning, Ag	84 \pm 1%	1061 \pm 3 1106 \pm 2
3	Corning, Ag	84 \pm 1%	1068 \pm 2 1114 \pm 1
573 K			
Sensor		pH response	$E_{Zr} - E_{H_2}$ (mV)
1		103 \pm 5%	966 \pm 1 972 \pm 16
3		102 \pm 6%	959 \pm 2 964 \pm 17
373 K (return)			
Sensor		pH response	$E_{Zr} - E_{H_2}$ (mV)
1		100 \pm 2%	1116 \pm 2 1117 \pm 2
3		98 \pm 0%	1118 \pm 0 1122 \pm 0

A more serious problem is their performance below 473 K. Currently, for a pH sensor to be used below 473 K, it must first be subjected to an autoclaving of 523-573 K in order for its potential to become poised. Sensors not autoclaved above 523 K will still have pH response, but their pH response is superior and their calibration more stable when they are poised. Another separate problem is the degradation of their response below 473 K due to aging effects from extended autoclave exposure. We have only seen this behavior with a couple of sensors and have not been able to relate it to any other parametric changes. Other tubes have performed well at 373-473 K at a similar exposure age. It is uncertain whether we are dealing with a statistical failure or a general aging phenomena because the population of evaluated sensors is too small. However, even these degraded sensors perform well ≥ 523 K.

Presently, the pH sensors have too high an electrical resistance to have any practical use below 373 K. A fruitful study would be to examine other zirconia compositions or different ceramic oxide systems for improved pH response. Some guidelines for this study are

1. The major ceramic conduction process must be ionic. Electronic conductivity will result in the sensor responding to the redox environment.

2. The ac impedance of the ceramic must be low enough that the small current demands made by an electrometer will not result in a significant potential drop across it.

3. The hydrogen ion exchange reaction with the solution-ceramic interface must be kinetically fast enough to appear reversible. Judging from how common pH response is with metal-metal oxide systems in a corroding environment, adequate rates of the hydrogen ion reaction may be common with ceramic systems as well.

4. The electrical connection with the ceramic must be reversible so that space charges or other polarization effects will not occur when the sensor is interrogated by the electrometer. We feel this region will be the major problem area with all sensors because an electrochemical equilibrium must exist to interconnect the pure electronic conduction of the metal to the ionic conduction of the ceramic.

Conclusions

1. Good pH response was demonstrated throughout the temperature range of 373-573 K.

2. The internal half-cell of the pH sensors is reversible to oxygen. This behavior suggests that the sensors can be easily calibrated and maintain their calibration for useful periods of time.

3. The pH sensors have the same activation energy as high temperature oxygen sensors, implying that the conduction mechanism is by the oxide ion.

4. An improved electrical/mechanical seal is demonstrated.

Acknowledgment

This work is supported by the Department of Energy under the Basalt Waste Isolation Project of Rockwell Hanford Operations, Richland, Washington.

Manuscript submitted June 4, 1984; revised manuscript received Aug. 27, 1984.

Pacific Northwest Laboratories assisted in meeting the publication costs of this article.

REFERENCES

1. L. W. Niedrach, *Science*, **207**, 1200 (1980).
2. L. W. Niedrach, "Hydrogen Ion Sensor Having a Membrane Sheath of an Oxygen Ion Conducting Ceramic," U.S. Patent 4,264,424, April 28, 1981.
3. L. W. Niedrach and W. H. Stoddard, "The Development of a High Temperature pH Electrode for Geothermal Fluids—Task 1," prepared for the Pacific Northwest Laboratory operated by Battelle Memorial Institute for the U.S. Department of Energy, PNL-3857, March 1981.
4. L. W. Niedrach and W. H. Stoddard, "The Development of a High Temperature pH Electrode for Geothermal Fluids—Task III," prepared for the Pacific Northwest Laboratory operated by Battelle Memorial Institute for the U.S. Department of Energy, PNL-4651, February 1983.
5. L. W. Niedrach and W. H. Stoddard, *Ind. Eng. Chem. Prod. Res. Dev.*, **22**, 594 (1983).
6. T. Tsuruta and D. D. Macdonald, *This Journal*, **129**, 1221 (1982).
7. M. J. Danielson, *Corrosion*, **35**, 200 (1979).
8. D. J. G. Ives and G. J. Janz, "Reference Electrode," pp. 105-108, Academic Press, New York (1961).
9. C. F. Baes and R. E. Mesmer, "The Hydrolysis of Cations," John Wiley & Sons, New York (1976).
10. "Selected Values of Chemical Thermodynamic Properties," NBS Technical Note 270-3, National Bureau of Standards, Washington, DC (1968).
11. G. B. Naumov, B. N. Ryzhenko, and L. L. Khodakovskiy, "Handbook of Thermodynamic Data," p. 246, U.S. Geological Society, Report PB-226-722, Menlo Park, CA, January 1974.
12. A. H. Heuer and L. W. Hobbs, Editors, "Science and Technology of Zirconia," Vol. 3, pp. 364-379, American Ceramic Society, Columbus, OH (1981).
13. Jonathan Myers, Gene C. Ulmer, David E. Grandstaff, Robert Brodzinski, Michael J. Danielson, and Oscar H. Koski, "Recent Developments in the Monitoring/Control of Eh-pH Conditions in Hydrothermal Experiments," Geochemical Behavior of Disposed Radioactive Waste, American Chemical Society Symposium Series No. 246, Washington, DC (1984).

The Kinetics of Platinum-Oxygen Local Cells

James P. Hoare*

General Motors Research Laboratories, Electrochemistry Department, Warren, Michigan 48090-9055

ABSTRACT

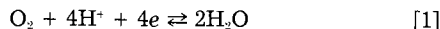
A model of the local cell established at bright Pt electrodes immersed in O₂-saturated acid solution was constructed from which the potential dependence on the partial pressure of O₂ and on the pH was determined. The calculated coefficients agreed with those experimentally determined so that $E_m = 1.06 - 0.048 \text{ pH} + 0.012 \log P_{O_2}$. The equilibrium O₂ potential can be observed by eliminating this local cell action by passivating the Pt surface.

An inert electrode behaves only as a sink or source of electrons and provides a catalytic surface on which the electrode process takes place. To construct an electrode system for which one of the reactants is a gas, one plunges an inert electrode into the proper electrolyte and

*Electrochemical Society Active Member.

bubbles the gas over the electrode. An oxygen electrode is made by immersing a Pt wire or gauze in a solution of H₂SO₄ or KOH and by bubbling O₂ gas over the Pt electrodes.

From thermodynamic studies, the standard potential for the oxygen electrode in acid solution

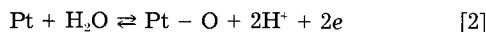


is calculated (1-4) to be 1.229V. When O_2 is bubbled around a Pt electrode immersed in 2N H_2SO_4 solution, the observed potential is no higher than 1.06V measured against a Pt/ H_2 reference electrode in the same solution.

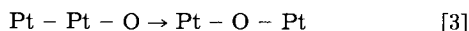
Although a number of explanations for this depressed potential of the O_2 electrode at rest have been put forth (5), it is generally agreed (6-10) that the potential is a mixed potential even though agreement about the nature of the oxidation and reduction processes responsible for the local cell is not met.

A Local Cell Model

It was concluded (11) from various rest potential studies that Pt is not inert to O_2 -saturated acid solutions. Consequently, a local cell is set up with the reduction of O_2 , Eq. [1], occurring at cathodic sites and the oxidation of Pt, Eq. [2], at anodic sites where Pt-O represents



a hydrated layer of adsorbed O atoms. Since the overall local cell reaction is $2\text{Pt} + \text{O}_2 \rightarrow 2\text{Pt-O}$, the Pt surface should become covered with the conducting layer of Pt-O, the local cell should not exist, the potential should be determined only by Eq. [1], and the rest potential should rise to 1.229V. Because this behavior is not observed, a complete layer of Pt-O must not be formed. Only a partial layer of Pt-O is formed since the adsorbed oxygen can be dissolved in the Pt through a place-change mechanism (12, 13)



producing an uncovered Pt site. When the rate of formation of Pt-O by local cell action equals the rate of oxygen dissolution by the place-change mechanism, a steady state is set up. Under these conditions, the Pt surface coverage with Pt-O is about 30% (9, 14), the rest potential is 1.06V (11), and the local cell current is about 10^{-7} A/cm² (15, 16). It has been estimated that it would require 190,000 days to saturate a 1 cm³ of Pt at the local cell corrosion rate (17).

At cathodic sites, the dissociative adsorption of oxygen from solution on the Pt surface is the first step in the reduction of O_2



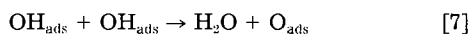
A square root relationship between the partial pressure of oxygen and the amount of oxygen adsorbed has been reported (9, 18). The next step is the first electron discharge step



and is considered to be the slow or rate-determining step. This step is followed by reaction with a hydrogen ion to form an adsorbed OH radical



Then two OH_{ads} can combine to form an H_2O molecule and an adsorbed O_{ads} , which can undergo Eq. [5], [6], and [7]



to form another molecule of H_2O and complete the overall reaction, Eq. [1]. This mechanism requires that the rate-determining step, Eq. [5], occur four times for each overall reaction, Eq. [1], to take place. That is, the stoichiometric number, ν , (19) is 4.

The rate of the cathodic reaction, v_c , is

$$v_c = k_2(\text{O}_{\text{ads}})e^{-\alpha_c(E-E_c^0)/FRT} \quad [8]$$

where α_c is the cathodic symmetry factor and E_c^0 is the equilibrium potential of Eq. [1]. According to steady-state

theory, the concentration of all intermediates is constant with time

$$\frac{\partial(\text{O}_{\text{ads}})}{\partial t} = 0 = k_1(\text{O}_2) - k_2(\text{O}_{\text{ads}})^2 e^{-2\alpha_c(E-E_c^0)/FRT} - k_{-1}(\text{O}_{\text{ads}})^2 \quad [9]$$

Note that Eq. [5] has to occur twice for each occurrence of Eq. [4]. Then

$$(\text{O}_{\text{ads}})^2 = \frac{k_1(\text{O}_2)}{k_2 e^{-2\alpha_c(E-E_c^0)/FRT} + k_{-1}} \quad [10]$$

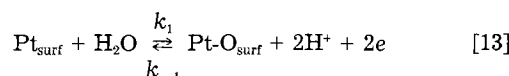
However, $k_2 \ll k_{-1}$, so that

$$(\text{O}_{\text{ads}}) = (k_1/k_{-1})^{1/2} (\text{O}_2)^{1/2} \quad [11]$$

With the substitution of Eq. [11] into Eq. [8], we obtain

$$v_c = k_2(k_1/k_{-1})^{1/2} (\text{O}_2)^{1/2} e^{-\alpha_c(E-E_c^0)/FRT} \quad [12]$$

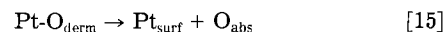
At anodic sites, "bare" Pt surface sites, Pt_{surf} react with water to form adsorbed oxygen atoms, $\text{Pt-O}_{\text{surf}}$



Some $\text{Pt-O}_{\text{surf}}$ sites can flip over by the place change mechanism, Eq. [3], to produce derisorbed (20) oxygen, $\text{Pt-O}_{\text{derm}}$ (oxygen dissolved in the surface layers or skin of the metal)



It is Eq. [14] that is considered to be the slow or rate-determining step. The derisorbed oxygen can diffuse into the bulk metal to regenerate Pt_{surf} sites and adsorbed oxygen, O_{abs}



and to maintain the local cell action.

The rate of the anodic reaction is

$$v_a = k_2(\text{Pt-O}_{\text{surf}}) \quad [16]$$

Then, at steady state

$$\frac{\partial(\text{Pt-O}_{\text{surf}})}{\partial t} = 0 = k_1(\text{Pt}_{\text{surf}})(\text{H}_2\text{O})e^{2(1-\alpha_a)(E-E_a^0)/FRT} - k_2(\text{Pt-O}_{\text{surf}}) - k_{-1}(\text{Pt-O}_{\text{surf}})(\text{H}^+)^2 e^{-2\alpha_a(E-E_a^0)/FRT} \quad [17]$$

where α_a is the anodic symmetry factor and E_a^0 is the equilibrium potential of Eq. [2]. By solving for $(\text{Pt-O}_{\text{surf}})$

$$(\text{Pt-O}_{\text{surf}}) = \frac{k_1(\text{Pt}_{\text{surf}})(\text{H}_2\text{O})e^{2(1-\alpha_a)(E-E_a^0)/FRT}}{(k_2 + k_{-1})(\text{H}^+)^2 e^{-\alpha_a(E-E_a^0)/FRT}} \quad [18]$$

and substituting into Eq. [16], noting that $k_2 \ll k_{-1}$, we obtain

$$v_a = \left(\frac{k_1 k_2}{k_{-1}} \right) \frac{(\text{Pt}_{\text{surf}})(\text{H}_2\text{O})}{(\text{H}^+)^2} e^{2(E-E_a^0)/FRT} \quad [19]$$

For the steady-state local cell shown in Fig. 1, $v_c = v_a$, E becomes the mixed potential, E_m , the activity of H_2O is unity, and $I_c = I_a = I_{\text{loc}}$, the local cell current. Equating Eq. [12] to Eq. [19]

$$K(\text{O}_2)^{1/2} e^{-\alpha_c(E_m-E_c^0)/FRT} = K' \frac{(\text{Pt}_{\text{surf}})}{(\text{H}^+)^2} e^{2(E_m-E_a^0)/FRT} \quad [20]$$

After rearranging terms

$$e^{-(2+\alpha_c)E_m/FRT} e^{(\alpha_c E_c^0 + 2E_a^0)/FRT} = \frac{K'(\text{Pt}_{\text{surf}})}{\text{O}_2^{1/2}(\text{H}^+)^2} \quad [21]$$

and take logarithms of both sides, we have

$$\alpha_c E_c^0 + 2E_a^0 - (2 + \alpha_c)E_m = \frac{2.3RT}{F} \log(\text{Pt}_{\text{surf}}) - \frac{2.3RT}{F} \log(\text{O}_2)^{1/2} - \frac{2.3RT}{F} \log(\text{H}^+)^2 + \frac{2.3RT}{F} \log K'' \quad [22]$$

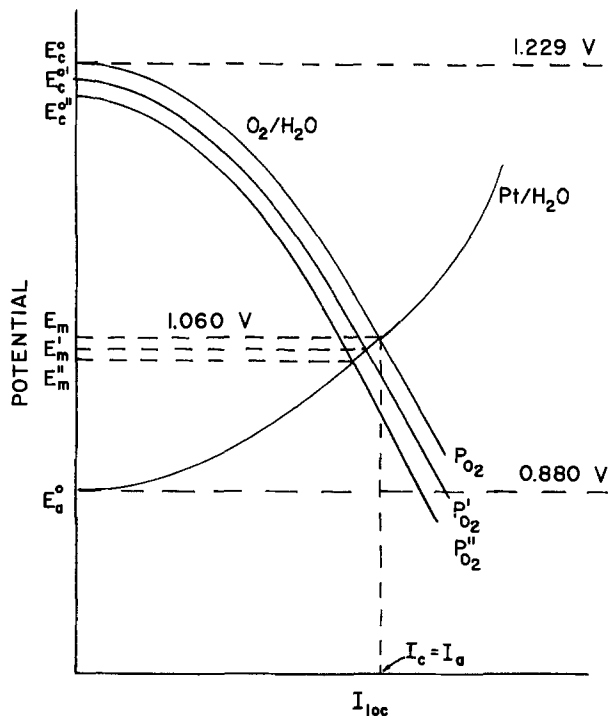


Fig. 1. Sketch of local cell diagram for the rest potential of a Pt/O₂ electrode showing curves for the reduction of O₂ at three values of P_{O₂} and for the oxidation of Pt. Where curves cross is the observed rest or mixed potential (1.06V at P_{O₂} = 1) and the current is the corrosion current (I_o - I_a = I_{loc}). The value for E_a⁰ is taken from Ref. (11). P_{O₂}' < P_{O₂} < P_{O₂} = 1 atm.

One now can obtain the coefficients for the dependence of E_m on the partial pressure of O₂, P_{O₂}, and the pH

$$\frac{\partial E_m}{\partial \log P_{O_2}} = \left(\frac{1}{2}\right) \frac{2.3RT}{F} \left(\frac{1}{2 + \alpha_c}\right) \quad [23]$$

$$\frac{\partial E_m}{\partial pH} = - \frac{4.6RT}{F} \left(\frac{1}{2 + \alpha_c}\right) \quad [24]$$

From electrochemical kinetic studies of the reduction of O₂ on a number of metals (21), α is found to be very close to 0.5. At 25°C, ∂E_m/∂ log P_{O₂} = 0.012V and ∂E_m/∂pH = -0.048V.

Test of the Model

According to the model, the equilibrium potential of Eq. [1] could be observed if the local cell could be eliminated. It has been found (22-23) that the Pt surface may be passivated by a complete layer of electronically conducting oxide or adsorbed oxygen atoms by exposing the Pt to concentrated nitric acid for periods of time greater than 30h. When such a passivated Pt electrode is immersed in O₂-saturated acid solution, a potential of 1.2295V is observed. A number of other workers have also reported this equilibrium potential using Pt electrodes passivated in various ways (24-28). The ∂E_c⁰/∂ log P_{O₂} is 0.015V and the ∂E_c⁰/∂pH is 0.060V (23) as warranted by the Nernst equation.

It was found (22) that passivation of Pt in HNO₃ caused the Pt to be charged with dissolved oxygen to a greater extent than that produced by anodization of Pt (14). Platinum which has been charged with dissolved oxygen will be referred to as the Pt-O alloy. Under the driving force of anodization or passivation in HNO₃, the bulk Pt reservoir becomes increasingly charged with dissolved oxygen. As a result, the rate of dissolution of adsorbed Pt-O into the bulk Pt decreases. To increase this dissolution rate to that of the local cell, the activity of Pt-O must be increased by increasing the steady-state coverage of Pt with Pt-O. According to Eq. [22], the rest potential, E_m, increases with an increase in the Pt-O coverage. Experimentally, it has been reported by a number of researchers (14, 15, 22, 29-31) that E_m does increase with surface coverage.

In a series of experiments, Pt diaphragms were mounted between the halves of a two-compartmented cell (17, 32). In the front side filled with O₂-saturated 2N H₂SO₄, the rest potential of the Pt foil was monitored. After steady state was reached, the back side of the foil was anodized in N₂-saturated 2N H₂SO₄ against a Pt gauze counterelectrode. As shown in Fig. 2, the rest potential increased towards E_c⁰ with the time of anodization, and the rate of increase in E_m depended on the thickness of the foil or volume-to-surface ratio.

When the potential of the front side of the Pt diaphragm had reached 1.148V, the partial pressure of O₂ in the front compartment was varied by using O₂-N₂ mixtures. The data are presented in Fig. 3 with a line of slope 0.012V to show that the data are not inconsistent with the 0.012V slope. By replacing a measured amount of solution drawn from the front compartment with a hypodermic syringe by the exactly same amount of water, the pH was varied. The rest potential as a function of the pH is plotted in Fig. 4 with a line of slope 0.048 drawn to demonstrate the consistency of the data with the 0.048V slope. These data lend strong support to the validity of the local cell model of the Pt/O₂ electrode. The local cell diagram for a Pt-O alloy appears in Fig. 5.

Since it was not possible to saturate the Pt metal with dissolved oxygen by anodization alone, the Pt diaphragm studies were continued with O₂-saturated 2N H₂SO₄ in the front compartment and air-saturated concentrated HNO₃ in the back compartment (33). After 54h, Fig. 6, the potential on the front side of the thinnest Pt foil reached a value of 1.227V and ∂E/∂ log P_{O₂} was 0.015V, as expected if Eq. [1] were potential determining. By saturating the Pt metal with dissolved oxygen, the local cell can no longer exist because "bare" Pt sites no longer exist and Eq. [1] is potential determining.

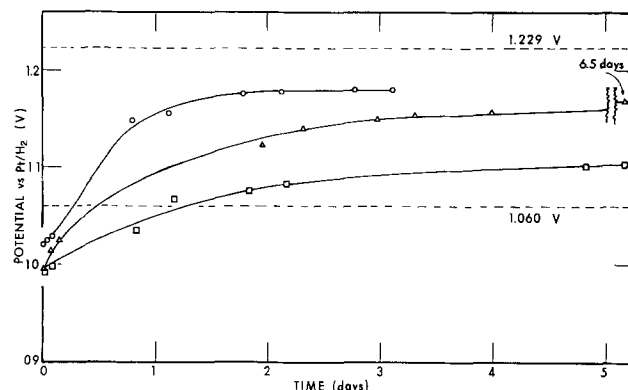


Fig. 2. A plot of the rest potential of the front side of a Pt diaphragm in O₂-saturated 2N H₂SO₄ for three thicknesses (0.00127 cm, circles; 0.00254 cm, triangles; 0.00508 cm, squares) as a function of the time for which the back side was anodized.

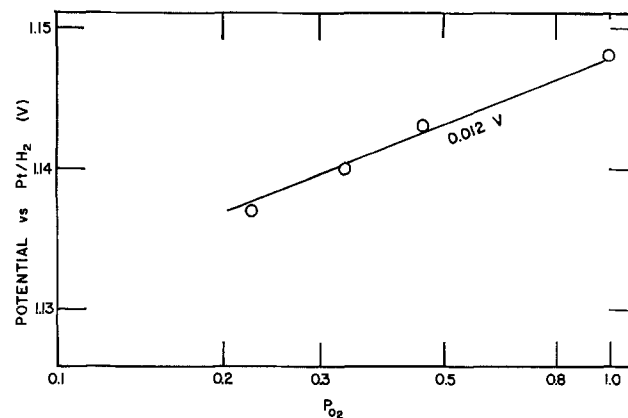


Fig. 3. A plot of the rest potential of the front side of a Pt-O alloy diaphragm in O₂-saturated 2N H₂SO₄ as a function of the log P_{O₂}. A line with a slope of 0.012V is drawn through the points.

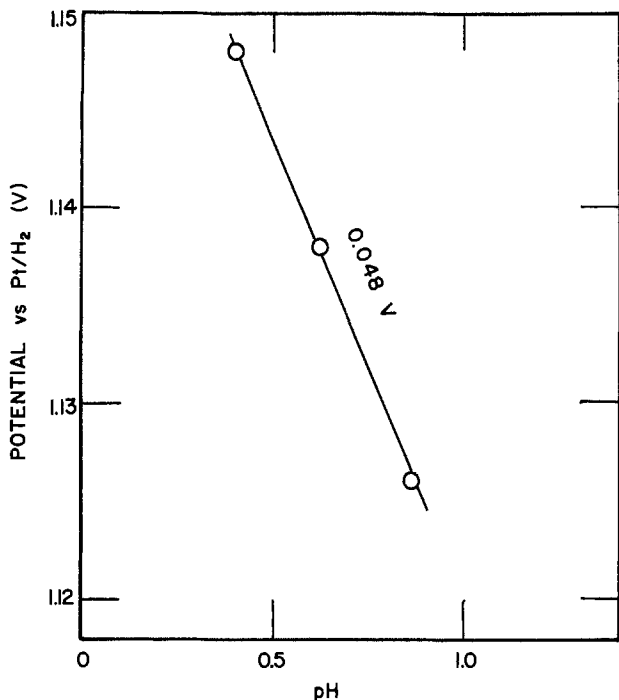


Fig. 4. A plot of the rest potential of the front side of a Pt-O alloy diaphragm in O₂-saturated 2N H₂SO₄ as a function of the pH. A line with a slope of 0.048V is drawn through the points.

At this point, the front side of the Pt diaphragm was polarized against a Pt-gauze counterelectrode. The oxygen overvoltage, O₂-η, at low current densities (34) is presented in Fig. 7. It is noted that the η passes from anodic to cathodic values through E_c⁰ without a change of slope. A value of 4.2 × 10⁴Ω is obtained for dη/di from which a value of the exchange current, i₀, can be obtained from i₀ = (RT/nF)(di/dη) = 1.40 × 10⁻⁶ A/cm², where n is the number of electrons transferred in the rate-determining step. In Fig. 8, the complete polarization curve for the reduction of O₂ is plotted. Extrapolation of the Tafel slope to η = 0 gives a value of 1.48 × 10⁻⁶ A/cm² for i₀. The good agreement between these two values for i₀ indicates that

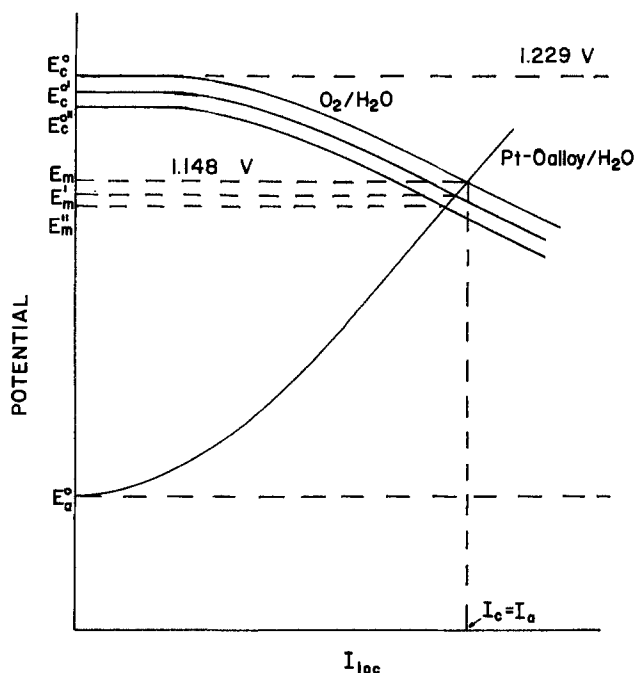


Fig. 5. Sketch of the local cell diagram for the rest potential of a Pt-O alloy/O₂ electrode, showing curves for the reduction of O₂ at three values of P_{O₂} (P_{O₂}¹ < P_{O₂}² < P_{O₂}³ = 1 atm). Explanation same as in Fig. 1. A value for E_a⁰ is not known, but probably lies near 1V (22).

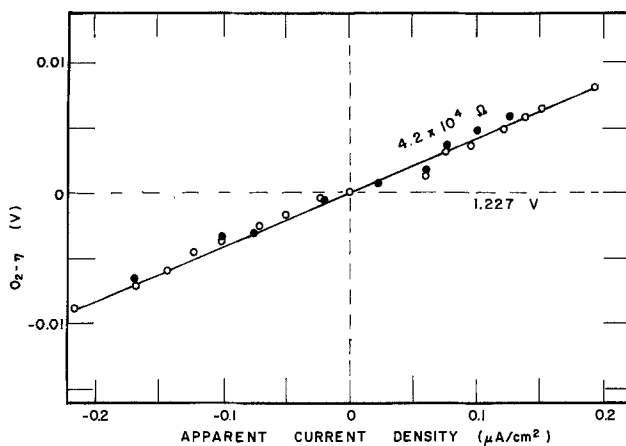


Fig. 6. Oxygen overvoltage obtained on the front side of a Pt-O alloy diaphragm (rest potential: 1.227V) in 2N H₂SO₄ at low current densities; open symbols for increasing and filled symbols for decreasing current.

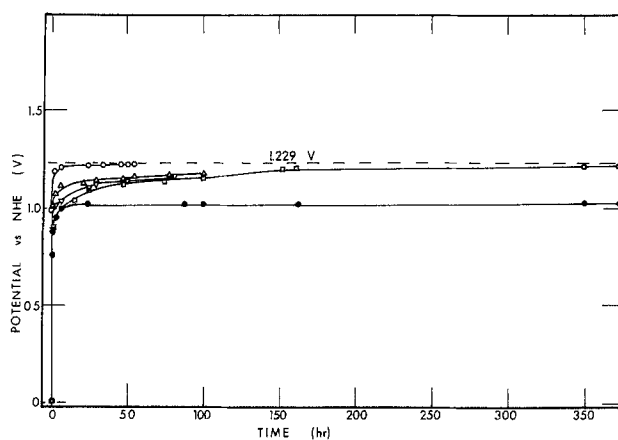


Fig. 7. A plot of the rest potential on the front side of a Pt diaphragm in O₂-saturated 2N H₂SO₄ for four thicknesses (0.00127 cm, circles; 0.00254 cm, triangles; 0.00508 cm, inverted triangles; 0.00762 cm, squares) as a function of the time the back side was in contact with air-saturated HNO₃. Potential of an auxiliary Pt gauze in the front compartment is given by the filled circles.

the same mechanism for O₂ reduction takes place at low and at high current densities on a Pt-O alloy cathode. A value for the stoichiometric number ν can be obtained (35) from

$$\nu = - (d\eta/di)(nF/RT)i_0 \quad [25]$$

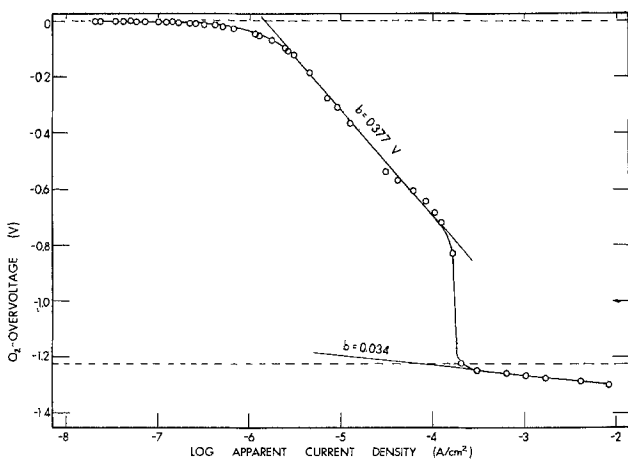


Fig. 8. Oxygen overvoltage obtained on the front side of a Pt-O alloy diaphragm (rest potential: 1.227V) in O₂-saturated 2N H₂SO₄ over entire range of current densities studied. At very high current densities, H₂ evolution takes place (low Tafel slope of 0.03); at medium current densities, high Tafel slope (0.38) shows influence of dissolved oxygen in Pt on reduction of O₂; Tafel slope extrapolates to 1.48 × 10⁻⁶ A/cm² for i₀.

where n is the number of electrons transferred in the overall electrode process and we take $d\eta/di$ from the low current data and i_0 from the high current data

$$\nu = -4.2 \times 10^4 \times 4 \times (-1.48 \times 10^{-6})/0.059 = 4.2$$

This experimentally found value for ν agrees very well with that value obtained from the proposed mechanism with Eq. [5] rate determining. A value of 3.5 has been reported (36) for the reduction of O_2 on Pt in 1N $HClO_4$.

The Pt-O Alloy

When the Pt diaphragm was removed from the two-compartmented cell after being saturated with dissolved oxygen ($E = 1.227V$), that portion of the foil exposed to the HNO_3 had buckled out (34, 37), indicating that the Pt lattice had expanded. This expansion of the lattice was confirmed by x-ray diffraction studies (37). Scanning electron micrographs (SEM) of a HNO_3 -passivated Pt surface show a surface covered with tiny hexagonal pits ($\sim 1 \mu m$ diam) (37). It is proposed (37) that the sides of the micro-etch-pits expose high index planes similar to the stepped surfaces studied by Somorjai and co-workers (38). They observed that both hydrogen and oxygen are more readily adsorbed and more readily dissolved in Pt with stepped surfaces. There was no sign of pitting on the SEM of an anodized Pt surface (39). These observations may account for the fact that Pt-O alloys with greater oxygen content are obtained by passivation in HNO_3 than by anodization. Most likely, the oxygen enters the octahedra holes of the face-centered cubic lattice of the Pt, causing the lattice to expand. Apparently, oxygen can also enter into the grain boundaries first (39) without lattice expansion, but with higher O contents, the oxygen enters the lattice.

Whenever Pt is anodized, it is charged with oxygen and is no longer Pt but a Pt-O alloy. The Pt-O alloy is a better catalyst for H_2 , O_2 , and various redox reactions (40). This observation accounts for the greater reversibility of freshly anodized, indicator electrodes (40) and for the required 5-10 cycles of polarization before a steady-state, cyclic voltammogram can be obtained (41) on Pt.

Conclusions

The rest potential of an oxygen electrode on bright Pt in acid solution is a mixed potential arising from a local cell composed of the reduction of O_2 at cathodic sites and the oxidation of Pt at anodic sites. The rest potential as a function of P_{O_2} and pH is

$$E_m = 1.060 - 0.048 \text{ pH} + 0.012 P_{O_2}$$

The thermodynamic equilibrium potential can be observed on Pt by eliminating the local cell by passivating the Pt surface or by saturating the bulk Pt with dissolved oxygen. In this case

$$E_c^0 = 1.229 - 0.059 \text{ pH} + 0.015 P_{O_2}$$

Oxygen may be dissolved in Pt to form a Pt-O alloy which offers a more catalytically active surface for a number of electrode reactions than pure Pt. The rest potential on a Pt-O alloy electrode is

$$E_m = E_m^0 - 0.048 \text{ pH} + 0.012 P_{O_2}$$

where E_m^0 has values, in general, between 1.1 and 1.2V, depending on the oxygen content of the alloy. On clean, bright Pt, the rate of the dissociative adsorption of O_2 is greater than the rate of electron transfer (42) and the four-electron reduction of O_2 takes place with $\nu = 4$.

Manuscript submitted Feb. 27, 1984; revised manuscript received ca. July 18, 1984. This was Paper 223 presented

at the New Orleans, Louisiana, Meeting of the Society, Oct. 7-12, 1984.

General Motors Research Laboratories assisted in meeting the publication costs of this article.

REFERENCES

1. W. Nernst and H. von Wartenberg, *Z. Phys. Chem.*, **56**, 534 (1906).
2. G. N. Lewis and M. Randall, *J. Am. Chem. Soc.*, **36**, 1969 (1914).
3. W. M. Latimer, "Oxidation Potentials, 2nd ed., p. 39, Prentice-Hall, Englewood Cliffs, NJ (1952).
4. D. D. Wagman, W. H. Evans, V. B. Parker, I. Halow, S. M. Bailey, and R. H. Schumm, NBS Tech. Note 270-3, U.S. Govt. Printing Office, Washington, DC (1968).
5. J. P. Hoare, "The Electrochemistry of Oxygen," pp. 15-46, Interscience, New York (1968).
6. T. P. Hoar, *Proc. R. Soc. London, Ser. A*, **142**, 628 (1933).
7. D. S. Gananamuthu and J. V. Petrocelli, *This Journal*, **114**, 1036 (1967).
8. D. Winkelmann, *Z. Elektrochem.*, **60**, 731 (1956).
9. H. Wroblowa, M. L. B. Rao, A. Damjanovic, and J. O'M. Bockris, *J. Electroanal. Chem.*, **15**, 139 (1967).
10. V. I. Nesterova and A. N. Frumkin, *Zh. Fiz. Khim.*, **26**, 1178 (1952).
11. J. P. Hoare, *This Journal*, **109**, 858 (1962).
12. N. Sato and M. Cohen, *ibid.*, **111**, 512 (1964).
13. B. E. Conway and S. Gottesfeld, *J. Chem. Soc. Faraday Trans. 1*, **69**, 105 (1973).
14. R. Thacker and J. P. Hoare, *J. Electroanal. Chem.*, **30**, 1 (1971).
15. K. J. Vetter and D. Berndt, *Z. Elektrochem.*, **62**, 378 (1958).
16. J. P. Hoare, *This Journal*, **112**, 602 (1965).
17. J. P. Hoare, *ibid.*, **121**, 872 (1974).
18. M. L. B. Rao, A. Damjanovic, and J. O'M. Bockris, *J. Phys. Chem.*, **67**, 2508 (1963).
19. J. O'M. Bockris and A. K. N. Reddy, "Modern Electrochemistry," p. 1100, Plenum Press, New York (1970).
20. S. Schuldiner and T. B. Warner, *This Journal*, **112**, 212, 853 (1965).
21. J. P. Hoare, in "The Encyclopedia of the Electrochemistry of the Elements," Vol. II, A. J. Bard, Editor, p. 208, Dekker, New York (1974).
22. J. P. Hoare, R. Thacker, and C. R. Wiese, *J. Electroanal. Chem.*, **30**, 15 (1971).
23. J. P. Hoare, *This Journal*, **110**, 1019 (1963); *ibid.*, **112**, 849 (1965).
24. J. O'M. Bockris and A. K. M. S. Huq, *Proc. R. Soc. London, Ser. A*, **237**, 277 (1956).
25. N. Watanabe and M. A. V. Devanathan, *This Journal*, **111**, 615 (1964).
26. G. Bianchi, F. Mazza, and T. Mussini, *Electrochim. Acta*, **7**, 457 (1962).
27. W. Visscher and M. A. V. Devanathan, *J. Electroanal. Chem.*, **8**, 127 (1964).
28. G. Bianchi and G. Caprioglio, *Electrochim. Acta*, **1**, 18 (1959).
29. W. Böld and M. W. Breiter, *ibid.*, **5**, 145 (1961).
30. F. P. Bowden, *Proc. R. Soc. London, Ser. A*, **125**, 446 (1929).
31. J. A. V. Butler and G. Armstrong, *ibid.*, **137**, 604 (1932).
32. J. P. Hoare, *J. Phys. Chem.*, **79**, 2175 (1975).
33. J. P. Hoare, *This Journal*, **125**, 1768 (1978).
34. J. P. Hoare, *ibid.*, **126**, 1502 (1979).
35. P. Delahay, "Double Layer and Electrode Kinetics," p. 12, Interscience, New York (1965).
36. A. Damjanovic, A. Dey, and J. O'M. Bockris, *Electrochim. Acta*, **11**, 791 (1966).
37. J. P. Hoare, *ibid.*, **26**, 225 (1981).
38. B. Lany, R. W. Joyner, and G. A. Somorjai, *Surf. Sci.*, **30**, 440, 445 (1972).
39. J. P. Hoare, *This Journal*, **127**, 1758 (1980).
40. J. P. Hoare, *J. Electroanal. Chem.*, **12**, 260 (1964).
41. J. P. Hoare, *Electrochim. Acta*, **27**, 1751 (1982).
42. J. P. Hoare, *ibid.*, **20**, 267 (1975).

Localized Corrosion of Fe-B-Si Glassy Alloys

M. Janik-Czachor

Institute of Physical Chemistry, Polish Academy of Sciences, Warsaw, Poland

ABSTRACT

The glassy alloys $\text{Fe}_{75}\text{B}_{25-x}\text{Si}_x$ with $x < 12\%$ at. exhibit a breakdown of passivity in borate buffer solution with no aggressive ions added. This instability of the passivating film, leading to a localized corrosion, ceases at $x \geq 12\%$ at. XPS analysis suggests that at $x = 12\%$ the passivating film consists mainly of SiO_2 , the minor components being Fe_2O_3 and B_2O_3 . At $x = 9\%$ the main constituents of the film are silicates, which exhibit a lower protective ability and cannot efficiently counteract the detrimental effect of boron compounds. Chlorides are harmful for passivity of the Fe-B-Si alloys; severe pitting occurs even at a chloride concentration as low as 10^{-4}M .

The passivating film cannot provide protection to the substrate metal when, for some reason, it becomes unstable and an activation follows. Activation can occur over a whole surface or can be confined to highly localized regions.

In the former case, general corrosion follows. Conditions for a total depassivation depend upon metal composition and environmental factors and are defined theoretically according to the thermodynamic diagrams of Pourbaix (1).

When activation occurs only at certain points on a metal surface, localized corrosion follows. The mechanism of this type of depassivation (breakdown of passivity) is still a subject of controversy (2-5). Therefore, it is of importance not only from a practical, but from a fundamental viewpoint to identify factors enhancing resistance of the passivating film to localized breakdown.

Some glassy alloys are remarkably corrosion resistant (6) and exhibit an extremely stable passivating film which does not undergo localized breakdown, even under very severe conditions. Detailed analysis of the existing experimental data suggests that the composition of the substrate is of much greater importance than its homogeneous structure. The corrosion resistant glassy alloys rely on passivating films formed by such metal elements as Cr, Ti, and W (7).

Corrosion resistance of glassy alloys which do not contain any of the above mentioned film-forming elements is rather poor (8-12). It has been found, however, that Si may improve it (11-13). Si, when substituted for B, in Fe-Ni-B or Fe-B glassy alloys enhances stability of the passive state. Enrichment of Si in the passivating film is responsible for this enhancement in Fe-Ni-B-Si alloys (11) and probably also in Fe base alloys (12, 13).

In this paper the effect of Si on the stability and composition of the passivating film on Fe-B-Si alloys is considered in more detail.

Experimental

A series of $\text{Fe}_{75}\text{B}_{25-x}\text{Si}_x$ glassy ribbons with $x = 6-18\%$ at. was investigated. $\text{Fe}_{80}\text{B}_{20}$ alloy was used for comparison. The amorphous nature of the ribbons was confirmed by x-ray diffraction.

Details concerning the samples preparation and electrochemical measurements are given elsewhere (11). Optical microscopy was used to examine the samples before and after the electrochemical measurements. XPS technique was employed for surface analysis.

XPS measurements were performed in a 555 XPS/AES/SIMS spectrometer (Physical Electronics) by using a Mg anode at 300W. Ar^+ ion etching was used to obtain information on composition as a function of depth into the passivating film. 1 keV ion beam with $1 \mu\text{A}/4 \text{mm}^2$ ion c.d. was used to remove the film gradually.

Results

Effects of Si on the stability of passivating film on Fe-B-Si alloys in borate buffer solution.—Si in Fe-B-Si alloys not only affects their ability to passivate, but also influences stability of the passive state. As can be seen

from Fig. 1, the maximum c.d. (the apparent critical c.d. for passivation, I_{cr}) and the critical passivation potential (E_{cr}) both decrease with Si content in the alloy. Moreover, the width of the stable passivity range increases with Si content, being only $\sim 300 \text{mV}$ for $\text{Fe}_{80}\text{B}_{20}$ alloy, and attaining a maximum width of $\sim 1300 \text{mV}$ practically at 12% Si; an estimate can be obtained from Fig. 1.

Microscopic examinations have revealed that a sharp increase in c.d. for the alloys with $< 12\%$ Si is caused by a breakdown of passivity followed by localized corrosion similar to pitting. The active spots grew quickly in depth and could perforate the ribbons (Fig. 2), although no aggressive ions were present in solution.

In order to obtain information about the relative resistance of the passivating film to general activation, the open-circuit potential decay curves for prepassivated samples were measured.

Figure 3 shows some examples of potential decay curves for the alloys prepassivated at -100mV (this potential value lies within the stable passivity range for all the alloys under investigation; see Fig. 1). The potential decays slowly and then, after a period of time which is longer the higher Si concentration is, it reaches the activation potential (E_a). Then it sharply drops down to E_{corr} .

Effect of Si on the composition of the passive film.—In order to gain some insight into the chemical state of the film components, as well as to distinguish between the signals from the substrate and from the film itself, XPS analysis of the prepassivated samples was performed. Attention was focused on the 9% Si and 12% Si alloys, since the first exhibits an unstable, and the second a stable, passivity in borate buffer solution (see Fig. 1). The analysis revealed presence of the following elements at the surface: silicon, iron, boron, oxygen, and carbon. The last element is an impurity and is not taken into account for the following analysis.

Identification of the chemical state of the surface constituents was made on the basis of the position of individual lines in the spectrum. Figure 4 gives some examples for 9% Si alloy. The Fe^0 , B^0 , and Si^0 signals come from the

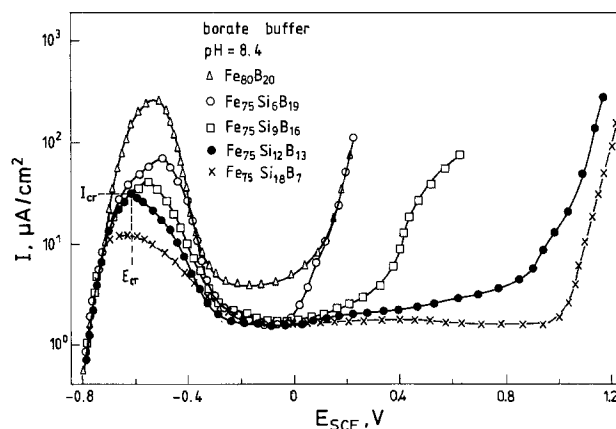


Fig. 1. Anodic polarization curves (2 V/h)

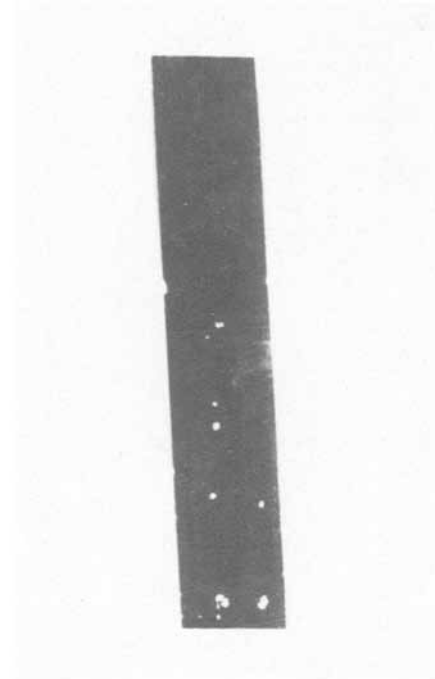


Fig. 2. Localized corrosion of Fe₇₅B₁₉Si₆ alloy in borate buffer solution at +120 mV.

substrate, whereas Fe_{ox}, B_{ox}, Si_{ox}, and O signals come from the passivating film. Since the signals from the substrate are quite visible in the spectrum, an assumption can be made that in this case the passivating film is thinner than the corresponding escape depth of photoelectrons. Under the present experimental conditions this is about 2 nm.

For the 12% Si alloy the B^o and Si^o signals are relatively smaller than for the 9% Si alloy and the Fe^o signal appears only as a shoulder. This suggests that the film thickness here is larger than that for the 9% Si substrate. This conclusion is in agreement with a previous finding (13). The AES/ion milling experiments have shown that the time necessary to sputter the passivating film away was longer the higher the Si content in the substrate.

Ar⁺ ion etching was used alternately with XPS analysis to obtain information on composition as a function of depth into the film material. Use of this method of surface removal is likely to change the chemical nature of the surface. Thus caution was exercised in analyzing the data.

Table I gives some examples of the binding energies of photoelectrons coming from the passivating film and from the substrate, for the two alloys. The positions of Fe^o2p, B^o1s, and Si^o1s signals coming from the substrate do not change with sputtering time. They compare with literature data for pure elements (14). On the other hand,

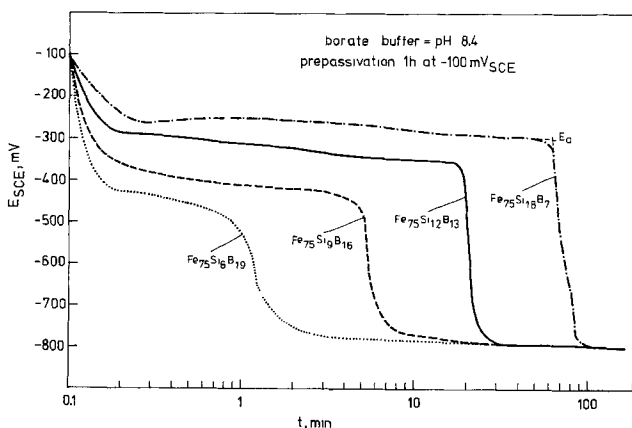


Fig. 3. Open-circuit potential decay curves

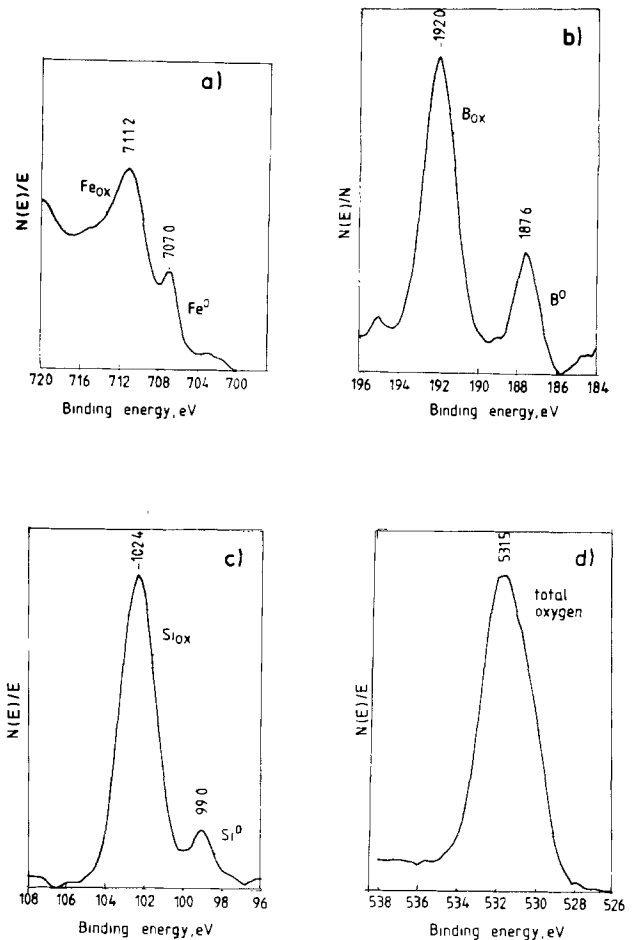


Fig. 4. XPS spectra obtained for Fe₇₅B₁₉Si₆ alloy prepassivated at -100 mV in borate buffer: a) Fe 2p_{3/2}; b) B 1s; c) Si 2p; d) O 1s.

the positions of some signals coming from the passivating film exhibit a variation with sputtering. It is not clear, however, whether this reflects the original changes in chemical state of various components, or some sputtering effects.

The relative concentrations of various constituents of the surface were estimated by quantifying the XPS measurements utilizing peak area sensitivity factors. This method is known to be more accurate than that using peak height (14). The following sensitivity coefficients were used: S_{Fe} = 3.0, S_B = 0.13, S_{Si} = 0.26, S_O = 0.67, each determined using special standards.¹

¹The data were kindly provided by Dr. J. A. Taylor from the University of Minnesota.

Table I. Photoelectron binding energies^a (eV) of the constituents of the Fe-B-Si substrates and of the superficial passivating film formed at -100 mV

t _{sputt} (min)	Fe-2p _{3/2} -Fe _{ox}	Si-2p-Si _{ox}	B-1s-B _{ox}	O 1s	O 1s-Si _{ox} 2p		
Fe₇₅B₁₉Si₆							
0	707.0	711.2	99.0	102.4	187.6 192.0	531.5	429.1
15	706.8	710.6	99.0	102.7	187.6 192.6	531.8	429.1
75	706.8	710.8	99.0	102.8	187.5 192.6	531.6	428.8
Bulk	706.8	—	99.0	—	187.6	—	531.9
Fe₇₅B₁₃Si₁₂							
0	707.0	711.0	99.4	103.0	187.6 192.0	532.1	429.1
21	706.8	710.8	99.0	103.0	187.6 193.0	532.5	429.5
78	706.8	710.8	99.0	102.8	187.6 192.8	532.3	429.5
Bulk	707.0	—	99.0	—	187.6	—	531.6

^a The binding energies were determined with an accuracy of ± 0.1 eV.

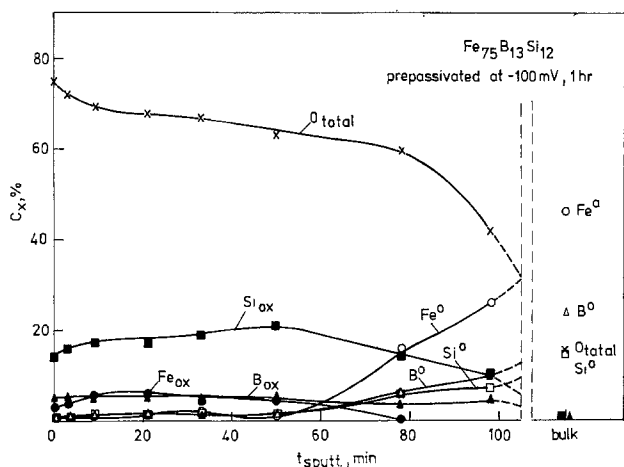
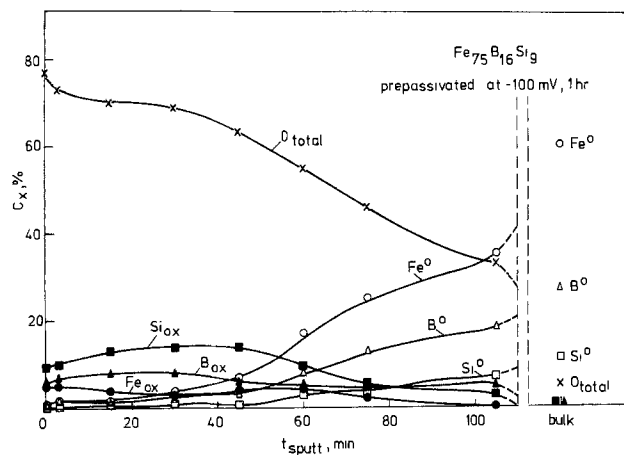


Fig. 5. Depth profiles of the passivating film formed on Fe-B-Si glassy alloys in borate buffer solution.

Composition profiles of the films are shown in Fig. 5. The main feature of these profiles is that the Si_{ox} concentration is much higher than that of Fe_{ox} and B_{ox} . The main difference between the two profiles is that the time necessary to produce a rise in the $\text{Fe}2p$ signal is much larger for the 12% Si containing substrate. This may again suggest that the film is thicker in this case, although structural factors may also affect the sputtering time (15).

For the 12% Si substrate the concentration of Si_{ox} is about 3.5-fold higher than that of Fe_{ox} and B_{ox} [Fig. 5 (bottom)]. Taking into account corresponding binding energies of the photoelectrons of $\text{Fe}_{\text{ox}}2p$, $\text{Si}_{\text{ox}}2p$, and $\text{B}_{\text{ox}}1s$, we assume that the constituents of the film are: SiO_2 , Fe_2O_3 , and B_2O_3 . Considering the concentrations of individual constituents in the middle of the composition profile, we obtain the following molar film compositions: $\sim 80\%$ SiO_2 , $\sim 10\%$ Fe_2O_3 , and $\sim 10\%$ B_2O_3 . The amount of the total oxygen in such a mixed film (62%) compares with the value of $\sim 65\%$ from the XPS data [Fig. 5 (bottom)].

For the 9% Si alloy the atomic concentration of Si_{ox} is 3-fold higher than that of Fe_{ox} and over 2-fold higher than that of B_{ox} . However, the above assumption about the mixed oxides as the constituents of the film does not seem to be reasonable in this case.

From the calculations it follows that only about 43% of oxygen could be engaged in the oxides. Since XPS analysis gives about 60-70% at. of oxygen in the passivating film [Fig. 5 (top)], the question arises as to what the chemical state of the remaining 20% of oxygen is. We can resolve this question, assuming that some oxygen reaches species, other than SiO_2 , are the main components of the passivating film on the 9% Si substrate. This subject will be discussed later in more detail.

Effect of chlorides.—The stable passivity of Fe-B-Si glassy alloys with $\geq 12\%$ Si breaks down easily in

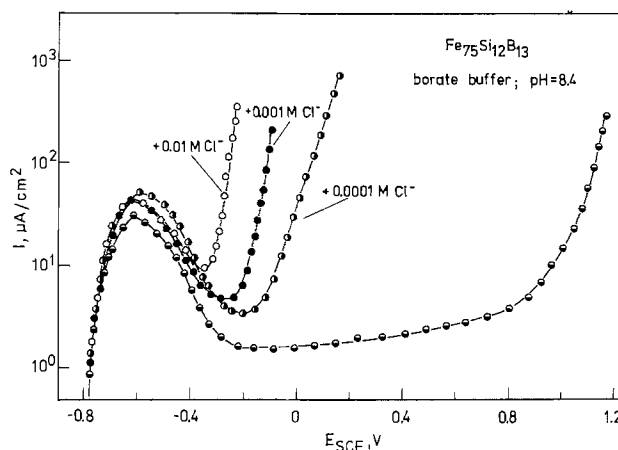


Fig. 6. Effect of chlorides on the anodic polarization curves

chloride-containing solutions. These alloys appear very susceptible to chloride attack; they undergo pitting at only $10^{-4}M$ Cl^- . One should note that the critical chloride concentration for pitting of crystalline iron is $3 \times 10^{-4}M$ (16, 17). An estimate of the effect of chloride concentration on the anodic behavior of 12% Si alloy can be obtained from Fig. 6. The results for 18% Si alloy are similar, but the increase in c.d. due to breakdown of passivity is not as sharp as that in Fig. 6.

Discussion

Fe-B-Si glassy alloys with $\leq 12\%$ Si exhibit a passivity in borate buffer solution that is partly unstable. They undergo a breakdown of passivity in this solution, in the absence of any halide ions. The breakdown potential increases with Si content in the substrate (Fig. 1), and only at $\geq 12\%$ Si does it attain the oxygen evolution potential value.

XPS analysis suggests that the film formed on the 12% Si alloy is relatively thicker and consists mainly of SiO_2 , the minor constituents being B_2O_3 and Fe_2O_3 . The film formed on 9% Si alloy is also enriched with Si, but its O/Si ratio seems to be higher than 2/1. In order to get an idea about the chemical composition of the main component of the film in this case, the O 1s and Si 2p line energy difference must be considered.

Studying various Si compounds, Wagner *et al.* (18) have found that the magnitudes of the O 1s and Si 2p binding energies have a high positive correlation. This can be seen from Fig. 7. All the oxides, hydroxides, and silicates lie in a narrow band corresponding to a line difference of 429.0-429.6 eV. However, for the oxides and hydroxides the binding energies are relatively higher than those for the silicates.

Three points for each passivating film are shown in Fig. 7: they represent the energy line differences (I) before sputtering, (II) after several minutes of sputtering, and (III) near the end of sputtering close to the film/substrate interface. The arrows indicate an evolution of the energy line difference with sputtering.

It is interesting to note that the location of the data points for the passivating film on 12% Si alloy confirms the assumption already made that the main constituent of the film is a silicon oxide. The location of the points does change a little with sputtering, but all the three points lie in the same narrow band where the other three points corresponding to oxides do.

The location of the data points for the 9% Si alloy suggests that silicates rather than oxides are the main components of the passivating film in this case. According to literature data, the O/Si ratio for silicates can attain 4/1 (19). Apparently oxygen-rich silicates are formed in the course of passivation. These silicates exhibit lower protective abilities than the oxides formed at the 12% Si substrate. In this way one can understand the difference in anodic behavior of both alloys.

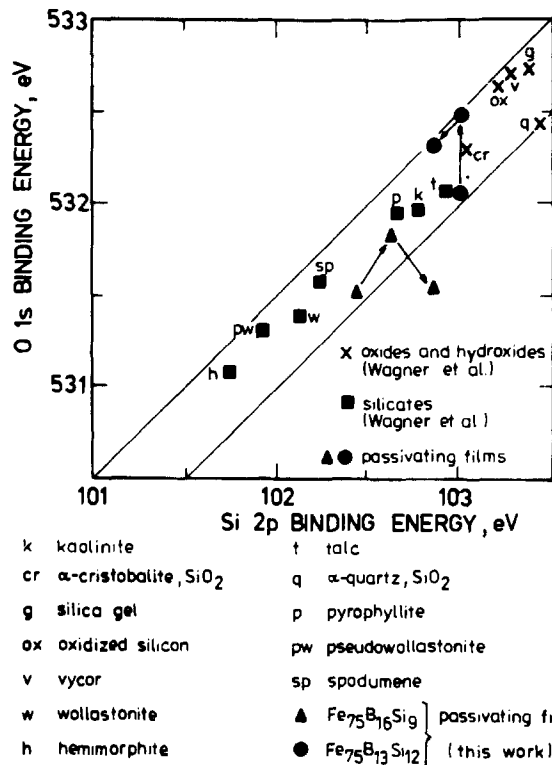


Fig. 7. O 1s binding energy vs. Si 2p binding energy for various oxides, silicates, and passivating films on Fe-B-Si alloys.

It has been found that B is detrimental for corrosion resistance of Fe-B alloys in acid solution (9) and for the stability of the passive state in borate buffer solution (20). The present results show that Si compounds in the passivating film on Fe-B-Si alloys can counteract the detrimental effect of B compounds. Evidently, silicon oxides are more effective than the silicates. Unfortunately, even the silicon oxide containing films are very susceptible to chloride attack.

A question may arise as to what is the effect of the amorphous structure on the behavior of these alloys in the passive state. Unfortunately, no direct comparison with a single phase crystalline alloy at the same composition can be made, since the Fe-B-Si alloys are multiphase systems after crystallization (21). One should note, however, that the stationary rate of the passive metal dissolution is determined by dissolution of metal ions from the passivating film. As pointed out by Kapusta and Heusler (9), the passivating film over both the glassy and crystalline substrate is in the vitreous state anyway. Thus, no difference of the dissolution rate is expected to be influenced by the substrate structure.

Conclusions

1. Si, when substituted for B in Fe-B glassy alloys, improves their ability to passivate. It extends the otherwise

narrow range of their stable passivity in borate buffer solution, thus eliminating localized corrosion, when the Si content attains 12% at.

2. XPS analysis suggests that at Si < 12%, silicates, and at Si ≥ 12%, silicon oxides, are the main components of the passivating film. The oxides efficiently counteract the detrimental effect of boron compounds in the film and provide much better protection to the metal substrate than the silicates.

3. Chlorides cause a severe breakdown of passivity of the Fe-B-Si alloys at concentration as low as 10⁻⁴M.

Acknowledgments

The author is greatly indebted to Professor R. A. Oriani for stimulating discussions and for making available the surface analytical facility. Helpful discussions with Dr. J. A. Taylor are also gratefully acknowledged. This work has been done under the research project 03.10.

Manuscript submitted June 15, 1984; revised manuscript received Oct. 15, 1984.

REFERENCES

1. M. Pourbaix, "Atlas of Electrochemical Equilibria in Aqueous Solutions," Pergamon Press, Oxford (1966).
2. J. Kruger, in "Passivity of Iron and Iron Base Alloys," p. 91, NACE-3 (1975).
3. J. Galvele, in "Passivity of Metals," J. Kruger and R. P. Frankenthal, Editors, p. 285, The Electrochemical Society Softbound Proceedings Series, Princeton, NJ (1978).
4. M. Janik-Czachor, G. C. Wood, and G. E. Thompson, *Br. Corros. J.*, **15**, 154 (1980).
5. N. Sato, *This Journal*, **129**, 255 (1982).
6. K. Hashimoto, in "Passivity of Metals and Semiconductors," M. Froment, Editor, p. 235, Elsevier (1983).
7. R. B. Diegle, N. R. Sorensen, T. Tsuru, and R. M. Latanision, in "Treatise on Materials Science and Technology," J. C. Scully, Editor, p. 59, Academic Press, New York (1983).
8. P. Kovacs, J. Farkas, L. Takacs, M. Z. Awad, A. Vertes, L. Kiss, and A. Lovas, *This Journal*, **129**, 695 (1982).
9. S. Kapusta and K. E. Heusler, *Z. Metallk.*, **72**, 785 (1981).
10. D. Huerta and K. E. Heusler, *J. Noncryst. Sol.*, In press.
11. M. Janik-Czachor, *Warkst. Korros.*, **34**, 47 (1983).
12. M. Janik-Czachor, *ibid.*, **34**, 451 (1983).
13. M. Janik-Czachor, in "Proceedings 9th ICMC," Toronto (1984).
14. C. D. Wagner, W. M. Riggs, L. E. Davis, and G. E. Muilenberg, "Handbook of X-Ray Photoelectron Spectroscopy," Perkin Elmer, Minnesota (1979).
15. M. Janik-Czachor, *Corrosion*, **35**, 360 (1979).
16. H. J. Engell and N. D. Stolice, *Z. Phys. Chem. N.F.*, **20**, 115 (1959).
17. K. E. Heusler and L. Fisher, *Werkst. Korros.*, **27**, 555 (1976).
18. C. D. Wagner, D. E. Passoja, H. F. Hiller, T. G. Kinisky, H. A. Six, W. T. Sansen, and J. A. Taylor, *J. Vac. Sci. Technol.*, **21**, 933 (1982).
19. W. Eitel, "Silicate Science," Vol. I, Academic Press, New York (1964).
20. M. Wisławska and M. Janik-Czachor, In preparation.
21. A. Załuska, Thesis, T.U., Warsaw (1983).

Transport Number Measurements in Silica

J. K. Srivastava,* V. B. Tare, and J. B. Wagner, Jr.*

Center for Solid State Science, and Departments of Chemistry, Physics, and Mechanical and Aerospace Engineering, Arizona State University, Tempe, Arizona 85287

ABSTRACT

Using an open-circuit emf method, the average transport number for ions, \bar{t}_i , has been determined for quartz crystals, vitreous silica, and amorphous silica grown thermally on silicon. Results for all types of silica show that \bar{t}_i increases with temperature between about 550° and 950°C.

Silica exists in three commonly occurring forms, namely, crystalline, amorphous, and a supercooled liquid or vitreous state (1). Schmalzried (2) reported that at 1000°C and between 10^{-16} and 1 atm of oxygen pressure, the transport number of ions in silica glass is close to unity. For silica thermally grown on silicon, Jorgensen (3) and Mills and Kroger (4) suggested that the charges associated with the transport of oxygen ions through SiO_2 are less than the conventionally accepted values of four per mole of oxygen under certain conditions.

Diffusion of oxygen through silica has been studied by several investigators (5). The results indicate that the diffusion of oxygen in quartz is strongly anisotropic. The diffusion of oxygen through various forms of silica has been suggested to be due to transport of oxygen as an uncharged molecule or as O_2^- or $\text{O}_2^{\cdot-}$ (4). When bulk diffusion of ions and electrons (to preserve electroneutrality) governs the kinetics of oxidation of silicon, the rate of oxidation can be calculated by C. Wagner's equation (6), provided the transport number of ions and electrons through the growing oxide layer is precisely known. The main reason for the observed discrepancy between the experimentally determined rates of oxidation and the rates estimated from the available data on transport number and the diffusion of oxygen is possibly the lack of reliable information on the transport numbers and diffusivities.

This paper describes the measurement of transport number by an emf method (2) in all three types of silica, namely, single-crystal quartz, vitreous silica, and amorphous silica thermally grown on single-crystal Si. This method essentially involves measurements of open-circuit emf of a cell in which silica is an electrolyte separating two different oxygen partial pressures. In the case of silica thermally grown on silicon, the partial pressure of oxygen at Si/SiO_2 interface is the dissociation pressure of SiO_2 . The other oxygen pressure was fixed by a metal/metal oxide mixture. For the vitreous and single-crystal quartz, the oxygen pressures on two sides of the electrolytes were fixed by a metal/metal oxide mixture.

Experimental Procedure

Single-crystal quartz used in the present investigation was obtained from Bell Laboratories and had $\langle 010 \rangle$ growth directions. It was free from sodium and potassium impurities (less than detectable level, < 1 ppm). The principal impurities were Fe, 30 ppm, and Al, 30-50 ppm. Rectangular pieces of $1.5 \times 1.5 \times 0.2$ cm with $\langle 010 \rangle$ orientation were cut from a large crystal with the help of a diamond saw. The pieces were cleaned with a HF-water mixture, degreased with acetone, finally washed with distilled water, and again cleaned in an ultrasonic cleaner in acetone.

Vitreous and SiO_2 thermally grown on silicon were obtained from Motorola. 20 kÅ thick SiO_2 was thermally grown on n-type silicon $\langle 100 \rangle$ with 3-4 Ωcm resistivity. The vitreous silica was 1 mm thick. These were cut into pieces in dimensions similar to the crystalline quartz, and were also cleaned by the same procedure described for crystalline quartz. The samples were of semiconductor-grade purity.

*Electrochemical Society Active Member.

Three different metal/metal oxide mixtures used to obtain different partial pressures of oxygen were $\text{Cu}/\text{Cu}_2\text{O}$, Ni/NiO , and Fe/FeO . These were prepared by using the metal and its oxide powder, both of 99.99% obtained from Alfa Products. They were mixed in 1:1 volume ratio in an agate mortar and were pressed into pellets of 3 mm thickness and 1 cm diam in a steel die. These pellets were sintered for 15h in purified argon at temperatures varying from 500° to 700°C to increase their density and improve the mechanical strength. These were then lightly polished with 3/0 emery paper and cleaned with acetone before use.

To obtain the open-circuit emf, the silica pellets were sandwiched between two different metal/metal oxide pellets. The whole assembly was held together by means of a spring assembly and an alumina sample holder. The details were similar to those described elsewhere (7). Platinum wires, spot-welded to platinum foils pressed on the metal/metal oxide electrodes, were used as leads to measure open-circuit emf. A Pt-Pt + 10% Rh thermocouple placed very near the electrolyte was used to measure temperature. The whole assembly was introduced in another alumina tube in which a continuous flow of argon purified by passing it over Drierite, phosphorous pentoxide, and copper heated at 400°C flowed. The complete assembly was kept in a resistance furnace whose temperature was kept within $\pm 1^\circ\text{C}$ with a proportional temperature controller. The cell was electrically shielded from the furnace to avoid external stray pickup.

The open-circuit emf was measured using a 117 Keithley Digital Voltmeter with an impedance of 10 MΩ. The following cell configurations were used to obtain the open-circuit voltages.

$\text{Cu}/\text{Cu}_2\text{O}$	Quartz crystal	Ni/NiO	I
Fe/FeO	Quartz crystal	Ni/NiO	II
Fe/FeO	Vitreous silica	Ni/NiO	III
Pt, Si	Thermally grown SiO_2	Ni/NiO	IV

Measurements were repeated on at least two cells of the same cell configuration. Measurements were restricted to 900°C, because above this temperature there was some evidence of the electrode-electrolyte reaction, particularly in cell I at the quartz $\text{Cu}-\text{Cu}_2\text{O}$ interface. The emf values were, however, reproducible during several heating and cooling cycles if the measurements were restricted to temperatures below 900°C.

Results and Discussion

According to C. Wagner (6), the open-circuit emf, E , of the above cells is given by

$$E = \frac{1}{nF} \int_{\mu'_{\text{O}_2}}^{\mu''_{\text{O}_2}} \bar{t}_i \cdot d\mu_{\text{O}_2} \quad [1]$$

where n is the charge per mole of oxygen ion migrating through the sample, F is Faraday's constant, and μ'_{O_2} and μ''_{O_2} are the chemical potentials of oxygen on each of the two sides of the electrolyte. The derivation of Eq. [1] assumes transport by ions.

The chemical potentials are given by

$$\mu_{\text{O}_2} = \mu''_{\text{O}_2} + RT \ln P_{\text{O}_2} \quad [2]$$

Table I. Ionic transport number for forms of silica, estimated from the experimentally observed (E_{obs}) and theoretically calculated (E_{ion}) emf's of cells I-IV at various temperatures

Cell	T (°C)	E_{obs} (mV)	E_{ion} (mV)	\bar{t}_i
I Cu/Cu ₂ O Quartz crystal Ni/NiO	545	75	284.88	0.26
	590	110	281.42	0.39
	600	125	280.59	0.44
	675	150	274.90	0.58
		160		
	725	235	271.07	0.90
		245		
	800	265	265.32	0.98
	850	235	261.48	0.95
		250		
	900	245	257.65	0.97
		250		
II Fe/FeO Quartz Ni/NiO	530	40	236.03	0.16
	570	75	240.50	0.31
	640	155	248.41	0.62
	675	190	252.30	0.75
	700	220	255.16	0.86
	725	250	257.97	0.99
	790	265	265.28	0.99
	840	265	271.13	0.97
III Fe/FeO Vit. silica Ni/NiO	645	130	248.97	0.52
	728	162	250.31	0.62
	790	185	265.28	0.69
	865	200	274.85	0.72
	915	201	279.35	0.71
	950	208	283.28	0.71
IV Pt, Si thermally grown SiO ₂ Ni/NiO	625	125	1121.08	0.11
		127		
	700	235	1120.39	0.20
	740	320	1120.01	0.28
	750	375	1119.92	0.33
	850	445	1118.99	0.39
950	438	1118.06	0.39	

where $\mu^{\circ}_{\text{O}_2}$ is the chemical potential of oxygen in its standard state, 1 atm of oxygen. Thus Eq. [1] can be written as

$$E = \frac{RT}{nF} \int_{P'_{\text{O}_2}}^{P''_{\text{O}_2}} \bar{t}_i \cdot \frac{dP_{\text{O}_2}}{P_{\text{O}_2}} \quad [3]$$

If an electrolyte is completely ionic, i.e., $\bar{t}_i = 1$, Eq. [3] becomes

$$E_{\text{ion}} = \frac{RT}{nF} \ln \frac{P''_{\text{O}_2}}{P'_{\text{O}_2}} \quad [4]$$

where E_{ion} is the theoretical voltage as calculated. The P'_{O_2} and P''_{O_2} can be easily calculated from the free energies of formation of respective oxides used to fix the oxygen pressures.

However, if $\bar{t}_i \neq 1$, the voltage will, in general, be a complex function of oxygen pressure [see Ref. (2)]. As a first approximation, however, we may take it outside the integral by replacing \bar{t}_i with \bar{t}_i , the average transport number at oxygen pressures between P'_{O_2} and P''_{O_2} .

Dividing Eq. [3] by Eq. [4], the expression for average transport number is

$$\bar{t}_i = \frac{E_{\text{obs}}}{E_{\text{ion}}} \quad [5]$$

where E_{obs} is the measured open-circuit emf.

The data obtained on all the cells are tabulated in Table I. To estimate E_{ion} , free energies of formation of the respective oxides were taken from the data compiled by Turkdogan (8). Also, in calculating E_{ion} , the value of n is assumed to be 4 per mole of oxygen.

Figure 1 shows the observed, as well as theoretical, open-circuit emf's (E_{ion}) for cell I. The corresponding values of \bar{t}_i are shown in Table I. It can be seen that the \bar{t}_i for quartz is nearly equal to 1 only between 700° and

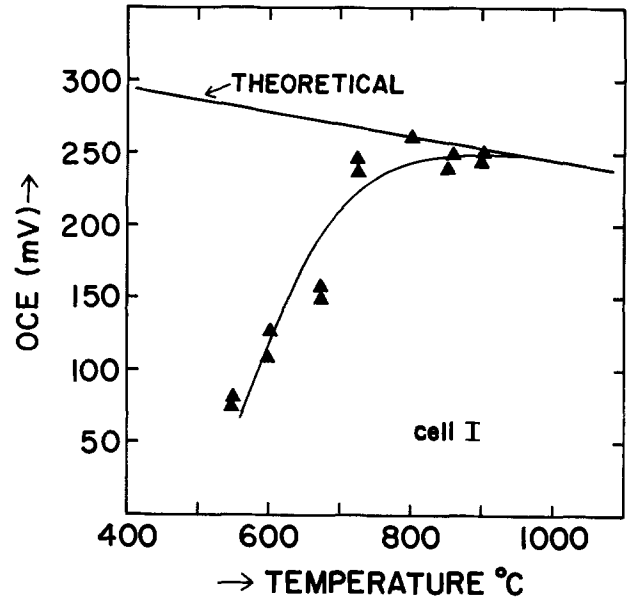


Fig. 1. Observed (E_{obs}) and theoretical (E_{ion}) open-circuit emf's (OCE) of cell I, Cu, Cu₂O|quartz crystal|Ni, NiO, in the temperature range 550°-900°C.

900°C. The values of \bar{t}_i at temperatures less than 700°C deviate considerably from unity.

Figure 2 shows the open-circuit emf, E_{obs} , for cells II and III as a function of temperature. E_{ion} is also shown for comparison. In this oxygen pressure range also, crystalline quartz has $\bar{t}_i \cong 1$ at the temperatures above 700°C. The values of \bar{t}_i drop steeply below 700°C. Data above 900°C could not be obtained because of the possible reaction of electrolyte with the electrodes. \bar{t}_i for vitreous silica (cell III) is much lower than 1 for all temperatures (see Table I). The transport number, however, increases with increase in temperature and attains a maximum value of 0.7 in the temperature range of 800°-900°C.

A similar trend in the variation of average transport number with the increase in temperature is observed for cell IV (Fig. 3). In this case, the average oxygen pressure is, however, very low. The maximum in average transport number is 0.4 and occurs also in the temperature range of 750°-950°C, although the scatter in the data is very large.

As mentioned earlier, the average transport number has been obtained assuming the value of n in Eq. [4] to be 4.

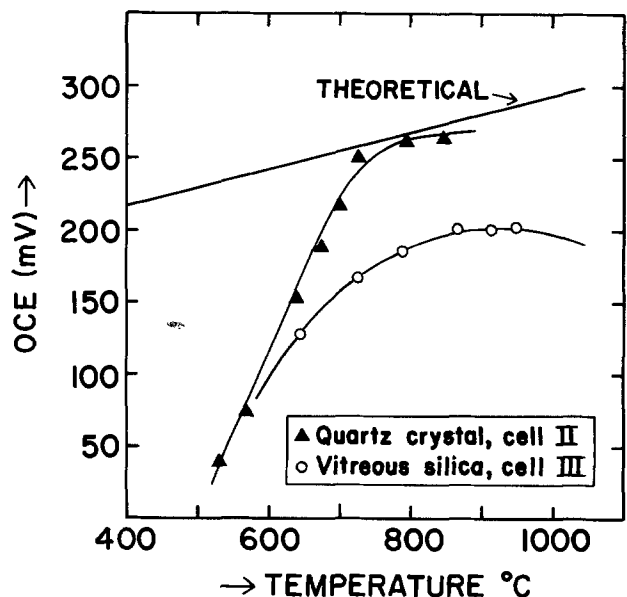


Fig. 2. Observed (E_{obs}) and theoretical (E_{ion}) open-circuit emf's (OCE) of cell II, Fe, FeO|quartz crystal|Ni, NiO, and cell III, Fe, FeO|vitreous silica|Ni, NiO, in the temperature range 500°-950°C.

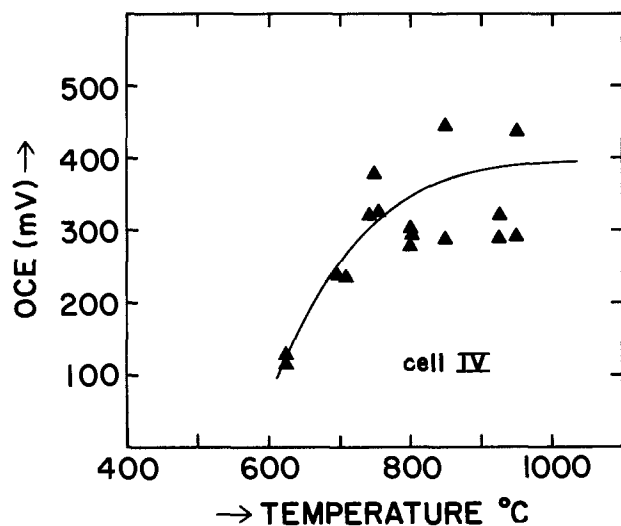


Fig. 3. Observed (E_{obs}) open-circuit emf's (OCE) of cell IV, Pt, Si|thermally-grown SiO_2 |Ni, NiO, in the temperature range 600°-950°C.

In the temperature range of 700°-900°C, these average ionic transport numbers were found to be maximum values for all the three forms of silica samples. The transport number of crystalline quartz is close to unity, while for vitreous silica $\bar{t}_i = 0.7$ and for SiO_2 thermally grown on Si, it is ~ 0.2 - 0.39 . A value of $\bar{t}_i = 1$ for crystalline quartz in the temperature range of 700°-900°C suggests that the assumption that $n = 4$ is justified. Lower values of \bar{t}_i for the vitreous silica at the same average oxygen activity as that for crystalline quartz may be caused by the electronic conductivity or by the deviation of n from 4. Vitreous silica is considered to be a supercooled liquid. Liquid-like structures generally favor higher ionic transference numbers. It is therefore suggested that lower transference number in vitreous SiO_2 may be due to a value of n different than 4. In other words, the oxygen ions migrating in these samples may have charges varying from almost 0 to 4 per molecule, as has been suggested earlier (5).

The small ionic transference number for SiO_2 thermally grown in silicon can also be explained in a similar way. In fact, this ionic transport number is so low that the possibility of the transport of neutral oxygen cannot be ruled out (9).

The above explanation is consistent with the one offered by several investigators on transport properties of

SiO_2 . However, further experiments are essential in resolving the nature of transporting species unambiguously. The ionic transport number in SiO_2 thermally grown on Si, obtained independently by polarization technique (7), is found to be approximately 0.9 in the temperature range of 750°-875°C. This is consistent with the hypothesis that uncharged oxygen is involved in the transport, as has been reported by Costello and Tressler (10) from oxidation studies at 1000°C. The polarization technique involving measurements of current-voltage characteristics on a material where the electronic conductivity is due to the electrons only is influenced by the transport of only charged species, whereas, as mentioned earlier, the open-circuit voltage data depends upon the effective charges n in the migrating oxygen.

Acknowledgments

This research was supported by the Army Research Office under Contract DAAG-29-82-K-0052. The authors thank R. A. Laudise of AT&T Bell Labs for furnishing the single crystal of quartz and E. Reed and J. B. Price of Motorola, Inc., for furnishing the vitreous silica and the oxidized silicon wafers and for helpful discussions.

Manuscript submitted June 4, 1984; revised manuscript received Oct. 22, 1984. This was Paper 656 presented at the New Orleans, Louisiana, Meeting of the Society, Oct. 7-12, 1984.

Arizona State University assisted in meeting the publication costs of this article.

REFERENCES

1. F. A. Cotton and G. Wilkinson, "Advanced Inorganic Chemistry," p. 387, John Wiley and Sons, New York (1980).
2. H. Schmalzried, *Z. Phys. Chem. Neue Folge*, **38**, 87 (1963).
3. P. J. Jorgensen, *J. Chem. Phys.*, **37**, 874 (1962).
4. T. G. Mills and F. A. Kroger, *This Journal*, **120**, 1582 (1973).
5. G. H. Frischat, "Ionic Diffusion in Oxide Glasses," p.29, Trans. Tech. Publication (1976).
6. C. Wagner, *Phys. Chem. (B)*, **21**, 25 (1933).
7. J. K. Srivastava, M. Prasad, and J. B. Wagner, Jr., Paper 305 presented at The Electrochemical Society Meeting, Washington, DC, October 9-14, 1983.
8. E. T. Turkdogan, "Physical Chemistry of High Temperature Technology," Table 1.2, Academic Press, New York (1980).
9. A. G. Revesz, *J. Non-Cryst. Solids*, **4**, 347 (1970).
10. J. A. Costello and R. E. Tressler, *This Journal*, **131**, 1944 (1984).

Effect of Rhodamine-B on the Electrodeposition of Lead on Copper

Joseph C. Farmer^{*,1} and Rolf H. Muller*

Materials and Molecular Research Division, Lawrence Berkeley Laboratory and Department of Chemical Engineering, University of California, Berkeley, California 94720

ABSTRACT

Rhodamine-B chloride ($10\ \mu\text{M}$) has been used as a model plating additive in a study of the electrodeposition of Pb from 1M NaClO_4 , 0.5 and 5 mM Pb^{2+} (pH 3) on Cu. Ellipsometer measurements during cyclic voltammetry have shown that the addition of dye results in a more compact bulk deposit than obtained in its absence. It also prevents complete monolayer coverage during formation of the Pb underpotential deposit and shifts the bulk deposition peak to more cathodic potentials during the first potential cycle. Dye effects on potential and micromorphology disappear during subsequent cycling, but reappear after relaxation periods at open circuit. Depletion and readsorption of dye on the surface have been confirmed by spectroscopic ellipsometry. Different optical film models have been investigated for the interpretation of spectroscopic ellipsometer measurements by use of multidimensional analysis.

Surface active agents (additives, inhibitors) have long been used on an empirical basis to control surface finish in electrolytic metal deposition. Indications are that uncontrolled impurities often cause similar effects. Few fundamental studies have been undertaken to define the role of these agents during the initial stages of electrocrystallization, despite the great technical importance of their use (1). The objectives of this work were to correlate variations in adsorbate coverage on the electrode with differences in overpotential and micromorphology of the deposit. Deposit thicknesses investigated ranged from a monolayer (the underpotential deposit, UPD) to thicknesses of about 100 nm . The principal experimental techniques used were cyclic voltammetry and ellipsometry (both spectroscopic and fixed wavelength). A self-compensating instrument with rapid spectral scanning capabilities for the visible range and automated data collection has been built for this purpose and is discussed elsewhere (2, 3).

Selection of Electrochemical System

The materials used in this study were selected to satisfy electrochemical and optical criteria. Most of the experimental investigations were conducted with Cu as the electrode substrate, Pb as the deposited metal, and rhodamine-B chloride as the model inhibitor. The supporting electrolyte was composed of 1M sodium perchlorate, acidified to pH 3 by use of perchloric acid. The inhibitor concentration was typically $10\ \mu\text{M}$ and Pb^{2+} ion concentration was 5.0 mM (as nitrate).

The materials chosen have optical constants which are distinguishable over the spectral range accessible to the optical instrumentation ($370\text{--}720\text{ nm}$). Cu shows a distinctive absorption in the visible (around 550 nm), which is believed to be due to electronic transitions from the filled d bands into the sp conduction bands (4-6). In contrast to Cu, Pb shows no such characteristic in the visible and has relatively flat optical constants (7). Dissolved rhodamine-B has a characteristic absorption band at about 555 nm , believed to be due to an electronic transition from a singlet ground state to an excited triplet state (8). The electronic transition moment related to this absorption process lies parallel to the three conjugated rings of the rhodamine-B molecule. Rhodamine-B can be expected to adsorb on the surface with a preferential orientation of the transition moment, resulting in a birefringent (dichroic) adsorbate layer. This birefringence, and its spectral dependence, can be interpreted in terms of molecular orientation of the adsorbate on the surface (9, 10).

Electrochemically, Cu is stable to dissolution and oxidation at the reversible potential for Pb deposition from acidic solutions (11), and Pb forms a well-defined underpotential deposit on Cu substrates (12). In screening studies with over 30 materials, 14 of which were indicators or

laser dyes, rhodamine-B was found to induce the largest increase in overpotential (125 mV) for bulk Pb deposition.

Experimental Procedure

The automatic spectroscopic ellipsometer used in this study employed the polarizer-compensator-sample-analyzer optical configuration. It was self-nulling by use of a magneto-optic polarizer and analyzer, and could be operated in either a spectroscopic or fixed wavelength mode (2, 3). The spectral range was $370\text{--}720\text{ nm}$, the angle of incidence used was 75° . A complete scan of spectroscopic measurements (Δ and Ψ at different wavelengths) could be made in 3s although improved signal-to-noise ratios were obtained with slower scanning (*e.g.*, one scan per 15s) or by averaging multiple scans. Slower scanning was essential to observe dye adsorption. Faster scanning gave sufficient signal quality for resolution of deposit micromorphology. Data acquisition was fully automated with a LSI-11/02 microcomputer system, which was also used for instrument calibrations and to interpret measurements by use of optical models.

The electrochemical cell used for experiments with Cu substrates was made of Teflon. It was designed for clean operation and low light absorption in the solution with a small liquid volume (2 ml) and a short optical path (2.5 cm) through the solution. The cell was pie-shaped, with windows made of polished and annealed optical-quality quartz, oriented normal to incident and reflected light beams for operation at an angle of incidence of 75° .

The round working electrodes were machined from polycrystalline oxygen-free Cu with an exposed surface of 1.27 cm diam. The electrodes were polished mechanically with a final alumina abrasive of $0.05\ \mu\text{m}$. Air-formed oxide on the electrode surface was removed by prepolarization in the acidic electrolyte. The counterelectrode consisted of a Pb wire (99.999% purity) wound into a flat spiral, positioned 0.8 cm from the working electrode and of equal diameter. Lead oxide resulting from the corrosion of the counterelectrode was removed by cathodic prepolarization, using a second Pb wire electrode and an initial electrolyte charge. The initial electrolyte charge was replaced when the Cu working electrode was inserted, without exposing the anode to air.

A double-junction Ag/AgCl reference electrode (Dow-Corning 476067), inserted into a Teflon reference electrode compartment, was connected to the electrochemical cell with a Teflon capillary (0.16 cm od). The reference electrode was connected to the potentiostat via an electrometer probe (PAR).

Two syringes (15 ml each) were used to supply electrolyte to and withdraw from the cell. The electrolyte consisted of $5\text{ mM Pb}(\text{NO}_3)_2$, 1M NaClO_4 at pH 3, with or without $10\ \mu\text{M}$ rhodamine-B addition. It was prepared from deionized, singly distilled ($10\text{ M}\Omega$) water and analytical-grade salts. The electrolyte was nitrogen stripped for about 15 min prior to experiments, and the cell was purged with nitrogen before filling. The syringes and a

*Electrochemical Society Active Member.

¹Present address: Sandia National Laboratory, Livermore, California 94550.

nitrogen purge stream were connected with Teflon capillaries.

The potential of the working electrode was controlled with a potentiostat (PAR 173), and the charge passed was determined with a digital coulometer (PAR 179). The coulombic efficiencies between deposition and dissolution were always greater than 95%. Film thickness d_q based on charge is that given for a compact lead layer. Cell potential and current, together with the measured ellipsometer parameters Δ and Ψ (measured as Faraday cell currents), were recorded by the LSI microcomputer system via an eight-channel analog-to-digital converter (Datel MST-LSI2).

Spectroscopic Ellipsometry

Electrochemical deposition of Pb films.—Thin films of lead on copper substrates were prepared by potentiostatic deposition (-600 mV vs. Ag/AgCl) from an electrolyte consisting of 5 mM $\text{Pb}(\text{NO}_3)_2$ and 1M NaClO_4 at pH 3, with deposition times of 1-8 min.

Based upon charge passed, the film thicknesses d_q would have been 31, 60, and 110 nm if the deposit had formed uniformly and had been compact. However, it was found that the deposit was not homogeneous and compact, and multilayer optical models had to be used to explain the spectroscopic ellipsometer measurements.

Single-layer optical models.—Film models investigated for the interpretation of measurements are illustrated in Fig. 1 (2). Examples of interpretations given below illustrate the use of the high information content of spectroscopic ellipsometer measurements for the derivation of wavelength-independent film parameters. Predictions based upon the following three optical models for single-layer films (Fig. 1a-1c) are compared to experimental spectroscopic ellipsometer measurements in Fig. 2-4. In the compact film model, the entire deposit was treated as bulk Pb and there was only one adjustable parameter, the deposit thickness. Figure 2 shows spectroscopic simulations of Δ for various assumed thicknesses (solid lines labeled 0, 1, 5, 10 nm, etc.). Comparison with experimental measurements also shown on the figure (dotted lines for 31, 60, and 110 nm compact thicknesses) illustrates that this model is inadequate.

The second single-layer optical model was that of a porous film in which porosity was taken into consideration by use of an effective refractive index. Pores were treated as microinclusions of electrolyte ($n = 1.34$) in a Pb host medium ($\hat{n} = 2.1-4.2i$), and the optical properties of an isotropic homogeneous film were computed by use of the Maxwell-Garnett or Bruggeman equations. These equations have been used in the literature for modeling rough

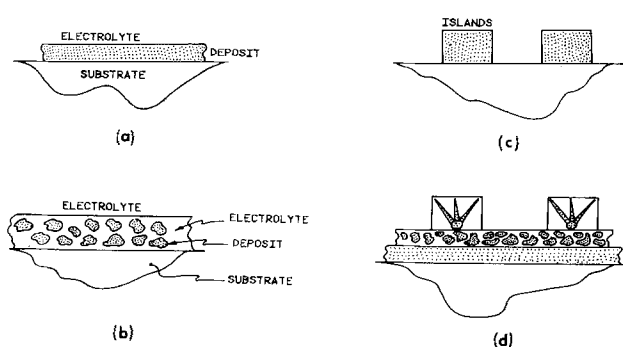


Fig. 1. Schematic of film models investigated for the interpretation of spectroscopic ellipsometer measurements of thin Pb deposits on Cu substrates. Number of adjustable parameters given in parentheses. (a): Compact single film (1). (b): Porous single film, optical constants of effective medium determined according to Maxwell-Garnett (2) or Bruggeman (2). (c): Island single film, reflection coefficient determined by coherent superposition of polarization states, islands compact (2), porous (3) or anisotropic (6). (d): Multilayer films, three layers: compact and porous layers, dendritic islands (6) or two layers: compact and porous films (3).

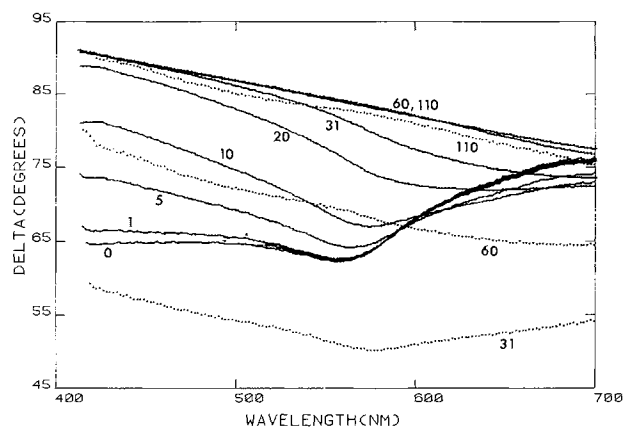


Fig. 2. Spectroscopic simulations for compact film model (solid lines). Pb deposits of thickness 0, 1, 5, 10, 20, 31, 60, 110 nm. Experimental measurements (dotted lines) for 31, 60, 110 nm equivalent compact Pb deposits (d_q , based upon coulometric measurements) on Cu.

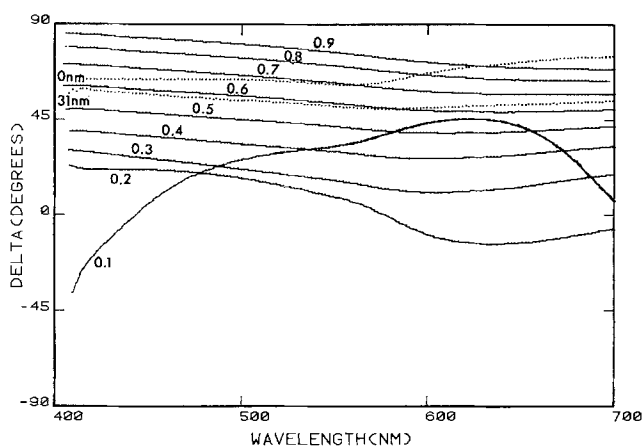


Fig. 3. Spectroscopic simulations of porous film model (solid lines). Volume fractions of Pb 0.1-0.9, amount of deposit corresponding to a 31 nm compact Pb layer on a Cu substrate. Simulations based upon the effective medium approximation (Bruggeman equation). Experimental measurements (dotted lines) for 0 and 31 nm equivalent compact film.

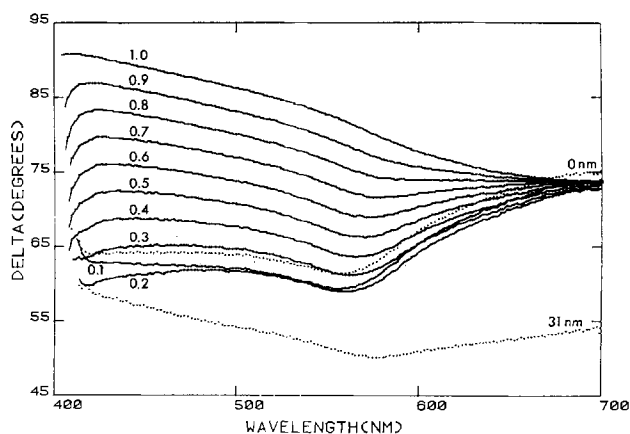


Fig. 4. Spectroscopic simulations of island film model (solid lines). Surface coverage 0.1-1.0, amount of deposit corresponding to 31 nm compact layer, Cu substrate. Simulations based on coherent superposition of polarization states. Experimental measurements (dotted lines) for 0 and 31 nm equivalent compact film.

surfaces and particulate films (13-16). This model involved two adjustable parameters: the deposit thickness and porosity. Spectroscopic simulations of the ellipsometer parameter Δ for this model are shown in Fig. 3 for an amount of deposit corresponding to a 31 nm thick, compact Pb layer (based upon coulometric measurements) redistributed on a Cu substrate as deposits of

various porosities. Simulations are represented by solid lines, and experimental measurements are represented by dotted lines. It is evident that this model alone is also inadequate to explain experimental measurements of delta and deposit thickness based on charge.

The third model was based on the coherent superposition of polarization states resulting from reflection of adjacent film-covered and bare elements of a patchwise covered surface (17-19). The island film may be compact, porous, or anisotropic. In the latter case, at least six unknown film parameters would have to be determined, which results in unacceptable parameter variances. The dimensions of the islands are assumed to be smaller than the transverse and longitudinal coherence of the incident light at the specimen surface. For the present spectroscopic ellipsometer, the longitudinal coherence ranges from 16 μm at 400 nm to 49 μm at 700 nm (20); the transverse (lateral) coherence ranges from 10 μm at 400 nm to 17 μm at 700 nm (21). These estimates assume (conservatively) a bandwidth twice that of the source (20 nm). Since complementary SEM studies of the films investigated here have shown the dimensions of dendritic islands to be less than 15 μm , use of the coherent superposition model is justified for the present experiments.

Spectroscopic simulations of delta for films corresponding to a 31 nm thick, uniform, compact Pb deposit (based upon coulometric measurements), redistributed on a Cu substrate as compact islands, are shown in Fig. 4. The island model used for these simulations employed two adjustable parameters: fractional surface coverage and island thickness. Combinations of these two parameters which were consistent with the amount of Pb known to be in the film from coulometric measurements were used. It can be seen that this model is also incapable of explaining the experimental measurements.

For all single-layer optical models, disagreement of the computed spectral dependence of psi was similar to that shown for delta. It is important to note that interpretations of measurements at a single wavelength often are possible, but the entire spectral range cannot be fitted with any of the models. This fact illustrates the greatly increased information content of spectroscopic measurements.

Multiple-layer optical models.—A three-layer model (2) is illustrated in Fig. 1d. The first layer was assumed to be an isotropic film representing the underpotential deposit. Optical properties of this layer were determined in a separate study (22).

The second layer was assumed to be a granular, porous deposit with optical constants computed from the properties of Pb and electrolyte, by use of the Bruggeman theory for a binary mixture, Eq. [1]-[5]. Incorporation of this layer into the optical model was motivated by light scattering measurements (22)

$$\frac{\hat{\epsilon}_{\text{ph}} - \hat{\epsilon}_f}{\hat{\epsilon}_{\text{ph}} + 2\hat{\epsilon}_f} \theta_{\text{ph}} + \frac{\hat{\epsilon}_s - \hat{\epsilon}_f}{\hat{\epsilon}_s + 2\hat{\epsilon}_f} (1 - \theta_{\text{ph}}) = 0 \quad [1]$$

$$\hat{\epsilon}_f = \frac{1}{2} [-\hat{A} \pm (\hat{A}^2 - 4\hat{B})^{1/2}] \quad [2]$$

$$\hat{A} = \frac{1}{2} [\hat{\epsilon}_{\text{ph}}(1 - 3\theta_{\text{ph}}) + \hat{\epsilon}_s(3\theta_{\text{ph}} - 2)] \quad [3]$$

$$\hat{B} = -\frac{1}{2} [\hat{\epsilon}_{\text{ph}}\hat{\epsilon}_s] \quad [4]$$

$$\hat{n}_f = \hat{\epsilon}_f^{1/2} \quad [5]$$

The root with the largest modulus was used as solution of Eq. [1] (23).

The third layer represents dendritic Pb islands, visible in scanning electron micrographs, and was modeled by an island film and coherent superposition of polarization states (Eq. [6]) resulting from reflection on adjacent surface elements with and without island coverage

$$\hat{r}_v = \theta_f \hat{r}_{v,f} + (1 - \theta_f) \hat{r}_{v,s} \quad [6]$$

Use of coherent superposition implies that the diameter of islands is smaller than the spacial coherence of the illuminating light. The total amount of Pb contained in the three layers was adjusted to agree with the coulometric measurements.

Although the three-layer model provides very good agreement between predictions and measurements, the computations have shown that the optical effect of the third (dendritic island) layer is often negligible, because the surface coverage by islands is small (5-10%). A simplified two-layer model was therefore used for interpretations. Only three unknown parameters have to be determined with this model (thickness of the first, compact layer, and thickness and porosity of the second, porous layer), as opposed to six parameters required for the three-layer model. Despite the insignificant optical effect of the dendritic island layer, it usually contained about two-thirds of the Pb deposit known to be present from coulometric measurement. All optical constants were determined experimentally from independent measurements, and were not treated as adjustable parameters.

Optimization of the two-layer model.—Optimized values of the wavelength-independent parameters of the two-layer model (thicknesses and porosity) were obtained by minimizing the sum-of-squares error between measurements and model predictions over the entire spectral range. As outlined in a previous paper (22), parameter confidence intervals are calculated from the variance of the measurements by use of the student t-statistic at a 95% confidence level for $2N-P$ degrees of freedom, where N is the number of delta-psi measurements over the spectral range (from a single spectroscopic scan) and P is the number of adjustable parameters. Wavelengths of individual measurements are spaced at intervals greater than the source bandwidth; measurements at each wavelength are treated as independent observations of the same surface.

Optimization of the wavelength-independent parameters required to specify only the first two layers resulted in smaller parameter variances than if all three layers were included, because the variance for any parameter increases dramatically as the total number of model parameters P approaches the number of data points ($2N$) used in the optimization. This strategy is based on the results of optical computations which had shown that the third (island) layer has an insignificant optical effect. All deposited Pb not accounted for in the first two layers after optimization was assumed to be contained in the dendritic islands.

Results of the optimization are shown in Fig. 5 and 6 (delta and psi vs. wavelength). The solid lines represent experimental measurements, and the circles represent points calculated by a multidimensional optimization routine. Very good agreement was obtained by optimization of the thickness and porosity of the second layer, which are wavelength-independent adjustable parameters. Table I summarizes the results of the optimization. Measured and calculated values of delta and psi at particular wavelengths are tabulated for three thicknesses. The amount of material, based on coulometric measurements,

Table I. Spectroscopic ellipsometry of Pb deposits: optimization of two-layer model. Confidence intervals for model parameters given for 95% confidence limits

Thickness of compact deposit d_c based on charge	30 nm	60 nm	110 nm
Thickness of porous layer (nm)	31 \pm 4.1	50 \pm 16.2	87 \pm 266.4
Vol. fraction Pb in porous layer	0.585 \pm 0.139	0.775 \pm 0.165	0.968 \pm 0.274
Thickness of compact (UPD) layer (nm)	0.48 \pm 0.11	0.48 \pm 0.11	0.48 \pm 0.11

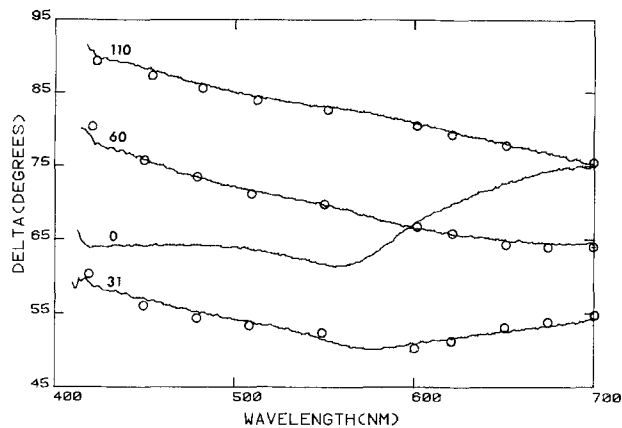


Fig. 5. Spectroscopic simulation for optimum fit of ellipsometer parameter delta for a two-layer film model (circles) and measurements (solid lines) for equivalent deposit thicknesses of 0, 31, 60, and 110 nm. Film parameters derived from optimum fit of model predictions to measurements given in Table I.

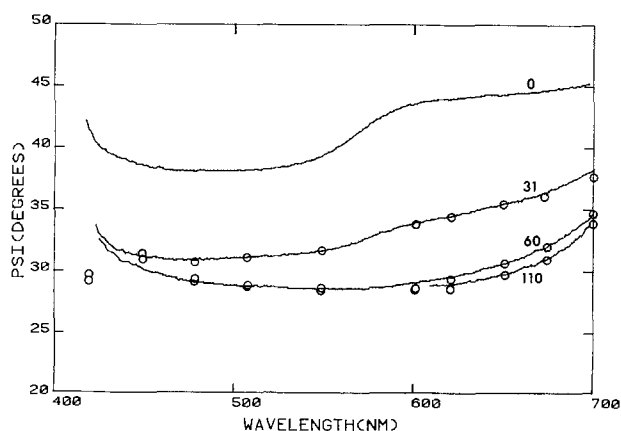


Fig. 6. Spectroscopic simulation for optimum fit of ellipsometer parameter psi for a two-layer film model; other comments as in Fig. 5.

present in these films corresponds to compact layers of thickness 31, 60, and 110 nm. By minimizing the sum-of-squares error (24) between the model predictions and measured values of delta and psi over the entire spectral range, one determines the optimum values of the wavelength-independent adjustable parameters (thickness and porosity). Table I shows the values of the thickness and porosity of the porous layer with their statistically determined confidence interval and the thickness of the compact layer which corresponds to that of the underpotential deposits (19, 22). Thicknesses and porosities of the second layer are thus found to be 31 nm and 41%, 50 nm and 22%, and 87 nm and 3%, respectively.

The large error limits given for the film thickness in the last column of Table I (87 ± 266 nm) are caused by the fact that a layer of that thickness is just barely penetrated by the light (conventional penetration depth for normal incidence 8 and 13 nm at wavelengths 400 and 700 nm, respectively) and behaves optically almost like bulk lead. The measurements are therefore insensitive to deposit thickness, resulting in a wide confidence interval.

Inhibitor Effects

Conclusions about the effect of rhodamine-B on deposit porosity were derived from spectroscopic ellipsometer measurements by the methods discussed in the preceding section. Figures 7 and 8 show, for a thin deposit (31 nm, based on charge), how the distinctive spectral properties of the Cu substrate, which are still visible through the deposit obtained without dye, were completely masked by a deposit of equal lead content obtained in the presence of the dye. The large optical difference is due to differences

Table II. Effect of rhodamine-B on the morphology of bulk Pb deposits during cyclic voltammetry. Comparison of thickness d_q of bulk deposit derived from charge passed with thickness d and volume fraction θ_{pb} obtained from ellipsometer measurements. Points B to F selected in first and second potential sweep identified in Fig. 11 and 12

Sweep no., point	E (mV)	d_q (nm)	d (nm)	θ_{pb}	$\frac{d \times \theta_{pb}}{d_q} \times 100(\%)$
No dye added					
1, B	-582	16.3	7.5	0.38	17
1, C	-430	37.9	50.6	0.56	75
2, E	-573	16.3	8.6	0.35	18
2, F	-400	37.9	50.9	0.55	74
10 μ M rhodamine-B					
1, B	-800	21.7	11.3	0.89	46
1, C	-439	37.9	29.6	0.85	66
2, E	-800	27.1	24.4	0.61	55
2, F	-388	43.3	42.0	0.66	64

in porosity (45% without dye, < 10% with dye). Spectral scans of delta for a thicker deposit (110 nm, based on charge) are shown in Fig. 9. Here, deposits made with and without rhodamine-B show similar optical characteristics, which can be interpreted as Pb layers too thick to be penetrated by the light, even for deposits obtained without dye. The optical interpretations were similar for deposits obtained with constant or cycling potential. The underpotential deposit can be represented as a compact monolayer in the absence of the dye and an incomplete monolayer in its presence.

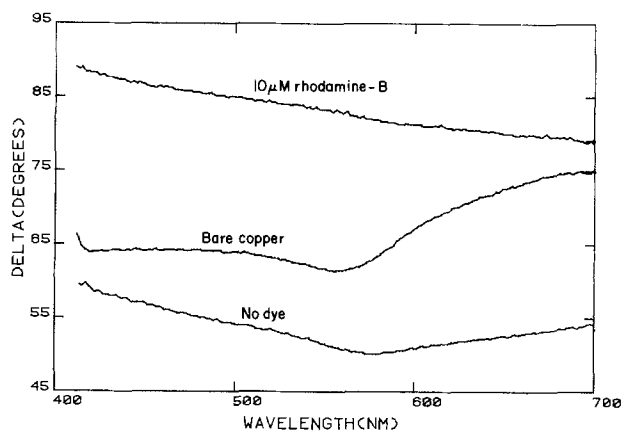


Fig. 7. Spectroscopic measurement of ellipsometer parameter delta for thin Pb deposit on Cu (corresponding to 31 nm compact thickness); effect of presence of dye, bare Cu substrate shown for comparison. Potentiostatic deposition, -600 mV vs. Ag/AgCl, electrolyte as in Fig. 1, except for dye. Substrate visible through porous deposit obtained without dye.

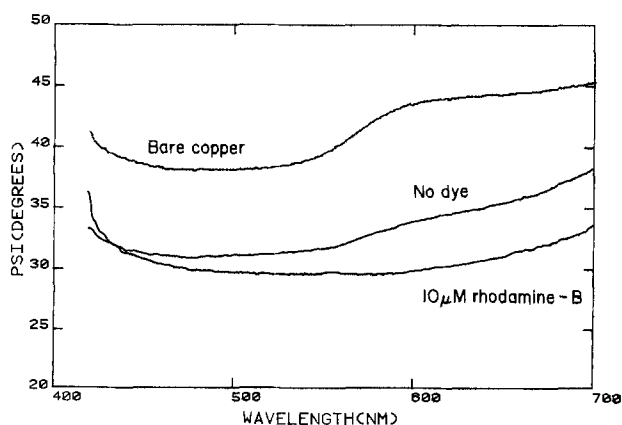


Fig. 8. Spectroscopic measurement of ellipsometer parameter psi, data as for Fig. 7.

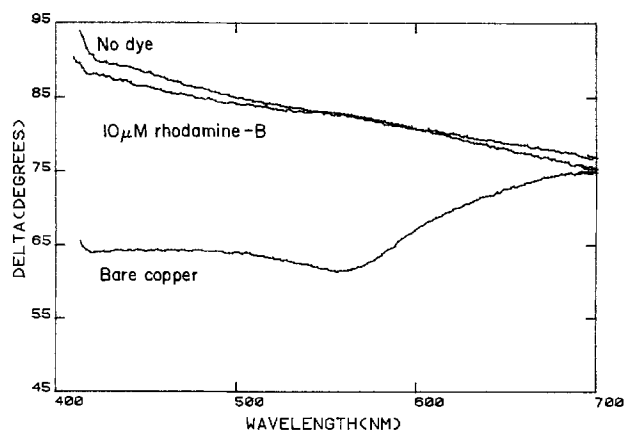


Fig. 9. Spectroscopic measurement of ellipsometer parameter delta for thick Pb deposit on Cu (corresponding to 110 nm compact thickness). Substrate obscured.

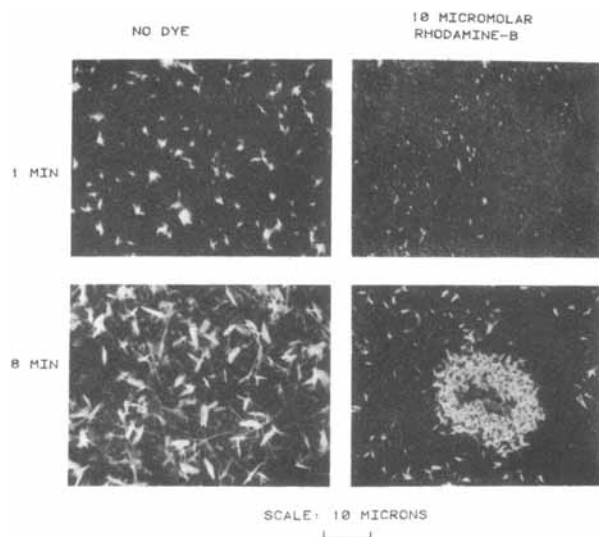


Fig. 10. Effect of rhodamine-B on the micromorphology of thin (1 min, 30 nm) and thick (8 min, 110 nm) Pb deposits; scanning electron micrographs. Potentiostatic deposition at -600 mV vs. Ag/AgCl.

The scanning electron micrographs shown in Fig. 10 illustrate the fine-grained initial (1 min, corresponding to 30 nm compact thickness) deposit obtained with the dye and the dendritic islands obtained without it. At a later stage of deposition (8 min, corresponding to 110 nm compact thickness) the effect of the dye begins to wear off and patches of porous deposit appear, while without dye the dendrites continue to grow into a matted layer. Energy dispersive x-ray analysis has shown that the dendrites are composed of lead, and that, without dye, the deposit between dendrites is very thin, while it is thick and uniform with the dye, as had been inferred from the ellipsometer measurements.

Ellipsometry and Cyclic Voltammetry

Cyclic voltammetry and ellipsometry measurements (at 550 nm wavelength) were conducted simultaneously. A potential ramp (+100 to -800 mV vs. 4M Ag/AgCl reference, 2.8 V/min) and current response are shown in Fig. 11. The corresponding ellipsometer measurements are given in Fig. 12. They show a response which coincides with the onset of a cathodic deposition current (points A and D for first and second sweep). The deposit thickness and porosity ($1 - \theta_{ph}$) were determined by fitting the ellipsometer measurements to the two-layer optical model discussed above.

Interpretations for selected measured points B-F, Fig. 11 and 12, are given in Table II. It can be seen that, during the first potential cycle, the presence of the dye results in

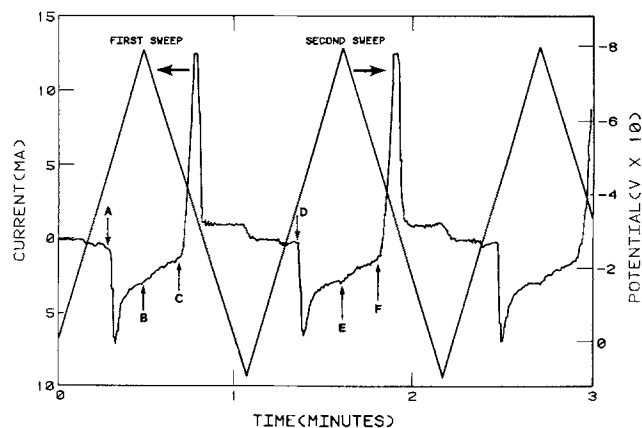


Fig. 11. Potential cycles (+100 to -800 mV vs. Ag/AgCl, sweep rate 2.8 V/min) applied to working electrode (1.13 cm²) and resulting current response. Pb deposition on Cu from 5 mM Pb(NO₃)₂, 1M NaClO₄, pH 3, 10 μM rhodamine-B. Evaluation of measurements at points B to F shown in Table II.

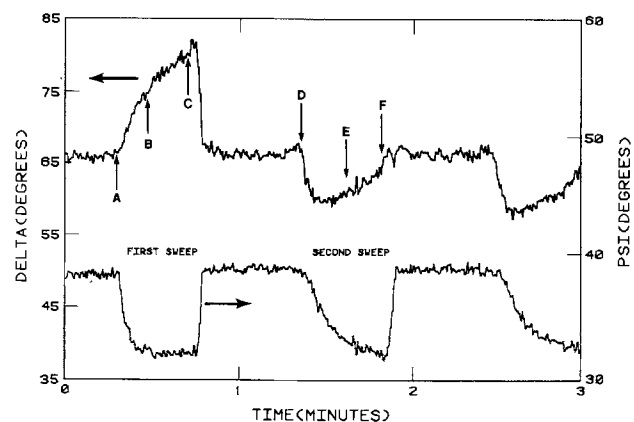


Fig. 12. Ellipsometer measurements collected during potential cycles shown in Fig. 11; wavelength 550 nm (10 nm bandwidth), angle of incidence 75°.

a higher volume fraction (lower porosity) of lead in the bulk deposit. The effect of the dye gradually disappears in the second and subsequent cycles, where volume fractions close to those without dye are obtained (22). Thus, a 15% porosity obtained in the first potential sweep for a layer 29.6 nm thick compares to a 34% porosity obtained in the second sweep at 42 nm thickness. This increase in porosity is responsible for the change from a positive to a negative response in delta to deposition between the first and subsequent sweeps. Depletion of dye at the electrode surface is the cause for this change in behavior. The effect of rhodamine-B on deposit porosity reappears after relaxation periods at open circuit. The optical constants of compact lead ($\hat{n} = 2.1-4.2i$) were combined with the refractive index of the electrolyte ($n = 1.34$) to compute the optical properties of the porous deposits by use of the Bruggeman equation. The optical constants of the copper substrate were measured as $\hat{n} = 0.7-3.4i$.

The amount of lead in the bulk deposit derived from the ellipsometer measurements (product of thickness d and volume fraction θ_{ph}) is always less than the amount based on the charge passed (thickness d_u), as shown in the last column of Table II. The ratio is lower for deposits without dye, in agreement with the formation of more dendritic islands, which are not measured optically (2).

Measurement of the Inhibitor Layer

Underpotential and bulk peaks in the cyclic voltammograms are shifted to more cathodic potentials by adsorbed rhodamine-B. Due to depletion of the dye, this potential shift disappears, however, after several uninterrupted potential cycles, but it reappears after relaxation periods (10-60 min) at open circuit, during which

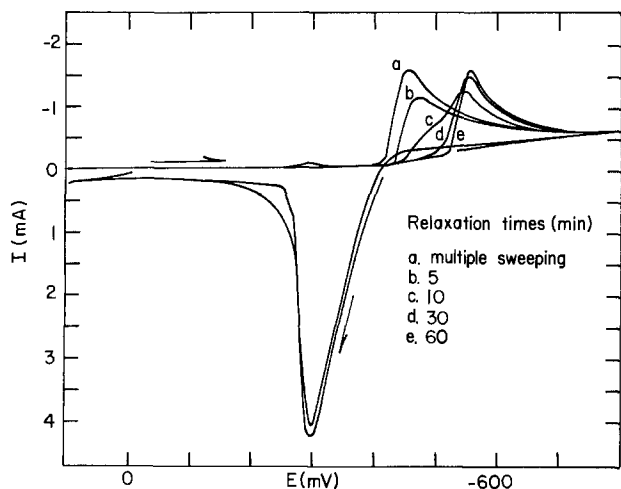


Fig. 13. Readsorption of rhodamine-B on Cu during 5-60 min relaxation at open circuit after removal by multiple potential sweeps; effect on cyclic voltammograms, 2 V/min, 1M NaClO₄, 5 mM Pb²⁺, 10 μM dye, pH 3, 1.27 cm².

adsorption can take place by diffusion from the electrolyte (Fig. 13). The repopulation of the electrode surface with rhodamine-B adsorbate has also been observed by spectroscopic ellipsometry; differential measurements with and without dye (Fig. 14 and 15) show the development of spectral features due to the adsorbed dye. These spectral scans were taken immediately preceding the corresponding cyclic voltammograms of Fig. 13, the relaxation times in minutes are indicated along the curves. A study of the adsorbed dye layer (25) which will be presented elsewhere, has shown that molecules oriented normal to the electrode surface, forming an adsorbate layer 32 Å thick, appear to be responsible for the inhibition of Pb deposition.

The long relaxation times required to restore rhodamine-B coverage of the surface are due to the slow diffusion from the very dilute (10 μM) solution (26). For a coverage between 4×10^{13} and 2×10^{14} molecules/cm², assuming a linear adsorption isotherm with an equilibrium constant of 0.01-0.03 cm (27), a 30 min time to half-coverage would require a diffusion coefficient between 5.6×10^{-8} and 5.0×10^{-7} cm² s⁻¹, which appears reasonable.

Conclusions

Rhodamine-B acts as a deposition inhibitor for the electrodeposition of Pb on Cu and Ag. Potentials required for deposition are more cathodic in the presence of rhodamine-B than in its absence.

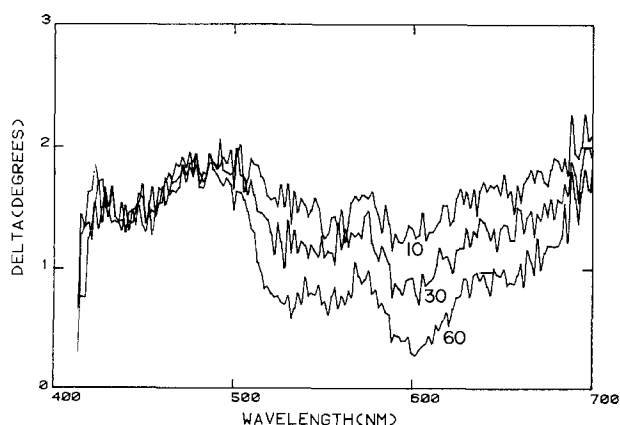


Fig. 14. Differential spectroscopic measurements of ellipsometer parameter Δ for readsorption of rhodamine-B on Cu after multiple potential sweeps. (Spectra for bare Cu in electrolyte without dye subtracted.) Relaxation periods at open circuit in minutes given along curves. Experimental conditions as in Fig. 13.

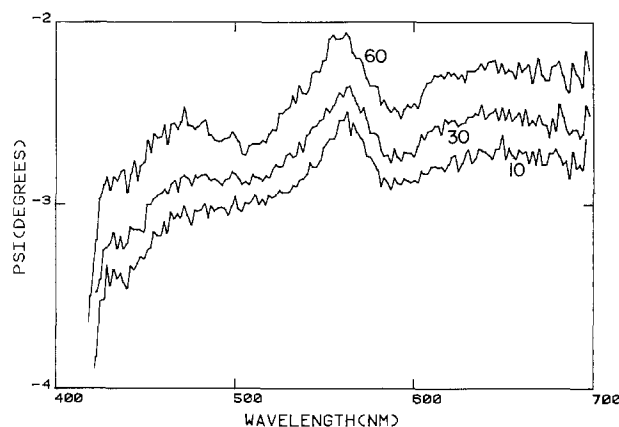


Fig. 15. Differential spectroscopic measurements of ellipsometer parameter ψ for readsorption of rhodamine-B on Cu. Experimental conditions as in Fig. 13.

Less porous deposits are formed in the presence of the dye and the underpotential deposit is less than a complete monolayer. The observed decrease in bulk deposit porosity resulting from the addition of rhodamine-B can be attributed to an increase in nucleation density on the surface and inhibition of dendrite growth.

If nucleation of the bulk deposit is favored at imperfections of the first monolayer of the underpotential deposit, the partial monolayer formed in the presence of rhodamine-B may provide a higher density of nucleation sites. Also, because deposition occurs at more cathodic potentials in the presence of the dye, the equilibrium size of nuclei on the surface is smaller and their number larger. Kinetic effects of the adsorbed dye molecules may involve a decrease in the surface diffusion of Pb adatoms, which would also result in a higher nucleation density.

The selective reduction of rhodamine-B at easily accessible (high activity) sites, such as tips of dendrites, in favor of Pb²⁺ reduction, could shift the deposition to less accessible sites close to the surface which would preferentially be supplied by Pb²⁺ because of its higher diffusion coefficient.

The dye is reduced at the surface and inhibitory effects on the deposit micromorphology disappear until the surface is repopulated with adsorbate during relaxation periods at open circuit.

Spectroscopic ellipsometry allows one to calculate confidence intervals of wavelength-independent parameters for micromorphological optical models and to justify the use of more sophisticated optical models on the basis of the greater degrees of freedom.

For three electrolytically formed Pb deposits (compact thickness 31, 60, and 110 nm) the best agreement between measurements and model predictions was obtained for a three-layer model or a two-layer simplification of it. The distribution of deposited material between compact, porous (granular), and dendritic island layers could be determined.

Acknowledgment

This work was supported by the Director, Office of Energy Research, Office of Basic Energy Sciences, Materials Sciences Division of the U.S. Department of Energy under Contract no. DE-AC03-76SF00098.

Manuscript submitted Dec. 6, 1983; revised manuscript received ca. Oct. 1, 1984. This was Paper 822 presented at the San Francisco, California, Meeting of the Society, May 8-13, 1983.

Lawrence Berkeley Laboratory assisted in meeting the publication costs of this article.

LIST OF SYMBOLS

- d thickness of deposit derived from ellipsometer measurements
 d_c thickness of deposit for a compact layer, based on charge

k	imaginary part of complex refractive index
n	real part of complex refractive index
\hat{n}_f	complex refractive index of porous film
\hat{n}_s	complex refractive index of substrate
\hat{r}_ν	complex Fresnel reflection coefficient for polarization ν (s or p)
$\hat{r}_{\nu,t}$	complex Fresnel reflection coefficient for film-covered surface
$\hat{r}_{\nu,s}$	complex Fresnel reflection coefficient for bare surface
\hat{A}, \hat{B}	complex parameters for quadratic equation
E	potential vs. 4M Ag/AgCl
N	number of pairs of Δ and ψ measurements
P	number of model parameters to be fitted
Q	charge passed
α	level of confidence (1-2 α)
$\hat{\epsilon}_f$	complex dielectric function of porous film
$\hat{\epsilon}_{Pb}$	complex dielectric function of metallic Pb
$\hat{\epsilon}_s$	complex dielectric function of electrolyte solution
θ_f	fraction of surface covered by film of refractive index \hat{n}_f
θ_{Pb}	volume fraction of Pb in porous film derived from ellipsometer measurements
Δ	ellipsometer parameter, phase difference between p and s electric field components after reflection, relative to the incident (degrees)
Δ_C	calculated value of Δ
Δ_M	measured value of Δ
ψ	ellipsometer parameter, amplitude ratio of p and s electric field components after reflection (tan ψ), relative to the incident (degrees)
ψ_C	calculated value of ψ
ψ_M	measured value of ψ

REFERENCES

- J. A. Harrison and H. R. Thirsk, in "Electroanalytical Chemistry," Vol. 5, A. J. Bard, Editor, pp. 67 ff, Marcel Dekker, New York (1971).
- R. H. Muller and J. C. Farmer, *J. Phys.*, **44**, C10 (1983).
- R. H. Muller and J. C. Farmer, *Rev. Sci. Instrum.*, **55**, 371 (1984).
- G. Hass and L. Hadley, in "American Institute of Physics Handbook," 2nd ed., D. E. Gray, Editor, pp. 6-103, McGraw-Hill, New York (1963).
- P. B. Johnson and R. W. Christy, *Phys. Rev. B*, **6**, 4370 (1972).
- D. M. Kolb and R. Kötz, *Surf. Sci.*, **64**, 698 (1977).
- P. Bousquet, *J. Phys. Rad.*, **21**, 873 (1960).
- J. B. Birks, "Photophysics of Aromatic Molecules," pp.193 ff, John Wiley and Sons, London (1970).
- W. J. Plieth, P. Gruschinske, and H. J. Hensel, *Ber. Bunsenges. Phys. Chem.*, **82**, 615 (1978).
- S. Schmidt and R. Reich, *ibid.*, **76**, 599 (1972).
- M. Pourbaix, "Atlas of Electrochemical Equilibria in Aqueous Solutions," pp. 387, 489, Pergamon Press, New York (1966).
- D. M. Kolb, in "Advances in Electrochemistry and Electrochemical Engineering," Vol. 11, H. Gerischer and C. W. Tobias, Editors, p. 139, John Wiley and Sons, New York (1978).
- D. E. Aspnes, J. B. Theeten, and F. Hottier, *Phys. Rev. B*, **20**, 3292 (1979).
- R. M. A. Azzam and N. M. Bashara, *ibid.*, **5**, 4721 (1972).
- R. H. Muller and C. G. Smith, *Surf. Sci.*, **96**, 375 (1980).
- D. E. Aspnes and J. B. Theeten, *Phys. Rev. B*, **20**, 3292 (1979).
- R. H. Muller, in "Advances in Electrochemistry and Electrochemical Engineering," Vol. 9, C. W. Tobias and P. Delahay, Editors, p. 220, John Wiley and Sons, New York (1973).
- C. G. Smith, Ph.D Thesis, University of California, Berkeley, CA (1978).
- R. H. Muller and J. C. Farmer, *Surf. Sci.*, **135**, 521 (1983).
- G. R. Fowles, "Introduction to Modern Optics," 2nd ed., p. 74, Holt, Rinehart, and Winston, New York (1975).
- M. Born and E. Wolf, "Principles of Optics," 2nd ed., p. 551, MacMillan, New York (1964).
- J. C. Farmer and R. H. Muller, Abstract 823, p. 1220, The Electrochemical Society Extended Abstracts, Vol. 83-2, San Francisco, CA, May 8-13, 1983; *This Journal*, **132**, 39 (1985).
- W. Kahan, Personal communication, Department of Electrical Engineering and Computer Science, University of California, Berkeley, August 1982.
- G. E. Box and G. A. Coutie, *Proc. Inst. Electr. Engrs.*, **103B**, Suppl. 1, 100 (1956).
- J. C. Farmer, Ph.D dissertation, University of California, Berkeley, CA (March 1983).
- T. K. Sherwood, R. L. Pigford, and C. R. Wilkie, "Mass Transfer," p. 34, McGraw-Hill, New York (1975).
- A. J. Bard and L. R. Faulkner, "Electrochemical Methods, Fundamentals and Applications," pp. 518-519, John Wiley and Sons, New York (1980).

Electrochemical Deposition of Cadmium Sulfide Thin Films from Organic Solution

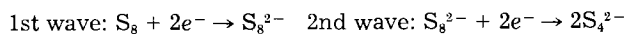
I. Sulfur Reduction and Cadmium-Polysulfide Complex Formation

François Mondon

Laboratoire de Spectrométrie Physique, CNRS et Université de Grenoble I, 38402 Saint-Martin d'Heres Cedex, France

ABSTRACT

The reduction of sulfur in an aprotic solvent (DMSO) is known to be a two-stage process; each stage involves a bielectronic electrochemical step followed by a chemical dismutation reaction. When reduction is performed at a rotating electrode, it is shown that the electrochemical steps alone are involved in the electrode process. The voltammetric waves then correspond to the simple scheme



The slower dismutation reactions appear only in the bulk of solution. They lead to electron numbers which differ from 2 when S_8 is electrolyzed. The addition of Cd^{2+} ions to a polysulfide ion solution yields soluble polysulfide-cadmium 2:1 complexes $[Cd(S_x)_2]^{2-}$ with $x = 8, 6,$ and 4 . The stability of the complex is increased when x decreases from 8 to 4, which leads to dismutation and exchange reactions between complexes, polysulfide ions, and sulfur.

Cadmium sulfide CdS is a potential material for fabrication of low-cost solar cells based on thin polycrystalline films (1, 2). Besides several chemical or physical processes (3-5), thin cadmium sulfide films are obtained by means of electrochemical reduction of an organic solution containing molecular sulfur S_8 and a cadmium salt (6-9). Although it is sometimes written as a simple reaction $(Cd^{2+} + 1/4 S_8 + 2e^- \rightarrow CdS)$ (7), the electrochemical deposi-

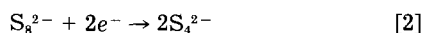
tion of CdS soon proves to be a rather intricate process. The purpose of this paper (and of our next one on the same topic) is to demonstrate how sulfur reduction is implied with further chemical and electrochemical reactions to yield CdS deposits.

Chemical reaction between molecular sulfur S_8 and monosulfide ion S^{2-} in various solvents yields a mixture of different polysulfide ions S_x^{2-} . The sulfuration index

x varies according to the $S_8 : S^{2-}$ ratio in a range which depends upon the solvent (10-13). An alternative way for polysulfides preparation is the electrochemical reduction of molecular sulfur dissolved into a suitable solvent, *e.g.*, dimethylsulfoxide (DMSO) or dimethylformamide (DMF). Both means of preparation yield similar mixtures of S_8^{2-} , S_6^{2-} , and S_4^{2-} ions.

Electrochemical reduction of sulfur in aprotic organic solvents proceeds through complex reaction paths. It was demonstrated in previous studies that the electrochemical steps of the process may be followed by chemical reaction between sulfur and polysulfides (14, 15).

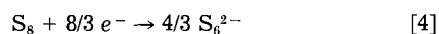
Scanning potential voltammograms for reduction of S_8 at a rotating electrode (*e.g.*, platinum electrode and DMSO) show two waves of equal amplitudes (Fig. 1). The simplest scheme consistent with this behavior is the following



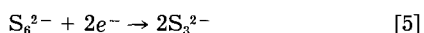
When reduction of S_8 is carried on at a potential corresponding to the first wave, the electrolysis first proceeds through a two-electron reaction. However, the current vanishes only when S_8 is reduced by $8/3$ electrons. This unusual behavior is related to the dismutation of S_8^{2-} (15)



At the end of the electrolysis, the whole process is then



The polysulfide S_6^{2-} may be reduced to S_3^{2-} at a potential corresponding to the second wave of the voltammograms



Besides the above-mentioned "two-electron" process (Eq. [1] and [2]), another interpretation of the two reduction waves is an "8/3-electron" process involving Eq. [4] and [5]. It is thus desirable to demonstrate clearly which process takes place at a rotating electrode, prior to investigating the role of S_8 reduction in CdS deposition.

Experimental

Chemicals.—Reagent grade DMSO was purified by means of distillation under reduced pressure. The supporting electrolyte, tetraethyl-ammonium-perchlorate (TEAP), was twice recrystallized from cold water and

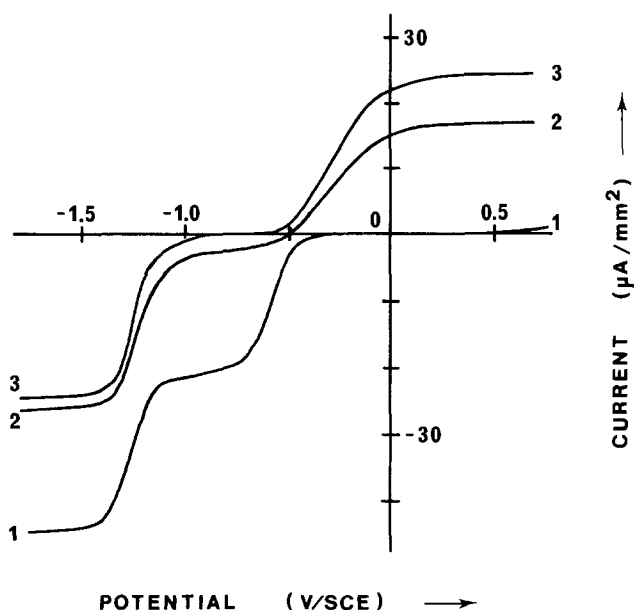


Fig. 1. Voltammetric plot for a sulfur solution in DMSO before and during electrolysis at $-0.9V$: (1) before electrolysis; (2) at $f = 2$ F/mol; and (3) at $f = 8/3$. $C_0 = 2.5 \times 10^{-3}$ mol/liter S_8 ; 4 mVs^{-1} ; 600 rpm ; 60°C .

thoroughly dried under vacuum. Sulfur was recrystallized from benzene. Cadmium salts were cadmium chloride or nitrate. Water was removed from cadmium nitrate solutions by means of molecular sieves and by nitrogen bubbling at 80°C . All solutions were deaerated by nitrogen bubbling before and during all experiments. The sulfur concentration was 2.5×10^{-3} mol S_8 /liter.

Apparatus and methods.—A Tacussel potentiostat and integrating coulometer (PRT 40-1X, IG6-N) were used in electrochemical measurements. Voltammetry was performed at a rotating platinum disk electrode (a 2 mm diam platinum wire fitted into a 10 mm PTFE rod). This electrode was polished with $0.3 \mu\text{m}$ alumina powder before each run. Unless otherwise specified, the electrode was rotated at 600 rpm. Controlled potential electrolysis was carried out at a large platinum foil cleaned in aqua regia. The auxiliary electrode was a platinum foil; it was isolated from the working solution by means of a bridge (filled with DMSO + TEAP) fitted with two glass frits. A commercial aqueous calomel reference electrode (SCE) was used in all experiments. In order to exclude any water diffusion, this reference electrode was connected to the working solution by means of a bridge containing DMSO + TEAP and molecular sieves. Most electrochemistry experiments were carried out at 60°C ; the water-jacketed airtight vessel was continuously flushed with purified nitrogen. Absorption spectra were recorded on a Beckman DB-GT spectrophotometer; the solutions were transferred from the electrolysis vessel to the spectrophotometric cells by means of PTFE tubing in a nitrogen-flushed airtight arrangement.

Sulfur Reduction in DMSO

Potentiodynamic plots.—Potentiodynamic scans were run at several temperatures from 20° to 110°C with voltage scan rates ranging between 2 and 20 mV s^{-1} . The scan rate had no effect on the voltammograms, and the ratio of the limiting currents of the two waves remained very close to 1 at any temperature. The rate of rotation ω of the electrode was varied between 200 and 5000 rpm at 20° and 60°C . In each case, the two limiting currents' variations satisfied the Levich equation (*i.e.*, proportional to $\omega^{1/2}$).

Controlled potential electrolysis.—Reduction of the working solution was performed at -0.9 V/ECS (*i.e.*, on the first wave). The concentration of unreduced sulfur was monitored from time to time by means of voltammetry at a rotating platinum electrode (Fig. 1). Figure 2 shows a plot of the remaining sulfur concentration against the charge flowing during electrolysis. This

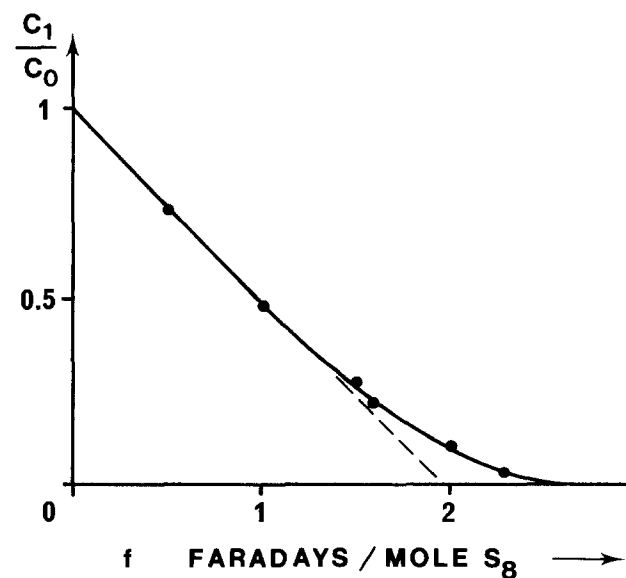
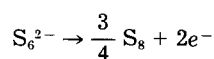
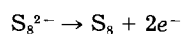


Fig. 2. Variation of the unreduced sulfur S_8 concentration during electrolysis at $-0.9V$ (60°C).

charge is expressed as the number f of F/mol of S_8 initially present in the solution.

Voltammetry is also used to monitor S_8^{2-} and S_6^{2-} evolution during electrolysis. These polysulfides are indeed oxidized into S_8 with loss of two electrons (13)



Whatever the stage of reduction, only one oxidation wave is obtained and the half-wave potential remains unchanged (-0.19 V/ECS). The oxidation limiting current increases linearly with f , and no variation of the slope occurs at $f = 1$ (Fig. 3). In addition, the current variation against electrode rotation speed satisfies Levich's law. The reduction of S_8^{2-} and S_6^{2-} takes part in the second wave limiting current i_2 , which displays a complex behavior, first decreasing, then increasing to ca. 10% above its initial value (Fig. 4).

When the electrolysis is performed at -1.5 V/ECS (second wave), identical results are obtained from voltammetric plots, as long as $f < 8/3$. The sulfur and polysulfide ion content of the solution thus depends only on f and not on electrolysis potential. As soon as f exceeds $8/3$, the rest potential of the Pt working electrode is shifted from -0.7 to -1.0 V/SCE, and a new oxidation wave appears ($E_{1/2} \approx$

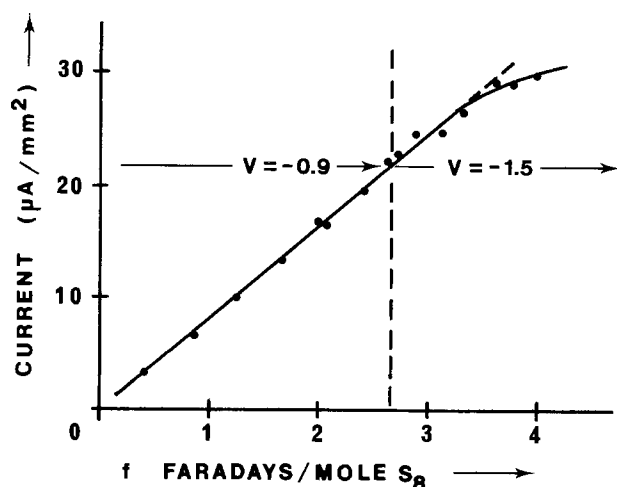


Fig. 3. Variation of the oxidation limiting current during controlled potential electrolysis (at -0.9 V until $f = 8/3$, and then at -1.5 V). Same conditions as Fig. 1.

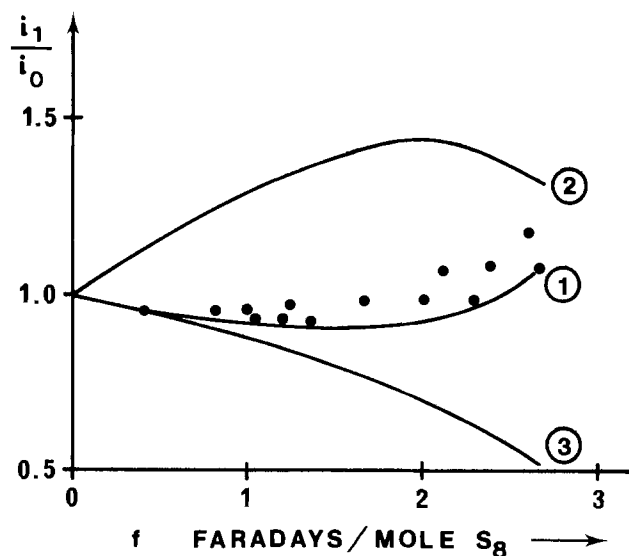
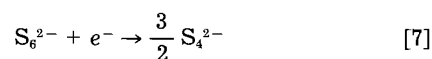
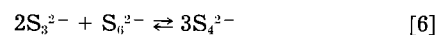


Fig. 4. Relative variation of the second wave limiting current during electrolysis at -0.9 V. Experimental points and calculated curves.

-0.8 V/SCE). Between $f = 8/3$ and $f = 3.8$, the reduction appears to be a one-electron process.

Discussion.—It can be concluded from the above results that the limitation of the current in potentiodynamic plots arises from diffusional transport of S_8 only. Therefore, it can be inferred either that the dismutation reaction [3] is slow and takes place only outside the diffusion limiting layer or, on the contrary, that this reaction is fast enough to go to completion inside the diffusion layer. This result precludes a middle hypothesis set between the former "two-electron" case and the latter "8/3-electron" one.

The results concerning the controlled-potential electrolysis are similar to those of Badoz-Lambling (15). The one-electron process occurring beyond $f = 8/3$ is the reduction of S_6^{2-} into S_3^{2-} [5], followed by the reaction between S_3^{2-} and S_6^{2-}



The limitation of the oxidation current is also a diffusional process. The lack of variation in the slope of the plot of the limiting current between $f = 0$ and $f = 3.5$, strongly suggests that the diffusion coefficients of S_8^{2-} and S_6^{2-} are equal, according to Levich's equation. Their value is then

$$D_2(S_8^{2-}) = D_3(S_6^{2-}) = (6.3 \pm 0.3) \times 10^{-6} \text{ cm}^2 \text{ s}^{-1} \text{ at } 60^\circ\text{C}$$

Assuming either $n = 2$ or $n = 8/3$ for the electron number for sulfur reduction in voltammetric conditions, two values of the S_8 diffusion coefficient are derived from the reduction limiting current

$$n = 2e^- : D_1 = (8.9 \pm 0.4) \times 10^{-6} \text{ cm}^2 \text{ s}^{-1} \quad \text{at } 60^\circ\text{C}$$

$$n = 8/3 e^- : D_1' = (5.8 \pm 0.3) \times 10^{-6} \text{ cm}^2 \text{ s}^{-1}$$

A previous study in our group (16) showed that, owing to electrostatic interactions and ion pairing, the diffusivity of a charged species in an electrolytic solution is lower than the diffusivity of a similar neutral species. For instance, with tetramethyl phenylenediamine (TMPD/TMPD⁺), the ratio $D(\text{neutral})/D(\text{charged})$ ranges from 1.3 to 1.9 in acetone, according to the supporting electrolyte concentration. The above-mentioned results concerning S_8 and S_8^{2-} yield the ratios $D_1/D_2 = 1.4 \pm 0.07$ (for $n = 2$) and $D_1'/D_2 = 0.9 \pm 0.04$ (for $n = 8/3$). The diffusion coefficients of S_8 and S_8^{2-} may be affected by the shape of the species (ring or chain). The comparison between several mono- or tetra-alkylammonium ions (chains or spheroids with the same molecular weight) shows that the ionic mobility of the spheroid is a few percent larger. The "two-electron" hypothesis then appears more likely than the "8/3-electron" one.

A final piece of evidence in favor of the two-electron process is obtained through the analysis of the variations of the second wave amplitude during electrolysis at -0.9 V. Provided that the concentrations and diffusivities of various species are known, the second wave current i_2 can be derived as a function of the number of F, f , in the various reaction schemes. Regardless of the scheme, the respective concentrations C_1 , C_2 , and C_3 of S_8 , S_8^{2-} , and S_6^{2-} may be derived at any stage of the electrolysis

$$C_1 = C_0 i_1/i_0$$

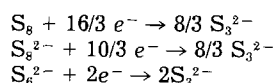
$$C_2 = 4(C_0(1 - 3f/8) - C_1)$$

$$C_3 = 2(C_0(f - 2) + 2C_1)$$

Reactions [3] and [6] are slow.—The dismutation reactions [3] and [6] take place only in the bulk of the solution. The first stage is then reaction [1], while the second wave involves reactions [1] + [2] and [5]. The limiting currents are derived by use of coefficients D_1 and D_2 and of proper electron numbers. In this first case the ratio i_1/i_0 is

$$Y_1 = \frac{i_2}{i_0} = \frac{i_1}{i_0} + \frac{1}{2} \left(\frac{D_2}{D_1} \right)^{2/3} f = \frac{i_1}{i_0} + 0.40f$$

Reaction [3] is fast and [6] is slow.—Reaction [3] now occurs inside the diffusion layer; the first voltammetric wave then corresponds to the formation of S_6^{2-} (Eq. [4]). In the bulk of the solution, S_6^{2-} is partly reconverted into S_8^{2-} as long as S_8 is present; this process takes place outside the diffusion layer and thus does not affect the first wave. Derivation of the second wave current in this case is more complicated. The reduction of S_8^{2-} proceeds through evolution of S_8 and S_6^{2-} , which are reduced into S_3^{2-} . The molecular sulfur S_8 (present in the bulk or evolved inside the diffusion layer) is indeed not reduced into S_4^{2-} , such a process not being consistent with two waves of equal amplitudes for S_8 reduction. The correct assumption here is reduction of S_8 into S_3^{2-} via a 16/3 electron process. The complete set of equations for the second wave is then



The ratio i_2/i_0 in this second case is

$$\begin{aligned} Y_2 &= \frac{i_1}{i_0} + 2 \left(\frac{D_2}{D_1'} \right)^{2/3} \left(1 - \frac{i_1}{i_0} - \frac{3}{16} f \right) \\ &= \frac{i_1}{i_0} + 2.66 \left(1 - \frac{i_1}{i_0} - \frac{3}{16} f \right) \end{aligned}$$

(note the use of coefficient D_1' for S_8).

Reaction [3] is slow and [6] is fast.—Reaction [6] now takes place inside the diffusion layer; reduction of S_6^{2-} thus yields S_4^{2-} (reaction [7]). The remainder of the process is the same as in the first case. The result is then

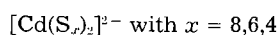
$$\begin{aligned} Y_3 &= \frac{i_1}{i_0} + 2 \left(\frac{D_2}{D_1} \right)^{2/3} \left(1 - \frac{i_1}{i_0} - \frac{1}{4} f \right) \\ &= \frac{i_1}{i_0} + 1.58 \left(1 - \frac{i_1}{i_0} - \frac{1}{4} f \right) \end{aligned}$$

The values Y_1 , Y_2 , and Y_3 of the ratio i_2/i_0 are plotted against f together with the experimental values in Fig. 4. It is clear from this plot that the first hypothesis is in quite good agreement with experiments, while calculated variations Y_2 and Y_3 bear no relation to them.

This last result supports the simplest model for S_8 reduction at a rotating electrode, i.e., two electrochemical steps involving two-electron transfers according to reactions [1] and [2].

Reactions Between Polysulfide Ions and Cd^{2+}

Discoloration of polysulfide solutions.—A solution containing S_8^{2-} and S_6^{2-} shows a deep blue color; when a solution containing Cd^{2+} [as $Cd(NO_3)_2$, for instance] is gradually added to the polysulfide solution, the blue color vanishes and turns to light yellow. When the initial content of the polysulfide solution is mainly S_4^{2-} , the initial color is yellow-green; again, it turns to light yellow upon Cd^{2+} addition. The discoloration is sharp enough to allow an accurate determination of the corresponding quantity of Cd^{2+} ions. Figure 5 shows a plot of this Cd^{2+} quantity against the total polysulfide content of the solution. The same linear variation is observed, irrespective of the reduction state of the polysulfide ions. The abscissa then can be either the mole number of S_x^{2-} or the number f of F/mol S_8 when the polysulfide solution is obtained by means of S_8 reduction. This implies that Cd^{2+} reacts in the same manner with S_8^{2-} , S_6^{2-} , and S_4^{2-} . The $S_x^{2-}: Cd^{2+}$ ratio at discoloration is ≈ 2.1 , thus we consider the formation of cadmium-polysulfide complexes with the formula



The difference between the stoichiometric ratio 2 in the formula and the experimental value 2.1 can be ascribed to

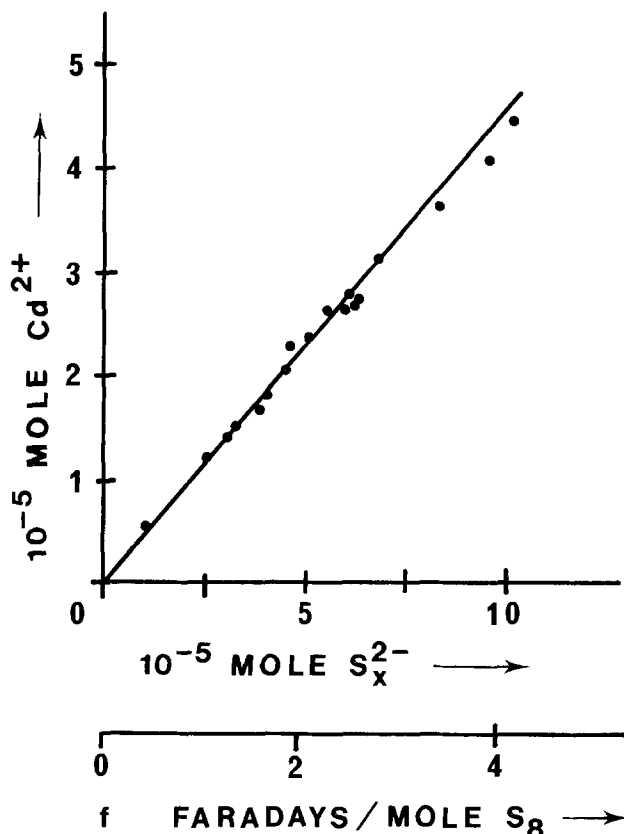


Fig. 5. Plot of the Cd^{2+} quantity required for discoloration of a polysulfide ion solution against the total polysulfide content. 60°C; initial sulfur content, 5×10^{-5} mol.

various causes, such as a systematic misinterpretation of the discoloration point or influence of oxygen introduced by the Cd^{2+} solution. The nonquantitative formation of S_4^{2-} leads to some deviation from the linear variation when f is close to 4 F/mol S_8 .

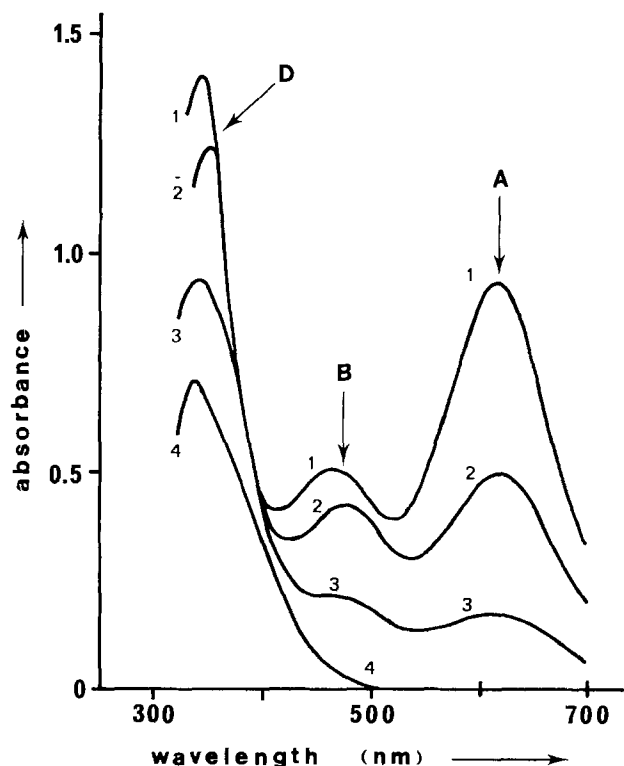


Fig. 6. Absorption spectra of a polysulfide solution containing S_8^{2-} ($\approx 2 \times 10^{-5}$ mol) and S_6^{2-} ($\approx 4 \times 10^{-5}$ mol) ($v = 20$ ml) before and during Cd^{2+} addition: 1, before addition; 2, $+10^{-5}$ mol Cd^{2+} ; 3, $+2 \times 10^{-5}$ mol Cd^{2+} ; 4, $+4 \times 10^{-5}$ mol Cd^{2+} (1 mm cell).

Polysulfide complex formation reactions.—The formation of cadmium dipolysulfide complexes and their behavior may be studied by means of spectroscopy and voltammetry. Figure 6 shows the absorption spectra of a solution containing S_8^{2-} and S_6^{2-} (obtained by electrolysis of S_8 with $f = 2.4$). According to Ref. (14) and (15), band B (490 nm) is due to S_8^{2-} , whereas band A (618 nm) is assigned to the radical $S_3^{\cdot-}$, issued from S_6^{2-} dissociation. Band D, at 355 nm, was also assigned to S_8^{2-} (15); however, we observed a strong absorption at this wavelength, even when S_8^{2-} was completely reduced into S_6^{2-} and S_4^{2-} . This observation can be compared to the absorption data concerning sulfanes H_nS_n . The first allowed transition wavelength of these compounds shows little dependence upon the chain length n (for $4 \leq n \leq 8$) and lies in the same domain (17). When Cd^{2+} is added to the polysulfide solution, the absorbance of bands A and B decreases and vanishes when discoloration is obtained; it should be pointed out that band D does not vanish (Fig. 6). The absorbance of band B is a linear function of S_8^{2-} concentration, whereas, owing to the dissociation of S_6^{2-} into $S_3^{\cdot-}$, the absorbance of band A is related to the square root of S_6^{2-} concentration (15). The variations of S_8^{2-} and S_6^{2-} concentrations upon Cd^{2+} addition can then be derived from the spectra of Fig. 6; they are plotted in Fig. 7. It is clear that S_6^{2-} concentration decreases much faster than S_8^{2-} concentration at the beginning of Cd^{2+} addition: this means that the complex $[Cd(S_6)_2]^{2-}$ is more stable than $[Cd(S_8)_2]^{2-}$.

A similar result is obtained with a solution containing S_6^{2-} and S_4^{2-} . The initial spectrum displays bands A, D, and C (430 nm), which is assigned to S_4^{2-} (15) (Fig. 8). There is a sharp decrease of band C upon a first addition of Cd^{2+} solution, while band A remains unaffected; S_4^{2-} thus reacts with Cd^{2+} prior to S_6^{2-} . When more Cd^{2+} is added, band A decreases in turn; in the same time, band C is altered as its maximum moves towards 490 nm, which is the position of band B (S_8^{2-}).

This stability difference is also displayed through voltammetric plots (Fig. 9). Solutions containing S_8^{2-} and S_6^{2-} (Fig. 9a) or S_6^{2-} alone (Fig. 9b) were prepared by electrolysis. In both cases, the limiting current of the first reduction wave increases when Cd^{2+} is added up to discoloration, the half-wave potential not being altered. This behavior is explained in terms of S_8 regeneration and implies the reactions

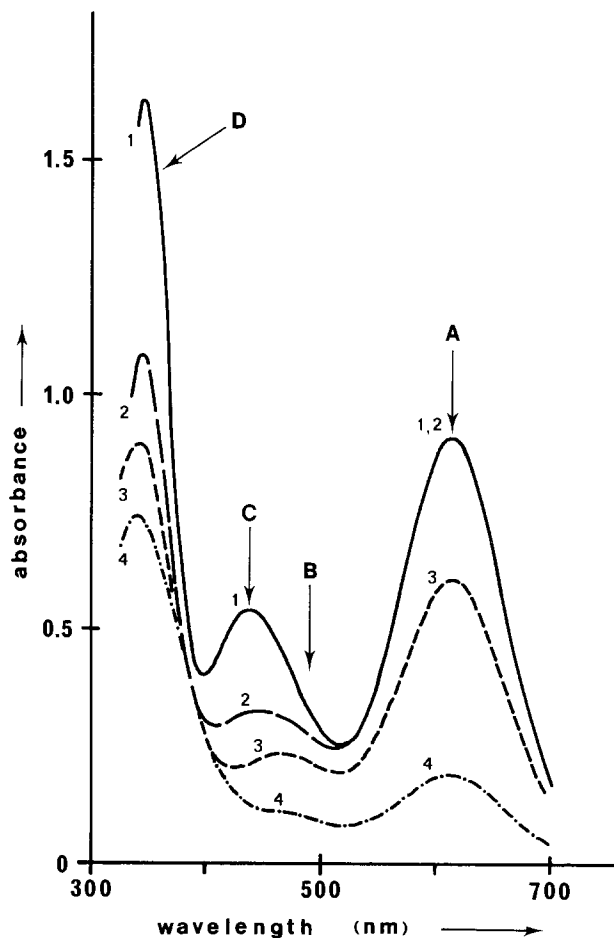
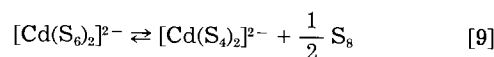
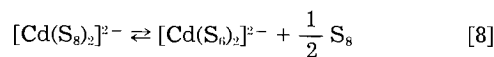


Fig. 8. Absorption spectra of a polysulfide solution containing S_6^{2-} and S_4^{2-} ($\approx 4 \cdot 10^{-5}$ mol each in 20 ml) before and during Cd^{2+} addition: 1, before addition; 2, $+10^{-5}$ mol Cd^{2+} ; 3, $+2 \times 10^{-5}$ mol Cd^{2+} ; 4, $+3 \times 10^{-5}$ mol Cd^{2+} . Discoloration takes place for 3.8×10^{-5} mol Cd^{2+} . (1 mm cell).

oration, the half-wave potential not being altered. This behavior is explained in terms of S_8 regeneration and implies the reactions



The shift of band C toward the position of band B in the spectra of Fig. 8 is consistent with reaction [9]: as $[Cd(S_6)_2]^{2-}$ is converted into $[Cd(S_4)_2]^{2-}$, the evolved sulfur S_8 reacts with S_6^{2-} to yield S_8^{2-} through dismutation reaction [3]. As S_8^{2-} in turn reacts with Cd^{2+} when discoloration takes place, the whole process can be described by the dismutation reaction

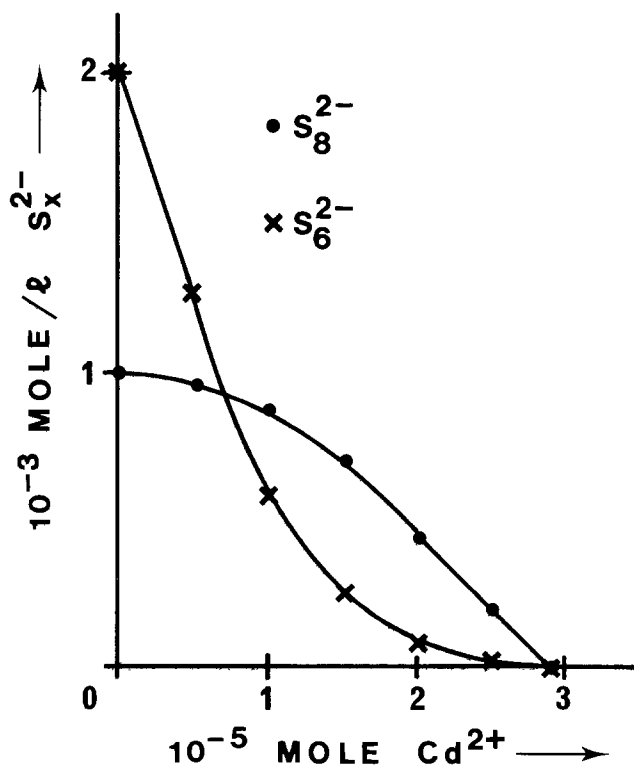
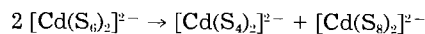


Fig. 7. Variation of S_8^{2-} and S_6^{2-} concentrations during Cd^{2+} addition (derived from the spectra of Fig. 6).

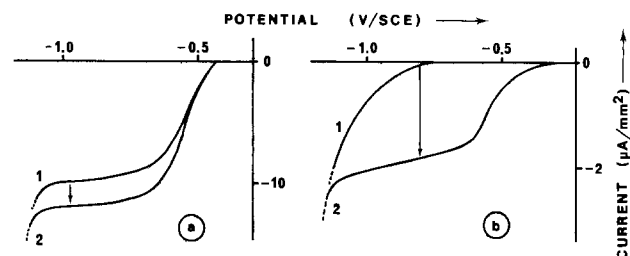
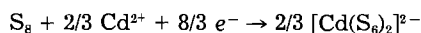


Fig. 9. Observation of the first wave limiting current increase when Cd^{2+} is added up to discoloration to a polysulfide solution. (a) After electrolysis until $f = 1$. (b) After electrolysis until $f = 8/3$ (same conditions as Fig. 1).

Complex formation with Cd²⁺ generated in situ.—Direct generation of Cd²⁺ ions inside the solution is achieved during S₈ electrolysis by oxidation of cadmium metal. For this purpose, the current is shared between two auxiliary electrodes: one is a cadmium wire set into the solution, the second is platinum foil with a junction bridge (Fig. 10). The cadmium oxidation current is set by means of a current splitter (two variable resistors) in order to obtain 1 mol Cd²⁺ for 2 mol S₈²⁻ or another ratio. The ratio is precisely monitored by means of two current integrators. This method rules out possible troubles arising from the oxygen or water content of the cadmium salt solution; in addition, it allows the precise monitoring of small Cd²⁺ quantities.

When the electrolysis is performed with a S₈²⁻: Cd²⁺ ratio of 2, the solution gradually turns yellow and the absorption spectra shows only one band at 340-350 nm. The distinctive colorations of polysulfide ions soon appear if the S₈²⁻: Cd²⁺ ratio is increased to a slight extent. This result confirms the exact value of the stoichiometric ratio in the formula of the complex.

The concentration of unreduced sulfur is again monitored by voltammetry during electrolysis at -0.9V. Figure 11 must be compared to Fig. 2. The slope of the S₈ concentration variation remains the same from $f = 0$ to $f \approx 8/3$, indicating transfer of 8/3 electrons. The reduction process is then



The complex $[Cd(S_8)_2]^{2-}$ thus does not appear, even at the beginning of the electrolysis ($f < 1$). Because there is no excess Cd²⁺ ions in the solution, the electrochemical stage remains S₈ reduction into S₈²⁻. When $f \leq 1$, the dismutation of S₈²⁻ into S₈ and S₆²⁻ is weak; the 8/3 electron

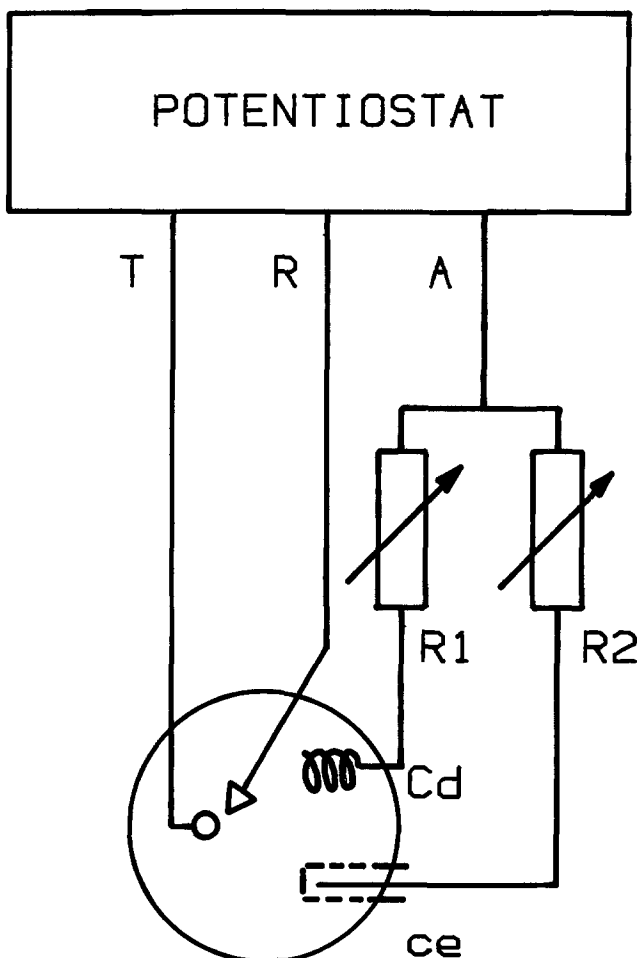


Fig. 10. Experimental setup for Cd²⁺ generation during S₈ reduction: (T) working electrode; (R) SCE reference electrode; (A) auxiliary electrodes circuit; (ce) platinum counterelectrode; (Cd) cadmium wire.

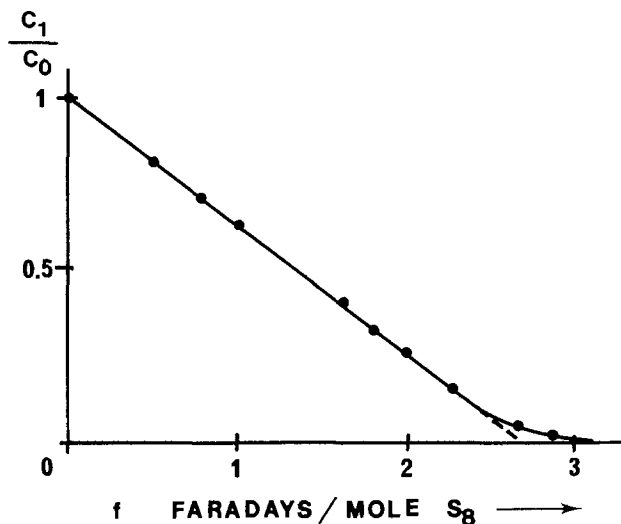


Fig. 11. Variation of the unreduced sulfur concentration during electrolysis at -0.9V with Cd²⁺ generation (S₈²⁻:Cd²⁺ ratio = 2).

number then results from the complete conversion of $[Cd(S_8)_2]^{2-}$ into $[Cd(S_6)_2]^{2-}$ according to reaction [8]. When f reaches 8/3 F/mol S₈, the first wave does not disappear; however, the electrolysis current is small and vanishes when f is about 3. This indicates a moderate conversion of $[Cd(S_8)_2]^{2-}$ into $[Cd(S_4)_2]^{2-}$ through reaction [9].

In order to complete the reduction and reach $f = 4$, the electrolysis potential must be raised to ca. -1.4V. The polysulfide complex $[Cd(S_4)_2]^{2-}$ is then obtained through reduction of $[Cd(S_6)_2]^{2-}$, which rids the process of the nonquantitative reduction of S₈ (or S₈²⁻) into S₄²⁻. This reduction is again studied by means of voltammetry and spectroscopy. The limiting current of the second wave shows a linear dependence against f , with an abrupt change of the slope at $f \approx 8/3$. Spectrophotometry yields additional information about the absorption band located around 340-350 nm, which is observed in both complex and polysulfide solutions (band D). The absorbance increases in a linear fashion as $[Cd(S_8)_2]^{2-}$ is evolved during electrolysis until $f = 8/3$ (Fig. 12). The molar absorptivity of $[Cd(S_8)_2]^{2-}$ is derived from this part of the curve: $\epsilon \approx 5200$ at 340 nm. When $f > 8/3$, $[Cd(S_8)_2]^{2-}$ is reduced into $[Cd(S_4)_2]^{2-}$; the absorption decrease implies that the absorptivity of the latter complex is smaller than the former. The linear variation of the absorbance as a function of f

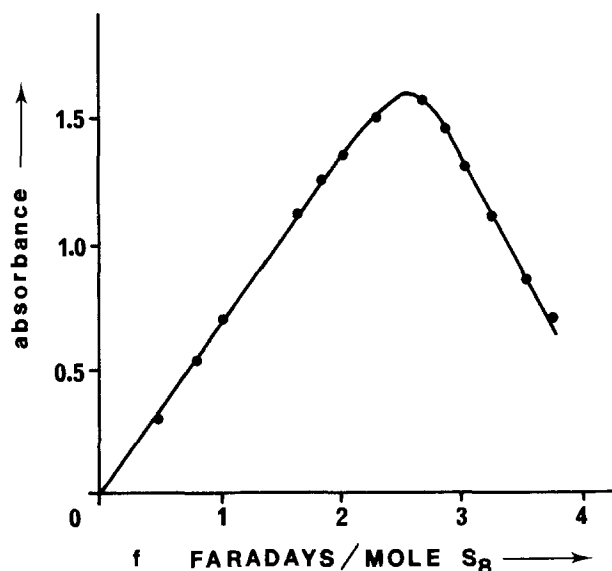


Fig. 12. Variation of the absorbance at 340 nm during electrolysis of a S₈ solution ($C_0 = 2.5 \times 10^{-3}$ mol/liter⁻¹) with Cd²⁺ generation (S₈²⁻:Cd²⁺ ratio = 2; 1 mm cell).

indicates that this reduction is quantitative. The molar absorptivity of $[\text{Cd}(\text{S}_x)_2]^{2-}$ can then be derived: $\epsilon' \approx 1200$ at 340 nm.

Conclusion

A full set of consistent electrochemical evidence supports the "two-electron" model for sulfur reduction at a rotating electrode in DMSO. The two voltammetric waves of same amplitude are thus assigned to the simple electrochemical reactions [1] and [2]. The chemical reactions which are likely to alter the electron number, *i.e.*, dismutation reactions [3] and [6], are slow and occur only in the bulk of the solution.

The addition of a cadmium salt to a solution of polysulfide ions leads to the formation of soluble and stable polysulfide-cadmium complexes. Their general formula is $\text{Cd}(\text{S}_x)_2^{2-}$, with $x = 8, 6,$ and 4 . The complex stability increases as the polysulfide chain length x decreases from 8 to 4, which leads to several reactions between complexes, polysulfide ions, and sulfur. These chemical reactions are similar to those involving polysulfide ions themselves. However, the trend towards short chain polysulfide-cadmium complex formation is more pronounced than for free polysulfide ions. For instance, there is a moderate conversion of $[\text{Cd}(\text{S}_6)_2]^{2-}$ into $[\text{Cd}(\text{S}_4)_2]^{2-}$ and S_8 , while the corresponding conversion of S_6^{2-} into S_4^{2-} is not observed. We are not aware of any other description of similar polysulfide-metallic ion complexes.

The behavior of polysulfide ions and polysulfide-cadmium complexes in presence of excess Cd^{2+} ions and the formation of other polysulfide-cadmium compounds will be examined in our next paper.

Manuscript submitted July 10, 1984; revised manuscript received Oct. 13, 1984.

CNRS assisted in meeting the publication costs of this article.

REFERENCES

1. W. E. Devaney, A. M. Barnett, G. M. Storti, and J. D. Meakin, *IEEE Trans. Electron Devices*, **ed-26**, 205 (1979).
2. T. W. F. Russell, A. M. Barnett, B. N. Baron, J. V. Masi, and R. E. Rocheleau, in "Proceedings of the 14th IEEE Photovoltaic Spec. Conference," p. 354, San Diego (1980).
3. M. Perotin, J. Bougnot, J. Marucchi, O. Maris, R. Dauree, C. Grill, and M. Savelli, in "Proceedings of the 14th IEEE Photovoltaic Spec. Conference," p. 172, San Diego (1980).
4. A. L. Fahrenbruch, *J. Cryst. Growth*, **39**, 73 (1977).
5. R. O. Loufty, L. F. McIntyre, D. K. Murti, and C. K. Hsiao, *Solar Energy Mater.*, **5**, 221 (1981).
6. A. S. Baranski and W. R. Fawcett, *This Journal*, **127**, 767 (1980).
7. A. S. Baranski, W. R. Fawcett, A. C. McDonald, R. M. de Nobrega, and J. R. MacDonald, *ibid.*, **128**, 963 (1981).
8. A. S. Baranski, W. R. Fawcett, K. Gatner, A. C. McDonald, J. R. MacDonald, and M. Selen, *ibid.*, **130**, 579 (1983).
9. A. S. Baranski, W. R. Fawcett, and A. C. McDonald, *J. Electroanal. Chem.*, **160**, 271 (1984).
10. G. Maronny, *J. Chim. Phys.*, **59**, 140, 202 (1959).
11. E. Zintl, S. Goubeau, and W. Dullekope, *Z. Phys. Ch.*, **154**, 26 (1931).
12. K. A. Paulsen and R. A. Osteryoung, *J. Am. Chem. Soc.*, **98**, 6866 (1976).
13. M. Delamar and J. C. Marchon, *J. Electroanal. Chem.*, **63**, 351 (1975).
14. R. P. Martin, W. H. Doubs, J. L. Roberts, and D. T. Sawyer, *Inorgan. Chem.*, **12**, 1921 (1973).
15. J. Badoz-Lambling, R. Bonaterre, G. Cauquis, M. Delamar, and G. Demange, *Electrochim. Acta*, **21**, 119 (1976).
16. R. Hérino, D.Sc. Thesis, University of Grenoble (1980).
17. B. Meyer, *Chem. Rev.*, **76**, 367 (1976).

Time-Dependent Energy Efficiency Losses at Nickel Cathodes in Alkaline Water Electrolysis Systems

H. E. G. Rommal^{*,1} and P. J. Moran^{**}

Department of Materials Science and Engineering, The Johns Hopkins University, Baltimore, Maryland 21218

ABSTRACT

Water electrolysis in alkaline solutions is an important hydrogen production method. One difficulty encountered in systems employing nickel electrodes in KOH electrolytes is the continual decrease in operating efficiency with time. The major component of this decrease is the rise in cathodic overpotential at constant cell current. It was found that the kinetic parameters of Tafel slope and exchange current density increase markedly with the decline of efficiency. Four mechanisms have previously been postulated as being responsible for this phenomenon. In the present work, it was found that the loss of efficiency can be completely recovered; and an examination of the recovery mechanism supports the theory of hydrogen absorption's being responsible for the efficiency decline.

Hydrogen is an important raw material for many industries and is regarded as a viable replacement for petroleum products as the world's primary future fuel (1-3). One method used to produce hydrogen is water electrolysis. Many commercial electrolysis systems employ nickel anodes and cathodes in aqueous potassium hydroxide electrolyte. Efficiencies of these systems have been improved substantially in the last five years (4) with the development of advanced high surface area nickel electrodes and modification of cell designs to minimize resistive losses.

One of the most persistent and least well-understood problems plaguing those systems is the continual decrease in energy efficiency with time during operation.

*Electrochemical Society Student Member.

**Electrochemical Society Active Member.

¹Present address: Department of Metallurgy and Materials Engineering, Lehigh University, Bethlehem, Pennsylvania 18015.

The energy efficiency E_o can be written (5)

$$E_o = E_{\max} E_v E_l$$

where E_{\max} is the maximum intrinsic efficiency of the reaction(s) in question derived from the thermodynamic considerations, E_v is the voltage efficiency, and E_l is the current efficiency. Current efficiencies in unipolar water electrolyzers are close to 100% since no side reactions occur (6). Since E_{\max} is a thermodynamic property which is nearly invariant at the temperatures of interest and E_l is close to unity, the only term which could be significantly degraded with time is E_v . Typical values of full cell voltage efficiencies, referenced to the 1.23V reversible full cell potential, in industrial alkaline systems are about 70%, and decline to approximately 60% after only 200h of operation (7). Voltage efficiency can be improved by reducing the magnitude of either cathodic or anodic overpotential or the resistive losses in the electrolyte.

Electrolyte conductivity was found to be invariant with time by other investigators (8). While both η_A and η_c increase with time, the rise in the magnitude of the cathodic overpotential is reputed to be more severe for nonactivated flat-plate electrodes (9), and reportedly represents the major component of the degradation of E_0 with time (henceforth referred to as cathodic time effects). The phenomenon of cathode voltage increase with time at constant current and temperature has, therefore, been pursued in this research.

Apparatus and Experimental Conditions

An electrochemical cell for investigation of cathodic voltage-time behavior was constructed of polypropylene and high density polyethylene and is illustrated in Fig. 1. A 10 cm² Ni 200 screen counterelectrode was surrounded by a woven polyethylene membrane to minimize gaseous oxygen transfer from anolyte to catholyte during electrolysis. Also, the catholyte was purged with prepurified nitrogen for 1h prior to and throughout each test to displace any dissolved oxygen present. These measures minimized the possibility of oxygen depolarization at the cathode. The electrolyte used was a 30 weight percent (w/o) aqueous KOH solution prepared from Baker Reagent Pellets or Hooker Chemical 45 w/o solution diluted with deionized or distilled water, and cleaned by pre-electrolysis. Reference electrodes were of the saturated calomel (SCE) type and were coated with Teflon, except at the frit, to minimize electrolyte contamination by dissolution of the glass body. To insure proper functioning, SCE's were checked against another SCE reference electrode in KCl solution before and after each test. The electrolyte temperature was maintained at 37° ± 1°C by placing the cell in a controlled-temperature bath. This temperature simulates commercial operation. A Teflon-coated thermometer was used to monitor electrolyte temperature.

Working electrodes (cathodes) were fashioned from 1.0 cm² square sections cut from 0.125 in. thick Ni 200 plate. These sections were metallographically mounted in an inert polymer resin and mechanically polished to expose a planar 1.0 cm² apparent geometric surface area. Mounted and polished electrodes were cleansed thoroughly in each of a series of solvents (ethanol, acetone, ethanol, distilled water) and dried in a stream of nitrogen.

Galvanostatic control was maintained with a Princeton Applied Research (PAR) Model 173 Potentiostat/Galvano-

stat or a Kepco Model CK 36-1.5 Regulated Power Supply. Controlled potential experiments were conducted using the PAR Model 173 Potentiostat and a PAR Model 175 Programmer. Unless otherwise indicated, data were corrected for IR drop in the electrolyte by a current interruption technique (10). Typical ohmic half-cell resistance values were 0.6-0.7Ω. Voltage or current vs. time data were averaged at logarithmically spaced time intervals.

Galvanostatic Experiments

Initial investigations of the increase of η_c with time were made galvanostatically. Cells were operated for a period of 6h, and the increases in the cathodic half-cell potential (cathode vs. SCE) were monitored. Tests were conducted at six apparent current densities ranging from 2.5 to 500 mA/cm².

Previous investigators have reported a linear behavior of cathode half-cell potential with log time with a slope of 100 mV/decade time (9). Tests made in this study at lower current densities, 2.5-25 mA/cm², typically showed this linear behavior with a slope of 90 mV/decade time. However, at higher current densities, 100-500 mA/cm², sharp increases in the cathode potentials occurred between 10³ and 10⁴s (16.67 min and 2.78h, respectively) with slopes of approximately 450mV/decade time. In the regions preceding and following this sharp increase, the potential was linear with log time with slope 90 mV/decade. A plot of average cathodic half-cell potential vs. log time for all current densities tested appears in Fig. 2. It can be seen that this sharp increase in the higher current density experiments (henceforth called the "jump") is responsible for approximately 50% of the total increase in cathode potential over 6h in each case. No data were recorded during the first minute of operation to allow for system stabilization. It can be seen that the magnitude of this increase is much larger for the 100 and 200 mA/cm² tests than for the experiments at lower current densities. It can also be seen, however, that the total increase in η_c is less for the runs at 500 mA/cm² than for the 100 and 200 mA/cm² tests.

The cathodes operated at 500 mA/cm² for 6h were covered with a black deposit. Energy dispersive x-ray microanalysis of this deposit with a Tracor Northern TN-2000 Energy Dispersive X-ray Analysis System mounted on an ISI-60A scanning electron microscope showed the deposit to be predominantly iron. Fe is a common trace impurity in all available forms of KOH and most deionized and distilled water. All four combinations of Baker KOH, Hooker KOH, deionized H₂O, and distilled H₂O were prepared in an attempt to identify the major source of the Fe. Cathodes were run at 500 mA/cm² for 6h in each electrolyte, and the surface examined afterward via scanning electron microscopy for extent of Fe deposition. These tests clearly indicated that the deposition was much greater from the Baker KOH than from the Hooker, with the choice between distilled or deionized water used for dilution being unimportant. Fe is roughly as electrocatalytic for the production of hydrogen as Ni (11), and the deposition of a rough layer of Fe onto a smooth Ni surface increased the active surface area, decreasing the true cur-

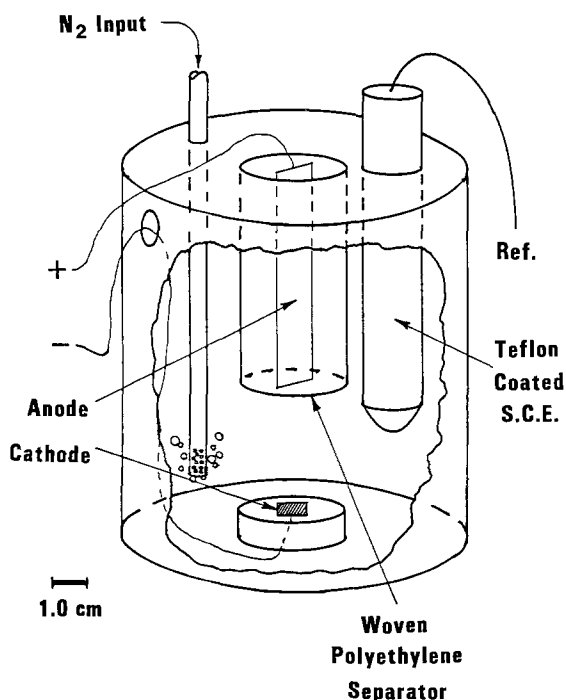


Fig. 1. Schematic of cell used for efficiency loss studies

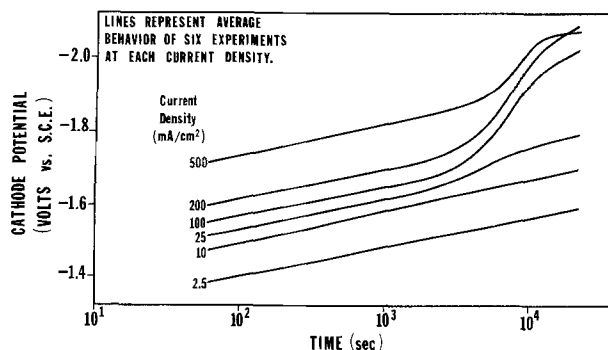


Fig. 2. Nickel cathode potential behavior with time under galvanostatic control as a function of current density in 30 w/o KOH at 37°C.

rent density (and, hence, η_c) and working against the time effects. This deposition is strongly dependent on current density, as expected, and, hence, had little effect on the tests made at 200 mA/cm² and below. Optical and scanning electron microscopy revealed no detectable deposits on all but the 500 mA/cm² cathodes. All subsequent tests were performed using Hooker 45 w/o KOH solution diluted with deionized H₂O, which was cleaned by pre-electrolysis using 50 cm² Ni 200 electrodes and a current of 10 mA for 24h. Electrolytes were checked for Fe content by a visible spectrophotometric technique. It was found that appreciable Fe did not accumulate and that the jump was fairly reproducible for solutions with Fe concentrations below 0.03 ppm. The location of the jump in time was found not to be readily correlated to current density, and its onset did not occur at a specific overpotential.

Potentiostatic Experiments

One would expect analogous behavior if similar tests were performed potentiostatically. Cathodes were held at a constant potential of $-2.00V$ vs. SCE (non-IR corrected) for 6h, and the decrease in cell current was recorded. The current shows a steady decay for the first 10^3 - 10^4 s, and then there is a sharp drop, which corresponds to the jump observed in galvanostatic tests. In these potentiostatic experiments, the cells lost, on the average, 90% of the initial current over 6h. Typical behavior of a potentiostatic test is shown in Fig. 3. In order to determine if the kinetic parameters of Tafel slope b and exchange current density i_0 , for the hydrogen evolution reaction are affected by the efficiency loss, average cathode overpotentials obtained from the preceding galvanostatic tests at various times were plotted vs. log current density. Values were taken from the first (1 min) and last (6h) data points and times just before (10^3 s) and just after (10^4 s) the jump for each current. Values for b and i_0 obtained from these plots are given in Table I. It can be seen that both b and i_0 increase dramatically with the advancement of time effects. Also, since the values are similar for 1 min and 10^3 s, and for 6h and 10^4 s, it is the jump which causes nearly all of this change in b and i_0 .

To further substantiate these findings, a set of Tafel experiments was devised. Cathode potential measurements were made at nine different current densities ranging from 10^{-3} to 0.6 A/cm². The potential was allowed to stabilize for only 2s at each current density before the value was recorded; thus, a Tafel plot was generated in approximately 20s. This short period allowed for almost no time effects to occur. The cathodes were then operated at 100 mA/cm² for 6h, allowing the jump to occur, and the fast Tafel experiment repeated without allowing hydrogen evolution to cease at the cathodes. The average data for these tests yielded values of $b = 125$ mV/decade and $i_0 = 1.9 \times 10^{-6}$ A/cm² before the jump and $b = 310$ mV/decade and $i_0 = 0.9 \times 10^{-4}$ A/cm² after the jump. Those values are nearly identical to those obtained from the previous galvanostatic tests. In addition, the IR drop in the cell was

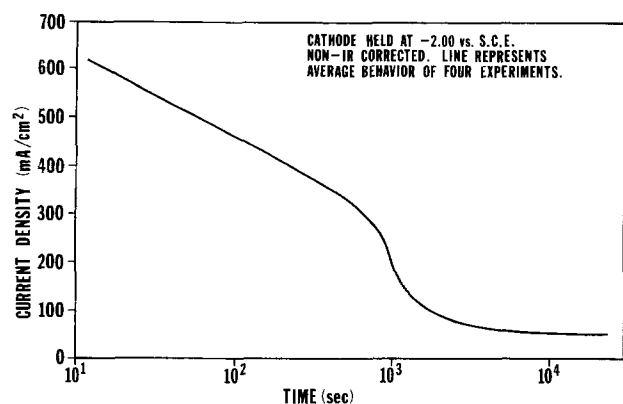


Fig. 3. Nickel cathode current density behavior with time for potentiostatic control at $-2.00V$ vs. SCE in 30 w/o KOH at 37°C.

Table I. Hydrogen evolution parameters for nickel cathodes at various times during cathode voltage increase with time

TIME	b (mV/decade)	i_0 (A/cm ²)
60 sec (1 min)	100	2×10^{-6}
10^3 sec	125	3×10^{-6}
10^4 sec	300	10^{-4}
2.16×10^4 sec (6hrs)	300	10^{-4}

checked both before each initial and after each final Tafel plot, and was found to be constant. This indicates that there is neither electrolyte resistivity component in the cathode voltage increases, nor resistive deposit accumulated on the electrode.

Recovery of Lost Efficiency

Since the cathodic overpotential increases occur during vigorous hydrogen evolution, it seems reasonable to infer that a cathodic reaction (or reactions) is responsible for the time effects. Given this, it also follows that a corresponding anodic reaction or reactions might reverse the process. Recovery of lost efficiency has, in fact, been observed. In commercial cells, a complete recovery of full cell voltage increases incurred during hundreds of hours of operation can be accomplished by simply removing the applied current for a period as short as 0.2h (7). Also, the increase in the cathodic overpotential seen after many hours of operation can be completely recovered by removal of the polarizing current for a period of one or two days or by shorting the anode to the cathode for a substantially shorter period, on the order of several minutes (9). Similar behavior has been observed qualitatively by the authors. It is presumed that, during open- or short-circuit decay, an anodic reaction (or reactions) is occurring at the cathode, undoing or reversing the mechanism responsible for time effects. Examinations of the recovery mechanism(s) were made in conjunction with tests similar to the 6h potentiostatic experiments described earlier. Cathodes were held at $-2.00V$ vs. SCE (non-IR corrected) for a period of 3h, allowing the jump to occur, and the drop in cell current recorded. The decrease in current ranged from 33% to a more typical 90%, as shown in Fig. 3. Shorting the anode to cathode for a period of 10 min and resuming the polarization to $-2.00V$ vs. SCE produced typically 95% recovery of the lost current.

In order to study the reaction(s) occurring during recovery, a set of cyclic voltammetric tests was devised. Electrodes were potentiodynamically swept from -2.00 to $-0.50V$ vs. SCE (non-IR corrected) and back at a scan rate of 1.0 mV/s and the cell current recorded. The electrodes (cathodes) were then held at $-2.00V$ vs. SCE (well into H₂ evolution) for 3h, and the cell current decay was observed. The sweep from -2.00 to 0.50V vs. SCE and back was then repeated. It was found that this sweep typically produced a recovery of 80-90% of the current lost during the previous 3h decay period. Figure 4 shows a plot of typical current behavior in the potential region anodic to reversible hydrogen potential ($-1.094V$ vs. SCE for 30 w/o KOH, pH 14.7) during the two potentiodynamic sweeps.

Several things can be observed in Fig. 4. First, the overall anodic activity is much greater in the postdecay sweeps than in the sweeps made before the 3h current decay. Second, in both cases there are two (potential-defined) regions of activity: one between the reversible hydrogen potential and $-0.8V$ vs. SCE, and other between $-0.8V$ and $-0.5V$ vs. SCE. Third, it is the first region, negative to $-0.8V$ vs. SCE, that shows the greatest increase in activity from pre- to postdecay sweeps. To test the initial hypothesis that it is indeed anodic activity which is responsible for the recovery of time effects, these same experiments were repeated, but the upper sweep limit was changed from $-0.5V$ vs. SCE to $-1.10V$

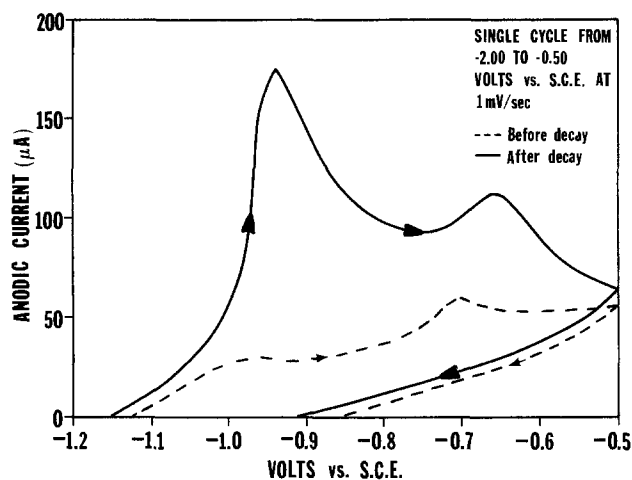


Fig. 4. Anodic portions of single-cycle voltammograms for nickel before and after decay of current density at -2.00V vs. SCE in 30 w/o KOH at 37°C .

vs. SCE (just cathodic to reversible hydrogen and before the occurrence of anodic current). These cathodic-only sweeps produced no current recovery whatsoever.

A reaction or reactions occurring in some or all of the potential region anodic to reversible hydrogen potential is therefore responsible for recovery. To determine which portion of the anodic region causes recovery, a slightly different set of controlled potential experiments was devised. Cathodes were held at -2.00V vs. SCE (non-IR corrected) for 3h, allowing the cell current to decay as before. Potentiodynamic sweeps were then performed from -2.00V vs. SCE to successively more anodic potentials, and back. These upper sweep limits varied from -1.20V vs. SCE to -0.50V vs. SCE in 100 mV increments. The scan rate used was 100 mV/s . The amount of anodic charge passed during each sweep was measured using a PAR Model 379 Coulometer or an Electroynthesis Corporation Model 640 Coulometer. The cathodic cell currents at -2.00V vs. SCE after each sweep (a measure of recovery) were also recorded. Figure 5 contains a plot of both the anodic coulombs contained in, and the cell current of -2.00V vs. SCE after each sweep vs. the upper sweep limit. 90% of the recovery typically occurred in the region between the reversible hydrogen potential and -0.80V vs. SCE , further indicating that it is this region which is primarily responsible for the recovery. However, the task of attempting to identify the mechanisms operating in the two regions of anodic activity still remained.

Proposed Efficiency Loss Mechanisms

Four possible mechanisms have been postulated by previous investigators as being responsible for the increase in cathodic overpotential with time.

1. Increases in η_c are caused by a loss of electrocatalytically active material from the cathode (12, 13).
2. Increases in η_c are caused by slow reduction of nickel hydroxide to nickel, which may be a poorer evolver of hydrogen (14).
3. Increases in η_c are caused by deposition of impurities from the electrolyte onto the cathode (7).
4. Increases in η_c are caused by the absorption of atomic hydrogen into the lattice of the nickel cathode (9, 15).

The first hypothesis was easily tested. Cathodes were examined by scanning electron microscopy; their surfaces were found to be unchanged during 6h of operation at 100 mA/cm^2 . In addition, this mechanism is usually common only in systems employing activated cathodes. Those in this study were flat-plate, unactivated Ni.

If second hypothesis were true, it would follow that the anodic activity responsible for recovery would correspond to reformation of $\text{Ni}(\text{OH})_2$ from nickel. To test this theory, an experiment was devised to yield the nickel hy-

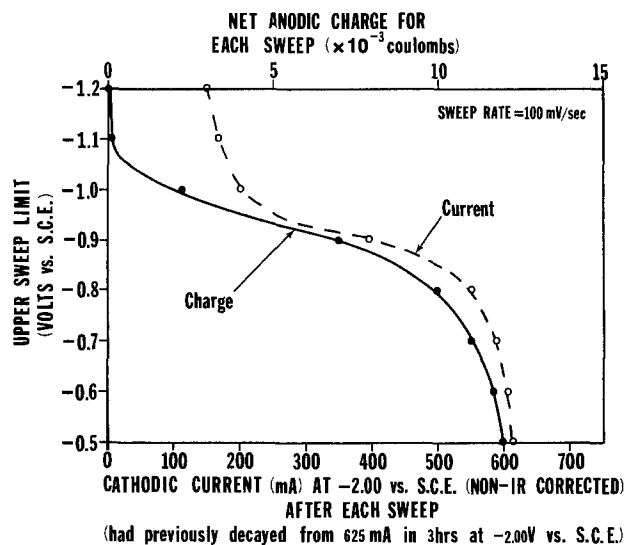


Fig. 5. Current recovered and associated anodic charge detected for successive single-cycle voltammetric sweeps from and after 3h at -2.00V vs. SCE for nickel in 30 w/o KOH at 37°C .

droxide formation peak alone. A piece of nickel used as a dummy electrode was held at -1.050V vs. SCE (slightly anodic to the reversible hydrogen potential). The working nickel electrode was electrically connected parallel with the dummy but not introduced into the cell yet. The working electrode was then abraded with dry 600 grit polishing paper to expose a fresh nickel surface. The grit was blown from the electrode surface with nitrogen, and it was inserted into solution under potentiostatic control at -1.050V vs. SCE . The dummy electrode was then disconnected and removed from solution. Since the working electrode was never polarized cathodically, no time effects occurred. Also, it is assumed that inserting a relatively oxide- and hydroxide-free nickel surface into solution under potentiostatic control preserved the nickel surface. The working electrode was then swept at 1.0 mV/s to -0.50V vs. SCE and back. Since no time effects have occurred, no recovery peak should appear. In fact, only one peak at approximately -0.70V vs. SCE was observed, and its position is in good agreement with potentials reported for nickel hydroxide formation peaks (16). This indicates that the anodic peak in the region between -0.80V vs. SCE and -0.50V vs. SCE (centered around -0.70V vs. SCE) in Fig. 3 corresponds to the formation of nickel hydroxide. No appreciable activity was observed in the potential region from reversible hydrogen potential to -0.80V vs. SCE responsible for recovery. This indicates that nickel hydroxide formation is not responsible for recovery, and, hence, that reduction of nickel hydroxide is probably not the mechanism responsible for time effects.

The hypothesis of impurity deposition was examined in the following way. If impurity deposition from solution is responsible for time effects, then the anodic activity negative to -0.80V vs. SCE (the "recovery peak") responsible for recovery should correspond to oxidation or dissolution of the deposited impurity. An examination of the coulombs contained in the recovery peaks yields an average value of $4 \times 10^{-2}\text{ C/cm}^2$. If it is assumed that the impurity is a metallic ion (such as Fe), a calculation of the amount dissolved during recovery and hence this amount deposited during decay can be made. If the atomic weight, valence, and density of Fe are used in this calculation, the result yields an estimated 300 \AA thick layer of deposit which would be present after 3h of evolution at 100 mA/cm^2 . This is more than enough to be easily detectable by scanning electron microscopy and energy dispersive x-ray microanalysis (EDS). The conventional detector utilized is capable of detecting all elements heavier than fluorine in the part per ten thousand range, and, as mentioned previously, the only element detected on any cathode surface (other than Ni) was Fe, which has been shown

to improve, not degrade, catalytic performance (17). In addition, these recovery identification experiments were performed using KOH solutions containing less than 0.03 ppm Fe, virtually eliminating its deposition. Although it is possible that non-EDS detectable monolayer impurities were present on the electrode surface, it should be realized that care was taken to construct the cell and components of inert materials and that the electrolytes were purified by pre-electrolysis.

The fourth proposed mechanism, hydrogen absorption, is supported by this research because the potential region where the anodic recovery reaction is observed is consistent with hydrogen oxidation potentials. The increase in both the Tafel slope and exchange current density is peculiar, as one would expect an increase in b but a decrease in i_0 to accompany a degradation of catalytic properties. If the mechanism is indeed hydrogen absorption, then perhaps this process itself influences the E vs. $\log i$ behavior of the cathode. It may even take the form of a competing electrochemical reaction, as proposed by Conway *et al.* (18), and it has been demonstrated (19) that even a small (current-wise) competing reaction can have a major influence on experimentally observed Tafel parameters.

Conclusions

Cathodic voltage-time effects on nickel in KOH are manifested as increases in cathodic overpotential at constant current or decreases in cell current at constant cathode half-cell potential. For galvanostatic tests at low current densities, η_c increases linearly with \log time. However, at higher current densities, there is a relatively rapid increase in η_c following an incubation period. This rapid increase was found to drastically increase the values of b and i_0 for the hydrogen evolution reaction. Four mechanisms to explain cathodic time effects have been previously proposed. They are (i) loss of catalyst, (ii) impurity deposition, (iii) reduction of $\text{Ni}(\text{OH})_2$, and (iv) absorption of atomic hydrogen by the cathode. Time effects are completely recoverable, and an investigation of the recovery mechanism has yielded evidence to contradict mechanisms (i), (ii), and (iii) and support the hydrogen absorption mechanism. A thorough investigation of hydrogen absorption and its relation to time effects will appear in a later paper.

Acknowledgments

This work was supported jointly by a grant from Teledyne, Incorporated, through the Teledyne Research Assistantship Program, and a Research Initiation Grant from the National Science Foundation (DMR-8006688).

Manuscript submitted Aug. 15, 1983; revised manuscript received July 31, 1984. This was Paper 453 pre-

sented at the Montreal, Quebec, Canada, Meeting of the Society, May 9-14, 1982.

The Johns Hopkins University assisted in meeting the publication costs of this article.

REFERENCES

1. D. P. Gregory, in "Symposium Papers: Hydrogen for Energy Distribution," p. 139, Institute for Gas Technology, Chicago (1978).
2. J. O'M. Bockris, "Electrochemistry of Cleaner Environments," pp. 226-279, Plenum Press, New York (1972).
3. J. H. Kelley and R. Manvi, in "Symposium Papers: Hydrogen for Energy Distribution," p. 9, Institute for Gas Technology, Chicago (1978).
4. J. N. Murray, Paper presented at the Chemical/Hydrogen Energy Storage Systems Program Semi-annual Contracts Review, Brookhaven National Laboratory, Upton, NY (1980).
5. P. J. Moran, Ph.D. Thesis, University of Virginia, Charlottesville, VA (1980).
6. D. H. Smith, in "Industrial Electrochemical Processes," A. T. Kuhn, Editor, p. 130, Elsevier, New York (1971).
7. J. N. Murray, J. B. Laskin, and W. C. Kincaide, in "Industrial Water Electrolysis," S. Srinivasan, F. J. Salzano, and A. R. Landgrebe, Editors, p. 39, The Electrochemical Society Softbound Proceedings Series, Princeton, NJ (1978).
8. R. J. Guanti and P. J. Moran, Paper 443 presented at the Electrochemical Society Meeting, Montreal, Que., Canada, May 9-14, 1982.
9. P. J. Moran, in "Proceedings of the ERDA Contractors' Review Meeting on Chemical Energy Storage and Hydrogen Energy Systems," p. 39, National Technical Information Service, Springfield, VA (1976).
10. H. E. G. Rommal, M.S.E. Thesis, The Johns Hopkins University, Baltimore, MD (1982).
11. J. O'M. Bockris and E. C. Potter, *This Journal*, **99**, 169 (1952).
12. K. Christiansen and T. Grundt, in "Industrial Water Electrolysis," S. Srinivasan, F. J. Salzano, and A. R. Landgrebe, Editors, p. 29, The Electrochemical Society Softbound Proceedings Series, Princeton, NJ (1978).
13. A. Nidola, P. M. Spaziante, and L. Giuffre, in "Industrial Water Electrolysis," S. Srinivasan, F. J. Salzano, and A. R. Landgrebe, Editors, p. 102, The Electrochemical Society Softbound Proceedings Series, Princeton, NJ (1978).
14. D. E. Hall, Private communication.
15. R. L. LeRoy, M. B. I. Janjua, R. Renaud, and U. Leuenberger, in "Industrial Water Electrolysis," S. Srinivasan, F. J. Salzano, and A. R. Landgrebe, Editors, p. 63, The Electrochemical Society Softbound Proceedings Series, Princeton, NJ (1978).
16. R. S. Schreiber Guzman, J. R. Vilche, and A. J. Arvia, *This Journal*, **125**, 1578 (1978).
17. M. A. Riley and P. J. Moran, Paper 447 presented at The Electrochemical Society Meeting, Montreal, Que., Canada, May 9-14, 1982.
18. B. E. Conway, H. Angerstein-Kozłowska, M. A. Sattar, and B. V. Tilak, *This Journal*, **130**, 1825 (1983).
19. M. Stern, *ibid.*, **104**, 645 (1957).

ESCA and Photoelectrochemical Studies of p-n Junction Silicon Electrodes Protected by Platinum Deposition for Use in Solar Energy Conversion

Yoshihiro Nakato, Masahiro Hiramato, Yasushi Iwakabe, and Hiroshi Tsubomura

Laboratory for Chemical Conversion of Solar Energy and Department of Chemistry, Osaka University, Toyonaka, Osaka 560, Japan

ABSTRACT

Layers of mixed platinum and silicon were formed on p⁺-n junction silicon single crystal wafers (hereafter abbreviated as p⁺-n-Si) by depositing Pt on the p⁺-Si surface, followed by heating at 320°-350°C. ESCA studies showed that Pt silicide (PtSi, or in some cases a mixture of PtSi and Pt₂Si) was formed when a 3-5 nm-thick Pt layer on Si was heated, whereas a nonstoichiometric, Si-rich Pt-Si intermixed layer was formed when an ultrathin Pt layer (1.0 nm thick) on Si was heated. It was also confirmed that, in the former case, a majority of the deposited Pt remained in the form of pure metal when Pt-deposited silicon was exposed to air for ca. one day before heating. The p⁺-n-Si photoanode covered with Pt silicide gave photocurrent-voltage characteristics nearly the same as the previously reported Pt-coated p⁺-n-Si photoanode in a hydrogen iodide/iodine solution, indicating that Pt silicide formation does not affect the photovoltage at the p⁺-n junction. The photocurrent of ca. 14 mAcm⁻² at the maximum power point was maintained for 400h under continued illumination and only slightly reduced after 4500h (~6.3 months). The p⁺-n-Si electrode covered with the Pt-Si intermixed layer gave a short-circuit photocurrent higher than that covered with Pt silicide by virtue of the higher light transmittance in the layer, but was somewhat inferior in photocurrent stability. ESCA studies of the electrodes after long-term stability tests revealed that some platinum was lost in the outermost layer, suggesting that the decay of the fill factor is mainly due to the chemical change at the top surface in both the case of Pt silicide and of the Pt-Si intermixed layer.

Many studies have been made on semiconductor photoelectrochemical (PEC) cells in view of the direct conversion of solar energy into storable chemical energy. It has become clear that the main difficulty in this method lies in the fact that all known semiconductor electrodes having suitable bandgaps are unstable in electrolyte solutions. Various attempts have been made to stabilize such semiconductor electrodes. A method applicable to chemical conversion is coating the electrodes with thin layers of protective materials such as noble metals (1), metal oxides (2, 3), metal silicides (4), organic materials (5-7), and boron phosphide (8). Some coating materials also act as catalysts for photoelectrode reactions (9-12).

We reported previously (13) that a p⁺-n-Si photoanode coated with 2-3 nm-thick Pd or Pt metal photoelectrolyzes hydrogen iodide into hydrogen and iodine without external bias, with a high solar-to-chemical conversion efficiency of ca. 8%. The photocurrent was stable for 500h in the case of Pt coating. Nearly the same results were obtained with n⁺-p-Si photocathodes (14). In the course of the work, we found that Pd atoms penetrate into Si during Pd deposition, resulting in a Pd-Si intermixed layer (13b, 14). The layer was electrochemically much more stable than the deposited Pd metal. Although these Pd layers were much less stable than the deposited Pt layers, this result suggested that Pt silicide might be much more stable than the deposited Pt metal layer.

It has been well known that metals deposited on Si react with it at relatively low temperatures such as from 100° to 700°C, forming metal silicides (15). Such silicides have good conductivity and adhesivity to the Si substrate and are promising as a protective layer for the Si electrodes. Noble or near-noble metal silicides have been well studied. According to recent literature, Pt₂Si grows first at temperatures above 200°C until entire Pt is consumed, and then PtSi starts to grow under ultrahigh vacuum conditions (16). The growth mechanism is strongly affected by the presence of oxygen in the ambient, and PtSi often grows rather predominantly under low vacuum (10⁻⁷ to 10⁻⁶ torr) (16, 17). PtSi on Si is stable at temperatures below 700°C (18). The formation of a Pt-Si intermixed layer in nonannealed samples is also reported (19).

Little work has been done on electrochemical properties of metal silicides in relation with their composition or structure. Recently, Bard *et al.* reported that an n-Si electrode covered with Pt silicide shows photocurrent stable for 8 or 185h for oxidation of bromide or ferrous ions, re-

spectively (4). They interpreted the AES and XPS results as showing the presence of PtSi intergrown with Si (4b, 20). They also reported (4b) that Ir silicide-covered or RuO₂-modified Ir silicide-covered n-Si electrodes are more stable.

In this paper we will report on the photoelectrochemical properties of Pt silicide and Pt-Si intermixed layers, thermally grown on p⁺-n-Si photoanodes. The latter are newly found in the present work and are interesting photoelectrochemically because they are formed from an ultrathin Pt layer deposited on Si, causing little attenuation of the incident light. ESCA studies and electrochemical measurements were made for investigating the surface mechanisms of the electrode degradation.

Experimental

Single crystal wafers of p⁺-n-Si, prepared by an ion implantation method, were obtained from Mitsubishi Electric Corporation. The concentration of doped boron was ca. 2 × 10²⁰ cm⁻³ and the p-n junction depth was 0.6-0.9 μm. Other details were described elsewhere (13b).

Pt was deposited on the p⁺-Si [100] side of the wafer at an average rate of 0.5 nm/min under 1-2 × 10⁻⁶ torr by electron beam evaporation. The p⁺-n-Si wafer was etched in a 46% HF solution for 2 min, quickly washed, dried, and put in the vacuum within 10 min after the etching. The average thickness of the deposited Pt was monitored with a quartz crystal oscillator. The temperature of the sample was monitored with a Chromel-Alumel thermocouple in contact with the sample holder. It did not exceed 90°C during the Pt evaporation.

Heating of the Pt deposited p⁺-n-Si wafer was performed by using a radiation heater in the electron beam evaporation chamber under 1-3 × 10⁻⁶ torr. In most cases, the Si wafer was heated immediately after the Pt evaporation without exposing it to air. In other cases, it was exposed to air for a while and then heated under vacuum. The temperature of wafer rose to 300-400°C within 6 min. The heated sample was removed from the evaporation chamber after it cooled to 50°C.

ESCA spectra were obtained with a Shimadzu ESCA 750 spectrometer (13b). The binding energies were corrected by using the C1s peak of contaminant carbon as a standard. The relative atomic concentrations were calculated from the integrated peak intensities corrected for the relative ionization cross sections. The depth profile was obtained from ESCA measurements combined with

the Ar⁺ ion sputtering technique. The sputter rates for Si and Pt in our apparatus were estimated to be ca. 0.04 and 0.09 nm/s, respectively, from reported sputtering yields (21) by the 2.0 keV Ar⁺-ion beam. The depth profiles in the present work are not corrected for the differences in the sputter rates.

The electrodes were prepared by making an ohmic contact on n-Si with indium-gallium alloy. A tungsten-halogen lamp or a Wacom Solar Simulator (AM1) was used as the light source (14). The cells were cooled by circulating water around them in cases where long-term stability tests were made. Further experimental details were described elsewhere (13b, 14).

Results

ESCA studies of p⁺n-Si coated with Pt and heated at 320°-350°C.—We reported previously (13b) that most of the Pt deposited on Si was in the form of pure metal after heating at 400°C for 10 min, contrary to the previous reports demanding platinum silicide formation (15). Therefore, we have investigated the detailed experimental conditions for the silicide formation.

Figure 1 shows Si2p and Pt4f ESCA spectra for a p⁺n-Si wafer which was coated with 5.0 nm-thick Pt and heated in vacuum at 350°C for 5 min. The spin-orbit splitting for the Si2p peak was too small to be resolved, contrary to that for the Pt4f. The Si2p peak observed with a short Ar⁺-ion etching time was somewhat broad (curves 1 and 2). It shifted toward lower binding energies with increase in etching time, finally approaching that of pure Si. The two Pt4f peaks also shifted in parallel to each other with increasing etching time.

Figure 2(A) shows relative atomic concentrations for the same electrode as in Fig. 1, as a function of the Ar⁺-ion etching time. The contribution of the contaminating carbon is not included in the figure. The oxygen concentration was kept at ca. 12%, even with long etching time, indicating that it is also due to the sample contamination. One can see from Fig. 2(A) that Si and Pt are present with an atomic ratio of nearly 1:1 in a region of the etching time from 0 to 100s, showing the formation of Pt silicide with a stoichiometry of PtSi. In this region, the Pt4f_{7/2} peak lies at 72.0 eV, ca. 0.7 eV higher than that for the Pt metal, and the Si2p peak lies between 100.2 and 100.3 eV, ca. 0.8 eV higher than that for elemental Si, as seen in Fig. 2(B).

The oxygen concentration is relatively high from 0 to 40s [Fig. 2(A)]. The Si2p peak shifted toward higher energies in this region [Fig. 2(B)]. The Pt4f_{7/2} peak also shifted toward higher energies at the surface [Fig. 2(B)]. It is also noted that the Si2p peak for a short etching time shows a broad swelling at the higher energy side, as seen in curve 1 of Fig. 1. All these results suggest that PtSi is covered with a thin oxide layer.

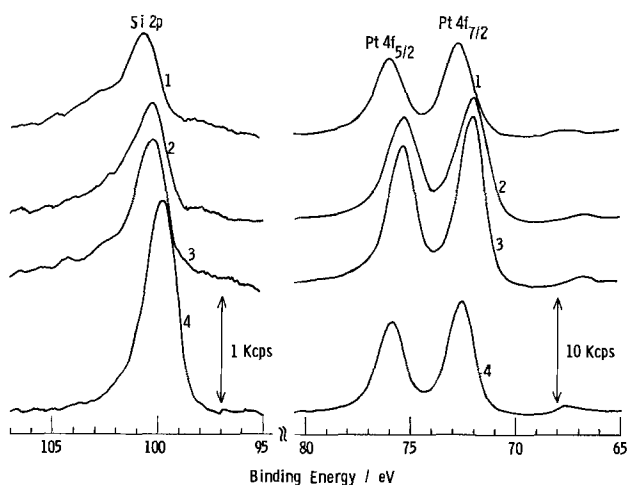


Fig. 1. ESCA spectra of p⁺n-Si coated by 5.0 nm-thick Pt and heated at 350°C for 5 min (curve 1) and of those after subsequent Ar⁺ ion etching, 20s (curve 2), 60s (curve 3), and 150s (curve 4).

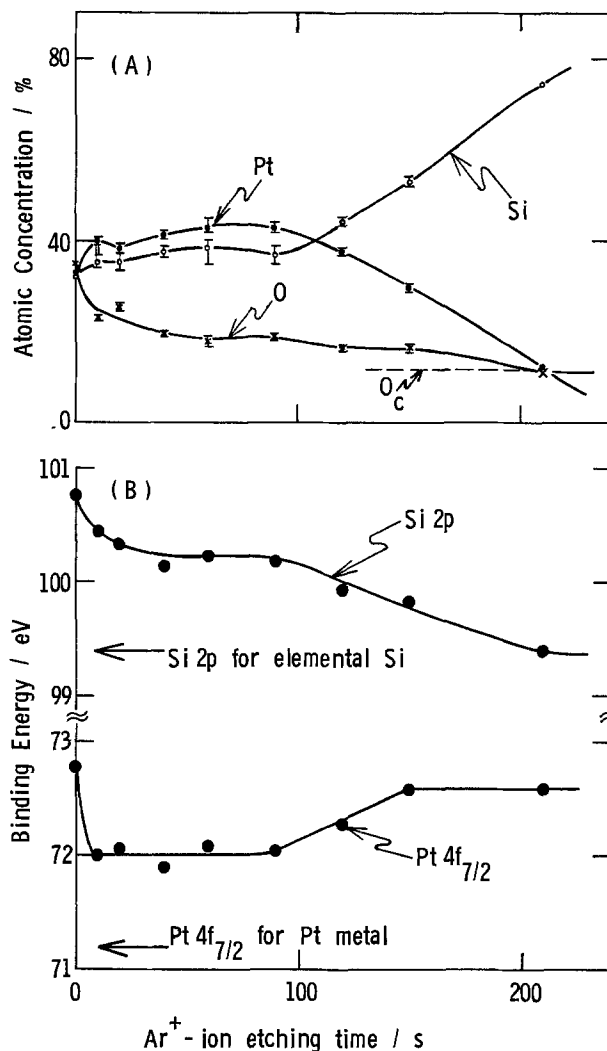


Fig. 2. Relative atomic concentrations (A) and binding energies (B) for the same p⁺n-Si as in Fig. 1, as a function of the Ar⁺ ion etching time. O_c in (A) refers to the oxygen concentration attributable to the contamination.

When Si was coated with Pt 3-5 nm thick and heated at 300°-350°C, the Pt silicide formed was in most cases PtSi. In some cases, however, the Pt to Si atomic ratio in the silicide region increased to 1.5. This indicates the formation of a mixture of PtSi and Pt₃Si (16, 17). The Pt4f_{7/2} peak for the Pt silicide layer with the Pt/Si ratio of 1.5 lay at 71.8 eV, ca. 0.2 eV lower than that for PtSi, being indicative of the Pt4f_{7/2} peak for Pt₃Si lying rather close to that for the Pt metal.

Figure 3 shows the results of ESCA studies for a p⁺n-Si wafer which was coated with 5.0 nm-thick Pt, exposed to air for one day, and then heated at 350°C for 5 min. In this case, the deposited Pt was in the form of pure metal, because the binding energy for the Pt4f_{7/2} peak for the Ar⁺-ion etching time from 0 to 50s agreed with that of the Pt metal [Fig. 3(B)]. A similar result was reported in our previous paper (13b), where Pt was evaporated at a high rate of 0.1 to 1.0 nm/s by using an electrically heated tungsten boat under 2 × 10⁻⁵ torr.

It is to be noted in Fig. 3(A) that the oxygen concentration increases at the interface between Si and Pt. The Si2p peak also exhibited a broad swelling at the higher energy side at this interface. These results indicate that a thin silicon oxide (SiO_x) layer is formed at the interface while Pt-deposited p⁺n-Si is exposed to air, and the oxide layer acts as a diffusion barrier to prevent the silicide formation. This explanation is supported by the fact that the less silicide formed, the longer the air-exposure time. ESCA studies also showed that both the oxygen concentration at the Si-Pt interface and the swelling at the higher energy side of the Si2p peak increased with longer

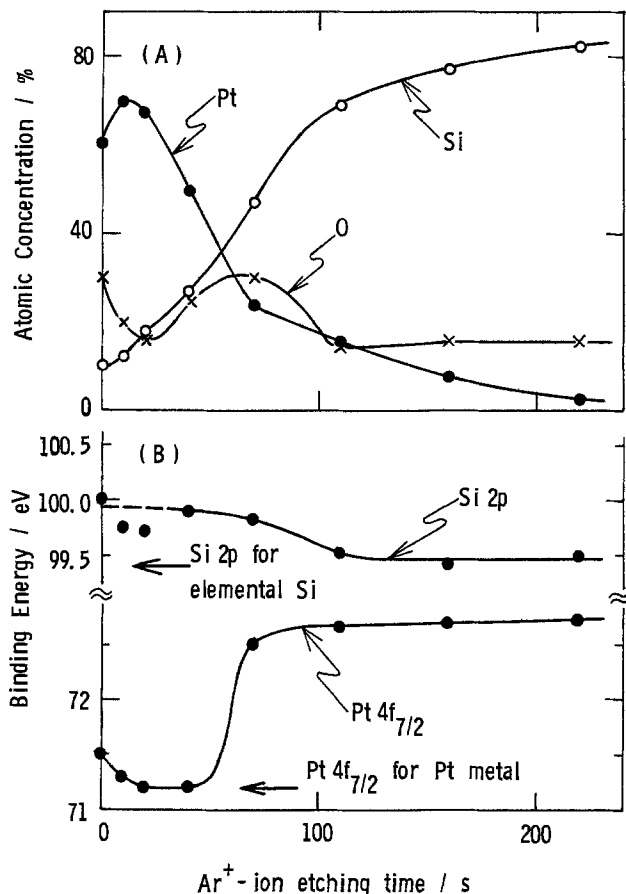


Fig. 3. Relative atomic concentrations (A) and binding energies (B) for p⁺n-Si which was coated with 5.0 nm-thick Pt, exposed to air for one day, and heated at 350°C for 5 min, as a function of the Ar⁺ ion etching time.

air-exposure. The interfacial SiO_x layer grew faster when Pt was deposited at a high evaporation rate. Goodnick *et al.* reported (17) that no PtSi was formed, even by heating at 400°C for 1h in a case where Pt was deposited on Si having a thermally grown, 3.0 nm-thick SiO₂ surface layer.

Figure 4(A) shows the depth profile for a p⁺n-Si wafer which was coated with an ultrathin Pt layer (ca. 1.0 nm thick) and heated immediately at 320°C for 5 min. The deposited Pt diffused into Si, but the Pt/Si atomic ratio was much less than unity, changing with the Ar⁺-ion etching time, in contradiction to the case of Fig. 2. This suggests that a nonstoichiometric, Si-rich Pt-Si intermixed layer was formed at the surface. The binding energy for the Pt4f_{7/2} peak was nearly constant, irrespective of the Pt/Si ratio, lying at 72.7 eV [Fig. 4(B)], ca. 0.7 eV higher than that for PtSi [Fig. 2(B)]. The Si2p peak, on the other hand, shifted little from that for elemental Si.

ESCA studies of a p⁺n-Si wafer coated with 1.0 nm-thick Pt, but not heated, showed a monotonic decrease of the Pt concentration from the surface into the interior, contrary to Fig. 4(A). The Pt4f_{7/2} peak in this case lay at 72.0 eV just at the surface (*i.e.*, in case of no Ar⁺-ion etching) and at ca. 72.7 eV in a region of the etching time longer than 10s, similar to that in Fig. 4(B). This suggests that all Pt intermixes with Si during the Pt deposition when the Pt layer is ultrathin.

Photoelectrochemical behavior of p⁺n-Si photoanodes covered with Pt silicide or Si-rich Pt-Si intermixed layers in hydrogen iodide/iodine solutions.—Figure 5 shows current density(*j*)-potential(*U*) curves for various p⁺n-Si photoanodes. Curve a is one of the best results for p⁺n-Si electrodes coated with 5.0 nm-thick Pt and heated at 350°C for 5 min. The depth profile of this electrode was similar to that of Fig. 2(A), except that the Pt/Si atomic ratio was about 1.5 in the silicide region. The electrode gave a reasonable open-circuit photovoltage (*V*_{oc} ~ 0.55V) but a small fill factor.

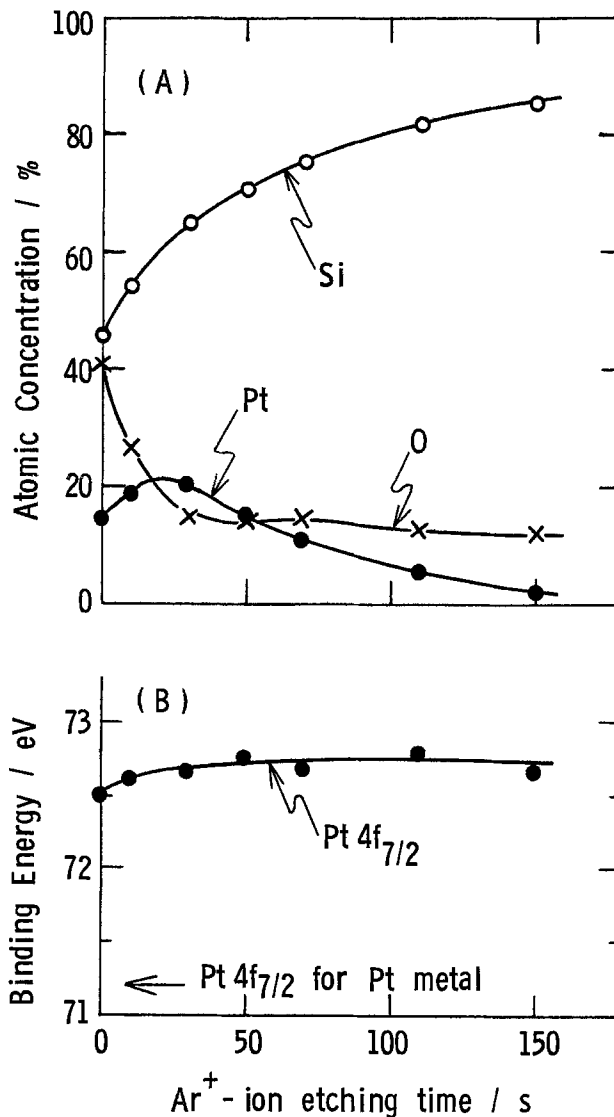


Fig. 4. Relative atomic concentrations (A) and binding energies (B) for p⁺n-Si coated with 1.0 nm-thick Pt and heated at 320°C for 5 min, as a function of the Ar⁺ ion etching time.

The fill factor was improved by etching the electrode in a 10% HF solution for 10s, as shown by curve b. The dark cathodic current also increased by the etching. No detectable changes, however, were observed in the depth profile and the binding energy for the Pt4f_{7/2} peak. It is to be noted here that the *j*-*U* curve for the etched electrode (curve b) nearly agreed with that for a p⁺n-Si electrode coated with 5 nm-thick Pt but not heated (curve c). The fill factor was generally small for electrodes prepared by heating at high temperatures (400°-500°C) for a long time (20-40 min) and was not sufficiently improved by HF etching in such cases.

Curve d in Fig. 5 shows the *j*-*U* curve for a p⁺n-Si electrode coated with 1.0 nm-thick Pt and heated at 320°C for 5 min, thus having a Si-rich Pt-Si intermixed layer as shown in Fig. 4. The electrode was etched in a 10% HF solution for 10s before measurements. The short-circuit current (*j*_{sc}) was higher than the cases of curves b and c, due to the thinner Pt layer, and the *V*_{oc} and the fill factor were nearly the same.

Figure 6 shows the results of photocurrent stability tests. The photocurrent was measured under continuous illumination in a PEC cell containing a 7.6M HI/0.2M I₂ stirred solution, with the Si electrode connected through an external 150Ω resistor to a Pt counterelectrode. The 150Ω resistor was employed to obtain the photocurrent at the maximum power point. Curve a stands for the Pt silicide-covered p⁺n-Si electrode, which gave curve b in Fig. 5. The photocurrent was quite stable for 400h, and

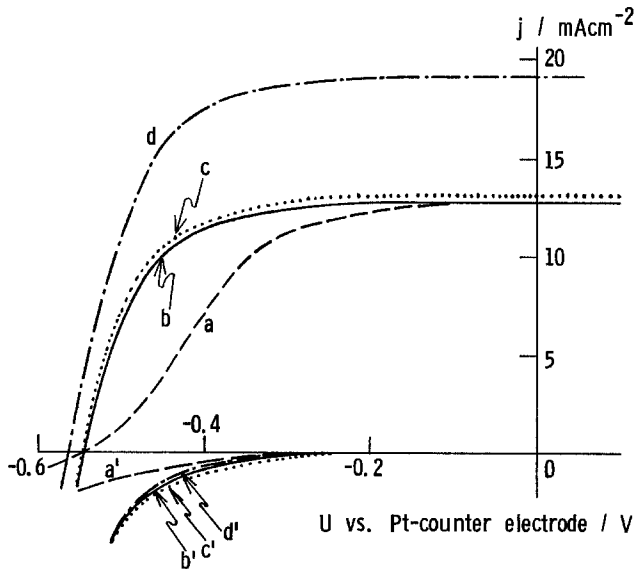


Fig. 5. Photocurrent density (j)-potential (U) curves: (curve a) for a p^+n -Si electrode covered with an as-formed Pt silicide layer; (curve b) for the same electrode as curve a, except that it was etched in a 10% HF solution for 10s; (curve c) for a p^+n -Si electrode coated with Pt, but not heated; and (curve d) for that covered with a Si-rich Pt-Si intermixed layer, after being etched in a 10% HF solution for 10s. Curves a', b', c', and d' are for the dark currents. The light source is a Wacom Solar Simulator (AM1 100 mWcm⁻²). The electrolyte is a 7.6M HI/0.05M I₂ stirred solution.

the j - U curve observed after the stability test agreed with the initial curve. ESCA measurements performed after this test, however, showed a decrease of the outermost Pt, as shown in Fig. 7.

Curve b in Fig. 6 is for another electrode which was prepared simultaneously under the same condition as that of the electrode which gave curve a. The photocurrent was maintained rather well during a very prolonged period of 4500h. No change was observed for the V_{oc} and j_{sc} .

Figure 8 shows the results of stability tests for electrodes covered with a Si-rich Pt-Si intermixed layer corresponding to Fig. 4. Experiments were made in the same way as in Fig. 6, except that a 100Ω external resistor was used instead of a 150Ω one by taking account of the higher j_{sc} in this case. Curve a is for the electrode which gave the j - U curve d in Fig. 5. No change in V_{oc} and j_{sc} was observed again in this case. ESCA studies of the degraded electrodes showed a decrease of Pt only at the surface, with little growth of silicon oxide at the surface, in the same way as indicated in Fig. 7. Curve b is for another electrode which was prepared under the same conditions as the electrode giving curve a. The fill factor of this electrode was somewhat small at the beginning, compared with that for the electrode of curve a, but the photocur-

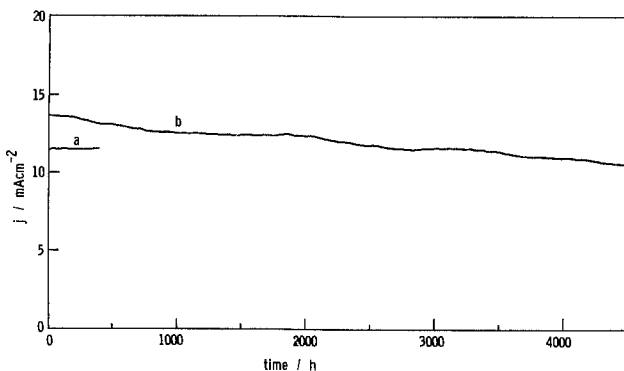


Fig. 6. Photocurrent density (j) vs. time for two Pt silicide covered p^+n -Si electrodes, prepared simultaneously under the same conditions. They were etched in a 10% HF solution for 10s before experiments. The light source is a tungsten-halogen lamp.

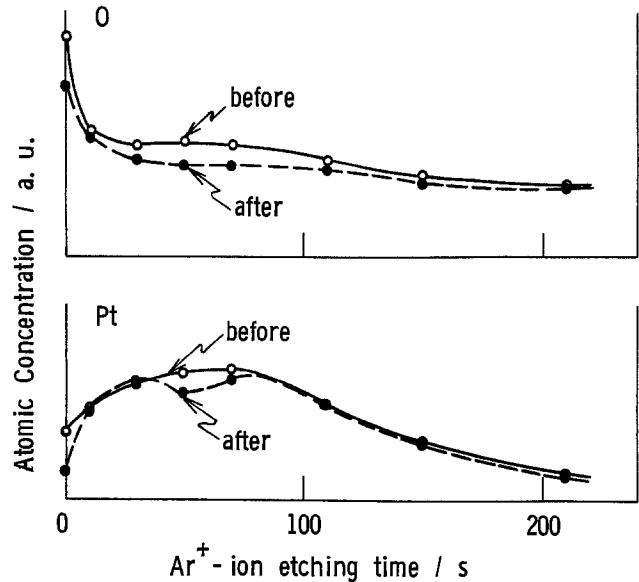


Fig. 7. Atomic concentrations of O and Pt for the Pt silicide-covered p^+n -Si electrode as a function of the Ar⁺ ion etching time, observed before (—○—) and after (—●—) the 400h photocurrent stability test shown in curve a of Fig. 6.

rent decayed rather gradually. The p^+n -Si electrode, coated with 1.0 nm-thick Pt and not heated, showed the j - U curve nearly the same as the heated one (curve d of Fig. 5), but the fill factor decreased faster during the stability tests.

Discussion

We have concluded that PtSi or a mixture of PtSi and Pt₂Si was grown in the case where a relatively thick (3-5 nm) Pt layer was deposited on p^+n -Si and heated, whereas a nonstoichiometric, Si-rich Pt-Si intermixed layer was grown in the case where an ultrathin (1.0 nm) Pt layer was deposited on p^+n -Si and heated. McGuire *et al.* (22) reported that the Pt4f_{7/2} peak for PtSi lies 0.4 eV higher than that for Pt metal, in relatively good agreement with the present result.

Some investigations have been made on the formation of thin nonstoichiometric intermixed layers at the metal/silicon or silicide/silicon interfaces (15, 19, 23), for the purpose of understanding the mechanism of silicide formation or its effect on the Schottky barrier height. Abbati *et al.* reported (19) that a Pt-Si intermixed layer with a concentration gradient was formed when 2-10 monolayers of Pt were deposited on clean Si at room temperature. A similar result was obtained in the present work. The result in Fig. 4 is the first to show that a nonstoichiometric Pt-Si intermixed layer exists even after heating the sample at 320°C. It seems reasonable that

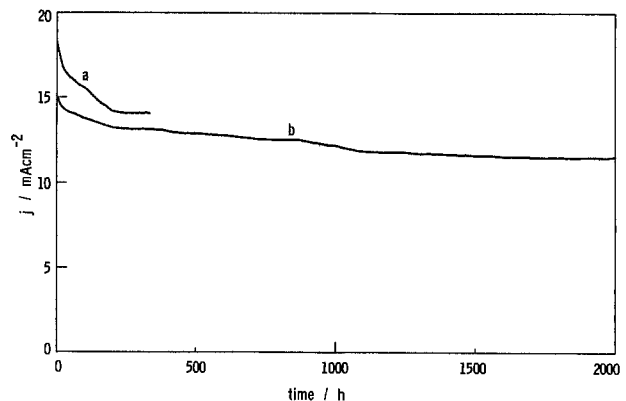


Fig. 8. Photocurrent density (j) vs. time for two p^+n -Si electrodes covered with the Si-rich Pt-Si intermixed layer, prepared under the same conditions. They were etched in a 10% HF solution for 10s before experiments.

such a layer is formed, even in heated samples when the amount of the Pt deposited is too small to form the silicide.

Figures 2 and 3 suggest that the Pt-Si intermixed layer similar to the case of Fig. 4 is also present at both the PtSi/Si and Pt/Si interfaces, as seen from the chemical shift of the Pt $4f_{7/2}$ peak to 72.7 eV. The presence of similar interfacial layers with graded concentrations was reported at Ni/Ni $_2$ Si and Ni $_2$ Si/Si interfaces (23). It is also noted that the Pt $4f_{7/2}$ peak at 72.7 eV in the present work is very similar to that reported by Bard *et al.* (20), though they interpreted it as due to PtSi.

It was reported by several workers (15a, 17, 20) that PtSi is covered with a thin oxide layer when it is formed under $\sim 10^{-6}$ torr, as observed in the present work (Fig. 2). The improvement of the fill factor of the Pt silicide-covered electrode by HF etching (curves a and b in Fig. 5) indicates that this oxide layer is responsible for the small fill factor. Since the ESCA analysis showed no detectable change in the surface chemical composition by the etching, it seems likely that the reaction kinetics are improved by the HF etching, which removes very thin oxide layers covering the Pt atoms at the top surface in contact with the electrolyte solution.

As mentioned in the preceding section, the ESCA studies of the p-n-Si electrodes covered with Pt silicide after long-term stability tests showed a loss of the outermost Pt (Fig. 7), even for the case where the photocurrent had been unchanged. A similar loss of the outermost Pt atoms was observed for electrodes covered with the Si-rich Pt-Si intermixed layer. It is reasonable that by such a change, the electrochemical active sites are decreased, thus increasing the overpotential for electrochemical reactions and decreasing the fill factor. The inferiority of the photocurrent stability for the electrode covered with the Si-rich Pt-Si intermixed layer, as compared with the electrode covered with Pt silicide, can be explained by assuming that the above effect of the decrease of the surface Pt atoms becomes more prominent as the Pt/Si atomic ratio at the surface becomes smaller.

As can be seen from Fig. 6, the p-n-Si electrode covered with Pt silicide has shown a good stability under illumination over a period of 4500h. However, further investigations should be necessary to decide whether the coating of this type is superior to the previously reported, Pt-coated electrodes.

Acknowledgment

The authors wish to express their thanks to Mitsubishi Electric Corporation for kindly offering p-n junction Si single crystal wafers.

Manuscript submitted June 4, 1984; revised manuscript received Oct. 2, 1984.

Osaka University assisted in meeting the publication costs of this article.

REFERENCES

- (a) Y. Nakato, T. Ohnishi, and H. Tsubomura, *Chem. Lett.*, 883 (1975); (b) S. Menezes, A. Heller, and B. Miller, *This Journal*, 127, 1268 (1980); (c) K. W. Frese, Jr., M. J. Madou, and S. R. Morrison, *ibid.*, 128, 1939 (1981).
- (a) P. A. Kohl, S. N. Frank, and A. J. Bard, *This Journal*, 124, 225 (1977); (b) M. Tomkiewicz and J. M. Woodall, *ibid.*, 124, 1436 (1977); (c) H. Morisaki, M. Ono, H. Dohkoshi, and K. Yazawa, *Jpn. J. Appl. Phys.*, 19, L148 (1980); (d) G. Nogami, H. Yamaguchi, G. Maeda, K. Beppu, Y. Ueda, and T. Nakamura, *J. Appl. Phys.*, 54, 1605 (1983).
- (a) F. Decker, J. Melsheimer, and H. Gerischer, *Israel J. Chem.*, 22, 195 (1982); (b) L. Thompson, J. DuBow, and K. Rajeshwar, *This Journal*, 129, 1934 (1982); (c) G. Hodes, L. Thompson, J. DuBow, and K. Rajeshwar, *J. Am. Chem. Soc.*, 105, 324 (1983).
- (a) F. -R. F. Fan, G. A. Hope, and A. J. Bard, *This Journal*, 129, 1647 (1982); (b) F. -R. F. Fan, R. G. Keil, and A. J. Bard, *J. Am. Chem. Soc.*, 105, 220 (1983).
- (a) J. M. Bolts, A. B. Bocarsly, M. C. Palazzotto, E. G. Walton, N. S. Lewis, and M. S. Wrighton, *J. Am. Chem. Soc.*, 101, 1378 (1979); (b) A. B. Bocarsly, E. G. Walton, and M. S. Wrighton, *ibid.*, 102, 3390 (1980).
- (a) Y. Nakato, M. Shioji, and H. Tsubomura, *J. Phys. Chem.*, 85, 1670 (1981); (b) P. Leempoel, M. Castro-Acuna, F. -R. F. Fan, and A. J. Bard, *ibid.*, 86, 1396 (1982).
- (a) R. Noufi, A. J. Frank, and A. J. Nozik, *J. Am. Chem. Soc.*, 103, 1849 (1981); (b) T. Skotheim, I. Lundström, and J. Prejza, *This Journal*, 128, 1625 (1981); (c) F. -R. F. Fan, B. L. Wheeler, and A. J. Bard, *ibid.*, 128, 2042 (1981); (d) A. J. Frank and K. Honda, *J. Phys. Chem.*, 86, 1933 (1982).
- D. S. Ginley, R. J. Baughman, and M. A. Butler, *This Journal*, 130, 1999 (1983).
- Y. Nakato, S. Tonomura, and H. Tsubomura, *Ber. Bunsenges. Phys. Chem.*, 80, 1289 (1976).
- R. N. Dominey, N. S. Lewis, J. A. Bruce, D. C. Bookbinder, and M. S. Wrighton, *J. Am. Chem. Soc.*, 104, 467 (1982).
- A. Heller, E. Aharon-Shalom, W. A. Bonner, and B. Miller, *ibid.*, 104, 6942 (1982).
- M. Szklarczyk and J. O'M. Bockris, *Appl. Phys. Lett.*, 42, 1035 (1983).
- (a) Y. Nakato, A. Tsumura, and H. Tsubomura, *Chem. Lett.*, 1071 (1982); (b) Y. Nakato, M. Yoshimura, M. Hiramoto, A. Tsumura, T. Murahashi, and H. Tsubomura, *Bull. Chem. Soc. Jpn.*, 57, 355 (1984).
- Y. Nakato, Y. Egi, M. Hiramoto, and H. Tsubomura, *J. Phys. Chem.*, 88, 4218 (1984).
- (a) K. N. Tu and J. W. Mayer, in "Thin Films-Interdiffusion and Reactions," J. M. Poate, K. N. Tu, and J. W. Mayer, Editors, Chap. 10, Wiley, New York (1978); (b) G. W. Rubloff, *Surf. Sci.*, 132, 268 (1983); (c) A. Hiraki, *Jpn. J. Appl. Phys.*, 22, 549 (1983).
- C. A. Crider, J. M. Poate, J. E. Rowe, and T. T. Sheng, *J. Appl. Phys.*, 52, 2860 (1981).
- S. M. Goodnick, M. Fathipour, D. L. Ellsworth, and C. W. Wilmsen, *J. Vac. Sci. Technol.*, 18, 949 (1981).
- S. P. Murarka, E. Kinsbron, D. B. Fraser, J. M. Andrews, and E. J. Lloyd, *J. Appl. Phys.*, 54, 6943 (1983).
- G. Rossi, I. Abbati, L. Braicovich, I. Lindau, and W. E. Spicer, *Phys. Rev. B*, 25, 3627 (1982).
- G. A. Hope, F. -R. F. Fan, and A. J. Bard, *This Journal*, 130, 1488 (1983).
- A. L. Southern, W. R. Willis, and M. T. Robinson, *J. Appl. Phys.*, 34, 153 (1963).
- S. Danyluk and G. E. McGuire, *ibid.*, 45, 5141 (1974).
- N. W. Cheung, P. J. Grunthaner, F. J. Grunthaner, J. W. Mayer, and B. M. Ullrich, *J. Vac. Sci. Technol.*, 18, 917 (1981).

The Chemistry of Li/SOCl₂ Cells

An ESR Study of Carbon Electrodes

S. S. Kim, Boyd J. Carter, and F. D. Tsay

Jet Propulsion Laboratory, Applied Mechanics Division, California Institute of Technology, Pasadena, California 91109

ABSTRACT

Carbon electrodes from Li/SOCl₂ cells were studied by electron spin resonance after various stages of discharge. Different behavior was observed in the temperature-dependent part of the ESR linewidth, defined as "intrinsic linewidth," ΔH_{int} , when two different electrolytes were used. With one electrolyte, 1.5M LiAlCl₄/SOCl₂, the ΔH_{int} value stayed constant or slightly decreased whereas with another electrolyte, 1.0M LiAlCl₄/14% BrCl in SOCl₂, the value increased as discharge progressed. The carbon electrodes are modified differently during discharge with these two electrolytes, and it is speculated that this may be due to changes in the carbon matrix functional groups. This difference in the carbon electrodes may explain the claimed differences in safety performance of the cells.

The lithium (Li)-thionyl chloride (SOCl₂) cell system has been of great interest for many applications because of its high specific energy and high discharge rates. However, there have been safety problems with these cells, since the cells have been found on occasion to vent (expel internal liquids and gases) or explode (1). It is of major importance to resolve these safety problems to provide safe cells. Previously, we have studied the cell chemistry during discharge to +0.5V (2). With the establishment of a mechanism for the reduction of SOCl₂ during discharge to +0.5V at 25°-30°C, we have eliminated the concern of a cell explosion due to buildup, and then rapid decomposition of a chemical intermediate formed during discharge. The research mentioned above only studied discharge to +0.5V, and did not address the hazardous conditions of voltage reversal of Li-SOCl₂ cells. Voltage reversal can occur in a battery if one cell in a series connected stacks of cells has less capacity than the other cells. During discharge, the cell with less capacity is fully discharged, but current continues to flow through the cell in the same direction, driven by the other cells in the stack. The voltage of this particular cell drops below 0 V, and new reactions occur in the cell. As an example, carbon-limited voltage reversal occurs when a cell has excess Li and electrolyte, and the cell is limited by the carbon electrode capacity. In this case, the carbon electrode is reported to be plugged with LiCl (3) and possibly S, products of the reduction of SOCl₂ which limit the ability of the electrode to reduce SOCl₂ at the rates required to support the discharge currents. When the cell voltage drops below 0 V, it is then possible for new reactions such as LiCl or LiAlCl₄ reduction to form Li metal to occur. These reduction reactions are reasonable based upon the cell voltage holding at -0.1 to -0.20V at 10 mA/cm².

Carbon-limited voltage reversal has been found to be a hazardous discharge condition for Li-SOCl₂ cells. A possible explanation for the observed ventings and explosion of carbon-limited cells during reversal is the exothermic reaction observed by Kilroy *et al.* (4) in their calorimetry research. Recently, a catalytic effect of carbon black on the reactivity of lithium with SOCl₂ electrolytes has also been reported (5). At low temperatures (<100°C), it was found that lithium-carbon samples would exhibit large exotherms when in contact with cell electrolytes. Thus it was suggested that during carbon-limited voltage reversal, when LiCl could be reduced to Li metal, the lithium-carbon/electrolyte reaction could occur raising the temperature in the cell, leading to thermal runaway.

The reaction between sulfur and Li metal was also found to be an exothermic reaction, initiating at ~130°C. This reaction could also account for the safety hazard, or react in addition to the lithium-carbon/electrolyte reaction. Liang *et al.* (6) have reported that adding BrCl to neutral LiAlCl₄/SOCl₂ electrolyte improves the safety performance of the cell. It was postulated that the BrCl can react with sulfur deposited on the carbon during reduction of SOCl₂, dissolving the sulfur. Thus, the sulfur is not

present during reversal to react with Li metal and possibly lead to thermal runaway.

In order to understand the changes occurring in the carbon electrode during discharge and their implication to cell safety, we have initiated ESR studies of the carbon electrode. Many researchers studied carbon crystals (7), polycrystalline carbon (8), ultrafine graphite particles (9), and metal-carbon intercalation compounds (10) by ESR. It was found that ESR linewidth is very sensitive to the variation of spin lattice relaxation processes of the charge carriers in the carbon samples. In this respect, it was of interest to use ESR spectroscopy as a unique tool to determine the changes in the carbon, as the discharge proceeds. By employing both 1.5M LiAlCl₄/SOCl₂ (A) and 1.0M LiAlCl₄/14% BrCl in SOCl₂ (B) as electrolytes, it should also be possible to better understand the safety hazards due to changes in the carbon electrode during reversal and, in particular, elucidate the manner in which BrCl possibly improves the safety of the cell.

Experimental

All cell components were handled under an argon atmosphere in a Vacuum Atmospheres Dry Box (<10 ppm O₂ and H₂O). Thionyl chloride (SOCl₂) was obtained from Aldrich and purified by vacuum distillation from triphenylphosphite. Lithium tetrachloroaluminate (LiAlCl₄) was obtained from Lithium Corporation of America and bromine chloride (BrCl) was obtained from Dow Chemical Company. Both were used without further purification.

1.5M LiAlCl₄/SOCl₂ electrolyte (A) was prepared by adding the necessary LiAlCl₄ to purified SOCl₂. Undissolved solids (LiCl) were separated by decanting the solution. 1.0M LiAlCl₄/14% BrCl in SOCl₂ (B) was prepared by adding a known amount of BrCl to purified SOCl₂, followed by addition of the necessary amount of LiAlCl₄. Again, separation of undissolved solids (LiCl) was effected by decanting.

Two different sets of carbon electrodes, commercial and JPL, were studied. The commercial carbon electrodes were purchased from Power Conversion, Incorporated (Mount Vernon, New York) and used without modification. The JPL carbon electrodes were prepared by applying a 10% Teflon-Shawinigan acetylene black mixture onto expanded nickel metal, rolling, drying, and finally sintering the electrode at 280°C for 1h. The Shawinigan acetylene black (average particle size ~42.5 nm) was purchased from Gulf Oil and Chemical Company (Englewood Cliffs, New Jersey).

Carbon electrodes for analysis were prepared by discharging carbons in a one-compartment cell shown in Fig. 1. Two lithium electrodes were used for each carbon electrode, and they were separated by Mead Glass Paper 935-BJH. Measured amounts of electrolyte (~1.4 ml) were added to the assembly, which was then sealed in a plastic bag to prevent electrolyte evaporation. Cells were discharged at constant current (10 mA/cm² of carbon) using

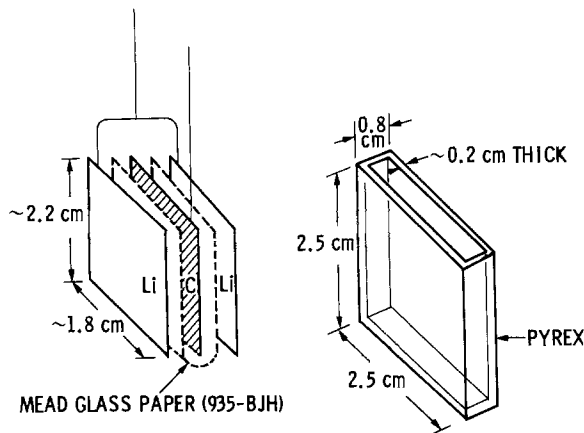


Fig. 1. One-compartment cell assembly

an Electronic Measurements Model C629 Constant Current Power Supply. A Fluke 8021 B multimeter was used to follow the current, and a Hewlett-Packard 7132 A recorder was used to follow voltage and time. Typical voltage vs. time plot during discharge is shown in Fig. 2.

All carbon electrodes sampled at different stages of discharge were dried at room temperature *in vacuo* for 2h or more in the antichamber of the dry box. Samples were collected by scraping carbon flakes off the dried electrodes. The carbon flakes showed different degrees of agglomeration. The flakes were ground slightly inside the dry box with a mortar and pestle to ensure homogeneous sampling. ESR spectra of these samples showed symmetrical lineshapes (C_2 symmetry with respect to the center of each spectrum), very close to Lorentzian (see Fig. 3). The symmetric lineshape ensured the carbon samples of particle size smaller than the microwave skin depth. The carbon samples (~20 mg) were transferred to ESR tubes (3 mm od, 2 mm id) equipped with ground joints. The tubes were sealed under argon with Apiezon N grease in the dry box.

An ESR spectrometer (Varian E-line Century Series) operating at X band (9.2 GHz) was used with 100 kHz field modulation. For most of the samples, ESR scans were made at two temperatures, at 77 and 294 K (room temperature). Some of the samples were also measured at 192 K. The intermediate temperature, 192 K, was obtained by blowing cold N_2 gas through a Dewar insert inside a microwave cavity.

Results and Discussion

The carbon samples show ESR lineshapes close to Lorentzian (see Fig. 3). All the observed spectra gave $g = 2.0032$. They are assigned as from charge carriers in carbon as reported earlier by several authors (7-9). The Lorentzian lineshape of the observed spectra shows that the major contribution to the linewidth is from the spin relaxation processes, the linewidth being inversely proportional to T_1 and T_2 , spin-lattice relaxation time and spin-spin relaxation time, respectively. In conductors (11, 12), the two processes are no longer distinguishable and can be regarded as $T_1 = T_2$. The relaxation times are affected by temperature, presence of impurities in the matrix, and also by particle size due to spin flipping at

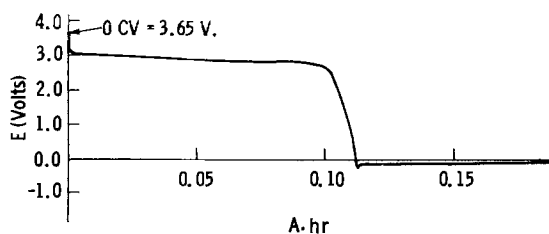


Fig. 2. A typical plot of voltage vs. Ah during discharge. In this case, current was kept at 80.7 mA (10 mA/cm²).

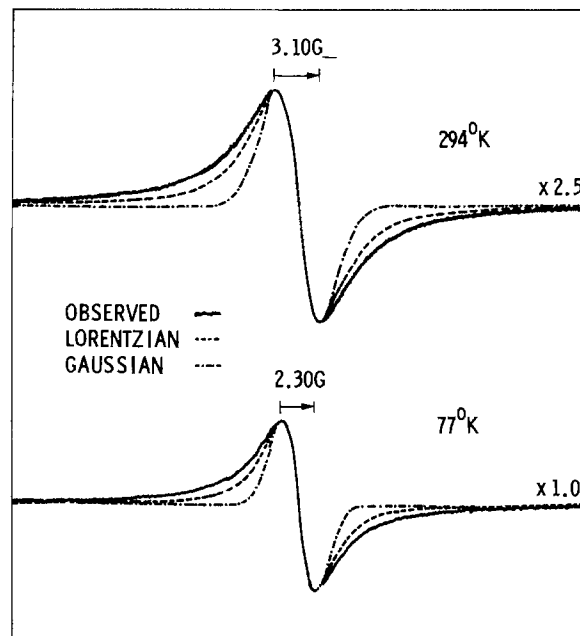


Fig. 3. ESR spectra of a carbon sample at 294 and 77 K. The carbon sample was collected from a cell containing electrolyte B discharged to 0.208 Ah. The observed spectra are compared with simulations of Lorentzian and Gaussian lineshape.

particle surfaces. The surface contribution to linewidth becomes more important with smaller particles. The observed ESR linewidth are thus a reflection of all these relaxation processes.

Each set of carbon electrodes, commercial or JPL, were prepared from one lot of carbon. Thus, one can assume a uniform distribution of particle size for each set of electrodes. However, after discharging processes, the carbon flakes from the electrodes showed different degrees of agglomeration, which effects the particle size of the sample. In order to filter out the effects of particle size on the observed linewidths and study the changes in the carbon matrices, we used the approach of Watts and Cousins (13). They proposed that the observed linewidth, ΔH_{obs} , can be broken down into three separate contributions

$$\Delta H_{\text{obs}} = \Delta H_{\text{int}} + \Delta H_s + \Delta H_c \quad [1]$$

or expressed in corresponding relaxation times

$$\frac{1}{T_2} = \frac{1}{T_{\text{int}}} + \frac{1}{T_s} + \frac{1}{T_c} \quad [1']$$

in which ΔH_{int} is the "intrinsic linewidth," (or T_{int} , the "intrinsic relaxation time") contribution from phonon modulated spin-orbit coupling mechanism. It is believed (14, 15) that this is the main interaction responsible for relaxation processes in carbon lattices intercalated with heavy atoms (*e.g.*, Br, Cl). The second term, ΔH_s (or T_s), is related to the spin flipping at the particle surface and is a function of particle size. The third term, ΔH_c (or T_c), is a temperature-independent term which may arise from crystalline defect centers or from impurities in the sample.

In Fig. 4, the observed linewidths are plotted as a function of temperature. The relationship is quite linear, within experimental error, for the temperature ranges studied. With the support of theoretical studies (16-18), one can regard the ΔH_{int} as proportional to temperature

$$\Delta H_{\text{int}} = k_1 T \quad [2]$$

The rest of terms will be regarded as constant in temperature

$$\Delta H_s + \Delta H_c = \text{const.} \quad [3]$$

It should be noted that the case discussed by Watts and Cousins (13), where ΔH_s was treated as inversely propor-

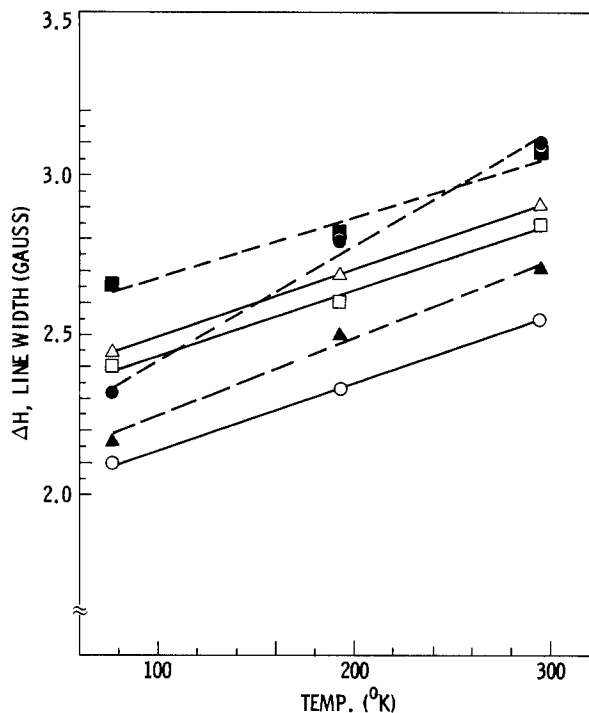


Fig. 4. Variation of ESR linewidth, ΔH , of carbon samples as a function of temperature. With A electrolyte, O = carbon-limited voltage reversal (CLVR), and Δ = normal discharge (ND). \square = Carbon wetted with electrolyte and dried (CW). With B electrolyte, \bullet = CLVR, \blacktriangle = ND, \blacksquare = CW.

tional to temperature, does not fit our observed linewidth data.

From relations [1]-[3], the ΔH_{int} values are calculated by Eq. [4]

$$\Delta H_{\text{int}} = \frac{\Delta H^{294} - \Delta H^{77}}{294 - 77} \times T, \quad 77 \leq T \leq 294 \quad [4]$$

in which ΔH^{294} and ΔH^{77} denote the observed derivative ESR linewidths (peak to valley) at 294 and 77 K.

Examples of observed ESR linewidth data and calculated ΔH_{int} values are listed in Table I. The carbon sample at 0.0 Ah was prepared by wetting the fresh electrode with corresponding electrolyte and dried under vacuum. These carbon samples showed larger ΔH_{int} value than fresh carbons. However, samples from carbon electrode wetted only by SOCl₂ showed ΔH_{int} value similar to the fresh carbons. It appears the difference is caused by the adsorption (deposition) of the solute material, LiAlCl₄, on the pores of carbon electrode. After pumping under vacuum in the process of drying, the solvent SOCl₂ evapo-

rated, but the solute material did not. The solute material with Al and Cl atoms then shortens the relaxation time through spin-orbit coupling, and broader ΔH_{int} values are observed. However, when another set of carbon samples is studied as a function of wetting time (up to 2.5h) without any electrical discharge, the samples did not show any change in ΔH_{obs} or ΔH_{int} value within experimental error.

If we now define

$$\Delta(\Delta H) = \Delta H^{294} - \Delta H^{77}$$

then, at a given temperature, T

$$\Delta H_{\text{int}} \propto \Delta(\Delta H) \quad [5]$$

Since they are proportional to each other, one can simply compare $\Delta(\Delta H)$ in place of ΔH_{int} . In Fig. 5, the $\Delta(\Delta H)$ values are plotted as a function of the total amount of charges passed in the units of ampere hours. For each set of discharged carbons, commercial and JPL carbon, a similar tendency was observed; the carbons discharged with A electrolyte tend to give narrower (or constant) ΔH_{int} [and $\Delta(\Delta H)$] value with discharge, and the carbons with B electrolyte give broader ΔH_{int} values with discharge.

The spin-orbit coupling is very weak in Li (13, 17, 18), and changes in Li concentration in the carbon matrix should not affect ΔH_{int} value significantly. Thus, the observation of slight decrease (or constant) in ΔH_{int} value with electrolyte A does not contradict the generally accepted discharge mechanism in which LiCl is deposited (or intercalated) in the carbon electrode during discharge, and later reduced to Li metal during voltage reversal.

Liang *et al.* (6) have speculated that sulfur may also be deposited in the carbon electrode during discharge with electrolyte A, and this sulfur may be the source for the safety hazard during voltage reversal of cells with electrolyte A. They also reported that cells with electrolyte B may be safer because the presence of BrCl in SOCl₂ may help dissolve sulfur in the carbon electrode. If the deposition of sulfur is in the form of intercalation through the carbon matrices, the observed ΔH_{int} value for the case of A electrolyte should increase with discharge because the intercalation would shorten the spin lattice relaxation time by spin orbit coupling mechanism. In case of B electrolyte, the ΔH_{int} linewidth should be narrower than the corresponding A electrolyte case because of less amount of sulfur deposition on the carbon electrode during discharge. Our results do not agree with this picture. However, if the deposition of sulfur is only an agglomeration on the carbon surface and segregated from the carbon matrix, the deposition should not affect the ESR linewidth significantly. Some heavy atoms must be electronically interacting with the carbon electrode, thus

Table I. The ESR linewidths (G) of carbon samples after discharge

Total charges passed (Ah)	Commercial carbon					Total charges passed (Ah)	JPL carbon				
	ΔH		$\Delta(\Delta H)$	ΔH_{int}			ΔH		$\Delta(\Delta H)$	ΔH_{int}	
	77 K	294 K		77 K	294 K		77 K	294 K		77 K	294 K
Electrolyte A											
0.205	2.19	2.69	0.50	0.18	0.68	0.271	2.02	2.24	0.22	0.08	0.30
0.170	1.96	2.46	0.50	0.18	0.68						
0.112	2.19	2.70	0.51	0.18	0.69	0.114	2.16	2.46	0.30	0.11	0.41
0.051	2.69	3.33	0.64	0.23	0.87						
0.0	2.27	2.80	0.53	0.19	0.72	0.0	2.28	2.60	0.32	0.11	0.43
Electrolyte B											
0.208	2.30	3.10	0.80	0.28	1.08	0.196	2.07	2.55	0.48	0.17	0.65
						0.170	2.20	2.68	0.48	0.17	0.65
						0.156	2.05	2.48	0.43	0.15	0.58
0.042	2.16	2.70	0.54	0.19	0.73	0.069	2.07	2.50	0.43	0.15	0.58
0.0	2.66	3.08	0.42	0.15	0.57	0.0	2.48	2.86	0.38	0.13	0.51
Carbon electrode no electrolyte	2.75	3.10	0.35	0.12	0.47		2.79	3.10	0.31	0.11	0.42

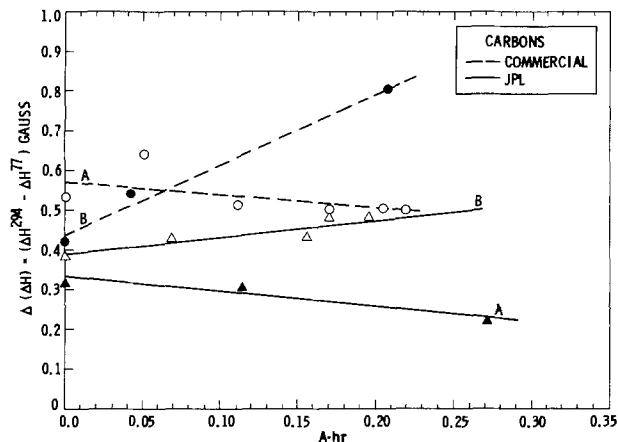


Fig. 5. A plot of $\Delta(\Delta H) = \Delta H^{294} - \Delta H^{77}$ vs. amount of discharge (Ah) for commercial and JPL carbon electrodes in two different electrolytes, A and B. Typically normal discharge is in the range of 0 ~ 0.11 Ah, voltage reversal from ~ 0.11 Ah.

broadening the ΔH_{int} linewidth with discharge when using electrolyte B. One possible explanation of the data appears to be an interaction between BrCl and the carbon electrode. As the discharge progresses, BrCl interacts with the carbon, possibly forming C—Br and/or C—Cl bonds. This interaction of carbon lattice with heavy elements will shorten the spin-lattice relaxation time (T_{int}) through stronger spin-orbit coupling and results in broader ΔH_{int} values. It seems that the possibly improved safety of cells with electrolyte B probably arises because of the change in the characteristics of the carbon (e.g., carbon functional groups) and the influence of these changes on the cell chemistry.

As suggested above, ESR is very sensitive to subtle changes in the carbon electrode. Indeed, the ESR method can be employed to study oxidation of carbon surfaces after prolonged (1 day) exposure to air. It was found in our laboratory that fresh carbon particles (Shawinigan acetylene black) give narrower ESR linewidth upon cooling from 294 to 77 K, i.e., $\Delta(\Delta H) > 0$, however, after prolonged exposure to air, the trend is reversed, i.e., the linewidth becomes broader upon cooling to 77 K, $\Delta(\Delta H) < 0$. This observation can be explained by oxidation of the carbon surfaces after exposure to air, as in the case of metal oxide particles studied by Bowring and Cousins (19). This result is important, since it points out the need to carefully control the handling of the carbon used in preparing electrodes to achieve reproducible cells. This result also shows the ESR as a valuable "quality control" tool to identify unknown causes for irreproducible results and performance of carbon electrodes.

In summary, it has been demonstrated that ESR spectroscopy is a valuable tool for investigating the chemistry in Li/SOCl₂ cells. Changes in characteristics of the carbon, due to exposure to oxygen or BrCl, have been identified. Moreover, changes in carbon functional groups will almost certainly impact the chemistry, safety, and performance of Li/SOCl₂ cells. In particular, the reported improved safety of Li/SOCl₂ cells with the BrCl additive is best explained by the changes in the characteristics of the carbon electrode because of reaction with BrCl.

Acknowledgments

The authors would like to thank other members of our battery research team, Roger Williams and Maggie Evans, for many helpful discussions. This research represents one phase of research performed at the Jet Propulsion Laboratory, California Institute of Technology, sponsored by the National Aeronautics and Space Administration under Contract NAS7-918.

Manuscript submitted Dec. 21, 1983; revised manuscript received Oct. 2, 1984.

Jet Propulsion Laboratory assisted in meeting the publication costs of this article.

REFERENCES

1. A. N. Dey, Final Report, Contract DAAB17-74-C-1119, for U.S. Army ERADCOM, Fort Monmouth, NJ, July 1978.
2. B. Carter, R. Williams, F. Tsay, A. Rodrigues, S. Kim, M. Evans, and H. Frank, *This Journal*, To be published.
3. A. N. Dey, *ibid.*, **123**, 1262 (1976).
4. S. Dallek, S. D. James, and W. P. Kilroy, *ibid.*, **128**, 508 (1981).
5. S. D. James, P. H. Smith, and W. P. Kilroy, *ibid.*, **130**, 2037 (1983).
6. C. C. Liang, P. W. Krehl, and D. A. Danner, *J. Appl. Electrochem.*, **11**, 563 (1981).
7. G. Wagoner, *Phys. Rev.*, **118**, 647 (1960).
8. L. S. Singer and G. Wagoner, *J. Chem. Phys.*, **37**, 1812 (1962).
9. R. J. Bobka and L. S. Singer, *J. Solid State Chem.*, **2**, 218 (1970).
10. P. Lauginie, H. Estrade, J. Conard, D. Guerard, P. Lagrange, and M. El Makrini, *Physica B*, **99**, 514 (1980).
11. T. R. Carver and C. P. Slichter, *Phys. Rev.*, **102**, 975 (1956).
12. G. Feher and A. F. Kip, *ibid.*, **98**, 337 (1955).
13. A. J. Watts and J. E. Cousins, *Phys. Status Solidi*, **30**, 105 (1968).
14. K. A. Muller and R. Kleiner, *Phys. Lett.*, **1**, 98 (1962).
15. M. Ya Gen and V. I. Petinov, *Sov. Phys. JETP*, **21**, 19 (1965).
16. Y. Yafet, *Solid State Phys.*, **14**, 1 (1963).
17. A. W. Overhauser, *Phys. Rev.*, **89**, 689 (1953).
18. R. J. Elliott, *ibid.*, **96**, 266 (1954).
19. C. S. Bowring and J. E. Cousins, *Phys. Status Solidi B*, **50**, 553 (1972).

Improved High-Purity Arc-Furnace Silicon for Solar Cells

J. A. Amick,* J. P. Dismukes,* R. W. Francis,* L. P. Hunt,* P. S. Ravishankar,* and M. Schneider*

Exxon Research and Engineering Company, Solar Electric Conversion Unit, Annandale, New Jersey 07701

K. Matthei and R. Sylvain

Solar Power Corporation, Woburn, Massachusetts 01801

K. Larsen and A. Schei*

Elkem a/s, Research and Development Center, N-4620 Vaagsbygd, Norway

ABSTRACT

Single-crystal silicon solar cells having efficiencies within 1% of those prepared in semiconductor-grade silicon have been fabricated in twice-recrystallized, high purity metallurgical silicon. Produced in a 100 kW experimental arc furnace by carbothermic reduction of pure silica with pelletized carbon black, the best "solar-grade" silicon contained 50-100 ppmw Al, 50-100 ppmw Fe, 10 ppmw Ti, 1.8 ppma B, and 2.1 ppma P. Following two Czochralski (Cz) recrystallizations, the metal impurity levels in the final ingot were indistinguishable from those in once Cz-recrystallized semiconductor-grade silicon, while the boron and phosphorus contents were 1.5 ppma and 0.6 ppma, respectively. The average efficiency of 4 cm² test solar cells prepared in twice-recrystallized "solar-grade" materials was 13.7%, compared to 14.4% for semiconductor-grade controls. The average efficiency of unencapsulated, production-type 100 mm diam solar cells made in this material was 11.8%. Compared with earlier experiments, this represents a nearly 2% improvement in efficiency, which is attributed largely to the factor of two lower boron content in the starting silicon.

Since 1976, the average price of photovoltaic modules fabricated from crystalline silicon solar cells has decreased from about \$40/W_{pk} (1980 dollars) to about \$8.50/W_{pk} (1980 dollars). However, substantial reductions in module manufacturing cost and price are believed necessary to provide impetus for any major potential market expansion. Since the cost of silicon wafers is a major ingredient in module cost, a joint research program to explore the feasibility of one promising route to low cost crystalline silicon for high efficiency solar cells was undertaken jointly by Exxon and Elkem, AG.

The generic sequence of manufacturing steps selected for evaluation consists of: (i) preparation of pure C and SiO₂ feedstocks, (ii) arc furnace reduction of the feedstocks to pure metallurgical silicon (PMS), (iii) metallurgical purification of PMS to solar-grade polysilicon (SGP), at a price goal of \$14/kg in 1980 dollars (1), (iv) crystal growth of silicon ingot from SGP, (v) slicing of silicon wafers from the silicon ingot, and (vi) processing of the wafers into solar cells.

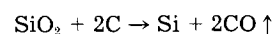
Similar research and development efforts, starting with pure feedstocks (2-5), and related efforts, starting with conventional metallurgical silicon (6-7), have been reported, with the common objective to reduce solar cell cost. This paper describes recent advances made in feedstock selection and arc furnace operation which result in lowered boron concentration in the silicon and in improved efficiency in solar cells made from it.

Experimental

SiO₂ and C feedstocks.—Impurity analyses of the principal SiO₂ and C feedstocks evaluated in this work are shown in Tables I and II, respectively. The methodology of feedstock selection and the methods for cleaning the quartz and the pelletization of SiO₂ and carbon black powders are described elsewhere (3, 8, 9). Two sources of lump quartz and two sources of granular quartz were evaluated. The lump quartz sources from British Columbia and Arkansas, which were previously analyzed (3) with results similar to those shown in Table I, are of equivalent purity and moderate projected cost (\$0.25-\$0.50/kg). The type-"A" granular quartz, is a relatively high cost (\$2.00/kg) material upgraded to high purity from pegmatite, whereas the type-"B" granular quartz is low cost (\$0.10/kg) commercial-type feedstock from quartz rock.

*Electrochemical Society Active Member.

For the overall arc furnace reaction



cleaned lump quartz or silica/sucrose pellets was used together with C-black/sucrose or C-black/sucrose/silica pellets. Granular quartz was further ground and pelletized either with C-black and sucrose, or with sucrose alone. The particular combination of SiO₂ and C feedstocks is identified for each test reported in Table III.

Two carbon blacks, type I, a thermal black from natural gas, and type II, a furnace black from residual oils, were selected for evaluation. Since in pelletized form both ma-

Table I. Impurity analysis of SiO₂ sources evaluated in arc-furnace tests (spark-source mass spectroscopy)

Impurity (ppmw)	Lump quartz (1-2 cm)		Granular quartz (0.01 cm)	
	Mt. Rose ^a	Malvern ^b	Type A	Type B
Al	30	60	20	>1000
Fe	20	30	10	500
Ti	1	<1	5	50
B	<1	1	0.5	2
P	<1	1	1	<1

^a Mount Rose Mining Company Limited, Armstrong, British Columbia, Canada.

^b Malvern Minerals Company, Hot Springs, Arkansas.

Table II. Impurity analysis of carbon sources evaluated for arc-furnace tests (spark-source mass spectroscopy)

Impurity (ppmw)	Carbon blacks		Carbon electrodes ^c	
	Type I ^a	Type II ^b	Pure	Impure
Al	2	20	<1	30-300
Fe	10	80	1	1600-5000
Ti	<1	10	<1	10-200
V	<1	<1	<1	30-60
Ca	<1	80	5	80-200
Mg	2	50	<2	1-5
B	1	<1	<0.5	1
P	<1	<1	<1	—

^a Selected "thermal black" from natural gas.

^b Selected "furnace black" from residual oil.

^c Union Carbide Corporation, Sweden.

Table III. Energy consumption and PMS impurity analysis as a function of raw material feedstocks for representative arc-furnace tests

	Energy Consumption (kWh/kg-Si)	Raw material feedstocks			Impurity analysis of PMS				
		C-pellet ^a	C/SiO ₂ - pellet ^a	Lump SiO ₂	B (ppma)	P (ppma)	Al (ppmw)	Fe (ppmw)	Ti (ppmw)
50 kW furnace ^b									
Run no.									
PMS-4	45	Type I	—	Mt. Rose	5.7	7.5	2000	1000	100
PMS-5	33	Type I	—	Mt. Rose	8.9	19.0	700	800	200
PMS-7	33	Type I	—	Malvern	8.7	11.1	300	400	200
PMS-9	24	—	3.7/1 (Type I/ Type B)	Malvern	16.3	12.6	3400	700	100
100 kW furnace ^b									
Run no.									
PMS-15	71	Type I	—	Mt. Rose	9.2	7.3	770	730	250
PMS-17	24	—	3.5/1 (Type I/ Type A)	Mt. Rose	3.6	2.4	190	160	16
PMS-19	31	—	3.5/1 (Type I/ Type A)	Mt. Rose	4.1	1.4	290	190	22
PMS-20	22	—	3.5/1 (Type I/ Type A)	Type A	1.8	2.1	70	90	10
PMS-24	33	—	1.6/1 (Type I/ Type A)	Malvern	2.8	1.9	130	160	13

^a Pelletized with sucrose binder.

^b Impure electrode for 50 kW and pure electrode for 100 kW furnace.

materials behaved similarly in arc furnace operation, most of the tests, including all those reported here in Table III, were conducted using type I. The carbon black powder was converted into 1-2 cm size pellets using water-sucrose solutions in a pilot-size, 1m diam disk pelletizer. The purchased carbon electrodes were used without further treatment.

Submerged-arc-reduction furnace operation.—The selected C and SiO₂ feedstocks, described above, were converted into PMS in two different single-phase, laboratory-size, one-electrode arc furnaces of split-body design having nominal 50 and 100 kW power ratings, respectively. The construction of the smaller furnace is similar to one of fixed-body design previously described (9), but incorporates the split-body design in addition. The larger furnace incorporates the split-body design (10), as shown in Fig. 1. The tests in the 50 kW furnace were designed to establish suitable smelting conditions and to develop the appropriate materials of construction for subsequent use in the 100 kW, split-body furnace under the purest operating conditions. For simplicity, the graphite electrode, which is positioned vertically and centered in the 100 cm id cavity, is omitted from the drawing. Likewise, the graphite tapping spout has been omitted for clarity. A feedback loop on the 100 kW furnace allowed for automatic position adjustment of the electrode in order to maintain constant electrical load to the furnace. The duration of the smelting tests varied from about 1 to 2.5 days, with PMS production rates of about 1.5 kg/h in the 50 kW furnace and of about 5 kg/h in the 100 kW furnace.

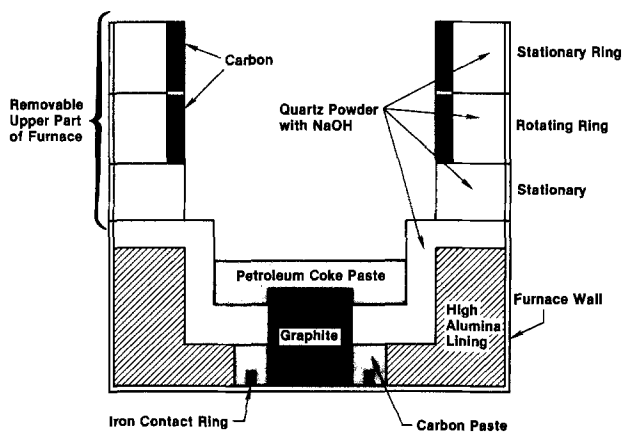


Fig. 1. Schematic illustration of experimental 100 kW arc furnace. The sketch is simplified, and not to scale.

Metallurgical purification of PMS to SGP.—From previous work on metallurgical-grade silicon (MG-Si) (6, 7, 11) and on pure metallurgical grade silicon (PMS) (3), we concluded that there was little hope of obtaining high efficiency solar cells on any silicon material taken directly from an arc furnace and then recrystallized once. The silicon from an arc furnace, even under the best possible operating conditions, contains too much silicon carbide and metal impurities. Accordingly, an intermediate low cost metallurgical or hydrometallurgical step is needed to convert high purity arc-furnace silicon (PMS) into solar-grade polysilicon (SGP) ready for final recrystallization. One aim of this program was to explore intermediate purification steps which could meet the overall cost goal of \$14/kg (1980 dollars) and still provide the requisite purity (13) so that high efficiency solar cells could be obtained.

As an initial standard for comparison, we have employed Czochralski recrystallization for conversion of arc-furnace silicon to solar-grade polysilicon ready for final recrystallization. At the same time, we conducted a separate investigation of alternative approaches to upgrading arc-furnace silicon which would meet cost and purity goals.

Drawing on the experience of Hunt (3) and Secco d'Aragona (11), we adopted the following procedure. Each PMS batch was given a two-step etch, first in aqueous HF and then in an HNO₃-HF-HOAc(acetic) acid mixture to remove oxide, slag, and extraneous iron particles introduced during crushing of the silicon. About 15 kg of the etched PMS was charged into a standard quartz crucible in the growth chamber of a commercial crystal puller. After melting, the silicon was observed to be covered with a thick layer of silicon oxide and silicon carbide slag. The oxide slag was removed by reducing the Ar pressure in the chamber to less than 1 torr and increasing the melt temperature, to "boil" the melt. The "boiling" action occurs because of the rapid evolution of SiO gas.

To remove most of the remaining SiC slag, silicon seeds were introduced and crowns were grown to occlude the SiC floating on the surface. However, because of SiC dislodged from the walls during growth, only polycrystalline ingots could be grown. The typical growth rate employed for ~11 cm diam ingots was 6.4 cm/h, with 15 rpm seed rotation and 8 rpm crucible counter-rotation. The polycrystalline ingot was cylindrically ground to remove about 3 mm from its outer surface, and cropped at the seed and the tang. After being etched in a mixture of hydrofluoric, nitric, and acetic acids, the resulting rod served as prototype SGP for crystal growth into the final silicon ingot.

Table IV. Metal impurity content in Czochralski once-recrystallized ingots^a (spark-source mass spectroscopy)

Arc furnace run	Ingots	Position ^b	Al (ppmw)	Fe (ppmw)	Ti (ppmw)
PMS-4	SPC-6	Seed Tang	10 (20) >1000	1 (10 ⁻³) 1000	< 1 (10 ⁻⁴) 100
PMS-5	SPC-4	Seed Tang	10 (7) >1000	5 (8 × 10 ⁻⁵) 500	< 1 (2 × 10 ⁻⁴) 100
PMS-7	SPC-13	Seed Tang	2 (3) 100	20 (4 × 10 ⁻³) 100	< 1 (2 × 10 ⁻⁴) 100

^a The numbers in parenthesis = $k_{eff} \times [\text{metal}]$ in the arc-furnace run. $K_{eff} = 0.01$ (Al); 10^{-5} (Fe); 10^{-6} (Ti).

^b Seed at 0.1 of melt pulled; tang at 0.7 of melt pulled.

Impurity analyses from the seed and tang of several of the once-recrystallized polycrystalline ingots are shown in Table IV. The numbers in parentheses indicate the product of distribution coefficient of the metal impurity and the metal impurity content in the PMS melt, at the seed of the ingot. The analysis for Al suggests that quite large Al concentrations can be incorporated due to the relatively large distribution coefficient. The analyses for Fe at the seed suggest that constitutional supercooling may already be occurring for this impurity. As indicated, small Ti concentrations were measured at the seed. A pronounced increase in the concentrations of Al, Fe, and Ti is noted at the tang of the ingots due to constitutional supercooling. The plot of the metal impurity concentrations in the PMS melt in Fig. 2, together with a theoretical curve similar to that of Hopkins *et al.* (12) for the onset of constitutional supercooling as a function of crystal growth rate, substantiates the expectation that supercooling and a strong increase in impurity content of the ingot would occur at or near the seed of the ingot. Once this behavior was understood, the attempt was made to grow ~11 cm diam polycrystalline Czochralski ingots at lower growth rates in order to eliminate the occurrence of constitutional supercooling. However all attempts were unsuccessful owing to the difficulty in maintaining diameter control at low growth rates in the commercial Czochralski furnace under normal operating conditions

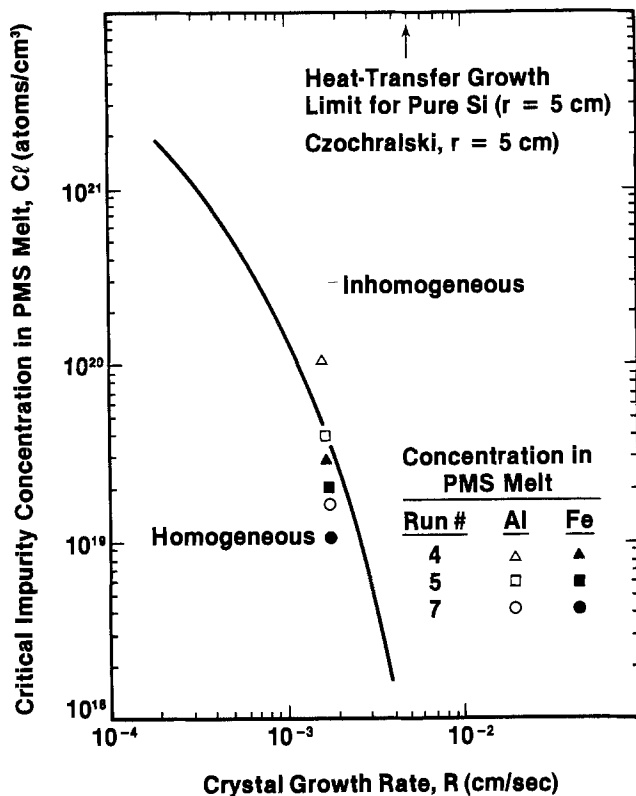


Fig. 2. Metal impurity concentrations in the PMS melt

without extensive improvement in the feedback and control systems. Thus, in all the work reported here, a growth rate of about 6.4 cm/h was employed.

Growth of silicon ingot from SGP.— In principle, conversion of low cost SGP to low cost silicon wafers might be carried out by any one of several crystal growth methods, including Czochralski, Bridgman, float zone, and ribbon techniques. For the purpose of evaluating the feedstock preparation, arc furnace operation, and solar cell processing steps in the overall manufacturing sequence, in the present paper we focus on the Czochralski single-crystal growth method in order to make possible the simplest and most direct correlation with current production technology for single-crystal solar cells employed by much of the terrestrial photovoltaic industry.

Most of the Czochralski ingots for this study were ~11 cm diam boules grown in a commercial crystal growth apparatus under standard conditions for operation of this type equipment. No significant differences in Czochralski growth were observed from SGP compared to growth from semiconductor silicon.

Solar cell processing.—Solar cells of the production design and size shown in Fig. 3a were fabricated in 100 mm diam, 500 μm thick wafers sliced from the single-crystal ingots grown from arc-furnace silicon. In addition, a few Czochralski and float zone wafers, prepared from semiconductor silicon either in house or by outside vendors, were fabricated into 100 mm diam solar cells to provide a comparison. Junction formation was performed in the p-type wafers by the well-known POCl_3 process (14), followed by low cost Ni/solder metallization and AR coating. Hence, the results reported for 100 mm diam wafers provide a good indication of what may be expected in factory production without optimization.

In order to gain some indication of the solar cell performance which might be expected with further solar cell optimization, small test cells 2 × 2 cm size (see Fig. 3b) were fabricated.¹

¹Cells were fabricated by Applied Solar Energy Corporation, City of Industry, California 91749.

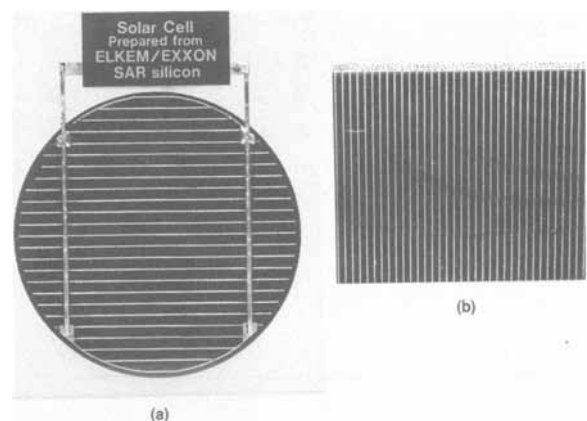


Fig. 3. a: A cell produced in 100 mm diam 500 μm thick wafers sliced from single-crystal ingots grown from arc-furnace silicon. b: 2 × 2 cm test cell.

The solar cell efficiency was measured with a Spectrolab XT-10 Type 1 simulator. Light intensity was 100 mW/cm² (AM1) calibrated with a test cell. The simulator uses an arc lamp with a water filter to cut off the long wavelengths, and chuck temperature is kept at 28°C.

Results and Discussion

Impurity levels in PMS from arc-furnace tests.—General considerations from this and previous work (3-5, 9) suggest that there are probably three main contributions to impurities in the PMS. The first contribution is contamination from the materials of construction of the arc furnace and from the stoking and tapping operations. The second is extraneous contamination during handling and preparation of the feedstocks. The third is the base level of impurities in the raw feedstocks, shown in Tables I and II. For the 50 kW furnace tests, a combination of the first two factors appears to determine the impurity levels in the final PMS, as indicated by the analytical data in Table III. One exception to this trend is run no. PMS-9, for which additional boron and aluminum appear to have been incorporated from the type-B granular quartz. This run, however, did exhibit exceptionally low energy consumption. For this reason, most of the runs in the 100 kW furnace were conducted using mixed C/SiO₂ pellets, which appear to offer a reactivity advantage over pellets made from carbon black alone.

The first run in the 100 kW arc furnace, PMS-15, appears to suffer the same contamination problems experienced in the 50 kW furnace tests. The other four runs, however, probably reflect a residual contribution of impurities from the furnace itself, which is difficult to quantify, plus a contribution from the raw material feedstocks. No measurable difference in B, P, Al, Fe, or Ti can be attributed to the use of Malvern as compared to Mt. Rose lump quartz. However, the use of type-A granular

quartz as the sole source of SiO₂ appears to have been the major factor contributing to the two-fold reduction in these impurities in PMS-20. The method in which we have the best confidence for determining the impurity contribution from feedstocks is to convert them to PMS in an arc furnace of the purest construction possible and then to measure the B and P in the PMS by an analysis of Hall measurements along silicon ingots (15).

At this time, we cannot give a firm answer as to the availability of low cost granular silica sources which could be substituted for the relatively high cost type-A granular quartz. Nor can we determine whether still further reductions in B content of PMS would be possible either by feedstock selection, improvement in feedstock preparation, or in the purity and size of the arc furnace. But it is clear that the results achieved in this work with granular quartz represent a factor of two improvement over the best previously reported arc-furnace silicon from pure feedstocks, as reported by Hunt and Dosaj (3): B, 4.7 ppma; P, <1 ppma. As discussed in the next sections, this factor of two reduction in B content leads directly to an approximate 2% improvement in solar cell efficiency.

Solar cell performance as function of B and P level in arc-furnace silicon and semiconductor silicon.—Figure 4 shows the dependence of short-circuit current density upon B concentration over a three orders of magnitude range of boron concentration. This dependence of short-circuit current, with a change in slope at the 1-2 ppma boron concentration level, results in a similar variation in solar cell efficiency with boron concentration. For all except the two lowest data points for twice Cz recrystallized PMS, there is little or no difference between the behavior of ingots from PMS or semiconductor-grade silicon. For these two ingots, a third recrystallization, as indicated by the arrows in the figure, raised the short-circuit current to the range observed for semiconductor-grade ingots.

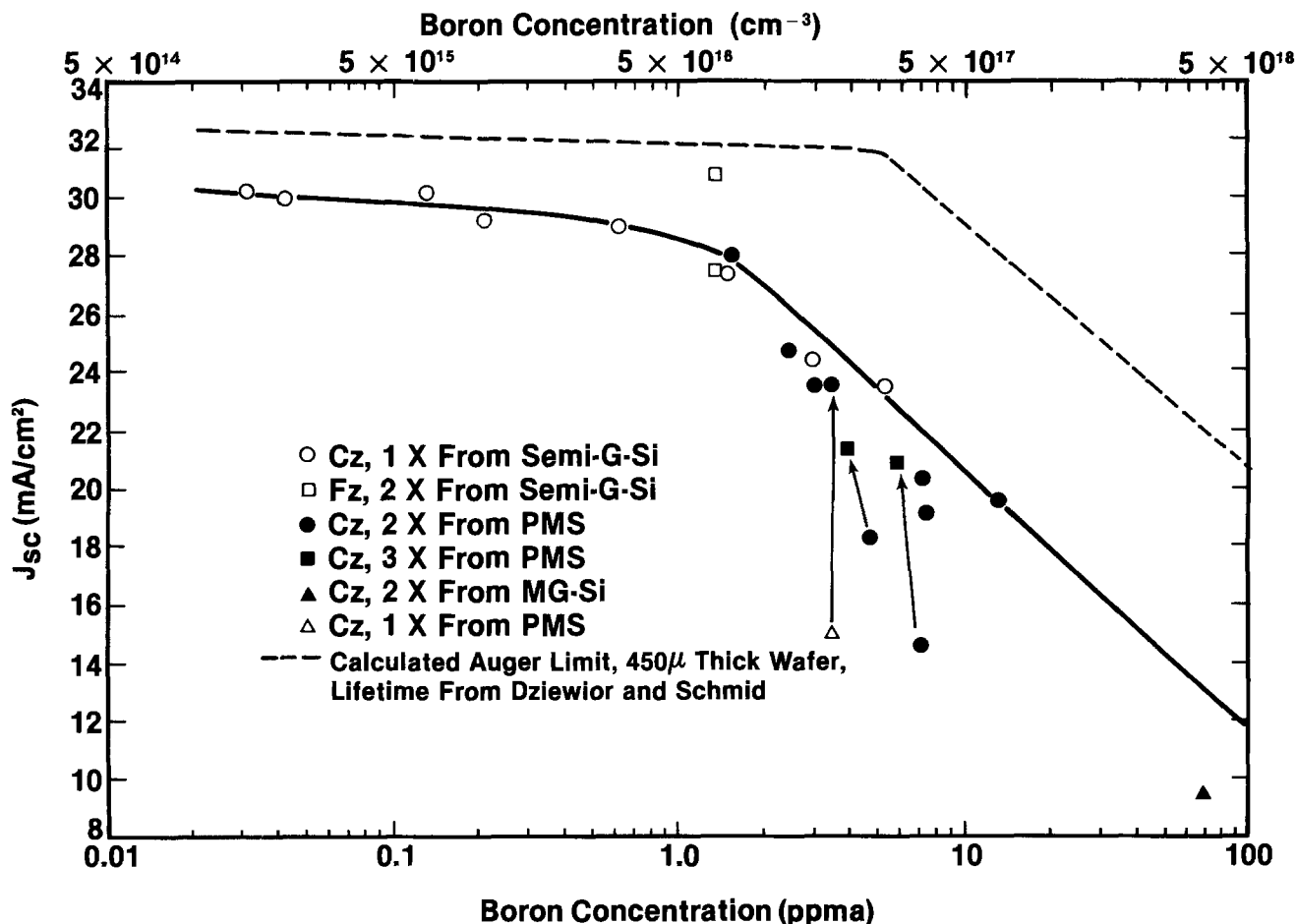


Fig. 4. Short-circuit current density dependency on B concentration

Hence, it appears that for these two cases, the first Cz purification of the PMS was not sufficiently effective in removing metal impurities or carbon. As also indicated in Fig. 4, a similar improvement was generally noted in short-circuit current density when once recrystallized PMS was given a second recrystallization to a Cz single crystal.

Table V shows the best solar cell performance obtained in production-size 100 mm diam solar cells of the construction shown in Fig. 3a. These results indicate strong correlation with B level, and weak or no correlation with P level. For B levels exceeding 4 ppma (average) in the twice recrystallized Czochralski ingot, the best efficiency achieved was 9.5%. For B levels in the range 2.4-3.3 ppma, it was possible to achieve about 10.5% efficiency. When the B level was reduced to 1.5 ppma, as described above using type-A granular quartz, efficiency of 12.5% was achieved, representing an absolute increase of 2% efficiency in these production-size cells.

The data on production-size solar cells in Table VI provide further confirmation that short-circuit current and hence efficiency depend strongly on boron concentration in solar cells derived both from semiconductor-grade silicon and from solar-grade silicon. Hence we conclude that, after appropriate upgrading, residual metal impurity concentrations in single-crystal Czochralski ingots are due to the crystal-growth operations (16) rather than the original arc-furnace silicon. While impurities and/or structural defects may be directly responsible for the observed degradation of performance with increasing boron content, we conclude that the boron is directly involved in their formation. They might be due, for instance, to complexes or precipitates of boron oxide, boron nitride, or metallic borides.

Solar cell performance as a function of diffusion length in arc furnace and semiconductor silicon.—Although the decrease of solar cell efficiency at high B levels, corresponding to electrical resistivity levels lower than

0.1 Ω -cm, has long been recognized (17), the experimental data in Fig. 4 show a threshold behavior at much lower B levels ($\sim 5 \times 10^{16} \text{ cm}^{-3}$ on 1 ppma) than would be calculated assuming classical Auger recombination ($\sim 10^{18} \text{ cm}^{-3}$ or 20 ppma) as the limiting degradation mechanism (18, 19). Hence, to investigate this effect further, we have prepared a number of Cz ingots from semiconductor-grade silicon, with different B levels, and measured their diffusion length and solar cell performance compared to that of Cz ingots twice recrystallized from PMS. Figure 5 shows a plot of short-circuit current as a function of diffusion length, obtained on wafers prior to solar cell processing by the measurement of capacitively coupled, charge carrier lifetime (20). The solid curve is calculated for 450 μm thick solar cells according to the methodology of Amick and Ghosh (21). The experimental points appear well fitted by a curve representing a 20% loss for reflection and shadowing. Thus, it is apparent that semiconductor-grade silicon wafers and arc-furnace silicon wafers show a similar increase in short-circuit current with increasing diffusion length (*i.e.*, decreasing B concentration). Suitably recrystallized arc-furnace silicon behaves identically to semiconductor-grade silicon. The occurrence of the threshold behavior in Fig. 4 at lower B levels than expected for Auger recombination is, therefore, probably related to as-yet uncharacterized effects of residual metal impurities (16, 22) from the crystal-growth apparatus, to carbon or oxygen contamination (23), to point defects, or to complexes or precipitates of these entities with boron.

Performance of production-size solar cells in single-crystal Czochralski ingots from the highest purity PMS.—As discussed above, production-size solar cells from ingots SPC-76, SPC-77, and SPC-83, prepared by two recrystallizations of PMS-20, showed the best efficiency of all the arc-furnace tests. The correlation of the improved efficiency with decreased boron concentration appears well founded.

Table V. Best solar cell performance as a function of B and P level in arc-furnace silicon

Arc-furnace silicon source	Twice-recrystallized Cz ingot				Best solar cell performance			
	Ingot (no.)	B (ppma)	P (ppma)	ρ (Ω -cm)	V_{oc} (V)	J_{sc} (mA/cm ²)	FF	Efficiency (%)
50 kW furnace								
PMS-4	SPC-8	4.6	2.0	0.17	0.580	18.2	0.71	7.5
PMS-5	SPC-5	7.1	5.0	0.23	0.570	14.6	0.76	6.3
PMS-7	SPC-15	6.9	2.9	0.18	0.600	20.4	0.78	9.5
PMS-9	SPC-19	13.4	3.7	0.08	0.600	19.5	0.75	8.7
100 kW furnace								
PMS-15	SPC-44	7.2	1.8	0.11	0.593	19.1	0.69	7.8
PMS-17	SPC-59	2.9	<0.6	0.17	0.585	23.6	0.76	10.5
PMS-19	SPC-70	3.3	<0.4	0.17	0.576	23.5	0.68	9.2
PMS-20	SPC-76	1.5	0.6	0.48	0.594	28.3	0.75	12.6
	SPC-77	1.5	0.6	0.55	0.593	28.6	0.76	12.9
	SPC-83	1.5	0.6	0.50	0.598	27.5	0.76	12.5
PMS-24	SPC-100	2.4	0.7	0.29	0.595	24.7	0.68	10.0
Commercial MG-Si Elkem, Fiskaa	SPC-23	72	12	0.02	0.565	9.6	0.70	3.8

Table VI. Comparison of the performance of production-size solar cells^a with silicon source used for growth of Czochralski ingot

Silicon source	Cz ingot	[B] (ppma)	[C] (ppma)	Number of solar cells	ρ (Ω -cm)	Average performance			
						Efficiency (%)	J_{sc} (mA/cm ²)	FF	V_{oc} (V)
Semiconductor grade	SPC-28 ^b	3.0	<1	5	0.16	11.0	24.5	0.752	0.597
PMS-17	SPC-59 ^c	2.9	1-3	10	0.17	10.0	24.3	0.700	0.592
Semiconductor grade	SPC-27 ^b	1.4	<1	8	0.3	11.6	26.3	0.743	0.595
Semiconductor grade	SPC-A ^b	0.5	<1	3	0.7	12.1	28.0	0.728	0.594
PMS-20	SPC-83 ^c	1.5	1-3	21	0.6	11.8	27.8	0.711	0.596

^a 100 mm diam.

^b One Czochralski recrystallization.

^c Two Czochralski recrystallizations.

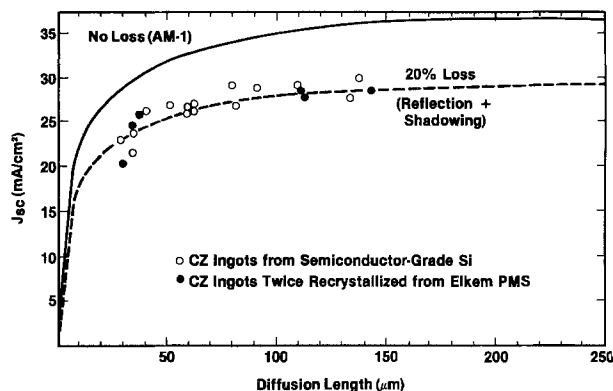


Fig. 5. Short-circuit current as a function of diffusion length

The best individual cell fabricated had an efficiency of 12.9%, as indicated in Table V. To gain some indication of the distribution of efficiency, which can be expected in production, we fabricated a total of 99 solar cells using procedures similar to those employed in production. The three ingots evaluated had seed-to-tang resistivities that collectively ranged from 0.53 to 0.76 Ω -cm. In analyzing the results, we were interested in evaluating two factors. The first was the overall distribution of efficiencies. The second was the variation of efficiency along the length of the Czochralski ingot, since any metallic impurities or carbon, possibly carried over from the PMS to the SGP, might be expected to raise the levels of these impurities towards the tang of the ingot.

The distribution of efficiencies of the 99 cells is shown in Fig. 6. Two-thirds of the cells fall in the efficiency range between 11.5% and 12.5%. Three-eighths of the cells have solar cell efficiencies \geq 12%. Only one-twelfth of the cells have efficiencies below 10%. The principal reason for the low efficiency tail is low fill factor, which was discussed above. Hence, improvement in fill factor should be a key objective of further development work on solar-grade silicon ingots such as those investigated here.

Cell parameters for ingot SPC-77 are shown in Fig. 7 as a function of the fraction of the melt pulled. The decrease in cell efficiency and diffusion length for fractions of the melt pulled greater than 0.5 is attributed to the disloca-

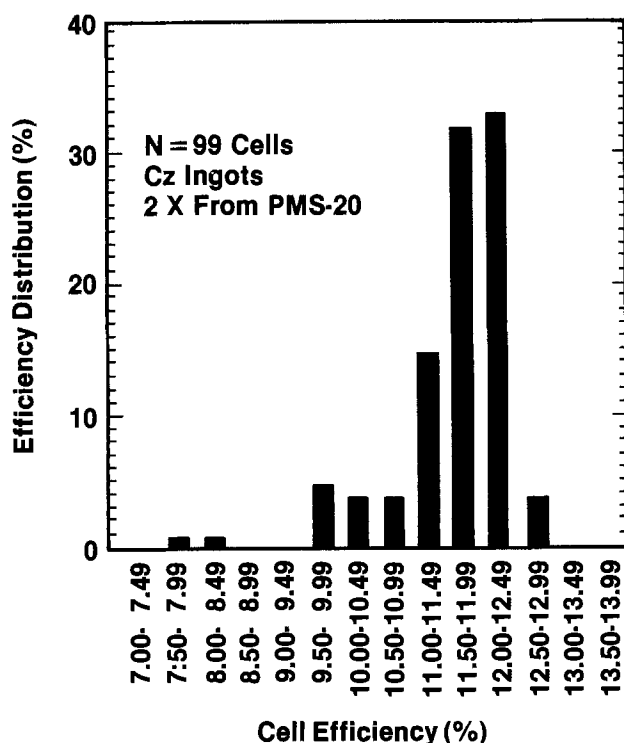


Fig. 6. Distribution of efficiencies of the 99 cells

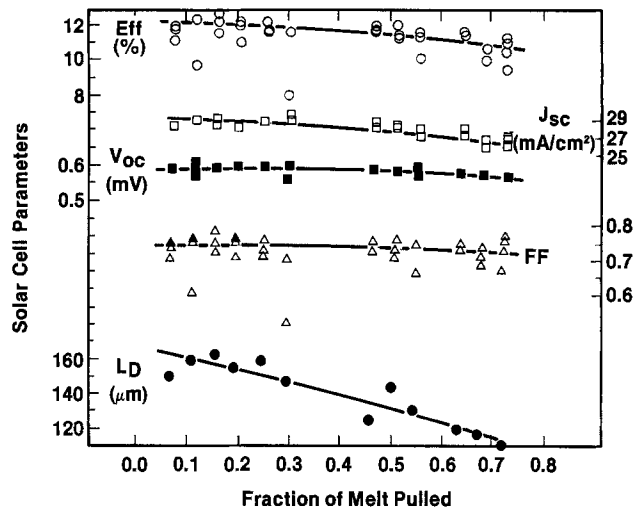


Fig. 7. Cell parameters for ingot SPC-77 as a function of the fraction of the melt pulled.

tion density, which increased from zero to about 10,000/cm² at the tang. The cause of the high dislocation density appears related to the thermal history of this ingot, rather than due to impurities, since a relatively small 10 kg charge was used, resulting in poor growth control toward the tang. Another ingot, SPC-83, was essentially dislocation free from seed to tang, and exhibited relatively constant efficiency along the length of the ingot.

Solar cell performance in laboratory-scale 4 cm² test cells in ingot from highest purity PMS.—Table VII shows the comparison of performance, including average, maximum, and minimum values for 4 cm² test cells fabricated by Applied Solar Energy Corporation from semiconductor Cz ingot and from ingot SPC-83 derived from the best arc-furnace silicon reported here, PMS-20. The principal reason for a difference in the average efficiency in SPC-83, 13.7%, and that in SPC-B, 14.4%, is the low fill factor of the one low value cell.

The average test cell efficiency on 4 cm² cells (13.7%) exceeds that obtained on production-size 78 cm² cells (11.8%) for three reasons. The first is lower reflection due to a two-layer AR coating. The second is lower shadowing (~7%) as compared to the production-size cells (~15%). The third factor is a statistical effect in the material or the processing of larger area cells. The results on small area cells do suggest, however, that it should be possible to produce production-size cells with efficiencies of about 14% from twice-recrystallized PMS.

Conclusions

The technical feasibility of reacting pelletized granular quartz and carbon black in a specially constructed 100 kW arc-furnace, to produce purified metallurgical silicon (PMS) having 1.8 ppma B has been demonstrated. This is a factor of 2.5 lower B concentration than previously reported for PMS. The production of this quality of PMS at low cost appears feasible since MG-Si is produced commercially in large submerged arc reduction furnaces. Increasing the size of the arc furnace should, if anything, improve the purity of PMS silicon.

Comparison of solar cell performance in once- and twice-recrystallized PMS ingots confirms our initial working hypothesis that for high efficiency solar cells, an intermediate upgrading step is necessary to convert PMS to a solar-grade polysilicon (SGP) feedstock suitable for final recrystallization into ingot. The successful use of the Czochralski process for this intermediate purification demonstrates the feasibility of directional solidification as a generic metallurgical upgrading step. However, to accomplish this economically will require development and scale-up of alternative, *e.g.*, Bridgman, processes, since Czochralski upgrading does not appear economical at any scale for producing \$14/kg SGP.

Table VII. Comparison of the performance of laboratory-size test solar cells^a with silicon source used for growth of Czochralski ingot

Silicon sources	Cz ingot	[B] (ppma)	[C] (ppma)	ρ (Ω -cm)	Number of solar cells	Efficiency (%)	J_{sc} (mA/cm ²)	FF	V_{oc} (V)
Semiconductor	SPC-B ^b	0.1	<1	2	8 Average	14.4	31.5	0.780	0.589
					Maximum	14.7	31.5	0.800	0.588
					Minimum	14.2	31.5	0.750	0.588
PMS-20	SPC-83 ^c	1.5	1-3	0.6	12 Average	13.7	30.3	0.754	0.597
					Maximum	14.8	31.3	0.790	0.600
					Minimum	9.3	29.5	0.530	0.597

^a 2 × 2 cm area, fabricated by ASEC.

^b One Czochralski recrystallization.

^c Two Czochralski recrystallizations.

We have shown that the efficiency of crystalline-silicon solar cells depends critically upon boron concentration. The lowered boron content in the present PMS results in a net 2% improvement in solar cell efficiency compared to previous work on solar cells derived from PMS.

Acknowledgments

The authors give special recognition to Rolf Nordheim and Hans Storegraven, of Elkem, and to Dewi Jones, Don Kahn, and Al Skopp, of Exxon, for guidance in structuring the joint technical program between our two companies. We acknowledge technical support from Chris Carson, Joel Haberman, Marty Pope and Earl Shipp, at Exxon, and from the technical staff at Elkem Research and Development Center. Amal Ghosh at Exxon and Gunnar Halvorsen at Elkem made significant contributions through frequent technical consultations. The authors also express appreciation to Bob Hull of Mulab Incorporated, Basking Ridge, New Jersey, for special technical projects and consultation. Finally, the authors recognize the wise counsel provided by Paul Caruso, Frank Pasterczyk, Joseph Shropshire, Ole Vanberg, and John Wurmser, of Exxon, and by Eric Dahl and Stig Lyng, of Elkem, in the technical management of the program.

Manuscript submitted Oct. 11, 1983; revised manuscript received Oct. 9, 1984. This was Paper 208 presented at the San Francisco, California, Meeting of the Society, May 8-13, 1983.

Exxon Research and Engineering Company assisted in meeting the publication costs of this article.

REFERENCES

- D.O.E., J.P.D., and NASA, "Low Cost Solar Array Project," brochure from the 15th IEEE Specialists Conference, May 1981; J. R. Lay and S. K. Iya, in "Proceedings of the 15th IEEE Photovoltaics Specialists Conference," May 1981, p. 565, IEEE, New York (1981).
- D. Helmreich, E. Sirtl, and J. Dietl, in "Crystals, Growth, Properties and Applications," Vol. 5, J. Grabmaier, Editor, Springer-Verlag, Berlin (1981).
- L. P. Hunt and V. D. Dosaj, Final Report, D.O.E. Report DOE/JPL/954559-78/7, D.O.E. Technical Information Center (1979).
- S. Pizzini, in "Materials and New Processing Technologies for Photovoltaics," J. P. Dismukes, P. Rai-Choudhury, E. Sirtl, and L. P. Hunt, Editors, p. 26, The Electrochemical Society Softbound Proceedings Series, Pennington, NJ (1982).
- H. A. Aulich, K.-H. Eisenrith, H.-P. Urbach, and J. C. Grabmaier, in "Materials and New Processing Technologies for Photovoltaics," J. P. Dismukes, P. Rai-Choudhury, E. Sirtl, and L. P. Hunt, Editors, p. 177, The Electrochemical Society Softbound Proceedings Series, Pennington, NJ (1982).
- J. Dietl, in "Materials and New Processing Technologies for Photovoltaics," J. A. Amick, P. Rai-Choudhury, E. Sirtl, and J. P. Dismukes, Editors, p. 48, The Electrochemical Society Softbound Proceedings Series, Pennington, NJ (1981).
- S. Pizzini, *Solar Energy Mater.*, **6**, 253 (1982).
- V. D. Dosaj and J. P. Hunt, U.S. Pat. 4,247,528 (1981).
- V. D. Dosaj, L. P. Hunt, and A. Schei, *J. Metals*, **30**, 8 (1978).
- H. Krogsrud, N. C. Bugge, and K. Piene, in "Proceedings of the 35th Electric Furnace Conference," p. 15 (1977).
- F. Secco d'Aragona and H. M. Liaw, in "Materials and New Processing Technologies for Photovoltaics," J. A. Amick, P. Rai-Choudhury, E. Sirtl, and J. P. Dismukes, Editors, p. 119, The Electrochemical Society Softbound Proceedings Series, Pennington, NJ (1981).
- R. H. Hopkins, R. G. Seidensticker, J. R. Davis, P. Rai-Choudhury, P. D. Blas, and J. R. McCormick, *J. Cryst. Growth*, **42**, 493 (1977).
- J. R. Davis, R. H. Hopkins, and A. Rohgatgi, in "Materials and New Processing Technologies for Photovoltaics," J. P. Dismukes, E. Sirtl, P. Rai-Choudhury, and L. P. Hunt, Editors, p. 14, The Electrochemical Society Softbound Proceedings Series, Pennington, NJ (1982).
- See, for example, E. L. Ralph, in "Proceedings of the 11th IEEE Photovoltaic Specialists Conference, p. 315, IEEE, New York (1975); V. K. Kapur, J. E. Avery, and C. F. Gay, in "Materials and New Processing Technologies for Photovoltaics," J. A. Amick, E. Sirtl, P. Rai-Choudhury, and J. P. Dismukes, Editors, p. 140, The Electrochemical Society Softbound Proceedings Series, Pennington, NJ (1981).
- L. P. Hunt, R. W. Francis, and J. P. Dismukes, To be published.
- P. J. Ward, *This Journal*, **129**, 2573 (1982).
- P. A. Iles and S. I. Soclof, in "Record of the 11th IEEE Photovoltaics Specialists Conference," p. 19, IEEE, New York (1975).
- J. Dzewior and W. Schmid, *Appl. Phys. Lett.*, **31**, 346 (1977).
- L. Passavi and E. Susik, *J. Appl. Phys.*, **54**, 3935 (1983).
- T. Tiedje, J. O. Haberman, R. W. Francis, and A. K. Ghosh, *ibid.*, **54**, 2499 (1983).
- J. A. Amick and A. K. Ghosh, in "Materials and New Processing Technologies for Photovoltaics," J. A. Amick, P. Rai-Choudhury, E. Sirtl, and J. P. Dismukes, Editors, p. 196, The Electrochemical Society Softbound Proceedings Series, Pennington, NJ (1981).
- K. Graff and H. Pieper, in "Lifetime Factors in Silicon," ASTM STP 712, p. 136, ASTM, Philadelphia, PA (1980).
- D. C. Wong and G. F. Wakefield, in "Lifetime Factors in Silicon," ASTM STP 712, p. 86, ASTM, Philadelphia, PA (1980).

The Current-Voltage Characteristics of a Photoelectrochemical Cell Using p-Type Porous Si

Nobuyoshi Koshida, Masahiro Nagasu, Takashi Sakusabe, and Yuji Kiuchi

Department of Electronic Engineering, Tokyo University of Agriculture and Technology, Koganei, Tokyo 184, Japan

ABSTRACT

Fundamental characteristics of a photoelectrochemical cell using p-type porous-Si layer (PSL) as a semiconductor photoelectrode were measured. The PSL electrode exhibited stable photodiode characteristics. The increase in the PSL thickness was very useful in suppressing the dark current, although it resulted somewhat in reducing the photosensitivity, due to the increase in surface recombination losses of photogenerated carriers.

The surface of n-type semiconductors with small bandgaps suitable for solar energy conversion is unfortunately unstable in photoelectrochemical cell. For example, a n-type Si electrode operated in aqueous electrolytes is rapidly passivated under illumination (1). In order to suppress photoanodic surface corrosion of n-type semiconductors and to stabilize the operation, several attempts based upon thin film coating (2-8) and chemical derivatization (9) have been made.

The porous-Si layer (PSL) applied here was found in the 1950s by Uhlir (10) and Turner (11) in the course of the anodization studies of Si in HF solution. Recently, the formation mechanism of PSL and its structure were studied by Unagami (12, 13) in detail. According to those results, PSL is formed by local dissolution during anodization in HF solution. It consists of many micropores formed uniformly in the thickness direction. The diameter of micropores ranges from about 50 to 300Å, depending on the resistivity of Si substrate and the condition of anodic reaction. This PSL, which can be oxidized easily by thermal process (14, 15), has been applied to the isolation technique in integrated circuits (16).

The PSL can be obtained in either n-type or p-type Si substrate. In n-type Si, however, the anodic reaction needs to be carried out under illumination to generate holes which are necessary for the formation of PSL. In this paper, we report the application of PSL as a photoelectrode of a photoelectrochemical cell using p-type Si substrates.

Experimental

Formation of PSL electrodes.—Silicon wafers used in this experiment were (111) p-type single crystals (0.3-0.5 Ω cm) with a mirror surface. Prior to anodization, the wafers were cleaned, a thin Al film was deposited on the back side, and they were alloyed to form an ohmic contact. Nonanodized parts of the wafers were then covered with acidproof wax. Anodization was done in 50 weight percent (w/o) HF solution under a constant current density. The current densities i_A were adjusted to the values below those used for electropolishing. After rinsing the anodized wafers in deionized water and removing the wax, the HF solution left in PSL was released by heat-treatment at 100°-150°C in vacuum. The thickness of PSL was measured separately by microscopic observation of level lapped surfaces.

Measurements of the characteristics of PSL electrodes.—The wafers were covered again with the wax and then used as photoelectrodes of the cell with Pt counterelectrode and SCE reference. The electrolyte was 0.005M Na_2HPO_4 (pH = 7.8). The light source was a 150W tungsten lamp; the maximum exposure intensity was 60 mW/cm² (in 0.4-0.9 μm wavelength range). The current-voltage curves of PSL photoelectrodes were measured under different light intensities. N_2 bubbling was done throughout the measurements in order to prevent the sticking of the H_2 bubbles at the PSL surface. Quantum efficiencies were measured using He-Ne laser of 6328Å wavelength and 1 mW power. The stability of PSL elec-

trodes was also evaluated by the change in the dark current with passed charge during the continuous photo-cathodic operation.

Results and Discussion

PSL thickness.—Figure 1 shows the thickness of PSL formed under various conditions as a function of the anodic reaction time t_A . The PSL thickness d , which is larger for higher current density of anodization and for lower resistivity of the Si substrate, increases nearly in proportion to t_A . These results are consistent with those reported previously (12).

The local-dissolution of Si resulting in PSL is ensured by the steady hole supply from the substrate. The formation of PSL, therefore, proceeds more easily for lower-resistivity substrates. In fact, PSL formed in the low-resistivity substrate becomes deeper than that in the high-resistivity one, even if anodization was done at the same current density and reaction time, as shown in Fig. 1. This means that the porosity of PSL is decreased as the resistivity of the substrate is lowered. Under the experimental conditions in Fig. 1, the porosity of PSL ranges between 40% and 50% (12).

The scanning electron micrograph of cleaved cross section of PSL is shown in Fig. 2. A uniform PSL is formed in the thickness direction. The porosity appears to be independent of the PSL thickness.

Current-voltage curves.—A typical example of photo-current-voltage characteristics under bias obtained from the PSL photoelectrode is shown in Fig. 3. The PSL in this case was formed under the conditions of $i_A = 50$ mA/cm², $t_A = 20$ min, and $d = 57$ μm . In the backward (cathodic) bias region, photocurrent behaves in a way similar to that of a normal photodiode. These curves were stable and reproducible. The rising voltage of photocurrent was -0.75V (vs. SCE) and open-circuit photovoltage was

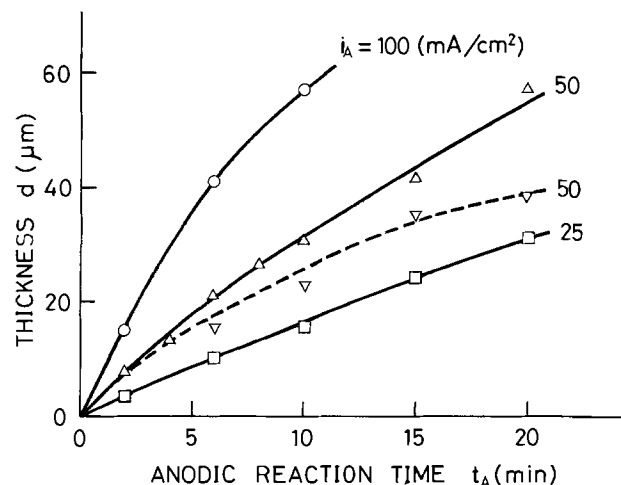


Fig. 1. Thickness of PSL formed at different current densities as a function of anodic reaction time. The result obtained from a high-resistivity (3-5 Ω cm) substrate is also shown by the dotted line.

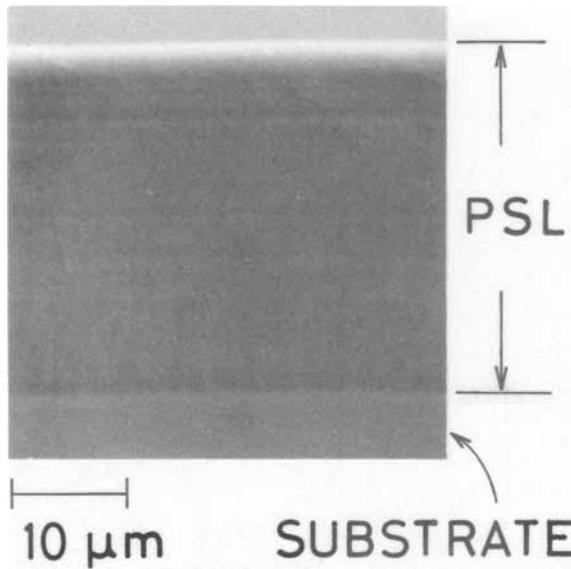


Fig. 2. Scanning electron micrograph of cleaved cross section of anodized PSL.

0.50V. Reversible hydrogen and oxygen evolution potentials in this cell are -0.70 and 0.53V (vs. SCE), respectively. Under photocathodic operation, H₂ and O₂ evolutions were observed at PSL and Pt electrodes, respectively. Similar results were obtained from the photoelectrodes with different PSL thickness.

Sensitivity.—Figure 4 shows the saturated photocurrent i_s of some PSL electrodes as a function of the light intensity. The linearity between i_s and the light intensity is consistently maintained over a wide illumination range. The sample of $d = 0$ represented in Fig. 4 is the naked Si electrode prepared only by a conventional chemical etching process. As the PSL thickness was increased, photosensitivity, S , defined as the ratio of i_s to the light intensity, was reduced. Figure 5 shows the change in S obtained from Fig. 4 with the PSL thickness. Quantum efficiencies η are also shown in Fig. 5. It should be noted that both S and η become almost constant in the region of the PSL thickness beyond 30 μm . The final values of S and η correspond to the intrinsic values of PSL. This is

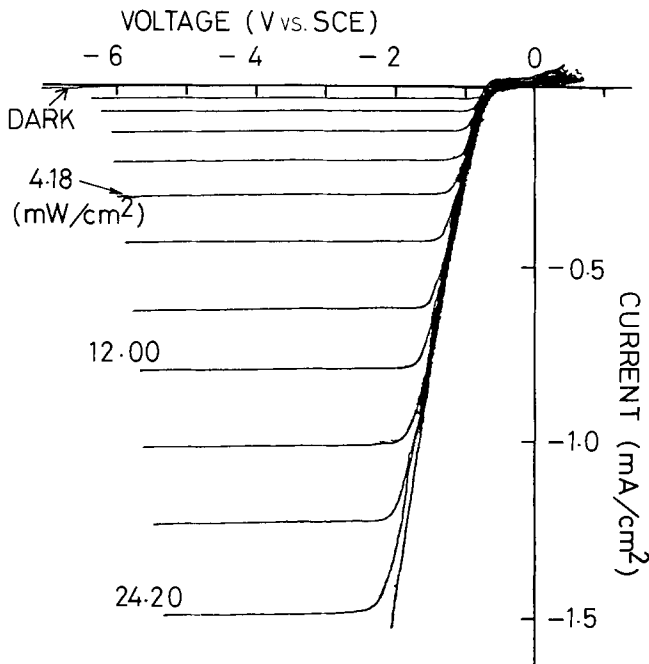


Fig. 3. Current-voltage curves of a p-type PSL photoelectrode

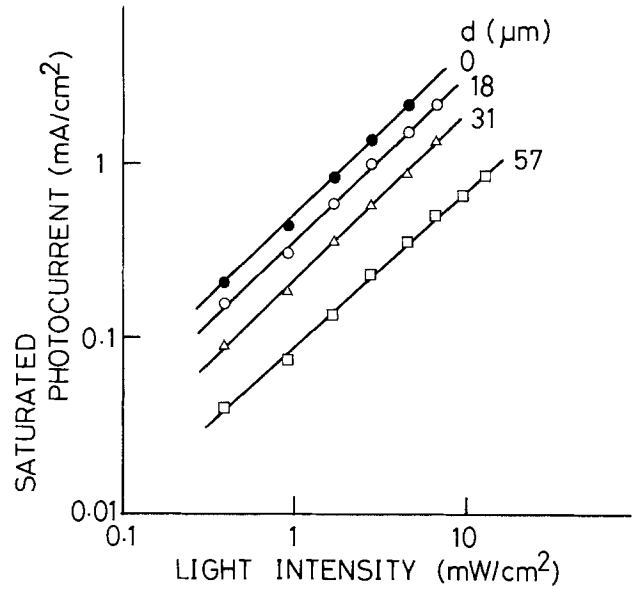


Fig. 4. Saturated photocurrents of some PSL electrodes as a function of the light intensity.

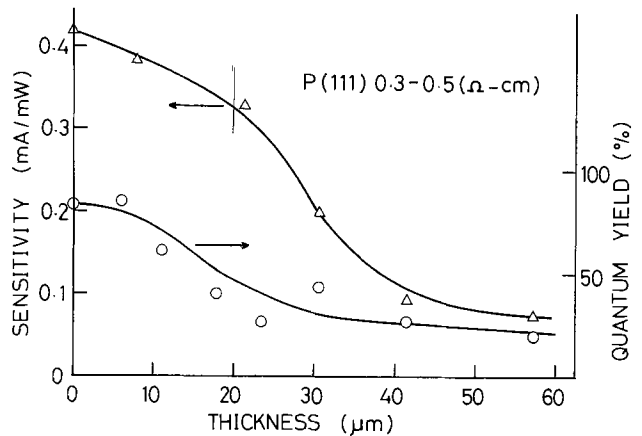


Fig. 5. Photosensitivity and quantum efficiency as a function of the PSL thickness.

reasonable, considering that single or polycrystalline structure remains in PSL (13) and that the absorption coefficient of single-crystal Si for visible light is 10^3 - 10^5 cm^{-1} (17).

At the surface of PSL, thin surface porous film (SPF) is formed at the early stage of anodization (12). The local dissolution of Si resulting in PSL is initiated by this SPF. The SPF can easily be etched by HNO₃ + HF solution. In order to investigate the influence of SPF, photocurrent-voltage curves of the SPF etched sample were also measured. The results were similar to those shown in Fig. 3-5.

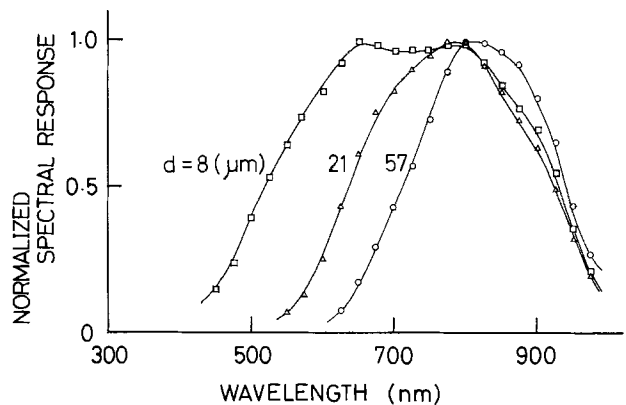


Fig. 6. Normalized spectral response of photosensitivity for three different PSL electrodes.

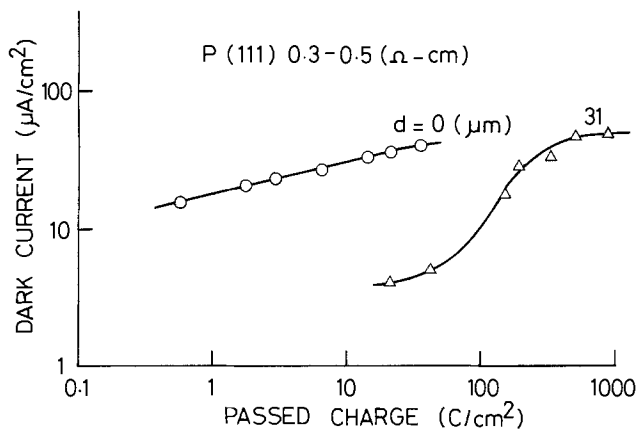


Fig. 7. Suppressing effect of PSL on the dark current

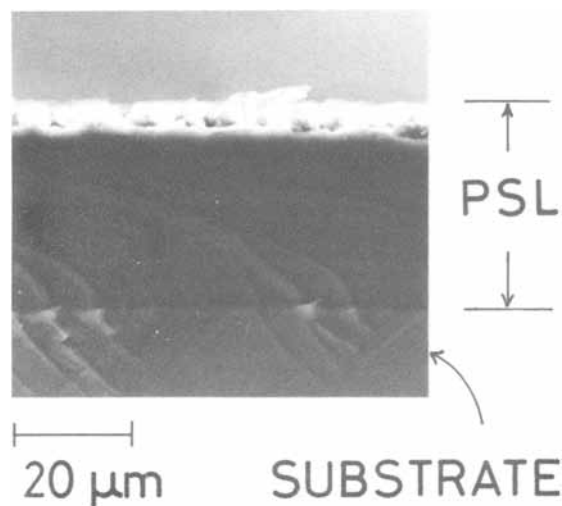


Fig. 8. Scanning electron micrograph of cleaved cross section of PSL after photocathodic operation.

Therefore, SPF itself has no significant effects on the photoelectronic process.

Spectral response.—Figure 6 shows the spectral response of some PSL electrodes. It can be seen that as the PSL thickness is increased, the sensitivity in the short-wavelength region is reduced. This suggests that the increase in the PSL thickness results in higher surface recombination rate of photogenerated carriers. The reduction in photosensitivity with increasing PSL thickness shown in Fig. 5 can thus be explained from this result.

Stability.—The most important characteristic of the PSL electrode was the stability of operation. Figure 7 compares the dark current of PSL with that of the naked Si substrate as a function of passed charge of electricity through the sample at an average current density of 2 mA/cm² under illumination. These dark currents were measured at a terminal voltage of 5V between PSL and Pt electrodes. It is apparent from Fig. 7 that the formation of a thick PSL produces a pronounced suppressing effect on the dark current.

Figure 8 shows a cross-sectional view of PSL after a long-time photocathodic operation. A certain degree of dissolution of PSL can be seen. Further operation resulted in the development of dissolution toward the substrate and the subsequent increase in the dark current. The final current-voltage curves are shown in Fig. 9. Although the dark current is considerably increased, both the stability and the net photocurrent are comparable with those at the initial stage shown in Fig. 3.

During the formation of PSL, the working face of local dissolution was the bottom of the micropores (12). Similarly, the dark current controlled by the majority carrier

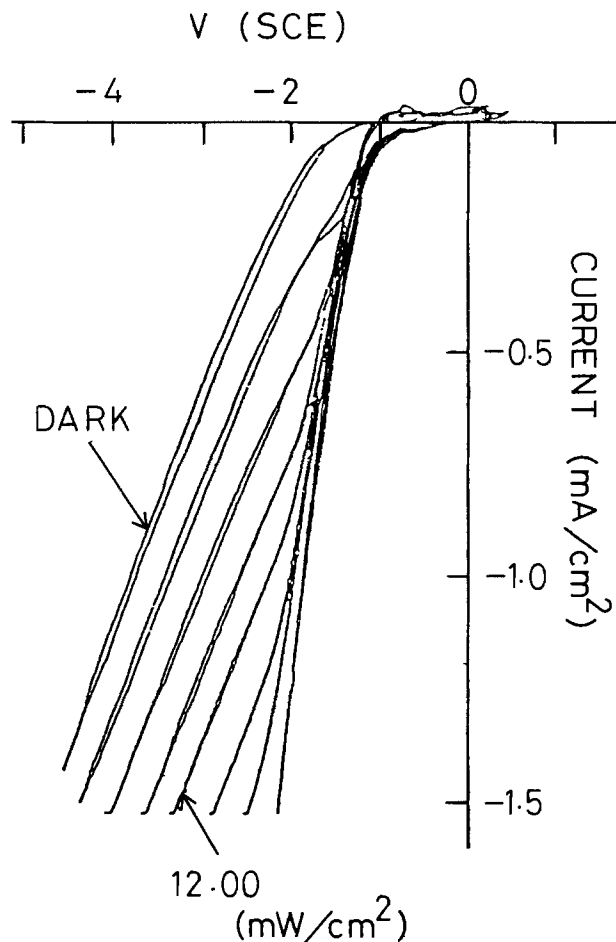


Fig. 9. Current-voltage curves of the PSL photoelectrode at the final stage of operation. The sample is the same as the one shown in Fig. 3.

holes is thought to be governed by the rear surface of PSL. While PSL remains thick enough, the interfacial charge transfer occurs only near the surface of PSL. At that time, the dark current is negligible. As the dissolution of PSL due to the out diffusion of holes proceeds under illumination, the PSL thickness is gradually decreased. As the consequence of this, the dark current is increased. Finally, it reaches the original value of the naked Si substrate. If the initial PSL is thick enough, the dark current will be suppressed successfully over a long period of time because of the requirement of a large amount of charges for dissolution. This picture explains the result of Fig. 7 qualitatively.

Conclusion

Fundamental characteristics of PSL photoelectrodes have been shown. The formation of a porous structure at the p-type Si surface is very useful in suppressing the dark current of the photoelectrochemical cell. The PSL electrode can provide a basis in the understanding of the photoelectrolysis at semiconductor-liquid interfaces, although p-type PSL itself does not show net energy conversion of light. Further studies concerning the interfacial charge transfer process in PSL and the application of PSL to n-type Si substrates are in progress.

Acknowledgments

The authors would like to thank Dr. T. Unagami for his helpful suggestions and Professor S. Yoshida for his continuous guidance and encouragement.

Manuscript submitted April 23, 1984; revised manuscript received Sept. 15, 1984.

Tokyo University of Agriculture and Technology assisted in meet the publication costs of this article.

REFERENCES

1. V. A. Myamlin and Y. V. Pleskov, "Electrochemistry of Semiconductors," Chap. IV, Plenum Press, New York (1967).
2. Y. Nakato, T. Ohnishi, and H. Tsubomura, *Chem. Lett.*, 883 (1975).
3. P. A. Kohl, S. N. Frank, and A. J. Bard, *This Journal*, **124**, 225 (1977).
4. M. Tomkiewicz and J. M. Woodall, *ibid.*, **124**, 1436 (1977).
5. H. Morisaki, H. Ono, H. Dohkoshi, and K. Yazawa, *Jpn. J. Appl. Phys.*, **19**, L148 (1980).
6. S. Menezes, A. Heller, and B. Miller, *This Journal*, **127**, 1268 (1980).
7. R. Noufi, A. J. Nozik, J. White, and L. F. Warren, *ibid.*, **129**, 2261 (1982).
8. D. S. Ginley, R. J. Baughman, and M. A. Butler, *ibid.*, **130**, 1999 (1983).
9. J. M. Bolts, A. B. Bocarsly, M. C. Palazzotto, E. G. Walton, N. S. Lewis, and M. S. Wrighton, *J. Am. Chem. Soc.*, **101**, 1378 (1979).
10. A. Uhler, *Bell Syst. Tech. J.*, **35**, 333 (1956).
11. D. R. Turner, *This Journal*, **105**, 402 (1958).
12. T. Unagami, *ibid.*, **127**, 476 (1980).
13. T. Unagami and M. Seki, *ibid.*, **125**, 1339 (1978).
14. Y. Watanabe, Y. Arita, T. Yokoyama, and Y. Igarashi, *ibid.*, **122**, 1351 (1975).
15. T. Unagami, *Jpn. J. Appl. Phys.*, **19**, 231 (1980).
16. T. Unagami and K. Kato, *ibid.*, **16**, 1635 (1977).
17. S. M. Sze, "Physics of Semiconductor Devices," 2nd edition, p. 42, John Wiley & Sons, New York (1981).

Maximum Power Spectroscopy of n-Type a-Si:H, c-Si, CdSe, and InP in Nonaqueous Photoelectrochemical Cells

J. M. Rosamilia and B. Miller*

AT&T Bell Laboratories, Murray Hill, New Jersey 07974

ABSTRACT

Amorphous silicon photoanodes in a nonaqueous photoelectrochemical cell show wavelength dependence of their power outputs. This behavior has been studied by maximum power spectroscopy (MPS) and compared to similar experiments with conventional short-circuit spectroscopy. The derivative maximum power output under constant chopped input power (MPS) shows dependence on the wavelength distribution in superimposed fixed beams, whereas the conventional short-circuit measurements do not. Single-crystal substrates of n-Si, n-CdSe, and n-InP do not show any differences between the spectroscopies. Rotating ring-disk electrode studies confirm the regenerative behavior of the n-CdSe and n-InP electrodes with the $\text{Fe}(\text{HOCH}_2\text{Cp})_2 - \text{Fe}(\text{HOCH}_2\text{Cp})_2^+$ couple in $\text{LiClO}_4/\text{methanol}$ solution. [$\text{Fe}(\text{HOCH}_2\text{Cp})_2$ = hydroxymethyl ferrocene.]

Photoelectrochemical cells (PEC's) with semiconductor-electrolyte junctions have attracted much attention as candidate systems for the conversion of solar energy into electricity. The spectral response of these systems is a fundamental characterization usually taken as the set of monochromatic quantum efficiencies under short-circuit photocurrent (I_{sc}) collection. We have elsewhere (1) discussed an alternative approach called maximum power spectroscopy (MPS), which measures the derivative maximum power output response to a selected spectral intensity distribution of a scanned monochromatic chopped beam superimposed on one from a fixed source.

PEC's are sensitive in light to electricity conversion to many factors (*viz.*, electrode kinetics, recombination of photogenerated hole-electron pairs, counterelectrode behavior, internal resistances, solution absorbance, and surface reflectivity). The last two of this list will directly influence spectral response at zero power (short circuit), as may significant recombination effects. All, however, will affect the maximum power output.

In the introduction of MPS (1), we studied a p-n Si diode, using added series resistance to simulate these advantages of response realizable in maximum power efficiency spectra. We wish to devote our attention here to photoelectrochemical cells having a common nonaqueous electrolyte phase (20 mM $\text{Fe}(\text{HOCH}_2\text{Cp})_2/1.0\text{M}$ $\text{LiClO}_4/\text{CH}_3\text{OH}$) (2, 3) and four different n-type doped semiconductor photoelectrodes, amorphous hydrogenated silicon (a-Si:H), crystalline silicon (c-Si), CdSe, and InP. Silicon electrodes of both forms have been stabilized to a considerable degree in nonaqueous solvents (2-7), and developments following the introduction of ethanolic ferrocene/ferrocenium solutions by Legg *et al.* (4) have been especially promising.

Recent investigations indicate that the a-Si:H junctions exhibit wavelength-dependent fill factors (2), and this behavior would be particularly interesting to study by MPS.

Both crystalline and amorphous silicon photoanodes in 1.5M LiClO_4 -methanol solution with 0.02-0.20M ferrocene or hydroxymethyl ferrocene/0.5 mM oxidized form are capable of significant solar power conversion efficiencies of 10.1% (3) and 2.7-3.3% (2), respectively.

For further comparison, we chose also to study a semiconductor (CdSe) of bandgap similar to that of a-Si:H and one (InP) whose surface properties in this system would be of additional interest from the viewpoint of stability. For these latter two materials, we felt it necessary to document independently the nature of the reactions proceeding under illumination. Therefore, rotating ring-disk electrode (RRDE) studies were applied to examine whether the photogenerated holes at n-CdSe and n-InP react efficiently to oxidize solution redox species of the ferrocene type.

The MPS technique measures the modulated maximum power output response, ΔP_o , of the photovoltaic system to a chopped monochromatic power input, ΔP_i , superimposed on a steady input power, P_s . The P_s source gives flexibility to the choice of operating levels and allows probing of nonlinearity and saturation effects as a function of intensity. In the present case, the spectral content of P_s would also be significant. In all situations, we compare MPS results to those of short-circuit current spectroscopy under the same conditions.

Experimental

Electrodes.—0.5-0.6 μm thick films of a-Si:H deposited on stainless steel substrates and doped n-type were made available to us as epoxy-mounted electrodes by N. S. Lewis of Stanford University. Their preparation has been previously described (2). The photoelectrode area exposed to the electrolyte was ~ 0.3 cm². Electrodes of single-crystal n-type silicon (c-Si) were prepared from polished wafers of 1-10 Ω -cm resistivity. The a-Si:H and c-Si photoanodes were etched in 5% aqueous HF for 10s, followed by a methanol rinse immediately before use. n-Type CdSe (Cleveland Crystals, Incorporated) 1.8 Ω -cm,

* Electrochemical Society Active Member.

(0001)-face photoanodes were etched for 30s in 4-1 HCl:HNO₃, then rinsed in distilled water. Next they were immersed for 30s in a 10% aqueous KCN solution (to dissolve any selenium that may have been present following oxidation by the aqua regia), with final rinse in methanol. n-InP (Czochralski-grown, kindly supplied by W. A. Bonner) photoanodes were etched in concentrated HCl for 10s, then rinsed with methanol just prior to use.

Reagents.—Anhydrous methanol (0.007% H₂O) was obtained from J. T. Baker, and hydroxymethylferrocene was obtained from Strem Chemical, Incorporated Reagent grade LiClO₄ (Aldrich Chemical Company, Incorporated) and the hydromethylferrocene were used without further purification. All solutions were stored over activated Linde 3A molecular sieves.

Spectroscopy.—The circuitry and instrumentation for obtaining maximum power spectral response were as recently described (1, 8). The input light consisted of a 5 Hz chopped monochromatic beam of power P_i superimposed on a constant beam of power P_s . The bandpass averaged 10 nm (50% of intensity) over the spectrum. The level of P_i was kept constant, independent of wavelength (12 μ W). A 50W tungsten-halogen lamp equipped either with a 600 nm longwave transmitting filter for $\lambda > 600$ nm or a 500 nm shortwave transmitting filter for $\lambda < 500$ nm was the P_s source. The transmitting filters were interference types from Melles Griot. The optical path length through the solution was ~ 5 mm, and no corrections were made for solution absorbance. The cell was operated in a 3-electrode configuration, using graphite rods for both counter and reference electrodes. The reference zero is therefore the solution redox level. The cell solution contained 20 mM Fe(HOCH₂Cp)₂/1.0M LiClO₄/CH₃OH, unless otherwise indicated, and the redox level was established by oxidation of some Fe(HOCH₂Cp)₂ to Fe(HOCH₂Cp)₂⁺ prior to measurement. Solutions were stirred using a magnetic spin bar. Input power regulation, spectral scanning, and data acquisition and plotting were performed under Apple IIe computer control in conjunction with the necessary servo instrumentation (1).

Because inputs are controlled for constant power, spectra of short-circuit current (ΔI_{sc}) have to be corrected for the number of photons (multiplied by photon energy) to be quantum efficiency displays. When there are no wavelength dependent internal losses to cause a normalized difference between ΔI_{sc} and ΔP_o spectra, these spectra also are the same, in spite of different units (current vs. power), because the voltage effect of each absorbed photon is the same, as earlier seen (1).

RRDE.—Rotating ring-disk electrode (RRDE) experiments employed a Pine Instrument Model RDE3 bipotentiostat with graphite rods both as reference and counter-electrodes. n-CdSe and n-InP disks were provided with a Au ring by means of epoxy seals. The areas of the n-CdSe and n-InP disks were 0.175 cm². The geometric collection efficiency, N , of each electrode (9) was determined experimentally by controlling the current at the disk for Fe(HOCH₂Cp)₂ reduction (forward diode direction, dark reaction) and by measuring the disk shielding of the limiting cathodic current at the ring. The cells were equipped with an optical flat bottom to permit illumination of the disk with a 100W tungsten-halogen lamp. A rotation speed of 1600 rpm and a scan rate of 10 mV/s were maintained in all such experiments.

Results

a-Si:H.—Shown in Fig. 1 are the current-voltage and the corresponding $V \times I$ (power) curves for a-Si:H in 20 mM Fe(HOCH₂Cp)₂ for shortwave ($\lambda < 500$ nm) and longwave ($\lambda > 600$ nm) irradiation. Intensities are adjusted to provide identical short-circuit currents in each case.

Fill factors (ff) and maximum power outputs are summarized in Table I. For such experiments, these quantities are 20% greater for lower wavelength irradiation. These data are consistent with those of Gronet *et al.* (2). Displayed in Fig. 2 are plots of I_{sc} vs. P_o for different levels

Table I.

P_s λ , nm	I_{sc} mA	ff	P_o mW
>600	0.68	0.47	0.24
<500	0.68	0.56	0.29

of irradiation at $\lambda > 600$ nm and $\lambda < 500$ nm. P_o is a linear function of I_{sc} over the input power range examined for long and short excitation wavelengths, but the slope, dP_o/dI_{sc} , is steeper under shorter wavelength irradiation. Total internal losses are a function of incident wavelength (2). This factor is emphasized in maximum power output, as opposed to short-circuit (I_{sc}) measurements, because of the role of photoconductivity in the response of this material.

Observing these trends with a-Si:H prompted us to examine the wavelength effect in more detail with maximum power spectra (ΔP_o vs. λ). The spectral cutoffs of the P_s beams were the same in these experiments as those in Fig. 1 and 2. Again these intensities were adjusted to provide the same short-circuit photocurrent density for $\lambda > 600$ nm and $\lambda < 500$ nm sources. The level of I_{sc} was that indicated by the arrow on the abscissa of Fig. 2. It is clear

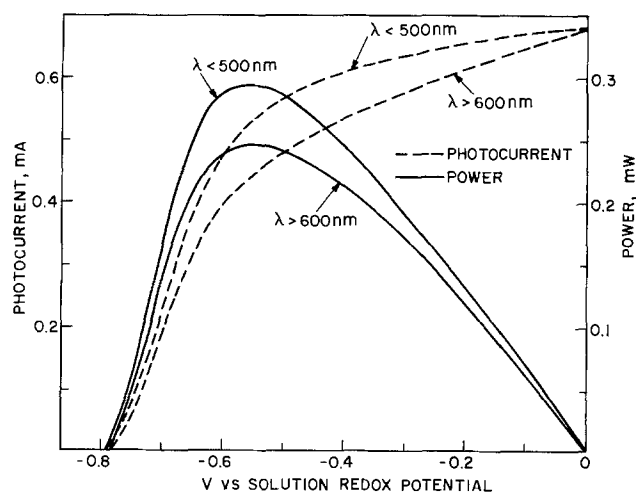


Fig. 1. Current-voltage (---) and power-voltage curves (—) for irradiation of $\lambda < 500$ nm and $\lambda > 600$ nm, a-Si:H cell.

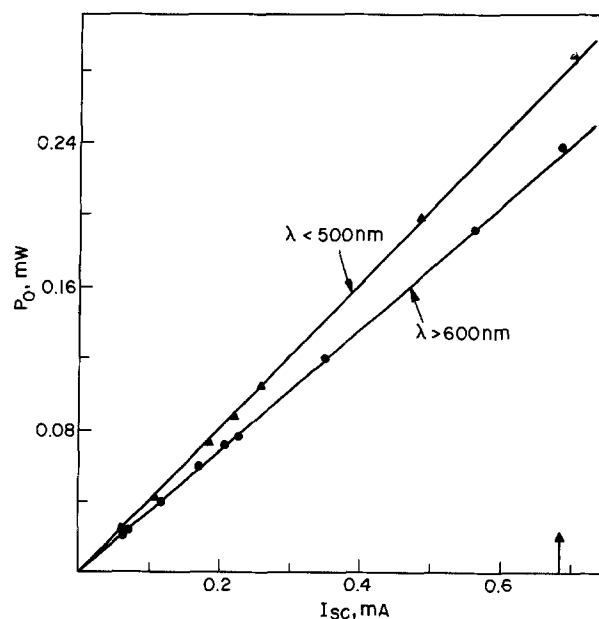


Fig. 2. Plot of P_o vs. I_{sc} for irradiation of $\lambda < 500$ nm (Δ) and $\lambda > 600$ nm (\circ), a-Si:H cell. The arrow indicates the level of P_s employed in Fig. 3.

that the choice of I_{sc} will modify the modulated spectra, depending on the nature of internal voltage losses, as shown for our earlier model experiments (1).

Figure 3A, curve I, shows the modulated power spectrum ΔP_o vs. λ for a-Si:H using $\lambda < 500$ nm for P_s . ΔP_o declines below 530 nm because of solution absorption (λ maximum for $Fe(HOCH_2Cp)_2$ absorption is 435 nm), whereas the longer wavelength limit is that expected from the 1.7 eV bandgap of a-Si:H. Curve II in Fig. 3A is that for P_s at $\lambda > 600$ nm, and it shows a reduced ΔP_o response relative to curve I at wavelengths between 540 nm and the bandgap edge. The ΔP_o responses for both P_s beams are much closer at $\lambda < 530$ nm. The integrated spectral responses are consistent with the wavelength-dependent fill factors for a-Si:H semiconductor liquid junctions given in Fig. 1 and 2. Modulated short-circuit (ΔI_{sc}) spectra employing P_s of $\lambda > 600$ nm and $\lambda < 500$ nm for constant total dc short-circuit current are shown in Fig. 3B. There is no significant effect traceable to the spectral distribution of P_s intensity.

n-Si.—When the experiments of Fig. 3A and 3B are repeated with n-Si and are normalized to the peak value, a single curve is found within experimental resolution for the combinations of $P_s > 600$ nm and $P_s < 500$ nm with ΔP_o and ΔI_{sc} , as illustrated in Fig. 4A and 4B. There is no P_s source wavelength effect with the n-Si single crystal, in contrast to that with the a-Si:H substrate.

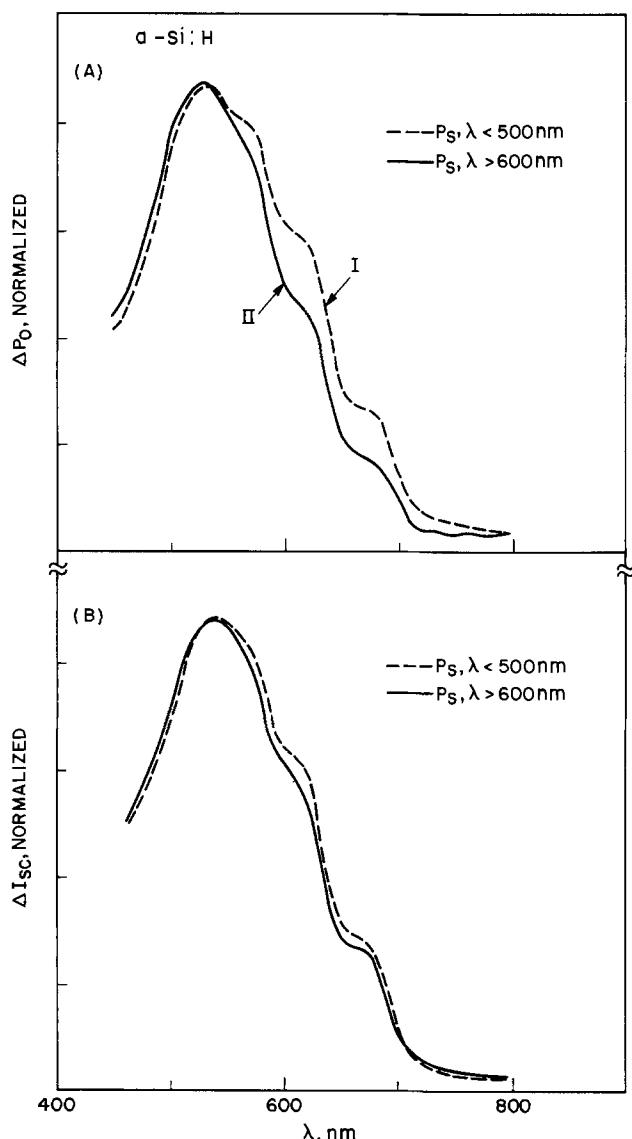


Fig. 3. Modulated spectra (A) ΔP_o vs. λ and (B) ΔI_{sc} vs. λ for a-Si:H employing P_s $\lambda < 500$ nm (---), and P_s $\lambda > 600$ nm (—).

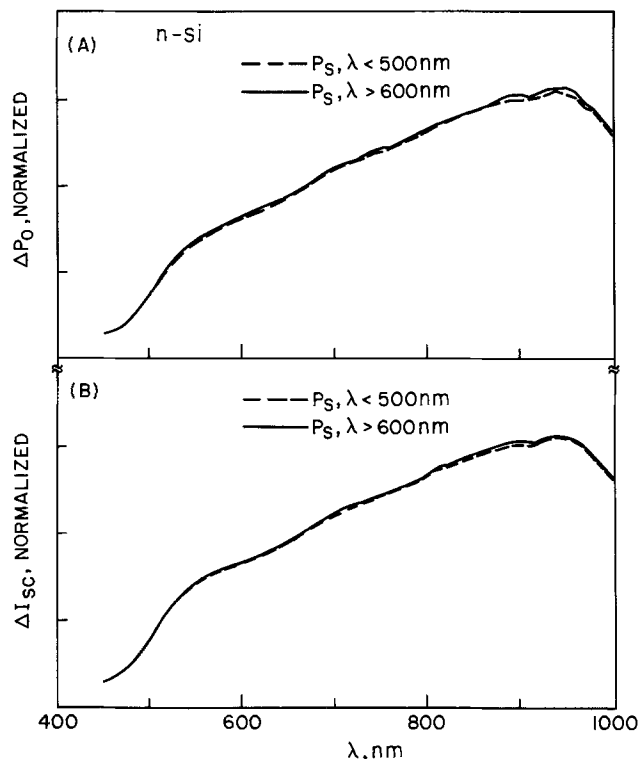


Fig. 4. Modulated spectra (A) ΔP_o vs. λ and (B) ΔI_{sc} vs. λ for n-Si employing P_s $\lambda < 500$ nm (---), and P_s $\lambda > 600$ nm (—).

n-CdSe.—RRDE experiments were first performed to establish if the photogenerated holes produced at a n-CdSe photoanode interface are consumed by hydroxymethylferrocene in 1.0M $LiClO_4/CH_3OH$ solution, rather than by photocorrosion of the semiconductor itself. Figure 5 shows i_D-E_D and the corresponding i_R-E_D curves for a n-CdSe/Au RRDE in 20 mM $Fe(HOCH_2Cp)_2$ under photon flux limited conditions. The ring is controlled at a potential to collect $Fe(HOCH_2Cp)_2^+$ generated at the semiconductor disk. The i_R-i_D relation from this data is shown as the lower line in the insert. The shielding technique for calibration of the collection efficiency (N) at the ring is shown as the dashed line in the insert (note that the current scales are different but proportional). The plot of ring reduction current vs. controlled disk currents under illumination (lower trace) has a slope of 0.342, in agreement with the experimental N of 0.352 for the dark shielding data (dashed trace). These results indicate that, within experimental accuracy, the photogenerated holes react to oxidize the ferrocene derivative at the n-CdSe surface un-

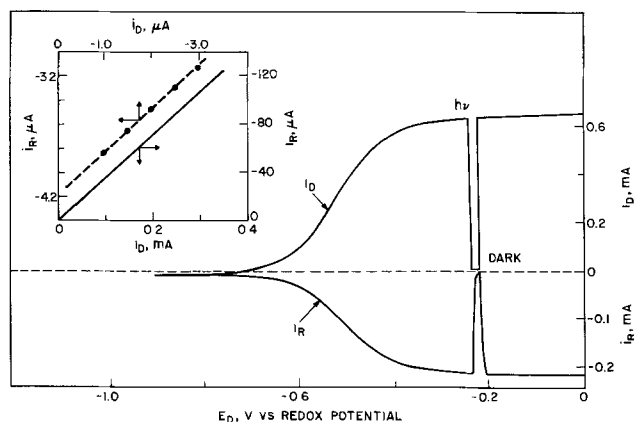


Fig. 5. i_D-E_D and i_R-E_D curves for an illuminated n-CdSe disk-Au ring electrode in 20 mM $Fe(HOCH_2Cp)_2$. E_D scan at 10 mV/s, $E_R = -0.2$ V, $\omega = 1600$ rpm. The insert is the i_R-i_D curve (—) for the potential scan under $h\nu$ conditions. The dotted trace is i_R-i_D for ring shielding in the dark under controlled i_D .

der these illumination conditions. The cell thus operates in a nominally regenerative manner. The stabilization of the surface against corrosion is further evidenced by reproducible cycling behavior between open and short circuit over the short term (hours) tested.

The maximum power spectrum was recorded for n-CdSe under conditions as described for a-Si:H to compare the behavior of a single-crystal semiconductor of virtually the same direct bandgap as a-Si:H. ΔP_0 vs. λ for n-CdSe under the two incident wavelengths of P_s conditions is shown in Fig. 6. The steep edge at the n-CdSe bandgap of 1.7 eV and the solution absorption determine the spectral shape. There is no difference in results for P_s , $\lambda > 600$ nm and $\lambda < 500$ nm. n-CdSe in this medium exhibits no wavelength dependence of fill factors. The Δi_{sc} vs. λ spectra on normalization were identical to the maximum power spectra, as was the case with c-Si, and they are not shown here.

During our investigation, we observed spectral effects due to excess Se on the surface of a freshly oxidatively etched electrode. In Fig. 6 (dotted-dash trace) is the maximum power spectrum of such an electrode if the described KCN solution treatment is not applied. Before immersion in KCN, there is a decrease in the spectral response below 600 nm attributable to the red film of excess Se formed on the surface by aqua regia. The KCN dip has also been used previously for the semiconductor electrode in the n-CdSe/Na₂S-S-NaOH/C solar cell to yield a more reproducible initial electrode state (10).

n-InP.—Parallel studies to those on n-CdSe were performed with n-InP. The equivalent study to that in Fig. 5, but for an n-InP disk with Au ring, is displayed in Fig. 7. A collection efficiency of 0.312 is obtained for the plot of i_R vs. controlled photoanodic values of i_D from the insert of Fig. 5. This corresponds adequately to the N value of 0.329 calculated from the shown dark reaction ring shielding. Further confirmation that charge is being efficiently transferred to the redox system was obtained from a plot of i_R vs. i_D while controlling E_D , as in the Fig. 7 scan ($N = 0.308$).

Photogenerated holes thus oxidize the solution species ($\text{Fe}(\text{HOCH}_2\text{Cp})_2$) under these circumstances, within ring detectability. Maximum power stability for n-InP photoanodes at suitable P_s levels is sufficient for the periods necessary to obtain spectra. The presence of water in the methanol solution significantly contributes to surface oxidation and early cell degradation. Thus, the oxidation wave in this system usually corresponds to a higher fill

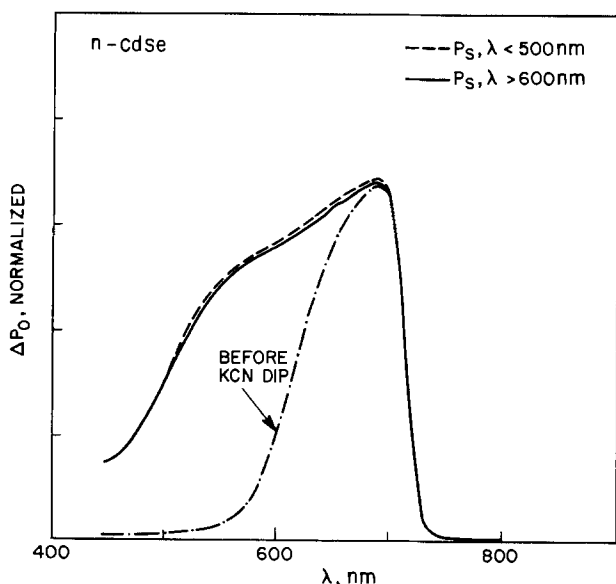


Fig. 6. Modulated power spectra ΔP_0 vs. λ of n-CdSe. The solid line shows the spectra under low energy excitation; the dashed line, under high energy excitation. The dash-dotted line is a spectrum obtained before KCN treatment.

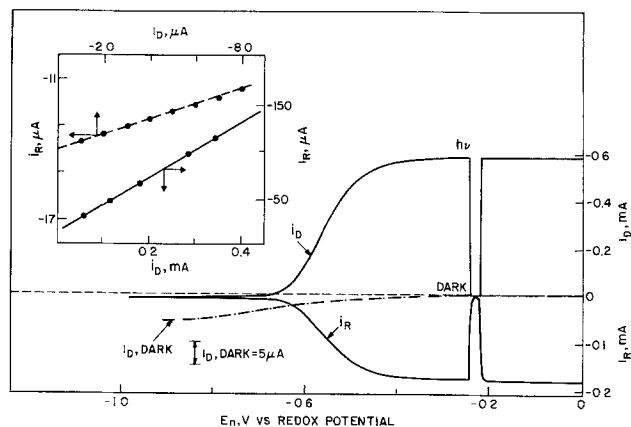


Fig. 7. i_D - E_D and i_R - E_D curves for an illuminated n-InP disk-Au ring electrode in 20 mM $\text{Fe}(\text{HOCH}_2\text{Cp})_2$. E_D scan at 10 mV/s, $E_R = -0.2$ V, $\omega = 1600$ rpm. The insert is an i_R - i_D (—) plot for an illuminated disk at controlled i_D . The i_R - i_D (---) plot was obtained by controlling cathodic disk currents in the dark and measuring the ring shield currents.

factor at a freshly etched disk and decreases slowly on cycling. Efficient collection of $\text{Fe}(\text{HOCH}_2\text{Cp})_2^+$ at the ring (constant i_R/i_D ratio) is retained while i_D declines. More careful drying with molecular sieves and the use of drier methanol sources promote stability. Competitive oxide film formation at the disk eventually leads to passivating thickness which inhibit the oxidation of $\text{Fe}(\text{HOCH}_2\text{Cp})_2$. The occurrence of parallel processes in which the surface oxidation of n-InP cannot be initially suppressed, but which subsequently promote the tunneling transfer of charge to the redox system, have been discussed elsewhere (11, 12). When the film thickness increases, this transfer is inhibited and passivity is observed. The potential scan in Fig. 7 is of a surface on which a thin oxide film initially exists because the electrode was previously cycled. When higher light intensities are applied, degradation is much faster. These effects are shown in Fig. 8 for potential scan and constant potential conditions. The parallel process of surface oxidation is slow in drier solutions. The degradation (oxide) component of disk current is, however, then too low to alter the collection efficiency for the disk $\text{Fe}(\text{HOCH}_2\text{Cp})_2^+$ product within ring accuracy.

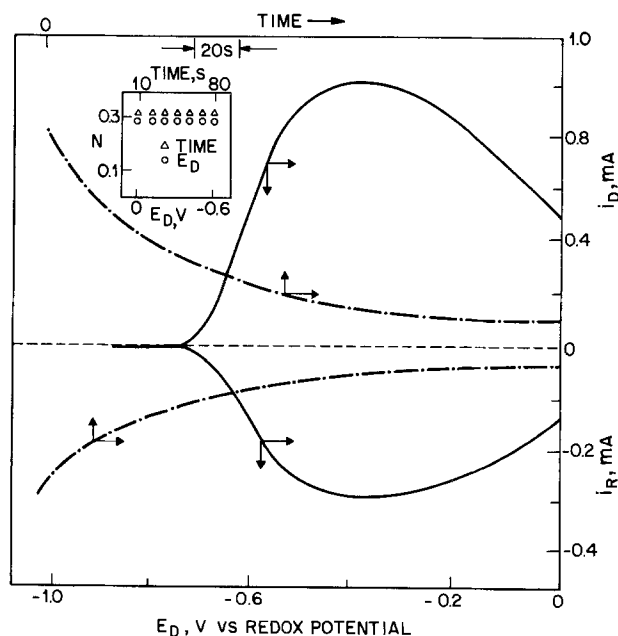


Fig. 8. i_D and i_R vs. E_D (—) and i_D and i_R vs. time (---) curves for an illuminated n-InP disk-Au ring electrode in 20 mM $\text{Fe}(\text{HOCH}_2\text{Cp})_2$. All conditions are the same as in Fig. 7, except for the more intense irradiance. The insert is collection efficiency N vs. E_D or time Δ obtained from i_R - i_D vs. E_D and the respective i_D - i_R vs. time curves.

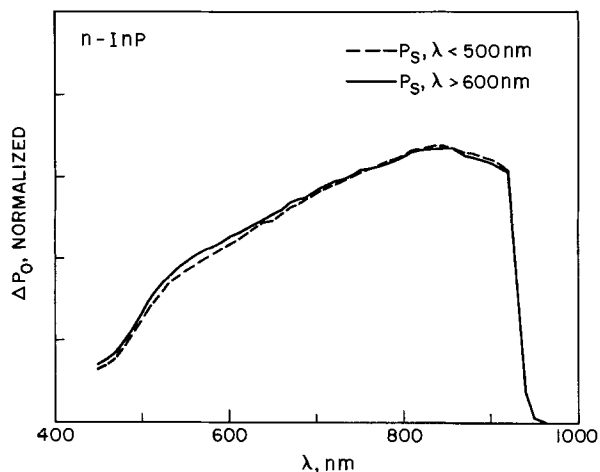


Fig. 9. Modulated power spectra ΔP_0 vs. λ of n-InP. The solid line shows the spectra under low energy excitation; the dash line, under high energy excitation.

Thus, the current efficiency for surface oxidation is indicated to be less than a few percent.

Maximum power spectra for n-InP in this system, shown in Fig. 9, were analogous to those for n-CdSe and c-Si, except for the bandgap (1.35 eV). P_s beams with either short or long wavelength photons in equal numbers have no differentiating effect on the ΔP_0 response. All three examples of crystalline semiconductors studied here were thus parallel in this regard. This would be the classical expectation: all photons of greater than bandgap energy produce the same output and thus show no excitation wavelength differentiation.

Conclusions

The recently introduced method of maximum power spectroscopy has been used to characterize amorphous silicon and three n-type crystalline Si, CdSe, and InP semiconductor photoelectrodes. With a superimposed beam of either short or long wavelength excitation, the thin film of a-Si:H was the only material to exhibit a

wavelength dependent effect in the differential power output spectrum. However, under the same conditions, the differential short-circuit quantum efficiency spectrum displays no dependence on the wavelength distribution of the steady beam when it is normalized to constant dc cell output.

RRDE studies evidence that n-CdSe and n-InP photoanodes in this methanolic medium operate in a regenerative manner. Photocorrosion and/or photopassivation processes at these electrodes are largely circumvented under these operating conditions. The stability of n-InP is more sensitive to light intensity and electrolyte purity and decreases on extended potential cycling.

Acknowledgment

The authors wish to express their appreciation to N. S. Lewis of Stanford University for generously supplying us with epoxy-mounted a-Si:H photoelectrodes.

Manuscript submitted May 14, 1984; revised manuscript received Sept. 10, 1984.

AT&T Bell Laboratories assisted in meeting the publication costs of this article.

REFERENCES

1. B. Miller and J. M. Rosamilia, *This Journal*, **131**, 2266 (1984).
2. C. M. Gronet, N. S. Lewis, G. W. Cogan, J. F. Gibbon, G. R. Moddel, and H. Weismann, *ibid.*, **131**, 2873 (1984).
3. C. M. Gronet, N. S. Lewis, C. Cogan, and J. Gibbons, *Proc. Nat'l Acad. Sci., USA*, **80**, 1152 (1983).
4. K. D. Legg, A. B. Ellis, J. M. Bolts, and M. S. Wrighton, *ibid.*, **74**, 4116 (1977).
5. D. Laser and A. J. Bard, *J. Phys. Chem.*, **80**, 459 (1976).
6. Y. Avigal, D. Cohen, G. Hodes, J. Manassen, B. Vainas, and R. A. G. Gibson, *This Journal*, **127**, 1209 (1980).
7. G. S. Calabrese, M-S. Lin, J. Dresner, and M. S. Wrighton, *J. Am. Chem. Soc.*, **104**, 2412 (1982).
8. B. Miller, *This Journal*, **127**, 184 (1980).
9. W. J. Albery and S. Bruckenstein, *Trans. Faraday Soc.*, **62**, 1920 (1966).
10. A. Heller, G. P. Schwartz, R. G. Vadimsky, S. Menezes, and B. Miller, *This Journal*, **125**, 1156 (1978).
11. L. F. Schneemeyer and B. Miller, *ibid.*, **129**, 1977 (1982).
12. B. Miller, *J. Electroanal. Chem.*, **168**, 91 (1984).

Polymer Films on Electrodes.

XVI. *In Situ* Ellipsometric Measurements of Polybipyrazine, Polyaniline, and Polyvinylferrocene Films

Clifford M. Carlin, Larry J. Kepley, and Allen J. Bard*

Department of Chemistry, The University of Texas at Austin, Austin, Texas 78712

ABSTRACT

Ellipsometry was used to study the electrodeposition of polymer films formed by oxidation of bipyrazine, polyvinylferrocene, and aniline. For polymeric films of limited thickness displaying good optical characteristics (*i.e.*, high reflectivity, uniform coverage, and homogeneity), the film refractive index and thickness were determined. Nonideal ellipsometric behavior was observed when film morphology varied with film growth. Polyvinylferrocene films in 0.1M TBABF₄/acetonitrile were shown to be 15% thicker in the oxidized form than in the reduced form.

Polymer-modified electrodes are prepared by coating thin (100Å-2 μm) films of polymers on conductive substrates (1, 2). These polymers can be electronically conductive ones (*e.g.*, polypyrrole or polyaniline) or those that contain electroactive centers (*e.g.*, polyvinylferrocene or doped Nafion).

The electrochemical investigation and characterization of electron and mass-transport processes in polymer-

*Electrochemical Society Active Member.

coated electrodes has suffered from the lack of a simple and accurate technique for the determination of the polymer film thickness, *d*. Although the thickness of films in solution can be estimated from mechanical stylus profilometer (*e.g.*, Dektak) measurements of dry film thicknesses or from integrated voltammetric currents and assumed densities, uncertainties in the estimated film density, swelling factors, coulometric efficiency for film deposition, and redox processes lead to a low degree of

confidence in the values of d obtained. Recently, *in situ* profilometer measurements of the change in thickness upon reduction of a film have been reported (3). The development of a generally applicable optical technique to determine d would be desirable, since optical methods are inherently precise and often suitable for measurements *in situ*.

Of the optical methods available for making thin film measurements, perhaps the most attractive for this purpose is ellipsometry (4). It has several advantages over other optical techniques: (i) it has already been successfully applied in the study of passivating and adsorbed layers in various electrochemical systems (4-8) [e.g., in the anodic growth of passivating oxide layers on metal electrodes (8)], as well as in the study of electroinactive polymers on semiconductors (9, 10); (ii) it does not require a transparent electrode, only an optically smooth electrode surface; (iii) it does not require the determination of absolute light intensities; and (iv) it can be used to determine the thicknesses of layers much less than the wavelength of visible light. Although ellipsometry has been applied to the study of a wide variety of surfaces under various experimental conditions, it has not been used to characterize polymer-modified electrodes. In this paper, we describe *in situ* ellipsometric measurements on a series of polymer-modified electrodes and gauge its utility and limitations for several types of conductive and electroactive polymer coatings.

Experimental

Instrumentation.—Ellipsometry measurements were obtained on a modified O. C. Rudolph and Sons, Incorporated, Model 437 research ellipsometer [PSCA optical arrangement (4)]. The source was a tungsten/iodine lamp, and wavelengths suitable for the quarter-wave plates available were isolated with interference bandpass filters. Detection was accomplished with a Hamamatsu R928 photomultiplier tube by passing the output photocurrent through a variable resistance box and measuring the resulting voltage with a digital voltmeter. Measurements were made for a range of compensator/analyzer settings around the null-point, which, by interpolation, could generally be determined to within 0.3° for either the compensator or analyzer azimuth. Inaccuracies due to optical components' nonideality and improper alignment were somewhat larger than this and were functions of the reflection polarizations. These errors could be largely eliminated by averaging the calculated optical parameters obtained with the two unique compensator positions which allowed the reflection to be extinguished (*i.e.*, fast axis along the major or minor ellipse of polarization). The procedure was generally not applied, however, because it required doubling of an already lengthy (approximately 10 min per point) data collection time and because the corrections had little effect on the estimated film thickness or morphology.

The cell used during the ellipsometry measurements is shown in Fig. 1. The cell top and base were constructed of either stainless steel or Plexiglas. The window openings are 1/8 in. holes positioned so that incident light can strike the electrode at 45° , 60° , or 75° angles. The cell tops were machined so that glass windows could be cemented in place perpendicular to the direction of propagation of the incident or reflected radiation. Glass or Plexiglas side plates were also cemented in place. The electrode was a 0.5 cm diam piece of glassy carbon attached with conductive epoxy cement to the end of a brass rod. This assembly was inserted into a heat-softened Teflon tube which was cooled and threaded. The electrode surface was polished with increasingly finer diamond paste and alumina, ending with $0.05 \mu\text{m}$ alumina. Electrodes were sonicated for at least 10 min in deionized water before use.

Materials.—Acetonitrile, MeCN (Fisher Scientific), was dried with 0.4 nm molecular sieves (M-512, Fisher Scientific). Tetrabutylammonium tetrafluoroborate, TBABF₄ (Southwestern Analytical Chemicals), and methylene

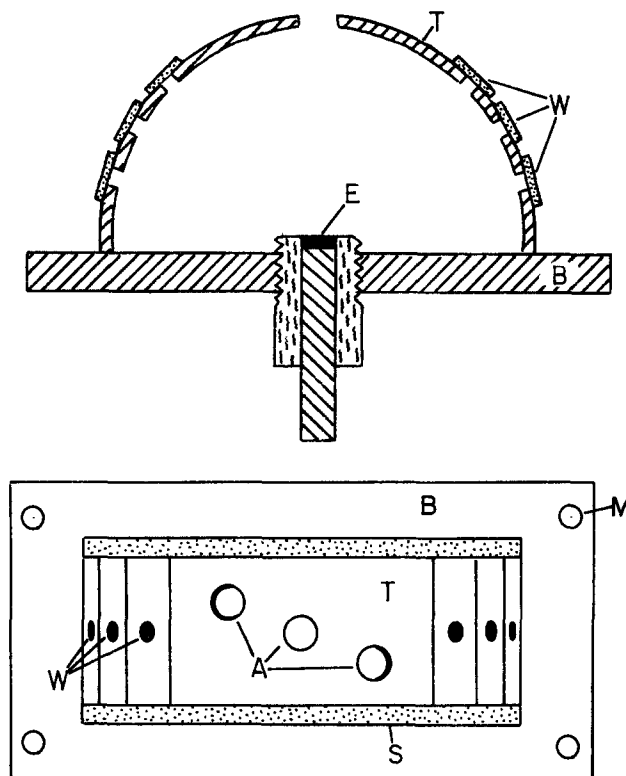


Fig. 1. Ellipsometer cell. Indicated are the cell top (T) and base (B), windows (W), sides (S), electrode (E), and mounting hole (M) and access ports (A) through which pass the counter and reference electrodes.

chloride, CH₂Cl₂ (Fisher Scientific), were used as received. Aniline (MCB) was distilled once from calcium hydride under nitrogen. Bipyrazine, bpz, was used as received from Professor A. B. P. Lever (York University). Polyvinylferrocene, PVF, was prepared and characterized (MW = 15,700; degree of polymerization = 74) by T. W. Smith *et al.* (11). Copolymers of vinylferrocene and vinylcyclopentadienylmanganeses tricarbonyl, VF-VCM (80/20 and 22/78 mole percent [m/o] ratio), were prepared and characterized by Dr. C. U. Pittman, Jr., *et al.* (12).

Film deposition.—Bipyrazine was electrochemically polymerized onto glassy carbon (13) from 3 mM bpz/10% aqueous H₂SO₄ by cycling the electrode potential at 500 mV/s between 1.5 and 2.1V *vs.* a saturated calomel electrode (SCE). The potential for bipyrazine oxidation is close to that of water, so a clearly defined wave for bpz oxidation cannot be resolved in the cyclic voltammograms and bpz oxidation currents cannot be monitored. Ellipsometry measurements were made both on the dry electrode and *in situ* with the potential held at 1.5V *vs.* SCE. For the former experiments, the polymer was deposited outside of the ellipsometer cell and the electrode was rinsed with deionized water and dried with a stream of nitrogen gas.

Polyaniline films (14) were deposited by electrochemical oxidation of aniline from 100 mM aniline/1M aqueous H₂SO₄ solutions either potentiostatically (at 0.8V *vs.* SCE) or by cycling the applied potential between -0.2 and 0.8V *vs.* SCE. Ellipsometry measurements were made *in situ* with the potential held at -0.2 V *vs.* SCE.

Polyvinylferrocene and the VF-VCM copolymers were anodically precipitated from 0.1M TBABF₄/CH₂Cl₂ containing 0.2 mg of polymer per ml of solution (15). Deposition potentials were generally 200 mV positive of the PVF redox potential, *i.e.*, about 0.7V *vs.* a silver wire reference electrode. Ellipsometry measurements were made with the electrode in either the deposition solution or a 0.1M TBABF₄/MeCN solution. For the latter method, optically higher quality films were obtained by dipping the film-coated electrode once into each of the following rinses: 0.1M TBABF₄/MeCN, 0.05M TBABF₄/MeCN, and neat MeCN.

Analysis.—The optical constants of the polymer films generated by the above techniques were obtained by simulating a series of ellipsometry curves (ψ vs. Δ) and visually choosing the best fit of the experimental ψ and Δ . In general, there are four constants (the refractive indexes of the solution or gas phase contacting the film, N_0 , and of the substrate, N_2 ; the angle of incidence, ϕ ; the wavelength, λ), one variable (thickness, d), and one parameter (film refractive index, N_1) necessary in generating a particular curve. In all cases, N_0 was determined independently with an Abbe refractometer and ϕ and λ set to values appropriate to the experiment. The assignment of N_2 was made by determining ψ and Δ for the bare electrode and calculating a bulk refractive index. For this study, it was assumed that displacement of any adsorbate or chemical modification of the electrode surface upon polymer deposition caused no significant change in N_2 . Ignoring the correction procedure described above did not have a significant effect on the choice of N_1 (and, therefore, the calculated d), but did lead to a small, finite deviation of the experimental data from ideal behavior for films of high optical quality. For the films described below as being nonideal (i.e., inhomogeneous or nonuniform), this instrumental error can be considered insignificant.

Results

Polybipyrazine.—Electrochemical formation and deposition of a polymer film on an electrode is especially convenient because the ellipsometric parameters can be determined as the film grows. For a film of uniform density, refractive index, and thickness (d), the expected ψ vs. Δ plot would be periodic with one complete cycle occurring when d equals about one-half the wavelength of the incident light wave. Typical data obtained for the *in situ* deposition of polybipyrazine are shown in Fig. 2. The refractive index of the deposition solution was 1.387, and the calculated N_2 for the glassy carbon electrode immersed in that solution was $1.82-i0.67$. The experimental data shown in Fig. 2 do not follow the expected ideal behavior for a nonabsorbing film because the points are not exactly periodic as the film thickness approaches 250 nm. The particular values of N_1 for the simulations in Fig. 2 were chosen by fixing the real part and determining the imaginary part that provided the best fit of the data in the first cycle of the polarization curve. It was difficult to determine the exact precision in N_1 (and d), but based on a series of simulations that provide a reasonably good fit to the experimental data, d is probably known to within $\pm 10\%$ for the thinnest (<50 nm) films and within $\pm 3\%$ for the thicker films. The two best fits, for $N_1 = 1.63-i0.022$ and $1.64-i0.017$, are those shown in Fig. 2. There is an obvious deviation of the experimental from the simulated curves for the thickest films. Such behavior is characteristic of a nonuniform or variable thickness film (see "Discussion" section), and in general the

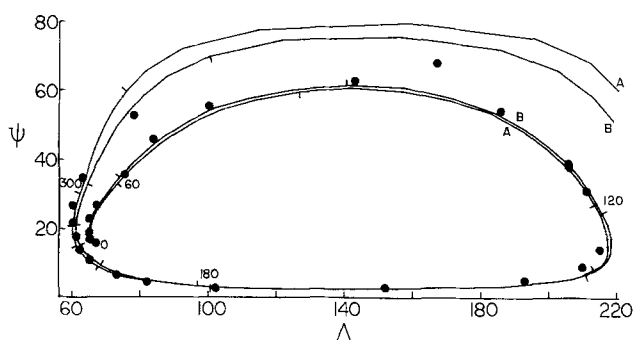


Fig. 2. *In situ* experimental (●) and simulated (—) data for reduced (1.5V vs. SCE) polybipyrazine deposited from 3 mM bipyrazine in 10% aqueous H_2SO_4 ($N_0 = 1.387$). The simulations consist of line segments connecting calculated points for films in 3 nm increments. The complex refractive indexes are (A) $1.63-i0.022$ and (B) $1.64-i0.017$. Indicated d are in nm.

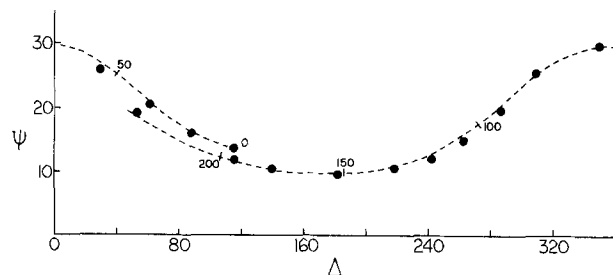


Fig. 3. Experimental (●) and simulated (---) data for dry polybipyrazine films. The simulation is for $N_1 = 1.64-i0.035$. Indicated d are in nm.

bipyrazine films grown in the ellipsometer cell were often visibly nonuniform. Since similar data for thicker polymer films is consistent with an imaginary component of N_1 of about 0.025, curve A ($N_1 = 1.63-i0.022$) probably represents the best fit of the data in Fig. 2. The results for dry polybipyrazine appear in Fig. 3. The dotted line demonstrates the excellent fit of the data to the simulated curve for $N_1 = 1.64-i0.035$ ($N_2 = 1.84-i0.70$).

Figure 4 contains plots of estimated thickness of wet and dry polybipyrazine layers as a function of number of deposition cycles. In general, it was difficult to control the deposition rate of these films from day to day. The bipyrazine oxidation wave is buried under that of the solvent, so small relative changes in deposition potential (due, perhaps, to electrode pretreatment) or in the reference electrode potential could lead to significant changes in deposition rate. Measurements on a particular film in both the wet and dry states indicate that polybipyrazine exhibits very little swelling, so that most of the difference in the observed deposition rates in Fig. 4 can be attributed to variations in experimental parameters or deposition technique. Figure 4 contains two notable features: a wide linear growth region and an initial stage of apparently more rapid deposition. The significance of these characteristics is discussed below.

Polyaniline.—All attempts to obtain ideal plots of ψ vs. Δ for the polyaniline deposition were unsuccessful. Figure 5 contains the best set of results for the reduced polymer which was obtained for films deposited by cycling the working electrode potential between -0.2 and $0.8V$ vs. SCE. A good fit, dashed line, of the early data (to a half-cycle) was obtained for $N_0 = 1.346$ and $N_1 = 1.60$. The spi-

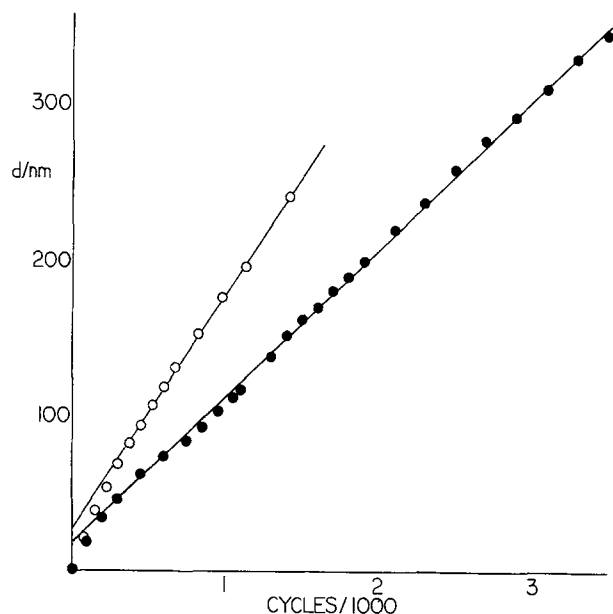


Fig. 4. Growth curves for reduced *in situ* (●) and dry (○) polybipyrazine films. Films were grown under different conditions (see text).

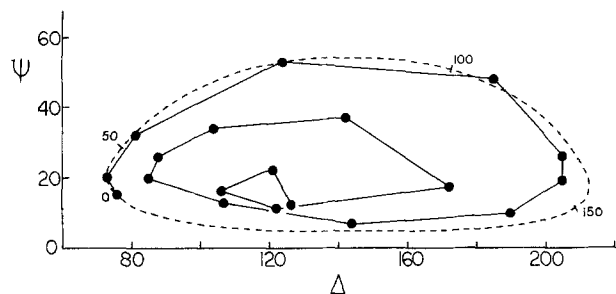


Fig. 5. Reduced (-0.2V vs. SCE) polyaniline which was deposited from 100 mM solutions in $1\text{M H}_2\text{SO}_4$ by cycling the electrode potential between -0.2 and 0.8V vs. SCE . The curve (---) is that predicted for $N_1 = 1.61$. Indicated d are in nm.

raling inward of the ψ vs. Δ data after a half-cycle was accompanied by a marked decrease in the absolute reflectivity and the increasingly hazy appearance of the electrode surface. Potentiostatically growing the polymer produced a coating with obviously poorer optical properties.

Polyvinylferrocene and VF-VCM copolymers.—Attempts to monitor film deposition of PVF in $0.1\text{M TBABF}_4/\text{CH}_2\text{Cl}_2$ solution were unsuccessful. Although a steady increase of oxidized polymer on the electrode surface could be verified by cyclic voltammetry and typical surface waves were observed, there were only very small changes in the reflection polarization of 546 nm light. Oxidation for several hours resulted in the appearance of a blue-green flocculent material on the electrode surface and a decrease in absolute reflectivity, but little change in the reflection polarization. These results suggest that PVF deposits as a highly solvated layer on the electrode surface.

Ellipsometric measurements on films deposited in $0.1\text{M TBABF}_4/\text{CH}_2\text{Cl}_2$ and transferred with rinsing to $0.1\text{M TBABF}_4/\text{MeCN}$ for measurement produced plots of ψ vs. Δ from which d could be determined. Rapid growth ($5\text{--}10\text{ nm/min}$) was apparent from both electrochemical and optical measurements. Figure 6 contains results for an accumulative deposition in which the electrode was repeatedly transferred between deposition and observation solutions. Starting with the bare electrode and proceeding around the dashed curves, each point represents the reflection polarization observed for a film grown thicker between points. The circular and triangular points correspond to the film in the oxidized and reduced (neutral) states, respectively. Simulations are shown by solid lines

connecting points calculated for 10 nm film thickness increments. Each simulated curve represents a fit of the first five data points for each oxidation state with $N_0 = 1.347$ (measured) and $N_2 = 1.81 \pm 0.66$ (calculated). These data indicate that the oxidized form of the polymer film has a lower refractive index (1.48 vs. 1.53) and is 15% thicker than the reduced form (Fig. 7). The experimental ψ vs. Δ plots in Fig. 6 are clearly aperiodic and spiral inward in a fashion similar to that of polyaniline.

Figure 8 is a plot of measured thickness vs. integrated reduction current for a reduced PVF film that displayed good optical properties up to a thickness of 325 nm . This film was grown and studied in the same manner as the film discussed above, except that it was not allowed to dry during the rinsing and transferring procedure. In addition to having reflection polarizations which were close to the ideal behavior for $N_1 = 1.51$, it exhibited, for a scan rate of 10 mV/s , thin-layer cyclic voltammetric waves from which integrated reduction currents were obtained. The plot is fairly linear, as would be expected for a film depositing with uniform density and electroactivity.

Unlike the homopolymer, the deposition of the copolymers could be monitored directly in the deposition solution. Very slow deposition (several hours being required to obtain the data shown) of the 22% ferrocene VF-VCM yielded a reasonable plot of ψ vs. Δ to about 150 nm (Fig. 9). The refractive index of the film was about 1.52 , and N_0 was 1.424 . Also shown in Fig. 9 is a plot of thickness vs. integrated reduction current. The deposition of optically detectable polymer film becomes very inefficient at a thickness of about 150 nm . The surface became noticeably hazy when growth of thicker films was attempted. A spiraling inward of the ellipsometry plot may be occurring, but scattering caused the loss of so much signal that additional data could not be obtained. If the electrodes were washed in acetonitrile, however, a partial restoration of surface reflectivity was observed, without removal of all of the polymer layer. Similar behavior was observed with $80\%/22\%$ VF-VCM.

Discussion

Polybipyrazine.—Of the films studied, polybipyrazine exhibited the best optical characteristics. The deviation of the experimental data in Fig. 2 from that expected for a single layer of refractive index 1.63 ± 0.022 is most likely due to a nonuniform film thickness across the electrode surface. Because of instrumental limitations, a relatively large area, 0.1 cm^2 , or approximately 50% , of the electrode surface had to be included in any optical measurement. If this film is not passivating (as Fig. 4 suggests), non-uniform deposition due to, for example, edge effects, may

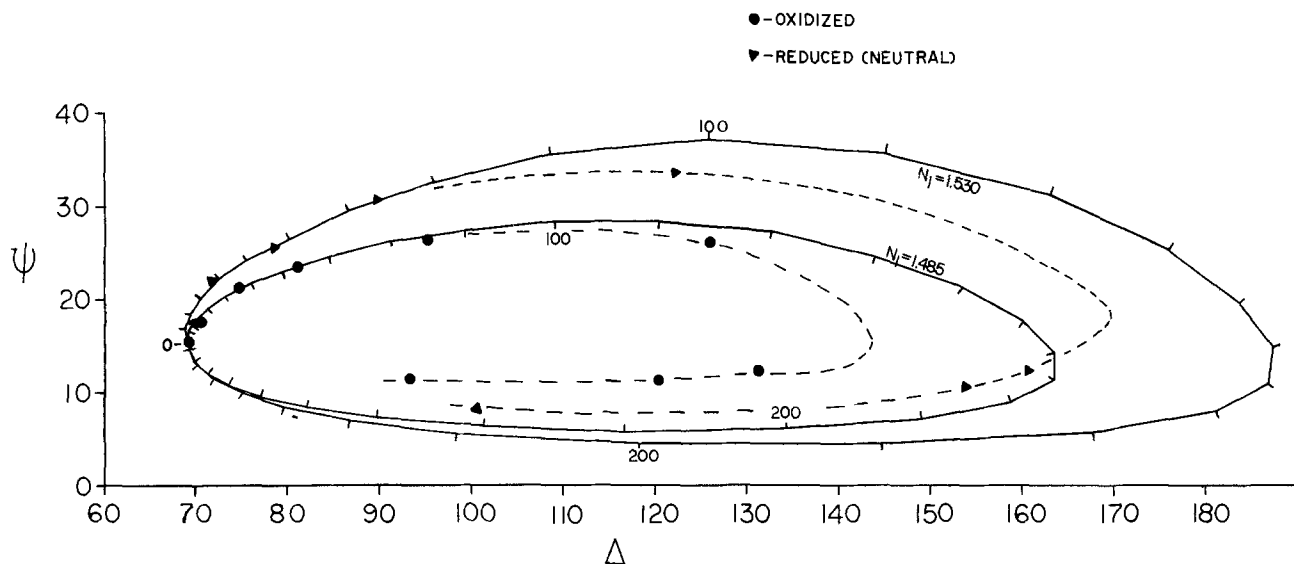


Fig. 6. Experimental and simulated polarizations for PVF films deposited from methylene chloride and transferred to acetonitrile. The simulations are the best fits of the first five points for each oxidation state. Tic marks are placed every 10 nm . The dashed lines are included only for clarity.

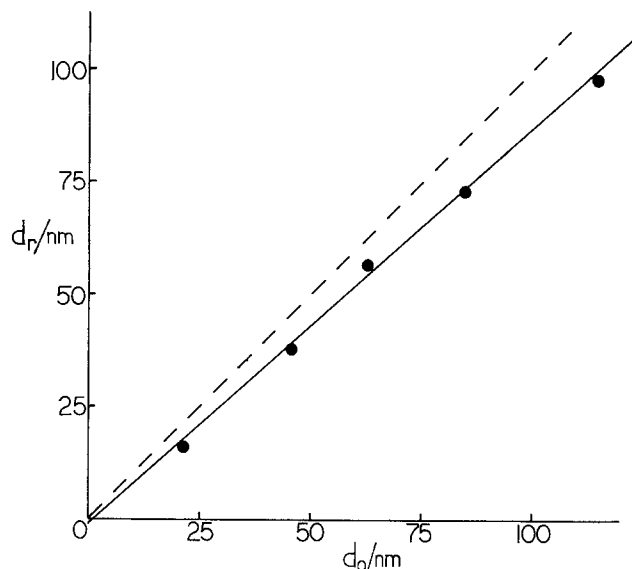


Fig. 7. Reduced (d_r) vs. oxidized (d_o) PVF polymer film thicknesses from data and simulations in Fig. 6.

lead to a relative variation in film depth, d , which is independent of the effective mean thickness. The theoretical plots of ψ vs. Δ shown in Fig. 2 were made by drawing straight lines between calculated points every 3 nm; the effects of nonuniformity would be expected to be most apparent in the regions of these curves where both ψ and Δ are strongly dependent on thickness. In Fig. 2, this occurs when ψ is close to its maximum for a particular cycle. In this region, a spread of reflection polarizations (i.e., depolarization) would lead to an observed ψ which is lower than expected for a uniform film. The effect is much more noticeable in the second cycle because the absolute variation in film thickness could be considerably greater (because the film is three times thicker) and, for absorbing films, the dependence of ψ and Δ on d is somewhat greater. Instrumental designs (14) which permit higher spatial resolution would be required to study thicker films, because this type of variability in d will eventually lead to depolarization sufficient to render thickness information unobtainable. Alternatively, the use of a profiling ellipsometer system (17) could provide coverage information for the entire electrode surface.

The data for the dry polybipyrazine film (Fig. 3) is interesting, because its refractive index is very similar to that of the wet film (i.e., the real part of N_1 equal to 1.64 vs. 1.63 for the wet polymer). Since little swelling was observed between the wet and dry polymer, this behavior suggests either that solvent is mostly excluded from the reduced polymer layer, as might be expected for a neutral

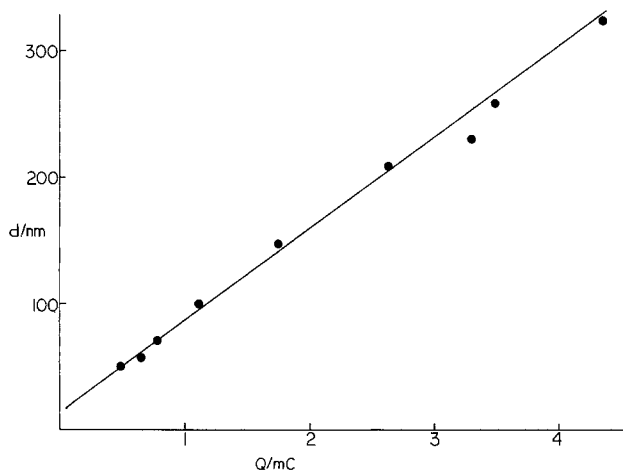


Fig. 8. Thickness vs. integrated reduction currents for PVF

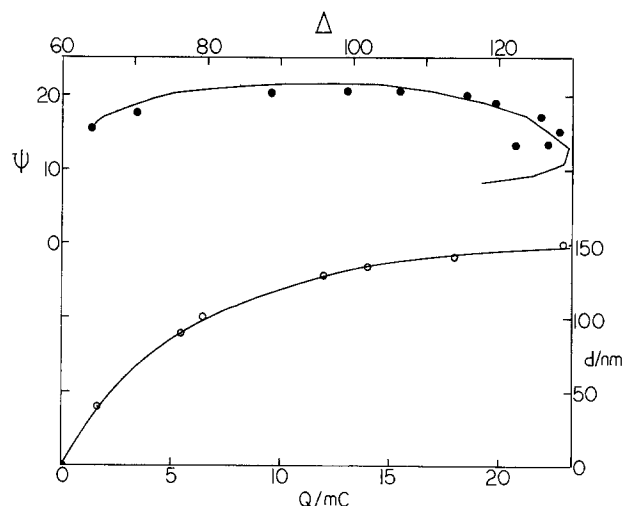


Fig. 9. Data for the *in situ* deposition of 22/78 PVF/VF-VCM in methylene chloride. The top curve represents an attempted fit with $N_1 = 1.52$. The bottom curve is a plot of estimated thickness vs. total deposition charge passed.

organic film, or that the air-dried film retained a significant amount of solvent. The former seems unlikely because rapid diffusion of hydroquinone through the reduced polymer has been observed (13).

Another interesting result of the polybipyrazine experiments is contained in Fig. 4. A plot of the ellipsometrically determined coating thickness vs. the number of deposition cycles clearly indicates that the polymer layer is not passivating toward continued deposition for layers of up to 325 nm. This implies that electron transport is rapid within the oxidized film (and the film is capable of oxidizing the monomer) and/or that mass transport of the monomer to the electrode surface (through the film) is not significantly limited by the presence of the polymer layer. These results are consistent with the electrochemical findings (13). Although, taken alone, these ellipsometry data cannot be used to deduce the mechanism of film deposition for polybipyrazine, they do show that ellipsometry may provide supportive evidence about the nature of the film in such an investigation. For example, the initial deposition rate for films <70 nm thick is twice that of the limiting rate (see Fig. 4).

Polyaniline.—Although ellipsometry does not yield useful thickness measurements for $d > 150$ nm, the polyaniline results are significant in that they demonstrate the sensitivity of the ellipsometric technique to film morphology. For the data presented in Fig. 5, reasonably precise film thicknesses can be obtained during the early stages of film growth. Optically, this film behaves well to about 150 nm, as is evident by the good fit of the data to a curve for $N_1 = 1.60$ and by the fact that macroscopic examination of the electrode surface showed a highly reflective surface. For thicker films, the optical characteristics of the polyaniline layer changed, as is evident from the inward spiral of the ellipsometry data. Simulations using various combinations of real and imaginary components for N_1 confirm that the unusual behavior of the measured ψ and Δ in Fig. 5 cannot be described by ellipsometry theory for homogeneous films, so effects of inhomogeneity and/or surface roughness must be considered. The theory for inhomogeneous coatings has been developed (4), but in general, closed-form solutions for the ellipsometry equation cannot be obtained, even if a functional description of the depth-dependent refractive index is available (18). Calculations may be made if the film is approximated by a series of discrete homogeneous layers. If the refractive index of these layers is assumed to decrease with distance from the substrate/film interface, the simulated curves spiral inward in a fashion similar to the observed polyaniline curves. However, optical and electron microscopy (not shown) indicate that

the deposition of a relatively dense polymer layer up to 150 nm is followed by the growth of loosely packed fiberlike structures which have diameters of about 200 nm. Fibrous structures of this size cause roughness effects that would preclude the use of a multiple layer (microscopic) approach to the simulation of the ellipsometry data and would force the use of theories for the treatment of gross roughness (19). Additional data, such as multiple angle measurements, will be required to determine whether a particular model is valid.

The optical properties of the polyaniline films depend on the deposition technique. The data in Fig. 5 are for a film deposited by cycling the electrode potential as described in the experimental section, while potentiostatically-grown films exhibited much poorer optical characteristics. The fiberlike structures found in the thicker films are clearly electronically conductive, since microscopic examination of the film during oxidation and reduction shows rapid changes in the color of the fibers during electrochemical cycling. Growth of these fibers may be analogous to the growth of needlelike crystals of conductive tetrathiafulvalenium bromide in Nafion films (20, 21). These results suggest a changing mechanism for film deposition. The initially deposited film is much more dense, because the possibility of monomer oxidation directly at the electrode is high. As it becomes increasingly difficult for monomer to reach the electrode surface, oxidation at the termini of the conductive aniline chains becomes the dominant Faradaic process, leading to fiber production. Attempts have been made to improve the homogeneity of the aniline polymers by using different potential pulse or controlled current deposition programs, but little improvement in the optical characteristics of the films above 150 nm has been realized.

Polyvinylferrocene and VF-VCM copolymers.—PVF films produced by prolonged oxidation in methylene chloride could not be detected *in situ*, indicating that PVF deposits as a very diffuse, highly solvated layer. A film was obviously being formed, because the blue-green flocculent material was observed on the electrode, and large cyclic voltammetric surface-waves resulted when the applied potential was scanned negatively. The lack of change in the reflection polarization indicates, however, that the oxidized film had a refractive index that was not significantly different than that of the deposition solution.

The copolymers deposited more densely than PVF in methylene chloride, and it was possible to monitor their growth *in situ* up to thicknesses of 150 nm (see Fig. 9). At this point, deposition either effectively ceased or the density of newly deposited film became too low to be optically detected. These films grew much more slowly (about 50 nm/h) than PVF, which may have enhanced their ability to pack more densely, thus permitting one to monitor their growth in the deposition solution. The limiting factor in measuring the thickness of these films appears to be their inherent nature to grow inhomogeneously.

Films grown in methylene chloride and directly transferred into acetonitrile without rinsing resulted in ψ vs. Δ curves which spiraled quickly inward and cyclic voltammetric waves that showed diffusional tailing. This kind of ellipsometric behavior would be expected, as discussed above, of a film whose refractive index (and, therefore, density) decreases with distance from the electrode or whose surface is becoming increasingly rough. A precise description of the inhomogeneity would be important to know if one expects to model the electrochemical behavior of this redox polymer successfully.

The sensitivity of ellipsometry to roughness and/or inhomogeneity dictated that procedures be found to improve the quality of PVF films. Variability of film quality was a persistent problem, and ellipsometric characterization proved a useful diagnostic tool for ascertaining if a film was depositing uniformly. Nonideal growth could be observed early, long before the appearance of any light

scattering or tailing cyclic voltammetric waves. Since PVF is slightly soluble in neat MeCN, but insoluble in 0.1M TBABF₄/MeCN, the films were rinsed as described in the "Deposition" section. The films were ellipsometrically observed to become thinner by this procedure. MeCN probably dissolves any loosely-bound outer layer and also solvates the film, thus improving its homogeneity. Films of improved optical and electrochemical quality could be grown to 300 nm by rinsing the electrode between depositions in this fashion, and ellipsometry curves (not shown) spiraled inward less dramatically. High surface reflectivity could generally be restored by this procedure with minimal concurrent loss of polymer.

Although homogeneous and uniform films were difficult to grow, Fig. 7 and 8 indicate that useful information could be obtained over a limited range of d . Figure 7 is especially interesting in that it represents the first reliable measurement of an oxidation/reduction swelling coefficient for an electroactive polymer. The observed decrease in film refractive index and increase in thickness that occurs upon oxidation of the polymer suggests that PVF is swelled by the uptake of counterions and attendant solvent molecules. The measured swelling coefficient (determined from the slope of the line in Fig. 7) is 1.15. Although allowance for film absorptivity has not been made, it is believed that this would be small, because the films in Fig. 7 are rather thin, and measurements on thicker (though somewhat inhomogeneous) films do not indicate that absorption is a problem.

The data in Fig. 8 allow comparison to be made between PVF film thicknesses determined ellipsometrically and by a nonoptical technique. The slope of the line in Fig. 8 provides a thickness/charge relationship given by

$$d = (1.9 \times 10^{-3} \text{ cm}^3 \text{ C}^{-1}) Q/A \quad [1]$$

where d is the thickness, in cm, Q is the charge passed to reduce the totally oxidized film, in coulombs, and A is the electrode area, in cm². This finding is consistent with previously published results (22) for thicker PVF polymer films. The concentration of electroactive redox centers, C , is approximated (assuming $n = 1$) by

$$C = Q/dAF \quad [2]$$

where F is Faraday's constant. From the experimental expression for d , one obtains

$$C = (F \times 1.9 \times 10^{-3} \text{ cm}^3 \text{ C}^{-1})^{-1} \approx 5M \quad [3]$$

which is consistent with a reasonably densely packed array ($\sim 1.1 \text{ g/cm}^3$) of ferrocene moieties.

Conclusion

It has been shown that the ellipsometric technique can be applied successfully to the *in situ* study of electroactive polymer-modified electrodes. Data have been presented on three classes of electroactive polymer materials.

The conductive polymer, polyaniline, exhibits a very inhomogeneous morphology and at best displays ideal optical properties only up to 150 nm. Thickness and structural information for polyaniline films with a thickness greater than this will require multiple angle studies in order to apply microscopic or gross roughness theories to this system. Ellipsometry may prove to be useful in attempts to monitor and control the morphology of conductive films.

In situ measurements for the electroprecipitated redox polymers (PVF and the copolymers) have proven to be capable of providing redox site concentrations (necessary for electrochemical studies), as well as information on morphological changes that occur upon oxidation or reduction of these films. Detailed ellipsometric studies will eventually assist in the understanding of the mechanisms of charge transport in this important class of compounds.

Electropolymerized bipyrazine yielded the best films for the ellipsometric determination of thickness. Al-

though instrumental and sample problems limited our ability to make precise measurements for thicknesses beyond about 400 nm, analysis of much thicker layers is well within reach.

As a general tool for the study of polymer modified electrodes, ellipsometry will eventually be limited by effects of gross roughness and film nonuniformity. Implementation of improved cell designs and more complex theoretical considerations may improve its utility in this field. Data acquisition with an automatic ellipsometer and at multiple wavelengths should also aid in the elucidation of the structure and behavior of polymer films on electrodes.

Acknowledgments

The authors wish to thank Dr. Frank Fan, Dr. Pushpito Ghosh, Dr. Johna Leddy, and Dr. Alex McDonald for their helpful assistance and comments. The support of this work by the National Science Foundation (CHE84-02135) and the Robert A. Welch Foundation (F-079) is gratefully acknowledged.

Manuscript submitted May 14, 1984; revised manuscript received Sept. 24, 1984.

REFERENCES

1. R. W. Murray, in "Electroanalytical Chemistry," A. J. Bard, Editor, pp. 191-368, Vol. 13, Marcel Dekker, New York (1984).
2. W. J. Albery and A. R. Hillman, *Chem. Soc. Annu. Rep. C.*, **377** (1981).
3. T. Lewis, H. S. White, and M. Wrighton, Private communication.
4. R. M. A. Azzam and N. M. Bashara, in "Ellipsometry and Polarized Light," pp. 269-363, North-Holland Publishing Co., New York (1977).
5. W. Paik, M. A. Genshaw, and J. O'M. Bockris, *J. Phys. Chem.*, **74**, 4266 (1970).
6. E. Yeager, *Surf. Sci.*, **101**, 1 (1980).
7. J. Kruger, in "Advances in Electrochemistry and Electrochemical Engineering," P. Delahay and C. W. Tobias, Editors, pp. 227-280, Vol. 9, John Wiley and Sons, New York (1973).
8. Several recent examples include: W. Kozlowski and A. Szklarska-Smialowska, *This Journal*, **131**, 723 (1984); J. L. Ord, *ibid.*, **129**, 767 (1982); C.-T. Chen and B. D. Cahan, *ibid.*, **128**, 17 (1982); S. Silverman, G. Cragnolino, and D. D. MacDonald, *ibid.*, **129**, 2419 (1982); T. Ohtsuka and N. Sato, *ibid.*, **128**, 2522 (1981).
9. R. Scheps, *ibid.*, **129**, 2273 (1982).
10. R. Scheps, *ibid.*, **131**, 540 (1984).
11. T. W. Smith, J. E. Kuder, and D. Wychik, *J. Polym. Sci., Polym. Chem. Ed.*, **14**, 2433 (1976).
12. C. U. Pittman, Jr., G. V. Marlin, and T. D. Rounsefell, *Macromolecules*, **6**(1), 1 (1973).
13. P. K. Ghosh and A. J. Bard, *This Journal*, In press.
14. A. F. Diaz and J. A. Logan, *J. Electroanal. Chem.*, **111**, 111 (1980).
15. A. Merz and A. J. Bard, *J. Am. Chem. Soc.*, **100**, 3222 (1978).
16. K. Sugimoto and S. Matsuda, *This Journal*, **130**, 2323 (1983).
17. M. Stenberg and H. Nygren, *Anal. Biochem.*, **127**, 183 (1982).
18. F. Abeles, in "Ellipsometry in the Measurement of Surfaces and Thin Films, Symposium Proceedings, Washington, 1963," E. Passaglia, R. R. Stromberg, and J. Kruger, Editors, pp. 41-58, National Bureau of Standards Miscellaneous Publication 256 (1964).
19. T. Smith, *J. Electroanal. Chem.*, **150**, 277 (1983).
20. T. P. Henning, H. S. White, and A. J. Bard, *J. Am. Chem. Soc.*, **103**, 3937 (1981).
21. T. P. Henning, H. S. White, and A. J. Bard, *ibid.*, **104**, 5862 (1982).
22. J. Leddy and A. J. Bard, *J. Electroanal. Chem.*, **153**, 223 (1983).

Electrocatalytic Oxidation of As(III)

II. Kinetic Studies at Pt Electrodes

Tim D. Cabelka,¹ Deborah S. Austin, and Dennis C. Johnson*

Department of Chemistry and Ames Laboratory,² Iowa State University, Ames, Iowa 50011

ABSTRACT

The empirical rate law for the electrocatalyzed oxidation of As(III) at a Pt RDE in acidic media was determined from potentiostatic measurements to be

$$k = k_0(t/t_0)^{-b} \exp \{-E/E_0\}$$

where $t_0 = 1.0$ s and $E_0 = 0.161$ V vs. SCE. For an electrode surface covered with less than the equivalent of a monolayer of PtO (*i.e.*, $Q_{ox}/Q_H < ca. 2$), $b = 0.30$, whereas for an extended oxide coverage (*i.e.*, $Q_{ox}/Q_H > 2$), $b = 0.5$. The coefficient k_0 is independent of time (t) and electrode potential (E), but decreases as a function of the log of As(III) flux, *i.e.*, $\omega^{1/2}C^b_{As(III)}$. It is PtOH and not PtO that is the active agent for oxygen-atom transfer in the electrocatalytic mechanism. The finite rate of oxidation of As(III) observed for $Q_{ox}/Q_H \gg 2$ is concluded to result from $\cdot OH$ generated as the first step in the mechanism for continued oxide growth. It is concluded also that the generation of $\cdot OH$ at a highly oxidized Pt surface occurs at a rate independent of applied potential.

A brief review of the electrochemical literature for As(III) was presented in part I of this work (1), together with our results of voltammetric studies at Pt rotating disk and ring-disk electrodes. The irreversible oxidation of As(OH)₃ at Pt electrodes in acidic media is electrocatalyzed dramatically by the anodic discharge of adsorbed $\cdot OH$ (*i.e.*, PtOH) as the first step in (i) the production of surface oxide (*i.e.*, PtO) and (ii) the evolution of O₂(g) at an oxide-covered Pt surface. The rate of oxidation of As(III) is substantially lower at a surface covered by a well-developed layer of PtO with a rate constant (k), mea-

sured during the negative potential scan, which is independent of potential in the range $0.9 \leq E \leq 1.2$ V vs. SCE. Hence, for a fixed quantity of surface oxide, the rate-determining step (rds) is not a charge-transfer step. The value of k measured at 1.0V on the negative potential scan for an oxide covered electrode decreases with increasing value of the anodic scan limit (E_a) for the preceding positive scan as described by

$$k = M \cdot \exp \{-E_a/E_0\} \quad [1]$$

where M and E_0 are constants; the value of M was not studied for time dependence in part I (1). The charge corresponding to the total surface oxide (Q_{ox}) formed during a cyclic potential scan for $E_a \geq 1.0$ V in the presence of As(III) is approximately the same as for the absence of As(III). Since Q_{ox} is a linear function of E_a (2), Eq. [1] can

*Electrochemical Society Active Member.

¹Present address: Dow Chemical Company, Midland, Michigan 48640.

²Operated for the U.S. Department of Energy by Iowa State University under Contract no. W-7405-ENG-82.

be rewritten as

$$k = N \cdot \exp \{-Q_{ox}/Q_0\} \quad [2]$$

where N and Q_0 are constants under the conditions of measurement.

Gilroy (2) has reviewed the literature pertaining to the kinetics of oxide growth at Pt electrodes and provided additional data to demonstrate the time dependence of Q_{ox} as described by

$$Q_{ox} = a\eta \ln(t/t_0) \quad [3]$$

where a and t_0 are constants, and η is the applied overpotential for oxide formation. Combining Eq. [2] and [3] to eliminate Q_{ox} gives the anticipated dependence of k on t following a potential step to a fixed value of η

$$\ln k = \ln N - (a\eta/Q_0) \ln(t/t_0) \quad [4]$$

Here, we report the results of a kinetic study of the electrocatalyzed oxidation of As(III) in acidic media to test the validity of Eq. [4].

Experimental

Instrumentation and chemicals.—Most conditions and devices described in Ref. (1) apply. The electrode was Model AFMD/8 Pt RDE ($A_d = 0.166 \text{ cm}^2$) in conjunction with the MSR rotator (Pine Instrument Company). In some experiments, speed control was by an analog signal from a linear ramp generator; in others, control was by a Model 6800 Southwest Technical Products Corporation computer (Pine Instrument Company) using a 12-bit D/A converter.

All chemicals were analytical reagent grade and solutions were prepared from triply distilled water. The NaClO_4 used to regulate ionic strength was recrystallized twice from distilled water to minimize the level of trace Cl^- .

Procedures.—The reproducibility of the electrode surface activity was insured for potentiostatic i - t studies by the customary voltammetric pretreatment under a triangular-sweep potential waveform applied 10-20 times or until the i - E curves were reproducible. Conditions for the pretreatment were: $E_p = 1.2$ - 1.3 V , $E_c = 0.1$ - 0.2 V , $\phi = 3$ - 6 V/min ; ω and C^b were the values to be applied in the subsequent potentiostatic study. A value of E_c less than 0.1 V was not chosen to avoid electrodeposition of bulk As⁰. The pretreatment was terminated on the negative scan at $E = E_c$; then, E was stepped immediately to the potentiostatic value of interest and the i - t curve recorded.

The faradaic response was modeled after the treatment of coupled kinetics (3) as given by

$$i = \frac{nFADC^b}{\delta + D/k} \quad [5]$$

where $\delta = 1.61D^{1/3}\nu^{1/6}\omega^{-1/2}$ and all terms have their customary electrochemical significance for the RDE. The constant k is taken to be a generalized rate constant and was determined to be a function of t , E , C^b and $\omega^{1/2}$. Two specific applications of Eq. [5] were used for calculating k as a function of t .

Method A.—The value of i was recorded as a continuous function of t and k was calculated for selected values of t using

$$k = \frac{1}{nFAC^b(1/i - 1/i_{lim})} \quad [6]$$

where i_{lim} corresponds to the calculated transport-limited current for the RDE. As will be demonstrated, large error in k can result at small t , *i.e.*, when $i \approx i_{lim}$, due to a small error in the estimation of i_{lim} .

Method B.—For some kinetic studies of long duration (*i.e.*, $t > \text{ca. } 500 \text{ s}$), k was calculated from the intercept of the $i^{-1}\omega^{-1/2}$ plot made according to

$$i^{-1} = \frac{\omega^{-1/2}}{0.62nFAD^{2/3}\nu^{-1/6}C^b} + \frac{1}{knFAC^b} \quad [7]$$

from the i - ω curve recorded at selected values of t . The time to sweep the range of ω (*i.e.*, 30 - 525 rad/s) was *ca.* 45 s , which was small in comparison to the large values of t involved in these i - t studies. Hence, the quantity of surface oxide was estimated to be constant during the course of each ω scan. Twelve specific values of i^{-1} were plotted *vs.* $\omega^{-1/2}$ from each i - ω curve for eight values of t , and the slopes and intercepts were obtained by linear regression.

The Pt RDE electrode was polished with $1.0 \mu\text{m}$ alumina for all experiments. The average roughness factor was determined to be 2.0 , based on measurements of the charge for hydrogen adsorption (Q_H).

Results and Discussion

Dependence of k on t .—Representative current-time (i - t) curves for 2.00 mM As(III) are shown in Fig. 1 for E in the region of electrocatalysis (see Fig. 1 and 7, part I). The calculated i_{lim} is shown for comparison (*i.e.*, $465 \mu\text{A}$). Of the numerous plotting methods tested, the best linear plots were obtained for $\log k$ *vs.* $\log t$, as illustrated in Fig. 2 for Method A with $t = 10$ - $10,000 \text{ s}$. The plots are adequately approximated by a linear correspondence for the regions of $t < \text{ca. } 200 \text{ s}$ (slope = *ca.* -0.3) and $t > \text{ca. } 500 \text{ s}$ (slope = *ca.* -0.5).

Method B was applied to the evaluation of k in the range 360 - 7200 s and plots of i^{-1} *vs.* $\omega^{-1/2}$ are shown in Fig. 3. The fact that these plots are parallel with that for i_{lim}^{-1} *vs.* $\omega^{-1/2}$ supports the choice of D for calculating i_{lim} . The plot of $\log k$ *vs.* $\log t$ for eight values of t was linear with a slope of -0.49 , in agreement with Method A for $t > \text{ca. } 500 \text{ s}$ (Fig. 2).

Consideration of error.—Values of k calculated from i at small t (Method A) can have large error when $i \approx i_{lim}$ (see Eq. [6]). Since i_{lim} cannot be measured directly using the Pt RDE, it was calculated based on the value of D ($1.026 \times 10^{-5} \text{ cm}^2 \text{ s}^{-1}$ for $0.5 \text{ M H}_2\text{SO}_4$) from measurements of i_{lim} at a Au RDE, where the oxidation of As(III) is transport limited. Consider the plots of $\log k$ *vs.* $\log t$ in Fig. 2 for $E = 1.0$ and 1.2 V which are redrawn in Fig. 4. Also shown in Fig. 4 are the plots for k calculated using i_{lim} estimated to be *ca.* 6% lower than the "correct" value used for Fig. 2. The shaded area between the two curves illustrates the extent of uncertainty in $\log k$; *i.e.*, the 6% decrease in i_{lim} produces an increase of k of $\geq 50\%$ for $t < \text{ca. } 20 \text{ s}$ at $E = 1.0 \text{ V}$. The error in k for small t is much less at larger E because i decreases more rapidly from i_{lim} (see Fig. 1).

Dependence of k on E .—Of greatest consequence in electroanalysis is the rapid decrease in response at relatively short times (*i.e.*, $t < 100 \text{ s}$). Representative plots of $\log k$ *vs.* $\log t$ are shown in Fig. 5 for E increased by 50 mV increments in the range 0.90 - 1.25 V for $\omega^{1/2} = 10.23 \text{ rad}^{1/2} \text{ s}^{-1/2}$; the statistics for such plots are given in Table I for two values of ω . The slopes exhibit negligible dependence on

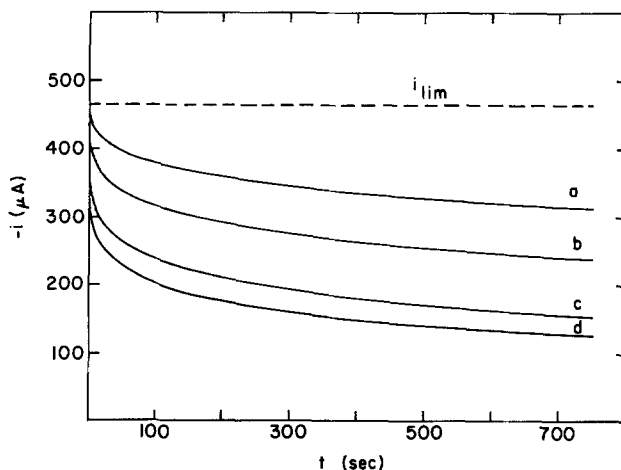


Fig. 1. Current-time (i - t) curves for As(III) at E (V vs. SCE): a = 1.00 , b = 1.10 , c = 1.20 , and d = 1.30 . Conditions: $C^b = 2.00 \text{ mM As(III)}$ in $0.50 \text{ H}_2\text{SO}_4$, $\omega^{1/2} = 10.23 \text{ rad}^{1/2} \text{ s}^{-1/2}$.

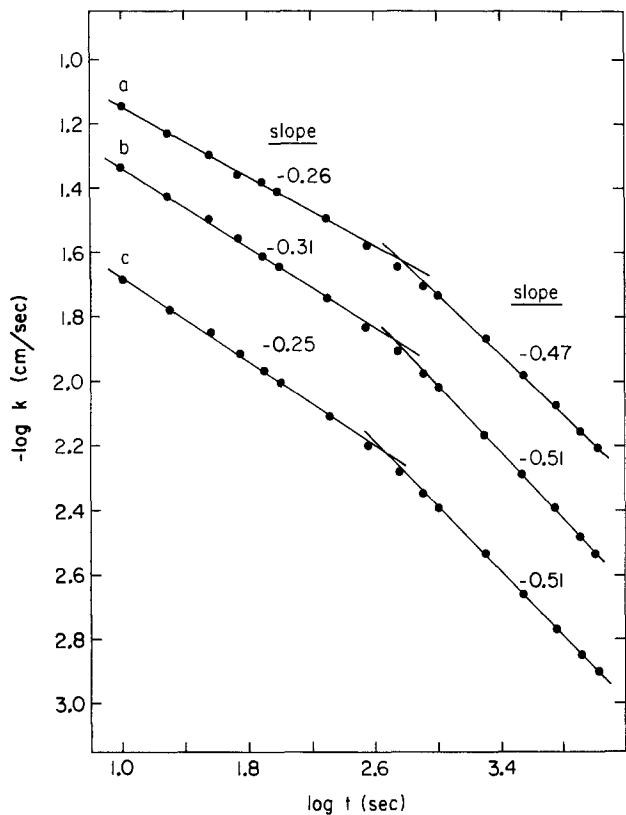


Fig. 2. Plots of $\log k$ vs. $\log t$ for $t = 10-10,000s$ (Method A). E (V vs. SCE): a = 1.00, b = 1.10, and c = 1.20. Conditions: $C^b = 2.00$ mM As(III) in $0.50M$ H_2SO_4 , $\omega^{1/2} = 10.23$ $rad^{1/2} s^{-1/2}$.

E , and the average value is -0.30 . The intercepts (I) of $\log k$ - $\log t$ plots (i.e., $\log k$ for $t = 1s$) are linearly dependent on E (Fig. 6, curves A and B). Because of the large uncertainty of the intercept calculated from $\log k$ - $\log t$ plots, for

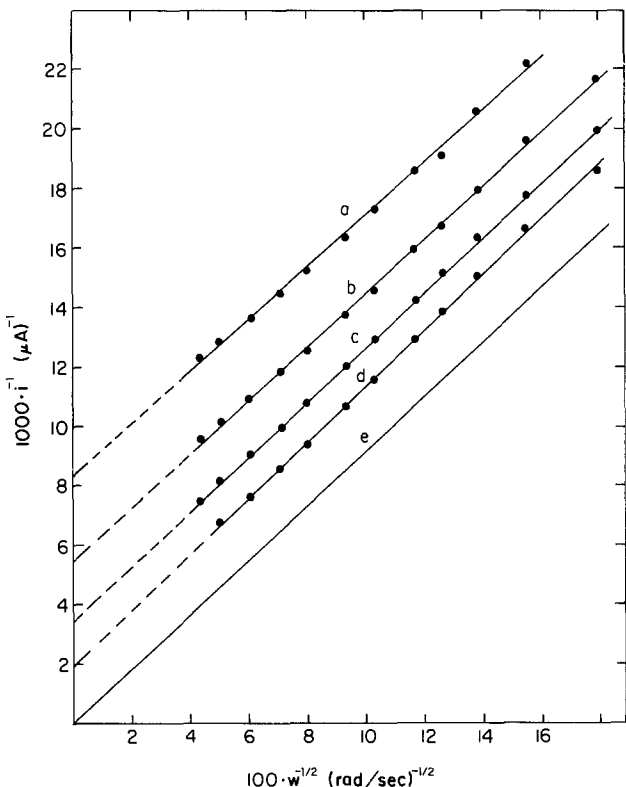


Fig. 3. Plot of i^{-1} vs. $\omega^{-1/2}$ (Method B). t (min): a = 6, b = 24, c = 60, and d = 120; e = theoretical for $D/k = 0$. Conditions: $C^b = 0.515$ mM As(III) in $0.50M$ $HClO_4$; $\omega^{1/2} = 5.60$ $rad^{1/2} s^{-1/2}$ between values of t ; $E = 1.10V$ vs. SCE.

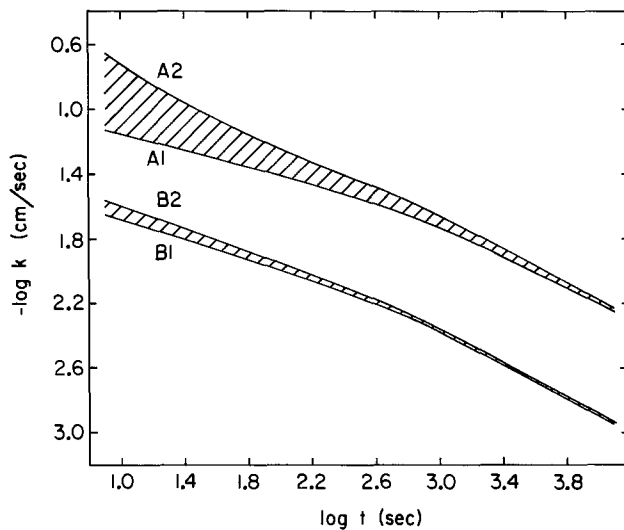


Fig. 4. Plots of $\log k$ vs. $\log t$ and consideration of error. Conditions: $C^b = 2.00$ mM As(III) in $0.50M$ H_2SO_4 , $\omega^{1/2} = 10.23$ $rad^{1/2} s^{-1/2}$; E (V vs. SCE): A = 1.00; B = 1.20; i_{lim} (μA): A1, B1 = $465 \mu A$ (as shown in Fig. 2) A2, B2 = $427 \mu A$.

which all data is taken for $t \geq 10s$, values of $\log k$ at $t = 100s$ for these same experiments are plotted also in Fig. 6 (curves C and D). The slopes of the plots in Fig. 6 are: -2.34 (A), -3.09 (B), -2.71 (C), and -2.74 (D); the average is -2.7 ± 0.3 .

The dependence of k on E and t for $t < 100s$ is described by

$$k = k_0(t/t_0)^{-b} \exp \{-E/E_0\} \quad [8]$$

where $t_0 = 1.0s$, $b = 0.30$, and $E_0 = (1/2.7) \ln 10 = 0.161V$. This value of E_0 is in satisfactory agreement with the value $0.177V$ reported for Eq. [6] of Ref. (1). This agreement may seem surprising at first thought because of the differences in the two experimental techniques. In Ref. (1), k was found to be virtually independent of E in the range $1.2-0.9V$ during the negative scan of E . This results because Q_{ox} is established by the value of E_a for the posi-

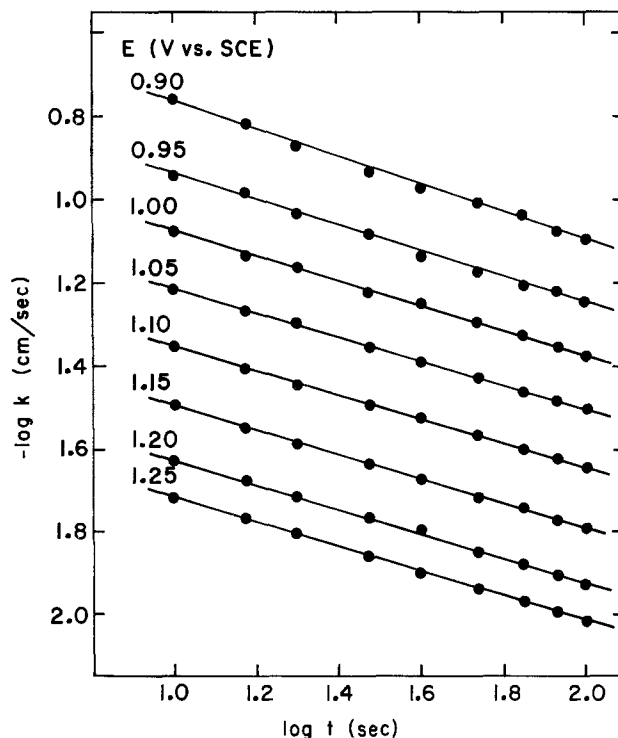


Fig. 5. Plots of $\log k$ vs. $\log t$ as a function of E for $t = 10-100s$. E (V vs. SCE) given in figure. Conditions: $C^b = 2.00$ mM As(III) in $0.50M$ H_2SO_4 , $\omega^{1/2} = 10.23$ $rad^{1/2} s^{-1/2}$.

Table I. Dependence of k on E^*

E (V vs. SCE)	$\omega^{1/2} = 10.23 \text{ rad}^{1/2} \text{ s}^{-1/2}$		$\omega^{1/2} = 22.88 \text{ rad}^{1/2} \text{ s}^{-1/2}$	
	$d \log k/d \log t$	Intercept (I)	$d \log k/d \log t$	Intercept (I)
0.09	-0.324	-0.445	-0.338	-0.551
0.95	-0.308	-0.633	-0.340	-0.653
1.00	-0.294	-0.784	-0.322	-0.813
1.05	-0.280	-0.941	-0.306	-0.980
1.10	-0.285	-1.073	-0.298	-1.132
1.15	-0.290	-1.208	-0.299	-1.277
1.20	-0.296	-1.329	-0.296	-1.423
1.25	-0.296	-1.421	-0.286	-1.528
Avg.	-0.297		-0.310	
Std.dev.(s)	± 0.014		± 0.020	

* Conditions: 2.00 mM As(III) in 0.50M H_2SO_4 .

negative scan and remains virtually constant during the negative scan within the potential range specified. The dependence of k on E from potentiostatic experiments reported here ($t < 100\text{s}$) is virtually identical to that from cyclic voltammetry (1), and we conclude that Q_{ox} controls the value of k for both experiments.

The value of k_0 in Eq. [8] was calculated from the data for 2.00 mM As(III) (Table I), and the results are shown in Table II; \bar{k}_0 represents the average of k_0 for nine values of t in the range 10-100s. The values of k_0 at $E = 0.90$ and 1.25V differ significantly from the values for $E = 0.95$ -1.20V and are ignored in computing the grand average of \bar{k}_0 . The value of k_0 at $E = 1.25\text{V}$ deviated from \bar{k}_0 because of the significant rate of $\text{O}_2(\text{g})$ evolution for $E > 1.20\text{V}$ and the concomitant catalysis of As(III) oxidation [see Fig. 7 of Ref. (1)]. Justification for ignoring the value of k_0 at $E = 0.90\text{V}$ is nonexistent at this time, as this potential seems well within the range for the electrocatalyzed reaction.

Dependence of k_0 on C^b and $\omega^{1/2}$.—Although b in Eq. [8] was found to be independent of C^b and $\omega^{1/2}$, k_0 decreased with increased flux of As(III) for all values t and E . Representative $\log k$ - $\log t$ plots are shown in Fig. 7 as a function of $\omega^{1/2}$ for 2.0 mM As(OH)₃. The value of k_0 is adequately given by

$$k_0 = -d - e \log (\omega^{1/2} C^b / M \text{ rad}^{1/2} \text{ s}^{-1/2})$$

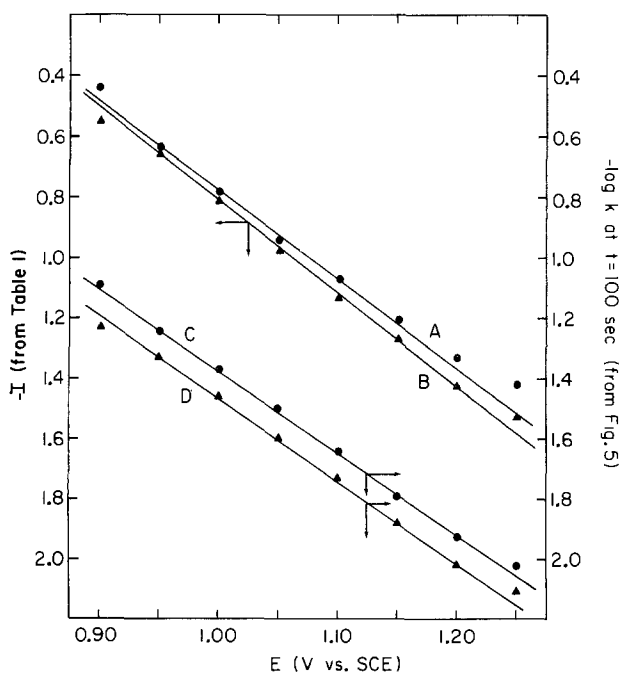


Fig. 6. Plots of I (from Table I) and $\log k$ (from Fig. 5) vs. E . $\omega^{1/2}$ ($\text{rad}^{1/2} \text{ s}^{-1/2}$): A, C = 10.23; B, D = 22.88.

Table II. Test of equations for potential dependence*

E	$\omega^{1/2} = 10.23 \text{ rad}^{1/2} \text{ s}^{-1/2}$		$\omega^{1/2} = 22.88 \text{ rad}^{1/2} \text{ s}^{-1/2}$	
	\bar{k}_0 (cm/s)	($m = 9$)	\bar{k}_0 (cm/s)	s ($m = 9$)
0.90	87.1	1.9	64.8	2.2
0.95	81.5	1.4	69.4	0.7
1.00	82.7	0.7	70.2	1.3
1.05	82.5	1.5	68.6	1.0
1.10	81.8	1.1	68.0	0.3
1.15	80.0	0.7	66.1	0.5
1.20	81.1	0.8	65.1	0.3
1.25	89.0	0.7	71.7	0.8
Avg. (0.95-1.20V)	81.6 ± 1.0		67.9 ± 1.0	

* $C^b = 2.0 \text{ mM As(III)}$ in $0.5\text{M H}_2\text{SO}_4$.

where $d = 110 \pm 10 \text{ cm s}^{-1}$ and $e = 38 \pm 6 \text{ cm s}^{-1}$. The large uncertainties in d and e are the result of difficulty in reproducing results from run to run as C^b was varied. This could be the consequence of an impurity problem. An additional consideration of the uncertainty is the fact the convenient variation of flux was limited approximately to only one decade.

The fundamental cause of the decreasing value of k with increasing flux of As(III) is not clear. Perhaps the product As(V) is adsorbed on and/or occluded in the rapidly growing oxide. As a result, the accessibility of As(OH)_3 for the adsorbed $\cdot\text{OH}$ might be decreased substantially. We note again that the rate of oxide growth is virtually unaffected by the presence of As(III) in solution and, therefore, the presence of As(V) in the diffusion layer.

Dependence of b on Q_{ox} .—From square-wave modulated voltammetry [Fig. 7 of Ref. (1)], it was concluded that the maximum rate for the surface-controlled oxygen-transfer reaction between the surface "oxide" and As(OH)_3 corresponds to a surface with adsorbed $\cdot\text{OH}$ as the predominate form of "oxide" at a coverage less than the equivalent of one monolayer (*i.e.*, $Q_{\text{ox}}/Q_{\text{H}} < 1$). Since As(OH)_3 is readily adsorbed at oxide-free Pt sites, the most favorable reaction mechanism is concluded to involve co-adsorbed $\cdot\text{OH}$ and As(OH)_3 . Hence, it was suspected that the transition of the slope of $\log k$ - $\log t$ plots from -0.30 to -0.50 might correspond to a change in the predominate reac-

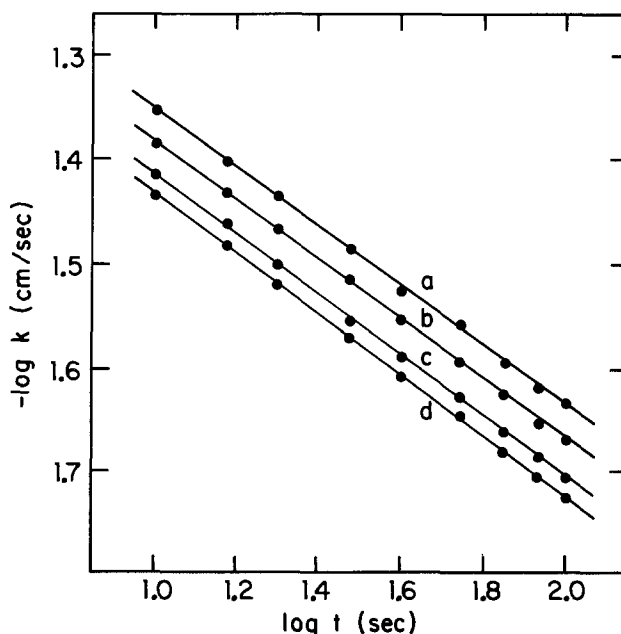


Fig. 7. Plots of $\log k$ vs. $\log t$ for $t = 10$ -100s as a function of $\omega^{1/2}$. $\omega^{1/2}$ ($\text{rad}^{1/2} \text{ s}^{-1/2}$): a = 10.23, b = 14.47, c = 20.47, and d = 25.07. Conditions: $C^b = 2.0 \text{ mM As(III)}$, $E = 1.10\text{V}$.

tion mechanism as a consequence of the growth of surface oxide beyond the equivalent of a monolayer of PtOH (i.e., $Q_{ox}/Q_H > 1$) when the number of available Pt sites for adsorption of As(OH)₃ is minimal and the oxygen transfer reaction is between PtOH and As(OH)₃ in the outer Helmholtz plane, as suggested pictorially in Ref. (1).

Values of i as a function of Q_{ox} from the voltammetric experiments of Ref. (1) are replotted in Fig. 8. Recall that the corresponding plot of $\log k$ vs. Q_{ox} is linear [Fig. 8 of Ref. (1)]. The values of Q_{ox} corresponding to the equivalent of a monolayer of PtOH (i.e., $Q_{ox}/Q_H = 1$) and a monolayer of PtO (i.e., $Q_{ox}/Q_H = 2$) are indicated in Fig. 8. Clearly, $i = i_{lim}$ for $Q_{ox}/Q_H \leq 1$. Furthermore, $i < 0.5 i_{lim}$ for $Q_{ox}/Q_H > 2.0$ and the corresponding values of $\log k \ll -1.5$ [see Fig. 8 of Ref. (1)]. From Fig. 2, $b = 0.50$ when $\log k \ll -1.5$, and the transition in the value of b corresponds apparently to an extent of surface oxide substantially beyond the equivalent of a monolayer of PtO. We note that the concept of a perfect monolayer for a polycrystalline surface having a substantial degree of surface roughness undoubtedly is imaginary, at best. But, insofar as mechanistic proposals have validity for practical electrode surfaces, we conclude that $b = 0.30$ for $0 < \theta_{PtOH} < 1.0$ and $b = 0.50$ for an extended surface oxide ($\theta_{PtO} \gg 1.0$) such that $\theta_{PtOH} \rightarrow 0$. Based on the conclusion that the extended growth of oxide for $Q_{ox}/Q_H > 2$ continues to involve generation of adsorbed $\cdot OH$, these sites of greatest reactivity are undoubtedly widely dispersed on the surface and the electrode can be characterized as not being uniformly accessible.

Consideration of nonuniform accessibility for the electrode.—The observation of a linear plot of i^{-1} vs. $\omega^{-1/2}$ having a nonzero intercept (I) is diagnostic evidence of "mixed control" of the faradaic process at a RDE (see Eq. [5]). For an electrode surface with uniform activity, mass transport within the diffusion layer is solely in a direction normal to the surface and a nonzero intercept (I) in Fig. 3 is representative of slow coupled chemical or electrochemical processes. For a partially blocked electrode surface, the electrode is not uniformly accessible, and appreciable curvilinear diffusional transport occurs to active surface sites. For this case, $I > 0$, even for rapid reaction kinetics at the reactive sites and I is a function of the geometry and spacing of the active surface sites. Landsberg *et al.* (4-6) characterized the $i-\omega^{1/2}$ response for partially blocked RDE surfaces based on a theory of curvilinear diffusion by Smythe (7) and noted (6) that diagnostic evidence for curvilinear diffusion is the constancy of the product DI for a given anolyte. Experimental verification was achieved for alteration of D by changing the viscosity of the media. The product $D_{As(III)}I$ (Method B) was examined for As(III) in 0.50M HClO₄ as a function of added NaClO₄; the data are summarized in Table III. The product $D_{As(III)}I$ increased by more than 60% in going from $\mu =$

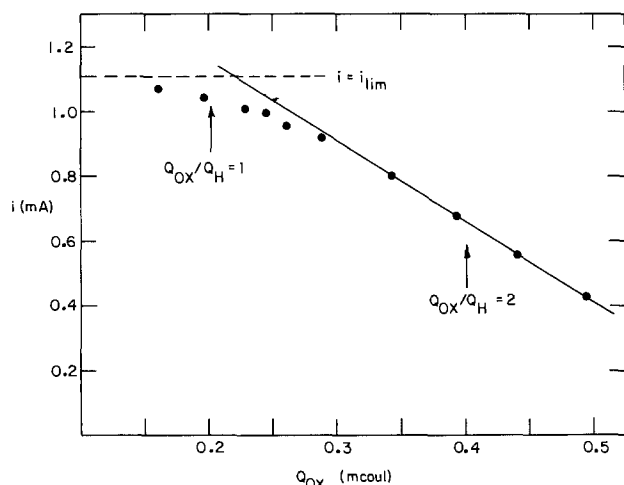


Fig. 8. Plot of i vs. Q_{ox} . $C^b = 1.11$ mM As(III) in 0.50M H₂SO₄, $\omega^{1/2} = 10.23$ rad^{1/2} s^{-1/2}, $Q_H = 200$ μC .

Table III. Product of diffusion coefficient (D) and intercept (I) of plots of i^{-1} vs. $\omega^{-1/2}$ as a function of ionic strength (μ)^a

t (min)	$D \cdot I \cdot 10^8$ cm ² μA^{-1} s ⁻¹		
	$\mu = 0.5M^b$	$\mu = 2.75M^c$	$\mu = 5.00M^d$
12	3.0	3.4	5.0
18	3.6	4.1	6.0
24	4.0	4.7	6.8
30	4.5	5.3	7.7
60	6.3	7.7	11.0

^a 2.0 mM As(III) in 0.50M HClO₄ + NaClO₄.

^b $D_{As(III)} = 1.15 \times 10^{-5}$ cm² s⁻¹.

^c $D_{As(III)} = 0.93 \times 10^{-5}$ cm² s⁻¹.

^d $D_{As(III)} = 0.66 \times 10^{-5}$ cm² s⁻¹.

0.5-5.0M. We conclude that curvilinear diffusion is not responsible exclusively for the nonzero intercepts of the $i^{-1}-\omega^{-1/2}$ plots, although its contribution cannot be excluded totally.

Possibility of oxygen abstraction from PtO.—It was estimated from cyclic voltammetry (1) that Q_{ox} is relatively unaffected by the presence of As(III) for $E_a > 1.0V$. A Pt flow-through detector was applied in a rigorous test of this conclusion. With a stream of 2.0 mM As(III) in 0.5M H₂SO₄ flowing through the detector at 0.5 ml min⁻¹, the value of E was scanned from $E_c = 0.0V$ to $E_a = 1.3V$ at 3.0V min⁻¹ and then to 1.0V, at which the negative scan was interrupted for $t = 10$ min. After the delay, the stream was switched to pure 0.5M H₂SO₄ and E was scanned to 0.0 V while recording the cathodic $i-E$ curve; the experiment was repeated in the absence of As(III). The areas of the two oxide reduction peaks were virtually identical ($\pm 1\%$). Hence, it is verified that the presence of As(III) does not alter Q_{ox} . Furthermore, it is demonstrated by this experiment that abstraction of O atoms by As(OH)₃ from PtO is negligible. If abstraction had occurred during the 10 min delay, the value of Q_{ox} would have steadily decreased in the presence of As(OH)₃ to the value corresponding to a scan to $E_a = 1.0V$. Additional evidence for this came from cyclic voltammetry: when the negative potential scan was halted at $E = 1.0V$ in cyclic voltammetry at the RDE, there was no increase in i with time beyond that value observed for the uninterrupted scan.

Diffusion of As(OH)₃ through the oxide film.—The potential-independent rate of As(III) oxidation observed on the negative scan in cyclic voltammetry [Fig. 7 of Ref. (1)] reflects the absence of an electron transfer in the rate-determining step. The possibility of slow molecular diffusion through the oxide film was considered. For such a mechanism, D/k in Eq. [5] would be replaced by the thickness of the oxide, which is proportional to Q_{ox} for $Q_{ox}/Q_H > 1$. If such is the controlling mechanism, linear plots would be obtained for $\log k$ vs. $\log Q_{ox}$.

Summary and Conclusion

The formation of chemisorbed $\cdot OH$ (i.e., PtOH), as the first step in production of surface oxide at Pt electrodes, is a reversible process (8, 9). The reversibly adsorbed $\cdot OH$ can be stabilized by place exchange with surface atoms of Pt, to give a species designated as OHPt, and ultimately oxidized further at high E to yield PtO. The kinetic results reported here are consistent with the conclusion that PtOH, but not OHPt nor PtO, is active as the O transfer agent in the electrocatalytic oxidation of As(OH)₃ to OAs(OH)₃. The dependence of k on E given here from potentiostatic measurements is virtually the same as for k on E_a from voltammetric studies (1), even though k in Ref. (1) was measured during the negative scan at $E < E_a$. In the voltammetric case, k is independent of E on the negative scan (1.1-0.9V) for $E_a > ca. 1.1V$ because Q_{ox} is fixed by E_a and remains virtually constant during the negative scan on the time scale of the voltammetric experiment.

Clearly, the time dependence of k from the potentiostatic measurements (Eq. [8]) is not consistent with that

predicted (Eq. [4]) on the basis of the observed $k - Q_{ox}$ dependence in Ref. (1) (Eq. [2]) and the known $Q_{ox} = t$ behavior (Eq. [3]). We had predicted that the $\ln k - \ln t$ slope would be a linear function of E and independent of t ; however, we observed the slope of $\ln k - \ln t$ plots to be independent of E and to undergo a transition (-0.30 to -0.50) in the region $t = 400$ - 600 s (see Fig. 2, 5). The explanation of this apparent conflict is that Q_{ox} represents the total charge for the three forms of surface oxygen, i.e., $Q_{ox} = Q_{PtOH} + Q_{OHPl} + Q_{PtO}$, and not just the active form, Q_{PtOH} . Furthermore, the $Q_{ox} - t$ behavior (Eq. [3]) does not correspond to the $Q_{PtOH} - t$ behavior, since the ratio Q_{PtOH}/Q_{ox} is not constant with time. The reaction between PtOH and adsorbed $As(OH)_3$ is very fast and $i \approx i_{lim}$ for small t when $Q_{PtOH} \approx Q_{ox}$ and $Q_{ox} < 1$, i.e., there are numerous adsorption sites available for $As(OH)_3$. But even in this case for $Q_{ox}/Q_H < 1$, Q_{PtOH} steadily decreases with time because of place exchange; hence, i decreases with time and we observe a $\ln k - \ln t$ slope of -0.30 . For large E where $Q_{OH}/Q_H \gg 1$, Q_{PtOH} is still significant at short t but O transfer is concluded now to occur by a slower reaction to $As(OH)_3$ in the outer Helmholtz plane, possibly by the mechanism suggested pictorially in Ref. (1). With increasing t , i decreases significantly below i_{lim} , and we observe a $\ln k - \ln t$ slope of -0.50 . We recall again from Ref. (1) that for E in the region of O_2 evolution, the surface coverage by adsorbed $\cdot OH$ is increased greatly and k increases accordingly; we observed signals for $As(OH)_3$ by hydrodynamically modulated voltammetry, in excess of $0.8 i_{lim}$ at heavily anodized electrodes, for which $i < 0.1 i_{lim}$ in the absence of O_2 evolution.

The electrocatalytic oxidation with O transfer for $As(OH)_3$ bears striking resemblance to the electrocatalytic production of IO_3^- from I^- at Pt in acidic media (10). In that case, production of IO_3^- occurs nearly at a mass-transport-limited rate simultaneously with oxidation of adsorbed iodine to IO_3^- during the rapid formation of surface oxide on the positive voltammetric scan; also, production of IO_3^- is at a transport-limited rate when O_2 is being evolved. In contrast to $As(OH)_3$, production of IO_3^- is negligible for $Q_{ox}/Q_H > 2$ in the absence of O_2 evolution and when $dQ_{ox}/dt \approx 0$, i.e., the negative voltammetric scan. We interpret this to reflect a very low rate of O transfer to I^- in the outer Helmholtz plane.

Experimental results from variation of solution viscosity do not confirm the possibility that the low reactivity of an oxide-covered electrode at large time can be characterized exclusively as conforming to the model of a non-uniformly accessible surface. We conclude that, even though Q_{PtOH} is small, $Q_{PtOH} \neq 0$, and it is the slow rate at which adsorbed $\cdot OH$ is regenerated on the oxide-covered surface after O transfer which is rate determining. If so, the $k - E - t$ dependencies are descriptive of the oxide-growth rate for $Q_{ox}/Q_H \gg 2$. But if this is true, we must conclude also that for an electrode with Q_{ox} fixed by application of $E > 1.1V$, the rate of oxide growth is independent of E for subsequent kinetic measurements at $0.9 < E < 1.1V$. The oxide growth mechanism could be controlled by the place-exchange reaction at the Pt-PtO interface (11) and the oxidation of $As(OH)_3$ may serve as a useful probe for further studies of oxide growth kinetics. We continue to investigate this possibility.

Acknowledgment

This work was supported by the Office of Basic Energy Sciences.

Manuscript submitted April 16, 1984; revised manuscript received ca. Oct. 19, 1984.

Ames Laboratory assisted in meeting the publication costs of this article.

REFERENCES

1. T. D. Cabelka, D. S. Austin, and D. C. Johnson, *This Journal*, **131**, 1595 (1984).
2. D. Gilroy, *J. Electroanal. Chem.*, **71**, 257 (1976).
3. V. G. Levich, "Physicochemical Hydrodynamics," pp. 72-78, Prentice-Hall, Englewood Cliffs, NJ (1962).
4. R. Landsberg and R. Thiele, *Electrochim. Acta*, **11**, 1243 (1966).
5. F. Scheller, R. Landsberg, and S. Muller, *J. Electroanal. Chem.*, **20**, 375 (1969).
6. F. Scheller, R. Landsberg, and H. Wolf, *Z. Phys. Chem. (Leipzig)*, **243**, 345 (1970).
7. W. R. Smythe, *J. Appl. Phys.*, **24**, 70 (1951).
8. H. A. Kozłowska, B. E. Conway, and W. B. A. Sharp, *J. Electroanal. Chem.*, **43**, 9 (1973).
9. S. Gottesfield and B. E. Conway, *J. Chem. Soc. Faraday Trans. 1*, **69**, 1090 (1973).
10. D. S. Austin, D. C. Johnson, T. G. Hines, and E. T. Berti, *Anal. Chem.*, **55**, 2222 (1983).
11. M. J. Weaver, *J. Electroanal. Chem.*, **51**, 231 (1974).

How to Reduce the Cointercalation of Propylene Carbonate in Li_xZrS_2 and Other Layered Compounds

W. R. McKinnon and J. R. Dahn

National Research Council of Canada, Division of Chemistry, Solid State Chemistry, Ottawa, Ontario, Canada K1A 0R9

ABSTRACT

Cointercalation of propylene carbonate (PC) into layered materials intercalated with lithium can be reduced with concentrated electrolytes. We show electrochemical and x-ray diffraction evidence for this reduction in Li/ZrS_2 cells with $LiAsF_6/PC$ electrolyte.

When Li intercalates into a host solid in an electrochemical cell, it sometimes carries with it molecules of the solvent from the electrolyte (1, 2). Such cointercalation of the solvent interferes with studies of intercalation of unsolvated Li. Moreover, if cointercalation occurs but is not recognized, experiments can be misinterpreted; in fact, cointercalation might be responsible for many of the discrepancies between reports of the electrochemical behavior of intercalation electrodes. Cointercalation is also a problem in commercial applications of intercalation batteries, because the large expansion of the lattice by the solvent degrades the host electrode. Propylene carbonate (PC) is an attractive solvent because it has a low vapor pressure and is easy to purify, but it cointercalates with

Li in layered compounds such as $TiS_2(1, 3)$. Many replacements for PC are volatile and sometimes explosive when combined with lithium salts in batteries.

The amount of host cointercalated with PC is reduced if high currents are used to discharge the cell initially (4). Apparently, unsolvated Li diffuses into the host more quickly than solvated Li, and PC will not enter a layer that contains enough unsolvated Li. Thus PC can still be used in experimental cells if the first discharge is done quickly; if too much Li is removed on subsequent charges, however, PC may cointercalate.

We have discovered that, in some cases, cointercalation of PC is nearly eliminated with a saturated solution of $LiAsF_6$ in PC. To illustrate this here, we compare

Li/Li_rZrS₂ cells made with 1M and saturated solutions of LiAsF₆ in PC. We have measured the voltage V vs. x in Li_rZrS₂, as well as the structure of the ZrS₂ host in these cells. At low currents, little PC cointercalates in cells made with the saturated solution, whereas PC cointercalates into almost all of the ZrS₂ in the 1M solution. We discuss these differences in terms of the chemical potential of PC in the electrolyte.

Experimental Procedure

Powdered ZrS₂ was made by reacting Zr and excess S at 900°C, then quenching. The particle size was less than 1 μm. Electrochemical cells with Li and ZrS₂ electrodes were prepared as described in Ref. (5), except that the electrolyte was either a 1M or a saturated solution of LiAsF₆ (used as received from U.S. Steel Agri-Chemicals) in PC (obtained from J. T. Baker then vacuum distilled). We also prepared cells with beryllium x-ray windows (4) to study changes in the structure of the ZrS₂ host *in-situ* in both 1M and saturated solutions.

A saturated solution of LiAsF₆ in PC has a lower conductivity than a 1M solution, so we could not use ZrS₂ electrodes flattened with rollers, as we did in our earlier work on TaS₂ (6). With the fine ZrS₂ powder used here, the pores of rolled electrodes are so small that cells made with these electrodes have very poor kinetics. In ZrS₂ electrodes that were not rolled, up to 60% of the host did not make good electrical contact to the electrode and so did not intercalate.

Experimental Results

The ZrS₂ powder used here gives results similar to those reported earlier for coarser powder (6). Figure 1 shows $-\partial x/\partial V$ vs. x for the third charge and fourth discharge of a Li/Li_rZrS₂ cell made with a saturated electrolyte. (The data have been normalized to a change $\Delta x = 1$ for the voltage range shown.) The peaks in Fig. 1 near 1.9V are broader than in our earlier results. This broadening is due to the smaller particles, not to the higher currents. The width of the peaks increases by only a few percent if the current is doubled. We chose the finer powder for this work because PC cointercalates into it more rapidly. The peaks in Fig. 1 are caused by the change in structure of ZrS₂ from the 1T polytype at $x = 0$ to the 3R polytype at $x = 0.23$ (6).

When PC is cointercalated, V vs. x is different than the behavior shown in Fig. 1. Figure 2 shows V vs. x for the first discharge of three Li/Li_rZrS₂ cells, two made with a saturated solution of LiAsF₆ in PC, and one with a 1M solution. The values of x in Fig. 2-5 have not been renormalized, but rather are calculated only from the current and the mass of ZrS₂ in each cell. We call this the "apparent" value of x , to stress that it measures only the average Li content of the entire electrode and so does not distinguish

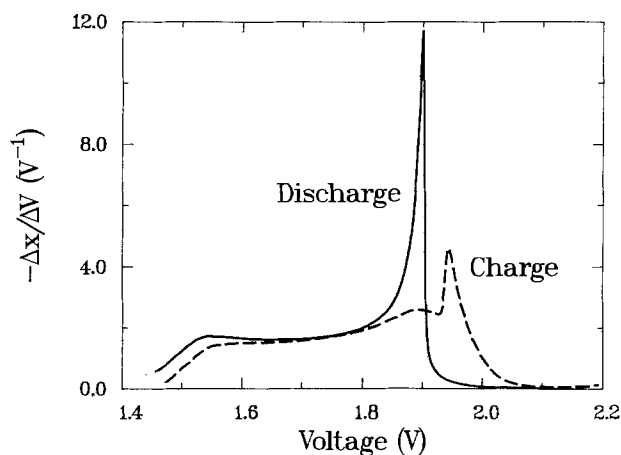


Fig. 1. $-\Delta x/\Delta V$ vs. voltage V for the third charge and fourth discharge of a Li/Li_rZrS₂ cell with saturated LiAsF₆/PC as electrolyte. The curves have been normalized so $\Delta x = 1$ over the range of voltage shown. For the currents used, the charge and discharge each took about 17h.

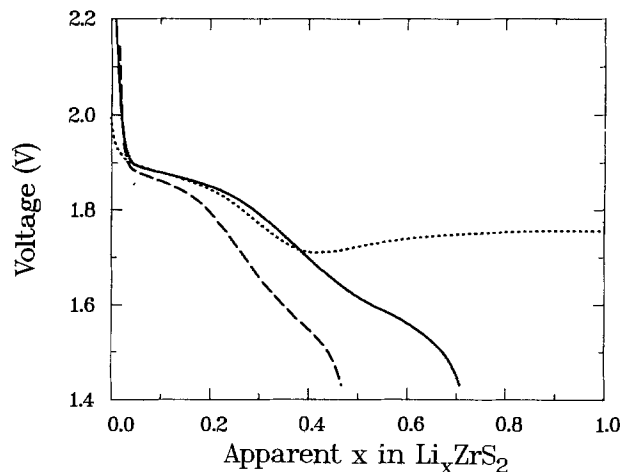


Fig. 2. Cell voltage V vs. the apparent value of x in Li_rZrS₂ for the first discharge of Li/Li_rZrS₂ cells. (····): 1M LiAsF₆/PC electrolyte, 25h rate. (—): Saturated LiAsF₆/PC electrolyte, 50h rate. (---): Saturated LiAsF₆/PC electrolyte, 18h rate. The apparent value of x was calculated only from the current and the mass of ZrS₂. The rate quoted corresponds to the time to change the apparent x by $\Delta x = 1$.

Li_rZrS₂ without PC, cointercalated ZrS₂, and unintercalated ZrS₂. For the cell made with 1M solution, the voltage rises with x between $x = 0.4$ and 0.6 , then remains constant well beyond $x = 1$. As we show below, cointercalation of PC begins at 1.9V in Fig. 1; the plateau at 1.75V in the cell with 1M electrolyte corresponds to a further reaction of the cointercalated material with lithium. Cointercalation of PC and lithium is much slower than intercalation of lithium alone, so the voltage in Fig. 1 probably does not measure the free energy of the cointercalation reaction, as we discuss below.

Figure 3 shows $-\partial x/\partial V$ vs. V for the same cells as in Fig. 2. For the cell with 1M solution, $-\partial x/\partial V$ diverges near 1.7V, corresponding to the rise in voltage near $x = 0.4$ in Fig. 2. ($-\partial x/\partial V$ for $x > 0.4$ has not been plotted for this cell.) The cells with saturated solution were run at 25 and 50h rates. (These rates correspond to the time to change the apparent x by $\Delta x = 1$.) Both these cells show peaks near 1.6V, not present in Fig. 1, which presumably correspond to the plateau at 1.8V in the cell with 1M solution. Hence, some of the ZrS₂ is being cointercalated with PC in the cells with saturated electrolyte. The peaks at the 50h rate are higher, implying that more of the host has been cointercalated at the slower rate.

We studied the degree of cointercalation using *in situ* x-ray diffraction. Figures 4 and 5 compare the changes in the x-ray diffraction spectra of Li_rZrS₂ for cells with saturated and 1M solutions, respectively. These spectra were taken on the first discharging at constant current. Figure 4 is similar to the results of Ref. (6). As x increases, Bragg

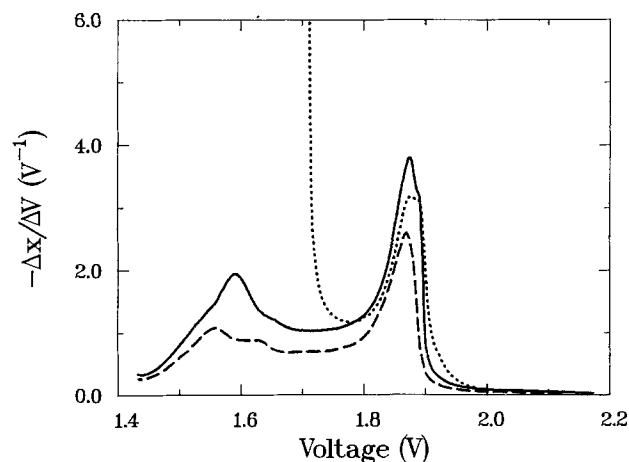


Fig. 3. $-\Delta x/\Delta V$ vs. cell voltage V for the curves in Fig. 2.

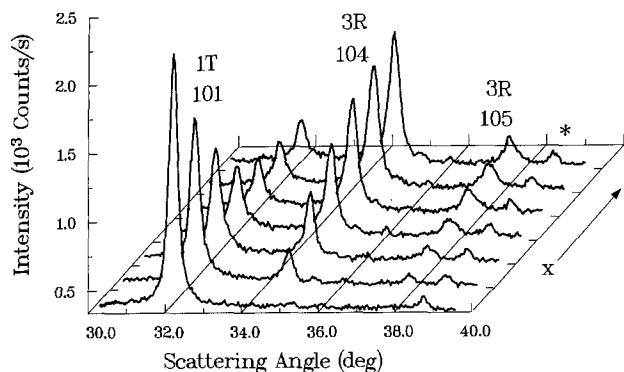


Fig. 4. X-ray diffraction spectra for ZrS_2 during the first discharge in a $Li/Li_{1-x}Zr_xS_2$ cell with saturated $LiAsF_6/PC$ electrolyte. The cell was discharged at constant current at a 25h rate. The apparent x for the scans, starting from the front, is 0.03, 0.12, 0.21, 0.29, 0.38, and 0.47. The 101 peaks from 1T- ZrS_2 and the 104 peak of 3R- ZrS_2 are shown, together with a peak from some component of the cell (*).

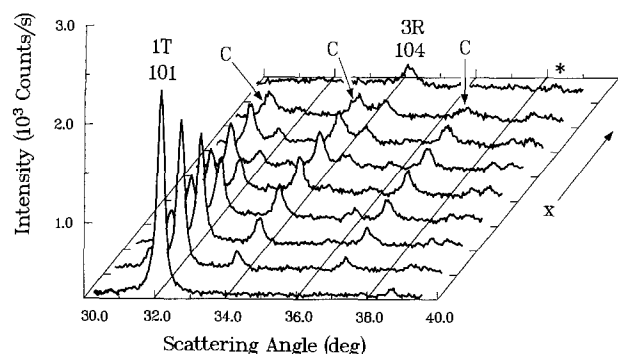


Fig. 5. As in Fig. 4, except for cells with 1M $LiAsF_6/PC$ electrolyte at a 40h rate (The last scan is from a different cell than the other eight). Starting from the front, the apparent x is 0.07, 0.12, 0.18, 0.24, 0.30, 0.35, 0.41, 0.51, 2.04. In addition to the peaks in Fig. 4 are peaks from cointercalated ZrS_2 (labeled as C).

peaks from the original 1T structure of ZrS_2 shrink, and those from the 3R structure grow. The remaining peaks in the 1T structure for $x > 0.2$ are from ZrS_2 that did not make good electrical contact to the electrode. There are no extra peaks in Fig. 4 from ZrS_2 cointercalated with PC. In contrast, Fig. 5 does show extra peaks from cointercalated ZrS_2 . These peaks grow until $x \approx 0.3$, then shrink again when the voltage reaches the plateau at 1.75V (Fig. 2). In the last curve in Fig. 5, which corresponds to an apparent x of 2.0, the peaks from cointercalated Li_xZrS_2 have completely disappeared. (We do not know what happened to this material during the plateau at 1.75V. If it decomposed, the decomposition products are not crystalline enough to give Bragg peaks). Note that the peaks for the cointercalated material are broad, so a small amount of cointercalation would not be seen in Fig. 4. The causes of the long plateau in $V(x)$ in Fig. 2 have not been studied.

Discussion

Our x-ray results show that less PC is cointercalated from a saturated solution of $LiAsF_6$ in PC than from a 1M solution. The electrochemical behavior in Fig. 2 and 3 is consistent with this reduction, for the features in $-dx/dV$ associated with the cointercalation are reduced in a saturated solution. The interpretation of Fig. 2 and 3, however, is complicated by kinetics. PC can be kept out of the host even in a 1M solution of $LiAsF_6/PC$ if the first discharge is done at high currents (4), indicating that cointercalation of Li and PC is slower than intercalation

of Li alone. Thus, when cointercalation of Li and PC is occurring in parallel with intercalation of Li alone, the measured voltage V corresponds to V_1 , the voltage of the intercalation reaction, and not to V_c , the voltage of the cointercalation reaction. This is probably why the voltages for the cells in Fig. 2 are similar at low x : intercalation of Li alone is almost at equilibrium, but cointercalation is far from equilibrium. Moreover, this argument implies that the rate of cointercalation will decrease as the difference $V_c - V_1$ decreases. This difference will decrease with increasing concentration of the electrolyte, as we now show.

For simplicity, suppose lithium in the host is either free of PC or solvated by n atoms of PC, so we only need to consider two types of guest: Li and $Li(PC)_n$. The voltage of intercalation of Li is related to the difference in μ and μ_0 , the chemical potentials of lithium in the host and in lithium metal, respectively, by (8)

$$V_1 = -(\mu - \mu_0)/e \quad [1]$$

where e is the magnitude of the electronic charge. For cointercalation of Li and PC, each atom of Li that enters the host carries with it n molecules of PC, so the voltage is

$$V_c = -[(\mu + n\omega) - (\mu_0 - n\omega_0)]/e \quad [2]$$

where ω and ω_0 are the chemical potentials of PC in the host and in the solution, respectively. The difference in potential of the two reactions is

$$V_c - V_1 = n(\omega_0 - \omega)/e \quad [3]$$

Since the chemical potential of any molecule decreases with the number of those molecules (9, 10), ω_0 should be lower in a saturated electrolyte solution than in a 1M solution, so $V_c - V_1$ should be smaller and cointercalation should be slower.

A complication in our experiments is that there are similar amounts of ZrS_2 and PC in our cells, so the concentration of the electrolyte increases as PC cointercalates (ω_0 decreases). Further work is needed to determine the ranges of stability of the various phases, and to study the kinetics of intercalation and cointercalation.

In conclusion, we have shown that less PC cointercalates into Li_xZrS_2 from a saturated solution of $LiAsF_6$ in PC than from a 1M solution. We have found similar reductions in cointercalation with Li_xZrSe_2 and Li_xTaS_2 . The use of concentrated solutions should extend the usefulness of PC as a solvent in experimental cells used in the study of intercalation, and possibly in cells for commercial applications.

Manuscript submitted June 18, 1984; revised manuscript received ca. Oct. 9, 1984.

REFERENCES

1. M. S. Whittingham, *Prog. Solid State Chem.*, **12**, 41 (1978).
2. R. Schöllhorn, in "Intercalation Chemistry," M. S. Whittingham and A. J. Jacobson, Editors, p. 315, Academic Press, New York (1982).
3. J. R. Dahn, M. A. Py, and R. R. Haering, *Can. J. Phys.*, **60**, 307 (1982).
4. J. R. Dahn and W. R. McKinnon, *This Journal*, To be published.
5. D. C. Dahn and R. R. Haering, *Solid-State Commun.*, **44**, 29 (1982).
6. W. R. McKinnon, J. R. Dahn, and C. Levy-Clement, *ibid.*, **50**, 104 (1984).
7. W. R. McKinnon and J. R. Dahn, *ibid.*, **48**, 43 (1983).
8. W. R. McKinnon and R. R. Haering, in "Modern Aspects of Electrochemistry," Vol. 15, R. E. White, J. O'M. Bockris, and B. E. Conway, Editors, p. 235, Plenum Press, New York (1983).
9. C. Kittel and H. Kroemer, "Thermal Physics," 2nd ed., p. 147, Freeman, San Francisco, CA (1980).
10. T. L. Hill, "Statistical Mechanics," p. 113, McGraw-Hill, New York (1956).

In Situ Production of Ozone in Water Using a Membrane Electrolyzer

S. Stucki, G. Theis,¹ R. Kötzi, H. Devantay, and H. J. Christen

Brown Boveri Research Center, CH-5405 Baden, Switzerland

ABSTRACT

The application of solid polymer electrolyte or Membrel water electrolysis cells with PbO_2 anodes for anodic generation of ozone in electrolyte-free water is reported. Maximum yields were obtained at a temperature of 25°-30°C and a current density of 1.0-1.3 Acm^{-2} . The current efficiency was not found to depend on ozone concentration in the feed water. Both, the perfluorinated membrane and the anode do not show any degradation of performance after 2500h of operation. The excellent stability and performance of the cell are correlated with properties of the membrane and its interface with the anode: exclusive transference of electric current by protons; absence of convection in the electrolyte; high oxygen oversaturation in the vicinity of the electrode.

Ozone is playing an increasingly important role as an environmentally clean oxidant in water treatment and several new processes in chemical and pulp industries. The application of ozone—unlike that of chlorine—does not leave harmful residues such as haloforms, etc., after reaction. The environmental advantages of ozone over chlorine justify its higher cost of generation for an increasing number of applications. Because ozone is highly reactive and cannot be stored over an extended period of time, it has to be generated on site. The usual technique is by silent electrical discharge in an ozonizer using dry air or pure oxygen as a medium. The specific energy consumption of classical ozonizers has been improved recently (1) to values of 14 Wh g^{-1} for air and 6 Wh g^{-1} for oxygen feed.

The literature on electrolytic ozone production was reviewed by Foller and Tobias (2). In terms of efficiency, the anodic formation of O_3 does not seem to be able to beat the classical gas-phase process; the best results have been obtained at technically impractically low temperatures, and these just about reach the efficiency of a modern air-driven ozonizer. Still, electrolytic ozone generation offers a couple of features that are not realized in the classical method and which make it an interesting alternative for various small-scale applications of ozone: investment costs for an electrolyzer (per unity mass of produced O_3) are expected to be considerably lower than for conventional equipment. The concentrations of O_3 in the product gas that can be achieved are higher for electrolytic systems. This reduces the gas volumes involved in ozone treatment or opens applications where high concentrations are a prerequisite.

The solid polymer electrolyte or Membrel cell design is a particularly interesting design for an electrolytic ozone generator, since it can be operated in electrolyte-free water and hence allows *in situ* ozonation in water streams.

Solid polymer electrolyte cells have been shown to offer a conceptually attractive approach to new or established electrochemical processes (3). In water electrolyzers, the ion conducting membrane electrolyte is in its H^+ form and is hence a strong acid. It was shown by Foller and Tobias (2) that electrolyte properties correlate strongly with the ozone yield and that the Lewis acidity of the electrolyte anion, in particular, correlates with current efficiency. The terminal $-\text{SO}_3\text{H}$ groups of the perfluorinated side chains of the Nafion membrane material seem to fit the electrolyte requirements of a good ozone generating cell. In the following, we report results obtained with a Membrel water electrolysis cell modified with a high overpotential anode.

Experimental

The cell used for these studies consisted of a membrane and electrode assembly known from Membrel water electrolyzer designs (4). The cathode consisted of a Pt catalyst deposited with a proprietary method onto the surface of a Nafion 120 membrane and contacted by a

porous graphite current collector. The membrane was allowed to swell in water at 130°C corresponding to a water uptake of ~30 weight percent (w/o). The anode was formed by a porous titanium sintered material covered with a PbO_2 layer and pressed onto the surface of the membrane. The complete membrane and electrode assembly had an area of 30 cm^2 and was contained in a monopolar circular cell housing made of titanium and stainless steel. Figure 1 shows a diagram of the cell used. Care was taken to provide sufficient volume of the housing to allow thermostating of the assembly. The cell was mounted in an all-glass and Teflon water circulating system. The same water was used for both feed and cooling agent.

Figure 2 shows the flow system of the experimental set up. Water was circulated in a closed anode loop by a PTFE circulation pump. A constant circulation flow was maintained throughout all experiments at ~50 $\text{liter}\cdot\text{h}^{-1}$. The loop was fed with demineralized water. The feed water flux (j_w) was adjusted by a metering valve between 5 and 60 $\text{liter}\cdot\text{h}^{-1}$. An overflow maintained a constant water volume in the anode loop. A small fraction of water (~0.1 $\text{liter}\cdot\text{h}^{-1}$ at the rated currents) was transported by electro-osmosis through the membrane to the cathode compartment and discarded. Circulation of water in the cathode loop was maintained by gas lift pumping only, which was sufficient for reasonable thermostating of the entire cell body.

Current efficiencies of ozone production were determined by measuring the ozone concentrations in the produced oxygen gas and in the water overflow from the anode loop. Concentration measurements were performed using a UV-vis spectral photometer (Shimadzu UV-120-02) with separate flow-through absorption cuvettes for the liquid and the gaseous phases. Concentra-

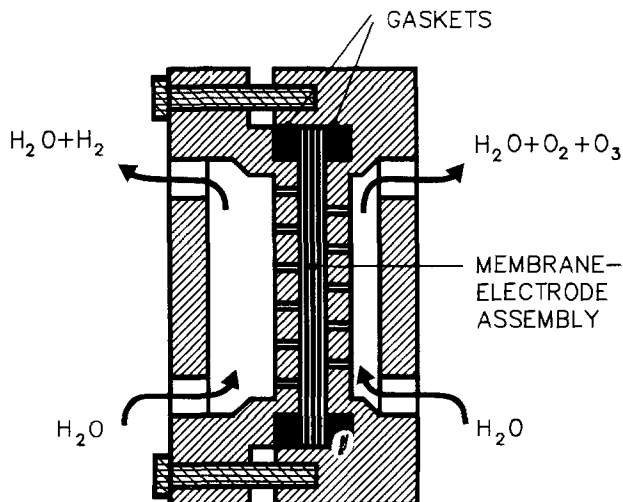


Fig. 1. Experimental cell for ozone generation in water. The hardware is made from titanium on the anode side and of stainless steel on the cathode side.

¹ Present address: Hoffmann La Roche, 4002 Basel, Switzerland.

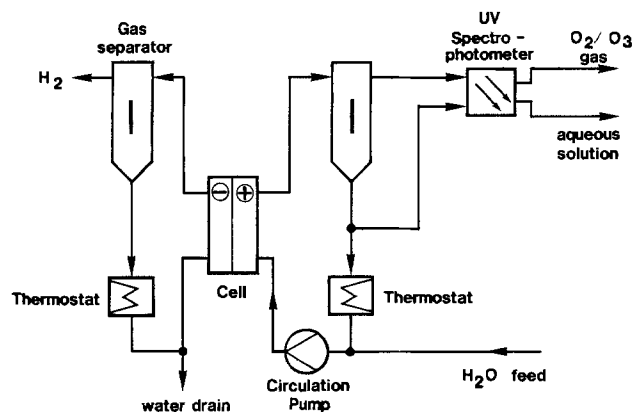


Fig. 2. Flow scheme of experimental rig

tion (gm^{-3}) was calculated from the measured extinction data using the coefficients from literature: $3024 \text{ cm}^{-1} \text{ mol}^{-1} \text{ liter}$ at 253.7 nm for the gas (5) and $2900 \text{ cm}^{-1} \text{ mol}^{-1} \text{ liter}$ at 258 nm for the aqueous solution (6). The PbO_2 electrode was characterized before and after service in the cell by x-ray diffraction at glancing incidence (2°) and scanning electron microscopy.

The feed water was demineralized by passing through a mixed bed ion exchange column. Conductivity was in the range of $1.2 \mu\text{S cm}^{-2}$.

Results

Ozone yield.—The current efficiency of the Membrel ozone generator was determined as a function of the process variables: current, temperature, and feed-water flow. All data are reported for one specific anode structure. The influence of the structural parameters of the anode such as porosity and thickness will be discussed in a later publication (7). The behavior of the generator (discussed here as a function of the above-mentioned process parameters) is qualitatively not affected by the anode geometry. The current efficiency η_i was calculated from the concentration data measured in the gas phase and in the aqueous phase after production had reached steady state, which happened after $\sim 100\text{h}$ of operation. The current efficiency is defined as

$$\eta_i = (j_w C^w + j_g C^g) z F i^{-1} \cdot 100\%$$

where j_w and j_g are the flow rates of water and anode gas, respectively, C^w and C^g the corresponding concentrations of ozone, i the current, F the Faraday constant, and z the number of electrons necessary for the formation of 1 mol of O_3 ($z = 6$).

In Fig. 3, current efficiency is plotted in percents against temperature. The current efficiency shows a maximum of $\sim 15\%$ at a temperature of $25^\circ\text{--}30^\circ\text{C}$. This temperature and its peak value are rather unexpectedly high. Efficiency maxima have been reported at much lower temperatures in concentrated solutions of oxyacids, *i.e.*, at -40°C in H_2SO_4 (2), -10°C in H_3PO_4 (2), and -30°C in HClO_4 (8). No explanation for these maxima has yet been found.

The dependence of the relevant data for O_3 formation on current density is shown in Fig. 4. The current efficiency (Fig. 4b) increases with increasing current density and levels off above $\sim 1.3 \text{ kAm}^{-2}$, reaching a saturation value. Qualitatively, the curve shape resembles the corresponding curves reported by Foller and Tobias (2) for sulfuric acid at 0°C . The specific power consumption P of the process expressed in watt-hours (dc power) per gram of produced ozone is calculated from the current efficiency η_i and the corresponding cell voltage U

$$P = \frac{UzF}{M\eta_i}$$

where M is the molecular weight of ozone, F the Faraday constant, and z the number of electrons transferred in forming O_3 .

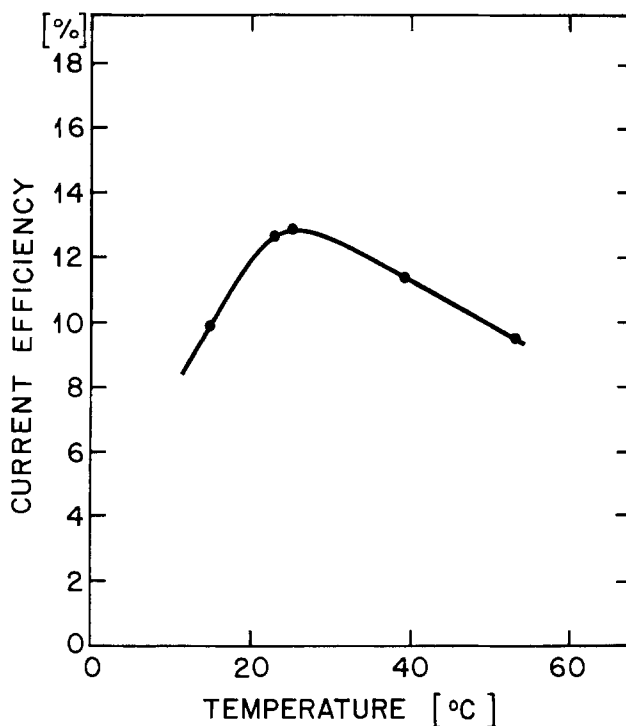


Fig. 3. Current efficiency as a function of temperature. Current density: $i = 1 \text{ Acm}^{-2}$; feed water: $j_w = 5 \text{ liter}\cdot\text{h}^{-1}$.

Combining the data of Fig. 4b with the current-voltage characteristics of the cell (Fig. 4c) yields the plot of P vs. current density (Fig. 4a), which shows a minimum around 1 A/cm^2 .

The concentrations of ozone that correspond to the efficiency data reported above are in the order of $150\text{--}180 \text{ gm}^{-3}$ in the gas phase and $20\text{--}30 \text{ gm}^{-3}$ in water. These concentrations depend, of course, on the amount of water that is fed to the system per unit time (j_w). At constant temperature (18°C) and current (30A), the water flux (j_w) was varied between 5 and $60 \text{ liter}\cdot\text{h}^{-1}$. The ratio of the concentrations of ozone in gas and in water (which, in the limiting case of $j_w = 0$ is ~ 5) increases with water flux. This indicates that, in the flow system used, an equilibrium partition of ozone between gas and liquid is only attained at very small fluxes. This is illustrated in Fig. 5a, which is a graph of the apparent Henry constant defined as

$$H_{\text{app}} = (C^g)(C^w)^{-1}$$

where C^g and C^w are both measured in grams per cubic meter of gas or liquid, respectively. The concentration of ozone in water in this experiment varied between 25 and 4 ppm (Fig. 5b). The total quantity of ozone produced per unit time (j_{O_3}), however, is independent of the water flux, as can be seen from the top curve of Fig. 5c. The other two curves of Fig. 5c show the fractions of the total ozone production: first, that which leaves the system as aqueous solution and, second, that which leaves in the gas phase. The independence of ozone yield from feed-water flux means that current efficiency is not influenced by the degree of saturation with ozone of the water passing through the cell.

Stability.—One problem generally encountered with ozone generating cells is the long-term stability of electrode materials and cell equipment. Nafion membranes are well known for their extraordinary stability against oxidants (9). The excellent oxidation stability is confirmed by our long-term testing of cells. No degradation of the membrane was detected after $>2000\text{h}$ of operation under a constant load of 1.3 Acm^{-2} . During operation, the effluent water was checked for fluoride ions. The levels measured with an ion-selective electrode were only just within its detection limit and were not indicative of significant decomposition.

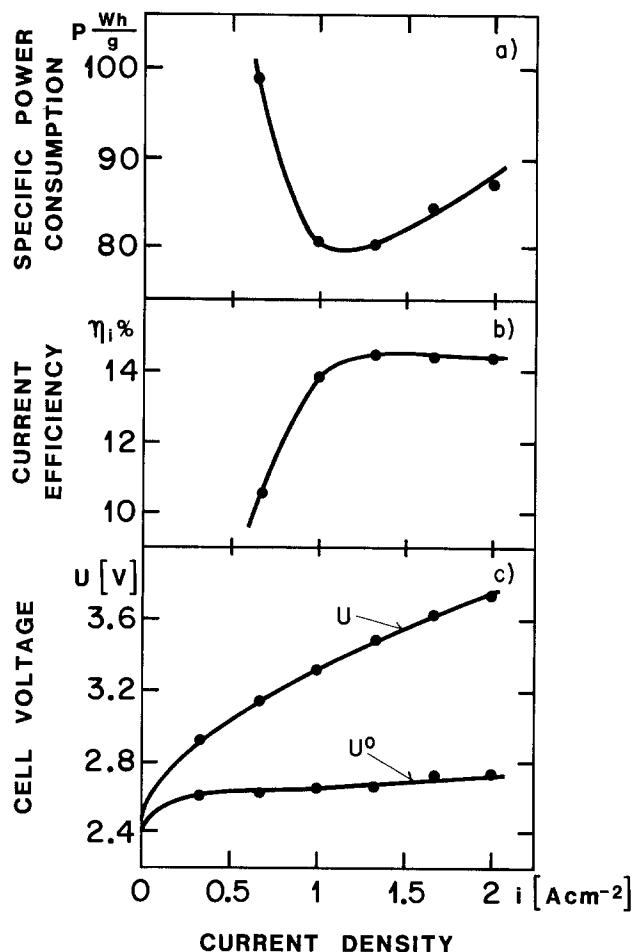


Fig. 4. Efficiencies and cell voltage of Membrel cell as a function of current density. Operating conditions: $j_w = 10 \text{ liter}\cdot\text{h}^{-1}$, $T = 25^\circ\text{C}$. a: Specific power consumption P for ozone generation. b: Current efficiency for ozone generation. c: Cell voltage (U) and iR corrected cell voltage (U^0). iR contribution evaluated from cell voltage decay after fast current interruption.

Lead dioxide is known to undergo corrosion in liquid acids under conditions of high anodic currents (10, 11). Long-term experiments with Membrel cells were performed in order to assess the corrosion behavior of PbO_2 deposited on titanium. For this purpose, an experiment was run over a period of 2500h under a load of 1.3 Acm^{-2} . The water from the anode loop was checked for lead ions by inverse voltammetry.² The lead level found did not differ significantly from the level of the deionized feed

² Analysis of Pb content in water were kindly performed by Dr. H. Siegenthaler of the Institut für anorgan. Chemie, Universität Bern, Switzerland.

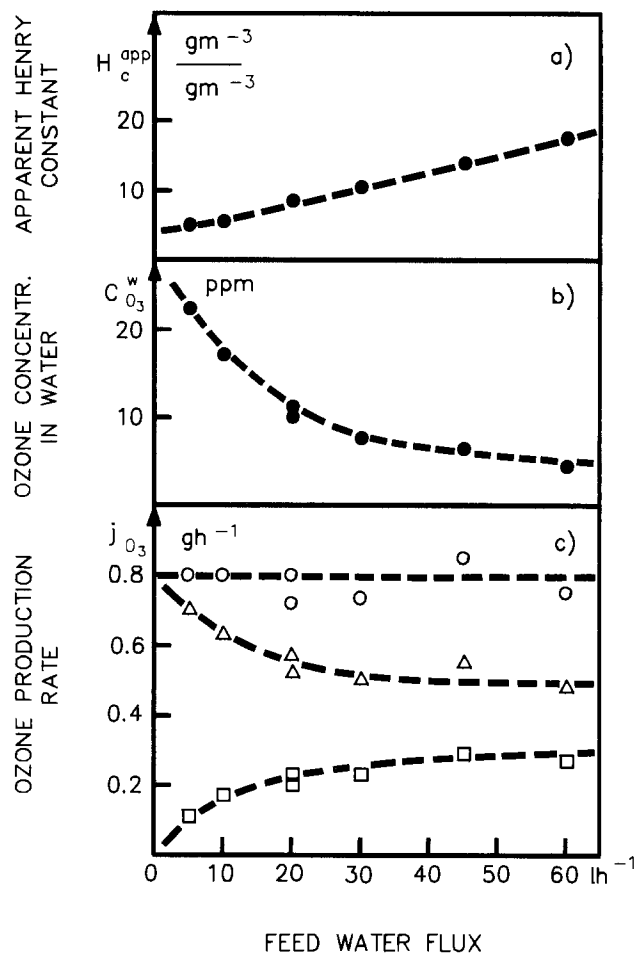


Fig. 5. Influence of feed water flux on cell performance data at $T = 30^\circ\text{C}$ and $i = 1 \text{ Acm}^{-2}$. a: Apparent Henry constant, expressed as the ratio of concentrations of ozone in the gas phase and in the water $H_c^{\text{app}} = (C_g/C_l)$. b: Concentration (ppm) of ozone in the anode water loop, analyzed by UV absorption at 258 nm. c: Ozone production rate in grams per hour, leaving the apparatus in \square : the aqueous phase ($j_{\text{O}_3}^w$), \triangle the gas phase ($j_{\text{O}_3}^g$) and \circ : overall ($j_{\text{O}_3} = j_{\text{O}_3}^w + j_{\text{O}_3}^g$).

water (feed water: 0.35 ppb; anode loop: 0.38 ppb). The cell voltage was stable within $3.45 \pm 0.1 \text{ V}$ at 30°C throughout the experiment.

After disassembling the cell, the PbO_2 layer was inspected using scanning electron microscopy. The micrograph of Fig. 6a shows the back of the electrode which was not in direct contact with the membrane, and Fig. 6b shows the electrode surface facing the membrane. The differences between the back and the front are evident. The crystallite morphology of PbO_2 is partly destroyed in the contact areas where the electrode reaction took place

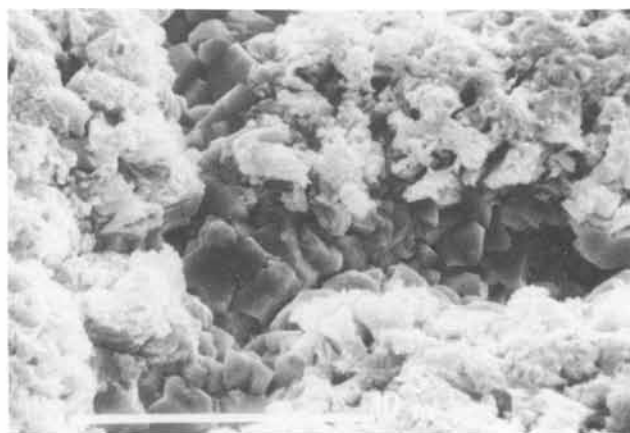
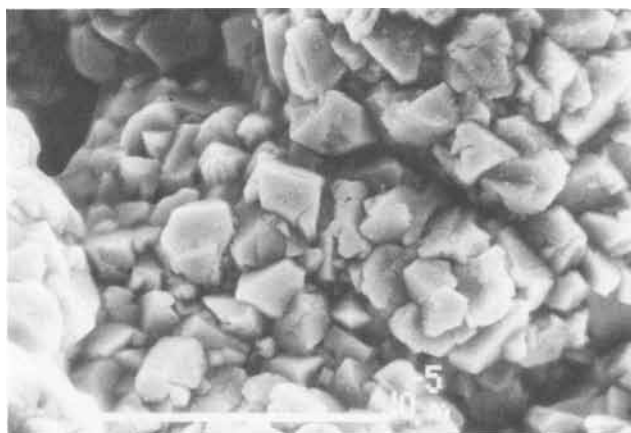


Fig. 6. Scanning electron micrographs of the PbO_2 layer of a Membrel anode after 2500h of service. a(left): Back of the electrode, not electrochemically active. b(right): Front of the electrode with areas of intimate contact with the membrane.

at a high rate. The estimated current density at the points of contact with the membrane (destroyed crystal morphology) was about 2.5 Acm^{-2} . The crystallography of the PbO_2 layer was studied by x-ray diffraction at glancing incidence ($\sim 2^\circ$), which samples a layer depth of $\sim 0.1 \mu\text{m}$. The diffractograms of Fig. 7 show the lines observed for both sides of the electrode after use in the cell. The rear surface consists of a mixture of $\beta\text{-PbO}_2$ and $\alpha\text{-PbO}_2$ due to the deposition process chosen. The lines originating from the $\alpha\text{-PbO}_2$ structure are strongly diminished on the front surface which was electrochemically active. It is known from the literature (10) that α - and $\beta\text{-PbO}_2$ usually corrode at the same rate, so preferential corrosion of $\alpha\text{-PbO}_2$ can be excluded. More likely is a transformation of $\alpha\text{-PbO}_2$ into $\beta\text{-PbO}_2$ via a solute species (discussed below).

Discussion

Comparing the results that were obtained using the Membrel water electrolyzer as an ozone generator with published work on comparable systems, one finds two features which are strikingly different. First, the PbO_2 coating in contact with Nafion seems to be more stable (by several orders of magnitude) than in liquid electro-

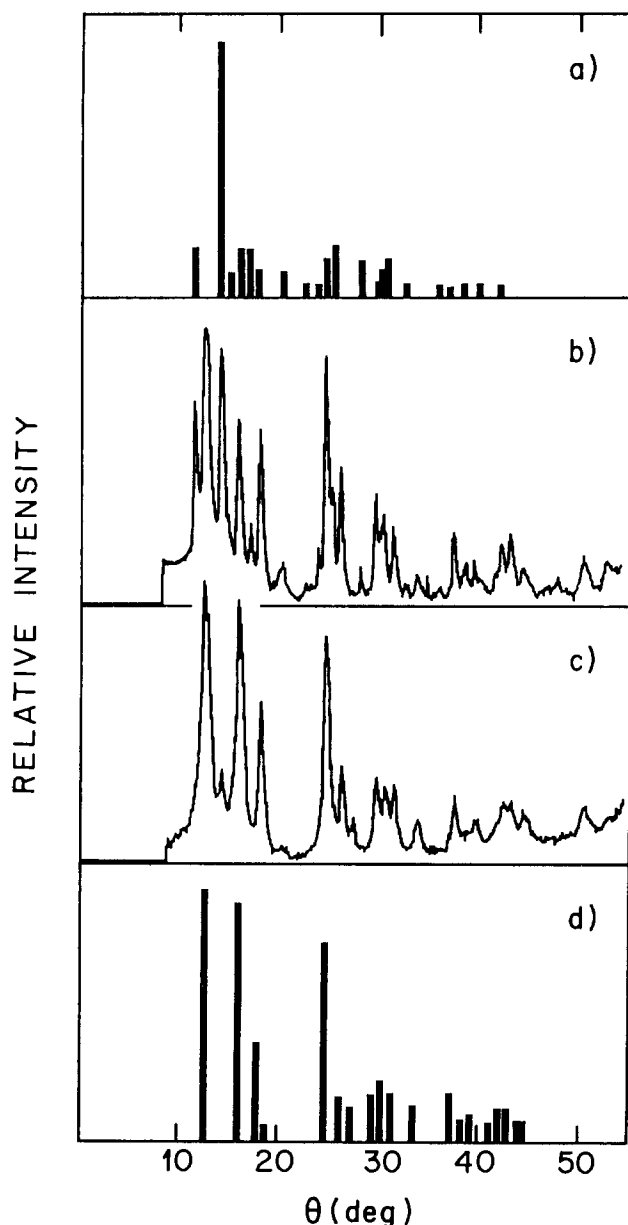


Fig. 7. X-ray diffraction at glancing incidence of the same electrode as Fig. 6. a: Expected lines for $\alpha\text{-PbO}_2$ (17). b: Diffractogram of the back of the electrode. c: Diffractogram of the front part of the electrode. d: Expected lines for $\beta\text{-PbO}_2$ (17).

lytes. Second, the system shows a distinct yield maximum at a comparably high temperature of $25^\circ\text{--}30^\circ\text{C}$. Both properties of the system are important for its technical application and must be deduced from specific properties of the ion exchange membrane used as an electrolyte and its interface to the PbO_2 anode. It is generally assumed that perfluorinated ionomer materials in contact with water segregate into one hydrophilic and into one (possibly two) hydrophobic phases (12). The hydrophilic phase contains the ionic groups and most of the water and forms a percolating network within the membrane. The electrolytic properties of Nafion membranes are given by this aqueous phase, formed by fixed anions, mobile cations (hydronium ions in the case of water electrolysis), and water. In many respects, Nafion does behave like an "ordinary" aqueous electrolyte: *i.e.*, cyclic voltammetry of Pt electrodes in contact with Nafion in pure water gives all the features that are well known in acidic liquid electrolytes (13).

With respect to the corrosion stability of lead dioxide, two properties of the membrane electrolyte seem to be decisive. The electrolyte is convection free and prevents mechanical wear of the electrode coating. The proton transference number in this application is 1.0, and, therefore, no concentration gradients of electrolyte species by transference will occur, even at extremely high current densities. The corrosion resistance can be rationalized assuming the validity of the model for PbO_2 corrosion in liquid acids proposed by Foller and Tobias (10). They assume chemical dissolution of PbO_2 as Pb^{2+} in a layer with very high proton activity near the anode (due to transference) and reformation of $\beta\text{-PbO}_2$ in the bulk of the electrolyte where pH is higher. Support for this model was deduced from the observed transformation of $\alpha\text{-PbO}_2$ as an electrode coating into $\beta\text{-PbO}_2$ as a corrosion product. Our results fit very well into that model. The absence of concentration gradients at the anode surface reduces drastically the chemical dissolution of PbO_2 . The little PbO_2 that does dissolve is redeposited immediately onto the surface because of unfavorable transport conditions for its removal from the electrode (absence of convection).

The mechanisms involved in the anodic evolution of ozone are not well understood. The reaction does not seem to depend much on specific electrocatalytic properties of the electrode material, the only prerequisite apparently being a sufficiently high overpotential for oxygen evolution. However, the ozone yield strongly depends on electrolyte properties, such as its concentration and the electronegativity of its anion. The different location of the temperature maximum of the ozone yield for lead dioxide electrodes in different electrolytes also suggests that the observed temperature dependence is mainly governed by the physical chemistry of the electrolyte solution, rather than by the surface properties of the electrode. The electrolyte influence on ozone yield has been rationalized in two ways by Foller and Tobias (2, 18). First, the adsorption of oxyanions competes with the adsorption of oxygen intermediates and hence influences the free energy of adsorption of oxygen. An optimum free energy of adsorption of oxygen exists at low to intermediate anion coverages. Ozone is believed to be formed by a heterogeneous catalytic mechanism on the electrode surface. Second, the electrolyte anions stabilize the free intermediate species that might be formed at high anodic potentials. This argument holds mainly for fluoroanion electrolytes. The kinetics of this process would then be determined mainly by a homogeneous mechanism in the electrolyte.

An electrocatalytic mechanism as suggested by the anion adsorption model seems improbable since any adsorbed intermediate irrespective of its adsorption energy would be an intermediate for both, O_2 and O_3 . A mechanism via solute species seems more probable. With platinum as a catalyst the cathode overpotential is estimated to be in the order of 50 mV (3). This means that the iR free anode potential derived from Fig. 4 is in the order of 2.5V over the current density range of maximum ozone yield. This is sufficiently high to form free or loosely adsorbed

atomic oxygen, which reacts readily with molecular oxygen to form ozone (14). Assuming a mechanism of the kind outlined above, one would expect the ozone current yield to depend on the oxygen concentration in the immediate vicinity of the electrode. It has been shown by gas diffusion measurements that supersaturation in the order of 10 bars can occur at gas evolving electrode-membrane interfaces (15). One reason for the relatively high current yield of the Membrel ozone generator at moderate temperatures might be connected with the high oxygen supersaturation of the solid polymer electrolyte structure. The assumption of a high supersaturation of oxygen at the electrode-membrane interface, and, consequently, of ozone as well, also explains the independence of the yield from ozone concentration in the feed water. The concentration range of ozone in the feed water was 5-25 ppm and probably smaller by at least an order of magnitude than in the region of supersaturation. Hence, no dependence on the concentration is to be expected. In order to get more information about the influence of the concentrations of dissolved gases, a pressure electrolysis system for ozone generation is being built (16).

Conclusions

Nafion membranes have some unique physical and chemical properties that make them suitable for use as electrolytes in solid polymer electrolyte cells for ozone generation: current efficiency of 15%; a relatively low cell voltage; operation at room temperature; and a long lifetime of the cell components. Together, these make this system an economically interesting new electrolytic technique. The main advantage is the fact that the Membrel cell directly produces an aqueous solution of ozone ready for various oxidizing and/or disinfectant applications.

The mechanisms of ozone formation are not well understood, and more fundamental and applied research is necessary to guide further improvement of the system.

Acknowledgment

The authors are grateful to Mrs. R. Loitzl for the preparation of PbO₂ anodes.

Manuscript submitted June 11, 1984; revised manuscript received ca. Sept. 19, 1984. This was Paper 573 presented at the San Francisco, California, Meeting of the Society, May 8-13, 1983.

Brown, Boveri & Cie assisted in meeting the publication costs of this article.

REFERENCES

1. H. P. Klein, *J. Am. Oil Chem. Soc.*, **61**, 306 (1984).
2. P. C. Foller and C. W. Tobias, *This Journal*, **129**, 506 (1982).
3. A. B. La Conti, in "Proceedings of the Oronzio De Nora Symposium on Chlorine Technology," p. 94, Venice (1979).
4. S. Stucki and R. Müller, in "Proceedings of the 3rd World Hydrogen Energy Conference," Vol. 4, p. 1799, Tokyo, Japan (1980).
5. De Mowe and Patapoff, *Environ. Sci. Technol.*, **10**, 9 (1976).
6. H. Bader and J. Hoigné, *Water Res.*, **15**, 449 (1981).
7. S. Stucki and H. Devantay, To be published.
8. D. P. Semchenko, E. T. Lyubushkina, and V. Lyubushkin, *Izv. Sco. Kavk. Nauchn. Tsentra Vyssh. Shk. Ser. Tekn. Nauk*, **3**, 98 (1975).
9. W. Grot. *Chem. Ing. Technol.*, **44**, 167 (1972).
10. P. C. Foller and C. W. Tobias, *This Journal*, **129**, 567 (1982).
11. D. Gilroy, *J. Appl. Electrochem.*, **12**, 171 (1982).
12. R. S. Yeo, *This Journal*, **130**, 533 (1983).
13. S. Stucki and A. Menth, in "Industrial Water Electrolysis," S. Srinivasan, F. J. Salzano, and A. R. Landgrebe, Editors, p. 180, The Electrochemical Society Softbound Proceedings Series, Princeton, NJ (1979).
14. M. Pourbaix, "Atlas of Electrochemical Equilibria," Section 19.1, National Association of Corrosion Engineers, Houston (1974).
15. R. Oberlin, S. Stucki, and H. J. Christen, p. 434, Extended Abstracts of the 33rd Meeting of the ISE, Lyon (1982).
16. S. Stucki and H. J. Christen, To be published.
17. Powder Diffraction File, Inorganic Phases, ICPDS (1981).
18. P. C. Foller and C. W. Tobias, *J. Phys. Chem.*, **85**, 3238 (1981).

Computer Simulation of Dendritic Electrodeposition

Richard F. Voss

IBM Thomas J. Watson Research Center, Yorktown Heights, New York 10598

Micha Tomkiewicz*

Department of Physics, Brooklyn College of CUNY, Brooklyn, New York 11210

ABSTRACT

We have generalized the single-particle diffusion-limited aggregation process to both multiparticles and aggregation on an initially smooth surface. The computer simulation is done as a function of "concentration" of the particles and the sticking coefficient to the surface. These parameters are correlated with electrochemical parameters such as overpotential, limiting current, exchange current, and electrolyte concentration. The correlations between the two sets of parameters permits direct comparison between simulation and experiment. The transition between "mossy" deposits and fully developed dendritic growth is recorded. The simulation reproduces the presence of a critical overpotential and an initiation time. The fundamental interdependence of these parameters and their dependence on the concentration of the electrolyte, quantitatively resemble that of the observed dendrite growth in electrodeposition of Zn and other metals.

The subject of dendritic growth during electrodeposition of metals has fascinated electrochemists for many years. Part of this fascination is, no doubt, due to the technological importance of this phenomenon, particularly in conjunction with battery technology. Equally important, however, is the challenge that is being presented in the complexity and the unique morphology that is be-

ing created and the realization that this unique morphology can be generated, under appropriate conditions, regardless of the metal involved.

The interdependence between ionic transport in the electrolyte, the kinetics of charge transfer at the metal solution interface and the solid state properties of the deposit was emphasized in numerous review articles on electrodeposition (1). Closer to home, the system in which dendrite formation was most thoroughly studied is the

*Electrochemical Society Active Member.

electrodeposition of Zn in alkali zincate electrolyte. All the comparisons with experiment that will be made in this paper are based on this system. In this system, three kinds of deposits are encountered (2): (i) smooth deposits at low overpotential in vigorously stirred electrolytes, (ii) in quiescent concentrated solutions, dark gray porous (mossy) deposits are formed at low overpotential, and (iii) at higher overpotentials, dendritic deposits are invariably formed. Phenomenologically, it was recognized that an initiation overpotential is required to produce dendrites, and at least one initiation time was observed. Beyond the initiation time, the velocity of dendrite propagation was found to be approximately constant. The issue of both an initiating time and overvoltage as two separate requirements is still unsettled. Their presence will imply a critical overvoltage with an infinite initiation time and a finite initiation time for an infinite overpotential.

Morphologically, it was observed that, after the initiation stage, the dendrite tips are parabolic in shape with approximately constant radius of curvature (3) that decreases with overpotential (4).

The most recent attempt at a comprehensive theoretical analysis of the phenomena can be found in a series of papers by Landau and his group (4) which expand on earlier concepts that were advanced by Bockris and his group (5).

These theories divide the dendrite growth into two stages: initiation and propagation. During the initiation stage arbitrary roughness at the substrate (1), or, more specifically, pyramids arising from rotation of screw dislocations (3), are being exponentially amplified by preferential transport of the deposited ions from the electrolyte. At the propagation stage, equations which include diffusion, reaction kinetics, and surface energy were solved for either maximum velocity at the tip (5) or to obey marginal stability criteria (4). From the results, it was possible to obtain the radius of the tip, the critical overpotential, and/or the induction time. Attempts were made to determine the interdependence of these parameters and their dependence on electrolyte concentration, temperature, and hydrodynamic conditions. It is not our intention in this paper to challenge any of these theories. We would like to explore here what aspects of the dendritic growth can be simulated without making any physical assumptions about the system. The system consists only of an arbitrary featureless surface in contact with an "electrolyte" at a given concentration. Each particle in the electrolyte undergoes random walk until it reaches the surface. At the surface, a finite, given probability will determine whether the particle will stick to the surface or will be reflected back to the solution.

Methodology

Our work was stimulated by the recent interest among physicists in growth or aggregation phenomena that result in fractal clusters (6, 7) with power-law correlations over wide ranges of length scales. Such correlations are reminiscent of those found in equilibrium-phase transitions at the critical point. Much of the recent widespread interest in understanding the computer simulations of simple aggregation processes (8-10) have been successful in reproducing the scale invariant properties. In particular, a simple model has been presented (8, 9) for the aggregation process when the limiting step is diffusion to the growth sites. This model is based only on local constraints (Brownian motion, connectivity to aggregate) yet it reproduces the long-range fractal behavior. This model and its variations have also stimulated theoretical treatments based on mean field (11) and continuum (12-14) approximations and real space renormalization (15).

The models presented here are a generalization of the single-particle diffusion-limited aggregation process (8) to both multiple particles and aggregation on an initially smooth surface. In the original model (8), a single particle would undergo a random walk until reaching the boundary of the aggregate of cluster. At this point, it became part of the cluster and a new particle began its walk.

Here, we begin with a two-dimensional square lattice (typically 600×400) where a fraction of the sites are initially occupied with mobile particles. The bottom edge is the initial active area for growth while the top edge is held at fixed concentration (9). The mobile particles undergo simultaneous diffusion (random walks) under the constraint that no two particles can occupy the same site at the same time. During a time step, each of the mobile particles is examined in random order. One of its four neighbor sites is selected by chance as a possible next position. If unoccupied, the particle moves to this new site. If occupied, the particle remains fixed. Periodic boundary conditions are used in the horizontal direction, particles that leave to the right enter from the left. If the new site borders a growth site, it becomes part of the aggregate with probability k . Once part of the aggregate, the particle is immobile and is itself a new growth site. The sticking probability k is related to the electrochemical parameters during electrolyte deposition. The process is repeated for different k and c , where c represents the fraction of occupied sites until an either fixed number of particles have aggregated (typically 100,000) or until a fixed number of time steps have elapsed.

Since this paper represents a collaborative effort between a theoretical physicist and an electrochemist, we feel that the appropriate procedure to present the results is in terms of intrinsic system parameters which are independent of electrochemical terminology. Thus, the kinetics at the interface is represented by sticking probability, the electrolyte concentration in terms of percentage of occupied sites and distance, and time in terms of arbitrary displacement units and number of steps in a Brownian motion in which the diffusion coefficient is taken as unity. These units have the advantage that they are independent of any particular system. In the discussion section, we will transform these units to the conventional electrochemical units, using the Zn system as an example.

Results

Figures 1 and 2 show the time evolution of the morphologies which develop with 10% electrolyte concentration and different sticking probabilities. In addition, one can observe the concentration gradient in the electrolyte as one approaches and enters the deposited surface.

By comparing the figures, one can observe the first important result from this work: at low sticking probability (1%), one observes a morphology which is similar to the mossy deposit that is observed with metal deposition at low overpotential and a "typical" dendrite formation with side branching, etc., at the higher sticking probab-



Fig. 1. Simulation of growth for concentration of 0.1 (fraction of occupied sites) and sticking coefficient of 0.3. The transition between black and gray indicates time evolution in units of 2×10^5 Brownian motion steps.

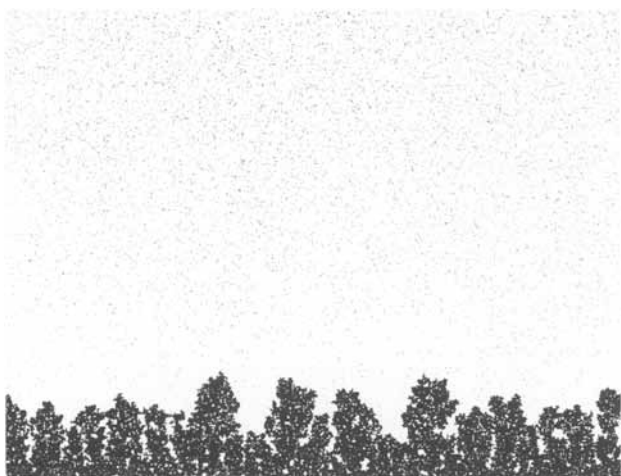


Fig. 2. The same conditions as Fig. 1, but with sticking coefficient of 0.01.

In Fig. 3, we show the time evolution of the surface height for various sticking probabilities at a fixed electrolyte concentration (10%). In Fig. 4, we show the time evolution of the surface height for various electrolyte concentrations at a fixed sticking probability (10%). Since both figures can be directly compared with experiment, all the quantitative analysis will be based on them. From Fig. 1, it is obvious that dendrites of various heights are formed across the surface. The surface height in Fig. 3 and 4 was calculated by taking an "average" of the dominating dendrites. This procedure clearly deviates from the experimental determination of this parameter (3), which was done by following the growth of an arbitrary, single dendrite. Figures 3 and 4 are presented in logarithmic scale; they cover at least three orders of magnitude in length and six orders of magnitude in time. Even without quantitative analysis of the data in these figures, the existence of an initiation time for dendrite growth, which changes with the sticking probability and the concentration of the electrolyte, is evident. The exact significance of the initiation time is not so obvious. One can observe that all the curves are approximately linear in the logarithmic scale, down to a height of 1. Below that height, the curves deviate from linear behavior in a non-systematic way with considerable amount of noise. In the linear portions of the curves, the slope is approximately constant, with value of 2/3 for the high electrolyte concentrations with increase in slope as we increase the concentration of the electrolyte. This is a clear deviation from the experimentally observed behavior (3), in which, over a

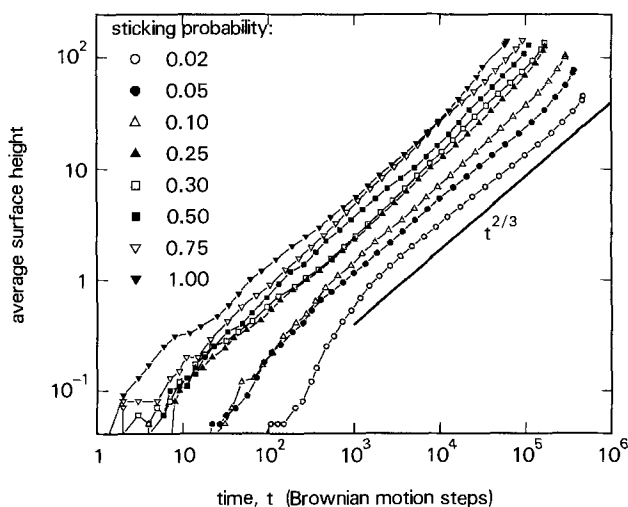


Fig. 3. The average surface height as a function of time in Brownian motion steps, for fixed concentration (0.1) and varying sticking probability.

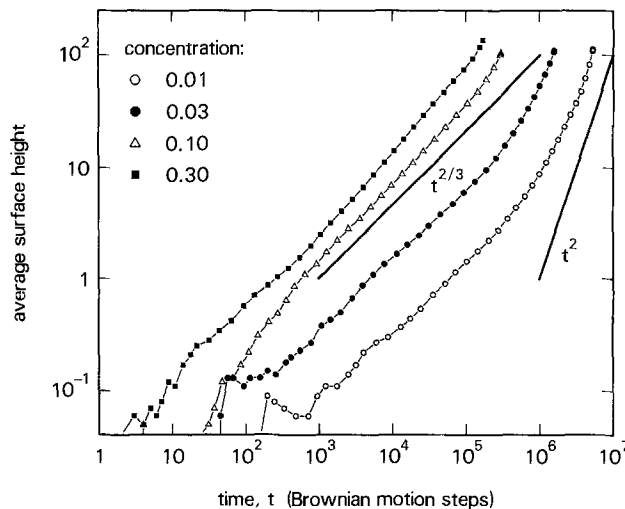


Fig. 4. The same as Fig. 3 with fixed sticking probability (0.1) and varying concentration.

much more limited range of time and distance, a linear dependence which implies constant rate of growth was observed. We do not wish to speculate here as to the possible origin of these differences. The dimensionality of the problem, the method of measurement of the height, the available range, are all different.

Arbitrarily, we will stipulate that a height of 1 is the threshold of dendritic growth. Figure 5 shows the time it takes to reach this height as a function of the sticking probability for $c = 0.1$, and at a sticking probability of 0.1 as a function of concentration. If we associate this time with the initiation time and the sticking probability with the overvoltage, this curve can also be directly compared with experiment. This will be done in the discussion section, after we introduce the correlation between the sticking probability and the overvoltage.

Discussion

Correlation Between the Numerical Calculations and Electrochemical Parameters

Sticking coefficients and overpotential.—Suppose that the deposition occurs under mixed activation and diffusion control (1). The current density is given by

$$I = I_0 \left\{ \left(\frac{I_{l,c} - I}{I_{l,c}} \right) f_c(\eta) - \left(\frac{I_{l,a} - I}{I_{l,a}} \right) f_a(\eta) \right\} \quad [1]$$

where

$$f_c(\eta) = \exp(\alpha_c F \eta / RT) \quad [2]$$

$$f_a(\eta) = \exp(\alpha_a F \eta / RT) \quad [3]$$

I_0 is the exchange current, $I_{l,c}$ and $I_{l,a}$ the limiting currents, α_a and α_c the transfer coefficients of the anodic and cathodic reactions, F the Faraday number, R the gas constant, T the absolute temperature, and η the overpotential. For the numerical simulation, we assume that when the reaction is diffusion controlled, i.e., $I = I_l$, the sticking coefficient of the solute on the electrode is 1. Under these conditions, every encounter between solute and substrate results in deposition. Following this assumption, we define the sticking coefficient at any potential as

$$\kappa = \frac{I}{I_l} \quad [4]$$

and assume that the limiting currents for the anodic and cathodic reactions are the same in magnitude and opposed in sign, then, by rearranging Eq. [1], we obtain

$$\frac{1}{\kappa} = \frac{f_c(\eta) + f_a(\eta)}{f_c(\eta) - f_a(\eta)} + \frac{I_l/I_0}{f_c(\eta) - f_a(\eta)} \quad [5]$$

For a stationary electrode the limiting current density is given by

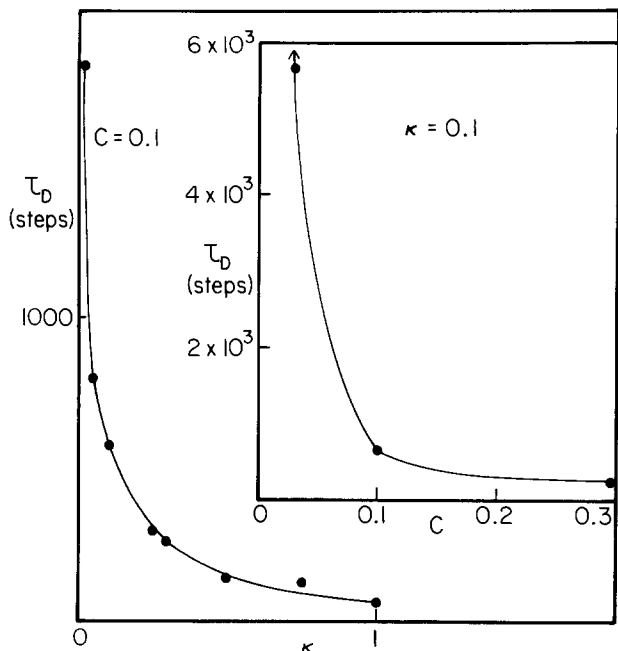


Fig. 5. The variation of the initiation time (taken at surface height of 1) with the sticking probability and concentration (insert). The data were taken from Fig. 3 and 4.

$$I_0 = ZFDC_0/\delta_0 \quad [6]$$

where D is the diffusion coefficient of the depositing ions, C_0 is their concentration, Z the charge, and δ is the thickness of the diffusion layer. For illustration purposes, let us take the Zn system as a prototype. Diggle *et al.* (3) have found that in zincate solutions $D/\delta = 6.8 \times 10^{-4}$ cm/s. If we now write the exchange current density as (1)

$$I_0 = FkC_0 \exp\left(\frac{-\alpha_c F}{RT} E_0\right) \quad [7]$$

where k is the rate constant of the rate-determining step, C_0 the concentration of the electrolyte, and E_0 the equilibrium potential of the reaction and take typical exchange current for the Zn electrode to be 5.5 A/cm² at $C_0 = 5.5$ M, which is approximately equivalent to the 10% concentration shown in Fig. 3. We will further assume that, for this electrode, $\alpha_c = 1 - \beta$ and $\alpha_a = \beta$, where $\beta \approx 0.5$ is the symmetry factor and $Z = 1$.

Using these data and Eq. [1] and [5], one can correlate the sticking coefficients with the overpotential for a given concentration of the electrolyte. For a quick reference, such a correlation is presented in Fig. 6.

Time and space.—The calculations are presented in units of Brownian steps with normalized diffusion coefficient, $D = 1$.

To convert these units into the conventional units of length and time, we will compare the calculated growth rate to the experimental growth rate of Zn dendrites and introduce the diffusion coefficient of zincate ion. The comparison is not exact because the experimental observations were carried out at considerably lower zincate concentrations and the numerical propagation velocities are not constant. Nevertheless, the comparison should be valid well within an order of magnitude and will add to the clarity of the qualitative comparisons that we try to make here between “theory” and experiment. Two equations will be used for this purpose: from random walk statistics, the root mean square displacement $\bar{\Delta}$ changes with time according to

$$\bar{\Delta} = \sqrt{2Dt} \quad [8]$$

and the “average” velocity of the dendrite propagation is given by

$$v = \frac{l}{t} \quad [9]$$

where l is the length of a dendrite.

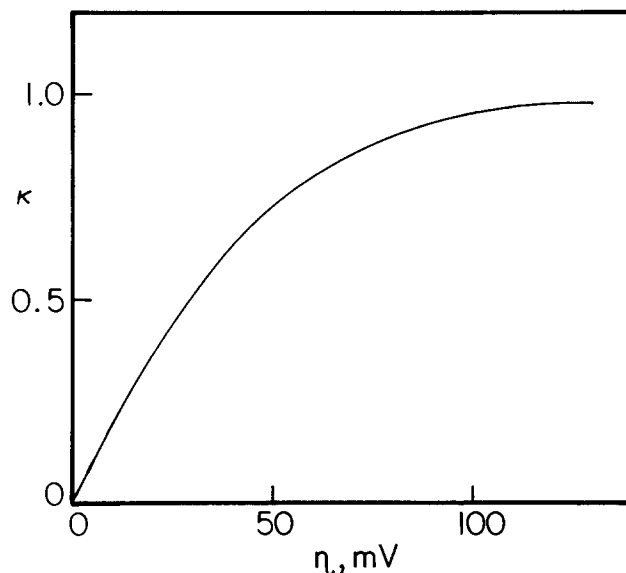


Fig. 6. The calculated variations of the sticking probability with the overpotential. The calculations are based on Eq. [1] and [5] and parameters which are given in the text.

Typical experimental value for v in the Zn system is 1 μ m/s, and a “typical” calculated value, taken from Fig. 3, is 5×10^{-3} displacements/no. of Brownian steps. Taking these values together with the measured diffusion coefficient of $D = 6.8 \times 10^{-6}$ cm²/s, we arrive at the following transformations: 1 Brownian displacement ≈ 7 μ m, and 1 Brownian step ≈ 0.03 s.

Comparison with Experiment

Most of the quantitative experimental work on dendritic electrodeposition was done in conjunction with the electrodeposition of Zn. The examples that we took in the previous section to establish the connection between this work and electrochemical systems have originated from the work on the Zn electrode. Most of the work on the Zn electrode was done with electrolyte concentration considerably lower (typically 0.1M) than the one that we have used here. The main reason for that is that considerably larger computer times are required for the lower concentrations and we did not feel that a full quantitative comparison between our results and the experimental observations was called for and would justify our additional expenditures. Morphologically, Fig. 1 and 2 show that the computer is able to reproduce the transition between mossy deposits and the dendritic deposits as one increases the overvoltage. However, on close inspection, the computer simulation results in growth which can best be described in terms of Mandelbrot’s fractal geometry (7) with power-law correlations over wide range of length scales, while, experimentally, the individual dendrites terminate in crystalline, parabolic fronts with optimized radius of curvature which varies with overpotential. This difference is intrinsic to the method of analysis and serves as a reminder that the real dendritic growth on a real substrate is considerably more complex than the simplified model which is presented here.

In addition to the kinetically dependent morphological changes in the deposits, the most convincing analogy with experiment is the dependence of the initiation times for the dendritic growth on the overvoltage and concentration of the electrolyte. Quantitatively, Fig. 4 has similar functional dependence of the initiation time on the sticking coefficient and concentration as the one that was observed experimentally between initiation time and overvoltage (3, 4). However, if we define the critical overvoltage at which the initiation time increases asymptotically to infinity, we find that while, experimentally, for electrolyte concentration of 0.1M, the value for Zn is around 70 mV, from Fig. 4, the critical sticking coefficient approaches zero. Whether this apparent lack

of critical sticking coefficient is due to the scaling relations that were introduced here or is intrinsic to the simplicity of the model that was presented here remains to be determined.

Acknowledgments

We would like to express our special gratitude to Dr. U. Landau from Case Western University and to Dr. S. Szpak from the Naval Ocean Systems Center for making available to us a yet unpublished documentation and photographs of dendritic growth on the Zn electrode. One of us (M. T.) would like to acknowledge the support of the Office of Naval Research.

Manuscript submitted May 1, 1984; revised manuscript received Sept. 20, 1984.

Brooklyn College assisted in meeting the publication costs of this article.

REFERENCES

1. See, for example, J. O'M. Bockris and A. R. Despic, in "Physical Chemistry: An Advanced Treatise," Vol. IXB, H. Eyring, Editor, Chap. 7, Academic Press, New York (1970).
2. J. McBreen and E. J. Cairns, in "Advances in Electro-

- chemistry and Electrochemical Engineering," Vol. 11, H. Gerischer and C. W. Tobias, Editors, p. 273, John Wiley & Sons, New York (1978).
3. J. W. Diggle, A. R. Despic, and J. O'M. Bockris, *This Journal*, **116**, 1503 (1969).
4. U. Landau and J. H. Shyu, *ibid.*, To be published.
5. See Ref. a and 3 and J. L. Barton and J. O'M. Bockris, *Proc. R. Soc. A*, **268**, 485 (1962).
6. S. R. Forrest and T. A. Witten, *J. Phys. A*, **12**, L109 (1979).
7. B. Mandelbrot, "The Fractal Geometry of Nature," Freeman, New York (1982).
8. T. A. Witten and L. M. Sander, *Phys. Rev. Lett.*, **47**, 1400 (1981); *Phys. Rev. B*, **17**, 5686 (1983).
9. P. Meakin, *Phys. Rev. A*, **27**, 604 (1983).
10. R. F. Voss, *Phys. Rev. B Rapid Commun.*, To be published; in "Proceedings of the Conference on Fractals in Physics," Gaithersburg, MD, 1983, To be published.
11. M. Muthukumar, *Phys. Rev. Lett.*, **50**, 839 (1983).
12. R. Ball, M. Nauenberg, and T. Witten, NSF ITP preprint.
13. M. Nauenberg, *Phys. Rev. B*, **28**, 449 (1983).
14. M. Nauenberg, R. Richter, and L. M. Sander, *Phys. Rev. B*, To be published.
15. H. Gould, F. Family, and H. E. Stanley, *Phys. Rev. Lett.*, **50**, 686 (1983).

Technical Notes



Anodic Dissolution of Zinc Electrodes in Alkaline Electrolyte: Mass Transport Effects

Yu-Chi Chang* and Geoffrey Prentice**

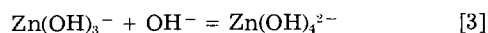
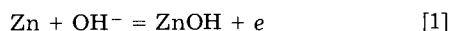
Department of Chemical Engineering, The Johns Hopkins University, Baltimore, Maryland 21218

In a previous investigation (1), we proposed a three-step mechanism for the anodic dissolution of zinc in dilute alkaline electrolyte. From that mechanism, we deduced the kinetic parameters, under the assumption that the system was kinetically controlled. Quantitative agreement between calculated and experimental results was obtained in the initial dissolution region, near $-1.23V$ vs. NHE.

In the present analysis, we incorporate mass-transport effects. Because the hydrodynamics and current distribution are well defined on the rotating disk electrode, data from this system are particularly appropriate for analysis. Studies conducted at constant potential show that the reciprocal of the current density vs. the reciprocal of the square root of the rotation rate yields a linear relation (2, 3), where both the slope and the intercept vary with potential. In the following analysis, we show that our proposed mechanism in conjunction with the Levich equation for species mass transport yields the proper relationship between rotation rate and current density. Certain mechanisms, which are valid under kinetic control, are incompatible with these experimental results and can be eliminated on that basis.

Proposed Model

Analysis of rate expressions.—Our proposed model for the anodic dissolution of zinc in dilute alkaline electrolyte is



*Electrochemical Society Student Member.

**Electrochemical Society Active Member.

When the fraction of adsorbed ZnOH (θ) is treated in accordance with Langmuir's hypotheses, the rate expressions become (1)

$$\tau_1 = i_1/\mathbf{F} = k_{a1} \exp [(1 - \beta_1)\mathbf{FV}/RT](1 - \theta)c_{\text{OH}^-} - k_{c1} \exp (-\beta_1\mathbf{FV}/RT)\theta \quad [4]$$

$$\tau_2 = i_2/\mathbf{F} = k_{a2} \exp [(1 - \beta_2)\mathbf{FV}/RT]c_{\text{OH}^-}^{2-\theta} - k_{c2} \exp (-\beta_2\mathbf{FV}/RT)c_{\text{Zn(OH)}_3^-}(1 - \theta) \text{ rds} \quad [5]$$

$$\tau_3 = k_{a3}c_{\text{Zn(OH)}_3^-}c_{\text{OH}^-} - k_{c3}c_{\text{Zn(OH)}_4^{2-}} \quad [6]$$

At steady state, all the reactions proceed at the same rate, and the net current density is

$$i = 2i_1 = 2i_2 \quad [7]$$

Since reaction [1] is assumed to be at equilibrium, the fractional surface coverage is obtained from Eq. [4]

$$\theta = k_{a1}c_{\text{OH}^-}/[k_{a1}c_{\text{OH}^-} + k_{c1} \exp (-\mathbf{FV}/RT)] \quad [8]$$

Substitution of Eq. [8] into Eq. [5] yields

$$i_2/\mathbf{F} = i/(2\mathbf{F}) = k_{a2}k_{a1}c_{\text{OH}^-}^{-3} \exp [(2 - \beta_2)\mathbf{FV}/RT] / [(H + 1)k_{c1}] - k_{c2}k_{c3}c_{\text{Zn(OH)}_4^{2-}} \exp (-\beta_2\mathbf{FV}/RT) / [(H + 1)k_{a3}c_{\text{OH}^-}] \quad [9]$$

where

$$H = k_{a1}c_{\text{OH}^-}/[k_{c1} \exp (-\mathbf{FV}/RT)] \quad [10]$$

Analysis of mass-transport effects.—The surface concentration of a reacting species can be estimated from Levich's equation

$$c_i = c_i^b - 1.6\nu^{1/6}\omega^{-1/2}i/(n_i\mathbf{F}D_i^{2/3}) \quad [11]$$

If we assume that the physical properties are constant,

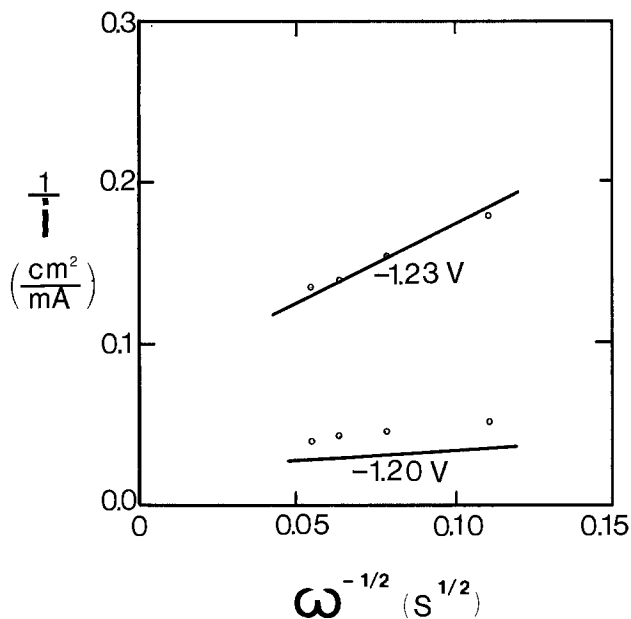


Fig. 1. Reciprocal of the current density vs. $1/\omega^{1/2}$. 1M KOH, 25°C, from Ref. (2).

the invariant quantities in the second term can be lumped, and Eq. [11] becomes

$$c_i = c_i^b - A_i \omega^{-1/2} i \quad [12]$$

The surface concentrations of OH^- and $\text{Zn}(\text{OH})_4^{2-}$ can be estimated from Eq. [12] (with the appropriate sign change for anodic dissolution)

$$c_{\text{OH}^-} = c_{\text{OH}^-}^b - A_{\text{OH}^-} \omega^{-1/2} i \quad [13]$$

$$c_{\text{Zn}(\text{OH})_4^{2-}} = c_{\text{Zn}(\text{OH})_4^{2-}}^b + A_{\text{Zn}(\text{OH})_4^{2-}} \omega^{-1/2} i \quad [14]$$

The term $c_{\text{OH}^-}^3$ calculated from Eq. [13], is

$$c_{\text{OH}^-}^3 = c_{\text{OH}^-}^{b3} - 3c_{\text{OH}^-}^{b2} A_{\text{OH}^-} \omega^{-1/2} i + 3c_{\text{OH}^-}^b (A_{\text{OH}^-} \omega^{-1/2} i)^2 + (A_{\text{OH}^-} \omega^{-1/2} i)^3 \quad [15]$$

The terms of order i^2 and i^3 are small compared to the term of order i in the active dissolution regime, where $i < 0.01 \text{ A/cm}^2$; therefore, for $c_{\text{OH}^-}^b \sim 10^{-3} \text{ mol/cm}^3$, the latter two terms in Eq. [15] can be neglected. Substitution of the surface concentrations from Eq. [13]-[15] into Eq. [9] yields

$$i = 2F \{ k_{a2} k_{a1} c_{\text{OH}^-}^{b3} \exp[(2 - \beta_2)FV/RT] / [(H + 1)k_{c1}] - k_{c2} k_{c3} c_{\text{Zn}(\text{OH})_4^{2-}}^b \exp(-\beta_2 FV/RT) / [(H + 1)k_{a3} c_{\text{OH}^-}] \} \{ 1 + 6Fk_{a2} k_{a1} c_{\text{OH}^-}^{b2} A_{\text{OH}^-} \omega^{-1/2} \exp[(2 - \beta_2)FV/RT] / [(H + 1)k_{c1}] + 2Fk_{c2} k_{c3} A_{\text{Zn}(\text{OH})_4^{2-}} \omega^{-1/2} \exp(-\beta_2 FV/RT) / [k_{a3}(H + 1)c_{\text{OH}^-}] \} \quad [16]$$

For rotation rates of the order of 100 rpm, $A_{\text{OH}^-} \omega^{-1/2} i$ is small compared to $c_{\text{OH}^-}^b$ in the initial dissolution region; therefore, the former term can be neglected when compared to $c_{\text{OH}^-}^b$. The second term in the numerator represents the cathodic component; it is generally much smaller than the first and can also be neglected. With these two simplifications, Eq. [16] can be cast in a form showing the explicit dependence of $1/i$ on $1/\omega^{1/2}$

$$1/i = 1 / \{ 2Fk_{a2} k_{a1} c_{\text{OH}^-}^{b3} \exp[(2 - \beta_2)FV/RT] / [(H + 1)k_{c1}] + \omega^{-1/2} [3A_{\text{OH}^-} / c_{\text{OH}^-}^b + k_{c1} k_{c2} k_{c3} A_{\text{Zn}(\text{OH})_4^{2-}} \exp(-2FV/RT) / (k_{a1} k_{a2} k_{a3} c_{\text{OH}^-}^{b4})] \} \quad [17]$$

Results and Discussion

Equation [17] shows that $1/i$ is linearly related to $1/\omega^{1/2}$ at fixed potential. Both the slope and the intercept vary with potential (Fig. 1). The rate constants and equilibrium constants are those that were calculated or estimated previously (1) when only kinetic limitations were taken into account; the values are summarized in Table I.

Table I. Summary of kinetic and thermodynamic quantities

Species	Standard free energy of formation (kcal/mol)	
ZnOH	-65.8	
OH^-	-37.6	
$\text{Zn}(\text{OH})_3^-$	-166.0 to -167.6	
$\text{Zn}(\text{OH})_4^{2-}$	-205.2 to -206.2	
Reaction	Standard free energy of reaction (kcal)	Kinetic rate constant ($\text{cm}^2/\text{s}\cdot\text{mol}$)
1	-28.2	9.3×10^9
2	-25.0 to -26.6	
3	-2.6 to 0	

Thermodynamic quantities were obtained (or derived) from data found in Ref. (5). The free energy of formation of ZnOH and the rate constant were estimated [see Ref. (1)].

Because the equilibrium constants are exponentially related to the free energy of reaction, Eq. [17] is particularly sensitive to the uncertainty in the thermodynamic data. The first term in Eq. [17] corresponds to the intercept of the $1/i$ vs. $1/\omega^{1/2}$ plot. This term depends on the rate constant for the second reaction and the equilibrium constant for the first reaction. The slope of the line, which is the coefficient of the second term, is related to the equilibrium constants of the three reactions. Variations in the values of the equilibrium constants result from assuming that $\text{Zn}(\text{OH})_2$ exists in different crystalline forms and from the uncertainty in the experimental determinations. The range of these values is shown in Table I. The sensitivity of the slope and the intercept to the thermodynamic values is shown in Table II.

Several assumptions were made in the derivation of Eq. [17]. The assumption that the bulk concentration of hydroxide is large compared to the term $A_{\text{OH}^-} \omega^{-1/2} i$ is generally valid. We are primarily interested in bulk hydroxide concentrations greater than 10^{-3} mol/cm^3 , rotation rates greater than 200 rpm, and current densities less than 10 mA/cm^2 . Within this range of parameters, the term $A_{\text{OH}^-} \omega^{-1/2} i$ is less than 10% of the bulk hydroxide concentration and can legitimately be neglected. The assumption that the second term in the numerator of Eq. [16] can be neglected is appropriate at low zincate concentrations and at relatively anodic potentials. At -1.20V vs. NHE and at a bulk zincate concentration of 10^{-9} mol/cm^3 , the second term is less than 0.01% of the first term; however, at more cathodic potentials (-1.23V vs. NHE), the current density becomes extremely sensitive to bulk zincate concentration (Fig. 2). This sensitivity occurs when approaching the reversible potential, which is approximately

Table II. Sensitivity of the $1/i$ vs. $1/\omega^{1/2}$ curve to thermodynamic quantities

Species	Free energy of formation (kcal/mol)		
	Case I	Case II	Case III
Zn	0	0	0
OH^-	-37.60	-37.60	-37.60
ZnOH	-65.85	-65.85	-67.00
$\text{Zn}(\text{OH})_3^-$	-166.0	-167.6	-166.0
$\text{Zn}(\text{OH})_4^{2-}$	-205.2	-206.2	-205.2
Potential vs. NHE			
	-1.23V		-1.20V
	Slope	Intercept	Slope
Case I	995	75.8	156
Case II	247	75.8	83.7
Case III	995	10.8	156
		Intercept	
Case I		23.0	
Case II		22.9	
Case III		3.26	

Case I represents the best estimate of the parameters.

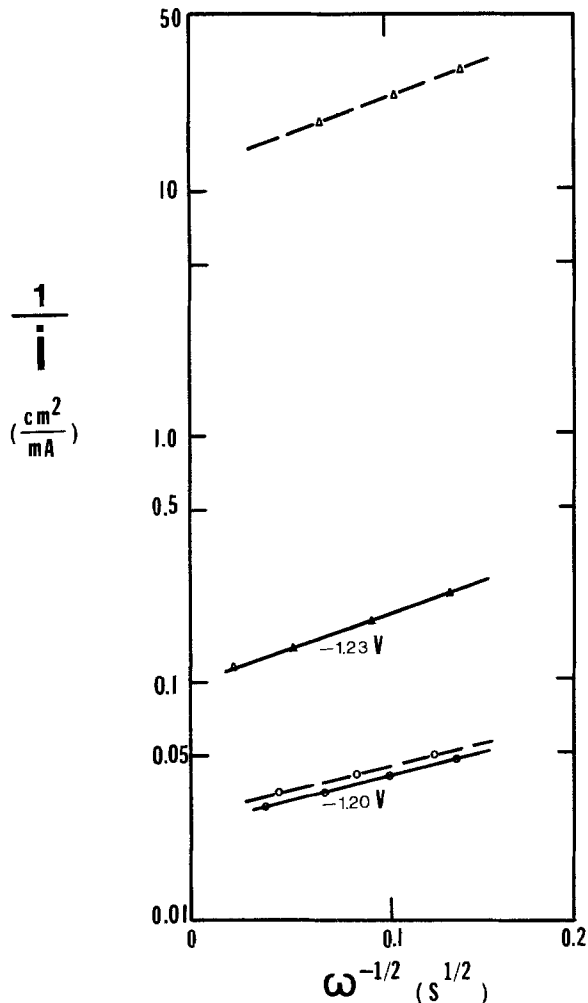


Fig. 2. Reciprocal of the current density vs. $1/\omega^{1/2}$. Solid curves represent simulated results for $c_{Zn(OH)_4^{2-b}} = 10^{-9}$; dashed curves for $c_{Zn(OH)_4^{2-b}} = 10^{-5}$. All simulations for 1M hydroxide. Upper curves (Δ) show high sensitivity to zincate concentration near the reversible potential. Lower curves (\circ) show that the current density is not sensitive to zincate concentration at more anodic potentials.

-1.23V vs. NHE (10^{-3} mol/cm³ KOH, 10^{-5} mol/cm³ zincate).

Armstrong and Bulman (3) assumed that the finite slope of the $1/i$ vs. $1/\omega^{1/2}$ plot is due to the diffusion of $Zn(OH)_4^{2-}$ from the electrode. Analysis of our model shows that the slope of this line is due to mass-transport limitations of both the zincate and the hydroxide ions. From the second term of Eq. [17], we can determine the contributions of the mass-transport limitations from each of the two species. At -1.20V vs. NHE (-1.31V vs. Hg/HgO), the contribution from each of the two sources is approximately equal, while at -1.23V (-1.34V vs. Hg/HgO) only 10% of the contribution is due to hydroxide ion mass-transport limitations. The change in the slope as a function of potential is related to the slow transport of the zincate ion.

Certain mechanisms are incompatible with the data displayed in Fig. 1. For example, if we postulate that we can neglect the reverse reaction in the rate-determining step, Eq. [17] becomes

$$1/i = 1/[2Fk_{a2}k_{a1}c_{OH}^{-b3} \exp[(2 - \beta_2)FV/RT] / \{(H + 1)k_{c1}\} + 1/\omega^{1/2}[3A_{OH} - c_{OH}^{-b}]] \quad [18]$$

Although a plot of this equation yields a straight line with a finite slope, the slope is no longer potential dependent. A similar analysis applied to the mechanism proposed by Bockris *et al.* (4) shows that the reverse reaction in the rate-determining step must also be included in order to obtain a potential-dependent slope.

From Eq. [17], the dependence of $d(1/i)/d(1/\omega^{1/2})$ on potential is given by

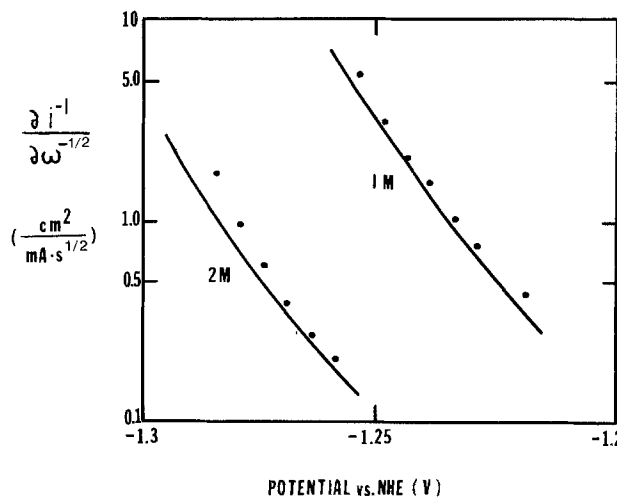


Fig. 3. $d(1/i)/d(1/\omega^{1/2})$ vs. potential. The solid lines are simulated, and the points represent data from Ref. (3). The data are for 1M NaOH and 2M NaOH.

$$S = d(1/i)/d(1/\omega^{1/2}) = k_{c1}k_{c2}k_{c3}A_{Zn(OH)_4^{2-b}}/$$

$$(k_{a1}k_{a2}k_{a3}c_{OH}^{-b4}) \exp(-2FV/RT) + 3A_{OH} - c_{OH}^{-b} \quad [19]$$

The derivative of the potential with respect to the logarithm of S is

$$dV/d(\log S) = -2.3RT\{3A_{OH} - k_{a1}k_{a2}k_{a3}c_{OH}^{-b3} / [A_{Zn(OH)_4^{2-b}} - k_{c1}k_{c2}k_{c3} \exp(-2FV/RT)] + 1\}/2F \quad [20]$$

Evaluation of Eq. [20] at 298 K yields a value of approximately 30 mV/decade. This is in agreement with experimental results (3) obtained with 1 and 2M NaOH (Fig. 3).

From Eq. [17], we can determine the effects of zincate concentration and of hydroxide concentration on current density

$$\begin{aligned} \partial \log i / \partial \log c_{Zn(OH)_4^{2-b}} &= 1/[1 - k_{a1}k_{a2}k_{a3}c_{OH}^{-b4} \exp(2FV/RT) / \\ &\quad (k_{c1}k_{c2}k_{c3}c_{Zn(OH)_4^{2-b}})] \quad [21] \end{aligned}$$

and

$$\begin{aligned} \partial \log i / \partial \log c_{OH}^{-b} &= \{(3 + 2H) / \\ &\quad (2Fk_{a2}K_1c_{OH}^{-b3} \exp[(2 - \beta_2)FV/RT] + \omega^{-1/2}3A_{OH} - c_{OH}^{-b} \\ &\quad + \omega^{-1/2} [4A_{Zn(OH)_4^{2-b}} \exp(-2FV/RT) / \\ &\quad (K_1K_2K_3c_{OH}^{-b4})])\}i \quad [22] \end{aligned}$$

These expressions represent an apparent reaction order when mass transport is taken into account. The apparent reaction order with respect to zincate is approximately 0 at relatively positive potentials; it only becomes significantly larger at more negative potentials, near the reversible potential. The apparent reaction order with respect to hydroxide is generally between 3 and 4 in the range of interest. In these calculations, we incorporated activity

Table III. Apparent reaction orders with respect to hydroxide and zincate

	Calculated	Experimental	Potential (vs. NHE)
$\partial \log i / \partial \log c_{OH}^{-b}$	3.33		V = -1.23
	3.66	3.6	V = -1.26
$\partial \log i / \partial \log c_{Zn(OH)_4^{2-b}}$	-0.01		V = -1.23
			$c_{Zn(OH)_4^{2-b}} = 10^{-7}$
			V = -1.20
	-9.6×10^{-6}		$c_{Zn(OH)_4^{2-b}} = 10^{-9}$

Values computed when mass transport is taken into account. Potentials are with respect to the NHE. Rotation rate is 800 rpm. The experimental value was computed from only two concentrations taken from Ref. (3).

coefficients appropriate for KOH: 0.76 for 1M KOH and 0.92 for 2M KOH (6). Values of calculated and experimental apparent reaction orders appear in Table III.

In further work, we plan to extend these results to more anodic potentials and to develop a more comprehensive model describing anodic dissolution and passivation for this system.

Acknowledgment

This material is based upon work supported by the National Science Foundation under Grant no. CPE-8202725.

Manuscript submitted Feb. 8, 1984; revised manuscript received ca. Sept. 26, 1984.

The National Science Foundation assisted in meeting the publication costs of this article

LIST OF SYMBOLS

A	lumped parameter (see Eq. [12])
c	concentration (mol/cm ³)
F	Faraday's constant (96,500 C/eq.)
H	special variable, see Eq. [10]
i	current density (A/cm ²)
i ₀	exchange current density (A/cm ²)
k	kinetic rate constant (cm ³ /s-mol) for reaction [2]
K	equilibrium constant, ratio of rate constants
r	reaction rate (mol/s cm ²)
R	gas constant (8.31 J/mol K)
S	slope of 1/i vs. 1/ω ^{1/2} curve, see Eq. [19]
T	temperature (K)

V	potential with respect to a given electrode (V)
α	transfer coefficient
β	symmetry factor
ν	kinematic viscosity (cm ² /s)
η	overpotential (V)
θ	fractional surface coverage
ω	rotation rate (rad/s)

Subscripts

a	anodic
c	cathodic
i	component
1, 2, 3	number of reaction, see Eq. [1]-[3]

Superscripts

b	bulk
o	equilibrium condition

REFERENCES

1. Y-C. Chang and G. A. Prentice, *This Journal*, **131**, 1465 (1984).
2. R. D. Armstrong and M. F. Bell, *J. Electroanal. Chem.*, **55**, 201 (1974).
3. R. D. Armstrong and G. M. Bulman, *ibid.*, **25**, 121 (1970).
4. J. O'M. Bockris, Z. Nagy, and A. Damjanovic, *This Journal*, **119**, 285 (1972).
5. "Selected Values of Chemical Thermodynamic Properties—Tables for the First Thirty-Four Elements in the Standard Order of Arrangement," NBS Technical Note 270-3, pp. 12, 233, National Bureau of Standards, Washington, DC (1968).
6. D. P. Boden, R. B. Wylie, and V. J. Spera, *This Journal*, **118**, 1298 (1971).

Passivation Behavior of Titanium-6Al-4V Alloy in Phosphoric Acid Solution

D. D. N. Singh

National Metallurgical Laboratory, Corrosion Section, Jamshedpur 831007, India

Titanium metal, because of its light weight, good mechanical properties, and excellent corrosion resistance, has been increasingly considered for various applications in the process industries through laboratory investigations. The corrosion resistance of the metal is due to its inherent nature to form stable titanium dioxide. The potential-pH diagram of titanium (1) indicates that the formation of oxide film on the metal becomes thermodynamically unstable in nonoxidizing acidic aqueous environments, which results in a general dissolution of the metal. This behavior limits the more widespread use of the metal in many nonoxidizing acids such as sulfuric, hydrochloric, phosphoric, and oxalic in different process industries. The stability of the metal in such environments can be restored by the adjustment of potential by the use of anodic passivation either by means of impressed current or by alloying with other metals, such as palladium or nickel, or by introducing a redox system in the environment (2). Out of all these methods, anodic passivation is considered superior because of high range of passivation potential observed for titanium in most of the environments. For a metal to be protected anodically in an environment, the necessary condition is a low order of passive dissolution current and passive potential.

The frequent failure of titanium materials in nonoxidizing acid solutions has attracted the attention of many workers to the study of the electrochemical behavior of the metal in such media (3-7). However, relatively less attention has been paid to the passivation behavior of titanium in phosphoric acid solution, which is an important chemical in industries. Phosphoric acid is a nonoxidizing acid and has a deleterious action towards titanium and its alloys. The present paper deals with the passivation tend-

ency of an industrially important titanium alloy, Ti-6Al-4V, in different concentrations of phosphoric acid at different temperatures.

Experimental

Titanium alloy of composition 6Al-4V in sheet form (18 SWG) embedded in epoxy resin with 3 cm² of working area was used as working electrode. Prior to immersion in the electrolyte, it was polished with 6/0 grade emery paper, dipped in 5% H₂SO₄ containing 0.01M NaF, followed by a thorough rinsing with distilled water, and then, finally, degreased with methanol. A platinum sheet was used as an auxiliary electrode. A Luggin probe saturated calomel reference electrode assembly was employed; it contained an isolating stopcock to avoid contamination by the chloride solution of the reference electrode. Electrode potentials are reported vs. saturated calomel electrode (SCE) uncorrected for liquid-junction potentials.

Anodic polarization studies were carried out using a Taccussel potentiostat (PRT 20-2X), and potential and current were recorded using a Houston X-Y-T recorder (Model 2000). The potential was swept at the rate of 1 V/h after a steady corrosion potential was achieved.

Analar-grade chemicals were used. NaF was used as a source of F⁻ in the solution. The experiments were performed at 32° ± 1°C.

Results and Discussion

Figure 1 shows the potential-time curves for the alloy in blank 85% H₃PO₄ as well as containing different concentrations of water and F⁻. In all cases, it is found that the potential moves in active direction with time, indicating the dissolution of pre-existing oxide film on the metal

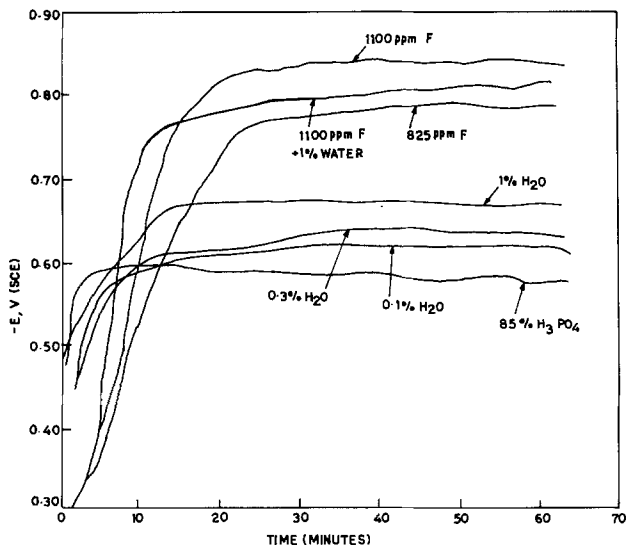


Fig. 1. Potential-time curves for the alloy in different concentrations of phosphoric acid.

surface. Attainment of the steady potential in the presence of fluoride ion is sluggish compared to the blank solution. The addition of small amounts of water in phosphoric acid does not alter the nature of the curves, but it does shift the potential in a more active direction as compared to blank solution.

The anodic polarization behavior of titanium in 85% H_3PO_4 and containing different concentrations of F^- is shown in Fig. 2. In the pure acid, the metal passivates after exhibiting a small range of active dissolution. The addition of F^- increases the critical current density and primary passivation potential considerably. The passive dissolution current is dependent upon the presence of F^- . It is noted that the active-passive curves for titanium (i.e., S-type curves) are recorded for acid solutions containing more than 450 ppm F^- . For solutions containing less F^- , the curves are similar to the one recorded in the absence of any F^- . However, the current increases with increasing F^- at any potential.

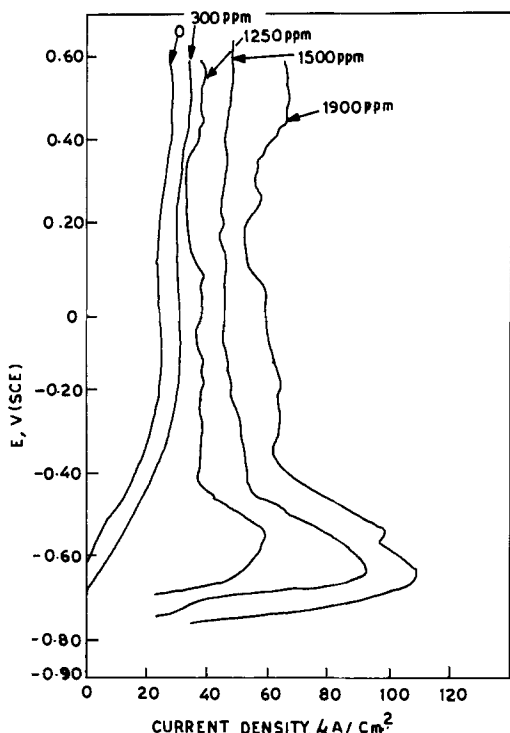


Fig. 2. Effect of fluoride ion on anodic polarization of the alloy in 85% H_3PO_4 .

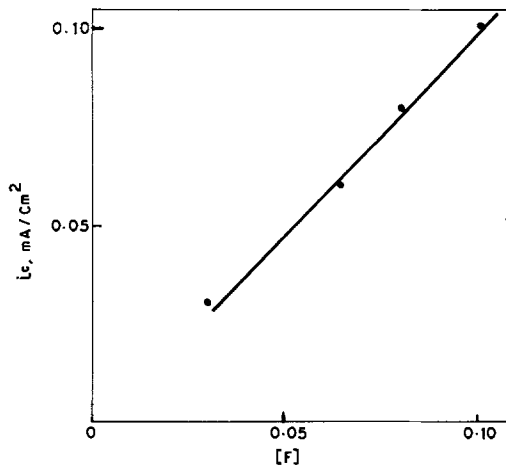


Fig. 3. Variation of critical current density with concentration of fluoride ion.

The dependence of critical current density for the onset of passivity (i_{cr}) on F^- concentration has been plotted in Fig. 3. A straight line with slope 1.0 is observed. That slope is less than the slope reported for titanium in H_2SO_4 solution (3). This may be attributed to the relatively mild corrosive action of H_3PO_4 as compared to H_2SO_4 and stronger adsorption capability of PO_4^{3-} than SO_4^{2-} on the metal surfaces, as well as to the differences in alloy composition. It was not possible to conduct the experiments precisely above F^- concentration of 0.1M because of large fluctuations in the active potential region. Such fluctuations are generally ascribed to the competitive depassivation-repassivation reactions taking place on the metal surfaces, the possibility of which exists in a solution containing PO_4^{3-} and F^- ions.

The influence of the addition of triply distilled water on the steady-state corrosion potential of titanium in phosphoric acid is recorded in Fig. 4. The steady-state corrosion potential initially moves in active direction with the addition of water and subsequently in nobler direction. This indicates that the presence of water (up to 70% of the acid) has a deleterious effect on titanium dissolution. This was further confirmed by the plot of anodic polarization (Fig. 5), where it has been found that the active as well as the passive dissolution rate in 70% H_3PO_4 is considerably higher as compared to lower and higher acid ranges. This change in corrosiveness of the acid is probably related to its change in structure with dilution. In a solution containing 86% H_3PO_4 , the phosphate ions are interconnected by hydrogen bonds. But, in a diluted solution, the phosphate ions are hydrogen bonded to the

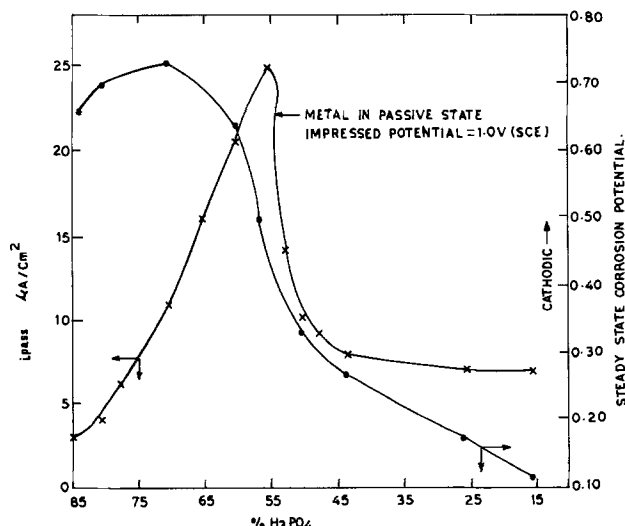


Fig. 4. Effect of the acid dilution on the passive dissolution current density and steady-state corrosion potential of the alloy.

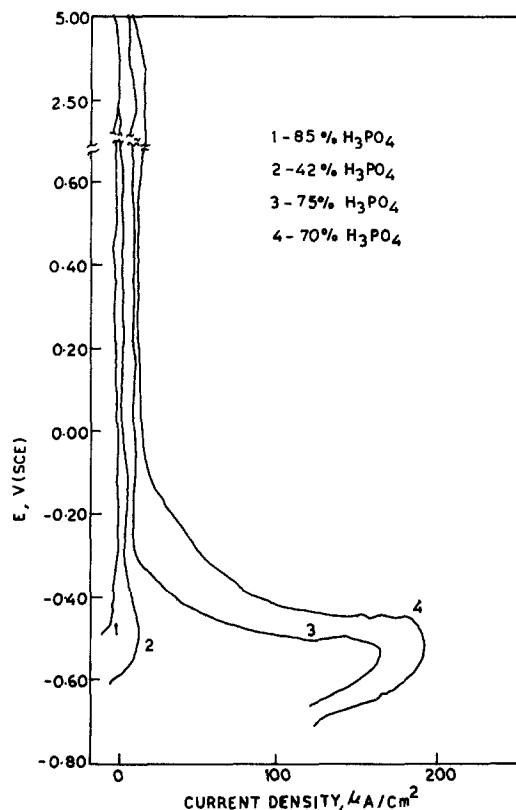


Fig. 5. Anodic polarization behavior of the metal in different concentrations of the acid.

water liquid lattice, rather than to other phosphate ions (8, 9). It is, therefore, expected that a dilute solution of phosphoric acid should have poorer solvation effect as compared to a concentrated acid. The reasons for a higher dissolution current observed at and above 70% acid solution is, however, not clear. The possibility of interaction of the newly added water molecule (10), which is considered as a Lewis base, with pre-existing Lewis acid regions in the oxide layer of titanium (10-12) is ruled out because of the presence of excess of water molecules in 85% H_3PO_4 and also because of the presence of Bronsted acid, *i.e.*, hydronium ion in the solution.

Variation of the passive dissolution current with dilution of the acid is shown in Fig. 4. The highest and the lowest current density are observed in an acid concentration range of 60%-55% and in 85%, respectively.

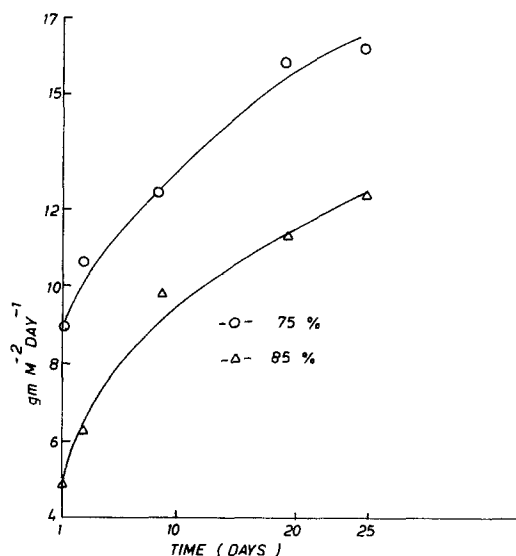


Fig. 6. Weight loss vs. time plot for the corrosion of the metal in 85% and 75% H_3PO_4 .

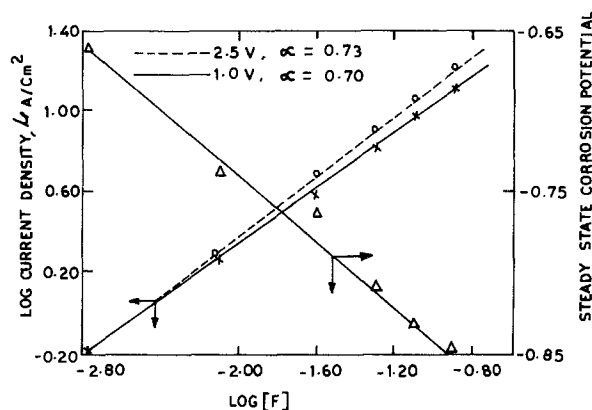


Fig. 7. Effect of the fluoride ion on the passive dissolution of the alloy in 85% H_3PO_4 .

To determine the nature of the kinetics of corrosion of the metal, some weight loss experiments were conducted for free dissolution in 85% and 75% H_3PO_4 . Weight loss vs. time plots are shown in Fig. 6. The dissolution of the metal in higher acid concentration (85%) is considerably lower than that in 75% acid. Optical microscopic examinations of the corroded surface showed uniform attack by the acid on the metal surface at both concentrations.

Influence of fluoride ion on the passive dissolution of titanium alloy in 85% H_3PO_4 is plotted in Fig. 7. In these experiments, the electrode potential was fixed in the passive range (*i.e.*, at 1.00V or at 2.50V SCE). The passive current density i_{pass} is strongly dependent upon the fluoride concentration but does not change much with potential, indicating a strong and stable passive film on the surface. i_{pass} varies with fluoride concentration $[F]$ as

$$i_{pass} = A [F]^\alpha$$

where A and α are constants at a fixed potential. The value of α was found to be of the order of 0.7 and is not dependent on potential. Nonintegral orders for dissolution of oxides have been reported for other metals oxides (13, 14). A dissolution order of 1.8 has been reported for passive titanium in sulfuric acid containing NaF (15). It has been suggested that the adsorption of fluoride ion on the surface and the role of surface reactions are important factors in the dissolution of such type of oxides (13). As expected, the order of dissolution in passive state of the metal (0.70) is lower than that in the active state (1.0).

Figure 8 shows the effect of temperature on the anodic polarization behavior of titanium in concentrated phosphoric acid (85%) solution. With increasing temperature,

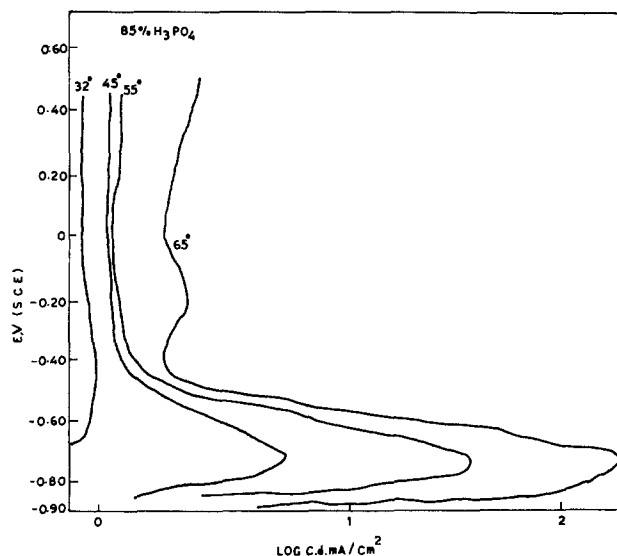


Fig. 8. Influence of temperature on the anodic behavior of the metal.

the active corrosion region is lengthened. The passive current density also increases gradually with temperature. This indicates that the passive film is less resistant in concentrated acid solution at higher temperatures. The initial potential ($-0.40V$ SCE) of stable passivity, however, remained constant at all the temperatures studied.

Conclusion

The passive film on titanium-6Al-4V alloy in different concentrations of phosphoric acid is stable over a wide range of potentials with a low passive dissolution current density. Additions of low percentages of water are found to accelerate the active as well as the passive dissolution of the metal in the acid solution. A sufficiently diluted acid, however, reduces the corrosive action. Metal dissolution in the acid in active region is found to be first order, with respect to fluoride ion; it is less than unity in the passive state. The potential has hardly any effect on the passive dissolution of the metal in the acid solution containing fluoride ion. Increases in temperature accelerate metal dissolution in the active as well as in the passive regions.

Acknowledgments

This paper is published by the permission of the Director, National Metallurgical Laboratory, Jamshedpur, India. The author is also thankful to Mr. K. P. Mukherjee, Head, Corrosion Division, for his valuable support and discussions.

Manuscript submitted March 26, 1984; revised manuscript received Sept. 4, 1984.

REFERENCES

1. M. Pourbaix, "Atlas of Electrochemical Equilibria in Aqueous Solution," p. 213, Pergamon Press, Oxford, England (1966).
2. B. H. Hanson, "Titanium Science & Technology," Vol. 4, p. 2419, Plenum Press, New York (1973).
3. M. J. Mandry and G. J. Rosenblatt, *This Journal*, **119**, 29 (1972).
4. M. Stern and H. J. Wissenberg, *ibid.*, **106**, 755 (1959).
5. L. B. Golden, I. R. Lane, and W. L. Acherman, *Ind. Eng. Chem.*, **4**, 1930 (1952).
6. H. H. Uhlig and A. J. Geary, *This Journal*, **101**, 215 (1954).
7. D. D. N. Singh, M. K. Banerjee, and P. S. Nag, *NML Tech. J.* (1983).
8. O. Bastiansen and C. Finback, cited in J. R. V. Wazer, "Phosphorus and Its Compounds," Vol. 1, p. 488, Interscience, New York (1958).
9. A. Simon and M. Z. West, *Z. Anorg. Allg. Chem.*, **268**, 301 (1952).
10. P. Fuguassi and E. G. Nancy, in "Titanium Science and Technology," Vol. 4, R. I. Jaffee and H. M. Burte, Editors, p. 2611 (1973).
11. G. D. Parfett, J. Ramsbotham, and C. H. Rochester, *Trans. Faraday Soc.*, **67**, 1500 (1971).
12. G. D. Parfett, J. Ramsbotham, and C. H. Rochester, *ibid.*, **67**, 84 (1971).
13. T. Takeuchi, C. K. Hauson, and M. E. Wadsworth, *J. Inorg. Nucl. Chem.*, **33**, 1089 (1971).
14. M. E. Shying, T. M. Florence, and D. J. Carswell, *ibid.*, **32**, 3492 (1970).
15. J. J. Kelly, *Electrochim. Acta*, **24**, 1273 (1979).

A Degradation due to Surface Oxidations in GaAlAs Red Light Emitting Diodes and a Prevention of It

H. Yamanaka and S. Koike

Matsushita Electronics Corporation, Semiconductor Division, Nagaokakyo, Kyoto, 617 Japan

Ga_{1-x}Al_xAs red light emitting diodes (LED's) of 650 ~ 660 nm wavelength are being developed due to interest in new applications such as outdoor signs, crosswalk signals, and light sources for optical plastic fiber communications. This is because of high brightness and the fact that their emission wavelength just corresponds to the wavelength region of low attenuation in plastic fibers (1-3). This technical note describes a degradation due to surface oxidation in these GaAlAs red LED's and gives a method for prevention.

The GaAlAs red LED consisted of p-type Ga_{0.65}Al_{0.35}As and n-type Ga_{0.35}Al_{0.65}As layers grown by a conventional liquid-phase epitaxial method on a p-type GaAs substrate as shown in Fig. 1. The thickness of the epitaxial p- and n-GaAlAs layers are 30 ~ 40 μm and 15 ~ 20 μm, respectively. Figure 2 shows degradation characteristics of epoxy-encapsulated present LED's aged at a current density of $J_f = 16.3$ A/cm² at 85°C with atmospheric relative humidity of 85% (dashed line) and without humidity (solid line), respectively. In the humid atmosphere, there were remarkable fluctuations of output power at about 100h and an output power decrease of 20 ~ 50% at 1000h. However, this degradation could not be observed in the LED's after enforcing a boil test with no bias voltage (no current). These results prove that applying voltage under the humid atmosphere causes this degradation.

A cross-sectional photograph of the degraded LED is displayed in Fig. 3. An absorptive dark layer, which interrupted the radiative light to be emitted outside, formed on the surface of the Ga_{1-x}Al_xAs layer. Figure 4 (left) gives an Auger electron spectroscopy (AES) in-depth profile of the absorptive layer, showing the presence of Al, Al₂O₃, Ga, and As. However, it is not possible to determine whether the Ga and As exist in elemental form or as ox-

ides. Considering that Ga₂O₃, Al₂O₃, and As₂O₃ are optically transparent oxides for the emission wavelength, ele-

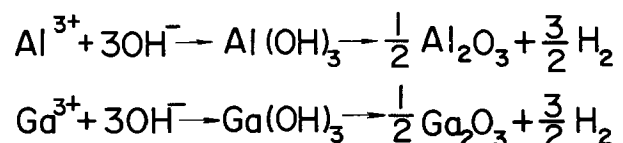
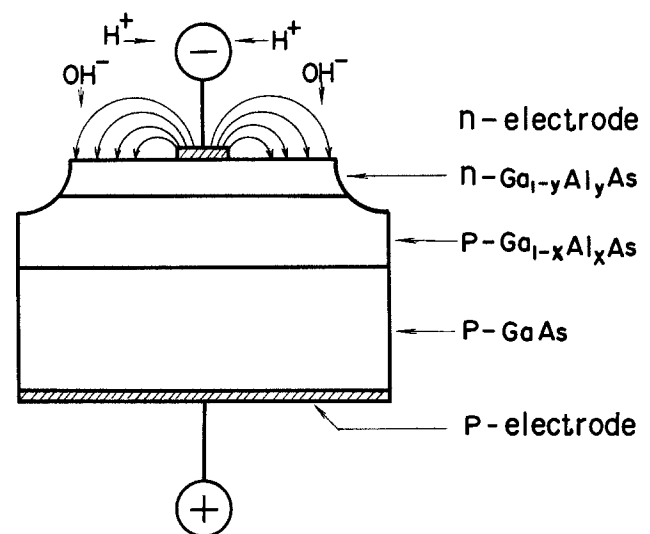


Fig. 1. Schematic illustrations of a GaAlAs red LED and a mechanism for the formation of the absorptive layer.

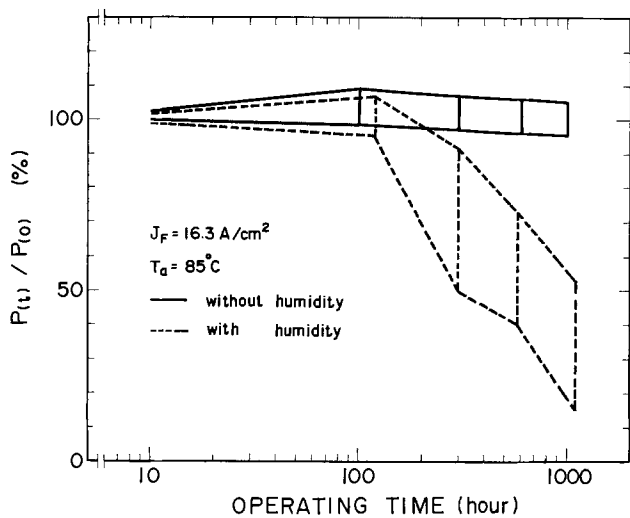


Fig. 2. Degradation characteristics of GaAlAs LED's after aging with and without humidity.

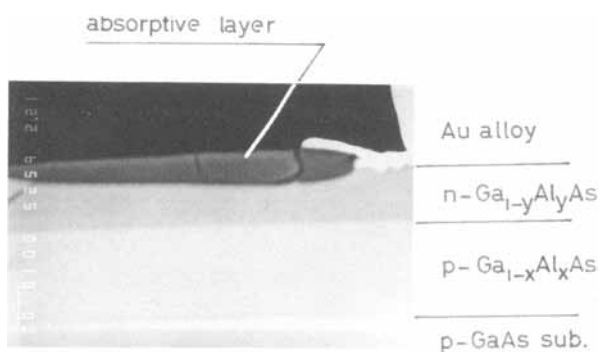


Fig. 3. A cross-sectional photograph of the degraded LED

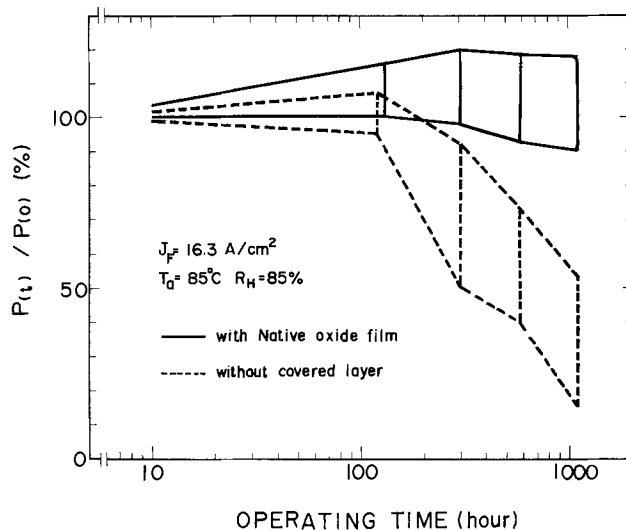


Fig. 5. Degradation characteristics of GaAlAs LED's with and without native oxide films.

mental Ga, Al, and As seem to act as sources of the absorptive function for the emitting light (4). It should also be noted that in Fig. 3 the absorptive layer grew thicker near the n-electrode. These facts suggest a mechanism for the formation of the absorptive layer, based on an electrochemical process using current paths from the n-electrode to the surface. This is associated with (OH)⁻ ions transported through the medium of the epoxy mold as shown in Fig. 1.

Therefore, in order to prevent the absorptive layer from forming, the surface of GaAlAs LED's must be covered with an optically transparent insulator film to cut off the current path. For this purpose, a native oxide film was grown in a solution with NH₄OH and H₂O₂ in 1:100 volume ratio. It could be formed easily on lateral parts, as well as on the upper part of the LED's surface at the same time. It was verified that the resulting film, uniformly blue and about 30 nm thick, was transparent to emission

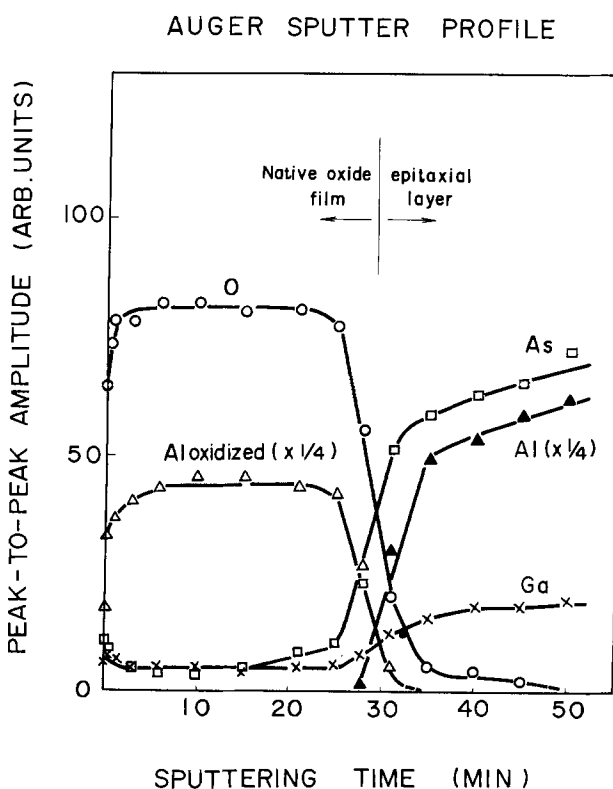
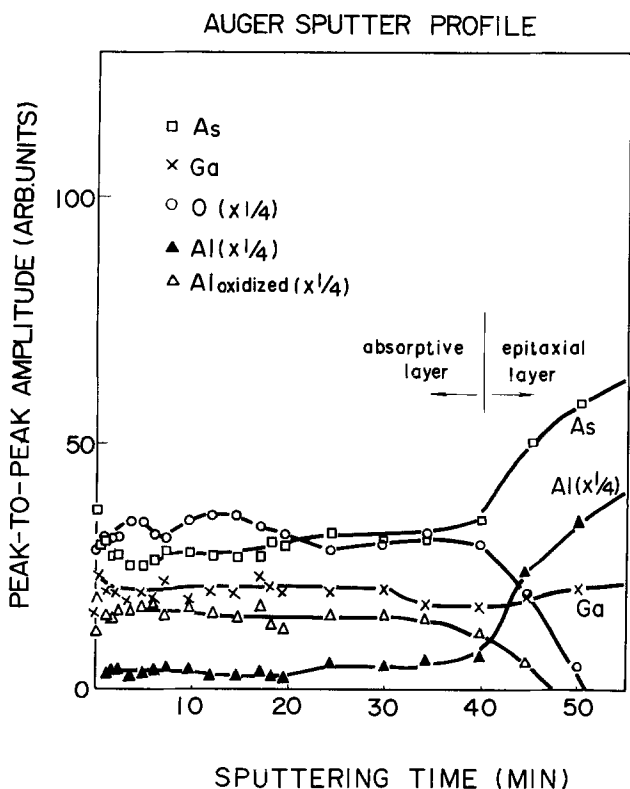


Fig. 4. Auger electron spectroscopy (AES) in-depth profile of an absorptive layer (left) and a native oxide film (right)

wavelength by measurement of output power. The AES in-depth profile of the native oxide film is represented in Fig. 4 (right). The elemental Al and products including Ga and As in the native oxide film are easily reduced in comparison with GaAlAs epitaxial layers, which is reasonable because the solution employed is one of well-known etchants for GaAs (5, 6). The solid lines in Fig. 5 show degradation characteristics of the GaAlAs red LED's covered with the former native oxide film aged in the same humidity as that of Fig. 2. The dashed lines in the figure, the characteristics of the LED's without covered layer, are also represented. The fluctuations of the output power of the oxide covered LED did not occur after 1000h, even under the humid atmosphere. These results support the described formation mechanism of the absorptive layer and the presumption that elemental Al, Ga, and As are involved in the absorption of the emitting light. The method described here is one which provides effective prevention.

Acknowledgments

The authors wish to thank H. Mizuno, H. Iwasa, S. Ohyabu, and S. Fujiwara for useful discussions and encouragements through the course of this work.

Manuscript submitted July 2, 1984; revised manuscript received Sept. 5, 1984.

Matsushita Electronics Corporation assisted in meeting the publication costs of this article.

REFERENCES

1. H. Ishiguro, K. Sawa, S. Nagao, H. Yamanaka, and S. Koike, *Appl. Phys. Lett.*, **43**, 1034 (1983).
2. J. Nishizawa, K. Sato, and T. Teshima, *J. Appl. Phys.*, **48**, 3484 (1977).
3. K. Takahashi, *J. Electron. Eng.*, **19**, 50 (1982).
4. G. P. Schwartz, B. V. Dutt, and G. J. Gualtiev, *Appl. Phys. Lett.*, **39**, 52 (1981).
5. J. C. Dymant and G. A. Rozgonyi, *This Journal*, **118**, 1346 (1971).
6. J. J. Gannon and C. J. Nuese, *ibid.*, **121**, 1215 (1974).

Chromium-Doped Raney Nickel Catalyst for Hydrogen Electrodes in Alkaline Fuel Cells

T. Kenjo

Department of Applied Science for Energy, Muroran Institute of Technology, Mizumoto-cho, Muroran, Japan 050

Raney nickel is a relatively inexpensive and highly active non-noble metal catalyst for hydrogen electrodes in alkaline fuel cells. Sturm, Richter, and Mund found that its catalytic activity was enhanced by doping transition metals such as titanium, iron, and molybdenum (1, 2).

During the course of attempting to add various dopants to Raney alloys, we have found that tenth percents of chromium markedly enhance the activity of Raney nickel. In this study, hydrogen electrodes catalyzed with this new Raney nickel have been prepared, and their polarization characteristics have been measured. For comparison, the polarization data are shown with those for titanium-doped and nondoped Raney nickels which undergo the same electrode processing.

Experimental

Preparation of the catalyst.—A melt possessing a mass fraction of 60% aluminum and 40% nickel + dopant was prepared with an induction furnace at 0.4 torr using an alumina crucible. It was quenched by pouring into an iron cylinder. The ingot obtained was powdered to a particle size smaller than 37 μm . Aluminum was leached with 6M KOH solution ($1M = 1 \text{ mol/dm}^3$) at 80°C for 12h. Raney nickel obtained as a black precipitate was washed alternatively with water and methylalcohol several times. The BET surface area for 0.4% chromium-doped catalyst was 64.7 m^2/g at this stage.

Preparation of the electrodes.—Polytetrafluoroethylene (PTFE) binder (Polyflon dispersion D-1, Daikin Industrial Company) was mixed with the Raney nickel precipitate, which was covered with water to prevent air exposure. The content of PTFE added was 10% in weight against the dry catalyst. The mixture was milled under blowing at room temperature. It became a paste as the water vaporized off. The paste obtained was callender-rolled by hand into sheets. After dried in air overnight, they were washed in boiled acetone to remove the surfactant which had been originally contained in the PTFE dispersion. This electrode processing results in a natural depyrophorization of Raney nickel catalyst so that the catalyst layer thus obtained can be handled safely in air. The BET surface areas of the nondoped, 0.4% chromium-doped, and 0.4% titanium-doped Raney nickels at this stage are 14.0 m^2/g , 10.8 m^2/g , and 8.8 m^2/g , respectively.

The gas-side layers were prepared by binding nickel black powder (prepared by heating nickel formate at 250°C in hydrogen atmosphere) with PTFE in the same manner as in the catalyst layers. They were reinforced with 100 mesh stainless-steel screens and then heated at 380°C in nitrogen atmosphere. They were attached to the catalyst layers by pressing at 630 kg/cm^2 . The double-layered electrodes thus obtained were heated at 180°C in hydrogen atmosphere to activate the catalyst. The BET surface areas for nondoped, 0.4% chromium-doped, and 0.4% titanium-doped Raney nickels at this stage are 47.7 m^2/g , 59.3 m^2/g , and 64.6 m^2/g , respectively. Most of the surface area loss during the electrode processing is recovered in this activating process.

Measurement of the polarization.—The geometrical working area of the test electrodes was 7 cm^2 . The counterelectrode used was a silver-catalyzed oxygen electrode. The electrolyte used was 6M KOH solution and was circulated between both electrodes at a rate of 5 ml/min. The electrode potential was measured against the Hg/HgO reference electrode. The IR voltage drop was eliminated by the current-interruption method.

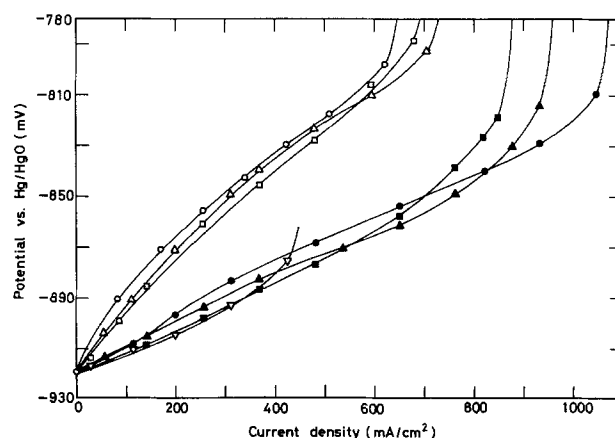


Fig. 1. Influence of the chromium content on the polarization curves. Catalyst loading: 40 mg/cm^2 . Electrolyte: 6M KOH 60°C. Chromium content: (○) nondoped; (△) 0.05%; (□) 0.1%; (●) 0.2%; (▲) 0.4%; (■) 0.8%; (▽) 2%. IR drop eliminated.

Results and Discussion

Polarization curves of the hydrogen electrodes catalyzed with chromium-doped Raney nickels are shown in Fig. 1 with variation of the chromium content in the starting alloys. There are no significant doping effects in a chromium content less than 0.1%, but on exceeding 0.2%, the polarization drops caused by doping become marked.

The polarization curves observed are essentially linear in a load less than 100 mA/cm². The polarization resistance can therefore be calculated from the slope in this load range and used as a measure for the catalytic activity. Figure 2 shows the plots of polarization resistance vs. chromium content in comparison with the similar plots for titanium-doped Raney nickel. Chromium lowers the polarization resistance by a factor of about 4, whereas titanium does so by a factor of 2.4 at the minimum. This indicates that the chromium-doped Raney nickel is more active than the titanium-doped catalyst.

Although high activities are maintained at chromium contents ranging to 2%, the upper limit for practical use should be 1% because the alloy powder becomes too soluble in 6M KOH solution when it exceeds this limit.

As seen in Fig. 2, the polarization resistance for the titanium-doped catalyst is minimized at a content of 0.4%, and the bottom of the curve is very narrow. According to the study done by Mund, Richter, and Sturm, the minimum value is found at higher titanium contents of 1.5-2%, and the bottom of the curve is much wider than that in the present study. The discrepancy between these two seems to be ascribable to different depyrophorization methods. Mund, Richter, and Sturm exposed dried catalyst slowly to oxygen. In this study, mixing the wet catalyst with the PTFE dispersion in air results in a natural depyrophorization. The surface oxidation in wet probably maintained the catalytic surface at a lower temperature than that in dry, resulting in a different surface condition.

The limiting current density (i_L) also is increased by doping chromium, as seen in Fig. 1, but the optimum dopant concentration is lower than that for the polariza-

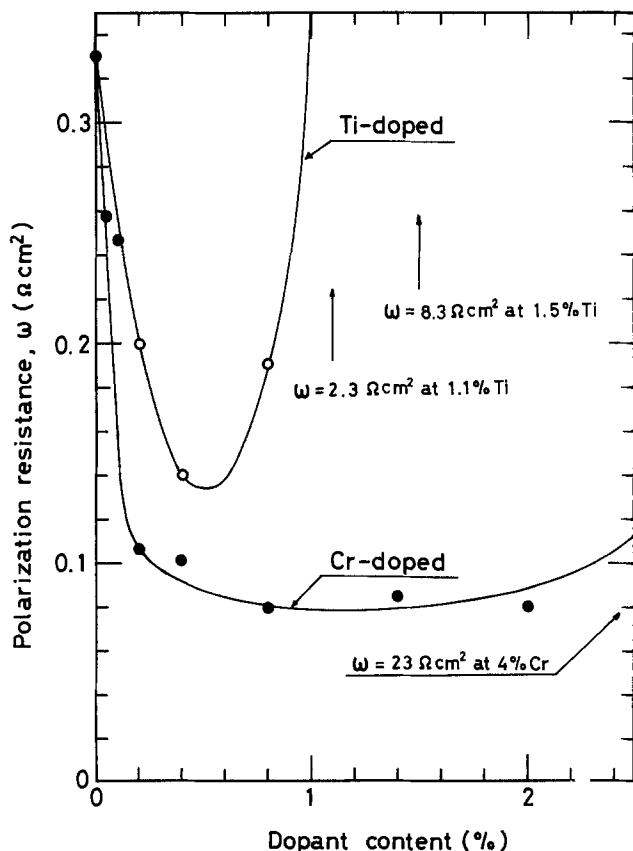


Fig. 2. Effect of the dopant content in Raney alloy on the polarization resistance. Catalyst loading: 40 mg/cm². Electrolyte: 6M KOH 60°C. IR drop eliminated.

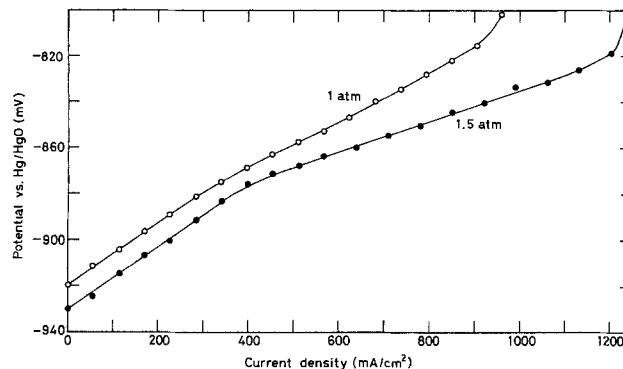


Fig. 3. Pressure dependence of the polarization characteristics. Catalyst loading: 30 mg/cm². Electrolyte: 6M KOH 60°C. Chromium content: 0.2%. IR drop eliminated.

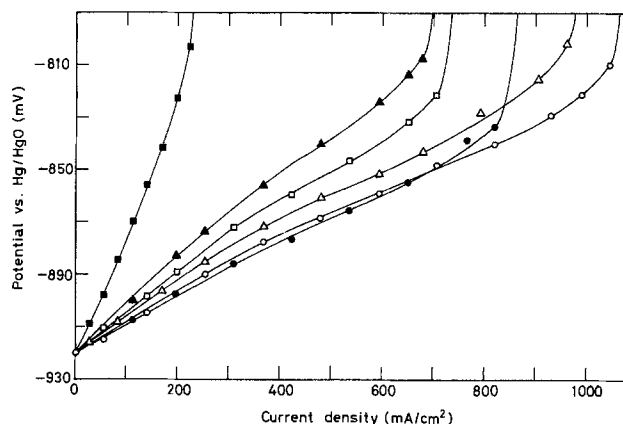


Fig. 4. Influence of the catalyst loading on the polarization characteristics. Chromium content: 0.2%. Electrolyte: 6M KOH 60°C. Catalyst loading: (■) 13.3 mg/cm²; (▲) 24.6 mg/cm²; (□) 30.5 mg/cm²; (△) 37.6 mg/cm²; (○) 39.3 mg/cm²; (●) 91.5 mg/cm². IR drop eliminated.

tion resistance. The i_L value is maximized at a dopant content as low as 0.2%, where the polarization resistance is still decreasing. This suggests that the i_L value obtained is very close to the upper limit of Raney nickel electrodes that can be attained by the activity improvement alone. A further increase is possible when a higher gas pressure is applied; 1.2 A/cm² is sustained at 1.5 atm, as shown in Fig. 3. This is probably due to an accelerated gas transportation through the electrode pores.

The dependence of polarization characteristics on the catalyst loading is shown in Fig. 4 for 0.2% chromium-doped catalyst. The polarization observed is lowered with increasing catalyst loading. This can be explained on the basis of the electrolyte film model (2). The polarization resistance ω is expressed as a function of the thickness of catalyst layer d

$$\omega = \sqrt{\rho \cdot k} \coth \sqrt{\rho \cdot d^2/k} \quad [1]$$

where ρ is the resistivity of the electrolyte film covering the catalytic surface, k the interfacial resistance at the film/catalyst interface. The catalyst loading is proportional to the thickness; 1 mm = 300 mg/cm² in this case. The parameters k and ρ , which characterize the catalyst, are obtained as values providing the curve fitting best to the experimental data. Figure 5 contains such plots of ω^{-1} vs. d for the 0.2% chromium-doped catalyst. The best-fit curve (solid line) gives parameter values of $k = 1.3 \times 10^{-3} \Omega \text{cm}^2$ and $\rho = 7.5 \Omega \text{cm}^2$. With the nondoped Raney nickel catalyst, $k = 4.5 \times 10^{-3} \Omega \text{cm}^2$ and $\rho = 11 \Omega \text{cm}^2$ were obtained with the same procedure. The k value is a measure of the catalytic activity such that a smaller value corresponds to a higher activity. An activating effect of the chromium dopant has thus been shown from the comparison of these two k values.

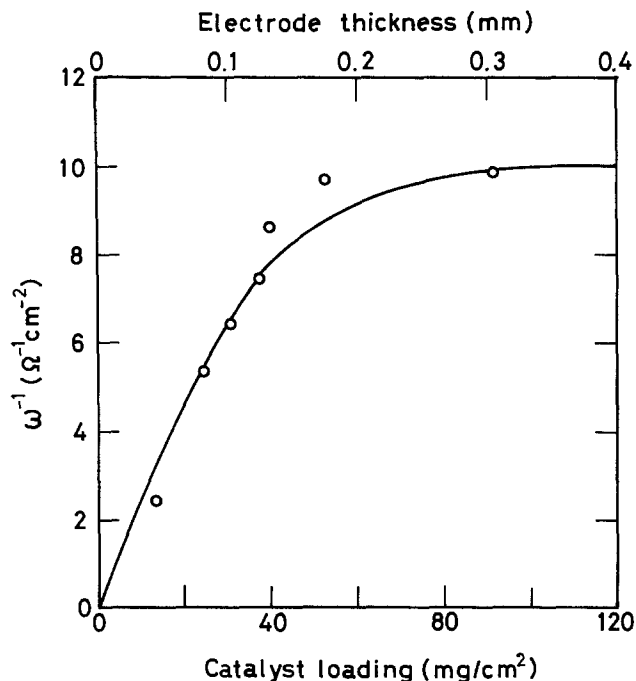


Fig. 5. Reciprocal polarization resistance ω^{-1} as a function of the catalyst loading. Chromium content: 0.2%. Electrolyte: 6M KOH 60°C. Solid line calculated from Eq. [1]. IR drop eliminated.

The Arrhenius plots of the polarization resistance for 0.8% chromium-doped catalyst are shown in Fig. 6 in comparison with the plots for 0.8% titanium-doped catalyst. The activation energies calculated from the slopes are 34.5 and 31.6 kJ/mol for the titanium-doped and chromium-doped catalysts, respectively. This suggests that the lower activation energy results in a lower polarization resistance at a temperature range studied. Their BET surface areas are very close to each other, as described in the experimental section. The chromium-induced high activity is thus attributed to a low activation energy for the polarization.

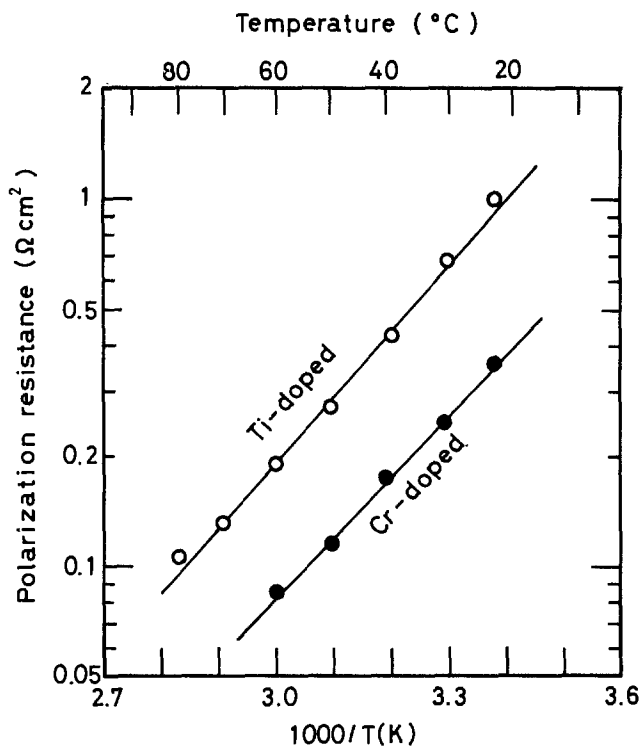


Fig. 6. Arrhenius plots of the polarization resistance for chromium- or titanium-doped Raney nickel. Dopant content: 0.8%. Catalyst loading: 40 mg/cm². Electrolyte: 6M KOH 60°C. IR drop eliminated.

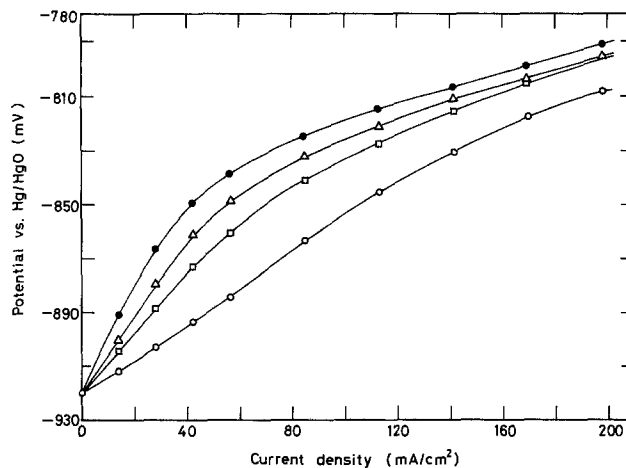


Fig. 7. Polarization change of the nondoped Raney nickel electrodes when the loading-unloading cycle is repeated. Catalyst loading: 21 mg/cm². Electrolyte: 6M KOH 60°C. (○) 1st run; (□) 2nd run; (△) 3rd run; (●) 4th run. IR drop eliminated.

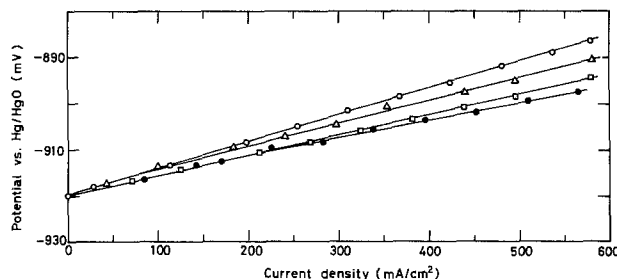


Fig. 8. Polarization change of the 0.8% chromium-doped Raney nickel electrodes when the loading-unloading cycle is repeated. Catalyst loading: 52 mg/cm². Electrolyte: 6M KOH 60°C. (○) 1st run; (△) 2nd run; (□) 3rd run; (●) 4th run. IR drop eliminated.

The limiting current density for the electrode with the chromium-doped catalyst is not very dependent upon temperature. The electrode catalyzed with 0.2% chromium-doped Raney nickel sustains a load of 900 mA/cm² at 60°C (Fig. 3) and still maintains a value as large as 500 mA/cm² at 30°C.

The polarization for the nondoped Raney nickel increases with repeating loading-unloading cycle, as Fig. 7 shows. This polarization change is probably due to an unstable surface condition of the nondoped catalyst. The chromium doping can prevent this. Figure 8 shows the case of 0.8% chromium-doped Raney nickel. In contrast to the case of nondoped Raney nickel, the polarization essentially does not change with every cycle, although a slight decrease can be seen. This is a stabilizing effect of the chromium dopant.

Figure 8 also shows the best performance obtained in the present study. In this case, 52 mg/cm² and 0.8% were chosen as a catalyst loading and chromium content, respectively. A polarization of 20 mV is attained at a load of 500 mA/cm² and 60°C. The polarization resistance calculated from the slope is 0.04 Ωcm². This is one-fifth as large as the lowest value for nondoped catalyst.

In conclusion, we can say that chromium is a good dopant for Raney nickel used for hydrogen electrodes. It improves and stabilizes the polarization characteristics of Raney nickel electrodes. The chromium-doped Raney nickel is more active than the titanium-doped catalyst and provides a high activity over a wide range of the dopant content.

Acknowledgment

The author expresses his appreciation to Professor K. Fujikawa of Muroran Institute of Technology for making

the measurement of BET surface area possible for this work.

Manuscript submitted March 12, 1984; revised manuscript received Oct. 18, 1984.

Muroran Institute of Technology assisted in meeting the publication costs of this article.

Porous Anodic Films on Aluminum at Low Potentials

D. Y. Jung* and M. Metzger*

Department of Metallurgy and Mining Engineering and Materials Research Laboratory, University of Illinois at Urbana-Champaign, Urbana, Illinois 61801

There exists a considerable literature on the formation conditions and structures of thick porous anodic films formed on aluminum in sulfuric, phosphoric, oxalic, or chromic acids at high potentials. As formed at room temperature at cell voltages from about 10 to > 100V with respect to a platinum cathode, these films are composed of columnar cells (typically 2.5-2.8 nm/V diam) with a central pore (diameter varies somewhat, near 1 nm/V), which terminates in a barrier layer of thickness about 1.0 nm/V (1-5). The "cell voltage" here serves as an approximation to the forming overpotential across the film. Film growth, i.e., pore lengthening, occurs across the barrier layer the thickness of which is maintained constant by electrochemical decomposition of the layer at its external surface (6, 7). There is also a slow purely chemical dissolution of the pore walls, causing them to taper during film growth, and the film reaches a limiting total thickness at the pore length at which the cell wall has tapered to zero thickness (8, 9). This body of information may have value as a guide in investigating and understanding the behavior of films on aluminum at potentials in the corrosion range.

In the course of a study on selective dissolution in Al-Cu alloys, some capacitance and other observations on aluminum in sulfuric acid pertinent to this question were made, and these are reported here. The differential capacitance of aluminum electrodes in 1, 5, and 10N H₂SO₄ was measured some years ago by Petrocelli (10), who found evidence of films he estimated as 1-5 nm thick, with 1/C linear with potential increment above the corrosion potential (near -0.9 V_{SCE}) over a 3V range. Films formed in 2.4M H₂SO₄ at 1.0 V_{SCE} have been examined by transmission electron microscopy by Zahavi *et al.* (11), who found them to be porous, although the details of the pore structure were too fine to measure. The total thickness of these films was much greater than the values given by Petrocelli, which would be expected if his films were porous and the measured capacitances sensed only the barrier layer thicknesses (12).

The capacitance of annealed specimens of 99.999% Al sheet mechanically polished through 0.05 μm alumina was measured at various potentials by modulating the control potential (from a PAR 373 potentiostat with risetime < 10⁻³s) with a 1 kHz 1 mV peak to peak signal from a lock-in amplifier (Ithaco 391A) and measuring the out-of-phase current. Measurements were made at 25.0 ± 0.2°C without deaeration or stirring. The specimen was allowed a few minutes to come to its steady corrosion potential near -1.04 V_{SCE}, and then it was scanned upward at 0.1 V/12 min and the scan reversed at 1.0 or 1.2 V_{SCE}. In the case of the porous films formed at higher potentials, it is known that a substantial reduction in cell voltage, say, from 10 to 5V, produces a period of low current lasting many minutes ("recovery"), during which the barrier layer thins, initially only by slow chemical dissolution, until the field across it increases sufficiently for the

*Electrochemical Society Active Member.

REFERENCES

1. F. von Sturm, in "Proceedings of the Symposium on Electrode Materials and Processes for Energy Conversion and Storage," J. D. E. McIntyre, S. Srinivasan, and F. G. Will, Editors, pp. 247-264, The Electrochemical Society, Softbound Proceedings Series, Princeton, New Jersey (1977).
2. K. Mund, G. Richter, and F. von Sturm, *This Journal*, **124**, 1 (1977).

forming current to reach the new steady state (13). In the present experiments, steady state was achieved in a few minutes because of the small potential step of 0.1 or 0.2V, and the currents and capacitances attained the same steady-state values for upward or downward scans. Duplicate runs gave almost identical results.

Inverse capacitance *vs.* potential at steady state is shown in Fig. 1. 1/C was linear in potential down to 0 V_{SCE}, but the slope decreased at lower potentials. The nonlinear region had not been observed by Petrocelli. His values for 5N H₂SO₄ lay below the values in Fig. 1, presumably because his surfaces had been finished on coarser abrasive and were rougher, and his slope for this concentration was lower than that of the linear part of Fig. 1. The present observations could be extended to somewhat lower potentials than his and were terminated at -1.3 V_{SCE} because of fluctuations in the measurements accompanying increased hydrogen evolution at lower potentials.

The measured capacitance represents the film capacitance, C_f, in series with the double-layer capacitance, C_{dl}, at its external surface. If the latter is assumed independent of potential, then 1/C_f has the shape of the 1/C curve of Fig. 1 but lies below this by 1/C_{dl}. This would not affect the linearity or slope of the region above 0 V_{SCE}. With the estimated dielectric constant 9 and a roughness factor 1, this linear region gives for barrier layer thickness a ratio 1.0 nm/V, which agrees with the value determined electronmicroscopically at much higher potentials [for films formed in phosphoric or oxalic acids (2, 5)]. This suggests that classical porous film behavior applies down to 0 V_{SCE}.

It is readily deduced that the films formed in the nonlinear region of Fig. 1 must also have been of some porous type. As part of the study of electrode structure, AES depth profiles had been determined after exposure at

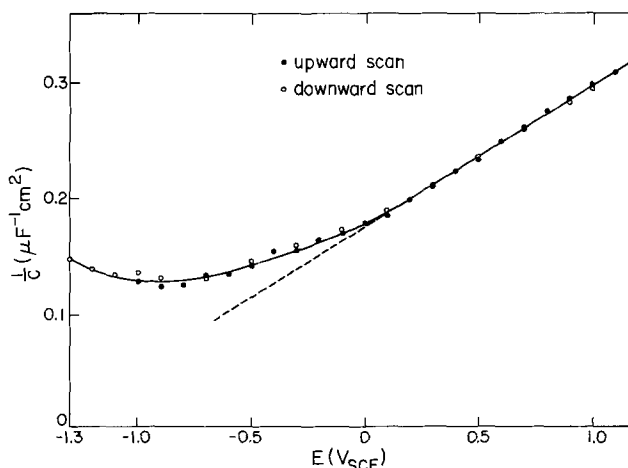


Fig. 1. Steady-state inverse capacitance at 1 kHz vs. potential for aluminum in 2.4M H₂SO₄.

two potentials in this region. The sputtering rate had been calibrated employing a compact anodic film, and it was found that the steady-state total film thickness at $-0.50 V_{SCE}$ was equivalent to a 4 nm thick compact film and at $-0.10 V_{SCE}$ to a 30 nm compact film. At these potentials, the capacitance measurements yielded apparent film thicknesses of ≤ 1 nm. The formation of a porous film is consistent with other evidence. When a specimen is potentiostated at these potentials, the cell current is initially high and passes through a minimum and a shallow maximum before leveling off; this behavior is characteristic of porous film formation by constant-voltage anodizing (14, 15). The rapid increase in steady-state total film thickness with increasing potential is also a characteristic of porous films, since the pore wall is thicker and the rate of pore lengthening higher, so that the limiting thickness determined by tapering of pore walls through chemical dissolution is reached at greater pore lengths. The steady-state total thickness increased to a compact film equivalent of 110 nm at $+0.5 V_{SCE}$, at which point it became inconvenient to measure by sputtering under the calibrated conditions.

Another point of comparison is the known incorporation of sulfur into sulfuric acid anodic films (6, 14). Cherki and Siejka (6), for example, found by Rutherford backscattering 3.6 atomic percent (a/o) S in films formed in 15% sulfuric acid at 10V. In the present work, AES spectra on the surface of films formed at -0.50 , -0.10 , or $+0.50 V_{SCE}$ confirmed the presence of S at ~ 0.5 a/o (within a factor of two). This would not be directly compared with figures in the literature, which are bulk analyses.

The nonlinear behavior in the lower part of the curve of Fig. 1 is thought to arise in two ways. For $E \leq -1.0 V_{SCE}$, i.e., on attaining potentials near and below the corrosion potential, the rise of $1/C$ would reflect blocking of many pores by trapped hydrogen gas bubbles so that the apparent capacitance is lowered. Such an explanation is not applicable in the higher part of the nonlinear region of Fig. 1, which extends a little above the hydrogen reversible potential. However, another reason for a deviation from the classical behavior comes from consideration of the dimensions of the classical pore structure. In this potential range, the film forming potential difference can be at most something like 1V, and this would make the pore diameter only about 1 nm, according to the classical ratio. It is not realistic that the electrochemical behavior and the geometry of such a fine structure will remain quantitatively the same as that of much coarser structures. Even at slightly higher potentials in the linear part of Fig. 1, where the slope of $1/C$ agreed with the classical ratio for barrier-layer thickness, the pore and cell dimensions may not have conformed to their classical values.

For formation of the supposedly classical porous film above $0 V_{SCE}$, the minimum potential which is required for the presence of a forming overpotential, η_{ox} , across the barrier layer may be examined with reference to the linear region in Fig. 1. Without correction for the unknown double-layer capacitance (i.e., for very large C_{dl}), this line would extrapolate to $1/C = 0$ at about $-1.4 V_{SCE}$. The potential for zero classical film thickness cannot be lower than this. If C_{dl} were 40 or $20 \mu F/cm^2$ independent of potential, $1/C$ would extrapolate to zero film thickness at -1.2 or $-1.0 V_{SCE}$. The reversible Al/Al_2O_3 potential depends slightly on the form of oxide assumed; it may be taken for the present solution as $-1.7 V_{SCE}$. Thus, if the total overpotential is written as the sum of the overpotentials at the interfaces plus that across the barrier layer of the film, $E - E_{eq} = \eta_m + \eta_s + \eta_{ox}$ (16, 17), the two interface overpotentials would add to at least 0.3V and probably

substantially more. Siejka *et al.* (17) examined this question in studies employing nuclear microanalysis of oxygen for compact films formed in ammonium citrate and found the interface overpotentials to add to zero within $\sim 0.1V$ for unpolished aluminum. This is to be expected in the absence of significant film dissolution, according to the analysis of Dignam and Kalia (18). That the sum of the interface overpotentials was larger in the present case can be attributed to the formation of a porous film requiring a substantial overpotential at the barrier layer-solution interface to effect the rapid electrochemical decomposition of the film occurring there.

From the above, the formation of a classical porous film is possible only above a certain minimum potential, which is higher than $-1.4 V_{SCE}$. The film, which is present according to Fig. 1 from 0 to $-1.3 V_{SCE}$, may be considered a nonclassical porous film. This would be able to form below the minimum potential for the classical film if the sum of the interface overpotentials were smaller for the nonclassical film. A nonclassical porous film could also form above the minimum potential for the classical film if the kinetics were favorable. According to the present interpretation, this situation prevails over much of the nonlinear range of $1/C$ below $0 V_{SCE}$.

From the considerations presented here, it is concluded that for aluminum in sulfuric acid the classical porous film formalism developed in anodizing studies at high potentials is not quantitatively valid at potentials in the corrosion range, but this information has value in understanding at least the qualitative aspects of film-formation behavior in this range.

Acknowledgments

This work was supported by the National Science Foundation under Contract DMR 80-20250. The authors are indebted to R. S. Alwitt for a discussion of data on the dielectric constant.

Manuscript submitted July 9, 1984; revised manuscript received ca. Sept. 28, 1984.

The University of Illinois assisted in meeting the publication costs of this article.

REFERENCES

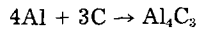
1. F. Keller, M. F. Hunter, and D. L. Robinson, *This Journal*, **100**, 411 (1953).
2. J. P. O'Sullivan and G. C. Wood, *Proc. R. Soc. London Ser. A.*, **317**, 511 (1970).
3. G. C. Wood and J. P. O'Sullivan, *Electrochim. Acta*, **15**, 1865 (1970).
4. G. C. Wood in "Oxides and Oxide Films," J. W. Diggle, Editor, p. 167, Dekker, New York (1973).
5. G. Bailey and G. C. Wood, *Trans. Inst. Metal Finish.*, **52**, 187 (1974).
6. C. Cherki and J. Siejka, *This Journal*, **120**, 784 (1973).
7. J. Siejka and C. Ortega, *ibid.*, **124**, 883 (1977).
8. M. Nagayama and K. Tamura, *Electrochim. Acta*, **12**, 1097 (1967).
9. M. Nagayama, K. Tamura, and H. Takahashi, *Corros. Sci.*, **10**, 617 (1970).
10. J. V. Petrocelli, *This Journal*, **106**, 566 (1959).
11. J. Zahavi, I. D. Ward, and M. Metzger, *ibid.*, **125**, 574 (1978).
12. A. J. Dekker and H. M. A. Urquhart, *Can. J. Res.*, **28**, Sect. B, 541 (1950).
13. J. W. Diggle, T. C. Downie, and C. W. Goulding, *This Journal*, **116**, 737 (1969).
14. R. B. Mason, *ibid.*, **102**, 671 (1955).
15. T. P. Hoar and J. Yahalom, *ibid.*, **110**, 614 (1963).
16. L. Young, "Anodic Oxide Films," p. 8, Academic Press, New York (1961).
17. J. Siejka, J. P. Nadai, and G. Amsel, *This Journal*, **118**, 727 (1971).
18. M. J. Dignam and R. K. Kalia, *Surf. Sci.*, **100**, 154 (1980).

Electrical Resistivity of Aluminum Carbide at 990-1240 K

W. R. King and R. C. Dorward

Kaiser Aluminum and Chemical Corporation, Center for Technology, Pleasanton, California 94566

In the conventional aluminum electrolytic reduction process, a molten metal pool is contained in a carbon cell bottom. Since the standard free energy of the reaction



is about -145 kJ/mol at 1273 K (1), it is not surprising that aluminum carbide (Al_4C_3) can form at the interface between the metal and the carbon. An Al_4C_3 reaction layer is thought to be responsible for a significant voltage drop, thereby reducing the energy efficiency of the reduction process (2). To gain a better understanding of the voltage drop that could be expected in this region, the electrical resistivity of Al_4C_3 was measured at temperatures of interest (990-1240 K).

Several methods of preparing Al_4C_3 , including reactions of carbon with Al_2O_3 , AlPO_4 , and aluminum metal at tem-

peratures up to 1770 K , were tried before one was found that produced material of sufficient purity and yield. The process finally used consisted of heating a mixture of 0.5 mm diam aluminum shot, high purity graphite, and natural cryolite in a graphite boat to about 1570 K in purified argon. The temperature was then raised to about 1770 K , allowing the cryolite to volatilize. The amount of carbon used was only 97.8% of theoretical stoichiometric quantity, as it was found that a slight excess of aluminum was necessary, especially when conducting the reaction in a graphite boat. When the boats were removed from the furnace, a dark crust covered the Al_4C_3 , which was bright orange in color. The Al_4C_3 reaction product was analyzed for aluminum and carbon and found to contain 75.0 weight percent (w/o) Al and 24.2 w/o C, indicating that the purity was at least 99% . X-ray diffraction analysis of the material suggested a trace of carbon impurity.

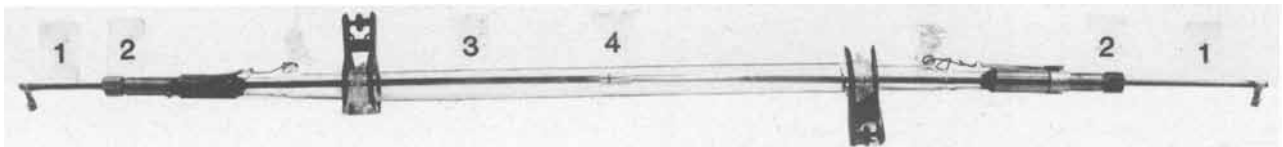


Fig. 1. Electrical resistance apparatus for measurement of elevated temperatures. 1: Inconel rods (0.635 cm diam). 2: Brass collets. 3: Quartz tube. 4: Alumina tube sample holder.

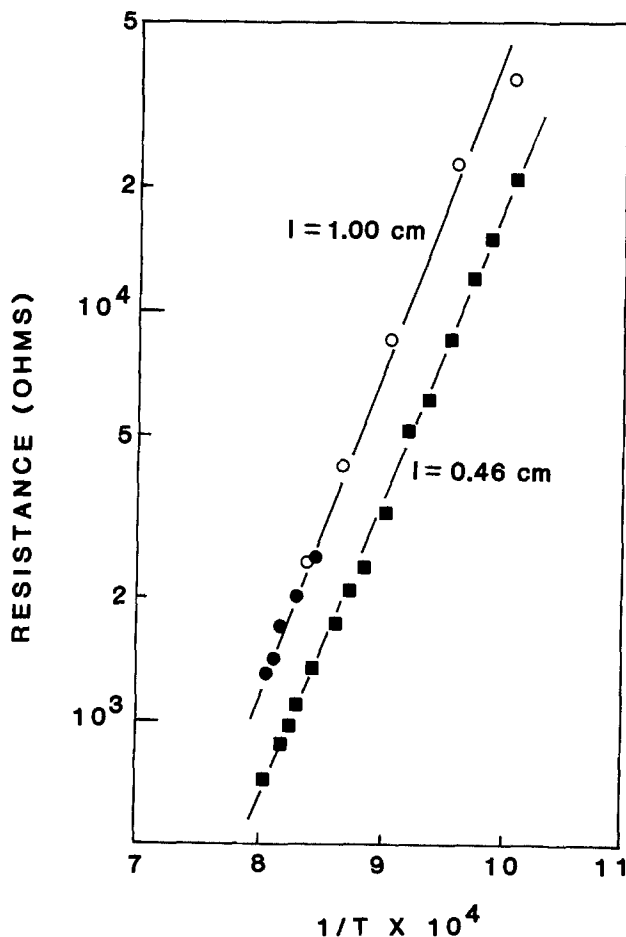


Fig. 2. Resistance of Al_4C_3 as a function of temperature. Solid symbols: heating. Open symbols: cooling. 1.00 cm specimen 57% dense, 0.46 cm specimen 61% dense.

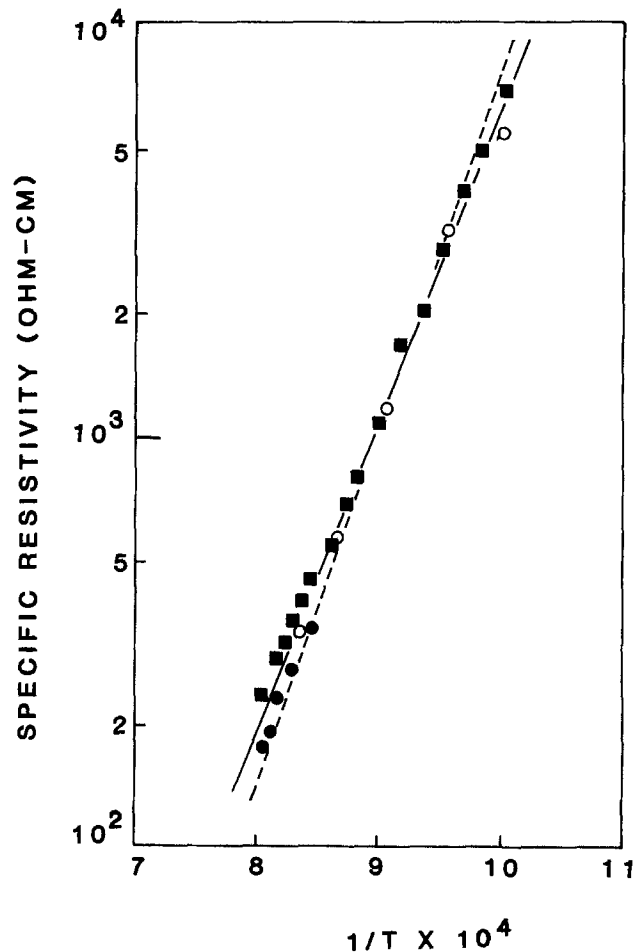


Fig. 3. Specific resistivity of Al_4C_3 as a function of temperature. Circles (1.00 cm specimen) and squares (0.45 cm specimen) based on $\rho = AR/l$. Dashed line based on $\rho = A\Delta R/\Delta l$, assuming both specimens 60% dense. Data were corrected for density by Bruggemann equation.

Pellets of 0.635 cm diam and 0.5-1.0 cm length were pressed from powder wetted with petroleum ether in a steel die at a pressure of about 650 MPa. The pellets had apparent densities of about 60% of theoretical (2.99 g/cm^3), and were not strong enough to allow surface contacts to be made as in the conventional four-point resistivity method. They had sufficient strength, however, to hold together when restrained between two Inconel rods in the electrical resistivity apparatus shown in Fig. 1. The Inconel rods, sample holder, and pellet were enclosed in a quartz tube, which had provision for flowing argon gas through it. One of the Inconel rods was hollow, but closed on one end allowing a thermocouple to be placed within a few millimeters of the sample. The apparatus was placed in a Leco tube furnace so that the center portion could be heated. Before heating, the system was flushed with purified argon for several hours. The electrical resistance measurements were made with a Wheatstone bridge connected across the ends of the Inconel rods.

The resistance data for two samples of lengths (l) 0.46 and 1.00 cm are shown in Fig. 2 as $\ln R$ vs. $1/T$ plots. Apparent resistivities were calculated by two procedures: (i) from the one-dimensional conduction equation $\rho = AR/l$, and (ii) from the differential relation $\rho = A\Delta R/\Delta l$, where ΔR and Δl are the differences in resistance and length of the two specimens. The latter method eliminates any potential contact resistance effects, provided they are the same in each test. An attempt was also made to correct for density using the Bruggemann equation, which has been shown to apply in aqueous systems containing non-conducting spheres (3)

$$\rho_0 = \rho(1 - \epsilon)^{1.5}$$

ρ_0 and ρ are the specific and apparent (measured) resistivities, respectively, and ϵ is the void fraction. The results in Fig. 3 show good agreement between the two samples, and indicate that contact resistance effects were minimal. The data are well represented by the expression

$$\rho_0 = 2.17 \times 10^{-4} \exp(1.71 \times 10^4/T)$$

The activation energy of 143 kJ implies a bandgap of almost 3 eV (290 kJ).

At a typical reduction cell temperature of 1225 K, the resistivity of Al_4C_3 is about 250 $\Omega\text{-cm}$. The thickness of Al_4C_3 corresponding to a voltage drop of 0.1V is therefore only 4 μm at a current density of 1 A/cm^2 .

Acknowledgment

This work was sponsored in part by the U.S. Department of Energy, Conservation and Renewable Energy, Office of Industrial Programs, under Contract DE-AC07-76CS40215.

Manuscript received Sept. 10, 1984.

Kaiser Aluminum and Chemical Corporation assisted in meeting the publication costs of this article.

REFERENCES

1. W. L. Worrell, *Can. Met. Quart.*, **4**, 87 (1965).
2. Y. V. Baimakov, *Legkie Metall.*, **6**, 22 (1937).
3. R. E. DeLaRue and C. W. Tobias, *This Journal*, **106**, 827 (1959).



Modeling of the Reaction for Low Pressure Chemical Vapor Deposition of Silicon Dioxide

Arthur J. Learn*

Anicon, Incorporated, San Jose, California 95134

ABSTRACT

A reaction model developed by Hitchman and Kane for semi-insulating polysilicon (SIPOS) deposition is adapted to the case of silicon dioxide growth on silicon wafers at low temperature and pressure. The model is used to explain the radial nonuniformities associated with the oxide deposition process and the function of a cage surrounding the wafers. The effect of providing openings in the cage for introduction of reactants is examined. The proportionality of oxide growth rate and silane flow rate, as well as a near-linear dependence of growth rate on wafer spacing, are also interpretable in terms of the reaction model.

The significant benefits resulting from chemical vapor deposition at reduced pressures are generally recognized (1). Mass-transfer limitations become relatively unimportant under this condition. Consequently, close wafer spacing on the order of a few millimeters can be utilized, and large processing load sizes result. In addition, excellent deposit-thickness uniformities are typically achieved. One exception (1) in this regard has historically occurred in the deposition of silicon dioxide at temperatures near 400°C. Reasonable within-wafer uniformities are achieved in this case only by placing a tube (cage) around the wafers. The necessity for a similar configuration in the case of semi-insulating polysilicon (SIPOS) deposition at low pressures has been established (2). A reaction model to explain the radial nonuniformity was proposed, which involves the generation of a homogeneous intermediate (SiH_2) on a heterogeneous oxygen containing site. The depositions were performed in a horizontal, hot-wall tube-type reactor with gas flow parallel to the axis of the wafer carrier.

In the present study, deposition of silicon dioxide at low pressure and temperature with a different flow pattern was investigated. In this case, reactant gases are introduced perpendicularly to the axis of the wafer carrier. The SIPOS model of Ref. (2) was adapted to the growth of oxide, where similarities to the SIPOS growth were noted. The results obtained for oxide growth are largely interpretable on this basis.

Experimental

The reactor design used is shown schematically in Fig. 1. The silane and oxygen reactants are introduced into the deposition chamber through separate injection tubes located at the center of the system. Wafers are held in caged carriers (boats) on either side of the injectors. A series of holes in the cage allows for introduction of reactants to the wafers. Typical deposition parameters were flow rates for each reactant of $250 \text{ cm}^3 \text{ min}^{-1}$, total pressure of 100 mtorr and temperature of 400°C.

Thickness measurements were made with a NanoSpec/AFT (Nanometrics, Incorporated, Sunnyvale, CA) using a refractive index of 1.46. The correct refractive index was separately determined by ellipsometry. Normally, thickness readings were taken at the wafer center and four

points (top, bottom, left, right) 6 mm inside the wafer edge. The ratio of the center thickness, t_c , to the average of the edge thicknesses, \bar{t}_e , was utilized as a measure of thickness uniformity. A more conventional uniformity parameter is the one-standard-deviation value divided by average thickness. As revealed in Fig. 2, there is a very good correlation between these two measures of uniformity. The data points shown are averages for a number of experimental runs. The solid lines are least mean squares fits to the data.

Theoretical Background

The deposition of SIPOS is performed by reacting SiH_4 and N_2O at temperatures of 600°-700°C. In this case, it is postulated (2) that four gaseous species can be adsorbed on the substrate surface. These are SiH_4 , N_2O , H_2 , and SiH_2 . It is proposed, and given empirical substantiation, that SiH_2 arises from pyrolysis of SiH_4 on an oxygen containing site at the growth surface. The formation of SIPOS occurs on the surface through reaction of Si (arising from pyrolysis of adsorbed SiH_4 at a silicon site) and adsorbed N_2O . Adsorption of SiH_2 at silicon sites can alter the rate of the SIPOS reaction. Because of the two

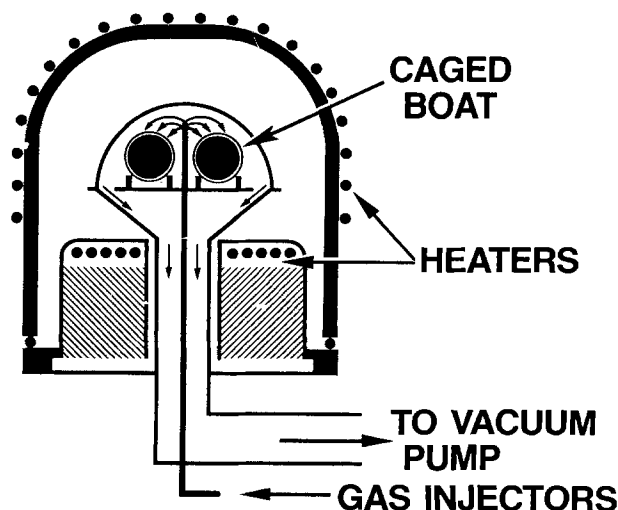


Fig. 1. Schematic of the reactor configuration

*Electrochemical Society Active Member.

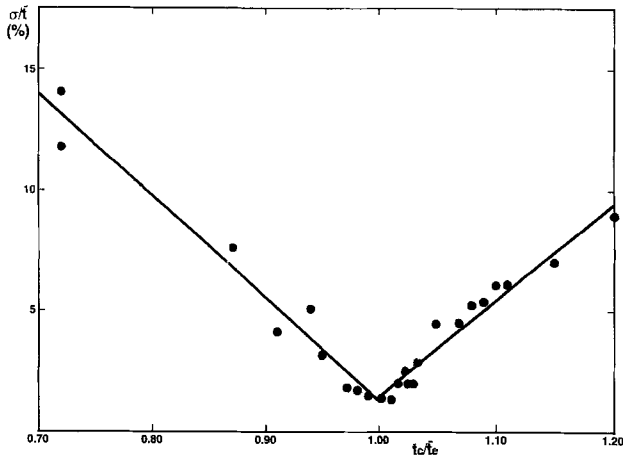


Fig. 2. Correlation of the within-wafer uniformity on a one-sigma basis to the ratio t_c/t_s .

types of adsorption sites and the multiplicity of adsorbed species, the SIPOS growth rate is expected to have contributions related to each of the species.

The considerations for silicon dioxide growth are not substantially different from those above. Rather than the oxygen bearing species N_2O , O_2 is the second reactant. Making the appropriate substitutions, Eq. [30] of Ref. (2) then yields as the growth rate, GR, for SiO_2

$$GR = \frac{kK_s}{2} (1 - X_s) \left[\frac{2(1 + X_s)}{n_s} + 2K_h + K_o \gamma(1 - X_o) + K_c k_m (1 + X_s) \frac{n_m A}{n_s V} \right]^{-1} \quad [1]$$

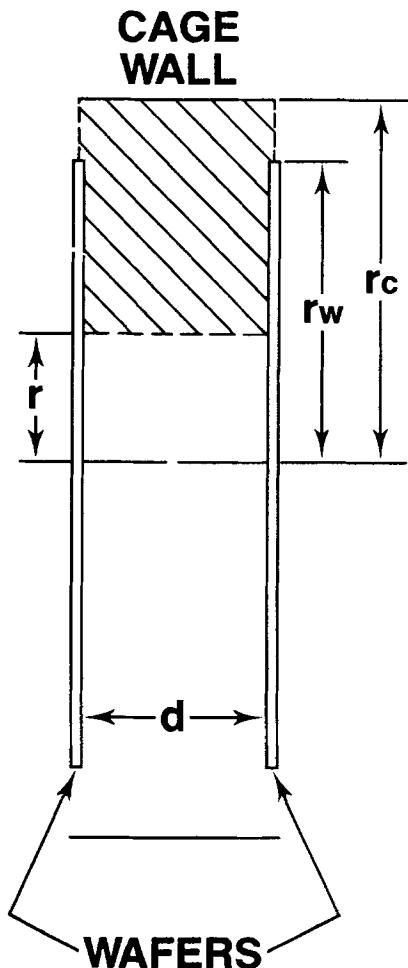


Fig. 3. Unit cell for silane-oxygen reaction in a caged boat

where k is rate constant for decomposition of adsorbed SiH_4 , K_s is equilibrium constant for SiH_4 adsorption, X_s is SiH_4 depletion, n_s is input SiH_4 concentration, K_h is equilibrium constant for desorption of H_2 , K_o is equilibrium constant for adsorption of O_2 , γ is flow rate O_2 /flow rate SiH_4 , X_o is oxygen depletion, K_c is equilibrium constant for SiH_2 desorption, k_m is a modified rate constant, n_m is density of oxygen containing surface sites, and A and V are an area and volume defined with the aid of Fig. 3. The total area on which deposition can occur is A and V is the volume of the hatched region in Fig. 3. Certain of the results discussed in the following section imply that the last term in Eq. [1] is predominant. Chief among these are a weak dependence of GR on γ for $\gamma \approx 1$ and an approximately linear dependence of GR on wafer spacing. Under this assumption

$$GR = \frac{k}{2k_m} \frac{K_s}{K_c} \frac{(1 - X_s)}{(1 + X_s)} \frac{n_s}{n_m} \frac{V}{A} \quad [2]$$

The term V/A can be expressed as a function of radial position r on a wafer as follows

$$V/A = \frac{d}{2} \frac{(r_c^2 - r^2)}{r_c d + r_w^2 - r^2} \quad [3]$$

where, as defined in Fig. 3, d is wafer-wafer spacing, r_w is wafer radius, and r_c is the inner radius of the cage surrounding the wafers. In general, this term will result in a radial variation of GR and hence thickness. The positioning of the cage can, however, be optimized to eliminate such a variation. The required condition is that $d(GR)/dr = 0$, i.e., $d(V/A)/dr = 0$. From Eq. [3], this translates into the condition that $r_c^2 - r_c d - r_w^2 = 0$. Therefore

$$r_c = 1/2 [d + (d^2 + 4r_w^2)^{1/2}] \quad [4]$$

For dimensions such that $d \ll r_w$, Eq. [4] becomes

$$r_c = r_w + d/2 \quad [5]$$

Thus, in the ideal case, the spacing, X , of the cage from the wafer edge is approximately one-half of the wafer spacing. For larger X , the deposit is thicker at the wafer edge than at the center. For smaller X , the converse is true.

In addition, for the ideal case, $V/A = d/2$ and from Eq. [2], GR is directly proportional to wafer spacing. Under other than ideal conditions, the form of V/A (and hence GR_c) at the wafer center ($r = 0$) is

$$GR_c \propto d \frac{r_c^2}{r_c d + r_w^2} \quad [6]$$

Again, for $d \ll r_w$ and $r_c \approx r_w$, $GR_c \propto d$, as before.

If introduction of reactant gases must occur through the cage, as in the system of this study, then, obviously, holes must be present in the cage. This to some degree increases V and decreases A so that V/A is increased. The consequence is to produce a relatively thicker deposit near the wafer edge than at the center.

Results and Discussion

Growth rate is shown as a function of d in Fig. 4 for r_c and r_w equal to 52.5 and 50.0 mm, respectively. Growth rate is proportional to spacing for the smaller d and is sublinear for the larger d . This behavior is functionally consistent with Eq. [6]. Somewhat less falloff of GR is, however, observed than expected from Eq. [6]. For example, for d equal to 19 mm a GR of 36 nm min⁻¹ would be expected.

Two implications of this particular dependency of GR on d are noteworthy. Where wafers are held in slots within the boat, the effective d will be relatively small and little deposition will occur in such areas. This is the origin of the "boat marks" that appear for low pressure oxide deposition. The variation of GR with d also dictates strict parallelism of the wafer surfaces. Random tilting of some wafers will result in thicker or thinner deposits in certain

LSSS

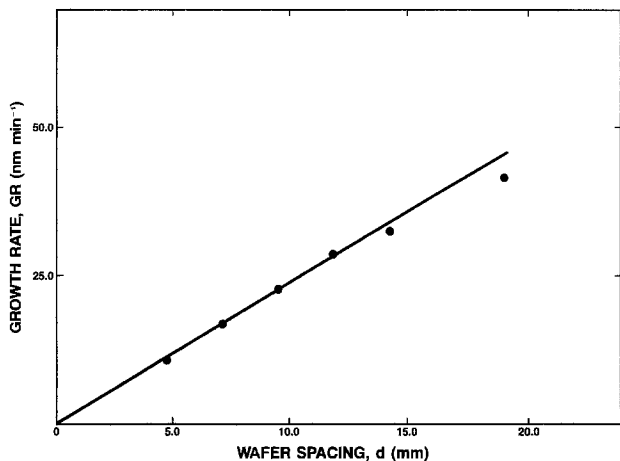


Fig. 4. Growth rate at wafer center as a function of wafer spacing

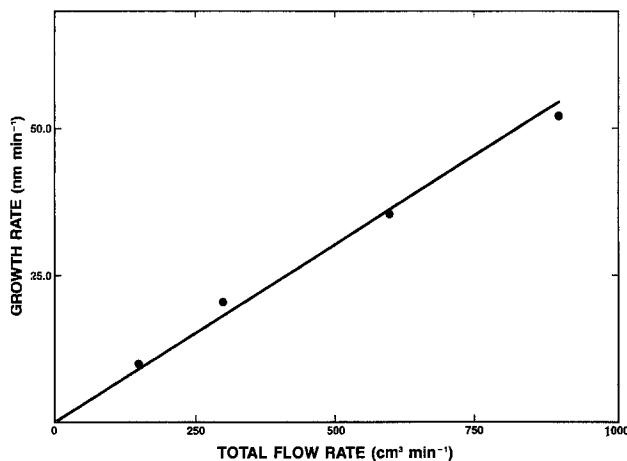


Fig. 5. Growth rate at wafer center as a function of total flow rate for O_2/SiH_4 mole ratio = 1.

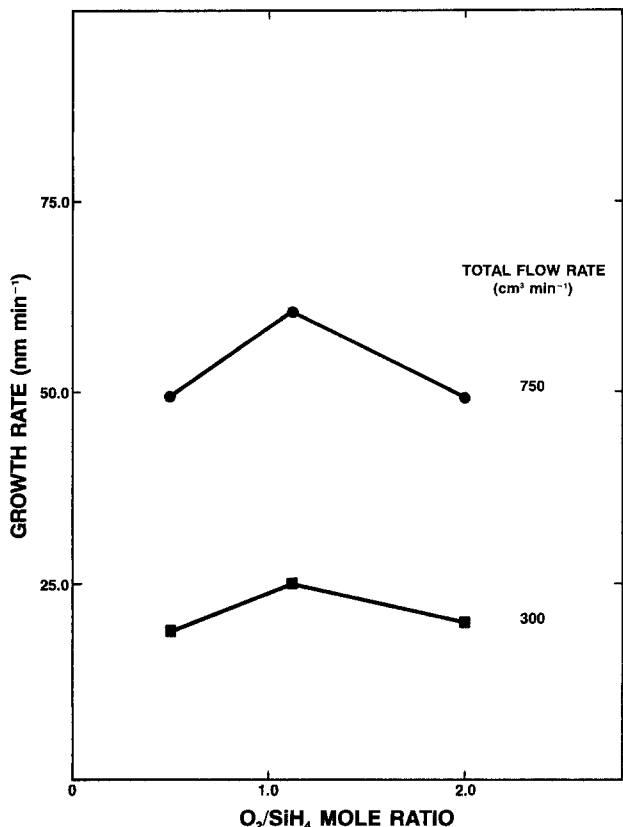


Fig. 6. Growth rate at wafer center as a function of O_2/SiH_4 mole ratio at two total flow rates.

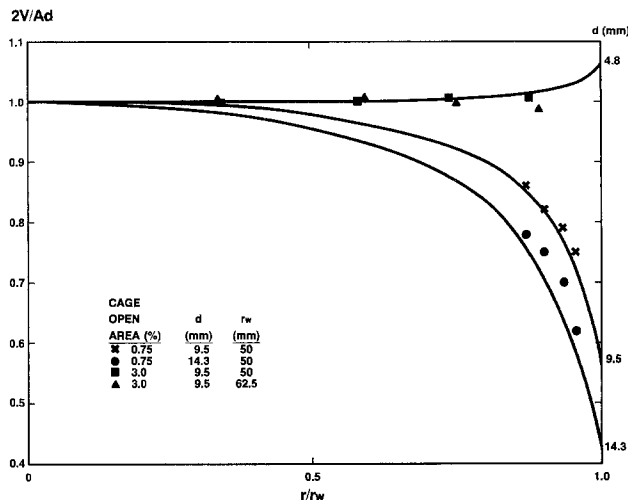


Fig. 7. Radial thickness profiles according to Eq. [3]. Data presented are for conditions indicated in the inset.

regions of these wafers. Accordingly, the within-wafer uniformity will be degraded.

Growth rate as a function of total volumetric flow rate is presented in Fig. 5 for d equal to 9.5 mm. To a good approximation, GR is directly proportional to the total flow rate. Such a dependency is consistent with Eq. [2]. A linear dependence of GR on the SiH_4 concentration n_s is predicted.

Growth rates are presented in Fig. 6 as a function of O_2/SiH_4 mole ratio γ for d equal to 9.5 mm and two total flow rates. Again, the approximate proportionality of GR to total flow rate is noted. There is about a 20% change in GR over the range of γ from 0.5-2.0 with a peak value for $\gamma \approx 1$. Comparable results were obtained in an earlier investigation under similar deposition conditions (3). This weak dependency on γ , in conjunction with the above results for flow rate and d , lends credence to the assumption made in arriving at Eq. [2].

Additional verification of the correct functionality of Eq. [2] is gained through examination of thickness uni-

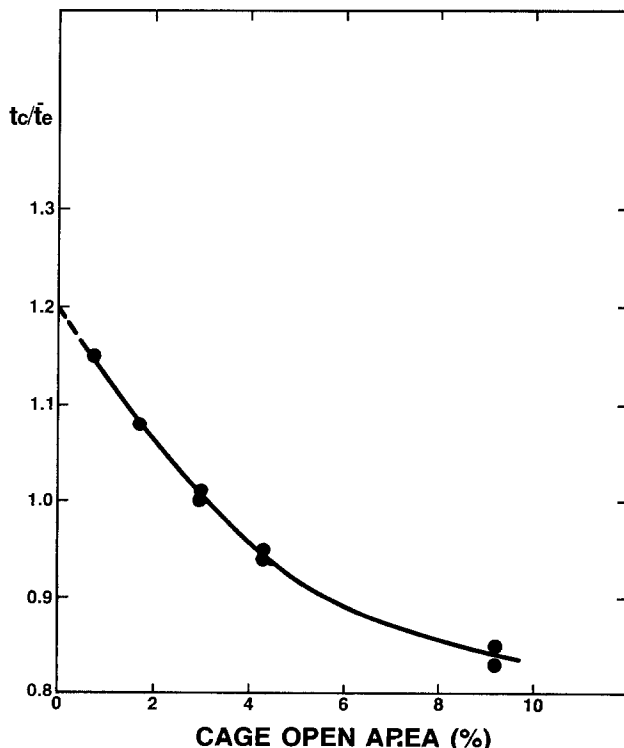


Fig. 8. Within-wafer uniformity as a function of cage open area for $d = 9.55$ mm and $X = 2.5$ mm.

formity of the deposits. Equation [3] is plotted in Fig. 7 as a function of normalized wafer radius for $r_c - r_w$ equal to 2.5 mm. Three values of d are considered. Data are shown for 100 mm diam wafers with an open area on the cage of approximately 0.75% of the total cage area. The functional form of the data closely approximates that of Eq. [3] although actual values are somewhat larger. Increasing the open area to 3% greatly reduces the thickness variation along the wafer radius, as shown in Fig. 7. The plot for d equal to 4.8 mm in Fig. 7 illustrates that the same degree of uniformity is achievable only for the percent open area approaching zero, *i.e.*, for the ideal case of Eq. [3].

Uniformity as a function of open area on the cage is further explored in Fig. 8 for d equal to 9.5 mm. The measure of uniformity used is t_c/\bar{t}_c , which ideally should be unity. Consistent with the data of Fig. 7, this condition is satisfied for an open area of about 3%. As mentioned in the preceding section, increased open area results in increased thickness at the wafer edges. The value of t_c/\bar{t}_c extrapolated to zero open area is 1.20. This is in excellent agreement with the value of 1.19 calculated from Eq. [3] and plotted in Fig. 7.

A final comment may be made regarding the apparent similarity in type of the SIPOS and oxide reactions. Both are strongly temperature-activated, characteristic of heterogeneous reaction. The activation energy for the SiH₄, N₂O reaction is on the order of 1 eV, with the exact value depending on the ratio of flow rates for the two reactants (2). The activation energy for oxide growth (4) in the reactor of this study is 0.52 eV for γ equal to one.

Conclusions

The reaction model of Ref. (2) for SIPOS deposition was found to be equally applicable to the deposition of silicon dioxide at lower temperatures. In particular, the linear dependence of oxide growth rate on silane flow rate and near-linear dependence on wafer spacing are explained by such a model. The necessity for opening holes in the cage surrounding wafers, because of the unique reactant-gas-flow pattern in the reactor used, allows comparison of uniformity data to the model only for results extrapolated to a closed cage. Agreement is, however, excellent in this case.

Acknowledgment

The technical assistance of Ron Jackson in performance of depositions and measurements is gratefully acknowledged.

Manuscript submitted June 25, 1984; revised manuscript received Sept. 25, 1984.

Anicon, Incorporated assisted in meeting the publication costs of this article.

REFERENCES

1. R. S. Rosler, *Solid State Technol.*, **20**(4), 63 (1977).
2. M. L. Hitchman and J. Kane, *J. Cryst. Growth*, **55**, 485 (1981).
3. P. J. Tobin, J. B. Price, and L. M. Campbell, *This Journal*, **127**, 2222 (1980).
4. A. J. Learn, *ibid.*, **132**, 405 (1985).

Electrophoretic Deposition of Glass Powder for Passivation of High Voltage Transistors

Masaru Shimbo* and Katsujiro Tanzawa

Toshiba Research and Development Center, Komukai Toshiba-cho, Saiwai-ku, Kawasaki, Japan

Masafumi Miyakawa and Takao Emoto

Toshiba Microelectronics Center, Komukai Toshiba-cho, Saiwai-ku, Kawasaki, Japan

ABSTRACT

Zinc borosilicate glass was electrophoretically deposited on silicon substrates in IPA solutions containing Y⁺⁺⁺ and Mg⁺⁺ additives. The deposition rate as well as the surface structure of deposits was greatly influenced by the Mg/Y ratio in the solution. Most of the deposits formed in the Y⁺⁺⁺ ion-rich solutions can be removed by rinsing, whereas the glass deposits formed in the Mg rich solutions are tightly attached to the substrates. Preferable deposits for filling of the moats between high voltage transistors are formed at Mg/(Mg + Y) = 0.5.

Glass passivation, a technique for protecting junction surfaces with multicomponent glass, is known to promote semiconductor device reliability (1-6). Many glass passivated diodes (5), thyristors (3, 6), and power transistors (4) have been developed and are commercially available. The authors also developed glass passivated high voltage power transistors, which are used in the horizontal oscillation circuits for color television sets (7). In this device development, it was necessary to improve a new glass coating method which enables filling the glass in deep beveled moats. A cross-sectional photograph of the device moat is shown in Fig. 1.

This paper describes an improved electrophoretic coating method which is utilized in high voltage power transistor production. There have been several reports published concerning electrophoretic coatings of the passivation glass (8-11). Sheldom (8) and Miwa *et al.* (9) described the deposition of zinc borosilicate glass dispersed in isopropanol (IPA), with ammonium hydroxide

or hydrofluoric acid as the additives. The deposition of lead borosilicate glass in ethyl acetate or acetone with a small amount of methanol is reported in Ref. (10). Trap (11) cited the deposition of the germania containing lead aluminosilicate glass in IPA with aluminum chloride. The author's method uses yttrium and magnesium ion additives in alcohol (IPA) solutions. The concentration ratio for each cation plays an important role in the deposition rate, as well as the surface features of the deposit. Several other factors which affect deposition rates were also examined, and their deposition mechanisms are discussed.

Experimental

The glass of SiO₂ 10, B₂O₃ 25, ZnO 59, PbO 5.0, and Al₂O₃ 1.0 weight percent (w/o) composition was prepared using the standard glass making method; reagent-grade raw materials were mixed and melted in a platinum crucible with an electric furnace at about 1450°C for 4h. The melt was then poured between two water-cooled rollers to make thin glass foils. The glass was crushed and pulver-

*Electrochemical Society Active Member.

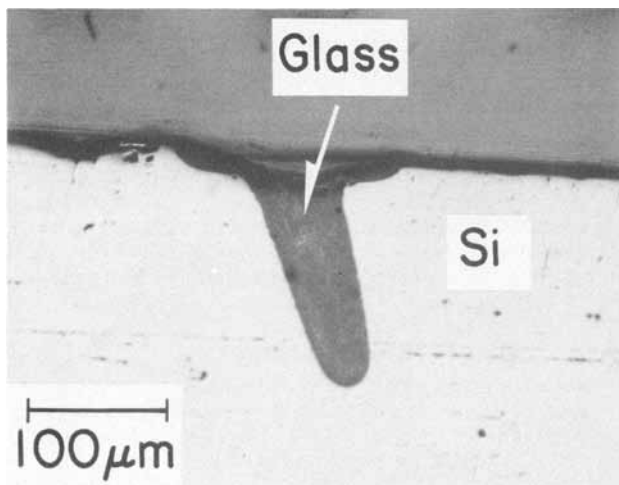


Fig. 1. A cross-sectional photograph at the moat of the finished high voltage power transistor.

ized in a ball mill. With one side polished, (100) silicon wafers (p type, 2-3 Ωcm) 50 mm in diameter were chemically cleaned (12) and used for deposition-rate studies. For surface-morphology studies, grooves with rectangular crossing were formed on polished silicon surfaces with 5 mm pitches, using a diamond saw after thermal oxidation in wet oxygen atmosphere. Width and depth of the grooves were 100 and 150 μm , respectively. Thickness of the oxide layer was about 1.2 μm .

The electrophoretic deposition vessel was a 600 ml Teflon beaker with a platinum-plate counterelectrode. The substrate wafer was fixed on a vacuum holder, which permitted retaining electric contact, and immersed in the vessel vertically. The distance between the wafer and the electrode was 2 cm. Negative electric potential was applied to the wafer, with a regulated dc power supply (max 300V) at constant voltage. Electrophoretic current was measured by using a laboratory recorder. The glass powder, passed through a 325 mesh sieve, was dispersed in IPA, in which magnesium nitrate and/or yttrium nitrate had been dissolved. Total concentration of the electrolytes was 0.25 or 0.5×10^{-3} mol/l.

The usual glass/solvent ratio and water content in the solutions were 10g/100 ml and 0.5%, respectively. The dispersed solutions were decanted before the electrophoresis studies in order to eliminate large particles ($>10 \mu\text{m}$). The solution was not stirred during deposition. After deposition, the substrate was rinsed with ethyl acetate, dried, and weighed. The glass firing temperature was 700°C.

For *in situ* deposition-rate measurement, wafer weight change during deposition was measured (10). A silicon wafer, 2 in. in diameter, was hung from a load cell (Kyowa Electric Instruments Company) in the electrophoresis vessel containing the solution using 0.6 mm diam Pt wire and a quartz glass hook. The wire was fixed on the rear surface of the wafer with electroconductive silver paste. The rear surface and the wire in the solution were insulated with Apiezon wax. An electric potential was applied through the Pt wire. The counterelectrode was the Pt plate. The electrophoretic conditions and concentration for the solutions were similar to those described previously.

The cation concentration in the solutions before and after glass dispersion were chemically analyzed, and concentration differences obtained were considered to correspond to the adsorbed cations on the glass particles. For the glass-dispersed solutions, the glass was precipitated by centrifuge before analysis. A glass deposit, formed by electrophoresis, was dissolved in concentrated nitric acid, and the amount of Y and Mg ions in it was also chemically analyzed.

Results

Deposit surface morphology.—Figure 2 shows microscopic photographs of glass deposited on the surface at

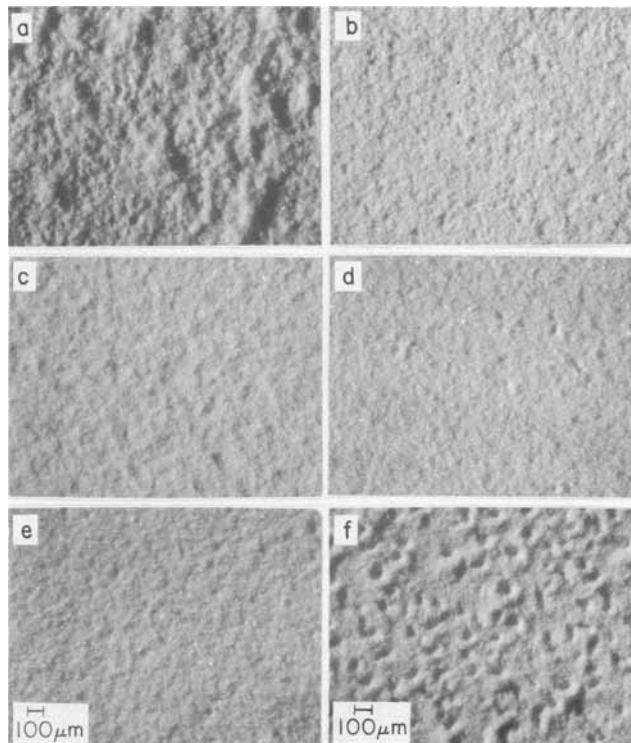


Fig. 2. Microscopic photographs of the deposit surface on silicon wafers. Electrophoretic conditions: 300V, 2 min. Total cation concentration: a) 0.25×10^{-3} mol/l, b to f) 0.5×10^{-3} mol/l. Cations ratio (Mg/Mg + Y): a and b) 0; c) 0.25; d) 0.5; e) 0.75; and f) 1.0.

various Mg/Mg + Y ratios. When the additive cation is Y ions only, the deposits become rough and nonuniform in their appearance. However, the surface roughness is improved when the Y ion concentration increases.

When Mg ions are dominant in the solutions, crater-like pits are formed on the deposits. Smooth and uniform de-

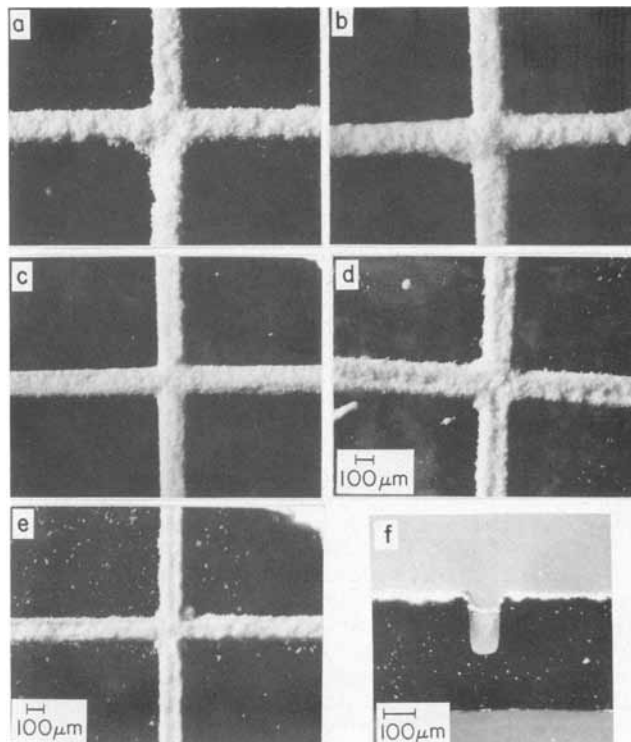


Fig. 3. Microscopic photographs of glass deposits on the grooves. Electrophoretic conditions: 300V 2 min. Total cations concentration: 0.5×10^{-3} mol/l. a) Mg/Mg + Y = 0, b) = 0.25, c) = 0.5, d) = 0.75, and e) = 1.0. f) Cross-sectional photograph of the groove after firing the c deposits.

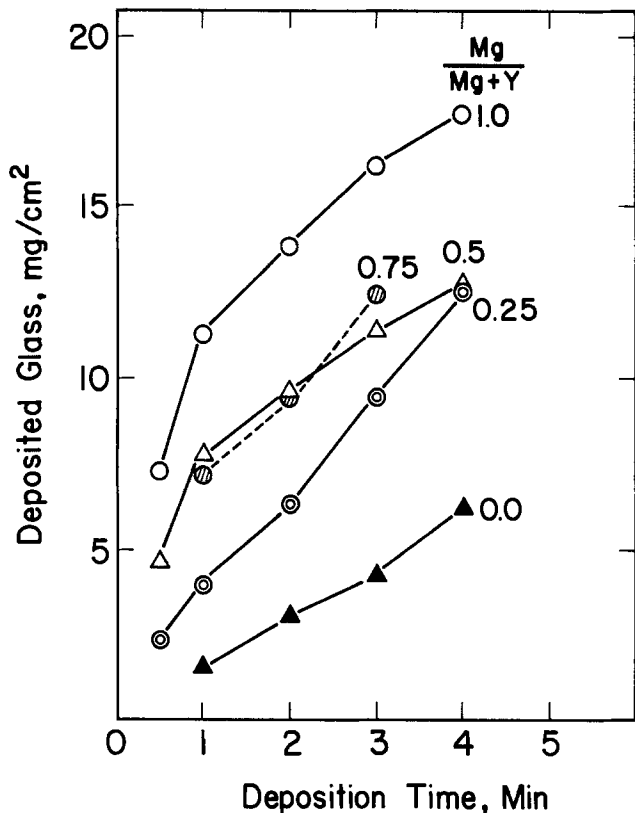


Fig. 4. Glass deposition rate on grooveless wafers in various Mg/Mg + Y ratios with 0.25×10^{-3} mol/l total cation concentration at 300V.

posits are formed when both Y and Mg ions are present. The mixed cation additives effect is more distinct when grooved substrates are used, as shown in Fig. 3. The opti-

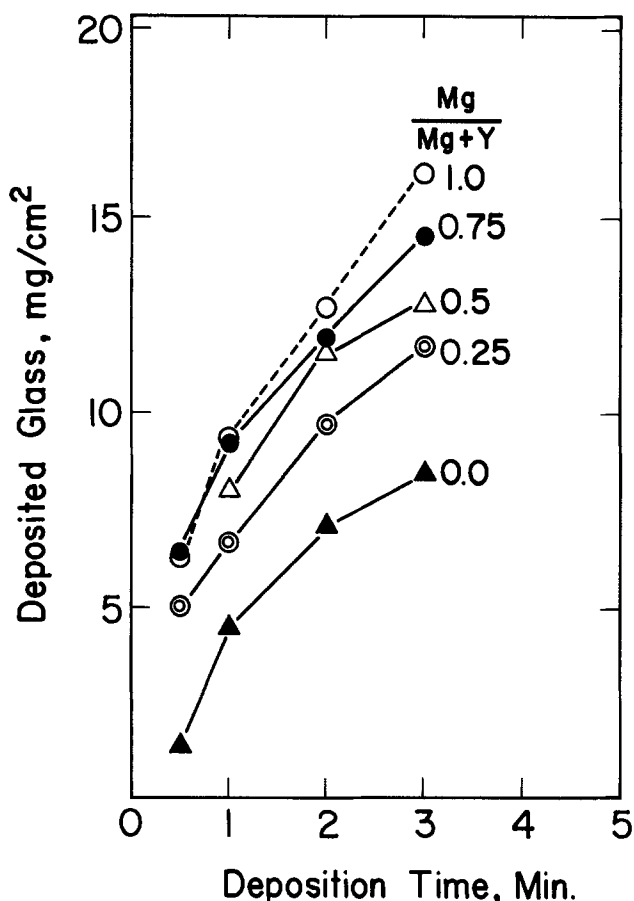


Fig. 5. Glass deposition rate on grooveless wafers in various Mg/Mg + Y ratios with 0.5×10^{-3} mol/l total cation concentration at 300V.

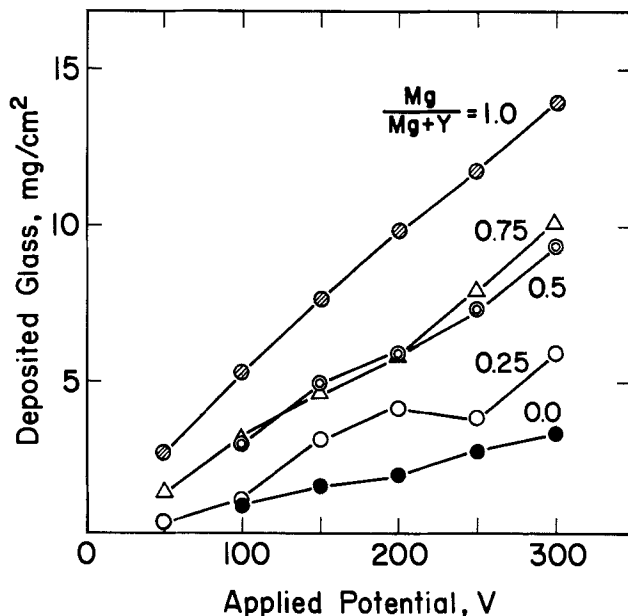


Fig. 6. Deposition rate vs. applied potential with various Mg/Mg + Y ratios. Total electrolyte concentration: 0.25×10^{-3} mol/l. Deposition time: 2 min.

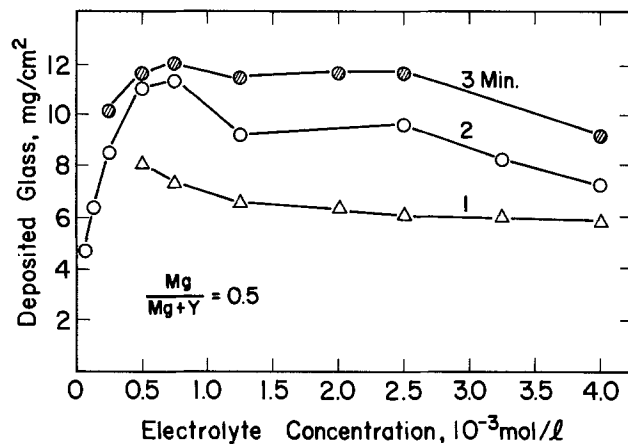


Fig. 7. Total cation concentration effect on deposition rate. Mg/Mg + Y = 0.5. Applied potential: 300V.

mum conditions seem to be near the Mg/Mg + Y = 0.5 point. Figure 3f is a cross-sectional photograph of the groove after firing the glass deposits shown in Fig. 3c. The amount of glass in the groove was able to be controlled within 10% of meniscus height if proper solution conditions were chosen.

Deposition rate studies.—Figures 4 and 5 show deposition rates for wafers without grooves at various Mg/Mg + Y ratios with two different total electrolyte concentrations. The accuracy of this study is about $\pm 20\%$. Some of this low reproducibility may be caused by breakoff of the deposits attached around wafer fringes. The rate increases with increasing Mg ion percentages. The deposition rate increases linearly with the applied voltage, as is shown in Fig. 6. The electrolyte concentration effect at Mg/Mg + Y = 0.5 is shown in Fig. 7. The deposition rate increases with an increase in the concentration, up to 0.5×10^{-3} mol/l, then gradually reduces. The glass content effect in the solutions is shown in Fig. 8. The rate has a maximum at about 10g glass/100 ml IPA. The deposition rate vs. Mg/Mg + Y ratio with two different water contents in the solutions is shown in Fig. 9. The rate increases with increased water content, especially at the low Y ions range.

Glass deposition in situ measurement.—Figure 10 shows the results of *in situ* deposition measurement for

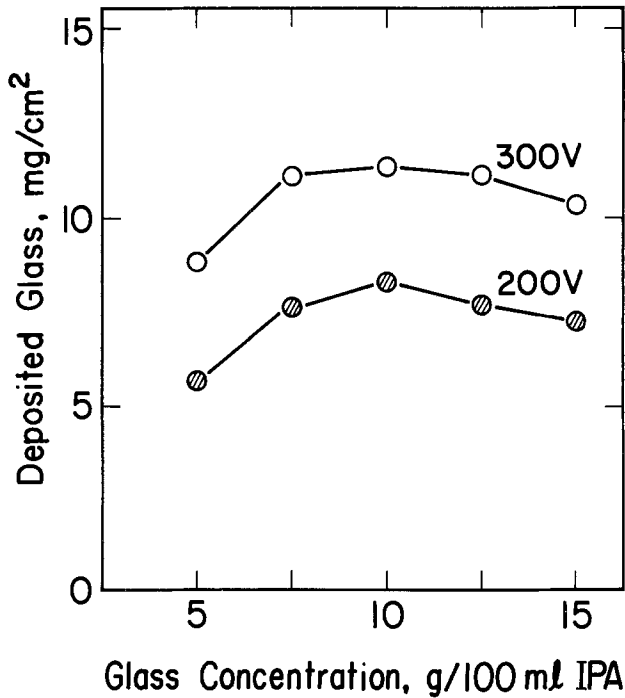


Fig. 8. Glass concentration effect on deposition rate. $Mg/Mg + Y = 0.5$. Total cation concentration: 0.5×10^{-3} mol/l. Deposition time: 2 min.

grooveless wafers. Contrary to the previous measurement, the deposition rate increases with increasing Y ions content when the $Mg/Mg + Y$ ratio is less than 0.5. However, a considerable amount of glass is removed when the applied voltage is removed (dashed lines in Fig. 10). In this concentration range, most of the deposit is washed off after shaking and rinsing the substrates. In the $Mg/Mg + Y \geq 0.5$ range, the deposition rate becomes small, but the deposits adhere strongly to the substrates.

Reproducibility of this measurement was about $\pm 10\%$. Hence, final weight difference between each curve in Fig. 10 in this low $Mg/Mg + Y$ range has little meaning.

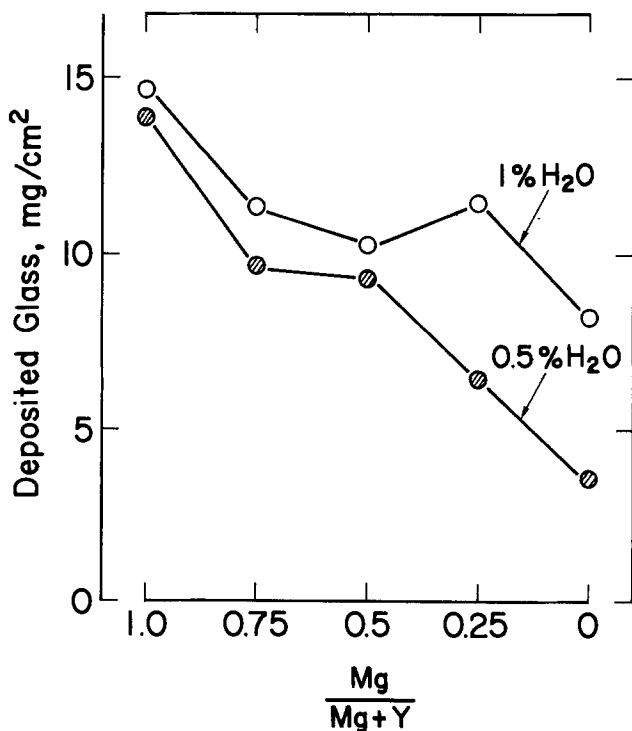


Fig. 9. Deposition rate vs. $Mg/Mg + Y$ ratio with different water concentrations. Total cation concentration: 0.25×10^{-3} mol/l. Applied potential: 300V. Deposition time: 2 min.

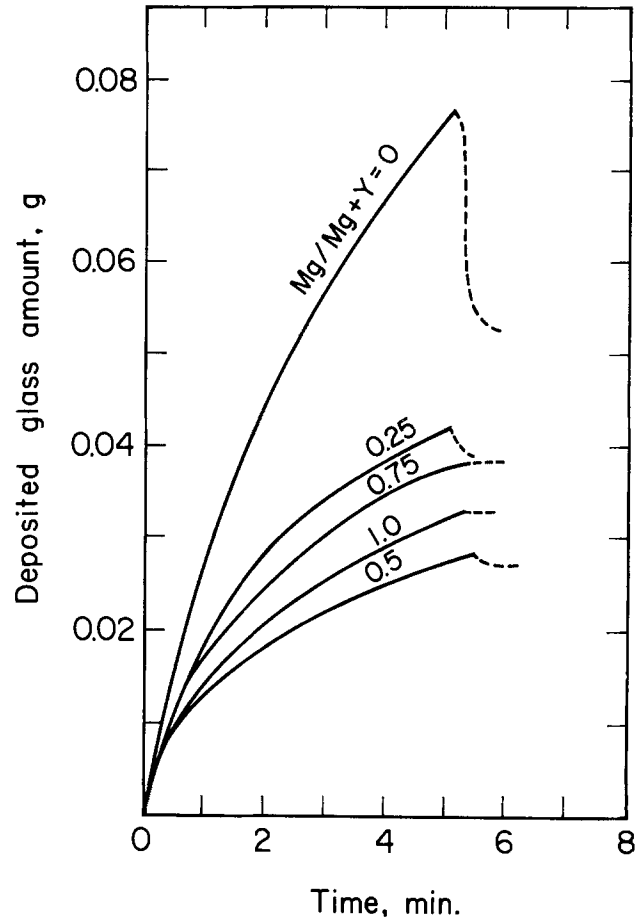


Fig. 10. *In situ* measurement of the deposition rate with various $Mg/Mg + Y$ ratios. Total cation concentrations: 0.5×10^{-3} mol/l. Applied potential: 300V. Substrate: 2 in diam silicon wafer.

Current measurements and adsorbed cations estimation.—Electric conductivities (electrolytic currents) were measured for solutions with cation additives but without glass dispersion. Results are shown in Fig. 11. The conductivity increases with $Mg/Mg + Y$ ratio increase. Dur-

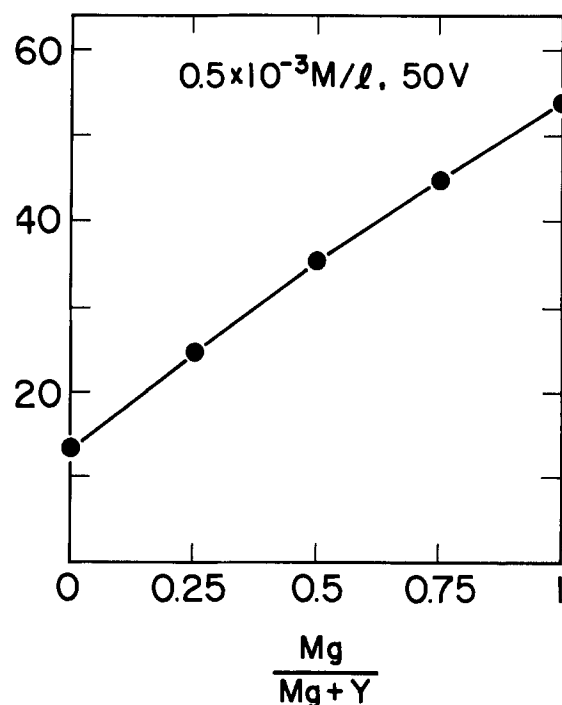


Fig. 11. Electrolytic currents vs. $Mg/Mg + Y$ ratio in solutions before glass addition.

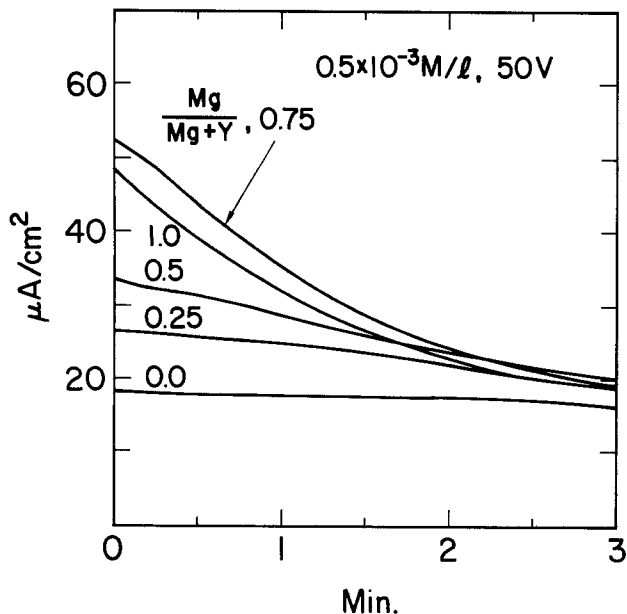


Fig. 12. Electrophoretic currents during glass deposition with various Mg/Mg + Y ratios.

ing these current measurements, the cathode wafers are covered with Mg and/or Y hydroxides. The electrophoretic currents during the glass deposition are shown in Fig. 12. The initial current increases with increasing Mg ions content, but current decay with time also increases.

The amount of adsorbed cations, estimated from concentration difference in the solution, is shown in Fig. 13 in relation to Mg/Mg + Y ratio of the additive electrolytes. A considerable amount of each cation is adsorbed from each solution. However, Y ions are selectively adsorbed when both Mg and Y ions are in the solutions.

The amount of the cations included in the electrophoresis deposits changed within about 0.1-0.01% when solution conditions and/or electrophoresis conditions were changed.

However, the amount always exceeded that of the adsorbed cations from the solution.

Discussions

General mechanisms of electrophoretic coating were briefly discussed by With (13). Grosso *et al.* (14) reported

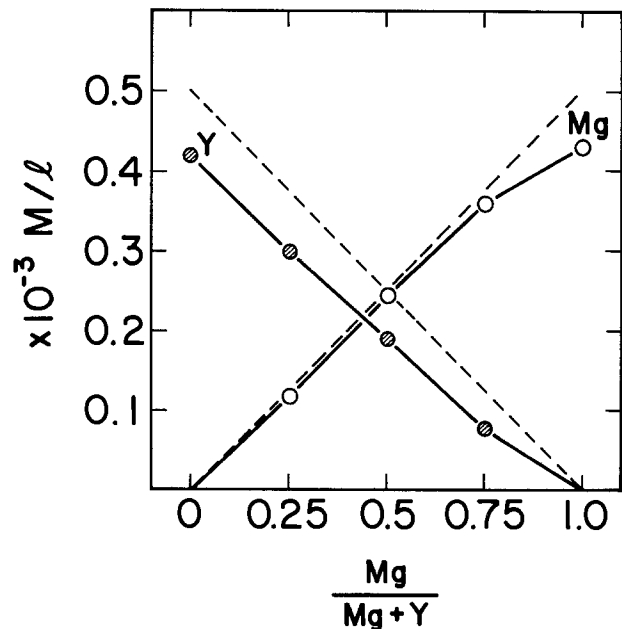


Fig. 13. Adsorbed amount of cations per unit glass in relation to Mg/Mg + Y ratio. Total cation concentration: 0.5 × 10⁻³ mol/l. Glass concentration: 10g/100 ml solution.

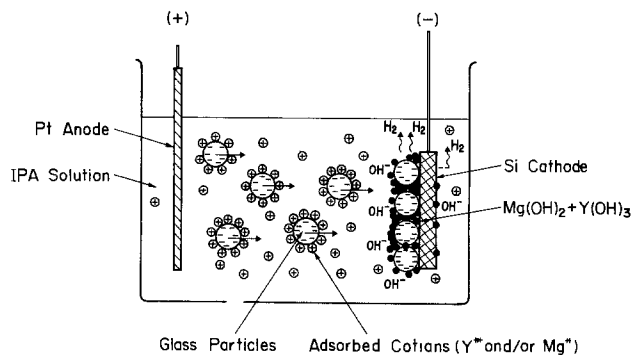


Fig. 14. A schematic view of glass powder electrophoretic deposition process.

the electrophoretic deposition of phosphor powders in polar organic solvents with inorganic cation additives. Similar mechanisms can be applied to the results described here. The additive cations are adsorbed on the glass particles to make positive charges and stabilize the dispersion. When an electric field is applied, the particles are transported toward the cathode and agglomerate on it. During this process, water in the solutions is electrolyzed to produce OH ions around the cathode. Then, cation hydroxides precipitate between the particles and bind them tightly on the substrates. This process is shown in Fig. 14.

When Y ions are dominant in the solution, the deposits are attached loosely on the substrate. In this case, electrode polarization by the deposited layers is small, so the deposition rate becomes large, in spite of the small electric conductivity of the solution. However, the deposits are released during rinsing, and only a small layer remains. When Mg ions dominate, dense and highly adhesive deposition layers are formed. However, the deposition rate reduces with time caused by the insulating nature of the deposits. Besides, large electric conductivity of the solution may promote the hydrogen evolution reactions which cause pits in the deposited glass. When using grooved substrates, the deposited layers spread out from the grooves along the equipotential lines, because the electric potential concentrates on the fringes of the grooves. However, if the deposit's binding force is reduced by selecting the proper ratio of Mg to Y in the solution, glass deposited away from the grooves is washed off during rinsing, and remaining layers are localized on the grooves. Moderate electric conductivity for solutions containing both cations may also contribute to the proper deposition rate without hydrogen evolution.

Conclusion

Electrophoretic deposition of zinc borosilicate glass powder in IPA solution containing Y and Mg ions enables the glass passivation of high voltage power transistors at more than 1500V breakdown voltage.

The Y/Mg composition ratio in the solution has a great effect on the surface structure of the deposits and the deposition rate. When Y ions are dominant in the solution, weak-bonded deposits, most of which fall off during rinsing, are formed. In the range where Mg ions are dominant, tightly bonded deposits are formed, but hydrogen gas evolution causes pits in the glass surface. For glass deposition in the device moats, adding the same amounts of Y and Mg ions is preferable, since glass deposited away from the moats was washed off and the remaining glass was localized on the moat. The glass deposits contain 0.1-0.01% of additive cations. Incorporation of small amounts of additive Y⁺⁺⁺ and Mg⁺⁺ cations in the deposited and fused glass films was shown to have no influence on device characteristics.

Acknowledgments

The authors wish to thank M. Uchida, K. Gotoo, and T. Ozawa for planning and developing the glass passivated transistors, which was the motivation for this work. S. Iiri

and I. Suzuki carried out chemical analysis, and S. Tai produced the glass powder.

Manuscript submitted June 5, 1984; revised manuscript received Sept. 19, 1984.

Toshiba Research and Development Center assisted in meeting the publication costs of this article.

REFERENCES

1. W. A. Pliskin and E. E. Conrad, *Electrochem. Technol.*, **2**, 196 (1964).
2. M. Dumesnil and R. Hewitt, *This Journal*, **117**, 100 (1970).
3. T. Shibuya, T. Miwa, Y. Sato, and K. Hadano, "IVth International Congress on Glass," Vol. 8, p. 111, Kyoto, Japan, (1974).
4. A. H. Berman, *Solid State Technol.*, **19**, 29 (1976).
5. D. L. Flowers and H. G. Hughes, *This Journal*, **129**, 154 (1982).
6. S. Ohr, *Electronic Design*, **29**, 34 (1981).
7. M. Uchida, T. Emoto, S. Morita, T. Yonesawa, and M. Miyakawa, *Toshiba Review (Jpn. Edition)*, **33**, 769 (1978).
8. G. S. Sheldon, U.S. Pat. 3,642,597 (1972).
9. K. Miwa, M. Kanno, S. Kawamura, and T. Shibuya, *Denki Kagaku*, **40**, 478 (1972).
10. Y. Watanabe, Y. Kajiwarra, and H. Gamoh, "10th Symposium of Semiconductors and Integrated Circuits Technology," p. 24, Tokyo, Japan (1976).
11. H. J. L. Trap, *Verr. Refract.*, **32**, 17 (1978).
12. W. Kern and D. A. Puotinen, *RCA Rev.*, **31**, 187 (1970).
13. A. With, in "Science and Technology of Surface Coatings," B. N. Chapman and J. C. Anderson, Editors, p. 60, Academic Press, London (1974).
14. P. F. Grosso, R. E. Rutherford, Jr., and D. E. Sargent, *This Journal*, **117**, 1456 (1970).

Dangling Bonds in Memory-Quality Silicon Nitride Films

Shizuo Fujita and Akio Sasaki

Department of Electrical Engineering, Kyoto University, Kyoto 606, Japan

ABSTRACT

Origin of memory traps in chemically vapor-deposited silicon nitride films was investigated. Electron-spin resonance and infrared absorption measurements revealed the existence of silicon dangling bonds which have three-folded configuration. Correlation between the spin density and the metal-nitride-oxide-semiconductor (MNOS) memory characteristics was studied, and it was suggested that silicon dangling bonds are responsible for the trap states which cause not only hopping conduction, but also memory behavior. A model is presented suggesting that the dangling bonds are positively, neutrally, or negatively ionized. The MNOS memory behavior and the energy level of the traps were well interpreted by taking into account the transition of the dangling bonds.

A great interest has been focused on a metal-nitride-oxide-semiconductor (MNOS) field-effect transistor as an electrically alterable nonvolatile memory device (1-4). Its write-in, erasure, and retention behavior are indebted to the charging and discharging of trap states at silicon oxide-silicon nitride interface and in silicon nitride bulk. Because memory characteristics greatly depend on silicon nitride deposition conditions (5), investigation of trap characteristics and understanding of trap origin are indispensable in realizing high-quality, reliable memory devices.

Various microscopic models have been proposed as the memory traps. Kirk (6) suggested variation of electron configurations around nitrogen atoms as the charge storage mechanism in a silicon nitride layer. Kapoor *et al.* (7) showed association of the trapped charges' density with oxygen impurity concentration. More recent studies reported that excess silicon atoms (8) or hydrogen bondings (Si-H and N-H) (9) are responsible for memory behavior. Other reports suggested that the memory traps originate from silicon dangling bonds (10, 11) whose charged states are changed by electron trapping and detrapping (11).

However, we have to mention that the model should clearly illustrate the following fundamental characteristics of the memory traps: (i) they are both negatively and positively ionized due to capture or emission of carriers, because the flatband voltage (V_{FB}) in a MNOS device is changed for both positive and negative values; (ii) they can be judged to lie deep in the forbidden gap of silicon nitride (12, 13). From these points of view, the idea of silicon dangling bonds being considered as the memory traps seems to be well supported by Robertson and Powell (14), who have theoretically showed that silicon dangling bonds create energy levels almost in the middle of the forbidden gap of silicon nitride. However, experimental investigation of the dangling bonds and of the correlation between the dangling bonds' density and the memory behavior have not been fully carried out.

In this paper, we will present observation of existence of silicon dangling bonds in chemically vapor-deposited (CVD) silicon nitride from electron-spin resonance (ESR) and infrared absorption measurements. The results are discussed in terms of the silicon nitride deposition conditions, and the memory behavior is well interpreted by taking into account the transition of charged states of silicon dangling bonds in the silicon nitride layer.

Silicon Nitride Deposition

Silicon nitride films were prepared by the pyrolysis of SiH_4 and NH_3 with Ar carrier gas at 700°C in a conventional normal-pressure CVD system. The flow ratio $R = \text{NH}_3/\text{SiH}_4$ was varied between 10 and 1000. Quartz and (100)-oriented p-type silicon substrates were used for ESR measurements and fabrication of MNOS diodes, respectively.

Electron-Spin Resonance

Typical spectrum.—ESR measurements were performed at room temperature with the use of an x-band spectrometer with a magnetic field modulation of 100 kHz frequency and 2.5 Gauss width. The microwave power was 100 μW , because the absorption intensity tends to saturate when increasing the power beyond this value.

Figure 1 shows an absorption derivative of typical ESR signal for our CVD silicon nitride. The ESR signal will be attributed to silicon or nitrogen dangling bonds. However, nitrogen dangling bonds should largely split the signal into three lines, because nitrogen atoms have nuclear spin of unity (15). A large number of N-H bonds with the order of 10^{20} cm^{-3} has been observed in CVD silicon nitride through the infrared absorption studies (10, 16), and thus nitrogen dangling bonds would be effectively passivated with hydrogen due to higher bonding energy of N-H than Si-H. Therefore, the results suggest that the ESR signal originates mainly from silicon dangling bonds whose silicon atoms have three-folded configuration and are symbolized as T_3^0 (17, 18). We have

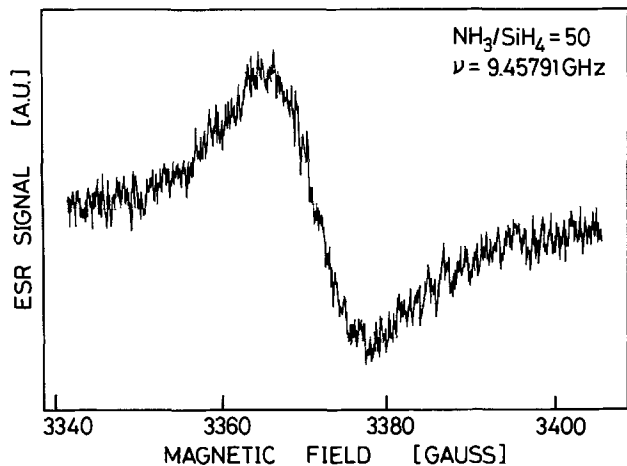


Fig. 1. Absorption derivative of typical ESR signal observed at room temperature.

confirmed that the dangling bonds exist in silicon nitride bulk, because the absorption intensity is larger for thicker films.

g-value and linewidth.—The *g* value and the peak-to-peak linewidth were determined by referring the spectrum from Mn^{2+} in MgO . The *g* value was found to be 2.002, which is lower than that of amorphous silicon, 2.0055 (19). The linewidth was 12.6 Gauss for the sample shown in Fig. 1, and this value is twice as large as that of amorphous silicon having similar spin density to the present silicon nitride (20). The lowering of *g* value and the spread of linewidth would be attributed to interaction between silicon and nitrogen atoms, as was theoretically calculated and experimentally observed in sputtering-deposited (21) or plasma-deposited (22) silicon nitride films.

Variation of spin density and linewidth.—The spin density N_s and the linewidth ΔH_{pp} are shown in Fig. 2 as a function of NH_3/SiH_4 ratio. The dangling bond decreases with the increase of the NH_3/SiH_4 ratio. One of the reasons for this result would be approach of the film composition from slightly silicon-rich to more complete stoichiometric value (23), although the composition variation was not so large that it could be identified by Auger-electron spectroscopy. However, we would like to mention here that

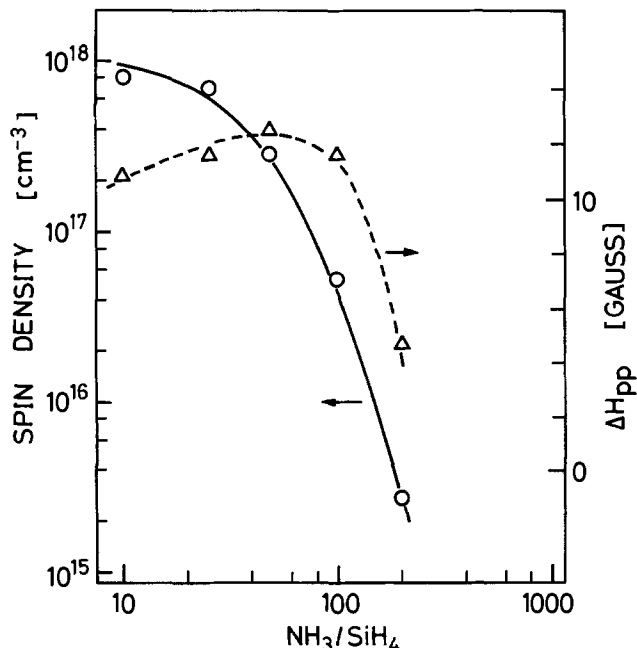


Fig. 2. Spin densities (solid line) and peak-to-peak linewidths (dashed line) obtained from ESR measurements against NH_3/SiH_4 ratio.

there is no inevitability of the dangling bonds' density being decreased with the approach to the stoichiometric composition, because the film is amorphous. If the silicon nitride is crystallized, lack of a nitrogen atom creates a vacancy surrounded by three silicon atoms, and thus three silicon dangling bonds remain. Amorphous films have various types of disorder, and the relationship between the defect density and the composition cannot be directly stated. We can only say that much incorporation of nitrogen would relax somewhat the atomic network to create more complete bonding.

It is interesting that these spin-density values are comparable to or smaller than those in the plasma-deposited silicon nitride (22). It is well known that spin density in CVD amorphous silicon is many orders of magnitude greater than that in a plasma-deposited film, because the latter contains many hydrogen atoms passivating silicon dangling bonds (24). However, in the CVD silicon nitride, the atomic network of silicon and nitrogen atoms itself would be much more complete than that in the plasma-deposited film, and thus, without much hydrogen passivation, the dangling bonds' density could be reduced to an order comparable to that in plasma-deposited, *i.e.*, hydrogen-passivated, silicon nitride.

Correlation between spin density and memory behavior.—Thin-oxide MNOS diodes, whose silicon nitride and oxide thicknesses were 950 and 20 Å, respectively, were fabricated. Figure 3 shows flatband-voltage hysteresis loops subjected to the pulse voltage of 100 ms width applied to the metal electrodes. The retention characteristics were evaluated by the decay rate of the flatband voltage $\partial V_{FB}/\partial \log t$ measured at 10^3 min after write-in, and they are shown in Fig. 4 as a function of initial flatband voltage measured just after write-in. The experiments were performed at room temperature. Larger memory

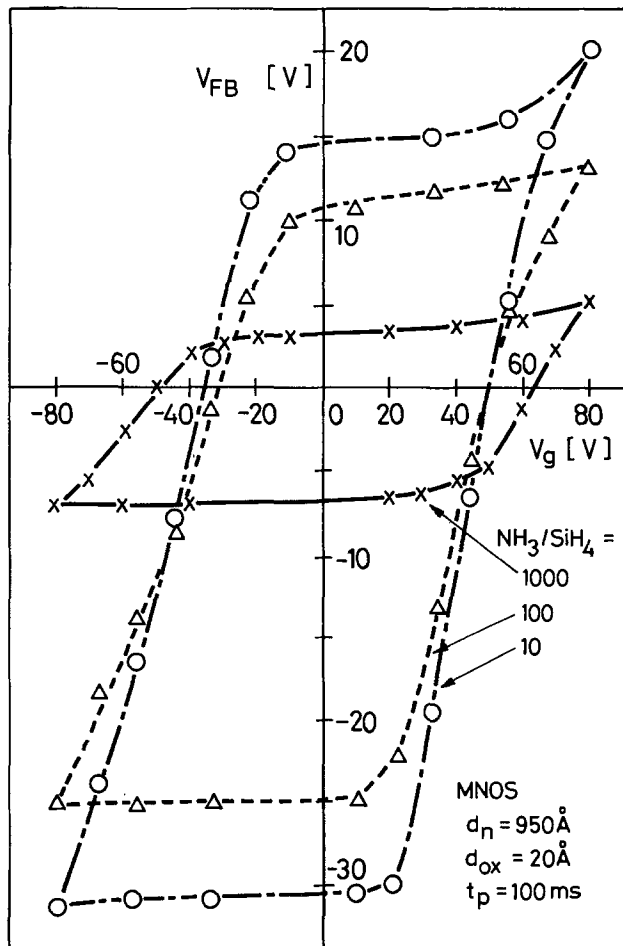


Fig. 3. Flatband voltage hysteresis loops of thin-oxide MNOS diodes under application of 100 ms pulse.

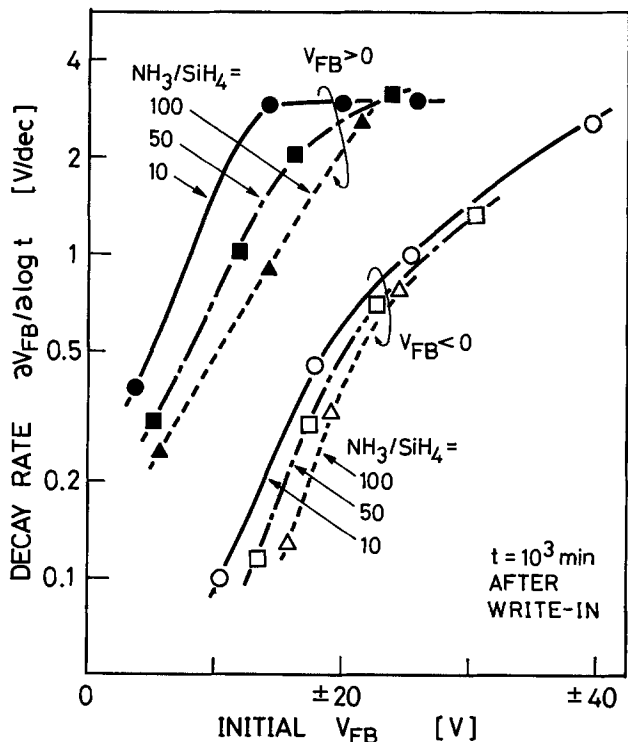


Fig. 4. Decay rates of the flatband voltage $\Delta V_{FB}/\Delta \log t$ measured at the time 10^3 min after write-in.

window and larger decay rate were observed, as the silicon nitride layer was deposited with smaller NH_3/SiH_4 .

Figure 5 represents the memory window, the decay rate, and the leakage current as a function of the spin density in the silicon nitride. The memory window is defined as the flatband-voltage difference between those achieved by +80 and -80V pulse application. For the decay rate, the values in Fig. 3 obtained when the initial flatband voltage was set at +10 and -20V were plotted. The leakage current was measured at the electric field of 5 MV/cm in the silicon nitride layer.

With increase of the spin density, the memory window increases, *i.e.*, more electrons or holes are trapped in the silicon nitride, suggesting that silicon dangling bonds are responsible for deep trap states which cause memory behavior. Further, increase of the leakage current with the spin density shows that the silicon dangling bonds can also be hopping sites. The larger decay rate for higher spin density is attributed to stronger Coulombic repulsion among trapped charges and/or larger conductivity of the film.

Discussions

Theoretical backing.—Robertson and Powell (14) theoretically calculated local density of states by the tight binding recursion method (25) for principal defects in silicon nitride, namely, silicon and nitrogen dangling bonds (neutral and charged centers), $\equiv\text{SiH}$ and $=\text{NH}$ units, and $\equiv\text{Si}-\text{Si}\equiv$ unit. Among these, silicon dangling bonds can produce a density-of-states peak near midgap. The long-term traps for memory behavior (memory traps) should be energetically localized away from both the conduction band and the valence band, because if their density of states is much overlapped with the tail states, trapped charges will be fairly easily released to the conduction band or to the valence band obtaining thermal energy and/or electrostatic energy. In fact, Robertson and Powell proposed that silicon dangling bonds can become the long-term (memory) traps of silicon nitride in MNOS devices. These theoretical results support quite well our considerations experimentally derived from the correlation between the ESR and memory characteristics.

Calculations by Robertson and Powell showed that neither $=\text{NH}$ nor $\equiv\text{SiH}$ centers produce localized states in the bandgap. From these results, it becomes apparent

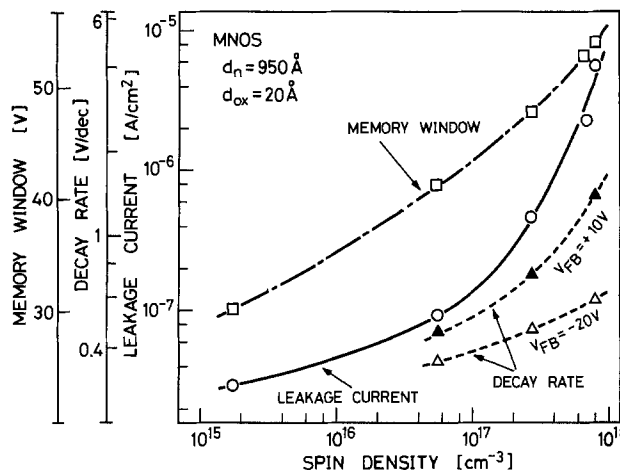
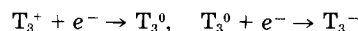


Fig. 5. Variations of V_{FB} windows, decay rates, and leakage currents against the spin densities in the silicon nitride films.

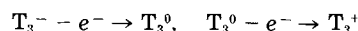
that hydrogen-related defects cannot be responsible for memory behavior. However, a distinct relationship between the hydrogen density and the trapped charge density has been reported (9). Therefore, further discussions on origin of memory traps will be continuously required.

Model for charging and discharging of traps.—We will consider carrier trapping and detrapping phenomena of silicon dangling bonds. In an amorphous silicon, silicon dangling bonds are negatively or positively ionized depending on the Fermi-level position. They are symbolized as T_3^- and T_3^+ , respectively (17, 18). The similar behavior can be expected in the CVD silicon nitride. In other words, silicon dangling bonds have either T_3^+ , T_3^0 , or T_3^- states, and thus the flatband voltage is shifted according to the charged states of the memory traps.

When the memory traps capture electrons, their charged states change as



and when they emit electrons



Here, note that if the trap states capture electrons from or emit electrons to the valence band, they are equivalent in that they emit or capture holes, respectively. The transition is shown schematically in Fig. 6.

More precisely, we can consider by taking into account thermal equilibrium states the following two possibilities.

(i) See Fig. 7(a). At thermal equilibrium, silicon dangling bonds have a T_3^0 state. When positive voltage is first applied to the metal electrode of an MNOS structure, they capture electrons and transit as $T_3^0 \rightarrow T_3^-$. After the transition, when negative voltage is applied, the

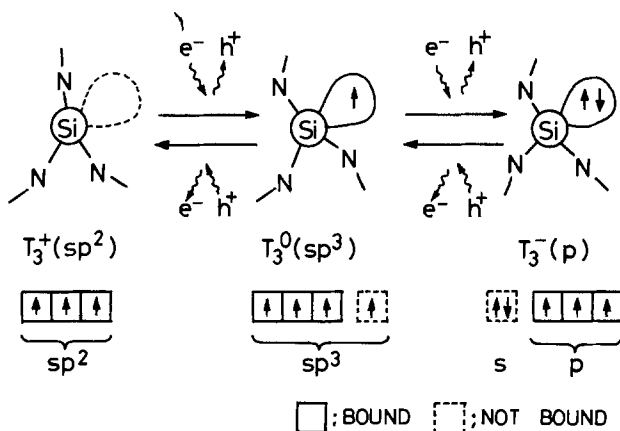


Fig. 6. A model for transition of the dangling bonds among three charged states: positive, neutral, and negative, symbolized as T_3^+ , T_3^0 , and T_3^- , respectively.

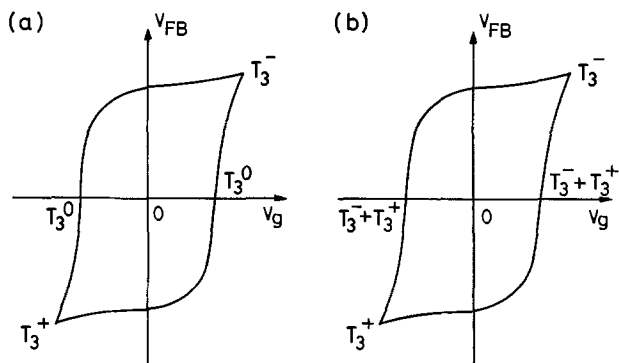
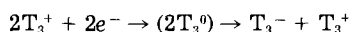


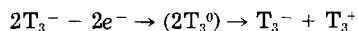
Fig. 7. Transition of charged states of dangling bonds is shown besides the V_{FB} hysteresis. Two possibilities, (a) and (b), can be considered.

dangling bonds emit one of the electrons occupying the orbital and transit as $T_3^- \rightarrow T_3^0$. If the negative voltage of higher intensity is further applied, they emit another one of the electrons remaining there, and transit as $T_3^0 \rightarrow T_3^+$. When the voltage polarity is reversed, the dangling bonds capture electrons to become T_3^0 , then capture another electron to become T_3^- .

(ii) See Fig. 7(b). This model is based on negative correlation energy (U) concepts (26). Adler (27) and Elliot (28) proposed the negative U for $2T_3^0 \rightarrow T_3^- + T_3^+$. If this model can be also applied to the dangling bonds in silicon nitride, they will have T_3^- and T_3^+ states in the film rather than T_3^0 at thermal equilibrium condition. When positive voltage is applied to the metal electrode of an MNOS structure, the dangling bonds having T_3^+ state capture electrons to its empty orbital to become T_3^0 , then two T_3^0 's exchange their electrons to make one T_3^- and one T_3^+ . The resultant transition may be written as



After reversing voltage polarity, T_3^- emit electrons to become T_3^0 , and two T_3^0 's make one T_3^- and T_3^+ , i.e.



The total amount of charges in silicon nitride or the flatband voltage of an MNOS structure is determined by the ratio of the T_3^- to the T_3^+ states' densities.

Trap density.—Various authors have investigated the trap density in CVD silicon nitride. Here, we will discuss one correlation between the trap density and the spin density.

Ross and Wallmark (29) investigated charge transfer in an MNOS structure under direct tunneling mode and derived a memory trap density of $6 \times 10^{19} \text{ cm}^{-3}$. We have studied the dependence of the memory trap density determined by a technique similar to theirs (10). The results are shown in Fig. 8 as a function of the spin density. Arnett and Yun (30) measured the charge propagation in a silicon nitride layer in a MNOS structure and reported the memory trap density to be $6 \times 10^{18} \text{ cm}^{-3}$. Krause (31) investigated the transient current due to filling-up of the traps, and Kapoor *et al.* (7-9, 32) studied the amount of charges ionized by ultraviolet light illumination. Their results on the memory trap density were $4.4 \times 10^{17} \sim 1.5 \times 10^{19} \text{ cm}^{-3}$ and $3 \times 10^{17} \sim 2 \times 10^{18} \text{ cm}^{-3}$, respectively.

We recognize that the reported memory trap density values differ so much by authors. These differences would not completely arise from the difference of the deposition conditions, but from the problems involved in the measurement techniques. For example, when we deposited the sample with $\text{NH}_3/\text{SiH}_4 = 100$, the trap density shown in Fig. 8 was $3.5 \times 10^{19} \text{ cm}^{-3}$, whereas if we measured it by the photoionization technique (33), it was found to be $5 \times 10^{17} \sim 6 \times 10^{18} \text{ cm}^{-3}$, depending on the layer thickness. One of the reasons for this dependence on the measurement techniques would be lack of knowledge of spatial distribution of the memory traps and of detailed charge-transport phenomena.

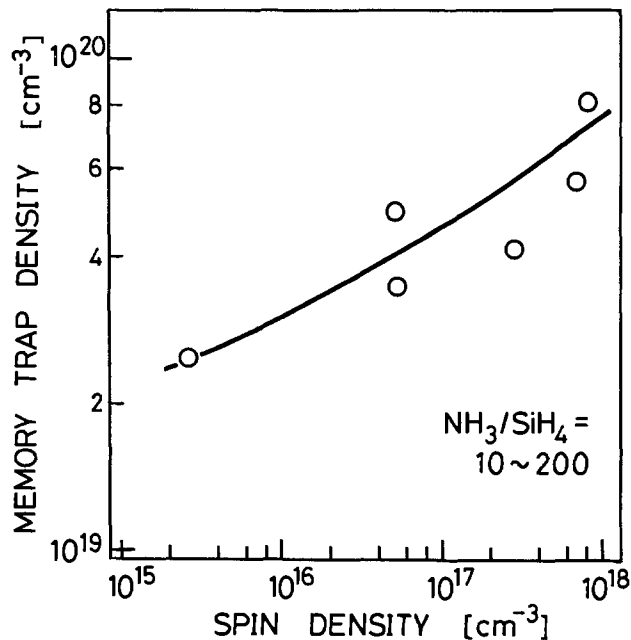


Fig. 8. Memory trap density, determined by the procedure proposed by Ross and Wallmark (29), as a function of the spin density.

Because many silicon nitride layers for MNOS memory devices have been conventionally deposited with $\text{NH}_3/\text{SiH}_4 = 30 \sim 1000$ (11, 34 ~ 36), we can see that the reported memory trap density values are somewhat larger than the spin density. In addition, we cannot see in Fig. 8 the linear relationship between the memory trap density and the spin density.

However, we would like to emphasize here that these differences do not deny our conclusion that the silicon dangling bonds become the memory traps, because there seem to be no inevitability of the memory trap density's coinciding with the spin density, due to following reasons.

(i) The memory traps would not be uniformly distributed in the silicon nitride (31, 37). Those which exist close to the silicon oxide-silicon nitride interface are mainly responsible for the memory behavior. It might be possible that the dangling bonds density is higher around here than in the bulk, due to oxygen incorporation (7) and/or mechanical stress arising from difference of thermal expansion coefficients between silicon oxide and silicon nitride. The ESR has been measured on the sample whose thickness is more than $1 \mu\text{m}$, because the signal intensity was under detectable limit when the sample was thinner. Therefore, the averaged spin density might become much smaller than that close to the interface.

(ii) Such T_3^- and T_3^+ states have no spin, and only the dangling bonds having T_3^0 state can be identified by ESR. If the memory traps are the negative U defects, i.e., most of them have T_3^- or T_3^+ states, the spin density becomes much lower than the memory trap density.

Photoinduced ESR, or dependence of the spin density on the V_{FB} or on the nitride thickness, would give further information on the origin, distribution, and properties of the memory traps.

Conclusions

In this paper, we have described the origin of memory traps in CVD silicon nitride films. Electron-spin resonance revealed the existence of silicon dangling bonds in the film. Correlation between the spin density and the MNOS memory behavior was studied and discussed, and the following results have been obtained.

(i) Silicon dangling bonds can be an origin of trap states in CVD silicon nitride which are responsible for not only hopping conduction, but also memory behavior in MNOS devices. (ii) Transition of the dangling bonds among positive, neutral, and negative states causes nonvolatile memory behavior in MNOS devices. (iii) The trap density

might be higher near the silicon oxide-silicon nitride interface region and/or the memory traps might be the negative U defects.

More precise ESR measurements would disclose more detailed characteristics of the memory traps in the silicon nitride films.

Acknowledgments

The authors would like to thank Dr. Takashi Kawamura of the Division of Molecular Engineering, Kyoto University, for his valuable assistance in the ESR measurements. This work was supported in part by a Grant in Aid for Special Project Research on Nanometer Structure Electronics from the Ministry of Education, Science and Culture of Japan.

Manuscript submitted Aug. 15, 1984.

Kyoto University assisted in meeting the publication costs of this article.

REFERENCES

1. P. C. Y. Chen, *IEEE Trans. Electron Devices*, **ed-24**, 584 (1977).
2. S. Koike and G. Kambara, *IEEE J. Solid State Circuits*, **sc-11**, 303 (1976).
3. J. J. Chang, *Proc. IEEE*, **64**, 1039 (1976).
4. F. A. Sewell, Jr., *IEEE Trans. Electron Devices*, **ed-20**, 563 (1973).
5. H. Nakayama and T. Enomoto, *Jpn. J. Appl. Phys.*, **18**, 1773 (1979).
6. C. T. Kirk, Jr., *J. Appl. Phys.*, **50**, 4190 (1979).
7. V. J. Kapoor, R. S. Bailey, and S. R. Smith, *J. Vac. Sci. Technol.*, **18**, 305 (1981).
8. R. S. Bailey and V. J. Kapoor, *ibid.*, **20**, 484 (1982).
9. V. J. Kapoor, R. S. Bailey, and H. J. Stein, *ibid.*, **1**, 600 (1983).
10. S. Fujita, H. Toyoshima, M. Nishihara, and A. Sasaki, *J. Electron. Mater.*, **11**, 795 (1982).
11. K. L. Ngai and Y. Hsia, *Appl. Phys. Lett.*, **41**, 159 (1982).
12. S. Fujita, M. Nishihara, W. L. Hoi, and A. Sasaki, *Jpn. J. Appl. Phys.*, **20**, 917 (1981).
13. V. J. Kapoor and S. B. Bibyk, *Thin Solid Films*, **78**, 193 (1981).
14. J. Robertson and M. J. Powell, *Appl. Phys. Lett.*, **44**, 415 (1984).
15. C. L. Ultee, *Phys. Chem.*, **64**, 1873 (1960).
16. H. J. Stein and H. A. R. Wegener, *This Journal*, **124**, 908 (1977).
17. D. Adler, *Phys. Rev. Lett.*, **41**, 1755 (1978).
18. M. Kastner, D. Adler, and H. Fritzsche, *ibid.*, **37**, 1504 (1976).
19. M. H. Brodsky and R. S. Title, *ibid.*, **23**, 581 (1969).
20. R. S. Title, M. H. Brodsky, and J. J. Cuomo, in "Amorphous and Liquid Semiconductors," W. E. Spear, Editor, p. 424, CIGL, University of Edinburgh (1977).
21. T. Shimizu, S. Oozora, A. Morimoto, K. Kumeda, and N. Ishii, *Solar Energy Mater.*, **8**, 311 (1982).
22. S. Yokoyama, M. Hirose, and Y. Osaka, *Jpn. J. Appl. Phys.*, **20**, L35 (1981).
23. T. Makino, *This Journal*, **130**, 450 (1983).
24. N. F. Mott and E. A. Davis, "Electronic Processes in Non-Crystalline Materials," p. 315, Clarendon Press (1979).
25. J. Robertson, *J. Appl. Phys.*, **54**, 4490 (1983).
26. P. W. Anderson, *Phys. Rev. Lett.*, **34**, 953 (1975).
27. D. Adler, *ibid.*, **41**, 1755 (1978).
28. S. R. Elliott, *Philos. Mag. B*, **38**, 325 (1978).
29. E. C. Ross and J. T. Wallmark, *RCA Rev.*, **30**, 366 (1969).
30. P. C. Arnett and B. H. Yun, *Appl. Phys. Lett.*, **26**, 94 (1975).
31. H. Krause, *Phys. Status Solidi A*, **36**, 705 (1976).
32. V. J. Kapoor and R. A. Turi, *J. Appl. Phys.*, **52**, 311 (1981).
33. V. J. Kapoor, F. J. Feigl, and S. R. Butler, *ibid.*, **48**, 739 (1977).
34. Y. Misawa and H. Yagi, *Jpn. J. Appl. Phys.*, **15**, 1045 (1976).
35. J. A. Topich and E. T. Yun, *This Journal*, **123**, 535 (1976).
36. R. Hezel and E. W. Hearn, *ibid.*, **125**, 1045 (1978).
37. J. S. Johannesssen, C. R. Helms, W. Spicer, and Y. E. Strausser, *IEEE Trans. Electron Devices*, **ed-24**, 547 (1977).

Difficulties with the Lag-Time Measurement of Oxygen Diffusion in Thermally-Grown SiO₂

Chien-Jih Han* and C. R. Helms**

Stanford Electronics Laboratory, Stanford University, Stanford, California 94305

ABSTRACT

The diffusion coefficient of oxygen in SiO₂ during thermal oxidation was recently measured by Irene using a "lag-time" method and found to be $D = 2.3 \times 10^{-13}$ cm²/s at 1000°C, much smaller than values obtained by Norton for oxygen permeation through fused silica. We have found a subtle difficulty with the "lag time" formalism which appears to explain this discrepancy. In addition, our reanalysis of Irene's results shows a "memory effect" for the parabolic rate constant for sequential oxidations first observed by Hamasaki for the linear rate constant.

Many experiments have been performed in the past to determine the diffusion coefficient for oxygen molecules through SiO₂. Using measurements of O₂ permeation through vitreous SiO₂, Norton (1) found diffusion coefficients of 4.2×10^{-9} - 1.2×10^{-8} cm²/s over a temperature range of 950°-1078°C. In contrast to these results, numerous investigators, using exchange methods, found diffusion coefficients $\sim 10^5$ times smaller than Norton's results (2-4). This discrepancy is related to the assumed diffusion mechanism for O₂ diffusion through SiO₂. It is clear from Ref. (5-8) that the majority flux of oxygen through SiO₂ during the oxidation of SiO₂ in dry O₂ is due to "interstitial" diffusion, with little exchange with the previously grown SiO₂. The exchange experiments mea-

sure only that component of the diffusing oxygen that has exchanged with the SiO₂. Additional evidence for the correct relationship between Norton's results and Si oxidation in dry O₂ comes from the good agreement between Norton's value for the product of the diffusion coefficient and the oxygen solubility compared to the parabolic rate of Si oxidation (9).

In order to independently measure the diffusion rate for oxygen in SiO₂ layers responsible for the oxidation process, Irene (10) applied a "lag time" method to determine the diffusivity of oxygen, with *in situ* ellipsometry measurements of the oxide thicknesses during the oxidation of silicon. His measurements of the lag time for subsequent oxidation of 1 μm-thick SiO₂ layers on Si showed a measureable lag time only for the highest temperature investigated (1000°C over a 600°-1000°C range), exactly the opposite of what might be expected for a simple singly

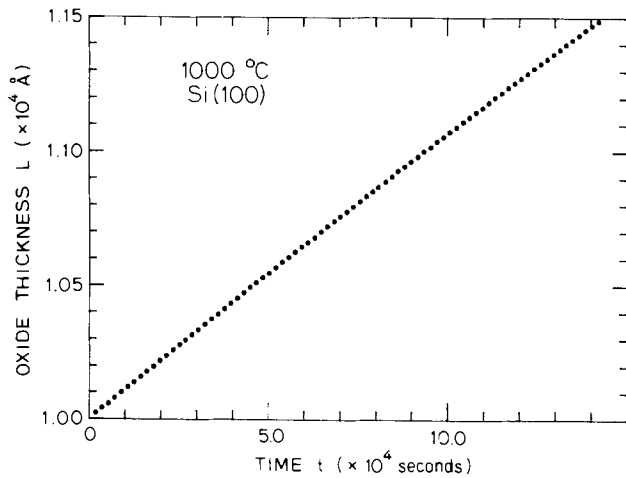
*Electrochemical Society Student Member.

**Electrochemical Society Active Member.

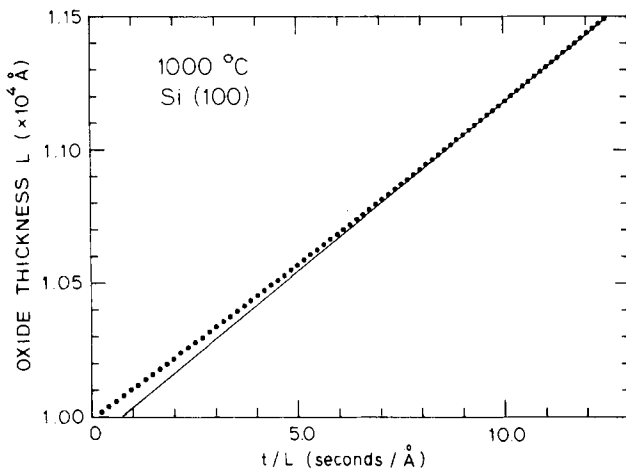
activated diffusion process through a medium with temperature independent properties. We previously suggested that these results may be due to the nature of the sequential oxidations performed, rather than to an actual lag time for a constant-temperature process (11), but more recently we have found a subtle difficulty with the "lag time" formalism which appears to explain Irene's findings. In addition, our reanalysis of Irene's results shows a "memory effect" for the parabolic rate constant first observed by Hamasaki for the linear-rate constant (12). This "memory effect," which appears in the linear and parabolic-rate constants has significant consequences for

the values of the activation energy and the pre-exponential factor associated with the constants.

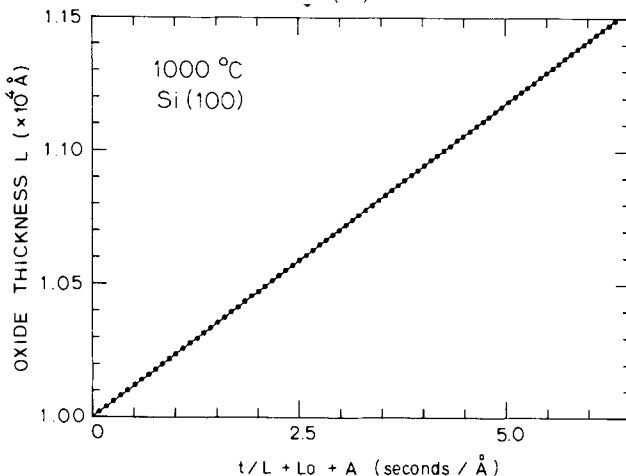
The lag-time method assumes that the oxygen diffusion through a silicon-dioxide layer obeys Fick's law for diffusion. For large thicknesses where the interface reaction rate is much faster than the diffusion rate, the growth rate of the silicon-dioxide corresponds to the permeation rate of the oxygen through silicon dioxide. As described by Irene, during a sequential oxidation process where the dissolved oxygen is removed from the initial oxide during an intervening annealing step, there is an inherent time



(a)

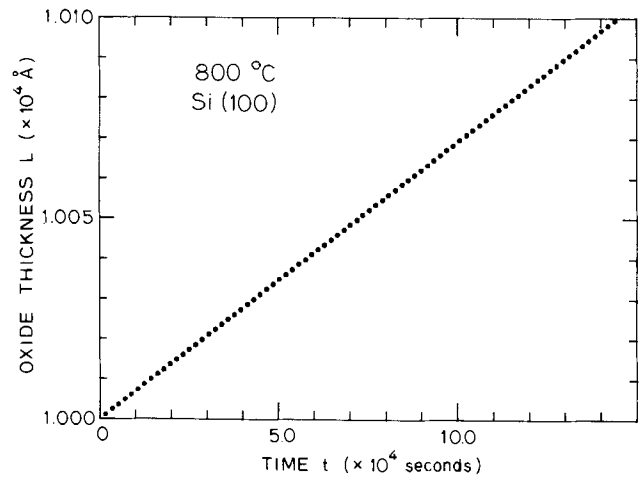


(b)

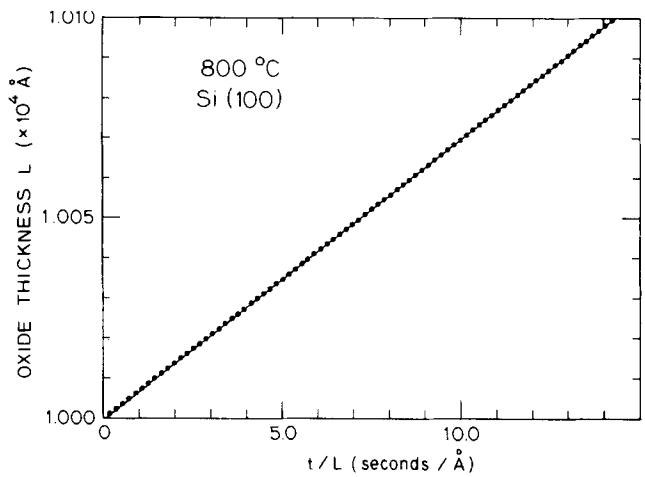


(c)

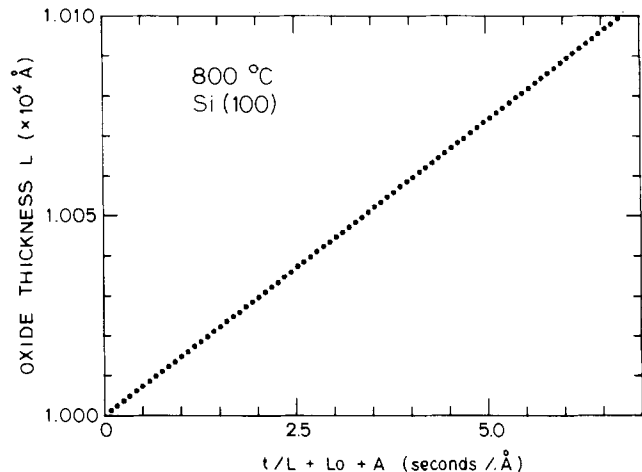
Fig. 1. Steady-state growth rate of a SiO_2 layer on a Si(100) surface at 1000°C after an initial 10,000 \AA thick oxide. (a) Thickness, L , vs. time, t . (b) L vs. t/L . (c) L vs. $t/(L + L_0 + A)$. (Note, the ordinate begins at $L = 10,000\text{\AA}$.)



(a)



(b)



(c)

Fig. 2. Steady-state growth rate of a SiO_2 layer on a Si(100) surface at 800°C after an initial 10,000 \AA thick oxide. (a) Thickness, L , vs. time, t . (b) L vs. t/L . (c) L vs. $t/(L + L_0 + A)$. (Note, the ordinate begins at $L = 10,000\text{\AA}$.)

delay between the time of the first exposure to the oxygen gas and the time the oxidation rate reaches a steady-state value caused by the finite diffusion rate of oxygen.

In the lag-time analysis, the oxide thickness is assumed to remain constant during the oxidation to make the diffusion equation solvable in an analytic form. Hence, the second oxide layer grown must be thin, compared to the initial oxide, for the analysis to be valid. A plot of the total thickness, L vs. time over thickness, t/L , is made, and a linear extrapolation of this curve from the steady-state growth region down to the initial oxide thickness L_0 , should intercept the t/L axis at a point corresponding to the lag time. This value is related to the diffusion coefficient by the expression $\tau = (L_0^2/6D)$. In Irene's analysis, this "constant-thickness" assumption led to significant errors in the interpretation of the experimental results.

To illustrate these errors, we generated two sets of data for oxides grown at 1000° and 800°C, assuming steady-state conditions which have zero lag times. Initial oxide thicknesses of 10,000Å were used to compare with Irene's conditions. In the steady-state limit, the growth may be characterized by the linear-parabolic rate law (13)

$$\frac{(L^2 - L_0^2)}{B} + \frac{(L - L_0)}{B/A} = t \quad [1]$$

where L is the oxide thickness during the second oxidation step, L_0 is the initial oxide thickness and B and B/A are the parabolic and linear rate constants. The fitting parameter in the Deal-Grove model that corresponds to the native oxide thickness is incorporated in the term L_0 . The values used for B and B/A were 235 Å²/s and 0.247 Å/s at 1000°C and 14.8 Å²/s and 0.0113 Å/s at 800°C (14). Plots of the thickness as a function of time are shown in Fig. 1(a) and 2(a) for the 1000°C case and the 800°C case, respectively. (Note, the ordinate begins at $L = 10,000$ Å.)

Figures 1(b) and 2(b) show plots of L vs. t/L for the data in Fig. 1(a) and 2(a), respectively. Rather than a straight line, Fig. 1(b) has a noticeable curvature caused by the error in the "constant-thickness" approximation. The lag time one finds from extrapolating the data in Fig. 1(b) is $\tau \approx 8000$ s, even though the "data" were generated with zero lag time. At 800°C, the L vs. t/L plot is linear and goes through the origin because the additional oxide grown on top of the 10,000Å oxide is very thin, which makes the "constant-thickness" approximation reasonably good. These results can be compared with those obtained by Irene and can explain the large "lag time" observed at 1000°C and the small "lag time" observed at 800°C. There is an alternative to plotting L vs. t/L which can eliminate the nonlinearity shown above. If we rearrange Eq. [1], we obtain

$$L - L_0 = \frac{B(t - \tau)}{L_0 + L + A} \quad [2]$$

where $\tau \approx (L_0^2/6D)$. Hence, a plot of L vs. $t/(L_0 + L + A)$ for the two sets of steady-state data should give straight lines with the intercept on the $L = L_0$ axis at τ . Figures 1(c) and 2(c) show these results. The spurious lag time from the L vs. t/L analysis at 1000°C disappears in this new plot.

Based on this type of plot, however, Irene's results still seem inconsistent with the steady-state growth model. Using the new analysis technique, a slight curvature is

still observed for his 1000°C data. It is unlikely that this rate increase was caused by a lag-time delay from the diffusion process because of the results of the isotopic tracer experiments (5-7). The solubility of oxygen molecules in thermally grown SiO₂ was below the detectability limit of these experiments ($<10^{20}$ cm⁻³). In order to attain the reported oxidation rate, the diffusion coefficient must be two orders of magnitude greater than Irene's reported value. This diffusion rate would be too fast for Irene's lag-time experiment to measure. A more likely explanation for the increase is a result of variations in the diffusion coefficient and the solubility of oxygen in SiO₂ caused by a structural change in the oxide during the anneal and the subsequent oxidation.

Another result from Irene's experiment is the permeation rate obtained at 1000° and 800°C. The oxidation rate from his experiment at 1000°C was approximately the same as the rate obtained from Lie *et al.* (14) or Irene's previous work (15). At 800°C, however, Irene found an oxidation rate which is more than four times greater than the calculated rate from Lie *et al.* (14). (A comparison to Irene's previous work does not exist at this temperature.) As we previously suggested (11), this discrepancy may be attributed to the same "memory effect" observed by Hamasaki (12). Hamasaki's finding, however, were for thinner oxides and therefore related primarily to the linear rate constant B/A . Our reanalysis of Irene's data for thicker oxides indicated that this same memory effect is present in the parabolic-rate constant as well. This "memory effect" in the parabolic-rate constant indicates that the transport properties of oxygen in SiO₂ depend on the growth temperature of the oxide.

Acknowledgments

The authors wish to thank E. A. Irene for his comments and discussions during the writing of this paper. This work was supported by the Defense Advance Research Project Agency Contract no. MDA903-79-C-0257.

Manuscript submitted June 21, 1984; revised manuscript received Sept. 21, 1984.

Stanford University assisted in meeting the publication costs of this article.

REFERENCES

1. F. J. Norton, *Nature (London)*, **171**, 701 (1961).
2. E. L. Williams, *J. Am. Ceram. Soc.*, **48**, 190 (1965).
3. E. W. Suecov, *ibid.*, **46**, 14 (1963).
4. K. Muehlenbachs and H. A. Schaeffer, *Can. Mineral.*, **15**, 179 (1977).
5. J. W. Rouse, C. R. Helms, and C. J. Han, in "Computer Aided Design of Integrated Circuit Fabrication Processes for VLSI Devices," Final Report, p. 261, Stanford University, Stanford, CA (1982).
6. E. Rosencher, A. Straboni, S. Rigo, and G. Amsel, *Appl. Phys. Lett.*, **34**, 254 (1979).
7. J. A. Costello and R. E. Tressler, *This Journal*, **131**, 1944 (1984).
8. A. G. Revesz and H. A. Schaeffer, *ibid.*, **129**, 357 (1982).
9. R. H. Doremus, *J. Phys. Chem.*, **80**, 1773 (1976).
10. E. A. Irene, *This Journal*, **129**, 413 (1982).
11. C. R. Helms, *ibid.*, **129**, 2883 (1982).
12. M. Hamasaki, *Solid-State Electron.*, **25**, 479 (1982).
13. B. E. Deal and A. S. Grove, *J. Appl. Phys.*, **36**, 3770 (1965).
14. L. N. Lie, R. R. Razouk, and B. E. Deal, *This Journal*, **129**, 2828 (1982).
15. E. A. Irene, *ibid.*, **125**, 1146 (1978).

Phosphorus Incorporation Effects in Silicon Dioxide Grown at Low Pressure and Temperature

Arthur J. Learn*

Anicon, Incorporated, San Jose, California 95134

ABSTRACT

The manner and effects of phosphorus incorporation in oxides grown from silane and oxygen at low pressure and low temperature were investigated. Phosphine incorporation is avoided through proper selection of the oxygen/hydride mole ratio. Typical reflow processing results in removal of phosphine from oxides grown under other than optimum conditions. Although the majority of the phosphorus appears in the form of phosphorus pentoxide in all cases, the trioxide also is present, except when the total phosphorus content is less than approximately 2 weight percent. The efficiency of phosphorus incorporation is reduced for increased growth temperature, flow rate, or pressure. This temperature effect, as well as a reduction in activation energy for doped-oxide growth, is in large part interpretable in terms of a temperature-insensitive phosphine/oxygen reaction. The oxide growth rate is increased and the stress level is reduced through phosphorus incorporation.

Phosphorus-doped silicon dioxide has a wide range of applications in integrated circuit manufacture (1). Among these are use as reflow glass layers, interlevel dielectrics in multilevel metallization systems, and passivation over metallization. Early films were provided by chemical vapor deposition in reactors operated at atmospheric pressure. More recently, low-pressure chemical vapor deposition of oxide, as well as of other materials, has come into common use. In addition to the lower pressure, other deposition parameters can differ significantly for the newer process. Accordingly, it would be anticipated that the details of phosphorus incorporation in the oxide may differ for the two processes. Recently refined analytical techniques (2) aid in studies of this phenomenon. Also, the nature of the reactant-gas flow can affect the phosphorus incorporation. The reactor (3) utilized in this study directs flow parallel to the wafer surface, rather than perpendicular to it, as in most conventional low-pressure systems. In particular, this can result in different reactant depletion effects for the two configurations.

The effects associated with phosphorus incorporation in oxides deposited in a vertical-flow reactor were investigated. The manner of phosphorus incorporation was determined as a function of mole ratio of oxygen to hydride, phosphine mole ratio, deposition temperature, total mass flow rate, pressure, and reflow conditions. Tracking of the growth rate with many of these deposition parameters aided in the data analysis. Finally, the effect of phosphorus incorporation on stress was established.

Experimental

The reactor configuration is described in detail elsewhere (3). Briefly, wafers reside in quartz boats, with their axes aligned parallel to elongated reaction-gas injectors. Line of sight between the injectors and exhaust slots on either side of the injectors passes through the centers of the wafer stacks. One injector is used for oxygen, and a second for the hydrides. The PH_3 mole ratio is adjusted by combining a PH_3/SiH_4 mixture with pure SiH_4 upstream of the injector. Here, as in subsequent discussion, the PH_3 mole ratio is defined as the ratio of PH_3 flow rate to the total hydride flow rate. The PH_3 mole ratio was varied up to 0.15. Deposition temperatures of 300°-500°C and total flow rates of up to 1200 $\text{cm}^3 \text{min}^{-1}$ were investigated. The typical system pressure was 100 mtorr.

Thickness measurements were made with a NanoSpec/AFT (Nanometrics, Incorporated, Sunnyvale, California) using a refractive index of 1.46. The refractive index was separately determined by ellipsometry. Stress was determined from wafer bow measurements. Curvature of a given wafer was measured before and subsequent to deposition, after removal of the deposit from the wafer back side.

* Electrochemical Society Active Member.

The majority of analyses for phosphorus content were performed by Balazs Laboratories, Mountain View, California, using wet-chemical methods (2). This approach distinguishes between phosphorus incorporated as P_2O_5 , P_2O_3 , or PH_3 . In other cases, electron beam x-ray microprobe analysis (EDX) was employed to determine total phosphorus content. As may be seen from Fig. 1, an almost 1:1 correlation of total phosphorus is noted for the two techniques.

Results and Discussion

Different boat designs were utilized in the course of this investigation which can alter the details of the chemical vapor deposition process (3). Consequently, total self-consistency of the data may be lacking from one series of experiments to another. Within a series, however, care was taken to insure the comparative validity of results.

Mole ratio effects.—It is known (2) that phosphorus can be incorporated in oxides deposited at low pressure in compound form as P_2O_5 , P_2O_3 , or PH_3 . Initial studies were devoted to elimination of PH_3 because of the concomitant safety issues. As is illustrated in Fig. 2, for a PH_3 mole ratio of 0.15 (corresponding to a doping level of about 10

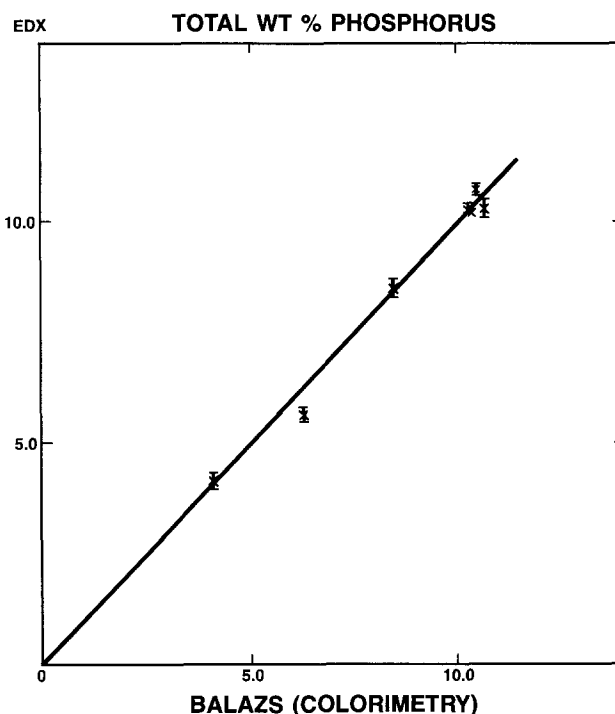


Fig. 1. Correlation of measurement techniques for total phosphorus content in phosphorus-doped oxide.

weight percent [w/o] phosphorus), detectable PH_3 can be present in the deposit. For O_2 /hydride mole ratios ≤ 1.5 , the PH_3 level decreases as this ratio increases and falls below the detectability limit of 0.05 w/o at an O_2 /hydride mole ratio of 1.5. When the O_2 /hydride mole ratio is increased to 2.0, however, PH_3 reappears. Consequently, an O_2 /hydride mole ratio of 1.5 was selected for all subsequent experimentation requiring such high phosphorus doping concentration. The P_2O_5 content passes through a minimum, and the P_2O_3 content through a maximum, for an O_2 /hydride mole ratio of 1.5. The sum of the phosphorus contributions from the two oxides, however, remains relatively constant at the 10.5 w/o level, independent of O_2 /hydride mole ratio. This result differs from that obtained in another study (4) of oxides deposited at low, though unspecified, pressures. In that case, the phosphorus content decreased with increased O_2 /hydride mole ratio over the range shown in Fig. 2.

The effect of reflow conditions on those films with the highest PH_3 content was also determined. As indicated in Table I, procedures in either an inert ambient or an oxidizing ambient were tested. Regardless of ambient, exposure to a temperature of 920°C is apparently sufficient to remove PH_3 . Another notable effect is the reduction of P_2O_5 content in the oxidizing ambient. Somewhat surprisingly, the trioxide is not further oxidized to appear as P_2O_3 , but rather is abstracted from the film.

For phosphorus doping levels less than 10 w/o, the O_2 /hydride mole ratio was scaled to match a ratio of 1:1 for undoped oxide. For example, at a PH_3 mole ratio of 0.09, an O_2 /hydride mole ratio of 1.3 was used. On this basis, results for a range of phosphorus concentrations down to 2 w/o are presented in Fig. 3. No PH_3 is detectable in any of these deposits. A monotonic increase in P_2O_5 and in total phosphorus content is observed with increasing mole ratio of PH_3 . A tendency toward saturation at the highest concentrations is indicated. The P_2O_3 content is maximum near midrange concentrations of 6-8 w/o for the data of Fig. 3. Presumably, further optimization of the O_2 /hydride mole ratio could reduce the P_2O_3 levels for such concentrations.

Growth rate, under the above conditions, as a function of total phosphorus content is presented in Fig. 4. As with

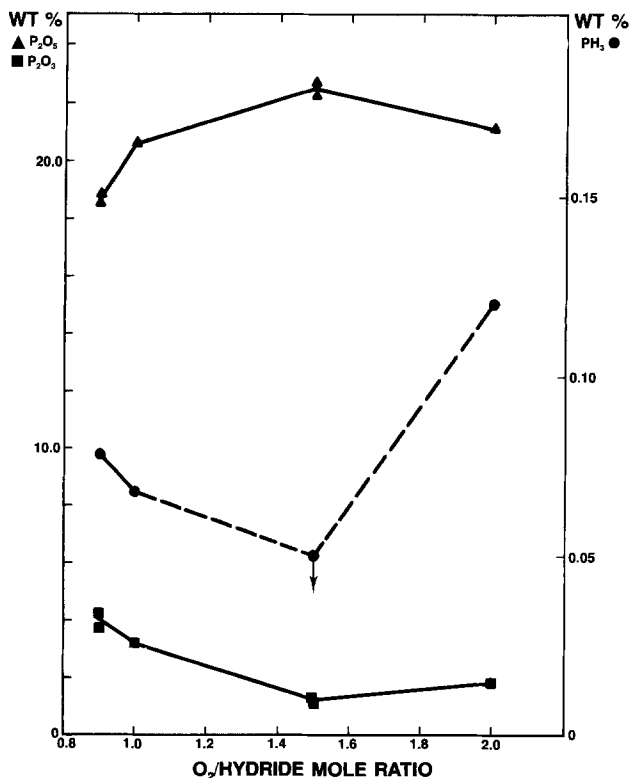


Fig. 2. Concentration of phosphorus bearing compounds as a function of O_2 /total hydride mole ratio.

Table I. Effect of reflow processing on concentration of phosphorus-bearing compounds

Reflow process	PH_3 (w/o)	P_2O_3 (w/o)	P_2O_5 (w/o)
None	0.12	21.2	1.8
920°C , 30 min N_2	BDL ^a	21.2	1.8
920°C , 10 min O_2 + 5 min steam + 10 min N_2	BDL ^a	20.8	0.3

^a Below detectable limit of 0.05 w/o.

undoped oxide (3), the growth rate is roughly proportional to wafer spacing. To a good approximation, growth rate also depends linearly on phosphorus content, with a slope of 0.86 nm min^{-1} per w/o. Similar results are obtained when the O_2 /hydride mole ratio is held constant. Such a dependence is different than previously observed (4-6) where a minimum in growth rate appears at a few weight percent phosphorus. The difference may be accounted for by a lower pressure used in the present work or by less depletion with the single-pass gas flow at each wafer.

The latter property provides quite uniform incorporation of phosphorus within a wafer and from wafer to wafer. Such uniformities are shown in Fig. 5 for different phosphorus doping levels. For within-wafer uniformity determination, four points 6 mm from the wafer edge were measured, as well as the wafer center. Wafer-to-wafer data are for centerpoint readings. All uniformities are within ± 0.2 w/o phosphorus. On a rather limited data base, the within-wafer uniformity does not exhibit a dependence on phosphorus content. Wafer-to-wafer uniformity, however, appears to degrade somewhat with increased phosphorus content.

Temperature effects.—Arrhenius plots of the logarithm of growth rate *vs.* the reciprocal of absolute deposition temperature are shown in Fig. 6 for undoped and phosphorus-doped oxide. In the lower temperature regime ($T < 400^\circ\text{C}$), an activation energy E_a can be defined for the different films. The values of E_a are presented in Fig. 6 and are seen to decrease with increasing phosphine mole ratio, *i.e.*, increasing phosphorus concentration. If it is assumed that the PH_3/O_2 reaction is relatively temperature independent, then a reduced effective E_a would be expected for the phosphorus-doped films, as observed. At the higher temperatures shown, growth rate saturates for undoped and doped films. Presumably, this occurs as a consequence of nearly complete utilization of the SiH_4 under the flow conditions for the experiments. The incremental increases in saturation growth rate would thus arise from the PH_3/O_2 reaction. The percentage of SiH_4

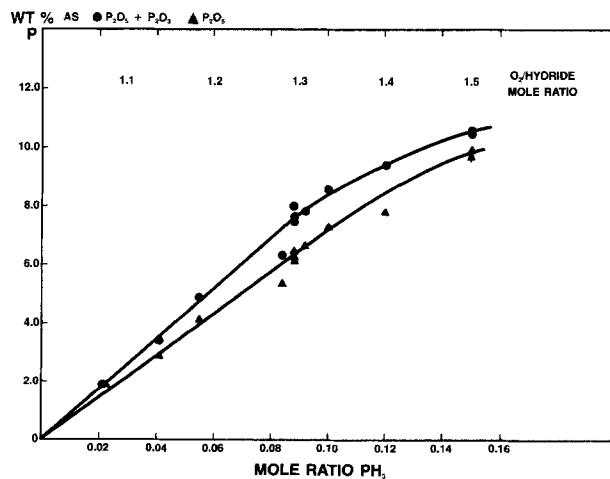


Fig. 3. Phosphorus concentration incorporated as P_2O_5 or as P_2O_5 plus P_2O_3 as a function of PH_3 mole ratio and the oxygen/total hydride mole ratios indicated.

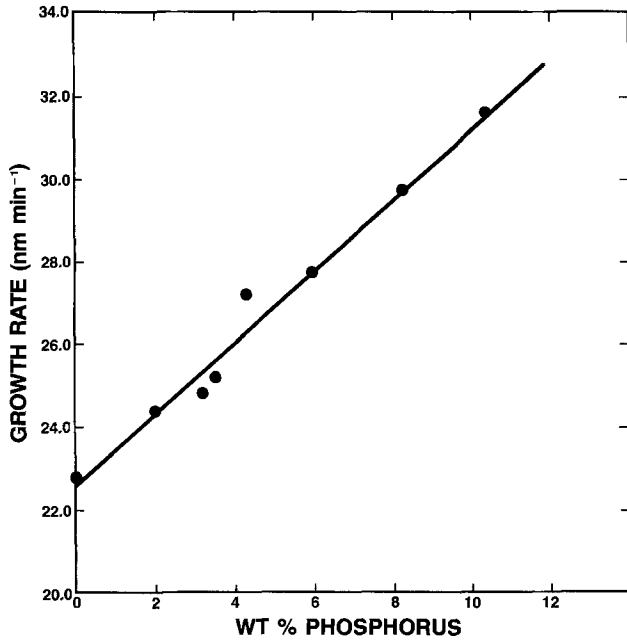


Fig. 4. Growth rate as a function of total phosphorus content

consumed in the deposition chamber can, of course, be calculated if the surface area and associated growth rate are known. Because, as mentioned above, the latter depends on spacing of the deposition surfaces and there is some roughness on chamber surfaces, such a calculation is not quantitative. With these uncertainties in mind, about 50% consumption of the SiH₄ is indicated for the saturation condition.

The efficiency of phosphorus incorporation in the films increased with decreased growth temperature, as shown in Fig. 7. Saturation of the phosphorus content occurs at the highest temperature of 500°C. The trend is similar for the two doping levels and is primarily accounted for by increased P₂O₅ content at reduced temperatures. A similar trend was observed for doped oxides grown at atmospheric pressure (7, 8). Tests performed for PH₃ at the temperature extremes proved negative. The increase in phosphorus content at lower temperatures is again qualitatively explainable in terms of a temperature-insensitive PH₃/O₂ reaction. The ratio of growth rate for P₂O₅ and SiO₂ would then increase with decreased temperature.

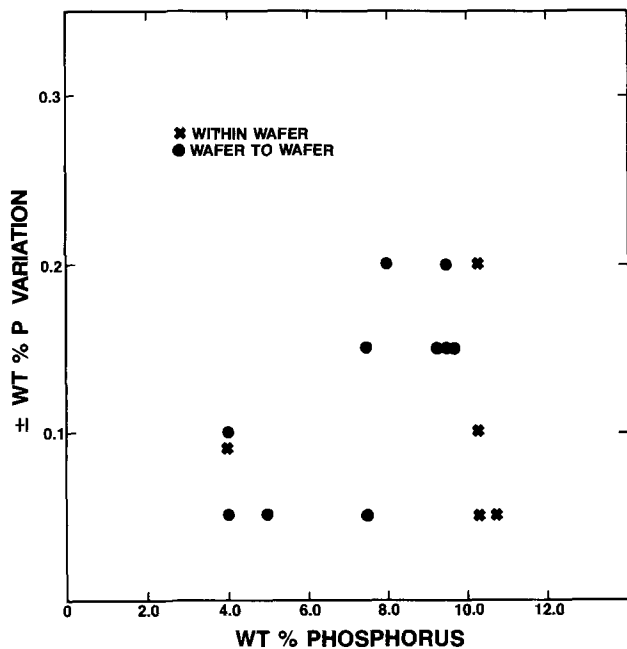


Fig. 5. Phosphorus-incorporation uniformity variation with total phosphorus concentration.

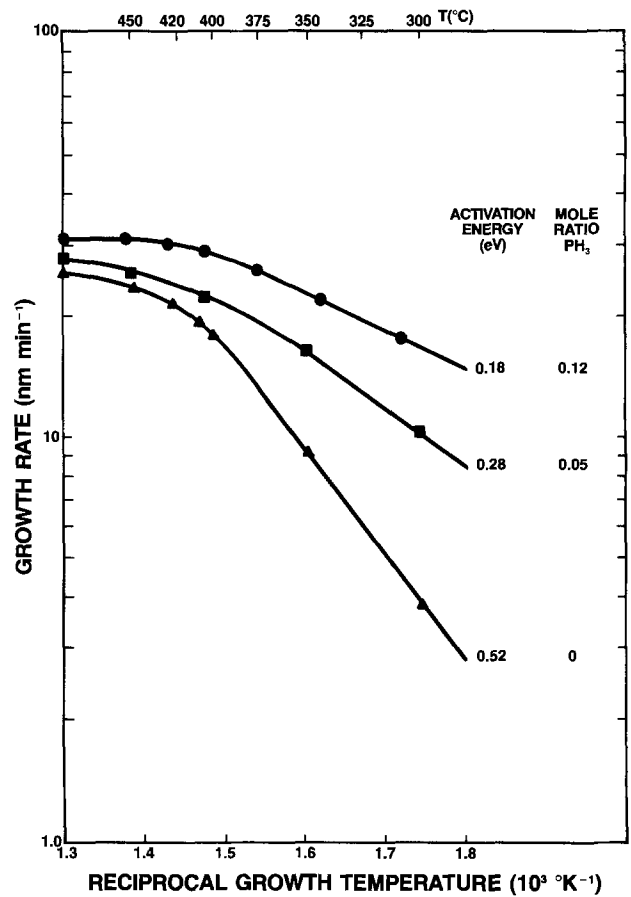


Fig. 6. Arrhenius plots of growth rate for undoped and phosphorus-doped oxide.

Additional information concerning phosphorus incorporation can be extracted from the saturation growth rates discussed above. The assumptions made are that the SiH₄/O₂ and PH₃/O₂ reactions contribute independently to growth rate, that the densities are equal for SiO₂ and P₂O₅, and that all phosphorus is incorporated as P₂O₅. The growth-rate ratio for P₂O₅ and P₂O₅ + SiO₂ is then proportional to the weight-content ratio of P₂O₅. In addition, the latter is 2.29 times the weight ratio of phosphorus in the oxide. From Fig. 6, the saturation growth rates for undoped, moderately doped, and heavily doped films are approximately 25.5, 27.5, and 31.0 nm min⁻¹, respectively. The corresponding phosphorus concentrations calculated are 3.2 and 7.7 w/o for the films of medium and heavy doping. These values are in reasonable agreement with

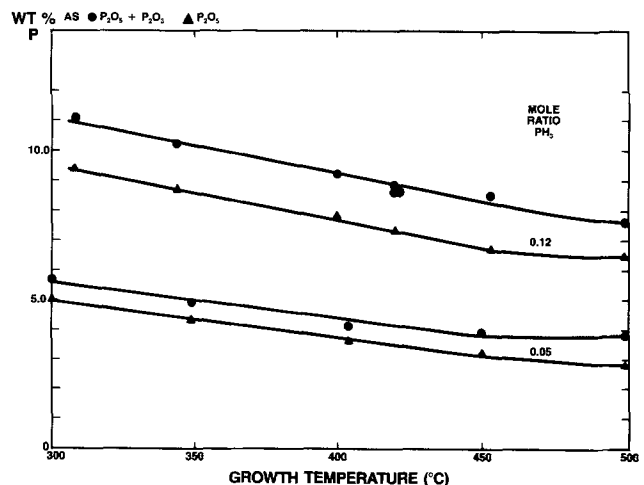


Fig. 7. Phosphorus concentration incorporated as P₂O₅ or as P₂O₅ plus P₂O₃ as a function of growth temperature.

the measured values of 3.8 and 7.6 shown in Fig. 7 at the highest growth temperature. The assumption of independent contributions from the PH_3/O_2 and SiH_4/O_2 reactions is apparently invalid at lower temperatures, where utilization of the SiH_4 is less complete. The differential growth rate above then becomes much larger than the weight content ratio of P_2O_5 .

It is noteworthy that the near-saturation doping levels are approximately those expected for stoichiometry of the combined $\text{SiH}_4/\text{PH}_3/\text{O}_2$ reaction. The values calculated in that case are 2.6 and 6.8 w/o. The calculated values are roughly independent of whether the reaction product is P_2O_5 or P_2O_3 because the stoichiometry is identical for the two reactions and the mole percent ratio is approximately equal to the w/o phosphorus for each of the oxides. A similar concurrence of calculated and measured phosphorus concentration for comparable growth temperature was observed (7) for oxides grown at atmospheric pressure. Phosphorus concentrations exceeding the stoichiometric values at lower temperatures, as in Fig. 7, were also noted previously (4) for low pressure growth at 360°C . This effect was interpreted (4) as kinetic inhibition of the silane oxidation relative to the phosphine oxidation.

Flow rate and pressure effects.—The growth rate exhibits a linear dependence on total mass flow in the $300\text{--}1200\text{ cm}^3\text{ min}^{-1}$ range for a phosphine mole ratio of 0.12 and an $\text{O}_2/\text{hydride}$ mole ratio of 1.4. This dependency is the same as for undoped oxide and is consistent with the model established for such growth (3). Phosphorus incorporation as a function of total flow is illustrated in Fig. 8. The P_2O_5 content decreases with increased flow, whereas the P_2O_3 content increases. The latter increase is insufficient to balance the P_2O_5 decrease, so the total w/o phosphorus decreases with increased flow. The decrease in total phosphorus and P_2O_5 concentrations may be attributable to the PH_3 becoming less competitive for adsorption sites as the SiH_4 concentration increases with increased flow. Such a reduced reaction rate could also account for the greater prevalence of the suboxide, P_2O_3 .

Increasing the total system pressure from 100 to 300 mtorr yielded an increase in growth rate from 28 to 32 nm

min^{-1} . This result is for films grown with the same mole ratios listed in the preceding paragraph. The weight percent phosphorus incorporated as P_2O_5 and P_2O_3 is reduced from 7.8 to 6.0 and from 1.4 to 1.2, respectively, at the higher pressure. Similar to the effect of high flow rate, the longer residence time at higher pressure may favor SiH_4 over PH_3 adsorption.

Film stress.—The room-temperature stress in deposits is shown as a function of phosphorus content in Fig. 9. The stress becomes less compressive as phosphorus content increases to about 8.5 w/o. For larger concentrations, the stress is tensile. The compressive stress for undoped films is reduced for lower deposition temperature. Such a decrease is largely attributable to differential thermal expansion of oxide and silicon. The stress arising from this source (9) is proportional to $(\alpha_o - \alpha_{\text{si}})(T - T_r)$, where α_o and α_{si} are the thermal expansion coefficients for silicon dioxide and silicon, T is the growth temperature, and T_r is room temperature. The values of α_o and α_{si} are 0.5 and 2.5×10^{-6} per degree centigrade, respectively. Thus the stress is expected to be negative (compressive), as observed for undoped films. The stress ratio calculated from the above expression as T is reduced from 400° to 300°C is 0.73. The ratio of 0.60 observed is not substantially different. The indication, therefore, is that the majority of the stress in undoped films is a consequence of differential thermal expansion and there is little intrinsic stress. The role of phosphorus is not certain, but may be to increase α_o . For phosphorus concentration greater than 8.5 w/o, the effect is sufficient to reverse the sign of the stress and place the film in tension at room temperature.

Conclusions

Phosphine can be eliminated from phosphorus-doped oxides grown at low pressures through optimized adjustment of the growth conditions. The same goal is achieved with conventional reflow processes. The ratio of P_2O_3 to P_2O_5 incorporated in the silicon dioxide can also be minimized through proper choice of growth parameters. The efficiency of incorporation of phosphorus under

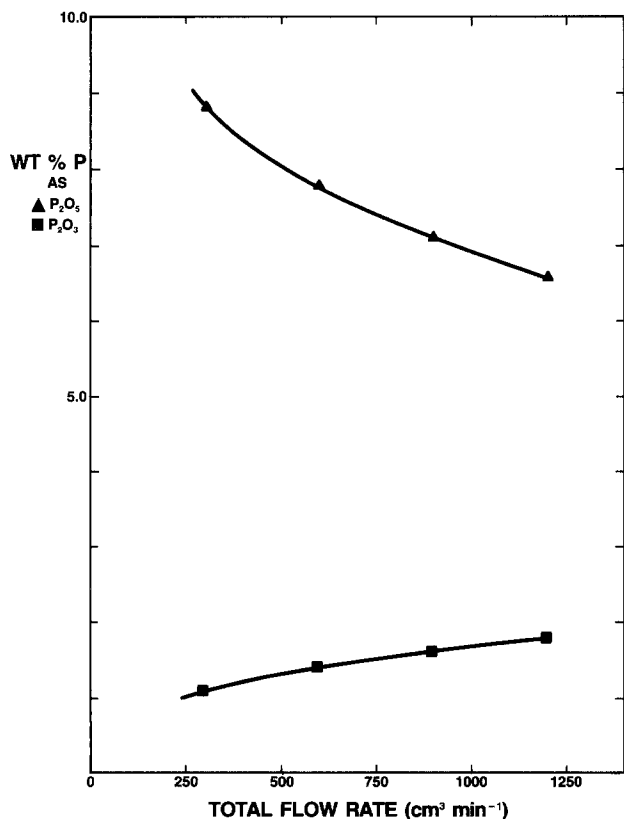


Fig. 8. Phosphorus concentration incorporated as P_2O_5 or P_2O_3 as a function of total flow rate.

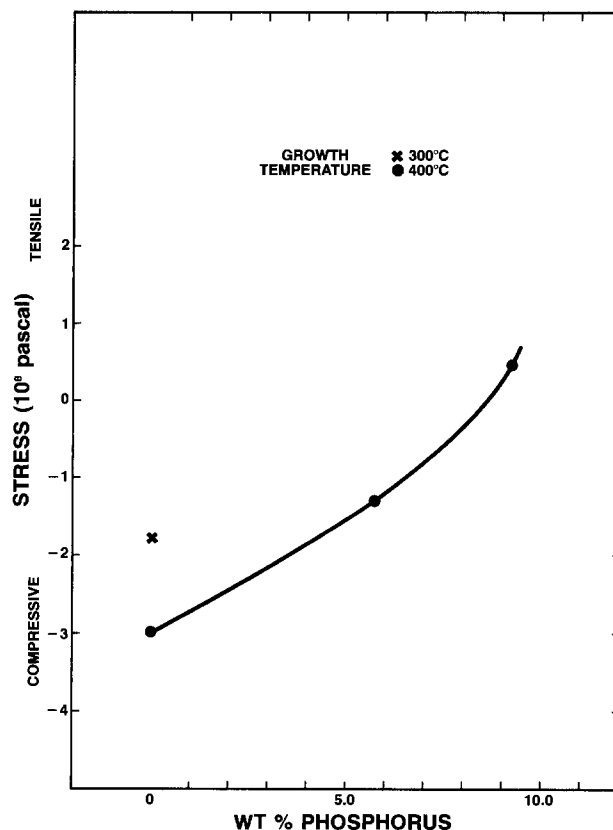


Fig. 9. Room-temperature film stress as a function of total phosphorus concentration and growth temperature.

standard conditions is no worse than 80% up to a PH_3 mole ratio of 0.15. The efficiency is reduced by increasing growth temperature, flow rate, or pressure. The growth rate exhibits a decreased activation energy with increased phosphorus content at low temperature, and it saturates at high temperatures. The temperature effects can be largely explained by a temperature-insensitive PH_3/O_2 reaction. The flow rate and pressure effects may be related to relative PH_3 - SiH_4 adsorption properties. The film stress becomes less compressive through phosphorus additions and, at least for undoped oxide, arises primarily from differential thermal expansion. Finally, the ability to discern the above trends is in substantial measure due to the tight control of growth conditions in the vertical reactor used.

Acknowledgments

The author is grateful to Ron Jackson for performance of the depositions and for aid in data acquisition and analysis. Informative discussions with Nick Miller are also acknowledged. Bill Baerg of Intel Corporation was helpful in obtaining the reflow and stress data.

Manuscript submitted June 25, 1984; revised manuscript received Aug. 20, 1984.

Anicon, Incorporated, assisted in meeting the publication costs of this article.

REFERENCES

1. W. Kern and G. L. Schnable, *IEEE Trans. Electron Devices*, **ed-26**, 647 (1979).
2. J. Houskova, K.-K. N. Ho, and M. K. Balazs, in "Materials Characterization in Microelectronics and Processing," To be published by the American Chemical Society.
3. A. J. Learn, *This Journal*, **132**, 390 (1985).
4. P. J. Tobin and J. B. Price, Paper 204 presented at The Electrochemical Society Meeting, Montreal, Que., Canada, May 9-14, 1982.
5. M. Shibata, T. Yoshimi, and K. Sugawara, *This Journal*, **122**, 157 (1975).
6. G. Wahl, in "Chemical Vapor Deposition," J. M. Blocher, Jr., H. E. Hintermann, and L. H. Hall, Editors, pp. 391-406, The Electrochemical Society Bound Proceedings Series, Princeton, NJ (1975).
7. A. S. Tenney and M. Ghezzeo, *This Journal*, **120**, 1276 (1973).
8. J. Wong and M. Ghezzeo, *ibid.*, **122**, 1268 (1975).
9. K. Kinoshita, *Thin Solid Films*, **12**, 17 (1972).

Modified Phosphosilicate Glasses for VLSI Applications

K. Nassau, R. A. Levy,* and D. L. Chadwick

AT&T Bell Laboratories, Murray Hill, New Jersey 07974

ABSTRACT

In this study, the glass transition temperature T_g is determined from thermal expansion measurements in a series of glass compositions prepared by bulk fusion of a phosphosilicate matrix to which oxides of boron, germanium, or arsenic are added. On a per-molar basis, addition of boron was observed to be the most effective in lowering the glass transition temperature of the phosphosilicate matrix, as compared to arsenic or germanium, which is found to be the least effective. For borophosphosilicate glass with concentrations of B_2O_3 less than 13 m/o, values of T_g are observed to be reduced by increasing the P_2O_5 content. Near 13 m/o B_2O_3 , the temperatures become independent of P_2O_5 , while at a still higher B_2O_3 content they are actually raised upon increasing the P_2O_5 concentration. For the germanophosphosilicate glass, no such reversal is noted as values of T_g decrease slightly with P_2O_5 additions at all GeO_2 concentrations. Glass compositions with potential VLSI applications can, thus, have the P_2O_5 content reduced to the minimum value required to provide gettering without significantly affecting the glass transition or associated viscous flow parameters. From a comparison of the measured values of T_g in bulk glasses with reported values of the flow temperature T_f for films with corresponding compositions, a correlation factor relating those two parameters is established. Thus, the relatively simple thermal expansion technique can now be used to survey for glass compositions with promising flow characteristics without the rigorous and time consuming effort of conducting the more difficult bulk viscosity experiments or developing deposition processes for films with possibly unsuitable viscous characteristics.

Phosphosilicate glass (PSG) deposited by low pressure chemical vapor deposition (LPCVD) is widely used in the fabrication of integrated circuits (1). It serves as a dielectric to insulate gate interconnects from metallization, as a passivation overcoat to provide mechanical protection, and as a solid diffusion source to dope silicon with phosphorus. In the processing of 2.5 μm Twin-Tub CMOS devices (2), PSG is exclusively used for its function as an intermediate dielectric providing, due to the phosphorus presence, added capabilities for effective gettering of sodium and other rapidly diffusing metal ions (3). Following deposition, PSG films typically undergo two high temperature processing steps (*i.e.* flow and reflow) to smooth the topography and drive in the junctions (4). The ability of PSG to undergo viscous deformation at a given temperature is primarily a function of the phosphorus content in the glass (5). With the ongoing emphasis on fine line geometries with design rules requiring short channel lengths ($\leq 1 \mu\text{m}$) and shallow junctions ($\leq 0.25 \mu\text{m}$), a reduction in thermal cycle to minimize lateral and vertical diffusion of dopants becomes essential. Reduction of the flow and/or reflow temperature can generally be achieved by an increase in the phosphorus concentration of PSG, with a decrease of 50°C requiring an addi-

tional 3 weight percent (w/o) P(6). However, glasses with high P concentrations become extremely hygroscopic and may, due to chemical as well as electrochemical reactions, corrode the Al metallization (7).

Reported studies of CVD dielectric films for potential applications in silicon devices have focused on the investigation of silica with oxides of boron, phosphorus, boron plus phosphorus, aluminum, boron plus aluminum, zinc, boron plus zinc, arsenic, and several other combinations (8, 9). To meet future VLSI requirements, the initial development of a ternary glass system ought to retain the well-characterized phosphosilicate glass matrix for gettering purposes and also for minimizing major process changes. The choice of an additional oxide component should then be based on the overall properties and process compatibility of the ternary glass system.

In this study, we examine a series of glass compositions prepared by bulk fusion of a phosphosilicate matrix to which oxides of boron, germanium, or arsenic were added. The purpose here is to evaluate the contributory effect of these oxide additions on the viscous properties of the matrix. Since determination of the glass transition temperature T_g from thermal expansion data is known to yield a measure of viscosity, we shall demonstrate that values of T_g can be empirically correlated to flow temperature by addition of a constant factor equal to $\sim 288^\circ\text{C}$.

*Electrochemical Society Active Member.

Furthermore, we shall establish that this technique offers a relatively quick way of surveying glass compositions with promising flow temperatures without the arduous effort of developing and characterizing a possibly unsuitable LPCVD process.

Sample Preparation and Measurement Technique

Materials used in the preparation of the bulk glasses included hydrolized silica powder (Cab-O-Sil, G. L. Cabot, Incorporated), 99.999% GeO_2 (Apache Chemicals Incorporated), and ACS grade As_2O_3 (Alfa Products); boron was used in the form of a reagent grade ammonium pentaborate $(\text{NH}_4)_2\text{B}_{10}\text{O}_{18}\cdot 8\text{H}_2\text{O}$ (Fisher Scientific Company) and phosphorus as reagent-grade dibasic ammonium phosphate $(\text{NH}_4)_2\text{HPO}_4$ (Baker Chemical Company).

Batches to produce 25g of glass were prepared first by mixing the ingredients with 100 to 200 ml of distilled water (the quantity depending on the amount of Cab-O-Sil); these batches were then ball-milled for a minimum of 10h, dried in an oven at 120°C , ground, and heated in a platinum or a high purity alumina crucible in accordance with the following procedure. After initial firing for 1h at 1000°C , each sample was reground and refired at 1150°C ; this sequence was repeated at 150°C intervals until glass formation was achieved to a maximum temperature of 1600°C . Bulk glass could not be obtained at this temperature in a few high silica concentrations samples which sintered into granular material; since x-ray diffraction showed no signs of crystallinity in these samples, they were pressed at 2500 psi into 9 mm diam pellets suitable for the thermal expansion measurements.

One percent of As_2O_3 was purposely added to each glass composition as a fining agent to remove gas bubbles and assist in homogenizing the melt. This ingredient is not shown in Tables I and II and is expected to have a small and approximately constant effect on the results. Clear glasses were obtained only in the case of low melting compositions, but this is not expected to affect the glass transition measurements. Weighing samples before and after melting showed no significant weight loss due to vaporization of components, except for the two highest arsenic-containing compositions of Table III.

Semiquantitative analysis by x-ray fluorescence on two representative specimens of Table II showed the expected major ingredients, including the arsenic. Other detectable elements were not exhibited; this includes aluminum, a possible contaminant from the ball milling and crucible, which has a detectability limit of less than 0.1% by this technique.

Quantitative analysis of these same specimens by inductively coupled plasma optical emission analysis in mole percent (m/o) oxides (the number in parenthesis is the nominal composition) were as follows. Sample 1: $\text{SiO}_2 = 68.8$ (69), $\text{GeO}_2 = 21.2$ (23), $\text{P}_2\text{O}_5 = 7.1$ (8), $\text{B}_2\text{O}_3 < 0.01$ (0), $\text{As}_2\text{O}_3 = 0.66$ (1), $\text{Al}_2\text{O}_3 = 0.05$ (0), total recovery = 97.8%. Sample 2: $\text{SiO}_2 = 77.1$ (81), $\text{GeO}_2 = 0.11$ (0), $\text{P}_2\text{O}_5 = 2.0$ (2), $\text{B}_2\text{O}_3 = 17.0$ (17), $\text{As}_2\text{O}_3 = 0.69$ (1), $\text{Al}_2\text{O}_3 = 0.01$ (0), total recovery = 96.9%. The standard deviation for these results is about one percent of the result for each value. It can be seen that some arsenic is lost as expected and that a little phosphorus is lost as well at high concentration. In both cases, the aluminum contamination is acceptably low and total recovery as well as agreement with nominal values is very satisfactory.

Thermal expansion measurements were performed on a du Pont 1090 thermoanalyzer using a heating rate of 5 degrees per minute. At least two runs were performed on each sample, the first generally serving as an annealing step. In this technique, a sample typically 3 mm thick is placed on a fused silica holder in a furnace. A fused silica plunger rests on top of the sample and transmits the sample expansion to a linear transducer located outside the furnace. The expansion coefficient of fused silica ($0.55 \mu\text{m}/\text{m}^\circ\text{C}$) was added in all cases to the observed expansion coefficient as is appropriate for the geometry used in this thermoanalyzer.

The glass transition temperature (also known as the glass transformation temperature) specifies a temperature region where many of the properties of a glass change significantly. The glass transition temperature is generally associated with the slowing down of molecular rearrangements in the glass structure during cooling. When these rearrangements occur rapidly within the time frame of an experimental measurement, the glass has the properties of a fluid melt; when the measurements are fast, the glass structure is "frozen" and the glass behaves like a solid. The rate of these molecular rearrangements is closely associated with viscous flow and, as generally noted (10), T_g occurs in all oxide glasses at a viscosity of $\sim 10^{13}\text{P}$ (1 Poise = $1 \text{ g}/\text{cm}\cdot\text{s}$). The softening point of a glass is the temperature at which it has a viscosity of $10^{7.6}\text{P}$. At that viscosity a rod 24 cm in length and 0.7 mm in diameter elongates 1 mm/min under its own weight. The flow temperature T_f in glass films would expectably be close to that softening point. For glass systems in which the viscosity exhibits an Arrhenius-type behavior (or one close to it), differential variations in viscosity η can be directly correlated to differential variations in temperature. Thus, the difference in values of the viscosity at the glass transition temperature and at the flow temperature (i.e. $\eta_{T_g} - \eta_{T_f}$) would reflect from the slope of the η vs. $1/T$ curve, the difference in the values of T_g and T_f (i.e. $T_g - T_f$). It is interesting to note that the phase change from the liquid to the glassy state is a continuous transition. The second-order quantities, such as the coefficient of thermal expansion or specific heat, rather than the corresponding first-order quantities, such as volume or enthalpy, show a discontinuity at T_g . Thus, measurements of the coefficient of thermal expansion as a function of glass composition would specify, in the present investigation, not only changes in the corresponding values of T_g but also the associated changes in the viscosity of the system.

A typical thermal expansion curve, obtained in this case for the ternary 81 m/o SiO_2 , 17 m/o B_2O_3 , 2 m/o P_2O_5 glass system is shown in Fig. 1. Generally, such curves tend to exhibit first a linear increase in length with increasing temperature followed by a slight bend in the curve and then another sharp bend towards a steeper slope; the curve then heads toward a peak before shifting direction toward smaller lengths. This latter shift is due to the slumping of the fluid melt under its own weight as well as the compression of the softened glass by the weight of the plunger and is therefore not really an essential part of the expansion curve. If methods were used where the softening of the sample did not interfere with the measurement, the curve would continue rising with higher temperatures. To a first approximation, the volume of most solids is known to increase linearly with

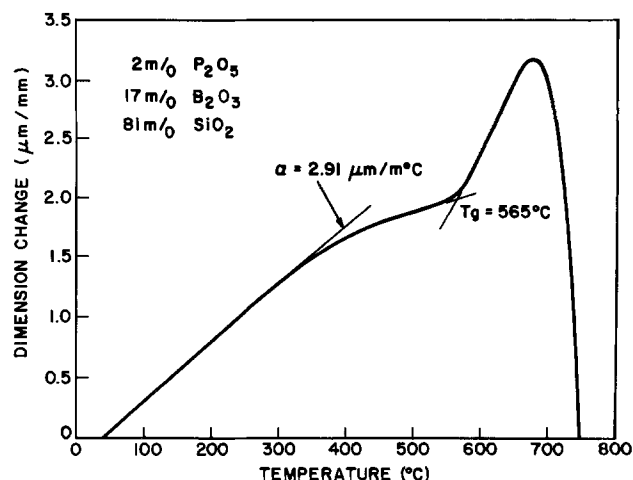


Fig. 1. Thermal expansion curve illustrating the linear, stabilization, and glass transition regions for the ternary 81 m/o SiO_2 , 17 m/o B_2O_3 , 2 m/o P_2O_5 glass system.

temperature with the thermal expansion adequately represented by a series expression with a small quadratic term (10)

$$l = l_0 (1 + \alpha T + \beta T^2)$$

where α is the linear expansion coefficient. However, a second contribution to thermal expansion may arise from a change in the molecular arrangement of the material. In most crystalline solids, such changes are restricted to abrupt alterations in crystal form at phase transitions, while in the case of glasses, at sufficiently high temperatures, the molecular rearrangements change continuously with temperature and contribute a major portion of the observed expansion. Thus, at the point where structural changes begin to take effect, changes in the slope of the expansion curve are to be expected. Based on such considerations, T_g is then measured, as shown in Fig. 1, at the extrapolated onset point at which the curve shows a sharp bend towards a steeper slope. Glass transition temperatures, recorded by this technique, were generally reproducible to $\pm 10^\circ\text{C}$ and are here given to the nearest 5°C , usually as an average of at least two measurements. In the temperature range between the linear region and T_g , the slight bend observed in the expansion curve is associated with the thermal history of the sample. For rapidly cooled samples this departure from linearity reflects large deviation from thermodynamic equilibrium of the structure. Only small effects are expected for samples slowly cooled from the melt, but then the risk of triggering crystallization also becomes higher. Below this so-called stabilization range, the slope of the linear portion of the expansion curve extending down to room temperature yields the coefficient of thermal expansion.

Since the elemental concentration in a glass may be listed in mole percent (m/o), cation percent (cat/o), or as weight percent (w/o) of the element or compound oxide (*i.e.*, w/o P or w/o P_2O_5), calculations describing the conversion technique as well as some illustrative conversion tables are presented in the Appendix. For sake of consistency, glass compositions will be referred to in m/o throughout this investigation.

Results and Discussion

The glass transition temperature data obtained are summarized in Tables I to III. The smoothed constant P_2O_5 concentration curves of Fig. 2 and 3 were constructed from the data of Tables I and II. Points were next taken from these curves at 25° or 50°C intervals and used to draw the three-component T_g curves of Fig. 4 and 5.

For the binary $\text{SiO}_2\text{-P}_2\text{O}_5$ system, T_g is observed in Fig. 2 or 3 to decrease from 1160°C for pure SiO_2 down to 725°C for PSG with 8 m/o P_2O_5 . That is indeed consistent with the observed decrease in viscous flow with additional P in the glass. For glasses with constant phosphorus concentrations of 0, 2, 4, or 8 m/o P_2O_5 , the effect of adding B_2O_3 results, as shown in Fig. 2, in a monotonic decrease of the glass transition temperature for both the binary $\text{SiO}_2\text{-B}_2\text{O}_3$ and ternary $\text{SiO}_2\text{-B}_2\text{O}_3\text{-P}_2\text{O}_5$ glass systems. For

Table I. Glass transition temperatures of some binary oxide glasses

m/o P_2O_5	m/o B_2O_3	m/o GeO_2	m/o SiO_2	T_g ($^\circ\text{C}$)
8			100.0	1160
			92.0	725
	5.0		95.0	815*
	9.3		90.7	700*
	11.0		89.0	685*
	15.7		84.3	540*
	17.0		83.0	535*
		4.1	95.9	800*
		7.0	93.0	750*
		13.3	86.7	730*
		13.5	86.5	725*
		31.0	69.0	650*
		45.0	55.0	660

* Data courtesy of J. W. Fleming (22).

Table II. Measured values of glass transition temperature for multicomponent glasses involving SiO_2 with P_2O_5 , B_2O_3 , and GeO_2

m/o P_2O_5	m/o B_2O_3	m/o GeO_2	m/o SiO_2	T_g ($^\circ\text{C}$)
2	6		92	820
2	17		81	565*
2	40		58	375
4	6		90	700
4	17		79	555
4	40		56	415
7	6		87	675
8	17		75	610
8	30		62	500
8	43		49	420
8	60		32	310
2		12	86	710
2		23	75	675
4		12	84	680
4		25	71	665
4		45	51	610
7		6	87	720
7		12	81	700
8		23	69	665*
7		46	47	595
8		92	0	515
8	10	10	72	640
8	10	20	62	610

* Analyses given in the text.

Table III. Glass transition temperatures of some As_2O_3 containing glasses

m/o P_2O_5	m/o B_2O_3	m/o GeO_2	m/o As_2O_3	m/o SiO_2	T_g ($^\circ\text{C}$)
2.0		23	23.0	52	525
7.5			7.5	85	635
8.0			20.0	72	715
8.0	10		10.0	72	620
8.0		20	10.0	62	570

instance, in the case of ternary glasses with a 4 m/o P_2O_5 concentration, values of T_g are seen to vary from 700° to 555° and 415°C with corresponding additions of 6, 17, and 40 m/o B_2O_3 . A similar but less pronounced effect is observed in Fig. 3 as the result of adding GeO_2 to the SiO_2 or to the $\text{SiO}_2\text{-P}_2\text{O}_5$ glass matrix. In this case, for a constant 4 m/o P_2O_5 concentration, values of T_g are seen to vary from 680° to 665° and 610°C for corresponding concentrations of 12, 25, and 45 m/o GeO_2 . The difference in the glass structure between these two glass systems presumably produces this variation in the viscous behavior. The strengths of the oxygen-central atom bonds in the simple oxides such as SiO_2 , GeO_2 , P_2O_5 , and B_2O_3 are all of the order of 100 kcal/mol (11). The very large difference in viscosity of these oxides, summarized by Doremus (11) and shown here in Fig. 6, is therefore quite unexpected since the mechanism of viscous flow undoubtedly involves the breaking of oxide bonds. On the other hand, the melting points of the crystalline oxides parallel the variations in viscosity: SiO_2 (cristobalite), 1710°C ; GeO_2 (hexagonal), 1116°C ; P_2O_5 , 580°C ; B_2O_3 , 450°C . Thus, the differences then indicate that the detailed structure of the oxide network is also important in determining the ease of viscous flow. The linked-ring structure of B_2O_3 (12) is probably the reason for the low viscosity of this oxide (at 550°C , $\eta \sim 10^8\text{P}$), since the bonds between rings are expectably weaker than those in the rings. The P_2O_5 network possibly contains sheets of PO_4 tetrahedra where each tetrahedron is bonded to three others instead of four as for SiO_2 and GeO_2 . The lower viscosity (at 550°C , $\eta \sim 10^7\text{P}$), and melting point of crystalline P_2O_5 may then result from this particular structure. One would expect, from the similarity in the structure of GeO_2 and SiO_2 , that these oxides would have a similar viscosity and melting point, since each apparently forms a random three-dimensional network in the glassy state. Thus, the significant difference

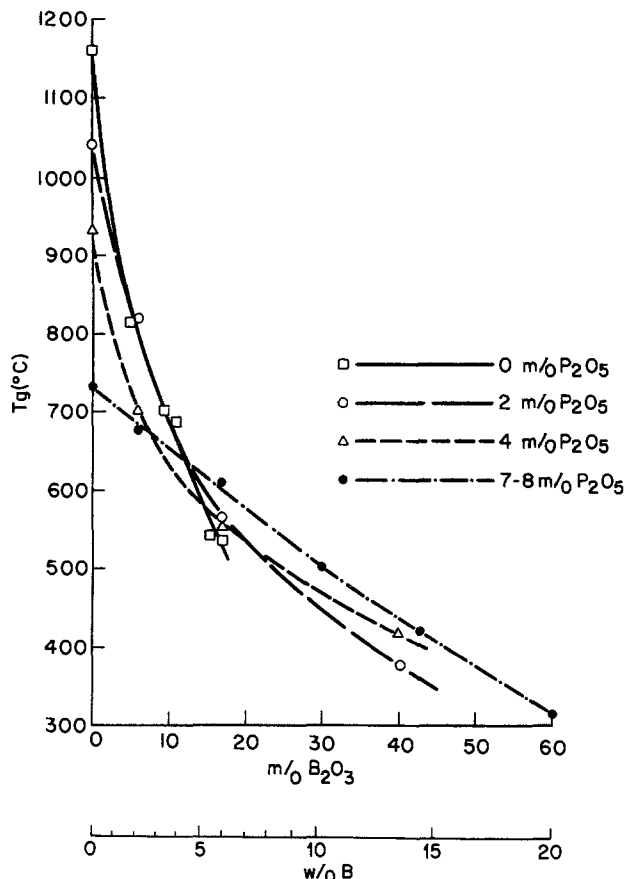


Fig. 2. Functional dependence of glass transition temperature on m/o B₂O₃ content in a phosphosilicate glass matrix with 0, 2, 4, and 7-8 m/o P₂O₅.

in the viscosity and melting point between SiO₂ (at 1100°C, $\eta \sim 10^{13}$ P) and GeO₂ (at 1100°C, $\eta \sim 10^6$ P) raises doubt on the presumed structure similarity. Although the random-network structure for vitreous silica is well established, there may be some subtle discrepancies in the germania network accounting for its lower viscosity.

In the process of mixing oxides, such as that being done in the present investigation, the silica network-forming lattice gets broken up resulting in local distortions of the structure and consequently a lower viscous flow. Oxides with vastly different structures from SiO₂, particularly such as in the case of B₂O₃, would then be most effective in distorting the silica structure and achieving low flow characteristics.

In Table IV, published values of flow temperature T_f , for borosilicate (13), phosphosilicate (3-5), and borophosphosilicate (13) glass systems, have been assembled with the corresponding measured values of T_g . Determination of $(T_f - T_g)$ for each of these available data points yielded an average value for the set of 288°C with a standard deviation of 16°C. This, indeed, indicates a very satisfactory fit to the data, especially since T_f is a rather subjective measurement at best determined only to $\pm 25^\circ\text{C}$. Further-

Table IV. Values of T_g and T_f for some borophosphosilicate glass compositions

Ref.	Composition		Temperatures		
	m/o B ₂ O ₃	m/o P ₂ O ₅	T_f (°C)	T_g (°C)	$T_f - T_g$ (°C)
4, (PSG)		7.5	1050	750	300
13, (BPSG-A)	11.9	4.2	925	645	280
13, (BSG)	18.9		825	515	310
13, (PSG)		6.9	1075	800	275
5, (PSG)		8.0	1000	725	275
		Average			288
		Standard deviation			16

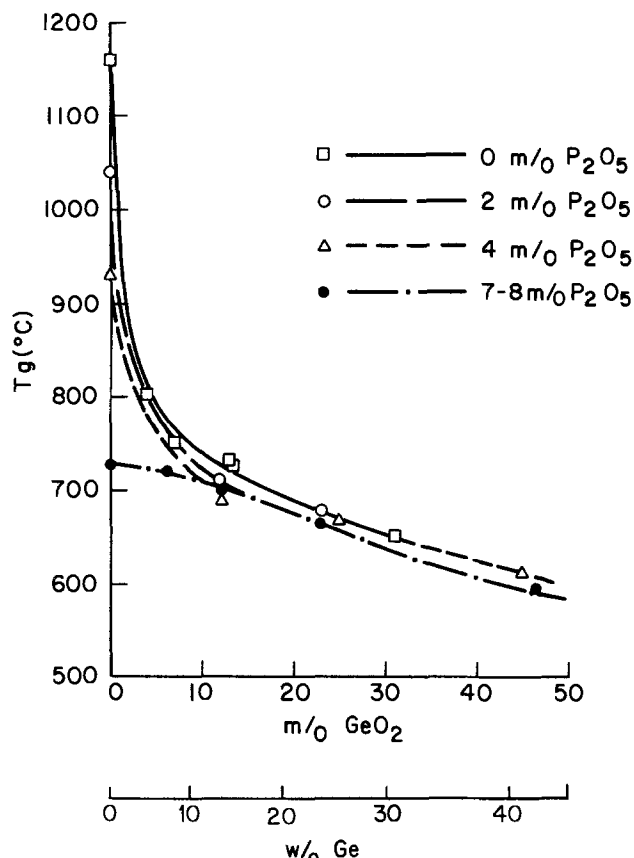


Fig. 3. Functional dependence of glass transition temperature on m/o GeO₂ in a phosphosilicate glass matrix with 0, 2, 4, and 7-8 m/o P₂O₅.

more, the minor variations observed in $(T_f - T_g)$ may derive from differences in the nature of glasses prepared by these different techniques (*i.e.*, CVD *vs.* bulk melting), as well as other factors such as the presence of the 1 m/o As₂O₃ and the occurrence of mixed valencies in P (*i.e.*, P₂O₃ and P₂O₅) and As (*i.e.*, As₂O₃ and As₂O₅). Thus, through determination of the glass transition temperature, with the use of the relatively simple thermal expansion technique, an estimate for the corresponding flow temperature can be achieved by addition of a constant factor. That, indeed, facilitates the task of surveying for glass compositions with promising flow characteristics, without the rigorous and time consuming effort of con-

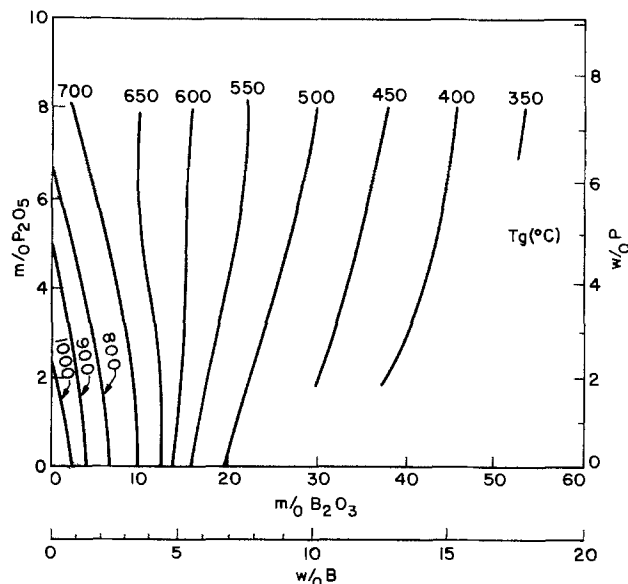


Fig. 4. Glass transition isotherms for the borophosphosilicate glass system.

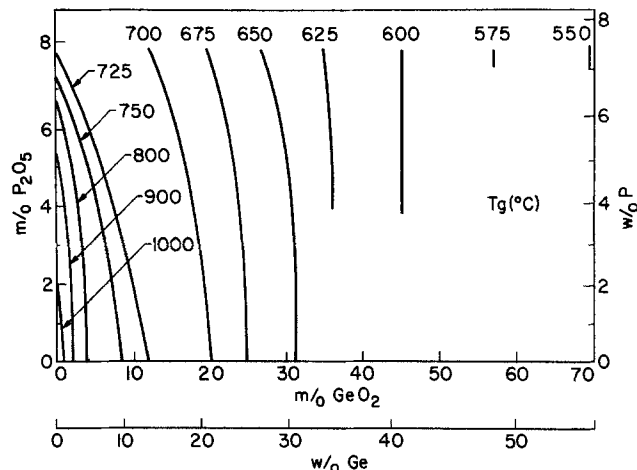


Fig. 5. Glass transition isotherms for the germanophosphosilicate glass system.

ducting the more difficult bulk viscosity viscous experiments (14) or developing deposition processes for films with possibly unsuitable viscous characteristics.

An examination of Fig. 4 indicates that at less than about 13 m/o B_2O_3 concentration, borophosphosilicate glasses can have their T_g and therefore their T_f reduced by increasing the P_2O_5 concentration. Near 13 m/o B_2O_3 these temperatures appear to become independent of P_2O_5 content, while at a still higher B_2O_3 content these temperatures are actually raised on increasing the P_2O_5 concentration. Thus, glasses under present consideration for VLSI applications, with typical concentrations of about 13 m/o B_2O_3 , could have the P_2O_5 content reduced to the minimum value necessary to provide gettering (*i. e.*, even possibly as low as 2 m/o) without significantly affecting the flow characteristics. In view of the fact that these glasses are expected to be densified during flow and/or reflow at a relatively low temperature ($\leq 950^\circ C$) where the surface depletion of P becomes less pronounced, the beneficial option of reducing the phosphorus in the glass would minimize corrosion-related problems with Al and furthermore allow for reliable encapsulation of devices in economical plastic packages.

Although borophosphosilicate glass appears now to be the choice material for meeting the reduced thermal glass requirements, there may still be, associated with its use, a few technological challenges to overcome. One of the present problems worth noting is the lack of reliable analytical techniques for determining the boron content in the glass. The fact that B is a light element ($Z = 5$, AMU ≈ 11) excludes the use of x-ray related techniques (*i. e.*, x-ray fluorescence, electron microprobe analysis, EDS,...) since most of the emitted energy is low and absorbed by

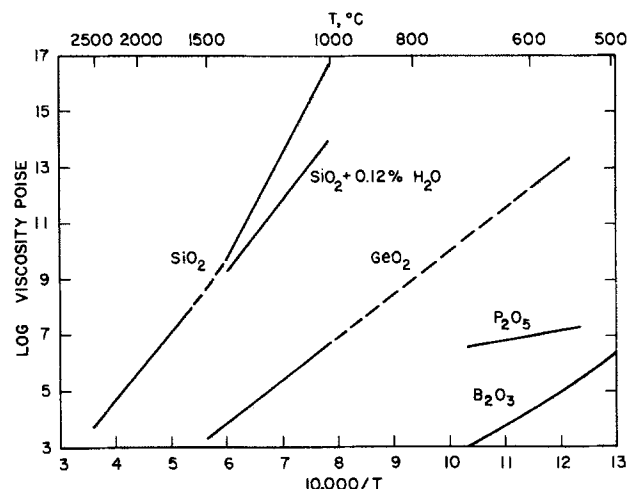


Fig. 6. Viscosities of various glass forming oxides as a function of reciprocal temperature.

the detector window. Although there are ongoing efforts by equipment manufacturers to develop windowless detectors, the technology is still in its infancy. On the other hand, the insulating character of borophosphosilicate glass hampers the use of surface techniques (*i. e.*, AES, XPS, SIMS,...) because of the inevitable interference of electronic or ionic charging effects. Furthermore, the presence of both P and B in the glass complicates the interpretation of results generated from indirect analytical methods (*i. e.*, refractive index determination, etch rate variation, diffusion techniques,...). Thus, the choice of available techniques narrows down to possibly neutron activation, infrared absorption, and/or chemical analysis. Neutron activation requires the use of an accelerator, not generally available on premises and extensive monitoring equipment, a situation certainly not suitable for a VLSI production environment. Infrared absorption has been extensively used in the characterization of borophosphosilicate glass films and appears at this stage to be one of the more promising techniques. However, inherent problems associated with poor resolution of overlapping bands and the limited sensitivity of the technique to dilute concentrations are recognized drawbacks. Furthermore, as typical of all other analytical techniques which yield relative results, IR absorption requires proper standardization, a task hard to achieve with the current lack of absolute standards. The focus, thus, becomes chemical analysis, which is now being extensively explored and promises to be the only accurate, if nonetheless destructive, procedure for determining boron in borophosphosilicate glass.

Another area of concern arising from the use of borophosphosilicate glass in VLSI devices pertains to the high nuclear cross section of B^{10} (4017 ± 32 barns) for thermal neutrons (15). Through an (n, α) reaction B^{10} which is $\sim 20\%$ naturally abundant in B dissociates following neutron capture, releasing in the process α particles which in turn may trigger soft errors within the device. However, based on background count rate measurements of thermal neutrons in a laboratory environment, calculations by Yaney and Filo (16) have predicted such nuclear transmutations to have a negligible effect on device performance.

The possibility of phase separation in borophosphosilicate glass is another potential complication resulting from the significant difference in the molecular structures of the oxides (*i. e.*, B_2O_3 , SiO_2 , and P_2O_5) (17). In the B_2O_3 - SiO_2 system, Charles and Wagstaff (8) have predicted and experimentally confirmed the occurrence of a sub-liquidus miscibility gap below $520^\circ C$ that extends across the complete binary. The addition of P_2O_5 would presumably further enhance such phase separation due to the relatively high ionic potential (defined as the ratio of ionic charge to ionic radius) of phosphorus (19). Thus, devices with borophosphosilicate glass heat-treated below the metastable two-liquid coexistence boundary, as typically done, for instance, at the H_2 annealing steps, could precipitate a borate-rich phase leachable during subsequent wet chemical or dry etching.

Another limiting feature associated with the use of B_2O_3 is the hygroscopic character of the oxide. In general, borate glasses are known to react readily with atmospheric water and degrade. However, borophosphosilicate glass films containing ≤ 4 w/o B have been shown to be relatively stable chemically during storage and exposure to humid ambients. At higher B concentrations, the extended exposure of undensified films at high humidity has been reported to cause some surface devitrification and in the case of the fused glass, some leaching of the boron and phosphorus oxides. Thus, as in the present case of phosphosilicate glass where control of P concentration is essential to prevent Al corrosion, control of both B and P concentrations in borophosphosilicate glass now becomes imperative for fabrication of a reliable product.

Most of these technological difficulties, associated with the use of borophosphosilicate glass, can be avoided by considering the alternate selection of a phosphogermano-

silicate glass. Germanium, being a relatively heavier element ($Z = 32$, $AMU = 73$), can be readily detected by standard analytical x-ray techniques (*i. e.*, x-ray fluorescence, electron microprobe, EDS,...). The nuclear cross section of all Ge isotopes (*i. e.*, Ge^{70} , Ge^{72} , Ge^{73} , Ge^{74} , and Ge^{76}) for thermal neutrons is relatively low (15) (in worst case situation, $\sigma = 14 \pm 1$ barns for Ge^{73}), thus eliminating the potential threat of nuclear transmutations affecting device performance. The reported tendency (20) of both germanium and phosphorus to substitute for silicon in the silicon-oxygen network eliminate the risk of phase separation. Finally, based on working knowledge of the chemical behavior of crystalline and amorphous phases, the tendency of GeO_2 to react with moisture is considered significantly lower than that of P_2O_5 or B_2O_3 but still higher than that of As_2O_3 , ZnO , Al_2O_3 , or SiO_2 .

Examination of Fig. 5 reveals that the glass transition temperature for the germanophosphosilicate glass decreases with P_2O_5 additions at all GeO_2 concentrations. However, the decrease is relatively modest in the region of interest, so that a reduction in the P_2O_5 concentration to minimize hygroscopicity could again be achieved with no significant changes in the viscous behavior of the system. Thus, the choice of a silica glass containing 35 m/o GeO_2 and 4 m/o P_2O_5 , exhibiting an interpolated value of $T_g \approx 635^\circ C$, is predicted to have a flow temperature below $950^\circ C$. That would, indeed, provide us with the necessary margin to optimize the flow and/or reflow cycle so as to achieve the desirable junction depths.

The characteristic properties of the phosphogermanate system are worth noting within the context of the present discussion. The measured value of T_g for the $GeO_2 - 8$ m/o P_2O_5 composition was $\sim 515^\circ C$, which would suggest a value of T_f close to $800^\circ C$. The possibility of reducing the flow temperature to such levels is attractive from a processing standpoint. It would decouple the diffusion from the flow and/or reflow requirements. Implants could first be thermally driven to required depths, and the glass subsequently deposited, flowed, and/or reflowed to generate the desirable topographical profile. Furthermore, for such a chemically stable binary system, the characterization and control of glass composition could be significantly simplified. The commercial availability of a source gas such as germane, compatible with present CVD deposition equipment, provides added justification for exploring the developmental feasibility of a CVD process for phosphogermanate glass films.

Examination in Table III of the T_g values for As_2O_3 containing glasses indicates that the effect of arsenic on the viscous characteristics of the system lies, on a per-molar basis, between that of boron and that of germanium. However, due to the fact that some volatilization did occur during the fusing process, and since the $As^{3+} - As^{5+}$ equilibrium in arsenic-containing glasses depends on the specific processing atmosphere and temperature (21), there is expressed doubt for this particular case in the premise of translating bulk results directly into actual flow temperatures for corresponding CVD films.

Conclusions

In this study, we have determined the glass transition temperature from thermal expansion measurements in a series of glass compositions prepared by bulk fusion of a phosphosilicate matrix to which oxides of boron, germanium, or arsenic were added. On a per-molar basis, addition of boron was observed to be the most effective in lowering the glass transition temperature of the phosphosilicate matrix, as compared to arsenic or germanium, which was found to be the least effective. For borophosphosilicate glass with concentrations of B_2O_3 less than 13 m/o, values of T_g were observed to be reduced by increasing the P_2O_5 content. Near 13 m/o B_2O_3 , these temperatures became independent of P_2O_5 , while at a still higher B_2O_3 content they were actually raised upon increasing the P_2O_5 concentration. For the germanophosphosilicate glass, no such reversal was noted, as values of T_g decreased slightly with P_2O_5 additions at all GeO_2 concentra-

tions. Glass compositions with potential VLSI applications could, thus, have the P_2O_5 content reduced to the minimum value necessary to provide gettering without significantly affecting the phase transition and associated viscous flow parameters. The anticipated difficulties in the use of borophosphosilicate glass in devices have been outlined, and ways of avoiding them have been proposed by exploring the alternate use of a germanophosphosilicate or even the simple binary phosphogermanate glass system. From a comparison of the measured values of T_g in bulk glasses with reported values of T_f for films with corresponding compositions, we have established empirically a correlation factor relating the two parameters. Thus, the relatively simple thermal expansion technique can now be used to survey for glass compositions with promising flow characteristics, without the rigorous and time consuming effort of conducting the more difficult bulk viscosity experiments or developing deposition processes for films with possibly unsuitable viscous characteristics.

Acknowledgments

The authors wish to thank T. Y. Kometani for the emission analysis, S. M. Vincent for the x-ray fluorescence data, and A. E. Miller for assistance in various parts of this project.

Manuscript submitted July 10, 1984; revised manuscript received Oct. 22, 1984.

AT&T Bell Laboratories assisted in meeting the publication costs of this article.

APPENDIX

Consider a glass containing A grams of M_xO_y plus S grams of SiO_2 . If W_M is the atomic weight of M , W_O of O , etc., then $W_{M_xO_y} = xW_M + yW_O$ is the molecular weight of M_xO_y , and so on. Then

$$\text{w/o of } M_xO_y = \frac{100 \cdot A}{A + S} \quad [\text{A-1}]$$

$$\text{w/o of } M = \frac{100 \cdot A}{A + S} \times \frac{W_M}{W_{M_xO_y}} \quad [\text{A-2}]$$

$$\text{m/o of } M_xO_y = \frac{100 \cdot A/W_{M_xO_y}}{A/W_{M_xO_y} + S/W_{SiO_2}} \quad [\text{A-3}]$$

$$\text{cat/o of } M (= \text{m/o } MO_{y/x}) = \frac{100 \cdot x \cdot A/W_{M_xO_y}}{x \cdot A/W_{M_xO_y} + S/W_{SiO_2}} \quad [\text{A-4}]$$

For a glass containing multiple ingredients A , B , C , ..., and SiO_2 it is only necessary to replace A by $A + B + C + \dots$ in Eq. [A-1] and [A-2], and $A/W_{M_xO_y}$ by $A/W_{M_xO_y} + B/W + \dots$, in Eq. [A-3] and [A-4]. For a GeO_2 based glass, W_{GeO_2} would replace W_{SiO_2} , and so on. In the following table the conversions are given for various oxides present one at a time at the 10 m/o level in silica and in germania.

Table A-I. Various ways of expressing the concentration of 10 m/o M_xO_y in SiO_2

M_xO_y	m/o	cat/o	w/o M	w/o M_xO_y
Al_2O_3	10.0	18.2	8.4	15.9
As_2O_3	10.0	18.2	20.3	26.8
B_2O_3	10.0	18.2	3.5	11.4
GeO_2	10.0	10.0	11.2	16.2
P_2O_5	10.0	18.2	9.1	20.8
ZnO	10.0	10.0	10.5	13.1

Table A-II. Various ways of expressing the concentration of 10 m/o M_xO_y in GeO_2

M_xO_y	m/o	cat/o	w/o M	w/o M_xO_y
Al_2O_3	10.0	18.2	5.2	9.8
As_2O_3	10.0	18.2	13.2	17.4
B_2O_3	10.0	18.2	2.1	6.9
P_2O_5	10.0	18.2	5.7	13.1
SiO_2	10.0	10.0	2.8	6.0
ZnO	10.0	10.0	6.4	8.0

REFERENCES

- G. L. Schnable, W. Kern, and R. B. Comizzoli, *This Journal*, **122**, 1092 (1975).
- L. C. Parrillo, L. K. Wang, R. D. Swenumson, R. L. Field, R. C. Melin, and R. A. Levy, "Twin-Tub CMOS II—An Advanced VLSI Technology," IEEE Tech. Dig., Int. Electron Device Meet., p. 706 (1982).
- D. R. Kerr, J. S. Logan, P. J. Burkhardt, and W. A. Pliskin, *IBM J. Res. Dev.*, **8**, 376 (September 1964).
- W. E. Armstrong and D. C. Tolliver, *This Journal*, **121**, 307 (1974).
- R. A. Levy, S. M. Vincent, and T. E. McGahan, Submitted to *This Journal*.
- A. C. Adams and C. D. Capio, *This Journal*, **128**, 423 (1981).
- N. Nagasima, H. Suzuki, K. Tanaka, and S. Nishida, *ibid.*, **121**, 434 (1974).
- W. Kern and R. C. Heim, *ibid.*, **117**, 562, 568 (1970).
- J. Wong, *ibid.*, **119**, 1071 (1972).
- J. M. Stevels, "The Structure and the Physical Properties of Glass," *Encyclopedia of Physics*, Vol. XIII, p. 510, Springer-Verlag, Berlin (1962).
- R. H. Doremus, "Glass Science," p. 105, John Wiley and Sons, New York (1973).
- J. D. Mackenzie, "Modern Aspects of the Vitreous State," Vol. I, p. 188, Butterworths, London (1960).
- W. Kern and G. L. Schnable, *RCA Rev.*, **43**, 423 (1982).
- H. E. Hagy, *J. Am. Ceram. Soc.*, **46**[2], 93 (1963).
- "Handbook of Chemistry and Physics," R. C. Weast, Editor, p. B-4 (1969-70).
- D. S. Yaney and A. J. Filo, Private communication.
- D. R. Uhlmann and A. G. Kolbeck, *Phys. Chem. Glasses*, **17**, 146 (1976).
- R. J. Charles and F. E. Wagstaff, *J. Am. Ceram. Soc.*, **51**, [1], 16 (1968).
- M. Tomozawa, "Advances in Crystallization and Nucleation in Glasses," p. 41, American Ceramic Society (1971).
- R. H. Doremus, "Glass Science," p. 49, John Wiley and Sons, New York (1973).
- R. Pyare, S. P. Singh, A. Singh, and P. Nath, *Phys. Chem. Glasses*, **23**, 158 (1982).
- J. W. Fleming, Ph.D. Thesis, Rutgers University, New Brunswick, NJ (1981).

Dependence of Partial Pressure of H₂O on Pyrogenic Growth of Silicon Dioxide

A. N. Chandorkar

Department of Electrical Engineering, Indian Institute of Technology, Bombay 400076, India

V. T. Karulkar and K. V. Ramanathan

Solid State Electronics Group, Tata Institute of Fundamental Research, Bombay 40005, India

ABSTRACT

The growth of silicon dioxide film is one of the major steps in any silicon IC fabrication. The quality of the silicon dioxide film is of paramount importance in MOS LSI/VLSI circuits, just as the "process design" many times requires tailoring of oxidation time and temperatures of the growth. Pyrogenic growth of oxide films is an ideal aid in achieving both of these objectives. A large number of "nomograms" giving oxide growths at various partial pressures of water vapor and temperatures are presented here as an aid to process design. Also, a simple model of pyrogenic oxide growth is given here which can be used for computer simulation of the process.

Until the advent of MOS technology, the silicon-dioxide films were generally used only as a mask during diffusions of impurity atoms in the fabrication of bipolar devices and integrated circuits. But due to present day emphasis on MOS LSI/VLSI circuits, the techniques for obtaining good quality films of silicon dioxide have received a great deal of attention. Apart from dry-oxygen ambient, water containing ambients have been used during oxidation of silicon to obtain SiO₂ films (1-6). The wet oxidation, however, is liable to contamination from the water container and is due to presence of undesirable impurities dissolved in water itself. Another technique, suggested first in 1967 (7) and called "pyrogenic oxidation," is now widely used. In this case, oxidation of silicon is carried by direct reaction of H₂ and O₂ at elevated temperatures in the oxidation furnace itself. Due to *in situ* water formation and the fact that oxygen is never saturated with water vapors, the pyrogenically grown oxides are "cleaner" oxides. Despite wide use of pyrogenic technique for SiO₂ growth, it is rather surprising that little data are available in literature on growth rates and other properties of pyrogenically grown oxide films. For example, Deal *et al.* (8, 9) have reported growth rates and other properties for a maximum of 10% partial pressure of H₂O, and Enomoto *et al.* (10) have given similar data at a fixed temperature and at three partial-pressure values. The purpose of this work, therefore, is to report extensive data acquired by us on silicon dioxide films pyrogenically grown at temperatures varying from 800° to 1200°C and at partial pressures of H₂O varying from 0 to 100%. The data

obtained by us are further presented here in simple nomograms. The importance of this work lies in the fact that by use of these nomograms, it is possible for anybody now to choose a growth rate of oxide films consistent with other technological considerations, such as diffusion temperature. Also, standard dry-wet-dry drive-in cycles can easily be simulated by changing one of the gas-flow rates.

Silicon wafers used for the present experiment were of (100) orientation and were n-type phosphorous-doped, with resistivity of 4-6 Ωcm. The wafers were cleaned by standard RCA procedure, rinsing in deionized water (18M Ωcm resistivity), and spin drying, prior to loading in oxidation furnace. The oxidation setup is shown in Fig. 1. The system consists of a quartz capillary of 2 mm diam enveloped by another quartz tube of 15 mm diam. This can be easily fitted to standard furnace tube (75 mm ID) with the help of a ball-and-socket joint. The furnace used in the experiment was "Thermco Brute XL," which keeps the temperature within ± 0.5°C of any set temperature. Hydrogen gas is passed through the capillary tube extending into the end zone of the furnace, which is maintained above 600°C. The oxygen is passed through the enveloping tube into the furnace. The combustion of hydrogen thus occurs in oxygen ambient, providing *in situ* water vapors. The partial pressure of H₂O vapor is a function of ratio of hydrogen to oxygen gas and is defined as

$$(H_2O)_p = (2 \times \text{Vol. of } H_2) / (2 \times \text{Vol. of } O_2 + 1 \times \text{Vol. of } H_2)$$

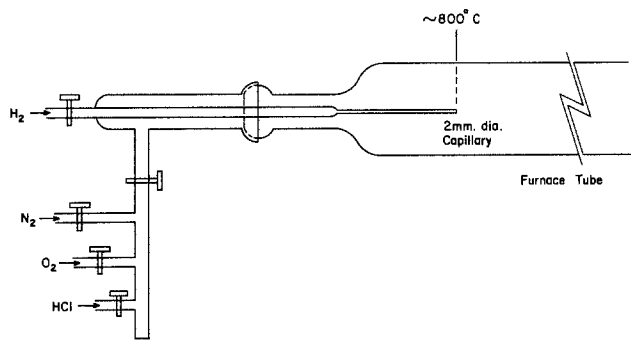


Fig. 1. Pyrogenic oxide-growth system

The oxide-growth tube was purged with 5% HCl gas in presence of O₂ for half an hour prior to each set of oxide growths. However, no HCl was passed during oxide growth because it was found to affect the partial pressure of the water vapor generated. Total gas flow of 2.25 l/min was maintained throughout this experiment by use of standard flowmeters which are calibrated to gas inputs at 14 psi pressure. To obtain oxide-growth rates at various values of temperature, time, and partial pressure, the following sequence was followed: (i) partial pressure was set

to a fixed value by choosing oxygen-to-hydrogen gas ratio; (ii) furnace temperature was set to a value, and oxide films were grown for times of 300, 600, 900, 1800, 3600, 5400, 7200, and 10,800s; (iii) for the same partial pressure, sequence (ii) was repeated for various temperature values from 800° to 1200°C at an interval of 100°C; and (iv) sequences (ii) and (iii) were then repeated for various values of partial pressures, namely, 0, 0.25, 0.4, 0.5, 0.75, and 1.0. Clearly, the use of 0.0 partial pressure implies absence of hydrogen and hence simulates dry-oxidation, while the case of 1.0 partial pressure corresponds to "steam" oxidation.

The thickness of each oxide film grown as discussed above was measured using an ellipsometer (Gaertner Scientific Corporation Model no. L 117). A computer program simulating ellipsometry was used to compute oxide thickness and refractive index of the film. The input to the program are the measured values of positions of "polarizer" and "analyzer" in two modes, expressed in degrees. Each of Fig. 2-7 gives oxide thickness in angstroms (Å) at various times of growth, having temperatures and partial pressures as variable parameters.

The quality of the oxides was judged by making C-V (high frequency) measurements on MOS capacitors fabricated on oxides grown at 1000°C for thickness of ~1000Å at each of the specified partial pressures. The results of

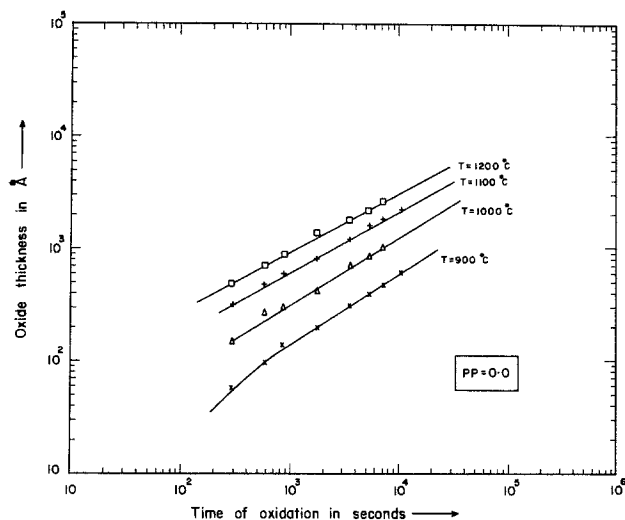


Fig. 2. Oxidation thickness against oxidation time for silicon, (100) orientated n-type, at partial pressure of 0.0% (dry oxidation) for various temperatures.

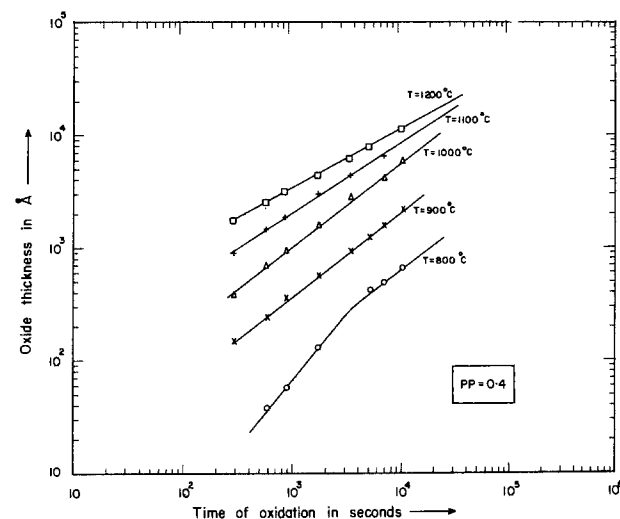


Fig. 4. Oxidation thickness against oxidation time for silicon, (100) orientated n-type, at partial pressure of 40% for various temperatures.

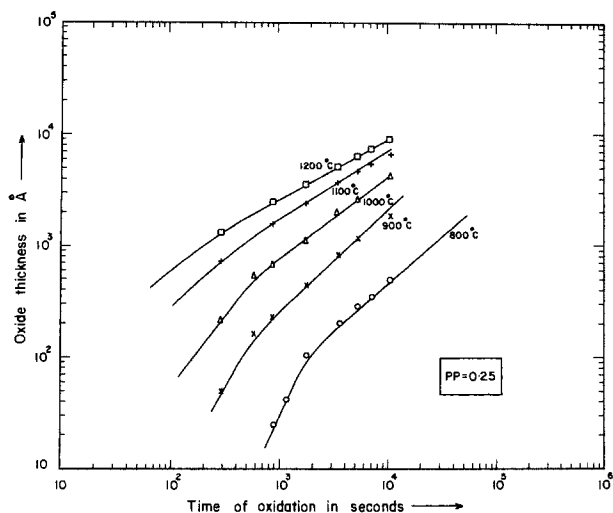


Fig. 3. Oxidation thickness against oxidation time for silicon, (100) orientated n-type, at partial pressure of 25% for various temperatures.

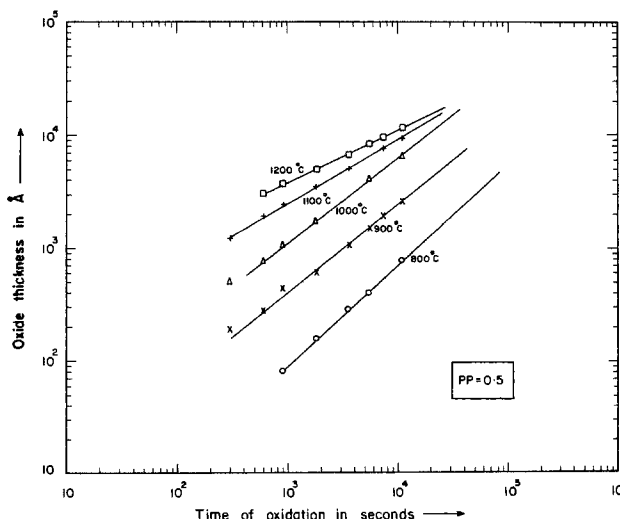


Fig. 5. Oxidation thickness against oxidation time for silicon, (100) orientated n-type, at partial pressure of 50% for various temperatures.

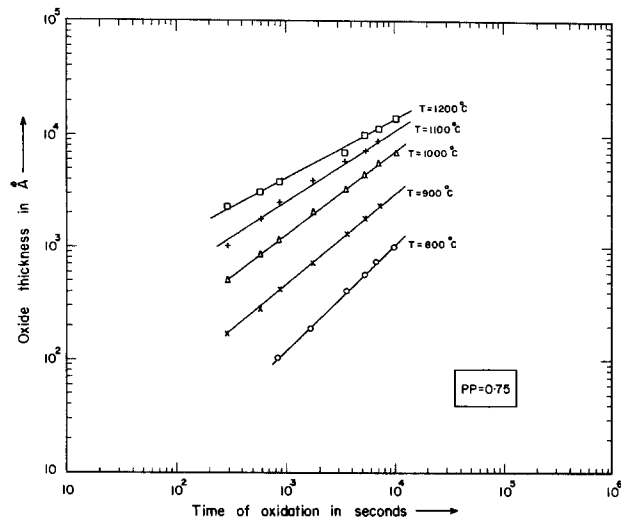


Fig. 6. Oxidation thickness against oxidation time for silicon, (100) orientated n-type, at partial pressure of 75% for various temperatures.

C-V measurements show Q_{ox}/q values of approximately $2 \times 10^{19}/\text{cm}^2$ for all the oxides under study. MOS capacitors were fabricated on oxides grown under various partial pressures and having thicknesses of 600Å, 1000Å, 6000Å and 1μm. These were subjected to high voltages to test the dielectric strengths of the oxides. It was found that almost all the types of oxides show a dielectric strength of the order of 6×10^6 V/cm. The refractive index of films grown was observed to be between 1.44 and 1.45. These results indicate that the pyrogenically grown oxides have properties which are compatible to standard MOS technology requirements, with the aided advantage of flexibility in choice of temperatures and times for desired oxide-thickness growth.

To simulate the pyrogenic oxide growth, we have been able to fit the data, (total of 240 points) within $\pm 5\%$ rms error, into the oxidation model suggested by Deal *et al.* (8, 11). The model presented by Deal *et al.* gives oxide thickness as

$$2Z_{ox} = (-K_p/K_l) + [(K_p/K_l)^2 + 4K_p(t + t_0)]^{1/2} \quad [2]$$

where K_p and K_l are the parabolic rate constant and linear rate constant, respectively. Using curve fitting techniques, the rate constants for pyrogenic oxide were evaluated and given as

$$K_p = 2.438 \times 10^6 (0.05 + p^{0.75}) \exp(-0.58q/kT) \quad [3]$$

$$K_l = 1.408 \times 10^6 (0.096 + p^{0.75}) \exp(-1.5q/kT) \quad [4]$$

and $t_0 = 400$

where p is the partial pressure of the H₂O vapor given by Eq. [1].

Because in the case of pyrogenic oxide growths the partial pressure of H₂O varies from 0 to 100%, the model given in (8, 11) is not strictly valid for our case. A generalized two-species model is more appropriate for this case,

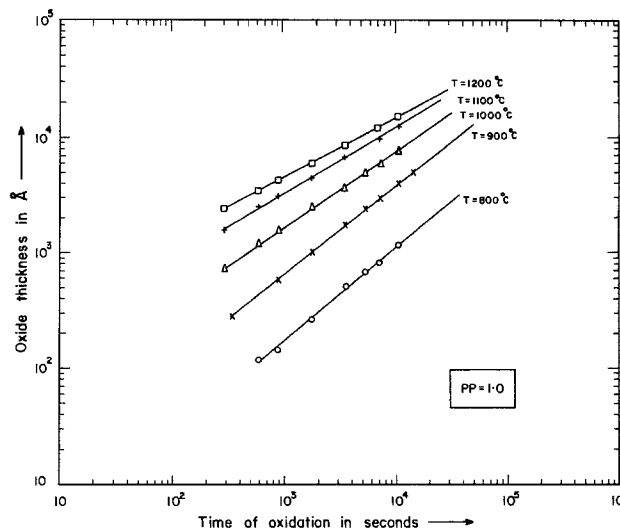


Fig. 7. Oxidation thickness against oxidation time for silicon, (100) orientated n-type, at partial pressure of 100% for various temperatures.

but for simplicity of use in a computer simulation model, we have accepted the model given by Eq. [2]. The choice is justified because the data of oxide growths could easily be simulated through this model within $\pm 5\%$ rms error.

Therefore, we presume that the extensive data in the form of nomograms, as well as the simple process-simulation computer model for pyrogenic oxides in the present form will be of great help to device technologists.

Acknowledgments

We wish to thank Shri Dinesh Sharma and Shri P. R. Apte for their help in the curve fitting of the data. We would also like to acknowledge the help rendered by Shri S. Pai and Miss A. M. Patel during experimental work. Discussions with Dr. A. S. Vengurlekar have helped a great deal in refining the presentation of this paper.

Manuscript submitted July 28, 1982; revised manuscript received Aug. 10, 1983.

REFERENCES

1. J. R. Ligenza and W. G. Spitzer, *J. Phys. Chem. Solids*, **17**, 196 (1961).
2. P. S. Flint, Paper 94 presented at The Electrochemical Society Meeting, Los Angeles, CA, May 6-10, 1962.
3. B. E. Deal, *This Journal*, **110**, 527 (1963).
4. R. J. Kriegler, *Denki Kagaku*, **41**, 466 (1973).
5. A. Rohatgi, S. R. Butler, F. J. Feigle, H. W. Kraner, and K. W. Jonez, *Appl. Phys. Lett.*, **30**, 104 (1977).
6. Y. J. Van der Meulen, C. M. Osborn, and J. F. Ziegler, *This Journal*, **122**, 284 (1975).
7. R. M. McLouski, Paper 177 presented at The Electrochemical Society Meeting, Chicago, IL, Oct. 15-20, 1967.
8. B. E. Deal, D. W. Hess, J. D. Plummer, and C. P. Ho, *This Journal*, **125**, 334 (1978).
9. B. E. Deal, *ibid.*, **125**, 576 (1978).
10. T. Enomoto, R. Ando, H. Morita, and H. Nakayama, *Jpn. J. Appl. Phys.*, **17**, 1049 (1978).
11. B. E. Deal and A. S. Grove, *J. Appl. Phys.*, **36**, 3770 (1965).

Novel Passivation Dielectrics—The Boron- or Phosphorus-Doped Hydrogenated Amorphous Silicon Carbide Films

C. Y. Chang,* Y. K. Fang, C. F. Huang, and B. S. Wu

Department of Electrical and Computer Engineering, National Cheng Kung University, Tainan, Taiwan, China

ABSTRACT

Hydrogenated amorphous silicon carbide (a-SiC:H) thin films were prepared and studied in a radio-frequency glow-discharge system, using a gas mixture of SiH₄ and one of the following carbon sources: methane (CH₄), benzene (C₆H₆), toluene (C₇H₈), *o*-xylene (C₈H₁₀), trichloroethane (C₂H₃Cl₃), trichloroethylene (C₂HCl₃), or carbon tetrachloride (CCl₄). The effect of doping phosphorus and boron into those a-SiC:H films on chemical etching rate, electrical dc resistivity, breakdown strength, and optical refractive index have been systematically investigated. Their chemical etching properties were examined by immersing in 49% HF, buffered HF, 180°C H₃PO₄ solutions, or in CF₄ + O₂ plasma. It was found that the boron-doped a-SiC:H film possesses five times slower etching rate than the undoped one, while phosphorus-doped a-SiC:H film shows about three times slower. Among those a-SiC:H films, the one obtained from a mixture of SiH₄ and benzene shows the best etch-resistant property, while the ones obtained from a mixture of SiH₄ and chlorine containing carbon sources (*e.g.*, trichloroethylene, trichloroethane, or carbon tetrachloride) shows that they are poor in etching resistance (*i.e.*, the etching rate is higher). By measuring dc resistivity, dielectric breakdown strength, and effective refractive index, it was found that boron- or phosphorus-doped a-SiC:H films exhibit much higher dielectric strength and resistivity, but lower etching rate, presumably because of higher density.

Recently, hydrogenated amorphous silicon carbide (a-SiC:H) films have been investigated intensively (1-8) because of their applications in photovoltaic devices. Some properties of undoped hydrogenated amorphous silicon carbide films were reported by Anderson and Spear in 1977 (9). However, only few efforts have been made to discover the effect of doping boron or phosphorus into hydrogenated amorphous silicon carbide films. Therefore, for the first time, properties of boron- or phosphorus-doped a-SiC:H films have been systematically investigated which include chemical etching rate, dc resistivity, breakdown strength, pinhole density, and optical refractive index.

In previous articles (9, 10), hydrogenated amorphous silicon carbide films have been prepared by radio-frequency glow-discharge decomposition of a gas mixture of silane (SiH₄) and one of the following hydrocarbon gases: methane (CH₄), ethylene (C₂H₄), or propane (C₃H₈), or decomposition of tetramethylsilane (Si(CH₃)₄) alone. It was believed that optical, electrical, and chemical properties of a-SiC:H film might be significantly dependent on the kind of hydrocarbon gas source (3) used.

Hydrogenated amorphous silicon (a-Si:H) alloy has been shown to be an excellent passivant for pn junction (11) in which two-order-of-magnitude reduction in reverse leakage current and sharper breakdown behavior were revealed, compared with the one passivated only by thermally grown silicon dioxide. Furthermore, Bind *et al.* and others (12-15) reported that 1 weight percent (w/o) of boron or boron carbide was found to be effective additive to enhance density of silicon carbide material, and thus can be used as a barrier material from Na⁺ ions or moisture contamination.

It is the purpose of this study to develop a new passivation material by doping boron or phosphorus into various kinds of amorphous silicon-carbon alloy, which were prepared from a mixture of silane and different kinds of carbon-based organic materials, *i.e.*, methane (CH₄), *o*-xylene (C₈H₁₀), toluene (C₇H₈), benzene (C₆H₆), trichloroethylene (C₂HCl₃), trichloroethane (C₂H₃Cl₃), or carbon tetrachloride (CCl₄). Chemical etching rate, electrical dc resistivity, dielectric breakdown strength, pinhole density, and optical refractive index of those films were systematically investigated.

Film Preparation

The films were prepared by 13.56 MHz RF plasma-enhanced chemical vapor deposition from a gas mixture of silane (SiH₄) and methane (CH₄), *o*-xylene (C₈H₁₀), toluene (C₇H₈), benzene (C₆H₆), trichloroethylene

(C₂HCl₃), trichloroethane (C₂H₃Cl₃), or carbon tetrachloride (CCl₄) by adding up to 1% doping species of phosphine or diborane. Corning 7059 glass plates or single-crystal silicon wafers were used as substrates. Typical preparation conditions of these samples are listed in Table I. An Anelva Plasma CVD-301 system was used in our experiment. The diameter of the electrode was 200 mm. Spacing between electrodes was adjustable from 15 to 45 mm. A capacitively coupled glow-discharge plasma was created by a radio-frequency generator with a power of 300W and frequency of 13.56 MHz. Figure 1 shows the schematic diagram of plasma CVD system.

Initially, substrates were subjected to a standard cleaning process before loading into the reaction chamber. Prior to the onset of deposition, nitrogen plasma is ap-

Table I. Preparation condition of a-SiC:H films (top) and parameters used for radio-frequency glow-discharge deposition of a-SiC:H films (bottom)

Sample	Composition
1A	SiH ₄ (5.0 sccm) + CH ₄ (5.0 sccm) + B ₂ H ₆ (1 w/o)
1B	SiH ₄ (5.0 sccm) + CH ₄ (5.0 sccm) + PH ₃ (1 w/o)
2A	SiH ₄ (8.8 sccm) + C ₈ H ₁₀ (1.1 sccm) + B ₂ H ₆ (1 w/o)
2B	SiH ₄ (8.8 sccm) + C ₈ H ₁₀ (1.1 sccm) + PH ₃ (1 w/o)
3A	SiH ₄ (8.7 sccm) + C ₇ H ₈ (1.3 sccm) + B ₂ H ₆ (1 w/o)
3B	SiH ₄ (8.7 sccm) + C ₇ H ₈ (1.3 sccm) + PH ₃ (1 w/o)
4A	SiH ₄ (8.6 sccm) + C ₆ H ₆ (1.4 sccm) + B ₂ H ₆ (1 w/o)
4B	SiH ₄ (8.6 sccm) + C ₆ H ₆ (1.4 sccm) + PH ₃ (1 w/o)
4C	SiH ₄ (8.6 sccm) + C ₆ H ₆ (1.4 sccm)
5A	SiH ₄ (6.6 sccm) + C ₂ HCl ₃ (3.3 sccm) + B ₂ H ₆ (1 w/o)
5B	SiH ₄ (6.6 sccm) + C ₂ HCl ₃ (3.3 sccm) + PH ₃ (1 w/o)
6A	SiH ₄ (6.6 sccm) + C ₂ H ₃ Cl ₃ (3.3 sccm) + B ₂ H ₆ (1 w/o)
6B	SiH ₄ (6.6 sccm) + C ₂ H ₃ Cl ₃ (3.3 sccm) + PH ₃ (1 w/o)
7A	SiH ₄ (5.0 sccm) + CCl ₄ (5.0 sccm) + B ₂ H ₆ (1 w/o)
7B	SiH ₄ (5.0 sccm) + CCl ₄ (5.0 sccm) + PH ₃ (1 w/o)

Parameter	Range
RF power	40W
Substrate temperature	250°-270°C
Deposition pressure	1-1.5 torr
Gaseous SiH ₄	25.9% in H ₂
B ₂ H ₆ , PH ₃	1% in H ₂
CH ₄	1% in H ₂
Solution C ₈ H ₁₀ , C ₇ H ₈	Extra pure
C ₆ H ₆ , C ₂ HCl ₃	Reagent
C ₂ H ₃ Cl ₃ , CCl ₄	
Total flow rate	10 sccm
Deposition rate	90-125 Å/min
Deposition time	30 min
Film thickness	500-3500Å

*Electrochemical Society Active Member.

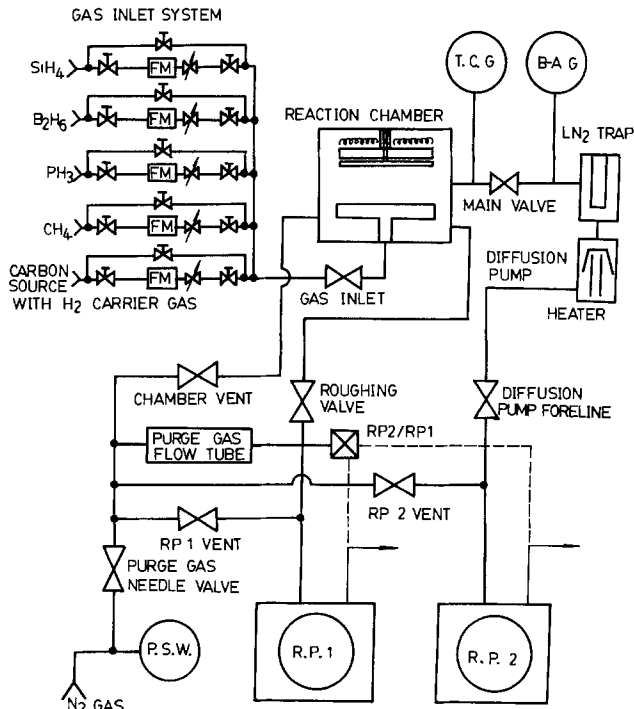


Fig. 1. Schematic diagram of the plasma CVD system used in this experiment.

plied in order to clean the substrate. Then, the chamber was evacuated to a pressure lower than 10^{-7} torr. Substrate temperature was raised up to 250°-270°C, RF power to 40W, chamber pressure to 1-1.5 torr, and the total gas flow rate to 20 sccm.

The reaction gases were SiH_4 (25.9% in H_2) and one of the following carbon sources: CH_4 , C_6H_{10} , C_7H_8 , C_6H_6 , C_2HCl_3 , $\text{C}_2\text{H}_3\text{Cl}_3$, or CCl_4 . The doping gas was B_2H_6 (1% in H_2) or PH_3 (1% in H_2). After deposition, H_2 plasma treatment was performed for 10 min.

The various carbon sources used in this study were all extra-pure reagent solution, except for CH_4 (1% H_2 based), which was in gaseous form. The carrier gas was pure hydrogen. The flow rates of various carbon sources were properly controlled in order to obtain stoichiometric compositions, which are shown in Table I.

Measurement and Discussion

Measuring techniques, results, and interpretation of the results concerning the properties of boron- or phosphorus-doped a-SiC:H film are presented below.

Chemical etching rate.—Chemical etching properties of B-doped, P-doped, and undoped a-SiC:H film were examined by immersing a-SiC samples in concentrated HF

acid (49%), buffered HF solution, 180°C H_3PO_4 solution or by $\text{CF}_4 + \text{O}_2$ plasma etching. The average etching rate was determined conventionally by measuring the time required to remove the entire film completely.

Table II shows the wet etching rate for a-SiC:H films obtained from different carbon sources. Benzene and methane groups reveal lowest etching rate; while chlorine containing groups, *i.e.*, trichloroethylene, trichloroethane, and carbon tetrachloride, reveal higher etching rates. Groups of σ -xylene and toluene show that they are also good candidates of carbon source.

Investigating boron or phosphorus doping effect on chemical properties of a-SiC:H film shows that benzene may be a good carbon source because of its excellent etching resistance, availability, and convenience in processing. It was found that boron-doped a-SiC:H films possessed five times slower etching rate than the undoped one; while phosphorus-doped films possessed only about three times slower. From this evaluation, it suggested that boron doping is superior to phosphorus doping in a-SiC:H film for device passivation. However, phosphorus impurity also reveals a prevailing effect in a-SiC:H film than the undoped one, as etching resistance was concerned.

Etch rate may be used as a sensitive indicator of dielectric film quality (16, 17). Film density, stoichiometry, and composition of the film can be directly revealed by etching. It is believable that the surface free energy in grain boundary of the doped a-SiC:H film is modified, which leads to a more dense state. Thus, protection against moisture and contamination can be improved (12, 13).

A "Plasmaline" plasma etching system was employed for dry etching by using tetrafluorine-oxygen gas mixture as etchant. Typical plasma etching conditions were: RF power = 100W, pressure = 1 torr, and total gas flow rate = 100 sccm. The etching rates are shown in Table III. Both the etching rates of doped and undoped a-SiC:H films vary dramatically for different carbon sources. There are similar tendency with that of wet etching. Table IV also shows that of G.D. doped a-SiC:H films obtained from benzene source exhibits a slightly smaller etch rate than that of a-SiC_x films (20).

DC resistivity.—DC resistivity was determined by using a six-point-probe meter (Four Dimension Company, Model 101), as shown in Fig. 2. This is an excellent tool for measuring higher sheet resistivity films like hydrogenated amorphous silicon layer, which would be impossible to measure by using conventional four-point probe method.

The six-point probe method can measure resistivity from 10^{-1} to 10^{12} Ω/\square , which is accomplished by using a low probing force (about 10g force with 500Å penetration depth) with an extremely high insulation.

Table IV is a summary of the measured dc resistivity of boron- or phosphorus-doped a-SiC films which were pre-

Table II. Etching rates for a-SiC:H films prepared from different carbon sources. Top: 49% HF etch rate. Center: buffer HF etch rate. Bottom: 180°C H_3PO_4 etch rate
Unit: Å/min^a

Carbon source Dopant	CH_4	C_6H_{10}	C_7H_8	C_6H_6	C_2HCl_3	$\text{C}_2\text{H}_3\text{Cl}_3$	CCl_4
B-doped	48	52	89	30	148	118	159
P-doped	75	81	141	54	805	6500	6000
	Unit: Å/h ^b						
B-doped	17	65	120	30	63	2140	3660
P-doped	50	68	1230	30	67	3900	3600
	Unit: Å/h ^c						
B-doped	650	1000	900	740	1000	1100	1200
P-doped	750	1000	950	800	1200	1100	1000

^a Etch rate for undoped a-SiC:H (C_6H_6 carbon source) is 160; G.D. SiN_x film is 2000-3000.

^b Undoped a-SiC:H (C_6H_6 carbon source) is 90. G.D. SiN_x film is 6000.

^c Undoped a-SiC:H (C_6H_6 carbon source) is 1700. G.D. SiN_x film is 3600.

Table III. $CF_4 + O_2$ Plasma etch rate of a-SiC:H films prepared from different carbon sourcesUnit: Å/min^a

Carbon source Dopant	CH ₄	C ₃ H ₁₀	C ₇ H ₈	C ₆ H ₆	C ₂ HCl ₃	C ₂ H ₃ Cl ₃	CCl ₄
	B-doped	160	392	317	320	980	530
P-doped	420	540	520	450	1280	810	1000

Undoped a-SiC:H (C₆H₆ carbon source) is 530; G.D. SiN_x is 450.

Table IV. Measured dc resistivity of a-SiC:H films prepared from different carbon-based sources

Unit: Ω-cm

Carbon source Dopant	CH ₄	C ₃ H ₁₀	C ₇ H ₈	C ₆ H ₆	C ₂ HCl ₃	C ₂ H ₃ Cl ₃	CCl ₄
	B-doped	9.9×10^{10}	2.3×10^9	9.1×10^{10}	9.0×10^{10}	2.2×10^9	3.7×10^7
P-doped	9.0×10^9	1.3×10^9	5.4×10^9	8×10^9	1.1×10^9	5.8×10^7	3.9×10^6

The undoped a-SiC:H (C₆H₆ carbon source) is 5×10^{12} Ω-cm, while the G.D. SiN is 6×10^{12} Ω-cm.

pared from different carbon-based sources and silane. As can be seen from this table, films with dc resistivity in the range of 10^{10} - 10^{11} Ω-cm were obtained by adding 1 w/o diborane or 1 w/o phosphine into the main flow of SiH₄ gas. The resistivity of the undoped one is around 5×10^{12} Ω-cm, which is higher. However, the doped ones are still good enough as a passivation material.

Dielectric breakdown strength.—a-SiC:H films prepared from various carbon sources exhibit different breakdown strength. A metal-silicon carbide n-type crystalline Si capacitor (18) was fabricated and was biased in the accumulation region by applying a ramp voltage. Since the sheet resistivity of n-type crystalline silicon is as low as 2-5 Ω-cm, the value of the dielectric breakdown strength was measured by assuming that the dc voltage is uniformly distributed across the silicon carbide layer, and no voltage drop is developed beyond the metal dot.

As is seen from Table V, the dielectric breakdown strength of doped a-SiC:H film is improved by one order of magnitude than the undoped one. It also exhibits a better result compared with conventional glow-discharged

a-SiN_x film (18). The boron-doped a-SiC:H film prepared by decomposing silane and methane reveals the best and stable results among these carbon-based films.

The same effects of boron- and phosphorus-doped films on breakdown strength have also been found for BPSG, PSG (19), and doped a-SiN_x film (20). For comparison, dielectric constants which were calculated from refractive index (21) are listed in Table VI. Among these, it is found that boron doped G.D. a-SiC:H film possesses higher dielectric constant than the others, with an average value of 7.

Pinhole density.—The pinhole test is one of the important methods for both locating defects in dielectric film and evaluating quality of the films. Many methods for decorating the dielectric film defects have been explored, including replica electron microscopy, electrochemical autograph, etc. (22). However, none of these methods are found to be both simple and reproducible except the copper decoration technique.

A copper decoration setup which consists of a constant-voltage power supply and a dc ampere meter was em-

Table V. Dielectric breakdown strength of a-SiC:H films varied with different carbon sources

Unit: V/cm $\times 10^6$

Carbon source Dopant	CH ₄	C ₃ H ₁₀	C ₇ H ₈	C ₆ H ₆	C ₂ HCl ₃	C ₂ H ₃ Cl ₃	CCl ₄
	B-doped	3.4	3.2	1.2	1.4	1.3	5.0
P-doped	3.3	3.1	1.3	1.2	1.2	4.9	2.5

Undoped a-SiC:H (C₆H₆ carbon source) is 6.4×10^5 ; G.D. SiN_x is 1×10^6 .

Table VI. Refractive index and dielectric constant of a-SiC:H films obtained from different carbon sources

Refractive index^a

Carbon source Dopant	CH ₄	C ₃ H ₁₀	C ₇ H ₈	C ₆ H ₆	C ₂ HCl ₃	C ₂ H ₃ Cl ₃	CCl ₄
	B-doped	2.85	2.50	2.65	2.65	2.70	2.45
P-doped	2.65	—	2.55	2.60	2.65	2.60	2.40
Dielectric constant ^b							
B-doped	8.12	6.25	7.02	7.02	7.29	6.62	—
P-doped	7.02	—	6.50	6.76	7.02	6.76	5.76

^a Undoped a-SiC:H (C₆H₆ carbon source) is 2.4; G.D. a-SiN_x is 2.0; thermally grown SiO₂ is 1.4.^b Undoped a-SiC:H (C₆H₆ carbon source) is 5.76; G.D. a-SiN_x is 4.

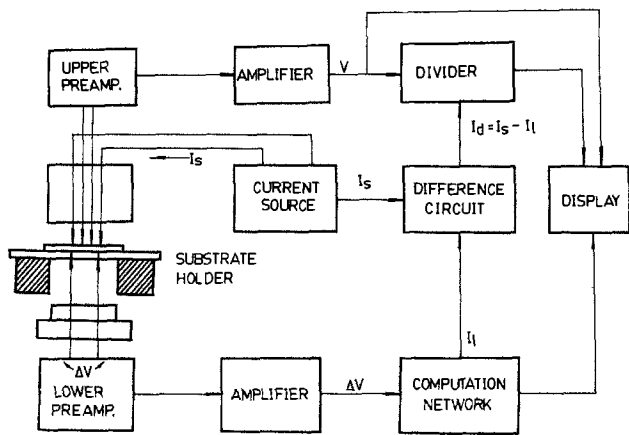


Fig. 2. Block diagram of the six-point-probe system

ployed. A low resistivity silicon wafer deposited the dielectric film and was placed on a conductive, flat aluminum plate, then was put into a glass beaker in which acetic acid (CH_3COOH) solution was employed as electrolyte. A copper plate was used as another electrode.

The experimental results are listed in Table VII, which shows that boron-doped a-SiC:H films possess substantially fewer decoration sites than phosphorus-doped and undoped ones. The thickness of the films are around 1000Å.

Optical refractive index.—In order to investigate optical refractive index and thickness of the films, the ellipsometer was used to characterize the a-SiC:H films with layer thickness ranging from 3000 to 3500Å.

Table VII shows that the refractive index also changes with different kinds of carbon source employed. Typical refractive indexes for thermally grown silicon dioxide (SiO_2) and plasma-enhanced CVD silicon nitride (SiN_x) are about 1.45 and 2.0, respectively. In the present work, all of the doped a-SiC:H films are larger than 2.5, and even the undoped one possesses a value of 2.4.

Interestingly, the boron-doped films obtained from silane and methane exhibit the highest refractive index of 2.85. This high value may be due to the higher carbon content in the a-SiC:H film or boron doping, which affects the surface free energy of the film (12). Further study is underway.

There is some relationship between film quality and deposition rate, which can be derived from film-thickness measurement. The low deposition rate of the doped films is presumably due to their higher density.

Table VIII shows the deposition rates of the a-SiC:H films for different kinds of carbon sources. In each case, pressure during the deposition process was kept at the same conditions as described in Table I. The experimental results coincide with the previous experimental studies, that is: the boron-doped a-SiC:H film using methane or benzene as carbon source exhibits the slowest deposition rate, though almost all of the deposition rates of the a-SiC:H film are varied within a range of 90-125 Å/min.

Conclusions

In this paper, plasma-enhanced chemical vapor deposited amorphous silicon carbide films were prepared by using wide variety of carbon sources. The effects of boron or phosphorus doping were also investigated. Some newly discovered results are as follows.

1. Hydrogenated amorphous SiC films which were boron- or phosphorus-doped or undoped can be successfully prepared from silane and organic carbon-based sources, including methane, *o*-xylene, toluene, benzene, trichloroethylene, trichloroethane, and carbon tetrachloride in a glow-discharge deposition system.

2. It is concluded that only methane and benzene are good candidates from the point of view of chemical, electrical, and optical properties, while chlorine containing carbon sources, *e.g.*, trichloroethylene, trichloroethane, and carbon tetrachloride, reveal poorer properties. However, benzene is highly recommended because of availability and ease of handling.

3. Boron-doped films always show chemical, electrical, and optical properties superior to phosphorus-doped ones. This may be due to surface free energy modification by dopant participation. In addition, owing to the fact that the ionic radius of boron is smaller than that of phosphorus, the modification effect is more evident in boron-doped a-SiC:H film.

4. The deposition temperature is low (250°-270°C). The best G.D. a-SiC:H film for passivation has been obtained from silane and benzene gas mixture with 1 w/o boron doping, which possesses the following properties: HF etching rate = 30 Å/min, buffered HF etching rate = 30 Å/h, 180°C H_3PO_4 etching rate = 740 Å/h, $\text{CF}_4 + \text{O}_2$ plasma etching rate = 320 Å/min, resistivity = 10^{11} (Ω-cm), and refractive index = 2.65. These data are superior or competitive to the conventional passivation films, *e.g.*, thermally grown SiO_2 , G.D. SiN_x , CVD SiN_x , and thus the boron-doped G.D. a-SiC:H film may be adopted as a novel passivant for semiconductor devices or optical dielectric film.

5. It is believable that MNS and MNOS devices using boron-doped a-SiC:H film as the insulator layer may pos-

Table VII. Pinhole density of a-SiC:H films prepared from different carbon sources

Unit: $1/\text{cm}^2$

Carbon source Dopant	CH_4	C_8H_{10}	C_7H_8	C_6H_6	C_2HCl_3	$\text{C}_2\text{H}_3\text{Cl}_3$	CCl_4
	B-doped	—	8	20	6	15	39
P-doped	—	25	12	10	20	39	25

Undoped a-SiC:H (C_6H_6 carbon source) is 26.

Table VIII. Deposition rate of a-SiC:H films prepared from different carbon sources

Unit: Å/min

Carbon source Dopant	CH_4	C_8H_{10}	C_7H_8	C_6H_6	C_2HCl_3	$\text{C}_2\text{H}_3\text{Cl}_3$	CCl_4
	B-doped	—	105	100	95	98	106
P-doped	—	108	123	107	107	112	125

Undoped a-SiC:H (C_6H_6 carbon source) is 115.

sess the better diffusion barrier against environmental contamination and radiation (*i.e.*, ion implantation, etc.) because of its better passivation performance and less leakage.

It is also presumably applicable to VLSI device passivation. Nevertheless, its use as an active part in energy conversion devices, sensors, or light emitting diodes are also promising.

Acknowledgments

The authors are grateful to L. Wu and M. K. Lee for assisting in building the experimental system, to R. H. Lee for the assistance in sample preparation, and to Y. K. Su, Y. H. Wang, and W. C. Liu for their generosity in providing the unpublished AES data. This work was supported by the National Science Council, Republic of China.

Manuscript submitted March 4, 1983; revised manuscript received Aug. 15, 1984.

National Cheng Kung University assisted in meeting the publication costs of this article.

REFERENCES

1. Y. Tawada, H. Okamoto, and Y. Hamakawa, *Appl. Phys. Lett.*, **39**, 237 (1980).
2. S. Nishino, Y. Hazuki, H. Matsunami, and T. Tanaka, *This Journal*, **127**, 2674 (1980).
3. Y. Tawada, K. Tsuge, M. Kondo, H. Okamoto, and Y. Hamakawa, *J. Appl. Phys.*, **53**, 5273 (1980).
4. I. Watanabe, Y. Hata, A. Morimoto, and T. Shimizu, *Jpn. J. Appl. Phys.*, **21**, L613 (1982).
5. A. Morimoto, T. Miura, M. Kumeda, and T. Shimizu, *ibid.*, **21**, L119 (1982).
6. K. Nakazawa, S. Ueda, M. Kumeda, A. Morimoto, and T. Shimizu, *ibid.*, **21**, L176 (1982).
7. T. Shimada, Y. Katayama, and K. F. Komatsubara, *J. Appl. Phys.*, **50**, 5530 (1979).
8. A. Morimoto, T. Miura, M. Kumeda, and T. Shimizu, *ibid.*, **53**, 7299 (1982).
9. D. A. Anderson and W. E. Spear, *Philos. Mag.*, **35**, 1 (1977).
10. H. Munekata, S. Murasato, and H. Kukimoto, *Appl. Phys. Lett.*, **37**, 536 (1980).
11. I. Weitzel, R. Primig, and K. Kempter, *Thin Solid Films*, **75**, 143 (1981).
12. J. M. Bind and J. V. Biggers, *J. Appl. Phys.*, **47**, 5171 (1976).
13. J. M. Bind and J. V. Biggers, *J. Am. Ceram. Soc.*, **58**, 304 (1975).
14. N. D. Antonova, A. A. Kalinina, and V. I. Kudryavtsev, *Sov. Powder Met. Metal Ceram.*, **6**, 444 (1962).
15. P. T. B. Shaffer, *Mater. Res. Bull.*, **4**, 213 (1969).
16. A. K. Sinha, H. J. Levinstein, T. E. Smith, G. Quintana, and S. E. Haszko, *This Journal*, **125**, 601 (1978).
17. C. A. Deckest, *ibid.*, **125**, 320 (1978).
18. C. E. Morosanu, *Thin Solid Films*, **65**, 171 (1980).
19. W. Kern and G. L. Schnable, *RCA Rev.*, **43**, 423 (1982).
20. C. Y. Chang, Y. K. Fang, C. F. Huang, and R. H. Lee, To be published.
21. K. M. Mar and G. M. Samuelson, *Solid State Technol.*, **137**, April 1980.
22. W. J. Shannon, *RCA Rev.*, **31**, 431 (1970).

Crystallographic Growth Forms of Silicon on a Free Melt Surface

T. F. Ciszek*

Solar Energy Research Institute, Golden, Colorado 80401

ABSTRACT

Crystallographic growth forms and radial growth-rate anisotropies of point-nucleated, dislocation-free silicon sheets spreading horizontally on the free surface of a silicon melt have been measured for (100), (110), (111), and (112) sheet planes. 16 mm movie photography was used to record the growth process. Analysis of the sheet edges has lead to predicted geometries for the tip shape of unidirectional, dislocation-free, horizontally growing sheets propagating in various directions within the above-mentioned planes and provides a crystallographic description of the radial leading edges of the solid/liquid interface during flat-top transition growth in Czochralski pulling.

Two applications of silicon crystal growth from the melt which involve lateral growth on the free melt surface are flat-top transition growth in the Czochralski process (1) and horizontal ribbon growth with a large-area solid/liquid interface (2). In this paper, observations of (100), (110), (111), and (112) sheets propagating radially from small-diameter sources on a free melt surface are presented. From 16 mm films and postgrowth examination of the crystals, it was possible to deduce the idealized polygonal growth shapes of the sheets. In addition, information about growth rate anisotropies in the sheet planes has been obtained. Generally, the crystal faces that grow most slowly are those with the closest packing. As Jackson pointed out (3), these should also be the faces with the lowest specific surface free energy. Thus, there is reason to expect that the equilibrium form and the observed macroscopic growth form will be similar.

Equilibrium forms are governed by the variation of surface free energy with crystal orientation, as described by the classic work of Wulff (4). Further amplification of Wulff's concepts was provided by Herring (5). In these treatments, a polar plot of specific surface free energy *vs.* crystal orientation (called a Wulff plot) is constructed. The distance from the origin in a particular direction is proportional to the surface free energy for the crystal orientation corresponding to that direction. In general, the plot is a three-dimensional closed surface with a number

of minima and maxima. If planes perpendicular to the radius vector are imagined at each point on the closed surface, then the volume that can be reached from the origin without crossing any planes defines the equilibrium shape or form of the crystal. Since sharp minima or cusps in the polar plot have the shortest radius vectors, planes normal to the radius at these cusp positions will dominate the equilibrium shape.

Sheet crystals are approximately two-dimensional; hence, a planar section through the Wulff plot coincident with the sheet surface plane is useful in describing the equilibrium shape. On the hypothesis that growth forms and equilibrium forms are similar for the crystals grown in this study, qualitative Wulff plots that locate the cusp minima in the various sheet planes were constructed. Detailed data for the variation of surface free energy with orientation is not available for silicon. However, it is generally acknowledged that the (111) planes have the lowest surface free energy, and vestiges of these planes are responsible for the observable "growth lines" on crystals constrained to grow in a cylindrical ingot form. As mentioned earlier, the value of the surface free energy for a particular crystal plane is a function of the free bond density. This is lowest for (111) planes.

From the geometry of the sheet edges, a crystallographic description of faceting effects during flat-top Czochralski transition growth was obtained. Similarly, it is possible to determine the criteria that govern the tip

* Electrochemical Society Active Member.

shapes of single-crystal silicon ribbons growing horizontally from a melt surface.

Experimental

Silicon was melted in a quartz crucible of 60 mm diam and 25 mm height. Induction heating with a graphite susceptor was used. The susceptor was insulated by a cylindrical opaque quartz tube with a 6 mm wall thickness. An inert atmosphere of argon was maintained in the growth chamber. Sheet growth was initiated by dipping a seed crystal of the desired orientation into the melt and growing a thin neck from the seed at 15 rpm rotation rate in order to produce a dislocation-free, small (0.5-1.5 mm diam) cylindrical crystal. A sheet was then allowed to propagate radially in all directions on the melt surface by setting the vertical pulling speed to zero, dropping the RF generator power level to 94.7% of the value at which the neck was grown, and lowering the rotation rate to 1 rpm. A slow rate was used to avoid imposing a round shape on the spreading sheet. However, a nonzero rate was needed to allow measurements of all crystal faces on movie films of the growth. For each seed orientation, a second sheet was grown from a larger diameter (3.8-6.2 mm), dislocation-free, round cylindrical starting condition. Since the transformation from round to equilibrium shape occurs in a distance which is a function of initial round diameter, this allowed the transformation to be viewed on two different size scales.

The sheets did not grow perfectly flat and tended to have a slightly convex bottom since some growth occurred downward into the melt while the sheets were spreading radially. The radial growth rate of the sheets as they approached their equilibrium shapes typically ranged from 7 to 15 mm/min for the 5.3% power reductions used in these studies. At some point in the growth, icing from the crucible walls moved radially inward to close proximity with the spreading sheets. The sheets were removed from the melt at this time by quickly pulling the seed upward.

Records of the sheet growth experiments were made with 16 mm movie photography. The camera was located outside a window of the growth chamber, and a polished silicon mirror was used to direct light rays from the growth area to the camera. A filming speed of 10 frame/s was used in the sheet growth studies. The typical growth duration was 140s and, since a rotation rate of 1 rpm was used, the crystal revolved just over two times during the filming. This allowed any particular diameter of the growing sheet to be measured five times. Measurements were made of the distance between parallel flat faces and of the diameters of the faster growing diagonally opposed regions located angularly between two successive flat faces. Figure 1 is the view the camera sees. In this case, a (110) sheet growing at its limiting shape is shown. The measurements were made from the film by passing it un-

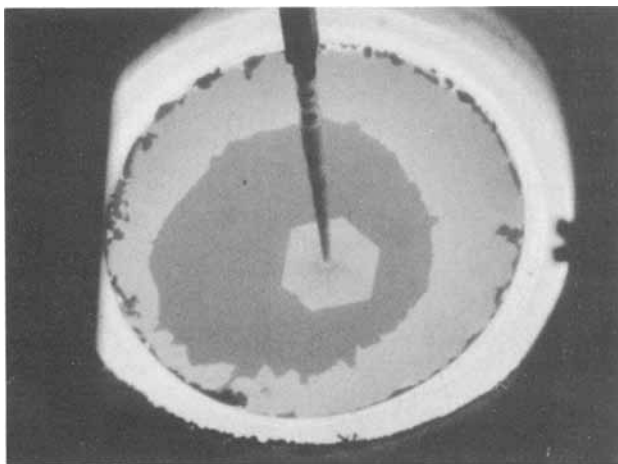


Fig. 1. A 16 mm frame from a film showing the limiting growth shape of a (110) sheet.

der a low-power (8-40 \times) microscope with a reticle placed over the film.

Sheet Shapes

The limiting shape of a (100) dislocation-free silicon sheet is a square. Figure 2a shows this form for a sheet grown from a 1.2 mm diam, round starting shape. The transformation to the square shape occurs in about 3-4 seed diameters; thus, the sheet is square at a small size. The idealized square shape is shown in Fig. 2b. The edges are in the four $\langle 011 \rangle$ directions, and the corners lie along the four $\langle 001 \rangle$ directions. The Wulff plot in the (100) plane is expected to have minima at the four (011) planes normal to the sheet surface and larger values in other directions. This is qualitatively shown by the curved, four-lobed figure surrounding the equilibrium shape.

Sheets nucleated in the (111) plane transform from round to hexagonal with equal 120° angles (Fig. 3a). The sides of the hexagonal shape are in $\langle \bar{1}\bar{1}2 \rangle$ radial directions, while the corners are in $\langle \bar{1}10 \rangle$ directions. The hypothetical Wulff plot is drawn with six cusps on the $(\bar{1}\bar{1}2)$ planes bounding the idealized sheet shape shown in Fig. 3b.

At first glance, the growth form of (110) sheets also appears to be a regular hexagon (Fig. 4a). However, closer examination shows that there is less symmetry in the (110) shape. Four of the six polygonal sides lie in $\langle \bar{1}11 \rangle$ directions, and the angle between two such adjacent sides is only 109.471° , as shown in Fig. 4b. The corners between two such sides lie in $[\bar{1}10]$ and $[1\bar{1}0]$ directions. Two sides of the polygonal shape are opposite each other and in the $[001]$ and $[00\bar{1}]$ directions. These sides make an angle of

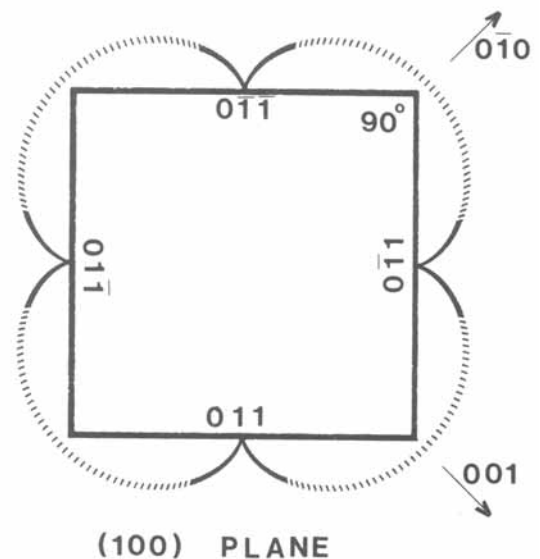
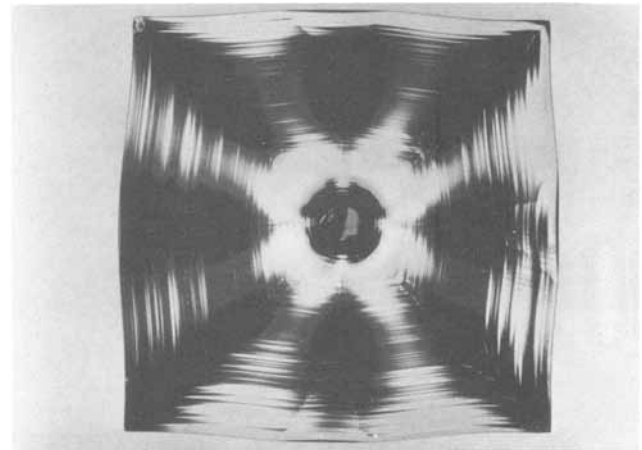


Fig. 2. a(top): Final shape of a (100) sheet. b(bottom): Idealized growth form and qualitative Wulff plot for a (100) sheet.

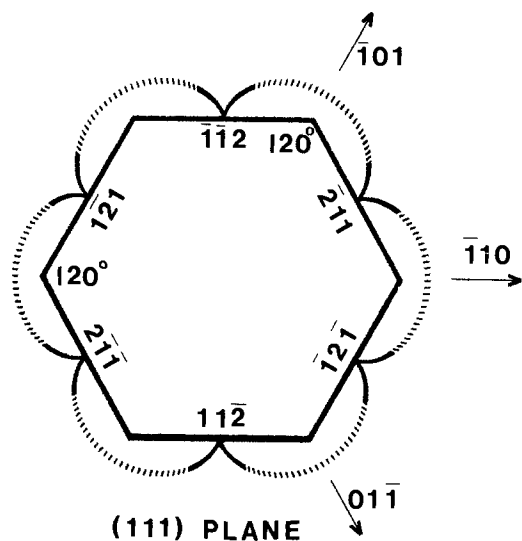
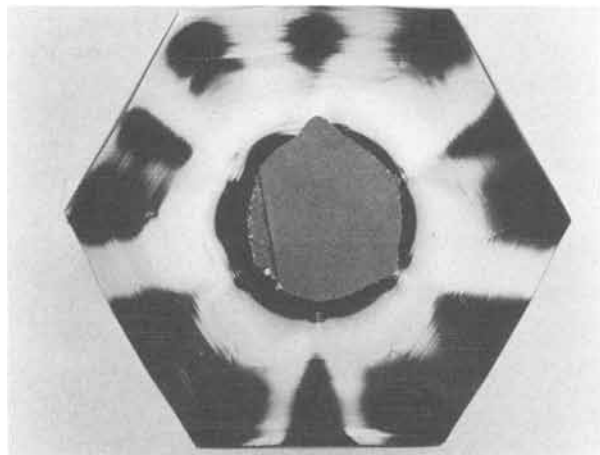


Fig. 3. a(top): Final shape of a (111) sheet. b(bottom): Idealized growth form and qualitative Wulff plot for a (111) sheet.

125.264°, with the $(\bar{1}11)$ type sides. Minima occur on both (001)- and $(\bar{1}11)$ -type planes in the qualitative Wulff plot. Since growth in the $[001]$ -type directions appears to proceed more rapidly than growth in the $[\bar{1}11]$ -type directions (Fig. 4a), it is possible that after long growth times the (001) faces may vanish, leaving only $(\bar{1}11)$ bounding planes.

The (112) plane sheets are observed to also have six sides, as can be seen in the sheet crystal of Fig. 5a. However, the bounding faces and included angles are different from both the (111) and (110) sheet cases. Two opposite sides are in $\langle \bar{1}11 \rangle$ directions. The other four sides correspond to predicted Wulff plot cusps on $(2\bar{4}1)$ -type planes. Two adjacent sides of this type make an angle of 135.585° with each other. The corners between these sides are in $[\bar{1}10]$ and $[\bar{1}10]$ directions. The angle between $(2\bar{4}1)$ - and $(\bar{1}11)$ -type sides is 112.208°. The deduced Wulff plot shows minima on both $(\bar{1}11)$ - and $(2\bar{4}1)$ -type planes (Fig. 5b). The growth rates in the $[2\bar{4}1]$ - and $[\bar{1}11]$ -type directions appeared to be very similar (Fig. 5a). However, it is again possible that for long growth times one or the other may dominate.

The Wulff plots in Fig. 2-5 are only hypothetical. It is reasonably certain that minima occur where they are shown. Whether the minima are sharp cusps or only shallow valleys is not known. There is more uncertainty about the nonminima portions of the plots. Thus, they are shown as dotted lines in the figures. Since no special effort was made to reduce thermal asymmetry in the hot zone, the sheet crystal forms were sometimes asymmetrical. That is, the distance from the seed to two equivalent flat edges was not always equal.

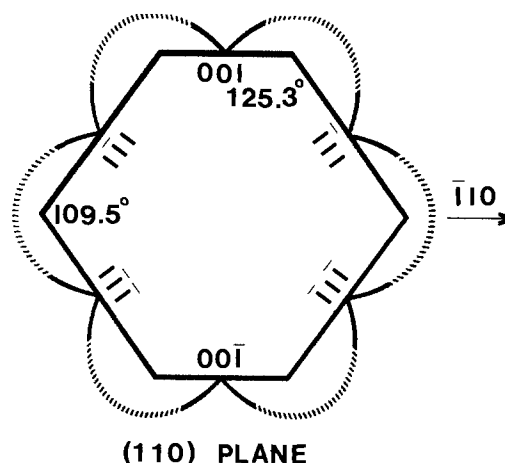
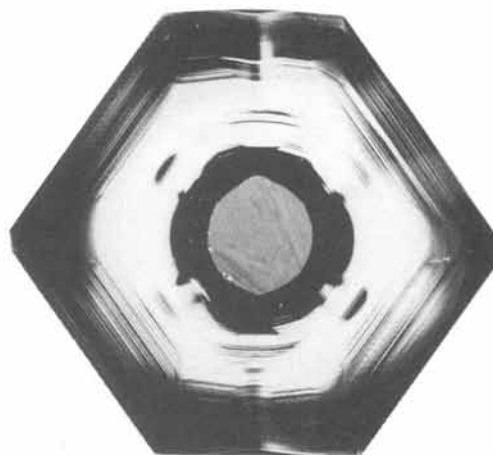


Fig. 4. a(top): Final shape of a (110) sheet. b(bottom): Idealized growth form and qualitative Wulff plot for a (110) sheet.

Sheet Edge Geometries

A strong (111) faceting effect was observed on the edge regions of the sheets, largely because dislocation-free growth was employed for the sheet experiments. In the absence of dislocations, nucleation of new growth is more difficult, and larger levels of supercooling arise at the leading edges of the growth front. Faceting accompanies this situation. One (100) sheet was grown from a dislocated starting configuration. Two effects were noted with this sheet. The edge faceting was much less pronounced and, in fact, was nearly absent. Also, the idealized square shape did not completely form, at least not in the growth times available in our experimental setup. The corners of the sheet remained well-rounded.

The edge faceting in dislocation-free sheets always appeared on (111) planes. An example is depicted in the photograph of Fig. 6, which shows a (111) sheet mounted in wax to allow viewing of the edge. The central edge facet in the photograph makes a 70.5° acute angle with the top of the sheet. It is located in a $\langle 2\bar{1}\bar{1} \rangle$ -type direction from the seed. To the left and right of this facet are other edge facets that make a 109.5° obtuse angle with the sheet's top surface. These are in $\langle 2\bar{1}1 \rangle$ directions from the seed. All told, there are three obtuse facets and three acute facets alternating around the sheet edge. Careful scrutiny of Fig. 6 also reveals a (111) facet on the sheet top adjacent to the central edge facet. There are six of these, one adjacent to each edge facet.

In addition to describing the radial growth crystallography for flat-top Czochralski transition growth, these observations have implications for high perfection sheet growth solid/liquid interfaces in the horizontal growth mode. It is possible to predict, for example, the sheet tip geometries for a large number of growth orientations

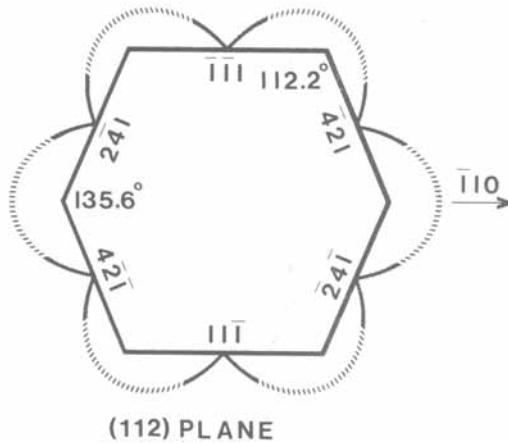
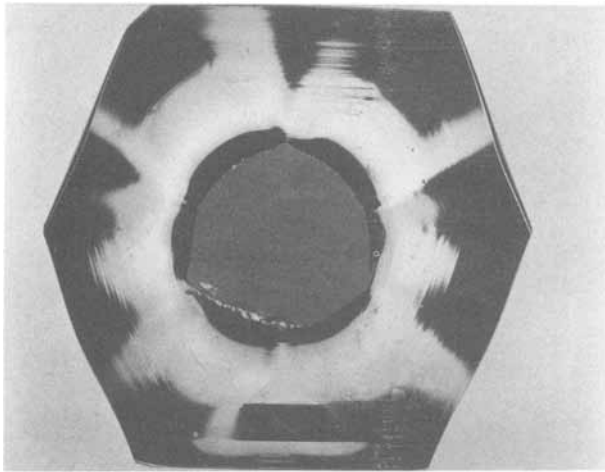


Fig. 5. a(top): Final shape of a (112) sheet. b(bottom): Idealized growth form and qualitative Wulff plot for a (112) sheet.

from the observations on radially spreading sheets. Figure 7 shows the expected tip geometries for (111) dislocation-free sheets growing in the $\langle 2\bar{1}\bar{1} \rangle$ - and $\langle \bar{2}1\bar{1} \rangle$ -type directions, with a 5° pulling angle. Note the retrograde tip angle for $\langle \bar{2}1\bar{1} \rangle$ growth.

For (100) sheets, four (111) edge facets appear in $\langle 011 \rangle$ directions from the seed. All make 54.7° acute angles with the top of the sheet. The expected tip geometry for dislocation-free (100) silicon sheets growing in one of these four directions is given in Fig. 8.

The edges of (110) sheets displayed two types of (111) facets. In the four $\langle 1\bar{1}\bar{1} \rangle$ -type directions, a 90° facet with respect to the sheet plane was found. In the two $\langle 001 \rangle$ directions, the facet made a 35.3° acute angle with the

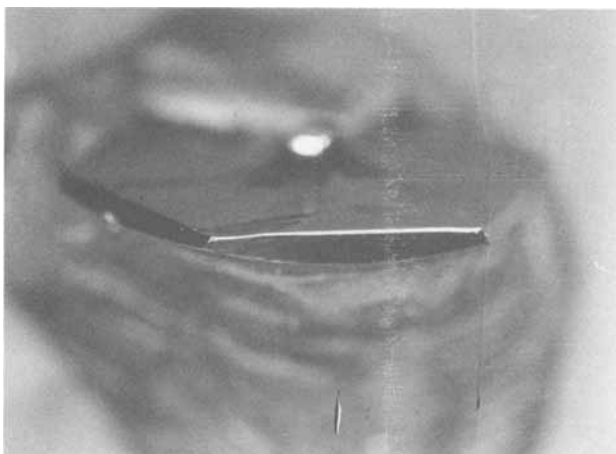


Fig. 6. Edge facets on a (111) dislocation-free sheet mounted in wax

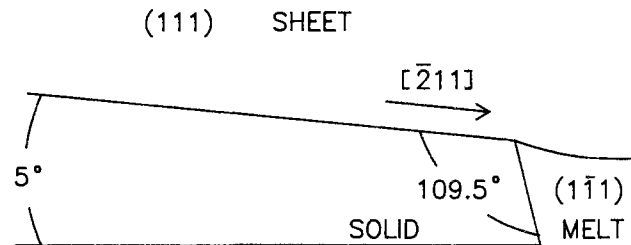
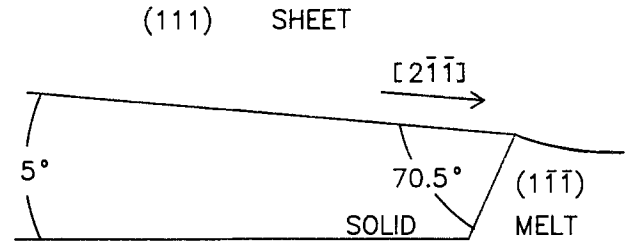


Fig. 7. Predicted tip geometries for horizontally grown (111) sheets pulled in the $\langle 2\bar{1}\bar{1} \rangle$ and $\langle \bar{2}1\bar{1} \rangle$ directions.

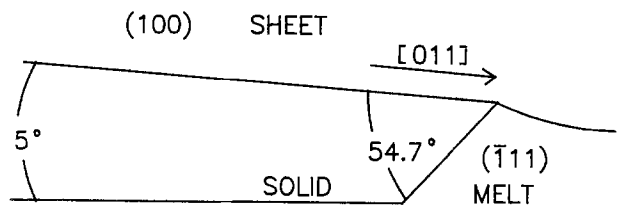


Fig. 8. Predicted tip geometry for horizontal (100) sheets growing in the $\langle 011 \rangle$ directions.

sheet top. The 144.7° obtuse (111) facets were not observed. Predicted sheet tip geometries for horizontal growth are drawn in Fig. 9.

The greatest variety of edge facets was seen in (112) sheets. Figure 10 shows these in the way they would define the tip geometries of horizontal sheets. In the $[1\bar{1}\bar{1}]$ direction, a facet at 90° to the sheet plane was seen, while in the $[\bar{1}\bar{1}\bar{1}]$ direction, two facets appeared. One was at 90° to the sheet plane, and a second was at 19.5° . These two facets meet at an included angle of 109.5° . In the $\langle 4\bar{2}\bar{1} \rangle$ directions, acute angle facets of 61.9° were seen, while in the $\langle \bar{4}2\bar{1} \rangle$ directions, the angles were retrograde with a 118.1° value.

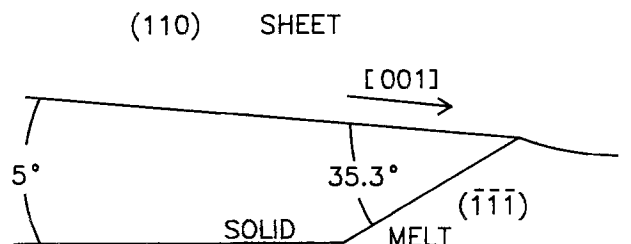
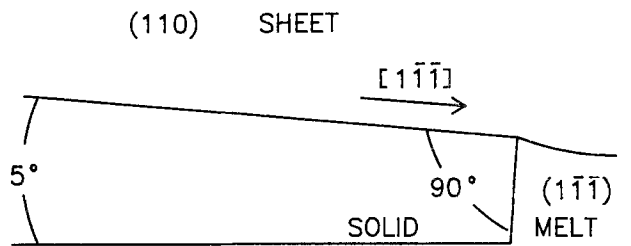


Fig. 9. Predicted tip geometries for horizontal (110) sheets growing in the $\langle 1\bar{1}\bar{1} \rangle$ and $\langle 001 \rangle$ directions.

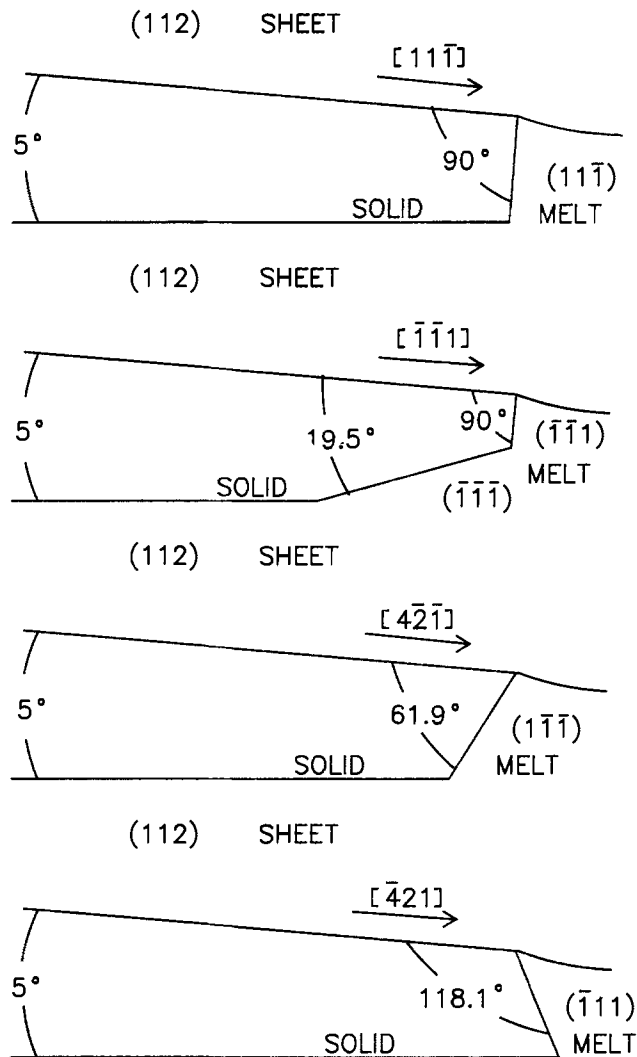


Fig. 10. Predicted tip geometries for (112) sheets growing in the $[11\bar{1}]$, $[\bar{1}\bar{1}1]$, $\langle 4\bar{2}\bar{1}\rangle$, and $\langle 421\rangle$ directions.

Growth Rate Anisotropies

As the radially spreading sheets described in this study evolve from the round initial geometry to the polygonal growth form, it is evident that the growth rates in the directions toward the polygon corners must be greater than the growth rates in directions toward the flat polygon sides. Neither of the rates are constant with time. Initially, the growth rate is slow, since the melt temperature does not respond immediately to the drop in RF generator power. The rate increases slowly at first, and then more rapidly, as the expanding top surface of the solid, with its higher emissivity, becomes an increasingly more effective heat radiator. The slope of a size vs. time plot for a particular direction from the seed, at any given time, is the growth rate in that direction at that time. The ratio between rates in different directions is the ratio of slopes of the two size vs. time curves at the same instant.

Figure 11 shows the size of a (100) sheet along the $\langle 011\rangle$ and $\langle 001\rangle$ directions as a function of time for a dislocation-free starting diameter of 1.2 mm. All $\langle 001\rangle$ directions were considered to be equivalent, and all $\langle 001\rangle$ directions were considered to be equivalent. Thus, four measurements for each set of directions were made for each revolution of the crystal. The initially round (100) sheet eventually became square, and the ratio of slopes in the $\langle 011\rangle$ and $\langle 001\rangle$ directions, for large times, is expected to be the geometrically limited value 0.71. The growth rate ratios were determined by evaluating the derivatives of the second-order polynomial regression best fit curves for the diameter vs. time data, for each of the two directions, and taking their ratios. The $\langle 011\rangle/\langle 001\rangle$ growth rate ratio in the (100) sheet plane ranges from 0.4

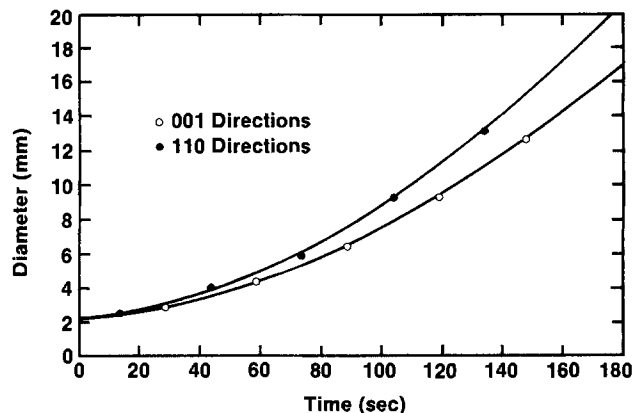


Fig. 11. Size vs. time for a (100) sheet in two different radial directions.

to a final value of 0.74 over the 150s growth time (Fig. 12) with a relatively quick rise to 0.6 and then a slower approach to 0.74. A growth model for a growth rate in the $\langle 011\rangle$ direction 0.6 times the growth rate in any other direction is shown in Fig. 13. The transformation from a round to a square shape is seen to happen in about three seed diameters.

Similar behavior, but generally with less anisotropy, was seen for the other sheet planes. For example, the $\langle 11\bar{2}\rangle/\langle 01\bar{1}\rangle$ growth rate ratio in the (111) plane ranged from an initial value near 0.6 to a final value of 0.9 (Fig. 12), which is in good agreement with the geometrically limited value of 0.87. The change of growth rate ratios

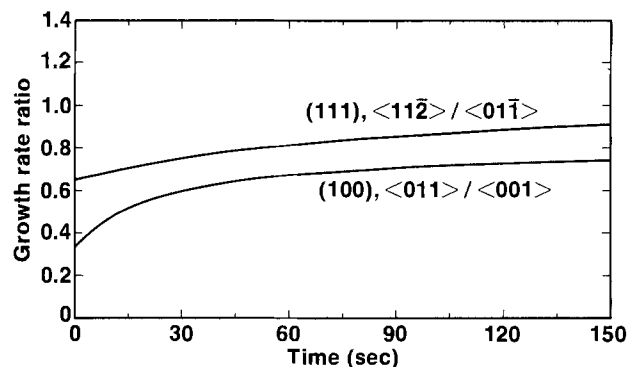


Fig. 12. Two examples of the change of growth rate ratios with time. a: (Growth rate in $\langle 011\rangle$ direction)/(growth rate in $\langle 001\rangle$ direction) for the (100) sheet plane (lower curve). b: (Growth rate in $\langle 11\bar{2}\rangle$ direction)/(growth rate in $\langle 01\bar{1}\rangle$ direction) for the (111) sheet plane (upper curve).

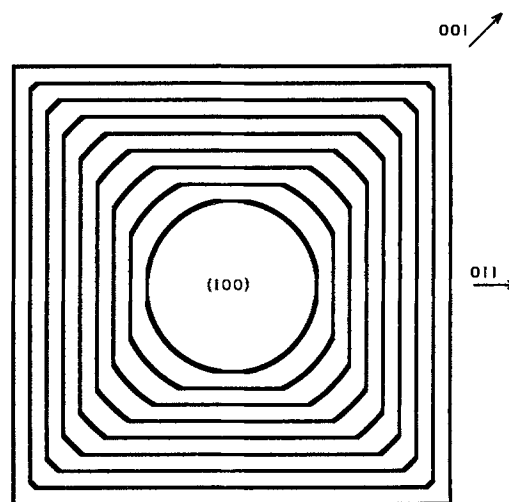


Fig. 13. (100) sheet growth model for growth rate in $\langle 110\rangle$ directions equal to 0.6 times the rate in all other directions.

with time is probably related to the changing temperature. However, the change is moderate, and the growth rate ratios appear to asymptotically approach final values at high growth speeds.

Summary and Discussion

The technique of studying rapid silicon sheet growth via free spreading of point-nucleated sheets on a super-cooled horizontal melt surface has yielded a large amount of information about idealized growth forms, solid/liquid interface sheet tip morphologies, qualitative Wulff surface free energy polar plots, and growth rate anisotropies. The method is versatile in that both very high perfection (dislocation-free) effects and less structured (polycrystalline and dendritic) effects can be studied. In this paper, only dislocation-free growth with (100), (111), (110), and (112) surface planes is discussed in detail.

The low surface free energy (111) planes dominate the sheet tip geometry at the solid/liquid interface, determine the growth form of radially growing sheet crystals (through their intersection with the sheet plane), and contribute to growth rate anisotropies due to the relative difficulty of new growth nucleation on the low free bond density (111) surface. They also play a determining role in fast dendritic growth by virtue of the high free bond density associated with reentrant edges at a (111) twin boundary. Earlier work on edge-supported pulling of silicon sheets (6) showed that (111) twin planes can block the spreading of spurious random grains. A similar mechanism has recently been found to be important in stabilizing the crystal structure of horizontally grown sheets. In dendritic web growth, (111) twin planes are key elements of the growth process and the (111) web surface is very high in quality. The equilibrium structure of long multicrystalline silicon sheets is dominated by longitudinal grains with (111) boundaries and near $\langle 110 \rangle$ surface normals. In summary, the properties of the (111) surface

in silicon are of major importance for sheet crystal growth. In addition, (111) plane faceting dominates the edge geometry for radially spreading growth during the flat-top transition phase of Czochralski crystal pulling.

Acknowledgments

The technical assistance of several individuals is deeply appreciated. M. Schietzelt helped in the crystal growth experiments, the 16 mm film analysis, and the preparation of figures for the manuscript. J. Hurd also assisted in the film measurements. Support for this work was provided by the U.S. Department of Energy and DOE/JPL contract W08746-83. The content of this paper is derived from a presentation by the author at the JPL Research Forum on High-Speed Growth and Characterization of Crystals for Solar Cells, Port St. Lucie, Florida, July 25-27, 1983.

Manuscript submitted April 23, 1984; revised manuscript received Sept. 21, 1984.

The Solar Energy Research Institute assisted in meeting the publication costs of this article.

REFERENCES

1. W. Zulehner and D. Huber, in "Crystals—Growth, Properties, and Applications," Vol. 8, J. Grabmaier, Editor, pp. 1-143, Springer-Verlag, Berlin (1982).
2. B. Kudo, *J. Cryst. Growth*, **50**, 247 (1980).
3. K. A. Jackson, in "Crystal Growth: A Tutorial Approach," W. Bardsley, D. T. J. Hurle, and J. B. Mullin, Editors, pp. 139-155, North Holland, Amsterdam (1979).
4. G. Wulff, *Z. Krist.*, **34**, 449 (1901).
5. C. Herring, *Phys. Rev.*, **82**, 87 (1951).
6. T. F. Ciszek and J. L. Hurd, in "Electronic and Optical Properties of Polycrystalline or Impure Semiconductors and Novel Silicon Growth Methods," K. V. Ravi and B. O'Mara, Editors, p. 213, The Electrochemical Society Softbound Proceedings Series, Princeton, NJ (1980).

Epitaxial Growth Rate of GaAs: Chloride Transport Process

J. C. Hong and H. H. Lee

Department of Chemical Engineering, University of Florida, Gainesville, Florida 32611

ABSTRACT

A rate expression is developed for the growth rate of gallium arsenide based on a postulated mechanism of the growth kinetics. This rate expression, when applied to the experimental data reported by Shaw (4), describes the growth rate quite accurately over wide ranges of temperature and concentrations. In particular, it describes in a quantitative manner the temperature and GaCl concentration dependence of the growth rate, which goes through a maximum with the temperature and the concentration. The growth rate as affected by diffusion is given in terms of concentration boundary layer and the intrinsic growth rate obtained. A criterion of negligible diffusional effect is developed. The effect of physical orientation of substrate surface on the growth rate is also presented. These results allow one to determine rather completely the growth rate as affected by temperature, vapor-phase composition, fluid velocity, and the substrate orientation.

The vapor-phase epitaxial growth of GaAs in the Ga/HCl/As/H₂ system has received considerable attention in the literature, and review articles (1, 2) are available. One major interest in the epitaxial growth is the effects of various conditions on the growth rate. In the studies dealing with the effects, the usual approach is to assume equilibrium conditions (2). In this approach, the etching rate at the source is related to the thermodynamic equilibrium constant for the reaction leading to the formation of GaCl, chloride flow rate and the inlet partial pressure of AsCl₃. This etching rate is used for the difference in the etching rates between the source and the substrate to represent the thermodynamic term in the growth rate. Thus, the growth rate is typically expressed as a product of the thermodynamic term and hydrodynamic term in the form used for the growth of Si. The equilibrium approach has been used in one form or another by Hollan *et al.* (3) and

Shaw (4) in the use of a quasi-equilibrium method (5) to diffusion-limited growth rate (6, 7).

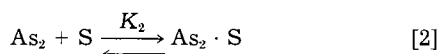
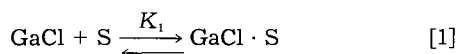
The growth process is considered kinetically controlled if the surface reactions are rate-limiting or transport (diffusion)-controlled if the diffusion through the boundary layer on the substrate is the rate-limiting step. Thus, the growth is either kinetically controlled or diffusion controlled, depending on the relative magnitude of rate constant and mass-transfer coefficient in the simplest case in which the growth rate is proportional to concentration. Although the distinction between kinetically controlled and diffusion-controlled growth is based on the relative speed of the two rate processes, this distinction is often used to explain the temperature dependence of the growth rate. In the region where the growth rate increases with increasing temperature, the growth process is considered to be under kinetic control, whereas it is un-

der diffusion control in the region where the growth rate decreases with increasing temperature. It appears that such a distinction is improper since the growth rate would not decrease with increasing temperature if indeed the diffusion process is the rate-limiting step.

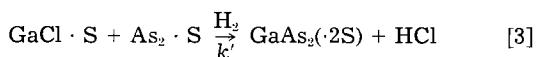
The factors that affect the growth rate are temperature, vapor-phase gas composition, physical orientation of substrate with respect to gas flow, flow rate, and crystallographic orientation of substrate surface. For a given crystal plane, the first two factors determine the growth rate in the absence of diffusional effect. This growth rate in the absence of diffusion limitation may be termed "intrinsic growth rate," since it is the intrinsic rate unaffected by diffusion. The latter two factors determine in what manner the intrinsic rate is altered by diffusion for the actual growth rate observed. In this paper, we present results for a quantitative description of the growth rate. For the results, we first develop an expression for the intrinsic growth rate based on a postulated growth mechanism. We then determine the manner in which the intrinsic growth rate is affected by diffusion. This leads directly to the effect of physical substrate orientation on the growth rate. The results are compared with the data reported in the literature. This comparison leads to some insights into the growth mechanism.

Intrinsic Growth Rate

Consider the deposition of GaAs onto the substrate surface. We postulate that the incorporation of vapor-phase molecules onto the substrate requires adsorption of arsenic and GaCl onto the substrate sites as suggested by Shaw (4) and that arsenic is molecularly adsorbed in the form of As_2 . These competitive adsorption steps can be represented as



where K_1 and K_2 are the ratios of the forward rate constant to the reverse rate constant for the elementary steps shown. Here, the vacant site is denoted by S and the adsorbed states are represented by $GaCl \cdot S$ and $As_2 \cdot S$. We postulate further that the adsorbed species interact in the presence of hydrogen, which abstracts chlorine, for the incorporation into GaAs crystal structure



where $GaAs_2(\cdot 2S)$ denotes the lattice state of GaAs already incorporated into the crystal structure. It is postulated that in building up the zinc blende crystal structure of GaAs, one additional As atom is required for successive incorporation of Ga atom into the structure. In reality, there could be several surface reactions for the incorporation. Hence, the reaction shown represents the controlling step in an overall surface reaction scheme rather than the controlling elementary step. In addition, we postulate that two vacant sites can react with HCl, resulting in the etching of GaAs



where the pair of vacant sites is denoted by (2S). Here again, this reaction represents an overall surface reaction scheme rather than an elementary step, as we shall see. According to the postulation, then, the rate of incorporation per unit surface area, r , in mole/(time · area) is

$$r = k' C_{H_2} C_{GaCl \cdot S} C_{As_2 \cdot S} - k_e C_v^2 C_{HCl} \quad [5]$$

where $C_{GaCl \cdot S}$ and $C_{As_2 \cdot S}$ are the surface concentrations of the adsorbed species, $GaCl \cdot S$ and $As_2 \cdot S$. C_v is the surface concentration of vacant sites and C_{H_2} and C_{HCl} are the volume concentrations of hydrogen and HCl. If we use

the site balance per unit surface area given by

$$C_t = C_v + C_{GaCl \cdot S} + C_{As_2 \cdot S} \quad [6]$$

the elementary steps given by Eq. [1] and [2] yield

$$\frac{C_v}{C_t} = \frac{1}{1 + K_1 C_{GaCl} + K_2 C^{1/2}_{As_4}}, \quad K_2 = K_2' K_{As}^{1/2} \quad [7]$$

where K_{As} is the equilibrium constant for $As_4 \rightleftharpoons 2As_2$. Here, C_t is the surface concentration of total sites. Equation [7] can be used in Eq. [5] with the aid of Eq. [1] and [2] for $C_{GaCl \cdot S}$ and $C_{As_2 \cdot S}$ to arrive at the following rate of incorporation

$$r = \frac{k C_{H_2} C_{GaCl} C^{1/2}_{As_4} - k_e C_{HCl}}{(1 + K_1 C_{GaCl} + K_2 C^{1/2}_{As_4})^2} \quad [8]$$

where k and k_e are given by

$$k = k' C_t^2 K_1 K_2 = k' C_t^2 K_1 K_2' K^{1/2}_{As} \quad [9]$$

$$k_e = k_e' C_t^2$$

Since the incorporation rate is given in terms of moles GaAs/(time · area) or length/(time · area), the growth rate G can be expressed as

$$G = Ar \quad [10]$$

where A is a constant. If G is expressed in terms of weight GaAs/(time · area), for instance, the constant A is simply the molecular weight of GaAs. The growth rate G is often given in terms of partial pressure. Thus, we write the growth rate as follows

$$G = \frac{\bar{k} p_{H_2} p_{GaCl} p^{1/2}_{As_4} - \bar{k}_e p_{HCl}}{(1 + \bar{K}_1 p_{GaCl} + \bar{K}_2 p^{1/2}_{As_4})^2} \quad [11]$$

where p_i is the partial pressure of species i and the overbar denotes the quantity including ($R_g T$) factor resulting from the application of ideal gas law ($p_i = C_i R_g T$) in converting C_i to p_i . The rate constants \bar{k} and \bar{k}_e also include the constant A .

Consider the application of the growth rate given by Eq. [11] to experimental data. In particular, consider the extensive data reported by Shaw (4). The data are suitable for determining the intrinsic growth rate since the total

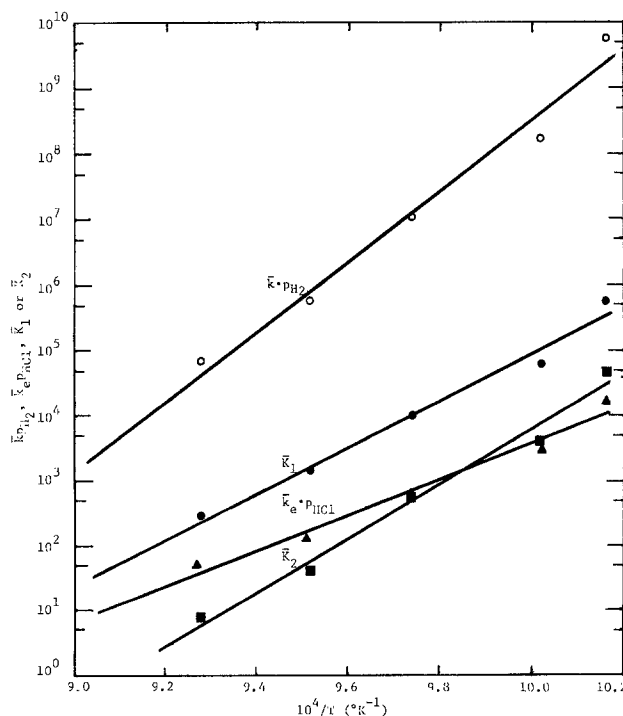


Fig. 1. Arrhenius plots for the rate and equilibrium constants in Eq. [12] as a function of reciprocal temperature for GaAs growth rate.

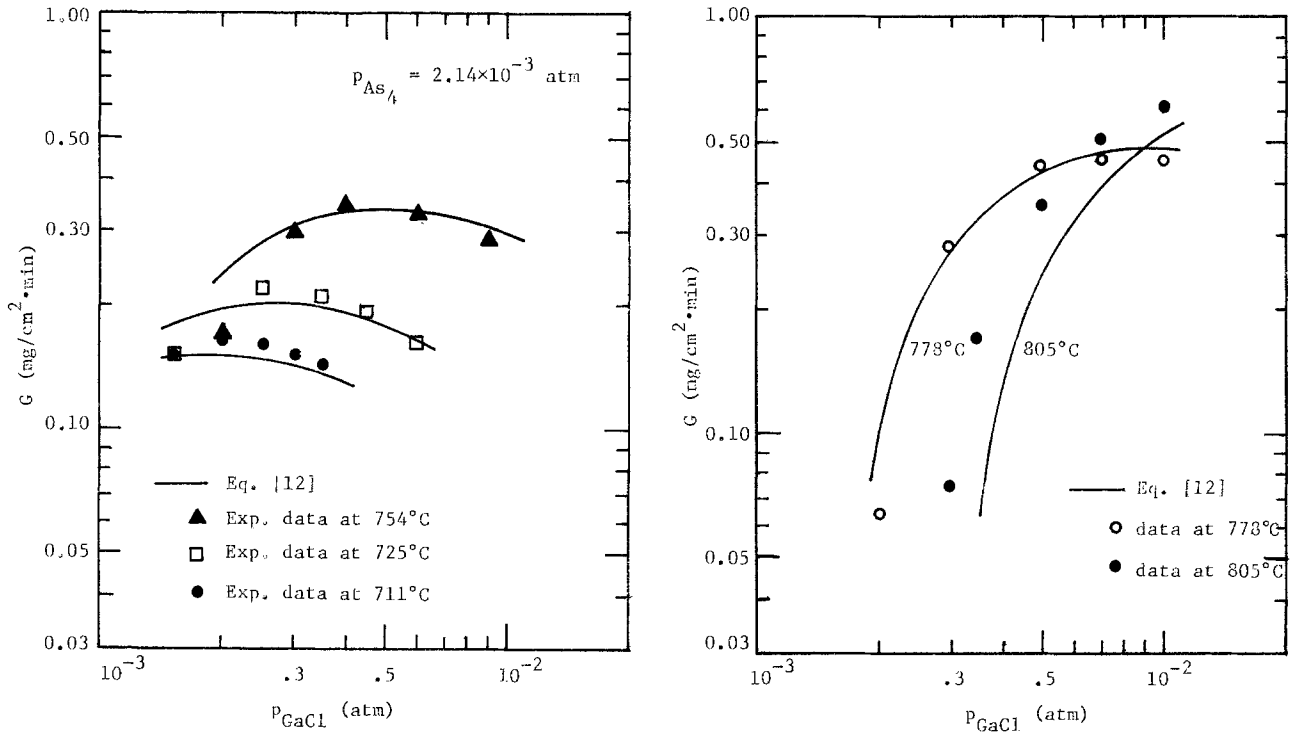


Fig. 2. Comparison between experimental growth rates of GaAs and those predicted by Eq. [12] as a function of GaCl partial pressure at (a, left) low and (b, right) high temperatures.

flow rate is such that the growth rate is unaffected by diffusion (8) and the reactant partial pressures were independently varied. In order to determine the rate and equilibrium constants in Eq. [11], the growth rates reported in Fig. 4 and 5 in the paper by Shaw (4) at temperatures 711°, 725°, 754°, 778°, and 805°C were utilized. A nonlinear regression program was used to calculate the rate and equilibrium constants at each temperature and these results in turn used to obtain the Arrhenius plots shown in Fig. 1. Since p_{H_2} and p_{HCl} in all cases are essentially constant, these were lumped with the rate constants k and \bar{k} , as shown in Fig. 1. Based on the Arrhenius plots, the growth rate can now be written as follows

$$G = \frac{(\bar{k}p_{H_2})p^{1/2}_{As_4}p_{GaCl} - (\bar{k}_e p_{HCl})}{(1 + \bar{K}_1 p_{GaCl} + \bar{K}_2 p^{1/2}_{As_4})^2}, \text{ (mg/cm}^2 \cdot \text{min)}, p_i \text{ in atm} \quad [12]$$

$$\begin{aligned} (\bar{k}p_{H_2}) &= 8.059 \times 10^{-46} \exp(123,400/T), p_{H_2} = 1 \text{ atm} \\ (\bar{k}_e p_{HCl}) &= 2.643 \times 10^{-38} \exp(95,200/T), p_{HCl} = 9.7 \times 10^{-4} \text{ atm} \\ \bar{K}_1 &= 2.337 \times 10^{-31} \exp(81,900/T) \\ \bar{K}_2 &= 1.511 \times 10^{-23} \exp(63,000/T) \end{aligned} \quad [13]$$

Comparisons between the growth rate predicted by Eq. [12] and [13] and the experimental data reported by Shaw (4) are shown in Fig. 2 and 3. It is seen in Fig. 2, which corresponds to Fig. 5 in the paper by Shaw (4), that the growth rate expression of Eq. [12] predicts the experimental growth rates quite accurately at the temperatures 711°, 725°, 754°, and 778°C, although the prediction is higher at 778°C at low pressures when p_{GaCl} is varied at constant p_{As_4} . At 805°C, however, the prediction is lower than the experimental growth rate. An important observation that can be made in Fig. 2 is that the growth-rate expression predicts quite accurately the maximum growth rate with respect to p_{GaCl} at all temperatures. The comparison given in Fig. 3, which corresponds to Fig. 4 in the paper by Shaw (4), shows similar behavior as in Fig. 2, *i.e.*, quite accurate predictions at 711°, 725°, 754° (except at low p_{As_4} pressures), and 778°C, but not as good at 805°C, when p_{As_4} is varied at constant p_{GaCl} . The major characteristics of the epitaxial growth of GaAs by the chloride transport process are that the growth rate goes through a maximum as p_{GaCl} is increased and that it also goes through a maxi-

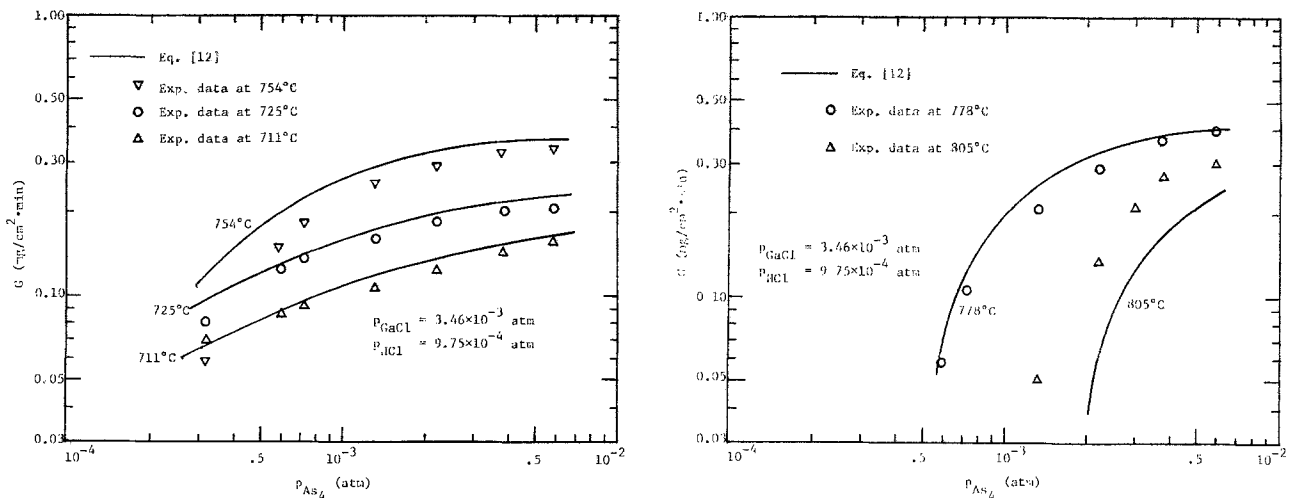


Fig. 3. Comparison between experimental growth rate of GaAs and those predicted by Eq. [12] as a function of As₄ partial pressure at (a, left) low and (b, right) high temperatures.

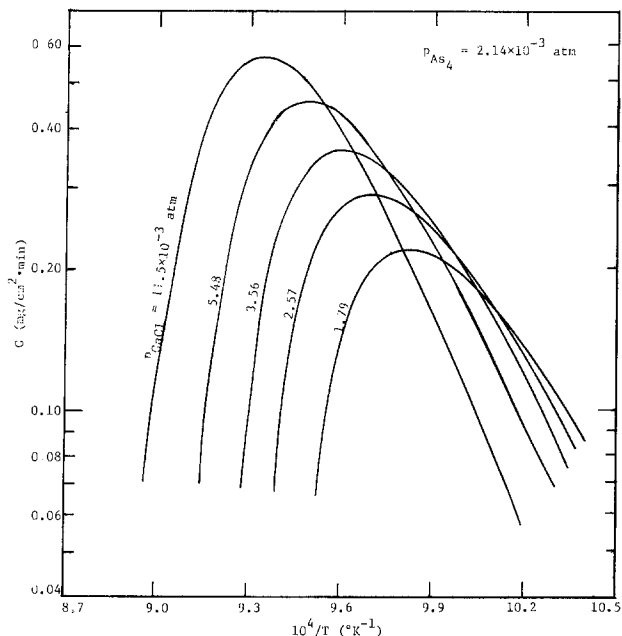


Fig. 4. Growth rate of GaAs as a function of reciprocal temperature at various partial pressures of GaCl.

imum as the substrate temperature is raised. Although the results shown in Fig. 2 and 3 should reveal the temperature dependence upon close examination, we show for comparison in Fig. 4 the growth rate given by Eq. [12] as a function of reciprocal temperature at various p_{GaCl} values. A comparison of Fig. 4 with Fig. 3 in the paper by Shaw (4) should reveal that there is a good agreement between the two, in particular with respect to the maximum values of the growth rates and the temperatures at which these maxima occur. While not presented, the same can be concluded about the temperature dependence of the growth rate at various arsenic partial pressures.

We have seen that the growth rate given by Eq. [12] describes the epitaxial growth rate satisfactorily and that it can explain quantitatively the major characteristics of the growth. In light of this, let us consider implications of the results as related to the postulated mechanism. According to the temperature dependence of \bar{K}_1 in Eq. [13], which is essentially K_1 , the heat of adsorption for the adsorption/desorption step of Eq. [1] is very high, indicating highly activated adsorption/desorption of GaCl. \bar{K}_2 is essentially K_2 , which is the product of K_2 , the equilibrium constant for the adsorption/desorption step for As_2 , and $K^{1/2}_{\text{As}}$, the equilibrium constant for $\text{As}_2 \rightleftharpoons 2\text{As}$. According to the temperature dependence given in Eq. [13], the heat of adsorption of As_2 is much less than that of GaCl since \bar{K}_2 is a composite of two equilibrium constants. This indicates that the adsorption of GaCl plays a much more important role than the adsorption of As_2 . In this regard, it is noteworthy that the growth-rate expression based on dissociative adsorption of As_2 , which leads to $p^{1/4}_{\text{As}_2}$ dependence of the growth rate rather than $p^{1/2}_{\text{As}_2}$, described the growth quite poorly. While only adsorption experiments would clearly resolve the nature of adsorption, the kinetic information nevertheless points to molecular adsorption of As_2 rather than dissociative adsorption. It is of interest that the apparent rate constants \bar{k} and \bar{k}_c decrease rather than increase with increasing temperature, as is evident from the expressions in Eq. [13]. This is not surprising at least for \bar{k} in light of the fact that the heats of adsorption for K_1 and K_2 (see Eq. [9] for k) are very high since the apparent activation energy given for \bar{k} is the sum of the activation energy of k' and the heats of adsorption for K_1 and K_2 , which are positive. Thus, the rate constant k' can be expressed as $k' = k'_0 \exp(-21,500/T)$, where k'_0 is a pre-exponential factor, the activation energy being 43 kcal/mol. The fact that \bar{k}_c decreases with increasing temperature indicates that the etching of GaAs represented by Eq. [14] is not simple as indicated earlier, but would represent an

overall surface process consisting of several surface reactions.

Transport (Diffusion) Effects

The intrinsic growth rate given by Eq. [13] is the growth rate when the diffusional effect is absent. The diffusional effect on the growth rate is usually treated in terms of boundary layer forming from the leading edge of the substrate (9), the theory of which is due to Schlichting (10). This diffusional effect is important not only for determining the actual growth rate, but also for growing uniform films, as demonstrated by Kuiper *et al.* (11) and Komeno *et al.* (12). The boundary-layer thickness through which the gas molecules have to diffuse to the substrate surface for subsequent incorporation into crystal structure is usually taken as the hydrodynamic (velocity) boundary-layer thickness (2, 12). At steady state, the concentration gradient in the boundary layer is linear and, therefore, the mass-transfer coefficient k_g is given by

$$k_g(x) = \frac{D}{\delta(x)} \quad [14]$$

when the flux through the layer is expressed as the product of k_g and the concentration difference. Here D is the molecular diffusivity of diffusing species, δ is the concentration boundary-layer thickness, and x is the distance from the leading edge of the substrate, which is taken as zero.

While the velocity boundary-layer thickness has been used in the literature for the mass-transfer coefficient, the boundary layer of interest is rather the concentration boundary layer, which is different from the velocity layer. The velocity boundary-layer thickness δ_h is related to the concentration boundary-layer thickness through Schmidt number, Sc , as follows (13)

$$\frac{\delta}{\delta_h} = Sc^{-1/3}; Sc = \nu/D \quad [15]$$

where ν is kinematic viscosity. According to Schlichting (10), the velocity boundary-layer thickness is given by

$$\delta_h = 5(\nu x/v_x)^{1/2} \quad [16]$$

if the thickness is defined as that at which the velocity becomes 99% of the bulk fluid velocity v_x . This can be combined with Eq. [14] and [15] to give

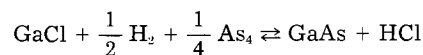
$$k_g = \frac{v_x^{1/2} D^{2/3}}{5 \eta^{1/6} x^{1/2}} \quad [17]$$

The theoretical value of the mass-transfer coefficient for any species of interest can be calculated from Eq. [17] with the aid of the Chapman-Enskog formula (14) for the theoretical value of the molecular diffusivity D . For the binary diffusivity calculation, the molecular diffusivity (for GaCl, for instance) can be taken as that of GaCl in H_2 since the mole fraction of H_2 is close to unity.

Consider now the effect of diffusion. At steady state, the mass flux through the boundary layer should be equal to the rate of reaction at the surface for any species

$$(k_{g,i}[(C_x)_i - C_i] = b_i r, i = \text{GaCl}, \text{As}_4, \text{H}_2, \text{HCl} \quad [18]$$

where C_x is the bulk gas concentration, r is that given by Eq. [8], and b_i is the stoichiometric coefficient for the overall reaction



with the sign convention that it is positive for reactants and negative for products since r is based on the species GaAs. Thus, b_i for As_4 , for instance, is 1/4, whereas it is -1 for HCl. In order to determine the actual growth rate based on bulk gas concentrations $(C_x)_i$, Eq. [8] and [18] written for each i have to be solved simultaneously for the surface concentrations C_i , which in turn can be used in Eq. [8] for the actual growth rate. It is immediately clear

that closed-form expressions cannot be obtained for the diffusional effect on the growth rate because of the non-linearity involved in Eq. [8].

Before proceeding to an examination of the diffusional effect, we consider two items that are noteworthy. If the growth rate is determined in terms of weight or average thickness, the mass-transfer coefficient averaged over the substrate length L may be used

$$(\bar{k}_d)_i = \frac{1}{L} \int_0^L \frac{v_x^{1/2} D_{im}^{2/3}}{5\nu_m^{1/6} x^{1/2}} dx = \frac{0.4v_x^{1/2} D_{im}^{2/3}}{\nu_m^{1/6} L^{1/2}} \quad [19]$$

where $(\bar{k}_d)_i$ is the average k_d for species, ν_m is the kinetic viscosity of the gas mixture, and D_{im} is the diffusivity of species i in the gas mixture. Use of this average mass-transfer coefficient also allows us to arrive at a criterion that can be used to determine whether the growth is affected by diffusion. For this, we consider Eq. [18] rewritten for the limiting reactant j in the following form

$$(\bar{k}_d)_j(C_{xj})[1 - C_j(C_{xj})] = b_jAG \quad [20]$$

where A is the constant relating r to the growth rate G (Eq. [10]). If the diffusional effect is negligible, the surface concentration c_j is very close to the bulk gas concentration and thus $C_j(C_{xj})$ should be very close to unity. If we consider 98% approach of C_j to (C_{xj}) as diffusion-free, we have from Eq. [20]

$$\frac{|b_j|AG}{(\bar{k}_d)_j(C_{xj})} < 0.02 \quad [21]$$

That is, if the criterion of Inequality [21] is satisfied, the concentration of the limiting reactant at the substrate surface is higher than 98% of the bulk concentration. This criterion is particularly useful for planning an experiment under diffusion-free conditions or for determining the extent of diffusion limitation of the growth rate obtained experimentally. It is noted that all quantities involved are readily available. This criterion was applied to the experimental results obtained by Shaw (8), in which total flow rate was varied at 750°C. GaCl was taken as the limiting reactant for which $|b_j| = 1$, A is the molecular weight of GaAs since the growth rate is in terms of weight. Equation [19] was used for \bar{k}_d , and the experimental growth rate of 65 $\mu\text{g/h}$ was used. The value of the left-hand side of Inequality [21] thus calculated is 0.004 at $v_x = 0.315$ cm/s, indicating that the surface concentration of GaCl approaches 99.6% of the bulk GaCl concentration for the total flow rate of 383 ml/min.

In order to assess the effect of diffusion, the growth conditions used by Shaw (4) were used along with Eq. [13], [18], and [19] for the growth rate as affected by diffusion. As detailed in the Appendix, the temperature dependence of physical properties can be expressed as

$$D_{im,T} = D_{im,1000} \left(\frac{T}{1000} \right)^{1.75}, \text{ (cm}^2/\text{s)}$$

$$\nu_{m,T} = \nu_{m,1000} \left(\frac{T}{1000} \right)^{1.65}, \text{ (cm}^2/\text{s); } \nu_{m,1000} = 8 \text{ cm}^2/\text{s}$$

$$(\bar{k}_d)_i = \frac{0.4v_x^{1/2} D_{im}^{2/3}}{\nu_m^{1/6} L^{1/2}}, \text{ (cm/s)}$$

In terms of consistent units, Eq. [18] can be written as

$$\left[\frac{(\bar{k}_d)_i}{R_g T} \right] (p_{zi} - p_i) - 1.657 \times 10^{-6} b_i G = 0$$

(mol /cm² · s), $i = \text{As}_4, \text{GaCl, H}_2, \text{HCl}$

With the aid of Eq. [12] and [13], these equations can be solved for p_i , which in turn can be used in Eq. [12] for the growth rate as a function of fluid velocity and temperature for given vapor-phase composition. The results are shown in Fig. 5 along with the vapor-phase composition used in the calculations. It is seen that for the vapor composition given, the growth rate is practically independent of transport effect, regardless of temperature if the fluid velocity is sufficiently high.

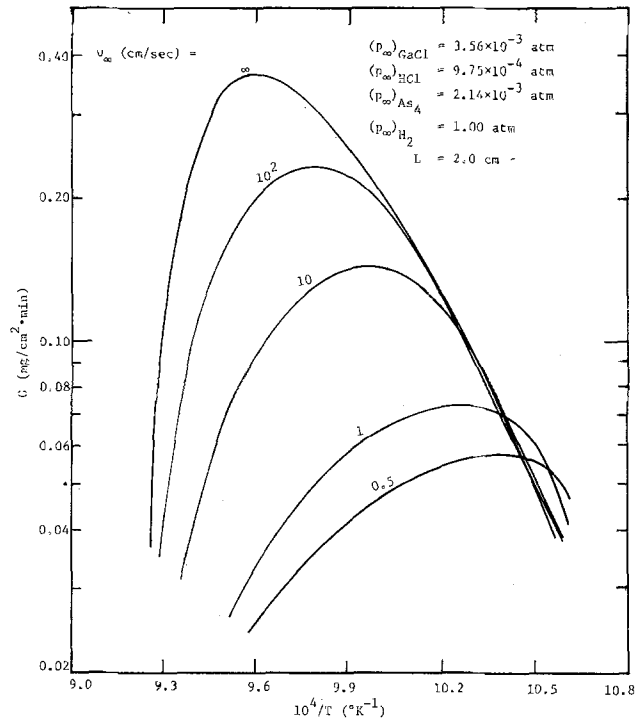


Fig. 5. Effect of diffusion on GaAs growth rate as affected by fluid velocity.

Perhaps the most important lesson to be drawn from Fig. 5 is that diffusion in the usual sense of transport limitation cannot cause the growth rate to decrease with increasing temperature at high temperatures. The growth rate's being diffusion limited simply means that the growth rate cannot reach the intrinsic rate. It is of interest to note in Fig. 5 that the diffusion-limited growth rate can be higher than the intrinsic rate at low temperatures, *i.e.*, $v = \infty$ vs. $v = 0.5$. This is due to the fact that the diffusional effect on the inhibition term for the growth rate (denominator of Eq. [12]) is larger than the effect on the numerator terms in Eq. [12]. Therefore, if a low temperature is preferred for a purer crystal, for instance, it may be advantageous to use a very low flow rate. This would have the added advantage of minimizing the thickness variation in a grown crystal.

Effect of Physical Orientation of Substrate

Consider the effect of substrate orientation with respect to gas flow on the mass-transfer coefficient. Let us define the angle of inclination β as shown in Fig. 6. The diffusional effect considered in the previous section is for $\beta = 0^\circ$. The change of velocity boundary-layer thickness with the angle was obtained by Hartree (15), and the results were given in a tabular form for selected values of β . While the results were obtained for the symmetrical case of two plates separated by $\beta\pi$, they can be used for our purpose provided that deposition occurs only on the side of substrate facing the flow (Fig. 6). The velocity boundary-layer thickness obtained for various β values can be well approximated by

$$\frac{\delta_n(\beta)}{\delta_n(\beta = 0)} = \left(\frac{2 - \beta}{2} \right)^{1/2} \exp(-\sqrt{\beta}/3)$$

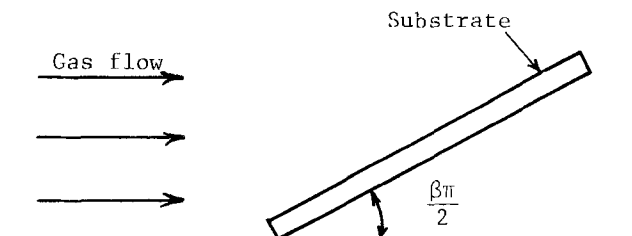


Fig. 6. Substrate orientation with respect to gas flow

where $\delta_h(\beta = 0)$ is that given by Eq. [16]. If we assume that Eq. [15] still applies, the mass-transfer coefficient is given by

$$k_{tr} = \frac{1}{\left(\frac{2-\beta}{2}\right)^{1/2} \exp(-\sqrt{\beta/3})} \left[\frac{v_x^{1/2} D^{2/3}}{5\nu^{1/6} x^{1/2}} \right], \beta < 2 \quad [22]$$

Now that the mass-transfer coefficient contains the effect of the substrate orientation, the diffusional effect on the growth rate can be determined in the same manner as in the previous section with the use of Eq. [22].

Concluding Remarks

An intrinsic kinetics of GaAs growth has been developed based on a postulated growth mechanism, which involves molecular adsorption of both GaCl and As₂, surface reaction of these adsorbed species for GaAs formation, and dissociation of two vacant sites to GaCl with vapor-phase HCl. The growth-rate expression thus obtained has been shown to describe the growth behavior quite accurately for the experimental data of Shaw (4) obtained under widely varying temperature and concentrations. In particular, the expression explains the major characteristics quantitatively such as the temperature and GaCl-concentration dependence of the growth rate, which goes through a maximum with respect to both the temperature and the GaCl concentration. The rate and equilibrium constants determined from the experimental data indicate that GaCl adsorption/desorption is a highly selective and activated process. The effect of diffusion on the growth rate has been determined based on concentration boundary layer and the intrinsic growth rate obtained earlier. A simple criterion for negligible diffusion effect has been derived. This criterion can be used for selection of experimental conditions under which the diffusional effect is negligible. The effect of substrate orientation has also been given for the growth rate. The results presented here, when taken together, describe rather completely the growth rate as affected by vapor-phase gas composition, temperature, fluid velocity, and physical orientation of substrate surface.

Manuscript received March 7, 1984.

LIST OF SYMBOLS

A	constant for conversion from mol/cm ² · s to wt/cm ² · s or length/cm ² · s
b	stoichiometric coefficient, positive for reactants and negative for products
C _i	volume concentration of species i (i = As ₂ , H ₂ , HCl, GaCl)
C _v	surface concentration of total sites
C _v	surface concentration of vacant sites
C _{GaCl-s}	surface concentration of adsorbed GaCl
C _{As₂-s}	surface concentration of adsorbed As ₂
C _∞	bulk fluid concentration
D	molecular diffusivity
D _{im}	D for species i in gas mixture
G	growth rate
k	k' C ₂ ² K ₁ K ₂
k'	rate constant for the reaction in Eq. [3]
k _e	k _e C _v ²
k _e '	rate constant for the reaction in Eq. [4]
$\frac{k}{k'}$	Ak/R _g T
$\frac{k_e}{k_e'}$	Ak _e R _g T
k _g	film mass-transfer coefficient
K ₁	equilibrium constant for the step in Eq. [1]
K ₂	K' ₂ K _{As} ^{1/2}
$\frac{K_1}{K_2}$	equilibrium constant for the step in Eq. [2]
$\frac{K_1}{K_2}$	K ₁ /R _g T
$\frac{K_2}{K_2}$	K ₂ /R _g T
K _{As}	equilibrium constant for As ₂ ⇌ 2As
L	length of substrate
p _i	partial pressure of species i
r	rate of growth in mol/cm ² s
R _g	gas constant
S	vacant active site
Sc	Schmidt number (ν/D)
T	temperature
v _∞	bulk fluid velocity

x distance from the edge of substrate

Greek letters

β	angle in radian shown in Fig. 6
δ	concentration boundary-layer thickness
δ _h	velocity boundary-layer thickness
ν	kinematic viscosity
ν _m	ν for gas mixture

Subscripts

i	species
j	limiting reactant

APPENDIX

Physical Properties

The values of D_{im}(=D_{iH₂}) were calculated by the Chapman-Enskog relationship

$$D_{iH_2} = 1.858 \times 10^{-3} T^{3/2} \frac{[(M_1 + M_{H_2})/(M_1 M_{H_2})]^{1/2}}{P \sigma_{iH_2}^2 \Omega_{iH_2}(T)} \quad (\text{cm}^2/\text{s})$$

where M is the molecular weight. For the calculations, the binary Lennard-Jones parameters σ and Ω were obtained from

$$\sigma_{iH_2} = \frac{1}{2} (\sigma_i + \sigma_{H_2})$$

$$\epsilon_{iH_2} = (\epsilon_i \epsilon_{H_2})^{1/2}$$

The values thus calculated along with the parameter values are given below

Species (i)	σ	ε/k _B	D _{iH₂,T = 1000 K}	D _{iH₂,T = 300 K}
GaCl	(6)	(1000)	3.04	0.370
H ₂	2.827	59.7	10.8	1.31
As ₂	(5)	(1000)	3.02	0.367
HCl	3.339	344.7	5.61	0.682

where k_B is the Boltzmann constant. The parameters were obtained from Ref. (13). The parentheses are used in the table to denote estimated values. The viscosity was obtained from

$$\eta = 26.69 \frac{\sqrt{MT}}{\sigma^2 \Omega_V(T)} \quad (\mu p)$$

The kinematic viscosity ν is η/ρ, where ρ is density. The temperature dependence of ρ and Ω is as follows

$$\rho \propto T^{-1}$$

$$\Omega_{iH_2} \propto T^{-0.25}$$

$$\Omega_V \propto T^{-0.15}$$

Use of these temperature dependences led to the temperature dependences for D_{im} and ν_m given in the text.

REFERENCES

- D. W. Shaw, *J. Cryst. Growth*, **31**, 130 (1975).
- T. Arizumi, in "Current Topics in Materials Science," Vol. 1, E. Kaldis, Editor, pp. 343-420, North-Holland (1978).
- L. Hollan, J. M. Durand, and R. Cadoret, *This Journal*, **124**, 135 (1977).
- D. W. Shaw, *ibid.*, **117**, 683 (1970).
- T. O. Sedgwick, *ibid.*, **111**, 1381 (1964).
- A. Boucher and L. Hollan, *ibid.*, **117**, 932 (1970).
- H. Seki, K. Moriyama, I. Asakawa, and S. Horie, *Jpn. J. Appl. Phys.*, **7**, 1324 (1968).
- D. W. Shaw, *This Journal*, **115**, 405 (1968).
- S. E. Bradshaw, *Int. J. Electron.*, **21**, 205 (1966).
- H. Schlichting, "Boundary Layer Theory," 4th ed., McGraw-Hill, New York (1960).
- A. E. T. Kuiper, C. J. H. van den Brekel, J. de Groot, and G. W. Veltkamp, *This Journal*, **129**, 2288 (1982).
- J. Komeno, S. Ohkawa, A. Miura, K. Dazai, and O. Ryuzan, *ibid.*, **124**, 1440 (1977).
- R. C. Reid, J. M. Prausnitz, and T. K. Sherwood, "The Properties of Gases and Liquids," Appendix C, McGraw-Hill, New York (1975).
- J. O. Hirschfelder, C. F. Curtiss, and R. B. Bird, "Molecular Theory of Gases and Liquids," p. 359, John Wiley and Sons, New York (1954).
- D. R. Hartree, *Proc. Camb. Philos. Soc.*, **33**, Part II, 223 (1937).

Electrochromism in Sputtered Li-W-O Compounds and a Layered Structure

Makoto Kitabatake, Kumiko Hirochi, and Kiyotaka Wasa

Matsushita Electric Industrial Company, Limited, Central Research Laboratories, Moriguchi, Osaka 570, Japan

ABSTRACT

The electrochromic behavior of sputtered Li-W-O thin films was studied. Two types of transparent film were selectively prepared under different sputtering conditions. A clear blue film (film A) was deposited under pure argon gas and a colorless film (film B) was obtained under a mixed gas of argon and oxygen. The blue coloration of film A bleached into another type of colorless film (film A') by heating in an atmosphere of oxygen. Using these films, a new type of electrochromic device (Au/film B/film A'/ITO) was proposed and fabricated with a simple process.

WO₃ has been known as one of the most common electrochromic materials. In general, the electrocoloration in the WO₃ film results from the formation of a tungsten bronze (M_xWO₃, x = 0 ~ 1) (1). The M represent, for example, H, Li, or Na (2). The formation of the tungsten bronze is caused by the double injection of the M⁺ ions and electrons to the WO₃. The blue coloration of the tungsten bronze is attributed to the intervalence transfer of electrons between W⁶⁺ and W⁵⁺ (1, 3, 4). Two types of Li-W-O compounds have been known. One is blue Li₁WO₃, which exhibits tungsten bronze structure (5), and the other is colorless Li₂WO₄, which contains only W⁶⁺. Li₂WO₄ is applicable to a Li electrolyte which supplies Li⁺ ions to the electrochromic materials (6).

We have prepared thin films of the Li-W-O compounds by a sputtering deposition under various sputtering gas compositions. This paper describes their optical properties and their applications to electrochromic devices.

Sample Preparations

An RF sputtering apparatus was employed for the deposition of the Li-W-O thin films. The sputtering conditions are shown in Table I. The sputtering gas was pure argon (purity 6N) or a mixture of argon and oxygen (purity 6N). The mixing ratio (O₂/Ar) of the sputtering gas was varied from 0 to 1. The sintered powder synthesized from Li₂CO₃ (purity 4N) and WO₃ (purity 4N) was put in a stainless steel dish and used as the target. The powder of Li₂CO₃ and WO₃ was mixed in a ratio of 1:1 (molecule). The substrates were fused quartz plates with smooth surfaces of 0.2 mm thickness.

The Sputtered Li-W-O Films

Two types of transparent film were prepared by sputtering deposition. Film A was deposited under the sputtering gas of pure argon. Film B was deposited under the mixture of argon and oxygen. The same sputtering targets were used for the preparation of these films. Film A was colored blue and film B was colorless. Figure 1 shows the absorption of red light (He-Ne laser: 6328Å) of the films sputtered under different sputtering gas compositions. Film A, deposited under pure argon sputtering gas, strongly absorbs red light. The absorption decreases abruptly with the small addition of oxygen to the sputtering gas. Film B deposited under the mixed gas of argon and oxygen scarcely absorbs the red light. Figure 2 shows the visible light-absorption spectra of film A and film B. Film A strongly absorbs from red to infrared regions, compared with film B.

Table I. Sputtering conditions for the Li-W-O film preparation

Target dimension	80 mmφ
Target composition	Li ₂ CO ₃ , WO ₃ (1:1 molecule) mixed powder
Sputtering gas	Ar or Ar + O ₂ (3 × 10 ⁻² torr)
Substrate temperature	R.T. ~ 100°C
Sputtering power	100W
Deposition rate	30 ~ 60 Å/min

Figures 3(A) and (B) are the RHEED pattern of film A and film B, respectively. From the RHEED patterns, film A is amorphous due to the halo pattern and film B is polycrystalline due to the ring pattern. The Auger anal-

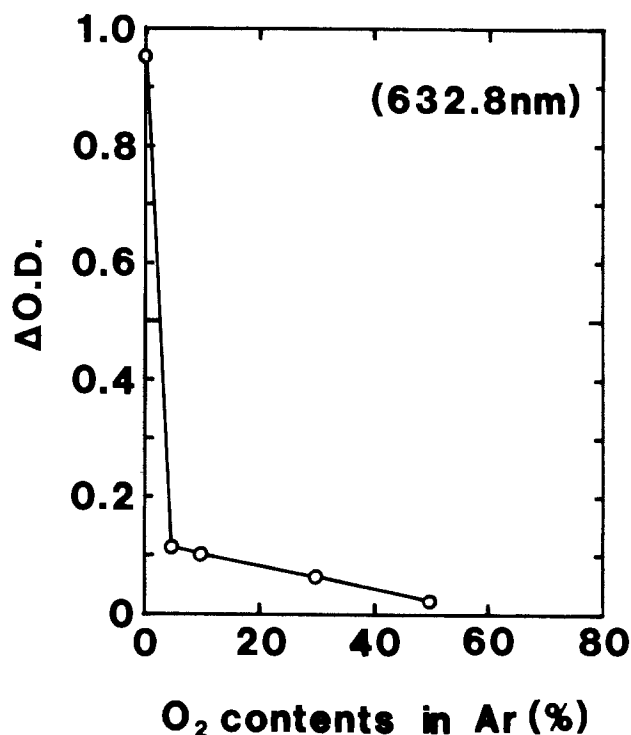


Fig. 1. Absorption of the red light of the films sputtered using different sputtering gas. Film thickness is about 3000Å.

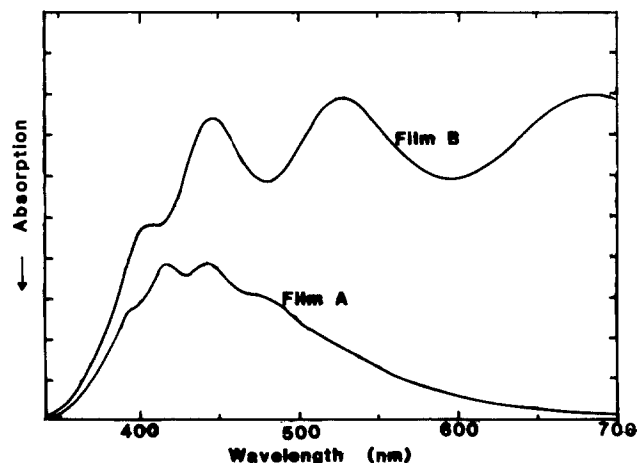


Fig. 2. Absorption spectra of the film A and the film B. Film thickness is about 3000Å.

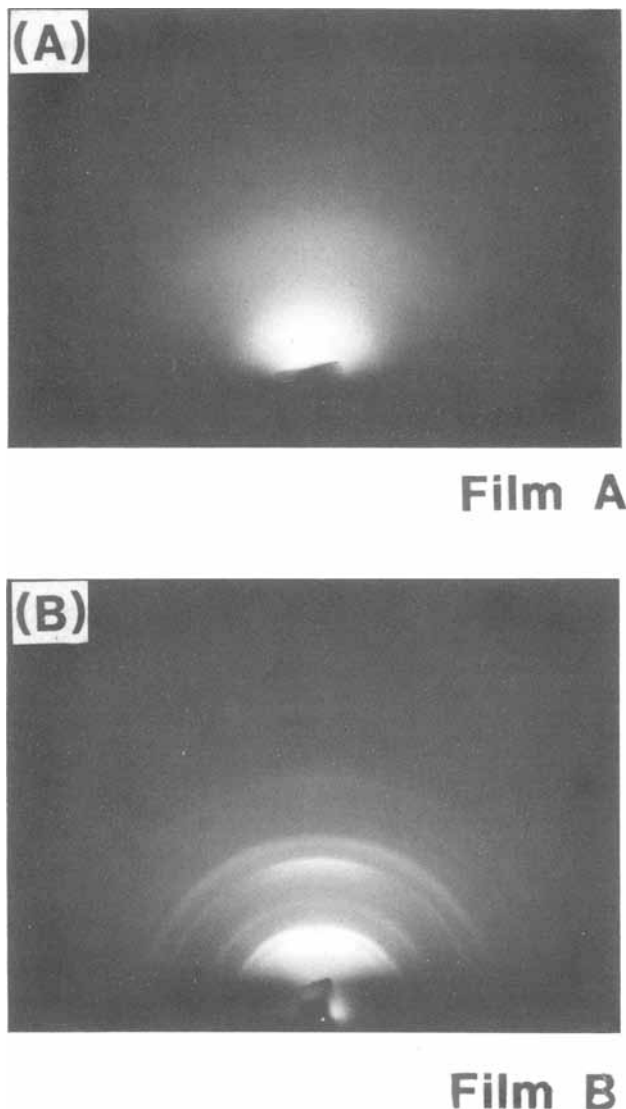


Fig. 3. RHEED patterns of film A and film B. Film thickness is about 3000\AA .

yses suggested that the compositions of film A and film B were almost the same. The blue coloration of film A was bleached by the radiation of a CO_2 laser ($> 0.5 \text{ W/mm}^2$). Film A crystallized and was changed to film B by this radiation. It is considered that the state of the W^{5+} which causes the coloration is nonequilibrium in comparison with that of the W^{6+} . In the sputtering process, there is a possibility of constructing the nonequilibrium microstates by the effects of the impinging ions and nuclei with high energy on the deposited film during the film growth. In film A of amorphous Li-W-O prepared by sputtering, there are so many nonequilibrium microstates that the density of the W^{5+} , which causes the coloration, is high. In film B of polycrystalline Li-W-O, the presence of

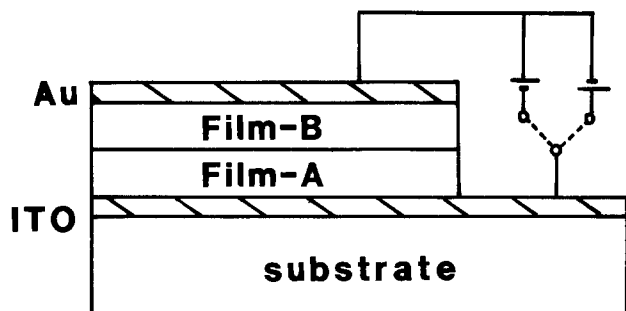


Fig. 4. Structure of the new electrochromic device

oxygen in the sputtering gas plays an important role in the coloration and the crystallization of the film. These considerations suggest that the crystallization of the film is equivalent to the moderation of the nonequilibrium states and the reduction of the density of the W^{5+} .

The coloration of film A was bleached without crystallization when the film was slightly heated at 200°C in an atmosphere of oxygen; in the atmosphere of pure argon, film A was not bleached. This slightly heated film remained amorphous. Oxygen facilitates the moderation of the nonequilibrium microstates in film A in the heating process. We call this slightly heated colorless amorphous film "film A'." The W^{5+} in film A can easily change to the W^{6+} without crystallization. Detailed analysis of the light absorption spectra indicated that film A' weakly absorbed the region similar to that of film A. The density of the W^{5+} in film A' was much smaller than that in film A.

Electrochromic Device Fabrication

We prepared the electrochromic devices with the Au/film B/film A/ITO layered structure shown in Fig. 4. This layered structure was fabricated by the control of the sputtering gas composition during the sputtering deposition. Film A was first deposited under the pure argon gas on the ITO electrode, which was deposited on the fused quartz substrate. Subsequently, film B was deposited on film A under the mixed gas of argon and oxygen without breaking the vacuum. The first-deposited film A was initially colored blue. During the deposition of film B on film A, film A changed to transparent. Film A changed to film A' in the layered structure because film A was slightly heated in the atmosphere of oxygen during the deposition of film B. The thicknesses of film A and film B were 0.7 and $0.3 \mu\text{m}$, respectively. The Au electrode was vacuum deposited on the layered structure.

Figure 5 shows the interrupted voltammogram of the Au/film B/film A/ITO layered structure. The sweeping rate of the applied voltage was 0.2 V/s . The initially transparent layered structure was colored blue under the positive bias to the Au electrode and bleached again under the negative bias to the Au electrode. Film A' reversibly changed to film A by the alternation of the bias voltage. This coloration bleaching was either cycled or memorized in a similar manner to other electrochromic devices already reported (7). Film A operates as the electrochromic layer. Film B operates as the electrolyte layer which supplies the Li^+ ions to the electrochromic layer (film A). Figure 6 shows the time response of this new electrochromic device under different bias voltages. The change in the optical density ($\Delta\text{O.D.}$) of the device was measured

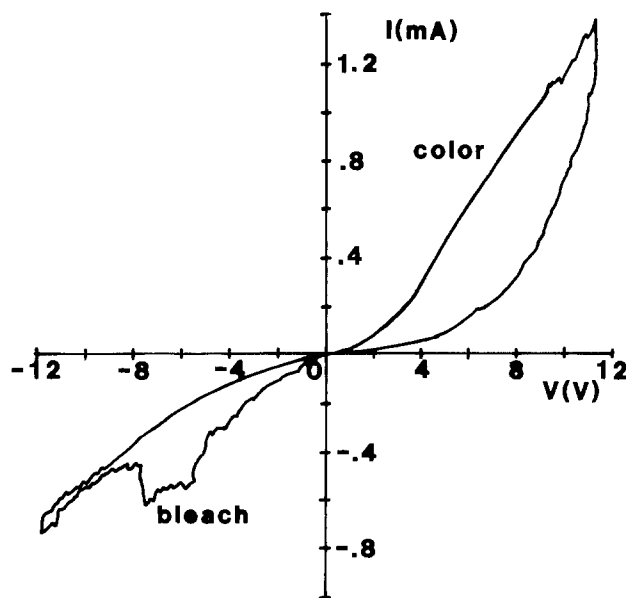


Fig. 5. Interrupted voltammogram of the device. The sweeping rate of the applied voltage is 0.2 V/s .

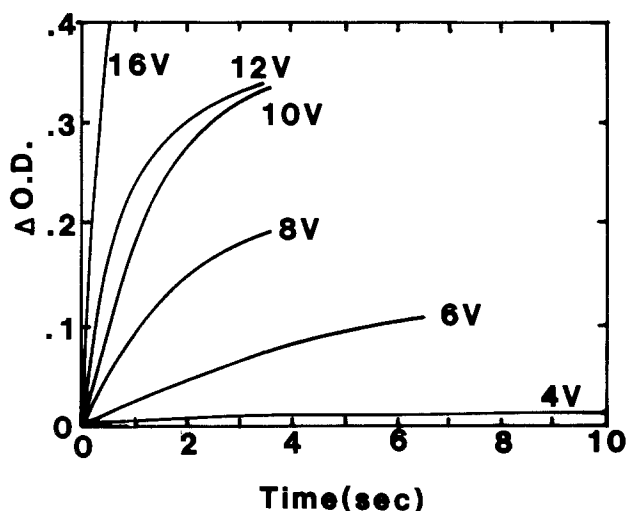


Fig. 6. Time response of the device

in the reflection mode using the He-Ne laser. Under the bias voltage above 16V, the response time is 200 ms or less.

Conclusions

The electrochromic material and device were prepared by the sputtering deposition of the Li-W-O compound. The deposited or heated films of the Li-W-O compounds can be classified as follows

Film A: deposited using pure argon sputtering gas; amorphous and colored blue.

Film B: deposited using the mixed (O₂, Ar) sputtering gas; polycrystalline and colorless.

Film A': the slightly heated film of film A; amorphous and colorless.

The presence of oxygen played an important role in the coloration and the crystallization of films during both the sputtering deposition and the heating process.

The device fabrication was very simple. The electrochromic and electrolyte layers were fabricated by the selection of the sputtering gas composition. The layered structure Au/film B/film A/ITO operated as the electrochromic device, and its response time was 200 ms or less.

Acknowledgments

The authors wish to express their sincere thanks to K. Kusao for his Auger analyses and to S. Hayakawa for his continuous encouragement. This work was performed through Special Coordination Funds for Science and Technology of the Japanese Government.

Manuscript submitted June 11, 1984; revised manuscript received Sept. 28, 1984.

Matsushita Electric Industrial Company, Limited, assisted in meeting the publication costs of this article.

REFERENCES

1. B. W. Faughnan, R. S. Crandall, and P. M. Heyman, *RCA Rev.*, **36**, 177 (1975).
2. T. C. Arnoldussen, *This Journal*, **128**, 117 (1981).
3. O. F. Schirmer and E. Salje, *J. Phys. C*, **13**, L1067 (1980).
4. O. F. Schirmer, V. Wittwer, G. Baur, and G. Brandt, *This Journal*, **124**, 749 (1977).
5. S. K. Mohapatra, *ibid.*, **125**, 284 (1978).
6. T. Yoshimura, M. Watanabe, Y. Koike, K. Kiyota, and M. Tanaka, *Jpn. J. Appl. Phys.*, **22**, 152 (1983).
7. T. Oi, *Appl. Phys. Lett.*, **37**, 244 (1980).

A Structural and Electrical Comparison of BCl and BF₂ Ion-Implanted Silicon

M. Delfino* and M. E. Lunnon

Philips Research Laboratories, Signetics Corporation, Sunnyvale, California 94088

ABSTRACT

The molecular ions BCl⁺ and BF₂⁺ are implanted into <100> silicon at an energy of 16 keV per boron atom in the dose range of 6 × 10¹⁴–1.2 × 10¹⁵ cm⁻² to form shallow p⁺/n junctions. Cross-sectional transmission electron microscopy shows that chlorine is at least four times as effective as fluorine in amorphizing silicon. The increase in thickness of the amorphous layer, however, has a small effect in the reduction of axial channeling of boron as measured by secondary ion mass spectrometry. After annealing for 30 min at 900°C, diffusion of interstitial boron is enhanced by chlorine relative to fluorine, whereas the electrical activity of boron is inhibited. Diodes made with both BCl⁺ and BF₂⁺ implantations have comparable I-V characteristics with low reverse-bias junction leakage currents that are not affected by a band of dislocation loops which remain near the original amorphous-crystalline interface.

The use of ionized molecules such as BF₂⁺, BF⁺, BCl₂⁺, and BCl⁺ for p-type doping silicon by ion implantation was first proposed in 1971 (1). This work and subsequent studies by others (2-5) have demonstrated that BF₂⁺ implantation in particular can be a useful alternative to B⁺ implantation for the formation of shallow junction devices. The increased mass of BF₂⁺ results in a shorter intrinsic range and leads to a reduced ion-dose threshold with an accompanying higher critical temperature for amorphizing the substrate. The amorphous layer, in turn, minimizes channeling and lowers the activation energy for postimplantation annealing. Thus the residual defect density is, in general, reduced, which in principle lowers the sheet resistance and the junction leakage. Also, the trapped fluorine does not appear to be detrimental to device performance or reliability.

In spite of the extensive studies of BF₂⁺ implantation in silicon and its widespread acceptance in integrated cir-

cuit fabrication, a limited amount of work (4, 5) has been done with implanting other molecular boron ions into silicon. This appears to be due to the fact that the accompanying chlorine (4, 5) or bromine (4) adversely affects the electrical activation of the co-implanted boron. More recently (6), implanted chlorine at concentrations on the order of 10²⁰ cm⁻³ has been found to retard the solid-phase epitaxial regrowth of silicon. Nonetheless, in this paper, we demonstrate that, while chlorine does indeed inhibit boron electrical activity, shallow p⁺/n junction diodes with excellent I-V characteristics can be formed by furnace annealing BCl⁺-implanted silicon.

Experimental

BCl⁺ was implanted at 67 keV to a dose of 6.0 × 10¹⁴ or 1.2 × 10¹⁵ cm⁻² into Czochralski-grown n-type <100> silicon doped with phosphorus to a resistivity of 3.4-5.0 Ω-cm. The same dose BF₂⁺ implantations were done at the equivalent energy, i.e., 16 keV per B atom, of 71 keV for

*Electrochemical Society Active Member.

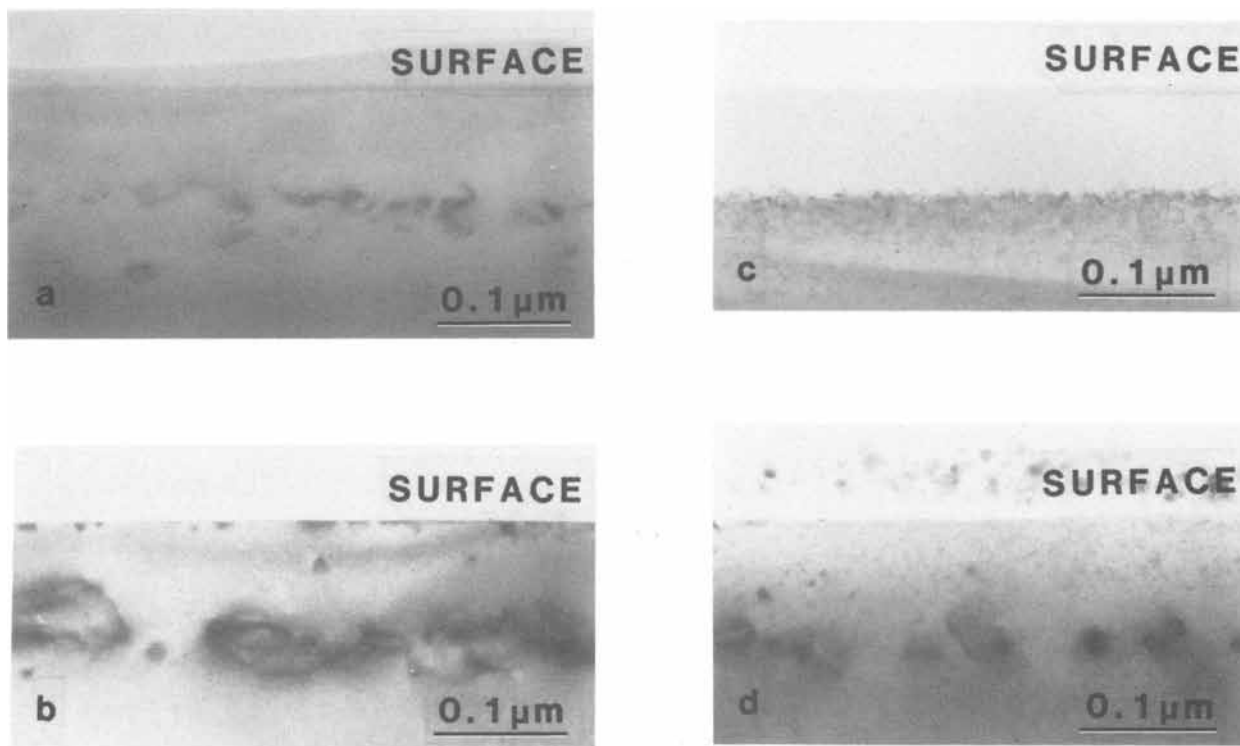


Fig. 1. TEM $\langle 110 \rangle$ cross-sectional micrographs of $\langle 100 \rangle$ Si. a: As-implanted $6 \times 10^{14} \text{ BF}_2^+ \text{ cm}^{-2}$ at 71 keV. b: Furnace annealed at 900°C for 30 min. c: As-implanted $6 \times 10^{14} \text{ BCl}^+ \text{ cm}^{-2}$ at 67 keV. d: Furnace annealed at 900°C for 30 min.

comparison. A beam current density of $0.8 \mu\text{A cm}^{-2}$ was used to reduce the degree of self-annealing during implantation with the substrates held at room temperature. The ion beam was tilted 7° from the $\langle 100 \rangle$ in a random crystallographic direction to minimize axial channeling.

After implantation, the samples were annealed for 30 min at 900°C in dry nitrogen.

The structure of the as-implanted and postannealed samples was examined by both planar and cross-sectional transmission electron microscopy (TEM). Secondary ion

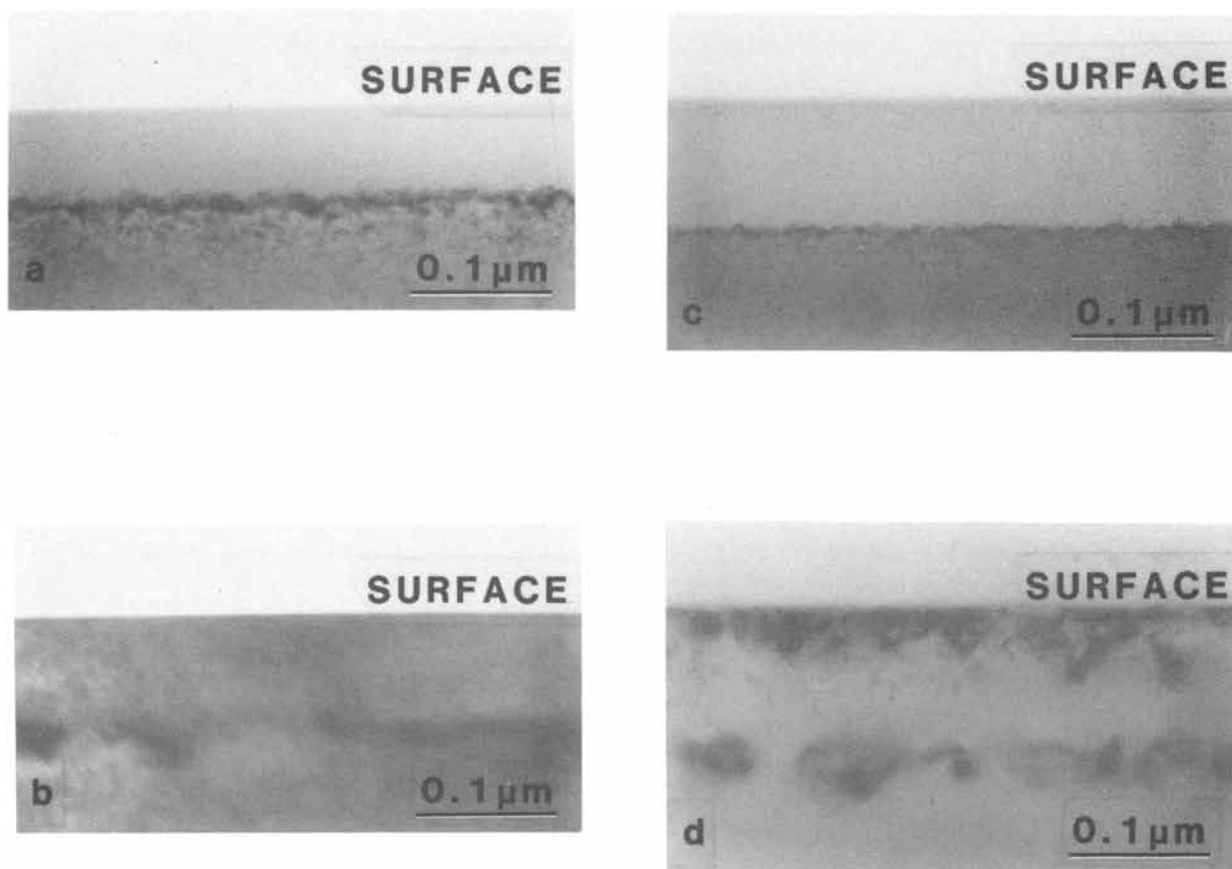


Fig. 2. TEM $\langle 110 \rangle$ cross-sectional micrographs of $\langle 100 \rangle$ Si. a: As-implanted $1.2 \times 10^{15} \text{ BF}_2^+ \text{ cm}^{-2}$ at 71 keV. b: Furnace annealed at 900°C for 30 min. c: As-implanted $1.2 \times 10^{15} \text{ BCl}^+ \text{ cm}^{-2}$ at 67 keV. d: Furnace annealed at 900°C for 30 min.

mass spectrometry (SIMS) employed both O₂⁺ and Cs⁺ primary beams depth to profile the atomic concentration of boron and halogens, respectively.¹ Carrier concentration profiles, assuming bulk mobility, were obtained from spreading resistance measurements of beveled samples.² A 0.7 μm thick chemically vapor deposited oxide on the backsurface of the wafer prior to beveling improved depth resolution. Junction measurements were reproducible to within ±0.02 μm. The electrical quality of the p/n junction was evaluated by measuring, in darkness, the I-V characteristics of 0.01 cm diam diodes. The diodes were fabricated using standard photolithographic techniques. A 0.6 μm thick thermal oxide served as a mask during implantation. Aluminum-silicon was sputter deposited, etched, and annealed for 30 min at 410°C in forming gas to form contact pads.

Structural Characterization

Figure 1a-1d shows TEM <100> cross-sectional micrographs of <100> silicon implanted with 71 keV BF₂⁺ and 67 keV BCl₂⁺ to a dose of 6 × 10¹⁴ cm⁻², before and after annealing. The as-implanted samples show that a continuous amorphous layer is formed with BCl₂⁺ implantation only. The thickness of the amorphous layer is 0.078 μm. By comparison, BF₂⁺ at the identical dose and at the same beam current density only forms a thin buried damaged layer, suggesting the onset of an amorphous layer. After furnace annealing, a band of dislocation loops corresponding to the original amorphous-crystalline interface remains.

Results for an implantation dose of 1.2 × 10¹⁵ cm⁻² are shown in Fig. 2a-2d. In this case, BF₂⁺ forms a continuous amorphous layer with an abrupt amorphous-crystalline interface. The thickness of the amorphous layer is 0.072 μm, whereas the same dose BCl₂⁺ implantation amorphizes the surface to a depth of 0.092 μm. After annealing, both samples epitaxially regrow perfect single-crystal material. A band of dislocation loops similar to that observed with the low dose implantations is found.

Figure 3a-3d shows TEM <100> planar-view micrographs after furnace annealing. All samples show a uni-

¹Charles Evans and Associates, San Mateo, California 94402.

²Solecon Laboratories, Sunnyvale, California 94089.

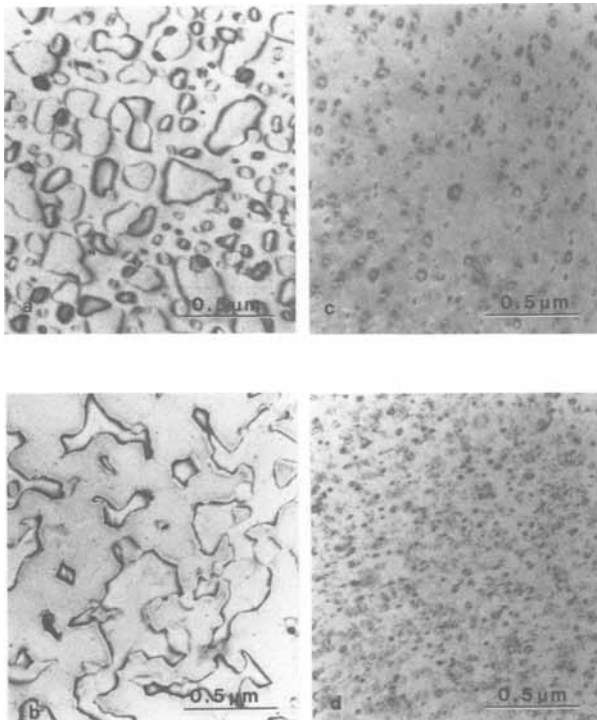


Fig. 3. TEM <100> planar-view micrographs of <100> Si after furnace annealing at 900°C for 30 min. a: 6 × 10¹⁴ BF₂⁺ cm⁻² at 71 keV. b: 1.2 × 10¹⁵ BF₂⁺ cm⁻² at 67 keV. c: 6 × 10¹⁴ BCl₂⁺ cm⁻² at 67 keV. d: 1.2 × 10¹⁵ BCl₂⁺ cm⁻² at 67 keV.

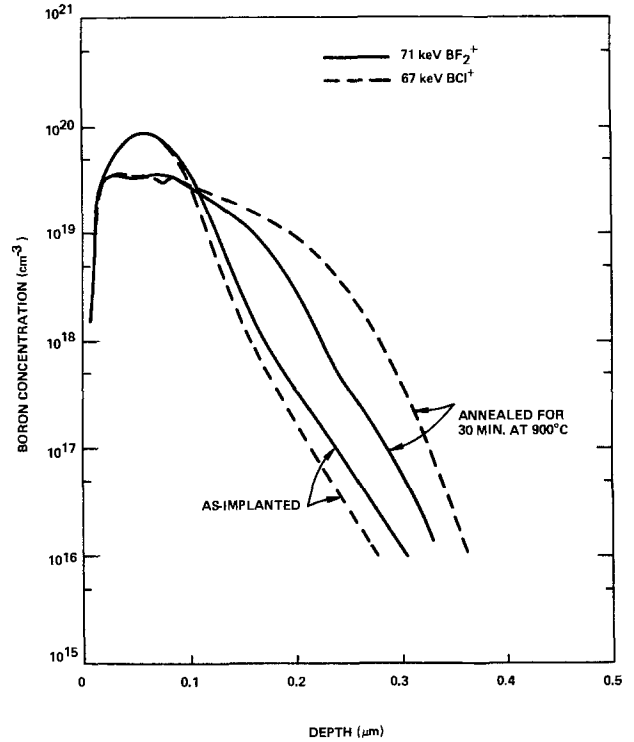


Fig. 4. Atomic boron depth profiles from SIMS for an implantation ion dose of 6 × 10¹⁴ cm⁻².

form density of dislocation loops corresponding to the defect band observed in the cross-sectional specimens. The dislocation loop density of the post-annealed BCl₂⁺ implanted samples is proportional to the implantation dose but four orders of magnitude lower in density. The average diameter of the dislocation loops in both BCl₂⁺ implanted samples is approximately 0.02 μm, whereas the BF₂⁺ implantations result in much larger dislocation loops of irregular shape. These larger dislocation loops arise from a tendency of the smaller loops to coalesce during annealing. The growth of the dislocations appears to be

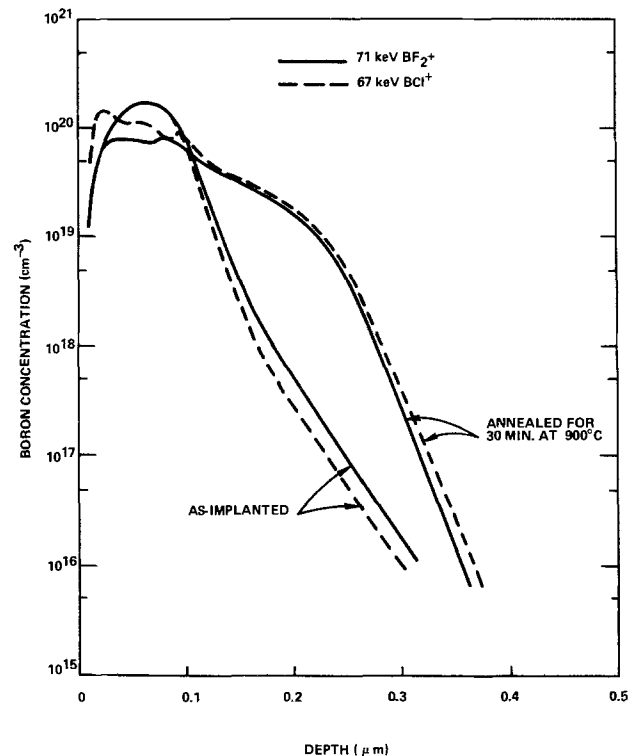


Fig. 5. Atomic boron depth profiles from SIMS for an implantation ion dose of 1.2 × 10¹⁵ cm⁻².

related to the higher diffusivity of fluorine compared to chlorine as discussed later. There is no evidence of gas bubbles in any samples, suggesting that the retained halogen is chemically bonded.

The atomic concentration profiles of boron, before and after annealing, are shown in Fig. 4 for BCl^+ and BF_2^+ implanted to a dose of $6 \times 10^{14} \text{ cm}^{-2}$. The boron gaussian-like peaks are in coincidence as expected from the energy equivalence of the dissociated molecular ions. The formation of an amorphous layer by BCl^+ implantation affects axial boron channeling with a reduction of the boron tail by $0.026 \mu\text{m}$. After annealing, boron diffuses more than twice as deeply in the BCl^+ -implanted sample. This enhanced boron diffusion is primarily due to the presence of an amorphous layer which increases the diffusivity by a factor of four (7).

At an ion dose of $1.2 \times 10^{15} \text{ cm}^{-2}$, where both BCl^+ and BF_2^+ amorphize silicon, the difference in the boron channeling tail is only $0.017 \mu\text{m}$. The $0.02 \mu\text{m}$ thicker amorphous layer formed with BCl^+ appears to contribute little to any further reduction in boron channeling. The SIMS profiles after annealing show that boron diffuses $0.03 \mu\text{m}$ deeper in the BCl^+ -implanted sample. This enhanced boron diffusion is attributed to the presence of chlorine. In addition there is a pile-up of boron towards the surface in the BCl^+ -implanted sample.

It appears, however, that the boron diffusion does not track the movement of the chlorine. Figure 6 shows that virtually no chlorine diffuses out after the furnace annealing, although slightly more is lost with the higher dose

implantation. By comparison, the BF_2^+ -implanted samples show considerable loss of fluorine after annealing, resulting in a characteristic two peak profile (8, 9). The minima correspond approximately to the original amorphous-crystalline interface in the high dose implanted sample and the buried damaged layer in the low dose implanted sample. It is interesting to note that even the thin damaged layer formed by implanting $6 \times 10^{14} \text{ BF}_2^+ \text{ cm}^{-2}$ is sufficient to cause fluorine to segregate after annealing. The presence of an amorphous layer is not required to form this multiple-peak structure, as previously believed (9). The amorphous layer does, however, retard the outdiffusion of fluorine during annealing. Apparently, the fluorine bonds to silicon during solid-phase epitaxial regrowth. This bond is not easily broken at 900°C .

Electrical Characterization

The carrier concentration depth profiles measured after furnace annealing for 30 min at 900°C are shown in Fig. 7. The relevant parameters obtained from these data are summarized in Table I. In agreement with previous work (4), these results show that less electrical activity is achieved by implanting BCl and that this effect becomes more pronounced as the chlorine concentration increases. The electrical junctions produced with both BCl implantations are identical and $0.044 \mu\text{m}$ shallower than that formed with the high dose BF_2^+ implantation. In all cases, the electrical junctions obtained from spreading resistance measurements are shallower than the metallurgical

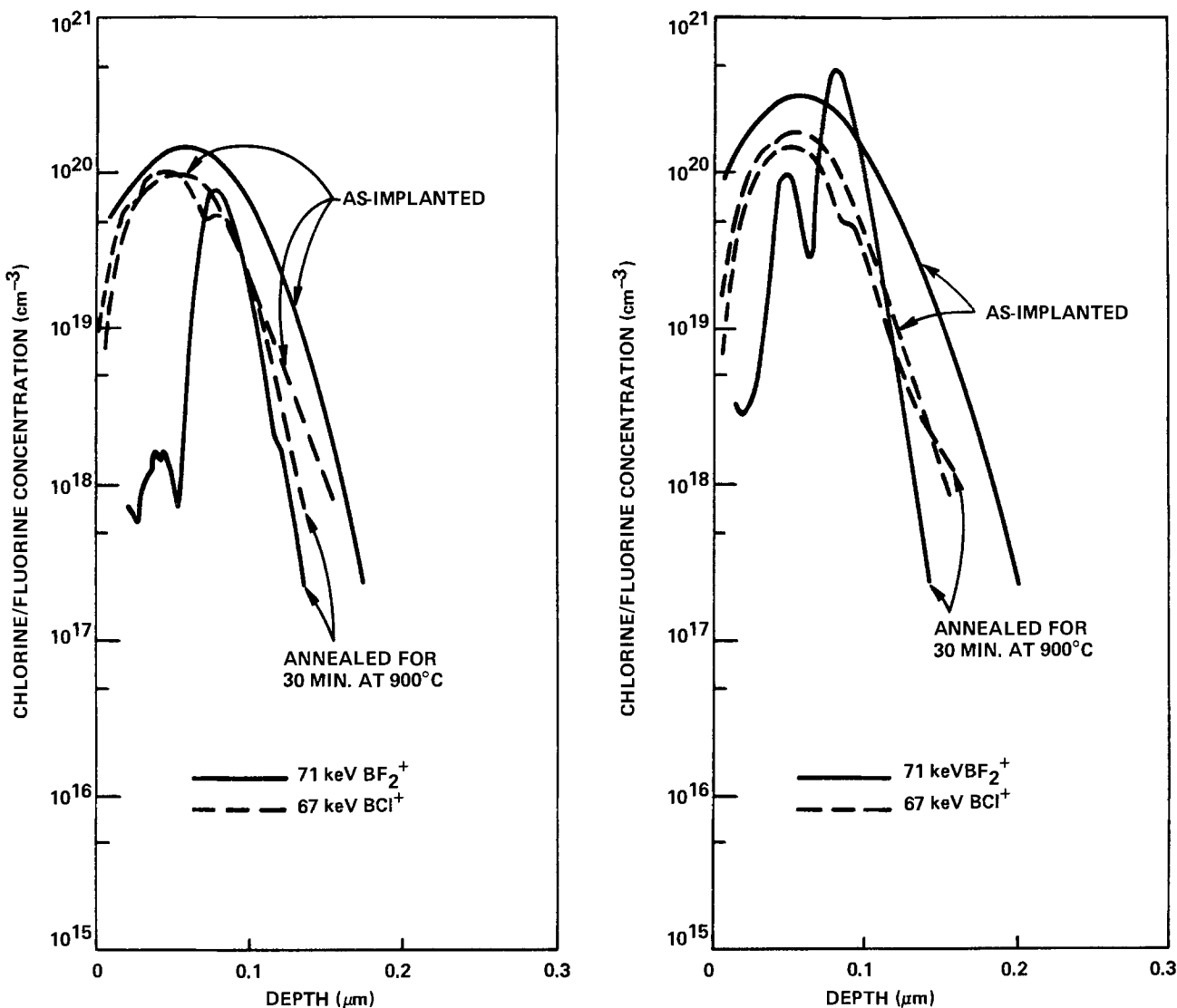


Fig. 6. Atomic chlorine/fluorine depth profiles from SIMS. a(left): Implantation ion dose of $6 \times 10^{14} \text{ cm}^{-2}$. b(right): Implantation ion dose of $1.2 \times 10^{15} \text{ cm}^{-2}$.

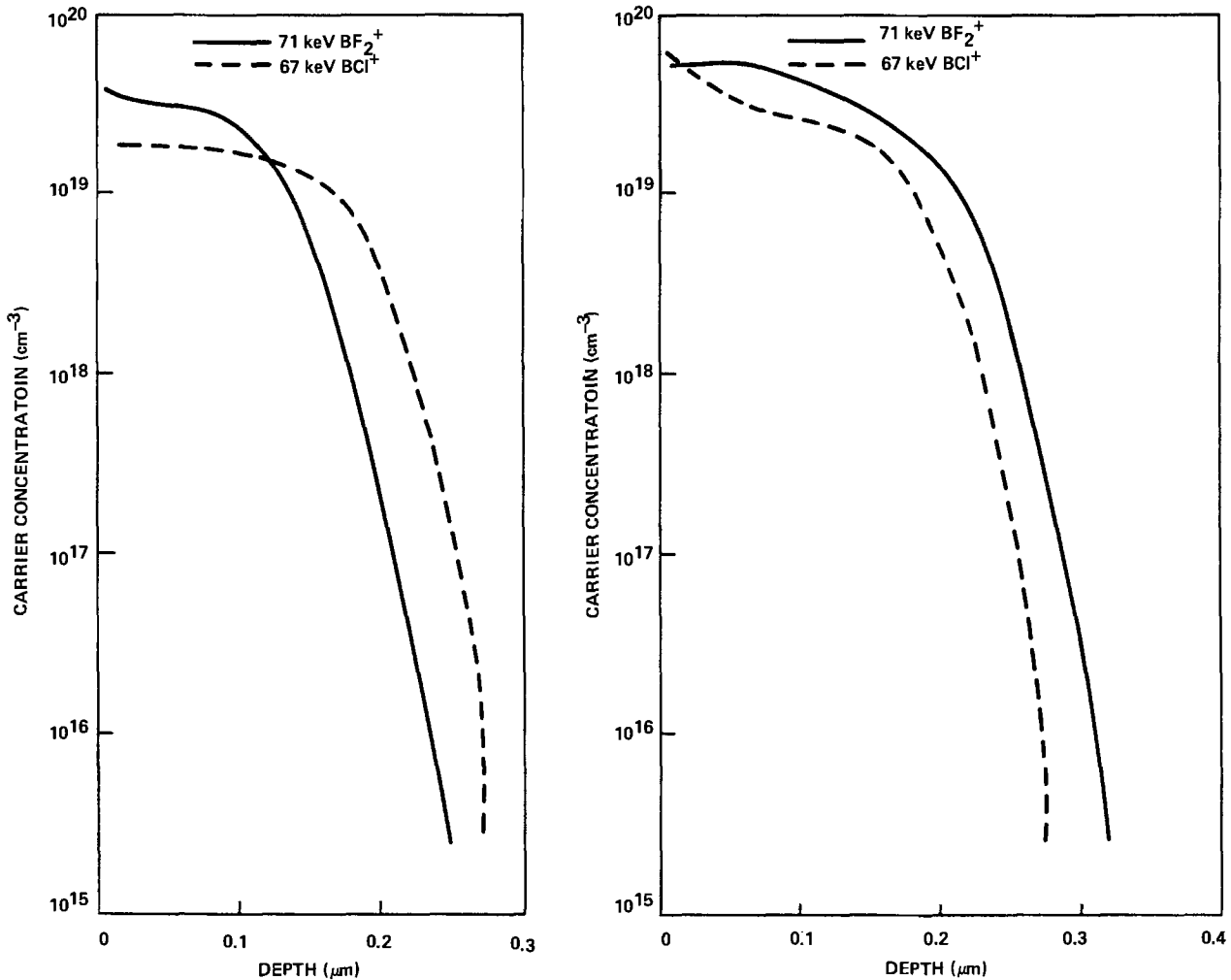


Fig. 7. Carrier concentration depth profiles from spreading resistance measurements made on beveled samples. a(left): Implantation ion dose of $6 \times 10^{14} \text{ cm}^{-2}$. b(right): Implantation ion dose of $1.2 \times 10^{15} \text{ cm}^{-2}$.

junctions measured by SIMS. The boron in the implanted tail region is therefore interstitial and does not enter substitutional sites during annealing. This effect is most pronounced with the high dose BCl⁺ implantation, where the metallurgical junction is approximately 0.1 μm deeper than the electrical junction.

The room temperature I-V characteristics of p⁺/n diodes fabricated by implanting either BCl⁺ or BF₂⁺ and furnace annealing for 30 min at 900°C are summarized in Table II. The measurements were made with the p electrode biased and the substrate at ground potential. The statistics are based on an analysis of 20 diodes on two wafers of each implantation. The reverse-bias leakage current density is lower with the BF₂ implantations and increases with an increase in ion dose of either BCl⁺ or BF₂⁺. The breakdown voltage is appreciably lower with the high dose BCl implantation only suggesting that chlorine acts as an ionized impurity scattering site. The forward-bias characteristics could be fit to the expression $J = J_0[\exp(qV/mkT)^{-1}]$ where $kT/q = 25.26 \text{ mV}$. Over the current range from 10^{-11} to 10^{-6} A , we find m equal to 1.01-1.03 with BF₂ and m equal to 1.08-1.11 with BCl. Nonlinearity above 10^{-6} A is attributed to excess diode resistance. The near-ideal behavior of the diodes suggests that current

transport is dominated by diffusion. An increased deviation from the ideal is noted with BCl relative to BF₂ which increases with the ion dose of either species. This implies that the halogen contributes to some minority recombination within the depletion layer and that chlorine is far worse than fluorine in this respect. This could explain the extremely poor electrical characteristics found for annealing high dose BCl₂ implantations in silicon (5). Nonetheless, the diode characteristics are in general excellent and comparable to furnace-annealed B-implanted p/n diodes (2, 10).

Summary and Conclusion

The use of BCl⁺ implantation as an alternative to BF₂⁺ implantation to form shallow p⁺/n junctions in <100> silicon is examined. Because of complete dissociation of the molecular ion upon impact with the lattice, any structural and electrical effects are explained in terms of the influence of the halogen alone.

Chlorine is found to be at least four times as effective as fluorine in amorphizing <100> silicon. The coamorphization of the silicon surface which accompanies a $6 \times 10^{14} \text{ BCl}^+ \text{ cm}^{-2}$ implantation has a small effect in the reduction

Table I. The sheet resistivity (ρ_s), effective surface carrier concentration (N_s), and junction depth (X_j) for 71 keV BF₂ and 67 keV BCl ion-implanted <100> silicon after furnace annealing for 30 min at 900°C

Ion dose (cm ⁻²)	6×10^{14}		1.2×10^{15}	
	BF ₂ ⁺	BCl ⁺	BF ₂ ⁺	BCl ⁺
ρ_s (Ω/\square)	230±5	288±6	121±3	189±4
N_s ($\times 10^{14} \text{ cm}^{-2}$)	4.48	3.25	9.0	5.52
X_j (μm)	0.25	0.27	0.32	0.27

Table II. The reverse-bias leakage current density (J), reverse-junction breakdown voltage (B_v), and forward-current recombination factor (m), for 71 keV BF₂ and 67 keV BCl ion-implanted p⁺/n diodes. The diode area is 0.032 cm².

Ion dose (cm ⁻²)	6×10^{14}		1.2×10^{15}	
	BF ₂ ⁺	BCl ⁺	BF ₂ ⁺	BCl ⁺
J (nA cm ⁻²) at -1V	-1.1±0.2	-1.8±0.4	-1.9±0.2	-3.5±0.5
J (nA cm ⁻²) at -5V	-4.4±0.4	-6.7±0.7	-6.4±0.6	-9.9±0.8
B_v (V)	-62±1	-64±2	-57±2	-54±3
m	1.01	1.08	1.03	1.11

of boron channeling compared to BF_2^+ . It is interesting that the amorphous layer does not suppress more of the boron channeling tail. The increase in thickness of the amorphous layer with BCl dose has essentially no effect on boron channeling.

Diffusion of interstitial boron during annealing is enhanced by chlorine relative to fluorine, whereas the transition to electrically active interstitial sites is retarded. This behavior tends to produce deeper metallurgical junctions and shallower electrical junctions with BCl^+ implantations in particular.

The mobility of fluorine during annealing is much higher than that of chlorine. Fluorine appears to segregate in regions of high lattice damage, whereas chlorine shows remarkably little diffusion and essentially maintains the as-implanted profile after annealing.

Shallow p⁺/n junction diodes fabricated with both BCl^+ and BF_2^+ implantations display excellent I-V characteristics, although the higher concentration of chlorine shows some degradation, suggesting minority carrier generation within the depletion region. The electrical properties are clearly more sensitive to the presence of the retained halogen than to the band of dislocation loops remaining near the original amorphous-crystalline interface.

Acknowledgments

The authors thank P. Contreras for the TEM sample preparation and G. de Groot for fabricating the diode ar-

rays. Helpful discussions with W. T. Stacy and the staff at C. Evans and Associates are appreciated. We thank M-A. Nicolet for sending a preprint of his paper.

Manuscript received July 16, 1984.

Philips Research Laboratories assisted in meeting the publication costs of this article.

REFERENCES

1. H. Muller, H. Ryssel, and I. Ruge, in "Ion Implantation in Semiconductors," I. Ruge and J. Graul, Editors, p. 85, Plenum Press, New York (1971).
2. A. E. Michel, F. F. Fang, and E. S. Pan, *J. Appl. Phys.*, **45**, 2991 (1974).
3. R. G. Wilson, *ibid.*, **54**, 6879 (1983).
4. D. G. Beanland, *Solid State Electron.*, **21**, 537 (1978).
5. G. Fuse, T. Hirao, K. Inoue, and S. Takayanagi, *J. Appl. Phys.*, **53**, 3650 (1982).
6. I. Suni, U. Shreter, M-A. Nicolet, and J. E. Baker, *ibid.*, **56**, 273 (1984).
7. B. L. Crowder, J. F. Ziegler, and G. W. Cole, in "Ion Implantation in Semiconductors and Other Materials," B. L. Crowder, Editor, p. 257, Plenum Press, New York (1973).
8. M. Y. Tsai, B. G. Streetman, P. Williams, and C. A. Evans, Jr., *Appl. Phys. Lett.*, **32**, 144 (1978).
9. M. Y. Tsai, D. S. Day, B. G. Streetman, P. Williams, and C. A. Evans, Jr., *J. Appl. Phys.*, **50**, 188 (1979).
10. J. B. Lasky, *ibid.*, **54**, 6009 (1983).

An Improved Test Structure and Kelvin-Measurement Method for the Determination of Integrated Circuit Front Contact Resistance

J. A. Mazer and L. W. Linholm*

Semiconductor Devices and Circuits Division, National Bureau of Standards, Washington, DC 20234

A. N. Saxena

American Microsystems, Inc., Santa Clara, California 95051

ABSTRACT

The use of an improved microelectronic test structure and associated Kelvin measurement method for determining front contact resistance (circuit loading resistance) of a metal/semiconductor ohmic contact is described. The values of front contact resistance for aluminum/silicon contacts are determined using this Kelvin-cross contact resistance test structure and are compared with values determined by a two-terminal contact chain method and with values determined by a Kelvin voltage divider method. The values of front contact resistance using the Kelvin-cross structure and associated measurement method are shown to be less sensitive to photolithographic process variations and electrical measurement errors than those determined using the other two structures and measurement methods.

The problem of ohmic contact resistance becomes increasingly significant as the critical feature size for VLSI technology decreases. The contact resistance encountered as the current passes between the metal and the semiconductor will increase as the contact-window size decreases, and it can lead to prohibitively large RC time constants. The circuit loading resistance of an ohmic contact is called the front contact resistance (1, 2). The front contact resistance is defined as the ratio of the voltage across the interfacial layer at the edge where the current density is greatest to the entire current through the contact; it is independent of the current polarity.

A common approach to the determination of front contact resistance has been to measure the total series resistance of a chain of alternating diffused layer and metal layer sections serially connected by contact windows. This is usually a two-point measurement in which a dc current is forced from one end of the chain to the other while the voltage is measured between the two ends.

A knowledge of the diffused-layer and metal-layer sheet resistances, the number of diffused-layer and metal-layer squares, and the number of contact windows is then used to calculate an average value for front contact resistance. Because this is not a Kelvin measurement, both the resistance in the current (voltage) taps and the probe-to-probe pad resistance are sensed in the measurement. A Kelvin measurement method can avoid the inclusion of these parasitic resistances because it employs separate pairs of taps to sense the current and the voltage. This paper describes the use of a recently reported microelectronic test structure and electrical measurement method for the Kelvin determination of front contact resistance (1). This improved test structure also allows the Kelvin measurement of the interfacial and end contact resistances. [These parameters are defined by means of a transmission-line model for the metal/semiconductor contact (1).] The sensitivity of this method to measurement interferences and misalignment has also been discussed (1). A comparison of the values of front contact resistance determined by this method and by the contact-chain method,

* Electrochemical Society Active Member.

for 10 μm-square Al/Si contacts, is made. A comparison is also made between values determined by this method and values determined by a Kelvin voltage-divider method (2).

Fabrication of Devices

Three 4 in. wafers patterned entirely with contact resistance test chips were fabricated. These chips contain cross-bridge sheet resistors for the determination of both the sheet resistance and electrical linewidth of diffused and metal layers (3, 4); two two-terminal contact chains which allow the non-Kelvin determination of front contact resistance (Fig. 1); two sizes of a Kelvin voltage-divider structure, previously reported in the literature (2), for the determination of front contact resistance (Fig. 2); and a Kelvin-cross contact resistance test structure for the direct measurement of the end and interfacial contact resistances and for the determination of the front contact resistance (1) (Fig. 3). Table I gives the design values for the contact chains and the Kelvin test structures.

For each of the three wafers, an n-type diffused layer was formed by a 75 keV implantation of arsenic into a p-type 19 Ωcm <100> substrate. The implant dose was 1 × 10¹⁶ cm⁻². The implantation was followed by a drive-in at 1000°C in an N₂ ambient. Drive-in times were 20, 40, and 80 min, respectively. Contact windows were opened by a wet-etching technique. The metallization was 99% Al/1% Si sintered for 20 min at 490°C in an N₂ ambient. The sheet resistance and linewidth, for both the diffused and metal layers, were determined from the cross-bridge sheet resistor structures. Measurements were made at approximately 130 sites on each wafer by means of an automated parametric measurement system. Measured values for resistance and linewidth are given in Table II.

Determination of Front Contact Resistance

Two-terminal contact chains.—For each contact chain (Fig. 1), a non-Kelvin determination of front contact resistance was made by forcing a dc current of 1 mA from one terminal to the other and measuring the voltage between the terminals. The front contact resistance R_f is given by

$$R_f = [VI - (R_{SD})(n_D) - (R_{SM})(n_M)]/N \quad [1]$$

where I is the forced current, V is the measured voltage, R_{SD} and R_{SM} are the sheet resistances of the diffused and metal layers, respectively, n_D and n_M are the number of diffused and metal layer squares, respectively, and N is the number of (10-μm-square-design) contact windows. Lateral diffusion of the dopant and imprecise metal-line etching can cause the true values for n_D and n_M to be significantly different than the design values listed in Table I. In the application of Eq. [1], calculated values for n_D and n_M , obtained by correcting the design values of these parameters for the electrically measured linewidth, are used in place of the design values. Table III gives the calculated values for n_D and n_M corrected for the electrically measured linewidth. For each contact chain, measurements of VI were made at approximately 130 sites across each wafer.

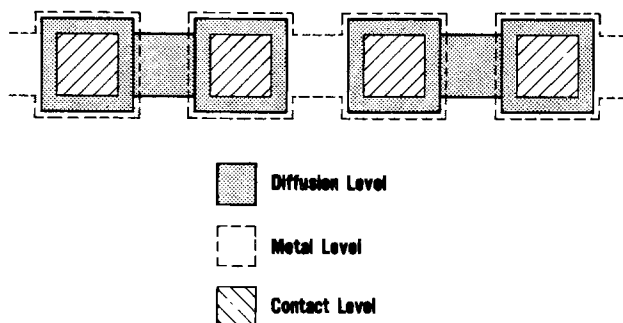
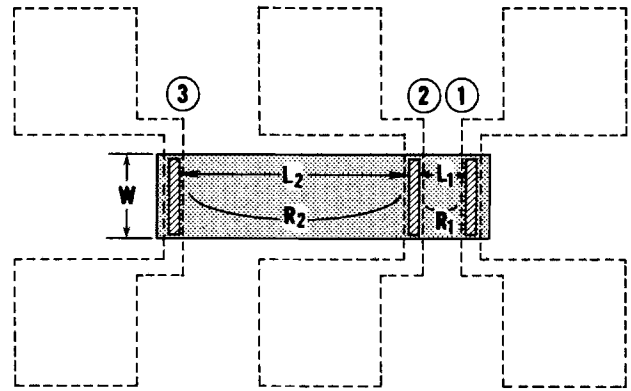


Fig. 1. Section of a two-terminal contact chain (chain B) for the non-Kelvin determination of front contact resistance.



$$R_f = \frac{R_1 L_2 - R_2 L_1}{2(L_2 - L_1)}$$

Fig. 2. Kelvin voltage-divider test structure proposed in Ref. (2) for the determination of front contact resistance. Front contact resistance is calculated from the measurement of R_1 and R_2 .

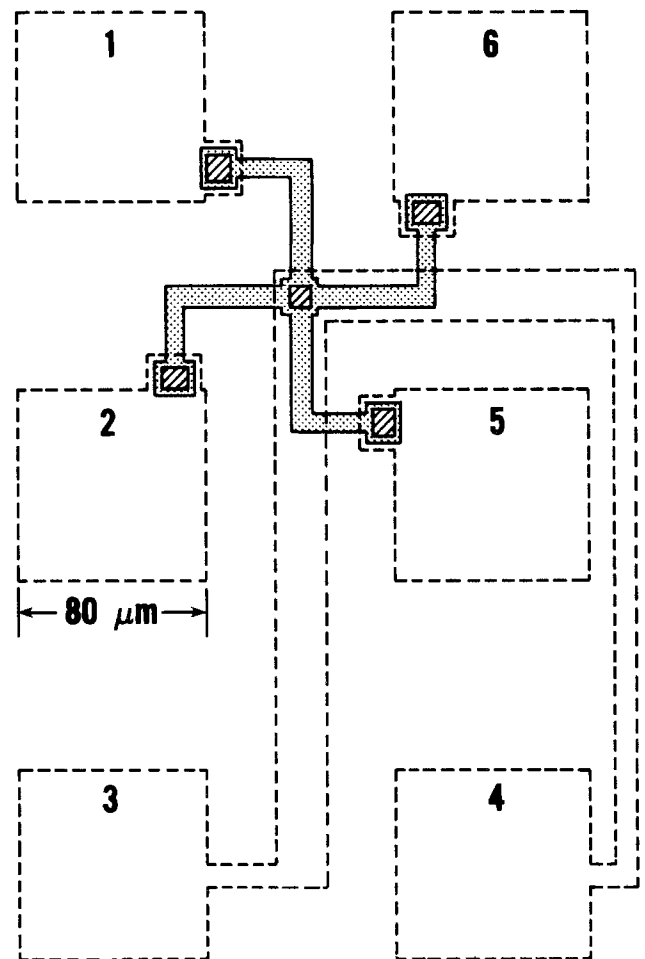


Fig. 3. Kelvin-cross contact resistance test structure for the determination of R_e , R_c , ρ_c , R_{SDUC} and R_f . The values of R_e and R_c are measured directly; ρ_c is determined indirectly from the measurement of R_e ; R_{SDUC} and R_f are determined indirectly from the measurement of R_e .

Table I. Design values for the contact chains and Kelvin structures. n_D and n_M are the number of diffusion-layer and metal-layer squares, respectively, in a chain. N is the number of contact windows in a chain. L_1 and L_2 are the lengths for the Berger structures (2). For the contact chains, diffused-layer squares under the contacts are not included, but metal-layer squares over the contacts are included.

Structure	n_D	n_M	N	Window size ($\mu\text{m} \times \mu\text{m}$)	L_1 (μm)	L_2 (μm)
Chain A	117.0	165.4	52	10 × 10	—	—
Chain B	85.5	198.2	114	10 × 10	—	—
Voltage divider A	—	—	—	7.5 × 50	15	150
Voltage divider B	—	—	—	7.5 × 50	30	150
Kelvin cross	—	—	—	10 × 10	—	—

Table II. Measured values for sheet resistance and linewidth. Sample standard deviations were about three percent of sample means. The design values for the diffused layer and metal layer linewidths were 6 μm and 8 μm , respectively.

Wafer	R_{SD} (Ω/\square)	Diffusion linewidth (μm)	R_{SM} (Ω/\square)	Metal linewidth (μm)
2395-1	24.0	7.03	3.91E-2	7.00
2395-5	19.5	8.03	2.90E-2	7.04
2395-9	15.8	7.04	3.13E-2	6.72

Kelvin voltage-divider structure.—The Kelvin test structure introduced by Berger (2), shown in Fig. 2, allows the determination of the front contact resistance from the measurement of two resistances, R_1 and R_2 . In Fig. 2, R_1 is measured by forcing a current of 1 mA between contacts 1 and 2 and measuring the voltage across the same. R_2 is measured in a similar fashion using contacts 2 and 3. The resistors R_1 and R_2 are diffused resistors. The resistance of a diffused resistor, including both contacts, is given by

$$R = R_s L/W + 2R_f \quad [2]$$

where R_s is the sheet resistance of the diffused resistor, L is the length between contacts, and W is the width of the resistor. The substitution of R_1 and R_2 and the corresponding lengths L_1 and L_2 into Eq. [2] yields a system of equations that can be solved for R_f

$$R_f = (R_1 L_2 - R_2 L_1) / [2(L_2 - L_1)] \quad [3]$$

The design values for L_1 and L_2 are listed in Table I. For each of these Kelvin test structures, measurements of R_1 and R_2 were made at approximately 130 sites across each wafer.

Kelvin-cross test structure.—The transmission-line analysis of the uniform interfacial contact (5, 1) allows the calculation of R_f from the measured value of the end contact resistance R_e

$$R_f = R_e \cosh [(R_{SDUC}/\rho_c)^{1/2} d] \quad [4]$$

where R_{SDUC} is the sheet resistance of the diffused layer directly under the contact window, d is the length of the contact window, and ρ_c is the specific contact resistance of the metal/semiconductor interfacial layer. The end contact resistance R_e is the ratio of the voltage across

Table III. Calculated values for n_D and n_M obtained by correcting the design values of these parameters for the electrically measured linewidth. Superscripts A and B refer to contact chains A and B, respectively.

Wafer	n_D^A	n_M^A	n_D^B	n_M^B
2395-1	106.08	182.71	77.52	219.66
2395-5	97.24	181.99	71.25	218.56
2395-9	106.08	188.23	77.52	226.26

the interfacial layer at the edge where the current density is least to the entire current through the contact (1). A direct Kelvin measurement of R_e can be made by using the six-terminal structure shown in Fig. 3. In Fig. 3, a current of 1 mA is forced from pad 1 to pad 3, while the voltage is measured between pad 5 and pad 4. The ratio of the voltage to the current is R_e . [Pads 2 and 6 are used for other measurements (1).] The value of R_{SDUC} is not necessarily the same as the value of the diffused-layer sheet resistance away from the contact window. This is because the sintering step alters the sheet resistance of the diffused layer directly under the contact window by forming an Al/Si composite. The values of R_{SDUC} and ρ_c are determined by the method described in Ref. (1) using this same structure. A necessary requirement for the validity of the transmission-line analysis is that the interfacial contact layer have areal uniformity. A method for determining the areal uniformity of the interfacial contact layer is described in Ref. (6, 1). The interfacial contact layer, for each of the three wafers used in this study, was determined to be uniform across its area by this method. The end contact resistance R_e was measured at approximately 130 sites across each wafer.

Discussion and Results

The values of front contact resistance determined by the contact-chain method are given in Table IV. The negative values of R_f are attributed to contact window overetching. Measurements of contact-window size at selected sites with an image-shear optical microscope showed that the contact windows (10 μm by 10 μm design) were overetched on each of the three wafers by an amount between 1.4 and 1.7 μm . For chains A and B on wafer 2395-1, overetching of the contact windows by approximately 0.54 and 0.48 μm , respectively, is enough to produce negative calculated values of R_f if this overetching is not taken into account. Calculation of R_f , using values of n_D that are corrected for both measured linewidth and measured contact-window size, yields positive values (Table IV). In the application of the contact-chain method, n_D is seldom corrected for both linewidth and contact-window size. Even with these two corrections, the contact-chain method tends to be highly inaccurate because the calculated value of R_f is always essentially the difference of two large numbers, namely, $R_{SD} n_D$ and V/I (7). It is seen in Table IV that even with the corrections for both linewidth and contact-window size (overetching), there is still great disagreement in the calculated values for R_f on each wafer. A small percentage error in the measurement of either R_{SD} or V/I will tend to cause a very large percentage error in the calculated value of R_f . As an example of this, consider chain A on wafer 2395-1. If, in Tables II and IV, the measured values of R_{SD} and V/I were 2% smaller and 2% larger, respectively, then the calculated value of R_f^A would be 0.783 Ω instead of -1.16 Ω .

Table V gives the values of front contact resistance determined by the Kelvin voltage-divider method (2). As with the contact chains, the calculations of negative values is attributed to overetching of the contact windows. Image-shear optical-microscope measurements

Table IV. Measured values of V/I and calculated values of R_f for the contact chains (10- μm -square-design contact windows). All values of R_f have been calculated using the measured value of linewidth. Superscripts A and B refer to the contact chains A and B, respectively. The prime notation (') refers to values which have been corrected for overetching. Sample standard deviations were less than four percent of sample means for measured values of V/I .

Wafer	Chain A (V/I) (Ω)	Chain B (V/I) (Ω)	R_f^A (Ω)	R_f^B (Ω)	$R_f'^A$ (Ω)	$R_f'^B$ (Ω)
2395-1	2493	1749	-1.16	-1.05	0.391	0.590
2395-5	1841	1282	-1.16	-1.00	0.241	0.411
2395-9	1653	1194	-0.557	-0.332	0.504	0.780

Table V. Measured values of R_1 and R_2 and calculated values of R_f by the Kelvin voltage-divider method (2). (Contact windows have a design value of $7.5 \mu\text{m}$ by $50 \mu\text{m}$.) The superscripts A and B refer to the two sizes of the voltage divider structures. The prime notation (') refers to values which have been corrected for overetching. Sample standard deviations were less than two percent of sample means for the measured values of R_1 and R_2 .

Wafer	R_1^A (Ω)	R_2^A (Ω)	R_1^B (Ω)	R_2^B (Ω)	R_f^A (Ω)	R_f^B (Ω)	$R_f'^A$ (Ω)	$R_f'^B$ (Ω)
2395-1	6.36	64.0	12.7	63.9	-0.022	-0.050	0.319	0.291
2395-5	5.06	50.8	10.1	50.7	-0.011	-0.025	0.277	0.280
2395-9	4.46	42.3	8.65	42.3	0.128	0.119	0.338	0.329

showed that the contact windows (7.5 by $50 \mu\text{m}$ design) were overetched on each of the three wafers by an amount between 1.5 and $2.2 \mu\text{m}$. For voltage-divider structures A and B on wafer 2395-1, overetching of the contact windows by as little as 0.10 and $0.23 \mu\text{m}$, respectively, is enough to produce negative calculated values of R_f if this overetching is not taken into account. Calculation of R_f , using the values of L_1 and L_2 that are based on measured contact-window size, yields positive values (Table V). The Kelvin voltage-divider method (2) shares a common source of error with the contact-chain method; namely, the calculated value of R_f is always essentially the difference of two comparably large numbers. As with the contact chains, a consequence of this fact is that the calculated value for R_f is very sensitive to errors in the measurements. To illustrate this, consider the voltage-divider structure A on wafer 2395-1. If, in Table V, the measured values of R_1 and R_2 were 2% larger and 2% smaller, respectively, then the calculated value of R_f would be 0.122Ω instead of -0.022Ω .

Table VI lists the values of R_{SDUC} , ρ_c , and R_e , and the subsequent calculated values of R_f obtained by using Eq. [4]. When R_f is determined by the Kelvin-cross method (1), i.e., Eq. [4], the primary source of error is the uncertainty in the contact-window length d . The sheet resistance of the diffused layer directly under the contact R_{SDUC} is calculated by means of a transmission line equation that involves the parameters R_e , ρ_c , and d (1). (Since the value of ρ_c is a material property of the interfacial contact layer, any pair of values (R_e , d) can be used to calculate the value of the material parameter R_{SDUC} .) For the $10 \mu\text{m}$ -square-design contact windows on wafer 2395-1, if the windows were overetched by $1 \mu\text{m}$, the method of Ref. (1) would yield a calculated value for R_{SDUC} of $1.91 \Omega/\text{square}$ instead of $2.64 \Omega/\text{square}$ and would yield a calculated value for R_f of 0.508Ω instead of 0.657Ω . It is seen that the value of R_f determined by the Kelvin-cross method, i.e., Eq. [4], is less sensitive to imprecise window etching (or imprecise photolithography) than is the value for R_f determined by either the contact-chain method or the Kelvin voltage-divider method. The Kelvin-cross method is also relatively insensitive to errors in the electrical measurements. For example, consider wafer 2395-1. If in Table VI the measured value for R_e was 2% larger than the value reported, the calculated value for R_{SDUC} would be $2.60 \Omega/\text{square}$ instead of $2.64 \Omega/\text{square}$ and the calculated value for R_f would be 0.652Ω instead of 0.657Ω . [R_{SDUC} is a function of R_e (1).]

Unlike the contact-chain method, both Kelvin methods have the advantage of being insensitive to linewidth. The Kelvin-cross method has the additional advantage of being relatively insensitive to photolithography process variations and to small errors in the electrical measurements. In principle, the contact-chain method and the voltage-divider method can yield accurate values for R_f . But, as illustrated above, the sensitivities of these two methods re-

Table VI. Direct-Kelvin-measurement values for end contact resistance R_e , values of R_{SDUC} and ρ_c determined by the method described in Ref. (1), and values of front contact resistance R_f obtained from Eq. [4]. (Contact windows have a design value of $10 \mu\text{m}$ by $10 \mu\text{m}$.) Sample standard deviations were about twenty percent of sample means for measured values of R_e .

Wafer	R_e (Ω)	R_{SDUC} (Ω/\square)	ρ_c ($\Omega\text{-cm}^2$)	R_f from Eq. [4] (Ω)
2395-1	2.38E-2	2.64	1.64E-7	0.657
2395-5	3.29E-2	2.16	1.67E-7	0.601
2395-9	3.87E-2	1.53	1.49E-7	0.479

quire very careful measurements and very accurate knowledge of various fabrication parameters. Differences between the results reported in Table VI, Table IV, and Table V, normalized for a $10 \mu\text{m}$ -square contact, are attributed to the accuracy with which these factors can be determined and to possible lateral current crowding effects. In particular, the determination of the exact contact-window size is very time consuming and, thus, probably infeasible in a production environment.

Conclusions

The front contact resistance is of significance to the circuit designer because it represents the actual circuit loading resistance of the contact. This paper has shown that the determination of R_f by means of a Kelvin-cross test structure (1) is inherently more accurate than the determination of R_f by means of either the non-Kelvin contact-chain method or the Kelvin voltage-divider method (2). The Kelvin-cross method is inherently more accurate than the other methods because it does not involve the subtraction of two comparably large numbers and because it does not require the precise measurement of linewidths and contact window size. The Kelvin-cross method is a completely electrical measurement procedure, is convenient to use, and is valid for a wide range of contact areas. It allows the measurement of R_f for contact windows with the same design dimensions as those used in production. Because this new structure is relatively small, it is feasible to include it on production chips. Use of the Kelvin-cross test structure and electrical measurement method will significantly improve the accuracy of contact resistance values that are used by circuit designers in circuit simulation codes.

Acknowledgments

The authors thank J. A. Horst, C. H. Ellenwood, M. R. Doggett, and B. L. Staton for assistance in obtaining the data for this study, and M. J. Candela for assistance in manuscript preparation.

Manuscript submitted March 15, 1984; revised manuscript received Oct. 22, 1984.

National Bureau of Standards assisted in meeting the publication costs of this article.

REFERENCES

1. S. J. Proctor, L. W. Linholm, and J. A. Mazer, *IEEE Trans. Electron Devices*, **ed-30**, 1535 (1983).
2. H. H. Berger, *Solid State Electron.*, **15**, 145 (1972).
3. M. G. Buehler, S. D. Grant, and W. R. Thurber, *This Journal*, **125**, 650 (1978).
4. L. J. van der Pauw, *Philips Res. Rep.*, **13**, 1 (1958).
5. H. Murrmann and D. Widmann, *IEEE Trans. Electron Devices*, **ed-16**, 1022 (1969).
6. S. J. Proctor and L. W. Linholm, *IEEE Electron Device Lett.*, **ed1-3**, 294 (1982).
7. C. Y. Ting and B. L. Crowder, *This Journal*, **129**, 2590 (1982).

Interfacial Structure of Tungsten Layers Formed by Selective Low Pressure Chemical Vapor Deposition

W. T. Stacy,* E. K. Broadbent,* and M. H. Norcott

Philips Research Laboratories Sunnyvale, Signetics Corporation, Sunnyvale, California 94086

ABSTRACT

We have analyzed the interfacial structure of selectively deposited LPCVD tungsten on monocrystalline silicon, polycrystalline silicon, and polycrystalline aluminum substrates. Cross-sectional specimens were examined by transmission electron microscopy to determine the amount of substrate consumed by the selective deposition process and to assess the degree of lateral encroachment under masking SiO_2 layers for different conditions of deposition and surface preparation. The tungsten-silicon interfacial structure was found to depend strongly on the initial surface preparation. Immersion in a dilute HF solution resulted in a smooth interface, while a glow-discharge treatment ($\text{CF}_4 + \text{O}_2$) led to highly irregular interfaces, which, in extreme cases, contained tunnels extending $1 \mu\text{m}$ or more into the silicon substrate. Layers formed in WF_6 plus H_2 were found to consist of two layers, of which the lower layer is formed by the substrate reduction of WF_6 .

The selective low pressure chemical vapor deposition (LPCVD) of tungsten involves the formation of a tungsten layer on exposed surfaces of silicon, aluminum, and various metal silicides without the tungsten forming on SiO_2 or Si_3N_4 (1-4). This results in a self-aligned tungsten pattern which does not require a lithographic masking step and, consequently, is an attractive option for a number of integrated circuit applications (5-10).

The process by which the tungsten deposits selectively, however, requires the chemical reduction of WF_6 by the substrate. Since this must entail some consumption of the substrate, the concern arises that the tungsten deposit may penetrate deeply into the substrate and disturb the underlying device structures. With this in mind, we have used transmission electron microscopy to characterize the interfacial structure of selectively deposited LPCVD tungsten films. Cross-sectional specimens have been employed to reveal the amount of substrate consumed and the degree of lateral encroachment under adjacent SiO_2 layers for different conditions of deposition and surface preparation.

Experimental

The deposition of the tungsten films was carried out in the low pressure (0.5 torr), horizontal flow, chemical vapor deposition (CVD) system described in a previous publication (4). The deposition gases were WF_6 (99.8%), purified H_2 , and Ar (99.9998%). The deposition substrates were 100 mm diam, p-type, 7-21 $\Omega\text{-cm}$, (111) silicon wafers. Three types of substrate coatings were used: patterned SiO_2 , patterned polycrystalline silicon, and patterned polycrystalline aluminum. For the SiO_2 coating, a $0.3 \mu\text{m}$ layer of thermally grown SiO_2 was etched into a repetitive stripe pattern with a pitch of $8 \mu\text{m}$ and a spacing of $4 \mu\text{m}$. The LPCVD polysilicon was defined in the same way on a $0.3 \mu\text{m}$ layer of SiO_2 . The aluminum layer was deposited by E-beam evaporation and patterned in the same way on a $0.45 \mu\text{m}$ layer of SiO_2 . All substrates were cleaned immediately prior to deposition by either a low pressure glow discharge (CF_4 and O_2) treatment or an immersion in dilute HF followed by a rinse in deionized water and spin drying.

The resulting samples were characterized by both scanning and transmission electron microscopy (SEM and TEM). The TEM specimens were prepared in cross section by a procedure involving metallographic sectioning followed by Ar ion beam milling. All TEM micrographs were taken at an accelerating voltage of 120 kV. In some cases, the chemical composition was probed in the TEM by means of an energy dispersive x-ray detector coupled with an electron beam scanning attachment (STEM-EDS).

Results

Hydrogen reduction of WF_6 .—Figure 1 is a cross sectional TEM micrograph of a specimen consisting of tung-

sten deposited onto a silicon substrate partially covered by SiO_2 . The deposition reactant gases were WF_6 and H_2 , and the deposition time and temperature were 20 min and 300°C . After the oxide pattern was formed, the substrate was cleaned just before deposition in a CF_4/O_2 glow discharge. It can be seen that the tungsten layer extends vertically to a depth of $0.1 \mu\text{m}$ and laterally about $0.2 \mu\text{m}$ under the oxide edge. It will be shown later in this section that this lateral encroachment consists mostly of a filamentary structure in the silicon which contains very little tungsten.

The lateral penetration of the bulk of the tungsten layer is only $0.085 \mu\text{m}$. The tungsten extends above the initial silicon surface approximately $0.05 \mu\text{m}$, resulting in a total thickness of $0.15 \mu\text{m}$. The SiO_2 thickness is $0.32 \mu\text{m}$.

The micrograph in Fig. 2 was taken in a thinner region of the specimen and consequently reveals more of the internal structure of the tungsten layer. It can be seen that two layers are involved: an upper layer $0.05 \mu\text{m}$ thick, and a lower layer varying in thickness from 0.02 to $0.1 \mu\text{m}$. The two tungsten layers are separated by a thin interfacial layer, possibly an oxide, approximately 3 nm thick. Note that the W/Si interface is extremely nonuniform. Results similar to those in Fig. 1 and 2 were obtained with polysilicon substrates. Again, a total thickness of $0.15 \mu\text{m}$ was found, and the films exhibited the same double layer structure.

In Fig. 3, the substrate was a $0.7 \mu\text{m}$ layer of polycrystalline aluminum. In this case, again for the same deposition conditions, the resulting tungsten film is thinner, 0.07 - $0.10 \mu\text{m}$. The higher magnification image in the inset

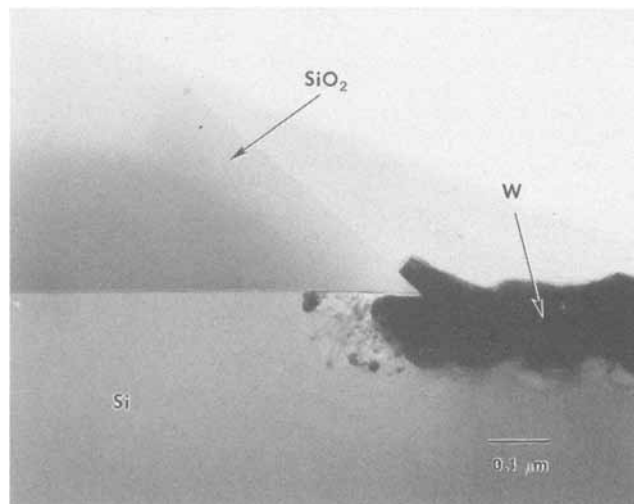


Fig. 1. TEM micrograph of a selectively deposited tungsten film in cross section. Deposition at 300°C , 20 min, $\text{WF}_6 + \text{H}_2$ reactant gases.

*Electrochemical Society Active Member.

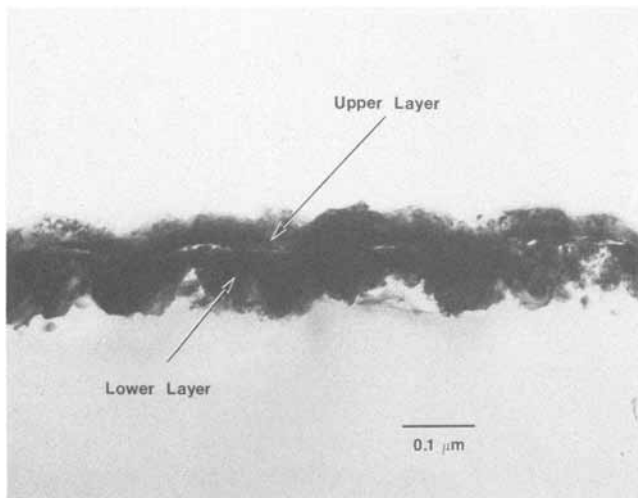


Fig. 2. Higher magnification view of the tungsten deposit in Fig. 1. Two layers separated by an oxide film can be seen.

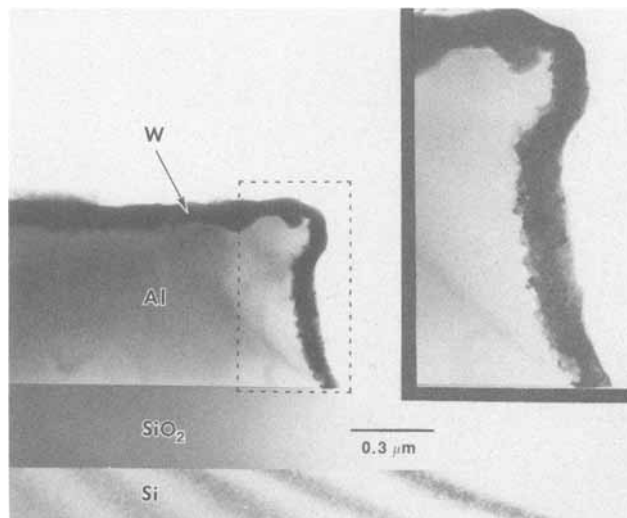


Fig. 3. Tungsten selectively deposited on aluminum, same deposition conditions as in Fig. 1. Inset shows the corner region at slightly higher magnification. Note that only one tungsten layer is visible.

shows only a single-layer structure. Note the irregular shape of the W/Al interface, which suggests that some consumption of Al has taken place.

Substrate reduction of WF₆.—Figure 4a is a SEM micrograph of tungsten selectively deposited onto monocrystalline silicon with only WF₆ and Ar as reactant gases. Again the deposition temperature was 300°C, and the surface was precleaned in a CF₄/O₂ glow discharge. The deposition time, however, was 40 instead of 20 min. Substantial encroachment of the tungsten under the SiO₂ stripe has occurred. The diffuse image of the tungsten edge, which is visible through the oxide, is presumably due to electrons backscattered from the tungsten and rescattered by the SiO₂. The TEM cross section of the same specimen (Fig. 4b) confirms that the lateral encroachment is 0.9 μm and the total layer thickness is 0.17 μm. Note that the tungsten layer is recessed; there is no tungsten formation above the original silicon surface. Also, there is no evidence of a double-layer structure. Higher magnification micrographs (not shown) showed only the presence of a single-layer structure when WF₆ and Ar were the reactant gases. Similar results were obtained with polysilicon substrates.

For the same deposition conditions (300°C, 40 min, WF₆ + Ar), a much thinner deposit was formed on polycrystalline aluminum. The TEM cross section in Fig. 5 reveals only a few grains of tungsten on an oxide layer about 5 nm thick.

Tunnels.—Another example of the filamentary structure in Fig. 1 is shown in detail in Fig. 6 for slightly differ-

ent deposition conditions (300°C, 40 min, WF₆ and H₂). The filaments appear to be individual tunnels in the silicon with diameters ranging from 20 to 40 nm. Each tunnel is constant in diameter over its entire length, and at the end of each tunnel is a particle equal in size to the tunnel diameter. We have analyzed several of the particles with STEM/EDS (4 nm probe beam diameter) and have found in each case a localized tungsten signal. Thus the tunnels appear to be the result of tungsten containing particles “burrowing” into the silicon substrate.

An examination of the tunnels via stereo pair micrographs has revealed many different shapes and lengths. Each particle appears to have had a unique pathway. In Fig. 7, for example, one sees evidence of straight, circular, and spiral trajectories. Note the particle which has reflected from the underside of the SiO₂ layer during its propagation.

In general, the tunnel structures were found at the edges of the tungsten deposits. In cases where the deposition was not uniform (e.g., due to a contaminated surface or a thicker surface oxide layer), the tunnels were observed over most of the tungsten-silicon interface. As the density of the tunnels increased, the tunnel lengths were found to decrease. Figure 8 shows an extreme case, where, owing to an inadequate cleaning procedure, only islands of tungsten were formed. The SEM micrograph (Fig. 8a) shows the isolated tungsten deposits; the TEM micrograph (Fig. 8b) reveals in cross section the underlying tunnel structures.

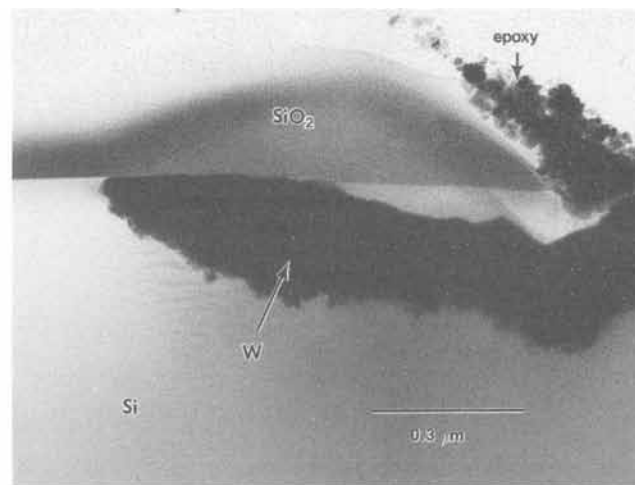
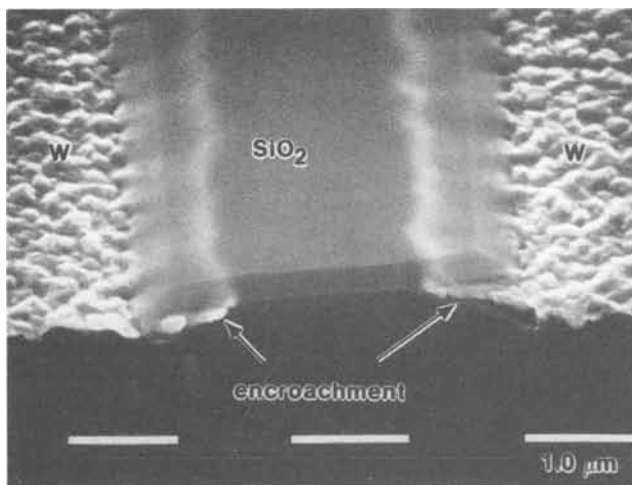


Fig. 4. An extreme case of tungsten encroachment under the neighboring SiO₂ layer. Deposition at 300°C, 40 min, WF₆ + Ar reactant gases (a, left) SEM micrograph, (b, right) TEM cross section.

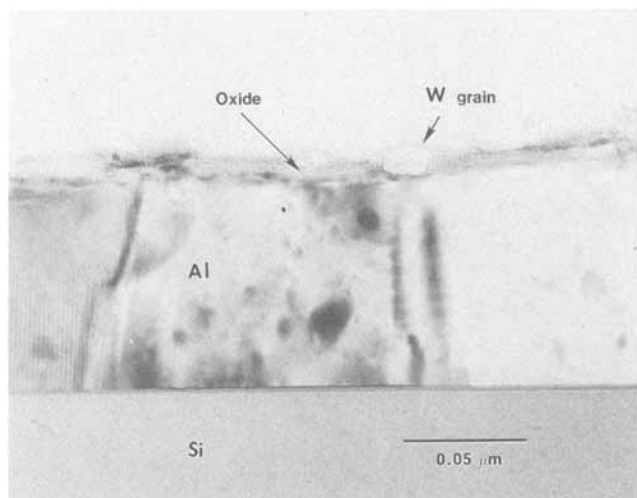


Fig. 5. Tungsten selectively deposited on aluminum in a $WF_6 + Ar$ reaction ambient ($300^\circ C$, 40 min). Note the presence of an oxide surface layer.

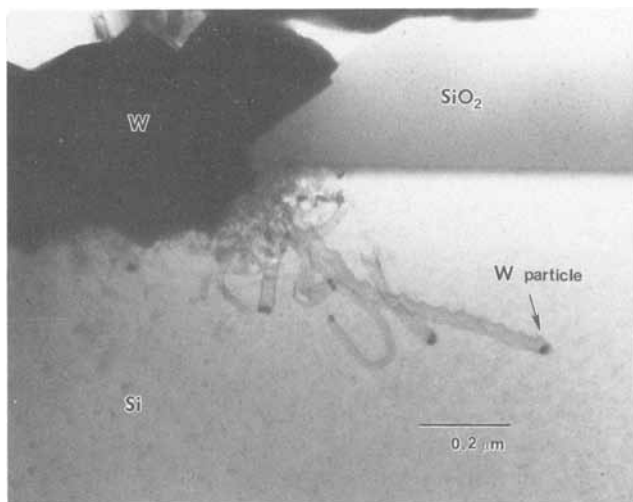


Fig. 6. Tunnel structures formed at the edge of the oxide stripe. TEM cross-sectional micrograph.

Surface preparation.—The importance of the substrate cleaning procedure is illustrated in Fig. 9a and 9b. The two films were deposited simultaneously under the same conditions ($300^\circ C$, 20 min, $WF_6 + Ar$); only the substrate surface preparation was different. The substrate in Fig. 9a

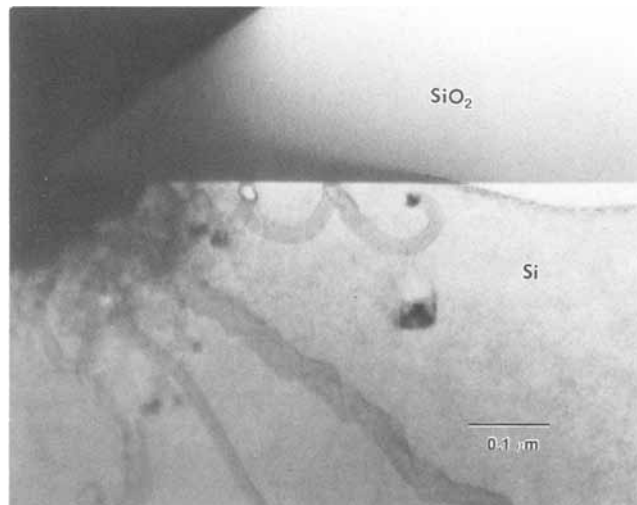


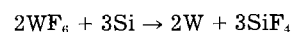
Fig. 7. Detail showing tunnel deflected by SiO_2 -Si interface

was cleaned prior to deposition in a CF_4/O_2 glow discharge, whereas that in Fig. 9b was immersed for 2 min in a dilute HF solution. The differences in the resulting layer thicknesses and interface smoothness are striking. The layer in Fig. 9a has a total thickness of $0.17 \mu m$, while the layer in Fig. 9b is only $0.02 \mu m$ thick.

This important result has been reported by one of us in a study of the growth kinetics of selectively deposited tungsten (4). It was found that when the silicon surfaces had been exposed to higher temperatures ($425^\circ C$) in the presence of an oxidizing ambient, the tungsten deposit was less uniform and much thicker. This was attributed to the presence of an oxide film of varying thickness which resulted in a nonuniform reduction of WF_6 . Consequently, all of the data in that paper were taken for wafers precleaned in HF.

Discussion

Double-layer vs. single-layer structure.—The tungsten films deposited on silicon were found to consist of two layers when the reactant gases were WF_6 plus H_2 , and one layer when WF_6 plus Ar were used. This can be attributed to the WF_6 reduction mechanisms involved. In the former case, both hydrogen reduction and silicon reduction of WF_6 occur, while in the latter only the silicon reaction takes place. Thus the lower layer is formed by the reaction with the substrate



and the upper layer of the reaction involving hydrogen

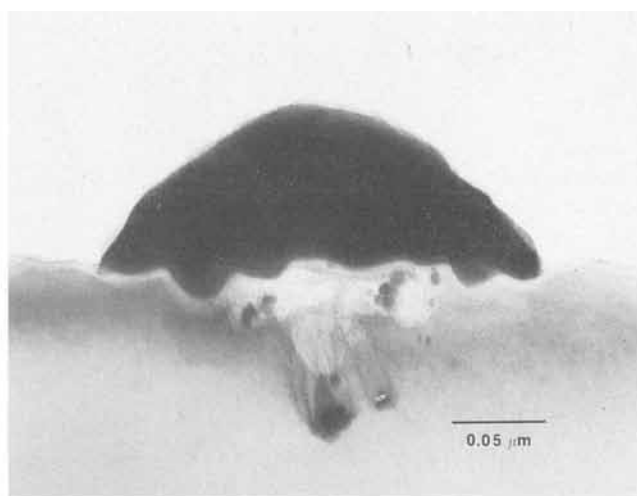
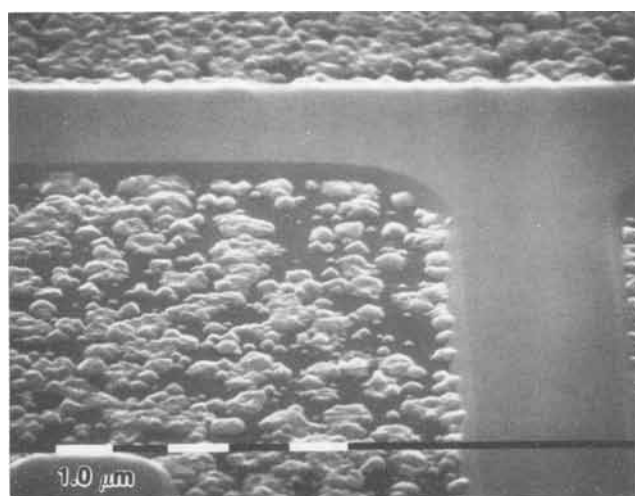


Fig. 8. Tunnel structures associated with incomplete coverage of the substrate. (a, left): SEM micrograph showing island growth. (b, right): TEM cross section of an individual "island."

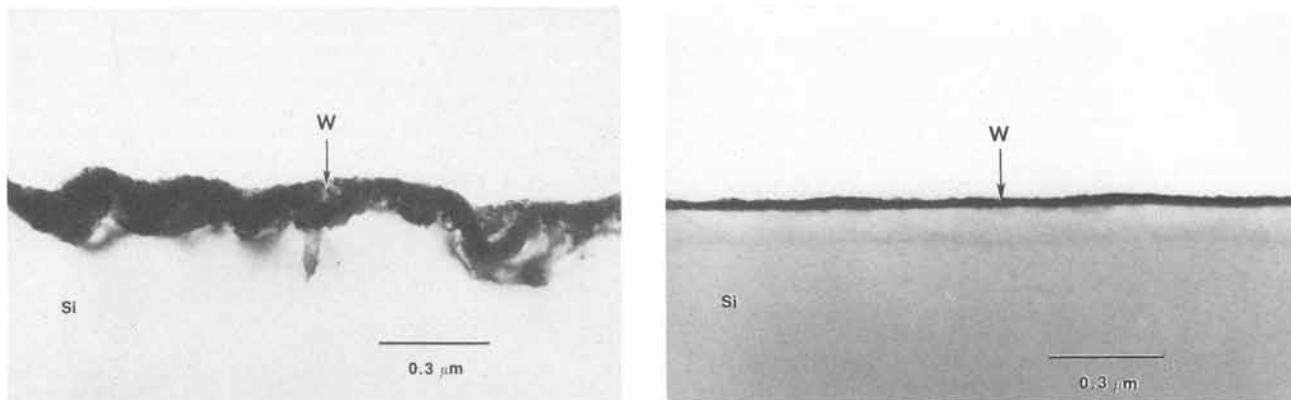
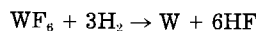
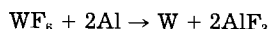


Fig. 9. TEM cross sections of two tungsten layers deposited under the same conditions, but for different substrate cleaning treatments. (a, left): CF_4/O_2 glow discharge clean. (b, right): Immersion in dilute HF.



The very thin, interfacial oxide layer (Fig. 2) may have originated at the original silicon surface. During the formation of the lower tungsten layer, WF_6 would diffuse through this oxide, react with Si to form W, and thus leave the oxide film on the surface of the lower layer. Once the lower layer reaches a thickness sufficient to substantially reduce the transport of WF_6 , the hydrogen reduction of WF_6 would become the dominant deposition reaction. The oxide film would be left behind to mark the transition from tungsten formation at the silicon surface to formation at the tungsten surface.

In the case of an aluminum substrate, the initial layer formed by the aluminum reduction of WF_6



is much thinner, possibly due to the presence of the oxide film seen in Fig. 5. Consequently, the lower layer is not visible in Fig. 3.

Tunnel structures.—The tunnels in Fig. 6, 7, and 8b bear a resemblance to the “channels” reported in studies of the catalytic gasification of graphite (11-14). Metal films (such as Ni or Pt), which have been deposited on cleaved graphite substrates and then heated, have been found to coalesce into droplets and then form pits in the substrate by catalyzing the oxidation or hydrogenation reaction. Using controlled-atmosphere electron microscopy, Baker and co-workers have shown that at certain temperature ranges the metal particles become mobile and actually cut grooves into the graphite surface. The resulting patterns are similar in appearance to the tunnel structures reported here.

Any model of the formation of the tunnels must explain two important experimental results: (i) the tungsten containing particle remains constant in diameter as the tunnel forms. It is neither consumed nor enlarged by the tunneling reaction. (ii) The tunnels are observed in silicon (but not in aluminum), both with and without H_2 in the reaction ambient. Since silicon must be consumed and removed to form the tunnels, and since H_2 is not required in the reaction, it is likely that the gas SiF_4 is a primary reaction product. A possible mechanism then is that silicon is etched by trapped fluorine or some fluorine containing product from the reaction between WF_6 and Si. The selective adsorption of fluorine onto tungsten would bring sufficient concentrations of fluorine in contact with the silicon such that etching could occur.

Thus, analogous to the channels in graphite, the role of the tungsten particle would be that of a reaction catalyst. This is plausible in light of data that F_2 forms an adsorbed film (on tungsten) which is stable to temperatures greater than 2000°C (15).

The location and density of the tunnels is presumably determined by the location and density of the reaction sites. Local inhomogeneities in thickness or structure of a substrate oxide film could lead to preferred nucleation sites of the tungsten deposit. With an increase in the density of the reaction sites, a continuous tungsten layer is formed sooner with less Si consumption, less trapped fluorine, and therefore less tunneling. It follows that the tunnel formation can be eliminated by depositing the tungsten onto either an oxide-free substrate or one whose native oxide layer allows a rapid uniform reaction.

Surface preparation.—As mentioned in Ref. (4), the effects of surface preparation can also be understood in

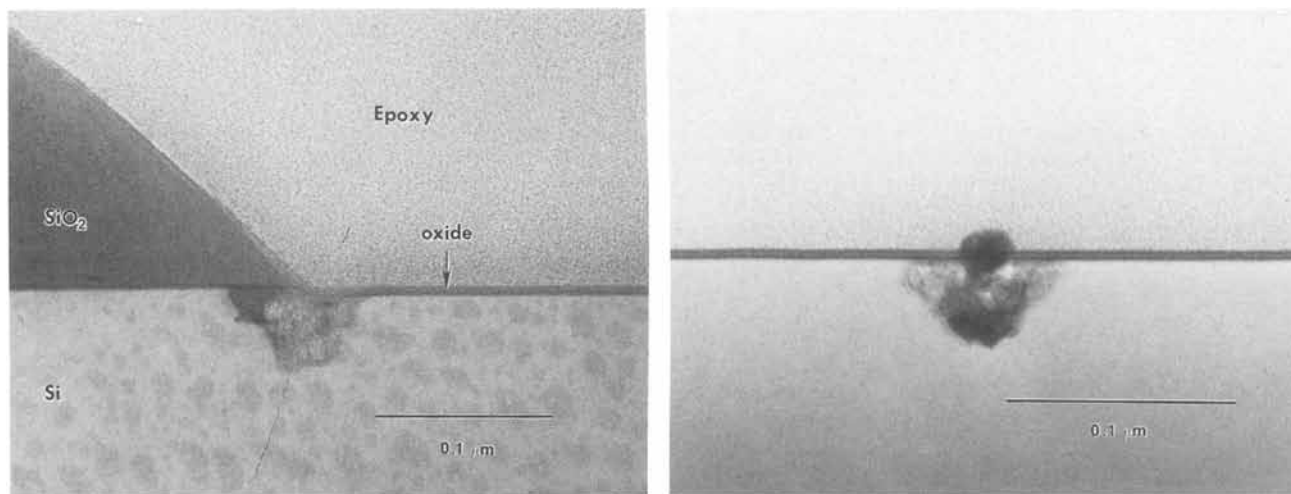


Fig. 10. TEM cross sections showing initial nucleation sites of the tungsten deposit. 300°C , 1 min, $\text{WF}_6 + \text{Ar}$. (a, left): Near the SiO_2 edge. (b, right): Away from the SiO_2 stripe.

terms of oxide films. Cleaning in a CF_4/O_2 glow discharge apparently leaves an oxide layer which results in a nonuniform reaction between WF_6 and the silicon substrate. The HF treatment followed by an unavoidable exposure to atmosphere must also produce a surface oxide layer, but one which is more readily broken up by the substrate reduction reaction.

To add credence to this theory, samples were prepared to reveal the initial tungsten nucleation sites. After a glow discharge surface treatment, a film was deposited at 300°C for only 1 min in $WF_6 + Ar$. Two TEM micrographs of this specimen in cross section are shown in Fig. 10. The micrographs show a surface oxide film as well as two nucleation sites, one near the perimeter and the other within the contact opening area. In contrast, after an HF treatment, we have found that for the same deposition conditions (300°C, 1 min, $WF_6 + Ar$) a continuous, uniform deposit layer is formed. Note that Fig. 10 also demonstrates how the oxide film is left on the surface of the lower tungsten layer as the Si reduction of WF_6 occurs (see above discussion).

Conclusions

The selective deposition of tungsten onto silicon by means of WF_6 and H_2 leads to two layers separated by a thin interfacial oxide. The lower layer is formed by the substrate reduction of WF_6 and is limited in thickness by the rate at which WF_6 reaches the substrate surface. In the case of silicon, the lower layer ranges in thickness from 20 to 150 nm; for aluminum, the lower layer consists of isolated grains of about 20 nm diam. This lower layer accounts for the selectivity of the deposition process and provides a nucleating surface for the subsequent tungsten formation (the upper layer) by the hydrogen reduction of WF_6 .

The important practical conclusion from this study is that the tungsten-silicon interface structure is strongly affected by the surface preparation. A cleaning procedure which results in a thin uniform oxide film (or no oxide film at all) will produce a smooth interface with the least amount of Si consumption. Other procedures, which leave nonuniform surface films, lead to highly irregular interfaces, which in extreme cases include tunnels extending 1 μm or more into the silicon substrate. We suggest that these tunnels are formed by the etching action of trapped fluorine adsorbed onto tungsten particles.

Acknowledgments

E. van de Ven, C. Werkhoven, and J. DeBlasi have provided valuable suggestions and encouragement. We are also grateful to D. Coulman (University of Illinois) for useful discussions of the tunnels and to W. Benzing and C. Ramiller (Applied Materials, Incorporated) for use of the LPCVD W deposition apparatus.

Manuscript received July 23, 1984.

Philips Research Laboratories assisted in meeting the publication costs of this article.

REFERENCES

1. P. Gargini and I. Beinglass, Abstract 380, p. 924, The Electrochemical Society Extended Abstracts, Vol. 81-2, Denver, CO, Oct. 11-16, 1981.
2. T. Moriya, S. Shima, Y. Hazuki, M. Chiba, and M. Kashiwagi, in "Proceedings of the IEEE 1983 International Electron Devices Meeting," p. 550 (1983).
3. T. Moriya, K. Yamada, T. Shibata, H. Iizuka, and M. Kashiwagi, in "Proceedings of the Symposium on VLSI Technology," p. 96 (1983).
4. E. K. Broadbent and C. L. Ramiller, *This Journal*, **131**, 1427 (1984).
5. P. Gargini and I. Beinglass, in "Proceedings of the IEEE 1981 International Electron Devices Meeting," p. 54 (1981).
6. N. E. Miller and I. Beinglass, *Solid State Technol.*, **25**, 85 (1982).
7. P. A. Gargini, *Ind. Res. Dev.*, 142 (March 1983).
8. K. C. Saraswat, S. Swirhun, and J. P. McVittie, Abstract 78, p. 114, The Electrochemical Society Extended Abstracts, Vol. 84-1, Cincinnati, OH, May 6-11, 1984.
9. S. Swirhun, K. C. Saraswat, and R. M. Swanson, *IEEE Electron Device Lett.*, **ed1-5**, 209 (1984).
10. J. De Blasi, C. Werkhoven, T. Brill, and P. Mayo, Abstract 517, p. 756, The Electrochemical Society Extended Abstracts, Vol. 84-2, New Orleans, LA, Oct. 7-12, 1984.
11. R. T. K. Baker, J. A. France, L. Rouse, and R. J. Waite, *J. Catal.*, **41**, 22 (1979).
12. R. T. K. Baker, in "Catalysis Reviews," Vol. 19, H. Heinemann and J. J. Carberry, Editors, p. 161 (1979).
13. R. T. K. Baker, R. D. Sherwood, and J. A. Domesic, *J. Catal.*, **62**, 221 (1980).
14. R. T. K. Baker and R. D. Sherwood, *ibid.*, **70**, 198 (1981).
15. M. Metlay and G. E. Kimball, *J. Chem. Phys.*, **16**, 779 (1948).

Analysis of Multicomponent LPCVD Processes

Deposition of Pure and *In Situ* Doped Poly-Si

Karl F. Roenigk* and Klavs F. Jensen**

Department of Chemical Engineering and Materials Science, University of Minnesota, Minneapolis, Minnesota 55455

ABSTRACT

A general model has been developed for multicomponent-multireaction systems in the hot-wall multiple-wafers-in-tube LPCVD reactor. The modeling equations describe the coupled convective and diffusive mass fluxes in the annular reactor flow region as well as those between each pair of wafers. Complex reaction mechanisms involving both gas-phase and surface reactions can be included in the model formulation. Multicomponent transport effects in the deposition of pure and doped polycrystalline Si are analyzed. The model predicts experimentally observed growth rates for pure polycrystalline Si quite well. However, because of insufficient data, a comparison of model predictions and experimental growth rates has not been feasible for *in situ* doped Si. The model is also used to predict the performance of a new continuous moving boat LPCVD reactor offering excellent film uniformity and process automation.

Low pressure chemical vapor deposition (LPCVD) is increasingly becoming a preferred method of depositing thin solid films of microelectronic materials because of the many advantages offered by the technique. LPCVD, which is predominantly carried out in tubular hot-wall reactors, allows a large number of wafers to be processed

with excellent film thickness and composition uniformity across each wafer as well as from wafer to wafer (1, 2). The large packing densities that can be realized in LPCVD reactors are possible because at the reduced pressures (~ 0.5 torr) diffusion is rapid so that the chemical reactions at the wafer surface are usually rate-controlling rather than mass-transfer processes. LPCVD is widely used to deposit thin films of polycrystalline Si,

*Electrochemical Society Student Member.

**Electrochemical Society Active Member.

SiO₂, and Si₃N₄ (1, 2). In addition, there is considerable interest in LPCVD of *in situ* doped polycrystalline Si (3, 4) as well as metallization by LPCVD of Al (5) and W (6).

The control and reproducibility of LPCVD reactor performance is crucial in obtaining films that satisfy the stringent demands imposed by modern microelectronic device structures. Nonuniformities in film thickness and composition (and implicitly resistivity) can make it impossible to realize the desired electronic device. LPCVD reactor operation has so far mainly relied on semiempirical design rules and operation regimes selected on the basis of trial and error experimentation. This limits the operation of existing reactors to certain fixed operating ranges and impedes the design of new LPCVD reactors. However, mathematical models incorporating the key physical and chemical process features should prove to be cost and time saving tools in the efficient operation of CVD reactors. In addition, the models should lead to an enhanced understanding of existing processes as well as provide new insight for the design of CVD reactors. In this work, a general mathematical model of LPCVD is presented. As a first application of the model, the deposition of pure and *in situ* doped polycrystalline Si is considered. These processes are suitable for illustrating the manner in which the model may be employed and for providing insight into its application to more complex LPCVD processes such as SiO₂ and Si₃N₄ deposition.

A number of reactor models have been proposed for both the cold-wall, atmospheric pressure CVD reactor and the hot-wall, tubular LPCVD reactor (7). The most complete treatment so far of LPCVD reactors appears to be that of Jensen and Graves (8). Their model, hereafter referred to as model I, combined the diffusive and convective fluxes in the annular flow region between the reactor wall and the wafer edges (cf. Fig. 1) with the diffusion between the wafers and subsequent reactions on the wafer surfaces. However, the change in gas velocity due to temperature variations and hydrogen production was approximated. Nevertheless, the model correctly predicted experimental observations from separate reactor studies of polycrystalline Si growth. Moreover, it allowed the authors to demonstrate the highly uniform deposition rates that were theoretically feasible in a LPCVD reactor with recycle of part of the reactor effluent.

As with previous LPCVD reactor descriptions, model I neglected the coupling of the diffusive fluxes in multicomponent systems through the Stefan-Maxwell relations (9). However, that simplification may lead to inaccurate model predictions for most LPCVD processes of interest (e.g., *in situ* doped polycrystalline Si, SiO₂, and Si₃N₄). Therefore, in this contribution, the original modeling concepts of Model I are extended to encompass multicom-

ponent diffusion effects. The resulting model is applicable to general LPCVD processes given a knowledge of the appropriate homogeneous and heterogeneous kinetics.

The detailed mathematical model is developed in the subsequent section. The model development is followed by an analysis of multicomponent effects in polycrystalline Si deposition including comparisons with predictions of model I. The model is then used to analyze a new continuous LPCVD reactor design where the wafers are conveyed countercurrently to the reactant gases. Finally, the deposition of *in situ* doped polycrystalline Si is discussed, with particular emphasis on the probable kinetics involved in the process.

Model Development

The model is based on the schematic representation of the typical commercial LPCVD reactor illustrated in Fig. 1. The wafers are placed perpendicular to the main direction of flow and concentrically inside the reactor (quartz) tube. The flow in the annular region formed by the tube wall and the wafer edges is laminar for the Reynolds numbers corresponding to typical LPCVD operating conditions. Because of the small wafer spacing relative to the wafer radius and the low pressures, mixing effects near the wafer edges may be neglected. In addition, it may be assumed that there is no imposed flow between the wafers, i.e., multicomponent diffusion and the associated Stefan flow are the dominant modes of transport in the wafer region. Calculations have shown that gas heat up lengths in typical LPCVD reactors are small compared to the reactor lengths. Furthermore, the heats of reaction associated with the growth processes are small because of the slow deposition rates (~100 Å/min). Thus, the temperature profile may be assumed fixed by the furnace settings. This approximation eliminates the need for an energy balance.

The steady-state species mole balance for component *j* has the general form

$$\frac{1}{r} \frac{\partial}{\partial r} (rN_{rj}) + \frac{\partial}{\partial z} N_{zj} = \sum_{i=1}^{n^s} \alpha_{ij}^s \mathcal{R}_i^s \quad [1]$$

for both the annular region and the space between the wafers. Here N_{rj} and N_{zj} are the radial and axial molar fluxes, respectively, of the *j*th species. The left-hand side of Eq. [1] represents the production of *j* in n^s independent gas-phase reactions. The α_{ij} 's are the stoichiometric coefficients of the *i*th reaction, \mathcal{R}_i . By convention the α_{ij} 's are positive for products. The boundary conditions on Eq. [1] are for the annular region

$$N_{zj} = v_0 c_0 x_{j0} \text{ at } z = 0 \text{ and } \frac{\partial x_j}{\partial z} = 0 \text{ at } z = L \quad [2a]$$

$$N_{rj} = - \sum_{i=1}^{n^s} \alpha_{ij}^s \mathcal{R}_i^s \text{ at } r = R_t$$

and

$$N_{rj} = a \left(\frac{R_t}{R_w} \right) \sum_{i=1}^{n^s} \alpha_{ij}^s \mathcal{R}_i^s + N_{rj} \Big|_{R_w} \text{ at } r = R_w \quad [2b]$$

The condition [2a] at $z = 0$ expresses the continuity of fluxes in the axial direction across the reactor inlet. The formulation of the condition at $z = L$ is difficult. The present choice implies that negligible reaction and back diffusion occur downstream of the wafer zone. The first radial condition in Eq. [2b] states that the flux of *j* to the wall equals the amount of *j* consumed in surface reactions on the wall. Similarly, the second condition states that the flux of the *j*th species to the wafer edge is the amount of *j* deposited on the wafer carrier boat plus the flux in between the wafers. The quantity *a* represents the boat area relative to the tube area.

The boundary conditions for the wafer space take the form

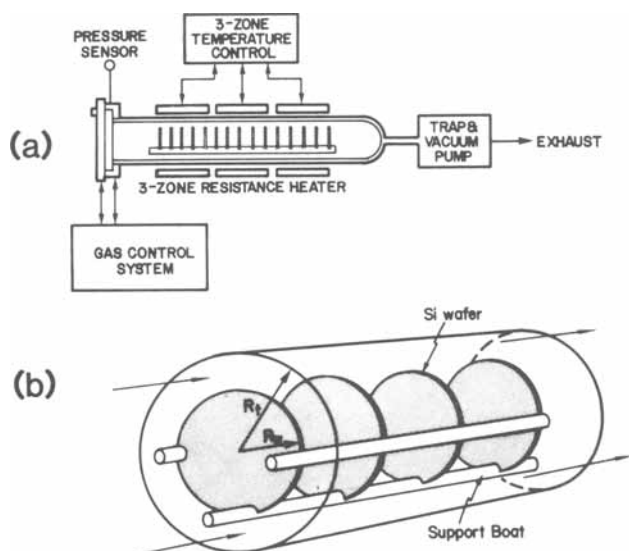


Fig. 1. LPCVD reactor

$$N_{zj} = \sum_{i=1}^{n^s} \alpha_{ij}^s \mathcal{R}_i^s \text{ at } z = z_k, k = 1, 2, \dots, N_{\text{wafer}} \quad [3a]$$

and

$$N_{zj} = -\sum_{i=1}^{n^s} \alpha_{ij}^s \mathcal{R}_i^s \text{ at } z = z_k +$$

$$\Delta x_j \Big|_{R_w^-} = x_j \Big|_{R_w^+} \text{ at } r = R_w, \text{ and } \frac{\partial x_j}{\partial r} = 0 \text{ at } r = 0 \quad [3b]$$

The two conditions on the axial direction express that the flux of material to the wafer surfaces equals that consumed in surface reactions on the wafers. The radial conditions represent continuity of mole fractions from the wafer edge to the annular flow region and symmetry, respectively. Equations [1]-[3] must be combined with appropriate expressions for the fluxes N_{rj} and N_{zj} . In an S component ideal gas, the molar fluxes are related through the Stefan-Maxwell equations (9)

$$\nabla x_i = \sum_{j \neq i}^s \frac{1}{cD_{ij}} (x_i N_j - x_j N_i) \quad [4]$$

Here D_{ij} is the i - j binary diffusivity and N_k represents a vector of the axial and radial components of the fluxes. Since the mole fractions must sum to unity, *i.e.*

$$\sum_{i=1}^s x_i = 1 \quad [5]$$

there are at most $S - 1$ independent Stefan-Maxwell relations.

Equations [1]-[5] combined with appropriate momentum balances form a complex set of partial differential equations which in principle can be solved by a suitable numerical technique. However, it is more useful in this investigation to make some physically reasonable assumptions which reduce the complexity of the model. The same approach was used in deriving model I. First, since the wafer spacing (Δ) is small relative to the wafer radius, the rapid diffusion at LPCVD conditions would be expected to essentially eliminate axial variations within each wafer cell. Therefore, we may average Eq. [1] over the z direction within each cell formed by the wafers. The resulting component balance for the wafer region is then

$$\frac{\Delta}{r} \frac{d}{dr} (rN_{rj}) = \Delta \sum_{i=1}^{n^g} \alpha_{ij}^g \mathcal{R}_i^g + 2 \sum_{i=1}^{n^s} \alpha_{ij}^s \mathcal{R}_i^s \quad [6]$$

with boundary conditions of Eq. [3b].

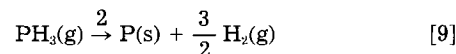
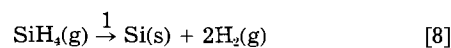
Secondly, the rapid diffusion is also expected to reduce radial variations in gas-phase concentrations in the annulus. Moreover, the time scale associated with deposition is larger than that for diffusion; therefore, perfect radial mixing may be assumed as also done in model I. Then by averaging Eq. [1] over the radial direction, the component balance for the annular flow region takes the form

$$\frac{d}{dz} (N_{zj}) = \frac{2}{(R_i^2 - R_w^2)} \left[R_i(1 + a) \sum_{i=1}^{n^g} \alpha_{ij}^g \mathcal{R}_i^g \right. \\ \left. + R_w N_{rj} \Big|_{R_w^-} \right] + \sum_{i=1}^{n^s} \alpha_{ij}^s \mathcal{R}_i^s \quad [7]$$

with boundary conditions of Eq. [2a]. The flux of species j in between the wafers, *i.e.*, $N_{rj}|_{R_w^-}$ is determined from the solution to Eq. [6].

Equations [6] and [7] with their respective boundary conditions form the general model for the LPCVD reactor. For S chemical species, n^g gas-phase reactions, and n^s surface reactions, there are at most $n^g + n^s \leq S - 1$ independent component balances, Eq. [6] and [7]. These must be solved with the Stefan-Maxwell relations (Eq. [4]) and the constraint (Eq. [5]). The model can be applied to any LPCVD reactor system given the chemical kinetics. To illustrate the use of the modeling approach, the deposition of pure and *in situ* doped polycrystalline Si are considered as examples.

LPCVD of pure and doped polycrystalline Si is usually carried out with SiH_4 and small amounts of dopant (*e.g.*, AsH_3 , PH_3 , or B_2H_6). The kinetics of polycrystalline Si deposition from SiH_4 have received considerable attention (10, 11). However, the detailed kinetics of dopant incorporation are poorly understood, as are the effects of dopants on the Si growth rate. It is known that SiH_4 can decompose in the gas phase to SiH_2 and H_2 and it is possible for SiH_2 to insert itself in both SiH_4 and the dopant gas. However, in view of the low pressures and the limited knowledge of those gas-phase reactions, the surface reactions are assumed to dominate the deposition process. Thus, the model is based on the overall heterogeneous reactions



with reaction rates \mathcal{R}_1 and \mathcal{R}_2 . PH_3 is used as an example, but the model development would be similar for other dopant gases. Because of adsorption/desorption effects it is possible that \mathcal{R}_1 and \mathcal{R}_2 each depend on all the gaseous reactants. The kinetics of these reactions will be discussed in a subsequent section. Since there are no gas-phase reactions and only two surface reactions, the mole balances over SiH_4 (1) and PH_3 (2) take the form for the annulus

$$\frac{dN_{zk}}{dz} = \frac{-2\mathcal{R}_k}{(R_i^2 - R_w^2)} \left[R_i(1 + a) \right. \\ \left. + \frac{R_w^2}{\Delta} \eta_k \right], k = 1, 2 \quad [10]$$

with boundary conditions

$$N_{zk}(z = 0) = v_0 c_0 x_{k0} \\ \text{and } \frac{dx_k}{dz} \Big|_L = 0 \quad k = 1, 2 \quad [10a]$$

where

$$\eta_k = \frac{2 \int_0^{R_w} r \mathcal{R}_k dr}{R_w^2 \mathcal{R}_k \Big|_{R_w}} \quad k = 1, 2 \quad [10b]$$

while for the wafer region

$$\frac{\Delta}{r} \frac{d}{dr} (rN_{rk}) = -2 \mathcal{R}_k \quad k = 1, 2 \quad [11]$$

with boundary conditions

$$\frac{dx_k}{dr} \Big|_0 = 0 \text{ and } x_k(R_w^-) = x_k(R_w^+) \quad [11a]$$

The quantity η_k is defined as the ratio of the average deposition rate on the wafer to that at the wafer edge. Thus, η_1 may be regarded as a measure of film thickness uniformity. When $\eta_1 \dot{=} 1$, η_2 becomes a measure of doping level uniformity. However, if $\eta_1 \neq 1$, it is not feasible to make a simple interpretation of η_2 . If diffusion effects are small, $\eta_1 \dot{=} 1$ and $\eta_2 \dot{=} 1$, whereas they differ from unity when diffusion effects are significant enough to produce nonuniform film thicknesses and doping levels.

The balance over the inert gas (3) gives

$$N_{z3} = v_0 c_0 x_{30} \text{ in the annular region} \quad [12a]$$

$$N_{r3} = 0 \text{ between the wafers} \quad [12b]$$

Because of the coupling of the fluxes and production of H_2 , the constant flux of inert gas does not lead to constant inert mole fractions through the reactor. Finally, the flux of the last component H_2 (4) may be expressed as follows by using the stoichiometry of the reactions [8] and [9]

$$N_{z1} = v_0 c_0 x_{z10} + 2(v_0 c_0 x_{z10} - N_{z1}) + \frac{3}{2}(v_0 c_0 x_{z20} - N_{z2}) \text{ in the annular region} \quad [13a]$$

$$N_{r1} = -2N_{r1} - \frac{3}{2}N_{r2} \text{ in the wafer region} \quad [13b]$$

By combining the modeling Eq. [10]-[13] with Stefan-Maxwell relations [4] for three components and the constraint [5], it is then possible to predict the growth rates and doping levels on each wafer as well as throughout the reactor. If the dopant, component (2), is eliminated, the equations may also be used to predict pure polycrystalline deposition. Both cases are considered below. The nonlinear modeling equations are solved by orthogonal collocation in similar manner to that used for model I (8). However, in the present cases, more than one interior collocation point is used to solve the local wafer deposition equations. Finally, growth rates, average growth rates, and standard deviations in growth rates may be calculated by formulas analogous to those presented in Ref. (8) (cf. Eq. [33]-[35]).

Deposition of Polycrystalline Si

The present model was used to predict reported experimental growth rates. The following rate expression was assumed

$$\mathcal{R} = \frac{kP_{\text{SiH}_4}}{1 + K_{\text{H}}P_{\text{H}_2}^{1/2} + K_{\text{S}}P_{\text{SiH}_4}} \quad [14]$$

This particular rate expression follows from the assumption of adsorption-desorption equilibria of silane and hydrogen and a rate-controlling first-order decomposition of silane on the surface. In addition, it reflects the experimental observations: (i) growth rate is proportional to SiH_4 pressures but saturated at high SiH_4 pressures and (ii) the growth rate is hindered by adsorbed atomic hydrogen. The rate expression [14] and the model were used in nonlinear regression of reported experimental growth rates (1, 10). The kinetic parameters with their 95% confidence intervals were found to be

$$k = (1.6 \pm 0.4) \times 10^9 \exp(-18,500/T) \text{ mol/m}^2/\text{s/atm}$$

$$K_{\text{H}} = (0.6 \pm 0.3) \times 10^2 \text{ atm}^{-1/2}$$

$$K_{\text{S}} = (0.7 \pm 0.1) \times 10^5 \text{ atm}^{-1}$$

The activation energy of k was not determined. Its value is generally agreed upon in previous studies (11). The model with the use of the kinetic parameters in the rate expression [14] correctly predicts both the effect of SiH_4 depletion and H_2 inhibition on the Si deposition rate. Furthermore, as illustrated in Fig. 2, the model predictions span data from two different reactor systems with two orders of magnitude variation in SiH_4 partial pressures. Classen *et al.* proposed that P_{H_2} rather than $P_{\text{H}_2}^{1/2}$ should be included in the rate expression [14]. However, we found significantly better representation of data with $P_{\text{H}_2}^{1/2}$, indicating that dissociatively adsorbed H_2 hinders Si growth. The $-1/2$ power dependence on hydrogen is also supported by experiments of Duchemin *et al.* (12).

The present multicomponent LPCVD reactor model makes it possible to evaluate approximations inherent in Model I (8). Multicomponent effects were neglected in the development of Model I and the conversion of $\text{SiH}_4(\chi)$ was related to the silane mole fraction through a simple algebraic relation (cf., Ref. (8), Eq. [13]). However, this relation is only strictly valid in a well mixed reactor or a plug flow reactor. It is an approximation for LPCVD reactor conditions where both diffusive and convective transport are important. The correct definition of the SiH_4 conversion in the present system is

$$\chi = 1 - \frac{N_{z1}}{N_{z10}} \quad [15]$$

where the flux N_{z1} is composed of diffusive and convective contributions; *i.e.*, $N_{z1} = J_{z1} + x_{z1}c_1v$. Thus, simple algebraic relations between SiH_4 mole fractions and conversion cannot be made without neglecting the diffusive flux, as is done in Model I.

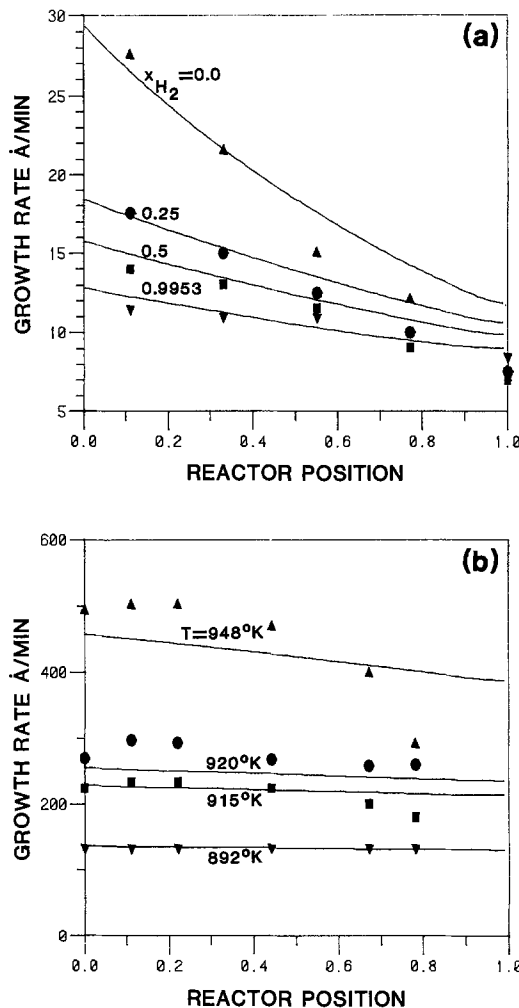


Fig. 2. Model predictions and experimental LPCVD poly-Si growth rates at: (a) various hydrogen feed compositions (10), $Q = 1000$ sccm, $T = 880$ K, 0.47% SiH_4 feed, balance H_2 and N_2 , $P = 0.525$ torr; (b) various temperatures (1), $Q = 650$ sccm, 23% SiH_4 feed in N_2 diluent, $P = 0.5$ torr.

To study the effects of the simplifications in Model I, its predictions for polycrystalline Si deposition from SiH_4 were compared to those obtained with the present multicomponent treatment. The calculations were carried out at varying inlet flow rates for a typical commercial LPCVD reactor and the chemical kinetics given above. Figure 3a shows the maximum and average percent error in growth rates as a function of the Peclet number for the case of pure SiH_4 feed to the reactor. The error is determined as

$$\epsilon = \left[\frac{g(\text{Model I}) - g(\text{new model})}{g(\text{new model})} \right] 100\% \quad [16]$$

The Peclet number, $Pe (= v_0L/D_{\text{SiH}_4, \text{H}_2})$ is a measure of the convective flux relative to the diffusive flux. For high flow rates, Pe is large, and the two models agree as expected since the approximation in Model I holds in the plug flow limit. However, for typical operating conditions, there is approximately 10% difference in the predicted growth rates. Model I consistently predicts higher growth rates than the present model because the velocity in Model I is artificially higher than for the detailed model. Figure 3b illustrates the difference in model predictions in dilute processing. (Here $Pe = v_0L/D_{\text{SiH}_4, \text{N}_2}$.) Again, the models agree at high flow rates, but differ approximately 5% at typical operating conditions.

Although the predictions of Model I differ from those of the detailed multicomponent treatment, Model I is still a useful approximation for simple systems where it is applicable. It is more tractable and gives a simpler picture

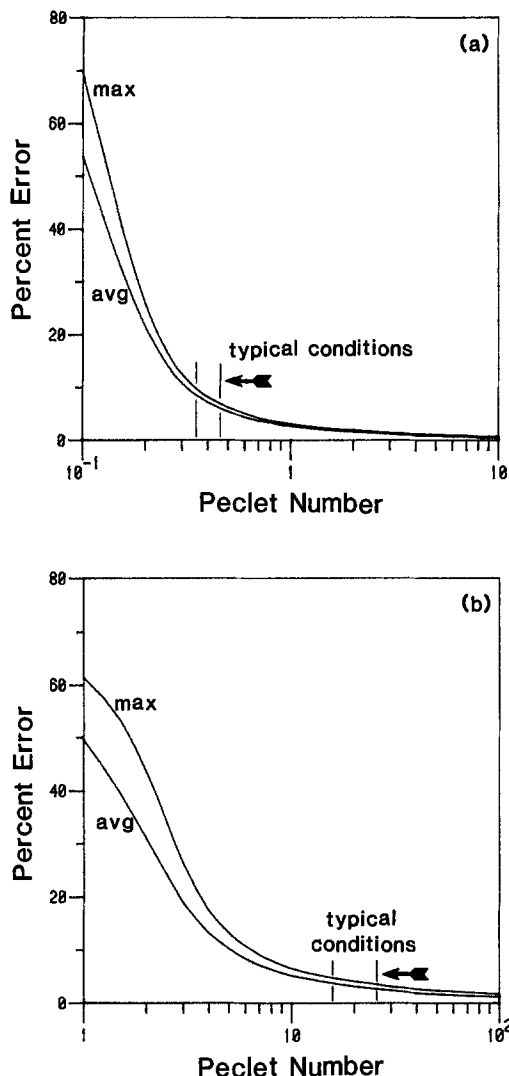


Fig. 3. Error of growth rate and average growth rate between Model I and present formulation for typical LPCVD reactor. $T = 800$ K, $P = 0.6$ torr. (a): Pure SiH_4 feed, $Pe = v_0 L / D_{\text{SiH}_4\text{-H}_2}$. (b): 23% SiH_4 feed in N_2 , $Pe = v_0 L / D_{\text{SiH}_4\text{-N}_2}$.

of LPCVD reactor behavior than the present model. However, for analysis of general LPCVD processes, the present formulation should be preferred.

A Continuous Moving Boat LPCVD Reactor

To further illustrate the utility of the developed LPCVD reactor model, it is employed in reactor design considerations. It is desirable to design and operate LPCVD reactors so that film thickness and composition variations are minimized within each wafer as well as from wafer to wafer. In this spirit, Model I was used to demonstrate the high levels of uniformities feasible with recycle of part of the reactor effluent. Similar results would be predicted by the present model. A continuous LPCVD reactor, where the wafers are conveyed through the reactor countercurrently to the reactant gases, is another attractive alternative to the conventional LPCVD reactor with furnace temperature ramps. Since each wafer would experience the same conditions in its travel through the reactor, each wafer would have identical average film thickness and wafer uniformity. Therefore, the need for adjusting the furnace profile to ensure wafer to wafer uniformity is eliminated and a flat temperature profile may be used. This case is illustrated schematically in Fig. 4. The constant deposition temperature has the advantage of more uniform film morphology and strain (19) than can be achieved in standard LPCVD reactors. This ultimately enhances electronic device uniformity and lessens

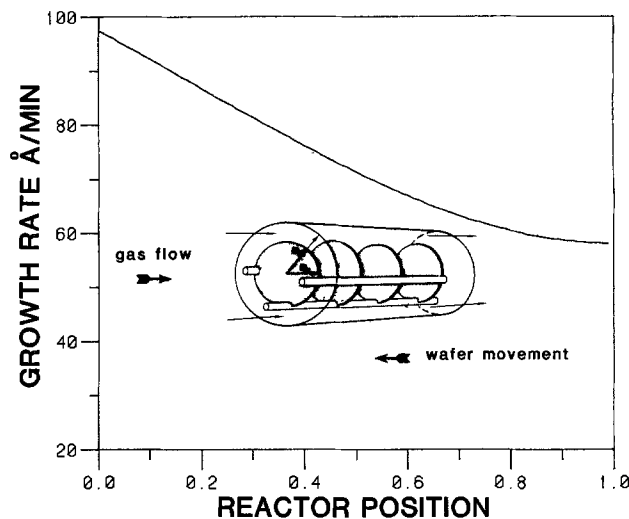


Fig. 4. Continuous LPCVD concept. Wafers conveyed countercurrent to gas flow experience reactor growth profile and exit with identical average film thickness and uniformity. $T = 893$ K, $P = 0.5$ torr, $Q(\text{SiH}_4) = 20$ sccm, $\bar{g} = 76$ Å/min, conversion = 0.9, $N_w = 100$.

doping and oxidation concerns in postdeposition process steps.

A continuous LPCVD reactor would have additional advantages associated with process automation. It would enable automatic loading and unloading of wafers and even sequencing with subsequent process steps, thereby decreasing the possibility for contamination. The main difficulty in the design of such a reactor lies in the mechanical handling of the wafers. However, these mechanical problems are beyond the scope of the present work, where process feasibility and performance are the important issues.

The developed model may be used to predict the film thickness and uniformity on the processed wafers by considering the growth rates experienced by any single wafer as it is conveyed through the reactor. If it is assumed that the wafers are stepped through incremental positions in the reactor, then a wafer spends a time Δt at each wafer position in the reactor. The film thickness on the exiting wafer, \bar{d} , would then be the sum of the thickness deposited at each wafer position

$$\bar{d} = \sum_{i=1}^{N_w} g_i \eta_i \Delta t_i \quad [17]$$

Since the wafer spacing is small, the sum may be approximated by an integral over the reactor to obtain

$$\begin{aligned} \bar{d} &= \sum_{i=1}^{N_w} g_i \eta_i \Delta \cdot \frac{\Delta t_i}{\Delta} \\ &= \frac{\Delta t_i}{\Delta} \int_0^L g \eta \, dz = \frac{\Delta t_i}{\Delta} L \bar{g} \end{aligned} \quad [18]$$

The wafer process rate, \dot{w} , is just $(\Delta t_i)^{-1}$ and $N_w = L/\Delta$. Thus, by rearranging Eq. [18], \dot{w} may be expressed as a function of the number of wafers in the boat, the desired average thickness \bar{d} , and the process variables determining the average growth rate, \bar{g}

$$\dot{w} = N_w \left(\frac{\bar{g}}{\bar{d}} \right) \quad [19]$$

Note that each wafer leaves the reactor with the same average thickness \bar{d} given by Eq. [18]. Thus, there is complete wafer-to-wafer uniformity. The in-wafer standard deviation in thickness may be shown to be

$$\begin{aligned} \left(\frac{\sigma}{\bar{d}} \right) &= \left[(\bar{g})^{-2} \int_0^L 2 \left(\frac{r}{R_w} \right) \right. \\ &\quad \left. \left[\frac{1}{L} \int_0^L g(r, z) \, dz \right]^2 d \left(\frac{r}{R_w} \right) - 1 \right]^{1/2} \end{aligned} \quad [20]$$

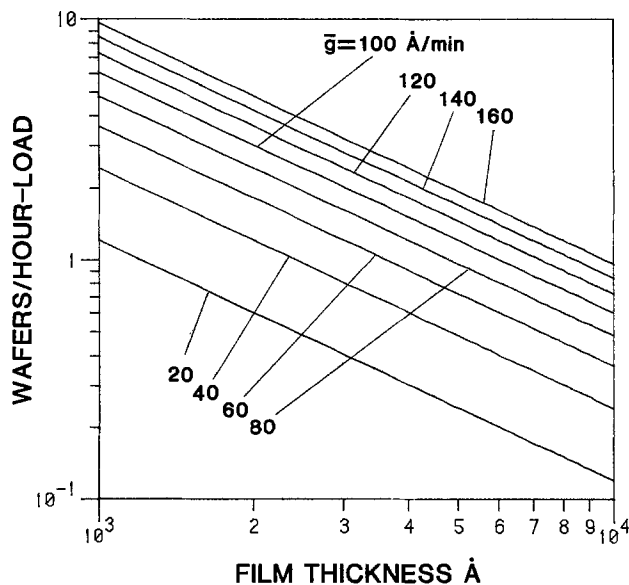


Fig. 5. Wafer production rate per wafer load for desired thickness and given average growth rate in a continuous LPCVD reactor. Example for $d = 5000\text{Å}$, $g = 80\text{Å/min}$, $NW = 100$, $\dot{w} = 100\text{ wafer/h}$.

By using Eq. [18] and [19], it is possible to construct operating charts, such as Fig. 5, relating the wafer process rate for a desired film thickness to the average growth rate. The model developed is then useful in determining optimal operating conditions where the average growth rate may be obtained with acceptable in-wafer uniformity as given by Eq. [20]. For most polycrystalline Si deposition conditions, the in-wafer film thickness variations are small ($< 2\%$). However, for more complex deposition schemes, such as SiO_2 , it may be necessary to use Eq. [20] to estimate in-wafer film thickness deviations. Extensive calculations indicate that for the poly-Si kinetics the in-wafer film uniformity is always better in the moving LPCVD than the conventional reactor. An additional attractive feature of the moving boat reactor is that essentially complete conversion of the reactant can be achieved.

Deposition of *In Situ* Doped Polycrystalline Si

The presence of dopants has been observed to significantly alter the growth kinetics of Si films (13-15, 19-20). The growth rate is decreased by AsH_3 and PH_3 , whereas it is enhanced by B_2H_6 . Different arguments have been presented to explain the observed effect in the case of n-type dopants. Farrow (14) argued that dopant slowed the Si growth by adsorption on active sites, while Chang (15) proposed that the dopant changed the surface potential so that the Si species were less easily adsorbed. Farrow suggested that B_2H_6 facilitated SiH_4 decomposition on the surface, but Chang again proposed that the change in surface potential due to adsorbed B_2H_6 enhanced adsorption of Si species. Recent surface science experiments by Yu and Meyerson (19) present strong evidence for the site blocking mechanism of rate suppression in *in situ* phosphorous-doped poly-Si deposition. They demonstrate that PH_3 strongly adsorbs on Si and that H_2 desorption from adsorbed PH_3 above 400°C leads to further increases in the phosphorous coverage, effectively blocking the coadsorption of SiH_4 . This is consistent with the appreciable suppression of the Si deposition rate by even small amounts of PH_3 observed experimentally. In addition, the effect has been shown to alter the activation energy of the overall deposition reaction (4, 13, 14, 16). In particular, the experiments by Baudrant and Sacilotti indicate a linearly varying activation energy with PH_3 partial pressure.

The present multicomponent model was used in an attempt to determine the appropriate kinetics of *in situ* P-doped poly-Si. The data of Baudrant and Sacilotti (2) and Kurokawa (3) were used to test proposed kinetic

schemes. However, many reactor parameters and experimental data necessary for simulation were not reported and therefore had to be estimated. It was found that typical Langmuir-Hinshelwood kinetic schemes would not allow satisfactory representation of the reported Si growth rates, although resistivity levels were approximated reasonably well (17). The failure of conventional Langmuir-Hinshelwood kinetics in modeling the data is consistent with Yu and Meyerson's (19) finding of a strong PH_3 adsorption. In fact, preliminary calculations predicted PH_3 surface coverage of approximately unity. Additional more complicated rate expressions were tested including the effect of dopant on the Si deposition activation energy. However, owing to the lack of complete experimental data, it was not possible to conclude about the probable kinetics. Nonlinear regression of *in situ* doping is complicated by the added problem of predicting doping levels. Unfortunately, most studies including that of Baudrant and Sacilotti report resistivities rather than actual solid concentrations. This means that a reliable correlation between resistivity and solid dopant concentration is needed. Nevertheless, the reasonable trends obtained with limited data (17) show good promise for future studies with a larger data base. The gas-phase chemistry of the $\text{SiH}_4/\text{PH}_3/\text{H}_2$ system will likely have to be included in these studies to provide a complete understanding of rate depression and nonuniformities observed in deposition of *in situ* doped polycrystalline Si.

Conclusion

A general model for multicomponent-multireaction LPCVD reactor systems has been developed and applied to specific examples. The model details the multicomponent transport processes in the annular flow region as well as those between the wafers. Complex kinetic schemes involving both gas-phase and surface reactions can readily be included in the model formulation. The multicomponent treatment was used to evaluate approximations made in an earlier model (8) for polycrystalline deposition from SiH_4 .

The utility of the model was further illustrated by the analysis of a countercurrent moving boat LPCVD reactor. This reactor gave excellent uniformity and had the additional advantage of process automation. However, the mechanical aspects of such a reactor need to be resolved.

Because of the lack of detailed kinetic data for *in situ* doped polycrystalline Si, it was not possible to verify the model to the same extent as done for pure polycrystalline Si deposition. In fact, the general scarcity of reliable kinetic mechanisms and rate constants constitutes a major problem in CVD reactor modeling. The good predictions of pure Si deposition and the additional process insights resulting from the LPCVD reactor model should serve as incentives for future combined kinetic and reactor modeling studies of more complex CVD systems, such as SiO_2 and Si_3N_4 . This is currently under investigation.

Acknowledgment

The authors are grateful to the National Science Foundation (DMR 8307924) and the Microelectronic and Information Sciences Center at the University of Minnesota for support.

Manuscript submitted March 6, 1984; revised manuscript received Oct. 23, 1984.

The University of Minnesota assisted in meeting the publication costs of this article.

LIST OF SYMBOLS

a	area of wafer carrier relative to reactor tube area
c	concentration
D_{ij}	binary diffusivity
g	growth rate
J_i	diffusive flux of component i
k_i	rate constant for component i
K_i	adsorption constant for component i
L	length of reactor
n	number of reactions gas phase, surface
N_r	radial molar flux

N_z axial molar flux
 r radial coordinate
 R_w radius of wafer
 R_t radius of reactor tube
 \mathcal{R}_i rate of reaction i
 S number of chemical species
 Δt_i time of each deposition step
 v linear velocity in annulus
 \dot{w} wafer processing rate
 x_i mole fraction component i
 z axial coordinate
 α_{ij} stoichiometric coefficient
 Δ wafer spacing
 σ standard deviation in in-wafer thickness

Superscripts

g gas phase
 s surface

REFERENCES

1. R. S. Rosler, *Solid State Technol.*, **20** (3), 63 (1977).
2. W. A. Brown and T. I. Kamins, *ibid.*, **22**, 51 (1979).
3. H. Kurokawa, *This Journal*, **129**, 2620 (1982).
4. A. Baudrant and M. Sacilotti, *ibid.*, **129**, 1109 (1982).
5. M. J. Cooke, R. A. Heinecke, R. C. Stern, and J. W. C. Maes, *Solid State Technol.*, **25** (12), 62 (1982).
6. N. Miller and E. Beinglass, *ibid.*, **23** (12), 79 (1980).
7. K. F. Jensen, in "Chemical Vapor Deposition," McD.
8. K. F. Jensen and D. B. Graves, *This Journal*, **130**, 1950 (1983).
9. R. B. Bird, W. E. Steward, and E. N. Lightfoot, "Transport Phenomena," Chap. 18, John Wiley and Sons, New York (1962).
10. W. A. P. Claassen, J. Bloem, W. G. J. N. Valkenburg, and C. H. J. van den Brekel, *J. Cryst. Growth*, **57**, 259 (1982).
11. W. A. Bryant, *Thin Solid Films*, **60**, 19 (1979).
12. M. J. Duchemin, M. M. Bonnet, and M. F. Koelsch, *This Journal*, **125**, 637 (1978).
13. F. C. Eversteyn and B. H. Put, *ibid.*, **120**, 106 (1973).
14. R. F. C. Farrow, *ibid.*, **121**, 899 (1974).
15. C.-A. Chang, *ibid.*, **123**, 1245 (1976).
16. T. B. Swanson and R. N. Tucker, *ibid.*, **116**, 1271 (1969).
17. K. F. Roenigk and K. F. Jensen, in "Chemical Vapor Deposition," McD. Robinson, C. H. J. van den Brekel, C. W. Cullen, J. M. Blocher, Jr., and P. Rai-Choudhury, Editors, p. 112, The Electrochemical Society Softbound Proceedings Series, Pennington, NJ (1984).
18. B. Harbeke, L. Krausbauer, E. F. Steigmeier, A. E. Widmer, H. G. Kappert, and G. Neugebauer, *RCA Rev.*, **44**, 287 (1983).
19. M. L. Yu and B. S. Meyerson, *J. Vac. Sci. Technol. A*, **2**, 446 (1984).

Vaporization Behavior, Phase Equilibria, and Thermodynamic Stabilities of Nickel Phosphides¹

Clifford E. Myers* and Thomas J. Conti

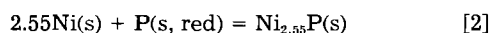
Department of Chemistry, State University of New York at Binghamton, Binghamton, New York 13901

ABSTRACT

The equilibrium vaporization reactions $12\text{Ni}_2\text{P}(s) = 2\text{Ni}_{12}\text{P}_5(s) + \text{P}_2(g)$ and $6.8\text{Ni}_{12}\text{P}_5(s) = 32\text{Ni}_{2.55}\text{P}(s) + \text{P}_2(g)$ have been studied by mass-loss effusion in the temperature range 1237–1401 K. The results were combined with published calorimetric data for nickel-rich samples and static phosphorus-dissociation pressure data for phosphorus-rich samples, with consideration of the requirements of the published phase diagram, to obtain enthalpies of formation (from red P), $\Delta H_f^\circ/R$, and enthalpies of atomization, $\Delta H_{at}^\circ/R$, respectively, in kilokelvins at 298.15 K: $1/4 \text{Ni}_3\text{P}(s)$, -5.94 ± 0.5 , 54.8; $1/3.55 \text{Ni}_{2.55}\text{P}(s)$, -6.65 ± 0.5 , 55.2; $1/17 \text{Ni}_{12}\text{P}_5(s)$, -6.73 ± 0.5 , 55.1; $1/3 \text{Ni}_2\text{P}(s)$, -6.87 ± 0.5 , 54.8; $1/9 \text{Ni}_2\text{P}_4(s)$, -6.39 ± 0.5 , 53.0; $1/2.22 \text{Ni}_{1.22}\text{P}(s)$, -6.32 ± 0.5 , 52.9; $1/2 \text{NiP}(s)$, -6.09 ± 0.5 , 52.1; $1/3 \text{NiP}_2(s)$, -5.38 ± 0.5 , 49.4; $1/4 \text{NiP}_3(s)$, -4.52 ± 0.5 , 47.6.

The nickel-phosphorus phase diagram has been well established in the definitive work of Larsson (1), but published data do not permit a complete working out of the thermodynamics of the system. Weibke and Schrag (2) measured directly the heat of reaction of nickel and phosphorus at about 630°C, but their studies were limited to metal-rich compositions. Biltz and Heimbrecht (3) measured dissociation pressures of phosphorus over phosphorus-rich samples, but the static method they employed did not allow an overlap in composition with the calorimetric study (2). Hence, a Knudsen effusion study of phosphorus-dissociation pressures was initiated for the central portion of the phase diagram.

The compositions of the intermediate phases and their temperature ranges of stability were taken from Larsson's study (1); the phase diagram is given in Fig. 1. In terms of this diagram, the reactions studied by Weibke and Schrag (2) are



Similarly, the reactions studied by Biltz and Heimbrecht (3) are

*Electrochemical Society Active Member.

¹Energy data in this paper are given in "rational" units; values in other units may be obtained by multiplying by the appropriate value of the gas constant, R .

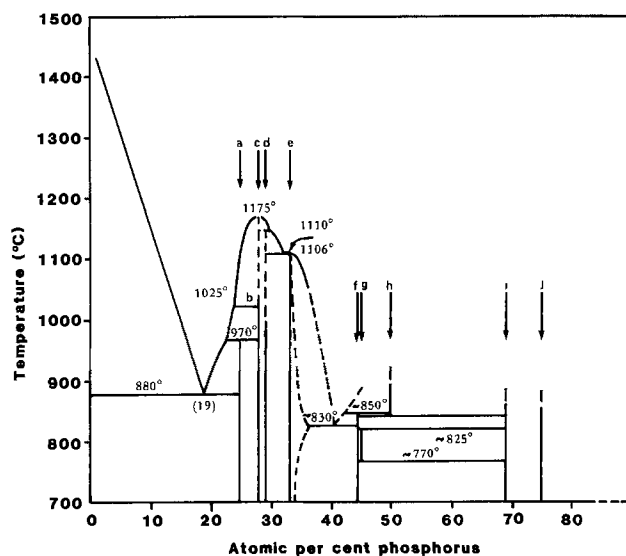
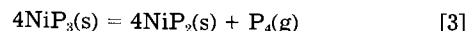


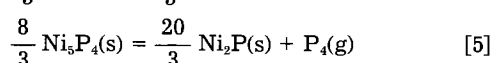
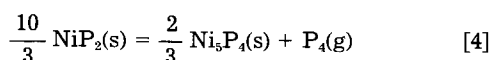
Fig. 1. Nickel-phosphorus phase diagram [after Larsson, Ref. (1)]. Phases: a, Ni_3P ; b, Ni_5P_2 (β); c, $\text{Ni}_{2.55}\text{P}$; d, Ni_{12}P_5 ; e, Ni_2P ; f, Ni_5P_4 ; g, $\text{Ni}_{1.22}\text{P}$; h, NiP ; i, NiP_2 ; j, NiP_3 .

Table I. Data for the reaction: $12\text{Ni}_2\text{P}(s) = 2\text{Ni}_{12}\text{P}_5(s) + \text{P}_2(g)$

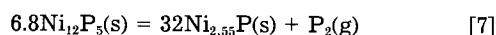
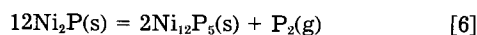
T	Cell	$10^3m(\text{mg}/\text{min})$	$P(\text{P}_2) \times 10^6(\text{atm})$	$-\log P$	$\Delta\Phi'/R$	$\Delta H_{298.15}^{\text{oll}}/R$ (kK)
Run A (~560 mg sample)						
1260	C-3	1.5	9.25	5.03	20.38	40.27
1360	C-3	21.0	134	3.87	20.47	39.96
1285	C-3	3.8	23.7	4.63	20.40	39.91
1323	C-3	8.3	52.4	4.28	20.34	39.95
1331	C-192	1.83	121	3.92	20.44	39.22
1304	C-192	0.61	40.0	4.40	20.41	39.83
1274	C-3	1.2	7.44	5.13	20.39	41.03
1286	C-3	1.44	8.97	5.05	20.31	41.07
Run B (~565 mg sample)						
1338	C-192	2.0	133	3.88	20.45	39.32
1322	C-192	1.1	72.6	4.14	20.43	39.61
1354	C-192	3.84	257	3.59	20.46	38.90
1322	C-3	6.22	39.3	4.41	20.43	40.43
1360	C-3	20.0	128	3.89	20.47	40.02
1347	C-4	7.39	158	3.80	20.46	39.35
1324	C-4	2.73	58.1	4.24	20.43	39.98
1359	C-4	10.2	220	3.66	20.47	39.27
1289	C-4	0.90	18.9	4.72	20.40	40.31
1302	C-4	1.1	23.2	4.63	20.41	40.46
1328	C-4	2.78	59.2	4.23	20.44	40.08
1302	C-4	1.50	31.6	4.50	20.41	40.07
1353	C-4	5.17	111	3.95	20.46	39.99
1331	C-4	3.5	74.7	4.13	20.44	39.87
Run C (~510 mg sample)						
1341	C-192	1.83	122	3.91	20.45	39.50
1362	C-192	3.69	247	3.61	20.47	39.20
1305	C-192	0.53	34.8	4.46	20.42	40.05
1237	C-4	0.17	3.50	5.46	20.36	40.74
1260	C-4	0.32	6.64	5.18	20.38	40.71
Effective orifice areas: C-3 $2.75 \times 10^{-4} \text{cm}^2$						Mean $\Delta H_{298.15}^{\text{oll}}/R = 39.97$
C-4 $8.17 \times 10^{-5} \text{cm}^2$						
C-192 $2.63 \times 10^{-5} \text{cm}^2$						

Table II. Data for the reaction: $6.80\text{Ni}_{12}\text{P}_5(s) = 32\text{Ni}_{2.55}\text{P}(s) + \text{P}_2(g)$

T	Cell	$10^3m(\text{mg}/\text{min})$	$P(\text{P}_2) \times 10^6(\text{atm})$	$-\log P$	$\Delta\Phi'/R$	$\Delta H_{298.15}^{\text{oll}}/R$ (kK)
Run D (~360 mg sample)						
1401	C-4	1.4	32.8	4.48	20.97	43.83
1400	C-4	1.3	28.4	4.55	20.97	44.03
1399	C-4	1.5	32.8	4.48	20.97	43.77
1399	C-192	0.48	32.6	4.49	20.97	43.80
Effective orifice areas: C-4 $8.17 \times 10^{-5} \text{cm}^2$						Mean $\Delta H_{298.15}^{\text{oll}}/R = 43.86$
C-192 $2.63 \times 10^{-5} \text{cm}^2$						



The effusion study reported here considered the reactions



which provide a link between the two previous studies.

Experimental

The effusion apparatus used in this study, together with calibration and operation procedures, has been described previously (4). It consists of a vacuum system, induction heater, temperature controller, and recording vacuum balance. The channel-orifice effusion cells were fabricated from 0.95 cm high-density graphite rod. The effective orifice areas were determined by direct measurement as previously described (4). The phosphide samples were prepared by direct combination of the elements in evacuated and sealed "Vycor" glass ampuls, using the procedures and precautions described earlier (4). The products of the preparations, as well as residues from the effusion runs, were characterized by x-ray powder diffraction (5-7). Observed intensity and d spacing data were compared with published data for Ni_2P (5), Ni_{12}P_5 (7), and $\text{Ni}_{2.55}\text{P}$ (6).

Results

The primary data were the temperature, corrected for thermocouple calibration, and the rate of mass loss, cor-

rected for nonorifice effusion (4) (less than 20%), obtained from the recording vacuum balance. Tables I and II list the results for the Ni_2P - Ni_{12}P_5 and Ni_{12}P_5 - $\text{Ni}_{2.55}\text{P}$ two-phase regions, respectively. The vaporization was found to be severely retarded, and long channels were required to reduce the effective orifice areas sufficiently to achieve equilibrium. Additionally, the measurements were greatly complicated by sintering of the samples which resulted in a decrease in the rate of effusion as the run progressed, even though two solid phases were still present. In order to cope with this difficulty, the sample was removed after every second or third point for re-grinding. While this procedure appeared to overcome the difficulty, the very low rates of mass loss, particularly at lower temperatures, made detection of a decrease in the rate very difficult. The slopes of the mass-time records could be measured with a reproducibility of about $\pm 10\%$. The total mass losses in runs A, B, and C were 3.3, 7.6, and 2.1 mg, respectively, which may be compared with the ~ 16 mg loss needed to cross the Ni_2P - Ni_{12}P_5 two-phase region. For run D, the total loss was 2.3 mg, with about 3 mg loss needed to cross the Ni_{12}P_5 - $\text{Ni}_{2.55}\text{P}$ two-phase region. Pressures of P_2 were calculated, assuming P_2 and P_4 to be in equilibrium in the vapor, with the modification of the effusion equation derived earlier (4)

$$P(\text{P}_2) = \frac{K}{2\sqrt{2}} \left\{ \left[1 + \frac{8m}{aK} \left(\frac{\pi RT}{M} \right)^{1/2} \right]^{1/2} - 1 \right\} \quad [8]$$

$$= \frac{K}{2\sqrt{2}} \left\{ \left[1 + \frac{Cm}{aK} \left(\frac{T}{M} \right)^{1/2} \right]^{1/2} - 1 \right\}$$

where K is the equilibrium constant (8) for $\text{P}_4(g) = 2\text{P}_2(g)$

and M is the molecular weight of P_2 . When $P(P_2)$ is given in atmospheres, m (the rate of mass loss) in mg/min, T as Kelvin temperature, and a (the effective orifice area) in cm^2 , the constant is $C = 2.127 \times 10^{-6}$. Because the calculated pressures do not show any apparent variation with effective orifice area, all the data were assumed to represent equilibrium conditions. There are no entropy nor high-temperature heat-capacity data for the nickel phosphides in the literature, and it was necessary to estimate these. The procedure used earlier (4), based on published data on transition metal silicides (9-13), was used to generate the estimates given in Table III. The value for the entropy of NiP was adjusted upward by 5% in order to obtain results consistent with the observed diagram (1).

Third-law enthalpy changes for reactions [6] and [7] were calculated using free-energy functions, $\Phi' = -(G_r^\circ - H_{298.15}^\circ)/T$, based on the entropy and heat capacity estimates. The second-law enthalpy change for reaction [6] was calculated to be 58.8 kK at 298.15 K, which is in poor agreement with the mean third-law value. The second-law value was rejected in favor of the third-law result. This choice was based on two considerations. First, the very low rates of mass loss at lower temperatures made detection of curvature in the mass vs. time record extremely difficult, and thus, the observed slopes in this range may be too small due to kinetic effects brought on by sintering of the sample. Second, attempts to force agreement of the second-law and third-law results would require increasing $\Delta\Phi'/R$ for reaction [6] by 13.9. It is unlikely that the entropy estimates for $Ni_{12}P_5$ and Ni_2P are in error by an amount sufficient to produce this difference, because similar estimates for other systems (4, 14) have produced acceptable agreement. Hence, the mean third-law value was used in subsequent calculations. The available temperature range for the study of reaction [7] was too small to permit determination of a meaningful second-law enthalpy change; hence, the mean third-law result was carried forward into subsequent calculations. Free-energy functions based on the estimates in Table III were used to obtain third-law enthalpy changes for reactions [3], [4], and [5] from the data of Blitz and Heimbrecht (3). The enthalpies reported by Weibke and Schrag (2) were corrected to 298.15 K by means of the heat capacity estimates in Table III. Enthalpies of reaction at 298.15 K are summarized in Table IV. The appropriate combination of these with the enthalpies of formation (8) of $P_2(g)$ and $P_4(g)$



yields enthalpies of formation

$$\Delta H_1 = \Delta H_f(Ni_3P)$$

$$\Delta H_2 = \Delta H_f(Ni_{2.55}P)$$

$$\Delta H_{13} = \Delta H_f(Ni_{12}P_5) = \frac{1}{6.8} (\Delta H_9 + 32\Delta H_2 - \Delta H_7)$$

$$\Delta H_{14} = \Delta H_f(Ni_2P) = \frac{1}{12} (\Delta H_9 + 2\Delta H_{13} - \Delta H_6)$$

$$\Delta H_{15} = \Delta H_f(Ni_5P_4) = \frac{3}{8} (\Delta H_{10} + \frac{20}{3} \Delta H_{14} - \Delta H_5)$$

$$\Delta H_{16} = \Delta H_f(NiP_2) = \frac{3}{10} (\Delta H_{10} + \frac{2}{3} \Delta H_{15} - \Delta H_4)$$

$$\Delta H_{17} = \Delta H_f(NiP_3) = \frac{1}{4} (\Delta H_{10} + 4\Delta H_{16} - \Delta H_3)$$

which are tabulated, together with enthalpies of atomization, in Table V. In this series of calculations, it is assumed that ΔH° , ΔS° , and ΔC° of phase formation are essentially constant across the Ni_2P single-phase region.

The enthalpies of formation of NiP and $Ni_{1.22}P$ may be deduced from data in Table V and consideration of the phase diagram (1). Because NiP(s) is formed spontaneously from Ni_5P_4 and NiP₂ above (but not below) about 850°C (1123 K), its formation from these compounds must proceed with positive changes in both enthalpy and en-

Table III. Estimated entropies and heat capacities

	$S_{298.15}^\circ/R$	A	$B \times 10^3 \text{ K}^{-1}$
Ni_3P	13.1	10.3	4.72
$Ni_{2.55}P$	11.8	9.10	4.00
$Ni_{12}P_5$	56.3	42.2	21.0
Ni_2P	9.9	7.50	3.20
Ni_5P_4	26.4	23.5	7.30
$Ni_{1.22}P$	6.63	5.69	1.75
NiP	5.6	5.23	1.41
NiP ₂	6.4	7.85	1.91
NiP ₃	8.4	10.5	2.26

$C_p/R = A + BT$

Table IV. Enthalpies of reaction at 298.15 K (kK)

Reaction		$\Delta H_{298.15}^\circ/R$	Notes
$3Ni(s) + P(s, \text{red}) = Ni_3P(s)$	(1)	-23.8 ± 2	a
$2.55Ni(s) + P(s, \text{red}) = Ni_{2.55}P(s)$	(2)	-23.6 ± 2	a
$4NiP_3(s) = 4NiP_2(s) + P_4(g)$	(3)	23.2 ± 3	b
$\frac{10}{3} NiP_2(s) = \frac{2}{3} Ni_5P_4(s) + P_4(g)$	(4)	31.0 ± 3	b
$\frac{8}{3} Ni_5P_4(s) = \frac{20}{3} Ni_2P(s) + P_4(g)$	(5)	31.6 ± 3	b
$12Ni_2P(s) = 2Ni_{12}P_5(s) + P_2(g)$	(6)	40.0 ± 3	c
$6.80Ni_{12}P_5(s) = 32Ni_{2.55}P(s) + P_2(g)$	(7)	43.9 ± 3	c
$\frac{1}{6} Ni_5P_4(s) + \frac{1}{6} NiP_2(s) = NiP(s)$	(11)	0.1 ± 0.1	d
$0.24Ni_5P_4(s) + 0.02NiP_2(s) = Ni_{1.22}P(s)$	(12)	0.1 ± 0.1	d

a) Calculated from the data of Weibke and Schrag (2).

b) Calculated from the data of Blitz and Heimbrecht (3).

c) This work.

d) Calculated from phase diagram (1).

trophy at that temperature, and $\Delta H_{11}^\circ = T\Delta S_{11}^\circ$ at 1123 K. Use of the estimated entropy and heat-capacity data in Table III leads to the enthalpy of reaction recorded in Table IV and the enthalpies of formation and atomization of NiP(s) given in Table V. According to the phase diagram (1), $Ni_{1.22}P$ is stable with respect to Ni_5P_4 and NiP₂ only between about 770°C (1043 K) and 825°C (1098 K). This requires not only that $\Delta H_{12}^\circ = T\Delta S_{12}^\circ$ at both these temperatures, but also that both ΔH_{12}° and ΔS_{12}° be posi-

Table V. Enthalpies of formation (from red P) and atomization (kK) at 298.15 K

	$\Delta H_f^\circ/R$	$\Delta H_{at}^\circ/R$
$\frac{1}{4} Ni_3P(s)$	5.94 ± 0.5	54.8
$\frac{1}{3.55} Ni_{2.55}P(s)$	6.65 ± 0.5	55.2
$\frac{1}{17} Ni_{12}P_5(s)$	6.73 ± 0.5	55.1
$\frac{1}{3} Ni_2P(s)$	6.87 ± 0.5	54.8
$\frac{1}{9} Ni_5P_4(s)$	6.39 ± 0.5	53.0
$\frac{1}{2.22} Ni_{1.22}P(s)$	6.32 ± 0.5	52.9
$\frac{1}{2} NiP(s)$	6.09 ± 0.5	52.1
$\frac{1}{3} NiP_2(s)$	5.38 ± 0.5	49.4
$\frac{1}{4} NiP_3(s)$	4.52 ± 0.5	47.6

tive at the lower temperature and negative at the higher temperature. These considerations, together with the estimated entropy and heat-capacity data in Table III, were used to deduce the value for ΔH_{12} in Table IV and the enthalpies of formation and atomization of $\text{Ni}_{1.22}\text{P(s)}$ given in Table V. Uncertainty limits were assigned in the manner described earlier (14).

It has been pointed out (14) that the atomization enthalpies per gram atom of the nickel phosphides are, at corresponding compositions, very nearly the same as those for the phosphides of iron (15) and cobalt (4); but, when valence-state energies (16) of the metal atom are taken into account (14), the atomization enthalpies to valence-state atoms per mole of monophosphides show a regular decrease in the series CrP(145.3 kK) (17), MnP(141.3 kK) (14), FeP(130.0 kK) (15), CoP(119.1 kK) (4), and NiP(104.2 kK). This decrease parallels the decrease in the number of bonding electrons per metal atom from six in CrP to two in NiP and suggests that chemical bonding is similar in this series of compounds.

Acknowledgments

The authors are pleased to acknowledge the support of the U.S. Office of Naval Research during the preparation of this study for publication. Thanks are also due Professor Leo Brewer and his research group for helpful discussions.

Manuscript submitted Aug. 24, 1984; revised manuscript received Oct. 16, 1984.

State University of New York at Binghamton assisted in meeting the publication costs of this article.

REFERENCES

1. E. Larsson, *Arkiv Kemi*, **23**, 335 (1965).
2. F. Wiebke and G. Schrag, *Z. Electrochem.*, **47**, 222 (1941).
3. W. Biltz and M. Heimbrecht, *Z. Anorg. Allg. Chem.*, **237**, 132 (1938).
4. C. E. Myers, *High Temp. Sci.*, **6**, 309 (1974).
5. H. Nowotny and E. Henglein, *Z. Phys. Chem. (Leipzig)*, **B40**, 281 (1938).
6. G. Saini, L. Calvert, and J. Taylor, *Can. J. Chem.*, **42**, 1511 (1964).
7. S. Rundqvist and E. Larsson, *Acta Chem. Scand.*, **13**, 551 (1959).
8. D. R. Stull and H. Prophet, *Natl. Stand. Ref. Data Ser., Natl. Bur. Stand.*, No. 37 (1971).
9. A. Frolov, Yu. Putintsev, F. Sidorenko, P. Gel'd, and R. Krentsis, *Izv. Akad. Nauk SSSR, Neorg. Mater.*, **8**, 468 (1972).
10. G. Kalishevich, P. Gel'd, and R. Krentsis, *Teplofiz. Vys. Temp., Akad. Nauk SSSR*, **2**, 16 (1964).
11. S. Letun, P. Gel'd, and N. Serebrennikov, *Zh. Neorg. Khim.*, **10**, 1263 (1965).
12. R. Krentsis and P. Gel'd, *Fiz. Met. Metalloved.*, **13**, 319 (1962).
13. G. Kalishevich, P. Gel'd, and R. Krentsis, *Zh. Fiz. Khim.*, **39**, 2999 (1965); *Teplofiz. Vys. Temp.*, **4**, 653 (1966).
14. C. E. Myers, E. D. Jung, and E. L. Patterson, *Inorg. Chem.*, **19**, 532 (1980).
15. G. Lewis and C. E. Myers, *J. Phys. Chem.*, **67**, 1289 (1963).
16. J. S. Griffith, *J. Inorg. Nucl. Chem.*, **3**, 15 (1956).
17. C. E. Myers, G. A. Kisacky, and J. K. Klingert, *This Journal*, **132**, 236 (1985).

Properties of LPCVD Aluminum Films Produced by Disproportionation of Aluminum Monochloride

R. A. Levy,* P. K. Gallagher, R. Contolini,*¹ and F. Schrey

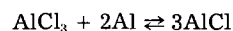
AT&T Bell Laboratories, Murray Hill, New Jersey 07974

ABSTRACT

This study describes the properties of LPCVD Al deposited by the disproportionation of AlCl_3 on Si and SiO_2 substrates. In contrast to the organometallic LPCVD Al processes, this deposition technique offers the advantages of a lower hazard potential and, possibly, the ability of simultaneously incorporating desired dopants such as Cu and/or Si. The Al deposits are shown to be chemically pure, as well as adherent, and to exhibit the normal structural and electrical properties of Al. Furthermore, the films exhibit, in local areas, signs of specularly reflecting the absence of the rough topographical structure typical of organometallic LPCVD Al processes. However, the difficulties associated with proper activation of the substrate surface remain, at the present, a significant problem in the viability of this metallization technology.

Aluminum and aluminum-alloy films are widely used in the metallization of integrated circuits. Such films have normally been deposited by electron-beam (E-Gun[®]) or RF induction-source evaporation (In-Source[®]), although recently the use of magnetron sputtering has become more prominent. All of these line-of-sight deposition techniques suffer, however, from poor step coverage, which often results in formation of microcracks and discontinuities at corners of deep steps. With the current growth in emphasis on multilevel structures for vertical integration, coupled with the incessant interest in devices with high packing densities and horizontally reduced dimensions, the need for deposition processes providing conformal step coverage now becomes essential. Recently, several studies pertaining to the characterization of aluminum films deposited by an LPCVD process using tri-isobutyl aluminum (TIBAL) as a source have been reported (1-4). The results show that this particular process does indeed provide conformal step coverage, exhibits excellent film properties in terms of chemical pu-

rity, adhesion, and electrical resistivity, is compatible with current VLSI processing, and appears to have no adverse effects on overall device performance. However, in a comparison with In-Source Al-0.5% Cu films (1, 5), differences for LPCVD Al were noted with respect to its surface roughness, fine grain size, and inferior electromigration resistance. Furthermore, the safety hazard associated with the use or disposal of TIBAL, a highly toxic and pyrophoric material, was emphasized as being of concern. In view of these recognized limitations, a study was undertaken to assess the feasibility of using alternate and safe Al sources. In this paper, we describe the properties of LPCVD Al films deposited by the disproportionation reaction



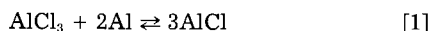
We shall demonstrate that, with the use of this process, the deposits exhibit a high degree of chemical purity, a randomly textured structure, the expected electrical properties of Al films, and, in select areas, evidence of a significant degree of optical reflectivity. However, as typical of other LPCVD metal processes, it was found

* Electrochemical Society Active Member.

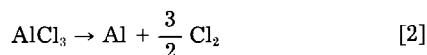
¹ Presently at Bell Communication Research, Incorporated.

that the development of a reliable procedure for activating the substrate surface to insure reproducible uniformity in nucleation and growth of the film is essential. Although attempts were made to develop such an activation process, discussions pertaining to this particular topic will not be included in this paper.

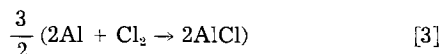
Physical properties and plating chemistry of AlCl_3 .—CVD methods based upon the transport of inorganic chlorides have been used in a wide variety of applications (6). As a CVD source, aluminum trichloride (7) is a colorless, crystalline solid with a melting point of 192.4°C , a sublimation point of 180°C at 1 atm, and a density of 2.44 g/cm^3 . The vapor pressure of solid AlCl_3 between 420 K and the melting point 467 K, is given by $\log p_{\text{cm}} = 15.115 - 6000/T$. For the liquid, between 467 and 482 K, $\log p_{\text{cm}} = 6.678 - 2070/T$. Despite its satisfactory vaporization characteristics, AlCl_3 does not readily decompose by a pyrolytic, displacement, or reduction reaction to yield metallic aluminum. However, it can partially react at high temperatures with molten Al ($>660^\circ\text{C}$) to form AlCl as follows.



This equilibrium equation may be viewed as the sum of two equations, namely



and



where standard free energy data (8) is available, in this case, for each. For Eq. [2]

$$\Delta G^\circ (\text{cal/mol}) = 140,000 - 2.5T \log T - 7.05 T$$

and for Eq. [3]

$$\Delta G^\circ (\text{cal/mol}) = \frac{3}{2} (-25,860 + 11.8T \log T - 71.9T)$$

yielding for the sum a value for

$$\Delta G^\circ (\text{cal/mol}) = 101,210 + 15.2T \log T - 114.9T$$

A computer plot for the standard free energy corresponding to Eq. [1] is shown in Fig. 1. Examination of the re-

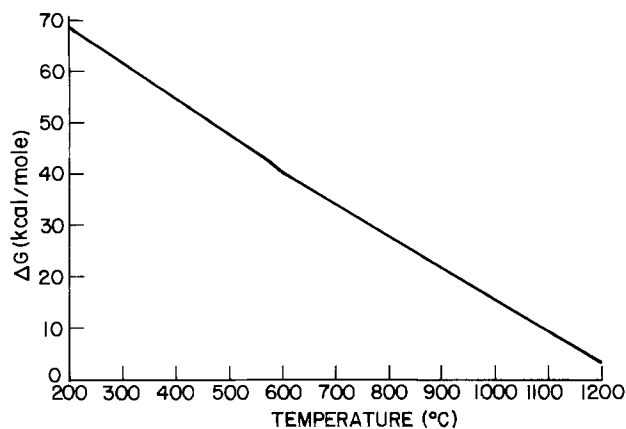


Fig. 1. Standard free-energy change (ΔG°) as a function of temperature for the reaction $\text{AlCl}_3 + 2\text{Al} \rightleftharpoons 3\text{AlCl}$.

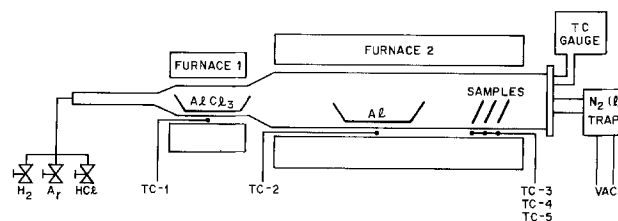


Fig. 2. Schematic diagram of the Al LPCVD reactor used in this project

sults indicates that the equilibrium in Eq. [1] is indeed displaced toward the right with increasing temperature, but the free energy does not become negative till above 1200°C . At lower temperatures, this equilibrium shifts back to the left, and the AlCl reverts to Al and AlCl_3 . For instance, at 1250 K and 0.5 torr of AlCl_3 , approximately 11% of this AlCl_3 vapor in contact with Al would be converted to AlCl at equilibrium. Upon cooling to 500 K , virtually all of this AlCl would disproportionate to Al and gaseous AlCl_3 , which may be recovered and recycled if desired.

Rather than contend with the problems and inconvenience of handling, vaporizing, and preventing the upstream condensation of AlCl_3 , the simpler and controllable process of introducing HCl into the carrier gas stream,

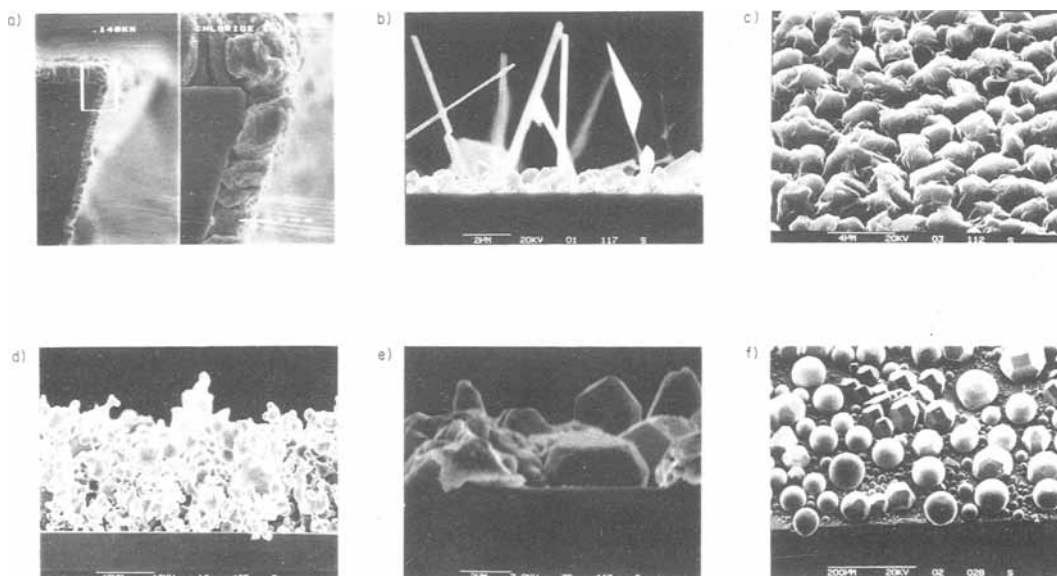
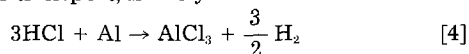
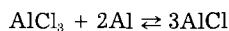


Fig. 3. Representative sampling of SEM photographs showing LPCVD Al films deposited under various experimental conditions: a) AlCl_3 source at 100°C , Al at 900°C , substrate at 400°C ; b) HCl source, Al at 900°C , substrate predipped in 1% H_2WO_4 solution, substrate temperature 220°C , cross-sectional view; c) same as b, but top view; d) AlCl_3 source at 100°C , Al at 975°C , predipped in 1% H_2WO_4 solution, substrate temperature 450°C ; e) AlCl_3 source at 100°C , Al at 900°C , substrate predipped in 100:1 HF, followed by 1% organosilane solution, substrate temperature 515°C ; f) HCl source, Al at 900°C , substrate at 600°C .

e.g., H₂ or Ar, to form AlCl₃ *in situ* by reaction with molten Al was tried in this study and found to be successful. Two simultaneous equilibrium reactions are believed to account for the transport, namely



and



For such a transport mechanism, we found it advisable to limit the flow of HCl so that it could be totally consumed in the hot zone and not be available downstream to etch the Al deposit. It is interesting to note that this AlCl disproportionation process is an atypical CVD method in the sense that instead of having, under normal conditions, the cool reactant gases decompose on a hot substrate surface, we have in this particular case hot reactant gases decomposing on a cool substrate surface. We believe that despite this difference, the conformality in step coverage is still to be expected of this process.

Experimental Procedure

A schematic representation of the apparatus used in the present investigation is shown in Fig. 2. In cases where AlCl₃ was used as a source material, it was heated in Furnace 1 over the temperature range of 120°-160°C. The molten aluminum was heated in Furnace 2 over the temperature range of 900°-1000°C. The samples were placed in the steep temperature gradient at the downstream end of the furnace, with their respective positions determining their temperature. In addition to the thermocouples used for monitoring the temperature of the AlCl₃ source and the molten Al, three others straddled the samples to establish the deposition temperature range. In all cases, the thermocouples were external to the reaction tube, due to the corrosive nature of the ambient. The 2.5 in. id of the quartz tube allowed for samples with approximately 3 cm² areas to be stacked one behind the other 1-2 cm apart or for long narrow strips to be exposed side-by-side so that the entire temperature gradient (150°-550°C) was achieved along a single sample. A small conventional mechanical pump was used to provide the modest vacuum requirements. A total operating pressure of 1 torr was used for most experiments. The base pressure achieved without the intentional addition of gases ranged from 0.02 to 0.05 torr. When HCl was used in the gas stream, there was no AlCl₃ present and, hence, no need for Furnace 1. This in turn simplified the experimental procedure and allowed, through measurement of flow rates, strict control on the composition of reactant gases. In some of the experiments where HCl was used, a small Alundum boat with Ti metal was added in hot zone just ahead of the other Alundum boat containing the Al. The Ti presumably served to getter the gas stream, particularly for O₂ and H₂O, and served to activate the substrate surface as reported in the case of LPCVD Al deposited from organometallics. Although numerous runs have been made using this disproportionation process with a wide range of experimental variables, Al films consistent with the standards required of device fabrication have not been reproducibly achieved. A representative sampling of SEM photographs, shown in Fig. 3, for the films deposited under various experimental conditions is useful here in illustrating the problems associated with improper nucleation and growth of the substrate and the effect on the structure of deposits. This investigation will, thus, solely focus on characterization of the best films produced to date with this process. Such films were deposited both on Si and SiO₂ substrates with HCl accounting for the transport (*i.e.*, no direct addition of AlCl₃). The temperature of Al and Ti (used for gettering) was controlled at 900°C, and the deposition temperature of the samples was monitored at ~400°C. The operational sequence of deposition normally proceeded as follows. Starting with a base pressure of 45 mtorr, H₂ was introduced at room temperature, raising the pressure to 800 mtorr, Furnace 2 was

then heated to 900°C, at which point HCl was added to raise the total pressure to 1 torr. The HCl flow was maintained for 45 min, and then both the flow of HCl and the power to the furnace were shut off and the reactor was allowed to cool at its own rate in the flow of H₂ at 800 mtorr. Approximately 0.6 of the 127.6g of Al was transported during such a run, whereas the loss from the 10.2g of Ti was >0.1g. Some attack of the quartz tube was obvious in the hot zone surrounding the Al. Controlled experiments with the HCl shut off, but all other conditions maintained the same, including pressure adjustment to 1 torr with H₂, failed reproducibly to produce Al deposits on the wafer, thus confirming the chloride transport nature of this process. The contributory effect of Al evaporation onto deposits was considered, but was dismissed in view of the exceedingly low vapor pressure of Al (4.7 × 10⁻⁴ torr at 1000°C) and the lack of material transport noted in the controlled experiments.

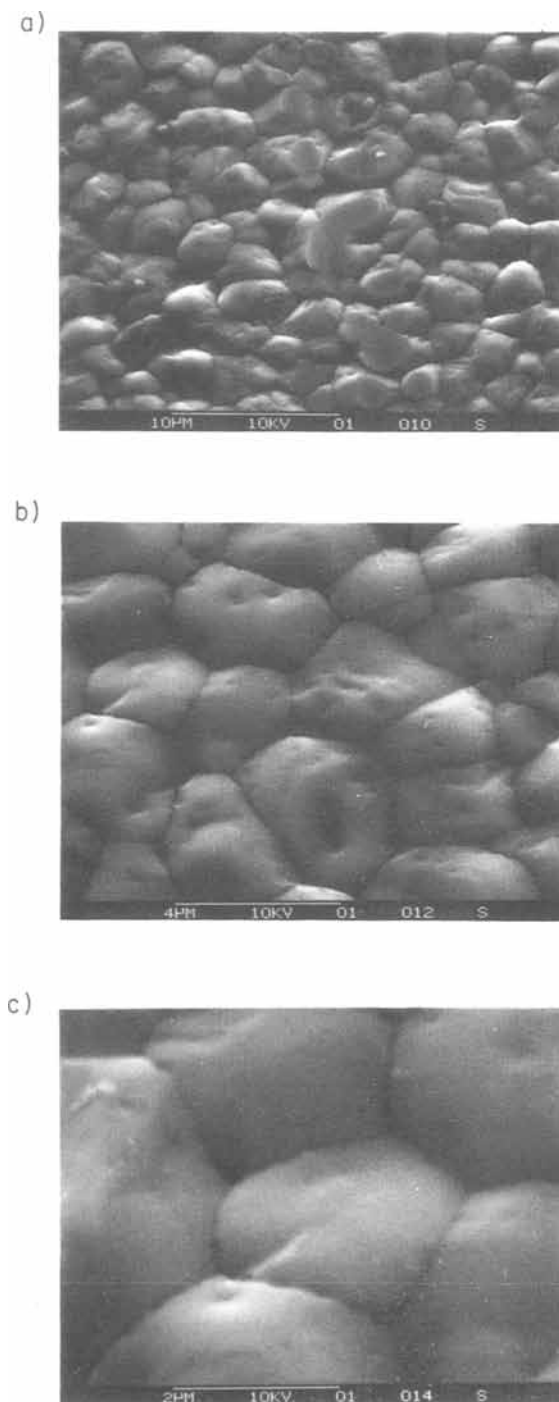


Fig. 4. SEM photographs taken at several magnifications of best LPCVD Al deposits.

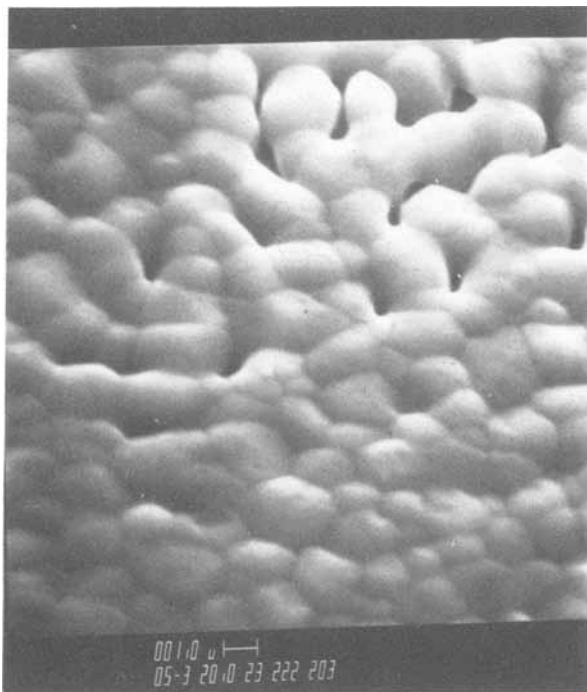


Fig. 5. SEM photograph of LPCVD Al deposit exhibiting both the coherent and incoherent regions of the film.

Film Characterization

The topography, the chemical composition, the adherence, and the structural, electrical, and optical properties of LPCVD Al deposited on blank wafers by disproportionation of AlCl₃ have been characterized. Each of these properties will now be described.

Topography.—In contrast to the cloudy appearance characteristic of LPCVD Al deposited from a TIBAL source (1-3), LPCVD Al produced by disproportionation of AlCl₃ exhibit in localized areas across the sample a significant degree of optical reflectivity. Typical SEM photographs of such areas, shown at several magnifications in Fig. 4, reveal a continuous network of grooved grains, with an average grain size of $\sim 4 \mu\text{m}$ and a rather uniform size distribution. The lack of steep peaks and valleys, which generally account for poor reflectance of a surface, is in this case clearly evident. The extent of these areas is observed, however, to be spatially limited to ≤ 1 cm, with the borders being marked, as seen in Fig. 5, by the presence of voids across the rest of the film. The grooving observed at the grain boundaries is presumably due to preferential etching of the boundary surface by chlorine ions in the gas stream, while the holes scattered through the imperfect regions of the film are believed to be, as previously noted, the result of improper activation of the substrate surface. Evidently, the concentration of nuclei on the substrate surface was not in this case ade-

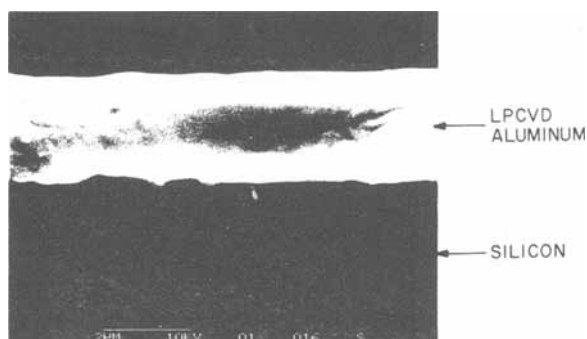


Fig. 6. Vertical SEM cross section across a coherent region of the LPCVD Al film.

quately uniform to insure proper growth and coalescence of the film. The vertical SEM cross section across a coherent region of the film, shown in Fig. 6, illustrates the smoothness, uniformity, and continuity of the Al deposit.

Chemical composition.—The purity of the Al deposit was investigated through the use of x-ray fluorescence (XRF), energy dispersive x-ray analysis (EDX), and Auger electron spectroscopy (AES).

The fluorescence data was gathered in an x-ray Milliprobe unit interfaced to a Li-drifted Si detector and a PGT-3 analyzing system. A Cr target operated at 50 kV and 3 mA provided the source of radiation. The sample was placed in a chamber flushed with He to minimize absorption of the emitted x-rays. A 0.75 mm aperture and 4.8 mm beam stop were used for enhancing count-rate efficiency. In cases where extraneous diffraction peaks were observed, the sample was reoriented to lessen their interference effect. The x-ray fluorescence spectra for

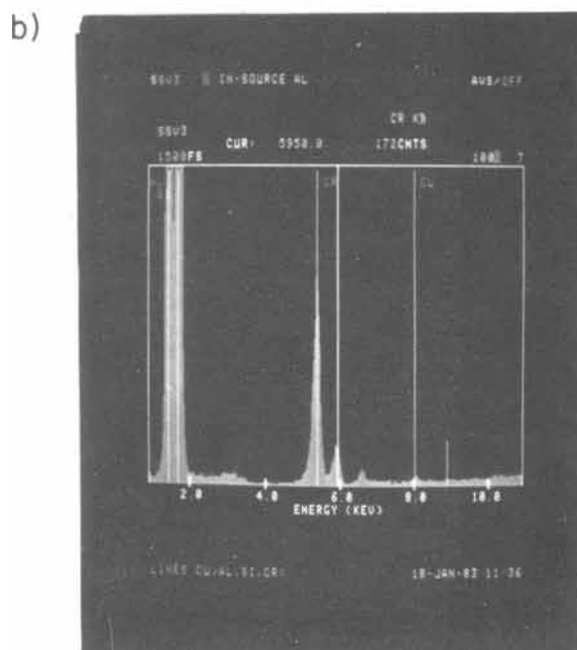
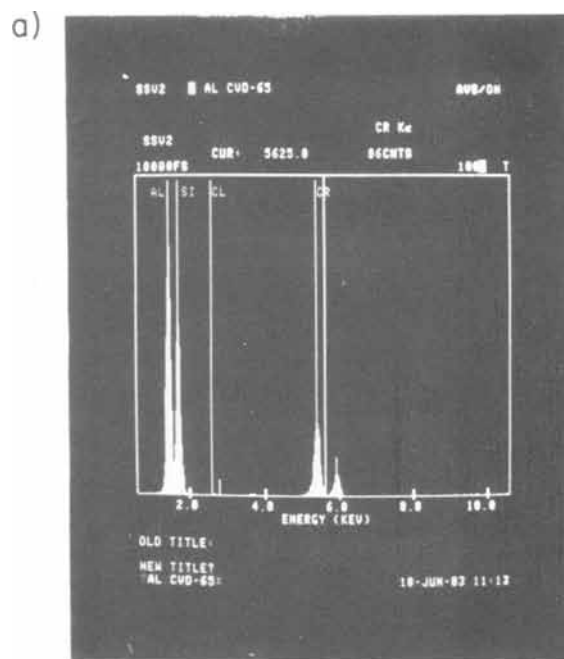


Fig. 7. X-ray fluorescence (XRF) spectra for Al deposited by a) disproportionation of AlCl₃ and by b) In-Source evaporation.

LPCVD Al deposited by disproportionation of AlCl and for In-Source Al-0.5% Cu, used here for control purposes, are shown in Fig. 7a and 7b, respectively. Besides the common occurrence of the characteristic K_{α} and K_{β} lines of the Cr target tube at 5.41 and 5.95 keV and the Cr K_{α} escape peak at 3.67 keV, the relevant K_{α} lines in both samples appear to be due to Al (1.49 keV) and, as a result of the SiO₂ substrate, Si (1.74 keV). In the case of the LPCVD Al sample, traces of Cl were noted while, for the In-Source Al-0.5% Cu film, the presence of the Cu K_{α} line at 8.05 keV is clearly evident.



Fig. 8. Energy dispersive x-ray (EDX) spectra of a) LPCVD Al at 10 keV, b) LPCVD and In-Source Al at 20 keV in the energy range of 0.80-3.36 keV, and c) same as b, but in an extension of the energy range to 10.96 keV.

While topographical information was being gathered in the SEM, the EDX attachment (KeveX-7000) on the system provided a compositional analysis of areas of interest. Accelerating potentials of 10 or 20 keV were used for the purpose of varying the penetration depth of the electron beam. For the LPCVD Al sample, an EDX spectrum taken at 10 keV over the range of 0.16-5.28 keV reveals in Fig. 8a a unique line at 1.49 keV attributed to the K_{α} transition of Al. At the higher accelerating potential of 20 keV, in the range of 0.80-3.36 keV, the spectra of Fig. 8b representing a superposition of LPCVD Al (dotted lines) and In-Source Al-0.5% Cu (solid lines) reveal in both cases the emergence of the Si K_{α} signal from the substrate at 1.74 keV. The higher intensity peak of Al and lower intensity peak of Si measured for LPCVD Al is a reflection of the thickness of the deposit, which in this case is $\sim 2.4 \mu\text{m}$ vs. $\sim 1 \mu\text{m}$ for the In-Source Al-0.5% Cu film. An extension of the energy scale to 10.96 keV is seen in Fig. 8c to yield the Cu K_{α} peak at 8.05 keV for the In-Source sample. The absence of extraneous peaks over this wide energy range is direct evidence of the compositional purity of both deposits. It is worthwhile noting at this point that one of the advantages of using electrons rather than x-rays in exciting the sample is that peaks generated from the target tube (i.e., Cr K_{α} and K_{β} , as well as other escape peaks) are eliminated, thus simplifying significantly the interpretation of results.

Using Auger electron spectroscopy, additional information about impurity elements below those of Na ($Z = 11$) was gathered for the surface, as well as for the bulk of the Al film. Figure 9 shows an elemental AES survey of the surface, which exhibits signals of aluminum, oxygen, chlorine, carbon, and sulfur. The tendency of aluminum to combine readily with oxygen in the environment to form a thin corrosion-resistant film of Al₂O₃ accounts for the presence of the oxygen in the spectrum. The weak chlorine peak at 181 eV reflects the adsorption of this specie during the final stage of Al deposition, whereas the carbon and sulfur are considered here to be surface contaminants.

A depth profile analysis achieved by ion-beam sputtering with Ne reveals in Fig. 10 the rapid decrease in the oxygen concentration below the surface level and the increase and subsequent stabilization of the pure Al signal within the bulk of the film. A second elemental survey taken at a depth of $\sim 3000 \text{ \AA}$ exhibits (Fig. 11), in addition to the expected aluminum and neon peaks, low levels of oxygen and, as shown on an expanded scale in Fig. 12, silicon. Both these signals are attributed to the SiO₂ substrate exposed to the incident electron beam in the incoherent regions of the films. By focusing the beam to within a single grain and using the undifferentiated energy distribution function $N(E)$, the oxygen and Si signals

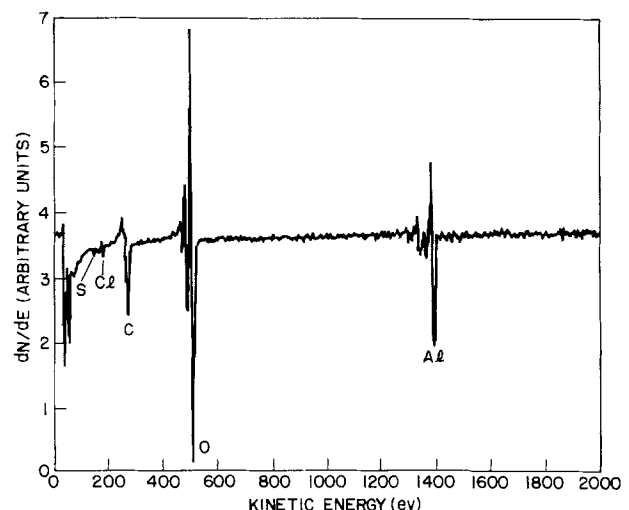


Fig. 9. Elemental Auger electron spectroscopy (AES) survey of surface of LPCVD Al deposit.

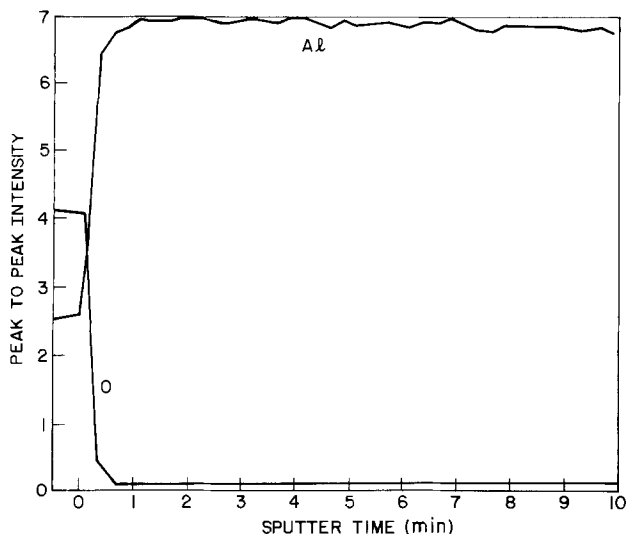


Fig. 10. AES depth profile of LPCVD Al deposit achieved by ion-beam sputtering with Ne.

are seen in Fig. 13 to vanish, and the only pertinent peaks remaining are those attributed to Al and Ne. In view of the recognized sensitivity of the AES technique to all elements above hydrogen, the impurity level within the film is conservatively established to be less than 0.5%, thus establishing an estimate of the Al purity of these deposits of better than 99.5%.

Adherence.—Several attempts to peel the Al film from the Si or SiO₂ substrate with the aid of scotch tape reproducibly yielded negative results. This method, however rudimentary, is helpful in illustrating the bonding quality of the present deposits. Regardless of the deposition technique, Al has generally been known to exhibit excellent adhesive qualities to SiO₂ because of its competition with silicon for oxygen (the heat of formation of Al₂O₃ is high than that of SiO₂, which results in formation of a strong chemical bond).

Structural properties.—The microscopic structure of the Al films deposited with the present process was inferred from x-ray diffraction measurements. The x-ray diffraction data were gathered in a Phillips Model APD 3600 using CuK_α radiation generated by a power supply operating at 45 kV and 30 mA. A diffraction pattern of an Al film deposited on a thermally oxidized Si wafer is shown in Fig. 14 along with the standard Al pattern from the JCPDS file. Besides the Si <400> and <200> K_α reflections detected at 69.17° and 33.09°, respectively, as

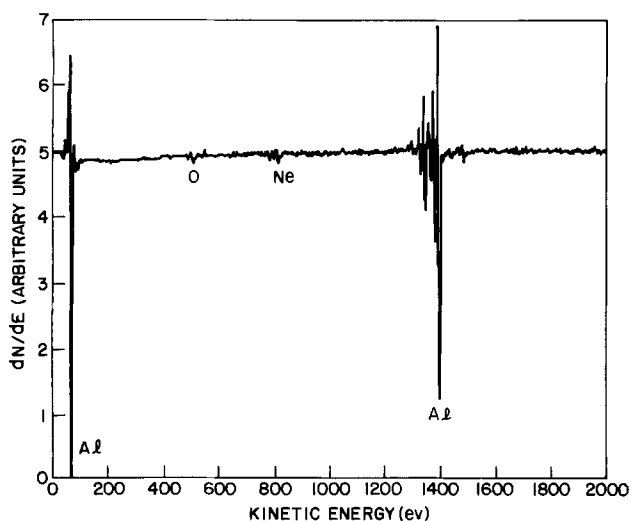


Fig. 11. Elemental AES survey at a depth of ~3000Å in the LPCVD Al film.

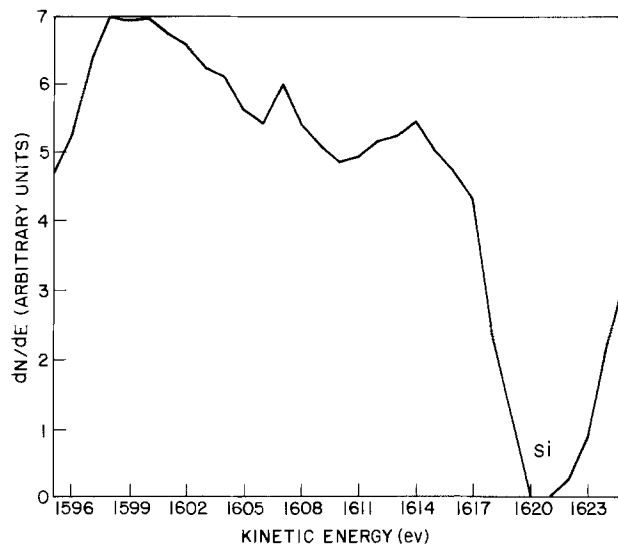


Fig. 12. Expanded scale of AES spectrum at a depth of ~3000Å in the LPCVD Al film showing Si.

well as the weak <400> K_β reflection detected at 61.73°, all other peaks of the x-ray pattern were attributed to Al. The relative intensities of all Al peaks followed closely the ratio predicted in the JCPDS card (4-787), establishing a random orientation for the microcrystalline structure of this Al deposit. Those results are in contrast to the microstructure of In-Source (5), E-Gun (9), and the other reported LPCVD Al films which generally show a highly textured <111> structure (1, 2).

Electrical properties.—The electrical resistivity of the deposited Al was determined from the calculated product of the sheet resistance and film thickness. The sheet resistance measurement was carried out with a square array of probes set 150 μm apart at each side. The geometry and spacing of the probes were dictated by the inherent nonuniformity in film thickness. A standard In-Source Al film was used for calibration purposes. A 50 mA constant current was fed through two of the probes, and the voltage was recorded with a microvoltmeter across the other two probes. The film thickness was determined with the aid of a Dektak[®] stylus at a step wet-etched in the vicinity of where the sheet resistance data were gathered. Values of the resistivity ranged from 3.4 to 3.7 μΩ-cm. That is higher than the ideal 2.7 μΩ-cm bulk resistivity value for pure Al, but it is in close agreement with values reported for sputtered (10) and other LPCVD Al deposits (1, 2).

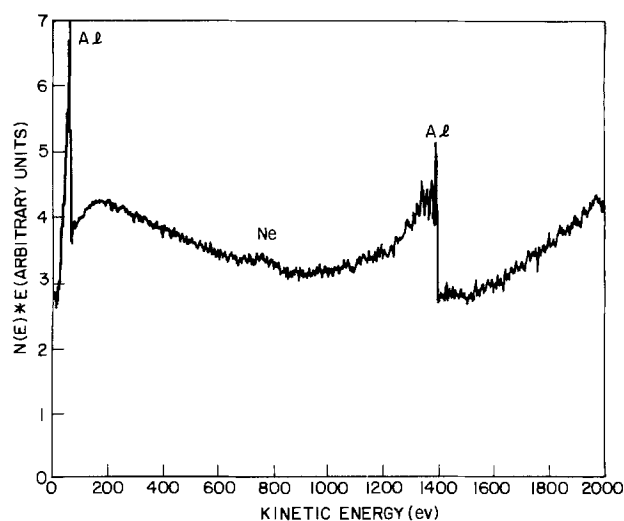


Fig. 13. Undifferentiated AES spectrum taken within a single grain of the LPCVD Al film.

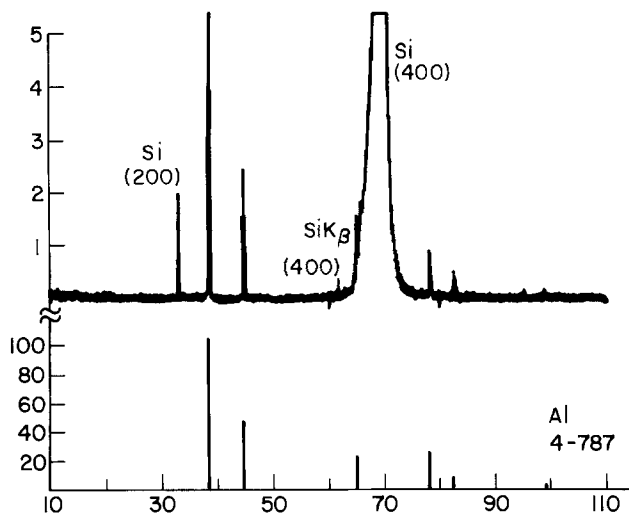


Fig. 14. X-ray diffraction pattern of LPCVD Al deposited on SiO₂.

Optical properties.—In order to investigate the optical properties of LPCVD Al deposited by disproportionation of AlCl₃, reflectance measurements were gathered at a fixed wavelength of 5145Å using a 200 μm wide focused Ar⁺ laser beam. The beam was adjusted to be incident on the sample at a 10° angle from the surface normal. The intensity of both the incident and reflected beams was determined using a Coherent Radiation Model 210 power meter. The reflectance was determined from the ratio of those two measurements. Three Al films were examined for comparison purposes: a sputtered pure Al film deposited in a Varian 3180 magnetron unit, an LPCVD Al film, deposited by decomposition of TIBAL, and the Al film under present investigation. As expected from visual inspection, the sputtered Al film exhibited the highest reflectance, with a value close to 86%, while the LPCVD Al film deposited by TIBAL decomposition showed the poorest, with a value close to 1%. In the shiny regions of the Al film under present investigation, the reflectance was recorded at close to 5%, with most of the light scattering being contributed by the receding grain boundaries and surface pits. Thus, elimination of these surface defects promised to lead to significant enhancement in the specularity of these Al deposits.

Conclusions

Our results have established that the use of an inorganic LPCVD process based upon the disproportionation

of AlCl₃ results in the deposition of Al films on Si or SiO₂ substrates. This deposition technique offers advantages: a lower hazard potential and, possibly, the ability to simultaneously incorporate desired dopants such as Cu and/or Si. The Al deposits have been shown to be chemically pure, as well as adherent, and to exhibit a randomly textured structure, as well as the expected electrical properties of Al thin films. Furthermore, in certain regions, the films exhibited a significant degree of optical reflectivity, pointing to the absence of the rough topographical structure typical of organometallic LPCVD Al processes. However, the difficulties associated with proper activation of the substrate surface still remain a problem in the viability of this metallization technology.

Acknowledgments

The authors wish to thank T. E. McGahon for the scanning electron microscopy work, S. M. Vincent for assistance with the x-ray fluorescence measurements, F. Ermanis for the energy dispersive x-ray analysis, E. Lane for gathering the Auger electron spectroscopy data, J. B. Hopkins for the optical measurements, L. J. Lecheler for assistance in various tasks of this project, and M. L. Green for many fruitful discussions.

Manuscript submitted Aug. 21, 1984; revised manuscript received Oct. 12, 1984.

AT&T Bell Laboratories assisted in meeting the publication costs of this article.

REFERENCES

1. R. A. Levy, M. L. Green, and P. K. Gallagher, *This Journal*, **131**, 2175 (1984).
2. M. L. Green, R. A. Levy, R. G. Nuzzo, and E. Coleman, *Thin Solid Films*, **114**, 367 (1984).
3. M. J. Cooke, R. A. Heinecke, R. C. Stern, and J. W. C. Maes, *Solid State Technol.*, **62** (1982).
4. A. Malazgirt and J. W. Evans, *Metall. Trans.*, **11B**, 225 (1980).
5. R. A. Levy, L. C. Parrillo, L. J. Lecheler, and R. V. Knoell, *This Journal*, **132**, 159 (1985).
6. W. M. Feist, S. R. Steele, and D. W. Readey, in "Physics of Thin Films," Vol. 5, G. Hass and R. E. Thun, Editors, Academic Press, New York (1969).
7. K. Wade and A. J. Banister, in "Comprehensive Inorganic Chemistry," p. 993, Pergamon Press, Oxford, England (1973).
8. H. Villa, *J. Soc. Chem. Ind.*, 59 (1950).
9. S. Vaidya, D. B. Fraser, and A. K. Sinha, *Proc. 18th Rel. Phys. Symp. IEEE*, 165 (1980).
10. P. S. McLeod and J. L. Hughes, *J. Vac. Sci. Technol.*, **16**, 369 (1979).

Electrical Conductivities of Er₂O₃ Stabilized HfO₂ Solid Solutions

G. W. Jordan and M. F. Berard

Ames Laboratory,¹ Department of Materials Science and Engineering, Iowa State University, Ames, Iowa 50011

ABSTRACT

The electrical properties of fluorite-structure solid solutions of HfO₂ fully stabilized by doping with Er₂O₃ were studied. The dependence of the total ac electrical conductivity and ionic transference number upon composition (10-50 mole percent (m/o) Er₂O₃), temperature (520°-1070°C), and oxygen partial pressure (1-10⁻¹⁹ atm) were investigated. Bulk electrical conductivities of polycrystalline specimens were separated from other polarizations by a complex impedance technique and were compared to conductivities of single crystals. The electrical conductivity generally decreased as the dopant level increased, although plateaus indicative of possible defect ordering were observed over the composition range of 20-35 m/o Er₂O₃. The effects of surface finish, aspect ratio, and porosity of the specimens were negligible. All Er₂O₃ stabilized HfO₂ compositions were shown to be electrolytic conductors below 1070°C for oxygen partial pressures less than 1 atm. Oxygen diffusion coefficients were calculated using the Nernst-Einstein equation.

Hafnium oxide fully stabilized by additions of alkaline-earth or rare-earth oxides presents many possibilities for exploitation because of its refractory, electrolytic, neutron-absorption, and chemical-inertness characteristics. Uses and studies of stabilized hafnia have been limited because of high cost. Even though hafnium is a moderately abundant element (1), and is present in zirconium containing minerals, typically at a level of 1.5-3.0 weight percent (w/o) hafnium referred to zirconium content (2), the chemical properties of Hf and Zr compounds are nearly identical, making separation of Hf difficult and costly.

Stabilized HfO₂ has several advantages over stabilized ZrO₂ because of superior physical properties, and it has been recommended for use in solid electrolyte oxygen probes in molten metals (3) and for use as high-temperature electrodes and low-temperature current leadouts for magnetohydrodynamic generators (4). Progressive decomposition into two phases caused by repeated cycling through the monoclinic/tetragonal polymorphic transformation temperature occurs at much higher temperatures in stabilized HfO₂ than in ZrO₂, and the volume change associated with the transformation is smaller. The driving force for this destabilization is smaller for rare-earth oxide stabilizing dopants than it is for alkaline-earth oxides, primarily because the rare-earth cations are larger and more electropositive (2).

The purpose of this investigation was to determine the bulk electrical transport properties of Er₂O₃ stabilized HfO₂ (ErSH) over wide ranges of composition (10-50 mole percent [m/o] Er₂O₃), temperature (520°-1070°C), and oxygen partial pressure (1-10⁻¹⁹ atm). This work was to establish a foundation for investigations of fluorite-structure solid solutions in the ternary HfO₂-Er₂O₃-Ta₂O₅ system.

Literature Review

Electrical conductivity investigations of HfO₂ containing systems have been relatively limited, although they were recently surveyed (5). In contrast, such investigations of stabilized ZrO₂ have been numerous and have been frequently reviewed (6-11). Binary systems of HfO₂ with oxides of all the alkaline-earth metals except radium have been studied (12); systems containing CaO [e.g., Ref. (13)] and MgO [e.g., Ref. (14) and (15)] have been most often investigated.

Binary systems containing HfO₂ and oxides of all rare-earth elements of the cerium subgroup, except promethium, have been studied. The most extensively studied components of this group have been La₂O₃ [e.g., Ref. (16)] and PrO_x [e.g., Ref. (17) and (18)]. Fewer investigations of binary systems containing oxides of rare-earth elements of the yttrium subgroup have been conducted. Only Y₂O₃ [e.g., Ref. (19)], Tb₂O₃ [e.g., Ref. (17)], and Er₂O₃ [e.g., Ref. (20)] have been employed as second components from this subgroup. Details of these investigations and several

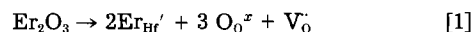
additional citations of literature pertaining to HfO₂ containing systems can be found in Ref. (5).

Johnstone (20) has made the only previous investigation of electrical transport properties of an extensive range of compositions in the HfO₂-Er₂O₃ system (8.6-90 m/o Er₂O₃), although Marchant (21) has measured the dc electrical conductivity of one high Er₂O₃ content composition in air to 1300°C. Johnstone determined ac electrical conductivities at a fixed frequency of 1592 Hz over a narrow temperature range (800-1000°C) and a fairly wide range of oxygen partial pressures (1-10⁻¹⁴ atm). Ionic transference numbers were determined using the open-circuit emf method, employing Cu-Cu₂O vs. Ni-NiO reversible coexistence electrodes. Predominantly ionic conductivity was exhibited by compositions within the fluorite domain. Evidence of possible ordering within the fluorite single-phase region was also observed.

Transport properties of cations in the HfO₂-Er₂O₃ system have been investigated by Berard and his co-workers in a series of diffusion studies (22-26). Only two of these, those of Tesch (25) and Tesch *et al.* (26), involved the HfO₂ rich fluorite solid solutions; the other studies involved Er₂O₃ rich compositions having the rare-earth oxide type-C structure.

Three investigations of phase equilibria in the HfO₂-Er₂O₃ system have been reported (20, 27, 28) and reviewed previously (29). In all three studies, the phase boundaries of the single-phase fluorite solid-solution region, which is of interest in this study, agreed fairly closely (Fig. 1), except Duran *et al.* (28) reported an ordered phase within the fluorite domain below 1500°C based on the hexagonal compound Er₃Hf₃O₁₂. The ordering process for the formation of the ι -phase² was reported to be very sluggish. Indeed, efforts to replicate these results did not produce any evidence of ordering (29).

The defect structure of ErSH fluorite solid solutions is consistent with an anion vacancy defect model, as was first shown by Johnstone (20). Recently, Tesch (25) presented a very detailed analysis of the defect chemistry in ErSH (which is strictly applicable only in the case of unassociated point defects). The predominating defects (using Kröger-Vink notation) are Er_{Hf}' and V_O°, as is shown by the incorporation reaction



Theoretical density is predicted by

$$\rho_{\text{true}} = \frac{4}{a_0^3 N_A} \left[\frac{(1-x)(MW_{\text{HfO}_2}) + x(MW_{\text{Er}_2\text{O}_3})}{1+x} \right] \quad [2]$$

where a_0 is the lattice parameter of a fluorite solid solution containing x mol fraction Er₂O₃, MW refers to molecular weight of the oxides subscripted, and N_A is Avogadro's number.

²This is the usual designation for the M₃O₁₂ phase; see, e.g., Ref. (30). Duran *et al.* (28) designated this the δ phase, which usually refers to an M₁₁O₂₀ phase (30).

¹Supported by USDOE, Office of Basic Energy Sciences, Division of Materials Sciences, under Contract No. W-7405-Eng-82.

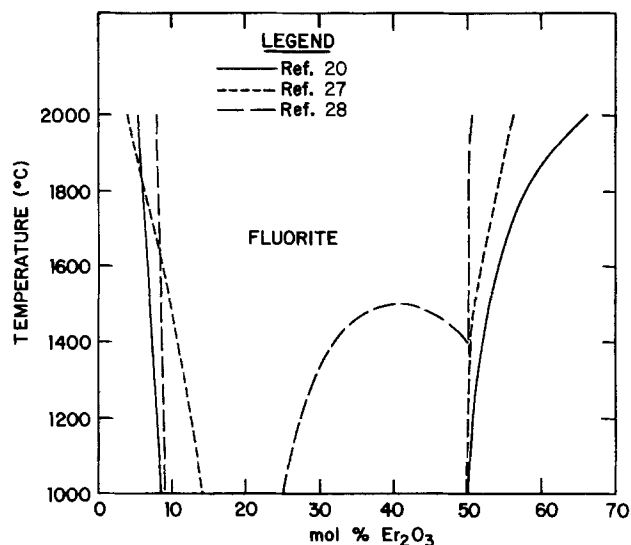


Fig. 1. Limits of the single-phase fluorite region in the HfO₂-Er₂O₃ system according to various investigators.

Experimental Procedure

Raw materials.—Impurity analyses of the Er₂O₃³ used throughout this investigation and of the reactor grade HfO₂⁴ used in the preparation of single crystals are shown in Table I. Qualitative emission spectrographic analysis of the reactor grade hafnium oxychloride⁴ used to prepare polycrystalline specimens indicated faint traces of Ba, Ca, Fe, Mg, and Ti.

Powder processing and specimen preparation.—Ten compositions in the HfO₂-Er₂O₃ system were prepared for polycrystalline specimens. Er₂O₃ contents ranged from 10-50 m/o Er₂O₃ in 5 m/o increments and also included the 33 1/3 m/o Er₂O₃ composition. Powders were prepared by calcination of coprecipitated hydroxide precursors. Precipitation was accomplished by adding aqueous ammonia

³Ames Laboratory Rare Earth Separation Group, Ames, Iowa.

⁴Teledyne Wah Chang Albany, Albany, Oregon.

Table I. Emission spectrographic analyses

Element	Er ₂ O ₃	HfO ₂
	Concentration (ppm) ^a	Concentration (ppm) ^a
Er	>99.9%	
Hf		>98.3%
Al		<35
Fe	≤40	<50
Si	≤30	<100
Ti		<25
Zr		1.6
Y	≤50	
Dy	≤200	
Ho	≤100	
Tm	≤100	
Yb	≤50	
B		0.4
Cd		<0.2
Co		<0.5
Cr		<20
Cu		<25
Mg	<20	<10
Mn		<25
Mo		<25
Ni		<25
Pb		<10
Sn		<10
V		<10
W		<10
Zn	<100	≤50
Ca	≤10	<20/HfO ₂
Na		<20/HfO ₂
U		21/HfO ₂

^a Impurities on Hf metal basis unless noted otherwise.

(2.5N) to blends of cation stock solutions. The stock solutions were prepared by dissolving HfOCl₂·8H₂O in distilled water (50g HfO₂/l) and Er₂O₃ in 2.35N HNO₃ (50g Er₂O₃/l). Final pH during precipitation ranged between 9 and 10.5. The gelatinous hydroxide precursors were de-watered using a series of organic washes to improve the sinterability of the powders (31, 32) and were then calcined at 1100°C in air for 2h.

Small cylindrical specimens were formed without binder, first using uniaxial pressing in a double acting die to approximately 42 MPa (6 ksi), followed by isostatic pressing to 207 MPa (30 ksi).⁵ Two sintering treatments were employed: vacuum sintering at 1880°C for 1h or air sintering at 1706°C for 1h. During sintering, temperatures were measured with an automatic optical pyrometer corrected for sight glass absorption. Specimens were contained in covered erbia crucibles; the air sintering treatments were performed inside an alumina muffle tube inserted into a natural gas-air furnace. After vacuum sintering, all specimens were heated in air for 2h at 1100°C to correct for small deviations from stoichiometry.

Specimen bulk densities were determined by standard water-immersion procedures and have been previously reported and discussed (32). The faces of the cylindrical specimens were generally polished through Linde A (0.3 μm), although some specimens were polished to a lesser degree or even not at all to evaluate the effect of surface finish on conductivity values.

Single-crystal specimens were sectioned from crystals of 10 and 25 m/o ErSH⁶ produced using a skull melting technique.⁷ Faces were polished through Linde A. X-ray diffraction was employed to verify that all compositions were single-phase and fluorite-structure.

Electrical Measurements.—For ac electrical conductivity measurements, porous platinum electrodes were painted onto the specimen faces and baked at 1000°C to create a strong ceramic-metal bond (33); multiple coats were applied until the resistance between any two points on the surface was less than 0.1Ω. The measurement cell, which consisted of one or often two specimens to replicate results, was mounted on an alumina pedestal inside two muffle tubes inserted into a noninductively wound electric furnace; this configuration has been described in detail by Schieltz (34). The outer muffle tube and the lead wires were shielded to eliminate induced EMF's.

Equivalent series resistance and capacitance were measured using the instrumentation shown schematically in Fig. 2(a). A microcomputer⁸ controlled data acquisition by the microprocessor-based bridge⁹ at numerous frequencies between 240 Hz and 20 kHz. Some measurements were made with an LCR meter¹⁰ at higher frequencies ranging from 10 kHz to 1 MHz. Temperature was measured with Pt-Pt10Rh thermocouples using the digital multimeter and was varied from 1070° to 520°C. Oxygen partial pressures ranging from 1 to 10⁻¹⁹ atm were established by a gas mixing and purification train similar to that described by Basler (35) and were verified with an oxygen analyzer.

The bulk (lattice) and interfacial contributions to the total conductances were separated by complex impedance spectroscopy¹¹ (37, 38), even though this generally accepted model has many parameters for which physical interpretations cannot be proven (39). An idealized complex impedance spectrum and equivalent circuit for an ionic conductor are shown in Fig. 3. The three semicircular arcs represent dispersions at low, medium, and high

⁵Typical green densities before and after isostatic pressing were 35 and 44% of theoretical density, respectively.

⁶These are nominal compositions. Wet chemical analyses indicated actual compositions of 10.54 and 23.73 m/o Er₂O₃.

⁷Ceres Corporation, Waltham, Massachusetts.

⁸Commodore PET Computer, Model 4032.

⁹GenRad Precision LC Digibridge, Model 1688.

¹⁰Hewlett Packard Multi-Frequency LCR Meter, Model 4275A.

¹¹Brailsford and Hohnke (36) have shown that complex impedance plots permit more accurate determinations of bulk electrical conductivities than do complex admittance plots.

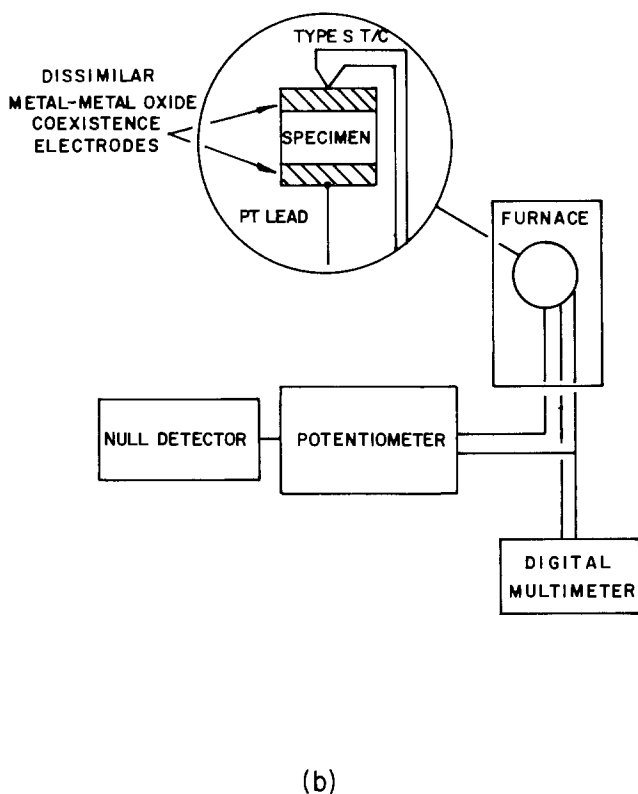
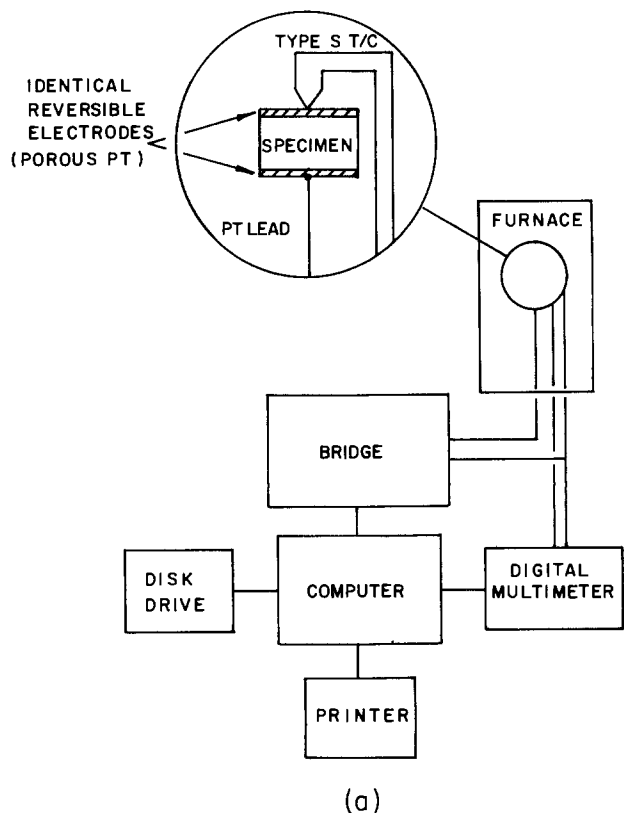


Fig. 2. Instrumentation block diagrams: (a) ac conductivity; (b) open-circuit EMF.

frequencies caused by electrode interfacial polarization, grain boundary polarization, and the bulk specimen, respectively. (Frequency f increases in the direction indicated: the capacitance corresponding to each dispersion can be calculated from the maximum reactance on each arc.) R_b is the bulk ionic resistance; C_g is the geometric capacitance; and R_{gb} , C_{gb} , R_e , and C_e are the lumped resistances and capacitances associated with the grain boundary and electrode interfaces. R_p , the resistance of a parallel electronic conduction path, is very large for an electrolytic

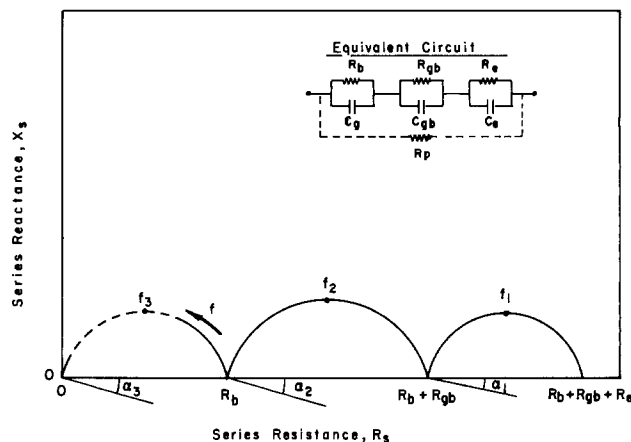


Fig. 3. Idealized complex impedance diagram and corresponding equivalent circuit model (insert).

conductor and can often be neglected for mixed conductors exhibiting high ionic transference numbers. The center of each dispersion arc is depressed by some angle α which is commonly attributed to the distribution of relaxation times associated with each polarization. Only portions of this idealized spectrum were observed at any one time, depending upon temperature and frequency. As would be expected for heavily doped compositions prepared from high purity raw materials, no dispersions due to grain boundary polarization were evident in this investigation. This was verified using the single-crystal specimens.

Transference numbers were determined utilizing duplicate cells and the instrumentation shown in Fig. 2(b). Reversible coexistence electrodes were fabricated from 10:1 mixtures of transition metals (Cu, Co, and Fe) and their oxides. Typical oxygen partial pressures established thus at various temperatures by the Cu-Cu₂O, Co-CoO, and Fe-FeO electrodes employed in this study are listed in Table II. These P_{O_2} values and theoretical EMF's for the various electrode pairs were calculated using the thermodynamic data of Wicks and Block (40). The potentiometer¹² and null detector¹³ measured the actual open-circuit EMF. Temperatures investigated ranged from 720° to 1020°C and were measured as described before.

Results and Discussion

Effects of composition and temperature.—Bulk electrical conductivities determined for various ErSH compositions between 521° and 1063°C in air are shown in Fig. 4. Total electrical conductivity generally decreased as dopant level increased at all temperatures investigated, but a plateau was observed over the composition range of 20-35 m/o Er₂O₃. This decrease in conductivity with increase in dopant is consistent with the immobilization of defects by ordering or clustering in the increasingly defective solid solutions. The plateaus were more pronounced at the lower temperatures and may be indicative of defect ordering in the neighborhood of the pyrochlore composition or one of the other ordered substructures known in some anion deficient fluorite systems (30).

Decreases in electrical conductivities as the defect concentration (dopant level) increases are typical for heavily

¹²Leeds & Northrup Type K-5 Potentiometer, Model 7555.

¹³Leeds & Northrup D. C. Null Detector, Model 9828.

Table II. $\log_{10} P_{O_2}$ of various M-MO reversible coexistence electrodes [based on Ref. (40)]

Electrode	Temperature, °C			
	720	820	920	1020
Cu-Cu ₂ O	-10.42	- 8.84	- 7.53	- 6.44
Co-CoO	-17.55	-15.29	-13.40	-11.81
Fe-FeO	-20.88	-18.32	-16.13	-14.32

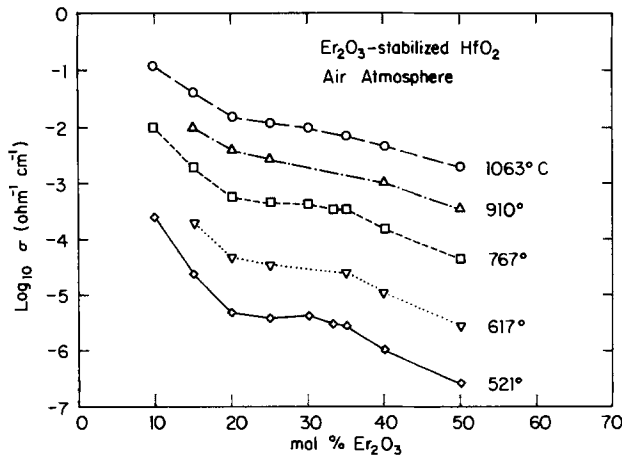


Fig. 4. Bulk electrical conductivities of ErSH solid solutions at various temperatures.

doped fluorite and defective fluorite-structure solid solutions. Several different types of defect-structure models involving clustering have been proposed for stabilized ZrO₂. Butler *et al.* (41) employed computer simulations to show that formation of clusters between low-valence dopants and charge compensating anion vacancies was energetically more favorable than formation of ordered microdomains, even though such microdomains consisting of fluorite-related compounds are commonly observed microstructural features (10). Early attempts to rationalize the decrease in conductivity with increasing anion vacancy concentration in stabilized ZrO₂ (and other defective fluorite structure compositions) have been reviewed several times (42, 43, 11) and generally have involved the introduction of configurational constraints to the motion of vacancies due to their mutual coulombic repulsion. Subbarao and Ramakrishnan (42) extended the earlier statistical models (for ThO₂ and ZrO₂ doped with CaO and YO_{1.5}) to include both anion vacancy trapping at lattice sites occupied by cation dopants and vacancy-vacancy repulsions. They assumed that only "free" vacancies (*i.e.*, those with no dopant ions as nearest neighbors) contribute to electrical conductivity, and they obtained better qualitative agreement than the earlier models. However, the conductivity reduction calculated with this model did not decrease as rapidly with increasing dopant level has been experimentally determined—presumably due to influences of long-range coulombic forces and formation of ordered phases. As Norwick (11) has indicated, the problem with a theory of conduction by only "free" vacancies is that, at high defect concentrations, connected paths of such "free" vacancies no longer exist. Nakamura and Wagner (43) considered contributions to electrical conductivity from anion vacancies which were adjacent to dopant ions (in CaO-stabilized ZrO₂). They obtained excellent quantitative agreement with experimental results by postulating that conduction proceeds by a multimode mechanism involving various degrees of association between dopant cations and oxygen vacancies and by assuming that the coordination number of the dopant cations (Ca_{Zr}²⁺) to each 24 second-nearest-neighbor anion site is 1/3.

Electrical conductivities determined in this study for various compositions are compared with those of other investigators at 1000°C in air for related rare-earth oxide (RE₂O₃)-HfO₂(ZrO₂) systems in Fig. 5. Only Johnstone, who also studied the HfO₂-Er₂O₃ system, observed a plateau in the conductivity *vs.* dopant concentration curve at such high temperatures. (Comparable data for related systems at lower temperatures where the plateaus are more pronounced are not available.) The reported conductivities of single-phase fluorite solid solutions containing between approximately 10 and 50 mol/o RE₂O₃ agree within about half an order of magnitude regardless of dopant or host and despite the different measurement techniques

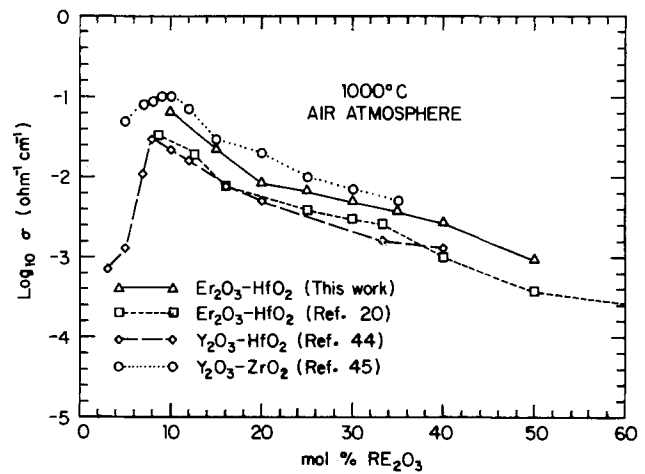


Fig. 5. Electrical conductivities of RE₂O₃-HfO₂(ZrO₂) compositions according to various investigators.

employed (complex impedance analysis was employed in this work; the other studies reported ac conductivities measured at different fixed frequencies). The variation in the electrical conductivities may possibly be due to differences in the reported sintered densities of the specimens on which the measurements were made; although, as is discussed below, the degradation of electrical conductivity due to porosity is much less than might be expected.

The activation energy for conduction increased as the dopant concentration was increased (Fig. 6). Thus, the conductivity values tended to converge at high temperatures, although not nearly as rapidly as Hohnke (46) has suggested for Y₂O₃ stabilized ZrO₂ and other materials. (Log σT has been plotted *vs.* reciprocal absolute temperature in Fig. 6 to determine the activation energy of conduction ΔH , as suggested by absolute reaction-rate theory, even though it is common practice to determine an activation energy we shall call Q from Arrhenius plots of log σ *vs.* $1/T$. Values of ΔH are approximately 0.09 eV higher than values of Q in this temperature range.¹⁴ Com-

¹⁴Schieltz *et al.* (19) have shown that $\Delta G^\ddagger = Q + C$, where $C = -R[d \ln T/d(1/T)]$.

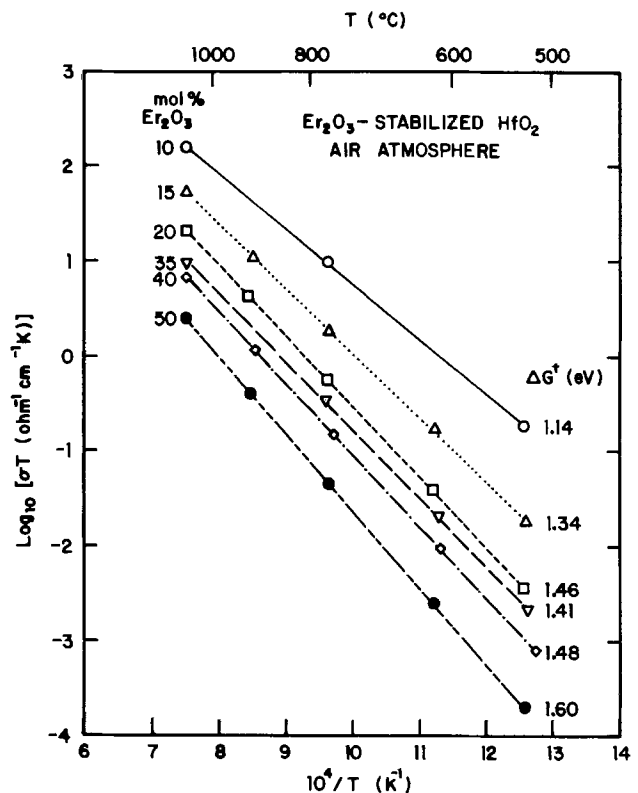


Fig. 6. Log σT vs. $1/T$ plot for selected ErSH compositions

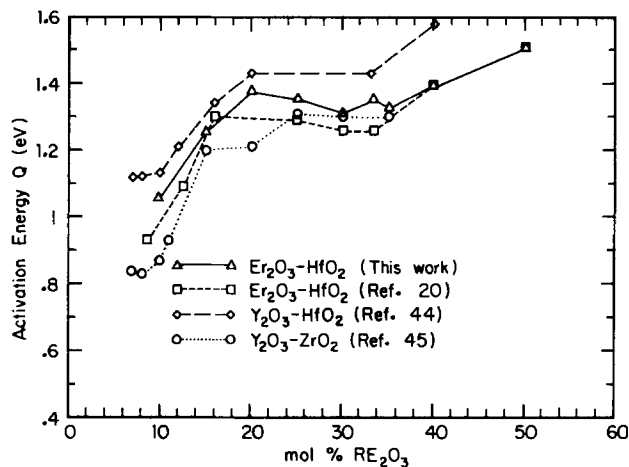


Fig. 7. Activation energies of $\text{RE}_2\text{O}_3\text{-HfO}_2(\text{ZrO}_2)$ compositions according to various investigators.

comparisons with other RE_2O_3 stabilized $\text{HfO}_2(\text{ZrO}_2)$ systems (Fig. 7) also indicate a general trend toward increased activation energies (Q) as the dopant level is increased. However, activation energy plateaus similar to the conductivity plateaus discussed previously (Fig. 5) are observed over the range of 20-35 m/o dopant for all these systems.

Effect of oxygen partial pressure.—Bulk electrical conductivities were found to be independent of P_{O_2} over the range of $1\text{-}10^{-19}$ atm for all temperatures (Fig. 8a) and nearly all compositions (Fig. 8b) investigated. This is usually an indication of predominantly ionic conduction. The 10 m/o single-crystal and 50 m/o polycrystalline ErSH compositions (*i.e.*, those near the fluorite single-phase limits) evidenced slight increases in conductivity above oxygen partial pressures of 10^{-3} atm, which may indicate the onset of p-type electronic conductivity.

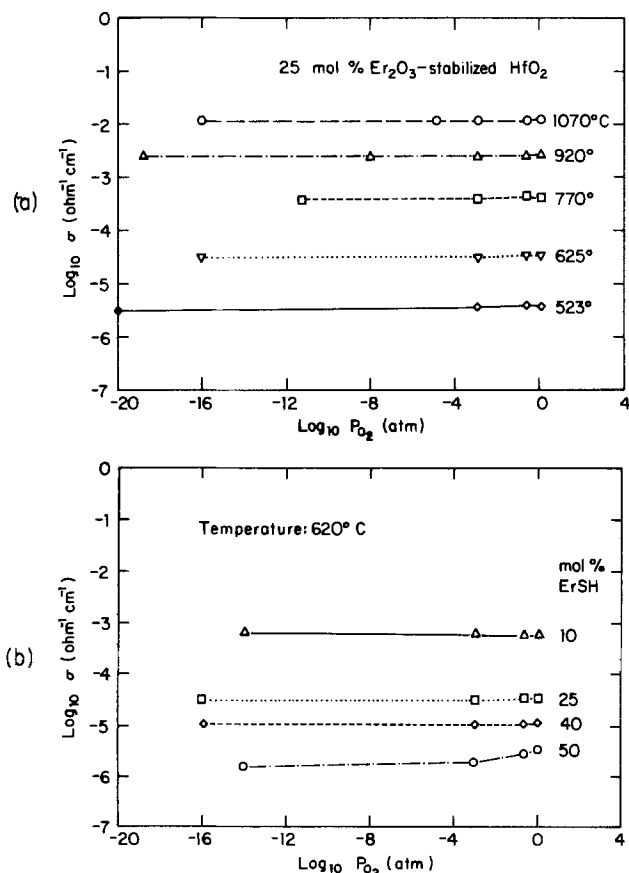


Fig. 8. P_{O_2} dependence of bulk electrical conductivities: (a) 25 m/o ErSH at various temperatures; (b) selected ErSH compositions at 620°C .

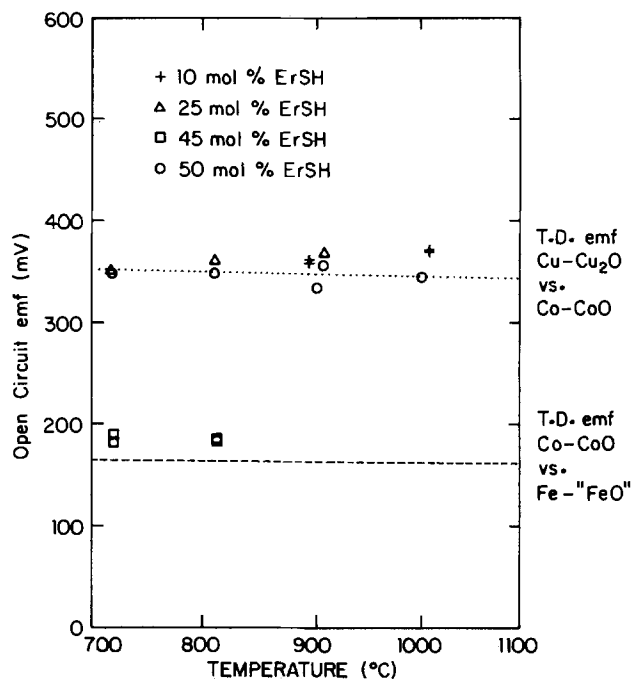


Fig. 9. Comparison of thermodynamic EMFs for various coexistence electrode pairs; measured open-circuit EMFs for selected ErSH compositions.

Open-circuit EMF results for 10, 25, 45, and 50 m/o ErSH are summarized in Fig. 9. The ionic transference numbers of these materials were confirmed to be near unity, because the measured open-circuit EMF values fell very near or even slightly above the dotted and dashed lines which represent the thermodynamic EMFs established by the indicated pairs of reversible coexistence electrodes. In particular, 10, 25, and 50 m/o ErSH are shown to be electrolytic conductors between 720° and 1020°C over the P_{O_2} range established by Cu-Cu₂O and Co-CoO electrodes (refer to Table II). Similarly, 45 m/o ErSH is shown to be an electrolytic conductor between 720° and 820°C at the lower oxygen partial pressures established by Co-CoO and Fe-FeO electrodes.

Oxygen self-diffusion coefficients (D_{Ox}) were calculated using the Nernst-Einstein equation

$$t_i k T \sigma = N z^2 e^2 D_{\text{Ox}} \quad [3]$$

where t_i is the ionic transference number (unity for a solid oxide electrolyte), k is Boltzmann's constant, T is absolute temperature, σ represents electrical conductivity, z is the valence of the diffusing species, and e signifies elementary charge. For ErSH, the concentration of oxygen ions, N , was computed from the relation

$$N = 2(x + 2) / [a_0^3(x + 1)] \quad [4]$$

where a_0 , the lattice parameter of a composition containing x mol fraction Er_2O_3 was estimated using the empirical equation¹⁵

$$a_0 \text{ (nm)} = 2.590x + 50.986 \quad [5]$$

Typical values of D_{Ox} for the ranges of temperature and ErSH compositions studied in this investigation are shown in Table III. These values for anion diffusion are

¹⁵Calculated from precision lattice parameter data measured by C. D. Wirkus, Ames Laboratory, Ames, Iowa.

Table III. Values of D_{Ox} in Er_2O_3 stabilized HfO_2

Mole fraction Er_2O_3	$D_{\text{Ox}}, \text{cm}^2 \text{s}^{-1}$		
	550°C	800°C	1050°C
0.10	1.28×10^{-9}	4.50×10^{-8}	3.88×10^{-7}
0.25	2.63×10^{-11}	2.99×10^{-9}	6.26×10^{-8}
0.40	9.52×10^{-12}	1.33×10^{-9}	2.81×10^{-8}
0.50	9.10×10^{-13}	2.40×10^{-10}	9.62×10^{-9}

approximately twenty orders of magnitude greater than estimates of cation diffusivities extrapolated from data obtained by Tesch *et al.* (25, 26), at higher temperatures.

Effects of porosity, surface finish, and aspect ratio.—Total bulk electrical conductivities (determined from complex impedance analysis) of polycrystalline specimens were virtually identical to those obtained for single crystals. Figure 10 includes data for single-crystal and polycrystalline 10 and 25 m/o ErSH of 83%-96% theoretical density, and shows that the expected degradation effect of porosity (47) was negligible. Casselton (48) has also observed virtually identical electrical conductivities for (Y₂O₃ stabilized ZrO₂) single crystals and polycrystals of 92%-95% theoretical density; this agreement was attributed to insignificant grain boundary conductivity in the polycrystals—the effect of porosity was not addressed. A number of tests were performed to determine whether surface finish or aspect ratio (*A/L*) of the specimens could have approximately offset the expected conductance degradation due to porosity. Bulk electrical conductivities were found to be the same regardless of whether electrodes were applied to unpolished (as-sintered) specimen faces or to faces polished through Linde A [Fig. 11(a)]; *i.e.*, the electrode/specimen contact area and effective *A/L* were not changed significantly by polishing. Similarly, electrical conductivities determined for 10 m/o ErSH single-crystal specimens with aspect ratios varying by up to a factor of eighteen were identical [Fig. 11(b)]; neither gas phase nor surface conduction was a problem.

Recently, Brailsford and Hohnke (36) presented an alternative to the usual equivalent circuit method of analysis and showed that intragranular pores should dilute the contribution to impedance arising from the high-conductivity bulk material, whereas intergranular porosity should augment the blocking effect of the high-impedance grain boundary regions. Because complex impedance spectroscopy separates the bulk and grain boundary contributions to the electrical conductivity, and because most porosity in the specimens used in this study appeared to be present intergranularly, it is not surprising that the electrical conductivities of porous polycrystalline and single-crystal specimens were virtually identical.

Conclusions

Erbia-stabilized hafnia (ErSH) exhibits high ionic conductivity similar to other fluorite-structure rare-earth oxide-stabilized HfO₂(ZrO₂) compositions. It is, in fact, an electrolytic conductor (*t_i* > 0.99) over wide ranges of composition, temperature, and oxygen partial pressures. The bulk electrical conductivities determined from complex impedance analysis for polycrystalline specimens are the same as those measured for single crystals; therefore, grain boundary and porosity effects are negligible. The effects of surface finish and aspect ratio of the specimens are also negligible. The electrical conductivity generally

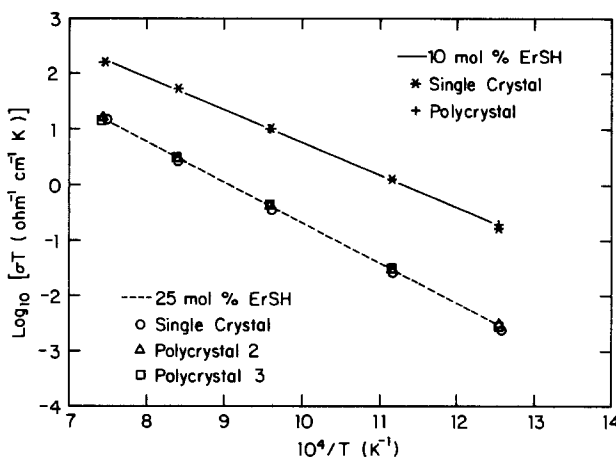


Fig. 10. Bulk electrical conductivities for single-crystal and polycrystalline specimens of two ErSH compositions.

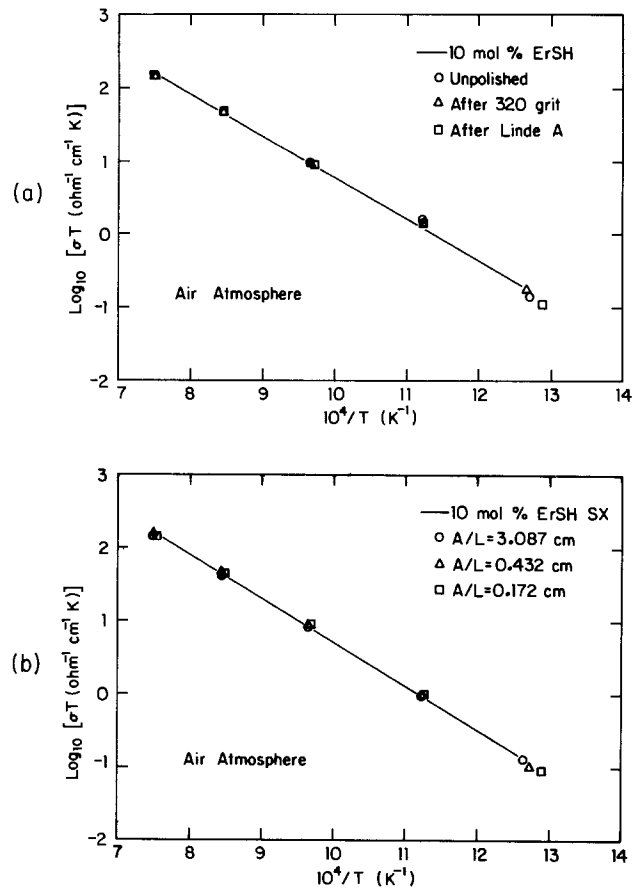


Fig. 11. Effect of specimen variables on bulk electrical conductivities: (a) surface finish; (b) aspect ratio.

decreases, and the activation energy for ionic conduction generally increases as the dopant level increases, although plateaus are observed over the composition range of 20-35 m/o Er₂O₃. (Values of electrical conductivities measured in this investigation ranged from approximately $1.2 \times 10^{-1} \Omega^{-1} \text{cm}^{-1}$ at 1070°C for 10 m/o ErSH to $2.6 \times 10^{-7} \Omega^{-1} \text{cm}^{-1}$ at 520°C for 50 m/o ErSH. Activation energies (ΔH) ranged from 1.14 eV for 10 m/o ErSH to 1.60 eV for 50 m/o ErSH.)

Manuscript submitted May 2, 1984; revised manuscript received Oct. 3, 1984.

Ames Laboratory assisted in meeting the publication costs of this article.

REFERENCES

- O. A. Songina, in "Rare Metals," p. 3, National Science Foundation, Washington, DC (1970).
- C. T. Lynch, in "High Temperature Oxides: Part II," A. M. Alper, Editor, p. 193, Academic Press, New York, (1970).
- D. Janke, *Metall. Trans. B*, **13**, 227 (1982).
- D. D. Marchant and J. L. Bates, in "The Rare Earths in Modern Science and Technology" Vol. 2, G. J. McCarthy, J. J. Rhyne, and H. B. Silber, Editors, p. 553, Plenum Press, New York (1980).
- G. W. Jordan and M. F. Berard, Iowa State University Report IS 4550, Ames Laboratory, Ames, Iowa (1984).
- T. H. Etsell and S. N. Flengas, *Chem. Rev.*, **70**, 339 (1970).
- A. Kvist, in "Physics of Electrolytes: Vol. 1," J. Hladik, Editor, p. 319, Academic Press, New York (1972).
- T. Takahashi, in "Physics of Electrolytes Vol. 2," J. Hladik, Editor, p. 989, Academic Press, New York (1972).
- C. B. Choudhary, H. S. Maiti, and E. C. Subbarao, in "Solid Electrolytes and Their Applications," E. C. Subbarao, Editor, p. 1, Plenum Press, New York (1980).
- J. A. Kilner and B. C. H. Steele, in "Nonstoichiometric Oxides," O. T. Sorensen, Editor, p. 233, Academic Press, New York (1981).
- A. S. Nowick, in "Diffusion in Crystalline Solids," G. E. Murch and A. S. Nowick, Editors, Academic Press,

- New York (1984).
12. Z. S. Volchenkova and S. F. Pal'guev, *Tr. Inst. Elektrokhim. Ural. Nauchn. Tsent. Fil. Akad. Nauk SSSR*, **5**, 133 (1964).
 13. H. A. Johansen and J. G. Cleary, *This Journal*, **111**, 100 (1964).
 14. A. K. Kuznetsov, P. A. Tikhonov, and M. V. Kravchinskaya, *Inorg. Mater. (Engl. Transl.)*, **10**, 1290 (1974).
 15. E. I. Zoz, E. B. Malets, and E. L. Karyakina, *Russ. J. Inorg. Chem. (Engl. Transl.)*, **24**, 1624 (1979).
 16. Z. S. Volchenkova and D. S. Zubankova, *Inorg. Mater. (Engl. Transl.)*, **18**, 1737 (1982).
 17. P. A. Tikhonov, L. V. Sazonova, V. B. Glushkova, and M. V. Kravchinskaya, *Russ. J. Phys. Chem. (Engl. Transl.)*, **54**, 1121 (1980).
 18. V. Patras, J. Krempasky, G. Vlasak, and F. Hanic, *Phys. Status Solidi A*, **63**, 79 (1981).
 19. J. D. Schieltz, J. W. Patterson, and D. R. Wilder, *This Journal*, **118**, 1257 (1971).
 20. J. K. Johnstone, Ph.D. Thesis, Iowa State University, Ames, Iowa (1970).
 21. D. D. Marchant, Private communication, Pacific Northwest Laboratory, Richland, Washington (1980).
 22. W. F. Schiavi, M.S. Thesis, Iowa State University, Ames, Iowa (1976).
 23. R. W. Scheidecker and M. F. Berard, *J. Am. Ceram. Soc.*, **61**, 399 (1978).
 24. R. W. Scheidecker and M. F. Berard, *ibid.*, **62**, 470 (1979).
 25. R. J. Tesch, M.S. Thesis, Iowa State University, Ames, Iowa (1981).
 26. R. J. Tesch, C. D. Wirkus, and M. F. Berard, *J. Am. Ceram. Soc.*, **65**, 511 (1982).
 27. F. M. Spiridonov and L. N. Komissarova, *Russ. J. Inorg. Chem. (Engl. Transl.)*, **15**, 445 (1970).
 28. P. Duran, C. Pascual, J.-P. Coutures, and S. R. Skaggs, *J. Am. Ceram. Soc.*, **66**, 101 (1983).
 29. G. W. Jordan, M. G. McTaggart, and M. F. Berard, Submitted to *J. Solid State Chem.*
 30. J. O. Sawyer, B. G. Hyde, and L. Eyring, *Bull. Soc. Chim. Fr.*, **1965**, 1190 (1965).
 31. S. L. Dole, R. W. Scheidecker, L. W. Shiers, M. F. Berard, and O. Hunter, Jr., *Mater. Sci. Eng.*, **32**, 277 (1978).
 32. G. W. Jordan, M. F. Berard, and C. D. Wirkus, in "Processing of Metal and Ceramic Powders," R. M. German and K. W. Lay, Editors, p. 123, The Metallurgical Society of AIME, Warrendale, PA (1982).
 33. H. J. DeBruin, A. F. Moodie, and C. E. Warble, *J. Mater. Sci.*, **7**, 909 (1972).
 34. J. D. Schieltz, Ph.D. Thesis, Iowa State University, Ames, Iowa (1970).
 35. D. B. Basler, M.S. Thesis, Iowa State University, Ames, Iowa (1972).
 36. A. D. Brailsford and D. K. Hohnke, *Solid State Ionics*, **11**, 133 (1983).
 37. J. E. Bauerle, *J. Phys. Chem. Solids*, **30**, 2657 (1969).
 38. J. R. Macdonald, in "Superionic Conductors," G. D. Mahan and W. L. Roth, Editors, p. 81, Plenum Press, New York (1976).
 39. A. K. Jonscher, *J. Mater. Sci.*, **16**, 2037 (1981).
 40. C. E. Wicks and F. E. Block, U.S. Bur. Mines, Bull., 605 (1963).
 41. V. Butler, C. R. A. Catlow, and B. E. F. Fender, *Solid State Ionics*, **5**, 539 (1981).
 42. E. C. Subbarao and T. V. Ramakrishnan, in "Fast Ion Transport in Solids," P. Vashishta, J. N. Mundy, and G. K. Shenoy, Editors, p. 653, Elsevier North Holland, Inc., New York (1979).
 43. A. Nakamura and J. B. Wagner, Jr., *This Journal*, **127**, 2325 (1980).
 44. J. Besson, C. Deportes, and G. Robert, *C. R. Seances Acad. Sci. Roum.*, **262**, 527 (1966).
 45. D. W. Strickler and W. G. Carlson, *J. Am. Ceram. Soc.*, **47**, 122 (1964).
 46. D. K. Hohnke, in "Fast Ion Transport in Solids," P. Vashishta, J. N. Mundy, and G. K. Shenoy, Editors, p. 669, Elsevier North Holland, Inc., New York (1979).
 47. D. R. Flynn, U.S. Nat. Bur. Stand., Spec. Publ. 303 (1969).
 48. R. E. W. Casselton, *Phys. Status Solidi A*, **2**, 571 (1970).

Finite Element Analysis of a Thermal-Capillary Model for Liquid Encapsulated Czochralski Growth

J. J. Derby and R. A. Brown

Department of Chemical Engineering, Massachusetts Institute of Technology, Cambridge, Massachusetts 02139

F. T. Geyling, A. S. Jordan,* and G. A. Nikolakopoulou

AT&T Bell Laboratories, Murray Hill, New Jersey 07974

ABSTRACT

A two-dimensional model for the coupled effects of heat transfer and capillarity in a liquid encapsulated Czochralski growth system is analyzed by solving the full free-boundary problem describing the temperature field in each phase, the shapes of the melt/solid and fluid/fluid interfaces, and the radius of a steadily growing crystal. Solutions are based on a finite element analysis with Newton iteration for all the variables. Heat transfer in the melt is taken to be dominated by conduction, and radiation to a uniform ambient is included for a transparent encapsulant. Calculations for a model GaAs system give reasonable predictions of crystal size and axial temperature gradient. The results are most sensitive to radiation through the encapsulant.

The liquid encapsulated Czochralski (LEC) method for growing single crystals of semiconductor materials with high vapor pressure has become an important method for producing GaAs, InP, and other semiconductor materials (1-3). Here a cylindrical crystal is pulled from the surface of a melt pool through a layer of liquid encapsulant, usually boric oxide B₂O₃, which prevents the escape of the vapor. Empirical advances in the technology of LEC growth have led to the production of moderate diameter boules of these materials with low dislocation densities (4-6); however, little progress has been made in the quantitative understanding of the transport processes important in LEC growth. The focus of this research is the de-

*Electrochemical Society Active Member.

velopment of a detailed model for the heat transport and capillarity in LEC growth of GaAs that will become the basis for both design calculations and the development of rational control algorithms.

In LEC and other free-meniscus crystal-growth techniques, the shape of the crystal and the temperature field in the melt, crystal, and encapsulant are controlled by the coupled effects of heat transfer throughout the growth system and the shapes of the melt/encapsulant and encapsulant/gas interfaces. Capillarity and the wetting of the crystal by its melt set the position and shape of the menisci. The mathematical description of this system is an extremely complicated free-boundary problem for the temperature field and the location of the fluid/fluid and

melt/crystal interfaces; the calculations of Ettouney *et al.* (7, 8) for edge-defined film-fed growth of thin silicon sheets are the only similar calculations for an entire free-meniscus crystal growth system. In this paper, we present a finite-element/Newton numerical method for simulating LEC crystal growth. The numerical scheme is modeled after the Isotherm/Newton finite-element method developed by Ettouney and Brown (9); the method was found to be the most efficient of several techniques tested in that report. The Isotherm/Newton method combines the flexibility of finite-element approximations for handling irregularly shaped domains with the efficiency of Newton's method for solving large sets of nonlinear algebraic equations.

The calculations are based on a simplified but realistic model for the growth of GaAs by LEC where heat transfer in the melt and B_2O_3 are dominated by conduction. Convective heat transfer in the melt caused by buoyancy forces and crystal rotation is insignificant on a macroscopic scale for low Prandtl number melts and even moderately intense flows, as pointed out by the hydrodynamic calculations of Langlois (10) and others (11, 12). Indeed, conduction-dominated models have been the basis for other simulations of the interaction of the crystal with a Czochralski melt pool in two-dimensional (13-16) and one-dimensional (17-19) heat-transfer models. The one-dimensional models were based on fin-type approximations to the temperature field which are strictly valid only when the temperature varies slowly across the radius of the crystal. As shown in this paper, this assumption is not met near the contact of melt, crystal, and encapsulant, and the results of these models predict unrealistic behavior for Czochralski growth systems. Neglecting convection in the B_2O_3 also seems justified because the velocity field there is mainly azimuthal, driven by crystal and crucible rotation, and has no influence on vertical and radial heat transfer.

The dependence of the crystal thickness on the pull rate for stable crystal growth was the most important feature of Czochralski growth estimated from these simplified models. The most often used result was derived by Billig (17) and is based on one-dimensional heat transfer to uniform surroundings from a growing crystal coupled to a melt which is just thermally supercooled at the solidification front moving at the solidification velocity. These assumptions lead to the result that the crystal radius is inversely proportional to the square of the pull rate. We will compare this estimate to the results from our detailed model.

Appropriate accounting of radiative heat transfer between the melt, crystal, encapsulant, and the surrounding furnace and modeling of the heat transfer through the surrounding crucible are crucial for quantitative prediction of the crystal shape and temperature fields. In the model presented here, we assume that the B_2O_3 is totally transparent to radiation emitted at the crystal and melt surfaces, and that these surfaces radiate to an average ambient temperature. While this is a considerable simplification of each of these radiative fluxes, particularly when the melt level is low and the hot crucible wall radiates to the crystal, meaningful insight into the response of the system to changes in heat-transfer conditions is obtained. The view factors along the surfaces appropriate for a particular furnace [e.g., see Ref. (18)] can be incorporated into our computational scheme; this work is currently underway. Meanwhile, the validity of the transparent model used here can only be estimated by comparison of the computed values of the axial and radial temperature gradients with the gradients measured recently in a similar liquid-encapsulated Czochralski system during the growth of InP (5). The 530 K difference in melting point between InP and GaAs and the idealized furnace configuration studied here make our comparison only approximate.

The shapes of the melt/encapsulant and encapsulant/gas menisci are determined by balancing surface tension and hydrostatic pressure, as given by the Young-

Laplace equation and by the wetting conditions at the crystal and crucible surfaces. Static meniscus shapes for different radii crystals in a Czochralski system have been calculated both exactly (20, 21) and approximately (22, 23). Heat transfer in the entire growth system determines which of these interfaces are attainable and connects the shape and stability of the crystal grown with the pull rate and thermal operating conditions of the furnace. Only the two-dimensional analysis of Crowley (16) has attempted to link the crystal radius with heat transfer through the shape of the meniscus in a conventional Czochralski system. Crowley solved a time-dependent heat-transfer model, similar in spirit to the one proposed in this paper's next section, in the regions of melt and crystal adjacent to the melt/solid interface. Heat transfer and crystal radius were linked through an approximate solution of the equation of capillary statics. Our analysis differs from the one in Ref. (16) in that the entire melt, crystal, and encapsulant for LEC growth are accounted for so that thermal boundary conditions used in the analysis can be determined from external inputs only.

Our heat-transfer model for LEC growth is described in the following section, and the finite-element method for calculating solutions to it is presented following that section. Sample calculations for the growth of GaAs in a small-scale LEC system are described in the "Results" section. The numerical method is equally applicable for modeling conventional Czochralski growth when the encapsulant layer is removed.

Thermal-Capillary Model for LEC Growth

We model the steady-state growth of a cylindrical boule of GaAs with radius R from a melt of volume \tilde{V}_m encapsulated with B_2O_3 of volume \tilde{V}_e in a crucible of inner radius R_c . The crystal is pulled continuously from the melt at a rate V_p . We imagine a quasi steady-state process in which the melt depth in the crucible, and hence the volume of the melt, changes much slower than the thermal transients in the system. Then it is valid to reconstruct the time history of a LEC growth run from a sequence of steady-state calculations with decreasing melt depths.

Our prototype LEC system is shown schematically in Fig. 1 with the notation needed to represent the melt (D_1), encapsulant (D_2), and the crystal (D_3). Each of these regions is characterized by a set of constant thermophysical properties. Segments of the boundary have been labeled as ∂D_i , where the value of i corresponds to the parts shown in Fig. 1. The energy balances and boundary conditions are put in dimensionless form by scaling lengths with the radius of the crucible, R_c , and temperature with the equilibrium melting point of the crystal, $\theta(r, z) = T(r, z)/T_i$. The dimensionless radius, melt volume, and encapsulant volume are defined by $R = R/R_c$, $V_m \equiv \tilde{V}_m/R_c^3$, and $V_e \equiv \tilde{V}_e/R_c^3$, respectively. All variables discussed below are given in dimensionless form, unless explicitly stated otherwise. The temperature field and the shapes of the melt/crystal [$H_0(r)$], melt/ B_2O_3 [$H_1(r)$], and B_2O_3 /gas [$H_2(r)$] interfaces are represented in the dimensionless cylindrical coordinate system (r, z) centered at the bottom of the crucible.

The energy balances in each of the phases are

$$K_1 \nabla^2 \theta = 0, \text{ in } D_1 \quad [1]$$

$$K_2 \nabla^2 \theta = 0, \text{ in } D_2 \quad [2]$$

$$\nabla^2 \theta - \text{Pe}(e_z \cdot \nabla \theta) = 0, \text{ in } D_3 \quad [3]$$

where $\nabla = e_r(\partial/\partial r) + e_z(\partial/\partial z)$ is the gradient operator in cylindrical coordinates and e_r and e_z are the unit vectors. In the equations above, K_i denotes thermal conductivity ratios and Pe represents the Peclet number, a dimensionless form of the steady-state growth rate; see the List of Symbols for a precise definition.

The conditions on the boundaries between melt, crystal, and B_2O_3 guarantee that temperature is continuous and that energy is conserved along each interface. At the melt/crystal interface (∂D_0), the interfacial energy balance is

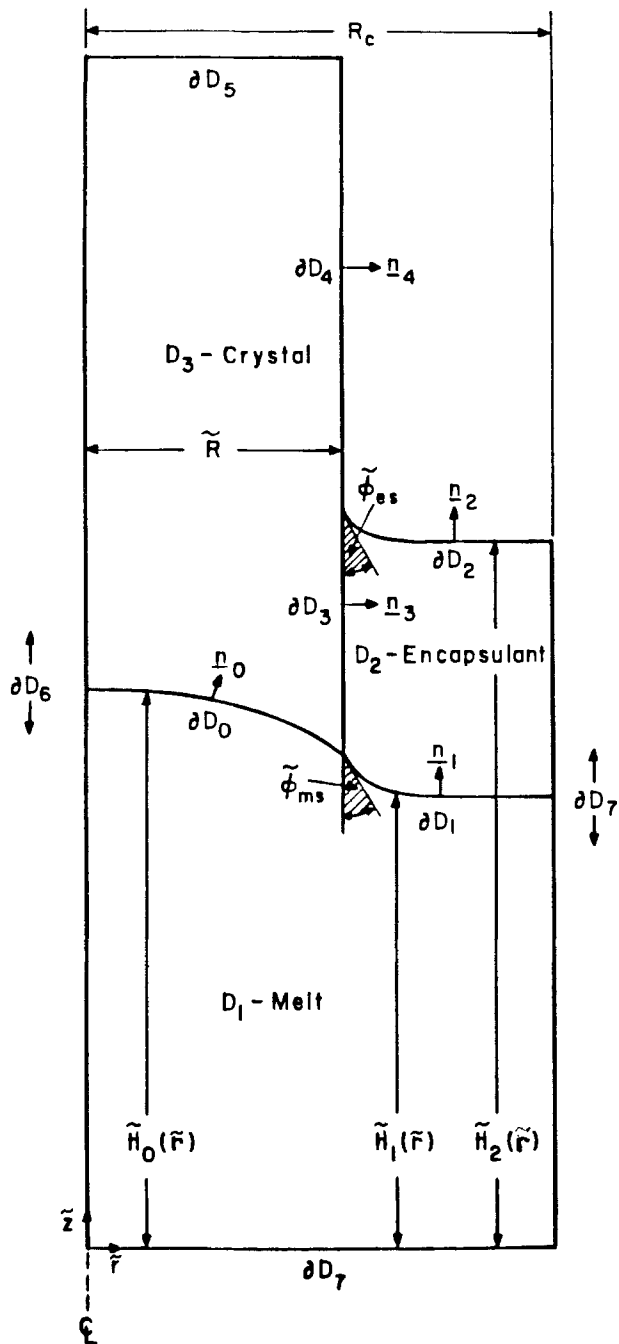


Fig. 1. Schematic of model for LEC system

$$K_1(\mathbf{n}_0 \cdot \nabla \theta)_m - (\mathbf{n}_0 \cdot \nabla \theta)_s = \text{Pe}S(\mathbf{n}_0 \cdot \mathbf{e}_z) \quad [4]$$

where the Stefan number S measures the latent heat of the phase transformation. The subscripts m and s refer to quantities evaluated in the melt and solid crystal, respectively, and \mathbf{n}_0 is the outward pointing normal along the melt/crystal interface (∂D_0) as detailed in Fig. 1.

At the melt/ B_2O_3 interface (∂D_1), the conductive fluxes between the two phases are balanced against the radiative heat loss through the glass to the surroundings. We model the B_2O_3 as being perfectly transparent so that energy radiates directly from this interface to a distant surface at temperature $\theta_a \equiv T_a/T_f$ representative of the furnace ambient. The dimensionless form of the energy balance on the segment ∂D_1 is

$$-K_1(\mathbf{n}_1 \cdot \nabla \theta) = Ra_1(\theta^4 - \theta_a^4) \quad [5]$$

where Ra_1 is the radiation number for this surface.

The energy balance along the crystal/encapsulant surface (∂D_3) also assumes the B_2O_3 to be totally transparent and nonreflective so that the condition is written as

$$-\mathbf{n}_3 \cdot \nabla \theta = Ra_3(\theta^4 - \theta_a^4) \quad [6]$$

where Ra_3 is the radiation number based on the emissivity of this surface. Heat transfer from the interfaces to the ambient include both radiation and convection as

$$-K_2(\mathbf{n}_2 \cdot \nabla \theta) = \text{Bi}_2(\theta - \theta_a) + Ra_2(\theta^4 - \theta_a^4) \quad [7]$$

$$-\mathbf{n}_4 \cdot \nabla \theta = \text{Bi}_4(\theta - \theta_a) + Ra_4(\theta^4 - \theta_a^4) \quad [8]$$

where Bi_j is the Biot number based on the heat-transfer coefficient for each surface; $j = 2$ for the encapsulant/gas interface (∂D_2) and $j = 4$ for the crystal/gas surface (∂D_4). The top of the crystal ∂D_5 is assumed adiabatic

$$\mathbf{e}_z \cdot \nabla \theta = 0 \quad [9]$$

where the length of the crystal is long enough so that the crystal has reached thermal equilibrium with the ambient.

Along the crucible wall (∂D_7) the temperature is set as

$$\theta(r, z)|_{\text{wall}} = \theta_c \quad [10]$$

where $\theta_c \equiv T_c/T_f$. In the calculation presented here, θ_c is taken to be constant, although the numerical methods generalize easily to either specified temperature or flux distributions. As is discussed below, proper accounting of the varying heat transfer through the bottom and sides of a crucible in a real crystal growth system is crucial for accurate prediction of interface shapes. The centerline of the system (∂D_6) is specified as a symmetry axis by

$$\mathbf{e}_r \cdot \nabla \theta = 0 \quad [11]$$

The boundaries of the phases are determined by the shapes of the three interfaces and the radius of the crystal. These are determined by a set of interface and contact conditions which must be satisfied simultaneously with the energy balances, Eq. [1]-[11]. The melt/solid interface shape is determined as the melting point isotherm for GaAs written as

$$\theta(r, H_0(r)) = 1 \quad [12]$$

in terms of the dimensionless location of this interface $H_0(r)$.

The melt/encapsulant and encapsulant/gas interfaces are determined from the Young-Laplace equations for each surface

$$2\mathcal{H}_i = \text{Bo}_i(H_i - \lambda_i), \quad i = 1, 2 \quad [13]$$

where \mathcal{H}_i is the mean curvature of the interface, defined as

$$2\mathcal{H}_i = \frac{\frac{d^2 H_i}{dr^2}}{\left[1 + \left(\frac{dH_i}{dr}\right)^2\right]^{3/2}} + \frac{\frac{dH_i}{dr}}{r \left[1 + \left(\frac{dH_i}{dr}\right)^2\right]^{1/2}} \quad [14]$$

where Bo_i is the Bond number and λ_i is an unknown reference pressure difference for the i th interface. The Bond number measures the relative importance of gravity and surface tension in setting the shapes of these surfaces. For the LEC GaAs system, gravity dominates the interface shape, and surface tension is important only within a small range of several millimeters from the crystal and crucible. Equation [14] has been derived assuming that the dynamic viscous and pressure forces caused by fluid motion in the encapsulant and melt are small with respect to surface-tension forces. The viscous tractions associated with the melt are certainly much smaller than those created by any motion in the B_2O_3 , where the viscosity is 300 times larger and the largest errors associated with our assumption of a hydrostatic interface originate.

The pressure differences arise because no datum location exists along either surface where the curvature is precisely zero. Thus, ambient pressure cannot be directly related to the pressures in the encapsulant and melt. The unknowns λ_i are determined by specifying the volumes of

melt and encapsulant as in other capillary problems (24). These volume constraints are for λ_1

$$\int_0^R H_0(r)rdr + \int_R^1 H_1(r)rdr = V_m/2\pi \quad [15]$$

and for λ_2

$$\int_R^1 (H_2(r) - H_1(r))rdr = V_e/2\pi \quad [16]$$

where V_m and V_e are the dimensionless volumes of melt and encapsulant, respectively.

Equations [13]-[16] are solved with edge conditions on both interfaces which specify the wetting angle ϕ of melt and encapsulant against the crystal and crucible. The B_2O_3 is taken to wet the crystal ($\phi_{es} = 5^\circ$), but not the crucible ($\phi_{ec} = 90^\circ$)

$$\left. \frac{dH_2}{dr} \right|_R = \tan(\bar{\phi}_{es} - 90^\circ) \quad [17]$$

$$\left. \frac{dH_2}{dr} \right|_1 = 0 \quad [18]$$

This last condition is incorrect because the encapsulant does wet the crucible; however, this assumption has no effect on the predictions pertaining to the growing crystal and considerably simplifies the calculations by preventing interfaces from becoming very steep at the crucible. At the three-phase contact between melt, encapsulant, and crucible, the angle is set to 90° , as for the encapsulant/gas interface, *i.e.*

$$\left. \frac{dH_1}{dr} \right|_1 = 0 \quad [19]$$

Along the melt/crystal/ B_2O_3 contact curve, the melt/solid and melt/ B_2O_3 interfaces join

$$H_0(R) = H_1(R) \quad [20]$$

and the wetting angle $\bar{\phi}_{ms}$ for equilibrium crystal growth is met

$$\left. \frac{dH_1}{dr} \right|_R = \tan(\bar{\phi}_{ms} - 90^\circ) \quad [21]$$

For GaAs, $\bar{\phi}_{ms}$ is approximately 15° (25). This last constraint, Eq. [21], overspecifies the melt/encapsulant interface meniscus unless the crystal radius is determined simultaneously. We use Eq. [21] as the condition for determining R .

Finite-Element Analysis

Equations [1]-[21] define a complex nonlinear free-boundary problem which taxes previously developed numerical methods for solution. We have developed a finite-element/Newton method based on the techniques described in Ref. (9) for simultaneously computing the interface shapes and temperature field in each phase.

The regions of melt, crystal, and encapsulant are divided into quadrilateral elements as shown in Fig. 2 for approximate locations of the three interfaces and the crystal radius. The finite-element mesh is defined so that the unknown interfaces always fall along rows of nodes. As the correct solution is approached, the mesh deforms to follow the interfaces. A continuous temperature field is defined over the regions of the system (D_1, D_2, D_3) using polynomial basis functions $\{\Phi^i(\tau, z)\}$ as follows

$$\theta(\tau, z) = \sum_{i=1}^N \alpha_i \Phi^i(\tau, z) \quad [22]$$

where the coefficients α_i are a subset of the solution vector.

Within each element, the basis functions are isoparametrically mapped into a square "unit element" defined in a coordinate system (ξ, η) where $(-1 \leq \xi \leq 1,$

$-1 \leq \eta \leq 1)$. The coordinate system (ξ, η) is related to the cylindrical coordinate system of the element by

$$r = \sum_{i=1}^9 r_i \phi^i(\xi, \eta) \quad [23]$$

$$z = \sum_{i=1}^9 z_i \phi^i(\xi, \eta) \quad [24]$$

The elemental basis functions $\{\phi^i(\xi, \eta)\}$ are standard nine-constant biquadratic Lagrangian polynomials (26), and (r_i, z_i) are the locations of the element nodes. Note that (r_i, z_i) are determined by the positions of the interfaces.

The shapes of the three unknown interfaces are interpolated by one-dimensional quadratic finite-element bases $\{\Psi^i(\tau)\}$ as

$$H_i(\tau) = \sum_{j=1}^{N_i} \beta_{ij} \Psi^j(\tau) \quad [25]$$

with N_i as the number of nodes along the i th surface, and the coefficients $\{\beta_{ij}\}$, $i = 0, 1, 2$, are determined along with R as part of the solution. As with the temperature equations, the interface equations are mapped to a one-dimensional unit element in the radial direction. The elemental quadratic polynomials $\{\psi^i(\xi)\}$ are expressed in the transformed coordinate ξ , where $-1 \leq \xi \leq 1$.

The energy balances in each phase are discretized by the Galerkin finite-element method following the formalism of the isotherm method developed in Ref. (9). This reduces the field equations and the energy balances along boundaries, Eq. [1]-[11], to a set algebraic equations in terms of the coefficients for temperature and interface shape. These equations are

$$\begin{aligned} & - \int_{D_j} K_j \nabla \Phi^i \cdot \nabla \theta \, dV - \int_{D_3} \text{Pe} \Phi^i \frac{\partial \theta}{\partial z} \, dV \\ & + \int_{\partial D_0} \text{Pe} S \Phi^i (n_0 \cdot e_z) \, dS - \int_{\partial D_1} R \alpha_1 \Phi^i (\theta^4 - \theta_a^4) \, dS \\ & - \int_{\partial D_2} [\text{Bi}_2 \Phi^i (\theta - \theta_a) + R \alpha_2 \Phi^i (\theta^4 - \theta_a^4)] \, dS \\ & - \int_{\partial D_3} R \alpha_3 \Phi^i (\theta^4 - \theta_a^4) \, dS - \int_{\partial D_4} [\text{Bi}_4 \Phi^i (\theta - \theta_a) \\ & + R \alpha_4 \Phi^i (\theta^4 - \theta_a^4)] \, dS = 0, \quad i = 1, \dots, N \end{aligned} \quad [26]$$

They are nonlinear because of the term θ^4 in the radiation condition and because of the implicit dependence of the basis functions and the Galerkin integrals on the interface shapes. We represent these equations more compactly as

$$\hat{R}_i(x) = 0, \quad i = 1, \dots, N \quad [27]$$

with \hat{R}_i representing the set of residual equations for the temperature unknowns $x_i = \alpha_i$, for $i = 1, \dots, N$.

The interface shapes are determined from the Galerkin integrals of Eq. [12] and [14], which incorporate all the wetting angle conditions except Eq. [21]. These equations are

$$\int_0^R \Psi^i [\theta(\tau, H_0(\tau)) - 1] \tau d\tau = 0 \quad [28]$$

$$- \int_R^1 \left\{ \frac{\frac{d\Psi^i}{dr} \frac{dH_1}{dr}}{\left[1 + \left(\frac{dH_1}{dr}\right)^2\right]^{1/2}} + \text{Bo}_1 \Psi^i(H_1 + \lambda_1) \right\} \tau d\tau = 0 \quad [29]$$

$$- \int_R^1 \left\{ \frac{\frac{d\Psi^i}{dr} \frac{dH_2}{dr}}{\left[1 + \left(\frac{dH_2}{dr}\right)^2\right]^{1/2}} + \text{Bo}_2 \Psi^i(H_2 + \lambda_2) \right\} \tau d\tau$$

$$- \frac{\Psi^i \tan(\bar{\phi}_{es} - 90^\circ) R}{[1 + \tan^2(\bar{\phi}_{es} - 90^\circ)]^{1/2}} = 0 \quad [30]$$

or more compactly

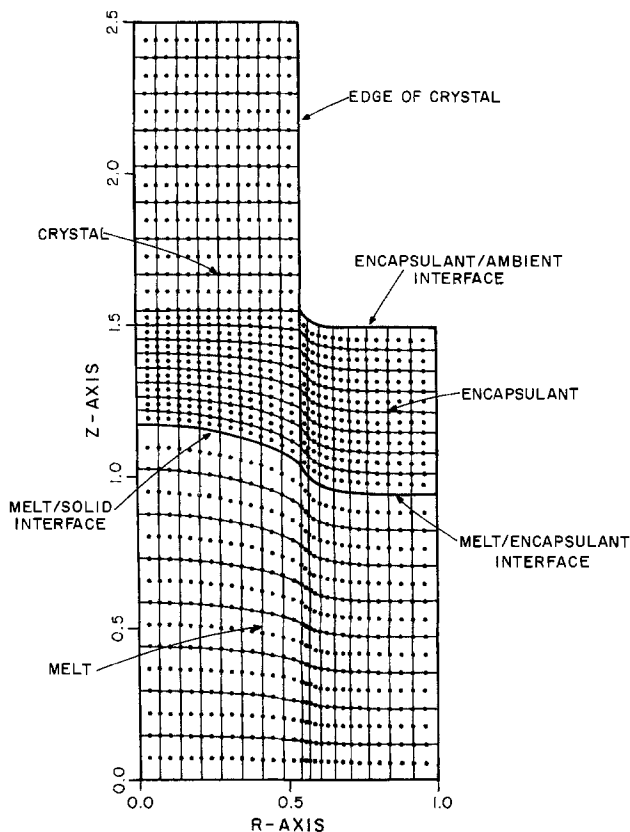


Fig. 2. Sample finite element mesh. Mesh contains 320 elements and 1361 nodes. There are a total of 1415 unknowns for this system.

$$\hat{R}_i(x) = 0, \quad i = N + 1, \dots, N_t \quad [31]$$

where x_i represent the interface unknowns $\{\beta_{ij}\}$ of Eq. [25]. The remaining volume constraints, Eq. [15] and [16], and the condition for the equilibrium growth angle, Eq. [21], form the remaining residual conditions denoted as \hat{R}_{N_t+i} , $i = 1, 2, 3$, respectively.

The complete set of nonlinear residual equations is

$$\hat{R}(x) = \hat{R}(\alpha, \beta, R, \lambda_1, \lambda_2) = 0 \quad [32]$$

where the entire vector of unknowns is $x^T = (\alpha^T, \beta^T, R, \lambda_1, \lambda_2)$. In this form, the coupling between the temperature field and the shapes of the phases is obvious, as is the

Table I. Operating parameters

Parameter	Reference case value	
	Dimensional	Dimensionless
Biot numbers (Bi_i)	—	$j = 1,3, \quad 0.0$ $j = 2,4, \quad 0.05$
Bond numbers (Bo_i)	—	$i = 1, \quad 150.0$ $i = 2, \quad 370.0$
Thermal conductivity ratios:		
Melt/solid (K_1)	—	2.0
Encapsulant/solid (K_2)	—	0.5
Radius of crucible (R_c)	5.0 cm	1.0
Radiation number (Ra_i)	—	all $i, \quad 0.8$
Stefan number (S)	—	1.0
Ambient temperature (T_a, θ_a)	1280 K	0.85
Crucible temperature (T_c, θ_c)	1660 K	1.1
Solidification temperature (T_f)	1511 K	1.0
Volume of encapsulant (V_e, V_e)	29.3 cm ³	1.18
Nominal thickness	2.5 cm	0.5
Volume of melt (V_m, V_m)	78.5 cm ³	3.14
Nominal depth	5.0 cm	1.0
Crystal pull rate (V_p, Pe)	2.3 cm/h	0.1
Equilibrium wetting angles:		
Melt/crystal/encapsulant (ϕ_{mc})	15°	—
Melt/crucible/encapsulant (ϕ_{ec})	0°	—
Encapsulant/crystal/ambient (ϕ_{ca})	5°	—
Encapsulant/crucible/ambient (ϕ_{ec})	0°	—

difficulty with convergence that one would expect with any iterative method for the solution of Eq. [32] which tries to satisfy the equations successively. The Newton method implemented here iterates simultaneously for the entire solution vector x .

At each iteration, the solution vector is updated according to the formula

$$x^{k+1} = x^k + \delta \quad [33]$$

where x^{k+1} is the new solution vector, x^k is the approximation to the solution vector from the previous iteration, and the correction vector δ is computed by solution of the matrix problem

$$\mathbf{J}\delta = -\hat{\mathbf{R}} \quad [34]$$

The Jacobian matrix \mathbf{J} has components $J_{ij} = \partial \hat{R}_i / \partial x_j$ which

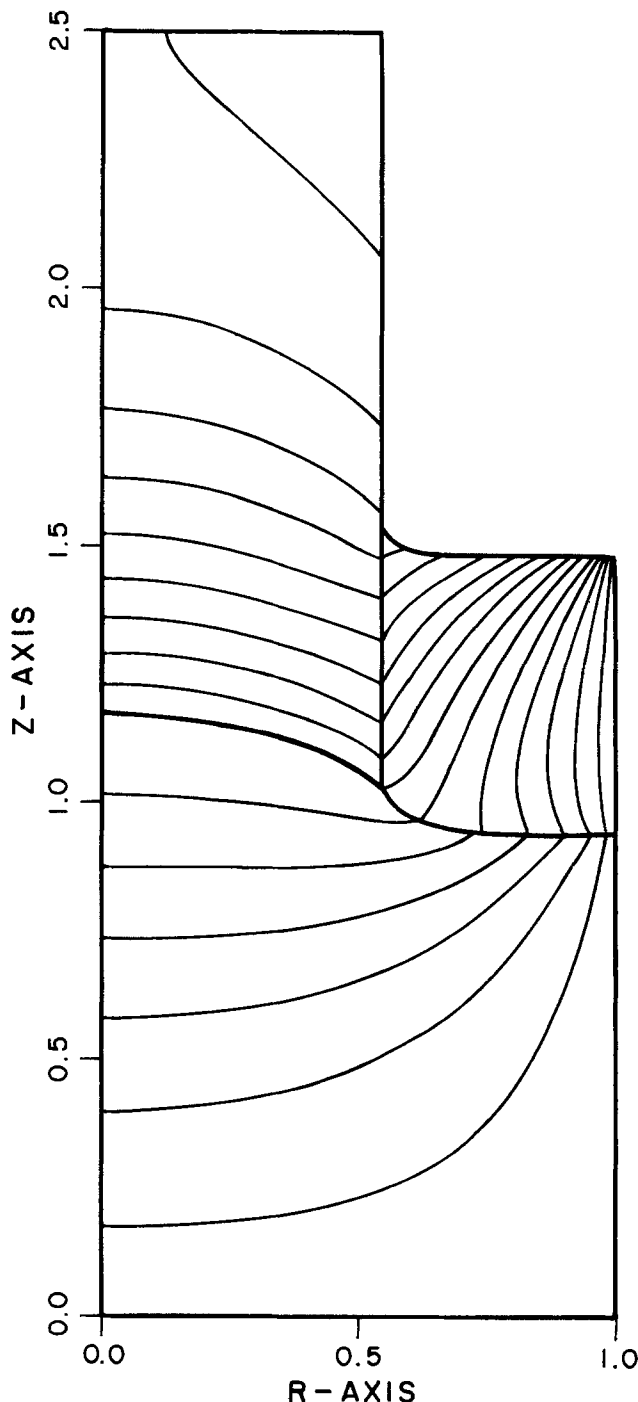


Fig. 3. Isotherms and interface shapes for reference case (parameters listed in Table I). The finite element mesh used in this calculation is shown in Fig. 2. Isotherms for all plots are incremented by 23K ($\Delta\theta = 1.5 \times 10^{-2}$).

represent the sensitivity of the residuals vector to perturbations in the solution vector and are obtained by analytical differentiation of the residual equations.

The sensitivity of the residual equation to the locations of the three interfaces includes the effects on the basis functions of displacing the finite-element mesh; these terms are computed by the isoparametric mapping technique suggested by Saito and Scriven (27) and used by others (28, 29). The evaluation of these terms is carried out in the transformed coordinates (ξ, η) where the dependence of the basis functions on the element shape is explicitly given by the mapping equations [23] and [24]. The derivatives are evaluated in closed form because the relationships between the position of the nodes (r_i, z_i) and the interface shapes and crystal radius are known. The equations for mesh construction allow the finite-element mesh to be preferentially refined near the crystal and melt/solid interfaces.

The dependence of the residual equations on the unknowns gives \mathbf{J} the "arrow" matrix structure typical of free-boundary problems (9, 27). We solve the equation set Eq. [34] by Gaussian elimination using a computer code for banded matrices with the arrow structure. For the discretization shown in Fig. 2, a mesh of 320 elements (a maximum of 16 in the radial direction and 24 in the axial dimension), the equation set had 1415 unknowns, and each iteration required 110 cpu seconds on the Cray-1 computer at Bell Laboratories; over 90% of the cpu time was used in the Gaussian elimination for this large system of equations. For all calculations reported, quadratic convergence of the residuals to the solution was observed, as is expected for Newton's method. The convergence of a particular calculation is displayed in Fig. 6 below.

Results

Calculations were carried out for a prototype of a small-scale GaAs experimental system using the 320-element mesh shown in Fig. 2. A crucible of 5 cm radius was used for all calculations; crucible and ambient temperatures were 1.1 and 0.85 times the melting point of GaAs, respectively; the reference-case pull rate was 2.3 cm/h. The dimensionless groups appropriate for modeling GaAs growth were based on our best estimates for thermophysical data and are listed in Table I. Isotherms

and interfaces for the reference case are shown in Fig. 3. The crystal filled almost half the radius of the crucible, and the melt/crystal interface was concave upward into the crystal. The elevation of the melt/encapsulant "shoulder" was approximately 0.45 cm, and the deflection stretched less than 1 cm away from the crystal surface. In the region of the three-phase contact at the edge of the crystal, the isotherms in all three phases were very curved. The existence of pronounced radial temperature gradients in this region casts doubt upon the validity of one-dimensional heat-transfer models. Radiation from the submerged surfaces through the encapsulant is an important heat-transfer mechanism. This radiative flux acts as a heat sink along the interfaces and is noted by the change in sign of the temperature gradient across the melt/encapsulant and crystal/encapsulant boundaries.

The accuracy of the finite-element calculations was estimated by repeating the calculation of the reference case for several finite-element meshes smaller than the one pictured in Fig. 2. These results are shown in Table II and show the reliability of finite-element approximations constructed with even coarser element discretizations. For example, the crystal radius predicted using a mesh with only 80 elements (391 unknowns) gave a prediction for radius that differed only 2% from the result for the 320 element mesh.

The response of the heat-transfer model to various operating and thermophysical input data was determined by varying parameters about the reference case shown in Fig. 3. These results are discussed in the subsections below for variations of pull rate (Peclet number) and radiative heat loss (radiation number).

Varying pull rate.—Increasing the pull rate increased the amount of heat liberated per unit area of the melt/solid interface and caused it to become more concave with respect to the crystal. The rearrangement of the temperature field necessary to accommodate the extra latent heat drove the melt/solid interface higher. The need to dissipate the greater release of latent heat, coupled with surface tension acting through the melt/encapsulant interface, then decreased the radius of the crystal. Results for varying the pull rate between the reference of 2.3 cm/h ($Pe = 0.1$) and 18.7 cm/h ($Pe = 0.8$) are shown in Fig. 4 as plots of the isotherms in the melt, crystal, and encapsulant. The configurations of the finite-element mesh for

Table II. Results of mesh refinement

	Mesh size		
	I 80 elements 391 unknowns	II 180 elements 823 unknowns	III 320 elements 1415 unknowns
Crystal radius, R	0.5575 (0.0222)*	0.5486 (0.0059)	0.5457
Melt/solid interface			
Centerline height, $H_0(O)$	1.1809 (0.0073)	1.1745 (0.0018)	1.1724
Deflection, $H_0(O) - H_0(R)$	0.1450 (0.0454)	0.1402 (0.0108)	0.1387
Melt/ B_2O_3 meniscus			
Height at crystal, $H_1(R)$	1.0359 (0.0021)	1.0343 (0.0006)	1.0337
Deflection, $H_1(R) - H_1(1)$	0.0989 (0.0928)	0.0925 (0.0221)	0.0905
Axial temperature gradient at melt/solid interface			
Centerline, $-(\partial\theta/\partial z)_m$	0.0928 (0.0153)	0.0919 (0.0055)	0.0914
Edge of crystal, $-(\partial\theta/\partial z)_m$	0.205 (0.0955)	0.212 (0.0230)	0.217
Crystal temperature at top of B_2O_3			
Centerline, $\theta(0, H_2(R))$	0.9231 (0.0018)	0.9218 (0.0004)	0.9214
Edge, $\theta(R, H_2(R))$	0.8977 (0.0012)	0.8969 (0.0003)	0.8966
CPU time, seconds on CRAY 1	10	—	109.8

* Numbers in parentheses are relative differences between results for smaller meshes and mesh III, computed as $|(I) - (III)|(III)$.

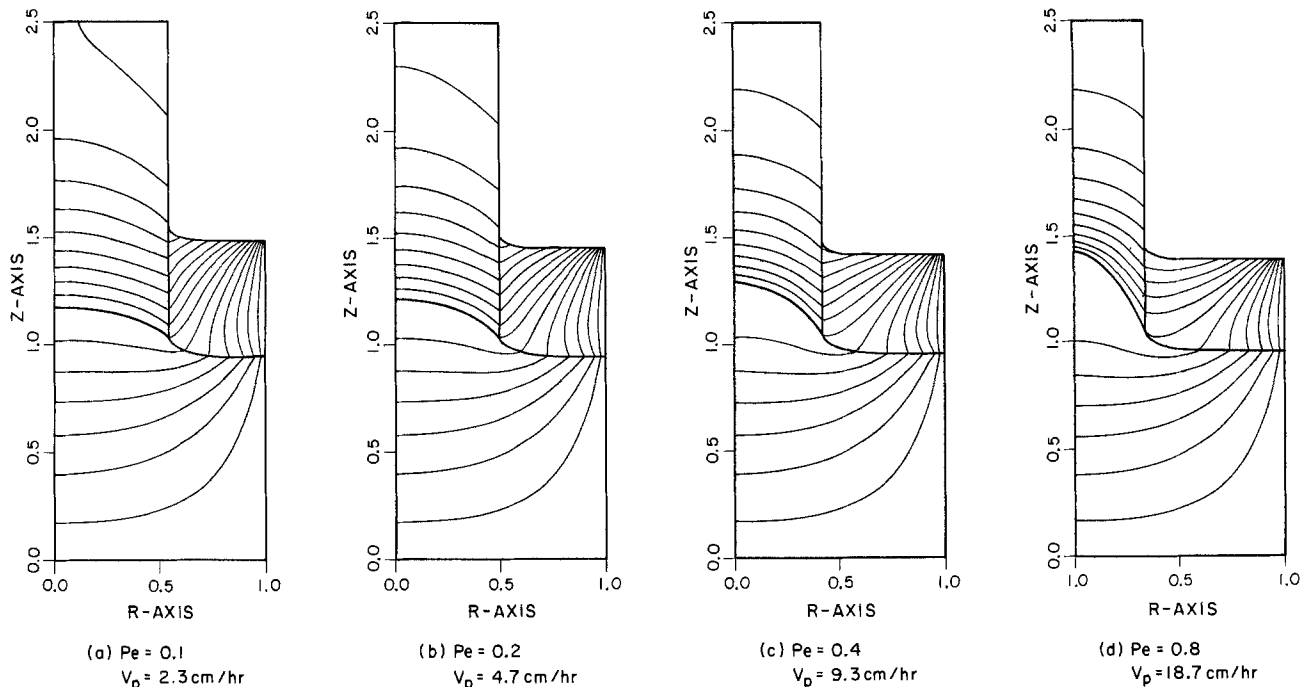


Fig. 4. Changes in isotherms and interface shapes with increasing pull rate. All other parameters are held fixed at those listed in Table I

these different pull rates are shown in Fig. 5. The convergence sequences with Newton iteration of the calculations for each growth velocity are shown in Fig. 6 for calculations with the same first guess. Each iteration displayed quadratic convergence, *i.e.*, its slope between at least the last two iterates was less than -2 .

The axial temperature profiles along the centerline ($r = 0$) and the crystal edge ($r = R$) are presented in Fig. 7. Increasing the pull rate was expected to increase the temperature gradient in the crystal and decrease the gradient in the melt at the solidification front. As seen in Fig. 7, these trends were evident at the crystal center, but not at the edge. Radiative and conductive heat transfer from the perimeter of the crystal to the surroundings was intense enough to counterbalance the local increase in heat flux caused by higher pull rates. At the pull rate of 2.3 cm/h, the gradient in the crystal at the centerline is -85.5 K/cm, a value which is reasonable for growth of GaAs. Although

the interfacial temperature gradient measured from the melt decreased with increasing Pe , it did not reach zero, even at the highest pull rate; for $Pe = 0.8$, the dimensional temperature gradient was -2.4 K/cm. Thermal supercooling must occur at a yet higher pull rate.

Over the range of pull rates, 2.3–18.7 cm/h, the crystal radius decreased from 2.73 to 1.70 cm, as shown separately in Fig. 8. The proposed relation between crystal radius and pull rate for Czochralski growth derived by Billig (17) predicted that the crystal radius was proportional to the inverse square of the pull rate, or in dimensionless form, $R \propto 1/Pe^2$. Fitting this form to the results of the model leads to the equation

$$R = 0.0776/Pe^2 \quad [35]$$

Kim *et al.* (30) suggested that the radius and pull rate of a Czochralski crystal be correlated as $R = A/(Pe + B)$, where A and B are constants set by the heat transfer in the fur-

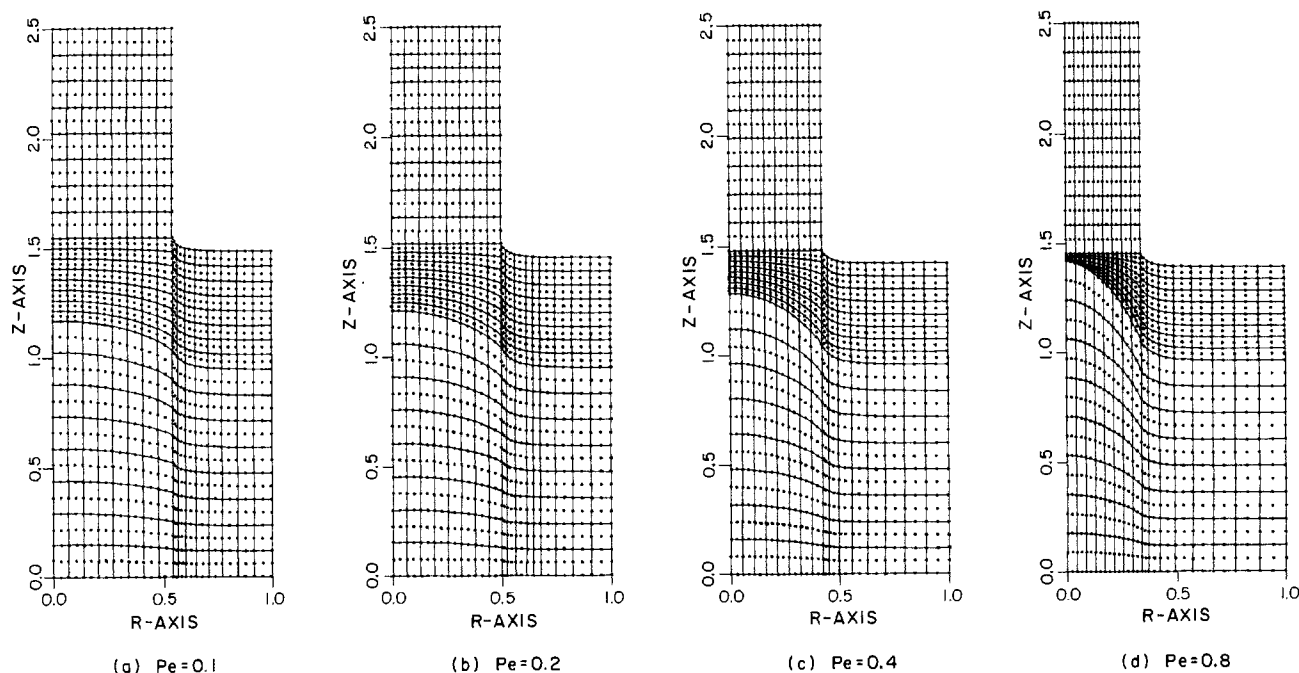


Fig. 5. Finite element meshes for the isotherms and interface shapes shown in Fig. 4

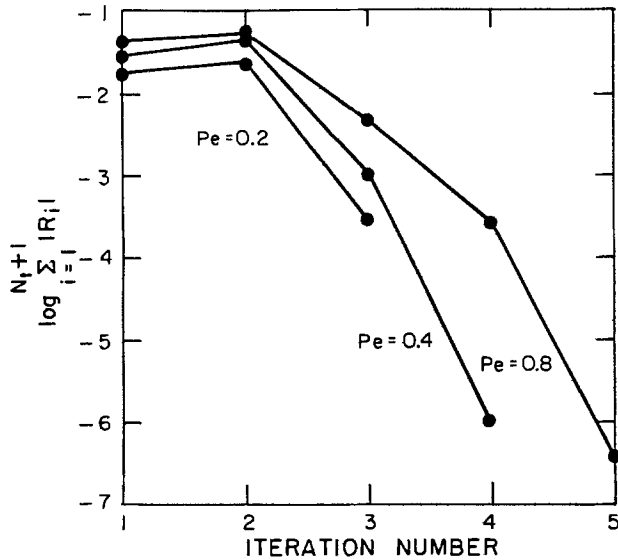


Fig. 6. Convergence of finite element solution with Newton iterations for calculations shown in Fig. 4.

nance. Fitting the data for $Pe = 0.1$ and $Pe = 0.2$ to determine A and B yields

$$R = 0.568/(Pe + 0.941) \quad [36]$$

Both of these relations are plotted, along with the finite-element results, in Fig. 8 for the entire range of growth rates. The agreement with the correlation of Kim *et al.* is excellent (the correlation coefficient was 1.0000), whereas the derivation of Billig does not fit the finite-element results at all (correlation coefficient was 0.68). This is not surprising, because Billig's assumptions of a thermally supercooled melt next to the melt/solid interface and a one-dimensional crystal temperature field in this region were not met by the results of the two-dimensional thermal-capillary model used here.

Varying volume of encapsulant.—The effect of increasing the volume of the encapsulant on the temperature field and the crystal radius was complicated by geometrical interaction of the depth of the B_2O_3 with the size of the crystal. The variation of this depth for the same volume of B_2O_3 and different growth rates is seen in Fig. 4. The depth of the layer measured at the crucible wall varied from 2.27 to 2.1 cm as the pull rate was changed from 2.3 to 18.7 cm/h.

Calculations were carried out for four volumes of encapsulant with all other operating parameters held fixed at the values for the base case; the isotherms and interfaces for these calculations are shown in Fig. 9. The calculations for $V_c = 0$ were for a system without the encapsulant layer and with radiation and convection directly from the now melt/gas meniscus to the ambient. As expected, increasing the amount of the low-conductivity encapsulant inhibited heat transfer from the melt and crystal and resulted in smaller crystals for a given pull rate (2.3 cm/h). Several other features of these calculations were much less obvious.

The melt/crystal interface was more concave with deeper encapsulant. Increasing the depth of the B_2O_3 caused a greater portion of the heat transfer from the melt to occur by conduction through the crystal. The increased heat flux into the crystal near the melt/crystal/ B_2O_3 contact caused the temperature field to be more two-dimensional there; however, the axial temperature gradient at the melt/crystal interface changed little with increasing depth of encapsulant. The magnitude of the radial temperature gradient was proportional to the curvature of the melt/crystal interface.

The axial temperature profiles along the centerline and perimeter of the crystal are shown in Fig. 10 for the base case and three different depths of B_2O_3 . The axially averaged radial temperature differences decreased with in-

creasing encapsulant depth, but the relative deflection of the melt/solid interface did not decrease because of the increased distortion of the temperature field there.

Varying radiative heat transfer.—The importance of the description of radiation through the encapsulant and to the environment was verified by the sensitivity of the results to changes in the emissivities along the surfaces. Isotherms and interface shapes are shown in Fig. 11 for two different sets of radiation numbers. The first corresponded to a factor-of-two decrease in ϵ along all radiating boundaries ($Ra_i = 0.4$), whereas the second was performed with lower emissivities on only the surfaces with the encapsulant, *i.e.*, $Ra_{1,3} = 0.4$ and $Ra_{2,4} = 0.8$. Halving the radiative flux along all the surfaces drastically decreased the radius of the crystal to $\bar{R} = 0.61$ cm [see Fig. 11(b)], flattened the melt/crystal interface, and increased the temperature gradient next to the solidification front. The added resistance to radiation along both menisci inhibited radiation through the B_2O_3 to the extent that the temperature gradients on either side of the boundaries with the encapsulant had the same sign.

Specifying the emissivity along interfaces with the B_2O_3 to be lower than along surfaces with the gas lowered the influence of radiation, but did not eliminate it, as is seen by examining the temperature gradients along the internal surfaces in Fig. 11(c). Here the crystal radius was decreased to 1.29 cm, compared to 2.73 cm for the reference case. The interface shape was flattened and the axial temperature gradient was increased. The largest value of the gradient along the center of the crystal still appeared at the solidification interface; however, the gradient was more uniform near the melt/crystal surface than in the reference case.

Discussion

The two-dimensional model for liquid-encapsulated Czochralski growth presented here is the first to give simultaneous predictions of the crystal shape and temperature field in this system. The accuracy of the calculations depends on the accuracy of the heat-transfer model used in each phase and across phase boundaries, and it depends on the reliability of the thermophysical properties used in the model. The calculations for the prototype of a small-scale growth system given in the "Results" section above predict reasonable dependence of the crystal radius on growth rate and reasonable axial temperature gradients. Müller *et al.* (5) have recently measured temperature gradients in an InP crystal growing in a LEC system. They report temperature gradients near 80 K/cm at the interface and higher gradients as the crystal is pulled through the B_2O_3 . The melt/crystal interface was convex to the crystal in all the experiments reported in Ref. (5). In our calculations, the maximum axial temperature gradient occurred at the solidification front and the interface was concave. The qualitative discrepancies between our results and these experiments may be linked to the method used by Müller *et al.* for measuring axial temperature profiles. In their experiment, the thermocouple was moved upward through the melt and incorporated into the growing crystal during seeding at the initial stages of growth. Enough crystal had not been grown, so the assumption of a uniform radius protruding from the encapsulant was not satisfied. Under these conditions, heat transfer to the ambient changes continuously with time, so the experiments can only be simulated using a transient analysis which accounts for the variations of the radius with time.

Also, the heat transfer through the crucible sides and bottom also plays an important role in setting the magnitude and curvature of the radial temperature gradients and the interface shape in a LEC system. Heat losses through the usually unheated bottom of the crucible cause the temperature at the center of the crucible to be lower than at the sides and can result in interfaces that are convex to the solid at the centerline and result in the formation of solid on the bottom of the crucible. Radiation from the wall of the bare crucible to the crystal also

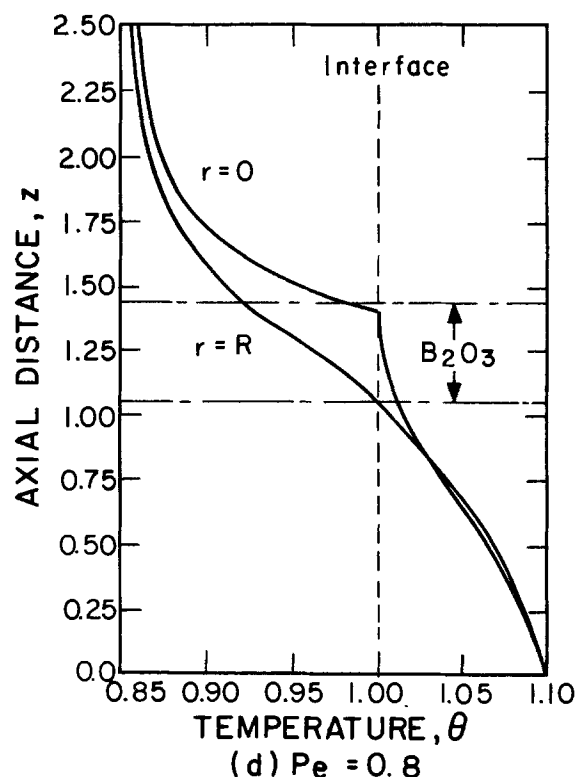
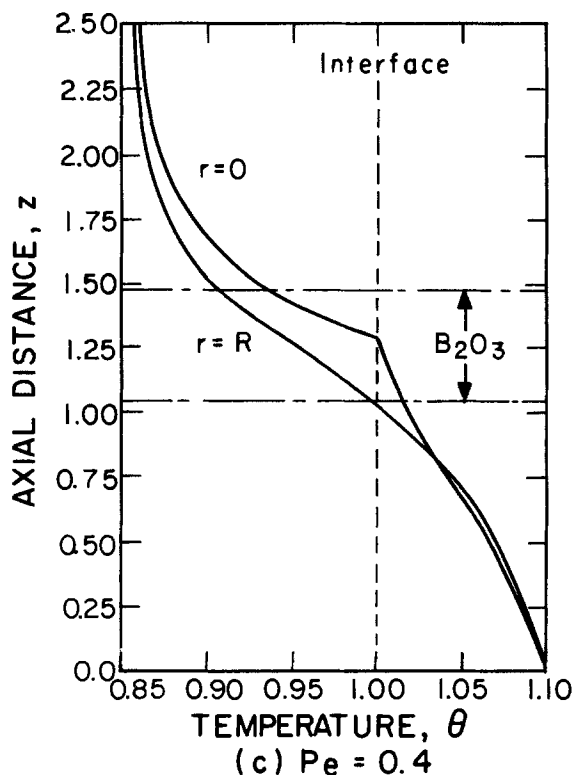
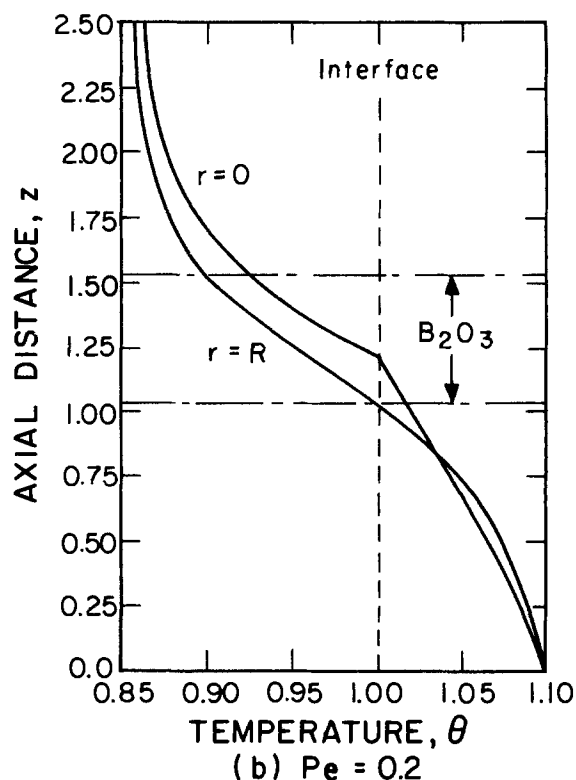
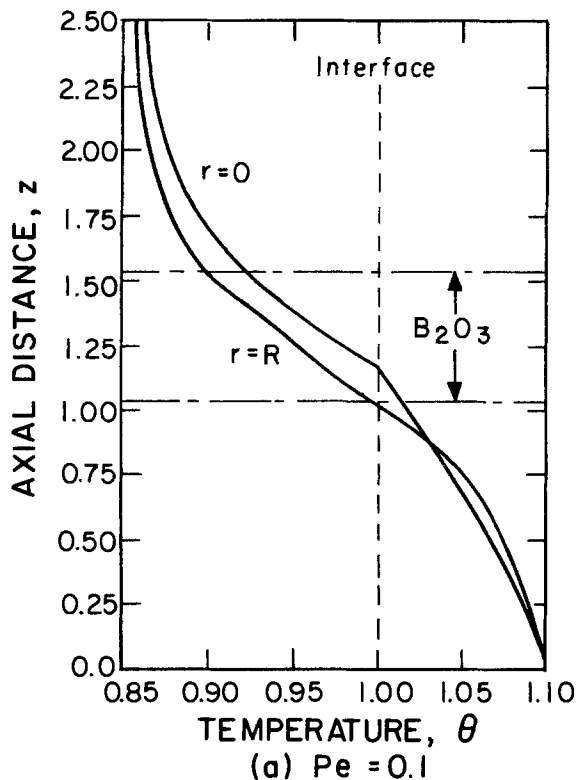


Fig. 7. Variations of axial temperature profiles along centerline ($r = 0$) and at the crystal radius ($r = R$) for pull rates of Fig. 4.

increases the temperature along the edge of the boule and makes the interface more convex. These effects may be responsible for the differences between the experimental results in Ref. (5) and our calculations, as will be discussed in another communication where the crucible is included in the calculations (31).

The simple model used for radiation through the B_2O_3 to the surroundings is a major source of error in the

finite-element modeling of LEC growth. The limited calculations on the sensitivity to the parameters in the radiation model suggest that small changes in the emissivities can make large differences in the crystal radius and in the temperature distribution in the crystal. A more complete model of radiation along these surfaces is probably needed before computations can be compared quantitatively with experiments. The most serious limitation of

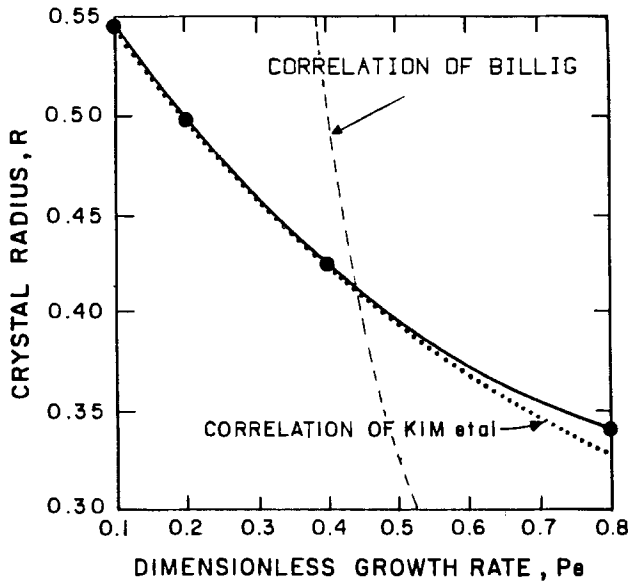


Fig. 8. Variation of crystal radius as a function of pull rate. All other parameters were held fixed at reference values. The dashed curves represent the relations of Billig, Eq. [35], and Kim et al., Eq. [36].

any modeling of LEC growth may be the lack of information on radiation through the B_2O_3 . The assumption of total transparency of this molten glass is undoubtedly poor, especially when even a small amount of water is present in the encapsulant layer (32). More complex heat-transfer models that account for absorption in the B_2O_3 and for reflected radiation are probably not justified without better experimental data on the radiation properties of B_2O_3 .

Even with the simple radiation model, the complete calculation of operating states for a LEC system is a powerful tool for understanding the interactions of various heat-transfer mechanisms and capillarity. Moreover, the numerical method described in the "Finite-Element Analysis" section above is the basis for studies of stability of the entire growth process, for the determination of transfer functions for control algorithms, and for complete simulation of transients in the process that occurs during

seeding of the melt. Each of these extensions is made feasible because of the use of the Newton iteration scheme. The Jacobian matrix used at each step in this iterative procedure is needed in computer-aided algorithms for the calculation of parametric sensitivity and stability (8, 33, 34) and in fully-implicit methods for time integration of the dynamic problem (35). Previous stability analyses for the Czochralski process and other meniscus-defined growth systems have either neglected the interactions of heat transfer with capillarity (19, 36) or have used entirely empirical expressions for the effects of heat transfer (37, 38). The stability analysis based on the entire two-dimensional model used here will give an accurate assessment of the importance of the thermal-capillary coupling in the control of conventional and liquid encapsulated Czochralski growth systems.

Acknowledgments

This research was supported by Bell Laboratories and by a National Foundation Fellowship awarded to J.J.D. We are extremely grateful to the late J. Nielson for his encouragement in the initial stages of our research.

Manuscript submitted Aug. 1, 1984; revised manuscript received Sept. 24, 1984.

AT&T Bell Laboratories assisted in meeting the publication costs of this article.

LIST OF SYMBOLS

- Bi_j Biot number = $h_j R_c / k_s$ for surface j
- Bo_i Bond number = $g R_c^2 \Delta \rho / \sigma_i$ for surface i
- Cp heat capacity [J/kg μ K]
- D_i mathematical domain: 1-melt, 2-encapsulant, 3-crystal
- ∂D_i boundaries of domains: see Fig. 1
- e_r unit radial coordinate vector
- e_z unit axial coordinate vector
- g gravitational constant [m/s²]
- h_j heat-transfer coefficient for surface j [W/m²K]
- H_i height of interface i from bottom of crucible [m]
- \bar{H}_i dimensionless interface height = H_i / R_c
- \mathcal{H}_i mean curvature of interface i
- J Jacobian sensitivity matrix
- J_{ij} individual component of Jacobian matrix
- k thermal conductivity [W/mK]
- K_i thermal conductivity ratio = k_i / k_s for region i
- n_i unit normal vector to surface i
- N number of temperature unknowns
- N_t number of temperature and interface unknowns

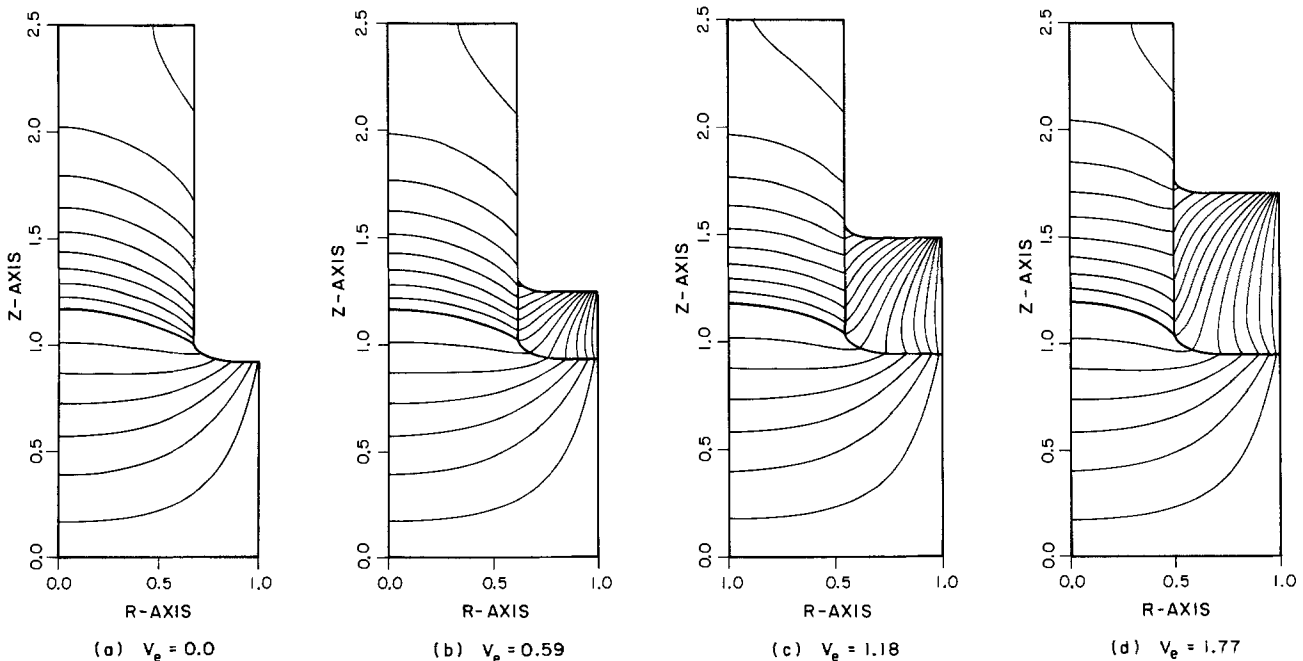


Fig. 9. Changes in isotherms and interface shapes with the volume of the encapsulant layer. All other parameters are held fixed at the values listed in Table I.

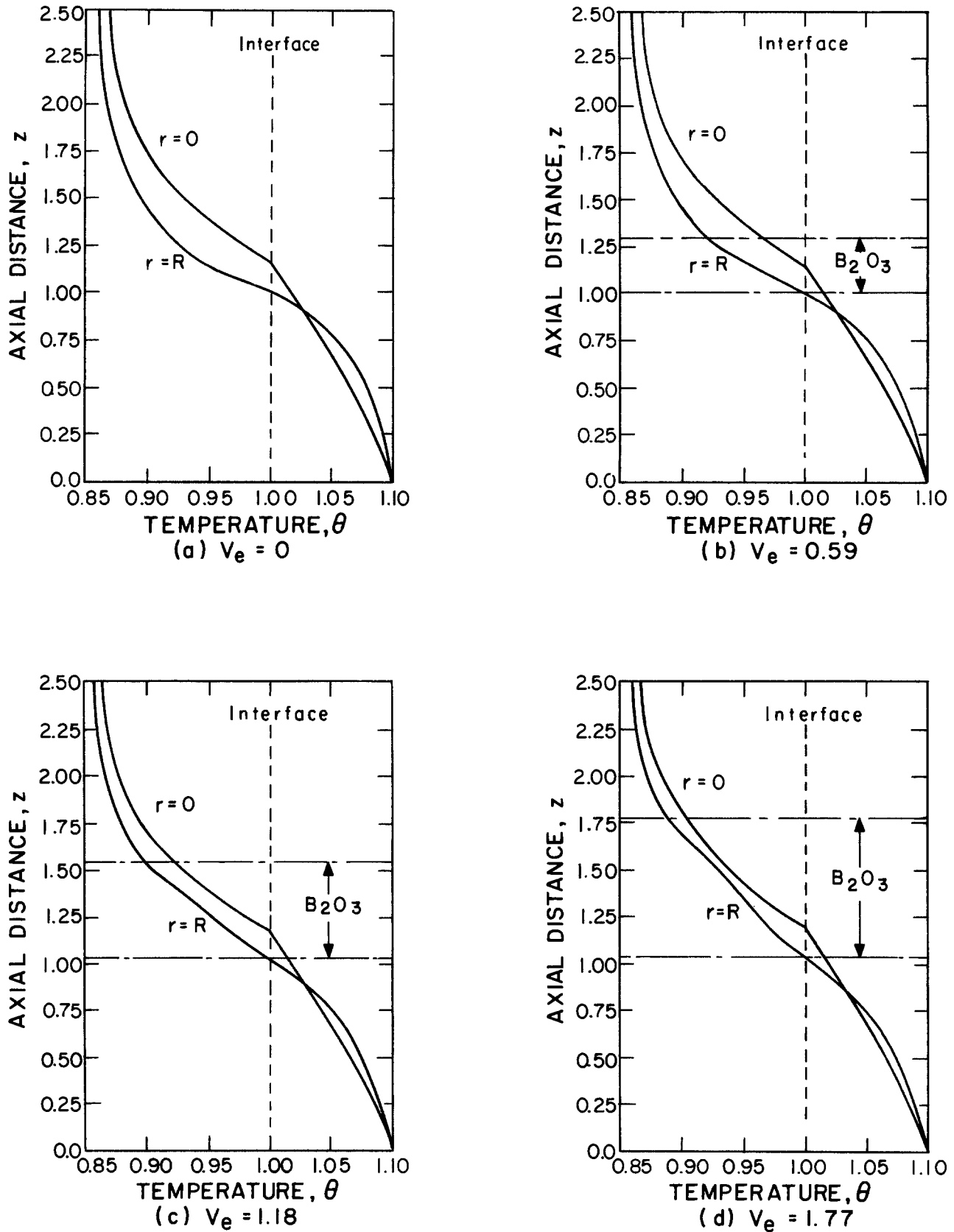


Fig. 10. Variation of axial temperature profiles along centerline and crystal radius with increasing depth of the encapsulant

p_i^0 datum pressure for interface i [N/m²]
 Pe Peclet number = $V_p R_c \rho_s C p_i / k_s$
 \tilde{r} radial coordinate measured from center of crucible [m]
 r dimensionless radial coordinate = \tilde{r} / R_c
 R crystal radius [m]
 \tilde{R} dimensionless crystal radius = \tilde{R} / R_c
 R_c crucible radius [m]
 \mathbf{R} residual vector

\hat{R}_i individual component of residual vector
 Ra_i radiation number = $\sigma^* \epsilon_i R_c T_i^3 / k_s$ for surface i
 S Stefan number = $\Delta H_f / C p_s T_i$
 T temperature [K]
 T_s solidification temperature [K]
 V_e volume of encapsulant [m³]
 \tilde{V}_e dimensionless volume of encapsulant = \tilde{V}_e / R_c^3
 \tilde{V}_m volume of melt [m³]

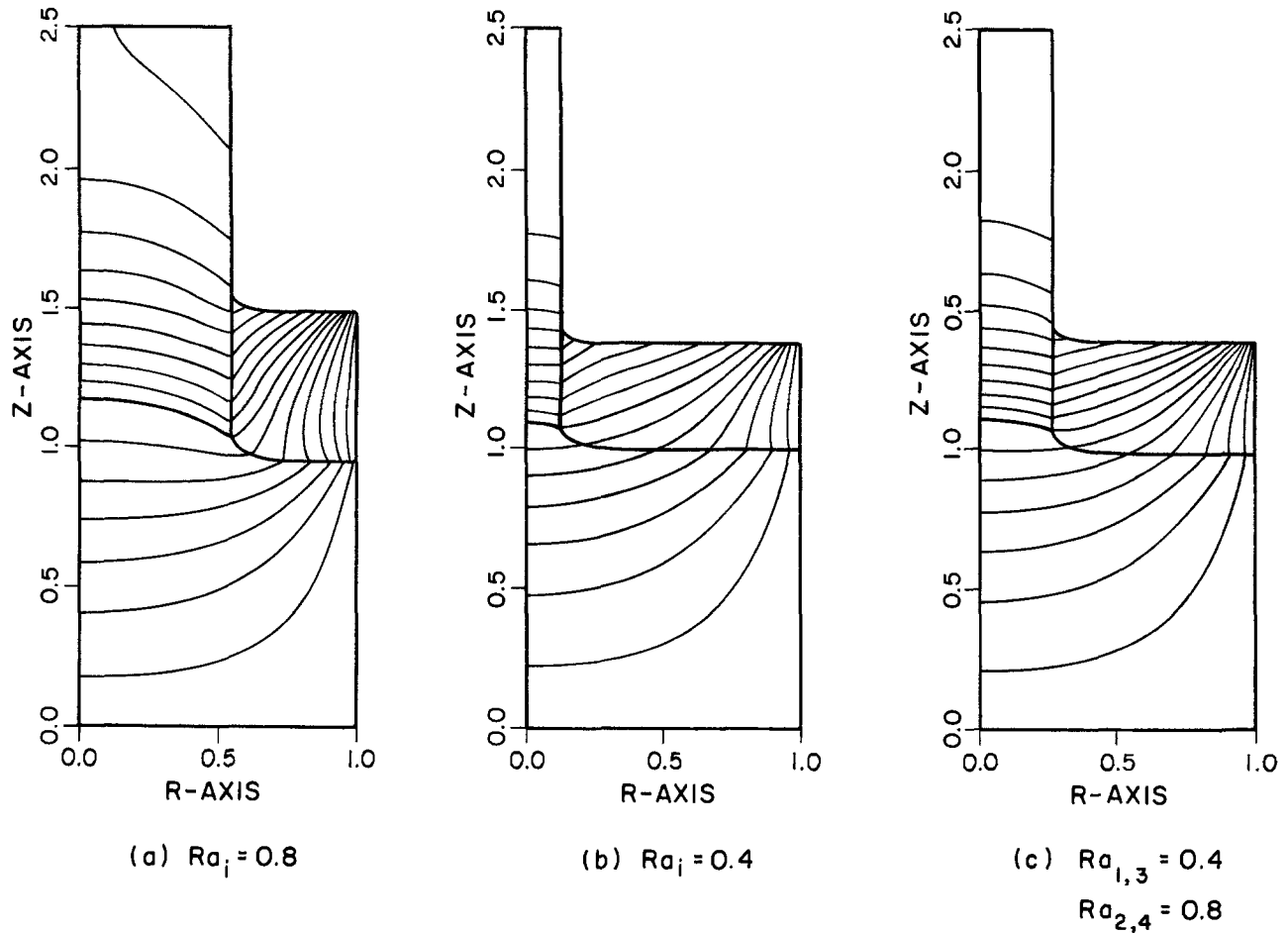


Fig. 11. Variation of isotherms and interface shapes with a decrease in the radiation numbers to $Ra_i = 0.4$ on all surfaces (b) and $Ra_{1,3} = 0.4$ and $Ra_{2,4} = 0.8$ (c).

V_m dimensionless volume of melt = \tilde{V}_m/R_c^3
 V_p steady-state crystal pull rate [m/s]
 x vector of solution unknowns
 x_i individual component of solution unknowns vector
 z axial coordinate measured from bottom of crucible [m]
 z dimensionless axial coordinate = \tilde{z}/R_c

Greek symbols

α temperature unknowns vector
 α_i individual component of temperature unknowns vector
 β interface unknowns vector
 β_{ij} j th component of unknowns vector for interface H_i
 δ correction vector used in Newton's method
 ΔH_f heat of fusion [J/kg]
 $\Delta \rho_i$ density difference across interface i [kg/m³]
 ϵ_i emissivity of surface i
 η axial coordinate in unit element
 θ dimensionless temperature = T/T_f
 λ_i dimensionless reference pressure = $p_i^0/\Delta \rho_i g R_c$
 ξ radial coordinate in unit element
 ρ density [kg/m³]
 σ_i surface tension for surface i [N/m]
 σ^* Stefan-Boltzmann constant [W/m²K⁴]
 ϕ equilibrium wetting angles
 ϕ^i two-dimensional elemental polynomial basis functions
 Φ^i two-dimensional global polynomial basis functions
 ψ^j one-dimensional elemental polynomial basis functions
 Ψ^j one-dimensional global polynomial basis functions

Superscripts

i, j numerical indexes
 k numerical index denoting iteration number
 T transpose of vector

Subscripts

a ambient
 c crucible

e encapsulant
 i, j indexes denoting surface, domain, or equation numbers
 m melt
 s solid

REFERENCES

1. E. P. A. Metz, R. C. Miller, and R. Mazelsky, *J. Appl. Phys.*, **33**, 2016 (1962).
2. J. B. Mullin, B. W. Straugham, and W. S. Brockell, *J. Phys. Chem. Sol.*, **26**, 782 (1965).
3. L. M. Foster, in "Preparation and Properties of Solid State Materials," Vol. 3, W. R. Wilcox, Editor, p. 153, Marcel Dekker, New York (1977).
4. K. Terashima and T. Fukudo, *J. Cryst. Growth*, **63**, 423 (1983).
5. G. Muller, J. Volkl, and E. Tomzig, *ibid.*, **64**, 40 (1983).
6. G. Jacob, in "Proceedings of the Semi-Insulating III-V Material Conference," p. 2, Evian (1982).
7. H. M. Ettouney and R. A. Brown, *J. Cryst. Growth*, **62**, 230 (1983).
8. H. M. Ettouney and R. A. Brown, *ibid.*, Submitted.
9. H. M. Ettouney and R. A. Brown, *J. Comp. Phys.*, **49**, 118 (1983).
10. W. E. Langlois, *Physiochem. Hydrodynamics*, **2**, 245 (1981).
11. C. J. Chang and R. A. Brown, *J. Cryst. Growth*, **63**, 343 (1983).
12. M. J. Crochet, P. J. Wouters, F. T. Geyling, and A. S. Jordan, *J. Cryst. Growth*, **65**, 153 (1983).
13. N. Kobayashi, in "Preparation and Properties of Materials," Vol. 6, W. R. Wilcox, Editor, p. 119, Marcel Dekker, New York (1981).
14. A. S. Jordan, R. Caruso, and A. R. von Neida, *Bell Syst. Tech. J.*, **59**, 593 (1980).
15. M. Duseaux, *J. Cryst. Growth*, **61**, 576 (1983).
16. A. B. Crowley, *IMA J. Appl. Math.*, **30**, 173 (1983).
17. E. Billig, *Proc. R. Soc. London, Ser. A*, **229**, 346 (1955).
18. S. N. Rea, *J. Cryst. Growth*, **54**, 267 (1981).
19. A. Van der Hart and W. Uelhoff, *ibid.*, **51**, 251 (1981).
20. C. Huh and L. E. Scriven, *J. Colloid Interface Sci.*, **30**, 323 (1969).
21. E. A. Boucher and H. J. Kent, *Proc. R. Soc. London, Ser. A*, **356**, 61 (1977).

22. S. V. Tsvinski, *Inzh.-Fiz. Zh. Akad. Nauk. Belorussk. SSR*, **5**, 59 (1962).
23. D. T. J. Hurle, *J. Cryst. Growth*, **63**, 13 (1983).
24. R. A. Brown, F. M. Orr, Jr., and L. E. Scriven, *J. Colloid Interface Sci.*, **73**, 76 (1980).
25. I. Y. Kashkooli, Z. A. Munir, and L. Williams, *J. Mater. Sci.*, **9**, 538 (1974).
26. G. Strang and G. L. Fix, "An Analysis of the Finite Element Method," p. 87, Prentice Hall, Englewood Cliffs, NJ (1973).
27. H. L. Saito and L. E. Scriven, *J. Comput. Phys.*, **42**, 53 (1981).
28. C. J. Chang and R. A. Brown, in "Numerical and Methodologies in Heat Transfer," T. Shih, Editor, p. 283, Hemisphere Press, New York (1983).
29. S. Kistler and L. E. Scriven, in "Computers in Polymer Processing," J. R. A. Pearson and S. M. Richardson, Editors, Chap. 7, Applied Science Publishers, London (1983).
30. K. M. Kim, A. Kran, P. Smetana, and G. H. Schwuttke, *This Journal*, **130**, 1156 (1983).
31. J. J. Derby and R. A. Brown, Submitted to *J. Cryst. Growth*.
32. Technical Brochure, RASA Industries, Ltd., Tokyo, Japan.
33. R. A. Brown, L. E. Scriven, and W. J. Silliman, in "Methods in Nonlinear Dynamics," P. Holmes, Editor, p. 289, SIAM, Philadelphia (1980).
34. Y. Yamaguchi, C. J. Chang, and R. A. Brown, *Philos. Trans. Soc. London, Ser. A*, **312**, 519 (1984).
35. J. J. Derby and R. A. Brown, Submitted to *Chem. Engng. Sci.*
36. T. Surek, *J. Appl. Phys.*, **47**, 4384 (1976).
37. T. Surek and S. R. Coriell, *J. Cryst. Growth*, **37**, 253 (1977).
38. V. A. Tatarchenko and E. A. Brener, *ibid.*, **50**, 33 (1980).

Infrared, Raman, and X-Ray Diffraction Studies of Silicon Oxide Films Formed from SiH₄ and N₂O Chemical Vapor Deposition

Minoru Nakamura, Yasuhiro Mochizuki, and Katsuhisa Usami

Hitachi Research Laboratory, 4026 Kuji-cho, Hitachi 319-12, Japan

Yoshiko Itoh and Tadashi Nozaki

Rikagaku Kenkyusho, Wako, Saitama 351, Japan

ABSTRACT

Infrared, Raman, and x-ray diffraction measurements were used to study films obtained by chemical vapor deposition from SiH₄ and N₂O gases. A wide range of N₂O/SiH₄ ratios (γ) were used to examine the existing phases inside the film, oxidation states of the oxide phases, and crystallite growth of the silicon phase on subsequent heat-treatment. The as-deposited films were composed of an amorphous genuine silicon phase and an oxide phase SiO_x, with x values from 1.38 to 1.63 for γ from 0.5 to 24. Reconstruction of both phases occurred by subsequent heat-treatment in N₂ atmosphere. The sizes of the silicon crystallites formed in the silicon phase by subsequent heat-treatment were related to oxygen content of the film. Comparing reported electric and optical properties with results obtained in this study, we proposed a new model of the films, in which the silicon and oxide phases formed a complicated three-dimensional network. The model consistently explained all the observed film properties.

Much interest has been directed towards chemical vapor deposited silicon oxide films, obtained from SiH₄ and N₂O gases, which can be used for passivation (1-2), nonvolatile memory devices (3), and heterojunction transistors (4). Such films are commonly referred to by the acronym SIPOS (semi-insulating polycrystalline silicon), or silicon-rich silicon dioxide. Through investigations using transmission electron microscopy (TEM) (5, 6), reflection high-energy electron diffraction (RHEED) (7), x-ray photoelectron spectroscopy (XPS) (6, 8), Raman (9), infrared (IR) (10), and IR-visible absorption (11) measurements, the structural image of the films has become clear to a certain extent. However, interesting points still remain regarding oxidation state of the films, morphology of the silicon phase, and structural arrangement of silicon and oxide phases when both are present in the films.

In this paper, accurate determinations of film oxygen content were made by radioactivation analysis. These results formed the basis for evaluation of film oxidation state and existing phases in the as-deposited film. Changes in oxidation state of the oxide phase and morphology of the silicon on subsequent heat-treatment of specimens in a N₂ atmosphere were examined through IR absorption, Raman, and x-ray diffraction measurements. A model was proposed to explain the electrical and optical properties of the films.

Experimental

Film deposition.—An ordinary chemical vapor deposition reactor was used to deposit the films at atmospheric pressure by reactive decomposition of silane (SiH₄) and nitrous oxide (N₂O) diluted in N₂ gas. The deposition tem-

perature was 650°C. In order to obtain a range of oxygen contents in the films, the reactant gas flow ratios N₂O/SiH₄ (designated γ) were varied from 0 to 24. As a matter of convenience for radioactivation analysis of oxygen, the film thickness was varied from 0.22 to 0.75 μ m. High purity (111) FZ silicon plates (oxygen content <10¹⁷ at./cm³) with thicknesses of 300 μ m and 1 mm were used as film substrates for radioactivation analysis and IR absorption measurements, respectively; 1 mm thick fused silica was used as a substrate for the Raman and x-ray diffraction measurements.

Radioactivation analysis.—For accurate determination of film oxygen content, a radioanalytical method using activation by the ¹⁶O(³He, p)¹⁶F reaction was employed. Steam oxidized silicon dioxide film 1.05 μ m thick and having a density of 2.12 \pm 0.02 g/cm³ was used as a reference. Details for activation analysis are given in the literature (12). The maximum error in the oxygen content (atomic percent [a/o]) was estimated to be within 10%.

Infrared measurements.—The IR spectra were recorded from 4000 to 400 cm⁻¹ by a Hitachi spectrometer (EPI-G3), with the reference being the same as the specimen (1 mm thick silicon plate).

Raman measurements.—For the Raman measurements, an argon ion laser line of 514.5 nm wavelength with 100-300 mW power was used as an incident beam with a spot diameter of about 10 μ m. The spectrometer was a JRS-400D (JEOL). The maximum spectral resolution was about 1.0 cm⁻¹, and the tracking error in the wave number was 0.3 cm⁻¹. The Raman scattering was measured with a backscattering configuration.

X-ray diffraction measurements.—In order to investigate sizes of the silicon crystallites in the film, x-ray diffraction patterns were taken of the film. The diffractometer was a Rigaku Geigerflex RAD-rA, and the incident x-ray line was $\text{CuK}\alpha$.

Results

Oxygen content as a function of gas flow ratio γ .—Oxygen content of the as-deposited films as obtained by radioactivation analysis are summarized in Table I. The film thickness measured by Taylor Hobson Talystep I are also given in the same table. The oxygen content increased with the gas flow ratio γ . The relationship between oxygen content α (atomic percent) and γ was approximately given by $\alpha = \beta \log \gamma + \epsilon$, where β and ϵ were about 11 and 20, respectively. This expression differed slightly from that given by Mochizuki *et al.* (2), probably owing to differences in the reactors employed. The oxygen content at $\gamma = 0$ was not zero, owing to oxygen contamination of the reactor walls and gas transfer tube.

Infrared spectra.—The IR absorption spectra for as-deposited films are shown in Fig. 1. The peaks located between $1000\text{--}1100\text{ cm}^{-1}$ shifted slightly to higher wave number with increasing γ , while the 875 cm^{-1} peak remained constant. The 800 cm^{-1} peak was scarcely observable for the $\gamma = 24$ specimen. As shown in Fig. 2, when there was no internal stress in a homogeneous oxide film SiO_x , there was a simple relation between x and the main peak position (between $980\text{--}1082\text{ cm}^{-1}$) (13). Comparing Fig. 1 with Fig. 2, the x values were from 1.38 to 1.63 for the films prepared from $\gamma = 0.5\text{--}24$, which were in good agreement with the $x = 1.4$ value obtained by XPS (5). Assuming that the whole film was composed of a homogeneous oxide, the oxygen contents were accordingly given from 58 to 62 a/o. These values were significantly different from those given in Table I, suggesting that the films were not composed simply of a homogeneous oxide phase.

X-ray, electron diffractions, and Raman spectra.—In order to investigate the phase (or phases) of the films, x-ray and electron diffraction patterns and Raman spectra of the films were measured. The x-ray and electron diffraction patterns indicated that the constituent phase (or phases) of all the films was amorphous, which was in agreement with the findings of Nagashima and Kubota (14) that the silicon phase was amorphous for chemical vapor deposition from SiH_4 under 650°C . As shown in Fig. 3, a broad but obvious peak was observed around 480 cm^{-1} in the Raman spectra for all the films on both silicon and fused silica substrates. It coincided with that of the amorphous silicon phase in the Si:H film prepared in a hydrogen plasma (15). Accordingly, the peak could be assigned to the amorphous silicon phase. Based on the IR and Raman results, the films were regarded as composed of a genuine silicon phase and a silicon oxide phase SiO_x , with $x = 1.38\text{--}1.63$.

Calculation of oxygen content from IR absorption.—When the films were composed of only genuine silicon and SiO_x phases, their oxygen content could be obtained

Table I. Gas flow ratio, thickness, oxygen content, and volume ratio of SiO_x . Deposition temperature: 650°C

No.	Gas flow ratio (γ)	Thickness (μm)	Oxygen content ^a α (a/o)	Volume ratio of SiO_x ^b (R)
1	0	0.75	2.2	0.028
2	0.5	0.57	17.5	0.23
3	1	0.53	18.5	0.29
4	2	0.50	23.3	0.35
5	4	0.31	29.7	0.38
6	8	0.27	35.9	0.47
7	16	0.36	37.2	0.58
8	24	0.22	41.8	0.63

^a Measured by radioactivation analysis.

^b See Results section.

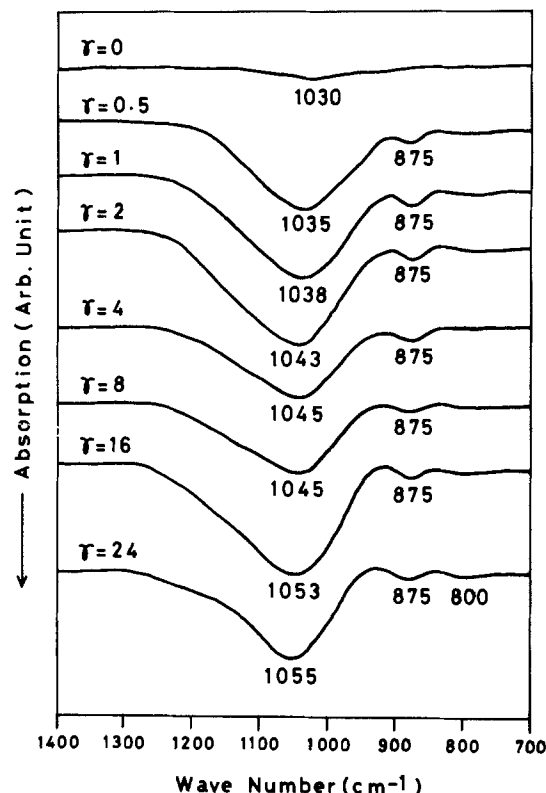


Fig. 1. Infrared absorption spectra for specimens deposited on silicon substrate.

independently of radioactivation analysis by using IR absorption intensities. The IR absorption intensities per unit thickness of integrated optical density between $700\text{--}1400\text{ cm}^{-1}$ for homogeneous oxide SiO_x has already been given as a function of the position (cm^{-1}) of the infrared main peak (13). The intensity ratio relative to SiO_2 is also shown in Fig. 2. From this relation, together with the integrated intensity between $700\text{--}1400\text{ cm}^{-1}$ of the experimental spectra shown in Fig. 1, R , the volume ratio of SiO_x to the entire film, was easily calculated. The values are summarized in Table I. The R values increased with increasing oxygen content. Using this ratio, the oxygen content of the film as an atomic ratio was given by $Rx B_{\text{SiO}_x} / [R(1+x)B_{\text{Si}} \rho_{\text{SiO}_x} + (1-R)(B_{\text{Si}} + x \cdot B_{\text{O}}) \rho_{\text{Si}}]$, where B

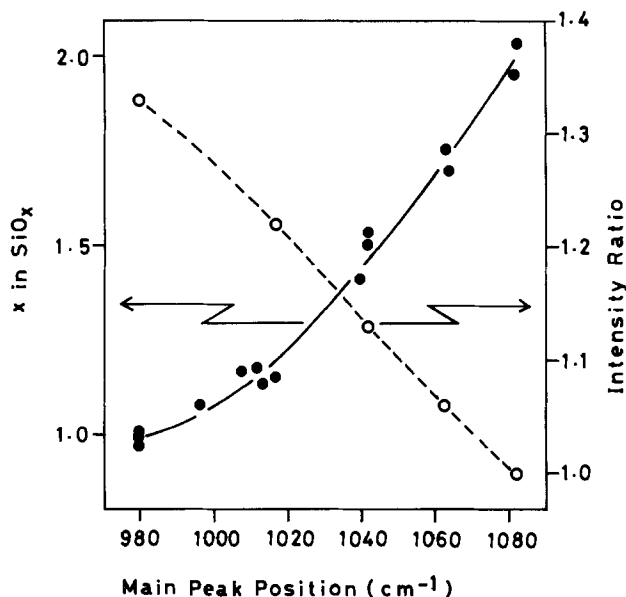


Fig. 2. Oxidation state and intensity ratio per unit thickness relative to SiO_2 vs. main peak position for homogeneous oxide specimens prepared by SiO evaporation.

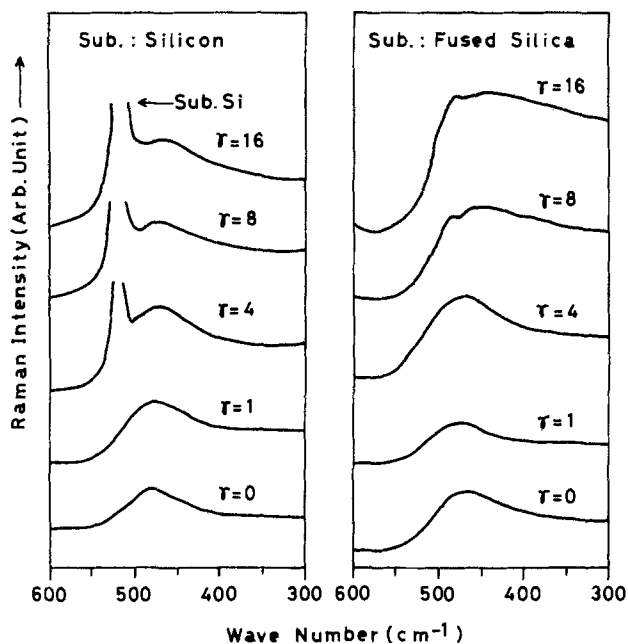


Fig. 3. Raman spectra for specimens deposited on silicon and fused silica substrates. The large peak seen for the specimens on the silicon substrate is the lattice vibration of silicon in the substrate.

and ρ indicated atomic weight and density, respectively, for the subscripted species. Since the actual density of SiO_x in the film was unknown, but differences in density among silicon, SiO, and SiO_2 prepared by heating SiO in air were small [e.g., 2.33 (16), 2.16 (13), and 2.27 (13) g/cm^3 , respectively, the last value coincides with that for thermal SiO_2 (16)], its value was approximated to be the mean of those for SiO and SiO_2 (e.g., 2.22 g/cm^3). The maximum error in oxygen content due to this approximation was estimated to be within 10%. The IR results are shown in Fig. 4 vs. those from radioactivation analysis. Deviation from 1:1 correspondence was within 15%, indicating that the films were composed of only genuine silicon and SiO_x phases.

Changes in IR spectra by heat-treatment—The films at $\gamma = 0, 1, 4,$ and 8 were heated from 700° to 1100°C for 1 h in an N_2 atmosphere. As shown in Fig. 5 for the $\gamma = 4$ specimen, the wave number of the main peak located between 1000 – 1100 cm^{-1} shifted to the higher wave number side with higher heat-treatment temperatures. The peaks at 875 – 880 cm^{-1} seen for the as-deposited and 700°C heat-treated specimens disappeared for the specimen heated at 800°C . Instead, a new peak appeared at around 800 cm^{-1} , which shifted to 815 cm^{-1} on heating at 1100°C . However,

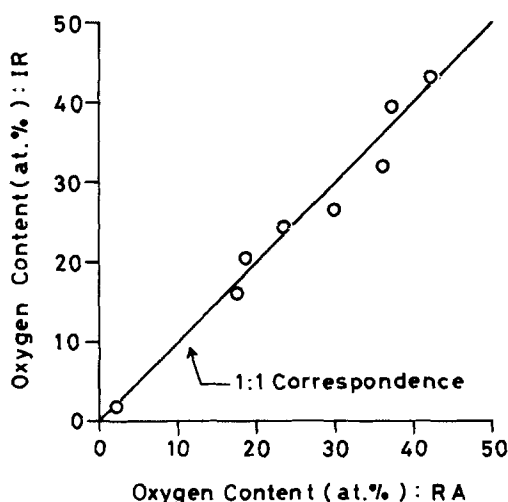


Fig. 4. Correlation of oxygen content obtained by IR and radioactivation (RA) analysis.

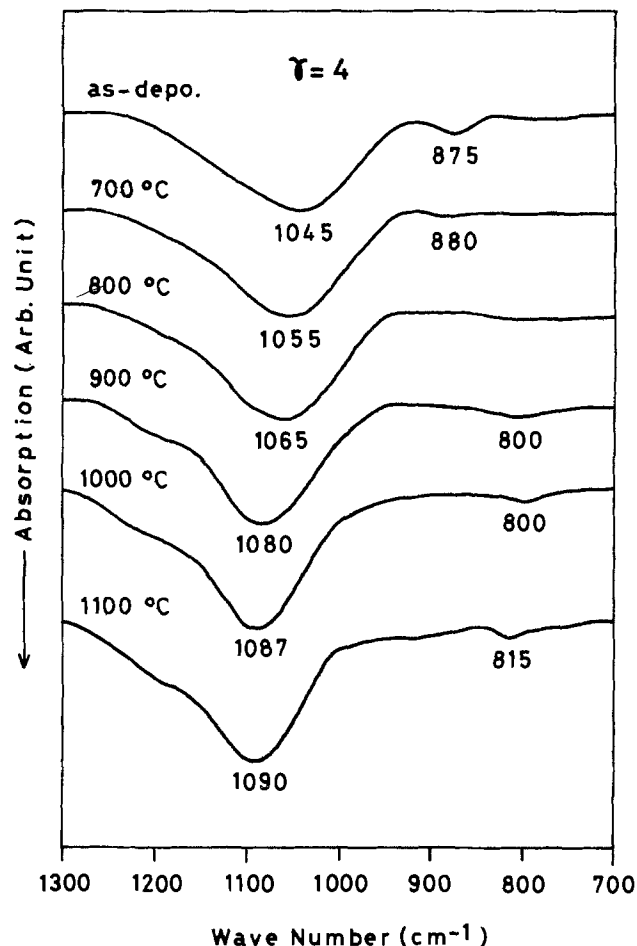


Fig. 5. Changes in the IR absorption spectra for various heat-treatment temperatures ($\gamma = 4$ specimen).

the absorption intensity in the 700 – 1400 cm^{-1} region was hardly changed by increased heat-treatment temperatures. Almost the same feature was seen for the other specimens. Changes in the main peaks are shown in Fig. 6. These results indicated that the oxidation state x of the film oxide phase increased up to SiO_2 when the heat-treatment temperature was increased, and suggested that the concentration of oxygen atom into the oxide phase, or escape of silicon atom from the oxide phase, occurred. Comparing this change of absorption intensity with the intensity ratio shown in Fig. 2, a slight amount of oxygen impurity appeared to be taken into the oxide phase by the

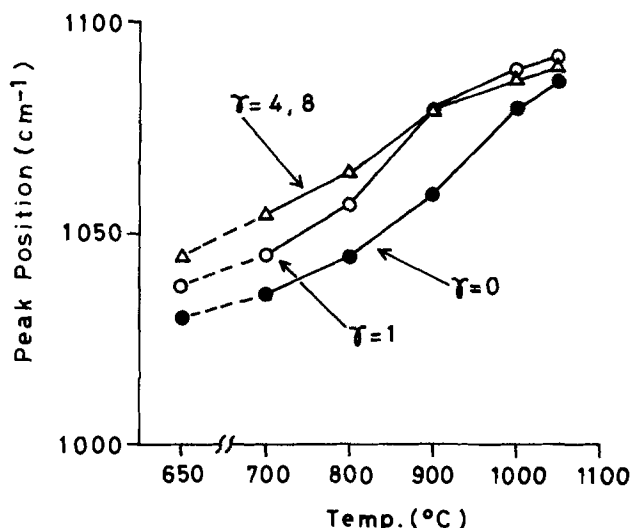


Fig. 6. Changes in main peak position with heat-treatment temperatures.

increased heat-treatment temperatures. The peak positions around 1100 and 800 cm^{-1} for the specimens heated above 1000°C were shifted to higher wave number over those for SiO_2 (e.g., 1082 and 800 cm^{-1} , respectively). These abnormal peak shifts were attributed, not to an increased oxidation state of $x > 2$, but to internal compressive stress in the oxide phase due to differences in thermal expansion coefficients between oxide and silicon substrates. However, since the changes in main peak positions on heating for peaks above 1080 cm^{-1} were smaller than those for peaks under 1080 cm^{-1} , the contribution from internal compressive stress to shifts in the main peak position was estimated to be small as compared to that from the increase in oxidation state x .

Changes in crystalline size of silicon.—Silicon crystallites appeared in the films after heat-treatment. The crystallite size of silicon, D , estimated by the Scherrer equation for x-ray diffraction

$$D = K \lambda / \beta \cos \theta \quad [1]$$

is shown in Fig. 7 vs. heat-treatment temperature, where K is a constant and selected as 0.90, λ is the incident x-ray wavelength, β the full width of the half maximum of the diffraction peak, and θ the Bragg angle. For the $\gamma = 0$ specimen, crystallites of about 10 nm appeared on both silicon and fused silica substrates when the specimen was heated at 700°C. The size remained fairly constant up to 900°C, and then increased rapidly on heating above 1000°C. For the other specimens which contained more oxygen, no crystallites appeared on heating, even at higher temperatures. For the $\gamma = 1$ specimen, a few crystallites, smaller than those for the $\gamma = 0$ specimen, appeared on heating at 900°C. The higher the oxygen content of the film was, the higher the temperature at which crystallites appeared was. The size of a (111) silicon crystallite and averaged size of (220) and (311) crystallites on silica substrate were almost the same. However, the (111) crystallite was easier to grow at lower temperatures than

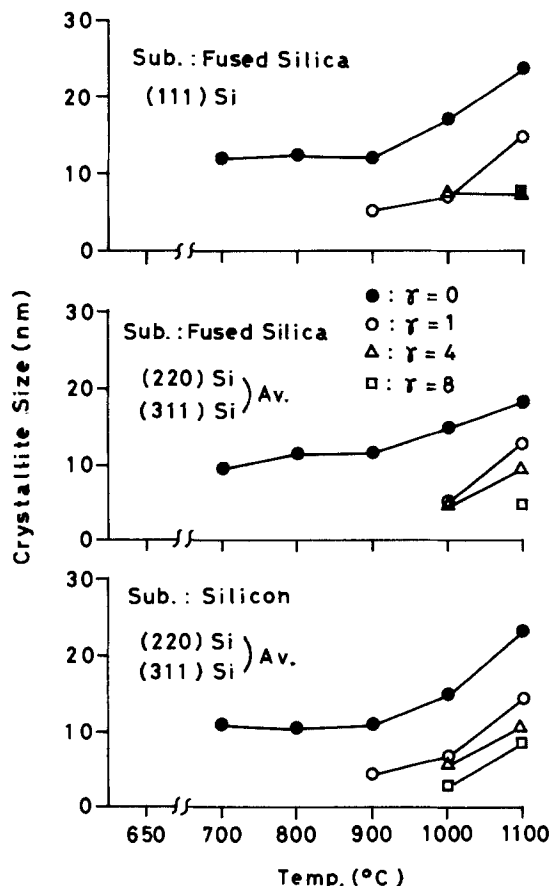


Fig. 7. Changes in crystallite sizes of silicon with heat-treatment temperatures.

(220) and (311) crystallites. The same features were observed for the specimens on the silicon substrate, although the size of the (111) crystallite was not (Fig. 7). The crystallite size at the nucleation temperature of the crystallite became smaller according to the increased oxygen content in the film. These observations were similar to those reported by Hamasaki *et al.* (5), although the exact sizes of the crystallites differed.

Changes in Raman spectra on heat-treatment.—The Raman spectra for the specimens for $\lambda = 0, 1$, and 4 heated at 700°-1100°C are shown in Fig 8-10, respectively. A sharp peak appeared around 500-520 cm^{-1} on heat-treatment. The intensity scale with the same laser power (about 150 mW) is given in the figures. The temperatures at which the sharp peak appeared coincided with those of the crystallite nucleation described in the preceding subsection. Accordingly, the sharp peak was assigned to the lattice vibration of the silicon crystallite, as demonstrated by Iqbal *et al.* (15) for Si:H prepared by glow discharge. The detection sensitivity for crystallite appearance was greater for Raman measurements than for x-ray diffraction measurements. In all the figures, the crystallite peak grew with the rise in heat-treatment temperatures, and a corresponding decrease in the amorphous peak. As shown by the dotted curves in Fig. 9, the intensity ratio (crystallite to amorphous phase) was separable for specimens on both substrates. Although silicon peaks (amorphous and crystallite) of the film became difficult to observe for the specimens with high oxygen content (thin film), owing to overlapping with the substrate peaks, they could be obtained by subtracting the substrate spectrum from the mixed spectrum. The width of the crystallite peaks for specimens on silica substrate was more than twice as broad as that for those on silicon substrate, although the mean crystallite sizes were the same on both. This must result from inhomogeneity of the crystallite size and the internal stress on the silicon crystallites, the latter of which is described below.

Raman peak position and crystallite size.—Accurate positions of the Raman peaks were observed. The relation-

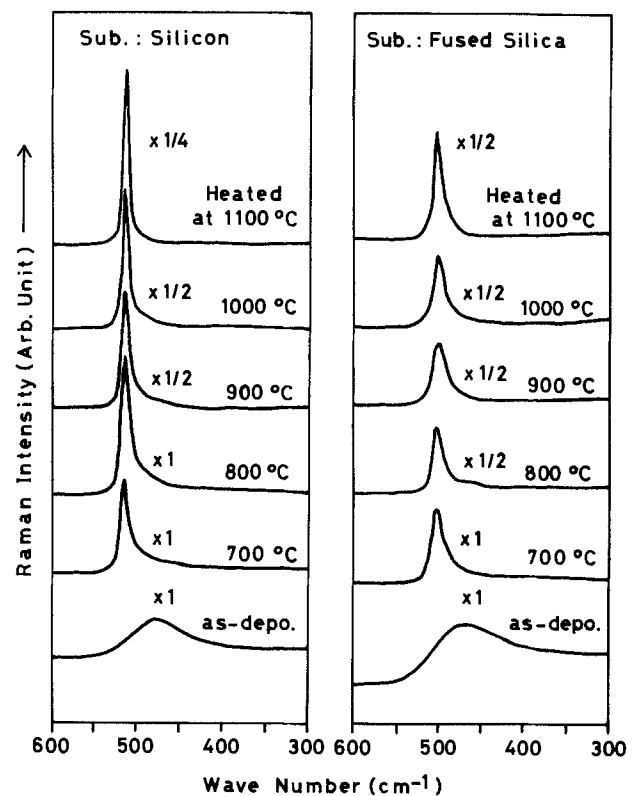


Fig. 8. Raman spectral changes with heat-treatment for $\gamma = 0$ specimens. The values in the figure indicate intensity scale for the same incident laser power.

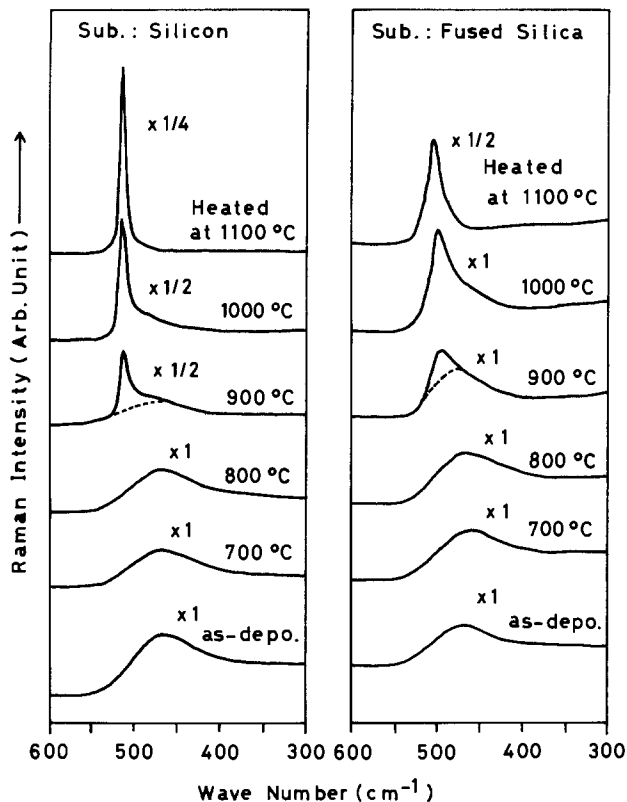


Fig. 9. Raman spectral changes with heat-treatment for $\gamma = 1$ specimens. The values in the figure indicate intensity scale for the same incident laser power.

ships between Raman peak positions and mean sizes of (111), (220), and (311) silicon crystallites, as obtained by x-ray diffraction, are summarized in Fig. 11. Correlations differed between specimens on silicon substrate and those on fused silica. The peak position (wave number)

for specimens on silicon substrate increased with increased crystallite size, and reached that of a single crystal of silicon (520.5 cm^{-1}) when crystallite size was more than 150 nm. This tendency was the same for Si:H as predicted by the slab model (17). However, the peak positions for specimens on silica substrate had a maximum of about 508 cm^{-1} at crystallite sizes around 11 nm, and decreased gradually with larger crystallites. The difference between both correlations could be attributed to the internal stress subjected to the silicon phase. When the thermal expansion coefficient of a substrate material is smaller than that of a film material, the film material is subjected to a tensile stress at room temperature after heating the specimen at high temperatures, and vice versa, as often seen for silicon on insulator (18). Since the thermal coefficient of the fused silica is much smaller than that of silicon crystal, the silicon crystallites should be subjected to a large tensile stress at room temperature after heat-treatments of the specimen; the higher the treatment temperature, the larger the tensile stress. The difference in peak positions on both substrates was explained by this effect. When the silicon crystallite is subjected to hydrostatic pressure τ , τ can be estimated by the shift $\Delta\nu$ of the Raman peak (F_{2g}) of the stressed crystal from that of an unstressed crystal (19) as

$$\tau (\text{N/m}^2) = -2.09 \times 10^8 \Delta\nu (\text{cm}^{-1}) \quad [2]$$

In derivation of Eq. [2], the values of elastic constants given by Kittel (20) and the parameters (p and q) given by Chandraseker *et al.* (21) were used. Since the silicon crystallites on the silicon substrate were subjected to no stress, the stress for the specimens on the silica substrate was given by the difference in peak positions for specimens on both substrates. Anomalous internal tensile stresses of $2.1 \pm 0.6 \times 10^9 \text{ N/m}^2$ for 5-10 nm size crystallites and $3.1 \pm 0.8 \times 10^9 \text{ N/m}^2$ for 15-20 nm size crystallites on fused silica were obtained. The decrease in peak wave number for increasing crystallite sizes over 11 nm was explained by the fact that the specimens which included large crystallites experienced higher temperatures than those which included small crystallites.

Discussion

Oxidation state of the oxide phase.—A number of opinions have been put forward regarding the oxidation state of films, especially for as-deposited amorphous specimens. Knolle and Maxwell (10) stated that the as-deposited film was composed of a homogeneous oxide phase, and the shift of the main IR peak located at $1000\text{--}1100 \text{ cm}^{-1}$ on changes in oxygen content of the film deposited at low pressure (LP SIPOS) occurred from mixing of SiO_2 character (mixture model). However, they used Philipp's statistical model (random bonding model) (22) for the films deposited at atmospheric pressure (AP SIPOS). There are some points to resolve in their discussion. First, the films are not composed of a homogeneous phase, but are heterogeneous phases of silicon oxide (SiO_x) and genuine silicon as demonstrated in this paper and Hartstein *et al.* (9). Second, the mixture model and random bonding model contradict each other; only one model must be employed to explain the oxide phase in the film. As for the oxidation state of the oxide phase, there has been proposed a model (6, 8) in which the oxide is composed of a mixture of the stoichiometric species of Si, Si_2O , SiO , Si_2O_3 , and SiO_2 (mixture model) as based on the chemical shifts observed in XPS studies. However, the stoichiometric intermediate phase between Si and SiO_2 is uncertain. The 875 cm^{-1} peak seen in Fig. 1 and assigned by Ritter (23) as the vibrational mode of Si_2O_3 , could be assigned to a vibrational mode from a structural combination of the species of silicon tetrahedra $\text{Si}(\text{O}_y\text{Si}_{4-y})$ (13) ($y = 2, 3, \text{ and } 4$) given by Philipp's bonding model (22). In the IR spectra, we could not observe any evidence for an intermediate phase between the Si and SiO_2 phases. In XPS studies, we can only observe the bonding character such as Si^0 , Si^+ , ..., Si^{4+} , which suggests no intermediate oxide phase. Accordingly, only Si

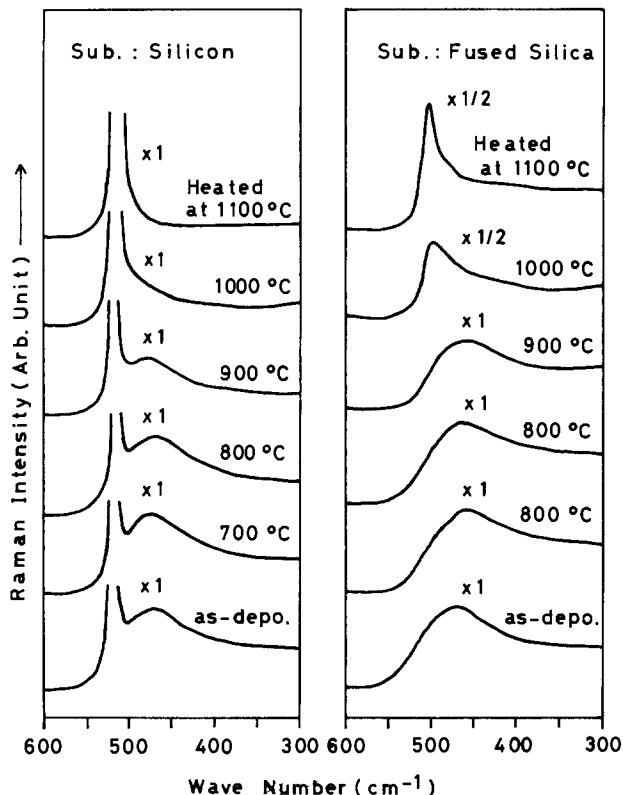


Fig. 10. Raman spectral changes with heat-treatment for $\gamma = 4$ specimens. The values in the figure indicate intensity scale for the same incident laser power.

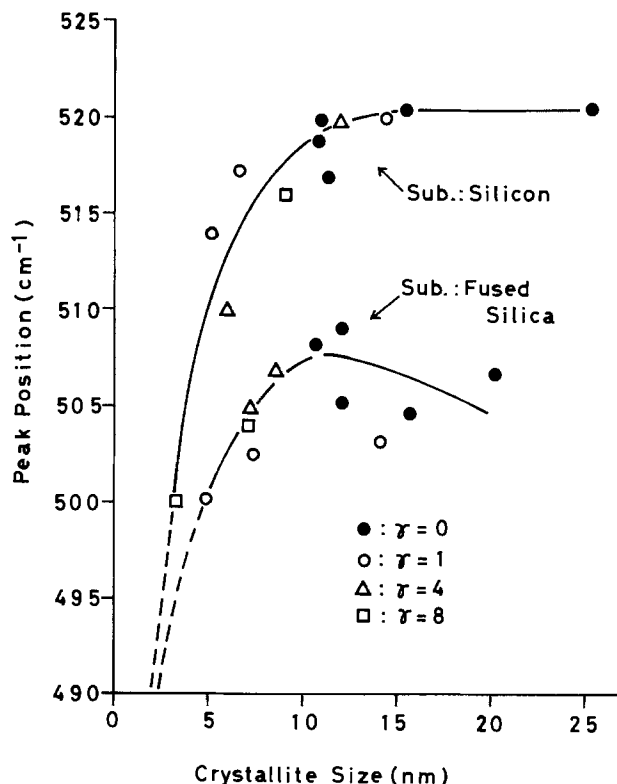


Fig. 11. Peak position of the Raman band vs. crystallite size for specimens on silicon and fused silica substrates.

and SiO_2 stoichiometric species remain in the mixture model. When the oxide is a mixture of Si and amorphous SiO_2 , we can always observe IR absorption peaks at around 1080, 800, and 450 cm^{-1} due to the SiO_2 phase, although peak shifts of several tens of cm^{-1} sometimes occur, owing to internal stress and porosity of the oxide (24). As seen from Fig. 1, we could not observe any evidence that the oxide was composed of Si and SiO_2 phases. Accordingly, the mixture model is inadequate to explain the oxidation state of our films. On the other hand, the shift of the main peak to higher wave number side and the disappearance and appearance of the 875 and 800 cm^{-1} peaks, respectively, according to increases in the oxidation state, could be reasonably explained with Philipp's bonding model. When the value x in oxide SiO_x is given, the probability P_y of each bonding type $\text{Si}(\text{O}_y\text{Si}_{4-y})$ ($y = 0, 1, \dots, 4$) is given by

$$P_y = N_y (1 - 0.5x)^{4-y} (0.5x)^y \quad [3]$$

where N_y indicates the number of possible arrangements in each type. Using Eq. [3], the mean probabilities for SiO_x character of the oxide phase of our as-deposited films were found to be from 0.22 to 0.47 for γ values from 0.5 to 24; these results were quite different from those of Knolle and Maxwell (10). Thus, the oxide phase in the films must be understood as SiO_x whose chemical bonds are given by the Philipp's bonding types $\text{Si}(\text{O}_y\text{Si}_{4-y})$. The chemical shifts seen in the XPS studies (6, 8) are reasonably explained by the random bonding model.

Microstructure of the film.—On the basis of TEM and x-ray diffraction observations of films, Hamasaki *et al* (5) proposed a microstructure film model; the grains of the oxide phase were separately embedded on the silicon phase (separate grain model). However, the question remains whether this simple model can consistently explain the electric and optical properties of the film and the crystal growth in the silicon phase. The large changes in resistivity (2) and bandgap (25) with change in oxygen content suggested that interruption of the electron current by the oxide phase was more influential than expected by the separate grain model.

Kwark and Swanson (11) observed absorption coefficients between 0.5–2.5 eV for films prepared with γ values

from 0.62 to 3.2. Comparing Table I, the volume ratios of silicon phase in their films could be estimated to be located from 0.77 ($\gamma = 0.5$) to 0.62 ($\gamma = 4$). From the data given by Kwark and Swanson [Fig. 1 in Ref. (11)], it could be found that a small amount of volume decrease of the silicon phase gave rise to a large decrease in the absorption coefficients at the energy region (1.5–2.3 eV) where absorption was mainly brought about by bulk silicon. This suggested that the interface between silicon and oxide phase was arranged so that the surface areas of both phases were much larger than those estimated by the separate grain model.

The fact that the crystallite sizes hardly grew with increasing heat-treatment temperatures up to 1000°C indicated that the crystal growth of the silicon phase was more restricted by the oxide phase than could be predicted by the separate grain model. From the viewpoint of the film growth kinetics, it was reasonable for each phase to grow continuously, in the growth direction, in the forms of columns or veins, as for Si:H (26). These columns or veins had branchings due to fluctuations in surface temperatures and reactant gas flows; they intersected each other at certain points.

From these considerations, we can imagine a model in which a considerable part of the surface of both phases is surrounded by the other phases in a manner such that both penetrate each other. However, one phase is not completely enclosed by the other. Accordingly, each phase forms a three-dimensional network with thinner and thicker parts within the mesh. We call our model the three-dimensional network model. With this model, we can consistently explain the electric and optical properties, the silicon crystallite growth, and the ease of reconstruction of both phases in the film on heat-treatment. The semi-insulating property of the film can be attributed to the interruption of electric currents at the thinner parts of the silicon veins enclosed by oxide phase. The increase in silicon crystallite size on heat-treatment over 1000°C must originate in a breakdown of the thinner part of the oxide network, and subsequent union of the silicon phase. The mean mesh sizes of the silicon phase for as-deposited specimens must be almost the same as the crystallite sizes of silicon at the nucleation temperatures.

Conclusion

Films obtained by chemical vapor deposition from SiH_4 and N_2O gases were studied. Infrared, Raman, and x-ray diffraction measurements were employed to evaluate the existing phases inside the film, the oxidation states of the oxide phase, and crystallite growth of the silicon phase on heat-treatment. The conclusions are as follows.

1. The as-deposited films were composed of an amorphous genuine silicon phase and an oxide phase SiO_x , with $x = 1.38\text{--}1.63$ for flow ratios ($\text{N}_2\text{O}/\text{SiH}_4$) = 0.5–24.
2. The oxidation state of the oxide phase increased with increasing heat-treatment temperatures in a N_2 atmosphere; the reconstruction of both phases occurred.
3. On heating the specimens in N_2 atmosphere, silicon crystallites grew inside the silicon phase. The sizes of the crystallites and the nucleation temperatures were closely related to the oxygen content of the films; the higher the oxygen content, the smaller the crystallites were, and the higher the nucleation temperatures.
4. The peak position of the Raman band due to silicon crystallites was closely related to the crystallite sizes and internal stress experienced by the film. When crystallite sizes were known, the stress could be estimated by the difference in Raman peak positions between stressed and unstressed films.
5. The silicon crystallites on silica substrate were subjected to a large tensile stress, *i.e.*, about $2.1\text{--}3.1 \times 10^9 \text{ N/m}^2$.
5. The oxidation states of the oxide phase could be analyzed by Philipp's bonding model. From this model, peak shifts in the infrared absorption and the chemical shifts in the XPS of the oxide phase were consistently explained as changes in the oxidation state x .

6. The silicon and oxide phases in the film formed a complicated three-dimensional network (network model). From this model, electric, optical properties, and crystallite growth of silicon from the amorphous silicon phase were consistently explained.

Acknowledgments

We thank H. Hachino and T. Suzuki of Hitachi Research Laboratory for their encouragement.

Manuscript received April 13, 1984.

Hitachi Limited assisted in meeting the publication costs of this article.

REFERENCES

1. T. Matsushita, T. Aoki, T. Ohtsu, H. Yamato, H. Hayashi, M. Okayama, and Y. Kawana, *Jpn. J. Appl. Phys. Suppl.*, **15**, 35 (1976).
2. H. Mochizuki, T. Aoki, H. Yamato, M. Okayama, M. Abe, and T. Ando, *ibid.*, **15**, 41 (1976).
3. D. J. Diamaria, *J. Appl. Phys.*, **50**, 5826 (1979).
4. T. Matsushita, N. Oh-uchi, H. Hayashi, and H. Yamato, *Appl. Phys. Lett.*, **35**, 549 (1979).
5. M. Hamasaki, T. Adachi, S. Wakayama, and M. Kikuchi, *J. Appl. Phys.*, **49**, 3987 (1978).
6. E. A. Irene, N. J. Chou, D. W. Dong, and E. Tierney, *This Journal*, **127**, 2518 (1980).
7. J. T. McGinn and A. M. Goodman, *Appl. Phys. Lett.*, **34**, 601 (1979).
8. J. H. Thomas, III and A. M. Goodman, *This Journal*, **126**, 1766 (1979).
9. A. Hartstein, J. C. Tsang, D. J. Diamaria, and D. W. Dong, *Appl. Phys. Lett.*, **36**, 836 (1980).
10. W. R. Knolle and H. R. Maxwell, Jr., *This Journal*, **127**, 2254 (1980); H. R. Maxwell, Jr. and W. R. Knolle, *ibid.*, **128**, 576 (1981).
11. Y. Kwark and R. M. Swanson, *ibid.*, **129**, 197 (1982).
12. T. Nozaki, M. Iwamoto, K. Usami, K. Mukai, and A. Hiraiwa, *J. Radioanal. Chem.*, **52**, 449 (1979).
13. M. Nakamura, Y. Mochizuki, K. Usami, Y. Itoh, and T. Nozaki, Submitted to *Solid-State Commun.*
14. N. Nagashima and N. Kubota, *Jpn. J. Appl. Phys.*, **14**, 1105 (1975).
15. Z. Iqbal, S. Veprek, A. P. Webb, and P. Capezuto, *Solid-State Commun.*, **37**, 993 (1981).
16. H. F. Wolf, "Silicon Semiconductor Data," p. 3, 602, Pergamon Press, New York (1976).
17. G. Kanellis, J. F. Morhange, and M. Balkanski, *Phys. Rev. B*, **21**, 1534 (1980).
18. T. Englert, G. Abstreiter, and J. Pontcharra, *Solid-State Electron.*, **23**, 31 (1980).
19. E. Anastassakis, A. Pinczuk, E. Burstein, F. H. Pollak, and M. Cardona, *Solid-State Commun.*, **8**, 133 (1970).
20. C. Kittel, "Introduction to Solid State Physics," 4th ed., p. 133, John Wiley and Sons, New York (1971).
21. M. Chandrasekhar, J. B. Renucci, and M. Cardona, *Phys. Rev. B*, **17**, 1623 (1978).
22. H. R. Philipp, *J. Phys. Chem. Solids*, **32**, 1935 (1971).
23. E. Ritter, *Opt. Acta*, **19**, 197 (1962).
24. W. A. Pliskin, *J. Vac. Sci. Technol.*, **14**, 1064 (1977).
25. M. Hamasaki, T. Adachi, S. Wakayama, and M. Kikuchi, *Solid-State Commun.*, **21**, 591 (1977).
26. R. Messier and R. C. Ross, *J. Appl. Phys.*, **53**, 6220 (1982), and references therein.

High Field Phenomena in Thermal SiO₂

C. Glenn Shirley¹

Motorola, Incorporated, Process Technology Laboratory, SRDL, Phoenix, Arizona 85008

ABSTRACT

High field phenomena in thermally grown SiO₂ have been investigated by a combination of three techniques: (i) current-voltage characterization, (ii) CV measurements, and (iii) forced-current voltage-time characteristics. Comparison with theoretical Fowler-Nordheim predictions was used in the current-voltage technique. Four oxide thicknesses were studied: 160, 345, 652, and 1452Å. All structures were nonrecessed Al/SiO₂/Si capacitors of various areas. The substrate was n-type silicon. Interface trap formation and charging with electrons near the cathode during injection from Si was observed for all oxides. Creation of immobile holes in the oxide valence band by impact ionization was observed for the thicker oxides, but not the thinnest. Bulk trapping was significant when electrons were injected from Al into the thicker oxides. The Al/SiO₂ interface was considerably leakier in thicker oxides than predicted by the Fowler-Nordheim theory. It is important to consider these high field phenomena in reliability questions because they constitute a true wear-out mechanism for intrinsic (*i.e.*, with no defects) thermal oxides. As oxides become thinner in devices, high field phenomena become a more practical concern.

As integrated circuits shrink, thinner thermal oxides of silicon are required to withstand higher electric fields. This is beginning to change the situation with regard to oxide reliability. Historically, oxide reliability has been limited by defects which have early breakdown characteristics. Much has been done to predict and minimize defect-related failure rates. Statistical methods have played a large role in this. A common procedure is to screen devices by applying a high voltage during an accelerated test. The surviving population has a large reduction in early failure rate at the cost of a small loss in manufacturing yield. This rationale does not apply if oxides fail by a true wear-out mechanism. This is because accelerated stress weakens the entire population. The thin oxides used in VLSI processing must be more nearly defect-free because they must withstand higher fields. Thus, increasingly, reliability is being limited not by defects but by the intrinsic high field processes we shall be examining in this report. The main problem is not that devices will suffer wear-out in operation, but that the likelihood of stressing devices into wear-out during the accelerated testing used to screen devices. Hence the importance of studying the high field behavior of thermal oxides.

The purpose of this paper is to review intrinsic high field phenomena in thermal oxides and to demonstrate

how they may be observed. With this report as a guide, we are in a good position to characterize quickly the high field behavior of any gate oxide system (silicides, etc.).

In this study, three kinds of data were acquired: (i) IV data, (ii) CV data, and (iii) the *V-t* characteristics obtained when a constant current is forced through the MOS capacitor. All three types of data were gathered as function of capacitor area and oxide thickness. No area dependence beyond simple scaling of current and capacitance with area was found. That is, edge effects were negligible. The study was carried out on the Al/SiO₂/n-type Si system.

Theoretical Background

Figure 1 shows a schematic of the well-known (1, 2) band structure of the Al/SiO₂/Si MOS diode. Electrons in Si or Al have high potential barriers at the interface to surmount before they can enter the SiO₂. As the potential difference across the oxide is increased, the barrier at the negative (electron injecting) electrode becomes sharply triangular. When the barrier thickness, *d*, at the Fermi level of the injecting electrode becomes of the order of 50Å, appreciable numbers of electrons can enter the oxide conduction band by quantum tunneling through the interfacial barrier. By simple trigonometry, this occurs at an electric field of about $\phi_{si}/d \approx 3.0 \text{ eV}/50 \times 10^{-8} \text{ cm} \approx 6 \times$

¹Present address: Intel Corporation, Chandler, Arizona 85224.

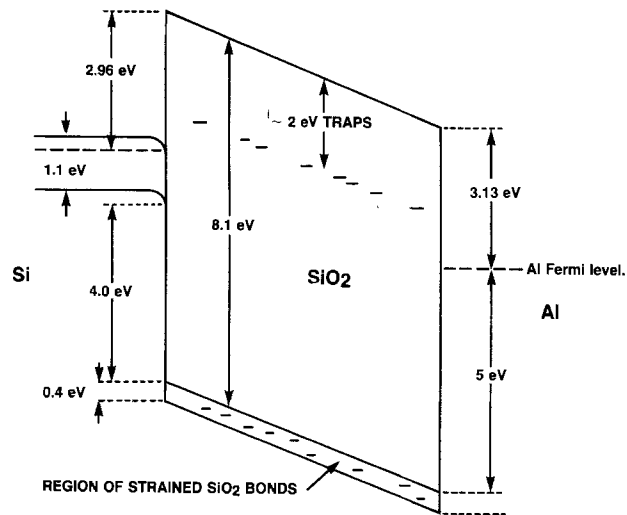


Fig. 1. Band diagram of Si/SiO₂/Al system shown with aluminum biased positive relative to silicon.

10⁶ V/cm. The barrier height for electrons at the Si/SiO₂ interface is denoted by ϕ_{Si} . Once in the conduction band of the oxide, the electrons have high mobility [20-40 cm²/V-s, Ref. (1)] and move rapidly to the anode. Some electrons may fall into the fairly numerous traps at about 2 eV below the oxide conduction band, but they will immediately tunnel out of them at the high electric fields necessary to cause injection from the cathode. Holes injected from the anode have a much higher barrier (4-5 eV) to surmount than electrons, and holes are known to have a very low mobility in the oxide [2 × 10⁻⁵ cm²/V-s, Ref. (1)]. The low hole mobility is probably due to the large number of shallow hole traps just above the valence band of SiO₂ due to strained Si-O bonds. Hence, the number of injected holes and their influence on conduction is negligible in our experiments. Hot holes can be injected into SiO₂ by avalanche injection from n-type silicon driven into deep depletion, but this condition does not occur in our experiments.

When a constant current is forced into a MOS capacitor, the leakage current-voltage-time characteristic appears as shown schematically in Fig. 2. The leakage current is the forced current less the displacement current. The displacement current can be calculated from $I(\text{disp}) = C(dV/dt)$ where C is the capacitance of the MOS capacitor and dV/dt is the instantaneous rate of increase in voltage. The IV characteristic of the oxide is shown as a projec-

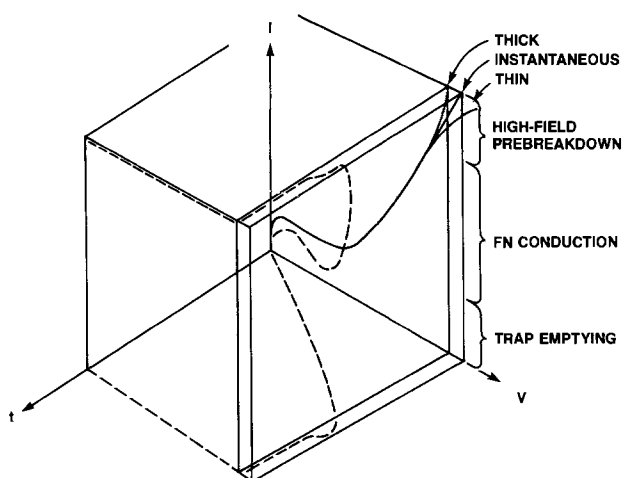


Fig. 2. Schematic of leakage current-voltage-time characteristic. At high fields, the IV characteristic changes with time as charge builds up in the oxide. The time-dependent deviation from the ideal Fowler-Nordheim law at high fields depends on oxide thickness.

Table I. Oxide thickness measured by IBM thin film analyzer

Wafer no.	Thickness (Å)
5	144 (160 ^a)
6	345
7	652
8	1452

^a Better agreement between theory and experiment for IV data was obtained with $t_{ox} = 160\text{Å}$.

tion on the IV plane, while the V-t characteristic obtained when a constant current is forced is shown as a projection on the V-t plane. Figure 2 summarizes the various regimes of importance in the electrical behavior of thermal oxide. At low electric fields, no charge is injected from the electrodes, but electrons will be ejected from shallow traps and will flow to the anode. This is the origin of the flat part of the IV curve labeled "trap emptying." We will not be examining this regime in this report, but we indicate in passing that techniques measuring trap filling and emptying transients at low fields can be used to gauge oxide quality. At higher electric fields, quantum tunneling at the electron injecting electrode (cathode) becomes dominant and the IV characteristic follows the Fowler-Nordheim (FN) law (3-5) (labeled "FN conduction" in Fig. 2). The FN characteristic can be extended to lower fields by maintaining a bias in the trap emptying regime to drain the shallow traps before taking the FN trace. This "uncovers" the FN characteristic at lower fields (4). At high fields, just prior to breakdown, the IV characteristic deviates from the FN law in a time-dependent fashion (4-6) labeled "high-field prebreakdown" in Fig. 2. It is important to realize that the measured injected current depends on the local electric field in the oxide at the cathode. This is the same as the average field across the oxide only if there is no charge in the dielectric. The average field is what is experimentally measured. Therefore, the high field deviations from the FN law are due to charging in the oxide. The charges take time to build up. Hence, the high field deviations from the FN law are time dependent. These charges are intimately related to the intrinsic (that is, nondefect-related) breakdown mechanism. This report is about the FN conduction regime, and the high field prebreakdown regime and the time dependence of the latter. This report does not consider the yield issues associated with defect-caused breakdowns. While this is of great importance, our focus is on the intrinsic properties of the oxide.

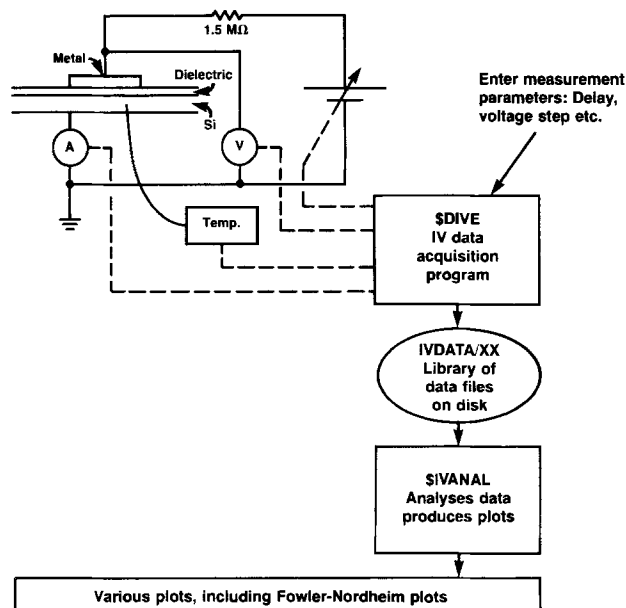


Fig. 3. Computer-automated IV data acquisition and analysis system

Sample Preparation

Four $\langle 100 \rangle$ n-type phosphorous-doped wafers with $N \approx 5 \times 10^{14} \text{ cm}^{-3}$ were separately thermally oxidized using a standard HCl cycle. Only the time in the growth part of the cycle was varied to change the thicknesses of the oxides. The oxide thicknesses were measured using an IBM Film Thickness Analyzer (FTA). The thicknesses obtained are shown in Table I. We shall see later that better agreement between theory and experiment for the IV data of wafer 5 was obtained if the thickness of the thinnest oxide is taken to be 160\AA rather than the 144\AA given by the IBM FTA. Much of the data analysis will use 160\AA instead of 144\AA . This is a reasonable correction, since the IBM FTA gives estimates consistently lower than other thickness measurement techniques such as ellipsometry, CV, etc. Next, 1000\AA of aluminum was deposited on the wafers and then patterned into arrays of rectangular capacitors of various areas. The wafers were then annealed at 450°C for 30 min in forming gas. Finally, the oxide was stripped from the backs of the wafers using an HF fume. All wafers were processed identically except for the growth part of the oxidation cycle.

Electrical Measurements

Current-voltage measurements.—Current-voltage characteristics were measured using the system shown in Fig. 3. A Tektronix 4051 computer controls a Kepco BOP500M bipolar power supply with 500V range. The current flowing from the chuck to ground is monitored by a Keithley 616 electrometer and transmitted to the computer by a

custom interface built in our laboratory. The voltage on the probe is measured by a Fluke 8502A digital multimeter and transmitted to the computer via the general purpose interface bus (GPIB). There is also provision for heating or cooling the sample under computer control, but this was not used in these experiments. All measurements were done at room temperature. The program \$DIVE controls the instruments and acquires the data. The voltage applied to a MOS capacitor was increased in approximately 1V steps until electrical breakdown of the oxide occurred. A 4s delay after each voltage step allowed displacement current transients to decay. IV characteristics were obtained in this way on 25 and 625 mil^2 capacitors in both positive and negative polarities. Each characteristic was obtained on a virgin capacitor, and measurements for any given set of conditions were repeated on virgin capacitors to ensure reproducibility.

Once the data were acquired, they were saved in a library of data files, IVDATA (Fig. 3), on a floppy disk reserved for data. Also saved are an identifying string, the area of the capacitor and the thickness of the oxide. These files can be read by the program \$IVANAL and various types of plots can be generated. Of particular importance in this study are Fowler-Nordheim (FN) plots: $\log J/E^2$ vs. $1/E$, where J is the current density and E is the average field across the dielectric (i.e., $E = \text{total voltage drop/oxide thickness}$). The FN plots for 25 mil^2 capacitors for four oxide thicknesses in both polarities are shown in Fig. 4 and 5. The plotting program ignores the sign of the voltage drop across the oxide except that data taken with

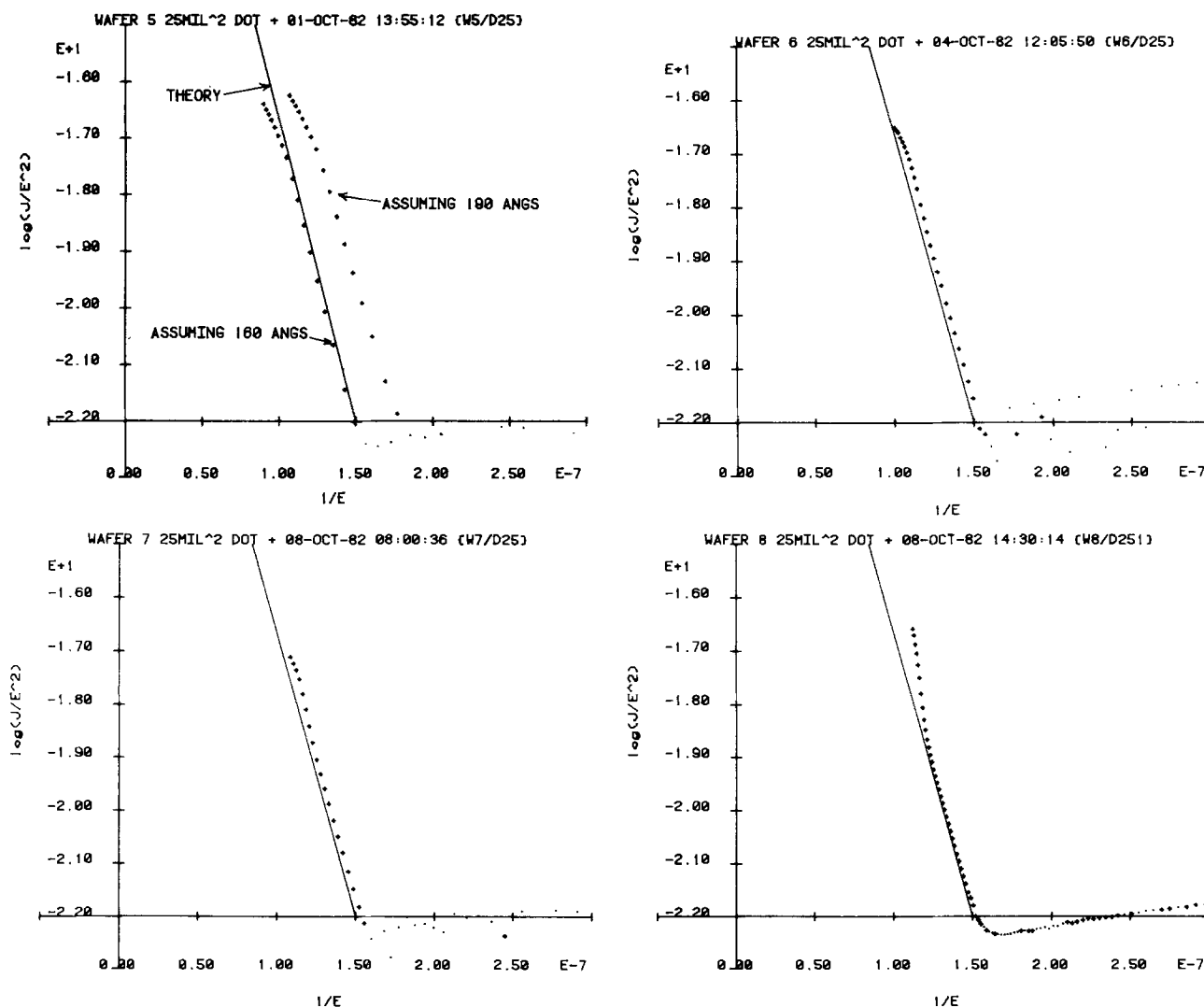


Fig. 4. Fowler-Nordheim plots for injection from silicon for various thicknesses of thermal SiO_2 . Theory shown as solid lines. Top left: Wafer 5 assuming $t_{\text{ox}} = 160\text{\AA}$ and $t_{\text{ox}} = 190\text{\AA}$. Best agreement with theory occurs for $t_{\text{ox}} = 160\text{\AA}$. Top right: Wafer 6, 345\AA . Bottom left: Wafer 7, 652\AA . Bottom right: Wafer 8, 1453\AA .

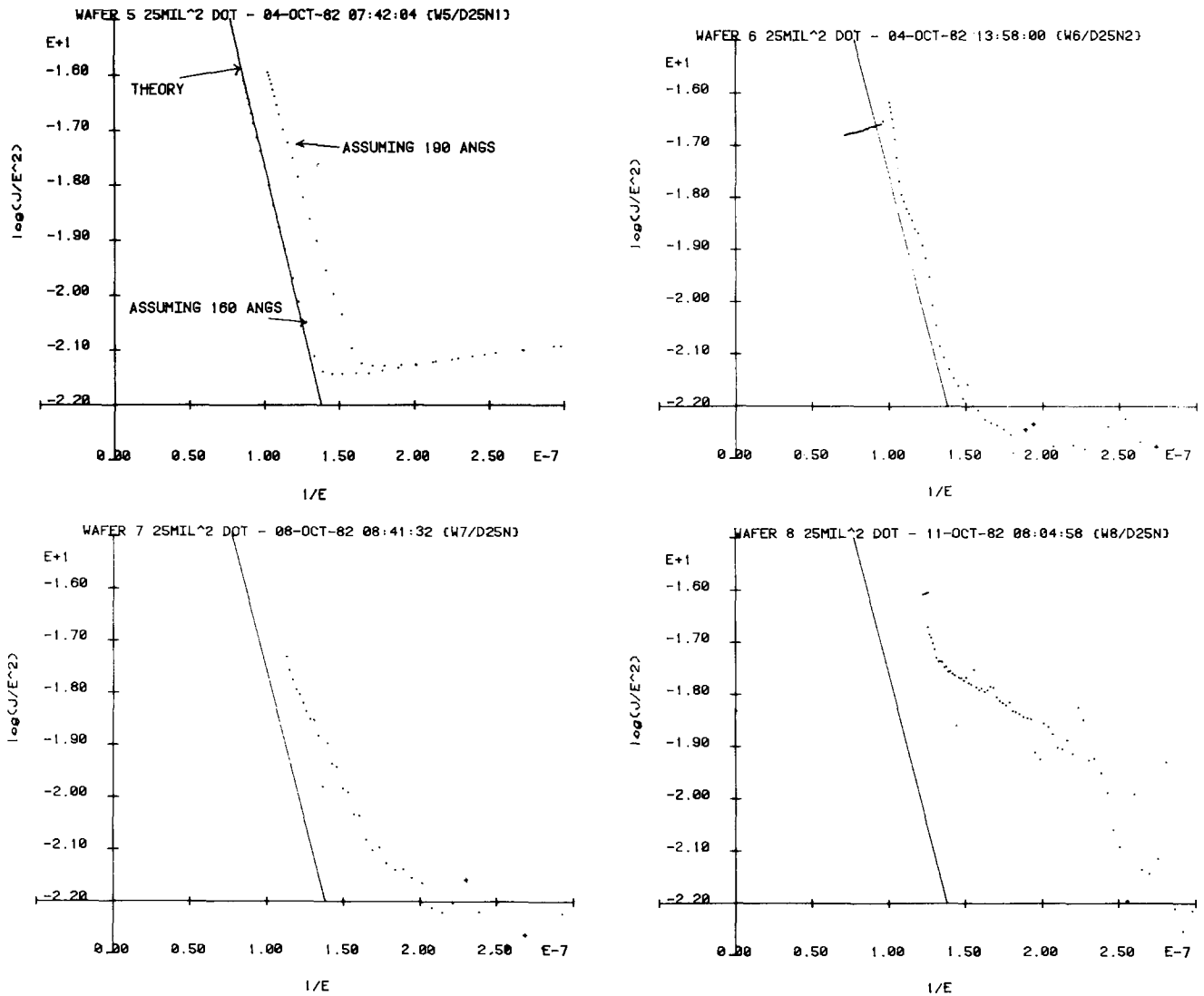


Fig. 5. Fowler-Nordheim plots for injection from aluminum for various thicknesses of thermal SiO₂. Theory shown as solid lines. Top left: Wafer 5 assuming $t_{ox} = 160\text{\AA}$ and $t_{ox} = 190\text{\AA}$. Best agreement with theory for $t_{ox} = 160\text{\AA}$. Top right: Wafer 6, 345Å. Bottom left: Wafer 7, 652Å. Bottom right: Wafer 8, 1453Å.

Al biased positive is plotted with “+” signs, while data with the opposite polarity is plotted with dots. Note also that many of the computer-generated plots have “E + 1” near the end of the x- or y-axis. This means that the appropriate scale numbers are to be multiplied by 10. In general $E + n$ means multiplication by 10^{+n} . The IV characteristic was taken to breakdown so that the smallest value of $1/E$ on a plot is taken as a measure of (the reciprocal of) the breakdown field, E_b . The same kind of data was obtained for 625 mil² capacitors and identical curves were obtained, except that E_b tended to be lower.

It is valuable to compare our experimental data with theoretical expectations. Fowler-Nordheim tunneling has received considerable attention in the literature over the years (3-5), so that there is now a good consensus of opinion regarding the J - E characteristic for various electrode materials. This is summarized in a recent paper by Weinberg (5). The FN characteristic is

$$J/E_c^2 = C \exp(-\beta/E_c) \tag{1}$$

where E_c is the cathode field, where

$$C = q^3 m / (16\pi^2 \hbar m_{ox} \phi_0) = 1.54 \times 10^{-6} (m/m_{ox}) / \phi_0 \text{ A/V}^2 \tag{2}$$

and

$$\beta = (4/3)(2m_{ox}\phi_0^3)^{1/2} / (q\hbar) = 6.83 \times 10^7 (m_{ox}/m)^{1/2} \phi_0^{3/2} \text{ V/cm} \tag{3}$$

In Eq. [2] and [3], q is the electronic charge, m is the elec-

tron rest mass, m_{ox} is the electron effective mass in the oxide, \hbar is Planck's constant divided by 2π , and ϕ_0 is the height above the electrode conduction band in electron volts of the barrier at the cathode. It is important to understand that it is the electric field at the electron injecting interface, the cathode, which governs the current density. In Fig. 1, the cathode electric field in the oxide is represented by the slope of the oxide energy bands at the cathode. A consensus of the literature (5) is that $m_{ox} = 0.5m$, $\phi_{Al} = 3.13 \text{ eV}$, and $\phi_{Si}(100) = 2.96 \text{ eV}$. The aluminum barrier height is to be used in Eq. [2] and [3] for injection from aluminum, i.e., aluminum biased negative relative to the substrate, while ϕ_{Si} is to be used for aluminum biased positive relative to the substrate. If we assume negligible charge in the oxide, then the cathode field, E_c , equals the average field and we may use Eq. [1] with the consensus parameters to compare the theoretical predictions with our data. This is done by superimposing the theoretical J - E relationship, shown as the solid straight lines, over our data in the FN plots in Fig. 4 and 5.

Corrections were applied to the raw IV data before plotting it in Fig. 4 and 5. The corrections caused an appreciable change from the raw data only for the thinnest oxide; nonetheless, the corrections were applied to all of the data. The measured voltage drop across the MOS diode should be corrected for band bending at the silicon surface and the metal-semiconductor work function difference to give the actual potential drop across the oxide (8). For Al negative, voltage was increased slowly enough that the inversion layer in the silicon always had time to

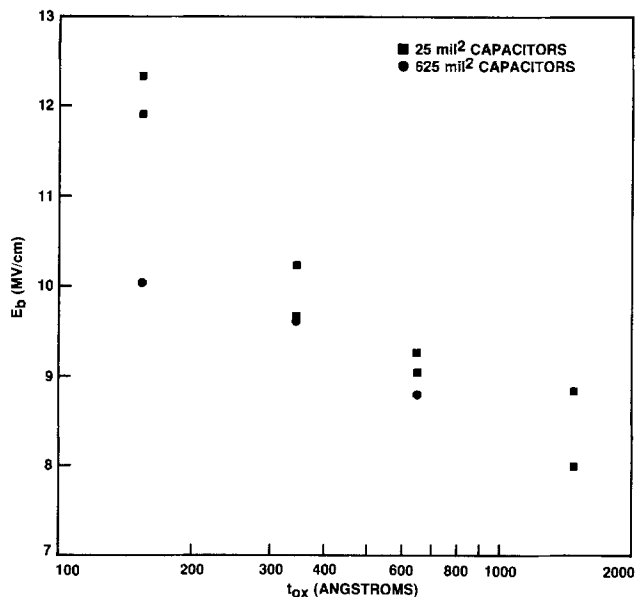


Fig. 6. Breakdown electric field for injection from aluminum. Thermal oxides on n-type silicon (Y58).

form. This means that the usual equilibrium theory (9) may be used to compute these corrections. The corrections amount to about a volt (a bandgap) in inversion, and less in accumulation. This can be an appreciable correction for thin oxides. Specifically, the total potential, V_{TOT} , of aluminum relative to bulk silicon is related to the voltage drop across the oxide, V_{ox} , by

$$V_{TOT} = \phi_{MS} + V_{ox} + \Psi_s(E_s) \quad [4]$$

where $\Psi_s(E_s)$ is the semiconductor surface potential relative to the bulk as a function of the field E_s at the semiconductor surface. E_s is related to V_{ox} by

$$E_s = (K_{ox}/K_s)(V_{ox}/t_{ox}) \quad [5]$$

Equation [4] assumes that there is no charge in the oxide. In strong inversion (9) ($V_{ox} < 0$), we have

$$\Psi_s = -(kT/q) \ln [(E_s^2 K_s \epsilon_0 n) / (2kT n_i^2)] \quad [6]$$

while in accumulation ($V_{ox} > 0$)

$$\Psi_s = (kT/q) \ln [(E_s^2 K_s \epsilon_0) / (2kT n)] \quad [7]$$

where ϵ_0 is the permittivity of the vacuum, k is

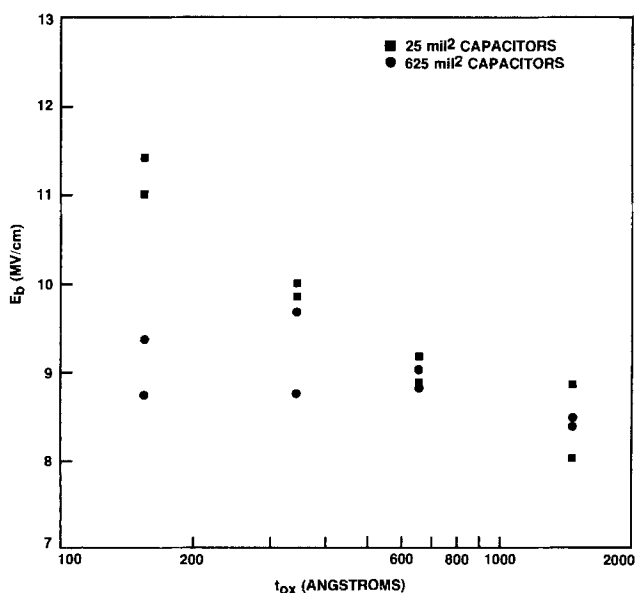


Fig. 7. Breakdown electric field for injection from silicon. Thermal oxides on n-type silicon (Y58).

CV PROCEDURE DEFINITION

OLD PROCEDURE NAME: INJ144N

Step#		Vstart=	Vstop=	R=	(V/s)	Freq=	(Hz)	T=	(deg C)	Bias=
1	(Trace)	1.00	-1.00	0.01		1.0E+004		25.0		
2	(Soak)							25.0		-7.20
3	(Trace)	1.00	-1.0	0.01		1.0E+004		25.0		
4	(Soak)							25.0		-8.64
5	(Trace)	1.00	-1.00	0.01		1.0E+004		25.0		
6	(Soak)							25.0		-10.08
7	(Trace)	1.00	-1.00	0.01		1.0E+004		25.0		
8	(Soak)							25.0		-11.52
9	(Trace)	1.00	-1.00	0.01		1.0E+004		25.0		
10	(Soak)							25.0		-12.96
11	(Trace)	1.00	-1.0	0.01		1.0E+004		25.0		
12	(Soak)							25.0		-14.40
13	(Trace)	1.00	-1.00	0.01		1.0E+004		25.0		

Fig. 8. A CV procedure typical of those used to produce the data in Fig. 9 and 10. Each trace step is identical. Each soak step is the same except for a linearly increasing stressing electric field.

Boltzmann's constant, q is the electronic charge, T is the absolute temperature, K_{ox} is the oxide dielectric constant, n_i is the intrinsic electron concentration, and n is the bulk electron density. The Eq. [4]-[7] give a relationship between V_{TOT} and V_{ox} . When parameters appropriate to the substrate and metal used in this experiment ($\phi_{MS} = -0.33V$, $n = 5 \times 10^{14} \text{ cm}^{-3}$) are substituted into the equations we find that over the range of voltages for which FN conduction occurs, the difference between V_{ox} and V_{TOT} is practically constant. In accumulation (fortuitously), $V_{TOT} = V_{ox}$, while in inversion $V_{TOT} = V_{ox} \times 1.26V$. This holds for all four oxides tested. Thus, in practice only the data for injection from aluminum was corrected. Even with this correction, the thinnest oxide FN data deviated appreciably from theory. It was possible to adjust the assumed thickness of the thinnest oxide upwards by 16 to 160Å and get excellent agreement with the FN theory simultaneously for injection from Si and from Al². It is known that the IBM FTA tends to underestimate the thickness of thin oxides, so careful ellipsometer measurements were made. With the refractive index forced to $n = 1.465$ (He-Ne laser), a thickness of 190Å was found. The ellipsometer data were definitely inconsistent with 160Å and, *a fortiori*, 144Å, provided $n = 1.465$. On the other hand, 190Å is inconsistent with the "consensus" parameters in the FN theory, as can be seen in Fig. 4 and 5. Thickness estimates from CV measurements agreed with the ellipsometer estimates. There are several possible explanations for these discrepancies: (i) the refractive index of the oxide is different from the $n = 1.465$ assumed in the

²It is worth noting that simultaneous agreement with theory for both polarities is not possible for any thickness unless the band bending and work-function difference corrections are applied.

ellipsometer calculations. If the refractive index is not forced to a value, then the ellipsometer data give $t_{\text{ox}} = 160\text{\AA}$ and $n = 1.8$. (ii) The oxide has a complicated graded optical structure. (iii) The thin oxide has a lower interfacial barrier than the thicker oxides. Adjustment of the barrier heights to give agreement with theory for both polarities assuming $t_{\text{ox}} = 190\text{\AA}$ gives $\phi = 2.67\text{ eV}$. (iv) The electronic effective mass is different for thin oxides or (v) some other reason. We are unable to resolve this discrepancy, but it seems that the IBM FTA reading is definitely low. We shall take 160\AA as the thickness of the thinnest oxide for much of the discussion which follows. The thicker oxides have good agreement with FN theory without any of these corrections. Nonetheless, the band bending and work-function difference corrections were applied to the data for the thicker oxides. This discussion shows that detailed interpretation of thin oxide FN data is considerably more complicated than for thicker oxides.

Several observations can be made from the FN plots in Fig. 4 and 5 and their deviations from theory.

1. For injection from Si, the IV data agree well with FN theory except at high fields just below breakdown. The nature of the deviation at high fields depends on oxide thickness. For the 1453\AA oxide, the data deviate from the FN theory to higher current densities. For the thinnest (160\AA) oxide, the deviation from the FN theory is to lower current densities. For intermediate oxide thicknesses, deviation is first to the high side of the FN curve and then lower as E increases.

2. For injection from aluminum, the current-voltage data agree well with the FN theory only for the thinnest oxide. As the oxides become thicker, the deviation from the FN theory increases, all in the direction of higher current densities. That is, the films are "leakier" than predicted by the FN theory. As the electric field increases,

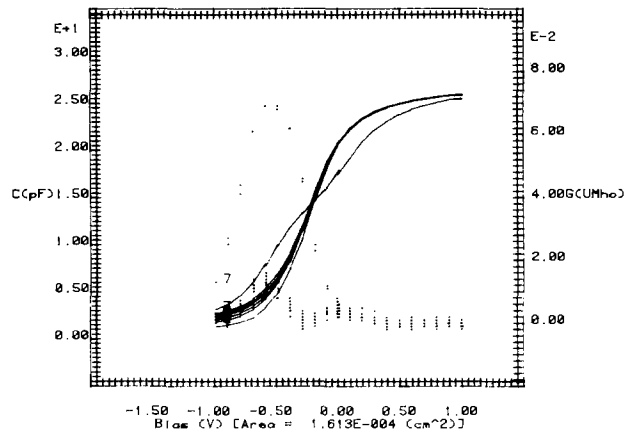
the IV characteristic for the thicker films approaches the FN curve.

3. The electric field at breakdown as determined from all of the IV data taken is shown as a function of oxide thickness in Fig. 6 and 7. Two main trends are apparent: (i) the well-known increase in breakdown field for decreasing oxide thickness (10), and (ii) the breakdown field for smaller capacitors tends to be higher than for larger capacitors, especially for thinner oxides. The IV characteristics for the large and small area capacitors are in excellent agreement when scaled according to area, but for the larger area capacitors the current density does not reach quite as high a value before breakdown occurs. It is difficult to interpret the area dependence of E_b without sampling a large number of dots to obtain statistical data.

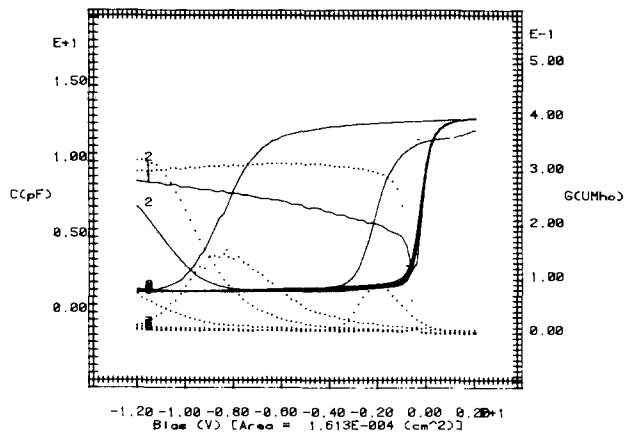
Capacitance-conductance-voltage measurements.—Because the IV data were so reproducible, it was feasible to carry out ac capacitance-conductance-voltage (CGV) measurements on virgin capacitors using stresses comparable with those used in the IV measurements. The CGV data give information on charging and interface state generation which occurs during the conduction process. Two types of CGV data are acquired: (i) data as a function of stress level held for fixed times at each level, and (ii) data as a function of time at a fixed stress.

Isochronal CV data with varying stresses.—The IV traces were examined and a series of stresses extending into the prebreakdown region, but avoiding breakdown, was chosen. The electric fields ranged from 5 MV/cm to 9 or 10 MV/cm in 1 MV/cm steps. An initial CGV trace was taken on a virgin capacitor. Then, an alternating series of stress and trace was carried out with increasing electric field stress but exactly the same trace conditions. Each stress level was held for 10s at room temperature. This

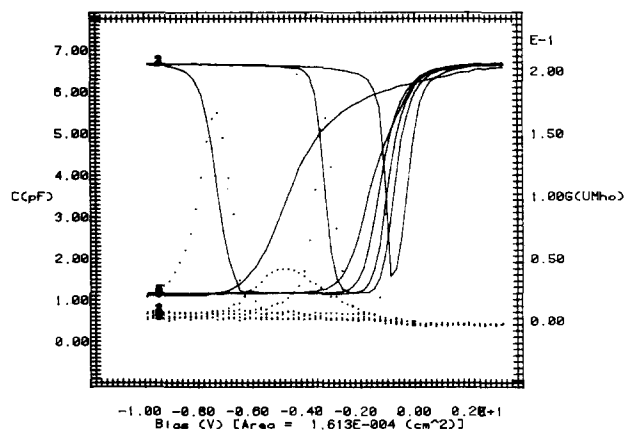
WAFS 144 ANG SID2 25 MIL² (N25C) INJ144P 14-DEC-82 14:53:38 (WS/P25E)



WAF 6 25MIL² DOT 345 A SID2 INJ345P16 18-FEB-83 18:07:17 (W6/I25P2)



WAF 7 25MIL² DOT 652 A SID2 INJ652P2 08-FEB-83 18:28:19 (V7/P25B)



WAFER 8 25MIL² DOT 1452 ANGS SID2 INJ1453P 08-FEB-83 15:59:38 (W8/N25)

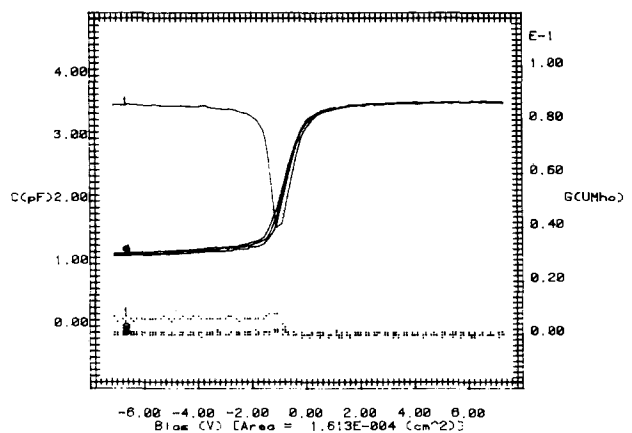


Fig. 9. CV data for injection from Si, i.e., Al was biased positive. Traces were taken at 10 kHz and 25°C. Trace 1 is for the virgin capacitor. Subsequent traces were made after successively higher electric field stresses starting at 5 MV/cm and increasing in steps of 1 MV/cm. Each stress was held for 10s at 25°C.

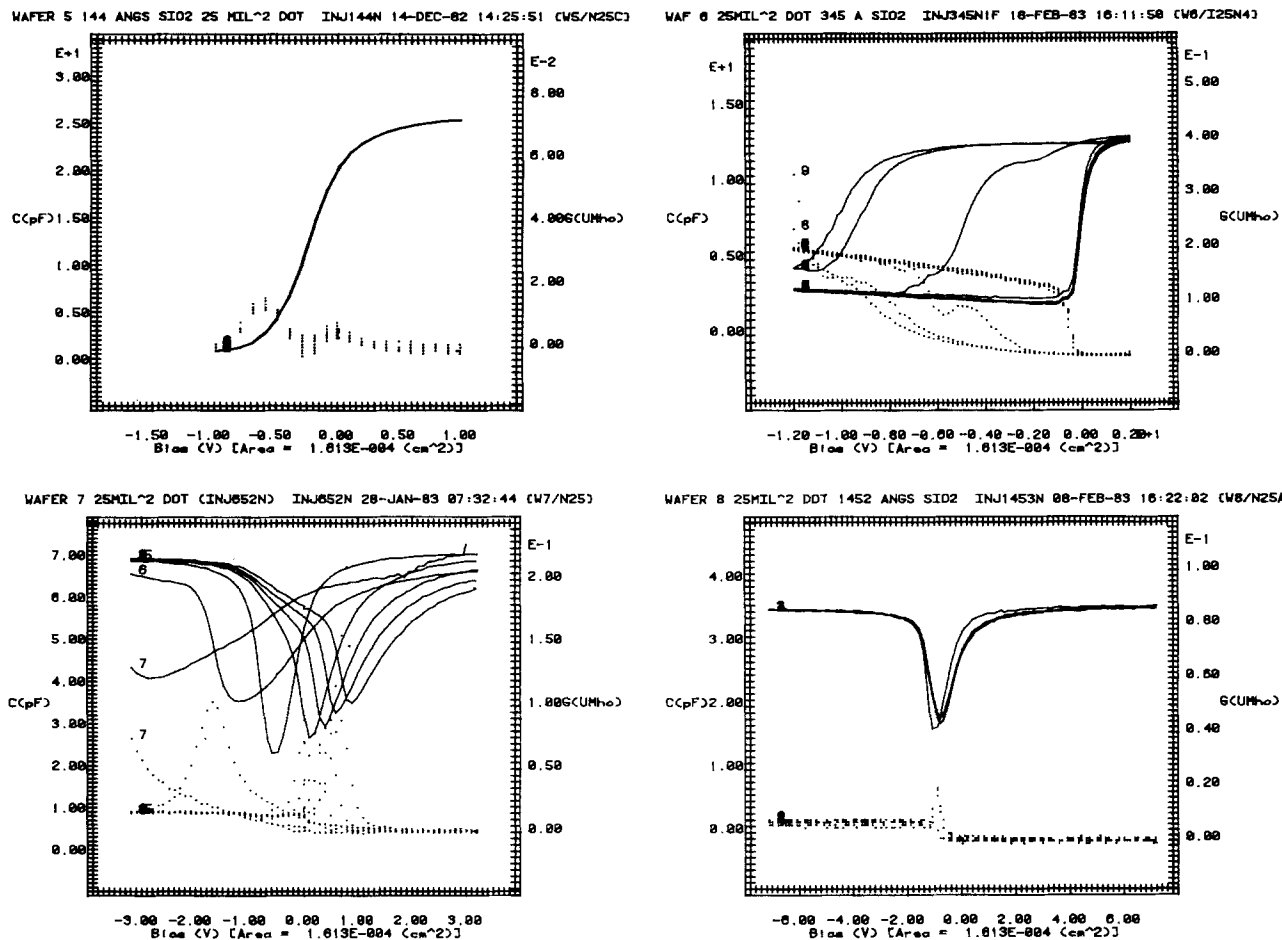


Fig. 10. CV data for injection from Al, i.e., Al was biased negative. Traces were taken at 10 kHz and 25°C. Trace 1 is for the virgin capacitor. Subsequent traces were made after successively higher electric field stress starting at 5 MV/cm and increasing in steps of 1 MV/cm. Each stress was held for 10s at 25°C.

was done in both polarities. There was insufficient bias capability in our CGV measurement equipment to stress the 1453Å oxide into the prebreakdown region. The automatic CV system in our laboratory is well suited to this

type of measurement because a complicated sequence may be set up off line and then executed whenever a measurement is needed. The system is described in detail elsewhere (11). A typical procedure definition is shown in Fig. 8.

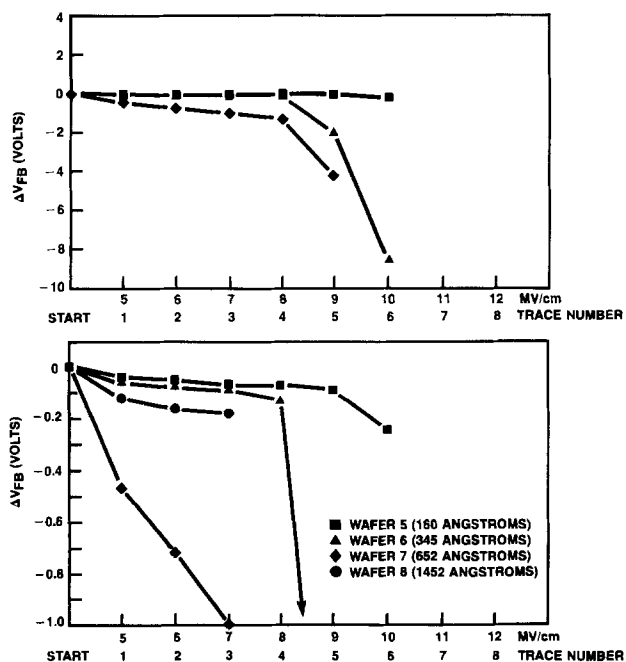


Fig. 11. Cumulative flatband voltage shifts after stress at successively higher electric fields. For injection from silicon. Taken from CV data in Fig. 9. Trace 1 is after 5 MV/cm stress for 10s, trace 2 is after 6 MV/cm stress for 10s, etc. Top: all data. Bottom: Expanded voltage scale.

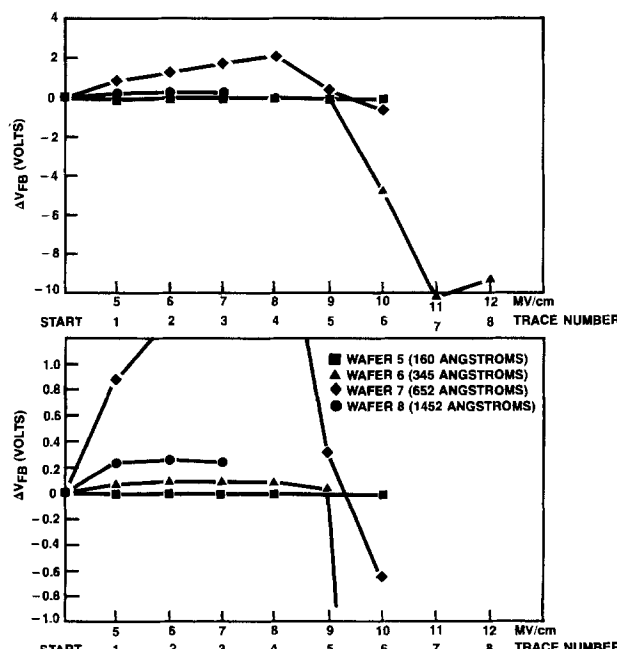


Fig. 12. Cumulative flatband voltage shifts after stress at successively higher electric fields. For injection from aluminum. Taken from CV data in Fig. 10. Trace 1 is after 5 MV/cm stress for 10s, trace 2 is after 6 MV/cm stress 10s, etc. Top: All data. Bottom: Expanded voltage scale.

CGV data obtained in this way were quite reproducible. Typical sets of traces are shown in Fig. 9 and 10. Figure 9 shows data for injection from silicon, while Fig. 10 shows data for injection from aluminum. The shifts of the flatband voltage from the flatband voltage of the first trace were obtained from the data of Fig. 9 and 10 and plotted vs. stress level in Fig. 11 for injection from Si and in Fig. 12 for injection from Al. This was done automatically, using a CV analysis utility in the CGV data acquisition system (11). In Fig. 11 and 12, a positive ΔV_{FB} corresponds to a rightward shift of the CV trace and a negative change in the oxide film. Quantitatively, the relation between ΔV_{FB} and charge induced in the film is

$$\Delta V_{FB} = -\bar{x}Q_{tot}/(\epsilon_0 K_{ox})$$

where Q_{tot} is the total charge induced in the film by the stress which caused the shift and \bar{x} is the location of the centroid of the distribution of the induced charge, measured from the Al/SiO₂ interface. In the following discussion, a flatband shift is interpreted qualitatively as charge in the film, but it must be kept in mind that the magnitude of the shift depends on the position of the charge as well as its magnitude. The data in Fig. 9-12 may be interpreted as follows.

Wafer 5, $t_{ox} = 160\text{\AA}$.—No flatband shifts occur for either polarity, so no charge was induced in the film, except, possibly, close to the Al/SiO₂ interface. For injection from Al no change occurs in the traces. But for injection from Si, the traces become more and more distorted (but unshifted) as the stress increases. The slight shifts shown in

Fig. 11 are just a reflection of the distortion of the traces in Fig. 9, rather than true shifts. Note particularly the large increase in the conductance peak (G) after the final 10 MV/cm pulse. This will be examined in more detail below.

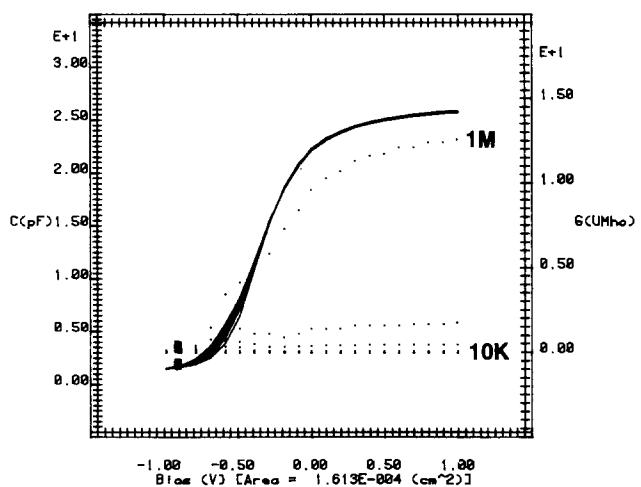
Wafer 6, $t_{ox} = 345\text{\AA}$.—For injection from Si, lower field strengths induce small positive charges until the 9 and 10 MV/cm pulses induce large positive charges. For injection from Al, lower field pulses induce small negative charges, but eventually the 10, 11, and 12 MV/cm produce large positive charges which swamp the earlier-induced negative charge.

Wafer 7, $t_{ox} = 652\text{\AA}$.—Flatband shifts of either polarity were relatively easy to induce. For injection from Si, increasing stress levels induced moderate positive charges until a 9 MV/cm stress caused a large amount of positive charge. For injection from Al, increasing strength pulses cause increasing amounts of negative charge until the 9 and 10 MV/cm pulses reduce the net charge, and even begin to make it positive.

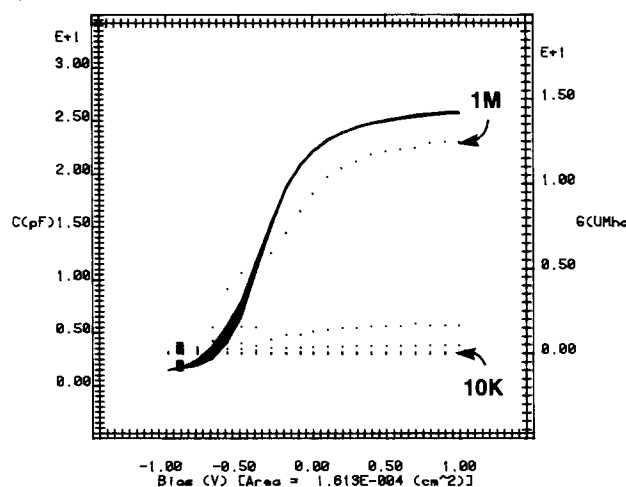
Wafer 8, $t_{ox} = 1453\text{\AA}$.—Slight negative charging occurred for injection from Al, and slight positive charging was seen for injection from Si. High fields could not be obtained because of the limits of our equipment.

CV data as a function of time at a fixed stress level.—A series of CGV measurements was undertaken to measure the accumulated change due to a given stress held for increasing accumulated time. This gives an idea of the times required to produce charging, etc. A trace (or

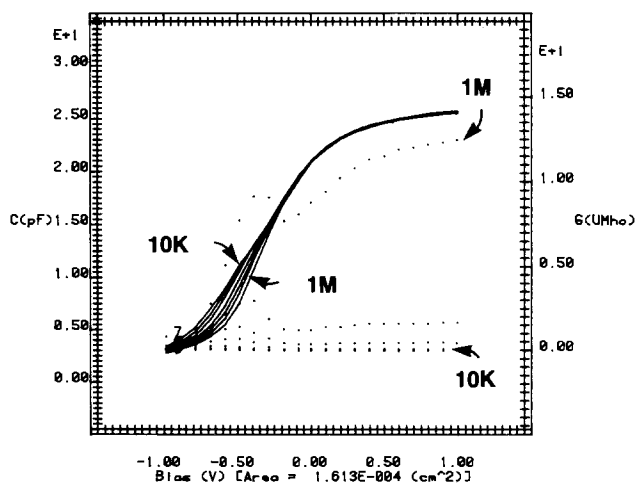
WAFS 144 ANG SIO2 25MIL^2 DOT B4 STRESS FREQ144N 14-DEC-82 17:02:41 (W5)



WAFS #F25C AFTER -14.4 V STRESS FREQ144N 14-DEC-82 17:18:28 (W5/F25D)



WAF 5 #F25D AFTER +14.4V STRESS FREQ144N 14-DEC-82 17:33:53 (W5/F25E)



WAFS #F25E AFTER ANOTHER +14.4V FREQ144N 14-DEC-82 17:48:57 (W5/F25F)

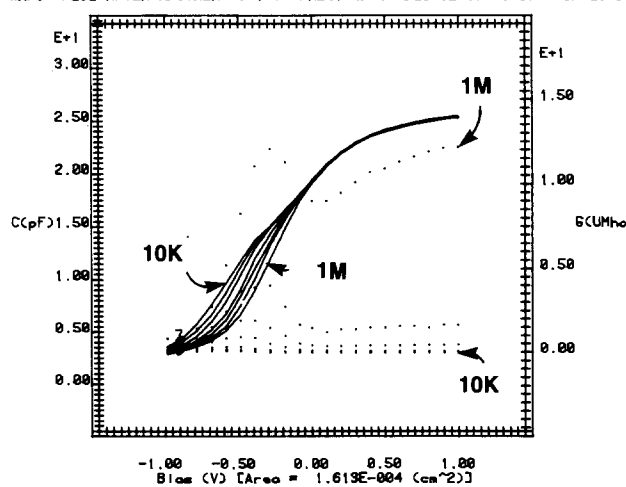


Fig. 13. CGV traces taken at a series of frequencies: 10 kHz, 20 kHz, 40 kHz, 100 kHz, 200 kHz, 400 kHz, and 1 MHz. Dotted lines are G (right-hand scale) and solid lines are C (left-hand scale). All data are taken on the same 25 mil² capacitor. Top left: virgin capacitor. Top right: after 10s of negative (on Al) 10 MV/cm. Bottom left: after a further 10s of positive 10 MV/cm pulse. Bottom right: after another 10s positive 10 MV/cm pulse.

traces) which characterize the oxide were alternated with stresses of fixed duration and voltage. All traces and stresses were done at room temperature.

Wafer 5, $t_{ox} = 160\text{\AA}$.—The changes in the thinnest oxide due to high field stresses show up as distortions in the CGV traces, Fig. 9 and 10 upper left, rather than as flatband shifts. We therefore decided to take a series of traces at different frequencies to display the effect of fast states being created at the injecting interface. In Fig. 13, we show frequency series CGV data. At the top left is the data for a virgin capacitor. After 10s at 10 MV/cm with injection from Al (top right, Fig. 13), there is no discernable change in the CGV characteristics. This capacitor was then stressed for 10s at 10 MV/cm with injection from Si (bottom left, Fig. 13) and distortion of the CV traces at low frequency was seen. Also, the conductance is seen to have a peak in the depletion region of the CGV plots. A further pulse of 10s at 10 MV/cm with injection from Si caused further distortion in the CV plots and further growth of the peak in G (bottom right, Fig. 13). This was repeated with injection from Si four additional times. The distortion of the low frequency C plot increased, as did the peak in G. The conductance data in Fig. 13 are replotted in Fig. 14 as $G/2\pi f$ vs. $\log f$ (f = frequency) with bias as a parameter. The density of interface traps, N_{it} , is proportional to $G/2\pi f$ (12). An increase in N_{it} causes a proportional increase in $G/2\pi f$. We have taken the height of the envelope of curves at 100 kHz in Fig. 14 as a measure of N_{it} in arbitrary units. In Fig. 15, we have plotted N_{it} in these arbitrary units after each of the pulses described above. It is clear from Fig. 15 that injection from Al causes no increase in the fast states at the Si/SiO₂ interface. However, injection from Si causes increases in N_{it}

which are beginning to saturate after about 60s of accumulated injection at 10 MV/cm. Another measurement was made in which a positive 10s, 10 MV/cm pulse was the first stress on a virgin capacitor. The increase in N_{it} due to this is also shown in Fig. 15. This demonstrates reproducibility and that injection from Al in the first series had no effect on subsequent developments, owing to injection from Si.

Wafer 6, $t_{ox} = 345\text{\AA}$ and wafer 7, $t_{ox} = 652\text{\AA}$.—For these wafers, the main effect of the stress in the prebreakdown region is to shift the flatband voltages. For both wafers, single 10 kHz CGV traces alternated with room temperature stresses. Each stress was held for 2s. The electric field was 10 MV/cm for wafer 6 and 9 MV/cm for wafer 7 since 10 MV/cm caused breakdown of the oxide on wafer 7. The results are shown in Fig. 16. Careful comparison reveals that the results of Fig. 16 are consistent with those of Fig. 11 and 12. We could not produce fields in the prebreakdown region of wafer 8 with our CV equipment. Therefore, there are no data for the time dependence of the flatband voltage for the thickest oxide.

For wafer 6, positive charge generation reaches a limit after 6s of injection from Si at 10 MV/cm. The time to reach the steady-state flatband shift is considerably slower (10s) for wafer 6 when injection is from Al, but the final flatband shift is the same whichever electrode is injecting.

An electric field of 9 MV/cm for injection from Al on wafer 7 does not seem to be enough to create any positive charge, but it does seem to be sufficient to detrapp any electrons (negative charge) trapped at lower fields. This seems to be true for all the oxides because all of the curves in Fig. 12 cross the X-axis near 9 MV/cm. Figure

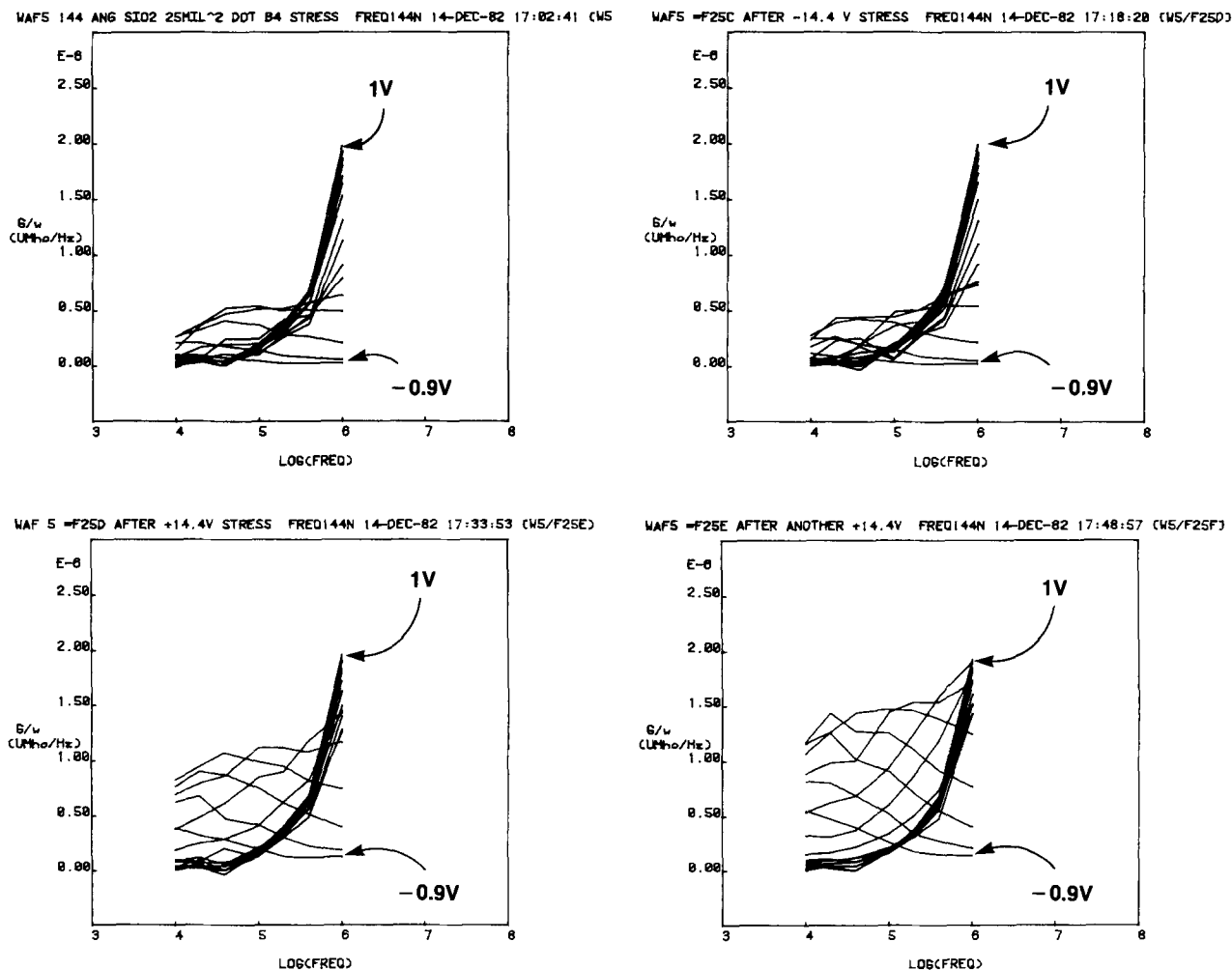


Fig. 14. GV data from Fig. 13 replotted as $G/2\pi f$ vs. $\log f$ (f = frequency) with bias as a parameter. The curves are plotted at 0.1V intervals for biases ranging from -1 to 1V.

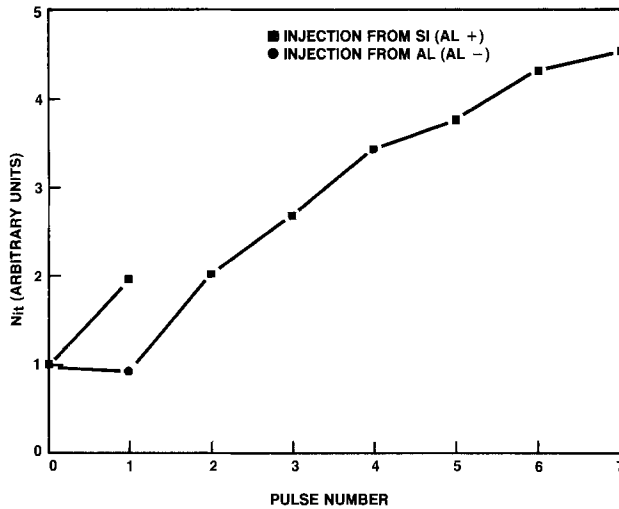


Fig. 15. The effect of high electric-field charge injection on N_{it} . For wafer 5: n-type (Y58), $t_{ox} = 160\text{\AA}$, capacitor area = 25 mil^2 . Pulse width = 10s, pulse height = 10 MV/cm.

16, bottom, shows that this condition can be maintained as a steady state. Injection from Si induces positive charges at lower fields than injection from Al, as can be seen from Fig. 11 and 12. Thus, for wafer 7, injection from Si at 9 MV/cm caused considerable positive charging within 2s, whereas injection from Al at the same field caused none (Fig. 16, bottom). The cause of the slow relaxation in the flatband voltage after 2s in Fig. 16, bottom, is not known.

Constant-current V-t characteristics.—The last set of data obtained was the voltage-time characteristic of a virgin test capacitor into which a constant current was forced. The characteristic is obtained by simultaneously unshorting the capacitor, redirecting a current from a constant-current supply onto the capacitor, triggering a high speed DVM, and monitoring the voltage across the capacitor as a function of time. At first, the voltage increase is linear with time as the test capacitor (and stray capacitance) charges. Eventually, conduction through the dielectric becomes appreciable, and the voltage is determined by the IV characteristic of the capacitor and by the current being forced. The voltage in this condition is constant if the IV characteristic of the capacitor does not change. However, space-charge buildup in the dielectric changes the IV characteristic and hence V, so the shape of the V-t characteristic in the conduction regime gives information on charging of the dielectric. This type of information, coupled with simultaneous flatband shift measurements, has been used by Meyer and Crook (16) to characterize trapping in thin oxides. We studied only injection from Si since this maintains the substrate in accumulation, thus avoiding the problem of accounting for the voltage drop across the depletion layer.

Examples of the data obtained for three thicknesses and three current densities are shown in Fig. 17. Several observations can be made: (i) the thicker oxides have an initial peak, whereas this is absent in the thinnest oxide, (ii) the initial peak, when it occurs, is sharper for higher current densities, (iii) all oxide thicknesses show a slow increase in voltage; this occurs after the initial peak for the thicker oxides, but starts immediately for the thinnest oxide, (iv) the slow increase in V is more rapid at higher current densities, and (v) not shown in Fig. 17 is the considerable scatter in time to breakdown, making generalization about times to breakdown difficult without better statistics. Still, the thinnest oxide seemed to have longer times to failure than the thicker oxides.

Discussion

The electrical results described in the previous section can be interpreted in terms of the band diagrams in Fig. 18. These diagrams incorporate the ideas of Harari (6, 7), Solomon (15), Shatzkes and Av-Ron (8), and DiStefano

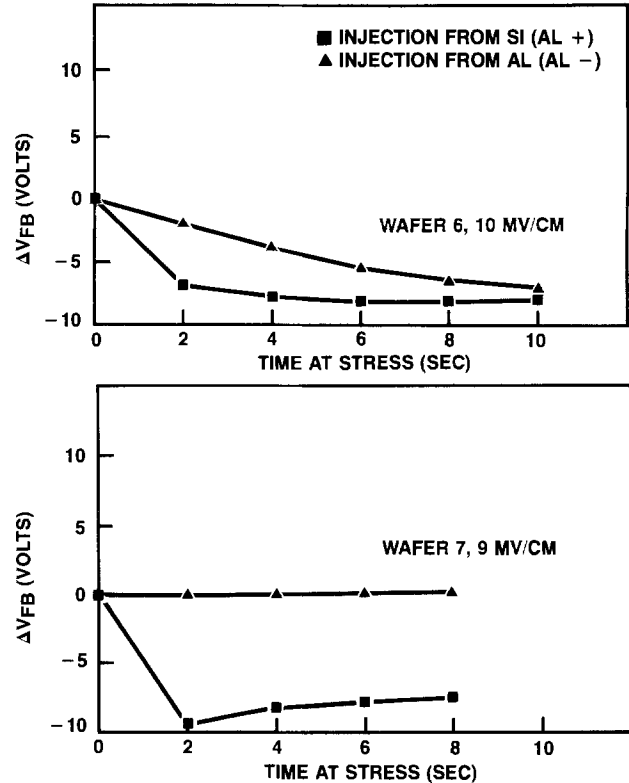


Fig. 16. Accumulated flatband voltage shifts vs. accumulated time at stress for wafer 6 ($t_{ox} = 345\text{\AA}$) and wafer 7 ($t_{ox} = 652\text{\AA}$). Stress was 10 MV/cm for wafer 6 and 9 MV/cm for wafer 7.

and Shatzkes (14). The diagrams are drawn for the case of a constant cathode field, that is, when a constant current is forced into the oxide and for high fields near breakdown. The time evolution of these bands is shown for thin oxides (6, 7, 16) and thick oxides (8, 14). Electrons injected from an electrode are accelerated by the internal field in the oxide and are scattered, forming a Poisson-shaped energy distribution which broadens and moves to lower energies as distance from the cathode increases. An electron in a part of this distribution which lies above the ionization threshold can create an electron-hole pair. The ionization threshold is one bandgap potential above the oxide conduction band. This is shown as dotted lines in Fig. 18. For thick oxides or high average fields, the peak in the hot electron distribution rises above the ionization threshold somewhere in the oxide causing ionization. The electrons so formed become part of the hot electron distribution, but the holes have very low mobility and so are practically fixed in position. For thin oxides or low average fields, there is insufficient distance or field strength to accelerate the hot electrons to a kinetic energy above the ionization threshold anywhere in the oxide, so no holes are formed. We shall call an oxide "thin" if a field high enough to cause impact ionization cannot be reached before the oxide breaks down. Thus there are two distinct types of behavior depending on oxide thickness. Oxides thinner than 250-300Å will never show a positive charge buildup due to immobile holes, whereas thicker oxides will.

The band diagrams in Fig. 18 can be used to interpret the V-t characteristics in Fig. 17 for injection from Si. The cathode field, that is, the slope of the bands at the cathode, is fixed by the current density being forced. The forced current density and the cathode field are related by the FN law. For thin oxide, traps near the cathode are generated and filled with electrons (6, 7, 15). This causes a downward bending of the oxide bands to the right of the trapped electrons (see Fig. 18). As trap creation and filling proceeds, this bending continues and causes the voltage difference across the capacitor to increase. This effect is seen for the 160Å oxide in Fig. 17. Eventually, breakdown occurs when the electric field exceeds some

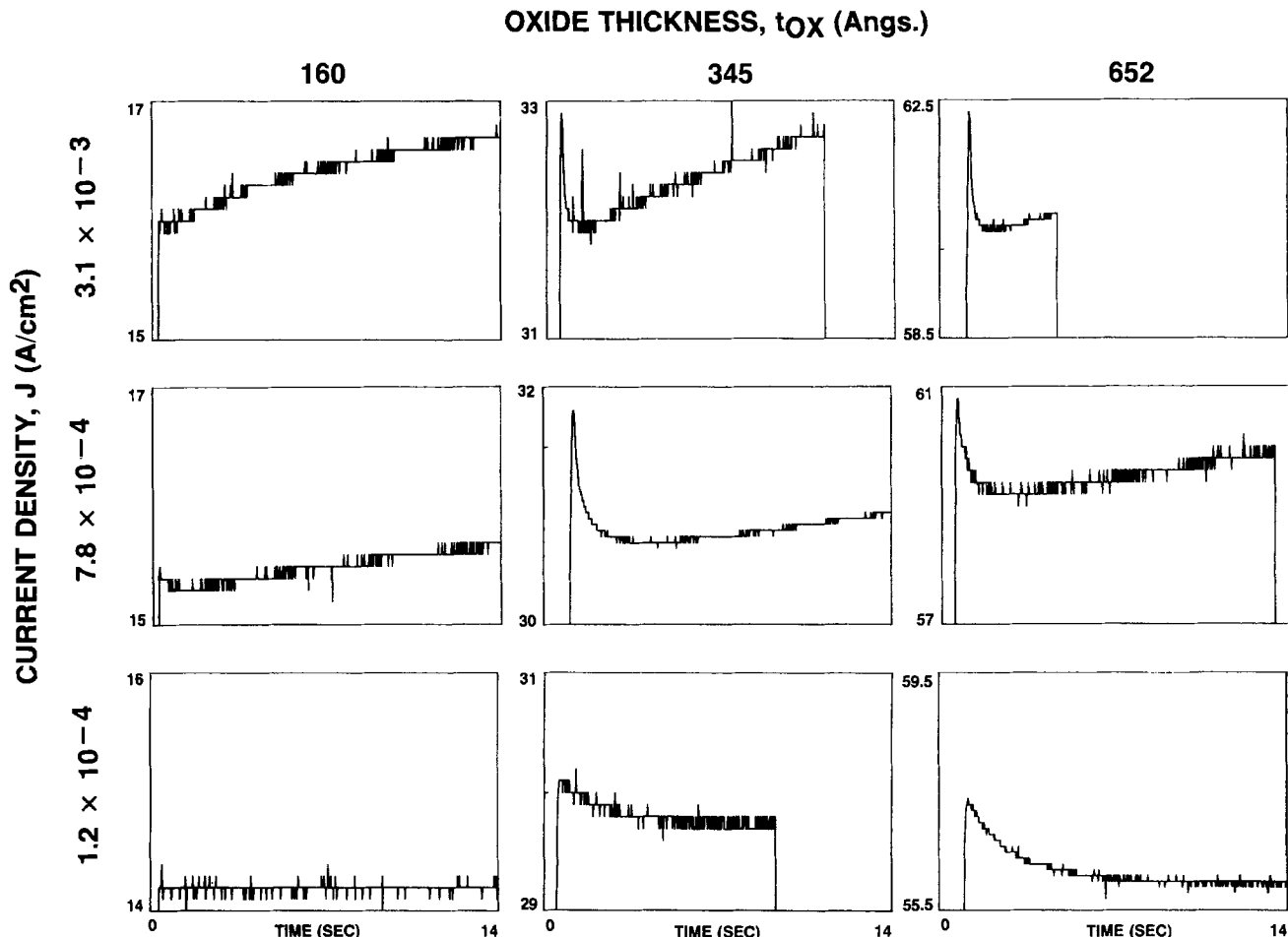


Fig. 17. Forced-current voltage-time characteristics for three oxide thicknesses (columns) and three current densities (rows). All data are for injection from silicon. Horizontal (time) axes are the same for all plots. Voltage range is shown on vertical axes.

critical value somewhere in the oxide, variously estimated as 30 MV/cm (7), 11.2 MV/cm (16), etc. For thick oxide, a relatively rapidly formed positive charge due to holes generated by ionization reduces the voltage drop across the oxide from its initial value (see Fig. 18). This is the origin of the initial peak in the $V-t$ characteristic for the thicker oxides. After this initial formation of positive charge, electron traps are generated and filled near the cathode, just as for the thin oxide, causing a slow rise in the voltage drop across the oxide (see Fig. 17). Both the positive charge and the negative charge build up more rapidly for higher current densities.

The effects of hole formation deep in the oxide and trap formation and filling near the cathode also show up in the IV and CV data. For the moment, our discussion is confined to injection from Si. The IV and CV data were taken under forced voltage, not forced current, conditions so the illustration in Fig. 18 does not strictly apply. For the thinnest oxide, the buildup of negative trapped charge at the cathode under fixed voltage conditions reduces the cathode field below the measured average field and hence reduces the injected current. This explains the deviation to lower current densities from the FN law observed in the thinnest oxide (see Fig. 4). However, for the thicker oxides, the rapid buildup of positive charge causes an enhancement of the cathode field above the average field, increasing the current above the FN prediction. Eventually, the slow buildup of trapped negative charge near the cathode tends to reduce the cathode field again bringing current back to the FN prediction, or lower. Thus the same mechanisms explain both the $V-t$ characteristics in Fig. 17 and the deviations from the FN law observed in Fig. 4. The difference is that one characteristic is observed under forced current conditions, while the other is observed under forced voltage conditions.

The CV characteristics for injection from Si, Fig. 11, show only negative flatband shifts. That is, they show

only the positive charge induced in the thicker oxides. In the CV traces for the thinnest oxide, there is no sign of the negative charge which was observed in the IV and $V-t$ characteristics. It seems that the traps created and filled with electrons during stress discharge when the stress is removed to make a CV trace. This means that they must be very close to the injecting interface and are in electrical communication with the bulk Si. Thus, at least some of the traps observed in the IV and $V-t$ data are the interface traps detected in the frequency CV data in Fig. 13-15. The conductance-voltage traces for the thicker oxides (Fig. 9) also show peaks which increase in height with increasing stress, thus showing the formation of interface traps. The CGV data are therefore entirely consistent with the IV and $V-t$ data if the negatively charged traps near the injecting interface are understood to be interface traps which discharge (but do not heal) when stress is removed.

The IV characteristics for injection from aluminum were "leakier" than the FN theory, except for the thinnest oxide (see Fig. 5). This may be due to degradation of the Al/SiO₂ interface by a chemical reaction. The increasing deviation from the FN theory as the oxide thickness increases is not understood. When the cathode field is large enough to cause appreciable charge injection through an ideal triangular barrier by the FN mechanism, the electric fields in the bulk of the oxide are large enough to cause immediate detrapping by tunneling out of the numerous grown-in traps at about 2 eV below the oxide conduction band. Thus, no charging of these grown-in traps will occur. The grown-in traps are distributed uniformly throughout the bulk of the oxide and are to be distinguished from the current-induced interface traps described above. However, if the interface is a more efficient injector than a simple triangular tunneling barrier, then large numbers of electrons will enter the oxide and fill traps at fields low enough that detrapping will not

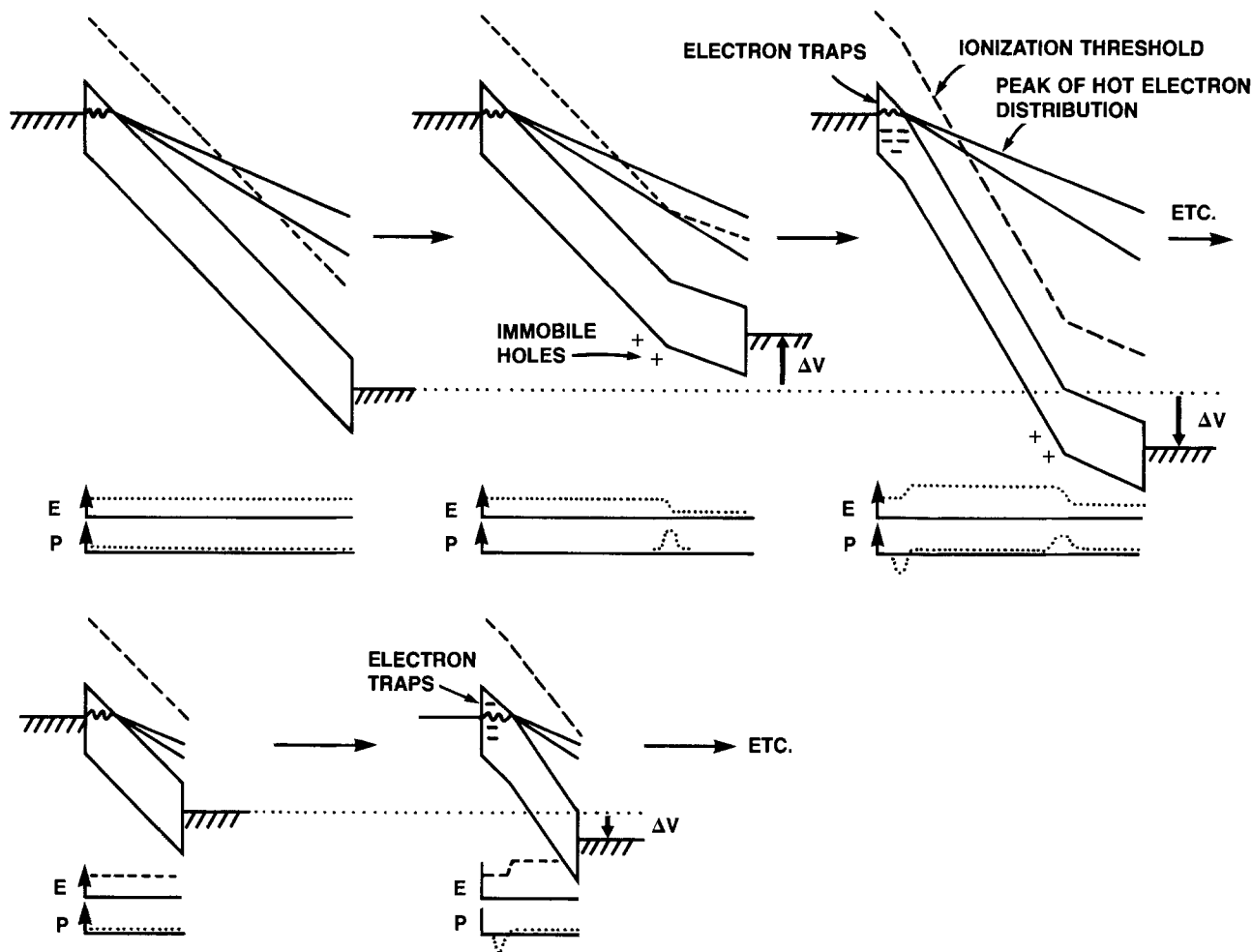


Fig. 18. Time evolution of bands, electric fields, and charges for thick oxide (top) and thin oxide (bottom). Drawn for constant forced current

occur (20). Thus, the negative charging evidenced by the positive flatband shifts shown in Fig. 12 is probably due to bulk trapping and is consistent with the "leakier" than FN current-voltage characteristics in Fig. 5. Notice that the thinnest oxide, which obeys the FN law, shows no evidence of bulk trapping. As the electric field increases the IV characteristics approach the FN characteristic (Fig. 5), bulk traps are emptied, and impact ionization produces holes which produce negative flatband shifts (Fig. 12).

This discussion has shown that all of the data can be explained in terms of a simple model with the following features: (i) impact ionization produces immobile holes in thicker oxides, (ii) interfacial trap formation and filling near the cathode occur in all of the oxides, and (iii) for "leaky" interfaces, such as the Al/SiO₂ interface in our particular oxides, bulk trapping occurs. These charges distort the bands in the oxide and create internal electric fields which differ from the average electric field. Whenever the electric field somewhere in the oxide exceeds a critical value, breakdown occurs. At a given average electric field, the relative rates of generation of charge formation by the above three mechanisms, especially the first two, determine the time to breakdown. Defects, weak or thin spots in the oxide, etc., will all contribute to a scatter in the times to breakdown. Another factor which determines the time to breakdown is the way in which the oxide is stressed: *viz.*, by forced current or forced voltage, the rate of charge buildup is different for each of these methods.

Conclusions

We have presented a qualitative picture of high field trapping and ionization phenomena in thermal oxides as a function of oxide film thickness. This was done by integrating three types of data: (i) IV data, (ii) CV data,

and (iii) forced-current voltage-time data. Interface trap formation and charging with electrons near the cathode during injection from Si was observed for all oxides. Creation of immobile holes in the oxide valence band by impact ionization was observed for the thicker oxides, but not the thinnest. Bulk trapping was significant when electrons were injected from Al into the thicker oxides. For the thicker oxides, the Al/SiO₂ interface was considerably leakier than predicted by the FN theory. This type of measurement is an important adjunct to long term reliability studies since these phenomena cause wear-out of intrinsic oxides.

There is still considerable controversy as to exactly what mechanisms occur in oxides at highfields (16-19). We have interpreted our data according to what seem to be the most likely mechanisms (7, 8, 15). A partial reason for many of the conflicting observations in the literature must be differences, documented and otherwise, in the processes which produce MOS test capacitors. This shows the importance of setting up the techniques described in this report as a process-development tool as opposed to making the measurements once with the hope of pinning down the mechanisms once and for all. Measurement techniques set up as a process-development tool must be highly automatic both in data acquisition and data analysis in order to facilitate throughput.

Most of the analysis in this report has been qualitative because our purpose has been to review and illustrate rather than to make a detailed quantitative analysis of a particular oxide. Still, it is clear that quantitative analysis such as calculation of cross sections, trapping efficiencies, etc., are quite straightforward since all the data are stored in digital form on floppy disks, and are easily accessible for computer analysis.

The discussion has shown the power of using multiple techniques in unraveling mechanisms. For example, the

CV shifts due to bulk trapping when electron injection was from aluminum would have been difficult to understand without the FN data. It is also worth emphasizing the value of FN data by itself as an analytical tool, especially when comparison is made with theoretical expectations. FN analysis is not as widely recognized as a process development tool as is, say, CV measurement.

Acknowledgments

Thanks are due to the following individuals: C. E. Wu for helpful discussions, Rick Cosway for supplying oxides, Kathy Ginn for processing, Dan McGuire for help with measurements, and Sue Trower for typing this paper.

Manuscript received Dec. 21, 1983.

Motorola, Incorporated, assisted in meeting the publication costs of this article.

REFERENCES

1. D. J. DiMaria, in "The Physics of SiO₂ and Its Interfaces," Pergamon Press, New York (1978).
2. H. F. Wolf, "Semiconductors," Interscience, New York (1971).
3. M. Lenzlinger and E. H. Snow, *J. Appl. Phys.*, **40**, 278 (1969).
4. C. M. Osburn and E. J. Weitzman, *This Journal*, **119**, 603 (1972).
5. Z. A. Weinberg, *J. Appl. Phys.*, **53**, 5052 (1982).
6. E. Harari, *Appl. Phys. Lett.*, **30**, 601 (1977).
7. E. Harari, *J. Appl. Phys.*, **49**, 2478 (1978).
8. M. Shatzkes and M. Av-Ron, *ibid.*, **47**, 3192 (1976).
9. S. M. Sze, "Physics of Semiconductor Devices," Wiley-Interscience, New York (1969).
10. C. M. Osburn and D. W. Ormond, *This Journal*, **119**, 597 (1972).
11. C. G. Shirley, *Semicond. Intl.*, **5**, 81 (1982).
12. E. H. Nicollian, A. Goetzberger, and A. D. Lopez, *Solid State Electron.*, **12**, 937 (1969).
13. C. M. Osburn and N. J. Chou, *This Journal*, **120**, 1377 (1973).
14. T. H. DiStefano and M. Shatzkes, *J. Vac. Sci. Technol.*, **12**, 37 (1975).
15. P. Soloman, *J. Appl. Phys.*, **48**, 3843 (1977).
16. W. K. Meyer and D. L. Crook, Paper presented at the International Reliability Physics Symposium, Phoenix, AZ (1983).
17. C. S. Jenq, T. R. Raganth, C. H. Huang, H. S. Jones, and T. T. L. Chang, *IEDM*, 388 (1981).
18. M. S. Liang and C. Hu, *ibid.*, 396 (1981).
19. M. Itsumi, *J. Appl. Phys.*, **52**, 3491 (1981).
20. D. J. DiMaria and D. W. Dong, *ibid.*, **51**, 2722 (1980).

The Atomic-Scale Origin of the Strain Enthalpy of Mixing in Zincblende Alloys

J. C. Mikkelsen, Jr.*

Xerox Palo Alto Research Center, Palo Alto, California 94304

ABSTRACT

The atomic-scale structure of Ga_{1-x}In_xAs solid solutions, previously experimentally determined by extended x-ray absorption fine structure, is used to model the strain energy associated with the local distortions in bondlengths and bond angles relative to those in the pure binary compounds. The distortion energy associated with the bondlength change was calculated to be 0.03X(1 - X) eV/cation-anion pair, where X is the InAs mole fraction, and adding the contribution from the bond-angle distortions leads to a total strain energy of 0.11X(1 - X) eV/atom-pair. The composition dependence of the strain energy is the same as the regular solution enthalpy of mixing, α_sX(1 - X), and the calculated value of the solid solution interaction parameter, α_s, is in good agreement with the reported experimental value of 0.13 eV/atom-pair for Ga_{1-x}In_xAs. Similar calculations are made for four other zincblende solid solutions for which the atomic-scale structure has been determined, and the results suggest that local bond strain is the major contribution to the enthalpy of mixing. Generalization of the strain calculations leads to a second-order dependence of the α_s on the normalized difference in endmember lattice constants, with no adjustable parameters, and this result is compared to semiempirical models for α_s.

Ternary and quaternary solid solutions of III-V semiconductors have received much attention as substrates and active layers of optoelectronic devices for applications such as optical communications. In particular, an enormous effort has been expended in determining many of the solid-liquid phase diagrams in order to develop suitable conditions for controlled crystal growth of the desired alloy compositions (1). In an attempt to predict the more complex quaternary phase relations and the ultimate stability of the solid solutions well below the solidus temperatures, various thermodynamic models have been used to parameterize the existing experimental temperature- and compositional-dependent phase equilibria. In an ideal binary solution (2), there is no enthalpy contribution to the solution free energy, and the ideal entropy of mixing is $-R(X_1 \ln X_1 + X_2 \ln X_2)$. The deviations from ideality are small in many III-V ternary systems, and many of the phase diagrams have been successfully modeled by assuming that the solids are regular solutions (1). A regular solution (2) is one in which the free energy of mixing has, in addition to the ideal entropy term, a composition-dependent enthalpy term of the form α_sX₁(1 - X₁), where α_s is the solid solution interaction parameter

(also called Ω) and must be independent of both temperature and composition. In the regular solution models for III-V phase diagrams the α_s's range from zero for Al_{1-x}Ga_xAs to 4.5 kcal/mol (0.195 eV/atom-pair) for GaAs_{1-x}Sb_x (1). Although more complex thermodynamic models have also been used to fit the experimental phase diagrams, the extent of improvement is difficult to assess.

Since the solid solution interaction parameter represents the deviation of zincblende alloys from ideal solid solutions, understanding its atomic-scale origin can improve the ability to predict more complex phase diagrams, the dependence of alloy crystal chemistry on crystal-growth technique, alloy stability against phase separation below the growth temperature, and, possibly, the mechanisms of device degradation. In standard thermodynamic texts, it is postulated that local strain associated with different atomic sizes of the constituents is a major contribution to the enthalpy of mixing in solid solutions. There have been semiempirical correlations of α_s with the difference between the lattice constants of the binary compounds which form the solid solution, Δ = a₁ - a₂. Stringfellow (3) and Brebrick and Panlener (4) have asserted that α_s is reasonably well correlated with square (3) or sixth (4) power dependences of α_s on Δ, respectively.

*Electrochemical Society Active Member.

Although these correlations imply that the deviation from ideality is due to a local lattice mismatch arising from the different "size" of the substituted ions, Stringfellow derived the Δ^2 dependence in the delta-lattice-parameter (DLP) model not on the basis of strain, but on the expected variation of the alloy electronic structure with lattice constant within the context of the dielectric band model of Phillips and Van Vechten (5) which is discussed in detail below.

An estimate of lattice strain energy has been compared to experimental values of α_s for three pseudobinary III-V systems, including $\text{Ga}_{1-x}\text{In}_x\text{As}$, by Foster and Woods (6), and they found that the calculated strain energy led to a calculated interaction parameter which was a factor of 5 too high. In their elastic model, it was assumed that the strain energy was that required to increase the Ga-As distance, and decrease the In-As distance, in order to make both distances equal to the average cation-anion distance defined by the alloy lattice constant. However, recent extended-x-ray-absorption-fine-structure (EXAFS) measurements on $\text{Ga}_{1-x}\text{In}_x\text{As}$ (7) and other III-V alloys (8) indicate this is not a good approximation to the alloy structure. Rather, there is always $\sim 0.13\text{\AA}$ difference between the Ga-As and In-As bondlengths at any given alloy composition. The availability of atomic-scale structural information on solid solutions now permits an examination of the contribution of bond strain to the enthalpy of mixing. We show that the bond distortion energy calculated from the EXAFS structural information for representative ternary zincblende alloys is in good agreement with the thermochemical interaction parameters which model the enthalpy of mixing.

Structural Model for Zincblende Solid Solutions

In the structural discussion which follows, we will compare the equilibrium alloy structure of $\text{Ga}_{1-x}\text{In}_x\text{As}$ as an example zincblende solid solution with two approximations, the deviations from which will provide the basis for the calculation of the bond-distortion energies. The two structural approximations are the virtual crystal approximation (9) (VCA) and what can be called the covalent radius approximation (CRA) after the chemical bond concepts of Pauling and Huggins (10), which suggest that a tetrahedral covalent radius, to first order, is invariant. In the VCA, the substituted and common atoms occupy their respective regular zincblende lattice sites, and at a given composition all cation-anion nearest neighbor (nn) bondlengths are equal to $a_0\sqrt{3}/4$, where a_0 is the alloy lattice constant. Thus, in the VCA description of $\text{Ga}_{0.5}\text{In}_{0.5}\text{As}$, all the Ga-As nn bondlengths are stretched and the In-As bondlengths are compressed by 0.087\AA to become equal to 2.535\AA . Since the zincblende crystal structure is strictly retained in the VCA (with random distribution of substituted ions), all interatomic bond angles are at the ideal tetrahedral value of 109.5° . In other words, the VCA is characterized by a zero bond angle distortion at the expense of large changes in the nn bondlengths. This approximation is equivalent to that used in the elastic model of Foster and Woods. Since the EXAFS results indicate that the Ga-As and In-As nn distances change by only 25% of that required to make them equal for any given alloy composition, it is obvious that the Foster-Woods estimate of the strain (which is proportional to the square of the bondlength change) will be much too high. In the CRA, however, local atomic displacements from the zincblende lattice sites are required to produce two different cation-anion nn distances, which correspond to the natural bondlengths in the pure binary endmembers. This condition is satisfied in the zincblende-like chalcopyrite structure (11), where the substituted sublattice can be approximately fcc, and the common sublattice atoms are displaced to accommodate two different cation-anion distances. Atomic displacements from fcc positions result in a deviation of the bond angles from 109.5° . Thus, the CRA is characterized by zero nn bondlength changes at the expense of large bond-angle distortions.

EXAFS measurements (7) indicate that the equilibrium alloy structure of $\text{Ga}_{1-x}\text{In}_x\text{As}$ is closer to the second approximation. The Ga-As nn distance is given by $2.448 + 0.044X_2$ (\AA) and the In-As nn distance by $2.622 - 0.044X_1$ (\AA), where X_1 and X_2 are the mole fractions of GaAs and InAs, respectively. By contrast, in the VCA all of the cation-anion nn distances are given by $2.448 + 0.174X_2$ (\AA). Thus, in $\text{Ga}_{0.5}\text{In}_{0.5}\text{As}$, the experimentally-determined Ga-As and In-As nn distances are 2.470 and 2.600\AA , respectively, compared to the VCA average distance of 2.535\AA .

Although the nn Ga-As and In-As distances are known with good accuracy ($\pm 0.005\text{\AA}$), the second neighbor (nnn) distances are less certain, due to both larger experimental error bars ($\pm 0.02\text{\AA}$) and the fact that the (gaussian) width of the alloy nnn pair-correlation functions are of the order of 0.05\AA broader than those in the pure binary compounds. The additional width can arise from both static (statistical distribution of local Ga-In concentrations) and dynamic (thermal vibration) contributions (the latter of which has been minimized by making the EXAFS measurements at 77 K). We cannot calculate an accurate distribution of bond angles from the nnn distance distributions without knowledge of the intermediate-range structure. If we use the mean distance (peak) of the nnn gaussian distributions, the bond angles in $\text{Ga}_{0.5}\text{In}_{0.5}\text{As}$ deviate from the ideal 109.5° by a maximum of 3.1° for In-As-In and a minimum of zero for In-As-Ga, with an rms value of 0.5° for all the bond angles. However, the real structure must contain a somewhat different distribution of bond angles which arise from the nnn distances which are either larger or smaller than the peak value of the nnn distributions. Although it would seem reasonable to assume that the shortest Ga-Ga nnn distances are associated with AsGa_4 tetrahedra and the longest In-In distances are associated with AsIn_4 tetrahedra, we have not determined a satisfactory self-consistent bond-angle model which accurately fits all of the EXAFS data.

An alternative estimate of the bond-angle distribution can be calculated for the chalcopyrite-like structural model (7) which gave a good fit to both the nn and nnn EXAFS data for $\text{Ga}_{0.5}\text{In}_{0.5}\text{As}$, except that the model cation-cation nnn distributions were too sharp. The change in bond angles for the As atom displacements ranged from 0° for In-As-Ga angle to a maximum of $+4.4^\circ$ for Ga-As-Ga and -4.4° for In-As-In. The rms change in the 12 bond angles associated with a (Ga, In)-As atom-pair is 2.0° , considerably larger than the 0.5 estimated from only the peaks in the EXAFS nnn distributions, but they are the actual bond angles observed in the cubic chalcopyrite compound ZnSnAs_2 , in which the nn and nnn distributions closely approximate those observed for $\text{Ga}_{0.5}\text{In}_{0.5}\text{As}$. Regardless of the estimates for the bond-angle displacements, it is obvious that the equilibrium alloy structure is a balance between bondlength and bond-angle distortions, *i.e.*, the two distortions oppose each other. In other words, in the absence of forces which resist changes in bond angles, the minimum energy would be satisfied by a zero bondlength change relative to the binary endmember compounds. The $\text{Ga}_{1-x}\text{In}_x\text{As}$ alloy nn bondlengths determined by EXAFS, along with estimates for the bond-angle contributions, are used below in a simple force constant model to calculate the bonding strain energy, and these results are compared to the thermodynamic analysis of the GaAs-InAs pseudobinary phase diagram.

Estimate of Strain Energy for $\text{Ga}_{1-x}\text{In}_x\text{As}$

Our principal objective is to obtain the excess enthalpy of mixing due to strained bonds, using as the reference state the bondlengths in the endmember binary compounds, *i.e.*, 2.448 and 2.622\AA for Ga-As and In-As, respectively, and ideal tetrahedral angles of 109.5° . If all of the atomic positions in the alloy were known with sufficient accuracy to determine the bond angles, a force constant model (12) could be used to compute the total displacement (strain) energy in terms of changes in bondlengths

and angles relative to the standard states. In the absence of accurate bond-angle information, we take a slightly different approach. We view the local forces as separable into those which resist bondlength changes (central) and the net of all the others, which resist bond-angle changes (noncentral). The strain energy from the former is straightforwardly determined from the isotropic dilation (increase in Ga-As bondlengths) or compression (decrease in In-As bondlength) compared to the reference Ga-As and In-As bondlengths. For example, the strain energy associated with radial changes in the Ga-As bondlength, $U_r(\text{Ga-As})$, is given by $1/2 k_r \Delta r_1^2$, where k_r is the central force constant and has a value of 128 N/m (12) derived from the bulk modulus and Δr_1 is the change in bondlength from 2.448Å. The parabolic dependence of U_r on Δr_1 is shown for a single Ga-As bond by curve (a) in the configuration energy diagram of Fig. 1. If there were no forces resisting the bond-angle distortions [no θ -dependent terms Eq. [1] of Ref. (12)], then the minimum energy would correspond to no change in Ga-As bondlength for any alloy composition, *i.e.*, the CRA model would be satisfied. However, at the experimentally determined Ga-As nn distance in the $\text{Ga}_{0.5}\text{In}_{0.5}\text{As}$ alloy, $\Delta r = 0.022\text{Å}$, and $U_r = 0.002$ eV per Ga-As bond (0.007 eV per Ga-As atom-pair). Since $\Delta r_1 = 0.044X_2$, the composition dependence of $U_r(\text{GaAs})$ is given by $0.007 X_2^2$ eV per Ga-As bond. There is a similar energy term from the corresponding decrease of the alloy In-As nn distance, $\Delta r_2(k_{r2} = 108$ N/m), which also contributes 0.002 eV per In-As bond. Since the rate of change in VCA average nn distance, Δr_{VCA} , is approximately four times that observed in Δr_1 or Δr_2 , the strain energy calculated for the virtual crystal structure, which has bondlength changes only, is approximately 16 times higher than that obtained from the experimentally determined alloy bondlength distortions. However, the correct value for the strain associated with only the bondlength distortions is approximately a factor of four smaller than the measured enthalpy of mixing (1, 6). [Fedders and Muller (13) recently obtained a similar result by considering only the changes in alloy bondlengths (7),

but they did not attempt to calculate the strain associated with bond-angle distortions.]

The next step is to estimate the bond-angle, or noncentral, contribution to the bond-strain energy. In the absence of known bond-angle distributions for the alloy, we make a semiempirical estimate of the effective bond-angle strain, U_{eff} , by equating the opposing central and noncentral forces at equilibrium bondlengths which are observed experimentally by EXAFS. In addition, we assume that the reference state for the bond angle is the ideal tetrahedral angle of 109.5° . Since this latter structural condition is satisfied at any alloy composition by the VCA model, we have $U_{\text{eff}}(\text{VCA}) = 0$. The Ga-As bond-angle distortion energy for the $\text{Ga}_{0.5}\text{In}_{0.5}\text{As}$ alloy is shown by curve (b) in Fig. 1 which satisfies the two constraints of equal forces at $\Delta r_1 = 0.022\text{Å}$ and zero energy at $\Delta r_{\text{VCA}} = 0.087\text{Å}$. The effective bond-angle distortion energy is 0.005 eV/bond, or 0.023 eV/atom-pair, and the total strain energy is 0.030 eV/(Ga-As) atom-pair in the $\text{Ga}_{0.5}\text{In}_{0.5}\text{As}$ alloy. By comparison, for $\text{Ga}_{0.5}\text{In}_{0.5}\text{As}$ the total strain energy at CRA, which arises from bond-angle distortions only, is 0.042 eV per atom-pair, whereas the total strain energy at VCA, which arises from bondlength distortions only, is 0.140 eV/atom-pair. Thus, the calculated total strain energy for the equilibrium structure is lower than that of either the VCA or CRA, and it is apparent that most of the strain energy actually arises from the distortion of the bond angles. As a matter of perspective, this strain energy of 0.03 eV/atom pair is certainly small compared with the GaAs cohesive energy of 5.8 eV/atom-pair, or the heat of formation of 0.75 eV/atom-pair (5).

A general form of the bond-angle strain energy is preferred in order to examine the composition dependence of the total strain energy. Curve (b) of Fig. 1 is of the form $U_{\text{eff}}(\text{GaAs}) = 1/2 k_{\text{eff}}(\Delta r_{\text{eff}})^2$, where $\Delta r_{\text{eff}} = \Delta r_{\text{VCA}} - \Delta r_1$. Since the central and effective noncentral forces are equal and opposite at the equilibrium value of Δr_1

$$k_{\text{eff}}/k_r = \Delta r_1/(\Delta r_{\text{VCA}} - \Delta r_1) \quad [1]$$

For later comparison with other zincblende alloy systems, it is useful to express the composition dependence of the bondlengths as $\Delta r_1 = S_1 X_2$ and $\Delta r_{\text{VCA}} = S_{\text{VCA}} X_2$, where S_1 (measured by EXAFS) and S_{VCA} (determined from the alloy lattice constants) equal 0.044 and 0.174Å, respectively, for $\text{Ga}_{1-x}\text{In}_x\text{As}$. Thus, $k_{\text{eff}} = k_r S_1/(S_{\text{VCA}} - S_1)$, and $\Delta r_{\text{eff}} = X_2(S_{\text{VCA}} - S_1)$, and the term in parentheses is independent of composition. Although curve (a) in Fig. 1 universally represents the radial strain energy for Ga-As bonds at any bondlength defined by Δr_1 , the bond-angle contribution is a family of curves like (b) which depend on composition, *i.e.*, which have their minima at the appropriate VCA distance.

Before proceeding with the expression for the composition-dependence of the total strain energy, consider the value of the "effective" angular displacement which is represented by Δr_{eff} and which is on the order of 0.065Å. Since the nn bondlengths are approximately 2.5Å, the effective angular displacements are 1.5° . This value is in better agreement with the above chalcopyrite estimate than that obtained from only the peaks of the EXAFS nnn distributions and at the respective equilibrium nn distances have derivatives equal to those of curve (A). For the sake of comparison, we put the various estimates of the bond-angle displacements in the θ -dependent terms of Eq. [1] in Ref. (12). The largest value of the bond-angle strain (0.020 eV/atom-pair) occurs for the 2.0° rms bond-angle change of the chalcopyrite model, and the smallest value (0.002 eV/atom-pair) occurs for the 0.5° rms displacement calculated from the peak in the EXAFS nnn distributions. It is beyond the scope of this study to make a theoretical analysis of all the terms which comprise the semiempirical parameter k_{eff} ; however, we note that it probably cannot be simply related to the k_θ 's (or to a β/α ratio) of Ref. (12), and that it probably does indirectly include coulombic terms, which may also be minimized at the VCA structure, owing to the periodicity of the lattice.

Addition of the Ga-As bondlength and bond-angle strain energy contributions (multiplied by four bonds per

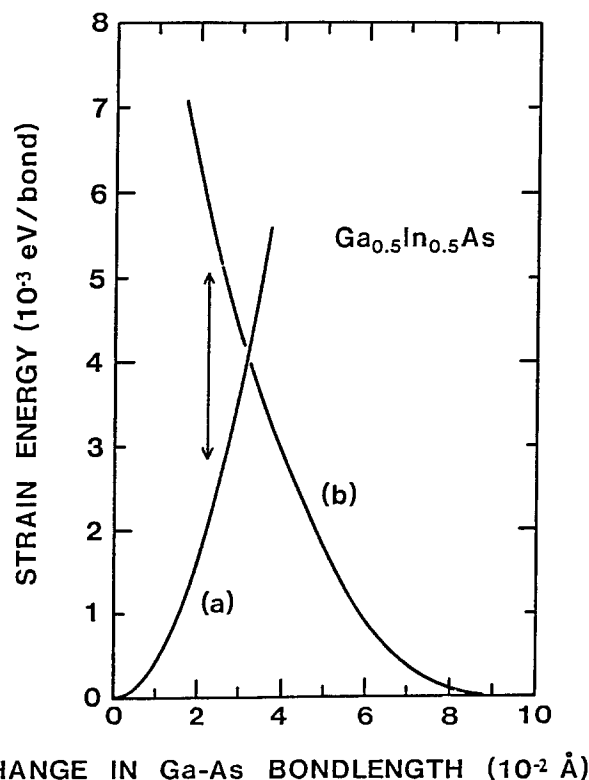


Fig. 1. Configuration energy diagram for distortions in $\text{Ga}_{1-x}\text{In}_x\text{As}$. Curve (a) is bond-stretching displacement energy per Ga-As bond vs. change in Ga-As nn distance; curve (b) is effective noncentral displacement energy per Ga-As bond in $\text{Ga}_{0.5}\text{In}_{0.5}\text{As}$. Arrow indicates the equilibrium Ga-As Δr in $\text{Ga}_{0.5}\text{In}_{0.5}\text{As}$ at 0.022Å.

Table I. Lattice parameter differences, Δ (11), atomic-scale structural parameters, S_1/S_{VCA} (defined in text) from EXAFS (7, 8) and Fukai model (14), central force constants (12), and calculated and experimental (1, 3, 4) regular solution interaction parameters for several zincblende alloys

Alloy	Δ (Å)	S_1/S_{VCA}		k_1	k_2	α_s (calc)	α_s (meas)
		EXAFS	Fukai	(N/m)	(N/m)	(eV/atom-pair)	
(Ga,In)P	0.418	0.204	0.208	147	132	0.11(8)	0.139-0.156
(Ga,In)As	0.382	0.252	0.212	128	108	0.11(4)	0.078-0.130
Ga(As,P)	0.203	0.250	0.240	128	147	0.03(4)	0.017
Zn(Se,Te)	0.421	0.244	0.153	107	96	0.10(6)	0.065
Cu(Br,I)	0.352	0.320	—	~70	~70	0.06(6)	—

Ga, As atom-pair) leads to the composition-dependent expression

$$U_{(Ga-As)} = 2k_{r12}S_{VCA}S_1X_2^2 \text{ (eV per Ga-As atom-pair)} \quad [2]$$

A similar expression exists for each In-As atom-pair. In order to compute a strain energy per alloy atom-pair, the Ga-As and In-As contributions are weighted by their respective mole fractions. Although, in principle, S_2 , the rate of change in In-As bondlength with composition, can differ from S_1 , the EXAFS results gave identical values for S_1 and S_2 . Furthermore, since the central force constants are similar (128 and 108 N/m), they can be replaced by an average value, k_{r12} . By combining terms the final approximate strain energy per alloy atom-pair is

$$U_{\text{strain}} = (S_{VCA}S_12k_{r12})X_1X_2 \text{ (eV per atom-pair)} \quad [3]$$

The form of this expression is the same as the regular solution excess enthalpy of mixing, with α_s given by the product of constants, $S_{VCA}S_12k_{r12}$. The calculated value of $S_{VCA}S_12k_{r12}$ is 0.11(4) eV/atom-pair, which is in excellent agreement with the reported value of α_s of 0.130 eV/atom-pair reported by Ilegems and Panish (1), but somewhat higher than the value of 0.087 obtained by Foster and Woods (6). The excess enthalpy of mixing appears to originate from the change in covalent bondlengths and bond angles in the solid solutions. Of course, it is possible to retain the composition dependence of α_s through the use of individual force constants, k_{r1} , rather than their average. In $Ga_{1-x}In_xAs$, for example, α_s varies by 20% from 0.124 to 0.104 eV/atom-pair for values of $x = 0$ and 1, respectively. If the composition dependence of the interaction parameter determined by Foster and Woods is approximated by a linear curve, the change is also a 20% decrease from GaAs to InAs.

Strain Enthalpy of Mixing for Other Zincblende Ternary Alloys

EXAFS measurements have been made on several zincblende solid solutions (8), and the values of S_1 (which were found to be nearly equal S_2) from preliminary data analyses are shown in Table I. The ratio of the observed change in nn distance (S_1) to the change in average nn distance (S_{VCA}) can be taken as a relative measure of the degree of bondlength distortion. This ratio is higher for the more ionic cuprous halides than the covalent III-V systems. Recently, Fukai (14) has applied a force constant model to estimate the bondlength distortions in zincblende solid solutions. He derived an expression for S_1/S_{VCA} (γ in his notation) which is given by $4/3(\beta/\bar{\alpha})/[1 + (\beta/\bar{\alpha})]$, where $\bar{\alpha}$ and $\bar{\beta}$ are the mean short range bond stretching and bond bending force constants given by Martin (12). The agreement between the Fukai model and experimental EXAFS results is very good for $Ga_{1-x}In_xP$ and $GaAs_{1-x}P_x$, and slightly less so for $Ga_{1-x}In_xAs$. However, the predicted trend with ionicity is in the wrong direction. Fukai reasoned that since $\beta/\bar{\alpha}$ decreased with increasing ionicity, S_1/S_{VCA} would therefore decrease with increasing ionicity. The experimental EXAFS data show that the opposite is true: the cuprous halides have much larger S_1/S_{VCA} ratios, and the value for $ZnSe_{1-x}Te_x$ is nearly a factor of two higher than predicted. Qualitatively, the reason why the bondlength distortions do not de-

crease with increasing ionicity is that electrostatic forces resist "ionic" displacements from ideal VCA lattice positions even though the bond-angle restoring force, β , is diminished. In fact, we have observed that S_1/S_{VCA} for alkali halide pseudobinary compounds (in which the ratio β/α approaches zero) is larger than those obtained for the zincblende solid solutions (15). Of course, long-range coulombic contributions are not included in an analysis based on α and β alone. However, all noncentral contributions are included in the above semiempirical determination of k_{eff} from the experimentally measured equilibrium bondlengths.

The calculated strain contributions to the enthalpy of mixing are compared to the (range of) experimentally measured values for the solid solution interaction parameter, α_s , in Table I. The calculated strain enthalpy for $Ga_{1-x}In_xP$ is in good agreement with the lower reported value of the interaction parameter, but those calculated for the $GaP_{1-x}As_x$ and $ZnSe_{1-x}Te_x$ solid solutions are approximately a factor of two higher than the reported values. No enthalpy of mixing has been reported for the $CuBr_{1-x}I_x$ alloy system, but it is interesting to note that the calculated value of 0.066 eV/atom-pair is comparable to the value of 0.081 eV/atom-pair measured for the analogous alkali halide solid solution, $RbBr_{1-x}I_x$ (16). Thermodynamic analysis of EXAFS measurements on alkali halide systems (15), such as $RbBr_{1-x}I_x$, are in progress. Preliminary results indicate that, although the changes in nn bondlengths (S_1) are higher for the alkali halides than the zincblende semiconductors, the smaller values of the bulk moduli lead to comparable values for the enthalpy of mixing.

Discussion

We next examine the similarities between Eq. [3] and the formulation for α_s given by Stringfellow, and then assess the simplifications used to relate the strain energy to experimental thermodynamic parameters. First, since the zincblende nn distance equals $a_0\sqrt{3}/4$, then $S_{VCA} = \sqrt{3}/4 \Delta$. The calculated form of α_s is $3/8 (S_1/S_{VCA})k_{r12}\Delta^2$. In order to generalize this expression to many zincblende solid solutions, note that (i) the values of S_1/S_{VCA} are approximately 1/4 for four of the alloys listed in Table I, and (ii) the values of k_{r12} are 120 ± 20 N/m. Thus, as an approximation $(S_1/S_{VCA})k_{r12}$ is a constant, and $\alpha_s = K\Delta^2$. If K is rewritten as $4.375K/\alpha^{4.5}$ according to Stringfellow's DLP model (3), our calculated values for K determined from the actual parameters for $Ga_{1-x}In_xAs$ and $GaAs_xP_{1-x}$ are 1.06 and 0.96×10^7 cal/mol-Å^{2.5}, respectively, compared to Stringfellow's value of 1.15×10^7 , which was obtained by fitting to the experimental values for 16 systems. Thus, if the strain energy is the major component of the interaction parameter, a second-order dependence of α_s on Δ is expected, in agreement with the correlation proposed by Stringfellow (3). By inspection, since the Δ 's for $Ga_{1-x}In_xAs$, $Ga_{1-x}In_xP$, and $ZnSe_{1-x}Te_x$ are approximately equal, their respective α_s 's should also be nearly equal. Since the Δ for $GaP_{1-x}As_x$ is a factor of two smaller than the other three systems, a factor of four smaller α_s is to be expected.

Although the present strain model and the DLP predict that the regular solution interaction parameters are approximately fit by a universal constant times Δ^2 , the DLP model did not explicitly originate from bond strain. Rather, the DLP model is based on the dielectric band model of Phillips and Van Vechten (5) (PVV). In the PVV model it is assumed that the semiconductor energy gaps are a function of two terms, the homopolar gap energy, E_h , which is proportional to $a_0^{-2.5}$ derived empirically from Si and Ge, and the ionic energy gap, C , which has a more complex dependence on lattice constant, ionicity, and metallization. The PVV model predicts reasonably accurate values of the bandgaps and heats of formation for zincblende compounds. The excess heats of formation of solid solutions relative to physical mixtures of the binary compounds were calculated by Van Vechten (17) and Stringfellow (18). However, the agreement with ex-

perimental values of the interaction parameter was not satisfactory. For example, the calculated value for $\text{Ga}_{1-x}\text{In}_x\text{As}$ was at least a factor of four too low, and the sign was wrong for $\text{Al}_{1-x}\text{Ga}_x\text{As}$ and $\text{Al}_{1-x}\text{In}_x\text{As}$. Stringfellow (3) obtained a significant improvement in the calculated values for the enthalpy of mixing by assuming that the heats of formation (or cohesive energies) have an $\alpha_0^{-2.5}$ dependence and other alloy variations in ionicity and metallization contained in the PVV theory could be ignored. Since the lattice constant of most zincblende pseudobinary solid solutions varies nearly linearly with composition, the composition dependence of the heat of formation (or any other property which varies sublinearly with lattice constant) will also be nonlinear. Since the Taylor series expansion of the alloy exponential term in the DLP model was truncated after the second term (linear term cancels), only the term in Δ^2 would remain for any negative exponent in the expression for ΔH_f dependence on α_0^{-x} (with a different form for the universal constant and a factor in the denominator). Thus, the DLP is only a semiempirical model for the enthalpy of mixing, and has only an indirect relationship to the original PVV dielectric theory. It is unclear what relationship should exist between the bandgap variation with composition and the enthalpy of mixing. The model presented above predicts that the enthalpy of mixing originates from local changes in bondlength and bond angle. However, the electronic band structure of these semiconductors averages the crystal potentials over many atomic sites. In fact, the use of the PVV model, through the dependence of the bandgaps (19) on an average lattice constant, implies the validity of the VCA to describe the atomic separation appropriate for the alloy. However, the EXAFS results indicate that the VCA is a poor description for the atomic-scale structure (7, 8). Elucidation of the correct relationship between the atomic-scale structure and the resultant band structure of alloy semiconductors is beyond the scope of the present work.

Although the major component of the solid solution enthalpy of mixing has been shown to originate from strain inherent in the atomic-scale structure of the solid solutions, it is important to examine some of the thermodynamic simplifications implicit in relating the model to experiment. The experimental values for the enthalpy of mixing were determined by modeling the phase diagrams with a regular solution model for the solid and generally with the simple solution model for the ternary liquids. Thus, as pointed out in Ref. (1), there usually are no unique values for either the liquid or solid interaction parameters, and there is some variation resulting from use of ternary as well as pseudobinary data to obtain a best fit to the model. For example, the values of α_s for $\text{Ga}_{1-x}\text{In}_x\text{As}$ vary by nearly 50% from 0.087 (6) to 0.130 (1).

As pointed out earlier, in the regular solution model, α_s is independent of composition and temperature. However, the strain model presented here has a composition dependence through the variation of the bulk modulus between the two binary compounds. The temperature-dependent interaction parameter obtained by Foster and Woods might be explained on the basis that the variation in α_s is actually a composition dependence through the temperature-composition solidus curve. Since the higher melting point binary compounds also have higher bulk moduli than the lower melting point compounds, this correlation would generally exist in pseudobinary phase diagrams. A temperature dependence to the calculated strain enthalpy is difficult to predict. The EXAFS measurements, upon which the present model is based, were made at 77 K (to reduce thermal vibrations), whereas the thermodynamic liquidus-solidus data were obtained at 1000-1500 K. A small decrease in the strain contribution to the enthalpy of mixing is expected due to the decrease in the bulk modulus at elevated temperature, unless there is a compensating change in S_i . It is possible that the bond strain can be reduced at elevated temperature due to anisotropic (anharmonic) atomic vibrations. This question might be suitably addressed by diffraction experiments at

elevated temperatures. If there is a vibrational contribution to the free energy of mixing, it is generally considered as an excess entropy term and is obviously ignored in the regular solution model. Since the phonon frequencies for III-V alloys do not show appreciable sublinear composition dependence, it might be argued that the vibrational entropy is unlikely to significantly add to the ideal entropy of mixing.

Finally, the regular solution model assumes that the entropy of mixing is ideal. A deviation from random occupation of the substituted sublattice, either through clustering or ordering, will reduce the ideal entropy of mixing term. In the quasichemical models for solutions (2), an excess enthalpy of mixing naturally leads to a deviation from randomness because like bonds are either more or less stable than mixed bonds. However, this model typically assumes that only the differences in chemical energy of just the first-neighbor bonds are important and it does not explicitly treat bond strain. Thus, if the reasoning is extended to second-neighbor interactions in pseudobinary systems because the number of different cation-anion bonds remains unchanged upon alloying, a positive excess enthalpy of mixing in all ternary zincblende solid solutions (except $\text{Al}_{1-x}\text{Ga}_x\text{As}$) means that unlike (Ga-In) bonds are less stable than the mean of like (Ga-Ga and In-In) bonds. This approach ignores the common (As) sublattice altogether. However, it is the As sublattice which undergoes the major displacements from the ideal (VCA) lattice sites to accommodate different Ga-As and In-As bondlengths (7). If the quasichemical model were modified to reflect the additional energy of each near-neighbor bond due to alloying, the approach would be similar to that used above, *i.e.*, the additional individual bond energy arises from changes in bondlengths and bond angles from their ideal values.

Even if the random alloys are not thermodynamically stable at temperatures substantially lower than their formation temperatures, it may not be kinetically possible to order or spinodally decompose the alloys. We have annealed several of the alloy systems below the calculated equilibrium critical temperatures and found no difference in the sublattice occupation using EXAFS. If ordering or clustering is limited by atomic diffusion over dimensions on the order of 10 Å, it means that diffusion coefficients must be less than 10^{-20} cm²s⁻¹. However, solid solutions grown at low temperatures from metal-rich solutions or by CVD methods may produce clustered or ordered alloys. Such experiments are presently underway. However, Stringfellow (20) has calculated that the coherency strain associated with developing critical nuclei from random fluctuations in composition dramatically reduces the critical temperature for alloy spinodal decomposition. For all of the systems included in Table I, the effective critical temperature is reduced to 0 K by this coherency strain. [Feddars and Muller (13) have arrived at a similar conclusion regarding the stability of random alloys once they have formed.] It is interesting to note that thermodynamic analysis of binary metallic alloys, such as Ni-Au (21), indicates both an excess enthalpy and a higher than ideal entropy of mixing in the absence of clustering or chemical ordering. It is presently difficult to assess the importance of the above factors because, since, even under the assumption that the solid solutions are strictly regular, experimental values of α_s for some alloys can vary by a factor of two.

Summary

We have calculated the bond strain associated with the atomic-scale structure as determined by EXAFS measurements for several zincblende solid solutions. It was found that the sum of the strain associated with bondlength and effective bond-angle distortions leads to an expression for the total strain energy which is equal to $\alpha_s X(1 - X)$, which has the same form of the regular solution enthalpy of mixing. The magnitude of the calculated value of α_s is in excellent agreement with experimentally measured values, and a generalization of the expression

leads to a predicted universal dependence of α_s on Δ^2 , in agreement with the semiempirical DLP model.

Acknowledgment

The author is grateful for the collaborative efforts of J. Boyce in the EXAFS analysis and the useful discussions with D. J. Chadi and C. Herring.

Manuscript submitted March 26, 1984; revised manuscript received Oct. 18, 1984.

Xerox Corporation assisted in meeting the publication costs of this article.

REFERENCES

1. M. B. Panish and M. Ilegems, in "Progress in Solid State Chemistry," Vol. 7, H. Reiss and J. O. McCaldin, Editors, pp. 39-84, Pergamon Press, Oxford, England (1972).
2. R. A. Swalin, "Thermodynamics of Solids," Chap. 8, John Wiley & Sons, New York (1962).
3. G. B. Stringfellow, *J. Phys. Chem. Solids*, **34**, 1749 (1973).
4. R. F. Brebrick and R. J. Panlener, *This Journal*, **121**, 932 (1974).
5. J. C. Phillips and J. A. Van Vechten, *Phys. Rev. B*, **2**, 2147 (1970).
6. L. M. Foster and J. F. Woods, *This Journal*, **118**, 1175 (1971).
7. J. C. Mikkelsen, Jr., and J. B. Boyce, *Phys. Rev. Lett.*, **49**,

- 1412 (1982); *Phys. Rev. B*, **28**, 7130 (1983).
8. J. C. Mikkelsen, Jr., and J. B. Boyce, in "Proceedings of the 17th International Conference on the Physics of Semiconductors," J. D. Chadi, W. A. Harrison, R. Z. Bachrach, Springer-Verlag, New York (1985).
9. L. Nordheim, *Ann. Phys.*, **9**, 607, 641 (1931).
10. L. Pauling and M. L. Huggins, *Z. Kristallog. Kristall. Kristallphys. Kristallchem.*, **87**, 205 (1934).
11. R. W. G. Wyckoff, "Crystal Structures," Vol. 2, p. 338, Interscience, New York (1964).
12. R. M. Martin, *Phys. Rev. B*, **1**, 4005 (1970).
13. P. A. Fedders and M. W. Muller, *J. Phys. Chem. Solids*, **45**, 685 (1984).
14. T. Fukai, *Jpn. J. Appl. Phys.*, **23**, L208 (1984).
15. J. B. Boyce and J. C. Mikkelsen, Jr., *Bull. Am. Phys. Soc.*, **28**, 490 (1983).
16. D. L. Fancher and G. R. Barsh, *J. Phys. Chem. Solids*, **30**, 2503 (1969).
17. J. A. Van Vechten, in "Proceedings of the 10th International Conference on the Physics of Semiconductors," Oak Ridge, TN, 1970, S. P. Keller, J. C. Hensel, and F. Stern, Editors, p. 602, U.S. Atomic Energy Commission (1970).
18. G. B. Stringfellow, *J. Phys. Chem. Solids*, **33**, 665 (1972).
19. J. A. Van Vechten and T. K. Bergstresser, *Phys. Rev. B*, **1**, 3351 (1970).
20. G. B. Stringfellow, *J. Electron. Mater.*, **11**, 903 (1982).
21. L. L. Seigle, M. Cohen, and B. L. Averbach, *J. Metals*, **7**, 1330 (1952).

Technical Notes



A Low Pressure BPSG Deposition Process

Thomas Foster,* Gary Hoeye, and Jon Goldman*

Thermco Systems, Incorporated, Orange, California 92668

Presently, the semiconductor industry uses deposited silicon dioxide glass for insulating layers between conducting polysilicon and metal layers in MOS fabrication (1). It has previously been found that flowing the glass to smooth out the surface before metal deposition tends to alleviate metal step coverage problems (1-3). Phosphosilicate glass (PSG) containing 6-8 weight percent (w/o) phosphorus flows adequately at temperatures of 1000°-1100°C (2). As geometries of integrated circuits decrease in size, it is becoming more important to reduce the flow temperature of the glass to decrease dopant redistribution. A 50°C reduction in flow temperature requires approximately 3 w/o more phosphorus, but too much phosphorus causes problems in IC's, including corrosion of aluminum conductors (1). It is important to lower the flow temperature without increasing phosphorus concentrations above present levels.

Previous work has shown that the addition of boron in making borophosphosilicate glass (BPSG) aids greatly in reducing the flow temperature (1, 2). In addition, BPSG has lower etch rates in buffered HF and has lower intrinsic tensile stress than PSG (2).

In most of the published work on BPSG up to this point, the films were deposited in atmospheric CVD systems employing rotating hot plates, belt drives, etc. (1, 2). The advantages of low-pressure deposition over these types of systems have been well documented. Films deposited at low pressure generally tend to be more uniform, have fewer particles and pinholes, and have better step coverage than their counterparts deposited at atmospheric pressure (4, 5). Recently, some plasma BPSG has been reported (6).

The intent of this work, therefore, was to attempt to develop an LPCVD process for deposition of BPSG.

* Electrochemical Society Active Member.

Experimental

The experiments were performed in a modified Thermco VLTO system utilizing a 145 mm id/151 mm od quartz tube which was approximately 6 ft long. The quartz process tube was enclosed in a resistance-heated furnace element. There were four stainless steel injectors located along the bottom of the tube, along with various mass-flow controllers and a vacuum pump. Two injectors brought oxygen into the deposition zone, and the other injectors brought in the remainder of the gases. A total wafer load of 90 wafers was utilized. Wafers were loaded into five covered boats. Grooves in the covers of the boats were precision cut with a laser and served the function of redirecting the gas flow, improving the film uniformity. B₂H₆ was tried as a boron source, but due to the configuration of the system, it decomposed and deposited inside the injectors. Wafers processed with B₂H₆ were analyzed for boron content, and it was found that they contained less than 1/2 w/o boron. BCl₃ was tried and found effective as a boron source.

Several wafers were analyzed by a commercial laboratory for boron and phosphorus concentrations using a wet chemistry technique. Some samples were analyzed using SIMS to obtain the concentration profile of boron, phosphorus, and chlorine as a function of depth in the film. Film thicknesses were measured with a Nanospec visible light spectrometer.

The BPSG process was run at 425°C and pressures ranging from 175-200 mtorr. The SiH₄/O₂ ratio was kept constant at 0.67 and the O₂ flow rate was constant at 68 sccm. Wafers for the flow tests were processed with approximately 7000Å of BPSG. The polysilicon steps of interest were 0.5 μm thick and 3 μm wide. The wafers were processed with BPSG containing 4 w/o phosphorus and 0.2, and 3.5 w/o boron, respectively. The PH₃ flow rate

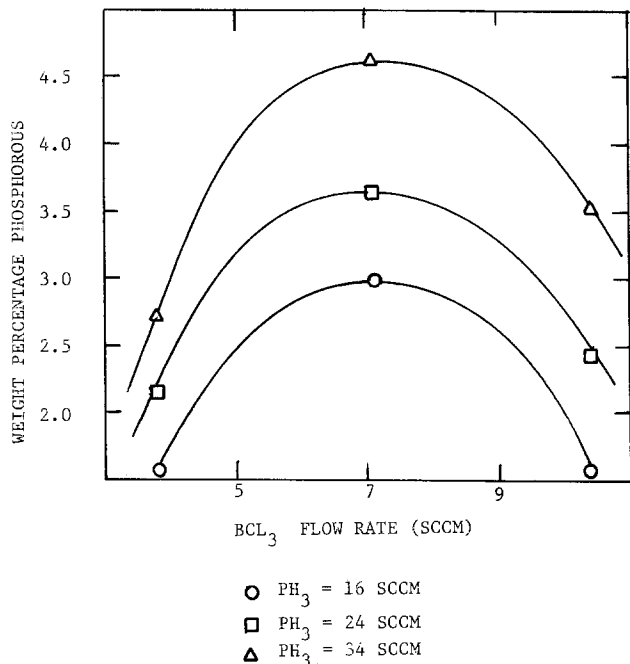


Fig. 1. Phosphorus weight percentage as a function of BCl₃ flow rate

was 50 sccm to obtain 0 w/o boron and 4 w/o phosphorus. The PH₃ flow rate was 42 sccm, and the BCl₃ flow rate was 3.6 sccm for 2 w/o boron and 4 w/o phosphorus. The PH₃ flow rate was 32 sccm, and the BCl₃ flow rate was 7.2 sccm for 3.5 w/o boron and 4 w/o phosphorus. A PH₃/N₂ mixture of 15% PH₃ and 85% N₂ was used in the experiments, and the PH₃ flow rates given include N₂. The flow tests were done at 850° and 925°C in steam and at 925°C in N₂ for a duration of 30 min.

Results and Discussion

Deposition rates ranged from 75 to 110 Å/min. The presence of boron and phosphorus in the process did not seem to affect the growth rate as reported in earlier work

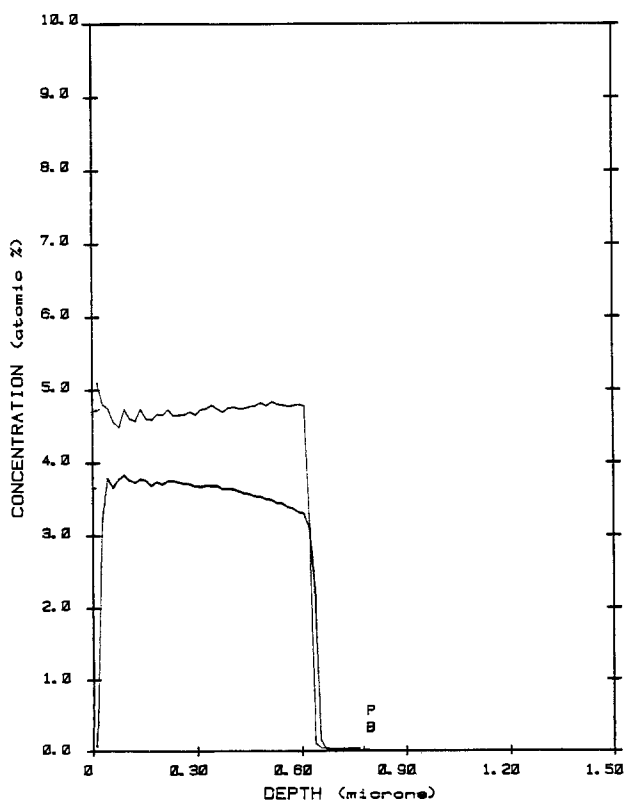


Fig. 2. Phosphorus and boron concentration profiles by SIMS

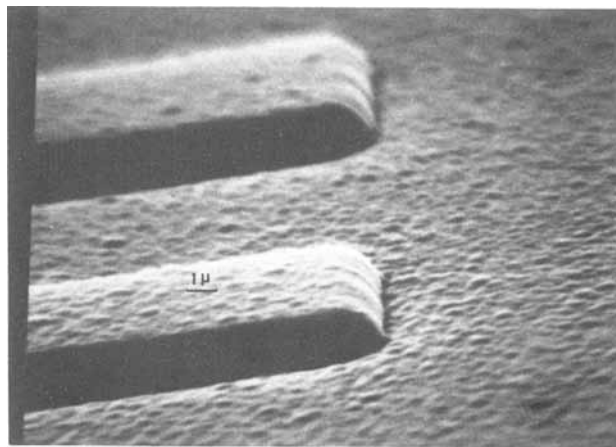


Fig. 3. SEM of as-deposited BPSG (3.5 w/o B, 4.0 w/o P)

(2). The variation in the deposition rate is attributable to differences in pressure caused by changes in the PH₃/N₂ flow rates.

Plotting the phosphorus weight percentage as a function of BCl₃ flow rate yields some interesting facts about this particular process (Fig. 1). It is apparent that as the BCl₃ flow rate is increased along a constant PH₃ flow rate line, the phosphorus incorporation is enhanced, but only up to a point. When the BCl₃ flow rate reaches approximately 7 sccm, the phosphorus incorporation begins to decrease.

A 100 mm wafer was analyzed at 4 points for phosphorus content and at 3 points for boron content. The phosphorus content varied from 4.4 to 4.7 w/o. The boron content varied from 3.3 to 3.6 w/o. From the same run, a wafer from each of the five boats was analyzed for boron and phosphorus concentrations. The phosphorus concentration varied from 4.0 to 4.7 w/o, whereas the boron concentration varied from 3.3 to 3.8 w/o.

The SIMS analysis indicates that the phosphorus and boron concentration profiles are flat, except that there seems to be a depletion of boron and an accumulation of phosphorus in the top 400 Å of film (Fig 2). However, initial charging problems during the SIMS analysis make the surface concentration data unreliable.

SIMS profiles indicate chlorine incorporation in the film varying from 0.3 to 1.0 w/o. Chlorine has been known to cause problems in LPCVD SiO₂ films deposited using SiH₂Cl₂ and N₂O (7). Similar problems have been observed in the present work. Delamination of films containing more than 4.0 w/o boron occurred upon annealing. These films contained the highest chlorine concentrations encountered in these experiments.

Samples composed of 0, 2, and 3.5 w/o boron and 4 w/o phosphorus were etched in 6:1 BOE etchant as-deposited and after annealing (925°C, N₂, 30 min). The as-deposited

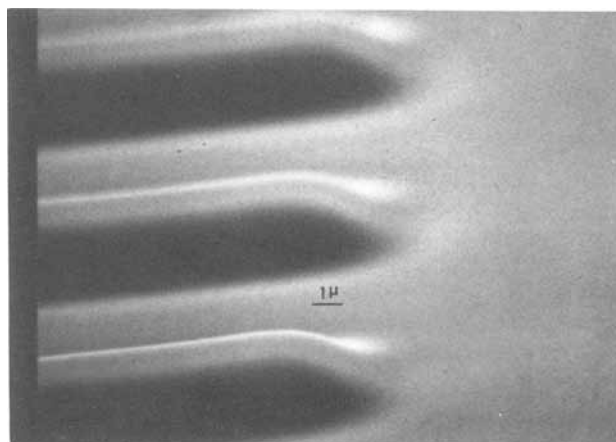


Fig. 4. SEM of BPSG annealed in steam at 925°C (2.0 w/o B, 4.0 w/o P)

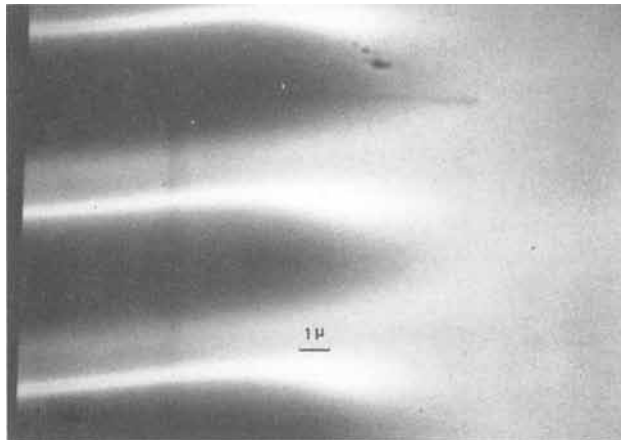


Fig. 5. SEM of BPSG annealed in steam at 925°C (3.5 w/o B, 4.0 w/o P)

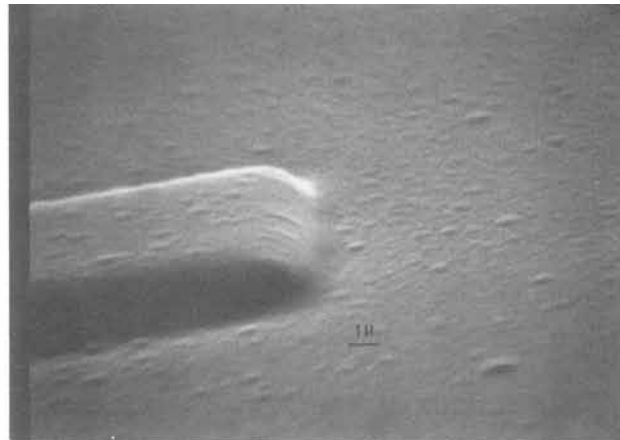


Fig. 6. SEM of BPSG annealed in nitrogen at 925°C (3.5 w/o B, 4.0 w/o P)

etch rates decreased from 105 Å/s (0 w/o B, 4 w/o P) to 35 Å/s (3.5 w/o B, 4 w/o P). The annealed film etch rates decreased from 47 Å/s (0 w/o B, 4 w/o P) to 18 Å/s (3.5 w/o B, 4 w/o P). These etch rate trends agree with previous work (2).

A 76 mm wafer was measured for film thickness at fifteen points spaced equidistant from top to bottom and from left to right. Taking the whole wafer into consideration, the deviation in thickness uniformity was $\pm 2.7\%$. Results on 4 in. wafers are comparable. The deviation in thickness uniformity across all 90 wafers on the paddle was $\pm 6.0\%$.

Figure 3 is a SEM of the as-deposited BPSG with no flow. Figure 4 is a sample containing 2 w/o boron and 4 w/o phosphorus that was annealed in steam at 925°C. A smooth film with gradual tapers is observed. Figure 5 shows a sample containing 3.5 w/o B and 4.0 w/o P annealed at 925°C in steam; it shows excessive flow, approaching planarization. Figure 6 shows a sample containing the same concentrations annealed at 925°C in N₂. The flow is adequate, but not as excessive as that which occurred in steam. Samples containing no boron showed no flow at 925°C. Also, the samples containing 4 w/o P and 3.5 w/o B studied exhibited no flow at 850°C in steam or nitrogen.

There is a difference in degree of flow between atmospheric pressure BPSG (AP BPSG) and low pressure BPSG (LP BPSG). The 2 w/o B, 4 w/o P LP BPSG flows well in steam at 925°C, whereas AP BPSG would require almost double the B concentration to achieve a similar flow (2). This could be due to differences in deposition pressure, reactor geometry, O₂/SiH₄ flow ratios, boron source gases, and deposition rates which lead to a different film chemistry and structure. Still, the exact cause of this difference is not understood.

Summary

Boron and phosphorus are readily incorporated into SiO₂ films at levels required to obtain excellent flow

characteristics at temperatures of 925°C. Increasing the boron concentration results in an increased amount of flow at that temperature, as in previous work. The films flow more in steam than in N₂. For this particular configuration, it was found that phosphorus incorporation was enhanced by the presence of boron until a certain BCl₃ flow rate, where the phosphorus incorporation began to be inhibited. The trends in the etch-rate tests conducted agree with those found in the 1982 paper by Kern *et al.*

The thickness uniformity across the wafer was found to be $\pm 2.7\%$, and uniformity down the boat was found to be $\pm 6\%$.

It appears that LP BPSG has different flow characteristics than AP BPSG. Although the exact reason for this phenomenon is not understood, it could be due to different film chemistry and structure that arises from different deposition parameters.

The incorporation of chlorine in films containing high boron concentrations poses potential problems. It has been observed that blisters formed upon annealing of films containing boron concentrations of greater than 4 w/o.

Manuscript submitted Feb. 6, 1984; revised manuscript received Aug. 23, 1984.

Thermco Systems, Incorporated, assisted in meeting the publication costs of this article.

REFERENCES

1. C. Ramiller and L. Yau, Paper presented at Semicon/West '82, May 25, San Mateo, CA, 1982.
2. W. Kern and G. Schnable, *RCA Rev.*, **43**, 423 (1982).
3. W. Kern, *ibid.*, **34**, 655 (1973).
4. M. Hammond and R. Gieske, Paper presented at Semicon/West '76, May 27, San Mateo, CA, 1976.
5. R. M. Levin and K. Evans-Lutterodt, *J. Vac. Sci. Technol.*, **B1**, 54 (1983).
6. J. E. Tong, K. Schertenleib, and R. A. Carpio, *Solid State Technol.*, 161 (1984).
7. K. Watanabe, T. Tanigaki, and S. Wakayama, *This Journal*, **128**, 2630 (1981).

A New Technique of Forming Thin Free Standing Single-Crystal Films

M. Tanielian, S. Blackstone, and R. Lajos

Gould Research Center, Rolling Meadows, Illinois 60008

The mechanical integrity of vacuum deposited thin films has been the subject of many investigations (1). Two effects that play a vital role in this respect are the adhesion of the thin film to the substrate and the large

stress that may be present in the thin film. Both properties are functions of the deposition conditions, and relate to the nature of the thin film and substrate. The resultant effect of large stresses is the presence of a large number

of defects and, in more severe cases, peeling of the thin film off the substrate. Since large stresses are undesirable (the general trend being that the stress is larger for thicker films), one tries to reduce the stress in thin films by reducing their thickness and improving the adhesion of the thin film to the substrate. Although desirable, this condition cannot often be met. For instance, the adhesion of sputtered films tends to be much better than those of evaporated films, but, at the same time, the stress in sputtered films is usually higher than in evaporated films.

Here, we report on a novel effect in which the large stress present in the thin film is coupled with excellent adhesion and results in the liftoff of the thin film from its substrate together with a layer of the substrate material attached to the thin film. When the thin film material is etched away, one obtains a thin, free standing layer of the substrate. In this particular case, the sputtered thin film material was Nichrome (80Ni/20Cr) and the substrate was a Si or GaAs wafer.

It seems unlikely that this effect is only an isolated incident limited to this specific thin film material and substrates. Since adhesion and stress can be altered by changing the deposition conditions and/or the materials involved, it is quite possible that this process will manifest itself in a variety of thin films and substrates.

Experimental

This investigation was carried out in a small bell jar system fitted with a dc magnetron sputter gun. The target was a Nichrome alloy with a composition of 80Ni/20Cr. The system was pumped typically to a base pressure 5×10^{-7} torr and backfilled with about 3 mtorr of ultrahigh purity argon. The substrates were at ambient temperature and comprised (111), (100), oxidized and unoxidized Si wafers, and in one case a GaAs wafer. The typical sputtering rate was about 100 Å/min. When the thickness of the Nichrome film exceeded about 6-7 μm , the Nichrome

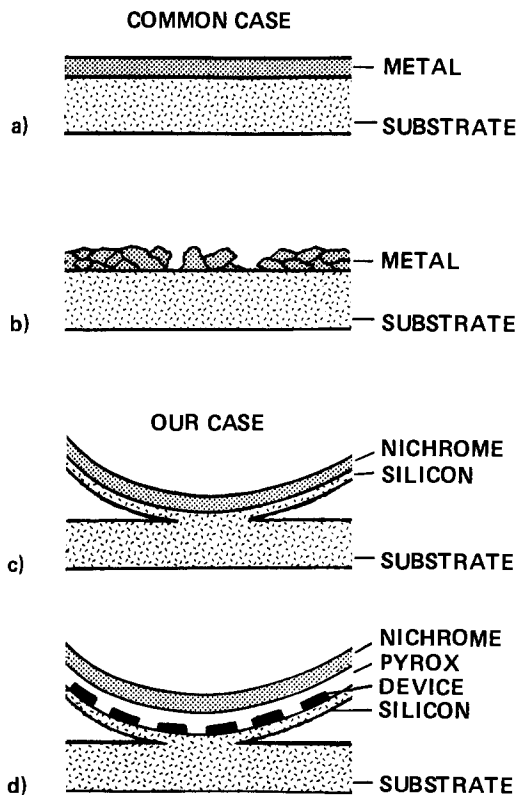


Fig. 1. Schematic representation of the peel-off process: (a) normal case; (b) a "thick" thin film which has large built-in stress thus resulting in cracking and peeling of the thin film; (c) in our case, a "thick" Nichrome film (typically 6-7 μm) which peels off the substrate with a layer of the substrate attached to it, (d) same situation as in (c), but with devices fabricated on the substrate surface.

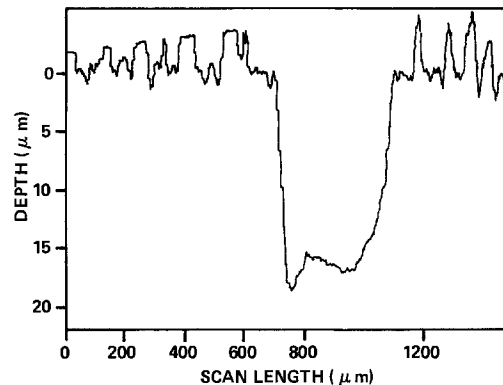


Fig. 2. Thickness profile of the back (rough) side of a Si wafer after a strip of material was peeled off. The roughness at the bottom of the pit (left by the peeled-off material) is comparable to the roughness of the wafer surface.

film peeled off the substrate together with a layer of Si from the wafer attached to it. The peeled Si thickness was roughly 15-20 μm . An example is shown in Fig. 1. When smaller or well-defined areas of the substrates were to be peeled, we deposited a somewhat thinner film, typically around 5 μm , which produced a stressed wafer but no spontaneous peeling. The areas to be peeled were then photolithographically defined and the excess film was etched away using an aqua regia solution. As soon as the

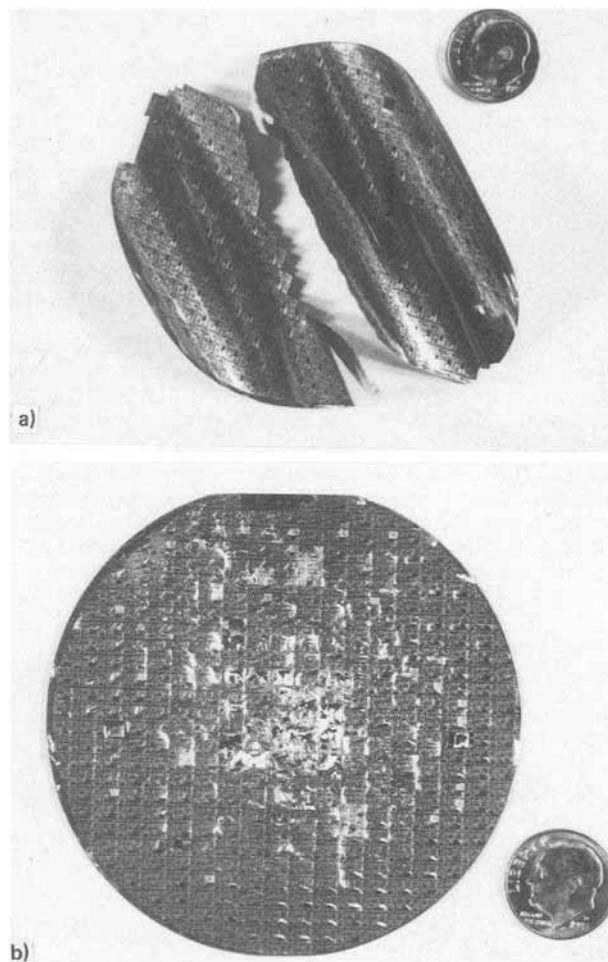


Fig. 3. Peeled-off Si layers with devices fabricated on them. (a): The whole underlayer of the devices was peeled by depositing a thick Nichrome layer (6-7 μm). (b): A thinner Nichrome layer does not produce enough stress to peel off a whole layer but only individual IC's. The individual IC's have peeled off because of high stress developed along the streets due to the absence of a field oxide.

excess film was etched off, those areas which were still covered by the Nichrome film peeled off on their own. A stylus thickness trace of the peel pits is given in Fig. 2. This spontaneous peeling may often, however, be undesirable. In this case, the deposited film was made somewhat thinner, of the order of $4\ \mu\text{m}$, so that the photodefined areas did not peel off during the etching of the excess Nichrome film. The peeling was instigated in this case by a thermal shock resulting from immersion of the wafer into liquid N_2 or heating the substrate to several hundred degrees centigrade.

Results

Using the above technique, we were able to peel off whole wafer-size layers from 2, 3, and 4 in. wafers and strips of various sizes and shapes. It is interesting to note that the presence of an oxide on the wafer, either thermally grown in the range of 900-4500Å, or deposited using an atmospheric CVD reactor system (Pyrox) with a thickness of 0.5-1.0 μm , did not affect the peeling. Thus whole finished IC's were peeled off a wafer that had a Pyrox layer deposited on top of them (see Fig. 3). Isolated IC's were also peeled off by decreasing the Nichrome thickness and immersing the wafer into liquid N_2 . This was possible because the stresses in a fabricated wafer present a high stress point due to the absence of a field oxide at those areas.

The peeled-off surface appears to be fractured along crystal planes, leaving a faceted texture. A profilometer trace of this surface shows a roughness of about $2\ \mu\text{m}$, which is comparable to the roughness of the back side of a wafer. The uniformity of a peeled off layer is related to the peel-off conditions. On the average it is about 10-20% of the layer thickness. Once a layer of the substrate was peeled off, a second layer could also be peeled following the same procedure. In fact, we observed that, the rougher the substrate surface, the better the adhesion of the Nichrome film to the substrate and the thinner the Nichrome layer needed to induce peeling. Although the peeling action produces a rough surface on the substrate, the peeled-off layers show a small number of defects. This was tested using a Sirtl etch, which showed that

most of the defects were localized along the periphery of the strips.

Discussion

This method of forming thin, low defect, free standing single-crystal silicon wafers could be useful for solar cell applications. It would allow the fabrication of wafers thinner than can be presently sawn, and because all of the starting material is used, the elimination of kerf loss could result in a cost savings. One could even envision skiving a boule to produce large sheets of single-crystal material. The roughened surface of the as-peeled wafers could possibly be optimized as an antireflective coating.

As entirely finished circuits have been peeled from the surface of the wafer, this technique could have applications in silicon-on-insulator technology. Alternatively, on-chip circuits could be isolated by patterning the Nichrome into isolation areas, then by thermal shock, *i.e.*, passing a current through the Nichrome wire, peeling trenches out of the silicon between the circuits. The trench isolation could have similar advantages to etched trenches. Finally, this technique could be useful for TEM sample preparation.

In summary, a method of fabricating thin, low defect, free standing single-crystal films is suggested. It is based on the deposition of a highly stressed film, which, with or without thermal shock, peels off of a substrate, taking a layer of the substrate with it. Although the highly stressed film discussed here is Nichrome, in principle many other thin films could exhibit these peeling phenomena. This technique could have applications in solar cells, in wafer fabrication, and in IC technology.

Manuscript submitted July 16, 1984; revised manuscript received Oct. 4, 1984. This was Paper 82 presented at the Cincinnati, Ohio, Meeting of the Society, May 6-11, 1984.

Gould Research Center assisted in meeting the publication costs of this article.

REFERENCES

1. K. L. Chopra, "Thin Film Phenomena," R. Kreeger, New York (1979).



COMMENTS

Each issue of the **Journal** will have a section of "Comments." In this section, we provide a means via short pieces, *i.e.*, one column or less, to applaud, dispute, or otherwise discuss the papers published in the **Journal**. Space will be provided for one response by the paper's author(s) to each comment.

Since space available in each issue for the "Comments" section is limited; it is important to be concise.

Comments should be sent to the Editor, Dr. Norman Hackerman, President's Office, Rice University, P.O. Box 1892, Houston, TX 77251.

Norman Hackerman
Editor

Precise Evaluation of Oxygen Measurements on Cz-Silicon Wafers

K. Graff

(pp. 1378-1381, Vol. 130, no. 6)

A. Baghdadi:¹ The paper by Graff is primarily concerned with corrections for multiple-reflection effects for optical absorption measurements in thin silicon slices with nonpolished back surfaces. As the author correctly points out, improved accuracy in the infrared absorption measurement of the oxygen content of such silicon wafers is needed in order to allow silicon suppliers to meet modern VLSI processing specifications. However, the methods the author suggests for including the effect of a nonpolished back surface on the intensity of the transmitted light do not adequately take into account losses due to surface roughness.

A better approach, which properly accounts for silicon-air interfaces and for the effects of multiple reflections, would be to start with the following equation²

$$I = \frac{I_0 T_f T_b e^{-\alpha x}}{1 - R_f R_b e^{-2\alpha x}} \quad [1]$$

where I is the intensity of the transmitted light, I_0 is the intensity of the incident light, T is the nonscattered transmittance, α is the sample absorptivity, x is the sample thickness, R is the nonscattered (*i.e.*, specular) reflectance, and the subscripts f and b refer to the front and back surfaces of the silicon slice, respectively. The loss of light due to scattering would result in lower values for both the transmittance and the reflectance of the rough surface as compared to the transmittance and reflectance of a polished surface. Starting from Eq. [1] and assuming that the front surface is polished so that

$$T_f = T \quad \text{and} \quad R_f = R$$

but the back surface is not polished, we can write

$$R_b = sR \quad \text{and} \quad T_b = sT$$

where s is the factor characterizing the scattering from the nonpolished back surface. Then we have

$$I = \frac{I_0 T^2 s e^{-\alpha x}}{1 - R^2 s e^{-2\alpha x}}$$

To put this equation in a form similar to that used by Graff, note that $T = (1 - R)$ and let $s e^{-\alpha x} = e^{-\alpha^* x}$. Then we have

$$\text{Transmittance} \equiv \frac{I}{I_0} = \frac{(1 - R)^2 e^{-\alpha^* x}}{1 - R^2 e^{-\alpha^* x} e^{-\alpha x}} \quad [2]$$

which is not Graff's Eq. [1]. In other words, his method of modifying the classical equation for transmission through a

parallel plate is not adequate, because α^* cannot consistently be substituted for α in both the numerator and the denominator in this equation. In addition, note that both Eq. [2] above and Graff's Eq. [1] would not be useful, because they do not respond properly to a variation in the sample thickness x .

In addition, there are some difficulties with the application of his method, as described in his Eq. [3]-[7]. These equations do not specify which of the reference wafers are designated by the subscripts f , b , and 3 . It appears that a key assumption is that a given back-side treatment, such as grinding or sandblasting, would produce similar results with both Czochralski (Cz) and float-zone (fz) silicon. Unfortunately, because the presence of oxygen in Cz silicon results in a material which is mechanically stronger than low-oxygen float-zone silicon,³ the assumption of equivalent damage in Cz and fz silicon cannot be accepted without experimental support. For example, as Graff points out, the ground Cz wafer transmitted 12% of the incident light, while the ground fz wafer only transmitted 5.6%.

K. Graff:⁴ In measuring the IR transmittance of common silicon wafers with polished front side and more or less rough reverse side, the following experimental facts must be taken into consideration.

According to the reflectance R of the silicon-air interface, the incident beam is reflected at both surfaces of the sample. The reflectance is a constant which depends only on the refractive index of silicon and is independent of the structure of the surface. Whereas the polished surface of the sample reflects the incident beam for perpendicular irradiation in the opposite direction, the rough reverse side does not. Here the radiation is scattered, effecting a divergent reflected beam. For a single-beam transmission (neglecting multiple reflections), this scattering does not affect the transmitted intensity. Therefore, the single-beam approach for thick samples and high absorption remains almost unaffected by rough surfaces.

However, taking into account multiple reflection within the sample to be measured, a considerable difference between a both-sides polished wafer and a common wafer with one rough surface is observed. The divergent reflected beam from the reverse side of the wafer causes a divergent transmitted beam after reflection at the polished surface. Only a small fraction of this divergent beam is monitored by common spectrometers. As a consequence, the absolute transmission is decreased compared to an equal wafer with polished surfaces.

In order to take into account these losses due to surface roughness, we assume an additional fictive absorption α^* within the volume of the wafer, which effects the same loss of intensity in the volume of the sample as scattering does at

¹ National Bureau of Standards, Washington, DC 20234.

² A Baghdadi in "Defects in Silicon," W. M. Bullis and L. C. Kimerling, Editors, p. 293, The Electrochemical Society Softbound Proceedings Series, Pennington, New Jersey (1983).

³ K. Sumino, in "Semiconductor Silicon/1981," H. R. Huff, R. J. Kriegler, and Y. Takeishi, Editors, p. 208, The Electrochemical Society Softbound Proceedings Series, Pennington, New Jersey (1981).

⁴ Telefunken electronic GmbH, D-7100 Heilbronn, Germany.

the rough reverse side. This fictive absorption α^+ can be determined by means of the well-established Eq. [1] using the measured reduced absolute transmittance T .

On the other hand, the proposed statements of Baghdadi

$$R_b = sR \quad T_b = sT \quad T = 1 - R$$

yield

$$T_b = s(1 - R) \quad \text{and} \quad T_b = 1 - R_b = 1 - sR$$

which is contradictory by statement because reflectance R_b and transmittance T_b at the back side are not reduced by the same factor s (for $s \neq 1$). Furthermore, the statement of Baghdadi

$$se^{-\alpha x} = e^{-\alpha^+ x}$$

is not suitable to compare his Eq. [2] with our Eq. [1] because

$$se^{-\alpha x} = e^{-\alpha x + \ln s} \neq e^{-\alpha^+ x}$$

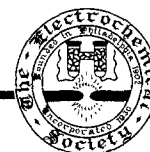
Because the statements of Baghdadi are contradictory, his conclusions must be misleading.

As already discussed in the original paper, a simple reduction of the reflectance R yields no suitable means for evaluating the beam scattering. Besides, by assuming a fictive absorption α^+ , the correction for intensity losses can also be done by assuming a higher fictive sample thickness

d^+ which is performed by the same mathematical formalism. This fictive sample thickness d^+ , however, must be determined using the absolute transmittance of sample at 1105 cm^{-1} where oxygen absorption takes place and not at any other wavelength, because scattering may considerably depend on the wavelength.

In conclusion, our proposed correction method for taking into account intensity losses at rough silicon surfaces has meanwhile been applied in several hundreds of measurements, yielding accurate results. Results obtained on highly scattering wafers with low transmittances approach those obtained by applying the equation for single reflection. On the other hand, results obtained on well-polished wafers approach those obtained by means of the equation for multiple reflection.

Although the mathematical formalism (Eq. [3]-[7]) for developing the rather simple final Eq. [9] seems rather complicated because the usually graphically constructed base line of the reference measurement must be simulated by introducing a further reference measurement on two additional reference samples ref_2 and ref_3 , the application of the final equation is quite simple and fast. The determination of the oxygen content on a single wafer which is composed of two spectra (an absolute air reference and a reference measurement), including evaluation by computer, takes less than 4 min.



V_2O_5 - P_2O_5 Glasses as Cathode for Lithium Secondary Battery

Y. Sakurai and J. Yamaki*

*Ibaraki Electrical Communication Laboratory, Nippon Telegraph and Telephone Public Corporation,
Tokai, Ibaraki-ken, 319-11, Japan*

INTRODUCTION

During past two decades, the importance of rechargeable lithium cells has been emphasized and a large variety of materials has been discovered and evaluated for use as reversible cathodes and electrolytes. Materials that undergo intercalation or topochemical reactions with lithium have been investigated as candidates for cathodes in nonaqueous secondary lithium cells (1). Recent interest in researching cathode active materials has mainly focussed on crystalline transition metal chalcogenides. On the other hand, electrochemical behaviors of several amorphous materials have been reported, for example MoS_2 , MoS_3 , V_2S_5 (2) and LiV_3O_8 (3). However, no successful cycling behavior has been obtained except for MoS_2 in the amorphous state. This paper reports electrochemical data on rechargeable vanadate glasses in the system V_2O_5 - P_2O_5 .

EXPERIMENTAL

Vanadate glasses in the V_2O_5 - P_2O_5 system with 95 and 90 mole% V_2O_5 were prepared by melting the oxides in platinum crucibles for 1 hr at 750°C followed by quenching at water temperature. X-ray diffraction studies indicated that these vitreous oxides were amorphous to X-ray.

Cathode characteristics of vanadate glasses were examined by using a coin type cell which has a conventional flat cell configuration (23 mm diameter and 2 mm thickness) and a cathode area of 2 cm². The cathode was a mixture of vanadate glass and ketjen black with a small quantity of polytetrafluoroethylene powder. The lithium content in each cell was ca. 200 mAh. The electrolyte used here was 1.5M-LiAsF₆/2-methyltetrahydrofuran. As a separator, Celgard 2402 was used.

*Electrochemical Society Active Member

Key words: Li secondary battery, cathode, vanadate glass.

The cells were assembled in a drybox filled with argon gas. The cell performance was evaluated at a constant current.

RESULTS AND DISCUSSION

Infrared absorption spectra of 95 and 90 mole% V_2O_5 - P_2O_5 glasses are shown in Fig. 1, together with that of V_2O_5 crystal. It should be noted that the absorption of V=O vibration around 1000 cm⁻¹ and V-O vibration around 800,600 cm⁻¹ remain in amorphous state, so similar bonds are present in vanadate glass.

Discharge curves of 95 mole% V_2O_5 - P_2O_5 glass at various currents are shown in Fig. 2. There was no clear appearance of the plateau followed by a slope. This suggests that in the amorphous state there is not any site preference for Li⁺ compared with crystalline V_2O_5 in which there are some energetically different reaction sites depending on crystal structure. Similar discharge behaviors were observed for 90 mole% V_2O_5 - P_2O_5 glass. These vanadate glasses showed high energy density of ca. 900 Wh/kg(glass weight) at 1.5 V cut-off and accommodate 3 Li/vanadate glass.

Typical cycling behavior of 95 mole% V_2O_5 - P_2O_5 glass at 1 Li/mole depth (150 Ah/kg) and 1 mA/cm² rate is given in Fig. 3. After several cycles, the cell showed good reversibility, resulting in a prolonged cycle life of over 145 times. And another deeper cycling test was carried out between 2 V and 3.5 V at 0.5 mA/cm² for the same cell system (Fig. 4). The cell has been cycled over 95 times at a depth of ca. 1.2 Li/mole and is still running.

In crystalline V_2O_5 , further reduction below 2.5 V ($x > 1$ in $Li_xV_2O_5$) leads to eventual breaking of the weak V-O bonds along cleavage plane (010) followed by a major structural reorganization, resulting in further irreversibility (4). To the contrary, although our vanadate glasses have similar V-O bonds to crystalline V_2O_5 as

seen in Fig. 1, the somewhat broad IR spectra are indicative of variations in bond length. This bond length variation seems to act as a structure-stabilizer and to sustain extended cycling without a significant rupture of V-O bonds. Indeed, SEM observation indicated that there was no cleavage in the vanadate glass studied here, in contrast with layer structure crystalline V₂O₅.

We are presently making studies of glass composition dependence and electrolyte effect for cathode properties, and in the course of the study we believe advanced rechargeable Li/vanadate glass cells with improved high energy density and cycle life will be discovered.

REFERENCES

- 1) K.M. Abraham, *J. Power Sources*, **7**, 1 (1981/2).
- 2) M.S. Whittingham, *J. Electroanal. Chem.*, **118**, 229 (1981).
- 3) K. Nassau and D.W. Murphy, *J. Non-Crystalline Solids*, **44**, 297 (1981).
- 4) D.W. Murphy and P.A. Christian, *Science*, **205**, 651 (1979).

Manuscript submitted Nov. 5, 1984.
Nippon Telegraph & Telephone Public Corporation assisted in meeting the publication costs of this article.

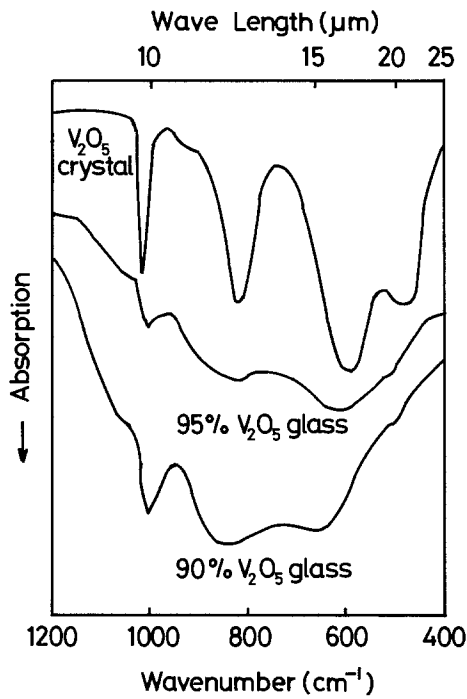


Fig. 1. IR spectra of V₂O₅ crystal and V₂O₅-P₂O₅ glasses

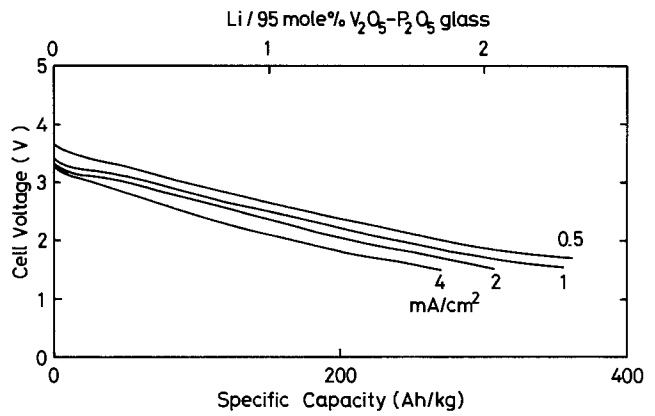


Fig. 2. Rate capability of 95 mole% V₂O₅-P₂O₅ glass

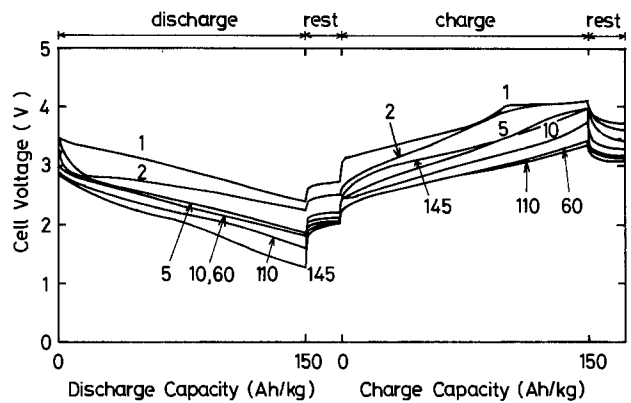


Fig. 3. Cycling behavior of 95 mole% V₂O₅-P₂O₅ glass at 1 mA/cm² (1 Li/mole) Cycle numbers are indicated

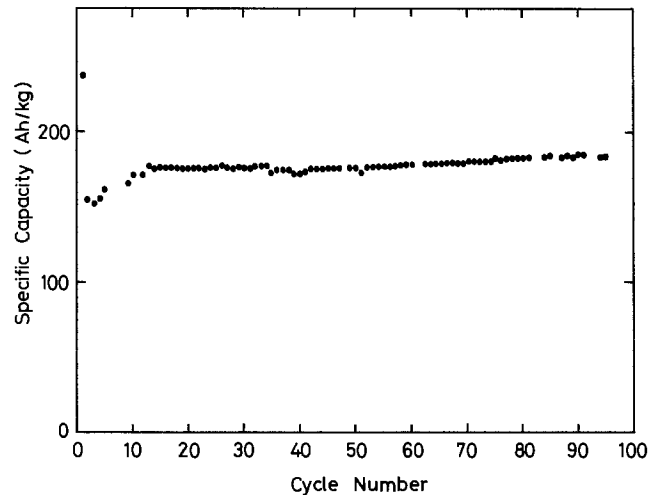


Fig. 4. Cycle life performance of 95 mole% V₂O₅-P₂O₅ glass at 0.5 mA/cm², 2.0-3.5 V voltage limited cycling

Ion Transporting Composite Membranes

I. Nafion-Impregnated Gore-Tex

Reginald M. Penner and Charles R. Martin*

Department of Chemistry, Texas A&M University, College Station, Texas 77843

Nafion is a family of extremely versatile cation transporting polymers (1). While they have many highly desirable chemical and mechanical features (1), the Nafion polymers have a potentially significant disadvantage — they are rather expensive. The high costs of these polymers have prompted an effort to develop membrane materials with the same desirable chemical and mechanical features, but which can be produced more cheaply (2).

It occurred to us that an ionically conductive membrane has two major functions, a structural/mechanical function (i.e., to serve as a chemically inert barrier to prevent bulk mixing of catholyte and anolyte solutions) and a chemical function (i.e., to selectively transport the desired ion from one solution to the other). It seemed likely that a cheaper membrane could be prepared by doping an inexpensive, nonconductive material (which serves the mechanical/structural function) with a small amount of an ion transporting polymer (which allows the membrane to accomplish its chemical function). In an effort to demonstrate the feasibility of this approach, we have impregnated commercially available porous polytetrafluoroethylene membranes (PTFE, Gore-tex) with small quantities of Nafion, to make cation transporting composites. The results of our initial studies of the transport properties of these composites are described here.

Nafion 117 and Gore-tex (0.2 μm mean pore diameter) membranes were donated by E. I. Du Pont and W. L. Gore Associates, respectively. Solutions of Nafion were prepared using the procedure of Martin, et al. (3). The transport properties of the native and Nafion-impregnated Gore-tex (NIGT) membranes were studied electrochemically (4) using wax-impregnated graphite (WIG) rods (5) as the substrate electrodes. Briefly, a section of Gore-tex membrane was stretched over the pretreated (6) WIG electrode surface and held in place by a collar of heat shrinkable Teflon tubing. The Gore-tex was

*Electrochemical Society Active Member.

then Nafion-impregnated by immersing the membrane-covered electrode in Nafion solution (0.7 to 2.5 w/V% in 95% ethanol) and ultrasonically for 30 min. The electrode was removed from the impregnating solution and the solvent was allowed to evaporate (room temperature, 5 hours).

Gore-tex membranes are made of porous PTFE and are available in a variety of porosities. Because of the chemical inertness and mechanical strength of PTFE, Gore-tex seems to be the ideal material for satisfying the mechanical/structural membrane function. Furthermore, Gore-tex is about an order of magnitude cheaper than Nafion. Native Gore-tex membranes are not wetted by water and, therefore, totally insulate a substrate WIG electrode from a contacting aqueous supporting electrolyte solution (Fig. 1, curve A). However, when Nafion-impregnated, the membranes become water swollen and ionically conductive; background cyclic voltammograms (Fig. 1, curve B) similar to those observed at the uncoated WIG electrodes are obtained. The ionic conductivity of NIGT is more dramatically demonstrated by the voltammograms shown in Fig. 2; a NIGT-WIG electrode was immersed in a solution 3 mM in $\text{Ru}(\text{NH}_3)_6^{3+}$ and the potential was scanned over the $\text{Ru}^{\text{III/II}}$ redox wave. A $\text{Ru}(\text{NH}_3)_6^{3+}$ "loading" voltammogram very similar to that obtained at a Nafion-film modified electrode (4) is observed (Fig. 2a).

When $\text{Ru}(\text{NH}_3)_6^{3+}$ loaded NIGT-WIG electrodes are transferred to supporting electrolyte solution, the majority of the $\text{Ru}(\text{NH}_3)_6^{3+}$ is retained by the NIGT membrane (Fig. 2b); this is again, analogous to results obtained with Nafion film-coated electrodes (4). As shown in Fig. 2b, the differences in potential between the anodic and cathodic peaks for the $\text{Ru}(\text{NH}_3)_6^{3+/2+}$ waves decrease as the quantity of Nafion impregnated increases. This suggests (as might be expected) that the ionic conductivity of NIGT increases with the quantity of

Manuscript submitted Oct. 30, 1984.

Nafion incorporated.

Finally, it is of particular interest to note that preliminary measurements of the apparent diffusion coefficients for $\text{Ru}(\text{NH}_3)_6^{3+}$ and $\text{Ru}(\text{NH}_3)_6^{2+}$ in NIGT membranes containing ca. 15 wt % Nafion have produced values which are over an order of magnitude larger than the corresponding diffusion coefficients in Nafion (4). This suggests that the open porous structure of Gore-tex allows for markedly enhanced ion transport rates. Further studies of these and related composite membranes are in progress.

ACKNOWLEDGEMENTS

This work was supported by the Office of Naval Research and the Robert A. Welch Foundation.

REFERENCES

1. A. Eisenberg and H. L. Yeager, Editors, "Perfluorinated Ionomer Membrane," ACS Symposium Series, No. 180, ACS, Washington, D.C. (1982), and references therein.
2. V. D'Agostino, J. Lee, and E. Lu, in "Ion Exchange: Transport and Interfacial Properties," R. S. Yeo and R. P. Buck, Editors, p. 148. The Electrochemical Society Softbound Proceedings Series, Pennington, N.J. (1981).
3. C. R. Martin, T. A. Rhoades, and J. A. Ferguson, *Anal. Chem.*, **54**, 1639 (1982).
4. C. R. Martin and K. A. Dollard, *J. Electroanal. Chem.*, **159**, 127 (1983), and references therein.
5. Ralph N. Adams, "Electrochemistry at Solid Electrodes," pp. 278, 279, Marcel Dekker, Inc., New York (1969).
6. While the general construction is as described in reference 5, details of pretreatment will be given in a forthcoming article.

Texas A&M University assisted in meeting the publication costs of this article.

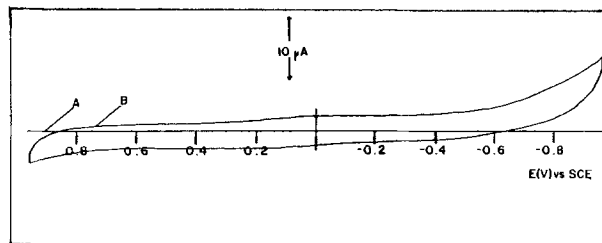


Figure 1. Background voltammograms (200 mV/s) in 0.1 M NaClO_4 . A. Native Gore-tex membrane-modified WIG electrode. B. Nafion-impregnated (14.6 w/w %) Gore-tex membrane-modified WIG electrode.

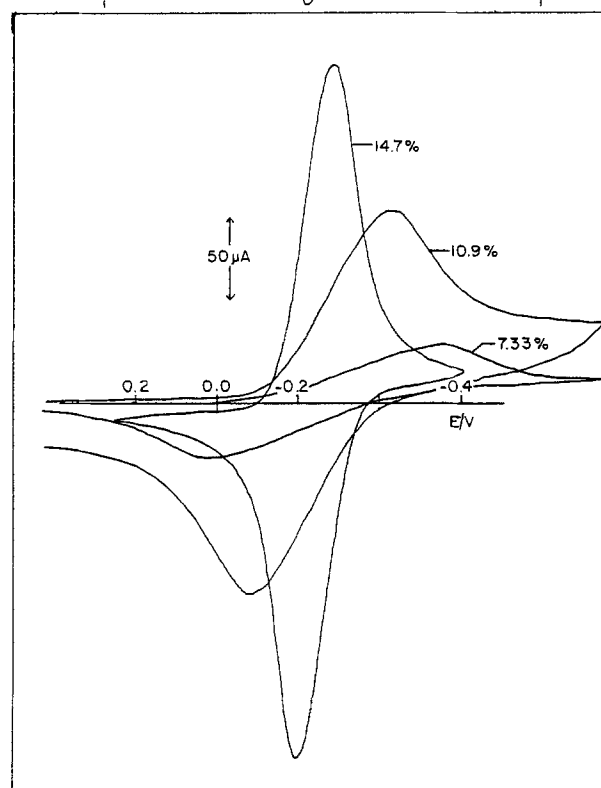
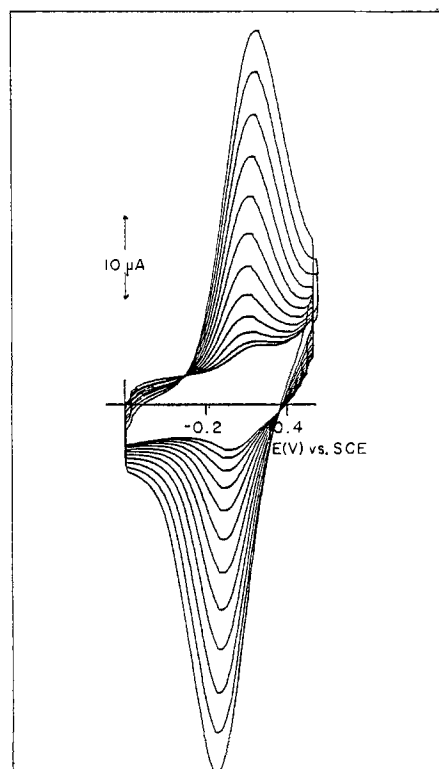


Figure 2. $\text{Ru}(\text{NH}_3)_6^{3+/2+}$ voltammograms (200 mV/s) for NIGT-WIG electrodes. A. Loading in 3 mM $\text{Ru}(\text{NH}_3)_6^{3+}$, 0.1 M NaClO_4 solution (every fifth scan recorded). B. Loaded electrodes in 0.1 M NaClO_4 . % Nafion in membranes as shown.

Activation Energy for the Parabolic Rate Constant during Sequential Si Oxidation

C. J. Han* and C. R. Helms**

Stanford Electronics Laboratories, Stanford University, Stanford, California 94305

In this communication we report on an analysis of recent experimental data (1) which clearly shows that transport properties of thermally grown SiO₂ change as a function of temperature. Our analysis is consistent with other observations where the refractive index (2,3), density (3), and interfacial stress (4) in SiO₂ vary with temperature. These changes account for the apparent anomalous effect of temperature on the activation energy for the parabolic rate constant, B, reported by several investigators (5-7). Figure 1 shows this effect in an Arrhenius plot of these data (5-8). The activation energy varies from 0.9 eV at 1150°C to 2.6 eV at 780°C.

Recent experiments by Irene (1) shed considerable light on the mechanism for this change in activation energy. He grew oxides in dry O₂ at 1000°C to 1µm thicknesses, then recorded oxidation rates for subsequent oxidations at lower temperatures. The rates measured at lower temperatures should have therefore exhibited the properties of a "1000°C" oxide, so long as the lower temperature oxidations did not significantly affect their structure.

In a reanalysis of Irene's data, using an improved lag time formulation, we indeed observe this effect (9). The oxidation rates were analyzed using the linear parabolic rate law:

$$\frac{dL}{dt} = \frac{B}{2L+A} \quad [1]$$

where L is the thickness, B is the parabolic rate constant B/A is the linear rate constant, and dL/dt is the growth rate. Since dL/dt and L are measured quantities, B can be determined if A is known; since L>>A for these experiments, the error caused by an uncertainty in A is not significant.

* Electrochemical Society Student Member

** Electrochemical Society Active Member

Key Words: Insulator, diffusion, oxidation

To verify this we evaluated the value for B in two limits. First, the B/A values from Ref. (5) provided one limit; second, B/A → ∞ provided the other limit for the minimum value for B. We plotted these B values for Irene's 800°C, 900°C, and 1000°C oxidation rates in Fig. 1 along with the previously reported B values (5-8). As mentioned above, previous results showed the familiar change in the apparent activation energy as a function of temperature. However, the parabolic rate constants from Irene's sequential experiments at 800°C and 900°C fall along a straight line tangent to the curve of B values at 1000°C with a slope of 1.1 eV! During the second oxidation, the oxide appeared to retain the activation energy and the preexponential factor from the 1000°C oxidation. In the 40 hours Irene oxidized his samples, the 1000°C oxide apparently did not change its form to equilibrate with the lower temperature. It retained a "memory" of the past oxidation process. The direction of the change to lower activation energy for higher temperature oxides is also not surprising since the lower density and the stress relaxation for higher temperature oxides would promote the lower activation energy.

There is also evidence that the linear rate constant exhibits a "memory effect" as well. Hamasaki (10) observed enhanced oxidation rates for thinner oxides in a sequential higher temperature/lower temperature oxidation sequence. In that case, however, the enhancement in oxidation rate decreased with oxidation time. This may not be surprising since the linear rate constant, being an interface property, may equilibrate rapidly at the new growth temperature.

This work supported by DARPA Contract No. MDA 903-79-C-0257.

REFERENCES

- (1) E. A. Irene, J. Electrochem. Soc., 129, 413 (1982).

- (2) E. A. Taft, J. Electrochem. Soc., 125, 968 (1978).
- (3) E. A. Irene, E. Tierney, and J. Angitello, J. Electrochem. Soc., 129, 2594 (1982).
- (4) E. P. EerNisse, Appl. Phys. Lett., 35(1), 8 (1979).
- (5) E. A. Irene, J. Electrochem. Soc., 125, 1146 (1978).
- (6) L. N. Lie, R. R. Razouk, and B. E. Deal, J. Electrochem. Soc., 129, 2828 (1982).
- (7) H. Z. Massoud, "Thermal Oxidation of Silicon in Dry Oxygen-Growth Kinetics and Charge Characterization in the Thin Regime", p. 132, Thesis presented to Stanford University (1983).
- (8) B. E. Deal and A. S. Grove, J. Appl. Phys., 36, 3770 (1965).
- (9) C. J. Han and C. R. Helms, accepted for publication, J. Electrochem. Soc.
- (10) M. Hamasaki, Solid State Electronics, 25, 479 (1982).

Manuscript submitted Nov. 20, 1984.

Stanford Electronics Laboratories assisted in meeting the publication costs of this article.

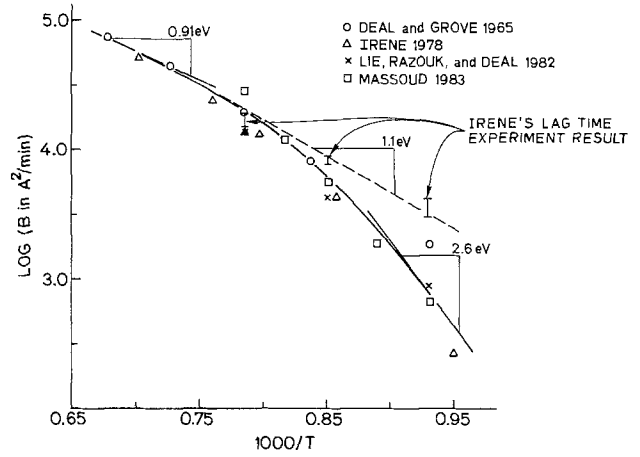


Figure 1.

Arrhenius plot of the parabolic rate coefficient from Refs. (5-8) and from Irene's sequential oxidation results (5). During the sequential oxidation process, the SiO_2 retains the activation energy and the pre-exponential factor from the 1000°C oxidation

Electrochemical Degradation of Polyacetylene Molecular Structure

Fritz G. Will*

General Electric Company, Corporate Research and Development, Schenectady, New York 12301

While the structural effects of thermal and oxidative treatments of polyacetylene have been the subject of a number of studies (1-3), the electrochemical stability of polyacetylene has not been similarly addressed. Evidently, the effect of repetitive charge and discharge and that of deep discharge and overcharge on the structural integrity of polyacetylene are significant for the potential use of polyacetylene electrodes in rechargeable cells or batteries (4). This communication presents results on the effect of deep discharge and heavy charge on the molecular structure of p-doped polyacetylene. Fourier-transformed photoacoustic infrared spectroscopy (PAS) is employed to evaluate structural changes in the polyacetylene resulting from the electrochemical treatment.

Polyacetylene film of 68 μ thickness had been prepared by the Rohm and Haas Company, using the standard Shirakawa technique (5). Details regarding the preparation have been published elsewhere (6). The film had an apparent density of 0.56 g/cm³ or 48% of theoretical and a specific surface area of 40 m²/g. Circular electrodes of 1.2 cm² area were provided on one side with a 1000 Å Au film and an Au wire, attached with Au-epoxy cement. Experiments were carried out in a PTFE cell using a Li counter and reference electrode. The electrolyte was a 10% b.w. solution of LiBF₄ in sulfolane. Handling, experimentation and transfer of samples were performed in dry, inert gas environment. To obtain good PAS data, electrode films were shredded after removal of the Au film. This enhanced the signal strength by improving the acoustic coupling. The PAS equipment employed has been described elsewhere (6).

Electrode 1 was charged with 0.24 mA/cm² for 1 h, corresponding to a BF₄ dopant level of 3 mole%. It was then left on open circuit for 1 h and discharged with 0.08 mA/cm² to 1.5V versus Li reference; 0.9 mole% dopant remained in the structure. The relevant potential-time curves are shown in Fig. 1. After an open circuit stand of 15 h, the

potential was 2.5V and the electrode was removed for IR-spectroscopy.

Electrode 2 was charged with 0.24 mA/cm² for 1 h, left on open circuit for 1 h and then cathodically polarized with 0.24 mA/cm² for 15 h. Only the first 3 h of discharge are shown in Fig. 1. Above about 1.2 V, p-dopant is removed and below 1.2 V n-doping of polyacetylene with Li occurs; n-doping was performed for 14 h to a level of 42 mole%. Subsequent anodic polarization with 0.24 mA/cm² for 9 h leads to the potential-time curve shown in Fig. 2; 13.5 mole% n-dopant, Li, is removed during the first 4.5 h and 13.5 mole% p-dopant, BF₄, incorporated during the next 4.5 h. After an open circuit stand of 15h, a potential of 3.4V was attained and the electrode was removed for IR spectroscopy.

Photoacoustic spectra of pristine polyacetylene film (6) and of electrodes 1 and 2 are shown in Fig. 3(a), (b) and (c), respectively. The wavenumbers of the major absorption bands are given in Table 1. Spectrum (a) is characteristic for undoped film comprising a mixture of the cis- and trans- isomer (6). Spectrum (b) for electrode 1, p-doped to 3 mole% and undoped to 0.9 mole% once, shows the characteristic polyacetylene features much reduced and the cis bands less pronounced than the trans-bands. These two effects are due to the strong free charge-carrier absorption and dopant-induced cis- to trans- isomerization (5,7). The dominating features of spectrum (b) are the strong bands at 1405 and 1295 cm⁻¹ which are not present in spectrum (a) for pristine polyacetylene. Two similar bands have been observed in gas phase-doped polyacetylene by others (8-10) and have been ascribed (8) to dopant-activation of Raman modes in the IR corresponding to C-C and C=C stretching.

Spectrum (c) for electrode 2, p-doped to 3 mole% followed by n-doping to 13.5 mole% and p-doping to 13.5%, shows the weak features of trans-polyacetylene similar to electrode 2. The dopant-activated bands at 1415 and 1297 cm⁻¹ are stronger, corresponding to the higher dopant level. The most significant features, however, are the two strong bands at 2920 and 2852 cm⁻¹ which were not present in the spec-

*Electrochemical Society Active Member

Key Words: Polymers, Electrode, Infrared

tra of pristine polyacetylene or of electrode 1. These bands are typical for the asymmetrical and symmetrical C-H stretching modes of methylene groups in long-chain aliphatic hydrocarbons. In agreement with this interpretation, the complex band structure between 1200 and 900 cm^{-1} can also be ascribed to C-C stretching modes in long-chain hydrocarbons.

Thus, we find clear evidence that a single overdischarge, resulting in 13.5 mole% n-doping, followed by heavy p-doping or charging to 13.5% mole% leads to irreversible attack on the molecular backbone of the polyacetylene structure. The nature of the attack is the breaking of the double bonds in the conjugated bond system $=\text{CH}-\text{CH}=\text{CH}-$ and the concurrent formation of long-chain aliphatic hydrocarbons $-\text{CH}_2-\text{CH}_2-\text{CH}_2-$.

Table I. Photoacoustic Spectra of Polyacetylene Films

Pristine Film cm^{-1}	Electrode 1 cm^{-1}	Electrode 2 cm^{-1}	Assignment
3040 W	-	-	C-H stretch in cis(CH) _x
3010 W	3010 W	3010 W	C-H stretch in trans(CH) _x
-	-	2920 S	asymm. C-H stretch in (CH ₂) _x
-	-	2852 S	symm. C-H stretch in (CH ₂) _x
1800 S	1800 W	-	1321 + 446 cis(CH) _x
-	1405 S	-	C-C stretch dopant-activated
1330 S	1330 W	1415 S	C-H in plane bend in cis(CH) _x
-	1295 M	1296 S	C-H in plane bend dopant-act. _x
1246 M	1260 W	1260 VW	C-H in plane bend in cis(CH) _x
1116 M	1116 W	1116 W	C-C stretch in cis(CH) _x
1018 M	1018 W	1018 W	C-H out plane bend in trans(CH) _x
748 S	748 W	748 VW	C-H out plane bend in cis(CH) _x
459 S	459 VW	-	C-C-C bend in cis(CH) _x

S = strong, M = medium, W = weak, VW = very weak

Manuscript submitted Nov. 5, 1984.

REFERENCES

1. T. Ito, H. Shirakawa and S. Ikeda, *J. Polymer Sci.* **13**, 1943 (1975).
2. S.P.S. Yen, R. Somoano, S.K. Khanna, and A. Rembaum, *Solid State Commun.*, **36**, 339 (1980).
3. F.G. Will and D.W. McKee, *J. Polymer Sci., Polymer Chem. Ed.* **21**, 3479 (1983).
4. P.J. Nigrey, D. MacInnes Jr., D.P. Nairns and A.G. MacDiarmid, *J. Electrochem. Soc.* **128**, 1651 (1981).
5. T. Ito, H. Shirakawa and S. Ikeda, *J. Polymer Sci.* **12**, 11 (1974).
6. F.G. Will, R.S. McDonald, R.D. Gleim, and M.R. Winkle, *J. Chem. Phys.*, **78**, 5847 (1983).
7. A. Montaner, M. Galtier, C. Benoit, and M. Aldissi, *Solid State Commun.*, **39**, 99 (1981).
8. J.F. Rabolt, T.C. Clarke, and G.B. Street, *J. Chem Phys.*, **71**, 4614 (1979).
9. I. Harada, Y. Furukawa, M. Tasumi, H. Shirakawa and S. Ikeda, *J. Chem. Phys.*, **73**, 4746 (1980).
10. S.I. Yaniger, S.M. Riseman, T. Frigo, and E.M. Eyring, *J. Chem. Phys.*, **76**, 4298 (1982).

General Electric Company assisted in meeting the publication costs of this article.

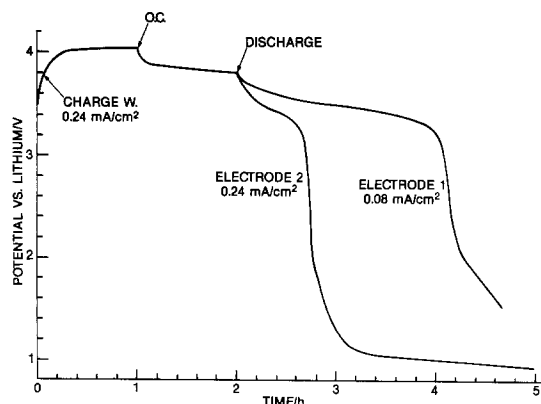


Fig. 1. Charge discharge curves: Electrode 1: 3 mole% p-doping, undoping to 0.9% Electrode 2: 3% p-doping, 1 h undoping, 14 h n-doping.

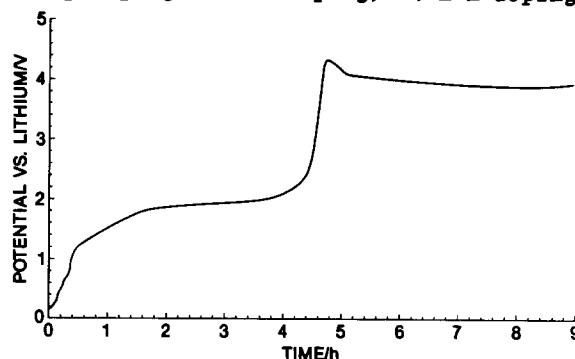


Fig. 2. Charging curve of electrode 2 following deep discharge: Removal of 13.5 mole% n-dopant followed by 13.5 mole% p-doping.

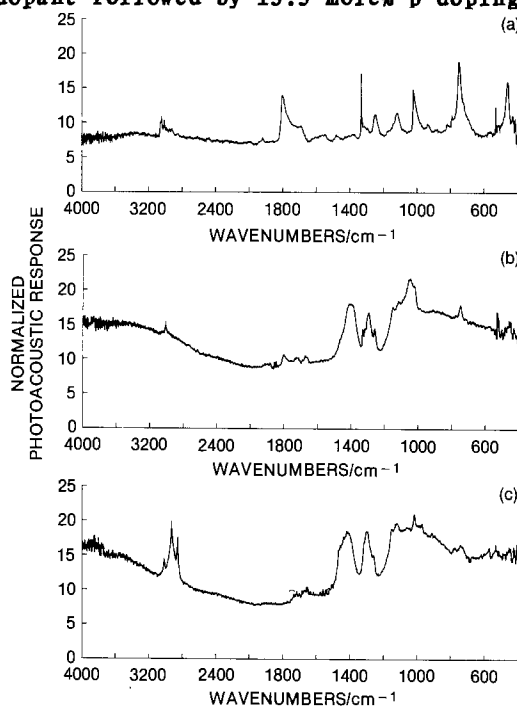


Fig. 3. Photoacoustic infrared spectra of polyacetylene films: (a) Pristine film. (b) Electrode 1: charged and discharged once. (c) Electrode 2: deep discharge-heavy charge.

A Two-Photoelectrode Solid-State Photoelectrochemical Cell

Anthony F. Sammells* and Sharon K. Schmidt

Eltron Research Incorporated, Naperville, Illinois 60540

The use of solid-electrolyte based photoelectrochemical (PEC) cells provides a unique approach for the PEC conversion and storage of selected redox species incorporated within the proximity of the semiconductor/solid electrolyte interface. For such interfaces, however, the efficient recombination of photogenerated carriers appears to be greatest when both polycrystalline semiconductor and solid electrolyte materials are present at the junction. As a consequence, PEC cells fabricated which contain such interfaces, frequently possess little or no effective photoactivity. To minimize such high populations of surface states, single crystal photoelectrodes in contact with solid polymer based electrolytes have been used. We have previously reported on the two photoelectrode cell p-InP/PEO·NaSCN, Na₂S, S/n-CdS where the sodium ion conducting solid polymer electrolyte (SPE) poly(ethylene oxide) PEO was used.¹ Upon illumination, this cell gave photopotentials up to 540mV, however current densities of less than 1 μA/cm² could only be achieved even under both biased and illuminated conditions. This was in part a consequence of the high resistivity of the SPE material used. PEO had earlier been used in the solid-state PEC cell n-Si/PEO, KI, I₂/SnO₂ glass, where the n-Si photoanode was initially coated with platinum and subsequently protected from photoanodic corrosion effects by a sequential layer of platinum and polypyrrole.² For PEO based PEC cells, small interelectrode spacings are desirable for not only minimizing cell IR losses but also for improving light transmission to the solid-state junction of interest. Achieving small well defined interelectrode spacings can, however, often be logistically somewhat difficult and can frequently lead to cell shorting.

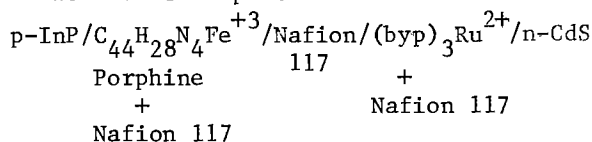
If we wish to introduce some faradaic storage capacity into a solid-state PEC cell, it will be necessary to provide for effective separation of the oxidant and reductant species which reside close to the appropriate photoelectrode. While this, in principle, could be achieved using PEO, the preparation of an interelectrode spacing with clearly

defined oxidant, separator and reductant regions can be expected to provide a formidable task. This problem has been addressed here by the use of the perfluorinated cation exchange membrane Nafion,³ as the SPE in a solid-state PEC cell containing potential storage capacity. The PEC activity of semiconductors incorporated onto Nafion in contact with aqueous solutions has been previously reported on, directed towards the photoelectrolysis of water.⁴

As is well known, this material has found extensive application in a variety of electrochemical cells. In addition, redox species such as (bpy)₃Ru²⁺ have been shown to be irreversibly coordinated into Nafion's polymeric matrix where they have exhibited electrochemical reversibility.⁵⁻⁸

Here it appears that the mobile conducting cations are exchanged by the introduced redox species. When such redox containing polymers are attached to an electrode, redox electrochemistry can take place via an electron self-exchange reaction involving the introduced redox species.⁹⁻¹¹ This SPE material can consist of essentially two phases¹² which contain respectively a bulk polymer and a lower density ionic cluster phase. It is in the lower density phase that introduced redox complexes appear to reside. In addition, the higher oxidation states of such complexes appear to be less strongly held than do their lower oxidation states.¹³

We wish to report on the cell



where the respective redox species are initially introduced in a Nafion 117 solution which is subsequently applied onto the surface of a sodium exchange Nafion 117 membrane. The materials and procedures followed for preparation of this cell will now be discussed.

Single crystal n-CdS was obtained from Cleveland Crystal. Ohmic contact to this

material was made by initially etching with H_2SO_4 and after rinsing with distilled water and drying, contacted with a gallium-indium eutectic. Current collection was achieved to this area via a nickel wire and silver epoxy, and the whole electrode assembly cured at $150^\circ C$ for one hour.

The p-InP single crystal was obtained from CrystaComm Inc. (Zn doped $\approx 10^{17} \text{ cm}^{-3}$). The $\langle 111 \rangle$ face was used. After etching the surface with bromine/isopropanol solution, ohmic contact was achieved by the sequential vacuum thermal evaporation of a Au/Zn/Au layer followed by an anneal under H_2 for one hour at $400^\circ C$. The cell was prepared by introducing a drop of a 5% Nafion 117 present in a mixture of lower aliphatic alcohols containing 0.005M iron (III) meso-tetraphenyl porphine chloride ($C_{44}H_{28}ClFeN_4$) and 0.01NaCl onto both the surface of an appropriately etched p-InP and a Na^+ exchanged Nafion 117 membrane. After both halves were allowed to nominally dry under ambient conditions for about one hour, they could be directly contacted by lightly pressing. A similar procedure was followed for the photoanode side where a 5% Nafion solution containing 0.01M $(byp)_3RuCl_2$ and 0.01M NaCl, was introduced onto both the Nafion 117 membrane and n-CdS single crystal before finally being contacted together. A schematic diagram of the finally assembled cell is shown in Figure 1. The simultaneous illumination of both the n-CdS and p-InP redox solid electrolyte junctions was achieved from the n-CdS photoanode side.

Selection of this two photoelectrode cell was preceded by a preliminary investigation of various redox species introduced into the SPE using cells of the configuration photoelectrode/redox, Nafion117/SnO₂ Cond. Glass. For the cells n-CdS/ $(byp)_3RuCl_2$ + Nafion 117/SnO₂ conducting glass, and p-InP/Tetraphenyl Fe^{3+} Porphine + Nafion 117/SnO₂ conducting glass, illumination through the conducting glass (100 mW/cm^2 quartz-iodine) to the photoelectrode/SPE interface of interest, photopotentials of respectively -750 mV and $+420 \text{ mV}$ were realized from each cell. In addition, upon potentiostatting each of these cells respectively 0.4 V cathodic or anodic of their illuminated rest potential, current densities in the 3 to $20 \text{ } \mu\text{A/cm}^2$ range were obtained.

The two photoelectrode cell
 p-InP/ $C_{44}H_{28}N_4Fe^{3+}$ /Nafion/ $(byp)_3Ru^{2+}$ /n-CdS
 Porphine 117 +
 + Nafion 117
 Nafion 117

approximately one hour after fabrication possessed a dark open circuit potential of 380 mV .

Upon illumination of this cell, an initial photopotential of 1130 mV was realized. The photopotential-time characteristics of this cell are shown in Figure 2A. The photo-current-voltage scan for this cell is shown in Figure 2B. Here the total cell potential is reported where cell charge is occurring over the voltage range shown. PEC charge currents up to $30 \text{ } \mu\text{A/cm}^2$ were realized upon cell bias. The half-cell reactions during cell charge will correspond to $TPPFe^{3+} + e^- \rightarrow TPPFe^{2+}$ at the p-InP photocathode and $(byp)_3Ru^{2+} + h^+ \rightarrow (byp)_3Ru^{3+}$ at the n-CdS photoanode. The photocurrent wavelength response of this cell was performed using a Rudolph Instruments Monochromator Model #681A31. The light source used was a Sylvania 300W ELH bulb. These cell characteristics are shown in Figure 3. The peak photocurrent occurs at $\approx 550 \text{ nm}$ or 2.25 eV , which is approximately 300 mV below the n-CdS band-gap. This may be a consequence of the ruthenium doped SPE sensitizing the n-CdS photoanode to larger wavelengths. This might be a result of the $(byp)_3Ru^{2+}/(byp)_3Ru^{3+}$ couple being somewhat positive of the n-CdS flat-band potential.¹⁴

In conclusion, we have identified a two photoelectrode solid-state PEC cell which is able to produce photopotentials in excess of one voltage and possesses some inherent storage capacity. This storage capacity is, of course, presently limited by the low concentration and thin SPE redox layers used between the photoelectrode and the SPE membrane. It is expected that this cell will be of potential value as not only a specialized storage device, but for specific detector applications.

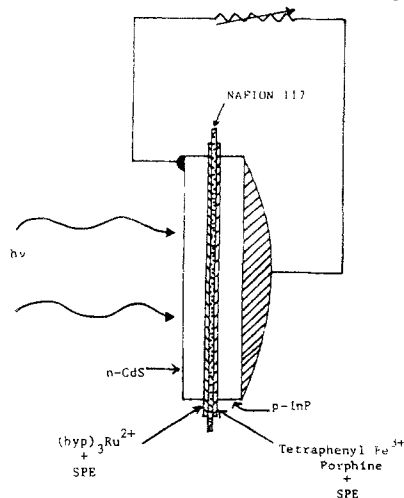


Figure 1.
 Schematic Diagram of p-InP/Tetraphenyl Fe^{3+}
 Porphine/Nafion 117/ $(byp)_3Ru^{2+}Cl_2$ /n-CdS
 Solid-State Photoelectrochemical Cell

The n-CdSe Photoelectrochemical Cell: Wavelength-Dependent Photostability

Holly-Dee Rubin, Douglas J. Arent, and Andrew B. Bocarsly*

Department of Chemistry, Princeton University, Princeton, New Jersey 08544

Much recent work has focused on $\text{Fe}(\text{CN})_6^{4-/3-}$ as a stabilizing electrolyte for n-CdX (X=S, Se) based photoelectrochemical cells (1-5). Prior studies performed in this laboratory (6) showed that irradiation of n-CdS in an electrolyte containing $\text{Fe}(\text{CN})_6^{4-/3-}$ can lead to formation of a surface layer of $[\text{Cd}^{\text{II/III}}\text{Fe}^{\text{II/III}}(\text{CN})_6]^{2-/1-}$. In the presence of the appropriate cations, this layer was associated with improved cell output parameters. These studies have now been extended to include the n-CdSe system. In this letter we wish to report an unprecedented wavelength dependence of the n-CdSe photoelectrochemical cell.

Figure 1 illustrates the dependence of the cell photocurrent stability on incident irradiation wavelength. Light intensity was adjusted so that similar current densities were obtained at the two wavelengths employed since some absorption by solution species occurs at 488nm. When the 488nm line of an Ar^+ laser is used, stable photocurrent output is achieved for periods in excess of several hours (7). However, when excitation is at 633nm (He-Ne laser) the photocurrent decreases with time. The extent to which this is observed is found to be concentration dependent. At high concentrations ($>0.5\text{M}$) of $\text{K}_4\text{Fe}(\text{CN})_6$, photostability at 633nm increases, so that the difference in stability between 488nm and 633nm is decreased but still evident.

Further experiments performed on both single crystal [(0001) face], and polycrystalline n-CdSe using a 2500W Xe lamp and a Schoeffel monochromator indicate that the onset of stability occurs at energies higher than about 550nm. All wavelengths studied are capable of exciting the band gap transition of CdSe ($E_{\text{BG}}=1.7\text{eV}$). Furthermore, it is found that if a sample is initially irradiated at 488nm and then later exposed to 633nm light, the resulting photocurrent is stable.

We believe that a $\text{Cd}^{\text{II}}\text{Fe}^{\text{II/III}}(\text{CN})_6$ surface layer is responsible for this behavior. In support of this conclusion diffuse reflectance FTIR spectroscopy of irradiated electrodes yields data which coincide with those obtained from authentic samples of $\text{K}_2[\text{Cd}^{\text{II}}\text{Fe}^{\text{II}}(\text{CN})_6]$.

Although it has been previously suggested that the corrosive formation of a selenium surface layer is the source of n-CdSe photostability in $\text{Fe}(\text{CN})_6^{4-/3-}$ electrolyte (5), such an overlayer cannot be invoked to explain the observed behavior. A selenium layer, were one to form, would be anticipated to develop at all wavelengths studied. This layer would be expected to exhibit the same behavior at a given wavelength, irregardless of irradiation pretreatment, i.e. preirradiation at 488nm should not affect electrode stability at 633nm, in contrast to the observed behavior.

Although a selenium overlayer may be present, the cation dependence of the systems under study also tends to rule out such a layer as responsible for either the electrode photostability or the wavelength dependent behavior. It has been suggested that addition of salts to the $\text{CdX}/\text{Fe}(\text{CN})_6^{3-/4-}$ solution should result in competitive adsorption (3) (i.e. the salt is able to displace adsorbed ferro-ferricyanide) with a concomitant decrease in cell output. Addition of Cs^+ salt to the n-CdSe cell does lead to instability. However, as previously reported (6), addition of CsNO_3 to the CdS/ferro-ferricyanide cell improves stability, in marked contrast to the results obtained at n-CdSe and to those predicted by the competitive adsorption model. These results are consistent with the hypothesis advanced previously that the role of the alkali cation is to influence the redox potential of the surface species, enhancing communication between this species and the semiconductor valence band (6). These observations also tend to support the conclusion that a selenium corrosion layer cannot be responsible for the wavelength dependence - selenium would not be expected to induce cation

*Electrochemical Society Active Member.

Key words: semiconductor, films, photoelectricity, energy conversion

dependent behavior.

Since a $[\text{CdII/III}(\text{CN})_6]^{1-/2-}$ layer appears to form at all wavelengths studied, it is logical to ascribe the wavelength dependence to the photochemical properties of the surface species. Alternately, solution based photochemistry might be considered as the source of the wavelength dependence. However, it is highly improbable that solution photochemistry could produce the wavelength dependence, since there is no observable change in the solution redox potential as measured before and after irradiation, and absorbance at these wavelengths is exceedingly low. If solution photochemistry is occurring, the concentration of products would be too low to have a major effect. Therefore, we propose that at $\lambda < 550\text{nm}$ the surface attached material undergoes a photochemical reaction leading to a product responsible for the improved output characteristics of the n-CdSe ferro-ferricyanide photoelectrochemical cell.

The wavelength dependence suggests ligand loss as the most likely process (8). Several possible outcomes resulting from ligand loss can be envisioned, all of which provide a mechanism for stabilizing the interface. Aquation could occur. The resulting aquated surface species would be expected to have a different film morphology than the parent complex. $\text{MFe}(\text{CN})_6$ species are known to possess a zeolitic structure (9); aquation could lead to a change in pore size. Were the pore size to increase, solution contact with the surface film could be enhanced. Since one function of the film is to mediate charge transfer from the semiconductor to the solution redox couple (6), increased solution contact could facilitate this process, thus providing a more stable interface. A second outcome of ligand loss could be that the iron centers are able to come in close proximity, again enhancing the charge transfer properties of the film. Finally, the introduction of an empty coordination site on the Fe center provides the possibility of direct Se-Fe bonding from a surface Se site. This bonding could promote charge transfer from the semiconductor to the surface attached species via an inner sphere mechanism.

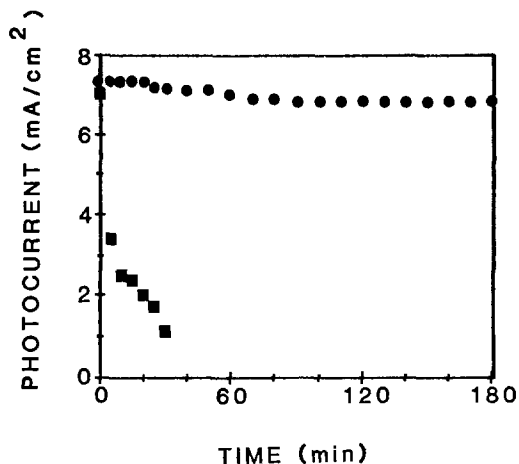
In conclusion, a $\text{CdFe}^{\text{II/III}}(\text{CN})_6$ surface layer on n-CdSe not only enhances photostability, but also induces wavelength dependent behavior in the photoelectrochemical cell composed of n-CdSe/ $\text{Fe}(\text{CN})_6^{4-/3-}$. The wavelength dependence appears to be due to a photochemical reaction which changes the properties of the surface film. Such changes appear capable of enhancing charge transfer

rates at the semiconductor interface, thus decreasing the relative importance of the photodecomposition pathway. The surface film can be prepared at 488nm with subsequent irradiation at much lower energy resulting in a stabilized photoelectrochemical cell.

Acknowledgments.-- H.-D. R. acknowledges the Electrochemical Society and the DOE for a Summer Research Fellowship.

REFERENCES

1. R. Noufi, D. Tench, L. F. Warren, *J. Electrochem. Soc.*, **128**, 2363 (1981).
2. R. A. L. Vanden Berghe, W. P. Gomes, and F. Cardon, *Z. Phys. Chem. N./F.*, **92**, 91 (1974).
3. R. Tenne, *J. Electrochem. Soc.*, **130**, 2163 (1983).
4. K. W. Frese, Jr., *J. Electrochem. Soc.*, **130**, 28 (1983).
5. J. Reichman and M. A. Russak, *J. Electrochem. Soc.*, **131**, 796 (1984).
6. H.-D. Rubin, B. D. Humphrey, and A. B. Bocarsly, *Nature*, **308**, 339 (1984).
7. Stable output for periods in excess of 20 hrs have been noted during preliminary studies.
8. A. W. Adamson, W. I. Waltz, E. Zinato, D. W. Watts, P. D. Fleischauer, and R. D. Lindholm, *Chem. Review*, **68**, 541 (1968).
9. K. Itaya, N. Shoji, I. Uchida, *J. Am. Chem. Soc.*, **106**, 3423 (1984).



Time dependence of the output photocurrent for a n-CdSe/(0.2M/0.01M) $\text{Fe}(\text{CN})_6^{4-/3-}$, 0.1M KOH photoelectrochemical cell potentiostatted at 0V vs. SCE.

- 22mW/cm², 488nm
- 14mW/cm², 633nm

Manuscript submitted Oct. 19, 1984.
Princeton University assisted in meeting the publication costs of this article.



Mechanistic Studies Related to the Safety of Li/SOCl₂ Cells

B. J. Carter,* R. M. Williams,* F. D. Tsay, A. Rodriguez, S. Kim, M. M. Evans, and H. Frank*

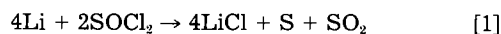
Jet Propulsion Laboratory, California Institute of Technology, Pasadena, California 91109

ABSTRACT

Mechanistic studies of the reactions in Li-SOCl₂ cells have been undertaken to improve understanding of the safety problems of these cells. The electrochemical reduction of 1.5M LiAlCl₄/SOCl₂ has been investigated using gas chromatography, electron spin resonance spectroscopy, and infrared spectroscopy. Cl₂ and S₂Cl₂ have been identified as intermediates in the reduction of SOCl₂, along with a radical species ($g_{xx} = 2.004$, $g_{yy} = 2.016$, $g_{zz} = 2.008$) and the proposed triplet ground-state dimer of this radical. SO₂ and sulfur have been identified as products. Based upon these findings, a mechanism for the electrochemical reduction of 1.5M LiAlCl₄/SOCl₂ has been proposed, and its implications for safety of Li-SOCl₂ cells during discharge to +0.5V at 25°-30°C are discussed.

There has been great interest in the lithium thionyl chloride battery system because of its high energy density. The solvent, thionyl chloride (SOCl₂), is also the cathode active material, so this cell has the potential for high rate discharge. Despite much progress in the areas of design and optimization of cells and elimination of voltage delay, safety problems still hinder the application of the cells. The cells pose a safety problem because they have been found to vent (expel internal liquids and gases) or explode (1). Many explanations have been offered to account for the venting and explosion phenomena.

One general explanation for the observed unsafe behavior of Li-SOCl₂ cells is the production, and violent decomposition, of intermediates formed during the discharge of the cell. The concentration of the metastable compounds increases to the point that their decomposition causes venting or an explosion, or produces sufficient heat to trigger the direct Li-liquid cathode reaction. Although the overall cell chemistry, Eq. [1], is generally accepted, there is disagreement over intermediates formed during discharge and the discharge reaction mechanism



Several intermediates have been proposed in the reduction of SOCl₂, such as SO, (SO)_n, S₂O, and S₂Cl₂ (2-6). Of these intermediates, S₂O has been identified by infrared spectroscopy (5), and S₂Cl₂ has been identified by gas chromatography (6). A method for overcoming the possible "chemical" safety problem is to identify the intermediates which are formed during cell discharge and to establish the reaction mechanism of discharge. With this fundamental understanding of the cell chemistry, it should be possible to establish safe discharge conditions, such as voltage limits, or to modify the cell chemistry to eliminate the unsafe behavior due to hazardous intermediates. This paper presents the results to date of our efforts to achieve this goal for Li-SOCl₂ cells discharged at 25°-30°C to a voltage of +0.5V.

Experimental

All cell components for chemical studies were handled under an argon atmosphere in a Vacuum Atmospheres dry box (<10 ppm O₂). SOCl₂ was obtained from Aldrich and purified by distillation from triphenylphosphite (7). LiCl was obtained from Alfa and dried in vacuo for 24h at 130°C before use. AlCl₃ was obtained from Fluka AG,

* Electrochemical Society Active Member.

Chemische Fabrik (puriss.), and used without additional purification. 1.5M LiAlCl₄/SOCl₂ electrolyte solutions were used in all the experiments, and the reduction experiments were carried out at 25°-30°C.

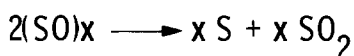
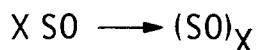
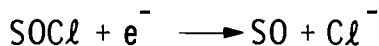
Gas chromatography (GC) experiments were carried out with a Hewlett-Packard Model 5880 GC, with a 6 ft-1/4 in. glass column packed with 10% QF-1 on 80/100 chromasorb G column. The temperatures of the injector port and column were kept below 130°C to prevent reaction between S and SOCl₂ (8). Samples for the GC experiments were prepared by reduction of the electrolyte solution at the carbon electrode of a Li-SOCl₂ cell at 10 mA/cm² and 25°-30°C. Aliquots were removed and the samples transported to the GC in sealed reactivials. Electron spin resonance (ESR) spectra were recorded at 77 K on a Varian E-line Century Series spectrometer operating at X-band frequency (9.1 to 9.5 GHz) employing 100 kHz field modulation. Samples for the ESR experiments were prepared by rapidly reducing the electrolyte solution at gold or carbon electrodes at 25°-30°C and quickly freezing the samples. Infrared (IR) spectra were recorded at room temperature with a Digilab FTS-15C spectrometer. Samples for IR analysis were prepared *in situ* by reduction of the electrolyte solution at a gold grid electrode, at voltages of 3.6 to +0.5V_{Li}, 0.1 to 0.5 mA/cm², and at 25°-30°C (9).

Results and Discussion

In order to understand what hazardous compounds might be formed during discharge of a Li-SOCl₂ cell, and their implication for cell safety, it is important to establish the mechanism for the electrochemical reduction of SOCl₂. Two mechanisms have previously been reported for this reduction process (Fig. 1). Bowden and Dey (4) have proposed reducing SOCl₂ to yield SO, which could form the polymer (SO)_n. This polymer is proposed to be hazardous. Blomgren *et al.* (6) have proposed reducing SOCl₂ to yield SOCl, which in subsequent reactions yields SCl₂ and S₂Cl₂. Our work has focused on identifying the intermediates of the electrochemical reduction of SOCl₂, employing a variety of complementary techniques. Because of the complexity of the chemistry, it is important to have the corroborating evidence of complementary techniques to provide convincing evidence for a mechanism of the reduction of SOCl₂ in Li-SOCl₂ cells.

The GC results for fresh and discharged 1.5M LiAlCl₄/SOCl₂ solutions have been obtained (Fig. 2). For the fresh samples, the major peak is SOCl₂, but some SO₂ and S₂Cl₂

I. BOWDEN AND DEY (4)



II. BLOMGREN, ET AL (6)

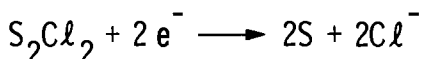
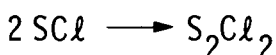
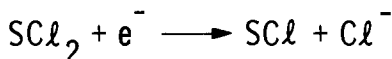
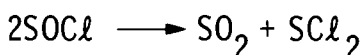


Fig. 1. Postulated mechanisms for reduction of SOCl_2 in Li-SOCl_2 cells.

are present. After discharge, the amounts of Cl_2 , SO_2 , and S_2Cl_2 have significantly increased. These results strongly suggest that S_2Cl_2 and Cl_2 are intermediates in the reduction of SOCl_2 and are possibly formed by the disproportionation of SCl_2 . However, SCl_2 is not positively identified in the chromatograms, but it does seem reasonable to propose SCl_2 as an intermediate in the reduction of SOCl_2 .

Most of the ESR samples were prepared by reduction of $1.5\text{M LiAlCl}_4/\text{SOCl}_2$ at a gold electrode because doing so gives clean samples at voltages of 3.6 to $+0.5\text{V}_{\text{Li}}$ and current densities as high as 0.1 to 0.5 mA/cm^2 . The samples prepared should mimic the Li-SOCl_2 cell chemistry during discharge. In particular, these experimental conditions should mimic cell chemistry at the beginning of discharge, when excess electrolyte is present, because only a small amount of SOCl_2 is utilized. It is not clear if these current densities approximate 10 mA/cm^2 on a Teflon-bonded carbon electrode. Samples are also prepared using a carbon fiber electrode, but there is a problem with the structural integrity of the carbon electrode, since carbon particles are found in the samples. These carbon particles provide a large ESR signal due to the graphitic carbon radical which dominates part of the spectrum obtained with these samples, but the remainder of the spectrum is essentially the same as that observed for samples prepared at the gold electrode. This is an important point because it supports application of the results obtained on gold electrodes to real cell chemistry in which the reduction occurs on carbon electrodes.

The overall ESR spectrum of discharged $1.5\text{M LiAlCl}_4/\text{SOCl}_2$ is shown in Fig. 3. The spectrum is very complicated and covers about 5000G . This is most unusual because most ESR spectra of radicals cover a region of a few hundred gauss. A great deal of interpretation has been necessary to assign most of the features of this spectrum. Figure 4, curve A, shows the region around $g = 2$,

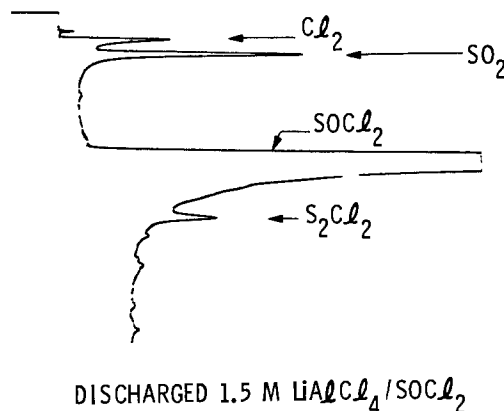
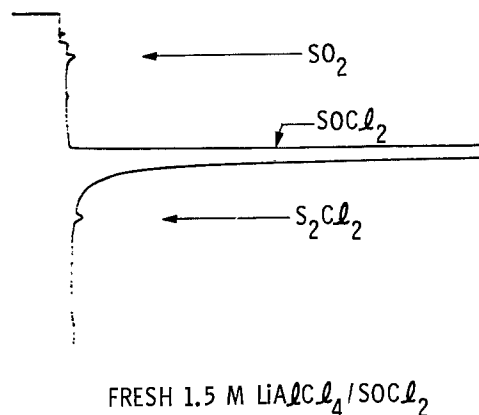


Fig. 2. Gas chromatograms of $1.5\text{M LiAlCl}_4/\text{SOCl}_2$

i.e., 3200G , expanded, and curve B shows the second derivative of the spectrum. The major points made by Fig. 4 are that the three g values are observed for the three principal axis, x , y , and z , because the sample is frozen. For each g value, a quartet is observed due to hyperfine splitting, the nuclear spin interaction with the electron spin angular momentum. Because of the quartet for each g value, it is concluded that the radical electron is localized on a nucleus of spin $3/2$. The most likely candidate for the nucleus is chlorine.

Table I summarizes the results from Fig. 4, along with presenting literature data of similar compounds. It is clear from Table I that these 19 valence electron molecules have similar g values. With these triatomic molecules, the unpaired electron should be largely localized on the central atom (10). As seen for OSCl , which was prepared by γ radiation of a frozen glass of SOCl_2 , there is very little hyperfine splitting because the radical electron is largely localized on sulfur (11). In ClO_2 , the radical electron is largely localized on chlorine, and a quartet is observed for each g value, with large hyperfine constants (12). The hyperfine constants for ClO_2 and the unknown are very similar and, thus, we conclude that the unknown

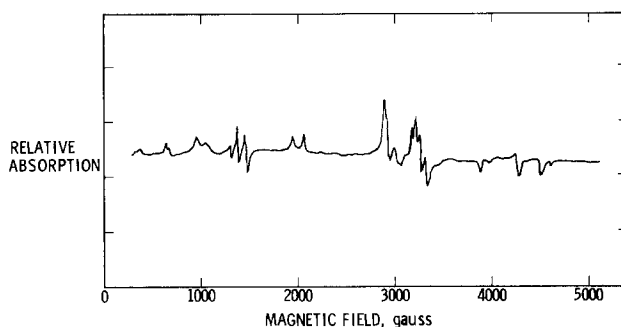


Fig. 3. ESR spectrum of discharge electrolyte at 77 K

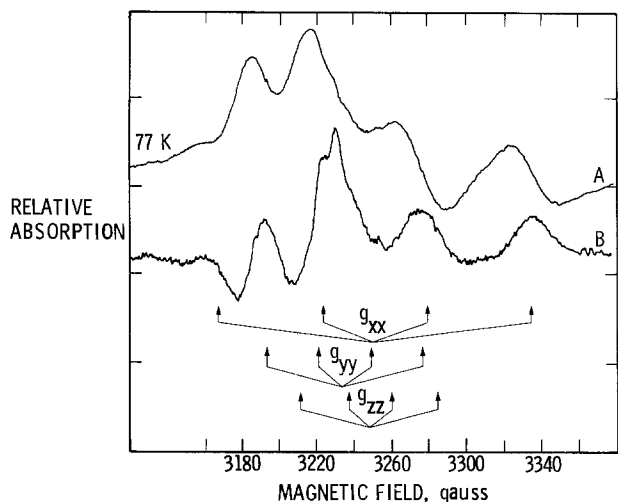


Fig. 4. ESR spectrum of discharged electrolyte at 77 K: curve A = first derivative; curve B = second derivative.

is OCIS, with chlorine being the central atom. OCIS should have chemistry similar to ClO₂, which is a known hazardous compound when present at a partial pressure greater than 50 torr (13). If OCIS is present in significant concentration in a cell, it could be a safety hazard.

The most reasonable explanation for the ESR spectrum covering 5000G is the existence (assumed) of a molecule with large zero-field splitting. In this case, two OCIS monomers come together, and the two radical electrons interact, in the strong field case, to yield a dimer with a triplet ground state. For this dimer, there should be four forms: two isomeric forms of planar conformation; and two isomeric forms of skewed conformation (see Fig. 5). The planar forms are D_{2h} symmetry in the highest reasonable case, assuming O and S are similar (14). The planar forms should have three unique axes. In the ESR spectrum then, two transitions should be observed for each unique axis, and a total of six transitions should thus be observed. Because there are two isomeric forms of the planar conformation, a perturbation on the simple explanation, one would expect each transition, as predicted above, to be split into a doublet, as observed in Fig. 8. Following similar logic, the skewed conformations have a highest reasonable symmetry of D_{2d} (14). There are only two unique axes, since *x* and *y* are degenerate. Thus, four transitions should be observed for this dimer. Again, adding the perturbation of the other isomeric form, one should expect each transition to be split into a doublet. However, the *x* and *y* axes are not actually degenerate, so the transitions in these polarizations are expected to be split again to yield a doublet of doublets. These transitions are also observed in Fig. 6.

To date, the only reasonable way to account for the ten transitions shown in Fig. 6 is with a triplet ground-state dimer of the OCIS monomer. Supporting further these assignments, when the temperature of the frozen sample is warmed, the above peaks move closer to *g* = 2.0 and decrease in intensity. This is expected because the electron-electron repulsion should separate the monomeric units at higher temperatures, reducing the zero-field splitting and the concentration of dimer species. These assignments of the dimer are also supported by calculations (9).

Table I. ESR parameters

RADICAL	g-VALUE			³⁵ Cl HYPERFINE CONSTANT (gauss)		
	g _{XX}	g _{YY}	g _{ZZ}	A _{XX}	A _{YY}	A _{ZZ}
UNKNOWN	2.004	2.016	2.008	57	29	25
O S Cl ₂ (13)	2.000	2.017	2.008		(A < 11)	
O Cl O (14)	2.0036	2.0183	2.0088	+57.6	-30.8	-26.8

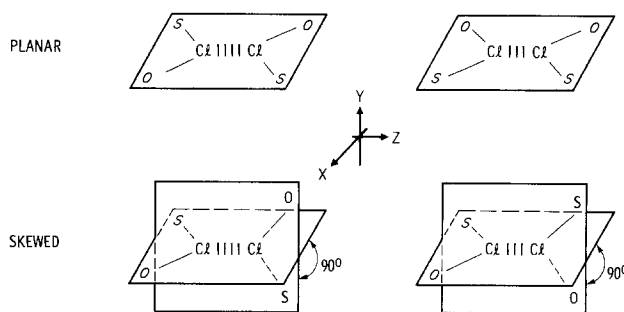


Fig. 5. Proposed structures of (OCIS) dimers

To obtain initial data on the lifetimes of the radical intermediates and to observe ESR active compounds formed later in the reduction sequence of SOCl₂, warming experiments were initiated. In these experiments, ESR samples were warmed for a specific length of time at a specific temperature, then cooled to 77 K to obtain the spectrum. Although these experiments have not been completed, one can estimate that the half-lives of OCIS and its triplet dimer are on the order of 4-10s at 25°-30°C. Much more research is required to accurately determine these half-lives. One other ESR active compound, which is formed later in the reduction sequence of SOCl₂, has been identified. Its spectrum, shown in Fig. 7, is always the last spectrum obtained in these warming experiments. The data from this spectrum are summarized in Table II, along with literature data for oligomeric sulfur (15). As can be seen, the data are in good agreement, and we are confident that the final product observed in the reduction of SOCl₂ is sulfur. This assignment is consistent with the established overall cell chemistry for Li-SOCl₂ cells, and it lends support to the claim that the chemistry of the laboratory cell is similar to that occurring in Li-SOCl₂ hardware cells.

Spectra from the IR investigations of 1.5M LiAlCl₄/SOCl₂ reduced *in situ* have shown that SO₂ (1330 cm⁻¹) and SO₂Cl₂ (1410 cm⁻¹) are present in the reduced solution. These results are reasonable because SO₂ has been observed in discharged solutions by GC, and SO₂ is generally accepted to be a product of the reduction of SOCl₂. With Cl₂ having also been detected in discharged solutions by GC, SO₂Cl₂ is probably formed by the well-known reaction of SO₂ and Cl₂ to yield SO₂Cl₂.

Based upon these results, the following mechanism, shown in Fig. 8, for the reduction of SOCl₂ is proposed. A one-electron reduction of SOCl₂ to yield OSCl, which we have not observed, is proposed as the first step. OSCl isomerizes to OCIS, which should have chemistry similar to ClO₂, a known hazardous compound. OCIS can "dimerize," *i.e.*, at least form a weakly bonded dimer, which should decompose to yield SO₂ and SCl₂. SCl₂ has not yet been identified as an intermediate, but because Cl₂ and S₂Cl₂ have been observed, the known

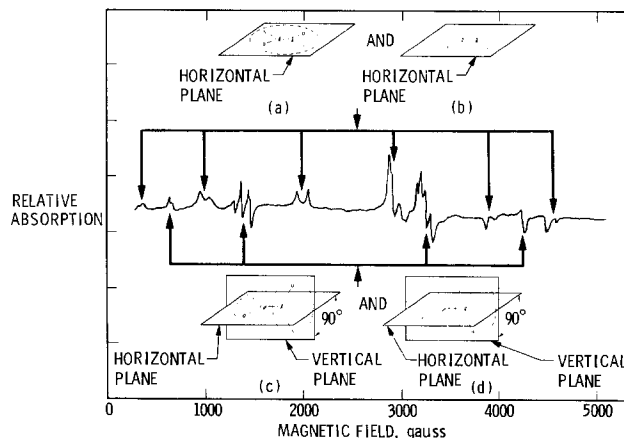


Fig. 6. ESR spectrum of (OCIS) dimers

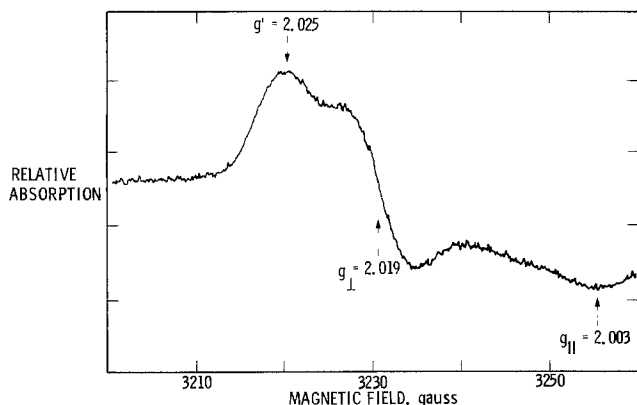


Fig. 7. ESR spectrum of discharged electrolyte heated to 228 K for 5 min, then cooled to 77 K.

disproportionation reaction of SOCl_2 to yield S_2Cl_2 and Cl_2 is the most plausible explanation for the occurrence of the latter compounds in the cell chemistry. Because SO_2 and Cl_2 are both present in the discharged solution, it is expected that SO_2Cl_2 will be present; this has been confirmed by IR. The remainder of the details of the reduction of SOCl_2 to yield the known final cell products, S, SO_2 , and Cl^- , have not yet been established. The subsequent overall reduction reactions of SOCl_2 , S_2Cl_2 , Cl_2 , and SO_2Cl_2 to yield S, SO_2 , and Cl^- are only listed for completeness, not because their mechanisms have been established. Since no evidence for other intermediates has been obtained, no additional reactions are included.

Even though this mechanism is not complete or fully proven, it is reasonable to speculate on its implications for safety of Li-SOCl₂ cells during discharge to +0.5V at 25°-30°C using 1.5M LiAlCl₄/SOCl₂. Although OCIS could be a hazardous intermediate, by analogy with the chemistry of ClO₂, if it is present in sufficiently high concentration, the lack of delay in formation of SO₂, observed by Istone and Brodd (5), and the relatively short lifetime of OCIS and (OCIS)₂ suggest that the concentration OCIS never gets high. Thus, it appears that there are no safety hazards due to intermediates formed during discharge of

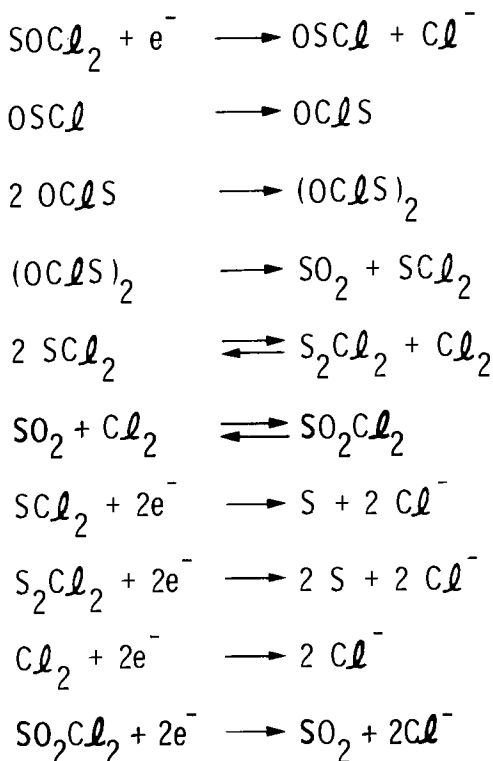


Fig. 8. Proposed mechanism

Table II. ESR parameters

RADICAL	g-VALUE		
	g_{\parallel}	g_{\perp}	g'
UNKNOWN FROM WARMED SOLUTION	2.003	2.019	2.025
S_5^+ (17)	2.003	2.019	
S_n^+ OPEN CHAIN (17)			2.025

Li-SOCl₂ under these conditions. However, if under other operating conditions, such as low temperature operation, SO₂ delay is observed in a cell, OCIS might form in concentrations sufficiently high to account for unsafe behavior of Li-SOCl₂ cells. Also, the mechanism has not been completed, so other hazardous intermediates may still be identified.

Clearly, more work is needed to fully understand the processes which govern the safety of Li-SOCl₂ cells. Both the identification of possible hazardous compounds (such as OCIS) formed during the discharge of a Li-SOCl₂ cell and the proposed mechanism for reduction SOCl₂ provide the basis for a fundamental understanding of the reactions which can cause venting or explosions. Although additional research is needed, this research also provides the basis for investigating the reactions which occur during voltage reversal, a hazardous condition for some Li-SOCl₂ cells, and it provides the foundation for modifying the chemistry of Li-SOCl₂ cells to improve cell safety.

Acknowledgments

The authors thank Dr. Richard Hammen for many helpful discussions and Lois Taylor for her assistance with the infrared studies. The authors also thank Larry Whitcanack for assistance in many of the experiments. This paper represents one phase of research performed by the Jet Propulsion Laboratory, California Institute of Technology, sponsored by NASA.

Manuscript submitted Sept. 23, 1983; revised manuscript received July 11, 1984.

California Institute of Technology assisted in meeting the publication costs of this article.

REFERENCES

- A. N. Dey, Final Report, Contract DAAB17-74-C-1119, for U.S. Army ERADCOM, July 1978.
- A. N. Dey and P. Bro, *This Journal*, **125**, 1574 (1978).
- C. R. Schlaikjer, F. Goebel, and N. J. Marincic, *ibid.*, **126**, 513 (1979).
- W. L. Bowden and A. N. Dey, *ibid.*, **127**, 1419 (1980).
- W. K. Istone and R. J. Brodd, *ibid.*, **129**, 1853 (1982).
- G. E. Blomgren, V. Z. Leger, T. Kalnoki-Kio, M. L. Kronenberg, and R. J. Brodd, *Power Sources*, **7**, 583 (1979).
- K. Friedman and L. Wetter, *J. Chem. Soc.*, 36 (1967).
- "Inorganic Electrolytes," Final Report by GTE for Office of Naval Research, Contract N00014-76-C-0524, p. 28, January 1979.
- R. Williams, F. D. Tsay, S. Kim, M. Evans, Q. Kim, A. Rodriguez, B. J. Carter, and H. Frank, in "Lithium Batteries," A. N. Dey, Editor, p. 60, The Electrochemical Society Softbound Proceedings Series, Pennington, NJ (1984).
- A. D. Walsh, *J. Chem. Soc.*, 2274 (1953).
- K. Nishikida and F. Williams, *J. Magn. Reson.*, **14**, 348 (1974).
- T. Cole, *Proc. Nat. Acad. Sci.*, **46**, 506 (1960).
- E. T. McHale and G. vonElbe, *J. Am. Chem. Soc.*, **89**, 2795 (1967); *J. Chem. Phys.*, **72**, 1849 (1968).
- F. A. Cotton, "Chemical Applications of Group Theory," 2nd ed., Wiley-Interscience, New York (1971).
- H. Low and R. Beaudet, *J. Am. Chem. Soc.*, **98**, 3849 (1976).

Lithium Cycling Performance in Improved Lithium Hexafluoroarsenate/2-Methyl Tetrahydrofuran Electrolytes

C. D. Desjardins,* T. G. Cadger, and R. S. Salter

Research and Productivity Council, Fredericton, New Brunswick, Canada E3B 5H1

G. Donaldson and E. J. Casey

Defense Research Establishment, Shirley Bay, Ottawa, Ontario, Canada K1A 0Z4

ABSTRACT

Lithium hexafluoroarsenate/2-methyl tetrahydrofuran electrolytes have been prepared, purified, and evaluated using half-cell galvanostatic lithium cycling, cyclic voltammetry, plus colorimetric, gas chromatographic, and UV absorption techniques. Superior electrolytes have been prepared yielding reproducible cycling efficiencies in excess of 97%. Static aging trials at ambient temperature clearly demonstrate deterioration in cycling performance with time. This decline in performance is related to electrolyte degradation, possibly arising from the formation of peroxides. However, studies of various battery testing regimes on 1M LiAsF₆/2Me-THF electrolyte support the system's battery potential with respect to both rate capability and shelf-life characteristics.

The reversibility of the lithium electrode in aprotic solvent-based electrolytes has improved substantially in the last five years, increasing from cycling efficiencies of approximately 80% in 1976 to efficiencies approaching approximately 98% in 1983. These aprotic, or more specifically "ether," solvents have been studied because of both their stability to alkali metals and their low temperature characteristics: namely, freezing point, solvating power, and viscosity. It has been established that ether solvent stability is not thermodynamic, but kinetic in origin (1). Recent evidence indicates that some ethers are chemically reactive towards lithium metal and, therefore, rely on the formation of insoluble, passivating films for lithium reversibility (2). These films would be beneficial, if they were conductive to lithium ions. However, the film generating reactions in electrochemical cells, in general, result in excessive consumption of electrodeposited lithium, and, ultimately, cell failure occurs.

The ether-based aprotic electrolyte systems that have demonstrated potential for secondary lithium battery development are molar solutions of lithium hexafluoroarsenate (LiAsF₆), lithium perchlorate (LiClO₄), and lithium bromide (LiBr) in propylene carbonate (PC) (3, 4), tetrahydrofuran (THF) (5), 1,3-dioxolane (6), 2-methyl tetrahydrofuran (2Me-THF) (7), and diethyl ether (DEE) (2). For example, the 2Me-THF and DEE based electrolytes have yielded cycling efficiencies greater than 96% and 98%, respectively (7, 2).

The improvements in lithium cycling efficiency for the systems cited above have been due, in large part, to the close attention that has been paid to the "quality" of electrolyte and electrode materials, in terms of purity, handling in "nonreactive" environments, and dryness (moisture free).

Our studies, conducted over the past four years on solvents such as PC, THF, and 2 Me-THF, have focused on the choice of superior solute/solvent combinations with emphasis on determining those factors influencing lithium reversibility as related to electrolyte preparation procedures and to the use of drying and purifying agents (8). This paper examines the LiAsF₆/2Me-THF electrolyte couple for: (i) static stability, (ii) purity, and (iii) lithium cycling in an effort to improve performance and further understand lithium anode behavior.

Experimental

General.—Electrolyte purification procedures and the electrochemical experiments were conducted at ambient temperature under an argon atmosphere in a Vacuum Atmospheres dry lab equipped with a Model HE-493 Dri Train. An additional activated carbon/molecular sieve recirculating chamber further purified the dry box atmo-

sphere. The atmosphere was checked with a bare light bulb filament, which operated continuously for at least 30 days in the box. Solvents and other electrolyte materials (e.g., solutes) were transferred to the box under vacuum through the use of a glass vacuum line and related accessories.

Ultraviolet (UV) spectra were recorded on a Beckman 25 Spectrophotometer. Gas chromatograms (GC) were obtained with a Varian 6000 GC equipped with a flame ionization detector (FID) (sensitivity approximately 10⁻¹¹ A/mV) and a Spectra Physics SP4100 Integrator. A 182 × 0.3175 cm Porapak QS column was used. Colorimetry results were obtained with a Spectronics 20. A Bascom Turner eight-channel X-Y or Y-t recorder was used for data acquisition. Conductivities were obtained with a Model 31 Yellow Springs Instrument Conductivity Bridge and a microcell having a cell constant of 1.0/cm.

Materials.—Lithium hexafluoroarsenate (LiAsF₆) (USS Agri-Chemicals) and lithium trifluoromethane sulfonate (LiCF₃SO₃) (Alfa Ventron) were used as received. Lithium foil (5, 15, 38 mil) was obtained from Foote Mineral Company sealed under Ar. Lithium hexafluorophosphate (LiPF₆) (Ozark Mahoning) was recrystallized from specially purified and dried acetonitrile (MeCN;BDH) prior to use (10). MeCN was purified by the method of Walter and Ramaley (11), followed by successive distillations from treated molecular sieve 3A. Neutral alumina (Fisher) and molecular sieve 3A (Davison Chemical) were treated under vacuum at 300°-350°C for 24h prior to use.

2Me-THF (Aldrich) was refluxed over CaH₂ and then distilled under Ar from a Nester Faust Auto Annular Still. The reflux ratio was generally 20:1. The actual fraction for collection was determined either by an impurity-free GC scan (e.g., 2Mefuran (2Me-F) and peroxide impurity levels to < 10 ppm) or by a minimum UV absorbance at 218 nm. The 2Me-THF was then vacuum distilled two times over treated molecular sieve 3A followed by transfer to the dry box.

Electrolyte preparation and purifications.—Molar solutions of electrolyte were prepared by adding the appropriate Li salt to the purified solvent at room temperature. These solutions were further treated by passage through an alumina column. The first 10-20% fraction was discarded and the electrolyte was stored in glass vials (Reacti Flasks; Pierce) in the presence of Li foil. Teflon (TUF-TAINER; Pierce) and polyethylene (NALGENE) vials were also used. Pre-electrolysis procedures for 2Me-THF-based electrolyte followed those carried out by Koch *et al.* (5).

Aging trials.—Aging experiments are defined as static electrolytes stored in glass, polyethylene, or Teflon vials at ambient temperatures. The vials were not protected

* Electrochemical Society Active Member.

from light unless specified otherwise. Old vials are those which had been used previously to store electrolyte. Comparative tests were run with and without Li foil present in the storage vials.

Cells and electrodes.—Glass rectangular cells [$1 \times 1 \times 4$ cm (full cell), $1 \times 0.5 \times 4$ cm (half-cell), $0.5 \times 0.5 \times 4$ cm (quarter cell), all constructed in house] or UV cuvettes were used for the galvanostatic cycling of Li in a half-cell configuration. In general, the working electrode was a 1×4 cm Ni sheet 0.127 mm thick (Alfa Ventron, m4N8). The auxiliary electrode was cut from Li ribbon foil to meet the cell dimensions. The reference electrode was a Li wire placed in a Pasteur pipette and held in place by a machined Teflon top. Exactly 1 ml of electrolyte was added to the cell, thereby defining the working and auxiliary electrodes as 1×1 cm and 1 cm apart. Solvent evaporation was minimized by sealing the top with Parafilm.

Chronopotentiometric plating and stripping of lithium was conducted using a constant current power supply, a controller relay for polarity reversal, a microprocessor (MOS technology) for timing control, and various monitoring equipment (all constructed in house).

The following procedure, similar to that described by Koch *et al.* (2), was used to determine Li cycling efficiencies: a known charge of Li, 2.9 C/cm^2 , was plated onto the Ni substrate working electrode. A smaller charge (1.3 C/cm^2) was then stripped and plated from this electrode. The excess amount of Li charge, 1.6 C/cm^2 , was then slowly consumed by the $< 100\%$ efficient stripping cycle. Prior to exhaustion of the excess Li and reaching the Ni substrate, many "100%" cycles can be achieved. Therefore, the average efficiency per cycle, \bar{E} can be calculated by Eq. [1], where Q_s is the charge of Li stripped, Q_{ex} is the amount of excess Li, and n is the number of 100% cycles. All cycling tests in this study are based on a 5 mA/cm^2 plating and stripping current density unless otherwise specified

$$\bar{E} = \frac{Q_s - \frac{Q_{ex}}{n}}{Q_s} \quad [1]$$

Results and Discussion

General.—The data presented below are based on different batches of $1\text{M LiAsF}_6/2\text{Me-THF}$ electrolytes. Therefore, cycling efficiencies vary as a result of changes in electrolyte quality during the test program.

Aging trials.— $1\text{M LiAsF}_6/2\text{Me-THF}$ electrolytes were aged in vials at room temperature, and their cycling performances were monitored with time. Li foil was found to have no effect on the cycling performance. The results obtained are illustrated for the case of "old" glass vials in Fig. 1a, "new" glass vials in Fig. 1b, and Teflon or polyethylene vials in Fig. 2. The best overall cycling efficiencies were observed for the "old" vial case. In all instances, cycling efficiencies peaked with time; this behavior is quite reproducible. The second consistent result is the decrease in 100% cycles with time to values ranging from 60% to 70% of the observed maximum. The old and new glass vials are of borosilicate construction. Consequently, further tests were completed to assess the effect of aging in the presence of borosilicate and Pyrex glass ground to a fine powder. These tests showed no difference within ± 2 cycles.

Pre-electrolyzed $1\text{M LiAsF}_6/2\text{Me-THF}$ electrolytes have shown inferior performance in our studies, and, therefore, the aging of the electrolytes, as seen in Fig. 3, would be expected to show no improvement over non-pre-electrolyzed solutions. Similar cycle peaking and slow decline in efficiency over 70 days were observed.

The effect of light on aging (*e.g.*, a 25W bulb) was also assessed. In Fig. 4, electrolyte aged in light showed improved performance relative to those aged in the dark. This evidence substantiates the positive role of light to both degradation of electrolyte and possibly complementary production of new electrolyte species.

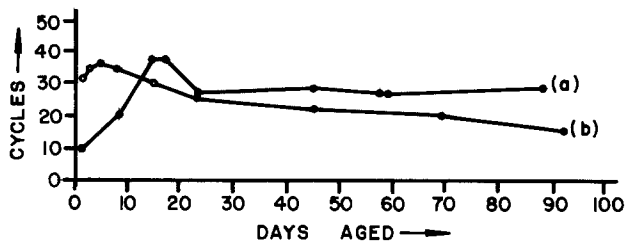


Fig. 1. Aging effects of $1\text{M LiAsF}_6/2\text{Me-THF}$ electrolyte. (a): Old vial. (b): New vial.

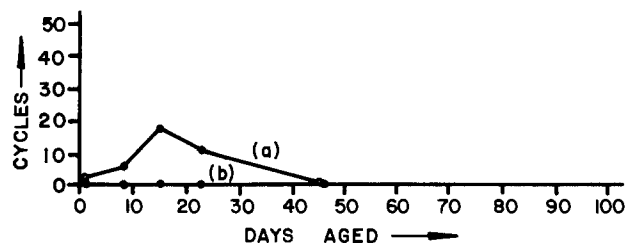


Fig. 2. Aging of $1\text{M LiAsF}_6/2\text{Me-THF}$ in Teflon (a) and polyethylene vials (b).

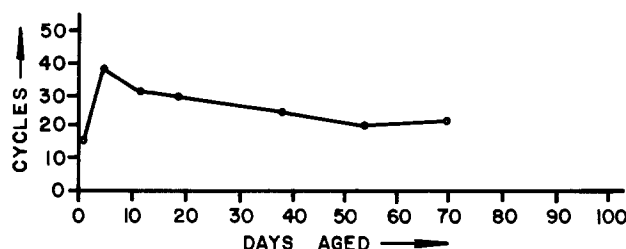


Fig. 3. Effect of aging $1\text{M LiAsF}_6/2\text{Me-THF}$ electrolyte after pre-electrolysis.

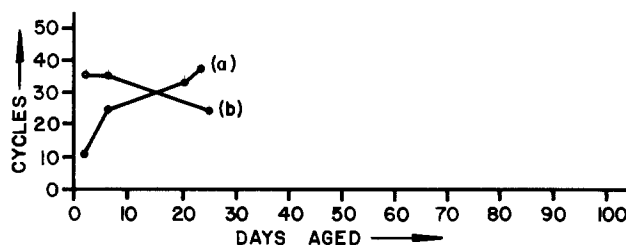
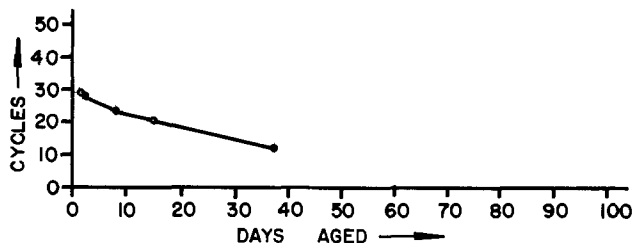
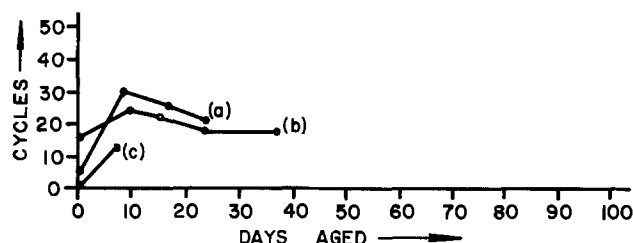


Fig. 4. Aging of $1\text{M LiAsF}_6/2\text{Me-THF}$ in glass vials stored in light (a) and dark (b).

Aging trials were also carried out for a $1.5\text{M LiAsF}_6/2\text{Me-THF}$ electrolyte (see Fig. 5). The cycle peaking phenomena observed for 1M solutions was not observed. The "usual" decline in cycling efficiencies, however, was observed, and the 1.5M electrolyte did not cycle as well as a 1M electrolyte.

Alumina electrolyte treatments were monitored for aging and their influence on cycling efficiency during aging. The $1\text{M LiAsF}_6/2\text{Me-THF}$ electrolyte in Fig. 6 clearly indicates the importance of discarding the first fraction (*e.g.*, Fig. 6c) of an alumina-treated electrolyte. Obviously, the amount of discard can be critical to the electrolyte performance. It is our observation that the best long-term cycling efficiency is obtained for the last fraction collected (*e.g.*, Fig. 6b).

Impurities in 2Me-THF solvent.— 2Me-THF (as received) contains approximately 300 ppm of detectable peroxide and approximately 1000 ppm of 2Me-F . Spinning band distillation under Ar atmosphere is very effective in removing these impurities. GC data (9) have verified that all impurities can be removed to detection limits. The detection limit for 2Me-F , based on standard curves, has been determined to be 10 ppm. Removal of 2Me-F impurities to < 10 ppm in 2Me-THF solvent was carried out to

Fig. 5. Aging of 1.5M LiAsF₆/2Me-THF electrolyteFig. 6. Effect of passing 1M LiAsF₆/2Me-THF electrolyte through a treated alumina column. (a): Fraction 2. (b): Fraction 3. (c): Fraction 1.

establish its effect on electrolyte cycling performance. Therefore, additions of 2Me-F ranging from 0 to 200 ppm to 2Me-THF electrolyte were studied. No adverse effects for 2Me-F addition (see Fig. 7) were noted for the electrolyte tested.

Peroxide impurities were assessed using colorimetric, GC, and UV absorption techniques. A colorimetric redox reaction employing the ferric/ferrous thiocyanate couple [e.g., absorption of the red Fe³⁺ thiocyanate complex at 512 nm (12)] was used to quantitatively detect peroxide. The detection limit of this technique was determined to be approximately 10 ppm. At present, the GC detection limit is also 10 ppm. Exposure of "peroxide-free" 2Me-THF solvent to the atmosphere at any point of transfer prior to introduction to the dry box will result in degradation. For example, a distillate fraction of 2Me-THF under argon was briefly exposed to air. The GC chromatograms of this solvent taken several weeks later showed additional peaks, which we have attributed to peroxide formation (9).

Both 2Me-THF solvent and 1M LiAsF₆/2Me-THF electrolyte absorb strongly in the UV at 218 nm. This absorbance is strong for as-received 2Me-THF (9) and falls rapidly with successive distillate fractions. Note that while colorimetric and GC techniques indicate solvent peroxide levels to be < 10 ppm, the UV absorbance of the solvent is strong (see Fig. 8). In one experiment, molecular sieve treatment (see Fig. 8b) marginally decreased the 218 nm absorption. Zeolites or molecular sieves have been reported to be efficient agents for removal of peroxides in ether solvent (13). However, whether these agents are effective at the 10 ppm level has not yet been established. Alumina stirred in 2Me-THF solvent showed, in Fig. 8c, an increase in UV absorption. However, we have also shown that successive fractions of electrolyte passed through alumina results in reduction of absorption levels. Alumina is another agent which has been reported to be effective in removing peroxide impurity in cyclic ethers

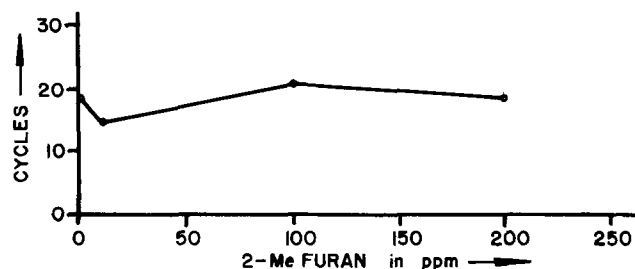
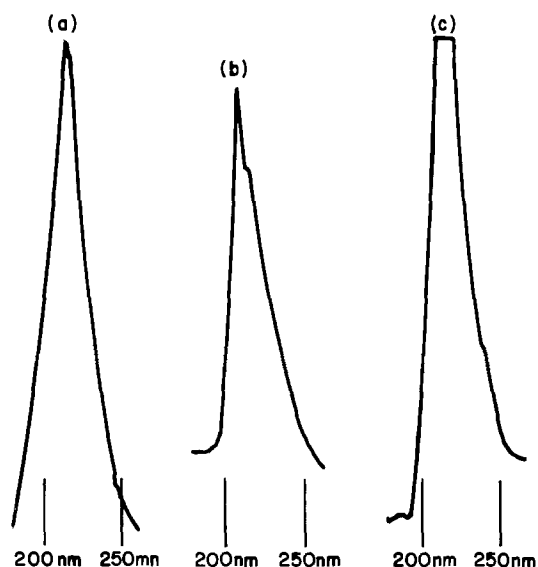
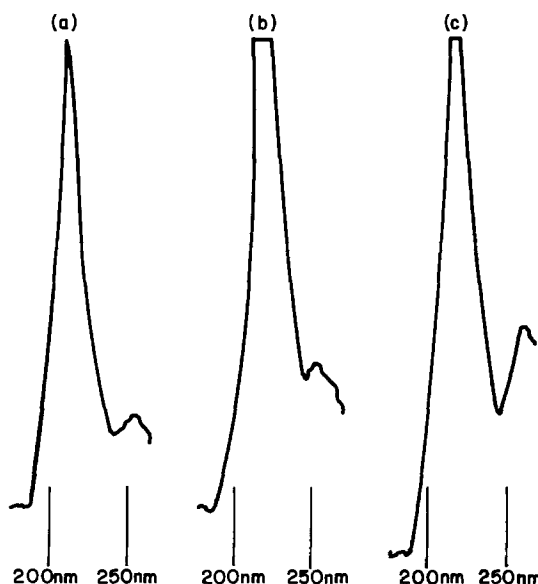
Fig. 7. 2-Methyl furan addition to 1M LiAsF₆/2Me-THF electrolyte.

Fig. 8. UV spectra of 2Me-THF solvent. (a): No treatment, spinning band purified. (b): Molecular sieve treatment. (c): Alumina stirred in solvent.

(14). It is probable that alumina performs two functions: (i) removal of water, and (ii) removal of peroxide. There is preliminary evidence which correlates cycling performance with UV absorption. The best electrolytes consistently show low absorbance levels. For example, as illustrated in Fig. 9, absorption differences are observed for a 42-cycle electrolyte, a 22-cycle electrolyte, and a pre-electrolyzed electrolyte.

UV absorption for cyclic ether electrolytes has been reported previously. In studies by Koch *et al.* (15) on LiAsF₆/THF electrolyte, an absorption maximum of 260 nm was obtained. No correlation between α -hydroperoxide and the UV absorbance was found. This correlation is expected to be less likely in the 2Me-THF case. However, the source of the 260 nm absorption band could not be ascertained. Nevertheless, LiAsF₆/2Me-THF or THF based electrolytes definitely show increases in UV absorbance with time. The corresponding pure solvents do not exhibit this characteristic. Consequently, Koch *et al.* (15) have speculated, and we concur, that LiAsF₆ or an impurity in the salt may be the source of degradation.

The linkage between the UV absorption band at 218 nm and the presence of peroxide cannot be firmly estab-

Fig. 9. UV spectra of 1M LiAsF₆/2Me-THF electrolyte. (a): 42-cycle electrolyte. (b): 22-cycle electrolyte. (c): Pre-electrolyzed electrolyte.

lished. However, recent preliminary GC data do show additional peaks on solvent degradation, which we have attributed to peroxide formation. Identification of these species is in progress.

Solute studies.—In past studies, lithium hexafluorophosphate (LiPF_6), lithium hexafluoroantimonate (LiSbF_6), and lithium hexafluorotungstate (LiWF_6) were prepared in house, purified, and 1M solutions tested in 2Me-THF solvent (8). Poor cycling performance was observed with these three solutes. Recently, other solute materials were examined.

Lithium trifluoromethanesulfonate, LiCF_3SO_3 , showed limited solubility ($< 0.4\text{M}$) in 2Me-THF, and the prepared electrolyte showed no lithium reversibility. Commercially available LiPF_6 was recrystallized from MeCN and retested. No improvements over material prepared in house were observed.

Cell dependencies.—The relationship of our cell system design to cycling efficiency was assessed. The purpose was to ensure experimental reproducibility. For example, different glass cells, cuvettes, and Ni foil substrate combinations were used under otherwise similar experimental conditions with 1M $\text{LiAsF}_6/2\text{Me-THF}$ electrolyte. These tests established a reproducibility of ± 2 -100% cycles. The lithium reference electrodes, either as a lithium plug in a glass tube or as a lithium wire in a Pasteur pipette, also yielded the same number of cycles. The reference to working electrode potential, however, does change. Pre-treatment of the lithium auxiliary electrode by scraping, anodic prestripping, etc., also showed no influence on cycling efficiency.

Cell geometry has a strong influence on the ratio of electrode surface area to edges. Therefore, the rectangular cell geometry was changed and a one-half cell and a one-quarter cell were tested. Since the cycling efficiency remained invariant (within ± 2 cycles) with changes in cell geometry, edge effects were eliminated as a significant variable for our test conditions.

Electrochemical effects.—Cyclic voltammograms of 1M $\text{LiAsF}_6/2\text{Me-THF}$ electrolyte showed good lithium reversibility (9).

The experimental regime chosen for all comparative studies was a 5 mA/cm^2 stripping/plating sequence. An independent study was performed to determine the influence of variations in the plating and/or stripping current density in 1M $\text{LiAsF}_6/2\text{Me-THF}$ electrolyte. Figure 10 illustrates the behavior of varying the plating current density (e.g., from 0.5 to 5 mA/cm^2) while holding the stripping current density at 5 mA/cm^2 . The lower plating current densities resulted in a significant decrease in cycling efficiency. In a complementary series of tests, the stripping current density was varied from 0.5 to 5 mA/cm^2 while the plating current density was held at 5 mA/cm^2 . As seen in Fig. 11, the same decline in cycling efficiency is observed. For the case where the stripping and plating current densities are kept equal, while the current density is varied from 1 to 10 mA/cm^2 (see Fig. 12), no real effect on cycling efficiency is observed. This result is, therefore, surprising in view of declines observed at < 2.5 mA/cm^2 in Fig. 10 and 11.

The shelf-life characteristics of the 1M $\text{LiAsF}_6/2\text{Me-THF}$ electrolyte systems are important to future battery development. Several experiments assessing this effect through open-circuit stands (OC) were completed. Preliminary results, which reflect both charge retention capabilities and shelf-life characteristics, show minimal differences, if any, in cycling efficiency with increasing OC times. For example, a comparison of the cycling efficiency at 0 OC stand vs. a 10 min OC stand (equivalent to a total open-circuit stand time of approximately 10h during the experiment) shows a decrease of less than 0.25%. It is also clear that further work is indicated.

Optimized cycling behavior.—All the data we have collected on solvent/electrolyte dependencies can be used to advantage. For example, with care in purification procedures and aging conditions, it is possible to prepare elec-

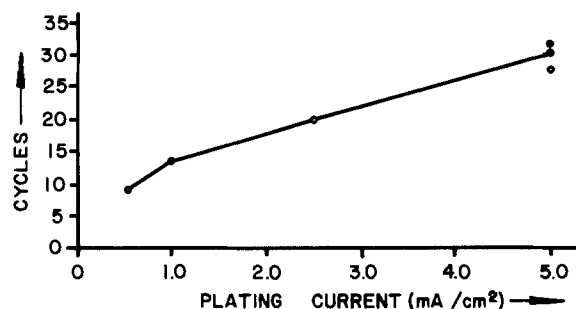


Fig. 10. Plating current effects

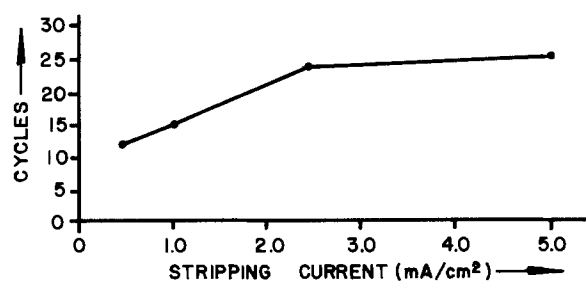


Fig. 11. Stripping current effects

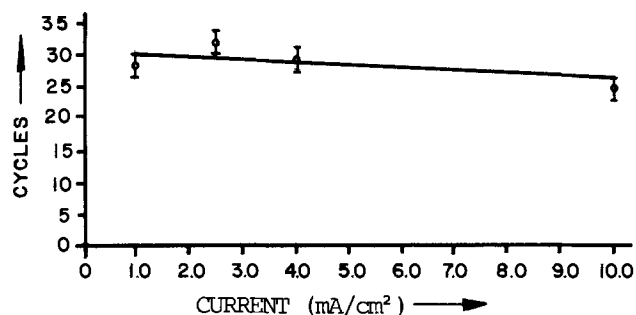


Fig. 12. Current density effects

trolytes that exhibit, reproducibly, 40 ± 2 -100% cycles or approximately 97% cycling efficiency at an average 45% depth of discharge in half-cell tests. In one isolated experiment, an optimized electrolyte actually gave 123 cycles or approximately 99% cycling efficiency; the experiment terminated only because of solvent evaporation. Observations at the 50 cycle mark revealed a lithium electrode that was smooth, and silvery gray in appearance. No further observations were made until cell failure, at which time the lithium electrode had turned mossy black.

Stability considerations.—2Me-THF solvent is more stable than THF to chemical breakdown. This has been demonstrated by Koch *et al.* (5) in static and dynamic experiments. In addition, it is known that THF can be easily polymerized in the presence of LiAsF_6 salt, a phenomena not yet observed for 2Me-THF. One argument advocated for this enhanced stability is the inductive effect of a methyl group in the position raising the energy of the lowest unoccupied molecular orbital (LUMO). We have carried out a series of CNDO molecular orbital calculations on these molecules using a program developed by Dobosh (17). LUMO values of 7.01 (THF) and 7.07 eV (2Me-THF) were obtained. These differences are marginal, considering the differences in their reactivity, and would suggest that nonthermodynamic effects play a major role.

Conclusions

Pure, reasonably stable 1M $\text{LiAsF}_6/2\text{Me-THF}$ electrolytes can be prepared. Although this electrolyte deteriorates with time, stable cycling efficiency plateaus can be obtained. Optimized 1M $\text{LiAsF}_6/2\text{Me-THF}$ electrolyte yields reproducible cycling efficiencies in excess of 97%. At present, LiAsF_6 is the best solute material for 2Me-THF solvent. Whether LiAsF_6 or an impurity in this salt is

responsible for electrolyte degradation has yet to be determined. The evidence is consistent for electrolyte degradation being linked to "peroxide" formation.

Acknowledgment

This work was supported by the Canadian Department of National Defence (DND).

Manuscript submitted Feb. 13, 1984; revised manuscript received ca. Nov. 7, 1984. This was Paper 811 presented at the San Francisco, California, Meeting of the Society, May 8-13, 1983.

The New Brunswick Research and Productivity Council of Canada assisted in meeting the publication costs of this article.

REFERENCES

1. I. A. Kendrinskii, S. V. Morosov, G. I. Sukhova, and L. A. Sukhova, *Sov. Electrochem.*, **12**, 1094 (1977).
2. V. R. Koch, J. L. Goldman, C. J. Mattos, and M. Mulvaney, *This Journal*, **129**, 1 (1982).
3. V. R. Koch and S. B. Brummer, *Electrochim. Acta*, **22**, 75 (1977).
4. R. R. Haering, J. A. R. Stiles, and K. Brandt, Can. Pat. 1,114,896; U.S. Pat. 4,251,606.
5. V. R. Koch and J. H. Young, *This Journal*, **125**, 1371 (1978); V. R. Koch, *ibid.*, **126**, 181 (1979).
6. G. H. Newman, R. W. Francis, L. H. Gaines, and B. M. L. Rao, Paper 7 presented at the Atlanta, GA, Meeting of the Society, Oct. 9-14, 1977.
7. V. R. Koch, *J. Power Sources*, **6**, 357 (1981); V. R. Koch and J. H. Young, *Science*, **204**, 499 (1979); V. R. Koch, U.S. Pat. 4,118,550 (1977).
8. C. D. Desjardins and R. S. Salter, Final Report, DSS Contract no. 2SR78-00065, March 31, 1980; C. D. Desjardins and R. S. Salter, Final Report, DSS Contract no. 19SR3230016, March 31, 1981; C. D. Desjardins and R. S. Salter, Final Report, DSS Contract no. 19SR3155-1-6606, March 31, 1982.
9. C. D. Desjardins, R. S. Salter, and T. G. Cadger, Abstract 811, p. 1200, The Electrochemical Society Extended Abstracts, Vol. 83-1, San Francisco, CA, May 8-13, 1983.
10. G. A. Heath, G. T. Hefter, T. W. Boyle, C. D. Desjardins, and D. W. A. Sharp, *J. Fluorine Chem.*, **11**, 399 (1978).
11. M. Walter and L. Ramaley, *Anal. Chem.*, **45**, 165 (1973).
12. S. Sigga, "Quantitative Organic Analysis via Functional Groups," p. 268, John Wiley and Sons, New York (1963).
13. M. Wortel and H. van Bekkum, *J. Org. Chem.*, **45**, 4763 (1980).
14. W. Dasler and C. D. Bauer, *Ind. Eng. Chem. Anal. Ed.*, **18**, 52 (1946).
15. V. R. Koch, J. L. Goldman, and R. M. Mank, in "Battery Design and Optimization," S. Gross, Editor, p. 377, The Electrochemical Society Softbound Proceedings Series, Princeton, NJ (1979).
16. P. A. Dobosh, *QCPE*, **13**, 141 (1969).

An Electrochemical Study of the Pit Initiation Resistance of Ferritic Stainless Steels

W. R. Cieslak*

Sandia National Laboratories, Albuquerque, New Mexico 87185

D. J. Duquette

Department of Materials Engineering, Rensselaer Polytechnic Institute, Troy, New York 12181

ABSTRACT

A variety of electrochemical techniques has been used to study the resistance of ferritic stainless steels to pit initiation in 1M NaCl at 80°C. Critical pitting potentials have been measured by potentiodynamic anodic polarization and by the "scratch" technique. The effectiveness of passivation potential and alloy content to promote formation of a film that is resistant to breakdown has been studied by pit induction time measurements. The ability of the passive surface to adjust to abrupt changes in passivating conditions has been studied by potential stepping experiments. It has been shown that the effect of Cr on passive film properties is disproportionately great with respect to that of Mo for alloys of comparable pitting resistance.

The use of critical pitting potentials measured potentiodynamically to determine pitting resistance has been widely criticized, particularly in the interpretation of polarization diagrams to locate the critical potential(s). A critical potential, V_c , may be defined as that potential noble to which pits, once initiated, will stably grow (1). However, a second critical potential, V_{pp} , may be defined for the reverse potential scan as that potential active to which growing pits cannot be maintained (2). There is no clear agreement as to the criteria required to define a critical potential or as to whether such potentials are theoretically meaningful (3-5). The issue is complicated by the sensitivity of measurements to experimental variables such as rate of polarization and surface treatment. Slow rates have been recommended for the most accurate measurement of V_c (5-8) because with increasing scan rate insufficient induction time for pit initiation is allowed at less noble potentials. However, with too slow a scan rate, the measured V_c shifts in the noble direction, possibly due to development and/or thickening of the passive layer (9). Similarly, a very fast scan may give a more active V_c if

* Electrochemical Society Active Member.

time for film development is not sufficient. The balance between film growth and surface activation may lead to a maximum in the V_c vs. scan rate curve (10) or to variable responses among a group of alloys (1, 11). Although the lack of a shift of V_c to active values as scan rate increases may signify relatively rapid film formation kinetics, it does not appear to be a sufficient criterion for distinguishing more resistant alloys.

Surface treatment affects film formation kinetics and, therefore, may affect V_c measurements (12). For example, 600 grit surfaces yield the most reproducible pitting data for Zr, as compared to chemical polish, electropolish, and air or vacuum anneal (10). Pitting resistance of stainless steels as measured by very rapid scanning also increases with finer grit finishes (13). However, this relationship was observed at slow scan rates only when the availability of pit initiation sites was affected by the surface finish (14).

To determine V_c precisely, in the absence of induction-time complications, the "scratch" technique was developed (15). By eliminating the induction period, this technique should provide better reproducibility than

potentiodynamic methods, for which variations of 100-500 mV are routinely reported (1, 6, 11, 16, 17).

The effect of Mo on the pitting properties of stainless steels is not fully understood. For example, it has been stated that Mo can aid the film's healing capability, but not the basic initiation resistance (18). However, Mo has little effect on V_{rp} and localized corrosion propagation resistance (6, 19), yet it improves crevice corrosion resistance (16, 20-26). To make a reasonable comparison of these results, variations in experimental techniques must be taken into account, as well as the fact that the effectiveness of Mo is not independent of the Cr content of the steel. The aim of the present study is to interpret the responses to different experimental techniques as an aid in understanding the effects of alloy composition and microstructure on pitting resistance. Properties of films formed under the same conditions as used in determining pitting resistance are tested. Electrochemical techniques are used to learn about film stability to provide insight into the nature of the passive film protectivity.

Experimental Procedure

The six heats of high purity ferritic stainless steel, listed in Table I and supplied by the Climax Molybdenum Company, are referred to as 18-0, 18-2, 18-5, 28-0, 28-2, and 28-5, respectively. Rectangular specimens ($13 \times 8 \times 1$ mm) were annealed in vacuum for 10 min at 1040°C and water quenched to produce a fully recrystallized single-phase ferritic microstructure.

Samples were wet ground on all sides on 240 through 600 grit SiC papers. For mounted samples, a stainless-steel wire was percussion welded to the sample, and the joint and the end of a plastic or glass tube shielding the wire were cast in epoxy (Maraglas no. 655 resin with no. 555 hardener, ACME Chemicals & Insulation Company, New Haven, Connecticut 06505). The mounts were cured at 80°C for a minimum of 8h. Immediately prior to use, each sample was again wet ground on 600 grit paper.

The test apparatus was a standard 1-liter six-necked flask. The specimen holder for the sheet samples was a platinum wire platform which created a three-point electrical contact (14). Test solutions were 1M NaCl prepared with distilled, deionized water. Electrolytes were deaerated with prepurified argon for a minimum of 4h before each test, and purging was continued throughout the test. A temperature of $80 \pm 1^\circ\text{C}$ was maintained by a transformer-controlled heating mantle. Potentials were measured against and are referred to a saturated calomel electrode (SCE).

The basic potentiodynamic anodic polarization test was begun by leaving the sample at open circuit for 10 min, during which time the corrosion potential attained a steady value between -500 and -650 mV. To save time, a rapid scan (3.6 V/h) was employed from -600 to -300 mV. This was followed by a slow scan (360 mV/h) from -300 mV until a sharp increase in current occurred, signaling the initiation of pitting. The steels did not exhibit active dissolution in the deaerated NaCl electrolyte. The effect of scan rate on V_c as measured potentiodynamically was investigated for the range 80 mV/h to 21.6 V/h. Critical pitting potentials were also measured by mechanical film rupture (scratch) testing (15), using 20 mV steps and scratches which generated 5-10 μA current spikes. Galvanostatic testing was conducted at an anodic

Table I. Compositions of ferritic stainless steels (w/o)

Cr	Mo	C	S	P	N	Al	O	Fe
17.95	0.010	0.002	0.004	0.004	0.0034	ND	0.0371	Bal.
17.95	1.98	0.001	0.004	0.004	0.0021	0.001	0.0367	Bal.
18.00	4.91	0.002	0.004	0.003	0.0022	0.003	0.0369	Bal.
27.65	0.10	0.002	0.003	0.004	0.0026	ND	0.0504	Bal.
27.87	1.99	0.002	0.003	0.005	0.0022	0.001	0.0499	Bal.
28.05	4.92	0.002	0.003	0.004	0.0027	0.004	0.0457	Bal.

ND = Not determined.

current density of 1 mA/cm², which was held for 15 min to allow pit growth (17, 18).

Induction times were measured on samples that had been anodically passivated for 2h at potentials of -600, -400, or -200 mV, each of which is active to the critical pitting potential. The potential was then stepped to +25, +100, or +250 mV, and the time, τ , to an abrupt rise in current was recorded.

Current transients following a potential step were measured using a Physical Data Model 514A transient recorder. Samples were left at open circuit for 2 min, held at -650 mV for 2 min, and then stepped to the potential of interest. A Princeton Applied Research Model 173/176 potentiostat/galvanostat was used for all studies.

Results

Critical pitting potentials, V_c .—The results of potentiodynamic testing at 360 mV/h and scratch testing (Table II) do not reveal identical trends of pitting resistance dependency on alloy composition. For example, 18-2 appears more resistant to pitting than 28-0 in the scratch test but no more resistant in scan testing. V_c measured by the scan technique was never active to that measured using the scratch technique. The difference in pitting potentials measured by the two techniques shows no clear dependence on alloy composition. Previously, it was shown that preferential localized attack at microstructural features, e.g., inclusions, is not observed under any of the experimental conditions (27, 28). Rather, the pit initiation resistance is controlled by alloy composition. For pitting at inclusions, the pits do not necessarily nucleate preferentially on the film-free surface created during scratch testing, and the comparison to scan testing is not valid (29, 30).

The critical pitting potentials are not a function of scan rate for rates more rapid than 360 mV/h but shift in the noble direction with decreasing scan rate. The scatter of data, however, is large at slow scan rates. Critical pitting potentials measured at a single scan rate shift in the noble direction and exhibit increased scatter with finer surface finishes. Those conditions producing nobler critical potentials also result in lower pitting densities (number per square centimeter). The influences of alloy composition and surface finish on pitting density were further investigated by galvanostatic testing (Table III). Pitting density was observed to be a function primarily of surface finish; a finer polish produced a surface which was more resistant to pit initiation. Therefore, pitting density cannot provide a basis for differentiating pit susceptibility among the experimental alloys.

Induction times.—The induction time, τ , for film breakdown was measured at several potentials after initial passivation at a less noble potential. The pit initiation potential of +25 mV is approximately 125 mV noble to V_c measured by scratch testing for 28-0; +100 mV provides the same ΔV for 18-2, and +250 mV for both 18-5 and 28-2.

Table II. Comparison of potentiodynamic anodic polarization (360 mV/h) to scratch technique, critical pitting potentials (mV vs. SCE)

Alloy	V_c		Difference scan-scratch
	Scan	Scratch	
18-0	-172	-230	58
18-2	-37	-33	-4
18-5	+142	+126	16
28-0	-40	-104	64
28-2	+274	+98	176
28-5	+985 ^a	—	—

Each V_c is the average of 5-10 tests.

Pooled standard deviation for scan testing = 30.1.

Pooled standard deviation for scratch testing = 26.9.

^a The critical potential was ill-defined due to the onset of transpassive dissolution.

Table III. Galvanostatic testing
1 mA/cm² anodic for 15 min

Alloy	Surface	Oscillation V range (mV vs. SCE)	Pit density (no./cm ²)
18-5	600 grit SiC	+50 to +130	55
18-5	600 grit SiC	+20 to +100	58
28-0	600 grit SiC	-190 to -120	56
28-0	600 grit SiC	-190 to -110	66
18-5	0.3 μm Al ₂ O ₃	0 to +100	20
18-5	0.3 μm Al ₂ O ₃	+20 to +80	—
28-0	0.3 μm Al ₂ O ₃	-180 to -120	24
28-0	0.3 μm Al ₂ O ₃	-190 to -140	—

Passivating the specimens at -600 mV did not provide protection from pit initiation (Table IV), τ being less than 1s in all cases. Better protection was obtained at more noble potentials. The full range of responses is clearly exhibited by 28-0, which is the only alloy whose critical pitting potential is noble to each passivation potential and active to each induction potential.

Those conditions that caused τ to increase also caused the pitting density to decrease. Numerous pits formed on samples passivated at -600 mV, while only one or two pits formed after passivation at -200 mV. The current rose much more steeply upon breakdown of a very protective film than upon breakdown of a less protective film, over a range of a few seconds to a few minutes to reach 1 mA. Similarly for potentiodynamic testing, more rapid scan rates produced larger numbers of smaller pits at a slower rate of increase in current. Tests were conducted to a constant final current; therefore, the amount of charge passed varied inversely with the rate of increase in current.

Potential step responses.—A potential step from -650 mV to -400, -200, or +200 mV was used to evaluate the ability of each alloy to adjust to an abrupt disturbance of the passivating condition. The initial rate of current decay following a potential step is approximately 1.5 decades in the first 10 ms and exhibits a linear relationship between $\log i$ and $\log t$

$$\log i = m \log kt \quad [1]$$

The slope, m , is lower for steps to more noble potentials, and higher currents are generated for larger steps

Table IV. Effect of alloy composition, passivation potential, and induction potential on induction time for pit initiation

Alloy	Passivation potential (mV vs. SCE)	Induction time (s)		
		+25 mV	+100 mV	+250 mV
18-0	-400	2	1	—
18-2	-600	—	<1	—
	-400	—	90; 100	2
	-200	—	61,200; 4500	120; 90
18-5	-600	—	—	<1
	-400	—	—	<1; 4
	-200	—	—	290; 450
28-0	-600	<1	<1	—
	-400	42,480	960; 330	<1; <1
	-200	100,800	2700; 1200; 13,200	170; 510
28-2	-400	—	—	510; 6
	-200	—	—	2020; 1330

Table V. Initial current decay
average slope, \bar{m} , of logarithmic i vs. t plot

Alloy	Step potential (mV vs. SCE)		
	-400	-200	+200
18-0	-1.05	-0.92	-0.75
18-2	-1.00	-0.90	-0.83
18-5	-1.05	-0.90	-0.72
28-0	-1.18	-1.07	-0.85
28-2	-1.13	-1.02	-0.87
28-5	-1.05	-1.03	-0.95

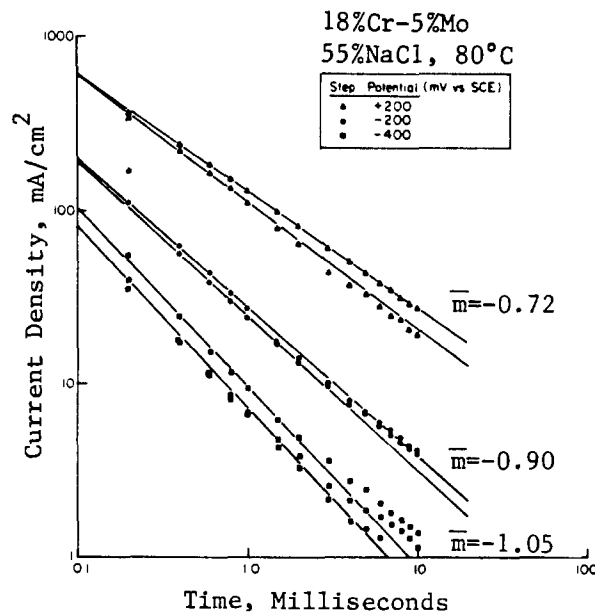


Fig. 1. Log i vs. $\log t$ plot for 18-5 at three step potentials

(Fig. 1). The charge passed is calculated by integrating the area under the curve

$$Q = \int_{t_1}^{t_2} i dt = k \int_{t_1}^{t_2} t^m dt \quad [2]$$

$$Q = \frac{k}{(m+1)} \left[t_2^{(m+1)} - t_1^{(m+1)} \right] \quad [3]$$

The calculation was performed from $t_1 = 0.1$ ms to $t_2 = 5$ ms. The slopes and charge densities for the initial current decay curves are presented in Tables V and VI, respectively.

The slopes of the decay transients are steeper for the 28% Cr alloys than for the 18% Cr alloys, at a given step potential. The experimental scatter produced an average difference between the minimum and maximum slopes of 0.06, measured in 2-3 replicates of each experiment. While the addition of Mo does not appear to affect the slope (Table V), it does reduce the amount of charge passed during the initial 5 ms (Table VI). This is shown consistently for the 5% Mo alloys, as compared to the Mo-free alloys, at all step potentials. The increase from 18% to 28% Cr, however, results in a greater decrease in charge density than does the addition of 5% Mo.

Charge density for 60s decays was measured using planimetry on the i - t curves. Just as for the 5 ms time period, the charge density for the 60s time period decreased with increasing Mo or Cr. No linear i - t relationships, even for a logarithmic or a semi-logarithmic plot (Fig. 2) were observed. If the step potential was noble to V_c , an increase in current would occur within this time period. Therefore, the data in Table VII are presented as charge density for those combinations of alloy and step potential resulting in only passive film growth and as the time at which the current began to increase for those conditions causing pitting. The times at which pitting started (current reversal) correlate well with the pitting resistances of the alloys, increasing with more noble V_c .

Table VI. Initial current decay charge density
($\mu\text{C}/\text{cm}^2$)

Alloy	Step potential (mV vs. SCE)		
	-400	-200	+200
18-0	45	121	521
18-2	51	128	536
18-5	34	96	447
28-0	27	85	297
28-2	25	65	313
28-5	22	65	234

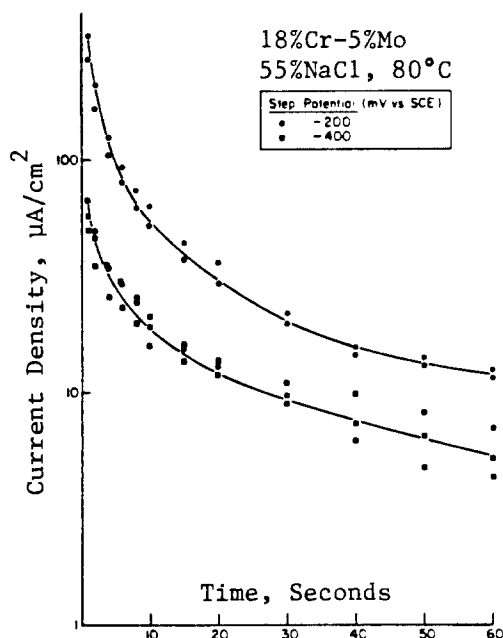


Fig. 2. Log i vs. t plot for 18-5 at nonpitting step potentials

Discussion

The stability of passive films formed on high purity ferritic stainless steels in a pitting electrolyte has been studied. The time to initiate pits depends upon the stage of development of the passive film and the driving force (pitting overpotential) for breakdown. The kinetics of film development play a major role in determining pitting parameters.

The induction-time experiments indicate that nobler potentials promote the development of more protective passive films. The Mo additions are effective in increasing the pit induction times measured at potentials at least 125 mV noble to potentials for stable pitting. Film self-repair is not a competitive process for the large driving force for breakdown at such noble potentials. Therefore, the ability of Mo to increase induction time must be a consequence of its ability to enhance film resistance to breakdown. In general, increased induction times may be attributed to the existence of more homogeneous films, regardless of thickness (31, 32).

The steeper slope of the current decay curves (Fig. 1) following a potential step for the 28% Cr alloys indicates that the films provide protection more quickly than those on the 18% Cr alloys. As noted in the Results section, this slope is not particularly sensitive to Mo content, although the charge density for this linear region decreases as a result of alloyed Mo. The magnitude of the charge density, a substantial portion of which may be attributable to charging of the electrical double layer, is less than needed for one monolayer of film growth (28). These effects of Mo in stainless steels in NaCl solution are different from those in acids, where Mo increases the charge density for formation (33) and the growth rate (34) of passive films. Additionally, for current decay following abrasion, Mo increases the rate of decay (35,

Table VII. Current decay 60s behavior

Alloy	Step potential (mV vs. SCE)		
	-400	-200	+200
18-0	1.7 mC/cm ²	18s	0.01s
18-2	1.9 mC/cm ²	2.7 mC/cm ²	0.07s
18-5	1.0 mC/cm ²	2.3 mC/cm ²	0.50s
28-0	0.6 mC/cm ²	4.6 mC/cm ²	0.10s
28-2	0.7 mC/cm ²	1.2 mC/cm ²	0.80s
28-5	0.4 mC/cm ²	1.3 mC/cm ²	3.5 mC/cm ²

36). In these and other studies of active dissolution or propagating pits (37-41), the effects of Mo may be attributed to MoO₄²⁻ surface enrichment, which could lower the anodic dissolution kinetics and promote (re)passivation. Under the present conditions, pits are not propagating nor is the surface film-free at any time, yet Mo still affects the electrochemical behavior. A decrease in charge passed indicates better efficiency of protection, whether related to composition, thickness, or structure. Obviously, less charge is needed to grow a Cr-rich film on the 28% Cr alloys than on the 18% Cr alloys, because more Cr is available. However, the smaller charge required for passivation of Mo containing alloys may be related to the defect structure of the film. Passive films on Fe-Cr alloys (of $\geq 19\%$ Cr) are primarily amorphous (42). If this amorphous film is assumed to exhibit short-range order, then the coordination of O²⁻ ions around Cr³⁺ may be somewhat deficient in oxygen because of Fe²⁺ ions in the film. A minimal Cr³⁺/Fe²⁺ ratio in the film is required to produce a protective film containing sufficient oxygen, and this ratio is achieved with lesser charge for alloys of higher Cr content. This model assumes that the O²⁻ defect structure controls the resistance of passive film to breakdown by the Cl⁻ ion. Interaction of Cl⁻ with O²⁻ vacancies has been suggested in a model of pitting corrosion (43), and the interaction has been considered to be the reason that oxygen-deficient (n-type semiconducting) films are pit-susceptible (44, 45). Although it is well known that little Mo is incorporated in the film, the incorporation of a small but significant number of Mo ions in the +6 oxidation state cannot be ruled out. The Mo⁶⁺ ion is expected to reduce the O²⁻ defect concentration of the passive film, resulting in a more protective film. Thus, the Mo⁶⁺/Cr³⁺ ratio of the film would primarily affect the resistance of the film to local breakdown. This could explain the synergistic effect of Mo and Cr for highly alloyed stainless steels.

The hypothesized effect of Mo is similar to that which is expected in the presence of the increasingly oxidizing conditions imposed by increasingly noble passivation potentials. Both a noble passivation potential and a greater Mo content enhance the resistance of the film to breakdown, while affecting the composition, as measured by Auger analysis, very little (28, 46). Therefore, both might act to decrease the susceptibility of film imperfections to breakdown.

Conclusions

1. Mo enhances the passivating capabilities of Cr, but to a lesser extent than is expected based on the effectiveness of Mo to promote pitting resistance.
2. Lower pitting densities are exhibited by passive films that are more resistant to pitting, implying that film sites at which pits initiate are less susceptible and/or less numerous. Film resistance, as measured by induction time, is increased by higher alloy content and by more noble passivation potential.
3. It is suggested that the resistance to pit initiation of passive film imperfections related to insufficient O²⁻ incorporation might be improved by Mo incorporation, much in the same manner as by nobler passivation potential.

Acknowledgments

The authors would like to acknowledge the financial support provided by the U.S. Department of Energy under Contract no. EY-76-S-02-2462-000 and by a Fannie and John Hertz Foundation Fellowship granted to one of the authors (WRC). This work was performed at Rensselaer Polytechnic Institute, Troy, New York 12181.

Manuscript submitted Dec. 28, 1983; revised manuscript received Nov. 5, 1984.

Sandia National Laboratories assisted in meeting the publication costs of this article.

REFERENCES

1. P. E. Manning, *Corrosion*, **36**, 468 (1980).
2. M. Pourbaix, L. Klimzack-Mathieu, Ch. Mertens, J.

- Meunier, Cl. Vanleughenaghe, L. DeMunsk, J. Laureys, L. Neelemans, and M. Warsee, *Corros. Sci.*, **3**, 239 (1963).
3. Ja. M. Kolotyrkin, *Corrosion*, **19**, 261t (1963).
 4. Z. Szklarska-Smialowska, *ibid.*, **27**, 223 (1971).
 5. J. R. Galvele, in "Passivity of Metals," R. P. Frankenthal and J. Kruger, Editors, p. 285, The Electrochemical Society Corrosion Monographs Series, Princeton, NJ (1978).
 6. G. Herbsleb and W. Schwenk, *Corros. Sci.*, **13**, 739 (1973).
 7. H. P. Leckie, *This Journal*, **117**, 1153 (1970).
 8. H. C. Man and D. R. Gabe, *Corros. Sci.*, **21**, 713 (1981).
 9. Z. Szklarska-Smialowska and M. Janik-Czachor, in "Localized Corrosion," p. 353, National Association of Corrosion Engineers, Houston (1974).
 10. D. R. Knittel, M. A. Maguire, A. Bronson, and J. S. Chen, *Corrosion*, **38**, 265 (1982).
 11. E. A. Lizlovs and A. P. Bond, *ibid.*, **31**, 219 (1975).
 12. D. Caplan, A. Harvey, and M. Cohen, *This Journal*, **108**, 134 (1961).
 13. P. E. Morris, ASTM STP 567, p. 261, American Society for Testing and Materials, Philadelphia, PA (1976).
 14. P. E. Manning, D. J. Duquette, and W. F. Savage, *Corrosion*, **35**, 151 (1979).
 15. N. Pessall and C. Liu, *Electrochim. Acta*, **16**, 1987 (1971).
 16. J. Degerbeck, *This Journal*, **120**, 175 (1973).
 17. T. M. Devine, *ibid.*, **126**, 374 (1979).
 18. M. A. Streicher, *ibid.*, **103**, 375 (1956).
 19. B. E. Wilde, *Corrosion*, **28**, 283 (1972).
 20. E. A. Lizlovs and A. P. Bond, *This Journal*, **118**, 22 (1971).
 21. E. A. Lizlovs, ASTM STP 516, p. 201, American Society for Testing and Materials, Philadelphia, PA (1972).
 22. N. Pessall and J. I. Nurminen, *Corrosion*, **30**, 381 (1974).
 23. R. J. Brigham, *Mater. Perform.*, **13** (11), 29 (1974).
 24. C. W. Kovach and L. S. Redmerski, Paper 123 presented at CORROSION/81, National Association of Corrosion Engineers Meeting, Toronto, April 1981.
 25. R. M. Kain, Paper 66 presented at CORROSION/82, National Association of Corrosion Engineers Meeting, Houston, March 1982.
 26. H. P. Hack, Paper 65 presented at CORROSION/82, National Association of Corrosion Engineers Meeting, Houston, March 1982.
 27. W. R. Cieslak and D. J. Duquette, in "Proceedings of the International Symposium on Environmental Degradation of Materials in Nuclear Power Systems-Water Reactors," p. 438, Myrtle Beach, SC, Aug. 1983, National Association of Corrosion Engineers, Houston (1983).
 28. W. R. Cieslak, PhD. Thesis, Rensselaer Polytechnic Institute, Troy, NY (1983).
 29. M. Barbosa and J. C. Scully, *Corros. Sci.*, **22**, 1025 (1982).
 30. R. C. Newman, H. S. Isaacs, and B. Alman, *Corrosion*, **38**, 261 (1982).
 31. K. J. Vetter and H. H. Strehblow, in "Localized Corrosion," p. 240, National Association of Corrosion Engineers, Houston (1974).
 32. J. R. Ambrose and J. Kruger, in "Proceedings of the Fourth International Congress on Metallic Corrosion," p. 698, National Association of Corrosion Engineers, Houston (1972).
 33. M. B. Rockel, *Corrosion*, **29**, 393 (1973).
 34. K. Sugimoto and Y. Sawada, *Corros. Sci.*, **17**, 425 (1977).
 35. J. Kruger and J. R. Ambrose, NBS Report no. NBS1R 74-583, Technical Summary Report no. 5 (1974).
 36. K. Hashimoto, K. Asami, and K. Teramoto, *Corros. Sci.*, **19**, 3 (1979).
 37. K. Sugimoto and Y. Sawada, *Corrosion*, **32**, 347 (1976).
 38. T. Kodama and J. R. Ambrose, *ibid.*, **33**, 155 (1977).
 39. H. Okada, H. Ogawa, I. Itoh, and H. Omata, in "Passivity and Its Breakdown on Iron and Iron-Base Alloys," p. 82, National Association of Corrosion Engineers, Houston (1975).
 40. H. Ogawa, I. Itoh, and H. Okada, *Corrosion*, **34**, 52 (1978).
 41. J. R. Galvele, J. B. Lumsden, and R. W. Staehle, *This Journal*, **125**, 1204 (1978).
 42. C. L. McBee and J. Kruger, *Electrochim. Acta*, **17**, 1337 (1972).
 43. L. F. Lin, C. Y. Choa, and D. D. Macdonald, *This Journal*, **128**, 1194 (1981).
 44. G. Bianchi, A. Cerquetti, F. Mazza, and S. Torchio, *Corros. Sci.*, **12**, 495 (1972).
 45. G. TrabANELLI, F. Zucchi, G. Brunoro, and G. P. Bolognesi, *Thin Solid Films*, **13**, 131 (1972).
 46. W. R. Cieslak and D. J. Duquette, *Corrosion*, **40**, 545 (1984).

A Theory of Perturbation-Initiated Pitting

T. Okada

Industrial Products Research Institute, M.I.T.I., Yatabe, Tsukuba, Ibaraki 305, Japan

ABSTRACT

It is shown that perturbation of the concentration of aggressive ions and also of an electrical field in a corrosive solution can initiate local activation and pitting nucleation in a passive metal. The linear stability theory was applied to the system in which a passive metal is kept at a constant potential in a solution containing aggressive ions. A critical condition was discovered where the possible disturbance in the solution caused the acceleration of local dissolution of the passive film. This process advanced autocatalytically until it reaches pit nucleation. Perturbations were found to grow with time above a critical wavelength. It was demonstrated that a high concentration of aggressive ions, a high electrical field in the solution, and a positive electrode potential promotes pit nucleation. The process was well explained as a probability event.

There is much current debate concerning the initiation step of pitting corrosion (1-5): on which part or in what stage does the nonuniform and localized corrosion process, which leads to film destruction, arise?

One approach is to assume the effects of heterogeneity present on the passive metal (4, 6), and the other is to assume an induced heterogeneity at the interface between a passive metal and corrosive media (1, 7, 8). The former approach is called an *a priori* assumption, because it puts an emphasis on the inherent microscopic defects on the metal surface: inclusions, grain boundaries, scratches, etc. The latter approach is called the *a posteriori* assumption, in that it acknowledges a nonuniformity on the metal surface and its development to the visible dimension, which occurs after a passive metal is placed in a cor-

rosive media. It should be recognized, however, that these assumptions might equally contribute to the occurrence of pitting phenomena.

In connection with *a posteriori* assumptions, the significance of stochastic (9-11) or fluctuation (12) processes have been stressed as the initial step of pitting. This presents the possible occurrence of series of processes initiated by perturbations in corrosive media, which then lead to passive film breakdown and pit initiation. However, very few mechanisms can satisfactorily explain the occurrence of this process. Also, it is necessary to specify the mechanisms which account for the feature of localization and isolation of pits.

In this study, the system of passive metal in a corrosive environment will be examined and its stability discussed,

in which aggressive ions are transported and adsorbed on the passive film with spatial fluctuations. The process of passive film destruction and pit initiation will also be discussed.

Theory

Suppose that a passive metal is kept at a constant potential in a solution containing aggressive ions. At the interface between the metal and the solution, the metal ion passes through a passive film which is in equilibrium between growth and dissolution. The current flows from the anodic part of the passive metal to the counterelectrode or to the cathodic part of the passive film (Fig. 1).

In the initial state, the metal ion dissolves uniformly through the passive film. Current flows through the solution by ionic transport. The halide ion moves by electric migration towards the surface of the passive metal, and this brings about the concentration of halide ions and their adsorption on the surface of the passive film. This further causes the increment of the rate of dissolution reaction of metal ions (5, 7, 13).

If the transport is perturbed, resulting in a concentration of aggressive ions on the passive film surface, the dissolution rate changes locally. This causes nonuniformity in the ion flux. The system becomes unstable and promotes local destruction of the passive film if the perturbation increases with time. If, however, the perturbation decreases, the passive metal dissolves uniformly and no pits appear. Whether the disturbance increases or decreases will determine the possibility of pit nucleation.

The instability of disturbed parameter systems is examined using the linear stability theory (14, 15). The theory has been successfully applied to the problem of convective transport (14), as well as to the problem of morphological instability in electrocrystallization (16, 17).

Parameters to be considered in the system are: (i) transport of ionic species in the solution, (ii) reaction current at the passive film-solution interface, and (iii) the electrical potential profile which governs the ionic current in the solution. The basic relationships for these parameters will be established first, from which perturbation equations around the steady state will be derived, and the instability of the system against infinitesimal perturbations can be examined from the analysis of normal modes (14, 15).

Basic equations.—Reactions which are occurring at the passive film-solution interface are

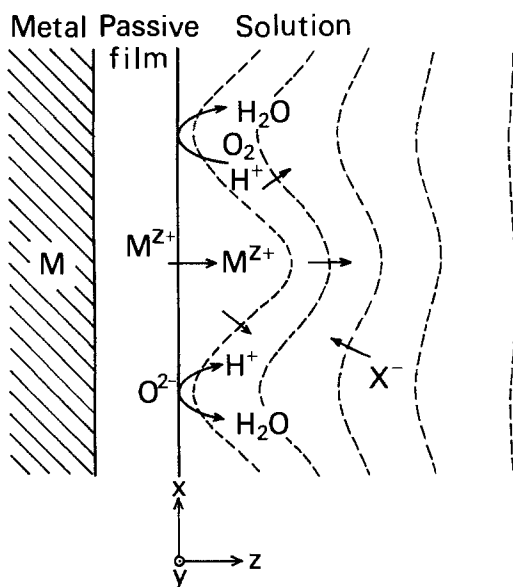
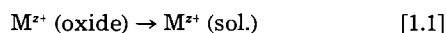
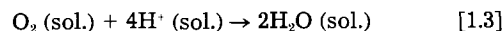
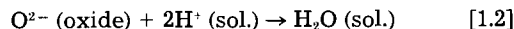


Fig. 1. Processes occurring in the passive metal-solution system. Broken line indicates perturbed potential profile in the solution. M^{z+} : metal ion. X^- : halide ion.



The current density of each reaction is designated as I_a , I_{c1} , and I_{c2} , respectively. In the present system, the passive film is in equilibrium between formation and dissolution, so that $I_{c1} = 0$. Also, I_{c2} is supposed to be very small compared with I_a : $|I_{c2}| \ll I_a$.

I_a is affected by the concentration of the halide ion X^- at the interface (7, 13). X^- is assumed to be adsorbed on the surface of the passive film following the Temkin-type isotherm, and it forms a complex with the lattice cation M^{z+} by which M^{z+} dissolves, so that it is obtained (Appendix A)

$$I_a = k_M C_X(0)^m \exp \left\{ \frac{\beta F \Delta \Phi_{\text{MO/S}}}{RT} \right\} \quad [2]$$

where $C_X(0)$ is the concentration of X^- at the interface and $\Delta \Phi_{\text{MO/S}}$ is the Galvani potential difference through the interface.

Ionic species move by diffusion and by electric migration in solution. The X-Y plane lies along the surface of the passive film and the Z axis normally extends into the solution. The concentration $C_j(x, y, z, t)$ of ion j at (x, y, z) and at time t is expressed by the following equation (18)

$$\frac{\partial C_j(x, y, z, t)}{\partial t} = -\nabla \cdot J_j \quad [3]$$

where ∇ is the gradient operator and J_j is the flux of ion j. J_j is composed of a diffusion component and a migration component (19)

$$J_j = -D_j \{ \nabla C_j + z_j C_j \nabla (f\Phi) \} \quad [4]$$

Here, $f \equiv F/RT$, D_j and z_j are the diffusion coefficient and the charge of the species j, respectively, and Φ is the electrical potential in the solution measured by a reference electrode. D_j is assumed to be a constant, independent of concentration or location. Equations [3] and [4] give

$$\frac{1}{D_j} \frac{\partial C_j}{\partial t} = \nabla^2 C_j + \nabla C_j \cdot \nabla (z_j f \Phi) + C_j \nabla^2 (z_j f \Phi) \quad [5]$$

For Φ , the Laplace equation is assumed to hold (20) as a first approximation, with no excess charge density in the solution

$$\nabla^2 \Phi = 0 \quad [6]$$

The perturbation equations.—Suppose that the system is subjected to small perturbations. Each parameter of the system can be divided into two parts

$$C_j = \bar{C}_j + c_j \quad [7.1]$$

$$\Phi = \bar{\Phi} + \phi \quad [7.2]$$

where \bar{C}_j and $\bar{\Phi}$ are steady-state components and c_j and ϕ are perturbations. \bar{C}_j and $\bar{\Phi}$ would be uniform in the X and Y directions and are functions only of Z. Ignoring the contributions by reactions other than [1.1] at the interface, Nernst's ionic mobility equation gives (19)

$$\frac{\nu_j}{nF} \bar{I}_a = -D_j \{ \nabla \bar{C}_j + \bar{C}_j \nabla (z_j F \bar{\Phi}) \} \quad [8]$$

Here n and ν_j are the charge transferred and the stoichiometric factors in the reaction [1.1]. In this case $n = z_M = z$, $\nu_M = 1$, and $\nu_{j \neq M} = 0$. It can also be written

$$\nabla^2 \bar{C}_j + \nabla \bar{C}_j \cdot \nabla (z_j F \bar{\Phi}) = 0 \quad [9]$$

$$\nabla^2 \bar{\Phi} = 0 \quad [10]$$

The amplitude describing the perturbation A ($A = c_j, \phi$) can be expanded in the manner (14)

$$A(x, y, z, t) = \int_{-\infty}^{\infty} \int_{-\infty}^{\infty} dk_x dk_y A_k(z, t) \exp [i(k_x x + k_y y)] \quad [11]$$

where k_x and k_y are the wave numbers associated with the perturbation $A_k(z,t)$, and can be related to the wavelength λ_x, λ_y of perturbation in the X and Y directions as follows

$$\lambda_x = 2\pi/k_x; \quad \lambda_y = 2\pi/k_y \quad [12]$$

The instability of the system will result from perturbations of even one wave number, so the analysis can be made in terms of two-dimensional periodic waves of an assigned set of wave numbers (k_x, k_y).

The perturbed components c_j and ϕ are described in the form

$$c_j(x,y,z,t) = c_j^\circ(z) \exp[i(k_x x + k_y y) + pt] \quad [13.1]$$

$$\phi(x,y,z,t) = \phi^\circ(z) \exp[i(k_x x + k_y y) + pt] \quad [13.2]$$

where p is a constant for the time variation of perturbations. Substitution of Eq. [7.1], [7.2], [9], [10], [13.1], and [13.2] into Eq. [5] and [6] yields

$$\left[D^2 + \left\{ D \left(\frac{z_j F \bar{\Phi}}{RT} \right) \right\} D - k^2 - \frac{p}{D_j} \right] c_j^\circ(z) + (D \bar{C}_j) D \{ z_j f \phi^\circ(z) \} = 0 \quad [14]$$

$$(D^2 - k^2) \phi^\circ(z) = 0 \quad [15]$$

where $D = d/dz$ and

$$k^2 = k_x^2 + k_y^2 \quad [16]$$

For simplicity, the electric field in the solution is assumed to be constant for the steady-state component¹

$$D(z_j f \bar{\Phi}) \equiv E_j = \text{const.} \quad [17]$$

Of ionic species which move through the solution, the metal ion M^{2+} and the halide ion X^- will be taken into consideration in the following treatment.² From Eq. [8]

$$D \bar{C}_x = - \bar{C}_x E_x \quad [18.1]$$

$$D \bar{C}_M = - \bar{C}_M E_M - \frac{\bar{I}_a}{z F D_M} \quad [18.2]$$

The boundary conditions.—The perturbation diminishes in the bulk of the solution, so that

$$c_j^\circ(z) = 0 \quad (j = M, X) \text{ at } z \rightarrow \infty \quad [19.1]$$

$$\phi^\circ(z) = 0 \quad \text{at } z \rightarrow \infty \quad [19.2]$$

Using Eq. [18.1] and [18.2], the general solutions for Eq. [14] and [15] are obtained as follows, which satisfy the conditions [19.1] and [19.2] (Appendix B)

$$c_X^\circ(z) = X_1 \exp(E_{X1} z) + X_2 \exp(E_{X2} z) \quad [20.1]$$

$$c_M^\circ(z) = M_1 \exp(E_{M1} z) + M_2 \exp(E_{M2} z) \quad [20.2]$$

$$\phi^\circ(z) = S \exp(-kz) \quad [20.3]$$

where³

$$E_{j1} \equiv -\frac{1}{2} E_j - \sqrt{\frac{1}{4} E_j^2 + k^2 + \frac{p}{D_j}} \quad (j = M, X) \quad [20.4]$$

$$E_{j2} \equiv -E_j - k \quad (|E_{M1}| < k) \quad (j = M, X) \quad [20.5]$$

¹Equation [8] together with the uniformity of $\bar{\Phi}$ in the x- and y- directions gives $d\bar{\Phi}/dz = \text{const.}$

²In general, several cationic and anionic species exist in the solution which come from the corrosive materials (HCl, etc.) or from the supporting electrolyte (Na_2SO_4 , etc.). However, perturbations of concentrations other than those of M^{2+} and X^- are disregarded for simplicity.

³ M_2 should be zero if $k < |E_{M1}|$. In the usual corrosive media, however, $|E_{M1}|$ is of the order of 1 so that the wavelength λ of perturbations should be larger than the order of a few centimeters in order for $k < |E_{M1}|$. Such waves will have no physical significance because they will be extinguished, e.g., by convection.

Continuity in terms of flux at the passive film-solution interface requires that

$$D_X \{ D c_X^\circ(z) - \bar{C}_X f D \phi^\circ(z) + c_X^\circ(z) E_X \} = 0 \text{ at } z = 0 \quad [21.1]$$

$$\frac{i_a^\circ}{zF} = -D_M [D c_M^\circ(z) + \bar{C}_M z f D \phi^\circ(z) + c_M^\circ(z) E_M] \text{ at } z = 0 \quad [21.2]$$

here i_a° is the amplitude of a normal mode of i_a , which is a perturbation of the current density I_a caused by perturbations in the solution, i.e.

$$I_a = \bar{I}_a + i_a \quad [22]$$

$$i_a = i_a^\circ \exp[i(k_x x + k_y y) + pt] \quad [23]$$

Using Eq. [2], i_a° can be expressed as follows (Appendix C)

$$i_a^\circ = \frac{\bar{I}_a}{1 + \frac{\beta}{\alpha_t}} \left\{ (\alpha z + m) \frac{c_X^\circ(0)}{\bar{C}_X(0)} - \beta f \phi^\circ(0) \right\} \quad [24]$$

where α_t is the transfer coefficient for conduction in the passive film and decreases with an increase in passive film thickness L ($\alpha_t \propto 1/L$).

Integrating the material balance Eq. [5] over the range of z [0, ∞] and using Eq. [18.1] and [18.2], the following is obtained

$$\begin{aligned} [(D + E_X) c_X^\circ(z)]_0^\infty - \bar{C}_X f \phi^\circ(0) \frac{k E_X}{k + E_X} \\ - \left(k^2 + \frac{p}{D_X} \right) \int_0^\infty c_X^\circ(z) dz = 0 \end{aligned} \quad [25]$$

$$\begin{aligned} [(D + E_M) c_M^\circ(z)]_0^\infty + \left\{ \bar{C}_M(0) E_M + \frac{\bar{I}_a}{z F D_M} \right\} z f \phi^\circ(0) \frac{k}{k + E_M} \\ - \left(k^2 + \frac{p}{D_M} \right) \int_0^\infty c_M^\circ(z) dz = 0 \end{aligned} \quad [26]$$

Applying the condition of electroneutrality to the range of z [0, ∞] where fluctuations of the charge density other than M^{2+} and X^- are assumed to cancel or to be negligible, the following is obtained

$$\int_0^\infty -\zeta F c_X^\circ(z) + z F c_M^\circ(z) dz = 0 \quad [27.1]$$

where

$$\zeta \equiv \frac{z \bar{C}_M(0)}{\bar{C}_X(0)} \quad [27.2]$$

is the factor to correlate the amplitude of perturbations of two ions in the presence of other ions.

Substitution of Eq. [20] into Eq. [21.1], [21.2], [24]-[26], and [27.1] yields

$$(E_X + E_{X1}) X_1 - k X_2 + \bar{C}_X(0) f k S = 0 \quad [28.1]$$

$$\begin{aligned} (\alpha z + m) \bar{K} (X_1 + X_2) + (E_M + E_{M1}) M_1 - k M_2 - \{ \bar{C}_M(0) z f k \\ + \beta f \bar{K} \bar{C}_X(0) \} S = 0 \end{aligned} \quad [28.2]$$

$$\begin{aligned} \left(E_X + E_{X1} - \frac{k^2 p}{E_{X1}} \right) X_1 + \left(-k + \frac{k^2 + \frac{p}{D_X}}{k + E_X} \right) X_2 \\ + \bar{C}_X(0) f \frac{k E_X}{k + E_X} S = 0 \end{aligned} \quad [28.3]$$

$$\begin{aligned} \left(E_M + E_{M1} - \frac{k^2 + \frac{p}{D_M}}{E_{M1}} \right) M_1 + \left(-k + \frac{k^2 + \frac{p}{D_M}}{k + E_M} \right) M_2 \\ - \left\{ \bar{C}_M(0) E_M + \frac{\bar{I}_a}{z F D_M} \right\} z f \frac{k}{k + E_M} S = 0 \end{aligned} \quad [28.4]$$

$$\frac{\zeta}{E_{X1}} X_1 - \frac{\zeta}{E_X + k} X_2 - \frac{z}{E_{M1}} M_1 + \frac{z}{k + E_M} M_2 = 0 \quad [28.5]$$

where

$$\bar{K} \equiv \frac{1}{zFD_M \bar{C}_X(0)} \frac{\bar{I}_a}{1 + \frac{\beta}{\alpha_f}} \quad [28.6]$$

The characteristic equation.—Equations [28] represent a system of linear homogeneous equations for the coefficients X_1 , X_2 , M_1 , M_2 , and S . For a nonzero solution of these equations to exist, the determinant H of the system must vanish (14). It can be shown that p is real and that the principle of the exchange of stabilities is valid in this system (Appendix D). The transition from stable to unstable state occurs via a stationary state, which corresponds to $p = 0$, as seen from Eq. [13.1] and [13.2]. Then H becomes at this marginal state

$$H(p = 0) = H_1 H_2 = 0 \quad [29.1]$$

here

$$H_1 \equiv \frac{k^2 E_X E_M}{E_{X1} E_{M1}} \left(\frac{k}{k + E_X} \right)^2 \frac{1}{k + E_M} \quad [29.2]$$

$$H_2 \equiv z f \left\{ -(\alpha z + m) \bar{K} \bar{C}_X(0) + \beta \bar{K} \bar{C}_X(0) + z k \bar{C}_M(0) \right. \\ \left. (k + E_X) + \zeta \bar{C}_X(0) f k^2 \right. \\ \left. - z^2 f k \left\{ \bar{C}_M(0) E_M + \frac{\bar{I}_a}{z F D_M} \right\} \frac{k + E_X}{k + E_M} \right\} \quad [29.3]$$

Conditions for perturbation to grow.—In order for Eq. [29.1] to be satisfied, at least one of the members H_1 , H_2 , must vanish. For $k > |E_M|$, $H_1 \neq 0$, so that $H_2 = 0$. Rewriting Eq. [29.3] with $E_M = -zE_X$ it is obtained

$$(1 + z) \zeta \omega^2 - h(\omega, W) \omega - (m + \alpha z - \beta) W = 0 \quad [30.1]$$

in which

$$h(\omega, W) \equiv \left\{ m + \alpha z - \beta + z \left(1 + \frac{\beta}{\alpha_f} \right) \frac{\omega + 1}{\omega - z} \right\} W \\ - z \zeta \left(1 + z \frac{\omega + 1}{\omega - z} \right) \quad [30.2]$$

and ω and W are dimensionless parameters

$$\omega \equiv \frac{k}{E_X}; \quad W \equiv \frac{z \bar{K}}{E_X} \quad [30.3]$$

W is expressed as follows, using Eq. [28.6] and [C-9]

$$W = k_a \bar{C}_X(0)^n \exp \left(\frac{\alpha_a F E}{RT} \right) / F D_M E_X \left(1 + \frac{\beta}{\alpha_f} \right) \quad [31]$$

where $n \equiv \{(\beta + m)\alpha_f / (\beta + \alpha_f)\} - 1$, $\alpha_a \equiv \beta \alpha_f / (\beta + \alpha_f)$, and E is the potential of the passive metal. W increases exponentially with the increase in E , so that $h(\omega, W)$ becomes large⁴ and k has a root in the range $k > zE_X$

$$k_c = \frac{E_X}{2(1+z\zeta)} \left\{ h(W) \right. \\ \left. + \sqrt{h(W)^2 + 4(1+z\zeta)(m + \alpha z - \beta)W} \right\} \quad [32]^5$$

The wave number of the perturbation at the marginal state is given by Eq. [32] and when k becomes short of k_c , the perturbation grows with time and the system

⁴In Eq. [30.2], the first term in the right-hand side becomes negative only in the case when the increase in the halide ion concentration at the passive film-solution interface brings about a decrease in the anodic current. This is not plausible for the system under consideration.

⁵ $(\omega + 1)/(\omega - z)$ was put to 1 for large $h(\omega, W)$, which is denoted as $h(W)$.

moves from the stationary to the unstable state (Appendix E). As seen from Eq. [31], the region of k specifying instability expands as the potential of the metal and/or the concentration of halide ion are increased (Fig. 2). For the fixed W in Eq. [31]

$$E = \text{const.} - \frac{nRT}{\alpha_a F} \ln \bar{C}_X(0) \quad [33]$$

which is the relationship between the potential of the metal and the concentration of aggressive ions. This shows a tendency for pitting to occur.

Current distribution and the localized attack.—When dissolution current arises locally at some point on the passive film by perturbation, the surroundings may become cathodic. Then dissolution is suppressed and this results in a localization of pits. This situation can be illustrated as follows.

Take a cylindrical coordinate system (r, ψ, z) with the Z -axis originating from the surface of the passive film normally into the solution. Disturbances c_X and ϕ shall be expressed as follows, by separation of variables

$$c_X(r, z, t) = c(r) c^o(z) \exp(pt) \quad [34.1]$$

$$\phi(r, z, t) = \phi(r) \phi^o(z) \exp(pt) \quad [34.2]$$

where symmetry around the Z -axis is assumed. From Eq. [5], [6], and [17] is obtained

$$(D^2 + E_X D) c^o(z) + \frac{c^o(z)}{c(r)} \nabla_z^2 c(r) - \frac{p}{D_X} \\ - (DC_X) \frac{\phi(r)}{c(r)} D \left\{ f \phi^o(z) \right\} = 0 \quad [35]$$

$$\frac{1}{\phi(r)} \nabla_r^2 \phi(r) = - \frac{1}{\phi^o(z)} D^2 \phi^o(z) \quad [36]$$

where $\nabla_z^2 \equiv \frac{d^2}{dr^2} + \frac{1}{r} \frac{d}{dr}$. The solution to Eq. [36] which satisfies $\phi = 0$ at $z \rightarrow \infty$ and nonzero at $r = 0$ is

$$\phi^o(z) = P_1 \exp(-kz) \quad [37.1]$$

$$\phi(r) = Z_0(kr) \quad [37.2]$$

where $Z_0(kr)$ is the Bessel function of 0th order. Substitution of Eq. [37.1] and [37.2] into Eq. [35] comes to Eq. [14], if it is put

$$\nabla_z^2 c(r) = -k^2 c(r) \quad [38]$$

then the solution exists in the form

$$c(r) = P_2 Z_0(kr) \quad [39]$$

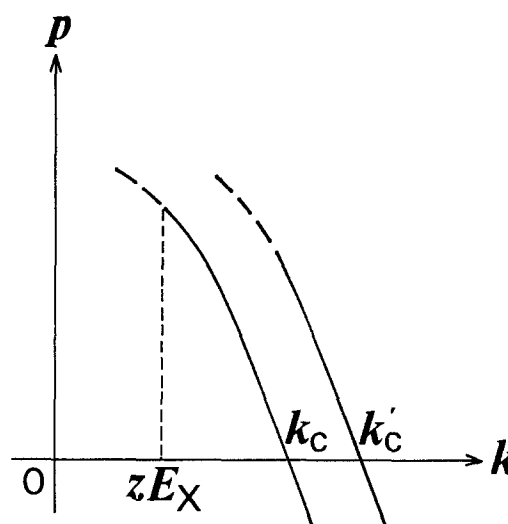


Fig. 2. Variation of p with k . Units are arbitrary. k_c : critical wave number for instability. $k_c = k_c(W)$, $k'_c = k'_c(W')$, $W' > W$.

Substituting these results into Eq. [24] and [11], the fluctuation of anodic current at the surface of the passive film is obtained

$$i_a(r,t) = \int_{z \in X} \frac{A_k \bar{I}_a}{1 + \frac{\beta}{\alpha_f}} \left\{ \left(\alpha z + m \right) \frac{c^0(0)}{C_X(0)} A_2 + \beta f A_1 \right\} Z_0(kr) \exp(pt) dk \quad [40]$$

In Fig. 3, the radial distribution of $i_a(r,t)$ was illustrated schematically. Because no assumptions were made for the cathodic reactions for this consideration, the case will be allowed where $\bar{I}_a - \bar{I}_{c2} = 0$. This indicates that cathodic current flows at the surroundings and the passivity is protected at these areas so that the pitting nucleation site is localized (21).

Discussion

Origin of localized attack.—There are several kinds of heterogeneities present on the surface of a passive film: inclusions, grain boundaries, dislocations, etc. These are sometimes believed to be related to the pitting nucleation site (5). However, it does not seem likely that pits always nucleate at these sites when the metal is immersed into a corrosive medium.

According to the probability concept of pitting corrosion, some stochastic process should precede pit nucleation (9-11). Fluctuations of the concentration of ionic species or of the electrical field in the solution would thus play a major role at the initial stage of pit nucleation, and if they grow with time, an unstable state results. Once this instability occurs, it would ultimately come to the state where localized concentration of aggressive ions and localized attack at the passive film start. As seen from Eq. [31] and [32], the system is more susceptible to pitting if there are a large halide concentration, a more positive metal potential, or higher electrical field in the solution. A rough estimation of the wavelength of perturbation where instability sets in was made for typical values of parameters (Table I).⁶ It is seen that a borderline exists for the possible occurrence of processes leading to pit nucleation.

The structural defects (4, 5) on the passive film would be favorable in the occurrence of perturbation or in the stimulation of following processes, if these defects "harmonize" the perturbations. The effects of the change in pH should also be significant in some cases, which is considered in Appendix F.

Pit initiation via the halide nuclei formation.—Pitting is expected to initiate when a localized attack by aggressive

⁶The electrical field in the bulk of the solution was adopted, for simplicity, for the calculation instead of the possible strong field at the vicinity of the interface.

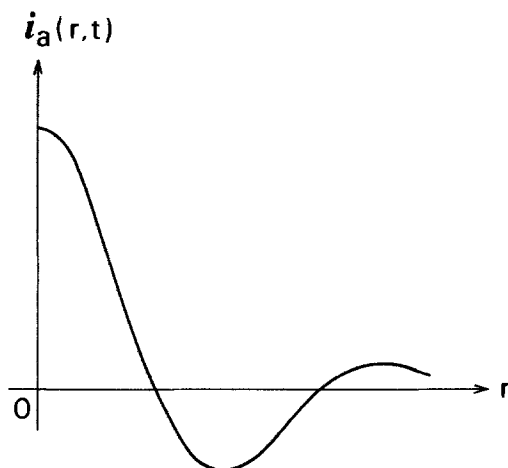


Fig. 3. The radial distribution of the perturbed current at time t around the anodic site. Units are arbitrary.

Table I. Estimated critical wavelength λ_c for perturbation. $z = 2, m = 3, \alpha = 0.5, \beta = 1.5, \alpha_f = 0.15$ or $0.3, \zeta = 0.1, D_M = 7 \times 10^{-6} \text{ cm}^2 \text{ s}^{-1}$, molar conductance = $6 \times 10^2 \Omega^{-1} \text{ cm}^2, T = 25^\circ \text{C}$.

\bar{I}_a	α_f	c		
		1 M	0.1 M	0.01 M
1×10^{-4} A cm ⁻²	0.15	12 cm	1.2 cm	0.12 cm
	0.3	11	1.1	0.11
1×10^{-3} A cm ⁻²	0.15	1.2	0.12	0.012
	0.3	1.1	0.11	0.011
1×10^{-2} A cm ⁻²	0.15	0.12	0.012	0.0012
	0.3	0.11	0.011	0.0011

λ_c
→ PIT NUCLEATION

sive ions starts by perturbation. However, in order to obtain the condition where aggressive ions break through the passive film of thickness L , the metal should be polarized above a certain critical potential. This potential is referred to as the pit-initiation potential, and often deviates positively from the repassivation potential at which pits stop (22, 23).

A process is assumed in which hemispherical halide nuclei form on the surface of the passive film and grow inwards. Whether the halide nuclei grow continuously or not determined the occurrence of pitting (12, 23).

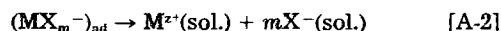
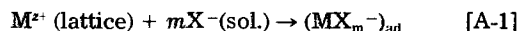
It should again be noted that the pit initiation process is a probability event, in that it requires the growth of perturbation in the solution and the formation of halide nuclei in the passive film, and that it implies a positive polarization of the passive metal.

Manuscript submitted May 14, 1984; revised manuscript received Oct. 31, 1984. This was Paper 237 presented at the New Orleans, Louisiana, Meeting of the Society, Oct. 7-12, 1984.

Industrial Products Research Institute assisted in meeting the publication costs of this article.

APPENDIX A

The significance of the adsorption process of aggressive ions in the passive film destruction was pointed out by several authors (7, 24, 25). Halide ions are adsorbed on the surface of a passive metal and form a complex with the lattice cation. This complex is then activated to dissolve the metal ion



Suppose that the number of metal ions per unit surface area of the passive film is S_M and that the number of coordination sites of the halide ions for each surface metal ion is N_X . Then the number of adsorption sites for X^{-} per unit surface area of the passive film is $S_M N_X$. Following the reaction [A-2], m halide ions are assumed to jointly adsorb on the surface metal ion ($0 < m < N_X$). The dissolution current density I_a depends on the surface concentration $C(MX_{\text{ad}})$ of the adsorbed complex. Neglecting the reverse rate (19, 26)

$$I_a = k_M' \exp\left(-\frac{\Delta G^{\ddagger}}{RT}\right) C(MX_{\text{ad}}) \exp\left[\frac{\alpha z F (\Delta\Phi_{\text{MO/S}} - \Delta\Phi_{\text{MO/S,rev}})}{RT}\right] \quad [A-3]$$

where k_M' is rate constant, ΔG^{\ddagger} the standard chemical free energy of activation, α the symmetrical factor, and $\Delta\Phi_{\text{MO/S}}$ and $\Delta\Phi_{\text{MO/S,rev}}$ are the Galvani potential difference at the passive film-solution interface and its equilibrium value.

$C(MX_{ad})$ is expressed as follows

$$C(MX_{ad}) = \text{const. } S_M \frac{N_X!}{(N_X - m)!m!} \prod_{i=1}^m \theta_i \quad [\text{A-4}]$$

where θ_i is surface coverage of X^- which come i th in the units of N_X coordination sites. θ_i is assumed to obey the following adsorption isotherm (27, 28)

$$\theta_i = \frac{K_i C_X(0)}{1 + K_i C_X(0)} \quad [\text{A-5}]$$

in which K_i changes with the change in θ_j ($j < i$)

$$K_i = K_0 \exp \left(-r \sum_{j=1}^{i-1} \theta_j / RT \right) \quad [\text{A-6}]$$

$$K_0 \equiv \exp \left(\frac{-\Delta G_{ad}^\circ(0) + F\Phi_1}{RT} \right) \quad [\text{A-7}]$$

here $\Delta G_{ad}^\circ(0)$ is the standard free energy of adsorption at $\theta_i = 0$, and r is the Temkin parameter, *i.e.*, the variation of standard free energy of adsorption with coverage (26, 28). Φ_1 is the potential at the inner plane of the electrical double layer (27)

$$\Phi_1 = \alpha_1 \Delta\Phi_{MO/S}, \quad (0 < \alpha_1 < 1) \quad [\text{A-8}]$$

Since $1/N_X > \theta_1 > \theta_2 > \dots, \theta_i$ in Eq. [A-5] can be approximated as follows

$$\theta_i \propto K_i C_X(0) \quad [\text{A-9}]$$

Only the interaction between adsorbed X^- in the units N_X coordination sites is significant, so that

$$K_i = K_0 \exp \{ r(i-1)/N_X RT \} \quad [\text{A-10}]$$

Substituting Eq. [A-9] and [A-10] into Eq. [A-4] and rewriting Eq. [A-3], Eq. [2] is obtained in which

$$k_M \equiv \text{const. exp} \left\{ \frac{-\Delta G_{ad}^\circ - m \Delta G_{ad}^\circ(0) - \alpha z F \Delta\Phi_{MO/S,rev}}{RT} \right\} \exp \left\{ \frac{m(m-1)r}{2N_X RT} \right\} \quad [\text{A-11}]$$

$$\beta \equiv \alpha z + \alpha_1 m \quad [\text{A-12}]$$

APPENDIX B

Equation [14] becomes using Eq. [17]

$$\frac{(D^2 + E_j D - k^2 - \frac{p}{D_j}) c_j^\circ(z)}{D \bar{C}_j} = D \left\{ \frac{z_j F \phi^\circ(z)}{RT} \right\} \quad [\text{B-1}]$$

from Eq. [17], [18.1], and [18.2]

$$D^2 \bar{C}_j = -E_j D \bar{C}_j \quad [\text{B-2}]$$

$$D^3 \bar{C}_j = E_j^2 D \bar{C}_j \quad [\text{B-3}]$$

Operating $(D^2 - k^2)$ to Eq. [B-1] and using Eq. [15], [B-2], and [B-3]

$$\frac{1}{D \bar{C}_j} (D^2 + 2E_j D - k^2 + E_j) \left(D^2 + E_j D - k^2 - \frac{p}{D_j} \right) c_j^\circ(z) = 0 \quad [\text{B-4}]$$

The general solution to the above equation is

$$c_j^\circ(z) = c_j^{\circ+}(z) + c_j^{\circ-}(z) \quad [\text{B-5}]$$

where

$$c_j^{\circ\pm}(z) \equiv J_1^\pm \exp(E_{j1}^\pm z) + J_2^\pm \exp(E_{j2}^\pm z) \quad [\text{B-6}]$$

$$E_{j1}^\pm \equiv -\frac{1}{2} E_j \pm \sqrt{\frac{1}{4} E_j^2 + k^2 + \frac{p}{D_j}} \quad [\text{B-7}]$$

$$E_{j2}^\pm \equiv -E_j \pm k \quad [\text{B-8}]$$

The general solution to Eq. [15] is

$$\phi^\circ(z) = S^+ \exp(kz) + S^- \exp(-kz) \quad [\text{B-9}]$$

Each member of the right-hand side of Eq. [B-5] makes a pair with those in Eq. [B-9]. In order for the solution [B-9] to satisfy the boundary condition [19.2], S^+ should be zero. Then $c_j^\circ(z) = 0$ in Eq. [B-5], and so $j_1^+ = J_2^+ = 0$. Also it is seen in order for Eq. [19.1] to be satisfied

$$E_{j1}^- < 0 \quad [\text{B-10}]$$

$$E_{j2}^- < 0 \quad [\text{B-11}]$$

Inequality [B-10] is always satisfied. From Inequality [B-11], it is obtained that $-E_j < k$. All these results are used in Eq. [20].

APPENDIX C

Suppose that I_a is subjected to a small change around the steady-state value \bar{I}_a . Substituting Eq. [2] into Eq. [22] and retaining only the first-order derivatives, it is obtained that

$$i_a = \bar{I}_a \left\{ \frac{\partial \ln k_M}{\partial C_X(0)} C_X(0) + m \frac{C_X(0)}{C_X(0)} + \frac{\beta F}{RT} \delta\Delta\Phi_{MO/S} \right\} \quad [\text{C-1}]$$

in which k_M is expressed as follows, according to Eq. [A-11]

$$k_M = \text{const. exp} \left[-\frac{\alpha z F \Delta\Phi_{MO/S,rev}}{RT} \right] \quad [\text{C-2}]$$

and

$$\Delta\Phi_{MO/S,rev} = -\frac{RT}{F} \ln \bar{C}_X(0) + \text{const.} \quad [\text{C-3}]$$

The potential E of the passive metal measured by a reference electrode in the solution is

$$E = \Delta\Phi_{M/MO} + \Delta\Phi_{MO/S} + \Delta\Phi_{sol.} + \text{const.} \quad [\text{C-4}]$$

in which $\Delta\Phi_{M/MO}$ is the potential difference across the passive film and $\Delta\Phi_{sol.}$ is the potential difference in the solution. In the case E is kept constant

$$\delta\Delta\Phi_{MO/S} = -\delta\Delta\Phi_{M/MO} - \delta\Delta\Phi_{sol.} \quad [\text{C-5}]$$

The current density which passes through the passive film is expressed as follows

$$\bar{I}_a = \text{const. exp} \left[\frac{\alpha_f F}{RT} \Delta\Phi_{M/MO} \right] \quad [\text{C-6}]$$

Then

$$i_a = \delta I_a = \frac{\alpha_f F}{RT} \delta\Delta\Phi_{MO/S} \bar{I}_a \quad [\text{C-7}]$$

$\delta\Delta\Phi_{sol.}$ can be equated to the change in electrical potential in the solution by perturbation

$$\delta\Delta\Phi_{sol.} = \phi(z=0) \quad [\text{C-8}]$$

Substituting Eq. [C-2], [C-3], [C-5], [C-7], and [C-8], into Eq. [C-1] and dividing by $\exp [i(k_x x + k_y y) + pt]$, Eq. [24] is obtained, in which \bar{I}_a is written as follows, using Eq. [2] and [C-6]

$$\bar{I}_a = k_a \bar{C}_X(0)^{m'} \exp \left\{ \frac{\alpha_a F \Delta\Phi_{M/S}}{RT} \right\} \quad [\text{C-9}]$$

where

$$m' \equiv \frac{(\beta + m) \alpha_f}{\beta + \alpha_f} \quad [\text{C-10}]$$

$$\alpha_a \equiv \frac{\beta \alpha_f}{\beta + \alpha_f} \quad [\text{C-11}]$$

$$\Delta\Phi_{M/S} \equiv \Delta\Phi_{M/MO} + \Delta\Phi_{MO/S} \quad [\text{C-12}]$$

APPENDIX D

Define $G(z)$ as follows

$$(D^2 + 2E_j D - k^2 + E_j^2) c_j^{\circ}(z) \equiv G(z) \quad [\text{D-1}]$$

It is written from Eq. [B-4]

$$\left(D^2 + E_j D - k^2 - \frac{p}{D_j}\right) G(z) = 0 \quad [\text{D-2}]$$

Multiply the complex conjugate G^* of G on both sides of Eq. [D-2] and integrate over the range of z , thereby using the boundary conditions

$$\begin{aligned} \int_0^{\infty} G^* \left(D^2 + E_j D - k^2 - \frac{p}{D_j}\right) G dz &= -G^*(0) DG(0) \\ &- \int_0^{\infty} |DG|^2 dz - E_j |G(0)|^2 \\ &- \int_0^{\infty} GE_j DG^* dz - \left(k^2 + \frac{p}{D_j}\right) \int_0^{\infty} |G|^2 dz = 0 \end{aligned} \quad [\text{D-3}]$$

Taking the imaginary part of Eq. [D-3]

$$\begin{aligned} im G^*(0) DG(0) + im \int_0^{\infty} GE_j DG^* dz + im \left(\frac{p}{D_j}\right) \\ \int_0^{\infty} |G|^2 dz = 0 \end{aligned} \quad [\text{D-4}]$$

$c_j^{\circ}(z)$ is adopted which takes real values according to Eq. [20], so that $G(z)$ is also real as seen from Eq. [D-1]. Then the first two terms in Eq. [D-4] vanishes and

$$im(p) \int_0^{\infty} |G|^2 dz = 0 \quad [\text{D-5}]$$

Since the integral is positive definite, it is seen that $im(p) = 0$ so that p is real.

APPENDIX E

The variation of p with k is determined by $H(p) = 0$. In the region $-E_M < k$, p passes through the axis $p = 0$ once at $k = k_c$ given by Eq. [32]. The gradient of $p - k$ curve around this point is to be examined. This can be done by noting the direction of shifting p from $p = 0$ when k goes over k_c by small amount.

To simplify the treatment, it would be reasonable to put

$$\int_0^{\infty} \frac{\partial}{\partial t} c_x dz = 0 \quad [\text{E-1}]$$

$$\int_0^{\infty} \frac{\partial}{\partial t} c_M dz = \frac{i_a}{zF} \{1 - \kappa(p)\} \quad (0 < \kappa(p) < 1) \quad [\text{E-2}]$$

$\kappa(p)$ is a function of p , and $\kappa = 1$ at $p = 0$.

The determinant $H(p)$ is then expanded

$$\begin{aligned} H(p) &= k^2 \frac{(E_N + E_{N1} + k)(E_{N1} - k)}{E_{N1}(k + E_N)} \\ &\frac{(E_M + E_{M1} + k)(E_{M1} - k)}{E_{M1}(k + E_M)} \frac{1}{k + E_N} \end{aligned}$$

$$\times \{H_2 + (1 - \kappa)zf(\alpha z + m - \beta) \bar{K} \bar{C}_X(0)(k + E_N)\} = 0 \quad [\text{E-3}]$$

Expanding each element of the above equation with respect to p around $p = 0$ and neglecting the second- and higher-order terms, it is obtained

$$\begin{aligned} H_p \equiv \left\{ \frac{kE_N}{E_{N0}} + \alpha_N(k)p \right\} \left\{ \frac{kE_M}{E_{M0}} + \alpha_M(k)p \right\} \left(\frac{k}{k + E_N} \right)^2 \frac{1}{k + E_M} \\ \times \{H_2 - \kappa_1 zf(\alpha z + m - \beta) \bar{K} \bar{C}_X(0)(k + E_N)p\} = 0 \end{aligned} \quad [\text{E-4}]$$

where

$$E_{X0} \equiv E_{X1}(p = 0), E_{M0} \equiv E_{M1}(p = 0), \kappa_1 \equiv \left(\frac{\partial \kappa}{\partial p} \right)_{p=0}, \text{ and}$$

$$\begin{aligned} \alpha_j(k) &\equiv \frac{1}{\sqrt{E_j^2 + 4k^2} D_j} \\ &\left\{ 1 + \frac{k(k + E_j)}{\frac{1}{2} E_j^2 + k^2 + E_j \sqrt{\frac{1}{4} E_j^2 + k^2}} \right\} \end{aligned} \quad [\text{E-5}]$$

H_p is a function of third order with respect to p

$$H_p = K(k)p^3 + L(k)p^2 + M(k)p + N(k) = 0 \quad [\text{E-6}]$$

$H_p - p$ makes a family of curves with k as a parameter. $N(k)$ is the value of H_p at $p = 0$, i.e., at the intersection of $H_p - p$ curve with the ordinate. At $k = k_c$, $N(k_c) = 0$. It is seen that $H_p - p$ curve goes through the origin for $k = k_c$. Obviously $N(k)$ is equal to $H(p = 0)$ in Eq. [29.1]

$$N(k) = H(p = 0) = H_1 H_2 \quad [\text{E-7}]$$

It is seen from Eq. [29.2] and [29.3] that $H_1 < 0$ and $H_2 > 0$. at $k = k_c + dk$ ($dk > 0$), so that

$$N(k_c + dk) < 0 \quad [\text{E-8}]$$

Whether the gradient of $H_p - p$ curve for $k = k_c + dk$ around $p = 0$ takes positive or negative values determines the sign of p which satisfies Eq. [E-6]. The gradient of $H_p - p$ curve around $p = 0$ will not change very largely if k increases from k_c to $k_c + dk$ by infinitesimal amount

$$\frac{dH_p}{dp}(k = k_c + dk) \approx \frac{dH_p}{dp}(k = k_c) \quad [\text{E-9}]$$

Also from Eq. [E-6]

$$\frac{dH_p}{dp}(k = k_c) = \frac{dH_p}{dp}(p = 0) = M(k_c) \quad [\text{E-10}]$$

Equation [E-4] is expanded and the coefficient $M(k)$ for the first order of p is obtained as follows

$$\begin{aligned} M(k) &= \left\{ \frac{kE_N}{E_{N0}} \alpha_M(k) + \frac{kE_M}{E_{M0}} \alpha_N(k) \right\} \left(\frac{k}{k + E_N} \right)^2 \frac{1}{k + E_M} H_2 \\ &- H_1 \kappa_1 zf(\alpha z + m - \beta) \bar{K} \bar{C}_X(0)(k + E_N) \end{aligned} \quad [\text{E-11}]$$

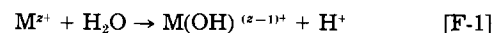
$H_2(k_c) = 0$, as seen from Eq. [29.1]. It is also seen from Eq. [E-2] that $\kappa_1 < 0$, so that

$$M(k_c) < 0 \quad [\text{E-12}]$$

because $H_1(k_c) < 0$. This shows that $p < 0$, i.e., p becomes negative when k goes over k_c . Then $p - k$ curve has a shape as depicted in Fig. 2.

APPENDIX F

The change in pH of the solution at the interface seems to play a major role on the initiation of pitting (5, 29). The H^+ activity will change by two processes. One is due to the hydrolysis of the dissolved metal ions (5)



The other is due to the change in activity coefficients caused by the increase in the halide ion concentration. These two effects will be considered briefly. The formula for the dissolution current density which includes H^+ activity a_H is

$$I_a = k_M'' C_X(0)^m a_H(0)^n \exp \left[\frac{\beta F \Delta \Phi_{M(OH)}}{RT} \right] \quad [\text{F-2}]$$

H^+ concentration is given by (5)

$$C_H = K_1 C_M / C_{M(OH)} \quad [\text{F-3}]$$

where K_1 is the equilibrium constant of reaction [F-1]. If the change in concentration of $M(OH)^{(z-1)+}$ which is produced by hydrolysis is neglected

$$C_H \propto C_M \quad [F-4]$$

The activity coefficient γ_H of H^+ can be expressed as follows, if it is not in dilute solutions (30)

$$\ln \gamma_H = -K_2 + K_3 C_X \quad [F-5]$$

Then Eq. [F-2] is written as

$$I_a = k_M C_X(0)^m C_M(0)^h \exp \{hK_3 C_X(0)\} \exp \left[\frac{\beta F \Delta \Phi_{M0/S}}{RT} \right] \quad [F-6]$$

For simplicity, the ionic transport equation for H^+ is not considered here except for the contribution of a_H to boundary conditions. In this case, Eq. [28.2] is replaced by the following equation

$$\begin{aligned} & \{(\alpha z + m) \bar{K} + hK_3 \bar{C}_X(0)\} (X_1 + X_2) \\ & + \left\{ E_M + E_{M1} + \bar{K}h \frac{\bar{C}_X(0)}{\bar{C}_M(0)} \right\} B_1 \\ & + \left\{ \bar{K}h \frac{\bar{C}_X(0)}{\bar{C}_M(0)} - k \right\} B_2 - \left\{ C_M(0)zfk + \beta f \bar{K} \bar{C}_X(0) \right\} S = 0 \end{aligned} \quad [F-7]$$

It is rather tedious to solve characteristic equations including Eq. [F-7]. In the special case where reaction [F-1] can be ignored and only the change in γ_H is taken into account, the results can be obtained with little alterations. In this case the critical wave number k_c for the growing perturbation is expressed similarly to Eq. [32], where $h(W)$ is replaced by $h_1(W)$

$$\begin{aligned} h_1(W) \equiv & \left\{ m + \alpha z - \beta + hK_3 \bar{C}_X(0) - z \left(1 + \frac{\beta}{\alpha_f} \right) \right\} W \\ & + z(z-1)\zeta \quad [F-8] \end{aligned}$$

REFERENCES

- N. D. Green and M. G. Fontana, *Corrosion*, **15**, 25t (1959).
- Ja. M. Kolotyrkin, *ibid.*, **19**, 261t (1963).
- H. Kaesche, "Die Korrosion der Metalle," Kap. 9, Springer-Verlag, Berlin (1966).
- Z. Szklarska-Smialowska, *Corrosion*, **27**, 223 (1971).
- J. R. Galvele, *Treat. Mater. Sci. Technol.*, **23**, 1 (1983).
- K. Osozawa, N. Okato, Y. Fukase, and K. Yokota, *Boshoku Gijutsu*, **24**, 1 (1975).
- Ja. M. Kolotyrkin, *This Journal*, **108**, 209 (1961).
- T. P. Hoar and W. R. Jacob, *Nature*, **216**, 1299 (1967).
- N. Sato, *This Journal*, **123**, 1197 (1976).
- T. Shibata and T. Takeyama, *Nature*, **260**, 315 (1976).
- T. Shibata and T. Takeyama, *Corrosion*, **33**, 243 (1977).
- T. Okada, *This Journal*, **131**, 241 (1984).
- M. Janik-Czachor and S. Kaszczyszyn, *Werkst. Korros.*, **33**, 500 (1982).
- S. Chandrasekhar, "Hydrodynamic and Hydromagnetic Stability," Oxford University Press, Oxford, England (1961).
- M. M. Denn, "Stability of Reaction and Transport Processes," Prentice-Hall, Englewood Cliffs, NJ (1975).
- R. Aogaki, K. Kitazawa, Y. Kose, and K. Fueki, *Electrochim. Acta*, **25**, 965 (1980).
- R. Aogaki, *This Journal*, **129**, 2442, 2447 (1982).
- J. Crank, "The Mathematics of Diffusion," Chap. 1, Oxford at the Clarendon Press, London (1957).
- K. J. Vetter, "Electrochemical Kinetics," Chap. 2, Academic Press, New York (1967).
- L. D. Landau and E. M. Lifshitz, "Electro Dynamics of Continuous Media," Chap. 3, Pergamon Press, London (1960).
- I. L. Losenfeld and I. S. Danilov, *Corros. Sci.*, **7**, 129 (1967).
- M. Pourbaix, *Corrosion*, **26**, 431 (1970).
- T. Okada, in "Passivity of Metals and Semiconductors," M. Froment, Editor, p. 281, Elsevier, Amsterdam (1983).
- T. P. Hoar, P. B. Mears, and G. P. Pothwell, *Corros. Sci.*, **5**, 279 (1965).
- P. Zaya and M. B. Ives, in "Passivity of Metals and Semiconductors," M. Froment, Editor, p. 287, Elsevier, Amsterdam (1983).
- B. E. Conway, "Theory and Principles of Electrode Processes," Chap. 6, Ronald Press, New York (1965).
- P. Delahay, "Double Layer and Electrode Kinetics," Chap. 4, Interscience, New York (1965).
- E. Gileadi (Editor) "Electrosorption," Chap. 1, Plenum Press, New York (1967).
- T. P. Hoar, *Discuss. Faraday Soc.*, **1**, 299 (1947).
- H. S. Harned and B. B. Owen, "Physical Chemistry of Electrolytic Solutions," Chap. 12, 14, Reinhold, New York (1957).

Semiconductor Electrodes

LVI. Principles of Multijunction Electrodes and Photoelectrosynthesis at Texas Instruments' p/n-Si Solar Arrays

James R. White, Fu-Ren F. Fan, and Allen J. Bard*

Department of Chemistry, The University of Texas Austin, Texas 78712

ABSTRACT

In photoelectrochemical (PEC) cells based on single junctions of semiconductors with solutions or metals, photopotentials are rarely above 0.6-0.8V. The higher photovoltages needed to drive more energetic reactions require multijunction cells involving multilayer electrodes or series connection of PEC cells. Such PEC cells are considered, and their behavior is shown to be predicted from the current-potential (i-V) behavior at each interface; the sum of the voltage drops at a given current yields the i-V characteristic of the overall PEC cell. These principles are illustrated with the Texas Instruments arrays based on silicon spheres and Si p/n junctions contacting a solution via a noble metal layer. Reactions considered include generation of Cl_2 with reduction of O_2 or the generation of H_2 , the photobromination of phenol, and the photochlorination of cyclohexene in acetonitrile.

Liquid-junction photoelectrochemical (PEC) cells are of interest in the direct utilization of solar energy to carry out useful chemical reactions (1-4). In most liquid-junction PEC cells, the photopotential arises at the semiconductor/solution interface. The maximum (open-circuit) photopotential, which represents the driving force of the cell chemical reaction, is rarely more than 0.8V, and is often below 0.6V. This rather low driving force limits the

range of possible photoelectrosynthetic reactions which can be carried out in PEC cells without the application of an external bias. Alternatively, the photoactive junction can be at a metal/semiconductor (Schottky barrier) interface with the faradaic reaction occurring at the metal (sometimes bearing an appropriate electrocatalyst). For example, PEC's with the following junctions have been described: Au/n-GaP (5, 6), PtSi/n-Si (7), and Pt/n-GaAs (8). Such cells have the advantage that the semiconductor is protected from the solution environment and show

* Electrochemical Society Active Member.

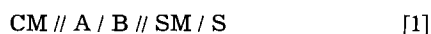
photopotentials that are independent of the redox potential of solution species. However, again the reported photopotentials are usually below 0.6V. Related PEC's involve photopotentials that arise at a p/n semiconductor junction, again protected from the solution by a metal overlayer. The most highly developed systems of this type are probably the p-Si/n-Si junctions separated from the solution by suitable noble metal overlayers that are used in the Texas Instruments Solar Energy System (TISES) (9-11). The photopotential developed at these junctions is about 0.55V. These latter p-Si/n-Si junctions are clearly related to solid-state photovoltaic cells (e.g., involving single-crystal Si) that are used for electricity production. In the TISES system, these junctions are produced on small (0.2 mm diam) Si spheres that are embedded in glass and backed by a conductive matrix to form arrays in contact with a solution. The relative advantages of these arrays compared to solid-state devices has been discussed (10, 11).

If more energetic reactions are to be driven in PEC cells without an external bias, cells with both photoactive anodes and cathodes can be employed. These two electrodes must be matched carefully to maximize the efficiency, since two photons are used to drive a single electron through the circuit. This strategy is employed in the TISES system, where both n-Si on p-Si spheres (photocathodes) and p-Si on n-Si spheres (photoanodes) are coupled to produce a total open-circuit voltage of 1.1V. These microspheres are coated with noble metal films which act as electrolytic contacts to the solution, stabilize the substrate Si, and catalyze the electrode reactions. The TISES system has been developed specifically for the overall conversion of solar to electrical energy in a system where HBr is decomposed by sunlight to form Br₂ at the photoanode and H₂ at the photocathode. The Br₂ and H₂ are stored and subsequently recombined in a fuel cell to produce electricity.

To form systems with higher output voltages, a number of junctions must be connected in series or the PEC cells must be coupled in a suitable way. Particularly interesting structures would involve multilayer devices with several photoactive junctions, especially if semiconductors with different bandgaps are employed. Structures of this type have been proposed in solid-state photovoltaic devices (tandem or cascade cells) (12), but few examples have been given in photoelectrochemical cells for direct utilization of radiant energy in chemical reactions. In this paper, we consider the principles of semiconductor electrode devices with interior photoactive junctions and the means of coupling PEC cells to increase the available voltage to levels consistent with a particular reaction. In particular, we demonstrate the application of the Texas Instruments solar arrays to electrosynthetic reactions, e.g., in the production of chlorine and oxygen and in the bromination of phenol. The utilization of these arrays in a nonaqueous solvent (MeCN) for the chlorination of cyclohexene is also described.

Principles of Operation

We suggest the following notation for multilayer semiconductor devices

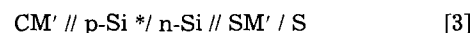


where CM represents the contact metal to the electrode (connected to an external lead), A and B represent other, often semiconductor phases, SM is the surface metal or layer contacting the solution phase, and S is the solution. As usual in electrochemical cells, a slash represents a junction; we represent an ohmic contact by //. For example, the Texas Instruments photoanode (TIA), which is part of the array used in this work, is represented as



where CM is the tantalum back contact, and SM is a surface metal (e.g., Pt or Ir) with a suitable catalyst. The photoactive junction (indicated by the asterisk) is the Si

n/p junction. This can also be denoted as an L₄P₁ electrode, where L represents the number of layers used and P the number of photoactive junctions. The TI photocathode (TIC) is thus



and the array is formed by contacting CM and CM'.

The operation and current-voltage (i-V) curves of a given electrode can be understood by examining the i-V characteristics of each junction and noting that these are connected in series. Operation of the total cell can then be obtained, as is usual for electrochemical devices, by combining the i-V characteristics of each electrode. Consider the TIA shown in Eq. [2]. The electrochemical behavior is described by that of the p/n junction, either in the dark or under irradiation, in series with the SM/S interface (Fig. 1). For the p/n junction the dark behavior (curve A) is given by the Shockley Eq. [4] (13)

$$j = j_s [\exp (eV_j/kt) - 1] \quad [4]$$

where j is the current density, j_s is the saturation current density for the junction as determined by the carrier density, mobility, and diffusion length, and V_j is the voltage drop across this junction. The illuminated p/n junction (curve B) behaves as a constant current source in parallel with the junction and the j - V relationship is given by

$$j = j_s [\exp (eV_j/kT) - 1] - j_L \quad [5]$$

where j_L is the constant current produced by photogeneration of carriers in the junction. The metal/solution junction shows behavior that depends upon the nature of the metal and solution components and is governed by the typical electrochemical thermodynamic, mass-transport, and kinetic considerations (14). A representative curve is given in Fig. 1C, showing the current across this junction as a function of the potential of SM *vs.* a reference electrode, V_{SM} . The j - V behavior of the multilayer structure is given by the summation of the j - V_j and j - V_{SM} curves, assuming a series connection (Fig. 1D). At any current density, j , the voltage drop between CM and the reference electrode, V , is $V_j + V_{SM}$ (plus any iR drops within the phases). Clearly, the light driven photopotential (or the underpotential for the electrode reaction because of the p/n junction), at any value of j , is V_j . The behavior of the TIC shown in Eq. [3] can be obtained in an analogous manner, as shown in Fig. 2. The characteristics of multilayer, multijunction devices, e.g., containing several photoactive junctions, can be obtained in a similar way by adding the j - V characteristics of each junction.

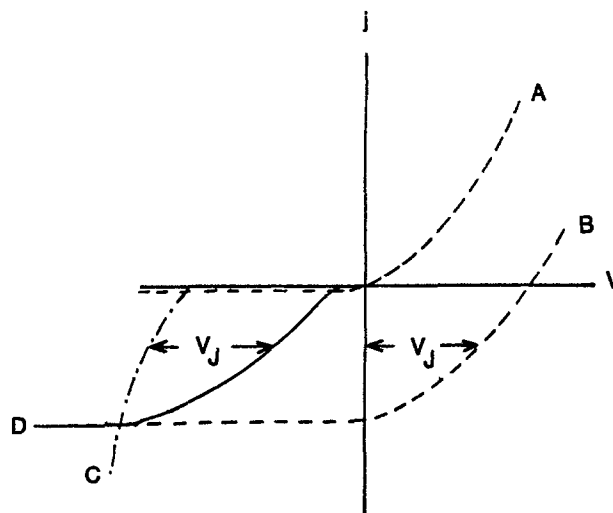


Fig. 1. Representative j - V curves for p on n-Si junction in the dark (A) and in the light (B). Voltage scale for curves A and B represents a voltage drop, ($\Delta V = V_j$) across the p/n junction. (C): j - V curve for a metal/solution junction. (D); j - V curve for total TIA. Potentials are *vs.* a reference electrode.

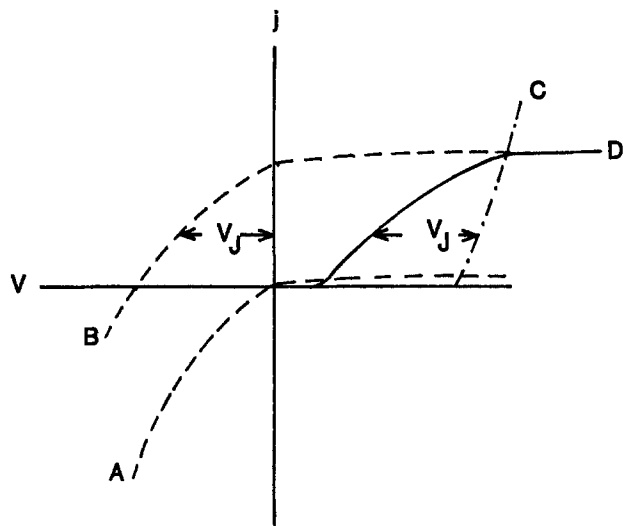


Fig. 2. Representative j - V curves for n on p-Si junction in the dark (A) and in the light (B). Voltage scale for A and B represents a voltage drop, $\Delta V = V_J$, across the n/p junction. (C): j - V curves for a metal electrode; (D): j - V curve for total TIC. Potentials are vs. a reference electrode.

Single photoelectrode cells.—The behavior of the overall photoelectrosynthetic cell, e.g., TIA/S/M, where M is the conductive counterelectrode, is determined by the i - V curve of the TIA discussed above, the i - V curve of electrode M (in the cathodic region) and any iR drop in solution, under the conditions that the total anodic current at the TIA is equal to the cathodic current at M at any given cell voltage, V_{cell} . Representative curves are given in Fig. 3. The maximum current in the absence of any externally applied voltage would be i_{sc} , the short-circuit current. Clearly, for a spontaneous reaction, good overlap of the anodic and cathodic i - V curves is required. The i - V curve for a variable load resistor, R_L , across the cell, represented by V_{cell} , or with an externally applied voltage, V_{appl} , can also be obtained (Fig. 3). The maximum photocurrent under any conditions [in the absence of current doubling effect (15)] is i_L , governed by the p/n junction characteristics. An analogous treatment applies for the TIC coupled in a cell with a metal anode.

Systems with two photoelectrode (dual-array PEC).—When one photoelectrode is coupled with a metal counterelectrode, the maximum open-circuit photovoltage, V_{oc} , is limited by the potential generated at a single p/n junction, e.g., for a silicon p/n junction, 0.55V. However, if a photoanode is coupled with a photocathode, V_{oc} is the sum of both photoactive junction potentials. Thus, for the cell TIC/S/TIA, $V_{\text{oc}} = 1.1\text{V}$. This allows more energetic reactions to be driven without an external bias. Again, the overall cell behavior can be predicted from the individual i - V curves for the TIA and TIC. This is shown in Fig. 4.

Multiple photoarray system.—To obtain even higher potentials to drive more energetic reactions, two (or more) photocells must be coupled. For example, by suitable coupling of the photocells: TIC/S/TIA and TIC/S'/TIA an open-circuit photovoltage of 2.2V can be obtained across solution S'. In this case, cell 1 would contain a single redox couple (e.g., Br_2/Br^-) and behaves as a photovoltaic cell which provides a bias to cell 2 and adds to the photovoltage developed in cell 2. The mode of connection of these cells and the relevant i - V curves are shown in Fig. 5, where a reaction involving $> 1.1\text{V}$ (e.g., $2\text{HCl} \rightarrow \text{H}_2 + \text{Cl}_2$) is carried out.

The experimental results that follow illustrate i - V curves for several redox couples at TI silicon arrays (TIA, TIC) and demonstrate several photoelectrosynthetic PEC's of the type outlined above.

Experimental

The multilayered semiconductor electrodes used in these experiments were the TISES silicon arrays pro-

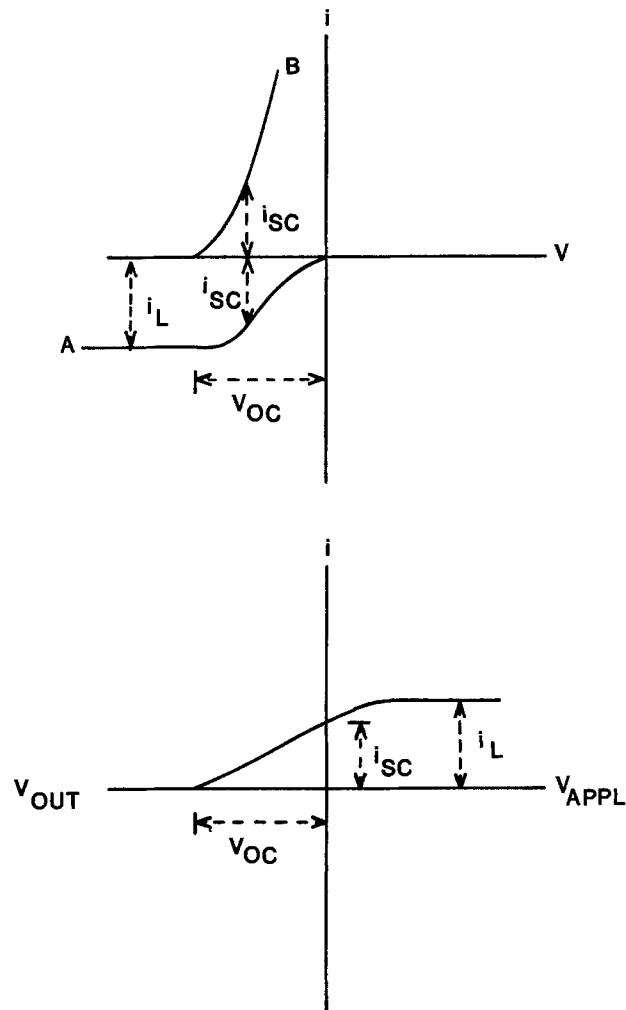


Fig. 3. Representative i - V curves for the cell TIA/S/M. Top: curves A and B represent TIA and M, respectively. Potentials are vs. a reference electrode. Bottom: i - V_{cell} behavior when electrodes are coupled through a load resistance, R_L . For $R_L = 0$, $i = i_{\text{sc}}$, and $V = 0$; for $R \rightarrow \infty$, $i = 0$, and $V = V_{\text{oc}}$. V_{out} represents a voltage produced by the cell under illumination. V_{appl} represents a voltage applied to the cell.

duced by Texas Instruments. Electrodes were made by contacting a copper wire to the conductive back surface of the panel arrays with conductive silver paint. The con-

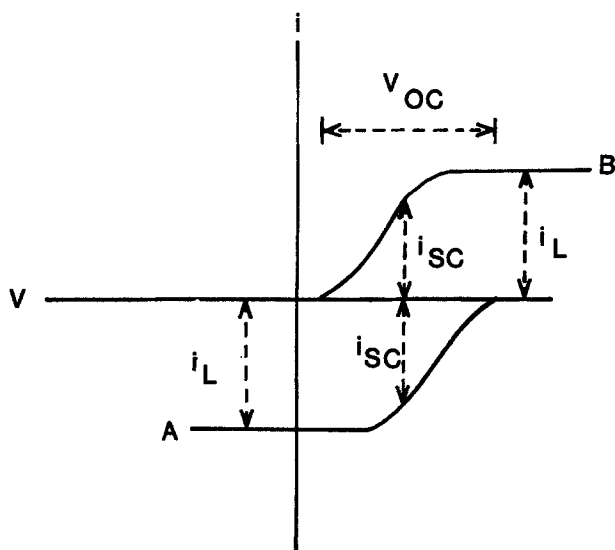


Fig. 4. Representative i - V curves for the cell TIA/M/TIC. Potentials are vs. a reference electrode. Curves A and B represent TIA and TIC, respectively.

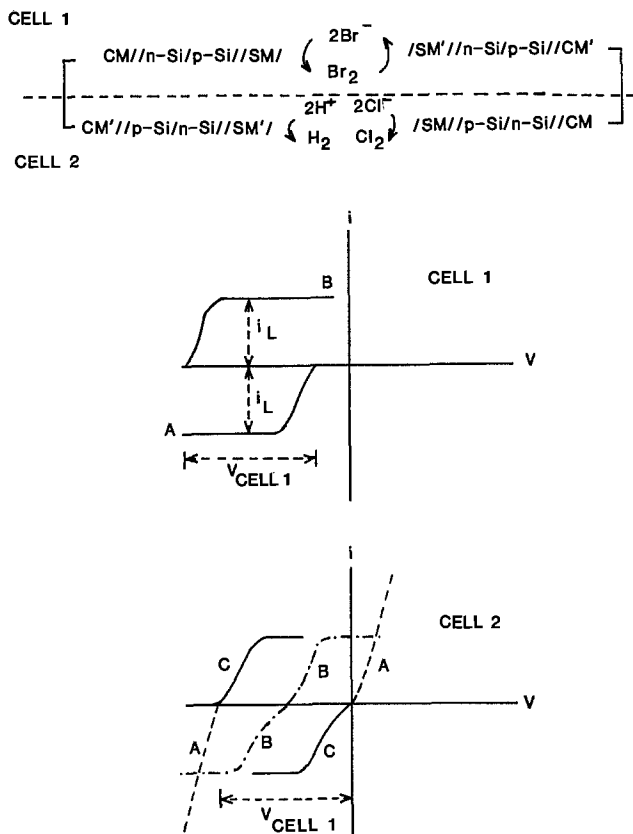


Fig. 5. Schematic representation of dual cell photoarray system. Top: *i-V* curves for cell 1; (A) TIA, (B) TIC. Bottom: *i-V* curves for cell 2. (A) (---): Pt electrode in HCl. (B) (-.-.-): TIA and TIC in HCl under illumination. (C) (—): as in B, under bias from cell 1.

tact was covered with epoxy cement which was insulated from solution with silicone rubber. The exposed front surface geometrical area was 0.25 cm^2 . RuO_2 films were prepared by decomposition of RuO_4 vapor, which was prepared chemically (16), onto ambient temperature substrates. XPS data showed that the binding energies for the Ru $3d_{5/2}$ line from samples prepared in this manner are in agreement with those obtained for anhydrous RuO_2 powder (17).

Voltammetric experiments were performed in a single-compartment Pyrex cell with a volume of 50 ml. All solutions were degassed with prepurified N_2 for 15 min prior to use unless indicated otherwise. Voltammograms were recorded with a Princeton Applied Research (PAR) Model 173 potentiostat/galvanostat, a PAR Model 175 Universal Programmer, and a Houston Instruments Model 2000 X-Y Recorder. The illumination source was a tungsten-halogen lamp with a 13 cm water filter.

A dual-compartment Plexiglas cell (40 ml each compartment) was used for experiments involving multiple photoelectrodes immersed in two solutions. For the experiment involving HCl electrolysis, one compartment contained HCl while the other contained the Br^-/Br_2 redox couple. Photoelectrodes were placed as close to the cell wall as possible to minimize absorption of light by the solution.

A Pyrex H-cell was used for the experiments in which Cl_2 was produced by reduction of O_2 (TIA/S/M). A fuel cell electrode (geometrical area, 3.1 cm^2), Teflon/carbon/platinum (donated by TI), was used as a cell divider. One compartment contained $5M$ HCl, and the other was kept dry and pressurized with O_2 .

Power characteristics were evaluated with a series, variable resistance box and a digital voltmeter. Short-circuit measurements were approximated by using a 15Ω resistance and measuring the corresponding voltage drop. All chemicals were reagent grade and were used without further purification. Triply distilled water was used in all

experiments. Acetonitrile was dried over molecular sieves.

Results and Discussion

Half-reactions at TIA's and TIC's.—We considered half-cells composed of a TIA immersed in different solutions (cell [2]) and compared the photoresponse of these to the *i-V* curves at a metal electrode.

Oxidation of chloride.—The voltammetric curves for a TIA in $10.0M$ LiCl are shown in Fig. 6. In the dark, curve A, essentially no current is observed, even at potentials where vigorous Cl_2 production is observed on a bare Pt electrode (curve C). Under illumination, at a light intensity of 170 mW/cm^2 , *j-V* curve B results. The limiting current density, j_L , was 38 mA/cm^2 . The open-circuit photopotential, V_{oc} , was $0.49V$, as measured from the differences between curves B and C. The platinum disk electrode operated near the reversible potential for the Cl/Cl_2 couple at low current densities. The fill factor was 0.42 . The stability of the TIA for Cl_2 evolution was tested by holding it at $\pm 1.0V$ vs. SCE under illumination of 170 mW/cm^2 for 48h; voltammograms taken intermittently during this time period showed no change in j_L or in the *j-V* curve. No apparent changes in the electrode surface were observed.

The effect of thin films of RuO_2 , a known catalyst for chlorine evolution, on the voltammetric response in Cl^- media was also examined. Films about 100\AA thick were deposited by chemical vapor deposition onto ambient temperature substrates. The TIA/ RuO_2 electrode showed a slightly more negative onset for chlorine evolution compared to an unmodified TIA (Fig. 7). The modified TIA also showed a larger cathodic peak on the reverse scan. These results suggest that the kinetics of the Cl^-/Cl_2 couple are somewhat improved by the RuO_2 treatment. The fill factor for the RuO_2 coated anode increased to 0.48 . There was, however, some attenuation of j_L because of light absorption by the RuO_2 layer (25% attenuation in the worst case). The RuO_2 modified TIA's were tested for stability by potential cycling for 1h under illumination. The films showed stable operation for solutions of $pH > 2$; however, for $pH < 1$, the *i-V* curves showed only resistive behavior with poor photoeffects, indicating deterioration of the surface film.

The Br^-/Br_2 couple.—This couple is of interest because photogenerated Br_2 could be employed in brominations of organics and because this couple could be used in a photovoltaic mode in the coupling of two PEC's. Typical *i-V* curves are shown in Fig. 8 for the TIA and TIC electrodes. The data pertaining to this couple are given in Table I.

$Fe(III)/Fe(II)$ couples.—We also investigated the $Fe^{3+/2+}$ couple in $1M$ HCl medium and the $Fe(CN)_6^{3-/4-}$ couple in $0.5M$ Na_2SO_4 for use in the photovoltaic biasing cell. The

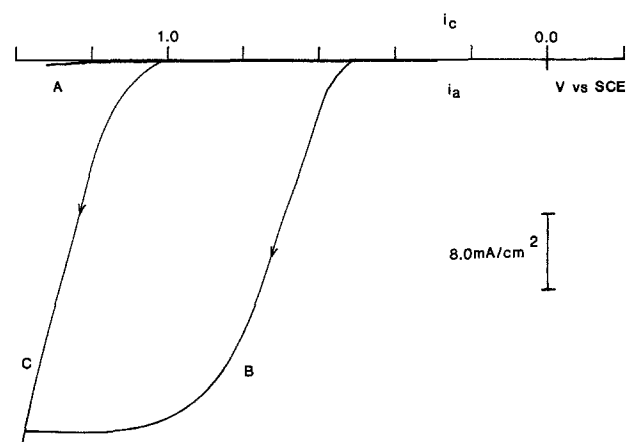


Fig. 6. *j-V* behavior for a TIA in $10M$ LiCl in the dark (A) and under illumination of 170 mW/cm^2 (B) and for a Pt electrode (C). Scan rate: 100 mV/s .

Table I. Photovoltaic parameters of two electrode configuration (photoelectrode vs. Pt electrode)^a

Electrolyte	Photoelectrode	V_{oc} (V) ^b	$j_i = j_{sc}$ (mA/cm ²) ^c	f.f. ^d	Efficiency (%) ^e
0.5M Fe(CN) ₆ ⁴⁻ } 0.5M Fe(CN) ₆ ³⁻ } 0.5M Na ₂ SO ₄	anode	0.48	9	0.65	4.3
	cathode	0.45	10	0.55	3.8
2M FeCl ₂ } 2M FeCl ₃ } 1M HCl }	anode	0.5	13	0.6	6.0
	cathode	0.48	15	0.6	6.7
48% HBr	anode	0.5	23	0.5	8.8
1M Br ₂	cathode	0.5	25	0.55	10.5

^a Light intensity = 65 mW/cm², from tungsten-halogen lamp.

^b Open-circuit photovoltage.

^c Short-circuit photocurrent.

^d Fill factor.

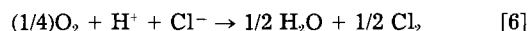
^e Maximal power conversion efficiency = $(V_{oc} \times j_{sc} \times f.f.) / \text{light intensity}$.

results are summarized in Table I. The efficiency with these couples was lower than that found with the Br⁻/Br₂ couple. This can primarily be attributed to lower values of j_i (and, hence, i_{sc}). For the Fe^{3+/2+} couple, this arises because of increased light absorption by the solution, while for the Fe(CN)₆^{3-/4-} couple the relatively low solubility causes j_i to be limited by mass transfer. The latter couple also suffers from some photochemical instability (18).

The O₂/OH⁻ system.—The *i*-*V* curves for the oxidation of hydroxide ion at a TIA are given in Fig. 9. For an unbuffered solution (curve A), the *i*-*V* is drawn out, probably because of pH changes in the vicinity of the electrode during the oxidation as well as sluggish electron-transfer rates at the metal/solution interface. Sharper *i*-*V* curves occur in 1M NaOH (curve B); these show some hysteresis on scan direction which, perhaps, is caused by blockage of electrode surface by oxygen bubbles. We also examined the effect of a chemically vapor deposited layer of RuO₂ on the TIA. While RuO₂ coating had only a small effect in the unbuffered solutions (pH = 8), for the 1M NaOH there was a significant improvement in behavior. The potential for the onset of photocurrent was shifted to more negative values and the current rose more steeply (*i.e.*, the fill factor improved).

Single photoarray cells.—Since the total driving force for a single photoarray cell is small (0.55V), only photo-

electrosynthetic reactions which have both a small positive ΔG° and good kinetics (low overpotential) are possible. An interesting reaction possibility is the photo-production of chlorine via the reaction



At pH = 0, ΔG° is 0.13 eV. This reaction can be accomplished in a cell represented as TIA/S/M, where the metal electrode, M, is a large area (geometric, 3.1 cm²) fuel cell cathode (Pt-C-Teflon) with the *i*-*V* characteristics shown in Fig. 10A; this showed a 0.7V overpotential for O₂ reduction. The TIA *i*-*V* response, Fig. 12A, shows poor overlap with that of M; thus, large photocurrents would not be expected upon coupling the two electrodes. Experimentally, i_{sc} was 0.5 mA/cm² and V_{oc} was 0.15V; these are comparatively low values, in agreement with the prediction based upon individual *i*-*V* characteristics. While the TIA demonstrated characteristic behavior for photo-oxidation of Cl⁻,

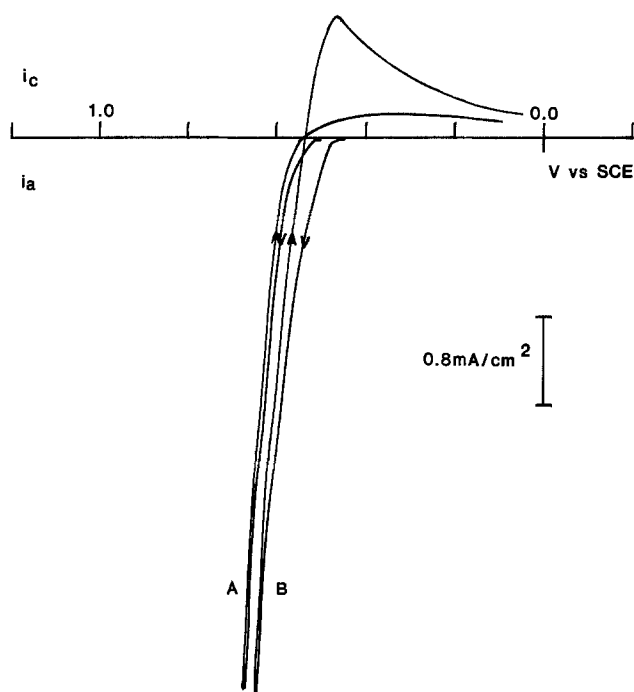


Fig. 7. *j*-*V* behavior for a TIA (A) and a RuO₂-modified TIA (B) in 10M LiCl. Light intensity: 170 mW/cm². Scan rate: 100 mV/s.

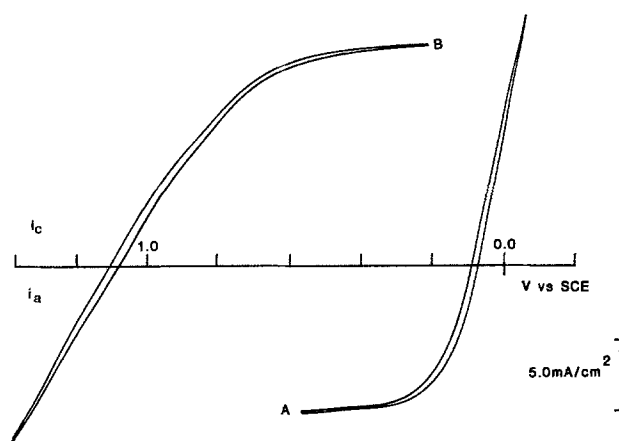


Fig. 8. *j*-*V* behavior for a TIA (A), TIC (B) in 48% HBr, 1.0M Br₂. 170 mW/cm² light intensity. Scan rate: 100 mV/s.

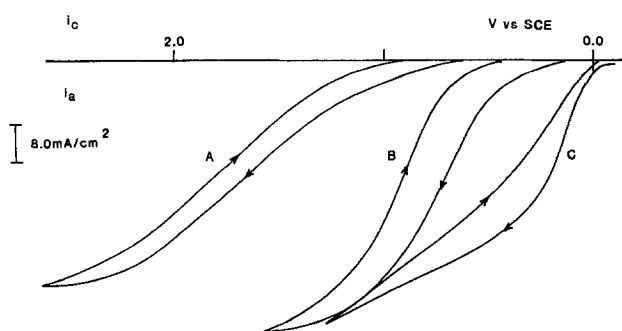


Fig. 9. *j*-*V* behavior for a TIA in 0.1M Na₂SO₄ (pH = 8) (A) and in 1M NaOH (B). (C): RuO₂-modified TIA in 1M NaOH. Light intensity: 170 mW/cm². Scan rate: 100 mV/s.

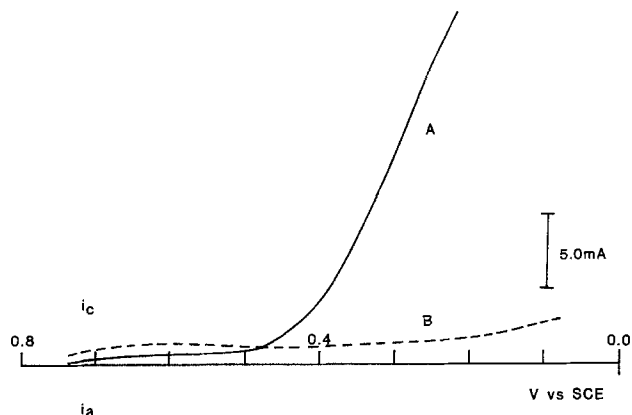
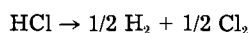


Fig. 10. *i*-*V* behavior for a fuel cell cathode (Pt-C-Teflon) with N_2 flow (B) and O_2 (A) in 5M HCl. Scan rate: 5 mV/s.

the cell was limited primarily because of poor kinetics for O_2 reduction at the metal cathode.

Dual photoarray cells.—The coupling of two photoarrays, TIA/S/TIC, allows the generation of ca. 1.1V during force for synthetic reactions. An example of a reaction in this type of cell is the bromination of phenol (18) at a TIA, coupled with the reduction of H^+ at a TIC. The photo-oxidation of Br^- in 48% HBr, has a V_{onset} shifted ca. 0.55V more negative compared to a Pt electrode (Fig. 11). On the reverse scan, a cathodic peak was observed, indicating at least some of the Br_2 being produced was rereduced. Addition of 1M phenol to the cell suppressed the cathodic wave and shifted V_{onset} about 50 mV more negative (curve C). The cathodic wave was absent even at scan rates of 10 V/s, indicating that the bromination of phenol is an efficient approach to preventing back electron transfer. Experiments performed with only phenol and supporting electrolyte showed no photoanodic current, indicating that the observed behavior was not due to direct oxidation of phenol. i_a for the TIA was attenuated by 20% in the presence of phenol; however, reduction of H^+ at a TIC, curve D, was unchanged by phenol addition. The two photoelectrodes when coupled give a V_{oc} of 0.42V with i_{sc} of 4.5 mA.

Multiple photoarray cells.—In order to drive more energetic reactions, individual photocells must be coupled to obtain larger potentials. The reaction



has a $\Delta G^\circ = 1.36$ eV ($pH = 0$), and would not occur in a cell of the type TIA/S/TIC, since the maximum available

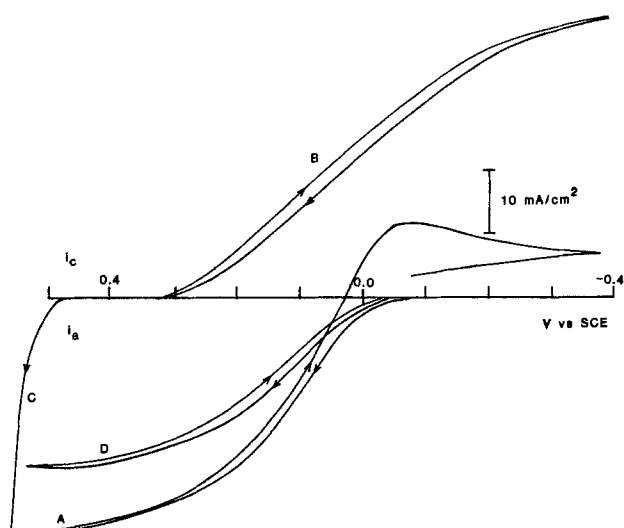


Fig. 11. *i*-*V* behavior in 48% HBr for a TIA (A), TIC (B), and Pt electrode (C). TIA response after addition of 1M phenol (D). Scan rate: 100 mV/s. Light intensity: 80 mW/cm².

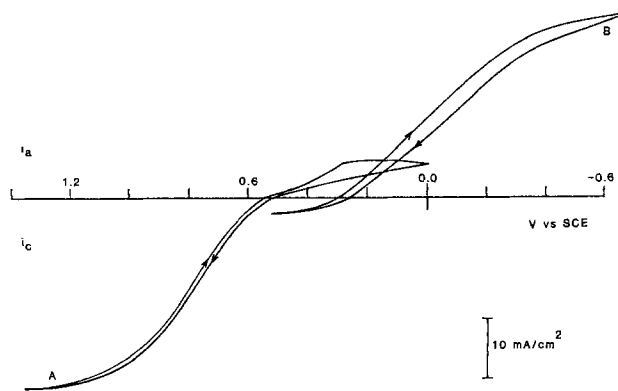


Fig. 12. *j*-*V* behavior for TIA (A) and TIC (B) in 5M HCl. Light intensity: 170 mW/cm². Scan rate: 100 mV/s.

photovoltage is only ca. 1.1V. The coupling of two cells, TIA/S/TIC (cell 2) and TIA/S/TIC (cell 1), where cell 1 contains a single redox couple, which provides a bias to cell 2, will produce a photopotential large enough for HCl electrolysis to occur in cell 2. The *i*-*V* curves for both a TIA and a TIC in 5M HCl are given in Fig. 12. The overlap is poor, and coupling these electrodes resulted in no observable short-circuit photocurrent. However, addition of the bias from cell 2 (coupled as in Fig. 5) did result in a net short-circuit photocurrent. For the case of cell 1 containing 1.0M $Br_2/1.0M$ KBr, the observed value of j_{sc} was 7.3 mA/cm² with V_{oc} being 2.0V with illumination intensity of 170 mW/cm². Table II gives values of j_{sc} for various conditions in cells 1 and 2. As predicted from the *i*-*V* characteristics for individual half-cells (Table I), the Br^-/Br_2 couple gave the best behavior. Moreover (see Table II), more acidic conditions favor the reaction, since the proton reduction reaction shifts towards more positive potentials with decreasing pH but the Cl^- oxidation is invariant with pH. Efficiencies for the coupled cell arrangement are also given in Table II. The efficiency, ϕ , is defined as

$$\phi = P_c/I \quad [7]$$

where P_c is the power stored as free energy in the electrolysis products and I is the incident light intensity. P_c was evaluated by assuming the products are consumed in a fuel cell reaction at the same current density as that for their production. Therefore, we take

$$P_c = j_{sc} \times E^\circ \quad [8]$$

where E° is the standard potential for rereaction, $-1.36V$.

Photoarrays in nonaqueous media.—Halogenation in nonaqueous media is possible at the TIA, as demonstrated by the following results for the chlorination of cyclohexene in acetonitrile (MeCN) (19). The photo-oxidation of Cl^- at a TIA occurs with V_{onset} ca. 0.5V vs. SCE (Fig. 13). The cathodic wave indicates that some of

Table II. Photoelectrolysis of HCl with different coupling solutions

Cell conditions ^a		j_{sc}	P_c	ϕ (%)
Compartment A	Compartment B	(mA/cm ²)	(mW/cm ²) ^b	
11.6M HCl	1.0M Br_2 1.0M KBr	7.3	9.9	5.8
5.0M HCl	1.0M Br_2 1.0M KBr	6.7	9.1	5.3
5.0M HCl	2.0M $FeCl_2$ 2.0M $FeCl_3$	3.3	5.4	3.2
1.0M HCl	1.0M HCl 2.0M $FeCl_2$ 2.0M $FeCl_3$ 1.0M HCl	2.7	3.7	2.2

^a Cell configuration as in Fig. 5; illumination intensity 170 mW/cm².

^b Short-circuit conditions approximated with $R_i = 15\Omega$.

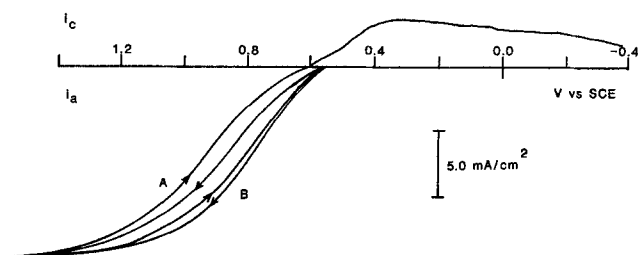


Fig. 13. j - V behavior for a TIA in 0.5M TBACl in MeCN (A) and after addition of 1M cyclohexene (B). Light intensity: 70 mW/cm². Scan rate: 100 mV/s. Potentials vs. SCE.

the Cl₂ produced was reduced on the reverse scan. Addition of 1M cyclohexene completely suppresses the cathodic wave, curve B, but had no effect on $i_{i,c}$, as in the bromination case. The wave was also shifted in a negative direction by 50-100 mV. The direct photo-oxidation of cyclohexene does not occur until ca. 1.6V vs. SCE and, therefore, does not influence the i - V behavior in Fig. 12.

Conclusions

Multilayer semiconductor electrode structures involving several photoactive junctions, such as the Texas Instruments arrays based on Si p/n junctions, can show stable operation and produce sufficient photovoltages to promote energetic reactions, such as the decomposition of HCl to H₂ and Cl₂. The i - V behavior at the interface with the solution is an important component of the cell performance, and metal surfaces can be selected to stabilize the electrode from photodecomposition and to catalyze the desired reactions. The behavior of multijunction devices can be obtained graphically from the i - V characteristics of each junction. Multijunction structures, such as coupled TI arrays, can produce photovoltages in excess of 2V, and can drive energetic reactions. The application of these arrays to nonaqueous solutions was also illustrated.

Acknowledgments

We are indebted to Texas Instruments, and especially Dr. I. Trachtenberg, Dr. T. Teherani, Dr. S. Frank, and Dr.

J. D. Luttmer, for TISES arrays and advice and comments. The support of this research by the National Science Foundation (CHE 8304666) and the Solar Energy Research Institute is gratefully acknowledged.

Manuscript received Dec. 21, 1983; revised manuscript received Sept. 24, 1984.

The University of Texas assisted in meeting the publication costs of this article.

REFERENCES

1. A. J. Bard, *J. Photochem.*, **10**, 59 (1979).
2. A. J. Bard, *Science*, **207**, 139 (1980).
3. M. Wrighton, *Acc. Chem. Res.*, **12**, 303 (1979).
4. A. Heller, *Science*, **223**, 1141 (1984).
5. Y. Nakato, T. Ohnishi, and H. Tsubomura, *Chem. Lett.*, 883 (1975).
6. R. H. Wilson, L. A. Harris, and M. E. Gerstner, *This Journal*, **124**, 1233 (1977).
7. F. R. F. Fan, R. G. Keil, and A. J. Bard, *J. Am. Chem. Soc.*, **105**, 220 (1983).
8. S. Menezes, A. Heller, and B. Miller, *This Journal*, **127**, 1268 (1980).
9. J. S. Kilby, J. W. Lathrop, and W. A. Porter, U.S. Pat. 4,021,323 (1977); U.S. Pat. 4,100,051 (1978); U.S. Pat. 4,136,436 (1979).
10. E. L. Johnson, *Proc. Intersoc. Energy Convers. Eng. Conf.*, **16**, 798 (1981).
11. E. L. Johnson, in "Electrochemistry in Industry," U. Landau, E. Yeager, and D. Kortan, Editors, pp. 299-306, Plenum, New York (1982).
12. J. J. Loferski, in "Photovoltaic and Photoelectrochemical Solar Energy Conversion," F. Cardon, W. P. Gomes, and W. Dekeyser, Editor, pp. 157-198, Plenum Press, New York (1981).
13. S. M. Sze, "Physics of Semiconductor Devices," Chap. 3, 12, Wiley-Interscience, New York (1969).
14. A. J. Bard and L. Faulkner, "Electrochemical Methods," John Wiley and Sons, New York (1980).
15. S. R. Morrison and T. Freund, *J. Phys. Chem.*, **47**, 1543 (1967).
16. P. Wehner and J. C. Hindman, *J. Am. Chem. Soc.*, **72**, 3911 (1950).
17. K. S. Kim and N. Winograd, *J. Catal.*, **35**, 66 (1974).
18. J. J. Lingane, "Electroanalytical Chemistry," p. 549, Interscience, New York (1958).
19. G. Faita, M. Fleischmann, and D. Pletcher, *J. Electroanal. Chem.*, **25**, 455 (1970).

Anodic Dissolution of Iron in Ammoniacal Ammonium Carbonate Solution

J. W. Lee, K. Osseo-Asare, and H. W. Pickering*

Metallurgy Program, Department of Materials Science and Engineering, The Pennsylvania State University, University Park, Pennsylvania 16802

ABSTRACT

The electrochemical behavior of iron has been characterized in aqueous ammoniacal ammonium carbonate solution. Pure iron anodically polarized in He- or O₂-saturated 2 kmol m⁻³ NH₃ + 1 kmol m⁻³ (NH₄)₂CO₃ solutions exhibits both stable active ($E = -650$ to -400 mV, SHE) and passive ($E = -330$ to 1000 mV) regions. A cathodic loop was observed in the potential range of -380 to 100 mV. It is suggested, on the basis of cathodic polarization curves of a graphite electrode in various concentrations of ammoniacal solution, that the cathodic loop is due to oxygen discharge. The addition of CoCO₃ to the ammoniacal solution has the same effect as oxygen in that it increases the cathodic current and potential range of the cathodic loop and, as such, functions as a strong oxidant.

Low grade oxide ores such as the land-based laterites and the ocean-floor manganese nodules, which contain only about 0.2% cobalt, are important cobalt resources (1, 2). When the reductive-roast ammonia leach process is applied to these materials, cobalt extraction rarely exceeds 50%, whereas nickel and copper recoveries of greater than 90% are attainable (3, 4). In this process, the roasting step produces alloys of Fe, Co, and other metals, which are

then involved in the subsequent leaching step. The low cobalt extraction can be attributed in part to coprecipitation of cobalt with iron and manganese and to the adsorption of cobalt on the oxide leach residues (5, 6). Adsorption experiments with model oxide powders have shown that the hydroxo species play a dominant role in cobalt uptake from aqueous ammoniacal solutions (6, 7). It has also been shown recently that the poor extraction of cobalt may be related to the electrochemical behavior of metallic iron (8). It was found during the anodic dissolu-

* Electrochemical Society Active Member.

tion of sintered iron-cobalt electrodes that cobalt dissolution was inhibited when the electrode potential was increased above 0.5V (SHE), which is in the passive region of the iron electrode in aqueous ammoniacal solutions (8). Additional indications of the possible influence of electrochemical processes are provided by the work of Kasherininov (9), Gong *et al.* (10), and Goeller *et al.* (11).

A detailed study of the electrochemical aspects of cobalt and iron dissolution in ammoniacal ammonium carbonate solutions is needed in order to understand better the behavior of these metals and in order to identify the conditions which would maximize cobalt extraction in ammonia hydrometallurgical systems. In this paper, electrochemical polarization techniques are applied to the study of iron dissolution in ammoniacal ammonium carbonate solutions with a view to laying the foundation for a study of iron-cobalt alloys.

Experimental Procedures

Samples of pure iron (99.7%) were prepared as cold-rolled polished, and annealed specimens, as described previously (8). Electrochemical characterization of the iron electrode was attained by determining (i) the current response to anodic or cathodic polarization under various controlled aqueous-phase conditions and (ii) the time dependence of the open-circuit potential.

Details of the electrochemical equipment and the procedures used for the polarization and open-circuit potential measurements are given elsewhere (8). Reagent-grade chemicals were used throughout, and, when needed, cobalt was introduced into the solution as CoCO_3 , but much of the cobaltous ion was likely converted to cobaltic ion during preparation of the solution (12). Following a period (~30 min) at open circuit, the electrode was swept at 6 mV min^{-1} in the more noble direction from a potential more negative than the open-circuit potential. This rate was slow enough to produce quasistationary values. In order to investigate the origin of the cathodic loop observed in the iron polarization experiment, cathodic polarization curves were measured potentiodynamically on graphite rod electrodes in various ammoniacal solutions, following a 30 min period at the open-circuit potential, after which time a quasistationary mixed potential was obtained. The electrochemical behavior of dissolved cobalt was also studied in this manner using the graphite electrode. All the experiments were conducted at room temperature (~25°C).

Results

Open-circuit potential behavior of iron.—The open-circuit potential of iron was monitored as a function of time (Fig. 1 and 2). The solutions were He- or O_2 -saturated $2 \text{ kmol m}^{-3} \text{ NH}_3 + 1 \text{ kmol m}^{-3} (\text{NH}_4)_2\text{CO}_3$ (pH = 9.90) with and without the addition of CoCO_3 . The values of the open-circuit potential presented in Table I are after 9h in the solutions.

In general, the open-circuit potential was more noble the higher the concentration of CoCO_3 . Another tendency was that the potentials were more positive in O_2 -saturated solution than in He-saturated solution. In the case of iron in the He-saturated cobalt-free (blank) solution, the potential initially decreased to less noble values and then increased in the more noble direction with increase in time. The minimum in the potential occurred at shorter and shorter times with increase in CoCO_3 in the solution, and was absent at the highest concentration (Fig. 1). In the case of the oxygen-saturated solutions (Fig. 2), no minima were observed; the potentials increased steadily with time.

Anodic polarization curves of iron.—The potentiodynamic anodic polarization curves of iron are presented in Fig. 3 to 5. The curves show three general regions of active, passive, and oxygen-evolution in addition to a cathodic loop. These same features were observed for sweeps in the opposite direction.

As the potential was swept in the noble direction, anodic current increased at first, but then

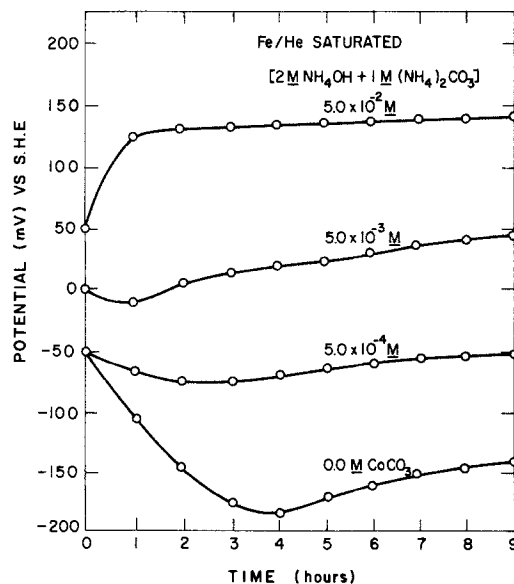


Fig. 1. Open-circuit potential vs. time for iron in He-saturated solution containing $2 \text{ kmol m}^{-3} \text{ NH}_3 + 1 \text{ kmol m}^{-3} (\text{NH}_4)_2\text{CO}_3$ and various concentrations of CoCO_3 .

leveled off, producing a yellow insoluble precipitate identified as a basic ferrous ammonium carbonate, $(\text{NH}_4)_2\text{Fe}_2(\text{OH})_4(\text{CO}_3)_2\text{H}_2\text{O}$ by x-ray diffraction. After that, the current density exhibited irregular oscillations within the range of $0.4\text{--}3.0 \text{ mA cm}^{-2}$ and a loosely adhering mixture of a yellow-and-brown-colored film formed on the corroding surface. As the potential was further increased, the iron electrode surface became covered with a shiny, dark-brown precipitate, which adhered tightly to the surface and could only be removed by application of a strong water spray. With additional increase in potential, a cathodic current was observed and the shiny dark brown film completely disappeared. Thus, the visible film is stable in the presence of high concentrations of ferrous ion (as exist at the surface during active dissolution), but apparently is not at the much lower current in the passive region. Its presence may be a necessary precursor for the passivating reaction. Table II shows the maximum values

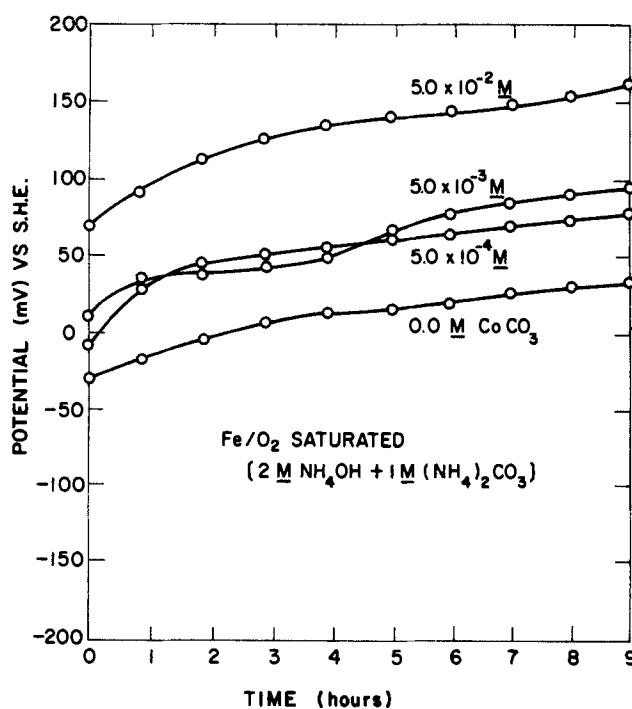


Fig. 2. Open-circuit potential vs. time for iron in O_2 -saturated solution containing $2 \text{ kmol m}^{-3} \text{ NH}_3 + 1 \text{ kmol m}^{-3} (\text{NH}_4)_2\text{CO}_3$ and various concentrations of CoCO_3 .

Table I. Open-circuit potentials for iron after 9h in He- or O₂-saturated 2 kmol m⁻³ NH₃ + 1 kmol m⁻³ (NH₄)₂CO₃ solutions

CoCO ₃ (kmol m ⁻³)	Potential (mV, SHE)	
	He-saturated solution	O ₂ -saturated solution
Blank	-140	35
5 × 10 ⁻⁴	-50	80
5 × 10 ⁻³	45	95
5 × 10 ⁻²	140	160

of the cathodic current density and the corresponding potential range in He- or O₂-saturated 2 kmol m⁻³ NH₃ + 1 kmol m⁻³ (NH₄)₂CO₃ solution.

As shown in Fig. 3-5 and Table II, as the concentration of CoCO₃ is increased or O₂ is added, the maximum cathodic current density and the range of potential across which the cathodic loop occurs increase and the maximum anodic current density decreases. The effect of cobalt in the electrolyte is illustrated also on graphite in Fig. 6, which shows a typical polarization curve for the Co(II)/Co(III) couple in ammonia-ammonium carbonate solution. According to this figure, reduction of Co(III) occurs below 45 mV (SHE).

As shown in Fig. 7, the cathodic polarization curves on a graphite electrode are not a strong function of the ammonia-ammoniacal solution composition. However, as O₂ is added to the solution, the cathodic current density in the -800 to 200 mV potential range increases by about an order of magnitude over that in He-saturated solution.

Discussion

General considerations.—The results presented above have shown that, in aqueous ammoniacal solution, the iron electrode exhibits active, passive, and oxygen evolution behavior, in addition to a cathodic loop. The onset of the anodic current in the neighborhood of -650 mV (SHE) is consistent with the thermodynamics of the Fe-

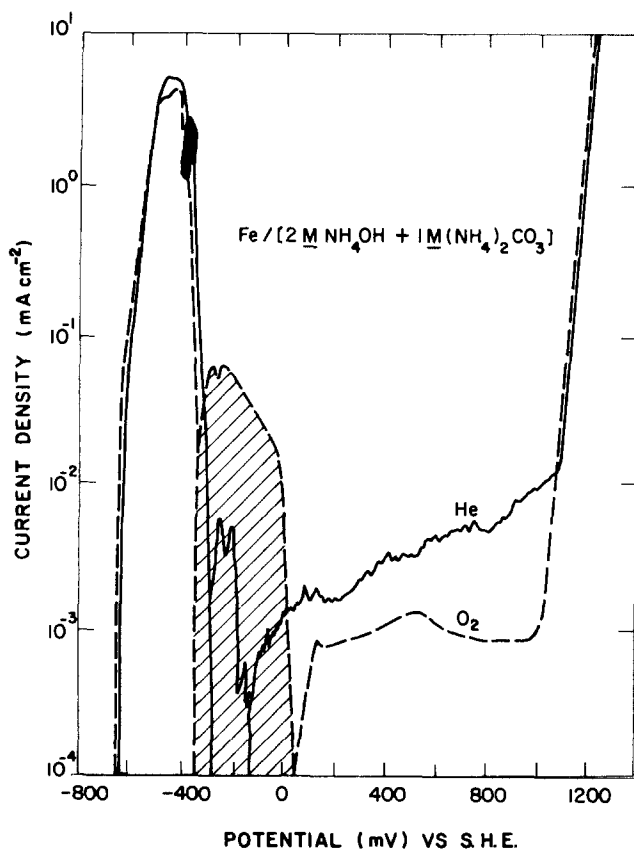


Fig. 3. Comparison of the anodic polarization curve of iron in He-saturated solution with that in O₂-saturated solution. Cross-hatched region is a cathodic loop.

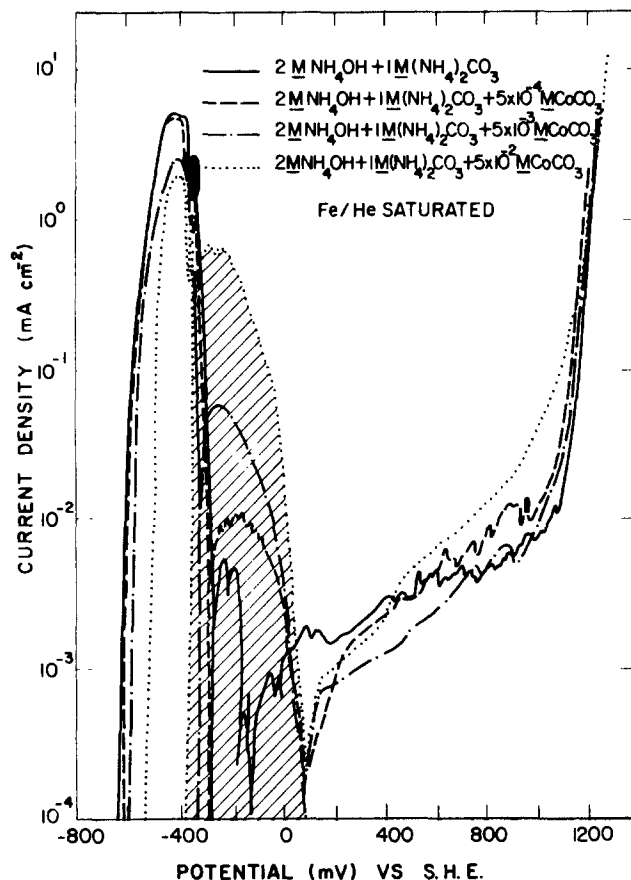


Fig. 4. Potentiodynamic polarization curves of iron in He-saturated solutions containing 2 kmol m⁻³ NH₃ + 1 kmol m⁻³ (NH₄)₂CO₃ and various concentrations of CoCO₃.

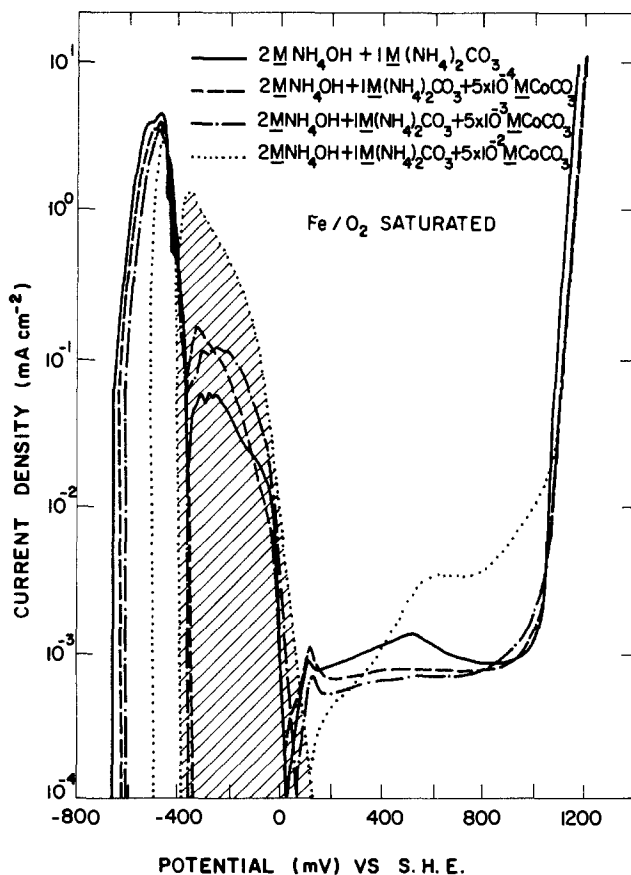


Fig. 5. Potentiodynamic polarization curves of iron in O₂-saturated solutions containing 2 kmol m⁻³ NH₃ + 1 kmol m⁻³ (NH₄)₂CO₃ and various concentrations of CoCO₃.

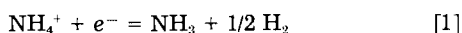
Table II. The maximum cathodic current density and the associated potential range during the potentiodynamic polarization of iron ($2 \text{ kmol m}^{-3} \text{ NH}_3 + 1 \text{ kmol m}^{-3} (\text{NH}_4)_2\text{CO}_3$)

He-saturated solution; CoCO_3 (kmol m^{-3})	Maximum current density ($\mu\text{A cm}^{-2}$)	Potential range (mV vs. SHE)	O_2 -saturated solution; CoCO_3 (kmol m^{-3})	Maximum current density ($\mu\text{A cm}^{-2}$)	Potential range (mV vs. SHE)
Blank	5	-270 to -150	Blank	60	-330 to 50
5×10^{-4}	10	-290 to 40	5×10^{-4}	150	-330 to 50
5×10^{-3}	60	-300 to 100	5×10^{-3}	130	-330 to 100
5×10^{-2}	800	-350 to 130	5×10^{-2}	1200	-360 to 150

$\text{NH}_3\text{-CO}_3\text{-H}_2\text{O}$ system. In a solution containing $10^{-4} \text{ kmol m}^{-3} \text{ Fe(II)}$ and $4 \text{ kmol m}^{-3} (\text{NH}_3 + \text{NH}_4^+)$, the $\text{Fe}(\text{NH}_3)_4^{2+}/\text{Fe}$ boundary occurs at $E_h = -780 \text{ mV}$ (8, 13). The maximum anodic current density of 4.3 mA cm^{-2} is much lower than that of 200 mA cm^{-2} obtained for the iron electrode in $1N$ sulfuric acid solution (14); in contrast, in basic solutions containing sodium borate or sodium benzoate, the maximum anodic currents are 10 and $230 \mu\text{A cm}^{-2}$, respectively (15). The decrease in anodic current observed at about -450 mV (SHE) is in qualitative agreement with the thermodynamic data and $E_h\text{-pH}$ diagrams presented in earlier papers (8, 13) which for $\text{pH } 10$, $10^{-4} \text{ kmol m}^{-3} \text{ Fe(II)}$ and $4 \text{ kmol m}^{-3} (\text{NH}_3 + \text{NH}_4^+)$ give the $\text{Fe}(\text{NH}_3)_4^{2+}/\text{FeOOH}$ boundary at $E_h = -380 \text{ mV}$. Characteristics of the surface films which form in this potential region are discussed elsewhere (16).

The cathodic loop.—The potentiodynamically produced anodic polarization curves for iron show a cathodic loop (Fig. 3-5). A few papers have treated the subject of the cathodic loop in the range of passive potentials in acid solutions and have shown that it is strongly related to the solution chemistry (17-22). In the CoCO_3 -free solutions, oxygen reduction may be the source of the loop (Fig. 3), even for the He-saturated solution, since it is difficult to completely eliminate oxygen from solution. Shams El Din *et al.* (23) have shown that NH_4^+ ions can facilitate the O_2 -reduction reaction. The hydrogen discharge reaction is also facilitated by the presence of NH_4^+ (24-26).

The following equation can be used to describe the discharge of hydrogen (13)



$$E_h(\text{V}) = -0.55 + 0.059 \log \frac{[\text{NH}_4^+]}{[\text{NH}_3]} \quad [2]$$

However, the cathodic loop at -380 to 100 mV in Fig. 3-5 cannot be attributed to this reaction since from Eq. [2] the equilibrium potential for reaction [1] is -550 mV for equal concentrations of NH_3 and NH_4^+ .

The oxygen reduction reaction can be written as follows

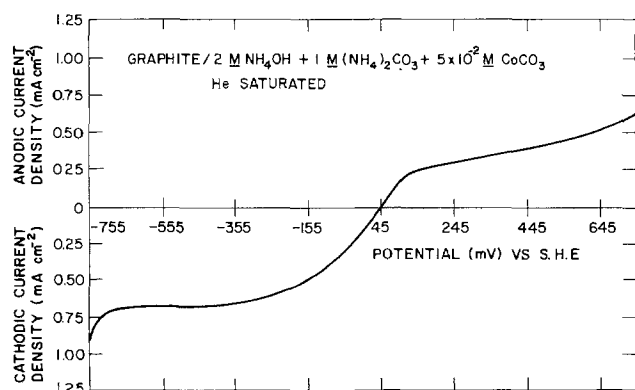
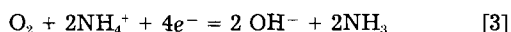


Fig. 6. Current-potential curve for the redox reaction of soluble Co(II)/Co(III) species at a graphite working electrode in He-saturated solution containing $2 \text{ kmol m}^{-3} \text{ NH}_3 + 1 \text{ kmol m}^{-3} (\text{NH}_4)_2\text{CO}_3 + 0.05 \text{ kmol m}^{-3} \text{ CoCO}_3$.

$$E_h(\text{V}) = 0.956 - 0.0296 \text{ pH} + 0.0296 \log \frac{[\text{NH}_4^+]}{[\text{NH}_3]} \quad [4]$$

The equilibrium potential for the $\text{pH } 9.9$ solution used in these experiments containing equal concentrations of NH_3 and NH_4^+ is 660 mV . Since this potential is more noble than the cathodic loop, it is possible for the oxygen reduction reaction to produce the loop. As shown in Fig. 3 and Tables I and II, with the introduction of oxygen into the solution, the open-circuit potential, the cathodic current at -250 mV (SHE), and the potential range of the loop are all increased. Also, Fig. 7 strongly suggests that oxygen reduction contributes to the cathodic loop; the shapes of the various current waves are almost the same while the introduction of oxygen into the solution substantially increases the cathodic current in the potential range -850 to 200 mV (SHE). Furthermore, it is significant to note that the maximum cathodic currents in the cathodic loops of the iron polarization curves in the He- and O_2 -saturated polarization curves of Fig. 3 are of the same order of magnitude as the respective cathodic polarization curves on a graphite electrode presented in Fig. 7 ($\sim 5 \times 10^{-3}$ for He and $\sim 5 \times 10^{-2} \text{ mA cm}^{-2}$ for O_2).

The effects of Co(II) and Co(III) amines on the polarization and open-circuit behavior of iron.—It is evident from the results presented in Fig. 1, 2, 4, and 5 and Tables

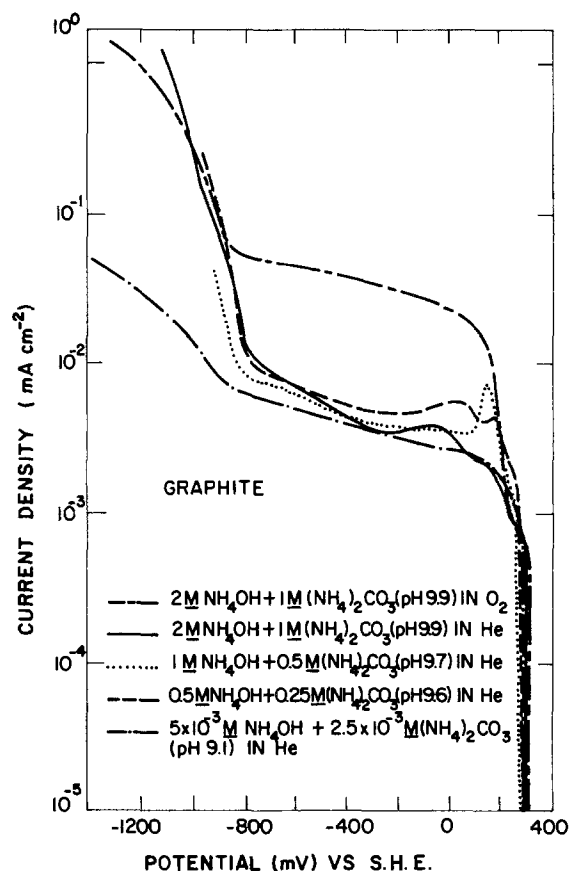
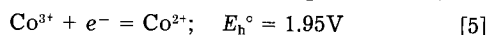
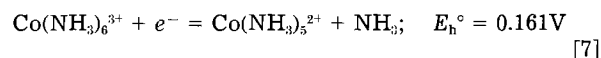
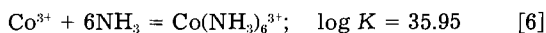


Fig. 7. Cathodic polarization curves on graphite in He- or O_2 -saturated solutions of ammonia-ammonium carbonate.

I and II that the presence of dissolved cobalt has a significant effect on the polarization behavior of iron. It is well known that in the Co-H₂O system, the oxidation of the cobaltous ion to the cobaltic ion is very unfavorable as can be understood from the standard potential (27)



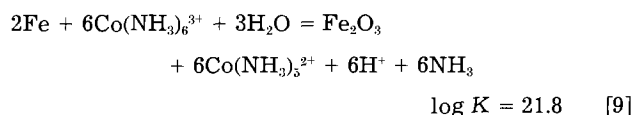
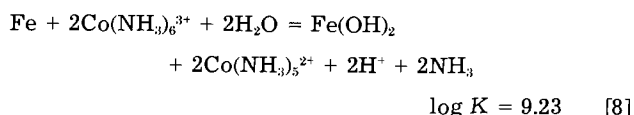
However, the oxidation of Co(II) to Co(III) becomes much more favorable in the presence of a variety of complexing ligands especially ammonia and may even be brought about by atmospheric oxygen (27). This is attributed to the formation of a stable complex of trivalent cobalt with NH₃ (8, 12, 27)



It should be noted that the cobaltic and cobaltous species are indicated in Eq. [7] as hexammine and pentammine species, respectively, since these have been indicated by thermodynamic analysis to be the stable forms under the present experimental conditions (8, 27).

The effect of cobalt addition to the electrolyte on the open-circuit potential (Fig. 1 and 2) and on the anodic polarization curves of Fe (Fig. 4 and 5) can be attributed to the reduction of Co(III) to Co(II); the oxidizing power of Co(III) is greater than that of oxygen based on a comparison of the relevant potential regions and maximum cathodic currents in Fig. 3-5. Comparison of the equilibrium potential of Fe/Fe(NH₃)₄²⁺ ($E_h^\circ = -0.548\text{V}$) with Co(II)/Co(III) ($E_h^\circ = 0.161\text{V}$) or OH⁻/O₂ ($E_h^\circ = 0.66\text{V}$) at equal concentrations of NH₃ and NH₄⁺ shows that spontaneous metal dissolution occurs with either oxidant, in accord with mixed potential theory. Thus, one expects the open-circuit potential to shift in the noble direction with increasing cobalt (or oxygen) content, as was found (Fig. 1 and 2). According to Fig. 6, below 45 mV (SHE), a significant cathodic reaction should be expected on a graphite electrode; at -200 mV, the cathodic current density is of the order of 0.5 mA cm⁻² in a solution containing 5 × 10⁻² kmol m⁻³ of cobalt. Examination of Fig. 4 reveals that the maximum current density of the cathodic loop is of the same magnitude (i.e., ~ 0.5 mA cm⁻²). Thus it appears that the cathodic loop in the CoCO₃ containing, He-saturated solutions is mainly due to the reduction of Co(III) amines. These explanations implicitly assume that during preparation of the solutions, most of the Co(II) added to the solution as CoCO₃ is oxidized to Co(III) by dissolved oxygen, in accord with other observations (12).

The shift of the open-circuit potential of Fe by cobalt addition to the electrolyte (Fig. 1 and 2) takes place wholly within the passive region of Fe (Fig. 3-5) and, therefore, has relatively little impact on the corresponding low corrosion rate of iron in this (passive) potential range. The direction of the potential shift, however, has far-reaching implications for Fe-Co alloys and reduction of roasted ferruginous oxide ores. In particular, a shift in the open-circuit potential of up to 300 mV in the noble direction could include the potential of the active/passive transition for these alloy materials, in which case, the addition of cobalt to the electrolyte would cause a marked decrease in the metal dissolution rate. Available polarization curves of Fe-10%Co and Fe-50%Co, indeed, show that the metal dissolution rate decreases with increasing potential above about -100 mV for the same electrolyte conditions (8). This is a potential range within the observed shift of the open-circuit value with increasing cobalt and/or oxygen concentration (Fig. 1 and 2). Thus, Co(NH₃)₆³⁺, even more so than oxygen, tends to promote the formation of passive films, as well as of bulk solid reaction products, on iron in its role as a strong oxidant, as the following reactions illustrate



Conclusions

1. Iron in ammonia-ammonium carbonate solution exhibits three general regions (active, passive, and oxygen evolution) in addition to a cathodic loop.

2. The cathodic loop is due to the discharge of oxygen. Cobalt additions to the electrolyte significantly increase the cathodic current in the loop. Co, even in a deoxygenated solution, provides a strong oxidizing power to the system.

3. The measured shift of the open-circuit potential in the noble direction by the Co(III) and O₂ reduction reactions is in accord with the mixed potential theory. The shift could have significance for Fe-Co alloy material produced by reductive roasted oxide ores, since the tendency for passivation sharply increases at more noble potentials as has already been found in laboratory tests on Fe-Co alloys.

Acknowledgment

The authors gratefully acknowledge the support of this work by the Department of the Interior under Grants no. G5105045 and G5115422.

Manuscript submitted April 9, 1984; revised manuscript received Nov. 2, 1984.

REFERENCES

1. D. J. I. Evans, R. S. Shoemaker, and H. Veltman, Editors, "Proceedings of the International Laterite Symposium," AIME, New York (1979).
2. G. P. Glasby, Editor, "Marine Manganese Deposits," Elsevier, Amsterdam (1977).
3. K. N. Han, M. Hoover, and D. W. Fuerstenau, *Int. J. Miner. Process.*, **1**, 215 (1974).
4. L. E. Slobtsov, V. Eerrera, E. Alfonso, O. G. Ibara, and P. Escobar, *Russ. J. Non-Ferrous Metal.*, **16**, 16 (1975).
5. M. H. Caron, *Trans. AIME*, **188**, 67 (1950).
6. K. Osseo-Asare and D. W. Fuerstenau, *Int. J. Miner. Process.*, **6**, 85 (1979).
7. K. Osseo-Asare and D. W. Fuerstenau, *ibid.*, **7**, 117 (1980).
8. K. Osseo-Asare, J. W. Lee, H. S. Kim, and H. W. Pickering, *Metall. Trans. B*, **14**, 571 (1983).
9. G. O. Kasherinov, *J. Appl. Chem. USSR*, **33**, 1225 (1960).
10. Q. Gong et al., *Nonferrous Metals Quart. (China)*, **32**, 17 (1980); C. Chen, in "Hydrometallurgy—Research, Development and Plant Practice," K. Osseo-Asare and J. D. Miller, Editors, pp. 65-85, TMS-AIME, Warrendale, PA (1982).
11. L. A. Goeller, C. D. Low, and D. C. Hale, in "International Conference on Cobalt: Metallurgy and Uses," Vol. 1, pp. 85-105, Brussels, Nov. 10-13, 1981, Benelux Metallurgie, Belgium (1981).
12. A. F. Trotman-Dickenson, "Comprehensive Inorganic Chemistry," Vol. 3, p. 1069, Pergamon Press, Oxford, England (1973).
13. K. Osseo-Asare, *Trans. IMM*, **90**, Sect. C, 159 (1981).
14. U. F. Franck, cited by K. J. Vetter, "Electrochemical Kinetics," p. 750, Academic Press, New York (1967).
15. J. G. N. Thomas and T. J. Nurse, *Br. Corros. J.*, **2**, 13 (1967).
16. J. W. Lee, H. W. Pickering, and K. Osseo-Asare, Paper in preparation.
17. C. Edeleanu, *Nature*, **173**, 739 (1954); *J. Iron Steel Inst.*, **188**, 122 (1958).
18. H. W. Pickering and R. P. Frankenthal, *This Journal*, **112**, 761 (1965).
19. J. M. West, *Br. Corros. J.*, **5**, 65 (1970).
20. J. G. N. Thomas and J. D. Davies, *ibid.*, **12**, 108 (1977).
21. I. L. Rosenfeld, L. V. Frolova, and N. N. Tavazde, *Prot. Met.*, **16**, 506 (1980).
22. I. L. Rosenfeld, *Corrosion*, **37**, 371 (1981).
23. A. M. Shams El Din and L. Holleck, *Ber. Bunsenges. Phys. Chem.*, **71**, 739 (1967).
24. I. K. Marshakov, Ya. A. Ugai, V. I. Vigdorovich, and M. I. Anokhina, *Sov. Electrochem.*, **1**, 1233 (1965).

25. S. E. Ostrovskaya, E. G. Tsventarnyi, and Ya. V. Durdin, *ibid.*, **9**, 1275 (1973).
 26. T. G. Nikiforova, E. G. Tsventarnyi, and Ya. V. Durdin, *ibid.*, **14**, 531 (1978).
 27. K. Osseo-Asare and D. W. Fuerstenau, in "Fundamental Aspects of Hydrometallurgical Processes," T. W. Chapman *et al.*, Editors, pp. 1-13, AIChE Symposium Series 74, AIChE, New York (1978).

Solute-Vacancy Interaction Model and the Effect of Minor Alloying Elements on the Initiation of Pitting Corrosion

Mirna Urquidi and Digby D. Macdonald*

SRI International, Chemistry Laboratory, Menlo Park, California 94025

ABSTRACT

A solute-vacancy interaction model (SVIM) is proposed to account for the effects of minor alloying elements (*e.g.*, Mo) on the breakdown of passive films. This model, which is an extension of the point-defect model (15-17) that was previously developed to account for the growth and breakdown of passive films, assumes that highly charged solutes (*e.g.*, Mo⁶⁺) form complexes with negatively charged cation vacancies ($V_{M\chi'}$). This interaction has the effect of reducing the flux of cation vacancies from the film/solution interface to the metal/film interface, and hence of increasing the breakdown voltage (V_c) and the induction time (t_{ind}) for pitting attack. By using experimental data for 18%Cr-1%Mo to calculate values for various parameters, we found that the SVIM accurately predicts the changes in V_c and t_{ind} for higher molybdenum concentrations in these ferritic stainless steels.

It is well known that minor alloying elements can have a profound effect on the susceptibility of a metal or alloy to localized corrosion, including pitting. By far the most important element is molybdenum, which, when added to austenitic and ferritic stainless steels at a concentration of a few percent, causes a significant shift in the breakdown (pitting) potential to more positive values (1-13). However, not all minor alloying elements are beneficial. For example, the addition of sulfur to carbon steels, particularly those containing manganese, increases the susceptibility of the matrix to localized attack (14). This has been attributed to the formation and subsequent electrodisolution of MnS particles in the passive film, but few details of how this occurs are known.

In spite of a considerable amount of work (1-13), no completely acceptable mechanism has been advanced to explain how small additions of elements such as molybdenum have such profound effects on the pitting resistances of metals and alloys. Thus, some workers propose that molybdenum increases the repassivation rate of the alloy and that because pitting occurs at a potential at which the breakdown rate exceeds the repassivation rate, the net effect is to shift the pitting potential in the positive direction. Other workers have advanced the hypothesis that molybdenum stabilizes a salt film (perhaps CrCl₂) on the metal surface, which, in turn, inhibits anodic dissolution of the underlying alloy and hence imparts some protective properties to the system. Still other researchers (8) have proposed that the beneficial effects of molybdenum and tungsten might be due to one, or to a combination of more than one, of the following: (i) thickening of the passive film, (ii) formation of a heteropoly-acid film that is less hydrolyzed and more readily polymerized than the existing passive film, (iii) an impeding of the adsorption of Cl⁻ onto the surface of the steel by increasing the oxygen affinity of the steel, or (iv) formation of an amorphous oxide film with a glassy structure. Bui *et al.* (8) finally attributed the beneficial effect of tungsten to the "formation of insoluble WO₃, which enhances the stability of oxide layers," but provided little experimental evidence that this is indeed the reason.

Over the past three years, we have developed the point-defect model for the growth and breakdown of passive films (15-17). This model has been particularly successful at explaining the growth kinetics of passive films on iron and nickel in aqueous solutions, and has been successful in accounting for chloride-induced breakdown of passive

films, in terms of the dependence of both the breakdown potential and induction time on the chloride activity (16). In this paper, we extend the point-defect model to explain the effects of certain alloying elements on the pitting behavior of metals and alloys. Since the basis for this extension is the interaction between the minor alloying element in the film (*e.g.*, Mo⁶⁺) and cation vacancies, this new model is hereafter referred to as the "solute-vacancy interaction model" (SVIM).

Pitting Characteristics of Metals and Alloys

Before discussing the theoretical basis for the solute/vacancy interaction model, it is advantageous to first summarize the experimental observations that must be explained by any satisfactory mechanism for the localized breakdown of passive films. These observations are as follows (18).

1. A critical pitting potential exists, above which localized attack is sustained, but below which pits spontaneously passivate.

2. In systems containing aggressive anions, such as Cl⁻, Br⁻, and I⁻, the breakdown potential (V_c) depends on the activity of the anion (a_x) according to

$$V_c = V_c^0 - B \log a_x \quad [1]$$

where B is normally greater than the Nernstian gradient of $2.303RT/nF$ (n = number of electrons involved in the dissolution reaction).

3. Breakdown involves an induction time between the point at which the aggressive anion is added to the system and when breakdown is observed. The induction time decreases with increasing pitting overpotential ($V - V_c$, where V is the applied voltage).

4. The addition of an aggressive anion, such as Cl⁻, to a solution in contact with a passive metal causes a "burst" of cations to be released from the oxide surface (19).

5. Little evidence exists that chloride or other aggressive anions penetrate barrier oxide films (18). However, penetration of "upper layer" films, which may form in certain systems as porous deposits on the base layer via dissolution/precipitation processes, may well occur, and this phenomenon probably accounts for the occasional report of chloride penetration into passive films.

6. A relationship appears to exist between the size of the aggressive anion, or its free energy of adsorption onto the passive film, and its ability to cause passivity breakdown.

7. In the case of Fe/Cr/Ni alloys, passivity breakdown coincides roughly with electrodisolution of chromium

* Electrochemical Society Active Member.

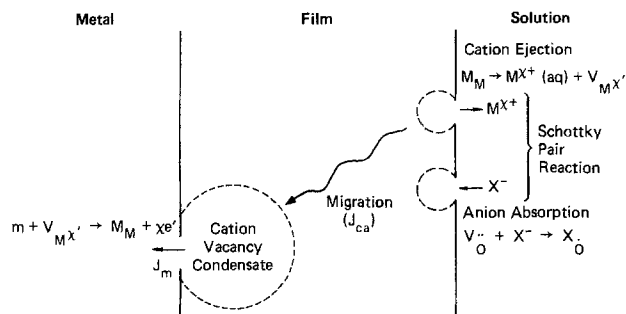


Fig. 1. Processes leading to the breakdown of passive films according to the point-defect model.

from the films (20), such that for potentials greater than the breakdown value (V_c) the concentration of Cr as Cr(III) in the film is greatly reduced. As we argue later, electrodisolution of Cr(III) leads to the formation of cation vacancies ($V_{Cr,3'}$) at the film/solution interface.

8. The addition of small amounts of certain alloying elements to the alloy phase, and, by implication, to the passive film, greatly increases the pitting resistance of the alloys. The most effective elements appear to be those that are capable of existing at oxidation states in excess of that for the cations in the host lattice. For example, Mo and W, both of which exist in the +6 state, are effective in protecting alloys (e.g., Fe/Cr) whose host cations in the passive film exist in the +3 state.

9. A synergistic relationship appears to exist between the chromium and molybdenum contents of the alloy, such that molybdenum is more effective at protecting Fe-Cr-Ni authentic stainless steels when the chromium content is high (6).

Any theory developed to account for the pitting characteristics of metals and alloys must explain the generalizations noted above, in addition to accounting for the properties of specific systems. However, the currently available theoretical treatments are either capable only of a semiquantitative explanation of some of the more important observations, or do not address the principal theme of this paper: the role of solutes in the film in determining the breakdown characteristics.

Solute-Vacancy Interaction Model

The solute vacancy interaction model described in this paper was developed to account for the effect of minor alloying elements, such as Mo and W, on the pitting resistance of iron-based alloys. The point-defect model (15-17), upon which the SVIM is based, proposes that passivity breakdown occurs because of an enhanced flux of cation vacancies from the film/solution interface to the metal/film interface, such that the excess vacancies arriving at the interface between the metal and the film cannot be absorbed into the metal at a high enough rate (Fig. 1). Accordingly, the vacancies accumulate to form a vacancy condensate at the metal/film interface, which then grows to a critical size. At this time, the film collapses locally to form a pit that will continue to grow provided that conditions are not conducive to repassivation. The point-defect model has led to the formulation of expressions for the two most important parameters that characterize the onset of pitting attack; the breakdown potential (V_c) and the induction time (t_{ind})

$$V_c = \frac{4.606RT}{\chi F \alpha} \log \left[\frac{J_m}{J_o u^{-\chi/2}} \right] - \frac{2.303RT}{\alpha F} \log [a_{Cl^-}] \quad [2]$$

$$t_{ind} = \xi' \left[\exp \left(\frac{\chi \alpha \Delta V}{2RT} \right) - 1 \right]^{-1} + \tau \quad [3]$$

where

$$\xi' = \xi / J_o u^{-\chi/2} [a_{Cl^-}]^{\chi/2} \exp \left(\frac{\chi F \alpha V_c}{2RT} \right) \quad [4]$$

$$\Delta V = V - V_c \quad [5]$$

and ξ is the critical size of the vacancy condensate, χ is the stoichiometry of the oxide ($MO_{\chi/2}$), and

$$u = \frac{N_v}{\Omega} \exp \left(\frac{\Delta G_{A-1}^0 - F\beta p H - F\phi_{fs}^0}{RT} \right) \quad [6]$$

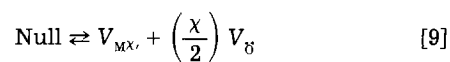
The parameter J_o is given by

$$J_o = \chi K D_{V_{M^{x'}}} [N_v/\Omega]^{(1+\chi/2)} \exp(-\Delta G_{sp}^0/RT) \quad [7]$$

where

$$K = \epsilon F/RT \quad [8]$$

and $D_{V_{M^{x'}}$ is the diffusivity of cation vacancies, N_v is Avogadro's number, Ω is the molar volume per cation of the film, α is the fraction of the total voltage applied between the metal and the solution that appears across the film/solution interface, F is Faraday's constant, ϵ is the electric field strength, ϕ_{fs}^0 and β are constants, and ΔG_{sp}^0 is the change in standard Gibbs energy for the Schottky pair reaction



The parameter ΔG_{A-1}^0 is the change in standard Gibbs energy for reaction [10]

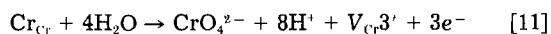


where $V_{M^{x'}}$ and V_{O} represent cation and anion vacancies, respectively, at the film/solution interface, and Cl_{O} represents a chloride ion (for example) occupying an oxide ion vacancy at the same location.

An enhanced flux of cation vacancies from the film/solution interface to the metal/film interface, which in turn may induce breakdown, can result from any process that gives rise to an increase in the concentration of cation vacancies at the film/solution interface. We identify three such processes below that we believe are of fundamental importance in determining the pitting characteristics of metals and alloys.

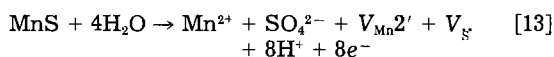
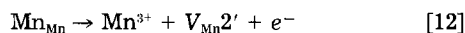
Anion adsorption.—Anions, which are comparable in size to oxide ions (e.g., Cl^-), may adsorb into anion vacancies at the film/solution interface according to reaction [10]. Thus, the removal of anion vacancies causes a concomitant increase in the concentration of cation vacancies according to the Schottky-pair reaction (Eq. [9]) and hence to an increase in the flux of these species toward the metal/film interface. Consideration of this process leads directly to Eq. [2] and [3] for V_c and t_{ind} , respectively. We believe that this is the primary process that is responsible for halide-induced breakdown because Eq. [2] and [3] are found to account quantitatively for the pitting of iron and nickel in sodium chloride solutions (16). This mechanism also accounts for the apparent dependence of V_c on the size of the aggressive anion, through the equilibrium constant for reaction [10].

Electrochemical cation dissolution.—In certain systems, cations may be ejected from the film/solution interface provided that the applied potential is high enough. This requires that the cation formed on dissolution exists in a higher oxidation state than it does in the film. An example of this phenomenon is the electrodisolution of chromium from the passive films on austenitic stainless steels



where Cr_{Cr} represents a chromium (III) cation occupying a cation site in the film at the film/solution interface, and $V_{\text{Cr},3'}$ represents the cation vacancy formed by the electrodisolution of that ion. Because this process is a charge-transfer reaction, the concentration of cation vacancies at the film/solution interface will increase dramatically (i.e., exponentially) above a certain voltage, which may be identified with the breakdown potential.

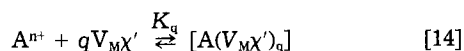
Electrodissolution of inclusions.—Pitting of carbon steels and stainless steels containing high concentrations of manganese sulfide inclusions frequently coincides with the dissolution of this second phase. In this case, pit nucleation probably occurs via the creation of cation vacancies according to reactions of the type



In the first case, the net effect of electrodisolution of the manganese from the sulfide particles is to create cation vacancies, which, in turn, may lead to film breakdown by condensing into voids at the metal/film interface. In the second case, destruction of the manganese sulfide matrix itself occurs, which will result in the formation of a local void. This void may then act as a nucleus for pitting attack.

Examination of Eq. [2]-[7] shows that any phenomenon that leads to a reduction in the diffusivity of the cation vacancies, $D_{V_{\text{Mn}}}$, will increase the breakdown potential (V_c) and induction time t_{ind} . Accordingly, the material should become more resistant to breakdown. In the SVIM, which is outlined below, we propose that complexes form between the mobile vacancies (V_{Mn}') and the immobile highly charged solute ions, such as Mo^{6+} and W^{6+} .

The interaction between cation vacancies (V_{Mn}') and a solute ion (A^{n+}) in a passive film can be represented as a chemical equilibrium



where K_n is the equilibrium constant

$$K_n = [P]/[A][V]^q \quad [15]$$

in which we represent the complex, solute, and vacancy concentrations by [P], [A], and [V], respectively. The condition for breakdown remains unchanged from that stated previously (16)

$$(J_{\text{ca}} - J_{\text{m}})_{\text{m}/f} (t_{\text{ind}} - \tau) > \xi \quad [16]$$

where J_{ca} and J_{m} are the fluxes of cation vacancies in the film and in the metal, respectively, at the metal/film interface, and τ is a relaxation time. The problem is now to compute J_{ca} as a function of solute concentration, recognizing that the concentration of cation vacancies is reduced by complex formation compared with the solute-free case.

Assuming that the complexes are immobile, the flux of cation vacancies in the film at the metal/film interface can be written as

$$(J_{\text{ca}})_{\text{m}/f} = -D_{V_{\text{Mn}}'} \left[\frac{\partial(n_v - q[P])}{\partial x} \right]_{\text{m}/f} - e\chi D_{V_{\text{Mn}}'} \frac{F\epsilon}{RT} (n_v - q[P])_{\text{m}/f} \quad [17]$$

where e is the electronic charge, ϵ is the electric field strength [assumed to be constant and independent of applied voltage (15-17)], and n_v is the concentration of vacancies that would exist if the solute was not present. The concentration of the complex can be obtained by solving Eq. [18], which is itself a restatement of Eq. [15]

$$[P] = K_n \{n_A - [P]\} \{n_v - q[P]\}^q \quad [18]$$

where n_A is the stoichiometric concentration of solute in the film.

Equation [17] can be rearranged to yield

$$(J_{\text{ca}})_{\text{m}/f} = -D \left(\frac{\partial n_v}{\partial x} \right) + D^* K^* (-e\chi) n_v \quad [19]$$

where D^* is the modified diffusivity coefficient and K^* is the modified K value ($K = F\epsilon/RT$). These functions must be calculated for specific values of q , i.e., for

various complex configurations. In this work, only $q = 1$ is considered, in which case

$$K^* = \frac{K \left(1 - \frac{\alpha}{2n_v} \pm \frac{1}{n_v} \left(\frac{\alpha^2}{4} - n_A n_v \right)^{(1/2)} \right)}{\frac{1}{2} \left\{ 1 \pm \left(\frac{\alpha}{2} - n_A \right) / \left(\frac{\alpha^2}{4} - n_A n_v \right)^{(1/2)} \right\}} \quad [20]$$

$$D^* = D \left[\frac{1}{2} \pm \frac{1}{2} \left(\frac{\alpha^2}{4} - n_A n_v \right)^{-1/2} \cdot \left(\frac{\alpha}{2} - n_A \right) \right] \quad [21]$$

where

$$\alpha = n_A + \frac{1}{K_q} + n_v \quad [22]$$

Only the real roots that produce positive values for D^* and ϵ^* are considered.

In order to quantify the effect of the solute on the pitting characteristics of an alloy, it is necessary to compute the change in breakdown potential and induction time as a function of solute (molybdenum) concentration. The appropriate functions are, therefore, given by

$$V_c(X_{\text{Mo}}) - V_c(X_{\text{Mo}} = 0) = \frac{4.606RT}{\chi F \alpha} \log \left[\frac{KD}{K^* D^*} \right] \quad [23]$$

$$\frac{t(X_{\text{Mo}})}{t(X_{\text{Mo}} = 0)} = \frac{\left[\xi + \tau \hat{J}_0 u^{-(\chi/2)} [\text{Cl}^-]^{(\chi/2)} \exp \left(\frac{\chi F \alpha V_c}{2RT} \right) \right] J_0}{\hat{J}_0 \left[\xi + \tau J_0 u^{-(\chi/2)} [\text{Cl}^-]^{(\chi/2)} \exp \left[\frac{\chi F \alpha V_c}{2RT} \right] \right]} \quad [24]$$

where \hat{J}_0 is defined by Eq. [7] with $D_{V_{\text{Mn}}'}$ and K replaced by $D^*_{V_{\text{Mn}}'}$ and K^* , respectively.

This last equation can be simplified for $t \rightarrow 0$ to read

$$\frac{t(X_{\text{Mo}})}{t(X_{\text{Mo}} = 0)} = \frac{KD}{K^* D^*} \quad [25]$$

The simplification $\tau \rightarrow 0$ is considered in this work.

Results and Discussion

Plots of V_c and the induction time ratio are shown in Fig. 2 and 3, respectively, as functions of X_{Mo} . In the first case, two sets of parameters n_v , q , and K_q have been used, and the values of n_v and K_q are such that the calculated values of $V_c(X_{\text{Mo}}) - V_c(X_{\text{Mo}} = 0)$ coincide with the experimental data for the breakdown potential for the 18%Cr-1%Mo alloy. As can be seen, reasonable agreement is obtained between the calculated and experimental data at other molybdenum concentrations, particularly considering the uncertainty in the experimentally determined breakdown potentials ($\pm 0.1V$). This model also predicts that the induction time is increased by complex formation between the solute and cation vacancies, as shown in Fig. 3. Thus, molybdenum not only shifts the breakdown voltage to more positive values, but also increases the induction time at any given breakdown overvoltage.

The point-defect model and the solute/vacancy interaction model discussed above have provided quantitative or semiquantitative explanations for most of the correlations discussed in the previous section. For example, the point-defect model (16) accounts quantitatively for the first six generalizations, and the SVIM developed in this work accounts for the next two, at least semiquantitatively. No explanation is currently available for the last observation (the synergistic relationship between the Cr and Mo contents of the alloy), but we believe that it may be due to the ability of chromium to establish a uniform molybdenum distribution in the film. This question will be addressed in a later paper.

Finally, we note that interactions between solutes (impurities) and charged species (eg. electrons and holes) in semiconductors and between point defects and solutes in crystalline solids have been well characterized in the literature (21). Accordingly, a firm theoretical basis exists for the SVIM developed in this work.

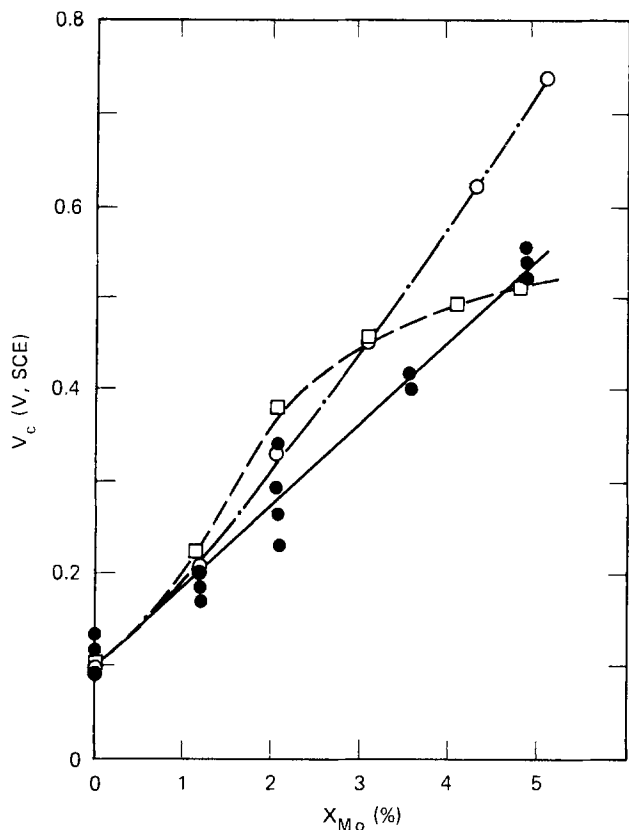


Fig. 2. Pitting potentials for 18% Cr ferritic stainless steels in 1M NaCl at 25°C. ●, ■: Lizlovs and Bond (6). This work: (○) $K_q = 10^{-4}$, $n_v = 4 \times 10^{20} \text{ cm}^{-3}$, $q = 1$; (□) $K = 10^{-17}$, $n_v = 4 \times 10^{19} \text{ cm}^{-3}$, $q = 1$.

Acknowledgments

The authors gratefully acknowledge the financial support of this work by the Office of Naval Research under Contract N00014-82-K-0265. This work was carried out at the Fontana Corrosion Center, Department of Metallurgical Engineering, Ohio State University, Columbus, Ohio.

Manuscript received Aug. 15, 1984.

SRI International assisted in meeting the publication costs of this article.

REFERENCES

1. R. C. Newman and E. M. Franz, *This Journal*, **131**, 223 (1984).
2. J. N. Wanklyn, *Corros. Sci.*, **21**, 211 (1981).
3. K. Hashimoto, K. Asami, and K. Teramoto, *ibid.*, **19**, 3 (1979).
4. R. Goetz and D. Landolt, *Electrochim. Acta*, **27**, 1061 (1982).

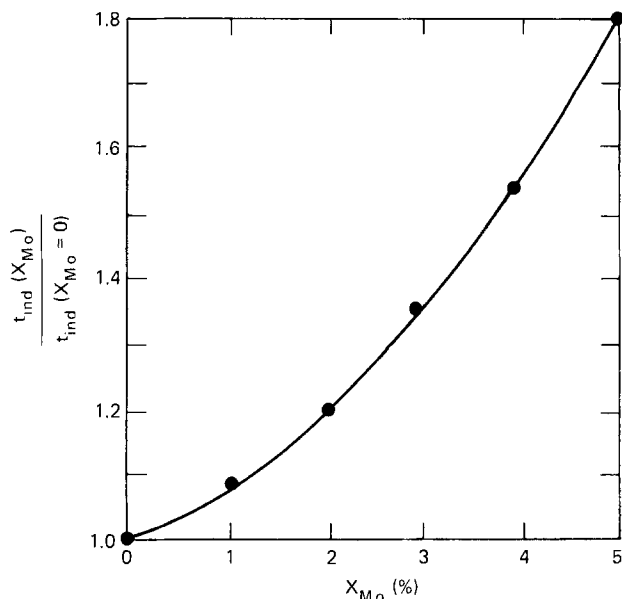


Fig. 3. Effect of molybdenum on induction time for pit initiation according to the SVIM ($K_q = 10^{-4}$, $n_v = 4 \times 10^{20} \text{ cm}^{-3}$, $q = 1$).

5. B. Brox and I. Olefjord, in "Proceedings of the 5th International Symposium on Passivity," Banbannes, France (1983).
6. E. A. Lizlovs and A. P. Bond, *This Journal*, **122**, 720 (1975).
7. J. B. Lumsden, in "Passivity of Metals," R. P. Frankenthal and J. Kruger, Editors, p. 730, The Electrochemical Society Corrosion Monographs Series, Princeton, NJ (1978).
8. N. Bui, A. Irhzo, F. Dabosi, and Y. Limouzin-Maire, *Corrosion*, **39**, 491 (1983).
9. L. Colombier, "Molybdenum in Stainless Steels and Alloys," Climax Molybdenum Co. (1968).
10. K. Sugimoto and Y. Sawada, *Corros. Sci.*, **17**, 425 (1977).
11. I. L. Rosenfeld, *Corrosion*, **37**, 371 (1981).
12. A. E. Yaniv, J. B. Lumsden, and R. W. Staehle, *This Journal*, **124**, 490 (1977).
13. M. Seo, Y. Matsumura, and N. Sato, *Trans. J.I.M.*, **20**, 501 (1979).
14. S. Smialowska, *Corrosion*, **28**, 388 (1972).
15. C. Y. Chao, L. F. Lin, and D. D. Macdonald, *This Journal*, **128**, 1187 (1981).
16. L. F. Lin, C. Y. Chao, and D. D. Macdonald, *ibid.*, **128**, 1194 (1981).
17. C. Y. Chao, L. F. Lin, and D. D. Macdonald, *ibid.*, **129**, 1874 (1982).
18. M. Janik-Czachor, *ibid.*, **128**, 513C (1981).
19. K. E. Heusler and L. Fischer, *Werkstoff. Korros.*, **27**, 551 (1976).
20. B. C. Syrett, D. D. Macdonald, and H. Shih, *Corrosion*, **36**, 130 (1980).
21. H. Reiss, *J. Chem. Phys.*, **21**, 1209 (1953).

Fluctuation Phenomena Studies in Chemically Sensitive Field Effect Transistors

I. Corrosion of Aluminum

Zheng Kang Li, Johannes M. Reijn, and Jiří Janata*

Department of Bioengineering, University of Utah, Salt Lake City, Utah 84112

ABSTRACT

It is shown that chemically sensitive field effect transistors can be used to study stochastic processes at the solution/solid interface which is not at equilibrium. Auto spectral densities and coherence functions for corrosion of aluminum-silicon alloy at zero-net current conditions have been obtained.

Noise in chemically sensitive field effect transistors (CHEMFET) originates both from the solid-state part of the device and from the electrochemical processes at each interface. In our previous work, we have shown that the analysis of noise of CHEMFET's with various ion selective membranes at chemical equilibrium yields an information about the exchange currents at the solution/membrane interface and about the bulk impedance of the membrane itself (1).

High signal-to-noise ratio, small input capacitance, small surface area of the electrode, and low parasitic impedance are the attractive features of CHEMFET's for the study of stochastic processes in electrochemical systems. Because each chip contains at least two transistors, it is possible to use multichannel analysis methods. These methods can yield a unique additional information about the whole system, and they reduce contributions from the solid-state part of the system.

In the first part of this series, we shall outline the theory of noise analysis in CHEMFET's and describe the experimental arrangement which was used in this and the subsequent studies.

Principle of Operation

The basic operation of CHEMFET's has been described elsewhere (2). The output, drain-to-source current I_D , for a n -channel transistor operated in the nonsaturated region [$V_D < (V_G - V_T)$] is

$$I_D = K \left[(V_G - V_T) - \frac{V_D}{2} \right] V_D \quad [1]$$

and in the saturation region where $V_D > (V_G - V_T)$

$$I_D = K' (V_G - V_T)^2 \quad [2]$$

The constants K and K' are characteristic of the geometry and material properties of the transistor shown in Fig. 1. The transconductance of the transistor is defined as

$$g_m = \left(\frac{\partial I_D}{\partial V_G} \right)_{V_D} \quad [3]$$

Because the magnitude of the solid-state part of the noise depends on the value of the drain current, it is preferable to operate the transistor in so-called feedback mode in which the average drain current is kept constant. In this case, the gate voltage fluctuations $v(t)$ are transformed into the drain current fluctuations $i(t)$ through the relationship

$$i(t) = g_m v(t) \quad [4]$$

Fluctuation Analysis Theory

In this section, a brief review of theory relevant to the present experiments is given. For a fuller account of the theoretical background, the reader is referred to textbooks (3-5). The drain current in the channel $I_D(t)$ of a CHEMFET can be expressed as (1)

$$I_D(t) = \bar{I} + i(t) \quad [5]$$

where \bar{I} is the mean value of the current and $i(t)$ is the fluctuating part of the drain current (noise). In the remaining part of this text, we will consider the fluctuations in the drain current only and for the sake of notation describe drain current fluctuations as $x(t)$ or $y(t)$.

When one is interested in the origin of the fluctuations, characterization of the signal (by means of parameters, for instance) is necessary. Before any meaningful signal characterization can be attempted, the signal has to be qualified.

This qualification can be carried out in the following way: Fig. 2 shows graphically the concept of a probability density function (PDF), which is defined for the signal $x(t)$ as

$$p(x) = \lim_{\Delta x \rightarrow 0} \frac{\text{Prob}[x < x(t) < x + \Delta x]}{\Delta x}$$

In general, $p(x, t)$ is a function of time. If this is not the case, that is when $p(x, t_1) = p(x, t_2)$ for all t_1, t_2 , it is said that the fluctuating signal is stationary. By its definition, the PDF $p(x, t)$ is normalized, i.e., $\int p(x, t) dx = 1$, where the integration is carried out over all values of the signal $x(t)$. For the PDF statistical moments can be calculated in the usual way, e.g., Eq. [6]. A large class of signals is formed by signals with a gaussian PDF, as illustrated in Fig. 2. When a fluctuating signal of this class has "direct" statistical moments defined by

Mean value

$$\langle x(t) \rangle = \lim_{T \rightarrow \infty} \left(\frac{1}{T} \int_0^T x(t) dt \right) \quad [6]$$

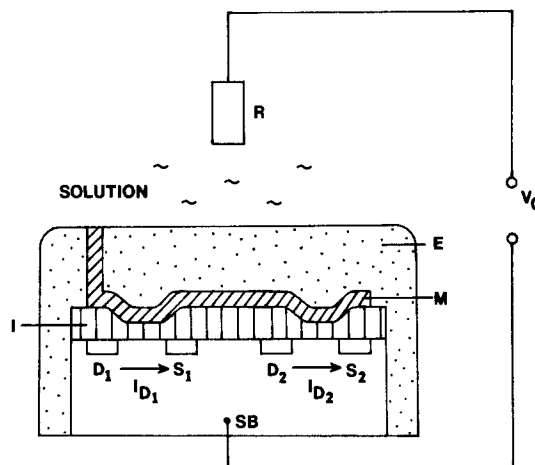


Fig. 1. Schematic diagram of the transistor chip (drawing not to scale). D: drain. S: source. I: insulator. M: metal. E: encapsulant. R: reference electrode. SB: substrate. I_D is drain-to-source current, and V_G is the applied gate voltage.

* Electrochemical Society Active Member.

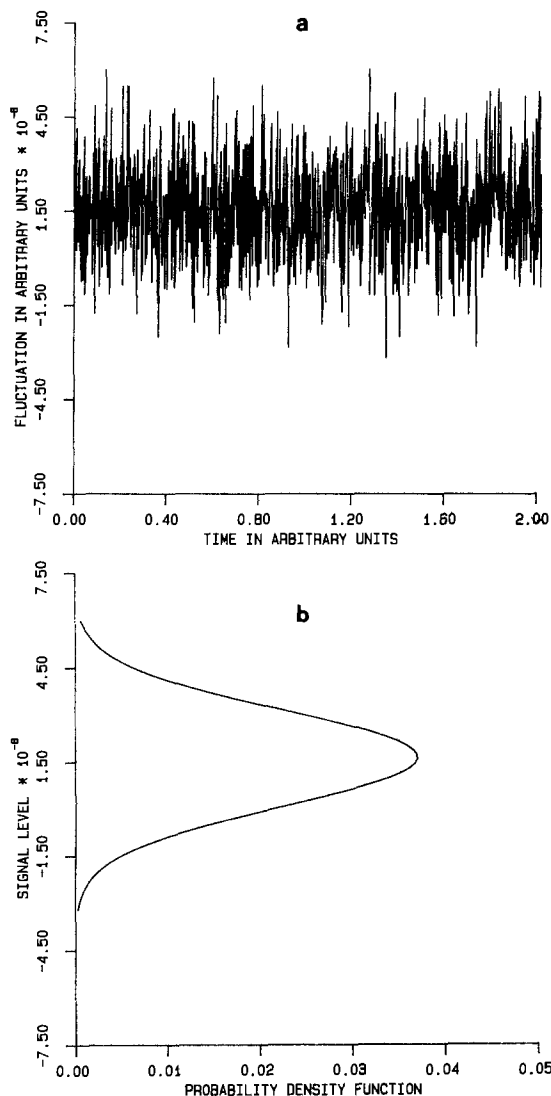


Fig. 2. Illustration of probability density function (PDF) for an arbitrary signal. a: Time record. b: PDF.

Mean value of the square

$$\langle x^2(t) \rangle = \lim_{T \rightarrow \infty} \left(\frac{1}{T} \int_0^T x^2(t) dt \right) \quad [7]$$

Variance

$$\sigma_t^2 = \langle x^2(t) \rangle - \langle x(t) \rangle^2 \quad [8]$$

When the measuring time is taken long enough (usually a limit $T \rightarrow \infty$ is involved) and the above defined moments equal the corresponding moments of the PDF for a stationary fluctuation, the signal is ergodic.

Frequency Domain Analysis

When the signal is stationary and ergodic, its parameters are independent of the observation time. This property allows for analysis of signal parameters from individual time records, e.g., mean and variance or from many different records as, for example, for frequency analysis using sampled portions of the signal of finite length (to be referred to as ensembles).

Suppose that one ensemble is represented by N samples, taken at time intervals Δt ; N is usually an integer power of 2. From the sequence of samples one calculates a discrete Fourier transform (DFT), usually using a fast Fourier transform algorithm (FFT) to save computation time (7). From the Fourier components estimates of spectral densities $G_x(k)$ are calculated as discrete frequencies $k f_s$, unique up to $k = N/2 - 1$. The sequence $G_x(k)$ is a discrete representation of the auto spectral density function for the signal $X(t)$. The true, continuous, signal-continuous, single-sided auto spectral density $G_x(f)$ is defined as

$$G_x(f) = 2 \lim_{T \rightarrow \infty} \frac{1}{T} \int_0^T X_k(f, T)^2 dT \quad [9]$$

The random part of the error in the spectral estimates is given by Bendat and Piersol (3) for the case of a signal with a gaussian PDF as a normalized standard error

$$\epsilon_T = \sqrt{2/M} \quad [10]$$

where M equals the number of degrees of freedom in statistical sense (each time record has two degrees of freedom, due to the fact that the spectral estimate has a real and an imaginary component). This implies that the standard deviation in a spectral estimate calculated from one time record is 100%, independent of the length of the record.

The number of degrees of freedom can be increased in two ways: by smoothing of the estimates at the expense of spectral resolution or by segment averaging. The latter technique requires a longer observation time, but preserves the spectral resolution, and is, therefore, adopted in this paper.

The bias part of the error in the spectral estimates is a function of the "shape" of the spectral density function. For flat spectra, $1/f$ noise, and lorentzian spectra this error is negligibly small at the frequencies of interest (3).

From the definition of the spectral density, it follows immediately that if a signal can be considered to be the sum of some stationary, ergodic signals the spectral density of the sum equals the sum of the spectral densities of the individual signals

$$\begin{aligned} x(t) &= \sum x_i(t) \quad i = 1, 2, 3 \dots \\ G_x(f) &= \sum G_{x_i}(f) \quad i = 1, 2, 3 \dots \end{aligned} \quad [11]$$

In a previous paper (1), this property was used by Haemmerli *et al.* to discriminate between noise originating in different parts of the CHEMFET/electrochemical cell system. It is clear from Eq. [11] that as soon as one of the different noise sources is stronger than the others this discrimination becomes impossible. The same conclusion was reached by Haemmerli.

Two-Channel Approach

In order to reduce the device noise in a CHEMFET/electrochemical system, a two-channel approach was developed based on the following reasoning: suppose that two CHEMFETs have an electrochemical noise source in common but that their "solid-state" noise is not correlated. For the fluctuations in the two drain currents, we can write

$$\begin{aligned} x(t) &= d_1(t) + e(t) \\ y(t) &= d_2(t) + e(t) \end{aligned} \quad [12]$$

$d_1(t)$ is the device noise for FET1, $d_2(t)$ is the device noise for FET2, and $e(t)$ is the (electrochemical) noise common to both channels. The true continuous single-side spectral density functions are

$$\begin{aligned} G_x(f) &= [D_1(f) + E(f)][D_1(f) + E(f)]^* \\ G_y(f) &= [D_2(f) + E(f)][D_2(f) + E(f)]^* \\ G_{xy}(f) &= [D_2(f) + E(f)][D_1(f) + E(f)]^* \end{aligned} \quad [13]$$

where (*) denotes a complex conjugate. $D_1(f)$ and $D_2(f)$ are Fourier transforms of signals $d_1(t)$ and $d_2(t)$, and $E(f)$ is the Fourier transform of the noise $e(t)$ common to both channels. If we drop the frequency dependence for convenience of notation, expanded Eq. [13] becomes

$$\begin{aligned} G_x &= D_1 D_1^* + E D_1^* + D_1 E^* + E E^* \\ G_y &= D_2 D_2^* + E D_2^* + D_2 E^* + E E^* \\ G_{xy} &= D_2 D_1^* + D_2 E^* + E D_1^* + E E^* \end{aligned} \quad [14]$$

If d_1 , d_2 , and e are uncorrelated noise sources, all cross-terms in Eq. [14]

$$E D_1^* = D_1 E^* = E D_2^* = D_2 E^* = D_1 D_2^* = D_2 D_1^*$$

are zero and hence

$$\begin{aligned} G_x &= D_1 D_1^* + EE^* \\ G_y &= D_2 D_2^* + EE^* \\ G_{xy} &= EE^* \end{aligned} \quad [15]$$

The cross spectral density function is thus a function of electrochemical noise common to both channels only.

A derived quantity is the coherence function defined as

$$\gamma(f)^2 = \frac{|G_{xy}(f)|^2}{G_x(f) G_y(f)} \quad [16]$$

Theoretically, this function has a range from zero for no coherence to one for complete coherence. It can be viewed as a measure for the amount of signal common to both channels.

The same considerations as above apply to the statistical errors in estimates of the auto spectral density functions obtained by Fourier analysis of time records. Error estimates in the cross power spectral density and in the coherence function are dependent on the amount of coherence between the two signals and are relatively complicated (3, 8). The number of degrees of freedom is important especially at low levels of coherence, as Table I shows.

Experimental

The transistor chips used in this study are identical to those used previously (1). They were mounted on 1.5 mm diam PVC tubing and encapsulated with a high grade epoxy resin (Epon 826 with Jeffamine D230 crosslinker). The two gates used for the cross-correlation measurements are connected as shown in Fig. 1. In this study, we have used 25 μm diam Al-Si (1%) wire, the geometrical area of the metal exposed to the solution was approximately $7 \times 10^{-6} \text{ cm}^2$. During etching experiments, this area was renewed by cutting the sample perpendicularly to the wire axis after each experiment. Unless stated otherwise, the measurements were done at room temperature. The actual temperature at the sensor site was determined by precalibration of one of the MOSFET's available on the transistor chip.

The noise measurements were done under two sets of experimental conditions: in pH 9.0, 0.1M borate buffer (no corrosion) and in etching solution consisting of 1600 ml H_3PO_4 (35% Fisher), 100 ml HNO_3 (69% Fisher), 100 ml acetic acid (glacial, Fisher), and 200 ml of water. This solution was diluted with distilled deionized water for concentration dependence studies as necessary. The solutions were degassed with nitrogen and stored in glass bottles under nitrogen. They were delivered to the transistor under constant pressure using the manifold shown in Fig. 3. The volumetric flow rate was controlled by adjusting the nitrogen pressure. Because of the irregular geometry of the encapsulated sample, the absolute face velocity of the flowing solution at the sample surface could not be determined. The electrical circuits used for monitoring the drain-to-source current are shown for a two-channel operation in Fig. 4b. The output signals were amplified with low noise, variable gain (1-10 K) preamplifiers (Princeton Applied Research, Model PAR 113A) and analyzed using Hewlett-Packard Signal Analyzer (HP 3582A). The accessible frequencies of this measuring setup were between 0.8 Hz and 25 kHz.

Results

In the preliminary experiments, we have used diluted hydrochloric acid (0.1 mM to 0.1M) has the reaction me-

Table I. Error estimate in coherence function at 99% confidence level and for coherence = 0.01

Degrees of freedom	Lower limit	Upper limit
100	0	0.06
1000	0.002	0.022
10000	0.007	0.013

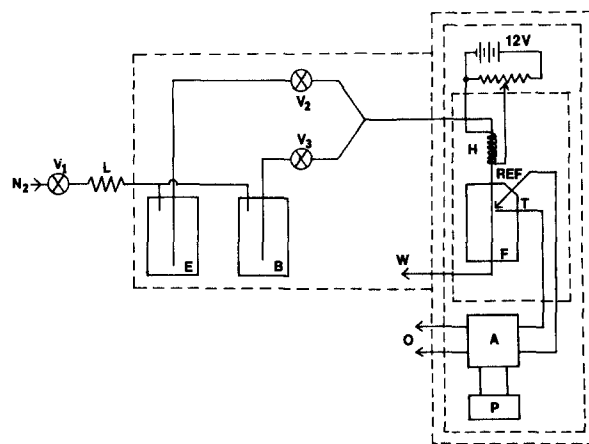


Fig. 3. Experimental arrangement. A: amplifier. P: battery pack. T: transistor under study. REF: reference electrode. F: flow cell. H: heater. S: solution inlet. W: outlet to waste. O: amplifier output. V: control valves. L: hydrodynamic load. E: etching solution. B: buffer. (---) Faraday shielding.

dium. For concentrations above 5 mM HCl, the reaction was too violent, yielding bubbles of hydrogen which created problems in the flow cell. For concentrations below 1 mM, the change of surface pH due to low buffering capacity led to irreproducible results. Nevertheless, the auto spectral densities in these experiments exhibited a pronounced maximum in the region between 1-10 Hz which increased with increasing concentration of the acid from $5 \times 10^{-18} \text{ A}^2 \text{ Hz}^{-1}$ for 0.1 mM HCl to $5 \times 10^{-17} \text{ A}^2 \text{ Hz}^{-1}$ for 0.1M HCl.

In order to control the surface concentrations better a buffered solution normally used for etching aluminum in the integrated circuit fabrication process (9) has been used in various dilutions. For undiluted solutions at room temperature, the typical etching rate is less than $1000 \text{ \AA min}^{-1}$. Therefore, for the duration of our experiment (~ 10 min), the removal of the material has not significantly altered the flow pattern around the sample.

The auto spectral densities for etching solutions of various dilutions are shown in Fig. 5. These are the results of 128 averages. There is a clear evidence of a lorentzian character of the spectrum (slope: -2) for the two highest concentrations. The intensity of the spectrum increases with the increasing concentration of the etching solution, in general agreement with the results obtained with hydrochloric acid.

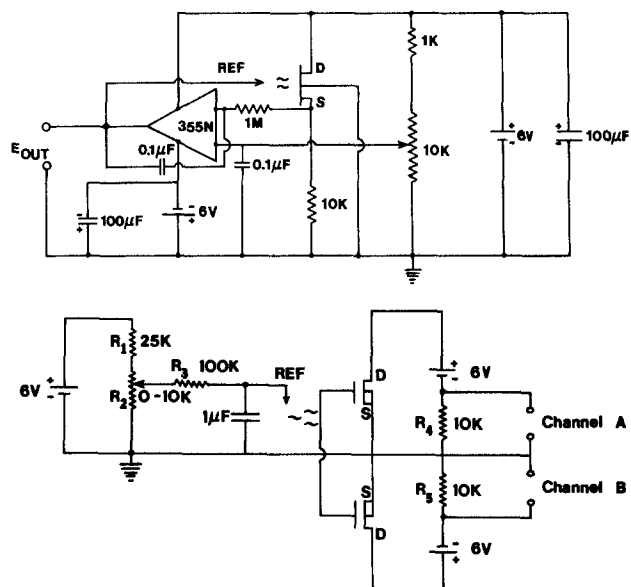


Fig. 4. Circuit used in two-channel measurements. REF: reference electrode. E_{OUT} : output voltage. D: drain. S: source.

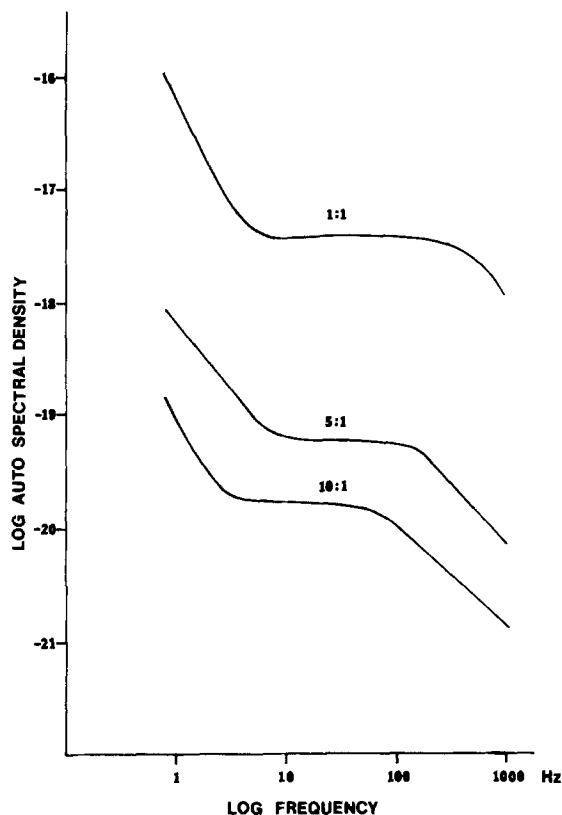


Fig. 5. Autospectral density for corrosion of aluminum at three different concentrations of etching solution. Vertical axis current density units are in A^2/Hz .

The coherence function (Eq. [16]) for the data presented in Fig. 5 is shown in Fig. 6. It again shows the expected concentration dependence. In buffer solution where no significant corrosion takes place, its value is 0.025 and independent of frequency up to 1 kHz. The fact that the coherence has a nonzero value indicates the presence of common electrochemical noise, which probably originates from the pseudo-exchange current (nonequilibrium) which takes place at the metal/solution interface. This statement has to be taken within the context of the statistical accuracy of the coherence function (Table D).

Conclusion

In this paper, we have outlined the framework for study of nonequilibrium fluctuation phenomena in chemically sensitive field effect transistors from both the theoretical and the experimental points of view. The corrosion of

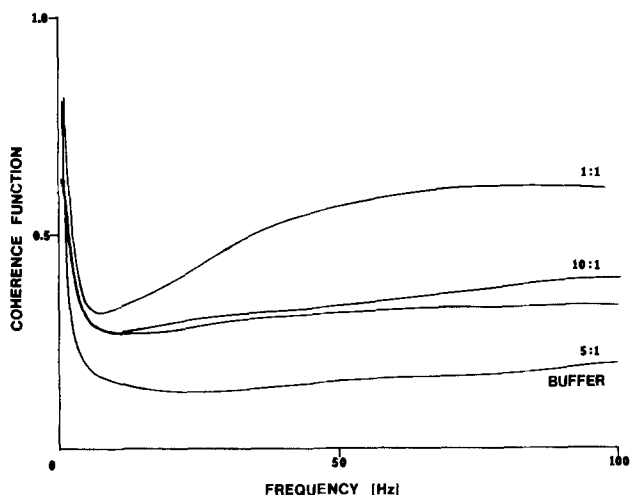


Fig. 6. Coherence function obtained in two-channel mode for three different concentrations of etching solution and for buffer solution.

aluminum/silicon alloy is used only as an illustration that this approach is feasible, and no interpretation of the experiments is attempted. The corrosion of metals and semiconductors is commonly studied by conventional electrochemical means in which the important corrosion parameters are derived from current-voltage characteristics which are extrapolated to zero net current conditions. Bertocci (10-12) has introduced the concept of coherence to corrosion measurements. It has allowed him to determine the causal relationship between current and voltage. The fundamental difference in our measurements is that they are performed at zero-net current condition. Thus, the only independent variables are surface concentrations, temperature, and pressure. This approach is possible because the coupling between the electrochemical process and the interface and the observable (fluctuation of the drain-to-source current) is through the electric field. In the following paper, we will show that this mode of operation yields a unique approach to the study of electrochemical reactions of various materials, including insulators.

Acknowledgments

This work was supported by the contract from the Office of Naval Research. We are indebted to our colleagues, Professors J. J. Brophy and Martin Fleischmann for stimulating discussions and encouragement.

Manuscript submitted July 16, 1984; revised manuscript received Oct. 1, 1984.

The University of Utah assisted in meeting the publication costs of this article.

LIST OF SYMBOLS

$D(f)$	Fourier transform of device noise
$E(f)$	Fourier transform of electrochemical noise
$d(t)$	device noise in time domain
$e(t)$	electrochemical noise in time domain
V_D	drain-source voltage
V_G	gate-source voltage
V_T	threshold voltage
I_D	drain current
\bar{I}_D	average value of drain current
$i(t)$	fluctuation in drain current in time domain
g_m	transconductance of FET
K, K'	constants of FET
$v(t)$	fluctuations in gate voltage
$x(t)$	fluctuating signal in time domain
$y(t)$	fluctuating signal in time domain
$p(x, t)$	probability density function for $x(t)$
$\langle x \rangle$	mean value of signal $x(t)$
$\langle x^2 \rangle$	mean value of the square for $x(t)$
σ_x	variance of $x(t)$
$G_x(f)$	auto spectral density for signal $x(t)$
$G_y(f)$	auto spectral density for signal $y(t)$
$G_{xy}(f)$	cross spectral density for signals $x(t)$ and $y(t)$
N	number of samples in finite length discrete time record
M	number of averages in spectral density estimate
$\gamma^2(f)$	coherence function

REFERENCES

1. A. Haemmerli, J. Janata, and J. J. Brophy, *This Journal*, **129**, 2307 (1982).
2. J. Janata and R. J. Huber, in "Ion Selective Electrodes in Analytical Chemistry," Vol. 2, H. Freiser, Editor, Plenum Press, New York (1980).
3. J. S. Bendat and A. G. Piersol, "Random Data: Analysis and Measurement Procedures," Wiley-Interscience, New York (1971).
4. R. N. Bracewell, "The Fourier Transform and its Applications," 2nd ed., McGraw-Hill, New York (1978).
5. C. W. Gardiner, "Handbook of Stochastic Methods for Physics, Chemistry and the Natural Sciences," Springer-Verlag, Berlin (1983).
6. M. Abramowitz and I. A. Stegun, "Handbook of Mathematical Functions," Chap. 26, Dover, New York (1963).
7. J. W. Cooley and J. W. Tukey, *Math. Comp.*, **19**, 297 (1965).
8. V. A. Benignus, *IEEE Trans. Audio Electroacoust.*, **au-17**, 145 (1969).

9. D. J. Elliott, "Integrated Circuit Fabrication Technology," Chap. 11, McGraw-Hill, New York (1982).
10. U. Bertocci, *This Journal*, **127**, 1931 (1980).
11. U. Bertocci, *ibid.*, **128**, 520 (1981).
12. U. Bertocci, in "Proceedings of the Sixth International Conference on Noise in Physical Systems," p. 328, National Bureau of Standards, Washington, DC (1981).

Fluctuation Phenomena Studies in Chemically Sensitive Field Effect Transistors

II. Corrosion of Silicon Oxynitride

Zheng Kang Li, Johannes M. Reijn, and Jiří Janata*

Department of Bioengineering, University of Utah, Salt Lake City, Utah 84112

ABSTRACT

Drain current fluctuations in a field effect transistor caused by the corrosion of silicon oxynitride have been measured and analyzed. It has been shown that under wet etching conditions the surface of silicon oxynitride becomes conducting. The equivalent electrical circuit corresponding to this situation has been proposed.

Analysis of equilibrium (1) and nonequilibrium noise (2) in CHEMFET's has shown that electrochemical information can be obtained from the solution/membrane (1) or solution/metal (2) interface without external electrical perturbation. The system is allowed to tell its own story, so to speak. The unique feature of CHEMFET lies in the fact that the electrochemical signal is coupled through the electric field directly to the transistor channel. In other words, there is no need for connecting the interface under study to the amplifier through a metal lead, which would introduce a parasitic impedance into the measurement. Under these conditions, any material, conductor, semiconductor, or insulator, deposited directly over the gate of the CHEMFET can be studied by this technique. In this paper, we will describe the study of electrochemical processes which are taking place at the surface of the gate insulator during a wet etching reaction. The theoretical background for this work has been outlined in the first paper of this series (2).

Experimental

Transistors used in this study were of the same type as used previously (2) except for the aluminum layer [Fig. 1 of Ref. (2)] which was not present. The size of the gates was $20 \times 400 \mu\text{m}$, and they were spaced $700 \mu\text{m}$ apart. The area of the chip exposed to the etching solution was typically $0.9\text{--}1.0 \text{ mm}^2$. A slightly different instrumentation approach has been used. The outputs from the two preamplifiers (PAR 113A) are connected to the signal analyzer HP 3582A (Hewlett-Packard) and also to a digitizing oscilloscope (Tektronix 5225). Signals were recorded on an FM tape recorder (Hewlett-Packard Model 3964A). This arrangement allows for on-line spectral analysis using the spectrum analyzer and for off-line analysis using our computer system.

The computer system used is an LSI 11/23-based minicomputer (Digital Equipment) running under an RT-11 5.1 operating system. Storage facilities are a 10 megabyte RL01 hard disk (Digital Equipment) and a dual RX02 floppy disk system (Data Systems Design) mainly used for backup purposes. Standard programming language is FORTRAN IV version 2.6 (Digital Equipment). We developed a Ratfor preprocessor to extend this language (3).

The computer performs a variety of tasks, as follows.

Data acquisition.—A Tektronix 5223 digitizing oscilloscope is connected through an HP-1B instrument interface bus. This arrangement allows for acquisition of two channel time records of 1016 points each, digitized to 10

bits, including sign. During the time needed for data transfer, the sampling is interrupted; thus, a discontinuous time series is obtained. As pointed out in the previous paper, this can be allowed for if the stochastic process is stationary and ergodic. For the nonstationary cases, we are studying alternatives to obtain continuous time series.

Data qualification.—Software is available to inspect time records for stationarity. The main test performs a fit of experimental data to a gaussian PDF. This test enables one to distinguish between "true" signals and unwanted disturbances. Furthermore, spectral analysis of nonstationary data yields results which have to be regarded very critically with respect to their interpretation. Use of the spectrum analyzer yields only averaged spectral estimates, and, therefore, information is lost in this computation. Even if the experimental data are expected to be stationary (for instance in equilibrium noise measurements) it is good practice to subject (part of) the time history of the experiment to statistical tests (4).

Data processing.—Programs are available for spectral analysis yielding estimates of the auto and cross spectral densities and the coherence function. In the time domain, auto and cross correlations can be calculated for individual time records.

Data presentation.—The software supports a HP 7220C digital plotter (Hewlett-Packard) for permanent copies of graphs and a graphical terminal MG8000 (Wicat) for quick visualization of results.

Data modeling.—The main programs in this group perform curve fitting as mentioned above for the PDF. The software is adapted from Bevington (5) and is written using the Marquardt algorithm.

Copies of programs are available upon request.

Solutions used in this study were $0.1M$ pH 7.00 phosphate buffer and etching solution containing 100 ml 85% w/w H_3PO_4 , A.C.S. Certified, Fisher and 5 ml 48-50% w/w HBF_4 , Purified, Fisher. Solutions were handled using the same manifold as described in the first paper of this series (2).

Results

The time records of the noise in buffer solution (equilibrium) and at 55°C in the etching solution (corrosion) are shown in Fig. 1. The temperature for etching of silicon oxynitride under normal processing conditions is 180°C . At that temperature, silicon oxynitride is removed at the rate of $\sim 50 \text{ \AA min}^{-1}$. We have found that the highest temperature under which our noise measurements could be done reproducibly was 55°C . At higher temperatures, the overall fluctuations were too violent and samples were

* Electrochemical Society Active Member.

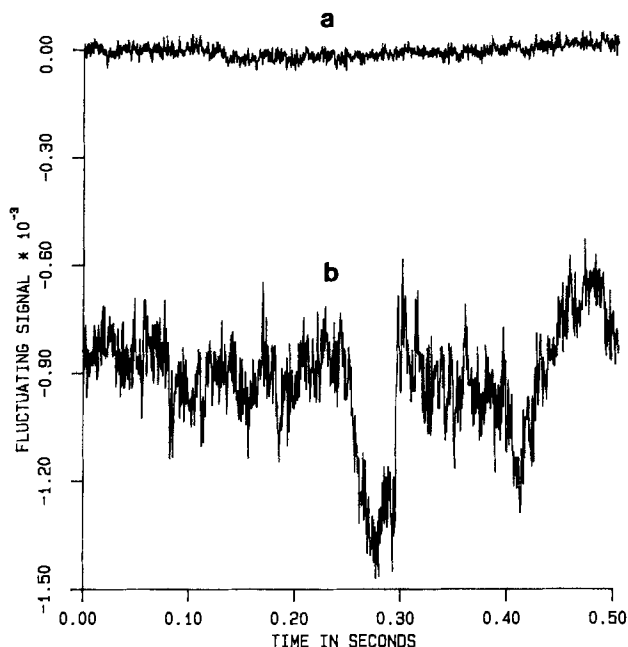


Fig. 1. Time record of the drain current fluctuations under (a) equilibrium (buffer) and (b) corrosion (55°C etching solution).

destroyed too quickly. The auto spectral density of corroding silicon oxynitride was found to be strongly dependent on temperature (Fig. 2a) and on mass transport (Fig. 3a).

The most surprising result of this work has been the strong correlation between signals from the gate A and the gate B [Fig. 1 of Ref. (2)] during corrosion conditions. As a matter of fact, the cross power spectral density and auto power spectral density calculated for the same corroding sample are almost identical. Consequently, the coherence function, $\gamma^2(\omega)$ has a nonzero value over broad range of frequencies, meaning that there is a strong correlation between these two signals. Thus, coherence is again strongly dependent on temperature (Fig. 2b), and on flow rate (Fig. 3b). The data in Fig. 2 and 3 are presented on different frequency scales in order to highlight the shapes of these frequency-dependent functions.

It has been found that the coherence function measured under mildest etching corrosion conditions (36°-38°C) slowly shifts towards lower frequencies with time. At

temperatures above 45°C, such shifts have not been observed. The time-dependent surface conductivity has been suspected to be the cause of this behavior. In order to verify this hypothesis, the following experimental sequence has been tried. The sample was first placed in the etching solution at 25°C. Under those conditions, no coherence occurs in the frequency range accessible to our measurements (0.8 Hz-25 kHz) (Fig. 4, curve 1). Without interrupting the flow of the etching solution, the heater was turned on and the temperature of the etching solution was raised to 38°C (Fig. 4, curve 2). After 4 min, the coherence has decreased gradually (Fig. 4, curve 3). The heater was then disconnected for 4 min and the coherence at 25°C was again measured; it had returned to near zero value. After 4 min, the temperature was again raised to 38°C. The coherence function has reached lower value than that obtained during the first cycle (Fig. 4, curve 4) and, again, gradually decreased with time. This behavior is consistent with formation (25°C) and removal (38°C) of surface conductive layer which is necessary for the nonzero value of the coherence function. It must be pointed out that zero value of coherence at 25°C does not imply the absence of surface conductive layer. It can mean the absence of the common correlated source of fluctuation, *i.e.*, the corrosion process, or it can mean that the surface resistance is so high that the coherence is shifted to frequencies below 0.8 Hz.

Discussion

There are two significant results of this study: the ability to investigate directly the electrochemical corrosion process taking place at the insulator/solution interface, and the finding that the entire surface of the silicon oxynitride becomes conductive during wet etching. The latter result, unfortunately, makes the interpretation of the fluctuation phenomena difficult at present. The time record of the corrosion process (Fig. 1) reflects the nature of the physical process itself. Each current excursion corresponds to an instantaneous charge imbalance at the gate capacitor. This can be due to random interaction of ions (both positive and negative) with the silicon oxynitride surface, ion exchange, or physical removal of charged material from the surface (etching). Any or all of these processes take place at the entire surface of the transistor chip. The original hypothesis has been that only the interactions taking place directly over the gate area A and B would be contributing to the fluctuations in those respective channels and be uncorrelated. This situation is in direct contrast to the experimental conditions

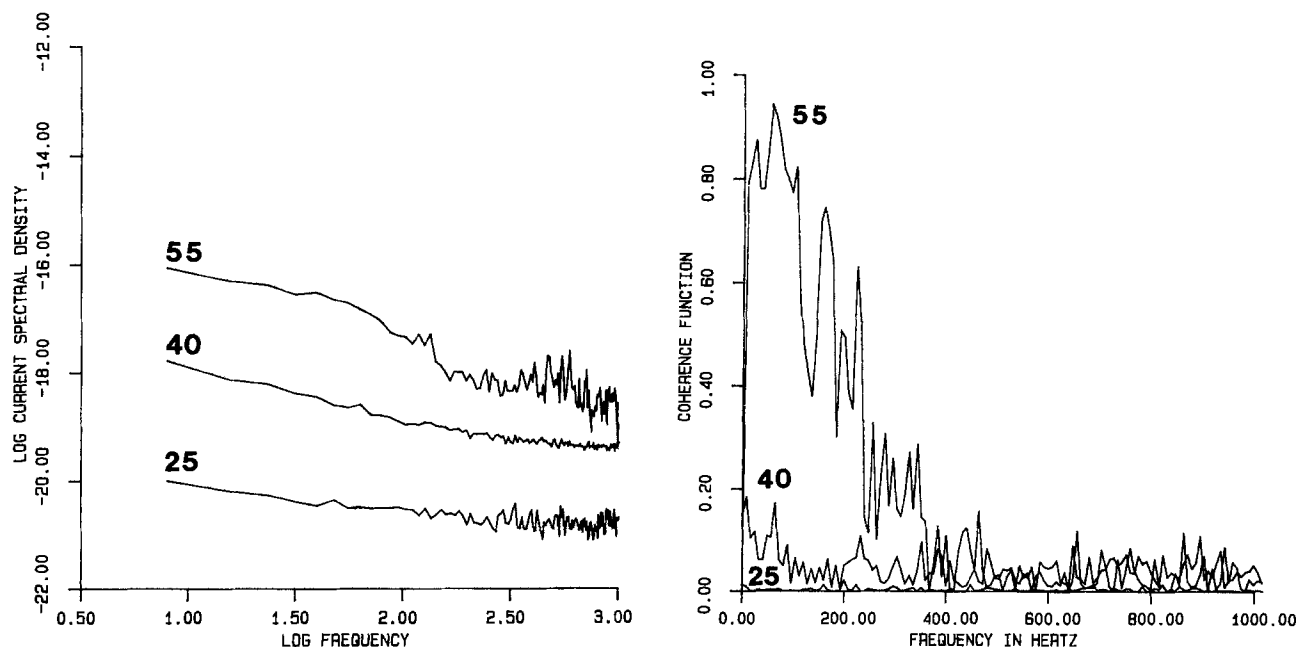


Fig. 2. The effect of temperature on corrosion of silicon oxynitride. a(left): Auto spectral density. b(right): Coherence function.

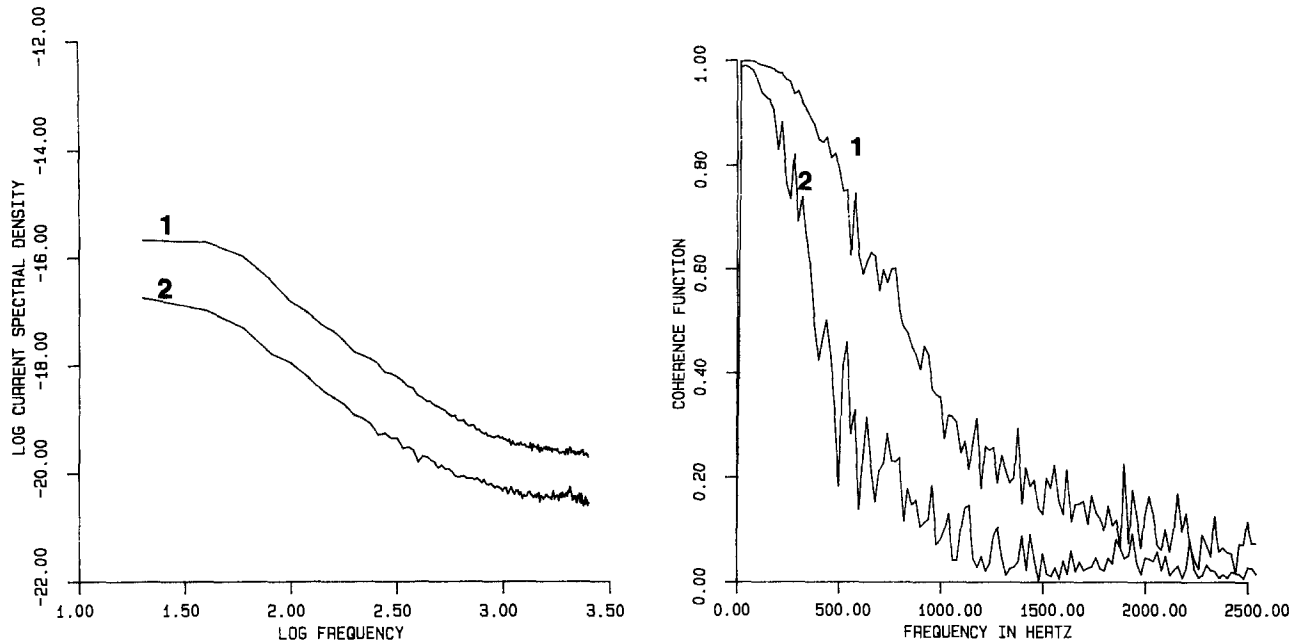


Fig. 3. The effect of mass transport on corrosion of silicon oxynitride. 1: Low flow rate. 2: High flow rate. a(left): Auto spectral density. b(right): Coherence function.

for the corrosion study of aluminum (2) in which the electrochemically generated fluctuations were made intentionally correlated to both gates through a common, metallic connection.

The presence of strongly correlated fluctuation source in the case of silicon oxynitride points to the existence of a conducting layer spread over the entire silicon oxynitride surface. Since this surface is laterally homogeneous chemically, it is reasonable to expect that the corrosion and hence the source of fluctuations is distributed uniformly over the entire surface. The process can be, therefore, modeled as a distributed impedance, as shown in Fig. 5a. In this model, the whole surface of the chip is subdivided into elementary complex impedance cells (Fig. 5b). In the first approximation, it is assumed that the conduction takes place in a two-dimensional conducting plane array of the elements Z_{jk} . It is further assumed that the elementary fluctuation sources, S_{jk} , are connected to the center of each impedance element Z_{jk} (Fig. 5b) and that the interconnections between neighboring elements are only orthogonal. Through this two-dimensional network each noise source anywhere on the chip surface contributes to the fluctuations measured in channels A and B.

The experiment described in Fig. 4 allows us to speculate about the nature of the plane conductor. At high tem-

perature ($> 45^\circ\text{C}$), the coherence function has a nonzero value which does not decrease in time. This means that the surface conductor is being formed continuously. At 38°C , the auto spectral density is high, meaning that the corrosion-related fluctuation source is operative but the coherence function gradually shifts to lower frequencies (Fig. 4, curves 2, 4, 5). This is consistent with the increase of the resistance value in the impedance element (Fig. 5b), which would effectively filter out the higher frequencies of the coherence function.

Periods 1, 3, and 6 in Fig. 4 represent time intervals in which the surface conductor can re-form. High values of the coherence function in the intervals 2, 4, and 5 support this hypothesis.

So far, we have been considering only a two-dimensional planar conductor, which is formed chemically. There is other evidence which suggests that this conductor is a three-dimensional layer of finite thickness. In that sense, the observed changes in the resistance as inferred from the time dependence of the coherence function can be due to the changes in the geometry of the layer (thickness) and/or of the volume density of charge carriers in that layer. At present, this question cannot be resolved on the basis of experimental evidence available to us.

The other supporting argument for the existence of the active surface layer comes from the analysis of concentration profiles of silicon oxynitride which has been done by both Auger spectroscopy (6, 7) and by ESCA (8) combined with argon ion sputtering. An oxygen-rich layer approximately 50\AA thick has been found to exist on the surface of silicon nitride. This layer re-forms spontaneously upon exposure to air at room temperature. This process resembles the formation of the passivation layer which is common to most metals and semiconductors.

It is well documented (9) that silicon oxynitride surface exhibits a linear pH sensitivity over a broad range of values (1-13 pH). Some authors have ascribed this sensitivity to ionization of silanol groups located in the surface plane. The linear character of the pH dependence would dictate the existence of at least 30 acid dissociation constants uniformly distributed over this pH range. The more likely explanation of the linear pH sensitivity is the existence of a hydration layer analogous to the one which forms on a glass pH electrode membrane (10).

The hydrated silicon oxynitride interface exhibits a typical nonpolarized behavior (11); it does not respond to adsorption of polyelectrolytes and is insensitive to the

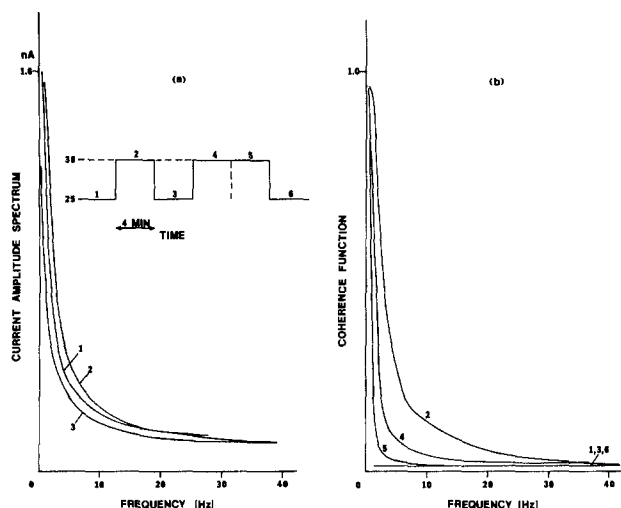


Fig. 4. Time dependence of the current spectrum (a) and coherence (b)

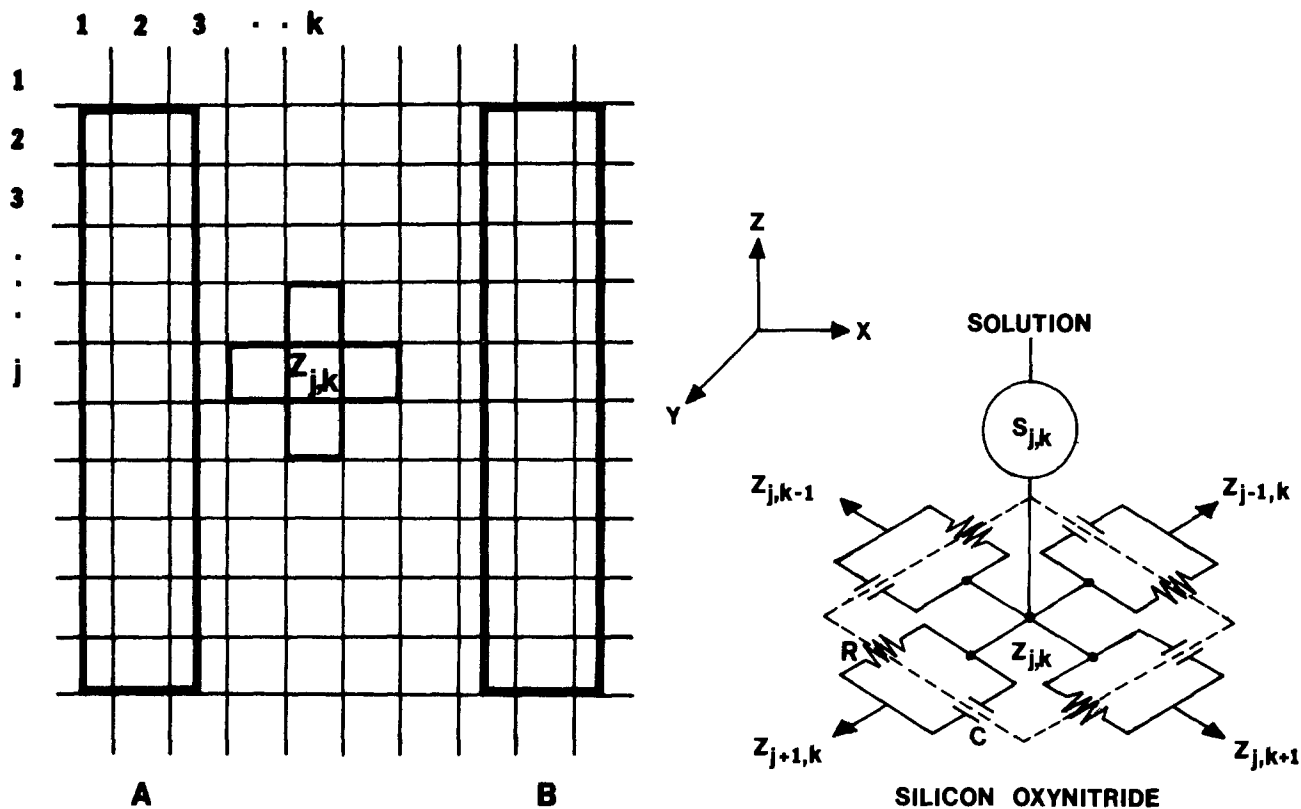


Fig. 5. Model of the transistor chip covered with silicon nitride under corrosion conditions. a(left): Distributed impedance superimposed on channels A and B. b(right): Model of the impedance cell $Z_{j,k}$ with the fluctuation source $S_{j,k}$. The reference point of the cell numbers is arbitrary.

motion of the solution. This is again consistent with the existence of a separate phase (hydrated layer) which has the boundary potential determined by the ion exchange process only.

Finally, our previous study has shown that silicon oxynitride allows migration of charge when exposed to water (12). The conduction properties of silicon nitride have been found to be strongly dependent on the degree of "wetness." While a dry surface would not allow charge migration for several hours, a wet surface dissipates charge from electrically floating transistor gate in a matter of seconds. From the time dependence of this charge migration, the surface resistivity of $10^{16} \Omega \square^{-1}$ has been found for a fully encapsulated transistor chip which has been immersed in water for several days. In contrast, the surface resistivity of the chip under etching conditions at 38°C is only $10^{11} \Omega \square^{-1}$ as estimated from the frequency dependence of the coherence function. The lower frequency roll-off of our experimental setup does not allow us to estimate the surface resistivity of silicon oxynitride under equilibrium conditions. However, the results of this work and of the charge migration studies which were mentioned above, point to a potentially serious problem due to the cross-talk in silicon oxynitride devices which would be used under aqueous conditions. It must be pointed out, however, that silicon oxynitride is a perfect insulator, for CHEMFET applications, in direction perpendicular to the surface as has been confirmed by repeated leakage tests done throughout this study.

Acknowledgments

The authors wish to acknowledge the support for this work from the Office of Naval Research.

Manuscript submitted July 16, 1984; revised manuscript received Oct. 1, 1984.

The University of Utah assisted in meeting the publication costs of this article.

REFERENCES

1. A. Haemmerli, J. Janata, and J. J. Brophy, *This Journal*, **129**, 2306 (1982).
2. Zheng Kang Li, J. M. Reijn, and J. Janata, *ibid.*, **32**, 559 (1985).
3. B. W. Kernighan and P. J. Plauger, "Software Tools," Addison-Wesley, Reading, MA (1976).
4. J. S. Bendat and A. G. Piersol, "Random Data: Analysis and Measurement Procedures," Wiley-Interscience, New York (1971).
5. P. R. Bevington, "Data Reduction and Error Analysis for the Physical Sciences," McGraw-Hill, New York (1969).
6. J. S. Johannessen, W. E. Spicer, and Y. E. Strausser, *Thin Solid Films*, **32**, 311 (1976).
7. M. G. Maguire and P. D. Augustus, *This Journal*, **119**, 791 (1972).
8. J. Janata and R. J. Huber, in "Ion-Selective Electrodes in Analytical Chemistry," Vol. 2, H. Freiser, Editor, Plenum Press, New York (1980).
9. J. Janata and R. J. Huber, in "Ion-Selective Electrodes in Analytical Chemistry," Vol. 2, H. Freiser, Editor, p. 150, Plenum Press, New York (1980).
10. G. Eisenmann, "Glass Electrodes for Hydrogen and Other Cations," Marcel Dekker, New York (1967).
11. J. Janata and R. J. Huber, in "Ion-Selective Electrodes in Analytical Chemistry," Vol. 2, H. Freiser, Editor, p. 131, Plenum Press, New York (1980).
12. R. M. Cohen and J. Janata, *Thin Solid Films*, **109**, 329 (1983).

Electrodeposition and Material Characterization of Cu_xS Films

R. D. Engelken*

Department of Engineering, Arkansas State University, State University (Jonesboro), Arkansas 72467

H. E. McCloud¹

Department of Computer Science, Mathematics, and Physics, Arkansas State University, State University (Jonesboro), Arkansas 72467

ABSTRACT

Thin films of Cu_{2-x}S and Cu_{1+x}S have been electrodeposited at temperatures from 21° to 120°C from propylene glycol solutions of CuNa_2EDTA , elemental sulfur, and KCl. The films were grown on a variety of substrates, including indium tin oxide (ITO) and tin oxide (TO) coated glasses, graphite, nickel, tin and titanium. The stoichiometry of those films grown at room temperature can be controlled through the electrolyte stirring rate which controls the rate of sulfur diffusion toward the cathode. Heterojunction-like double-layer structures of Cu_{2-x}S on Cu_{1+x}S and Cu_{1+x}S on Cu_{2-x}S were electrodeposited by changing the stirring rate midway through a deposition. Those films grown at room temperature had nearly structureless x-ray diffraction spectra, while those grown at high temperatures were polycrystalline. X-ray microanalysis data indicated a continuous copper-sulfur atomic ratio from 2.33 to 1.06. The Cu_{2-x}S -based films were brown to dark-gray, and the Cu_{1+x}S films were blue-green to black. The apparent absorbance edge minimum shifted continuously from 835 to 575 nm as the sulfur content of the films increased, and the apparent indirect or nondirect bandgaps of the least copper-deficient but nearly amorphous Cu_xS films electrodeposited at room temperature were in the 1.25-1.50 eV range.

Electrodeposition has emerged as an inexpensive, low temperature, and relatively simple method of producing thin semiconductor chalcogenide films, such as CdTe (1-14), CdSe (15-21), CuInSe_2 (22), CdS (14, 21, 23, 24), Bi_2S_3 (25), SnSe (26), etc., which are potential photovoltaic materials. Previous work involving the electroplating of copper sulfide-based material can be found in Ref. (21, 27, 28). Major problems with the method include difficulty in producing perfectly stoichiometric material as required for electronic purposes and in achieving large grain sizes.

We report the electrodeposition of thin films of the copper-sulfur system from solutions of ethylenediaminetetraacetic acid-disodium-copper (CuNa_2EDTA) and elemental sulfur dissolved in 1,2-propanediol (propylene glycol). The creation of a Cu_{2-x}S layer by ion displacement, chemical vapor deposition, evaporation, etc. in the fabrication of CdS/ Cu_{2-x}S solar cells is well known, and the successful controlled electrodeposition of Cu_{2-x}S might allow the fabrication of heterojunctions or Schottky barriers with Cu_{2-x}S as the base material. Good reviews of Cu_xS -based solar cells can be found in Ref. (29-32). Major problems with these cells include stability, the formation of Cu_{2-x}S with too large an x value, and electrochemical formation of shorting copper nodules.

Experimental Instrumentation and Procedure

The experimental apparatus included an IBM EC 225 voltammetric analyzer, Hewlett-Packard 7046-B X-Y-t recorder, Pine glassy carbon-glassy carbon ring-disk electrode and rotator, Fisher Thermix 600T stirring hot plate, Fisher Accumet 630 pH, temperature, and millivolt meter, and in-house constructed voltage followers, galvanostats, and potentiostats. The solution was typically 10^{-2}M in CuNa_2EDTA and 10^{-1} - 10^{-2}M in sulfur and contained 200 ml of propylene glycol. Occasionally, KCl or NH_4Cl (0.01-0.1M) was added for conductivity purposes. All chemicals were purchased from Alfa or Fisher and were reagent-grade. The solution and 1.5 in. long Teflon-covered stirring bar were contained in a 1325 ml Pyrex crystallizing dish covered with a polypropylene cover, which contained ports for cathode removal and for the insertion of a Corning double junction Ag/AgCl reference electrode, a Fisher temperature electrode, and a Poco graphite anode with sufficient area to completely "shadow" the 1 in.² cathodes. The cathode substrates were held by a Poco graphite clamp connected with Teflon bolts and nuts.

* Electrochemical Society Active Member.

¹ Present address: University of Missouri at Rolla, Rolla, Missouri 65401.

The IBM EC 225 voltammetric analyzer were normally used as the deposition power supply and was also used for the conduction of occasional voltammetric measurements in conjunction with the rotating electrode system and X-Y-t recorder. A battery-powered, floating OPAMP potentiostat/voltage follower circuit was used to control and measure the ring voltage and current.

A Perkin-Elmer/Hitachi Model 330 optical spectrophotometer was used for the measurement of optical absorbance vs. wavelength for those samples grown on the glass substrates. Conventional x-ray diffraction, x-ray microprobe analysis, and scanning electron microscope instrumentation located at the University of Missouri-Rolla and Arkansas State University were used for these measurements on the Cu_xS films.

Our deposition technique is similar to that developed by Baranski and Fawcett (21, 23, 25, 37, 38) and Roe *et al.* (24). In this technique, the film is formed by the plating of the metal and the subsequent reaction of the metal with the dissolved molecular chalcogen, and/or by the reduction of the chalcogen to a divalent anion and the precipitation of these anions with the metal cations. Baranski and Fawcett were successful in electrodepositing Cu_2S (21), but used hazardous CuCN due to the formation of "undesirable intermediates" when other copper salts were used.

Our copper sulfide films were produced by the electrodeposition of copper metal and subsequent reaction with sulfur at cathode voltages from -0.70 to -5.0V (Ag/AgCl). At -0.70V, the current densities varied from 3-16 $\mu\text{A}/\text{cm}^2$ at room temperature to 30-150 $\mu\text{A}/\text{cm}^2$ at temperatures near 100°C. The angular velocity of the stirring bar ranged from 0 to nearly 600 rpm, as measured with a strobe light or the period of the noise voltage induced in a nearby coil by the changing magnetic field of the stirring system.

The approximately 1 × 1 in. cathode substrates included PPG indium tin oxide (ITO) and tin oxide (TO) coated glasses, Poco graphite, nickel, tin, and titanium. The initial deposition voltage for the glass substrates was usually restricted to greater than -0.9V, owing to eventual electrochemical reduction of the conductive oxides at more negative voltages.

Substrate preparation was found to be critical to the uniformity and adherence of the deposits. After marking the conductive side with a diamond pen so that this side could be placed opposite the anode, the oxide-coated glasses were scrubbed with a test-tube brush and detergent. Graphite substrates were rubbed down to expose new material. Metal substrates were washed and then

etched in HCl or HNO₃. All substrates were rinsed in acetone, thoroughly dried, and handled with plastic forceps.

The finished deposits were carefully removed from the cathode clamp with the forceps and immediately rinsed with acetone, which was superior to water in removing the propylene glycol. The films were then rinsed in distilled/deionized water and dried before storage in sample boxes.

Experimental Results and Discussion

We have successfully electrodeposited Cu_xS films with x ranging from nearly 1 to >2 . The films with Cu/S ratios near unity are green to blue when thin, and dark black when thick and opaque. The films with Cu/S ratios near 2 are brown when thin and gray-brown when thick. Intermediate Cu/S ratios in the films produce either mixtures of brown and green colors on the same substrate or, more commonly, a homogeneous yellow-brown color. It was observed that the green Cu_{1+x}S material was favored near the solution-air interface; often, the brown deposits would yellow and turn green at the top one-third of the submerged substrate.

It was determined that the stoichiometry of the deposits could be controlled by varying the temperature, stirring rate, sulfur concentration, and current as a function of voltage. Evidently, the rate of reaction between the copper and sulfur is determined by the relative rates of mass transport of the sulfur and copper toward the cathode and their temperature-activated reaction rate constant. It is well known that the copper-chalcogen reaction rate is higher than such rates for most other metal-chalcogen reactions and may be up to 10⁴ that for tin and nickel (33). Of special significance is the fact that we were successful in depositing both green and brown films at room temperature, whereas most of the previous work utilizing this technique has been at temperatures greater than 90°C to avoid metal-rich deposits. This was possible because of the complexing nature of the EDTA ion, which allowed typical current densities of only 3-16 $\mu\text{A}/\text{cm}^2$, depending upon the stirring rate, at a deposition voltage near -0.7V vs. Ag/AgCl and because of the large Cu-S reaction rate constant. With sulfur concentrations between 10⁻³ and 10⁻²M, the color and composition could be well controlled through the angular velocity of the approximately 1.5 in. stirring bar. With no or very slow stirring (<50 rpm), the deposits were a rich but transparent brown color, and with rapid stirring were a blue-green color. Sulfur concentrations much less than 10⁻³M resulted in copper-rich deposits and rapid sulfur depletion due to film formation and oxidation of the sulfur at the anode. One disadvantage of the low current, room temperature depositions was that it often took over 12h to obtain reasonably thick deposits. This was especially a problem with the pulsed deposition method to be discussed below.

The fact that x in Cu_xS ranged from 1 to over 2 when there were no Cu⁺ ions deliberately added to the solution is evidence that the compounds are being produced primarily from the chemical reaction of plated copper and dissolved sulfur. If the primary reaction was the precipitation-like reaction of electrochemically produced S⁻ ions and Cu⁺ ions, the deposit would tend to be primarily CuS. This reaction could predominate in the electrodeposition of electronegative metal sulfides such as ZnS or MnS, where the sulfur reduction wave occurs at potentials more positive than the metal Nernst potential.

Those films grown at room temperature were smooth, shiny, and reasonably adherent. Rinses in water tended to produce more cracking of the films than did rinses in acetone. Those films grown on graphite and metal rarely cracked, while those grown on the oxide-coated glasses occasionally cracked and flaked, especially when very thick. A few depositions from a CuSO₄-based bath yielded powdery and nonadherent green-to-brown deposits, especially at high deposition temperatures and current densities greater than 100 $\mu\text{A}/\text{cm}^2$. The powdery nature was probably a consequence of the powdery copper deposition, as often occurs with noncomplexed copper ions.

At a temperature between 90° and 120°C, where the currents typically ranged from 30 to 150 $\mu\text{A}/\text{cm}^2$ at voltages near -0.7V (Ag/AgCl), thick, nearly opaque deposits could be obtained after 1-2h. Deposits grown at these temperatures, especially those grown on metal substrates, had a much more grainy texture than those grown at room temperature. It was difficult to obtain brown deposits at these temperatures because of the rapid reaction of the copper and sulfur, and there was a rapid transition from very copper-rich to green deposits as the sulfur concentration was increased from 10⁻⁴ to 10⁻³M. By using voltages negative of -1.0V , the copper current could be increased enough that the deposits would darken and become Cu_{2-x}S. It is likely that CuS is also directly reduced to Cu₂S at these very negative voltages. The high temperatures tended to change the color of the electrolyte from a bright blue to a dark blue-green when maintained for lengthy periods. Furthermore, a dark precipitate appeared in the crystallizing dish. After this precipitate formed, the subsequent deposits became very copper-like and nonuniform. Also associated with this phenomenon was the onset of a sweet, yeast-like odor from the solution. Although not rigorously investigated, we speculate that the high temperatures promote the in-solution formation of CuS from the reduction of Cu⁺⁺ to copper by the solvent and, thus, the removal of all of the sulfur from solution.

Annealing of the green CuS-based deposits in air at 200°-300°C quickly converted them to dark brown and very adherent Cu_{2-x}S-based deposits, probably with some oxides existing on the outer surface. However, we were unable to detect any oxygen in the microprobe analysis data due to oxygen's low atomic weight. There was always much sulfur remaining, as evidenced by microprobe analysis data, and, thus, Cu₂O formation was minor. We could also produce Cu_{2-x}S from Cu_{1+x}S by inserting the green deposits in a graphite clamp and placing them in a weakly acidic aqueous solution opposite a graphite anode. By generating small quantities of H₂ on the surface of the deposits, the "excess" sulfur reacted with the H₂ to form H₂S or HS⁻ and produced brown Cu_{2-x}S deposits. Large hydrogen currents and associated bubble formation tended to crack the films mechanically.

The solution used for this work was convenient to work with because of the very low toxicity of the propylene glycol and sulfur. Furthermore, the Cu⁺⁺ ions are complexed by the EDTA ions and rendered relatively nontoxic. The boiling point of propylene glycol is 187°C, so high temperatures can be used without boiling and rapid solvent evaporation and the associated flash ignition problems. This also allows for the melting of the submerged sulfur and greatly increases its rate of dissolution. Room temperature evaporation was negligible. A key advantage of this bath is that both the EDTA ions and the propylene glycol molecules complex most other heavy metal ions and strongly hinder or prevent their electrodeposition. Thus, metal impurities in the films are minimized.

Material Data

Table I shows experimental data for representative Cu_xS films. All of the samples in the table were grown from the same bath, which was 10⁻²M in CuNa₂EDTA, 10⁻²M in sulfur, and 10⁻²M in KCl. The films were grown in the same sequence as their sample numbers. The sequence E34-E50 was grown approximately in order of increasing stirring rate with all of the other parameters constant.

Those films grown at room temperature and those grown on the oxide-coated glasses were usually mirror-like and usually lacked definite x-ray diffraction structure because of, in part, the "brightening" effect of the EDTA ion and the very small grain sizes of the oxides on the glass. Figure 1 exhibits x-ray diffraction spectra typical for those films grown at temperatures greater than 90°C on metal substrates. The peaks are still rather weak and broad, consistent with small grain sizes. Sample E79 was grown on a nickel substrate at a temperature of

Table 1. Experimental conditions for and characteristics of representative electrodeposited Cu_xS films

SAMPLE	SUBSTRATE	T (°C)	E (V) Ag/AgCl	I (mA)	STIR RATE (RPM)	X(Cu) _x (S)	COLOR
34	ITO	20-23	-0.701	38	30	2.17	BROWN
35	ITO	22-27	-0.701	38	30	1.84	BROWN
37	ITO	21-23	-0.701	32	30	1.64	BROWN
39	ITO	22-25	-0.701	35	45	1.70	BROWN
40	ITO	21-23	-0.701	35	60	1.68	YELLOW-BROWN
42	ITO	21-23	-0.701	35	75	1.34	BOTH BROWN AND GREEN REGIONS
45	ITO	25-27	-0.701	42	100	1.14	GREEN
48	ITO	20-22	-0.701	60	85	1.48	BOTH BROWN AND GREEN REGIONS
49	ITO	20-22	-0.701	34	80	1.35	BROWN
50	ITO	20-23	-0.701 (PULSED)	52	430	1.39	GREEN
66	Sn	89-93	-1.400 (PULSED)	1200	465	1.23	GREEN
70	Ti	97-98	-1.400 (PULSED)	1100	550	1.06	GREEN
72	Ti	100-104	-5.000	4500	550	2.33	BROWN, BLUE AND GREEN REGIONS
75*	ITO	109-111	-1.400	800	375	2.06	GREEN BEFORE ANNEALING, BROWN AFTER ANNEALING.
77	Ni	98-111	-4.300	3500	550	1.81	BLUE-GRAY
78	GRAPHITE	97-103	-0.800	450	550	1.30	BROWN, BLUE AND GREEN REGIONS
79*	Ni	96-108	-1.600	1200	550	1.90	GRAY-BLACK

*ANNEALED; ITO - In₂O₃:Sn COATED GLASS, Ti - SnO₂ COATED GLASS.
APPROXIMATE FILM AREA = 0.5 IN².

96°-108°C, a voltage of -1.6V (Ag/AgCl), with a current density of 370 μA/cm² and a stirring rate of 550 rpm (determined from strobe light measurements). The sample was subsequently annealed in air at 213°C for 3h. The

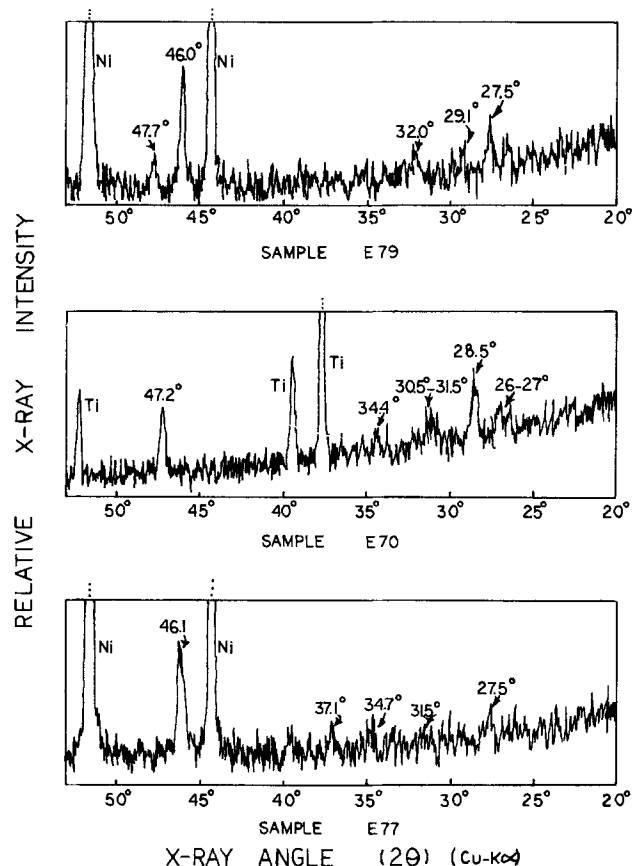


Fig. 1. X-ray diffraction spectra for Cu_xS films electrodeposited at high temperatures on metal substrates. The numbered peaks are possible Cu_xS structures while the substrate peaks are identified by the substrate material.

color of the film after annealing was gray-black. The peaks near 47.7° and 29.1° (2θ, Cu-Kα) are those associated with Cu_{1-x}S (covellite). The peaks near 46.0° and 27.5° are those associated with Cu_{2-x}S. The broad peak near 32.0° may be from either or both materials. Microanalysis data for this sample indicated a gross Cu/S elemental ratio of 1.90, but, evidently, more than one phase exists in the sample.

Sample E70, grown on titanium, exhibits peaks near 47.2° and 28.5°, which are probably characteristic of Cu_{1+x}S. Again, the broad peak near 31° may be due to either Cu_{1+x}S or Cu_{2-x}S. There is some indication of a small peak between 26° and 27°, consistent with anilite (Cu₃S₄). The x-ray microanalysis data for this sample indicated a Cu/S elemental ratio of 1.06. This sample was grown at 97°-98°C, with a deposition voltage of -1.40V (Ag/AgCl), a current density of 341 μA/cm², and a stirring rate of 550 rpm.

Sample E77 yielded peaks near 46.1°, 37.1°, and 27.5°, all characteristic of Cu_{2-x}S, and showed some indication of a peak near 31.5°. Microanalysis data indicated that the sample was Cu_{1.81}S, consistent with the digenite system. The conditions for the deposition of this film were a temperature of 98°-111°C, a deposition voltage of -4.30V (Ag/AgCl), a current density of 1.1 mA/cm², and a stirring rate of 550 rpm.

Figure 2 is a plot of typical graphical microanalysis data that accompanied the numerical printouts containing the elemental percentages. Sample E34 was grown on an indium tin oxide-coated glass substrate and E77 was grown on nickel, consistent with the indium, tin, and nickel peaks in the data. There were never any peaks in the microanalysis data for any film that were not attributable to copper, sulfur, or the substrate.

Although there is some scatter in the data points, Fig. 3 indicates an increase of sulfur content with increasing

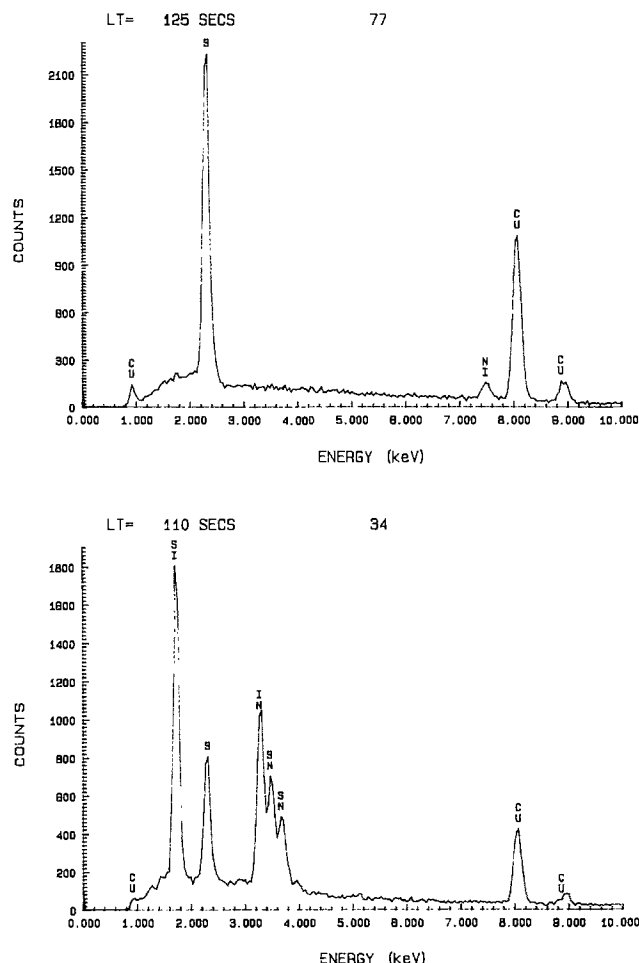


Fig. 2. Graphical x-ray microanalysis data for electrodeposited Cu_xS films.

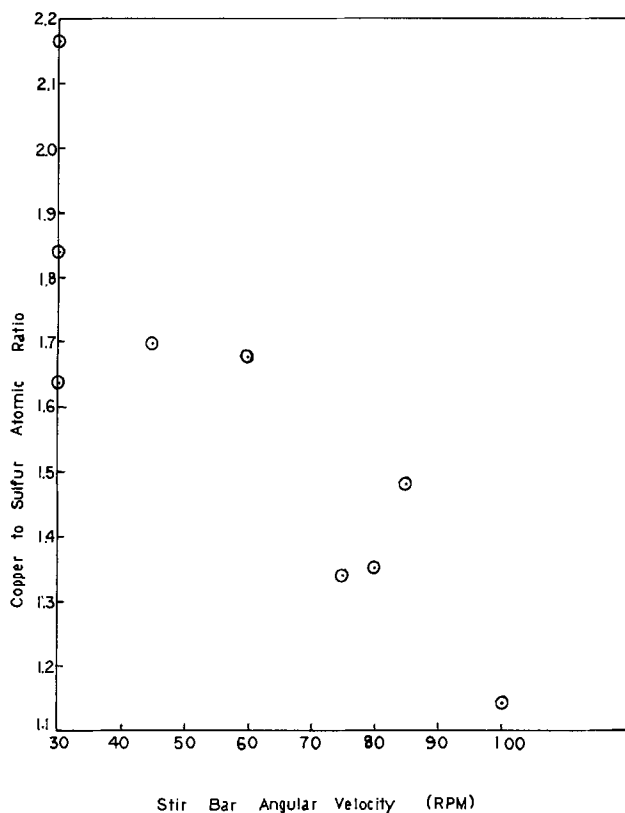


Fig. 3. Relative copper to sulfur atomic ratio vs. approximate stirring rate for electrodeposited Cu_xS samples E34-E49 that appear in Table I. All experimental conditions except the stirring rate were constant.

stirring rate as would be expected from the decreased sulfur diffusion-layer thickness and the increased cathode-surface sulfur concentration. Even with the lowest stirring rate (<50 rpm) and deposition voltages negative of the copper Nernst potential, no great excess of copper was indicated when the sulfur concentration was 10^{-2}M or greater.

Figure 4 shows the optical absorbance spectra for samples E34, E39, E48, E50, and E73. The spectra were compensated for substrate absorbance but not for reflectance. Referring to Table I, one notes that the bandgap absorbance edges, as approximately defined by the wavelength location of the spectra minima, move from 835 to 575 nm with increasing sulfur content. Thus, it should be possible to vary the bandgap of Cu_xS by controlling x with the stirring rate. These minima energies are not necessarily the bandgaps of the materials, as must be determined from various functional plots of the data.

Note that the gross absorbance also increases at the longest wavelengths and that the long wavelength absorbance seems to increase with increasing sulfur content. Rigorous comparison is hindered, however, by the slightly different film thicknesses. This low energy absorbance is probably due to free carrier absorption, but could also be partially due to interface reflectance between the sample and substrate. Most Cu_xS films, especially the green films, were very conductive and probably p-type degenerate with large hole concentrations leading to plasma resonance effects such as are discussed in Ref. (34). Note that the CuS -based samples on indium tin oxide-coated glass could serve as crude optical bandpass filters to the red end of the visible spectrum. The two competing "absorbance" processes make the determination of the actual material bandgap value difficult. Figure 5 plots $[\hbar\nu(A - A_0)]^{0.5}$ vs. $\hbar\nu$ for sample E34 and should yield linear plots if (35, 36)

$$A = A_0 + \frac{C(E - E_g)^2}{E}$$

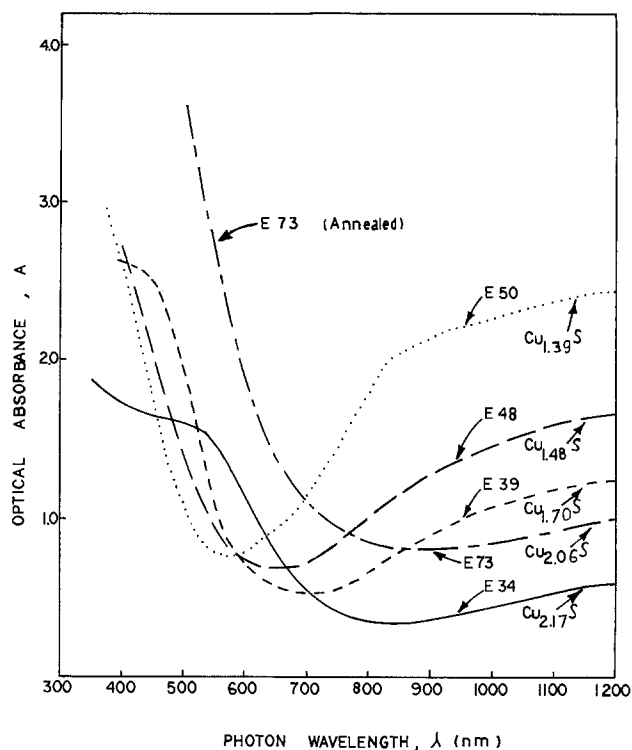


Fig. 4. Optical absorbance spectra for typical electrodeposited Cu_xS films. The apparent bandedge shifts consistently to shorter wavelengths with a decreasing copper-to-sulfur atomic ratio.

where $E = h\nu$ is the photon energy, E_g is the bandgap energy, and C is a constant. This functional form applies to materials exhibiting indirect or nondirect (amorphous-like) optical transitions. The uncertainty lies in A_0 , a background absorbance due to imperfect substrate compensation, sample reflectance, free carrier and impurity absorption, etc. Two values have been selected for A_0 , 0.0 and 0.34, the minimum absorbance of the sample. For $A_0 = 0.34$, a least squares fit of those points visually appearing linear yields a bandgap estimate of 1.5 eV, and A_0

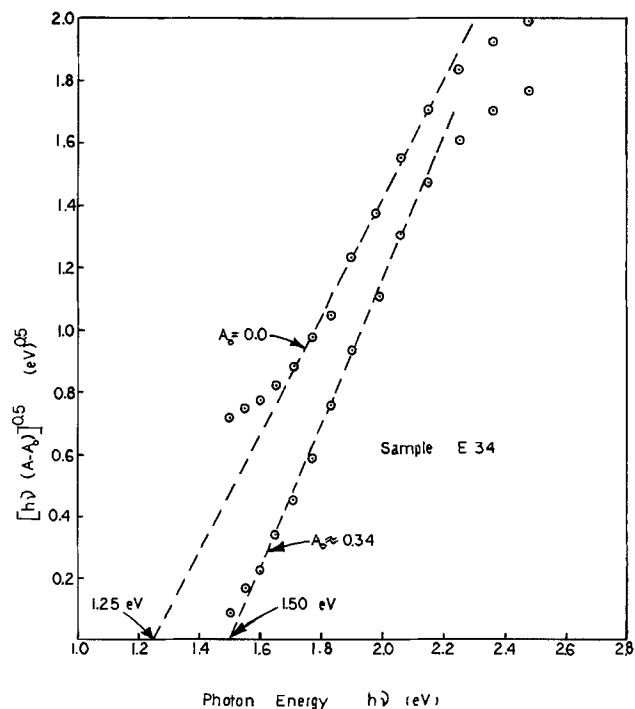


Fig. 5. Plots of $[\hbar\nu(A - A_0)]^{0.5}$ vs. $\hbar\nu$ for the slightly copper-rich sample E34 for two A_0 values. The extrapolated intercepts of the linear portions of the curves with the horizontal axis are estimates of the bandgap of the nearly amorphous sample.

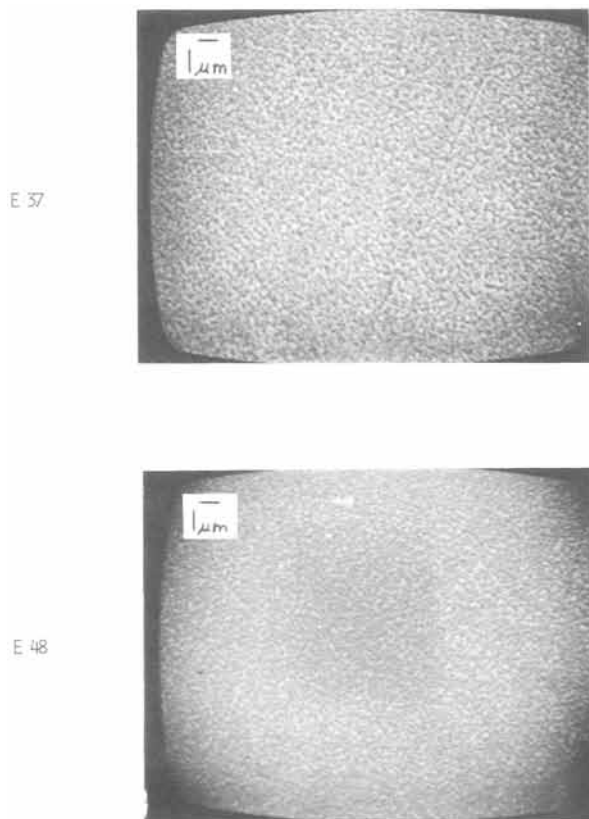


Fig. 6. Micrographs of Cu_xS samples E37 and E48, both yielding structureless x-ray diffraction spectra.

= 0.0 yields a bandgap estimate of 1.25 eV. We feel that the former estimate is more correct, but the actual E_g value could lie anywhere within this 0.25 eV range, which is consistent with that observed for Cu_{2-x}S produced by other methods (29, 30). Samples E34 and E73 were slightly copper-rich and were probably more nearly Cu₂S (chalcocite) than most of the other brown samples. Most brown samples with Cu/S ratios between 1.6 and 1.8 had absorbance minima occurring between 700 and 750 nm, consistent with the digenite phase. We feel that digenite is the most commonly electrodeposited form of Cu_{2-x}S. However, with more exact "fine tuning" of the experimental conditions, we hope that chalcocite can be consistently produced. A slight excess of copper might be required to achieve chalcocite, however, because djurleite ($x = 1.94-1.97$) is so close in composition and is considerably inferior to low chalcocite (Cu_{2.00}S) in photovoltaic properties. A very slight copper excess would shift the equilibrium toward copper interstitial atoms rather than vacancies and hinder the changes in crystal structure associated with increasing numbers of copper vacancies.

Figure 6 shows micrographs of samples E37 and E48, both grown at room temperature. Note the nodular appearance of the surfaces. The nodules range from 0.1 μm to 0.5 μm in breadth. The nodules for sample E37 exhibit a columnar structure when viewed at higher magnifications. However, the x-ray diffraction spectra for these samples were nearly structureless.

Figure 7 exhibits micrographs for sample E73 grown at 110°C on SnO₂-coated glass using a pulsed deposition technique. The dark green sample was then annealed in air at 213°C for 3h and transformed into a dark brown deposit (Cu_{2.06}S). The x values slightly greater than 2 could be due to a minor amount of Cu_xO formation at the surface of the film with annealing. Any oxygen present was not detected in the microprobe analysis data due to its low atomic weight and, thus, the Cu/S ratio calculated could be slightly in excess of the true x value.

These photographs are for the after-annealing case. Note the sponge-like structure of the deposit as opposed

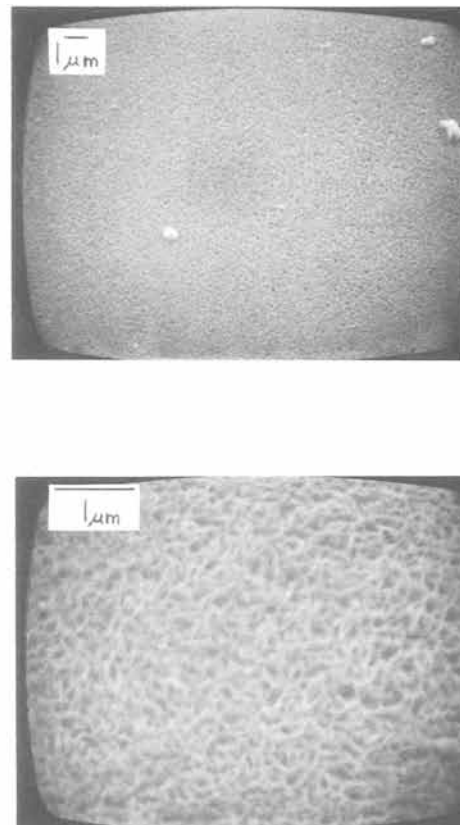


Fig. 7. Micrographs for sample E73 (Cu_{2.06}S) after annealing. This sample exhibited a weak Cu_{2-x}S x-ray diffraction structure.

to the nodular-like structures of samples E37 and E48. At higher magnifications, a brain-like structure is apparent. The x-ray diffraction spectrum for this sample showed a weak but definite peak between 45.5° and 46.0°, indicative of Cu₂S. Some of the brown samples, such as E45, grown at room temperature, also exhibited a similar structure when observed with magnification near 20,000×.

Figures 8 and 9 show micrographs for samples E66, E70, E77, and E79 grown at temperatures near 100°C on metal substrates. Sample E77 (Cu_{1.81}S) is composed of columnar crystals 0.5-1.0 μm wide and approximately 1.0 μm high. Sample E70 (Cu_{1.06}S) exhibits many needle-like or whisker-like crystals approximately 0.5 μm long and 0.05-0.1 μm wide. Sample E66 (Cu_{1.23}S) and E79 (Cu_{1.90}S) also exhibit these needle-like crystals, which sometimes clump together to form spheroids.

All of the samples viewed with the scanning electron microscope showed one or more of these four basic surface structures: (i) nodular (ii) sponge- or brain-like, (iii) columnar, and (iv) needle- or whisker-like. The nodular structure appears for both Cu_{1+x}S and Cu_{2-x}S and is indicative of nearly amorphous films. The sponge-like and columnar structures appear to arise from Cu_{2-x}S, and the needle-like structures seem to be indicative of Cu_{1+x}S. It is obvious that the high temperature depositions on metal substrates produce much larger crystallites than do the room temperature depositions.

Electrodeposition of Multiple-Layer Structures

We were also successful in plating heterojunction-like structures of Cu_{2-x}S/Cu_{1+x}S and Cu_{1+x}S/Cu_{2-x}S at room temperature simply by increasing or decreasing, respectively, the stirring rate midway through the deposition. By raising the cathode substrate slightly out of the electrolyte at this time, both film colors were visible at the end of the deposition. Thus, it is possible to electrodeposit two chemically similar but different (in band structure) semiconducting compounds with the same substrate and deposition voltage, and approximately the

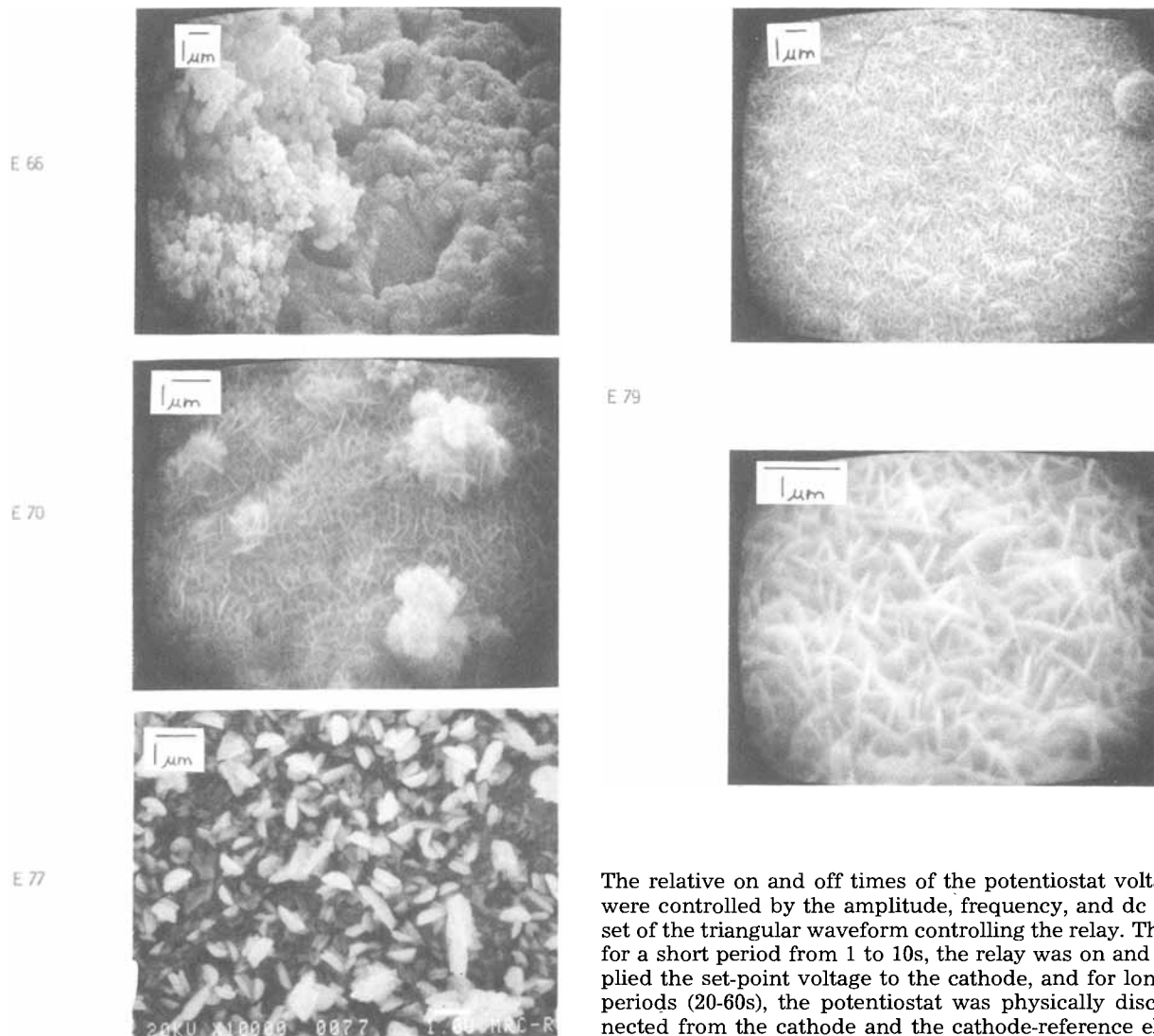


Fig. 8. Micrographs for samples E66, E70, and E77 grown on metal substrates at temperatures near 100°C and exhibiting substantial x-ray diffraction structure.

same current, simply by controlling the mass transport of the sulfur toward the cathode through the stirring rate. Such a technique would have many practical advantages in a commercial process. It would minimize the impurity problems associated with atomic diffusion across a heterojunction formed between two chemically unrelated compounds, and the associated doping of the depletion regions. Other multiple semiconductor compound systems such as the SnSe/SnSe₂ system (26) might be plated by this technique.

Furthermore, the same scheme might be used for depositing two different semiconductor layers and the top contact. Thus, a Cu_{1+x}S/Cu_{2-x}S/Cu device could be deposited through stirring rate variations. The copper layer adjacent to the Cu_{2-x}S would also tend to hinder its possible electrochemical transformation to a lower sulfur-content state under photovoltaic operation.

Pulsed Deposition Method

One fundamental advantage of the described electro-deposition technique is that it is nearly impossible to produce chalcogen-rich deposits, as is a likely possibility with cathodic deposition of the chalcogen from ions as occurs during CdTe electrodeposition. To take advantage of this fact, we developed a pulsed deposition scheme. The output of the potentiostat was connected to a relay. The relay coil was controlled by the triangular waveform of a Tektronix FG-504 low frequency function generator.

The relative on and off times of the potentiostat voltage were controlled by the amplitude, frequency, and dc offset of the triangular waveform controlling the relay. Thus, for a short period from 1 to 10s, the relay was on and applied the set-point voltage to the cathode, and for longer periods (20-60s), the potentiostat was physically disconnected from the cathode and the cathode-reference electrode voltage followed the open-circuit rest potential of the cathode and was sensed by a voltage follower circuit connected to the X-Y-t recorder. During the off portion of the cycle, the open-circuit voltage would nearly instantaneously increase to the quasi-rest potential of the deposited film and then quasi-exponentially increase from the quasi-rest voltage to an equilibrium value between 0.1 and -0.1V (Ag/AgCl), depending upon the experimental conditions. The apparent time constant of the "decay" was from 1 to 5s and resulted from the reaction of the plated copper with the dissolved sulfur, which caused a reduction of the copper activity in the deposit, and the relaxation of the copper ion activity in the Helmholtz layer to the bulk value. The reaction was essentially complete and produced nearly stoichiometric Cu_{1+x}S when the open-circuit potential reached a steady value.

It should also be possible to directly use a pulse generator as the set-point input to the potentiostat and alternately pulse the film anodically and cathodically. However, this would redissolve the Cu_xS during the anodic part of the cycle and slow the rate of deposition, although possibly decreasing the defect density and stress in the deposit. The relay scheme allows the sulfur to react with the deposited copper with no net change in the total copper content of the deposit. If the on times were long, the copper deposit might become too thick to allow sulfur diffusion through the deposit and, thus, complete reaction would be hindered. In this case, the anodic pulse might be beneficial to help remove excess copper which should dissolve at a more negative potential than would Cu_xS.

The pulsed mode is very attractive for the deposition of metal chalcogenide systems with only one compound, such as CdS, but for multiple-compound systems, such as

Cu_xS, would tend to produce the most sulfur-rich compound. The technique should allow the deposition of most metal chalcogenides at room temperature if there is a nonzero rate of reaction between the sulfur and metal. However, the required off time might be prohibitively long. It should be possible to deposit Cu_{2-x}S by closing the relay when the open-circuit potential just reaches the calculated equilibrium rest potential between stoichiometric Cu_xS and the electrolyte. As discussed previously, there is a continuous shift in the absorption edge of the Cu_xS to shorter wavelengths as x goes from 2 to 1. Thus, it might be possible to "tailor" the bandgap of the metastable Cu_xS deposits by switching the relay at the appropriate rest potential value. We are presently investigating this possibility.

Conclusions and Further Work

Both Cu_{2-x}S and Cu_{1+x}S thin films have been electro-deposited at temperatures from room temperature to 120°C from propylene glycol solutions of CuNa₂EDTA and sulfur. The stoichiometry of the films can be varied by controlling the rate of sulfur diffusion toward the cathode via the stirring rate. By changing the stirring rate midway through a signal deposition, both Cu_{2-x}S/Cu_{1+x}S and Cu_{1+x}S/Cu_{2-x}S structures have been deposited on the same substrate. The use of a pulsed deposition scheme allows nearly complete reaction of the copper and sulfur to form Cu_{1+x}S.

Those films grown at room temperature are usually amorphous, while those grown at temperatures near 100°C are polycrystalline. The amorphous films show a nodule-covered surface. Polycrystalline Cu_{1+x}S is composed of needle-like crystals, while polycrystalline Cu_{2-x}S exhibits a sponge-like or columnar surface. X-ray micro-analysis data indicated a continuous Cu/S ratio from 2.33 to 1.06. Furthermore, the optical absorbance edge minimum shifts continuously from 835 to 575 nm as the sulfur content increases. This might allow for bandgap "tailoring" even though the deposits may be metastable or mixtures in some cases. Plots of $[h\nu(A - A_0)]^{0.5}$ vs. $h\nu$ for the slightly copper-rich, amorphous sample E34 indicated an indirect or nondirect bandgap between 1.25 and 1.50 eV.

Future work includes deposition of Cu_xS films with an open-circuit potential controlled pulsed deposition system and a rotating cathode to better characterize the relationship between the stoichiometry and deposition conditions, so that photovoltaic-quality Cu₂S and, ultimately, junction devices can be consistently produced, as determined from structural, composition, optical, and electrical measurements.

Acknowledgments

The authors are grateful for the outstanding student assistance provided by Mr. Chuan Lee, Mr. Tim Martin, Mr. James Dodd, and Mr. Alan Copelin. We also thank Dr. Tom Van Doren, Dr. Jack Boone, Dr. J. Derald Morgan, Mr. Alok Berry, and Mr. Mike Norgerg at the University of Missouri-Rolla for their support and assistance. Also thanked are Dr. Albert Mink, Dr. Jerry Linnsteadter, Dr. Lawrence Mink, Dr. Dewey Sifford, Dr. Bill Wyatt, Dr. Ken Beadles, and Mr. John Hayenga at Arkansas State University for their cooperation and support, Sherry Engelken, Betty Minton, and Maxine Smith for the manuscript preparation, and Sunni Saleheddin for figure preparation. This work was funded primarily through a grant approved by the Arkansas State University Faculty Research Committee, whose support is gratefully acknowledged.

Manuscript submitted May 29, 1984; revised manuscript received Nov. 26, 1984. This was Paper 429 presented at the New Orleans, Louisiana, Meeting of the Society, Oct. 7-12, 1984.

Arkansas State University assisted in meeting the publication costs of this article.

REFERENCES

1. J. L. Boone and T. P. Van Doren, Final Report, Grant DE-FG02-79ER-10532, Solar Energy Research Insti-

- tute, Golden, CO (1982).
2. R. D. Engelken, Ph.D. Thesis, University of Missouri-Rolla, Rolla, MO (1983).
3. T. P. Van Doren, J. L. Boone, R. D. Engelken, and Z. Maczenski, in "Proceedings of the Eighth Annual University of Missouri-Rolla—Missouri Department of Natural Resources Conference on Energy," p. 35, University of Missouri-Rolla, Rolla, MO (1981).
4. M. P. R. Panicker, M. Knaster, and F. A. Kroger, *This Journal*, **125**, 566 (1978).
5. H. J. Gerritsen, *ibid.*, **131**, 136 (1984).
6. C. Ogden and D. Tench, Final Report, DOE Contract AC02-77CH00178, Rockwell International, Thousand Oaks, CA (1981).
7. G. Fulop, M. Doty, P. Meyers, J. Betz, and C. H. Liu, *Appl. Phys. Lett.*, **40**, 327 (1982).
8. J. Llabres, R. Noufi, R. J. Axton, and S. K. Deb, in "Photovoltaics Advanced Research and Development 5th Annual Meeting," p. 93, Solar Energy Research Institute, Golden, CO (1983).
9. B. M. Basol, E. S. Tseng, R. L. Rod, S. Ou, and O. M. Stafsudd, in "Proceedings of the Sixteenth IEEE Photovoltaic Specialists Conference," IEEE, New York (1982).
10. F. A. Kroger, *This Journal*, **125**, 2028 (1978).
11. M. P. R. Panicker, Ph.D. Thesis, University of California, Los Angeles, CA (1980).
12. R. N. Bhattacharya, K. Rajeshwar, and R. N. Noufi, *This Journal*, **131**, 939 (1984).
13. J. Llabres, *ibid.*, **131**, 464 (1984).
14. B. M. Basol and E. S. Tseng, in "Materials and New Processing Technologies for Photovoltaics," J. A. Amick, V. K. Kapur, and J. Dietl, Editors, p. 463, The Electrochemical Society Softbound Proceedings Series, Pennington, NJ (1983).
15. S. Chandra and R. K. Pandey, *Phys. Status Solidi A*, **59**, 787 (1980).
16. B. L. Funt, M. Leban, and A. Sherwood, in American Chemical Society Symposium Series no. 90, 242, American Chemical Society, Washington, DC (1979).
17. G. J. Houston, J. F. McCann, and D. Haneman, *J. Electroanal. Chem.*, **134**, 37 (1982).
18. M. S. Kazacos and B. Miller, *This Journal*, **127**, 869 (1980).
19. M. S. Kazacos and B. Miller, *ibid.*, **127**, 2378 (1980).
20. K. Colbow, D. J. Harrison, and B. L. Funt, *ibid.*, **128**, 547 (1981).
21. A. S. Baranski and W. R. Fawcett, *ibid.*, **127**, 766 (1980).
22. R. N. Bhattacharya, *This Journal*, **130**, 2040 (1983).
23. A. S. Baranski, W. R. Fawcett, A. C. McDonald, R. M. DeNobriga, and J. R. McDonald, *ibid.*, **128**, 963 (1981).
24. D. K. Roe, L. Wehzhao, and H. Gerischer, *J. Electroanal. Chem.*, **136**, 323 (1982).
25. A. S. Baranski, W. R. Fawcett, and C. M. Gilbert, *This Journal*, **130**, 2423 (1983).
26. R. D. Engelken, T. P. Van Doren, J. L. Boone, A. K. Berry, and A. Shahnazary, "Electrodeposition and Analysis of Tin Selenide Thin Films," To be published.
27. N. Nakayama, H. Matsumoto, A. Nakavo, S. Ikegami, H. Uda, and T. Yamashita, *Jpn. J. Appl. Phys.*, **19**, 703 (1980).
28. S. Saksena, D. K. Pandya, and K. L. Chopra, *Thin Solid Films*, **49**, 223 (1982).
29. K. L. Chopra and S. R. Das, "Thin Film Solar Cells," Plenum Press, New York (1983).
30. M. Savelli and J. Bougnot, in "Topics in Applied Physics," Vol. 31, p. 213, Springer-Verlag, New York (1979).
31. C. E. Backus, "Solar Cells," IEEE Press, New York (1976).
32. H. J. Hovel, "Solar Cells—Semiconductors and Semimetals," Vol. 11, Academic Press, New York (1975).
33. G. W. Kammlott, J. P. Franey, and T. E. Graedel, *This Journal*, **131**, 511 (1984).
34. K. Rajkanan, *Mater. Res. Bull.*, **14**, 207 (1979).
35. J. Tauc, in "Optical Properties of Solids," F. Abeles, Editor, p. 277, American Elsevier Publishing Company, New York (1972).
36. R. D. Engelken, M.S. Thesis, University of Missouri-Rolla, Rolla, MO (1980).
37. A. S. Baranski, M. S. Bennett, and W. R. Fawcett, *J. Appl. Phys.*, **54**, 6390 (1983).
38. A. S. Baranski and W. R. Fawcett, *This Journal*, **131**, 2508 (1984).

Electrochemical Study of the Autocatalytic Deposition of Gold-Copper Alloys

A. Molenaar and B. C. M. Meenderink

Philips Research Laboratories, 5600 JA Eindhoven, The Netherlands

ABSTRACT

The oxidation of formaldehyde was studied on a range of homogeneous copper-gold mixed crystals made by electroless deposition. The potential of passivation depends on the composition of the alloy. Electrochemical measurements were also performed for the deposition of alloys with a low, an equivalent, and a high gold-copper ratio. The catalytic activity of the gold-copper alloy for the oxidation of formaldehyde, and thus for autocatalytic metal deposition, is different from that of the pure metals. It is suggested that competition between the adsorption of formaldehyde and cyanide on the alloy surfaces at different potentials determines the catalytic properties.

A range of autocatalytic gold-copper alloys can be deposited from alkaline solutions containing $\text{KAu}(\text{CN})_2$, cupric ions complexed with EDTA and formaldehyde as reducing agent (1). Oxidation of formaldehyde does not take place on a gold surface in a wide potential range when cyanide ions are present in solution. It is, therefore, impossible to deposit, autocatalytically, pure gold from an electroless solution based on $\text{KAu}(\text{CN})_2$ and formaldehyde. However, cyanide has very little effect on the oxidation of formaldehyde on copper. In Ref. (1), we suggested that the copper acts as a catalyst for the oxidation and the electrons released at the copper or copper alloy surface can reduce both gold and copper ions. We have shown (1) that both copper- and gold-rich alloys can be deposited in this way. One of the surprising aspects of this work was that each gold-copper alloy, deposited from a stable electroless solution, has a characteristic lattice constant. A linear relationship was found between lattice constant and the alloy composition [Ref. (1), Fig. 7]. We must conclude that the gold-copper layers deposited from autocatalytic solutions are homogeneous mixed crystals in contrast to electroplated layers (2). Recent papers in the field of catalysis show that a metal in an alloy very often has catalytic properties similar to those of the bulk metal (3). De Jong (4) demonstrated that the catalytic properties of smaller stable metal particles can be studied in an alloy. Because we found that oxidation of formaldehyde in the presence of cyanide ions takes place on pure copper but not on pure gold, we tried to determine if, in the copper-gold alloy, only the copper atoms act as catalyst supplying the electrons for the reduction of the metal ions.

Experimental

Glass slides, roughened with silicon carbide and treated with 4% by weight hydrogen fluoride solution, were used as substrate. These were activated with stannous chloride-hydrochloric acid and palladium chloride-hydrochloric acid solution. The plating solutions had the following composition: copper sulfate 0.04M, tetrasodium salt of ethylenediaminetetraacetic acid 0.072M, gold(I) cyanide 10^{-2} - 10^{-4} M, potassium cyanide 10^{-3} M, sodium hydroxide 0.12M, and formaldehyde 0.10M. All solutions were prepared from analytical-grade chemicals. The experiments were carried out at 50°C. Plating rates were determined by weighing the deposits. The amount of hydrogen liberated during electroless metallization was measured with a gas burette. The copper/gold ratio was measured by low energy electron induced x-ray spectroscopy (LEEIXS) and in some cases by wet chemical analysis. Electrochemical measurements were carried out with the metallized glass slides. The working electrode was completely surrounded by a platinum sheet as counterelectrode. A saturated calomel electrode (SCE) was used as reference in combination with a Luggin capillary. The potential of the working electrode, given in V vs. SCE, was varied continuously with the aid of a Wenking ST 72 standard potentiostat and a Wenking VSG 72 voltage scan generator. The

scan rate was 1 mV/s in all cases. The current was recorded using a Philips PM 8141 X-Y recorder, and a Philips PM 2443 digital dc voltmeter was used to measure the potential.

Results

Using autocatalytic plating solutions at 50°C, we obtained a range of gold-copper alloys by changing the gold-cyanide concentration in the solution from $1.8 \cdot 10^{-4}$ to $1.4 \cdot 10^{-2}$ M. The metal content of the alloys and the lattice constants are given in Table I.

The potentials measured during plating (E_{pl}) shift to less negative values as the gold content is increased. We measured the plating rate and calculated the values as a current density (i_{pl}) using the measured copper/gold ratio (Fig. 1) in the layer and assuming that two electrons are required to form one copper atom and one electron for gold. The calculated current decreases as the gold content is increased.

The voltammograms for the oxidation of formaldehyde using a plating solution without metal ions are shown in Fig. 2 for the different alloys. When more gold is present in the alloy, not only is the current lowered in a wide potential range, but also the passivation of the alloy surface is also shifted to less negative values. Passivation is not observed on many alloys at potentials at which pure copper is oxidized. The plating potentials for the alloys with a copper content of less than 5% lies in this range. A reasonable agreement is found when the measured anodic current (i_M in Fig. 2) at the plating potential (E_{pl}) is compared with the currents (i_{pl}) deduced from the plating rate (Fig. 1 and Table I).

In Fig. 3-5, both the anodic and cathodic partial current-potential curves are given for alloy layers with 2.5, 49, and 98.5 atom percent (a/o) gold. The plating potentials (E_{pl}) are shown in the figures. The differences in the plating potential are not determined by the cathodic current, but correspond to the degree of inhibition of the oxidation of the formaldehyde. The overall cathodic current (Fig. 3-5)

Table I. Metal content and lattice constants of the metals

Cu (a/o)	Au (a/o)	<i>a</i> (Å)	E_{pl} (V)	i_{pl} (mA cm ⁻²)	i_M (mA cm ⁻²)	i_{Cu} (mA cm ⁻²)
100	—	3.62	-0.785	1.1	1.0	1.0
98.1	1.9	3.62	-0.780	1.0	1.3	1.0
97.5	2.5	3.63	-0.780	1.1	0.8	1.0
93.7	6.3	3.65	-0.761	1.1 ³	0.7	1.2
76.9	23.1	3.69	-0.728	0.9	0.7	1.6
51	49	3.86	-0.577	0.8 ³	0.8	5.6
16.5	83.5	4.02	-0.510	0.3	0.3	2.4
1.5	98.5	4.06	-0.470	0.1 ³	0.3	(0.01)
1	99	4.07	-0.470	0.1 ¹	0.1 ⁵	(0.01)

i_M is the current density measured from Fig. 2 at the plating potential (E_{pl}). i_{pl} is the plating rate calculated as current density. i_{Cu} is the current density at E_{pl} calculated assuming only copper acts as catalyst. a is the lattice constant. The values in brackets are at plating potentials when pure copper is passivated.

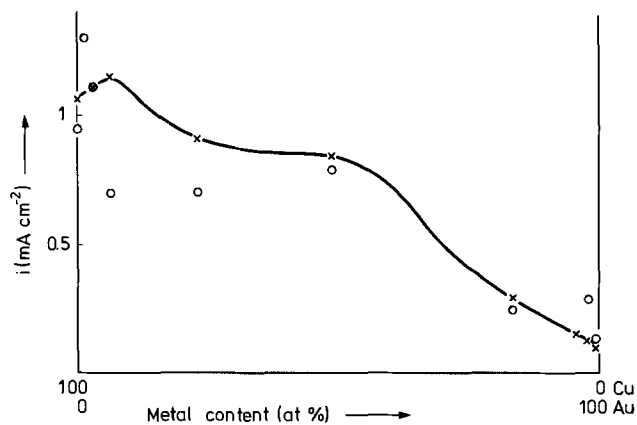


Fig. 1. The current at the mixed potential as a function of the metal content of the electroless Au-Cu deposits. X: Calculated from plating rate (i_{pl} in Table I). O: Measured from Fig. 2 (i_M in Table I).

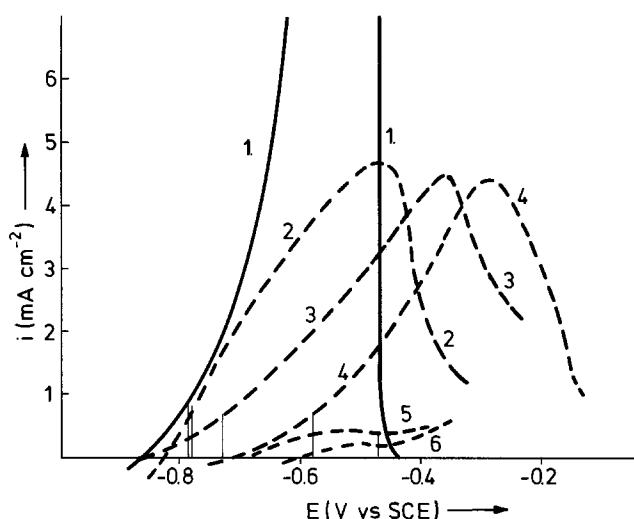


Fig. 2. Current-potential curves of the oxidation of formaldehyde measured at different Au-Cu deposits in solutions containing: 0.10M formaldehyde, 0.12M NaOH, 0.032M $\text{Na}_4\text{EDTA} \cdot 4\text{H}_2\text{O}$, 10^{-3}M KCN. 1: 100 a/o Cu. 2: 2.5 a/o Au-97.5 a/o Cu. 3: 23.1 a/o Au-76.9 a/o Cu. 4: 49 a/o Au-51 a/o Cu. 5: 98.5 a/o Au-1.5 a/o Cu. 6: >99 a/o Au-<1 a/o Cu. The current (i_M) at the plating potential (E_{pl}) is indicated by a vertical line in each case.

is not significantly changed when different alloy layers are used as electrodes in the corresponding solutions. Different plating potentials however, give different alloy compositions. We tried to measure the cathodic partial currents at the plating potential with the alloy as electrode and only gold or copper ions in solution. Because of changes in the electrode due to metal deposition, only the results for an alloy with approximately equivalent amounts of gold and copper are meaningful. The measured current densities at the plating potential ($E_{pl} = -0.577\text{V vs. SCE}$) in solutions containing 0.04M $\text{CuSO}_4 \cdot 5\text{H}_2\text{O}$, 0.072M $\text{Na}_4\text{EDTA} \cdot 4\text{H}_2\text{O}$, 0.12M NaOH, 10^{-3}M KCN, and $7 \cdot 10^{-3}\text{M}$ $\text{K Au}(\text{CN})_2$, 0.032M EDTA $4\text{Na} \cdot 4\text{H}_2\text{O}$, 0.12M NaOH, 10^{-3}M KCN, are as follows: $i_{\text{Cu}} = 0.36 \text{ mA cm}^{-2}$, and $i_{\text{Au}} = 0.22 \text{ mA cm}^{-2}$. These values lead us to expect an alloy composition of 53 a/o Au and 47 a/o Cu which is in good agreement with what we find (51 a/o Cu and 49 a/o Au). The composition of the autocatalytically deposited alloys can therefore be deduced from the cathodic partial reactions.

Hydrogen gas analyses were performed on a gold-copper alloy with about 1.5 a/o copper in a plating solution with the composition given in Fig. 5 (a + b) and a potential of -0.470V vs. SCE . In two experiments, 0.70 and 0.73 mol hydrogen gas were measured when two equivalents of gold and copper were deposited. On autocatalytic layers with a composition of 26 a/o copper and 74 a/o gold

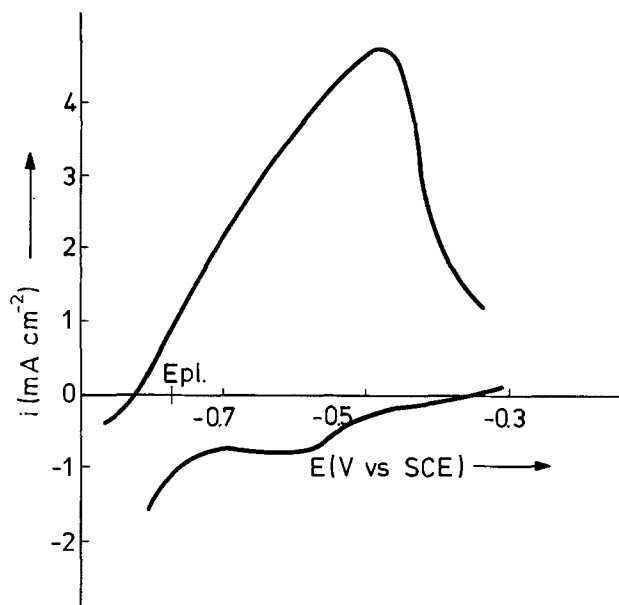


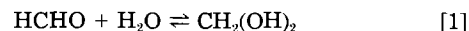
Fig. 3. The anodic and cathodic current-potential curves on a Au-Cu deposit with 2.5 a/o Au and 97.5 a/o Cu in solutions containing: top curve (anodic): 0.10M formaldehyde, 0.12M NaOH, 0.032M $\text{Na}_4\text{EDTA} \cdot 4\text{H}_2\text{O}$, 10^{-3}M KCN; bottom curve (cathodic): 0.04M $\text{CuSO}_4 \cdot 5\text{H}_2\text{O}$; $3.5 \cdot 10^{-4}\text{M}$ $\text{KAu}(\text{CN})_2$, 10^{-3}M KCN, 0.12M NaOH, 0.072M $\text{Na}_4\text{EDTA} \cdot 4\text{H}_2\text{O}$.

at a potential of -0.525V , we found about 0.90 mol hydrogen gas.

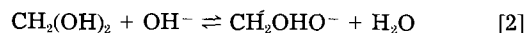
Discussion

In order to learn if the oxidation of formaldehyde takes place exclusively on copper or on the gold-copper alloy, we studied the reaction mechanism on the alloy. Van den Meerakker (5) found that the reaction on copper is different from that on gold.

Formaldehyde is completely hydrated in water



The hydrated formaldehyde is dissociated as a weak acid



It has been shown that the dissociated component, the methylene glycol ion, is the active reducing agent.

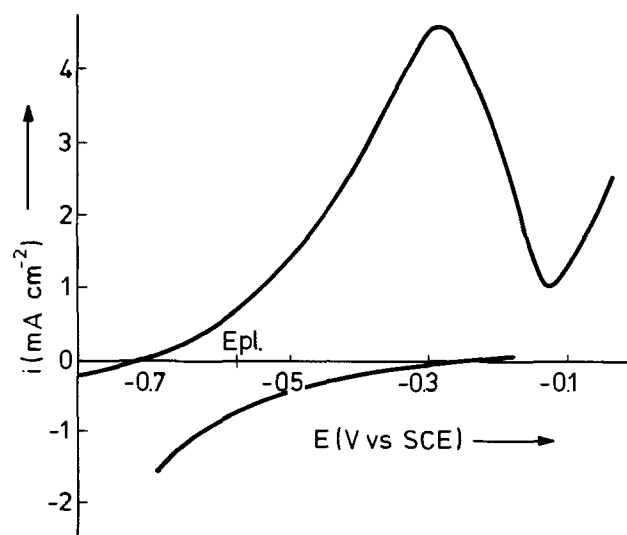


Fig. 4. The anodic and cathodic current-potential curves on a Au-Cu deposit with 49 a/o Au and 51 a/o Cu in solutions containing: top curve (anodic): 0.10M formaldehyde, 0.12M NaOH, 0.032M $\text{Na}_4\text{EDTA} \cdot 4\text{H}_2\text{O}$, 10^{-3}M KCN; bottom curve (cathodic): 0.04 $\text{CuSO}_4 \cdot 5\text{H}_2\text{O}$; $7 \cdot 10^{-3}\text{M}$ $\text{KAu}(\text{CN})_2$, 10^{-3}M KCN, 0.12M NaOH, 0.072M $\text{Na}_4\text{EDTA} \cdot 4\text{H}_2\text{O}$.

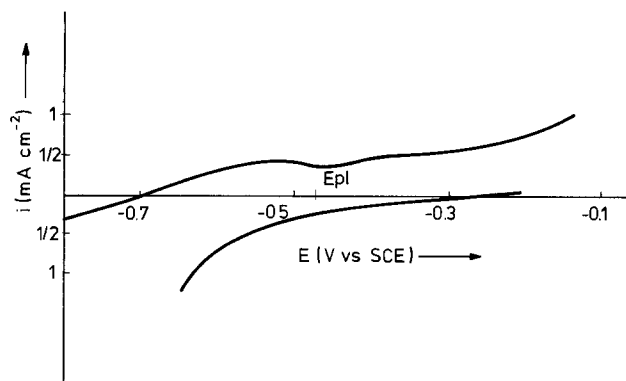
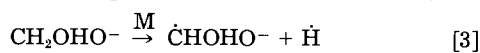


Fig. 5. The anodic and cathodic current-potential curves on a Au-Cu deposit with 98.5 a/o Au and 1.5 a/o Cu in solutions containing: top curve (anodic): 0.10M formaldehyde, 0.12M NaOH, 0.032M Na₄EDTA · 4H₂O, 10⁻³M KCN; bottom curve (cathodic): 0.04M CuSO₄ · 5H₂O, 1.4 × 10⁻²M KAUCN₂, 10⁻³M KCN, 0.12M NaOH, 0.072M Na₄EDTA · 4H₂O.

Atomic hydrogen is split from the adsorbed ions (5)



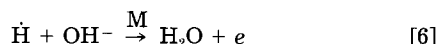
In a following reaction, an electron is released to the metal surface



and formate is formed in the solution. The atomic hydrogen at the metal surface can react in two ways



or



which gives an extra electron.

At a copper surface, only reaction [5] occurs, whereas on gold both reactions can take place; the ratio of the rates is dependent on the potential. Van den Meerakker (5) found on copper 100% reaction [5] and on gold at a potential of -0.500V vs. SCE 68% reaction [5] (0.68 mol hydrogen gas). During deposition of a gold alloy with 1.5 a/o copper at a plating potential of -0.470V vs. SCE , we determined 0.70 and 0.73 mol hydrogen gas. For an alloy with the composition of 26 a/o copper and 74 a/o gold (at a potential of -0.525V), we found 0.90 mol hydrogen. These results show that hydrogen gas is formed on the whole alloy and not only on the copper surface, as was suggested in Ref. 1.

A possible explanation could be that reaction [3] takes place on copper and the hydrogen atoms diffuse to the gold surface, on which reactions [5] and [6] then occur. This diffusion effect of hydrogen atoms over a large distance is called "spillover" and is mentioned frequently in recent discussions on catalysis (6). However, it is also possible that the overall oxidation reaction of formaldehyde takes place on the whole surface.

In Fig. 2, we have seen that the alloy layers have distinctive properties. Gold-copper layers do not passivate at potentials at which pure copper is oxidized. We compared the current at the plating potentials (i_M in Fig. 2) for each alloy with the current deduced from the deposition rate (i_{pl}) and found a reasonable agreement (Table I). From the current potential curve for the oxidation of formaldehyde at a pure electroless copper as electrode, we also calculated the current at the alloy plating potentials, assuming that only the copper in the alloy is responsible for the oxidation of formaldehyde and the copper atoms are homogeneously distributed throughout the layer. The resulting values (i_{Cu}) are given in the last column of Table I. The values in brackets are unreliable because pure copper is passivated at these potentials. A comparison of the calculated values with the plating rates indicates that the fraction of copper in the alloy cannot explain the low plating rates found in a range of gold-copper layers with more than 5 a/o gold (Table I).

It is possible that the concentration of copper at the surface is lower than in the bulk. The surface layer of an alloy is enriched in the component which has the lower surface free energy (7). The values for copper ($\gamma_{Cu} = 1800 \text{ mJ/m}^2$) and gold ($\gamma_{Au} = 1500 \text{ mJ/m}^2$) indicate that an enrichment of gold at the surface will take place; the effect is, however, not large (7). It is not likely that such an enrichment can explain our results. It is also possible that the copper in the alloy is less active than pure copper because of changes in the electronic structure of the metals. Since the work function of gold (5.1 eV) is larger than that of copper (4.65 eV), gold will accept negative charge from copper and the copper will be more positive in a gold-copper alloy. The electronic structure of the alloy may affect the competitive adsorption of cyanide and formaldehyde on the alloy surface. Cyanide ions inhibit the oxidation of formaldehyde on pure gold (1). Okinaka (8) has also shown that cyanide inhibits the oxidation of borohydride on gold. Horkans (9), using cyclic voltammetry, studied the effect of cyanide on the oxidation of formaldehyde on copper and gold at different potentials and found results similar to those reported in our earlier work (1). Cyanide ions poison the oxidation of formaldehyde on gold. On copper, however, higher formaldehyde currents can be sustained in the presence of cyanide. It is likely that the competition between the adsorption of formaldehyde and cyanide on the alloy determines the plating rate of the metallization.

Conclusions

In cyanide solutions, the oxidation current of formaldehyde on gold-copper alloys is lower when the alloys contain more gold. This decrease is accompanied by a shift of the passivation potential to more positive values. When the gold cyanide concentration in the plating solution is increased, the plating potentials are determined by the oxidation of formaldehyde (anodic current) and not by the deposition of gold and copper (cathodic current). The different plating potentials give a different cathodic current ratio for gold and copper. The currents at the plating potentials are generally in agreement with the plating rates, but not with the values calculated assuming that only the copper in the alloy is the active catalyst. Analyses of hydrogen evolution during electroless alloy plating lead us to conclude that hydrogen atoms are either formed on the whole alloy surface or that hydrogen atoms diffuse from the copper surface to the gold surface (spillover). It is suggested that the autocatalytic alloy deposition is determined by the competition between the adsorption of formaldehyde and cyanide on the alloy surface.

Acknowledgment

The authors would like to express their thanks to Dr. J. J. Kelly and Dr. G. Frens for helpful discussions.

Manuscript submitted Sept. 10, 1984; revised manuscript received Nov. 16, 1984.

Philips Research Laboratories assisted in meeting the publication costs of this article.

REFERENCES

1. A. Molenaar, *This Journal*, **129**, 1917 (1982).
2. A. Brenner, "Electrodeposition of Alloys," Vol. II, p. 520, Academic Press, New York (1963).
3. B. C. Cates, J. R. Katser, and G. C. A. Schuit, "Chemistry of Catalytic Processes," pp. 213-236, McGraw-Hill, New York (1979).
4. K. P. de Jong, Thesis, University of Utrecht, Utrecht, The Netherlands (1982).
5. J. v. D. Meerakker, *J. Appl. Electrochem.*, **11**, 387 (1981).
6. G. M. Pajonk, S. J. Tiechnev, and J. E. Germain, in "Proceedings of the International Symposium, Lyon-Villeurbanne 1983," Elsevier, Amsterdam.
7. M. J. Sparnaay and G. E. Thomas, *Surf. Sci.*, **135**, 184 (1983).
8. Y. Okinaka, *This Journal*, **120**, 743 (1973).
9. J. Horkans, *ibid.*, **131**, 1615 (1984).

Operational Study of a Phosphoric Acid Fuel Cell with Hydrogen and Methanol/Steam

M. Ratcliff, F. L. Posey, D. K. Johnson, and Helena L. Chum*

Solar Energy Research Institute, Thermochemical and Electrochemical Research Branch, Golden, Colorado 80401

ABSTRACT

Studies were performed comparing the operation of phosphoric acid fuel cells on hydrogen and air at constant load as a function of time and after operation under other conditions, namely: (i) periodic direct injection of methanol-water vapor, simulating failure of the steam re-forming unit, and (ii) open-circuit excursion. Tests were carried out on two 3W fuel cells (Energy Research Corporation, Danbury, Connecticut). Detailed organic product analyses of condensed effluent gases of both anode and cathode reveals that trimethylphosphate, a suspect carcinogenic compound, is released. After 5-6h, direct addition of methanol/water vapor at a rate sufficient to support constant 200-100 mA/cm² performance on hydrogen (steam re-former unit assumed 90% conversion) 0.5 mg of trimethylphosphate were detected from both anode and cathode effluents. These results translate into about 10-30 ppm/h of trimethylphosphate in the anode effluent and about one-third or less of that amount in the cathode effluent stream. These results may impact *in situ* methanol re-forming in phosphoric acid fuel cells and also external reforming at low methanol steam reforming conversion.

Methanol is a likely alternative to petroleum-derived fuels (1). It can be derived from a variety of resources both renewable and nonrenewable. In particular, when fuel cell power generation is considered, methanol is an attractive fuel since its steam reforming into hydrogen and carbon dioxide is favorable thermodynamically at moderate temperatures (< 300°C). The use of steam-reformed methanol in various types of fuel cells for vehicular applications has been reviewed recently (2-5). Methanol steam re-forming coupled to a palladium membrane for hydrogen separation from carbon dioxide has been described for use with an alkaline fuel cell (6). Methanol is also the fuel selected for the development of tactical fuel cell power plants in special military applications at brigade and forward areas (7). Investigation of some aspects of methanol steam re-forming coupled to phosphoric acid fuel cells has been carried out by Landsman and Luczak (8). The economics of biomass-derived alcohol applications in fuel cells has been reviewed recently (9). This paper presents further investigations of the combination: methanol steam re-forming to a state-of-the-art phosphoric acid fuel cell (from Energy Research Corporation, Danbury, Connecticut). We have simulated periodic failures of the steam re-forming unit by adding directly steam and methanol vapor to a phosphoric acid fuel cell which was otherwise continuously operated on hydrogen and air (or oxygen). These were more drastic conditions than one would expect in the operation of a fuel cell. A practical reformed methanol fuel cell is maintained at temperature by the enthalpy difference between ΔH and $-nFV$, where V is the terminal voltage per reacting mole of fuel. If a failure occurs, the cell would be expected to rapidly cool down. The data are pertinent to the operation of a cell with lower than 100% conversion efficiency, in which case both hydrogen and vapor methanol would be added to the operating fuel cell at the operating temperature. These results are also pertinent to *in situ* re-forming of methanol in phosphoric acid fuel cells. Data concerning cell performance degradation and the nature of the organic products that can be condensed from the anode and cathode effluent gases, as well as those remaining in the phosphoric acid matrix after methanol vapor addition, are reported.

Experimental

Materials.—UHP H₂, UHP O₂, and zero air were from Scientific Gas Products. High purity methanol is used as supplied from Burdick and Jackson. H₂O was deionized and distilled. 100% H₃PO₄ was prepared from Baker reagent-grade P₂O₅ and the stoichiometric amount of H₂O. Aqueous formaldehyde, trimethylphosphate, and formic acid were reagent grade from Aldrich. Methyl formate

was Baker reagent grade. A methanolic solution of formaldehyde was obtained from Celanese.

Equipment.—The fuel cell test bench is equipped with Matheson 600 Series Rotameters to control gas flows. Temperature control of the fuel cell is accomplished with an Omega 4000 Series temperature control with a K-type thermocouple. Polarization data are read from GE 800 Series digital panel meters. Polarization is changed with variable resistors in the test circuit and a toggle switch is used to consistently go to open-circuit condition. IR-free data were obtained with a Tektronics 7613 oscilloscope. An ESC 640 coulometer was employed.

The methanol/water vapor delivery system consists of a Sage Model 355 syringe pump with one or two gastight syringes (5-25 ml) adapted through Teflon plumbing (for two syringes) into a single 11 in. long 20 gauge SS needle. This needle passes through a septum into 1/8 in. stainless steel tubing. The tubing is about 8 ft long and coiled for about 6 ft so that the vapor is always rising. A pressure gauge and relief valve are incorporated into the boiler. The entire length is wrapped with heater tape and insulation. A thermocouple is installed at the boiler outlet and controls the temperature with a Watlow controller. A temperature difference of 90°-200°C exists in the line from liquid injection point to outlet. Flow rate settings from 0.25-12 ml/h were calibrated, and gas chromatographic analyses of the condensed vapor verified the ratios of methanol/water injected (1:1.2 or 1:0.6 mole ratio). At 200 mA/cm² (5A), the cells require 1.17×10^{-1} mol/h of hydrogen (assuming a current efficiency of 80%). Injection of 1.0:1.2 mole ratio of methanol in water at 2.6 ml/h meets this fuel requirement (assuming a steam re-forming conversion efficiency of 90%). Typically, the cells are fed methanol/water vapor at 2.6 ml/h or less; most experiments used 1.0:0.6 methanol:water mole ratio to increase the collection yields.

The phosphoric acid fuel cells used were supplied by Energy Research Corporation (Danbury, Connecticut). They were constructed in late 1982 and are optimized to run on H₂ and air. Electrode area is 25 cm² with a Pt loading of ~0.5 mg/cm² on the cathode and ~0.25 mg/cm² on the anode.

Operation on H₂/O₂ or air.—Cells that had never been run were pretreated by heating to 150°C for ~16h with no gas flow on load. After that time, the cell temperature was readjusted to 190°C and the fuel and oxidant gases turned on. The cell was connected to the gas lines with 1/4 in. × 28 threads/in. connectors, and gas pressure was 20 psi. The gas flow rates were ~55 ml/min H₂, 500 ml/min air (or ~30 ml/min O₂). There were four electrical leads to the current collectors: one set for the voltmeter and the other for the load through the variable resistors and ammeter. We operated the cell at 200 mA/cm² current

*Electrochemical Society Active Member.

density most of the time. For the freshly assembled cell the open-circuit voltage was 920-980 mV with H_2/O_2 or 900-950 mV with H_2/air . When the performance was lower than these values, it generally indicated that more electrolyte (100% H_3PO_4) was needed. The cell was recharged with 0.7-1.0 ml electrolyte with a gastight syringe into the fill tube.

Operation on methanol/water/air.—The operation of the fuel cell on methanol/water was similar to that on H_2/air , with the following exceptions. Methanol/water mixtures (1:1.2 or 1:0.6 mole ratio) were prepared gravimetrically and filtered before being drawn into the syringes. The syringes were placed in the pump and connected to the Teflon tubing/20 gauge needle and the boiler was warmed to 200°C (outlet temp.). The syringe pump was then turned on and usually adjusted to 2 ml/h. The system was allowed to equilibrate for ~30 min before connection to the fuel cell. The H_2 was shut off and disconnected. The boiler was then plumbed into the PTFE anode inlet tube and insulated with glass wool. The cell exhaust tubes were routed into round-bottom flasks equipped with reflux condensers to collect the vapors yielding the condensates for analyses. Alternatively, the exhaust tubes were immersed in round-bottom flasks filled with saturated barium hydroxide to precipitate the CO_2 evolved.

Data analysis.—The current voltage polarization curves were analyzed through a multiple linear regression analysis on a Hewlett-Packard Model 85 computer.

Identification and quantitation of effluent compounds.—Carbon dioxide from anode and cathode effluents was determined by passing the gases through solutions of saturated barium hydroxide. The $BaCO_3$ formed was filtered, washed with deionized water, and dried in a vacuum desiccator to constant weight.

Condensed organic volatile components were identified by mass spectroscopy. Mass spectral data were obtained on a Hewlett Packard 5985 GC/MS using both direct insertion and a packed column coupled to the mass spectrometer (electron-impact mode). In the direct insertion mode, the initial probe temperature was 25°C. This temperature was held for 5 min, after which the probe was heated to 250°C at 5°C/min. The following organic products have been detected (numbers in parentheses are the major mass peaks in the mass spectrum, electron-impact mode): formaldehyde ($m/z = 30, 29, 28$); methanol ($m/z = 32, 31, 29$); methylformate ($m/z = 60, 31, 29$); dimethoxymethane ($m/z = 75, 45, 29$); formic acid ($m/z = 46, 45, 29$); another possible compound detected was hydroxymethoxy methane ($m/z = 62$). In addition, trimethylphosphate was detected [$m/z = 140, 110$ (major) 96, 80, 79]. The best separation and resolution of peaks of the organic products was achieved with a 6 ft \times 1/4 in. glass column packed with a 50/50 mixture of Porapak QS and Porapak T, 80/100 mesh. The column was held at 120°C for 2 min then heated to 240°C at 20°C/min. Quantitation for all organic materials except trimethylphosphate was performed on the Varian 3700 gas chromatograph equipped with a VISTA 401 data acquisition system. The internal standard was dioxane. Helium flow rate was 25 ml/min. Thermal conductivity detector was MA:206. Quantitation of trimethylphosphate was performed on the mass spectral data from the Porapak QS/T column described above under the same conditions. Amounts were determined by the internal standard method using areas of selected ion peaks monitored by the system computer (see examples in Fig. 1). Errors in the quantitation are $\pm 10\%$ (GC) and $\pm 30\%$ (single-ion monitoring technique) due to the small amounts of the compounds.

GC and mass spectral assignments were verified by injecting the authentic pure compounds and comparing their retention times and fragmentation patterns with those of the condensed products. The library editor program for probability-based search of the HP5985 GC/MS system was also used in the identification of the condensed products. The probabilities of correct identifica-

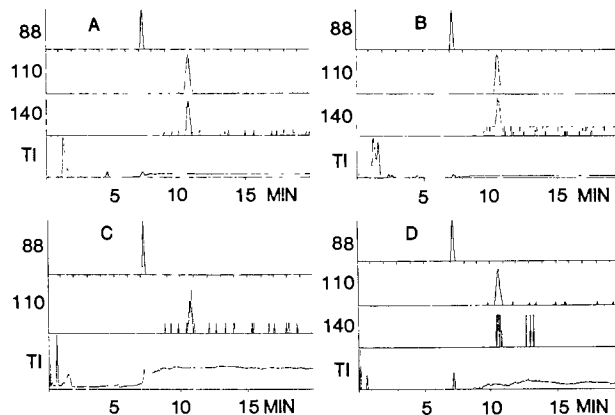


Fig. 1. Examples of single-ion monitoring of condensed anode (A, B) and cathode (C, D) effluent streams. Trimethyl phosphate ions: $m/z = 110$ and 140. Dioxane (internal standard): $m/z = 88$. TI = total ion. Injection of methanol/water vapor at 1:0.6 mole ratio at 2 ml/h for A and C: 7h and B and D: 5h.

tion of the various compounds ranged between 0.997 and 0.9999 (both in the standards and condensed effluent streams).

After cell shutdown, the phosphoric acid and possible esters were washed out of the silicon carbide matrix with D_2O and the proton NMR spectrum obtained. The spectrum obtained consists of one major doublet (3.63 ppm, $J = 11.2$ Hz) and another doublet of smaller intensity at 3.58 ppm ($J = 10.8$ Hz). The second doublet is probably due to the partially esterified products. Trimethylphosphate in D_2O presents a doublet (3.70 ppm, $J = 11.2$ Hz). (These chemical shifts are accurate to ± 0.05 ppm.) Under these conditions polyphosphates would most likely have hydrolyzed. Phosphorus NMR measurements confirmed the proton assignments.

Results and Discussions

Single cell performance.—A typical polarization curve of cell no. 1 is shown in Fig. 2 for hydrogen and air (or oxygen). The open-circuit voltage and the voltage on constant load to generate 200 mA/cm² as a function of time are displayed in Fig. 3. Also indicated in Fig. 3 is one period of 48h during which the cell was submitted to open circuit, a common condition in vehicular applications. After 120 days of operation on constant load, injec-

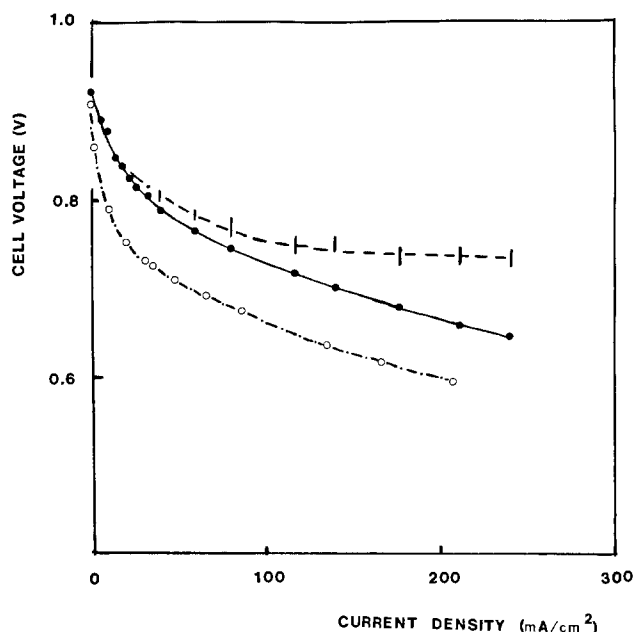


Fig. 2. Current-voltage polarization curves of phosphoric acid fuel cell no. 1 at 190°C. \circ : H_2/air . \bullet : H_2/O_2 . $I = iR_i$ corrected measurements.

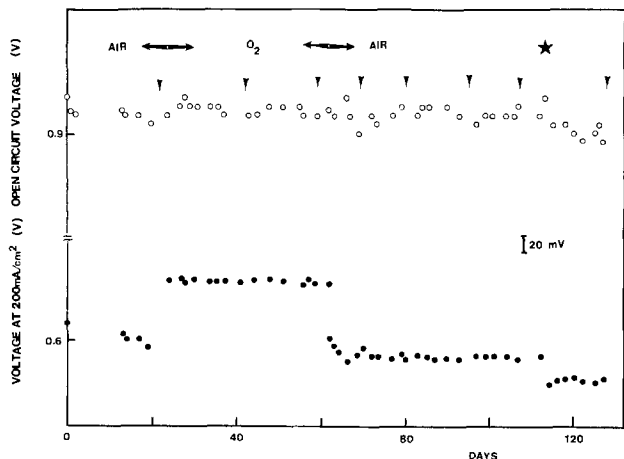


Fig. 3. Open-circuit voltage and voltage under load to produce 200 mA/cm² of fuel cell no. 1 as a function of time. Addition of phosphoric acid is represented by ∇. At *, the cell was left for 48h in open-circuit conditions. Cell temperature: 190°C.

tion of methanol/water vapor at 190°C was interspersed with operation on hydrogen (12 periods of ~6h [from 4 to 7h] over 35 days), as shown in Fig. 4. The amount of methanol added approximated that required to maintain 200 mA/cm² after steam re-forming (assumed 90% conversion). The upper curves display the open-circuit voltage and voltage on load on hydrogen and air. The lower curves indicate open-circuit voltage and voltage on load on methanol/water vapor and air. The second cell was also oper-

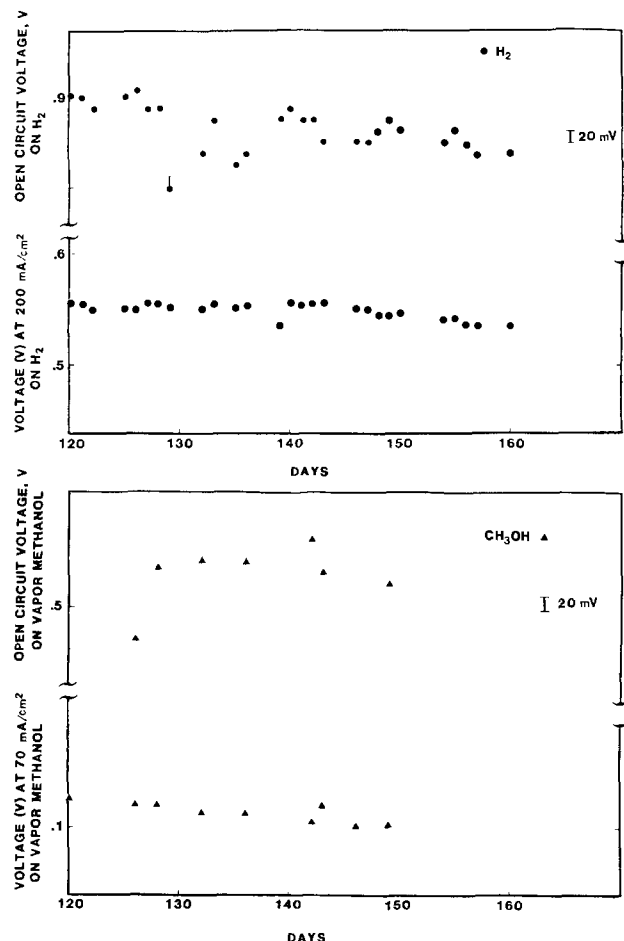


Fig. 4. Operation of fuel cell no. 1 on H₂/air (upper curve) interspersed with periods of addition of direct methanol/water vapor (at 190°C) (lower curve). Cell temperature: 190°C. Open-circuit voltage and voltage at 200 mA/cm² given for operation on hydrogen. For operation on methanol/water vapor, open-circuit voltage and voltage at 70 mA/cm² are given.

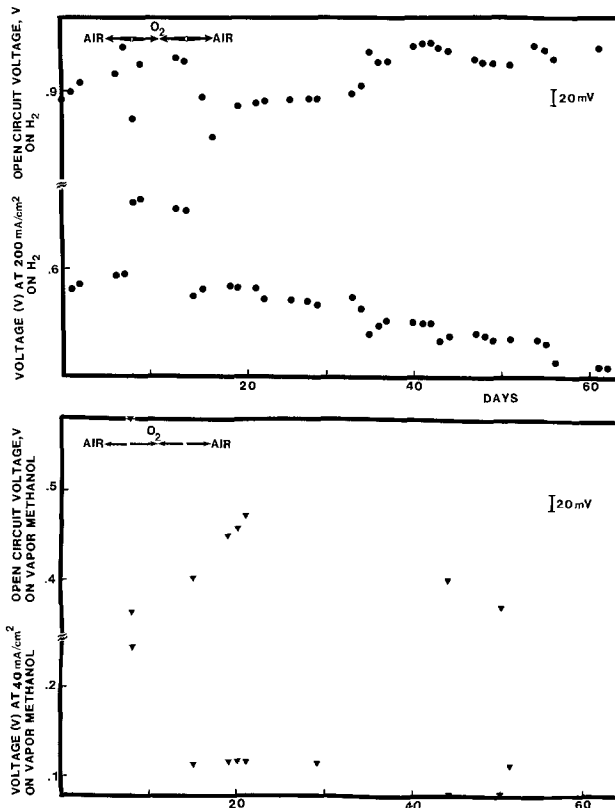


Fig. 5. Operation of fuel cell no. 2 on H₂/air (upper curve) interspersed with periods of addition of direct methanol/water vapor at 190°C (lower curve). Cell temperature: 190°C. Open-circuit voltage and voltage at 200 mA/cm² given for operation on hydrogen. For operation on methanol/water vapor, open-circuit voltage and voltage at 40 mA/cm² are given.

ated on constant load at 200 mA/cm² on hydrogen and air (or oxygen) except for ten (total 54h) periodic injections of methanol/water vapor in variable amounts (from equivalent amounts to produce 200-50 mA/cm²) over a period of 60 days (Fig. 5). Figure 6 shows an example of a polarization curve on CH₃OH/H₂O. In addition, one ethanol/water vapor injection was attempted. The cell performance on ethanol was much poorer than that shown for CH₃OH/water vapor in Fig. 6. After the ethanol addition, the anode was steamed to remove residual ethanol and methanol (air was continuously fed to the cathode). A substantial performance recovery of the anode was observed after steaming. After this experiment, four additional runs on methanol/water vapor were performed for collection of condensable products.

The cell voltage (V) can be expressed as a function of current density (i) by the equation

$$V = V_r - \frac{RT}{\alpha_a F} \ln \frac{i}{i_{0,a}} - \frac{RT}{\alpha_c F} \ln \frac{i}{i_{0,c}} - iR_i \quad [1]$$

assuming that the concentration overvoltage is negligible (10). V_r is the thermodynamic reversible voltage, α_a and α_c are the transfer coefficients, $i_{0,a}$ and $i_{0,c}$ the exchange current densities of the anodic and cathodic reactions, and R_i is the internal resistance of the cell. Equation [1] can be reduced to

$$V = A - B \ln i - iR_i \quad [2]$$

where

$$A = V_r + \frac{RT}{\alpha_a F} \ln i_{0,a} + \frac{RT}{\alpha_c F} \ln i_{0,c} \quad [3]$$

and

$$B = \frac{RT}{\alpha_a F} + \frac{RT}{\alpha_c F} \quad [4]$$

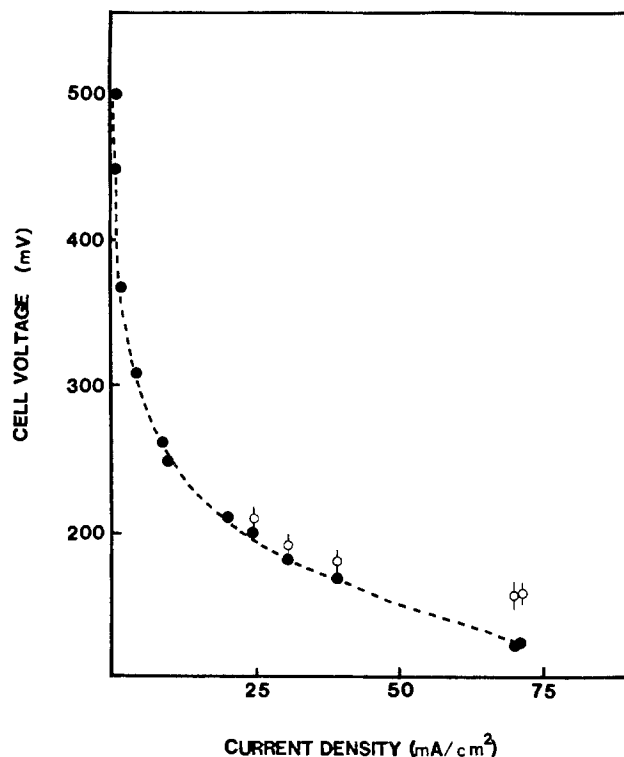


Fig. 6. Current-voltage polarization curve of cell no. 1 operated on direct methanol/water vapor added at 190°C in 1.0:1.2 mole ratio at 6 ml/h. ○: IR_1 -corrected measurements.

The values of A , B , and R_i were calculated by multiple linear regression analysis, and they are assembled in Table I. The value of A leads to an approximate value of the cathodic exchange current since the overpotential for hydrogen ionization is very small compared to that for oxygen reduction. For the same reason, the value of B effectively represents the Tafel slope for oxygen reduction. Larger experimental errors were associated with measurements of H_2/O_2 cells and those exposed to prolonged exposure to MeOH/ H_2O injection.

From Fig. 3, one can observe the performance degradation of cell no. 1 as a function of time compared to that

obtained after one period of 48h in open circuit. After 65 days on constant load, one observes degradation equivalent to that in the single open-circuit excursion. Similar faster degradation was observed after the periodic additions of methanol/water vapor, as shown in Fig. 4. When switching from the alcohol/water vapor fuel to hydrogen at the beginning of the test, voltage values at load recovered quickly (within a few minutes), and the voltages were stable. Towards the end of the test, the voltages were much less stable.

From the data in Table I, one can observe that, whereas the values of B are constant within the experimental errors, the values of A (± 10 mV), related mainly to the exchange currents, decrease faster both as a result of the open-circuit excursion and of methanol addition. At the same time the cell resistance increased 30%-40%. The decrease in A value is probably a result of the anode catalyst degradation possibly due to site reorganization and poisoning by the methanol oxidation intermediates. In addition, catalyst sites at the cathode are used in the chemical oxidation of methanol with air. Such utilization can lead to cathode catalyst degradation as well. The increased cell resistance is a result, among other factors, of trimethylphosphate (or methylpolyphosphate formation), which would contribute to the decreased conductance of the phosphoric acid electrolyte.

These trends were confirmed with the experiments using the second cell. This cell exhibited higher open-circuit voltages and A values; however, the initial cell resistance was 45% higher than that in cell no. 1 and increased significantly with addition of methanol/water vapor during one month (see Table I and Fig. 5). It is interesting to notice the remarkable performance recovery of the cell after steaming the anode. A values increased ~ 50 mV (cf. 10/11/83 with 9/26/83 data).

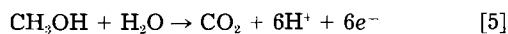
Collection of condensed products.—In most of the experiments described above, with addition of methanol/water vapor at constant load, the effluent gases from anode and cathode were condensed and analyzed. Initially, this test was performed on hydrogen/air to estimate the fraction of water vapor that can be effectively collected under our experimental conditions; 70% of the theoretically expected amount of water was condensed.

Direct injection of methanol/water vapor into a phosphoric acid fuel cell causes the following reactions to occur

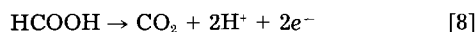
Table I. Analyses of voltage-current density measurements of H_2 /air or oxygen fuel cells no. 1 and no. 2 according to $V = A - B \ln i - iR$

Date	Conditions	Open-circuit voltage (V)	A (V) ± 0.01	B (mV)	R (Ω cm ²) ± 0.05
Cell no. 1 (operation started 3/15/83)					
3/29/83	Air	0.910	0.865	82 \pm 1	0.40
4/8/83	O ₂	0.920	0.897	73 \pm 5	0.40
5/23/83	Air	0.900	0.878	84 \pm 1	0.50
6/20/83	Air	0.915	0.885	89 \pm 1	0.49
7/5/83	Air	0.920	0.890	91 \pm 1	0.50
7/7/83	Air/after 48h open-circuit	0.890	0.873	92 \pm 1	0.55
7/8/83	Air	0.910	0.871	91 \pm 1	0.55
7/13/83	Air	0.900	0.868	88 \pm 2	0.64
7/25/83	After 9.3h injection CH ₃ OH/H ₂ O	0.860	0.839	76 \pm 10	0.55
7/28/83	After 6.8h injection CH ₃ OH/H ₂ O	0.840	0.825	70 \pm 30	0.57
8/24/83	After 46.6h injection CH ₃ OH/H ₂ O	0.890	0.825	72 \pm 3	0.60
Cell no. 2 (operation started 8/30/83)					
9/7/83	Air	0.950	0.903	86 \pm 4	0.55
9/8/83	O ₂	0.981	0.98	88 \pm 7	0.50
9/13/83	After 5.5h injection CH ₃ OH/H ₂ O	0.940	0.88	—	0.7
9/16/83	After 5.0h injection CH ₃ OH/H ₂ O	0.894	0.888	72 \pm 4	0.7
9/26/83	After 17.5h injection CH ₃ OH/H ₂ O	0.895	0.874	60 \pm 10	0.8
10/11/83	After 5h CH ₃ OH/H ₂ O injection, 4.5h of anode steaming, air in cathode	0.953	0.920	90 \pm 2	0.87

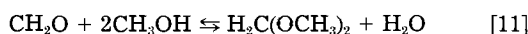
Overall anode:



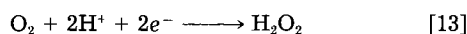
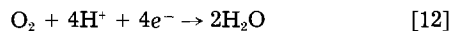
through the following overall intermediate reactions



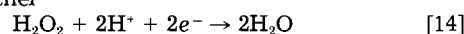
Chemical reactions with excess methanol:



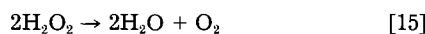
Cathode reactions:



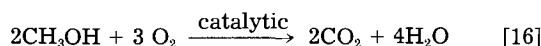
followed by either



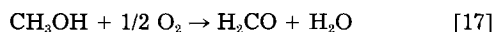
or



Other chemical reactions at the cathode:



through partial oxidations



In situ re-forming, $\text{CH}_3\text{OH} + \text{H}_2\text{O} \rightarrow \text{CO}_2 + 3\text{H}_2$, would not be favored under the experimental conditions.

Through GC and combined GC and MS (see experimental section) analytical techniques and NMR, we have evidence for reactions [5]-[11], [16], and [17].

Quantitation of reactions [5] and [16] is shown in Table II based on the precipitation of evolved carbon dioxide as barium carbonate. A comparison of the charge (current \times time) and that estimated from carbon dioxide evolution in the anode indicates that the mass and charge balance agree within 10%. The cathode released CO_2 indicates the amount of methanol which reaches the cathode and is chemically oxidized by oxygen in the presence of the catalyst. As seen from Table II, the higher the amount of methanol injected, the higher proportion of chemical oxidation. For instance, the ratio of methanol injected is 1:2:8 from C:B:A; it is closely followed in the amount of millimoles of carbon dioxide collected in the cathode. These two reactions account for 30% (A) to ~58%-65% (B and C) of the methanol injected. In parallel experiments, we have determined that 20%-30% of the excess methanol

can be condensed according to our experimental procedure. Therefore, we can account for 50%-70% of the methanol added, which compares well with the 70% recovered water from similar experiments on hydrogen and air.

The other organic intermediate products are present in small concentrations, in agreement with Landsman and Luczak (8) except for trimethylphosphate, which was not detected by these authors using infrared absorption spectroscopy. We positively identify trimethylphosphate both in the anode and cathode effluent streams and in the electrolyte matrix. Examples of the concentrations of the various organic compounds detected are shown in Table III.

Conclusions

The above results indicate that the 3W cell releases on the average a total of 4×10^{-3} mmol of trimethylphosphate, 88% of which is present in the anode effluent stream. This number represents ~0.56 mg of trimethylphosphate condensed after ~5h of addition of 195-295 mmol of methanol in an average of 6 milliliter of anode and cathode condensate. Since the collection efficiency of these experiments is ~70% for chemicals with lower boiling points (~100°C), it is expected that most of the trimethylphosphate was condensed, since its normal boiling point is 198°C. For experiments 6 and 9 described in Table III, our analytical results translate into approximately 10 and 30 ppm/h of trimethylphosphate in the anode effluent stream. The cathode stream effluent is estimated releasing one-third or less of that compound per hour.

Trimethylphosphate is a suspected carcinogenic compound. Some literature is available to date.¹ Our results show that this chemical could be released when cells are operated at 190°C when methanol vapor is added to the cells.

A large concentration of trimethylphosphate (see NMR data) and possible methylpolyphosphates is present in the electrolyte matrix. Ester formation could lead to power loss due to increased cell resistance. Benefits of steaming the anodes were derived, possibly by driving some of the excess alcohol from the cell.

Additional data for carcinogenicity of trimethylphosphate are necessary. Studies of the equilibria of ester formation in 100% phosphoric acid are underway, as well as the ester formation at lower level additions of methanol vapor simulating operating conditions (*e.g.*, 80% conversion efficiency in the presence of hydrogen).

Acknowledgments

The authors wish to thank Dr. S. Srinivasan, Professor K. Kordesch, Dr. J. Appleby, and Dr. J. Huff for many

¹Positive carcinogenicity as determined by the mammalian cytogenetic bone-marrow assay (12) and the *in vivo* mammalian cytogenetic leukocyte or lymphocyte assay (13) has been found. TMP is registered in the "Registry of Toxic Effects of Chemical Substances 1979," under no. TC8225000. The carcinogenesis bioassay is reported as completed with positive results for mouse and rat. For additional information on carcinogenicity of organic compounds, including TMP, see Ref. (14).

Table II. CO_2 collection experiments as barium carbonate

Experiment number ^a	Flow rate (ml/h) ^b	Total CH_3OH injected (mmol)	Avg. I (A)	Faradays ($I \times \text{time}/96,500$)	Faradays based on mmol anode CO_2	Anode CO_2 (mmol)	Cathode CO_2 (mmol)	Percent of methanol recovered as CO_2
A 10/14/83 ERC no. 2	2	39	1	3.7×10^{-2}	3.4×10^{-2}	5.7	5.9	30%
B 10/21/83 ERC no. 2	0.5	10	0.85	3.2×10^{-2}	3.0×10^{-2}	5.0	1.5	65%
C 10/26/83 ERC no. 2	0.25	5	c	—	1.2×10^{-2}	2.1	0.8	58%

^a All experiments with cell no. 2.

^b All experiments 1:0.6 mol ratio $\text{MeOH}:\text{H}_2\text{O}$.

^c Average I not measurable due to instability.

Table III. Quantitation of condensed anode and cathode effluents for organic products by GC or GC/MS

Date	Time on CH ₃ OH/H ₂ O vapor (h)	Average current (A)	Total H ₂ O injected (mmol)	Total CH ₃ OH injected (mmol)	MeOH condensed (mmol)	Estimate ^a of MeOH transformed into CO ₂ (anode and cathode)	Millimoles of organic products ^b								Volume (ml) condensed			
							PO(OCH ₃) ₃ (× 10 ³)		H ₂ CO (× 10 ¹)		HCOOH (× 10 ²)		HCO ₂ CH ₃ (× 10 ²)					
							A	C	A	C	A	C	A	C	A	C	A	C
7/29/83	6.0	1.5	140	235	45	120												
8/4/83	6.9	1.25	160	270	50	110	NM	NM	2.5	8	1	3	—		3.0	4.3		
8/9/83	7.0	1.25	165	275	65	115	NM	NM	2.6	7	4	22	2		2.6	5.8		
8/11/83	7.5	1.25	175	295	75	120	NM	NM	2.2	7	2	2	7		2.1	6.0		
9/8/83	5.5	2.0	130	215	80	125	1.6	traces	1.6	NM	NM	NM	9		3.0	5.8		
9/15/83	5.0 ^c	1.1	120	195	40	70	2.5	0.5	NM	4	NM	NM	7		1.5	3.1		
9/19/83	5.0 ^c	1.1	120	195	30	70	2.0	traces	NM	4	NM	NM	5		1.5	2.4		
9/20/83	7.5 ^c	1.1	175	290	50	110	1.5	0.4	NM	8	NM	NM	7		2.7	3.9		
9/20/83	5.0 ^c	1.1	120	195	45	70	9.0	traces	NM	8	NM	NM	8		2.3	3.7		

^a Anode CO₂ amounts were measured in most experiments. In some cases, both anode and cathode evolved CO₂ were measured. Amounts evolved in the cathode are roughly the same as those evolved in the anode at large methanol excess (for example, see Table II at 40 mmol).

^b The first four sets of analytical data were obtained by GC on a 6 ft × ¼ in. glass column packed with 80-100 mesh Porapak QS programmed from 100° to 200°C; the second set of data were obtained by GC or GC/MS on 50/50 mixture Porapak QS and T, as described in the experimental section.

^c Anode and cathode CO₂ measured in parallel experiments; condensates collected in these experiments.

NM: Not measured under the experimental conditions.

helpful suggestions and valuable discussions. The cooperation of Energy Research Corporation personnel, mainly Dr. H. Maru and Mr. M. George, is gratefully acknowledged. Thanks are also due to R. G. Nix, S. Black, P. Palasz, A. Swartzlander, and J. Veltrie for their cooperation during the experimental work. This work was supported by the Office of Alcohol Fuels, WPA 349, as part of the assessment of high efficiency methanol utilization routes.

Manuscript submitted Dec. 22, 1983; revised manuscript received Oct. 26, 1984.

The Solar Energy Research Institute assisted in meeting the publication costs of this article.

REFERENCES

1. T. B. Reed, Editor, "Biomass-to-Methanol Specialist's Workshop," March 3-5, 1982, Solar Energy Research Institute, Golden, CO (1982); Office of Technology Assessment, United States Congress, OTA-E-124 (1980); J. L. Ehrler and B. Juran, *Chemtech*, **13**, 188 (1983).
2. K. V. Kordesch, in "Renewable Fuels and Advanced Power Sources for Transportation Workshop," H. L. Chum and S. Srinivasan, Editors, p. 1-17, SERI/CP-234-1707, Solar Energy Research Institute, Golden, CO (1983).
3. D. K. Lynn, in "Renewable Fuels and Advanced Power Sources for Transportation Workshop," H. L. Chum and S. Srinivasan, Editors, pp. 167-182 and references therein, SERI/CP-234-1707, Solar Energy Research Institute, Golden, CO (1983).
4. H. C. Maru, D. N. Patel, and B. S. Baker, in "Renewable Fuels and Advanced Power Sources for Transportation Workshop," H. L. Chum and S. Srinivasan, Editors, pp. 109-126, SERI/CP-234-1707, Solar Energy Research Institute, Golden, CO (1983).
5. L. J. Nuttall, in "Renewable Fuels and Advanced Power Sources for Transportation Workshop," H. L. Chum and S. Srinivasan, Editors, pp. 93-108, SERI/CP-234-1707, Solar Energy Research Institute, Golden, CO (1983).
6. N. I. Palmer, B. Leiberman, and M. A. Vertes, in "Hydrocarbon Fuel Cell Technology," B. S. Baker, Editor, pp. 151-168, Academic Press, New York (1965).
7. J. A. Joebstl, in "Hydrocarbon Fuel Cell Technology," B. S. Baker, Editor, pp. 19-26, Academic Press, New York (1965); J. K. Stedman, S. Fanciullo, and S. S. Kurpit, in "Proceedings of the 30th Power Sources Conference," Atlantic City, NJ, June 7-10, 1982, The Electrochemical Society, Inc., p. 1 (1983).
8. D. A. Landsman and F. J. Luczak, Final Technical Report, Contract no. DAAK 70-80-C-0049 and references therein, United Technologies Power Systems, South Windsor, CT (1981).
9. S. P. Kothari and P. S. Patel, *Energy Prog.*, **2**, 187 (1982).
10. J. O'M. Bockris and S. Srinivasan, "Fuel Cells: Their Electrochemistry," McGraw Hill, New York (1969).
11. K. V. Kordesch, E. R. Gonzales, C. R. Derouin, K. L. Hseuh, and S. Srinivasan, in "Electrochemical and Surface Science Research on Fuel Cells, January 1-December 31, 1981," Progress Report LA-9345-PR, pp. 18-23, Los Alamos National Laboratory, Los Alamos, NM (1982).
12. I. D. Adler, G. Ramarao, and S. S. Epstein, *Mutation Res.*, **13**, 263 (1971).
13. G. Söderman, *Hereditas*, **71**, 335 (1972).
14. R. J. Preston, W. Au, M. A. Bender, J. G. Brewen, A. V. Carrano, J. A. Heddle, A. F. McFee, S. Wolff, and J. E. Wasson, *Mutation Res.*, **87**, 143 (1981).

A Close View of Gas Evolution from the Back Side of a Transparent Electrode

Paul J. Sides*,¹ and Charles W. Tobias**

Materials and Molecular Research Division and Department of Chemical Engineering, University of California, Berkeley, California 94720

ABSTRACT

Oxygen evolving on a transparent tin-oxide anode in aqueous potassium hydroxide was photographed by a high-speed motion-picture camera capable of 10,000 frames per second. With illumination by fiber optics and use of a microscope, sharp images of the emergence, growth, and coalescence of bubbles were obtained with a resolution as small as 1 μm . Bubbles grew by diffusion of oxygen and by coalescence with other bubbles still attached to the electrode. Detached bubbles in some cases reattached. Coalescing and detaching bubbles caused significant fluid motion close to the electrode surface. Bubbles in general were evolved in a cycle of growth by diffusion and various modes of coalescence.

Electrolytic gas evolution represents a significant and complicated problem in many electrochemical processes and devices. In spite of its scientific interest and economic importance, the physics of gas-bubble behavior is not well understood. The sequence of events in gas evolution can be divided into three stages: nucleation, growth, and detachment. Bubbles nucleate at electrode surfaces from solutions highly supersaturated with product gas, grow by mass transport of dissolved gas to the bubble surface or by coalescence with other bubbles, and detach from the electrode when forces pulling the bubbles away overcome the surface forces of adhesion. Many phenomena of gas evolution within each of these stages have been theoretically and experimentally investigated, but much remains to be understood.

Nucleation theory has been advanced for vaporization of pure substances (1) and for nucleation of bubbles from solutions containing dissolved gas (2, 3). Boiling nucleation on solid surfaces has been investigated (4) and reviewed (5), but there have been few studies of nucleation of electrolytically evolved bubbles. Westerheide and Westwater (6) reported that nucleation occurred at preferred sites such as pits and scratches on the electrode, and Janssen and Hoogland (7) observed that bubbles nucleated on a rotating platinum wire at specific sites which depended on pretreatment as well as current density. Other than the notable role of surface imperfections for nucleating bubbles, little is known about nucleation at an electrified interface.

The growth stage of gas-bubble evolution includes the mass transport of dissolved gas to the gas/liquid interface and the coalescence of bubbles to form larger bubbles. Scriven (8) gave a general analysis of the transport of dissolved gas to the bubble surface, which incorporated the approximate solutions of others, such as Plesset and Zwick (9) and Forest and Zuber (10). Using a microelectrode and a high-speed camera, Westerheide and Westwater (6) photographed single electrolytic hydrogen bubbles and quantitatively compared their growth data to the diffusive square-root-of-time growth dependence that is the result of the theoretical studies. They found agreement for a single bubble, but multiple bubbles interfered with each other's growth. Nevertheless, this work established diffusion of gas to the bubble surface as at least the initial mechanism by which bubbles grow. Of course, bubbles in practical gas-evolving processes stir the electrolyte close to the electrode and enhance mass transport to each other; nevertheless, diffusion is probably the controlling mechanism up to a bubble size of 1 to perhaps 10 μm , depending on the current density. Glas and Westwater (11) extended this work to include oxygen, chlorine, and carbon dioxide and various electrode materials.

The importance of mass transfer in the initial stage of growth being established, other investigators reported the equal significance of coalescence in gas evolution. Janssen and van Stralen (12) observed bubbles of oxygen evolved in aqueous potassium hydroxide on a transparent nickel electrode; photographing at 70 frames per second (fps), they observed frequent coalescence, lateral mobility of bubbles still attached to the surface, consumption of small bubbles by large ones at high current density, and a radial movement of small bubbles toward large ones. Putt (13) reported that hydrogen bubbles produced in acid grew large by a scavenging mechanism in which the bubbles slid along the electrode and consumed other smaller bubbles. One concludes from these studies that coalescence may largely determine the bubble size and that several modes of coalescence may be involved.

The third stage in the physics of gas evolution, detachment, also has been theoretically and experimentally investigated. Frumkin and Kabanov (14) found that bubbles detach when surface adhesive forces, related to bubble-contact angles, can no longer restrain them. In contrast to these equilibrium measurements, Westerheide and Westwater (6) observed the dynamics of gas evolution and noted that the bubble resulting from the coalescence of two large bubbles jumped off the electrode and sometimes even returned. They concluded that the expanding boundaries of the new bubble mechanically forced it off the electrode, and they speculated that bubbles' movement toward the electrode could be influenced by electrostatic forces operating on a moving bubble or by surface forces varying with concentration. Other investigators (13, 12) have also noted that coalescence often precedes departure. In an unusual and as yet unexplained mode of detachment, bubbles sometimes were ejected from the electrode in what Glas and Westwater (11) termed "rapid-fire emission." Janssen and Barendrecht (15) observed that hydrogen bubbles formed trains of noncoalesced small bubbles which left the electrode. Although the forces holding a bubble on the electrode at equilibrium and the role of coalescence in breaking bubbles away are established, the criteria or kinetics by which one may judge whether a given coalescence will lead to detachment or not are unclear; furthermore, the return of a detached bubble to the electrode surface and the rapid emission of bubbles await explanation.

The aim of our work was to photographically document bubble phenomena and to use these observations, in conjunction with the bewildering number of observations found in the literature, to establish an overall mechanism of oxygen-bubble growth and detachment in basic solutions. We used special techniques and materials to accomplish this because the events on gas evolving electrodes are microscopic, rapid, and obscured from the camera by the outer bubbles of the gas layer on the surface. Magnification and a high-speed camera can overcome the first two difficulties; we used a transparent electrode to over-

* Electrochemical Society Active Member.

** Electrochemical Society Honorary Member.

¹ Present address: Department of Chemical Engineering, Carnegie-Mellon University, Pittsburgh, Pennsylvania 15213.

come the third obstacle by viewing the phenomena close to the surface from the back side. Such an electrode also permits the microscope objective to approach the electrode without shielding it from current or affecting the dynamics at the surface. Furthermore, the electrode transmits light directly into the camera through the electrode, an important advantage when filming at high framing rates. The tin-oxide electrode used in this work transmitted essentially all of the incident light so that much faster framing rates could be used than were previously possible.

Experiments

We employed a $0.2\ \mu\text{m}$ antimony-doped film of tin oxide chemically vapor deposited on a 2 mm-thick glass substrate as a transparent electrode.² The electrode was incorporated into a cell which allowed electrical contact to parts of the surface but sealed off the contacts from the electrolyte. A cross section through the cell, shown in Fig. 1, shows two basins filled with silver epoxy for electrical contact to the "window electrode," the channel containing electrolyte, and the electrode itself which faces both silver epoxy and the electrolyte. The basins were sealed from the channel opening with insulating epoxy. The cell is shown in Fig. 2, which shows how the 2 cm square piece of the tin-oxide electrode fits into the opening in the Lucite body. The clear area in the center is where the electrode faces the electrolyte channel which was 0.3 cm wide, 0.5 cm deep, and 1.9 cm long. The wires leading out are copper electrical contacts. Because there was significant resistance in the tin-oxide film, the distance between the two contacts (of same polarity) on either side of the electrolyte channel was made as small as was practical for lowest resistance, easy departure of the bubbles, and avoidance of wall effects. There were holes leading out through the top and bottom of the cell for adding electrolyte and directing gas out of the cell. The counterelectrode was a platinum wire placed above the vertically positioned electrode so that gas evolving on it did not interfere with observation of the working electrode gas.

The arrangement of the apparatus is shown in Fig. 3 and 4. Intense light from an Ealing Corporation Model 22-0004 fiber optic light source passed through a clear Lucite plate which faced the window electrode across the channel of electrolyte. Images were magnified by a Bausch and Lomb microscope ($10\times$ objective and $15\times$ eyepiece) and received by a Red Lakes HYCAM high-speed camera. The 16 mm movie frame bounded an area 0.6 mm on a side as determined by photographing a calibrated microscope slide. Capable of framing rates from 10 to 10^4 fps, the camera accepted 100-400 ft rolls of KODAK TXR 430 high-speed camera film. Illuminated by a 250W slide-projector lamp, the fiber optic tip was placed 1 cm from the cell back and the power was turned on full. This transmitted enough light to produce clear images at film rates of around 10^4 fps after traveling through 1 cm of Lucite, electrolyte, and glass.

The cell was filled with aqueous potassium hydroxide from a reservoir above it and drained to a flask below. The electrode, polarized positively to produce oxygen, did not withstand electrolysis in acid or sodium chloride, but it performed well in alkaline solution; hence, oxygen was the only product investigated. When the microscope was focused, the distance from the camera to the eyepiece was set every time to the same length for optimum exposure of the film. An AMEL Model 551 potentiostat operated in galvanostatic mode provided the power for the reaction. After power was applied, the camera was manually activated and 400 ft of film was exposed in 5s; at the standard projection rate of 24 fps, 16 min is required to view the events. Many reels of film were taken

²Dr. Werner Kern at RCA Laboratories donated samples which had a film conductivity of $100\ \Omega/\square$. This unusual unit, used by thin film specialists, derives from the fact that the surface resistance of a square (measured from one side of the square to the other) is independent of the square's dimensions.

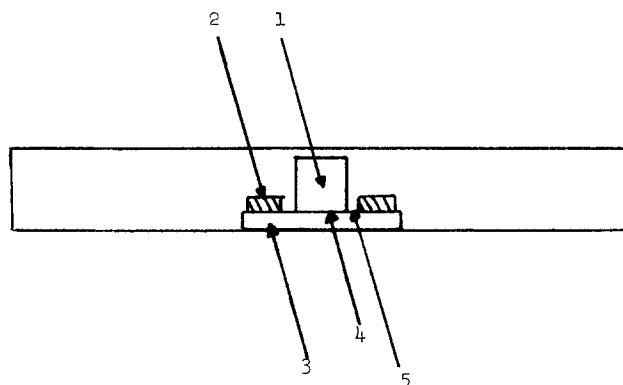


Fig. 1. Cross section of the transparent electrode cell: 1) electrolyte facing the tin oxide; 2) silver epoxy contact to electrode film; 3) glass substrate; 4) tin-oxide electrode film; 5) seal between silver epoxy and electrolyte.

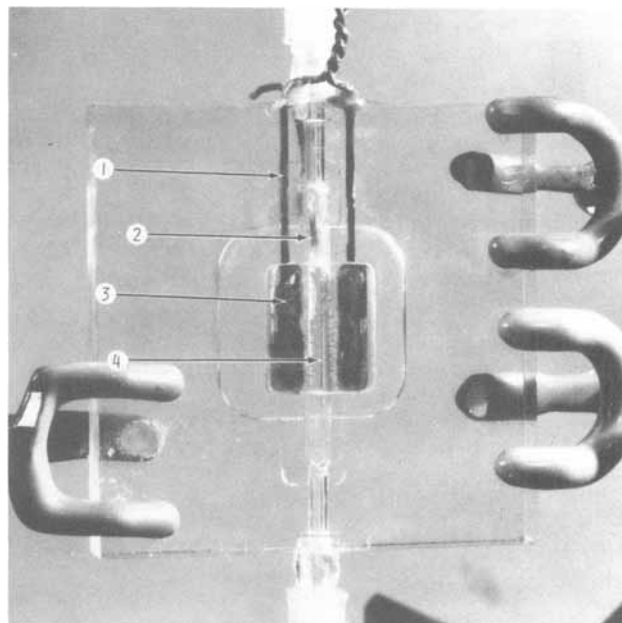


Fig. 2. Transparent electrode cell: (1) copper current collector; (2) Pt wire counterelectrode; (3) silver epoxy; (4) transparent electrode area.

at various speeds and concentrations of aqueous potassium hydroxide (21).

Results and Discussion

The tin oxide proved to be an effective window electrode that was stable to oxygen evolution in basic solution. It was not stable to chlorine evolution in neutral solution or, for obvious reasons, hydrogen evolution.

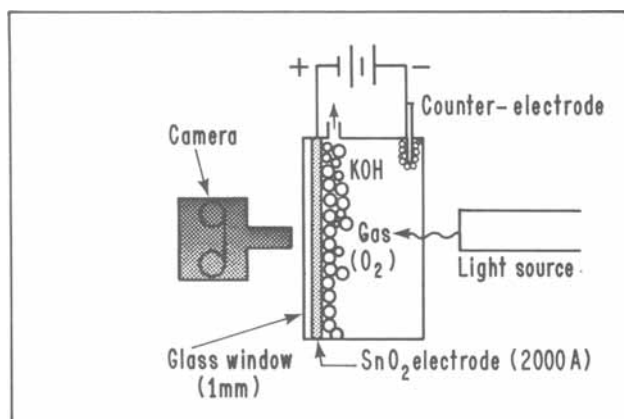


Fig. 3. Schematic of observation apparatus

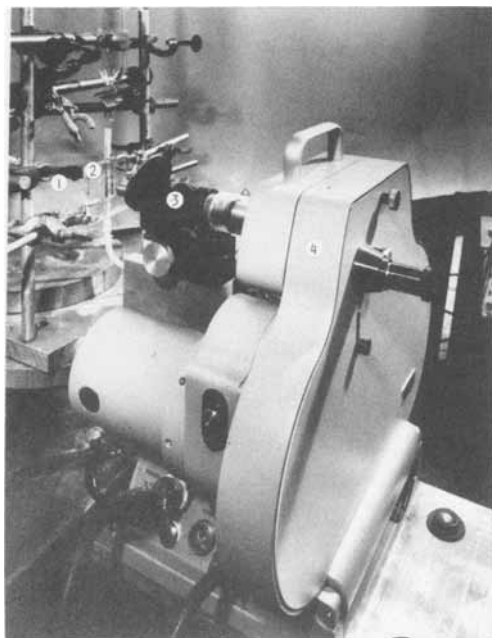


Fig. 4. Apparatus: (1) fiber optic light guide; (2) transparent electrode cell; (3) microscope; (4) Red Lakes HYCAM camera.

Despite the electrode's unusual properties of electronic conductivity and transparency, gas evolution on it had much in common with observations reported in the literature, thus it seems valid to draw general conclusions from its behavior. To study gas evolution quantitatively, one should know the local current density and, hence, the local gas-volume production rate; but the current distribution on the tin-oxide transparent electrode was nonuniform because of the surface resistance to current flow in the oxide film. Of course, electrode kinetics, especially serious in the case of oxygen evolution, mitigate the nonuniformity of the current distribution. In addition, the initially higher current density at the electrode/wall boundary produced bubbles that stuck there and further deflected the current to the center, where the pictures were taken. For these reasons and because direct observation did not indicate that the gas evolution rate at the point of observation was significantly different from other positions on the surface, the step of solving Laplace's equation in the electrolyte and on the semiconductor strip bounding it, which itself would be an approximation because the presence of bubbles, which introduces a formidable mathematical complexity, disturb the current distribution even further, was not taken. The current density was calculated as an average of the total current over the area of the electrode. The results are reported qualitatively.

The intense fiber optic light penetrated the bubbles' spherical caps but was deflected by the curved sides; thus, the image was a two-dimensional dark annulus as shown in Fig. 5. An additional light pointed at the cell from the side gave the bubble a highlight and made it appear three-dimensional. Difficult to describe in words and still pictures, the growth process of bubbles is best viewed continuously; a 30 min motion picture summarizing the transparent-electrode studies may be obtained for viewing by contacting either of the authors.

Movies taken at the standard speed, 24 fps, showed only blurred motion, but slowing the action by a factor of 10 revealed many of the phenomena reported in previous work, such as the preference for nucleation at surface imperfections and rapid initial growth by mass transfer where the bubble expanded with no apparent coalescences. Most interesting was the frequent bubble coalescence and the detachment of bubbles from the electrode. Identification, documentation, and organization of bubble growth and detachment phenomena are the core of this work.

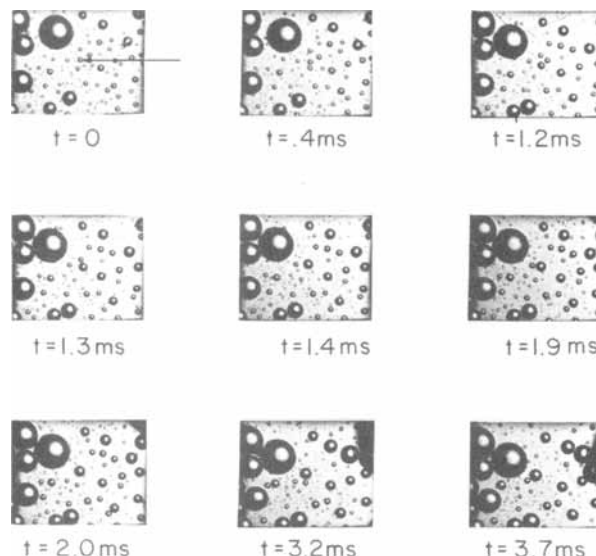


Fig. 5. Documentation of specific radial coalescence. The indicated bubble at time zero receives the four bubbles around it sequentially and visibly grows. One may observe this same effect around other bubbles in the sequence. Conditions: 10,000 frames per second; oxygen evolution; 298 K; no forced convection; 3% (wt) KOH; 500 mA/cm².

Coalescence of very small bubbles ensued after rapid initial growth by diffusion and marked the start of the coalescence phase of bubble growth. Bubbles nucleated, grew to a small size (<10 μm) by mass transfer and, upon touching, rapidly coalesced. There was no period of delay before the small bubbles in contact coalesced. Since coalescence between small bubbles and establishment of the final spherical boundary was always completed within 0.0001s, we never obtained images of intermediate stages. Although small bubbles coalesced almost immediately upon touching, large bubbles touched for many frames before coalescing. Perhaps the small newly formed bubbles did not have film stabilizing compounds adsorbed at their surfaces as did the large older ones. The bubble size in general depended on the number of coalescences, which means that one can limit bubble growth by controlling coalescence, that is, by removing the bubbles before they coalesce or somehow stabilizing the liquid film between the two touching bubbles so it cannot rupture.

Bubbles of a medium size, about 40 μm , established themselves as central collectors which received the smaller bubbles nucleating and growing around them. We call this "radial specific coalescence," a schematic of which appears in Fig. 6. The smaller bubbles translate radially across the electrode surface toward stationary central bubbles, two of which are represented in the schematic. A film sequence recording this mode of coalescence appears in Fig. 5. Small bubbles, while still attached, moved specifically in the direction of and coalesced with the medium bubble (at the arrow in Fig. 6) in whose sphere of influence, extending about three bubble diameters from the collector bubble, they were located. The central bubble swelled with the addition of the smaller bubbles but was not otherwise disturbed as it acquired them. Although there was an overall flow impressed on the system by movement of the buoyant bubbles, the radial movement of bubbles was symmetric 360° around the collector bubble, which remained anchored to the electrode; hence we concluded that the radial motion is a local phenomenon. The movement may have been a result of local flows established by continual coalescence, which entrains other bubbles toward the collector. Requiring a transparent electrode to be revealed, this phenomenon was also observed only by Janssen and van Stralen (12) on their transparent nickel electrode.

After the medium-size bubbles attained a size between 50 and 100 μm , large bubbles still attached to the surface and sliding from below the field of view scavenged them

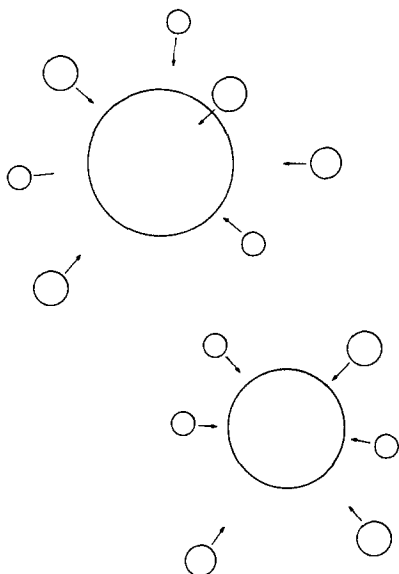


Fig. 6. Schematic of specific radial coalescence

or coalesced between themselves and moved out of view. (The bubbles' flattened areas of attachment were visible from behind the transparent electrode.) Scavenging of medium bubbles by large ones was the third mode of coalescence observable on the transparent electrode and was the mechanism by which bubbles attained their final size. A film clip, Fig. 7, demonstrates that after a group of large bubbles passes, new bubbles nucleated and grew to a size of 10-15 μm in diameter. These small bubbles coalesced to form medium-size bubbles which then grew further by specific radial coalescence. Large bubbles (200 μm) attached to and moving along the surface scavenged the small- and medium-size bubbles in their path.

We term this sequence of events (nucleation, growth by mass transfer, coalescence of small bubbles, coalescence by radial motion, and scavenging coalescence) the cyclic process of bubble growth because it is repeated continu-

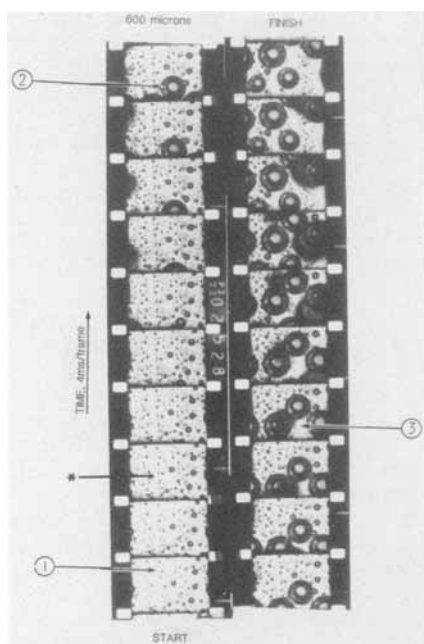


Fig. 7. Gas evolution slowed by a factor of 10. (1) Dispersion of small bubbles which grew on the electrode after a group of large bubbles swept through. (2) Several large bubbles travel along the surface and scavenge the small- and medium-size bubbles before them. (3) Empty area behind a large bubble showing its path. (*) Trail left by earlier scavenging bubble. Conditions: 240 frame per second; oxygen evolution; 298 K; no forced convection; 28% (wt) KOH; 100 mA/cm².

ally on the electrode and is the general way bubbles are "built." The period of the cycle, at a current density of 100 mA/cm², was approximately 0.1s. We hypothesize that this gas evolving electrode, and perhaps practical electrodes, are essentially a mosaic of regions in which this local mechanism governs the production of bubbles. Of course, this cannot be true for electrodes on which coalescence does not occur and can only be partly true for electrodes on which the bubbles are not mobile. If this cyclic mechanism of bubble evolution is valid, then modeling the mass-transfer enhancement due to bubble evolution is indeed a formidable task. In fact, the complexity of fluid motion induced by bubbles perhaps explains the divergent views on the model for mass-transfer enhancement.

Detachment of a bubble from the transparent electrode was also observed. Characterizing the detachment of a bubble from a vertical electrode is difficult because the buoyancy force does not act perpendicularly to the electrode; the only force continuously pushing the bubble away from the surface (at equilibrium) is exerted by the internal pressure of the bubble against the flattened bubble base. The sequence shown in Fig. 8 indicates that coalescence of two bubbles to form a new bubble, which being compressed against the electrode pushes away from it, is an important mechanism by which bubbles depart from vertical electrodes. This confirms the observation of Janssen and van Stralen (12). As mentioned by other investigators, especially by Glas and Westwater (11), the bubble, once detached, may return. This occurred on the tin-oxide electrode also. One can see the contact area under the bubbles in Fig. 8 as a slightly darkened spot on the left side of the light central area. When the bubbles coalesced and the new bubble had ceased its violent vibrations and had established its spherical boundary, the contact spot vanished but subsequently reappeared. Unfortunately, the still pictures cannot convey the impression one obtains from the motion pictures that there was indeed some kind of force which brought these oxygen bubbles back to the electrode because the bubble seemed to push its way back to the surface. Coehn and Neumann (23, 24) would argue that the return to the electrode was caused by the attraction of the charged bubble to the electrode surface. Glas and Westwater (11) speculated that a surface tension gradient caused the bubbles' return. A third possibility is that the bubble was still oscillating after the coalescence and then reattached when one part

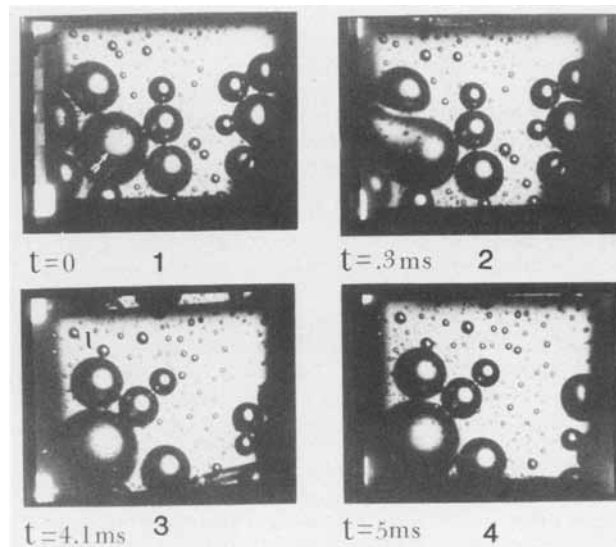


Fig. 8. Detachment and return of a bubble after coalescing with another bubble. 1) A bubble on the electrode touches another off the frame to the left. 2) The two bubbles coalesce. 3) The new bubble is off the surface. There are small bubbles on the surface between the large bubble and the surface. 4) The bubble has reattached. Conditions: 10,000 frames per second; oxygen evolution; 298 K; no forced convection; 3% (wt) KOH; 500 mA/cm².

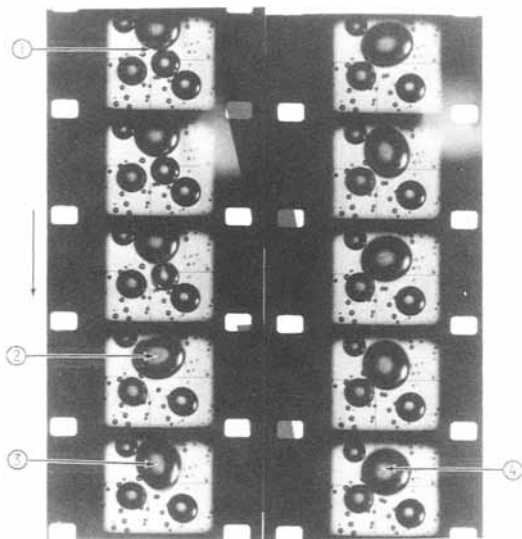


Fig. 9. Coalescence of two bubbles and subsequent vibration of the new bubble ($100 \mu\text{s}$ per frame). 1) Two bubbles touch for a number of frames while the film drains from between them. 2) The resulting bubble is compressed against the electrode. 3) The new bubble vibrates as it establishes its equilibrium boundaries. 4) The oscillations end after a half-millisecond. Conditions: 10,000 frames per second; oxygen evolution; 298 K; no forced convection; 28% (wt) KOH; 100 mA/cm^2 .

of it touched the electrode. The detachment and return of bubbles should be explored specifically.

The coalescence of large bubbles caused fluid motions close to the electrode surface, which may be important in mass-transport enhancement due to gas evolution reported by Ibl (22), Venczel (16), and Janssen and Hoogland (18). This mode joins the flow due to gas lift and fluid replacement due to bubble departure as an accelerator of mass transfer. A coalescence sequence between two large bubbles near the electrode and moving along it is shown in Fig. 9. The two bubbles appeared to touch for many frames as the film between them thinned and finally ruptured. The bubbles coalesced so quickly that the film rupture and the change from two bubbles to one occurred between two frames, that is, in less than $100 \mu\text{m}$. The new bubble was compressed along the axis of coalescence by the fluid rushing into the space behind the coalescing bubbles. The bubble vibrated like this for several frames before becoming spherical again. This is an example of coalescence of two relatively large bubbles, both traveling along the electrode surface.

Summary

The tin-oxide transparent electrode allowed observation of oxygen evolution in potassium hydroxide from the back side, a vantage from which to view the rapid and microscopic phenomena of gas evolution. Our study confirmed certain of the phenomena reported in the literature. Coalescence was most important in the overall process of gas evolution. The cycle of growth by mass transport and local coalescence followed by scavenging

coalescence determined bubble size on vertical electrodes. Small bubbles moved radially in toward a medium-size central bubble and coalesced with it; the new bubble in turn was scavenged by large bubbles moving along the surface. Coalescence also was important in bubble detachment. Some bubbles returned to the surface after leaving. In general, gas evolution on this electrode resembled a mosaic of local cycles of growth and detachment, the dimension of the localities being an order of magnitude greater than the largest bubbles.

Acknowledgments

This work was supported by the Director, Office of Energy Research, Office of Basic Energy Sciences, Materials Sciences Division of the U.S. Department of Energy under Contract no. W-7405-ENG-48 and by a Domestic Mining and Mineral Fellowship. We also wish to thank Dr. Werner Kern and RCA Laboratories, who supplied us with the electrodes.

Manuscript submitted July 9, 1984; revised manuscript received Oct. 25, 1984.

Carnegie-Mellon University assisted in meeting the publication costs of this article.

REFERENCES

1. M. Blander and J. L. Katz, *Am. Inst. Chem. Eng. J.*, **21**, 833 (1975).
2. T. W. Forest and C. A. Ward, *J. Chem. Phys.*, **66**, 2322 (1977).
3. C. A. Ward, A. Balakrishnan, and F. C. Hooper, *Trans. ASME*, **92**, 695 (1970).
4. H. B. Clark, P. S. Streng, and J. W. Westwater, *Chem. Eng. Prog. Symp. Ser.*, **55**, 103 (1957).
5. R. Cole, *Adv. Heat Transfer*, **10**, 85 (1974).
6. D. E. Westerheide and J. W. Westwater, *Am. Inst. Chem. Eng. J.*, **7**, 357 (1961).
7. L. Janssen and J. Hoogland, *Electrochim. Acta*, **15**, 1013 (1970).
8. L. E. Scriven, *Chem. Eng. Sci.*, **27**, 1753 (1959).
9. M. S. Plisset and S. A. Zwick, *J. Appl. Phys.*, **25**, 493 (1954).
10. H. K. Forster and N. Zuber, *ibid.*, **25**, 474 (1954).
11. J. P. Glas and J. W. Westwater, *Int. J. Heat Mass Transfer*, **7**, 1427 (1964).
12. L. Janssen and S. van Stralen, *Electrochim. Acta*, **26**, 1011 (1981).
13. R. Putt, M. S. Thesis, University of California, Berkeley (1975).
14. B. Kabanov and A. Frumkin, *Z. Phys. Chem.*, **165A**, 433 (1933).
15. L. Janssen and E. Barendrecht, *Electrochim. Acta*, **24**, 693 (1979).
16. J. Venczel, *ibid.*, **15**, 1909 (1970).
17. N. Ibl and J. Venczel, *Metalloberflache*, **24**, 365 (1970).
18. L. Janssen and J. Hoogland, *Electrochim. Acta*, **18**, 543 (1973).
19. D. Landolt, R. Acosta, R. Muller, and C. Tobias, *This Journal*, **117**, 839 (1970).
20. E. L. Littauer, U.S. Pat. 3,880,721 (1975).
21. P. J. Sides, Ph.D. Thesis, University of California, Berkeley (1981).
22. N. Ibl, *Chim. Ing. Tech.*, **43**, 202 (1971).
23. A. Coehn, *Z. Electrochem.*, **29**, 1 (1923).
24. A. Coehn and H. Neumann, *Z. Phys.*, **20**, 54 (1923).

The Reversibility of Sodium Insertion in Transition Metal Trisulfides

Margherita Zanini

Ford Motor Company, Dearborn, Michigan 48121

ABSTRACT

The effects produced by the insertion of sodium in the trisulfides of titanium, niobium, and tantalum were investigated by electrochemical techniques. Cyclic voltammetry measurements were carried out in these materials using high-temperature sodium cells which utilize the solid electrolyte β' -alumina. The data demonstrate that TiS_3 disproportionates into TiS_2 and sulfur during the first cycle. NbS_3 appears to gradually undergo irreversible transformations which decrease the amount of sodium that can be reversibly inserted. TaS_3 was found to be more stable. The transformations induced in the trisulfides by electrochemical titration with sodium are discussed in terms of the structural and chemical bonding properties of these materials.

Compounds that can react with alkali metals with a large free energy of reaction are potentially useful for battery applications (1, 2). The requirement that the process be readily reversible has put a premium on these reactions (called topochemical), which occur without appreciably modifying either the structure or the chemical bonding of the host material.¹ Typical examples are the layered transition-metal disulfides in which alkali metals are inserted between the weakly bonded layers of the compound (1). Because these intercalation compounds usually form nonstoichiometric phases with a wide compositional range, their energy density is large.

Many efforts have been devoted to finding other materials which meet the reversibility requirements, but for which the reaction product contains a ratio of alkali metal to transition metal of 2 or 3 in order to achieve larger energy densities (3). It was recognized early that materials such as TiS_3 and NbSe_3 could incorporate up to three lithium atoms per formula unit (4, 5). However, it was found that only about one-third of the lithium incorporated in TiS_3 could be removed (6). The reaction was found to be reversible in NbSe_3 , but although its volumetric energy density was large, its gravimetric energy density was comparable so that of TiS_2 (7). Past studies have not fully explained why different trichalcogenides show different degrees of reversibility for the reaction with lithium. Tests of the charge/discharge behavior of these compounds under galvanostatic conditions have indicated that the reaction with lithium is more complex than a topochemical reaction and induced structural transformations in the host materials. Unfortunately, x-ray diffraction measurements of the reacted trichalcogenides have typically shown patterns of weak and broad lines which hamper the complete identification of the reaction products.

In this paper we report electrochemical studies on the effects produced by the insertion of sodium in the trisulfides of titanium, niobium, and tantalum. The reaction was carried out by electrochemical titration in high-temperature sodium cells which utilize the solid electrolyte β' -alumina (8). Because β' -alumina is stable in the potential range of the experiment, we have been able to study the process without interference from side reactions with the electrolyte, and in addition we have avoided the problem of electrolyte cointercalation. We discuss how cyclic voltammetry measurements allow us to detect the occurrence of phase transformations in the electrode material with higher sensitivity than possible with conventional galvanostatic measurements. We also show that the reaction products for TiS_3 can be identified with this technique.

The electrochemical behavior of the trisulfides in sodium cells is shown to be profoundly different from that of the corresponding disulfides because sodium strongly interacts with the polysulfide group $(\text{S}_2)^{-2}$, which is characteristic in these materials. Our cyclic voltammetry data indicate that structural and chemical transformations oc-

cur in these materials, but the effects are dissimilar in each compound. XPS measurements of the sulfur 2p core level for the trisulfides are reported which indicate that the sulfur bonding characteristics in TaS_3 may be different from those of TiS_3 and NbS_3 . The observed chemical bonding differences can be correlated with the different behavior of the trisulfides upon electrochemical titration with sodium.

Sample Preparation

Titanium trisulfide was prepared by direct reaction between sulfur granules (Asarco) and titanium powders (Cerac mesh -325) in sealed quartz ampuls. A small sulfur excess above the stoichiometric composition was used. The ampul was then inserted in a two-zone furnace. The temperatures in the two zones were adjusted so that one end of the ampul was kept at 440°C to avoid high sulfur vapor pressure, and the other end with the metal powders was kept at 560°C. Formation of the undesired disulfide phase was observed if the reaction was carried above 570°C. When the powders had reacted, the temperature of the colder zone was raised to 500°C and the material was annealed for three days. The ampul was then cooled slowly, maintaining the temperature gradient to deposit the small excess sulfur at one end. In this way, blue-gray ribbons of TiS_3 were obtained, and the largest were roughly 1 cm long and 0.5 mm wide.

NbS_3 and TaS_3 were prepared in a similar way, starting with Cerac metal powders of -325 mesh. The temperature in the reaction zone was kept at 600°C for NbS_3 and at 650°C for TaS_3 , while the cold zone was maintained at 440°C in both cases. TaS_3 grew as a light felt of fine and short fibers which filled the inside of the ampul. NbS_3 also grew as fine needles, but with excess sulfur we were also able to obtain long, flat ribbons, similar to TiS_3 . The lattice constants of the synthesized trisulfides were derived by x-ray diffraction analysis of powder samples and were found to be in agreement with the data in the literature.

Experimental

The cells used for the electrochemical experiments were made of alumina tubing at the end of which a disk of β' -alumina was sealed with a soft glass. The other end of the ceramic tubing had a ceramic-to-glass transition so that sodium could be vacuum distilled in the container and sealed off. The temperature of the cell was measured with a shielded thermocouple sealed in the sodium compartment, with its tip close to, but not touching, the β' -alumina disk.

The positive electrode was made by pressing transition-metal sulfide fibers on a disk of thin aluminum foil with a die. Upon pressing, the fibers became a compacted felt with a geometrical surface area of 0.1-0.2 cm². The felt stuck slightly to the aluminum foil, which made the handling of the electrode easier. Typically, a few tenths of a milligram of active material were used for the electrode.

The precise amount was determined with an electronic balance by weight difference between the aluminum substrate alone and the pressed electrode. The electrode was then put in the center of a flexible aluminum cup which fitted the ceramic half-cell so that it could be easily positioned against the electrolyte. Contact between the solid electrode and the electrolyte was achieved by slightly pressing the aluminum cup with a flat, rigid cup holder. To apply the pressure, the ceramic half-cell was rigidly mounted by means of a metallic collar into one end of a threaded cylinder made of steel. A spring-loaded plunger was then screwed into the other end of the cylinder so that it pushed the cup holder. A pin was machined in the back of the cup holder to act as a point of contact with the plunger to compensate for the lack of parallelism between the β -alumina disk, cup holder, and plunger. In addition, to improve the contact between the sulfide electrode and the solid electrolyte, a pellet of graphite powders, slightly pressed into a 1 mm-thick disk, was added between the aluminum cup and the flat cup holder. When the pressure was applied, the graphite pellet flowed and pressed the electrode uniformly against the solid electrolyte. With this procedure of mounting the electrode, we were able to obtain an electrode-electrolyte interface with reproducible characteristics, as was demonstrated by the very good reproducibility of the data from sample to sample. At the temperature of operation (less than 320°C), we did not observe any reaction between the sulfide and the aluminum substrate. The cells were assembled and tested in a dry box. The cell assembly was heated in a cylindrical heater whose temperature was regulated within $\pm 1^\circ\text{C}$.

The measurements were carried out using PAR electrochemical instrumentation (Model 173 potentiostat, Model 371 coulometer, Model 175 programmer) controlled by a Tektronix 4051 computer. Sodium was inserted in the sulfide electrode and removed from it by discharging and charging the cell at low rates. The charge measured during the electrochemical titration is proportional to the amount of sodium inserted in the electrode material because no side reactions, such as reduction of the electrolyte, occur, and nonfaradaic effects, such as double-layer charging, are very small. These assumptions were verified in our case by changing the thickness of the electrode.

The reaction was carried out under the condition that the voltage of the cell should change at a constant rate with time. Thus, the titration current was observed to increase and decrease as a function of the voltage. The rate of the reaction, monitored by the current, was kept low enough to insure quasi-equilibrium conditions throughout the test. Specifically, the concentration gradients in the particles which compose the electrode were kept small so that the lineshapes of the voltammograms would not become broad and distorted. The use of micro-electrodes has the advantage of keeping the time of the experiments relatively short. Because the geometry of the cell did not allow the addition of a reference electrode, the sodium electrode was used as both a counter and a reference electrode. This configuration did not introduce a large error, because the polarization of the sodium electrode was low. This was verified by current step measurements using a sodium/ β -alumina/sodium cell. The IR drop of the sulfide cells was also checked with the same technique and found to be less than 20 mV at currents up to 1 mA.

The XPS spectra were obtained with a Vacuum Generator ESCA 3 system using a magnesium anode x-ray source (1253.6 eV). The instrument was operated in the constant pass energy mode with a typical resolution of 1.1 eV full width at half maximum peak height on the Au 4f_{7/2} line.

Results

We report in Fig. 1 the results of the first and second scan for TiS₃ obtained at 280°C. In this experiment the electrode was 0.3 mg and the scan rate was 0.1 mV/s. On

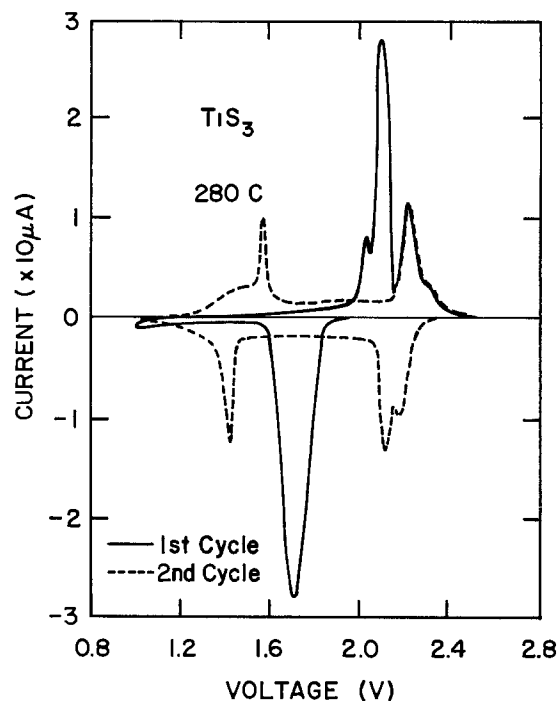


Fig. 1. Cyclic voltammetry curves for a TiS₃ electrode at a sweep rate of 0.1 mV/s. The negative curves correspond to the insertion of sodium in the electrode, the positive curves to its removal. The solid and dashed lines correspond to the first and second cycles, respectively.

discharge (cathodic wave), a broad current peak appears at 1.7V. The integrated current indicates that the process involves two electrodes per molecule. Below approximately 1.2V, the background current increases slowly. On charge (anodic wave), a complex lineshape, made of four peaks, is observed between 2.0 and 2.4V. The measured titration charge indicates that at least 95% of the sodium inserted in the electrode is removed on charge. Lower coulomb efficiency is observed if the cathodic scan is extended beyond 1V. The second scan is, however, different. Three cathodic peaks are observed at 2.2, 2.1, and 1.4V, respectively. Corresponding peaks, with very similar lineshapes, are observed in the anodic scan shifted by 80 mV toward higher energies. These peaks are the characteristic features observed for TiS₂. Similarly, the total charge measured during the second intercalation cycle is equivalent to only a one-electron process, and intercalation is reversible. Subsequent scans give identical results. After the cyclic voltammetry tests, the cell was opened to inspect the electrode. In the case in which the electrode was taken out after a full charge cycle, the color of the electrode was gold. Inspection under an optical microscope revealed that the electrode was now a compacted powder and had lost its originally fibrous appearance. X-ray diffraction data revealed some of the characteristic lines for TiS₂, although they were very broad. In another test, a TiS₃ electrode was removed from a cell after the first discharge to 1.2V. Its color was dark gray black. Part of the electrode was enclosed in a glass capillary for x-ray diffraction analysis while still in the dry box. Only a few broad lines were observed from which it was not possible to identify the reaction products.

The cyclic voltammetry curves for niobium and tantalum trisulfides show different features. In Fig. 2 we report the first and sixteenth complete scans for a NbS₃ electrode of 0.3 mg, and part of the second. The voltammograms were obtained at 280°C and at a scan rate of 0.1 mV/s. The first discharge curve shows a large current peak at 1.7V, similar to that observed for TiS₃, but narrower. The charge corresponding to the peak indicates a two-electron reduction process. At 0.9V, another peak corresponding to a one-electron process is observed. In the subsequent charge scan, a peak is observed at 1.5V, a doublet appears at 2.1-2.2V, and a small peak can be seen at 2.4V. The coulomb efficiency during the first cycle is

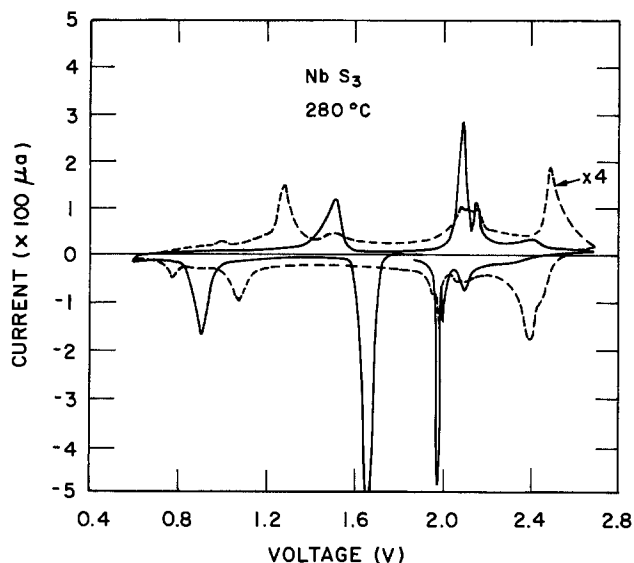


Fig. 2. Cyclic voltammery curves for a NbS_3 electrode at a sweep rate of 0.1 mV/s. The solid and dashed lines correspond to the first and sixteenth cycles, respectively.

about 90%. Although the lineshape of the first cathodic voltammogram is quite different from that of the first anodic voltammogram, on subsequent cycles the cathodic and anodic curves become more symmetrical. To illustrate this point, the first part of the second voltammogram is included in Fig. 2. Three peaks appear at 1.95, 2.10, and 2.34V, respectively, which are similar to the peaks observed in the first anodic scan. Quite different behavior is observed for the peak at lower voltages. In fact, the cathodic peak splits into two components, which grow at 0.8 and 1.1V, respectively, and have a 2:1 intensity ratio. The anodic peak at 1.5V instead starts decreasing in intensity, and another peak starts growing at 1.3V. The total charge associated with these peaks decreases monotonically and after a few cycles is roughly $0.5 e^-/\text{NbS}_3$. At higher voltages, the weak peaks at 2.4V in the cathodic scan and at 2.5V in the anodic scan gradually increase in intensity, while the other two peaks become weaker. By the tenth cycle, the total charge measured during a discharge cycle was $1.5 e^-/\text{mol}$ and kept decreasing. Separate scans over either the 0.6-1.6V or 2.0-2.7V region gave similar results, indicating that the processes are independent.

In Fig. 3 we show the first and eighth complete scans for a TaS_3 electrode taken at 280°C. Part of the second scan is also shown. The scan rate was 0.1 mV/s and the weight of the electrode was 0.4 mg. A peak at 1.7V and a small peak at 1.9V are observed on the first discharge. The total integrated current indicates a two-electron process. Another peak, corresponding to a one-electron process, is observed at 0.6V. On charge, two peaks appear at 1.0 and 1.3V respectively, and a very broad feature, which appears to be made of at least three components, is observed to be centered at 2.3V. The coulomb efficiency of the first cycle is about 95%. On the second discharge an asymmetric peak appears at 2.1V. This peak shifts on subsequent scans by 100 mV to higher voltages, splitting into two components of 3:1 intensity ratio. After a few cycles, the peak lineshape remains constant. During the transformation, the charge associated with the higher voltage processes decreases by 20%. The lower peak instead shifts by 50 mV to lower voltages, increasing its intensity, so that the total charge measured during the entire scan remains constant within 1-2%. The peaks in the anodic waves change to become more symmetrical with the cathodic peaks. The peak at 1.3V disappears and the one at 0.9V becomes stronger. The peak lineshape near 2.2V becomes sharper as if the central component grew at the expense of the others. Although the cyclic voltammery curves measured for TaS_3 showed lineshape transformations similar to those observed for NbS_3 , the two compounds

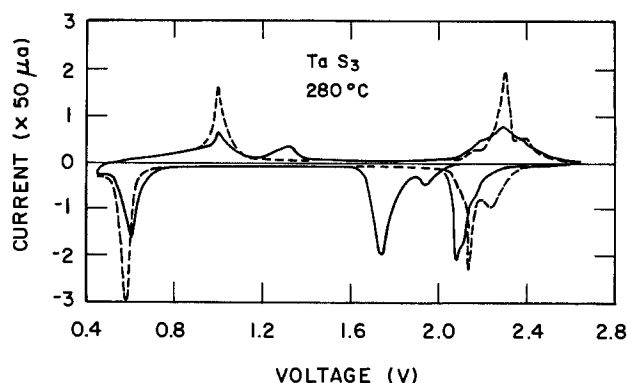


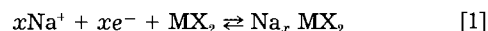
Fig. 3. Cyclic voltammery curves for a TaS_3 electrode at a sweep rate of 0.1 mV/s. The solid and dashed lines correspond to the first and eighth cycles, respectively.

behave differently in the following respects. First, in TaS_3 , the lineshape modifications occur without substantial loss in electrode utilization and coulomb efficiency. Second, the TaS_3 peaks change their intensity, but they do not shift substantially in voltage. And last, the changes in TaS_3 occur within the first three or four cycles, after which subsequent voltammograms do not change appreciably.

The NbS_3 and TaS_3 electrodes did not seem to have lost their fibrous appearance after the electrochemical tests, at least under low optical magnification. They did seem, however, to react with air, probably due to the remaining sodium that cannot be removed from the material during the electrochemical titration. X-ray diffraction measurements were performed on pieces of fully charged electrodes after they had been cycled several times. The samples were sealed in glass capillary while still in the dry box to prevent reaction with air. Their diffraction patterns showed only a few broad lines, suggesting that both materials had become highly disordered during the reaction. The presence of disulfide or trisulfide species could not be conclusively demonstrated.

Discussion

Our cyclic voltammery results demonstrate that the effects produced by the insertion of sodium in TiS_3 , NbS_3 , and TaS_3 are more complex than those observed in the disulfides (10). Titration of layered dichalcogenides with alkali metals has been shown to produce ternary phases according to the equation



where M is the transition metal and X is either sulfur or selenium. Stoichiometric and nonstoichiometric reaction products have been reported for the disulfides (12). The redox process described by Eq. [1] does not have a simple Nernstian behavior because it involves solid-state species. Typically, the equilibrium voltage of the titration cell is not a linear function of the alkali-metal concentration in the electrode material, and it changes discontinuously when a new phase is formed during the process. These discontinuities are resolved with the cyclic voltammery technique, with much higher sensitivity than possible with galvanostatic measurements, because this method, at very low rates, is equivalent to a differential measurement of the curve representing the sodium concentration in the electrode as a function of its equilibrium voltage. Thus, current peaks are observed when the free energy of reaction changes and can be correlated with changes in the electroaffinity of the host material, with changes in the site occupied by sodium and/or with structural transformations of the ternary compound formed during the process. In particular, very sharp current peaks are seen when two phases coexist. Conversely, the current is approximately constant when the reaction produces a homogeneous phase such as a solid solution (10).

We previously reported voltammograms for TiS_2 , NbS_2 , and TaS_2 obtained with the same cell configuration and

using microelectrodes (10). For each of the disulfides, we observed characteristic current peaks which did not appreciably change upon cycling. In addition, the cathodic and anodic waves were fairly symmetrical. We discussed how these features are characteristic for an intercalation process which affects the stacking of the disulfide layers but not their chemical bonding. The voltammograms for the trisulfides instead show modifications in lineshape and shifts in peak position as a function of cycling, which indicates that profound structural modifications occur during the reaction with sodium.

Before discussing the electrochemical data, it is useful to summarize the structural and chemical bonding properties of the materials under study. The structure of these trisulfides can be regarded as being built with chains of sulfur trigonal prisms, stacked to share their triangular faces, with the metal at the center of each prism. To satisfy the valence rules, sulfur-sulfur bonds are formed in such a way that two anions in each unit become paired (11). The chains are alternatively displaced along their axis by half a prism length. Their relative distance is such that the separation between the metal in one chain and one sulfur from each of the two adjacent chains is similar to the intrachain metal-sulfur distance. As a consequence, the metal becomes eightfold coordinated, and the resulting cross linking produces slabs of coupled chains. The slabs are weakly bonded by van der Waals forces because sulfur pairs form their outer layers and thus, the materials are pseudo two-dimensional. Details of intrachain or interchain interactions differ from one compound to another, giving rise to different layering patterns and different unit cells. While in TiS_3 (13) and NbS_3 (14), the chains are all equal and the unit cell contains two columns; the orthorhombic polytype of TaS_3 (15) has a more complicated unit cell, containing 24 chains. Although the structure of orthorhombic TaS_3 has not yet been exactly determined, it has been proposed that it contains several types of chains that differ from one another by the degree to which sulfur atoms are paired. The presence of such inequivalent chains has been determined in similar compounds, such as TaSe_3 and NbSe_3 (11), and in the less common monoclinic polytype of TaS_3 (16), which can be obtained at high pressure. In addition, when the anion-anion pairing is relaxed, interchain anion bonding occurs. As a result, the slabs formed by cross-linked chains become somewhat puckered, making the van der Waals gap less defined (11).

One important structural characteristic of these trisulfides is the presence of sulfur-sulfur bonds. This pair is usually referred to as the polysulfide group, because x-ray diffraction studies in TiS_3 and NbS_3 have shown that this bond length is equivalent to that found in other known polysulfides. Therefore, the trisulfides have been formally described by the ionic formula $\{\text{M}^{+4}(\text{S}_2)^{-2} \text{S}^{-2}\}$, although they are mostly covalently bonded. We also have verified with XPS measurements the presence of sulfur in different bonding configurations (17). In Fig. 4 we show the XPS spectra of the sulfur 2p core level that we measured for TiS_3 , NbS_3 , and orthorhombic TaS_3 . The spectra for TiS_3 and NbS_3 can be decomposed into two doublets. Each doublet corresponds to the 3/2 and 1/2 spin-orbit split components of the 2p core level. The intensity ratio between the two doublets is 2:1, the more intense one being at higher binding energies. This indicates that less charge is localized on the more abundant species, as suggested by the ionic formula of the compound. In contrast, the lineshape observed for TaS_3 cannot be decomposed into only two components, suggesting a more complex bonding configuration as indicated by x-ray diffraction studies.

We have observed pronounced differences in the lineshapes of the voltammograms of the trisulfides and in the behavior of their voltammograms upon cycling. However, it is possible to identify one common feature: on first discharge, the three materials all undergo a two-electron reduction process at approximately the same potential. We associate this process with the reduction of the

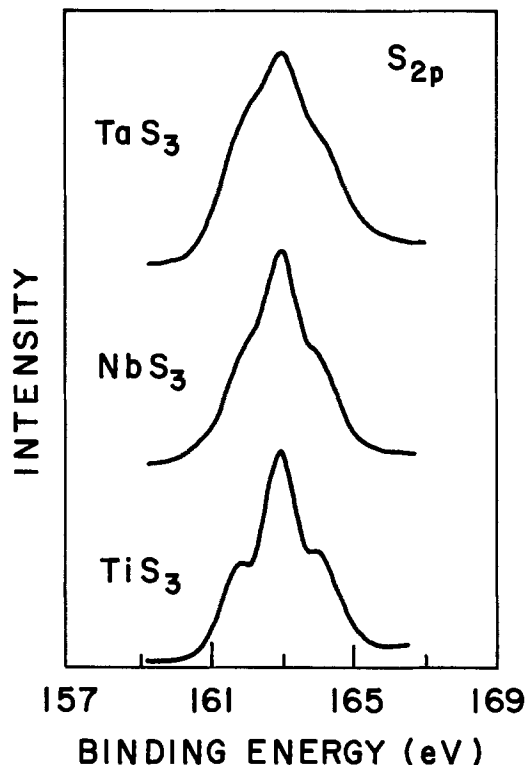


Fig. 4. XPS spectra of the S_{2p} core level for TiS_3 , NbS_3 , and TaS_3 .

polysulfide group with concomitant insertion of 2 Na/unit. It seems likely that sodium diffuses into the van der Waals gap of the material, although we were unable to confirm from our x-ray diffraction data that the unit cell expands along only one direction during this process. The initial reduction process breaks the polysulfide bond and produces different effects in each compound. For example, TiS_3 becomes unstable because the trigonal prismatic coordination of the cation is stabilized by the sulfur pair. Once the pair is broken, the structure tends to assume the more stable octahedral coordination which is found in TiS_2 (18). The disproportionation of TiS_3 to TiS_2 is clearly demonstrated by the cyclic voltammetry results because the curves obtained for scans subsequent to the first one are the same as the ones obtained for TiS_2 . It could be argued that the formation of TiS_2 occurs when the polysulfide is oxidized and the sodium is removed from the compound, because during the first anodic cycle, the characteristic disulfide peak at 1.5V is missing, while the peak at 2.1V is present. Moreover, because all of the sodium is removed during the first charge and the first oxidation peak is found above 2.0V, it seems unlikely that sodium sulfide and titanium disulfide are formed during the first discharge. The few broad lines observed in the x-ray diffraction pattern of an electrode discharged to 1.2V did not seem to correlate with those expected for Na_2S . It should be noticed that in the voltammograms of TiS_3 , the two peaks at 2.1V are resolved, indicating that the particle size of the product is small and that the disulfide is stoichiometric. Either excess of titanium or large particle size have the effect of broadening the peak linewidths. The spectra do not show any feature that can be associated with the presence of free sulfur liberated after the first cycle. However, a faint yellow deposit could be seen at the edge of the alumina disk after opening the cell. The absence of electrochemical activity from the free sulfur may be due to a loss of electrical contact. Because the quantity of sulfur is small, it is possible that it evaporates away during the experiment due to the relatively high temperature. We checked the transformation into the disulfide's not just being caused by the high temperature. A fresh electrode was kept at 300°C in a cell in open-circuit conditions for several days before being cycled, and it showed the same behavior.

Contrasting with the behavior of TiS_3 , no abrupt loss of capacity is observed in NbS_3 and TaS_3 after the first cycle. In both materials, the peaks in the first anodic scan and second cathodic scan above 2V are fairly symmetric, and the corresponding charge is greater than $1.5 e^-/\text{mol}$, indicating that the redox process is still associated with a polysulfide species. It also seems unlikely that the cation should change coordination, because the trigonal prismatic coordination is more stable than the octahedral one, at least in both niobium and tantalum disulfides (18). In addition, in all the scans these materials show another well-defined reduction process at voltages lower than 1V, not observed in TiS_3 . It is tempting to associate the low-voltage redox process with the oxidation and reduction of the cation. However, the trisulfides are largely covalent, and their atomic orbitals are well hybridized, so assignment of a specific valence state to the cation is purely formal. It could also be argued that TiS_3 can be further reduced below 1V because the titration current increases below this voltage. This process is, however, irreversible, because the anodic current is very small below $\sim 1.7\text{V}$, suggesting that sodium sulfide may be formed below 1V.

For the case of NbS_3 , our results suggest that this material undergoes irreversible transformations upon reaction with sodium. NbS_3 appears to transform slowly under repeated cycling, because new peaks in the voltammograms become more prominent and the electrode utilization decreases within ten cycles to almost half of its first-cycle value. However, the possibility that NbS_3 disproportionates to the disulfide seems contradicted by the fact that, even after fifteen cycles, the material can be inserted with more than 1 Na/Nb. The large sodium capacity would indicate that the polysulfide bond is still involved in the redox process, because the disulfides are typically found to reversibly incorporate 1 Na/unit at most (10). The lineshape of the voltammograms, even after several cycles, is different from that measured for rhombohedral NbS_2 (10). It should be noticed, however, that several nonstoichiometric phases have been identified in the sulfur-niobium phase diagram (19) and that their behavior in sodium cells has not been determined. Peculiar to NbS_3 is the very sharp peak at 1.95V, which is a characteristic potential for polysulfide reduction. The intensity of this peak decreases rapidly with cycling, while the peak at 2.4V increases to a comparable intensity. This feature might indicate that a disulfide phase is being formed at the expense of the trisulfide, because the typical potentials observed for sodium intercalation in the disulfides range between 2.2 and 2.4V, and the lineshape of the peak at 2.4V is similar to that observed for intercalation in those compounds (10). X-ray diffraction measurements on a fully charged electrode after sixteen charge/discharge cycles showed only a few diffuse lines from which the reaction products could not be identified.

TaS_3 is the most stable of the three sulfides. After the first few cycles, sodium seems to be inserted and removed from this compound with little loss in the electrode capacity, as is typically observed in an intercalation reaction. We suggest that the greater stability of TaS_3 when compared to the other two trisulfides may be related to the presence of relaxed sulfur pairs. The occurrence of relaxed polysulfide groups could be attributed to an increased charge transfer from the cation to the anion as if tantalum prefers the pentavalent configuration (16). Relaxation of intrachain sulfur-sulfur bonds may also promote interchain chalcogen interactions as it is observed, for instance, in TaSe_3 (11). Thus, the reduction process at high voltage may be quite complex, involving either different sulfide species or the compound as a whole. It should be noted, in fact, that the line shape of the peak above 2V is asymmetrical and is quite different from that observed for TiS_3 and NbS_3 . In addition, after several cycles, the charge associated with the lower redox process is found to be larger than $1 e^-/\text{Ta}$, suggesting the presence of pentavalent cations. Some degree of electrochemical irreversibility is present in the behavior of the

material because the anodic and cathodic peaks are widely separated. In particular, the peaks at low voltages are shifted by 400 mV. A large peak separation could result if the cation ligand field is distorted during the reduction process so that the oxidation potential is shifted to higher values.

The energy density of the TaS_3 electrode alone extrapolated from the tenth cycle is about 350 Wh/kg, which is similar to the one found for TiS_2 in a similar sodium cell (360 Wh/kg) (9). Because the density of TaS_3 is almost twice as large as that of TiS_2 , the utilization of TaS_3 could be more advantageous in applications in which the volumetric energy density needs to be high. In addition, the fibrous morphology of TaS_3 makes it easier than for the platelet-like disulfide materials to construct high surface-area electrodes which have good mechanical integrity.

Some of the trisulfides have been tested in the past as electrode materials in room-temperature lithium cells, but no tests have been performed in sodium cells. TiS_3 and NbS_3 showed poor reversibility with lithium (1, 20). It was found that three equivalents of lithium could be inserted electrochemically in 1 mol of TiS_3 , but that less than 1 eq/mol could be removed at very low current rates. The lack of reversibility observed in the galvanostatic charge/discharge data was ascribed to the formation of lithium sulfide and titanium disulfide (1). However, neither x-ray data nor the electrochemical data could conclusively show the presence of either compound. Similarly, it was found that 2.6 eq/mol of lithium could be inserted in NbS_3 on first discharge, only 80% of which could be removed (20). Our electrochemical data seem to indicate that no sodium sulfide is formed in the trisulfides during the first electrochemical discharge. We also found in our experiments that sodium can be removed from both TiS_3 and NbS_3 after the first discharge in much larger percentage than that measured in the case of titration with lithium. The greater degree of rechargeability observed in our experiments is probably due to the higher temperature of operation, instead of being related to intrinsically different effects occurring from the two alkali metals. In fact, it was shown in our earlier results that TiS_2 in a similar high-temperature sodium cell was much more reversible and had a deeper discharge range than in room-temperature sodium cells with a liquid electrolyte (9, 21). There are no data in the literature about the behavior of TaS_3 electrodes in lithium cells. Because in our experiments this compound is found to be rechargeable, it is possible that it may also have good rechargeability characteristics in room-temperature lithium cells, as was found for NbSe_3 (7). This material can be reversibly titrated with three equivalents of lithium per mole, and under galvanostatic discharge, it exhibits two plateaus. We found in our sodium cells that NbSe_3 behaves similarly to TaS_3 (22). In particular, three equivalents of sodium can be inserted in one mole of NbSe_3 and removed from it; the material can be cycled several times with little loss in electrode capacity, and only small changes in the voltammograms occur after repeated cycling. However, three separate redox processes seem to occur in NbSe_3 after the first cathodic scan. NbSe_3 was found to contain three kinds of chains which differ by the degree of anion pairing (11). These similarities between TaS_3 and NbSe_3 seem to point out that the characteristics of the anion bonding in the trichalcogenides may be the important factors in determining their stability toward the insertion of alkali metals.

Conclusion

We have shown that the electrochemical behavior of the trisulfides of titanium, niobium, and tantalum is dominated by the redox process on the polysulfide group. As a consequence, irreversible transformations are induced in the trisulfides, unlike what is observed in the corresponding disulfides. Although the trisulfides have similar structural characteristics, some differences in their bonding properties can be identified. We suggest that the different degrees of stability toward insertion of sodium

observed in these compounds are a consequence of different sulfur-sulfur bonding configurations. Our voltammograms clearly show the disproportionation of TiS_3 into the corresponding disulfide. It is not possible, on the basis of our data, to identify the precise mechanisms by which NbS_3 loses electrode capacity, although decomposition to the disulfide cannot be ruled out. The electrochemical behavior of TaS_3 instead resembles more what is expected for an intercalation process: only small changes are observed in its voltammograms upon cycling. TaS_3 may be potentially useful as an electrode material for applications in which a high volumetric energy density is required.

Acknowledgments

The author is deeply indebted to G. J. Tennenhouse for many helpful discussions and for providing the β'' -alumina disks. The help of J. E. deVries in the XPS data acquisition and the assistance of F. R. Runkle in making the ceramic cells are gratefully acknowledged.

Manuscript submitted Jan. 13, 1984; revised manuscript received Sept. 12, 1984.

Ford Motor Company assisted in meeting the publication costs of this article.

REFERENCES

1. M. S. Whittingham, *This Journal*, **123**, 315 (1976).
2. D. W. Murphy and F. A. Trumbore, *J. Cryst. Growth*, **39**, 185 (1977).
3. K. M. Abraham, *J. Power Sources*, **7**, 1 (1981).
4. R. R. Chianelli and M. B. Dines, *Inorg. Chem.*, **14**, 2417 (1975).
5. D. W. Murphy and F. A. Trumbore, *This Journal*, **123**, 960 (1976).
6. G. L. Holleck and J. R. Driscoll, *Electrochim. Acta*, **22**, 647 (1977).
7. J. N. Carides and D. W. Murphy, *This Journal*, **124**, 1309 (1977).
8. J. T. Kummer and N. Weber, *S. A. E. Trans.*, **26**, 1003 (1968).
9. M. Zanini, J. L. Shaw, and G. J. Tennenhouse, *This Journal*, **128**, 1647 (1981).
10. M. Zanini, J. L. Shaw, and G. J. Tennenhouse, *Solid State Ion.*, **5**, 371 (1981).
11. F. Hulliger, in "Physics and Chemistry of Materials with Layered Structures," Vol. 5, F. Levy, Editor, Reidel (1976).
12. M. S. Whittingham, *Solid State Chem.*, **12**, 41 (1978).
13. F. K. Mctaggart and A. D. Wadsley, *Aust. J. Chem.*, **11**, 445 (1958); S. Furuseth, L. Brattas, and A. Kjekshus, *Acta Chem. Scand.*, **A29**, 623 (1975).
14. J. Rijnsdorp and F. Jellinek, *J. Solid State Chem.*, **25**, 325 (1978).
15. E. Bjerkelund and A. Kjekshus, *Z. Anorg. Allg. Chem.*, **328**, 235 (1964); A. Bjerkelund, J. H. Femor, and A. Kjekshus, *Acta Chem. Scand.*, **20**, 1836 (1966).
16. A. Meerschaut, L. Guemas, and J. Rouxel, *J. Solid State Chem.*, **36**, 118 (1981).
17. M. Zanini and J. E. deVries, Internal Report, Ford Motor Company (1983).
18. F. R. Gamble, *J. Solid State Chem.*, **9**, 358 (1974).
19. F. Kadijk and F. Jellinek, *J. Less Common Metals*, **19**, 421 (1969).
20. G. L. Holleck, F. S. Shuker, and S. B. Brummer, Proceedings 10th IECEC, Newark, Delaware (1975).
21. G. H. Newman and L. P. Klemann, *This Journal*, **127**, 2097 (1980); K. M. Abraham, L. Pitts, and R. Schiff, *ibid.*, **127**, 2545 (1980).
22. M. Zanini, Unpublished results.

The Photoelectrochemical Behavior of $CuIn_5S_8$

B. Scrosati* and L. Fornarini

Department of Chemistry, University of Rome, 00185 Rome, Italy

G. Razzini and L. Peraldo Bicelli*

Department of Applied Physical Chemistry, The Milan Polytechnic, Research Centre on Electrode Processes of the CNR, 20133 Milan, Italy

ABSTRACT

The photoelectrochemical behavior of n- $CuIn_5S_8$, a chalcogenide having a spinel-type structure, has been studied in various electrolytes by measuring the spectral response, the current-potential characteristics, and the differential capacitance. The best results have been obtained in an aqueous sulfide-polysulfide solution, where the $CuIn_5S_8$ semiconductor electrode shows an excellent stability. The flatband potential of this semiconductor electrode has been found to depend on the solution composition. The most negative values have been observed in the sulfide-polysulfide solution, owing to specific adsorption of S^{2-} ions on the electrode surface. Preliminary results on the output power characteristic of the $CuIn_5S_8$ photoelectrochemical cell are also discussed.

Progress in the development of photoelectrochemical cells has required the investigation of new semiconductor electrodes exhibiting a good stability against photodecomposition and a high absorption in the visible portion of the solar spectrum. Some ternary semiconducting compounds have been shown to satisfy the above conditions, and, in particular, analogues of II-VI compounds, obtained by cross-substitution of the electropositive constituent, have lately been the subject of growing scientific interest.

In this work, we report the photoelectrochemical performance of $CuIn_5S_8$, whose optical and electrical properties are known (1). This n-type semiconductor has a cubic spinel-type structure similar to that of $CdIn_2S_4$ (2).

The ideal spinel structure can be viewed as a cubic close-packed partial structure of anions in which one-

eighth of the tetrahedral and one-half of the octahedral sites are occupied by cations.

Considering the general formula $M_{1/2}^+M_{1/2}^{3+}[M_2^{3+}]X_4^{2-}$ of a normal 1-3 spinel where the cations in the brackets occupy octahedral sites and the remaining cations occupy tetrahedral sites, $CuIn_5S_8$ may be written as $Cu_{1/2}In_{1/2}[In_2]S_4$. This formula can also be deduced by substituting monovalent copper cations and trivalent indium cations for divalent cadmium cations in $CdIn_2S_4$, which is, however, a partial inverse thio-spinel: $Cd_{1/2}In_{1/2}(Cd_{1/2}In_{3/2})S_4$ (3).

$CuIn_5S_8$ crystallizes in the space group $F\bar{4}3m$ (T^3d_h), has a cubic structure with lattice dimension $a = 10.6858\text{\AA}$ and has eight molecules per unit cell (4). Moreover, according to complete x-ray structural determinations, the tetrahedral sites are split into two nonequivalent groups with an unequal distribution of copper and indium ions. In fact, one site is occupied to the extent of 52.4% by cop-

* Electrochemical Society Active Member.

per ions and 47.6% by indium ions, whereas the opposite situation is found for the other site (4). However, Robbins and Miksovky (5) consider copper and indium ions to be crystallographically disordered on the sites having tetrahedral coordination, as usually occurs in 1-3 spinels.

The width of the forbidden bandgap of CuIn_5S_8 (1.26 eV, see below) is much closer to the optimal value for solar energy utilization than that of its structural analogue CdIn_5S_4 [2.28 eV (1)]. Following Usujima *et al.* (1), these values may be correlated with cationic atoms occupying the tetrahedral sites. For example, the large energy gap of CdIn_5S_4 seems to be connected with the strong ionicity of the cations at the tetrahedral sites, which is due to the large difference of the electronegativity between cadmium and sulfur. Up to now, ternary chalcogenides showing the spinel structure have scarcely been considered in photoelectrochemical studies, in comparison with ternary semiconductors showing a structure related to the zincblende type (e.g., a chalcopyrite structure), which either have a completely tetrahedral coordination [e.g., CuInS_2 (6-8), CuInSe_2 (9), CdGeP_2 (10), or a cation-deficient lattice], so that a smaller part (3/8 instead of 1/2) of the tetrahedral sites is occupied [e.g., CdIn_2Se_4 (11-12)].

Experimental

Single-crystal samples of n- CuIn_5S_8 , synthesized from the constituent elements, were kindly provided by Dr. J. L. Shay of AT&T Bell Laboratories. Some of the specimens gave a very low photoelectrochemical response, probably as a consequence of faults in their composition. In fact, sulfur vacancies have been shown to create donor levels in CuIn_5S_8 and thus to influence its resistivity and photosensitivity (1).

The material was also very sensitive to defects introduced during mechanical deformation; hence, the preparation conditions of the samples to be mounted on the sample holder were rather critical. As an example, often the mere action of cutting the crystals had a detrimental effect on the sample photoactivity, which practically decayed to zero. Therefore, the electrode surface was never polished.

Before mounting in the measurement cell, the electrodes were submitted to chemical etching. Various conventional etchants were tested, but the best results were obtained with a 1:1 $\text{H}_2\text{SO}_4\text{:H}_2\text{O}_2$ solution. Hence, all electrodes were treated with this solution for several minutes and then rinsed in bidistilled water.

The ohmic contact was established by soldering pure indium on the back surface of the crystal, taking care that no cracks formed during this operation. A copper wire was attached to the crystal by means of a silver paste, and insulating epoxy cement was used to seal the electrode except for its front surface.

A conventional three-electrode glass cell having a platinum foil (50 cm^2) as a counterelectrode and a saturated calomel electrode (SCE) as reference electrode were employed for studying the photoelectrochemical behavior of CuIn_5S_8 . This behavior was mainly examined in three different solutions, 1M Na_2SO_4 (pH = 4.8), 1M Na_2S + 1M S + 1M NaOH (in the following indicated as polysulfide solution), and 0.1M KI + 10^{-2} or 10^{-3} M I_2 . The various solutions were prepared from AR-grade reagents (Merck and Carlo Erba) and doubly distilled water.

The instrumentation included a standard photoelectrochemical setup with an Oriol 150 Xe-arc lamp, a UDT 61 radiometer, an Amel 553 potentiostat-galvanostat, an Applied Photophysics monochromator Model 7300 having 1200 grooves mm^{-1} , and a Wayne Kerr B 331 Mk 11 autobalance precision bridge (at a frequency of 1.6 kHz). A set of neutral density filters was used for changing the light intensity (13).

Results and Discussion

Spectral response.—Figure 1 shows the wavelength dependence of the short-circuit photocurrent of the n- CuIn_5S_8 electrode in the sulfide-polysulfide solution. Normalization was made for the spectrum of the lamp. The

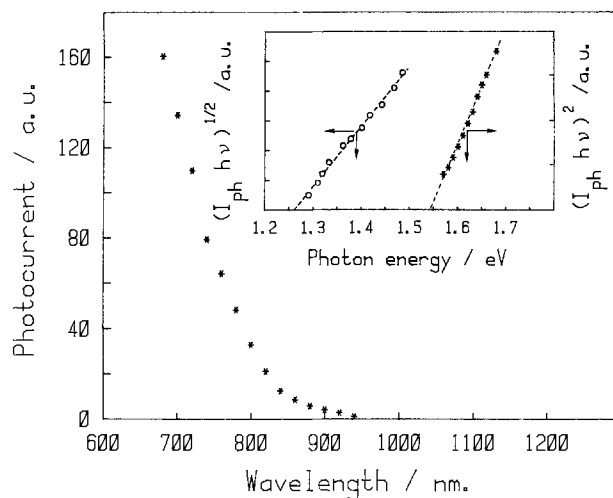


Fig. 1. Normalized spectral response of CuIn_5S_8 in 1M Na_2S , 1M S, 1M NaOH. In the insert is shown the determination of the bandgap of the indirect (1.26 eV) and of the direct (1.54 eV) transition.

threshold photoresponse at a wavelength of approximately 970 nm corresponds to a bandgap of about 1.28 eV, whereas practically no sub-bandgap photoresponse was observed.

For the evaluation of the photoelectrochemical behavior of a semiconductor electrode, not only the bandgap energy but also the type of electronic transition must be considered. In general, semiconductors with direct transitions are preferred due to the large absorption coefficient for photons having energies higher than the bandgap.

In the case of CuIn_5S_8 , both direct and indirect transitions have been reported (1). According to the simplified Gärtner equation (14), which is assumed to apply also in this case, the plot of $(I_{ph}h\nu)^{1/n}$ (where $n = 2$ or 0.5 for an indirect or a direct transition, respectively) is a linear function of $h\nu$ for wavelengths close enough to the transition energy. The bandgap energy can be determined from the Gärtner plot. In the case here under study, the plot is shown in the insert of Fig. 1. The linear behavior indicates the validity of the equation and allows one to determine the two energy gaps of CuIn_5S_8 , the lowest at 1.26 eV, due to an indirect-allowed transition, and the other at 1.54 eV, due to a direct mode. The results are in agreement with those obtained by Usujima *et al.* (1) from optical absorption measurements (1.30 and 1.51 eV, respectively).

The width of the forbidden gap is close to the optimal value for terrestrial photovoltaics. Its value is clearly influenced by the presence of indium atoms [compare the 1.5 eV value of CuInS_2 (7)]. Knowing the energy gap values, the correctness of the results regarding the transition modes could be further verified by plotting $\log(I_{ph}h\nu)$ vs. $\log(h\nu - E_g)$ (14). In the case here under study, two straight lines having slopes of 2.1 and 0.5, respectively, were obtained. This confirms that the transition occurring at the lowest wavelength is indirect (theoretical slope equal to 2) whereas the other is direct (theoretical slope equal to 0.5).

The occurrence of both indirect and direct transitions is common for the CdIn_2X_4 (with X = S, Se, Te) materials. The difference between the energy of the two bands decreases from 0.34 eV for CdIn_2S_4 (1) to 0.22 eV for CdIn_2Se_4 (11) and to 0.1 eV for CdIn_2Te_4 (11). However, for the structural analogues CdIn_2S_4 and CuIn_5S_8 , such difference goes from 0.34 (1) to 0.28 eV.

Photocurrent-voltage characteristics and photocorrosion.—The current-voltage curve of CuIn_5S_8 in the sulfide-polysulfide aqueous solutions shows the typical trend of an n-type semiconductor (Fig. 2). In the dark (curve d) no current flows up to an applied voltage of approximately 0.2V vs. SCE. Large photocurrents are obtained under illumination, with an onset depending upon the nature of the redox couple in solution. The photo-

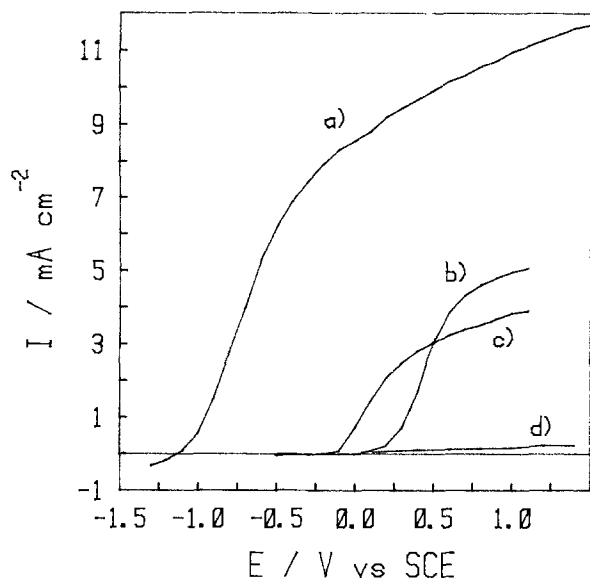
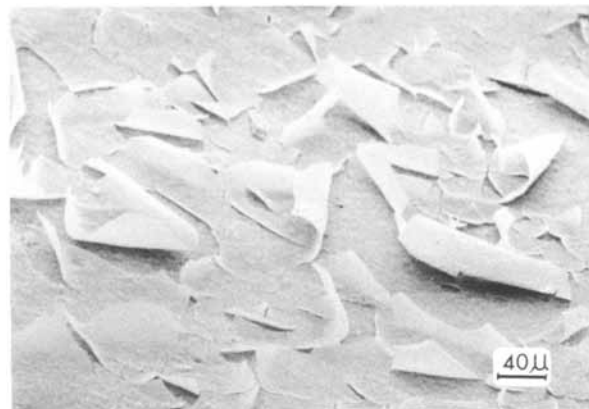


Fig. 2. Current-potential curves of CuIn_3S_8 in 1M Na_2S , 1M S , 1M NaOH (curve a); in 1M Na_2SO_4 , pH = 4.8 (curve b); in 0.1M KI , 0.001M I_2 (curve c). The dark curve in the polysulfide electrolyte is shown in curve d. Illumination: 100 mW/cm^2 white light. Scan rate: 4 mV/s.

current onset progressively shifts towards more negative voltages passing from the Na_2SO_4 solution (curve c) to the KI , I_2 solution (curve b) and to the polysulfide solution (curve a). The passage of current in the presence of the Na_2SO_4 , a "nonprotecting electrolyte" (2), indicates a photocorrosion process of the CuIn_3S_8 electrode. This process leads to the formation of sulfur on the electrode surface, as will be discussed below. This photocorrosion is consistently prevented not by the iodine-iodide couple, but rather by the polysulfide electrolyte, which shifts the onset potential to a very negative value.

The sulfide-polysulfide redox couple, which is known to give the best photoelectrochemical results in conjunction with cadmium calcogenide photoanodes, appeared then to be well-suited also for the CuIn_3S_8 electrodes. The large shift towards negative voltages is accompanied by a steep increase of photocurrent. The square of the photocurrent density vs. the applied potential for the CuIn_3S_8 electrode illuminated with 700 nm light chopped at 96 Hz in a polysulfide solution and in a Na_2SO_4 solution was measured. In both cases, a linear dependence is found, in agreement with the Gärtner equation (14), thus showing the absence of charge-carrier recombination in the near-surface region, when the charge-transfer reaction is not the limiting step. By extrapolating the I - V curve to the potential axis, a value of -1.2 V vs. SCE is obtained for the flatband potential of CuIn_3S_8 in polysulfide solutions, a value which is coincident with that determined from capacitance experiments (see below). Instead, the I - V characteristic in the Na_2SO_4 solution (see Fig. 2) had the typical delayed onset of the photocurrent indicative of surface recombination (due to the presence of surface states) or of a slow electron-transfer reaction, both preventing the semiconductor bands from flattening at potentials close to the flatband potential (15). Indeed, the latter is 0.25 V vs. SCE , a value less negative than the -0.55 V vs. SCE resulting from capacitance measurements (see below).

In order to determine the previously mentioned photocorrosion process, the CuIn_3S_8 electrode was polarized at 1 V vs. SCE in the Na_2SO_4 solution, and the photocurrent was measured as a function of time. A continuous decrease (the photocurrent decreased to one-half of its initial value in 1h) clearly indicated a progressive worsening of the photoelectrode due to the deterioration of its surface. After 3h of polarization, the electrode surface was examined by scanning electron microscopy (SEM). This observation showed that the entire sample surface was



(A)

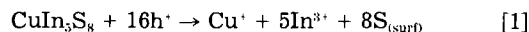


(B)

Fig. 3. SEM micrographs of the CuIn_3S_8 electrode surface after 3h polarization at 1 V vs. SCE in Na_2SO_4 at pH = 4.8 under 100 mW/cm^2 illumination (A) and after a subsequent treatment with carbon disulfide (B).

covered with a yellow film with partly peeling flakes (Fig. 3a). Microprobe analysis indicated that both film and flakes were sulfur-based compounds, very likely elemental sulfur. This initial sulfur film seems unable to protect the electrode surface from further corrosion, as is the case for the selenium corrosion layer on CdSe (16). In fact, after having reached a certain thickness, the sulfur layer peels off from the substrate, thus reexposing fresh surface portions to the electrolytic solution. After partial dissolution of the film with carbon disulfide, the electrode surface was again examined in the SEM. Typical etch pits are clearly noticeable on the specimen surface (Fig. 3b).

At the end of the polarization test, a plasma emission analysis was run, showing that 6 ppm copper ions were present in the electrolyte. All these results agree with CuIn_3S_8 photocorrosion via the overall reaction



A similar polarization test (0 V vs. SCE) was also performed in the sulfide-polysulfide solution. As expected, no corrosion phenomena were detected: the photocurrent remained constant, the appearance of the electrode surface remained unchanged, with no sign of elemental sulfur, and no copper ions were detected in the electrolyte. The CuIn_3S_8 electrode is thus expected to be highly stable in this electrolyte (see below).

This is not the case for other redox electrolytes. For instance the I/I_2 redox couple appears to act as a protecting electrolyte in a limited range, the onset potential being more negative than the photodecomposition potential (about 0.2 V vs. SCE , see Fig 2c). Effectively, in a range of values starting from the onset potential up to approximately the redox potential of the I/I_2 couple, the photocurrent remains stable at high values (i.e., at about 2.5

mA/cm²). However, going to progressively higher potentials, photocorrosion takes place, producing the typical sulfur coverage of the electrode surface accompanied by a remarkable decay of photocurrent.

Since it has been reported (2) that, for CdIn₂S₄, the aqueous ferri-ferrocyanide redox couple gave better results than the sulfide-polysulfide solution, the former electrolyte was also tested for the CuIn₃S₈ electrode. However, also, in this case, photodecomposition of the electrode with the formation of elemental sulfur on its surface was clearly observed. Consequently, the sulfide-polysulfide electrolyte has been selected for all the CuIn₃S₈ photoelectrochemical tests which necessitated a prolonged operation.

Light intensity influence.—In Fig. 4 is shown the plot of short-circuit photocurrent *vs.* input light power, on a double logarithmic scale, for the CuIn₃S₈ electrode in the sulfide-polysulfide solution. The striking feature of this plot is the linear dependence of photocurrent on light intensity over more than two decades. In agreement with Gärtner theory (14), a linearity over at least two orders of magnitude shows that the rate of charge transfer across the interface between the CuIn₃S₈ semiconductor and the electrolytic solution is very fast, the rate-determining step being the photogeneration of the charge carriers.

Flatband potential.—Differential capacitance measurements were performed on the CuIn₃S₈ electrode in various electrolytic solutions. A typical Mott-Schottky plot of CuIn₃S₈ in the 1M Na₂SO₄ solution is shown in Fig. 5. The 1/C²-V dependence is strictly linear over a wide range; hence, the flatband potential U_{FB} could be determined from the intercept of the curve on the X-axis. A value of -0.55V *vs.* SCE was obtained, which, as already stated, is more negative than that deduced from the onset of the current-potential curve (about -0.25V *vs.* SCE). The value of the flatband potential determined from capacitance measurements is in fairly good agreement with that (-0.6V *vs.* SCE) calculated from Mulliken electronegativities of the constituent atoms of CuIn₃S₈, following the method proposed by Butler and Ginley (17) (see Appendix). As often done in these calculations, the potential drop across the Helmholtz double layer due to specific adsorption of positively and negatively charged potential-determining ions at the interface has been ignored. Therefore, it was implicitly assumed that the adsorbed surface charge was zero. This hypothesis seems to be justified in the case of the Na₂SO₄ solution where OH⁻, H⁺, and other ions are expected not to be specifically adsorbed on the electrode surface. As a matter of fact, no differences in flatband potential were observed as a function of the solution pH.

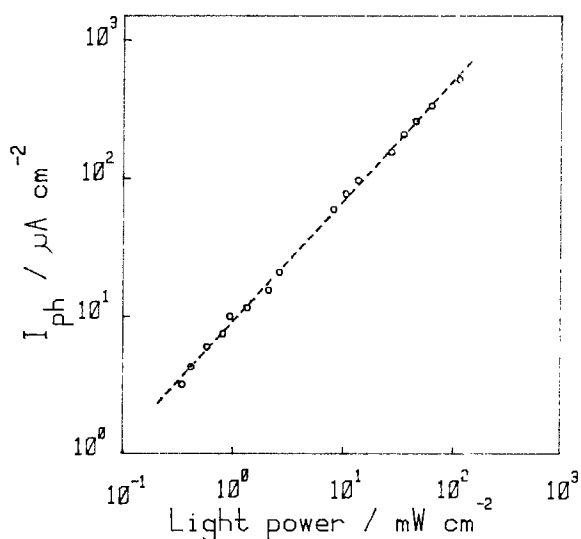


Fig. 4. Short-circuit photocurrent *vs.* light power for CuIn₃S₈ in 1M Na₂S, 1M S, 1M NaOH. White light.

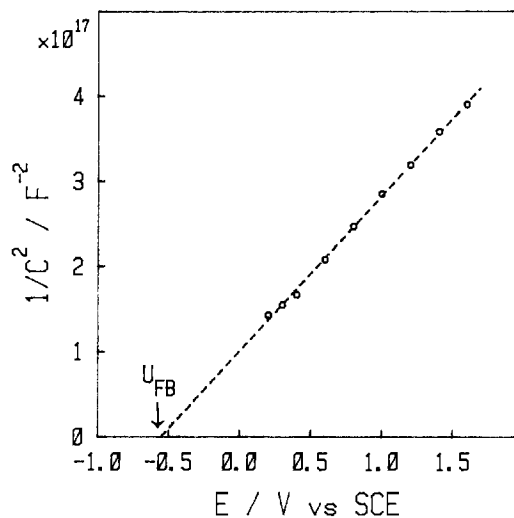


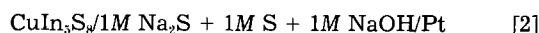
Fig. 5. Typical Mott-Schottky plot of CuIn₃S₈ in Na₂SO₄, pH = 4.8 and at 1.6 kHz.

The other important parameter usually estimated from Mott-Schottky plots, *i.e.*, the density of the majority carriers, could not be calculated in the present case, since the dielectric constant of CuIn₃S₈ is unknown.

The Mott-Schottky plots of CuIn₃S₈ in the sulfide-polysulfide solution showed that the flatband potential is shifted towards a more negative value (-1.2V *vs.* SCE) than that obtained in the Na₂SO₄ solution.

This difference is explainable by considering the specific adsorption of solution sulfide species. These adsorbed ions produced an additional potential drop across the Helmholtz double layer, thus shifting the flatband potential to more negative values. Similar shifts in flatband potential have been observed for cadmium chalcogenide photoelectrodes, in particular for the spinel analogue CdIn₂S₄ (2) and for CdS (18).

Output power characteristic and stability tests.—The power characteristics of the following photoelectrochemical cell



obtained under an illumination intensity of 100 mW/cm² are reported in Fig. 6 both for pristine and etched CuIn₃S₈ specimens. The short-circuit photocurrent (~4 mA/cm²), the maximum power efficiency (~0.4%), and the fill factor (~0.3) are still unsatisfactory for practical applications.

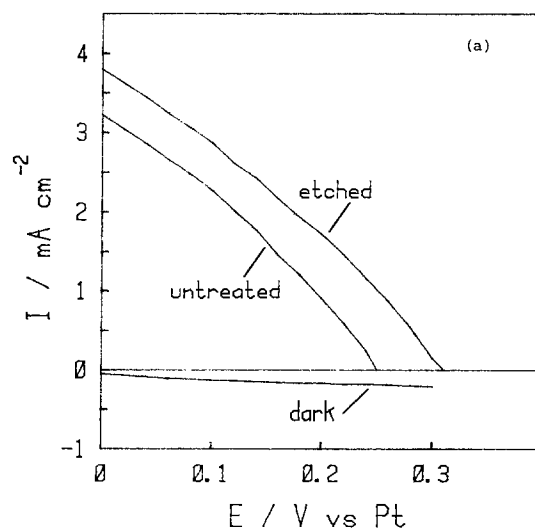


Fig. 6. Output power characteristics of the CuIn₃S₈/1M Na₂S, 1M S, 1M NaOH cell under 100 mW/cm² white light and in the dark. The characteristics are reported for both untreated and etched (1:1 H₂SO₄:H₂O₂) CuIn₃S₈ crystals.

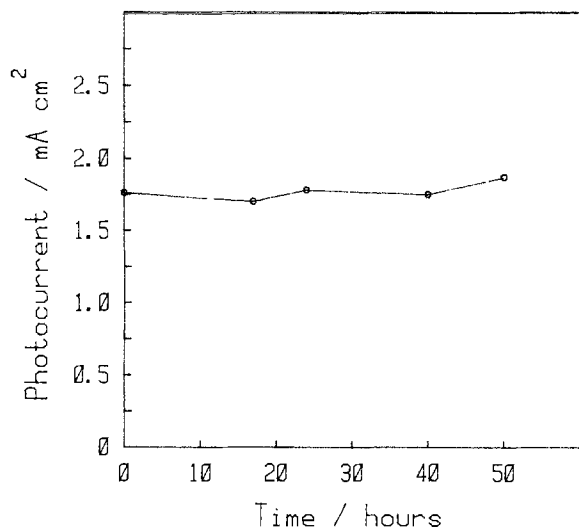


Fig. 7. Short-circuit photocurrent vs. time for a $\text{CuIn}_5\text{S}_8/1\text{M Na}_2\text{S}$, 1M S , 1M NaOH cell under continuous 100 mW/cm^2 white light illumination.

However, work is in progress to improve this performance with the study of the effects of various etching treatments.

The power characteristics were also measured in the presence of the $0.1\text{M KI} + 0.01\text{M I}_2$ solution, and comparable results were obtained. However, as already pointed out, this electrolyte solution cannot be used for prolonged operation. Therefore, stability tests of the CuIn_5S_8 electrodes were carried out using the sulfide-polysulfide solution, by monitoring the short-circuit photocurrent as a function of time during a 50h experiment (Fig. 7). Fairly constant values (around 1.8 mA/cm^2) were obtained, and no changes of the electrode surface morphology was observed after the test, thus confirming the stability of the semiconductor electrode in the polysulfide electrolyte.

Conclusions

The following conclusions can be drawn from the results discussed in this work.

1. The CuIn_5S_8 photoanode is stable in the sulfide-polysulfide electrolyte. Such extraordinary stability exceeds that of its structural analogue CdIn_2S_4 and may be attributed to a photodecomposition potential lying outside the bandgap of the semiconductor electrode.

2. The very negative value of the flatband potential of CuIn_5S_8 (-1.2V vs. SCE) in the sulfide-polysulfide electrolyte is not far from the value measured for cadmium-chalcogenide photoelectrodes in the same solution [i.e., 1.6V vs. SCE for CdS (2)]. This seems to indicate that, in the CuIn_5S_8 case also, adsorbed sulfide ions pin the semiconductor bandedges with respect to the redox potential of the solution, and it predicts a limiting open-circuit photovoltage.

3. Owing to the low photocurrents so far obtained, the solar conversion efficiency remains around 0.4%, a value lower than that obtained for other operating photoelectrochemical regenerative cells. Nevertheless, the initial results here reported appear sufficiently encouraging for promoting further work, particularly that directed to the enhancement of photocurrent values. In this respect, a systematic research of improved, *ad hoc* etching solutions, should be carried out.

Acknowledgments

The authors are highly indebted to Dr. J. L. Shay of AT&T Bell Laboratories for kindly providing the single-crystal samples and to Ms. E. Bet for assistance in performing the experiments. The financial support from the Consiglio Nazionale delle Ricerche, Progetto Finalizzato Energetica II, Sottoprogetto Energia Solare, Eolica e Idraulica, is also acknowledged.

Manuscript submitted July 18, 1984; revised manuscript received Oct. 26, 1984.

The University of Rome assisted in meeting the publication costs of this article.

APPENDIX

Following Butler and Ginley (17), the flatband potential (U_{FB}) of a semiconductor can be predicted from its bulk electronegativity (χ) when the bandgap (E_g) of the material is known. In fact, assuming that the potential drop across the Helmholtz double layer is zero

$$eU_{\text{FB}} (\text{SCE}) = \chi - E_g/2 - 4.75 + \Delta E \quad [3]$$

where the flatband potential is referred to the saturated calomel electrode, e is the electronic charge, 4.75 eV is the constant relating the reference electrode to the vacuum level, and ΔE is the difference between the Fermi level of the semiconductor and the bottom of the conduction band. Clearly, ΔE depends on the doping level. However, for heavily doped semiconductors, commonly employed in photoelectrochemical cells such as metal oxides (19) and cadmium chalcogenides (20), this term is only about 0.1 eV .

The bulk electronegativity of the compounds is assumed to be the geometric mean of Mulliken electronegativities of the constituent atoms. Hence, for CuIn_5S_8 , it is given by

$$\chi(\text{CuIn}_5\text{S}_8) = [\chi(\text{Cu}) \chi^5(\text{In}) \chi^8(\text{S})]^{1/14} \quad [4]$$

introducing this relationship in Eq. [3] and assuming $\Delta E = 0.1 \text{ eV}$, $U_{\text{FB}} = -0.6\text{V vs. SCE}$, as already reported in the text.

Recently, Halouani and Deschamvres (20) suggested a modified calculation method, in which both Eq. [3] and [4] were empirically adjusted to better match experimental results on flatband potentials. Moreover, they also considered other atomic electronegativity scales, such as those of Pauling, of Simons (21) and of Phillips (22). First of all, expression [3] was simplified in

$$\chi(\text{CuIn}_5\text{S}_8) = [\chi(\text{Cu}) \chi(\text{In}) \chi(\text{S})]^{1/3} \quad [5]$$

and Eq. [4] was modified introducing a constant C that was experimentally determined

$$eU_{\text{FB}} (\text{SCE}) = C\chi - E_g/2 - 4.75 + \Delta E \quad [6]$$

where C is equal to 1.03 or to 2.5, respectively, when Mulliken or Pauling electronegativities are utilized. Following this approach, $U_{\text{FB}} = -0.7\text{V vs. SCE}$ in the first case, and $U_{\text{FB}} = -0.3\text{V vs. SCE}$ in the second one.

Although Halouani and Deschamvres (20) consider that the best results are achieved with Pauling electronegativities, the latter suffer from uncertainties too great, particularly when heavy metal atoms are involved, to obtain reliable data.

REFERENCES

1. A. Usujima, S. Takeuchi, S. Endo, and T. Frie, *Jpn. J. Appl. Phys.*, **20**, 505 (1981).
2. G. F. Epps and R. S. Becker, *This Journal*, **129**, 2628 (1982).
3. F. Cerrina, I. Abbati, L. Braicovich, F. Lévy, and G. Margaritondo, *Solid-State Commun.*, **26**, 99 (1978); F. Cerrina, C. Quaresima, I. Abbati, L. Braicovich, P. Picco, and G. Margaritondo, *ibid.*, **33**, 429 (1980).
4. L. Gastaldi and L. Scaramuzza, *Acta Crystallogr., Sect. B*, **35**, 2283 (1979); C. Paorici, L. Zanotti, and L. Gastaldi, *Mater. Res. Bull.*, **14**, 469 (1979); L. Gastaldi and L. Scaramuzza, *Acta Crystallogr., Sect. B*, **36**, 2751 (1980).
5. M. Robbins and M. A. Miksovsky, *Mater. Res. Bull.*, **6**, 359 (1971).
6. M. Robbins, K. J. Bachmann, V. G. Lambrecht, F. A. Thiel, J. Thomson, Jr., R. G. Vadimsky, S. Menzes, A. Heller, and B. Miller, *This Journal*, **125**, 831 (1978).
7. Y. Mirovsky, D. Cahen, G. Hodes, R. Tenne, and W. Giriat, *Solar Energy Mater.*, **4**, 169 (1981).
8. H. J. Lewerenz and H. Goslowky, in "4th International Conference on Photochemical Conversion and Storage of Solar Energy," Jerusalem, Israel, 1982.
9. Y. Mirovsky and D. Cahen, *Appl. Phys. Lett.*, **40**, 727 (1982); K. J. Bachmann, S. Menezes, R. Koetz, M. Fearheily, and H. J. Lewerenz, *Surf. Sci.*, **138**, 475 (1984).
10. B. Scrosati and L. Fornarini, *This Journal*, **131**, 948 (1984).

11. R. Tenne, Y. Mirovsky, Y. Greenstein, and D. Cahen, *ibid.*, **129**, 1506 (1982).
12. L. Fornarini, F. Stirpe, E. Cardarelli, and B. Scrosati, *Solar Cells*, **11**, 389 (1984).
13. G. Razzini, M. Lazzari, L. Peraldo Bicelli, F. Lévy, L. De Angelis, F. Galluzzi, E. Scafé, L. Fornarini, and B. Scrosati, *J. Power Sources*, **6**, 371 (1981).
14. W. Gärtner, *Phys. Rev.*, **116**, 84 (1959); M. A. Butler, *J. Appl. Phys.*, **48**, 1914 (1977).
15. H. Gerischer, *J. Electroanal. Chem.*, **150**, 553 (1983).
16. K. W. Frese, Jr., *This Journal*, **130**, 28 (1983).
17. M. A. Butler and D. S. Ginley, *ibid.*, **125**, 228 (1978).
18. H. Minoura and M. Tsuiki, *Electrochim. Acta*, **23**, 1377 (1978).
19. M. A. Butler and D. S. Ginley, *Chem. Phys. Lett.*, **47**, 319 (1977).
20. F. El Halouani and A. Deschanvres, *Mater. Res. Bull.*, **17**, 1045 (1982).
21. J. St-John and A. N. Block, *Phys. Rev. Lett.*, **33**, 1095 (1974).
22. J. C. Phillips, "Bonds and Bonds in Semiconductors," p. 27. Academic Press, New York (1973).

An Ambient Temperature Secondary Aluminum Electrode: Its Cycling Rates and Its Cycling Efficiencies

J. J. Auborn* and Y. L. Barberio

AT&T Bell Laboratories, Murray Hill, New Jersey 07974

ABSTRACT

Electrochemically active aluminum can be cathodically deposited and anodically stripped from acidic mixtures of 1-methyl-3-ethylimidazolium chloride and aluminum chloride at room temperature. The rates of deposition can be high (25 mA/cm²), and the deposited aluminum can be quantitatively cycled in large amounts (>25 C/cm²) at high efficiency (>99%).

Ambient temperature chloraluminatate ionic liquids are formed from mixtures of organic chlorides such as n-butyl-pyridinium chloride (BuPyCl) (1) or 1-methyl-3-ethylimidazolium chloride (ImCl) (2) and aluminum chloride (AlCl₃). When the Lewis acid, AlCl₃, is added to the organic chloride in less than a stoichiometric amount, a basic melt results in which the principal anionic species are AlCl₄⁻ and Cl⁻. An acidic melt containing principal anionic species Al₂Cl₇⁻ and AlCl₄⁻ is obtained when AlCl₃ is in excess.

We have previously shown that aluminum can be cathodically deposited from acidic 1-methyl-3-ethylimidazolium chloraluminatate melts containing reducible Al₂Cl₇⁻. Here we show that electroplated aluminum can be cycled efficiently without irreversibly decomposing the chloraluminatate melt. Electrodeposited aluminum is crystalline, nondendritic, and adherent to a variety of substrates (3). Figure 1 shows SEM photographs of aluminum deposits on a copper substrate plated at 20 mA/cm² from 0.67 mole fraction AlCl₃ melt. The maximum current density for both deposition and stripping of aluminum depends on the melt composition. Cycling rates were also found to be dependent on cell orientation and solution mixing because of the formation of dense, lower conductivity AlCl₃ rich melt near an aluminum electrode on stripping when it is located on the bottom of the cell. Both deposition and stripping may be performed at higher rates in stirred melts or at rotating electrodes.

Apparatus

The electrochemical experiments were performed in thin film and flooded cells. The thin film cell, shown in Fig. 2, consisted of an insulated micrometer head containing a 0.635 cm diam high purity aluminum rod as the counterelectrode, axially aligned with a 0.635 cm diam copper- or tungsten-rod working electrode in a Teflon holder. For experiments with the electrodes inverted, the micrometer head can be fitted with a tungsten or copper rod as a working electrode with the aluminum rod fixed in the holder. The faces of both counter and working electrodes were polished and aligned carefully to achieve a uniform current distribution when a 15.8 μl drop of melt was placed on the lower electrode and the micrometer was closed to leave a 0.05 cm gap between the electrodes.

*Electrochemical Society Active Member.

This configuration achieves a uniform current distribution across the surfaces.

The flooded cell used for cycling studies, shown in Fig. 3, consisted of a 5-50 ml Princeton Applied Research (PAR) polarographic cell modified with a no. 15 O-ring joint on the bottom to hold a high purity aluminum sheet (Alfa) counterelectrode. The reference electrode consisted of a high purity aluminum wire immersed in stoichiometric ImAl₂Cl₇ melt in a glass capillary tube with an asbestos fiber junction separating it from the 10-15 ml melt contained in the cell. The working electrode was a 0.635 cm diam tungsten rotating-disk electrode at 1000 rpm in a Pine MSR rotator.

The electrochemical experiments were controlled with a PAR 173 potentiostat/galvanostat containing a PAR 179 coulometer plug-in. This instrument was controlled with a Keithley 230 voltage programmer for the cycling studies. The electrometer output of the potentiostat was monitored with a Hewlett-Packard 7100B strip chart recorder.

Experimental

1-methyl-3-ethylimidazolium chloride was prepared by reacting stoichiometric amounts of distilled 1-methylimidazole (Alfa) and dry, condensed ethyl chloride (Matheson Gas Products) at 70°C according to Wilkes (2). This process produces pressure of about 50 psig within the reaction vessel. The salt was then recrystallized several times in acetonitrile and ethyl acetate (Fischer Scientific, HPLC) to remove impurities.

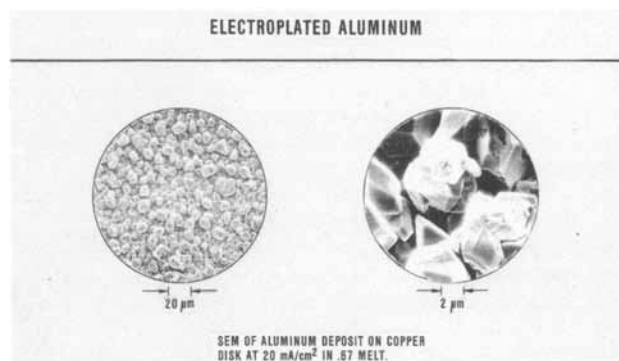


Fig. 1. SEM of aluminum deposit on a copper substrate at 20 mA/cm² in 0.67 mol fraction AlCl₃ melt.

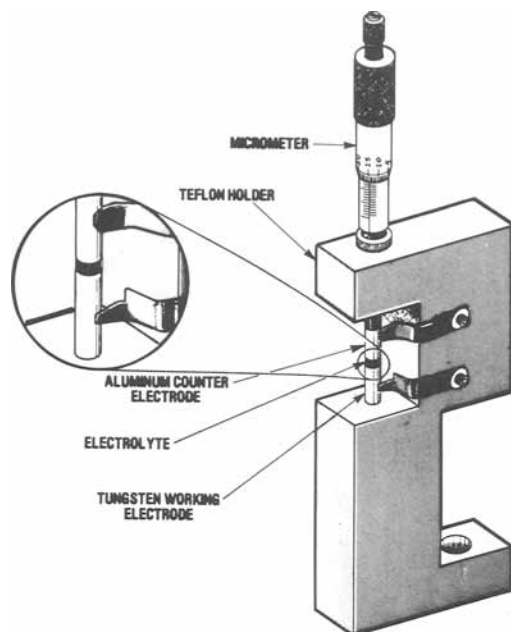


Fig. 2. Diagram of thin film cell used for aluminum deposition and stripping studies in 1-methyl-3-ethylimidazolium chloraluminum melt.

We found that the salt can also be prepared by continuously stirring the reactants at room temperature with a slight excess of ethyl chloride (10-20% by volume). The pressure produced at this temperature is only about 10 psig, greatly reducing the risk of explosion. At room temperature, the reaction should be carried out for a week to ten days for a good yield. With this method of preparation, the salt needed only one recrystallization before use.

Binary melts are formed by mixing the purified ImCl with sublimed AlCl_3 (Fluka, puriss.) in a helium-filled glove box controlled to <1 ppm O_2 and H_2O . Because the mixing process is highly exothermic, the melt must be prepared in small batches and cooled to prevent decomposition of the organic cation.

Acidic melts can be cleaned up by electrolyzing at low rates between two high purity aluminum electrodes. An ECO electroprep cell (ECO Incorporated, Cambridge, Massachusetts) was used at rates of 0.1-1 mA/cm^2 for extended periods of time to prepare the melts for cycling

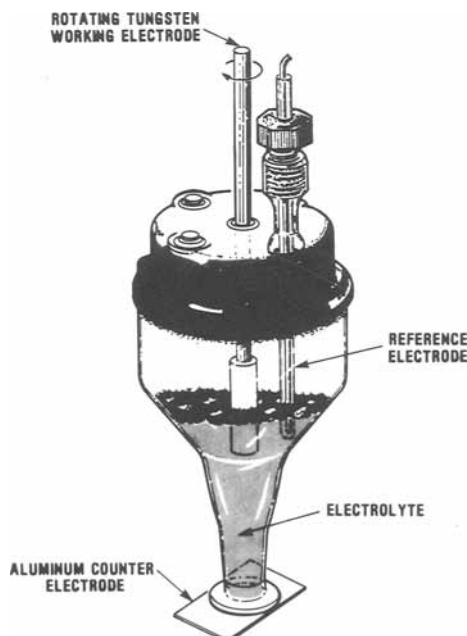


Fig. 3. Diagram of flooded cell used for aluminum cycling studies at a rotating tungsten electrode in 0.60 AlCl_3 melt.

studies. The cell consists of two high purity (99.983%) aluminum-plate electrodes (supplied by Reynolds Aluminum) separated by a Teflon gasket. Electrolyte is circulated through the cell by an external pump and reservoir. With this method of purifying melts, acidic mixtures can be made with unsublimed AlCl_3 , and then electrolyzed before use. Freshly prepared melt has a distinct yellow color which fades as the electrolyte is purified. When the melt is ready for use, it should be colorless. NMR spectroscopy can also be used to check the composition and purity of the melts (4).

The thin film cell was used to study the relationship between melt composition and maximum current density for plating and stripping aluminum. Varying the melt composition between 0.57 and 0.67 mole fraction AlCl_3 , the highest current density for plating and stripping aluminum without polarization was determined for each composition. Experiments were typically run for 30 min at each current density. The thin film cell was also used for electrolysis studies of the melt contained between the electrodes. Aluminum was continuously plated onto a copper substrate until the cell shorted out by the growth of a crystallite.

We checked the reversibility of a practical aluminum battery electrode by cycling aluminum from 0.60 melt onto a tungsten electrode. Plating and stripping current densities were controlled at rates varying from 2 to 25 mA/cm^2 . 2-25 C/cm^2 aluminum was cycled with 20-100% excess aluminum plated on the first cycle. The cells were cycled at equal plating and stripping rates until the working electrode polarized on stripping. Longer experiments were usually terminated after 100-200 cycles, and the remaining amount of aluminum was determined by stripping the electrode to polarization.

Initial cycling studies in the thin film cell proved to be troublesome. The experiments were limited to low currents (<10 mA/cm^2) and were frequently shorted out prematurely by crystallite formation. The electrolyte also began to evaporate during longer experiments (>24 h), changing the electrode contact area and current distribution across the surface.

Cycling experiments in the flooded cell were much more successful. The rotating electrode eliminated the problem of cell polarization by minimizing concentration gradients. In unstirred cells, dense, lower conductivity acidic melt (5) tended to collect at the bottom of the cell, impeding aluminum stripping from the lower electrode. In well-mixed electrolytes or at a rotating electrode, the orientation of the electrodes does not affect the plating or stripping process, because the concentration is homogeneous. The configuration of the flooded cell also made the addition of an $\text{Al}/\text{Al}_2\text{Cl}_7^-$ reference electrode possible and eliminated the problems of cell shorting.

Results

The maximum current density for plating and stripping aluminum from chloraluminum melts depends on the concentration of the melts. In an unstirred flooded cell, the maximum rate for aluminum deposition ranges from <1 mA/cm^2 for ImAlCl_4 to 20 mA/cm^2 for ImAl_2Cl_7 . Aluminum may be stripped at rates varying from 50 mA/cm^2 for ImAlCl_4 to <1 mA/cm^2 for ImAl_2Cl_7 (6).

Chronopotentiometric studies of acidic melts were used to determine the optimum composition for plating and stripping aluminum in the thin film cell. We found that we could sustain 10 mA/cm^2 without mixing in the thin film cell at a melt composition of 0.63 mole fraction AlCl_3 , with the aluminum anode on the top. We noted that polarized cells would recover if the cell were turned over and, therefore, repeated the above experiments with the cell inverted. The optimum composition for highest sustained current density (still 10 mA/cm^2) with the anode on the bottom was 0.60 mole fraction AlCl_3 . Figure 4 shows maximum current density vs. composition for stripping and plating in an unstirred flooded cell (6) and stripping-plating in the thin film cell with the aluminum anode on the bottom.

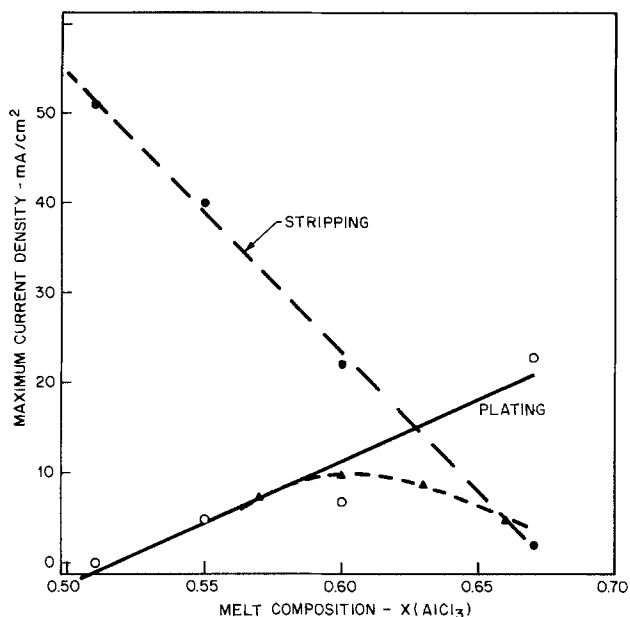


Fig. 4. Maximum current density vs. melt composition for aluminum plating (○) and stripping (●) in an unstirred flooded cell; aluminum cycling (▲) in a thin film cell with the aluminum anode on the bottom.

Exhaustive electrolysis of the 15.8 μl of 0.60-0.67 mole fraction AlCl_3 melt containing about 30 C ($\sim 100 \text{ C/cm}^2$) total aluminum could be sustained in the thin film cell at 5 mA/cm^2 for 17-30h with the aluminum anode on top. This corresponded to a 3-5 times complete turnover of the aluminum contained in the melt before the cell shorted out by the growth of an aluminum crystallite.

Cycling studies in the flooded cell demonstrated the efficiency of a secondary aluminum electrode. The cycling efficiency (E) of the aluminum electrode could be determined from the number of cycles to failure (N), the number of coulombs of aluminum plated or stripped on each half-cycle (A), and the excess number of coulombs plated on the first cycle (X), according to

$$E = (A - X/N)/A \quad [1]$$

We consistently obtained cycling efficiencies >0.99 at current densities up to 25 mA/cm^2 for cycling up to 25 C/cm^2 of aluminum if a 5-10 C/cm^2 excess amount of aluminum were plated on the first half-cycle. The results for a series of cycling experiments are shown in Table I. The best reported efficiency for a secondary lithium electrode is much lower (0.975) and requires a large excess capacity of lithium and a low current density (1 mA/cm^2) (7).

Discussion

Relatively large quantities (25 C/cm^2) of aluminum, suitable for battery-electrode applications, can be electrode-

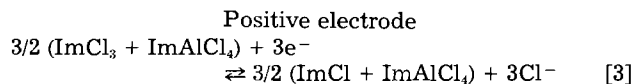
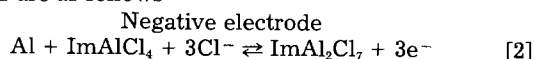
Table I. Aluminum cycling efficiency at a rotating tungsten electrode in 0.60 mol fraction AlCl_3 melt in a flooded cell

Current density (mA/cm^2)	Capacity cycled (C/cm^2)	Capacity excess (C/cm^2)	Cycling efficiency (%)	Turnover number
5	5	2.5	98.6	71
5	12.5	6.25	99.2	119
10	10	5	98.6	70
10	10	5	98.8	84
10	10	5	99.4	162
10	25	12.5	99.3	135
20	20	5	99.8	435
20	20	10	99.6	278
20	20	10	99.8	400
20	20	20	99.3	143
25	25	10	99.4	167
Best reported lithium data (7)				
1	5	25	97.5	40

posited and cycled efficiently (>0.99) at moderate rates (10 mA/cm^2) in acidic 1-methyl-3-ethylimidazolium chloraluminum melts at ambient temperature. The cycling efficiency does not significantly decrease as the current density is increased to 25 mA/cm^2 . The melt is not irreversibly decomposed by plating and stripping aluminum. A minimal quantity ($\sim 10 \text{ C/cm}^2$) of excess aluminum is required on a tungsten substrate to prevent the cell from polarizing after >100 cycles.

Although the cycling efficiency of aluminum is excellent compared to lithium as a secondary battery electrode, aluminum in acid melt is nearly 3V positive of lithium (8) and not useful with many of the positive-electrode materials used in lithium batteries. A strongly oxidizing, reversible positive-electrode material, compatible with acid chloraluminum melts, is required for a secondary aluminum battery. Several strongly oxidizing metal oxides, chalcogenides, and halides considered as possible positive-electrode materials (9) are limited by solubility in acidic melt. CuCl and AgCl are both reversible in acidic imidazolium chloraluminum melts at potentials positive of aluminum. However, they are both slightly soluble in acidic melt, limiting their usefulness as positive-electrode materials.

If the positive electrode is chosen to allow charging and discharging to change the acidity of the chloraluminum melt (10), large amounts of electrolyte would be necessary to keep the melt within the reversible (acidic) limit. As an example, consider an aluminum/chlorine formation cell. At the negative electrode, aluminum is reversibly oxidized and reduced in acidic melt, and at the positive electrode, chlorine is reduced and oxidized in basic melt. The reactions are as follows



with the free chloride ion allowed to pass through an ion-exchange membrane. The volume of melt needed is determined by the composition change of the catholyte and the solubility of chlorine in the anolyte. Here we have assumed that each Cl_2 complexes with a free chloride ion, forming a Cl_3^- ion. The actual solubility of chlorine in basic melt is higher and may approach twice this concentration. Using only the weight of active material (disregarding structural weight), the energy density of this cell as written would be 107 Wh/kg. Assuming an upper limit of two times this chlorine solubility, the energy density would be 153 Wh/kg. Alternatively, a cell which passes the Im^+ ion through an ion exchange membrane (Nafion) (11) would have a lower energy density (31.5 Wh/kg), assuming 1 dissolved Cl_2 per chloride ion. With Im^+ ion transport, the stoichiometry requires more melt than is needed for Cl^- ion transport. For comparison, a similar calculation for the conventional lead-acid battery yields an energy density of 169 Wh/kg. With the large amount of melt required, a cell of this type has a relatively low energy density. If a battery system is chosen where the melt is not affected by charge and discharge and serves only as a carrier for ionic charge, a more energetic cell would result.

Most of the polarization in an aluminum/imidazolium chloraluminum/aluminum cell results from the IR drop across the melt. Electrode polarization is low on both plating and stripping. This is favorable for a storage-battery electrode, but can be interpreted as low "throwing power" for electrodeposition. Therefore, uniform current density and very smooth electrode surfaces are essential for a smooth, even electroplated aluminum layer. Even slight irregularities on the plating surface will be exaggerated in the electroplated layer.

Summary

Large amounts of aluminum can be electroplated and stripped from acidic mixtures of 1-methyl-3-ethylimida-

zoliun chloride and aluminum chloride at ambient temperature. The plating and stripping rates are high for an ambient-temperature, nonaqueous system, and the quantity of aluminum is energetically useful for battery applications. The aluminum electrode shows high cycling efficiency which does not deteriorate as the rate is increased. The chloraluminum melt is stable and does not decompose on cycling. The relatively high positive potential of aluminum and the requirement of large quantities of melt to accommodate composition changes limit its application as a practical, high energy secondary battery.

Manuscript submitted Sept. 20, 1984.

AT&T Bell Laboratories assisted in meeting the publication costs of this article.

REFERENCES

1. R. Gale and R. Osteryoung, *Inorg. Chem.*, **18**, 1603 (1979).
2. J. S. Wilkes, J. A. Levisky, R. A. Wilson, and C. L. Hussey, *ibid.*, **21**, 1263 (1982).
3. J. S. Wilkes and J. J. Auburn, Abstract 242, p. 381, The Electrochemical Society Extended Abstracts, Vol. 83-2, Washington, DC, Oct. 9-14, 1983.
4. A. A. Fannin, L. King, J. A. Levisky, and J. S. Wilkes, *J. Phys. Chem.*, **88**, 2609 (1984).
5. A. A. Fannin, D. A. Floreani, L. A. King, J. S. Landers, B. J. Piersma, D. J. Stech, R. L. Vaughn, J. L. Williams, and J. S. Wilkes, *ibid.*, **88**, 2614 (1984).
6. J. S. Wilkes, Unpublished data.
7. K. M. Abraham and S. B. Brummer, in "Lithium Batteries," J. P. Gabano, Editor, p. 379, Academic Press, London (1983).
8. K. T. Ciemiecki and J. J. Auburn, in "Lithium Batteries," A. N. Day, Editor, p. 363, The Electrochemical Society Softbound Proceedings Series, Pennington, NJ (1984).
9. B. J. Piersma and J. S. Wilkes, FJSRL-TR-82-0004, ADA122840, September 1982.
10. C. J. Dymek, Jr., J. L. Williams, D. J. Groeger, and J. J. Auburn, *This Journal*, In press.
11. J. J. Auburn and C. J. Dymek, Jr., Unpublished data.

Two-Phase Mass Transfer in Channel Electrolyzers with Gas-Liquid Flow

Demetre J. Economou** and Richard C. Alkire*

Department of Chemical Engineering, University of Illinois, Urbana, Illinois 61801

ABSTRACT

The electrochemical limiting current method was employed to study the mass transfer to a solid electrode in cocurrent gas-liquid flow through a vertical parallel-plate electrolyzer. Three systems were investigated: aqueous ferricyanide, aqueous ferricyanide containing a dispersion of nitrogen bubbles, and aqueous electrolyte containing a dispersion of oxygen bubbles in equilibrium with the liquid phase. The total mass-transfer rate was found to be the sum of three contributions: (i) the one-phase convective rate associated with the liquid as if it were flowing alone through the cell; (ii) the enhancement of mass transfer owing to disruption of the mass-transfer boundary layer, even by bubbles containing inert gas; and (iii) the further enhancement owing to penetration of the mass-transfer boundary layer by bubbles containing reactive gas. A series of controlled experiments was conducted to determine the dependence of these enhancement mechanisms upon operating variables such as gas and liquid flow rates, bubble size, and electrode material. It was found that, although the conversion per pass through the cell was negligible, a sevenfold increase in the mass transfer, as compared to one-phase flow with the same liquid velocity, was obtained with a reactive gas void fraction as low as 10%.

Because electrochemical reactions are heterogeneous, industrial processes require high mass-transfer rates to minimize capital investment and, simultaneously, large electrode surface areas to achieve high production rates. Strategies for obtaining high mass-transfer rates include increasing the concentration driving force, as by improving reactant solubility, and augmenting the mass-transfer coefficient, as by vigorous stirring. In the case of parallel-plate electrolyzers, such strategies include operation in turbulent flow, evolution of gas which causes vigorous agitation at the electrode surface, use of turbulence promoters, and judicious employment of two-phase flow phenomena. In particular, two-phase processes can meet competing requirements for high mass-transfer rates while maintaining low pressure drop through the cell and also high loading of reactive species, which may be sparingly soluble in the continuous conductive phase.

In the present work, a study was undertaken of the mass transfer to a solid electrode in upward, cocurrent flow of a gas-liquid mixture introduced into a channel electrolyzer (1). In such flows, the presence of gas bubbles results in an enhancement of the mass-transfer rates over those which would be obtained with one-phase liquid flow alone. This enhancement may be attributed to two effects. First, there is the physical disruption of the mass-transfer boundary layer, caused by the stirring action of dispersed gas bubbles, even by electrochemically inert gases. This type of enhancement will be referred to

as the "disturbance mechanism." Second, when the gas is electrochemically reactive, there is a further enhancement by extraction of reactive material from those bubbles which penetrate to regions very close to the electrode surface. This type of enhancement arises from the replenishment of reactants in depleted regions of the mass-transfer boundary layer and will be referred to as the "extraction mechanism." The purpose of this work was to conduct a series of controlled experiments to determine the dependence of these enhancement mechanisms upon operating variables.

Analysis of electrochemical mass-transfer limiting current data can provide information on the individual elements of the overall mass-transfer mechanism. For example, Lu and Alkire (2) studied mass transfer to solid electrodes in the presence of a second dispersed liquid phase and found that addition of individual coefficients could be used to predict the overall rate. With nomenclature applicable to gas-liquid systems, the concept would be

$$i_t = i_o + i_d + i_e = nF(k_o c_{bl} + k_d c_{bl} + k_e c_{bl}) \quad [1]$$

The first term within the parentheses represents the mass-transfer rate owing to the one-phase convective flow. The second gives the enhancement by the disturbance mechanism, and the third gives the further enhancement by the extraction mechanism. While k_o may be calculated from first principles for simple flow configurations, there is no such theory for prediction of k_d and k_e .

*Electrochemical Society Active Member.

**Electrochemical Society Student Member.

The different concepts for enhancing mass transfer in industrial or large-scale cells have been reviewed by Houghton and Kuhn (3). A detailed description of mass transfer in parallel-plate electrochemical reactors is available (4, 33). Transport processes to the walls of narrow gap channels have been studied by Acosta *et al.* (34). Mass (or heat) transfer from a two-phase mixture to a heterogeneous boundary such as pipe wall or electrode surface has been actively investigated. Postlethwaite and Holdner (5) obtained an enhancement of the mass transfer of dissolved oxygen to a pipeline wall of up to 100% when sand particles were suspended in the flowing liquid. Dworak *et al.* (6, 7) observed weakly enhanced mass transfer by dispersing CCl_4 in aqueous ferricyanide flowing past a horizontal Ni electrode. Furthermore, by using a micro-electrode and the reactant in the dispersed second phase only, they found that under the experimental conditions used the dispersed droplets did not wet the electrode surface.

However, Lu and Alkire (2) found a mass-transfer enhancement of up to 170% by dispersing inert toluene droplets in aqueous ferricyanide in laminar flow past vertical planar electrodes. In the presence of a reactive second phase, it was found that a nonpolar electrode (graphite) gave significantly higher mass-transfer rates when compared to a polar electrode (DSA[®]), which suggests that wetting occurred. It was further found that for reactants which are sparingly soluble in the aqueous phase, mass transfer could be augmented by orders of magnitude by using a reactive second phase.

Gas-liquid systems have been widely studied owing to their relevance to many chemical engineering operations. The literature on interfacial mass transport, bubble columns (8), and gas-liquid flows in general (9) is voluminous. Heat-transfer studies from the two-phase mixture to the walls of a bubble column have been reported by Mersmann (10), Steiff and Weinspach (11), and Deckwer (12), among others.

From the electrochemical engineering point of view, one may distinguish between two situations involving gas-liquid mixtures: (a) gas evolving electrodes and (b) gas sparging. Gas evolution is commonly found in the electrochemical industry (H_2O electrolysis, chlor-alkali cell, chlorate cell, etc.) and has been reviewed by Vogt (13). As the bubbles form and break away, they stir the solution adjacent to the electrode enhancing mass transport. The case of superimposed external hydrodynamic flow has been considered by Beck (14) and Vogt (15). In particular, Beck proposed an additive mass-transfer model to account for simultaneous gas evolution and fluid flow. The additivity of the mass-transfer coefficients was subsequently verified (16), and the same concept was used to describe mass transfer in two-phase flows (Ref. (2, 17) and Eq. [1]). Gas sparging is an attractive mode of artificial stirring in electrochemical processes (18, 24). For example, open-topped tanks with widely spaced electrodes used in the metal finishing industry are agitated by introducing air at the bottom of the tank. Significant contributions to the field have been made by Ibl and co-workers. Ibl *et al.* (18) introduced N_2 through porous frits at the bottom of a vertical parallel-plate cell having a sectioned cathode. The mass-transfer coefficient was uniform throughout the electrode surface and the mass-transfer rate increased with increasing gas flow rate, although the rate leveled off at high gas flow rates. Frit pore size and, therefore, bubble size had no effect on mass transfer. The authors noted that mass-transfer coefficients one order of magnitude higher than those in natural convection can be achieved.

In another study, Ibl (19) injected gas through porous frits in the annular space between two concentric cylinders and obtained mass-transfer coefficients of up to $5.2 \cdot 10^{-3}$ cm/s. The influence on the working electrode of gas bubbles generated by the counterelectrode in a parallel-plate cell was investigated by Sigrist *et al.* (20). The study was conducted with and without superimposed electrolyte flow. It was found that, irrespective of the mode of

operation, the mass-transfer coefficient was dependent on the gas void fraction alone. The experimental data were correlated with an equation resembling that of turbulent free convection. Ibl (21) presented a model to explain these results.

Several laboratory and micropilot scale experiments in two-phase flow with reactive gas have been reported. Examples include the production of H_2O_2 by O_2 reduction on graphite particles in fixed bed reactors (22) and the production of oxalic acid from CO_2 in a parallel-plate reactor (23). However, these studies concentrated on problems related to current efficiency and cell voltage and did not address fundamental mass-transport processes.

In summary, transport literature exists for a wide variety of multiphase processes involving gas-liquid-solid systems, but there are no known works on transport to a solid reactive surface exposed to two-phase flow in which the gas phase contains the reactant. This type of system, however, is encountered in the electrolysis of gaseous feedstocks. The present study was therefore carried out to improve fundamental understanding of the sequence of events which occurs and to establish correlations for multiphase transport processes in channel electrolyzers.

Apparatus

The parallel-plate electrolyzer was similar to that used previously by Lu (2) and consisted of a divided cell having two flow circuits as illustrated schematically in Fig. 1. The cell was machined from two polypropylene blocks. Working electrodes of DSA[®] (2.7×27 cm exposed, Diamond Shamrock Corporation) or of Pt (2.7×26 cm, pressed against a 316 SS sheet) were used. Adjacent to and coplanar with the working electrode were two additional electrodes made of DSA[®] (2.7×10 cm) which served to eliminate entrance and exit effects; of these electrodes, the downstream electrode was used as the reference electrode for the ferricyanide reduction experiments. The counterelectrode was made of porous DSA[®] (3.1×27 cm, Diamond Shamrock Corporation) and was positioned so that electrolyte flowed through the pores toward the working electrode compartment (Fig. 1). Electrical contact to electrodes was made by titanium screws pressed onto the back side of the electrodes and was found to have a contact resistance of less than 0.1Ω .

A microporous polypropylene separator (Daramic, W.R. Grace & Company) was used to prevent bulk flow between the anolyte and catholyte compartments. The separator had support ribs in the direction of flow to avoid buckling and was held at a distance of 0.2 cm from each electrode surface. On the working electrode side, there

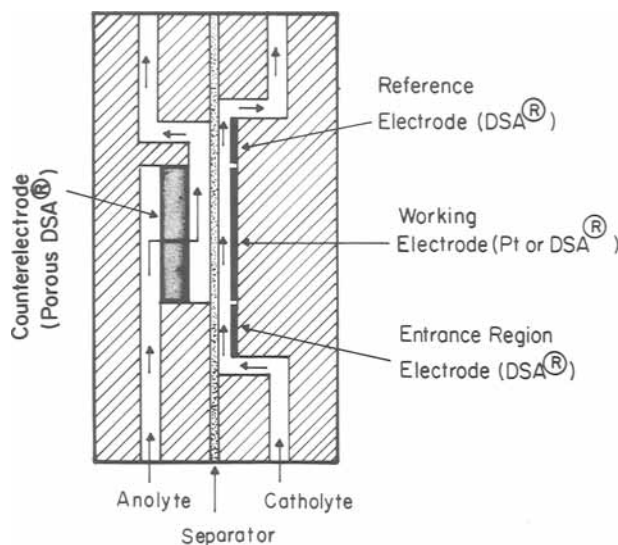


Fig. 1. Schematic of the flow circuits inside the cell (not drawn to scale). Reference electrode shown was used for the ferricyanide reduction experiments.

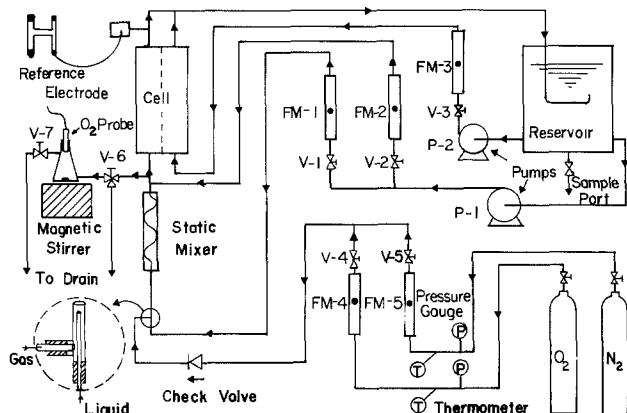


Fig. 2. Schematic of the flow system. Oxygen measuring system and reference electrode used for the oxygen-reduction experiments are included.

were three ribs dividing the catholyte chamber into two identical channels, each with cross-sectional dimensions of 1.35×0.2 cm. While in operation, the cell was positioned vertically.

Flow-visualization experiments were performed by replacing the separator and polypropylene counterelectrode block by a transparent Plexiglas sheet, of which the surface facing the working electrode was machined to exactly simulate the separator geometry.

The flow circuit illustrated in Fig. 2 consisted of delivery lines for gas and liquid streams which were combined in a Static Mixer[®] and passed to the working electrode compartment of the cell. Pump P-1 (March, no. TE-MDX-MT-3) fed the Static Mixer[®] with liquid electrolyte taken from the reservoir (4 liter capacity) at a rate controlled by valve V-1 and measured by meter FM-1 (Gilmont no. 4, Ti float). A second liquid metering system, V-2 and FM-2, was used to augment the flow from the Static Mixer[®] in order to achieve a wider range of variables. There were two gas-delivery systems containing calibrated flowmeters FM-4 (Gilmont no. 1, glass float) and FM-5 (Gilmont no. 2, glass float). Either or both systems could be used to control delivery rate of a single gas or of a gas mixture of known composition. The pressure of the gas was kept at 7 psig, determined by pressure gauges \textcircled{P} , while the gas temperature was measured with thermometers \textcircled{T} . The pressure in the cell was essentially 1 atm absolute.

The Static Mixer[®] (Kenics) used to generate a homogeneous dispersion of bubbles had a 3/16 in. id with 20 elements of 316 SS in a housing of the same material. The mean bubble size was measured from pictures of the two-phase mixture flowing through the working electrode compartment.

Pump P-2 (March, no. TE-MDX-MT-3) fed the counterelectrode compartment through flowmeter FM-3 (Gilmont no. 4, Ti float). After passing through the cell, the anolyte and catholyte streams merged and returned to the reservoir, where the gas was vented to the atmosphere and the liquid was recirculated. Anode and cathode reactions of ferri and ferrocyanide exhibited 100% c.e., so

there was no net concentration change in the recirculating system.

In experiments which involved oxygen reduction, the concentration of oxygen was measured just before the cell entrance with use of a calibrated dissolved- O_2 probe (Lazar, no. DO-166) in connection with the mV scale of a pH meter (Metrohm/Brinkmann pH-104). The O_2 concentration thus obtained was accurate to within ± 0.2 ppm.

Power to the cell was provided by a potentiostatic supply (Wenking, no. 70TS1) controlled by a function generator (PAR, no. 175). A cathodic-potential ramp was used to measure the limiting current plateau, which was displayed on an X-Y recorder (Houston, no. 2000).

Procedures

Table I lists the experimental systems that were used in this study. All solutions were prepared by mixing analytical-grade reagents with deionized, distilled water (conductivity $< 3 \times 10^{-6}$ ($\Omega\text{-cm}$)⁻¹). For the ferricyanide-reduction experiments, equimolar solutions of the redox couple were used in concentrations which ranged between 1 and 10 mM, as determined by iodometric titration (25).

The physical properties of the electrolyte solutions and the transport properties of the electrochemical reactants were measured and compiled in Table II. The density was measured by weighing a known solution volume, while the viscosity was found with an Ostwald viscometer. Diffusivities were determined with a Pt RDE (Pine, no. ASR, 366).

In order to obtain reproducible results, the Pt electrode was washed in acetone and distilled water, immersed in a chromic-sulfuric acid cleaning solution for 20 min, rinsed thoroughly, placed in the cell and activated in supporting electrolyte by sweeping five times between -1.2 and 0.8V vs. Hg/HgO (0.5M KOH), and then set at -1.2V vs. Hg/HgO for 2 min to reduce surface oxides. The DSA[®] electrode was degreased in trichloroethylene and rinsed with acetone and then water before being placed in the cell. No activation was necessary. The DSA[®] electrode was used for ferricyanide-reduction experiments only.

All electrolyses were carried out at about 25°C . For one-phase experiments with ferricyanide, the flow system was rinsed with distilled water and refilled with supporting electrolyte. An aliquot of stock solution containing reactant was then added, and the resulting solution was deaerated for 1h prior to use. The voltage scan was carried out at 5 mV/s . After completion of experiments at a given reactant concentration, an additional ali-

Table II. Physical and transport properties of the solutions used (at 25°C)

	0.2M Na_2SO_4	0.1M Na_2SO_4 + 0.2M KOH
Density (g/cm^3)	1.05	1.02
Kinematic viscosity (cm^2/s)	9.45×10^{-3}	9.28×10^{-3}
Ferricyanide diffusivity (cm^2/s)	0.65×10^{-5}	—
Oxygen diffusivity (cm^2/s)	—	1.85×10^{-3}
Oxygen concentration in air-saturated solution (mM)	—	0.220
Sc number	1450	500

Table I. Experimental format for separating the mass-transfer mechanisms

Liquid phase	Gas phase	Mechanism contributing to the current measured	Working-electrode reaction
Ferri/ferrocyanide in 0.2M Na_2SO_4 Air-saturated 0.2M KOH	—	One-phase convective flow mechanism	$\text{Fe}(\text{CN})_6^{3-} + e \rightarrow \text{Fe}(\text{CN})_6^{4-}$
Ferri/ferrocyanide in 0.2M Na_2SO_4 Saturated solution of 0.2M KOH + 0.1M Na_2SO_4	N_2 $\text{O}_2 - \text{N}_2$ mixtures	One-phase convective flow + disturbance mechanism One-phase convective flow + disturbance + extraction mechanism	$\text{O}_2 + 2\text{H}_2\text{O} + 4e \rightarrow 4\text{OH}^-$

quot of stock solution containing reactant was added to increase the concentration to a new level, and the procedure was repeated.

For two-phase ferricyanide-inert gas experiments, the procedure was identical, except than N_2 gas was metered into the Static Mixer[®], and the scan rate was 10 mV/s. Limiting currents were measured in sequence of experiments, each at constant liquid flow rate with successively increasing gas flow rates.

For one-phase experiments with dissolved oxygen as the reactant, the electrolyte was circulated through the flow system for 30 min while air was sparged into the reservoir. The Pt electrode was then activated, the O_2 concentration was measured with the dissolved oxygen probe, and current-potential curves were recorded at a scan rate of 5 mV/s. A Hg/HgO (0.5M KOH) reference electrode (built in-house) was used for all the experiments involving the O_2 reduction reaction.

For two-phase experiments with reactive gas bubbles, air, or other N_2 - O_2 mixtures (depending on the desired O_2 concentration) were dispersed in the electrolyte phase. The procedure was similar to that followed for the two-phase inert-gas experiments, except that special care was taken to ensure that the Pt electrode remained active. The electrode was periodically reactivated, and the gas was periodically shut off and a one-phase experiment was carried out to confirm reproducibility of the Pt surface. Repeated experiments were reproducible to within 3% for one-phase flow and to within 12% for two-phase flow with reactive gas. Two-phase inert-gas experiments were reproducible to within 5%.

Results

Flow visualization.—Flow-visualization experiments indicated several types of flow patterns, depending upon the flow rates of the two phases, as shown in Fig. 3. In the bubbly-flow regime, the gas was uniformly distributed as a swarm of tiny bubbles. In the slug-flow regime, some gas was in large bullet-shaped bubbles which almost spanned the interelectrode gap; these large bubbles were separated by slugs of liquid containing tiny gas bubbles. In the region of low liquid flow rates, the flow patterns were not reproducible; this nonreproducible region was avoided in the measurement of mass-transfer coefficients.

It was found that the electrolyte composition had a strong influence on bubble coalescence. For example, the bubbles formed in 0.2M Na_2SO_4 were extremely fine in comparison with those formed, under otherwise iden-

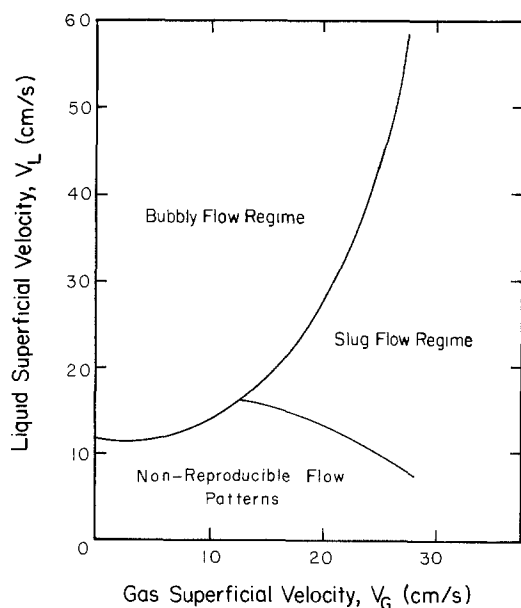


Fig. 3. Flow-pattern map for N_2 -0.2M Na_2SO_4 two-phase flow through the working electrode compartment.

tical conditions, in distilled water or in 0.2M H_2SO_4 . It was further found that the mixed electrolyte solution (0.2M KOH + 0.1M Na_2SO_4) used for two-phase oxygen-reduction experiments displayed the same behavior, with respect to bubble sizes, as the 0.2M Na_2SO_4 solution used for the two-phase ferricyanide-reduction experiments.

Analysis of limiting current data.—The one-phase mass-transfer coefficient, k_o , was obtained from cathodic limiting current measurements on solutions having known concentrations of reactant, ferricyanide, or oxygen, as shown in Table I

$$k_o = \frac{i_o}{nF c_{bl}} \quad [2]$$

Under the conditions investigated, the O_2 reduction reaction proceeded by a 4-electron pathway. The two-phase disturbance-mechanism coefficient, k_d , was found from limiting current data obtained with ferricyanide solutions containing dispersed N_2 ; by subtracting the limiting current owing to the one-phase convective flow as found previously for the same liquid flow rate, the current attributable to the disturbance mechanism was obtained

$$k_d = \frac{(i_o + i_d)}{nF c_{bl}} - k_o \quad [3]$$

As indicated in Table I, the two-phase extraction-mechanism coefficient, k_e , was found by dispersing air (or other O_2 - N_2 mixtures) in a solution of mixed KOH- Na_2SO_4 electrolyte. The limiting current thus measured was due to all three mechanisms. After subtracting the limiting current measured under the same hydrodynamic conditions, with N_2 dispersed in ferricyanide solution (corrected for differences in diffusivity, concentration, and n value), the extraction-mechanism mass-transfer coefficient could be obtained

$$k_e H = \frac{(i_o + i_d + i_e)}{nF c_{bl}} - (k_o + k_d) \quad [4]$$

Equation [4] is obtained after manipulating Eq. [1], assuming that the equilibrium between gas- and liquid-phase compositions can be described for the O_2 system by Henry's law, $c_{bG} = H c_{bl}$.

One-phase convective flow mechanism.—The theoretical average limiting current density for mass transfer in laminar flow between infinite parallel plates is (4)

$$i_o = 1.85 \frac{nFD c_{bl}}{s} \left[\frac{V_L}{dDL} \right]^{1/3} \quad [5]$$

where $d = 2h$. However, as verified by Pickett and Stanmore (26), the same equation can also be used for channels with finite dimensions, provided that the hydraulic diameter of the duct replaces the equivalent diameter, i.e., $d = 2Wh/(W + h)$. Figure 4 indicates that data for both the ferricyanide and the dissolved oxygen electrode were in good agreement with Eq. [5] for Reynolds numbers up to 2100 (55 cm/s), where transition to turbulent flow sets in (4). A further consequence of Eq. [5] is that a graph of $i_o/V_L^{1/3}$ vs. c_{bl} should give a straight line through the origin. This relation was verified for ferricyanide reduction on both DSA[®] and Pt electrodes over the range of 1-10 mM.

The mass-transfer coefficient for one-phase flow is therefore

$$k_o = \frac{1.85D}{s} \left[\frac{V_L}{dDL} \right]^{1/3} \quad [6]$$

and can be used to estimate the diffusion-layer thickness, $\delta = D/k_o$. At the highest flow rate, the diffusion-layer thickness (50 μm) was ten times larger than the DSA[®] electrode-surface roughness (5 μm), so the electrode may be characterized as "smooth" for the one-phase ex-

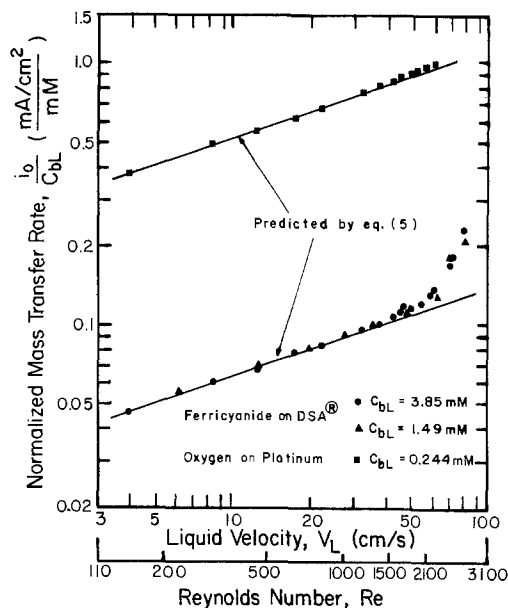


Fig. 4. Normalized mass-transfer rate vs. liquid velocity in one-phase flow. Re refers to the ferricyanide-0.2M Na_2SO_4 solution Reynolds number.

periments. The shiny Pt electrode was essentially "smooth" for the one- and two-phase experiments.

The effect of a turbulence promoter (VEXAR 549V300, du Pont) was to increase the mass-transfer coefficient. In the range $6 < V_L < 60$ (cm/s), the mass-transfer limiting current density followed the correlation

$$i_0 = 0.0177 V_L^{0.70} c_{bl} \quad [7]$$

The exponent on velocity (0.70) is larger than in Eq. [5] and is indicative of the increased stirring effect. Over the range investigated, the limiting current was increased as much as threefold by the presence of the turbulence promoter.

Two-phase disturbance mechanism.—Because the gas bubbles rise with respect to the liquid during transit through the electrolyzer, they impart a transverse momentum to the surrounding fluid which is absent in single-phase laminar flow and which influences the mass-transfer processes near the electrode surface. Additional sources of mixing action would include sudden motions imparted during bubble coalescence and/or breakup in the shear region near the electrode surface, as well as agitation in the wake region behind rising bubbles. For these reasons, the mass-transfer enhancement by the disturbance mechanism cannot be solely attributed to decreased channel cross-sectional area available for liquid flow and to consequentially increased liquid velocity. This situation is especially true for the narrow channel used in this work (0.2 cm channel gap).

For the case of two-phase flow with inert gas, Eq. [1] is simplified ($c_{ng} = 0$) to

$$i_0 + i_d = nF(k_o + k_d) c_{bl} \quad [8]$$

where the left-hand side represents the experimentally measured current density, k_o is given by Eq. [6], and c_{bl} was measured experimentally. Figure 5 illustrates that the form of Eq. [8] correctly correlates the mass-transfer behavior of the disturbance mechanism, in that data fall upon straight lines which pass through the origin and exhibit slopes that depend upon liquid- and gas-flow velocities.

Figure 6 illustrates how the mass-transfer rate due to both the one-phase convective flow mechanism and the disturbance mechanism varies with gas superficial velocity for several values of liquid superficial velocity. The superficial velocities of both phases were calculated by dividing the corresponding flow rate (that for the gas at 25°C and 1 atm) by the channel cross-sectional area. The

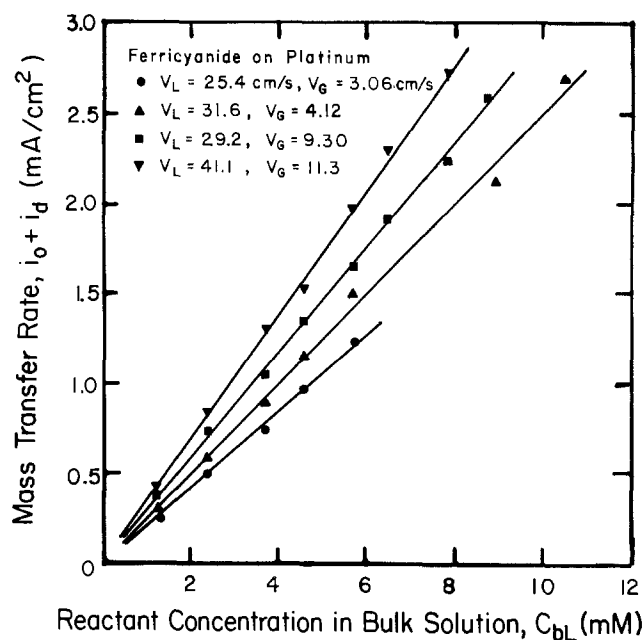


Fig. 5. Mass-transfer rate in two-phase flow with inert (N_2) gas vs. ferricyanide concentration in bulk solution.

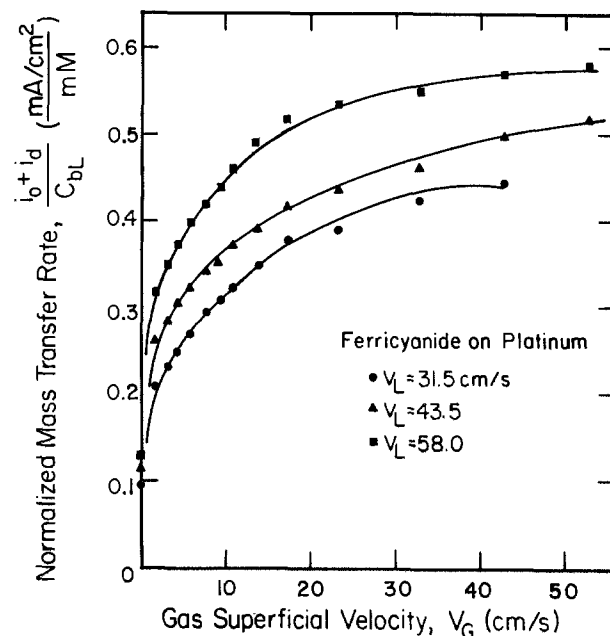


Fig. 6. Normalized mass-transfer rate in two-phase flow vs. nitrogen superficial velocity with the liquid superficial velocity as a parameter.

points on the $V_G = 0$ axis correspond to one-phase flow data. A substantial increase in the mass-transfer rate is obtained even when the gas flow rate is very small. For example, the limiting current is essentially doubled by gas velocities which are only 5% of the liquid velocity. This suggests that increased mass-transfer rates can be achieved for low gas-void fractions for which solution resistivity and pressure drop do not differ appreciably from the one-phase flow values.

Figure 6 also illustrates that the mass-transfer coefficient increases to a limiting value. For high gas velocities, a flow transition occurs from bubbly to slug flow, as indicated previously in Fig. 3. It is known (27) that slug flow is not as effective as bubbly flow in enhancing mass transport. A similar leveling of the transport rate in bubble columns has been reported by Ibl *et al.* (18), Novosad (27), Mersmann (10), and Steiff and Weinspach (11).

Figure 6 further shows that, for a given gas velocity, the mass-transfer coefficient increases with increasing liquid

velocity, a result which is in contrast to that reported by Sigrist *et al.* (20). However, in their experimental system, the interelectrode gap was at least five times wider than that used here, and, additionally, the liquid velocity employed was too low to be used in the present system while remaining in the bubbly flow regime. The explanation of these data by Ibl (21) was based on turbulent natural-convection concepts. Sigrist *et al.* realized that a decrease in the mass transfer with increasing liquid velocity (at constant gas velocity) would be observed provided that the liquid velocity is not too large. In studies of heat transfer in two-phase flow, others have reported conditions where the heat-transfer coefficient increases with liquid velocity (28) at high gas flow rates and where the coefficient is insensitive to liquid velocity (11) at low liquid flow rates. Thus it may be concluded that the disturbance effect is complex and that it depends upon the particular flow regime of operation. In the present work, the liquid velocity is appreciably higher than considered previously (20, 21), so explanations of behavior cannot be based on natural-convection phenomena.

Figure 6 also demonstrates that the disturbance mechanism can enhance the one-phase mass-transfer rate by up to 400%. Similarly, large enhancement factors have been reported elsewhere (11). In contrast, in studies on two-phase liquid-liquid systems, Lu and Alkire (2) reported an increase of up to 170%. The substantially greater enhancement in gas-liquid systems results from the significantly greater bubble-rise velocities in comparison with liquid droplets, owing to a greater density difference.

When the data in Fig. 6 are replotted on log-log coordinates, a slope of approximately 0.25 is found, which compares favorably to experimental and theoretical results reported for bubble columns (12).

After subtracting the contribution of the one-phase convective flow, the enhancement of mass transfer by the disturbance mechanism was found to be expressed by the empirical correlation

$$i_d = 0.007 V_L^{0.74} V_G^{0.36} C_{bL} \quad [9]$$

which describes the data, for the bubbly-flow regime, to within 8%.

For the two-phase inert-gas experiments, the DSA® electrode gave currents which were about 10% higher than on the Pt electrode. Because the two-phase mass-transfer boundary layer can be as thin as 10 μm , this effect was attributed to the roughness of the DSA® material (about 5 μm), while the shiny Pt was essentially smooth.

By using two different Static Mixers®, it was possible to vary the mean bubble diameter by a factor of two. For the 3/16 in. unit, the diameter ranged between 200 and 600 μm , and for a 1/4 in. unit, the diameter ranged between 400 and 1200 μm . The effect of bubble size upon the mass-transfer rate was smaller than 5%. Others have reported similar observations in both gas-liquid (18, 29) and liquid-liquid systems (2).

When a turbulence promoter was placed in the flow channel, the influence upon two-phase inert-gas mass transfer was negligible. These results suggest that the two-phase mixture was by its nature "well mixed" and that the turbulence promoter provided little additional mixing. While the promoter might be expected to alter the mean bubble size, the results of the previous paragraph indicate that the mass-transfer enhancement is insensitive to bubble size.

Two-phase extraction mechanism.—When an electrochemically reactive gas is introduced as the second phase, a further mass-transfer enhancement occurs, as is depicted in the upper portion of Fig. 7. The gas-side mass-transfer resistance is negligible (30), so the oxygen concentration at the gas-liquid bubble interface is at the saturation concentration. Furthermore, the solution far from the electrode is saturated in oxygen as well. However, a bubble may penetrate the mass-transfer boundary layer near the electrode surface and may provide, by extraction of oxygen from the bubble, an increase in local oxygen

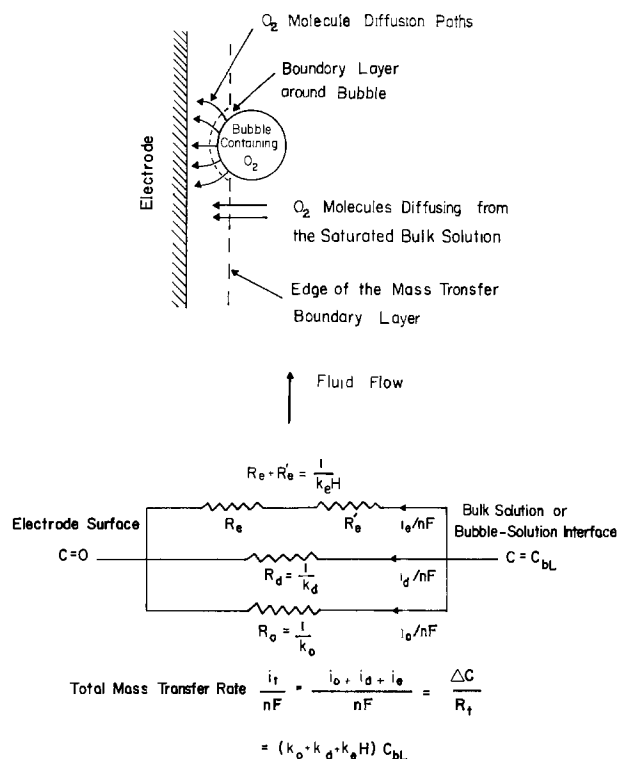


Fig. 7. (top) Mass-transfer mechanism in two-phase flow with reactive gas. (bottom) Equivalent resistive network.

concentration which would enhance the overall mass-transfer rate above that experienced by the disturbance mechanism of unreactive bubbles. It is to be expected that attachment of gas bubbles to the electrode is unlikely to occur at the polar electrode materials used in this study, so there will always be a liquid film separating the bubbles from the electrode. The lower portion of Fig. 7 indicates an equivalent resistive network describing the mass-transfer processes which are operative in the case of two-phase reactive-gas experiments. The extraction mechanism has been represented by two resistors in series, one of which (R'_e) accounts for the gas-to-liquid interfacial resistance, the other (R_e) for the further transport of the reactant to the electrode surface.

With use of Henry's law, Eq. [1] becomes

$$i_t = i_o + i_d + i_e = nF(k_o + k_d + k_e H) C_{bL} \quad [10]$$

For the conditions investigated in this study, the Henry's law constant for oxygen, $H = C_{bL}/C_{bL}$, had a value of 39. Data in Fig. 8 verify that the proposed additive correlation is appropriate. The variation in intercept may be attributed to drift in the "zero" of the oxygen probe and to uncertainty (at a level of 6.25×10^{-3} mM) in measurement of dissolved oxygen concentration by the probe. The data which follow were obtained at oxygen-saturation concentrations of 0.220 mM, for which probe errors were less than 8%.

The dependence of the measured total limiting current density on air superficial velocity is shown in Fig. 9 for three liquid superficial velocities. It is remarkable that for a given liquid velocity, the overall mass-transfer coefficient can be increased over the one-phase value by almost one order of magnitude by introduction of reactive gas. Indeed, the limiting current can be increased over the one-phase value by a factor of 7 with only 10% gas-volume ratio. The data shown in Fig. 9 exhibit similar behavior to the two-phase inert-gas data (Fig. 6) and, for the bubbly-flow regime, can be correlated by the empirical expression

$$i_t = 0.40 V_L^{0.60} V_G^{0.23} C_{bL} \quad [11]$$

which is good for $V_G > 1.8$ cm/s and describes the data to within 10%.

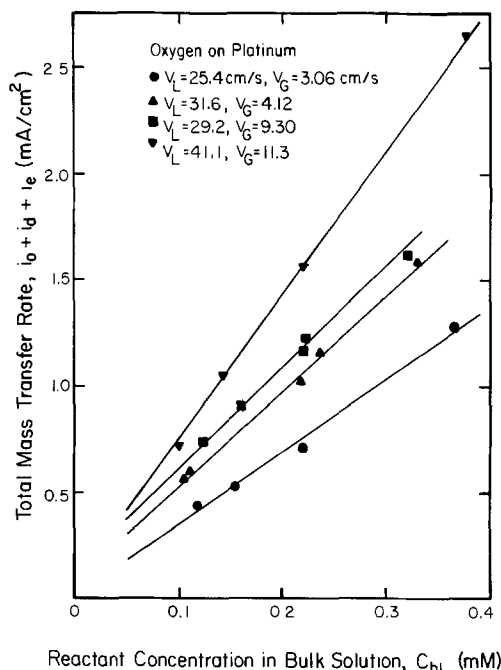


Fig. 8. Total mass-transfer rate in two-phase flow with reactive (O_2) gas vs. dissolved-oxygen concentration in bulk solution.

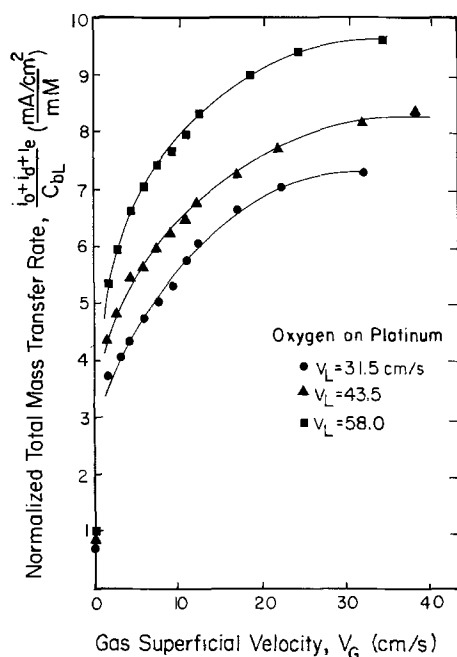


Fig. 9. Normalized mass-transfer rate in two-phase flow vs. air superficial velocity with the liquid superficial velocity as a parameter.

The relative importance of the extraction mechanism was found to be as follows

$$k_a H = (1.19 \pm 0.10) (k_o + k_d) \quad [12]$$

One intuitively expects that larger values of $(k_o + k_d)$ correspond to smaller bubble-electrode distances and, therefore, larger k_e . However, the linear relationship between i_e and $(i_o + i_d)$ implied by Eq. [12] may not be true in cases where, owing to high conversion of the reactant, replenishment of the bulk solution by the reactive bubbles occurs in addition to replenishment of the mass-transfer boundary layer.

Variation of bubble size, created with use of two different Static Mixers[®], had no influence on mass-transfer rates in two-phase reactive-gas systems. This is in contrast to data obtained in two-phase liquid-liquid systems

with reactive droplets (2). The difference may be attributed to the wettability of the electrode used by the dispersed organic phase. Similarly, the presence of a turbulence promoter in the working electrode compartment did not contribute additional mass-transfer enhancement beyond that afforded by the two-phase reactive gas in the absence of the promoter.

Conclusions

The limiting current method was used to study the mass transfer to a solid electrode in cocurrent gas-liquid flow through a vertical parallel-plate cell. Both an inert gas and a reactive gas were investigated. Flow visualization experiments showed that for the flow rates of gas and liquid used, the cell was in either the bubbly-flow or slug-flow regime. The total mass-transfer rate was expressed as the sum of the contributions of three different mechanisms: (i) the one-phase convective flow mechanism associated with the liquid as if it were flowing alone through the cell; (ii) the disturbance mechanism associated with the presence of bubbles "disturbing" the boundary layer; and (iii) the extraction mechanism associated with the presence of reactive bubbles replenishing the mass-transfer boundary layer. An experimental format was developed which enabled the contribution of each of the mechanisms to the total mass-transfer rate to be measured separately and enabled the additive model to be verified. Operating variables investigated included gas and liquid flow rates, bubble size, and electrode material. In addition, the effect of placing a turbulence promoter in the channel was determined.

The experimental results support the following conclusions.

1. The one-phase flow results compared well with theoretical expectations.

2. The mass-transfer rate due to the disturbance mechanism, as well as the mass-transfer rate due to the extraction mechanism, was proportional to the reactant concentration in the bulk solution.

3. At a constant liquid superficial velocity, the mass-transfer rate due to both the one-phase convective flow mechanism and the disturbance mechanism (i) reached values up to five times larger than those corresponding to the same liquid velocity in one-phase flow, (ii) increased sharply with increasing gas superficial velocity at low gas velocities, (iii) approached a constant value at high gas velocities, (iv) was dependent on the gas superficial velocity to the 0.25 power, (v) was independent of the bubble size for bubbles with diameters in the range 200-1200 μm , (vi) did not change significantly when a turbulence promoter was placed in the channel, and (vii) was always higher on an electrode with rough surface (DSA[®]) when compared to the rate on a "smooth" electrode (Pt).

4. The mass-transfer rate due to the disturbance mechanism was dependent on the liquid superficial velocity to the 0.74 power and on the gas superficial velocity to the 0.36 power (for the bubbly-flow regime).

5. At a constant liquid superficial velocity, the total mass-transfer rate in two-phase flow with reactive gas (i) reached values one order of magnitude higher than those corresponding to the same liquid velocity in one-phase flow, (ii) increased dramatically with increasing gas superficial velocity at low gas velocities, (iii) approached a constant value at high gas velocities, (iv) was dependent on the gas superficial velocity to the 0.23 power (for the bubbly-flow regime), (v) was independent of the bubble size for bubbles with diameters in the range 200-1200 μm , and (vi) changed insignificantly when a turbulence promoter was placed in the channel.

6. For a given gas superficial velocity, the total mass-transfer rate in two-phase flow with reactive gas was dependent on the liquid superficial velocity to the 0.60 power (for the bubbly-flow regime).

7. The mass-transfer rate due to the extraction mechanism was proportional to the mass-transfer rate due to both the one-phase convective flow mechanism and the

disturbance mechanism, the proportionality factor being 1.19 ± 0.10 .

The results of this study showed that the use of two-phase flow in electrochemical reactors incorporating a gas which is sparingly soluble in the liquid phase may be highly advantageous. In particular, high mass-transfer rates can be achieved at low gas-volume fractions. Thus, the solution resistivity and the pressure drop through the system do not differ significantly from the corresponding values in one-phase flow. Consider for example the case of a gas-void fraction $\epsilon = 10\%$. The conductivity of the solution (31) will be $\kappa = \kappa_0(1 - \epsilon)^{1.5} = 0.85\kappa_0$, and the energy consumption due to IR drop will increase by about 15%. Moreover, the pressure drop (32) will be

$$\frac{dP}{dx} = \left(\frac{1 + \epsilon}{1 - \epsilon} \right) \left(\frac{dP}{dx} \right)_l = 1.22 \left(\frac{dP}{dx} \right)_l$$

and the energy consumption for pumping will be 22% higher than that when operating in one-phase flow with the same liquid velocity. However, even at $\epsilon = 10\%$, the mass-transfer rate can be up to seven times that in one-phase flow (Fig. 9), which amounts to a 600% increase in productivity if the process is mass-transfer limited.

This work dealt with the case of negligible conversion per pass of the reactant through the cell. The enhancement due to the extraction mechanism was solely attributed to bubbles resaturating depleted regions within the mass-transfer boundary layer. In situations where the reactant conversion is high, however, the presence of the reactive bubbles resaturating the bulk solution as well will make the contribution of the extraction mechanism even more significant.

Acknowledgments

Financial support of this work was provided by the National Science Foundation (CPE 80-08947) and by a University of Illinois Fellowship.

Manuscript submitted April 5, 1984; revised manuscript received July 31, 1984.

University of Illinois assisted in meeting the publication costs of this article.

LIST OF SYMBOLS

c	reactant concentration, mM
d	equivalent diameter, cm
D	reactant diffusivity, cm ² /s
F	Faraday constant, 96,500 C/g-eq
h	gap of flow channel, cm
H	constant in Henry's law (= c_{ht}/c_{hl})
i	current density, mA/cm ²
k	mass-transfer coefficient, cm/s
L	electrode length, cm
n	number of electrons exchanged in electrode reaction
P	pressure, dyn/cm ²
R	equivalent mass-transfer resistance, s/cm
Re	Reynolds number in one-phase flow (dV_1/ν)
s	stoichiometric coefficient of reacting species
V	superficial velocity, cm/s
W	electrode width, cm

Greek Symbols

δ	diffusion-layer thickness, cm
ϵ	gas-void fraction

κ	solution conductivity, ($\Omega\text{-cm}$) ⁻¹
ν	solution kinematic viscosity, cm ² /s

Subscripts

b	bulk of gas or liquid phase
d	due to the disturbance mechanism
e	due to the extraction mechanism
G	gas phase
L	liquid phase
o	one-phase flow
t	total (all three mechanisms)

REFERENCES

- D. Economou, M.S. Thesis, University of Illinois (1983).
- P.-Y. Lu and R. C. Alkire, *This Journal*, **131**, 1059 (1984).
- R. W. Houghton and A. T. Kuhn, *J. Appl. Electrochem.*, **4**, 173 (1974).
- J. Lee and J. R. Selman, *This Journal*, **129**, 1670 (1982).
- J. Postlethwaite and D. N. Holdner, *Can. J. Chem. Eng.*, **54**, 255 (1976).
- R. Dworak, H. Fees, and H. Wendt, *AICHE Symp. Ser.*, **75**, 38 (1979).
- R. Dworak and H. Wendt, *Ber. Bunsenges. Phys. Chem.*, **81**, 728 (1977).
- Y. T. Shah, B. G. Kelkar, S. P. Godbole, and W.-D. Deckwer, *AICHE J.*, **28** (3), 353 (1982).
- G. B. Wallis, "One-Dimensional Two-Phase Flow," McGraw-Hill, New York (1969).
- A. Mersmann, *Chem.-Ing.-Tech.*, **47**, 869 (1975).
- A. Steiff and P.-M. Weinspach, *Ger. Chem. Eng.*, **1**, 150 (1978).
- W.-D. Deckwer, *Chem. Eng. Sci.*, **35**, 1341 (1980).
- H. Vogt, in "Comprehensive Treatise of Electrochemistry," Vol. 6, E. B. Yeager, J. O'M. Bockris, B. E. Conway, and S. Sarangapani, Editors, p. 445, Plenum Press, New York (1983).
- T. R. Beck, *This Journal*, **116**, 1038 (1969).
- H. Vogt, *Electrochim. Acta*, **23**, 203 (1978).
- R. Alkire and P.-Y. Lu, *This Journal*, **126**, 2118 (1979).
- P.-Y. Lu, Ph.D. Thesis, University of Illinois (1982).
- N. Ibl, R. Kind, and E. Adam, *Anales De Quimica*, **71**, 1008 (1975).
- N. Ibl, *Chem.-Ing.-Tech.*, **35**, 353 (1963).
- L. Sigrist, O. Dossenbach, and N. Ibl, *J. Heat and Mass Transfer*, **22**, 1393 (1979).
- N. Ibl, *Electrochim. Acta*, **24**, 1105 (1979).
- C. Oloman and A. P. Watkinson, *Can. J. Chem. Eng.*, **54**, 312 (1976); U.S. Pat. 3,969,201 (1976) and 4,118,305 (1978).
- J. Fischer, Th. Lehmann, and E. Heitz, *J. Appl. Electrochem.*, **11**, 743 (1981).
- A. S. Gendron and V. A. Ettel, *Can. J. Chem. Eng.*, **53**, 36 (1975).
- A. I. Vogel, "Quantitative Inorganic Analysis," 3rd ed., Longman, London (1961).
- D. J. Pickett and B. R. Stanmore, *J. Appl. Electrochem.*, **2**, 151 (1972).
- Z. Novosad, *Collect. Czech. Chem. Commun.*, **20**, 477 (1955).
- S. R. Ravipudi and T. M. Godbold, *Heat Transfer 6th Int. Heat Transfer Conf.*, **1**, 505 (1978).
- H. Kobel, W. Siemes, R. Mass, and K. Muller, *Chem.-Ing.-Tech.*, **30**, 400 (1958).
- M. Motarjemi and G. J. Jameson, *Chem. Eng. Sci.*, **33**, 1415 (1978).
- D. A. G. Bruggemann, *Ann. Phys.*, **24**, 636 (1935).
- H. Vogt, *J. Appl. Electrochem.*, **12**, 261 (1982).
- J. R. Selman and C. W. Tobias, in "Advances in Chemical Engineering," Vol. 10, T. Drew, Editor, p. 211, Academic Press, New York (1978).
- R. E. Acosta, R. H. Muller, and C. W. Tobias, *AICHE J.*, In press.

A Comparison of Photochemical Properties of Amorphous and Polycrystalline Fe₂O₃

F. A. Benko, J. Longo, and F. P. Koffyberg*

Department of Physics, Brock University, St. Catharines, Ontario, Canada L2S 3A1

ABSTRACT

A comparison is made of the photoelectrochemical properties of Fe_{1.996}Sn_{0.004}O₃ in two forms: as polycrystalline sintered compacts and as amorphous thin films prepared by RF sputtering. There is no essential difference in optical bandgaps, Mott-Schottky intercepts, band-edge positions, and optical absorption spectra. For the photo-oxidation of water, the difference between instantaneous and steady-state photocurrents is much larger for the amorphous than for crystalline form, which indicates a difference in the density and/or effectiveness of surface states. This difference between instantaneous and steady-state currents disappears, for both amorphous and crystalline Fe₂O₃, on adding the S²⁻/S_n²⁻ redox couple to the solution. The dark current of the amorphous form is larger, and its quantum efficiency in the ultraviolet is smaller.

Ferric oxide has been studied extensively as a photoanode; its relatively small bandgap, good chemical stability, and easy preparation makes it an interesting material for application in liquid-junction solar cells. However, its properties as a photoanode for water oxidation are apparently far from simple: on exposure to light, the photocurrents show strong transient excursions, and they do not set in at the flatband potential. Moreover, the Mott-Schottky plots are often found to be curved, and dependent on the measuring frequency as well. These deviations from simple behavior have been reported for Fe₂O₃ in the form of single crystals (1, 2), polycrystalline ceramics (3-5), and flame-oxidized iron (6, 7). The extent to which these complexities occur seems to depend sensitively on the sample preparation conditions; this points towards an important role for defect states, either in the bulk or at the surface.

In this paper, we report a comparison of the photoelectrochemical behavior of polycrystalline and amorphous Fe₂O₃. Our basic result is that the absence of long-range order in amorphous Fe₂O₃ has no influence on those properties which are normally associated with the crystalline electronic band structure. Only those parameters which control the kinetics of the forward and back-reactions of the photo-oxidation of water (without added redox couples) differ significantly between the amorphous and crystalline forms.

Experimental

Polycrystalline samples of Fe_{1.996}Sn_{0.004}O₃ (labeled c-Fe₂O₃ from here on) were prepared from Fe₂O₃ and SnO₂ (both better than 99.999%, Johnson & Matthey, Puratronic grade). The oxide mixture was pressed into disks and fired in air for 16h at 1300°C, followed by a fast air quench. Sample area was 1.2 cm², and its thickness was 0.2 cm. X-ray diffraction showed only lines of α-Fe₂O₃ (hematite structure). Amorphous samples (a-Fe₂O₃) of the same composition were prepared in thin film form by using some of these disks as sputtering targets. Sputtering took place in a small RF triode sputtering system (Plasmax 121) in an argon atmosphere, onto stainless-steel disks for the samples used in the electrochemical experiments and onto fused silica substrates for control samples. Very low plasma power was used, resulting in a growth rate of only ≈ 1.0 μm/day, onto the water-cooled substrates. X-ray diffraction of a 3 μm thick control sample showed neither discernible lines nor broad bands. The excellent stability of the a-Fe₂O₃ films was tested by heating this control sample for a few hours in air at successively higher temperatures without crystallizing; only during heating at 950°C did the sample transform to the crystalline state, as was seen by the appearance of sharp α-Fe₂O₃ x-ray diffraction lines and by the roughening of the previously mirror-smooth surface. Previous experience with preparing amorphous compound oxides in our

equipment has shown that the chemical composition of the sputtered film is equal (within ±5%) to the target composition. The a-Fe₂O₃ films were insoluble in strong acid and base; only 35% HJ etched the film at a rate of ≈ 3 μm/h.

The resistivity (ρ), Hall coefficient (R_H), and thermoelectric power (S) were measured by standard techniques. Ohmic contacts were made with indium applied with an ultrasonic soldering iron. The electrochemical measurements were made in a one-compartment cell; the samples were properly masked and the counterelectrode was 7 cm² of freshly platinized Pt. Potentials were measured with respect to the SCE. Solutions were continuously flushed with hydrogen. Current-voltage curves were measured potentiostatically; illumination was with a pulse of xenon-arc light (0.90 W/cm² at the sample surface) and time-dependent currents were recorded with a storage oscilloscope. The quantum efficiency was measured, on an arbitrary scale, with chopped monochromatic light and a lock-in amplifier over the entire wavelength range 300-900 nm; in the sub-bandgap region, great care was taken to avoid spurious effect due to second-order radiation and stray light from the monochromator. The results were then put on an absolute scale (with a possible ±10% error) by measuring directly with the oscilloscope the instantaneous and steady-state currents, at the same sample potential, under monochromatic illumination at $\lambda = 400$ nm. Light intensities were measured with a calibrated radiometer, and were corrected for reflectivity losses at the sample surface. The electrode impedance was measured in 1M NaOH and 0.1M Na₂HPO₄ in the range $7 \times 10^{-1} < f < 7 \times 10^4$ Hz using a system similar to that described in Ref. (8).

Results

Both a- and c-Fe₂O₃ samples were n-type semiconductors with properties reproducible to ±5%. The room temperature electrical parameters for c-Fe₂O₃ were: $\rho = 40$ Ω-cm, $R_H = 15$ cm³/C, and $S = 580$ μV/K. For the 3 μm a-Fe₂O₃ film, $\rho = 4.5 \times 10^2$ Ω-cm; R_H and S could not be measured.

The real and imaginary parts of the complex impedance were both frequency dependent according to $Z_{i,R} \sim f^{-\alpha}$, with $\alpha \approx 0.8$ for both a- and c-Fe₂O₃; similar results have been reported previously (5). Interpreting the imaginary part as a pure capacitance, $Z_i = (\omega C)^{-1}$, then a slightly curved Mott-Schottky plot of C^{-2} vs. V at a given frequency can be obtained; for $f = 14.7$ Hz, such a plot is shown in Fig. 1. At this low frequency, the value of $C = (\omega Z_i)^{-1}$ at $V - V_{FB} = 0.5V$ is 0.44 F/m² for the polycrystalline sample. This compares with a theoretical depletion layer capacitance of 0.06 F/m² and a Helmholtz capacitance of $C_H = 0.2$ F/m². However, the significance of the measured capacitance is doubtful, since the Mott-Schottky slopes were found to be frequency dependent. The intercept voltages V_0 were found to be independent

*Electrochemical Society Active Member.

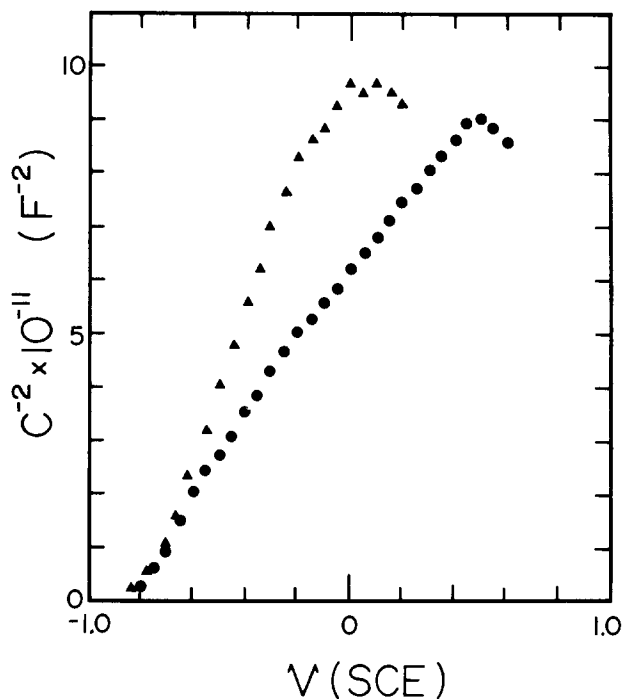


Fig. 1. The Mott-Schottky plots of C^{-2} vs V (SCE) for amorphous (\blacktriangle) and crystalline (\bullet) $\text{Fe}_{1.996}\text{Sn}_{0.004}\text{O}_3$. Electrolyte: 1M NaOH. Measuring frequency: 14.7 Hz. Sample area: 3.6 mm².

of frequency. In the frequency range $2 < f < 3 \times 10^4$ Hz, V_0 is identical for a- and c- Fe_2O_3 , and equal to -0.85 ± 0.05 V (SCE) in 1M NaOH and -0.55 ± 0.05 V (SCE) in 0.1M Na_2HPO_4 (pH = 9.2) solution.

The time dependence of the photocurrent is shown in Fig. 2a, which also gives the definitions of the instantaneous (i_t), steady-state (i_s), and dark (i_d) currents. i_t and i_s were proportional to the incident light intensity in the range of 0.2-0.9 W/cm² for all solutions. i - V characteristics were reproducible to $\pm 10\%$ between different samples.

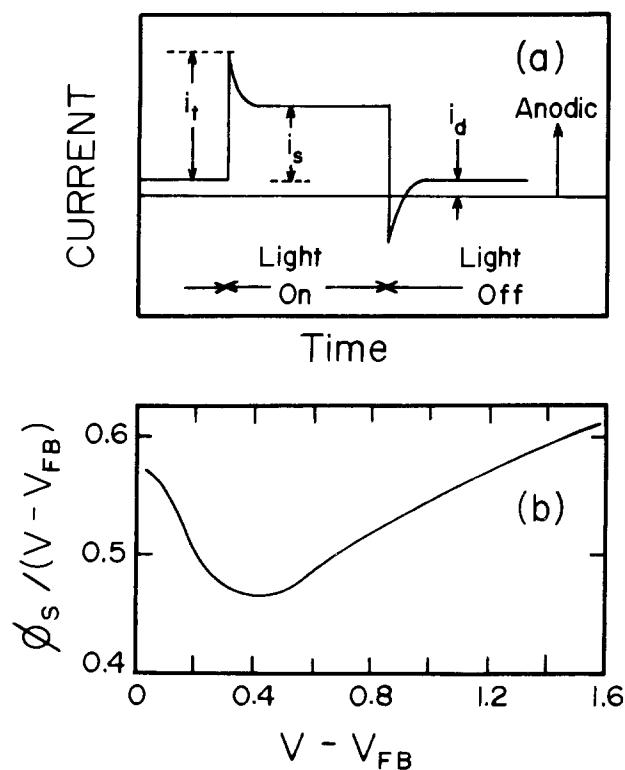


Fig. 2. (a): The time dependence of the currents. (b): The potential drop over the depletion layer (ϕ_s) as a function of the total potential drop ($V - V_{FB}$).

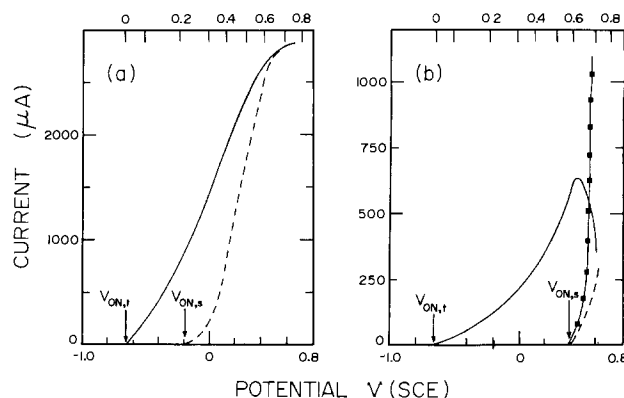


Fig. 3. The current-voltage curves of (a) crystalline and (b) amorphous $\text{Fe}_{1.996}\text{Sn}_{0.004}\text{O}_3$ in 1M NaOH. (—): i_t , (---): i_s , (· · ·): i_d . The top scale is ϕ_s , the potential drop over the depletion layer.

The risetime of i_t was ≤ 1 ms, the risetime of the light pulse; the decay time is of the order of 5-10 ms. Figure 3 shows the potential dependence of the currents in 1M NaOH.¹ For c- Fe_2O_3 , i_t sets in at $V_{ON,t} = -0.65$, but i_s becomes measurable only when $V \cong V_{ON,s} = -0.2$ V. Only at much higher anodic potential, $V \cong +0.5$ V, do the sharp transient current spikes disappear; there i_t and i_s are identical. The dark current is less than 10 μA over the entire potential range.

For a- Fe_2O_3 , i_t sets in also at $V_{ON,t} = -0.65$ V, but the steady-state currents cannot be observed until a potential of $V_{ON,s} = +0.4$ V (SCE) is reached. At higher potentials, i_s and i_d increase sharply, but i_t decreases. For $V \cong (V_{ON,s} + 0.2)$, the currents for a- Fe_2O_3 become very noisy and are not reproducible. The i - V curves of Fig. 3 do not change when changing the electrolyte to HClO_4 , H_2SO_4 , Na-acetate, Na-phosphate, or NaNO_3 solutions, except for a horizontal shift of approximately 60 mV/pH unit change. Saturating the solutions with O_2 instead of H_2 does not change the curves appreciably. Adding 0.01M KBr to the 1M HClO_4 solution reduced the difference between i_t and i_s by $\cong 80\%$. In 1M HClO_4 + 0.01M KI solution, the i_s curve was identical to the i_t curve for the c- Fe_2O_3 samples; data could not be obtained for the a- Fe_2O_3 samples since in this solution they dissolved very quickly as soon as the potential was increased from $V_{ON,t}$. The nearly complete disappearance of the transient current peaks was also observed in 1M NaOH + 0.1M Na_2S + 0.01M S_8 solutions; Fig. 4 shows the i - V curves. The a- and c- Fe_2O_3 samples

¹An anonymous referee has pointed out that the photocurrents of 2% Si-doped Fe_2O_3 samples are dependent on the quenching conditions. No such effect was found for our samples, as long as during preparation no Fe_3O_4 was formed by too high a temperature or too reducing an atmosphere during sintering.

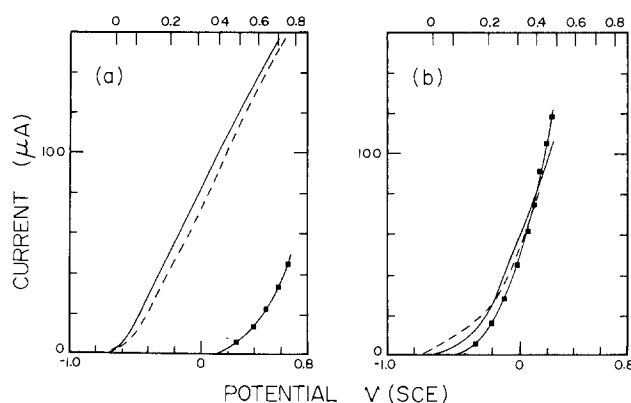


Fig. 4. The current-voltage curve of (a) crystalline and (b) amorphous $\text{Fe}_{1.996}\text{Sn}_{0.004}\text{O}_3$ in 1M NaOH + 0.1M Na_2S + 0.01M S_8 . (—): i_t , (---): i_s , (· · ·): i_d . The top scale is ϕ_s , the potential drop over the depletion layer.

have now nearly identical i_t and i_s curves; they only give different i_d curves. In contrast, the photocurrents in 1M NaOH are always larger for c- than for a- Fe_2O_3 .

The quantum efficiency η for the instantaneous current [$\eta = i_t/(\text{photon flux at surface})$] is shown in Fig. 5. These measurements were performed in 0.1M Na_2HPO_4 (pH = 9.2) solution at a potential $V = +0.75\text{V}$ (SCE). At this potential i_d and i_s for a- Fe_2O_3 are still zero, and the other currents are very stable and noise free, allowing a reliable determination of η over 6 orders of magnitude. Figure 5 also shows the optical absorption coefficient α for c- Fe_2O_3 from Ref. (9) and the preliminary results of our measurements of α for a- Fe_2O_3 . Over the limited common wavelength range, α for a- and c- Fe_2O_3 are essentially identical. The energy of the interband transitions was determined from plots of $(\eta h\nu)^m$ vs. $h\nu$. In the range $2.1 < h\nu < 2.7$ eV, a linear plot was obtained for $m = 1/2$, giving an indirect allowed bandgap transition at $E_{g,1} = 1.96 \pm 0.03$ eV. For $2.9 < h\nu < 4.2$ eV, we found $m = 2$ and $E_{g,2} = 2.73 \pm 0.05$ eV. These energies were identical for a- and c- Fe_2O_3 and are in good agreement with values reported for single-crystal Fe_2O_3 (10). The $(\alpha h\nu)^m$ plots gave $E_{g,1} = 1.95 \pm 0.08$ eV for both a- and c- Fe_2O_3 . All samples showed a small subsidiary maximum in the η -spectrum at $h\nu = 1.50 \pm 0.1$ eV; very careful checking showed that this was not an artifact of the measuring procedures.

Discussion

In the simplest model (11) of photoelectrolysis, the photocurrent is basically determined by the solid-state properties of the semiconductor: the position of the conduction and valence bandedges, the bandgap(s), and optical absorption coefficients, and the depletion layer width and hole diffusion coefficient. The photocurrent is then equal to the flux of photogenerated holes arriving at the semiconductor-solution interface; the charge-transfer and chemical-reaction kinetics are not supposed to be rate limiting. From numerous experiments (3, 4, 7), it is clear that this is not valid for mono- and polycrystalline Fe_2O_3 ; specifically, the existence of transient photocurrents shows that transfer kinetics can be rate limiting

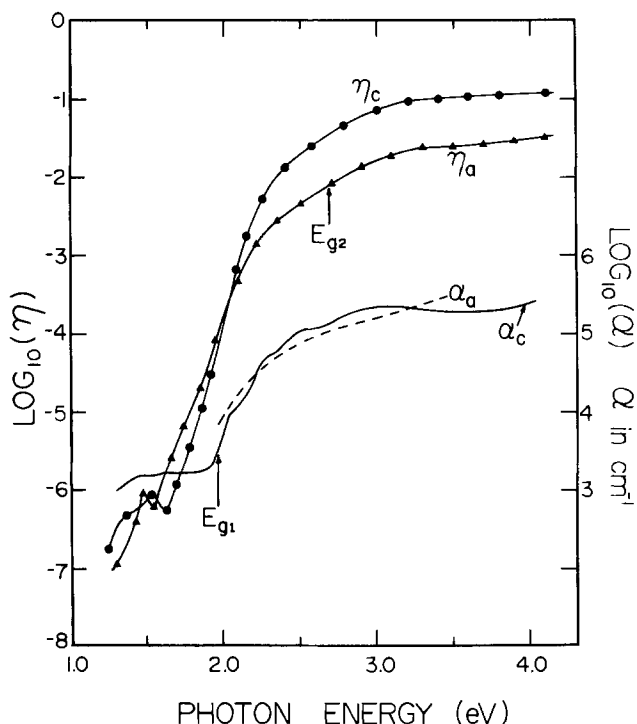


Fig. 5. Left scale: the quantum efficiency η of the instantaneous current for amorphous (\blacktriangle) and polycrystalline (\bullet) $\text{Fe}_{1.996}\text{Sn}_{0.004}\text{O}_3$, measured in 0.1M Na_2HPO_4 at $V = +0.75$ (SCE). Right scale: The absorption coefficient α for polycrystalline (—) Fe_2O_3 , [Ref. (9)] and for amorphous (-----) $\text{Fe}_{1.996}\text{Sn}_{0.004}\text{O}_3$.

with surface states playing an essential role. Only for the photo-oxidation of redox species such as I^- ions does Fe_2O_3 behave ideally (12). We will now discuss how the various parameters which influence the photoelectrochemical behavior differ between a- and c- Fe_2O_3 .

An exhaustive review (13) of the experimental data relating to electronic transport in c- Fe_2O_3 has shown that, most likely, the electrons, ionized from the Sn donors, move as large polarons with low mobility in a rather narrow 3d-conduction band. The electron effective mass is $(m^*/m_0) \cong 6$, and at the Sn doping level used in our samples the donor ionization energy is $E_D \cong 0.20$ eV. These parameters give a density of states $N_D \cong 3.65 \times 10^{20}$ cm^{-3} ; for a donor concentration $N_D = 8.0 \times 10^{19}$ cm^{-3} , the calculated carrier concentration is $n = 2.5 \times 10^{18}$ cm^{-3} and the Fermi level is $\Delta E_F = 0.13$ eV below the conduction bandedge. The calculated mobility is $\mu = 0.6$ cm^2/Vs , an acceptable value for a large polaron. The Hall effect is anomalous in Fe_2O_3 , and n cannot be calculated directly from R_H . An independent value of ΔE_F can be obtained from the thermoelectric power $S = (k/q)(A + \Delta E_F/kT)$, although the reliability of the result is somewhat doubtful due to impurity conduction effects. With $A = 2$ (13), the measured S value gives $\Delta E_F = 0.12$ eV, consistent with the previous estimate. For a- Fe_2O_3 , the conductivity mechanism is unknown, but oxides such as WO_3 which show large polaron conduction in the crystalline form are low mobility small polaron conductors in the amorphous form (14). The larger resistivity of a- Fe_2O_3 , as compared to c- Fe_2O_3 , indicates that such may be the case for Fe_2O_3 as well. For both a- and c- Fe_2O_3 , however, the resistivity is sufficiently small that photocurrents are not limited by slow carrier transport in the solid.

The experimental data show that for Fe_2O_3 the absence of long-range order has no discernible influence on the bandgap energies $E_{g,1}$ and $E_{g,2}$, whether they are determined from straight absorption or from quantum efficiency measurements. The absolute position of the bandedges can be determined from the flatband potential, which is, as we will show later, equal to -0.65V (SCE) in 1N NaOH for both a- and c- Fe_2O_3 . At the pH of zero charge [7.1 for Fe_2O_3 (15)], the Fermi level therefore lies $-0.65 + (14-7.1) \times 0.06 + 4.74 = 4.50$ eV below the vacuum level. This puts the conduction bandedge at 4.37 eV and the valence bandedge at 6.33 eV, in fair agreement with the value of 5.9 eV found from photoemission measurements (16). Presumably, the valence band wave functions are derived primarily from Fe^{3+} ($3d^5$) atomic terms; the band lies about 1V deeper than the 3d-valence bands in CuO (17) and NiO (18). Speculatively, we assign the $E_{g,2} = 2.73$ eV energy to a transition from a deeper lying O-2p valence band to the conduction band. This puts the O-2p band at 7.1 eV below the vacuum level, close to the position (7-7.5 eV) found for most metal oxides.

The quantum efficiency η for the instantaneous current (which is not limited by surface reaction kinetics) (7) will be proportional to the optical absorption coefficient α if both the depletion layer width W and the hole diffusion length L_p are smaller than the optical penetration depth α^{-1} (11). Close to the $E_{g,1}$ bandgap, η_a and η_c are nearly identical, but at higher photon energies they differ increasingly, even though α_a and α_c are essentially identical. It is unlikely that this difference is due to a difference in either W or L_p , since the samples are doped equally and since one expects L_p to be smaller, if anything, in the amorphous state. We have no explanation for this difference. Near and below $E_{g,1}$, the proportionality of α and η breaks down, since absorption processes which do not create hole-electron pairs contribute to α . The slope of $\log \eta$ vs. $h\nu$ near $E_{g,1}$ is larger for a- Fe_2O_3 than for c- Fe_2O_3 ; this may indicate that in a- Fe_2O_3 the bandedges are less sharp. We ascribe the small maximum at $h\nu = 1.5$ eV to a transition involving a state inside the bandgap, either from an occupied state 0.4-0.5 eV above the valence band or to an empty state below the conduction band [at the measuring potential of $V = +0.75\text{V}$ (SCE) in a pH = 9.2 solution the Fermi level lies between these two possi-

ble states]. c-Fe₂O₃ has two weak and broad absorption bands in this region (9), at $h\nu = 1.60$ and 1.43 eV, which are due to forbidden d-d crystal field transitions of the Fe³⁺ ion. Although it is, in principle, possible that the small η maximum at $h\nu = 1.5$ eV is due to a heating effect (19) from these crystal field absorptions, the sharpness of the maximum and the absence of any effect of increased stirring or chopper speed on the magnitude of η makes this very unlikely.

The strong frequency dependence of the complex impedance for both a- and c-Fe₂O₃ has been observed also in single crystals (2), polycrystalline (5), and thermally oxidized (6) iron samples; a satisfactory model for it is lacking. The slopes of the often curved Mott-Schottky plots cannot be used to determine donor densities N_D in any reliable manner. However, the intercept voltages V_o , at a given pH, are nearly equal for all different forms of Fe₂O₃; our value, $V_o = -0.85 \pm 0.05$ V (SCE) at pH ≈ 14 is valid for both a- and c-Fe₂O₃ and independent of frequency. V_o is related to the flatband potential according to (20, 21)

$$V_o - V_{FB} = \left(\frac{-kT}{q} r + \frac{kT}{q} \ln r \right) - (q\epsilon\epsilon_0 N_D / 2C_H^2) \quad [1]$$

with $r = N_D^+ / N_D$ the fraction of ionized donors in the bulk and C_H the Helmholtz layer capacitance. The first rhs term, due to incomplete donor ionization at flatband potential, can be calculated from the electronic properties determined previously and equals -0.09 V. The value of the second term, which comes from the contribution of the Helmholtz layer capacitance to the overall measured capacitance, depends strongly on the values adopted for ϵ and C_H . For Fe₂O₃, reported values of ϵ range from 20 (22) via 80 (4, 6) to 120 (1), depending on measuring frequency and sample preparation; we will use $\epsilon = 80$, measured (4) by a direct substitution method on undoped polycrystalline samples. A reliable value of C_H for oxide semiconductors is not available; we will use the generally accepted value $C_H = 0.2$ F/m² (23). We note that a recent report (2) shows a very large shift of V_o with N_D (determined from a MS slope) for single-crystal Zr-doped Fe₂O₃, leading to a value $C_H = 0.055$ F/m² with $\epsilon = 120$. This pair of values would give a second rhs term in Eq. [1] of 2.2 V, and lead to the conclusion that 90%-95% of the applied potential appears as a voltage drop over the Helmholtz layer; both consequences are difficult to accept. With $\epsilon = 80$ and $C_H = 0.2$ F/m² the correction term equals 0.11 V; therefore, the flatband potential in 1M NaOH is -0.65 ± 0.05 V (SCE).

If C_H is not very large compared to the depletion-layer capacitance C_s , then the applied potential $V - V_{FB}$ will partition itself between the Helmholtz layer (ϕ_H) and the depletion layer (ϕ_s). Values of $\phi_s / (V - V_{FB})$ can be calculated from the expressions (20, 21)

$$V - V_{FB} = \phi_s + \phi_H \quad [2]$$

$$\phi_H = Q_s C_H^{-1} \quad [3]$$

$$Q_s = (2N_D \epsilon \epsilon_0 kT)^{1/2} [(q\phi_s / kT) + r \{ \exp(-q\phi_s / kT) - 1 \} + \ln \{ r + (1 - r) \exp(-q\phi_s / kT) \}]^{1/2} \quad [4]$$

where the expression used for Q_s , the surface charge density, is valid for $(V - V_{FB}) \geq kT/q$. For the parameters $\epsilon = 80$, $C_H = 0.2$ F/m², and $N_D = 8 \times 10^{25}$ m⁻³, approximately half the applied total potential drop is over the depletion layer (Fig. 2b). We note that therefore the bandedges are not fixed on the energy scale when a potential is applied, but that they will shift by an amount $q\phi_H$ which can be obtained from Fig. 2b.

The onset voltages $V_{ON,i}$ for the instantaneous photocurrent i_i are equal for a- and c-Fe₂O₃, and are equal within experimental error to the flatband voltage V_{FB} ; Fig. 3 shows i_t , i_s , and i_d as a function of $(V - V_{FB})$ and ϕ_s . The smaller i_t values for a-Fe₂O₃ are a result of the smaller

η in the UV. A significant difference between a- and c-Fe₂O₃ shows up at larger bandbending. For a-Fe₂O₃, the potential $V_{ON,s}$ is 0.6V larger and coincides with the onset of a large dark current and a decrease in instantaneous current. The difference between i_t and i_s is generally attributed (3, 7) to the back-reaction (reduction) of an intermediate formed by the anodic photocurrent i_t . The cathodic reduction process under anodic bias has been shown (24, 25) to be a two-step process: transfer of electrons (surface concentration n_s) at a rate k_1 to surface states (density N_{ss}), followed by an isoenergetic transfer (rate k_2) to the solution species (concentration C_{ox}). The reduction current is given by

$$j_r = -qN_{ss}k_1n_s k_2 C_{ox} / (k_1 n_s + k_2 C_{ox}) \quad [5]$$

At small band bending, $k_1 n_s > k_2 C_{ox}$ and $j_r = -qN_{ss}k_2 C_{ox}$ independent of potential. At larger band bending, the current is limited by the transfer to the surface states and is given by $j_r = -qN_{ss}k_1 n_s$ with $n_s = n \exp(-\phi_s / kT)$. With this model $|j_r| = |j_t - j_s|$ and the onset voltage $V_{ON,s}$ is determined by a kinetic condition: $k_1 n_s \approx k_2 C_{ox}$. Now, C_{ox} is proportional to i_t and N_{ss} , and at the steady-state current onsets we have $(i_t)_a \approx (i_t)_c$. Therefore, the model parameters N_{ss} , k_1 , and k_2 for a- and c-Fe₂O₃ are related by

$$[(N_{ss}k_1/k_2)_a] / [(N_{ss}k_1/k_2)_c] \approx \exp[(\phi_{s,a}^* - \phi_{s,c}^*) / kT] \approx 5 \times 10^6$$

where $\phi_{s,a}^*$ and $\phi_{s,c}^*$ are the potential drops over the depletion layer at steady-state current onset. It is clear that the surface states are much more numerous and/or effective in a-Fe₂O₃ than in c-Fe₂O₃. We note, however, that this model has a serious difficulty in accounting for the magnitude of the current from the conduction band to the surface states; this is even more so for a-Fe₂O₃, where just before $V_{ON,s}$ the surface density of electrons is only 1.5×10^9 cm⁻². Tunneling through the depletion layer is unlikely to be important, since its width is at least 8×10^{-9} m.

Specifically, for a-Fe₂O₃, the simultaneous onset of i_s and i_d suggests that the position of the Fermi level determines $V_{ON,s}$. At small ϕ_s , the Fermi level will lie above the surface states which are then efficient electron transfer centers from the solid to the solution. At larger ϕ_s , the level is below the surface states, and the now unoccupied states become, in the dark, efficient centers for the reverse transfer, giving rise to a large dark current. The unoccupied states could also act as recombination centers for photogenerated holes, so that i_t starts to decrease for $V > V_{ON,s}$. These states must then lie $\phi_{s,a}^* + \Delta E_f \approx 0.5$ eV below the conduction bandedge, and they may be responsible for the small maximum in η at $h\nu = 1.5$ eV. Although this model may be valid for a-Fe₂O₃, it obviously cannot provide a common explanation for the different i - V curve of c-Fe₂O₃.

The addition of the S²⁻/S_n²⁻ redox couple to the solution results in the nearly complete absence of transient currents (7). Except for the early onset of a large dark current, the difference between a- and c-Fe₂O₃ also disappears. All photocurrents are small due to the absorption of UV by the yellow solution. The absence of a back-reaction is puzzling; the standard redox potential S²⁻/S_n²⁻ lies, at pH = 14, only ≈ 0.05 V below the conduction bandedge. There is, therefore, an appreciable overlap of the conduction band states with the sulfur states, so that a back-reaction could take place without the necessity of surface states. Whatever the reason for the absence of the back-reaction, the results show that for this photochemical reaction amorphous and crystalline Fe₂O₃ are not noticeably different.

Summary

The differences between amorphous and polycrystalline Fe₂O₃ are most pronounced in those photoelectrochemical properties which relate directly to defects; this shows clearly in differences in dark currents and in back-reaction current in the photo-oxidation of water. Proper-

ties which are not controlled by defects, such as S²⁻-photo-oxidation currents, absorption spectra, bandgaps, and bandedge positions are nearly identical for a- and c-Fe₂O₃. The only exception to this is the smaller quantum efficiency for the instantaneous currents in the UV for a-Fe₂O₃.

Acknowledgment

The work was supported financially by an Operating Grant from the National Science and Engineering Research Council of Canada.

Manuscript submitted May 1, 1984; revised manuscript received Sept. 12, 1984.

Brock University assisted in meeting the publication costs of this article.

REFERENCES

1. R. K. Quinn, R. D. Nasby, and R. J. Baughman, *Mater. Res. Bull.*, **11**, 1011 (1976).
2. J. C. Launay and G. Horowitz, *J. Cryst. Growth*, **57**, 118 (1982).
3. K. L. Hardee and A. J. Bard, *This Journal*, **124**, 215 (1977).
4. J. H. Kennedy and K. W. Frese, Jr., *ibid.*, **125**, 723 (1978).
5. J. F. McCann and S. P. S. Badwal, *ibid.*, **129**, 551 (1982).
6. K. S. Yun, S. M. Wilhelm, S. Kapusta, and N. Hackerman, *ibid.*, **127**, 85 (1980).
7. P. Iwanski, J. S. Curran, W. Gissler, and R. Memming, *ibid.*, **128**, 2128 (1981).
8. M. Tomkiewicz, *ibid.*, **126**, 3320 (1980).
9. L. A. Marusak, R. Messier, and W. B. White, *J. Phys. Chem. Solids*, **41**, 981 (1980).
10. F. P. Koffyberg, K. Dwight, and A. Wold, *Solid-State Commun.*, **30**, 433 (1979).
11. M. A. Butler, *J. Appl. Phys.*, **48**, 1914 (1977).
12. M. Anderman and J. H. Kennedy, *This Journal*, **131**, 21 (1984).
13. A. J. Bosman and H. J. van Daal, *Adv. Phys.*, **19**, 1 (1970).
14. F. P. Koffyberg and F. A. Benko, *J. Non-Cryst. Solids*, **40**, 7 (1980).
15. G. A. Parks, *Chem. Rev.*, **65**, 177 (1965).
16. S. V. Koshcheev and A. E. Cherkashin, *Inorg. Mater.*, **16**, 856 (1980).
17. F. P. Koffyberg and F. A. Benko, *J. Appl. Phys.*, **53**, 1173 (1982).
18. F. P. Koffyberg and F. A. Benko, *This Journal*, **128**, 2476 (1981).
19. F. Decker, J. F. Julião, and M. Abramovich, *Appl. Phys. Lett.*, **35**, 397 (1979).
20. J. F. Dewald, *Bell System Tech. J.*, **39**, 615 (1960).
21. R. De Gryse, W. P. Gomes, F. Cardon, and J. Vennik, *This Journal*, **122**, 711 (1975).
22. O. Jantzen, *Z. Angew. Phys.*, **18**, 560 (1965).
23. D. C. Grahame, *Chem. Rev.*, **41**, 441 (1947).
24. J. Vandermolen, W. P. Gomes, and F. Cardon, *This Journal*, **127**, 324 (1980).
25. P. Salvador and C. Gutiérrez, *ibid.*, **131**, 326 (1984).

The Effects of Surface Energetics and Surface Oxide Layers on the Cyclic Voltammetry of Metallocenes at Nonilluminated p-InP Electrodes

Carl A. Koval and Robin L. Austermann*

Department of Chemistry, University of Colorado, Boulder, Colorado 80309

John A. Turner** and Bruce A. Parkinson**

Solar Energy Research Institute, Photoconversion Research Branch, Golden, Colorado 80401

ABSTRACT

Electron-transfer processes at highly doped p-InP electrodes were investigated by monitoring the cyclic voltammetric dark currents of a series of metallocenes in acetonitrile solutions. The formal reduction potentials of the metallocenes span the bandgap of InP, allowing a comparison of the cyclic voltammetric response as a function of the formal reduction potential and the energetic condition of the electrode surface. Since the electron transfer of all of the metallocenes was electrochemically reversible on the timescale of cyclic voltammetry at a platinum electrode, differences in the voltammetric responses at p-InP were attributed to processes within the semiconductor or to surface phenomena. The energetic condition of the electrode surface during the cyclic voltammetric experiments was monitored by measurements of the capacitance of the space-charge region. Although a simple chemical etching and electrochemical cycling procedure yielded reproducible surface energetics, the p-InP/oxide/CH₃CN interface responded ideally to changes in electrode potential over a range of only about 0.8V. Metallocene redox couples with E⁰ located within that range exhibited reversible cyclic voltammetry when the experiment was performed within that range. The couples with E⁰ located outside of the ideal range displayed irreversible cyclic voltammetry. Voltammetric responses for p-InP electrodes with different crystal orientations and doping densities were compared.

Kinetics of electron-transfer processes occurring at metal electrode/solution interfaces have been studied for many years (1-5); however, kinetic processes at semiconductor electrode/solution interfaces have not received the same level of experimental scrutiny (6-12). This situation is a result of the relatively new use of semiconductor electrodes in electrochemical systems (13-16), the kinetic complexity of photoelectrochemical current flow, and the diversity of properties found for different semiconducting materials (8) and for different crystals of the same semiconducting material. In addition to the factors

that control the rates of electrochemical reactions at metals (e.g., diffusion of solution species, reorganization energies, and double-layer effects) (1-5), the rates of photoelectrochemical reactions are affected by processes that occur within the electrode (e.g., carrier diffusion and recombination) and by the dependence of these processes on light intensity and photon energy (6-12).

To investigate the ways that heterogeneous kinetics at semiconductor electrodes are affected by various combinations of the formal reduction potentials of solution species and the energetic condition of the electrode surface, we have measured cyclic voltammetric dark currents in acetonitrile solutions for cobaltocene and a number of ferrocene derivatives at highly doped p-InP electrodes.

*Electrochemical Society Student Member.

**Electrochemical Society Active Member.

Proper interpretation of the cyclic voltammetric data requires specific knowledge of the energetics at the semiconductor electrode/solution interface. This information has been derived from capacitance data that was obtained in the same solutions and within the same potential regions as the cyclic voltammetry experiments.

Indium phosphide was chosen as the electrode material in these studies because single-crystal samples are available from commercial sources with a variety of crystallographic orientations and doping densities. Furthermore, earlier reports indicate that if nonaqueous solvents are used in the electrochemical cell, InP electrodes with reproducible, stable, and nearly ideal surface characteristics can be prepared (17-19). There has been much interest in InP recently because it is a small bandgap material (1.35 eV) which allows for nearly optimal overlap with the solar spectrum. This makes InP a likely candidate for use in efficient photoelectrochemical devices (20).

Cobaltocene and a series of substituted ferrocenes were chosen to probe the heterogeneous kinetics at InP electrodes, because the reduction potentials for the couples involving the cation and neutral forms of these complexes span the bandgap of InP (Fig. 1). Although series of redox couples that include ferrocenes have been used in many photoelectrochemical studies, the sole use of metallocenes has several advantages. In addition to having identical charge types, the redox couples undergo outer-sphere electron-transfer reactions (21) because the metals are inert to substitution in both oxidation states.¹ Furthermore, the complexes are structurally similar, resulting in similar reorganization energies as evidenced by similar homogeneous self-exchange rate constants (22) and similar heterogeneous standard rate constants (23-24). The rates of heterogeneous charge transfer are rapid enough to ensure that the redox reactions at platinum will be diffusion controlled on the timescale of the cyclic voltammetry experiments. It can be assumed, therefore, that any differences in the heterogeneous kinetics as discerned by the voltammetric responses at p-InP can be attributed to processes within the semiconductor or to surface phenomena.

¹Cobaltocene and the ferricenium ions eventually undergo solvolysis reactions, but not within the timescale of these experiments.

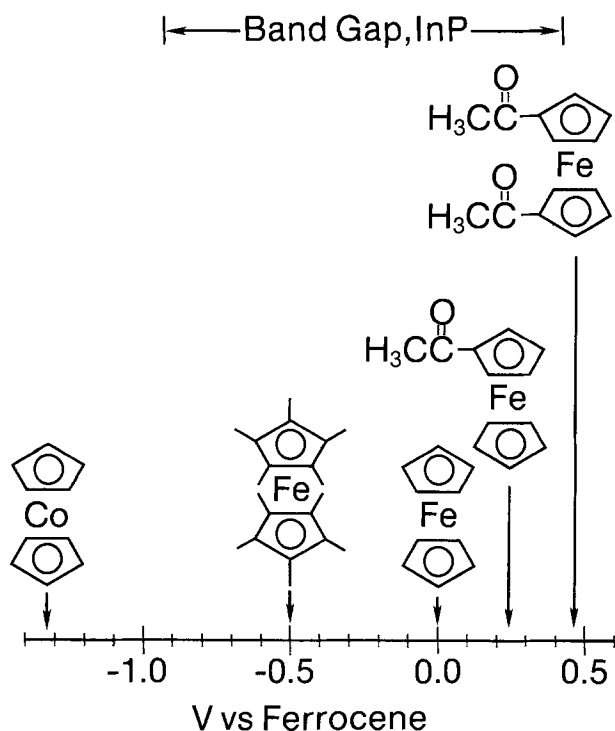


Fig. 1. Formal reduction potentials of the metallocenes in relation to the energy of the bandgap of InP.

Experimental

Reagents and materials.—Gold-label acetonitrile (Aldrich) was thoroughly dried by refluxing over calcium hydride for 14h in a nitrogen atmosphere.² The supporting electrolyte, tetrabutylammonium fluoroborate, TBABF₄, (Southwestern Analytical Chemicals, Incorporated) was dried under vacuum for 2 days at 25°C. Ferrocene, acetylferrocene, 1,1'-diacetylferrocene (Aldrich), and decamethylferrocene (Strem) were purified by sublimation. Cobalticinium hexafluorophosphate (Strem) was used without further purification.

Electrochemical measurements.—All electrochemical measurements were performed in a Vacuum Atmospheres Controlled-Atmosphere Glove Box containing helium. An opaque, one-compartment cell was used for all electrochemical measurements. The acetonitrile solutions contained 0.5M TBABF₄ as the supporting electrolyte. The reference electrode was a silver wire immersed in a solution of 0.01M AgNO₃ and 0.5M TBABF₄ in acetonitrile, which was contained in a glass tube that was sealed at one end with a Vycor glass disk (Princeton Applied Research). This reference electrode has a potential of 0.29V vs. SCE (25). Its potential was monitored daily by comparison with the formal reduction potential, E^o, of the ferricenium/ferrocene couple, which occurred at approximately 0.07V vs. the Ag/Ag⁺ reference electrode. All potentials herein are reported against the E^o for ferrocene^{••} (26). The counterelectrode was a platinum foil.

Cyclic voltammetry, CV, was performed with a Princeton Applied Research Model 175 universal programmer and Model 173 potentiostat/galvanostat. The data were recorded on a Houston Instruments Model 2000 X-Y recorder. In experiments involving p-InP electrodes, the total capacitance of the electrochemical cell was measured by using a Princeton Applied Research Model 5204 lock-in analyzer and a Hewlett Packard Model 3325A synthesizer/function generator interfaced to a computer acquisition system.

The formal reduction potentials of the metallocenes were determined from CV data measured at the platinum electrode as the average of the anodic and cathodic peak potentials. The values of E^o so determined were within ± 70 mV of previously reported measurements (27-29). The approximate concentrations of the ferrocene derivatives were determined by comparing the magnitudes of the CV peak currents obtained at a platinum electrode with peak currents obtained in a solution containing a known concentration of ferrocene. In each CV experiment, the peak current densities obtained at the p-InP electrode were compared with the peak current densities obtained at a platinum electrode in the same solution.

Electrode construction, pretreatment, and characterization.—The platinum disk electrode was constructed by attaching a copper wire to one end of a 1 cm piece of platinum wire with conducting silver epoxy. The copper wire and the sides and back of the platinum wire were sealed in a glass tube with insulating epoxy to isolate them from the solution. The exposed platinum disk was polished with 5.0, 1.0, 0.3, and 0.05 μ m alumina until examination under a microscope revealed a smooth surface. The area of the disk was determined from the diameter of the platinum wire and was found to be 0.00817 cm².

A copper wire was attached to the back of a p-InP crystal (Varian) with conducting silver epoxy, after an ohmic contact was made, as described elsewhere (19). The copper wire and the sides and back of the InP crystal were sealed in a glass tube with insulating epoxy to isolate them from the solution. Prior to each experiment, the electrodes were etched for 1 min in a 50/50 solution of

²In some of the initial experiments, the acetonitrile was passed through a column of activated alumina prior to solution preparation. This procedure was discontinued because it was found to have no effect on the electrochemical behavior.

Table I. Electrode characteristics

Electrode	Orientation	Area (cm ²)	E_{FB} (V)	Doping density (cm ⁻³)
P19(100)1	(100)	0.29	0.44 ^a	1.1×10^{19} ^b 3.4×10^{18} ^c
P19(100)2	(100)	0.18	0.4 ^d	1.5×10^{19} ^e 3.4×10^{18} ^c
P19(111)1	(111)	0.15	0.4 ^d	1.5×10^{19} ^e 1.8×10^{18} ^c
P19(111)2	(111)	0.14	0.4 ^d	1.5×10^{19} ^e 1.8×10^{18} ^c
P18(100)1	(100)	0.12	0.4 ^d	2.4×10^{18} ^e 8.5×10^{17} ^c
P18(100)2	(100)	0.11	0.4 ^d	2.4×10^{18} ^e 8.5×10^{17} ^c

^a Averaged value from the X-intercept of 11 MS plots, ± 0.04 V.

^b Averaged value from the slopes of 11 MS plots, $\pm 0.1 \times 10^{19}$ cm⁻³.

^c Determined from Hall conductivity measurements, $\pm 10\%$.

^d Determined from the X-intercept of a MS plot, ± 0.1 V.

^e Determined from the slope of a MS plot, $\pm 20\%$.

CH₃OH/concentrated HCl, rinsed with CH₃OH, and dried in a stream of argon. The areas of the InP electrodes were measured by using a photographic procedure.

The doping densities, N_A , and flatband potentials, E_{FB} , of the InP electrodes were determined from capacitance/potential data by using the Mott-Schottky equation (30)

$$1/C_{sc}^2 = (2/e\epsilon\epsilon_0 N_A) (E - E_{FB} - k_B T/e)$$

where C_{sc} is the capacitance of the space charge region, ϵ_0 is the permittivity of free space, ϵ is the static dielectric of the semiconductor, E is the electrode potential, and k_B is the Boltzmann constant. The data were modeled to a series RC circuit, and the total cell capacitance was assumed to be equal to C_{sc} (19). Values of C_{sc} were recorded at 100 mV intervals using a cyclic staircase potential program with the step time equal to 10s, which was superimposed upon an ac signal with a frequency of 5 kHz and an amplitude of 20 mV peak to peak. Since the response was found to be independent of frequency, the same frequency was used for all experiments.

The samples of p-InP employed in these studies were highly doped and had either a (100) or a (111) crystal orientation. The reproducibility of the voltammetric responses for different electrodes constructed from the same material was quite good. The characteristics of the various electrodes used in these studies are summarized in Table I. Despite the high doping densities, electrodes constructed from pieces of the same p-InP crystals as the electrodes in this study have been used to study photoelectrochemical phenomena (19, 31).

Results

Surface energetics in the absence of electroactive species.—A cyclic voltammogram of the P19 (100) 1 p-InP electrode (Table I) in electrolyte solution featured essentially no faradaic current between approximately -0.9 and -0.1 V vs. ferrocene (Fig. 2). Positive of -0.1 V, an anodic wave was observed which dramatically increased in magnitude when the electrode potential was swept positive of about 0.4 V. When the electrode potential was then swept negative of about -0.9 V, a small cathodic wave appeared. Similar scans utilizing a platinum electrode indicate that these waves are not due to electroactive impurities. Instead, the waves at p-InP appear to be a result of the oxidation of the electrode surface during the positive scans and the subsequent reduction of the surface during the negative scans. Typical Mott-Schottky (MS) plots for this electrode in electrolyte solution at three different frequencies are also shown (Fig. 2). The data were collected in the range of -0.9 to -0.1 V, which is within the bandgap of p-InP where the electrode exhibited essen-

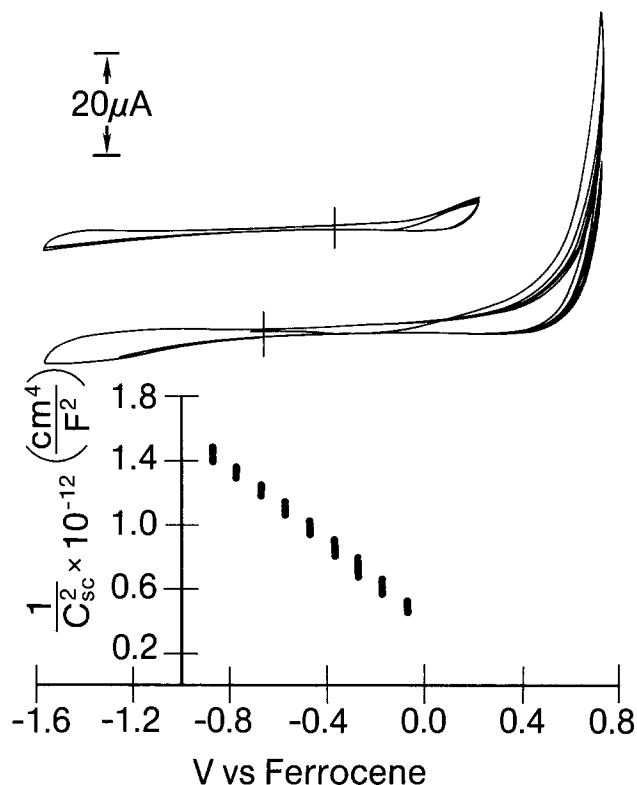


Fig. 2. Cyclic voltammograms for five consecutive cycles and Mott-Schottky plots for the P19(100)1 electrode in a solution of 0.5 M TBABF₄ in acetonitrile. The Mott-Schottky plots represent three sets of forward (positive) and reverse (negative) scans at three frequencies: 1, 5, and 10 kHz.

tially no faradaic background current. Capacitance data collected in this voltage range resulted in linear MS plots with no hysteresis between the forward (positive) scans and the reverse (negative) scans. The slopes and intercepts of the MS plots were independent of frequency.

Capacitance data collected in electrolyte solution within potential ranges in which the electrode featured anodic and cathodic faradaic background currents resulted in MS plots that exhibited hysteresis (Fig. 3). As the electrode potential was swept positive of about -0.1 V during the forward scan, C_{sc} became constant and independent of potential. This behavior suggests that positive charge resided at the electrode surface at potentials corresponding to the appearance of anodic current in the CV

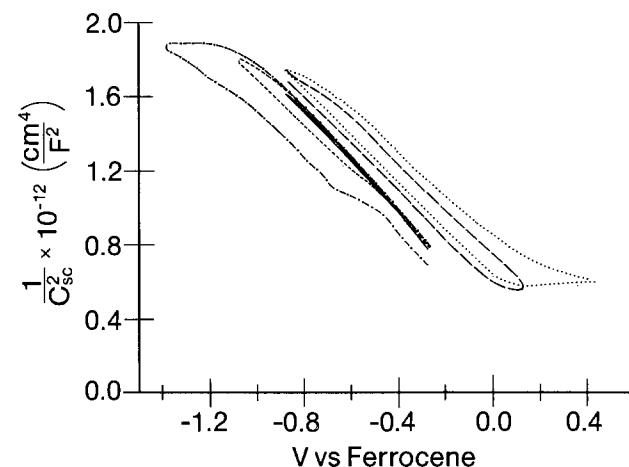


Fig. 3. Mott-Schottky plots for the P19(100)1 electrode in a solution of 0.5 M TBABF₄ in acetonitrile. The curves represent three sets of data collected with an initial potential of -0.3 V and switching potentials of -0.9 V (—), -1.1 V (---), and -1.4 V (-·-·-), and two sets of data with an initial potential of -0.9 V and switching potentials of 0.1 V (—) and 0.4 V (·····).

scans (Fig. 2). When the direction of the potential scan was reversed, the MS plot did not retrace itself. Although $1/C_{sc}^2$ vs. potential for the reverse (negative) scan was linear, it had a different X-intercept than it did for the forward scan, which indicates that the flatband potential had shifted in a positive direction during the forward scan. It was possible to remove the positive surface charge at the electrode surface and return the surface to its initial state by momentarily holding the electrode potential at $-0.9V$. A second capacitance vs. potential scan would then retrace the initial scan. This experiment indicates that the surface energetics could change during the cyclic voltammetry experiments if the switching potential, E_{λ} , was positive of about $-0.1V$. The result would be that the positions of the bandedges on the reverse scan might not be the same as they were on the forward scan.

Similar effects occurred when the electrode potential was swept more negative than about $-0.9V$. In this case as well, C_{sc} became constant and independent of potential, and the intercept of the MS plot on the reverse (positive) scan indicated a negative shift in E_{FB} . This behavior suggests that negative charge resided at the electrode surface at potentials corresponding to the appearance of cathodic current in the CV scans (Fig. 2). It was possible to remove the negative surface charge and restore E_{FB} to its original value by momentarily holding the electrode potential at $-0.3V$.

Permanent changes in E_{FB} resulted if the electrode potential was cycled repeatedly to potentials positive or negative of the initial positions of the bandedges (Fig. 4). If the electrode was cycled between -0.9 and $0.4V$, E_{FB} reached a constant value after a few CV scans and remained constant for more than 50 CV scans (triangles). If the electrode was cycled between -0.9 and $0.7V$, the flatband potential shifted in a positive direction during each CV scan and never reached a constant value (squares). Similarly, E_{FB} could be shifted to more negative values by repeated CV scans between -0.3 and $-1.6V$ (circles). After repeated cycling of an electrode between -0.9 and $0.7V$ or between -0.3 and $-1.6V$, the original E_{FB} could only be restored by re-etching the surface.

In the CV experiments reported below, each freshly etched electrode was cycled 5-10 times between -1.6 and $0.4V$ before data were collected in order to attain a stable E_{FB} . If the experiment required a switching potential posi-

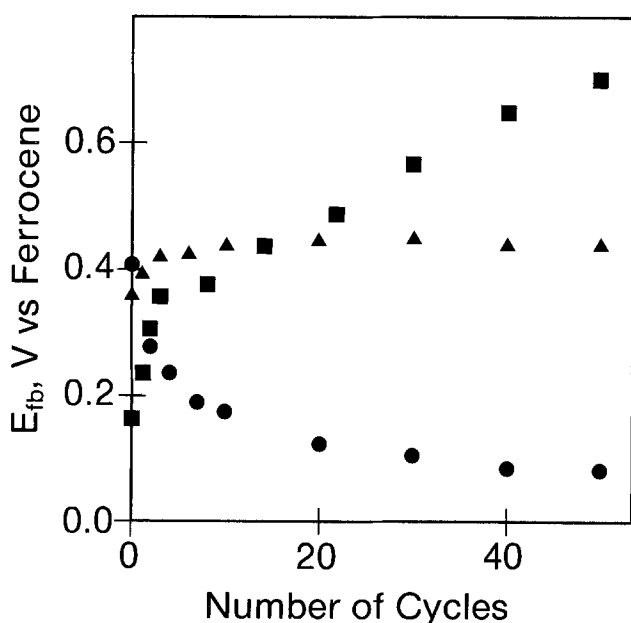


Fig. 4. The flatband potential as a function of the number of cyclic voltammograms done between three different pairs of switching potentials at the P19(100)1 electrode in a solution of $0.5M$ TBABF₄ in acetonitrile. The squares are switching potentials of -0.9 and $0.7V$. The triangles are switching potentials of -0.9 and $0.4V$. The circles are switching potentials of -0.3 and $-1.6V$.

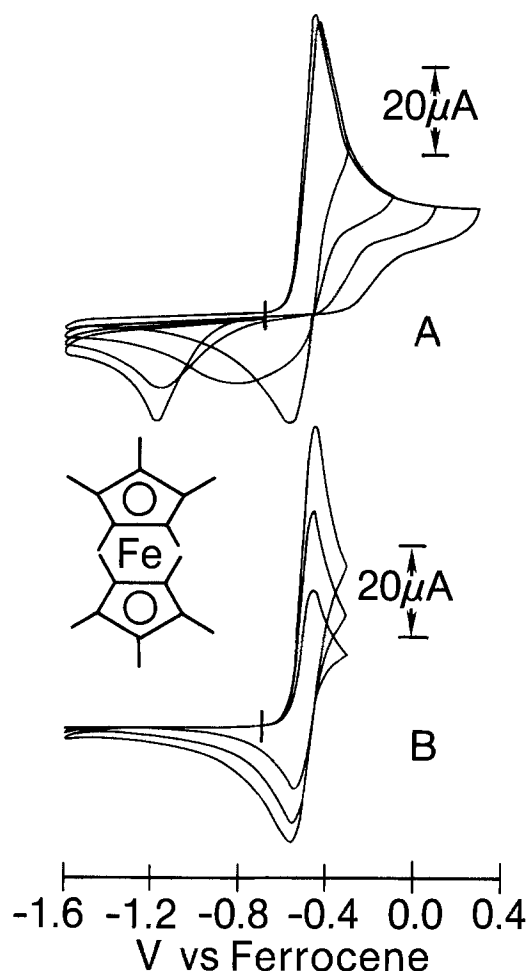


Fig. 5. Part A shows the switching potential dependence of 1 mM decamethylferrocene at the P19(100)2 electrode with $0.5M$ TBABF₄ supporting electrolyte in acetonitrile at a scan rate of 100 mV/s. Part B shows its scan rate dependence at 100 , 50 , and 20 mV/s with a switching potential of $-0.30V$.

tive of $0.4V$ or negative of $-1.6V$, fewer than ten scans were performed before the electrode was re-etched. Rapid loss of electrode response occurred if the electrode potential was swept positive of $0.7V$.

The effect of switching potential and scan rate on the cyclic voltammetry of metallocenes at P19 (100) p-InP electrodes.—Several aspects of the data described in the previous section indicated that the voltammetric behavior of the metallocenes would be affected by changes in the surface energetics of the semiconductor electrode and by changes in the surface oxide that occurred during the CV experiments. Decamethylferrocene would be expected to be the most sensitive probe for these changes, because its E° occurred within the region where there was neither bandedge movement nor surface charging, -0.9 to $-0.1V$. The E° value of ferrocene occurred just positive of that region, and the E° values of acetylferrocene and $1,1'$ -diacetylferrocene were found in the region where oxidation of the p-InP surface occurred in electrolyte solution. The E° value of cobaltocene was found in the region where reduction of the p-InP surface occurred in the electrolyte solution. The importance of the effects of surface energetics and surface redox reactions can be seen in Fig. 5A and 6A, in which the CV behavior of decamethylferrocene and ferrocene at P19 (100) 2 was recorded for different switching potentials. For decamethylferrocene, nearly reversible CV behavior was observed (Fig. 5B) until E_{λ} was made positive of about $-0.30V$. For more positive switching potentials, the cathodic waves became broader and decreased in magnitude, and the cathodic peak potential, E_{pc} , shifted to more negative potentials; however, when E_{λ} was made positive of $0.10V$, the cathodic wave began to

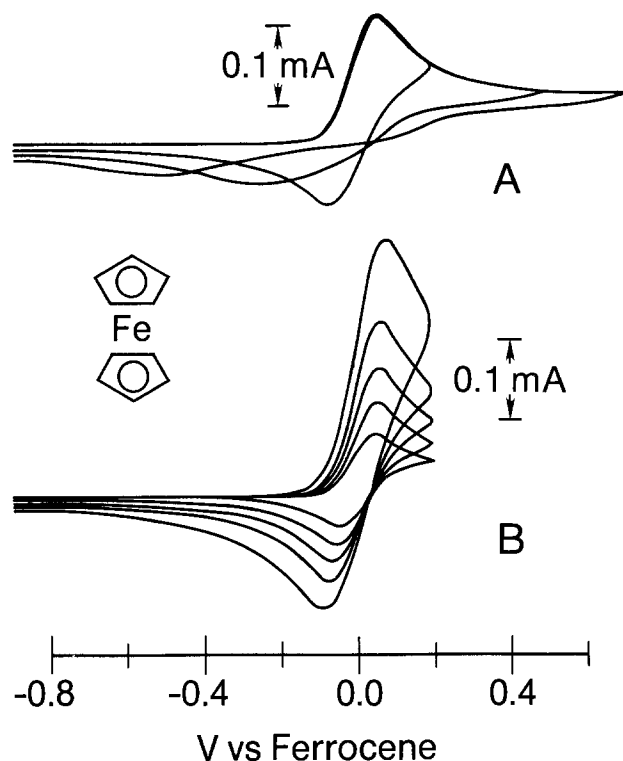


Fig. 6. Part A shows the switching potential dependence of 2 mM ferrocene at the P19(100)2 electrode with 0.5M TBABF₄ supporting electrolyte in acetonitrile at a scan rate of 100 mV/s. Part B shows its scan rate dependence at 500, 200, 100, 50, and 20 mV/s with a switching potential of 0.20V.

sharpen and increase in magnitude once again, and E_{pc} attained an approximately constant value of $-1.1V$. Nearly reversible CV behavior was also obtained for ferrocene when E_{λ} was 0.2V (Fig. 6B). For switching potentials positive of 0.2V, the cathodic peak became increasingly broad and decreased in magnitude, and E_{pc} shifted to more negative potentials. The switching potential dependence for acetylferrocene and 1,1'-diacetylferrocene was similar to that for ferrocene, except that the cathodic peaks were broader.

Close inspection of the currents observed during the reverse scans in Fig. 5A and 6A revealed another unusual feature that accompanied the changes in the cathodic waves. When E_{λ} was relatively positive, the Cottrell current for the oxidation of the metallocenes, which should decay as $t^{-1/2}$, suddenly decayed to zero at potentials that were well positive of $E^{o'}$. In general, the potential at which this current decay occurred tracked the switching potential.

For comparison between the responses of the ferrocene derivatives, cyclic voltammetry was performed in an extended potential range that was similar for each redox couple (Fig. 7 and 8). The oxidation waves for the ferrocenes occurred with only 100-200 mV overvoltages, with the larger overpotentials for the couples which had the most negative $E^{o'}$ within the bandgap. Plots of the anodic peak current, i_{pa} , vs. (scan rate)^{1/2} were linear. A plot of i_{pa} vs. ferrocene concentration from 10^{-4} to $10^{-2}M$ was linear as well, with a current density of 3.6 mA/cm² at the highest concentration when the scan rate was 100 mV/s. The magnitudes of the anodic current densities at P19(100) were at least 90% of the anodic current densities obtained at a platinum electrode in the same solution. These data suggest that the oxidations of the ferrocenes are controlled by the diffusion of solution species to the electrode surface.

When E_{λ} was several tenths of a volt positive of E_{pa} (Fig. 7 and 8), the reduction waves for the ferricenium⁺ ions occurred with substantial overvoltages. The overvoltages tended to be greater for the ferrocene derivatives with

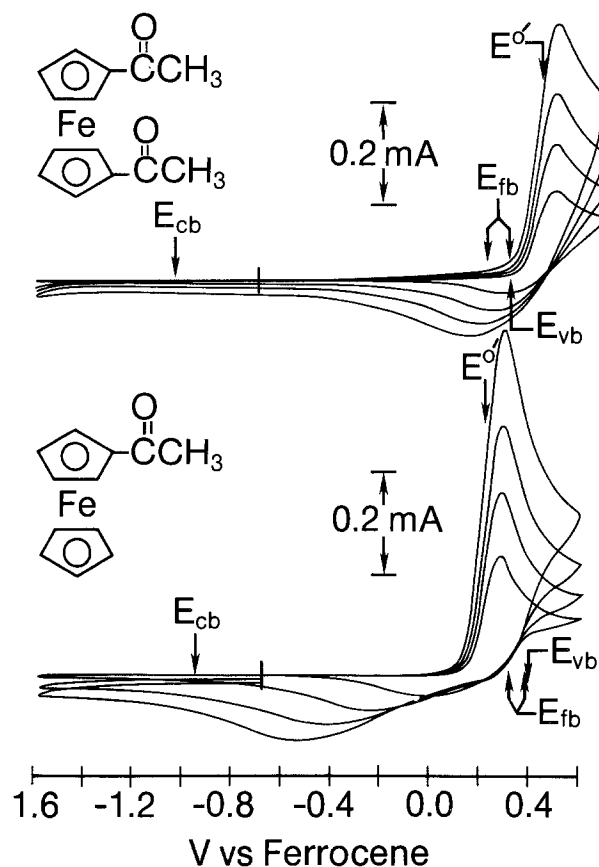


Fig. 7. Cyclic voltammograms of 4 mM 1,1'-diacetylferrocene and 5 mM acetylferrocene at the P19(100)1 electrode with 0.5M TBABF₄ supporting electrolyte in acetonitrile. The response at 200, 100, 50, and 20 mV/s is shown for each redox couple. The formal reduction potentials, the approximate potentials of the bandedges, and the flat-band potential as determined from capacitance data before and after the cyclic voltammetric scans are shown.

more negative reduction potentials. The cathodic peak current, i_{pc} , was less than 50% of the magnitude of i_{pa} for all of the ferrocenes. Nevertheless, plots of i_{pc} vs. (scan rate)^{1/2} and i_{pc} vs. ferrocene concentration from 10^{-4} to $10^{-2}M$ were linear. The current density at the highest concentration was 0.83 mA/cm² when the scan rate was 100 mV/s. For the CV scans with more positive switching potentials, the values of E_{pc} for ferricenium⁺ and acetylferrocenium⁺ were more dependent on scan rate than the values of E_{pc} for 1,1'-diacetylferricenium⁺ and decamethylferricenium⁺.

Figures 5A and 6A clearly indicate that the CV behavior of the cathodic waves in Fig. 7 and 8 was a result of the effect of the switching potential on the condition of the electrode surface. When E_{λ} was just positive of $E^{o'}$ for decamethylferrocene or ferrocene, the values of E_{pc} were not dependent on scan rate, and values of i_{pa}/i_{pc} obtained using the equation proposed by Nicholson were close to unity at all scan rates (Fig. 5B and 6B) (32).

In cyclic voltammograms for the reduction of ferricenium⁺ in solutions of ferricenium tetrafluoroborate (Fig. 9), the initial potential was 0.4V. (This resulted in surface charging similar to that which occurred during the cyclic voltammograms of ferrocene with an anodic switching potential of 0.4V.) The surface charging caused the cathodic wave on the forward (negative) scan to occur with a 1.0V overpotential and a current magnitude that was approximately 50% of that obtained for the one-electron reversible wave at a platinum electrode in the same solution, indicating kinetic control. On the reverse (positive) scan, the anodic wave occurred just positive of $E^{o'}$. The values of i_{pc}/i_{pa} were close to unity at all scan rates, and plots of i_{pc} and i_{pa} vs. (scan rate)^{1/2} were linear. Although the anodic peak current magnitude on the reverse scan

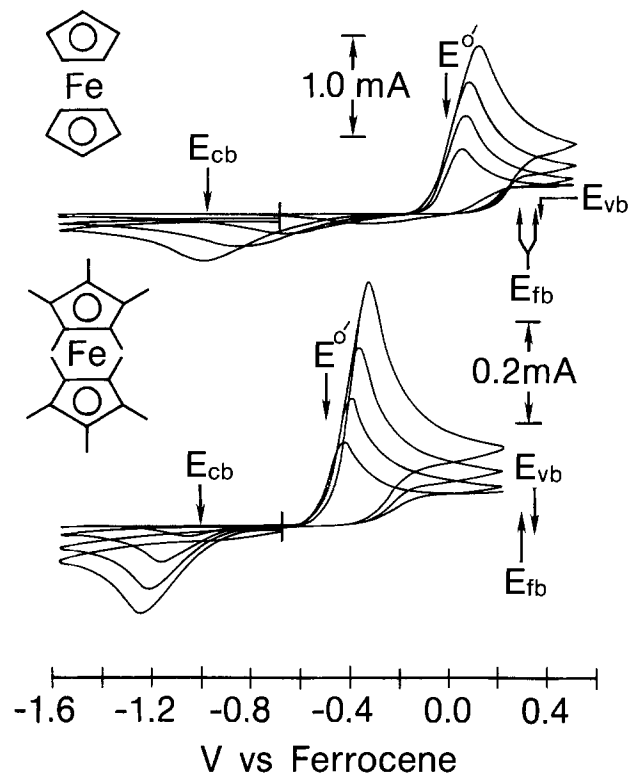


Fig. 8. Cyclic voltammograms of 13 mM ferrocene and 3 mM decamethylferrocene at the P19(100)1 electrode with 0.5M TBABF₄ supporting electrolyte in acetonitrile. The response at 200, 100, 50, and 20 mV/s is shown for each redox couple. The formal reduction potentials, the approximate potentials of the bandedges, and the flatband potential as determined from capacitance data before and after the cyclic voltammetric scans are shown.

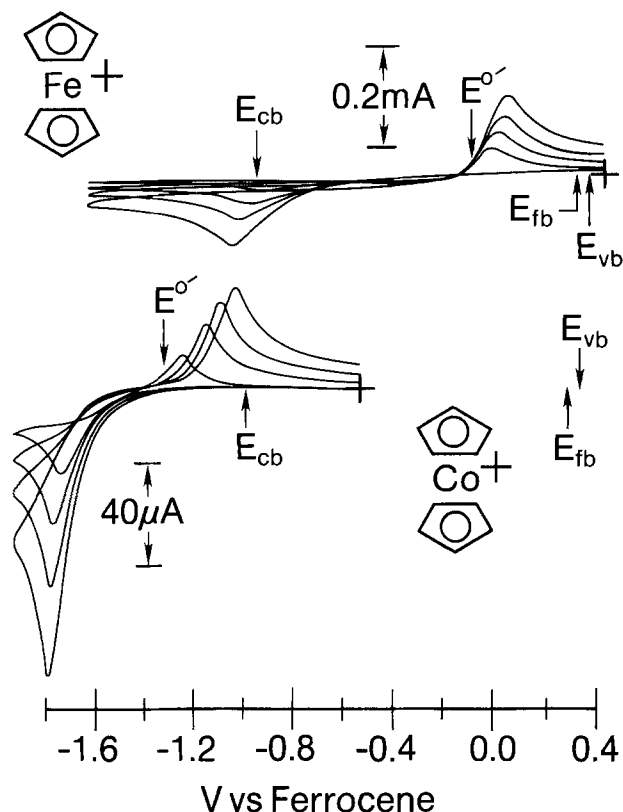


Fig. 9. Cyclic voltammograms of 2 mM ferricenium BF₄ and 1 mM cobalticenium PF₆ at the P19(100)1 electrode with 0.5M TBABF₄ supporting electrolyte in acetonitrile. The response at 200, 100, 50, and 20 mV/s is shown for each redox couple. The formal reduction potentials, the approximate potentials of the bandedges, and the flatband potential as determined from capacitance data before and after the cyclic voltammetric scans are shown.

was only 50% of that obtained at platinum, the peak current was limited by the concentration of ferrocene in the diffusion layer and not by electrode kinetics. These results indicate that although the reduction of ferricenium⁺ in a scan with an initial potential of 0.4V is kinetically controlled, the oxidation of ferrocene is diffusion controlled.

The $E^{o'}$ value of cobaltocene⁺⁰ occurs far negative of the conduction bandedge of p-InP. Reduction and oxidation of this complex occurred with overvoltages of 100-500 mV (Fig. 9). The value of E_{pc} had a very small dependence on scan rate. A plot of i_{pc} vs. (scan rate)^{1/2} was linear, and the magnitude of i_{pc} was within 10% of the value calculated for a one-electron reversible wave at a platinum electrode in the same solution. The value of E_{pa} had a larger dependence on scan rate. A plot of i_{pa} vs. (scan rate)^{1/2} was linear, but the magnitude of i_{pa} was less than 50% of the value calculated for a one-electron reversible wave at platinum in the same solution. No dependence on cathodic switching potential was observed for the cobaltocene⁻⁰ couple.

Effects due to lattice orientation and doping density.—Analogous experiments were performed to compare the responses at the P19 (100) electrodes with electrodes having a similar doping density but a different crystal orientation, P19 (111) 1 and P19 (111) 2, and with electrodes having the same orientation but a lower doping density, P18 (100) 1 and P18 (100) 2. In acetonitrile solutions containing only electrolyte, these electrodes yielded background currents and capacitance vs. potential data that were nearly identical to the P19 (100) electrodes. The flatband potentials for all of the p-InP electrodes, which had been freshly etched and then cycled between -1.6 and 0.4V in electrolyte solution, were within the range of 0.4 +/- 0.1V (Table I).

When P19 (111) electrodes were used to examine the cyclic voltammetry of the metallocenes, the results were

virtually identical to those obtained for the P19 (100) electrodes. This indicates that lattice orientation did not have an effect on the kinetics of charge transfer at the highly doped electrodes.

Major differences in the voltammetry of the metallocenes were observed when the P18 (100) p-InP electrodes were used. Both decamethylferrocene and ferrocene could be oxidized near their reversible potentials at the P18 (100) electrodes (Fig. 10 and 11), but the heterogeneous kinetics associated with the reduction of the two redox couples were quite different. At the P18 (100) electrodes, the CV of decamethylferrocene showed only a small amount of cathodic current on the reverse scan that was independent of scan rate when E_{λ} was -0.2V. No cathodic current appeared when E_{λ} was positive of -0.2V. In addition, a CV with a switching potential positive of -0.2V resulted in a change in the electrode surface that caused the anodic wave of the next CV to be shifted positive with respect to the one in the previous scan. The absence of a cathodic peak indicates that the reduction of decamethylferricenium⁺ was controlled by processes within the semiconductor. Ferrocene exhibited a nearly reversible looking cathodic wave on the reverse scan at the P18 (100) electrodes if E_{λ} was not positive of about 0.2V, similar to the response at the P19 (100) electrodes. Acetylferrocene exhibited a similar response to that of ferrocene at the P18 (100) electrodes, but the CV of 1,1'-diacetylferrocene showed only a broad anodic wave and a small, broad cathodic wave at all switching potentials. Cathodic current for the reduction of cobalticenium⁺ could barely be observed at the P18 (100) electrodes at potentials negative of -1.6V. Two extremely small oxidation peaks were observed on the reverse scan at -1.2 and -0.6V. The magnitudes of the current densities of the anodic peaks were less than 0.60% of the anodic current density at the platinum electrode in the same solution.

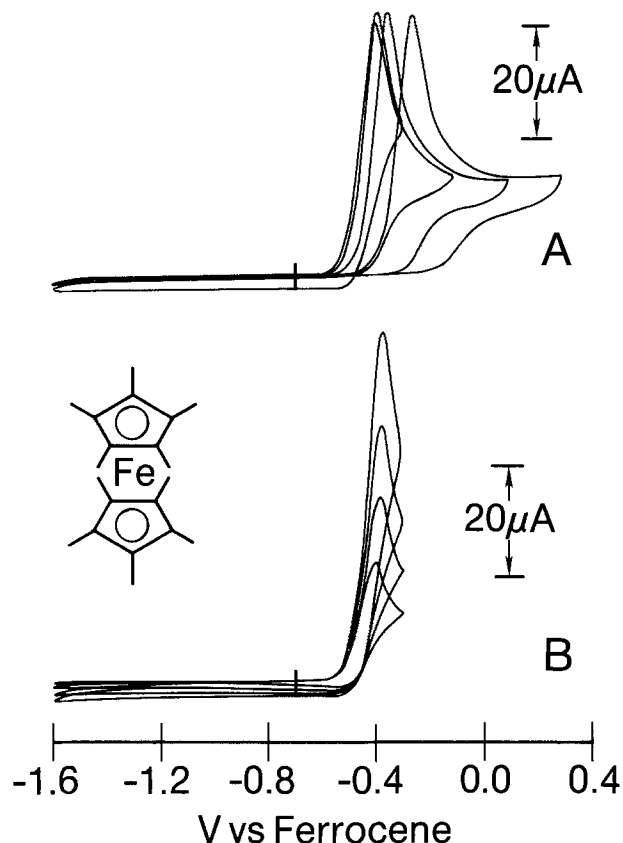


Fig. 10. Part A shows the switching potential dependence of 1 mM decamethylferrocene at the P18(100)1 electrode with 0.5M TBABF₄ supporting electrolyte in acetonitrile at a scan rate of 100 mV/s. Part B shows its scan rate dependence at 200, 100, 50, and 20 mV/s with a switching potential of $-0.30V$.

Discussion

The p-InP/oxide/CH₃CN interface as a function of electrode potential.—The kinetics and mechanisms of electron transfer across a semiconductor/solution interface are heavily influenced by the position of the Fermi level with respect to the valence band and conduction band edges at the electrode surface. The three surface energetic conditions of an ideal p-type semiconductor/solution interface in the dark, which can be achieved by changes in the Fermi level, are depicted in Fig. 12. These diagrams represent the electrochemical potential of an electron as a function of distance into the electrode with respect to redox levels in solution (33). Although dark current flow for each of these energetic conditions has been addressed experimentally and theoretically (9, 12) many questions remain unanswered.

One factor that influences the surface energetics and the rate of electron transfer at many semiconductor electrodes is the presence of an oxide layer at the interface. Oxide layers form spontaneously at room temperature when most metals and semiconductors are exposed to air (34). In the case of InP and other III-V semiconductors (35, 36), the native oxide layer can vary in depth from 1 to 5 nm. The composition of the oxide layer will vary with thickness and growth conditions. In air-saturated aqueous acid, Heller and others have shown that the surfaces of p-InP electrodes become covered with a thin layer of hydrated, conducting indium oxide (20, 37-39). Other studies have emphasized the importance of the oxide film in determining the utility of p-InP as a photocathode (20, 40-43). Formation of the film prevents other undesirable anodic corrosion processes in water and retards surface recombination of electron/hole pairs, yet the film is conducting to photogenerated conduction-band electrons (20). At this time, the effects of surface oxide on the rates and mechanisms of faradaic reactions at semiconductor or metal electrodes are not clearly understood. These ox-

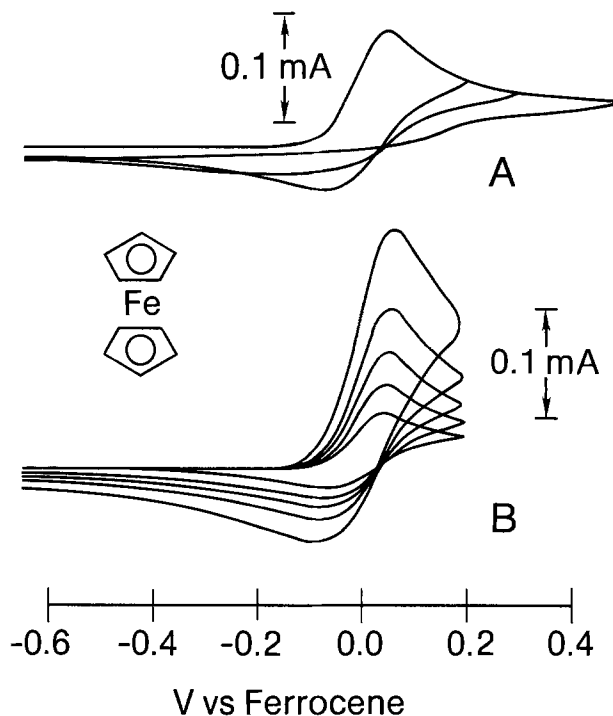


Fig. 11. Part A shows the switching potential dependence of 2 mM ferrocene at the P18(100)1 electrode with 0.5M TBABF₄ supporting electrolyte in acetonitrile at a scan rate of 100 mV/s. Part B shows its scan rate dependence at 500, 200, 100, 50, and 20 mV/s with a switching potential of 0.20V.

ides are generally either wide bandgap semiconductors or insulators; therefore, they represent a possible barrier to charge transfer.

Since the electrodes used in this study were etched in aqueous acid, it can be assumed that the lattice was terminated with an oxide film prior to immersion in the acetonitrile solutions. In order to obtain reproducible capacitance or voltammetric behavior, it was necessary to cycle the electrode several times between -1.6 and $0.4V$ in electrolyte solution. During these cycles, the current-

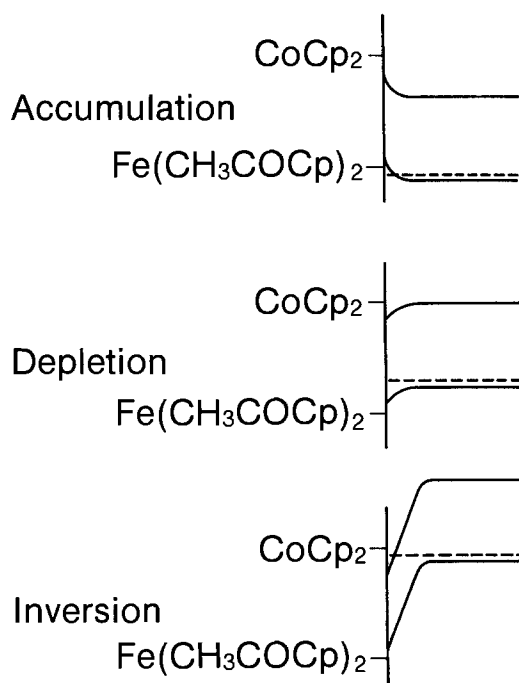


Fig. 12. Accumulation, depletion, and inversion as pictured for an ideal p-type InP/solution interface in the dark with respect to solution redox levels.

potential curves showed the passage of small currents. Because the addition of a small amount of water to the solution resulted in a dramatic increase in the background current, we interpret the anodic current flow to be a result of the oxidation of trace amounts of water present in the CH_3CN , causing the subsequent growth of additional surface oxide. The cathodic background current is interpreted as the subsequent reduction of the surface oxide. The p-InP/oxide/ CH_3CN interface prepared in this manner was relatively stable, as judged by the reproducibility (Table I) and stability (Fig. 4) of E_{FB} and by the consistency of the voltammetric responses observed for the series of metallocenes.

In principle, it should be possible to study faradaic redox processes at semiconductor electrodes under accumulation, depletion, or inversion conditions by adjusting the externally applied potential. Our data indicate that the positions of the bandedges at the p-InP/oxide/ CH_3CN interface are only stable within a limited potential range. The Mott-Schottky plots in Fig. 2 indicate that the interface responded to changes in the potential in a nearly ideal manner as long as the electrode potential was kept within the range of about -0.9V (near the conduction bandedge) and about -0.1V . Within this range, the electrode was in the depletion condition. As the electrode potential was swept positive of about -0.1V , the capacitance of the space charge region did not continue to increase but became nearly constant (Fig. 3). While a relatively potential-independent capacitance could result at an electrode under accumulation, our measurement of E_{FB} indicates that accumulation should not occur at the p-InP/oxide/ CH_3CN interface until the electrode potential is positive of 0.4V . Our data suggest that the potential-independent capacitance is associated with the anodic background current which occurs positive of -0.1V and is presumably due to the growth of surface oxide. Since Fig. 3 indicates that movement of E_{FB} accompanies the anodic background current, we conclude that accumulation is not achieved at p-InP/oxide/ CH_3CN interfaces.

Voltammetric scans to potentials negative of the conduction bandedge did not appear to result in chemically irreversible reduction of the electrode surface, such as the formation of metallic indium. The cathodic background voltammogram during negative scans was featureless, and sharp peaks that could be attributed to the oxidation of metallic indium were not observed on the reverse scans. The capacitance data in Fig. 3 reveal that the space-charge capacitance reached a nearly constant value at potentials negative of about -0.9V . This minimization and potential independence of C_{sc} is expected for ideal metal/insulator/semiconductor (MIS) devices if the capacitance is measured at high frequencies (44). This behavior has been observed at p-Si/ SiO_2 / CH_3OH and p-Si/ SiO_2 / CH_3CN interfaces (45). At an inverted p-type semiconductor/solution interface, excess electrons are stored near the electrode surface in the depletion layer, in surface states (46), or in interface states arising from the oxide layers (47). In any case, the excess surface charge causes the bandedges to become unpinned, that is, they shift with respect to the solution redox levels as the electrode potential is changed.

Figure 3 shows that during experiments in which the electrode potential was swept positive of about -0.1V or negative of about -0.9V , hysteresis in the capacitance of the space-charge region as a function of potential invariably occurred. The chemical processes responsible for this hysteresis are unknown, but a reasonable hypothesis would be that the storage and removal of charge in the oxide layer are not facile processes, owing to the chemical reactions that must accompany this redistribution of charge. Since the voltammetric and capacitance measurements were performed with similar effective scan rates and within similar potential ranges, it can be assumed that the hysteresis in the surface energetics also occurred during the cyclic voltammetry experiments.

Interpretation of cyclic voltammograms.—The CV experiments were designed to elucidate the factors that

control the voltammetric dark currents at a highly doped p-InP electrode for a series of structurally similar redox couples. Cyclic voltammetry is quite useful for qualitative experiments such as these, and it has been used extensively for such purposes in photoelectrochemical studies; however other studies involving cyclic voltammetry have typically not been closely paired with measurements of the capacitance of the space-charge region.

Decamethylferrocene⁺⁰ and ferrocene⁺⁰.—Based on capacitance measurements, the p-InP/oxide/ CH_3CN interface behaves as an ideal semiconductor/solution interface in the depletion condition when the applied potential is between about -0.9 and -0.1V . Figure 1 indicates that only the decamethylferrocene⁺⁰ couple can be examined under these conditions; however, the electrochemistry of the ferrocene⁺⁰ couple can be examined when the potential is close to the ideal region. Since the concentration of majority carriers at the electrode surface is extremely small when the electrode potential is within or near the ideal region, and since the electrons must transfer through a surface oxide layer, the observation of reversible cyclic voltammetry (Fig. 5B) is somewhat surprising. The mechanism of this facile redox process cannot be distinguished without further experiments (9, 12), however, the CV data reveal qualitative factors relevant to this issue. As shown in Fig. 10B, the rate of reduction of decamethylferrocenium⁺ is much more sensitive to the doping density of the electrode than the rate of oxidation of decamethylferrocene. This sensitivity of the cathodic process to N_A is apparently dependent upon the relationship between $E^{0'}$ and the bandedges, because the CV waves for ferrocene⁺⁰ remain symmetric when the doping density of the electrode is lowered (Fig. 6B and 11B). The behavior described above indicates that the p-InP/oxide/ CH_3CN interface is not a rectifying junction for the P19 (100) or P19 (111) electrodes. As the doping density is lowered and the width of the space-charge region increases, the interface becomes rectifying for decamethylferrocene⁺⁰ but not for ferrocene⁺⁰.

This behavior can be explained by drawing an analogy between the current flow across the p-InP/oxide/ CH_3CN interface and the current flow across a semiconductor/metal interface. A barrier to electron transfer is present at the p-InP/oxide/ CH_3CN interface, which is similar to the barrier at a semiconductor/metal interface. This barrier is a result of the gradient in potential across the space-charge region. At a p-type semiconductor, electron transfer between the solution species and the valence band is accomplished either by thermionic emission-diffusion over the barrier, which depends on the barrier height, or by quantum mechanical tunneling through the barrier, which depends on the width of the barrier as well as the barrier height (48). The barrier height ($E^{0'} - E_{\text{vb}}$ on the solution side of the interface and $E_{\text{F}} - E_{\text{vb}}$ on the semiconductor side of the interface) determines the concentration of holes at the interface at the energy of the valence bandedge that are available to accept the transferring electrons. The width of the barrier is related to the doping density of the electrode. The higher the doping density, the thinner the barrier.

Figure 13 illustrates the reason for the difference in rectifying behavior for decamethylferrocene and ferrocene. When the electrode potential is swept positive of the $E^{0'}$ of decamethylferrocene⁺⁰ so that oxidation is thermodynamically favorable, the barrier height in question is $E_{\text{F}} - E_{\text{vb}}$ (Fig. 13A), where E_{F} is the Fermi level. The concentration of holes in the semiconductor at the interface near the energy of E_{vb} is sufficient to accept electrons from the decamethylferrocene in solution via thermionic emission-diffusion at a rate controlled by the diffusion of decamethylferrocene to the electrode surface. When the electrode potential is swept negative of the $E^{0'}$ of decamethylferrocene⁺⁰ so that reduction is thermodynamically favorable, the barrier height in question is $E^{0'} - E_{\text{vb}}$ (Fig. 13B). This barrier height is larger, and the concentration of "holes" (empty states of decamethylferrocen-

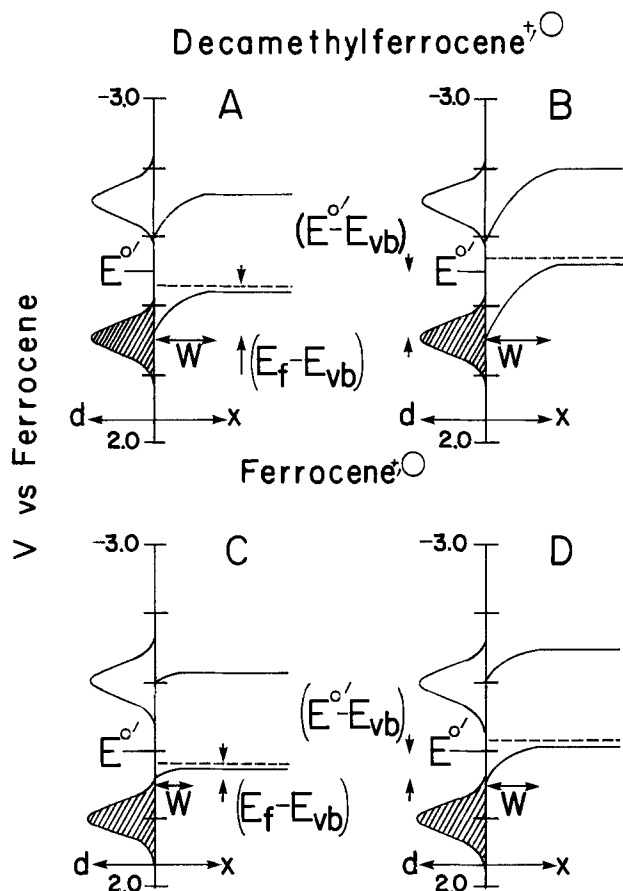


Fig. 13. Relationship between the height of the barrier to anodic current, $E_f - E_{vb}$ (parts A and C), or the height of the barrier to cathodic current, $E^{o'} - E_{vb}$ (parts B and D), and the distribution of the density of states, d , of decamethylferrocene $^{+0}$ (parts A and B) or ferrocene $^{+0}$ (parts C and D) in solution. The width of the space charge region, W , and the distance from the surface of the electrode, x , are also shown.

ium) near the energy of the valence bandedge is insufficient for thermionic emission-diffusion to be a facile process. At the P19 (100) and P19 (111) electrodes, the high doping density causes the barrier width, W , to be relatively small (about 200Å at the top of the valence band near E_f). Quantum mechanical tunneling of electrons from the semiconductor through the barrier into empty states of decamethylferrocene in solution becomes the dominant electron-transfer process for these electrodes. The rate is controlled by the diffusion of decamethylferricenium $^+$ to the electrode surface, resulting in a reversible cyclic voltammogram. At the P18 (100) electrodes, however the lower doping density causes the barrier to be too wide (about 400Å at the top of the valence band near E_f) for tunneling to be a facile process. Very little cathodic current appears at these electrodes for decamethylferrocene, resulting in an electrochemically irreversible wave.

In a similar way, when the electrode potential is swept positive of $E^{o'}$ for ferrocene $^{+0}$ so that oxidation becomes thermodynamically favorable, the barrier height in question is $E_f - E_{vb}$ (Fig. 13C). The concentration of holes in the semiconductor at the interface near the energy of E_{vb} is sufficient to accept electrons from the ferrocene in solution via thermionic emission-diffusion at a rate that is controlled by the diffusion of ferrocene to the electrode surface. In contrast to decamethylferrocene $^{+0}$, when the electrode potential is swept negative of $E^{o'}$ for ferrocene $^{+0}$ (Fig. 13D), the barrier height $E^{o'} - E_{vb}$ is low enough for a sufficient concentration of "holes" (empty states of ferricenium) to be present at the interface near the energy of E_{vb} to accept electrons from the semiconductor via thermionic emission-diffusion at a rate that is controlled by the diffusion of ferricenium $^+$ to the semiconductor. Because the doping density has little effect on the height of

the barrier, thermionic emission-diffusion is the dominant process for the electron transfer of ferrocene $^{+0}$, regardless of the doping density of the electrode.

The use of additional metallocenes which have $E^{o'}$ between the decamethylferrocene $^{+0}$ and ferrocene $^{+0}$ couples to explore this phenomenon further is desirable to further elucidate the relationship between the shape of the barrier and the voltammetric response.

Reasons for apparent electrochemical irreversibility.—When the electrode potential is swept outside of the region from about -0.9 to -0.1 V, electrochemically irreversible cyclic voltammograms are the result. The experiments depicted in Fig. 5A and 6A demonstrate that the irreversibility is not inherent to the heterogeneous kinetics. The apparent irreversibility is an artifact of the way that the CV experiment is performed. The most straightforward explanation for the onset of this pseudorectifying behavior is that it is directly caused by the oxidation and reduction of surface oxide during the CV experiment. The CV's for the ferrocene derivatives suggest two models by which the surface oxide may affect the electrochemical kinetics. The first model involves the formation of a thicker or less conducting oxide on the forward (positive) scan that would, by itself, subsequently inhibit the reduction of the ferricenium $^+$ ions on the reverse (negative) scan. In contrast, the second model involves only the movement of E_{FB} that occurs when the electrode potential is positive of about -0.1 V (Fig. 3). The timescales involved with the shifts in E_{FB} can result in different positions of the bandedges during the forward and reverse scans of a CV experiment. Figure 14 depicts the shift in E_{FB} that occurs during the cyclic voltammetry of decamethylferrocene at 19 (100) electrodes. The initial barrier to the reduction of decamethylferrocene, $(E^{o'} - E_{vb})_i$, is approximately 0.9V in magnitude (Fig. 14A). As the electrode potential is swept positive of -0.1 V, the surface oxide begins to charge and E_{FB} begins to shift in a positive direction, pushing E_{vb} to approximately 0.7V (Fig. 14B and 14C). As indicated by the hysteresis in the capacitance data (Fig. 3), E_{vb} remains at around 0.7V during the reverse (negative) scan (Fig. 14D). This results in a final barrier to the reduction of decamethylferrocene, $(E^{o'} - E_{vb})_f$, of approximately 1.2V. The final barrier is so high that neither thermionic emission-diffusion nor quantum mechanical tunneling is facile, resulting in no cathodic current. As the electrode is swept negative, charge is removed from the electrode surface and E_{vb} returns to its initial potential (Fig. 14E and 14F). The potential barrier is once again $(E^{o'} - E_{vb})_i$. As discussed previously, quantum mechanical tunneling of electrons through this barrier from the electrode to decamethylferrocene is a facile process, so cathodic current is observed at a large cathodic overpotential. A similar description can be used for the other ferrocenes.

The irreversibility associated with CV's of the cobaltocene $^{+0}$ couple (Fig. 9) is more difficult to interpret because mechanisms for electron transfer at inverted surfaces are not well understood (9). Here also, hysteresis in the space-charge capacitance occurs during the CV experiments when the electrode potential is negative of about -0.9 V (Fig. 3). The hysteresis could be responsible for the irreversible voltammograms in this case as well.

Mediation of electron transfer by surface states.—At the P19 (100), P19 (111), and P18 (100) electrodes, the oxidation waves for all of the ferrocene derivatives appeared to be diffusion controlled or nearly so. This behavior implies that the rate of oxidation was not limited by the rate of electron transfer between solution levels and vacant levels in the electrode (holes). An important question is whether the oxidation processes occurred by direct electron transfer between the ferrocenes and valence-band holes or via surface states that could mediate the electron-transfer process. Many theoretical and experimental studies have favored the latter explanation (47, 49-51). For reductions at n-InP/CH $_3$ CN interfaces, Kohl and Bard presented convincing evidence for the intermediacy of a

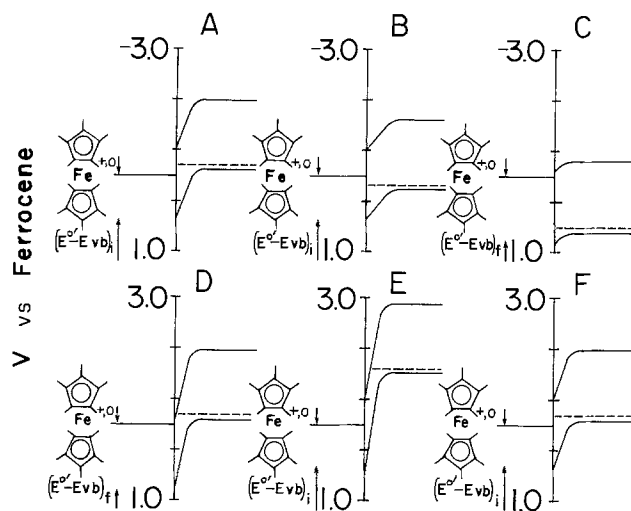


Fig. 14. Illustration of the shift in the valence band edge and the change in the height of the barrier to cathodic current, $E^{o'} - E_{vb}$, during a cyclic voltammogram of decamethylferrocene at a P19(100) electrode with an anodic switching potential of 0.6V and experimental conditions as reported herein. Part A: initial conditions. Part B: electrode potential swept positive of $E^{o'}$, oxidation of decamethylferrocene occurs. Part C: positive shift in the band edges and increase in the height of $E^{o'} - E_{vb}$ at positive potentials. Part D: the band edges remain at the more positive potential and the barrier height remains large during the reverse scan, so that no reduction of decamethylferrocene occurs when the electrode potential is swept negative of $E^{o'}$. Part E: sweeping the electrode to negative potentials returns the band edges and the barrier height to their initial conditions, allowing reduction of decamethylferrocene to occur. Part F: at the final potential, final conditions are identical to the initial conditions.

surface state (17). The reduction of many compounds occurred only after a certain negative potential was applied, and it was argued that this negative potential was

Table II. Result summarized

Electrode potential (V) ^a	Surface energetic condition ^b	Stability of surface energetics	CV dark currents
-2.0 to -0.9	Inversion	1. E_{FB} shifts negative with time 2. $1/C_{sc}^2$ vs. E exhibits hysteresis	1. Irreversible waves 2. Currents decrease with N_D
-0.9 to -0.1	Depletion	1. E_{FB} stable 2. $1/C_{sc}^2$ vs. E exhibits no hysteresis	1. Reversible waves 2. Reduction currents decrease with N_D
-0.1 to 0.4	Depletion	1. E_{FB} shifts positive but can be restored to initial value 2. $1/C_{sc}^2$ vs. E exhibits hysteresis	1. Waves begin to appear irreversible
0.4 to 0.8	Unknown because of anodic corrosion	1. E_{FB} shifts positive and can be partially restored to its initial value, but a permanent shift remains 2. $1/C_{sc}^2$ vs. E exhibits hysteresis	1. Irreversible waves
>0.8	Unknown because of anodic corrosion	1. E_{FB} shifts positive with time and cannot be restored to initial value	1. Electrode passivates

^a Potential vs. $E^{o'}$ for ferrocene⁺⁰ in CH_3CN .

^b See Fig. 12 and text.

required to fill the surface state. This resulted in the "leveling effect" for the reduction of compounds with $E^{o'}$ positive of E_{CB} . A leveling effect was not observed in the present study, since the various ferrocenes were oxidized at p-InP at their individual values of $E^{o'}$ and not at a common potential that could be associated with the emptying of a surface state. Nevertheless, surface-state mediation cannot be ruled out, because surface states with a wide range of energies may be available.

The relationship of this work to previous studies.—The results of this study are summarized in Table II. Dark currents that are independent of experimental parameters can only be observed within a small range of electrode potentials. When the electrode potential is outside of the range of about -0.9 to -0.1V, the dark currents are controlled by experimental parameters such as the initial potential and the switching potential. Most of the qualitative differences in the cyclic voltammetry reported here and by Kohl and Bard (17) can be attributed to the fact that the potential regions identified in Table II were not identified in the earlier study.

Photovoltages and photocurrents at p-InP/oxide/ CH_3CN interfaces are affected by the surface energetics and dark currents. In this regard, it is interesting to examine the photovoltages reported by Dominey *et al.* for various redox couples in CH_3CN at p-InP photocathodes (18). Couples with $E^{o'}$ negative of -1.2V displayed a nearly constant photovoltage of -0.8V. Our data indicate that all of those couples have $E^{o'}$ negative of the E_{CB} of p-InP/oxide/ CH_3CN and that the band bending becomes constant at negative potentials. For couples with $E^{o'}$ between -0.6 and -0.1V, the photovoltages were smaller than 0.8V and were dependent on $E^{o'}$. Our data indicate that those couples have $E^{o'}$ in the range where p-InP/oxide/ CH_3CN behaves like an ideal semiconductor/solution interface.

Conclusions

Reproducible flatband potentials and cyclic voltammetric behavior at highly doped p-InP electrodes in CH_3CN solutions in the dark depend upon the formation of a stable oxide layer on the surface. The capacitance of the p-InP/oxide/ CH_3CN interface behaves ideally between -0.9 and -0.1V vs. the formal reduction potential of ferrocene⁺⁰. Surface redox reactions that occur outside of this potential range lead to potential independent and hysteretic space-charge capacitances and irreversible cyclic voltammetry for metallocene redox couples. Reversible CV behavior can be observed for decamethylferrocene⁺⁰ ($E^{o'} = -0.5V$) and ferrocene⁺⁰ ($E^{o'} = 0.0V$) at the electrodes with the highest doping densities. The heterogeneous kinetics observed are affected by the doping density of the electrode, but they are not affected by the crystal orientation.

Acknowledgments

We wish to thank Arthur J. Nozik (SERI) and Nathan S. Lewis (Stanford University) for useful discussions and Brad Thacker (SERI) for obtaining the Hall measurements of the doping densities of the p-InP crystals. This project was supported in part by a grant in aid from the Council on Research and Creative Work, University of Colorado in Boulder; in part by BRSG Grant number RR07013-18 awarded by the BRSG program, Division of Research Resources, NIH; and in part by the Department of Energy (Division of Chemical Sciences) Contract no. DE-FG02-84ER13247.

Manuscript submitted July 23, 1984; revised manuscript received Oct. 15, 1984.

REFERENCES

- W. J. Albery, "Electrode Kinetics," Clarendon Press, Oxford (1975).
- J. O'M. Bockris and A. K. N. Reddy, "Modern Electrochemistry," Plenum Press, New York (1970).
- K. J. Vetter, "Electrochemical Kinetics," Academic Press, New York (1967).
- P. Delahay, "Double-Layer and Electrode Kinetics,"

- Interscience Publishers, New York (1965).
5. A. J. Bard and L. R. Faulkner, "Electrochemical Methods," Chap. 3, 12, John Wiley and Sons, New York (1980).
 6. H. Gerischer, *Adv. Electrochem. Electrochem. Engr.*, **1**, 139 (1961).
 7. H. Gerischer, *Top. Appl. Phys.*, **31**, 115 (1979).
 8. S. R. Morrison, "Electrochemistry at Semiconductor and Oxidized Metal Electrodes," Plenum Press, New York (1980).
 9. R. H. Wilson, *Crit. Rev. Solid State Mater. Sci.*, **1** (1980).
 10. A. J. Nozik, *Ann. Rev. Phys. Chem.*, **29**, 189 (1978).
 11. H. Reiss, *This Journal*, **125**, 937 (1978).
 12. R. Memming, *Electroanal. Chem.*, **11**, 1 (1979).
 13. A. J. Bard, *J. Phys. Chem.*, **86**, 172 (1982).
 14. M. S. Wrighton, *Acc. Chem. Res.*, **9**, 303 (1979).
 15. A. Heller, *ibid.*, **14**, 154 (1981).
 16. K. Rajeshwar, P. Singh, and J. Dubow, *Electrochim. Acta*, **23**, 1117 (1978).
 17. P. A. Kohl and A. J. Bard, *This Journal*, **126**, 598 (1979).
 18. R. N. Dominey, N. A. Lewis, and M. S. Wrighton, *J. Am. Chem. Soc.*, **103**, 1261 (1981).
 19. G. Cooper, J. A. Turner, B. A. Parkinson, and A. J. Nozik, *J. Appl. Phys.*, **54**, 6463 (1983).
 20. A. Heller, *Science*, **223**, 1141 (1984).
 21. H. Taube, "Electron Transfer Reactions of Complex Ions in Solution," Chap. 2, Academic Press, New York (1970).
 22. E. S. Vang, M-S. Chan, and A. C. Wahl, *J. Phys. Chem.*, **84**, 3094 (1980).
 23. W. E. Geiger and D. E. Smith, *J. Electroanal. Chem.*, **50**, 31 (1974).
 24. T. Saji, Y. Maruyama, and S. Aoyagui, *ibid.*, **86**, 219 (1978).
 25. C. K. Mann, *Electroanal. Chem.*, **3**, 57 (1969).
 26. R. R. Gagne, C. A. Koval, and G. C. Lisensky, *Inorg. Chem.*, **19**, 2854 (1980).
 27. J. L. Robbins, N. Edelstein, B. Spencer, and J. C. Smart, *J. Am. Chem. Soc.*, **104**, 1882 (1982).
 28. D. W. Hall and C. D. Russel, *ibid.*, **89**, 2316 (1969).
 29. W. F. Little, C. N. Reilly, J. D. Johnson, and A. P. Sanders, *ibid.*, **86**, 1382 (1964).
 30. A. J. Bard and L. R. Faulkner, "Electrochemical Methods," p. 636, John Wiley and Sons, New York (1980).
 31. A. J. Nozik and B. Thacker, Unpublished results.
 32. R. S. Nicholson, *Anal. Chem.*, **37**, 1351 (1965).
 33. A. J. Bard and L. R. Faulkner, "Electrochemical Methods," p. 634, John Wiley and Sons, New York (1980).
 34. T. L. Barr, *J. Phys. Chem.*, **82**, 1801 (1978).
 35. C. W. Wilmsen, *J. Vac. Sci. Technol.*, **19**, 279 (1981).
 36. G. P. Schwartz, "Insulating Films on Semiconductors," M. Schulz and G. Pensl, Editors, pp. 270-280, Springer-Verlag, Berlin (1981).
 37. H. J. Lewerenz, D. E. Aspnes, B. Miller, D. L. Malm, and A. Heller, *J. Am. Chem. Soc.*, **104**, 3325 (1982).
 38. H. C. Casey and E. Buehler, *Appl. Phys. Lett.*, **30**, 247 (1977).
 39. W. E. Spicer, P. Lindau, P. Skeath, C. Y. Su, and P. W. Chye, *Phys. Rev. Lett.*, **44**, 420 (1980).
 40. L. F. Schneemeyer and B. Miller, *This Journal*, **129**, 1977 (1982).
 41. A. Heller, B. Miller, H. J. Lewerenz, and K. J. Bachmann, *J. Am. Chem. Soc.*, **102**, 6556 (1980).
 42. A. Heller, B. Miller, and F. A. Thiel, *Appl. Phys. Lett.*, **38**, 282 (1981).
 43. S. Menezes, H. J. Lewerenz, F. A. Thiel, and K. J. Bachmann, *ibid.*, **38**, 710 (1981).
 44. S. M. Sze, "Physics of Semiconductor Devices," Chap. 9, John Wiley and Sons, New York (1969).
 45. J. A. Turner, J. Manassen, and A. J. Nozik, *Appl. Phys. Lett.*, **37**, 488 (1980).
 46. A. J. Bard, A. B. Bocarsly, F. F. Fan, E. G. Walton, and M. S. Wrighton, *J. Am. Chem. Soc.*, **102**, 3671 (1980).
 47. R. N. Noufi, P. A. Kohl, S. N. Frank, and A. J. Bard, *This Journal*, **125**, 246 (1978).
 48. S. M. Sze, "Physics of Semiconductor Devices," Chap. 5, John Wiley and Sons, New York (1969).
 49. R. Memming and G. Schwandt, *Electrochim. Acta*, **13**, 1299 (1968).
 50. K. Rajeshwar, *This Journal*, **129**, 1003 (1982).
 51. P. A. Kohl and A. J. Bard, *J. Am. Chem. Soc.*, **99**, 7531 (1977).

On the Origin of the Bandshifts in the Action Spectra of Polycrystalline TiO₂ Electrodes Prepared by Thermal Oxidation of Titanium

S.-E. Lindquist* and A. Lindgren

Institute of Physical Chemistry, University of Uppsala, S-751 21 Uppsala, Sweden

Zhu Yan-Ning

Institute of Photographic Chemistry, Academia Sinica Beijing, Beijing, China

ABSTRACT

The spectral distribution of the quantum efficiency in the range 250-550 nm has been determined for a number of TiO₂ electrodes prepared by thermal oxidation in air (temperature range 500°-700°C). A red shift in the action spectra and an extensive decrease in the quantum efficiency in the short wavelength range (250-300 nm) were observed with increasing oxidation. The effect of different polishing procedures on the electrodes before and after the formation of the TiO₂ layers was also investigated. A marked increase in quantum efficiency, especially in the short wavelength range, was registered with increasing surface finish of the electrodes. The observed changes in the action spectra are discussed in terms of electron-hole recombination mediated via surface states and recombination in the rough surface. It was possible to describe the registered action spectra in the wavelength range 300-400 nm in terms of the known absorption coefficient and a modified Gärtner-Butler equation with three adjustable parameters. The experimental data also give evidence of a gradient in doping density normal to the surface of the TiO₂ layer electrodes.

Action spectra of single-crystal and polycrystalline TiO₂ as electrode material in photoelectrochemical (PEC) cells varies strongly with method of preparation (1-14) and history of the electrode (15-17). Some of these variations are well understood and can be described in terms of parameters of the electrode material and properties of the

* Electrochemical Society Active Member.

interface between electrode and electrolyte (18-24). The often-observed decrease in quantum efficiency of TiO₂ electrodes in the short wavelength range (250-300 nm), however, is still the cause of some controversy. Different and sometimes conflicting ideas of its origin can be found in the literature (3, 7, 15, 16). It is well known that variations in surface morphology can substantially affect

the efficiency of the photoactive electrode(s) in a PEC cell (1, 2, 15, 25-29).

In an attempt to clarify to what extent changes in the surface morphology contribute to the observed variations in the spectral response of polycrystalline TiO₂ layer electrodes, different oxidation conditions and polishing procedures were utilized to achieve electrodes with different surface finishes. The registered action spectra of the electrodes are compared with earlier published spectra. The observed changes in spectral distribution of the photoreponse are discussed with reference to models proposed in the literature. The concept of a "recombination layer" at the surface of the electrode is introduced and a semi-empirical equation, based on the Gärtner-Butler expression (18, 19), is utilized to describe the registered action spectra in the wavelength range 300-400 nm.

Materials

Titanium plate, which, according to the manufacturer, contains Fe < 0.10%, O < 0.35%, N < 0.07%, C < 0.10%, and H < 0.012%. An etching solution was made from 1 part 40% HF solution, and 1 part conc HNO₃ and 3 parts distilled water. Phosphate buffer solutions were prepared from p.a. Baker reagent chemicals and distilled water. These solutions were pasteurized and stored at 4°C.

Preparation of the TiO₂ Layers

1 mm thick circular (20 mm diam) titanium plates were mechanically polished to mirror brightness with aluminium oxide (Tornerde, Jean Wirtz, Dusseldorf, Germany) in a sequence down to a grain size of 0.25 μm. Some of the mirror bright plates were etched for 20s in the etching solution (see previous section). All plates were carefully cleaned and finally rinsed in distilled water before they were placed in the preheated oven. The oxidation was carried out in air at atmospheric pressure. The temperature was measured close to the samples with a Pt/Pt, Rh (10%) thermocouple. Zero time was taken when the samples were placed in the oven. [A more detailed description of the preparation procedure is given in Ref. (29, 39).]

Experimental

The TiO₂ film thickness was determined from the interference fringe pattern of reflection spectra recorded in the range 400-15,000 nm. (Zeiss DMR 10, Beckman DK-2a, and Perkin Elmer 157 IR spectrophotometers were used.)

A conventional three-electrode cell was used. The TiO₂ electrodes were mounted in a specially constructed O-ring (Viton) sealed plexiglass holder, exposing a circular area of 0.8 or 1.8 cm² to the electrolyte. Ohmic contact (metal to metal) was made by pressing a spring-supported stainless steel pin or a copper wire against an oxide-free spot at the back of the Ti plate. The surface of the TiO₂ electrode was placed in the cell behind an optically flat fused quartz (suprasil) window. A calibrated saturated calomel electrode (0.242 ± 0.001V vs. NHE) was used as reference electrode (RE). The counterelectrode (CE) was platinized Pt-foil (area approximately 3 cm²) separated from the TiO₂ working electrode (WE) and RE by a porous glass filter. The arrangement of the light source, the monochromator, and the arrangement for measuring the light intensity have been described elsewhere (13). Corrections for reflection losses at the window of the cell and absorption losses in the electrolyte were made. Those cases where correction for reflection losses at the TiO₂/electrolyte interface were made, will be specially noted in the following. A Schott filter UG5 was used to eliminate stray light in the wavelength region 250-350 nm. The second-order spectrum from the grating monochromator (Schoeffel GM 252) was filtered off with a Schott GG15 cutoff filter.

The potentiostatic measurements were performed with a PAR 173 instrument. Action spectra (at constant WE potential) were determined from alternating point by point measurements of the photocurrent and the light flux. Photocurrent registration was also made on a Hewlett-Packard Model 7044A X-Y recorder. All measurements

were performed at room temperature (approximately 20°C).

The surface profile measurements were made on a Sloan Detak surface profile measuring instrument (Sloan Technology Corporation, Santa Barbara, California).

Results and Discussion

Estimation of film thickness.—The TiO₂ film thickness was estimated using Eq. [1]

$$\frac{n}{\lambda} = \frac{1}{4d} \left(M - \frac{k}{\pi} \right) \quad [1]$$

Here n is the refractive index, λ is the wavelength at maxima and minima, d is the film thickness, M is an integer, and k is a constant equal to 0 or π , depending on the phase difference between the beams reflected at the two interfaces air/oxide and oxide/metal. Refractive indexes of polycrystalline TiO₂ (rutile) given by Hass (30) and Cardona and Harbecke (31) were used in the calculations.

Figure 1 shows some typical plots from which the film thickness d was determined. The Tolansky method recently used by Stillwell and Park (32) was also applied and gave (except for two very thin films) the same results within 5%.

Measured values are collected in Tables I and II. They agree well (29) with the results of the more extensive studies by Kofstad *et al.* (33, 34) and Dechamps and Lehr (35).

The effect of increased oxidation of the titanium plate.—Figure 2 shows the action spectra of 12 polycrystalline TiO₂ electrodes prepared by thermal oxidation in air in the temperature range 500°-700°C. All twelve electrodes were made from carefully polished titanium plates, which were slightly etched (ca. 20s) before oxidation. SEM pictures give evidence of an increasing surface roughness with increasing oxidation (29). The action spectra in Fig. 2 were registered point by point, going from longer towards shorter wavelengths at a working electrode potential of 1.25V vs. SCE (pH = 6.75). The quantum efficiencies

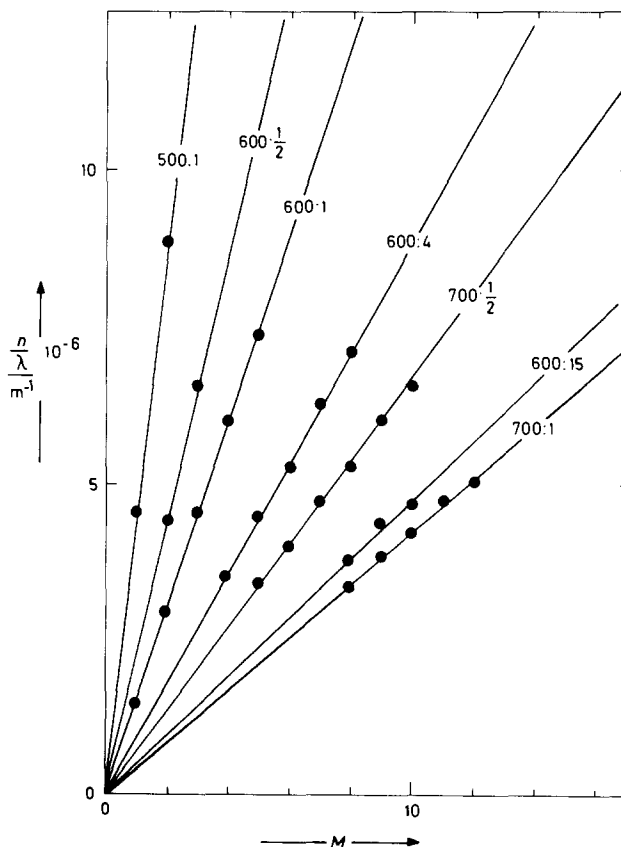


Fig. 1. Optical reflection data plotted according to Eq. [1]

Table I. The obtained values of the parameters w , d_f , and f are given for best fit of Eq. [2] to the action spectra in Fig. 2. No restrictions were imposed on the allowed values of the parameters. Details of the calculations are given in the text. The table also gives the TiO₂ layer thickness, as estimated from Fig. 1, CHISQ for best fit, and the preparation parameters for temperature, T_{ox} , and oxidation time, t_{ox}

T_{ox} (°C)	t_{ox} (h)	d (nm)	f (%)	d_f (nm)	w (nm)	CHISQ
502	0.50	48	0	2.5	11	0.91
	1.00	55	0	3.7	11	2.2
	4.0	83	0	10	16	2.5
	15.0	108	0	11	20	5.7
598	0.50	114	0	19	25	5.0
	1.00	165	$5 \cdot 10^{-4}$	24	33	3.9
	4.0	280	$1.5 \cdot 10^{-3}$	68	40	5.0
	15.0	530	2.1	107	48	4.2
704	0.50	370	6.3	102	68	3.7
	1.00	585	3.6	156	99	1.5
	4.0	1290	0.43	355	125	3.1
	15.0	2990	0.13	800	(63)	1.3

were calculated from the difference between the steady-state photocurrent and the dark current. A systematic change in the spectral distribution of the photoresponse with increasing oxidation can be seen. The trend of an overall increase in quantum efficiency with increasing oxidation (or TiO₂ film thickness) is succeeded by a rapid decrease in the range 250-300 nm (starting with the plate oxidized at 598°C for 4h). A shallow minimum at approximately 300 nm is seen. The maximum in the short wavelength region remains at approximately 270 nm, while the maximum in the long wavelength region (300-400 nm) undergoes a red shift with increasing oxidation.

A similar red shift has been observed by a number of workers (3, 5-9, 15, 16), e.g., by Matsumoto *et al.* (3) at thermally grown polycrystalline TiO₂ electrodes, and by Möllers *et al.* (7) at electrodes prepared by chemical vapor deposition. Liou *et al.* (16) and Wilson *et al.* (15), who investigated the aging of hydrogen-reduced single crystals of TiO₂, also report similar red shifts with increasing illumination time. Similarly, Mac Aleer and Peter (8) observed a red shift in the action spectra in their study of anodic oxide films on titanium. The shallow minimum near 300 nm is also present in the "anodic" action spectra of untreated polycrystalline TiO₂ electrodes (prepared much in the same way as in the present work) presented by Sprünken *et al.* (14), and in the action spectra of single-crystal TiO₂ electrodes registered by Wilson *et al.* (1). The minimum can be attributed to the higher reflection losses due to the large index of refraction (31) in this range (*vide infra*).

Different explanations of the observed changes in action spectra are proposed. Matsumoto *et al.* explain the observed red shift upon increased oxidation by referring to a model proposed by Goodenough. They suggest that the broadness and position of the photocurrent peak will mainly be determined by the degree of interaction be-

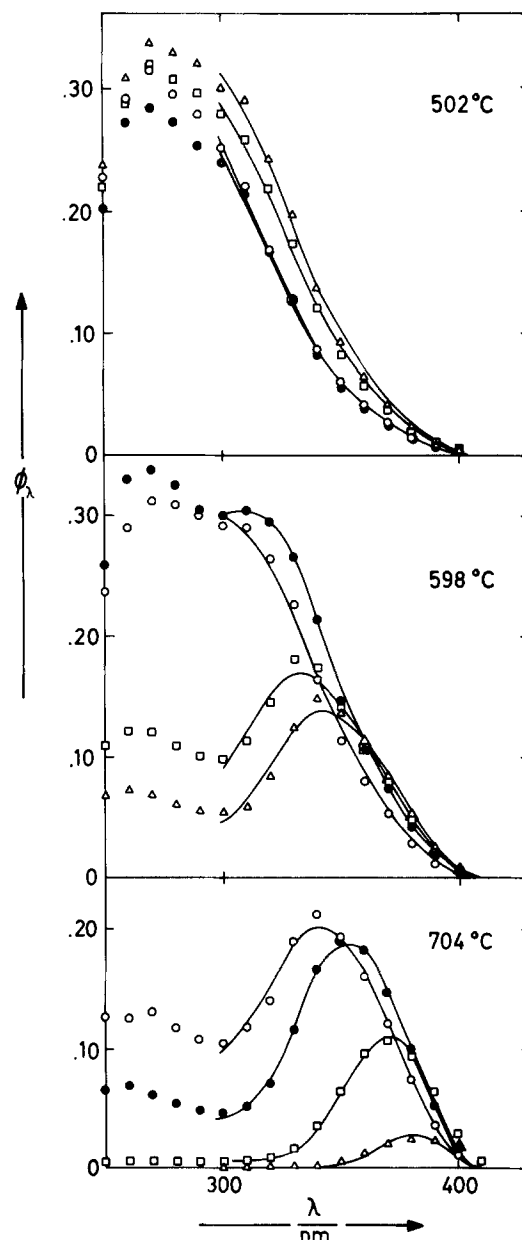


Fig. 2. Action spectra of 12-layer electrodes prepared by thermal oxidation of highly polished titanium plate. At each temperature (502°, 598°, and 704°C) the oxidation periods were: ○ 0.50h, ● 1.00h, □ 4.0h, and △ 15.0h. The solid lines show best fit of Eq. [2] to the experimental data. Electrode potential 1.25V vs. SCE; pH = 6.75.

tween the t_{2p} orbital of the Ti cation and the p orbital of the oxygen ion. If the interaction becomes weak, the peak becomes sharp and shifts towards longer wavelengths, and they propose that this is the case for samples prepared at temperatures above 700°C.

Table II. The obtained values of the parameters w and d_f are given for best fit of Eq. [2] to registered action spectra, as described in the text. In these calculations the parameter f was fixed at zero. Data collected from five different stages of polishing and six different electrode potentials, U vs. SCE.

The table also gives the thickness d at each stage of polishing. α_λ values from Ref. (13) were used in these calculations. $E_g = 3.05$ and $B = 8.7 \times 10^7$ eV⁻¹m⁻¹ were used to calculate α_λ in the wavelength range 340-400 nm. (See Eq. [3].) Allowed ranges of the parameters were: $0 < d_f < 2000$ nm, $0 < w < 2000$ nm

Stage	1			2			3			4			5		
d (nm)	d_f (nm)	w (nm)	CHISQ	d_f (nm)	w (nm)	CHISQ	d_f (nm)	w (nm)	CHISQ	d_f (nm)	w (nm)	CHISQ	d_f (nm)	w (nm)	CHISQ
0.20	156	197	22	77	150	111	26	112	65	11	105	50	24	68	28
0.50	165	273	33	85	221	209	21	210	168	5	189	180	25	103	98
0.75	171	329	40	90	267	277	21	271	262	6	250	264	26	123	161
1.00	170	361	46	92	302	312	21	321	337	6	289	297	27	139	214
1.25	168	389	49	93	330	322	21	357	390	6	327	379	27	151	260
1.50	184	436	125	92	351	320	21	390	481	—	—	—	27	161	304

In the qualitative discussion of aging effects in H_2 -reduced single-crystal rutile anodes, Harris and Wilson explained some of the observed changes in the spectral distribution of the photocurrent by the formation of an "inert" layer which absorbs photons without contributing to the current. They also discussed the effects of surface roughness and "pores" at the surface of the crystal.

A narrowing bandgap and shifts in the refractive index are proposed by Liou *et al.* as an explanation of the red shift observed in their aging experiments. Sprünken *et al.* do not discuss the bandshift mentioned above, but do give interesting comments on the charge exchange and the reactions at the electrode/electrolyte interface. In terms of a slightly modified model proposed by Gerischer (36) and Bard (37), a qualitative explanation to the "anodic" and "cathodic" action spectra was given, which was registered at working electrode potentials close to the flatband potential. The model includes surface states in the bandgap as well as the existence of different energy states of reduced and oxidized species (*e.g.*, O^{2-}/O_2) in the liquid phase. Their experiments showed that when oxygen or other reducible species like Fe^{3+} are present in the solution, electrons generated close to the electrode surface by short wavelength light with small penetration depth, $1/\alpha_\lambda$, are transferred to the solution and contribute to a "cathodic photocurrent."

Electrons generated deeper in the TiO_2 electrode by long wavelength light with low absorption coefficient, however, are drained into the electrode. Sprünken *et al.* did not make any systematic investigation of the effect of surface roughness, but assumed that the less pronounced cathodic effects on single crystals compared with polycrystalline materials arise from the smaller surface area of the former. We will return to the ideas of Wilson *et al.* and Sprünken *et al.* in the following discussion.

The effect of different polishing procedures.—The effects of different polishing procedures on the photoresponse are illustrated in Fig. 3-6. The data presented in these figures were collected from electrodes made from the same titanium plate and oxidized under identical conditions (4h in air at 685°C).

The electrodes A, B, and C (Fig. 3 and 4) were prepolished with powders of grain sizes 150 μm (100 mesh), 50 μm (280 mesh), and 0.25 μm , respectively, before the oxidation procedure. Electrode D was subjected to the same prepolishing procedure as C, but after oxida-

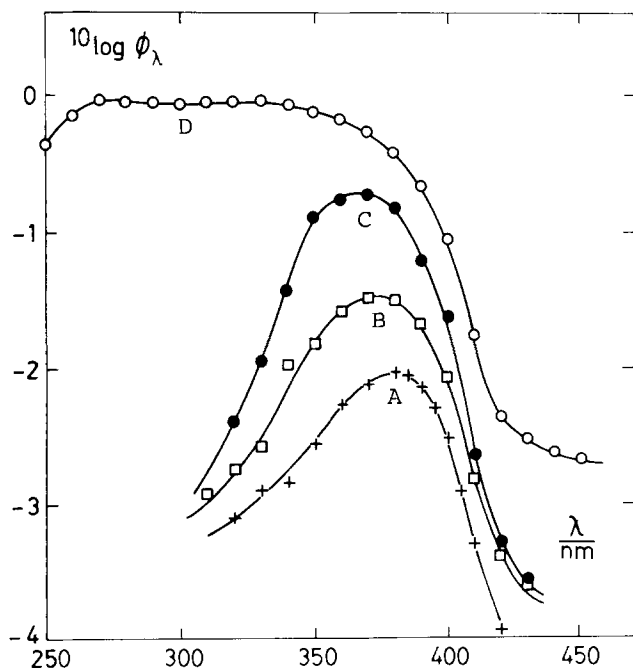


Fig. 3. Action spectra of polycrystalline TiO_2 electrodes showing the effect of different preparation procedures. Corresponding electrode surface profiles and detailed preparation parameters are given in Fig. 4.

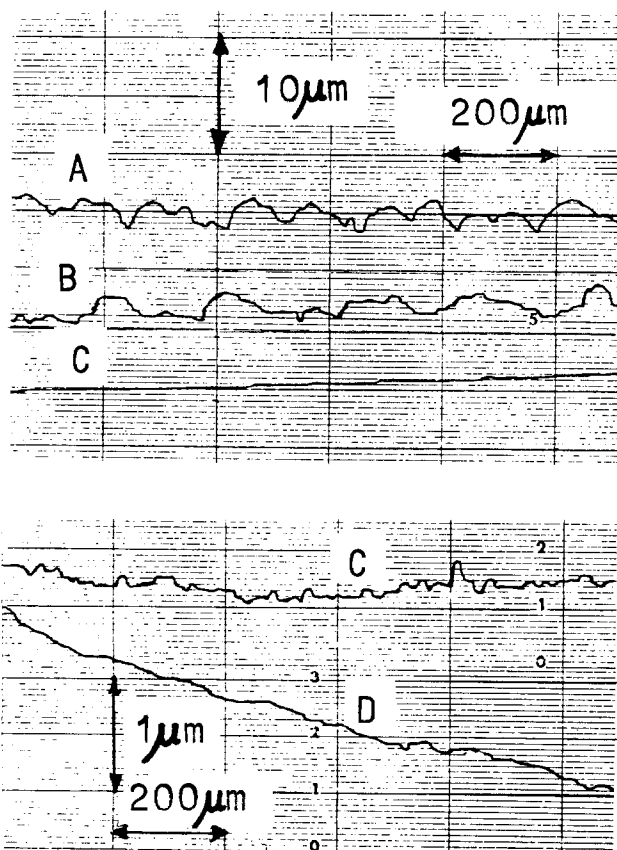


Fig. 4. Surface profiles of polycrystalline TiO_2 layer electrodes. The final polishing of the titanium plates before oxidation was made with the following grain sizes of the polishing media: A: 150 μm (100 mesh). B: 50 μm (280 mesh). C and D: 0.25 μm . After the oxidation procedure (4h at 685°C, air at 1 atm), D was polished to mirror brightness with 0.25 μm diamond paste.

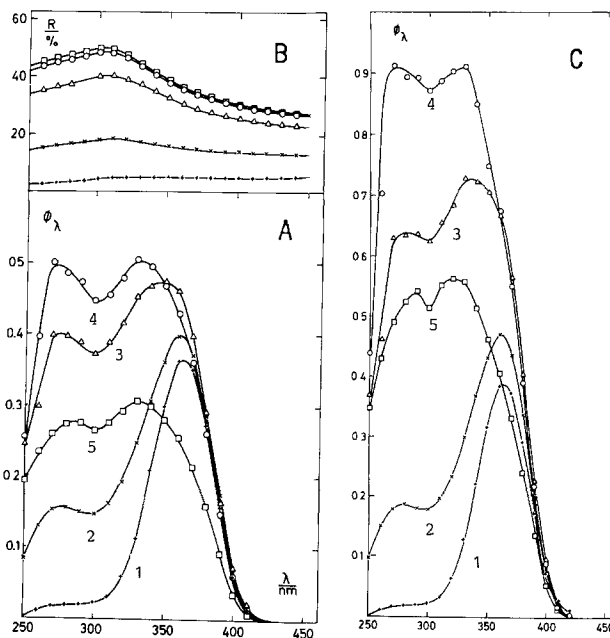


Fig. 5. The quantum efficiency (ϕ_λ) and the reflectance (R) as a function of wavelength (λ) of a polycrystalline TiO_2 electrode at different stages of surface finish. Corrections, except for reflection losses at the TiO_2 /electrolyte interface, had been made in A. In C, ϕ_λ has also been corrected for the specular reflection, as described in the text. Spectra of the unpolished electrode are in the different parts of the figure denoted with 1. Curves 2-5 represent different stages in the polishing procedure. The depth (d) of the layers, which decrease as the polishing proceeds, are given in Table II. The action spectra were all recorded at 1.0V vs. SCE at pH = 4.7. Note that the minima in the ϕ_λ curves coincide with the maxima in the reflectance spectra.

tion it was further polished with 0.25 μm diamond paste. The latter treatment will be discussed in detail below. The surface profiles of electrodes A-D are shown in Fig. 4. It is evident from these figures that there is a close connection between the surface structure and the registered changes in action spectra.

In addition to the overall decrease in quantum efficiency, a pronounced decrease in the efficiency of short wavelength light and a shift of the maximum towards longer wavelengths is registered with increasing surface roughness.

Figure 5 shows action spectra and reflectance spectra of a single polycrystalline TiO₂ electrode oxidized at 685°C for 4.0h in air at atmospheric pressure. This electrode was subject to successive surface polishing with 0.25 μm diamond paste after the oxidation. The polishing procedure was interrupted and the specular reflectance in air (Fig. 5B) and the action spectra were registered at five different stages of surface finish. From the interference pattern in the visible and infrared region of the reflectance spectra (not shown), the electrode thicknesses were determined as described above. The resulting film thicknesses, d , are collected in Table II.

In the action spectra shown in Fig. 5A, all corrections have been made except the correction for reflection losses at the TiO₂/electrolyte interface. The specular reflectance (Fig. 5B) was used to correct for these losses of light (see Fig. 5C). The latter correction is crude for two reasons: (i) the difference in refractive index between electrolyte and air has not been taken into account, and (ii) the diffuse part of reflection has been omitted.

As can be expected, the specular reflectance increases with polishing time. Curves 4 and 5 in Fig. 5B are almost identical, which indicates that the upper limit in specular reflection is reached. The reflectance at this stage is also very close to the value calculated from refractive index data given in the literature. The diffuse reflection is apparently very small and the electrode shows a mirror-like surface. The error introduced by omitting the diffuse reflectance at this stage is negligible. Note that the maxima in the reflectance spectra (at ca. 300 nm) correspond very well to the minima in quantum efficiency in curves 2-5 in Fig. 5A. For this reason, the minima in the corrected curves in Fig. 5C are less pronounced.

Examining the action spectra in the sequence from stage 1 to stage 5 (Fig. 5A and 5C), the following features are noticeable: (i) in spite of the increasing specular reflectance, the quantum efficiency in Fig. 5A increases with increasing polishing up to curve 4. The increase is most apparent in the range 250-300 nm. (ii) When the quantum efficiency decreases again (curve 5), the relatively larger quantum efficiency at short wavelengths persists and the spectrum more closely resembles curve 4 than curve 1. (iii) The edge of the action spectra just below the bandgap wavelength shifts towards longer wavelengths and then back again (curve 5) with increasing polishing.

As can be seen from Fig. 6, there is a marked increase in the sub-bandgap response after the first polishing procedure. The sub-bandgap response then remains fairly independent of further polishing.

Interpretation of action spectra.—Focusing our attention on the action spectra of the TiO₂ electrodes investigated in the present work, we will first consider the development of the TiO₂ layer as the oxidation proceeds. Starting with a highly polished Ti plate, a moderate oxidation (at low temperature for a short time) will result in a fairly smooth polycrystalline TiO₂ layer (Fig. 7A), in which the number of vacancies (or oxygen deficiencies expressed by y in TiO_{2-y}) rapidly increases inwards into the layer until the metal is reached. Thus an inhomogeneous doping density N_D will result. N_D will increase with the distance x from the surface. Increasing oxidation will give thicker TiO₂ layers (Fig. 7B and 7C), but also larger crystallites and a rougher surface. At high temperatures and long oxidation times, the rough surface region will be nearly completely oxidized. This means that the doping

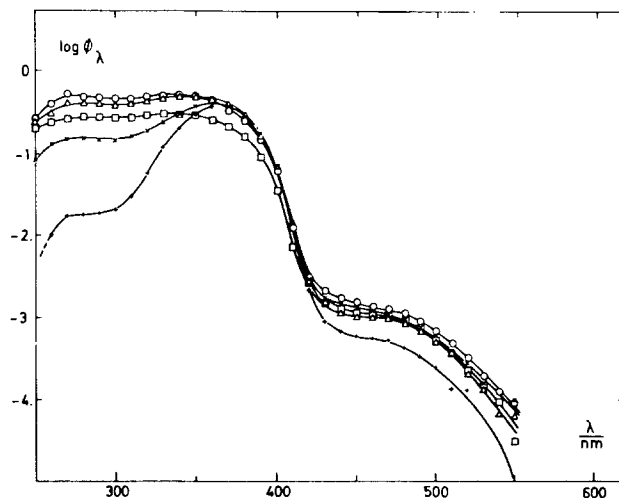


Fig. 6. Same action spectra as in Fig. 5A extended into the sub-bandgap region. Note the overall increase in sub-bandgap response after the first polishing procedure.

density N_D will be low at the surface and then gradually increase with layer depth, but now with a smaller gradient than in the case of the more moderately oxidized electrodes. Thus, the increase in efficiency with increasing oxidation for long wavelength light (with large penetration depth) can be qualitatively understood in terms of decreasing doping density, which results in a wider space-charge region.

Furthermore, as proposed by Harris and Wilson (15), electron-hole recombination in the poorly doped surface region could make this region function as an "inert" layer, which like an optical filter absorbs light without

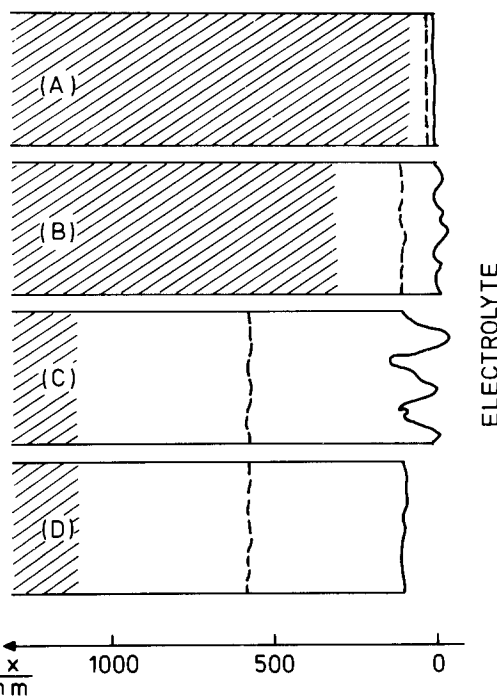


Fig. 7. Schematic representation of cross sections (normal to the macroscopic electrode surface) of TiO₂ layers formed by thermal oxidation of highly polished titanium plates. Shaded areas denote titanium, and unshaded TiO_{2-y}, where y is a small number representing oxygen deficiencies. y is a function of the distance (x) from the surface as described in the text. A-C illustrate the evolution of a layer electrode in a sequence of stronger oxidation conditions. The broken line gives the position of the border between the SCR and the bulk of the electrodes. Keeping the oxidation time constant, e.g., at 4h, A, B, and C may represent layers formed in air at ca. 500°, 600°, and 700°C, respectively. D shows the same electrode as C, but polished.

contributing to the photocurrent. The decreasing quantum efficiency (Fig. 2) of short wavelength light must, thus, according to this idea, be explained by electron-hole recombination in this surface "filter" region.

This is, however, not the only possible reason for low efficiency in the short wavelength range (250-300 nm) for the strongly oxidized titanium plate, e.g., electrodes prepared at temperatures above ca. 600°C (see Fig. 2). Recombination of charge carriers via states at the surface is another. Such states have been observed by a number of workers. For example, Sprünken *et al.* (14) and Wilson (38) have observed reduction peaks in their *i*-*V* curves just positive of the flatband potential. The reducible states observed by these workers were induced by light with energy exceeding the bandgap energy and at potentials positive of the flatband potential. The states were long lived and probably neutral (38). The observations of the referred author have been confirmed for polycrystalline TiO₂ electrodes at our laboratory. These experiments will be discussed further in a separate paper. Filling and unfilling such states may lead to recombination of electrons and holes.

At a rough, low doped surface (with irregular grains projecting into the electrolyte) a lateral transport of charge carriers to the interface is most probable [Compare the mechanism proposed by Lewerenz *et al.* for layered compounds (26).] Electrons and holes formed by short wavelength light will be generated predominantly in this low doped rough region and experience any field built up at the interface by surface states. Even if the bandbending is high deep in the electrode, at strong positive polarization (see Fig. 8), and a good charge separation is at hand in this particular region of the electrode, the photogenerated charge carriers in the low doped rough surface will experience not this field, but, rather, the field built up by the surface states. At positive polarization, the holes formed deep in the electrode, in the depletion layer, will be forced to the surface and the surface will become saturated with "oxidized" surface states. In the field created by these surface states, photoexcited electrons formed in the rough surface region will be

drained to the surface and consumed in a cathodic backreaction. The resulting "reduced" surface state will be rapidly reoxidized, since there is an excess of holes reaching the surface. The recombination thus mediated by the surface states will be experimentally registered as a decrease in quantum efficiency in the short wavelength range.

A mechanism such as the one proposed above may also explain the changes in action spectra with increasing TiO₂ layer thickness registered by Möllers *et al.* (7). Their TiO₂ layer electrodes made by chemical vapor deposition (CVD) show a similar decrease in quantum efficiency at short wavelengths with increasing layer thickness as observed for the electrodes in the present work (Fig. 2).

The aging experiment of reduced single-crystal TiO₂ electrodes performed by Harris and Wilson (15) shows that the surface roughness increases with time when the electrodes are illuminated under polarization. This increased surface roughness may be connected with the decrease in photocurrent below 300 nm. The red shift in spectral response registered by Harris and Wilson (15) and by Liou *et al.* (16) seems also to be associated with a decrease in doping density of the reduced electrodes in the course of the aging under illumination, as discussed by Butler (17).

The effects of different polishing and etching procedures of single-crystal TiO₂ electrodes reported by Wilson *et al.* (1) are somewhat puzzling. They propose in their report that mechanical polishing produces near the surface of the electrode a disturbed layer which (in contrast to the polycrystalline electrodes of the present work, Fig. 5) decreases the quantum efficiency in the entire spectral range observed. The sub-bandgap response observed at the polycrystalline TiO₂ electrodes in the present work (Fig. 6) and by Chang *et al.* (40) at polycrystalline SrTiO₃ might indicate a shearing of the crystallites during the polishing procedure. This shearing might, as proposed by Chang *et al.*, introduce new bulk levels in the bandgap.

The action spectra of single-crystal electrodes given by Wilson (1) also reveals that etching in molten NaOH gives a decrease in photoresponse in the short wavelength range, in much the same way as found for rough electrodes in the present work, while etching in sulfatesulfuric acid at 340°C does not. Only a more detailed analysis can clarify if these differences can be referred to differences in surface morphology.

A semiempirical equation to describe the action spectra.—An equation that fully describes the action spectra of the TiO₂ electrodes of the present work should include parameters that account for (i) a gradient in doping density normal to the electrode surface, (ii) recombination via surface states and via reactions at the surface, (iii) recombination in the bulk of the electrode as well as in the space-charge region (SCR) and in "the rough surface region," and (iv) effects of the variation of the morphology of the surface.

Models dealing with these phenomena have been proposed (20-24). Wilson (20) has considered surface recombination. Reichmann (21) has given a model for recombination in the SCR. In a recent paper, Allongue *et al.* (22) have incorporated both recombination in SCR and at the surface in a detailed analysis of redox stabilization of liquid-junction solar cells. Schoonman *et al.* (23) discussed the effect of surface roughness, and presented a modified Mott-Schottky equation to account for the lower donor density in a region near the surface of the electrode. None of the models fulfill all the demands stated above at the same time. A complete description of the action spectra in terms of existing models is thus not easily achieved. A combination of existing models would result in an equation with a large number of parameters. It is doubtful if adjusting experimental data to such an equation is meaningful.

We have therefore chosen to describe registered spectra in a simple "semi-empirical" equation. The quantum efficiency was thus expressed by

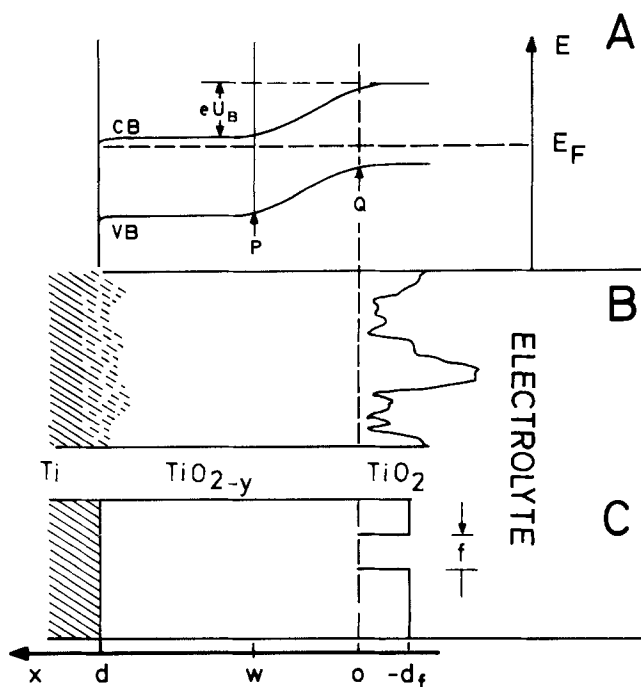


Fig. 8. A model of the TiO₂ layer electrode prepared by thermal oxidation of titanium. A shows the energy (*E*) diagram with the valence band (VB), the conduction band (CB), the Fermi level (*E_F*), and the band bending (eU_B). B visualizes a "real" electrode as illustrated in Fig. 7. C shows the corresponding idealized model on which Eq. [2] is based. The symbols (the layer thickness, *d*, the depletion layer width, *w*, the "recombination layer," *d_f*, the fraction of the surface not covered with the "recombination layer," *f*) as well as P and Q are all explained in the text.

$$\phi_\lambda = [f + (1 - f) \exp(-\alpha_\lambda d_r)] [1 - \exp(-\alpha_\lambda w)] \quad [2]$$

This equation is based on the well-known Gärtner-Butler expression (18, 19) and the proposed picture of the physical structure and energetic situation at the interface, as illustrated in Fig. 8. The figure shows a cross section (normal to the macroscopic surface) of an electrode prepared by thermal oxidation. Assuming an increase in doping density normal to the electrode surface, as discussed above, no simple expression for the depletion layer width, w , can be used. For our further discussion of the registered variation in the action spectra, however, such an equation need not necessarily be formulated. Assuming the existence of a smallest gradient in potential dU/dx needed to effectively separate photoinduced electron-hole pairs, we can at a given electrode potential choose to define w as a region, *e.g.*, between P and Q (see Fig. 8A), where this condition is fulfilled.

In Eq. [2], the concept of a "recombination layer,"¹ d_r , is introduced. The "recombination layer" is here defined as the region of the electrode, close to the surface, from which there is no net contribution to the photocurrent. As discussed above, recombination of charge carriers photo-generated in the rough surface region, via surface reactions, is a most probable process. If the recombination takes place via surface reactions, as proposed, or in the rough surface region itself, has, however, not been regarded in Eq. [2].

The parameter f has been introduced to account for the fraction of the surface not covered by the "recombination layer."

Figure 8B shows a "real" interfacial region, and Fig. 8C a model visualizing the parameters d_r and f in Eq. [2].

The absorption coefficient, α_λ , was in the indirect transition region 410-335 nm calculated from (13, 31)

$$\alpha_\lambda = B \frac{(h\nu - E_g)^2}{h\nu} \quad [3]$$

where h is Planck's constant, ν the frequency of the light, and E_g the bandgap. B is a constant which was adjusted to fit experimental data of α_λ , as described below.

The diffusion length of minority carriers, L_p , in polycrystalline materials is usually small. The Gärtner equation (18) has thus in Eq. [2] been approximated by assuming $\alpha_\lambda \times L_p \ll 1$. It can be argued that the approximation is not fully justified, especially in the short wavelength range, where the absorption coefficient is large. In the case of the investigated electrodes, short wavelength light will, however, be preferentially absorbed in the "recombination layer" and the depletion layer, and only to a minor extent contribute to diffusion currents. At wavelengths < 335 nm, the penetration depth $1/\alpha_\lambda$ is smaller than 100 nm (31, 13), a depth that can be judged to be in the range of, or smaller than, the sum of d_r and w for the investigated electrodes. Although not conclusive, the outcome of the calculations justifies the approximation for most of the electrodes, *vide infra* Tables I and II.

Application of Eq. [2] to experimental data.—Absorption coefficient data from both Cardona (31) and Lindquist *et al.* (13) were alternatively used. Different E_g values in the range 2.95-3.05 eV were used to calculate α_λ values from Eq. [3] in the range 340-400 nm.

The solid lines in Fig. 2 are the best fit of Eq. [2] to the experimental data in the range 300-400 nm.² The value of α_λ used in these calculations were in the range 340-400 nm determined from Eq. [3]. $E_g = 3.03$ eV and $B = 8.2 \times 10^7$ m⁻¹eV⁻¹ were used. Otherwise, the α_λ values were taken from Ref. (13). Resulting values of w , d_r , and f are col-

lected in Table I. Note that both d_r and w increase with increasing layer thickness d .

As can be seen from Table I, the parameter f reaches a maximum value of 0.063 (704°C, 0.50h). However, Eq. [2], with $f = 0$, fits the data almost equally well. The significance of f can therefore be discussed.

When interpreting the values in Table I, it should be remembered that the corrections for the reflection at the TiO₂/electrolyte interface have not been made.

In addition to the spectra shown in Fig. 5, which were recorded at 1V *vs.* SCE, action spectra were also registered at another five different electrode potentials at each stage of polishing. Two main sets of minimization calculations were made to adjust Eq. (2) to these data: (i) only d_r and w were adjusted, and f was fixed at zero, and (ii) all parameters (f , d_r , and w) were adjusted. Only the results of one of the sets of minimization calculations on the data from the polished electrode (compare Fig. 5), keeping f constant, will be discussed in some detail. Table II summarizes, as an example, a set of such runs on corrected ϕ_λ values (see Fig. 5C), in which f in Eq. [2] was fixed at zero. It can be deduced from Table II and Fig. 9 that the d_r values are almost independent of the electrode potential. The d_r values also decrease with decreasing layer thickness (that is, increased mechanical polishing). A minor increase in d_r is however found for the thinnest (837 nm) layer. The depletion layer width, w , at each stage of polishing increases with increasing electrode potential, as expected. The unpolished electrode gives the highest w values (see Fig. 9B). The w values then decrease with polishing. It is interesting to note (see Table II) that the change in layer thickness of the electrode and the decrease in d_r are of the same magnitude and that d_r is almost zero at stage 4—a fact which might indicate that the "recombination layer" has been polished away. On further polishing, the d_r values remain low and a noticeable decrease in w is registered (899 nm curve, Fig. 9). The latter, as mentioned, is consistent with a doping density gradient normal to the layer of the thermally grown TiO₂ electrodes.

In Fig. 9B, it is seen that the w values achieved in the calculations at each stage of polishing are gathered around lines which can be extrapolated close to or just above the flatband potential ($U_{FB} \sim -0.5$ V at pH = 4.7) (41-43). The main features of all runs with f fixed at zero were the same and independent of the set of α_λ values used.

Allowing all three parameters, f , d_r , and w , in Eq. [2], for the same set of data as used above, to be adjustable in the minimization gives a somewhat better fit of the calculated curve to the experimental data in Fig. 5C. The parameters f increases regularly, being only a few percent for the unpolished electrode and reaching approximately 90% at stage 4 in the polishing procedure. The values of w and d_r are at each polishing step both larger than in Table II (f fixed at zero). The w values increase in much the same way, as shown in Fig. 9. The values of d_r at each stage of polishing are surprisingly constant. A more complete description of the calculations is given in Ref. (39).

Summary

In an attempt to clarify the origin of the frequently observed variations in the distribution of the quantum efficiency of polycrystalline TiO₂ electrodes, action spectra and surface profiles from electrodes prepared under different conditions were registered. Three main sets of experiments were made: (i) highly polished titanium plates were oxidized at different temperatures and periods of time. Action spectra were registered. (ii) The surface of a few electrodes were deliberately made rough before oxidation by polishing with powders of larger grain sizes. The conditions of oxidation were kept constant. Action spectra (Fig. 3) and surface profiles (Fig. 4) were registered. (iii) A TiO₂ electrode with a rough surface was in a sequence of experiments carefully polished. Action spectra and reflectance spectra were recorded after each polishing procedure (Fig. 5 and 6).

¹ The name "recombination layer" (instead of "dead layer") has been used to emphasize the mechanism by which the photocurrent is believed to be suppressed, and to avoid the impression of a layer impenetrable for charge carriers.

² A computer program, UNIFIT, written by Peter Stilbs (Institute of Physical Chemistry, S-751 21 Uppsala, Sweden), was used. UNIFIT utilized the general minimization routine stepit version 7.4, written by J. P. Chadler, Department of Computer Science, Oklahoma State University, Stillwater, Oklahoma.

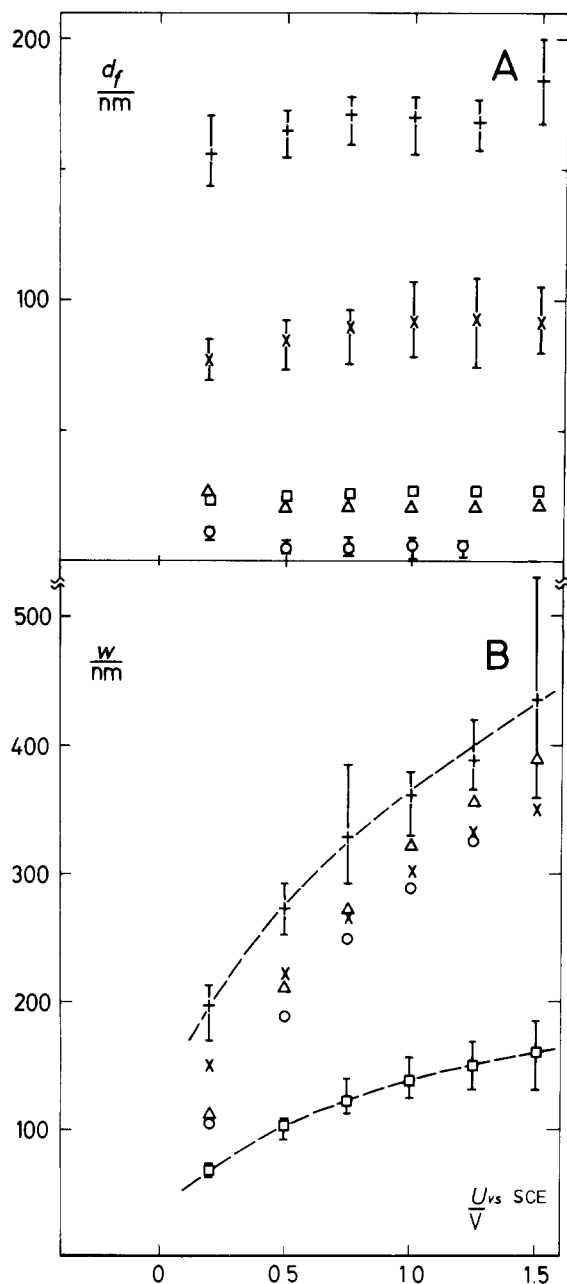


Fig. 9. The adjustable parameters d_f and w in Eq. [2] at five different stages of surface finish of the TiO_2 electrode, as a function of electrode potential U vs. SCE. The parameter f was fixed at zero. The layer thicknesses were: + 104, nm, \times 99, nm, \triangle 95, nm, \circ 89, nm, and \square 83, nm. The two lines drawn in that diagram are given to visualize the possible extrapolation to U_{FB} . For clarity, some error bars have been omitted.

It is evident from these experiments that the surface morphology of polycrystalline TiO_2 layer electrodes, prepared by thermal oxidation of titanium plate, is of the utmost importance for the performance of the electrode. As shown by other workers (3, 4) and in the present work, the spectral distribution of the quantum efficiency is for this reason strongly dependent on oxidation conditions. With increasing oxidation of highly polished titanium plates, the electrode surface gets rougher and a gradual decrease in quantum efficiency in the short wavelength range (250-300 nm) is registered. In this work, we have shown that the treatment of titanium plate prior to the oxidation procedure is also of importance. Starting with an already rough titanium surface before oxidation results in very poor photoresponse. Of more interest, however, is that careful surface polishing of the TiO_2 layer with a rough surface (e.g., formed at 700°C) gives a dramatic increase in photosensitivity of the electrode, especially in the short wavelength range.

To explain the observed changes in the action spectra and relate them to experimental data the effects of recombination of charge carriers, photogenerated in the rough surface region, was considered. It was proposed that the charge carriers, photogenerated in the low doped surface region of the electrode, are laterally transported to the interface. At a positive polarization of the electrode, the surface is saturated by "oxidized" surface states. In the field created by these states, the electrons photoexcited in the rough surface region are drained to the surface, where they are consumed in cathodic backreactions. As short wavelength light has small penetration depth in TiO_2 , it is mainly absorbed in the rough region. Thus, the quantum efficiency in the short wavelength range will decrease comparatively more than in the long wavelength range even at electrode potentials well positive of the flatband potential.

The action spectra were described by a modified Gärtner-Butler equation at different stages of oxidation and polishing of the electrodes. The best fit of the equation gave reasonable values of the adjustable parameters, although the significance of the parameter f can be discussed in some cases.

The increase in quantum efficiency in the range 250-300 nm due to the polishing of the polycrystalline TiO_2 electrodes prepared by thermal oxidation, is in contrast with what has been observed with SrTiO_3 (40) and TiO_2 single crystals (44). The changes in sub-bandgap response upon polishing are, however, the same.

The increase in quantum efficiency achieved by surface polishing is probably not unique for polycrystalline TiO_2 layer electrodes. Surface polishing can be expected to be equally important for the photoresponse of other commonly used polycrystalline electrode materials. Work in this direction is in progress.

Acknowledgments

We thank Dr. C-G. Ribbing and his colleagues at the Institute of Technology, Uppsala University, Uppsala Sweden, for their assistance in the optical measurements and research engineer Kjell Magnusson (at the same institute) who performed the surface profile measurements. This work was supported by the Swedish Natural Science Research Council. A grant from the Swedish Institute (SI) made Zhu Yan-Ning's visit in Uppsala possible.

Manuscript submitted Nov. 29, 1982; revised manuscript received Oct. 1, 1984.

The Institute of Physical Chemistry assisted in meeting the publication costs of this article.

REFERENCES

1. R. H. Wilson, L. A. Harris, and M. E. Gerstner, *This Journal*, **126**, 844 (1979).
2. M. P. Dare-Edwards and A. Hamnett, *J. Electroanal. Chem.*, **105**, 283 (1979).
3. Y. Matsumoto, J. Kurimoto, Y. Amagasaki, and E. Sato, *This Journal*, **127**, 2148 (1980).
4. K. Yazawa, H. Kamogawa, and H. Morisaki, *Int. J. Hydrogen Energy*, **4**, 205 (1979).
5. J. G. Mavroides, D. I. Tchernev, J. A. Kafalas, and D. F. Kolesar, *Mater. Res. Bull.*, **10**, 1023 (1975).
6. J. G. Mavroides, *ibid.*, **13**, 1379 (1978).
7. F. Möllers, H. J. Tolle, and R. Memming, *This Journal*, **121**, 1160 (1974).
8. J. F. McAleer and L. M. Peter, *ibid.*, **129**, 1252 (1982).
9. J. F. Houlihan, R. F. Bonaquist, R. T. Dirstine, and D. P. Madacsi, *Mater. Res. Bull.*, **16**, 659 (1981).
10. J. F. Julião, F. Decker, and M. Abramovich, *This Journal*, **127**, 2264 (1980).
11. J. Gautron, P. Lemasson, and J. F. Marucco, *Faraday Discuss.*, **70**, 81 (1980).
12. A. K. Ghosh and H. P. Maruska, *This Journal*, **124**, 1516 (1977).
13. S.-E. Lindquist, B. Finnström, and L. Tegner, *ibid.*, **130**, 351 (1983).
14. H.-R. Sprünken, R. Schumacher, and R. N. Schindler, *Faraday Discuss.*, **70**, 55 (1980); *Ber. Bunsenges. Phys.*

- Chem.*, **84**, 1040 (1980).
15. L. A. Harris and R. H. Wilson, *This Journal*, **123**, 1010 (1976).
 16. Fu-Tai Liou Ciang, Y. Yang, and S. N. Levine, *ibid.*, **130**, 893 (1983).
 17. M. A. Butler, *ibid.*, **126**, 338 (1979).
 18. W. W. Gärtner, *Phys. Rev.*, **116**, 84 (1959).
 19. M. A. Butler, *J. Appl. Phys.*, **48**, 1914 (1977).
 20. R. H. Wilson, *ibid.*, **48**, 4292 (1977).
 21. J. Reichman, *Appl. Phys. Lett.*, **36**, 574 (1980).
 22. P. Allongue, H. Cachet, and G. Horowitz, *This Journal*, **130**, 2352 (1983).
 23. J. Schooman, K. Vos, and G. Blasse, *ibid.*, **128**, 1154 (1981).
 24. H. Reiss, *ibid.*, **125**, 937 (1978).
 25. B. A. Parkinson, A. Heller, and B. Miller, *ibid.*, **126**, 954 (1979); *Appl. Phys. Lett.*, **33**, 521 (1978).
 26. H. J. Lewerenz, A. Heller, and F. J. DiSalvo, *J. Am. Chem. Soc.*, **102**, 1877 (1980).
 27. R. Tenne, Y. Mirovsky, Y. Greenstein, and D. Cahen, *This Journal*, **129**, 1506 (1982).
 28. A. Hamnett, in "Photogeneration of Hydrogen," A. Harriman and M. A. West, Editors, p. 147, Academic Press, London (1982).
 29. S.-E. Lindquist, C. Edström, and A. Lindgren, "Origin of Bandshifts in the Action Spectra of Polycrystalline TiO₂ Layer Electrodes Prepared by Thermal Oxidation. I." Internal report.
 30. G. Hass, *Vacuum*, **2**, 329 (1952).
 31. M. Cardona and G. Harbecke, *Phys. Rev. A*, **137**, 1467 (1965).
 32. D. E. Stilwell and Su-Moon Park, *This Journal*, **129**, 1501 (1982).
 33. P. Kofstad, K. Hauffe, and H. Kjöllesdal, *Acta Chem. Scand.*, **12**, 239 (1958).
 34. P. Kofstad, P. G. Anderson, and O. J. Krudtaa, *J. Less-Common Met.*, **3**, 89 (1961).
 35. M. Dechamps and P. Lehr, *ibid.*, **56**, 193 (1977).
 36. H. Gerischer, in "Advances in Electrochemistry and Electrochemical Engineering," Vol 1, P. Delahay, Editor, p. 139, Interscience, New York (1961).
 37. P. A. Kohl and A. J. Bard, *J. Am. Chem. Soc.*, **99**, 7531 (1977).
 38. R. H. Wilson, *This Journal*, **127**, 228 (1980).
 39. S.-E. Lindquist, A. Lindgren, and Zhu Yan-Ning, "Origin of Bandshifts in the Action Spectra of Polycrystalline TiO₂ Electrodes Prepared by Thermal Oxidation of Titanium. II. Effects of Surface Polishing." Internal report.
 40. B. T. Chang, G. Campet, J. Claverie, P. Hagenmuller, and J. B. Goodenough, *J. Solid State Chem.*, **49**, 247 (1983).
 41. B. Reichman and C. E. Byvik, *This Journal*, **128**, 2601 (1981).
 42. J. F. McCann and J. Pezy, *ibid.*, **128**, 1735 (1981).
 43. J. M. Bolts and M. S. Wrighton, *J. Phys. Chem.*, **80**, 2641 (1976).
 44. P. Salvador, *J. Appl. Phys.*, **55**, 2977 (1984).

Technical Notes



The Electrochemical Oxidation and Polymerization of Polycyclic Hydrocarbons

Robert J. Waltman and A. F. Diaz*

IBM Research Laboratory, San Jose, California 95193

Joachim Bargon

Institut für Physikalische Chemie, Universität Bonn, 5300 Bonn-1, Germany

The electrochemical oxidation reactions of polycyclic aromatic hydrocarbons are complex and usually irreversible (1,2). Although the more usual reaction pathway is the formation of soluble products whereby $n = 1$ (1), some compounds will undergo multielectron oxidations (2). In most cases, their oxidation is inevitably coupled with a rapid irreversible chemical reaction. This is often further complicated by the formation of an insulating film on the electrode surface. For example, the electro-oxidation of pyrene or triphenylene gives rise to such films (2). While formation of these films have often been ignored, it is only recently that interest has actually shifted to these films. For example, the recent finding that the polycyclic nonbenzenoid hydrocarbon azulene undergoes electrochemically induced polymerization (3-8) and, furthermore, that its polymer films are electrically conducting ($10^{-2} - 1$ S/cm) and display electrochromic behavior (8) has stimulated an investigation of the polymerization aptitude of other aromatic hydrocarbons. The electrical properties that these materials possess have been of interest both for the case of the polycyclic hydrocarbons which display modest intrinsic electrical conductivity (9) and their crystalline radical cation salts which exhibit high electrical conductivities (10). Accordingly, we report

*Electrochemical Society Active Member.

herein electropolymerization studies of the polycyclic hydrocarbons pyrene, triphenylene, fluorene, and fluoranthene. In considering the oxidation reactions of these compounds and the properties of their corresponding polymer films, pyrene is found to be considerably different from the other three aromatic compounds.

Experimental

All monomers were obtained from commercial sources and recrystallized prior to use. Electrochemical measurements were achieved in a three-electrode, single- or two-compartment cell using platinum, gold, and a saturated sodium chloride calomel (SSCE) as the working, counter, and reference electrodes, respectively. The solutions typically contained $10^{-3}M$ of monomer in 0.1M tetraethyl ammonium fluoroborate (TEAFB)/acetonitrile solution. The acetonitrile (Burdick and Jackson, spectrometric grade) was used as obtained without further purification. The electrical conductivities of pressed pellets were measured utilizing a Magne-Tron Instruments Model 700 four-probe apparatus.

Results and Discussion

Electro-oxidation reaction.—The electro-oxidation reactions of the four polycyclic hydrocarbon compounds

Table I. Cyclic voltammetric data for 2.5-4.0 $\mu\text{mol}/\text{cm}^3$ of compound in 0.1M TEAFB/acetonitrile. Sweep rate equals 40 mV/s.

Compound	E_{pa} (V)	$i/AC\nu^{1/2}$ ($\text{A} \cdot \text{cm} \cdot \text{mol}^{-1/2} \text{V}^{-1/2}$)	n^a	n^b
Pyrene	1.33	2003	1.7	^c
Pyrene ^d	1.30	2034	1.7	2.31
Fluorene	1.82	3676	2.5	2.23
Fluoranthene	1.68	2726	2.0	2.28
Triphenylene	1.83	4155	2.7	2.20

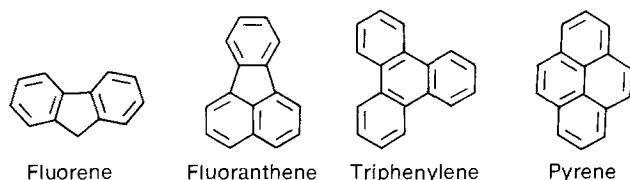
^a Value from cyclic voltammetry.

^b Value calculated using elemental analysis data.

^c No analysis due to poor quality of film.

^d Measured using perchlorate electrolyte.

shown below were measured using TEAFB electrolyte. These data are summarized in Table I. All of the compounds electro-oxidize irreversibly, and produce complicated cyclic voltammograms. The voltammograms



contain multiple peaks which are broad and overlapping. Even the first oxidation wave for all of the compounds listed in Table I is ill-defined and occurs as a shoulder on a much larger peak, which probably results from the oxidation of the polymeric product being formed on the electrode surface. The current response for the first oxidation reaction of pyrene, although a shoulder, is more distinguishable than with the other compounds. The voltammogram shown in Fig. 1 was measured using TEAFB and provides a value for E_{pa} of 1.33V. The oxidation of pyrene was also measured using tetrabutylammonium perchlorate electrolyte. The resulting voltammogram is very similar to that with the TEAFB electrolyte, but the E_{pa} value is slightly shifted to 1.30V. This result is not unexpected since our experiences with the electro-oxidation of azulene (5), pyrrole (11, 12), and thiophene (6) have revealed that the electropolymerization reaction is insensitive to the difference between the BF_4^- and the ClO_4^- electrolyte. The E_{pa} value for pyrene of 1.30V compares well with a previous literature value (2) of 1.24V (in a perchlorate/acetonitrile solution). Since it is known that the E_{pa} value for EC reactions are slightly dependent on both solution concentrations and sweep rate (13), reproducibility of the E_{pa} values for these polycyclic hydrocarbon compounds is not expected to be better

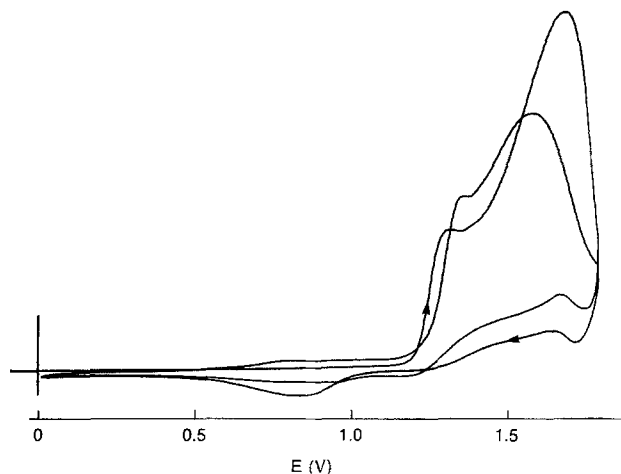


Fig. 1. Cyclic voltammogram of 3 $\mu\text{mol}/\text{cm}^3$ pyrene in 0.1M TEAFB/ CH_3CN at sweep rate of 100 mV/s, with 60% iR compensation.

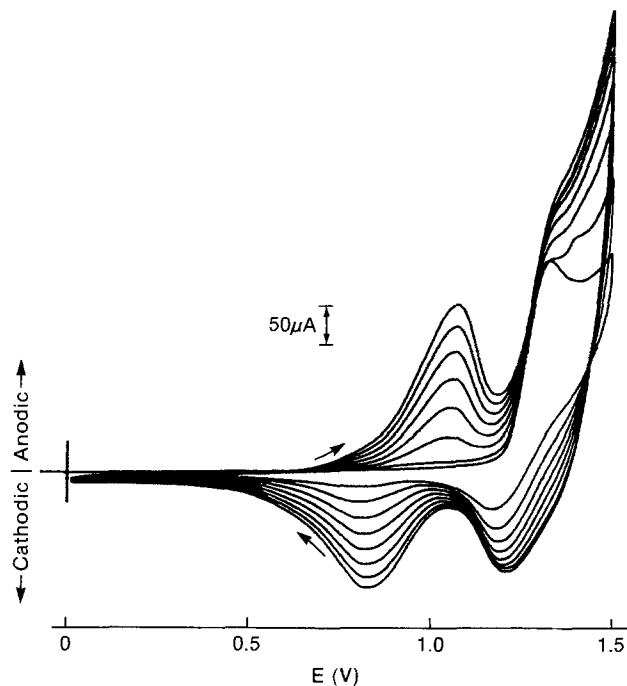


Fig. 2. Cyclic voltammogram of 3 $\mu\text{mol}/\text{cm}^3$ pyrene in 0.1M TEAFB/ CH_3CN at sweep rate of 200 mV/s, with 60% iR compensation. Successive sweeps reveal growth of polymer film on electrode surface.

than ± 10 to 20 mV, unless all experimental parameters are identical (13). The n value of the first oxidation peak for pyrene was estimated utilizing the Nicholson and Shain treatment (14) for a totally irreversible oxidation reaction. The diffusion constant was assumed to be $D = 2 \times 10^{-5}$ and $\alpha = 0.5$. The same n value of 1.7 was obtained with both the BF_4^- and the ClO_4^- electrolyte. This value is low (less than 2.0) and suggests that only a fraction of the monomer electropolymerizes. As is shown below, only half of the reaction produces film on the electrode. Because the electro-oxidation reaction of these compounds produces polymeric films on the Pt anode, each successive sweep in the cyclic voltammogram is different due to a buildup of polymer film. This is seen in Fig. 2 for pyrene in 0.1M TEAFB/acetonitrile, where the peaks for the oxidation-reduction reaction of the film product increase and there is a corresponding distortion of the current response for the oxidation of pyrene.

The E_{pa} values for fluorene, fluoranthene, and triphenylene are more difficult to determine, even at very slow sweep rates. For these three compounds, the E_{pa} values were estimated by deconvolution and, therefore, should be considered to be approximate. However, they appear to be consistent with literature values (15). The n values for fluorene, fluoranthene, and triphenylene are 2.5, 2.0, and 2.7, respectively. These values are consistent with values obtained for other film forming reactions (6, 17) and suggest that, within experimental error, the reaction that produces polymer film is the only reaction and it has a value for n equal to 2. As with pyrene, the buildup of the polymer film on the electrode can be followed in their cyclic voltammograms by successive cycles.

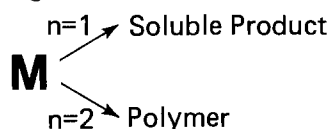
Polymeric films.—At constant potential electro-oxidation of the monomers, thicker films deposit at the electrode surface. Upon drying, these thick polymeric films become brittle and crack easily. They can be scraped off from the electrode surface to yield black, amorphous powders. The elemental composition of these materials indicate that the polymeric films are polymer-anion composites which contain ca. 12% anion by weight (Table II). This corresponds to a stoichiometry of 0.2-0.3 anions per repeating aromatic unit. This stoichiometry is in the range observed for the conducting polypyrrole films (12)

Table II. Elemental composition and electrical conductivity (σ) for some polymers derived from polycyclic hydrocarbons

Monomer	Polymer composition	σ (S/cm)
Pyrene (C ₁₆ H ₁₀)	C _{16.0} H _{12.0} (ClO ₄) _{0.31}	10 ⁻¹⁻¹
Fluorene (C ₁₃ H ₁₀)	C _{13.0} H _{9.3} (BF ₄) _{0.23}	10 ⁻⁴
Fluoroanthrene (C ₁₆ H ₁₀)	C _{16.0} H _{9.6} (BF ₄) _{0.28}	10 ^{-6-10⁻³}
Triphenylene (C ₁₈ H ₁₂)	C _{18.0} H _{11.4} (BF ₄) _{0.20}	10 ⁻⁴

and polyazulene films (5), but is higher than the stoichiometry found for the conducting polythiophene films (8). From these results, n values of 2.23, 2.28, and 2.20, can be calculated for the reactions producing polyfluorene-BF₄, polyfluoroanthrene-BF₄, and polytriphenylene-BF₄, respectively. These values are somewhat smaller than those estimated from the electrochemical data and are still consistent with the range of values obtained for other electropolymerization reactions of aromatic heterocyclic compounds (3). For example, pyrrole (16), thiophene (8), azulene (6), indole (17), or carbazole (18) all electropolymerize with n values between 2.0 and 2.8.

The tetrafluoroborate film of polypyrene, *i.e.*, polypyrene-BF₄, was much too brittle to handle. Therefore, the perchlorate film was prepared for elemental analysis. From this analysis, the stoichiometry of 0.31 anions/aromatic unit and an n value of 2.31 for the film forming reaction is calculated. This value which is a closer estimate of the electrochemical stoichiometry of the film forming reaction is greater than the n value for the overall reaction, 1.7. This difference may result from the presence of competitive reaction pathways with different electrochemical stoichiometries and different products, *e.g.*, polymer *vs.* soluble products. Thus, in the electro-oxidation of pyrene, film formation on the electrode surface occurs, but the solution also becomes discolored, indicating the production of soluble products. Since n_{app} (1.7) for the total reaction, and n_p (2.31) for the film forming reaction are known for pyrene, the fraction of pyrene which leads to polymer can be estimated, assuming that reaction leading to the formation of the soluble product, *i.e.*, dimerization, has an $n_s = 1$ (19), and that it is the only competing reaction.



Thus, if f is the fraction of pyrene which electropolymerizes, then $(1 - f)$ is the fraction which forms soluble species, and the following relationship can be written

$$n_{app} = n_p f + n_s(1 - f) \quad [1]$$

Thus, considering the above values, the fraction of pyrene which gives rise to polypyrene is 0.54, *i.e.*, only half of the reaction yields polymer film during electro-oxidation. The separation of the first peak in the voltammogram for pyrene, which is not observed with the other compounds, may simply be due to smaller current levels for the film products due to their low yield.

The elemental compositions of the polymers also reveal that they are all somewhat hydrogen-rich. Polypyrene is again different from the other polycyclic hydrocarbon polymers in that it is highly hydrogenated. The C/H elemental ratio for this compound is 16/12 and is consistent for an oligomer of polymeric material whereby the pyrene structure is *bis*-coupled and has two double bonds hydrogenated. The amount of hydrogen in the film produced from fluorene, fluoroanthrene, and triphenylene is also high. It is 10%-20% higher than the amount anticipated for a polymer or for a blend of low molecular weight oligomers where the aromatic rings are simply *bis*-coupled. The structure of these polymeric materials remains to be determined.

Of particular concern with polypyrene is the large excess of hydrogen content as revealed by the elemental

analysis data. The ESCA results of neutral polypyrene-BF₄ revealed the presence of only C and O, and the absence of any N or F. The absence of F is certainly expected in the neutral polymer, whereby an ionic complex is not formed with the BF₄ electrolyte. The lack of nitrogen reveals no contribution from alkyl ammonium ions or acetonitrile, both of which could be a source of high H content. The ESCA results also reveal the presence of oxygen uptake at the surface of the neutral film. For pyrene, an oxygen content of 0.3-1.3 oxygens per sixteen carbons (*i.e.*, one pyrene unit) is revealed.

The films are also electrically conducting, and the conductivity of the pressed pellets is summarized in Table II. Again, polypyrene is unique in that its electrical conductivity is in the range of 0.1-1 S/cm, similar to polythiophene (20) and polyazulene (5). The same conductivity level was measured for both the perchlorate and tetrafluoroborate film. The polyfluorene, polyfluoroanthrene, and polytriphenylene films are not as conducting and have values in the range 10⁻⁵-10⁻³ S/cm.

Scanning electron micrographs (SEM) for polyfluorene-BF₄, polyfluoroanthrene-BF₄, polytriphenylene-BF₄, and polypyrene-BF₄ are shown in Fig. 3. The brittle character of the polymer films can be seen in the SEM of polyfluorene-BF₄, where the cracking can be clearly seen. Otherwise, all exposures show nonspecific amorphous surface features found previously in polypyrrole (14), polythiophene (20), and polyazulene (5). Before any practical application can be considered for these materials, their intrinsic brittleness must be overcome. Although the mechanical properties of these films is not the subject of this paper, such properties may be improved by combining these electrically conducting polymers with an otherwise insulating, compatible matrix polymer with appropriate mechanical properties. For example, we have found (21) that incorporation of an electrically conducting polymer such as polypyrrole (PPY) into polyvinyl chloride (PVC), which has excellent mechanical properties, yields a composite material with the following properties: its electrical conductivity is governed predominantly by the PPY content, whereas the

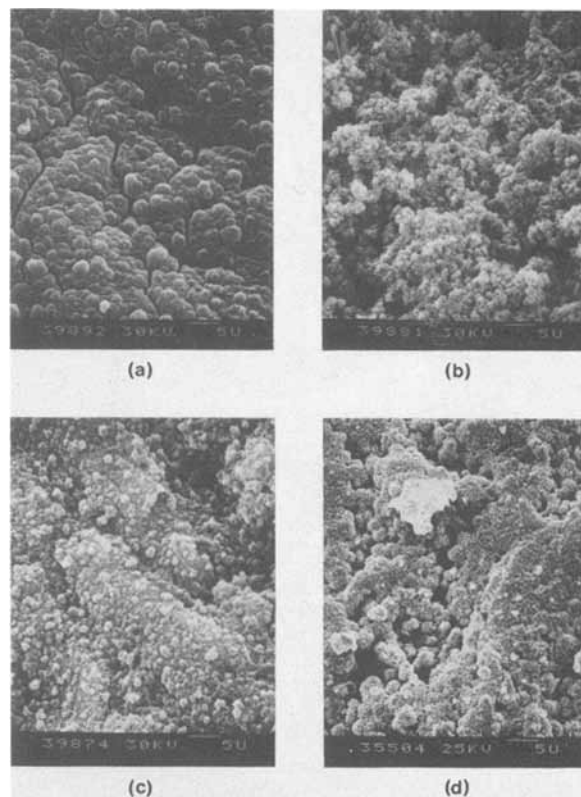


Fig. 3. Scanning electron micrographs of (a) polyfluorene-BF₄, (b) polyfluoroanthrene-BF₄, (c) polytriphenylene-BF₄, and (d) polypyrene-BF₄.

mechanical properties of the composite are effectively those of the PVC matrix polymer (21). Thus, electrochemically produced composites of this type allow one to overcome the shortcomings of the often very brittle yet highly conducting films, such as of PPY or even of polypyrrole. Further details about the preparation of these conducting composites and their electrical and mechanical properties will be described elsewhere (21).

Conclusion

The stoichiometric electrochemical polymerization reaction first described with polypyrrole appears to be quite general (6, 12). It is applicable not only to other heterocyclic systems such as thiophene (8), indole (17), and thianaphthene (17), and even a non-benzenoid aromatic hydrocarbon such as azulene (5), but also to polycyclic aromatic hydrocarbons. The electrochemical polymerization reaction proceeds with an electrochemical stoichiometry of 2.0 electrons/aromatic unit and the charge in excess of 2.0 is consumed in the partial oxidation of the polymeric film which forms on the electrode surface. As with any other preparative procedure, the yield of the desired product varies with the starting compound. While the heterocyclics produce 100% polymer film, the yields can be low as is observed with pyrene (50% film product). The principal difference between the aromatic hydrocarbon and the heterocyclic compounds lies in the quality of the resultant films. The former tend to be brittle and easily cracked. However, the incorporation of these films within a host matrix appears a viable and promising solution (21).

Acknowledgments

We thank J. Duran of this laboratory for taking the SEM pictures, and Professor M.-A. DePaoli, University of Campinas, SP, Brasil, for stimulating discussions.

Manuscript submitted April 30, 1984; revised manuscript received ca. Nov. 12, 1984.

IBM Corporation assisted in meeting the publication costs of this article.

REFERENCES

1. L. S. Marcoux, J. M. Fritsch, and R. N. Adams, *J. Am. Chem. Soc.*, **89**, 5766 (1967); J. Phelps, K. S. V. San-

- thanam, and A. J. Bard, *ibid.*, **89**, 1752 (1967); R. N. Adams, *Acc. Chem. Res.*, **2**, 175 (1969).
2. M. E. Peover and B. S. White, *J. Electroanal. Chem.*, **13**, 93 (1967).
3. A. F. Diaz, J. Bargon, and R. J. Waltman, in "Membranes and Ionic and Electronic Conducting Polymers," E. B. Yeager, B. Schumm, Jr., K. Mauritz, K. Abbey, D. Blankenship, and J. Akridge, Editors, p. 332, The Electrochemical Society Softbound Proceedings Series, Pennington, NJ (1982).
4. G. Tourillon and F. Garnier, *J. Electroanal. Chem.*, **135**, 173 (1982).
5. J. Bargon, S. Mohmand, and R. J. Waltman, *Molec. Cryst. Liq. Cryst.*, **93**, 279 (1983).
6. J. Bargon, S. Mohmand, and R. J. Waltman, *IBM J. Res. Dev.*, **27**, 330 (1983).
7. J. Bargon, S. Mohmand, and R. J. Waltman, To be published.
8. R. J. Waltman, A. F. Diaz, and J. Bargon, *This Journal*, **131**, 1452 (1984).
9. H. Akamatu and H. Inokuchi, *J. Chem. Phys.*, **18**, 810 (1950); H. Inokuchi, *Bull. Chem. Soc. Jpn.*, **24**, 222 (1951).
10. H. Eichele, M. Schwoerer, C. Krohnke, and G. Wegner, *Chem. Phys. Lett.*, **77**, 311 (1981); H. J. Keller, D. Nothe, H. Pritzkow, D. Wehe, M. Werner, P. Koch, and D. Schweitzer, *Mol. Cryst. Liq. Cryst.*, **62**, 181 (1980).
11. A. F. Diaz, M. Salmon, J. A. Logan, M. Krounbi, and J. Bargon, *ibid.*, **83**, 1297 (1982).
12. A. F. Diaz and K. K. Kanazawa, "Extended Linear Chain Compounds," Vol. 3, J. Miller, Editor, p. 417, Plenum Press, New York (1982).
13. R. N. Adams, "Electrochemistry at Solid Electrodes," Marcel Dekker, New York (1969).
14. R. S. Nicholson and I. Shain, *Anal. Chem.*, **36**, 706 (1964).
15. M. E. Peover, in "Electroanalytical Chemistry," Vol. 2, A. J. Bard, Editor, pp. 1-51, Marcel Dekker, New York (1967).
16. A. F. Diaz, *Chem. Scr.*, **17**, 145 (1981).
17. R. J. Waltman, A. F. Diaz, and J. Bargon, *J. Phys. Chem.*, **88**, 4343 (1984).
18. J. F. Ambrose and R. F. Nelson, *This Journal*, **115**, 1159 (1968).
19. A. F. Diaz, A. Martinez, K. K. Kanazawa, and M. Salmon, *J. Electroanal. Chem.*, **130**, 181 (1981).
20. R. J. Waltman, J. Bargon, and A. F. Diaz, *J. Phys. Chem.*, **87**, 1459 (1983).
21. M.-A. DePaoli, R. J. Waltman, J. Bargon, and A. F. Diaz, *J. Chem. Soc. Chem. Commun.*, 1015 (1984); M.-A. DePaoli, R. J. Waltman, J. Bargon, and A. F. Diaz, *J. Polym. Sci. Chem. Ed.*, To be published.

Long-Term Stabilization of Polythiophene-Protected n-GaAs Photoanodes in Aqueous Solution

G. Horowitz and F. Garnier

Laboratoire de Photochimie Solaire, C.N.R.S., 94320 Thiais, France

Among the different approaches that have been used to stabilize small bandgap n-type semiconductors against photocorrosion in photoelectrochemical (PEC) cells, the grafting of electrogenerated conducting polymers have been reported for Si (1-3), GaAs (4-6), CdS (7), and CdSe (4) photoanodes. Although long-term stabilization, up to 450h, has been reported for polypyrrole (PP)-coated n-Si in I^-/I_3^- aqueous solution (3), the stabilization of n-GaAs is limited by a phenomenon of film peeling that occurs after 10-20 min for PP (4) and 2h for polystyrene pendant $Ru(bpy)_3^{2+}$ (5). We have recently reported a 17h stabilization, with no film peeling, on poly(3-methylthiophene) (PMeT)-coated GaAs (6), but a continuous decrease of the photocurrent was observed, together with the appearance of corrosion holes visible to the naked eye after removal of the film. The lack of long-term stabilization of PP (4) and PMeT (6) covered GaAs was attributed to porosity of the polymer, which allows molecules of the solvent to reach the electrode surface.

However, recent experiments carried out in our laboratory have shown that hydrogen evolution does not occur at a reduced (quasi-insulating) PMeT-coated platinum electrode in 1N HCl aqueous solution (pH = 0) even at potentials as negative as -0.6 V/SCE (7). This result tends to prove that the permeability of PMeT to solute/solvent species is questionable. The origin of the photodegradation of polymer-coated GaAs has then to be reconsidered. We show in this paper that this photodegradation can be attributed mainly to breakings of the film and to its lack of intimate contact with the electrode surface. An improvement of both the solidity and adherence of the polymer allowed us to obtain a long-term stabilization of PMeT-coated n-GaAs in $Fe(CN)_6^{4-}$ aqueous solution.

Experimental

Semiconductor electrodes were prepared from nonintentionally doped (100)-oriented n-GaAs wafers purchased from RTC-Caen (France). The doping level was 2

$\times 10^{16} \text{ cm}^{-3}$ and the thickness 0.35 mm. Ohmic contact was obtained by evaporating Au-Ge alloy and annealing at 400°C under N_2 . The wafers were then cut into 1 cm diam disks and attached to brass disks with Ag paint. The disks were mounted in a Teflon holder, in which an O-ring delimited a 0.26 cm^2 circular active surface. This holder has been designed in order to allow the electrodes to be dismounted for scanning electron microscope (SEM) observation.

As mentioned in a previous paper (6), platinization of GaAs enhances PMeT growth rate (50 nm are then grown in less than 1 min), thus preventing concomitant photo-corrosion of the semiconductor, and allowing homogeneous films to be obtained. Prior to platinization, the electrodes were dipped into concentrated (30%) HCl, in order to remove the oxide layer, and rinsed thoroughly in twice-distilled water. Electroplating of Pt was then carried out at -0.6 V/SCE in a $(\text{NH}_4)_2\text{Pt Cl}_6/\text{LiClO}_4$ aqueous solution. The amount of deposited Pt, which was followed with the help of a digital coulometer, would correspond to a 1-2 nm thick continuous layer. SEM observation showed that the platinum formed in fact disconnected islands. The PMeT electrodeposition was performed in 0.5M distilled 3-methylthiophene, 0.02M $\text{Bu}_4\text{N SO}_3 \text{ CF}_3$, acetonitrile solution, at $+1.5 \text{ V/SCE}$ under a 150W Xe arc lamp illumination ($15 \pm 5 \text{ mW/cm}^2$). Again, the film thickness was controlled by using a digital coulometer. Since we need relative, rather than exact, values of the thickness, we assumed that the linear variation of 1 nm per mC/cm^2 observed on Pt electrodes (8) is also true for platinized n-GaAs.

Stability tests were made in 0.1M $\text{K}_3\text{Fe}(\text{CN})_6/0.25\text{M K}_4\text{Fe}(\text{CN})_6$ aqueous solutions ($\text{pH} = 6$) under illumination by the xenon arc lamp equipped with a 515 nm long pass filter in order to avoid the photodecomposition of ferricyanide by short wavelength light (9), and a water filter to cut the undesirable IR radiations.

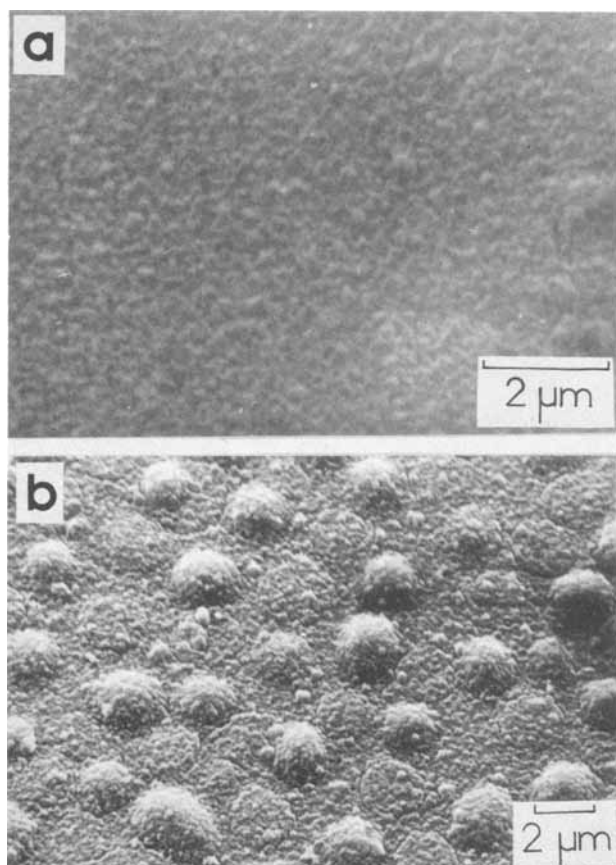


Fig. 1. Scanning electron micrographs of PMeT films grown on platinized n-GaAs electrodes. Thickness of the films: 70 (a) and 220 nm (b).

Results and Discussion

Scanning electron micrographs of 70 and 220 nm thick PMeT films grown on platinized n-GaAs, shown in Fig. 1, reveal a decrease of the homogeneity of the film as its thickness increases. A short-term stability test (ca. 15 min) was performed for both of these films. The charge passed during that test was about 2 C/cm^2 . No change of the polymer surface could be detected on the 70 nm film by SEM observation, and the electrode surface presented its original topography after removal of the PMeT film. This was not the case for the 220 nm film, for which corroded areas were visible to the naked eye. Figure 2 shows SEM photographs of a corroded area before and after film removal. The corrosion clearly occurs at micro-cracks of the film, through which the solution is able to reach the semiconductor surface. The fact that a corrosion of the electrode is observed is noteworthy, since at the value of the pH of the solution used for this experiment, passivation of GaAs should result, rather than corrosion. Although this phenomenon is not understood, it can be compared to a classical corrosion behavior of layer-protected metals. The swell of the polymer film at corrosion sites is probably due to a penetration of the solution under the film, which also explains the fact that the size of the corroded areas largely exceeds the width of the cracks. Importantly, the GaAs surface remained unchanged where no bursting of the polymer occurred.

These results indicate that the photodegradation of PMeT-coated GaAs is not due to an inherent porosity of the film, in which case one should observe a corrosion of the whole surface of the electrode, but rather that it initiates at places where cracking of the polymer occurs. Moreover, it appears that thin films present a better homogeneity and intimate contact with the semiconductor electrode. No interpretation can yet be given to this behavior. However we have observed similar topographies

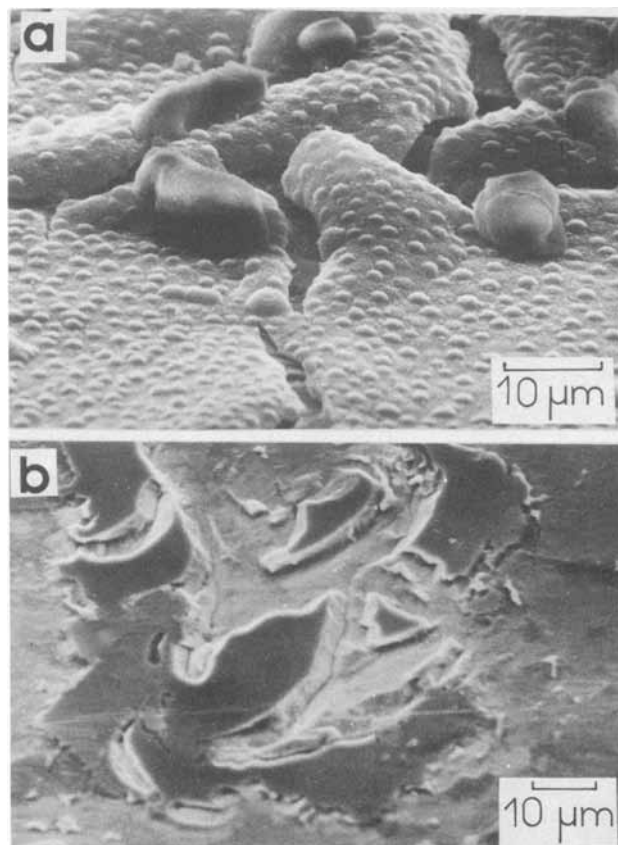


Fig. 2. Corrosion pictures on a 220 nm PMeT film-covered n-GaAs photoanode operated 15 min in aqueous $\text{Fe}(\text{CN})_6^{4-\beta-}$ solution. Charge passed: 1.85 C/cm^2 . Micrographs taken before (a) and after (b) PMeT film removal. Some ferra/ferricyanide crystals that have not been washed away by water rinsing can be seen on the polymer film (photograph a).

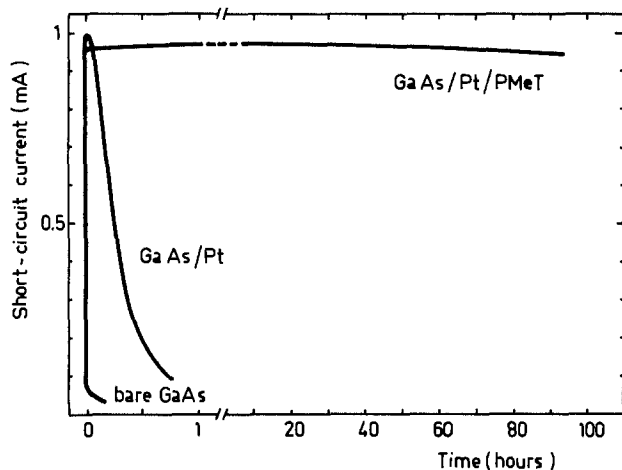


Fig. 3. Short-circuit current vs. time for bare, platinized, and 40 nm PMeT-coated n-GaAs photoanode in 0.1M $K_3Fe(CN)_6/0.25M K_4Fe(CN)_6$ aqueous solution. Illumination by Xe arc lamp with 515 nm long-pass filter. Electrode area: 0.26 cm^2 .

on PMeT grown on Pt electrodes (10). Our results clearly showed that thin films (some tens of nanometers) are very smooth and adherent, whereas thicker films present morphological inhomogeneities and losses of adherence.

A long-term stability test was then carried out with a 40 nm PMeT-coated electrode in $Fe(CN)_6^{4-3-}$ aqueous solution. This test consisted in measuring the short-circuit current, at a load resistance of 1Ω , of a PEC cell constituted with the polymer-coated GaAs photoanode and a platinum counterelectrode. The incident light power was 14 mW/cm^2 . The results are shown in Fig. 3. The photocurrent remained very constant for 90h, whereas it decays to negligible values within 1 min for bare GaAs, and within less than 1h for platinized GaAs. The charge passed during the test is 280C, i.e., 1100 C/cm^2 . This last value is noteworthy since it corresponds to the corrosion of almost twice the part of the electrode in contact with the solution. Figure 4 shows that only very slight degradation of the power characteristic of the cell is observed. The corresponding power efficiencies under filtered Xe illumination are 10.9% before and 9.4% after the stability test, which can be compared to the 12% solar efficiency of redox-stabilized n-GaAs-based PEC cells (11-13). The decrease of the power efficiency can originate, at least in part, from an increase of the light absorption by the polymer, due to its redoping by ferricyanide ions. This assumption is argued for by the change of the color of the film from red-brown to green, and by the possibility of doping PMeT grown on Pt in aqueous solutions (14). This implies that water molecules are able to penetrate the bulk of the polymer, which is in contrast to a nonpermeability of the polymer. We then think that the nonporosity of PMeT is limited to the first layers close to the substrate. Importantly, the decay of the fill factor is very slight, indicating that no oxide film has grown on the electrode. Also shown in Fig. 4 is the power characteristic of a platinized GaAs electrode after only 45 min operation. The shape of this characteristic is typical of an oxide covered (passivated) electrode.

No weight loss of the protected electrode could be measured but SEM observation showed a few tiny corrosion sites, mainly near the edge of the polymer-coated area. This corrosion was probably due to the presence of some pinholes in the polymer film. It must be noted that this very localized corrosion did not induce any loss of the intimate contact between the polymer and the semiconductor substrate. The great adherence of PMeT thin films on both metal and semiconductor electrodes seems then to be at the origin of the possibility of stabilizing GaAs photoanodes. The mechanism of this high adhesion power, which could be due to the presence of a sulfur atom in the thiophene ring, is presently under study in our laboratory.

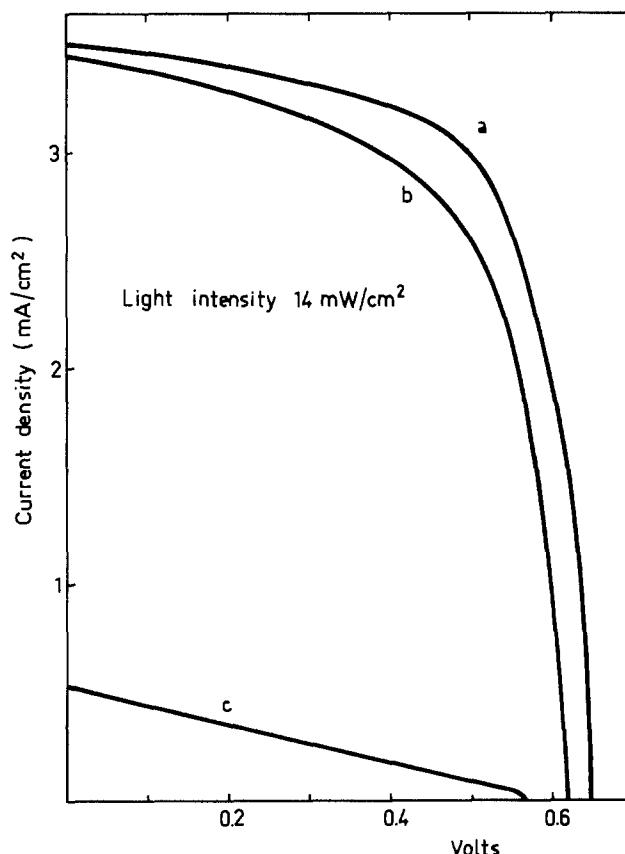


Fig. 4. a: Power characteristic for PMeT-coated n-GaAs in aqueous $Fe(CN)_6^{4-3-}$ solution, under 14 mW/cm^2 Xe arc lamp illumination. Open-circuit voltage: $V_{oc} = 0.655 \text{ V}$; short-circuit current density: $J_{sc} = 3.52 \text{ mA/cm}^2$; fill factor: $FF = 0.66$. b: Same as curve a after 90h of continuous operation. $V_{oc} = 0.625 \text{ V}$; $J_{sc} = 3.46 \text{ mA/cm}^2$; $FF = 0.61$. c: Power characteristic for a platinized n-GaAs photoanode in the same solution after 45 min of operation. $V_{oc} = 0.57 \text{ V}$; $J_{sc} = 0.52 \text{ mA/cm}^2$; $FF = 0.27$.

In conclusion, we have reported the first example of long-term stabilization of polymer-protected n-GaAs in aqueous solution. This result was obtained by using thin film of polymer, which appeared to be more homogeneous and adherent. Corrosion sites that form on thick-film-coated electrodes initiate at cracks of the film, which means that the photodegradation of the semiconductor is not due to a porosity of the polymer. Work is presently under way on GaAs-based photoelectrolytic cells.

Acknowledgment

Use of the scanning electron microscope of the Laboratoire de Physique des Liquides et Electrochimie du C.N.R.S., Université Pierre et Marie Curie, Paris, France (Dr. M. Froment) is gratefully acknowledged.

Manuscript submitted June 8, 1984; revised manuscript received Oct. 22, 1984.

REFERENCES

1. R. Noufi, A. J. Franck, and A. J. Nozik, *J. Am. Chem. Soc.*, **103**, 1849 (1981).
2. F. R. F. Fan, B. L. Wheeler, A. J. Bard, and R. N. Noufi, *This Journal*, **128**, 2042 (1981).
3. T. Skotheim, I. Lundström, and J. Prejza, *ibid.*, **128**, 1625 (1981); T. Skotheim, L.-B. Petersson, O. Inganäs, and I. Lundström, *ibid.*, **129**, 1737 (1982).
4. R. Noufi, D. Tench, and L. F. Warren, *ibid.*, **127**, 2310 (1980); *ibid.*, **128**, 2596 (1981).
5. K. Rajeshwar, M. Kaneki, and A. Yamada, *ibid.*, **130**, 38 (1983).
6. G. Horowitz, G. Tourillon, and F. Garnier, *ibid.*, **131**, 151 (1984).
7. G. Tourillon and F. Garnier, *J. Phys. Chem.*, To be published.
8. S. Glenis, G. Horowitz, G. Tourillon, and F. Garnier, *Thin Solid Films*, **111**, 93 (1984).

9. V. Balzani and V. Carassiti, "Photochemistry of Coordination Compounds," p. 162, Academic Press, London (1970).
10. G. Tourillon and F. Garnier, *J. Polymer Sci.*, **22**, 33 (1984).
11. B. A. Parkinson, A. Heller, and B. Miller, *Appl. Phys. Lett.*, **33**, 521 (1978); *This Journal*, **126**, 954 (1979).
12. R. Noufi and D. Tench, *ibid.*, **127**, 188 (1980).
13. A. Bourrasse, H. Cachet, G. Horowitz, and S. Le Crom, *Rev. Phys. Appl. (Paris)*, **17**, 801 (1982).
14. G. Tourillon and F. Garnier, *J. Electroanal. Chem.*, **161**, 407 (1984).



The Minority Carrier Recombination Resistance: A Useful Concept in Semiconductor Electrochemistry

J. E. A. M. van den Meerakker, J. J. Kelly, and P. H. L. Notten

Philips Research Laboratories, 5600 JA Eindhoven, The Netherlands

ABSTRACT

The impedance characteristics for redox reactions involving minority carrier recombination at semiconductor electrodes differ markedly from those involving majority carriers. In this work, holes were generated in the valence band of n-GaAs by illumination or injection from solution. A recombination resistance is used to characterize the process by which these holes recombine with electrons from the conduction band. This resistance is shown to be independent of the method of hole generation, the pH of the solution, and the nature of the injecting species, but dependent on the generation rate.

In semiconductor electrochemistry, it is of considerable importance to know which of the bands in the solid is involved in the reaction with a redox system in solution. For example, an oxidizing agent may be reduced either by electron capture from the conduction band or by hole injection into the valence band. On the basis of the standard potential of the redox system and the flatband potential of the semiconductor, it is generally obvious which of the two bands is important. However, the situation becomes more complex when an unstable intermediate is involved in the charge-transfer reaction (1) or when charging of an inversion layer or of surface states causes a considerable change in the Helmholtz potential and thus in the position of the semiconductor bandedges (2). In such cases, more sophisticated methods are often necessary to elucidate the reaction mechanism.

In a previous paper (3), we described how, in the photoanodic dissolution of an n-GaAs electrode, hole transfer to the solution was inhibited by an oxide film on the electrode surface. We showed an analogy between the impedance characteristics of this electrolyte-oxide-semiconductor (EOS) system, with enhanced minority carrier recombination, and that of an illuminated MOS device. The concept of a "recombination resistance" was used in the description of the recombination of the minority carriers created by illumination. The dependence of this resistance on light intensity was very similar to that found for the Si MOS transistor (4).

In principle, it should be possible to use such a concept more generally in semiconductor electrochemistry for cases in which recombination of minority carriers is important, irrespective of how these carriers are created. In this work, we describe the generation of holes in the valence band of n-GaAs by two methods, injection from solution and illumination, and we consider the effect of this generation and subsequent recombination on the impedance characteristics of the electrode. A comparison with results involving hole injection into p-GaAs, for which recombination can be disregarded, emphasizes the significance of the recombination resistance. We suggest that this concept may be useful, in certain cases, for deciding which type of charge carrier in the solid is determining for the electrochemical reaction.

Impedance of GaAs Electrodes under Depletion Conditions

In order to clarify what we mean by the recombination resistance, we shall first briefly consider the creation, recombination, and Faraday reactions of minority carriers in n-GaAs under depletion conditions.

Hole reactions at GaAs electrodes.—Under depletion conditions, the extent of the band-bending at the electrode surface determines what happens to holes injected from an oxidizing agent in solution into the valence band of n-GaAs. At relatively large band-bending [Fig. 1(a)], the holes are held at the surface by the electric field, and rupture of surface bonds occurs; the injection is compensated by dissolution of the GaAs, and the resultant net current is very small (5). At lower band-bending, the injected holes can recombine with electrons either at the surface or within a diffusion length of the surface [Fig. 1(b)]. A net cathodic current, carried by electrons in the bulk, is observed in this case.

In an n-type semiconductor, minority charge carriers can also be created by light. In this case, dissolution gives an anodic (photo-) current whose magnitude is determined by the light intensity [Fig. 1(c)], while recombination results in a net zero current [Fig. 1(d)].

Holes, injected under depletion conditions into a p-type GaAs electrode move away from the surface under influence of the electric field [Fig. 1(e)]. This hole-flow through the valence band of the solid is registered as a cathodic current. Recombination is, of course, not important in this case.

Equivalent circuits for GaAs electrodes.—Myamlin and Pleskov (6), using the analogy with MOS devices (7), propose a complete equivalent circuit for the impedance of an n-type semiconductor electrode under depletion conditions. In Fig. 2, the situation is shown for the case in which the recombination rate in the space-charge layer equals zero. C_D , C_S , and C_I are the capacitances of the depletion layer, the surface states, and the inversion layer, respectively. The Helmholtz capacitance C_H replaces the oxide capacitance of the MOS transistor. $R_{n,D}$ and $R_{p,D}$ are the resistances which characterize the transfer of elec-

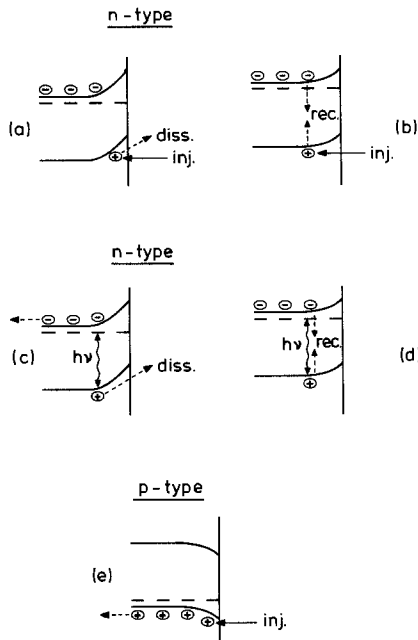


Fig. 1. Band diagrams for a semiconductor electrode under depletion conditions. (a) and (b) refer to hole injection (inj.) into an n-type electrode. At large band bending, (a) dissolution (diss.) dominates, while at moderate band bending, (b) recombination (rec.) dominates. (c) and (d) are the analogous cases when holes are generated by light. (e) shows hole injection into a p-type electrode.

trons and holes through the depletion layer, while $R_{n,s}$ and $R_{p,s}$ represent the transfer of electrons from the conduction band and of holes from the valence band to surface levels. R_B is the bulk semiconductor resistance. The impedance Z_r describes the generation and recombination of holes and their flow rates in the region of quasi neutrality in the bulk adjacent to the space-charge layer (7). Finally, if an electrochemical reaction occurs at the electrode, current flow through the surface must be taken into account. i_n and i_p represent the electron and hole currents.

In this work, we are mainly interested in the case in which recombination within the space-charge layer is dominant, i.e., the recombination rate is very high. Here the current in the space-charge layer changes from a predominantly electron current at the bulk side to a predominantly hole current near the surface. It becomes meaningless then to represent the current flow through the depletion layer by separate impedances for holes and electrons. The complex impedance Z_r together with $R_{n,D}$ and $R_{p,D}$ can therefore be replaced by a frequency-independent resistance R_D (7) [Fig. 3(a)]. Since, for the

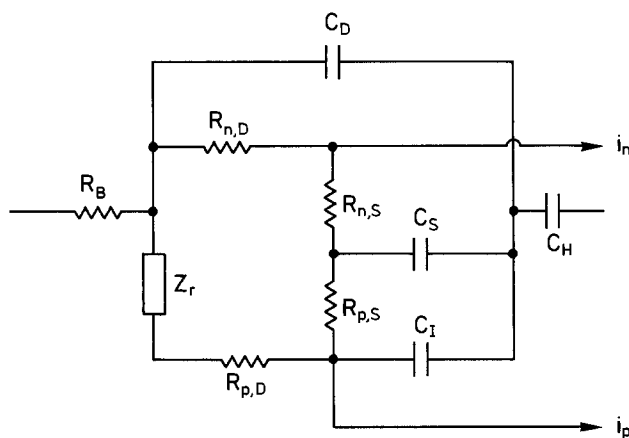


Fig. 2. Equivalent circuit for an n-type semiconductor under depletion or inversion conditions with zero recombination rate in the space-charge layer.

hole injection experiments described here, the rate of reduction of the oxidizing agent may be diffusion controlled, a Warburg impedance W is introduced into the hole injection path.

The equivalent circuit given in Fig. 3(a) is too complex for practical use, but can be further simplified. Pierret and Sah have shown (8) that the resistance R_D is essentially determined by the recombination process in the space-charge region. We now assume that one of the interface capacitances, C_I or C_S , is dominant, and we represent it by C_{if} [Fig. 3(b)]. If inversion can be disregarded, which is very likely to be the case here, then the space charge and surface resistances can be combined into a single recombination resistance which we denote by R_r . Alternatively, when surface states are unimportant, then inversion may determine the interface capacitance C_{if} . If the impedance is measured using a rotating disk electrode at potentials at which reduction of the oxidizing agent is completely diffusion limited, then the Warburg impedance becomes purely resistive and has a very high resistance value (R_w). For measuring frequencies in the range 1-10 kHz, this part of the circuit may be omitted and current will flow through the Helmholtz capacitance. Finally, on combining the electrolyte and bulk semiconductor resistances R_e and R_B into a term $R_{e,B}$, we obtain the simplified circuit shown in Fig. 3(b). This circuit also covers the generation/recombination case in which minority carriers are created by light instead of injection. The circuit is, in fact, the circuit deduced from composite impedance theory by Pierret and Sah for the illuminated MOS transistor without external current flow (8) and used by us for the GaAs EOS system; in the present case, the oxide capacitance is replaced by C_{if} .

For a p-type electrode under depletion conditions, the recombination resistance R_r appears in the current path for electrons. Since holes are being injected from solution [Fig. 1(e)], the Warburg impedance is found in the current path for majority carriers. Mott-Schottky measurements with p-GaAs show no evidence of surface state or inversion effects under depletion conditions in the dark. Since minority carrier processes are not important, a circuit equivalent to that shown in Fig. 2 can be simplified to one containing C_D , C_{if} , R_w , and $R_{p,D}$. The Helmholtz capacitance should be much larger than that of the depletion layer, and $R_{p,D}$ is negligible with respect to R_w . So, a simple circuit results: the depletion layer capacitance C_D is short-circuited by a large resistance R_w and is connected in series to the solution/bulk semiconductor resistance $R_{e,B}$.

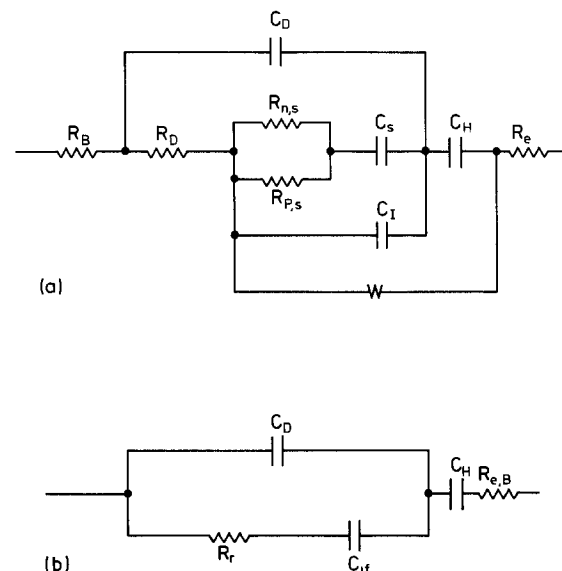


Fig. 3. (a) Equivalent circuit for an n-type semiconductor under depletion or inversion conditions with infinite recombination rate in the space-charge layer. (b) Simplified circuit of a, when the generation rate is diffusion controlled.

SSST

In order to characterize the recombination resistance R_r , we measured the frequency dependence of the impedance of an n-GaAs electrode in which holes were created by illumination or injected from Ce^{IV} or $Fe(CN)_6^{3-}$ ions in solution. Current-potential curves were used to distinguish the regions in which recombination and dissolution were dominant, and the results were compared with those of hole injection into p-GaAs.

Experimental

The GaAs single-crystal wafers were obtained from MCP Electronics, England, and had the 100 orientation. The n-type material was Si doped ($8.6 \times 10^{16} \text{ cm}^{-3}$) and had a resistivity of $0.019 \Omega\text{-cm}$. The p-type wafers were Zn doped ($8.4 \times 10^{17} \text{ cm}^{-3}$) and their resistivity was $0.042 \Omega\text{-cm}$. The diameter of the rotating disk electrodes made from these materials was 4 mm. Prior to use, all electrodes were etched at room temperature in a mixture of $H_2SO_4(98\%)-H_2O_2(30\%)-H_2O(3-1-1)$ and dipped in a 6N HCl solution.

The measurements were made in a conventional electrochemical cell using a platinum disk as a counter-electrode and a saturated calomel electrode (SCE) as a reference. All potentials are given with respect to this SCE. Impedance measurements were done under potentiostatic control with the aid of a Solartron 1172 Frequency Response Analyser and an rms signal of 10 mV. For illumination, a Spectra Physics 1 mW 133 He-Ne laser was used in combination with a glass fiber light cable. The penetration depth of this light is small compared to the diffusion length of holes in n-GaAs.

All solutions were prepared with reagent-grade chemicals and deoxygenated using a nitrogen flow. The measurements were performed at room temperature.

Results

Current-potential measurements.—The reduction of Ce^{IV} at pH 0 and $Fe(CN)_6^{3-}$ at pH 14 occurs at GaAs electrodes by means of hole injection into the valence band (9). The reduction reaction is diffusion controlled in a wide potential range, as is clear from the current-potential curves measured at p-GaAs [dashed lines in Fig. 4(a)]. An identical limiting current is found at n-GaAs [solid lines in Fig. 4(a)] at potentials more negative than -0.60V . In this range, which corresponds to moderate band bending [Fig. 1(b)], holes injected into the electrode recombine with electrons from the conduction band. At more anodic potentials, the band bending increases, the electron concentration at the surface is greatly reduced, and dissolu-

tion competes with recombination [Fig. 1(a)]. At potentials more positive than -0.35V , all holes injected into the electrode are used for the dissolution reaction, and the current tends to zero. The current-potential curves for $K_3Fe(CN)_6$ at pH 14 are similar to those given in Fig. 4(a) but are displaced by approximately 0.8V on the potential axis as a result of the higher pH.

Minority carriers can also be created in n-GaAs by illumination in an inert electrolyte [Fig. 1(c) and (d)]; in this case, the current-potential characteristics are "reversed" [Fig. 4(b)]. Efficient recombination at negative potentials results in very low current. At more positive potentials, the increased electric field at the surface ensures an efficient separation of charge carriers, and a photoanodic current resulting from dissolution is found. The ranges in which recombination or dissolution dominates are exactly the same as in the previous case. From these current-potential curves, the potential range can be deduced in which recombination of minority carriers is important. This is, of course, determined by the nature and the density of the recombination centers at and near the electrode surface and is therefore sensitive to the state of the electrode. The kinetics of the oxidation reaction involving the minority carriers (dissolution of GaAs in this case) are also important. In the present case, we have available a potential range of a few tenths of a volt, in which recombination dominates.

An important parameter in this work is the minority carrier generation rate I_g , which can be assessed from the limiting currents. In the case of illumination, this is given by the limiting photocurrent and is directly proportional to the light intensity. For hole injection from solution, the diffusion-controlled reduction current determines I_g ; its value can be varied by changing the concentration of the oxidizing agent in the solution and the rotation rate of the electrode [Fig. 4(a)].

Impedance measurements.—The equivalent circuit shown in Fig. 3(b) should be valid for n-GaAs when recombination is dominant. An analysis of this circuit gives two equations

$$\frac{1}{Z_{re} - R_{e,B}} = \frac{(C_D + C_{if})^2}{R_r C_{if}^2} + R_r C_D^2 \omega^2 \quad [1]$$

$$\frac{-\omega Z_{im}}{Z_{re} - R_{e,B}} = \frac{(C_D + C_{if})(C_D + C_{if} + C_H)}{R_r C_{if}^2 C_H} + \frac{R_r C_D(C_D + C_H)}{C_H} \omega^2 \quad [2]$$

in which Z_{re} and Z_{im} are the real and imaginary components of the complex impedance. $R_{e,B}$ could be obtained from the high frequency limit of Z_{re} . Plots of $1/(Z_{re} - R_{e,B})$ and $-\omega Z_{im}/(Z_{re} - R_{e,B})$ as a function of ω^2 should give straight lines. For all cases involving efficient recombination, we indeed found this to be the case. An example is shown in Fig. 5 for $Ce(SO_4)_2$. This implies that our assumptions with respect to the circuit of Fig. 3(a) are correct, and that the impedance behavior of n-GaAs can be represented by the simplified circuit of Fig. 3(b), when the recombination process dominates.

As C_D is negligible compared to C_{if} , R_r and C_D could be deduced from the slope of the lines in Fig. 5. The recombination resistance, R_r , depends strongly on the generation rate. Figure 6 summarizes the results both from the illumination and hole injection experiments. The slope of this log-log plot is approximately -1.1 . The most striking aspect of these results is that R_r is independent of the method of minority carrier generation (by illumination or injection from the solution). It is also independent of the species which injects the holes, the pH of the solution, and the potential in the recombination range.

The values of C_D measured during injection increased with decreasing potential, as might be expected. These values, however, were somewhat higher than those measured in an indifferent electrolyte in the dark, and showed an increase with increasing generation rate.

Since R_r and C_D are known, C_{if} could be calculated from the intercept of the plot of Eq. [1]. Its value varied from

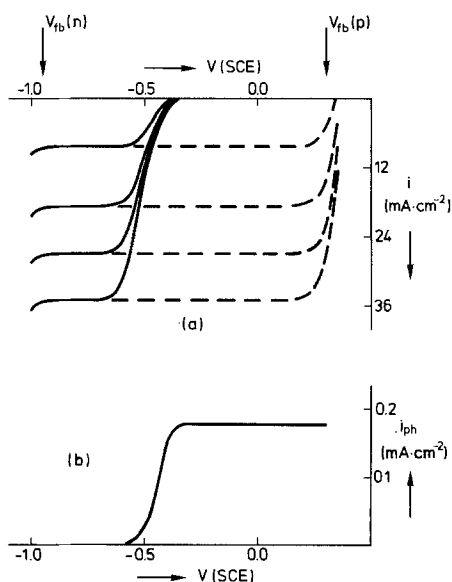


Fig. 4. (a) Current-voltage curves of p-type (dashed lines) and n-type (solid lines) GaAs at different rotation speeds (300, 1500, 3000, and 5000 rpm) in $0.05M Ce(SO_4)_2/1N H_2SO_4$ solution. (b) Photocurrent of n-GaAs in $1N H_2SO_4$ solution.

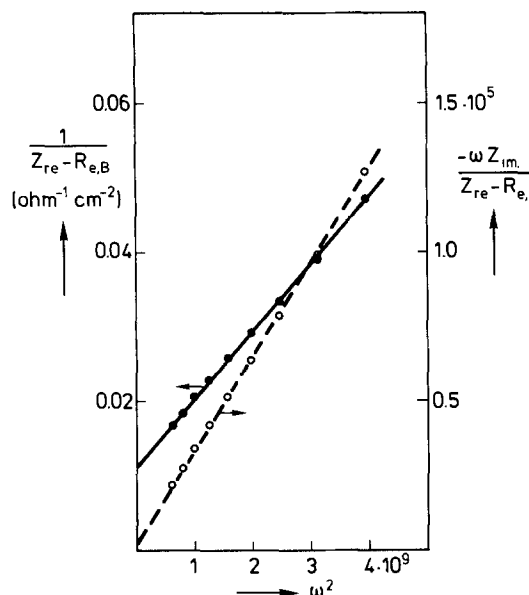


Fig. 5. Impedance results, plotted according to Eq. [1] and [2] for n-GaAs in $5.10^{-4}M$ $Ce(SO_4)_2/1N$ H_2SO_4 solution at $-0.70V$ (SCE) and 100 rpm. $\omega = 2\pi f$, where f is the measuring frequency in Hz.

approximately $0.1 \mu F \cdot cm^{-2}$ at very low injection rates to $15 \mu F \cdot cm^{-2}$ at the highest rates.

The impedance behavior of a p-GaAs electrode was, of course, totally different. It was consistent with a capacitance (C_D) shunted by a very large resistance (R_w), as expected. Recombination is not important in this case. For n-GaAs under conditions in which dissolution dominates (at potentials more positive than $-0.35V$), recombination also does not occur. In this situation, the impedance picture was similar to that for p-GaAs.

Discussion

These results show clearly the importance of recombination for the impedance characteristics of GaAs electrodes. In the absence of such recombination, as when holes are injected into p-GaAs or when dissolution ac-

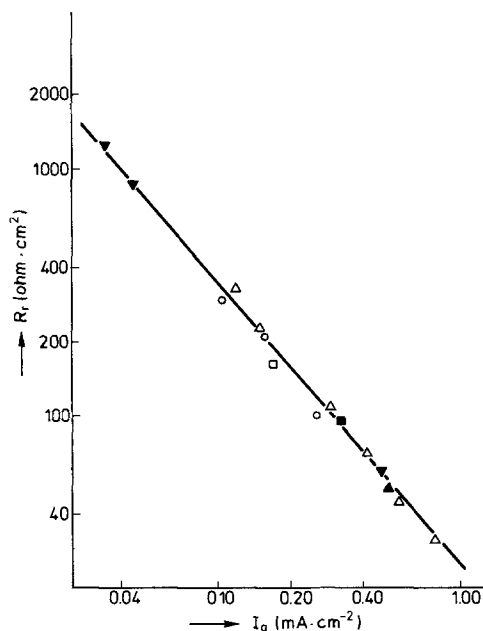


Fig. 6. Recombination resistance as a function of the generation rate for n-GaAs. $Ce(SO_4)_2/1N$ H_2SO_4 solutions at different $Ce(SO_4)_2$ concentrations and rotation speeds at $-0.60V$ (\blacktriangledown), $-0.65V$ (\blacktriangle), or $-0.70V$ (\triangle) vs. SCE. $K_3Fe(CN)_6/1N$ NaOH solutions at different $K_3Fe(CN)_6$ concentrations and rotation speeds at $-1.50V$ vs. SCE (\circ). $0.5M$ K_2SO_4 solution at $pH = 5.0$ under illumination at $-1.00V$ vs. SCE (\square). $1N$ H_2SO_4 solution under illumination at $-0.70V$ vs. SCE (\blacksquare).

counts for all holes introduced into n-GaAs, the depletion layer capacitance is shunted by a large Warburg-type impedance. On the other hand, when recombination within the space-charge layer or at the surface is important, the impedance of the electrode resembles that of the MOS and EOS devices (3, 4). This impedance is characterized by a capacitance associated with charge storage at the electrode/electrolyte interface and by a resistance which describes the recombination of minority carriers in the valence band with electrons from the conduction band [Fig. 3(b)].

The relatively large values of C_{if} found at higher injection rates indicate a considerable charge localization at the interface. This is supported by the increased value of the space-charge capacitance C_D relative to the value found when injection does not occur. This points to a shift in potential from the space-charge layer of the semiconductor to the Helmholtz layer. This change can be calculated from Mott-Schottky theory and used to determine the interface charge density (3). On assuming a value of $20 \mu F \cdot cm^{-2}$ for C_H , we obtain charge densities ranging from $6.10^{12} cm^{-2}$ at low injection rates to $3.10^{13} cm^{-2}$ at the highest injection rates used.

The recombination resistance R_r , measured here at potentials at least $0.2V$ positive with respect to the flatband potential, depends on the minority carrier generation rate but not on the method of generation. Since R_r is also insensitive to the electrode pretreatment and the pH and composition of the electrolyte, we may conclude that it is mainly determined by recombination not at the surface but in the space-charge layer; R_r is thus an intrinsic property of the material. The recombination resistance is therefore not coupled directly to the interface capacitance. This is also supported by the fact that such a coupling would lead to a time constant τ ($= R_r C_{if}$) in the range $0.1-1$ ms, which is much too high to account for the very efficient recombination occurring in this case.

Pierret and Sah have developed a quantitative model for the band-to-band communication in illuminated MOS devices under depletion and inversion conditions (8). Their treatment is based on Shockley-Read theory assuming a single-level recombination center. The theory is valid at low injection levels (8), i.e.

$$\frac{\Delta p}{n_i} < \exp \frac{|E_i(\text{bulk}) - E_F|}{kT} \quad [3]$$

where Δp is the deviation from the equilibrium minority carrier concentration as induced by light, n_i is the intrinsic carrier concentration, and E_i and E_F are the intrinsic and equilibrium Fermi levels, respectively. If the injection level is low, the model is obviously applicable to the present case in which the electrode is illuminated in an indifferent electrolyte at potentials negative with respect to the photocurrent-onset potential; in this range, recombination is dominant so that no external current flows [Fig. 1 (d)]. From Eq. [3] it is clear that the condition of a low injection level is indeed satisfied in the present case ($\Delta p < 10^{17} cm^{-3}$, i.e., $\Delta p < n_0$); light intensities were such that the photocurrent was linearly dependent on photon density (10). Sah has shown (11) that, for an extrinsic semiconductor, the nonequilibrium equivalent circuit for the case involving external current flow is identical to the equilibrium case with regard to carrier trapping, recombination, and generation, provided the steady-state carrier concentrations are considered instead of the equilibrium values. This means that the recombination model for the illuminated MOS device (8), also involving steady-state carrier concentrations, must be applicable to hole injection from solution when recombination of minority carriers dominates [Fig. 1 (b)]. Pierret and Sah derive an expression for the recombination resistance on the basis of a transition, within a narrow spatial region in the space-charge layer, from a predominantly hole current at the surface to an electron current in the bulk. This resistance is shown to be potential independent in a wide range. The relationship between the recombination resistance and the generation rate is deter-

mined by the nature of the recombination center. For an efficient level located near midgap with approximately equal capture cross sections for electrons and holes, an inverse square root dependence is predicted ($R_r \propto 1/\sqrt{I_g}$). An inverse linear dependence ($R_r \propto 1/I_g$), as found in the present work, indicates a dominant recombination center somewhat displaced from midgap and with a ratio of capture cross sections considerably different from unity. A similar dependence was found for the Si MOS device and the GaAs EOS system (3, 4).

In this work, we have only considered the two extreme cases: negligible and complete recombination. For an n-GaAs electrode at potentials in the intermediate range at which the anodic photocurrent and cathodic reduction current increase to their limiting values, the recombination resistance increases and the impedance picture becomes more complicated (12). Nevertheless, the presence of a recombination resistance in the equivalent circuit is a clear indication that minority carriers are responsible for the electrochemical reaction. In a subsequent paper, we shall show how this approach can be used to obtain information concerning a more complex reduction reaction at GaAs (13).

Acknowledgments

The authors wish to thank Dr. R. Memming (Philips Forschungslabor, Hamburg) and Dr. C. J. M. van Oordorp for helpful discussions.

Manuscript submitted Nov. 23, 1983; revised manuscript received Nov. 8, 1984.

Philips Research Laboratories assisted in meeting the publication costs of this article.

REFERENCES

1. R. Memming, *This Journal*, **116**, 785 (1969).
2. H. Gerischer, *Faraday Discuss. Chem. Soc.*, **70**, 137 (1980).
3. J. J. Kelly and P. H. L. Notten, *This Journal*, **130**, 2452 (1983).
4. R. F. Pierret and C. T. Sah, *Solid-State Electron.*, **13**, 289 (1970).
5. H. Gerischer and I. Wallem-Mattes, *Z. Phys. Chem. N.F.*, **64**, 187 (1969).
6. V. A. Myamlin and Yu. V. Pleskov, "Electrochemistry of Semiconductors," pp. 316-320, Plenum Press, New York (1967).
7. K. Lehovec and R. Slobodskoy, *Solid-State Electron.*, **7**, 59 (1964).
8. R. F. Pierret and C. T. Sah, *ibid.*, **13**, 269 (1970).
9. S. Menezes and B. Miller, *This Journal*, **130**, 517 (1983).
10. R. A. Smith, "Semiconductors," pp. 342-343, Cambridge University Press, Cambridge (1978).
11. C. T. Sah, *Solid-State Electron.*, **13**, 1547 (1970).
12. P. Allongue and H. Cachet, *J. Electroanal. Chem.*, **119**, 371 (1981).
13. J. E. A. M. van den Meerakker, *Electrochim. Acta*, In press.

Epitaxial Growth and Characterization of β -SiC Thin Films

P. Liaw^{*1} and R. F. Davis

Department of Materials Engineering, North Carolina State University, Raleigh, North Carolina 27695-7907

ABSTRACT

Crack-free monocrystalline β -SiC films having very smooth final surfaces may be reproducibly grown at 1600 K and 760 torr on (100) Si substrates using SiH₄ and C₂H₄ and H₂ if the Si is initially reacted with the C₂H₄ alone. This initial step produces a buffer layer which reduces the mismatches in expansion coefficients and lattice parameters and thus allows the subsequent growth of the β -SiC film to a thickness exceeding 5 μ m. It is necessary to heat the Si wafers from room temperature to the reaction temperature in a C₂H₄ and H₂ environment rather than preheating the substrates to the reaction temperature. An off-axis orientation of the Si in excess of approximately 3° results in a very rough final growth surface on the β -SiC film.

Silicon carbide (SiC) possesses a unique combination of properties which are not available from other more common semiconductor materials. In addition to its high thermal conductivity and melting point, extreme hardness and excellent resistance to chemical attack and mechanical damage, it is also characterized by a range of high energy bandgaps [2.2-3.3 eV, depending on the structure type; (see following discussion and Ref. (1) and (2))] and a high saturated drift velocity [$2.2.7 \times 10^7$ cm/s (3-5)], which are particularly important for electronic applications. As such, this material has, for several years, been considered the leading candidate material for future employment in thin film solid-state electronic devices which would be subjected to high temperatures or high frequencies or high power loads or a combination of these severe conditions.

Silicon carbide may exist in one particular crystallographic structure, if grown under carefully selected and controlled conditions. However, as a result of its low stacking fault energy, this material frequently occurs as a collection of several slightly different one-dimensional polymorphs or "polytypes" having different stacking sequences along the directions perpendicular to the closest packed planes. Alpha SiC forms in more than 140 identified hexagonal or rhombic polytypes, whereas, β -SiC possesses only the cubic zinc blende structure. An excel-

lent review of these polytypes and their formation has recently been published by Jepps and Page (6).

The common occurrence of the β polytype as a product of vapor and liquid growth processes, its transformation to one or more of the alpha forms at high temperatures and its recent commercial availability have caused it to be considered almost as a separate material. Because of its small bandgap (2.3 eV) and ease of growth at relatively low temperatures, the β form is currently considered the most desirable polytype for microelectronic applications.

The previous (1956-1973) major research periods concerned with the growth of SiC as an electronic material concentrated heavily on very high temperature sublimation-condensation (Lely) processes which formed an unreproducible variety of alpha polytypes within each crystal. Solution growth via the reaction of molten Si with its graphite container was a common method of growing β -SiC; however, these crystals were invariably small and highly twinned and therefore of little use for electronic applications. Chemical conversion of the Si surface and chemical vapor deposition (CVD) processes were also employed. However, the results in terms of thickness, single crystallinity, and/or device quality of the films were not sufficient to engender continued substantial funding of this research. For an essentially complete record of these earlier studies, the reader is referred to the published proceedings of the three previous SiC conferences (7-9) and their bibliographies.

Research in SiC for semiconductor applications has continued, albeit at a reduced level of effort, with positive

*Electrochemical Society Active Member.

¹Present address: Advanced Micro Devices, Sunnyvale, California 94088.

results in thin film growth, characterization, and the fabrication of simple devices. The most active group has been Matsunami and co-workers with the development of blue LED's by liquid-phase epitaxy (10) and chemical vapor deposition (11), photoluminescence studies of Al, Ga, and B acceptors in 4H, 6H, and 3C polytypes grown from a Si melt (12), the determination of site dependent impurity levels in 4H, 6H and 15R polytypes (13), the thermal oxidation (14) and C-V characterization of Al-SiO₂-SiC MOS structures (15), and the structure and properties of sputtered amorphous SiC films (16). Research in Germany directed by Münch has also led to the fabrication of blue LED's (17) as well as field effect and bipolar transistor (18) via vapor growth and liquid-phase epitaxy, additional understanding concerning thermal oxidation and electrolytic etching of SiC (19), and the determination of the high field saturated electron drift velocity (5) and the breakdown field in vapor-grown SiC p-n junctions (20). Finally, research has continued in the Soviet Union, primarily in the laboratory for Wide Band Gap Semiconductors in Leningrad, directed by Tairov. In addition to the solid-state physics studies on doped SiC [e.g., see Ref. (21)], considerable progress has been reported in the controlled growth of SiC single crystals having a preselected polytype [see Ref. (22) for a review of this work].

Essentially, all the studies noted above were concerned with the growth or characterization of selected α -SiC forms. However, very recently, Nishino and co-workers in Japan and the U.S. (23, 24) and Addamiano and Sprague (25) have employed a two-step CVD process whereby a "buffer" or "converted" layer is initially formed on a Si substrate surface via a reaction with propane followed by the growth of thin films of β -SiC.

The objectives of the research program reported herein have been: (i) the extension of the aforementioned two-step approach to determine the exact conditions for the formation of single-crystal β -SiC films of sufficient thickness and quality for microelectronic applications, and (ii) the characterization of these films by a variety of techniques. The following sections present the experimental aspects of this program, a discussion of the results obtained, and the major conclusions drawn from this research.

Experimental

An RF heated cold-wall barrel-type CVD reactor was designed and constructed in house especially for the growth of the β -SiC films. Highest purity silane (SiH₄), ethylene (C₂H₄), and H₂ (further purified to 0.1 ppm total impurities via Pd/Ag cell) were used as the Si and C source gases and carrier gas, respectively. HCl provided *in situ* gas phase etching of the (100) and (111) Si single-crystal substrates prior to deposition. Argon was employed for purging the input gas lines and the reaction chamber after each deposition. Nitrogen continually purged the mechanical pumps and the exhaust line to prevent the pyrophoric reaction of SiH₄. The use of the cold-wall vertical reactor noted above contrasts with the uncooled horizontal reactors used by other investigators (23-25). Our use of the former not only allowed films of excellent quality to be produced but also forced a change in the scenario for the two-step deposition process used by others which is described below. This type of reactor was also necessary because of the endothermic nature of SiH₄.

The total pressure in the reaction chamber and the flow rates of each of the gases were independently measured and set-point controlled using a capacitance manometer² and servo-mechanical valves³ for the former and mass flowmeters⁴ and magnetically proportioning valves⁵ for the latter. In this way, fluctuations in the nucleation rates of the reactant species were minimized.

²Model 220 BHS-2A1-B-1000, MKS Instruments, Incorporated, Burlington, Massachusetts.

³Model 253, MKS Instruments, Incorporated, Burlington, Massachusetts.

⁴Model FM-260, Tylan Corporation, Carson, California.

⁵Model 5835A, Brooks Instruments, Hatfield, Pennsylvania.

Both n-type ($\rho = 37$ -420 Ω -cm) and p-type ($\rho = 10$ -50 Ω -cm) Si wafers, having a nominal 1.1 cm diam, were ultrasonically trepanned from larger wafers using 30-40 volume percent (v/o) SiC in distilled H₂O as the abrasive. One side of the as-cut wafers was simultaneously chemically and mechanically polished using the Silver-Rugh-Gardiner method (26). All wafers had a thickness of 0.064 cm and were 1° or 6° off axis from the (100) plane and 2° and 4° off axis from the (111) plane.

Up to 16 of the Si wafers were loaded onto a tapered (3°) 8.9 cm long SiC-coated graphite⁶ susceptor having less than 10 ppm total impurities. The impervious SiC coating eliminated both the possibility of auto-doping and the diffusion of excess C from the susceptor onto the Si substrate.

Prior to each CVD step, the reaction chamber was three times pumped to 10 torr and purged with high purity Ar. Furthermore, the reactant and carrier gases initially bypassed the 6.3 cm id H₂O-cooled, double-wall quartz deposition chamber and were mechanically pumped into a lower stainless-steel chamber. When the preset flow rates were established, the gas mixture was switched via pneumatic valving into the top of the reaction chamber, where it subsequently reacted with the Si substrates. The deposition temperatures were measured on the SiC-coated graphite with an optical pyrometer because of the changing emissivity of the Si with the progressive deposition of SiC.

Initially, a single-step CVD process involving the simultaneous deposition of Si and C directly on the Si surface at 1 atm as well as reduced (to 38 torr) total pressures was employed. The occurrence of more than one phase at low total pressures prompted subsequent computer-aided thermodynamic calculations for the deposition of β -SiC as a function of total pressure, Si/Si+C ratios, and temperature. These results (27) showed that the limits of formation of the β -SiC phase field gradually narrow to essentially a straight line as the total pressure is reduced. Thus, 1 atm was used for the remainder of the experiments. The poor surface quality and the high residual stresses in the films (28) produced by this process promoted the use of the much more successful two-step approach noted in the introduction. In this latter process, approximately 0.30 v/o of C₂H₄ in flowing (3000 sccm) H₂ was introduced into the cold reaction chamber. The substrates were immediately and rapidly heated at approximately 500 K/min from room temperature over a total period of 2.5 min. The maximum possible temperature of 1600 K was achieved during the last 30s of this step. The chamber was subsequently flushed with H₂ for 5-10 min. A standard CVD process was then employed using 0.20 v/o SiH₄ and 0.10 v/o C₂H₄ in flowing (3000 sccm) H₂ at 1600 K. The growth rate was ~ 0.04 μ m/min. When the desired growth had been achieved, the SiH₄ and C₂H₄ valves were closed, the chamber allowed to flush for 5 min with H₂ and the temperature reduced to ambient. No etching of the final growth surface by the final H₂ flush was chemically or visually detected.

Surface characterization and thickness measurements were conducted using SEM and optical microscopy (OM). Conductive coatings or staining was unnecessary as the films were sufficiently conductive for the SEM studies and easily distinguished from the Si in the OM. For structural characterization, both x-ray and selected area electron diffraction techniques were employed. A reflection-type pole-figure device (Schulz goniometer) was used to determine the single- or polycrystallinity and the existence of epitaxy of the grown films. The transmission Laue method was also extensively used for more complete characterization of the crystal structure of the β -SiC films. As both the diamond cubic structure of Si and the zinc blende structure of β -SiC give exactly the same Laue patterns, it was necessary to wax⁷ the entire specimen,

⁶Ultra "F" grade UT-22 graphite, Ultra Carbon, Corporation, Bay City, Michigan.

⁷Apiezon Type W, James G. Biddle Company, Plymouth Meeting, Pennsylvania. The wax was removed using trichloroethylene.

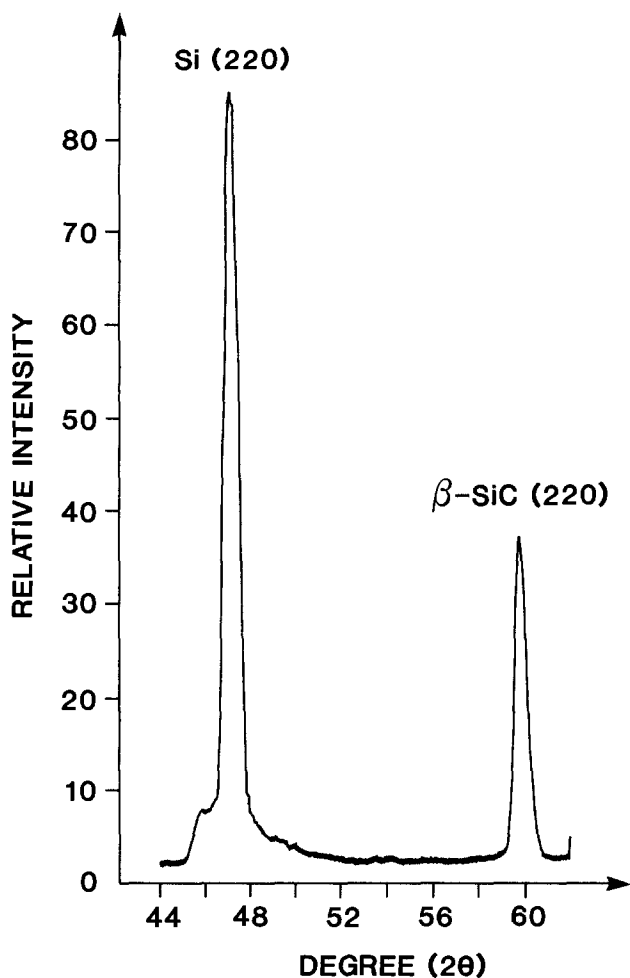


Fig. 1. X-ray diffraction spectrum of an epitaxial β -SiC thin film grown on a (111) Si substrate (this sample was first tilted 35° on the Schulz goniometer and then scanned from 44° - 62°).

except for a 2 mm central spot in the back of the Si substrate, and immerse the sample in an $\text{HF}+\text{HNO}_3$ (2:3 ratio) mixture until a hole was etched in the Si. The remaining Si substrate served as a support for the film. A 16h exposure at 35 kV and 20 mA was usually required to obtain the pattern. The distance between the specimen and the film was 5 cm.

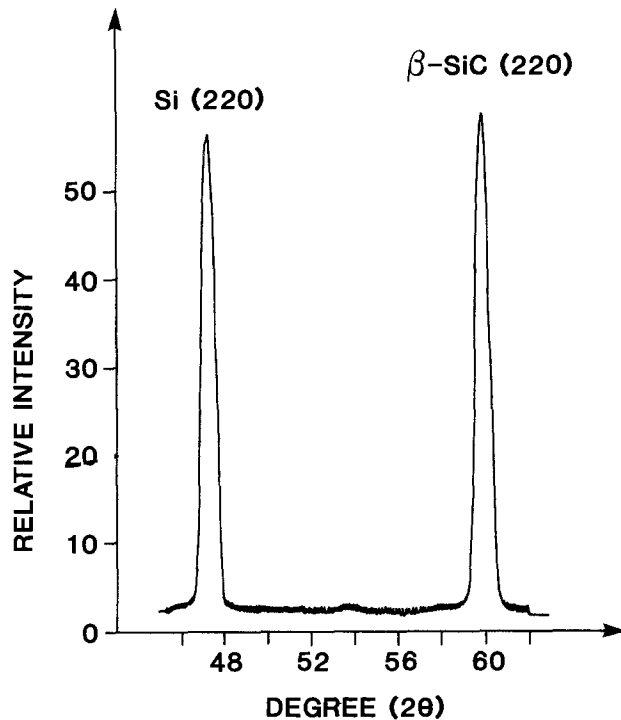


Fig. 2. X-ray diffraction spectrum of an epitaxial β -SiC thin film grown on a (100) Si substrate (this sample was first tilted 45° on the Schulz goniometer and then scanned from 45° - 62°).

Transmission electron diffraction (TED) samples were prepared by ion milling from the Si side at an angle of 15° to the surface. No sample preparation was necessary for the RED diffraction research.

Electrical properties of the films were measured by the van der Pauw technique. These intentionally undoped samples were n-type in character. Ohmic contacts were obtained by sintering an electron-beam evaporated 2000\AA Ni film at 1373 K for 5 min in vacuum. After the measurement, a very thin Ni film was burned into the β -SiC film as a result of Joule heating.

Results and Discussion

Reproducible epitaxial growth of single-crystal β -SiC thin films on (100) and (111) Si has been achieved via the initial reaction of C with the Si surface and the subsequent deposition of a SiC film. Using only the latter half

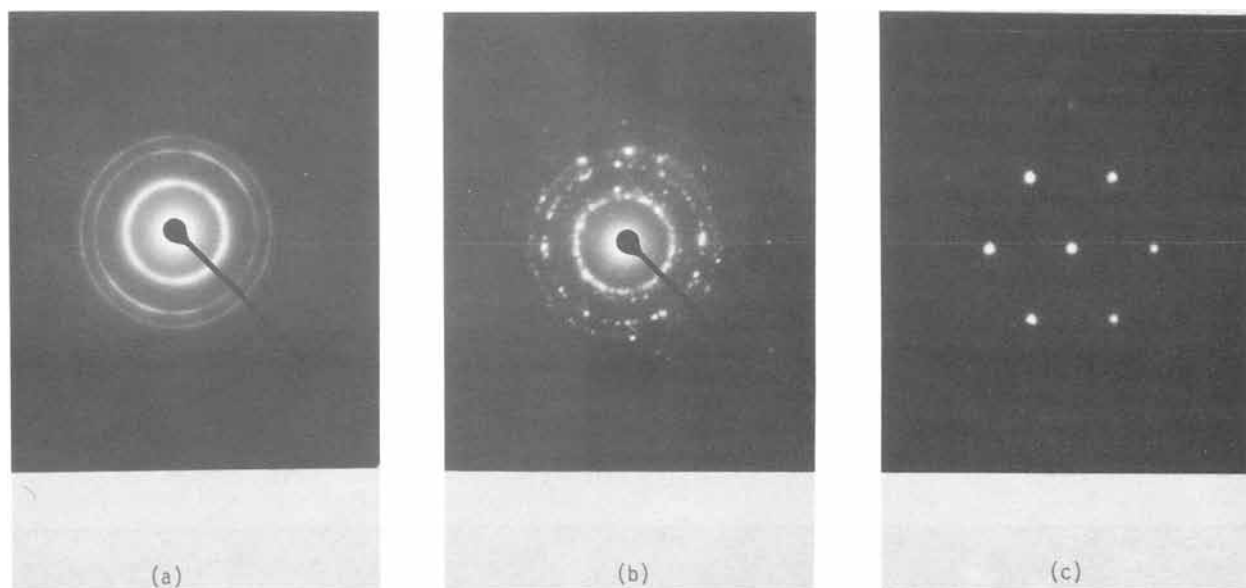


Fig. 3. Transmission electron diffraction patterns of β -SiC thin films grown on (111) Si substrates under the conditions of $P = 1$ atm and $T = 1343$ K (a), 1408 K (b), and 1633 K (c).

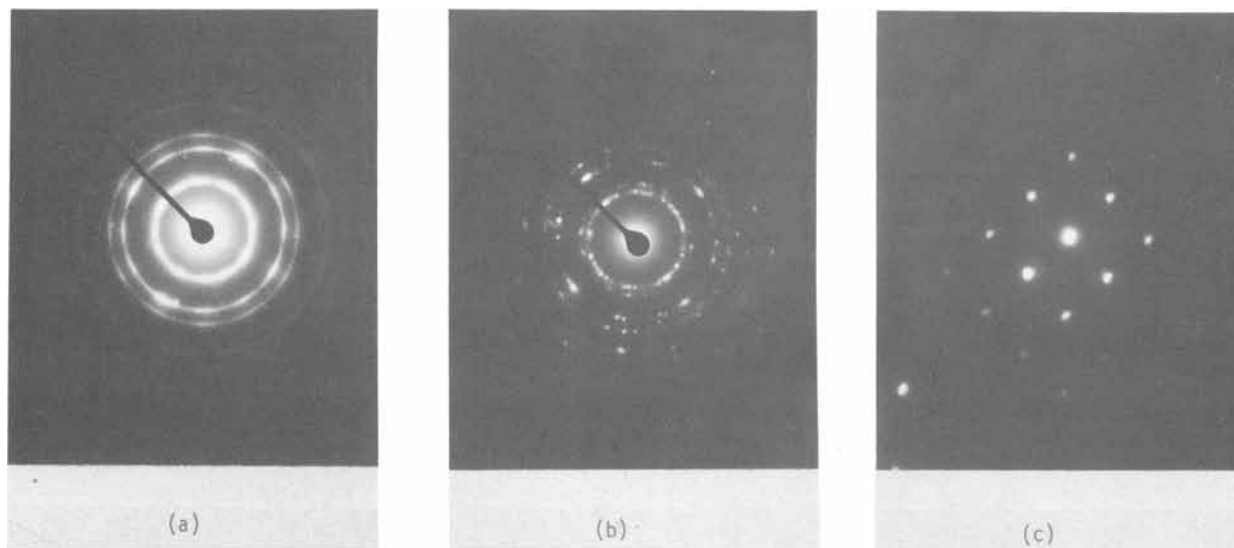


Fig. 4. Transmission electron diffraction patterns of β -SiC thin films grown on (100) Si substrates under the conditions of $P = 1$ atm and $T = 1343$ K (a), 1408 K (b), and 1633 K (c).

of this process did not allow reproducibility or equivalent quality to the two-step process on either of the Si planes.

Figure 1 shows a 2θ scan from 44° to 62° for an epitaxial β -SiC film grown on a (111) Si substrate. In this 2θ range, the (220) peaks resulting from both the β -SiC film and the Si substrate are included if the sample is tilted 35° on the Schulz goniometer so that the (220) is the diffracting plane. By rotating the sample one turn about its normal axis, one can detect three peaks of (220) β -SiC reflections which are separated 120° from each other. This indicates the normal three-fold symmetry of the (220) about the $\langle 111 \rangle$. One may surmise from this study that the crystal structure of the grown (111) β -SiC film is single crystalline in nature.

As for the β -SiC film grown on the (100) Si substrates, Fig. 2 shows the results of a 2θ scan from 45° to 62° . As in the example noted above, the (220) again becomes the principal diffracting plane when the sample is tilted 45° . However, with the (100) Si substrate orientation, the (220) β -SiC peaks are monitored at a 90° separation because of the four-fold symmetry of (220) about [100]. The presence of this symmetry as revealed by the diffraction pattern allows one to conclude that the crystal structure of the grown (100) β -SiC film is also a single crystal.

The above results were also supported by transmission Laue patterns (TLP) for the same film and substrate combinations (28). The (111) pattern also contained twelve spots in three groups of four spots each, which were very close to the (111) spots and which were more difficult to identify. Further investigations showed that these satellite-like spots were on three zone axes and on two rings, which correspond to the (111) β -SiC reflections from the K_α and K_β characteristic radiations of the Cu target. Normally, bending of crystallographic planes as a result of residual stresses causes streaks along the zone axis. However, because a Cu target was used to produce the "white" radiation, wherever the reflections from the characteristic radiation satisfied Bragg's law, a spot occurred instead. Thus these satellite spots note the existence of residual stresses in the grown (111) film.

The (100) pattern also contained extra spots very close to the (221) spots. In this case, it was determined that the extra spots were on two zone axes and on two rings, which correspond to the (220) β -SiC reflections from the K_α and K_β characteristic radiations of the Cu target. Again this indicated the existence of curved planes which formed as a result of stresses in the (100) β -SiC films. A complete discussion of this residual stress phenomena is given in Ref. (28).

Growth temperature was a very important factor in the attainment of single crystallinity in the films. As shown in the TED patterns of Fig. 3a and 4a, the β -SiC films

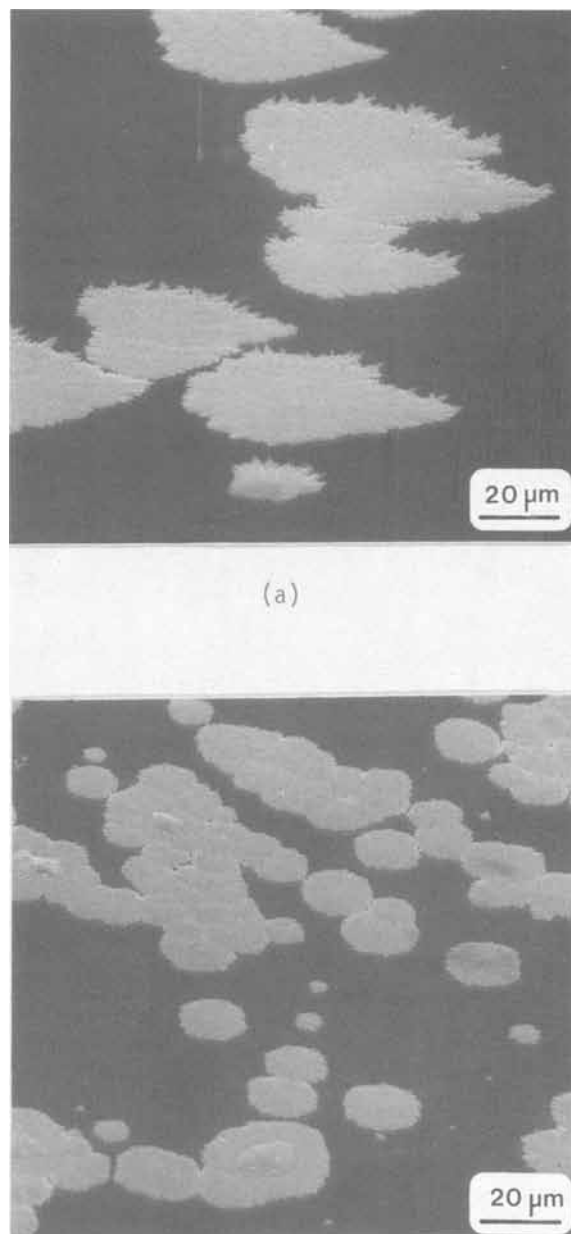
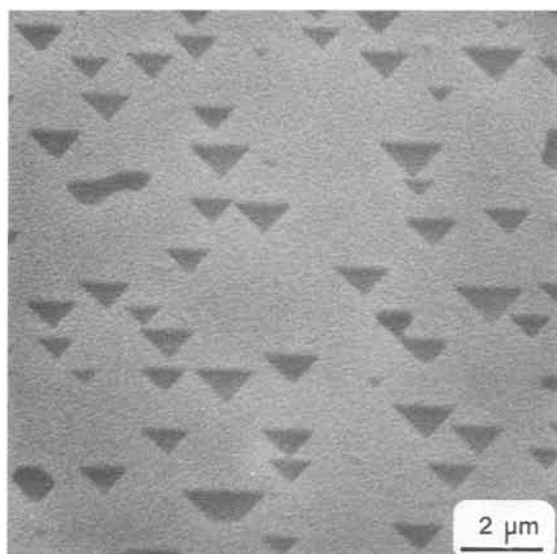
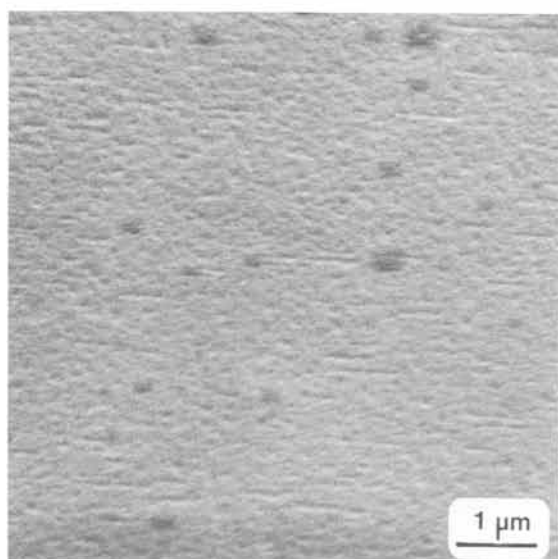


Fig. 5. SEM micrographs of (a) (111) Si and (b) (100) Si substrate surfaces after 3 min chemical conversion at 1600 K with a 1 sccm flow of C_2H_4 and 3000 sccm flow of H_2 .



(a)

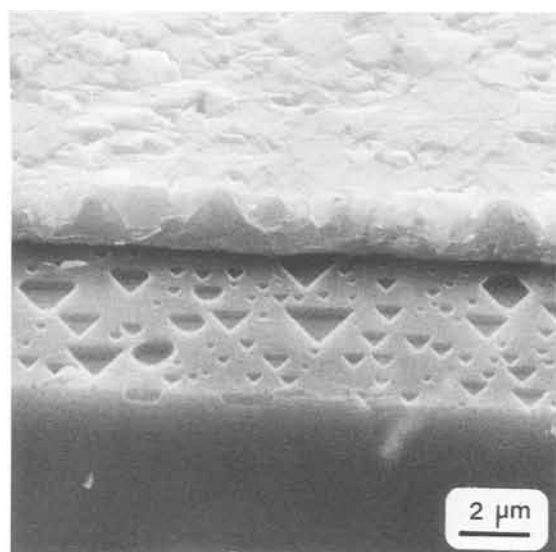


(b)

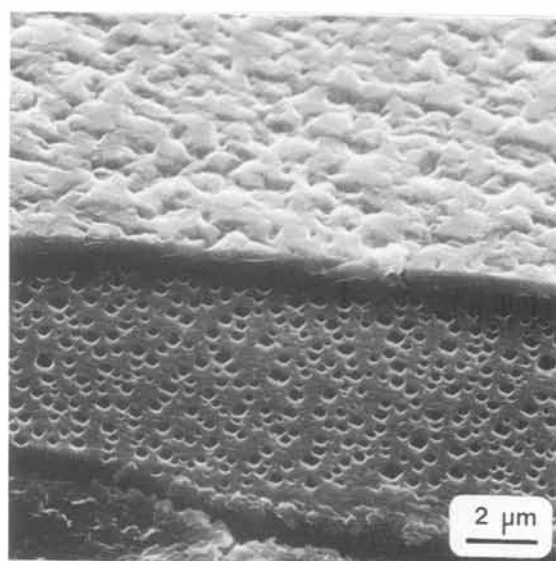
Fig. 6. SEM micrographs of the chemically converted Si surface on (a) (111) Si and (b) (100) Si after a 3 min chemical conversion conducted from room temperature to 1600 K with $C_2H_4 = 1$ sccm and $H_2 = 3000$ sccm and a total pressure of 760 torr.

grown on the (111) and (100) Si substrates, respectively, were polycrystalline when the growth temperature was 1343 K. As the substrate temperature increased to 1408 K, the grain size increased and spot-containing rings were observed, as revealed by Fig. 3b and 4b. Increasing the temperature further to 1633 K allowed monocrystalline films to grow on both substrates (see Fig. 3c and 4c). Additional x-ray Laue research showed that monocrystallinity could be achieved on the (111) Si at temperatures as low as 1583 K. However, the critical temperature for similar results on (100) Si was approximately 1600 K. Thus, the epitaxial growth of (111) β -SiC films can be achieved at a relatively lower temperature than that required for the (100) films using the two-step deposition process.

Scanning electron microscopy was also used extensively to characterize both the chemical conversion process and the growth of the β -SiC thin films. The former



(a)



(b)

Fig. 7. SEM micrographs showing the β -SiC film surface and the fractured side surface (top portion of the photographs) as well as the Si substrate upper surface and the fractured side surface (bottom portion of the photographs) for films grown on (a) (111) Si and (b) (100) Si.

was initially conducted under isothermal conditions at 1600 K with all other conditions being the same, as in the rapid heating procedure noted above. This produced relatively large localized deposits of C, as shown in Fig. 5. These deposits were triangular in shape on the (111) Si and rectangular on the (100) Si substrates. These shapes are characteristic of the voids found in the Si in these orientations, as noted below. It is believed that these areas acted as nucleation sites for the subsequent CVD growth, as the β -SiC films tended to be polycrystalline with very rough surfaces. By contrast, heating the Si substrates from room temperature to 1600 K in flowing C_2H_4 in H_2 at 760 torr produced thin but much more uniform deposits, as shown in Fig. 6. The voids revealed in the micrographs are principally on the Si surface; however, some portion of these defects may also extend to the surfaces of the converted layers as well as the final films. An acute example of this phenomenon is shown in Fig. 7. It is be-

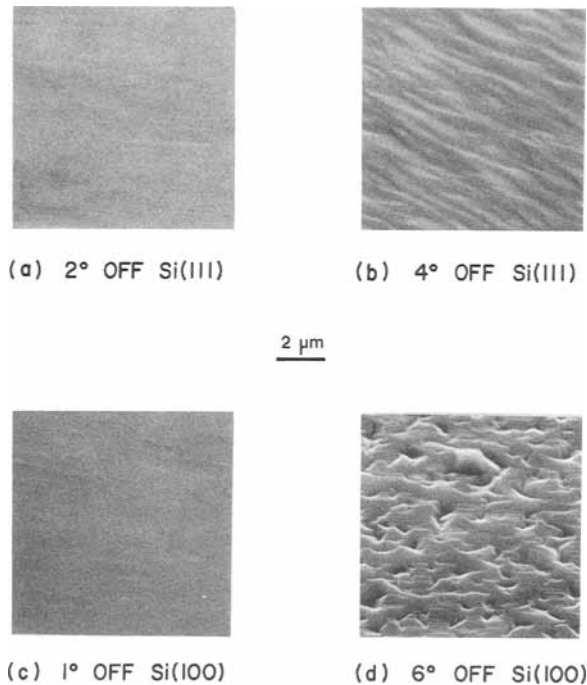


Fig. 8. Surface morphology of epitaxial β -SiC thin films grown on Si substrates with various off-axis orientations.

lieved that the existence of the voids is related to the growth mechanism involved in the chemical conversion of the Si substrate. In this process, the Si atoms diffuse out through the converted layer to react with the C atoms at the growth surface (29, 30). Thermal etching of the Si during heating was not responsible for the pitted Si surfaces; no such depressions were found in several (111) and (100) Si wafers heated to 1600 K in flowing H_2 for 10 min.

Abnormal needle-type growth also occurred but only in the polycrystalline β -SiC films having either (111) or (100) orientation. The initial growth conditions were found to be very critical to the presence of these needles. For example, no such needles were found in the subsequent β -SiC layers when the initial chemical conversion of the Si substrate was conducted from room temperature to 1600 K for 2.5 min. However, needles were observed when the chemical conversion was performed under isothermal conditions at 1600 K for 1 min. The nucleation in the latter case was much less controlled and resulted in the formation of occasional needles. Finally, it was also found that using a prolonged (e.g., 10 min) conversion time resulted in a very rough final surface on the β -SiC films.

During the latter stages of this research program, the growth techniques were sufficiently refined so as to produce very smooth final growth surfaces on both the (111) and (100) β -SiC films. However, the degree of smoothness decreased markedly with increase in off-axis orientation of the Si substrates. Using the same growth conditions and two-step growth procedure noted in the section on experimental procedure for all samples, it was found that the final surface of the films on (111) Si and (100) Si hav-

ing 2° and 1° off-axis orientations, respectively, were very smooth, as shown in Fig. 8a and 8c. However, films grown on similar wafers with 4° and 6° off-axis orientations had a moderate or very rough appearance.

The results of preliminary van der Pauw measurements are given in Table I for typical (100) β -SiC films having different thicknesses. All films were n-type, which may have been caused by the incorporation of nitrogen, which is a donor impurity, or by the existence of defects in the films. Additional study concerned with the correlation of defect substructure with electrical properties is now ongoing.

Summary

Reproducible growth of high purity monocrystalline thin films of β -SiC have been produced on Si using a unique cold-wall barrel-type reactor and a two-step process of surface conversion and subsequent film deposition. Direct growth of monocrystalline β -SiC films on (111) or (100) Si at temperatures up to 1600 K was difficult and nonreproducible. However, crack-free films having very smooth final surfaces can be grown on (100) Si if the Si surface is initially reacted with C_2H_4 carried in H_2 . This step is then followed by conventional CVD of the β -SiC using a mixture of SiH_4 and C_2H_4 , which are separately decomposed on the initial converted layer. It was found necessary to rapidly heat the Si substrates from room temperature to the conversion temperature in a C_2H_4 and H_2 environment rather than preheating the substrates to the reaction temperature. The off-axis orientation of the Si substrate was also found to be important in the smoothness of the final surface.

Acknowledgments

The authors wish to thank Dr. H. H. Stadelmaier for his valuable assistance with the x-ray diffraction research. The support of the Office of Naval Research via Grant no. N00014-79-C-0121 is also gratefully acknowledged.

Manuscript submitted June 18, 1984; revised manuscript received Nov. 12, 1984.

North Carolina State University assisted in meeting the publication costs of this article.

REFERENCES

- W. F. Knippenberg, *Philips Res. Rpt.*, **18**, 161 (1963).
- J. W. Faust, Jr., in "Silicon Carbide—1973," R. C. Marshall, J. W. Faust, Jr., and C. E. Ryan, Editors, p. 668, University of South Carolina Press, Columbia, SC (1974).
- H. W. Berman, T. M. Heng, N. C. Nathenson, and R. B. Campbell, in "Silicon Carbide—1973," R. C. Marshall, J. W. Faust, Jr., and C. E. Ryan, Editors, p. 500 University of South Carolina Press, Columbia, SC (1974).
- D. K. Ferry, *Phys. Rev. B*, **12**, 2361 (1975).
- W. v. Münch and E. Pettenpaul, *J. Appl. Phys.*, **48**, 4823 (1977).
- N. W. Jepps and T. F. Page in "Progress in Crystal Growth and Characterization," Vol. 7, P. Krishna, Editor, pp. 259-308, Pergamon Press, New York (1983).
- "Silicon Carbide, A High Temperature Semiconductor," by J. R. O'Connor, and J. Smiltens, Editors, Pergamon Press, New York (1960).
- "Silicon Carbide—1968," H. K. Henisch and R. Roy, Editors, Pergamon Press, New York (1969).
- "Silicon Carbide—1973," R. C. Marshall, J. W. Faust, Jr., and C. E. Ryan, Editors, University of South Carolina Press, Columbia, SC (1974).
- A. Susuki, M. Ikeda, N. Nagao, H. Matsunami, and T. Tanaka, *J. Appl. Phys.*, **47**, 4546 (1976).
- S. Nishino, A. Ibaraki, H. Matsunami, and T. Tanaka, *Jpn. J. Appl. Phys.*, **19**, L353 (1980).
- A. Susuki, H. Matsunami, and T. Tanaka, *This Journal*, **124**, 241 (1977).
- M. Ikeda, H. Matsunami, and T. Tanaka, *Phys. Rev. B*, **22**, 2842 (1980).
- A. Susuki, H. Matsunami, and T. Tanaka, *This Journal*, **125**, 1896 (1978).
- A. Susuki, K. Mamenno, N. Furui, and H. Matsunami, *Appl. Phys. Lett.*, **39**, 89 (1981).
- H. Matsunami, H. Masashiro, and T. Tanaka, *J. Elec-*

Table I. Electrical properties of n-type (100) β -SiC samples having three different thicknesses and grown on p-type (100) Si substrates

Sample no.	810916	810917	810919
Epitaxial film thickness (μm)	1.25	5.0	7.5
Resistivity ($\Omega\text{-cm}$)	0.13	0.38	0.22
Hall coefficient	-11.4	-97.4	059.5
Hall mobility ($\text{cm}^2/\text{V}\cdot\text{s}$)	88.0	256.0	270.0
Carrier concentration (cm^{-3})	5.5×10^{17}	6.5×10^{16}	1.1×10^{17}

- tron. Mater.*, **8**, 249 (1979).
- 17a. W. v. Münch, W. Kurzinger, and I. Pfaffender, *Solid State Electron.*, **19**, 871 (1976).
 - 17b. W. v. Münch and W. Kurzinger, *ibid.*, **21**, 1129 (1978).
 - 17c. W. v. Münch, *J. Electron. Mater.*, **6**, 449 (1977).
 18. W. v. Münch, Private communication.
 19. W. v. Münch and I. Pfaffender, *This Journal*, **122**, 642 (1975).
 20. W. v. Münch and I. Pfaffender, *J. Appl. Phys.*, **48**, 4831 (1977).
 21. G. K. Safaraliev, Yu. M. Tairov, V. F. Tsvetkov, and Yu. Kriger, *Sov. Phys. Semicond.*, **10**, 226 (1976).
 22. Y. M. Tairov and V. F. Tsvetkov, in "Progress in Crystal Growth and Characterization," Vol. 7, P. Krishan, Editor, p. 111, Pergamon Press, New York (1983).
 23. H. Matsunami, S. Nishino, and H. Ono, *IEEE Trans. Electron. Dev.*, **ed-28**, 1235 (1981).
 24. S. Nishino, J. A. Powell, and H. A. Will, *Appl. Phys. Lett.*, **42**, 460 (1983).
 25. A. Addamiano and J. A. Sprague, *ibid.*, **44**, 525 (1984).
 26. L. H. Blake and E. Mendel, *Solid-State Technol.*, **42** (1970).
 27. A. I. Kingon, L. J. Lutz, P. Liaw, and R. F. Davis, *J. Am. Ceram. Soc.*, **66**, 558 (1983).
 28. P. Liaw and R. F. Davis, *This Journal*, **131**, 634 (1984).
 29. J. Graul and E. Wagner, *Appl. Phys.*, **21**, 67 (1972).
 30. C. J. Mogab and H. J. Leamy, *J. Appl. Phys.*, **45**, 1075 (1974).

Transient Behavior during Film Removal in Diffusion-Controlled Plasma Etching

Richard C. Alkire* and Demetre J. Economou**

Department of Chemical Engineering, University of Illinois, Urbana, Illinois 61801

ABSTRACT

A mathematical model is formulated to analyze transient behavior during film removal from closely spaced wafers in a barrel plasma etching reactor. The model incorporates diffusion and simultaneous reactions which include the etching process as well as recombination reactions of both volume and surface types. The analysis relates the effect of geometric and operating variables to process characteristics such as etch uniformity, over-etch exposure, and throughput. Dimensionless system parameters are identified and are used to express computed results in general form. Regions of operating conditions that permit etch uniformity within specified tolerances are found, and optimum settings for inter-wafer spacing and reactor pressure to achieve maximum throughput are calculated.

Important goals for plasma processing include yield, throughput, and uniformity. Variables which are commonly controlled to achieve these goals include reactor geometry, design and operating conditions, choice of chemicals introduced into the plasma, and adjustment of wafer position within the reaction zone. It is the nature of such complex systems that engineering trade-offs exist in identifying "optimum" settings. Often, however, a seemingly minor adjustment in a sensitive variable can cause a major change in performance. Also, it is invariably difficult to translate successful experience with one system to a new system on the basis of intuition alone. For these reasons, purely empirical programs of development can be time consuming.

Mathematical methods have been used to model a wide variety of chemical reactor systems, and have been found useful in guiding development strategies for improvement. In the present study, a mathematical model was developed to predict transient behavior during film removal from closely spaced wafers in a barrel etcher.

The barrel plasma etching reactor, shown schematically in Fig. 1, consists of a cylindrical quartz chamber that has input gas manifolds and a vacuum pumping outlet. RF power, commonly at 13.56 MHz, is coupled to the reactor through external electrodes and an impedance matching network. The wafers are loaded on a boat in a stand-up configuration with the wafer axes along the barrel axis. In order to achieve high throughput, the interwafer spacing is made small so that the reactor may hold dozens of wafers in a single batch. During operation, gas is continuously introduced into the reactor. Active species, which are generated by electron-impact dissociation in the plasma region, diffuse in the interwafer space and react with the film on the wafer surface. At the same time, the active species may degrade by recombination reactions within the reactor volume or on the walls. Since etching is solely due to neutral species, the resulting edge-profile exhibits mask "undercut" characteristic of isotropic etching. Hence, the barrel etcher cannot be used for etching

fine line geometries. Sometimes an Al perforated cylinder is placed coaxially around the wafers. With the "etch tunnel" present, the plasma is confined in the annular region between the metal cylinder and the reactor wall; active species have then to diffuse through the perforations and, since the diffusion path is lengthened, the etch rate is smaller with the etch tunnel.

Stripping of photoresist in an oxygen plasma in a barrel-type reactor was the first application of plasma etching in semiconductor processing (1). Etching of Si, poly-Si, and Si₃N₄ in fluorine containing plasmas (especially in CF₄/O₂ mixtures) quickly found widespread applications (2). Similar reactors are also used for LPCVD processes (4, 18).

Etch uniformity and throughput are of particular importance in any plasma etching process. Across-wafer and wafer-to-wafer uniformity are both critical in etching patterned films since local loading can rapidly enhance mask undercut after the end point has been reached. Parameters that affect uniformity and throughput include RF power input, chamber pressure, gas flow rate and distribution, wafer spacing, wafer diameter, and tem-

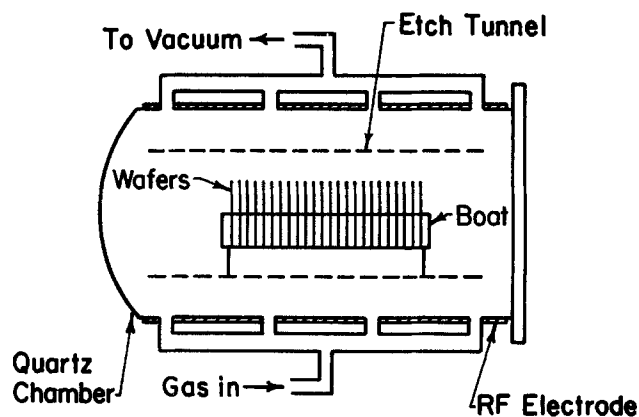


Fig. 1. Schematic of a barrel plasma etching reactor

*Electrochemical Society Active Member.

**Electrochemical Society Student Member.

perature. Several investigators have reported models for diffusion-controlled plasma etching in barrel reactors (5, 6). With assumption of steady-state conditions, the effect of process parameters on etch uniformity was studied.

In the present work, transient removal of a film from a wafer stacked in a barrel plasma etcher is investigated. Transport and reaction phenomena are used to predict behavior and to identify dimensionless scale-up parameters. This study differs from past work in that transient behavior is included so that the duration of etch cycle (throughput) and of over-etch exposure may be investigated. While actual plasma systems are more complex, the following model provides a basic framework which may be expanded as additional refinements are added.

Theoretical Formulation

Let us for the moment concentrate on events happening in the interwafer space, regarding the gas discharge outside the wafer stack as simply the source of etchant species. The plasma region is treated later. Figure 2, not drawn to scale, is a schematic representation of the radially symmetric cell formed by two wafers facing each other. Prior to the onset of etching, a film of uniform thickness exists on the wafer surfaces. The rate of film removal depends on the concentration distribution in the interwafer gap. To an extent that depends upon operating conditions, the etch rate is highest on the periphery of the wafer. Film in this region thus clears first, and subsequent film removal would then take place in more inaccessible regions. Figure 2 illustrates the situation part way through the process, where film has been cleared entirely from the outer portion of the wafer, while the inner region is yet to clear. As etching proceeds, the concentration distribution changes to conform to the reactivity distribution along the wafer surface. While the film may eventually be removed everywhere, the peripheral regions would meanwhile be exposed to overetching conditions which, in many systems, adversely affect product quality.

The following assumptions preserve the salient features of the system and also streamline the task of computation. 1. The spacing between adjacent wafers is sufficiently smaller than the wafer radius so that significant concentration variations occur only in the radial direction. 2. Convection is negligible with respect to diffusion

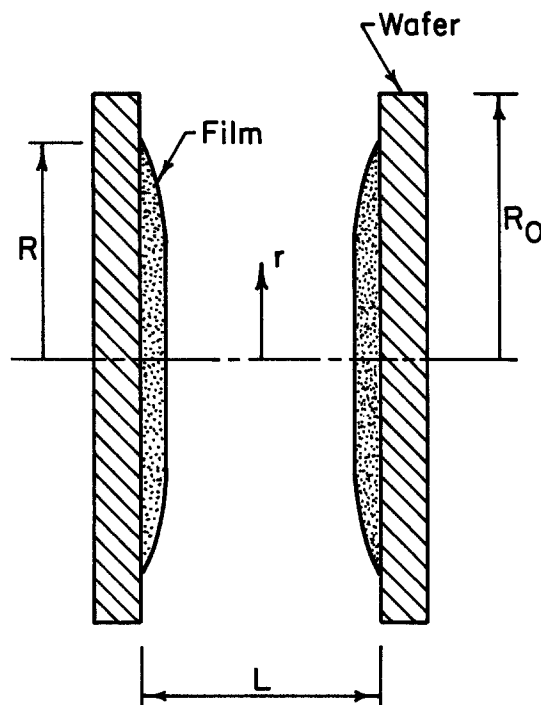


Fig. 2. Schematic of the radially symmetric region between two successive wafers.

in the interwafer region owing to the large value of the diffusion coefficient. An order of magnitude calculation showed that, even if all the gas were flowing parallel to the wafer surfaces, the Pe number ($=R_0 u_0 / D$) would be less than 0.05. In practical systems, with the gas outlet at the back of the quartz barrel, most of the gas flow is normal to the wafer surfaces. Thus, practical Pe numbers are even smaller. 3. The etching reaction is first order; this has been shown for photoresist stripping in oxygen (6) and Si etching in fluorine (7). 4. The etching reaction proceeds to completion at or near the film surface (6) over a distance much smaller than the diffusion length of the etching species, and the reaction products do not affect the etching process (8). 5. The substrate is not etched. Hence the model is applicable to processes such as photoresist stripping in an O_2 plasma or Si etching in a CF_4/O_2 plasma with SiO_2 as the substrate. 6. The pressure remains constant during an etch cycle; this can be achieved by using a pressure feed-back control system. 7. Operation is isothermal with no spatial variations of diffusivity or reaction rate constants. This assumption will not be valid in cases of highly exothermic etching reactions. For example, in etching Si at $0.5 \mu\text{m}/\text{min}$ in a F containing plasma, the adiabatic temperature rise of a 10 cm diam 0.5 mm thick slice will be $1.3^\circ\text{C}/\text{s}$. Furthermore, severe temperature variations will occur during start-up, unless a preheat-treatment with a N_2 or Ar plasma is applied. 8. The concentration of etchant at the wafer edge remains constant during the etch cycle. However, if the etching reaction is the main loss mechanism for the etchant species, and the reaction rate distribution along the wafer surface is nonuniform, the etchant concentration at the wafer edge (c_0) will change with time during a single etch cycle. This is because the amount of film remaining on the wafers will also change with time (loading effect). Such a change in c_0 could be predicted by Eq. [19] to be derived later. The calculations presented in this work did not account for any changes in c_0 during an etch cycle (see also "Conclusions" section). 9. The concentration profiles adjust rapidly to the gradual movement of the film front during depletion. Therefore, at any particular moment, the concentration distribution is at the steady-state distribution which corresponds to the reactivity conditions prevailing at that moment. This "pseudo-steady-state" approximation is valid provided that the time scale over which film depletion occurs (equal to $\chi h_0 / k_2 c_0$, see also expression for τ in Eq. [5]) is much greater than the "characteristic" diffusion time (R_0^2 / D). In other words, the following inequality should hold: $\chi h_0 D / k_2 c_0 R_0^2 \gg 1$. For typical values of the parameters (Table I), this ratio is found to be greater than 10^3 .

During etching, the thickness of etchable material left at a certain location and time will be given by

$$h(r,t) = h_0 - \int_0^t \frac{k_2}{\chi} c(r,t) dt \quad [1]$$

The concentration distribution $c(r,t)$ varies with time during the etching process and is calculated by application of transport laws to the movement of etchant species. The remaining text in this section consists of three segments: the general model, a limiting case valid in the absence of recombination reactions, and a method for determining the concentration of etching species at the edge of the wafer stack.

General model.—Under the foregoing assumptions stated above, the conservation equation for the etching species is

$$D \frac{1}{r} \frac{d}{dr} \left(r \frac{dc}{dr} \right) = \frac{2k_2}{L} c + 2k_1 c^2 [A_2] + \frac{v_0 \omega}{2L} c \quad [2]$$

with the boundary conditions

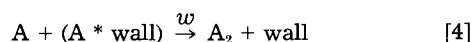
$$c = c_0 \text{ at } r = R_0$$

$$\frac{dc}{dr} = 0 \text{ at } r = 0$$

The left-hand side of Eq. [2] represents the radial diffusion of etchant into the region between the wafers, while the right-hand side (rhs) corresponds to the various reactions which occur. The first term on the rhs of Eq. [2] represents etching. Since only radial concentration gradients are assumed to exist, the heterogeneous reaction rate k_2c is transformed to a homogeneous rate term by multiplication by the surface to volume ratio $2/L$. Both surfaces have been assumed reactive, *i.e.*, the wafers stand back to back during etching. When etching patterned films, this term has to be multiplied by the fraction of the surface occupied by etchable material. Note that $k_2 = 0$ for $r > R$, where the film no longer exists (Fig. 2). The second term on the rhs of Eq. [2] represents volume recombination reactions of the active species of the form



A_2 is the parent molecule which gives A, the etching species, by electron-impact dissociation. A_2 acts as a third body for recombination to occur. The presence of a third body is required to conserve momentum and energy during recombination. The reverse of reaction [3] proceeds at negligibly small rates at the low temperatures used in plasma etching [*e.g.*, the equilibrium constant for the reaction $F_2 \rightleftharpoons 2F$ is $\approx 10^{-24}$ mol/cm³ at 300 K (19)]. When the concentration of the etching products is low, $[A_2] \approx P/R_g T - [A] = P/R_g T - c$. The third term on the rhs of Eq. [2] accounts for wall recombination of the active species in reactions of the form



This term results by multiplying the random flux of etchant striking the wafer surface ($1/4 v_0 c$) by the surface to volume ratio ($2/L$) and by the wall recombination coefficient w , which is assumed constant throughout the wafer surface. The wall recombination reaction is first order since an impinging atom recombines with an atom already adsorbed on the surface (9).

Before proceeding further, it is convenient to rewrite the governing equations in terms of dimensionless quantities based on the following definitions

$$\begin{aligned} \zeta &= \frac{r}{R_0} & H &= \frac{h}{h_0} \\ C &= \frac{c}{c_0} & \tau &= \frac{k_2 c_0}{\chi h_0} t \end{aligned} \quad [5]$$

When the variables defined in Eq. [5] are introduced into Eq. [1] and [2], the following dimensionless equations arise

$$H = 1 - \int_0^r C d\tau \quad [6]$$

$$\frac{d^2 C}{d\zeta^2} + \frac{1}{\zeta} \frac{dC}{d\zeta} = \phi_0^2 C + \alpha C^3 + \beta C^2 + \gamma C \quad [7]$$

with

$$\begin{aligned} \alpha &= -\frac{2k_1 R_0^2 c_0^2}{D} & \gamma &= \frac{v_0 w R_0^2}{2LD} \\ \beta &= \frac{2k_1 P R_0^2 c_0}{(R_g T) D} & \phi_0^2 &= R_0^2 \frac{2k_2}{LD} \end{aligned} \quad [8]$$

The dimensionless boundary conditions become

$$C = 1 \text{ at } \zeta = 1$$

$$\frac{dC}{d\zeta} = 0 \text{ at } \zeta = 0$$

Dimensionless number ϕ_0 is comparable to the Thiele Modulus found in catalytic reactor design (17); ϕ_0 represents the relative importance of the kinetics of etching as

compared to diffusion. If $\phi_0 \gg 1$, for example, diffusion is the controlling step, and one may expect concentration gradients to develop in the interwafer space and the etch rate distribution to be nonuniform. Under such conditions, the outer edge of the wafer would be exposed to overetching, while the center is yet to clear. If $\phi_0 \ll 1$, the etching reaction is sluggish and the reaction rate distribution is uniform all over the reacting surface.

Dimensionless groupings α and β describe volume recombination *vs.* diffusion effects. For example, if $\beta \gg 1$, the reactive species recombine before they have any chance to diffuse and etch the wafer surface. Volume recombination reactions are strongly dependent on pressure. For instance, α and β increase with the third power of pressure. Notice that since the partial pressure of the etching species is usually less than 10% of the reactor total pressure, $|\alpha| \leq 0.1\beta$. Finally, grouping γ describes surface recombination *vs.* diffusion effects and is affected by both the surface to volume ratio and the wall recombination coefficient. The latter depends critically on the nature and the condition of the surface.

By solving Eq. [6] and [7], the effect of process parameters (c_0 , P , D , k 's) and of geometric factors (L , R_0) on etch uniformity, overetch exposure, and total etch time can be determined. In particular, optimum conditions for high throughput can be identified. The above model extends previous studies by accounting for both volume and surface recombination reactions. In addition, the model includes transient effects owing to the pseudo-steady-state clearing of the film.

Note that Eq. [7] is general enough to handle more complex recombination reaction schemes. An example concerning an oxygen plasma is given in the Appendix.

The solution to Eq. [6] and [7] was obtained in a stepwise manner. The wafer was divided in a number of concentric rings of equal width. At each time step, the concentration profile was found by linearizing Eq. [7] about a trial solution and casting the linearized equation into finite difference form by using the central difference approximation. The resulting tridiagonal system was inverted in a CDC Cyber 175. Calculations started about the trial solution obtained analytically when all reaction terms are assumed to be first order in concentration. After the true concentration profile was found, the time required to completely strip the outer ring was determined, and a new film thickness distribution was computed by using Eq. [6]. A new concentration profile was then determined for which the wafer surface was reactive everywhere except for the ring already etched away. With the revised concentration distribution, the time necessary to completely strip the second ring was found. In a like manner, the time needed to strip each successive ring was calculated. The total etch time was the sum of the partial times. For each time step but the first, the solution found in the previous time step was used as the trial solution. No convergence problems were experienced for the values of the parameters used. Results did not differ appreciably by changing the number of rings from 150 to 200. Results were checked against the analytic solution for the limiting case of no recombination reactions discussed below.

Limiting case: no recombination reactions.—When recombination reactions can be neglected ($k_1 = w = 0$), *i.e.*, when the etchant has a long lifetime in the absence of etchable material, Eq. [2] can be simplified into the following two equations

$$D \frac{1}{r} \frac{d}{dr} \left(r \frac{dc}{dr} \right) = \frac{2k_2 c}{L} \quad [9]$$

for $0 \leq r \leq R$, *i.e.*, for the region still occupied by the film, and

$$r \frac{dc}{dr} = \text{const.} \quad [10]$$

for $R \leq r \leq R_0$, *i.e.*, for the film-free region near the periphery of the wafer.

It is convenient to introduce the following dimensionless variables

$$\psi = \frac{r}{R}, C = \frac{c}{c_0}, \text{ and } \phi^2 = R^2 \frac{2k_2}{LD}$$

The film radius R (and not the wafer radius R_0) was used in these definitions so that, although R is changing, the value of ψ is pinned at 1 for $r = R$. The dimensionless form of Eq. [9] is

$$\frac{d^2C}{d\psi^2} + \frac{1}{\psi} \frac{dC}{d\psi} = \phi^2 C \quad [11]$$

which is a Bessel equation. The boundary conditions are

$$C = C_R \text{ at } \psi = 1$$

$$\frac{dC}{d\psi} = 0 \text{ at } \psi = 0 \quad [12]$$

The dimensionless form of Eq. [10] is

$$\zeta \frac{dC}{d\zeta} = \text{const.}$$

with $\zeta = r/R_0$ as before in the general model. The pertinent boundary conditions are

$$C = 1 \text{ at } \zeta = 1$$

$$C = C_R \text{ at } \zeta = \frac{R}{R_0} = \sigma$$

C_R is eliminated by requiring the flux to be continuous at $r = R$. The final result for the concentration distribution is

$$C = \frac{I_0(\phi\psi)}{I_0(\phi) - \phi I_1(\phi) \ln \sigma} \quad 0 \leq r \leq R \quad [13]$$

$$C = 1 + \frac{\phi I_1(\phi) \ln \zeta}{I_0(\phi) - \phi I_1(\phi) \ln \sigma} \quad R \leq r \leq R_0 \quad [14]$$

where

$$I_0(x) = \sum_{n=0}^{\infty} \frac{(x/2)^{2n}}{(n!)^2}$$

is the modified Bessel function of the first kind of order zero and

$$I_1(x) = \sum_{n=0}^{\infty} \frac{(x/2)^{2n+1}}{n!(n+1)!}$$

is the modified Bessel function of the first kind of order one. Since $R = R(t)$, Eq. [13] and [14] have a time dependence built into the equations.

The overall etch rate at any given time is

$$2\pi R_0 LD \left. \frac{dc}{dr} \right|_{r=R_0} = 2\pi LD c_0 \frac{\phi I_1(\phi)}{I_0(\phi) - \phi I_1(\phi) \ln \sigma}$$

If the concentration of the etchant were c_0 throughout the wafer surface, the etch rate would be

$$2k_2 c_0 (\pi R^2)$$

Thus, the "effectiveness factor" η is

$$\eta = \frac{2\pi R_0 LD \left. \frac{dc}{dr} \right|_{r=R_0}}{2k_2 c_0 \pi R^2} = \frac{2I_1(\phi)}{\phi [I_0(\phi) - \phi I_1(\phi) \ln \sigma]} \quad [15]$$

The effectiveness factor is an expression of the actual overall reaction rate as compared to the reaction rate that would be obtained if the concentration were at the bulk value throughout the reacting surface (17). A more general expression for the effectiveness factor is

$$\eta = \frac{2 \int_0^R r e(c) dr}{R^2 e(c_0)} \quad [16]$$

When the reaction rate is first order in concentration, $e = k_2 c$, Eq. [16] becomes

$$\eta = \frac{2 \int_0^R r c dr}{R^2 c_0} = 2 \int_0^1 \psi C d\psi \quad [17]$$

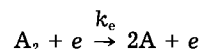
The effectiveness factor concept is used below for the prediction of the etchant concentration in the plasma space surrounding the wafer rack.

The analysis up to this point has concentrated on events occurring in between the wafers. A similar analysis can be applied to LPCVD processes. The recent work by Meyerson and Olbricht (24) is quite relevant. Up to this point, the plasma existing outside the wafer stack has been regarded as simply the source of etchant species. The only parameter, related to the plasma region, that is required for the solution of Eq. [6] and [7] is the etchant concentration at the edge of the wafer stack, c_0 . This quantity depends on a complex way on reactor geometry and operating parameters such as power, pressure, flow rate, etc. Prediction of c_0 would be less difficult for "clean" systems involving a single gas. An example of such a system is photoresist stripping in an O_2 plasma. The procedures for evaluating c_0 are given below.

Etchant concentration in the plasma.—The bulk etchant concentration (c_0) can be predicted by writing a conservation equation for the etchant species (10, 20). These species are generated by electron-impact dissociation of the parent molecules and are eliminated by recombination reactions (Eq. [3] and [4]), etching, and gas flow. Rapid backmixing tends to eliminate concentration gradients in the annular region outside the wafer rack where the plasma exists, particularly when the gas is symmetrically fed through manifolds parallel to the barrel axis. A conservative order of magnitude calculation gave a value for the Pe number less than 0.1. Thus, complete mixing can be assumed in that region (continuous stirred tank reactor model, CSTR). The species balance equation will then read

$$2k_e \langle n_e \rangle [A_2] V_p = \eta k_2 c_0 (N \pi R^2) + \frac{v_0 w}{4} S_p c_0 + 2k_1 c_0^2 [A_2] V_p + F c_0 \quad [18]$$

The term on the left-hand side of Eq. [18] represents production of etchant species via the reaction



The electron density has been assumed constant at the average value within the annular plasma space. This may be a good approximation if the thickness of the annular space is small compared to its length. Thus, the assumption is better if an etch tunnel is present. In addition, if the principal loss of electrons is a volume process (e.g., attachment), the electron density will tend to be uniform irrespective of the geometry.

The first term on the right-hand side of Eq. [18] represents loss of etchant in the etching reaction. This term depends on the number of wafers (N) and on the area of etchable material left on each wafer (πR^2). The last term in Eq. [18] represents etchant loss by flow. Under the assumption that the gas is essentially composed of A_2 and A (i.e., low loading of wafers), $[A_2] \approx P/R_g T - c_0$. Then, Eq. [18] gives

$$-c_0^3 + \frac{P}{R_g T} c_0^2 + \frac{\eta k_2 \pi R^2 N}{V_p} + \frac{v_0 w}{4a} + \frac{F}{V_p} + 2k_e \langle n_e \rangle + \frac{k_e \langle n_e \rangle P}{k_1 (R_g T)} = 0 \quad [19]$$

The solution to the cubic Eq. [19] provides c_0 . Note that since both R and η are functions of time, c_0 will be time dependent except in the case $\eta k_2 \pi R^2 N / V_p < < v_0 w / 4a$ or F / V_p or $2k_e < n_e >$. Neglecting the volume recombination reaction ($k_1 \equiv 0$) results

$$c_0 \approx \frac{2k_e < n_e > \left(\frac{P}{R_e T} \right)}{\frac{\eta k_2 \pi R^2 N}{V_p} + \frac{v_0 w}{4a} + \frac{F}{V_p} + 2k_e < n_e >} \quad [20]$$

This equation correctly predicts the loading effect in that a plot of $1/c_0$ vs. N results in a straight line (10).

Both the average electron density $<n_e>$ and the dissociation reaction rate constant k_e depend on pressure. In particular, k_e depends on the E_d/P ratio which is a unique function of the electron temperature. In general, determination of $<n_e>$ or k_e is an extremely difficult task. The presence of "hot" electrons, the multiplicity of the reaction channels, and the large number of chemical species involved make the problem of analyzing a gas discharge a very complicated one. The papers by Kushner (21, 22) illustrate the complexity of the problem. A rigorous analysis of the discharge requires knowledge of cross-sectional data for the various collisional processes occurring. Such data are scarce for most of the plasmas used in practice. However, the situation is less complicated when dealing with discharges of a single gas. For the O_2 discharge, in particular, the required physical data are available and a reasonably accurate analysis of an O_2 plasma can be realized. For such a discharge, the effective electric field-to-pressure ratio E_d/P as well as the average electron density $<n_e>$ can be evaluated for given pressure, power density, and reactor geometry from Fig. 1.19 of Ref. (11). After finding the E_d/P ratio, k_e can be obtained from Fig. 1.26 of the same reference. Then c_0 can be computed by using Eq. [20] or the more complicated Eq. [19], if necessary. Hence, the effect of reactor pressure and power input on the bulk etchant concentration can be evaluated for this particular discharge. The plots in Fig. 1.19 and 1.26 of Ref. (11) can be used for analyzing etching in an O_2 plasma as long as the byproducts of etching (CO_2 , CO , H_2O , etc.) are in low enough concentrations not to alter the discharge properties. Measurement of $<n_e>$ is usually done with Langmuir probes and is associated with certain experimental difficulties (23). The etchant concentration can be measured by optical emission spectroscopy (12) or by gas-phase titration (13, 14).

Results and Discussion

The foregoing model was employed to predict across-wafer uniformity, etch cycle duration, optimum throughput, and overetch exposure.

Consider first the situation where recombination reactions are negligible, and where steady-state concentration profiles have become established but film clearing has not yet begun. Such a situation corresponds to the simple limiting case described by Eq. [13] with $\sigma = 1$. Figure 3 illustrates how the concentration distribution in the interwafer region depends upon the Thiele Modulus (ϕ_0). For values of ϕ_0 less than 0.3, the concentration distribution (and thus the etching rate distribution) is nearly uniform. That is, the wafer surface is uniformly accessible to the etchant species. For a given wafer diameter and reactor pressure, small ϕ_0 values can be achieved by increasing the wafer spacing, although such action serves also to decrease the throughput. For high ϕ_0 values, diffusion is sluggish compared to the etching reaction so that etching species become depleted from the interwafer region and large radial concentration gradients build up. This will be the case when the wafer spacing is small, or the diffusivity is low (i.e., pressure is high), or the etching reaction is rapid.

A plot of the effectiveness factor η vs. the Thiele Modulus ϕ_0 (Eq. [15]) for two values of the dimensionless film radius $\sigma (= R/R_0)$ is shown in Fig. 4. When $\phi = \phi_0$, $\sigma \ll 1$ (i.e., $\phi < 0.1$), Eq. [15] reduces to

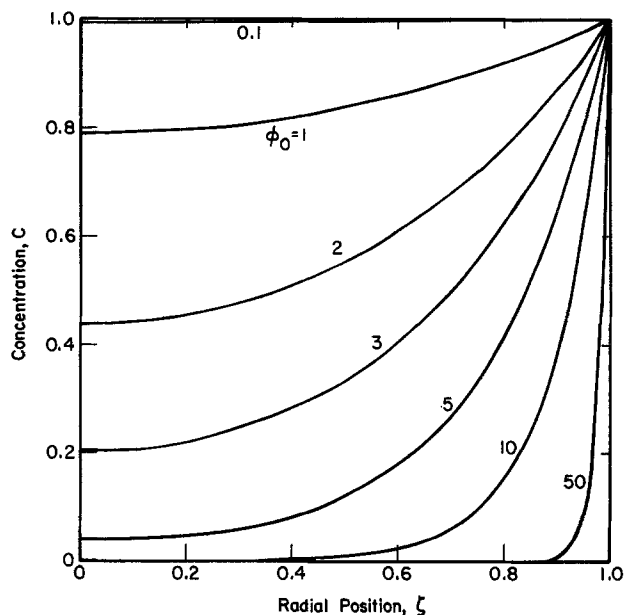


Fig. 3. Effect of Thiele Modulus ϕ_0 on the concentration distribution in the interwafer region prior to film depletion ($\sigma = 1$, $\alpha = \beta = \gamma = 0$).

$$\eta = \frac{4}{4 + \phi_0^2 \sigma^2 (1 - 2 \ln \sigma)} \quad [21]$$

For any value of σ , the effectiveness factor tends to unity for small values of the Thiele Modulus ϕ_0 . This agrees with the fact that for small ϕ_0 the concentration is at its bulk value (c_0) throughout the wafer surface (e.g., Fig. 3 with $\phi_0 = 0.1$).

When $\phi \gg 1$ (i.e., $\phi > 10$), Eq. [15] reduces to

$$\eta = \frac{2}{\phi_0 \sigma (1 - \phi_0 \sigma \ln \sigma)} \quad [22]$$

Before film depletion sets in, $R = R_0$ or $\sigma = 1$. Then Eq. [22] becomes

$$\eta = \frac{2}{\phi_0} \quad [23]$$

and a log-log plot of η vs. ϕ_0 will result in a straight line with a slope of -1 . (Fig. 4 for $\sigma = 1$.)

For any film radius R less than the wafer radius R_0 , ($\sigma < 1$), and for high enough values of the Thiele Modulus ϕ_0 so that $-\phi_0 \sigma \ln \sigma \gg 1$, Eq. [22] becomes

$$\eta = -\frac{2}{\phi_0^2 \sigma^2 \ln \sigma} \quad [24]$$

and a log-log plot of η vs. ϕ_0 will result in a straight line with slope of -2 . (Fig. 4 for $\sigma = 0.2$.)

Figure 5 depicts the concentration distribution in the interwafer space for several values of, in essence, the vol-

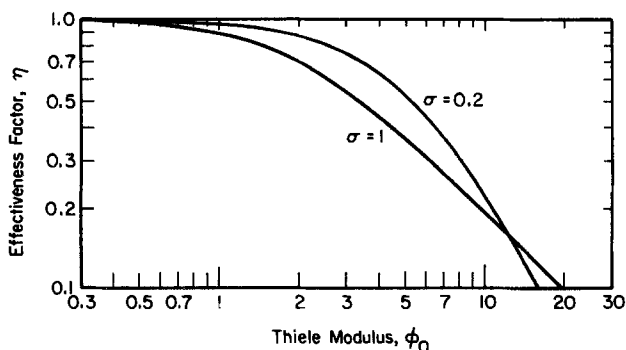


Fig. 4. Effectiveness factor η as a function of the Thiele Modulus ϕ_0 with the dimensionless film radius σ as a parameter (Eq. [15]).

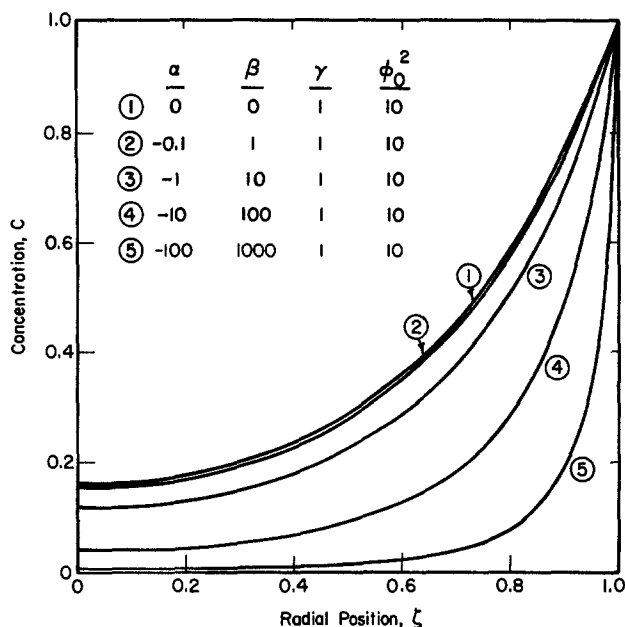


Fig. 5. Effect of volume recombination reactions on the concentration distribution in the interwafer space prior to film depletion ($\sigma = 1$).

ume recombination reaction rate constant k_1 . As k_1 increases so that $|\alpha| \gg 1$ and $\beta \gg 1$, strong concentration gradients develop which result in a highly nonuniform etch rate and a longer etch time. That is, reactants recombine to inactive species before they can diffuse into the wafer stack and etch the film. However, if k_1 is low enough so that $\beta < 1$, volume recombination reactions can be completely neglected (compare cases ① and ② in Fig. 5). This is true for the commonly employed O_2 or/and CF_4 discharges at pressures less than 1 torr. However, it may not be true for Cl_2 discharges, where the volume recombination rates are faster.

Figure 6 shows the film thickness distribution during transient film clearing with the dimensionless time as a parameter. Initially, the film has a uniform thickness h_0 ($H = 1$). After a dimensionless time of 1, the film begins to recede from the periphery. For this particular example, the film will be completely cleared after a dimensionless time of 10.1 has elapsed. The intersects with the ordinate provide the film radius R as a function of time.

Figure 7 shows the time dependence of the concentration profile during transient clearing of the film. After the outer rings have been cleared, the reactant penetrates more readily to the inner portion of the wafer and thus the concentration increases with time at a given radial position. This increase is less pronounced close to the center of the wafer since this region stays reactive almost throughout the cycle. Figure 6 gives the film thickness distribution as a function of time under the same conditions.

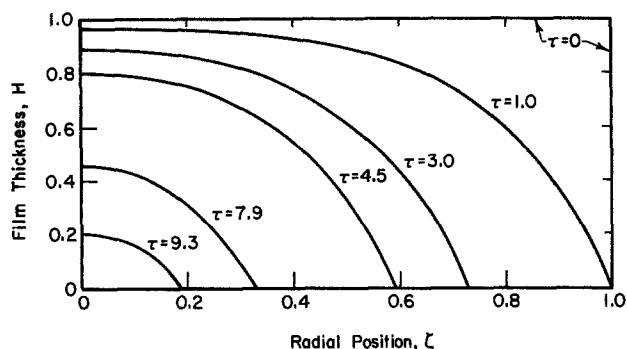


Fig. 6. Film thickness distribution at different cumulative etch times τ ($\alpha = -1$, $\beta = 10$, $\gamma = 0$, $\phi_0^2 = 25$ and total etch time $\tau_0 = 10.1$).

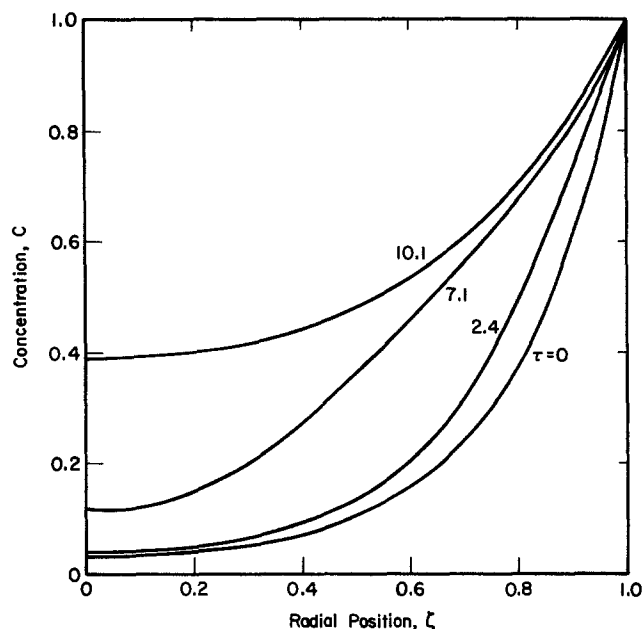


Fig. 7. Concentration distribution in the interwafer space at different cumulative etch times τ (parameter values are the same as in Fig. 6).

Exposure to overetch is to be avoided in etching most patterned films since local loading can result in rapid mask undercut after the end point has been reached. The percent overetch exposure as a function of the Thiele Modulus ϕ_0 is shown in Fig. 8 for four different radial positions on the wafer surface ζ ($=r/R_0$). In constructing Fig. 8, only surface (not volume) recombination reactions have been included ($\alpha = \beta = 0$, $\gamma = 1$). The percent overetch was computed by

$$\% \text{ overetch} = \frac{\tau_0 - \tau}{\tau} \times 100$$

where τ_0 is the total etch time (shown in the insert Table in Fig. 8), and τ is the time required to clear the film up to a given radial position ζ . Since the portion of the wafer closer to the periphery clears first, the overetch exposure is higher for larger ζ values. Furthermore, as the Thiele Modulus ϕ_0 increases, the radial distribution of the reaction rate becomes nonuniform, resulting in an increase of the overetch exposure.

A related plot is shown in Fig. 9, where the total etch time τ_0 has been plotted against the Thiele Modulus ϕ_0 .

Table I. Typical parameter values for barrel plasma etchers

Parameter value	Comments
$[A_2] = 6 \times 10^{-8} \text{ mol/cm}^3$	Parent gas partial pressure of 1 torr
$c_0 = 6 \times 10^{-9} \text{ mol/cm}^3$	Etchant partial pressure of 0.1 torr
$D \approx 350 \text{ cm}^2/\text{s}$	Estimated for O in O_2 at 400 K and 1 torr. Varies as P^{-1} and approximately at $T^{1.5}$
$h_0 = 10^{-4} \text{ cm}$ (1 μm)	—
$k_1 = 10^{15} \text{ cm}^3/(\text{mol})^2/\text{s}$	Corresponds to the reaction $O + O + O_2 \rightarrow 2 O_2$ (11)
$k_2 \approx 50 \text{ cm/s}$	Calculated from the value of $k_2/D = 0.158 \text{ cm}^{-1}$ given by Battey (6)
$L_r = 1 \text{ cm}$	Reference interwafer spacing
$P_r = 1 \text{ torr}$	Reference reactor pressure
$Q = 100 \text{ sccm}$	Corresponds to 1850 cm^3/s at 400 K and 1 torr
$R_0 = 5 \text{ cm}$	—
$T = 400 \text{ K}$	—
$v_0 \approx 7 \times 10^4 \text{ cm/s}$	Thermal velocity of O at 400 K
$w = 3 \times 10^{-4}$	For O recombining on silica at 400 K (9)
$\chi = 0.33$	very sensitive to surface conditions
	Corresponds to the reaction $Si + 4F \rightarrow SiF_4$

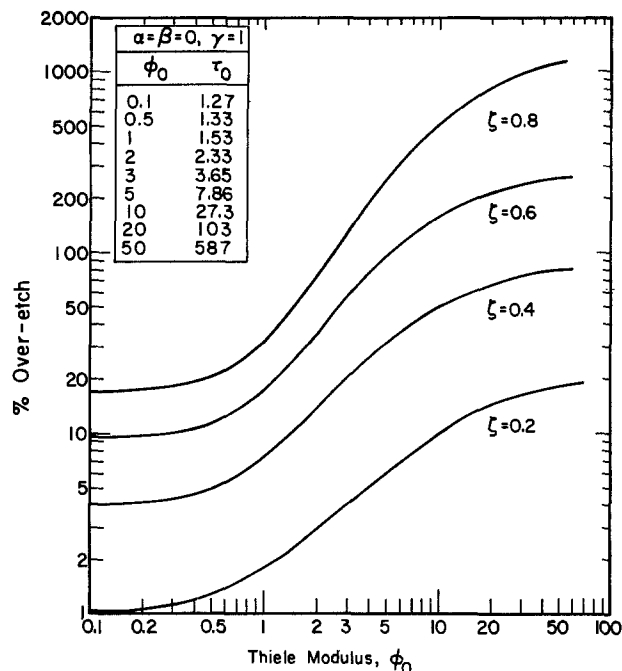


Fig. 8. Overetch exposure (%) vs. Thiele Modulus ϕ_0 for different radial positions on the wafer surface ζ ($\alpha = \beta = 0$, $\gamma = 1$).

with the surface recombination number γ as a parameter. No volume recombination reactions are considered. Since the edge of the wafer clears at a time $\tau = 1$, the percent maximum overetch will be $(\tau_0 - 1) \times 100$ and is also shown on the vertical axis. From Fig. 9, we observe that for $\gamma < 0.1$ and $\phi_0 < 0.3$ the film clears uniformly, i.e., there is no overetch exposure. As one expects, etch time and overetch increase as γ or/and ϕ_0 increase. In addition, for a particular value of γ , the corresponding curve approaches asymptotes for $\phi_0 \ll 1$ and $\phi_0 \gg 1$.

The effect of wafer spacing on throughput is illustrated in Fig. 10, where $1/L^*\tau_0$ (multiplied by 100) has been plotted against the dimensionless wafer spacing L^* . If the wafer thickness and the turnaround time are neglected, $1/L^*\tau_0$ is proportional to the throughput. The curve has been constructed by assigning a value of 5 to ϕ_0^2 and a value of 1 to γ for a dimensionless wafer spacing of $L^* =$

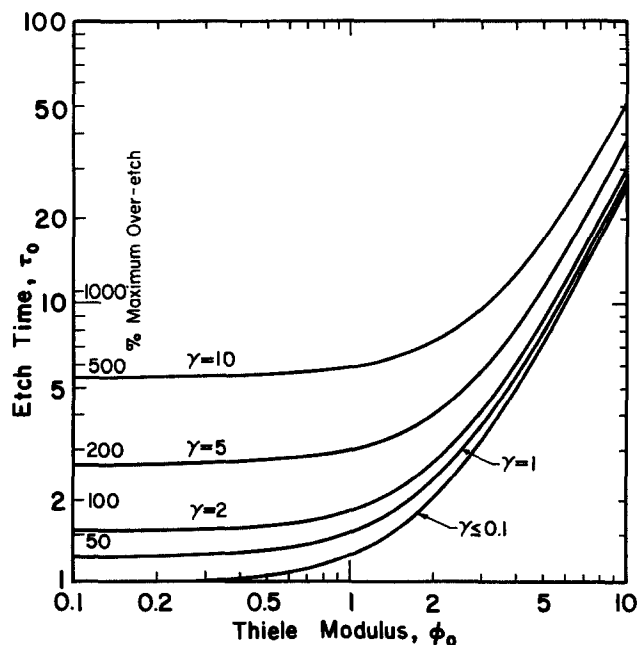


Fig. 9. Total etch time τ_0 and maximum overetch exposure (%) vs. Thiele Modulus ϕ_0 with the surface recombination number γ as a parameter ($\alpha = \beta = 0$).

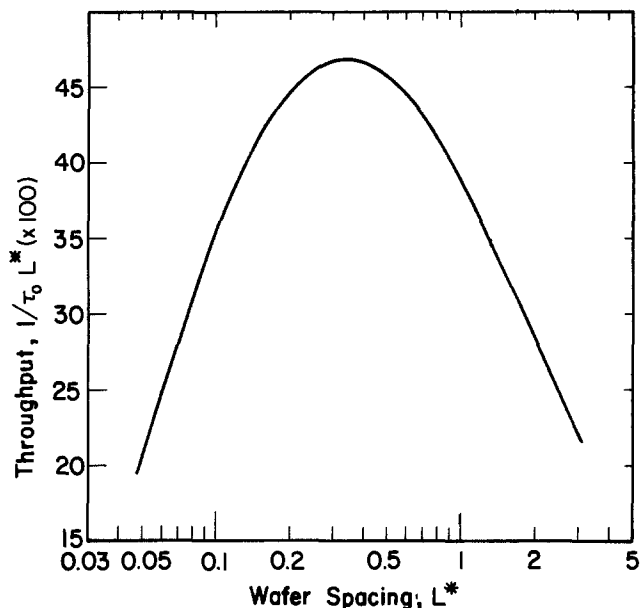


Fig. 10. Effect of wafer spacing on throughput

1. The values chosen for ϕ_0^2 and γ have been calculated by using typical values for the system parameters shown in Table I. By changing the wafer spacing L , γ and ϕ_0^2 change inversely proportionally. No volume recombination reactions have been considered since the corresponding dimensionless groups have no L dependence. The maximum in the plot can be explained as follows. As L^* becomes large, the total etch time $\tau_0 \rightarrow 1$ and by further increasing L^* the ratio $1/L^*\tau_0$ decreases. However, as L^* becomes small, τ_0 increases more rapidly, resulting in decreasing throughput $1/L^*\tau_0$. Thus, there is a maximum in the throughput as a function of the wafer spacing. For the parameter values used, this maximum is found from Fig. 10 to occur at $L = 0.4$ cm. This is to be compared with a spacing of 3/16 in. usually employed in stripping photoresists in an O_2 plasma. Direct quantitative comparison with published experiments is difficult since not all of the required system parameters (for example, wall recombination coefficient) are known.

Another parameter affecting the throughput is reactor pressure. Figure 11 depicts the dependence of the total etch time τ_0 on the dimensionless pressure P^* . In constructing Fig. 11, base values of $\alpha = -0.005$, $\beta = 0.05$, $\gamma = 1$, and $\phi_0^2 = 5$ have been assigned for a value of pressure $P^* = 1$. Again, the parameter values have been calculated by using Table I. In order to correctly determine the effect of pressure on τ_0 , the dependence of the bulk etchant con-

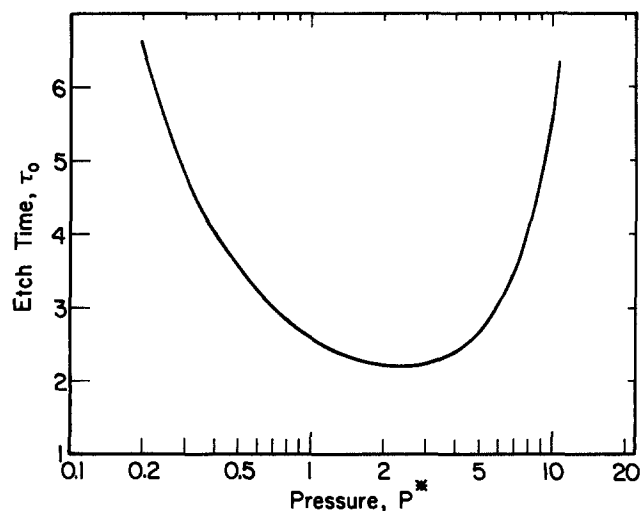


Fig. 11. Effect of reactor pressure on total etch time

centration c_0 , on pressure must be known. A linear relationship is assumed here (Eq. [20] and Ref. (15) and (16)), so that the dimensionless groups depend on pressure P as follows: $\alpha \sim P^3$, $\beta \sim P^3$, $\gamma \sim P$, $\phi_0^2 \sim p$ (diffusivity $\sim P^{-1}$), and $\tau \sim P$ (since $\tau \sim c_0$). The minimum in the etch time can be explained as follows: at high pressures, the etchant concentration is high but recombination reactions and low diffusivity establish large concentration gradients in the interwafer space. As a result, the etch time increases. However, at low pressures, diffusion is facile and recombination reactions are sluggish but there is not enough etchant species to etch the film. Thus, the strip time is again high. For this particular choice of the parameter values, the minimum in etch time is found from Fig. 11 to occur at about $P^* = 2$ or $P = 2$ torr. Note that $\tau = t/t_0$, where $t_0 = (k_2 c_0 / \chi h_0)^{-1}$ (Eq. [5]) is the "characteristic" etch time equal to 1.85 min for the parameter values of Table I. Hence, the minimum etch time of Fig. 11 would correspond to an etch duration of about 4 min.

The optima shown in Fig. 10 and 11 have been obtained under otherwise no constraints. For example, maximum allowances in overetch exposure are not accounted for. Thus, a pressure of 2 torr (resulting in $\phi_0^2 \sim 10$ for the case considered) would be too high for etching a patterned film.

The present analysis has limitations with respect to the range over which wafer spacing L and pressure P can vary. For example, for wafer spacings comparable to the wafer radius, the one-dimensional model is no longer valid. Furthermore, at low pressure and small wafer spacing, the diffusion mode may be of "Knudsen diffusion" when the mean free path becomes comparable to wafer spacing. This will happen for $PL < 0.05$ torr-cm. Nonetheless, the optimum L and P values are within the range where the model assumptions are valid. For instance, for the optimum wafer spacing of 0.4 cm, the pressure value below which Knudsen diffusion prevails is 0.125 torr. This is far from the optimum pressure value.

Conclusions

A mathematical model for transient clearing of films from restricted geometries has been developed. Dimensionless groupings of system parameters were used to compile behavior and to reveal scale-up principles. The effect of these parameters on etch uniformity, overetch exposure, and throughput was determined, and optima were identified. The model can be extended without much difficulty to handle more complex situations such as: (i) arbitrary etching reaction kinetics, (ii) other types of volume or surface recombination reactions, (iii) non-uniform initial film thickness, (iv) etchable substrate (reaction rate nonuniformities are critical in this case, since the substrate layer may be seriously damaged), (v) time varying bulk concentration (this requires solution of Eq. [19] at each time step after the effectiveness factor has been found from Eq. [15]), and (vi) spatial dependence of the wall recombination coefficient.

The model represents a simplified view by virtue of several assumptions. For example, the wafer temperature may change during etching if the reaction is accompanied by heat effects. Furthermore, the wafer temperature may depend on the reactor pressure. Since chemical reactions are affected by temperature, the reaction rate constant (k_2) may not be a constant. Other assumptions include one-dimensional concentration distribution and pseudo-steady state. Both assumptions can be relaxed, but at the expense of much higher computation time. Finally, detailed analysis of the plasma region is, for the majority of situations, extremely difficult.

Despite its simplicity, the model can serve as a basis for studying more complex systems. An example is removal of polymer drill smear from the holes of multilayer printed-circuit boards (3). Experimental work aimed at testing the model predictions is currently in progress in our laboratory.

Plasma processing systems are complex in the sense that several different phenomena may control overall be-

havior depending upon the choice of operating conditions. As a consequence, the efficient design and scale-up of plasma systems is usually difficult to accomplish by intuition alone. The use of mathematical models can assist in organizing scientific concepts into strategies for engineering design.

Acknowledgments

This study was supported by an IBM Departmental Grant and by a University of Illinois Fellowship.

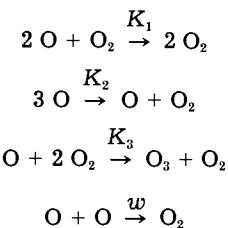
Manuscript submitted June 8, 1984; revised manuscript received Nov. 6, 1984.

The University of Illinois assisted in meeting the publication costs of this article.

APPENDIX

Recombination Reactions in an Oxygen Plasma

Oxygen plasmas are frequently employed for stripping photoresist masking layers. If the wafer load is small enough so that the stripping products are at negligible concentration, the pertinent recombination reactions will be (11)



For this system, Eq. [7] will be of exactly the same form but with the dimensionless groupings redefined as follows

$$\begin{aligned} \alpha &= \frac{2(K_2 + K_3 - K_1)R_0^2 c_0^2}{D} \\ \beta &= \frac{2(K_1 - 2K_3)PR_0^2 c_0}{(R_g T)D} \\ \gamma &= \left[\frac{v_0 w}{2L} + \frac{2K_3 P^2}{(R_g T)^2} \right] \frac{R_0^2}{D} \end{aligned}$$

with ϕ_0 remaining the same as before.

LIST OF SYMBOLS

a	specific volume of plasma space (V_p/S_p) (cm^3/cm^2)
A_2	etchant species
A_2	parent molecule
c_0	etchant concentration at the wafer edge (mol/cm^3)
c	etchant concentration (mol/cm^3)
C	dimensionless etchant concentration (c/c_0)
c_R	etchant concentration at $r = R$ (mol/cm^3)
D	etchant diffusivity (cm^2/s)
e	etch rate ($\text{mol}/\text{cm}^2/\text{s}$)
E_e	effective electric field in the plasma region (V/cm)
F	gas volumetric flow rate (cm^3/s)
h	film thickness (cm)
h_0	initial film thickness (cm)
H	dimensionless film thickness (h/h_0)
k_1	volume recombination reaction rate constant ($\text{cm}^6/(\text{mol})^2/\text{s}$)
k_2	etch rate constant (cm/s)
k_e	electron-impact dissociation rate constant ($\text{cm}^3/\text{mol}/\text{s}$)
L	wafer separation distance (cm)
L_r	reference interwafer spacing (1 cm)
L^*	dimensionless wafer separation distance (L/L_r)
$\langle n_e \rangle$	average electron density (mol/cm^3)
N	number of wafers
P	pressure (torr)
P_r	reference pressure (1 torr)
P^*	dimensionless pressure (P/P_r)
r	radial position (cm)
R	film radius (cm)
R_0	wafer radius (cm)
R_g	gas constant ($62,360 \text{ torr}\cdot\text{cm}^3/\text{mol}/\text{K}$)
S_p	surface area in contact with plasma (cm^2)
t	time (s)

T temperature (K)
 u_g gas velocity in interwafer space (cm/s)
 v_0 random thermal velocity of etchant species (cm/s)
 V_p volume occupied by the plasma (cm³)
 w wall recombination coefficient

Greek characters

α, β, γ dimensionless groups defined in Eq. [8]
 ζ dimensionless radial position, r/R_0
 η effectiveness factor (Eq. [15])
 σ dimensionless film radius, R/R_0
 τ dimensionless time, $k_2 c_0 t / \chi^2 h_0$
 τ_0 dimensionless total etch time
 ϕ Thiele Modulus based on the film radius, $R(2k_2/LD)^{1/2}$
 ϕ_0 Thiele Modulus based on the wafer radius, $R_0(2k_2/LD)^{1/2}$
 χ moles of A consumed per cm³ of film etched (mol/cm³)
 ψ dimensionless radial position, r/R

REFERENCES

1. S. M. Irving, *Solid State Technol.*, **14**, 47 (June 1971).
2. R. G. Poulsen, *J. Vac. Sci. Technol.*, **14**, 266 (1977).
3. R. D. Rust, R. J. Rhodes, and A. A. Parker, in "Plasma Processing," G. S. Mathad, G. C. Schwartz, and G. Smolinsky, Editors, p. 584, The Electrochemical Society Softbound Proceedings Series, Pennington, NJ (1983).
4. A. C. Adams, in "VLSI Technology," S. M. Sze, Editor, McGraw-Hill, New York (1983).
5. M. Doken and I. Miyata, *This Journal*, **126**, 2235 (1979).

6. J. F. Battey, *ibid.*, **124**, 437 (1977).
7. D. L. Flamm and V. M. Donnelly, *Plasma Chem. Plasma Proc.*, **1**, 317 (1981).
8. J. F. Battey, *This Journal*, **124**, 147 (1977).
9. J. C. Greaves and J. W. Linnett, *Trans. Faraday Soc.*, **55**, 1355 (1959).
10. C. J. Mogab, *This Journal*, **124**, 1262 (1977).
11. A. T. Bell, in "Techniques and Applications of Plasma Chemistry," J. R. Hollahan and A. T. Bell, Editors, John Wiley and Sons, New York (1974).
12. J. W. Coburn and M. Chen, *J. Vac. Sci. Technol.*, **18**, 3134 (1981).
13. A. Jacob, *Solid State Technol.*, **31** (June 1977).
14. P. C. Nordine and D. E. Rosner, *J. Chem. Soc. Faraday Trans.*, **72**, 1526 (1976).
15. A. Jacob, *Solid State Technol.*, **95** (April 1978).
16. A. A. Parker, R. J. Pachter, and R. D. Rust, in "Plasma Processing," G. S. Mathad, G. C. Schwartz, and G. Smolinsky, Editors, p. 596, The Electrochemical Society Softbound Proceedings Series, Pennington, NJ (1983).
17. E. E. Petersen, "Chemical Reaction Analysis," Prentice-Hall, Englewood Cliffs, NJ (1965).
18. K. F. Jensen and D. B. Graves, *This Journal*, **130**, 1950 (1983).
19. A. C. Lloyd, *Int. J. Chem. Kinetics*, **3**, 39 (1971).
20. D. L. Flamm, D. N. K. Wang, and D. Maydan, *This Journal*, **129**, 2755 (1982).
21. M. J. Kushner, *J. Appl. Phys.*, **53**, 2923 (1982).
22. M. J. Kushner, *ibid.*, **53**, 2939 (1982).
23. B. Chapman, "Glow Discharge Processes," p. 62, John Wiley and Sons, New York (1980).
24. B. S. Meyerson and W. Olbricht, *This Journal*, **131**, 2361 (1984).

Reaction Kinetics of Hg_{1-x}Cd_xTe/Br₂-CH₃OH

R. T. Talasek* and A. J. Syllaios*

Texas Instruments, Incorporated, Equipment Group, Dallas, Texas 75266

ABSTRACT

Bromine methanol solutions are extensively used in HgCdTe device processing technology. The relative reaction rates of Hg, Cd, and Te and HgCdTe with bromine in methanol have been studied. The reaction rate constants, reaction order, and some conclusions about the mechanisms of the reactions of the elements with bromine are reported here. The anisotropic nature of the reaction of the semiconductor with bromine has been demonstrated. The effects of mechanical action on the relative rates of the semiconductor constituents have been studied and are also discussed.

Mercury cadmium telluride is a semiconductor widely used in the fabrication of infrared detectors. Since it is a compound, HgCdTe is especially sensitive to chemical processing, and some processing may leave the semiconductor surface depleted of one or more elements. This depletion may affect the performance of devices dependent on the surface behavior of the semiconductor. One of these processes is the chemical etching or polishing of HgCdTe, which uses solutions of bromine in methanol. Electrolyte electroreflectance (EER) measurements indicate that the surface of HgCdTe is left tellurium rich after such chemical treatments (1). To study the chemistry of this polishing further, the chemical kinetics of the HgCdTe/Br₂-CH₃OH system were investigated by studying the reactions of the elements Hg, Cd, and Te and of HgCdTe with Br₂ in CH₃OH. The semiconductor reaction was studied under noncontact (etch) conditions and by making contact to a Pelon polishing pad.

The extent of a reaction in a kinetic study is generally monitored by some physical constant of the system proportional to the concentration of a particular component (2). In this case, the amount of product (metal in solution) was monitored by measuring the UV-visible absorption of metal ion complexes formed with diphenylthiocarbazonate (dithizone) for Hg and Cd and with sodium diethyldithiocarbamate for Te (3-5). The reactions were quenched at various time intervals, rather than continuously moni-

toring absorption, so that nothing was added to the etch solution that might affect the reaction.

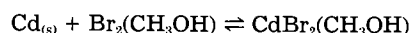
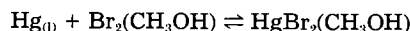
For any physical measurement, λ (in this case, metal complex absorption) that is proportional to reaction extent, the following relation holds (2)

$$\frac{\lambda_{\infty} - \lambda}{\lambda_{\infty} - \lambda_0} = \frac{C}{C_0} \quad [1]$$

where λ_{∞} is the measurement at full extent of reaction, λ_0 the measurement at reaction initiation, λ the measurement at time t , C_0 the initial concentration of limiting reactant, and C the concentration of limiting reactant at time t .

Reactions of Hg, Cd, and Te with Br₂/CH₃OH

The following elemental oxidation reduction reactions were studied



The reactions were studied by reacting the elemental metal with solutions of bromine in methanol in concentrations approximately equal to the effective metal concentration under convection-controlled conditions ($10^{-4}N > [\text{Br}_2] > 10^{-7}N$). For each reaction, a specific rate equa-

*Electrochemical Society Active Member.

tion can be written for each metal M

$$\frac{d[M^{n+}]}{dt} = k[M]^x[Br_2]^y \quad [2]$$

In the case of heterogeneous reactions such as these, the effective elemental metal concentration is

$$[M] = \frac{\text{Surface atoms}}{\text{Volume of solution}}$$

and was held constant throughout the reaction by maintaining a constant surface area of metal exposed to the solution. The rate equation can then be simplified to

$$\frac{d[M^{n+}]}{dt} = k'[Br_2]^y \quad [3]$$

where k' is an experimentally observed rate constant. Integrating this rate expression yields for $y = 1$

$$-\ln \frac{[Br_2]}{[Br_2]_0} = k't \quad [4]$$

and for $y = 2$

$$\frac{1}{[Br_2]} = k't + \frac{1}{[Br_2]_0} \quad [5]$$

or

$$\frac{[Br_2]_0}{[Br_2]} - 1 = k'[Br_2]_0 t$$

The reactions were quenched by removing the methanol solution from the reaction vessel. Determination of metal ion concentrations using the previously described complexing agents was done immediately.

By following the reaction extent at various time periods, reaction orders and rates were determined (Fig. 1a-1c). Resulting observed rate constants and orders were

Hg $k' = 2.9 \pm 0.5 \times 10^{-3} s^{-1}$; pseudo-first order

Cd $k' = 2.5 \pm 0.6 \times 10^{-3} s^{-1}$; pseudo-first order

Te $k' = 8.4 \pm 1.1 \times 10^{-4} M^{-1} s^{-1}$; pseudo-second order

From this data, it was concluded that, for the elemental reactions, the Hg and Cd reaction rates were equivalent within experimental error and that both rates were much faster than the Te reaction rate.

Although a mechanism could not be confirmed by such a limited study, some conclusions were drawn from this data. Obviously, the Te reaction proceeded by a different mechanism than the other reactions since it was second order. Also, given that (from transition-state theory)

$$k = CK_{eq}^\alpha \quad [6]$$

where k is a rate constant, C an integration constant, K_{eq} an equilibrium constant, and α a constant (for a particular reaction) related to the nature of the transition state $0 < \alpha < 1$, a comparison of the Hg and Cd mechanisms can be made (2). From reduction potentials, the following equilibrium constants were calculated (8)

$$K_{eq} (CdBr_2) \approx 10^{26}$$

$$K_{eq} (HgBr_2) \approx 10^3$$

Although C is not known, the wide variation in the values of K_{eq} for $CdBr_2$ and $HgBr_2$ indicate a large difference in α values for Cd and Hg. Therefore, it can be concluded that the mechanisms for the Hg and Cd reactions must be different, since the mechanism is related to the nature of the transition state.

Reaction of HgCdTe with Br₂/CH₃OH

Etch.—The material used for the semiconductor reactions was Hg_{1-x}Cd_xTe with $x = 0.225 \pm 0.003$ ($E_g \approx 0.12$ eV at 77 K), grown by solid-state recrystallization techniques (6). Nominal carrier concentrations and mobilities (by Hall effect measurements) were $7 \times 10^{14} cm^{-3}$ and $1.2 \times$

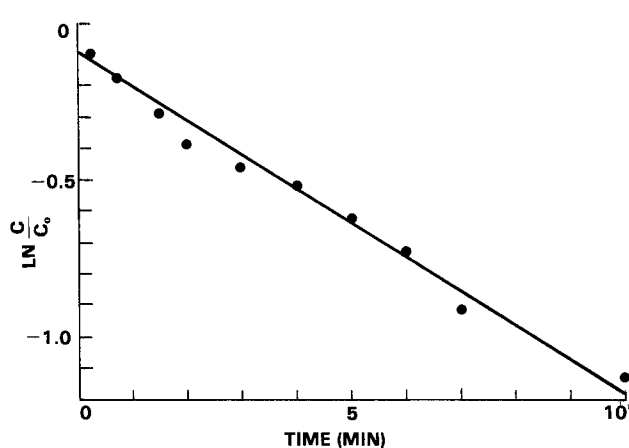
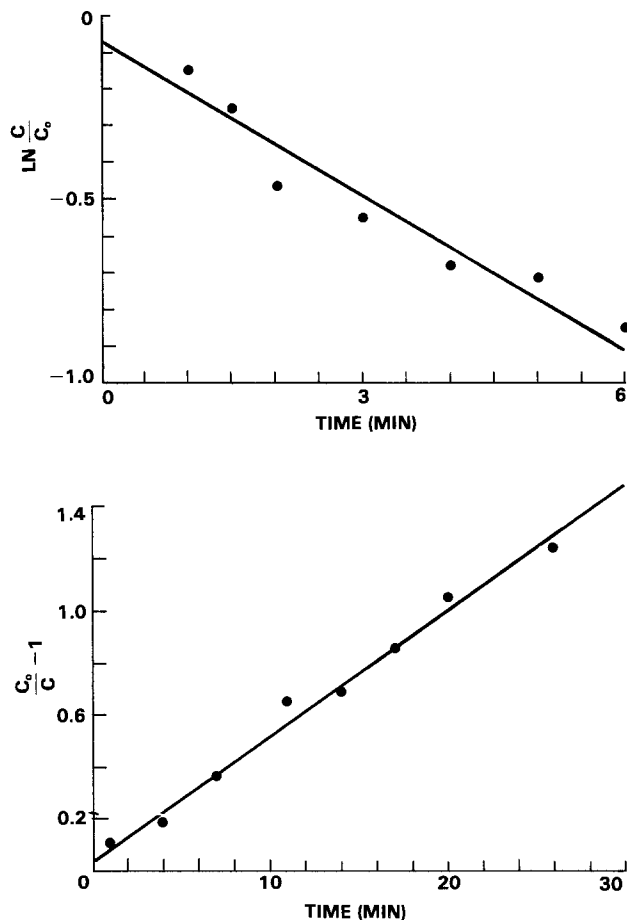


Fig. 1. a (top left): Reaction rate of mercury with bromine in CH₃OH. C is the concentration of bromine at time t . C_0 is the initial bromine concentration. $\lambda_{meas} = 486$ nm. b (top right): Reaction rate of cadmium with bromine in CH₃OH. $\lambda_{meas} = 516$ nm. c (left): Reaction rate of tellurium with bromine in CH₃OH. $\lambda_{meas} = 428$ nm.

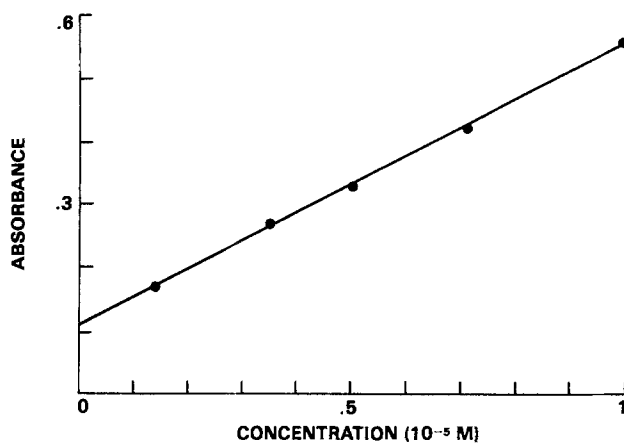
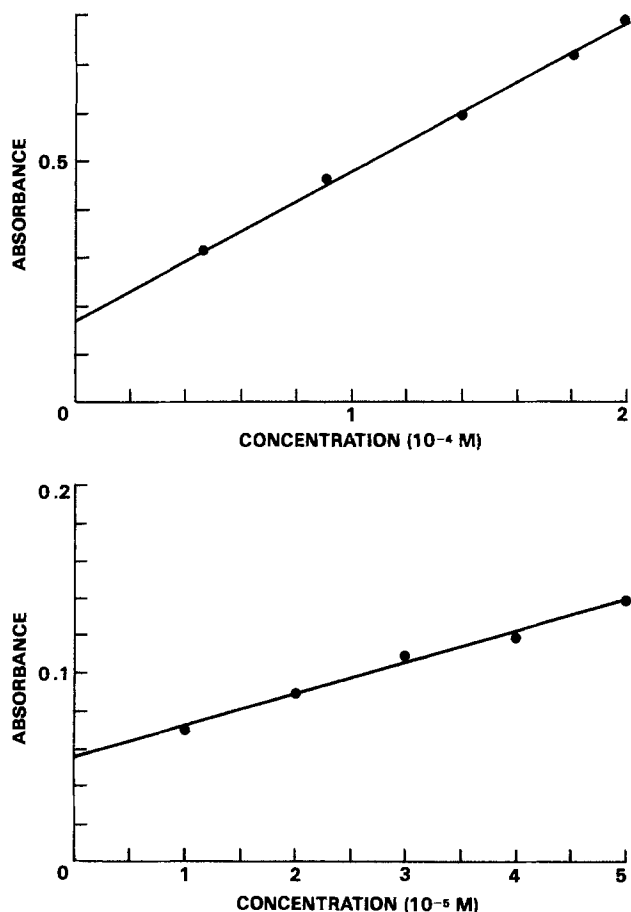


Fig. 2. a (top left): Mercury standard curve. b (top right): Cadmium standard curve. c (left): Tellurium standard curve.

10^5 $\text{cm}^2/\text{V}\cdot\text{s}$, respectively. No effort was made to orient crystals; however, an averaging effect would be observed on any orientation dependent rate effects.

For normal processing conditions, *i.e.*, $[\text{Br}_2] \approx 0.1N$, $[\text{Br}_2] \gg [\text{metal surface atoms}]$. Therefore, $[\text{Br}_2]$ can be assumed to be constant for normal processing times and it follows directly from Eq. [3] that

$$\frac{d[\text{M}^{n+}]}{dt} = k' \quad [7]$$

which can be described as pseudo 0th order (constant rate conditions). Any deviation from this would yield a nonlinear plot of product formation *vs.* time. Since all three products (Hg^{2+} , Cd^{2+} , Te^{4+}) were in the same solution, it was necessary to separate the ions prior to determination. Separation techniques using dithizone in CHCl_3 for Hg and Cd, and sodium diethyldithiocarbamate in CCl_4 for Te are detailed elsewhere (7). Standard curves from these separations are shown in Fig. 2. By following

the reaction *vs.* time, the rate plot (Fig. 3) was determined for Hg, Cd, and Te. From this data, experimental rate constants were calculated for the constituents of the semiconductor

$$\begin{aligned} k'_{\text{Te}} &= 5.3 \times 10^{-8} \text{ M s}^{-1} \\ k'_{\text{Hg}} &= 1.8 \times 10^{-7} \text{ M s}^{-1} \\ k'_{\text{Cd}} &= 5.3 \times 10^{-7} \text{ M s}^{-1} \end{aligned}$$

The relative rates of reactions of the elements comprising the semiconductor serve to illustrate the anisotropic nature of the reaction at the surface.

Chemical mechanical polishing.—A common technique in processing HgCdTe is chemical-mechanical polishing, whereby $\text{Br}_2/\text{CH}_3\text{OH}$ is flowed across a Pelon polishing pad, and the sample is polished using normal (hand) polishing techniques. Although pseudo-0th order kinetics should be observed as in the etching process, two important differences exist which may cause differences in the kinetics of the two processes. First, disturbance of the

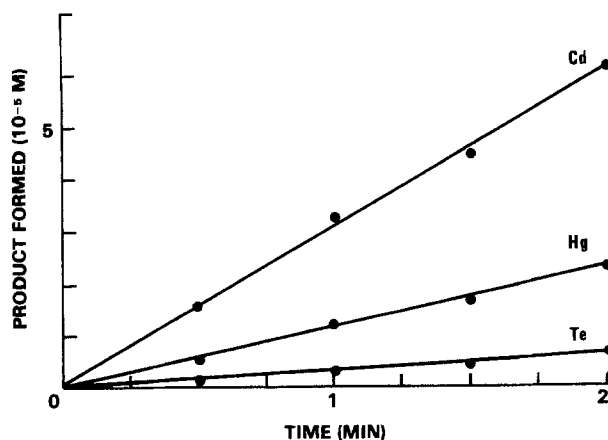


Fig. 3. Reaction of HgCdTe with bromine in CH_3OH under etch conditions.

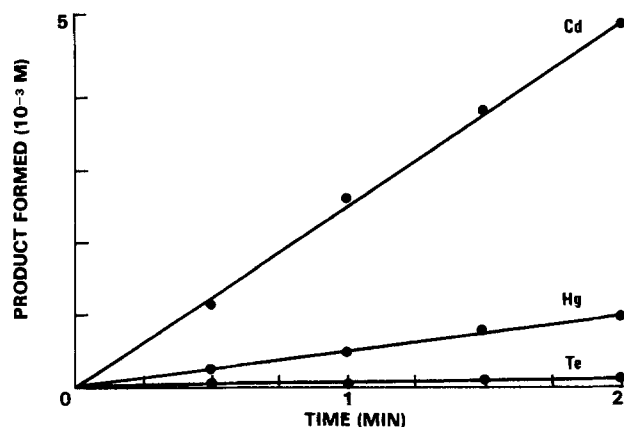


Fig. 4. Reaction of HgCdTe with bromine in CH_3OH under chemical-mechanical polishing conditions.

boundary layer may cause a deviation from the relative rates observed for etching. Also, since larger amounts of material are removed during the polishing process than the etching process, anisotropy is magnified. The resulting rate plots from this reaction are shown in Fig. 4. The experimentally determined rate constants were

$$\begin{aligned}k''_{\text{Te}} &= 8.3 \times 10^{-7} \text{ M s}^{-1} \\k''_{\text{Hg}} &= 8.3 \times 10^{-6} \text{ M s}^{-1} \\k''_{\text{Cd}} &= 4.2 \times 10^{-5} \text{ M s}^{-1}\end{aligned}$$

Normalizing the rates to Te yields rates of 1, 10, and 50 for Te, Hg, and Cd. These results demonstrate an accentuation of the anisotropic nature of the semiconductor reaction by the addition of mechanical action. The results also indicate a faster reaction rate for Te in the chemical-mechanical reaction than for any of the components in the etch reaction, indicative of the larger amount of material removed in the former.

Conclusion

The rate constants and reaction orders of Hg, Cd, and Te with Br₂ in methanol solutions have been determined. From these results, it was also determined that the three reactions proceed by entirely different mechanisms. The reaction of HgCdTe with Br₂ was also studied. The results show that this reaction is anisotropic, depleting Cd and, to a lesser extent, Hg from the semiconductor surface, in agreement with EER data mentioned earlier. It was also shown that the addition of mechanical action to the surface during the reaction enhanced the anisotropic nature of the reaction.

Acknowledgment

The authors would like to acknowledge M. J. Williams of Texas Instruments for providing the material for this study.

Manuscript submitted July 16, 1984; revised manuscript received Nov. 14, 1984. This was Paper 301 presented at the Washington, DC, Meeting of the Society, Oct. 9-14, 1983.

Texas Instruments, Incorporated assisted in meeting the publication costs of this article.

REFERENCES

1. A. Lastras-Martinez, U. Lee, J. Zehnder, and P. M. Raccach, *J. Vac. Sci. Technol.*, **21**, 157 (1982).
2. J. W. Moore and R. G. Pearson, "Kinetics and Mechanism," 3rd ed., John Wiley and Sons, New York (1981).
3. E. G. Sandell, "Colorimetric Metal Analysis," 3rd ed., Interscience Publishers, New York (1965).
4. E. B. Sandell and H. Onishi, "Photometric Determinations of Traces of Metals," 4th ed., John Wiley and Sons, New York (1978).
5. F. D. Snell and C. T. Snell, "Colorimetric Methods of Analysis," Vol. IIA, Van Nostrand, New York (1959).
6. M. J. Brau, U.S. Pat. 3,656,944 (1972).
7. G. H. Morrison and H. Freiser, "Solvent Extraction in Analytical Chemistry," John Wiley and Sons, New York (1957).
8. P. W. Atkins, "Physical Chemistry," W. H. Freeman, San Francisco, CA (1978).

Influence of Substrate Preparation on the Morphology of GaSb Films Grown by Molecular Beam Epitaxy

Mitsuru Kodama, Jun Hasegawa, and Morihiko Kimata

Department of Electrical Engineering, School of Science and Engineering, Waseda University, Shinjuku, Tokyo, Japan

ABSTRACT

The chemical etching of (100)-oriented GaSb substrate by several different treatments has been studied. The morphology of the MBE-grown GaSb films strongly depends on the substrate preparation prior to epitaxial growth. It is shown that some defects which originate at the substrate propagate to the surface of the films, in case of the improper chemical treatment, and degrade the morphology of the films. The excellent surface morphology of the film could be obtained reproducibly by treating the substrate with CH₃COOH-HNO₃-HF and subsequent HNO₃-HCl solutions.

In order to obtain high quality films grown by molecular beam epitaxy, the chemical treatment of the substrate prior to epitaxial growth is important. GaSb has been used as a substrate material for AlSb-GaSb superlattices (1) and GaSb-AlGaSb double heterostructure lasers (2). Moreover, it is a lattice-matched substrate for AlGaAsSb and InGaAsSb quaternary compounds, which are applicable for optoelectronic devices. However, the detailed chemical treatment of GaSb substrate prior to epitaxial growth has not been reported. In a state of equilibrium such as liquid- or vapor-phase epitaxy, the meltback (3) and vapor-etch technique (4) is usually used for the preparation of GaSb substrate prior to the epitaxial growth. Very little material, however, is removed from the substrate surface in the vacuum chamber prior to MBE growth. Therefore, improper substrate preparation can lead to poor epitaxial films. It has been previously reported that some morphological defects exist at the film surface and substrate-film interface in MBE-grown GaAs films (5).

The present work is conducted to determine the most proper chemical processing for the preparation of nondoped GaSb (100) substrates with reproducible smooth surfaces and to obtain MBE-grown GaSb films with reproducible excellent surface morphology.

Experimental Procedure

Nondoped (100)-oriented GaSb substrates (Sumitomo, a residual carrier concentration of $1 \times 10^{17} \text{ cm}^{-3}$) were used for experiments. At first, specimens were polished with 3.0 μm SiC and subsequent 0.3 μm alumina powder on a polishing pad. Then the polishing on a pad with fresh water was done to reduce the mechanically damaged surface effectively. As a result, we expect that the damaged layer on the surface is less than 1 μm . These were approximately 300 μm thick and $10 \times 10 \text{ mm}^2$ in area. The specimens were cleaned in trichlorethylene, acetone, and methanol, and etched by several treatments listed in Table I. The etched depth of each sample was evaluated by a conventional photolithography and a scanning electron micrography (SEM). The surface condition of chemically etched substrates was evaluated by an optical micrograph. Just after the samples were etched, they were inserted in an MBE apparatus such as reported previously (6). The GaSb substrate was mounted on a Mo substrate holder using Ga for adhesion. Ga is effective in keeping the substrate surface less oxidized during the process for adhesion (7). After the bakeout of a vacuum system, base pressure could be reached of less than 1×10^{-9} torr. The surface condition of the substrates was studied *in situ* by RHEED observation at a beam voltage

Table I. Chemical treatment procedures for nondoped GaSb(100) surface

Treatment	Composition and etching condition
I	2%Br ₂ -CH ₃ OH (R.T., 2 min)
II	CH ₃ COOH-HNO ₃ -HF (40:18:2, R.T., 40s)
III	CH ₃ COOH-HNO ₃ -HF (40:18:2, R.T., 40s) + Hot HCl (10 min)
IV	CH ₃ COOH-HNO ₃ -HF (40:18:2, R.T., 40s) + 2% Br ₂ -CH ₃ OH (1 min)
V	CH ₃ COOH-HNO ₃ -HF (40:18:2, R.T., 40s) + HNO ₃ -HCl (1:30, 5°C, 1 min)

R.T. indicates room temperature.
The post-treatment sequences are rinsing in methanol and drying with a spinner.

of 20 keV. After the heat-treatment of the substrates, a nondoped GaSb film was grown at a growth rate of 0.5-1.0 $\mu\text{m/h}$. The source materials for molecular beams were Ga (7N) and Sb (6N), which were evaporated from PBN and quartz Knudsen cells, respectively. The growth temperature has been used in the range of 420°-480°C. The morphology of MBE-GaSb films was evaluated by an optical micrograph. The cleaved and stained sections of the films using HF-HNO₃-H₂O solution were evaluated by SEM.

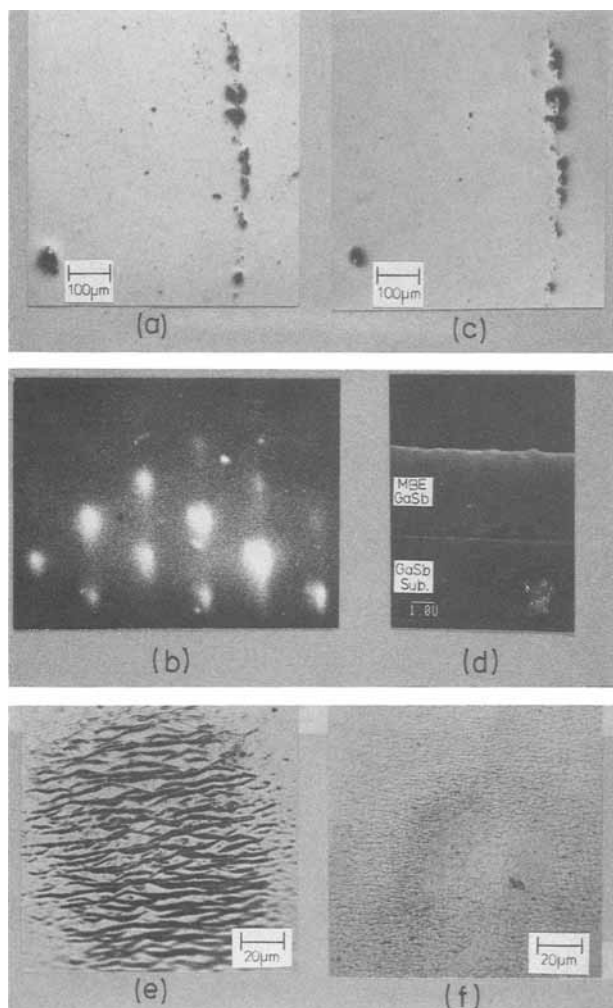


Fig. 1. (a): Surface of GaSb substrate etched by the treatment I. (b): RHEED pattern ($\langle 0\bar{1}1 \rangle$ azimuth) of substrate etched by the treatment I at heat-cleaning temperature T_{HC} about 535°C. (c): Surface morphology of deposited GaSb film. Thickness of film is about 3 μm . (d): SEM photograph of stained-cross sectional view of GaSb film. (e) and (f): Polycrystalline growth region which substrate contamination has produced.

Results and Discussion

Figure 1(a) shows an example of the etched surface by treatment I. The etching rate using 2% Br₂-CH₃OH solution, which was approximately 0.05 $\mu\text{m/s}$, was nearly constant. In this figure, small pits and scratches due to the selective etching at the damaged area on mechanically polished surface were observed on the surface. Such typical defective surfaces were sometimes observed independently of Br₂ content in the solution. Similar results were previously reported for the chemical etching of InP substrates using Br₂-CH₃OH solution (8). As the heat-cleaning temperature T_{HC} was raised to about 535°C, a spotty diffraction pattern started to appear as shown in Fig. 1(b). The appearance of such pattern can be regarded as a clear evidence of surface oxide being removed by a thermal decomposition process. However, it means that the initial, thermally cleaned surface is rough in an atomic scale, which produces a diffraction pattern of spots (9). It is shown in Fig. 1(c) that the surface of the MBE-GaSb film grown on the substrate shown in Fig. 1(a) is the same defect pattern as that of the substrate shown in Fig. 1(a). Therefore, it is clear that these surface defects propagate from the substrate. Figure 1(d) shows the stained cross-sectional view of the film. Some defects exist at the substrate-film interface. Moreover, Fig. 1(e) and 1(f) show the typical region where the substrate contamination has produced polycrystalline growth (5, 10), which is attributed to the involatile contaminants on the surface such as carbon. Oxide on the surface could be removed by the thermal treatment. However, it was found in our preliminary XPS observation that carbon could not be reduced effectively by the thermal treatment. The carbon remaining on the surface receiving treatment I was about 5% of a monolayer or more. Cho and Arthur (9) previously reported the polycrystalline GaAs over area with carbon contamination, and pointed out that carbon is the most troublesome contamination for MBE growth. Such

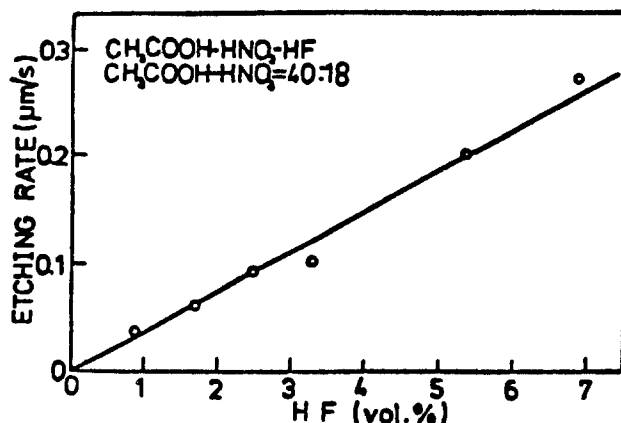


Fig. 2. HF content dependence for etching rate of nondoped GaSb(100) etched by CH₃COOH-HNO₃-HF solution.

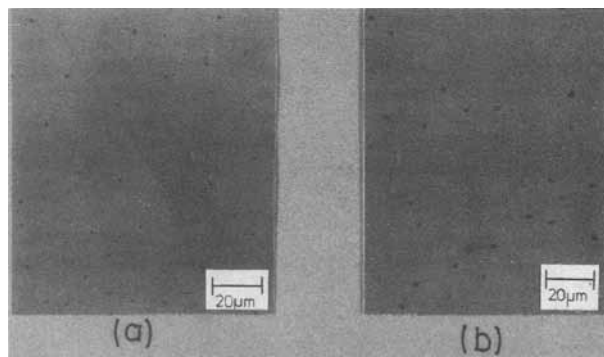


Fig. 3. (a): Surface of GaSb substrate etched by the treatment III. (b): Surface of GaSb film grown on the same substrate as shown in (a). Thickness of film is about 2 μm .

defects at the substrate-film interface and polycrystalline growth region were sometimes observed in case of treatment I. Therefore, the chemical etching of GaSb substrates by $\text{Br}_2\text{-CH}_3\text{OH}$ solution is not a proper procedure for the MBE growth. However, no pits and scratches were observed on the substrate surface etched by treatment II. The etching rate using $\text{CH}_3\text{COOH-HNO}_3\text{-HF}$ solution which was approximately $0.12 \mu\text{m/s}$ was nearly constant. The etching mechanism of this solution is not clear at this time. However, it was found in our experiments that this solution was most proper to remove the damaged surface completely. Figure 2 shows the HF content dependence of etching rate. The etching rate increases linearly with increasing HF content. However, with HF content of more than 7.0 volume percent, the etched surface was not smooth. Moreover, the residual surface oxide which degrades the morphology of the films sometimes remained on the substrate surface, irrespective of any HF content in the solution. This residual surface oxide was identified as Sb_2O_3 and Ga_2O_3 , as determined by XPS (11). In order to effectively remove this residual oxide, treatment III, IV, and V in Table I were applied. Treatment III and IV give rise to small pits. Figure 3(a) shows an example of the etched surface by the treatment III. Figure 3(b) shows the morphology of the film grown on the substrate shown in Fig. 3(a). A number of small pits which were in nearly the same order of density with that of the substrate were observed similar to treatment I. However, in case of treatment V, such small pits were not observed, and reproducible smooth etched surfaces were obtained as shown in Fig. 4(a). A subsequent $\text{HNO}_3\text{-HCl}$ solution could reduce the residual surface oxide content to the amount of about 20%, which was convinced by XPS. The resulting oxide which could be removed by the subse-

quent thermal treatment was estimated to be less than 10Å thick. The RHEED pattern of the substrate surface at the heat-cleaning temperature T_{HC} about 525°C was streaky as shown in Fig. 4(b), suggesting that the initial, thermally cleaned surface is atomically flat. Under Sb_4 flux (Sb cell temperature about 600°C) supplied by an evaporation cell, the substrate surface exhibited surface reconstruction. Figure 4(c) shows a $\text{C}(2 \times 6)$ structure along $\langle 0\bar{1}1 \rangle$ azimuth, already observed in MBE studies (12). The same sharp streaking RHEED pattern was maintained throughout the MBE growth of GaSb film. Figure 4(d) shows a typical surface morphology of the film grown on the substrate etched by treatment V. The surface is smooth relative to the former cases, and does not show any microscopic defects. Figure 4(e) shows the SEM photograph of the stained cross-sectional view of the film. The interface between the substrate and film was flat, and no defects exist at the interface. This result using treatment V was very reproducible as far as the morphology, substrate-film interface, and RHEED pattern were concerned. The streaky RHEED pattern of the substrate etched by treatment V was maintained to the substrate temperature about 580°C , and changed to a fairly diffuse spotty pattern about 590°C , due to the thermal faceting of the substrate surface. This may be attributed to the desorption of volatile atoms from the substrate surface due to the difficulty of maintaining a congruent evaporation. Figure 5(a) shows the thermally damaged substrate surface after the prolonged heat-treatment at 600°C . Figure 5(b) shows the corresponding RHEED pattern. Such a thermal faceting is also a source of defects in grown films (5).

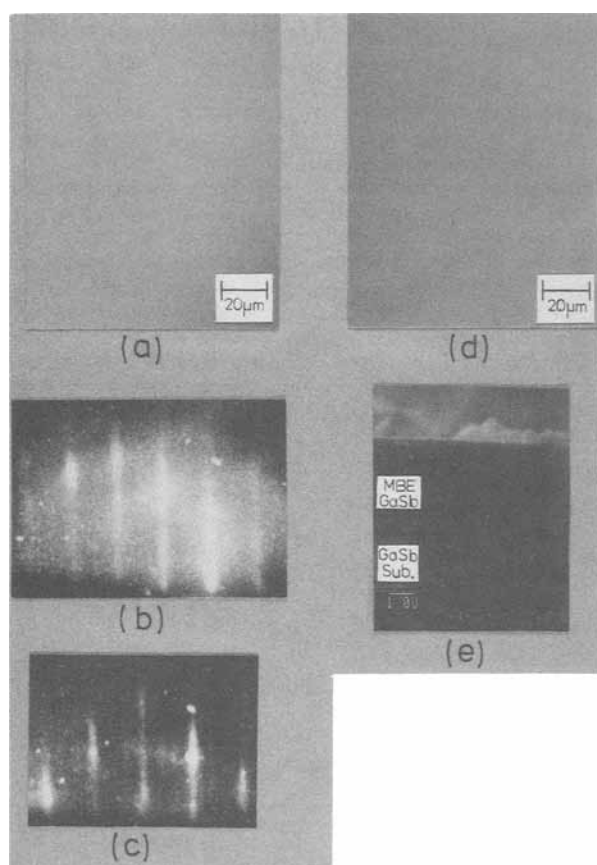


Fig. 4. (a): Surface of GaSb substrate etched by the treatment V. (b): RHEED pattern ($\langle 0\bar{1}1 \rangle$ azimuth) of substrate etched by the treatment V at heat-cleaning temperature T_{HC} about 525°C . (c): RHEED pattern ($\langle 0\bar{1}1 \rangle$ azimuth) of substrate under Sb_4 flux. (d): Surface of GaSb film grown on the same substrate as shown in (a). Thickness of film is about $2 \mu\text{m}$. (e): SEM photograph of stained-cross sectional view of GaSb film.

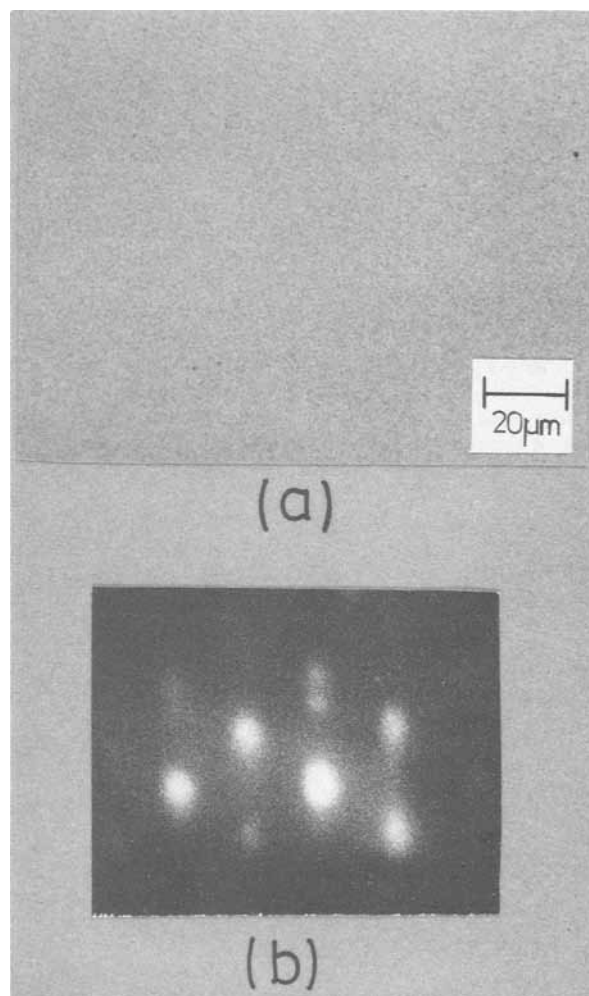


Fig. 5. (a): Surface of GaSb substrate after the heat-treatment about 600°C . (b) RHEED pattern ($\langle 0\bar{1}1 \rangle$ azimuth) of substrate at heat-treatment about 600°C .

Summary

The chemical etching of (100)-oriented nondoped GaSb substrates by several different treatments has been studied. The morphology of the MBE-grown GaSb films strongly depends on the substrate preparation prior to the growth. The conventional $\text{Br}_2\text{-CH}_3\text{OH}$ etching is not proper treatment for the substrate preparation. It is shown that some defects which originate at the substrate propagate to the surface of the films and degrade the morphology of the films. The excellent surface morphology of the film can be obtained reproducibly by treating the substrate with $\text{CH}_3\text{COOH-HNO}_3\text{-HF}$ and subsequent $\text{HNO}_3\text{-HCl}$ solutions.

Acknowledgments

The authors wish to thank A. Ryoji and A. Uda for technical assistance. They also wish to thank Dr. Matsushima for his encouragement.

Manuscript submitted April 9, 1984; revised manuscript received Nov. 14, 1984.

Waseda University assisted in meeting the publication costs of this article.

REFERENCES

1. M. Naganuma, Y. Suzuki, and H. Okamoto, *Inst. Phys. Conf. Ser.*, **63**, 125 (1981).
2. W. T. Tsang and N. A. Olsson, *Appl. Phys. Lett.*, **43**, 8 (1983).
3. F. Capasso, M. B. Panish, W. A. Bonner, and S. Sumski, *Inst. Phys. Conf. Ser.*, **56**, 125 (1981).
4. N. Kitamura, M. Takechi, J. Shen, and T. Wada, *Jpn. J. Appl. Phys.*, **20**, 995 (1981).
5. R. Z. Bachrach and B. S. Krusor, *J. Vac. Sci. Technol.*, **18**, 756 (1981).
6. H. Gotoh, K. Sasamoto, S. Kuroda, T. Yamamoto, K. Tamamura, M. Fukushima, and M. Kimata, *Jpn. J. Appl. Phys.*, **20**, L893 (1981).
7. G. Okumura, T. Misawa, S. Yoshida, and S. Gonda, Paper presented at the Annual Meeting of the Japanese Applied Physics Society, Sendai, Japan, October 1983.
8. Y. Nishitani and T. Kotani, *This Journal*, **126**, 2269 (1979).
9. A. Y. Cho and J. R. Arthur, in "Progress in Solid State Chemistry," G. Somorjai and J. McCaldin, Editors, Pergamon Press, New York (1975).
10. C. E. C. Wood, L. Rathbun, H. Ohno, and D. Desimone, *J. Cryst. Growth*, **51**, 299 (1981).
11. M. Kodama, J. Hasegawa, and M. Kimata, Paper presented at the Annual Meeting Japanese Applied Physics Society, Tokyo, March 1984.
12. C. A. Chang, H. Takaoka, L. L. Chang, and L. Esaki, *Appl. Phys. Lett.*, **40**, 983 (1982).

Large-Scale Growth of GaAs Epitaxial Layers by Metal Organic Chemical Vapor Deposition

J. L. Tandon and Y. C. M. Yeh

Applied Solar Energy Corporation, City Of Industry, California 91749

ABSTRACT

Physical and electronic properties of both p- and n-type GaAs layers grown by metal organic chemical vapor deposition (MOCVD) are discussed and correlated with reactor control parameters. Crucial questions about the uniformity and reproducibility of layer growth in a large-scale reactor are addressed. Data are presented which demonstrate large-scale viability of MOCVD technology. Under optimized operating conditions, good quality layers with thickness and carrier concentration variations of $\leq 10\%$ and $\leq 50\%$, respectively, have been grown on 60×4 cm wafers at a time. Such large-volume growth of GaAs layers has important implications in the production of GaAs devices and circuits.

In recent years, growth of epitaxial GaAs layers by MOCVD has received considerable attention (1). Since the first demonstration of the concept in 1968 (2), many laboratories have reported successful growth of doped layers using a variety of dopants (1, 3). The quality of layers grown by MOCVD has now attained a level which is as good, if not better, than that claimed by liquid-phase epitaxy, vapor-phase epitaxy, or molecular beam epitaxy (1, 4). This can be attributed primarily to a significant advancement in the availability of highly pure AsH_3 and organic sources for Ga (trimethyl-gallium and triethyl-gallium).

Although good success of the MOCVD technique has been achieved in small laboratory-type reactors, and large-scale reactors have been contemplated (5), the potential of the technology in production is yet to be realized. In this paper, large-scale growth of high quality GaAs epitaxial layers by MOCVD is reported. The properties of the layers as a function of flow rates of gases, temperature, and pressure are discussed. Specific questions about the uniformity and reproducibility of layer growth are addressed. Variations in the layer properties in a single growth run are correlated with temperature gradients and gas-flow dynamics within the reactor. Optimized control parameters for the reactor are determined, and data are presented which demonstrate good quality growth on 60×4 cm wafers at a time, with thickness and carrier concentration variations of $\leq 10\%$ and $\leq 50\%$, respectively.

Experimental Methods

Growth of epitaxial GaAs layers was carried out in a modified large-scale low pressure (< 760 torr) MOCVD reactor MR-200 built by Cambridge Instruments. The schematic diagram of the system is shown in Fig. 1. The reactor consists of a hollow SiC-coated graphite susceptor which sits on a quartz dome. The vertical lamp heating elements are arranged uniformly inside the quartz dome, and the heating of the susceptor is accomplished by radiation. Stabilization of the susceptor temperature is attained by controlling the power to the lamp heating elements, and the temperature is measured by a pyrometer. The pressure inside the reacting chamber is controlled by a throttle valve in front of the vacuum pump. The susceptor has an outer diameter of about 30.5 cm and has ten facets on its periphery, each comprising of four pockets [see Fig. 1(b)]. The dimensions of each pocket are 7.6×4.6 cm. Three wafers, each 2×4 cm, can be loaded in each one of the pockets. Thus, if desired, growth can be carried out on 120×4 cm wafers at one time. The vertical distance between the entry and the exit points of the gases in the reactor is about 25 cm. During growth the susceptor was rotated with a speed of ~ 5 rpm, and was covered with a stationary water-cooled barrel. The flow rate of carrier gas H_2 was ~ 120 liter/min for most growth runs.

GaAs wafers (semi-insulating or n-type ($n \sim 2 \times 10^{18} \text{ cm}^{-3}$) oriented $2^\circ\text{-}3^\circ$ off $\langle 100 \rangle$ axis) were used as substrates for growth experiments. The flow rates of the gases were controlled by mass flowmeters and microprocessor-

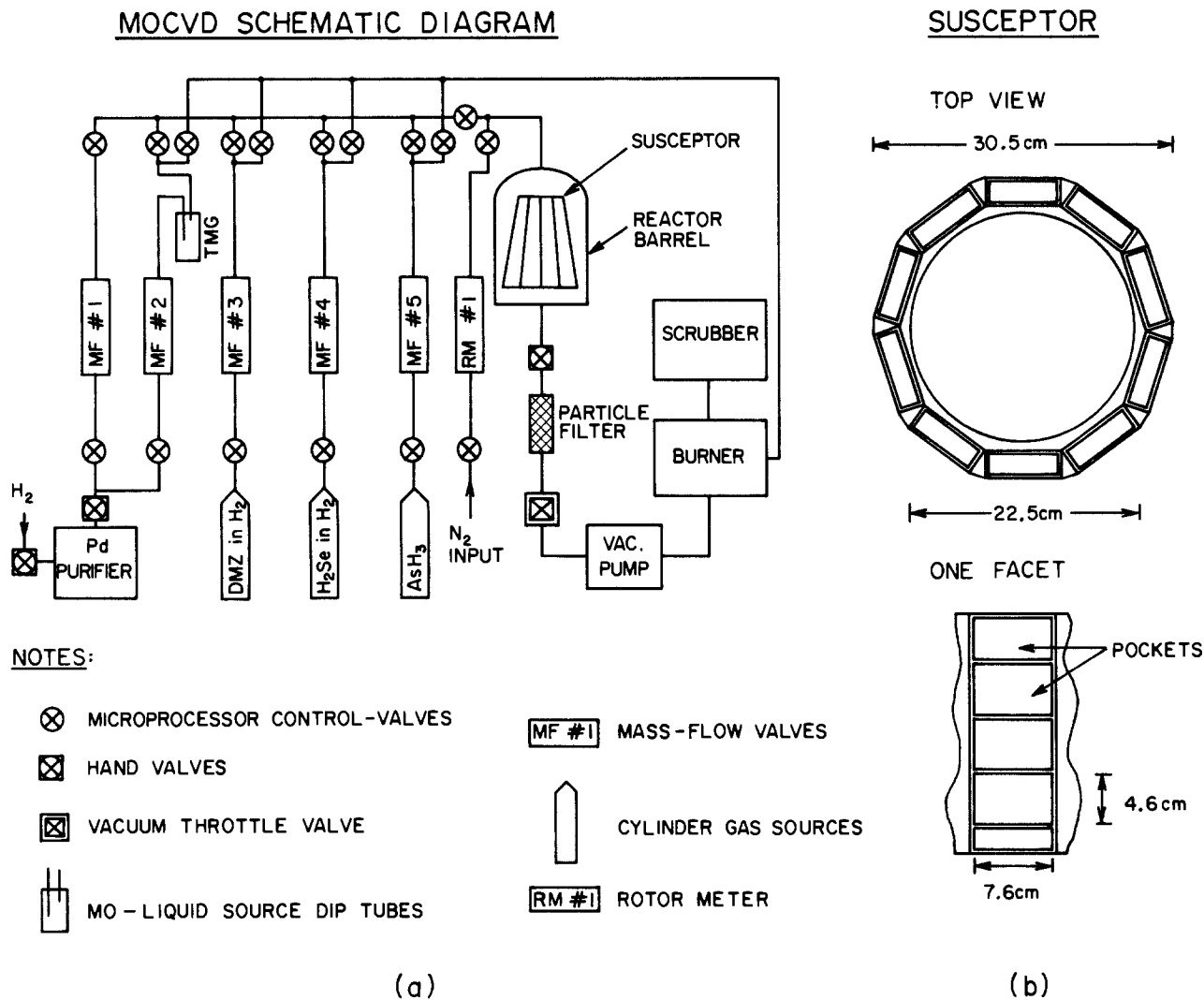


Fig. 1. Schematic diagrams of the MOCVD reactor system (a) and of the susceptor (b). The susceptor has ten facets (b) on its periphery, each containing four pockets for loading wafers. If desired, growth could be carried out on 120×4 cm wafers at one time.

activated valves. After growth, the surface morphology of the grown layers was examined by optical and secondary electron microscopy. Free carrier concentration and mobility values were determined by Hall-effect measurements performed on layers grown on semi-insulating GaAs wafers. The depth profiles of carrier concentrations and the thicknesses of the grown layers were measured by a Polaron British Post Office profiler. This instrument calculates and automatically plots carrier concentration as a function of depth. The carrier concentration is determined by measuring the capacitance *vs.* voltage of the reverse biased Mott-barrier formed between the GaAs wafer and an electrolyte. *In situ* depth measurements are obtained by controlled etching (in the same electrolyte), accomplished by passing a current generated either by a light source or by applying a bias. The carrier concentration values measured by the Polaron profiler cross checked very well (better than $\pm 20\%$) with the values obtained from Hall-effect measurements. As estimated by "alpha-step" stylus-type measurements performed on the etch pits created after Polaron profile measurements, the inaccuracy in the depth scale of the Polaron Profiler was less than $\pm 3\%$.

Results and Discussion

Surface morphology and crystalline quality of layers.—Epitaxial layers were grown in the temperature range 660 – 800°C . In some cases, island-type growth was observed in isolated regions. Figure 2 shows an example of such growth. This type of growth occurred around contaminant particles which clung to the surfaces of

GaAs wafers prior to growth. By energy dispersive x-rays these contaminant particles were found to be rich in Si and O concentration, indicating that they were SiO_x particles. Electrostatic charge is believed to be associated with these particles, which accounts for their strong clinging to the GaAs surface. Conventional cleaning procedures (rinsing with organic solvents) were found to be insufficient to remove them. An automated scrubbing procedure, whereby the wafers were scrubbed with nylon brushes in acetone, was developed and adopted, which considerably reduced their density. Such an automated procedure was especially required in the batch-process cleaning of a large number of wafers for growth.

In addition to the surface morphology features described above, growth defects comprising of pits and hill-locks (6) were also occasionally observed in localized areas. The origin of these defects and their relationship to growth parameters and/or substrate quality are not well understood yet. However, layers grown at high temperatures possessed less density of these defects.

The crystalline quality of the grown layers was measured by backscattering spectrometry with channeling, employing a 2 MeV He^+ beam. In all cases examined, the epitaxial layers were single crystalline with crystalline quality as good as the substrates.

Growth rate vs. trimethyl-gallium (TMG) mole fraction.—With the AsH_3 mole fraction maintained a factor 4-100 higher than the TMG mole fraction, the growth rate was found to be linearly dependent on the TMG mole fraction. Figure 3 confirms this result, where growth rate

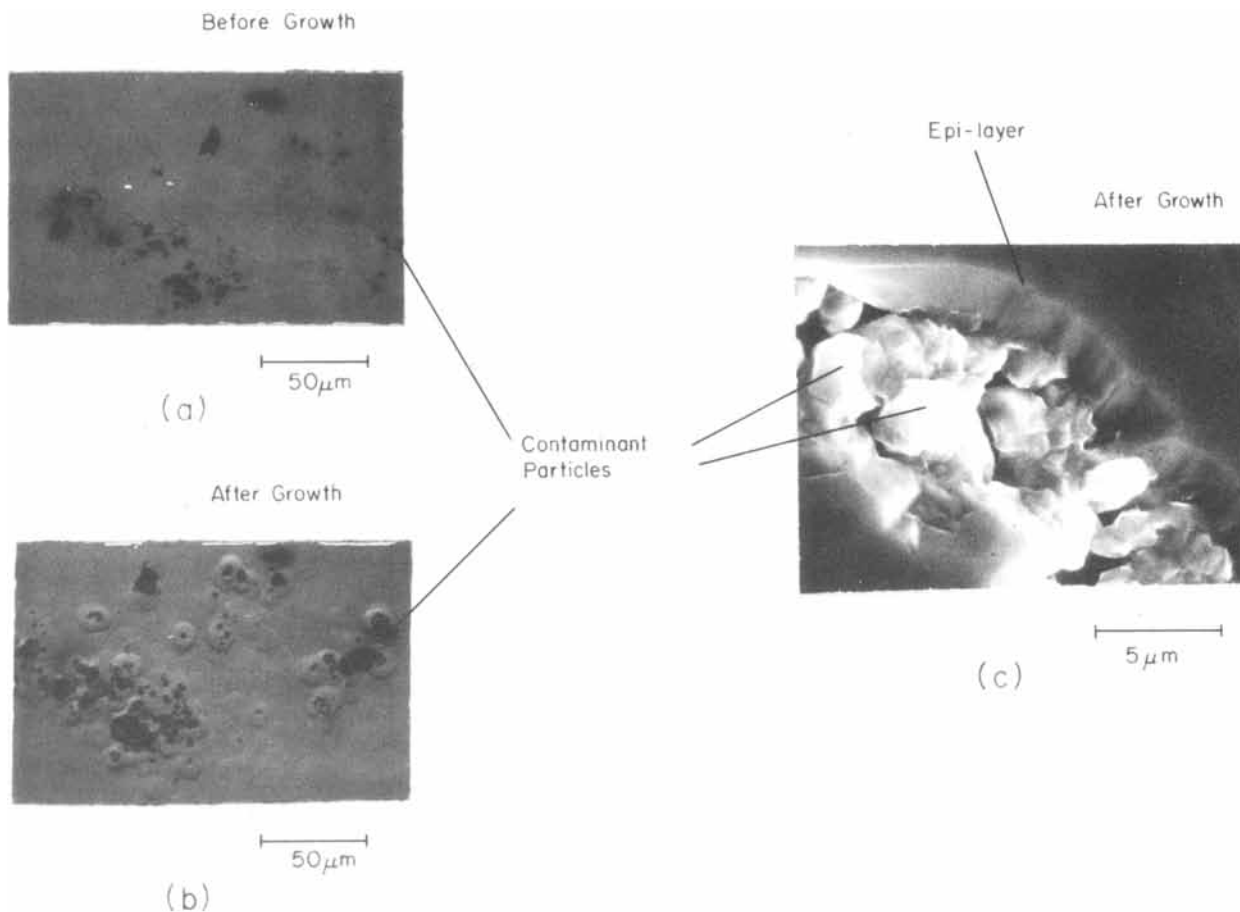


Fig. 2. Micrographs showing contaminant particles before growth (a), and morphology around these particles after growth (b) and (c). The micrographs (a) and (b) were obtained using an optical microscope (with Nomarski interference), and (c) using an SEM. The island-type growth around contaminant particles is evident from (c). By energy dispersive x-ray measurements, the contaminant particles were found to be rich in Si and O concentration, indicating that they were SiO_x particles.

is plotted as a function of TMG mole fraction for both n- and p-type layers. Similar observations have also been reported elsewhere (7-10).

n-type layers.—Several n-type layers were grown with various concentrations of H_2Se in the gas stream, while keeping all other parameters constant. Two identical growth runs were carried out for each concentration of H_2Se . In the runs, samples were placed all across the sus-

ceptor in the third and fourth pockets from the top [see Fig. 1(b)]. Figure 4 shows free-electron concentration (n)

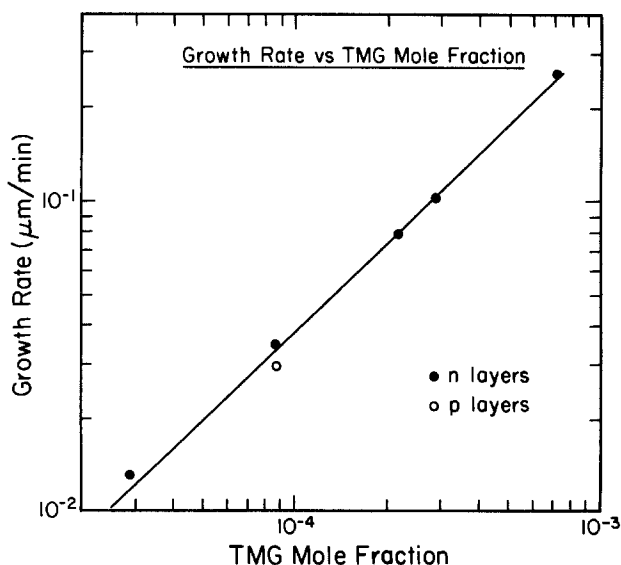


Fig. 3. Growth rate as a function of TMG mol fraction (x_{TMG}). All other parameters were kept constant: $x_{\text{AsH}_3} = 3.25 \times 10^{-3}$, $T = 730^\circ\text{C}$, $P = 132$ torr.

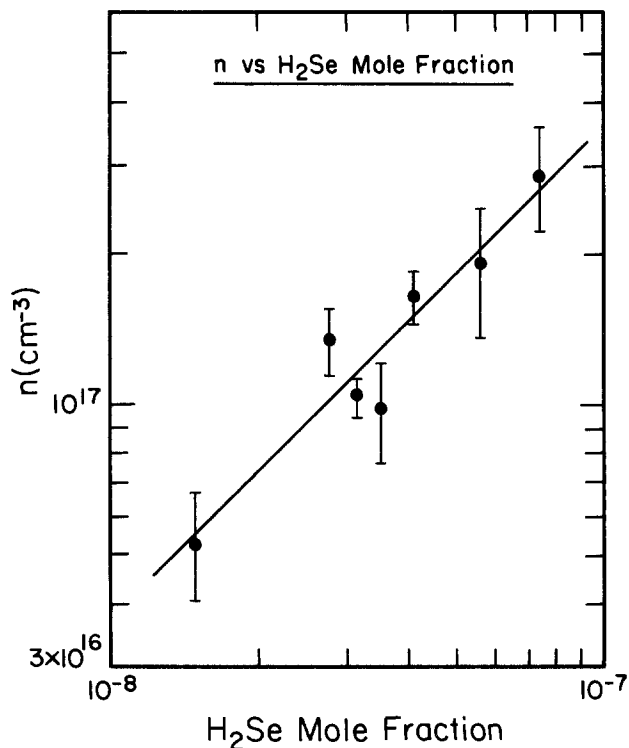


Fig. 4. Free electron concentration (n) in the grown layers as a function of H_2Se mole fraction ($x_{\text{H}_2\text{Se}}$). Other parameters: $x_{\text{TMG}} = 2.87 \times 10^{-4}$, $x_{\text{AsH}_3} = 3.25 \times 10^{-3}$, $T = 730^\circ\text{C}$, $P = 132$ torr.

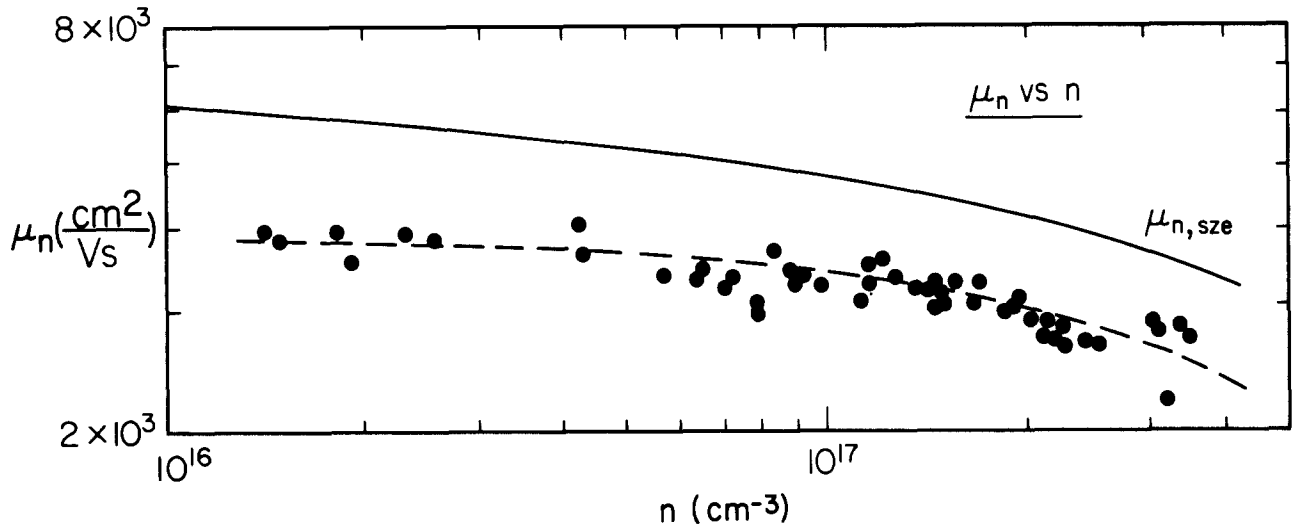


Fig. 5. Free electron concentration (n) of MOCVD grown n-type layers as a function of electron mobility (μ_n). The solid line ($\mu_{n, sze}$) is obtained from Ref. (11).

measured in these samples as a function of H_2Se mole fraction. Each point plotted in Fig. 4 is an average of four to five measurements made on randomly picked samples from the various pockets in the two identical runs. The error bars indicate scatter in the measurements. An analysis of the scatter revealed that variations across the susceptor and from run to run were small ($< \pm 20\%$), and within measurement errors. Most of the scatter in the data points could be attributed to a systematic variation in the doping of layers grown on samples placed at different vertical locations in the susceptor. This variation in a single growth run is discussed below. The straight line in Fig. 4 is a least-mean-square fitted line with a slope very close to 1. Thus, for the range of H_2Se mole fraction considered, n is found to vary linearly with H_2Se mole fraction.

The room temperature mobility of the grown n-type layers as a function of electron concentration is given in Fig. 5. The measurements reported here were made on samples loaded in the various pockets of the susceptor during several growth runs carried out with different concentrations of H_2Se . As expected, the mobility decreases with the increase in n , and the trend is similar to the estimated $\mu_{n, sze}$ given in Ref. (11) (solid line). However, the mobility values in the grown layers are lower than $\mu_{n, sze}$. This may be due to compensating impurities in gases which could get incorporated in the layers during growth.

p-type layers.—Figure 6 gives the hole concentration (p) measured in p-type layers as a function of dimethyl-zinc (DMZ) mole fraction. The data plotted here were collected on samples prepared in a similar fashion as described in the previous section. Again, a linear dependence is observed for the range considered, with the slope of the fitted line close to 1. The room temperature mobility decreases with increasing hole concentration (Fig. 7), following a trend similar to $\mu_{p, sze}$ (11). However, the measured mobility values in the grown layers are somewhat lower, which may again be due to compensating electronic impurities.

Doping vs. growth rate.—Free carrier concentrations were measured in both p- and n-type layers grown with varying growth rates. Different growth rates were obtained by changing the TMG mole fraction, while keeping the mole fractions of AsH_3 and the dopants constant. Figure 8 shows the dependence of hole concentration (p) on the growth rate of p-type layers. The error bars ascribed to the data again represent scatter in the measurements made on samples in different pockets of the susceptor and from run to run (see the "n-type layers" section). A significant increase in p is observed for higher growth rates. Similar results were also obtained on n-type layers grown with Se as dopant. Higher doping efficiency of

both p- and n-type dopants with higher growth rates is not intuitively clear. This behavior cannot be explained by variations in the buried compensating impurities alone during growth. The increase in both n and p with the increase in growth rate is most likely due to the increase in the incorporation of respective dopant atoms during growth. The dopant incorporation appears to be linked with the mass transport of Ga atoms which controls the growth rate. This effect, also reported elsewhere (7), has been attributed to surface kinetic effects. More diagnostic studies of the reacting species during growth are, however, required to understand this phenomenon better.

Spatial variation in carrier concentrations and thicknesses of grown layers at different growth temperatures.—n-type layers were grown on samples loaded all across the susceptor. Vertically, the samples spanned a distance of approximately 14 cm from the location of the injection of gases to the exit point where the gases were

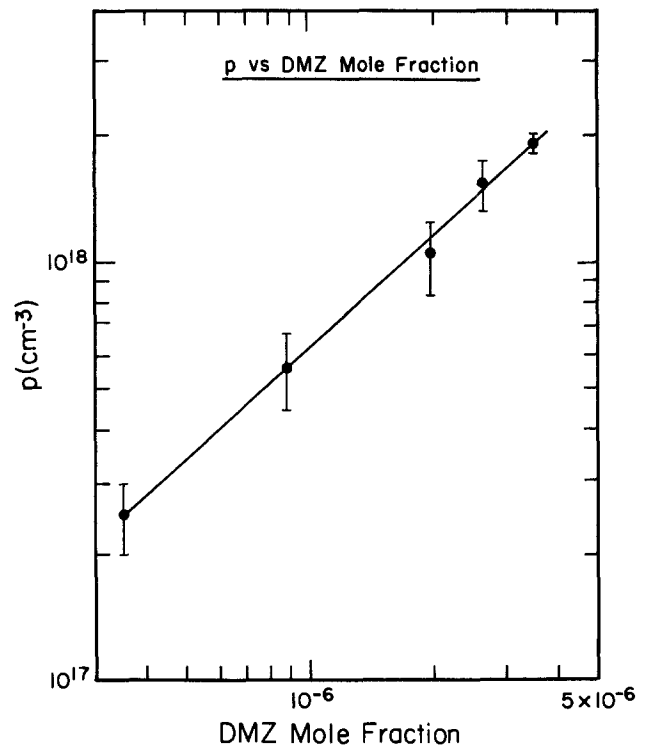


Fig. 6. Free hole concentration (p) in the grown layers as a function of DMZ mole fraction (x_{DMZ}). Other parameters: $x_{TMG} = 2.87 \times 10^{-4}$, $x_{AsH_3} = 3.25 \times 10^{-3}$, $T = 730^\circ C$, $P = 132$ torr.

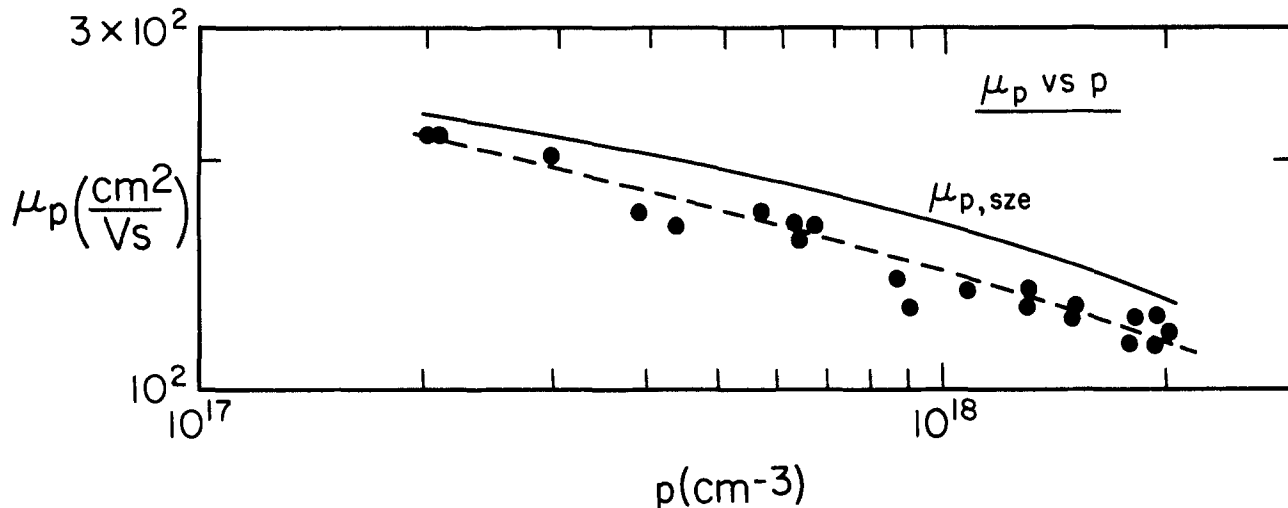


Fig. 7. Free hole concentration (p) of MOCVD grown p-type layers as a function of hole mobility (μ_p). The solid line ($\mu_{p, size}$) is obtained from Ref. (11).

pumped out. The pressure inside the reacting chamber was kept constant by manipulating the throttle valve (see Fig. 1). Three growth runs were carried out at three different temperatures measured at about the center of the susceptor. Other parameters (mole fractions of reacting gases and flow rates) were kept constant. Figure 9 shows the distribution in the free electron concentrations (n) and in the thicknesses of the grown layers as a function of vertical distance in the reactor (zero distance corresponds to the point of injection of the gases). Variations across the susceptor, at a fixed vertical distance, were within measurement errors (see "n-type layers" section). The three curves are for three different temperatures of growth. The value of n , at a fixed vertical distance, for constant mole fractions of reacting gases, pressure, and flow rates, decreases with increasing temperature of growth. Similar behavior was also observed for p-type layers with Zn doping. Decreased dopant incorporation with increased temperature of growth has also been reported earlier (7), and is related to increased kinetic energy of reacting species. Again, for better understanding of this effect, detailed characterization of chemical species at the growth surface is needed.

Another important feature of Fig. 9 is the variation in n with spatial vertical distance in the reactor. An identical trend for the three cases of growth temperatures implies an establishment of a steady-state spatial temperature gradient during growth. [The not-so-conspicuous trend in the lowest temperature case may be due to n-type dopant saturation effects at $\sim 2 \times 10^{18} \text{ cm}^{-3}$ level (12)]. The injection point is cooler than the exit point. The hottest point is located close to, but not at, the exit point. The existence of this temperature gradient was also verified by

measurements performed with a pyrometer under simulated growth conditions. The cooling of the surfaces of the samples near the injection point can be explained by the heat taken away by the cold gases entering the reacting chamber. At the exit point, the slight increase in n appears to be due to a slight drop in the temperature resulting from increased velocity of gases caused by pumping.

It is interesting to point out that spatial carrier concentration distribution, as measured and plotted in Fig. 9, serves as a sensitive probe for detecting temperature gra-

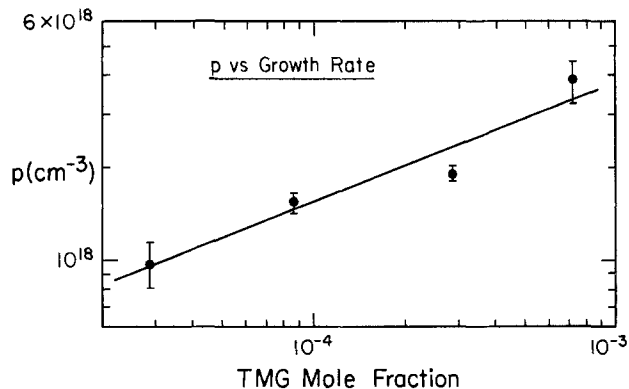


Fig. 8. Free hole concentration (p) as a function of TMG mole fraction (x_{TMG}), or growth rate (see Fig. 3). Constant parameters: $x_{AsH_3} = 3.25 \times 10^{-3}$, $x_{DMZ} = 3.47 \times 10^{-6}$, $T = 730^\circ\text{C}$, $P = 132 \text{ torr}$.

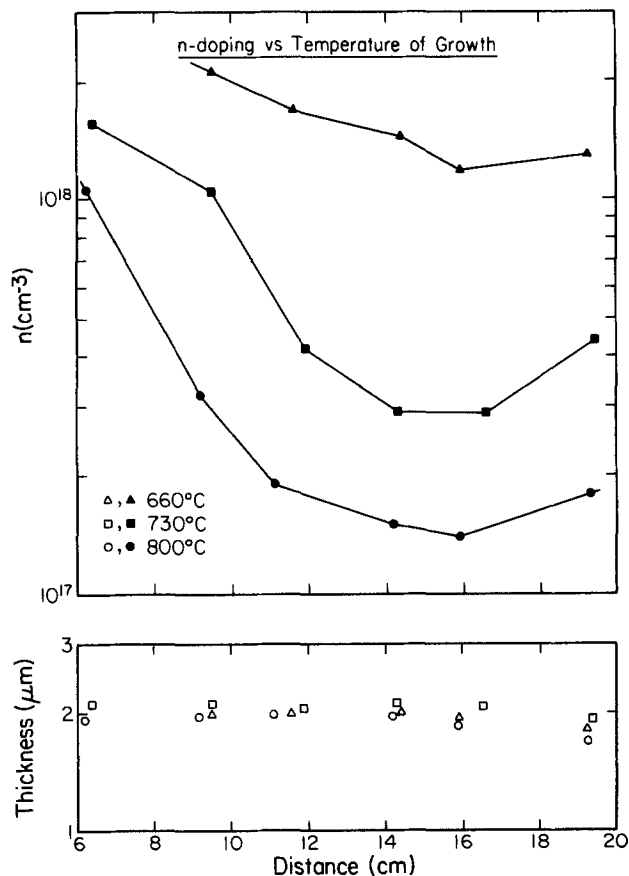


Fig. 9. Free electron concentration (n) and thicknesses of grown layers as a function of spatial distance in the reactor (see Fig. 1 and text for details). The three curves are for three different temperatures of growth, measured about the center of the susceptor. Constant parameters: $x_{TMG} = 2.87 \times 10^{-4}$, $x_{AsH_3} = 3.25 \times 10^{-3}$, $x_{H_2Se} = 5.63 \times 10^{-8}$, $P = 132 \text{ torr}$.

dients within the reactor. From the dependence of the carrier concentration on the temperature of growth, and from pyrometer measurements, a temperature gradient of $\sim 70^\circ\text{C}$ was estimated at an operating total pressure of 132 torr.

The spatial variation in the thicknesses of the grown layers is not as dramatic as the carrier-concentration variation. This implies that the growth rate is not a function of the temperature of growth. The drop ($\sim 30\%$) in the thicknesses of the layers near the exit point of the gases can be explained by a reduction in the growth rate due to a decrease in the available concentration of TMG per unit time. This decrease in TMG concentration may be caused by depletion and/or by the mechanism of differential pumping used in the reactor which increases the velocity of reacting gases at the exit point.

Spatial variation in carrier concentrations and thicknesses of grown layers at different pressures of growth.—To investigate the effect of total pressure on the carrier concentrations and the thicknesses of the grown layers, four growth runs were made with four different values of pressure. Other parameters, such as temperature, mole fractions of the reacting gases, and flow rates, were kept constant. Loading of the samples for growth in the reactor was carried out in a similar fashion as described in the previous section. Figure 10 shows the vertical spatial distribution in the electron concentrations (n), and in the thicknesses of the grown n-type layers. Similar behavior was also observed for p-type layers. For low values of total pressure, a large variation in the distribution of n is observed, which is due to a steady-state temperature gradient established in the reactor during growth (see the previous section, Fig. 9). An increase in the pressure of growth results in a reduction of temperature gradient. With the growth pressure of 400 torr, the gradient collapses, resulting in fairly uniform distribution of n . This behavior can be explained by the effect of total pressure

inside the reacting chamber on the temperature at the reacting surfaces of loaded wafers. An increase in pressure reduces the velocity of reacting gases, so that the gases become less effective in taking the heat away from the loaded wafers. This results in an increase in temperature, more significantly near the injection point of the gases in the reactor. A total pressure of 400 torr, for the operating growth parameters chosen in this case, thus homogenizes the temperature distribution within the reactor.

It should be noted that with the "optimized" operating conditions, good uniformity ($\leq 50\%$) in doping concentration is achieved over a region of about 14 cm in the reactor. Considering the geometry and dimensions of the susceptor (see Fig. 1), this implies that growth with a uniform distribution in carrier concentration can be carried out on 90×4 cm wafers at a time. The "optimized" conditions should not be considered as universal conditions, and indeed would depend on flow rates of gases, spatial distribution of lamp heating elements in the reactor, pumping speed in the below-atmosphere system, geometrical construction of the reactor, angle of susceptor facets with respect to the direction of flow of gases, etc.

As with the variation with temperature (see Fig. 9), the spatial variation in the thicknesses of the grown layers does not depend strongly on the pressure of growth. Again, thin growth near the exit point of gases results from the decreased concentration of available TMG per unit time (see the previous section). As can be seen from Fig. 10, layers with thickness variations of $\sim 10\%$ can be grown over a distance of ~ 10 cm, which corresponds to 60×4 cm wafers at a time (see Fig. 1).

Conclusions

Large-scale viability of a low pressure MOCVD system in the growth of epitaxial GaAs layers has been demonstrated. The reactor has the capability of handling 120×4 cm wafers at a time. Physical and electronic properties of the grown layers as a function of reactor operating parameters have been measured. Under "optimized" conditions, layers with doping and thickness variations of $\leq 50\%$ and $\leq 10\%$, respectively, have been grown on 60×4 cm wafers at a time.

The spatial uniformity in the properties of grown layers depends strongly on the gas-flow dynamics and the physical construction of the reactor. In the real growth cycle, establishment of temperature gradients are found to be most influential in producing nonuniformities. When designing and constructing large-scale reactors, to assure uniformity, dynamical growth conditions should be considered to obtain a laminar flow with constant temperature distribution. It should be pointed that a simulation of exact growth conditions is rather difficult because of the complicated processes involved. Thus, in this respect, another approach whereby modifications are made on the basis of feedback provided from layer measurements should be more useful and appropriate. Modifications along these lines are continually being carried out in our operating of the reactor.

Large-scale growth of epitaxial GaAs layers, as reported in this paper, has important implications in the production of GaAs devices. Currently, Applied Solar Energy Corporation is engaged in the production of GaAs solar cells using the MOCVD technology.

Acknowledgments

We would like to thank D. A. Smith, A. Mehta, and J. Wendt at Applied Solar Energy Corporation for their assistance with the preparation of samples. I. Suni and A. H. Hamdi at California Institute of Technology, Pasadena, California, are thanked for backscattering spectrometry measurements.

Manuscript submitted May 29, 1984; revised manuscript received Nov. 12, 1984.

Applied Solar Energy Corporation assisted in meeting the publication costs of this article.

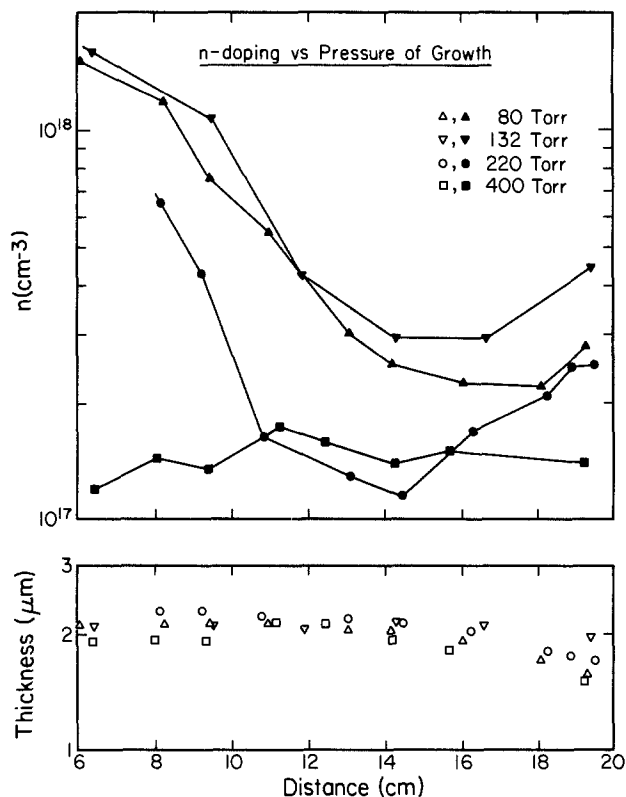


Fig. 10. Free electron concentration (n) and thicknesses of grown layers as a function of spatial distance in the reactor (see Fig. 1 and text for details). The four curves are for four different pressures of growth, measured near the exit point of gases in the reactor. Constant parameters: $x_{\text{TMG}} = 2.87 \times 10^{-4}$, $x_{\text{AsH}_3} = 3.25 \times 10^{-3}$, $x_{\text{H}_2\text{Se}} = 5.63 \times 10^{-8}$, $T = 730^\circ\text{C}$. Uniform growth takes place over the distance range 6-16 cm in the susceptor, with a pressure of 400 torr.

REFERENCES

1. See, for example, papers and references in the special issue on the First International Conference on MOCVD, *J. Cryst. Growth*, **55**, 1 (1981).
2. H. M. Manasevit, *Appl. Phys. Lett.*, **12**, 156 (1968).
3. H. H. Manasevit, *J. Cryst. Growth*, **55**, 1 (1981).
4. J. E. Andrews, *Res./Dev.*, **35**, 183 (1984).
5. S. D. Hersee, M. Baldy, P. Assenat, D. Huyghe, M. Bonnet, and J. P. Duchemin, in "Epitaxial Growth of Semiconductor Material," J. P. Noblanc and A. Mircea, Editors, p. 119, Les Editions, Paris (1982).
6. D. H. Reep and S. K. Gandhi, *J. Cryst. Growth*, **61**, 449 (1983).
7. S. J. Bass and P. E. Oliver, *Inst. Phys. Conf. Ser. B*, **33**, 1 (1977).
8. J. P. Duchemin, M. Bonnet, F. Koelsch, and D. Huyghe, *This Journal*, **126**, 1134 (1979).
9. R. R. Saxena, C. B. Cooper III, M. J. Ludowise, S. Hikido, V. M. Sardi, and P. G. Borden, *J. Cryst. Growth*, **55**, 58 (1981).
10. M. R. Leys and H. Veenvliet, *ibid.*, **55**, 145 (1981).
11. S. M. Sze, "The Physics of Semiconductor Devices," p. 29, John Wiley and Sons, New York (1981).
12. See, for example, T. Inada, M. Miwa, S. Kato, E. Kobayashi, and T. Hara, *J. Appl. Phys.*, **49**, 4571 (1978); T. D. Banwell, M. Maenpaa, M. A. Nicolet, and J. L. Tandon, *J. Phys. Chem. Solids*, **44**, 507 (1983).

Thermal Annealing of Si-N Absorption Bands in Nitrogen-Implanted Silicon

H. J. Stein*

Sandia National Laboratories, Albuquerque, New Mexico 87185

ABSTRACT

The behavior of nitrogen in silicon after implantation and annealing has been investigated by infrared (IR) absorption. Concentrations of N were chosen to represent those implanted into the Si layers in the formation of buried silicon nitride layers. Local mode frequencies similar to those for Si doped with N in the melt are observed after implantation. Intensities for the IR bands associated with the local modes increase when displacement damage is removed by annealing at temperatures between 200° and 600°C. Precipitation of implanted N upon annealing at 750°C is suggested to explain the appearance of additional Si-N bands with frequencies near those for Si-N absorption in crystalline Si₃N₄. Annealing at 900°C is required to remove Si-N absorption bands, whereas 600°C annealing removes Si-O bands in O-implanted Si. This difference may be important for ion and temperature selection when forming buried dielectric layers by ion implantation since impurity-defect accumulation must be controlled to maintain crystallinity in the Si overlayer.

Ion implantation is pervasive in the semiconductor industry. Conventional uses for implantation of electrically active dopants include doping for drive-in diffusion, self-aligned gates, and threshold voltage adjustment. These uses typically require energies < 100 keV and fluences of $\approx 10^{15}$ cm⁻². There has also been limited use of electrically active dopant implants at higher energies to achieve retrograde doping (1) and buried grids (2). Another potential use of ion implantation is the formation of buried dielectric layers in Si by implanting nitrogen or oxygen at high fluences and high energies (3). Typical depth dimensions for implanted silicon-on-insulator (SOI) structures are illustrated in Fig. 1. Circuits may be formed directly in the crystalline overlayer, or an epitaxial layer may be grown on the overlayer before circuit fabrication.

In contrast to conventional uses, buried dielectric layer formation requires energies > 100 keV and ion fluences of $\approx 10^{18}$ cm⁻². Implanting with a fluence sufficient to form a buried dielectric layer subjects the overlayer to high levels of energy into displacement processes and to concentrations of O or N which are above solid solubility limits in crystalline Si (4, 5). The present paper reports (6) studies of the chemical bonding and thermal stability of implanted N in Si at concentrations representative of those in the Si overlayer when a buried Si₃N₄ layer is formed. Infrared absorption was used for the studies, and the annealing characteristics for Si-N absorption bands are compared to the characteristics for Si-O absorption bands in O-implanted Si.

Background

Implantation with 2×10^{18} 200 keV N ion/cm² introduces sufficient N to produce a silicon nitride buried layer $\approx 2000\text{\AA}$ thick, as illustrated by the solid line in Fig. 2 for the N profile calculated using the Brice transport code (7). Sputtering, which is expected (8) to remove about 300 \AA , was not included in the calculation. In addition

to changes in Si produced by specific implanted ions, properties of the overlayer are also affected by displacement damage that accompanies ion implantation. The calculated energy deposited into displacement processes (7) is illustrated by the dashed line in Fig. 2. It is known (9) from previous work that crystalline Si is converted to an amorphous phase by an energy deposition of 10^{24} eV/cm³ into displacement processes at 300 K. Fortunately, significant dynamic annealing occurs for implantations performed above room temperature (9), so that crystallinity can be maintained in the Si overlayer by performing buried layer implantations at temperatures $\geq 400^\circ\text{C}$ for beam currents on the order of 10 μA .

The linear scale for the N concentration in Fig. 2 illustrates the expected buried nitride layer and Si overlayer. However, the same calculated profile plotted on a log scale (Fig. 3) shows N concentrations which are orders of magnitude above the solid solubility limit for N in Si (4.5×10^{15} cm⁻³). Nitrogen affects mechanical (10), electrical (11, 12), and optical properties (5, 13) of crystalline Si. Luminescence (13) and DLTS (14) studies have shown that N produces deep levels, and a deep level associated with substitutional N was identified (SL5 center) in EPR studies (15) of N-implanted Si.

A previous study (16) showed that N implanted into Si forms Si-N bonds which have vibrational modes detectable by infrared absorption. Absorption bands for implanted N in Si appear at the same frequencies as those for Si doped in the melt with N, even though the implanted N concentrations after implantation are orders of

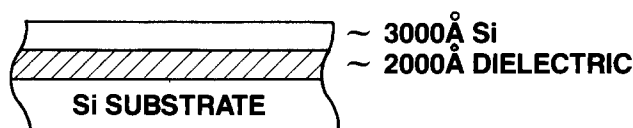


Fig. 1. Illustration of thickness for an implanted dielectric layer and crystalline silicon overlayer for SOI formed by implantation.

* Electrochemical Society Active Member.

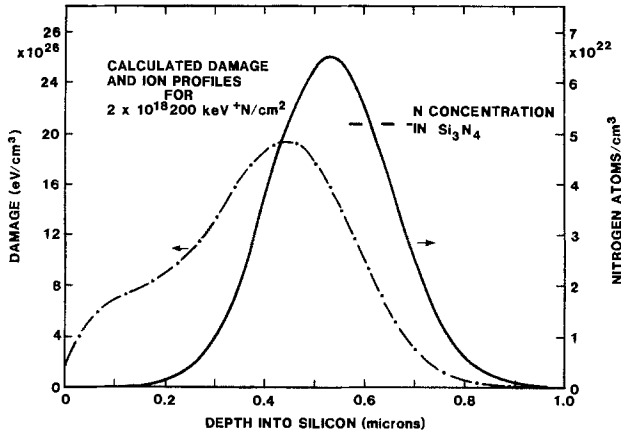


Fig. 2. Calculated depth distributions for nitrogen concentration and energy into displacement processes.

magnitude above equilibrium solid solubility. Absorption by Si-N local modes is used in the present investigation to characterize the effects of postimplantation annealing on Si-N local modes for high concentrations of implanted N in crystalline Si.

Experimental Details

A high resistivity p-type float zone <111> Si wafer 0.5 mm thick and polished on both sides was diced into 1/4 x 1/4 in. samples for implantations with N and Ne. An entire second wafer was implanted with O and subsequently diced into samples. Implantations were performed at ~50°C with scanned ion beams. Infrared absorption spectra were measured at room temperature at 2 cm⁻¹ resolution with a Nicolet 60SX FT-IR spectrometer. Annealing was performed in flowing N₂ for 1h periods and 100°C steps below 600°C, and 150°C steps above 600°C. Samples were given an HF dip after annealing to remove surface oxides.

Results and Discussion

An absorption spectrum for N implanted Si is shown in Fig. 4. Maximum intensities for Si-N bands are observed after a fluence of ~ 2 x 10¹⁵ N/cm² for ion energies between 100 and 200 keV. In order to increase the measured absorbance for Si-N bands, each of the two polished faces

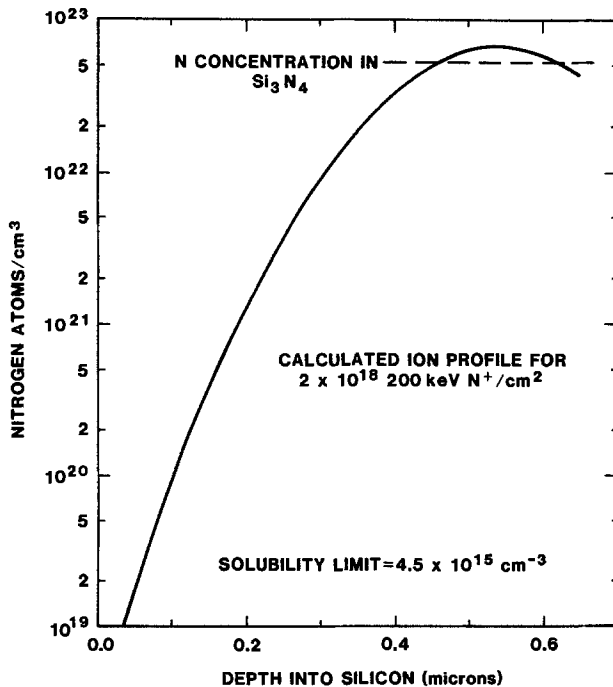


Fig. 3. Illustration of the nitrogen concentration profile implanted into the silicon overlayer.

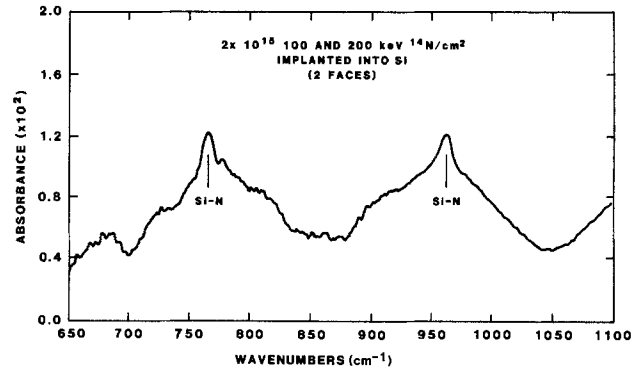


Fig. 4. Infrared absorption bands for Si-N centers in nitrogen-implanted crystalline silicon.

was implanted with 2 x 10¹⁵ of both 100 and 200 keV ¹⁴N/cm². Isotopic substitution was utilized in a previous study (16) to confirm that bands at 764 and 963 cm⁻¹ are associated with Si-N bonds. The broad features in Fig. 4 are interference effects which are not specific to N implantation. Mode frequencies, and therefore the force constants, for N in Si are higher than those for substitutional impurities such as carbon and boron, and they are more comparable (16) to those for oxygen-vacancy and interstitial carbon defects in Si. The 963 cm⁻¹ band is also close in frequency to major absorption bands for Si-N in crystalline Si₃N₄ (17, 18).

Absorption spectra taken after annealing the implanted samples at 600°, 750°, and 900°C are compared in Fig. 5. Spectra have been displaced along the absorbance axis for presentation. Intensities for the 963 and 764 cm⁻¹ bands increase upon annealing at 600°C and the peak for the lower frequency band shifts to 767 cm⁻¹. Henceforth, this band will be referred to as the 767 cm⁻¹ band. Annealing at 750°C decreases the intensities for the 767 and 963 cm⁻¹ bands but new bands appear at 790, 807, 895, and 1025 cm⁻¹. Frequencies for Si-N bands in crystalline Si₃N₄ are indicated in Fig. 5 for comparison to those in the implanted layer after annealing at 750°C. Similarities are evident between 856, 895, 963, and 1025 cm⁻¹ bands in annealed N-implanted Si and the strong bands in Si₃N₄. This similarity is taken as evidence for small precipitates of Si₃N₄ in the implanted layer. No bands appear in crystalline Si₃N₄ near the bands at 767, 790, and 807 cm⁻¹. Absorption in this frequency range has been reported for

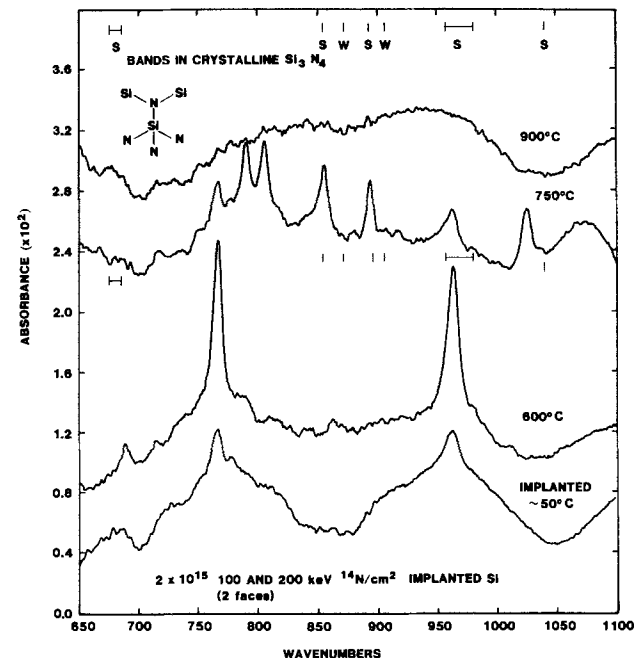


Fig. 5. Annealing effects on Si-N absorption bands in nitrogen-implanted crystalline silicon.

N-doped α -Si (19), and may, therefore, be a consequence of embedding Si-N oscillators in a Si host. Intensities for the Si-N bands are decreased to below the detection limit by annealing at 900°C.

Thermal stability of the implanted impurity in the overlayer is a factor in the choice of ions for buried-layer SOI. Consequently, spectra for Si-O absorption after O implantation and annealing at 300°, 400°, and 600°C are shown in Fig. 6 for comparison to annealing of Si-N bands. Bands at 830 and 1103 cm^{-1} are associated with neutral charge state oxygen-vacancy, O-V, and interstitial oxygen, O_i , centers, respectively (20). The additional band at 889 cm^{-1} after annealing at 300°C is associated with the negative charge state of O-V centers. Similar intensity for the 830 and 889 cm^{-1} bands indicates that the Fermi level is near the $E_c - 0.17$ eV level for O-V centers (20). Absorption bands for O-V centers are nearly removed by annealing at 400°C, and both the O-V and O_i centers are removed by annealing at 600°C. These centers, therefore, would be essentially eliminated by dynamic annealing during implantations near 500°C, which is a typical substrate temperature for buried dielectric layer formation. However intensities for Si-N absorption bands are at a maximum after annealing at 600°C.

More detailed isochronal annealing characteristics for the 767 and 963 cm^{-1} Si-N bands are shown in Fig. 7 where peak absorbance is plotted vs. isochronal annealing temperature. Increase in band intensities occurs primarily between 200° and 600°C. Nitrogen concentrations determined from the intensity of the 963 cm^{-1} band using a previously published calibration (5) are plotted on the right ordinate in Fig. 7. Comparing deduced densities to the density of implanted N atoms indicates about 12% of the implanted N incorporated into the local mode centers after annealing at 600°C. It should be emphasized that the concentration of Si-N inferred from the IR data is only approximate because of potential matrix effects in the IR cross sections. Annealing characteristics for the IR bands are quite different from those for the substitutional N SL5 center (15), and the centers must therefore be structurally different. The general characteristics for the 767 and 963 cm^{-1} bands are similar even though the ratios of their intensities are somewhat dependent upon the annealing temperature. Two modes for a single defect would obviously explain similar annealing characteristics; annihilation of two different defects by a common process is also a possibility.

Implanted samples annealed at 600° and 900°C were subjected to bombardment by 10^{15} 180 keV Ne/cm² and subsequently annealed. No Si-N bands were regenerated in the sample annealed at 900°C by the bombardment/anneal sequence. Bombardment with Ne reduced intensities

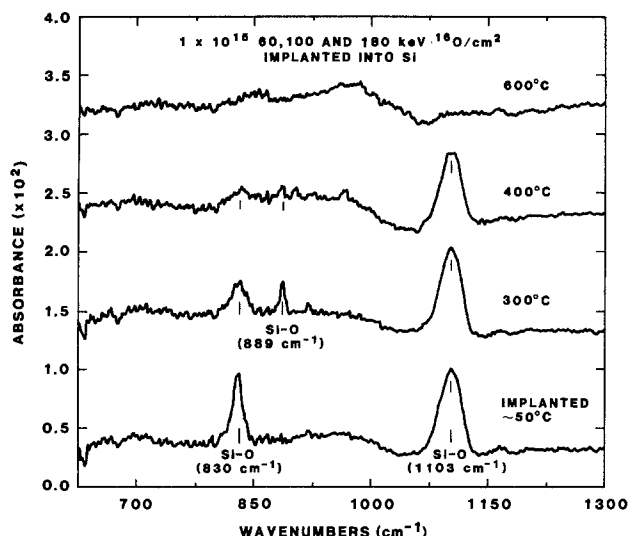


Fig. 6. Annealing effects on Si-O absorption bands in oxygen-implanted crystalline silicon.

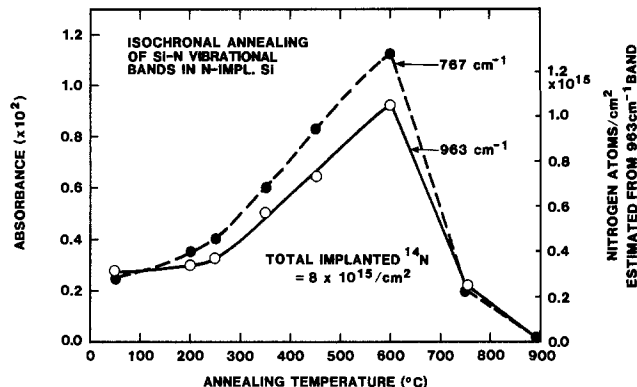


Fig. 7. Isochronal annealing of 767 and 963 cm^{-1} Si-N bands in nitrogen-implanted crystalline silicon.

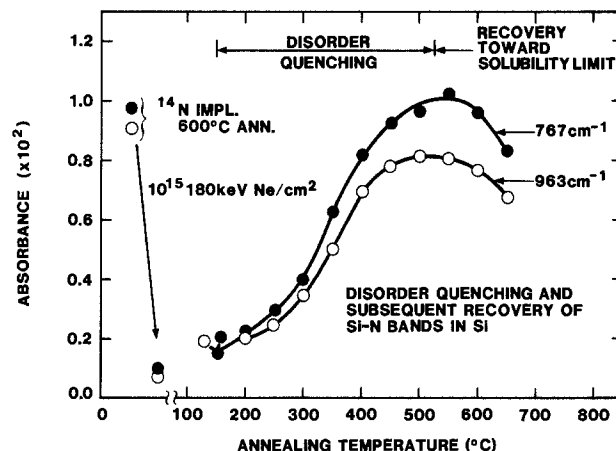


Fig. 8. Effects of Ne bombardment and annealing on previously annealed nitrogen-implanted silicon.

for Si-N bands in the sample annealed at 600°C as illustrated by the data in Fig. 8. Intensities for the bands recover upon subsequent annealing, similar to the results shown in Fig. 7 for the as-implanted sample. The 200°-600°C temperature range for recovery of the Si-N modes corresponds to the temperatures required to remove major defects produced by displacement damage (21). It is concluded, therefore, that disorder caused by displacement damage quenches local mode band intensities.

Intensities for the 767 and 963 cm^{-1} bands decrease, and additional bands form with annealing above 600°C in both the as-implanted and Ne-bombarded samples. These changes are attributed to motion of N on a local scale, resulting in precipitation of implanted N in Si. Growth and loss of the additional IR bands parallel annealing characteristics reported for shallow donors (11, 12) in N-implanted Si so that a relationship is suggested between precipitates and shallow donors. Loss of Si-N absorption bands at temperatures $> 750^\circ\text{C}$ agrees with the temperature reported for diffusion of N from Si layers toward free and internal surfaces (22).

Summary

Absorption bands associated with Si-N vibrational modes are introduced by implantation of N into crystalline Si. The implanted N concentrations are representative of those in the Si overlayer when implanting to form a buried silicon nitride layer. The Si-N bands are quenched by displacement damage and increase upon annealing between approximately 200° and 600°C for both as-implanted and samples which are rebombarded after annealing at 600°C. Similarities are apparent between frequencies for bands in crystalline Si_3N_4 and for Si-N bands in N-implanted Si after 750°C annealing. It is suggested, therefore, that precipitation of implanted N in Si occurs at 750°C. Measurements of N profiles by secondary ion

mass spectroscopy and of defect structures by transmission electron spectroscopy are needed to confirm N motion and precipitation in implanted layers.

Heating at 900°C is required to remove Si-N absorption bands in N-implanted Si, compared to 600°C for removal of Si-O bands in O-implanted Si. This difference in the annealing behavior may be important when selecting the implantation temperature and the species to optimize for dynamic annealing during buried layer SOI formation. In particular, it may be necessary to perform N implants at higher temperatures than those for O implants to achieve comparable defect annealing and impurity gettering.

Acknowledgment

This work was performed at Sandia National Laboratories under U.S. Department of Energy Contract no. DE-ACO4-76DP00789.

Manuscript submitted July 23, 1984; revised manuscript received Oct. 15, 1984.

Sandia National Laboratories assisted in meeting the publication costs of this article.

REFERENCES

1. R. D. Rung, C. J. Dell'Oca, and L. G. Walker, *IEEE Trans. Electron. Devices*, **ed-28**, 1115 (1981).
2. M. R. Wordeman, R. H. Dennard, and G. A. Sai-Halasz, *IEDM*, **81**, 40 (1981).
3. R. J. Dexter, S. B. Watelski, and S. T. Picraux, *Appl. Phys. Lett.*, **23**, 455 (1973); for a recent review, see, R. F. Pinizzotto, in "Ion Implantation and Ion Beam Processing of Materials," MRS Vol. 27, G. K. Hubler, O. W. Holland, C. R. Clayton, and C. W. White, Editors, p. 265, North-Holland, New York (1984).
4. H. J. Hrostowski and R. H. Kaiser, *Phys. Rev.*, **107**, 966 (1957).
5. T. Abe, K. Kikuchi, S. Shirai, and S. Murako, in "Semiconductor Silicon 1981," H. R. Huff and R. J. Kriegler, Editors, p. 54, The Electrochemical Society Softbound Proceedings Series, Pennington, NJ (1981).
6. H. J. Stein, Paper 117 presented at The Electrochemical Society Meeting, Cincinnati, OH, May 6-11, 1984.
7. D. K. Brice, *Rad. Eff.*, **11** (1971); private communication.
8. G. Zimmer and H. Vogt, *IEEE Trans. Electron. Devices*, **ed-30**, 1515 (1983).
9. F. L. Vook, in "Radiation Damage and Defects in Semiconductors," J. E. Whitehouse, Editor, p. 60, The Institute of Physics, London, England (1973).
10. K. Sumino, I. Yonenaga, M. Imai, and T. Abe, *J. Appl. Phys.*, **54**, 5016 (1983).
11. E. I. Zorin, P. V. Pavlov, and D. I. Tetel'baum, *Sov. Phys. Semicond.*, **2**, 111 (1968).
12. J. B. Mitchell, J. Shewschun, D. A. Thompson, and J. A. Davies, *J. Appl. Phys.*, **46**, 335 (1975).
13. M. Tajima, T. Masui, T. Abe, and T. Nozaki, *Jpn. J. Appl. Phys.*, **20**, L423 (1981).
14. Y. Tokumaru, H. Okushi, T. Masui, and T. Abe, *ibid.*, **21**, L443 (1982).
15. K. L. Brower, *Phys. Rev. B*, **26**, 6040 (1982).
16. H. J. Stein, *Appl. Phys. Lett.*, **43**, 296 (1983).
17. Y. N. Volgin and Y. I. Ukhanov, *Opt. Spectrosc.*, **38**, 412 (1975).
18. N. Wada, S. A. Solin, J. Wong, and S. Prochazka, *J. Non-Cryst. Solids*, **43**, 7 (1981).
19. G. Lucovsky, J. Yang, S. S. Chao, J. E. Tyler, and W. Czubatjy, *Phys. Rev. B*, **28**, 3234 (1983).
20. R. C. Newman, "Infra-red Studies of Crystal Defects," Taylor and Francis Ltd., London, England (1973).
21. H. J. Stein, in "Neutron Transmutation Doping in Semiconductors," J. M. Meese, Editor, p. 279, Plenum Press, New York (1979).
22. C. I. Drowley and T. I. Kamins, in "Laser-Solid Interactions and Transient Thermal Processing of Materials," MRS Vol. 13, J. Narayan, W. L. Brown, and R. A. Lemons, Editors, p. 511, North-Holland, New York (1983).

Preferential Etching of InP for Submicron Fabrication with HCl/H₃PO₄ Solution

S. Uekusa and K. Ōigawa

Meiji University, Faculty of Engineering, 1-1-1 Higashi-mita, Tama-ku, Kawasaki-shi, Kanagawa 214 Japan

M. Tacano

Electrotechnical Laboratory, 1-1-4 Umezono, Sakura-mura, Niihari-gun, Ibaraki 305 Japan

ABSTRACT

Etching rates of HCl/H₃PO₄ preferential etchant for the InP (100) surface are determined experimentally, particularly at low HCl concentration suitable for submicron fabrication processes. A very slow but reproducible etching rate of 1000 Å/min is obtained at 5% HCl concentration at room temperature with almost vertical (011) facets on a (100) plane. Concentration dependence of the etching rates and surface pretreatment effects are also investigated.

The chemical etching of InP crystals with HCl/H₃PO₄ etchant seems to be favorable for fabricating a submicron pattern which is essential for making optoelectronic or millimeter-wave electronic devices. It is expected that an InP crystal can be etched preferentially with use of HCl/H₃PO₄ etchant (1), but little is known about the etching characteristics relevant to submicron fabrication. Those characteristics on the (100) surface are essential because most of the device structures are fabricated on it. In order to find a slow but preferential etchant of the InP (100) surface, HCl/H₃PO₄ etchants, particularly with low HCl concentration, are investigated in the present paper together with some SEM (scanning electron microscope) observations of the etched facets at various crystal orientations.

Experimental

Multiple processes of photoresist coating/baking and etching with use of AZ1350 photoresist were applied to a Fe-doped semi-insulating InP wafer (supplied from SUMITOMO, resistivity larger than 10⁶ Ω-cm and etch-pit density below 1 × 10⁴ cm⁻² cut to the orientation (100) ± 0.5°) to form a steplike pattern on it for the purpose of determining the etching speed of the solution. The chemicals used were all of reagent grade, 12N with HCl (purity 35.0%), 15N with H₃PO₄ (purity ≥ 85.0%). The etching solution at various HCl concentrations ranging from 5% to 25% volume ratio was kept in a glass beaker and stirred at room temperature (23°C), while the wafer was face down at the bottom and frequently hand shaken in the solution. The etched depths on the (100) surface were measured by

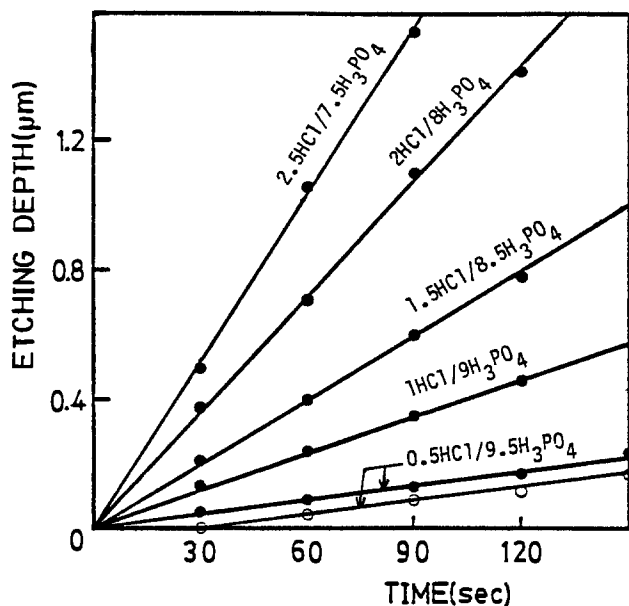


Fig. 1. Etched depths as a function of etching time with HCl/H₃PO₄ solution at 23°C, HCl concentration as a parameter. ● with pre-etching, ○ without pre-etching; 5% HCl concentration. Experimental standard deviations are within circles.

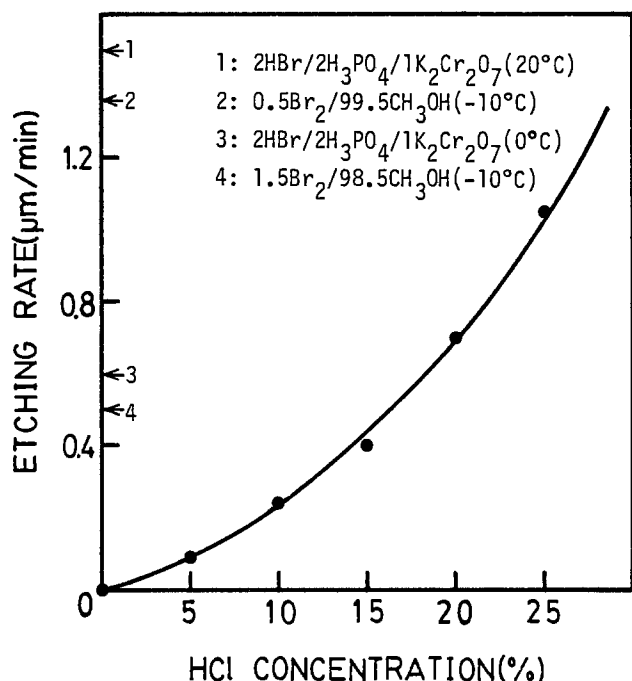


Fig. 2. Etching rates of (100) surface as a function of HCl concentration. Insets give those of other typical etchants.

a surface profiler with a stylus sweep speed at 0.01 mm/s on the sample surface. The etched samples were cleaved on (011) or (01 $\bar{1}$) surfaces, and the etched surfaces appearing on the cleavage were observed by a SEM (Akashi type ISI-DS130).

Results

The etched depths measured by the surface profiler are shown in Fig. 1 as a function of the etching time at low HCl concentration. In order to remove the native-oxide layer formed on the as-bought wafers, the wafers were pre-etched by a 10% HCl concentration for 60s just before the application of photolithographical processes for the etching depth measurements. As the open circles indicate, the wafers without pre-etching treatment have about a 30s delay time to start etching, i.e., we need about 30s to remove the native-oxide layer. Once the native-oxide layer

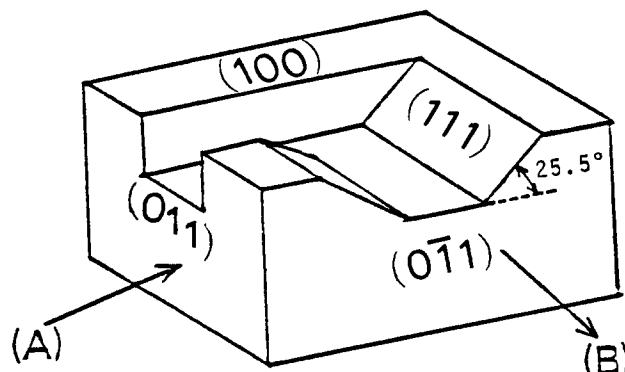


Fig. 3. Schematic diagram of etched pattern with respect to crystal orientation.

ers are removed, the surfaces are etched with the same etching speed as that of pre-etched surfaces (marked as the closed circles). At various HCl concentrations up to 25% volume in H₃PO₄, the etching depth in the pre-etched surfaces was measured as a function of etching time and plotted in Fig. 1. No saturation of the etching speed was observed with any of these solutions, and the etching speeds were determined from the slopes of the curves and plotted as a function of the HCl concentration ratio in Fig. 2. The etching speeds are 0.09 $\mu\text{m}/\text{min}$ for 5% HCl, 0.24 $\mu\text{m}/\text{min}$ for 10% HCl, 0.40 $\mu\text{m}/\text{min}$ for 15% HCl, 0.70 $\mu\text{m}/\text{min}$ for 20% HCl, and 1.05 $\mu\text{m}/\text{min}$ for 25% HCl. The etching speed of the (01 $\bar{1}$) and (111) surfaces are 3.4 $\mu\text{m}/\text{min}$ and 2.6 $\mu\text{m}/\text{min}$ for 20% HCl concentration, respectively. These are 4.9 and 3.8 times faster than that of the (100) surface at the same HCl concentration. Comparison with some other etching solutions, also shown in Fig. 2, makes clear the characteristics of the present solution. The etching speed of Br solutions (2, 3) seems to have a rather large dependence on both the temperature and Br concentration and must be cooled to below 0°C in order to attain a slow etching speed. We may therefore make a

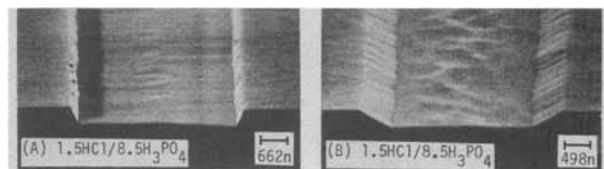


Fig. 4. SEM photographs of etched patterns. (A) (011) cleave; (B) [01 $\bar{1}$] cleave.

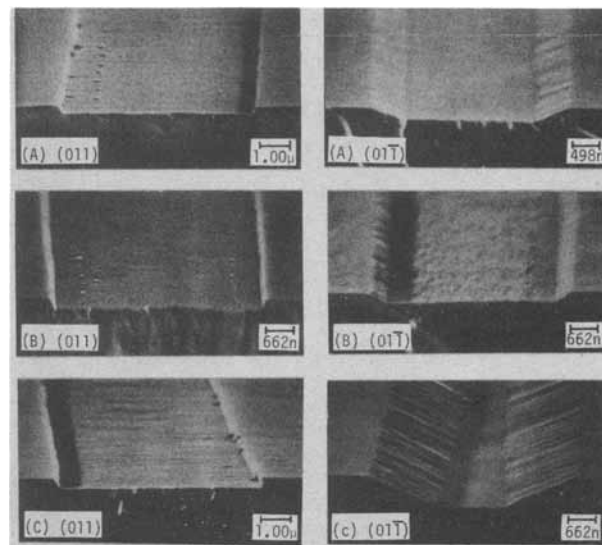


Fig. 5. SEM photographs of (011) and (01 $\bar{1}$) cleave of etched patterns at various HCl concentration. (A) 20% HCl/80% H₃PO₄; (B) 10% HCl/90% H₃PO₄; (C) 5% HCl/95% H₃PO₄.

fine submicron pattern with good reproducibility by using the present solution.

An optical ridge waveguide 2 μm in width was patterned parallel and perpendicular to the (100) surfaces and was cleaved to observe the facets by SEM. The crystallographic orientation and observation are schematically shown in Fig. 3. As shown in the following photographs, we have nearly vertical (01 $\bar{1}$) facets on the (100) plane, while (111) facets have an angle to the (100) plane. Figure 4 shows SEM photographs of the etched surfaces which are mechanically cleaved. The (01 $\bar{1}$) facets on the (100) surface give nearly vertical planes, as shown in Fig. 4(A), while (111) facets make an angle about 25.5° to the (100) plane, as shown in Fig. 4(B). The (01 $\bar{1}$) oriented ribs on the (100) InP surface therefore seem to be suitable for fabricating low-scattering optical waveguides with smooth (01 $\bar{1}$) facet vertical sidewalls. Forms of the (01 $\bar{1}$) and the (111) facets are further observed by SEM at various HCl concentrations, and the results are summarized in Fig. 5. Both (01 $\bar{1}$) and (111) facets change little in their forms with HCl concentration while maintaining smooth (100) etched surfaces. By changing either the HCl concentration or the etching time, therefore, we may fab-

ricate fine optical waveguides with smooth (01 $\bar{1}$) vertical sidewalls.

Summary

The etching rates of InP substrates with HCl-H₃PO₄ solution, especially with low HCl concentration, are studied experimentally, and the facets formed on the substrate surfaces are observed with use of SEM. Nearly vertical (01 $\bar{1}$) sidewalls with [011] ribs are fabricated by the present preferential etchant with good repeatability, indicating a promising technique for fabricating submicron structures like optical waveguides and other electronic devices.

Manuscript submitted June 28, 1984; revised manuscript received Sept. 11, 1984.

Meiji University assisted in meeting the publication costs of this article.

REFERENCES

1. P. Buchmann and A. J. N. Houghton, *Electron. Lett.*, **18**, 850 (1982).
2. S. Aytac and A. Schlachetzki, *Solid State Electron.*, **25**, 1135 (1982).
3. S. Adachi, *This Journal*, **129**, 609 (1982).

The Chemical Mass of Holes in Semiconductors

Carl D. Thurmond*

807 San Juan de Rio, Rio Rancho, New Mexico 87124

ABSTRACT

The equation $0 \rightleftharpoons e^- + e^+$ is a legitimate chemical equilibrium equation. Because the conservation of mass equation holds, the hole, e^+ , has a chemical mass that is the negative of the mass of the electron. The fact that the equation is not balanced with respect to charged particles is consistent with chemical equilibrium equations of charged particles in general. The hole is an abstraction. It has two masses. One mass, arising from its physical dynamic properties, is positive. The other, arising from its chemical thermodynamic properties as expressed in equilibrium chemical equations, is negative.

Is the equation



representing the formation of holes and electrons in semiconductors a legitimate chemical equation? Kröger, Stieltjes, and Vink, in an important paper in 1959 (1), have demonstrated that it is. But the question can be asked, "Isn't something surely wrong?" The conservation of mass condition that applies to all chemical equations apparently does not apply here because the mass of the hole is known to be about the same as the mass of the electron. Furthermore, chemical equations always have reactants and products. What are the reactants of Eq. [1]? Certain rules are used to write the equilibrium constant of chemical equations in terms of the concentrations of products and reactants. These rules do not seem to apply to Eq. [1].

These questions have led to a reconsideration of the source of Eq. [1]. Based on the approach used by Kröger, Stieltjes, and Vink (1) [also see Kröger (2)], it can be shown that Eq. [1] follows all the rules applicable to the usual equilibrium equation for charged particles. The major clarifying conclusion is that the chemical mass of the hole is not the same as the physical mass, the so-called effective mass of the hole. Rather it is the negative of the mass of the electron.

The primary intent of this paper is to prove this conclusion. While this conclusion is of no great scientific import, it is an interesting curiosity. It also makes clear that Eq. [1] is a legitimate chemical equation. The secondary intent of this paper is pedagogical. The means by which it will be proven that the mass of the hole as used in chemical equations must be the negative of the mass of

the electron will serve to clarify the meaning and use of chemical equilibrium equations. For chemists and chemical engineers, this should serve as a review with certain clarifying features. For semiconductor physicists, electrical engineers, and others, it may serve as an illustration of the use of chemical thermodynamics, as well as an explanation of the meaning and use of the chemical equilibrium equation.

Shockley has stated that "the hole is really an abstraction which gives a convenient way of describing the behavior of electrons" (3). This description leads to the conclusion based on the physical dynamic properties of semiconductors that the hole has a mass, called the effective mass. The mass of the hole is introduced as a convenient mathematical description of the movement of electrons in a nearly filled valence band. Just as in the description of the movement of electrons in the conduction band, where the acceleration produced by a force defines an effective mass for the electron by Newton's law, the hole is a convenient way of describing the acceleration of the valence electrons produced by a force. The effective masses of the electron and hole are, in general, of the same order of magnitude as the mass of the free electron, although in some cases the discrepancy is larger. It is to be shown that, based upon the chemical thermodynamic properties of semiconductors, the chemical mass is the negative of the mass of the electron. There is no conflict. The abstraction leads to two masses for the hole, one based upon the physical properties of the semiconductor, the other on its chemical properties.

Experimental evidence will be cited in support of the conclusion that the chemical mass of the hole is the negative of the mass of the electron.

*Electrochemical Society Active Member.

The method of proof follows the method used by Kröger, Stieltjes, and Vink (1), but with significant points of clarification. The method is based upon the properties of the chemical potential of atoms, molecules, and charged particles. In the next section, only neutral atoms and molecules are considered. A following section considers charged particles.

Chemical Thermodynamic Properties of Atoms and Molecules

The well-known thermodynamic function, the Gibbs energy, has been defined for any group of atoms and molecules (4). The group must be large enough in size so that the properties assigned to each kind of atom or molecule are not a function of size. This function has a minimum value as a function of the numbers of atoms and molecules present, and this can be shown to correspond to an equilibrium condition for this group of atoms and molecules. Gibbs showed that a function called the chemical potential could be defined (5) for each type of atom or molecule that leads to a very useful way to describe the equilibrium condition. The chemical potential of a particular atom or molecule is the change in the Gibbs energy of the total number of atoms and molecules when one atom or molecule is added. The numbers of each of the other kinds of atoms or molecules must not be changed when this is done. The temperature and pressure must also be held constant.

Gibbs then showed that a condition that must be met when equilibrium occurs is that the sum of the chemical potentials of the products of a reaction must equal the sum of the chemical potentials of the reactants. Each chemical potential will have the appropriate coefficient that assures that the law of conservation of mass is obeyed.

The Gibbs condition for equilibrium can be written in a concise way. If μ_i is the chemical potential of a particular atom or molecule (in units of energy per atom or per molecule) and ν_i is the appropriate coefficient called the stoichiometric coefficient, for each atom or molecule that assures conservation of mass in the reaction, the following equation is the Gibbs condition (6)

$$0 = \sum_i \nu_i \mu_i \quad [2]$$

In this form, the statement is that the sum of the chemical potentials, each taken with the appropriate coefficient, is equal to zero, with the convention that the stoichiometric coefficients, ν_i , are positive numbers for the products and negative numbers for the reactants.

The chemical reaction that corresponds to the Gibbs condition describes the conversion of a particular group of atoms and molecules to another group of atoms and molecules, as if all of the original group, the reactants, were converted to all of the final group, the products. This chemical reaction implies the conservation of mass, which can be stated as

$$0 = \sum_i \nu_i M_i \quad [3]$$

M_i is the mass of each atom or molecule in the reaction. When the number of atoms or molecules is Avogadro's number, 6.023×10^{23} , the masses, M_i , are the atomic and molecular weights. The ν_i 's are the same stoichiometric coefficients as in Eq. [2].

The chemical equation can be written as

$$0 = \sum_i \nu_i A_i \quad [4]$$

A_i is the chemical symbol or group of chemical symbols representing the atoms and molecules of the reactants and the products. For example, consider the reaction describing the formation of water vapor from the gaseous elements



Equation [5] follows from Eq. [4], with $A_1 = \text{H}_2\text{O}$, $A_2 = \text{O}_2$, $A_3 = \text{H}_2$, $\nu_1 = +1$, $\nu_2 = -1/2$, and $\nu_3 = -1$.

A general property of Eq. [4], illustrated in Eq. [5], is that the number of each kind of atom in the reactants is the same as the number of each kind in the products. This conservation of atom condition may be represented by the following equation

$$0 = \sum n_\alpha \quad [6]$$

The subscript α stands for a particular atom. The number of those atoms is n_α ; it is positive if from the products, negative if from the reactants. For example, in Eq. [5], n_{O} (products) is +1, n_{O} (reactants) is -1; n_{H} (products) is +2, n_{H} (reactants) is -2. Equation [6] is implied by the conservation of mass condition, Eq. [3], and justifies the use of the equal sign in chemical equations, Eq. [4] and illustrated in Eq. [5].

Equilibrium Constant

The equilibrium constant follows from Eq. [2] when the dependence of the chemical potentials on composition is included. G. N. Lewis (7) has defined a function called the activity, α_i , that is related to the chemical potential by the equation

$$\mu_i = \mu_i^\circ + RT \ln \alpha_i \quad [7]$$

When the activity, α_i , is unity, the phase is pure and the chemical potential of the atoms or molecules, μ_i , is that of the pure phase, μ_i° , solid or liquid, which is a function of temperature and pressure, not composition. For the gas phase, the activity is replaced by the fugacity. Equation [7] implies Avogadro's number of atoms or molecules because R , the gas constant, is used, rather than k , the Boltzmann constant, which is per atom or molecule.

The usefulness of Eq. [7] lies in the fact that for some cases of interest, α_i is equal to the atom fraction or molecule fraction of a component present in a solution, the mole fraction. In other cases of interest, it is proportional to the concentration, and the chemical potential is related to the concentration by

$$\mu_i = \mu_i^* + RT \ln C_i \quad [8]$$

For many gas phases, the fugacity is simply the partial pressure.

Substituting Eq. [7] into Eq. [2], the Gibbs condition for equilibrium, the equation for the equilibrium constant is obtained

$$\prod_i \alpha_i^{\nu_i} = \exp \left(- \sum_i \nu_i \mu_i^\circ / RT \right) = K \quad [9]$$

When activities are proportional to concentrations, Eq. [9] becomes

$$\prod_i C_i^{\nu_i} = \exp \left(- \sum_i \nu_i \mu_i^* / RT \right) = K_c \quad [10]$$

In a somewhat more familiar form, Eq. [10] becomes

$$\frac{C_1^{\nu_1} C_2^{\nu_2} \dots}{C_3^{\nu_3} C_4^{\nu_4}} = K_c \quad [11]$$

This equation was first obtained by Guldberg and Waage. It follows from their law of mass action, which states that the rate of a reaction is proportional to the active masses of the reactants and that at equilibrium the rate of the forward reaction equals the rate of the reverse reaction.

The equilibrium constant for Eq. [5] is simply

$$\frac{P_{\text{H}_2\text{O}}}{P_{\text{H}_2} P_{\text{O}_2}^{1/2}} = K_p \quad [12]$$

Equation [2], the Gibbs condition, was written before Eq. [4], the chemical reaction. Given Eq. [2], Eq. [4] fol-

lows. Usually the reverse situation occurs. The chemical reaction is written first, from which the stoichiometric coefficients of the Gibbs condition for equilibrium are obtained. But for electrons and holes, the Gibbs condition can first be written, followed by the chemical equation.

The proof that the chemical mass of the hole is the negative of the electron mass first requires the proof that Eq. [1] is legitimate. This proof cannot be made, however, without recognizing that the electron and the hole are charged particles. One of the important properties of chemical reactions has been expressed in Eq. [6], namely, the number of atoms of one kind in the products must equal the number of atoms of the same kind in the reactants. This rule does not apply to a reaction of charged particles and explains why Eq. [1] does not obey Eq. [6]. The Gibbs condition, Eq. [2], and the conservation of mass, Eq. [3], both apply to chemical reactions of charged particles. But Eq. [6] does not apply; the reaction equation, Eq. [4], must be modified, and a new condition must be introduced, the conservation of charge.

Chemical Thermodynamic Properties of Charged Particles

First, some comments about the chemical potential of charged particles should be made. As long as the group of charged particles of interest, which may include neutral particles, *i.e.*, atoms and molecules, is electrically neutral, the total Gibbs energy of the group of particles possesses "all of the properties which we have established for non-ionic systems" (8). Again, the group of particles must be large enough so that the properties of each kind of particle are not dependent on the size of the group.

The chemical potential of charged particles is frequently called the electrochemical potential to call attention to the fact that if an electric field is imposed and the group of particles of interest is no longer electrically neutral, the chemical potential and the electrochemical potential are no longer equal.

The chemical potential of a charged particle is, as before, the change in the Gibbs energy of the total number of particles when one of the charged particles is added. But for charged particles, the numbers of each of the other particles cannot be held constant. They are not independent variables if the charge of the total group of particles is to be kept zero. The chemical potential of each charged particle can be defined, but it will always occur in combinations of particles that assure electroneutrality.

The Gibbs condition for equilibrium of charged particles can then be written as in Eq. [2], as can the chemical potential of the electron. The conservation of mass equation, Eq. [3], still applies. The chemical reaction with charged particles may now be written as

$$0 = \sum_i \nu_i A_i^{z_i} \quad [13]$$

where z_i is the charge on the i th particle and may be zero. In addition, the condition of electroneutrality must be met

$$0 = \sum_i \nu_i Z_i \quad [14]$$

But the conservation of atoms, Eq. [6], is not observed. An atom is not equivalent to an ion. They differ in mass by the mass of the electron. This difference is generally ignored by chemists in the use of charged-particle equations because the mass of the electron is so small compared to that of an atom. But concerning the argument that the chemical mass of the hole is the negative of the mass of the electron, this difference cannot be ignored. Consequently, charged-particle equations are generally unbalanced and the equal sign in Eq. [13] is inappropriate.

The double arrow symbol, \rightleftharpoons , rather than the equal sign, is frequently used by chemists to emphasize the dynamic properties of an equilibrium reaction, *i.e.*, that the rate of the reaction in the forward direction equals the

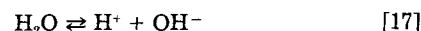
rate of the reaction in the reverse direction at equilibrium. Kröger (2) uses it for both atom and charged-particle equations. Prigogine (4) uses it sometimes for charged particle equations and sometimes not. Lewis, Randall, Pitzer, and Brewer (7) always use the equal sign. The double arrow sign will be used here to imply that Eq. [6] does not hold for charged particle reactions. It also implies a dynamic equilibrium. Consequently, the general equilibrium reaction equation for charged particles should be written as follows, rather than as in Eq. [13]

$$0 \rightleftharpoons \sum_i \nu_i A_i^{z_i} \quad [15]$$

To give some examples, first consider the ionization of the compound AB



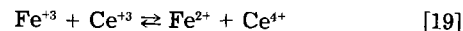
Neither A^+ nor B^- appear on the left side of the equation. In some cases, it would be appropriate to consider AB as made up of A^+ and B^- , but that need not be necessarily so. The equation for ionization of water



is not balanced; the species H^+ and OH^- are not thought to exist in H_2O as useful conceptual entities. The ionization of a donor in a semiconductor



is not a balanced equation. Nor is a charge-transfer reaction



The Gibbs equilibrium condition, the conservation of mass, and the conservation of charge conditions all hold, but an atom or particle conservation condition does not hold for charged particle equations.

Equilibrium Between Electrons and Holes in Semiconductors

The chemical potential of the electron can always be written in the form of Eq. [8] over some concentration range

$$\mu(e^-) = \mu^*(e^-) + RT \ln C(e^-) \quad [20]$$

The concentration of electrons can be varied under the electroneutrality condition by the addition of positive charge. The source of the positive charge is the donor impurity. Its presence need not be explicitly stated, but it is implicitly recognized.

The band model of a semiconductor leads to the following equation for the Fermi level, E_F , as a function of the electron concentration at thermal equilibrium (9)

$$E_F = E_c - RT \ln N_c + RT \ln C(e^-) \quad [21]$$

Equation [21] holds as long as $C(e^-)$ is significantly less than N_c , the effective concentration of states in the conduction band. E_c is the energy of electrons at the bottom of the conduction band. By comparing Eq. [21] with Eq. [20], it is seen that the Fermi level is the chemical potential of electrons (10)

$$E_F = \mu(e^-) \quad [22]$$

Similarly, the chemical potential of holes can always be written in the form of Eq. [8] over some concentration range

$$\mu(e^+) = \mu^*(e^+) + RT \ln C(e^+) \quad [23]$$

In this case, it is to be remembered that the hole concentration is varied by the addition of an acceptor impurity which, when ionized, has a negative charge.

The band model of a semiconductor can also be used to obtain a relationship between the chemical potential of holes and the concentration of holes at thermal equilibrium (11)

$$-E_F = -E_v - RT \ln N_v + RT \ln C(e^+) \quad [24]$$

This relationship holds as long as $C(e^+)$ is significantly less than N_v , the effective concentration of states at the top of the valence band of energy E_v . By comparing Eq. [24] with Eq. [23], it is found that the Fermi energy is the negative of the chemical potential of the hole

$$E_F = -\mu(e^+) \quad [25]$$

Consequently, at thermal equilibrium, the negative of the chemical potential of the hole is equal to the chemical potential of the electron

$$-\mu(e^+) = \mu(e^-) \quad [26]$$

Equation [26] may be rewritten in the form

$$0 = \mu(e^-) + \mu(e^+) \quad [27]$$

It is this equation, expressing the Gibbs condition for thermal equilibrium between electrons and holes, that implies, from Eq. [15], the charged particle equilibrium equation

$$0 \rightleftharpoons e^- + e^+ \quad [28]$$

The conservation of charge condition is met. The conservation of mass is implied, and consequently

$$M(e^+) = -M(e^-) \quad [29]$$

Equation [28] can be demonstrated to have other properties of any equilibrium equation. According to Eq. [10], the equilibrium constant is the product of the electron and hole concentrations

$$C(e^-) C(e^+) = K_c \quad [30]$$

There are no reactants, only products. Equation [28] may be written in the reverse direction

$$e^- + e^+ \rightleftharpoons 0 \quad [31]$$

The equilibrium constant for this equation, according to the rules applying to all equations, is just the reciprocal of the equilibrium constant of the forward direction

$$\frac{1}{C(e^-) C(e^+)} = \frac{1}{K_c} = K_c' \quad [32]$$

There are no products, only reactants.

The equilibrium constant obtained from the band model is

$$C(e^-) C(e^+) = N_c N_v \exp(-\Delta E_{cv}/RT) \quad [33]$$

where ΔE_{cv} is the bandgap energy, $E_c - E_v$. One of the factors in the term N_v , appearing in the equilibrium constant, is the effective mass of the hole, a positive number. But the equilibrium constant is derived from the Gibbs condition and the equilibrium equation that imply the mass of the hole is a negative number. There is no contradiction. The mass occurring in the N_v term is obtained from a consideration of the dynamic properties of electrons in a nearly filled valence band. Newton's law is used. The hole has two masses, one obtained from its physical dynamic properties, the other from its chemical thermodynamic properties as expressed in an equilibrium chemical equation.

Experimental Confirmation

When photons of energy larger than the bandgap energy are absorbed by a semiconductor, excess electrons and holes are generated. There are a number of mechanisms by which the energy absorbed by the crystal is redistributed, but one process is the annihilation of electrons and holes, which may be represented by the equation



The energy of the photons emitted from a semiconductor by this process is the energy of the bandgap, ΔE_{cv} . If a hole had a positive mass, its annihilation, along with the annihilation of the electron, would generate a photon en-

ergy of approximately half a million electron volts rather than the bandgap energy of an order of magnitude of an electron volt. The annihilation of a hole proceeds by a chemical process analogous to the annihilation of a positron by an electron. But the hole must have a mass which is the negative of the electron mass.

Comments

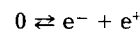
The chemical thermodynamic significance of Eq. [1] can be underscored by noting that important thermodynamic functions can be obtained as functions of temperature for this reaction, such as the standard Gibbs energy (the bandgap energy), the standard enthalpy, the standard entropy, and the standard heat capacity (12). These thermodynamic functions, on the other hand, can be used to stimulate the conception of physical models for the fundamental processes occurring in a semiconductor crystal (13-15).

The conclusion has been reached that the mass of the hole is the negative of the mass of the electron. What is meant, the effective mass of the electron or the mass of the free electron? Pragmatically, it does not matter. Philosophically it does, and the question can be simply answered. The effective mass of the electron has potential-energy terms in it which make no contribution to the mass equivalence of the electron. The average velocity of the electron in the conduction band is so small compared to the velocity of light that this contributes no significant equivalent mass to that of a free electron. The mass of the hole is the negative of the mass of the free electron.

As a final point of clarification, the conservation of mass condition is only an approximation. It is the conservation of energy condition that is implied. But because the Gibbs energy released or absorbed in a chemical reaction under all circumstances of interest has a negligibly small mass equivalent, the conservation of energy condition becomes the conservation of mass condition. This is also true for chemical reactions involving electrons.

Conclusions

It is generally believed that chemical equations must be balanced, i.e., that the number of atoms of each kind on each side of the equation must be the same. This condition, in fact, does not apply to charged-particle equations in general and accounts for the fact that the formation equation of electrons and holes is not balanced with respect to particles. This equation



is a legitimate equilibrium chemical equation. A consequence is that in chemical reactions, the hole acts as if it had a mass that is the negative of the mass of the electron. The "convenient abstraction" of the hole has two masses. In chemical thermodynamic equilibrium reactions, it is the negative of the free electron mass; in physical dynamic processes, it is the effective mass, a positive number, the order of magnitude of the mass of a free electron.

Acknowledgments

I wish to thank Peter Esherick for his helpful comments and Trylla Esherick for the word processing.

Manuscript submitted June 29, 1984; revised manuscript received Sept. 24, 1984.

REFERENCES

1. F. A. Kröger, F. Stieltjes, and H. J. Vink, *Philips Res. Rep.*, **14**, 557 (1959).
2. F. A. Kröger, "The Chemistry of Imperfect Crystals," Vol. 2, 2nd rev. ed., p. 77, North-Holland, Amsterdam (1974).
3. W. Shockley, "Electrons and Holes in Semiconductors," p. 178, D. Van Nostrand Co. Inc., New York (1950).
4. I. Prigogine and R. DeFay, "Chemical Thermodynamics," p. 34, Longmans Green, New York (1954). See also any text on chemical thermodynamics.
5. I. Prigogine and R. DeFay, *ibid.*, p. 68, Longmans Green (1954).
6. I. Prigogine and R. DeFay, *ibid.*, p. 69, Longmans Green (1954).

7. G. N. Lewis and M. Randall, "Thermodynamics," 2nd ed., revised by K. S. Pitzer and L. Brewer, p. 243, McGraw Hill, New York (1961).
8. I. Prigogine and R. DeFay, "Chemical Thermodynamics," p. 438, Longmans Green, New York (1954). The comment refers to the Helmholtz energy, F , but an equivalent statement applies to the Gibbs energy, G .
9. W. Shockley, "Electrons and Holes in Semiconductors," p. 240, D. Van Nostrand Co. Inc. (1950).
10. H. Reiss, *J. Chem. Phys.*, **21**, 1209 (1953).
11. I. Prigogine and R. DeFay, "Chemical Thermodynamics," p. 241, Longmans Green, New York (1954).
12. C. D. Thurmond, *This Journal*, **122**, 1133 (1975).
13. J. A. Van Vechten, in "Lattice Defects in Semiconductors," F. H. Huntley, Editor, p. 212, Institute of Physics, London (1975).
14. V. Heine and J. A. Van Vechten, *Phys. Rev. B*, **13**, 1622 (1976).
15. J. A. Van Vechten and C. D. Thurmond, *ibid.*, **14**, 3539 (1976).

Mass Spectrometric Study of $\text{Ga}(\text{CH}_3)_3$ and $\text{Ga}(\text{C}_2\text{H}_5)_3$ Decomposition Reaction in H_2 and N_2

M. Yoshida and H. Watanabe

NEC Corporation, Fundamental Research Laboratories, Miyazaki 4-chome, Miyamae, Kawasaki 213, Japan

F. Uesugi

NEC Corporation, Opto-Electronics Research Laboratories, Miyazaki 4-chome, Miyamae, Kawasaki 213, Japan

ABSTRACT

Decomposition of trimethylgallium (TMG) and triethylgallium (TEG) in hydrogen and nitrogen atmospheres was studied by a quadrupole mass analyzer. The decomposition reactions of TMG in H_2 and in N_2 and of TEG in H_2 and in N_2 take place in the temperature ranges $370^\circ\text{--}460^\circ$, $450^\circ\text{--}570^\circ$, $220^\circ\text{--}330^\circ$, and $270^\circ\text{--}380^\circ\text{C}$, respectively. The reaction mechanisms are hydrogenolysis for TMG in H_2 , homolytic fission for TMG in N_2 , and β elimination for TEG in both H_2 and N_2 . The hydrogenolysis of TMG follows homogeneous first-order kinetics on TMG concentration.

Almost two decades have passed since the use of metal-organics as source materials for chemical vapor deposition (CVD) was first described in the preparation of III-V materials (1). Now, the metalorganics which spread throughout the periodic table of elements have been used for growth of III-V compounds (2-4) and II-VI compounds (5), doping to III-V compounds (6-8), microdeposition of metals (9), and so on. The nature of decomposition reaction of these metalorganics has also been studied (5, 10-13). It is important to investigate the reaction of metal-organics further to find the optimum condition for the growth, especially for the low temperature CVD of semiconductors, metals, and insulators.

The purpose of this paper is to describe mass spectrometric study of trimethylgallium (TMG) and triethylgallium (TEG) decomposition reaction in hydrogen and nitrogen atmospheres. The mass spectroscopy is of great advantage to both identification of species and quantitative analysis (14).

Experimental

An experimental apparatus made with a hot-wall reactor and an ANELVA AGA-360 quadrupole mass analyzer is shown in Fig. 1. The inner diameter of the reactor was 55 mm. The organometallics (TMG and TEG) were introduced into the reactor through a 65°C water-cooled quartz tube. Gas flow of hydrogen or nitrogen from the opposite side kept the reactor wall at the low temperature region clean, and its flow rate was 600 sccm (standard cubic centimeter per minute) throughout the experiment. Sampling of the reacted gas was done downstream at a temperature less than 100°C by means of a quartz pinhole adjusted to accomplish the pressure of 1×10^{-5} torr in the mass analyzer. Upstream from the sampling pinhole, quartz wool was set to prevent the pinhole being choked with higher paraffins ($C \geq 5$) produced from the TMG and the TEG. In the beginning of this experiment, the sampling was done in the reaction region and the pinhole was choked with liquid gallium. In contrast to the reaction in a hydride system (14), the decomposition reaction of TMG and TEG is frozen under a critical temperature, and this temperature was found to be higher than 200°C

in this study. Therefore, post sampling reaction (14, 15) is not a problem here. The sampled gas entered the ion source of the mass analyzer passing through a 3/32 in. id, 2m-long stainless tube at room temperature. Argon was added into the gas flow to compensate the signal intensity for changing condition of the ion source and the ion collector by taking the relative ion current to the ion current of mass 40.

Results and Discussion

Mass spectra of TMG and TEG in H_2 at room temperature are shown in Fig. 2(a) and 2(b). The flow rates of hydrogen (without the opposite flow) were 700 sccm in (a) and 670 sccm in (b). Those of TMG, TEG, and Ar were 7.7, 1.2, and 1.2 sccm, respectively. In Fig. 2(a), parent peaks of TMG are at masses 114 and 116, corresponding to a natural $^{69}\text{Ga}/^{71}\text{Ga}$ ratio of 3/2. Between Ga^+ and $\text{Ga}(\text{CH}_3)_3^+$, GaCH_3^+ and $\text{Ga}(\text{CH}_3)_2^+$ -related fragment peaks are observed. The peaks at masses 40 and 20 show the argon. Methyl ion at mass 15 reacts with H_2 , and CH_4^+ is formed in the ion source. Figure 2(b) shows parent peaks of TEG at masses 156 and 158. Between Ga^+ and $\text{Ga}(\text{C}_2\text{H}_5)_3^+$, GaC_2H_5^+ and $\text{Ga}(\text{C}_2\text{H}_5)_2^+$ are observed. The peaks of $\text{Ga}(\text{CH}_3)_2^+$ at masses 99 and 101 are higher than those of GaC_2H_5^+ . The fragments of GaCH_3^+ and $\text{Ga}(\text{C}_2\text{H}_5)\text{CH}_3^+$ are also observed. The signal of $\text{Ga}(\text{C}_2\text{H}_5)_2\text{CH}_3^+$ is very weak and not seen in the spectrum. Ethyl ion at mass 29 reacts

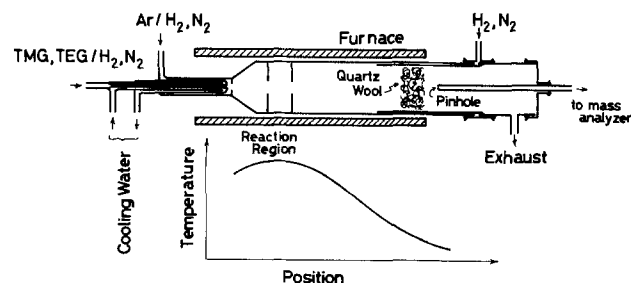


Fig. 1. Schematic of experimental apparatus

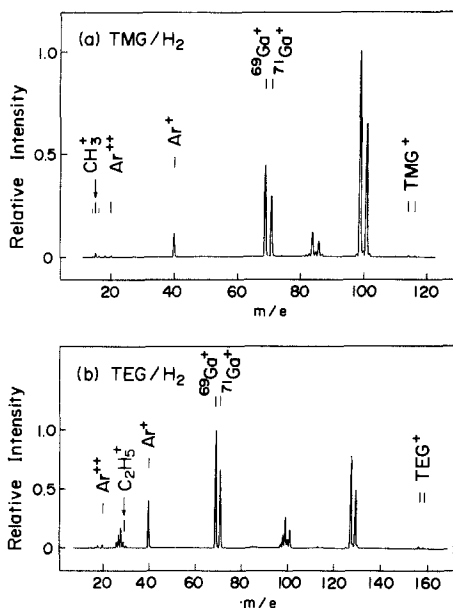


Fig. 2. Room temperature spectra of TMG and TEG in H_2

with H_2 , and $C_2H_6^+$ is formed in the ion source. No ethane was produced in the reactor at room temperature.

The relation between the normalized ion current ratio of mass 69 to mass 40 (unreacted TMG or TEG concentration normalized by that at room temperature) and the reaction temperature is shown in Fig. 3. The flow rates of H_2 , N_2 , TMG, TEG, and Ar were 670, 670, 4.6, 1.2, and 1.2 sccm, respectively. The pressures in the mass analyzer were 8×10^{-6} torr for H_2 and 1×10^{-5} torr for N_2 . The decomposition of TMG in H_2 took place at temperatures over $370^\circ C$ and was completed at $460^\circ C$. Those of TMG in N_2 , TEG in H_2 , and TEG in N_2 took place around temperature ranges of $450^\circ-570^\circ$, $220^\circ-330^\circ$, and $270^\circ-380^\circ C$, respectively. The temperature ranges of the TMG decomposition in both H_2 and N_2 agree with the study by infrared spectroscopy (13). TEG decomposed at lower temperatures than TMG, and the difference between H_2 and N_2 atmospheres in the TEG decomposition was less than that in the TMG decomposition.

The difference in the temperature range in which the decomposition reaction takes place means the difference in the reaction mechanism. To discuss this point, note is taken of hydrocarbons produced by the TMG and TEG decomposition. Figures 4(a) and (b) show mass spectra of TMG in H_2 at $450^\circ C$ and of TMG in N_2 at $550^\circ C$ in the mass range of 10-60. Figures 5(a) and (b) show those of TEG in H_2 and of TEG in N_2 at $300^\circ C$. In these measurements, the argon for the intensity reference was excluded to simplify the spectra.

Figure 4(a) shows that the TMG decomposition in H_2 produces methane (mass 12-16) and a small amount of ethane (mass 24-30). Propane (mass 37-44) and butane

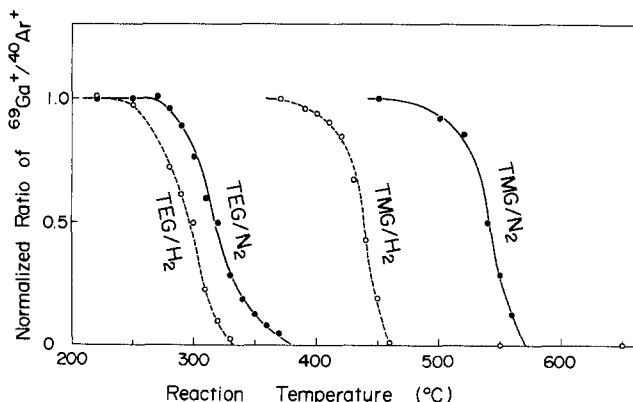


Fig. 3. Relation between normalized ion current ratio of mass 69 to mass 40 and reaction temperature.

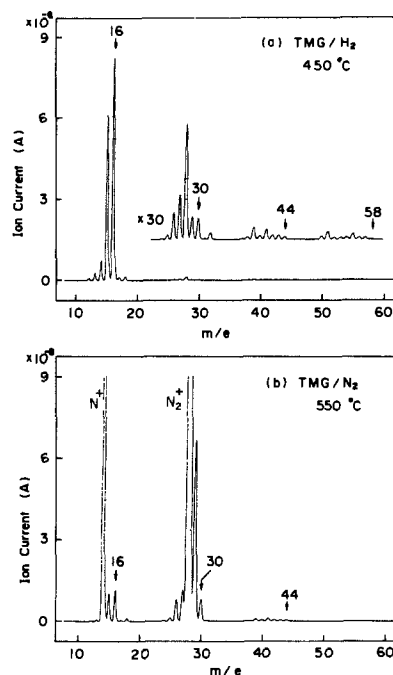


Fig. 4. Spectra of (a) TMG in H_2 at $450^\circ C$ and (b) TMG in N_2 at $550^\circ C$ in the mass range of 10-60.

(mass 50-58) observed in the spectrum were within background level of the analyzer. In contrast to TMG in H_2 , the TMG decomposition in N_2 produces methane, ethane, and propane, as shown in Fig. 4(b). Intense peaks at masses 14, 28, and 29 show $^{14}N^+$, $^{28}N_2^+$, and $^{29}N_2^+$. The peak at mass 30 equivalent to those at 26 and 27 in height shows ethane formation well. Therefore, it is concluded that the TMG decomposition in H_2 is hydrogenolysis which forms methane. The decomposition in N_2 is real pyrolysis, in which methyl radical formed by homolytic fission reacts with itself (forming ethane), TMG (forming methane or ethane), and products (forming propane and higher paraffins). The hydrogenolysis takes place at lower temperatures than the homolytic fission. The homolytic fission of TMG in H_2 also occurs as a subreaction. The radical mainly reacts with hydrogen forming methane, and a small amount of ethane is formed by radical-radical or radical-TMG reaction.

In Fig. 5, a noticeable feature in spectra is that the peak at mass 30 is small compared to the peaks at 26 and 27.

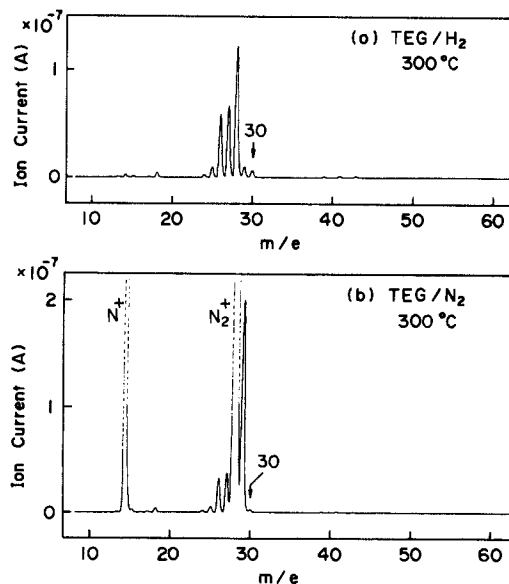


Fig. 5. Spectra of (a) TEG in H_2 and (b) TEG in N_2 at $300^\circ C$ in the mass range of 10-60.

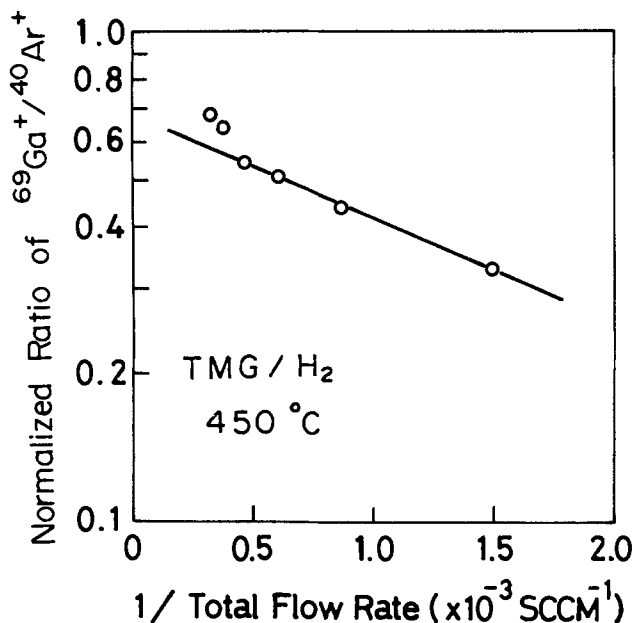


Fig. 6. Plot for logarithm of normalized ratio of ⁶⁹Ga⁺/⁴⁰Ar⁺ vs. inverse of total flow rate.

This feature means that the TEG decomposition in H₂ and N₂ produces not ethane, but ethylene. Therefore, the reaction mechanism of the TEG decomposition in both H₂ and N₂ is not ethane forming hydrogenolysis or homolytic fission. The mechanism is β elimination (16) forming ethylene. The β elimination mechanism makes the decomposition temperature fairly lower. Probably, the peak at mass 30 comes mainly from the reaction between ethyl ion and H₂, or ethyl ion and TEG in the ion source. The slight difference in the decomposition temperature between TEG in H₂ and TEG in N₂ needs further discussion.

Figure 6 shows a plot for logarithms of the normalized ratio of ⁶⁹Ga⁺/⁴⁰Ar⁺ vs. inverses of the total flow (excluding the opposite flow) rate. The decomposition of TMG in H₂ at 450°C was measured. It should be noted that the increase in the total flow rate by 4.6 times, by means of adding H₂ flow, only shifted the high temperature region downstream without changing the value and the width of the reaction-temperature profile. That means the residence time for the reaction is proportional to the inverse of the total flow rate. Then, the linearity in Fig. 6 shows first-order reaction mechanism $-d[\text{TMG}]/dt = k[\text{TMG}]$. Over the total flow rate of 2200 sccm, the unreacted ratios of TMG (normalized ⁶⁹Ga⁺/⁴⁰Ar⁺ ratio) were larger than those on the linear relation, probably because the gas flow passed through the reaction region without perfect mixing at the high flow rates. Expansion of the quartz surface by 30 times, by means of putting 3g quartz wool (~8 μm φ) in the reaction region, caused only a slight shift (~10°C) of the curve for TMG in H₂ (in Fig. 3) to the higher temperature side. Therefore, it is concluded that the TMG decomposition in H₂ follows homogeneous first-order kinetics on TMG concentration.

The result gives suggestion for low temperature CVD of GaAs using TMG and TEG. The low temperature CVD of GaAs using TMG in H₂ (17-19) must also be limited by the decomposition of TMG.

Summary

The decomposition reactions of TMG in H₂ and in N₂ and TEG in H₂ and in N₂ take place in the temperature ranges 370°-460°, 450°-570°, 220°-330°, and 270°-380°C, respectively. The reaction mechanisms are hydrogenolysis for TMG in H₂, homolytic fission for TMG in N₂, and β elimination for TEG in both H₂ and N₂. The hydrogenolysis of TMG follows homogeneous first-order kinetics on TMG concentration.

Acknowledgments

The authors wish to thank D. Shinoda for his interest and encouragement throughout this work. Helpful discussions with T. Mizutani on mass spectrometric analysis are duly recognized. Frequent and useful discussions with T. Maeda of Sumitomo Chemical Company Limited on chemistry of organometallics are also gratefully acknowledged.

Manuscript received Aug. 24, 1984.

NEC Corporation assisted in meeting the publication costs of this article.

REFERENCES

- H. M. Manasevit, *J. Cryst. Growth*, **55**, 1 (1981).
- P. D. Dapkus, H. M. Manasevit, and K. L. Hess, *ibid.*, **55**, 10 (1981).
- G. B. Stringfellow, *ibid.*, **55**, 42 (1981).
- J. P. Duchemin, J. P. Hirtz, M. Razeghi, M. Bonnet, and S. D. Hersee, *ibid.*, **55**, 64 (1981).
- J. B. Mullin, S. J. C. Irvine, and D. J. Ashen, *ibid.*, **55**, 92, (1981).
- S. J. Bass, *ibid.*, **44**, 29 (1978).
- C. R. Lewis, W. T. Dietze, and M. J. Ludowise, *J. Electron. Mater.*, **12**, 507 (1983).
- M. K. Lee, C. Y. Chang, and Y. K. Su, *Appl. Phys. Lett.*, **42**, 88 (1983).
- D. J. Ehrlich and J. Y. Tsao, *J. Vac. Sci. Technol. B*, **1**, 969 (1983).
- M. G. Jacko and S. J. W. Price, *Can. J. Chem.*, **41**, 1560 (1963).
- M. R. Leys and H. Veenliet, *J. Cryst. Growth*, **55**, 145 (1981).
- J. Nishizawa and T. Kurabayashi, *This Journal*, **130**, 413 (1983).
- M. R. Leys, Abstracts of 2nd International Conference on MOVPE, Sheffield (1984).
- V. S. Ban, *This Journal*, **118**, 1473 (1971).
- D. W. Kisker and D. A. Stevenson, in "Chemical Vapor Deposition," J. M. Blocher, Jr., G. E. Vuillard, and G. Wahl, Editors, p. 212, The Electrochemical Society Softbound Proceedings Series, Pennington, NJ (1981).
- M. E. O'Neill and K. Wade, in "Comprehensive Organometallic Chemistry, Volume 1," G. Wilkins, F. G. A. Stone, and E. W. Abel, Editors, p. 1, Pergamon Press, New York (1982).
- A. Escobosa, H. Kräutle, and H. Beneking, *J. Cryst. Growth*, **57**, 605 (1982).
- H. Kräutle, H. Roehle, A. Escobosa, and H. Beneking, *J. Electron. Mater.*, **12**, 215 (1983).
- K. P. Pande and A. C. Seabaugh, *This Journal*, **131**, 1357 (1984).

Secondary Electron Effect on Electric Potential of Insulator Surface during Ion Implantation

Masahiro Yoshizawa, Masayasu Miyake, Hiroyuki Harada,* Kazuhide Kiuchi, and Satoshi Tazawa

Nippon Telegraph and Telephone Public Corporation, Atsugi Electrical Communication Laboratory, 1839, Ono, Atsugi-shi, Kanagawa Pref., 243-01, Japan

ABSTRACT

The effects of secondary electrons on the electric potential of a thick SiO₂ surface during ion implantation are studied by measuring the potential using MOSFET's. Secondary electrons emitted from electrodes on an ion-implanted SiO₂ layer reduce its potential. The potential decreases as the implantation energy increases, because secondary electron emission yield increases with implantation energy. The potential distribution is trapezoidal for a SiO₂ layer with secondary electron emission electrodes, while the distribution is parabolic for a SiO₂ layer without electrodes. The potential is slightly dependent on beam current when a large number of secondary electrons are emitted. The potential is proportional to $I^{0.68}$, where I is the beam current, if the secondary electron emission is negligible. A potential reduction method, which involves applying a negative voltage to a Faraday tube, is proposed for practical use.

Ion implantation has been widely and effectively used in LSI fabrication. Its basic disadvantage is that the electric potential on an insulator increases because of charging. The increase in potential can cause problems, such as the breakdown of the insulator layer, which results in gate leakage in MOSFET's.

A few studies have been reported on the potential or electric properties of an insulator during ion implantation (1, 2). Wada *et al.* (1) observed current paths for ion implantation into a quartz wafer and reported that the substrate current, the current which flowed through the substrate, was dominant when the insulator thickness was less than the projected range of the implanted ions. Mori *et al.* (2) studied the potential in a thick insulator layer in which the substrate current did not flow. In these previous studies (1, 2), the effect of secondary electrons has not been studied. It is well known that a metal emits a greater number of secondary electrons than incident ions during ion implantation (3, 4). These secondary electrons have a great influence on potential.

This paper reports on effects of secondary electrons on potential during ion implantation, particularly on the potential distribution in a SiO₂ layer and the potential dependence on beam current. First, secondary electron emission yield is examined. Then, the effect of secondary electrons on the potential is studied. Finally, a method of potential reduction using secondary electrons is described.

Experimental Procedure

Sample preparation.—A silicon dioxide layer on a silicon wafer was used as an insulator layer. The oxides used were grown on a 30 ~ 50 Ω-cm <100> p-type 3 in. silicon wafer to a thickness of 7500Å by wet O₂ oxidation or 1000Å by dry O₂ oxidation. A 1000Å dry oxide layer was prepared only for measuring potential when the substrate current was dominant. An unpatterned 1 μm-thick aluminum or 0.45 μm-thick arsenic-doped polysilicon electrode was deposited on the SiO₂ layer for secondary electron emission yield measurement. For the potential distribution measurement, aluminum stripe patterns were fabricated on the SiO₂ layer using photolithographic techniques.

A medium current ion implanter with an electrostatic scanning system was used. The vertical scan frequency was about 1 kHz and the horizontal scan frequency was 100 Hz. Potential dependence on the scan frequency was studied, and it was confirmed that the potential was independent of horizontal scan frequency above 30 Hz.

Potential measurement.—The potential of the electrode during ion implantation was measured using a MOSFET. Figure 1 shows the potential measurement method. This measurement method causes no disturbance of the poten-

tial distribution because of the high input impedance. The electrode for measurement is connected to the FET gate. A positive voltage (V_s) is applied to the FET source in order to protect it from breakdown. Bias voltage (V_D) is initially applied so that the drain current does not flow, then V_s is decreased till the suitable drain current flows. The difference between V_s and the electrode potential is determined from the drain current of the FET.

The SiO₂ surface potential was only about 1V when 150 keV boron ions were implanted into a 1000Å SiO₂ layer at a beam current of 5 μA. In this case, the projected range of the ions is larger than the thickness of the SiO₂ layer (5), and substrate current was confirmed to be dominant. Therefore, problems related to the induced potential would only occur when the insulator layer thickness was so thick that substrate current would not flow. It was confirmed that substrate current does not flow for boron implantation with less than 100 keV energy into a 7500Å SiO₂ layer at a beam current of 5 μA. The measurements of potential were performed mainly for a boron implantation energy of 50 keV into a 7500Å SiO₂ layer, so as to distinguish the effects of secondary electrons (SE's) from those of the substrate current.

Secondary electron yield measurement.—An unpatterned aluminum or polysilicon electrode was deposited on a 7500Å SiO₂ layer. The method of measuring the secondary electron yield is illustrated in Fig. 2. The implantation area is limited to the hatched area (3.5 × 3 cm²) in order to eliminate the effect of SE's emitted from an aluminum wafer holder. The ion implanter Faraday cup is used as a secondary electron collector, which collects SE's emitted from the electrode. The Faraday cup con-

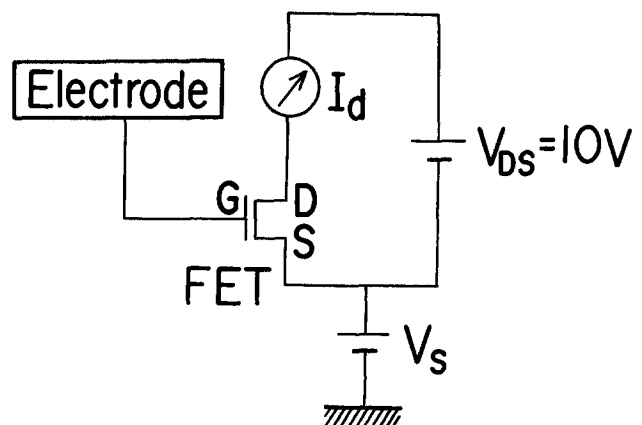


Fig. 1. The measurement method of the electrode potential using an FET. A bias voltage is applied to the FET source to protect it from breakdown. The difference between the electrode potential and the applied voltage is measured from the drain current of the FET.

*Electrochemical Society Active Member.

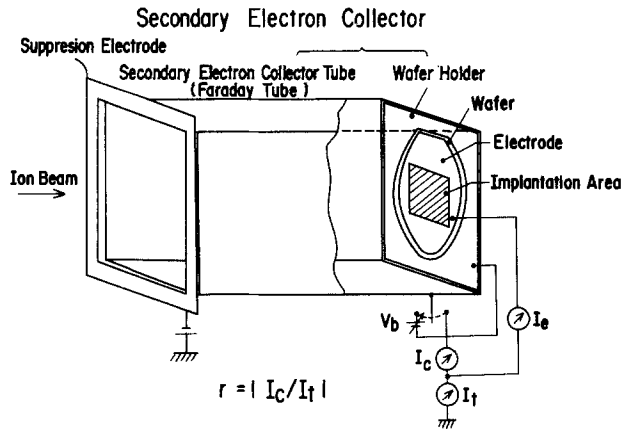


Fig. 2. The method of measuring the secondary electron yield. A Faraday cup is used for a secondary electron collector tube. A bias voltage (V_b) can be applied to the tube. A suppression voltage of $-300V$ is applied in front of the Faraday tube.

sists of the wafer holder and a tube (the tube is called a Faraday tube hereafter). A $-300V$ electron suppression voltage is applied to the suppression electrode in front of the Faraday tube in order to keep the SE's in the Faraday tube. Collector current (I_c) is due to the SE's, whereas electrode current (I_e) is due to both the incident ions and the SE's. Beam current (I_i) can be obtained as the sum of I_c and I_e . The secondary electron yield (γ) is defined by the ratio of I_c to I_i : $\gamma = |I_c/I_i|$. Secondary electron emission yield dependences on boron and arsenic ion implantation energy were measured for aluminum and polysilicon electrodes.

Potential distribution measurement of an insulator with secondary electron emission.—The potential distribution was measured using aluminum patterns with 7 stripe electrodes. Figure 3 shows two kinds of electrode patterns for measuring the effects of SE's on potential distribution. Pattern (a) has two secondary electron emission electrodes (S), which have wide areas, while pattern (b) does not have them. Stripe electrode width is 0.1 mm, and the distance between them is 1 mm. The electrodes (E) are earth electrodes, and the distance between electrodes (S) and (E) is 2 mm. The wafers were set so that the electrodes were parallel to the vertical scanning direction. The implantation area is limited to the hatched area ($3 \times 2.5 \text{ cm}^2$), so as to eliminate the SE effects from a wafer holder. Implantation area of electrodes (S), which emit SE's, is about 60% of the total implantation area. The potential distribution of the insulator is obtained by measuring the potentials of electrodes 1, 2, and 3 in patterns (a) and (b). The effects of SE's on the potential distribution were studied by comparing the potential of pattern (a) with that of pattern (b). Since the width of the potential measurement electrode is small, it is expected that the effects of SE's on potential distribution are negligible for pattern (b).

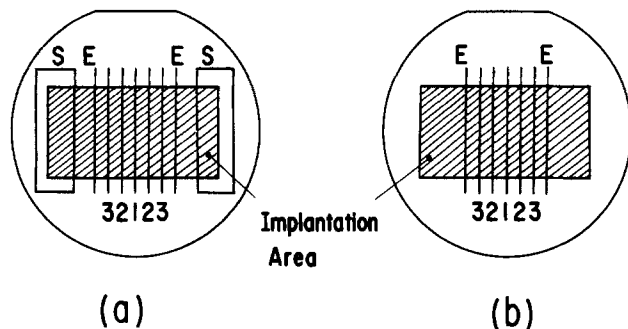


Fig. 3. The electrode patterns for measuring the effect of secondary electrons. Pattern (a) has secondary electron emission electrodes (S). Pattern (b) does not have them. Electrodes (E) are the earth electrodes. Stripe electrode width is 0.1 mm, and the distance between them is 1 mm. The distance between electrodes (S) and (E) is 2 mm.

Results and Discussion

Secondary electron yield.—Implantation energy dependences of secondary electron yields for aluminum and polysilicon are shown in Fig. 4. From this figure, it is found that (i) secondary electron (SE) yield increases with implantation energy, (ii) the yield for boron implantation is larger than that for arsenic implantation, (iii) the yield of the aluminum electrode is more than that of the polysilicon, and (iv) the number of SE's emitted from aluminum or polysilicon electrodes is more than, or about the same as, the number of incident ions. It was also confirmed that SE collector current (I_c in Fig. 2) was not observed when ions were implanted into a SiO_2 layer without an electrode.

It has been reported that kinetic emission is dominant in the velocity range above 10^7 cm/s , and the yield of the kinetic emission increases with incident ion velocity and decreases with work function of the material (3, 6). The velocity of a 25 keV arsenic ion is $6.6 \times 10^7 \text{ cm/s}$, which is the slowest velocity in the present work. Thus, secondary electrons are mainly due to the kinetic emission for the energy shown in Fig. 4. The difference between the yield of the boron ions and that of arsenic ions is caused by the velocity of boron ions being greater than that of arsenic ions at the same implantation energy. The yield difference between aluminum and polysilicon is caused by the difference of the work functions.

Secondary electron effects on insulator potential.—Potential distributions were obtained from potential measurements of electrodes 1, 2, and 3 in patterns (a) and (b) in Fig. 3. Figure 5 shows the potential distributions, where boron implantation was performed at 50 keV with a beam current of $0.5 \mu\text{A}$. The center electrode potential for pattern (a) is about 10 times less than that for pattern (b). The potential distribution for pattern (a) with secondary electron emission electrodes is trapezoidal, whereas that for pattern (b) without the electrodes is parabolic.

The potential distribution, when the effects of SE and those of substrate current are negligible, is parabolic as shown in the following equation (2)

$$V(X) = -\frac{iR_s}{2}(X-L)^2 + \frac{iR_sL^2}{2} \quad [1]$$

where R_s is the sheet resistance of the insulator layer, L is the distance between the earth electrodes, i is the beam density, and X is the distance from the earth electrode. The sheet resistance of the implanted SiO_2 layer is obtained by substituting the peak potential shown in Fig. 6 into Eq. [1]. The sheet resistance obtained is $6.5 \times 10^9 \Omega/\square$. A broken line in Fig. 5 was calculated using Eq. [1] and setting $R_s = 6.5 \times 10^9 \Omega/\square$. The difference between the po-

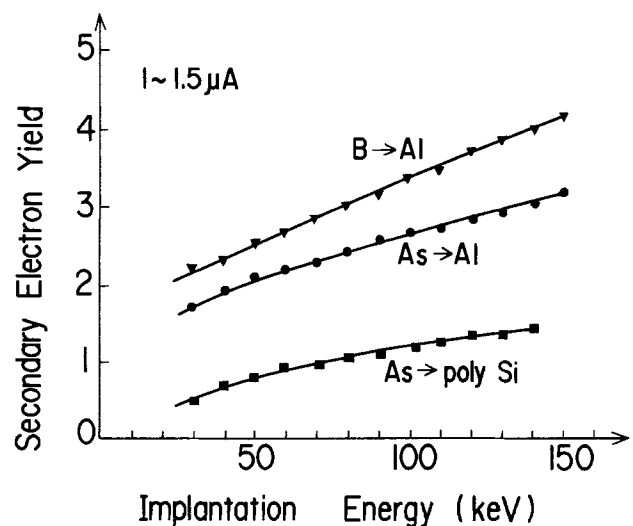


Fig. 4. Implantation energy dependences of secondary electron emission yield. Samples are grounded. Beam current is $1 \sim 1.5 \mu\text{A}$.

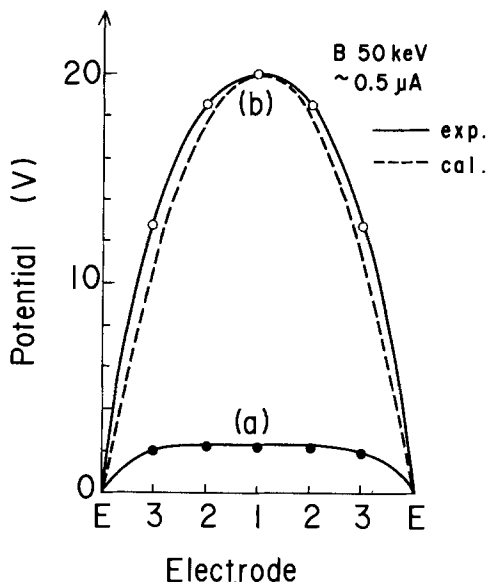


Fig. 5. The potential distribution on a SiO_2 layer for 50 keV. Boron implantation is performed at 50 keV with a beam current of $0.5 \mu\text{A}$. (a) Pattern with secondary electron emission electrodes (S). (b) Pattern without electrodes (S). The broken line is calculated using $R_s = 6.5 \times 10^9 \Omega/\square$ in Eq. [1].

tential distribution for pattern (b) and the calculated parabolic potential distribution is within 6%. Thus, it was confirmed that the SE effect was negligible for pattern (b).

Figure 5 indicates that a large number of SE's emitted from the aluminum electrodes decrease the potential and result in a trapezoidal potential distribution, since the number of SE's attracted to the insulator surface increases with surface potential.

Figure 6 shows center electrode potential dependence on the beam current. The potential for pattern (a) is less than one-tenth of that for pattern (b). The slope of the potential vs. beam current curve in pattern (b) is 0.68, and that in pattern (a) is 0.09. The potential for pattern (b) is greatly dependent on the beam current, whereas the potential for pattern (a) is slightly dependent on it. This difference is caused by the presence or absence of SE emission electrodes. Since the number of SE's increases with the beam current, potential dependence on the beam current is small for pattern (a) with SE emission electrodes.

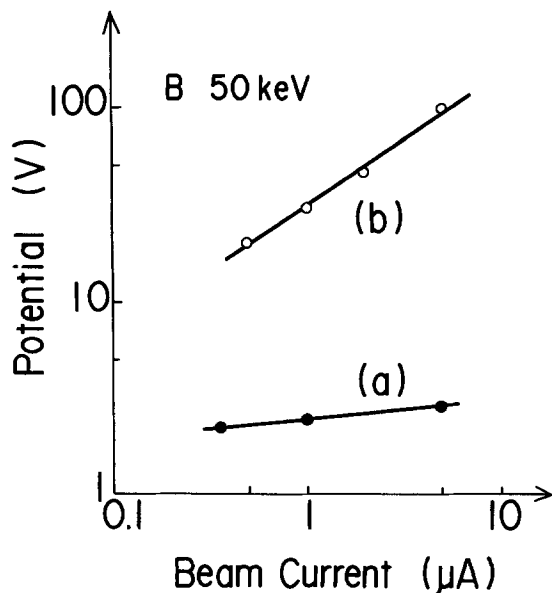


Fig. 6. Beam current dependence of potential for a 50 keV B implant. (a) Pattern with electrodes (S), which emit many secondary electrons. (b) Pattern without electrodes (S).

Then, it was confirmed that SE's emitted from metal electrodes decreased the potential and resulted in a slight dependence of the potential on beam current.

The potential dependence on beam current for pattern (b) is mainly caused by a sheet resistance dependence on beam current, since the SE effect on potential is negligible for pattern (b). The obtained sheet resistance is in the order of $10^9 \Omega/\square$ and is proportional to $I^{-0.32}$, where I is the beam current. The electron hole pairs generated in the SiO_2 layer by ion beam irradiation increase with the beam current, which causes an increase in SiO_2 conductivity.

Method for potential reduction.—The number of SE's repelled back to a wafer varies with the bias voltage applied to the Faraday tube: a negatively biased tube repels the SE's to the wafer, and the positively biased tube attracts them. This variation of the number of SE's causes the insulator surface potential variation. Figure 7 shows bias voltage dependence of the potential of the center electrode 1 shown in Fig. 3(a). Boron ions were implanted in the pattern (a) at 50 keV with $5 \mu\text{A}$. An increase in V_b leads to an increase in the potential, since the number of SE's repelled back to the wafer decreases. Potential decreases with a decrease in the bias voltage and it has a minimum value at a bias voltage of about -10V . This fact indicates that the potential of a wafer can be reduced by applying a negative voltage to the Faraday tube.

Secondary electrons emitted from the secondary electron emission electrodes have three trajectories as shown in the upper left side of Fig. 7. In trajectory 1, the SE's are attracted to the Faraday tube. In trajectory 2, the SE's are attracted to their own electrodes. In trajectory 3, the SE's are attracted to the SiO_2 layer on the wafer. The potential of the SiO_2 surface is decreased by the trajectory-3 SE's. The number of SE's of trajectories 1, 2, and 3 are represented by n_1 , n_2 , and n_3 , respectively. The effective number of SE's emitted from the electrodes is $n_1 + n_3$. The potential has a minimum value as shown in Fig. 7. This fact indicates that n_3 has a maximum value. The reason for the presence of maximum value in n_3 is considered as follows. In the high positively biased region, n_3 becomes 0, since all SE's are attracted to the Faraday tube. In the high negatively biased region, n_3 also becomes 0, since SE's are no longer emitted from the electrodes, owing to high electric field. Since n_3 becomes 0 in both the limiting regions (the high positively and negatively biased regions) and has positive finite value in other regions, n_3 has a maximum value.

Secondary electron emission electrodes were fabricated in a wafer in the present experiment. Secondary electrons emitted from a wafer holder can be utilized for potential reduction in practical use, since the wafer holder is exposed to the ion beam by over scan.

In order to examine the effects of this potential reduction method, the potential of the insulated electrode at

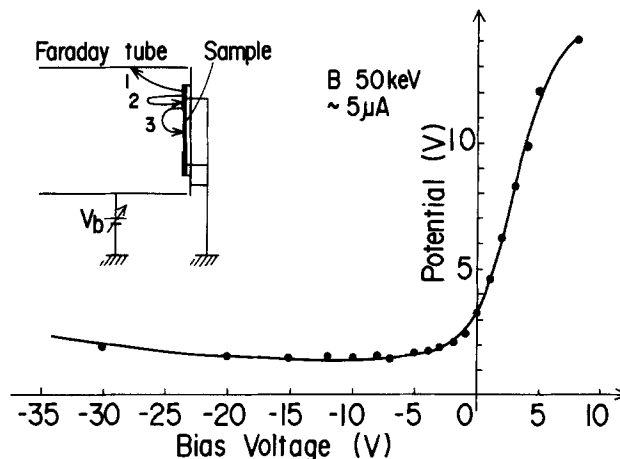


Fig. 7. Potential dependence on bias voltage applied to a Faraday tube. The potential of electrode 1 for pattern (a) shown in Fig. 3 is measured.

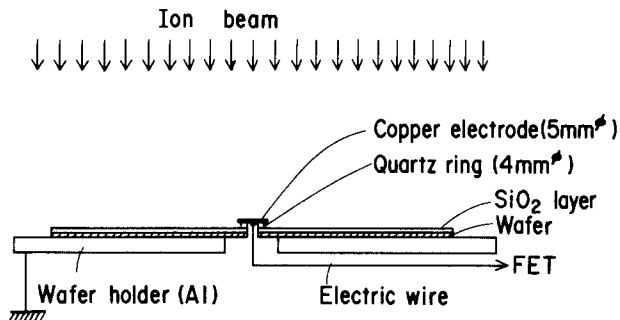


Fig. 8. The experimental arrangement for measuring potential of an insulated electrode at the wafer center. A center electrode made of copper is insulated by a quartz ring.

the wafer center was measured as illustrated in Fig. 8. A 7500Å oxide layer is grown on a 3 in. silicon wafer. The aluminum wafer holder area is $8 \times 8 \text{ cm}^2$, which is equal to the implantation area. The center electrode made of copper is insulated from the wafer by a quartz ring. The diameter of the ring is 4 mm, and that of the electrode is 5 mm. The SiO_2 layer area masked by the electrode, which is not irradiated by the ion beam, is not conductive. The potential of the wafer center is maximum in the wafer during ion implantation, because the distance between wafer center and wafer holder is maximum and only the SE's emitted from the holder can reduce the potential.

If we assume that no secondary electrons are emitted, the potential of a 3 in. wafer center with a SiO_2 layer can be estimated to be over 1000V using Eq. [1] and the order of $10^9 \Omega/\square$ sheet resistance. Further, the potential of the insulated electrode will become higher than 1000V. Figure 9 shows the insulated electrode potential dependence on the beam current as a function of implantation energy. Bias voltage was not applied to the tube. The potential is less than 30V and decreases with an increase in implantation energy, and slightly increases with the beam current. The fact that the resulting potential was less than the estimated value shows that the potential was decreased by the secondary electrons emitted from the wafer holder. The reason for this potential decrease with the implantation energy is an increase in SE emission from the wafer holder with the increase in implantation energy.

The potential becomes still smaller for practical ion implantation, since electrodes are not usually isolated from the SiO_2 layer and metal electrodes in the wafer emit SE's. However, it is necessary to reduce the SiO_2 surface potential even more to avoid problems such as gate leakage in MOSFET's. Figure 10 shows the insulated electrode potential dependence on the bias voltage applied to the Faraday tube, where boron ions were implanted at 50 keV with $5 \mu\text{A}$. The potential has a minimum value at a

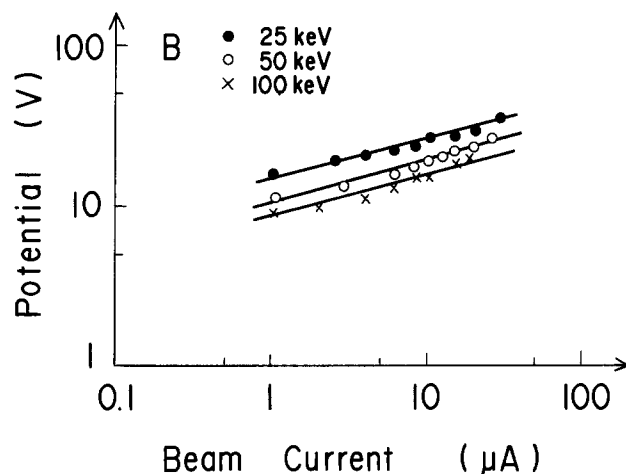


Fig. 9. Potential dependences of beam current as a function of implantation energy for the insulated electrode at a 3 in. wafer center.

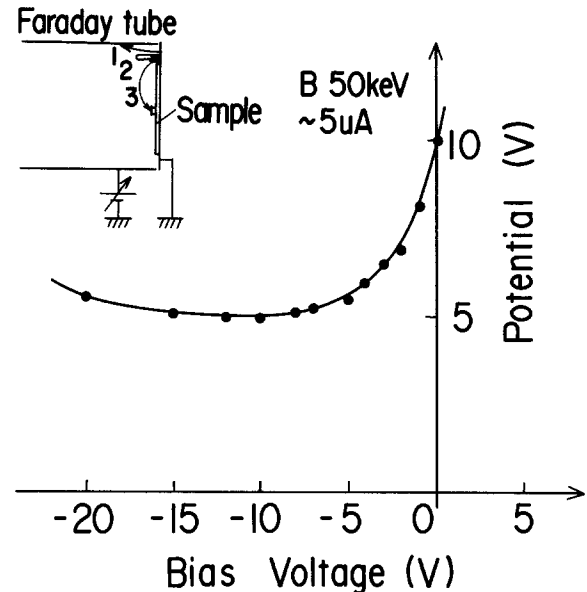


Fig. 10. Potential reduction by applying a negative voltage to a Faraday tube. Bias voltage dependence of the potential for the electrode illustrated in Fig. 8 is shown.

bias voltage of about -10V and slightly increases with a decrease in the bias voltage. This indicates that there is an optimum bias voltage to reduce the potential. The potential in Fig. 10 is more sensitive to bias voltage than that in Fig. 7, since the distance from the Faraday tube to the wafer holder is smaller than the distance to the secondary electron emission electrode in Fig. 7. This potential reduction method is advantageous in that the low potential can be maintained even when the ion beam is unstable, because the secondary electrons reduce the dependence of the potential on beam current.

Summary

The effects of secondary electrons on the electric potential of an insulator surface, during ion implantation, have been studied for an electrostatic scanning ion implanter. Results are summarized as follows.

1. Secondary electrons emitted from metal electrodes or a wafer holder during ion implantation decrease the insulator potential and result in a trapezoidal potential distribution. Secondary electrons also result in a slight dependence of the potential on beam current.

2. The potential distribution on an SiO_2 layer surface is parabolic, when the effect of the secondary electrons is negligible. In this case, the potential is in proportion to $I^{0.68}$, where I is the beam current. The sheet resistance of SiO_2 during ion implantation is on the order of $10^9 \Omega/\square$ in the beam density range of $0.01 \sim 1 \mu\text{A}/\text{cm}^2$.

3. The maximum potential of an insulated electrode on a 3 in. wafer is measured in the $1 \sim 30 \mu\text{A}$ beam current range when ion implantation is performed with overscan. The potential is less than 30V and decreases with the implantation energy, owing to the secondary electrons emitted from a wafer holder.

A potential reduction method, which employs applying a negative voltage to a Faraday tube, is proposed for practical use. This potential reduction method is advantageous in that low potential can be obtained even when the beam current is unstable, because the secondary electrons result in only a weak dependence of insulator potential on beam current.

Acknowledgment

The authors wish to thank Dr. Eisuke Arai for his encouragement and discussion.

Manuscript submitted July 9, 1984; revised manuscript received Nov. 28, 1984.

Nippon Telegraph and Telephone Public Corporation assisted in meeting the publication costs of this article.

REFERENCES

1. Y. Wada and K. Sato, *Jpn. J. Appl. Phys.*, **15**, 2289 (1976).
2. N. Mori, "Ion Implantation and Submicron Fabrication," p. 7 (1979).
3. G. Carter and J. S. Colligoni, "Ion Bombardment of Solids," Chap. 3, Heinemann Educational Books, London (1968).
4. B. Svensson and G. Holmen, *J. Appl. Phys.*, **52**, 6928 (1981).
5. J. F. Gibbons, W. S. Johnson, and S. W. Mylroie, "Projected Range Statistics, Semiconductors and Related Materials," 2nd ed., Halsted Press (1975).
6. R. J. Beuhler and L. Freidman, *J. Appl. Phys.*, **48**, 3928 (1977).

Correlation Between the Photosensitivity Changes of CdS Films and the Surface Chemical Modifications Analyzed by XRFS and LEEIXS

P. Josseaux and A. Kirsch-De Mesmaeker*

Faculté des Sciences, Université Libre de Bruxelles, B-1050 Brussels, Belgium

A. Roche and M. Romand

Laboratoire de Chimie Appliquée du CNRS, Université Claude Bernard, Villeurbanne Cedex, France

H. Montes

Laboratoire de Mécanique des surfaces du CNRS, Ecole Centrale de Lyon, 69130 Ecully, France

ABSTRACT

The photocurrent increase as a function of the illumination time of a CdS film in contact with basic aqueous solutions, in the absence and in the presence of cysteine 1M, is correlated to the intensity of the X emission of Cd and S in XRFS and of O in LEEIXS. The evolution of the photocurrent spectra is also examined. This correlation and the comparison of the X emission spectra of O of illuminated CdS with those of CdO and Cd(OH)₂ indicate that the CdS photosensitivity increase is due to hydroxylated intermediates of the CdS photocorrosion. CdO, an end product of the photodegradation, is responsible for the slow photocurrent decrease, which occurs after longer irradiation times of the junction.

The photoanodic behavior of CdS electrodes in contact with different redox electrolytes has been extensively studied (1). The main limiting factor for these systems is the CdS photocorrosion (2). The authors have studied previously the photoelectrochemical behavior of amorphous and polycrystalline CdS films in contact with basic aqueous solutions of sulfur organic reducing agents (3). Although the photocorrosion is not inhibited by these reductants, an interesting characteristic was observed with cysteine (3a, b): as a function of the illumination time of the CdS-solution junction under a constant applied bias, the photocurrent increases by a factor of 3-4, reaches a maximum, and then decreases slowly. XPS analyses of the electrode surface showed that this photosensitivity increase is not related to the photoelectrochemical attachment of cysteine on the surface (3b). The comparison of the photoelectrochemical behavior of the amorphous CdS films in H₂O/NaOH alone and in H₂O/NaOH/cysteine 1M suggested that the chemical modification of the electrode would originate from the accumulation of oxygen derivatives of Cd on the surface (3b). However, no direct experimental evidence had been obtained in favor of specific oxygenated compounds. In this paper, in order to determine the chemical species responsible for the photosensitivity increase, the illuminated electrodes are analyzed by complementary techniques, such as x-ray fluorescence spectrometry (XRFS), XPS, and low energy electron-induced x-ray spectrometry (LEEIXS), and the results are correlated with the photocurrent evolution.

Experimental

Photoelectrochemistry.—CdS film preparation by chemical precipitation and photoelectrochemical methodology have been described previously (3a, b). The CdS film thickness is of the order of 1.8 μm. The amorphous CdS precipitates on a conducting SnO₂ layer of 0.32 μm deposited on a glass support. The surface analyses are

performed on electrodes illuminated during different times, with a 2000W quartz-halogen lamp (Osram 64788) and under an applied bias of 0V (SCE). Only a part of the beam is focused on the samples. The light intensities are measured with a solarimeter Kipp & Zonen CM 5/6. After irradiation, the electrodes are washed in H₂O/NaOH pH 14, rinsed with tridistilled water, dried in a dessicator, and analyzed by the various techniques.

The photocurrent spectra, after different polychromatic illumination times, are recorded with a high intensity Bausch & Lomb monochromator and a quartz-halogen lamp with dichroic mirror (Philips 13117). They are corrected, taking into account the emission spectrum of the lamp.

The thermal treatment of CdS to form CdO has been examined in the literature (4). In this case, the CdS electrodes are put in an oven at 110°C during variable times. This treatment leads to a bathochromic shift of the absorption spectrum of the film. Subtraction of the spectra before and after the treatment gives an absorption spectrum with a λ_{max} around 500 nm. The CdS absorption spectrum shifts bathochromically as a function of the heating time in the oven. After 10h, however, the bathochromic shift has reached its maximum value of 15 nm.

LEEIXS.—A detailed description of the LEEIXS instruments has been given elsewhere (5-9). Only the basic principles of such an apparatus will be mentioned here. It consists of a wavelength-dispersive x-ray fluorescence spectrometer equipped with a cold cathode tube (CCT). This gas-discharge tube is an open-window device which operates directly in the primary vacuum of the spectrometer. Normal operating vacuum is 1.5 × 10⁻² torr. The CCT is used to bombard the sample surface with a monoenergetic electron beam selectable over the range 0.5-5 keV. The beam spot size at the surface is limited by the aperture of the anode. Typically, this spot is 1 cm in diameter. For a given accelerating voltage, the current is stabilized by an automatic pressure regulator in the range from

*Electrochemical Society Active Member.

0 to 2 mA. Both voltage and current are digitally controlled during the experiment. The soft x-ray spectrometer employed in the present measurements uses flat analyzing crystals or pseudocrystals. The detector is a flow-proportional counter with an ultrathin ($0.5 \mu\text{m}$) polypropylene window and an argon-methane (P-10) flow gas at atmospheric pressure. The bombarding electron-beam incidence angle is 70° and the takeoff angle for x-rays is 35° .

The effective analysis depth of LEEIXS is determined by the material thickness at which characteristic x-rays are produced within the sample. Obviously, this depends on the target material, the energy and the incidence angle of the electron beam, and the x-ray takeoff angle. Typically, the information depth is in the range of some hundred angstroms.

XRFS.—X-ray fluorescence is the conventional x-ray emission technique. This simple spectrochemical technique is usually regarded as a bulk analytical method. Actually, it is also a near-surface analysis technique when the x-rays, emitted and detected, originate from a near-surface layer of finite thickness. The instrument employed in this work (Philips PW 1540) is a flat-crystal spectrometer equipped with a flow-proportional counter using the P10 gas flow. The x-ray tube used has a chromium target.

XPS.—The XPS measurements are performed with a vacuum generators-CLAM 100 ESCA spectrometer using nonmonochromatic $\text{AlK}\alpha$ radiations (1486, 6 eV). The carbon C1s binding energy of contamination (285 eV) is used for calibration. Measurements are carried out at a pressure of less than 2×10^{-9} torr in the spectrometer vessel. Sample etching is performed in a preparation chamber by 5 keV argon ions. The density of the ion current is approximately $10 \mu\text{A}\cdot\text{cm}^{-2}$ at the sample surface.

Results and Discussion

Figure 1 shows the photocurrent density as a function of the polychromatic illumination time, at a bias of 0V (SCE), with $\text{H}_2\text{O}/\text{NaOH}$ alone and with $\text{H}_2\text{O}/\text{NaOH}/\text{cysteine}$ 1M. Eight electrodes per photocurrent-time curve, all prepared in the same precipitation bath, have been illuminated, each one in the same conditions but during different times, and analyzed by XRFS, XPS, and LEEIXS.

XRFS.—Because the thickness analyzed by XRFS is of the order of a few micrometers to a few millimeters, this technique gives information on the elementary chemical composition of the CdS film and of the SnO_2 coating the glass support (see Experimental section). Figures 2 and 3 show the results of the XRFS analyses of electrodes irradiated in $\text{H}_2\text{O}/\text{NaOH}$ alone and in $\text{H}_2\text{O}/\text{NaOH}/\text{cysteine}$ 1M. The $\text{CdL}_{\beta}/\text{SnL}_{\alpha}$ emission ratios decrease in both cases as a function of the irradiation. This corresponds to a slight

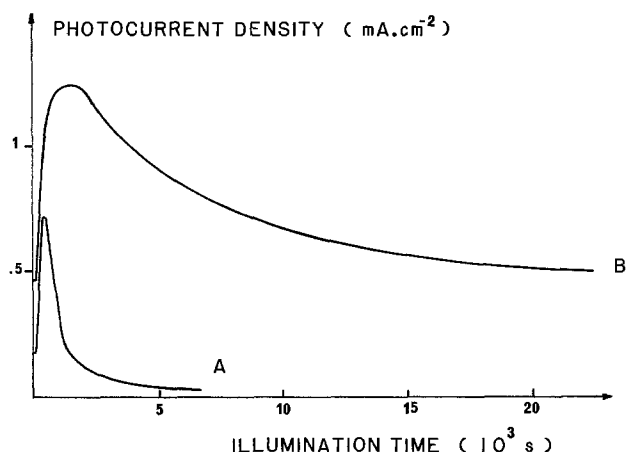


Fig. 1. Photocurrent density as a function of the polychromatic illumination time with (A) $\text{H}_2\text{O}/\text{NaOH}$ and (B) $\text{H}_2\text{O}/\text{NaOH}/\text{cysteine}$ 1M.

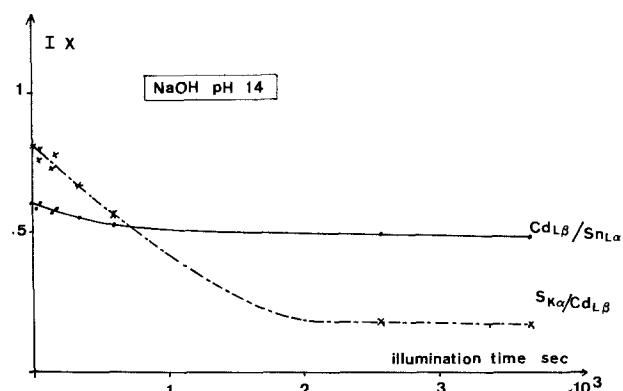


Fig. 2. Intensity ratio of $\text{CdL}_{\beta}/\text{SnL}_{\alpha}$ and $\text{SK}_{\alpha}/\text{CdL}_{\beta}$ in XRFS for the electrodes illuminated in contact with $\text{H}_2\text{O}/\text{NaOH}$ pH 14.

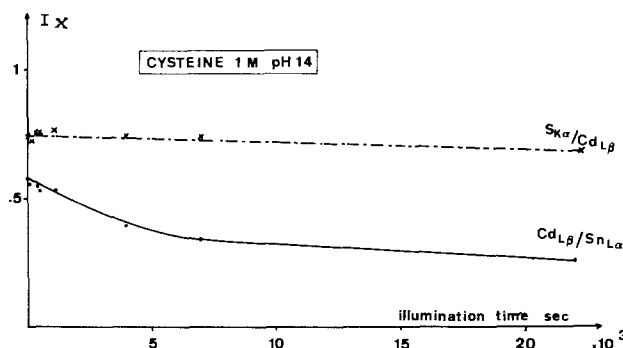


Fig. 3. Intensity ratio of $\text{CdL}_{\beta}/\text{SnL}_{\alpha}$ and $\text{SK}_{\alpha}/\text{CdL}_{\beta}$ in XRFS for the electrodes illuminated in contact with $\text{H}_2\text{O}/\text{NaOH}/\text{cysteine}$ 1M, pH 14.

decrease of the CdS film thickness, which indicates that the electrode photodegradation is not inhibited by cysteine, as already found (3a). The $\text{SK}_{\alpha}/\text{CdL}_{\beta}$ ratio decreases on irradiating in the absence of reductant, whereas it remains quasi constant with cysteine. This is incompatible with a production of sulfur S^0 from the photoanodic decomposition and indicates that the sulfur is further oxidized into sulfate (3b, c, d) and solubilized. A Cd enrichment of the film in contact with NaOH alone could be responsible for the $\text{SK}_{\alpha}/\text{CdL}_{\beta}$ decrease. The Cd^{2+} ions liberated from the lattice would thus remain in the film as $\text{Cd}(\text{OH})_2$ or CdO. On the other hand, the addition of cysteine solubilizes the Cd^{2+} into cadmium cysteinate, very soluble in basic solution (3a, b), which explains the constancy of the $\text{SK}_{\alpha}/\text{CdL}_{\beta}$ ratio in this case.

XPS.—The XRFS data are not inconsistent with the formation of $\text{Cd}(\text{OH})_2$ or CdO in the film as a function of the illumination with NaOH alone. This could also be the case with cysteine; however, the oxygenated cadmiums would be formed to a lesser extent through the film and still not detected by XRFS. The detection of some chemical changes more localized near the surface requires XPS analyses which allow investigation of about 5 nm of the film.

The electrodes supposedly most modified chemically, i.e., the ones which have reached the maximum photocurrent with cysteine, were thus examined by XPS. The characteristics are studied as a function of depth, thanks to an ion sputtering. Figures 4 and 5 show the modifications of the Cd 3d and S 2p photopeaks, respectively, as a function of the sputtering time. The occurrence of a Cd 3d $_{5/2}$ binding energy splitting can result from two factors acting either separately or simultaneously: a chemical effect due to a modification of the cadmium atom environment or a charging effect resulting from the isolating nature of one of the chemical species. In order to eliminate this ambiguity, the study of the Auger parameters (10) can be useful. An Auger parameter for a given atom is equal to the difference between the kinetic energy of the Auger line and the photoelectron peak

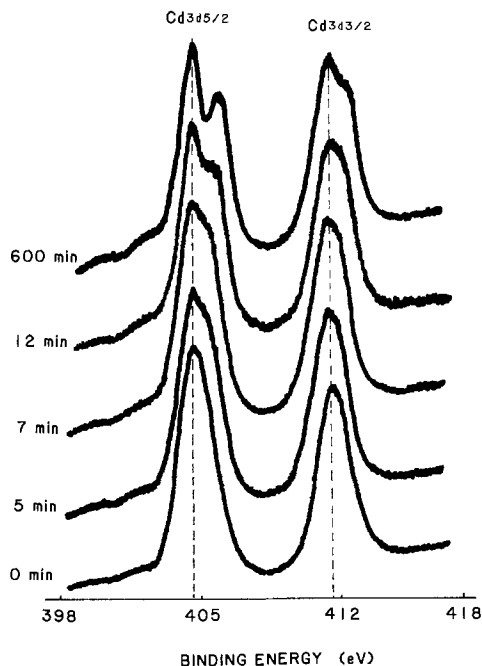


Fig. 4. Evolution of the Cd 3d signals in XPS as a function of the sputtering time of the CdS electrode illuminated in contact with cysteine 1M.

energy; it allows determination of the sample chemical nature during an in-depth profiling, independently of the charging effects. The Cd 3d5/2 and S 2p binding energy differences and the oxygen Auger parameters ($O_{1s} - O_{KLL}$) for different standards and for the CdS electrode, at different ion sputtering times, are listed in Table I. These values have been measured from data obtained within a minimum x-ray irradiation time (less than 150s) to prevent or minimize any possible x-ray damage of the sample (11). For the CdS electrode, the binding energy of the main Cd 3d5/2 photopeak (≈ 404 eV) is associated with the sulfide. Figure 5 and Table I show the presence at the electrode surface of cadmium sulfide, cadmium sulfate in small amount, and cadmium hydroxide. After a 5 min sputtering, the CdSO₄ disappears and the Cd(OH)₂ and CdS remain present within the total sputtered layer.

Consequently, even with cysteine, a new Cd species, Cd(OH)₂, is formed.

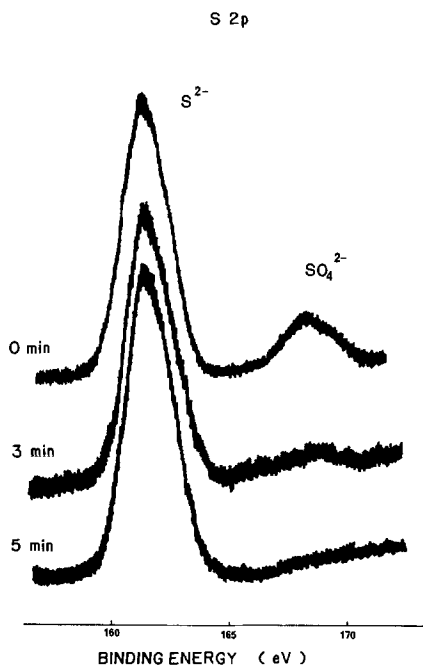


Fig. 5. Evolution of the S 2p signals in XPS as a function of the sputtering time of the CdS electrode illuminated in contact with cysteine 1M.

Table I. Cd 3d5/2 and S_{2p} binding energy differences and oxygen Auger parameters. (a) Cd S only dipped in H₂O/NaOH is not different from the CdS standard (3b). (b) The CdS electrode has been illuminated in contact with cysteine 1M

Sample	Cd 3d5/2 - S _{2p} (eV)	O _{1s} - O _{KLL} (eV)
CdS (a)	243.4	—
CdSO ₄	236.2	444.9
CdO	—	444.6
Cd(OH) ₂	—	446.4
CdS electrode (b)		
Sputtering time (min)		
0	243.6 and 236.3	446.4
5	243.1	446.5
7	243.1	446.4
600	242.8	446.4

LEEIXS.—Because Cd(OH)₂ and probably CdO occur on the films, the OK_α emission in LEEIXS of all the illuminated samples was analyzed. With this technique, for the OK_α signal and for an incident electron-beam energy of 3.5 eV, about 120 nm of the CdS film is analyzed.

The identification by LEEIXS of an oxygenated product at the surface must be performed by comparison with spectra of reference products. Therefore, the oxygen X emission spectra of CdO and Cd(OH)₂ have been recorded (Fig. 6). For CdO, the OK_α band is fairly symmetric, whereas the one for Cd(OH)₂ is characterized by a low energy shoulder (518 eV). Furthermore, Fig. 6 shows also that Cd(OH)₂ is unstable under the electron beam and that it changes rather quickly into CdO. The cadmium hydroxide decomposition into cadmium oxide is obviously associated with a OK_α intensity decrease. The OK_α spectra for electrodes illuminated in the presence of the reductant are shown in Fig. 7; they are similar to the ones for electrodes illuminated in absence of the reductant. They present the characteristics of the Cd(OH)₂ spectrum, *i.e.*, the shoulder at low energy and its disappearance as a function of the analysis time. The illuminated electrode surfaces are thus enriched in a Cd(OH)₂ type compound.

Then examined was the correlation between the intensity of the OK_α line and the changes of photocurrent *vs.*

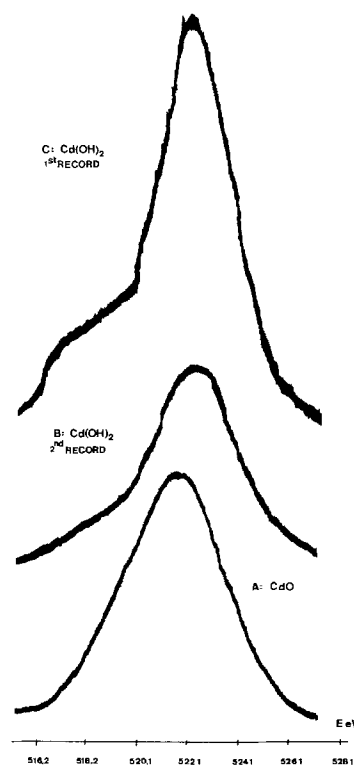


Fig. 6. Oxygen K_α emission spectra in LEEIXS for CdO and Cd(OH)₂ samples. (A) CdO. (B) Cd(OH)₂, second record. (C) Cd(OH)₂, first record.

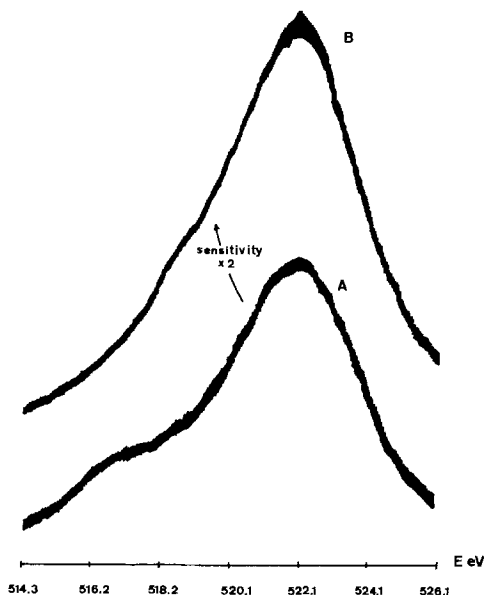


Fig. 7. Oxygen K_{α} emission spectra in LEEIXS for CdS illuminated in contact with cysteine 1M. (A) first record; (B) second record.

time, without and with cysteine. Figures 8 and 9 show the evolution of the OK_{α} line intensity as a function of the illumination time, with $H_2O/NaOH$ alone and with cysteine, respectively. The curves a, b and c correspond to three successive countings of 20s. In both figures, the photocurrent increase corresponds to an intensity increase of the OK_{α} line; however, the photocurrent decrease does not correspond to any decrease of the OK_{α} signal. With NaOH alone, the OK_{α} intensity is more or less constant

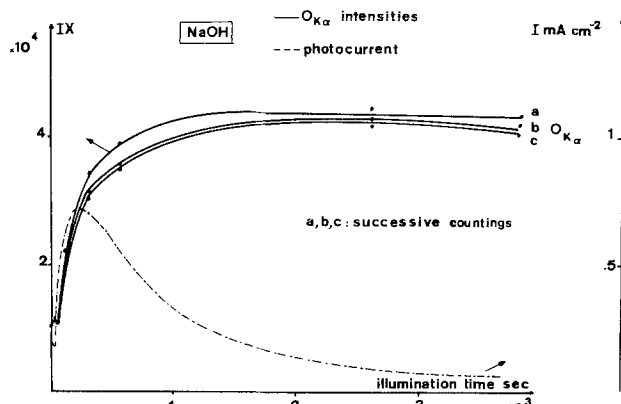


Fig. 8. Three successive countings of 20s (a, b, c) of the OK_{α} signal in LEEIXS as a function of the illumination time of CdS in contact with NaOH alone. Dotted line: photocurrent evolution as a function of the illumination time, with NaOH alone.

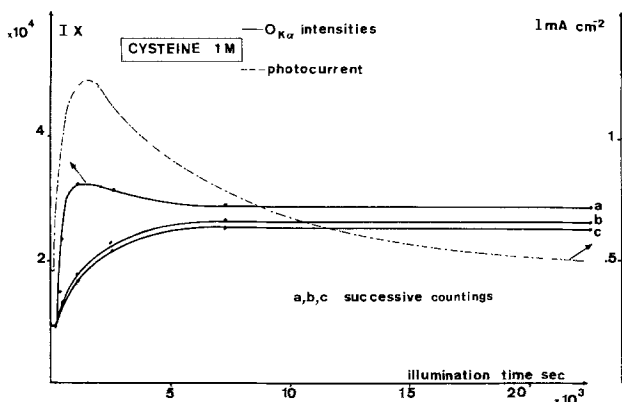


Fig. 9. The same as Fig. 8, but as a function of the illumination time with cysteine 1M.

for successive countings, with differences of 12% at most at the times near the maximum photocurrent. On the other hand, with cysteine, the OK_{α} line decreases with the successive countings, with a difference as high as 50% at times close to the maximum photocurrent. This shows that $Cd(OH)_2$, unstable under the electron beam, would be present on the electrodes illuminated with cysteine, whereas CdO, stable under the electron beam, would correspond to the main species formed on the electrodes irradiated with NaOH alone.

If we compare Fig. 8 and 9, it is observed that for the illuminations with NaOH alone, corresponding to lower photocurrents, the OK_{α} intensities are higher and, as mentioned above, they do not vary as the photocurrent. For the illuminations with cysteine, it is clear also that the photocurrent does not follow the OK_{α} signal, but increases with the variations of the OK_{α} intensities in the successive countings. Consequently, the photocurrent increase would be related to the increase of a $Cd(OH)_2$ -type compound on the surface. This would be an intermediate component formed during the CdS photoanodic decomposition, which is present in greater amount with cysteine than with NaOH alone. On the other hand, the higher stability of the OK_{α} signal would be correlated to the photocurrent decrease and, thus, to the formation of CdO.

Photocurrent spectra.—We confirmed the conclusions from the XRFs, XPS, and LEEIXS by *in situ* analyses of the interface, such as photocurrent spectra. The evolution of the photocurrent spectra as a function of the polychromatic illumination does not depend very much on the presence of cysteine 1M. During the photocurrent increase, under white light, the photocurrent spectra recorded from 400 to 550 nm increase also in intensity, more so with cysteine than with NaOH alone. When they are normalized at 450 nm for short illuminations, only the disappearance of a slight absorption around 515 nm is observed (see further); otherwise during the photocurrent increase there are no important changes from one spectrum to the other. This indicates that the CdS photosensitivity enhancement is not related to the formation on the electrode of a product which absorbs in the visible region. This is in agreement with the LEEIXS analyses indicating the occurrence of a $Cd(OH)_2$ type compound which is colorless.

As shown by Fig. 10, near the maximum photocurrent and during the photocurrent decrease, the normalized spectra change: the photocurrents decrease at shorter wavelengths, with a bathochromic shift of the absorption edge. The changes are the same with cysteine, though to a

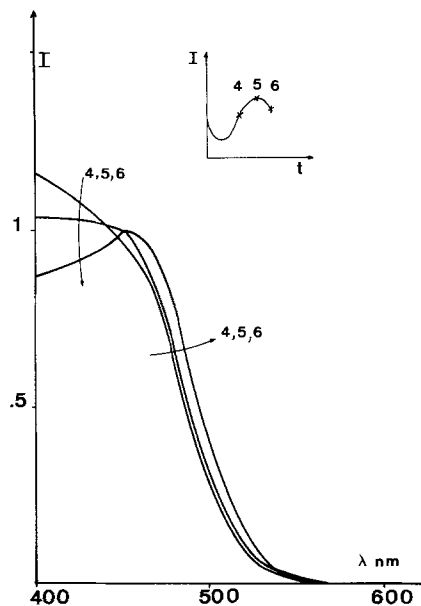


Fig. 10. CdS action spectra normalized at 450 nm as a function of the polychromatic illumination time at 0V (SCE). The analyzed samples are indicated on the curve photocurrent vs. the illumination time (4, 5, 6).

lesser extent. The bathochromic shift and the increase of the electron-hole recombinations at the surface, responsible for the photocurrent decreases at short wavelengths, could be attributed to the occurrence of CdO in the CdS lattice. The CdO bandgap differs throughout the literature [e.g., 590 nm (12); 500 nm (13)]. The authors obtained for a CdO powder an absorption λ_{max} of 540 nm. Because the gap of the CdS powder corresponds to about 510 nm, the formation of CdO in the CdS is thus compatible with these spectral data and in agreement with the LEEIXS conclusion.

In order to characterize better the CdS films enriched in CdO, thermally oxidized CdS (see Experimental) was prepared and its photoelectrochemical behavior was studied. The photocurrent spectra in NaOH, before any illumination, show that the thermal treatment shifts bathochromically the absorption edge (Fig. 11). The subtraction of the spectrum of the untreated electrode from the one of the treated CdS gives an absorption maximum around 515 nm which increases with the duration of the thermal treatment. Figure 12 shows for a thermally oxidized film the action spectra before illumination and after an irradiation corresponding to the maximum photocurrent. The evolution of the spectra is similar to that described for the untreated CdS. The absorption initially present at 515 nm, characteristic of the thermally generated CdO, disappears after illumination. Moreover, the longer the thermal treatment, the lower is the initial photocurrent in the first seconds of the polychromatic illumination, indicating some blocking of the electrode by CdO.

The experiments with thermally oxidized CdS films clearly indicate that the thermal CdO is different from the one formed photoelectrochemically. The thermal CdO probably forms a superficial film on the CdS, which disappears photoelectrochemically during the CdS photocorrosion. Besides, as mentioned above, this CdO film is also detected on the untreated electrode, before the polychromatic illumination. On the other hand, the photoelectrochemical CdO would form a mixed CdS-CdO lattice which penetrates deeper into the film and starts inhibiting the photoelectrochemistry.

Conclusion

The surface chemical analyses and photocurrent spectra lead to the conclusion that the photocurrent enhancement as a function of the illumination time, under a bias of 0V (SCE), is due to the accumulation of an intermediate species of the CdS photodegradation, which favors the electron transfer at the semiconductor-liquid interface. This species corresponds to Cd(OH)₂ or derivatives

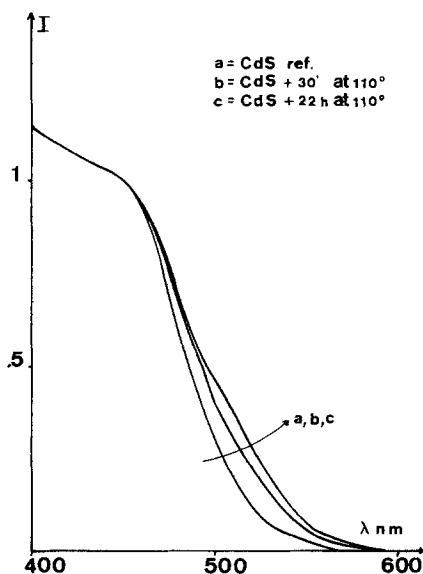


Fig. 11. Action spectra normalized at 450 nm of CdS in contact with H₂O/NaOH pH 14. (a) reference CdS; (b) CdS treated 30 min at 110°C; (c) CdS treated 22h at 110°C.

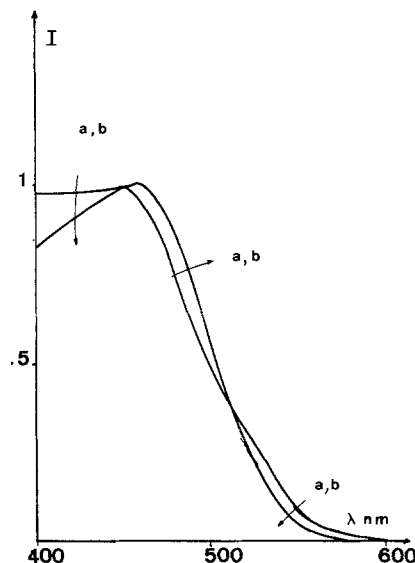


Fig. 12. Action spectra normalized at 450 nm of CdS in contact with H₂O/NaOH/cysteine 1M, pH 14, treated 22h at 110°C. (a) spectrum before the polychromatic illumination; (b) spectrum when the photocurrent under white light at 0V (SCE) has reached the maximum value

of hydroxylated cadmium which are converted into a final product: CdO. The accumulation of CdO within the CdS lattice leads to the slow photocurrent decrease. The greater amount of oxygenated cadmium in the samples illuminated in NaOH alone, as evidenced by LEEIXS, is mainly due to CdO, responsible for the lower photocurrents in NaOH compared to those with cysteine. It has to be noted that elemental sulfur has not been detected by XPS and LEEIXS during the blocking of the electrode surface.

The nature of the CdS chemical modification is not influenced by cysteine. However, this reductant does play a role. Indeed, in its presence, the photocurrent increase is more pronounced and more Cd(OH)₂-type species are formed. The reductant would thus stabilize the degradation intermediate responsible for the photosensitivity increase, or in other words, would decrease the rate of formation of CdO from Cd(OH)₂ within the CdS lattice. If Cd²⁺ ions are liberated from the lattice during the photocorrosion, in the presence of cysteine 1M, these ions would rather solubilize into cadmium cysteinate than precipitate on the electrode as Cd(OH)₂. However, the greater amount of Cd(OH)₂-type species with cysteine than with NaOH alone would suggest that the hydroxylated species look more like hydroxylated cadmiums still belonging to the CdS lattice than like precipitated Cd(OH)₂.

There are two possible explanations for the photosensitivity increase due to hydroxylated cadmiums: (i) as already proposed previously (3a, b), a passivation of surface states related to cadmium's dangling bonds, by reaction with OH⁻ ions, similar to Heller's interpretation (14) for Ru³⁺ on GaAs; and (ii) a higher rate of photo-oxidation of cysteine on an hydroxylated CdS surface.

Acknowledgments

One of the authors (P. J.) thanks the Institut pour l'Encouragement de la Recherche Scientifique dans l'Industrie et l'Agriculture (IRSIA) and the European Photochemistry Association (EPA) for a travel grant.

Manuscript submitted May 14, 1984; revised manuscript received Oct. 22, 1984.

Université Libre de Bruxelles assisted in meeting the publication costs of this article.

REFERENCES

- (a) A. B. Ellis, S. W. Kaiser, and M. S. Wrighton, *J. Am. Chem. Soc.*, **98**, 1635 (1976); (b) G. Hodes, J. Manassen, and D. Cahen, *Bull. Isr. Phys. Soc.*, **22**, 100 (1976); *Nature*, **261**, 403 (1976); (c) A. Heller, K. C. Chang, and B.

- Miller, *This Journal*, **124**, 697 (1977); (d) H. Minoura, T. Tsuiki, and T. Oki, *Ber. Bunsenges. Phys. Chem.*, **81**, 588 (1977); (e) H. Gerischer and J. Gobrecht, *ibid.*, **80**, 327 (1976).
2. H. Gerischer and J. Gobrecht, *Ber. Bunsenges. Phys. Chem.*, **82**, 520 (1978).
 3. (a) A. Kirsch-De Mesmaeker, A. M. Decoster, and J. Nasielski, *Sol. Energy Mater.*, **4**, 203 (1981); (b) A. Kirsch-De Mesmaeker, P. Josseaux, J. Nasielski, and C. Defosse, *ibid.*, **6**, 429 (1982); (c) P. Josseaux, A. Kirsch-De Mesmaeker, J. Riga, and J. Verbist, *This Journal*, **130**, 1067 (1983); (d) R. Dewitt and A. Kirsch-De Mesmaeker, *ibid.*, **130**, 1995 (1983).
 4. S. A. Kukuskin, L. A. Sergeeva, and I. P. Kalinkin, *Zh. Tekh. Fiz.*, **52**, 388 (1982).
 5. M. Romand, R. Bador, A. Roche, and G. Bouyssoux, *J. Microsc. Spectrosc. Electron.*, **2**, 627 (1977).
 6. R. Bador, A. Roche, G. Bouyssoux, and M. Romand, *Spectrochim. Acta*, **33B**, 437 (1978).
 7. A. Roche, A. Cachard, R. Bador, F. Buiguez, M. Charbonnier, and M. Romand, *J. Microsc. Spectrosc. Electron.*, **4**, 351 (1979).
 8. R. Bador, M. Romand, M. Charbonnier, and A. Roche, *Adv. X-ray Anal.*, **24**, 351 (1981).
 9. A. Roche, M. Charbonnier, F. Gaillard, M. Romand, and R. Bador, *Appl. Surf. Sci.*, **9**, 227 (1981).
 10. C. D. Wagner, W. M. Riggs, L. E. Davis, and J. F. Moulder, in "Handbook of X-ray Photoelectron Spectroscopy," G. E. Muilenberg, Editor, p. 18, Perkin-Elmer Corp., MN (1979).
 11. A. Roche, H. Montes, J. Brissot, M. Romand, P. Josseaux, and A. Kirsch-De Mesmaeker, *Appl. Surf. Sci.*, In press.
 12. A. K. Vijk, *J. Phys. Chem. Solids*, **30**, 1999 (1969).
 13. T. K. Lakshman, *This Journal*, **110**, 548 (1963).
 14. (a) B. A. Parkinson, A. Heller, and B. Miller, *ibid.*, **126**, 954 (1979); (b) A. Heller and B. Miller, *Electrochim. Acta*, **25**, 29 (1980).

Sidewall Tapering in Reactive Ion Etching

A. G. Nagy

Motorola, Incorporated, SPS, Process Technology Laboratory, SRDL, Phoenix, Arizona 85008

ABSTRACT

This paper reports for the first time the existence of a sidewall tapering phenomenon in reactive ion etching (an oxide process in a commercially available hex-type system) which is akin to that seen in sputter etching or ion milling. A facet forms in the photoresist mask because of an angular dependence of the resist loss rate. The facet angle is about 16° off vertical, and its downward propagation rate is more than twice the vertical etch rate of the resist. If this facet is allowed to reach the etching material during the course of the etch, it will replicate significantly into this material. When an initially vertical unmasked silicon step is exposed to the same oxide etch process, an identical facet is formed. However, when a bare silicon dioxide step is exposed to the process, no faceting is seen.

Close examination of the profiles of certain samples after silicon dioxide etching in a conventional reactive ion etching (RIE) system has shown a taper of slightly more than 15° off vertical (75° sidewall angle). This paper will examine some of the possible causes of this tapering.

In the past, slight tapering of a feature etched by RIE was not considered a serious problem, and indeed may even aid subsequent step coverage. However, current interest in processes such as selective epitaxy (1), and schemes where a sidewall mask is needed, such as sidewall masked isolation (SWAMI) (2) and self-aligned silicide processes (3), all of which require vertical sidewalls, demands that the causes of RIE-induced tapering be investigated.

In reactive ion etching, the chemical etch process is assisted by ion bombardment normal to the substrate, such that the resulting etch rate is higher than would be expected from simply superimposing a physical sputtering mechanism onto the chemical etch process (4). This bombardment-assisted mechanism, which is believed to be responsible for most of the anisotropy in RIE, leads one to expect vertically etched profiles, contrary to what has been observed here.

Tapering has been observed in ion milling or sputter etching (in which material removal is by physical sputtering only) when initially vertical steps are milled at normal incidence (5), and tilting a sheet film relative to the ion beam at the sidewall taper angle usually gives the highest milling rate. It has never been reported whether the ion-assisted process in RIE shows a similar angular dependence.

Three possible causes of the observed tapering were investigated: an initially tapered mask profile reproducing itself into the etching film, a lateral pull-back of the mask during the course of the etch, and replication into the etching film of a facet (akin to that seen in ion milling) formed in the mask during the course of the etch. The first two causes are well known and have, in fact, been

used in RIE to generate tapered vias for improved step coverage (6).

The tapering phenomenon was studied in a hex-type RIE system using photoresist, silicon, and silicon dioxide samples. An explanation of the phenomenon is presented, and a solution is proposed.

Equipment, Samples, and Experimental Methods

A fluorine-based ($\text{CHF}_3 + \text{O}_2$) oxide etch process in a hex-type reactor was used in this work because it is in this system that the tapering was first seen. The hex-type configuration gives a very large anode-to-cathode area ratio, resulting in a high degree of ion bombardment. The oxide etch rate in this process is 550 Å/min, the silicon etch rate is 110 Å/min, and the photoresist loss rate is 170 Å/min.

Tapering in positive photoresist, single-crystal silicon, and thermal oxide samples was studied. The degree of tapering was determined through the use of cross-sectional photos taken with a scanning electron microscope, and some of the processes were modeled using SAMPLE (7), a computer program which simulates dry etch processes and prints the resulting profiles.

Results and Discussion

The following three sections examine in turn each of the possible causes of tapering mentioned in the introduction. A solution to the problem is proposed. In the third section, a mechanistic explanation of the phenomenon based upon the fundamental differences between silicon dioxide, silicon, and organic etching is presented.

Initial mask taper replication.—It is well known that conventional photolithography does not produce vertical resist edge profiles. Figure 1a shows a rather extreme example of a tapered resist profile, approximately 1.0 μm of patterned resist sloped about 45°, masking a 1.5 μm thick thermal oxide film. Figure 1b shows the film after etch-

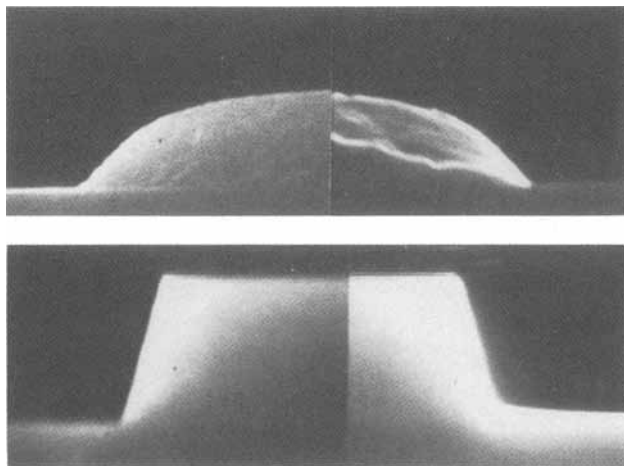


Fig. 1. a(top): $1.0\ \mu\text{m}$ photoresist over $1.5\ \mu\text{m}$ thermal oxide prior to oxide etch. 45° resist taper. b(bottom): Above wafer after 50 min oxide etch, resist removed. Approximately 16° oxide taper.

ing in the reactor for 50 min (mask has been stripped). The sidewall taper is about 16° off vertical.

To help determine if mask taper replication is a major cause of feature sidewall tapering, the etching of an oxide film beneath a tapered mask was modeled using SAMPLE for the following conditions: oxide thickness of $1.5\ \mu\text{m}$; resist thickness of $1.0\ \mu\text{m}$; opening width at base of mask of $1.25\ \mu\text{m}$; oxide vertical etch rate of $550\ \text{\AA}/\text{min}$; oxide lateral etch rate of $0\ \text{\AA}/\text{min}$; resist vertical loss rate of $170\ \text{\AA}/\text{min}$; resist lateral loss rate of $0\ \text{\AA}/\text{min}$; mask selectivity of 3:1; etch time of 50 min; and resist taper of 45° .

Figure 2 shows the printout of this modeling. The oxide taper after etch is 15° . Figure 3 shows the profile which results when a more realistic resist taper of 30° is used in the modeling with all the other parameters held constant. The sidewall taper is now 10° .

Selectivity of the etching film relative to the mask was also suspected to be a major factor in mask taper replication, so a selectivity of 6:1 was next substituted for the 3:1 value in the modeling. Figure 4 shows that the resultant sidewall angle is now 7.5° . This illustrates that there is a strong relation between the final etch profile and the selectivity, and, indeed, that under ideal conditions, the final taper angle in the film is simply the mask taper angle divided by the selectivity value.

Consequently, a large mask selectivity may be expected to give relatively vertical etch profiles, even if the mask is severely tapered. SAMPLE modeling of the etch of an oxide film masked with 45° tapered resist assuming a (unrealistic) 20:1 selectivity revealed virtually vertical oxide sidewalls.

Though vertically etched sidewalls can, in principle, be produced by using a highly selective etch, it is usually

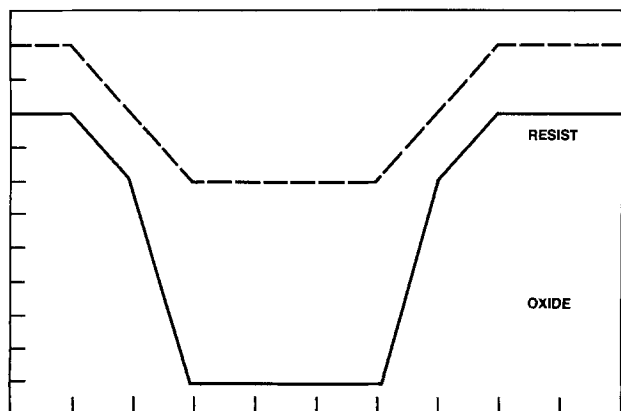


Fig. 2. SAMPLE modeling of 50 min etch of $1.5\ \mu\text{m}$ oxide masked with $1.0\ \mu\text{m}$ resist, tapered 45° . Selectivity: 3:1. Final oxide taper: 15° .

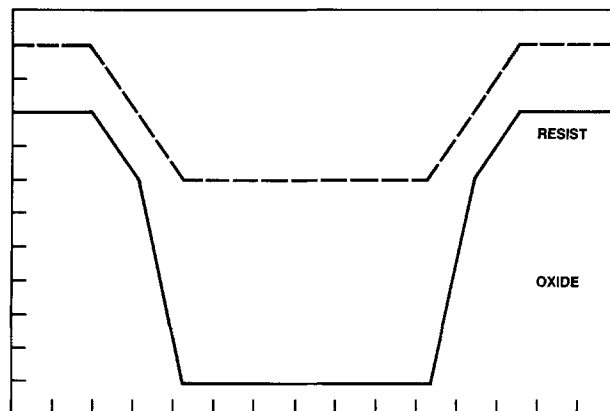


Fig. 3. SAMPLE modeling of 50 min etch of $1.5\ \mu\text{m}$ oxide masked with $1.0\ \mu\text{m}$ resist, tapered 30° . Selectivity: 3:1. Final oxide taper: 10° .

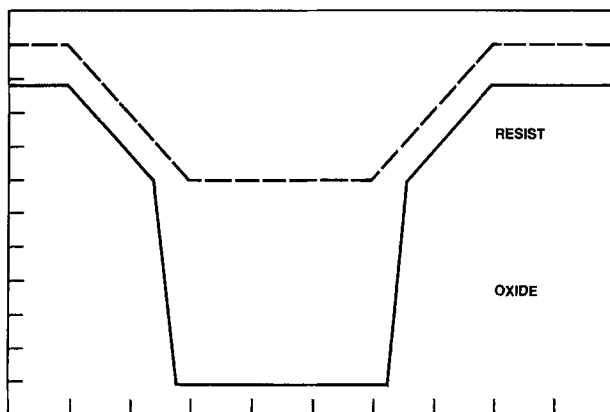


Fig. 4. SAMPLE modeling of 50 min etch of $1.5\ \mu\text{m}$ oxide masked with $1.0\ \mu\text{m}$ resist, tapered 45° . Selectivity: 6:1. Final oxide taper: 7.5° .

very difficult to make large changes in selectivity within the framework of an established process. Therefore, the possibility that tapered etching can be eliminated by using a mask with vertical sidewalls, a modification which at least in principle is feasible, was next studied. A $1.5\ \mu\text{m}$ thermal oxide film, patterned with approximately $1.0\ \mu\text{m}$ of resist using a standard tri-level technique (8) to ensure vertical resist profiles (Fig. 5) was etched for 50 min in the reactor. Figure 6 shows that a 15° taper, which SAMPLE does not predict, forms in the oxide. This implies that initial resist taper, while it is a factor, is not nec-

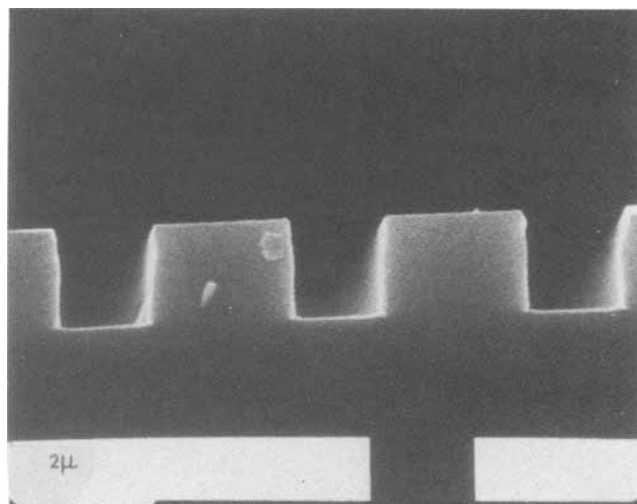


Fig. 5. $2.0\ \mu\text{m}$ tri-level resist patterned over bare silicon

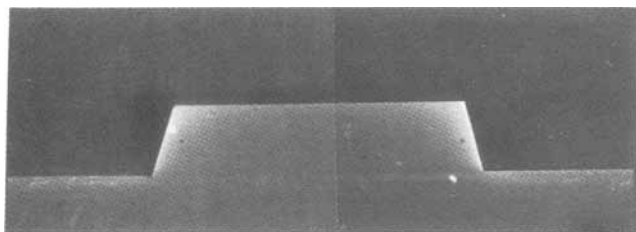


Fig. 6. Tri-level patterned thermal oxide ($1.5 \mu\text{m}$) after 50 min RIE. Mask has been stripped. 15° final oxide taper.

essarily the dominant cause of tapered etch profiles, and that some other mechanism is clearly operating.

Lateral resist loss during etching.—Lateral erosion of the resist mask during anisotropic oxide etching could plausibly result in tapered sidewalls. Fluorine is believed to catalyze the surface reaction of oxygen with organic materials (9), which could lead to lateral resist loss.

Figure 7 shows a SAMPLE-generated profile of a $1.5 \mu\text{m}$ thick oxide film patterned with $1.5 \mu\text{m}$ of vertical-walled resist with a $100 \text{ \AA}/\text{min}$ isotropic loss rate, meaning that both the vertical and horizontal resist loss rates were equal. The resist thickness and loss rate were chosen rather arbitrarily, as was the $500 \text{ \AA}/\text{min}$ oxide etch rate. A 10° oxide sidewall taper results.

An experiment was next performed to determine if significant lateral resist loss was occurring during the oxide etch process. $2.0 \mu\text{m}$ thick resist was patterned on bare silicon using the tri-level technique. The sample was then exposed to the etch process for 105 min. Figure 8 shows that, instead of a uniform lateral pull-back of the resist, a tapered profile results. The resist taper angle is 16° , and that of the underlying silicon is slightly greater (about 19°). Given the silicon and resist etch rates in this process, the relation between the resist and silicon taper angle is not surprising.

The above results show that the resist loss process is not isotropic, meaning that lateral resist erosion is not the cause of tapered etching.

Faceting in the mask.—The resist taper shown in Fig. 8 looks very much like that seen in ion milling, in which tapered profiles result in the film being milled if the facet produced in the mask is allowed to reach this film during the course of the run (5). An analogous phenomenon has apparently occurred in Fig. 8, as evidenced by the taper in the underlying silicon.

To cure the tapering problem in ion milling, the mask thickness and run time are chosen such that the facet does not reach the underlying material during the run. The result of etching a tri-level patterned resist-over-

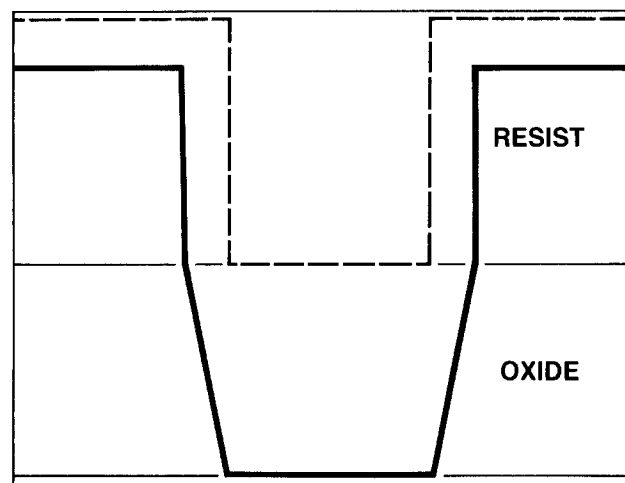


Fig. 7. SAMPLE modeling of $1.5 \mu\text{m}$ oxide masked with $1.5 \mu\text{m}$ vertical-walled resist. Resist lateral loss rate = resist vertical loss rate = $100 \text{ \AA}/\text{min}$. Mask selectivity: 5:1. 10° final oxide taper.

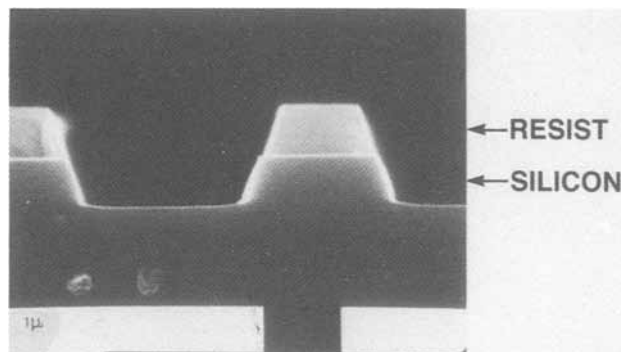


Fig. 8. Tri-level patterned resist over silicon after 105 min exposure to oxide etch process. Final resist taper: 16° . Silicon taper: 19° .

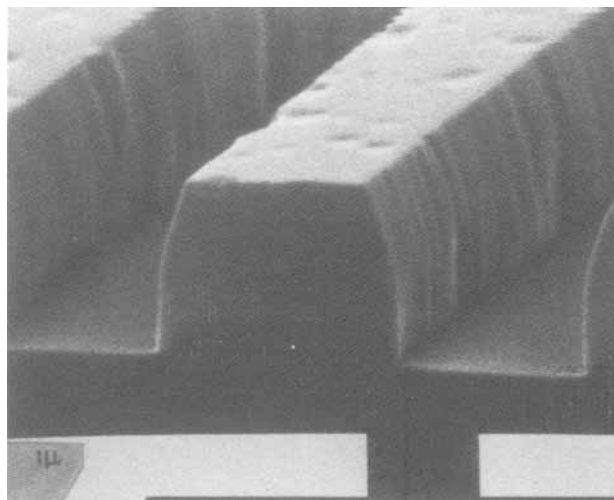


Fig. 9. Tri-level patterned resist over silicon after 50 min exposure to oxide etch process. Facet propagation rate: $310 \text{ \AA}/\text{min}$.

silicon sample for 50 min is shown in Fig. 9. The facet has not propagated all the way through the mask, leaving a vertical sidewall to protect the underlying silicon.

Knowing how far the facet has moved through the resist allows the facet downward propagation rate to be easily determined: $310 \text{ \AA}/\text{min}$, nearly twice the vertical etch rate. At this point, it should be mentioned that the high measured facet propagation rate explains the magnitude of the taper seen when etching an oxide film masked with vertical resist in relation to the apparent mask selectivity. While the ratio of the oxide etch rate to the vertical resist loss rate is about 3:1, which SAMPLE predicts should prevent serious mask taper replication into the etching film, substituting the resist facet propagation rate for the simple vertical loss rate gives an actual mask selectivity of only 1.8:1, producing the larger-than-expected oxide taper angle.

Now that the facet propagation rate in the photoresist was known, the tapering occurring in oxide etching could be eliminated by choosing an appropriate resist thickness and etch time: $1.0 \mu\text{m}$ thick thermal oxide samples were patterned with $1.0 \mu\text{m}$ of resist (tri-level), and the oxide was etched for 22 min, which only allowed the facet in the resist to propagate $0.68 \mu\text{m}$ downward through the mask. Figure 10 shows the wafer after the resist was removed. Vertical oxide sidewalls are seen.

Tapering mechanism.—In ion milling, the angular dependence of the milling rate leading to faceting is present regardless of the type of material being milled. To determine if the faceting observed in RIE is also common to all etchable materials, or if the fundamental differences in the mechanisms leading to material removal in photoresist, silicon, and silicon dioxide RIE might yield different profiles, unmasked vertical steps in silicon and oxide

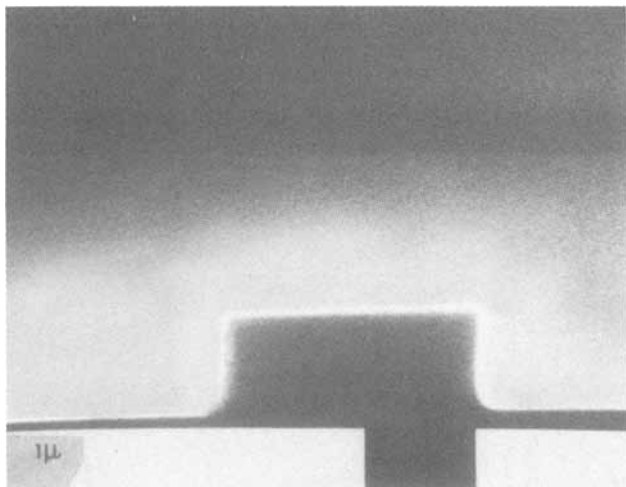


Fig. 10. μm oxide step masked with tri-level resist, etched for 22 min. Mask has been stripped.

were next exposed to the oxide etch process and checked for tapering.

Figure 11a shows a $1.5\ \mu\text{m}$ high step etched into single-crystal silicon, and Fig. 11b shows a cross section of the same step after exposure to the oxide etch process for 2h. The same facet as in photoresist was observed, with a 16°

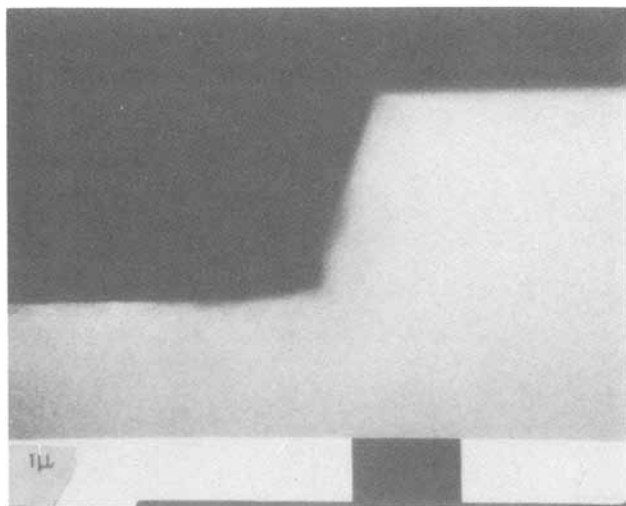
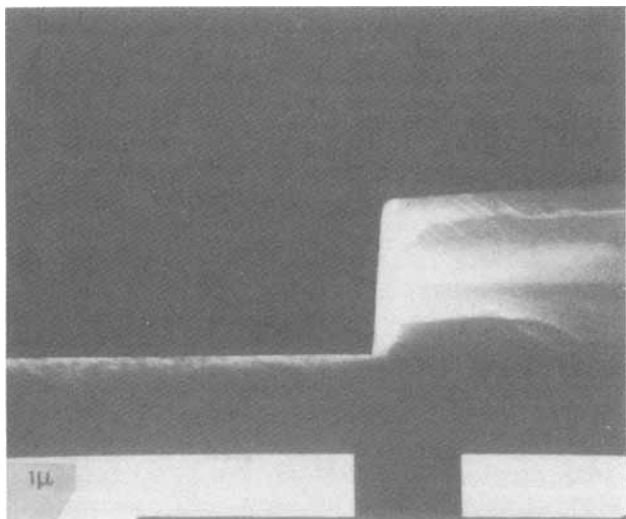


Fig. 11. a (top): $1.5\ \mu\text{m}$ high single-crystal silicon step. b(bottom). Wafer in Fig. 11a after 2h exposure to oxide etch process. 16° final silicon taper. Facet propagation rate: $180\ \text{\AA}/\text{min}$.

taper angle. The facet propagation rate is $180\ \text{\AA}/\text{min}$, again nearly twice the vertical etch rate.

Interestingly, however, when the vertical oxide steps produced as described above were exposed to the oxide etch process (for 8 min) after the mask was stripped, no faceting was seen (Fig. 12).

An explanation for the above observations is next presented.

Coburn and Winters have proposed that the following sequence of steps takes place during plasma etching (10): (i) nondissociative adsorption of gas-phase species at the surface of the solid being etched, (ii) dissociation of this adsorbed gas (*i.e.*, dissociative chemisorption), (iii) reaction between adsorbed atoms and the solid surface to form an adsorbed product molecule, *e.g.*, $\text{SiF}_4(\text{ads})$, (iv) desorption of the product molecule into the gas phase, and (v) the removal of nonreactive residue (*e.g.*, polymer) from the surface.

The key to tapering seems to be whether the rate-determining step in the etch mechanism of the particular material is strongly dependent upon purely physical sputtering, which is known to proceed more rapidly at preferential angles. Steps *iv* and *v* above are the only two which depend upon sputter ejection of material, so if either of these steps is dominant in a particular etch, an angular dependence would be expected.

Coburn and Winters concluded that the rate-limiting step in the etching of SiO_2 is step *iii*, the formation of the product molecule. The means by which ion bombardment may promote the reaction include damage-enhanced diffusion, knock-on collisions, and bond breaking (10). Sputter ejection and its corresponding angular dependence (11) do not come into play.

In silicon etching, Coburn and Winters proposed that step *ii*, the dissociative chemisorption of the etch species, is the rate-limiting step. This step would also appear not to be related to sputtering. However, step *v*, residue removal, may well be important. In Coburn and Winters' experiments, in which a XeF_2 beam and an ionized Ar beam were coincidentally directed at the surface (10), no polymer formation or residue (*e.g.*, carbon) deposition was possible. This is certainly not the case in the oxide etch process chemistry used here. Indeed, the anisotropy of the silicon and resist etching in the reactor could conceivably be aided by a polymer sidewall protection mechanism, as has been reported for other systems (12). If physical sputtering is the mechanism responsible for polymer removal from the top of features, as has been proposed (13), this would explain the observed angular dependence of silicon and photoresist RIE, provided the polymer deposition/removal process is a rate-limiting step. In oxide etching, oxygen released during the course

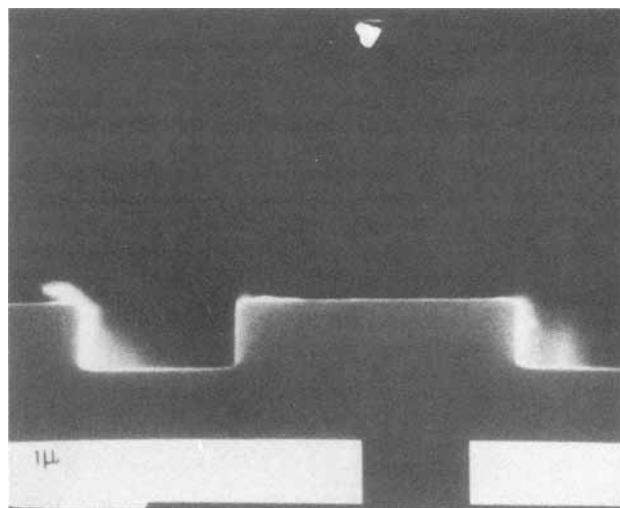


Fig. 12. Initially vertical oxide step exposed to oxide etch process for 8 min.

of the etch results in only a negligible buildup of polymer on the oxide surface (15). Consequently, a polymer deposition/removal mechanism is unlikely to occur in oxide RIE.

Conclusions

The tapered profile seen after etching a film which is known to etch anisotropically, such as oxide masked with vertical-walled photoresist, may now be explained. A facet forms in the resist mask, probably due to the angular dependence of the physical sputtering responsible for the removal of the polymer from the top of the resist. The facet propagates downward through the resist at a rate of approximately 310 Å/min, at an angle of slightly less than 20° off vertical. The resist facet starts to replicate into the oxide when it reaches the resist/oxide interface, because from this point on the oxide is no longer protected by a vertical mask.

To obtain vertically-etched sidewalls, then, one needs (i) a fairly vertical mask profile, (ii) good selectivity between the etching film and the mask material, and (iii) a mask thickness and etch time chosen such that at no time during the etch does the facet in the mask reach the interface between the mask and the etching film.

Faceting is also seen when bare vertical silicon steps are exposed to the same oxide etch process because of the angular dependence of polymer removal (sputtering) from the silicon surface. No faceting occurs when bare oxide steps are exposed to the process, however, because the oxygen liberated during oxide etching does not allow an appreciable amount of polymer to form on the oxide surface. The rate-limiting step in oxide etching, the formation of the adsorbed product molecule, SiF₄(ads), is not dependent upon sputter ejection.

Acknowledgments

The author is indebted to Dr. Clarence Tracy for many clarifying discussions, to F. J. Robinson for his assistance with much of the processing, and to R. Alvarado for taking several of the SEM's.

Manuscript submitted July 16, 1984; revised manuscript received Nov. 19, 1984. This was Paper 397 presented at the New Orleans, Louisiana, Meeting of the Society, Oct. 7-12, 1984.

Motorola, Incorporated, assisted in meeting the publication costs of this article.

REFERENCES

1. L. Jastrebski, A. Ipri, J. Corboy, and R. Metzyl, Paper presented at the IEEE VLSI Conference, Maui, HI, Sept. 1983.
2. K. Y. Chiu, *Hewlett-Packard J.*, 31, (Aug. 1982).
3. C. K. Lau, Y. C. See, D. B. Scott, J. M. Bridges, S. M. Perna, and R. D. Davies, *IEDM Tech Dig.*, 714 (1982).
4. J. W. Coburn, H. F. Winters, and T. J. Chuang, *J. Appl. Phys.*, 48, 3532 (1977).
5. R. W. Light and H. B. Bell, *This Journal*, 130, 1569 (1983).
6. H. I. Smith, *Proc. IEEE*, 62, 1361 (1974).
7. J. L. Reynolds and A. R. Neureuther, *J. Vac. Sci. Technol.*, 16, 1772 (1979).
8. M. M. O'Toole, E. D. Liu, and G. W. Ray, *Hewlett-Packard J.*, 5 (1982).
9. Y. Horiike and M. Shibigaki, Abstract 243, p. 619, The Electrochemical Society Extended Abstracts, Vol. 771, Philadelphia, May 8-11, 1977.
10. J. W. Coburn and H. F. Winters, *J. Appl. Phys.*, 50, 3189 (1979).
11. B. N. Chapman, "Glow Discharge Processes," Chap. 6, John Wiley and Sons, New York (1980).
12. M. Sato and H. Nakamura, *J. Vac. Sci. Technol.*, 20, 186 (1982).
13. J. W. Coburn and H. F. Winters, *ibid.*, 16, 391 (1979).

Czochralski Silicon Crystals Grown in a Transverse Magnetic Field

Kinji Hoshi, Nobuyuki Isawa, Toshihiko Suzuki, and Yasunori Ohkubo

Sony Corporation, Semiconductor Group, Atsugi, Kanagawa 243, Japan

ABSTRACT

Turbulent convection in silicon melts used in the Czochralski crystal-growth method was found to be effectively suppressed by applying a transverse magnetic field over 2000G. When turbulent convection is suppressed, it was found that the oxygen concentration in the resulting silicon crystals could be precisely controlled within a range of $0.5\text{-}12 \times 10^{17} \text{ cm}^{-3}$. The oxygen concentration distribution in the crystals is more uniform than that obtained by the conventional Czochralski method. As-grown n-type silicon crystals with a resistivity as high as 5000 Ω-cm were obtained. Resistivity distribution along the radius of the crystals is more uniform than that produced by the floating zone method. Silicon crystals with low oxygen concentration prepared by the present method have few thermal-induced defects, which cause the degradation of generation lifetime. The characteristics and yield of p-i-n photodiodes and planar-type GTO's are superior to that obtained in wafers prepared by the floating zone method. We conclude that the Czochralski method using a transverse magnetic field is an effective method of producing high quality silicon crystals which can improve the characteristics of semiconductor devices and their production yield.

Crystal growth in a magnetic field is a relatively new notion and only a few studies had been carried out until 1980.

InSb crystals grown in a horizontal boat in a magnetic field were reported by Chedzey *et al.* (1) and Utech *et al.* (2) in 1966. They reported the suppression of temperature fluctuations in the InSb melt and the decrease of growth striations in the crystal. In 1970, Witt *et al.* (3) reported InSb crystal growth by the Czochralski method in a transverse magnetic field. The temperature difference in the melt was enhanced, and the resulting striations adversely affected the crystal properties. In 1980 and 1981, we reported a silicon crystal grown in a transverse magnetic field by the Czochralski method (MCZ method) (4, 5). The MCZ method can produce crystals with a specific oxygen concentration within a range of $0.5\text{-}12 \times 10^{17} \text{ cm}^{-3}$, and reduce convection-generated (nonrotational) growth changes in the crystal, inhibit defect generation, and reduce warping during heat-treatment.

Since then, the method has received much attention and several studies have been carried out (6-10).

Experimental Procedure

Figure 1 shows an outline of the pulling machine used. The device has almost the same structure as that used in the conventional Czochralski method. A transverse magnetic field of up to 3700G is applied to the silicon melt between a pair of pole pieces with a diameter of 70 cm and a gap of 60 cm. The pulling machine is mostly made of nonmagnetic stainless steel. DC power, with a ripple component of less than 4%, is applied to the graphite heater to prevent the heater from vibrating in the magnetic field.

The diameter of the crystal was controlled by the weighing method reported by Hoshi *et al.* (11). The pulling operation is the same as that used in the conventional CZ method except for the application of a transverse magnetic field to the silicon melt. The magnet was

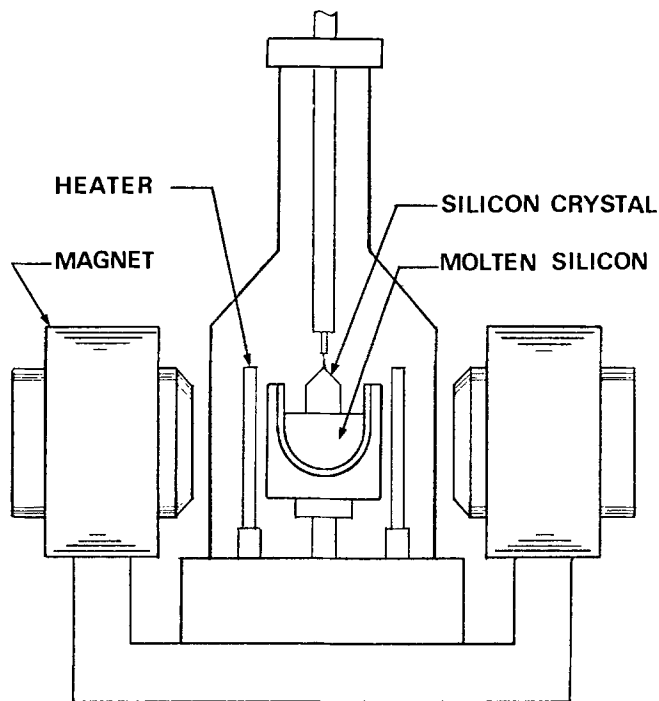


Fig. 1. Schematic cross section of MCZ apparatus

turned on after the charged silicon had melted. A silicon crystal with a diameter of 7.6 cm was grown from a melt of 4.5 kg in argon gas kept at 1 atm, and a silicon crystal with a diameter of 10 cm was grown from a melt of 20 kg in argon gas kept at about 10 torr. The pulling rate ranged from 0.9 to 1.1 mm/min, the crystal rotation rate from 0 to 30 rpm, and the crucible rotation rate from 0 to 20 rpm. The magnetic field strength ranged from 0 to 3700G. The magnetic field did not affect the automatic diameter control.

The resistivity was measured by the four-point probe method and the spreading resistance method.

Oxygen concentration was measured by the infrared absorption method using a beam spot size of 5 mm. All samples used were cut perpendicular to the growth axis and polished on both sides to yield a sample 2 mm thick. Oxygen concentration was calculated by using an infrared absorption coefficient of 2.45×10^{17} at. cm^{-3} (ASTM F121-80).

The carrier generation lifetime was measured by the MOS C-t method reported by Zerbst *et al.* (12).

Copper decoration was carried out to observe the crystal defects. A polished wafer was immersed in a dilute solution containing 1 ppm of copper ions and annealed in a furnace at 900°C for 30 min, after which it was polished, etched by Wright etchant, and inspected with an optical microscope.

Photoluminescence was measured by using a grating monochromator of SPEX Company, Limited, with an argon laser emitting at a wavelength of 5145Å as the light source. Photoluminescence intensity was converted into the corresponding impurity concentration in accordance with the working curve given by Tajima (13).

When wafer warping was less than 30 μm , the measurement was carried out by using a Model LSF-500 flatness tester of Canon Company, Limited, which employs the reflection and interference of laser beams. When wafer warping was more than 30 μm , the measurement was done in accordance with ASTM F657-80.

Results and Discussion

Stability of the melt surface.—In order to investigate the stability of the melt surface, a transverse magnetic field was applied to the silicon melt of 4.5 kg and the melt surface was observed without crucible rotation while the magnetic field strength was gradually increased. To more easily observe the vibration of melt surface, a mo-

lybdenum ring was set above the melt surface to act as a visual reference. Figure 2a shows the silicon melt surface at zero magnetic field, and Fig. 2b shows the surface at 3700G. Figure 2a indicates that the melt surface strongly vibrates at zero magnetic field due to thermal convection. Thermal convection and surface vibration decrease with the application of a magnetic field. Thus, at about 1000G, the reduction in vibration is apparent, although there are still some waves caused by vibration on the melt surface. Continuous vibration essentially ceased in a magnetic field of 1500G, at which point the ring edge could clearly be seen reflected on the melt surface. No significant change was observed over 1500G. Intermittent vibrations occurring at intervals of several seconds, however, were still observed on the melt surface. These intermittent vibrations might have some other cause than thermal convection, such as the Marangoni flow, which is caused by the difference in surface tension of points with different temperatures in the melt surface, or the melt flow caused by the wetting of the silicon melt to the quartz crucible.

Temperature fluctuation and temperature distribution in the silicon melt.—The following experiment was carried out to investigate the relations between vibrations on the melt surface, temperature fluctuations within the melt, and the speed of melt flow due to thermal convection. A Pt-Rh(13%) thermocouple with a diameter of 0.5 mm, protected by a quartz tube of 6 mm od, was placed 1 cm beneath the unseeded melt surface at the center of the 4.5 kg melt. The temperature was then measured at magnetic fields from 0 to 3700G without crucible rotation.

Figure 3 shows that the temperature fluctuations within the melt start decreasing at or near 1500G, and they are minimized at about 2000G. No significant change occurs in magnetic fields over 2000G. When the

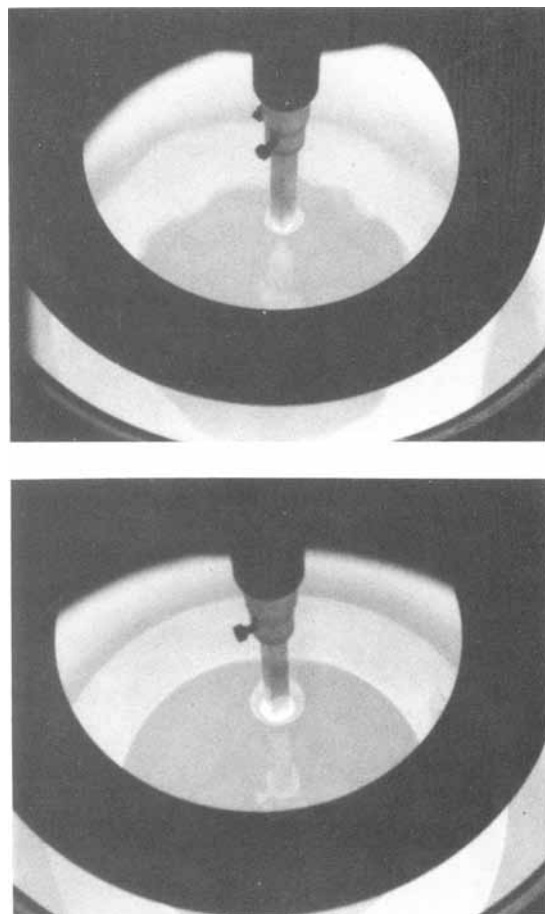


Fig. 2. Silicon melt surface. a(top): The melt vibrates due to thermal convection under 0G. b(bottom): The melt has a mirror-like surface at about 3700G.



Fig. 3. Effect of magnetic field on temperature fluctuations in silicon melt, measured at 10 mm below the melt surface of the crucible center.

magnetic field strength was changed stepwise, some spike noises were recorded on the chart, possibly caused by the induction current caused by the change in the field strength.

Utech *et al.* (14) measured the speed of flow in tin melts caused by thermal convection. No speed-of-flow measurement has been reported for silicon melt used in the CZ method. Two sets of Pt-Rh thermocouples were inserted into the 2.5 kg silicon melt, and were respectively placed at 10 (point a) and 20 mm (point b) beneath the melt surface with a clearance of about 10 mm from the crucible wall. Figure 4 shows the temperature fluctuations at points a and b at zero magnetic field. As the melt flows upward from point b to point a, the temperature at point a follows that at point b in the melt after a short period of time. One can calculate the speed of upward flow caused by thermal convection by measuring the time which has elapsed between X and X' shown in Fig. 4. The speed thus calculated was from 3.9 to 5.8 mm/s. When the 4.5 kg melt was used, the speed was calculated to be from 5 to 25 mm/s. In a magnetic field of 2000G, the upward flow was too slow to measure.

To measure the temperature distribution, three sets of thermocouples were placed about 20 mm beneath the surface at points A, B, and C, as is shown in Fig. 5. The temperature difference between point B and C was 0.5°C at 0G and 2.5°C at 3700G. This suggests that an increase in the magnetic field increases temperature gradients in the melt. Witt *et al.* (3) have previously reported similar increases of temperature differences in a magnetic field in a InSb melt used in the CZ method.

Temperature distribution is less of a problem than temperature fluctuations caused by thermal convection, be-

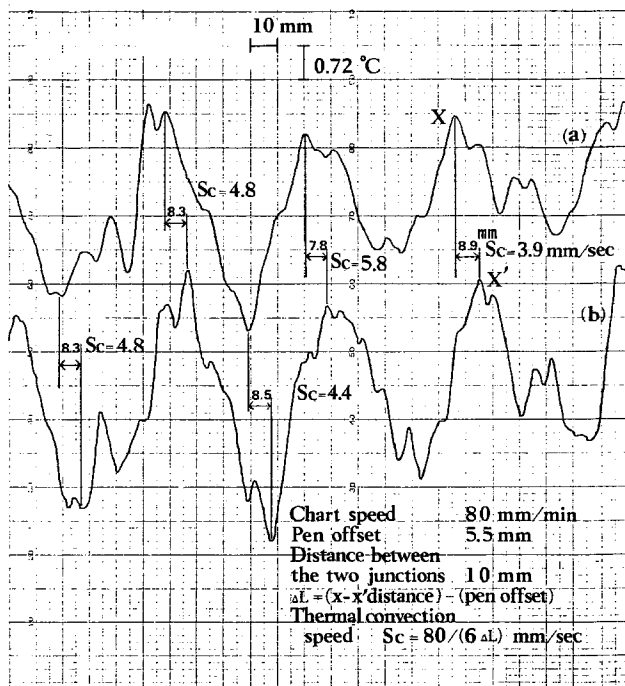
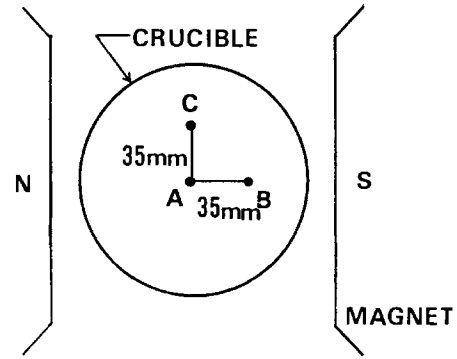


Fig. 4. Temperature fluctuations in 2.5 kg silicon melt measured at 10 mm (a) and 20 mm (b) below the melt surface at 10 mm from the crucible wall. Crucible is 200 mm diam. The speed of upward flow due to thermal convection was calculated by subtracting pen offset from the distance between X and X'. The recording direction is from right to left.



MAGNETIC FIELD (gauss)	TEMPERATURE (°C)			
	A	B	C	B - C
0	1423	1431.5	1432	0.5
3700	1422	1429	1431.5	2.5

Fig. 5. Temperature distribution in a 4.5 kg silicon melt at 20 mm below the melt surface. Crucible size is 200 mm diam, the silicon melt is 70 mm deep.

cause temperature distribution can be made more even by rotating the crystal and crucible in the CZ and MCZ method.

Growth striations and dopant concentrations.—Figure 6 shows the smooth surface of the crystals obtained by the present method.

Figure 7 shows a photograph of growth striations in a crystal cut along the growth axis, together with a graph of

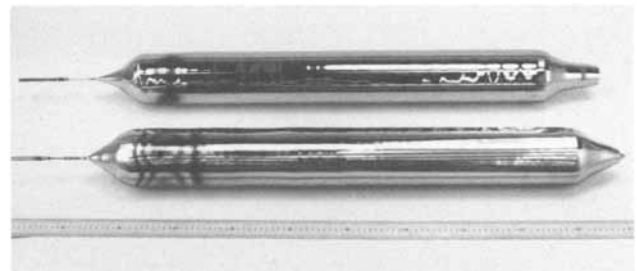


Fig. 6. MCZ silicon crystals with a diameter of 10 cm and a length of 100 cm grown in a transverse magnetic field of 3500G.

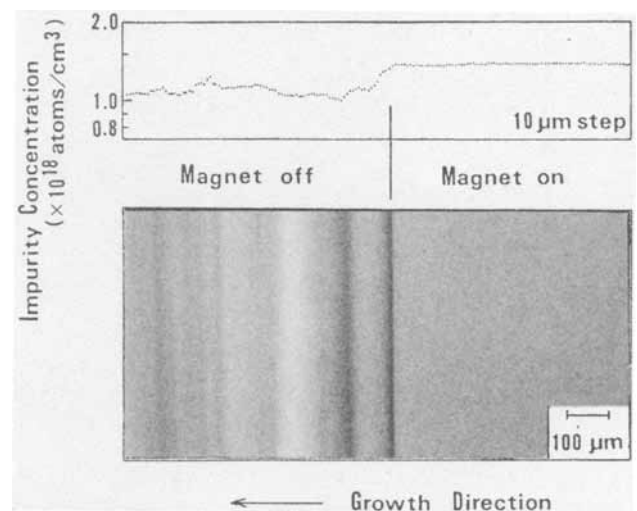


Fig. 7. Dopant concentration and growth striations in a crystal cut along a growth axis. Note that the magnet on region shows a uniform dopant distribution.

the corresponding phosphorus dopant concentrations measured at 10 μm steps using the spreading resistance method. This crystal, which has a diameter of 7.6 cm, was pulled into an orientation $\langle 111 \rangle$ without seed rotation at a growth rate of 1.1 mm/min. Irregular growth striations and an irregular phosphorus concentration were observed in the area grown without a magnetic field. In the area grown in the magnetic field of 3700G, growth striations were absent and phosphorus concentration distribution was uniform and about 33% greater than in the area grown without magnetic field. When a crystal was pulled with seed rotation, growth striations with a regular interval were observed in the crystal grown in a magnetic field, and complicated growth striation patterns were observed in the crystal grown without a magnetic field. Crystals grown with seed rotation also showed increases in phosphorus concentration of 38.1% at a seed rotation rate of 1 rpm, of 7.5% at 10 rpm, and of 0.13% at 30 rpm. Similar results were obtained with antimony-doped crystals, which were grown with and without a magnetic field (5). The effect of magnetic fields on rotational striations is now under investigation.

The increase of dopant concentration may be attributed to the increase of diffusion boundary-layer thickness caused by the suppression of turbulent convection and forced convection by a magnetic field.

Control of oxygen concentration.—Figure 8 shows the oxygen concentration in a crystal grown in a magnetic field of 0-3500G. The crystal, 7.6 cm diam and 30 cm long, was pulled at a rate of 0.9 mm/min from the 4.5 kg melt into an $\langle 100 \rangle$ direction at a crystal rotation rate of 30 rpm and a crucible rotation rate of 0.3 rpm. The oxygen concentration gradually decreases as the magnetic field increases to about 1500G, at which point it levels off and thermal convection almost disappears. This suggests that

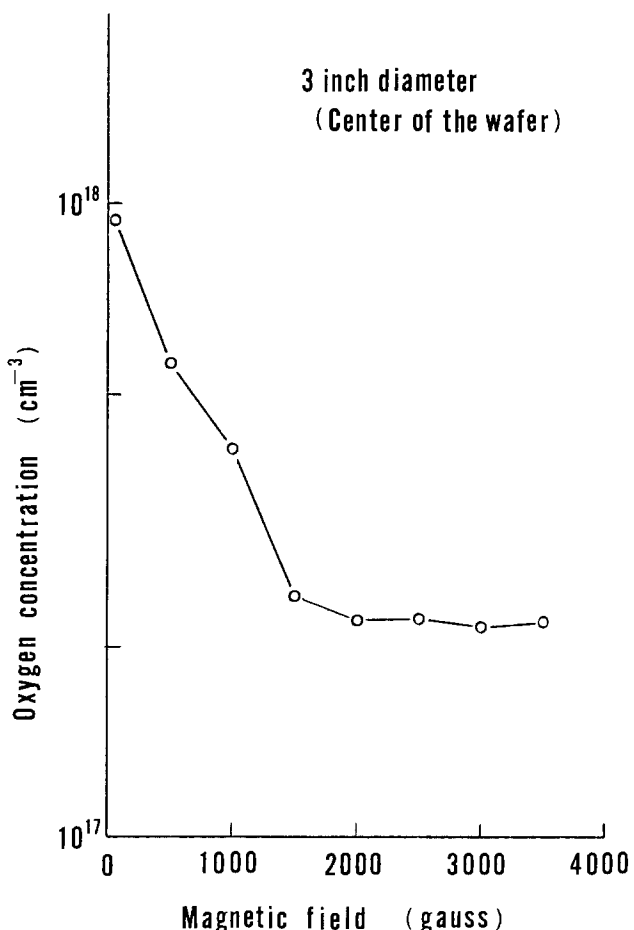


Fig. 8. Typical oxygen concentration in silicon crystal grown at various magnetic fields. Oxygen concentration does not depend on the magnitude of the magnetic field over 2000G at which point the thermal convection in the silicon melt almost disappears.

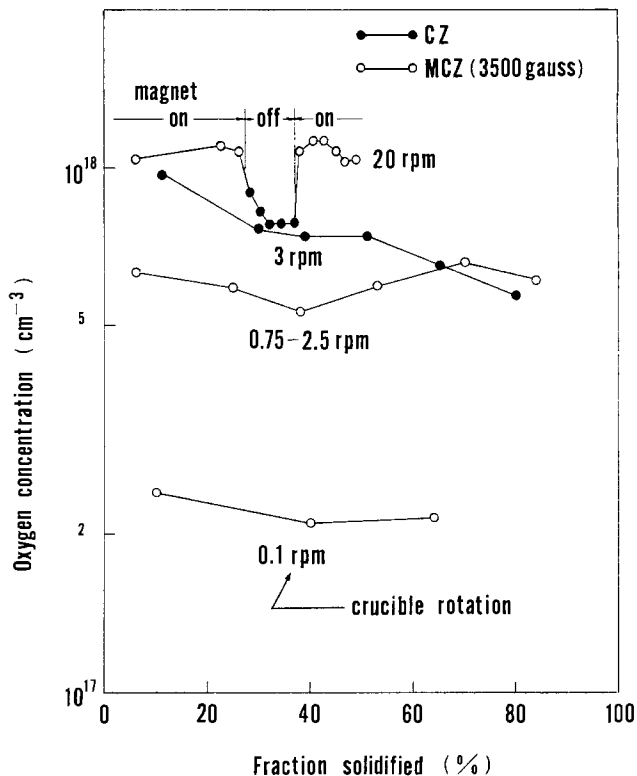


Fig. 9. Oxygen concentration along the growth direction. The oxygen concentration can be controlled by setting the crucible rotation rate in a magnetic field. Note the variation in oxygen concentration in the crystal grown at rotation rate of 20 rpm.

thermal convection plays an important role in the incorporation of oxygen atoms into the growing crystals.

Figure 9 shows the oxygen concentration in the growth direction of crystals grown with various crucible rotation rates. When a crystal is grown at a constant rate, the oxygen concentration decreases from top to bottom. When a magnetic field is applied to the melt, the level of oxygen concentration strongly depends on the crucible-rotation rate, the oxygen concentration decreasing as the rate decreases. At a high crucible-rotation rate of 20 rpm, the oxygen concentration in a crystal was found to increase to $1.2 \times 10^{18} \text{ cm}^{-3}$, while it remained at $7.8 \times 10^{17} \text{ cm}^{-3}$ without a magnetic field.

We have reported that oxygen concentration decreases as the distance between the crystal periphery and crucible wall increases in a magnetic field (5). The lowest oxygen concentration we obtained was $5 \times 10^{16} \text{ cm}^{-3}$ with a distance between the crystal periphery and crucible wall of 69 mm with no crucible or crystal rotation at 3500G.

Figure 10 shows variations in oxygen concentration along the radial direction in crystal grown by CZ and MCZ with crystal-rotation rate as a parameter. Crystals with a diameter of 7.6 cm were pulled at a growth rate of 1.0 mm/min from crucibles with a diameter of 19 cm. It is evident that the magnetic field does not degrade radial uniformity in crystals grown at a high rotation rate of 30 rpm. Crystal rotation, with or without magnetic field, improves the radial uniformity of oxygen as well as dopant impurity concentration. With the CZ method, the crystal-rotation rate is closely related to the oxygen concentration; that is, a high rotation rate gives a high oxygen concentration, even at a low crucible rotation rate. With the MCZ method, however, the oxygen concentration is kept low even at high crystal-rotation rates, and it can be effectively controlled by adjusting the crucible rotation rate. In this way, crystals with a good uniformity in the radial direction can be easily obtained in a wide range of oxygen concentration.

Crystal defects and lifetime.—We investigated the effect of oxygen concentration on stacking fault density within

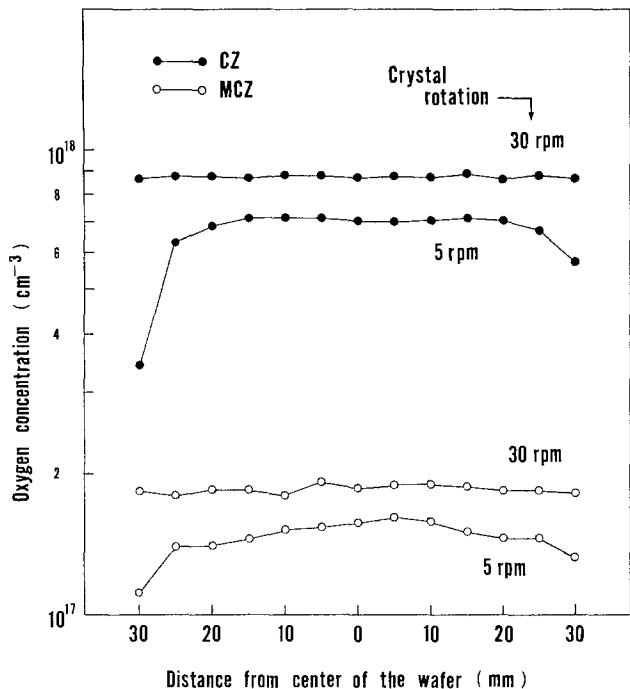


Fig. 10. Oxygen concentration along the radial direction of crystals grown with and without a magnetic field. MCZ used a field strength of 3500G.

a bulk crystal and on generation lifetime. Samples were cut from the center of boron-doped <100> crystals with a resistivity of 10-15 Ω-cm and an oxygen concentration in the range of $1 \times 10^{17} \text{ cm}^{-3}$ to $1 \times 10^{18} \text{ cm}^{-3}$. One sample with an oxygen concentration of $1 \times 10^{18} \text{ cm}^{-3}$ was prepared by the CZ method, and another was by the MCZ method.

Figure 11 shows the stacking fault density and the generation lifetime obtained by the MOS C-t method after samples were annealed at 1100°C in dry oxygen for 36h. The generation lifetime is inversely proportional to the stacking fault density and to the oxygen concentration. A remarkable change occurs near an oxygen concentration of $5 \times 10^{17} \text{ cm}^{-3}$.

Table I summarizes the generation lifetime after annealing at 1100°C in dry oxygen, using samples with an oxygen concentration in the range of $3.4\text{-}9.2 \times 10^{17} \text{ cm}^{-3}$. Ten test MOS capacitors were made from each sample. As the table shows, the generation lifetime decreases as the annealing time increases. The rate of decrease in the generation lifetime is related to the oxygen concentration.

High resistivity silicon crystals.—Undoped <100> silicon crystals were grown using an n-type polycrystalline silicon charge of resistivity of 1000 Ω-cm or more produced by High Silicon Company, Limited, and a quartz crucible of Toshiba Ceramics Company, Limited, containing a boron content of 10 ppb or less. Pulling conditions were at a crystal rotation of 10 rpm, a crucible rotation of 0.1 rpm, and at 3500G. n-Type crystals with a resistivity of up to 5000 Ω-cm and an oxygen concentration of $1.5 \times 10^{17} \text{ cm}^{-3}$ were obtained. Photoluminescence measurements showed that these crystals contained phosphorus of $7.6 \times 10^{12} \text{ cm}^{-3}$ and boron of 3.9×10^{12}

Table I. Generation lifetime after annealing at 1100°C in dry oxygen. MCZ-T and MCZ-B indicate the top and bottom of the crystal, respectively

Sample	Oxygen concentration (10^{17} cm^{-3})	Generation lifetime (μs)		
		As grown	1h	16h
CZ	8.2-9.2	1650-1700	450-580	175-310
MCZ-T	3.4-3.9	1240-1400	1060-1260	680-870
MCZ-B	5.2-5.5	1160-1450	960-1200	820-1000

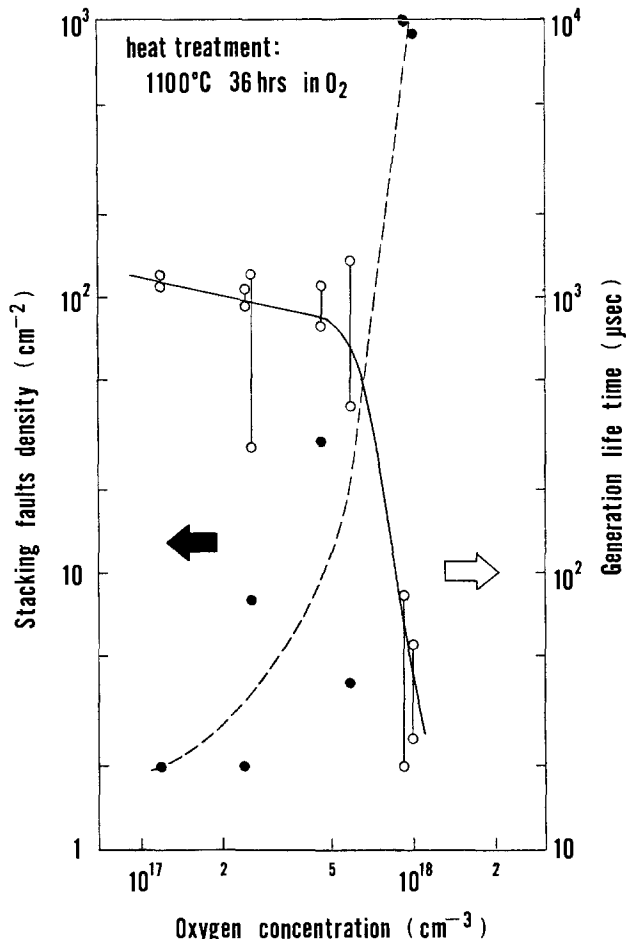


Fig. 11. The effect of oxygen concentration on stacking fault density and on generation lifetime after heat-treatment. Wright etchant was used to reveal the stacking faults.

cm^{-3} , the former mainly coming from the polycrystal and the latter from the quartz crucible.

As the suppression of thermal convection by a magnetic field reduces the quantity of oxygen and boron from the quartz crucible, the MCZ method can provide high resistivity silicon crystals with a low oxygen concentration, leading to low thermal donor generation.

Figure 12 shows resistivity distribution in the periphery of CZ and floating zone (FZ) phosphorus-doped wafers with a resistivity of about 80 Ω-cm. Resistivity was measured in 10 μm steps by the spreading resistance method. Resistivity within the measured range varied 2.6% for a

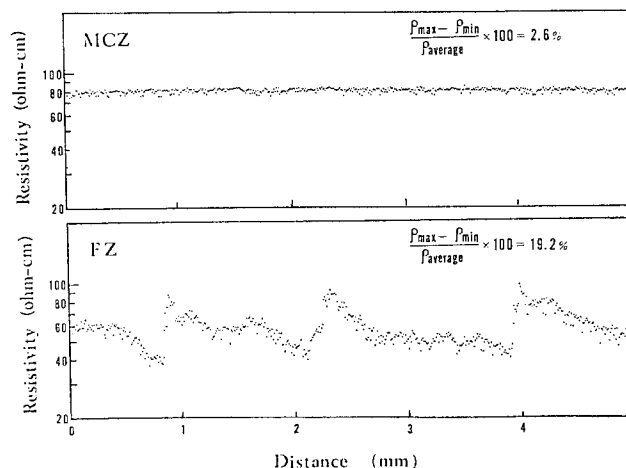


Fig. 12. Micro distribution of resistivity in MCZ and FZ wafers, measured at in 10 μm steps using the spreading resistance method.

MCZ wafer and 19.2% for an FZ wafer, presumably because the thermal convection and surface tension gradient-induced convection (Marangoni convection) which occurs in FZ crystal growth can cause a fluctuation in growth rates, resulting in variations in dopant concentration.

Wafer warpage caused by heat cycle.—The degree of warpage caused by heat cycles was found to be related to the oxygen concentrations in wafers, as is shown in Fig. 13 and 14. Samples with an oxygen concentration of 7.6×10^{17} , 2.5×10^{17} , and less than $1 \times 10^{16} \text{ cm}^{-3}$ were cut from three types of $\langle 100 \rangle$ boron-doped silicon crystals grown by CZ, MCZ, and FZ methods, respectively. Mirror-polished wafers of 5.0–5.2 cm diam and $380 \mu\text{m}$ thick were used. Heat cycles between room temperature and 1100°C were applied to the wafer, keeping the wafers at each temperature for 30 min. The transition time between room temperature and 1100°C was 6s. FZ wafers showed the largest warpage, as is shown in Fig. 13. After the heat-cycle test, the largest number of slip lines were observed in FZ wafers. FZ wafers contain too low an oxygen concentration to cause SiO_2 precipitation, which can prevent dislocations from moving and multiplying in the crystals during the heat cycles.

Figure 14 shows the effect of preannealing on warpage. The samples were preannealed at 1050°C for 100h, then heat cycled. At this point, CZ wafers showed the largest warpage. In the present experiment, it was seen that oxygen in CZ wafers can easily precipitate to form SiO_2 , because the oxygen concentration exceeds the solubility limit of oxygen in silicon at this preannealing temperature.

Figure 15 shows x-ray Lang topographs of CZ and MCZ wafers with oxygen concentrations of 7.6×10^{17} and $2 \times 10^{17} \text{ cm}^{-3}$, respectively. The wafers were thermally oxidized in dry oxygen at 1100°C for 16h. Dislocations caused by precipitated SiO_2 were in much evidence in the CZ wafer while there were few in the MCZ wafer. Dislocations

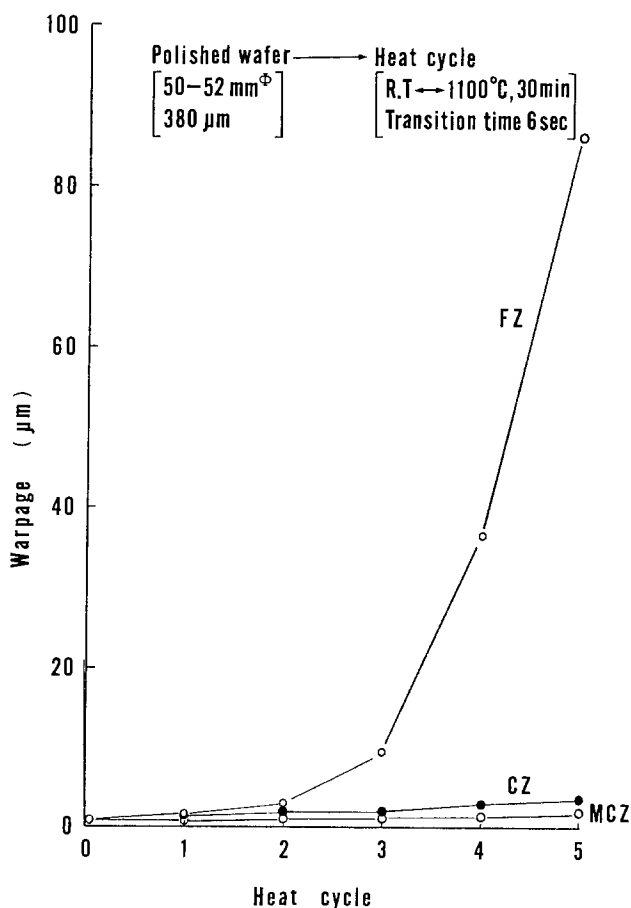


Fig. 13. Wafer warpage after heat cycle. The initial warpage was subtracted from warpage after heat cycle.

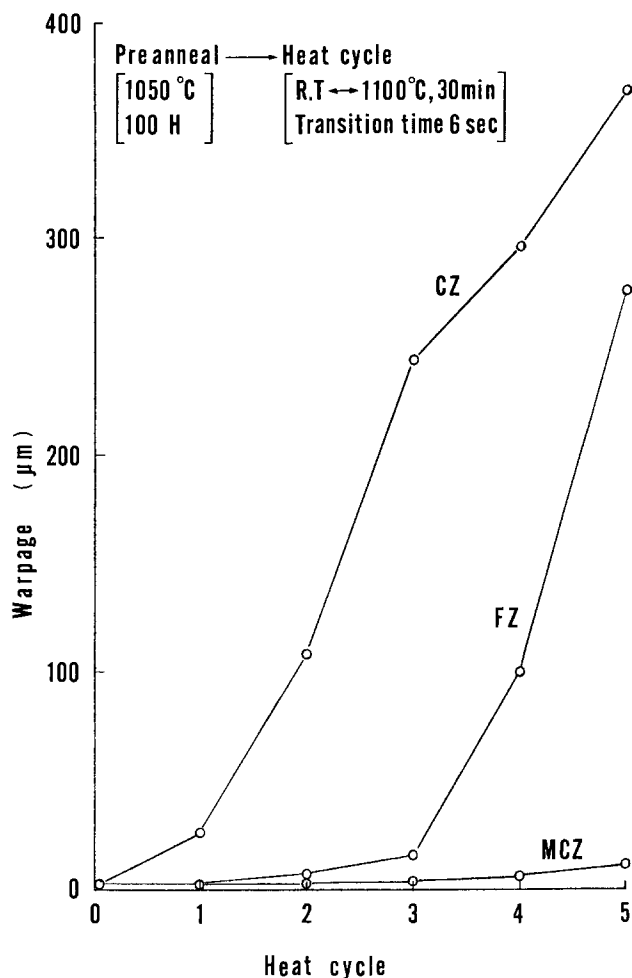


Fig. 14. Preannealing effect on wafer warpage after heat cycle. The initial warpage caused by preannealing was subtracted from the warpage after heat cycle. The initial warpages were almost the same in the three types of crystals.

punched out due to precipitated SiO_2 have been found to cause strains in wafers (15), suggesting that a high density of precipitated SiO_2 can cause warping in silicon wafers.

Application to devices.—A high sensitivity photodiode with a chip size of $3 \times 3 \text{ mm}$ was fabricated by using n-type MCZ and FZ wafers with a resistivity of 1000 $\Omega\text{-cm}$. The MCZ wafers had an oxygen concentration of $1.5 \times 10^{17} \text{ cm}^{-3}$, and the FZ wafers less than $1 \times 10^{16} \text{ cm}^{-3}$. Phosphorus was diffused into the wafers at 1280°C

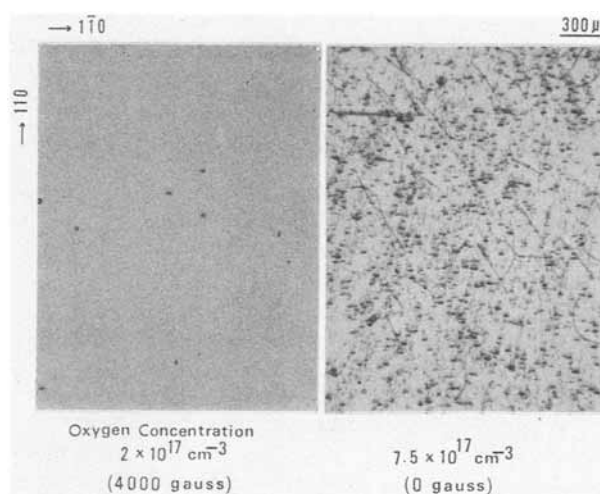


Fig. 15. X-ray Lang topographs of MCZ and CZ wafers after heat-treatment.

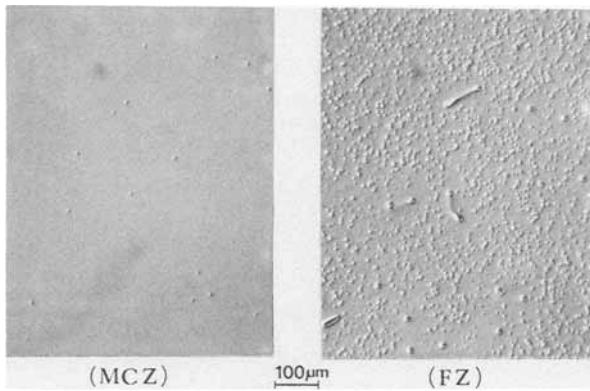


Fig. 16. Defects observed by optical microscopy. The samples were decorated with copper after completing the device processes.

for 155h before device fabrication to reduce the series resistance of the device, then one surface was polished to remove the phosphorus diffusion layer. The wafers, after being subjected to a course of heat-treatment, were diffused with copper, then polished to obtain a mirror surface. Wright etching was carried out to observe the defects in the wafers. Dislocations and microdefects were found in the order of 10^5 cm^{-2} in FZ wafers, but only microdefects were found in the order of 10^2 cm^{-2} or less in MCZ wafers, as is shown in Fig. 16. These microdefects may be caused by precipitation of metal coming from the furnace tube, heater elements, or carrier gas during the phosphorus-diffusion process.

Dark currents were measured at a bias voltage of 30V, at which the depletion layer width in the diode was about 80 μm . The dark current is lower and more concentrated in MCZ wafers than in FZ wafers, as is shown in Fig. 17. The dark current magnitude and distribution seem to be closely related to the density of the defects generated in the wafers during the phosphorus diffusion process and the course of heat-treatment.

Figure 18 shows the relationship between the resistivity and the breakdown voltages of planar-type GTO's fabricated using phosphorus-doped $\langle 111 \rangle$ MCZ and FZ wafers. Gold was diffused into the wafers to reduce the turn-off time. Figure 18 shows that the devices prepared using

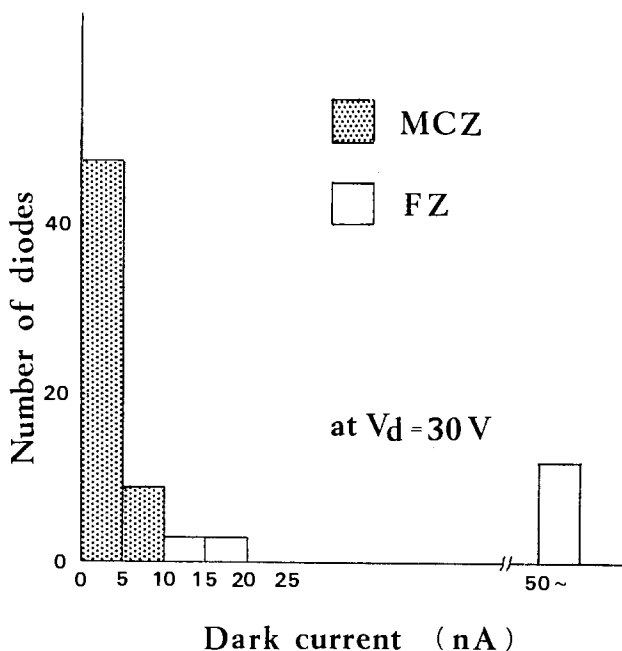


Fig. 17. Dark current of high sensitivity photodiodes fabricated using n-type MCZ and FZ wafers with a resistivity of 1000 $\Omega\text{-cm}$. The dark current is lower in MCZ wafers, showing more concentrated values than those in FZ wafers.

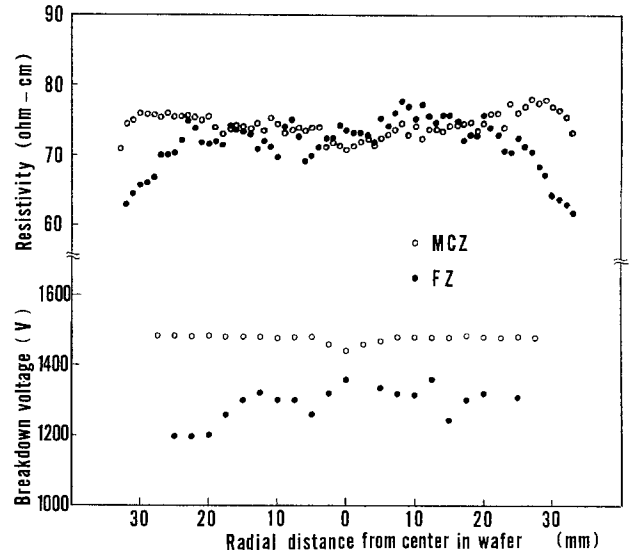


Fig. 18. Relationship between the resistivity and the breakdown voltages of the planar-type GTO's fabricated using n-type $\langle 111 \rangle$ MCZ and FZ wafers.

an MCZ wafer have more uniform and higher breakdown voltages than those prepared using an FZ wafer.

Summary

Turbulent convection within a silicon melt used in the CZ method is effectively suppressed and temperature fluctuations in the melt are reduced to 0.1°C or less by applying a transverse magnetic field over 2000G to the melt. As a result, the crystal is grown with higher thermal stability and less contamination from the crucible as compared to a crystal grown using the conventional CZ method.

Silicon single crystals prepared by the present method have the following advantages.

1. The oxygen concentration within the crystal can easily be controlled within the wide range of $0.5\text{-}12 \times 10^{17} \text{ cm}^{-3}$.
2. High resistivity crystals with up to 5000 $\Omega\text{-cm}$ can be obtained.
3. Resistivity along the radius of the crystals is more uniform than that of crystals produced by the FZ method.
4. Nonrotational growth striations are few.
5. The change in carrier lifetime after heat-treatment is small.
6. Oxygen precipitation and defect generation are reduced in crystals with a low oxygen concentration.
7. The degree of wafer warpage after heat cycles is small.
8. High sensitivity photodiodes and planar-type GTO's with very uniform device characteristics can be obtained.

These advantages indicate that this new method provides silicon wafers which produce devices of higher production yield than the FZ method. In addition, this method can provide wafers which satisfy the strict requirements for producing the very high speed integrated circuits (VHSIC), which will be needed soon. To realize VHSIC, low temperature processing is required in order to make possible the fine patterning techniques. Low temperature processing requires wafers with little precipitation of oxygen atoms and thermal donor generation. Precipitation notably occurs at 900°C or lower and leads to defect generation. Thermal donor generation which leads to a change in resistivity in the wafer is also a problem in low temperature processing. Thus, a crystal with a precisely controllable oxygen concentration should be used as a starting material. However, it should be noted that the silicon wafers with a low oxygen concentration do not contain any intrinsic gettering region in the wafer; therefore, extrinsic gettering technology is required for the high temperature processes currently in use.

Acknowledgments

The authors wish to thank Mr. H. Sato, Mr. T. Sato, and Mr. Y. Kato for their helpful assistance in experiments, Mr. H. Hayashi and Mr. H. Sone for device fabrication, and Dr. K. Morizane for fruitful discussions. Thanks are also given to Ms. H. Takamizawa for assistance in preparation of the materials.

Manuscript submitted July 10, 1984; revised manuscript received Oct. 4, 1984. This was Paper 324 presented at the St. Louis, Missouri, Meeting of the Society, May 11-16, 1980.

Sony Corporation assisted in meeting the publication costs of this article.

REFERENCES

- H. A. Chedzey and D. T. J. Hurle, *Nature*, **239**, 933 (1966).
- H. P. Utech and M. C. Flemings, *J. Appl. Phys.*, **37**, 2021 (1966).
- A. F. Witt, C. J. Herman, and H. C. Gatos, *J. Mater. Sci.*, **5**, 822 (1970).
- K. Hoshi, T. Suzuki, Y. Okubo, and N. Isawa, Abstract 324, p. 811, The Electrochemical Society Extended Abstracts, Vol. 80-1, St. Louis, MO, May 11-16, 1980.
- T. Suzuki, N. Isawa, Y. Okubo, and K. Hoshi, in "Semiconductor Silicon 1981," H. R. Huff, R. J. Kriegler, and Y. Takeishi, Editors, p. 90, The Electrochemical Society Softbound Proceedings Series, Pennington, NJ (1981).
- K. M. Kim, G. H. Schwuttke, and P. Smetana, *IBM Tech. Discl. Bull.*, **24**, 3376 (1981).
- K. M. Kim, *This Journal*, **129**, 427 (1982).
- K. Hoshikawa, *Jpn. J. Appl. Phys.*, **21**, L545 (1982).
- W. E. Langlois and K. J. Lee, *IBM J. Res. Dev.*, **27**, 281 (1983).
- K. Terashima and T. Fukuda, *J. Cryst. Growth*, **47**, 423 (1983).
- K. Hoshi, T. Suzuki, and Y. Tamate, *Denki Kagaku*, **40**, 521 (1972).
- M. Zerst, *Z. Angew. Phys.*, **22**, 30 (1966).
- M. Tajima, *Appl. Phys. Lett.*, **32**, 719 (1978).
- H. P. Utech, W. S. Browner, and J. G. Early, "Crystal Growth," pp. 201-205, Pergamon, Oxford, England (1967).
- K. Sumino, I. Yonenaga, and K. Hoshi, *J. Appl. Phys.*, **56**, 2346 (1984).

Photoactive Melt-Grown Group VI Transition Metal Dichalcogenides

H. J. Lewerenz* and H. Tributsch

Hahn-Meitner-Institut für Kernforschung Berlin, Bereich Strahlenchemie, D-1000 Berlin 39, Germany

M. Spiesser

Laboratoire de Physico-chimie des Solides, Université de Nantes, 44072 Nantes, France

ABSTRACT

Growth of two-dimensional patches of photosensitive layered transition metal dichalcogenides (MoSe_2 , WSe_2 , MoTe_2) from tellurium melts is reported. The material exhibits a substantially different morphology compared to vapor-transported crystals. Single-crystalline hexagons grow together along their edges and can form larger polycrystalline films with relatively few surface defects. No rosette-type growth is observed. The first electrochemical solar cells made with these materials did not yield conversion efficiencies exceeding 1%. Scanning laser spot analysis on smooth crystals reveals deficiencies concerning doping profile, stoichiometry, and impurity content. Better control of the growth process promises the development of high quality thin films.

The optical and electronic properties of layered Group VI transition metal dichalcogenides make these semiconductors promising candidates for efficient solar energy conversion (1, 2). With low energy indirect transitions followed by highly absorptive direct transitions ($\alpha \approx 10^5 \text{ cm}^{-1}$) at photon energies around 1.5 eV (WSe_2 , MoSe_2) and minority carrier diffusion lengths of about $2 \mu\text{m}$ (3, 4), it appears possible to convert solar to electrical energy efficiently in thin film structures. Investigations in semiconductor/liquid junction solar cells revealed that, although exceptional stability against photocorrosion is obtained with these semiconductors (5), large differences and irreproducibilities in photocurrent (i_{sc}), photovoltage (V_{oc}), and fill factor (ff) are observed (6). These differences have been attributed to variations in surface morphology (7-9) and deviations in stoichiometry (10). In particular, it turned out that steps on the surfaces of layered compounds are deleterious for the solar cell performance and that doping profiles can result in p- and n-conducting areas on the same crystal.

Extensive materials preparation work, however, resulted in the development of a photoelectrochemical solar cell with n- WSe_2 , which converts solar to electrical energy with an efficiency of 10% (11). Such crystals, grown by chemical vapor deposition (CVD), have to be selected with respect to their surface texture and doping profiles since this preparation method lacks reproducibility and

uniformity of the crystals. In addition, only relatively small polycrystalline material (50 mm^2) is obtained with CVD.

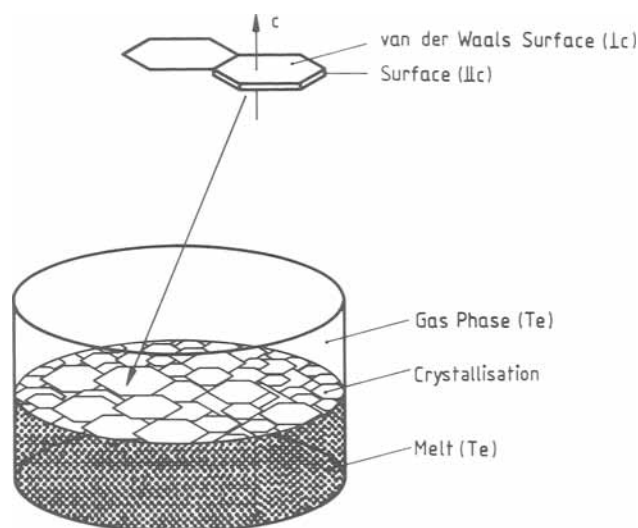


Fig. 1. Scheme explaining the lateral attachment of crystallites on the surface of a melt.

* Electrochemical Society Active Member.

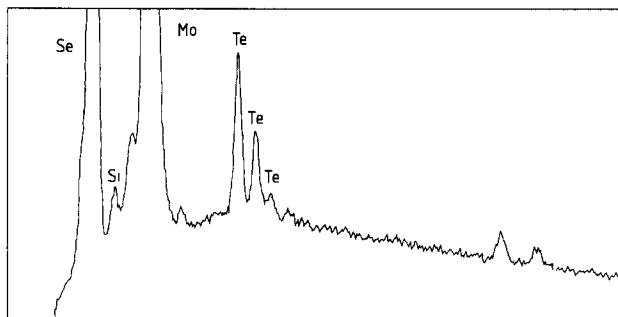


Fig. 2. X-ray fluorescence spectrum of Te-grown MoSe_2 indicating impurities of Te, Si, and transition metal.

Hence, considerable effort has been made to improve the performance of samples with a highly textured surface (11-14). An alternative possibility is given by changing the growth process of these semiconductors. Recently, Te has occasionally been used as melt for the growth of semiconducting crystals. Both the synthesis of II-VI compounds (15) and of transition metal dichalcogenides (16) have been successful. Whereas these studies emphasized improved quality and size of crystals, the present work focuses on the possibility of predominantly lateral growth at a melt/vapor interface.

The technical realization of large grain polycrystalline thin films of MoSe_2 and WSe_2 would be highly attractive

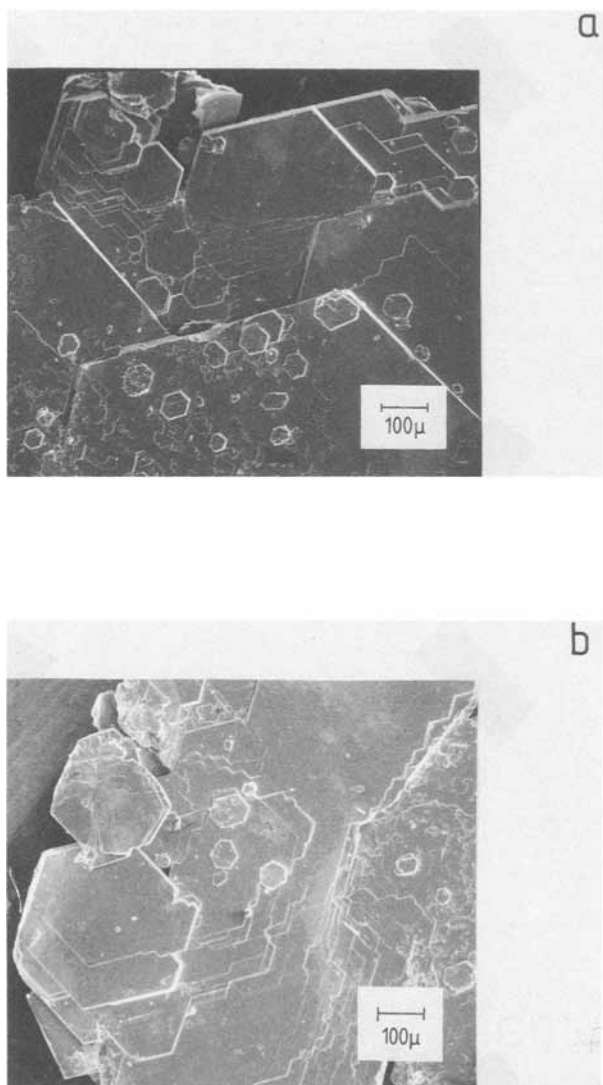


Fig. 3. Scanning electron micrographs of differently structured regions of Te-grown MoSe_2 layers. a: Comparably smooth. b: Highly textured surface.

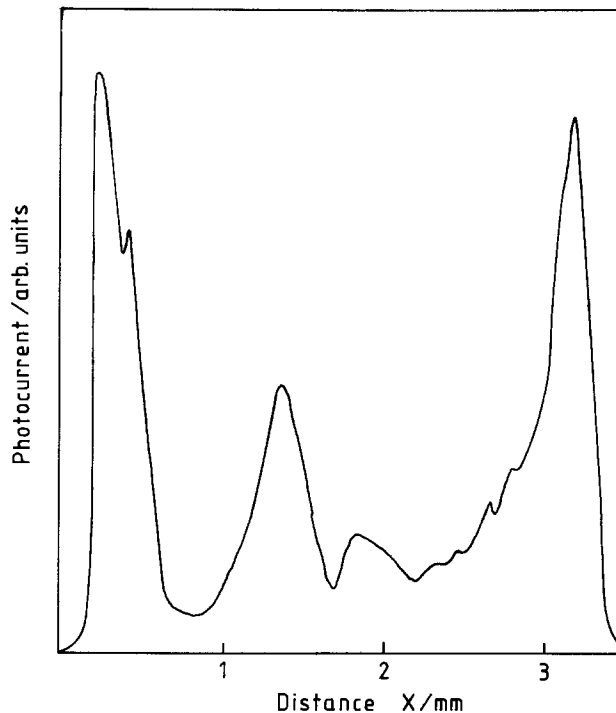


Fig. 4. Scanning laser spot pattern of an optically smooth region of Te-grown MoSe_2 . Illumination 633 nm with He-Ne laser; spot diam $\sim 50 \mu\text{m}$. Electrolyte: 0.5M K_2SO_4 . Electrode potential +0.4V vs. Hg_2SO_4 .

for the development of practicable, alternative solar energy converting devices.

Material Preparation

Powdered transition metal diselenide is added to double distilled Te (Koch-light no. 8698 h, 5N purity) in a ratio of 1:100, respectively. To 10g of this mixture, 100 mg of Se (Koch-light no. 8982-60, 5N) are added for better control of the desired reaction. The starting material is then encapsulated in a quartz tube (20 mm diam) evacuated and heated to 1050°C. Subsequent cooling is done with a gradient of 4°-5°C/h (16). During the cooling process, transition metal dichalcogenide crystals begin to nucleate in the bulk of the liquid as well as at the melt/vapor interface. A mechanism involving convection and surface tension (see below) appears to facilitate crystallization along the Te/vapor interface (Fig. 1), although the density of the semiconducting material exceeds the density of the melt. After termination of the growth process, the Te melt is eliminated by sublimation.

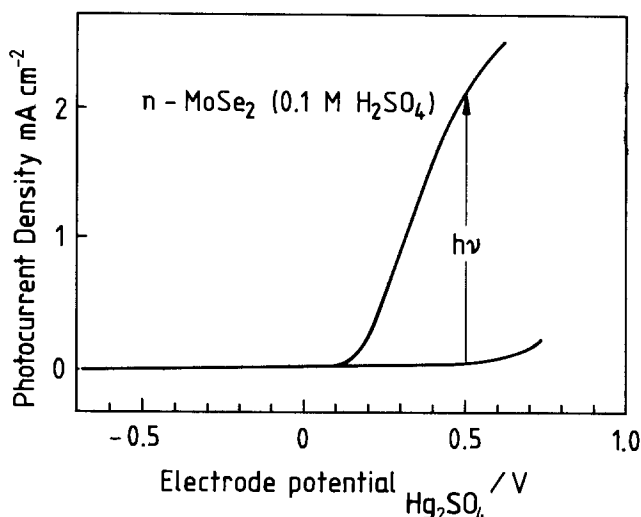


Fig. 5. Photo- and dark current-voltage characteristics of Te-grown MoSe_2 ; electrolyte 0.1M H_2SO_4 .

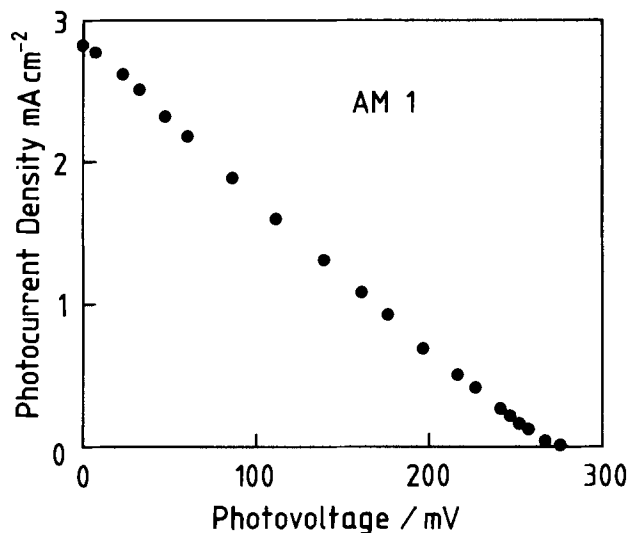


Fig. 6. Power output characteristic of Te-grown MoSe_2 electrode in $1\text{M KI}/0.1\text{M I}_2$ redox solution. Illumination by Solar Simulator (Oriental Corporation) under $\sim\text{AM 1}$ conditions.

MoSe_2 , MoTe_2 , and WSe_2 have been prepared. Crystal sizes range from typically $20\ \mu\text{m}$ up to $6\ \text{mm}$ diam with a thickness of approximately $0.3\ \text{mm}$. The transition metal diselenides obtained with the above described procedure had the stoichiometry $\text{MeSe}_{2-x}\text{Te}_x$ ($\text{Me} = \text{Mo}, \text{W}$) with $x \leq 0.1$. The Te content of the crystals could be reduced by heating the samples in Se atmosphere to 650°C . The MoSe_2 material investigated in this publication still showed detectable amounts of Te and some Si (Fig. 2).

All prepared materials were photoactive; MoSe_2 and MoTe_2 were n-type and WSe_2 showed p-type conductivity. The semiconductors exhibited photocurrent densities of several milliamperes per square centimeter at simulated AM 1 conditions. MoSe_2 was chosen for investigation because of its higher photopotential. It is of interest to note that large melt-grown layer-type MoS_2 crystal plates are found in pegmatitic deposits (17).

Results and Discussion

Compared to vapor transport grown and synthesized crystals, our samples show strong lateral attachment of hexagonal crystallites along their edges. The morphology of two differently and quite heavily structured MoSe_2 samples is displayed in Fig. 3. No rosette-type growth is observed, but the crystallites appear to be partially superposed, resulting in the formation of steps. These defects, however, do not appear to be predominantly responsible for the still moderate photoactivity of the material as compared to selected high quality vapor-grown crystals. This is evident from scanning laser spot experiments

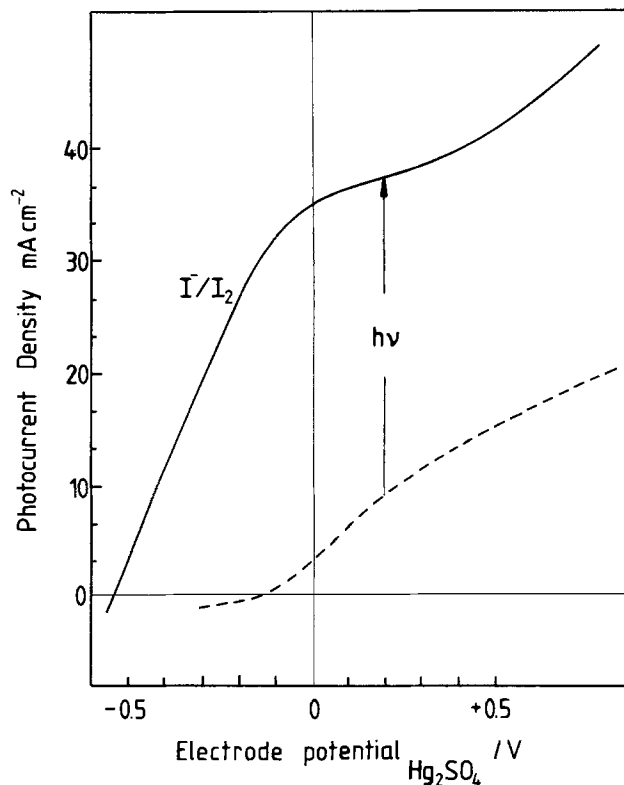


Fig. 7. Photo- and dark current-voltage characteristics of Te-grown MoSe_2 under $900\ \text{mW}/\text{cm}^2$ illumination in I^-/I_2 redox solution.

(Fig. 4) on optically smooth MoSe_2 electrodes which show pronounced variations in photoresponse across the surface. This could result from lateral differences in stoichiometry, impurity concentration, and doping level and has also been observed on vapor grown material (10).

Figure 5 shows current-voltage (*i*-*V*) characteristics of a structured MoSe_2 electrode in the dark and under simulated AM 1 illumination. In presence of the I^-/I_2 redox couple energy conversion is possible. As can be seen in Fig. 6, a relatively low photocurrent, a fill factor *ff* of ~ 0.25 , and a photovoltage of approximately $0.3\ \text{V}$ is obtained in a two-electrode solar cell experiment. The relatively low performance is obviously associated with a high density of states within the forbidden energy region which mediate electron transfer from iodide to the conduction band in the dark as shown in Fig. 7. In this case, higher photocurrents and photovoltages can only be reached under intense illumination. These defects could arise partly from the impurities found in the material as shown in Fig. 2 which could be reduced by better control of growth parameters, cleaning procedures, and annealing processes.

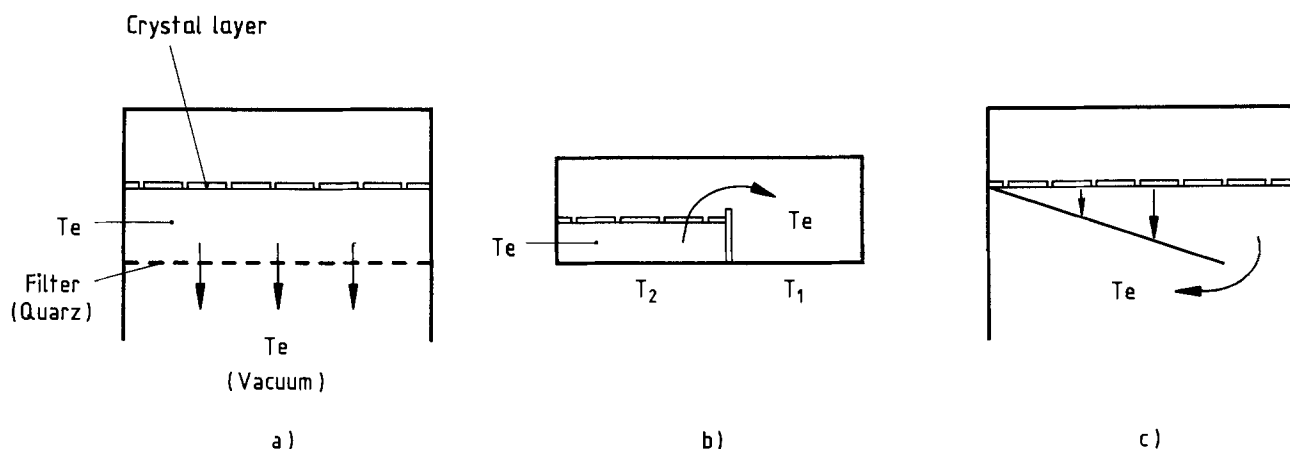


Fig. 8. Schematic representation of possibilities for extraction of transition metal dichalcogenide crystallites from Te melts. a: Filtration. b: Distillation (used in this work). c: Draining with subsequent sublimation.

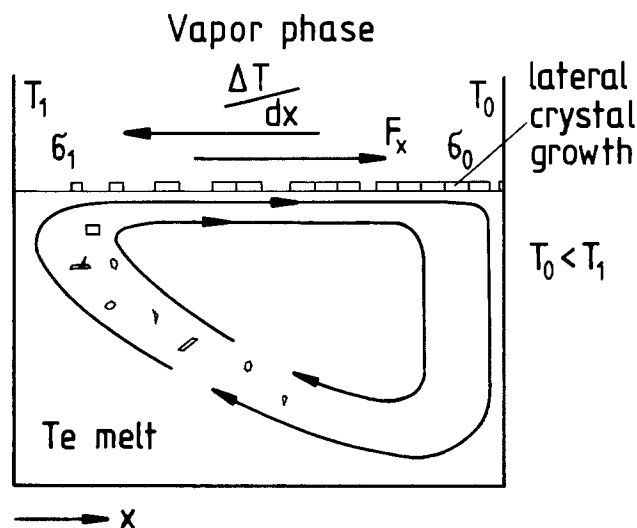


Fig. 9. Scheme illustrating surface accumulation of crystals for lateral growth due to the Marangoni effect. σ : Surface tension. F_x : Resulting force. $\Delta T/\Delta x$: Temperature gradient.

The preparation of large area smooth crystalline thin films of transition metal dichalcogenides appears to be possible by the described method. Different possibilities for separation of the Te from the crystallized phase are schematically shown in Fig. 8. A better understanding of the physical chemistry of crystal growth by this method is essential. It has to be emphasized that the mechanism involved is not trivial; the density of the nucleated layered crystallites exceeds that of the Te melt. In view of the experimental geometry, it appears plausible to assume a Marangoni type (18) of mechanism (Fig. 9): the surface tension which is a critical parameter for nucleation does not only depend on the concentration of a mixture but also on the temperature. A temperature gradient in the surface layer results in a force parallel to the surface, F_x , whose origin is the difference in surface tension. A convection results which transports nucleation centers from the bulk of the melt to the surface at the higher temperature site of the tube with subsequent transport of the slowly growing crystals along the interface. The larger crystallites at the sites with higher surface tension do not follow the convection path of the melt since the increased

surface tension probably inhibits their sinking. Further studies in well-designed crystal-growth vessels are necessary to test this hypothesis quantitatively.

Acknowledgment

We are indebted to Dr. S. Fiechter for providing us with information on the Marangoni effect.

Manuscript submitted Feb. 15, 1984; revised manuscript received Nov. 26, 1984.

Hahn-Meitner-Institut für Kernforschung Berlin assisted in meeting the publication costs of this article.

REFERENCES

1. H. Tributsch, *Ber. Bunsenges. Phys. Chem.*, **81**, 361 (1977).
2. H. Tributsch, *This Journal*, **125**, 1086 (1978).
3. H. J. Lewerenz, S. D. Ferris, C. J. Doherty, and H. J. Leamy, *ibid.*, **129**, 418 (1982).
4. W. Kautek, H. Gerischer, and H. Tributsch, *ibid.*, **127**, 2471 (1980).
5. H. Tributsch, *Z. Naturforsch.* **32a**, 972 (1977).
6. J. Gobrecht, H. Gerischer, and H. Tributsch, *Ber. Bunsenges. Phys. Chem.*, **82**, 1331 (1978).
7. H. J. Lewerenz, A. Heller, and F. J. DiSalvo, *J. Am. Chem. Soc.*, **102**, 1877 (1980).
8. H. J. Lewerenz, A. Heller, H. J. Leamy, and S. D. Ferris, in "Photoeffects at Semiconductor-Electrolyte Interfaces," A. J. Nozik, Editor, ACS Symposium Series, 146, Washington, DC (1981).
9. H. J. Lewerenz, H. Gerischer, and M. Lübke, *This Journal*, **131**, 100 (1984).
10. S. Menezes, L. F. Schneemeyer, and H. J. Lewerenz, *Appl. Phys. Lett.*, **38**, 949 (1981).
11. B. A. Parkinson, T. E. Furtak, D. Canfield, K. Kain, and G. Kline, *Faraday Discuss. Chem. Soc.*, **70**, 233 (1980).
12. G. Razzini, L. Peraldo Bicelli, G. Pini, and B. Scrosati, *This Journal*, **128**, 2134 (1982).
13. H. S. White, H. D. Abruna, and A. J. Bard, *ibid.*, **129**, 265 (1982).
14. L. Fornarini, F. Stirpe, and B. Scrosati, *ibid.*, **130**, 2184 (1983).
15. M. Aoki, in "Research in Photosynthesis and Photoconversion of Solar Energy," Reports of Special Project Research, Ministry of Education, Science and Culture, p. 229, Japan (1982).
16. M. Spiesser and J. Rouxel, *C. R. Acad. Sci. Paris Ser. II*, 1497 (1983).
17. P. Ramdohr and H. Strunz, "Lehrbuch der Mineralogie," pp. 467 ff., Enke Verlag, Stuttgart, Germany (1980).
18. D. Schwabe, *Mitteilungs. Deutsche Ges. Kristall. Kristallz.*, **37**, 5 (1983).

Thermodynamics of ZrC—Equilibrium Condition Calculated for Deposition from a CH₄-ZrCl₄-H₂ Gaseous Mixture

M. Ducarroi*

Labòratoire des Ultra-Réfractaires, Centre National de la Recherche Scientifique, Odeillo—66120 Font-Romeu, France

P. Salles and C. Bernard

Centre d'Information de Thermodynamique Chimique Minérale, Laboratoire de Thermodynamique et Physico-Chimie Métallurgiques, Domaine Universitaire, 38402 St-Martin-d'Herès, France

ABSTRACT

Chemical vapor deposition of the nonstoichiometric zirconium carbide is computed by minimization of the Gibbs free energy of the system. Analytical expressions for the Gibbs free energy of formation of Zr_xC_{1-x} f.c.c. solid and liquid phases are set up, and the deposition diagram with "isostoichiometric curves" is presented as a function of ZrCl₄, CH₄, and H₂ pressures in the input gas mixture.

For several years, thermodynamic computations based on the minimization of the total free energy of a complex chemical system involving a gas phase and several condensed species have been developed in order to predict the conditions of deposition. They were essentially applied to pure solid phases and/or stoichiometric compounds such as intermetallic oxides and carbides.

In recent years, such an approach has been enlarged in order to determine the deposition conditions of nonstoichiometric refractory solid solutions such as titanium carbides or nitrides and titanium carbonitrides.

In order to obtain CVD coats of ZrC having a well-defined stoichiometry, previously published activity values for Zr were fit by a model based on the Redlich-Kister formalism. The variation of Zr activity with composition, based on the model, was used to calculate the optimum conditions for producing Zr_xC_{1-x} from a mixture of CH₄, ZrCl₄, and H₂.

Thermodynamics of the Phase Zr_xC_{1-x}

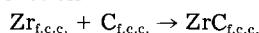
Zirconium carbide has an f.c.c. structure with a large homogeneity range due to carbon vacancies (1, 3-8). Very few studies are concerned with the thermodynamic properties of Zr_xC_{1-x} over its homogeneity domain. The only high temperature thermodynamic data available are the measurements of the activity of zirconium over the whole range of homogeneity of Zr_xC_{1-x}, referred to liquid zirconium, made by Storms and Griffin (1) for temperatures between 1700 and 2000 K.

These values, referred to b.c.c. Zr, allow the calculation of the activity of carbon (referred to graphite) by integration of the Gibbs-Duhem equation and, consequently, the determination of the Gibbs free energy of formation of Zr_xC_{1-x} (f.c.c.) from graphite and Zr (b.c.c.), namely

$$\Delta G_{\text{Zr}_x\text{C}_{1-x}}^{\text{f.c.c.}} = X_{\text{Zr}} RT \ln a_{\text{Zr}} + X_{\text{C}} RT \ln a_{\text{C}}$$

$$\text{ref. } \left| \begin{array}{l} \text{C graphite} \\ \text{Zr b.c.c.} \end{array} \right.$$

When using the Redlich-Kister formalism to represent the Gibbs free energy of formation of the f.c.c. solid solution Zr_xC_{1-x}, it is easier to fit the experimental results with the elements referred to the same structure, that is, to consider the reaction



whose Gibbs free energy is related to the former by

$$\Delta G_{\text{Zr}_x\text{C}_{1-x}}^{\text{f.c.c.}} = \Delta G_{\text{Zr}_x\text{C}_{1-x}}^{\text{f.c.c.}} - X_{\text{Zr}} [\Delta G_{\text{Zr}}^{\text{f.c.c.}} - \Delta G_{\text{Zr}}^{\text{b.c.c.}}]$$

$$\text{ref. } \left| \begin{array}{l} \text{C f.c.c.} \\ \text{Zr f.c.c.} \end{array} \right. \quad \text{ref. } \left| \begin{array}{l} \text{C graphite} \\ \text{Zr f.c.c.} \end{array} \right. - X_{\text{C}} [\Delta G_{\text{C}}^{\text{f.c.c.}} - \Delta G_{\text{C}}^{\text{graphite}}]$$

where $\Delta G_{\text{Zr}}^{\text{f.c.c.}} - \Delta G_{\text{Zr}}^{\text{b.c.c.}} = -961.4 + 3762 T$ (J/mol) corresponding to the free energy (2) of the reaction Zr_{b.c.c.} →

*Electrochemical Society Active Member.

Zr_{f.c.c.} and $\Delta G_{\text{C}}^{\text{f.c.c.}} - \Delta G_{\text{C}}^{\text{graphite}} = 138,523 - 14.6 T$ (J/mol) corresponding to the free energy (2) of the reaction C graphite → C f.c.c. Then the Gibbs energy as a function of the concentration may be expressed in the following form

$$\Delta G_{\text{Zr}_x\text{C}_{1-x}}^{\text{f.c.c.}}(T) = X_{\text{Zr}} \cdot X_{\text{C}} [A(T) + B(T)(X_{\text{C}} - X_{\text{Zr}})]$$

$$\text{Ref. } \left| \begin{array}{l} \text{C f.c.c.} \\ \text{Zr f.c.c.} \end{array} \right.$$

$$+ C(T)(X_{\text{C}} - X_{\text{Zr}})^2 + RT[(X_{\text{C}} \ln X_{\text{C}} + X_{\text{Zr}} \ln X_{\text{Zr}})] \quad [1]$$

$$\text{where } A(T) = -6.962 \cdot 10^5 + 73.6 \times T \\ B(T) = 8.561 \cdot 10^4 - 12.4 \times T \\ C(T) = 14.793 \cdot 10^5 - 243.3 \times T$$

in J/mol of Zr_xC_{1-x}.

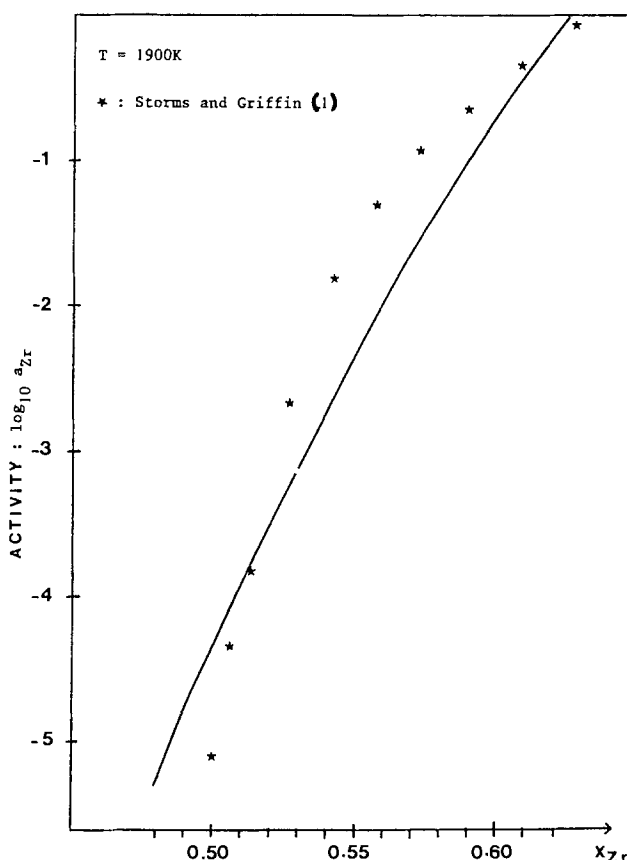


Fig. 1. Experimental (*) and calculated Zr activity vs. composition at 1900 K. *: Storms and Griffin (1).

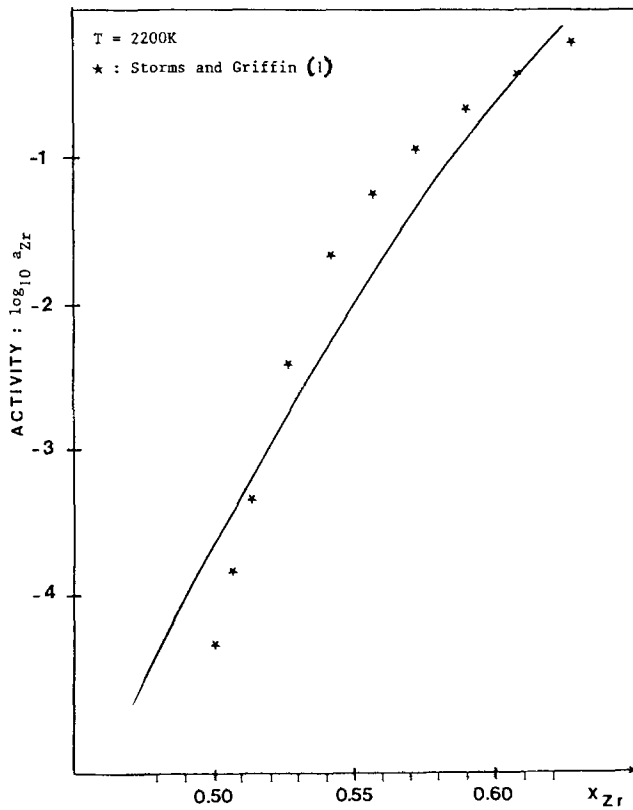


Fig. 2. Experimental (*) and calculated Zr activity vs. composition at 2200 K. *: Storms and Griffin (1).

Using Eq. [1], the activity of Zr can be calculated and compared to the measured a_{Zr} by Storms and Griffin (1) as shown in Fig. 1 and 2, and Gibbs free-energy values can be determined for $Zr_{0.5}C_{0.5}$, which are in good agreement with the values published in the literature, as illustrated in Table I.

The model can be used to calculate a tentative Gibbs energy for the liquid phase. Although this quantity was not needed in this paper, it may provide useful information for other studies. However, it cannot be used to calculate the phase diagram with a precision any greater than is currently available from published measurements.

After use of different optimization computer programs, the following expression was selected

$$\Delta G_{(Zr_xC_{1-x})}^{(l)} = X_{Zr}X_C[A(T) + B(T)(X_C - X_{Zr}) + C(T)(X_C - X_{Zr})^2] + RT[X_C \ln X_C + X_{Zr} \ln X_{Zr}] \quad [2]$$

ref. $\left\{ \begin{array}{l} \text{C liquid} \\ \text{Zr liquid} \end{array} \right.$

where $A(T) = -3.46 \cdot 10^5 + 30.0 \times T$
 $B(T) = 2.15 \cdot 10^4 - 5.5 \times T$
 $C(T) = 9.82 \cdot 10^4 - 3.8 \times T$

in J/mol of liquid ZrC.

Table I. Comparison between different values of the Gibbs free energy for $Zr_{0.5}C_{0.5}$ fcc phase

$\Delta G_{Zr_{0.5}C_{0.5}}$ ref.	Temperature (K)	1900	2000	2100	2200
From Storms and Gibbs-Duhem Polynomial, Eq. [1]		-92 688	-92 204	-91 725	-91 245
JANAF magnetic tape 1976		-88 923	-88 401	-87 880	-86 990
Hultgren, Ref. (6)		-87 232	-86 455	-85 753	-85 602

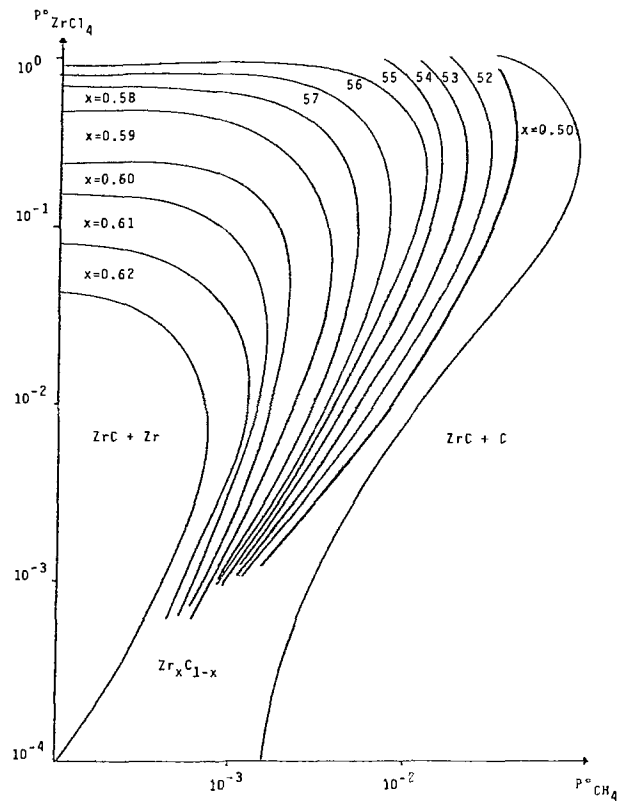


Fig. 3. "Isostoichiometric curves" as function of the input gas composition: $T = 1900 \text{ K}$; $P_{CH_4}^\circ + P_{ZrCl_4}^\circ + P_{H_2}^\circ = 1$.

CVD Diagram of Zr_xC_{1-x} from a CH_4 - $ZrCl_4$ - H_2 Gaseous Mixture

Thermodynamic calculations based on the minimization of the total free energy of a complex chemical system have been used by others to determine conditions for chemical vapor deposition (10-12). In the present case, the conditions for deposition of zirconium carbide have been calculated as a function of the input gas pressures ($P_{ZrCl_4}^\circ$, $P_{CH_4}^\circ$, $P_{H_2}^\circ$) at 1400 and 1900 K, under a total pressure of 1 atm.

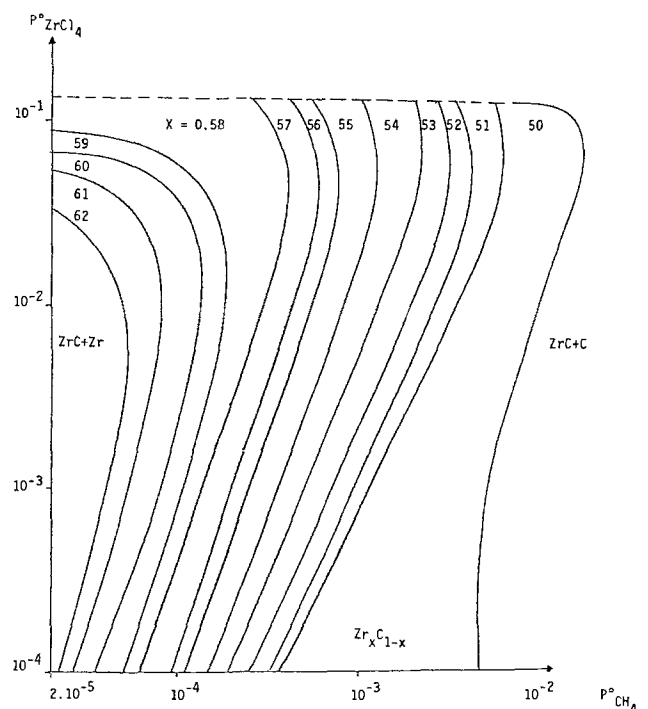


Fig. 4. "Isostoichiometric curves" as function of the input gas composition: $T = 1400 \text{ K}$; $P_{CH_4}^\circ + P_{ZrCl_4}^\circ + P_{H_2}^\circ = 1$.

The calculation requires thermodynamic data for all the chemical species which may be present: Zr_xC_{1-x} solid solutions, Zr and C, which are considered as pure condensed phases, and the gaseous species Zr, Cl, Cl_2 , $ClZr$, Cl_2Zr , Cl_3Zr , Cl_4Zr , CCl_4 , C_2Cl_2 , C_2Cl_4 , H, H_2 , HZr , CH, CH_2 , CH_3 , CH_4 , C_2H , C_2H_2 , C_2H_4 , ClH , $CClH$, $CClH_3$, CCl_2H_2 , CCl_3H , and C_2ClH .

The previously determined relation (1) Gibbs integral energy of mixing is used as input thermodynamic data for Zr_xC_{1-x} .

The various deposits and their deposition fields as a function of input gas composition are presented in Fig. 3 and 4. Isostochiometric curves are also reported in the deposition domain of the pure Zr_xC_{1-x} solid solution. This very large domain is limited by the boundary associated with $Zr_{0.5}C_{0.5}$ on the $ZrC + C$ side and by the boundary associated with $Zr_{0.62}C_{0.38}$ on the $ZrC + Zr$ side.

For equilibrium, the deposited phase ($ZrC + C$, ZrC , $ZrC + Zr$) and the composition of the pure solid solution may be easily varied by adjusting the input partial pressure of CH_4 for a constant $ZrCl_4$ feed.

At 1900 K, the field of interest is located in the following range (atm units)

$$5 \cdot 10^{-3} < P_{CH_4} < 10^{-2} \text{ and } 6 \cdot 10^{-2} < P_{ZrCl_4} < 10^{-1}$$

In conclusion, diagrams of this type allow specification of the gas composition, leading to the deposition of a zirconium carbide phase of controllable stoichiometry under equilibrium conditions. Work is in progress to estimate more precisely the thermodynamic properties of this nonstoichiometric monocarbide by use of a sublattice model to provide a better fit of the measured activities and the phase boundaries. Preliminary results indicate that the calculated CVD diagram is not changed greatly.

Manuscript submitted Feb. 8, 1984; revised manuscript received Sept. 18, 1984.

CNRS assisted in meeting the publication costs of this article.

REFERENCES

1. E. K. Storms and J. Griffin, *High Temp. Sci.*, **5**, 291 (1973).
2. L. Kaufman and M. Bernstein, "Computer Calculation of Phase Diagram," Academic Press, New York (1970).
3. R. V. Sara, *J. Am. Ceram. Soc.*, **48**, 243 (1965).
4. E. Rudy, Air Force Materials Laboratory AFML-TR-65-2 Part I, Vol. 2 (1965).
5. J. Farr, reported in E. K. Storms: Los Alamos Scientific Laboratory Lams 2674, March 15, 1962.
6. R. Hultgren, P. D. Desai, D. T. Hawkins, M. Gleiser, and K. K. Kelley, "Selected Values of Thermodynamic Properties of Metals and Alloys," American Society for Metals, Metals Park, Ohio (1973).
7. L. M. Adelsberg, L. M. Cadoff, and J. M. Tobin, *Trans. AIME*, **236**, 972 (1966).
8. E. K. Storms, in "The Refractory Carbides," J. L. Margrave, Editor, Academic Press, New York (1967).
9. F. A. Shunk, "Constitution of Binary Alloys," (Second Supplement), McGraw Hill Book Company (1960).
10. M. Ducarroi, M. Jaymes, C. Bernard, and Y. Deniel, *J. Less-Common Met.*, **40**, 173 (1975).
11. K. E. Spear, in "Chemical Vapor Deposition," T. O. Sedgwick and H. Lydtin, Editors, pp. 1-16, The Electrochemical Society Softbound Proceedings Series, Princeton, NJ (1979).
12. C. Bernard, in "Chemical Vapor Deposition," J. M. Blocher, Jr., and Guy E. Vuillard, Editors, The Electrochemical Society Softbound Proceedings Series, Pennington, NJ (1981).

Experimental Study of Equilibrium Conditions in the Si-H-Cl System

David W. Woodruff* and Rony A. Sanchez-Martinez

Corporate Research and Development, General Electric Company, Schenectady, New York 12345

ABSTRACT

Thermodynamic studies of the Si-H-Cl system are widely available. The results of these studies vary due to differences in the number of gas-phase components used and differences in the basic thermodynamic data employed. This work describes the first experimental study to determine the equilibrium Si/Cl ratio as a function of Cl/H and temperature. The experimental results fall near those which are calculated, though they do not uniquely support any one of the theoretical studies. Computational studies make the assumption that the Cl/H ratio is constant for the silicon CVD reaction. It is shown in this study that this is not always the case, particularly when there is substantial condensation of polychlorosilanes.

There have been a number of thermodynamic studies (1-5) of the Si-H-Cl system with specific application to the CVD of silicon. The results of such studies vary depending on which of the possible gas-phase components are included in the calculation and on the source of the primary thermodynamic data. Herrick and Sanchez-Martinez (1), for example, used 18 gas-phase components in their calculation; Hunt and Sirtl (2, 3) used 14, and Lever (4) used 9. These investigators also used different values of the enthalpy of formation for many of the components that their studies shared in common. These differences manifest themselves not only in the calculated partial pressures of the components at the solid surface, but also in the equilibrium Si/Cl ratio. Figure 1 shows the dependence of the Si/Cl ratio on the Cl/H ratio at 1350 K as calculated by the three sets of investigators mentioned above (1, 2, 4).

Experimental verification of these calculations is inadequate. Most comparisons (6-9) are from experiments done under conditions not designed to bring the bulk of the reactant gases to equilibrium with solid silicon. This

work describes the results of an experiment specifically designed to measure the equilibrium value of the Si/Cl ratio as a function of the Cl/H ratio and the temperature at atmospheric pressure.

An important feature of any equilibrium experiment is the assurance of achieving the equilibrium state. One way to assure this is to approach the equilibrium Si/Cl ratio starting with both higher and lower values of the initial Si/Cl ratio. Accordingly, this work presents results of both silicon deposition and silicon etching experiments. Another important assurance that equilibrium has been achieved is the independence of the results with reaction time. This independence has been demonstrated.

One of the premises of the thermodynamic calculations described above is that the Cl/H ratio remains constant for the silicon CVD reaction. This premise is based on the assumption that solid silicon is the only condensed material to be formed in this reaction thus leaving the amounts of Cl and H unchanged. This assumption ignores the formation of polychlorosilane materials which also condense and in doing so change both the Si/Cl and Cl/H ratios. The extent to which this reaction can occur has been observed experimentally and is presented herein.

*Electrochemical Society Active Member.

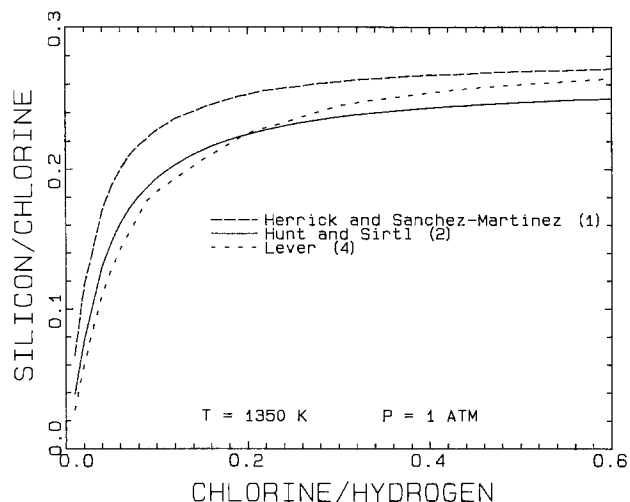


Fig. 1. Dependence of equilibrium Si/Cl on Cl/H as calculated by three investigators (1, 2, 4) at 1350 K and 1 atm total pressure.

Experimental

The equilibrium experiments were conducted in a horizontal hot-wall reactor consisting of a 0.64 cm-id, 1.22m-long quartz tube supported by an alumina tube in a three-zone furnace (see Fig. 2). The furnace hot zone was 0.61m long. Silicon deposition or etching occurred on the inside surface of the quartz tube. Trichlorosilane (TCS) and silicon tetrachloride (TET) were introduced from separate saturators with hydrogen carrier gas. HCl and additional hydrogen were fed directly from gas cylinders. The gases were mixed prior to delivery to the furnace.

The apparatus had two basic flow modes. The first allowed straight flow-through of the gases from the mixer through the furnace to the scrubber. This mode was used both to establish the concentration of reactant gas along the entire flow path and to put an initial deposit of silicon on the quartz tube. The second mode allowed recirculation of the gases through the furnace. The recycle was driven by a small, Teflon bellows pump. Gas samples were taken in 75 ml stainless-steel gas sampling cylinders, which by valving could be either included or excluded from the flow path. Gas analysis was performed on a gas chromatograph equipped with a gas sampling valve and a thermal-conductivity detector. By making multiple injections of each sample and averaging the results, the Si/Cl and Cl/H ratios were determined to an accuracy of $\pm 3\%$.

The experiments presented here were accomplished in three to five distinct steps. The first step was to establish an atmosphere of pure hydrogen in the entire flow circuit. This was done by evacuating and refilling, first four times with nitrogen, then four times with hydrogen. Following this, the system was purged with a constant hydrogen flow while the reactant gas flow was established to the scrubber.

Step two was the establishment of the reactant gases in the furnace flow circuit. The reactant flow was switched to the furnace line for 60 min, during which the flow was

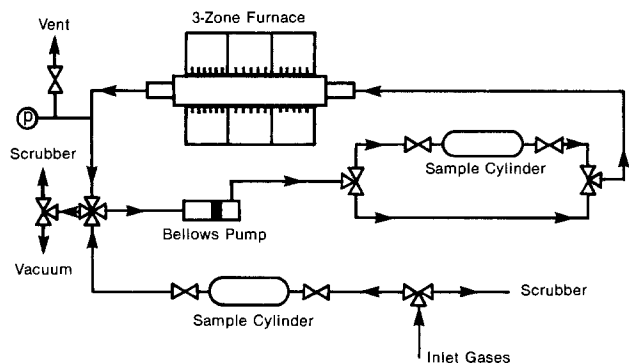


Fig. 2. Schematic diagram of the apparatus

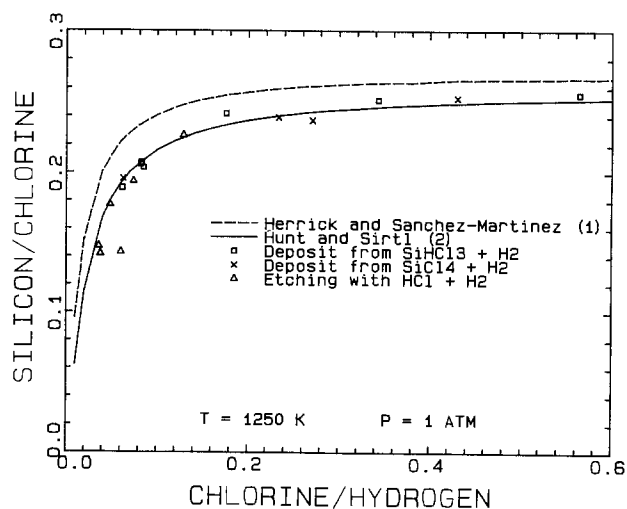


Fig. 3. Comparison of experimental data with theoretical data (1, 2) at 1250 K and 1 atm total pressure. Recycle time was 15 min.

directed straight through the tube to the scrubber with no recycle. This procedure not only established the desired concentration in the lines, but also built an initial deposit of silicon on the reaction-tube inner wall.

The equilibration of the reactant gases was the third step. The valving was switched so that the bellows pump recycled the gases through the sample cylinders to the furnace and then back. The recycling was generally done for 15 min, though some tests were performed to determine the extent of reaction as a function of recycle time. 15 min was more than adequate to reach equilibrium under these conditions.

Steps four and five were used only for those tests where etching was performed. Step four was a hydrogen purge to remove the deposition gases followed by a procedure similar to step two where the hydrogen/HCl mixture was introduced to the flow circuit. After the etching mixture flowed for 15 min, the valve was switched for recycle (step five). Because the etching step was slower than deposition, this recycle step was run for 2h, during which equilibrium was established.

Results and Discussion

The primary result of the experiments described herein is the dependence of the equilibrium Si/Cl ratio on the temperature and Cl/H ratio, pressure being constant. Experiments were conducted at temperatures of 1250, 1350, and 1450 K and covered a range of 0.01-0.6 in the Cl/H ratio. The results are presented in Fig. 3-5 along with calculated results using the data from Herrick and Sanchez-Martinez (1) and from Hunt and Sirtl (2). The experi-

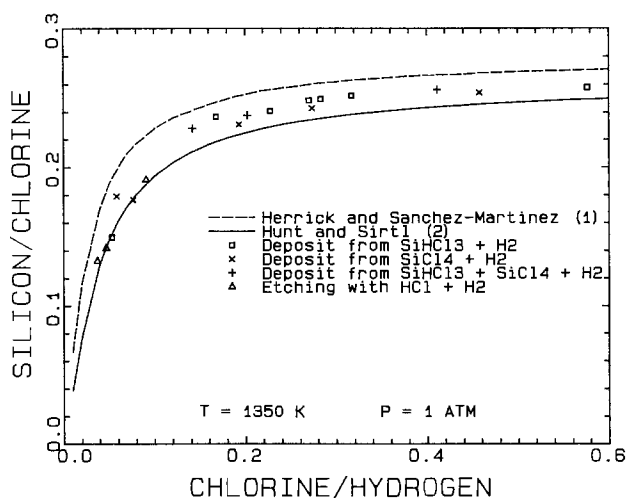


Fig. 4. Comparison of experimental data with theoretical data (1, 2) at 1350 K and 1 atm total pressure. Recycle time was 15 min.

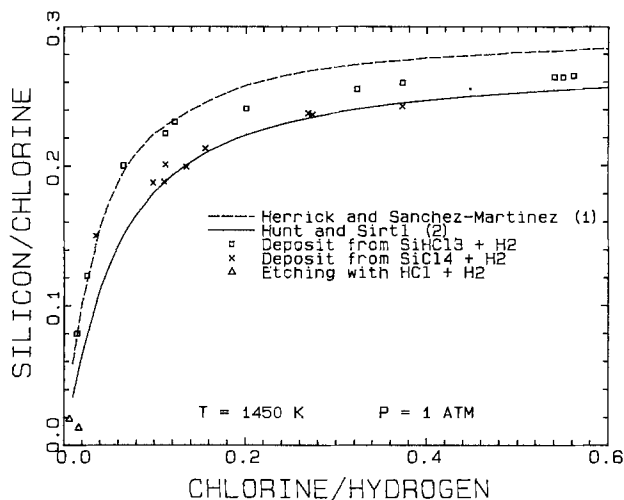


Fig. 5. Comparison of experimental data with theoretical data (1, 2) at 1450 K and 1 atm total pressure. Recycle time was 15 min.

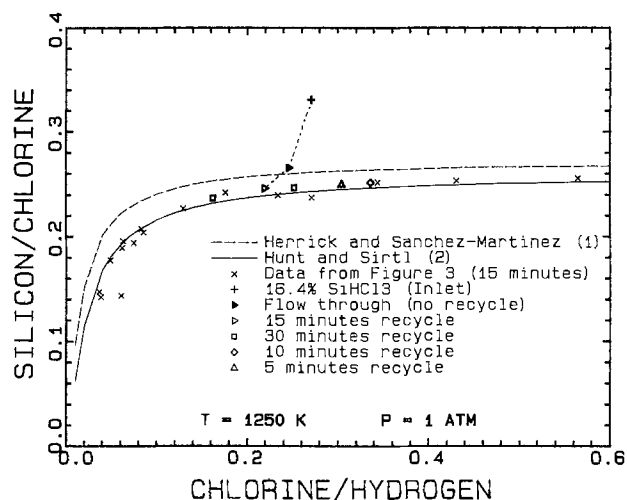


Fig. 6. Time dependence of experimental results compared with Fig. 3. All results were at 1250 K and 1 atm total pressure.

mental results follow closely the general shape of the calculated results. They do not, however, coincide with one or the other of the calculations at all conditions tested. The results of experiments at 1250 K coincide closely with the calculated results of Ref. (2), whereas at 1350 and 1450 K, the experimental data fall between the two calculated curves.

One test of the extent to which this experimental system reached equilibrium is the comparison of results from both etching with HCl and deposition from a variety of chlorosilane sources. The results of both 1250 and 1350 K coincide regardless of the reactant gas used for deposition. The etching and deposition results also agree well. At 1450 K, the results from depositions using TCS were slightly different from depositions using TET. Because of excessive formation of polychlorosilanes, etching experiments at 1450 K were not directly comparable to the deposition results.

Another test of the achievement of equilibrium is to compare results obtained using a variety of recycle times. Results for experiments with sufficient recycle times should all fall on the same locus of points. In Fig. 6, results are shown for recycle times of 5, 10, 15, and 30 min, all of which fall on the same curve. Also shown are the results of a test where samples were taken of the inlet gas, of gas which made only one pass through the oven (no recycle), and of the normal 15 min recycle run (these are connected by dashed lines). These results taken together show that the recycle is necessary to achieve equilibrium and that 5 min is sufficient recycle time to reach equilibrium for this particular set of conditions. These tests were repeated for each of the temperatures of interest, with the same results.

The comparison of results between no recycle and 15 min recycle also points out a major misconception in the understanding of the silicon CVD reaction. Note that not only does the Si/Cl ratio change over the course of the reaction, but the Cl/H ratio does as well. This observation has never been reported before, but was very consistent throughout these tests. It indicates that Cl is being removed from the gas phase in addition to the silicon. Because the chlorosilanes would not condense at the temperatures and pressures present in this apparatus, it is concluded that the change comes about because of the condensation of polychlorosilanes, a family of polymeric compounds with the general formula $(\text{Si-Cl}_x\text{-H}_{2-x})_n$. An oily substance of this type was observed at the outlet end of the reactor tube. This condensation would reduce all

three of the atomic species to various degree, depending on the amounts and degrees of chlorination of these materials. The formation of the polychlorosilanes could explain the differences seen in the results at 1450 K. It is expected that different reaction systems would form polychlorosilanes to varying degrees, depending on the amount of time the gases are held at reaction temperature. Because of this change in the Cl/H ratio, the results are presented using the outlet value of Cl/H as the independent variable, the condition at which the gases come to equilibrium.

Conclusions

This work has shown, for the first time, experimental results of the equilibrium Si/Cl ratio as a function of Cl/H ratio and of temperature. That the results are true equilibrium values was supported by the time invariance of the results and by the coincidence of results from various chlorosilane deposition sources as well as from HCl etching experiments. Experimental results also show that the Cl/H ratio is not necessarily constant for the silicon CVD reaction due to the condensation of polychlorosilanes. The experimental results fall near those which are calculated, though they do not uniquely support any one of the theoretical studies.

Acknowledgments

The authors would like to acknowledge D. K. Dietrich for his technical assistance and C. S. Herrick for technical discussion.

Manuscript submitted Aug. 21, 1984; revised manuscript received Oct. 16, 1984.

General Electrical Company assisted in meeting the publication costs of this article.

REFERENCES

1. C. S. Herrick and R. A. Sanchez-Martinez, *This Journal*, **131**, 455 (1984).
2. L. P. Hunt and E. Sirtl, *ibid.*, **119**, 1741 (1972).
3. E. Sirtl, L. P. Hunt, and D. H. Sawyer, *ibid.*, **121**, 919 (1974).
4. R. F. Lever, *IBM J. Res. Develop.*, **8**, 460 (1964).
5. M. Diana, L. DeMarino, L. Mastrantuono, and R. Rossi, *Rev. Int. Hautes Temp. Refract.*, **18**, 203 (1980).
6. K. R. Sarma and M. J. Rice, *This Journal*, **128**, 2647 (1981).
7. V. S. Ban and S. L. Gilbert, *ibid.*, **122**, 1382 (1975).
8. J. Nishizawa and H. Nihira, *J. Cryst. Growth*, **45**, 82 (1978).
9. V. S. Ban, *This Journal*, **122**, 1389 (1975).

GREG: A New Hotwall-Close-Spaced Vapor Transport Deposition System

Cornelius Menezes

Centro de Investigación y de Estudios Avanzados del IPN, México 7000, Mexico

Charles Fortmann and Sean Casey

Department of Materials Science, Stanford University, Stanford, California 94305

ABSTRACT

We describe a new hotwall-C.S.V.T. deposition system, GREG, which is especially suitable for high temperature deposition of large grained, high quality layers of II-VI compounds on common substrates. High growth rates and large deposited area are among the advantages claimed for this technique, which produced layers of CdTe and CdS with good crystalline orientation and large grain size.

The close-spaced vapor transport (C.S.V.T.) method has been utilized as a useful technique for epitaxial deposition of II-VI and III-V compound semiconductors (1-5). The advantage of the C.S.V.T. method (it allows deposition to be carried out at relatively high substrate temperatures, with a small temperature gradient between source and substrate, thus approaching equilibrium crystal growth conditions) makes the use of this, or improved techniques, attractive.

It is the aim of this report to present details of a deposition system, GREG (gradient recrystallization and growth), which is suitable for the deposition of semiconductor layers (especially of II-VI compounds, though not restricted to them) on a variety of common low cost substrates such as Pyrex glass slides, metals, and ceramics. The main improvement is the incorporation of a hotwall chamber that surrounds the source and reaches up to the substrate, so that the evaporant species is continuously surrounded by a high temperature envelope, such that the temperature gradient maintained during growth of the layer is uniform from source to substrate. The hot wall helps to maintain a high partial pressure of the condensing species adjacent to the substrate (23). The following are the salient features of the method.

1. The hotwall chamber, constructed of conductive graphite, maintains the required distance between source and substrate. In contrast with the C.S.V.T. method, which uses small spacings (0.1-1 mm), we use several tenths of a centimeter (0.3-0.8) as a spacing between source and substrate.

2. The surrounding ambient which is Argon gas at a low pressure, from 1 to 0.1 torr, maintains the delicate balance between the deposition and evaporation from the substrate; at the same time, the low pressure reduces collision events and decreases loss of incident energy of evaporant material by thermalization.

3. Large grained (30-50 μ) layers can be obtained rapidly with the GREG technique even on glass substrates at temperatures between 500° and 600°C. The very short deposition times required to obtain an appreciable thickness of the deposit allow Pyrex or other glass substrates to be used without much deformation.

A summary of the advantages claimed for the GREG method follows.

1. Ability to obtain well-oriented (see x-ray data), large grained layers (of CdTe, CdS, ZnSe) on low cost, commonly available glass substrates.

2. Large area of deposition, because of the use of a hotwall chamber which surrounds both source and substrate in a temperature gradient. Layers of 30-40 cm² can be grown with the existing GREG system.

3. Rapid growth rates (6-10 μ /min) make the method especially suitable for applications requiring thick layers, such as for thermoelectric modules, on large area substrates.

4. Ease of doping the layers using the GREG cycling mode (17) where a very thin film of dopant metal (*e.g.*, Al or Ag) is first deposited onto the substrate. By reversing the temperature gradient repeatedly, the dopant can be incorporated into the layer.

The GREG system, as suggested by its name, can also be used for the gradient recrystallization of previously grown films lacking in crystalline structure. The application of a temperature gradient during recrystallization improves the layer quality, as seen from data in Fig. 3(b). Thus the GREG system has two main applications: growth of semiconductor layers from suitable sources and recrystallization of random or structureless layers of films to obtain better layer characteristics.

On single-crystal CdTe (111) or (100) substrates, good quality epitaxial layers were obtained even though the growth rate was about 7-8 μ m/min (20).

The GREG system consists of three graphite blocks shown in schematic view in Fig. 1. The lower block (A) is termed the source block and the upper one (B) is the substrate block. The third and important element of this design is the hotwall chamber (C). The use of a hotwall chamber in high vacuum evaporation has been described by Behrnt and Moreno (8) for ZnTe, by López-Otero (9), and by Menezes (10) for CdTe, but has not so far been used in C.S.V.T. systems. Thermocouples are provided in each of the three blocks to monitor temperatures, which are controlled by S.C.R. controllers.

Although diffusion seems to play an important role in the transport mechanism (19), the deep etching, in regular planes of the source material (when single-crystal material is used), indicates that thermal etching of the source in the presence of argon may also be important.

Experimental

The general procedure for deposition of CdTe, CdS, and ZnSe using the GREG technique is as follows.

The substrates were thoroughly cleaned (11) using TCE, acetone, and a final rinse in an ultrasonic cleaner with alcohol. The hotwall chamber was loaded with the sub-

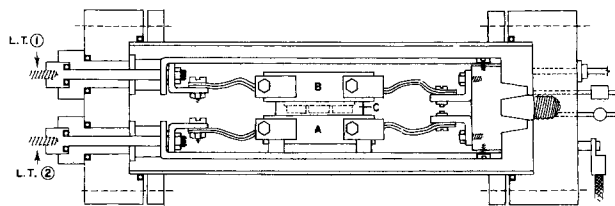


Fig. 1. Schematic of the GREG deposition system. The following labels refer to components of interest: (A) source block; (B) substrate block; (C) hotwall with chambers for source material; (L.T.1) low tension supply for substrate heater; (L.T.2) low tension supply for source heater.

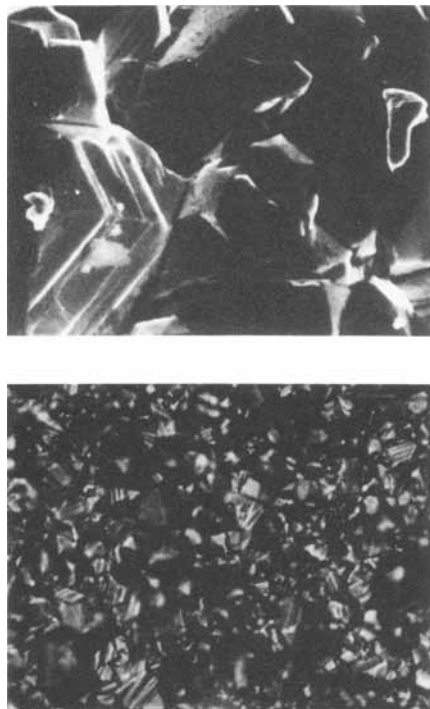


Fig. 2. (bottom) Photomicrograph of a CdTe layer deposited at 600°C on a glass substrate ($\times 600$). (top) Electron micrograph of a CdTe layer deposited by the GREG system at 650°C on a glass substrate ($\times 3000$).

strates and the source block with the evaporant (CdTe). The chamber was then evacuated to a pressure of less than 10^{-5} mm. Argon gas was introduced till a steady

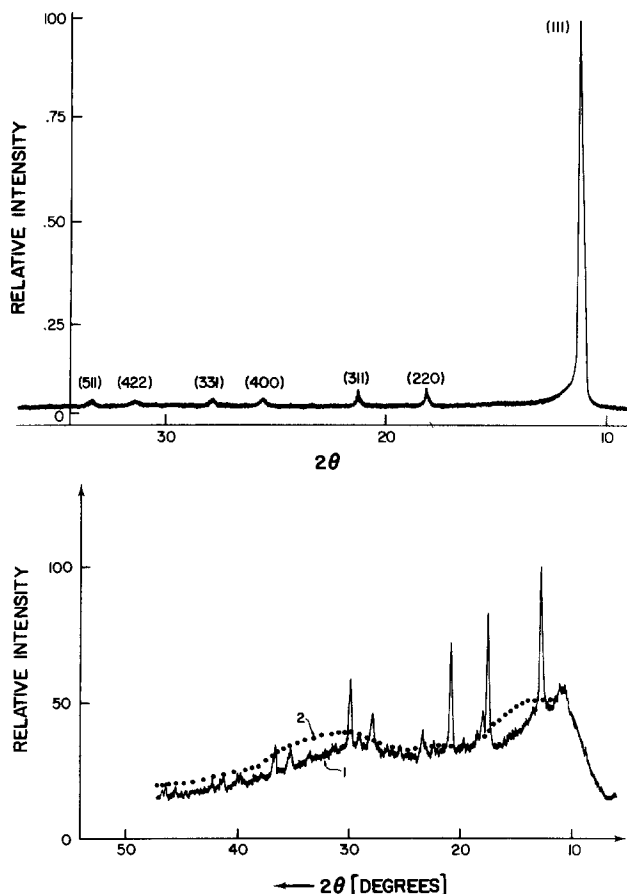


Fig. 3. (top) X-ray diffractometer trace of a CdTe layer deposited at 500°C substrate temperature and 625°C source temperature. (bottom) Recrystallized layer (1) and original amorphous layer (2).

pressure of 500-700 mtorr was obtained in the chamber. The pressure was monitored by a thermocouple vacuum gauge.

The deposition temperature was in the range 400°-600°C for the substrate block and 470°-650°C for the source block. Since the substrate is in intimate contact with the substrate block, we assume only a negligible temperature difference between the substrate and the substrate block heater whose temperature is continuously measured.

Characterization of Layers

Electron and photomicroscopy.—Figure 2 (bottom) shows a photomicrograph of a CdTe layer deposited at 500°C on a glass substrate. Figure 2 (top) shows an electron micrograph taken with a scanning electron microscope of a GREG-deposited CdTe layer which was deposited at 650°C on a glass substrate. The clean facets of the cubic CdTe crystals are clearly seen in the photograph. The (100) and (111) planes can be clearly distinguished in the picture.

X-ray diffraction.—All CdTe layers deposited by the GREG method show a cubic structure with the (111) plane being more usually the oriented plane. Most layers showed highly oriented crystal structure with the (111) plane being the principal plane of orientation. Figure 3 (top) shows a typical trace taken on an x-ray diffractometer of a specimen of CdTe deposited by the GREG technique with 75°C gradient.

Energy of activation.—In Fig. 4, we have plotted the log transport ratio ($\text{mg}/\text{cm}^2\text{-min}$) against temperature of source. The lower activation energy (34 K cal/mol) for deposition may be due to the geometry of the GREG system and the lower argon ambient pressure.

Thermoelectric power.—Preliminary thermoelectric power measurements were carried out on some specimens of CdTe deposited by the GREG method. Using the technique described by Arnoldussen (12), we obtained carrier concentrations of $\sim 10^{13}/\text{cm}^3$ for undoped specimens of CdTe and of $10^{16}\text{-}10^{17}/\text{cm}^3$ for aluminum and indium doped specimens. These values were in good agreement with the known doping concentration of the source material.

Electroreflectance.—Electroreflectance spectra taken for specimens of CdTe on conducting glass substrates show the characteristic line shape for CdTe (13). The measurements confirm the optical bandgap of the deposited CdTe to be 1.45 eV at room temperature (14).

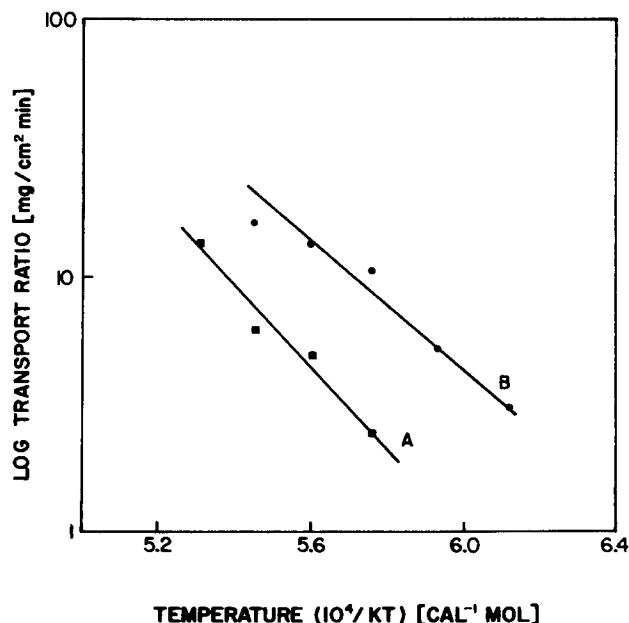


Fig. 4. Log transport ratio vs. temperature of source

Photoluminescence.—CdTe layers deposited by the GREG method showed strong photoluminescence. The photoluminescence spectrum of CdTe on ordinary glass showed an interesting structure which is very similar to that obtained with single crystals (15). Photothermal deflection spectroscopy was also used, to study the stoichiometry characteristics of these layers (16). Strong photoluminescence was also obtained with ZnSe and ZnS layers produced by the GREG method (21, 22).

Conclusions

We have demonstrated an improved hotwall-C.S.V.T. growth technique (GREG) which can also be used for gradient recrystallization of previously grown films. The advantages are: the use of commonly available substrates, large grain size and lower grain boundary concentration, large area, growth conditions approaching equilibrium as compared to high vacuum deposition, fast deposition rate without loss of layer quality, and applicability to many semiconductor materials. On single-crystal substrates, good quality epitaxial layers can be produced at a fast growth rate. CdTe layers have been used in experimental solar cells in a simple process (18).

Acknowledgments

Thanks are specially due to Dr. Richard Bube and Dr. A. F. Fahrenbruch for discussion and several useful suggestions in the course of this work. We also wish to thank my colleagues Dr. Feliciano Sánchez Sinencio, Dr. Ciro Falcony, Dr. Alfonso Lastras, and Dr. Julio Mendoza. Special thanks are due to Mr. Orlando Zelaya Angel, who carried out many of the depositions and made measurements of the thermoelectric power, optical absorption, and x-ray diffraction. This work was supported by a grant from the CONACYT and NSF (International Programs) and by O.A.S.

Manuscript submitted Jan. 17, 1984; revised manuscript received Oct. 31, 1984.

Centro de Investigacion y de Estudios Avanzados del IPN assisted in meeting the publication costs of this article.

REFERENCES

1. F. H. Nicoll, *This Journal*, **110**, 1165 (1963).
2. P. H. Robinson, *RCA Rev.*, **24**, 574 (1963).
3. R. F. Lever and F. Jona, *J. Appl. Phys.*, **34**, 3189 (1963).
4. J. Sarie, M. Akiyama, and T. Tanaka, *Jpn. J. Appl. Phys.*, **11**, 1758 (1972).
5. A. L. Fahrenbruch, V. Vasilchenkov, F. Buch, K. Mitchell, and R. H. Bube, *Appl. Phys. Lett.*, **10**, 605 (1974).
6. D. de Nobel, *Philips Res. Rep.*, **14**, 361 (1959).
7. J. Mimila-Arroyo, A. Bonazzi, and G. Cohen-Solal, Second International Symposium on CdTe, Strasbourg (1976).
8. M. E. Behrndt and S. C. Moreno, *J. Vac. Sci. Technol.*, **8**, 494 (1971).
9. A. López-Otero, *Thin Solid Films*, **49**, 3 (1978).
10. C. Menezes, *This Journal*, **127**, 159 (1980).
11. P. Lindquist, Ph.D. Thesis, Stanford University (1970).
12. T. A. Arnoldussen, Ph.D. Thesis, Stanford University (1973).
13. D. E. Aspnes, in "Handbook on Semiconductors," T. S. Moss, Editor, p. 109, North Holland, NY (1980).
14. See also "Semiconductors and Semimetals," Vol. 13, K. Zanio, Editor, Academic Press (1978).
15. J. G. Mendoza, *J. Appl. Phys.*, **56**, 10 (1984).
16. J. G. Mendoza-Alvarez, B. S. H. Royce, F. Sánchez Sinencio, O. Zelaya Angel, C. Menezes, and R. Triboulet, *Thin Solid Films*, **102**, 259 (1983).
17. C. Menezes, *J. Cryst. Growth*, to be published.
18. C. Menezes, F. Sánchez-Sinencio, C. Vázquez-López, and A. Sosa-Estrada, *Solar Energy Materials*, To be published.
19. T. C. Anthony, A. L. Fahrenbruch, and R. H. Bube, *J. Vac. Sci. Technol.*, To be published.
20. C. Menezes, *J. Cryst. Growth*, to be published.
21. C. Falcony, F. Sánchez-Sinencio, J. S. Helman, O. Zelaya, and C. Menezes, *J. Appl. Phys.*, In print.
22. C. Falcony, F. Sánchez-Sinencio, O. Zelaya, and C. A. Menezes, VIII Interamerican Conference on Materials Technology, San Juan, Puerto Rico, June (1984).
23. Private communication.

Transient Properties of the Luminescence of Eu^{3+} and Tb^{3+} in Oxysulfide Matrices

Jeannette Dexpert-Ghys and Yves Charreire

Laboratoire des Elements de Transitions dans les Solides, Equipe de Recherche du CNRS, F-92190 Meudon-Bellevue, France

Markku Leskelä and Lauri Niinistö

Department of Chemistry, Helsinki University of Technology, SF-02150 Espoo 15, Finland

ABSTRACT

Transient properties of Eu^{3+} emitting levels $^5\text{D}_2$, $^5\text{D}_1$, and $^5\text{D}_0$ in an yttrium oxysulfide matrix have been studied at various activator concentrations and under different excitation modes. Eu^{3+} was excited either to the charge-transfer state (CTS) by UV light or selectively to the $^5\text{D}_1$ levels by laser. At low Eu^{3+} concentrations, the results can be explained by a step process, $^5\text{D}_2 \rightarrow ^5\text{D}_1 \rightarrow ^5\text{D}_0$; the values calculated from rate equations are in agreement with the measured ones. The decrease of the lifetimes of $^5\text{D}_2$ and $^5\text{D}_1$ with increasing Eu^{3+} concentration can be explained by a cross-relaxation process between the Eu^{3+} ions. The lifetime of $^5\text{D}_0$ level decreases linearly with concentration when excited to CTS or with cathode rays; with selective excitation, the lifetime of $^5\text{D}_0$ is constant. The quenching of $^5\text{D}_0$ seems to be more complex than energy transfer to a sink and is possibly connected to the presence of Eu^{3+} ions excited into CTS, or is caused by the electronic structure of $(\text{YO})_2\text{S}$. In Tb^{3+} -activated oxysulfides, no step process $^5\text{D}_3 \rightarrow ^5\text{D}_4$ was observed. $(\text{GdO})_2\text{S}:\text{Tb}^{3+}$ compounds contained Eu^{3+} as an impurity, and an effective energy transfer $\text{Tb}^{3+}(^5\text{D}_4) + \text{Eu}^{3+}(^7\text{F}_0) \rightarrow \text{Tb}^{3+}(^7\text{F}_4) + \text{Eu}^{3+}(^5\text{D}_0)$ was noticed.

The fluorescence-decay studies of luminescent materials have been used to determine parameters such as energy-transfer rates, as well as radiative and nonradiative transition probabilities [e.g., Ref. (1), (2)]. On the other hand, many applications of inorganic phosphors have

specific requirements for the lifetime of luminescence. For instance, the afterglow of the phosphor cannot be too long in cathode-ray tubes. The measurement of the lifetime thus belongs to the quality control of commercial phosphors.

The dependence of intensity on Eu^{3+} and Tb^{3+} concentrations in rare-earth oxysulfides has been extensively studied, mainly under cathode-ray excitation (3-7), but also under ultraviolet light (4, 8, 9). Different aspects of the interaction mechanisms between the host lattice and the activator ion, or even between different activator ions, have been clarified. The characteristics of the Eu^{3+} emission *vs.* temperature in rare-earth oxysulfides have also been investigated by Struck *et al.* (10, 12). These experiments have shown the importance of the charge-transfer state (CTS) in the thermal quenching of Eu^{3+} luminescence. A crystal-field analysis of an Eu^{3+} spectrum in oxysulfides has been performed by Sovers (13).

The present study is a continuation of our previous one on the lifetimes of Eu^{3+} emission lines in an yttrium oxysulfide matrix and on the concentration dependence of lifetimes (14). In comparison with our previous observations under cathode-ray excitation, we present here detailed measurements under pulsed laser beam excitation. Ultraviolet light emitted by the nitrogen laser permits excitation into the CTS, whereas the use of tunable dye laser allows selective excitation into the $^5\text{D}_j$ levels of Eu^{3+} . The study of temporal evolution of Eu^{3+} emission in these different cases thus gives a better insight into the various phenomena occurring in the luminescence process which is the aim of the present work. The lifetime studies are also extended to other activator-matrix combinations than $(\text{YO})_2\text{S}:\text{Eu}^{3+}$, *viz.*, $(\text{GdO})_2\text{S}:\text{Tb}^{3+}$.

Experimental

The preparation of the rare-earth oxysulfide samples has been described elsewhere (14, 15). The europium and terbium concentrations varied between 0.1 and 12 mole percent (m/o). The purity of the host oxides was 99.99% and that of activators was 99.9%. This means that at higher activator concentrations, the trace elements of activator may play a role in the luminescence measurements. Particularly, Eu, Gd, and Tb can contain each other as impurities because they are the successive elements in the periodic system. Therefore, in $(\text{GdO})_2\text{S}:\text{Tb}^{3+}$ (10%), *e.g.*, the europium concentration can be several ppm.

The cathode-ray equipment has been described earlier (14). The photonic excitation was performed either by a JOBIN-YVON pulsed nitrogen laser ($\lambda = 3370\text{\AA}$, corresponding excitation into the CTS of Eu^{3+}) or by a JOBIN-YVON pulsed dye laser (selective excitation into the $^5\text{D}_j$ levels of Eu^{3+}). A schematic representation of the equipment used is shown in Fig. 1. The pulse duration is about 8 ns and the repetition rate is 10 Hz. The dye laser is tunable

within a wavelength range characteristic for the dye; its linewidth is 0.2\AA at 5800\AA .

The luminescence spectra were measured through a Jarrel-Ash monochromator of 1m focal length. The rising and decay curves were analyzed in a Boxcar integrator (ATNE) connected to a photomultiplier via an amplifier. The signal was digitalized and stored in a minicomputer (COMMODORE CBM 3032). The intensity fluctuations of the laser beam were corrected by the use of a photodiode reference. The signal/noise ratio was improved by summing over several pulses, generally 10 pulses.

The determinations of τ were made by the computer either by linear regression of $\log I(t)$ for exponential decays or by computing the mean duration $T_m = \int_0^\infty I(t)tdt / \int_0^\infty I(t)dt$. The uncertainty is experimentally estimated to be 3% for measurements with the same excitation and mode of computation.

Results and Discussion

Several points have to be specified before discussing experimental results. The positions of the Eu^{3+} energy levels in oxysulfide and the different notations used in the following are presented in Fig. 2. Let us first consider the case where ion-ion interactions (here, $\text{Eu}^{3+}-\text{Eu}^{3+}$) are not effective, *i.e.*, low europium concentrations. An excited level (say, $^5\text{D}_2$) may relax radiatively ($^5\text{D}_2 \rightarrow ^7\text{F}_j$ emission) and nonradiatively ($^5\text{D}_2 \rightarrow ^5\text{D}_{j<2}$) by a multiphonon process or quench via the CTS (10-12). The emission intensity $I(t)$ for a given level i is proportional to $n_i(t)$, the number of ions excited at time t . $n_i(t)$ follows the general evolution (16)

$$n_i(t) = \sum_{j=1}^k A_j^i e^{-t/T_j} \quad [1]$$

where i and j refer to given levels within the k -levels system. A_j^i are determined by the initial conditions and T_j are the inverse decay (radiative + nonradiative) probabilities. The reverse transitions $i \rightarrow j$ are neglected, which in the particular case of oxysulfide matrices implies working at low temperature to avoid $^5\text{D}_1 \rightarrow \text{CTS} \rightarrow ^5\text{D}_j$ processes. Although exact solutions do exist for the equations system (1), the relation between the decay function of one given level and the various individual probabilities are too complex to be of physical use when $k > 4$, and several approximations are then necessary. Even without searching for exact solutions, Eq. [1] shows that decay functions differ with the excitation mode. In the case of ultraviolet excitation of Eu^{3+} into the CTS (level 5), for example, $n_i(t) = f(P_{51}, P_{41}, P_{31}, P_{21}, P_{10})$, whereas under selective excitation, $n_i(t) = f(P_{i0}) = n_i(t_0)e^{-t/\tau_i}$.

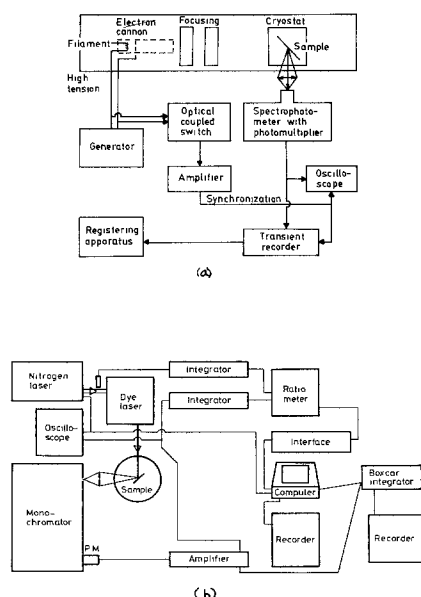


Fig. 1. Schematic representation of the equipment: (a) cathode-ray excitation; (b) pulsed-laser excitation.

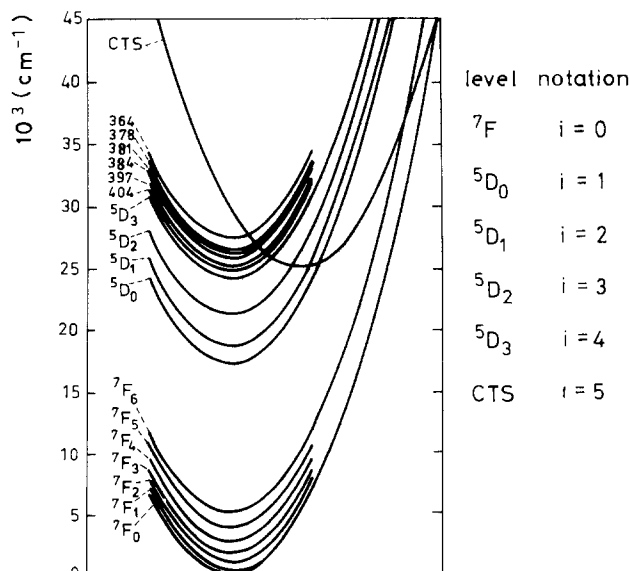


Fig. 2. Schematic representation of Eu^{3+} levels from Ref. (11) and notations used in the text.

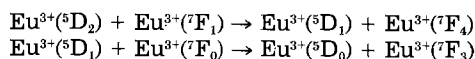
In the low concentration limit, the so-called rate equations may apply. The simple case of a three-level system is treated in the Appendix with reference to the Eu³⁺ ⁵D₁ (*i* = 2), ⁵D₀ (*i* = 1), and ⁷F₁ (*i* = 0) levels. It is shown that the consideration of the "mean duration of luminescence"

$$T_m = \int_0^\infty tI(t)dt / \int_0^\infty I(t)dt \quad [2]$$

permits one to discuss in a simple quantitative way the validity of rate equations in a given experimental case. The final equations ([A-8], [A-9]) can be verified only by using selective excitation. *T*₂ and *T*₁ are the ⁵D₁ and ⁵D₀ lifetimes measured successively under the ⁵D₁ and ⁵D₀ excitations. (*T*_m's are equal to 1/*e* lifetimes.) *T*_{1m} is the mean ⁵D₀ duration under ⁵D₁ excitation.

Equation [A-8] applies for any given three-level system, provided that the appropriate *T*'s are known. For instance, in the case of ⁵D₂ (*i* = 3) and ⁵D₁ (*i* = 2) levels, *T*_{2m} = *T*₂ + *T*₃ where *T*₂ and *T*₃ are determined under selective excitation of ⁵D₁ and ⁵D₂, respectively; *T*_{2m} refers to ⁵D₁ emission under ⁵D₂ excitation.

When the activator concentration increases, ion-ion interactions become more effective and the equations above are no longer valid. Eu³⁺-Eu³⁺ interaction causes ⁵D₂ and ⁵D₁ emission quenching by cross-relaxation processes like (17)



The emptying of upper levels causes the feeding of lower levels, and the overall effect is that *P*₂₁ and *P*₃₂, which include Eu-Eu energy-transfer probabilities, increase with concentration. In this case, as explicitly formulated by Inokuti and Hirayama (18), the decay function of donor luminescence is not exponential and

$$n_2(t) \sim \exp[-t/T_0 - \Gamma(1 - 3\theta)(c/c^*)(t/T_0)^{3/\theta}] \quad [3]$$

where *T*₀ is the (*i* = 2) radiative lifetime at low concentration, *Γ* a function of argument unity, *c* the dopant ion concentration, and *c** the critical activator concentration. *θ* defines the index of multipolar interaction. Experimental determination of *θ* has been made for numerous rare-earth-doped systems [see, e.g., Ref. (19) and references therein].

The above formulation (Eq. [3]) is still an approximation because the diffusion between identical levels without energy degradation has not been considered. When the diffusion of energy is very effective, the donor ion system (Eu³⁺ excited on ⁵D₁ level, for instance) exhibits a simple exponential decay and rate equations analogous to Eq. [A-2] and [A-3] apply. The intermediate case of diffusion-limited relaxation has been evidenced, for example, by Weber for Eu³⁺-Cr³⁺ doped samples (20).

The recent investigations, where emission from selected activator pairs has been monitored, give new information from ion-ion energy transfer (21-24). There are, however, many problems when these results are applied to the real samples.

Europium-activated yttrium oxysulfide (Y_{1-x}Eu_xO)₂S.—Figure 3 shows the concentration dependence of the lifetime of excited ⁵D₂ and ⁵D₁ levels of Eu³⁺ in (YO)₂S, excited with two different modes into the CTS of Eu³⁺ (3370Å). The shapes of the curves are similar in both excitation modes, but the lifetime values depend on the excitation mode. The lifetimes measured with UV excitation are shorter in the cases of ⁵D₁ and ⁵D₂ than those obtained by cathode ray excitation. Ozawa (3, 5) has given evidence that relaxation mechanisms are different when exciting luminescence by cathode ray or by photons (into CTS or ⁵D levels), which may explain the differences in *T*_m. Moreover, the pulse duration of electron beam (~1 ms) is much longer than the laser pulse, so the initial conditions for Eq. [A-3] should be modified (*N*₁⁰ ≠ 0); this leads to a different expression for *n*₁(*t*).

The lifetime (*T*_m) vs. Eu³⁺ concentration curves are nearly exponentially decreasing in the ⁵D₁ and ⁵D₂ cases. When the europium concentration is increased from 0.1 to

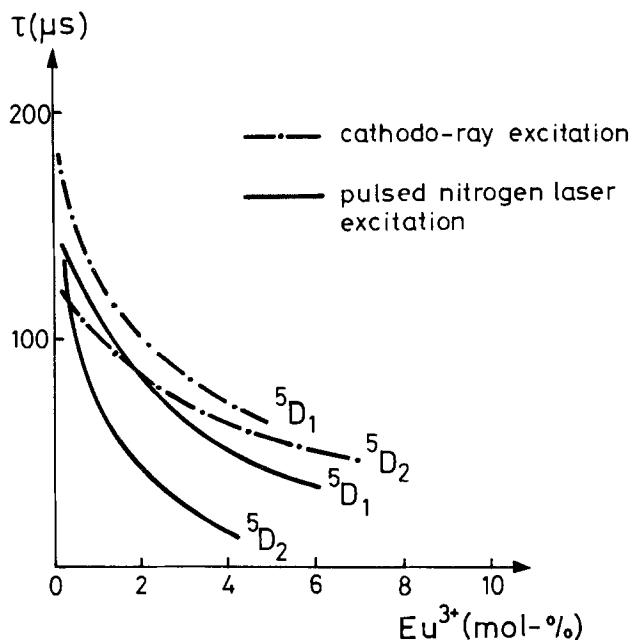


Fig. 3. Comparison of the lifetime vs. Eu³⁺ concentration curves of ⁵D₁ and ⁵D₂ levels when excited by both cathode rays and nitrogen laser (*λ* = 3370Å) at 300 K.

6%, the lifetimes are decreased from 180 and 110 μs to 50 μs and from 130 and 120 μs to 40 and 20 μs for ⁵D₁ and ⁵D₂ cases with both cathode ray and UV excitation, respectively. With higher europium concentrations, the intensity of these levels is so low that the lifetime measurements were impossible.

In our previous work (14), we reported the linear decay of *T*_m(⁵D₀) vs. Eu³⁺ concentration in the range 2-10% Eu³⁺. However, the experimental determination of *T*_m according to Eq. [2] has proven to be a simple and more precise method for the determination of activator concentrations. Figure 4 shows the evolution of *T*_m(⁵D₀) at 300 K vs. concentration for cathode ray, UV, and dye laser selective excitations. Most striking is that under direct selective excitation, *T*_m(⁵D₀) remains almost constant in the range 0.5% ≤ *x* ≤ 10% (*T*_m = 470 ± 20 μs) and suddenly falls at *x* = 12% (*T*_m = 400 μs). The observed discrepancies will be discussed in the following.

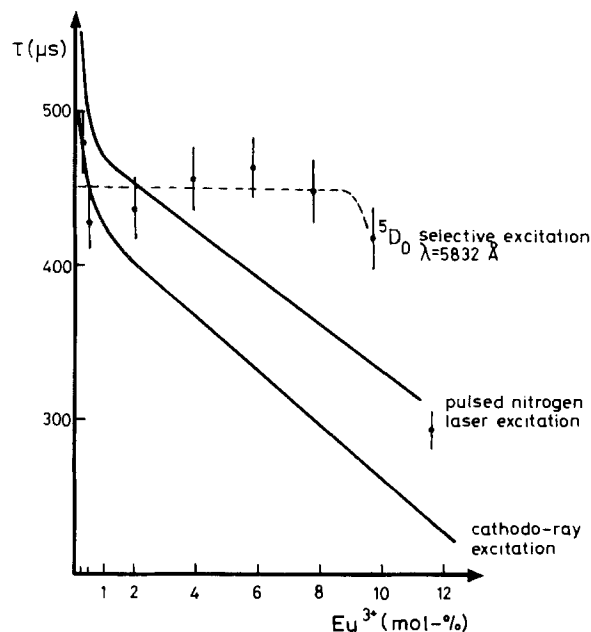


Fig. 4. The effect of excitation mode on the lifetime vs. concentration curves of ⁵D₀ of Eu³⁺ at 300 K: Cathode-ray excitation; pulsed nitrogen-laser excitation into the CTS level (3370Å); selective laser excitation into the ⁵D₀ level (5832Å).

We have investigated in detail the emission properties at relatively low dopant concentrations ($x = 0.005$). Because the phosphor characteristics are changed with temperature (10), the sample is immersed in liquid nitrogen and then has a constant temperature of 77 K. The main observations are the following.

Practically no differences were observed in the rise and decay curves when Eu^{3+} was excited into CTS (3370Å) or $^5\text{D}_2$ (4767Å), and $^5\text{D}_{2-0}$ emission was monitored. According to Struck and Fonger (10-12), at this composition and temperature, CTS excitation feeds instantaneously the $^5\text{D}_2$ and $^5\text{D}_1$ levels by passing $^5\text{D}_3$ and higher levels. This is in agreement with the observation of the same transient characteristics for both excitations. Selective excitation into $^5\text{D}_3$ level ($\lambda = 4130\text{Å}$) (13) at 77 K has proven to be impossible. Instead we observed the same weak fluorescence signal when tuning the laser between 4100 and 4150Å. On the other hand, Eu^{3+} is selectively excited with $\lambda = 3970\text{Å}$ corresponding to an upper 4f state observed but unidentified (11). This excitation mode leads to the same characteristics as did UV and $^5\text{D}_2$ excitation. The levels situated above $^5\text{D}_2$ have decay times too short to influence the lifetimes of the lower lying levels.

Under direct selective excitation, the decay curves of $^5\text{D}_2$, $^5\text{D}_1$, and $^5\text{D}_0$ levels are exponential within our experimental precision. The values are reported in Table I. By exciting $^5\text{D}_1$ ($i = 2$) and monitoring the evolution of $^5\text{D}_0$ ($i = 1$) fluorescence with time, we may discuss the applicability of Eq. [A-8]. The curve is presented in Fig. 5 and clearly shows a delayed buildup when compared with direct excitation. The numerical values are $T_1 = 1/P_{10} = 458 \mu\text{s}$, $T_2 = 1/(P_{21} + P_{20}) = 160 \mu\text{s}$, and $T_{1m}(\text{calc.}) = 618 \mu\text{s}$ instead of experimental $553 \pm 17 \mu\text{s}$. In the same way, we may study the values T of $^5\text{D}_2$ ($i = 3$) and $^5\text{D}_1$ ($i = 2$) under respective direct excitations as $1/(P_{32} + P_{31} + P_{30}) = 151 \mu\text{s}$ and $1/(P_{21} + P_{20}) = 160 \mu\text{s}$ giving $T_{2m}(\text{calc.}) = 311 \mu\text{s}$. The corresponding experimental value is $263 \mu\text{s}$.

The maximum $^5\text{D}_1$ intensity is reached experimentally at $\Delta t = 200 \mu\text{s}$, and by applying Eq. [A-4], the maximum is at $\Delta t(\text{calc.}) = T_2 T_1 / T_2 - T_1 \ln T_1 / T_2 = 258 \mu\text{s}$. The measured values are then 10%-20% lower than the theoretical ones. The difference is appreciably greater than our experimental uncertainty. Nevertheless, the general trend is that successive $^5\text{D}_2 \rightarrow ^5\text{D}_1 \rightarrow ^5\text{D}_0$ cascade process is effective at a Eu^{3+} concentration of 0.5% and that the order of magnitude of these measured mean lifetimes justifies the use of so-called rate equations at this Eu^{3+} concentration (and of course at smaller concentrations). The possible reasons for the observed discrepancies will be discussed in the following. On the contrary, at higher concentrations (6% Eu^{3+}), Eq. [A-8] gives $T_{1m}(\text{calc.}) = 595 \mu\text{s}$ instead of the $495 \mu\text{s}$ obtained experimentally. For this concentration, the observed T_{1m} are equal for any excitation mode, although upper levels have a non-negligible decay time ($100 \mu\text{s}$ for

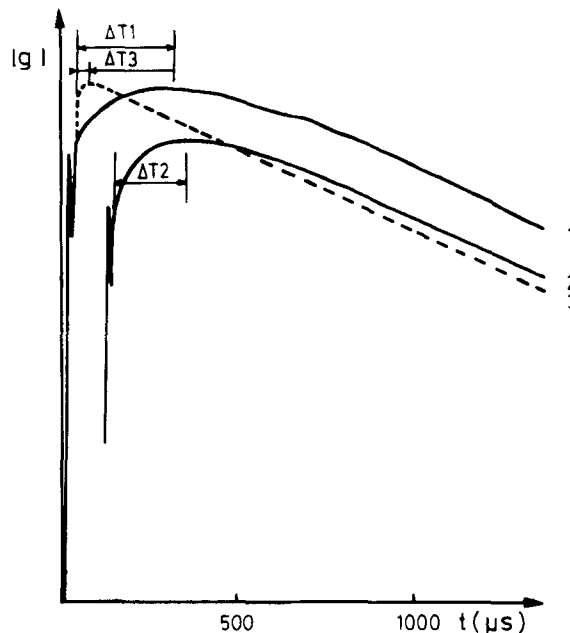


Fig. 5. Comparison of the transient properties of the $^5\text{D}_0$ level in $(\text{YO})_2\text{S}:\text{Eu}^{3+}$ (0.5%) at 77 K when excited by different methods: (1) into the CTS level; (2) $^5\text{D}_1$ level; and (3) $^5\text{D}_0$ level. ΔT_1 is the risetime of $^5\text{D}_0$.

$^5\text{D}_1$, Table I). This clearly shows that at this concentration, Eq. [A-2] and [A-3] are no more applicable due to ion-ion interactions which seem to be effective above the activator concentration of 1%.

Terbium-activated gadolinium oxysulfides ($\text{Gd}_{1-x}\text{Tb}_x\text{O}_2\text{S}$).—The behavior of the $^5\text{D}_4$ level of terbium was studied with the transition $^5\text{D}_4 \rightarrow ^7\text{F}_5$ (5440Å). The excitation wavelengths used were 3370 and 4897Å. The first value hits an f-f transition of Tb^{3+} and the second corresponds to the selective excitation of $^7\text{F}_6 \rightarrow ^5\text{D}_4$. The exponential decay curves are independent of the excitation way.

Yamamoto *et al.* (7) have observed the $^5\text{D}_3 \rightarrow ^5\text{D}_4$ step process in cathodoluminescence of Tb^{3+} at concentrations as low as 0.1%. In the present measurements, no delayed buildup of $^5\text{D}_4$ level was observed under any excitation condition with Tb^{3+} concentrations between 1% and 10%. This means that the cross-relaxation process $\text{Tb}^{3+}(^5\text{D}_3) + \text{Tb}^{3+}(^7\text{F}_6) \rightarrow \text{Tb}^{3+}(^5\text{D}_4) + \text{Tb}^{3+}(^7\text{F}_6)$ (25) is effective and that above 1% of Tb^{3+} the rate equations do not apply.

The concentration quenching of $^5\text{D}_4$ level in $(\text{GdO})_2\text{S}:\text{Tb}^{3+}$ samples is presented in Fig. 6. The shapes of the lifetime vs. Tb^{3+} concentration curves are similar in both excitation modes. Strong quenching was observed: the measured lifetime with 10% of Tb^{3+} was approximately 80% shorter than that with 1% of Tb^{3+} . In literature, the quenching of $^5\text{D}_4$ level in oxysulfide matrices has been reported to begin at concentrations of about 5%-6% (9, 26). In other high purity Tb^{3+} -activated compounds, a weak $^5\text{D}_4$ quenching has been observed (27, 28). The shortening of T in these compounds has been only about 10% when the Tb^{3+} amount varied between 0.1% and 100%.

In the present oxysulfide samples, at least a part of the additional quenching is due to the presence of a significant amount of Eu^{3+} , estimated to be 0.05%-0.1%. Europium probably originates from the impurities of gadolinium oxide. The fluorescence spectra of these compounds exhibit both Tb^{3+} and Eu^{3+} emissions. The relative intensities of the emissions vary with the excitation mode (Table II).

In $\text{Tb}^{3+}\text{-Eu}^{3+}$ interaction, the enhancement effect of Eu^{3+} emission by a small amount of Tb^{3+} in oxysulfide phosphors (7, 29) is well known. Yamamoto *et al.* (7) point out, however, that the simple multipolar energy transfer is not preponderant, at least for cathode ray excitation. On the contrary, this mechanism seems to be effective in experi-

Table I. Measured lifetimes (μs) for $(\text{Y}_{1-x}\text{Eu}_x\text{O})_2\text{S}$ samples at 77 K. (a) Direct selective excitation ($T_e = T_m$); (b) indirect excitation (T_m).

Emission	x (%)	Excitation level			
		CTS (3370Å)	$^5\text{D}_2$ (4690Å)	$^5\text{D}_1$ (5290Å)	$^5\text{D}_0$ (5830Å)
(a)					
4767Å	0.5		151		
$^5\text{D}_2 \rightarrow ^7\text{F}_1$	6		*		
5870Å	0.5			160	
$^5\text{D}_1 \rightarrow ^7\text{F}_3$	6			100	
6165Å	0.5				458
$^5\text{D}_0 \rightarrow ^7\text{F}_2$	6				497
(b)					
5870Å	0.5		263	160	
$^5\text{D}_1 \rightarrow ^7\text{F}_3$					
6165Å	0.5	658	635	553	458
$^5\text{D}_0 \rightarrow ^7\text{F}_2$	6	485	480	494	497

* Intensity too low.

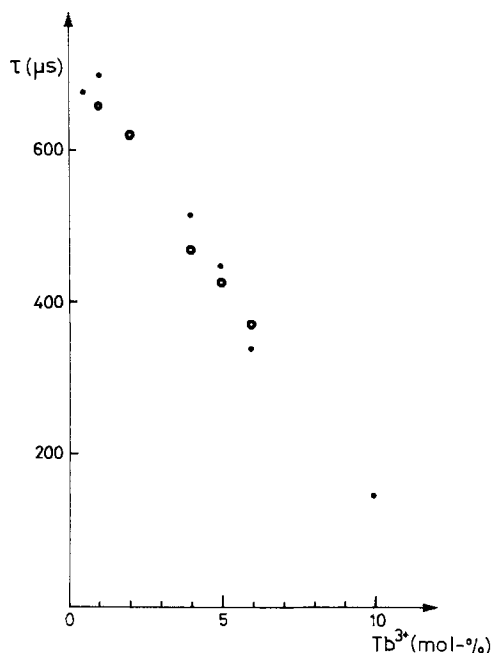


Fig. 6. Lifetime of 5D_4 vs. Tb^{3+} concentration in $(GdO)_2S$ matrix when excited with wavelengths 3370 Å (○) and 4897 Å (●) at 300 K. Note that the samples contain a small amount of europium as impurity.

mental conditions employed in the present work. The excitation spectra recorded between 4800 and 5000 Å for ${}^5D_4 \rightarrow {}^7F_5$ of Tb^{3+} at 5440 Å and ${}^5D_0 \rightarrow {}^7F_2$ of Eu^{3+} at 6165 Å show exactly the same shape with a line at 4897 Å corresponding to ${}^7F_6 \rightarrow {}^5D_4$ transition of Tb^{3+} (Fig. 7). This indicates that the energy transfer occurs via process $Tb^{3+}({}^5D_4) + Eu^{3+}({}^7F_0) \rightarrow Tb^{3+}({}^7F_4) + Eu^{3+}({}^5D_0)$. However, this process is probably not the only one in this system, as shown in Ref. (7). In particular, the results from the relative fluorescence intensities of Tb^{3+}/Eu^{3+} presented in Table II show that the intensity ratio is strongly dependent on the excitation mode, indicating complex interaction phenomena.

Discussion

We will now discuss in more detail the Eu^{3+} -activated oxysulfides. As shown in the previous paragraph, our Tb^{3+} -activated samples are in fact codoped with Eu^{3+} ions; thus there is a risk that the results on Tb^{3+} concentration quenching are altered by the Tb^{3+} - Eu^{3+} ion-ion interactions which we are not dealing with in this paper.

Let us consider the results collected in Fig. 4. By comparing the data measured under UV and direct selective excitation at room temperature, it can be seen that at very low Eu^{3+} concentrations (0.25% and 0.5%), the mean duration T_{im} of 5D_0 luminescence is longer under UV excitation, due to the slow buildup of 5D_0 when Eu^{3+} is excited into higher energetic levels. For $x = 1\%$, the values are equal, whereas for higher concentrations, T_{im} becomes shorter under UV excitation. The difference between the two values increases with x . This indicates that excitation of 5D_0 via the CTS provides an additional pathway for 5D_0 nonradiative relaxation, which becomes more and more effective for higher Eu^{3+} concentrations. Several investi-

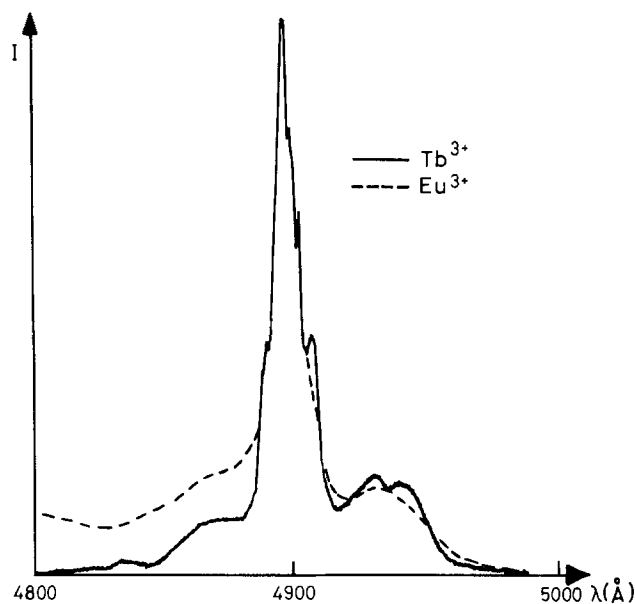


Fig. 7. Excitation spectra of transition ${}^5D_4 \rightarrow {}^7F_5$ (5440 Å) of Tb^{3+} (full line) and transition ${}^5D_0 \rightarrow {}^7F_2$ (6165 Å) of Eu^{3+} (dashed line) between 4800 and 5000 Å.

gations of 5D_0 concentration quenching have been reported. Generally they present the 5D_0 fluorescence yield under UV or cathode ray excitation. The 5D_0 quenching does not occur via the usual ion-ion multipolar interactions, because the ${}^5D_0 \rightarrow {}^7F_5$ energy gap cannot be matched by a transition within the 7F_5 multiplet. According to van Uitert (19), the 5D_0 self-quenching is related to exchange between identical Eu^{3+} ions: energy migrates until it reaches a sink. The nature of such sinks is very difficult to disclose, and there may be another rare-earth ion present in the sample as impurity, or the sample may contain crystal defects or grain boundaries.

Another type of concentration-related quenching mechanism proposed in Ref. (19) is more-efficient ion-phonon coupling for paired Eu^{3+} ions. This mechanism may well be the origin of the observed overall diminution of 5D_0 radiative lifetime at 300 K (520 μs for $x = 0.25\%$ vs. 400 μs for $x = 12\%$), but it has no reason to be more effective under CTS than under 5D_0 excitation. Another way to depopulate 5D_0 is up-conversion. Imanaga *et al.* (8) have observed a decrease in Eu^{3+} 5D_1 decay times with strong excitation into the CTS by pulsed nitrogen laser. Their observations are qualitatively in agreement with ours because, moreover, the shortening is stronger for higher Eu^{3+} concentrations. The nonradiative relaxation of 5D_1 states is attributed in Ref. (8) to interactions between Eu^{3+} (5D_1) and Eu^{3+} (CTS). In the absence of more experimental data, we cannot exactly define the mechanism responsible for additional 5D_0 quenching under UV and cathode ray excitation. It is obvious from experimental data, however, that it is directly linked to the presence of CTS-excited Eu^{3+} ions.

At moderately high Eu^{3+} concentrations (6%), rate equations are not available and the differential equations governing even the simple (5D_1 , 5D_0 , 7F) three-level system have not been established. The decay observed for the 5D_1 (donor) system is exponential within the experimental precision so that a donor time evolution following the Inokuti-Hirayama formulation (Eq. [3]) does not apply. The ${}^5D_1 \rightarrow {}^5D_0$ energy transfer occurs instantaneously because no 5D_0 delayed buildup is observed under 5D_1 excitation. Such apparent inconsistencies would probably be resolved only by establishing a correct set of differential equations for $n_i(t)$ and by fitting with experimental results.

Conclusion

Previous measurements dealing with lifetimes or quantum yields of Eu^{3+} -excited levels in $(YO)_2S$ under different excitation modes led to apparently incoherent results. In

Table II. Relative fluorescence intensities of Tb^{3+} and Eu^{3+} in $(Gd_{1-x}Tb_xO)_2S$ samples excited with different modes

x (mole per- cent)	Short UV 2537 Å		N ₂ laser 3370 Å		Long UV 3650 Å		Dye laser 4897 Å	
	I_{Tb}	I_{Eu}	I_{Tb}	I_{Eu}	I_{Tb}	I_{Eu}	I_{Tb}	I_{Eu}
0.5	100	—	15	100	100	70	—	—
1	100	—	40	100	100	14	—	—
2	100	—	100	25	100	7	—	—
4	100	7	100	45	100	12	100	16
5	100	9	100	22	100	14	100	22
6	100	17	100	20	100	20	—	—
10	100	76	100	76	100	84	—	—

particular, the 5D_0 -level lifetime evolution vs. concentration seemed abnormal.

In this work, we have tried to study in some detail the $\text{Eu}^{3+}({}^5D_{j=0-2})$ temporal time evolutions in $(\text{YO})_2\text{S}$. This was made possible by selectively exciting each of the 5D_j levels by means of a pulsed dye laser. The so-called decay time for a given level (i) is not strictly the inverse radiative probability of this level, but is a complex function $T = f(P_{ij})$ which depends on the initial conditions (excitation mode) and the concentration (quenching). At low concentrations (experimentally $< 1\%$ Eu^{3+}), we have shown that the time evolutions of excited levels' populations follow in first approximation the differential equations (rate equations) described in the literature. The function $T = f(P_{ij})$ differs following the way of calculating [mean duration or linear regression of $\log I(t)$]. Only the experimental case of a real three-levels system (observed under selective excitation) leads to a simple relation between T and the P_{ij} 's. For higher Eu^{3+} concentrations, the differential equations' systems describing the excited levels' populations are not known. Experimentally we have drawn the 5D_j fluorescence time evolution and computed the mean durations T_m vs. concentration.

The present study thus complements our previous measurements of T_m under cathodic excitation. In that work, it is shown that the experimental linear evolution of T_m (5D_0) vs. Eu^{3+} concentration is an indirect way of determining the activator concentration in oxysulfide matrices within the usual range $2\% \leq x \leq 10\%$. In the present study, we have observed approximately the same evolution of T_m (5D_0) vs. concentration when excited through the charge-transfer state CTS by means of UV nitrogen laser light. On the other hand, by direct 5D_0 selective excitation a quite different evolution is observed, namely, an almost constant T_m value over the composition range $0.5 \leq x \leq 10\%$. The physical reason for this additional 5D_0 quenching under CTS excitation as well as cathode ray has till now not been elucidated and may be linked to the particular electronic structure of $(\text{YO})_2\text{S}:\text{Eu}^{3+}$. Nevertheless, these comparative measurements prove that the 5D_0 quenching phenomenon is more complex than simple energy migration toward sinks and necessitates further investigation to be fully understood.

For terbium-activated gadolinium oxysulfide, we have evidenced the presence of Eu^{3+} as impurity in the samples as a cause for the 5D_4 concentration quenching. In these compounds, we observe no difference for 5D_4 and 5D_3 time evolution when excitation is made by UV light or selectively within each of the 5D_j levels.

The present work has clearly shown that the use of dye laser selective excitation permits clarifying to some extent the problem of transient properties of Eu^{3+} emission in the yttrium oxysulfide matrix by measuring reliable T_m (mean durations of luminescence) numerical values. Further investigation is, however, needed mainly at relatively high Eu^{3+} concentrations to establish the differential equations ruling the system. In this first step, we have evidenced that the excitation mode (cathode ray, CTS, or direct 5D_j) as well as the mathematical definition for the so-called lifetime have to be carefully defined before comparing different sets of experimental data.

Preliminary report was given at the 16th Rare Earth Research Conference, Tallahassee, Florida (31).

Manuscript submitted June 11, 1984; revised manuscript received Nov. 13, 1984.

Helsinki University of Technology assisted in meeting the publication costs of this article.

APPENDIX

The time evolutions of Eu^{3+} 5D_1 and 5D_0 levels follow the general formulation (see Fig. 2 for notations)

$$\begin{matrix} n'_0 & = & 0 & P_{10} & P_{20} & n_0 \\ n'_1 & = & 0 & -P_{10} & P_{21} & n_1 \\ n'_2 & = & 0 & 0 & -(P_{20} + P_{21}) & n_2 \end{matrix} \quad [\text{A-1}]$$

The solution is

$$n_2(t) = N_2^0 \exp [-(P_{21} + P_{20})t] \quad [\text{A-2}]$$

$$n_1(t) = \left(N_1^0 + \frac{P_{21}N_2^0}{P_{21} + P_{20} - P_{10}} \right) \exp(-P_{10}t) - \left(\frac{P_{21}N_2^0}{P_{21} + P_{20} - P_{10}} \right) \exp [-(P_{21} + P_{20})t] \quad [\text{A-3}]$$

N_2^0 and N_1^0 are initial values of n at $t = 0$. In case of pulsed excitation, $N_2^0 = N_2$ and $N_1^0 = 0$ can be assumed. P_{ij} is the $i \rightarrow j$ transition probability. From Eq. [A-2] and [A-3] the following conclusions can be obtained.

1. The emission intensity at level 1 shows an initial rise and then a decay formed in general by the sum of two exponentials. However, when $P_{10} \ll P_{21} + P_{20}$, the slope of $\ln [n_1(t)] = f(t)$ gives $T_e = 1/P_{10}$, the 5D_0 radiative lifetime.

2. $n_1(t)$ is at maximum at time

$$t = \frac{1}{P_{10} - P_{21} - P_{20}} \ln \frac{P_{10}}{P_{21} + P_{20}} \quad [\text{A-4}]$$

3. When $N_1^0 = 0$, Eq. [A-4] can be written

$$n_1(t) = \frac{P_{21}N_2^0}{P_{21} + P_{20} + P_{10}} [\exp(-P_{10}t) - \exp(-(P_{21} + P_{20})t)] \quad [\text{A-5}]$$

if $K = \frac{P_{21}N_2^0}{P_{21} + P_{20} - P_{10}}$

$$\int_0^\infty t n_1(t) dt = K \left[\left(\frac{1}{P_{10}} \right)^2 - \left(\frac{1}{P_{21} + P_{20}} \right)^2 \right] \quad [\text{A-6}]$$

and

$$\int_0^\infty n_1(t) dt = K \left(\frac{1}{P_{10}} - \frac{1}{P_{21} + P_{20}} \right) \quad [\text{A-7}]$$

taking T_m from Eq. [2] follows

$$T_{1m} = \frac{\int_0^\infty t n_1(t) dt}{\int_0^\infty n_1(t) dt} = \frac{1}{P_{10}} + \frac{1}{P_{21} + P_{20}} \quad [\text{A-8}]$$

Experimentally, P_{10} may be measured as $1/T_1$, and $(P_{21} + P_{20})$ may be measured as $1/T_2$ under selective excitation.

Then

$$T_{1m} = T_1 + T_2 \quad [\text{A-9}]$$

In many rare-earth systems, the decay times of the levels are very different so that various approximations can be employed. For example, if $T_2 \ll T_1$ in Eq. [A-8], $T_{1m} = T_1$ and may be determined as the 1/e decay time. In the case of Eu^{3+} , however, the 5D_0 lifetime is only about twice the lifetimes of 5D_1 and 5D_2 , which are almost equal. So the above approximation cannot be used.

REFERENCES

- W. W. Anderson, *J. Chem. Phys.*, **44**, 3283 (1966).
- J. M. Dishman and I. Camlibel, *Phys. Rev. B*, **6**, 1340 (1972).
- L. Ozawa, *Appl. Phys. Lett.*, **33**, 586 (1978).
- L. Ozawa, *This Journal*, **126**, 105 (1979).
- L. Ozawa, *ibid.*, **129**, 1535 (1982).
- D. J. Robbins, B. Cockayne, B. Lent, and J. L. Glasper, *ibid.*, **126**, 1556 (1979).
- H. Yamamoto and T. Kano, *ibid.*, **126**, 305 (1979).
- S. Imanaga, S. Yokono, and T. Hoshina, *Jpn. J. Appl. Phys.*, **19**, 41 (1980).
- J. Hölsä, M. Leskelä, and L. Niinistö, *Mater. Res. Bull.*, **14**, 1403 (1979).
- C. W. Struck and W. H. Fonger, *J. Lumin.*, **12**, 456 (1970).
- W. H. Fonger and C. W. Struck, *J. Chem. Phys.*, **52**, 6364 (1970).
- W. H. Fonger and C. W. Struck, *This Journal*, **118**, 273 (1971).
- O. J. Stovers and T. Yoshioka, *J. Chem. Phys.*, **51**, 5330 (1969).
- Y. Charreire, M. Leskelä, L. Niinistö, and J. Loriers, *Anal. Chim. Acta*, **118**, 123 (1980).
- M. Leskelä, L. Niinistö, Y. Charreire, and H. Dexpert, *Mater. Res. Bull.*, **14**, 455 (1979).
- M. J. Weber, *Phys. Rev.*, **156**, 231 (1967).

17. L. Ozawa and P. M. Jaffe, *This Journal*, **118**, 1678 (1971).
18. M. Inokuti and F. Hirayama, *J. Chem. Phys.*, **43**, 1978 (1965).
19. L. G. van Uitert, *This Journal*, **114**, 1048 (1967).
20. M. J. Weber, *Phys. Rev. B*, **4**, 2932 (1971).
21. R. Buisson and C. Vial, *J. Phys.*, **42**, L-115 (1981).
22. J. C. Vial and R. Buisson, *ibid.*, **43**, L-745 (1982).
23. R. Flach, D. S. Hamilton, P. M. Selzer, and W. M. Yen, *Phys. Rev. Lett.*, **35**, 1034 (1975); *Phys. Rev. B*, **15**, 1248 (1977).
24. J. Hegarty, D. L. Huber, and W. M. Yen, *Phys. Rev. B*, **25**, 5638 (1982).
25. G. Blasse, *J. Lumin.*, **12**, 766 (1970).
26. L. Ozawa, H. Forest, P. M. Jaffe, and C. Ban, *This Journal*, **118**, 482 (1971).
27. C. Fouassier, B. Saubat, and P. Hagemmuller, *J. Lumin.*, **23**, 405 (1981).
28. F. Auzel, J. Dexpert-Ghys, and C. Gautier, *ibid.*, **27**, 1 (1982).
29. M. R. Royce, U.S. Pat. 3,418,246 (1968).
30. L. G. van Uitert and S. Iida, *J. Chem. Phys.*, **37**, 986 (1982).
31. L. Niinistö, M. Leskelä, J. Dexpert-Ghys, and Y. Charreire, *J. Less-Common Met.*, **93**, 103 (1983).

Comparative Study of Sensitization of the Luminescence of Trivalent Rare Earth Ions by Ce³⁺ in LaOBr

Li You Mo,¹ F. Guillen, C. Fouassier, and P. Hagemmuller

Laboratoire de Chimie du Solide du CNRS, Université de Bordeaux I, 33405 Talence Cedex, France

ABSTRACT

Energy transfer from cerium to the Pr³⁺, Nd³⁺, Tb³⁺, Dy³⁺, Ho³⁺, and Er³⁺ ions has been observed in LaOBr. Comparison of the effect of the activator ions on the cerium emission intensity suggests that transfer occurs mainly by an exchange mechanism, after migration of the excitation among donor ions. With increasing cerium concentration, the ³P₀ praseodymium, ⁵S₂ holmium, and ⁴S_{3/2} erbium emissions are quenched, the energy difference between the transition to the next lowest level and the ²F_{5/2} → ²F_{7/2} cerium transition being sufficiently small for energy transfer. The cerium emission is quenched at room temperature by the Sm³⁺, Eu³⁺, Tm³⁺, and Yb³⁺ ions without sensitization of the activator as a result of the formation of a charge-transfer (Ce⁴⁺-divalent activator ion) state.

The use of rare earth phosphors in lamps has developed in recent years. Only two rare earth elements, europium and terbium, are used as activators. Both of them are expensive, so it is worthwhile investigating the possibility of using other lanthanides. Several reasons account for the remarkable properties of Eu³⁺ and Tb³⁺: (i) Eu³⁺ can be made (by high concentration) to emit dominantly from ⁵D₀ with the favorably placed ⁵D₀ → ⁷F₁, ⁷F₂ most prominent, and, similarly Tb³⁺ can be made to emit dominantly from ⁵D₄ with the favorably placed ⁵D₄ → ⁷F₅, ⁷F₄, ⁷F₃ most prominent; (ii) the large gap between the emitting level and the next-lowest excited state precludes nonradiative losses by multiphonon processes; (iii) the UV excitation radiation can be strongly absorbed, since Eu³⁺ shows a charge-transfer band and Tb³⁺ allowed f → d transitions around 250 nm; the Tb³⁺ emission can also be efficiently excited through a sensitizer like Ce³⁺; and (iv) concentration quenching is weak (no cross relaxation). Most other trivalent rare earths do not possess allowed transitions above 250 nm, so a high efficiency requires a sensitizer. Although the Ce³⁺ → Tb³⁺ transfer has been extensively studied, transfer from cerium to other luminescent rare earth ions has drawn much less attention. However, the importance of Ce → Ce migration for avoiding concentration quenching of the Sm³⁺ or Dy³⁺ ions has been emphasized (1, 2).

For cations like Ho³⁺ or Er³⁺ whose energy levels are closely spaced, a high probability for radiative emission in the visible requires weak phonon energies or weak coupling to phonons. This is the case for lanthanum oxybromide, LaOBr. Hölsa (3) has recently published the visible emission spectra of the trivalent rare earths in this host lattice. The emitting levels under UV excitation are indicated in Fig. 1 for some of those ions.

Ce³⁺ shows an intense blue emission peaking at 435 nm at room temperature (5-7). Rabatin and Sieger (8), Hölsa *et al.* (7), and H. Wang *et al.* (19) have shown that energy transfer from Ce³⁺ to Tb³⁺ occurs in LaOBr. However, despite the presence of several f-f absorption lines in the wavelength range of the cerium emission, no sensitization

of the samarium, holmium, dysprosium, or thulium emissions was observed (8).

For determining the parameters which govern the efficiency of the transfer from Ce³⁺ to other trivalent rare earth ions we have undertaken an investigation of the luminescence of the Pr³⁺, Nd³⁺, Sm³⁺, Eu³⁺, Tb³⁺, Dy³⁺, Ho³⁺, Er³⁺, and Tm³⁺ ions in the presence of this ion.

Experimental

The starting rare earth materials (Rhône-Poulenc) were La₂O₃ (99.99%), preheated for removing H₂O and CO₂, CeO₂ (99.99%), and other trivalent oxides (>99.9%). They were ground in an agate mortar with 30% excess of the calculated amount of NH₄Br and 0.3M KBr for 1M rare

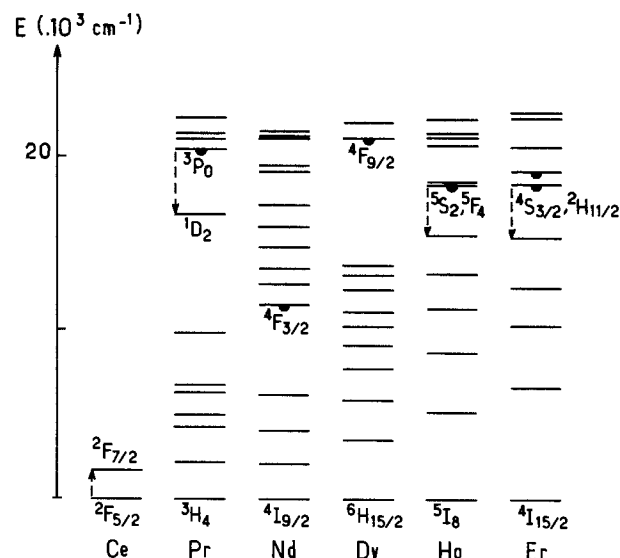


Fig. 1. Lower energy levels of Ce³⁺, Pr³⁺, Nd³⁺, Dy³⁺, Ho³⁺, and Er³⁺ (4). The half-circles point out the emitting levels of these ions in LaOBr for UV excitation. The arrows show the transitions responsible for quenching by cerium ions.

¹Permanent address: Changchun Institute of Applied Chemistry of the Chinese Academy of Science, Changchun, Jilin, China.

earth oxide, then fired at 900°C in a stream of nitrogen for 1h. After cooling, the flux is washed away with water.

Excitation and emission spectra were corrected for variation of lamp flux and detector response, respectively. A 6 ns pulsed nitrogen laser was used for determination of the fluorescent lifetimes. The signal was fed into a box-car averager (PAR Model 162).

Results

Energy migration among Ce³⁺ ions.—Figure 2 shows the emission spectra of Ce³⁺ in LaOBr at 300 and 90 K. Previous authors mention the existence of one band at room temperature. As a matter of fact, for low cerium concentrations, a shoulder on the short wavelength side can be clearly distinguished. When cooling, the high energy component becomes the most intense one. The two bands correspond to the transitions from the lowest 5d states to the ²F_{5/2} and ²F_{7/2} 4f levels. The decrease of the 5d → ²F_{5/2} 4f component intensity with cerium concentration indicates energy migration (9). Broadening of the absorption and emission bands with rising temperature results in increased overlapping, leading also to decrease of the high energy component. At low concentration, the luminescence shows weak thermal quenching at 300 K, as expected from the rather small Stokes shift (3400 cm⁻¹) (ratio of the integrated *I*(*hν*) curves: *I*_{300 K}/*I*_{90 K} = 0.92).

The high efficiency at room temperature and the existence of energy migration are two characteristics favorable for use of cerium as a sensitizer.

Effect of the incorporation of other trivalent rare earth ions on the cerium emission.—Figure 3 shows the cerium emission dependence on the activator concentration at 300 K in the La_{0.995-x}Ce_{0.005}A_xOBr compounds (A = Pr, Nd, Sm, Eu, Tb, Dy, Ho, Er, Tm, Yb). For each activator, the cerium emission intensity decreases rapidly with *x*. The effect of the incorporation of samarium and thulium is particularly strong since the cerium emission is nearly entirely quenched for *x* = 0.002.

Influence of cerium on the activator emission.—A = Pr, Nd, Tb, Dy, Ho, Er.—Figure 4 compares the excitation spectra of some of these ions in LaOBr- and Ce-doped LaOBr samples. As observed for Tb³⁺ by Hölsa *et al.* (7), the excitation spectra of Pr³⁺, Nd³⁺, Dy³⁺, Ho³⁺, and Er³⁺ in the cerium-doped samples contain the Ce 4f → 5d bands, indicating energy transfer.

Figure 5 shows the influence of the cerium concentration on the visible emission intensity of levels indicated in Fig. 1 for Pr, Dy, Ho, Er, excited through the f-d Ce bands. While, in the case of dysprosium, the intensity increases up to high cerium concentration, for praseodymium, holmium, and erbium, it reaches a maximum for a low content (*x* ≈ 0.01 for Pr, 0.005 for Ho and Er), then rapidly decreases. Such a dependence was also reported for terbium by Rabatin (8) and Hölsa *et al.* (7). However, as observed for dysprosium, the ⁴F_{3/2} infrared neodymium emission increases with cerium concentration.

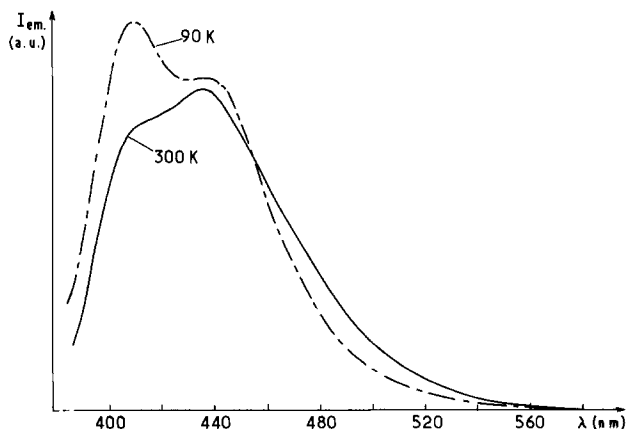


Fig. 2. Emission spectrum of La_{0.99}Ce_{0.01}OBr at 90 and 300 K for excitation into the 5d bands.

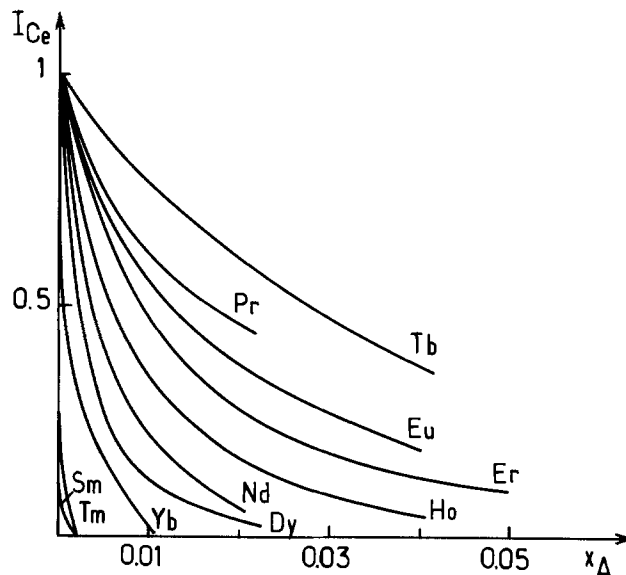


Fig. 3. Effect of the incorporation of other rare earths (A) on the cerium emission intensity for the La_{0.995-x}Ce_{0.005}A_xOBr series.

A = Sm, Eu, and Tm.—The excitation spectra of the Sm³⁺, Eu³⁺, and Tm³⁺ ions displayed in Fig. 6 show that the emission of these ions is not sensitized by Ce³⁺. The energy of photons absorbed by cerium ions is lost, so for excitation in the UV the presence of this element has a detrimental effect.

Discussion

Quenching of the Ce³⁺ emission by Sm³⁺, Eu³⁺, Tm³⁺, and Yb³⁺.—Blasse and Brill (1) have investigated the energy

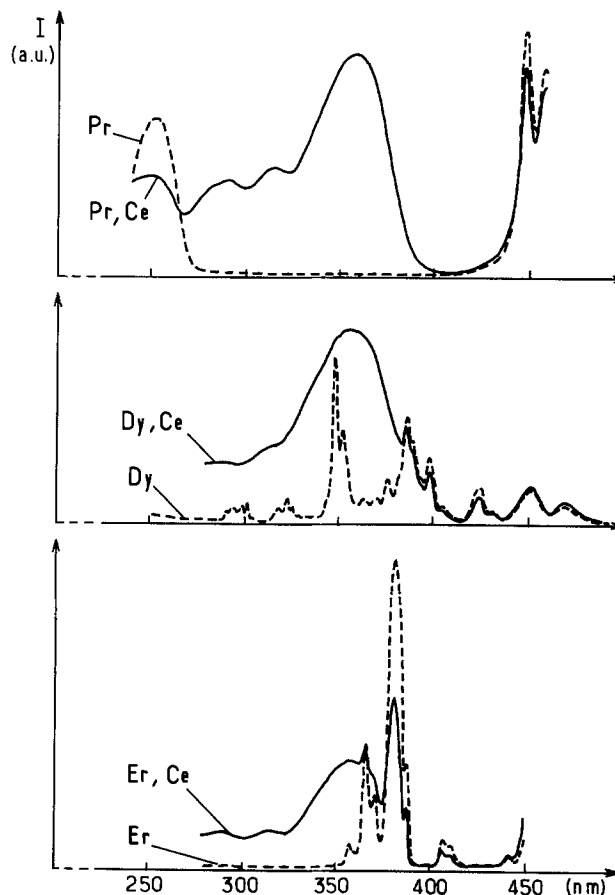


Fig. 4. Excitation spectra of the Pr³⁺, Dy³⁺, and Er³⁺ emissions in LaOBr and Ce-doped LaOBr at 300 K (Compositions: La_{0.99}Pr_{0.01}OBr and La_{0.985}Pr_{0.015}Ce_{0.005}OBr, La_{0.99}Dy_{0.01}OBr and La_{0.985}Dy_{0.015}Ce_{0.005}OBr, La_{0.99}Er_{0.01}OBr and La_{0.985}Er_{0.015}Ce_{0.005}OBr. Emission wavelengths: Pr-501, Dy-568.7, Er-542 nm.)

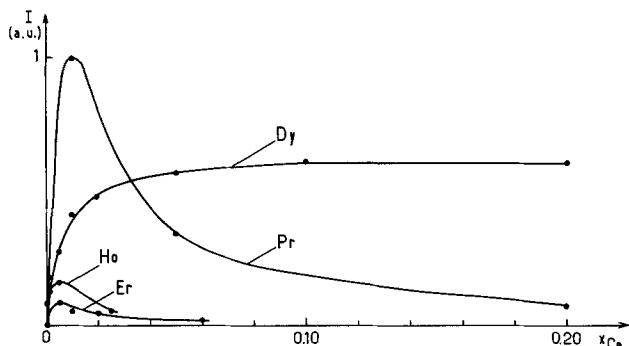


Fig. 5. Dependence of the visible emission intensity of the acceptor on cerium concentration for excitation into a f-d Ce band in the $\text{La}_{0.99-x}\text{Ce}_x\text{A}_{0.01}\text{OBr}$ ($\text{A} = \text{Dy}, \text{Ho}, \text{Er}$) and $\text{La}_{0.98-x}\text{Ce}_x\text{Pr}_{0.02}\text{OBr}$ series. The excitation wavelength lies near the maximum of the most intense f-d band in a region where the acceptor shows little absorption: $\lambda = 348 \text{ nm}$ for Pr, Ho, Er; $\lambda = 353 \text{ nm}$ for Dy. The measured intensity corresponds to transitions below 680 nm originating from the levels indicated in Fig. 1.

transfer from Ce^{3+} to Sm^{3+} or Eu^{3+} in borate and phosphate host lattices and in YOCl . In samples doped with europium, the cerium emission was quenched without sensitization of the activator. With samarium, sensitization was observed in the oxides but not in the oxychloride. In oxide glasses, Reisfeld *et al.* (17, 18) have observed energy transfer from Ce^{3+} to Tm^{3+} . The absence of sensitization for Sm^{3+} and Eu^{3+} was ascribed by Blasse *et al.* (i.c.) to the weak energy difference between the states ($\text{Ce}^{3+} + \text{A}^{3+}$) and ($\text{Ce}^{4+} + \text{A}^{2+}$) with $\text{A} = \text{Sm}, \text{Eu}$. The present study shows that the oxidizing character of the

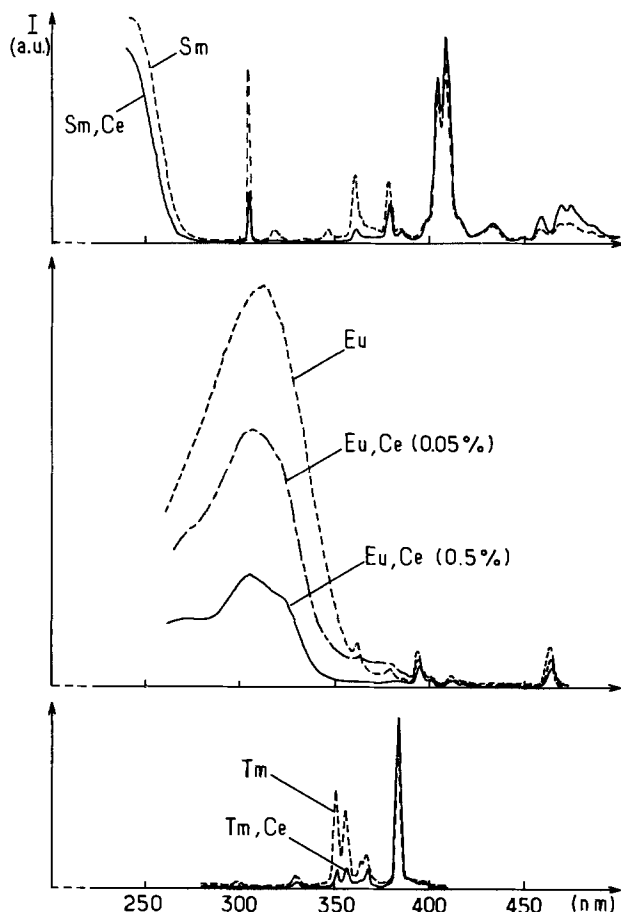


Fig. 6. Excitation spectra of the Sm^{3+} , Eu^{3+} and Tm^{3+} emissions in LaOBr and Ce -doped LaOBr at 300 K. (Compositions: $\text{La}_{0.99}\text{Sm}_{0.01}\text{OBr}$ and $\text{La}_{0.985}\text{Sm}_{0.01}\text{Ce}_{0.005}\text{OBr}$, $\text{La}_{0.98}\text{Eu}_{0.04}\text{OBr}$, $\text{La}_{0.9595}\text{Eu}_{0.04}\text{Ce}_{0.0005}\text{OBr}$ and $\text{La}_{0.955}\text{Eu}_{0.04}\text{Ce}_{0.005}\text{OBr}$, $\text{La}_{0.99}\text{Tm}_{0.01}\text{OBr}$ and $\text{La}_{0.985}\text{Tm}_{0.01}\text{Ce}_{0.005}\text{OBr}$. Emission wavelengths: Sm-609 nm, Eu-618 nm, Tm-460 nm.)

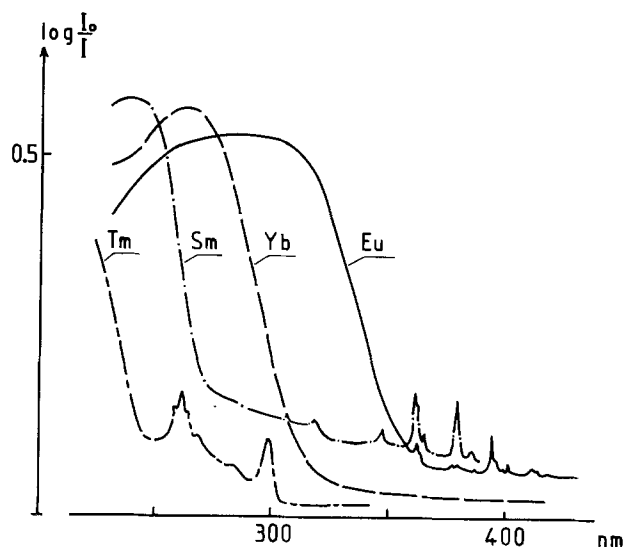


Fig. 7. Reflectance spectra of the lanthanum oxybromide doped with samarium, europium, thulium, and ytterbium (composition: $\text{La}_{0.99}\text{A}_{0.10}\text{OBr}$).

Tm^{3+} and Yb^{3+} ions in LaOBr is also sufficiently high for causing quenching of the cerium emission by such a mechanism. The tendency to reduction to the divalent state for the Sm^{3+} , Eu^{3+} , Tm^{3+} , and Yb^{3+} ions is given by the position of the band corresponding to electron transfer from a ligand in the $\text{A}_x\text{La}_{1-x}\text{OBr}$ phases. Owing to the weak electronegativity of bromine, the charge-transfer band for these four cations lies above 200 nm. As expected, its energy varies according to the sequence $\text{Eu} < \text{Yb} < \text{Sm} < \text{Tm}$ (Fig. 6 and 7). The strong effect of the acceptor on the cerium emission implies energy transfer between Ce^{3+} ions to a $\text{Ce}^{3+}\text{-A}^{3+}$ pair.

Figure 8 shows that in samarium- and thulium-doped samples the cerium emission reappears at low temperature. Such a thermal dependence was not observed for the Ce-Eu and Ce-Yb samples. Two mechanisms can be considered for interpreting the strong variation with temperature of the cerium emission in the samples containing samarium or thulium.

As shown by the changes in the shape of the cerium emission spectra (Fig. 2), Ce-Ce migration decreases at low temperature, reducing the probability of transfer to acceptor ions. This has been observed for instance for the $\text{Ce}^{3+} \rightarrow \text{Tb}^{3+}$ energy transfer in LaPO_4 (10). However, this process cannot account for the different behavior of the Ce-Eu and Ce-Yb samples.

Another explanation is that the reaction $\text{Ce}^{3+}(5d) + \text{A}^{3+} \rightarrow \text{Ce}^{4+} + \text{A}^{2+}$ ($\text{A} = \text{Sm}, \text{Tm}$) requires an activation energy

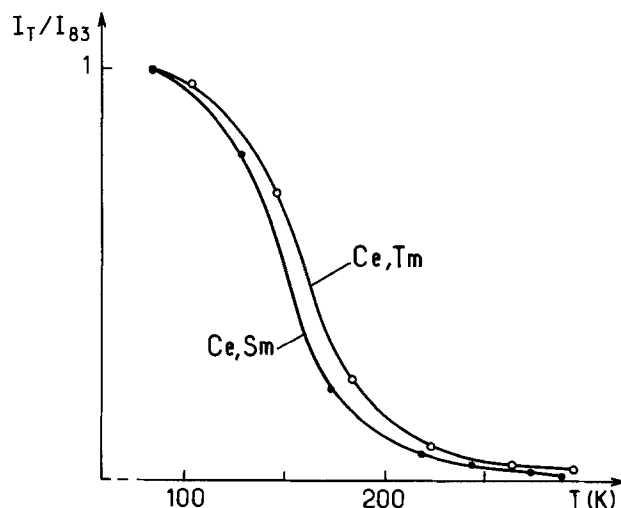


Fig. 8. Thermal dependence of the cerium emission in $\text{La}_{0.993}\text{Ce}_{0.005}\text{Sm}_{0.002}\text{OBr}$ and $\text{La}_{0.993}\text{Ce}_{0.005}\text{Tm}_{0.002}\text{OBr}$.

E_A , the trivalent states being more stable for samarium and thulium than for europium and ytterbium. From the thermal dependence of the cerium emission a value of about 900 cm^{-1} can be derived for E_A . The similarity of the thermal quenching curves for $A = \text{Sm}$ and Tm is surprising since thulium is less oxidizing than samarium. However, the variation of the equilibrium interatomic distance after the change of oxidation states may lower the charge-transfer state more strongly in the case of thulium than in that of samarium. It is known that when a lanthanide ion is substituted for a larger cation, the number of phonons emitted after absorption in the charge-transfer band increases with the difference in size (11).

The effect of the incorporation of other lanthanides on the cerium emission was similar when GdOCl was used as the host lattice. In a recent paper, Blasse (12) shows that in the $(\text{Y}, \text{Gd})\text{F}_3$ fluoride the europium emission can be sensitized by Ce^{3+} , owing to an energy transport of the type $\text{Ce}(\text{Gd})_n\text{-Eu}$. Such a transfer is not possible in chloride or bromide compounds since the $5d$ cerium levels are lowered below the first excited gadolinium level (${}^6\text{P}_{7/2}$) by the nephelauxetic effect.

$\text{Ce}^{3+} \rightarrow \text{Pr}^{3+}, \text{Nd}^{3+}, \text{Tb}^{3+}, \text{Dy}^{3+}, \text{Ho}^{3+}, \text{Er}^{3+}$ energy transfers.—The quenching of the Ce^{3+} emission increases in the sequence $\text{Tb} < \text{Pr} < \text{Er} < \text{Ho} < \text{Nd} < \text{Dy}$. Radiative transfer occurs since the Ce emission band shows dips corresponding to the f - f absorption lines of the acceptor (Fig. 9). However the magnitude of the quenching does not correlate with the variation of the oscillator strengths in the wavelength range of the donor emission; thus the effect of the incorporation of Pr^{3+} which possesses intense absorption lines around 450 nm is much less pronounced than that of Dy^{3+} and Nd^{3+} which show weaker absorption properties in this region. For the same reason, nonradiative transfer by multipolar interactions cannot be the primary cause of the quenching of the cerium emission.

According to Blasse and Brill (1), energy transfer from Bi^{3+} or Ce^{3+} to Sm^{3+} , Eu^{3+} , Tb^{3+} , Dy^{3+} in YOCl occurs mostly by exchange interaction. The probability of such a transfer is given by the formula derived by Dexter (13)

$$P = \frac{2\pi}{h} Z^2 \int f_s(E) F_A(E) dE$$

where Z is an exchange integral and $f_s(E)$ and $F_A(E)$ represent the normalized shape of the emission band of the sensitizer and the absorption band of the acceptor. Z cannot be derived from optical experiments. Blasse has suggested that the transfer probability is enhanced by mixing of anionic and cationic orbitals. The mixing is related to the energy necessary to promote an electron from the ligand to the $4f$ orbitals. Charge-transfer transitions have been recently observed in wide-gap sulfides for neodymium, dysprosium, holmium, and erbium (14).

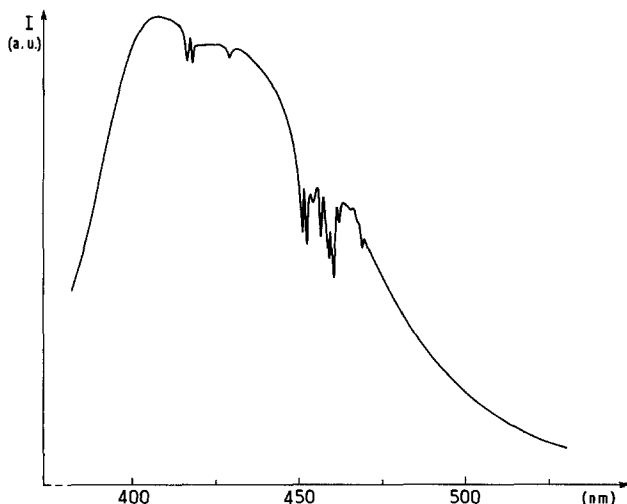


Fig. 9. Emission spectrum of cerium in $\text{La}_{0.985}\text{Ce}_{0.005}\text{Ho}_{0.010}\text{OBr}$ ($\lambda_{\text{exc}} = 362 \text{ nm}$) at 300 K .

Their energy increases according to the sequence $\text{Dy} < \text{Ho} < \text{Nd} < \text{Er}$; from the Jorgensen's spin-pairing theory (20), the charge-transfer bands of Pr^{3+} and Tb^{3+} are expected at higher energy ($\text{Pr} < \text{Tb}$). This is in nearly complete agreement with the influence of these ions on the cerium emission in LaOBr , the only difference being the relative positions of Nd and Ho . The results, therefore, support the mechanism proposed by Blasse.

The dependence of the activator emission intensity on cerium concentration shown in Fig. 5 can be related to the possibility of deexcitation of the emitting level by energy transfer to cerium ions. The separation between the ${}^2\text{F}_{5/2}$ and ${}^2\text{F}_{7/2}$ cerium levels is 1650 cm^{-1} . Measurements of the activator emission intensity for excitation into its $4f$ levels show that quenching occurs when the energy gap between the emitting level and the next-lower level, ΔE , is lower than 4000 cm^{-1} , i.e., for praseodymium, holmium, and erbium ions (Fig. 1). The activator ion decays to the next-lower level, while, simultaneously, cerium ions are excited from ${}^2\text{F}_{5/2}$ to ${}^2\text{F}_{7/2}$, the excess energy being given up to the lattice. Such a mechanism was proposed for explaining the quenching of the ${}^3\text{P}_0$ emission of praseodymium by cerium in LaF_3 (15, 16). As a consequence, at high cerium concentration in the oxybromide, the ${}^1\text{D}_2$ Pr^{3+} emission becomes predominant. The emission of dysprosium and neodymium for which ΔE amounts to about 7000 and 5000 cm^{-1} , respectively, is not affected by the incorporation of cerium. While no change was detected in the decay of the dysprosium fluorescence for $0 < x_{\text{Ce}} < 0.05$, Fig. 10 shows that over this composition range the erbium decay is strongly influenced by cerium concentration.

For dysprosium, despite the absence of nonradiative process involving the ${}^2\text{F}_{5/2}$ and ${}^2\text{F}_{7/2}$ cerium levels, at 300 K for the optimum composition the quantum yield of the visible emission for excitation into the cerium absorption bands is only about 10%. Neglecting the infrared transitions and concentration quenching cannot account for such a low value. The efficiency of the transfer increases with decreasing temperature: for the $\text{La}_{0.98}\text{Ce}_{0.01}\text{Dy}_{0.01}\text{OBr}$ composition, the intensity is multiplied by 5 at 85 K . An explanation may be the existence of nonradiative losses due to the mechanism proposed for Sm^{3+} , Eu^{3+} , Tm^{3+} , Yb^{3+} ions since Dy^{3+} is the most oxidizing of other rare earth cations (like these four elements dysprosium can occur in halides in the divalent state) (21).

Conclusions

From the present study, the following conclusions can be drawn.

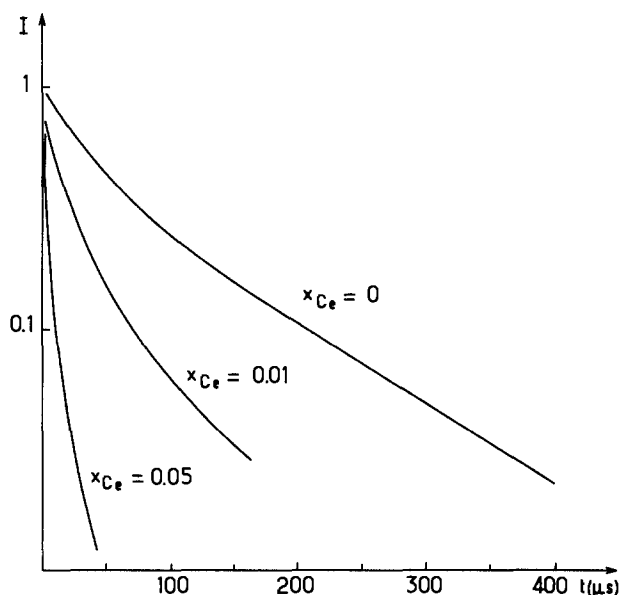


Fig. 10. Decay of the ${}^4\text{S}_{3/2}$, ${}^2\text{H}_{11/2}$ erbium emission in $\text{La}_{0.99-x}\text{Ce}_x\text{Er}_{0.01}\text{OBr}$ oxybromides at 300 K .

1. Ce-doped LaOBr is an efficient phosphor. Owing to the importance of energy migration between cerium ions, a high purity of the starting materials is required to avoid quenching by transfer to impurities. The presence of samarium and thulium is particularly detrimental.

2. Ce³⁺ cannot sensitize the emission of the most oxidizing Ln³⁺ ions (Sm³⁺, Eu³⁺, Tm³⁺) when incorporated in host lattices containing chloride or bromide ions.

3. Energy transfer from Ce³⁺ to Pr³⁺, Nd³⁺, Tb³⁺, Dy³⁺, Ho³⁺, and Er³⁺ occurs in LaOBr. However, when the energy gap between the emitting level and the next-lower level is less than 4000 cm⁻¹, the efficiency of the acceptor emission is affected by nonradiative losses due to an energy transfer involving the ²F_{5/2} → ²F_{7/2} cerium transitions.

Acknowledgment

We are indebted to M. Fu Wen Tian for lifetime measurements.

Manuscript submitted July 25, 1984; revised manuscript received Nov. 13, 1984.

CNRS assisted in meeting the publication costs of this article.

REFERENCES

- G. Blasse and A. Bril, *J. Chem. Phys.*, **47**, 1920 (1967).

- J. L. Sommerdijk and A. Bril, *This Journal*, **122**, 952 (1975).
- J. Hölsa, *Finn. Chem. Lett.*, 201 (1980).
- G. H. Dieke and H. M. Crosswhite, *Appl. Opt.*, **2**, 675 (1963).
- G. Blasse and A. Bril, *J. Chem. Phys.*, **47**, 5139 (1967).
- R. A. Buchanan, T. G. Maple, and A. F. Sklensky, U.S. Pat. 4,297,584 (1981).
- J. Hölsa, M. Leskelä, and L. Niinistö, *J. Solid State Chem.*, **37**, 267 (1981).
- J. G. Rabatin and R. A. Sieger, U.S. Pat. 3,617,743 (1971).
- G. Blasse and A. Bril, *J. Chem. Phys.*, **51**, 3252 (1969).
- J. C. Bourcet and F. K. Fong, *ibid.*, **60**, 34 (1974).
- C. W. Struck and W. H. Fonger, *ibid.*, **64**, 1784 (1976).
- G. Blasse, *Phys. Status Solidi A*, **75**, K41 (1983).
- D. L. Dexter, *J. Chem. Phys.*, **21**, 836 (1953).
- A. Garcia, F. Guillen, and C. Fouassier, *J. Lumin.*, To be published.
- M. R. Brown, J. S. S. Whiting, and W. A. Shand, *J. Chem. Phys.*, **43**, 1 (1965).
- E. G. Reut and A. I. Ryskin, *Opt. Spectrosc.*, **26**, 471 (1969).
- R. Reisfeld and Y. Eckstein, *Appl. Phys. Lett.*, **26**, 253 (1975).
- L. Boehm, R. Reisfeld, and B. Blanzat, *Chem. Phys. Lett.*, **45**, 441 (1977).
- H. Wang, C.-S. Shi, L.-R. Lou, W.-P. Zhang, X.-P. Lu, and J.-F. Zhang, *Lumin. Displ. Devices*, **5**, 36 (1984).
- C. K. Jørgensen, *Solid State Phys.*, **13**, 375 (1962).
- B. Johansson, *J. Phys. Chem. Solids*, **39**, 467 (1978).

Dye-Laser Spectroscopy of Commercial Y₂O₃:Eu³⁺ Phosphors

R. G. Pappalardo* and R. B. Hunt, Jr.

GTE Laboratories, Physical Electronics Technology Center, Waltham, Massachusetts 02254

ABSTRACT

Commercial Y₂O₃:Eu phosphors, formulated at constant europium content, exhibit under 254 nm excitation plaque-brightness variations of up to 10%. Several working models are proposed to explain this variation in emission brightness, and their physical implications on the spectral behavior of the Y₂O₃:Eu materials under discussion are explored by means of the techniques of low temperature, time-resolved emission and excitation spectroscopy, following dye-laser excitation. The following physical models were considered, as affecting the emission brightness of the Y₂O₃:Eu phosphors: sample-specific, nonradiative deactivation of the ⁵D₀ level; preferential site occupation (C₂ or C₃) by Eu³⁺; and the presence of secondary crystalline phases, or sites, of low emission efficiency. None of these models satisfactorily explains the variation in emission brightness for 254 nm excitation. However, a variety of spectral observations suggest that the Eu³⁺ content is lower in Y₂O₃:Eu materials of reduced brightness. This conclusion has been confirmed by high sensitivity, visible-reflectance spectroscopy on the phosphor powders.

The emission properties of Eu-doped Y₂O₃:Eu³⁺ were first reported in 1964 by Wickersheim and Lefever (1) of GTE Laboratories. Shortly afterward, this material (and its oxy-sulfide analog, Y₂O₃S) found extensive commercial application as efficient red emitting phosphors in CRT picture tubes (2, 3).

In the early 1970's, researchers at Philips extended to the area of low pressure fluorescent lamps a scheme familiar in color television technology: namely, the creation of a high efficacy white field by combining the narrow-band emission from three rare earth-activated phosphors (4, 5) emitting in the spectral regions of maximum sensitivity of the human color receptors. One such phosphor was Y₂O₃:Eu³⁺, chosen for its narrow emission in the red, at ≈612 nm and for its high emission-efficiency under 254 nm excitation. Later, this concept was extended to the development of higher brightness deluxe fluorescent lamps, again coated with phosphor blends (6) containing Y₂O₃:Eu³⁺.

Since both the Y₂O₃ host matrix and the Eu activator are very expensive chemicals, a large volume utilization of such materials in a mass-production item, such as the fluorescent lamp, entails high production costs and ultimately a great strain on the market availability of these materials. In many industrial laboratories, these cost considerations are presently the driving force behind efforts

aimed at: (i) replacing the Y₂O₃:Eu³⁺ phosphor with a less expensive material capable of comparable performance, (ii) reducing the yttrium content in the host lattice by partial substitution with a cheaper cation, (iii) ensuring the optimum utilization of the expensive Eu activator, and (iv) maintaining phosphor performance while reducing the Eu³⁺ content.

The present article is concerned in particular with point (iii) of the above listing, in view of observed variations in plaque brightness under 254 nm excitation, for commercial phosphors formulated at constant Eu. Working models to explain these observations were tested using mainly the techniques of pulsed dye-laser spectroscopy. The models in question were: (i) preferential occupation by Eu³⁺ of one of the two cation sites, (ii) enhanced nonradiative deactivation of the dominant (⁵D₀) emitting level of Eu³⁺ in the low brightness materials, and (iii) segregation of Eu³⁺ in distorted sites, or in secondary phases of low emission efficiency.

Results on the dye-laser spectroscopy of the Y₂O₃:Eu phosphors are reported and discussed in what follows, to assess the validity of such models.

Experimental Details

Phosphor samples and their preparation.—A variety of samples were studied in the course of the present investigation. All the samples had 4.7 mole percent (m/o) nomi-

*Electrochemical Society Active Member.

nal Eu^{3+} content. Phosphors fired under similar conditions often showed considerable variations (more than 10%) in plaque brightness for excitation at 254 nm.

Some of the materials studied were supplied by the GTE Products Corporation (Towanda, Pennsylvania), and were prepared there according to procedures perfected by Chenot and Kasenga (7). Their recommended procedure was also followed by Peters of GTE Laboratories in the preparation of some additional phosphors, as described next.

The required quantities of luminescent-grade Y_2O_3 and Eu_2O_3 , with total approximate weight of 25g, were dissolved in hot 10.5M nitric acid. Mixed oxalates were subsequently co-precipitated from the nitrate solutions by means of oxalic acid. After washing and drying, the oxalate precipitate was decomposed in a 1h-1000°C air firing, and the final luminescent materials were developed in a second firing in air at 1600°C for 4h.

Spectral instrumentation.—The powder samples were excited by the output of a Molelectron nitrogen-laser-pumped dye laser, Model UV24 and DL-II respectively. Time-detection of the luminescence relied on PAR boxcar integrators; measurements of the emission spectra, excitation spectra, and decay kinetics were performed under computer control, using APL language software, as described elsewhere (8). Steady-state spectral measurements were performed using a Perkin-Elmer spectrofluorimeter MPF-44A, while a Tektronix J16 photometer was used for plaque-brightness measurements.

For spectral measurements at room temperature the powder samples were pressed into circular cavities milled in anodized aluminum disks. For measurements at low temperature (to 4 K), the powders were deposited onto nickel disks from acetone slurries, and were then mounted on the cold finger of an Air Products Helitran cryostat (8).

Energy Levels of Eu^{3+} in Y_2O_3

A preliminary interpretation of the observed spectra of Eu^{3+} in the condensed phase, in terms of the excited en-

ergy levels of the $4f^6$ configuration, can be found, for instance, in Dieke's book (9). A more detailed spectral investigation of the energy levels of Eu^{3+} in Y_2O_3 was reported by Chang and Gruber (10), with emphasis on transitions involving C_2 sites (see below).

From x-ray diffraction studies (11), it is known that the point symmetry at the cation sites of Y_2O_3 is either C_2 or C_{3i} , the latter site possessing a center of inversion. Early work on rare earth-activated Y_2O_3 single crystals and powder materials (10, 12) established that both cation sites in Y_2O_3 are occupied by the $4f^6$ rare earth activators. The presence of a center of inversion at the C_{3i} site has far-reaching consequences, in the sense of greatly reducing the absorption cross section and the emission rate of the pertinent, forced-electric-dipole transitions, thus favoring the appearance of magnetic-dipole transitions, when the latter are allowed by the selection rules for the crystal-field wavefunctions (13, 14). A detailed energy-level scheme for the ${}^7\text{F}_0$, ${}^7\text{F}_1$, ${}^5\text{D}_1$, and ${}^5\text{D}_0$ levels of Eu^{3+} in Y_2O_3 , for both the C_2 and C_{3i} sites, was derived by Heber *et al.* (15) (Fig. 1) as a result of investigations on single crystals of Y_2O_3 containing Eu^{3+} (up to 5 m/o concentration). The details of the ${}^5\text{D}_1 \rightarrow {}^5\text{D}_0$ relaxation with $\text{C}_{3i} \rightarrow \text{C}_2$ energy transfer were also reported by Heber and Koebler (16). Extensive spectroscopic investigations of $\text{Y}_2\text{O}_3:\text{Eu}$ single crystals, using polarized light, have been recently reported by Dexpert-Ghys and Faucher (17).

The excited electronic states reached on exciting $\text{Y}_2\text{O}_3:\text{Eu}$ at 254 nm belong to a dense distribution of states associated with a charge-transfer process, involving the Eu^{3+} ions and the adjacent oxygen ions. The excitation energy then relaxes from the charge-transfer states to the excited levels of Eu^{3+} proper; hence, emission and nonradiative de-excitation from the ${}^5\text{D}$ term drive the electronic system of Eu^{3+} back to its equilibrium condition.

Spectral Results under UV Excitation

The values of the plaque brightness under 254 nm excitation for the phosphors investigated are collected in Table I. Inspection of the table shows that the plaque

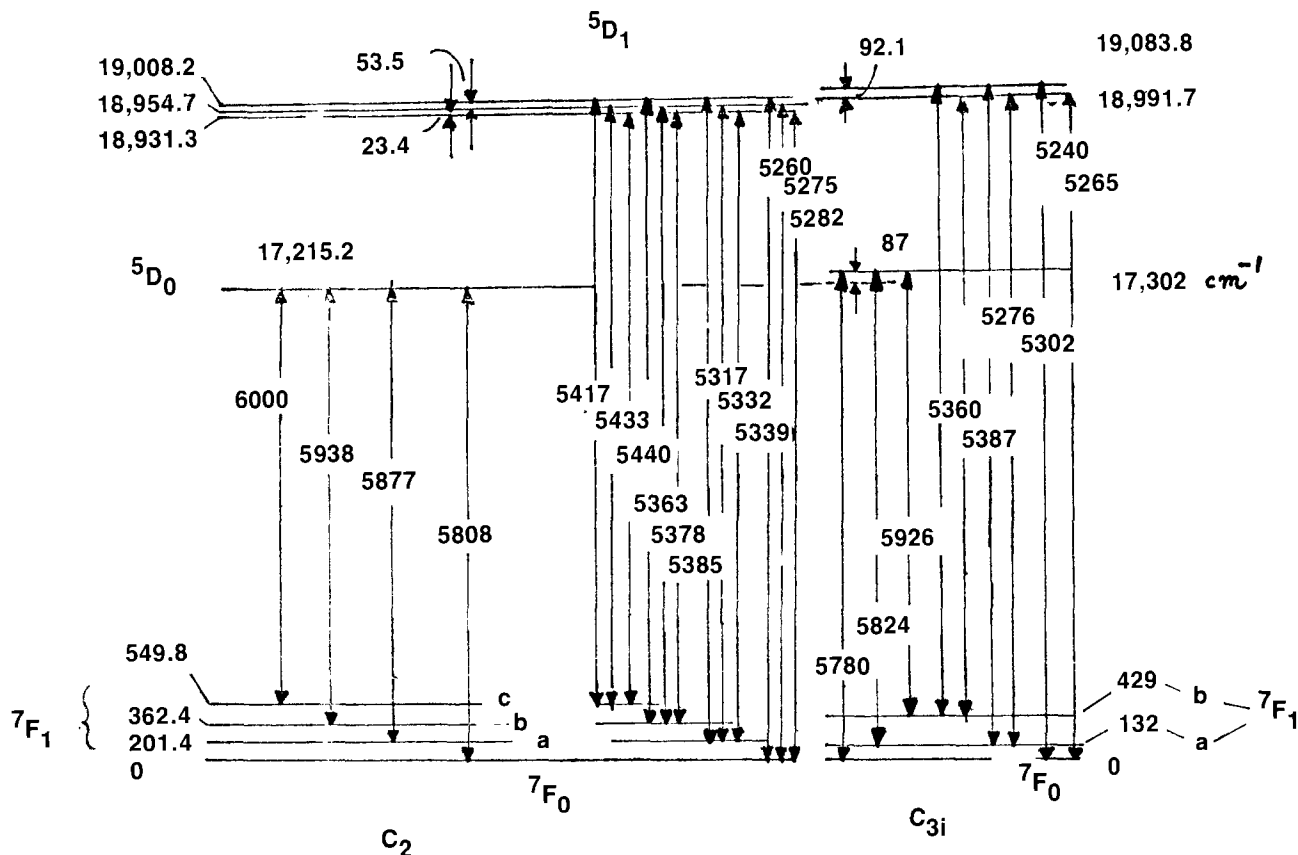


Fig. 1. Energy-level scheme for the lowest manifolds of the ${}^5\text{D}$ and ${}^7\text{F}$ terms in $\text{Y}_2\text{O}_3:\text{Eu}$. On the left, the level scheme for the C_2 site; on the right, that for the C_{3i} site.

Table I. Phosphor plaque-brightness under steady-state excitation at 254 nm (normalized to Yellow Halo and sample YCX-6)

Lot no.	Composition	Relative brightness	
YH PPP9780	CaFAP:Sb;Mn (Yellow Halo)	100	
GTE Labs W4117-54-1	Y ₂ O ₃ :Eu	63.7	98.8
Towanda ^a YRO-6	Y ₂ O ₃ :Eu	56.6	87.8
II-04A	Y ₂ O ₃ :Eu	57.9	89.8
YCX-6	Y ₂ O ₃ :Eu	64.4	100

^a In chronological order of preparation.

brightness of commercial materials formulated at constant Eu content (4.7 m/o) has gradually increased in time by more than 10%, as a result of improved synthesis procedures.

Emission after laser excitation in the UV.—Time-resolved detection of the emission after nanosecond-long excitation in the neighborhood of 254 nm shows, at delays of the order of a few microseconds after excitation, a large number of emission lines originating from upper levels of the 4f⁶ configuration. At later times ($\approx 100 \mu\text{s}$ after excitation), many of these lines are strongly reduced in intensity, or totally extinguished. Figures 2 and 3 show examples of emission curves in the spectral region 400-650 nm. The relative intensity of the various emission groups, at different detection times after excitation, gives an approximate measure of the lifetime of the relevant levels: namely, ⁵D₃, ⁵D₂, ⁵D₁, and ⁵D₀. The emission lifetime is of course longest for the low lying ⁵D₀ level (emission group from 580 nm to longer wavelengths) and decreases progressively for the ⁵D₁, ⁵D₂ levels, and for levels still higher in energy.

For our specific concerns, we would like to draw attention to the marked relative-intensity drop (between 10 and 100 μs) for the line at 588 nm, compared to the other emission components between 580 and 600 nm (Fig. 4; spectra individually normalized at the intensity of the 611 nm emission line). We attribute this intensity drop to the wavelength overlap between an emission line of ⁵D₀ and an intense emission line of ⁵D₁.

This wavelength overlap also affects the shape of the emission pattern measured in this spectral region under

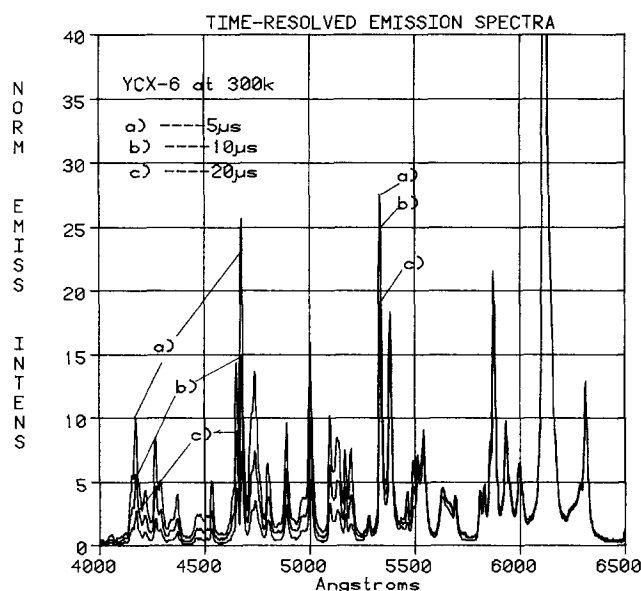


Fig. 2. Overview of the time-resolved emission spectra from 400 to 650 nm, following nanosecond laser excitation at 260 nm. Sample YCX-6 at room temperature. a): Emission detected during the first 5 μs . b): Some, first 10 μs . c): Some, first 20 μs . All curves are normalized to the peak of the strong emission line at 611 nm, which is truncated in plotting to enhance the weaker emission lines.

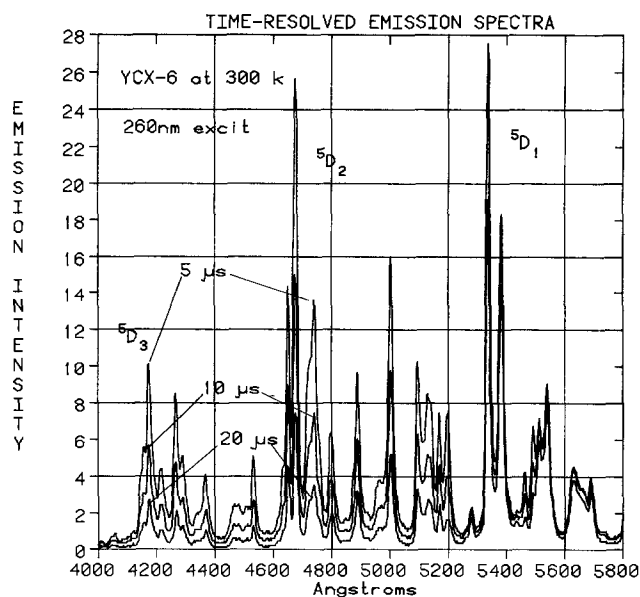


Fig. 3. Detail of Fig. 2 over the spectral range 400-580 nm. The emitting levels responsible for the main emission groups are identified.

steady-state excitation. While sample-to-sample differences in this emission pattern in steady-state emission measurements are often construed as indicative of structural differences between samples, the time-resolved spectra show that the shape of the emission pattern is also determined by the relative contribution of the ⁵D₁ level.

Emission decays after UV excitation.—An overview of the emission kinetics of ⁵D levels of interest is given in Table II, which lists relevant parameters, such as temperature, wavelength, transition assignments, the time after excitation at which detection was started, the risetime, and the time for emission to reach 1/e of the peak value. All measurements refer to 5-10 ns long laser excitation.

Some comments on the entries of Table II are now appropriate, in the context of correlating plaque brightness and decay kinetics of the phosphors. In Fig. 5 are plotted the normalized decay curves for emission at 611 nm (from

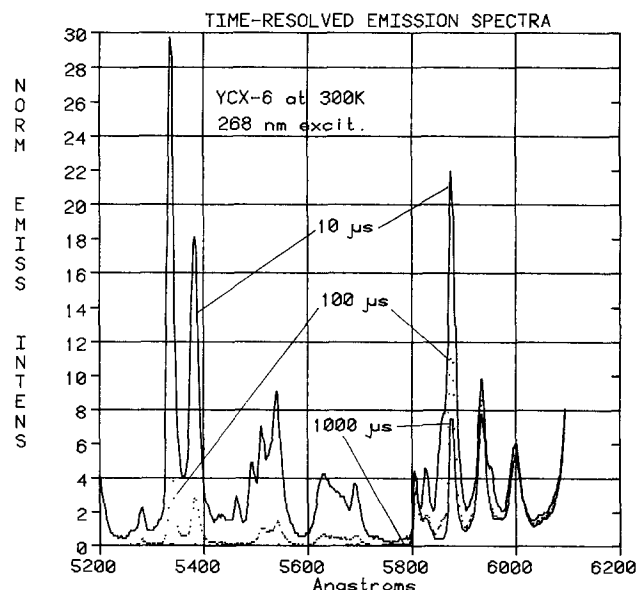


Fig. 4. Detail of the time-resolved spectra from 520-620 nm, to emphasize the unusual intensity behavior with detection time in the emission group between 580 and 600 nm. Sample YCX-6 at room temperature, excited with nanosecond pulses at 268 nm. Detection times are, respectively, 10, 100, and 1000 μs . Spectra are individually normalized at the peak of the 611 nm line. Note the rapid, relative-intensity drop of the 588.8 nm line between 10 and 100 μs .

Table II. Emission-decay parameters for various yttrium oxide:Eu phosphors

Sample	Run	Temp. (K)	Excitation (nm)	Transition	Emission (nm)	Transition	Detection start ^c	I/e time	Rise time ^d
YCX-6	H374	300	265	charge-transfer	611	$^5D_0 \rightarrow ^7F_3(C_2)$	0.5 ms	1.1 ms	
YCX-6	H376	300	265	charge-transfer	611	$^5D_0 \rightarrow ^7F_3(C_2)$	0.5 ms	1.1 ms	
YCX-6	H393	300	265	charge-transfer	611	$^5D_0 \rightarrow ^7F_3(C_2)$	0 ms		22 μ s
II-04A	H375	300	265	charge-transfer	611	$^5D_0 \rightarrow ^7F_3(C_2)$	0.5 ms	1.11 ms ^b	
W4117 ^a	H395	300	265	charge-transfer	611	$^5D_0 \rightarrow ^7F_3(C_2)$	0 ms		15 μ s
YCX-6	H401	300	265	charge-transfer	533.8	$^5D_{11} \rightarrow ^7F_{11}(C_2)$	0 μ s	43-46 μ s	8 μ s
II-04A	H402	300	265	charge-transfer	533.8	$^5D_{11} \rightarrow ^7F_{11}(C_2)$	0 μ s	49 μ s	8 μ s
W4117 ^a	H403	300	265	charge-transfer	533.8	$^5D_{11} \rightarrow ^7F_{11}(C_2)$	0 μ s	34 μ s	6 μ s
YCX-6	H409	300	265	charge-transfer	467.8	$^5D_2 \rightarrow ^7F$	0 μ s	5.5 μ s	0.3 μ s
II-04A	H410	300	265	charge-transfer	467.8	$^5D_2 \rightarrow ^7F$	0 μ s	6.5 μ s	0.3 μ s
W4117 ^a	H411	300	265	charge-transfer	467.8	$^5D_2 \rightarrow ^7F$	0 μ s	4.5 μ s	0.3 μ s
YCX-6	H308	300	582.4	$^7F_{11} \rightarrow ^5D_0(C_{31})$	611	$^5D_0 \rightarrow ^7F_3(C_2)$	0.35 ms	1.58 ms	
YCX-6	H356	300	582.4	$^7F_{11} \rightarrow ^5D_0(C_{31})$	611	$^5D_0 \rightarrow ^7F_3(C_2)$	0.35 ms	1.58 ms	
YCX-6	H319	77	582.4	$^7F_{11} \rightarrow ^5D_0(C_{31})$	611	$^5D_0 \rightarrow ^7F_3(C_2)$	0.35 ms	1.44-1.48	
II-04A	H305	300	582.4	$^7F_{11} \rightarrow ^5D_0(C_{31})$	611	$^5D_0 \rightarrow ^7F_3(C_2)$	0.35 ms	1.5 ms	
II-04A	H292	77	582.4	$^7F_{11} \rightarrow ^5D_0(C_{31})$	611	$^5D_0 \rightarrow ^7F_3(C_2)$	0.35 ms	1.64-1.68	
W4117 ^a	H355	300	582.4	$^7F_{11} \rightarrow ^5D_0(C_{31})$	611	$^5D_0 \rightarrow ^7F_3(C_2)$	0.35 ms	1.44 ms	
II-04A	H290	77	582.4	$^7F_{11} \rightarrow ^5D_0(C_{31})$	582.4	$^5D_0 \rightarrow ^7F_{11}(C_{31})$	0.35 ms	2.0 ms	
YCX-6	H309	300	580.	$^7F_0 \rightarrow ^5D_0(C_2)$	611	$^5D_0 \rightarrow ^7F_3(C_2)$	0.35 ms	1.2 ms ^b	
YCX-6	H318	77	580.	$^7F_0 \rightarrow ^5D_0(C_2)$	611	$^5D_0 \rightarrow ^7F_3(C_2)$	0.35 ms	0.84 ms	
YCX-6	H328	4	580.8	$^7F_0 \rightarrow ^5D_0(C_2)$	611	$^5D_0 \rightarrow ^7F_3(C_2)$	0.35 ms	0.93 ms ^b	
YCX-6	H499	5	580.8	$^7F_0 \rightarrow ^5D_0(C_2)$	611	$^5D_0 \rightarrow ^7F_3(C_2)$	0.35 ms	0.92 ms ^b	
YCX-6	H349	300	580.6	$^7F_0 \rightarrow ^5D_0(C_2)$	611	$^5D_0 \rightarrow ^7F_3(C_2)$	0.35 ms	1.1-1.2 ms	
II-04A	H304	300	580.7	$^7F_0 \rightarrow ^5D_0(C_2)$	611	$^5D_0 \rightarrow ^7F_3(C_2)$	0.35 ms	1.18 ms	
II-04A	H293	77	580.9	$^7F_0 \rightarrow ^5D_0(C_2)$	611	$^5D_0 \rightarrow ^7F_3(C_2)$	0.35 ms	1.04-1.08	
II-04A	H502	5	580.9	$^7F_0 \rightarrow ^5D_0(C_2)$	611.5	$^5D_0 \rightarrow ^7F_3(C_2)$	0.10 ms	0.97 ms	
YCX-6	H417	300	528.1	$^7F_0 \rightarrow ^5D_{11}(C_2)$	538.2	$^5D_{11} \rightarrow ^7F_{11}(C_2)$	0 μ s	39 μ s	2 μ s
YCX-6	H424	300	526.6	$^7F_0 \rightarrow ^5D_{11}(C_{31})$	538.2	$^5D_{11} \rightarrow ^7F_{11}(C_2)$	0 μ s	46 μ s	
II-04A	H416	300	528.1	$^7F_0 \rightarrow ^5D_{11}(C_2)$	533.8	$^5D_{11} \rightarrow ^7F_{11}(C_2)$	0 μ s	20 μ s	
W4117 ^a	H418	300	528.1	$^7F_0 \rightarrow ^5D_{11}(C_2)$	533.8	$^5D_{11} \rightarrow ^7F_{11}(C_2)$	0 μ s	16 μ s	
W4117 ^a	H525	10	528.1	$^7F_0 \rightarrow ^5D_{11}(C_2)$	611.5	$^5D_{11} \rightarrow ^7F_3(C_2)$			90 μ s
W4117 ^a	H516	10	528.1	$^7F_0 \rightarrow ^5D_{11}(C_2)$	611.5	$^5D_{11} \rightarrow ^7F_3(C_2)$	0.10 ms	1.0 ms	
W4117 ^a	H516	10	528.1	$^7F_0 \rightarrow ^5D_{11}(C_2)$	611.5	$^5D_{11} \rightarrow ^7F_3(C_2)$	0.10 ms	0.98 ms ^b	
W4117 ^a	H517	10	528.2	$^7F_0 \rightarrow ^5D_{11}(C_2)$	611.5	$^5D_{11} \rightarrow ^7F_3(C_2)$	0.10 ms	0.98 ms	
W4117 ^a	H520	10	527.0	$^7F_0 \rightarrow ^5D_{11}(C_2)$	611.5	$^5D_{11} \rightarrow ^7F_3(C_2)$	0.10 ms	1.02 ms	

^a W4117-54-1.^b Curve fitting with single-exponential decay.^c After excitation pulse.^d Between 10% and 90% intensity.

the 5D_0 level of the C_2 sites) for three different $Y_2O_3:Eu$ phosphors formulated with the same Eu content, but exhibiting a range of $\approx 10\%$ difference in plaque brightness under steady-state excitation at 254 nm (Table I). The normalized decay curves, resulting from dye-laser excitation at 265 nm, in the charge-transfer band of Eu^{3+} , were not appreciably different in the three materials. The decay was exponential, and its constant was measured as 1.1 ms (see Table II).

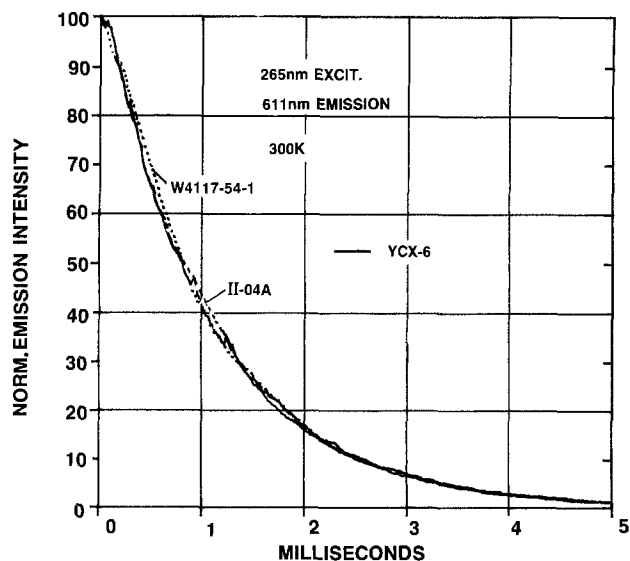


Fig. 5. Normalized emission decays at room temperature, measured at 611 nm for various $Y_2O_3:Eu$ samples, following laser excitation at 265 nm. See also Tables I and II.

The area under the actual emission-decay pulse of sample II-04A was measured as $\approx 89\%$ of the analogous quantity of YCX-6, in agreement with the relative brightness values of Table I. However, when we consider the areas under the curves (individually normalized at peak intensity), they differ by only 2%, the area for the dimmer II-04A being actually greater. Therefore, for UV excitation at room temperature no correlation appears to exist between 5D_0 emission lifetime and steady-state emission intensity at 611 nm (the dominant emission component). In other words, sample-specific nonradiative quenching of the 5D_0 population is apparently not responsible for the observed variation in steady-state plaque brightness for UV excitation.

In Fig. 6, the room temperature decays of the emission line at 533.8 nm are given for excitation at 265 nm of samples from lots YCX-6, II-04A, and W4117-54-1. By reference to the energy-level scheme of Fig. 1, this particular emission line is assigned to $^5D_1 \rightarrow ^7F_{11}$ transitions for C_2 sites.

Contrary to the case of the emission at 611 nm, a pronounced spread is observed in the emission decays of Fig. 6. The dimmest sample (II-04A; Table I) exhibited the slowest decay, with a decay constant of 49 μ s (to I_0/e intensity; Table II). Lowering of the sample temperature to 77 K produced a marked lengthening of the emission lifetime (92 μ s to I_0/e intensity for sample YCX-6) and a longer buildup time for emission to reach its maximum (≈ 20 μ s).

A trend in emission lifetimes similar to that of Fig. 6 is also observed, on a more compressed time scale, for emission from the 5D_2 manifold, as monitored at room temperature for the 467.8 nm emission line, the dominant transition of this group (see Fig. 2).

Of the three samples, the one with lowest steady-state brightness again exhibits the longest decay (*i.e.*, 6.5 μ s;

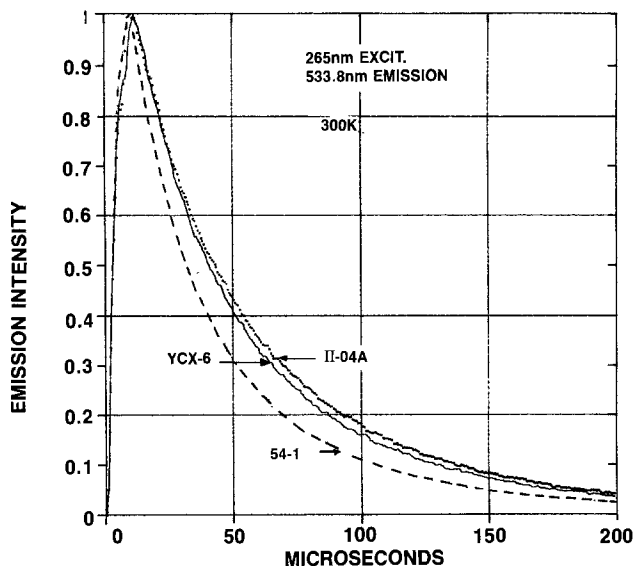


Fig. 6. Same as Fig. 5, but emission at 533.8 nm from C₂ sites of ⁵D₁. Sampling window 2 μs. The longest decay is observed for a sample of relatively low brightness for 254 nm excitation (see Table I).

Fig. 7). The decays were nonexponential, and the time required for the peak intensity to decay to its I₀/e value ranged in Fig. 7 from 4.5 to 6.5 μs (Table II). This time increased to ≈8 μs when the II-04A phosphor was cooled to 77 K.

Table II also lists the risetimes for emission, defined as the time between the 10% and 90% values of the emission intensity. A related quantity, namely the buildup time required for emission to reach its peak, was of the order of 10 μs for the ⁵D₁ emission resulting from UV excitation. The buildup time was definitely longer in the case of the ⁵D₀ emission at 611 nm, as a result of the gradual feeding of this level by higher lying levels; even at room temperature, the buildup time was of the order of 100 μs (Fig. 8; excitation at 265 nm), and it was appreciably longer for sample II-04A, in correlation with the ⁵D₁ lifetimes of the individual samples.

In summary, under UV excitation the emission decays at room temperature for the ⁵D₁ and ⁵D₂ manifolds (but not for ⁵D₀) were generally of longer duration for the low brightness II-04A material.

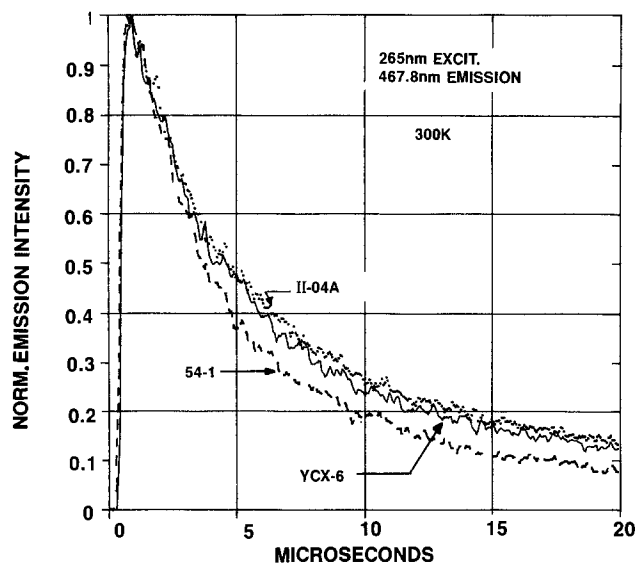


Fig. 7. Emission from the ⁵D₂ manifold at room temperature. Again, the longest decay is exhibited by the least bright material of the three.

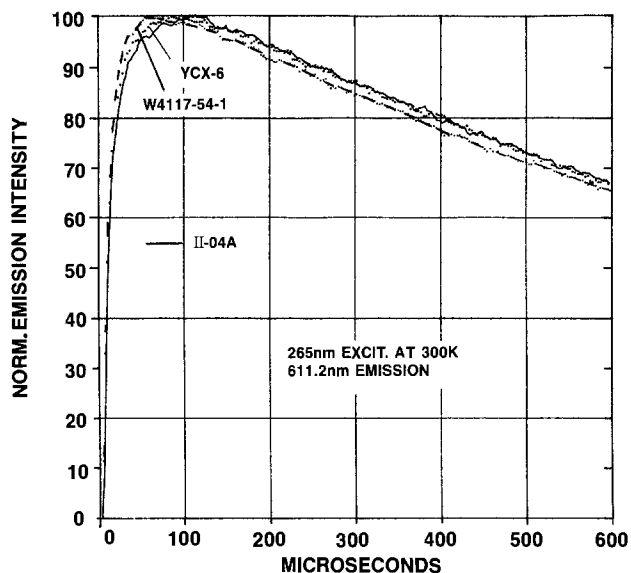


Fig. 8. Detail of the initial portion of the normalized emission decay at 611.2 nm at room temperature, for excitation at 265 nm. The emission from sample II-04A has an appreciably longer buildup time to reach its peak (≈100 μs).

Spectral Results for Level-Selective Excitation

Emission and excitation characteristics of the ⁵D manifolds will be now reconsidered for the case of selective excitation into specific levels of the ⁵D term.

Emission spectra for selective excitation into ⁵D₀.—We refer now to the energy-level scheme of Fig. 1. On excitation at 580.8 nm, energy is absorbed in the ⁷F₀ → ⁵D₀ transition of the C₂ sites. The emission at 77 K in the case of the YCX-6 material (Fig. 9, dotted curve) is found to consist of the resonant line at 580.8 nm, a weaker line at 582.4 nm, followed by a triplet at 587.4, 593.0, and 599.7 nm, and the intense line at ≈611 nm used for normalization in plotting. There are, in addition, emission groups at wavelengths longer than 611 nm, not considered here.

The assignment of the emission lines to specific electronic transitions is shown in Fig. 9 (see also the energy-

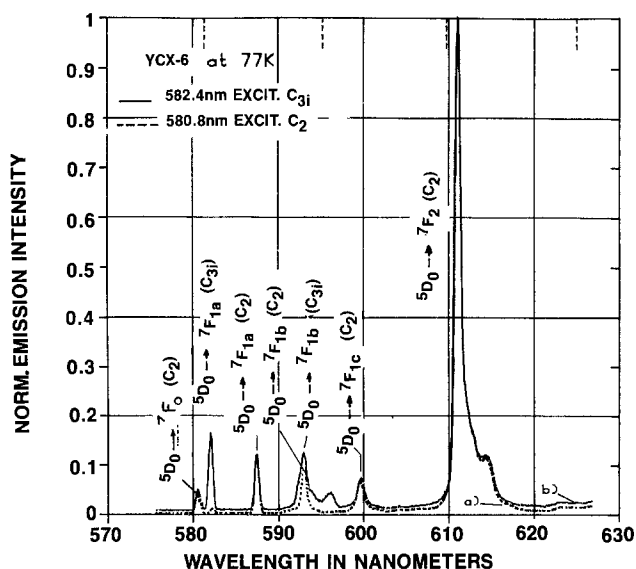


Fig. 9. Emission spectra ⁵D₀ → ⁷F₀, ⁷F₁, ⁷F₂ for selective excitation into the ⁵D₀ level of sample YCX-6 at 77 K. a) C₂ excitation at 580.8 nm (⁵D₀ → ⁷F₀; dashed trace). b) C_{3i} excitation ⁵D₀ → ⁷F_{3i} at 582.4 nm (continuous trace). The emission spectra are normalized at the peak of the 611 nm emission line. Note the strong C₂-type emission lines, especially at 611 nm, even for C_{3i}-type excitation, and the additional structure on the long wavelength side of the ⁵D₀ → ⁷F_{1b} emission line of C_{3i} type. Sampling: 1 ms long, starting 0.2 ms after excitation.

level scheme of Fig. 1). Excitation into the C_2 site produces, as expected, the corresponding ${}^5D_0 \rightarrow {}^7F_0, {}^7F_1, {}^7F_2, {}^7F_3, {}^7F_4, {}^7F_5$ emissions for the C_2 site. In addition, as evidenced by the weak line at 582.4 nm [${}^5D_0(C_{31}) \rightarrow {}^7F_{1a}(C_{31})$], only a modest energy transfer takes place at this temperature from ${}^5D_0(C_2)$ to the ${}^5D_0(C_{31})$ level, higher in energy by $\approx 90 \text{ cm}^{-1}$ (see Fig. 1).

On excitation at 582.4 nm (C_{31} -site absorption), a mixture of emission lines of C_2 and C_{31} origin is observed (Fig. 9, continuous trace). Among the former is the anti-Stokes emission at 580.8 nm, and all the remaining ${}^5D_0 \rightarrow {}^7F_0, {}^7F_1, {}^7F_2$ transitions for the C_2 site, including the dominant line at 611 nm, which is used for the normalization of the emission spectrum resulting from C_{31} -type excitation. The emission lines for transitions originating from Eu^{3+} ions in the C_{31} -sites are: the resonant ${}^5D_0 \rightarrow {}^7F_{1a}$ line at 582.4 nm; and the ${}^5D_0 \rightarrow {}^7F_{1b}$ transition at ≈ 592.9 nm, accompanied by some additional structure, which we shall assume to be of vibronic nature, for the time being. The point we want to emphasize is the efficient energy transfer from C_{31} to C_2 sites, even at 77 K, in the sense that excitation energy pumped into the C_{31} subsystem of 5D_0 ends up predominantly as C_2 emission at 611 nm.

For the purpose of the discussion to follow, it should be noted that, in comparing the emission spectra at 77 K for YCX-6 and II-04A following C_{31} excitation at 582.4 nm, the resonant emission line at 582.4 nm was found to be relatively stronger in II-04A, after the emission spectra were individually normalized at the intensity of the 611 nm line.

No evidence of additional emission lines, diagnostic of Eu^{3+} in secondary crystalline phases, was found on contrasting the emission spectra for level-selective excitation of the two materials YCX-6 and II-04A of different plaque-brightness.

Emission decays from 5D_0 .—The intrinsic emission kinetics of the important 5D_0 level are considered next. In Fig. 10, the solid curve shows the measured decay at 5 K of the emission line at 611.5 nm for sample YCX-6, after C_2 -type excitation at 580.8 nm; the dotted curve corresponds to a normalized curve for single exponential decay with 0.92 ms constant. The agreement is seen to be excellent. A different low temperature run with the same sample at 4 K gave on fitting a decay constant of 0.93 ms (Table II). The decay of the 611.5 nm emission of sample II-04A was also measured at 5 K after C_2 -type excitation at

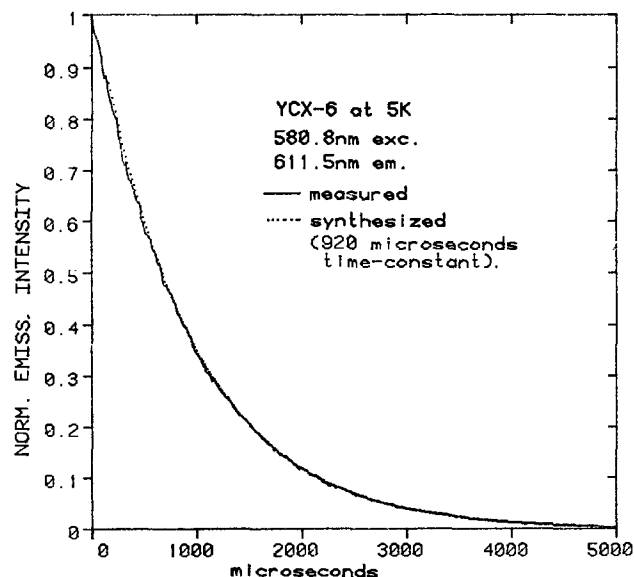


Fig. 10. Decay at 5 K of the emission at 611.5 nm from sample YCX-6 for C_2 -type excitation at 580.8 nm. The curve (normalized at its peak) was recorded with a $50 \mu\text{s}$ aperture, starting at $100 \mu\text{s}$ after excitation. By comparison, the dotted curve represents an exponential decay with a time constant of 0.92 ms. The overlap of the two curves is remarkably good.

580.8 nm. The decay was closely exponential with a decay constant of ≈ 0.97 ms, namely, longer than the 0.92-0.93 ms value for sample YCX-6.

In a separate series of measurements at various temperatures, we recorded the decay at 611.2 nm from sample YCX-6, after C_2 -type excitation at 580.0 nm (Fig. 11). Again, the decay was exponential at ≈ 4 K and at 300 K, but it had a more complex behavior at the intermediate temperature, presumably because at 77 K the upward energy transfer between C_2 and C_{31} sites, and back-transfer, become possible. Self-trapping of the emitted radiation could also play a role in the observed emission kinetics, especially at room temperature. The time associated with the first e folding of the emission (*i.e.*, to I_0/e) was 0.92 ms at 4 K and 1.2 ms at 300 K (see Table II).

Next, the decay curves for the main emission line at 611 nm were considered at room temperature both in the case of C_2 excitation at 580.6 nm and C_{31} excitation at 582.4 nm. In the former case, the decays of YCX-6 and W4117-54-1 were very similar, and were both somewhat longer than the decay of II-04A. In the latter case of C_{31} excitation, the decays were all generally longer, in view of the $C_{31} \rightarrow C_2$ transfer, and the decay constant of YCX-6 was measured as 1.58 ms, $\approx 5\%$ longer than for II-04A. Since the decay of YCX-6 was also longer than that of W4117-54-1 (Fig. 12), no correlation was found between plaque brightness for 254 nm excitation and decay time for C_2 emission resulting from C_{31} excitation in 5D_0 .

Excitation spectra for 5D_0 emission.—On monitoring the emission at 611.2 nm and scanning the excitation region corresponding to the ${}^7F_1 \rightarrow {}^5D_0$ absorptions in the YCX-6 material, peaks corresponding to both C_{31} and C_2 transitions are observed (Fig. 13). As the temperature is lowered, the short wavelength excitation peak of Fig. 13 (C_2 -transition ${}^7F_0 \rightarrow {}^5D_0$) increases in intensity at the expense of the remaining two lines, partly because of accumulation of population in the fundamental 7F_0 level.

As for the $C_{31} \rightarrow C_2$ transfer, as shown by the presence in the excitation spectra of lines corresponding to absorptive transitions within both C_{31} and C_2 sites, it continues even for temperatures as low as 55 K (Fig. 13; excitation line at 582.4 nm, namely ${}^7F_{1a} \rightarrow {}^5D_0$ transition for the C_{31} sites). When the temperature is further lowered to 4 K, the excitation pattern of Fig. 13 simplifies to one line at 580.8 nm, because the electronic population is effectively concentrated on the 7F_0 fundamental level, while the ${}^7F_{1a}$ level is depopulated.

In conclusion, since efficient $C_{31} \rightarrow C_2$ transfer occurs within 5D_0 at low temperatures, it can be expected to be

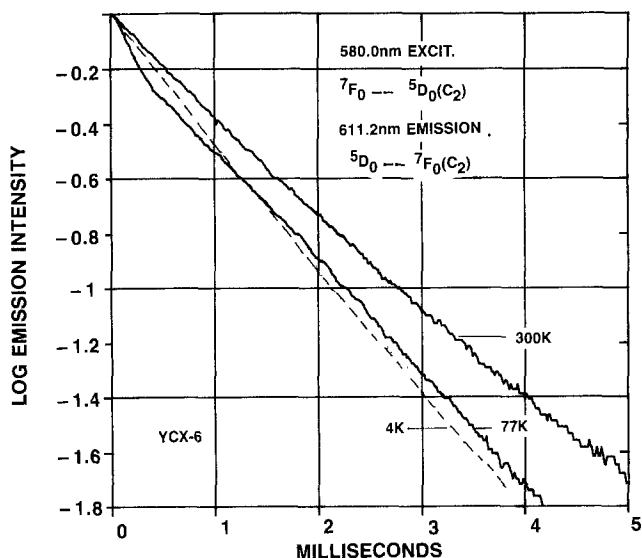


Fig. 11. Semilog plot of the emission decay for sample YCX-6 measured at 4, 77, and 300 K for C_2 -type excitation at 580 nm. The decay is exponential both at 4 and 300 K (definitely longer in the latter case), but nonexponential in its initial portion at 77 K.

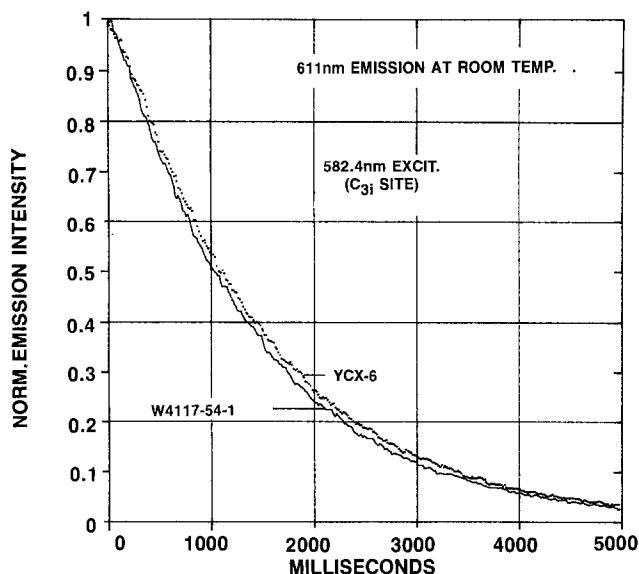


Fig. 12. Emission decays at room temperature for C_{3i}-type excitation at 582.4 nm. C₂-type emission monitored at 611 nm. The decay for the YCX-6 sample appears to be consistently slower.

even more effective at room temperature, thereby coupling the population of the two cation subsystems.

Excitation spectra measured while monitoring the emission along the spectral contour of the dominant emission line at ≈ 611 nm, revealed no new excitation peaks in samples exhibiting lower brightness under UV excitation. In the particular case of the ${}^7F_0 \rightarrow {}^5D_0$ excitation line of C₂ sites, we did not observe either the broadening or the splitting that would arise from Eu³⁺ in distorted sites or in secondary phases.

Similarly, no evidence of additional emission lines, diagnostic of Eu³⁺ in secondary crystalline phases, was found on contrasting the emission spectra for level-selective excitation of the two materials YCX-6 and II-04A of different brightness.

Discussion

Emission brightness for UV excitation.—As already mentioned, several mechanisms could be invoked as rele-

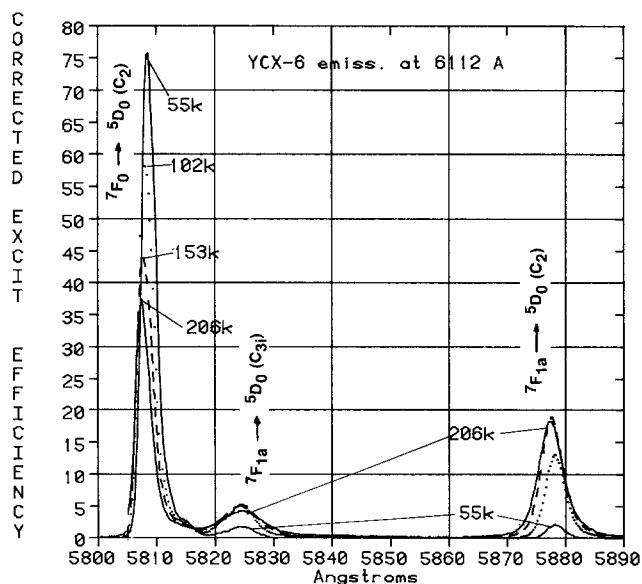


Fig. 13. Excitation spectra at various temperatures for the 611.2 nm emission in sample YCX-6, in the spectral region for 7F_0 , ${}^7F_{1a} \rightarrow {}^5D_0$ transitions. The excitation line at 580.8 nm increases monotonically with the decrease in temperature, as a result of thermal population-redistribution in the ground manifold of levels. Contributions to the C₂ emission originating from C_{3i}-type absorption (excitation line at 582.4 nm) are noticeable even at temperatures as low as 55 K. Detection: 1 ms long, starting 0.2 ms after excitation.

vant to the question of sample-to-sample variation in plaque brightness for 254 nm excitation in Y₂O₃:Eu, and appropriate measurement techniques would have to be used to verify experimentally the implications of such models. In this context dye-laser spectroscopy is especially suitable for checking mechanistic models, whose operation affects the emission-decay kinetics and/or fine details of the emission spectra and of the excitation spectra. Among these, we have considered: (i) preferential occupation by Eu³⁺ of one of the two cation sites (C_{3i} or C₂), (ii) enhanced nonradiative deactivation of the emitting 5D_0 level of Eu³⁺ in the low brightness materials, and (iii) segregation of Eu³⁺ in distorted sites or in secondary phases of low emission efficiency.

These models are now assessed on the basis of the experimental information gathered in the present study.

Nonradiative deactivation of 5D_0 .—It was already noted in previous sections that the bulk of the emission intensity in Y₂O₃:Eu phosphors originates from the 5D_0 level, and that the emission-decay kinetics from 5D_0 , following room temperature UV excitation (Fig. 5) do not differ sufficiently from sample to sample (Table II) to account for the observed 10% brightness differential (Table I).

On the contrary, for selective excitation into the C_{3i} level at 582.4 nm (Fig. 12) a somewhat longer emission decay is observed for the YCX-6 material than for the material W4117-54-1 (and II-04A). The reasons for the different decay behavior under UV excitation and 5D_0 excitation are not clear at present.

However, even for level-selective excitation, no correlation was found between plaque-brightness (for 254 nm excitation) and emission lifetimes of the 5D_0 levels.

One of the reasons for the lack of correlation between 5D_0 decay kinetics and phosphor brightness is the coupling in 5D_0 between two systems of ions (in C_{3i} sites and in C₂ sites) decaying at different rates. In view of the efficient C_{3i} \rightarrow C₂ intersite energy transfer in 5D_0 at room temperature, slower decays for the 611 nm emission do not necessarily indicate the absence of deleterious nonradiative deactivation processes. Longer decays may simply reflect an oscillatory-type migration of excitation energy back and forth between the C_{3i} and C₂ sublattices. No correlation between plaque brightness for 254 nm excitation, and the duration of the 5D_0 , C₂-type decay is expected *a fortiori* for UV excitation of the materials, since the emission kinetics of the 611 nm line are further complicated by intersite transfer and nonradiative deactivation along the ladder of electronic levels funneling the excitation energy down to the 5D_0 level.

Preferential site occupation by Eu³⁺.—Another mechanism impacting the emission brightness was initially postulated to be the following: let us assume that Eu³⁺ is preferentially situated in the C_{3i} site of the host matrix. Then these effects would be anticipated: (i) the relative intensity of the "hypersensitive" (18) C₂-type emission line at 611 nm will be reduced, while an increase would be expected in the relative intensity of the emission lines of C_{3i}-type, ${}^5D_0 \rightarrow {}^7F_{1a}$ and ${}^5D_0 \rightarrow {}^7F_{1b}$ at ≈ 582 and ≈ 593 nm, respectively. In addition, the longer lifetime of the C_{3i}-type 5D_0 level would enhance the probability of its nonradiative deactivation, resulting in reduced emission brightness.

The spectral measurements on the materials in question have shown that efficient coupling between C_{3i} and C₂ sites occurs even at temperatures as low as 55 K. Evidently, the intersite exchange of excitation energy will be even more effective at room temperature. Even assuming that such site occupation actually occurs, it will not affect significantly the emission from 5D_0 , which is predominantly in the form of the hypersensitive line at 611 nm.

Crystalline sites (or phases) of low emission efficiency.—As another working model, one could envisage that some of the Eu³⁺ ions are present either in distorted sites of the Y₂O₃ host matrix, or segregated in secondary crystalline phases. Both effects are expected to lead to re-

duced emission efficiency at 611 nm, by arguments similar to those outlined in the previous section on C_{31} vs. C_2 site occupation.

Assuming the model to be correct, we expect to find changes in the excitation and emission spectra in comparing $Y_2O_3:Eu$ phosphors of different brightness. In particular, if the hypothetical distorted sites of Y_2O_3 were occupied by Eu^{3+} , one would anticipate either a broadening, or a multiplicity of excitation and emission lines associated, for instance, with the easily detectable ${}^7F_0 \rightarrow {}^5D_0$ and ${}^5D_0 \rightarrow {}^7F_0$ transitions for the C_2 sites. Neither expectation is validated by the observations of the present study.

As for the presence of secondary crystal phases, the evidence to this effect is inconclusive, either from the x-ray diffraction data or from the overall absence of additional spectral features in the emission and excitation spectra.

The question of the actual Eu^{3+} content.—We list now some differences observed in the spectral behavior of the YCX-6 material and the dimmer II-04A material.

1. On UV excitation, the room temperature emission decays from 5D_2 and 5D_1 were slower in II-04A.

2. Again in II-04A, a longer buildup time after UV excitation was observed at room temperature for the 611 nm emission to reach its peak.

3. Longer 5D_0 emission decay of C_2 -type was measured at 5 K in II-04A, for C_2 -type selective excitation at 580.8 nm.

4. On excitation at 77 K into the C_{31} levels of 5D_0 , the resonant, C_{31} -type emission ${}^5D_0 \rightarrow {}^7F_{1a}$ was relatively stronger in II-04A.

5. The emission from II-04A had a relatively weaker intensity in the long-wavelength structure of the dominant emission line at 611 nm.

Most of these effects can be viewed as being caused by a less rapid energy transfer in the excited states of II-04A, which we attribute to a lower Eu^{3+} content in II-04A. This conclusion is quite unexpected. Measurements of the Eu content in the three phosphor materials of main interest in this report were obtained from atomic-absorption measurements, and are listed in Table III. The analytical data reveal that, while the early-vintage YRO-6 sample of low brightness (Table I) has a definitely lower Eu content (and this would explain the reduced brightness value), there appears to be no significant difference (only a relative $\approx 4\%$) in Eu content between YCX-6 and II-04A.

For our purposes, we are interested rather than in the total Eu content, as listed in Table III, in the fraction of Eu that is actually present as the trivalent ion. Since the analytical data do not differentiate between these two quantities, we have resorted to high sensitivity reflectance spectroscopy to assess qualitatively the relative concentration of Eu^{3+} in the II-04A and YCX-6 materials. Examples of reflectance spectra in the long-UV and visible regions are given in Fig. 15 and 16. In both figures, we are plotting diffuse reflectance spectra of two $Y_2O_3:Eu$ samples, using the reflectance of a suitable standard (Eastman Kodak Reflectance Standard 6091) as the base line for the measurements. In order to discriminate reflectance from luminescence signals, two monochromators (locked at the same wavelength) were

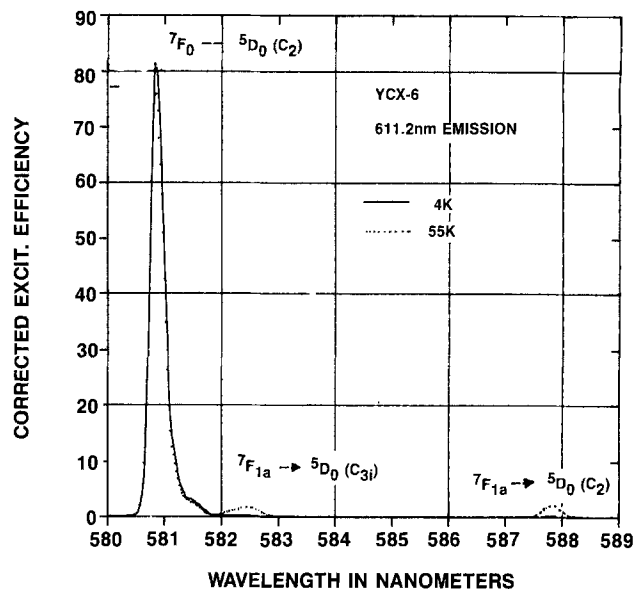


Fig. 14. Same as Fig. 13, but comparing excitation spectra at 55 and 4 K. At the latter temperature only, the contribution from the C_2 -type ${}^7F_0 \rightarrow {}^5D_0$ transition at 580.8 nm is observed.

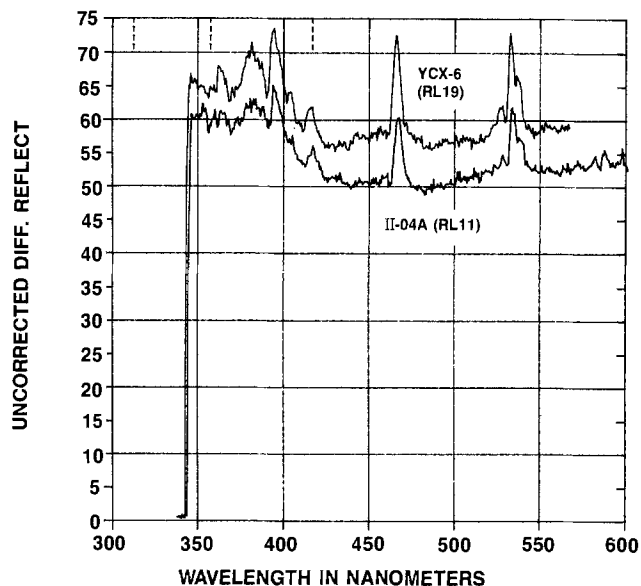


Fig. 15. Weak absorption lines contributed by Eu^{3+} , as detected from reflectance measurements at room temperature in the visible spectral region of sample YCX-6 and sample II-04A. Ordinates: difference reflectance spectra vs. the Eastman Kodak Reflectance Standard 6081. Absorption is in the direction of increasing ordinates.

scanned in tandem to supply the direct radiation and to detect the reflected radiation, respectively. The resulting spectra are plotted so that decreased reflectance (*i.e.*, increased absorbance) is in the direction of increasing values of the ordinates.

Table III. Eu content in various phosphors. Also reflectance at 254 nm, particle size, and quantum yield for emission

Lot no.	Composition	Eu content (w/o) ^a	254 nm reflect	Particle size ^b	Relative quantum yield ^c
GTEL W4117-54-1	$Y_2O_3:Eu$	6.98 6.92 6.91	0.25	6.82	131.7
Towanda YRO-6	$Y_2O_3:Eu$	4.98 4.54 4.53	0.28	6.93	121.9
II-04A	$Y_2O_3:Eu$	5.40 5.50 5.35	0.28	8.36	124.7
YCX-6	$Y_2O_3:Eu$	5.58 5.75 5.69	0.17	8.38	120.5

^a Results from three different analyses, using atomic absorption techniques.

^b Median diameter in micrometers from Coulter Counter measurements.

^c Relative quantum yield, from 254 nm reflectance and brightness values from Table I.

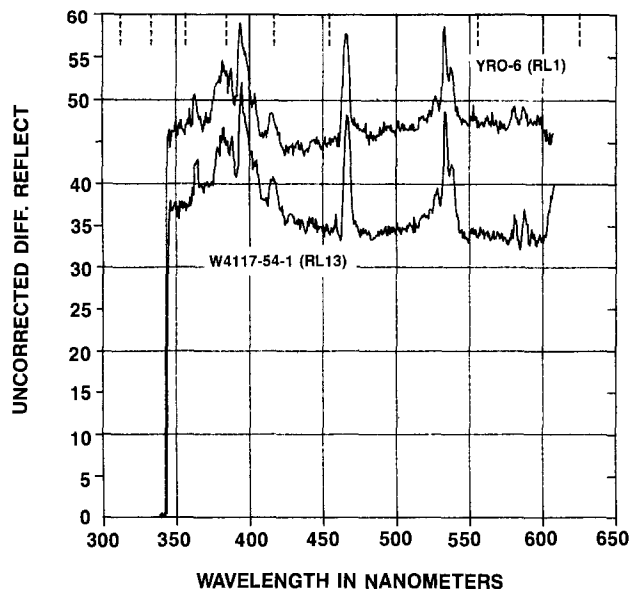


Fig. 16. Same as Fig. 15, but for samples W4117-54-1 and sample YRO-6.

Figure 15 shows a comparison of such spectra for samples II-04A and YCX-6, that have almost the same particle size (Table III). In spite of the comparable total Eu content, the Eu³⁺ content in II-04A seems lower, by almost a factor of two, judging from the reduced strength of the absorption lines. A similar comparison in Fig. 16 for W4117-54-1 and YRO-6, again with similar particle size (Table III), highlights the more intense Eu³⁺ absorption in the former, as expected simply from the difference in total Eu content.

Table III also lists the reflectance at 254 nm for the relevant samples. Here again, the objective of the measurement was to correlate UV absorbance with total Eu³⁺ content. Such correlation is apparently absent. Since the UV absorption at 254 nm is contributed not only by the charge-transfer transitions of Eu³⁺, but also by lattice defects/vacancies, a simple measurement of the reflectance at 254 nm may be insufficient for the stated aim. Instead, a careful study of the absorption throughout the entire UV spectral region would be required to separate the contributions to the absorption originating from Eu³⁺ and those caused by centers associated with lattice defects.

Conclusions

The present investigation on the dye-laser spectroscopy of commercial Y₂O₃:Eu phosphors has uncovered several spectral features of interest, associated with the excited state relaxation of Eu³⁺, and has clarified some effects observed in conventional optical spectroscopy of these materials. Such effects will now be summarized.

1. In the steady-state measurements of emission after 254 nm excitation, the intensity pattern of the line group from 580 to 600 nm is often observed to change from sample to sample. On the basis of the time-resolved emission spectra, we attribute these changes to variations in relative emission intensity from the upper ⁵D₀ level. In other words, these spectral effects are associated with changes in Eu³⁺ concentration.

2. Efficient coupling exists between the Eu³⁺ ions in the two C_{3i} and C₂ sublattices of the dominant ⁵D₀ emitting level. Differences from sample to sample in ⁵D₀ decay kinetics depend, via the Eu³⁺ concentration and the temperature, on the rates of the energy exchange back and forth between the C_{3i} and C₂ sublattices.

The following observations are pertinent to the specific question of plaque brightness for 254 nm excitation of the materials under consideration.

1. The decay time of the ⁵D₀ emission at room temperature does not correlate with emission brightness for 254 nm excitation.

2. No evidence was uncovered for secondary crystalline phases, or for Eu³⁺ sites of intrinsically low emission efficiency.

3. Dye-laser spectroscopy suggests that low-brightness materials contain lower concentrations of Eu³⁺.

4. High sensitivity reflectance spectroscopy confirms the model of a correlation of plaque brightness for 254 nm excitation and strength of the Eu³⁺ reflectance lines in the visible spectral region.

The techniques of dye-laser spectroscopy have been useful in suggesting a lower Eu³⁺ content in the sample of lower plaque brightness. Rather than the decay kinetics of the ⁵D₀ level, the key factors determining the emission brightness for 254 nm excitation in Y₂O₃:Eu appear to be: first, the actual Eu³⁺ concentration, as distinct from the total Eu content detected by analytical techniques; and, second, the nature of the short-UV absorptions in the materials in question: namely, whether they are contributed by Eu³⁺ charge-transfer processes or by absorbing centers that decay nonradiatively and do not transfer the absorbed UV radiation to Eu³⁺ emitting centers.

At this stage, the problem of plaque brightness under 254 nm excitation must be tackled by techniques other than dye-laser spectroscopy, with a shift to conventional excitation and reflectance spectroscopy in the UV, and high resolution reflectance spectroscopy in the visible region.

Acknowledgments

The authors wish to express their thanks to the following technical personnel of the GTE Corporation. From GTE Laboratories (Waltham, Massachusetts), M. Downey for the x-ray diffraction measurements; F. Durkin and C. Persiani for the analytical determination of the Eu content; T. Peters for the preparation of some of the phosphor samples and for many discussions on phosphor properties; and A. Vetrovs for assistance in the preparation of the phosphors. From GTE Products Corporation, Chemical and Metallurgical Division (Towanda, Pennsylvania), C. Chenot and A. Kasenga for providing the phosphor samples, for advice on procedures for the phosphor synthesis, and for discussions on the problem of emission brightness in Y₂O₃:Eu phosphors. From GTE Products Corporation, Lighting Products (Danvers, Massachusetts), E. Dale, for suggesting models relevant to the question of emission efficiency in Y₂O₃:Eu phosphors.

Manuscript submitted June 15, 1984; revised manuscript received ca. Oct. 22, 1984. Sections of this article were presented as Paper 512 at the Montreal, Quebec, Canada, Meeting of the Society, May 9-14, 1982.

GTE Laboratories assisted in meeting the publication costs of this article.

REFERENCES

1. K. A. Wickersheim and R. A. Lefever, *This Journal*, **111**, 47 (1964).
2. S. S. Trond, J. S. Martin, J. P. Stanavage, and A. L. Smith, Abstract 53, p. 132, The Electrochemical Society Extended Abstracts, Vol. 68-1, Boston, MA, May 5-9, 1968.
3. H. Forest, *This Journal*, **120**, 695 (1973).
4. J. M. P. J. Verstegen, D. Radjelovic, and L. E. Vrenken, *ibid.*, **121**, 1627 (1974).
5. L. E. Vrenken, *Lighting Research and Technology*, **8211** (1976).
6. T. F. Soules, Abstract 339, p. 845, The Electrochemical Society Extended Abstracts, Vol. 78-1, Seattle, WA, May 21-26, 1978.
7. C. F. Chenot and A. Kasenga, Private communication.
8. R. B. Hunt Jr. and R. G. Pappalardo, Submitted to *J. Lumin.*
9. G. H. Dieke, "Spectra and Energy Levels of Rare-Earth Ions in Crystals," Interscience, New York (1968).
10. N. C. Chang and J. B. Gruber, *J. Chem. Phys.*, **41**, 3227 (1964).
11. R. Wyckoff, "Crystal Structures," Vol. 2, p. 5, Interscience, New York (1964).

12. H. Forest and G. Ban, *This Journal*, **116**, 474 (1969).
 13. K. H. Hellwege, *Ann. Phys.*, **6.4**, 97, 127, 136, 143, 150 (1948).
 14. J. L. Prather, "Atomic Energy Levels in Crystals," p. 19, NBS Monograph, National Bureau of Standards, Washington, DC (1961).
 15. J. Heber, K. H. Hellwege, U. Koebler, and H. Mur-

- mann, *Z. Phys.*, **237**, 189 (1970).
 16. J. Heber and U. Koebler, *Bull. Acad. Sci. SSR*, **37**, 379 (1973).
 17. J. Dexpert-Ghys and M. Faucher, *Phys. Rev. B*, **20**, 10 (1979).
 18. C. K. Jorgensen and B. R. Judd, *Mol. Phys.*, **8**, 281 (1964).

Technical Notes



Selective Reactive Ion Etching of TiW

P. M. Schaible and G. C. Schwartz*

IBM Corporation, General Technology Division, Hopewell Junction, New York 12533

TiW is used as a barrier to interdiffusion between aluminum or aluminum copper thin films (used as interconnections in integrated circuits) and silicon or PtSi contacts, thereby preventing junction short circuits (1). One method of defining VLSI interconnection patterns is by a lift-off technique. A stencil is defined (2), and after evaporation, the unwanted metal is removed with the stencil, leaving the interconnection metallization. However, TiW is most practically deposited by sputtering, which is not compatible with this method. If TiW were sputtered through a lift-off mask, the pattern would have sloped walls (3), and coverage of the walls of the lift-off stencil is a potential problem. A more practical process for the formation of patterns in TiW is subtractive etching, following lift-off formation of the aluminum or aluminum copper on top of a blanket layer of TiW. To insure the absence of undercutting, reactive ion etching (RIE) is used to etch the TiW.

Although TiW can be etched in a CF_4 plasma, the etch-rate ratios, $R(TiW)/R(SiO_2)$ and $R(TiW)/R(Si_3N_4)$, are unfavorable, so severe attack of the substrate occurs.

This note describes the optimization of an alternate TiW RIE process, first proposed by Kitcher *et al.* (4). The process, RIE in CCl_4/O_2 mixtures, results in a favorable etch-rate ratio with respect to the nitride (or oxide) substrate. An overlying pattern of aluminum or AlCu (formed by lift-off or by a previous RIE step in CCl_4) is not etched in the CCl_4/O_2 mixture. Al_2O_3 , grown during the TiW etch is easily removed by an *in situ* RF sputter clean prior to deposition of the next level of metal (5).

*Electrochemical Society Active Member.

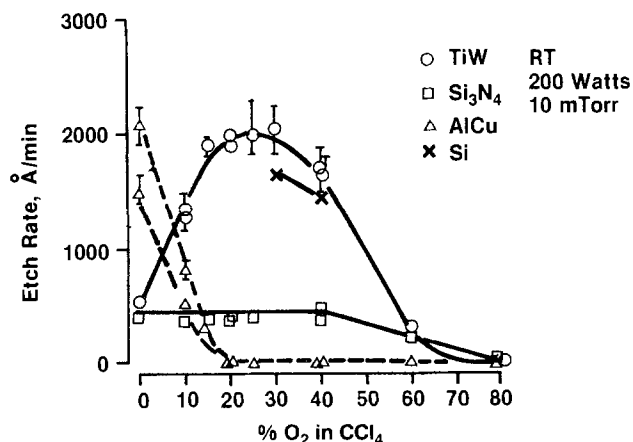


Fig. 1. Etch rates of TiW, Si_3N_4 , AlCu, and Si vs. $\%O_2$ in CCl_4 at room temperature, 200W, 10 mtorr total pressure. The two curves in the AlCu data represent the minimum and maximum etch rates observed.

The reactor used in these experiments has been described previously (6). In order to achieve, in this system, the maximum etch rate and the maximum selectivity, we investigated (at small loads) the effect of gas composition, input RF power, system pressure, and cathode temperature. The temperature of the etching samples (thin films deposited onto silicon-wafer substrates) is not controlled; it will depend on the cathode temperature and the RF power density (7).

Figure 1 shows the dependence of the etch rates of TiW, AlCu, and Si_3N_4 on the concentration of O_2 in CCl_4 , $\{C(O_2) = P(O_2)/[P(O_2) + P(CCl_4)]\}$; the input RF power density was 0.4 W/cm^2 , the total pressure was 10 mtorr, and the cathode was not heated by an external source. The etch rates of SiO_2 are not shown. We had found in previous experiments that Si_3N_4 always etched at a higher rate than SiO_2 in these plasmas (8). In pure CCl_4 , AlCu etches about 3-4 times more rapidly than TiW and Si_3N_4 . As $C(O_2)$ is increased, the etch rate of AlCu decreases rapidly; the etch rate becomes equal to the sputter etch rate at $C(O_2) = 0.2$. On the other hand, the etch rate of TiW, $R(TiW)$, increases with increasing $C(O_2)$ and reaches a broad maximum at $C(O_2) = 0.2-0.3$. When $C(O_2)$ is increased beyond 0.3, $R(TiW)$ decreases rapidly. The etch rate of Si_3N_4 , $R(Si_3N_4)$, is independent of $C(O_2)$ for values of $C(O_2)$ less than about 0.4; above $C(O_2) = 0.4$, $R(Si_3N_4)$ decreases gradually. The maximum value of $R(TiW)/R(Si_3N_4)$ is approximately 5 and occurs at $C(O_2) = 0.2$. In this gas mixture, the etch

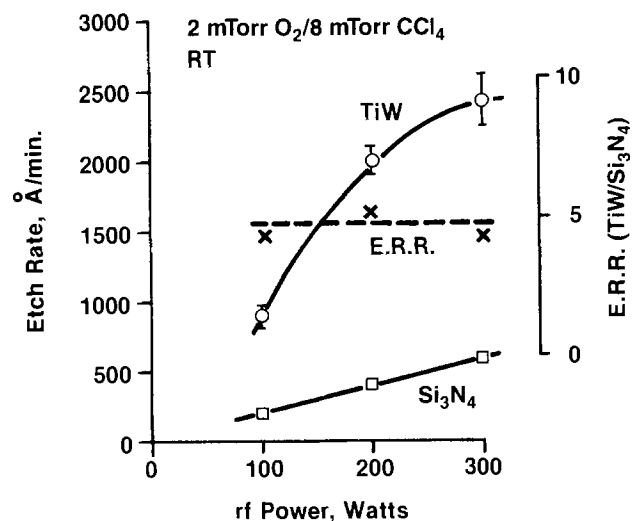


Fig. 2. Etch rates of TiW, Si_3N_4 , and ERR vs. RF power at room temperature, 2 mtorr $O_2/8$ mtorr CCl_4 .

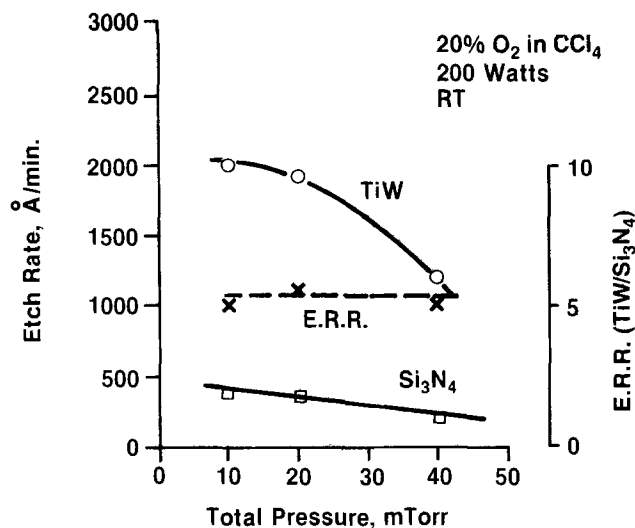


Fig. 3. Etch rates of TiW, Si₃N₄, and ERR vs. pressure at room temperature, 20% O₂ in CCl₄, 200W.

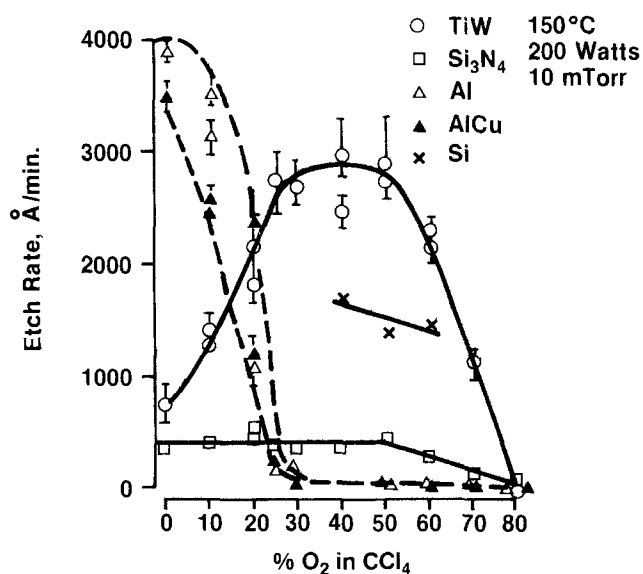


Fig. 4. Etch rates of TiW, Si₃N₄, Al, AlCu, and Si vs. %O₂ in CCl₄ at 150°C, 200W, 10 mtorr.

rate of silicon is approximately 0.9 $R(\text{TiW})$, so that uncovered contacts would be attacked.

At a constant value of $C(\text{O}_2) = 0.2$, we investigated the dependence of $R(\text{TiW})$, $R(\text{Si}_3\text{N}_4)$, and $R(\text{TiW})/R(\text{Si}_3\text{N}_4)$ on RF power and total pressure. At constant pressure, an increase in input power causes an increase in both etch rates, but the etch rate ratio remains unchanged. At constant input power, an increase in total pressure results in a decrease in both etch rates, but again, the etch rate ratio remains unchanged. This is illustrated in Fig. 2 and 3.

As seen in Fig. 4, increasing the cathode temperature to 150°C results in increases in both $R(\text{TiW})$ and $R(\text{AlCu})$ but no increase in $R(\text{Si}_3\text{N}_4)$. Figure 5 shows that the maximum value of $R(\text{TiW})/R(\text{Si}_3\text{N}_4)$ is 7.5 and that it remains constant as $C(\text{O}_2)$ changes from 0.3 to 0.7; at these values of $C(\text{O}_2)$, $R(\text{AlCu})$ is negligible and $R(\text{Si}) = 0.5R(\text{TiW})$, which decreases the attack on uncovered contacts. It can also be seen that a further increase in cathode temperature produces no further increase in $R(\text{TiW})/R(\text{Si}_3\text{N}_4)$.

Substitution of Cl₂/O₂ or Cl₂/CO₂ for CCl₄/O₂ resulted in similar trends of $R(\text{TiW})/R(\text{Si}_3\text{N}_4)$ vs. $C(\text{O}_2)$, but the etch rate ratios were lower than in CCl₄/O₂.

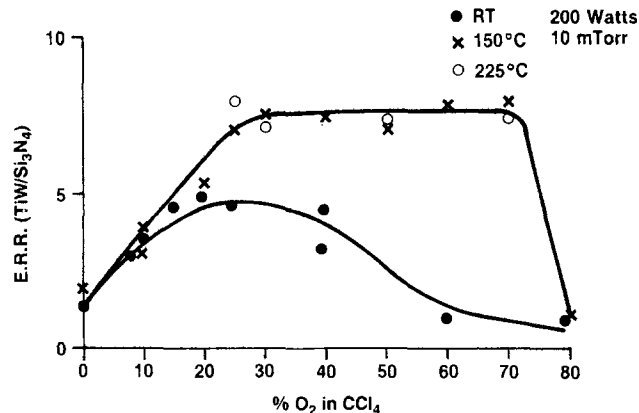


Fig. 5. ERR (TiW/Si₃N₄) vs. %O₂ in CCl₄ as a function of temperature at 200W, 10 mtorr pressure.

It has been proposed that Cl, formed in a CCl₄ plasma, is responsible for etching aluminum and AlCu (9). Burton *et al.* have shown that addition of O₂ to a CCl₄ plasma increases the amount of atomic Cl in the plasma until the dilution effect predominates (10). Nevertheless, Tokunaga *et al.* (9) reported that increasing additions of O₂ to CCl₄ plasmas reduced the etch rate of aluminum until, finally, no further etching was observed. They suggested that the species responsible for etching aluminum oxide were consumed by the O₂ so that the aluminum surface was protected from etching. Another view of the role of oxygen is that it reoxidizes the aluminum surface as fast as it is exposed, thereby preventing attack by Cl. We assume that the TiW is not subject to passivation by the added oxygen; therefore, the higher concentration of atomic Cl results in a higher etch rate.

Use of a gas mixture of 40%-50% O₂ in CCl₄ and a cathode temperature of 150°C permits etching of TiW with minimal attack of Al or AlCu and SiO₂ or Si₃N₄. The etch rate of silicon is about one-half the etch rate of TiW.

Acknowledgment

The authors thank J. P. Anderson for technical assistance.

Manuscript submitted June 11, 1984; revised manuscript received Nov. 2, 1984.

IBM Corporation assisted in meeting the publication costs of this article.

REFERENCES

1. P. B. Ghate, J. C. Blair, C. R. Fuller, and S. E. McGuire, *Thin Solid Films*, **53**, 117 (1978); C. Canali, G. Celotte, F. Fantini, and E. Zanoni, *ibid.*, **88**, 9 (1982); P. C. Parehk, R. C. Surine, and P. Lemieux, *Solid State Electron.*, **19**, 493 (1976).
2. J. P. Franco, J. R. Havas, and J. Rompala, U.S. Pat. 4,004,044 (1975).
3. T. Sakurai and T. Serikawa, *This Journal*, **126**, 1257 (1979).
4. J. R. Kitcher, G. M. Ozols, and B. N. Singerman, U.S. Pat. 4,203,800 (1980).
5. J. H. Bauer, in "The Eighth International Vac. Conference," Vol. 1, p. 649 (1980).
6. P. M. Schaible, W. C. Metzger, and J. P. Anderson, *J. Vac. Sci. Technol.*, **15**, 334 (1978).
7. G. C. Schwartz and P. M. Schaible, in "Plasma Processing," R. G. Freiser and C. J. Mogab, Editors, p. 133, The Electrochemical Society Softbound Proceedings Series, Pennington, NJ (1981).
8. Unpublished results.
9. K. Tokunaga and D. W. Hess, *This Journal*, **127**, 928 (1980).
10. R. H. Burton and G. Smolinsky, *ibid.*, **129**, 1599 (1982).

In Situ Preparation of p-Type CdTe Thin Films by Cathodic Electrodeposition

R. N. Bhattacharya and K. Rajeshwar*

Department of Chemistry, The University of Texas at Arlington, Arlington, Texas 76019

R. N. Noufi*

Solar Energy Research Institute, Golden, Colorado 80401

Recent studies on n-CdS/p-CdTe heterojunction solar cells (1) have reported solar-to-electrical conversion efficiencies approaching the 10% benchmark. Thin films of CdTe required for these devices are fabricated by a variety of methods (e.g., vacuum deposition, screen printing, close-spaced sublimation). Electrodeposition is another candidate technique receiving scrutiny (1b, 2). Although earlier studies had prescribed conditions for cathodic deposition of both n- as well as p-type CdTe (3), more recent work reveals difficulties with electrodeposition of p-type layers from acidic baths [cf. Ref. (1g, 4)]. These difficulties have led to the need for post-deposition thermal treatment of electrodeposited films to induce n → p-type conversion. Preliminary evidence for p-type electronic conductivity in the as-deposited films was presented in previous communications (2c, 2d). These experiments, however, were conducted on deposition baths containing no intentionally added acceptor impurity (e.g., Cu). The purpose of this note is to present further evidence for p-type conductivity in CdTe thin films containing Cu as well as some data bearing on the direct applicability of these films to n-CdS/p-CdTe heterojunction fabrication.

Experimental

Procedures for bath preparation and electrodeposition have been described in previous papers from these laboratories (2d, 5). Glass slides coated with Sn-doped indium oxide (ITO) (nominal sheet resistance: 10 Ω/□) and Mo were used as substrates for electrodeposition. These were obtained from commercial sources; the surfaces of these substrates were ultrasonically cleaned prior to use in the electrochemical cell. For acceptor doping of the electrodeposited CdTe thin films, requisite amounts of CuSO₄ were added to the deposition bath.

Ohmic contacts or barrier metals on devices were fabricated in a high vacuum metallization chamber. The intervening CdS layer in the n-CdS/p-CdTe heterojunction devices was prepared by a solution-growth technique described in Ref. (6). This layer was subsequently annealed in H₂ atmosphere at 250°C for ca. 1h to lower its resistivity. Typical characteristics of the annealed samples were the following: van der Pauw resistivity of 1.09 Ω-cm; Hall mobility of 6 cm²/V-s; and donor concentrations of ~10¹⁸ cm⁻³.

The thickness of the electrodeposited CdTe layers was nominally in the range 0.5-4 μm. For heterojunction CdS/CdTe devices, CdS layers 1000-3000 Å thick were employed. Cross-sectional examination of these structures by electron microscopy reveal columnar CdTe grains atop a fine-grained layer of CdS.

Results and Discussion

Table I contains representative compositional data obtained by electron probe microanalyses (EPMA) for CdTe thin films fabricated on ITO and Mo substrates. Additionally, data on two samples of CdS on glass are also shown. The CdTe thin films on ITO invariably contain Te as a separate phase; this is reflected in the high Te: Cd ratio for these samples (cf. sample no. 87 and 17 in Table I). Evidence for the presence of Te is also obtained from

Table I. Representative compositional characteristics of CdTe and CdS thin films from EPMA

Sample no.	Substrate	Composition (atom percent) ^a			
		Cd	Te	Cu	S
87	ITO	37.44 (2.71)	61.34 (4.43)	1.23 ^b (0.09)	—
17	ITO	29.73 (0.60)	62.37 (1.27)	7.90 ^c (0.16)	—
23	ITO	38.70 (4.38)	47.22 (5.35)	13.28 ^d (1.50)	—
37	Mo	47.11 (7.02)	48.16 (7.18)	4.73 ^e (0.71)	—
38	Mo	48.33 (7.36)	47.17 (7.18)	4.50 ^b (0.69)	—
39	Mo	46.16 (7.35)	49.55 (7.89)	4.29 ^e (0.68)	—
81 ^e	Glass	51.98 (2.84)	—	—	47.75 (2.61)
87b ^e	Glass	53.84 (5.27)	—	—	46.11 (4.51)

^a The values shown are averaged from those obtained by spot scanning several (nominally 10-12) positions.

^b Deposition bath contained 2 × 10⁻³M Cu²⁺.

^c Deposition bath contained 3 × 10⁻³M Cu²⁺.

^d Deposition bath contained 5 × 10⁻³M Cu²⁺.

^e Films prepared by solution growth method [cf. Ref. (6)].

x-ray diffraction analyses and is further confirmed by the tailing of the long-wavelength optical absorption response of these thin films. Precedence for formation of Te precipitates in CdTe is found in previous work (7). Excess Te is also implicated in device behavior wherein oxidative etching of the CdTe surface was employed (1f). In our experience, electrodeposition of device-quality CdTe thin films which are intrinsically p-type (i.e., those which contain interstitial Te in slight excess from the stoichiometric composition) is invariably accompanied by the formation of Te as a separate phase. In this regard, acceptor doping of CdTe during electrodeposition is a more viable approach as demonstrated below.

A typical Auger electron spectrum (differential form) and a depth profile for a doped thin film on Mo substrate are shown in Fig. 1a and 1b, respectively. Along with the ubiquitous C, S, and Cl are seen as impurities in Fig. 1a. The former is undoubtedly a consequence of SO₄²⁻ incorporation during film growth; a possible source for Cl⁻ ions is the internal solution of the saturated calomel reference electrode. A further point with acceptor doping is illustrated in Table I. The Cu uptake of the film increases with Cu²⁺ content in the bath as expected. However, the Cu content of the film is seen to be a sensitive function of the substrate material for a given Cu²⁺ loading of the bath (cf. Table I).

That our films thus prepared are indeed p-type in the as-deposited condition is shown by representative data shown in Fig. 2 and 3. Figure 2 shows the current voltage (i-E) characteristics of a Schottky barrier constructed from a CdTe film on ITO substrate. Indium [work function, φ = 3.97 eV, Ref. (8)] is a known Schottky barrier inducing contact on p-CdTe [electron affinity, EA: 4.28 eV, cf. Ref. (9)]. Consistent with this expectation, the i-E characteristics show good rectification on reverse bias of

*Electrochemical Society Active Member.

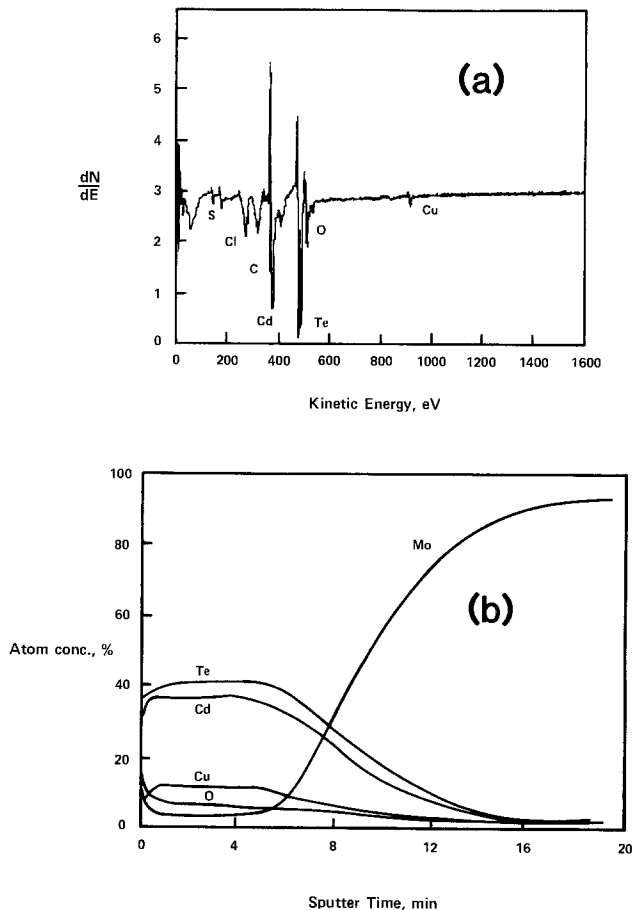


Fig. 1. (a): Auger electron spectrum of an electrodeposited CdTe/Cu thin film on Mo substrate. (b): Auger depth profile of an electrodeposited CdTe/Cu thin film on Mo substrate.

the junction. Figure 3 shows the behavior of a n-CdS/p-CdTe heterojunction fabricated from another Cu-doped CdTe thin film. In this case, note that the heavily doped ITO layer [$EA = \phi = 4.40$ eV, cf. Ref. (10)] functions as an ohmic contact for n-CdS [$EA = 4.50$ eV, cf. Ref. (9)], which is also heavily doped (see above). Gold [$\phi = 5.2$ eV, cf. Ref. (8)], however, forms an ohmic contact to p-type CdTe. Again, the high degree of rectification on reverse bias of the junction is consistent with p-type conductivity in the CdTe film and consequent formation of an n-CdS/p-CdTe heterojunction.

The absence of a buried n-CdTe/p-CdTe homojunction [cf. Ref. (1b)] in our ITO/CdS/CdTe/Au device structure is

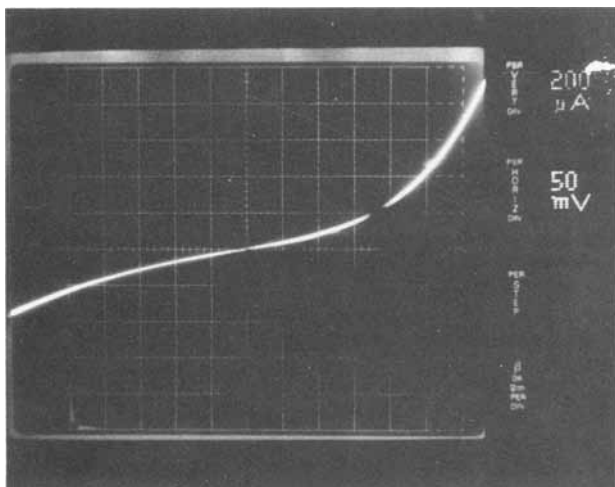


Fig. 2. Current-voltage (i-E) characteristics of an ITO/CdTe/In Schottky barrier.

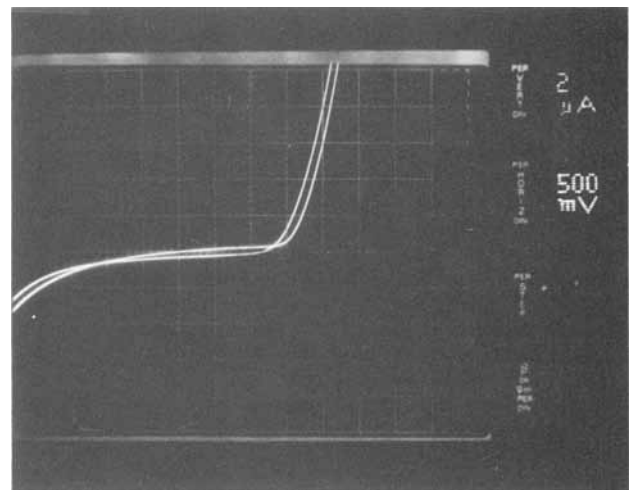


Fig. 3. Typical i-E characteristics of an ITO/CdS/CdTe/Au heterojunction device utilizing electrodeposited and Cu-doped p-CdTe layers. The two curves as shown denote scans in opposite directions.

shown by spectral response data. The short-wavelength cut-off and long-wavelength fall-off (ca. 500 and 850 nm, respectively) match the known absorption characteristics of CdS and CdTe. Additionally, measurement of the electron-beam induced current for the structure locates the photoactive junction at the CdS/CdTe interface.

Summary and Conclusion

The data presented in Fig. 1-3, when taken as a unit, are unequivocal evidence for the fact that our CdTe films are p-type when deposited under the conditions described above and in Ref. (5). We emphasize that these films show the typical behavior illustrated in Fig. 2 and 3 in the as-deposited condition; i.e., they received no thermal treatment to induce $n \rightarrow p$ conversion [cf. Ref. (1g)]. This may be an important advantage in the device fabrication stage given the extreme sensitivity observed for interfacial phenomena in comparable devices and the consequent deleterious effects in cell efficiencies on heat-treatment (11).

In conclusion, acceptor doping of electrodeposited CdTe thin films yield p-type films which show satisfactory rectification behavior when fabricated into CdTe/In Schottky barriers and CdS/CdTe heterojunctions.

Acknowledgments

This research was made possible by a subcontract (no. XL-3-03140-01) from the Solar Energy Research Institute (SERI). The authors (R. N. B. and K. R.) thank Satyen Deb and Gene Blakeslee of SERI for access to their laboratory facilities. EPMA and Auger electron spectroscopy were performed by Chuck Herrington and Amy Schwartzlander, respectively, at SERI. Dick Axton of SERI provided much technical assistance throughout the course of this work.

Manuscript submitted July 2, 1984; revised manuscript received Oct. 22, 1984.

The University of Texas assisted in meeting the publication costs of this article.

REFERENCES

- (a) A. L. Fahrenbruch, V. Vasilchenko, F. Buch, K. Mitchell, and R. H. Bube, *Appl. Phys. Lett.*, **25**, 605 (1974); (b) N. Nakayama, H. Matsumoto, K. Yamaguchi, S. Ikegami, and Y. Kioki, *Jpn. J. Appl. Phys.*, **15**, 2281 (1976); (c) Y. Y. Ma, A. L. Fahrenbruch, and R. H. Bube, *Appl. Phys. Lett.*, **30**, 423 (1977); (d) K. Mitchell, A. L. Fahrenbruch, and R. Bube, *J. Appl. Phys.*, **48**, 4365 (1977); (e) H. Uda, H. Taniguchi, M. Yoshida, and T. Yamashita, *Jpn. J. Appl. Phys.*, **19**, 703 (1980); (f) J. Werthen, A. Fahrenbruch, R. Bube, and J. C. Zesch, *J. Appl. Phys.*, **54**, 2750 (1983); (g) B. M. Basol, *ibid.*, **55**, 601 (1984) and references therein.

2. (a) G. Fulop, M. Doty, P. Meyers, J. Betz, and C. H. Liu, *Appl. Phys. Lett.*, **40**, 327 (1982); (b) K. Uosaki, M. Takahashi, and H. Kita, *Electrochim. Acta*, **29**, 279 (1984); (c) J. Ilabres, *This Journal*, **131**, 464 (1984); (d) R. N. Bhattacharya, K. Rajeshwar, and R. N. Noufi, *ibid.*, **131**, 939 (1984).
3. (a) F. A. Kroger, *ibid.*, **125**, 2028 (1978); (b) M. P. R. Panicker, J. Knaster, and F. A. Kroger, *ibid.*, **125**, 566 (1978).
4. R. L. Rod, R. Bunshah, O. Staffsudd, B. M. Basol, and P. Nath, Final Report to U.S. Department of Energy, Report no. DOE/ET/23008-T1, May 15, 1980.
5. R. N. Bhattacharya and K. Rajeshwar, *This Journal*, **131**, 2032 (1984).
6. A. Mondal, T. K. Chaudhuri, and P. Pramanik, *Solar Energy Mater.*, **7**, 431 (1983).
7. S. H. Shin, J. Bajaj, L. A. Moudy, and D. T. Cheung, *Appl. Phys. Lett.*, **43**, 68 (1983) and references therein.
8. E. H. Rhoderick, "Metal-Semiconductor Contacts," p. 54, Clarendon Press, Oxford, England (1980).
9. A. G. Milnes and D. L. Feucht, "Heterojunctions and Metal-Semiconductor Junctions," p. 8, Academic Press, New York (1972).
10. E. Y. Wang and L. Hsu, *This Journal*, **125**, 1328 (1978).
11. See, for example, H. P. Maruska, A. K. Ghosh, D. J. Eustace, and T. Feng, *J. Appl. Phys.*, **54**, 2489 (1983).

Solubility of α - Fe_2O_3 in Fused Na_2SO_4 at 1200 K

Y. S. Zhang and Robert A. Rapp*

Department of Metallurgical Engineering, The Ohio State University, Columbus, Ohio 43210

Iron-, nickel-, and cobalt-base alloys used at high temperatures are sometimes subjected to accelerated corrosion attack when covered by a thin layer of fused salt. This type of accelerated oxidation is called hot corrosion. Fused Na_2SO_4 , or a mixed alkali sulfate melt, is often responsible for this hot corrosion attack of metals. A knowledge of the solubilities of metal oxides, and the dependencies of the solubilities on acid/base melt chemistry assists in evaluating any oxide fluxing mechanism (1). The dissolution behavior of a metal oxide is also important for elucidating any electrochemical mechanism of hot corrosion in which soluble metal species are involved (1). Solubilities of the oxides NiO (2, 3), Co_3O_4 (2), Al_2O_3 (4), and Y_2O_3 (5) have been measured in fused Na_2SO_4 . In this work, the solubility of α - Fe_2O_3 at 1200 K and 1 atm oxygen has been measured as a function of the Na_2SO_4 melt basicity defined as $\log a_{\text{Na}_2\text{O}}$.

Experimental Procedure

About 0.5g of α - Fe_2O_3 powder (99.9% purity) and 25-30g of reagent-grade Na_2SO_4 were mixed and contained in an alumina crucible inside a closed-end cylindrical mullite chamber. Different compositions of catalyzed SO_2 - O_2 mixed gases were used to adjust the basicity of the Na_2SO_4 melt. Varying amounts of Na_2O_2 from 0.002 to 0.2 mole percent (m/o) Na_2O_2 were added to the melt to change its basicity in the basic direction from 9.5 to 7.3. As described in detail earlier (2, 4), the melt basicity was measured by two solid-state reference electrodes: a Na sensor and an oxygen probe. The Na sensor was composed of a Ag wire immersed in a fused Na_2SO_4 -10 m/o Ag_2SO_4 solution at the bottom of a Na^+ ion conducting mullite tube which was sealed at the top by ceramic cement. A Pt wire was welded to the Ag wire to serve as the lead wire. The oxygen probe was an internally platinized ZrO_2 (3.5 weight percent CaO) tube with a Pt lead wire. The internal electrode contacted air. The open-circuit potential between these two reference electrodes is given by (2)

$$E(\text{V}) = 1.4943 + 0.119 \log a_{\text{Na}_2\text{O}}(\text{melt}) \quad [1]$$

at 1200 K if the melt is in internal equilibrium (lacks concentration gradients). In addition, a Pt wire working electrode contacted the melt. Another Pt electrode was painted onto the outside surface of the zirconia tube just above the melt to monitor the P_{O_2} of the gas phase. After about two days, the P_{O_2} in the melt and above the melt became approximately equal and the melt basicity remained constant. Samples of the salt were taken by quenching some melt onto a cool alumina rod. The sampling rod did not contact either of the electrodes or the inside wall of the alumina crucible. The tip of the

sampling rod was kept 4-5 mm above the bottom of the crucible, so that no solid (dense) α - Fe_2O_3 powder was incorporated along with the salt sample. Each salt sample of about 0.2g was weighed to 0.1 mg accuracy and dissolved in 0.02N HCl to a volume of 100 or 1000 ml, depending upon the Fe concentration in the salt. The contents of soluble Fe were determined by using an atomic absorption spectrophotometer (Perkin-Elmer, Series 360) with a graphite furnace. The salt solutions introduced into the graphite furnace were limited to a 10 microliter volume, so that the Na_2SO_4 in the solutions did not affect the analytic results.

Results and Discussion

Figure 1 is the thermodynamic phase stability diagram for the Na-Fe-S-O system at 1200 K, which shows that α - Fe_2O_3 is stable at $8.1 < -\log a_{\text{Na}_2\text{O}} < 17.7$. Most of the data used for the construction of Fig. 1 are provided in

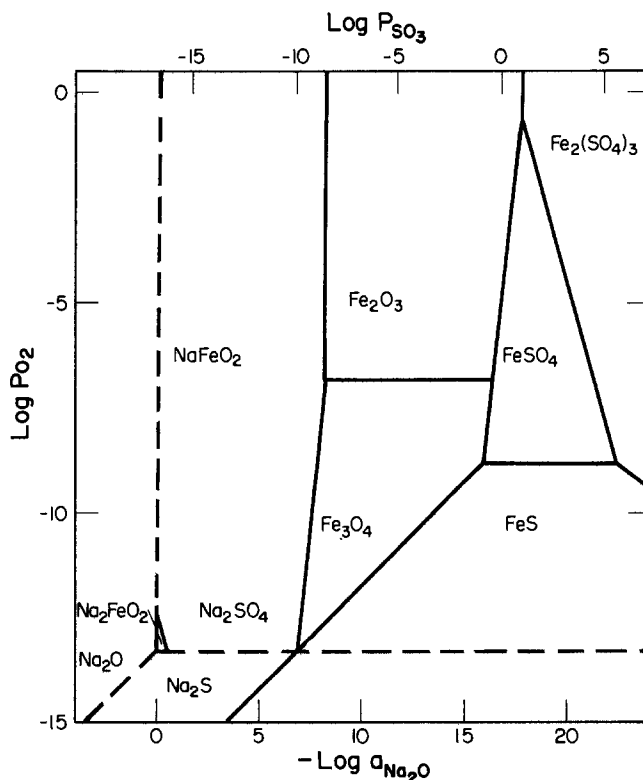


Fig. 1. Thermodynamic phase stability diagram for the Na-Fe-S-O system at 1200 K.

*Electrochemical Society Active Member.

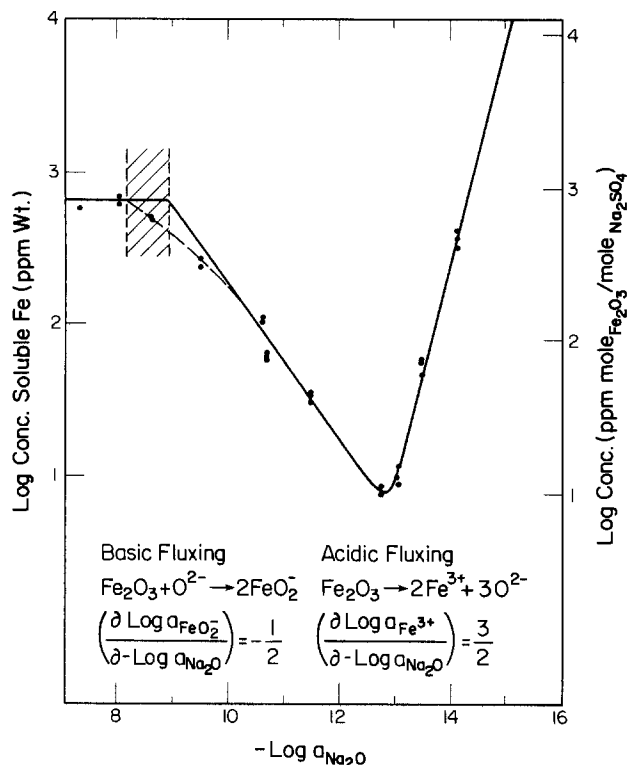
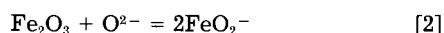


Fig. 2. Solubility of α -Fe₂O₃ in fused Na₂SO₄ at 1200 K and $P_{\text{O}_2} = 1$ atm.

the succeeding note (4). The dual designations for the abscissa are valid only in the regime where Na₂SO₄ is stable. Additionally, for 1200 K, $\Delta G^\circ_{\text{Fe}_2\text{O}_3} = -512.2$ kJ/mol (6), $\Delta G^\circ_{\text{Fe}_3\text{O}_4} = -731.9$ kJ/mol (6), $\Delta G^\circ_{\text{FeS}} = -85.8$ kJ/mol (6), $\Delta G^\circ_{\text{Fe}_2(\text{SO}_4)_3} = -1216.9$ kJ/mol (6), $\Delta G^\circ_{\text{FeSO}_4} = -488.7$ kJ/mol (6), $\Delta G^\circ_{\text{NaFeO}_2} = -474.1$ kJ/mol (7), and $\Delta G^\circ_{\text{Na}_2\text{FeO}_2} = -527.2$ kJ/mol (7). The data points in Fig. 2 are the measured solubilities of α -Fe₂O₃ in molten Na₂SO₄ at 1200 K and 1 atm oxygen. Each data point in Fig. 2 represents the average analysis for a separate salt sample compared against a certified standard solution. The high precision of the solubility values is indicated by the reproducibility of the data. In basic dissolution, the Na₂O dependence of the solubility indicates that the solute species of Fe₂O₃ is FeO₂⁻. The dependence of the FeO₂⁻ concentration upon the melt basicity is consistent with the following dissolution reaction

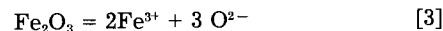


$$\left\{ \frac{\partial (\log a_{\text{FeO}_2^-})}{\partial (-\log a_{\text{Na}_2\text{O}})} \right\} = -\frac{1}{2} \quad [2a]$$

The solubility plateau to the left of about $-\log a_{\text{Na}_2\text{O}} = 9$ is expected because the dissolution of the equilibrium

NaFeO₂ phase to form FeO₂⁻ ions does not involve O²⁻ ions in the reaction. The cross-hatched transition indicates the thermodynamic uncertainty in the location of the phase stability boundary.

For acidic dissolution of Fe₂O₃, the solute correlates to Fe³⁺. The dependence of the Fe³⁺ concentration on the melt basicity is consistent with the reaction



$$\left\{ \frac{\partial (\log a_{\text{Fe}^{3+}})}{\partial (-\log a_{\text{Na}_2\text{O}})} \right\} = \frac{3}{2} \quad [3a]$$

Close to 1 atm O₂, both the basic and acidic solutes of Fe₂O₃ involve trivalent iron. Because no oxidation step is involved in such dissolution reactions, no dependence of solute concentrations upon P_{O_2} is expected near $P_{\text{O}_2} = 1$ atm.

Figure 2 shows that the solubility minimum lies at $-\log a_{\text{Na}_2\text{O}} = 12.9$. Thus, α -Fe₂O₃ is an oxide considerably more acidic than Co₃O₄ and NiO (2) but more basic than α -Al₂O₃ (4). The activity coefficients of the soluble species NaFeO₂ and Fe(SO₄)_{1.5} were calculated by methods used previously (2, 4) to be 250 and 3.6×10^{-3} , respectively. But these values possess considerable uncertainties arising from the uncertainties in the thermodynamic data (6, 7) for $\Delta G^\circ_{\text{NaFeO}_2}$ and $\Delta G^\circ_{\text{Fe}_2(\text{SO}_4)_3}$.

In order to evaluate and test the P_{O_2} dependence of the solubilities of iron oxides, and to relate the data to the hot corrosion of iron-base alloys, the solubilities of iron oxides are being measured at lower oxygen pressures in a continuing study.

Acknowledgments

This research was sponsored by the National Science Foundation, Metallurgy Program of the Division of Material Research under Grant DMR 791190. Y. S. Zhang is supported as a Visiting Scientist from People's Republic of China.

Manuscript submitted Aug. 6, 1984; revised manuscript received Nov. 12, 1984.

The National Science Foundation assisted in meeting the publication costs of this article.

REFERENCES

1. R. A. Rapp and K. S. Goto, in "Molten Salts," J. Braunstein and J. R. Selman, Editors, p. 159, The Electrochemical Society Softbound Proceedings Series, Pennington, NJ (1981).
2. D. K. Gupta and R. A. Rapp, *This Journal*, **127**, 2194, 2656 (1980).
3. M. L. Deanhardt and K. H. Stern, *ibid.*, **128**, 2577 (1981).
4. P. D. Jose, D. K. Gupta, and R. A. Rapp, *ibid.*, **132**, 735 (1985).
5. M. L. Deanhardt and K. H. Stern, *ibid.*, **129**, 2228 (1982).
6. JANAF Thermochemical Tables, 2nd ed., National Bureau of Standards 37, U.S. Dept. of Commerce (1971) and supplements.
7. B. J. Shain, P. C. S. Wu, and P. Chiotti, *J. Nucl. Mater.*, **67**, 13 (1977).

Solubility of α -Al₂O₃ in Fused Na₂SO₄ at 1200 K

P. D. Jose, D. K. Gupta, and Robert A. Rapp*

Department of Metallurgical Engineering, The Ohio State University, Columbus, Ohio 43210

Many alloys and coatings owe their resistance to high temperature oxidation to the slow growth of adherent Al₂O₃ scales. However, the dissolution of this protective oxide scale could represent an important step in the accelerated corrosion of engineering alloys in contact with a thin layer of fused salt. A number of salt films are known to cause such "hot corrosion." Because of its high stabil-

ity in oxidizing sulfur-bearing gases, sodium sulfate is particularly aggressive toward protective coatings in aircraft and marine gas turbines and in other engineering systems. A knowledge of the solubility of the protective oxide and its dependence on the fused salt chemistry may aid the interpretation of hot corrosion mechanisms and in the development of new protective materials.

Liang and Elliott (1) have reported a few values for the solubilities of Cr₂O₃, Al₂O₃, and NiO in Na₂SO₄ over a lim-

*Electrochemical Society Active Member.

ited range of salt compositions. Stroud and Rapp (2) reported solubilities for $\alpha\text{-Al}_2\text{O}_3$ and Cr_2O_3 in Na_2SO_4 at 1200 K as a function of P_{O_2} and $\log a_{\text{Na}_2\text{O}}$. However, their results were inconsistent with thermodynamic expectation, because the observed minimum in the oxide solubility occurred at too high a value for $a_{\text{Na}_2\text{O}}$. It now appears that because of a reaction of Na_2SO_4 with their platinum electrode in the Na_2SO_4 melts, a faulty potential was indicated for the Pt/melt electrode. The present study reports measurements for Al_2O_3 solubility using improved methods. Two solid electrolyte probes were used to infer the basicity of Na_2SO_4 melts as suggested by Watt *et al.* (3), and used by Gupta and Rapp (4) in a determination of the solubilities of NiO and Co_3O_4 in Na_2SO_4 at 1200 K. Deanhardt and Stern (5) have employed two pairs of such probes to determine the solubility products for NiO in Na_2SO_4 at 1200 K. Misra *et al.* (6) calculated the solubilities and the interaction energy parameters for the acidic solutes of NiO and Co_3O_4 by use of existing phase diagrams and a regular solution model. They found good agreement with experimental solubility results.

The acid-base character of Na_2SO_4 can be described by the equilibrium



in which Na_2O can be considered as the basic component and SO_3 the acidic component. The thermodynamic data listed in Table I were used to construct the Na-Al-S-O phase stability diagram of Fig. 1, which is analogous to the Pourbaix diagram of E vs. pH for aqueous solutions. The oxidation potential is plotted as the ordinate against the negative of salt basicity (defined as $\log a_{\text{Na}_2\text{O}}$) as the abscissa. The dashed lines show that liquid Na_2SO_4 is stable over a large area in this diagram. Alternate abscissa variables of $-\log a_{\text{Na}_2\text{O}}$, or else $\log P_{\text{SO}_3}$, can be used within the range of Na_2SO_4 stability at essentially unit activity. The diagram could provide quantitative values for the solubility of the metal oxide in the fused salt if the identity and the activity coefficients of the solute species were known. Conversely, if the solubility were known, the activity coefficients of the respective solutes in solution could be calculated. The reliability of activity coefficients obtained in this way depends greatly on the accuracy of the Gibbs energy of formation data for the soluble metal salts and the metal oxide and also on the accuracy of the experimental measurements. In the present study, the solubility of α -alumina in fused Na_2SO_4 at 1200 K was measured as a function of the thermodynamic activity of Na_2O for a fixed oxygen pressure of 1 atm. The results are related to the phase stability diagram and are used to infer the ionic solute species as well as the activity coefficients for the solute species of alumina.

Experimental Procedure

As in the preceding study by Gupta and Rapp (4), the voltage between two solid-state electrochemical probes was used to measure the basicity of the Na_2SO_4 melt. A closed-end mullite ($3\text{Al}_2\text{O}_3 \cdot 2\text{SiO}_2$) tube (McDanel MV30) with glassy grain boundaries is known to be an exclusive conductor of sodium ions at high temperatures. Within this tube, a small amount of liquid salt with composition 90 mole percent (m/o) Na_2SO_4 , 10 m/o Ag_2SO_4 contacted a Ag wire which was welded within the hot zone to a Pt lead wire. The working electrode for this cell was either a

Table I. Thermodynamic data relevant to Na-Al-S-O system

Compound	ΔG_f° (1200 K) (kJ/mol)	Ref.
Na_2O (s)	-250	(8)
Na_2S (s)	-282	(8)
Na_2SO_4 (l)	-893	(8)
SO_2 (v)	-273.7	(8)
SO_3 (v)	-260.3	(8)
$\alpha\text{-Al}_2\text{O}_3$ (s)	-1294	(8)
NaAlO_2 (s)	-862	(8)
$\text{Al}_2(\text{SO}_4)_3$ (s)	-1980	(9)
Al_2S_3 (s)	-657	(10)

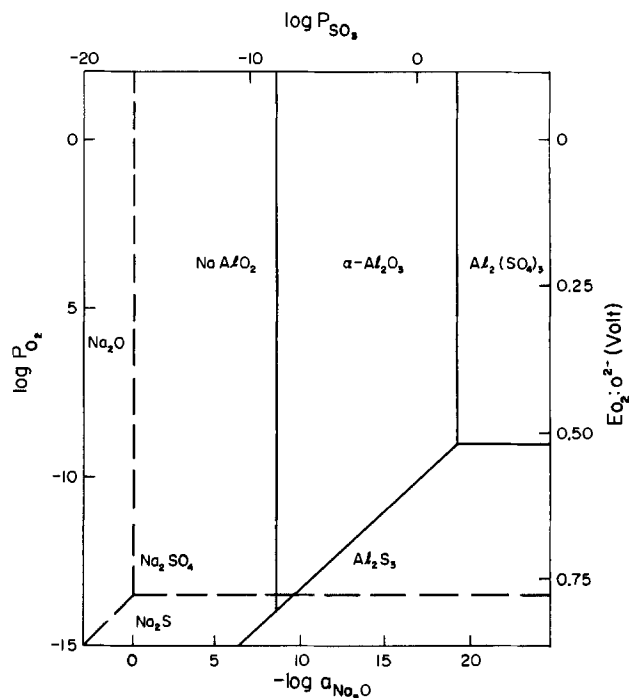


Fig. 1. Thermodynamic phase stabilities in the Na-Al-S-O system at 1200 K

Au or Pt wire contacting the Na_2SO_4 melt external to the mullite tube and remote from the gaseous environment; again, a Pt lead wire was attached. A closed-end 3.5 weight percent (w/o) CaO partially stabilized zirconia tube contacted the Na_2SO_4 melt. This zirconia tube was platinized on its aerated inside surface and provided with an internal Pt lead wire. The voltage between the zirconia electrode and the Au or Pt working electrode in the melt indicated the P_{O_2} of the melt (4). At 1200 K, the open-circuit voltage between the mullite and the zirconia electrodes is given by (4)

$$E(\text{V}) = 1.4943 + 0.119 \log a_{\text{Na}_2\text{O}} \quad [2]$$

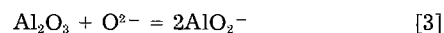
Strictly speaking, the $a_{\text{Na}_2\text{O}}$ is measured at the $\text{ZrO}_2/\text{fused Na}_2\text{SO}_4$ interface (7), but this Na_2O value is valid for the entire melt under equilibrium conditions.

Excess amounts (30-40g) of $\alpha\text{-Al}_2\text{O}_3$ powder were added to 100g of sodium sulfate in an alumina crucible placed within the mullite reaction tube. After drying the salt for a few days at 200°C, the temperature was raised to 1200 K. Salt samples were taken after various times by freezing salt onto a cold alumina tube after the electrochemical probes indicated equilibrium for oxygen between the fused salt and the gas, and after the salt basicity became constant. The salt samples were weighed, dissolved in distilled water, and analyzed by atomic absorption spectroscopy (Perkin-Elmer, Series 360) using a graphite furnace. For neutral water at $\text{pH} = 7$, the solubility of $\text{Al}(\text{OH})_3$ is a factor of at least 150 times higher than the highest Al solute concentration from the dissolved salt.

Results and Discussion

Figure 2 presents the results of solubility measurements for $\alpha\text{-Al}_2\text{O}_3$ in fused Na_2SO_4 at 1200 K in $P_{\text{O}_2} = 1$ atm. Although only a few points were obtained for the acidic segment of the solubility curve, the plot is well described by lines for one basic solute, AlO_2^- , and one acidic solute Al^{3+} . The minimum solubility occurs at about $\log a_{\text{Na}_2\text{O}} = -15.4$ and 13 wt ppm dissolved Al. A single datum point from Liang and Elliott (1) is in good agreement after conversion of their measurement to a common value for $\Delta G_{\text{Na}_2\text{SO}_4}^\circ$ (reported in Table I).

For the dissolution of $\alpha\text{-Al}_2\text{O}_3$ as a basic solute



so that

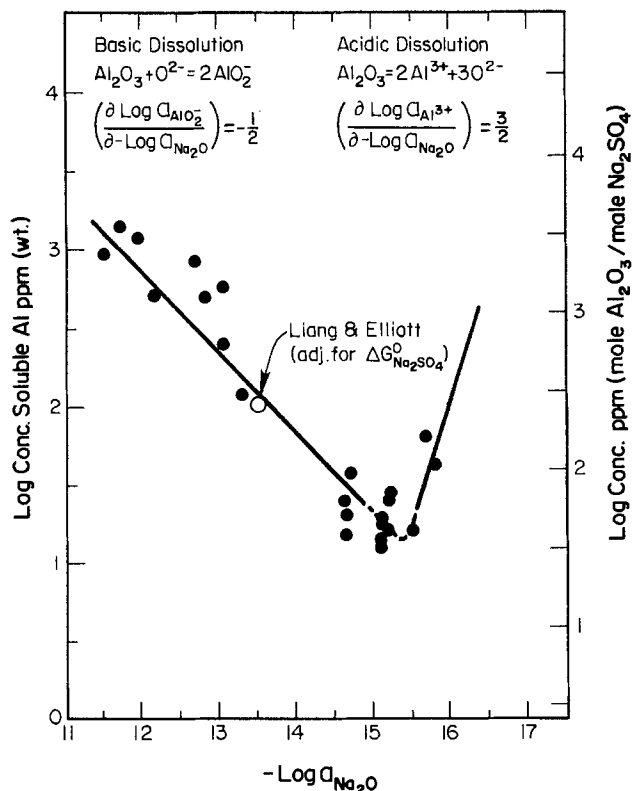


Fig. 2. Solubility of α - Al_2O_3 in fused Na_2SO_4 at 1200 K and $P_{\text{O}_2} = 1$ atm

$$\left(\frac{\partial \log a_{\text{AlO}_2^-}}{\partial -\log a_{\text{Na}_2\text{O}}}\right) = -\frac{1}{2} \quad [4]$$

With the assumption of a constant activity coefficient for the dissolved NaAlO_2 in these dilute solutions, the same dependence is expected for the plot of log concentration vs. $-\log a_{\text{Na}_2\text{O}}$, as shown in Fig. 2. Correlation of the data with the theoretical slope is good, implying that only the AlO_2^- ion is formed in basic dissolution. Any pair of values of salt basicity and oxide solubility can be used to calculate the activity coefficient for the dissolved NaAlO_2 component through the equilibrium



For the presence of Al_2O_3 at unit activity

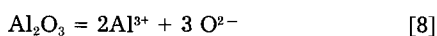
$$2 \log a_{\text{NaAlO}_2} - \log a_{\text{Na}_2\text{O}} = 8.10 \quad [6]$$

From Fig. 2, for $\log a_{\text{Na}_2\text{O}} = -13$ and therefore $a_{\text{NaAlO}_2} = 3.55 \times 10^{-3}$, the soluble mole fraction of NaAlO_2 (equal to twice the soluble Al_2O_3) equals 10^{-3} . Then, the activity coefficient for NaAlO_2 in dilute solution in Na_2SO_4 is given by

$$\gamma_{\text{NaAlO}_2} = \frac{a_{\text{NaAlO}_2}}{N_{\text{NaAlO}_2}} = 3.6 \quad [7]$$

Except for the indicated single solubility measurement from Liang and Elliott (1), previous measurements are not available for comparison.

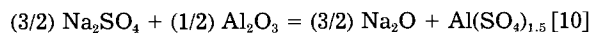
For the dissolution of α - Al_2O_3 as an acidic solute



and

$$\left(\frac{\partial \log a_{\text{Al}^{3+}}}{\partial -\log a_{\text{Na}_2\text{O}}}\right) = +\frac{3}{2} \quad [9]$$

Only a few data for acidic dissolution are shown in Fig. 2, but they are consistent with the presence of a single Al^{3+} acidic solute. Acidic dissolution of Al_2O_3 in Na_2SO_4 can also be described in terms of an $\text{Al}(\text{SO}_4)_{1.5}$ solute



For the presence of Al_2O_3 and Na_2SO_4 at unit activities

$$(3/2) \log a_{\text{Na}_2\text{O}} + \log a_{\text{Al}(\text{SO}_4)_{1.5}} = -27.05 \quad [11]$$

For $\log a_{\text{Na}_2\text{O}} = -16$, $a_{\text{Al}(\text{SO}_4)_{1.5}} = 8.91 \times 10^{-4}$, and the measured solubility (equal to twice the molar Al_2O_3 solubility) is about $N_{\text{Al}(\text{SO}_4)_{1.5}} = 2.5 \times 10^{-4}$, so that

$$\gamma_{\text{Al}_2(\text{SO}_4)_3} = \frac{a_{\text{Al}(\text{SO}_4)_{1.5}}}{N_{\text{Al}(\text{SO}_4)_{1.5}}} = 2.3 \quad [12]$$

No previous values have been reported in the literature. Indeed, the uncertainty in each activity coefficient is large, as previously mentioned.

In this study, it has been shown that at 1200 K and $P_{\text{O}_2} = 1$ atm α - Al_2O_3 dissolves in fused Na_2SO_4 as one acidic and one basic solute species, with the minimum solubility occurring at $\log a_{\text{Na}_2\text{O}} = -15.4$. Because neither dissolution reaction involves a change in aluminum valence, the solubility plot of Fig. 2 should not depend upon P_{O_2} .

Acknowledgment

This research was sponsored by the National Science Foundation, Metallurgy Program of the Division of Material Research under Grant DMR 791190.

Manuscript submitted Aug. 6, 1984; revised manuscript received Nov. 12, 1984.

The National Science Foundation assisted in meeting the publication costs of this article.

REFERENCES

- W. W. Liang and J. F. Elliott, *This Journal*, **125**, 572 (1978).
- W. P. Stroud and R. A. Rapp, in "High Temperature Metal Halide Chemistry," D. L. Hildenbrand and D. D. Cubicciotti, Editors, p. 574, The Electrochemical Society Softbound Proceedings Series, Princeton, NJ (1978).
- G. W. Watt, R. E. Anderson, and R. A. Rapp, in "Molten Salts," J. Braunstein and J. R. Selman, Editors, p. 81, The Electrochemical Society Softbound Proceedings Series, Pennington, NJ (1981).
- D. K. Gupta and R. A. Rapp, *This Journal*, **127**, 2194, 2656 (1980).
- M. L. Deanhardt and K. H. Stern, *ibid.*, **128**, 2577 (1981).
- A. K. Misra, D. P. Whittle, and W. L. Worrell, *ibid.*, **129**, 1840 (1982).
- C. O. Park, R. W. Geist, and R. A. Rapp, in "Equilibrium Diagrams; Localized Corrosion," R. P. Frankenthal and J. Kruger, Editors, p. 228, The Electrochemical Society Softbound Proceedings Series, Pennington, NJ (1984).
- JANAF Thermochemical Tables, 2nd ed., National Bureau of Standards 37, U.S. Dept. of Commerce (1971).
- H. H. Kellog, *Trans. Met. Soc. AIME*, **230**, 1622 (1964).
- I. Brian, O. Knacke, and D. Kubaschewski, "Thermochemical Properties of Inorganic Substances," Springer-Verlag, New York (1977).



COMMENTS

Each issue of the **Journal** will have a section of "Comments." In this section, we provide a means via short pieces, *i.e.*, one column or less, to applaud, dispute, or otherwise discuss the papers published in the **Journal**. Space will be provided for one response by the paper's author(s) to each comment.

Since space available in each issue for the "Comments" section is limited; it is important to be concise.

Comments should be sent to the Editor, Dr. Norman Hackerman, President's Office, Rice University, P.O. Box 1892, Houston, TX 77251.

Norman Hackerman
Editor

Experimental Determination of the Passive-Active Transition for Iron in 1M Sulfuric Acid

Philip P. Russel and John Newman
(pp. 547-553, Vol. 130, no. 3)

C. Gabrielli, M. Keddam, C. Rakotomavo, and H. Takenouti:¹ In this paper, the authors claim to have verified a previously developed model² concerning the active-passive transition of an iron electrode in 1M sulfuric acid solution first described by Epelboin *et al.*³ This model accounts for the Z-shaped polarization curve in terms of an ohmic drop overvoltage on an active disk whose radius r_p decreases as the passive state is approached (A-P configuration). A nearly parabolic I-E relationship in the transition region is used as a validity criterion of the model.

As a general criticism, a fitting of the experimental data to this law does not seem to us a very accurate way of testing the model, since, at least in the low current range, I-E plots are independent of the electrode diameter, as established in this paper, but also of the rotation speed Ω (see Fig. 6 of Epelboin *et al.*,³ reproduced in Fig. 1 of Law and Newman²), whereas the repartition of passive and active zones are dependent on Ω .³ Hence, whatever the elementary process involved to set the geometry of the dissolution and the ohmic drop, the parabolic law will fit the data satisfactorily.

Let us limit the discussion to more particular points.

1. It should be emphasized that the model is only consistent with the A-P configuration observed at high rotation speeds ($\Omega > 3600$ rpm) and high currents ($I \geq 180$ mA for 5 mm diam electrode). Have the authors really observed the A-P configuration to 1600 rpm?

2. It is extremely surprising that the paper deals with computed values of i_{avg} and r_p as presented in Table IV with no reference to direct measurements of r_p on the attacked surface [see (1) above]. It seems to us that a comparison of the data shown in Table IV with the real-life values of i_{avg} and r_p is of basic importance to substantiate the model and to establish definitely the increase of i_{avg} when I decreases in the transition range. It must be noted that our finding of i_{avg} decreasing with I is hardly questionable, since it is based on direct determinations of the active area, regardless of any model and hazardous assumptions on the electrode kinetics.

3. We agree with the authors that the ohmic drop may be the determining effect under extreme conditions where little mass-transfer limitation occurs (large Ω values, Fe-Ni alloy⁴). This is perfectly verified, as shown

¹ Groupe de recherche no. 4 du CNRS, "Physique des Liquides et Electrochimie," associé a l'université Pierre et Marie Curie, 75230 Paris Cedex 05, France.

² C. G. Law and J. Newman, *This Journal*, **126**, 1251 (1979).

³ I. Epelboin, C. Gabrielli, M. Keddam, J. C. Lestrade, and H. Takenouti, *ibid.*, **119**, 1632 (1972).

⁴ F. Wenger and J. Galland, in "Proceedings of the Fifth Symposium on Passivity," pp. 649-655, Elsevier, Amsterdam (1983).

in our Fig. 1 by complex impedance⁵ performed in the transition range under conditions where the model is likely to be valid (A-P). The diagram exhibits the usual shape related to a passivation process. The apparently positive polarization resistance (positive slope of the I-E curve) is entirely due to the electrolyte resistance shifting the diagram in the positive direction.

For lower rotation speeds, where a passive disk is always present at the center of the electrode (PAP or PA), impedance data reveal a more complicated behavior involving mass transfer in the Z-shaped feature.

This is also supported by recent estimations of the ohmic drop profiled along the disk radius by means of a Haber-Luggin capillary adapted to the rotating disk device.⁶ The AP configuration is the only case where the potential of the active area lies cathodic to the Flade potential.

It must be recognized that the general behavior of iron in the transition range from active to passive state involves some kind of coupling between mass transfer and passivation which remains to be incorporated in a more sophisticated form of the model.

Philip P. Russel⁶ and John Newman⁷ We appreciate the comments of Dr. Gabrielli and his co-workers. They are critical of the fact that we did not measure specifically the active area for use in the calculation of i_{avg} . We agree with their claim that our results would have been stronger if the active area had been measured instead of calculated. This statement is made in the conclusions section of our paper. However, we question the accuracy of

⁵ I. Epelboin, C. Gabrielli, M. Keddam, and H. Takenouti, "Kinetics of Physicochemical Oscillations," pp. 297-306, Aachen, Germany (1979).

⁶ To be published.

⁷ Weyerhaeuser Technology Center, Tacoma, Washington 98477.

⁸ Department of Chemical Engineering, University of California, Berkeley, California 94720.

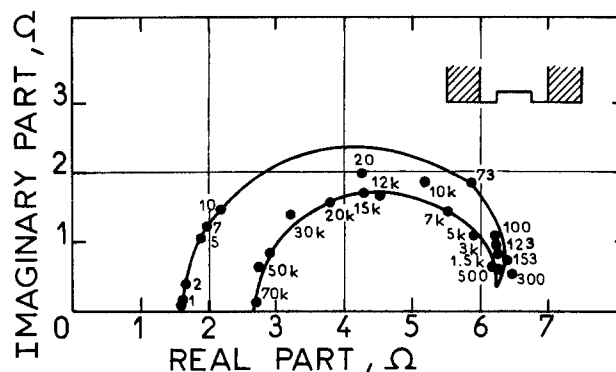


Fig. 1. Impedance diagram of an iron disk of 5 mm diam. Transition region: 4000 rpm, 250 mA. Frequency in Hz.

such a measurement, should one attempt to make it. Specifically, it is not clear that one may be able to determine that there is a central passive disk in a passive-active-passive configuration, as explained below.

First, consider a large central active area and an outer passive ring. The current density on the active area will approach a primary distribution for a sufficiently large active area.⁸ This will result in a high rate of dissolution near the periphery of the active region and a much smaller rate of dissolution near the center. We conclude that it may be difficult to differentiate between a low current density region in the center of the disk and a truly passivated central region in light of the $\pm 1 \mu\text{m}$ depth measurement accuracy given by Epelboin *et al.*³

As the active area decreases, the current density distribution will become more nearly uniform. This change is accompanied by a continuous decrease in the nonuniformity of the potential distribution. The maximum potential variation from the center to the edge of the passive zone is given as

$$\Delta\Phi_0 = 0.363 r_p i_{\text{avg}}/K \quad [1]$$

Assuming a value of 1 mm for the radius, 1.3 A/cm² for the average current density on the active portion, and a conductivity of 0.4 mho/cm, the potential may vary by up to 120 mV. The active dissolution kinetics of iron follow the Tafel law with a slope of 60 mV/decade.^{9, 10} This large difference in potential may produce much lower dissolution rates at the center of the disk even though the entire distribution is more uniform than it was in the nearly primary case. Again, this would make differentiation between a low dissolution rate and true passivation difficult in the small central region of the disk.

The high dissolution rates encountered on the peripheral area of the active zone provide additional complications in analyzing experimental results. The rapid recess of selected parts of the electrode surface will alter both the mass transfer and the ohmic potential drop in a manner that is difficult to quantify exactly. However, in the absence of this effect, the disk surface is uniform from a mass-transfer point of view, so that the current density distribution is controlled by the nonuniform potential field, which is directly related to the ohmic potential drop.

A Thermodynamic Theory of Electric Potential Generated on Crystallization of Electrolytes

R. P. Rastogi and S. A. Khan
(pp. 1327-1334, Vol. 130, no. 6)

B. N. Tripathi¹¹ In the above-mentioned and related paper,¹² Rastogi and Khan have presented an interesting theory of the development of electric potential on the precipitation and dissolution of electrolytes. In the paper under discussion, they tried to give a semiquantitative check of an inequality based on their thermodynamic theory. However, a quantitative check of their theory (Eq. [40]) can easily be made by substituting appropriate

⁸ J. Newman, *This Journal*, **113**, 1235 (1966).

⁹ J. O'M. Bockris, D. Drazic, and A. Despic, *Electrochim. Acta*, **4**, 325 (1961).

¹⁰ P. Russell, Ph.D. Thesis, University of California, Berkeley, CA (1984).

¹¹ Department of Chemistry, St. Andrew's College, Gorakhpur, India.

¹² R. P. Rastogi and S. A. Khan, *This Journal*, **127**, 1989 (1980).

values of transport numbers t_1^0 and t_2^0 . As already pointed out by the authors, the ions are dehydrated before they are added on to the crystal lattice. Therefore, it is quite reasonable to assume that the transport numbers t_1^0 and t_2^0 associated with the migration of ions from liquid/crystal interface to the crystal lattice are different from the conventional transport numbers. The supersaturated solution/crystal interface may be supposed to consist of mostly unhydrated cations and anions. Therefore, the layers closest to the crystal lattice may be supposed to behave like ionic melt. Hence, t_1^0 and t_2^0 should be equivalent to the transport numbers of bare ions in the molten salt. Therefore, we can make use of such transport numbers in order to have a theoretical estimation of $(\Delta\Phi)_{PP}$.

Rastogi and Khan have theoretically calculated the values of $(\Delta\Phi)_{PP}$ of KCl, KBr, and NaCl (Table II.) Their theoretical values (-284, -272, and -310 mV, respectively) are much higher in comparison to the experimental values (-54, -52, and -56 mV, respectively). However, the values of $(\Delta\Phi)_{PP}$ calculated on the basis of transport numbers of ions in the ionic melts of their respective salts (-67, -87, and -74 mV, respectively) are found to be in an excellent agreement with the experimental data.

R. P. Rastogi¹³ The significance of t_1^0 in the above paper has not been comprehended correctly by the above author. t_1^0 is not the conventional transport number since U_+^0 and U_-^0 are the mobilities of cations and anions on the crystal lattice. This is amply clarified by the paragraph preceding Eq. [40] in the paper under discussion. Hence, the mobilities of attachment of ions on the crystal lattice cannot be equated with the conventional mobilities of the bare ions in molten salt as such.

The theoretical values of precipitation potential in Table II of my paper are the expected upper limits of precipitation potential when t_1^0 is put equal to unity and $(\Delta H)^0$ is put equal to (i) $(\Delta H)_l$ and (ii) $-(\Delta H)_s$. Thus the meaning of the theoretical values has also not been correctly appreciated by the author. Such a calculation had to be devised since the mobilities of attachment of ions are not available in literature and only inequality [44] could alone be subjected to test.

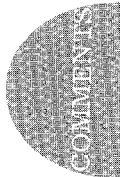
Some calculated values of precipitation potential have been quoted by the author when t_1^0 and t_2^0 are put equal to the transport number of corresponding ion in the molten salt for which no theoretical justification has been given. It should be noted that this procedure does not provide excellent agreement as claimed, particularly when the recent experimental values¹⁴ obtained with microelectrode are considered. The agreement as regards order of magnitude is perhaps due to the fact that the mobilities of attachment of the ions on the crystal lattice is likely to be inversely proportional¹⁴ to ionic radii and that the mobilities of the ions in molten salt obey a similar relationship¹⁵ approximately. It is difficult to comment further on the values obtained by the author since neither the source nor the data on the transport number of bare ions in molten salts has been reported.

Thanks are due to University Grants Commission (India) for Departmental Research Support.

¹³ Department of Chemistry, Gorakhpur University, Gorakhpur, India.

¹⁴ R. P. Rastogi, P. C. Pandey and A. K. Tripathi, submitted to *This Journal*.

¹⁵ H. Bloom, "The Chemistry of Molten Salts," p. 97, W. A. Benjamin, New York (1967).



ERRATUM

In the paper by A. Reisman, C. J. Merz, J. R. Maldonado, and W. W. Molzen, Jr. [*This Journal*, **131**, 1404 (1984)], the authors discovered subsequent to the paper's publication that a calculation error had been made which in turn led to an erroneous conclusion. In evaluating 10 keV electron damage effects on thin IGFET gate insulators, we had calculated that the insulators had absorbed 3×10^6 (SiO₂) and 3×10^7 rad (SiO₂) in two experiments employing 20 and 200 μ C doses, respectively. Comparing the measured insulator damage at these assumed rad doses with those observed for x-rays at the same rad doses led to the conclusion that electron-induced damage is greater for a given rad dose than is x-ray damage. The comparisons were made with 1.5 and 8.03 keV x-rays.

The correct numbers for the electron rad doses should have been 4.9×10^7 and 4.9×10^8 rad, respectively. The original, incorrect, and present recalculated numbers were based on the use of the Terrill equation [Ref. (14)]. Use of the Snow *et al.* energy-loss equation [Ref. (2)], or the Everhart relationship [Ref. (14)], gives, within experimental limits, similar results to the recalculated ones. Finally, using

energy-loss statistics obtained with 2×10^4 electrons in a Monte Carlo calculation by M. Rosenfield (IBM, T. J. Watson Research Center), we obtained a number of 5.5×10^7 rad for the 20 μ C case, in good agreement with the other recalculated value. The Monte Carlo calculations were made using the program developed by Rosenfield for his thesis titled "Analysis of Backscattered Electron Signals for X-ray Mask Inspection" (1984), Department of Electrical Engineering and Computer Science, University of California, Berkeley, California.

If the recalculated data point, 4.9×10^7 rad, is placed in its correct location in Fig. 1 (positive charge), or Fig. 2 (neutral traps), it falls within the data band of the x-ray curves. The 4.9×10^8 rad data point cannot be plotted since it lies outside the rad dose range studied for x-rays.

Consequently, the conclusion that, at the same dose, electrons create more damage than x-rays is incorrect. It should be concluded that similar electron and x-ray rad doses appear to give rise to similar levels of fixed positive charge and neutral trap damage, when particle and photon energies are similar.



Macroscopic Mechanical Oscillation Associated with Electrochemical Periodic Variation

O. Teschke,* D. M. Soares, and F. Galembeck

Inst. de Física and Inst. Química, Universidade Estadual de Campinas, 13100 Campinas S. P., Brazil

A number of electrochemical systems display oscillatory behavior (1-8). One example is iron anode in dilute sulphuric acid (9,10), in which case current oscillations are concurrent with oxide/salt films formation and removal (11).

Now, we have found that the level of the liquid (dilute H_2SO_4) surrounding an (wire) iron anode moves up and down, in synchronism with the current oscillations. That means, electrochemical oscillations are associated to mechanical oscillations, in this case.

The experimental set-up used is in Figure 1. Reagent-grade chemicals were used without further purification. 0.3 mm-thick, 99.99% iron wire was from C. Erba. Iron tips cut normal to the wire axis, washed with methanol and rinsed with double-distilled water were used as the anodes. The iron electrode was grounded. Voltage was applied between the counter electrode (a piece of 9.999% platinum wire with a drowned area 20 times larger than the area of the iron tip) and a saturated calomel electrode (SCE). Operational amplifiers kept the electrode voltages at the desired level, independently of current changes; a constant + 300 mV was applied between the iron and calomel electrode. Current-time curves were recorded on a 7100 BM Hewlett Packard recorder and pictures of the liquid-air-iron contact line were taken with a Nikkon F-2 camera (fitted with approximation rings). Reproducible current-time curves could only be obtained following this routine: i) a fresh solution is placed in the apparatus; ii) an iron tip is introduced in the solution and polarized (- 300 mV) against the SCE, allowing electrolysis to proceed for 15 minutes; iii) the iron tip is replaced by a new tip; iv) this is polarized (+ 300 mV) against the SCE and positioned to contact the liquid

meniscus.

As soon as iron touched the liquid this ascended around the metal, by capillary action. After an induction period of a few minutes, mechanical oscillations of the liquid level could be observed. Their appearance was concurrent with that of current-time oscillations and they led to considerable geometric changes in the iron tip-liquid contact region, as shown in Figure 2. Figure 3 shows typical current-time oscillations. Peak maxima were affected by a number of factors: solution stirring rate, solution concentration, shape of the iron tip and its exact position at the liquid interface. In the experiments reported here the iron tip (cut normal to the wire axis) was positioned with micromanipulators just to touch the meniscus at its center.

It has been reported (11) that electrochemical oscillations in the iron-sulphuric acid system are associated with the cyclic formation and destruction of a hydrous iron sulphate deposit, over the electrode metal. Contact angles between the electrolyte - i) bare iron wire and ii) sulphate-covered iron wire were measured from enlarged pictures, and they are 83° and 30° , respectively. Consequently, wetting ability of the surface changes in phase with the observed chemical changes.

The observed steps may be identified in the overall process: i) iron is corroded; its surface is covered with hydrophylic corrosion products, and becomes rougher; ii) liquid moves up, in a more wettable surface than bare metal, assessing new, unattached regions and originating slow current increase; iii) liquid reaches a higher point; suddenly, the liquid column falls, together with solid particles and leaving the metal surface clean -

the strong current pulse is detected at this point; iv) the current falls quickly to a low value and starts to increase slowly as the liquid moves up again.

It seems that the main factor leading to the oscillatory behavior are the iron surface wettability changes and the poor adhesion between iron, iron sulphate and aqueous solution, which at a point is unable to sustain the ascending liquid column. We believe that a better understanding of electrochemical-mechanical coupled oscillations depends on the evaluation of the involved adhesion forces.

REFERENCES

1. J. Wojtowicz, "Modern Aspects of Electrochemistry", vol. 8, B.E. Conway and J.O'M. Bockris, Ed. Plenum Press, New York, N.Y. 1972, Chapter 4.
2. K.F. Bonhoeffer and G. Langhammer, *Z. Electrochem.* **52**, 60, 67 (1948).
3. J. Wojtowicz, N. Marincic and B.E. Conway, *J. Chem. Phys.* **48**, 4333 (1968).
4. H.F. Honger, *This Journal* **115**, 492 (1968).
5. D. Gilroy and B.E. Conway, *J. Phys. Chem.* **69**, 1269 (1965).
6. M. Thalinger and M. Volmer, *Z. Physik Chem.* 1930, 150, 401.
7. G. Armstrong and J.A. Butler, *Disc. Faraday Soc.*, 1947, 1, 122.
8. S.W. Lin, J. Keizer, P.A. Rock, H. Stenschke, *Proc. Nat. Acad. Sci.* **71**, 4477 (1974).
9. P.P. Russell and J. Newman, *This Journal* **130**, 547 (1983). I. Epelboin, C. Gabrielli, M. Keddon, J.C. Lestrode and H. Takenouti, *This Journal* **119**, 1632 (1972).
10. U.F. Franck, *Symp. Faraday Soc.* **9**, 137 (1974).
11. T.R. Beck, *This Journal* **129**, 2412 (1982).

FIGURE CAPTIONS

- Fig. 1 Experimental set-up.
 Fig. 2 Photograph of the liquid level variation at the iron electrode interface. (a) Lower level, (b) Upper level.
 Fig. 3 Current-time profile for an iron

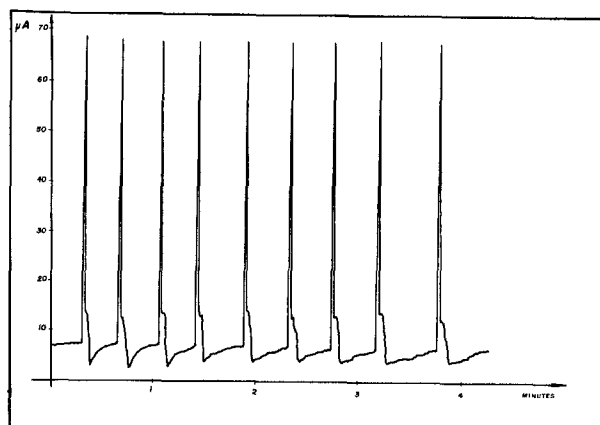
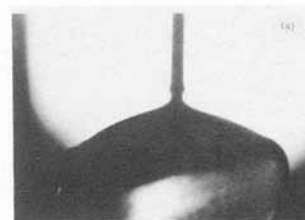
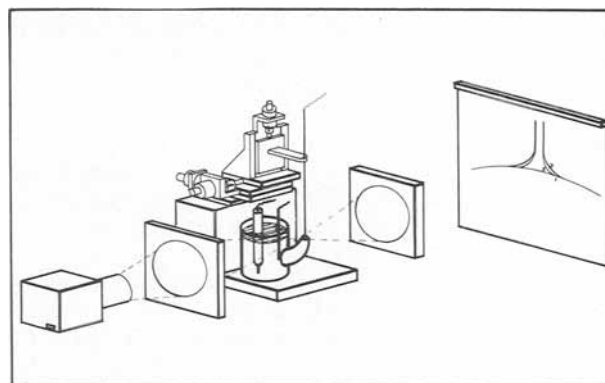
electrode in a solution 1N of H_2SO_4 at constant external potential, 300 mV (SCE).

Key words: Capillary oscillations, iron electrode.

* Electrochemical Society Member.

Manuscript submitted April 30, 1984; revised manuscript received Oct. 19, 1984.

Universidade Estadual de Campinas assisted in meeting the publication costs of this article.



Diffusion Coefficient of Dopants in Polyacetylene

Fritz G. Will*

General Electric Company, Corporate Research and Development, Schenectady, New York 12301

INTRODUCTION

There have been few attempts so far to establish the diffusion coefficient of dopants in polyacetylene (1-3), and published values show a ten order of magnitude discrepancy with values ranging from 4×10^{-18} to 2×10^{-8} cm²/sec. The low value is an estimate based on the open circuit voltage decay of polyacetylene electrodes following doping with Li or ClO₄ (1). The high value was determined from the I₂ uptake of polyacetylene films in organic I₂ solutions (2). In fact, however, one would expect the diffusion coefficient of various dopant molecules to be of the same order of magnitude.

In this communication, we report the diffusion coefficient of BF₄ in polyacetylene from electrochemical current pulse measurements and show that simultaneous determination of the solution-wetted surface area of the polyacetylene is mandatory to arrive at correct values. The wetted surface area was unknown in previous studies (1,2), and we demonstrate that different degrees of wetting of the microporous fibrous structure of polyacetylene readily accounts for the widely differing literature values.

EXPERIMENTAL

Polyacetylene film of 89 μ thickness had been prepared by the Rohm and Haas Company, using the standard Shirakawa technique. Details regarding the preparation have been published elsewhere (4). The film had 48% of theoretical density, the void space being comprised of interstices of several hundred Angstrom dimensions between polyacetylene fibers of 200 to 400 Å diameter. The specific surface area was determined by low temperature N₂ adsorption as 40 m²/g. Circular electrodes of 2 cm² area were prepared by sputtering 1000 Å Au films on one side and making pressure contact to a coiled Au wire. Experiments were

performed at room temperature in a PTFE cell employing a Li counter and reference electrode. The electrolyte was a 30% b.w. solution of LiBF₄ in sulfolane. Galvanostatic pulses were applied to electrodes pre-doped with approximately 7 mole% BF₄.

RESULTS AND DISCUSSION

Fig. 1 shows anodic and cathodic polarization-time transients, corresponding to p-doping and undoping with 100 sec current pulses of 1 mA. Both the wetted surface area and the diffusion coefficient can be determined from these transients.

The slope $d\eta/dt$ at $t=0$ yields the double layer capacity $C_D = I/d\eta/dt = 22 \mu\text{F}$. Such a value is only compatible with solution wetting the exterior surface, comparable in size to the projected area of 2 cm². If the large interior surface of 4000 cm² were wetted, then the capacity would have the unreasonably small value of 0.005 μF/cm². Based on the relevant solute and dopant concentrations, an estimate of the double layer capacity on the solution side of the polyacetylene and of the capacity associated with the space charge region within the polyacetylene yields values in the range of 10 to 50 μF/cm² for each. The total predicted capacity is therefore 5 to 25 μF/cm² of wetted area. Hence, the observed value of 22 μF corresponds to between 1 and 4 cm² of wetted area.

In the present case of only one exterior surface wetted by solution and pulse times short compared to the time constant for diffusion through the entire film thickness, semi-infinite diffusion analysis applies. Accounting for slow interface reaction (I₀), the solution (5) for small polarizations η is

$$\eta = (RT/F)(I/I_0 + 2I\sqrt{t}/\sqrt{\pi F c_0 A D}), \quad (1)$$

where t = time, c_0 = initial dopant concentration, A = wetted area, D = diffusion coefficient

*Electrochemical Society Active Member

Key Words: Polymers, Electrode, Kinetics

Manuscript received Nov. 19, 1984.

cient, I_0 = exchange current, I = applied current, F = Faraday, R = gas constant, T = temperature. A straight line should result in a plot of η vs \sqrt{t} with slope proportional to $1/\sqrt{D}$. Fig. 2 shows that this is indeed the case, and a value of 6×10^{-12} cm²/sec is determined from the slope from either anodic or cathodic transient. The fact that the extrapolated straight lines do not intersect the origin is due to the finite rate of charge transfer through the polyacetylene-solution interface (3).

It is important to note from Eq. (1) that identical transients are observed for identical values of $A\sqrt{D}$. Hence, D cannot be determined unless the wetted surface area A is known. Kaufman et al. (1) estimated 4×10^{-18} cm²/sec for the diffusion coefficient of Li and ClO₄ in polyacetylene, based on open circuit voltage decay measurements. Without knowing the wetted surface area, they assumed complete wetting of the interior surface. However, if one assumes only wetting of the exterior surface, the diffusion coefficient becomes 10^{-12} cm²/sec, in good agreement with the value determined in this study. Beniere et al. (2) derived diffusion coefficients of 2×10^{-10} to 2×10^{-8} cm²/sec for I₂ diffusion in polyacetylene, based on I₂ absorption from dilute I₂ solutions in pentane. They assumed wetting of the exterior surface only. If 0.1 to 1% of the interior surface were wetted, then the data of Beniere et al. would result in a diffusion coefficient of 6×10^{-12} cm²/sec.

In conclusion, we have established the diffusion coefficient of BF₄ dopant in polyacetylene as 6×10^{-12} cm²/sec and have shown that simultaneous determination of wetted surface area is mandatory. Grossly disparate literature values can be reconciled if allowance is made for different wetted surface areas.

REFERENCES

1. J.H. Kaufman, E.J. Mele, A.J. Heeger, R. Kaner and A.G. MacDiarmid, *J. Electrochem. Soc.* **130**, 571 (1983)
2. F. Beniere, S. Haridoss, J.P. Louboutin, H. Aldissi and J.M. Fabre, *J. Phys. Chem. Solids* **42**, 649 (1981)
3. F.G. Will, *Electrochem Soc. Ext. Abstracts* **83-1**, 838 (1983)
4. F.G. Will, R.S. McDonald, R.D. Gleim and M.R. Winkle, *J. Chem. Phys.* **78**, 5847 (1983)
5. T. Berzins and P. Delahay, *Z. Elektrochem.* **59**, 792 (1955)

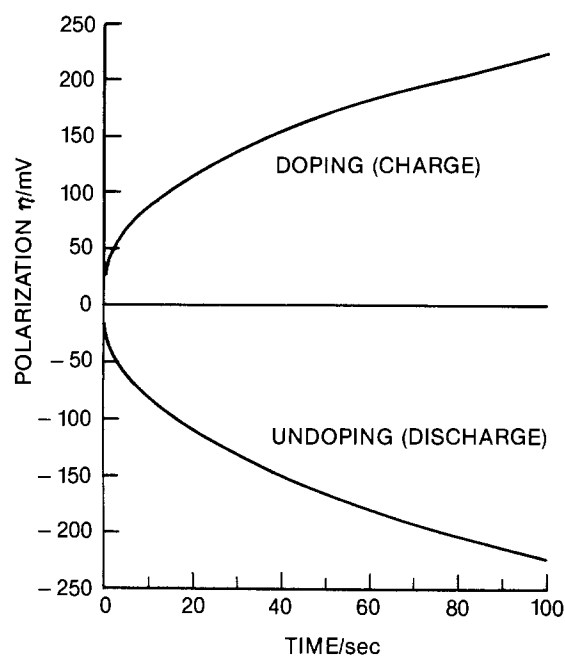


Fig. 1. IR-free overvoltage-time transients for anodic doping and cathodic undoping of polyacetylene; initial doping level 7 mole% BF₄; 1 mA current pulse of 100 sec duration.

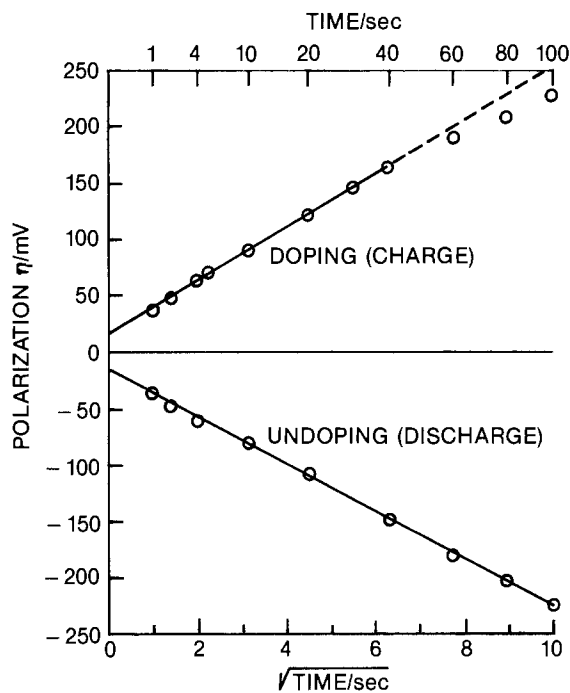


Fig. 2. Polarization data of Fig. 1 plotted vs. \sqrt{t} to determine diffusion coefficient.

General Electric Company assisted in meeting the publication costs of this article.

Multichannel Optical Analysis for the Study of Rapid Film Growth

Application to the Anodic Oxidation of Titanium

S. Djemai-Gadi, M. Froelicher, and A. Hugot-Le Goff

Laboratoire "Physique des Liquides et Electrochimie" du C. N. R. S., Université Pierre et Marie Curie, 75230 Paris Cedex 05, France

The multichannel optical analysis is now a means to investigate rapid phenomena, for instance the beginning of growth of an anodic oxide. Here, we will study the potentiostatic oxidation of the titanium in a sulfuric acid solution. We will show that the growth law during the first seconds is different from a classical high field law.

EXPERIMENTAL

The synopsis of the equipment is shown on figure 1. The titanium sample (E) has been mechanically and electrolytically (1) polished to be proper for optical studies, and it is polarised in 1N H₂SO₄ by a high power potentiostat (2) which allows passage of the large transient currents present at the beginning of the polarisation. The sample is illuminated by a 150 W Xenon source (S), focused by (L). After reflection, two other lens (L) focus the light on an entry slit (FE). The grating disperses the light between 200 and 800 nm, and the Reticon diode array detector (CAMERA) receives a plane scattered spectrum having a width of 25 mm. The array consists of 1024 diodes, each of them having a width of 25 μ m. Each diode can be read in 64 μ s, and the complete spectrum can be obtained in 64 ms.

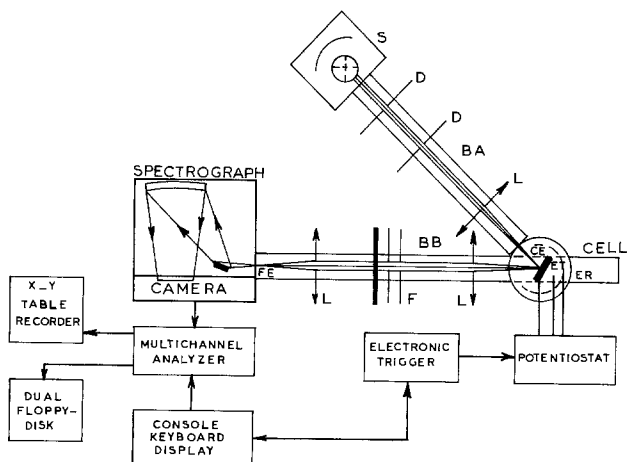


Fig. 1 : Synopsis of the equipment

Key Words : multichannel optical analysis, anodic oxidation, titanium

The beginning of the spectrum acquisition is synchronised with the beginning of the oxidation by an electronic trigger. A new spectrum can be taken immediately after the end of the first acquisition, and one can then obtain a reflectance spectrum of the titanium sample under oxidation every 64 ms.

RESULTS

In figure 2 are plotted some reflectance spectra obtained at different oxidation times for a 7 V potential. One sees the appearance of an interference minimum (λ_{m1}), which shifts towards the higher wavelengths when the oxidation time (and, then, the film thickness) increases. We have previously (3) determined the relation between the wavelength of the minimum and the film thickness. Then we can obtain the growth law of the oxide from the positions of the minimum.

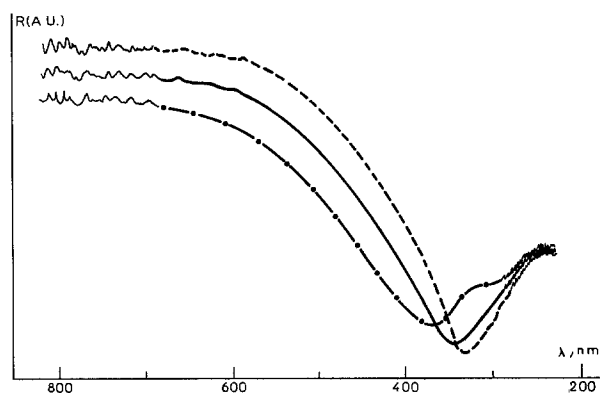


Fig. 2 : Reflectance spectra during an oxidation at 7 V ; -- : 64 ms ; — : 1.97 s ; -.- : 12 min.

When the thickness is greater than about 50-70 nm, one has to deal with the second interference minimum (λ_{m2}), as shown in figure 3 for a 50 V potential.

Plotting the values of thickness as function of the oxidation time, at a serie of voltages between 7 and 50 V, one observes two different growth laws, one after about 0.4 s,

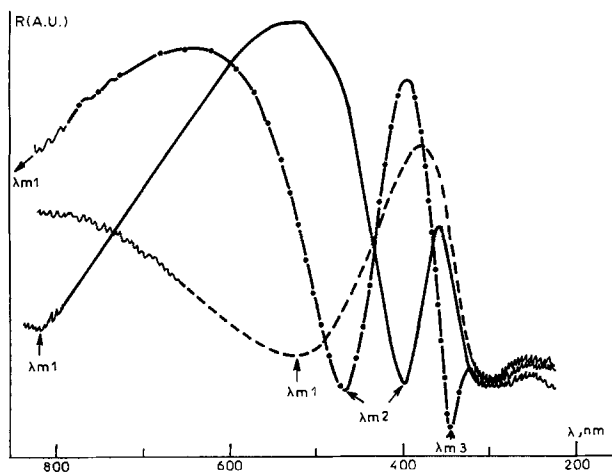


Fig. 3 : Reflectance spectra during an oxidation at 50 V. -- : 64 ms ; — : 0.38 s ; -.-. : 6.50 min.

and the other during the first hundred ms. The beginning of the growth is not dependent on the electric field since, as shown in figure 4, it is the same at every voltage. The growth rate is very high ; about one monolayer of oxide is built in 1 ms. The demand for material at the interface is great and needs a rapid transport of anions towards this interface. The transport processes in the electrolyte phase control the beginning of the growth.

In the second time range, as seen in figure 5, where the values of d/V are plotted in function of $\log t$, all the experimental points fall on the same straight line. We have fitted by least square this line, and found :

$$d/V = 2.19 + 0.217 \log t \text{ nm.V}^{-1}$$

One can write also $\delta d/\delta t = 0.217 \text{ V}/t$

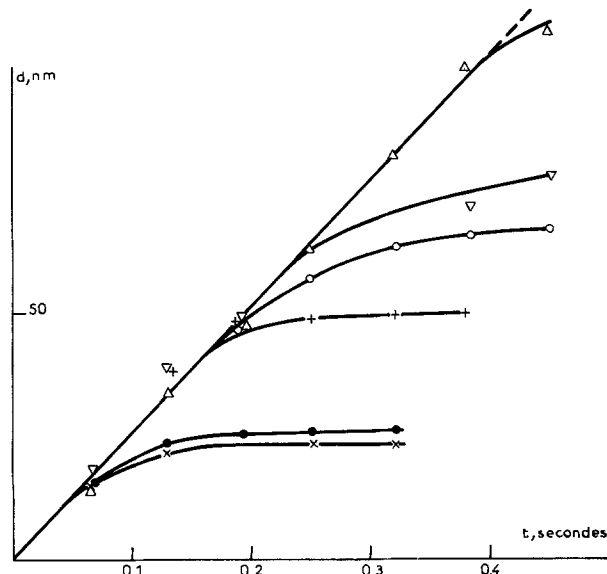


Fig. 4 : Beginning of the growth law of films. x : 7 V ; ● : 8 V ; + : 10 V ; o : 20 V ; ∇ : 30 V ; Δ : 50 V.

The thickness increment by time unit is proportional to the voltage, and in inverse ratio with the time. In this case, the growth of film is merely controlled by the electric field at the interface.

REFERENCES

- (1) A. Di Paola, F. Di Quarto, C. Sunseri, *Corr. Sci.*, **20**, 1067 (1980)
- (2) M. Froelicher, C. Gabrielli, J.P. Toqué, *J. Appl. Electrochem.*, **10**, 71 (1980)
- (3) Lj Arsov, M. Froelicher, M. Froment, A. Hugot-Le Goff, *J.Chim.Phys.*, **72**, 275 (1975)

Manuscript submitted Sept. 4, 1984; revised manuscript received Nov. 25, 1984.

CNRS assisted in meeting the publication costs of this article.

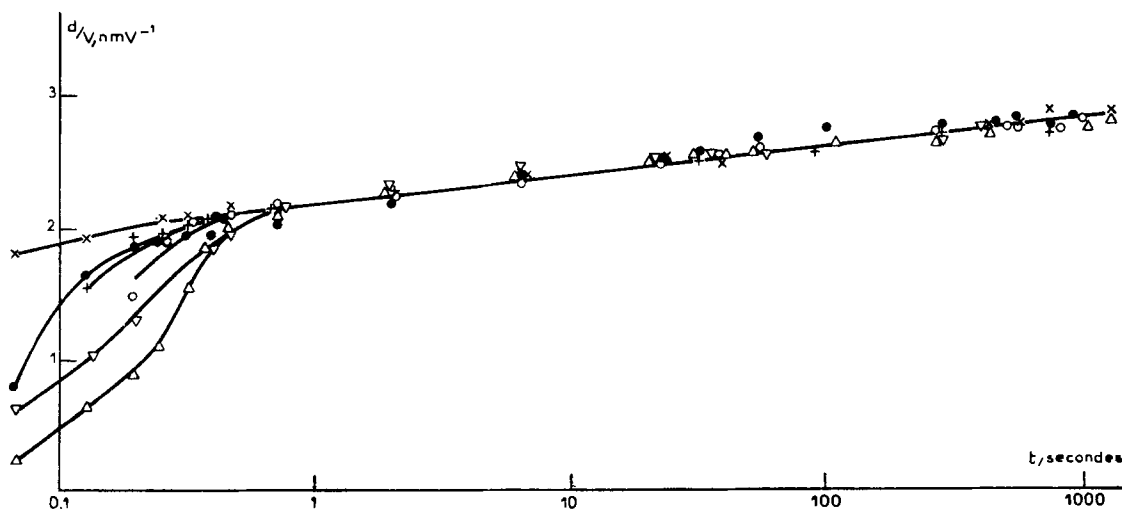


Fig. 5 : Growth law of films : values of the thickness "normalized" by the oxidation voltage, vs the logarithm of oxidation time.

x : 7 V ; ● : 8 V ; + : 10 V ; o : 20 V ; ∇ : 30 V ; Δ : 50 V.



An Improved Interrupter Circuit for Battery Testing

A Function Generator for the Resistance-Free Recording of Current/Voltage Curves

J. Gsellmann and K. Kordesch*

Technische Universität Graz, A-8010 Graz, Austria

ABSTRACT

The use of current interrupter circuits for the determination of the "resistance-free potential" of a cell under load condition is a well-known practice. One of the authors (K. K.) and A. Marko (1) designed a line-frequency (50/60 Hz) pulse-current circuit (2-4), which has been widely used since the 1960's. In the meantime, many electronic components have been improved and miniaturized. A new measuring circuit, which can be used in combination with any potentiostat or galvanostat, has been designed and tested in our laboratory.

Current/voltage characteristics of single electrodes, cells, and batteries are measured routinely in order to study the electrochemical processes occurring in galvanic systems. For this purpose, a potentiostat or galvanostat is used in combination with a function generator, which produces a triangular (smooth-ramp) or a saw-tooth voltage pattern, the latter determined by a certain frequency and showing the desired potential steps. The resulting electrode or cell voltages and corresponding currents can be obtained simultaneously and plotted by an X/Y recording system.

Such chronopotentiometric diagrams are "voltammograms." The obtained curves are usually showing the combined effects of several electrochemical processes, following the different physical chemical laws of thermodynamic or kinetic nature, like polarization or mass-transport phenomena. The limiting process will always dominantly show its characteristic parameter.

Superimposed on all these processes, expressed by the shape of the potential or current curves is the relationship between voltages and currents, given by Ohm's law: $U = IR$, whereby U stands for the potential, I for the current, and R for the resistance or the ohmic part of the impedance of the system. The purely ohmic value of R has its origin in no electrochemical reaction and sometimes completely overshadows the electrode system's response to the potentiostatic or galvanostatic test circuit. For that reason, it is often necessary to eliminate the ohmic components from all the test data before they can be properly evaluated.

However, in many technical cell systems, great significance is given to the ohmic resistance, it should be as small as possible, for a high electrical output, but especially to minimize the heat (I^2R) losses. Large electrolyte spaces or bad external or internal electronic contacts (*e.g.*, between particles) can result in a very poor cell performance and this may be blamed wrongly on electrochemical inefficiencies. Therefore, one needs to know at least the total of the values of the ohmic resistance components. Also, the influences of cell operating parameters, such as temperature, pressure, etc., must be known, but separated from the effects on the electrochemical processes.

In the electrochemical literature, the voltage difference caused by the current flow was named "polarization" or, as the effect is called more recently, "overvoltage." The terminology divides the phenomena further, in "resist-

ance overvoltage," into "chemical polarization" and "concentration polarization," etc. The direction of the current (charging or discharging a cell) determines if the voltage drops below, or rises above, the open-circuit voltage, as a result of the polarization of the electrodes, causing the overvoltage.

In this paper, we distinguish between the instantly (with electronic speed) occurring voltage step caused by the current flow through the ohmic resistance components of the cell and the slow (mass-transport determined, equilibrium seeking) voltage changes caused by the electrochemical reactions or physical processes at the interface or in the electrodes. "Resistance overvoltage" and "chemical (kinetic) polarization" have, therefore, principally different properties related to the speed at which they appear as soon as the current is switched on. Furthermore, the chemical (kinetic) polarization stays constant (in fuel cells) or increases slowly (in batteries) while the current continues to flow.

Methods to Eliminate the Ohmic Resistance Overvoltage

The resistance can be measured with an alternating current bridge-circuit while the cell is discharged or charged. With separate probes, it is possible to locate the partial resistances of, *e.g.*, the electrolyte, certain layers, or components. The effects of temperature or pressure can be determined similarly. The correction of the current/voltage curves obtained from the X/Y recorder is only a matter of calculating the resistance-free voltages, using Ohm's law, and redrawing the curves with the new voltage values.

Resistance can be measured with separate current and voltage leads (four-point ac measurements). This method is very accurate across metallic or good conductive carbon electrodes. Difficulties arise with less good conductive materials, *e.g.*, conductive plastic sheets, where the current may go another path than the voltage probe is measuring. Area averaging measurements are helpful; sometimes surface films give very different measurements in dry conditions and in electrolyte-wetted situations. Measuring the resistance overvoltage across electrode/electrolyte interfaces in operating cells requires the use of Luggin capillaries as close as possible to the electrode. In critical cases (with a low conductivity electrolyte), one must extrapolate to the distance zero.

Effects of the ohmic resistance can be eliminated by providing a "negative ohmic resistance" compensation. Such a negative impedance converter (NIC) can be built

*Electrochemical Society Active Member.

into the electronic measuring circuit of test instruments. One of the disadvantages is that the NIC can only compensate the ohmic resistance of the whole cell; another is that the value is only approximated because the circuit has a tendency to oscillate near the compensation point.

The ohmic portion of the overvoltage can be very accurately determined by the use of pulse measurements. The simplest way to do it galvanostatically is as follows: first, set the current through the cell at the desired constant level and then apply a negative voltage pulse to the control input of the same galvanostat so that the current drops to zero. At the end of the negative pulse, the previous control setting establishes the current flow again. The voltage of the cell is measured during the short time period when the current is zero. The voltage measurement can be made in different ways. A storage or delay oscilloscope may be used, or the trace of the pulse on the screen can be photographed and evaluated.

It is also feasible to use an analog storage circuit consisting of a condenser and a periodically operating mechanical (5), electronic (6), or thermal switch (7). The simplest circuit producing high current pulses periodically consists of a transformer and a diode. In order to obtain the voltage between the pulses, a diode bridge-circuit which is opened and closed by the opposite-phase voltage is very practical (1).

The pulse measurement method described above can be automated by establishing a certain timing control sequence (with an electronic timer or with a computer program) for the current interruptions. The current flowing from or into the cell can also be changed according to a test program profile. The result is current/voltage curves which are free of the voltage difference caused by the ohmic resistance. Simultaneously, of course, the terminal voltages can be recorded. The difference can be very indicative, especially if reference electrodes are employed.

Automatic Current Interrupter Devices

Potentiostatic and galvanostatic circuits are well known in the electrochemical test practice and are commercially available. The principal diagram of a V/I control circuit is shown in the left part of Fig. 1. A potentiostat is a direct current (dc) amplifier which works as a voltage following circuit. It has a differential input; if the (-) input is connected to the output, then the amplifier will act in such a way as to reduce the voltage difference between (+) and (-) to zero (inverting mode). If the test cell, in Fig. 1 consisting of a counterelectrode CE and a working electrode WE, is put into the circuit between output and ground G, then a current will be driven through the cell; it may flow in the charge or discharge direction, depending on the test purpose. This current is controlled by the voltage supplied from a constant source (CP) and adjusted by means of the variable resistor VR (a precision ten-turn potentiometer) between (+) and the ground. The (-) input

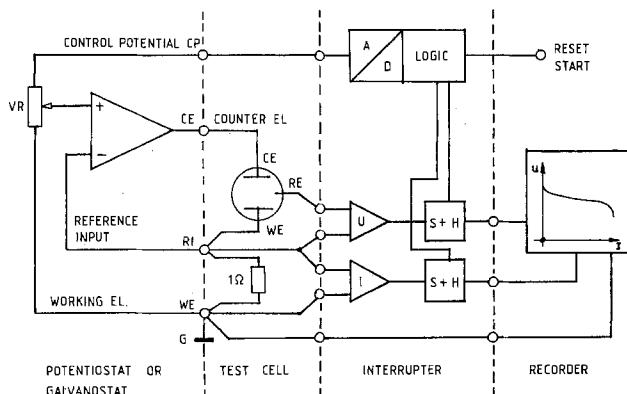


Fig. 1. Principal circuit for the "resistance-free" voltage measurements by the interruption method. CE: Counterelectrode. WE: Working electrode. RE: Reference electrode. RI: Reference input. G: Ground. A/D Analog/digital converter. U: Instrument amplifier for V. I: IA for I. VR: Variable resistor. S+H: Sample and hold circuit.

terminal (reference input RI) follows this voltage, impressed on the circuit via the variable resistor VR and holds it (potentiostat).

Arranging a 1.0Ω resistor between ground G and allowing the potentiostat to control the voltage difference across this constant 1.0Ω resistor, one obtains the characteristic behavior of a "galvanostat." Controlling to a $1.0V$ differential corresponds to a current flow of $1.0A$.

The characteristic features of a potentiostat are maximum current output, voltage range, actual control accuracy, which is determined by the stability of the electronic circuits, and the noise level. The reference voltage source must also be considered in respect to its true accuracy and reproducible long-time stability.

The achievable steepness of the voltage step (expressed in volts per microsecond) for the case of an ideal square pulse is of special importance for the design of interrupters. The speed of the response (risetime) determines how fast the current will be able to go to zero. The time needed is usually in the range of microseconds (μs). This time is negligible compared with the time requirements of electrochemical reactions and faradic transport processes, which do show differential changes (mV) in milliseconds (ms) but may reach final equilibria only in seconds to minutes.

Figure 2 shows graphically how the current, which flows through the test cell, drops from the value i to zero. Design calculations indicated that a time period of $100\mu s$ is sufficient for the measurement of the potential while no current is flowing. The "resistance-free" voltage obtained that way may have an uncertainty of less than 1% if one does not want too severe requirements with respect to precision and cost of the circuit components. Only electrodes which have a strong tendency to form passive surface films (magnesium, for example) need special attention.

In order to measure potentials independent of the ground connections, so-called "instrument amplifiers" are used. The counterelectrode and the reference electrode of the cell to be measured are not connected to ground. Good instrument amplifiers are commercially available; if they have to be made from single components, care must be taken to adjust resistors to very close tolerances in order to achieve a high "common mode rejection." The literature describes the selection of suitable components (8, 9).

Similar considerations are applicable to the current amplifiers. Exchanging the (+) and (-) input terminals makes it possible to adapt the recorded curves to the corresponding quadrant of the X/Y recorder.

The circuit diagram shown in Fig. 3 pictures the now-available (10) complete Sample and Hold Integrated Cir-

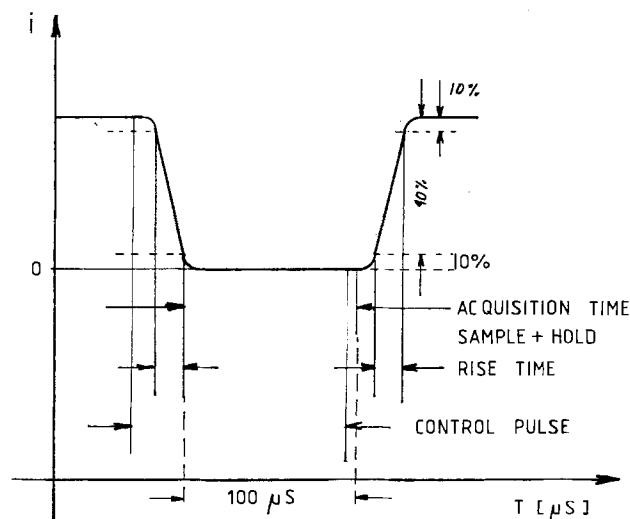


Fig. 2. Current/time diagram: trace of the current going from the constant value I to zero and back. This profile shows the slopes of the I/T lines due to the limitations imposed by the switching speed.

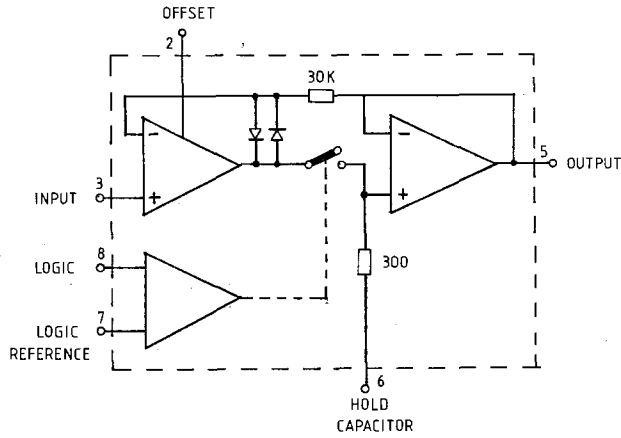


Fig. 3. Principal diagram of the sample and hold integrated circuit LF398 by National Semiconductor Corporation.

circuit designated S&H-IC-LF 398 which we used. The potential of the cell to be measured is first applied to the Fet input of an impedance converter with a very high resistance input and a low resistance output. In this way, a condenser can be charged very fast to the level of the cell voltage ("sample" mode). The capacitor can be separated from the charging circuit by means of a very high resistance electronic switch and exists then in the "hold" mode. A second impedance converter with a high resistance input and a low resistance output supplies the condenser voltage to the output terminal. The impedance converters are coupled with a feedback resistor to reduce possibilities for faulty operation. The electronic switch is actuated by an operational amplifier with differential input in order to be flexible in the choices of voltages and polarities to operate the switch.

The condenser charge current is limited by a 300Ω resistor. The charge time $T = RC$; therefore, we know the necessary charge time with a given capacity. A compromise must be chosen for the ratio of charge time (that is, the acquisition time in the sample mode) and the self-discharge time in the hold mode, which must be small compared to the intervals between the pulses. A frequency of, e.g., 1 pulse in 10s, needs already a two-stage

sample and hold circuit in which the first S&H uses a small capacitor and needs an extremely short time for being charged, but keeps the voltage accurately enough for about 100 μs for charging the following, perhaps a hundred times larger capacitor. The quality of the capacitors (type of dielectric) is very important.

The integrated circuit ADC-MC8BC is used as the digital/analog converter (11). It is an 8 bit converter with built-in counter and a reference potential source of 2.55V. The unit can be utilized in two ways: the pulses reaching the input of the counter are registered as dual value and converted into an analog voltage. Vice versa, 8 bit data can be supplied as input and converted into analog voltages. The counter can be set back with the reset input.

The buffer amplifier is a sensitive component; it must have a very small drift at zero input if the temperature changes and should have a low noise level at low frequencies. We chose an LF 13741 amplifier (12), but there are higher-quality IC's available (13).

Discussion of the Complete Measuring Instrument

Figure 4 is a flow diagram of the circuits to be shown in more detail later (in Fig. 6). The numbers correspond to the IC blocks discussed. 1 is a square wave generator, using an LM 555 to produce 256 Hz oscillations (12). The next IC, 2, is a 14-step binary divider. Its steps are used to provide the following frequencies: 64, 32, 16, 8, 4, 2, 1, 0.5, 0.25, 0.125, 0.0625, 0.03125, and 0.015625 Hz. In this way, we can obtain curves with a time axis of 4s-34 min. The various frequencies are selected with the step switch S-1. The switch has also an open position in which no pulses are transmitted. The selected pulses go to three parallel, monostable (MS-IC) multivibrators (no. 3, 4 and 5), each containing an RC circuit which triggers the MS-IC timers with the negative edge of the pulses. The delay times are adjusted with an oscilloscope to the following values: no. 3, 100 μs; no. 4, 90 μs; and no. 5, 10 ms. The output pulse of no. 3 is connected to the counter input of the D/A converter (IC no. 6) via the Nand gate IC-8. The same pulses are also reaching the CMOS Gate 74C00, in which a double conversion is made in order to operate the semiconductor switch CD4066, marked as no. 9, in the correct phase relation, required at that time.

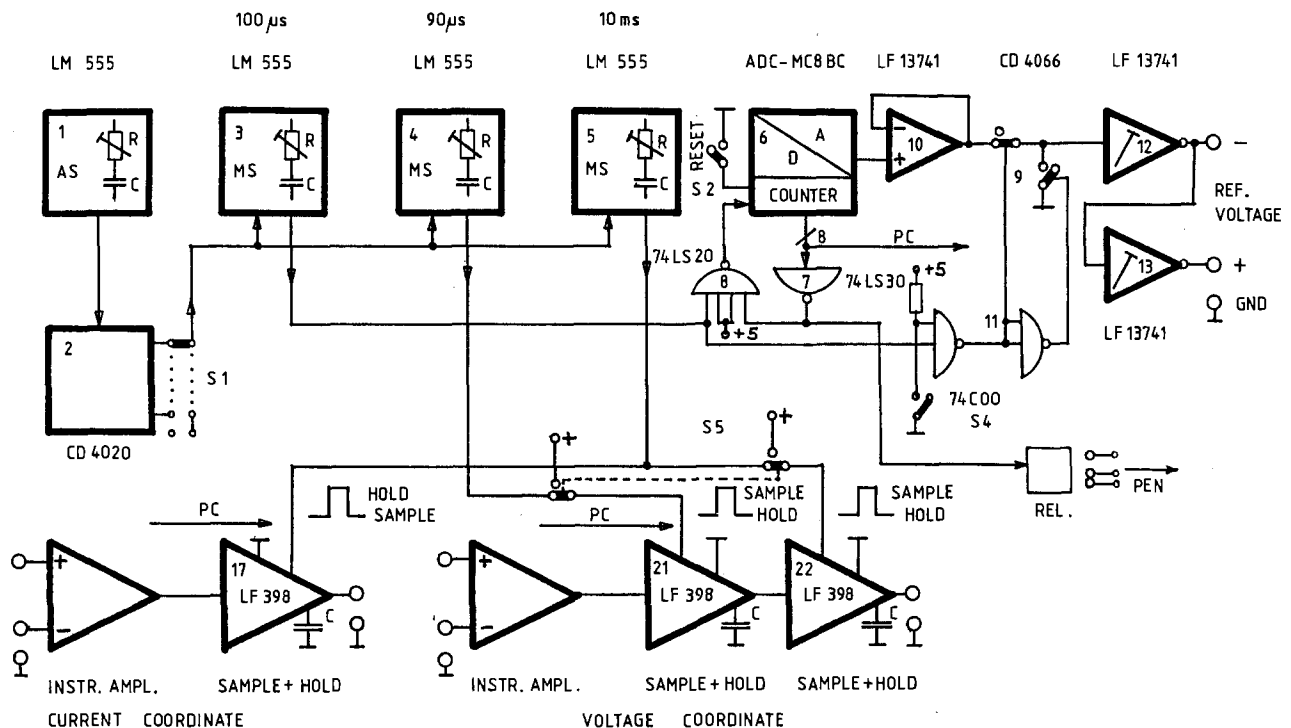


Fig. 4. Flow diagram of the frequency-controlled current interrupter circuit and voltage sensing system. The numbers in the circuit blocks correspond to the IC numbers in Fig. 6.

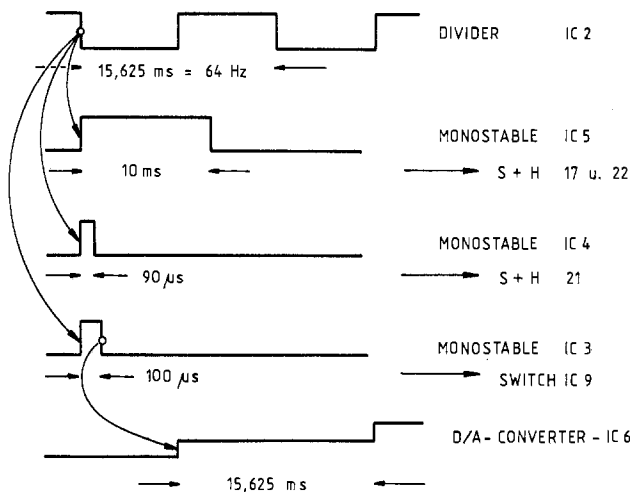


Fig. 5. A comparative diagram, showing the durations of the pulses and their timing sequences. The notations for the IC's corresponds with the numbers in Fig. 4 and 6.

As long as the Reset-Input of the D/A converter is on ground, no change occurs in the state of the counter and the output voltage is zero. As soon as S-2 is opened, the counter starts and a stepwise rising potential appears at the output. Once the counter reaches its highest decimal value (255), all eight data outputs go into the high state. The eight values are then going to a Nand gate with eight inputs and the outputs of the gate go into low state, locking the gate IC-8 for further pulses and storing the maximum values in the counter. Now the reference voltage for stationary measurements is available.

IC-12 and IC-13 amplify (and invert) the voltage to the desired value, so that the output terminals of the instrument can supply a buffered reference potential in positive and negative directions for the input of the galvanostat. Switch S-4 can prevent the pulses from going to IC-9 and the circuit measures the cell voltage with the ohmic resistance included. The output of gate IC-7 controls also a relay for the lifting of the recorder pen, as soon as the counter reaches 225.

Figure 5 is a comparative diagram, showing the durations of the pulses (the length of milliseconds in relation to microseconds is not drawn to scale!) and their timing sequences. The notations for the IC's correspond with the numbers in Fig. 4 and 6. The binary divider (IC-2) produces (in the 64 Hz position) pulses of 15,625 ms length. MS timer IC-5 controls one S&H circuit in the current circuit (17), and the second S&H in the voltage circuit (22) with pulses of 10 ms length. It should be noted that at high pulse, the S&H in the current circuit is in hold mode and the S&H in the voltage circuit is in sample mode. IC-4 controls the first S&H in the voltage circuit (21) with a 90 μ s sample period.

Figure 6 shows the power supply for the whole instrumentation. IC-6, IC-7, and IC-8 are operated with 5V and all others with 10V, split in +5 and -5V against ground. That is the reason why the input of IC-8, which gets the 10V pulses, must be connected to ground with a diode/resistor combination for the case that there is a negative voltage.

Control Circuit Including a Computer

A few changes to the circuit shown in Fig. 5 or 6, respectively, allow the use of a personal computer (PC), making the testing procedures far more flexible. The suggested changes are as follows.

Input 2 of the A/D converter must be grounded to make the converter accept 8 bit words and produce the corresponding voltage at the output. The switch IC-9 will be operated with the switch S-4. The pulses will be turned off with S-1. The logic inputs of the S&H IC's are to be switched over to the computer inputs marked PC. The logic level must be adapted with voltage dividers (8). The following features must be provided for operation with a PC: (i) 8 bit data channel for the control of the D/A-converter, (ii) 3 bit data channel for controlling the 3 S&H-stages, and (iii) two channel A/D converter for the current and voltage measurements.

Manuscript received Nov. 16, 1984. This was Paper 93 presented at the New Orleans, Louisiana, Meeting of the Society, Oct. 7-12, 1984.

REFERENCES

1. K. Kordesch and A. Marko, *This Journal*, **107**, 480

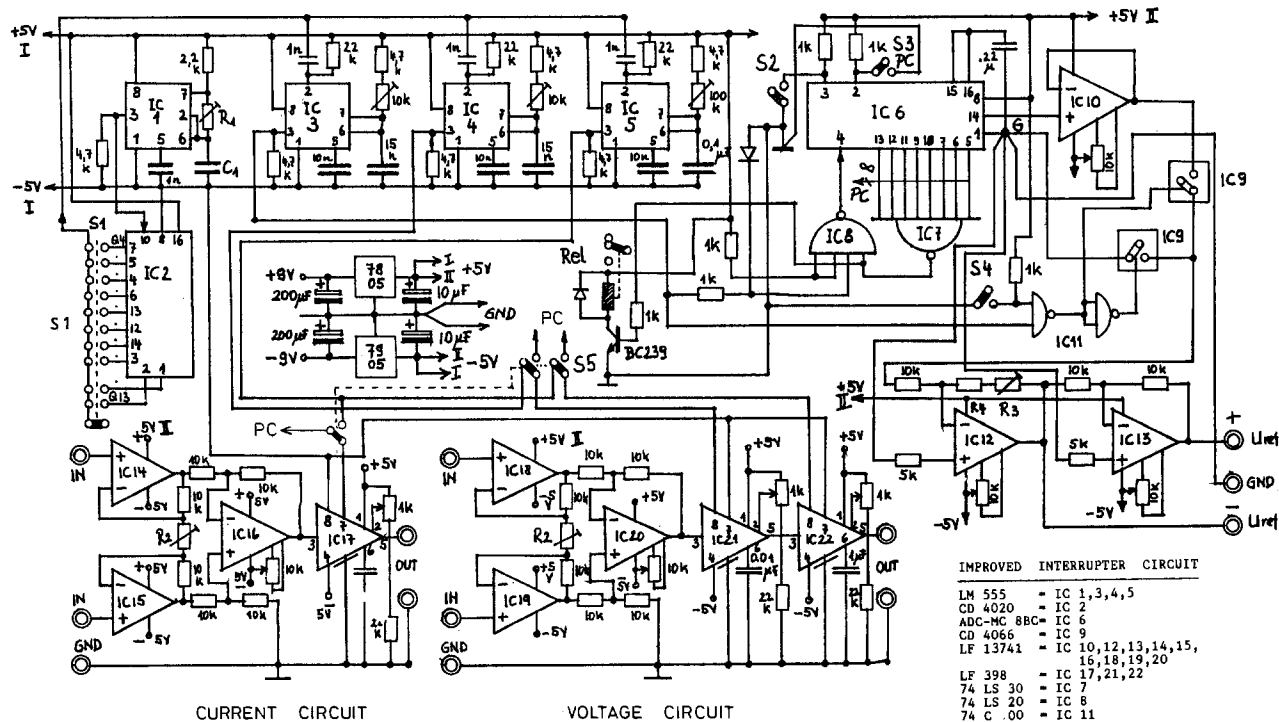


Fig. 6. The complete circuit diagram of the instrumentation to measure the voltage of a galvanic system under operating conditions (being discharged or charged), free of the effects of the ohmic overvoltage.

- (1960).
2. M. Lurie, H. N. Seiger, and R. C. Shair, in "Proceedings of the 17th Power Sources Conference," Atlantic City, NJ, May 21-23, 1963, p. 11 (1963).
 3. E. J. Cairns and H. A. Liebhavsky, "Fuel Cells and Fuel Cell Batteries," see pp. 223-238, John Wiley and Sons, New York (1968).
 4. K. V. Kordesch, *This Journal*, **119**, 1053 (1972).
 5. K. V. Kordesch and A. Marko, U.S. Pat. 2,662,211 (1953).
 6. K. V. Kordesch and F. Kornfeil, U.S. Pat. 2,864,055 (1958).
 7. F. H. Mullersman, U.S. Pat. 3,531,706 (1970).
 8. "Linear Data Book," Chap. 7.5-7.3, National Semiconductor Corp., Santa Clara, CA (1982).
 9. U. Tieze and Ch. Schenk, "Halbleiterschaltungstechnik," Chap. 7, 10, 24, Springer Verlag, Berlin (1983).
 10. "Linear Data Book," LF 398, National Semiconductor Corp., Santa Clara, CA (1982).
 11. ADC-MC8BC from "Electronic Design," Vol. 3, pp. 34-37, Engineering Production Handbook, Datel Systems, Inc., 1977/78 (1977).
 12. LF 1374 and LM 555, "Linear Data Book," National Semiconductor Corp., Santa Clara, CA (1982).
 13. "Data Acquisition Handbook," Chap. 2, Intersil, Inc. Munich, Germany (1980).

Complex Plane and ^7Li NMR Studies of Highly Conductive Sulfide-Based Lithium Glasses

Steven J. Visco, Peter Spellane, and John H. Kennedy*

Department of Chemistry, University of California, Santa Barbara, California 93106

ABSTRACT

The activation energy for lithium diffusion in highly conductive $\text{LiI-Li}_2\text{S-P}_2\text{S}_5$ glasses with varying lithium concentrations is measured by ^7Li NMR linewidth techniques, and is compared to activation energies for ionic conductivity obtained by complex plane techniques. The ^7Li NMR spectra for the glasses have been examined as a function of temperature; the HB equation for motional narrowing was used to calculate the activation energies for lithium movement in the various glasses. From the NMR data, two activation energies were observed over the temperature range of -100°C to room temperature. The low temperature, high activation energy values correlate well with the activation energies obtained from ionic conductivity measurements, while the high temperature, low activation energy process is apparently due to some sort of short-range motion detected only by the ^7Li NMR measurements.

The desire for reliable high energy density batteries has led to exciting developments in the field of solid-state electrolytes. Batteries utilizing solid electrolytes for ionic conduction may provide the most efficient means of storing energy. Much of the work in this field to date has focused on crystalline materials; however there has been a recent shift into new areas such as glass and polymeric electrolytes. Glass electrolytes offer many advantages over polycrystalline ceramic electrolytes, including isotropic conductivity, absence of grain boundary resistance, wide compositional ranges, and ease of fabrication.

The use of lithium as an anode material offers obvious benefits; lithium has a low equivalent weight, yields high cell voltages, and is relatively easy to handle. Consequently, there has been a substantial amount of research effort devoted to finding suitable lithium electrolytes. The search for crystalline lithium electrolytes has not been very satisfactory. However, there have been recent exciting advances in the development of lithium ion conductive glasses (1-14). Various glasses have been synthesized (such as $\text{LiI-Li}_2\text{S-P}_2\text{S}_5$ and $\text{LiI-Li}_2\text{S-B}_2\text{S}_3$) that have Li^+ conductivities matching the best crystalline electrolytes ($\sigma = 10^{-3} \text{ S-cm}^{-1}$ at 25°C) and stability ranges appropriate for their use in lithium anode batteries (1-5, 10).

The structures and mechanisms for conduction in glass electrolytes have been less studied and consequently less understood than their crystalline counterparts. In order to further explore the nature of the ionic conductivity in glasses, we have applied the techniques of both solid-state NMR and ac impedance to study the highly conductive $\text{LiI-Li}_2\text{S-P}_2\text{S}_5$ glasses (1-5).

The application of NMR in solid electrolyte studies is a potentially powerful tool for exploring both the structural and dynamic nature of these materials (15-19). ^7Li NMR has been used effectively to study the diffusion of Li^+ in Li_3N , and very recently to study Li^+ movement in the conductive lithium borate glasses (17-19) and $\text{Li}_2\text{S-GeS}_2$ glasses (20). A predominant cause of NMR line broadening in solids is the magnetic dipole-dipole interaction between nuclei. Thermal activation of ions with increasing temperature tends to remove the dipole-dipole inter-

action between nuclei of activated ions, and the corresponding NMR line narrows. This phenomenon is called motional narrowing. From the NMR linewidth *vs.* temperature data, the Hendrickson-Bray (HB) equation can be used to calculate the activation energy for Li^+ motion in the solid (18, 19).

Bray and his co-workers have determined the activation energies for Li^+ motion in the $\text{Li}_2\text{O-B}_2\text{O}_3$ and $\text{LiX-Li}_2\text{O-B}_2\text{O}_3$ ($\text{X} = \text{F, Cl}$) glasses (18, 19), and correlated them with activation energies reported from conductivity studies. It is important to realize that more meaningful comparisons between the two techniques can be obtained when conductivity and NMR measurements are made on the same sample.

We now present data obtained from both NMR and electrical conductivity measurements on $\text{LiI-Li}_2\text{S-P}_2\text{S}_5$ glasses having varying LiI concentrations. These glasses are of particular interest because they possess very high Li^+ conductivities at ambient temperatures (1-5).

Experimental

The $\text{LiI-Li}_2\text{S-P}_2\text{S}_5$ glasses were prepared according to the procedure of Malugani and Robert (2). The glass compositions are determined by holding the mole ratio of Li_2S to P_2S_5 at 2:1 while varying the mole ratio of LiI . Since starting materials and end products are extremely hygroscopic, all manipulations were performed inside a helium dry box equipped with a purification train to keep residual H_2O and O_2 to less than 1 ppm. The reagents were mixed in the appropriate proportions, sealed into thick-walled quartz tubes, placed in Inconel alloy pipe explosion shields, and heated to approximately 900°C for about 1h. The melts were then either air or water quenched, depending on the cooling rate desired. The quenched glass was ground to a fine powder, and, for the NMR study, a portion of the glass sample was sealed under vacuum into 5 mm NMR tubes. The remaining powder was then uniaxially pressed into 1/4 in. diam rods with TiS_2 electrodes on both faces. The vitreous electrolyte rod was finally isostatically pressed at approximately 40,000 lb/in.² prior to ionic conductivity measurements.

*Electrochemical Society Active Member.

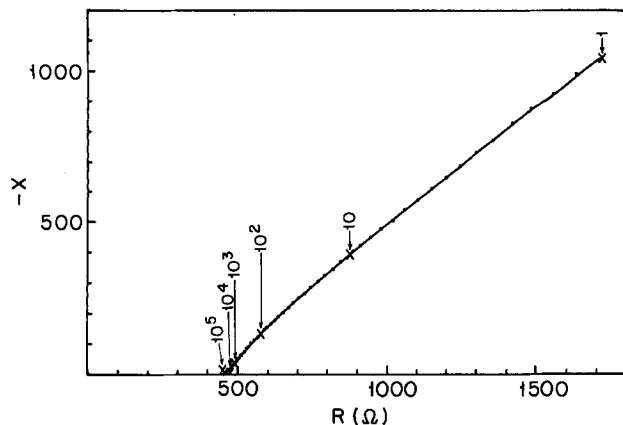


Fig. 1. The complex impedance diagram for 0.10LiI-0.60Li₂S-0.30P₂S₅ glass with TiS₂ electrodes ($T = 156^{\circ}\text{C}$).

The ionic conductivity of the glasses was determined using a Solartron 1174 Frequency Response Analyzer interfaced to a Hewlett-Packard 9845B desktop computer and a General Radio 1435 programmable decade resistance box. A correction program was incorporated to compensate for inductive effects arising from electrode leads observed at high frequency (10^5 - 10^6 Hz). The signal across the sample was 100 mV. Complex impedance measurements were recorded from 10^{-2} to 10^6 Hz over the temperature range 25° - 120°C .

⁷Li NMR spectra were obtained on a Nicolet NT-300 Spectrometer. A broad band probe was tuned to 116.6157 MHz on a solution sample of LiCl and the magnetic field homogeneity was optimized for this sample at room temperature. The lithium glass sample was then placed in the magnet and cooled gradually to -100°C . The sample was not spun, and no further attempt was made to improve field homogeneity. Thermal equilibration time varied from 15 to 60 min, depending on the selected temperature. A 90° pulse was applied, and data from 1000 transients was Fourier transformed to yield one broad resonance and fit to a Lorentzian curve.

Results and Discussion

The complex impedance plots of the LiI-Li₂S-P₂S₅ glasses consisted of a straight line intersecting the real axis at approximately a 45° angle (Fig. 1). The real axis intercept was taken to represent the bulk resistance of the glass sample. For all glass compositions, the ionic conductivities follow the classical Arrhenius law, $\sigma = \sigma_0 \exp(-E_a/RT)$ (Fig. 2). The ionic conductivities and corresponding activation energies of the vitreous electrolytes are governed by the glass composition. As previously reported by Malugani *et al.* (2-4), the ionic conduc-

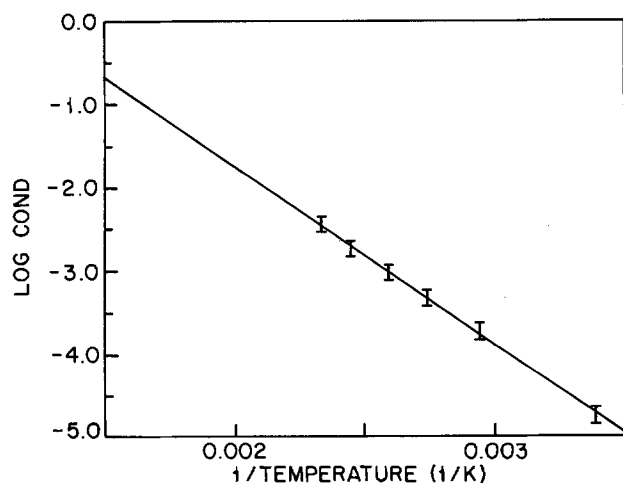


Fig. 2. Arrhenius plot of bulk conductivity for 0.10LiI-0.60Li₂S-0.30P₂S₅.

Table I. NMR parameters, conductivities, and E_a 's for lithium glasses

Glass composition	$B(\text{kHz})^a$	$E_a(\text{eV})^a$	$E_a(\text{eV})^b$	Cond. ($\text{S}\cdot\text{cm}^{-1}$) ^c
0.0LiI-0.67Li ₂ S-0.33P ₂ S ₅	3.3×10^{-11}	0.50	0.46	8.5×10^{-6}
	0.011	0.10		
0.10LiI-0.60Li ₂ S-0.30P ₂ S ₅	4.0×10^{-9}	0.38	0.42	2.2×10^{-6}
	0.011	0.10		
0.20LiI-0.53Li ₂ S-0.27P ₂ S ₅	1.6×10^{-7}	0.31	0.36	9.2×10^{-5}
	0.0058	0.11		
0.30LiI-0.47Li ₂ S-0.23P ₂ S ₅	1.5×10^{-7}	0.30	0.35	3.2×10^{-4}
	0.0080	0.10		

^a First listed value: low temperature, second value: high temperature.

^b From conductivity studies.

^c Conductivity at 25°C .

tivity of these glasses at a specific temperature increased and the activation energy decreased with increasing LiI concentration (Table I). The activation energies determined in this study were slightly higher than those reported in the literature (2-4). This could be the result of isostatically pressing the glass powders to less than maximum density.

The ⁷Li NMR spectra for the lithium glasses investigated exhibited a single ⁷Li resonance over the temperature range of -100° - 50°C (Fig. 3). The NMR linewidth *vs.* temperature data were analyzed using the HB equation for motional narrowing in solids written as

$$\ln(1/W-1/A) = -(E_a/kT) + \ln(1/B-1/A)$$

where W is the observed NMR linewidth, A is the experimentally determined rigid-lattice linewidth, and B is the high temperature linewidth. The rigid-lattice linewidth A is determined by lowering the sample temperature until the NMR linewidth no longer broadens. Due to the highly conductive nature of the LiI-Li₂S-P₂S₅ glasses and the fact that we are presently confined to a lower temperature limit of -100°C , it was necessary to extrapolate the rigid-lattice linewidth for the more conductive glasses containing high concentrations of LiI (*i.e.*, 30 mole percent). A plot of $\ln(1/W-1/A)$ *vs.* $1/T$ should produce a straight line with a slope of $-E_a$ and Y -intercept of $\ln(1/B-1/A)$.

The HB plots of the NMR data for the glass electrolytes clearly show two straight line segments, indicating that two types of motion in the glass are being observed (Fig. 4, 5). The low temperature line narrowing corresponds to

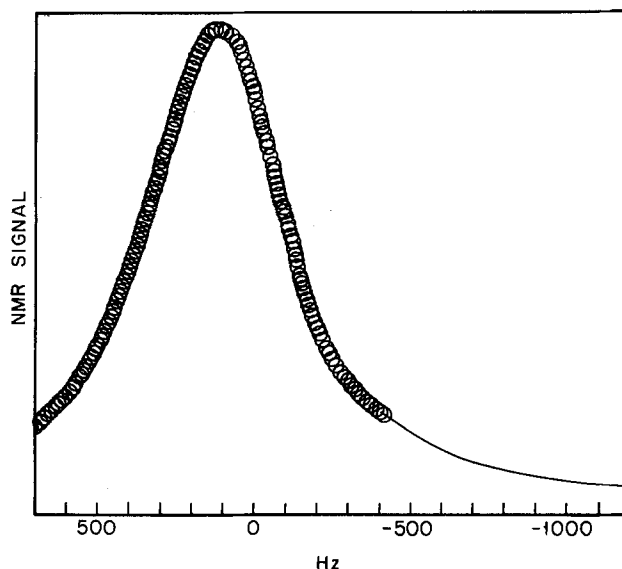


Fig. 3. ⁷Li nuclear magnetic resonance line obtained from sample of 0.20LiI-0.53Li₂S-0.27P₂S₅ glass at 10°C . Fit of 187 data points to Lorentzian function is shown.

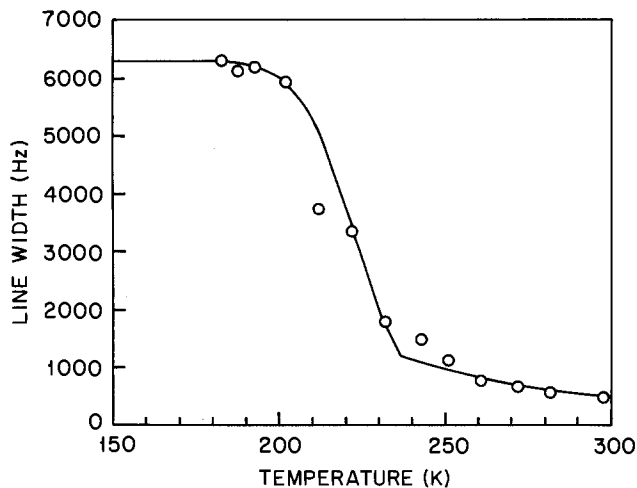


Fig. 4. ${}^7\text{Li}$ NMR linewidth vs. temperature for the $0.66\text{Li}_2\text{S}-0.34\text{P}_2\text{S}_5$ sample. *: Experimental points. Solid line: calculated curve.

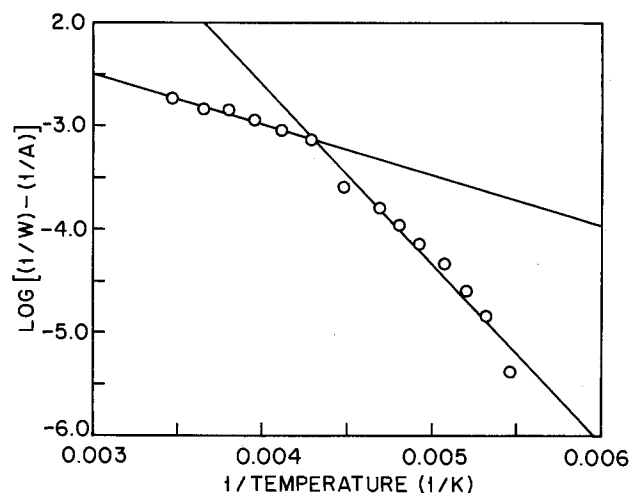


Fig. 5. The plot of $\ln[(1/W) - (1/A)]$ vs. $1/T$ for ${}^7\text{Li}$ motional narrowing data for the $0.10\text{LiI}-0.60\text{Li}_2\text{S}-\text{P}_2\text{S}_5$ glass exhibits two different processes that contribute to motional narrowing. The low temperature and high temperature activation energies obtained from this plot are 0.38 and 0.10 eV, respectively.

a high activation energy process, while the high temperature narrowing involves a low activation energy process (Table I). The activation energies for the low temperature narrowing correlate well with the activation energies obtained from the ionic conductivity measurements. The values for the parameter B corroborate this observation. Long-range motion (as in ionic conduction or diffusion) would eliminate the dipole-dipole interaction, whereas a local restricted motion would have far less effect in removing the interaction. Therefore, the value of B corresponding to long-range motion will be much smaller than that for short-range motion. As can be seen from Table I, the B values for the low temperature process exhibiting activation energies nearly equal to those obtained from conductivity measurements were several orders of magnitude smaller than the B values for the high temperature process. Bray *et al.* found the same trends for the lithium borate glasses (18, 19). The NMR results in Table I show

that the high activation energy for long-range motion in the glass decreased with increasing LiI concentration. This trend is mirrored by the activation energies for ionic conduction determined for the same glass samples.

The results in Table I also show that the low activation energy for short-range motion was essentially constant over the entire range of LiI concentrations, and little change was seen in the value of B . Thermal activation of the short-range motion in these glasses was apparently unaffected by the concentration of lithium ion, indicating that this process did not involve the presence of neighboring lithium ions. In addition, the constant low activation energy found in this study matched the analogous values determined by Bray *et al.* (19) for the $60\%\text{Li}_2\text{O}-40\%\text{B}_2\text{O}_3$ and $50\%\text{Li}_2\text{O}-\text{B}_2\text{O}_3$ glasses (0.11 eV).

Conclusion

It is clear that NMR investigations can yield useful information on the nature of the movement of Li^+ in solid electrolyte glasses. The activation energies for ${}^7\text{Li}$ motion determined from NMR line narrowing studies correlate well with the activation energies determined from ionic conductivity measurements on the same samples. Furthermore, the NMR measurements detect a type of short-range Li^+ motion that is apparently not detectable by electrical conductivity studies.

Acknowledgment

Financial support is acknowledged from the National Science Foundation (DMR 80-02676) and Union Carbide Corporation.

Manuscript received July 2, 1984.

REFERENCES

1. J. P. Malugani, R. Mercier, B. Fahys, and G. Robert, Abstract 709, p. 1136, The Electrochemical Society Extended Abstracts, Vol. 82-1, Montreal, Que., Canada, May 9-14, 1982.
2. J. P. Malugani and G. Robert, *Solid State Ionics*, **1**, 519 (1980).
3. G. Robert, J. P. Malugani, and A. Saida, *ibid.*, **3/4**, 311 (1981).
4. R. Mercier, J. P. Malugani, B. Fahys, and G. Robert, *ibid.*, **5**, 663 (1981).
5. J. P. Duchange, J. P. Malugani, and G. Robert, *Prog. Batt. Sol. Cells*, **4**, 46 (1982).
6. J. L. Souquet, *Ann. Rev. Mater. Sci.*, **11**, 211 (1981).
7. J. L. Souquet, *Solid State Ionics*, **5**, 77 (1981).
8. A. Levasseur, J. C. Brethous, J. M. Reau, and P. Hagemmuller, *ibid.*, **1**, 177 (1980).
9. M. Irion, M. Couzi, A. Levasseur, J. M. Reau, and J. C. Brethous, *J. Solid State Chem.*, **31**, 285 (1980).
10. H. Wada, M. Menetrier, A. Levasseur, and P. Hagemmuller, *Mater. Res. Bull.*, **18**, 189 (1983).
11. A. M. Glass, K. Nassau, and T. J. Negran, *J. Appl. Phys.*, **49**, 4898 (1978).
12. A. M. Glass and K. Nassau, *J. Appl. Phys.*, **51**, 3756 (1980).
13. K. Nassau, *J. Non-Cryst. Solids*, **42**, 423 (1980).
14. K. Nassau, R. J. Cava, and A. M. Glass, *Solid State Ionics*, **2**, 163 (1981).
15. B. C. Gerstein, *Anal. Chem.*, **55**, 781A (1983).
16. B. C. Gerstein, *ibid.*, **55**, 900A (1983).
17. S. G. Bishop and P. J. Bray, *J. Chem. Phys.*, **48**, 1709 (1968).
18. A. E. Geissberger, F. Bucholtz, and P. J. Bray, *J. Non-Cryst. Solids*, **49**, 117 (1982).
19. J. R. Hendrickson and P. J. Bray, *J. Mag. Resonance*, **9**, 341 (1973).
20. J. Senegas and J. Olivier-Fourcade, *J. Phys. Chem. Solids*, **44**, 1033 (1983).

The Pitting Corrosion of Nickel in Different Electrolyte Solutions Containing Chloride Ions

D. V. Vasquez Moll, R. C. Salvarezza, H. A. Videla, and A. J. Arvia*

Instituto de Investigaciones Fisicoquímicas Teóricas y Aplicadas, Sucursal 4, 1900 La Plata, Argentina

ABSTRACT

The pitting corrosion of nickel in different electrolytes containing chloride ions was studied by using potentiostatic and potentiodynamic techniques complemented with scanning electron microscopy. The breakdown potential depends linearly on the logarithm of the chloride ion concentration. The logarithm of the induction time for pit initiation decreases linearly with the reciprocal of the applied potential. The overall process can be described by two stages. The first stage of pitting is explained through the formation of the passive layer in competition with the nucleation and growth of a chloride layer. The second stage, which is diffusion controlled, occurs when the salt precipitation conditions is reached. The proposed reaction model reproduces the potentiostatic current transients of nickel pitting by chloride in near-neutral buffered and alkaline solutions.

The corrosion of nickel in chloride containing solutions has been studied in previous papers (1-5). Localized corrosion of nickel is observed at potentials more positive than a certain critical value (E_b). Pits as small as 1 μm diam growing with current densities of the order of 1-100 A/cm² were detected on the nickel surface (2). The initiation and growth of nickel pitting were attributed either to the presence of a thin salt film on the metal surface (2) or to a mass transport process due to local changes in pH (6). In principle, it should be expected that low pH values and high chloride concentrations be associated with large pits as is the case of ferrous alloys (7). Crystallographic and bright hemispherical pits, depending whether the current density is smaller or greater than the current density at which salt precipitation occurs, are observed on nickel 200 in concentrated chloride solutions (8). Pit stabilization on both iron and nickel was related either to the formation of a salt layer by precipitation or to a contaminated oxide on the pit surface (9). The formation of a nickel hydroxide layer would produce pit stabilization (10). It was recently claimed that chloride ions mainly interfere with the repassivation process instead of breaking the passive film in pitting corrosion of nickel (11).

The present paper deals with the pitting corrosion of nickel in different solutions containing chloride ions covering a relatively wide range of pH. The corrosion process is studied using electrochemical techniques complemented with scanning electron microscopy. Pit initiation of nickel in the various systems investigated can be interpreted through the same complex mechanism already applied to the pitting corrosion of iron (12).

Experimental

Working electrodes (specimens) were made of polycrystalline 99.99 nickel rods (5 mm diam) axially embedded in Araldite holders to obtain circular exposed areas of 0.2 cm². The pretreatment of each specimen consisted of a gradual polishing, starting with fine grained emery paper, followed with diamond paste, and, finally, with alumina paste (1 and 0.3 μm). The polished specimen was successively rinsed with acetone, twice-distilled water, and then dried in air at room temperature. A fresh specimen was used in each run. Measurements were made in a conventional Pyrex glass cell at 25 \pm 0.1°C. The potential of the specimen was measured against a saturated calomel electrode (SCE) connected through a Luggin-Haber capillary tip. In the text, potentials are referred to the SCE scale. A platinum plate was used as counter-electrode. The following electrolyte solutions were used: (i) phosphate-borate buffer (0.1M KH₂PO₄ + 0.05M Na₂B₄O₇, pH 8.00); (ii) borate-boric acid buffer (0.075M Na₂B₄O₇ + 0.15M H₃BO₃, pH 9.00); (iii) carbonate-bicarbonate buffer (0.05M Na₂CO₃ + 0.75M NaHCO₃, pH 9.00); and (iv) 10⁻³M NaOH. Sodium chloride was added to each electrolyte solution in the 0.1M \leq c_{NaCl} \leq 1M concentration

range. Solutions were prepared from twice-distilled water and AR chemicals and purged with purified nitrogen during 3h previously to each run.

Single triangular potential sweep (STPS) voltammograms run between the cathodic ($E_{s,c}$) and the anodic ($E_{s,a}$) switching potential at the sweep rate (v) 0.02 V/s, and potentiodynamic polarization curves ($v = 0.02$ V/min) were obtained in the conventional way and presented as current density (i) vs. potential (E) plots. Prior to each run, the specimen was held either at -1.00V in one of the buffer solutions or at 1.30V in the sodium hydroxide solution during 90s to achieve a reproducible electroreduced surface (14). Current transients (i/t) at constant potential (E_s) were also recorded. For this purpose, preceding the potential step at E_s the working electrode was successively potential stepped to -1.00V (E_c) during 90s and to -0.5V (E_a) during 90s to form a passive layer. Recent results in weakly alkaline phosphate solutions show that at potentials close to -0.5V (SCE) a thin film of $\approx 5\text{\AA}$ is formed at $t < 60\text{s}$ (13). Conventional microscopic and SEM observations were also made.

Results

Voltammetric response.—The first voltammetric scan of nickel both in borate-boric acid and phosphate-borate buffers at 0.02 V/s between $E_{s,c} = -1.00\text{V}$ and $E_{s,a} = 0.50\text{V}$ (Fig. 1a) shows a broad anodic current peak at ca. -0.45V which corresponds to Ni(OH)₂ electroformation (13) followed by a poorly defined hump in the -0.40 to 0.1V range. In carbonate-bicarbonate buffer, the anodic peak at -0.45V (Fig. 1b) and another well-defined anodic peak at -0.25V are observed (Fig. 1b).

The first positive potential going scan from $E_{s,c} = -1.00\text{V}$ to $E_{s,a} = 0.0\text{V}$ run in the buffer solutions containing 0.05M NaCl is qualitatively similar to that recorded in the absence of chloride ions (Fig. 1a and 1b). In the alkaline solution, the anodic peak related to Ni(OH)₂ electroformation appears at -0.65V and the potential of the anodic peak changes according to the solution pH (13). Likewise, when $E_{s,a}$ exceeds 0.05V, there is a sharp increase in the anodic current, which remains during the returning scan. In this case, the voltammetric loop is related to the localized corrosion of nickel. The potential associated with the activation process is more positive in carbonate-bicarbonate buffer than in other solutions.

The potentiodynamic E/I profiles recorded at 0.02 V/min in buffer solutions containing NaCl exhibit a breakdown potential (E_{bv}) associated with pitting corrosion of nickel. Current oscillations probably related to the nickel activation-repassivation processes are observed in a small potential region preceding E_{bv} (9).

The increase in NaCl concentration (c_{NaCl}) shifts E_{bv} toward more negative values according to the following equation

$$E_{bv} = a - b \log c_{\text{NaCl}} \quad [1]$$

*Electrochemical Society Active Member.

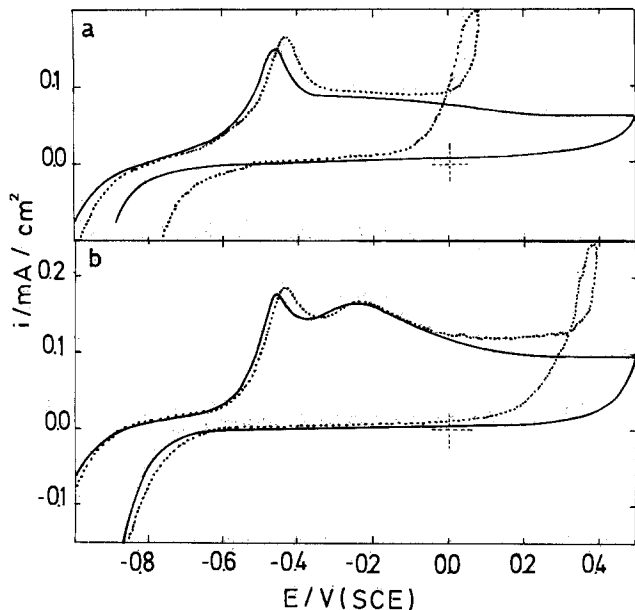


Fig. 1. STPS recorded at 0.02 V/s between $E_{s,c} = -1.00V$ and $E_{s,a} = +0.50V$ in: (a) (—) borate-boric acid buffer, (---) borate-boric acid + 0.5M NaCl; and (b) (—) carbonate-bicarbonate buffer, (---) carbonate-bicarbonate + 0.5M NaCl.

Equation [1] is fulfilled in both buffered and nonbuffered electrolytes (Fig. 2).

Current transients.—The current transients under a constant potential step in the $-0.50V < E_s < 0.40V$ range, in both buffer solutions and $10^{-3}M$ NaOH, in the absence of chloride ions, show a slow continuous decrease in current (Fig. 3). A similar behavior is observed in 0.5M NaCl when E_s is more negative than the potential range where current oscillations are observed.

When E_s falls within the region of current oscillations ($E_s \approx E_{bv}$), the current initially increases up to a maximum, and finally decreases again to approach a value which is slightly greater than that recorded in chloride-free solutions (Fig. 4). The maximum current may result from at least two competing processes such as those associated with pit formation and pit repassivation (10). In this case, few irregular pits are initially formed which are later repassivated. In the potentiostatic mode, pit stabilization occurs at $E_s \gg E_{bv}$.

When $E_s \gg E_{bv}$, the current initially decreases to a minimum and later increases to reach a large randomly

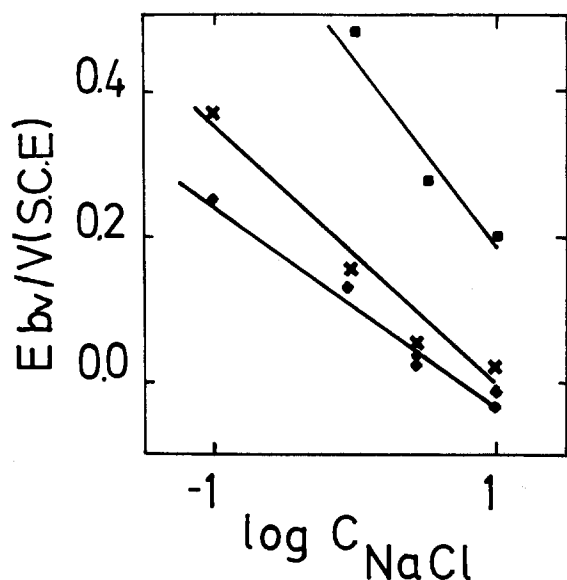


Fig. 2. E_{bv} vs. $\log C_{NaCl}$ in (◆) phosphate-borate buffer, (×) $1 \times 10^{-3}M$ NaOH, and (■) carbonate-bicarbonate.

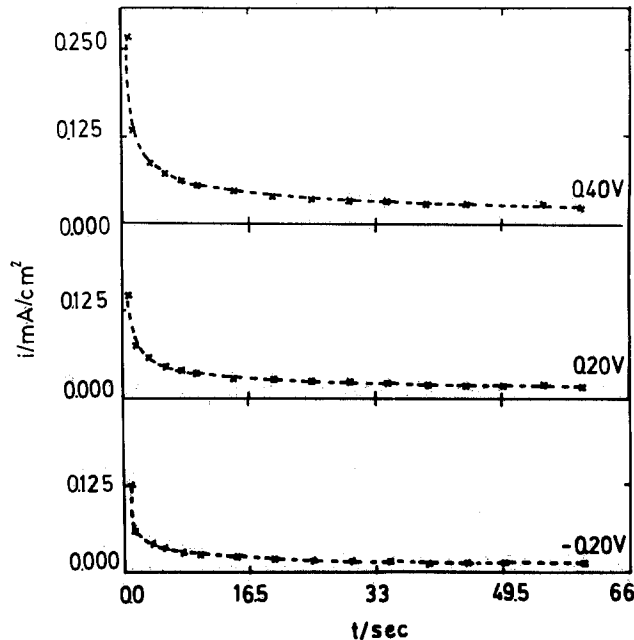


Fig. 3. Current transients at constant potential recorded in phosphate-borate buffer at different potential values. (●): Experimental data. (—): Obtained using Eq. [5] and [6].

fluctuating current value. The anodized test specimens become covered with a thick white-green product, probably hydrated $Ni(OH)_2$, which spalls away from the metal surface. In this case, solution stirring removes the corrosion product and slightly decreases the corrosion current. Microphotographs of the test specimens after anodization at 0.40V during 100s show large hemispherical bright pits. The initial part of the current transients ($E_s \gg E_{bv}$), in solutions containing 0.5M NaCl (Fig. 5a-5d), exhibits an induction time (t_i) which decreases as E_s increases. No pits were detected by conventional microscopic examination of electrodes anodized at $t < t_i$. At a constant E_s , the pitting current vs. time (t) relationships fit the Engell-Stolica equation (Fig. 6)

$$(i_t - i_c) = k_0(t - t_i)^b \quad [2]$$

where i_t is the overall current and i_c is the background current, and k_0 and b are constants. The values of b , which are in the 1.4-2.0 range for $t \rightarrow 0$, decrease later to the 0.33-0.76 range. The transition time (t_i) related to the change of b decreases as the applied potential increases.

The potential dependence of t_i is given by the equation

$$\log t_i/t_0 = k'(E_s - E_n)^{-1} \quad [3]$$

where E_n is taken as the potential value at which there is

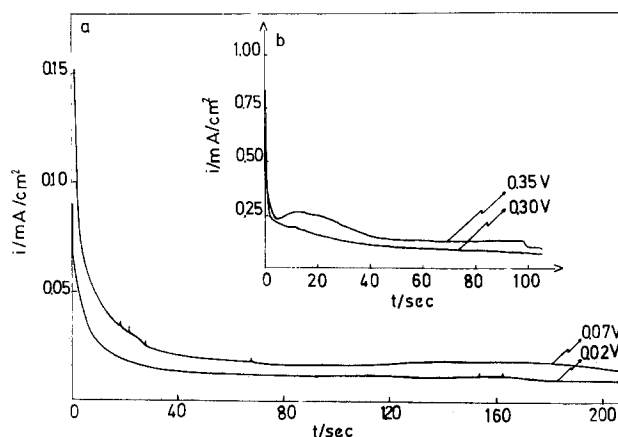


Fig. 4. Current transients recorded in different solutions containing 0.5M NaCl at potential values close to E_{bv} . a: $1 \times 10^{-3}M$ NaOH. b: Carbonate-bicarbonate.

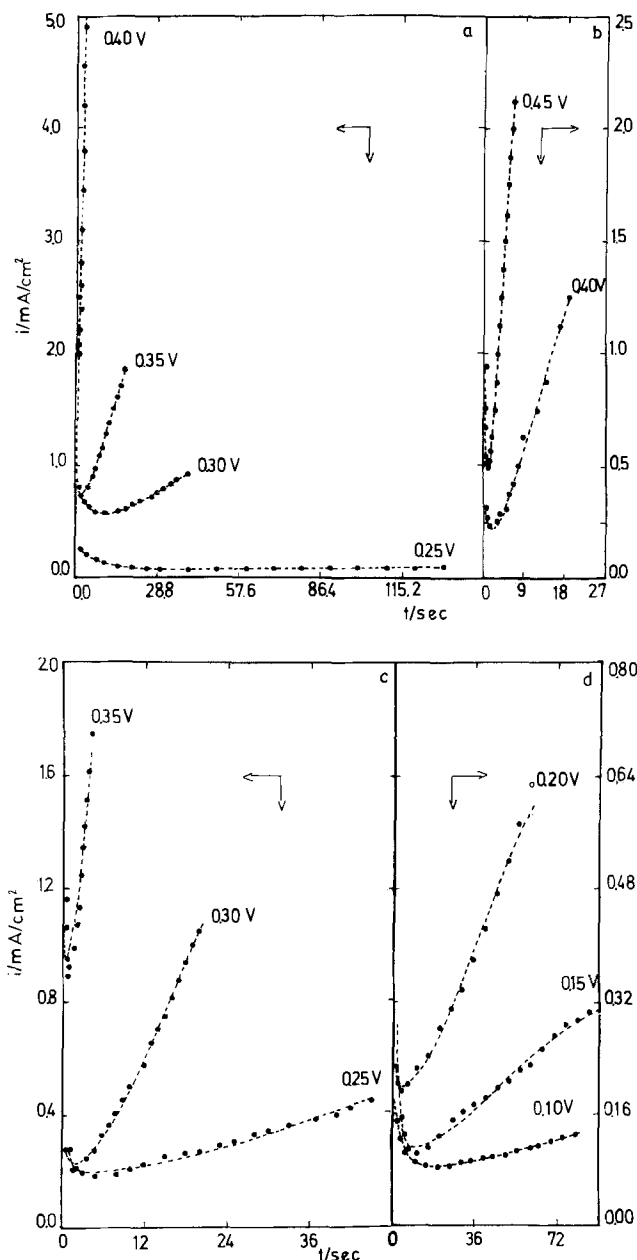


Fig. 5. Current transients at constant potential ($E_s \gg E_{bv}$) recorded in: (a) phosphate-borate + 0.5M NaCl, (b) carbonate-bicarbonate + 0.5M NaCl, (c) borate-boric acid + 0.5M NaCl, and (d) 1×10^{-3} M NaOH + 0.5M NaCl. (●): Experimental data. (—): Calculated using Eq. [5], [12], and [13].

no evidence of pit nucleation (absence of current oscillations), and k' and t_0 are constants.

SEM observations.—SEM patterns of test specimens anodized at $E_s \gg E_{bv}$, in phosphate-borate solution containing 0.5M NaCl, indicate the initial formation of crystallographic pits which during the pit growth transform into hemispherical bright pits (Fig. 7). The pit density in 10^{-3} M NaOH containing 0.5M NaCl increases slightly with the applied potential. In the 0.05-0.25V range, a linear pit density/potential relationship can be obtained (Fig. 8).

Discussion

The complex electrochemical response of nickel in nearly neutral buffered and alkaline solutions containing sodium chloride depends on the applied potential, as it involves nickel hydroxide formation, passivity onset, and pitting corrosion caused by the aggressive chloride ions. Besides, the change in both the morphology and kinetics of pit formation at $t = t_i$ points out that at least two stages should be distinguished in the pitting process.

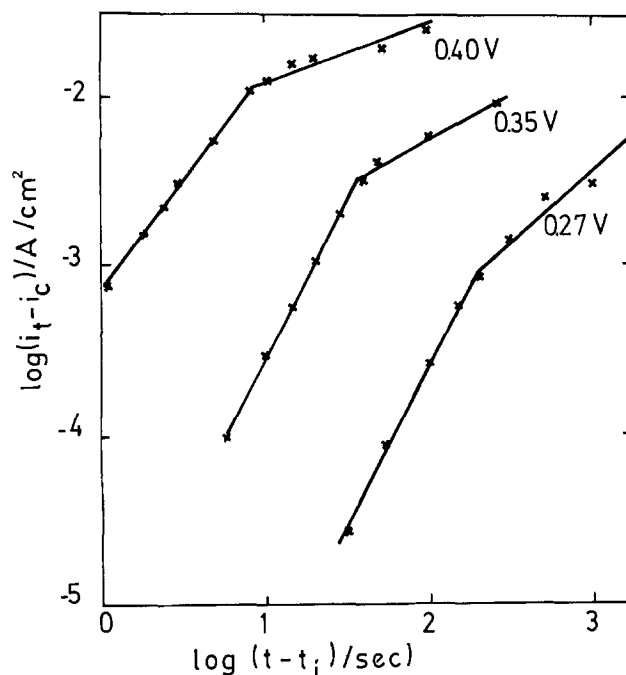


Fig. 6. $\log(i_t - i_c)$ vs. $\log(t - t_i)$ plots in (■) phosphate-borate + 0.5M NaCl, (×) carbonate-bicarbonate + 0.5M NaCl, and (+) 1×10^{-3} M NaOH + 0.5M NaCl.

The first stage of nickel passivation is related to the electroformation of a hydrous $\text{Ni}(\text{OH})_2$ (14) layer, which undergoes a series of chemical and electrochemical transformations, yielding the final passive NiO layer (15-16). The influence of chloride ions to promote pitting can be explained through the formation of nickel chloride nuclei interfering with the passive film formation (3) at potential values slightly lower than E_{bv} . Therefore, the initiation of pitting can be interpreted through the adsorption of chloride ions on a nickel surface which is nonhomogeneously covered with passive film. At $E_s > E_{bv}$ the interaction between the aggressive anion and the metal surface becomes strong enough to remove metal atoms as solvated complex ions out from the lattice.

The analysis of potentiostatic current transients can be used to estimate the extent of participation of the various processes during the anodization of nickel. The instantaneous average anodic current (i_t) can be associated with three main current contributions: namely, the passive layer growth (i_p), the metal corrosion through the passive film (i_c), and the randomly distributed salt nuclei growth (i_s) on the metal surface. Thus

$$i_t = i_p + i_s + i_c \quad [4]$$

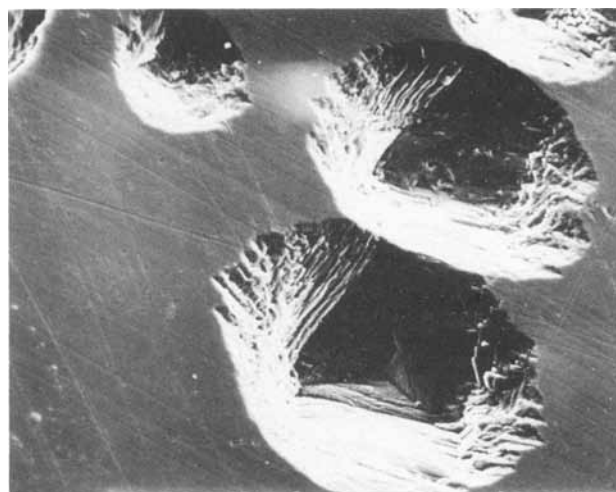


Fig. 7. SEM microphotograph of the metal surface after anodization at 0.35V during 50s in phosphate-borate + 0.5M NaCl.

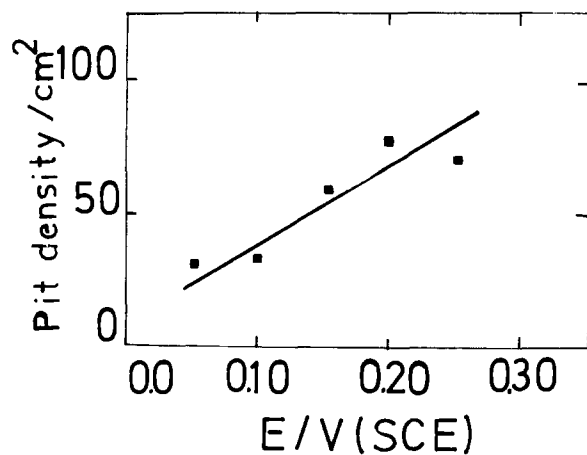


Fig. 8. Pit density vs. E_s plot in $1 \times 10^{-3} \text{ M NaOH} + 0.5 \text{ M NaCl}$. $t_s = 300\text{s}$.

where i_p and i_c are the relevant contributions in the absence of pitting. The passive layer growth can be interpreted in terms of an instantaneous nucleation and circular bidimensional growth under diffusion control (17). In this case, the instantaneous value of i_p is then given by an expression such as

$$i_p = P_1 \exp(-P_2 t) \quad [5]$$

where $P_1 = q_{\text{mon}} \pi K_e D N_0$, $P_2 = \pi K_e D N_0$, D is the diffusion coefficient of the reacting species, q_{mon} is the charge density required for the constant thickness full coverage of the metal surface by the passive layer, K_e is a proportionality constant, and N_0 is the number of sites available for nucleation.

However, the rate of metal corrosion through either the prepassive or passive layer appears as the dissolution of tridimensional nuclei under diffusion control following the rate equation (18)

$$i_c = \frac{P_3}{\sqrt{t}} [1 - \exp(-P_4 t)] \quad [6]$$

where $P_3 = zFD^{1/2} \Delta c/\pi^{1/2}$ and $P_4 = \pi N_0' k_e D'$. Δc is the concentration difference of the diffusion species. N_0' is the number of sites available for the dissolution process, D' is the diffusion coefficient of the species involved in the process, and k_e is a proportionality constant. When $P_4 t \rightarrow \infty$, Eq. [6] becomes

$$i_c = P_3/\sqrt{t} \quad [7]$$

In the absence of pitting, Eq. [5] and [6], with the parameters assembled in Table I, reproduce the current transients for the passive nickel within 1% (Fig. 3). The time dependences of i_c and i_p are considerably different (Fig. 9). The contribution of the passive film growth principally appears at $t < 2\text{s}$. At $t > 2\text{s}$ $i_c \rightarrow i_t$, in agreement with data already reported for nickel electrodisolution in borate-boric acid buffer (19).

The oxide growth can be assigned to the diffusion of oxygen containing species (20) through the prepassive layer. The P_1/P_2 ratio gives the charge density required to complete the passive layer. The value is comprised between 0.33 and 0.21 mC/cm^2 . The average thickness of the layer formed during the potential step can be roughly estimated from the equation

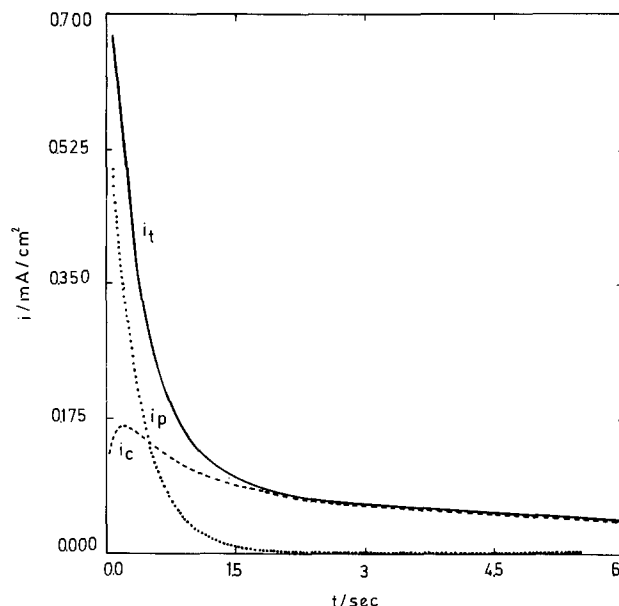


Fig. 9. Total anodic current (i_t), passive layer growth current (i_p), and dissolution current (i_c) for the current transient recorded at 0.20V in the phosphate-borate buffer.

$$h = \frac{M}{zF\rho} \frac{P_1}{P_2} \quad [8]$$

where M is the molecular weight and ρ is the density of the layer component. If the stoichiometry of the latter is taken as $\text{Ni}(\text{OH})_2$, then $M = 92.71 \text{ g/mol}$, $\rho = 4.10 \text{ g/cm}^3$, and a value of h of between 3 and 4\AA results.

The rate of metal corrosion (i_c) can be related to cation diffusion through the passive layer. The cation diffusion from the metal/layer to the layer/solution interface results in dissolution at the metal/layer interface (20). From the expression of P_3 , Δc (the difference of cation concentration between the metal/layer (c_0) and the layer/solution interface (c_h)) can be estimated. Taking $D' = 1.0 \times 10^{-15} \text{ cm}^2/\text{s}$ (21), the value of Δc calculated from $P_3 \approx 10^{-2} \text{ mol/cm}^3$. However, the c_0/c_h ratio can be estimated from the electrical potential gradient (ϵ) which, in layer of $h = 20\text{\AA}$, is close to 10^6 V/cm , through the equation

$$\epsilon h = \frac{kT}{ze} \ln \frac{c_0}{c_h} \quad [9]$$

where e is the electron charge and k is the Boltzmann constant.

As the c_0/c_h ratio comes out close to 10^6 , then $\Delta c \approx c_0 k_e$ can be calculated from the equation

$$k_e = \left(\frac{8\pi c_0 M}{\rho} \right)^{1/2} \quad [10]$$

For nickel, $M = 58.69 \text{ g/mol}$ and $\rho = 8.90 \text{ g/cm}^3$ and $k_e = 1.28$. Consequently, from the expression of P_4 , the value of N_0' can be estimated. Thus, for $P_4 = 330/\text{min}$, N_0' becomes equal to $10^{15}/\text{cm}^2$. This figure suggests that the corrosion process occurs practically on the whole metal/layer interface.

In the pitting region ($E_s \gg E_{\text{bv}}$), the rate equation of the corrosion process becomes more complex, as follows

$$i_c = \frac{P_3}{\sqrt{t}} [1.0 - \exp(-P_4 t)] + P_5 \quad [11]$$

Table I. Parameters used in simulation of potentiostatic current transients shown in Fig. 3

Electrolyte	E_s (V)	P_1 (mA/cm^2)	P_2 (min)	P_3 ($\text{mA min}^{1/2}/\text{cm}^2$)	P_4 (min)
Phosphate-borate	0.40	0.652	117	0.022	340
Phosphate-borate	0.20	0.507	143	0.010	315
Phosphate-borate	-0.20	0.647	173	0.014	339

where P_5 can be assigned to the corrosion current through either the prepassive or the passive layer induced by the accumulation of the aggressive anions at certain sites. Considering that

$$P_5 \gg \frac{P_3}{\sqrt{t}} | 1.0 - \exp(-P_4 t) |$$

Eq. [11] becomes

$$i_c \equiv P_5 \quad [12]$$

The large values of i_c suggest that at the sites of attack the prepassive layer was totally removed and at these points the nucleation and growth of a salt layer containing the aggressive anion takes place. Both SEM observation and the slight dependence of pit density on potential (Fig. 8) suggest that the mechanism of salt nuclei formation corresponds to an instantaneous nucleation and tridimensional growth. This process probably implies the electro-dissolution of nickel leading to pitting corrosion.

The instantaneous value of i_s can be calculated from the rate equation for conical pit growth under a charge-transfer control (22)

$$i_s = P_6 [1 - \exp(-P_7 t^2)] \quad [13]$$

where $P_6 = zFk_{3c}'$, $P_7 = \pi M_s^2 k_{3c}^2 N_{os} / \rho_s^2$, k_{3c} and k_{3c}' are the formal rate constants for the layer growth in the directions parallel and perpendicular to the metal plane, respectively, ρ_s is the salt (NiCl₂) density whose molecular weight in M_s , and N_{os} is the number of sites available for salt nuclei formation. When the salt nuclei formation implies an induction time (t_{is}), Eq. [13] becomes

$$i_s = P_6 | 1 - \exp[-P_7 (t - t_{is})^2] | \quad [14]$$

Equations [13] and [14], after a series expansion, yield the following relationships

$$i_s = P_6 P_7 t^2 \quad [15]$$

$$i_s = P_6 P_7 (t - t_{is})^2 \quad [16]$$

which correspond to particular cases of the Engell-Stolica equation, where $b = 2$. This value is approached at potentials close to E_{bv} in the early stages of pit growth.

The current transients recorded for $E_e \gg E_{bv}$ in solutions containing 0.5M NaCl are reproduced within a maximum error of 5% with Eq. [5], [12], and [13] using the parameters assembled in Table II (Fig. 5a-5d). In this case, the values of t_{is} are negligible in the time scale of the current transients. Consequently, large values of the nucleation rate are expected in agreement with an instantaneous nucleation process. The potential dependence of both P_6 and P_7 approach a linear semilogarithm relationship. The slope $dE/d \log P_6$ covers from 0.12 to 0.14 V/decade, and the slope $dE/d \log P_7$ is close to 0.06 V/decade. These results are comparable to the dependence of the pit current density on potential already reported by different authors (23-26). It is likely that P_6 and P_7 be related to the corrosion rate at the pit surface where a chloride condensed phase detected in small pits (27) impedes metal

repassivation. At this stage, pits are bounded by low crystal faces which are covered by chloride (28-29).

Considering that $k_{3c} \approx k_{3c}'$ and that at $t = t_i$ the pit area is close to 0.001% of the total metal surface area, the N_{os} values can be obtained from P_7 and P_6 through the following relationship

$$N_{os} = \frac{z^2 F^2 \rho_s^2 P_7}{\pi M_s^2 10^6 P_6^2} \quad [17]$$

For NiCl₂, $\rho_s = 3.55 \text{ g/cm}^3$, $M_s = 129.60 \text{ g/mol}$, and the N_{os} values are between 1×10^3 and $2.2 \times 10^4/\text{cm}^2$. These values, which are larger than those observed for the density of single pits, suggest that each large pit contains a relatively large number of overlapping sites during growth.

Bright nickel surfaces were observed during transpassive dissolution of nickel in the presence of a salt film (8). The transition from crystallographic to hemispherical pits and the change in the kinetics of pit growth at $t = t_i$ can be related to the precipitation of a layer of nickel chloride. As the total pit area at $t = t_i$ is about 0.001% of the total metal surface area, a penetration rate (v') ($v' = P_6/0.001$) of between 0.15 and 10 A/cm² results.

The pit depth (r) required to obtain the precipitation of nickel chloride can be estimated through the expression (9)

$$r = \frac{zFD_+ \Delta c_+}{2v'} \quad [18]$$

where D_+ is the cation diffusion coefficient.

By taking $D_+ = 10^{-5} \text{ cm}^2/\text{s}$ and $\Delta c_+ = 5 \times 10^{-3} \text{ mol/cm}^3$ from NiCl₂ solubility (2), the values of r are between 4.8 (10 A/cm²) and 320 μm (0.15 A/cm²). This means that deep pits are already formed when salt precipitation occurs. This conclusion is in agreement with the kinetic transition in pit growth already discussed.

In the absence of electrolyte convection, the instantaneous ion concentration at the flat metal surface dissolving at constant current density can be expressed by Sand's equation.

$$\Delta c_+ = 2v' \sqrt{t_i} / zF \sqrt{\pi D_+} \quad [19]$$

From this equation, the time (t_i) required to build up the concentration change $\Delta c_+ = 5 \times 10^{-3} \text{ mol/cm}^3$ becomes $t_i = 0.1\text{s}$ (10 A/cm²) and $t_i = 300\text{s}$ (0.15 A/cm²). These values of t_i are smaller than those resulting from the current transients (Fig. 6). The difference can be associated with the time required for salt supersaturation before precipitation (30-31).

During pitting, the pit cavity is covered by a thick layer of nickel hydroxide, which acts as a barrier to separate the pit electrolyte from bulk solution and contributes to pit stabilization (10).

The second stage of pitting occurring at $t > t_i$ is similar to the transpassive dissolution and becomes largely mass-transport controlled. In this case, Eq. [5], [12], and [13] are no longer valid (Fig. 10). The growth of salt nuclei under

Table II. Parameters used in simulation of the potentiostatic current transients shown in Fig. 5

Electrolyte	($E_s - E_{bv}$) (V)	P_1 (mA/cm ²)	P_2 (min)	P_3 (mA/cm ²)	P_4 (mA/cm ²)	P_7 (min ²)
Phosphate-borate buffer + 0.5M NaCl	0.36	12.02	3280	2.15	14.2	93.2
	0.31	2.44	148	0.691	1.88	10.6
	0.26	0.340	12.3	0.480	0.804	1.78
	0.21	0.213	7.78	0.065	0.154	0.04
Borate-boric buffer + 0.5M NaCl	0.31	6.20	673	9.29	4.28	39.7
	0.26	0.480	119	0.204	1.48	7.57
	0.21	0.383	91.8	0.193	0.557	1.14
Carbonate-bicarbonate + 0.5M NaCl	0.20	1.89	248	0.389	2.69	88.4
	0.15	0.253	96.0	0.202	1.47	12.2
$1 \times 10^{-3}\text{M NaOH} + 0.5\text{M NaCl}$	0.11	0.175	35.0	0.115	0.643	0.487
	0.06	0.254	35.7	0.103	0.236	0.871
	0.01	0.116	18.0	0.080	0.155	0.219

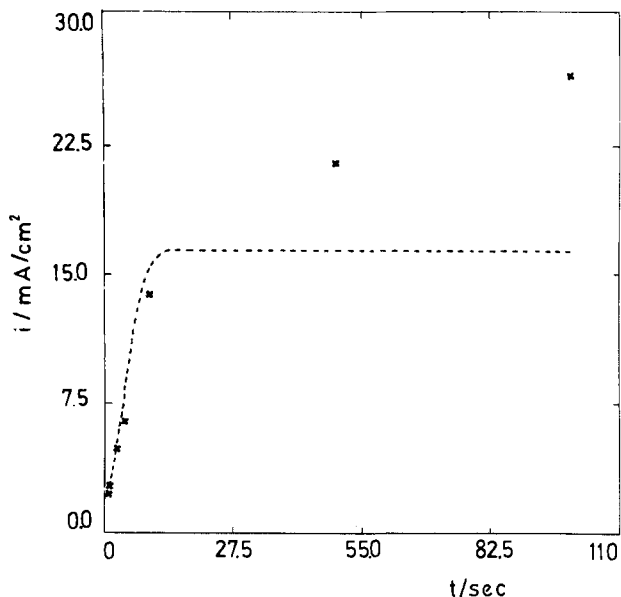


Fig. 10. Total current density. (---): Calculated using Eq. [5], [12] and [13]. (x): Experimental data.

diffusion control can be represented by instantaneous nucleation and tridimensional growth under diffusion control. The corresponding rate equation is (18)

$$i_s = \frac{P_8}{\sqrt{t - t_t}} [1 - \exp[-P_9(t - t_t)]] \quad [20]$$

where $P_8 = zFD_{-1/2} \Delta c_t / \pi^{1/2}$ and $P_9 = \pi N_{os}' k_s D_t$, N_{os}' denotes the number of sites available for the salt precipitation inside the pits, and k_s is a proportionality constant. When $P_9 t \rightarrow \infty$, Eq. (20) becomes

$$i_s = \frac{P_8}{\sqrt{t - t_t}} \quad [21]$$

The corresponding current transients can be simulated with Eq. [20] (Fig. 11) using the parameters assembled in Table III. Equations [20] and [21] explain the current decay observed in large artificial pits in acid solutions (31).

The cation diffusion coefficient from the bulk electrolyte can be estimated from P_8 .

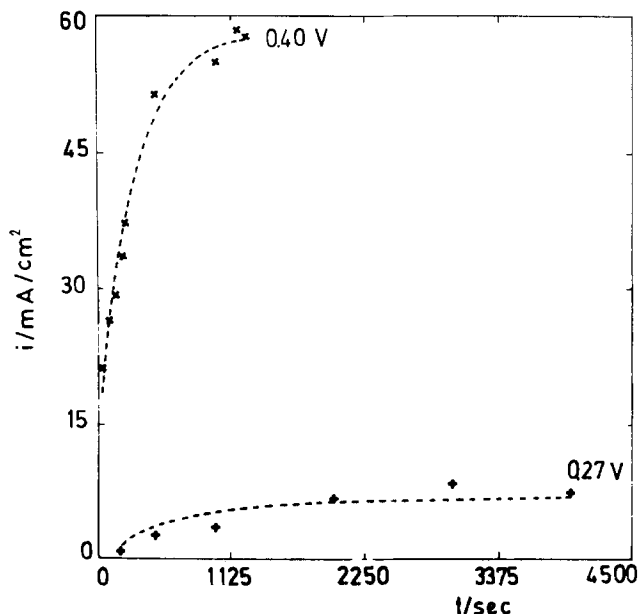


Fig. 11. Current transients recorded at different E_s values in phosphate-borate + 0.5M NaCl at $t > t_t$. (x +): Experimental data. (—): Calculated using Eq. [20].

Table III. Parameters used in simulation of the potentiostatic current transients shown in Fig. 11

Electrolyte	E_s (V)	P_8 (mA min ^{1/2} /cm ²)	P_9 (min)	t_t (min)
Phosphate-borate + 0.5M NaCl	0.400	383	0.055	0.05
Phosphate-borate + 0.5M NaCl	0.275	74.9	0.021	2.55

For $\Delta c_t = 5 \times 10^{-3}$ mol/cm³, at the lowest potential $D_t = 1.2 \times 10^{-6}$ cm²/seg. This is a reasonable figure for ionic diffusion from the bulk solution.

According to the localized acidification theory, pit stabilization occurs under diffusion control (6). The critical value of ri for pit initiation for all bivalent metals is close to 5×10^{-7} A/cm (32). However, in the presence of weak acid salts, the critical conditions for pit initiation are achieved at larger values of ri . In borate-boric acid solutions, the increase in the borax concentration from 10^{-4} to 10^{-3} results in an increase of about one order of magnitude in the ri value (6). Then, for 0.15M borax concentration as used in this work, the ri value must be greater than 10^{-4} A/cm. The penetration rate (v') obtained for nickel pitting in the borate-boric acid buffer at E_s close to E_{bv} is 0.3 A/cm². Consequently, using the value of 3×10^{-4} A/cm, localized acidification seems to contribute to pit growth only when the pit depth is greater than 10 μ m. This value is close to that required for the salt layer precipitation.

From the above discussion, it can be concluded that the nucleation and growth mechanism describes the phenomenology of the initial stages of nickel pitting by chloride in nearly neutral buffered solutions and alkaline solutions containing chloride. However, the above interpretation involves the limitations of the nucleation and growth mechanism which yields a macroscopic description of the corrosion process by taking into account the nucleation of a growth center, the corresponding geometry of the growing process, and the overlapping of nuclei (33).

Acknowledgment

INIFTA is sponsored by the Universidad Nacional de La Plata, the Consejo Nacional de Investigaciones Científicas y Técnicas, and the Comisión de Investigaciones Científicas (Provincia de Buenos Aires). D.V.M. acknowledges the fellowship granted by the Deutscher Akademischer Austauschdienst, through the University of Mainz-University of La Plata Cooperation Agreement and University of Concepción, Concepción, Chile.

Manuscript submitted June 11, 1984; revised manuscript received Dec. 26, 1984.

REFERENCES

1. J. R. Vilche and A. J. Arvia, *Corros. Sci.*, **15**, 419 (1975).
2. H. H. Strehblow and J. Weners, *Z. Phys. Chem. NF.*, **199** (1975).
3. H. H. Strehblow and M. B. Ives, *Corros. Sci.*, **16**, 317 (1976).
4. B. MacDougall, *This Journal*, **127**, 789 (1980).
5. B. MacDougall and M. J. Graham, *Electrochim. Acta*, **27**, 1093 (1982).
6. J. R. Galvele, *This Journal*, **123**, 464 (1976).
7. J. Mankowski and Z. Szklarska-Smialowska, *Corros. Sci.*, **15**, 493 (1975).
8. M. Datta and D. Landolt, *This Journal*, **129**, 1889 (1982).
9. N. Sato, *ibid.*, **129**, 260 (1982).
10. M. Kesten, *Corros. Sci.*, **14**, 665 (1974).
11. B. MacDougall, in "Passivity of Metals and Semiconductors," M. Froment, Editor, p. 275, Elsevier, New York (1983).
12. D. Vasquez Moll, R. C. Salvarezza, H. A. Videla, and A. J. Arvia, *Corros. Sci.*, To be published.
13. C. Y. Chao, Z. Szklarska-Smialowska, and D. D. Macdonald, *J. Electroanal. Chem.*, **131**, 279 (1982).
14. L. M. Gassa, J. R. Vilche, and A. J. Arvia, *J. Appl. Electrochem.*, **13**, 135 (1983).
15. B. MacDougall, D. F. Mitchell, and M. J. Graham, *This*

- Journal*, **128**, 1248 (1980).
16. S. G. Real, J. R. Vilche, and A. J. Arvia, *Corros. Sci.*, **20**, 563 (1980).
 17. W. Davison and J. A. Harrison, *J. Electroanal. Chem.*, **44**, 213 (1973).
 18. B. Scharifker and G. Hill, *Electrochim. Acta*, **28**, 879 (1983).
 19. N. Sato and G. Okamoto, in "Comprehensive Treatise of Electrochemistry," Vol. 4, J. O'M. Bockris, B. E. Conway, E. Yeager, and R. E. White, Editors, p. 210, Plenum Press, New York (1981).
 20. C. Y. Chao, L. F. Lin, and D. D. MacDonald, *This Journal*, **129**, 1187 (1981).
 21. Z. Szklarska-Smialowska and W. Kozlowski, *ibid.*, **131**, 234 (1984).
 22. M. Y. Abyaneh and M. Fleischmann, *Electrochim. Acta*, **27**, 1513 (1982).
 23. Z. Szklarska-Smialowska and M. Janik-Czachor, *Br. Corros. J.*, **4**, 138 (1969).
 24. W. Schwenk, *Corrosion*, **20**, 129 (1964).
 25. J. Weners, Diplomarbeit, Freie Universität Berlin, Berlin (1971).
 26. H. Kaesche, *Z. Phys. Chem. NF.*, **34**, 87 (1962).
 27. K. J. Vetter and H. H. Strehblow, in "Localized Corrosion," p. 240, NACE, Houston, TX (1974).
 28. K. J. Vetter and H. H. Strehblow, *Ber. Bunsenges. Phys. Chem.*, **74**, 1024 (1970).
 29. J. Tousek, *Corros. Sci.*, **12**, 799 (1972).
 30. H. C. Kuo and D. Landolt, *ibid.*, **16**, 915 (1976).
 31. T. R. Beck, *This Journal*, **129**, 2417 (1982).
 32. J. R. Galvele, *Corros. Sci.*, **21**, 551 (1981).
 33. D. E. Williams, C. Westcott, and M. Fleischmann, in "Passivity of Metals and Semiconductors," M. Froment, Editor, p. 219, Elsevier, New York (1983).

Electrochemical Studies of the Passive Film on 316 Stainless Steel in Chloride Media

M. G. S. Ferreira¹ and J. L. Dawson

UMIST, Corrosion and Protection Centre, Manchester, England M60 1QD

ABSTRACT

The kinetics of passive film growth on 316 stainless steel in 3% sodium chloride solution have been studied by dc and ac electrochemical measurements. The inverse logarithmic rates of current decay showed two stages of film growth, both controlled by a high field conduction mechanism. Impedance measurements were interpreted on the basis that diffusion of the metallic species through the film controlled the film growth-dissolution process. Capacitance data indicate that the film is 20–25Å thick, depending on potential, with a field strength of 6.66×10^6 V cm⁻¹.

The passivation of metals is of considerable technical importance, but, despite the considerable amount of research carried out on this topic, our understanding of the phenomena is still incomplete. The subject has been reviewed recently by Uhlig (1), and, although the present trend is to accept the formation of a film as being responsible for passivation, the important role of adsorption during the initial film formation stages should also be recognized (2).

In the case of stainless steels, many discrepancies appear to exist in the literature (3–11); the relationship between the composition of the films and the role of chromium and molybdenum on the protective properties still requires further study. Examination of publications relating to stainless steels shows that it is often difficult to compare results due to the various experimental conditions, different surface preparations, and limitation of the techniques used in the studies.

The composition, structure, and electrical properties of passivating films on austenitic stainless steels have been investigated using a range of different techniques: electron diffraction (3–6), x-ray photoelectron spectroscopy (ESCA) (7, 8), impedance measurements (7, 8), radioactive indicators (9, 10), ellipsometry (7, 8, 11), Auger electron spectroscopy (12–14), and chemical analysis of stripped films (3, 4). Of these methods, only the electrochemical and ellipsometric techniques provide *in situ* measurements.

There are also only a few publications concerned with the initiation of the film growth mechanism on iron (15) and stainless steel (7, 16), and virtually no evidence is available which indicates the mechanisms involved in the process of film growth and retention of passivity. However, recent impedance studies (19) at UMIST on 304 stainless steel in 3% sodium chloride solutions showed that a restricted diffusion process is obtained through the film, and this appeared to be a controlling factor in film stability.

The lack of quantitative data is a major problem in the development of detailed models. Nevertheless, Auger electron spectroscopy, x-ray photoelectron spectroscopy, and ellipsometry are providing semiquantitative results on the composition within the film and also on compositional changes with electrode potential.

Evaluation of the film thickness on stainless steel gave values between 5 and 60Å (3, 4, 7, 11, 17), and there is also evidence that these films possess semiconductive properties (17, 18).

The purpose of the present studies was to investigate the mechanism operating during passive film growth on 316 stainless steel and to study the changes with potential in the passive region. The ac impedance technique was the major investigative technique, since it provides *in situ* information on the mechanisms and kinetics of the processes.

DC measurements were also carried out, and the results obtained were assessed in terms of the kinetics of film growth. These were then correlated with impedance data to provide a model of the processes resulting in the formation of the passive film.

Experimental

Cell and electrodes.—A three-electrode cell consisting of a glass tube, 125 mm long and 25 mm diam, with three side arms was used in the experiments. A platinum foil and a saturated calomel electrode served as counter and reference electrodes, respectively. The working electrode was machined from bar stock of AISI 316 stainless steel with a composition

C	Si	Mn	P	S	Cr	Mo	Ni
0.04	0.23	1.65	0.030	0.016	16.87	2.49	12.72

In a preliminary series of experiments, considerable difficulties were experienced in achieving reproducibility of results due to the unpredictable onset of pitting and crevice corrosion. Electrode designs utilizing any form of masking procedure were found unsuitable; even the compression type of fitting, as used in the Makrides type of

¹ Present address: Laboratório de Electroquímica, Instituto Superior Técnico, 1096 Lisboa Codex, Portugal.

electrode (20), was not always satisfactory in eliminating crevice corrosion. It was also observed that with cylindrical electrodes, the site for pit initiation often occurred where the wall of the cylinder met the circular base. Reproducibility was only achieved by use of a truncated cone shaped electrode which was immersed to a fixed depth into the electrolyte and suspended from a leak-proof compression assembly incorporating a PTFE gasket (21). The truncated cone had an upper diameter of 10 mm, a lower diameter of 5 mm, and a height of 6 mm. The specimens were mechanically polished with emery paper to a 1000 grit silicon carbide finish under flowing water. Following this operation, the specimens were polished with a diamond paste to a 3 μm finish, degreased with acetone, and stored in a desiccator overnight prior to use.

Solutions.—Most studies were carried out in solution containing 3% sodium chloride, *i.e.*, 0.51M, with the pH adjusted to a value of 6.5 using 0.01M sodium hydroxide solution.

Comparison was also made with three solutions of pH = 0.6, but with varying chloride content: 0.5M H_2SO_4 + 0.1M NaCl, 0.5M H_2SO_4 + 0.3M NaCl, 0.5M H_2SO_4 + 0.5M NaCl, and 0.5M NaCl + 0.065M HCl.

Prior to an experiment, all solutions were deoxygenated overnight with pure nitrogen; the measurements were carried out at an ambient temperature of 291 K.

Electrochemical experiments.—Potentiokinetic measurements were carried out using an anodic sweep from the corrosion potential after the specimens had been immersed for half an hour to the depth required to give a working area of 60 mm^2 in the solution. The sweep rate was 10 mV min^{-1} , and the potential was reversed when the current density reached the value of 1 mA cm^{-2} or 400 mV . The equipment used in the experiments included a Chemical Electronics I. C. 20/05 potentiostat in conjunction with a Chemical Electronics linear sweep unit, a Sinclair DM 2 digital multimeter, and a Bryans Y-log X recorder which was used to monitor the current flowing through the cell.

Impedance measurements were made using a Solartron 1172 frequency response analyzer (FRA) over the frequency range 10 kHz–10 mHz and a 10 mV rms amplitude signal and the results were stored on a punch tape and subsequently analyzed on a Digital Equipment Corporation PDP 11/10 minicomputer. The circuitry used (21) made it possible for the experiments to be carried out at any required potential, the sweep rate from the initial corrosion potential being changed at a set rate (10 mV min^{-1}) until the desired value was reached.

Results and Interpretation

Polarization data.—The corrosion potential of the stainless steel specimens covered with the air-formed film produced by the overnight stand in the desiccator was typically $-150 \pm 20 \text{ mV vs. SCE}$. On polarization to more noble potentials, the anodic current density remained virtually unchanged at between 0.2×10^{-3} and $0.3 \times 10^{-3} \text{ mA cm}^{-2}$, the passivation current density. Above $+50 \pm 20 \text{ mV vs. SCE}$, the pitting potential, there was a rapid increase in current density with the increase in potential and pits could be seen on the metal surface. The potentiodynamic sweep was reversed at $+400 \text{ mV vs. SCE}$, and although there was an initial current increase the current decreased with the cathodic sweep until the alloy became passive again at a potential of -50 mV vs. SCE , the protection potential (see Fig. 1). These polarization results were similar to those found by previous workers (22, 23).

Film growth kinetics.—Freshly prepared electrodes, *i.e.*, ones relatively free from the air-formed film, were used to obtain the variation of current with time at a fixed potential. During these potentiostatic experiments, the current was observed to decrease progressively with time to the constant i_p value; then, by means of Faraday's law, the value of the charge passed, Q , was used to estimate the film thickness, x

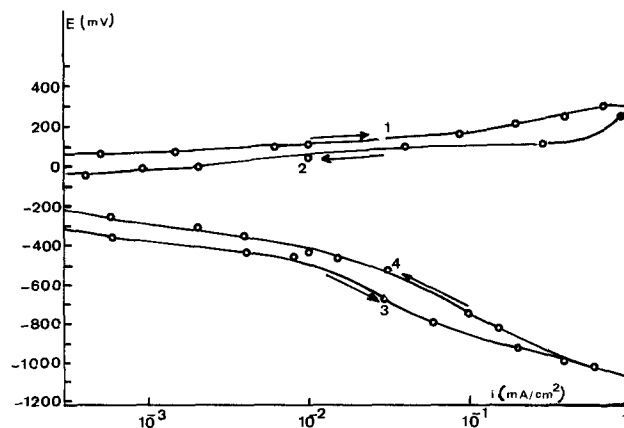


Fig. 1. Potentiodynamic plot of 316 stainless steel in 3% sodium chloride solution.

$$x = \frac{QM}{nF\gamma\rho} \quad [1]$$

Two estimates of the film thickness were made by assuming that the composition was either $\gamma\text{-Fe}_2\text{O}_3$ or $\text{Fe}(\text{OH})_3$. Thus, at a potential of -120 mV vs. SCE , $Q = 3.45 \times 10^{-3} \text{ C/cm}^2$, M for $\gamma\text{-Fe}_2\text{O}_3 = 159.7 \text{ g}$, assuming a surface roughness $\gamma = 1.2$, the film density $\rho = 5.6 \text{ g/cm}^3$, and $nF = 0.579 \times 10^6 \text{ C}$, which gave a thickness of 14.2 \AA . For $\text{Fe}(\text{OH})_3$, $M = 107 \text{ g}$; $\rho = 3.5 \text{ g/cm}^3$; and $nF = 0.289 \times 10^6 \text{ C}$, *i.e.*, a thickness of 26 \AA . These values appear to be reasonable for films on stainless steel in aqueous solutions and would only be modified slightly if account were to be taken of the other alloying elements in the steel.

Figure 2 shows an $\ln i$ vs. $\ln t$ plot, suggesting an experimental relationship of the type

$$\ln i = -a \ln t + b \quad [2]$$

but with two linear regions corresponding to two different stages of film growth. Rearrangement of Eq. [2] gives

$$\ln t = -\frac{\ln i}{a} + \frac{b}{a} \quad [3]$$

But at constant potential and temperature, the film thickness, x , is also proportioned to $\ln t$ (25)

$$\frac{1}{x} = -K \ln t + K' \quad [4]$$

where K and K' are constants. Substitution of Eq. [3] into [4] gives

$$\frac{1}{x} = -K \left(-\frac{\ln i}{a} + \frac{b}{a} \right) + K' \quad [5]$$

or

$$\ln i = \frac{a}{Kx} + b - a \frac{K'}{K} \quad [6]$$

This is the inverse logarithmic law as suggested (24) by the kinetic equation

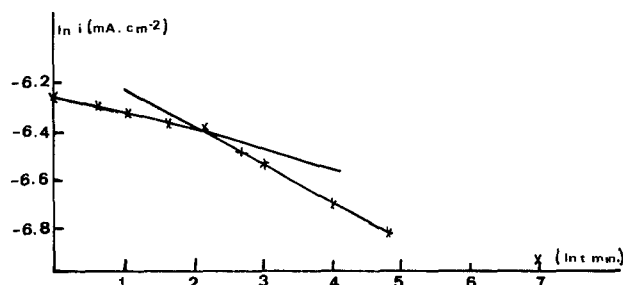


Fig. 2. Change of current with time at the potential of -120 mV

$$\ln\left(\frac{i}{i_0}\right) = B\left(\frac{E - E_0}{x}\right) \quad [7]$$

where i_0 , B , and E_0 are constants.

The correlation between $\ln i$ and $\ln t$, as predicted by the above equation, is shown to exist but involves a two-stage film growth, with the first occurring during the first 10 min of immersion. This change may be either the result of composition and structural changes within the film, as suggested for iron films (26, 27), or after 10 min the ionic current from the metal or film dissolution is no longer negligible and this is reflected in the film growth kinetics. Independent of the explanation, the inverse logarithmic law indicates that film growth occurs by a high field conduction mechanism which assists the movement of cations through the film.

AC measurements.—The ac data for the 316 stainless steel in 3% NaCl solution is presented in Fig. 3-5 for five different potentials: -130, -80, -20, +30, and +40 mV.

The three plots for the lower potential range of the passive region are shown in Fig. 3. These complex plane plots all have the same general shape which may correspond either to part of a large diameter charge-transfer semicircle or a charge-transfer-dominated region with some diffusion control, as found in other corrosion systems (28). Experimental plots were also compared with simulated plots obtained from computer-based equivalent circuit models as described later.

The data were also presented as a Bode diagram in the same figure, and it reflects the same features of the complex plane plots. Both show that the frequency responses are shifted to the left of the complex plot, indicating the large time constants for the system.

The plots shown in Fig. 4 and 5 deviate from those in Fig. 3. Since these correspond to potentials closer to the breakdown potential, they may reflect an increasing contribution from the anodic dissolution of the underlying metal through discontinuities or the weak points in the film (29-32); these processes are facilitated by the increase of potential. It can also be seen that the time constants decreased when compared to values obtained at the lower potentials, as revealed by the greater spread in the complex plane plot data.

Capacitance.—The capacity of the interface was determined as the slope of a plot of an imaginary part of the admittance Y'' , against angular frequency, ω . The results were then expressed as the reciprocal of the capacity vs. potential for the passive region as shown in Fig. 6. It can be seen that the reciprocal of capacity changes linearly with the potential from the rest potential up to +20 mV vs. SCE. Above this value, $1/C$ still increases with potential, although there is increasing scatter and a change in the slope. This is a reflection of the change in the complex plane plots with an alteration of reaction kinetics or a possible modification of the film for potentials higher than +20 mV vs. SCE or both.

The assumption is that the experimentally measured total capacitance, typically 7-10 μF , for the passive region is mainly due to the film because of the values obtained;

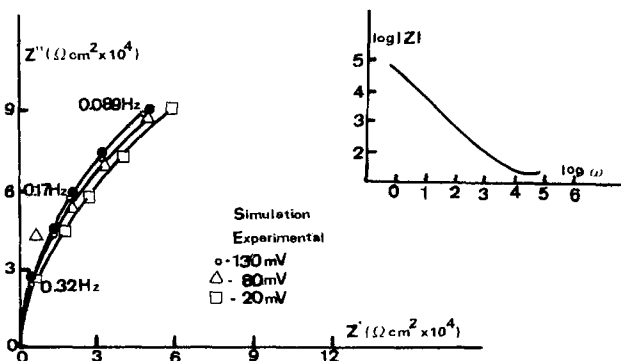


Fig. 3. Impedance plots between -130 mV and -20 mV

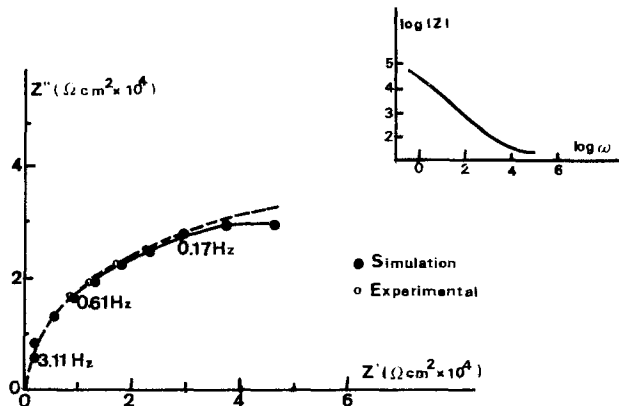


Fig. 4. Impedance plot at +30 mV

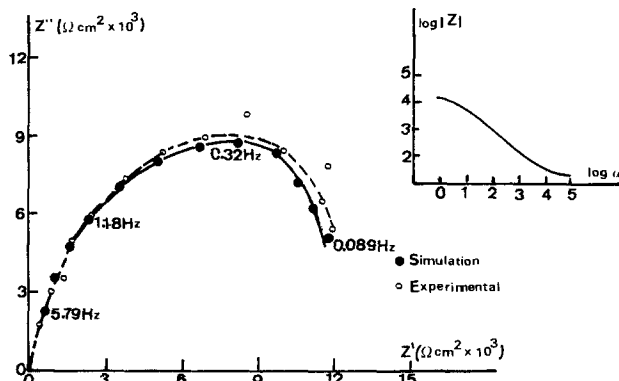


Fig. 5. Impedance plot at +40 mV

we could, therefore, neglect the contribution from the electrochemical double-layer capacity (17, 41).

A further assumption is that the surface film is homogeneous in its dielectric properties and that the thickness of the film, x , is inversely proportional to the capacity. Taking into account a surface roughness factor for the surface and the permittivity of vacuum, ϵ_0 , equal to $8.854 \times 10^{-14} \text{ F cm}^{-1}$, the capacity will be given by (17)

$$C = \frac{\epsilon\gamma}{0.113x} A \quad [8]$$

where C is the capacitance (μF), ϵ the dielectric constant, γ the surface roughness factor, and x the thickness of the film in angstroms. The constant 0.113 has the units $\text{cm}^2 \text{ F}^{-1} \text{ \AA}^{-1}$.

Using the roughness factor of 1.2 reported for an iron surface mechanically polished with 600 grit emery paper (33) [as used by Curley-Fiorino and Schmidt (17) for 304 stainless steel], a dielectric constant of 15.6, and a 2 \AA correction to account for any contribution of double-layer capacity to the measured capacity (17), the film thickness was estimated for the applied potentials, as shown in Fig. 7. It is seen that the thickness of the film increases line-

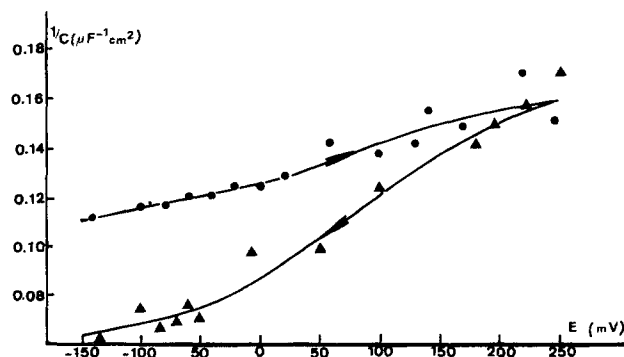


Fig. 6. Reciprocal of capacitance vs. potential

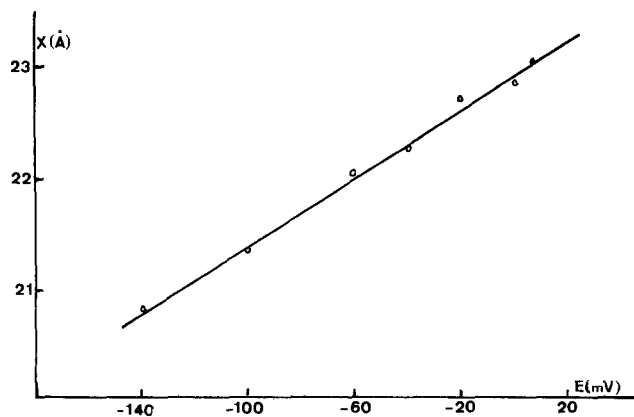


Fig. 7. Film thickness vs. potential

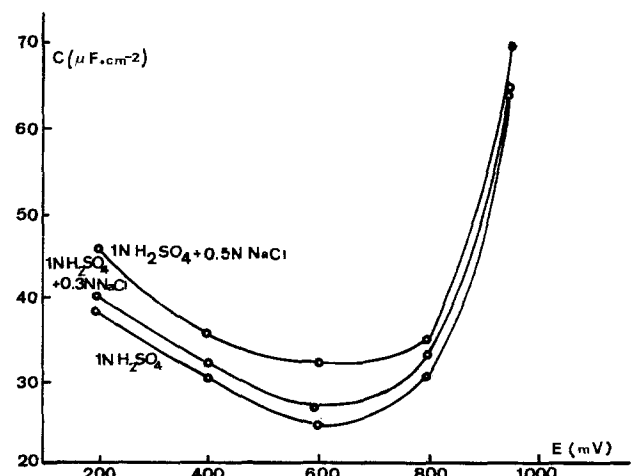
arly with potential from 20.5Å at -158 mV vs. SCE to 23.2Å at +20 mV vs. SCE.

The important feature of these results is the fact that the film properties were observed *in situ* in the chloride media because of the minor influence of the double-layer capacitance.

Impedance data in solutions containing sulfuric acid and hydrochloric acid.—In order to assess the influence of pH and change of chloride ion concentration, impedance plots in the passive region were obtained for the 316 stainless steel in 0.5M sulfuric acid and in mixed sulfuric, hydrochloric, and sodium chloride solutions, all of them with pH 0.6. The shape of these complex plane plots was very similar to those previously found for passive and pitting conditions, depending on the state of the metal.

For solutions containing 0.5M H₂SO₄, the metal was always passive, but in those containing 0.5M H₂SO₄ + 0.3M NaCl and 0.5M H₂SO₄ + 0.5M NaCl, the onset of pitting started for potentials around +600 and +500 mV, respectively. The value of capacitance was determined at various potentials, and the plots of capacitance vs. potential are shown in Fig. 8. It can be seen that, in general, the capacitance values were higher, indicating a thinner film, 5-10Å, in the 200-800 mV range. There was a decrease in capacity for potentials between +200 and +600 mV vs. SCE, followed by an abrupt increase. Identical results have been reported for AISI 304 stainless steel in sulfuric acid by Okamoto (7), who interpreted the increase of capacity on the basis of the adsorption of SO₄⁻ ion at potentials higher than the transition value.

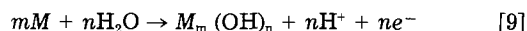
A solution containing a sulfate-free chloride mixture of 0.5M NaCl + 0.065M HCl was also examined, but in a more limited potential range due to the lower onset of pitting. The capacity values of the interface when plotted against the potential are shown in Fig. 9 conjointly with an iden-

Fig. 8. Effect of sodium chloride concentration on capacitance measurements in 1N H₂SO₄.

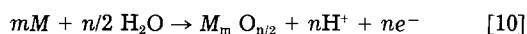
tical plot for a 3% NaCl solution (pH 6.5). It is seen that the capacity after first increasing with potential decreased slightly once pitting had started but increased again at higher potentials. A comparison of Fig. 8 and 9 suggests that the capacitance behavior is more related to the pH than to the solution composition. For the four plots corresponding to pH 0.6, the decrease in capacity is followed by an increase at the higher potentials, whereas, for the 3% NaCl solution, the capacity diminishes with potential for the whole range of potentials studied.

Discussion

The corrosion potential for 316 stainless steel in 3% NaCl solution is typically situated in the passive region. At more anodic potentials, and after short immersion times of freshly prepared electrodes, the major contribution to the current flow should be film growth, either



or



The impedance plots for the stainless steel polarized in the range of potentials between -130 and -20 mV in the passive region and shown in Fig. 3 should reflect the behavior of the metal dissolution or film formation at the potentials investigated. These complex plane shapes appeared to be well defined and could be considered as a straight line which bends slightly; or, the plot is part of a large diameter semicircle. Almost identical shapes were found by Epelboin *et al.* (34, 35) for nickel and chromium in sulfuric acid solution, by Armstrong *et al.* (36) for chromium in sulfuric acid solution, and also by Jibara (19) for 304 stainless steel in 3% NaCl solution. The first two interpreted the "almost vertical line" as the result of purely capacitive behavior, and Armstrong (36) interpreted this as a geometric capacity arising from a film where there is little mobile charge. Jibara (19) simulated this type of plot by assuming a restricted diffusion process in the film.

The present impedance data were interpreted by means of a computer simulation which has been developed by various members of the electrochemical group at UMIST over a period of years. This program can generate a simulation of a multicomponent equivalent circuit. For the present work it was found that the Randles equivalent circuit (see Fig. 10) gave a reasonable simulation provided that depression² of the plot was also incorporated. In this interactive computing procedure, the best estimate of the values of the different elements of the equivalent circuit was first made from experimental data. These values were used in a preliminary simulation, and the parameter values were then adjusted (Table I) until the simulation plot matched the experimental data as shown in Fig. 3-5.

Quantitative comparison of the data.—The charge-transfer resistance value of $1.26 \times 10^5 \Omega \text{ cm}^2$ is large compared to those found for freely corroding systems, and this indicates a low metal dissolution rate through the film. This was expected, since the passive current was $< 3 \times 10^4 \text{ mA cm}^{-2}$. This current flows across the interface and does not change significantly with the applied potential throughout the passive region, and, therefore, it should be valid to use the Stern-Geary equation (42) to estimate the corrosion current, especially as the corrosion potential is also situated in the passive region. Under these conditions, the Stern-Geary equation can be written as

$$\frac{1}{\theta} = i_{\text{corr}} \frac{\ln 10}{b_c} \quad [11]$$

The cathodic Tafel coefficient b_c was estimated from experimental data to have a value of 0.13V (see Fig. 1). The

² Depression of the impedance semicircle is ascribed to a distribution of time constants over the reaction surface; the angle of depression is that subtended by the semicircle center to the real axis.

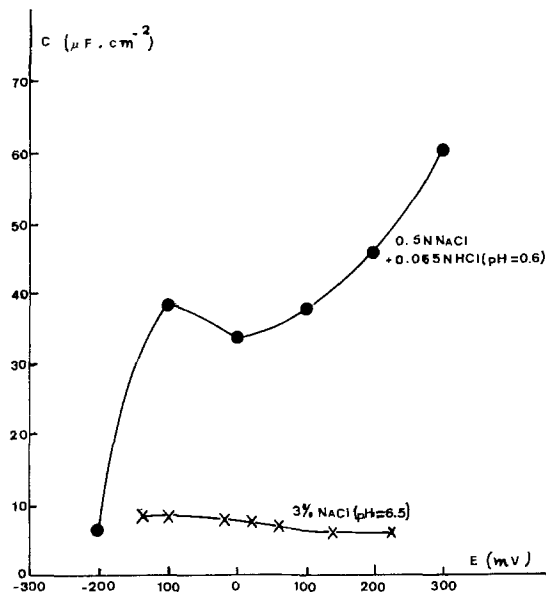


Fig. 9. Effect of pH on capacitance measurements

calculated value of $4.48 \times 10^{-4} \text{ mA cm}^{-2}$ for i_{corr} was found to be of a magnitude similar to that of the passive current.

The Warburg impedance was assessed as being a film diffusion process where the diffusion layer thickness, δ , was assumed to be equal to the film thickness, x . In this case, the diffusion factor (37) for the film, K_f , will be given by

$$K_f = x \left(\frac{2}{D_f} \right)^{1/2} \quad [12]$$

Thus, for a value of 21 \AA , the typical value of capacity at -130 mV , and for $K = 5$ (the value used in the simulation), a value for diffusion coefficient D_f of $3.45 \times 10^{-15} \text{ cm}^2 \text{ s}^{-1}$ is obtained for the mobile specimens in the film. This value of D_f is considered reasonable for diffusion through a film, being lower than the value corresponding to aqueous solutions, and is comparable with the values proposed by Armstrong *et al.* (38) for films on cadmium in KOH solutions.

The value of D_f was used to calculate the concentration, c_f , of the diffusing iron species in the film where the Warburg coefficient is

$$\sigma_f = \frac{RT}{\sqrt{2} n^2 F^2} \frac{1}{c_f D_f^{1/2}} \quad [13]$$

The value for the concentration of mobile species was thus found to be $c_f = 2.48 \times 10^{-5} \text{ mol liter}^{-1}$, and, since the diffusion appears to operate within the film, then Fick's law of diffusion may be written as

$$i_p = \frac{n F c_f D_f}{x} \quad [14]$$

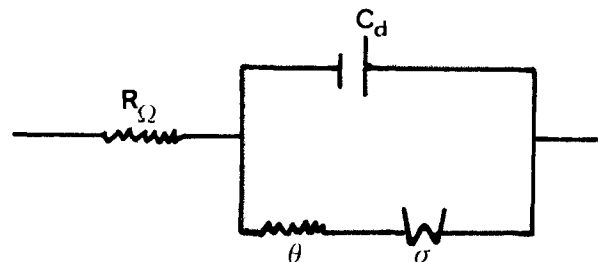


Fig. 10. Randles equivalent circuit

where i_p is the passivation current flowing through the film. Experimentally, the passivation current was less than $3 \times 10^{-4} \text{ mA cm}^{-2}$, and using a value of $2 \times 10^{-4} \text{ mA cm}^{-2}$ ($2 \times 10^{-7} \text{ A cm}^{-2}$), the concentration of species, c_f , in the film was estimated at $6.3 \times 10^{-5} \text{ mol liter}^{-1}$, which is comparable with the value estimated from the Warburg coefficient. The discrepancy may be due to the system not being entirely controlled by diffusion, since in a thin film with a high space charge, migration may also contribute to the mass transport. These correlations justify the modeling used for the simulation and also give support to the proposal that diffusion operates through the passive film.

The impedance plot in Fig. 4 at the potential of $+30 \text{ mV}$ vs. SCE was also simulated using the same equivalent circuit and the values for the different elements shown in Table I. Values of the film diffusion coefficient, D_f , and the concentration of the mobile species were also calculated using Eq. [8] and [9] and a film thickness of 23.5 \AA (see Fig. 7). At $+30 \text{ mV}$, $D_f = 1.2 \times 10^{-14} \text{ cm}^2 \text{ s}^{-1}$ and $c_f = 2.66 \times 10^{-5} \text{ mol liter}^{-1}$, which is higher than calculated at the lower potential, suggesting an increase in mobility of the species with increase in potential.

The inverse logarithmic law observed for the film growth process, Fig. 2, showed two different stages of film growth, the initial rate occurring during the first 10 min of immersion. As indicated previously in the Results section, the change in rate is either due to an increasing contribution by the ionic current of the metal dissolution rate or is the result of a change in the composition or structure of the film. A change in structure has been considered for the film growth on iron (26, 27) and was also used by Bulman and Tseung (11) to explain their ellipsometric data on austenitic stainless steel in sulfuric acid. An increasing ionic current and a composition or structural change are not mutually exclusive. Under the steady-state conditions of a fully grown film, our present impedance data and modeling provide conclusive evidence for metallic iron diffusion, and this is consistent with the film having a p-type semiconductor defect structure (39). However, the initial stages of film growth are more speculative, since other experimental evidence is not available and even Auger analysis of a change in the film composition near metal is as yet inconclusive (21). Some indication of the process involved in the film growth can be obtained from further examination of the present data.

Table I. Data from complex plane plot simulations

Electrode condition	θ Charge transfer resistance ($\Omega \text{ cm}^2$)	τ Time constant (s)	β Depression angle	σ_f Warburg coefficient ($\Omega \text{ cm}^2 \text{ s}^{-1/2}$)	K_f Diffusion factor ($\text{s}^{1/2}$)	R_n Solution resistance ($\Omega \text{ cm}^2$)
Passive (-130 to -20 mV) Fig. 3	1.26×10^5	2.25	8	3.2×10^4	5	24
Passive (30 mV) Fig. 4	2.5×10^4	0.35	8	1.6×10^4	3	24
Passive-pitting (40 mV) Fig. 5	1.6×10^4	0.28	10	5×10^3	0.6	24

The slope of the plot of film thickness, x , against potential, E , see Fig. 7, provides an estimate of the electric-field strength in the film of $6.66 \times 10^6 \text{ V cm}^{-1}$ ($6.66 \times 10^{-2} \text{ V \AA}^{-1}$). This gives a rate of increase of film thickness of 15\AA for each volt of potential increase, which is comparable to that found on other metals, particularly aluminum, although the potential range on stainless steel before breakdown prior to the onset of localized corrosion is obviously less. The present result suggests again that similar physical processes are involved in the film growth mechanism. More significantly, an indication of the initial film composition can be provided by Eq. [7]. Extrapolation of the thickness *vs.* potential plot to the zero film thickness intercept provides a value of E_0 , the equilibrium potential of the initial film. From Fig. 7, this was found to be -1.4V vs. SCE , which is comparable to the equilibrium potential of chromium oxide (40).

The important role of chromium in the passive film on stainless steel is well known and, in particular, it is interesting to note that the chromium-rich zone, as determined by Auger spectroscopy, is next to the metal (21). Hence, it is reasonable to envisage growth proceeding outward from the initial film.

Conclusions

1. For potentials between the corrosion potential (the lower limit investigated) and $+20 \text{ mV}$, there is a linear relation for the dependence of the reciprocal of capacity on potential. The thickness of the film, as measured by impedance measurements, assuming a parallel-plate condenser model, with the passive layer as dielectric, is in the range $20\text{-}25\text{\AA}$, depending on the applied potential.

2. In the same range of potentials, the passivation current was independent of potential. This is in accordance with film growth by a high field conduction mechanism as reflected by an inverse logarithmic law of current *vs.* time. Two stages of film growth can be distinguished, one below 10 min and the other for longer times.

3. Impedance measurements and computer simulations lead to the establishment of a model for the passivated steel, which shows that diffusion of the metallic species occurs through the passive film.

4. The field strength in the film is $6.66 \times 10^6 \text{ V cm}^{-1}$, corresponding to a rate of film formation of 15\AA for each volt of potential increase.

5. The equilibrium potential of the initial oxide film formation is -1.4V (SCE) , corresponding to chromium oxide, and this indicates the important role played by chromium in the formation and constitution of the film.

Acknowledgment

One of the authors, M. G. S. Ferreira, is grateful to the Instituto Nacional de Investigaço Cientfica, Portugal, for financial support while undertaking this work.

Manuscript submitted Jan. 11, 1983; revised manuscript received Nov. 26, 1984. Part of this article was presented as Paper 142 presented at the Denver, Colorado, Meeting of the Society, Oct. 11-16, 1981.

REFERENCES

- H. H. Uhlig, *Corros. Sci.*, **19**, 777 (1979).
- T. P. Hoar, *ibid.*, **7**, 341 (1967).
- R. Rhodin, *Corrosion*, **12**, 41 (1956).
- N. Nielsen and T. N. Rhodin, *Z. Elektrochem.*, **62**, 707 (1958).
- J. Yahalom and L. K. Ives, in "Japan-USA Seminar on Passivity and Its Breakdown on Iron and Iron Base Alloys, Honolulu," p. 69, NACE, Houston, TX (1975).
- C. L. McBee and J. Kruger, *Electrochim. Acta*, **17**, 1337 (1972).
- G. Okamoto, *Corros. Sci.*, **13**, 471 (1973).
- K. Sugimoto and Y. Sawada, *ibid.*, **17**, 425 (1977).
- K. Kudo, T. Shibata, G. Okamoto, and N. Sato, *ibid.*, **8**, 809 (1968).
- J. Siejka, C. Cherki, and J. Yahalom, *Electrochim. Acta*, **17**, 161 (1972); *This Journal*, **119**, 991 (1972).
- G. M. Bulman and A. C. Tseung, *Corros. Sci.*, **13**, 531 (1973).
- J. B. Lumsden and R. W. Staehle, *Scr. Metall.*, **6**, 1205 (1972).
- J. B. Lumsden and R. W. Staehle, in "Japan-USA Seminar on Passivity and Its Breakdown on Iron and Iron Base Alloys, Honolulu," p. 75, NACE, Houston, TX (1975).
- H. Okada, in "Japan-USA Seminar on Passivity and Its Breakdown on Iron and Iron Base Alloys, Honolulu," p. 82, NACE, Houston, TX (1975).
- G. T. Burnstein and D. H. Davies, *Corros. Sci.*, **20**, 1143 (1980).
- J. F. Rimbert and J. Pagetti, *ibid.*, **20**, 189 (1980).
- M. E. Curley-Fiorino and G. M. Schmid, *ibid.*, **20**, 313 (1980).
- J. L. Ord and J. H. Bartlett, *This Journal*, **112**, 160 (1965).
- S. M. Jibara, Ph.D. Thesis, UMIST, Manchester, England (1979).
- M. Stern and A. C. Makrides, *This Journal*, **107**, 782 (1960).
- M. G. S. Ferreira, Ph.D. Thesis, UMIST, Manchester, England (1981).
- V. Scotto, G. Ventura, and E. Traverso, *Corros. Sci.*, **19**, 237 (1979).
- Z. Szklarska-Smialowska, *Corrosion*, **27**, 23 (1971).
- R. V. Moshtev, *Ber. Bunsenges Phys. Chem.*, **72**, 452 (1968).
- A. K. Vijh, "Electrochemistry of Metals and Semiconductors," Marcel Dekker, Inc., New York (1973).
- N. Sato, K. Kudo, and T. Noda, *Electrochim. Acta.*, **16**, 1909 (1971).
- J. L. Ord and D. J. DeSmet, *This Journal*, **113**, 1258 (1966).
- D. G. John, Ph.D. Thesis, UMIST, Manchester, England (1979).
- Z. Szklarska-Smialowska, Z. Szummer, and J. Janik-Czakov, *Br. Corros. J.*, **5**, 159 (1970).
- A. Eklund, *This Journal*, **123**, 170 (1976).
- M. Kesten, *Corrosion*, **32**, 94 (1976).
- Z. Szklarska-Smialowska, *Br. Corros. J.*, **10**, 11 (1975).
- H. J. Engel and B. Ilschner, *Z. Elektrochem.*, **59**, 716 (1955).
- M. Boyer, I. Epelboin, and M. Keddam, *Electrochim. Acta*, **11**, 221 (1966).
- I. Epelboin, M. Keddam, and Ph. Morel, in "Proceedings of the Third International Congress on Metallic Corrosion," Vol. 1, p. 110, Mir, Moscow (1969).
- R. D. Armstrong and K. Edmondson, *Electrochim. Acta*, **18**, 937 (1973).
- J. L. Dawson and D. G. John, *J. Electroanal. Chem.*, **110**, 37 (1980).
- R. D. Armstrong and K. Edmondson, *ibid.*, **53**, 371 (1974).
- P. E. Manning and D. J. Duquette, *Corros. Sci.*, **20**, 597 (1980).
- M. Pourbaix, "Atlas of Electrochemical Equilibria in Aqueous Solutions," p. 256, NACE, Houston, TX (1974).
- J. O'M. Bockris and A. K. N. Reddy, "Modern Electrochemistry," Vol. 2, p. 816, Plenum Press, New York (1970).
- M. Stern and A. Geary, *This Journal*, **104**, 56 (1957).

Polarization of Aluminum during AC Corrosion in Sulfate Solutions

T. C. Tan^{*,1} and D-T. Chin^{*}

Department of Chemical Engineering, Clarkson University, Potsdam, New York 13676

ABSTRACT

An experimental study has been made of the effect of alternating voltage on the corrosion of aluminum in aqueous solutions of (i) 1N H₂SO₄, (ii) 1N Na₂SO₄, (iii) 1N NaOH, and (iv) 1N Na₂SO₄ containing 0-5010 ppm Cl⁻ ions. The polarization curves were measured with an alternating voltage (AV) modulation technique using sinusoidal waves, and the pitting behavior of aluminum was examined with constant potentiostatic coulometry and SEM photomicrography. The measurements were made over a range of AV magnitudes from 0 to 1500 mV rms, and AV frequencies from 20 to 600 Hz. The severity of AV effect was found to depend on the presence of an Al₂O₃ surface film. In alkaline solutions and in the sulfate solution containing a large amount of chloride ions, where no oxide was present on aluminum surface, AV exerted little or no effect on the anodic dissolution reaction of aluminum. In acidic and neutral sulfate solutions, AV enhanced the formation of oxide film at high anodic dc potentials as well as the dissolution of aluminum through the pores of the oxide film. Application of AV did not increase the pitting corrosion of aluminum in sulfate solutions.

Most published works on the corrosion of aluminum deal with its pitting potential, pit morphology, and pit mechanisms. Particular emphasis has been placed on the polarization of aluminum in chloride solutions. Some literature (1-7) is available on the corrosion of aluminum in the presence of alternating current (ac). Williams (1) reported that ac increased the corrosion rate of aluminum. French (2) suggested a critical ac current density of 0.0775 mA/cm², below which no appreciable corrosion of aluminum would occur in soil and chloride solutions. Hall and English (2) in their comments on French's work, reported that the corrosion rate of aluminum in 0.1% NaCl solution decreased to zero as the frequency of a 10V superimposed alternating voltage (AV) increased from 20 to 20,000 Hz (3). Thompson and Wood (4) studied the effect of 14V AV on the behavior of an aluminum electrode in 0.4M NaCl. Pitting was observed and the pit size and pit density increased with time. They attributed the pitting process to the positive half-cycle of the AV, and suggested that the pits were initiated by oxygen or hydrogen evolution at the flaws on the oxide film. The works by Serra and Mannheimer (5) and Chin *et al.* (6-7) indicated that ac exerted a greater influence on the corrosion of aluminum than copper and mild steel in soil.

The present project is a part of a continuing program in this laboratory looking into the ac corrosion of metals in aqueous environments (6-16). In this work, the effect of ac on the anodic and cathodic polarization curves of aluminum in sulfuric acid, sodium sulfate, sodium chloride, and sodium hydroxide solutions were measured with an AV modulation technique (13-16) using a sinusoidal wave. The corrosion behavior of aluminum under the influence of AV was also examined with constant potentiostatic coulometry and scanning electron photomicrography (SEM).

Experimental

The details of the experimental setup and electric circuit for AV modulation have been described in previous publications (10, 14-16), and will not be repeated here. The solutions used in this study were: (i) 1N H₂SO₄ (pH 0.1), (ii) 1N Na₂SO₄ (pH 7), (iii) 1N Na₂SO₄ plus 0-5010 ppm NaCl (pH 7), and (iv) 1N NaOH (pH 14). All solutions were deaerated by bubbling nitrogen gas for several hours before the experiment. During the experiment, the bubbling of nitrogen was continued at a slower rate, and the pH's of the solutions were maintained at a constant value by adding a small amount of dilute sulfuric acid or sodium hydroxide. A 1.5 liter Plexiglas cell equipped with a platinum screen counterelectrode, a silver/silver-chloride reference electrode (Ag/AgCl), and a Luggin capillary was used for the experiments. The working electrode was a stationary aluminum rod² (0.627 cm in diam), whose cylindrical side was insulated with a Teflon sheath leaving a

circular area of 0.309 cm² exposed to the electrolyte. For each experiment, the aluminum electrode was polished with 400 grit and then with 600 grit polishing paper. It was washed with alcohol, rinsed in distilled water, and soaked in concentrated nitric acid for 5 min. The electrode was again washed with distilled water and immediately placed in the cell and was positioned at approximately 2 mm from the tip of the Luggin capillary tube. To ensure good reproducibility in the polarization measurements, the electrode was further activated cathodically in the test electrolyte by polarizing at -3.0V vs. Ag/AgCl for 5 min. The electric circuit for AV modulation was then switched on, and the rest (corrosion) potential of aluminum was measured by adjusting the dc potential until no dc current flowed in the cell. The cathodic polarization curve was first obtained by incrementing the dc potential to -3.0V vs. Ag/AgCl with a step rate of 50 mV/min and a step size of 50 mV. The electrode potential was returned then to its rest potential, and the anodic polarization curve was obtained by stepping the potential toward the noble direction using the same step size and step rate until a potential of 6.0V vs. Ag/AgCl was reached. In this way, the dc polarization of the aluminum electrode under the influence of sinusoidal AV was measured in the test electrolytes for a range of AV magnitudes from 0 to 1500 mV rms, and AV frequencies from 20 to 600 Hz. Potentiostatic coulometry experiments were carried out with an aluminum stud having the same composition and exposed area as the electrode used in the polarization measurement. The aluminum samples were polarized with a constant AV in the test electrolyte at selected dc potentials in the active, passive, and transpassive regions of the polarization curve. After 5C of dc were passed, the electrode was removed from the cell and its surface was examined under a scanning electron microscope (SEM). All experiments were carried out at a room temperature of 26° ± 1°C.

Results

Polarization of aluminum without the influence of AV.—To establish a basis for comparing with AV modulation, a particular set of runs was made to determine the anodic and cathodic polarization of aluminum in the test electrolytes without any superimposed AV. The results showing the effect of pH on the behavior of aluminum in sulfuric acid, sodium sulfate, and sodium hydroxide solutions are given in Fig. 1. In neutral sodium sulfate solution, aluminum exhibited a narrow anodic active potential regime of 0-0.3V vs. Ag/AgCl with a critical current density of 0.023 mA/cm². The curve did not show a distinct passive-transpassive transitional potential. Instead, the dc current density increased slowly with increasing dc potential. At 5.6V vs. Ag/AgCl, the current rose to 0.1

² A commercial 6061-T6 aluminum was used for the experiment. Its chemical composition (w/o) was: Cu, 0.15-0.4; Si, 0.4-0.8; Mn, 0.15 max; Zn, 0.25 max; Fe, 0.7 max; Ti, 0.15 max; Mg, 0.8-1.2; Cr, 0.04-0.35; other impurities, 0.15 max; Al, remainder.

* Electrochemical Society Active Member.

¹ Present address: Department of Chemical Engineering, National University of Singapore, Kent Ridge, Singapore 0511.

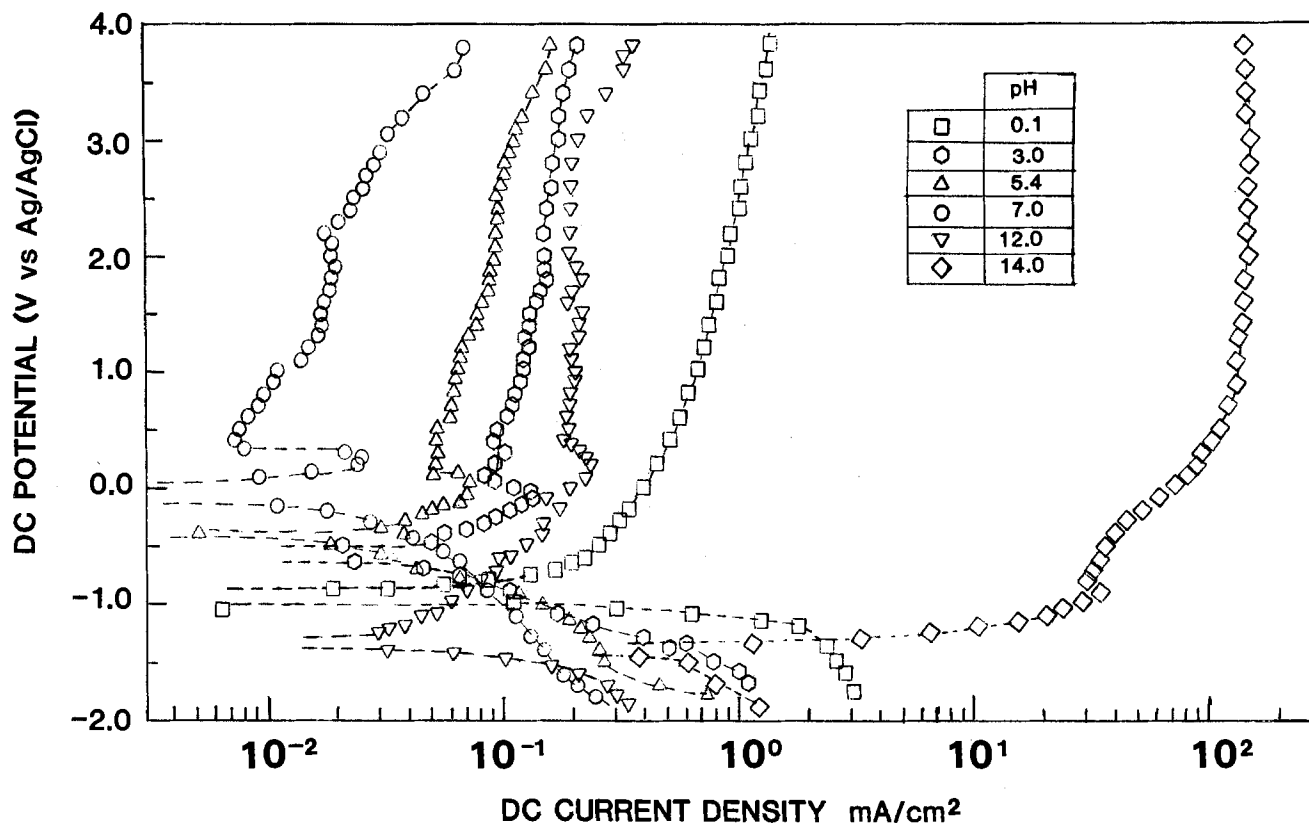


Fig. 1. DC polarization curves of aluminum in sulfate solutions at various pH values

mA/cm² as compared to 0.007 mA/cm² at 0.3 mV vs. Ag/AgCl. Although the increase was about 14 times, the dc current density was still small, and the aluminum could be considered to be passivated within the potential range investigated. As pH of the solution decreased from pH 7, the rest potential shifted to less noble values, and the dc current density in the anodic region increased. The anodic "nose," which characterized a transition from the active potential to passive potential, also diminished with decreasing pH, and completely disappeared in 1N sulfuric acid (pH 0.1). A similar trend was also observed as the pH of the solutions increased from 7.0; the anodic dc current density increased with increasing pH values. At pH 14, which corresponded to 1N sodium hydroxide, the anodic dc current density was 100 times greater than that in 1N sulfuric acid, which was again 100 times greater than that in neutral 1N sodium sulfate solution. Figure 2 shows the effect of pH on the rest potential of aluminum in sulfate solutions. The most positive rest potential was obtained for pH 7 sodium sulfate solution. As the pH values decreased or increased from this neutral value, the rest potential became more negative. Aluminum exhibited a higher corrosion tendency in alkaline environment than in acidic environment; this was indicated by a more negative rest potential of -1.4V vs. Ag/AgCl in pH 14 solution as compared to a value of -0.93V vs. Ag/AgCl at pH 0.1.

DC polarization curves of aluminum in neutral 1N sodium sulfate solutions containing various amounts of sodium chloride (0-5010 ppm) are given in Fig. 3. Chloride ions had a significant effect on the anodic polarization of aluminum. Below 38 ppm, chloride ions increased the critical current density for passivity by one order of magnitude, and shifted the active-passive transitional potential to a more positive value of 1.5V vs. Ag/AgCl. Above 100 ppm, chloride ion virtually eliminated the passivity of aluminum in neutral sulfate solution, and dc current density increased more than 1000 times on the anodic polarization curves. Pitting became visible on the specimen after the polarization measurements at chloride concentrations greater than 100 ppm. The pit size and pit density increased with increasing chloride concentrations. Figure 4 shows the rest potential of aluminum in 1N sodium sul-

fate in the presence of chloride ions. Similar to the pH effect, the rest potential became more negative with increasing chloride concentrations.

DC polarization curves with 60 Hz sinusoidal AV.—The effect of 60 Hz sinusoidal AV on the dc polarization curves of aluminum in (i) 1N Na₂SO₄, (ii) 1N H₂SO₄ or NaOH, and (iii) 1N Na₂SO₄ containing 38 ppm NaCl, respectively, are shown in Fig. 5, 6, and 7. Generally speaking, AV behaved as a depolarizer, and increased the dc current density at a given dc potential. The effect of AV increased with increasing AV magnitude. AV showed the

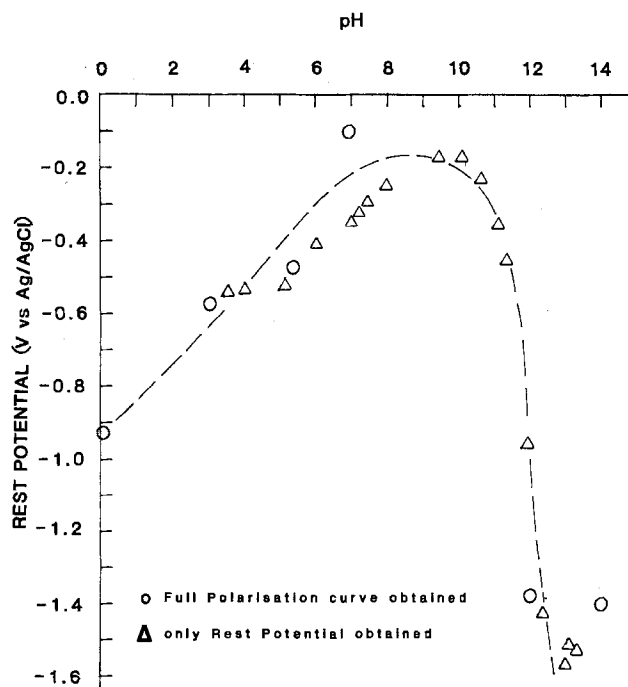


Fig. 2. Rest potential of aluminum in sulfate solutions at various pH values.

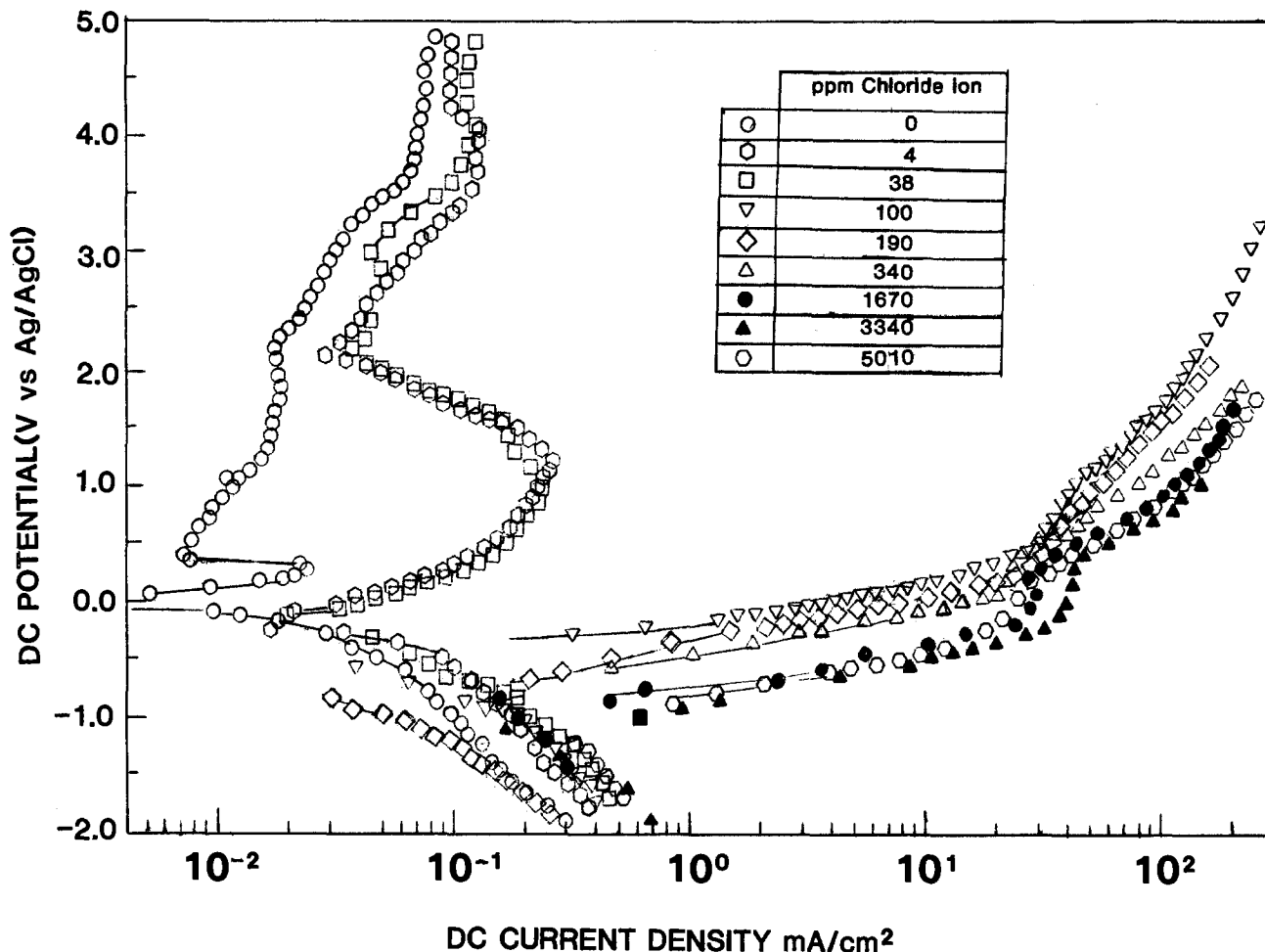


Fig. 3. DC polarization curves of aluminum in 1N sodium sulfate solution containing various amounts of chloride ions

greatest effect on the polarization of aluminum in 1N Na_2SO_4 solution, followed in turn by 1N H_2SO_4 , 1N Na_2SO_4 + 38 ppm NaCl, and 1N NaOH. For the neutral sodium sulfate solution, AV increased the critical current density and shifted the active-passive transitional potential toward the noble direction. The anodic dc current also increased with increasing AV; however, the increase was not as large as that of the pH effect or the addition of chloride ions (Fig. 1 and 3) to the sulfate solution. Application of a 1500 mV rms AV resulted in only a tenfold increase in dc current density in the anodic regime. The anodic dc current density with AV was smaller than 1 mA/cm^2 , and the polarization curves did not exhibit a dis-

tinct passive-transpassive transitional potential. This implied that the aluminum surface was still covered by an oxide layer even in the presence of AV. For 1N sulfuric acid and 1N sodium hydroxide solutions, the general characteristics of anodic polarization curves with or without AV were about the same except that AV slightly increased the dc current density. The effect of AV on the behavior of aluminum was less discernible in 1N sodium hydroxide than in 1N sulfuric acid. For the 1N sodium sulfate solution containing 38 ppm of chloride ion, application of AV appeared to eliminate the transition to passive potentials. Below the Flade potential of 1.0V vs. Ag/AgCl, AV did not affect the dc current density on the anodic curves.

Shifts in the rest potentials were observed upon the superimposition of AV. Figure 8 shows the rest potential shift for aluminum in 1N sodium sulfate, sulfuric acid, and sodium hydroxide solutions. Applications of AV caused the rest potential to shift toward the negative direction. The phenomenon agreed with an analysis of Chin *et al.* (9-10) that the shift in the rest potential resulted from an asymmetric behavior between the anodic and cathodic polarization of the corrosion system. For the present systems, the anodic polarization curves without AV possessed a Tafel slope in the active regime smaller than that on the cathodic polarization curves; according to the analysis, the rest potential would be shifted toward the negative direction.

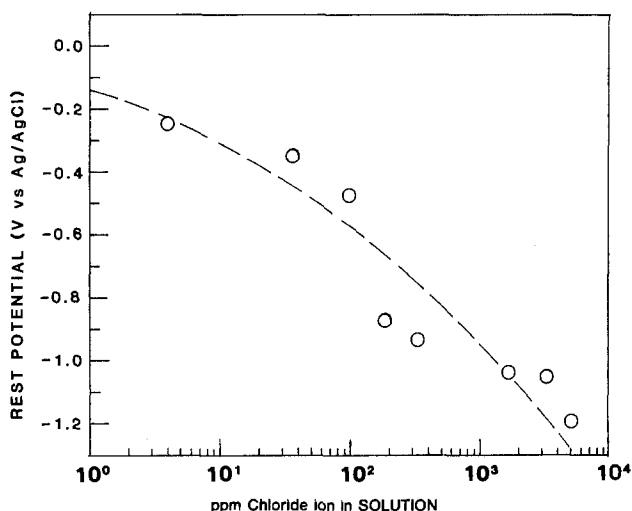


Fig. 4. Effect of chloride ion concentration on the rest potential of aluminum in 1N sodium sulfate solution.

Effect of AV frequency.—DC polarization curves showing the effect of AV frequency on the behavior of aluminum in 1N Na_2SO_4 are shown in Fig. 9. In these runs, the applied sinusoidal AV was maintained at a constant magnitude of 750 mV rms. and the frequency varied from 20 to 600 Hz. For comparison, the polarization curve without AV is also plotted in the figure as open squares. It can be seen that the highest effect was obtained with 20 Hz AV,

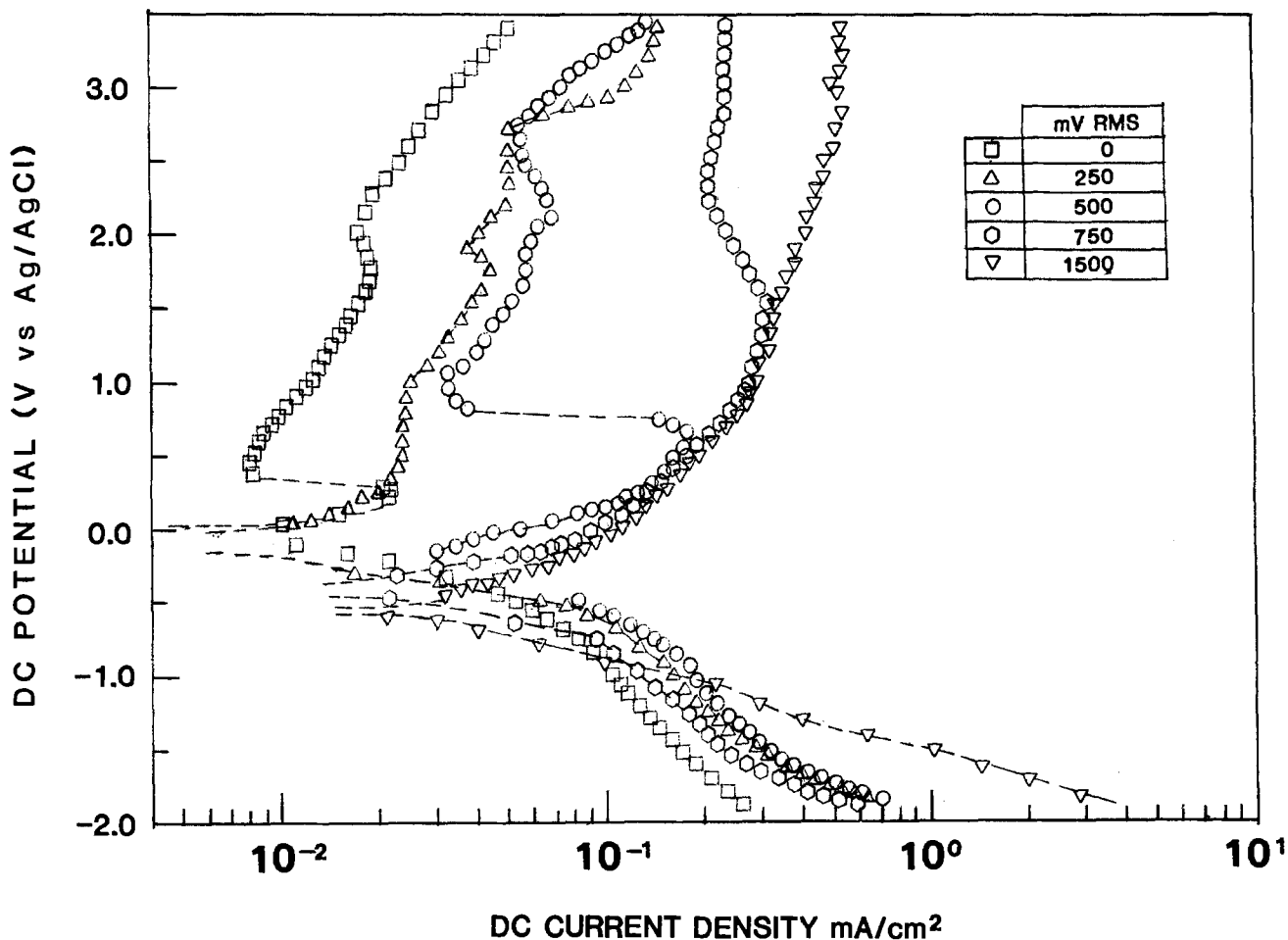


Fig. 5. Effect of 60 Hz sinusoidal AV on the dc polarization curves of aluminum in 1N sodium sulfate solution

and an increase in frequency shifted both the anodic and cathodic polarization curves toward the polarization curves without AV. Apparently, at high AV frequencies,

the double-layer impedance became smaller and more current was used in the charge and discharge of the electric double layer at the electrode-solution interface.

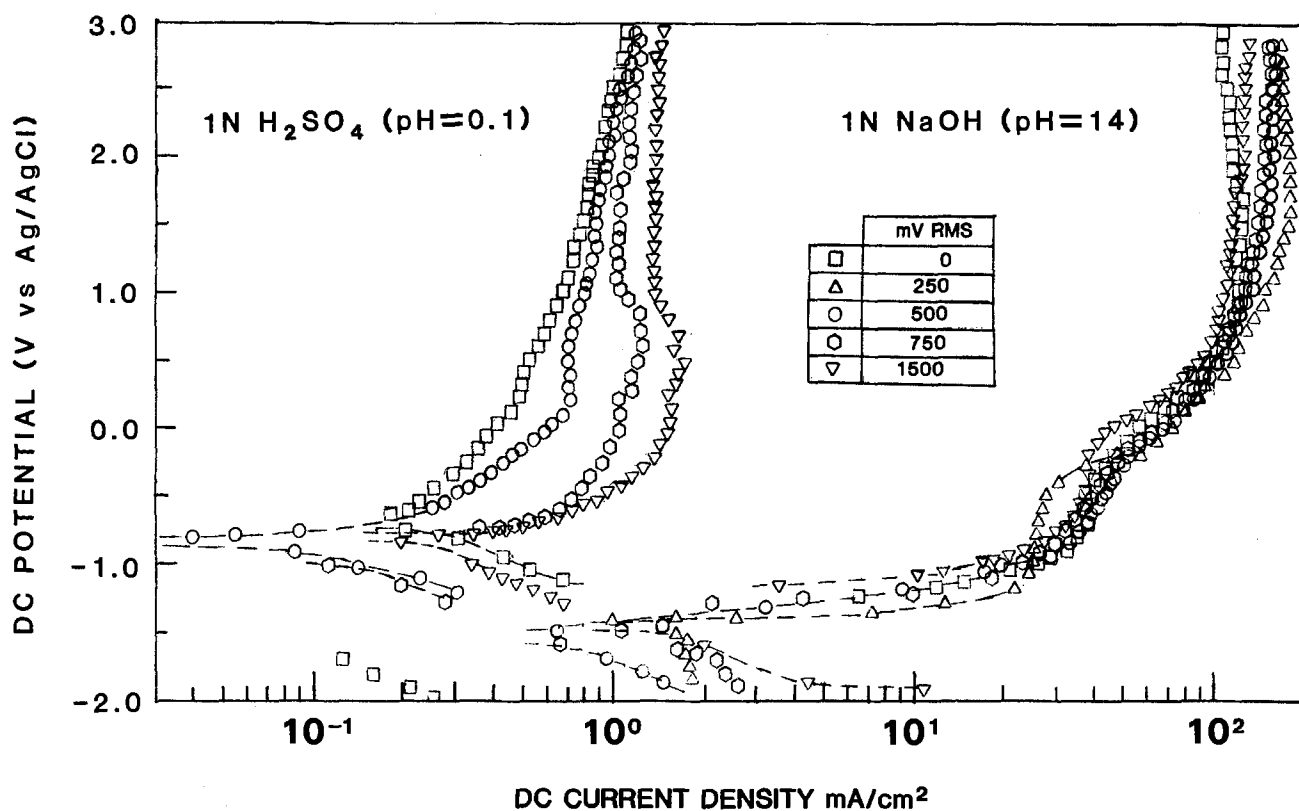


Fig. 6. Effect of 60 Hz sinusoidal AV on the dc polarization curves of aluminum in 1N sulfuric acid and 1N sodium hydroxide solution

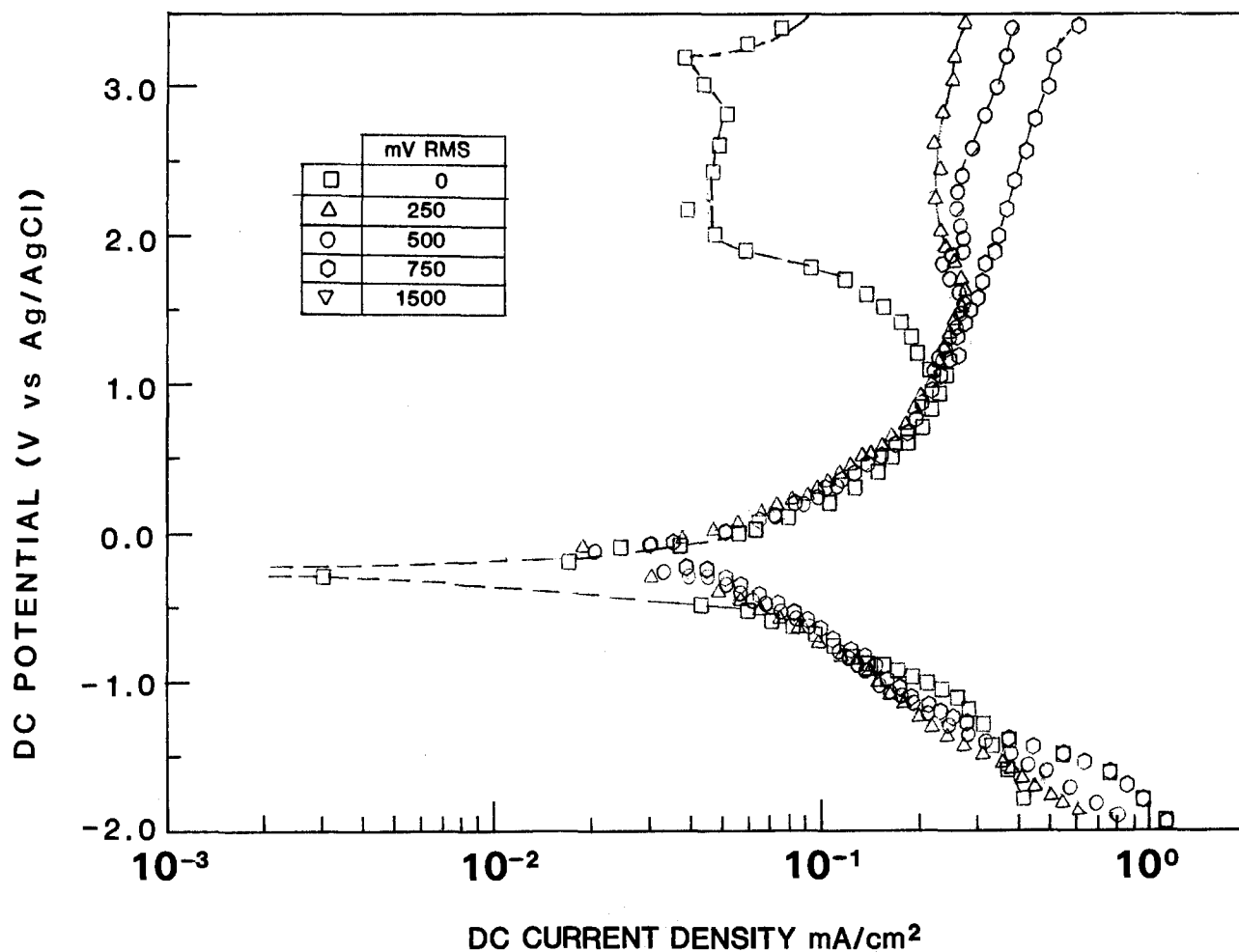


Fig. 7. Effect of 60 Hz sinusoidal AV on the dc polarization curves of aluminum in 1N sodium sulfate containing 38 ppm chloride ion

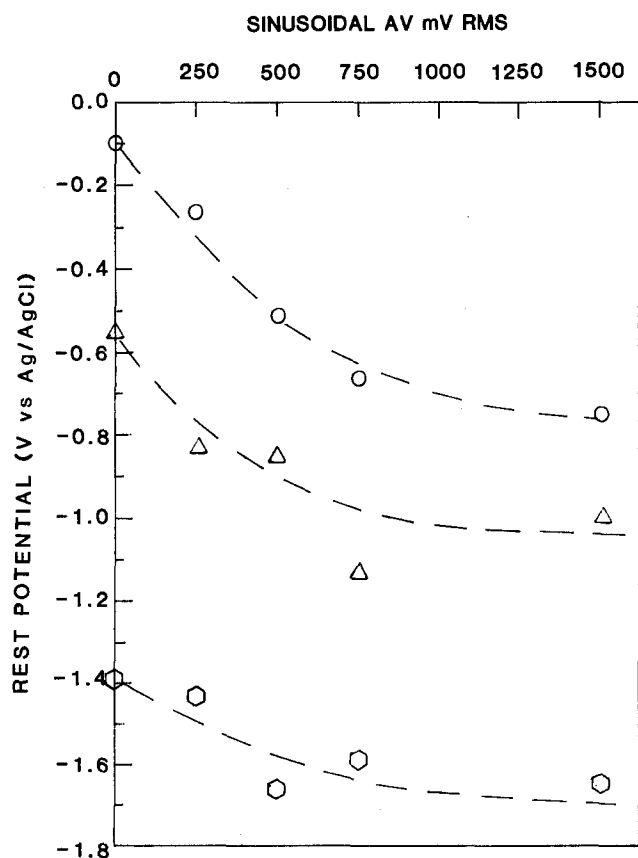


Fig. 8. Shift in the rest potential of aluminum by 60 Hz sinusoidal AV in 1N sodium sulfate (○), 1N sulfuric acid (△), and 1N sodium hydroxide (○).

SEM photomicrographs.—The SEM photomicrographs of aluminum samples after the potentiostatic coulometry experiments in 1N sodium sulfate solution are shown in Fig. 10. The experiments were carried out with 60 Hz sinusoidal AV. The specimens were potentiostatically held at selected anodic dc potentials, and the SEM analysis was made after 5C had passed through the cell. As a reference, Fig. 10a shows the surface with only a dc potential at 2.5V vs. Ag/AgCl, and Fig. 10b shows the effect of addition of 1670 ppm Cl⁻ ion at the same dc potential without any superimposed AV. Deep circular pits were

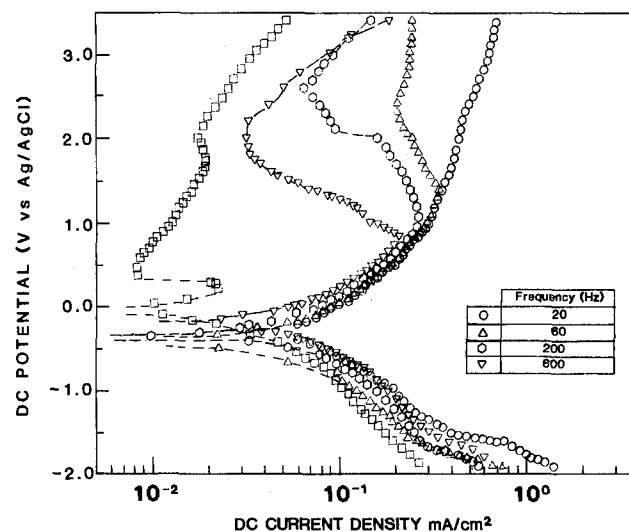


Fig. 9. Effect of AV frequency on the dc polarization of aluminum in 1N sodium sulfate solution. The sinusoidal AV was maintained at 750 mV rms.

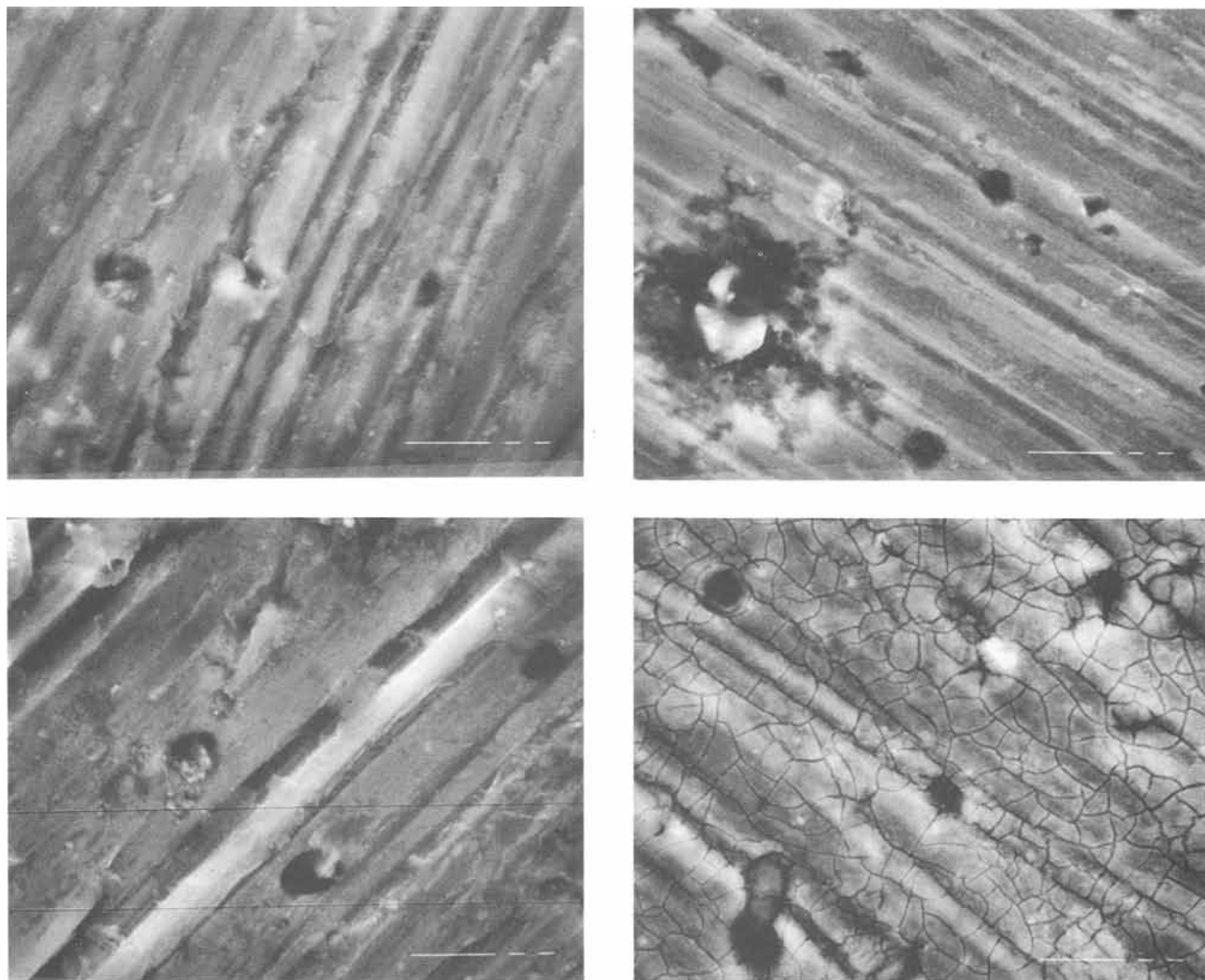


Fig. 10. SEM photomicrographs of aluminum surface after potentiostatic coulometry experiments with 60 Hz sinusoidal AV in 1N sodium sulfate solution (pH 7). a(top left): 0 AV at dc potential of 2.5V vs. Ag/AgCl. b(top right): 0 AV at dc potential of 2.5V vs. Ag/AgCl with 1670 ppm Cl^- . c(bottom left): 1500 mV rms AV at dc potential of 2.5V vs. Ag/AgCl. d(bottom right): 500 mV rms AV at dc potential of 0.5V vs. Ag/AgCl.

observed for all aluminum samples polarized at anodic dc potentials. The pit size and pit density increased as the pH of sulfate solution increased or decreased from a neutral value 7.0. The severest pitting of aluminum was obtained with 1N sodium hydroxide, followed by 1N sulfuric acid, and 1N sodium sulfate. Addition of chloride ions caused a lateral expansion of the pits on the oxide film as shown in Fig. 10b. The effect of AV on the pitting of aluminum is shown in Fig. 10c and 10d. The sample shown in Fig. 10c was superimposed with 1500 mV rms AV (60 Hz), and polarized at a dc potential of 2.5V vs. Ag/AgCl. For the same amount of dc coulombs passed, no discernible effect by AV was observed on the pitting of aluminum in 1N sodium sulfate solution. The pits with AV exhibited the same circular shape, size, and distribution; only the pitting rate was higher because of a higher dc current density with AV at the same dc potentials. An interesting topography on the oxide film is shown in Fig. 10d; this particular aluminum sample was superimposed with a 500 mV rms AV (60 Hz) and was held at a dc potential of 0.5V vs. Ag/AgCl, corresponding to an active-passive transitional potential shown in Fig. 5. The oxide film on this sample exhibited the dry mud-like cracks and grain boundaries. The pit shape and size on the sample were similar to those polarized at the same dc potential without superimposition of AV.

Discussion

In this laboratory, the method of AV modulation has been used to determine the effect of alternating current

(AC) on the corrosion of mild steel (10, 14) and stainless steels (15-16) in a number of aqueous environments. AV was found to destroy the passivity of the steels in sulfate, nitrate, chloride, perchlorate, and chlorate solutions. For the systems which exhibited an instantaneous passivation upon polarization at the anodic potentials, AV diminished the passive regime by shifting the passive-transpassive transitional potential toward the negative direction. In the solution where the electrodes exhibited distinct active, passive, and transpassive anodic potential regimes, AV increased the critical current density for passivity and decreased the passive regime by shifting the transpassive potential toward the negative direction and by increasing the dc current density in the passive regime. The passive current density of mild steel in sulfate, nitrate, and perchlorate solutions and of stainless steel in sulfuric acid was increased by AV by one to two orders of magnitude; whereas in chlorate solution, AV prevented the formation of oxide film on mild steel surface, and completely eliminated the passive regime on the polarization curve. The SEM photomicrographs revealed that AV destroyed the passive film and enhanced the pitting corrosion of mild and stainless steels. The effect was similar to the addition of chloride ions to the corrosion environments.

In the present results, there are three important features which differed from those of the previous investigations.

1. The anodic polarization curves of aluminum in sulfate solutions without AV did not have a distinct passive-transpassive transitional potential over a pH range of 0-12.

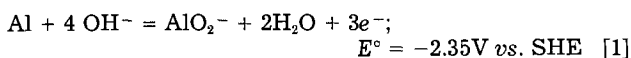
A small active potential region was obtained for the neutral sodium sulfate solution, and the addition of chloride ions of less than 38 ppm extended the active-passive transitional potential to 1.5V *vs.* Ag/AgCl. However, the critical current density for passivity was of the same order of magnitude as the dc current density in the passive regime. No passivation was observed for aluminum in 1N sodium hydroxide solution and in 1N sodium sulfate solution containing more than 100 ppm of chloride ions.

2. Although AV shifted the active-passive transitional potential toward the noble direction and increased the both anodic and cathodic current densities on the dc polarization curves in the present systems, AV did not seem to destroy the passivity of aluminum in acidic and neutral sulfate solutions or in the sulfate solutions containing less than 38 ppm of chloride ions. The anodic dc current density with 1500 mV rms AV was less than 1 mA/cm² in 1N neutral sodium sulfate solution, and was less than 2 mA/cm² in 1N sulfuric acid for all the dc potentials investigated, implying that the aluminum surface was covered with a layer of oxide film even in the presence of AV. No distinct transpassive potentials were observed on the polarization curves with applied AV.

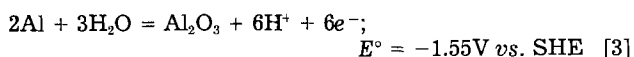
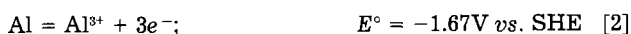
3. AV did not destroy the protective oxide film on aluminum surfaces in acidic and neutral sulfate solutions; nor did it enhance the pitting of aluminum by changing the pit shape, size, and distributions. Addition of chloride ions to the sulfate solutions caused more severe pitting of aluminum than did the application of AV.

The above features may be explained by the presence of an Al₂O₃ film on the aluminum surface. Al₂O₃ is amphoteric, and its solubility is smallest in neutral solutions (pH 6-7). It dissolves in acidic solutions to give Al³⁺ ions, and in alkaline solutions it reacts with hydroxyl ions to form soluble AlO₂⁻. Depending on the pH value, the following anodic reactions can occur during the corrosion of aluminum in aqueous solutions

in alkaline solutions



in acidic and neutral solutions



In alkaline solutions, no oxide film is present on the metal surface, and aluminum would dissolve at a high rate at anodic potentials. Application of AV would exert little or no influence on the anodic dissolution reaction of aluminum in 1N NaOH solution, as shown in Fig. 6. In acidic and neutral solutions, aluminum would first corrode according to reaction [2] at low anodic overpotentials. However, at sufficiently high anodic overpotentials, reaction [3] would start to take place, and an Al₂O₃ film formed on the aluminum surface would impede reaction [2] from continuing at a high rate. The present results seem to suggest that AV promoted both the reactions [2] and [3] for aluminum in acidic and neutral sulfate solutions. Periodically pulsating current has been used in the aluminum anodizing industry to improve the thickness of oxide film formed in sulfuric acid baths (17-18). AC was found to increase the rate of aluminum anodizing process and improve the color penetration into the oxide film. This fact agreed with the present SEM analysis shown in Fig. 10 that AV neither destroyed the oxide film nor increased the pitting corrosion of aluminum in sulfate solutions. The rates of metal dissolution and film formation processes were enhanced by AV at approximately equal magnitudes in acidic and neutral sulfate solutions.

The photomicrograph shown in Fig. 10d revealed an interesting effect of AV on the morphology of the oxide film on the aluminum surface. The experimental condition of this sample coincided with the critical current density of aluminum in 1N Na₂SO₄ when 500 mV rms si-

nusoidal AV (60 Hz) was superimposed onto the system. The photomicrograph revealed a dried mud-like matrix structure with circular pits evenly distributed on the surface. It should be noted that the cracks on the oxide film did not radiate from the pits, and some even circled around a pit in a concentric fashion. Similar morphological structure was reported by Galvele *et al.* (19) for the interior of pits on an aluminum sample polarized in deaerated sodium nitrate solution. Richardson and Wood (20) also found a similar structure for their aluminum sample after 20 days immersion in 1N KCl at pH 6 and under the influence of 14V AV. Michele (21) observed a similar oxide structure on the bottom of pits for aluminum polarized at a dc potential of -0.74V *vs.* SHE in deaerated HCl solution. The phenomenon was apparently associated with the active dissolution of aluminum near the Flade potential, where the film formation process started to compete with the metal dissolution reaction.

Conclusions

A study has been made of the effect of sinusoidal AV on the behavior of aluminum in aqueous sulfate solutions over a range of pH 0-14. The results revealed that the presence of an Al₂O₃ surface film played an important role on the corrosion of aluminum in the presence of AV. When no oxide film was present on the metal surface, such as in alkaline solutions and in the neutral sulfate solutions containing a large amount of chloride ions, AV exerted little or no influence on the anodic dissolution reaction. In acidic and neutral sulfate solutions which permitted the growth of Al₂O₃ at high anodic potentials, AV enhanced the film formation process as well as the metal dissolution reaction through the pores of the oxide film. Application of AV did not increase the pitting corrosion of aluminum in sulfate solution.

Acknowledgments

The authors would like to thank Tim Tyler and Bill Plunkett for their assistance on the fabrication of aluminum electrodes and the subsequent SEM analysis after corrosion tests. One of the authors (T.C.T.) received partial support from Lee's Foundation of Singapore and the Department of Chemical Engineering of the National University of Singapore for his visit to Clarkson University.

Manuscript submitted July 9, 1984; revised manuscript received Nov. 14, 1984.

REFERENCES

1. J. F. Williams, *Mater. Perform.*, **6**, 50 (1967).
2. W. H. French, *IEEE Trans. Power Apparatus Sys.*, **92**, 2053 (1973).
3. G. C. English, R. H. Brown, and R. R. Cope, Paper 57-852 presented at AIEE Summer General Meeting, Montreal, Canada (1957).
4. G. E. Thompson and G. C. Wood, *Corros. Sci.*, **18**, 721 (1978).
5. E. T. Serra and W. A. Mannheimer, Paper 55 presented at Corrosion/79, Atlanta, Georgia (1979).
6. S. Venkatesh and D-T. Chin, *Isr. J. Chem.*, **18**, 56 (1979).
7. D-T. Chin, in "Proceedings of the 9th International Congress on Metallic Corrosion, Toronto, Canada," Vol. 4, pp. 96-103 (1984).
8. S. R. Pookote and D-T. Chin, *Mater. Perform.*, **17**, 9 (1978).
9. D-T. Chin and T. W. Fu, *Corrosion*, **35**, 514 (1979).
10. D-T. Chin and S. Venkatesh, *This Journal*, **126**, 1908 (1979).
11. S. Venkatesh and D-T. Chin, *ibid.*, **128**, 2588 (1981).
12. D-T. Chin, R. Sethi, and J. McBreen, *ibid.*, **129**, 2677 (1982).
13. R. Sethi and D-T. Chin, *J. Electroanal. Chem.*, **160**, 79 (1984).
14. D-T. Chin and P. Sachdev, *This Journal*, **130**, 1714 (1984).
15. J. L. Wendt and D-T. Chin, *Corros. Sci.*, To be published.
16. J. L. Wendt and D-T. Chin, *ibid.*, To be published.
17. K. Yokoyama, H. Konno, H. Takahashi, and M. Nagayama, *Plating*, **69**, 62 (1982).

18. T. Takahashi and J. Saitoh, *ibid.*, **64**, 36 (1977).
 19. J. R. Galvele, S. M. de De Micheli, I. L. Muller, S. D. De Wexter, and I. L. Alanis, in "Localized Corrosion," R. F. Brown, J. Kruger, and A. Agarval, Editors, p. 580, NACE, Houston, TX (1974).
 20. J. A. Richardson and G. C. Wood, *Corros. Sci.*, **10**, 313 (1970).
 21. S. M. de De Micheli, *ibid.*, **18**, 605 (1978).

Study of Hydration Inhibitors on Aluminum Oxide Using Tunneling Spectroscopy and Molecular Electrostatic Potential Calculations

H. W. White,* C. D. Crowder, and G. P. Alldredge

Department of Physics and Astronomy, University of Missouri-Columbia, Columbia, Missouri 65211

ABSTRACT

Inelastic electron tunneling and *ab initio* molecular electrostatic potential calculations have been used to investigate the bonding of several phosphonate based hydration inhibitors adsorbed on aluminum oxide. Results are reported for phosphoric acid (PA), methylphosphonic acid (MPA), hydroxymethylphosphonic acid (HMP), and nitrotrismethylphosphonic acid (NTMP). Tunneling spectra were taken for PA, HMP, and NTMP and the observed frequencies compared to values obtained from FTIR, IR, and Raman spectra of similar compounds. Upward shifts in the P=O and P-O(H) stretch frequencies indicated that the phosphonates bond to the aluminum oxide surface through the phosphonate group. *Ab initio* quantum mechanical molecular electrostatic potentials (QMESP's) were calculated for PA, MPA, and HMP. Analysis of these results provided a means to understand on a molecular level the known variations in effectiveness for each of the inhibitors investigated.

Inelastic electron tunneling spectroscopy (IETS) and *ab initio* molecular electrostatic potential calculations have been used to investigate the bonding of several hydration inhibitors on aluminum oxide. The goal was to determine mechanisms whereby these molecules can inhibit the hydration of aluminum oxide in the presence of moisture. In this paper, results are discussed for the following phosphonate-type molecules: phosphonic acid (PA), methylphosphonic acid (MPA), hydroxymethylphosphonic acid (HMP), and nitrotrismethylphosphonic acid (NTMP).

Wedge tests of the type commonly used for adhesive bond testing have shown that NTMP in monolayer coverages on aluminum oxide can significantly increase bond strength and increase the lifetime of aluminum-aluminum oxide-polymer adhesive bonds. Similar tests on HMP and PA showed improvement but to a lesser extent. In contrast, recent tests on MPA showed that it provided no increase in performance.

IETS is a sensitive technique for measuring the vibrational frequencies of monolayer and submonolayer coverages of a molecular species adsorbed on a thin, insulating oxide surface, usually aluminum oxide.

The original intent of this work was to compare experimental and calculated IETS intensities for one or more small inhibitor molecules to obtain information on the orientation and bonding of the adsorbed species. Results for a more symmetrical, test-case molecule (thiourea) showed that the IETS intensity calculations could not be carried out because of the lack of complete vibrational analyses for the molecules of interest. However, methods developed for the model calculations have proved to be very useful for investigating variations in the molecular charge distribution for the inhibitors. Specifically, *ab initio* techniques have been used to determine the molecular structure, the quantum mechanical electrostatic potentials (QMESP's), and the charges which can be associated with each of the atoms in PA, MPA, and HMP. In this work, we exploit equipotential contour maps associated with QMESP's. This analysis is based, in part, on bonding information obtained while performing tunneling intensity calculations for thiourea (for which QMESP's were calculated as one step toward the determination of partial charges of thiourea); however, tunneling intensities were not calculated for the hydration inhibitors. Such calculations are too formidable.

Experimental

The IETS measurements were made on tunnel junctions prepared on insulating ceramic substrates. An alu-

minum electrode approximately 1000Å thick was evaporated onto the substrate at 10^{-7} - 10^{-8} torr. An oxide layer was grown on the aluminum and then doped with a water-based solution of the inhibitor. This doping process was done outside the vacuum chamber. The doped substrate was then returned to the vacuum chamber, and a top metal electrode of Pb was evaporated to complete the junction. Electrical leads were attached, the resistances were measured, and those junctions with good electrical characteristics were immersed in liquid helium for IETS measurements.

IETS spectra were obtained from 300 to 4000 cm^{-1} for PA, HMP, and NTMP. The observed frequencies and mode assignments are listed in Tables I, II, and III. The lower frequency portion of the spectrum obtained on a junction doped with a 0.3% solution of PA in water is shown in Fig. 1. Peak locations have been labeled in units of cm^{-1} . The HMP spectrum shown in Fig. 2 was taken on a junction doped with 10 mg of HMP per ml of water. The IETS spectrum for a 0.1% solution of NTMP is shown in Fig. 3.

Table I. Vibrational mode frequencies and assignments for PA adsorbed on aluminum oxide as measured by IETS

Frequency (cm^{-1})	Relative strength ^a	Group assignment
320	vs	Al phonon
410	s	
520	s	PO ₃ in-plane or P=O defm
610	s	P-O defm
629	vw	
655	vw	
690	s	
800	w	
865	sh	
920	vs	
945	sh	Al oxide phonon
1085	m	$\nu(\text{P}-\text{O}-(\text{H}))$
1170	b	$\nu(\text{P}=\text{O})$
1215	w, sh	$\nu(\text{P}=\text{O})$
1255	w, sh	
1315	vw	C-H (contamination)
1395	vw	C-H (contamination)
1458	m, b	C-H (contamination)
1700	m	
1680	w, b	
1855	s, b	2x Al oxide phonon
2490	w, b	$\nu(\text{C}-\text{H})$ (contamination)

^a w = weak, vw = very weak; m = medium; s = strong; vs = very strong; b = broad; sh = shoulder.

* Electrochemical Society Active Member.

Table II. Vibrational mode frequencies and assignments for HMP adsorbed on aluminum oxide as measured by IETS

Frequency (cm ⁻¹)	Relative strength ^a	Group assignment
320	vs	Al phonon
475	vw	PO ₃ in-plane or P=O defm
550	w	P-O or P=O defm
650	b	
790	vs	ν (P-O)
880	vs	CH ₂
935	sh	Al oxide phonon
1055	vs	ν (P-O-(H))
1210	vs	ν (P=O)
1235	w, sh	O-H defm
1350	vs	CH ₂ wag
1430	vs	CH ₂ defm
1605	s, b	
1860	m, b	2x Al oxide phonon
2445	m, b	Fermi resonance ?
2910	vs, b	ν (C-H)
3550	m, b	ν (O-H)

^a w = weak, vw = very weak; m = medium; s = strong; vs = very strong; b = broad; sh = shoulder.

Junctions doped by the same procedures as those used for the other molecules indicated that little, if any, MPA remained on the oxide layer. The general appearance of the oxide layer to the naked eye and also under a low power microscope suggested that the MPA did not absorb onto the oxide layer in the manner in which the other molecules did.

Results

An aluminum phonon near 320 cm⁻¹ and an aluminum oxide phonon near 945 cm⁻¹ occur in each of the spectra for PA, HMP, and NTMP. They are due to intrinsic features of the junction electrodes and will not be discussed further. All peak positions have been corrected for the presence of a superconducting top (Pb) electrode.

Weak bands appear at 475 and 455 cm⁻¹ in HMP and NTMP, respectively, whereas no peak occurs in PA in this region. Veken and Herman (1) assign a band as PO₃

Table III. Vibrational mode frequencies and assignments for NTMP adsorbed on aluminum oxide as measured by IETS

Frequency (cm ⁻¹)	Relative strength ^a	Group assignment
320	vs	Al phonon
455	b	PO ₃ or P=O defm
510	vw	PO ₃ or P=O defm
545	vw	P-O defm
585	b	P-O defm
652	vw	
780	s	ν (P-C)
880	vs	CH ₂
923	s, sh	Al oxide phonon
1040	vs	ν (P-O-(H))
1105	w, sh	
1200	b	ν (P=O)
1315	vs	CH ₂ wag
1430	vs	CH ₂ defm
2430	vs	
2935	vs	ν (C-H)

^a w = weak, vw = very weak; m = medium; s = strong; vs = very strong; b = broad; sh = shoulder.

in-plane motion which they observed near 480 cm⁻¹ (vw) in IR and at 498 cm⁻¹ (sh/w) in Raman spectra of dibasic methylphosphonic acid in water. The PO₃ in-plane assignment for PA near 520 cm⁻¹ is probably a PO₃ in-plane mode, but with different symmetry character. Thomas and Chittenden (2) give a possible alternative description to these peaks. They describe a weak, diffuse peak near 500 cm⁻¹ which they associate with P-O (OH) groups. Since the peaks are weak and can evidently be lost in some spectra, they cannot be considered significant.

The 545 and 585 cm⁻¹ peaks in NTMP, even though weak and broad, are of interest since FTIR results of NTMP adsorbed on aluminum oxide (3) show very strong, well-formed peaks at 547 and 585 cm⁻¹. The FTIR spectrum of dried NTMP (3) also shows a band near 554 cm⁻¹ which has been assigned as P-O motion. The IETS spectrum for HMP shows a weak peak at 550 cm⁻¹, and it is possible that the PA spectrum has a shoulder near 550 cm⁻¹, however, the results are not conclusive. These peaks are assigned as P-O deformation modes by compar-

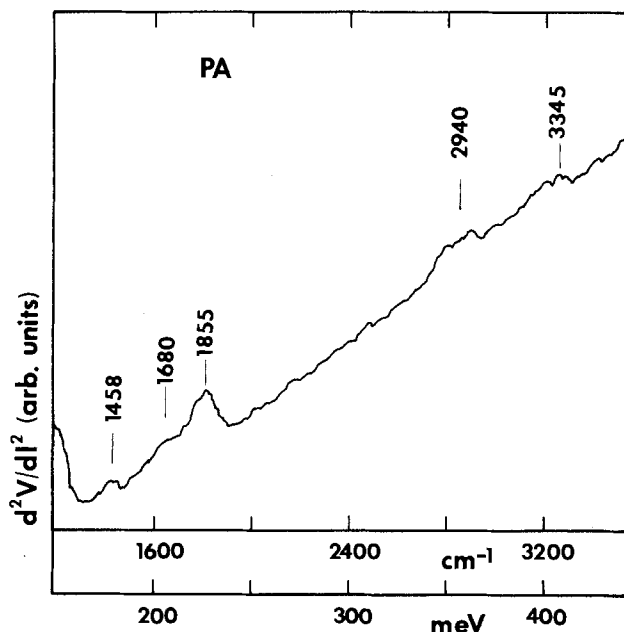
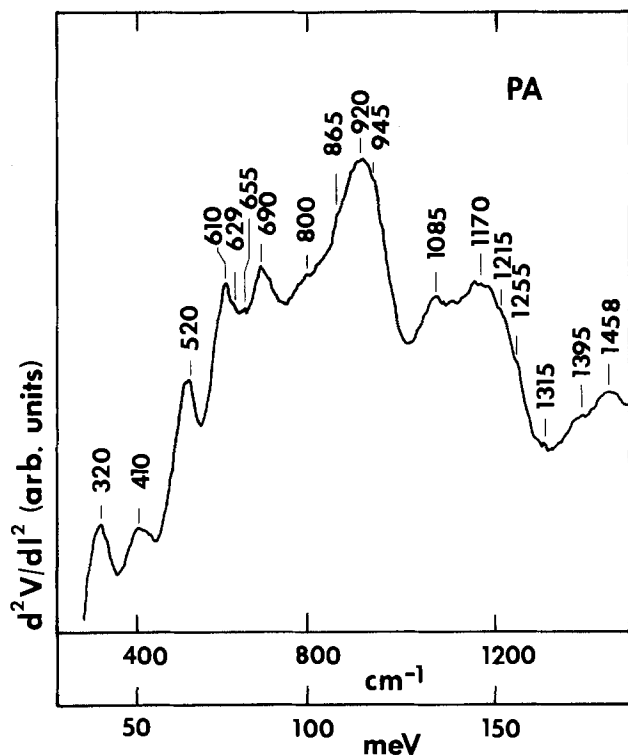


Fig. 1. IETS spectrum from 300 to 1500 cm⁻¹ for a 0.3% solution of PA in water.

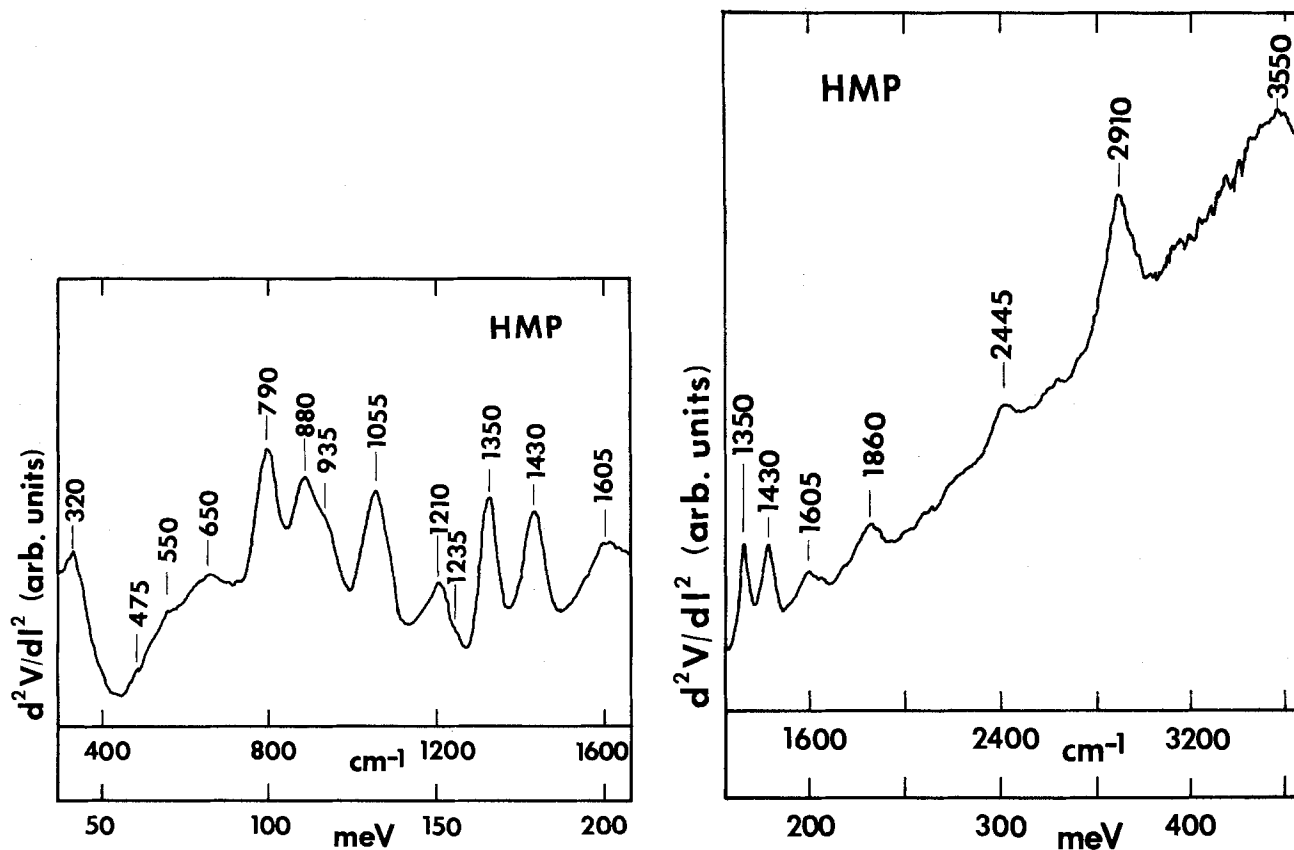


Fig. 2. IETS spectrum from 300 to 1650 cm^{-1} for a 1% solution of HMP in water.

ison with data by Veken and Herman (1). In Table I, we indicate a tentative assignment of this P-O deformation mode for the 610 cm^{-1} peak in PA.

There are several peaks in the PA spectra whose assignment is very unclear. Their locations are 629 (vw), 655 (vw), 690 (s), 800 (w), 865 (sh), and 920 (vs) cm^{-1} . Assignments of the strong peaks at 690 and 920 cm^{-1} were of special interest. No strong peaks occur in the 690 cm^{-1} region of either HMP or NTMP. There are strong peaks at 880 cm^{-1} in each; however, they are clearly associated with the CH_2 motion in HMP and NTMP. The strong

peaks at 790 cm^{-1} in HMP and at 780 cm^{-1} in NTMP can also be assigned to P-C stretch motion (1).

Peaks near 1085 (m) in PA, at 1055 (vs) in HMP, and at 1040 cm^{-1} (vs) in NTMP are undoubtedly $\nu(\text{P-O-H})$ which are known to occur near 1000 (± 100) cm^{-1} for molecules with these end groups. The FTIR data for NTMP adsorbed on aluminum oxide (3) has a very strong, broad band near 1050 cm^{-1} . FTIR on an Al-NTMP complex, formed by reacting $\text{Al}(\text{NO}_3)_3$ with NTMP (3), has a peak near 1160 cm^{-1} , both of which could have $\nu(\text{P=O})$ contributions.

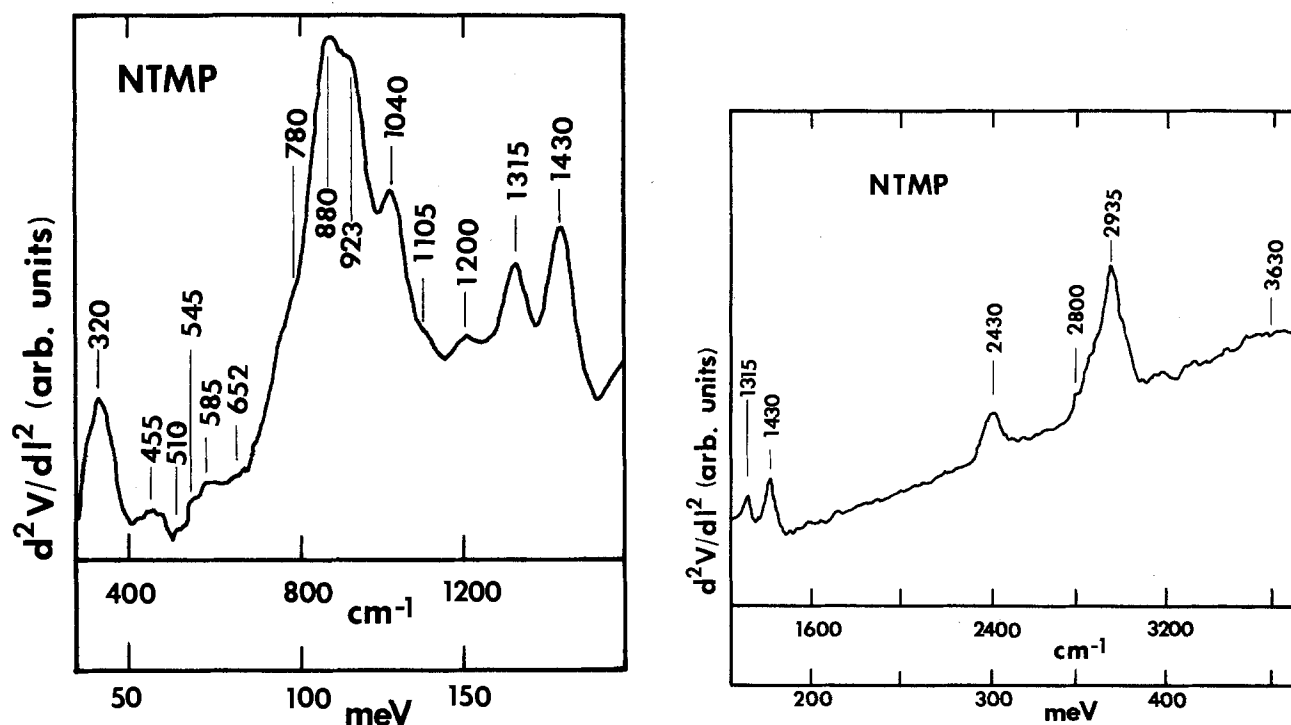


Fig. 3. IETS spectrum from 300 to 1600 cm^{-1} for a 0.1% solution of NTMP in water.

Peaks at 1210 (vs) in HMP and at 1200 cm^{-1} (b) in NTMP were assigned as $\nu(\text{P}=\text{O})$, in accordance with many literature discussions of the location of the phosphoryl frequency. According to Thomas and Chittenden (4), it sometimes occurs as a doublet and, as a result, can appear as such or as a broad peak. In their extensive analyses of $\nu(\text{P}=\text{O})$ shifts as a function of attached groups to phosphorus, they found that the mean value was sufficient to provide agreement with other data. In PA, a broad peak does occur at 1170 cm^{-1} , which was assigned as $\nu(\text{P}=\text{O})$. A weak shoulder at 1215 cm^{-1} was tentatively assigned as $\nu(\text{P}=\text{O})$ for lack of reasonable alternatives. The 1235 cm^{-1} peak in HMP is in the region expected for O-H deformations.

The location of the 1200 cm^{-1} $\nu(\text{P}=\text{O})$ peak in the IETS spectrum of NTMP was initially compared with a peak located at 1256 cm^{-1} as determined in an FTIR study of NTMP adsorbed on aluminum oxide (3). We now believe that this 1256 cm^{-1} peak is not due to $\nu(\text{P}=\text{O})$ since it is quite high. The FTIR of dried NTMP had a peak near 1188 cm^{-1} , and the Al-NTMP complex (3) showed a strong peak near 1160 cm^{-1} .

The 1350 (vs) and 1430 cm^{-1} (vs) peaks in HMP and the 1315 (vs) and 1430 (vs) peaks in NTMP were assigned as CH wag and C-H deformation modes, respectively. Veken and Herman (1) found CH wag and deformation modes at 1305 and 1430 cm^{-1} in dibasic $\text{CH}_3\text{PO}_3^{2-}$. The very weak peaks at 1315, 1395, and 1458 cm^{-1} in PA are likely to be due to CH contamination as suggested by the structure near 2940 cm^{-1} in PA.

Very strong $\nu(\text{C-H})$ modes were observed near 2910 cm^{-1} in HMP and near 2935 cm^{-1} in NTMP, as would be expected for molecules containing aliphatic CH bonds (*i.e.*, below 3000 cm^{-1} in almost all cases). A medium intensity, broad band near 3550 cm^{-1} in HMP was assigned as an O-H stretch.

There were interesting IETS peaks near 2445 cm^{-1} in HMP and 2430 cm^{-1} in NTMP which did not occur in PA. Although the nature of the modes is not clear, the fact that each was so strong and occurred in a region where no strong peaks were expected suggests that they are due to a Fermi resonance (overtone or combination occurring near a fundamental of the same symmetry type). In this case, the fundamental could be associated with an OH stretch mode since these can extend to much lower frequencies than 3550 cm^{-1} for phosphonic acid groups, as discussed by Thomas and Chittenden (2).

Of particular import to this work is the behavior of the $\nu(\text{P}=\text{O})$ and of the $\nu(\text{P-O-H})$ vibrations. The locations and relative strengths of the $\nu(\text{P}=\text{O})$ and $\nu(\text{P-O-H})$ IETS frequencies among PA, HMP, and NTMP are listed in Tables I, II, and III, respectively. The FTIR frequencies in cm^{-1} for dried NTMP, NTMP adsorbed on aluminum oxide, and the Al-NTMP complex were as follows for the $\text{P}=\text{O}$ and P-O-H modes, respectively: dried, 1188-970 and 1188-970; oxide adsorbed, (1256?) and 1052; and Al-complex, 1160 and (not observed). The assignment for the 1256 cm^{-1} peak is not clear, as stated above.

The IETS spectra for HMP showed much stronger features for these two modes than did the PA and NTMP. The locations of the IETS $\nu(\text{P}=\text{O})$ modes at 1170, 1210, and 1200 cm^{-1} for PA, HMP, and NTMP, respectively, when compared with the (maximum) value from the dried NTMP and Al-complex spectra suggested that the frequency for the $\text{P}=\text{O}$ mode was increased by adsorption on the oxide.

A similar shift which might have occurred in the $\nu(\text{P-O-H})$ frequencies cannot be determined on the same basis since the location of the $\nu(\text{P-O-H})$ frequency for the dried NTMP was not well determined by the FTIR data. Some progress can be made in the analysis of the $\nu(\text{P-O-H})$ modes, however, by comparison with solution data from the literature. Veken and Herman (1) found the $\nu(\text{P}=\text{O})$ frequency near 1140 cm^{-1} for dilute solutions of H_3PO_3 in water (*i.e.*, near the 1170 cm^{-1} value for IETS PA). The P-OH_2 antisymmetric and symmetric stretch frequencies were near 1010 and 950 cm^{-1} , respectively,

and the corresponding IR frequencies were near 1005 and 960 cm^{-1} , in good agreement with the Raman values. Since IETS $\nu(\text{P-O-H})$ frequency values were 1085, 1055, and 1040 cm^{-1} , respectively, for PA, HMP, and NTMP, the official data suggested that both the $\nu(\text{P}=\text{O})$ and $\nu(\text{P-O-H})$ observed frequencies were increased by adsorption. From these upward shifts, it was concluded that the phosphonate groups were significantly perturbed by adsorption on the oxide, and that in all those molecules these groups were active in the formation of bonds to the surface.

In summary, the observed upward shifts in the $\nu(\text{P}=\text{O})$ and $\nu(\text{P-O-H})$ frequencies observed in the IETS spectra as compared to values from FTIR, IR, and Raman data taken on dried, oxide adsorbed, complexed, and solution samples strongly suggests that PA, HMP, and NTMP bond to aluminum oxide through the phosphonate group. For further analysis, it would be useful to have frequency values for PA, HMP, and NTMP in solution. The absence of IETS intensities for tunnel junctions doped with MPA indicates that it does not bond nearly as strongly as do PA, HMP, and NTMP. On this basis, it would be judged as a poor inhibitor candidate. This conjecture was found to be in agreement with results from wedge tests (5).

Molecular Charge Distributions

In the discussion thus far, IETS vibrational frequencies and their shifts from values obtained independently (*e.g.*, optically) have been used to extract information on the adsorbed species. One of the original goals of this work was to compare measured and calculated relative peak intensities in an IETS spectrum to obtain information on the orientation and structure of the inhibitor molecules—MPA in particular. This goal could not have been achieved without extensive modeling and computer resources because the molecules are complex and complete vibrational analyses have not been made. As stated earlier, and discussed later, QMEP's instead could be utilized to obtain bonding information. They are considerably more straightforward to calculate than are tunneling intensities.

In the intensity calculations for thiourea, which were done to make IETS a more quantitative tool, an improved model was developed for calculating the intensities as a function of the orientation and structure of the adsorbate. It was called the floating valence model, the basis of which is the partial charge model of Kirtley *et al.* (6). In this model, the electron-molecule interaction is approximated by a coulombic interaction between the electron and partial charges assigned for each atomic site of the molecule. One of the major difficulties associated with this model was that there was no means to reliably assign the atomic partial charges, the values of which greatly influence calculated peak intensity ratios. Also, it was known from other calculations (7) that the pseudo-dipolar potential seen by the tunneling electron is not always oriented, as would be expected from charges moving along directions of atomic motion.

The floating valence model solved the two primary problems by the use of a two-step procedure first used by Momany (8) to determine partial charges. First, *ab initio* molecular QMEP's were calculated using an atomic orbital basis set. The second step was to determine the effective charge located at each atomic site, which would give a classical electrostatic potential equal to the QMEP.

To obtain reasonable tunneling intensities, we had to modify the fitting procedure to obtain more accurate partial charge values. This was done by dividing the charge on each atomic site into two portions. A core charge was forced to follow the motion of the atom while a valence charge was allowed to "float" in both direction and displacement magnitude to best fit the QMEP. We called these potential-derived (PD) charges. The development of the floating valence model and ensuing calculations for thiourea were extensive and are being published elsewhere (9, 10). The tunneling calculations clearly showed that the PD charges were very accurate.

The complete tunneling intensity calculations for thiourea (10) and the analyses of partial charges and QMEP's reported in this study provide three significant results relevant to the utilization of QMEP's, partial atomic charges, and calculated tunneling intensities to the study of inhibitors. First, there must exist an accurate and complete vibrational mode analysis for any molecule for which accurate tunneling intensities are to be calculated. For most large molecules, the analysis is either incomplete or has not been attempted. Second, molecular electrostatic equipotential contour plots through various symmetry planes give pictorial and quantitative information on the charge distribution for the inhibitor molecules. Although such plots are not generally available in the literature, plots can be produced for quite complex molecules, such as those in this study. The charge distribution in an inhibitor molecule affects its bonding characteristics, and hence its effectiveness. As such, they are useful for deducing information about the molecular orientation and relative bond strengths for various inhibitors. Studies of the systematic variations in the charge distributions with structure and with the substitution of various groups is a powerful tool for the development of better inhibitors and understanding inhibitor mechanisms. Third, accurate atomic partial charges for inhibitor molecules can be calculated from generated QMEP's. Although partial charges were calculated for the inhibitors in this study, attempts to correlate their variation with inhibitor effectiveness were unsuccessful. Additional work is required.

It should be made clear that our justification for utilizing QMEP's, rather than a complete comparison of experimental and calculated intensities, for hydration inhibitors stems directly from information gleaned from the complete tunneling intensity comparison for thiourea on aluminum oxide. Thiourea is a corrosion inhibitor for aluminum in dilute hydrochloric acid.

In the following section, the procedure for calculating QMEP's is presented in brief form. Results for PA, MPA, and HMP are reported. The large number of atoms in NTMP made it unsuitable for the *ab initio* calculations.

The *ab initio* electrostatic potentials were calculated using self-consistent Hartree-Fock theory. The basic equation for this theory is

$$\hat{F}\Psi_i = \epsilon_i\Psi_i \quad [1]$$

where Ψ_i is the *i*th molecular orbital, ϵ_i is the *i*th energy eigenvalue, and \hat{F} is the Fock operator (the effective one-electron operator) defined by

$$\hat{F}(p) = -\frac{1}{2}\nabla^2 - \sum_a \frac{Z_a}{r_{ap}} + \sum_j (2\hat{J}_j - \hat{K}_j) \quad [2]$$

where *p* is the electron index, *a* is the atom index, Z_a is the nuclear charge for the *a*th atom, r_{ap} is the distance from the *a*th nucleus to the *p*th electron, and \hat{J}_j and \hat{K}_j are the coulomb and exchange operators, which are as follows

$$\hat{J}_j\Psi_i(p) = \int \Psi_j^*(q) \left(\frac{1}{r_{qp}} \right) \Psi_j(q) d\tau_q \Psi_i(p) \quad [3]$$

$$\hat{K}_j\Psi_i(p) = \int \Psi_j^*(q) \left(\frac{1}{r_{qp}} \right) \Psi_i(q) d\tau_q \Psi_j(p) \quad [4]$$

where *q* and *p* are electron indexes, $d\tau$ is a volume element, and r_{qp} is the distance between the *q*th and *p*th electrons.

In our calculations, the linear combination of atomic orbital (LCAO) approach was used. It assumes that the molecular orbitals $\Psi_i(\vec{r})$ can be expanded in terms of atom-centered atomic orbitals $\phi_{\mu a}(\vec{r}_a)$ as

$$\Psi_i(\vec{r}) = \sum_a \sum_{\mu} \phi_{\mu a}(\vec{r}_a) C_i^{\mu a} \quad [5]$$

where *a* is the atom index, μ reflects the *n*, *l*, and *m* quantum numbers of the orbital, \vec{r} is a position vector

relative to the origin, \vec{R}_a is the position vector of the *a*th nucleus, and $\vec{r}_a = \vec{r} - \vec{R}_a$, and $C_i^{\mu a}$ are expansion coefficients which we wish to determine.

In atomic calculations, Slater-type orbitals (STO's) are often used to represent the radial dependence of the atomic orbitals. A normalized STO with principal quantum number *n* is given by

$$\text{STO}_n(r) = N_n r^{n-1} e^{-\zeta r} \quad [6]$$

where N_n is a normalization constant, and ζ is a parameter which is optimized to give the best fit to the radial dependence of a particular atomic orbital.

Unfortunately, STO's are too unwieldy to use for molecular calculations. One approach to alleviate this difficulty is to use a linear combination of gaussians to represent the exponential dependence of the STO's. If $\phi_{\mu}(r)$ represents the exponential dependence of an STO, then it can be expanded as follows

$$\phi_{\mu}(r) = \sum_{i=1}^N d_{i\mu} \exp(-\alpha_i r^2) \quad [7]$$

where *N* is the number of gaussians used in the expansion, $d_{i\mu}$ are contraction coefficients, α_i is the gaussian exponent.

This approach as implemented by Quantum Chemistry Program Exchange (QCPE) no. 437 (Gaussian 80) (11) was used to perform the computations. The gaussian contraction scheme for each orbital is referred to as the basis set. Two different basis sets were used for PA, MPA, and HMP, designated by STO-3G and STO 4-31G (or as 4-31G).

The Fock operator of Eq. [1] depends on the set of Ψ_i chosen. Gaussian 80 uses optimized atom-centered atomic orbital $[\phi_{\mu a}(\vec{r}_a)]$ along with a set of "guessed" $C_i^{\mu a}$ to calculate an initial $\Psi_i(\vec{r})$ via Eq. [5]. (The starting $C_i^{\mu a}$ are generated from a Hückel or projected Hückel guess.) The Fock matrix was determined from the $\Psi_i(\vec{r})$ via Eq. [2], [3], and [4] and was used in Eq. [1] to solve for new Ψ_i and ϵ_i . This process is repeated until the energy eigenvalues converge. The final wave functions yielded the optimal set of $C_i^{\mu a}$ which were used to calculate the electron density, $\rho(\vec{r})$, from the relationship

$$\rho(\vec{r}) = \sum_i^{\text{occ}} |\Psi_i(\vec{r})|^2 = \sum_{\substack{\mu, a \\ \nu, a'}} \phi_{\mu a}(\vec{r}_a) \phi_{\nu a'}(\vec{r}_{a'}) \sum_i^{\text{occ}} C_i^{\mu a} C_i^{\nu a'} \quad [8]$$

where \sum_i^{occ} indicates that the sum is over occupied orbitals only.

All calculations used restricted Hartree-Fock theory which assumes that both a spin up and a spin down electron occupy each spatial orbital. Once $\rho(\vec{r})$ had been obtained, the molecular electrostatic potential, $V(\vec{r})$, could be determined since

$$V(\vec{r}) = \sum_a \frac{Z_a e}{|\vec{r} - \vec{R}_a|} - e \int \frac{\rho(\vec{r}')}{|\vec{r} - \vec{r}'|} d\vec{r}' \quad [9]$$

In its original form, Gaussian 80 did not calculate $V(\vec{r})$. The STVINT section of Gaussian 80 was modified to do the appropriate integral calculations. Once this was done, it was a simple matter to add in the nuclear contributions to the potential (the first term in Eq. [9]) to calculate the QMEP's.

Equation [9] allowed the determination of the electrostatic potential at a point \vec{r} . To accurately fit the potential around a molecule, the potential must be known for a fairly large, representative set of field points. The electrostatic potential was calculated using a rectangular array of equally spaced points with the origin at the center of nuclear charge.

In order to calculate the QMEP's for the inhibitor molecules, it was necessary to first determine their structure by suitable methods since they were not available from the literature. The approach was to begin with a reasonable structure (or structures, in the case of MPA) with best guess values for bond lengths and angles and then to util-

ize the optimization features of the Gaussian 80 QCPE program to determine bond lengths and angles. One of the two structures assumed for MPA was the eclipsed methyl group, denoted as MPA-E. The other structure, denoted as MPA-S, had a methyl group staggered with respect to the P=O bond. The minimum energies obtained for MPA-E and MPA-S were so close as to preclude a decision on which structure was more stable.

The bond angles, bond lengths, and cartesian coordinates for PA, MPA-E, MPA-S, and HMP calculated with this technique are listed in Tables IV through XI. They are in reasonable agreement with values for angles and bond lengths of various related compounds.

Table IV. Calculated bond lengths and angles for PA

	Distance (Å)	Angles (degrees)	
P=O	1.50	O—P=O	116.53
P—O	1.55	P—O—H	110.32
O—H	1.00		

Table V. Calculated cartesian coordinates (Å) for the atoms of PA

Atom	X-coordinate	Y-coordinate	Z-coordinate
P	0.0	0.0	0.0
O	0.0	0.0	2.835
O	2.621	0.0	-1.309
H	3.999	0.0	-0.016
O	-1.309	-2.269	-1.312
O	-1.309	2.269	-1.312
H	-1.998	-3.464	-0.021
H	-1.998	3.464	-0.021

Table VI. Bond lengths and angles for MPA-E (eclipsed methyl group)

	Distance (Å)	Angles (degrees)	
P=O	1.50	C—P=O	122.21
P—O	1.55	C—P—O	100.88
O—H	1.00	O=P—O	113.30
C—P	1.78	P—O—H	110.38
C—H	1.10	O—P—O	103.98
		H—C—P	109.50
		H—C—H	109.43

Table VII. Calculated cartesian coordinates (Å) for the atoms of MPA-E

Atom	X-coordinate	Y-coordinate	Z-coordinate
P	0.0	0.0	0.0
O	0.0	0.0	2.835
O	2.690	0.0	-1.158
H	3.951	0.620	0.106
O	-1.269	2.373	-1.158
H	-1.316	3.776	0.106
C	-1.463	-2.441	-1.793
H	-2.302	-3.841	-0.505
H	-0.041	-3.369	-2.992
H	-2.952	-1.625	-2.992

Table VIII. Calculated bond lengths and angles for MPA-S (staggered methyl group)

	Distance (Å)	Angles (degrees)	
P=O	1.50	C—P=O	122.60
P—O	1.55	C—P—O	100.49
O—H	1.00	O=P—O	113.39
C—P	1.78	P—O—H	110.34
C—H	1.10	O—P—O	104.06
		H—C—P	109.50
		H—C—H	109.43

Table IX. Calculated cartesian coordinates (Å) for the atoms of MPA-S

Atom	X-coordinate	Y-coordinate	Z-coordinate
P	0.0	0.0	0.0
O	0.0	0.0	2.835
O	2.688	0.0	-1.163
H	3.957	0.573	0.115
O	-1.278	2.365	-1.163
H	-1.378	3.753	0.115
C	-1.451	-2.434	-1.812
H	-0.563	-4.259	-1.360
H	-1.210	-2.030	-3.836
H	-3.478	-2.521	-1.360

Table X. Calculated bond lengths and angles for HMP

	Distance (Å)	Angles (degrees)	
P=O	1.50	C—P=O	122.60
P—O	1.55	C—P—O	100.49
(P)—O—H	1.00	O=P—O	113.39
C—P	1.78	P—O—H	110.34
C—H	1.10	O—P—O	104.06
O—C	1.43	H—C—P	108.75
(C)—O—H	0.96	P—C—O	109.16
		C—O—H	104.34

Table XI. Calculated cartesian coordinates (Å) for the atoms of HMP

Atom	X-coordinate	Y-coordinate	Z-coordinate
P	0.0	0.0	0.0
O	0.0	0.0	2.835
O	2.688	0.0	-1.163
H	3.957	0.573	0.115
O	-1.278	2.365	-1.163
H	-1.378	3.753	0.115
C	-1.451	-2.434	-1.812
H	-0.597	-4.256	-1.289
H	-3.460	-2.549	-1.289
O	-1.130	-1.895	-4.440
H	-1.952	-3.274	-5.285

Molecular electrostatic potentials were obtained for each of the four structures described. Two basis sets, STO-3G and 4-31G, were used to investigate the effects of basis set selection. Plots of equipotential lines through the planes of reflection symmetry using the 4-31G basis set are shown in Fig. 4-7 for PA, MPA-E, MPA-S, and HMP. Inspection of these figures reveals significant changes in the molecular charge distributions which depend on the nature of the attached group. The effect of basis set (not shown) was also apparent; however, the 4-31G is deemed to be more accurate.

Discussion

There does appear to be some correlation of features observed in the molecular electrostatic equipotential contours and apparent bonding strength and inhibitor effectiveness as deduced from wedge tests and tunnel junction features. Analyses of peak shifts in the tunneling spectra indicate the phosphonate groups bond to the oxide layer. The bonding for MPA is very weak. The contours for PA in Fig. 4 show the existence of a large region just below the three P-O bonds which is very negative in potential. The -60 kcal/mol region which occurs just below the (single-bonded) oxygen would also appear below the other two oxygens which are out of the plane. These three oxygens would be even more negative if they were deprotonated and, as such, could form strong bonds to exposed aluminum cations in the oxide layer. The orientation and bonding arrangement for the adsorbed ion would be as schematically depicted in Fig. 8, with the P=O bond furthest from the oxide layer with its bond direction perpendicular to the layer. This bonding scheme seems quite reasonable.

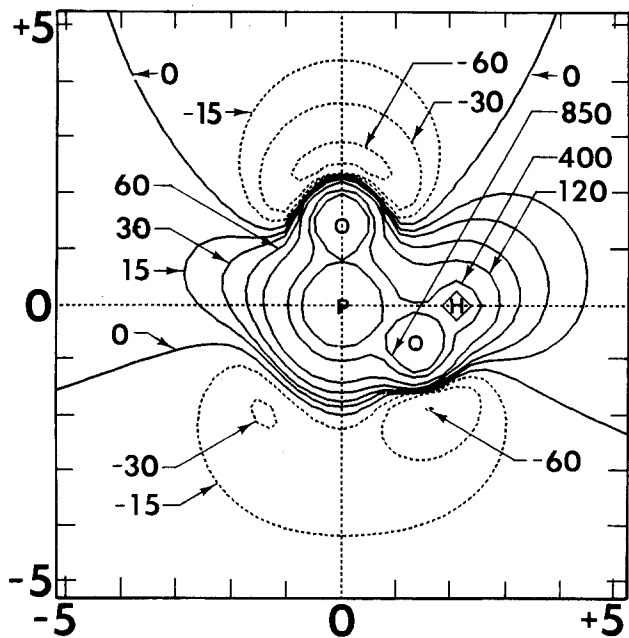


Fig. 4. Electrostatic potential contour plot for PA in the plane of reflection symmetry using a 4-31G basis set. Potential values are in kilocalorie per mole and distances are in angstroms.

Likewise, the equipotential contours for HMP in Fig. 7 also reveal the presence of a large negative potential region. The region is, however, formed by two single-bonded oxygens (which are out of the plane of reflection symmetry) and the oxygen in the C-O-H group. If HMP is considered to be as PA but with one of the O-H groups replaced by a C-O-H group, then the region of negative potential can be interpreted as being tipped toward the P=O bond direction. The -60 kcal/mol contour near the oxygen in the C-O-H group is larger than that shown for PA in Fig. 4 and indicates the possibility for the formation of a stronger Al-O bond for HMP than exists for PA. A possible orientation and bonding arrangement for HMP on aluminum oxide is shown schematically in Fig. 9. The P=O bond direction is tipped with respect to the plane of the oxide. It is not known whether the P=O bond would contribute significantly to the bonding in this orientation.

The contours for MPA-E and MPA-S shown in Fig. 5 and 6 are similar to each other except for the expected

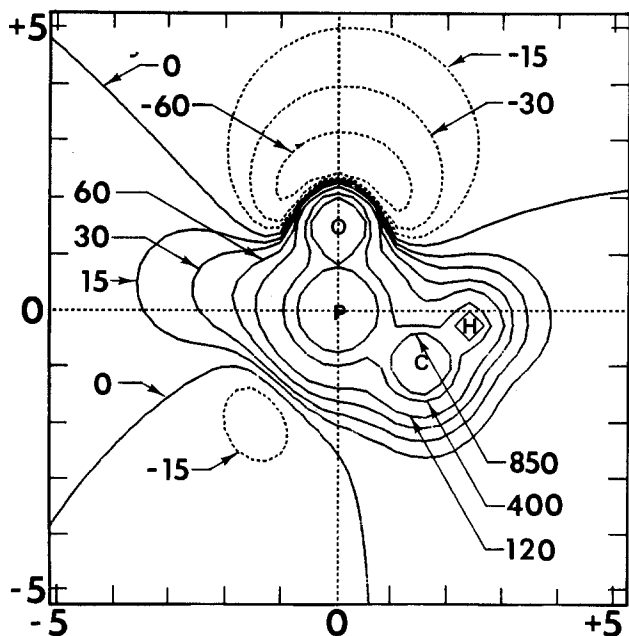


Fig. 5. MPA-E equipotential plot in the plane of reflection symmetry using the 4-31G basis set. Potential values are in kilocalorie per mole and distances are in angstroms.

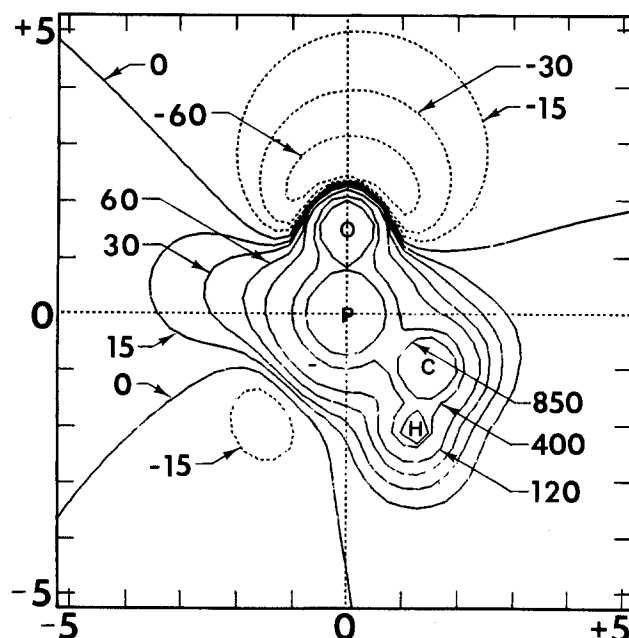


Fig. 6. MPA-S equipotential plot in the plane of reflection symmetry using the 4-31G basis set. Potential values are in kilocalorie per mole and distances are in angstroms.

differences due to the two configurations of the CH_3 group. There are two single-bonded oxygens in MPA. The most negative contour in the plane of reflection symmetry between them is only -15 kcal/mol. The negative potential region for MPA-E and MPA-S is much smaller and is less negative than for either PA or HMP. The region near the P=O bond does not vary appreciably among PA, MPA, and HMP. Therefore, the molecular equipotential contour plots for PA, MPA, and HMP indicate that MPA would not adsorb as strongly as either PA or HMP and, as a consequence, would be much less effective as a hydration inhibitor. This conclusion is in agreement with results from the IETS studies discussed earlier and with wedge test results on adhesive bonds.

Conclusions

The goal of this project to use a combined experimental and theoretical approach in the application of IETS to the study of hydration inhibitors on aluminum oxide. The

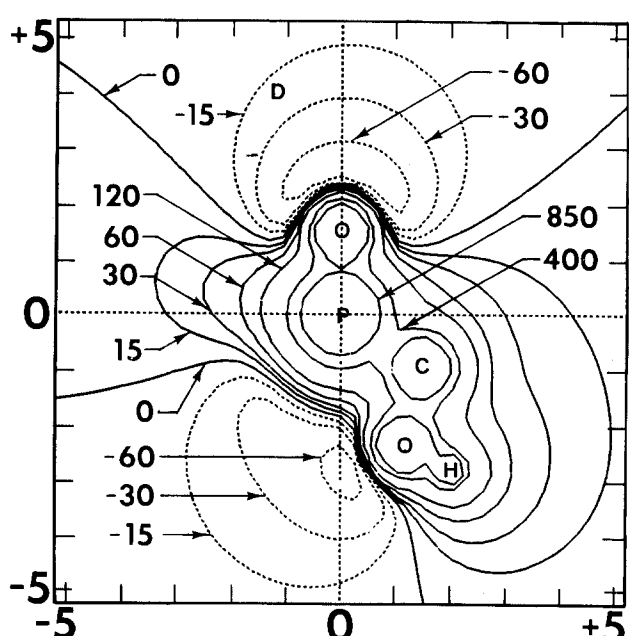


Fig. 7. HMP equipotential plot in the plane of reflection symmetry using the 4-31G basis set. Potential values are in kilocalorie per mole and distances are in angstroms.

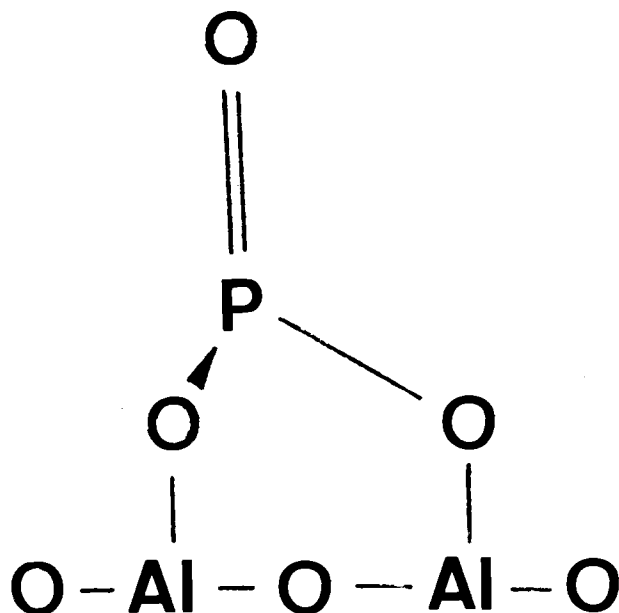


Fig. 8. A schematic showing the bonding and orientation of PA adsorbed on aluminum oxide.

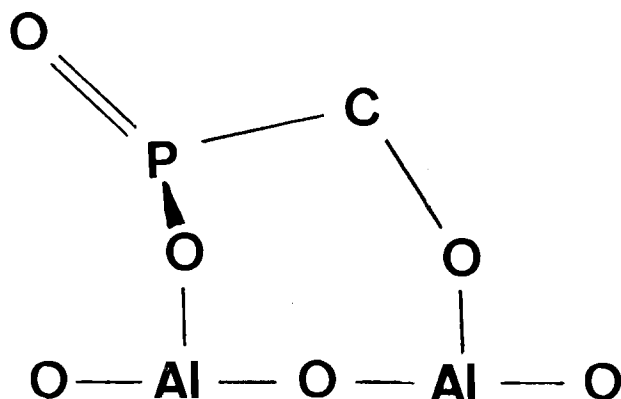


Fig. 9. A schematic showing the bonding and orientation of HMP adsorbed on aluminum oxide.

value of both tunneling spectroscopy and QMEP's for understanding inhibitor bonding has been established. For PA, HMP, and NTMP, observed shifts in $\nu(\text{P}=\text{O})$ and $\nu(\text{P}-\text{O}(\text{H}))$ tunneling frequencies from optical values strongly show that these molecules bond to the oxide layer through the phosphonate group. Tunnel junctions doped with MPA indicate that the bonding of MPA to the oxide is much weaker, and on this basis would be judged as a poor inhibitor candidate. This conjecture was found to be in agreement with wedge test results. Likewise, analysis of the equipotential contours for PA, MPA, and HMP indicated that PA and HMP could form strong bonds to exposed aluminum cations through the three single-bonded oxygens in PA, and through the two

single-bonded oxygens and the oxygen in the C-O(H) group in HMP. The equipotential contours for MPA indicated that it would form a much weaker bond than did PA and HMP. Since NTMP has three phosphonate groups, these results indicate that it would also be a strong adsorber and effective inhibitor.

The calculations in this work did not include the effects of electron transfer between the inhibitors and the oxide surface. A more complete model should include the effects of chemisorption on the structure and bonding properties of the inhibitors.

In future work, it would be informative to compare adsorbed and solution spectral frequencies for several of the large, effective phosphonate inhibitors having different substituted groups in order to more effectively determine any systematic behavior of frequency shifts upon adsorption. The use of semi-empirical methods could be used to more efficiently optimize molecular structures and to calculate molecular charge distributions for inhibitor molecules with as many as 100 atoms. *Ab initio* and semi-empirical calculations can be applied to a wide range of inhibitor types, including corrosion inhibitors on various metals.

Acknowledgments

We wish to thank J. S. Ahearn and G. D. Davis for providing information on wedge tests results, L. J. Matienzo for providing information on FTIR measurements prior to publication, and Lilian Xu for assistance in preparing samples. This work was supported in part by the Army Research Office, the Office of Naval Research, and Martin Marietta Corporation under Contract no. N00014-80-C-0718. One of the authors (C.D.C.) was supported in part by NSF Grants SPI 8019153, SPI 8166360, and SPE 8264085.

Manuscript submitted Dec. 28, 1983; revised manuscript received Nov. 26, 1984.

The University of Missouri assisted in meeting the publication costs of this article.

REFERENCES

1. B. J. Van der Veken and M. A. Herman, *J. Molecular Struct.*, **15**, 225 (1973).
2. L. C. Thomas and R. A. Chittenden, *Spectros. Acta*, **20**, 489 (1964).
3. L. J. Matienzo, Private communication.
4. L. C. Thomas and R. A. Chittenden, *Spectros. Acta*, **20**, 467 (1964).
5. J. S. Ahearn and G. D. Davis, Private communication.
6. John Kirtley, D. J. Scalapino, and P. K. Hansma, *Phys. Rev. B*, **14**, 3177 (1976).
7. J. Rath and T. Wolfram, in "Inelastic Electron Tunneling Spectroscopy," T. Wolfram, Editor, pp. 92-102, Springer-Verlag, Berlin (1978).
8. F. A. Momany, *J. Phys. Chem.*, **82**, 592 (1978).
9. C. D. Crowder, G. P. Alldredge, and H. W. White, *Phys. Rev.*, To be published.
10. C. D. Crowder, H. W. White, and G. P. Alldredge, *ibid.*, To be published.
11. P. N. van Kampen, F. A. A. M. de Lecus, G. F. Smits, and C. Altona, *QCPE*, **13**, 437 (1982).

Electrochemical Behavior of Passive Iron in Acid Medium

II. The Passive Film/Solution Interface

M. Keddou and C. Pallotta

Groupe de Recherche n° 4 du CNRS, "Physique des Liquides et Electrochimie," associé à l'Université Pierre et Marie Curie, 75230 Paris Cedex 05, France

ABSTRACT

The passive film on iron in acid media is investigated by means of a rapid change of electrolyte composition, with special attention to anion content, and by redox kinetics studies with a rotating disk under steady state and nonsteady state (electrohydrodynamic impedance). These techniques, associated with classical electrochemical impedance, allow one to establish the existence at the film-electrolyte interface of a loosely structured film limiting the rate of mass transfer in the case of ferrocyanide oxidation. Dynamic exchange of anions and most of the electrolyte composition effects take place in this layer. An attempt is made to relate the behavior of the passive film on iron in acid media to basic properties of iron oxides and oxyhydroxides in their colloidal state.

As shown in the first paper of this series (1), the impedance analysis of passive iron over a wide frequency range allows one to separate the transport properties in the film both from the charge transfer at interfaces and from film growth (1). A resistance linearly dependent on the potential is found. This dependence strongly supports the mechanism of high field assisted migration across the film, as suggested by Vetter.

A partially reversible charge transfer reaction at interfaces was evidenced by nonsteady-state experiments. The low frequency behavior of the impedance in the millihertz range led to the conclusion that diffusion is not the process controlling the passive current. The capacitance observed in this range is related to film growth and allows one to estimate the ratio of the film forming current to the dissolution current under nonsteady state.

The passive current acts as a scaling factor for the most important parameters involved in the electrochemical characterization of passivity. Its value depends strongly on electrolyte composition (anions and pH), probably through the charge carrier concentration in the film. This makes it possible to describe the passive system as a chemically dependent high field assisted ion migration (1).

Most of the data available from literature on the electrochemical response of passive iron to redox couples deal with neutral or alkaline media (2-6). Usually, only steady-state polarization curves were used to investigate the kinetics of these reactions, and the results were analyzed in terms of the semiconducting properties of the film or of tunneling. Furthermore, the possible modifications of the passive film as a result of redox reactions and its dependence upon anions were disregarded.

This part of the paper is aimed at analyzing the film/solution interface. This will be carried out by investigating the role of anions on the passive current and also the response of the passive system to redox couples in order to answer the following questions. Is there any correlation between the passive current value and the ability of the film to ensure electron charge transfer? Do the anions determine the kinetics of charge transfer on the film surface? Is the passive film-anion interaction dynamic or are the anions statically bonded to the film structure? Is there only a surface effect or is there penetration of anions in the film structure?

Experimental

Experimental conditions and devices are similar to the ones described in Ref. (1). A special cell was designed for performing a quasi-instantaneous and thorough change of electrolyte composition. As shown in Fig. 1, the cell is divided in two compartments separated by a glass frit, leaving the working electrode compartment isolated. The new solution enters the working electrode compartment as an impinging jet perpendicular to the electrode surface producing a composition transient. The stopcock at the cell

bottoms allows the new electrolyte to flow from a 1 liter reservoir placed on top of the cell. A Pt counterelectrode and a mercurous sulfate electrode in saturated K_2SO_4 (SSE) complete the cell. All potentials were referred to this reference electrode.

The solutions were deaerated by Ar bubbling and maintained at 25°C. A conventional electrochemical cell was used for other types of measurements. The working electrode, a disk of 0.2 cm², was prepared as explained in Ref. (1). A rotating disk setup was used with a range of angular velocities from 0 to 8000 rpm.

Procedure

The electrode was polarized at the working potential in the passivation domain for a given time. Then the electrolyte was suddenly changed and the current transient recorded as a function of time. Impedance measurements were carried out in this initial state and after the solution change, once the current attained its steady-state value in the new solution. In some instances, after about 15h of passivation in the full passive range, ions were incorporated into the electrolyte by adding different amounts of

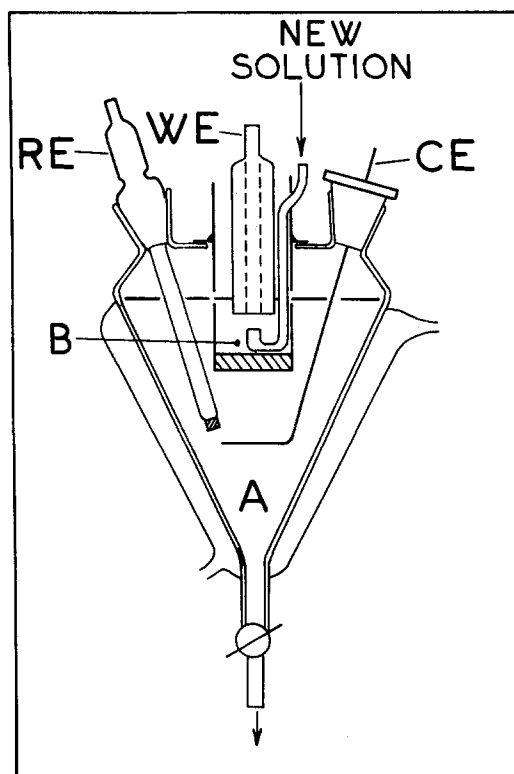


Fig. 1. Electrochemical cell for composition transients. Compartment A: 60 cm³. Compartment B: 10 cm³.

concentrated solutions. Care was taken in order to avoid pH changes. In the case of cation addition, the salt was chosen in order to avoid the introduction of foreign anions into the electrolyte.

Results and Discussion

Influence of the hydrodynamic conditions on the passive current.—Unexpectedly, the passive current of the Fe/H₂SO₄ and Fe/H₃PO₄ systems depends on the angular velocity of the electrode. As a consequence of an angular velocity transient, the current attains a limiting value showing an increase of between 10 and 30% of its stationary stagnant value, I_p , depending on potential. In the case of Fe/1M H₃PO₄, the I_p /time response to an angular velocity transient can be divided in two regions. The first, over a short interval of time, is characterized by a stepwise increase of the current as shown in Fig. 2. In the second region, over a long interval of time, the current tends slowly towards its limiting steady-state value following a staircase profile, as can be seen in Fig. 2. In this final state, the rotation of the electrode has practically no remaining effect on I_p . The duration of each of these two regions depends on the value of the angular velocity. For the opposite angular velocity transient, the current returns to about its initial value also following a staircase profile as shown in Fig. 3.

In the Fe/0.5M H₂SO₄ system, only the first stepwise increase of current is observed as a result of an angular velocity transient. A dependence of I_p vs. $\Omega^{-1/2}$ is found showing a limiting effect for angular velocities higher than 2200 rpm, as can be seen in Fig. 4. The electrode rotation has no effect on the passive current for the Fe/1M HClO₄ system.

The electrochemical properties of the passive iron system, and particularly its impedance behavior analyzed in Ref. (1), is not modified as a consequence of the electrode rotation.

Redox reactions on passive iron.—In order to analyze the film/solution interface from the viewpoint of its kinetic behavior, different ions were introduced into the solution after about 15h of passivation in a given electrolyte. Both Fe(II) and Fe(CN)₆⁴⁻ ions are in their oxidation domain in the full passive range (between ca. 0.2 and 1.0V). Ferrous ions were chosen with the idea of interfering with the ionics of the passive film.

Fe(CN)₆⁴⁻ to Fe(CN)₆³⁻ oxidation.—The kinetics of ferrocyanide oxidation are largely dependent on the electrolyte. In perchloric and phosphoric solutions, the reaction is diffusion controlled at moderate angular velocity ($\Omega = 110$ rpm) in the entire passive domain, while in sulfuric solutions a mixed kinetics is observed below 0.5V.

The I^{-1} vs. $\Omega^{-1/2}$ plots allow one to obtain at the same time kinetics and transport data. In the case where the electrode is coated by a solid layer, the following equation is valid (7)

$$I^{-1} = I_s^{-1} + I_{\Omega \rightarrow \infty}^{-1} + I_k^{-1} \quad [1]$$

where $I_s = nFD C^\infty / \delta$ is the Fick law, δ is the thickness of the concentration profile dependent on Ω according to the Levich equation, D the diffusion coefficient, and C^∞ is the concentration in the solution bulk, $I_{\Omega \rightarrow \infty} = nFD_L C^\infty / \delta_L$, δ_L is the thickness of the solid layer independent of Ω , and D_L the diffusion coefficient in this layer. Finally, I_k is the kinetic current. A nonzero intercept on the current axis then indicates either a kinetic limitation or a diffusion limitation originated in a diffusion layer of constant thickness.

As a comparison, the effect of the supporting electrolyte on the ferrocyanide oxidation on Pt was also analyzed. The results are shown in Fig. 5 and 6 and in Tables I and II. As expected from diffusion in the liquid phase, the same diffusion coefficient is obtained for Fe(CN)₆⁴⁻ on Pt and on passive iron electrodes. Regarding the $I_{\Omega \rightarrow \infty}$ limit, a larger dependence on the electrolyte composition is observed on passive iron in comparison with Pt.

In perchloric solutions, Pt and passive iron behave almost identically, whereas the difference between them increases in sulfuric and phosphoric solutions.

The relatively small influence of the electrolyte composition on the $I_{\Omega \rightarrow \infty}$ limit on Pt may be attributed to kinetic effects associated with a modification of the double-layer properties and/or of the active surface due to the different adsorption characteristics of anions. However, in the case of passive iron, the dependence of the $I_{\Omega \rightarrow \infty}$ limit on the electrolyte composition is so important that this interpretation hardly remains valid and a special interaction between passive iron and anions may be supposed in the case of sulfuric and phosphoric solutions. In contrast, in a perchloric solution, a metal-like behavior is observed.

For getting a deeper insight in the effect of anions on the passive film/solution interface, electrohydrodynamic impedance (EHD) was used. The method, based in the

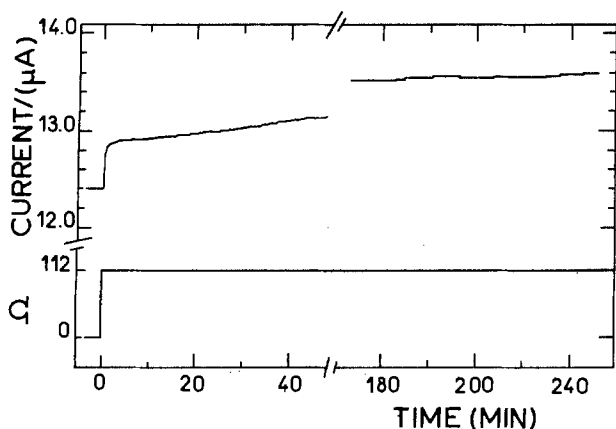


Fig. 2. Passive current/time transient in response to a step of angular velocity. Solid line: Fe/1M H₃PO₄; $E = 0.6V$.

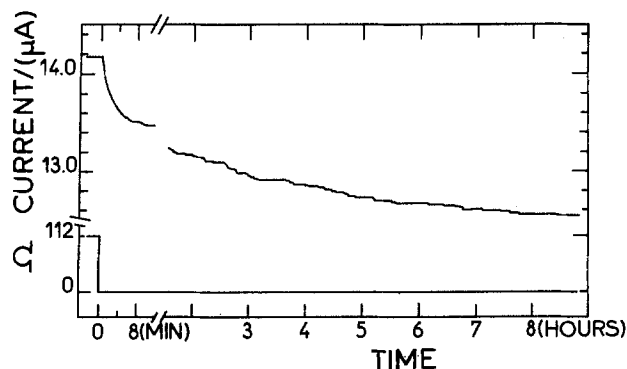


Fig. 3. Same as Fig. 2 but in the opposite direction.

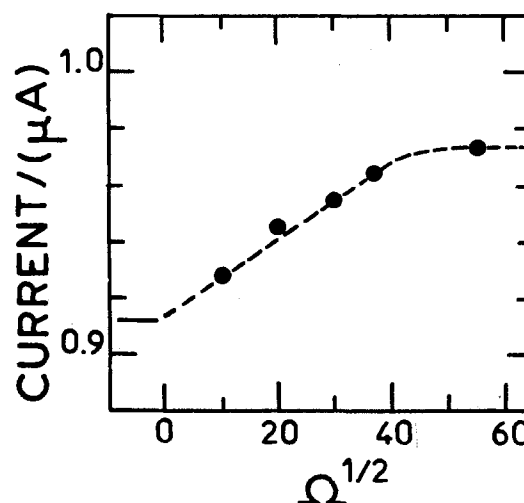


Fig. 4. Dependence of the passive current on the angular velocity. Fe/0.5M H₂SO₄; $E = 0.5V$.

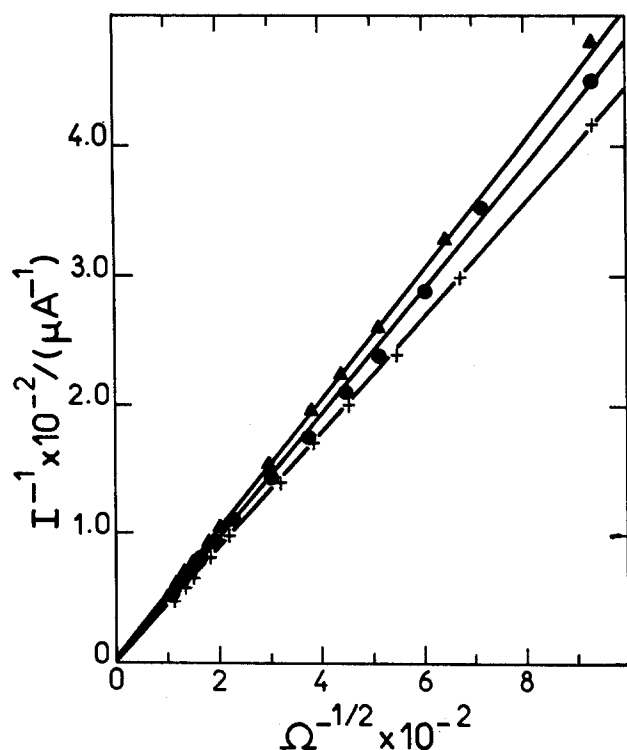


Fig. 5. I^{-1} vs. $\Omega^{-1/2}$ plots for the ferrocyanide oxidation on Pt for different supporting electrolytes. Electrode surface: 0.2 cm^2 ; $E = 0.4 \text{ V}$. ▲▲▲: $1 \text{ M H}_3\text{PO}_4$, ●●●: $0.5 \text{ M H}_2\text{SO}_4$, ++++: 1 M HClO_4 , $1 \text{ mM Fe(CN)}_6\text{K}_4$.

modulation of the angular velocity of the working electrode, was introduced (7) to investigate the coupling between heterogeneous kinetics and mass transport. The angular velocity Ω is modulated thus: $\Omega = \Omega^0 + \Delta\Omega \text{Re}(\exp \sigma jt)$ with $\Delta\Omega/\Omega^0 \ll 1$, σ being the angular frequency, $j = \sqrt{-1}$, and t is time. As a consequence, the different quantities related to mass transport are modulated allowing definition of an electrohydrodynamic impedance: $\partial I/\partial \Omega|_E$ under potentiostatic conditions (7-9).

EHD data obtained for different mean velocities and plotted as reduced amplitude $A(p)/A(o)$ vs. the reduced frequency p ($p = \sigma/\Omega^0$) are shown in Fig. 7, curves B, C, D, for the ferrocyanide oxidation on passive iron in perchloric, sulfuric, and phosphoric solutions. Fig. 7A represents the theoretical curve for a diffusion-controlled electrochemical reaction (7-9). Figure 7B and 7C shows that for

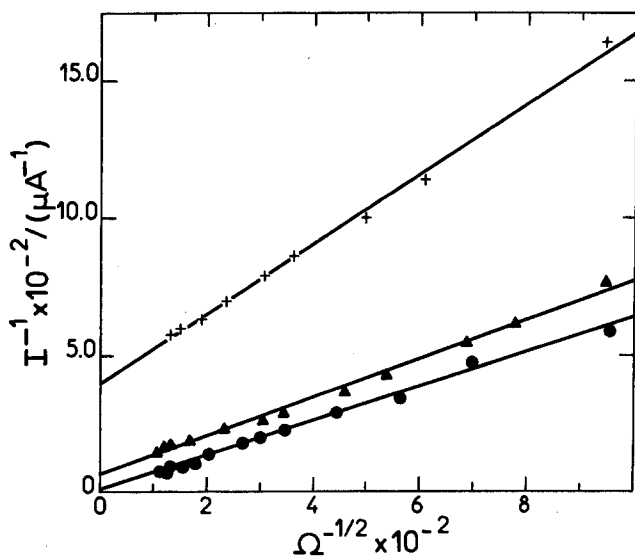


Fig. 6. I^{-1} vs. $\Omega^{-1/2}$ plots for the ferrocyanide oxidation on passive iron for different electrolytes. ++++: $1 \text{ M H}_3\text{PO}_4$; $E = 0.65 \text{ V}$. ▲▲▲: $0.5 \text{ M H}_2\text{SO}_4$; $E = 0.6 \text{ V}$. ●●●: 1 M HClO_4 ; $E = 0.35 \text{ V}$. $1 \text{ mM Fe(CN)}_6\text{K}_4$.

Table I. Diffusion coefficient and $I_{\Omega \rightarrow \infty}$ limit for the ferrocyanide oxidation on Pt in different supporting electrolytes. Ferrocyanide concentration: 1 mM ; $E = 0.4 \text{ V}$ (data obtained from Fig. 5)

Solution	D ($\text{cm}^2 \text{ s}^{-1}$)	$I_{\Omega \rightarrow \infty}$ (A cm^{-2})
1 M HClO_4	4.5×10^{-5}	3.8×10^{-2}
$1 \text{ M H}_2\text{SO}_4$	3.7×10^{-5}	4.1×10^{-3}
$0.5 \text{ M H}_2\text{SO}_4$	4.0×10^{-5}	2.5×10^{-2}
$1 \text{ M H}_3\text{PO}_4$	3.7×10^{-5}	2.0×10^{-2}

Table II. Diffusion coefficient and $I_{\Omega \rightarrow \infty}$ limit for the ferrocyanide oxidation on passive iron in different electrolytes. Ferrocyanide concentration: 1 mM (data obtained from Fig. 6)

Solution	D ($\text{cm}^2 \text{ s}^{-1}$)	$I_{\Omega \rightarrow \infty}$ (A cm^{-2})	E (V)
1 M HClO_4	2.0×10^{-5}	1.0×10^{-2}	0.35
$0.5 \text{ M H}_2\text{SO}_4$	2.2×10^{-5}	8.0×10^{-4}	0.60
$1 \text{ M H}_3\text{PO}_4$	1.0×10^{-5}	1.2×10^{-4}	0.65

perchloric and sulfuric acids the data can be reduced by the dimensionless parameter p , whatever the Ω value is, between 200 and 2000 rpm. Nevertheless, for sulfuric solution (curve B), the curves are translated from the theoretical curve (curve A) toward the low p values. In the case of phosphoric solution (curve D), in addition to the translation, a slight shift of the data is observed toward

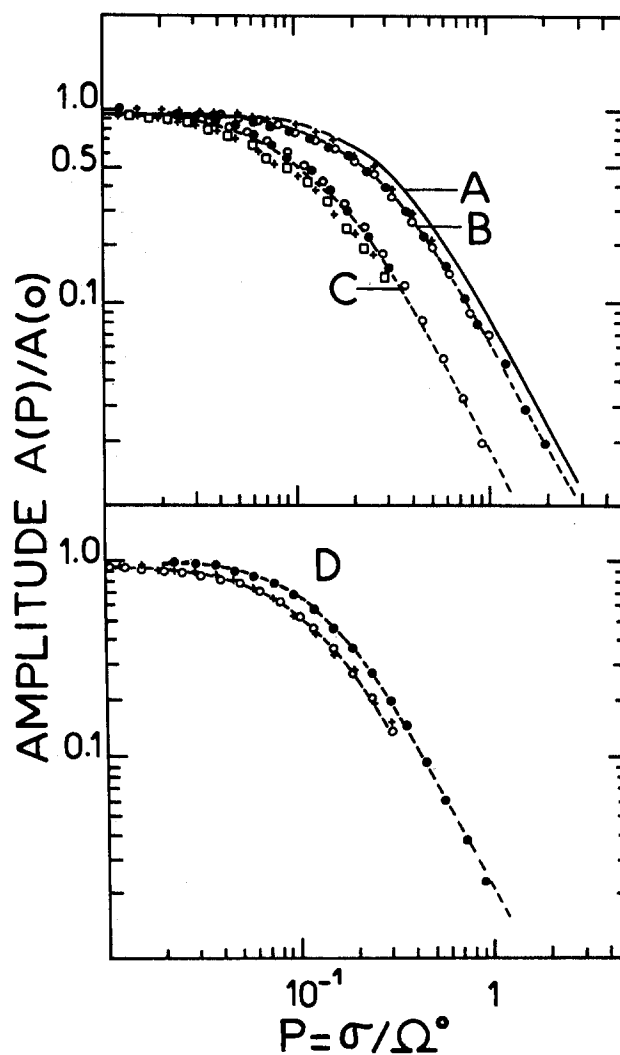


Fig. 7. Reduced amplitude of the potentiostatic EHD impedance. Ferrocyanide concentration: 1 mM . A: Theoretical curve. B: $\text{Fe}/1 \text{ M HClO}_4$; $E = 0.65 \text{ V}$. C: $\text{Fe}/0.5 \text{ M H}_2\text{SO}_4$; $E = 0.4 \text{ V}$. D: $\text{Fe}/1 \text{ M H}_3\text{PO}_4$; $E = 0.65 \text{ V}$. $\Omega = 200(\bullet)$, $600(\circ)$, $1200(+)$, $2000(\square)$.

the low p values when Ω changes from 200 to 600 rpm. However, changes of Ω from 600 to 2000 rpm produce no additional translation of the curves. Phase shift *vs.* reduced frequency plots confirm these observations.

It was shown that a translation of the data toward the low p values as Ω increases characterizes the EHD impedance of a reaction taking place on an electrode where a solid porous layer acts as a barrier between the active surface and the electrolyte (10). A new feature from the EHD impedance of the ferrocyanide oxidation on passive iron in sulfuric solutions is the reduction of the data at different Ω to a single curve translated from the theoretical one. The EHD results may be analyzed together with the observations described in Ref. (1). From the short time response of the current to an angular velocity transient (Fig. 2 and 3), it could be concluded that the electrode behaves like a usual mass-transfer-limited interface in the mixed kinetics domain. However, the long time current/time profile under constant angular velocity (staircase profile) suggests a simultaneous effect of erosion as a consequence of frictional shearing stress and/or centrifugal forces acting on a loosely structured film. A possible explanation of the EHD diagrams in the case of sulfuric solutions is also based on the presence of a loosely structured film whose thickness decreases as Ω increases. This film should attain a more solid structure, in the case of phosphoric solution, leading to a nonreducibility of the EHD experimental data for Ω values of 200 and 600 rpm. For greater angular velocities, the film thickness dependence on Ω reoccurs.

Mechanical damage to the passive iron/acid solution interface can also be induced by ultrasonic waves (11). This could be extremely relevant to erosion-corrosion processes.

The electrochemical impedance diagrams for the oxidation of ferrocyanide on passive iron in the different solutions can be analyzed as a parallel combination of the film response itself and of the electrochemical oxidation taking place on its surface. The impedance diagram characteristic of the iron passive system in acid media is shown in Fig. 8A. As discussed previously (1), it consists of three frequency domains: a capacitance loop at relatively high frequencies (HF capacitive loop), an inductive loop at medium frequencies (MF domain), and a capacitive domain at low frequencies (LF capacitive branch). The HF loop can be characterized by its real axis intercept R_{HF} .

In Fig. 8B is shown the impedance diagram for the oxidation reaction alone, calculated by subtracting the contribution of the passive electrode in the case of sulfuric acid at a potential where a mixed kinetics takes place. A fraction of a transfer reaction loop, at high frequencies, followed by a diffusion loop are observed. From the frequency spacing on the latter and the diffusivity coefficient (Table I), a δ value of 90 μm is found for $\Omega = 110$ rpm. It can be ascribed to the diffusion layer in the solution.

At low frequencies, there is an increase of the impedance in the frequency region interfering with the diffusion loop (Fig. 8B). If ferrous ions are present in the solution (from the active/passive transition), the mean current decreases during the impedance measurement in the low frequency domain ($f < 1$ mHz), changing the steady-state polarization conditions. Probably, the film growth process induces the precipitation of $(\text{Fe}(\text{CN})_6)_2\text{Fe}_3$, blocking the access of ferrocyanide to the active surface.

Fe(II) to Fe(III) oxidation.—Contrary to the observation in alkaline solutions (pH 8.4) (12, 13), the current of the passive iron/ferrous ion system in sulfuric and perchloric solutions depends on potential.

In the case of sulfuric solutions, two potential regions are distinguished, as shown in Fig. 9. In the first one, the current increases linearly with potential. In the second one, for potential more anodic than 0.7V, a Tafel relationship is verified. The presence of these two domains is independent of the polarization direction. Furthermore, the

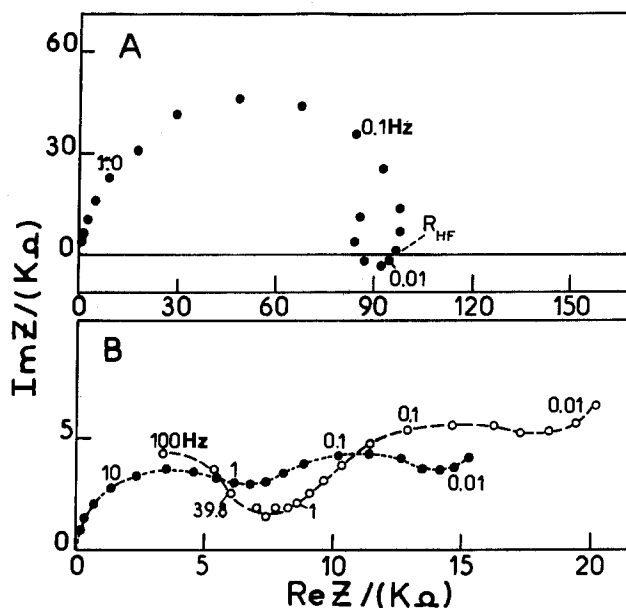


Fig. 8. A: Complex impedance diagram, Fe/0.5M H_2SO_4 ; $E = 0.3\text{V}$. B: (●●●) Experimental complex impedance diagram for the oxidation of ferrocyanide 1 mM on Fe/0.5M H_2SO_4 , $E = 0.3\text{V}$, $I = 14.6\ \mu\text{A}$, $\Omega = 112$ rpm. (○○○) Complex impedance diagram relative to the oxidation of ferrocyanide calculated by subtracting the contribution of the passive film (see text).

same results are obtained if the electrode is first passivated at each potential and then ferrous ions are added. In the case of the Fe/ HClO_4 system, only the first domain is accessible (Fig. 9) since at higher potentials a transpassive dissolution occurs.

At constant potential, the current increases linearly with the ferrous ion concentration (14). Nevertheless, the ratio of the oxidation current to the passive current is practically the same in sulfuric and perchloric media. In agreement with the passive current ratio, for the same potential and ferrous ion concentration, the oxidation current is 110 times greater in Fe/0.5M H_2SO_4 than in Fe/1M HClO_4 (Fig. 9). This behavior strongly differs from that observed in a solution containing ferrocyanide ions. The presence of ferrous ions seems to interfere with the film properties in such a way as to restrain the rate of charge transfer to a level correlated with the initial passive current. The formation of a ferrous-enriched layer is ex-

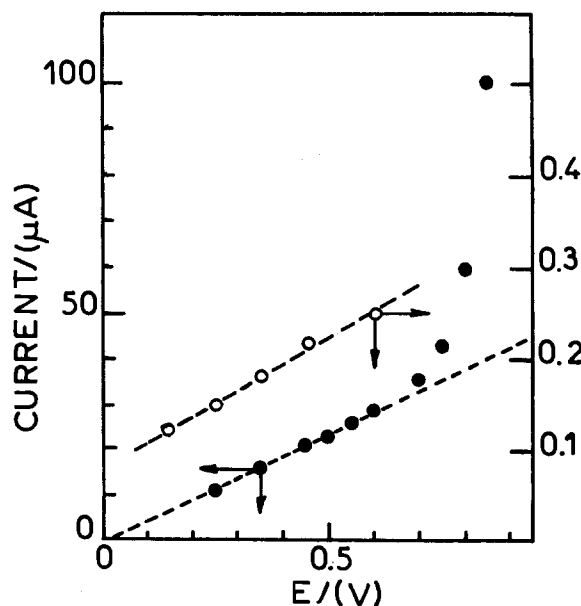


Fig. 9. Relation between potential and current for: (●●●) Fe/0.5M $\text{H}_2\text{SO}_4 + 0.14\text{M Fe(II)}$, and (○○○) Fe/1M $\text{HClO}_4 + 0.14\text{M Fe(II)}$.

pected from the cation substitution properties of iron oxides and oxyhydroxides (15). Consequently, the slow transformation of the film could lead to a change in the current. For instance, the Fe/0.5M H₂SO₄ system reacts stepwise to a ferrous ion addition. However, when the electrode is passivated in the first potential region, after the first sudden increase, the current evolves slowly. After 5 days of polarization, the current triples its initial stepwise value.

As proved by Raman spectroscopy, after 68h of polarization in the presence of ferrous ions, the layer transformation leads to pure magnetite as the potential approaches the transition domain in Fig. 9 (0.7V). Contrarily, at the same potential and polarization time, Raman spectroscopy reveals a mixture of hematite and magnetite in the absence of ferrous ions (16).

In other words, the transition observed around 0.7V may be interpreted as a critical potential at which percolation (17) gives rise to a bulk conductivity in the layer.

It is noticeable that this change in the film properties detected by redox and optical measurements is not related to any observable modification of the electrochemical behavior of passive iron. This could be easily understood by considering that optical and electronic behavior, on one hand, and ionic transport involved in passive corrosion, on the other hand, are related to the properties of the passive film material at two different scales.

As is shown in Fig. 10, the impedance diagram in this first potential domain consists of a high frequency capacitance loop and a LF domain, characterized by a 45° straight line, suggesting a diffusion limiting process. The $R_{HF}I$ product is close to 100 mV, as in the case of passive iron in absence of ferrous ions (1), in agreement with an oxidation current depending on the same process as the passive current.

In this potential domain as the current rises linearly with the potential (Fig. 9), the low frequency limit of the impedance must tend to a real constant value. From the I vs. E plot (Fig. 9), a resistance of 20 kΩ is calculated as the limiting value of the impedance for the Fe/0.5M H₂SO₄ + 0.14M Fe(II) system. For the Fe/1M HClO₄ + 0.14M Fe(II) system, a limiting resistance of 3 MΩ is obtained. Nevertheless, it is not possible to attain the low frequency limit of the impedance since at frequencies lower than 1 mHz the measuring signal by itself starts to increase the mean dc current, thus changing the polarization condition. There is an interaction, in the low frequency domain, between the film processes (film growth) and the kinetics of the oxidation reaction. This interaction is not expected from the potentiostatic polarization curves' showing little hysteresis.

Anion effect.—It is well known that the physicochemical properties of colloidal dispersions of iron oxides in aqueous solutions are strongly influenced by the counterion adsorption (18-24). Its influence depends on pH according to the point of zero charge value (pzc: pH at which the adsorbed H⁺ concentration equals the adsorbed OH⁻ concentration in the absence of specific ion adsorption). In the case of hematite, one of the possible film

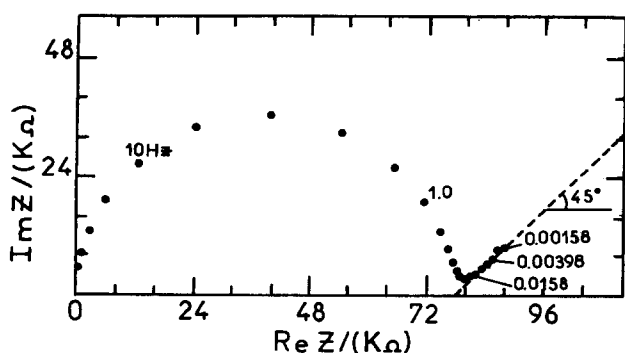


Fig. 10. Complex impedance diagram for Fe/0.5M H₂SO₄ + 0.05M Fe(II); $E = 0.5V$; $I = 14.7 \mu A$.

constituents, the pzc is placed at near neutral pH (pH 8.5) (18, 19, 22-24). Then, according to the pH of the solution, anions or cations will be adsorbed. The acid domain is influenced by anion adsorption. The ion-surface interaction is strongly related to the surface properties and to the nature of the ion, principally its electrostatic field strength (charge-to-size ratio); according to this, for a given surface there are two different types of interactions. The first one occurs with ions having a high electrostatic field, which is, therefore, a structure promoter for the surrounding water molecules. The second type includes large ions with relatively weak field strength, which are less heavily hydrated and therefore act as structure breakers (28).

According to adsorption studies on colloidal hematite, chloride, sulfate, perchlorate, and phosphate anions can be classified according to their increasing interactions with the surface as follows: chloride \approx perchlorate < sulfate < phosphate (19, 21, 28). Phosphate anion adsorption is so exceptionally strong that under special conditions the phosphate becomes a potential-determining ion (19). Contrarily, the anions leading to pitting corrosion are not specifically adsorbed on the oxide surface.

Anions are also known to play an important role in the chemical synthesis of iron oxides and oxyhydroxides (25-27). They even affect the chemical nature of oxyhydroxides (26, 27). For instance, chloride is known to induce β FeOOH formation.

Anions affect the crystallization process as well in the chemical formation of magnetite (25, 27). For instance, chloride yields only exceedingly small magnetite particles. In contrast, sulfate allows magnetite particles of a broad range of diameters.

It seems that this data can be extrapolated profitably to be applied to the passive film in various environmental conditions. Additional support is provided by the fact that anion sequences are the same according to either their surface interaction with colloidal iron oxide, as stated above, or their effect on passive current, as emphasized in Ref. (1). From these observations, it is possible to predict an important influence of cations on the iron passive current at pH > 8.5. It is noteworthy that pH 8.5, boric-borate buffered solutions, in which most of passivity investigations was carried out, corresponds precisely to the pzc of hematite and magnetite (18, 19, 23, 24). At this particular pH, the solubility of the oxides attains its minimum value (23,24).

Therefore, according to these basic properties of colloidal iron oxides, two interactions with the film material are to be considered: (i) surface interactions, (ii) bulk interactions during formation modifying the chemical and crystallographical properties of the film.

In order to investigate which of these effects is more relevant to the passive iron electrode, two types of experiments were performed: (i) measurement of the steady-state passive current as a function of the composition of a binary mixture of anions, (ii) analysis of composition transients.

Binary mixture.—Once the electrode is passivated in a given electrolyte (A), increasing amounts of a different acid solution (X) were successively added to the solution under potentiostatic conditions. A steady-state value is reached after each addition. Figure 11 shows the normalized current $I_p([X]/[A])/I_p([X])$ as a function of electrolyte composition $[X]/[A]$. In both cases investigated, the binary mixture is enriched in the acid giving rise to the higher passive current in pure solutions, and an increase of the normalized current is observed. Nevertheless, perchlorate is more easily displaced by sulfate than sulfate is by phosphate. Unfortunately, in contrast with colloid studies (21, 29), we have no access to the surface concentration of anions, making the analysis impossible in terms of adsorption isotherms.

Composition transients.—To study how anions influence the passive film to lead to a current strongly dependent on the solution composition (1), the effect of composition

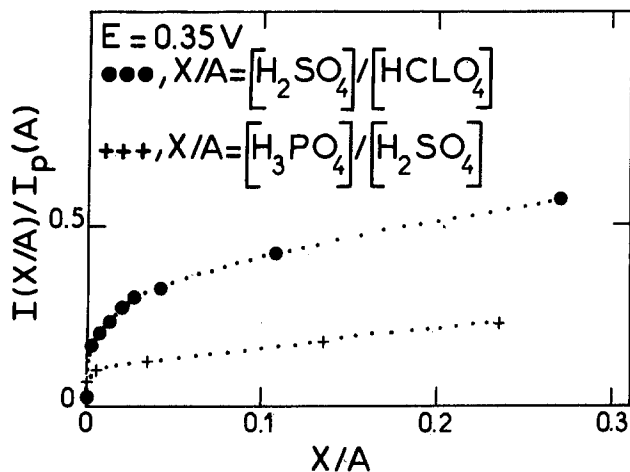


Fig. 11. Normalized current as a function of the composition of a binary acid mixture at constant pH.

transients was investigated. After 15h of passivation at 0.35V in 1M $H_2SO_4 + Na_2SO_4$, pH 0.95 solution, the electrolyte was changed to 1M H_3PO_4 under polarization using the electrochemical cell described in the Experimental section (Fig. 1). The current/time curve observed in Fig. 12A shows that the I_p value characteristic of the Fe/1M H_3PO_4 system is attained after about 30 min. The same type of curve is observed when 1M $HClO_4$ is replaced by 1M H_2SO_4 , i.e., when the replacement is in the direction of increasing I_p . However, when this sequence was inverted in the direction of diminishing I_p , the current/time profile strongly changes. The major part of the current change is recorded in the first minutes following the composition transient. Finally, a slow process lasting several hours leads to the steady-state I_p value characteristic of the passive iron in the new solution. As shown in Fig. 12B, 80% of the current change occurs in the first minute. The first region of the current/time curve is not influenced by the angular velocity of the electrode. Contrarily, the second region depends on the angular velocity: if the same experiment as shown in Fig. 12B is repeated with a rotating electrode ($\Omega = 2.800$ rpm), the second domain of the transient is reduced by about 4h.

These results clearly establish the dynamic behavior of the passive iron/acid solution interface with respect to an-

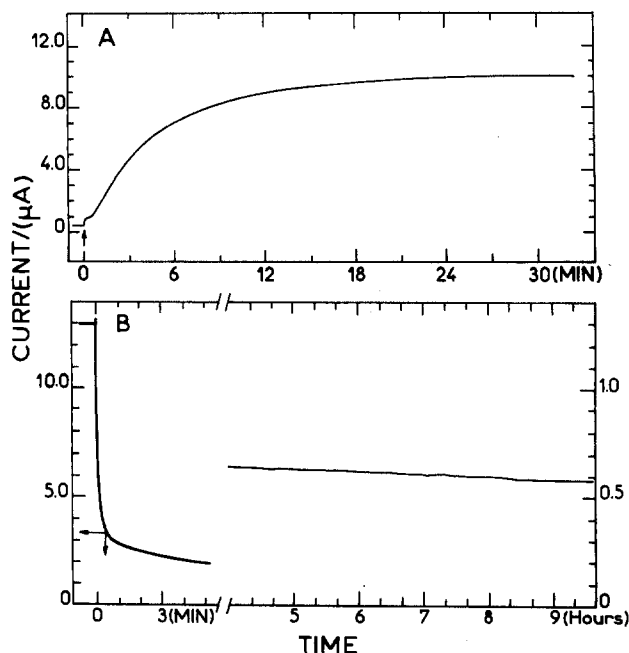


Fig. 12. Passive current/time response to a composition transient. A: From 1M $H_2SO_4 + Na_2SO_4$, pH = 0.95 to 1M H_3PO_4 . B: Opposite direction.

ions. However, both types of transients cannot be expressed as a unique analytical function in the full time range, which reveals the complexity of the process. Nevertheless, the transient toward lower passive current (Fig. 12B) clearly shows at least two types of interactions. The first one may be related to a fast anion bonding to the film surface which blocks the passive dissolution. The second slow part of the transient, affected by the angular velocity, may be related to anion penetration in the film itself. As supported by the effect of the angular velocity, the part of the film under hydrodynamic influence is involved to some extent in this bulk process. A change in the film composition induced by anions can be also considered (30).

Conclusion

A large amount of experimental data relevant to the properties of the film electrolyte interphase have been obtained, allowing one to define a transition region of appreciable thickness and cohesion. This view lies in the sensitivity of the electrochemical behavior to the angular velocity of the disk electrode under the following conditions: (i) dissolution in the passive state, (ii) redox kinetics for which the steady state and nonsteady state (EHD impedance) in the laminar flow regime show the existence of a loosely structured boundary layer, (iii) long-term response of the passive current to transients of electrolyte composition.

It is noticeable that the dependence of the layer on the electrolyte composition defined in terms of its transport and hydrodynamic behavior obeys the same sequence as the passive current densities. Hardly detectable in the perchloric solution, it reaches its maximum effect in the phosphoric medium. Anions penetrate this layer, contributing to its properties. They are incorporated into its structure in such a way that they are exchanged with anions in solution. Furthermore, redox reactions allowed by the good electronic conductivity of the internal film, are controlled by mass transfer across this region. An intricate situation is found in the case of ferrous anions, a possible constituent of the layer, probably inducing modifications of its ionic and electronic properties.

In this paper, a clear attempt is made to establish a connection between passive iron and some basic properties of iron oxides, especially in their colloidal state. It seems that this approach of passivity, even though straightforward in the framework of the oxide theory, was not explored in the literature. The main features of anion interaction with passive film have been related to their adsorbability on the surface of micelles. A conclusion regarding the existence of a transition layer on top of the passive film is not entirely original since the possible existence of a gel-like or polymeric structure in neutral media was invoked by other authors (31-33). A consideration of colloidal iron oxides also strongly supports this description and may provide some kind of new approach to passivity studies. It is known that hematite particles in aqueous solutions consist of a bulk anhydrous oxide surrounded by a hydrated interface (23). Goethite ($\alpha FeOOH$) is proposed (23) for the hydrated layer since it is a more stable oxyhydroxide and it has a structure related to hematite with a lower symmetry. The $\alpha FeOOH$ lattice is characterized by two FeO layers between OH planes, giving an alternate sequence as: OH—FeO—FeO—OH · OH—FeO. This lamellar structure, including H-bonds between OH neighbors, allows water molecules and ions to be intercalated, resulting in a material of a highly flexible composition (15). Protection conferred by some elements such as Mo may be attributed to their accommodation in this structure by cation substitution (34).

The resulting picture of the passive film is that of a two-layer structure: an inner region [dealt with in Ref. (1)], nearly independent of the solution composition, in which most of the electrical field is located; and an outer transition region accommodating the composition effects and defining a local environment in which growth and dissolution of the underlying layer take place.

Manuscript submitted May 30, 1984; revised manuscript received ca. Dec. 5, 1984.

REFERENCES

- M. Keddarn, J. F. Lizée, C. Pallotta, and H. Takenouti, *This Journal*, **131**, 2106 (1984).
- A. C. Makrides, *ibid.*, **111**, 392 (1964).
- W. Schmickler, in "Passivity of Metals," R. P. Frankenthal and J. Kruger, Editors, p. 102, The Electrochemical Society Corrosion Monograph Series, Princeton, NJ (1978).
- F. N. Delnick and N. Hackerman, in "Passivity of Metals," R. P. Frankenthal and J. Kruger, Editors, p. 116, The Electrochemical Society Corrosion Monograph Series, Princeton, NJ (1978).
- V. Stimming and J. W. Schultze, *Electrochim. Acta*, **24**, 859 (1979).
- W. Schmickler, in "Fifth International Symposium on Passivity," p. 23, Société de Chimie Physique, Bombannes, France (1983).
- C. Deslouis, C. Gabrielli, Ph. Sainte-Rose Franchine, and B. Tribollet, *This Journal*, **129**, 107 (1982).
- C. Deslouis, C. Gabrielli, and B. Tribollet, *ibid.*, **130**, 2044 (1983).
- B. Tribollet and J. Newman, *ibid.*, **130**, 2016 (1983).
- C. Deslouis, M. Duprat, M. Keddarn, F. Moran, and B. Tribollet, Abstract 198, p. 306, The Electrochemical Society Extended Abstracts, Vol. 83-2, Washington, DC, Oct. 9-14, 1983.
- R. C. Alkire and S. Perusich, *Corros. Sci.*, **23**, 1121 (1983).
- M. Nagayama and M. Cohen, *This Journal*, **110**, 670 (1963).
- M. Nagayama and S. Kawamura, *Electrochim. Acta*, **12**, 1109 (1967).
- M. Keddarn, J. F. Lizée, C. D. Pallotta, and H. Takenouti, in "Fifth International Symposium on Passivity," p. 51, Société de Chimie Physique, Bombannes, France (1983).
- P. Pascal "Nouveau Traité de Chimie Minérale," Tome XVII, pp. 615-687, M. Masson, Editor, Paris (1967).
- R. Dupeyrat, M. Froelicher, A. Hugot-Le Goff, M. Masson, and C. Pallotta, in "Fifth International Symposium on Passivity," p. 101, Société de Chimie Physique, Bombannes, France (1983).
- J. W. Essam, *Rep. Prog. Phys.*, **43**, 834 (1980).
- A. Breewisma and J. Lyklema, *Discuss. Faraday Soc.*, **52**, 324 (1971).
- A. Breewisma and J. Lyklema, *J. Colloid Interface Sci.*, **43**, 437 (1973).
- L. Bolistrien and J. Murray, in "Chemical Modeling in Aqueous Systems," E. A. Jenne, Editor, Chap. 14, ACS Symposium Series 93, American Chemical Society, Washington, DC (1979).
- A. Davis and J. O. Leckie, *J. Colloid Interface Sci.*, **74**, 32 (1980).
- S. Kittaka and T. Morimoto, *ibid.*, **75**, 398 (1980).
- F. Y. Onoda and P. L. De Bruyn, *Surf. Sci.*, **4**, 48 (1966).
- G. A. Parks and P. L. De Bruyn, *J. Phys. Chem.*, **66**, 967 (1962).
- T. Sugimoto and E. Matijevic, *J. Colloid Interface Sci.*, **74**, 227 (1980).
- M. Kiyama and T. Takada, *Bull. Chem. Soc. Jpn.*, **45**, 1923 (1972); T. Ishikawa and K. Inouye, *ibid.*, **45**, 2350 (1972); S. Music, A. Vertes, G. Simmons, I. Czako-Nagy, and A. Leidheiser, *J. Colloid Interface Sci.*, **85**, 256 (1982).
- E. Matijevic, *Corrosion*, **35**, 264 (1979).
- F. Dumont and A. Watillon, *Discuss. Faraday Soc.*, **52**, 352 (1971).
- F. J. Hingston, A. M. Posner, and J. P. Quirk, *ibid.*, **52**, 334 (1971).
- A. Hugot-LeGoff and C. Pallotta, Submitted to *This Journal*.
- W. Revie, B. G. Baker, and J. O'M. Bockris, *This Journal*, **122**, 1460 (1975).
- W. E. O'Grady, *ibid.*, **127**, 555 (1980).
- R. W. Hoffman, in "Fifth International Symposium on Passivity," p. 147, Société de Chimie Physique, Bombannes, France (1983).
- R. Berneron, J. C. Charbonnier, R. Namdai-Irani, and J. Manenc, *Corros. Sci.*, **20**, 899 (1980).

Ellipsometric Study of Anodic Oxide Films on Titanium in Hydrochloric Acid, Sulfuric Acid, and Phosphate Solution

Toshiaki Ohtsuka, Minoru Masuda, and Norio Sato*

Electrochemistry Laboratory, Faculty of Engineering, Hokkaido University, Sapporo 060, Japan

ABSTRACT

The anodic oxide film on titanium has been studied by ellipsometry and SEM observation. *Ex situ* multiple-angle-of-incidence and *in situ* ellipsometric measurements allow the complex refractive index to be estimated at $\bar{n} = 2.3 - 2.9i$ for the titanium substrate and at $\bar{n} = 2.1 - 0.03i$ for the anodic oxide film at wavelength 546.1 nm. The anodic oxide film thickness increases linearly with potential in a range from -0.55 to 7.5 V (RHE) at the rate of 2.8 nm V^{-1} in phosphate solutions of pH 1.6-12.1, 2.5 nm V^{-1} in $0.1M$ HCl solution, and 2.4 nm V^{-1} in $0.1M$ H₂SO₄ solution. At potentials more positive than 7.5 V, the film breaks down, leading to the formation of a thick oxide film probably due to an increased ionic current through the breakdown sites. The film composition is estimated to be TiO₂(H₂O)_{1.4} or TiO_{0.6}(OH)_{2.8}, which suggests the presence of hydroxyl bridge in its bonding structure.

The physicochemical properties of anodic oxide films formed on titanium are of importance in understanding the corrosion stability and photoelectrochemical activity of titanium oxide and oxide-covered titanium, which have attracted interest in recent years in the field of photoelectrode materials.

There has been a number of studies on the passivation of titanium dealing with the mechanism of active dissolution and active-passive transition in acidic aqueous media from electrochemical and impedance measurements (1-6). Armstrong *et al.* (1) and Harrison *et al.* (7) found that titanium dissolves producing Ti (III) ion in the active potential region and Ti (IV) ion in the passive potential region. Impedance measurements have shown that the electrode capacitance of titanium decreases when the passivation

manifests itself on the polarization curve (1, 7). The film formation accompanying passivation was investigated in aqueous and anhydrous solutions by Laser *et al.* (8) and Smith *et al.* (9) using ellipsometry.

Many attempts have also been made to produce thick oxide films by anodization at high current efficiency. In some respects, titanium behaves as a typical valve metal, but the anodic oxide film is electrochemically less stable than the barrier films formed on Al, Ta, and Nb (10). McAleer *et al.* (10) investigated by optical interferometry the breakdown phenomenon during potentiostatic anodization of titanium at high scan rate and found that both oxygen evolution and rapid film thickening take place when the film breaks down. Yahalom *et al.* (11) investigated by use of TEM the anodic oxide film of titanium stripped from the metal substrate and detected the anatase type of diffraction pattern for the anodized oxide

*Electrochemical Society Active Member.

film subjected to breakdown and crystallization. Dyer *et al.* (12) employed ellipsometry to study the film growth on titanium during galvanostatic oxidation and obtained the relationship between film thickness, cell voltage, weight gain, and anodic charge passed.

In this work, the relation between potential and film thickness is examined for the anodic oxide films formed on titanium in aqueous solution of various pH values in a wide range of potential from 0 to 15V, including the passivation and anodization regions. Furthermore, the film breakdown is discussed on the basis of the thickness measurements and electron microscopic observation of the film.

Experimental

A titanium sheet of 99.85 weight percent (w/o) purity (impurity: C = 0.009, N = 0.004, O = 0.101, H = 0.0013, and Fe = 0.036%) was cut to specimens 10 × 15 mm with a small handle. The specimens were mechanically polished through to 2000 grid emery paper, degreased with acetone in an ultrasonic cleaner, and annealed in vacuum at 1030 K for 3h. They were further polished by alumina abrasives through to 0.5 μm and finally etched in an aqueous mixture of HF (2 volume percent [v/o]) and HNO₃ (4 v/o) for 2s at room temperature. After polishing, the small handle of the specimen connected with a lead wire was covered with silicon rubber sealant.

Electrolytes used are aqueous solutions of 0.1M (mol dm⁻³) H₂SO₄ (pH 0.9), 0.1M HCl (pH 1.1), and four mixtures of 0.1M H₃PO₄ and 0.1M Na₃PO₄ (pH 1.6, 4.6, 6.9, and 12.1). The solutions were prepared from doubly distilled water and analytical-grade reagents. Before transfer into the cell, the solutions were deoxygenated by injecting purified nitrogen gas for more than 24h in solution reservoirs, each of which is connected with the cell through a stopcock.

The electrolytic cell was a Pyrex vessel 100 cm³ in capacity with two optical quartz windows fixed at an angle of 140.64°.

Titanium ion dissolved into the solution during anodic oxidation was analyzed by a colorimetric method using hydrogen peroxide. All measurements were carried out at 298.3 ± 0.5 K. The electrode potential of titanium was measured in reference to a Ag/AgCl electrode and converted into the reversible hydrogen electrode potential scale in the same solution at P_{H₂} = 1 atm (RHE).

Two types of manual ellipsometers were used, one of which was a vertical type of ellipsometer (Rudolf Company Type 43702-200E) for *ex situ* measurements in air by the multiple-angle-of-incidence (MAI) method (13) and the other a horizontal type of ellipsometer (Mizojiri Company Type DV 36) for *in situ* measurements in the electrolytic cell. For these ellipsometers, filters were used to isolate a 546.1 nm light beam for mercury lamps. The polarizer and compensator were placed in the incidence light path, and the analyzer and detector in the reflected light path. The *ex situ* MAI method was adopted to determine the optical unknown parameters of the oxide-covered titanium; *i.e.*, the complex refractive index of titanium substrate $\bar{n}_3 = n_3 - ik_3$, complex refractive index of oxide film $\bar{n}_2 = n_2 - ik_2$, and film thickness d . The MAI measurement was carried out at four different angles of incidence, $\phi_1 = 45.0^\circ, 55.0^\circ, 65.0^\circ,$ and 75.0° , for the electrode which had been anodically oxidized, rinsed with doubly distilled water, and then stored in a desiccator at room temperature. Calculation of five unknown parameters ($n_3, k_3, n_2, k_2,$ and d) or three unknown parameters ($n_2, k_2,$ and d) was made to minimize the standard deviation

$$\text{std dev} = \left[\frac{\sum_{i=1}^N (2\Psi_i^M - 2\Psi_i^T)^2 + (\Delta_i^M - \Delta_i^T)^2}{2N-1} \right]^{1/2} \quad [1]$$

where Ψ_i^M and Δ_i^M are, respectively, experimental values of the relative amplitude ratio and the relative phase difference at an angle of incidence $\phi_{1,i}$, and Ψ_i^T and Δ_i^T are the theoretical values. The reason for the use of a factor of

two for Ψ in Eq. [1] is that Ψ must have an error limit one-half as large as that of Δ , because the Ψ and Δ have been obtained from the azimuths of polarizer, P , and analyzer, A , under the extinction condition in what is known as the first zone: $\Psi = A$ and $\Delta = 2P + 90^\circ$, where A and P have been measured at a similar degree of error limit. The *in situ* measurement was conducted at an angle of incidence $\phi_1 = 70.32^\circ$, and analysis was made by making experimental loci of Ψ and Δ fit theoretical curves computed using the optical parameters estimated by the MAI method. All the ellipsometric analysis calculations were carried out at Hokkaido University Computing Center (14).

Results

Polarization curve.—Figure 1 shows the anodic current density (c.d.) measured after 1h polarization of the original specimen at every designated potential in 0.1M HCl solution and in 0.1M H₂SO₄ solution. The average dissolution current c.d., i_{diss} , is also plotted, which was determined from the amount of Ti(IV) ion dissolved into solution during 1h polarization in 0.1M H₂SO₄ solution. In 0.1M H₂SO₄ solution, the active-passive transition is observed to occur at -0.2V. In 0.1M HCl solution, however, no active dissolution is observed. The passivation manifests itself in a potential range from -0.2 to 3.0V, beyond which oxygen evolution takes place. In the oxygen evolution potential region the polarization curve exhibits the Tafel slope as large as 2.3 V decade⁻¹, which is much greater than that of other transition metals, such as iron, nickel, and cobalt. Such a large Tafel slope is probably due to the large bandgap energy of semiconductive oxide films formed on titanium. In 0.1M HCl solution, pitting corrosion was observed at potentials more positive than 11V, and the anodic current greater than 1×10^{-3} A cm⁻² produced white corrosion precipitates speckling the specimen surface slightly colored dark blue due to interference of light. The average dissolution c.d. measured for 1h polarization in 0.1M H₂SO₄ solution increases slightly with potential, reaching 1×10^{-6} A cm⁻² at 12V. In 0.1M H₂SO₄ solution, the amount of Ti dissolved in the active potential region was found to be equivalent to Ti(III) dissolution. The polarization curve was also measured in phosphate solutions, which was similar to that obtained in 0.1M HCl solution (see Fig. 6).

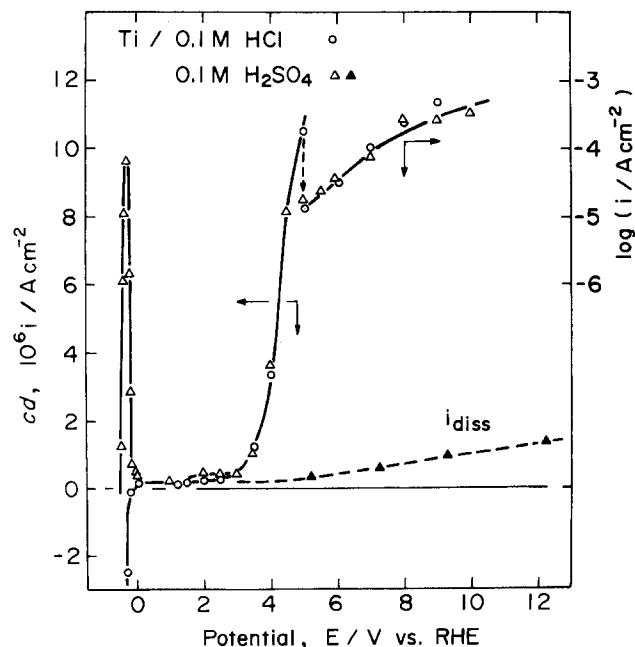


Fig. 1. Anodic current and average dissolution current as functions of potential for titanium electrode in 0.1M hydrochloric and 0.1M sulfuric acid solutions. The anodic current was measured at the end of 1h potentiostatic oxidation of the original specimen, and the average dissolution current was estimated from the amount of Ti(IV) ion dissolved into solution during 1h oxidation.

Ellipsometry.—To analyze the surface oxide film by ellipsometry, the complex refractive index, $\bar{n}_3 = n_3 - ik_3$, of the substrate metal must be known. In this work, the *ex situ* MAI method was applied to estimate the optical parameters of titanium metal and a thin air-formed oxide layer on the polished specimen surface. The result is shown in Fig. 2, where comparison is made between the measured values and the theoretical curves estimated by the least squares method. The optical parameters thus estimated with a mirror-like titanium surface provide the complex refractive index $\bar{n}_3 = 2.3(\pm 0.1) - 2.9(\pm 0.1)i$ for titanium metal, $\bar{n}_2 = 2.0(\pm 0.1) - 0.03(\pm 0.015)i$ for an air-formed oxide layer, and the film thickness $d = 2.9(\pm 0.5)$ nm. Figure 2 also shows the result obtained with a titanium electrode anodically oxidized at 7.35V in pH 6.9 phosphate solution, from which the values of $\bar{n} = 2.13 - 0.03i$ and $d = 25.3$ nm are determined with the above complex refractive index of titanium metal. Similar *ex situ* measurements by the MAI method were performed for a number of titanium electrodes anodically oxidized at various potentials in pH 6.9 phosphate solution and in sulfuric acid solution, and the average value of the complex refractive index of the anodic oxide film is found from the measurements to be $\bar{n}_2 = 2.2(\pm 0.1) - 0.03(\pm 0.005)i$.

Figure 3 shows the experimental loci of Ψ vs. Δ obtained from *in situ* ellipsometric measurements for a number of anodically oxidized titanium electrodes in a potential region from 1 to 10V in 0.1M HCl and 0.1M H₂SO₄ solutions. The solid line in Fig. 3 indicates a theoretical line along which a film with $\bar{n}_2 = 2.10 - 0.030i$ grows on the substrate with $\bar{n}_3 = 2.3 - 2.9i$. Similar loci of Ψ vs. Δ were obtained also in phosphate solutions at various pH values. The results are given in Fig. 4 along a theoretical line corresponding to the complex refractive index of the film formed in 0.1M H₂SO₄ and 0.1M HCl solution. As shown in Fig. 3 and 4, there is a fairly good agreement between the experimental loci and the theoretical line for the range of film thickness thinner than 30 nm. A slight deviation of the experimental loci from the theoretical line is observed for the film thicker than 30 nm, which may be attributed to the surface roughening described later. This deviation, however, appears to exert only a

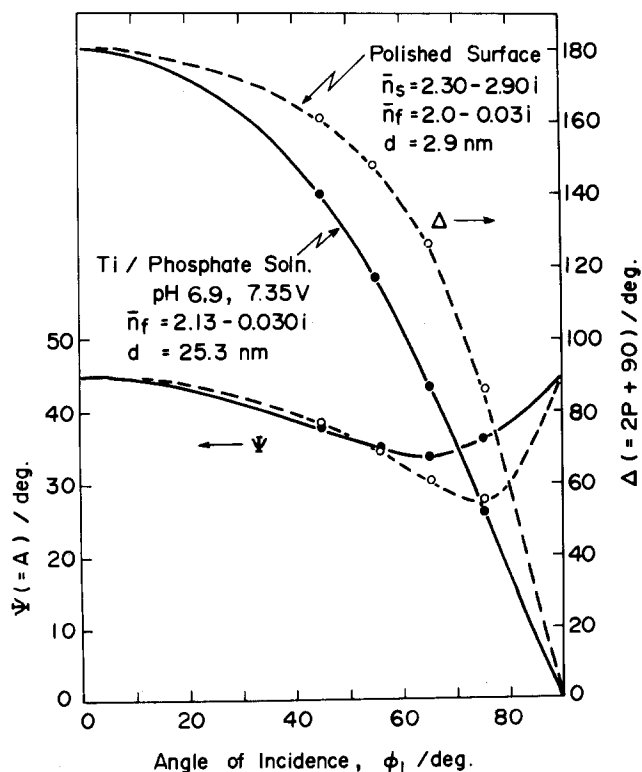


Fig. 2. Comparison between experimental Ψ and Δ at multiple angles of incidence and theoretical curves calculated from the optimum values of thickness and complex refractive index for the titanium substrate and the oxide film.

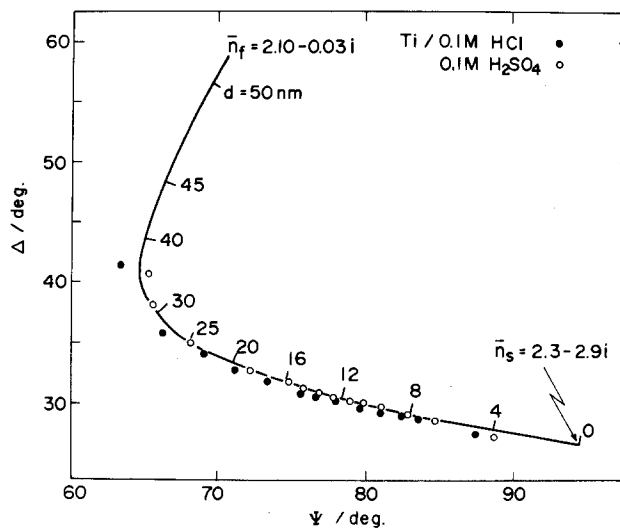


Fig. 3. Comparison between experimental Ψ and Δ measured *in situ* in 0.1M hydrochloric and 0.1M sulfuric acid solutions at an angle of incidence $\phi_1 = 70.32^\circ$ and a theoretical Ψ vs. Δ curve calculated for a growing film with $\bar{n}_2 = 2.1 - 0.03i$ on a substrate with $\bar{n}_3 = 2.3 - 2.9i$.

slight influence on the thickness estimation so that the same complex refractive index is used to evaluate the film thicker than 30 nm. The optical parameters estimated under this *in situ* condition is in agreement with the optical parameters obtained from the *ex situ* MAI measurement, except for a small difference in the refractive index of the oxide film, \bar{n}_2 . The change of the oxide film that might occur during storage was checked by MAI ellipsometry after removal of the specimen from the electrochemical cell and found to be inappreciable after 5 days of storage in desiccator.

Film thickness.—From the results shown in Fig. 3 and 4, the film thickness can be estimated. Figure 5 and 6 show the film thickness as a function of potential in 0.1M HCl, and 0.1M H₂SO₄, and phosphate solutions. Figure 6 also shows the anodic c.d. measured after 1h polarization at constant potential. The film thickness is observed to increase almost linearly with increasing potential up to 7.5V. At potentials higher than 7.5V, the thickness increases more steeply with potential and the reproducible results of thickness measurements are hardly obtained.

In the nearly linear thickness-potential curves a slight break is observed at about 3V, showing the film thickness/potential ratio 2.6 nm V⁻¹ at 0.0-3.0V, and 2.4 nm V⁻¹ at 3.0-7.5V in 0.1M HCl solution, and 2.5 nm V⁻¹ at 0.0-3.0V and 2.3 nm V⁻¹ at 3.0-7.5V in 0.1M H₂SO₄. No such break is seen in phosphate solutions, showing the thickness/potential ratio 2.8 nm V⁻¹ at 0.0-7.5V.

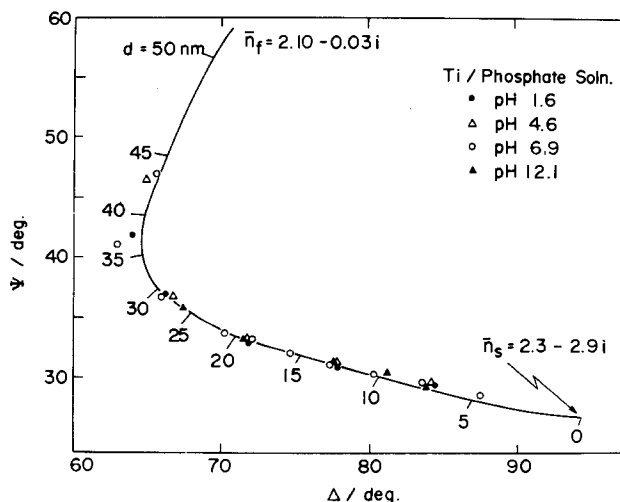


Fig. 4. Comparison between experimental Ψ and Δ measured *in situ* in phosphate solutions and a theoretical Ψ vs. Δ curve.

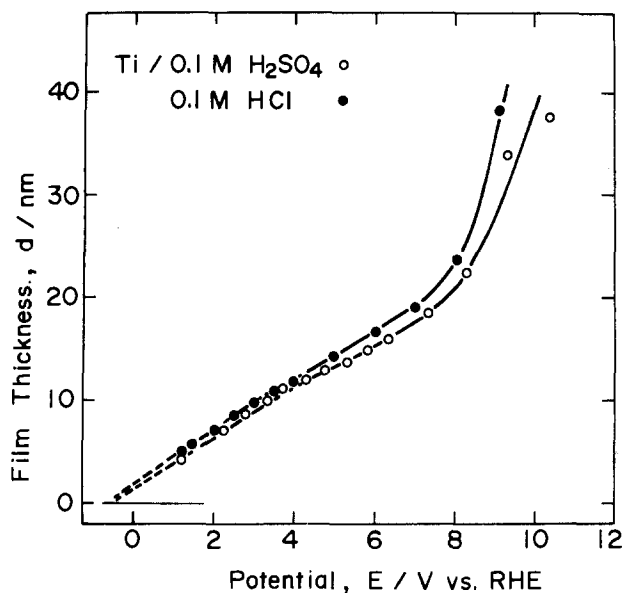


Fig. 5. Film thickness as a function of potential for the anodic oxide film formed on titanium by 1h potentiostatic oxidation in 0.1M hydrochloric and 0.1M sulfuric acid solutions.

The ratio of thickness to anodic charge passed was also measured by stepwise potential increase with a time interval of 1h. The result is shown in Fig. 7, from which the ratio is found to be $0.85 \text{ nm cm}^2 \text{ mC}^{-1}$ in pH 6.9 phosphate solutions. A slight scatter observed at 4.60V is due to the oxygen evolution reaction which consumes a part of anodic charge.

The galvanostatic film growth was also studied in pH 6.9 phosphate solution. Figure 8 shows the potential rise and film growth at constant anodic current. The thickness/charge ratio is $(d/Q) = 0.68 \text{ nm cm}^2 \text{ mC}^{-1}$ at $20 \mu\text{A cm}^{-2}$ and $(d/Q) = 0.71 \text{ nm cm}^2 \text{ mC}^{-1}$ at $5 \mu\text{A cm}^{-2}$, which are smaller than the $(d/Q) = 0.85 \text{ nm cm}^2 \text{ mC}^{-1}$ obtained for the potentiostatic film. This difference is probably caused by the film dissolution whose rate is dependent on the anodic c.d. (15). The linear potential rise and film growth are seen to level off at potentials more positive than 3V, where the oxygen evolution is taking place. The

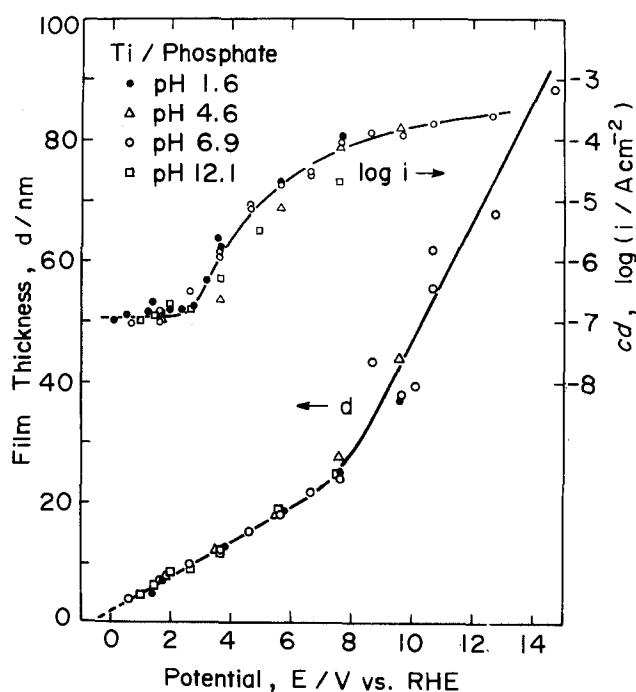


Fig. 6. Film thickness as a function of potential for the anodic oxide film formed on titanium by 1h potentiostatic oxidation in phosphate solutions at pH 1.6, 4.6, 6.9, and 12.1

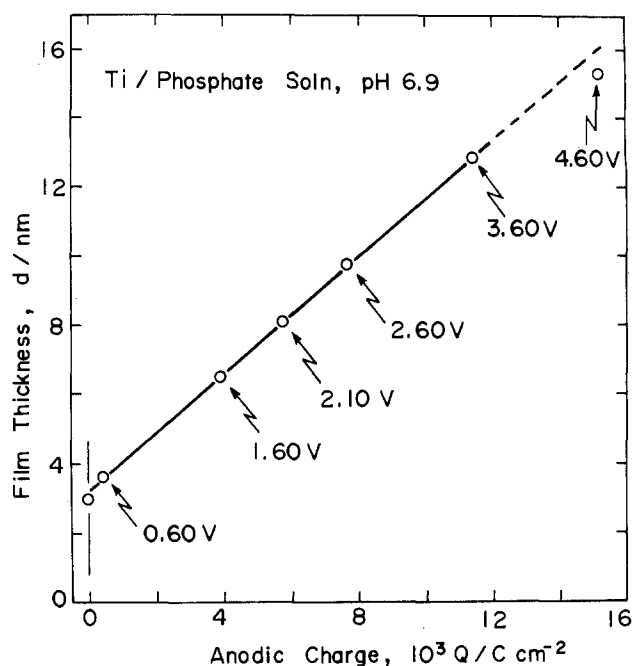


Fig. 7. Relationship between film thickness and anodic charge for the anodic oxide film on titanium by potentiostatic oxidation in pH 6.9 phosphate solution. The potential was increased stepwise at a time interval of 1h.

complex refractive index estimated for the galvanostatic film was found to be $n_2 = 2.10 - 0.03i$, which is consistent with the index obtained for the potentiostatic film.

Discussion

Complex refractive index.—The conventional ellipsometry at a fixed angle of incidence requires the oxide-free metal surface to estimate the complex refractive index of the metal. Smith *et al.* attempted to estimate by conventional ellipsometry the optical constant of a titanium electrode in HF solution where any surface oxide

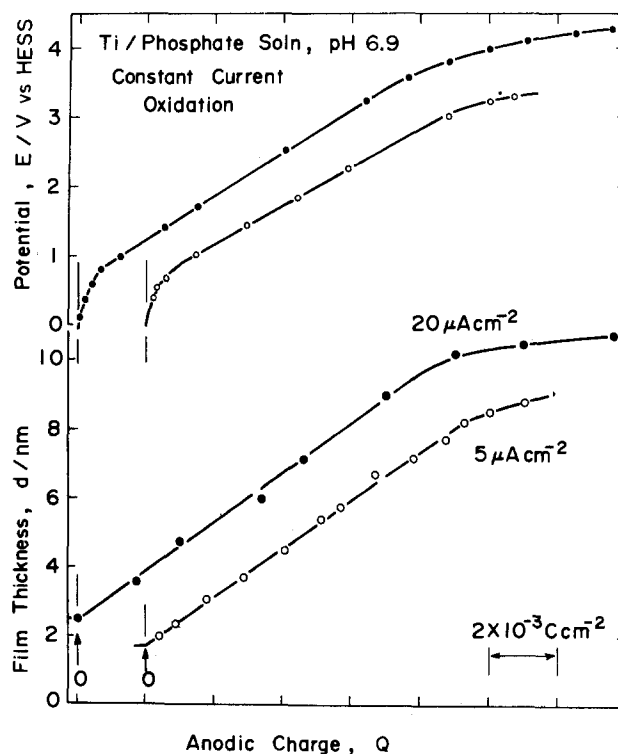


Fig. 8. Electrode potential and film thickness as functions of anodic charge passed during constant current oxidation of titanium in pH 6.9 phosphate solution.

layer would dissolve, leading to surface roughening. The electrochemical reduction of surface oxides, usually employed for iron and other metals, is incapable of producing the oxide-free bare titanium surface because of formation of surface hydride layer during cathodic reduction.

In this work, MAI ellipsometry has been employed to estimate the complex refractive index of titanium substrate covered with a surface oxide layer. This method is, in contrast with the conventional ellipsometry, capable of determining the five unknowns, n_2 , k_2 , d , n_3 , and k_3 , of a film-covered metal from a number of measurable parameters, Ψ and Δ , at different angles of incidence.

The complex refractive index of titanium at wavelength 546.1 nm found in the literature, shows some scatter ($n_3 = 2.0$ -3.1, $k_3 = 2.0$ -3.7), as listed in Table I. The index obtained in this work is relatively small compared with the reported values except by Andreeva (16) and Dyer *et al.* (12). It is known that the index measured by ellipsometry is sensitive to the specimen surface. In this work, the titanium specimen was slightly etched to remove a superficial polishing layer without roughening the surface.

The refractive index, n_2 , of the oxide film listed in Table I shows almost no scatter except for a value reported by Laser *et al.* (8). The anodic oxide film is found to possess the refractive index smaller than that of crystalline TiO_2 whose refractive index is larger than 2.5 for anatase, rutile, and brookite (21). The small refractive index may be attributed to the hydrated structure of the anodic oxide film.

The extinction index, k_2 , of the anodic oxide film obtained in this work indicates that the film is slightly light absorptive at wavelength 546.1 nm, though the film has been claimed to be transparent in literature. The slightly light absorptive nature may be explained by assuming the presence of ionic and electronic defects in the film.

Film growth.—The film growth of anodic oxide on titanium has been reported to obey the high field ion migration mechanism (22-24)

$$i = i_0 \exp(B\bar{E}) \quad [2]$$

where i_0 is ionic self-diffusion c.d. at zero field, \bar{E} electric field strength, and B a constant given as follows

$$B = zaF/RT \quad [3]$$

In Eq. [3], z and a indicate, respectively, the ionic valency and the half-jump distance (or the activation distance) of migrating ion. The validity of Eq. [2] can be examined on the results of galvanostatic oxidation (Fig. 8), where the electric field is calculated from the values of $(\partial E/\partial t)$ and $(\partial d/\partial t)$.

Table I. Complex refractive indexes of titanium and its anodic oxide film

Ref.	$n = n - ki$	Remarks
Titanium substrate ($\lambda = 546.1$ nm)		
(16)	2.10-2.02i	Ellipsometry
(9)	3.05-3.66i	Ellipsometry
(17)	2.5-3.4i ^a	Reflectance and transmittance spectroscopy
(18)	1.8-2.7i ^a	Reflectance spectroscopy
(19)	2.4-3.4i ^a	Reflectance spectroscopy
(12)	2.0-2.7i	Ellipsometry
(8)	(2.7 2.8)- (3.20 3.25)i	Ellipsometry
(20)	2.63-3.26i	Ellipsometry
Present work	2.3-2.9i	Ellipsometry
Anodic oxide film ($\lambda = 632.8$ nm)		
(9)	2.5-0.0i	Ellipsometry
(10)	2.5-0.0i	Reflectometry
Anodic oxide film ($\lambda = 546.1$ nm)		
(12)	2.1-0.0i	Ellipsometry
(8)	2.4-0.0i	Ellipsometry
(19)	2.2 (+0.05)- 0.0(+0.01)i	Ellipsometry
Present work	2.10-0.03i	Ellipsometry

^a Interpolated value.

$$\bar{E} = \left(\frac{\partial E}{\partial d} \right) = \left(\frac{\partial E}{\partial t} \right) \left(\frac{\partial d}{\partial t} \right)^{-1} \quad [4]$$

The \bar{E} vs. i relationship is given in Fig. 9, where the closed symbol indicates the result of potentiostatic 1h oxidation. From the plot in Fig. 9, the parameters of i_0 and B in Eq. [2] are found; $i_0 = 7.7 (\pm 2.0) \times 10^{-11}$ A cm⁻² and $B = 24 (\pm 5)$ nm V⁻¹. The value of i_0 is 100 times as large as that estimated by Johansen *et al.* (22) in aqueous ammonium borate solution and by Nishimura *et al.* (23) in aqueous chloride solution. Mizushima (24) reported a larger value of i_0 in anhydrous ethylene glycol. The value of B is fairly close to that obtained by other workers (22-24). From the value of B , the half-jump distance is found to be 0.16 nm for the migration of Ti(IV) ion, which is close to one-half of the distance between neighboring Ti ions in the lattice.

Film breakdown.—The linear relationship between film thickness and potential obtained under potentiostatic conditions has been shown to break at potentials more positive than 7.5V (Fig. 5 and 6). The abrupt thickening of the film above 7.5V may be attributed to the creation of lattice defects which increase the ionic leakage current. Observation with a scanning electron microscope (SEM; JEOL JSM-255) shows nearly the same surface morphology before and after oxidation at potentials more negative than 5V. At potentials more positive than 5.5V, a crater-conglomerate morphology with a single-crater diameter of about 3 μm is observed. Such a crater-like morphology was also reported by Yahalom *et al.* (11). At potentials more positive than 7.5V, the surface becomes rough, with a ripple-like appearance. From the surface observation described above, it appears that the breakdown of the anodic oxide film commences at 5.5V, producing a number of crater-like cracks, which will provide leakage paths for ionic current. The internal compressive stress induced by high field electrostriction will play an important role in the film breakdown, as proposed in a paper by Sato (25). At potentials more positive than 7.5V, the ionic current concentrates at the cracks, forming a thick oxide layer, whose thickness for unit voltage becomes greater than that of the film formed at more negative potentials.

Film composition.—Different models for the passive film on titanium have been proposed in literature, which assume either a unilayered or a multilayered structure. In this work, the unilayered model has been adopted, since the film was found to grow up along the theoretical curve

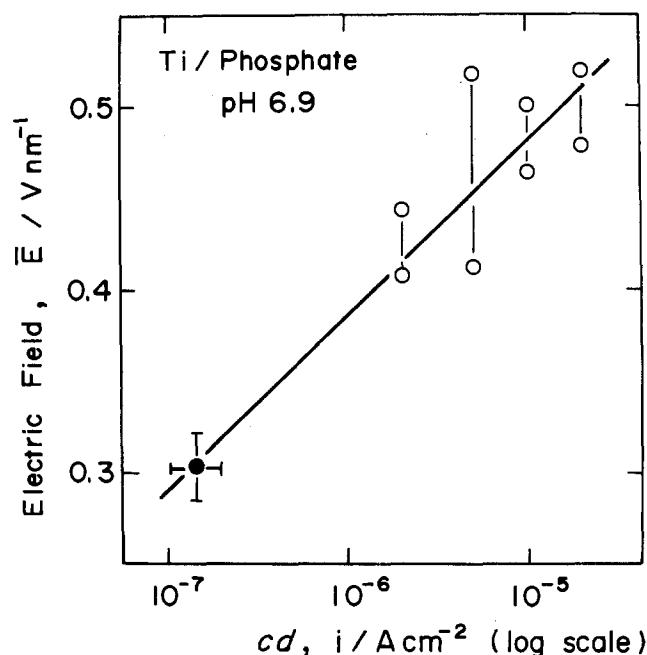


Fig. 9. Relationship between anodic current density and electric field strength for an anodic oxide film growing on titanium in pH 6.9 phosphate solution.

of the ellipsometric parameters drawn from a single-layer model.

The potential at zero film thickness is found to be $E = -0.55 \pm 0.10\text{V}$ from the linear thickness-potential plot shown in Fig. 5 and 6. This potential is very close to the transition potential from Ti_2O_3 to TiO_2 (26), suggesting that the passivation film is composed primarily of TiO_2 structure. From the large value of thickness-to-charge ratio and the small refractive index, it is suggested that the anodic oxide film contains some amount of water. Yahalom *et al.* (11) and Blondeau *et al.* (27) have observed electron diffraction patterns corresponding to anatase TiO_2 for the anodic films formed at potentials more positive than 50V, where the film breakdown takes place. Blondeau *et al.* (27) have also observed a quasiamorphous structure for the anodic oxide film formed at more negative potentials.

The thickness-to-charge ratio, $d/Q = 0.85 \text{ nm cm}^2 \text{ mC}^{-1}$, in a potential region less positive than 3.6V is 1.5 times as large as the theoretical value, $d/Q = 0.54 \text{ nm cm}^2 \text{ mC}^{-1}$, calculated from the density of crystalline anatase (21), $\rho = 3.84 \text{ g cm}^{-3}$, assuming the roughness factor, r , to be unity. This indicates that the anodic oxide film is hydrated. If we write the composition of the film as $\text{TiO}_2(\text{H}_2\text{O})_y$, the content of water, y , may be calculated by Eq. [5]

$$y = \left[\left(\frac{d}{Q} \right) \left(\frac{4F\rho}{r} \right) - M_{\text{TiO}_2} \right] \frac{1}{M_{\text{H}_2\text{O}}} \quad [5]$$

where M_{TiO_2} and $M_{\text{H}_2\text{O}}$ are the molecular weights of TiO_2 and H_2O , respectively. By use of $(d/Q) = 0.85 \text{ nm cm}^2 \text{ mC}^{-1}$ obtained above and $\rho = 3.2 \text{ g cm}^3$ measured by Dyer *et al.* (12), we obtain $y = 1.4$ and hence the composition of the anodic oxide film to be represented by $\text{TiO}_2(\text{H}_2\text{O})_{1.4}$ or $\text{TiO}_{0.6}(\text{OH})_{2.8}$. From the composition estimated above, it is evident that the film contains a large number of hydroxyl bridges in its bond structure. The presence of hydroxyl bridge may be confirmed by reversible absorption and desorption of hydrogen ions in the film observed by Dyer *et al.* (28).

Conclusion

The following conclusions may be drawn.

1. The complex refractive index at wavelength 546.1 nm is found to be $\bar{n} = 2.3-2.9i$ for the titanium substrate and $\bar{n} = 2.1-0.03i$ for the anodic oxide film formed on titanium in aqueous solution.

2. The anodic oxide film thickens linearly with increasing potential in a potential region from -0.55 to $+7.5 \text{ vs. RHE}$ under the condition of potentiostatic oxidation for 1h. The rate of thickness increase with potential is 2.8 nm V^{-1} in phosphate solutions (pH 1.6-11.5), 2.5 nm V^{-1} in 0.1M HCl solution, and 2.4 nm V^{-1} in 0.1M H_2SO_4 solution.

3. Breakdown of the anodic oxide film occurs at potentials more positive than 7.5V, beyond which a thick film

is formed. The thickening of the broken film is attributed to an increased ionic leakage current at breakdown sites.

4. The anodic oxide film is represented by $\text{TiO}_2(\text{H}_2\text{O})_{1.4}$ or $\text{TiO}_{0.6}(\text{OH})_{2.8}$, which contains a large density of hydroxyl bridge in its bonding structure.

Manuscript submitted July 23, 1984; revised manuscript received Nov. 27, 1984.

Hokkaido University assisted in meeting the publication costs of this article.

REFERENCES

1. R. D. Armstrong and R. E. Firman, *J. Electroanal. Chem.*, **34**, 391 (1972).
2. E. J. Kelly, in "Proceedings 5th International Congress on Metallic Corrosion," N. Sato, Editor, p. 137, NACE, Houston, TX (1974); *This Journal*, **123**, 162 (1976).
3. E. J. Kelly, *ibid.*, **126**, 2064 (1979).
4. J. P. Frayret, R. Pointean, and A. Caprani, *Electrochim. Acta*, **26**, 1783 (1981); *ibid.*, **26**, 1789 (1981).
5. C. Caprani and J. P. Frayret, *ibid.*, **24**, 835 (1979).
6. J. J. Kelly, *ibid.*, **24**, 1273 (1979).
7. J. A. Harrison and D. E. Williams, *ibid.*, **27**, 891 (1982).
8. D. Laser, M. Yaniv, and S. Gottesfeld, *This Journal*, **125**, 358 (1978).
9. T. Smith and F. Mansfeld, *This Journal*, **119**, 663 (1972).
10. J. F. McAleer and L. M. Peter, *ibid.*, **129**, 1252 (1982).
11. J. Yahalom and J. Zahavi, *Electrochim. Acta*, **15**, 1429 (1970).
12. C. K. Dyer and J. S. L. Leach, *This Journal*, **125**, 1032 (1978).
13. T. Ohtsuka, *Bull. Jpn. Inst. Metals*, **20**, 614 (1981).
14. K. Kudo and N. Sato, *Bull. Fac. Eng. Hokkaido Univ.*, **61**, 45 (1971).
15. K. D. Allard and K. E. Heusler, *J. Electroanal. Chem.*, **77**, 35 (1977).
16. V. V. Andreev, *Corrosion NACE*, **20**, 37 (1964).
17. P. B. Johnson and R. W. Christy, *Phys. Rev. B.*, **9**, 5056 (1974).
18. D. W. Lynch, C. G. Olson, and S. H. Weaver, *ibid.*, **11**, 3617 (1975).
19. G. Blondeau, M. Froelicher, M. Froment, and A. Hugot-Le Goff, *Thin Solid Films*, **38**, 261 (1976).
20. C. P. De Pauli, M. C. Giordano, and J. O. Zerbino, *Electrochim. Acta*, **28**, 1781 (1983).
21. "CRC Handbook of Chemistry and Physics," 61st., ed., R. C. Weast, Editor, p. B-159, CRC Press Inc., Boca Raton, FL (1980).
22. H. A. Johansen, G. B. Adams, Jr., and P. Van Rysselberghe, *This Journal*, **104**, 339 (1957).
23. R. Nishimura and K. Kudo, *Corros. Sci.*, **22**, 637 (1982).
24. W. Mizushima, *This Journal*, **108**, 825 (1961).
25. N. Sato, *Electrochim. Acta*, **16**, 1683 (1971).
26. P. Pourbaix "Atlas of Electrochemical Equilibria in Aqueous Solution," Pergamon Press, Oxford (1966).
27. G. Blondeau, M. Froelicher, M. Froment, A. Hugot-Le Goff, M. Brien, R. Calsou, and P. Larroque, *J. Microsc. Spectrosc. Electron.*, **2**, 27 (1977).
28. C. K. Dyer and S. S. L. Leach, *Electrochim. Acta*, **23**, 1387 (1978); *This Journal*, **125**, 23 (1978).

Analysis of Passive Films on Stainless Steel by Cyclic Voltammetry and Auger Spectroscopy

N. Ramasubramanian,* N. Preocanin, and R. D. Davidson

Atomic Energy of Canada Limited, Chalk River Nuclear Laboratories, Chalk River, Ontario, Canada K0J 1J0

ABSTRACT

Anodic passivation of Type 316L stainless steel in a borate-boric acid buffer solution was studied using cyclic voltammetry and Auger spectroscopy. Based on a comparison with the results obtained on the metals (iron, chromium, and nickel), the reduction peaks appearing in the voltammograms for the steel were attributed to the reductive dissolution of a ferric oxide and to valence transitions associated with chromium and nickel in the oxide. It is shown that cyclic voltammetry in the buffer solution provides a qualitative and semiquantitative analysis of the passive film growth. Okamoto's model of formation of two types of films, determined by the anodization potential, is found to be applicable; the mechanism of oxide growth is related to selective enrichment of iron or chromium, which is based on solubility relationships predicted by thermodynamic considerations.

In our catalyst development work, stainless steel (AISI 316L), in the passivated or oxidized condition, is used as a support material. Subsequent to the deposition of the catalytically active material on the oxidized steel, the catalyst is subjected to cyclic voltammetry and the surface area of the catalyst is evaluated from the hydrogen and oxygen adsorption/desorption peaks appearing in the voltammograms. In order to avoid the dissolution of the oxide film on stainless steel, a borate-boric acid buffer solution of pH 8.6 was selected, instead of the normally used 1N sulfuric acid solution, for the voltammetry measurements. Information on the passive film growth and its reduction characteristics in the borate-boric acid buffer solution was, therefore, essential to facilitate interpretation of the electrochemical data obtained with the catalyst.

Studies on passivity are primarily oriented toward understanding the corrosion behavior of metals and alloys. Detailed investigations on the electrochemical behavior of iron in the buffer solution are reported in the literature (1). In the case of stainless steels, however, a major part of the reported work is devoted to their behavior in acid and chloride solutions (2-5). Recently, surface analytical techniques, such as Auger spectroscopy and x-ray photoelectron spectroscopy, have been used extensively to elucidate the compositional changes in the passive film (3-7). For example, the enrichment or depletion of an alloying element in the passive film has been shown to depend on the pH of the anodizing solution (5). It has been proposed that the passive film is a duplex oxide (4); another conclusion is that two kinds of passive films are formed on the steel depending upon their formation potentials (3). If the passive film itself or a part of it is a reducible oxide and more than one type of oxide is present, then their cathodic reduction potentials could be expected to be different. Therefore, cyclic voltammetry in combination with a surface analytical technique, Auger spectroscopy, could provide information on the composition of the passive film.

The work reported here was undertaken to study the anodic oxidation of stainless steel and cathodic reduction of the oxides formed in a borate-boric acid buffer solution, characterize the oxide using cyclic voltammetry in the buffer solution, determine the composition of the oxide by Auger spectroscopy, and correlate the electrochemical and Auger results. For the sake of comparison, passive films grown in sulfuric acid and sodium hydroxide solutions were also tested in the buffer solution.

Experimental

The material was AISI Type 316L stainless steel. It was supplied by Sulzer Canada, Incorporated, (Sulzer packing BX) in the form of a corrugated sheet, 0.2 mm thick, having fine channels or grooves on the surface so as to provide a large exposed area. Samples 3-4 cm² in area were

* Electrochemical Society Active Member.

cut from these sheets, degreased, washed, and dried. A conventional glass cell with three compartments housing the working electrode, a saturated calomel reference electrode, and a platinum gauze counterelectrode was used for the electrochemical studies. The solution used was a buffer solution of pH 8.6 obtained by mixing required volumes of 0.15M boric acid and sodium borate solutions. Argon was kept bubbling through the solution in all the three compartments of the cell. All measurements were made at room temperature.

Prior to an experiment, the sample was reduced at a cathodic current of 1 mA cm⁻² for 1 min. It is expected that such a treatment would reductively dissolve any ferric oxide present on the as-received material; chromium-rich oxide, if present, is unlikely to be removed by this procedure. Anodic oxidation was done potentiostatically by holding the sample at the desired potential for 1h; galvanostatic reduction of the passive film was carried out at a constant current of 10 μ A cm⁻²; a scanning rate of 100 mV s⁻¹ was used for cyclic voltammetry measurements. Subsequent to the anodic oxidation, the sample was lifted up above the solution, the electrical connections were rearranged for cathodic reduction or cyclic voltammetry, and the sample was reimmersed in the solution. A potentiostat, Model 173, and a Universal programmer, Model 175, supplied by Princeton Applied Research, and a current source, Model 225, and electrometers, Model 600B, supplied by Keithley, formed part of the electrochemical system.

Auger analysis was carried out using a Physical Electronics Model 595 scanning Auger microprobe (SAM) equipped with a cylindrical mirror analyzer and a coaxial electron gun. Samples were mounted on holders so that the surface normals made an angle of 60° to the electron beam, and 30° to the ion beam.

Survey spectra and depth profile data were taken using a 5 keV, 50 nA electron beam rastered over a 100 μ m² area. Smooth regions on the sample surfaces were chosen in order to minimize any topographical effects. Depth profiles were obtained in the alternating sputter mode (10s cycles) using digital data acquisition. A 4 keV Ar⁺ ion beam rastered over a 4 mm² area yielded a current density of $\sim 20 \mu$ A/cm² (measured with an unbiased Faraday cup). Under these conditions, a sputter rate of $2.6 \pm 15\%$ nm/min was obtained. Calibration of sputter rate was based on an oxide film grown on 304 stainless steel, and its thickness determined by nuclear microanalysis (8). The base chamber pressure was 5×10^{-10} torr, and during sputtering the main chamber pressure rose to 2×10^{-8} torr.

For each profile, the elements C, O, Cr, Fe, and Ni were monitored at 273, 512, 529, 651, and 848 eV kinetic energy, respectively. The Auger peaks were computer differentiated and the peak-to-peak (p-p) height values for each element were normalized by dividing by the sum of the p-p values for Cr, Fe, and Ni.

Results

All the potentials were measured and are quoted relative to the saturated calomel electrode. Subsequent to the initial cathodic reduction of the air-formed oxide film, at 1 mA cm^{-2} and -1.4 V , the rest potential attained by the sample was usually at $\sim -0.7 \text{ V}$. After anodic oxidation, if the sample was left immersed in the solution, the open-circuit potential shifted steadily in the cathodic direction; for example, in the case of films grown at 0 and $+0.6 \text{ V}$, the potentials were at -0.45 and -0.25 V , respectively, in $\frac{1}{2} \text{ h}$. Thus, the possibility existed for the passive film to undergo autoreduction. Therefore, it was necessary to lift the sample up above the solution temporarily till the appropriate changes in the connections were made for the reduction of the passive films. Such changes were made within 1 min, and reduction was carried out immediately following reimmersion of the sample in the solution. The potential measured on reimmersion was cathodic to the anodization potential by about 0.2 V . In some experiments, after anodization, changes in the connections were made quickly without lifting the sample above the solution. The open-circuit potential measured and the voltammogram traced were quite similar to those obtained in the usual experiments, for the same anodizing conditions, where the sample was lifted above the solution for a short time.

In Fig. 1, the voltammograms obtained with the samples anodized at various potentials are compared. Initial scan was in the cathodic direction from the potential measured on reimmersion in the solution to -1.1 V , which was followed by the anodic scan to 0 V . The result ob-



Fig. 1. Voltammograms obtained in a borate-boric acid buffer solution for stainless steel, Type 316L, anodized 1h in the buffer solution; specimen areas in cm^2 and anodizing potential in volts, respectively, are as follows: a: 3.4, 0. b: 3.8, 0.3. c: 3.9, 0.6. d: 4, 0.75. e: 3.8, 0.9. f: Specimen 3.8 cm^2 in area exposed to air for 4h following initial cathodic reduction step.

tained for a sample that was exposed to air for 4h following the initial cathodic reduction step is also included in the figure. A reduction peak located at -0.64 V is observed with the film formed at 0 V ; this peak becomes more pronounced with the sample anodized at 0.3 V . Increasing the anodizing potential to 0.6 V leads to the appearance of a second reduction peak at 0 V and an increase in the current for the initial peak; the latter has shifted to -0.75 V . With further increase in the anodizing potential to 0.9 V , the peak currents increase and the reduction peaks show a shift toward more cathodic potentials; they are located at -0.2 and -0.8 V . All the passive films showed a broad anodic peak at $\sim -0.3 \text{ V}$, and this peak current increased with increase in the passive film thickness.

The variation in the thickness of the passive film, expressed as the equivalent amount of charge passed during anodization, with applied potential is shown in Fig. 2A. The amount of charge consumed in forming the film increases more rapidly at $\geq 0.5 \text{ V}$ than at lower potentials. In Fig. 2B are shown the galvanostatic reduction curves for the passive films formed at various potentials. The films formed at $\leq 0.3 \text{ V}$ show a single reduction wave at $\sim -0.55 \text{ V}$, whereas those formed at $\geq 0.3 \text{ V}$ show an additional wave at $\sim 0 \text{ V}$. In the case of the latter films, the final reduction potential attained is more cathodic by 200 mV when compared to the films formed at low potentials.

In Fig. 3, a selected set of voltammograms, obtained with a sample cycled several times in a range of potentials and over various ranges of potentials, is shown. The cathodic limit was set at -1.1 V , and the anodic limit was increased from 0 to 1.2 V in steps of 0.3 V during the scans. The results are quite similar to those shown in Fig. 1 for the passive films. With increasing anodic potential, the reduction peak currents at 0 and -0.6 V increase and the

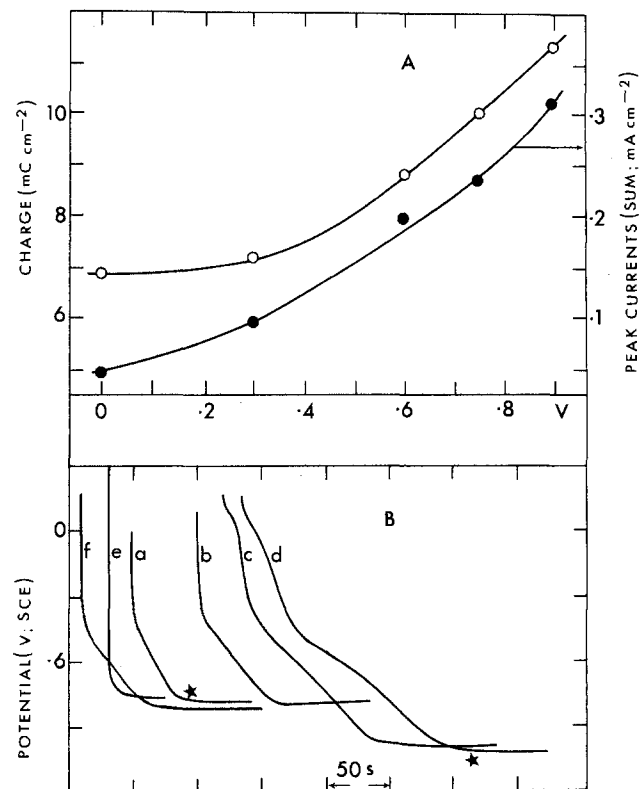


Fig. 2. A: Variation of the passive film thickness, for 316L stainless steel in borate-boric acid, with the anodizing potential; plotted as (\circ) charge passed during anodization and (\bullet) sum of the reduction peak currents obtained from Fig. 1. B: Galvanostatic reduction curves obtained in the buffer solution for the passive films; specimen areas in cm^2 and passivation potentials in volts are as follows: a: 3.8, 0. b: 4.2, 0.3. c: 3.8, 0.6. d: 3.6, 0.9. e: Specimen 3.9 cm^2 in area exposed to air for 4h after initial cathodic reduction step. f: As-received sample, 4.2 cm^2 in area.

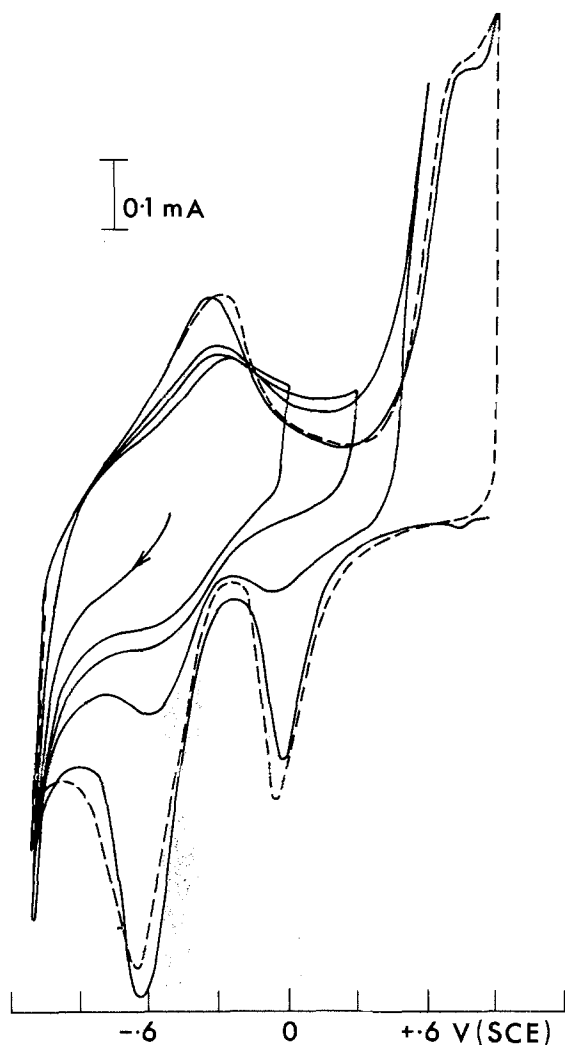


Fig. 3. Cyclic voltammograms obtained for 316L stainless steel, 4 cm² in area, in borate-boric acid buffer solution.

peaks shift slightly toward cathodic values; the reduction peak at 0 V is observed when the anodic scan limit is set at ≥ 0.6 V; all the curves show a broad anodic peak at -0.3 V. An anodic oxidation peak and also a cathodic reduction peak at $+0.75$ V become obvious when the potential is set at > 0.9 V during the anodic scans.

The results of the Auger analysis for passive films formed at 0 V, before and after the galvanostatic reduction, are shown in Fig. 4 and 5. Referring to the galvanostatic reduction curves shown in Fig. 2B, the reduction was followed just up to the knee (marked by an

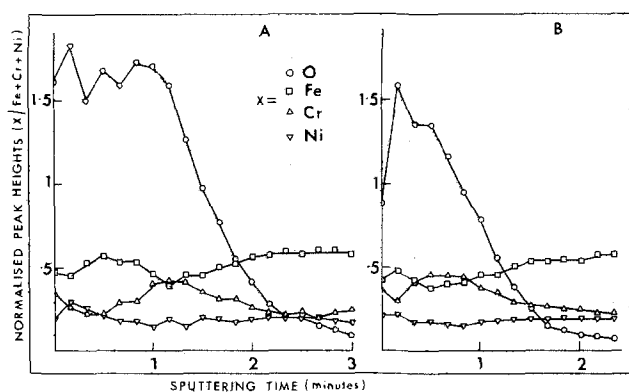


Fig. 4. Normalized Auger peak heights vs. sputtering time for passive films grown on 316L stainless steel at 0.9V for 1h in borate-boric acid solution. A: Passive film as grown. B: Passive film reduced galvanostatically in the buffer solution to a potential marked by an asterisk as shown in Fig. 2B.

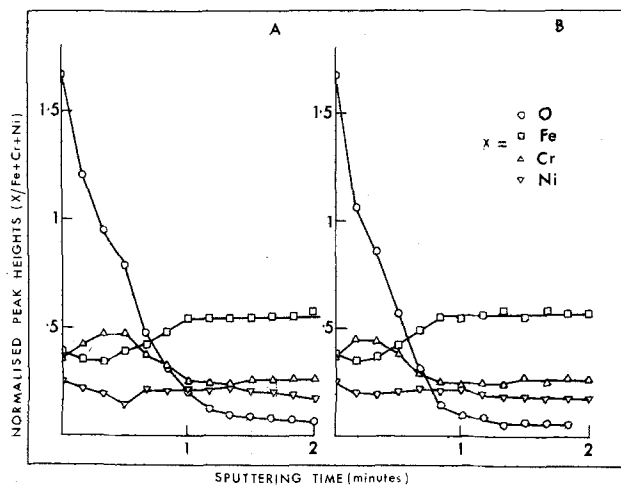


Fig. 5. Auger results for passive films grown on 316L stainless steel in borate-boric acid buffer solution; anodized at 0V for 1h. A: Passive film. B: Passive film reduced galvanostatically, following anodization, to a potential marked by an asterisk as shown in Fig. 2B.

asterisk), in the curves. In the case of the films grown at 0.9V, the oxygen profiles shown in Fig. 4A and 4B clearly indicate that a part of the oxide has been removed by the galvanostatic reduction step. Enrichment of chromium with a corresponding depletion of iron occurs in the oxide close to the steel-oxide interface; the relative levels of chromium and iron then gradually attain their values in the bulk of the steel at close to the oxide-solution interface. A slight enrichment of nickel is noticed in the outer layers of the oxide. The galvanostatic reduction has removed the outer oxide layers to a depth where the enrichment of chromium and depletion of iron had occurred; i.e., iron had been the major constituent of the part of the passive film that was reductively dissolved. In the case of films formed at 0 V, the galvanostatic reduction curve, Fig. 2B, shows that the charge equivalent to the reducible oxide is quite small when compared to the 0.9V film. This is also confirmed by the oxygen profiles shown in Fig. 5A and 5B. Chromium enrichment with the corresponding iron depletion occur in the oxide, and this region extends from one interface to the other.

Auger results for a sample cycled several times between -1.1 and $+1.2$ V are shown in Fig. 6; the sample was examined after a final scan in the anodic direction when the potential applied was 1.2V. Profiles for iron and chromium are quite similar to those for the 0.9V film in Fig. 4. Subsequent to an enrichment of chromium and depletion of iron close to the steel-oxide interface, the chromium level decreases and that of iron increases toward the oxide-solution interface. It is interesting to note that, even after a number of passivation and oxide reduction steps during the repeated cycling, the profiles are quite similar to a passive film formed at 0.9V in a single step. The profiles obtained for the air-formed oxide films, one existing on the as-received sample and that formed in 4h of exposure after the initial cathodic reduction step, are shown in Fig. 7; the latter were quite similar to those obtained for the 0 V film following the galvanostatic reduction step (cf. Fig. 7B and 5B). Chromium enrichment and iron depletion at the steel-oxide interface are seen to be common for both of the air-formed films. But, in the as-received condition, there is a reversal in the composition of the surface layers relative to the steel-oxide interface; they are enriched in iron and depleted in chromium. It must be pointed out that the oxide formed, even after 4h of exposure to air, following the initial cathodic reduction step did not show an arrest or a wave at -0.6 V during the galvanostatic reduction, whereas the oxide existing on the sample in the as-received condition always showed a distinct arrest (Fig. 2B, curve f) at -0.6 V, comparable to that obtained for a film formed at $+0.3$ V.

The voltammograms for the metals iron, chromium, and nickel and the alloy Nichrome are shown in Fig. 8. A

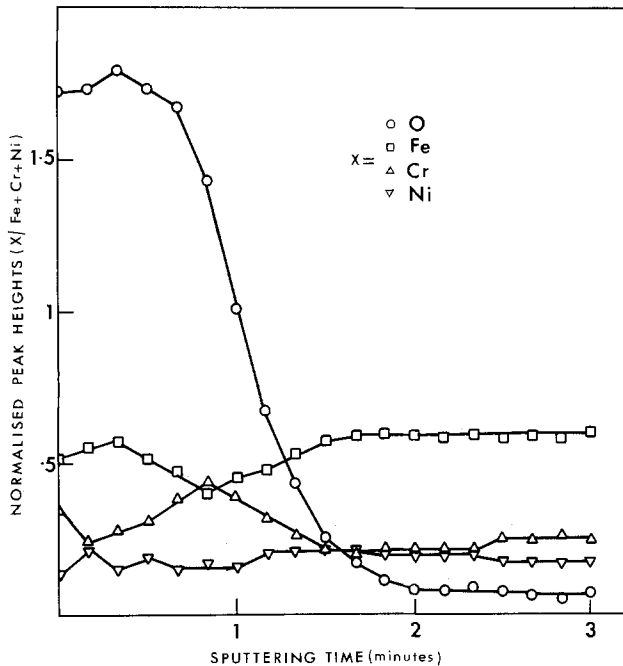


Fig. 6. Composition of the passive film formed on 316L stainless steel in borate-boric acid solution after repeated cycling as shown in Fig. 3; Auger analysis done after a final anodic scan when the potential was 1.2V.

composite of the curves of the three metals matches quite well with the voltammograms shown in Fig. 1 and 3 for the steel. Reduction peaks observed at -0.6V for iron, 0V for chromium, and $+0.7\text{V}$ for nickel and the anodic peaks (indicating the transition from an active to a passive state) at $\sim -0.3\text{V}$ obtained for all the three compare well with similar peaks obtained in the case of the steel. The galvanostatic reduction curves for the metals anodized to various potentials revealed a well-defined arrest at -0.6V , only in the case of iron; in the case of nickel and chromium, the potentials rapidly decreased to -1.4V ; a small inflection at 0V was noticed in the case of chromium.

Discussion

Auger analysis.—The mechanism of passive film formation on stainless steels is governed by the thermodynamic stability of the oxidation products, oxides and/or hydroxides, at the pH and the potential (3, 5); this conclusion is amply confirmed by the results presented here. When the equilibrium diagrams for iron, chromium, and nickel are compared, it is seen that at pH 8.6 and a potential of -1.35V (for the sake of consistency, potentials are

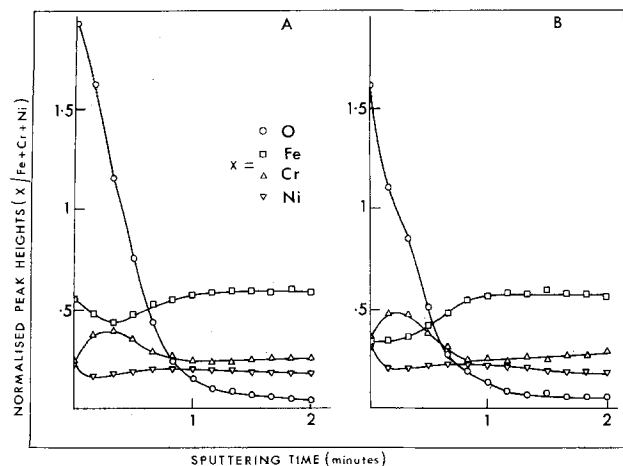


Fig. 7. Auger results for an air-formed oxide film on 316L stainless steel; A: As-received sample. B: Specimen reduced at -1.4V and 1 mA cm^{-2} and exposed to air for 4h.

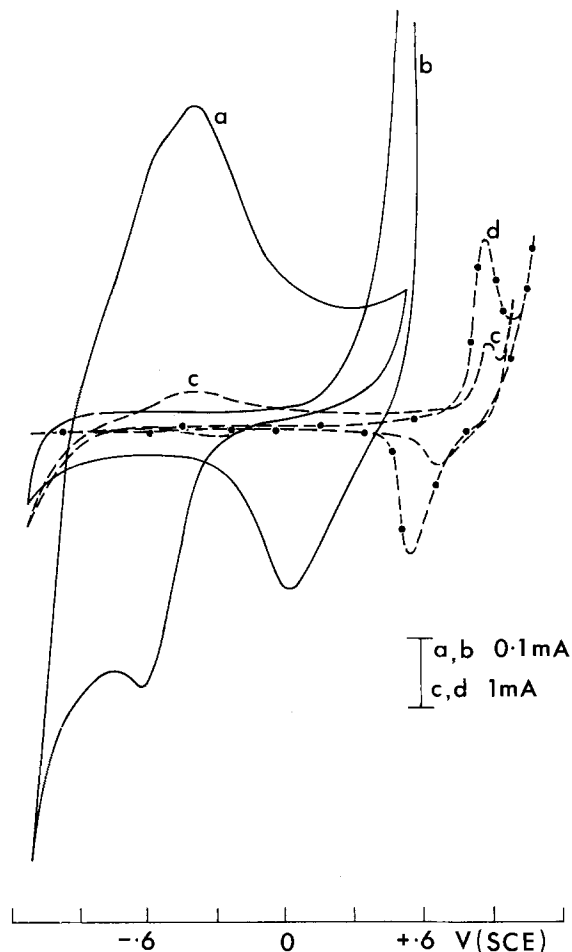


Fig. 8. Cyclic voltammograms for (a) iron 1.3 cm^2 , (b) chromium 2.4 cm^2 , (c) nickel 2 cm^2 , and (d) Nichrome, 1 cm^2 obtained in borate-boric acid buffer solution.

all referred to SCE), Cr_2O_3 is a stable oxide phase (9, 12). The Auger results obtained for the air-formed film (Fig. 7B) indicate a zone of chromium enrichment and iron depletion in the thin oxide layer. The profiles for the oxide that existed prior to the initial cathodic reduction step in the as-received condition (Fig. 7A) show a reversal in composition through the thickness of the film; the surface layers are rich in iron and depleted in chromium, relative to the inner interface, where the opposite is true. Cathodic reduction at 1 mA cm^{-2} and -1.4V , the initial surface preparation step, has thus selectively dissolved an oxide that was rich in iron. Galvanostatic reduction of the as-received sample indeed shows a distinct potential arrest at -0.6V , the characteristic reductive dissolution potential of a hydrated ferric oxide film (10, 11). Thus, the initial surface is not film free; passive film growth occurs on the surface carrying a thin ($\sim 1\text{ nm}$ thick) layer of chromium-rich oxide. From the equilibrium diagrams it is expected that at potentials anodic to 0V , chromium would dissolve preferentially in the buffer solution. The Auger results confirm this prediction; when the steel is passivated at potentials $\geq 0\text{V}$, the zone of chromium enrichment and iron depletion stays closer to the steel-oxide interface and the chromium level decreases and that of iron increases toward the oxide-solution interface (Fig. 4). When a sample was repeatedly passivated and the oxides formed were successively reduced, the final step of passivation still left the chromium-enriched and iron-depleted zone close to the steel-oxide interface (cf. Auger data in Fig. 6). During the passivation, half of a cycle chromium has preferentially dissolved, leaving an oxide richer in iron in the outer layers; this iron oxide has dissolved during the subsequent reduction half of the cycle. The final repassivation, which occurred between -0.3 and 1.2V (cf. Fig. 3 and 8; transpassive region for chromium) over a period of 15s, has led to the increase in iron

and decrease in the chromium levels toward the outer interface. The similarity in the composition of this passive film to that grown by a single-step anodization at +0.9V for 1h lends support to the proposal that passive film growth on the steel involves a selective dissolution process (3). The potential arrest at -0.6V observed during the galvanostatic reduction is characteristic of the reductive dissolution of Fe_2O_3 as Fe^{2+} in the solution (10, 11). The removal of outer oxide layers, rich in iron, during the galvanostatic reduction is also evidenced by the Auger results; the profiles obtained for a passive film, before and after the galvanostatic reduction, indicate reductive dissolution of outer oxide layers right up to the zone of chromium enrichment, near the steel-oxide interface, in the passive film.

Cyclic voltammetry.—The reduction peak appearing at -0.6 and -0.8V in the voltammograms of the passive films has to be attributed to the reductive dissolution of an oxide in the outer layers that is mostly of iron. A similar peak is observed in the voltammograms for pure iron; it corresponds to the potential arrest at -0.5 to -0.7V during the galvanostatic reduction; in the case of iron, this potential arrest is identified with the reduction of Fe_2O_3 and dissolution as Fe^{2+} (10, 11). With increasing anodic potential and, hence, the passive film thickness on the steel, the reduction peak current in the voltammogram increases; the galvanostatic reduction at this potential also corresponds to an increase in the amount of the reducible oxide. From the previous discussion based on solubility considerations, and confirmed by the Auger results, it is seen that thickening of the passive film with applied potential proceeds by the depletion of chromium and enrichment of iron in the outer oxide layers relative to the zone of chromium enrichment and iron depletion at the steel-oxide interface. The outer oxide layers of the passive film, reducible at -0.5 to -0.8V, are thus mostly ferric oxide (Fe_2O_3).

By comparison of the peaks obtained on the steel and pure chromium, the reduction peaks observed in the voltammograms at 0 to -0.2V are ascribed to chromium oxide in the passive film. In the galvanostatic reduction curves, a potential arrest at ~ 0 V is observed for both passivated chromium and the steel. Referring to the equilibrium diagram, it is seen that Cr_2O_3 is a stable oxide phase in the buffer solution at these potentials (9). Therefore, the reduction peak is not likely to be due to the reductive dissolution of the chromic oxide. However, the fact that this peak is observed only when passivation is done at $\geq 0.6\text{V}$ and that at these anodic potentials trivalent chromium can be oxidized to the hexavalent state (cf. equilibrium diagram) implies that this reduction peak is associated with the Cr^{6+} to Cr^{3+} transition occurring in the oxide. It is unlikely to be due to the reduction of Cr^{6+} species in the solution because samples passivated at $\geq 0.6\text{V}$ in a separate cell, washed in running water, and transferred to another cell containing a fresh quantity of the buffer solution still produced the same type of voltammograms showing the reduction peaks at 0 to -0.2V and -0.6 to -0.8V.

There were other interesting observations associated with this reduction peak at 0 to -0.2V. Samples anodized in 1M sulfuric acid solution, to various potentials up to 1V, when tested in the buffer solution, showed only the presence of a reduction peak at -0.7V, whereas voltammograms obtained with samples anodized in 0.1M sodium hydroxide solution of pH 12.8 and tested in the buffer solution revealed the presence of both reduction peaks, at -0.2 and -0.78V. With the samples anodized in the buffer solution and washed, dried, and tested immediately, the voltammograms showed both reduction peaks; however, after drying when aged for $\geq 1\text{h}$, the immersion potential of the sample in the buffer solution was cathodic at ~ -0.15V and only the reduction peak due to Fe_2O_3 at -0.6V was observed in the voltammogram. The passive film is believed to be a hydrated oxide (3); the hexavalent chromium species may be part of the bound water in the passive film and it undergoes autoreduction with aging.

When tracing cyclic voltammograms, anodic scans to potentials $> 0.9\text{V}$ led to the appearance of a reduction peak at +0.75V; this peak is very pronounced when thin oxide films, ~ 50 nm thick, grown thermally at 773 K on the steel are tested in the buffer solution. A reduction peak at about this potential is observed with pure nickel and Nichrome; these materials also show a corresponding anodic oxidation peak at +0.9V (cf. Fig. 8). The cathodic peak at +0.75V, therefore, reflects the reduction of nickel from a high to a lower valence state in the oxide; the equilibrium diagram suggests several oxidation states for nickel, stable as oxides, in the range of potentials from 0.4 to 0.8V at pH 8.6 (12).

In the case of passive films on the stainless steel, the oxides formed may not be identified individually as the oxides of the metals constituting the steel. For example, the shift in the cathodic direction of the reduction peak potentials in the voltammograms could be associated with compositional changes in the oxides making up the passive film. As a result, the efficiency of reduction of the hydrated ferric oxide on the steel could be different from that on iron. However, the sum of the heights of the two reduction peaks, attributed to chromium and iron oxides in the voltammograms, is seen to increase with the anodizing potential. This variation, shown in Fig. 2A, is similar to that of the charge passed in forming the passive film. This increase in the charge passed corresponds to an increase in the thickness of the total oxide, and reducible oxide is clearly evidenced by the Auger data (Fig. 4 and 5) and the galvanostatic reductions (Fig. 2B). The peak currents at 0 to -0.2V and -0.6 to -0.8V could thus be related to the relative amounts of the two oxides (chromium rich and iron rich) in the passive film. Additional work is necessary to relate quantitatively the peaks in the voltammograms with the composition of the passive film.

Structure of the passive film.—Anodic passivation of the stainless steel in the buffer solution bears a close analogy to that in acid solutions, and the results reported here support the model put forward by Okamoto for the structure of the passive film (3). In our study, steel carrying a thin film of chromium-rich oxide (nonreducible under the surface preparation conditions employed) is passivated. Depending on the anodization potential, two types of film are formed: at low potentials, $< 0\text{V}$, the oxide (hydrated) is mostly of chromium and, at high potentials, the outer oxide layers are mainly of iron. A zone of chromium enrichment and iron depletion is maintained close to the steel-oxide interface and film thickening with the applied potential proceeds by an increase in the level of iron and a decrease in the level of chromium toward the oxide-solution interface. The films formed at potentials $\geq 0\text{V}$ consist of at least two parts: outer layers of mainly ferric oxide, which could be reductively dissolved at ~ -0.6V, and inner layers rich in chromium oxide. The mechanism of growth of the passive films is governed by the solubility relationships of the oxides to the potential applied and pH of the solution.

Conclusions

Passivation behavior of 316L stainless steel in a borate-boric acid buffer solution of pH 8.6 was investigated by electrochemical means and Auger spectroscopy. Cyclic voltammograms obtained in the buffer solution showed characteristic reduction peaks. Similar peaks were also observed when the metals iron, chromium, and nickel were tested in the buffer solution. The reduction peak heights increased (proportionately) with increase in film thickness. A peak at -0.6 to -0.8V is identified with the reductive dissolution of a hydrated ferric oxide; reduction peaks at 0 to -0.2V and +0.75V are attributed to valence transitions, occurring in the solid state, associated with chromium and nickel, respectively, in the oxide.

Auger composition depth profiles revealed a zone of chromium enrichment and iron depletion close to the steel-oxide interface. Away from this zone and toward the oxide-solution interface, the level of iron increased and

that of chromium decreased with increase in passive film thickness. Auger data also confirmed the reductive dissolution of outer oxide layers occurring during the galvanostatic reduction at -0.6 to -0.8 V.

At potentials < 0 V, the passive film consisted mainly of chromium oxide; with increase in anodization potential, the outer layers were rich in the reductively dissolvable ferric oxide. Compositional changes in the passive film can be explained on the basis of selective solubility of the oxides at the applied potentials.

Cyclic voltammetry in the buffer solution, in combination with other surface analytical techniques, offers a qualitative and at least a semiquantitative analysis of passive film growth on stainless steels.

Manuscript submitted June 8, 1984; revised manuscript received Oct. 15, 1984.

Atomic Energy of Canada Limited assisted in meeting the publication costs of this article.

REFERENCES

1. Z. Szklarska-Smialowska and W. Kozłowski, *This Journal*, **131**, 234, 499 (1984).
2. G. M. Bulman and A. C. C. Tseung, *Corros. Sci.*, **13**, 531 (1973).
3. G. Okamoto, *ibid.*, **13**, 471 (1973).
4. M. da Cunha Belo, B. Rondot, F. Pons, J. LeHericy, and J. P. Langeron, *This Journal*, **124**, 1317 (1977).
5. A. E. Yaniv, J. B. Lumsden, and R. W. Staehle, *ibid.*, **124**, 490 (1977).
6. K. Asami and K. Hashimoto, *Corros. Sci.*, **19**, 1007 (1979).
7. I. Olefjord and B.-O. Elfstrom, *Corrosion*, **38**, 46 (1982).
8. R. L. Tapping, R. D. Davidson, and T. E. Jackman, "Surface and Interface Analysis," John Wiley and Sons, Ltd., Sussex, England (1985).
9. M. Pourbaix, "Lectures on Electrochemical Corrosion," Translated by J. A. S. Green, p. 151, Plenum Press, New York (1973).
10. M. Nagayama and M. Cohen, *This Journal*, **109**, 781 (1962).
11. N. Sato, K. Kudo, and T. Noda, *Corros. Sci.*, **10**, 785 (1970).
12. R. L. Cowan and R. W. Staehle, *This Journal*, **118**, 557 (1971).

Fluoride-Based Catalysts for the Electrodeposition of Chromium

J. P. Hoare and M. A. LaBoda*

General Motors Research Laboratories, Electrochemistry Department, Warren, Michigan 48090-9055

ABSTRACT

Steady-state polarization and transient cyclic voltammetric studies were carried out on bright Pt microelectrodes in chromic acid solutions catalyzed by NaF and Na_2SiF_6 . These data indicate that HF is the active agent in these plating baths and that it acts as both a blocking agent and a catalyst for the electrodeposition of Cr. Current efficiency studies in the high speed plating machine support these conclusions.

According to the model of Cr electrodeposition from chromic acid solution (1, 2), most of the Cr in solution exists as the trichromate ion, $\text{HCr}_3\text{O}_{10}^-$. Sulfuric acid is added to the bath in a regulated amount. The sulfate exists as bisulfate ions, HSO_4^- , which complex one end of the trichromate ion so that electrons are transferred from the cathode to the other end of the complex in the outer Helmholtz plane. In addition to this role as a blocking agent, the HSO_4^- ion acts as a catalyst by complexing with the decomposition product of the trichromate complex to form a dipolar chromous complex. This chromous species is adsorbed on the cathode surface where two electrons are transferred to produce a deposit of metallic Cr and the release of the HSO_4^- to solution.

It is known (3-6) that additions of fluoride ion, whether in the form of HF, a salt of an indifferent metal, or a fluorosilicate, to chromic acid will catalyze the conventional electrodeposition of metallic Cr. In an effort to understand the mechanism of fluoride-catalyzed chromic acid plating baths, an investigation was made of the polarization characteristics of Pt cathodes in various solutions of chromic acid to which small amounts of NaF or Na_2SiF_6 were added.

Experimental

The cathodes were made by melting small beads (~ 0.04 cm^2 in area) at the ends of Pt wires (99.99% pure) in an oxygen torch and were cleaned by the repeated heating in a burning hydrogen jet following by quenching in concentrated HNO_3 , as described earlier (1). The mounting of the test electrodes (three for duplicate runs) in the Teflon cell has been detailed previously (1, 7). After the cell was filled with 2.5M chromic acid (250g CrO_3 /liter), the required amount of NaF was added to the solution, which was stirred with purified N_2 (~ 150 cm^3 /min). In this series of runs, the cyclic voltammograms were obtained as a function of sweep rate as before (7). The cell was opened, another portion of NaF was added, and the cyclic

voltammogram was taken once more. This procedure was repeated until measurements were made in 2.5M chromic acid catalyzed by making the solution 0.04, 0.08, 0.12, 0.20, 0.28, and 0.36M in NaF.

In another series of experiments, the ratio of CrO_3 /NaF was maintained at about 10/1 while the concentration of chromic acid was varied. The solutions investigated were 0.1, 0.5, 1.0, 1.75, and 2.5M in CrO_3 . For each solution, the cyclic voltammogram was obtained on the Pt-bead electrode in N_2 -stirred solution, followed by the galvanostatic and potentiostatic steady-state polarization measurements. The details of such measurements have also been presented elsewhere (1, 7).

All potentials are recorded against the saturated calomel reference electrode (SCE), and all experiments were carried out at ambient temperature ($24^\circ \pm 1^\circ\text{C}$).

The steel-tube samples (length, 7.6 cm; od, 3.8 cm; wall thickness, 0.17 cm) were plated in the high speed plating (HSP) system (8) for 1 min in a sulfate-catalyzed solution [CrO_3 , 50 g/liter, H_2SO_4 , 0.5 g/liter, and boric acid, 10 g/liter as a brightness extender (9)] and in a sulfate-silico-fluoride solution (CrO_3 , 50 g/liter; H_2SO_4 , 0.4 g/liter; Na_2SiF_6 , 0.5 g/liter; boric acid, 10 g/liter). The electrolyte was pumped through the anode-cathode gap space of 3.8 mm by an air pressure range of 2.76-5.51 kPa, which yielded flow velocities of 2 and 4 m/s. The temperature range was 68° - 85°C and the voltage range was 5-15V. The cathode area was 83.6 cm^2 and the anode area was 89.7 cm^2 . All samples were weighed before and after plating to obtain the weight of deposit, and from a knowledge of the quantity of charge passed, the cathode efficiency for Cr plating was determined.

Results

The identification of the electrode processes responsible for the peaks observed on the cyclic voltammograms is aided by a knowledge of the electrode reactions determining the rest potential and the formation of the adsorbed films on the electrode surface (steady-state po-

* Electrochemical Society Active Member.

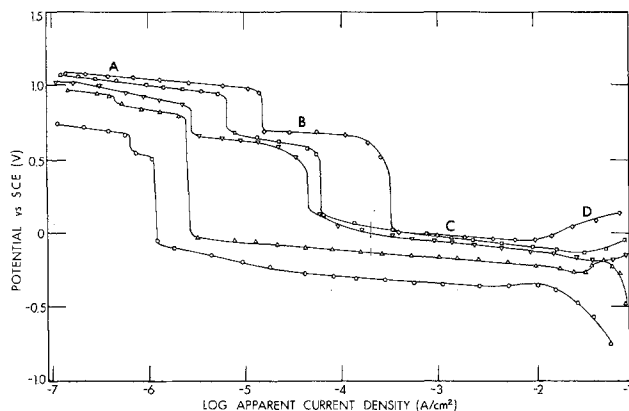
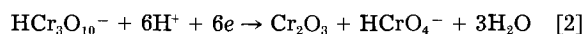


Fig. 1. Steady-state galvanostatic polarization curves obtained on Pt in various concentrations of CrO_3 and NaF such that the CrO_3/NaF ratio is near 10/1. 0.1M CrO_3 + 0.0096M NaF, circles; 0.5M CrO_3 + 0.05M NaF, triangles; 1.0M CrO_3 + 0.096M NaF, inverted triangles; 1.75M CrO_3 + 0.168M NaF, squares; 2.5M CrO_3 + 0.24M NaF, diamonds.

larization studies), and by surface analysis measurements (AES, XPS, SEM, etc.). The steady-state polarization curves at constant current on a Pt-bead cathode are plotted in Fig. 1 for five concentrations of chromic acid, all catalyzed by NaF such that the CrO_3/NaF ratio was close to 10/1. In general, the curves consist of three plateaus separated by limiting current regions. As suggested before (7), the first plateau at A corresponds to polarization of the local cell generated by the oxidation of Pt



and the reduction of Cr VI to Cr III at low current densities.



At higher current densities, the local cell is eliminated and the current falls to B through a limiting current where the current is consumed in the reduction of Cr VI to Cr III. With a high enough current density, the reduction of Cr VI can no longer support the demanded current and the current falls to C where the reduction of H^+ ions to H_2 gas supports the current. Finally, for the higher CrO_3 concentrations at D, a deposit is laid down on the Pt surface, shown by the bending upward of the curve in a so-called negative resistance region.

This negative resistance region produced by a change in surface area is more evident in the polarization curves obtained at constant potential in Fig. 2. These curves have the same general appearance as those in Fig. 1 with three plateaus, except that they are separated by negative resistance regions corresponding to the limiting current regions in Fig. 1. These area changes arise from the changes in the surface area produced by the reduction of the platinum oxides generated by the oxidizing power of

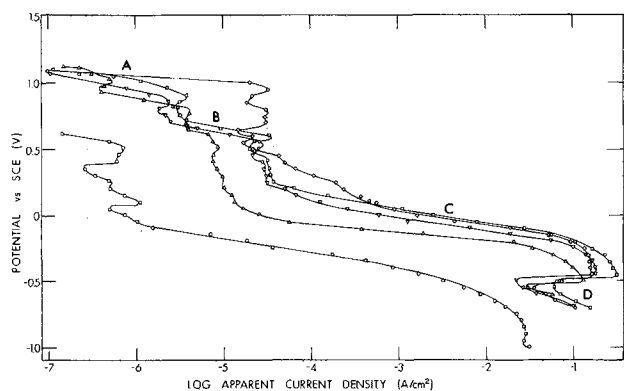


Fig. 2. Steady-state potentiostatic polarization curves obtained on Pt in the same solutions studied in Fig. 1.

the chromic acid. At D, the area changes are caused by the deposition of the Cr layer.

As the CrO_3 concentration increases, the length of the A plateau increases because more oxide is present in the more oxidizing environment. In the weak solution of 0.1M CrO_3 + 0.0096M NaF, the Cr VI concentration is so low that the system goes to H_2 evolution at low currents and a Cr metal deposit is not obtained (lack of negative resistance at D). A very thin porous deposit is obtained in the solution of 0.5M CrO_3 + 0.05M NaF as noted by the hump at D in Fig. 1. For the solutions of 1.0M CrO_3 + 0.096M NaF and stronger concentrations, good deposits of Cr metal are obtained at D but the area change or surface roughness increases with increasing concentration.

The surfaces of Pt-bead electrodes which had been cathodized in NaF-catalyzed chromic acid electrolyte were removed from the test cell, washed, dried, and analyzed with Auger electron spectroscopy (AES). The deposits obtained from 2.5M CrO_3 + 0.24M NaF, 1.75M CrO_3 + 0.168M NaF, and 0.5M CrO_3 + 0.05M NaF were investigated. The oxygen content of these Cr coatings range between 5 and 7 atomic percent (a/o). Although fluorine was detected in relatively very small amounts in the deposit, the height of the fluorine peak in AES spectra increased with increasing concentration of the electrolyte. From depth profiles obtained with argon sputtering, the thickness of these Cr deposits ranged between 20 and 50Å.

In Fig. 3, the cyclic voltammograms obtained on a Pt cathode in uncatalyzed 2.5M chromic acid are reproduced as a function of the sweep rate between -200 and 1500 mV. The two hydrogen desorption peaks, I_H and II_H on the anodic going sweep, the three complex polychromate reduction peaks, I'_O , II'_O , and III'_O on the cathodic going sweep, and the fact that the height of the major peaks indicated by Roman numerals are a linear function of the sweep rate indicate as before (7, 10) that the system is free of impurities. The large background current observed on the cathodic going sweep but not on the anodic going sweep arises from the reduction of Cr VI to Cr III. At a Pt anode, Cr III cannot be oxidized to Cr VI because the Cr III ions form a very stable hexaquo complex with water (7).

The cyclic voltammograms on Pt in 2.5M chromic acid containing 0.04M NaF as a function of sweep rate between -200 and 1500 mV are presented in Fig. 4. Here, at potentials below 0V, the current falls to very negative values where a thin layer of Cr metal is deposited on the Pt surface. This Cr layer, which does not exhibit the hydrogen reduction peaks, is removed at anodic potentials in peak V_O . Since the peak heights in Fig. 4 are a linear function of the sweep rate, the electrode processes which generate the peaks are surface reactions and do not arise from diffusion processes from solution.

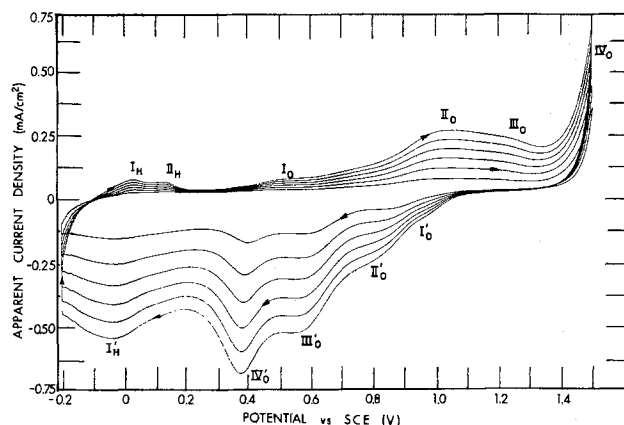


Fig. 3. A family of cyclic voltammograms obtained on Pt in 2.5M CrO_3 solution as a function of sweep rate (100, 83, 67, 50, 33, and 17 mV/s) between -200 and 1500 mV. The 100 mV/s curve is the outside curve. Roman numerals identify major peaks.

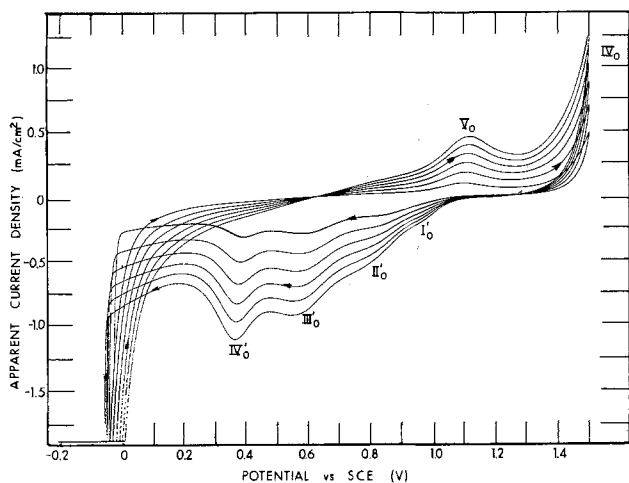


Fig. 4. Family of cyclic voltammograms obtained on Pt in 2.5M CrO₃ + 0.04M NaF solution as a function of the sweep rate (100, 83, 67, 50, 33, and 17 mv/s) between -200 and 1500 mV. The 100 mv/s curve is the outside curve. Roman numerals identify major peaks.

When the concentration of NaF was raised to 0.8M, the V₀ peak became more pronounced, but with further additions of NaF, little or no change in the peak area could be detected, even when the NaF concentration was raised to 0.24M shown in Fig. 5. In fact, at a NaF concentration of 0.45M, no change in V₀ was detected. The area under V₀ corresponds to the amount of Cr deposited on the Pt surface and appears to be virtually independent of the NaF concentration above about 0.1M. This observation is in agreement with that in the high speed plating machine where the rate of deposition is independent of the fluoride concentration above a given threshold value. In other words, one does not overcatalyze a Cr plating bath with F⁻ ion additions.

The presence of I₀' , II₀' , and III₀' in Fig. 4 and 5 and the negative resistance region at D in Fig. 1 and 2 give evidence that a cathodic film is formed in NaF-catalyzed chromic acid baths at the cathode. It is from this cathodic film that the Cr coating is deposited.

Figure 6 contains the cyclic voltammograms obtained on Pt-bead electrodes in 2.5M chromic acid (curve A) and in chromic acid catalyzed with Na₂SiF₆ addition (0.25M Na₂SiF₆) (curve B). Since the shape of curve B in Fig. 6 and that in Fig. 4 are highly similar, it is not critical to the quality of the product whether the fluoride catalyst is added as a salt of an indifferent cation or as a silicofluoride. A choice may be determined by the greater ease with which the silicofluorides can be handled and stored and by the greater solubility of the silicofluorides.

The high speed plating data of steel-tube samples in Na₂SiF₆-catalyzed chromic acid are plotted at two electro-

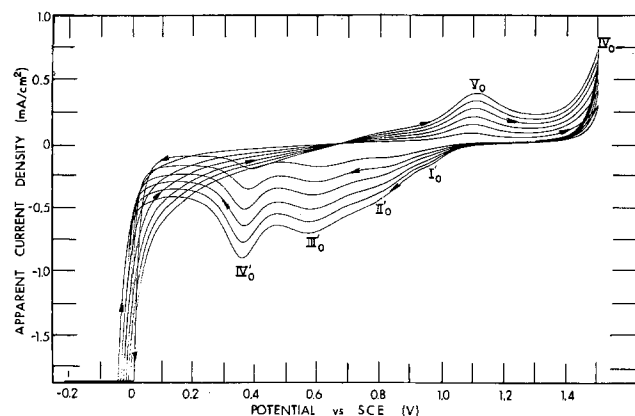


Fig. 5. Family of cyclic voltammograms obtained on Pt in 2.5M CrO₃ + 0.24M NaF solution as a function of sweep rate (100, 83, 67, 50, 33, and 17 mv/s) between -200 and 1500 mV. The 100 mv/s curve is the outside curve. Roman numerals identify major peaks.

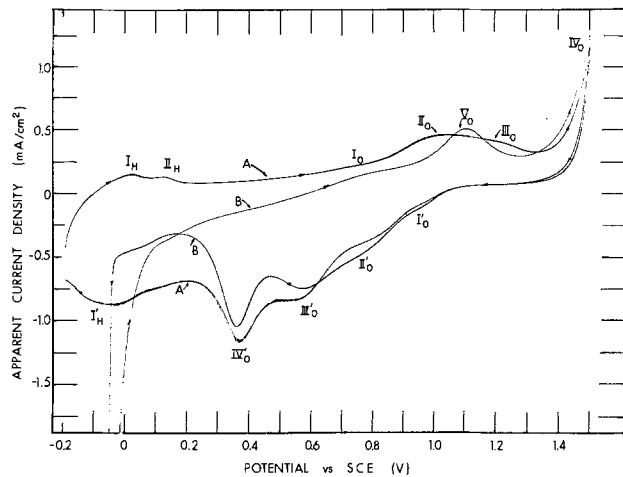


Fig. 6. Cyclic voltammogram obtained on Pt in N₂-stirred 2.5M chromic acid, (curve A) cycled from 200 to 1500 mV at a rate of 100 mV/s. Voltammogram on Pt in 2.5M CrO₃ + 0.25M Na₂SiF₆ (curve B). Major peaks identified by Roman numerals as in Ref. (11).

lyte flow rates (2 and 4 m/s) at 68°, 80°, and 85°C in Fig. 7 as the current efficiency for Cr plating as a function of the apparent current density. The current efficiency increases with the current density, decreases with the temperature, and is virtually independent of the flow rate.

Discussion

For metallic Cr to be deposited from the trichromate ion, a blocking agent must be present so that electrons will be transferred to only one end of the HCr₃O₁₀⁻ ion. In the case of sulfate-catalyzed CrO₃ electrolytes, the transfer of electrons to one end of the trichromate ion is hindered by the hydrogen bonding of HSO₄⁻ ion to the double-bonded oxygens at that end (1, 2). Since it makes little difference to the electrodeposition process how the fluoride is added (3-6) (see Fig. 2 and 6), a hydrogen containing species common to all the fluoride addition agents is HF and is considered to be the active catalyst for the electrodeposition of Cr. Fluoride ion hydrolyzes to HF according to Eq. [3]

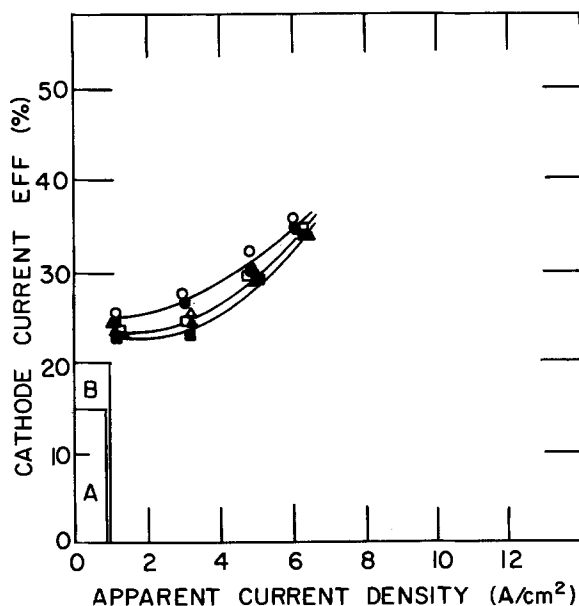
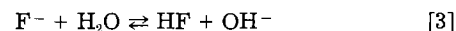
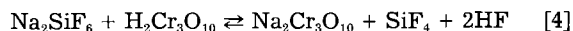
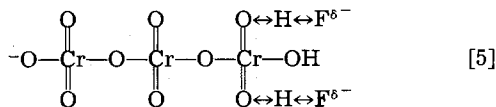


Fig. 7. Cathode current efficiency as a function of the apparent current density for Cr deposition on steel-tube samples in the mixed catalyst electrolyte at 68°C, circles; 80°C, triangles; and 85°C, squares. Open symbols, 2 m/s and filled, 4 m/s flow rate; (A) sulfate catalyst tank plating envelope; (b) mixed catalyst tank plating envelope.

and in the very strong acid medium of 2.5M chromic acid Eq. [3] is shifted to the right. In the case of the silicofluoride, it has been found (11) that metal silicofluorides are decomposed in concentrated H_2SO_4 to SiF_4 and HF. Possibly, in the strong acid environment of 2.5M chromic acid, Na_2SiF_6 disintegrates to HF by Eq. [4]

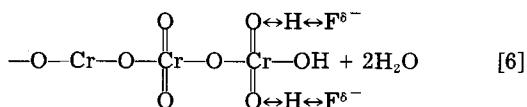


It is suggested, as in the case of sulfate-catalyzed chromic acid (2), that an equilibrium exists between all possible complexes formed by hydrogen bonding between HF and the polychromate ions where the distribution of complexes is determined by the ratio of CrO_3 to the catalyst concentrations. For sulfate-catalyzed systems, the greatest probability of obtaining a complex with one end blocked occurs at a CrO_3/H_2SO_4 ratio of 100/1. In the fluoride-catalyzed case, the ideal complex is

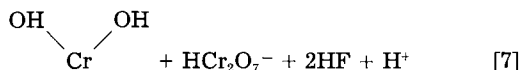


where the double-headed arrows indicate hydrogen bonding and the δ^- is the average negative charge resulting from resonance between the two hydrogen-bonded forms.

Electrons are transferred to the unblocked end of the complex in the outer Helmholtz plane by quantum mechanical tunneling through the potential energy barrier of the double layer. With the transfer of $4e$ and the reaction with $4H^+$ in six steps, one obtains a chromous complex



Decomposition of this complex takes place by an acid-catalyzed hydrolysis by reaction with H_3O^+ ions to give

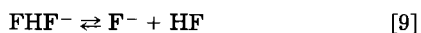


Since $Cr(OH)_2$ is in equilibrium with $Cr=O + H_2O$, the HF may hydrogen bond to $Cr=O$ to form the dipolar complex

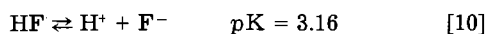


The positive end of this complex can be specifically adsorbed on the cathode surface. With the transfer of two electrons and the reaction with $2H^+$ ions, Cr metal is deposited and H_2O and HF are liberated. In this role, the HF acts as a catalyst.

In solutions containing F^- ions and HF, these species can combine to form the complex ion FHF^-



with a pK of 0.7 (12). As F^- ion is added to the system, the equilibrium (Eq. [9]) shifts to the left to form the HF_2^- ion. Since the hydrogen is tied up in the $F-H-F$ linkage, it cannot hydrogen bond with polychromate double-bonded oxygens. This behavior can account for the observed fact that a fluoride-catalyzed, chromic acid, plating bath resists overcatalyzation as in Fig. 4 and 5, in contrast to sulfate-catalyzed baths (2). The equilibrium constants for the ionization of HF (12)



and the ionization of HF_2^- , Eq. [9], maintains the CrO_3 /catalyst ratio in the range for acceptable Cr plating ($\sim 30/1$ from Fig. 4 and 5). Such a bath is self-regulated.

In the HSP machine, it was observed that an acceptable deposit of Cr was not obtained on steel-tube samples in fluoride-catalyzed chromic acid electrolytes at $68^\circ-85^\circ C$ and a flow rate of 2-4 m/s. Misplates such as patches and discolored smuts were deposited. In conventional plating from a fluoride-catalyzed bath, a viscous cathodic film could not be detected at the cathode surface, in contrast to that observed in sulfate-catalyzed baths (2). It is believed that the cathodic film is composed of a mixture of all possible complexes between HF, polychromates, and H_2O molecules. These HF-polychromate-complex films are much less viscous than the HSO_4^- -polychromate-complex films. As a result, the HF-polychromate films are relatively much thinner and can be swept from the cathode-electrolyte interface by the high flow rates used in the HSP system. Under these conditions, a poor deposit of metallic Cr would be expected, in agreement with the experimental observations, because Cr is deposited from the cathodic film (1).

When sulfuric acid was added to the fluoride-catalyzed chromic acid, excellent, bright, hard deposits of Cr were obtained on steel with this mixed-catalyst system in the HSP machine (see Fig. 7). In this case, the H_2SO_4 can form the more viscous cathodic film which is not easily swept from the cathodic surface by the high solution flow rates in the HSP machine.

It is concluded from these data that in fluoride-catalyzed Cr plating baths, HF acts as a blocking agent as well as a catalyst for the electrodeposition process. Although HF is a poorer blocking agent than HSO_4^- ion, it is a better catalyst for the reduction of the chromous complex (Eq. [8]) because of the higher electronegativity of the F atom. Since HF reacts with F^- ion to form the indifferent complex HF_2^- , a fluoride-catalyzed bath resists overcatalyzation, with further additions of fluoride producing a self-regulating bath.

Manuscript submitted Aug. 27, 1984; revised manuscript received Nov. 23, 1984.

General Motors Corporation assisted in meeting the publication costs of this article.

REFERENCES

1. J. P. Hoare, *This Journal*, **126**, 190 (1979).
2. J. P. Hoare, A. H. Holden, and M. A. LaBoda, *Plating Surf. Fin.*, **67**, 42 (June 1980).
3. T. A. Hood, *Metal Fin.*, **50**, 103 (1952).
4. P. Morisset, "Chromium Plating," p. 359, R. Drapes Ltd., England (1944).
5. R. Lowenheim, "Modern Electroplating," p. 97, John Wiley and Sons, New York (1963).
6. G. Dupernell, *Plating*, **47**, 35 (1960).
7. J. P. Hoare, *This Journal*, **130**, 1475 (1983).
8. M. A. LaBoda, *Surf. Technol.*, **11**, 91 (1980).
9. J. P. Hoare, *Plating Surf. Fin.*, **71**, 50 (March 1984).
10. A. Angerstein-Kozłowska, W. B. A. Sharp, and B. E. Conway, *J. Electroanal. Chem.*, **43**, 9 (1973); in "Electrocatalysis," M. W. Breiter, Editor, p. 94, The Electrochemical Society Softbound Proceedings Series, Princeton, NJ (1974).
11. J. H. Simons, "Fluorine Chemistry," Vol. I, p. 127, Academic Press, New York (1950).
12. F. A. Cotton and G. Wilkinson, "Advanced Inorganic Chemistry," p. 178, Interscience, New York (1972).

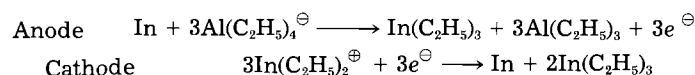
The Electrorefinement of Indium Through an Aluminum Alkyl Complex Electrolyte

M. S. Su, J. S. Gentry, C. B. Boss, C. G. Moreland, and K. J. Bachmann*

Department of Chemistry, North Carolina State University, Raleigh, North Carolina 27695-8204

ABSTRACT

High purity indium metal has been prepared by electrolysis at constant potential from a mixed Al + In complex electrolyte that contains typically 2 mol $\text{Al}(\text{C}_2\text{H}_5)_3$ and 0.06 mol $\text{In}(\text{C}_2\text{H}_5)_3$ per mol $\text{C}_6\text{H}_5\text{CH}_2\text{N}(\text{CH}_3)_3\text{F}$. Based on the results of cyclic voltammetry applied to the pure Al complex electrolyte and to the mixed electrolyte, a mechanism for the cathodic and anodic steps in the electrorefinement process is proposed. This mechanism is described by the following net electrode reactions



It is the opinion of the authors that the $[\text{Al}_2\text{F}(\text{C}_2\text{H}_5)_6]^\ominus$ and $[\text{Al}_3\text{F}(\text{C}_2\text{H}_5)_9]^\ominus$ ions that are shown by NMR studies to exist in equilibrium with uncomplexed $\text{Al}(\text{C}_2\text{H}_5)_3$ and $\text{Al}_2(\text{C}_2\text{H}_5)_6$, respectively, serve merely as supporting electrolyte. The indium metal obtained by electrorefinement in a mixed Al + In alkyl electrolyte is suitable for the synthesis and bulk crystal growth of In containing compound semiconductors. However, a further reduction of the ~ 2 ppm Al contamination level is required for making the electrorefined In a useful source material for epitaxial growth processes.

The ability of aluminum alkyl compounds, AlR_3 , to form complex electrolytes with alkali halides was discovered in 1955 by Ziegler *et al.* (1, 2), who recognized the potential of these electrolytes for the electrorefinement of aluminum (3). In subsequent patent applications, the replacement of the alkali halides by quaternary ammonium halides (4) and the extension of the electrorefinement to other Group IIIA metals (4) and Group IIB and Group IVA-VIA elements (5) have been disclosed.

Two series of complexes of the form $\text{M}^+[\text{AlR}_3\text{X}]^-$ and $\text{M}^+[\text{Al}_2\text{R}_6\text{X}]^-$, termed 1:1 and 1:2 complexes, respectively, have been reported with generally higher conductivity of the halide to aluminum ratio 1:2 complexes (6-9). For the $\text{K}^+[(\text{C}_2\text{H}_5)_3\text{Al-F-Al}(\text{C}_2\text{H}_5)_3]^-$ complex salt, x-ray diffraction studies show colinearity for the Al-F-Al atoms and tetrahedral coordination about the Al atoms (10). This result was interpreted in Ref. (10) in terms of a partial π character of the F-Al bond and an sp hybridization of the fluorine atom, which was supported by a subsequent NMR study of the electroneutral isoelectronic compound $(\text{CH}_3)_3\text{Si-F-Al}(\text{C}_2\text{H}_5)_3$ (11).

Ultraclean Group IIIA metals and metal alkyl compounds are presently of considerable technological interest for fabricating III-V compound semiconductors. In view of the advanced state of III-V compound bulk-crystal growth and epitaxy, the controlled reduction of the impurity background in the source materials is a key issue for the improvement of both optoelectronic devices and FET structures. The indium containing III-V compounds and alloys are currently of particular interest in the context of light sources and detectors for optical communications (12), thus motivating our work on the purification of this metal.

Experimental

The aluminum alkyl electrolyte was prepared according to the procedures of Dotzer (14). An excess of trimethylamine gas was passed over a 57g charge of triethylaluminum in a 1 liter flask. The triethylamine:triethylaluminum one-to-one adduct, obtained in a considerably exothermic reaction, was distilled under vacuum at 120°C . The clear, colorless distillate was heated to 50°C and stirred. A 55g sample of benzyl fluoride was added, dropwise. The mixture was then heated to 100°C and stirred for 30 min and served as a stock for the preparation of complex solutions by further additions of triethylaluminum. The electrolyte used for electrorefinement experiments consists of at least 2 mol $\text{Al}(\text{C}_2\text{H}_5)_3$ and 6 mol toluene per mol $\text{C}_6\text{H}_5\text{CH}_2\text{N}(\text{CH}_3)_3\text{F}$. In some cases, $\text{In}(\text{C}_2\text{H}_5)_3$

was added to this electrolyte. For the NMR studies described below, we prepared, also, complex solutions of NaF in triethylaluminum. The NMR spectra were taken on a EM-390 NMR spectrometer. Where not stated, the spectra shown in Fig. 1-6 were recorded at room temperature. All sample preparations and solution transfers were performed in an atmosphere of dry nitrogen.

A two-electrode galvanostatic or a three-electrode potentiostatic configuration was used for deposition of indium onto a platinum sheet cathode. The anode was either a pure aluminum wire or a block of indium metal. For the three-electrode potentiostatic experiments, the reference electrode was an aluminum wire in a pure triethylaluminum electrolyte. The electrolytes in the electrorefinement cell and in the reference electrode compartment contact in a sintered Vycor plug.

Samples of the electrolyte and deposited metal were analyzed by plasma-emission methods. Aliquots of the electrolyte, representing less than 0.05% of the total mass of the electrolyte in the cell, were removed and immediately weighed under an N_2 atmosphere. The samples were then hydrolyzed, similar to previously described procedures (13), by the addition of aqueous HCl, extracted from the toluene phase, and reweighed.

Samples of the deposited metal were taken by removing the Pt cathode from the cell, rinsing thoroughly with toluene followed by benzene, mechanically removing the metal from the electrode, melting under decahydronaphthalene, etching with 6M HCl, and weighing. The samples were then dissolved in concentrate HCl and diluted with deionized water.

The hydrolyzed electrolyte and dissolved metal samples were analyzed utilizing a Beckman spectraspan IV direct current argon plasma spectrometer.

Identification of the Complex Equilibria by NMR

Figure 1 shows the $^1\text{H-NMR}$ spectra for (a) triethylaluminum and (b) molar ratio of NaF to $\text{Al}(\text{C}_2\text{H}_5)_3 = 1:m$ solution, where $m = 2.5$, and further dilution of this solution with $\text{Al}(\text{C}_2\text{H}_5)_3$ to (c) $m = 3$ and (d) $m = 4$. Note that spectra b, c, and d were recorded at -10°C and these solutions also contained 3 mol toluene per mol NaF. This is important since in the absence of toluene a phase separation occurs at $m = 2$ (7). This phase separation is prevented in toluene containing solutions. Also, the phase separation established at $m \geq 2$ in the absence of toluene is reversed upon addition of toluene. Therefore, the toluene diluted solutions are thermodynamically stable to at least $m = 4$. Due to the influence of the electropositive Al atom, the CH_2 quartet is shifted upfield from the position of the CH_3

*Electrochemical Society Active Member.

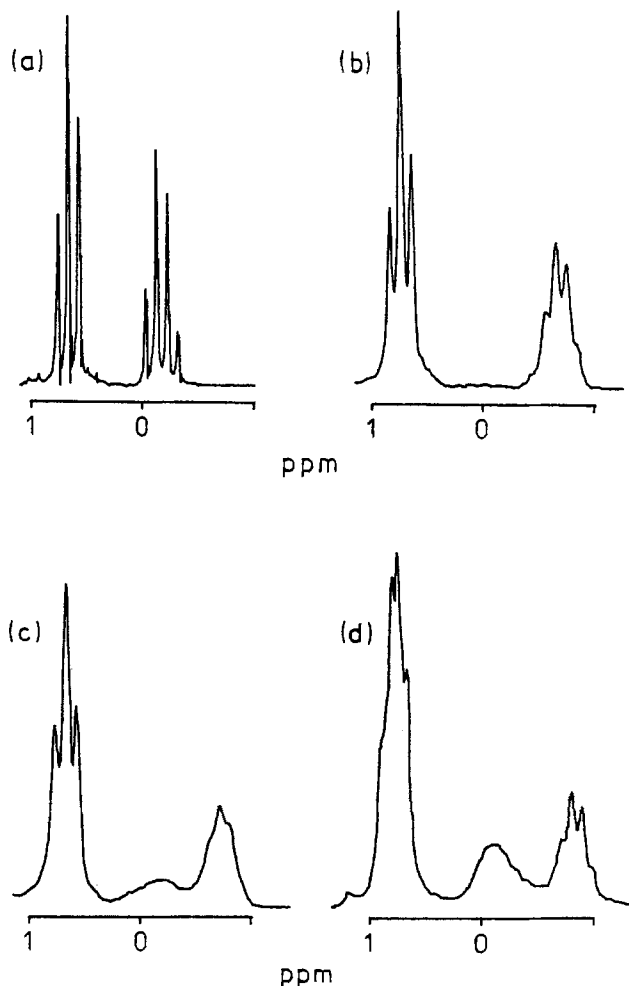


Fig. 1. $^1\text{H-NMR}$ spectra of $\text{NaF} + \text{Al}(\text{C}_2\text{H}_5)_3 + \text{toluene}$ solutions

triplet. At dilution $m = 2.5$, the upfield shift of the CH_2 signal is enhanced as expected from the F-Al interaction. Dilution beyond $m = 2.5$ results in the appearance of two CH_2 signals at fields that are characteristic for the complex and the pure triethylaluminum, respectively.

Figure 2 shows the $^1\text{H-NMR}$ spectra of molar ratio of trimethylbenzyl ammonium fluoride to triethylaluminum = $1:m$ solutions for various values $1 \leq m \leq 3$. As in the spectra for the Na^+ complex, the quartet associated with the CH_2 group of the ethyl groups in the anion complex is shifted upfield as compared to this position for pure $\text{Al}(\text{C}_2\text{H}_5)_3$. However, for $m \geq 3$, the fine structure due to the interaction of the CH_2 protons with the protons of the methyl group in the C_6H_5 group is reduced and a broadening occurs in the single line associated with the protons of the aromatic ring in the benzyl group. This phenomenon may be due to signal averaging and/or Al-proton coupling, but coincides, also, with the onset of a phase separation that is observed upon replacing Na^+ by $[\text{C}_6\text{H}_5\text{CH}_2\text{N}(\text{CH}_3)_3]^+$ for dilutions $m \geq 3$.

Figure 3 shows the $^{19}\text{F-NMR}$ spectra for molar ratio of toluene to NaF to $\text{Al}(\text{C}_2\text{H}_5)_3 = 3:1:m$ solutions with (a) $m = 2$, (b) $m = 2$, (c) $m = 2.5$, and (d) $m = 4$. A single peak at $\phi = 183$ ppm is observed for the $m = 1$ solution and is associated with the 1:1 complex $\text{Na}[\text{FAl}(\text{C}_2\text{H}_5)_3]$ reported previously (1-3, 5). For the $m = 2$ solution, a predominant peak at 172 ppm and a weak second peak at 166 ppm are recorded. The peak at 166 ppm increases relative to the peak at 172 ppm upon further dilution of the solution by $\text{Al}(\text{C}_2\text{H}_5)_3$. As pointed out in the above discussion of the ^1H spectra up to $m = 2.5$, no excess of uncomplexed $\text{Al}(\text{C}_2\text{H}_5)_3$ is detectable. Using this fact and the integrated intensities of the ^{19}F signals at 166 and 172 ppm for a solution with $m = 2.5$, we conclude that the signal at 172 ppm is associated with the previously reported 1:2 complex

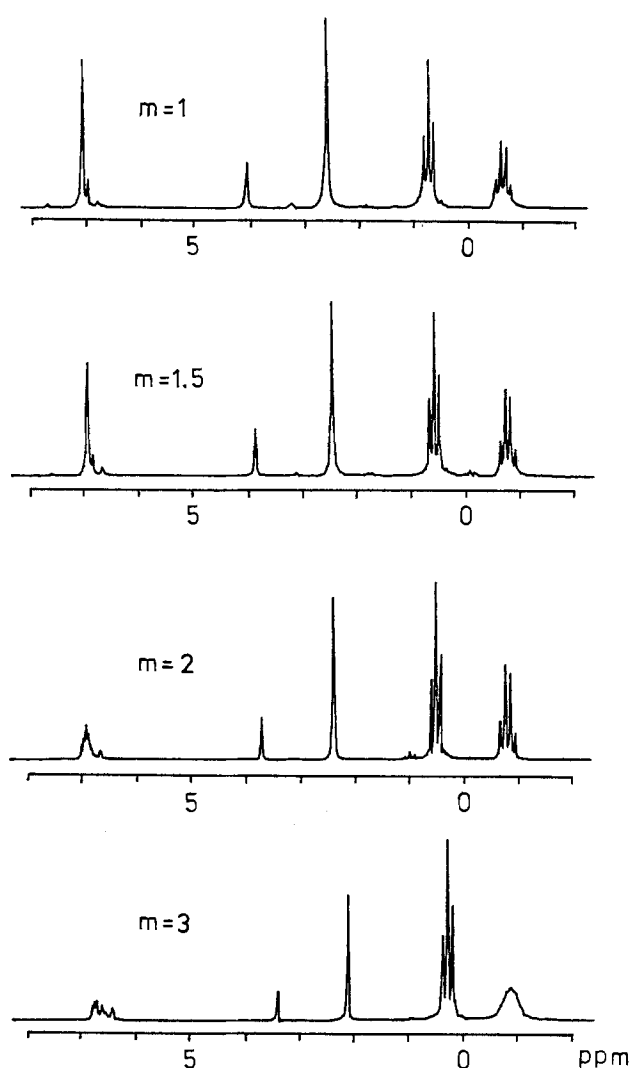


Fig. 2. $^1\text{H-NMR}$ spectra of $\text{C}_6\text{H}_5\text{CH}_2\text{N}(\text{CH}_3)_3\text{F} + \text{Al}(\text{C}_2\text{H}_5)_3$ solutions

(1-3, 5, 9) and the signal at 166 ppm is associated with a heretofore not recognized 1:3 complex.

Figure 4 shows a plot of the ratio of the integrated ^{19}F signals for the 1:2 and 1:3 complexes as a function of the molar ratio of $\text{Al}(\text{C}_2\text{H}_5)_3$ to $\text{NaF} = n$. As expected from the mass action law, the concentration of 1:3 complex increases as the concentration of free $\text{Al}(\text{C}_2\text{H}_5)_3$ increases (cf. discussion of Fig. 1).

Figure 5 shows the $^{19}\text{F-NMR}$ spectra for molar ratio of trimethylbenzyl ammonium fluoride to triethylaluminum = $1:m$ solutions where (a) $m = 1$, (b) $m = 1.5$, (c) $m = 2$, and (d) $m = 3$. The spectrum Fig. 5a was measured at -10°C . For the most diluted solution, $m = 3$, two dominant peaks at 172 and 166 ppm are observed that, in analogy to the NaF complex solutions, are associated with the 1:2 and 1:3 complexes, respectively. Also, a small additional peak at 162 ppm is observed, indicating the possible formation of higher-order complexes in the trimethylbenzyl ammonium fluoride solutions. In the $m = 2$ solution, this signal is absent and the signal associated with the 1:2 complex is dominant. However surprisingly, the signal at 162 ppm appears as a broadened significant feature in Fig. 5a, which shows an additional sharp peak at 153 ppm plus a broad peak at 175 ppm. The stoichiometry of the F compounds associated with the signals at 162 and 153 ppm is presently unknown. The broad signal at 175 ppm we interpret as an average between the signals associated with the lower order complexes.

Figure 6 shows the change in the $^{19}\text{F-NMR}$ spectra of $\text{C}_6\text{H}_5\text{CH}_2\text{N}(\text{CH}_3)_3\text{F} + \text{Al}(\text{C}_2\text{H}_5)_3$ complex electrolyte at constant $m \approx 3$ upon dilution by toluene. Clearly, the ratio of the 1:2 to 1:3 complex concentrations increases with dilu-

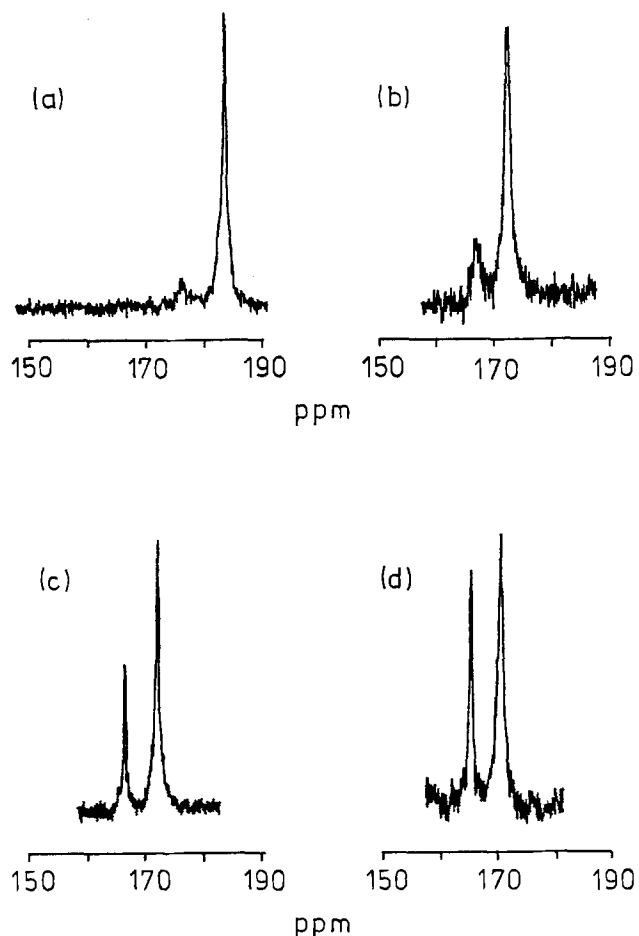


Fig. 3. ^{19}F -NMR spectra of $\text{NaF} + \text{Al}(\text{C}_2\text{H}_5)_3 + \text{toluene}$ solutions

tion. Assuming maximum conductivity for the 1:2 complex, this observation accounts for the previously unexplained increase in the conductivity of the halide:aluminum alkyl = 1:2 electrolytes upon dilution with toluene. Also, the shift of the equilibrium between 1:2 and 1:3 complex in toluene towards higher 1:2 complex concentration combined with a segregation coefficient $k \ll 1$ for 1:3 complex incorporation during crystal growth from such toluene solutions reconciles our results with the x-ray data of Natta *et al.* (6), which refer to pure

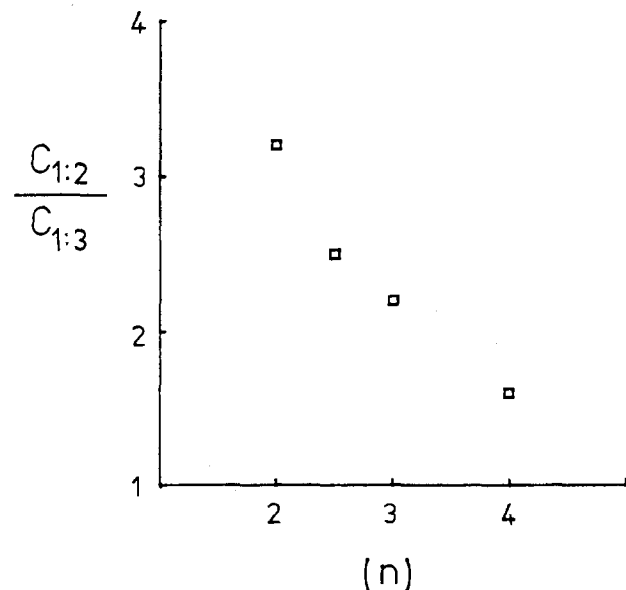


Fig. 4. Relative concentration $C_{1:2}/C_{1:3}$ of $\text{Na}[\text{Al}_2(\text{C}_2\text{H}_5)_6]$ and $\text{Na}[\text{Al}_3(\text{C}_2\text{H}_5)_9]$ as a function of the molar ratio of $\text{Al}(\text{C}_2\text{H}_5)_3$ to $\text{NaF} = n$.

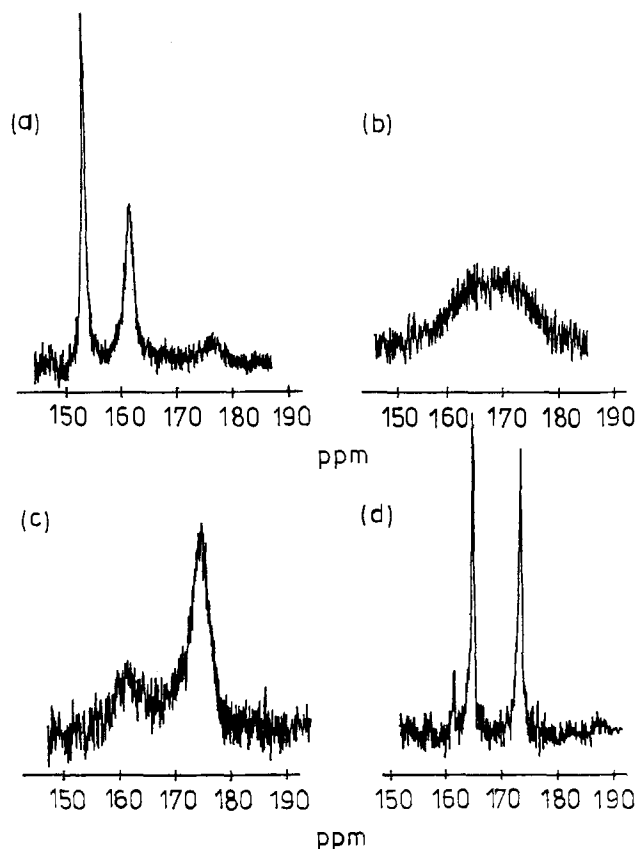


Fig. 5. ^{19}F -NMR spectra of $\text{C}_6\text{H}_5\text{CH}_2\text{N}(\text{CH}_3)_3\text{F} + \text{Al}(\text{C}_2\text{H}_5)_3$ solutions

single crystals of $\text{K}[\text{Al}_2\text{F}(\text{C}_2\text{H}_5)_6]$ grown from toluene solutions containing KF and $\text{Al}(\text{C}_2\text{H}_5)_3$ additions in a molar ratio of 1 to 2.

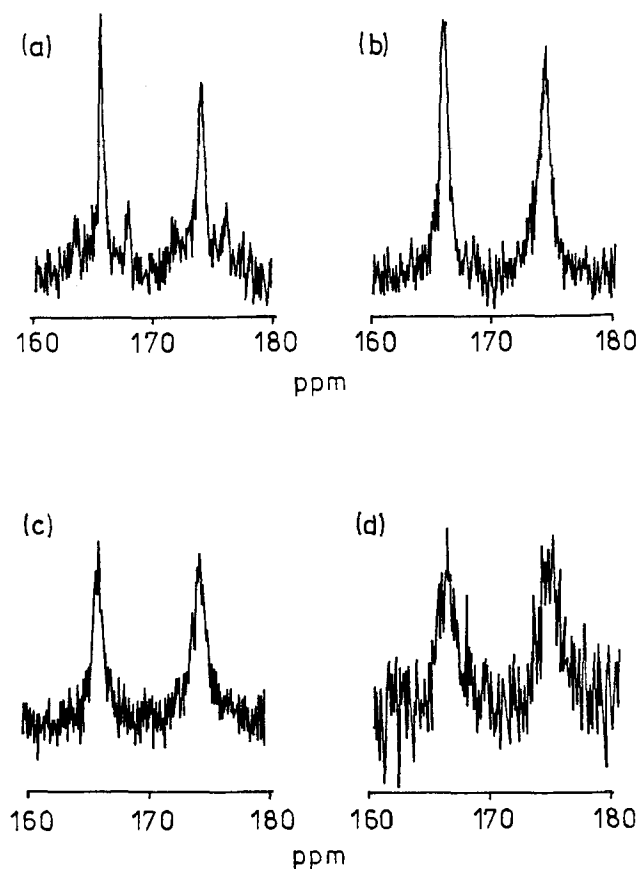
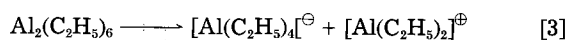
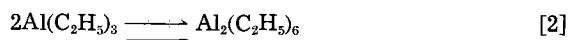
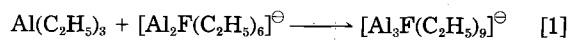


Fig. 6. ^{19}F -NMR spectra of $\text{C}_6\text{H}_5\text{CH}_2\text{N}(\text{CH}_3)_3\text{F} + \text{Al}(\text{C}_2\text{H}_5)_3$ solutions at $m = 3$ diluted with toluene (a) neat, (b) 25% toluene, (c) 50% toluene, and (d) 75% toluene.

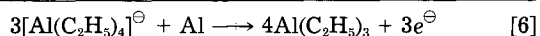
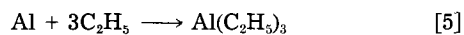
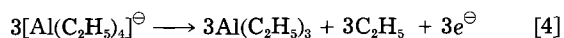
Electrorefinement Studies

Figure 7 shows the cyclic voltammograms for trimethylbenzyl ammonium triethylaluminum fluoride electrolyte using an Al anode for various dilutions m in the range $2.00 \leq m \leq 2.13$. The peak anodic and cathodic current densities for Al dissolution and Al deposition, respectively, are proportional to the amount of $\text{Al}(\text{C}_2\text{H}_5)_3$ added. According to the above NMR study, at $m = 2$ most of the $\text{Al}(\text{C}_2\text{H}_5)_3$ is complexed, but the concentration of free $\text{Al}(\text{C}_2\text{H}_5)_3$ increases substantially with increasing m , suggesting that the peak anodic and cathodic current densities for Al dissolution and Al deposition, respectively, are related to the concentration of excess $\text{Al}(\text{C}_2\text{H}_5)_3$ that is coupled to the following equilibria



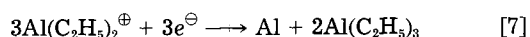
We propose the following overall anodic and cathodic partial reactions.

For the anodic reaction

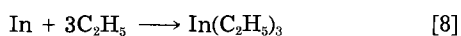


The formation of ethyl radicals in the anodic step, as assumed in Eq. [3], is a proven experimental fact and leads, in the case of inert metal anode, to the formation of the disproportionation products ethane and ethylene, as previously reported (9).

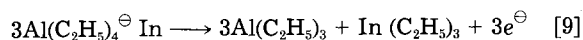
For the cathodic reaction



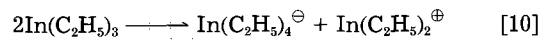
Since a replacement of the Al anode by an In anode leads to the chemical dissolution of In according to Eq. [8]



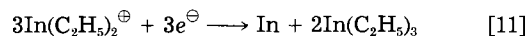
the overall anodic reaction is in this case



Consequently, upon electrolysis under galvanostatic conditions, the initially pure aluminum complex electrolyte becomes enriched in triethylindium, which, according to the equilibrium



is coupled to net cathodic reaction



This suggests the possibility of In deposition from an initially pure Al complex electrolyte, which has been verified previously (9) and has been explored here in more detail.

Table I shows the increase of the In concentration in the electrolyte during a typical galvanostatic experiment at a current density of 20 mA/cm² at the cathode which corresponds to ~5 mA/cm² at the In anode. The following features were observed: (i) the indium concentration increased very slowly to a steady-state value of $\sim 9 \times 10^{-3}M$, (ii) there were considerable fluctuations in the In concentration close to the cathode particularly during the initial period of the electrolysis. These fluctuations may have been related to changes in the flow conditions in the cell.

Figure 8 shows the cyclic voltammograms of $m = 2.4$ aluminum electrolyte with various additions of triethylindium. Two cathodic and two anodic peaks were observed, corresponding to the deposition of In and Al and the reoxidation of the reduced species, respectively. In view of the small In:Al ratio in the electrolyte, the height of the Al peaks were far less sensitive to changes in the In concentration than were the In peak heights, which increased linearly with the In concentration.

The peak separation between Al and In deposition was ~0.8V, offering thus an excellent opportunity for separation by electrolysis at controlled potential. Analyses of deposits obtained at the In-peak potential revealed an Al level of, typically, 2 ppm, which we believe is primarily due to difficulties in completely cleaning the Al electrolyte off the surface of the cathodic deposit. No other impurities were detected. In particular, Ga that was found as a trace metal impurity in the commercial 5N and 6N pure In metal available to us was absent in the electrorefined In. This material is well suited for the growth of bulk single crystals of the indium containing III-V compounds where small levels of isoelectronic impurities do not significantly affect the lattice constant and the band structure. In fact, currently, the deliberate addition of isoelectronic impurities as a means for increasing the yield stress of III-V substrate crystals is being explored in several laboratories with the aim at reducing the density of dislocations due to thermal stress during crystal growth. However, for the purpose of epitaxial growth, further work on the reduction of the Al impurity level is required because of its relatively large distribution coefficient and sticking coefficient under the conditions of liquid phase epitaxy and molecular beam epitaxy, respectively. Of

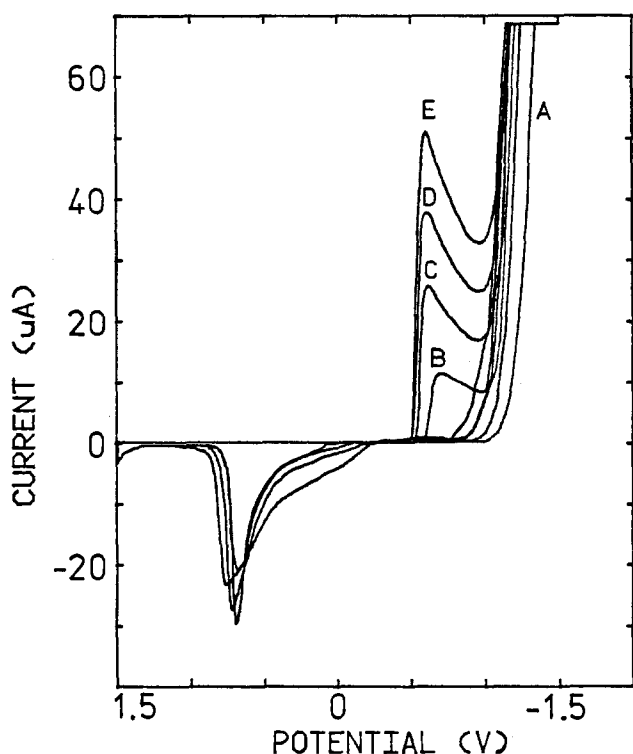


Fig. 7. Cyclic voltammograms at 25°C of $\text{Al}(\text{C}_2\text{H}_5)_3$ to $\text{C}_6\text{H}_5\text{CH}_2\text{N}(\text{CH}_3)_3\text{F}$ to toluene = $m:1:3$ solutions. Traces (A) $m = 2.00$, (B) $m = 2.05$, (C) $m = 2.08$, (D) $m = 2.11$, and (E) $m = 2.13$.

Table I. Electrolyte

Time (min)	[Al] (M)	[In] $\times 10^{-3}$ (M)
2	2.0	0.40
10	2.0	0.44
20	2.0	1.4
30	1.9	1.8
37	2.2	0.83
44	1.9	1.1
51	1.8	0.80
58	2.0	1.6
65	1.9	3.1
75	—	0.35
1278	—	9.3
2058	—	9.3

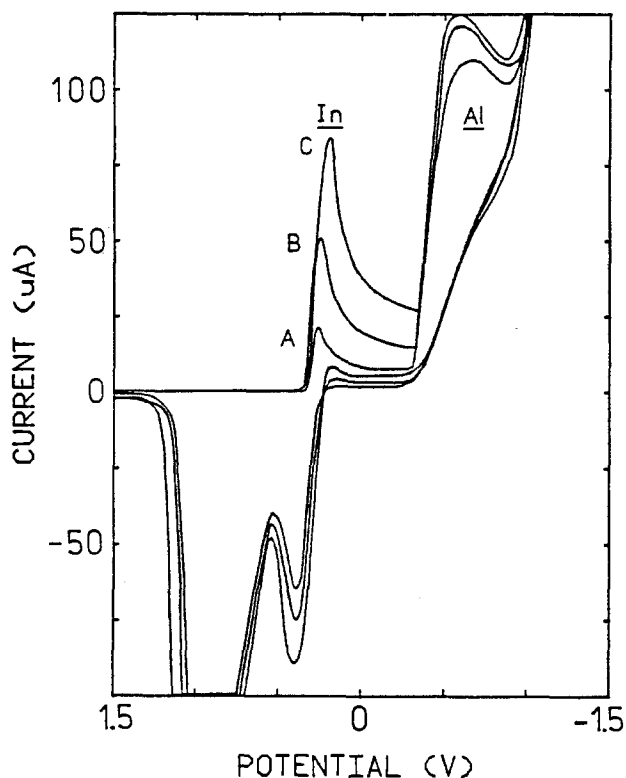


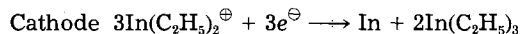
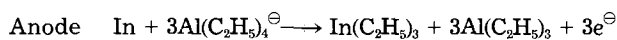
Fig. 8. Cyclic voltammograms at 25°C of $\text{Al}(\text{C}_2\text{H}_5)_3$ to $\text{In}(\text{C}_2\text{H}_5)_3$ to $\text{C}_6\text{H}_5\text{CH}_2\text{N}(\text{CH}_3)_3\text{F}$ to toluene = 2.40x:1:3 solutions. Traces (A) $x = 0.003$, (B) $x = 0.010$, and (C) $x = 0.017$.

course, this restriction does not apply to the growth of Al and In containing III-V alloy epilayers, where In electrorefined through the above described mixed Al + In alkyl electrolyte is a potentially useful source material.

Summary

High purity indium metal has been prepared by electrolysis at constant potential from a mixed Al + In complex electrolyte that contains typically 2 mol $\text{Al}(\text{C}_2\text{H}_5)_3$ and 0.06 mol $\text{In}(\text{C}_2\text{H}_5)_3$ per mol $\text{C}_6\text{H}_5\text{CH}_2\text{N}(\text{CH}_3)_3\text{F}$. Based on the results of NMR measurements that provide insight into the complex equilibria and of cyclic voltammetry applied to the pure Al complex electrolyte and to the mixed electrolyte, a mechanism for the cathodic and anodic steps in the electrorefinement process is proposed. This

mechanism is described by the following net electrode reactions



It is the opinion of the authors that the $\text{C}_6\text{H}_5\text{CH}_2\text{N}(\text{CH}_3)_3^+$, $[\text{Al}_2\text{F}(\text{C}_2\text{H}_5)_6]^-$, and $[\text{Al}_3\text{F}(\text{C}_2\text{H}_5)_9]^-$ ions that exist in equilibrium with uncomplexed $\text{Al}(\text{C}_2\text{H}_5)_3$ serve merely as supporting electrolyte. The indium metal obtained by electrolysis in a mixed Al + In alkyl electrolyte is suitable for the synthesis and bulk crystal growth of III-V compounds and other In containing compound semiconductors. However, a further reduction of the ~2 ppm Al contamination level is required for making the electrorefined In a useful source material for epitaxial growth processes.

This work was supported by NSF Grant DMR-8210367.

Manuscript submitted Aug. 6, 1984; revised manuscript received Nov. 26, 1984.

North Carolina State University assisted in meeting the publication costs of this article.

REFERENCES

1. K. Ziegler, E. Holzkamp, R. Köster, and H. Lehmkuhl, *Angew. Chem.*, **67**, 213 (1955); K. Ziegler and H. Lehmkuhl, *ibid.* **67**, 424 (1955).
2. K. Ziegler and H. Lehmkuhl, *Z. Anorg. Allg. Chem.*, **283**, 414 (1956).
3. K. Ziegler and H. Lehmkuhl, DAS 1056, 377, April 30, 1959.
4. R. Dötzer, F. Engelbrecht, and E. Todt, DBP 1 236 208, August 9, 1960.
5. E. Todt and H. Hauschildt, DBP 1 170 658, June 13, 1961.
6. K. Ziegler, *Experientia*, Suppl. II, 274 (1955).
7. K. Ziegler, R. Köster, H. Lehmkuhl, and K. Reinert, *Liebigs. Ann. Chem.*, **629**, 33 (1960).
8. K. Ziegler, and H. Lehmkuhl, DAS 1 056 377, April 30, 1959.
9. R. Dötzer, *Chem.-Ing.-Tech.*, **36**, 616 (1964).
10. G. Natta, G. Allegra, G. Perego, and A. Zambelli, *J. Am. Chem. Soc.*, **83**, 5033 (1961).
11. H. Schmidbaur and H. F. Klein, *Angew. Chem. Int. Ed.*, **5**, 726 (1966).
12. K. J. Bachmann, *Ann. Rev. Mater. Sci.*, **111**, 441 (1981).
13. T. R. Crompton, in "Analysis of Organoaluminum and Organozinc Compounds," R. Belcher and H. Freiser, Editors, p. 153, Pergamon Press Ltd., New York, (1968).
14. K. Ziegler, H. Lehmkuhl, and A. Lindner, *Chem. Ber.*, **92**, 2320 (1959).
15. R. Dötzer, Bundesrepublik Deutschland, Pat. 1200817, April 21, 1966.

Cyclic Voltammogram of Formaldehyde and Its Related Species in Electroless Copper Solution

Thomas M. Tam*

Lockheed Missiles and Space Company, Incorporated, Sunnyvale, California 94086

ABSTRACT

The cyclic voltammetric method that allows the evaluation of formaldehyde concentrations in electroless copper solution is described. In this study, evidence is provided to show that methylene glycolate anion and its copper (II) complex are electroactive species in the solution. These species give a peak centered around $-0.25\text{V vs. Ag/AgCl}$. It is also proposed that this technique can easily be integrated into a remote monitoring system.

Electroless copper plating solutions are widely used in the fabrication of printed circuit boards. This solution has three critical chemical components requiring control: the copper concentration, the formaldehyde concentration, and the alkalinity of the solution. The goal of this study is

* Electrochemical Society Active Member.

to identify chemical probes that will allow monitoring of these parameters via a computer control system. The ideal probes are those that can measure the process solution *in situ*. For an electroless copper solution, it was found that the concentration of copper and alkalinity can be conveniently measured by color and pH probes. How-

ever, no probe is available to measure formaldehyde in this solution.

Recently, there have been a few publications discussing the cyclic voltammetric method for studying the chemistry of electroless copper plating solution (1-4). These authors were able to identify voltammetric peaks that could be assigned to formaldehyde. Some of these voltammograms were either too complicated or lacking in quantitative data and therefore unsuitable for our purpose. It was found that by using a rotating platinum working electrode and scanning the voltage within a narrow range (i.e., -0.60 to $+0.8V$), an anodic peak is obtained and can be assigned to formaldehyde. Data are presented in this paper that validate assignments of this peak to formaldehyde and related species.

Experimental

Solutions.—The sample solution used in this study was a one-month-old Shipley electroless copper solution obtained from the plating shop. This was originally prepared by using Shipley's Cuposit 328A, S, and Y solutions² (Shipley Company, Incorporated). The purpose in using this solution is that the results can be directly applied to a production solution.

For experiments where the formaldehyde was the variable, 80 ml of the process solution was diluted to 100 ml by using varying amounts of Shipley 328S and deionized water.

For experiments where copper (II) is the variable, copper sulfate (2-10 g/l) and a constant weight of Rochelle salt (25 g/l) were added to 20 ml process solution. An appropriate amount of Cuposit 328S was added to adjust the concentration of formaldehyde to 0.1-0.2M. These solutions were then diluted to 100 ml.

The pH of these solutions was adjusted using either concentrated H_2SO_4 or NaOH solutions.

Analysis of the solution.—The total concentration of formaldehyde, $[\Sigma CH_2O]$, was obtained using a procedure recommended by Shipley (5). The total copper concentration was obtained by iodometric titration (6) and is represented by $[\Sigma Cu(II)]$.

The pH of these solutions was adjusted using either concentrated H_2SO_4 or NaOH solutions.

Cyclic voltammetric measurements.—A 200 ml Brinkmann titration vessel was used to hold the working, auxiliary, and reference electrodes. The working electrode was prepared by pressing a 1/8 in. diam platinum rod into a 3/8 in. diam stainless steel rod. The electrode body was sealed using Microstop (Michigan Chrome and Chemical Corporation). The exposed platinum surface was polished with 600 grit silicon carbide grinding paper. A Dietzen motor equipped with a rotating mercury contact (Mercotac Incorporated) was used to rotate the electrode. The auxiliary electrode used was a piece of 1/6 in. diam copper wire, and the reference electrode was a gel-type double junction Ag/AgCl electrode (Graphic Control). The potential was driven by a cyclic voltammetric unit. A Soltec X-Y recorder (UP6432S) was used to record the voltage and current change, and the potential was scanned between -0.6 and $+0.8V$ at a rate of 40 mV/s.

Curve analysis.—Intensity of the peak at $-0.25V$ was obtained by integrating the area under the recorded curve. If the scan rate in obtaining the voltammogram is known, the time element (seconds) along the X-axis can be determined. The current at a given time gives the total number of coulombs, Σq , which is proportional to the concentration of electroactive species of interest. The cyclic voltammetric system currently used does not have an integrator. To obtain the area, the voltammogram obtained from the X-Y chart recorder is photocopied. On the photocopied voltammogram, a base line was drawn to

connect the minima at -0.15 to $-0.45V$. The peak was then cut out along the trace and weighed. Using a proportionality factor, the weight was then converted to Σq .

Results

Separate voltammograms of electroless copper solutions have been published (1, 2, 4). The peaks of these voltammograms are due to the plating of copper onto the electrode surface during cathodic scan, and to the reduction of copper to its oxide during anodic scan (7, 8). In addition, there are peaks that can be assigned to formaldehyde. These formaldehyde peaks seem to be affected by copper plated on the electrode surface; therefore, they are difficult to use for quantitative data. It was found by using a platinum electrode and scanning the voltage in a narrower range ($-0.6-0.8V$) that copper will not deposit on the electrode surface. As a result, a relatively clean voltammogram, as shown in Fig. 1, was obtained. When the voltage is scanned in a cathodic direction, a single sharp peak centered at -0.20 to $-0.25V$ is observed, and will be designated as peak A. If the voltage is scanned beyond the mixed potential ($-0.70V$), copper deposition will result (9, 10).

On the anodic scan, a different broad-band centered around $+0.2V$ is also observed. For a freshly prepared solution, this broad-band's intensity is rather high. As the solution is left to stand for a period of time (e.g., overnight), the intensity of the band decreases significantly. This band could be due to oxidation of formaldehyde and is inhibited by the formation of platinum oxide (3, 11). This change has no effect on peak A. The intensity of peak A depends upon the total concentration of formaldehyde, $[\Sigma CH_2O]$, copper, $[\Sigma Cu(II)]$, and the pH of the solution. By varying one of these parameters at a time, a series of quantitative data have been obtained. With this data, we attempt to assign peak A to specific electroactive species that are related to formaldehyde.

Intensity of peak A vs. $[\Sigma CH_2O]$ and pH.—In this study, the sample solution was a one-month-old electroless solution obtained from the plating shop. Peak intensity, Σq , can be obtained by keeping the pH and $[\Sigma Cu(II)]$ of the solution constant. The $[\Sigma CH_2O]$ can be varied by adding concentrated CH_2O solution (Cuposit 328S) to the electroless copper solution. The intensity of the peak increases linearly with respect to $[\Sigma CH_2O]$. Figure 2 shows three examples where the pH of the solutions were maintained at 11.82, 12.28, and 12.51. When pH of the solution is changed, the linear relationship of the two parameters still exists, but the slope of the straight line, S , changes. Also note that none of the straight lines can be extrapolated to a zero intercept. The intercepts, I , are dependent upon the change in pH of the solution. The values of I and S at different $[OH^-]$ (calculated from pH measurements) are shown in Table I. By plotting S^{-1} vs. $[OH^-]^{-1}$,

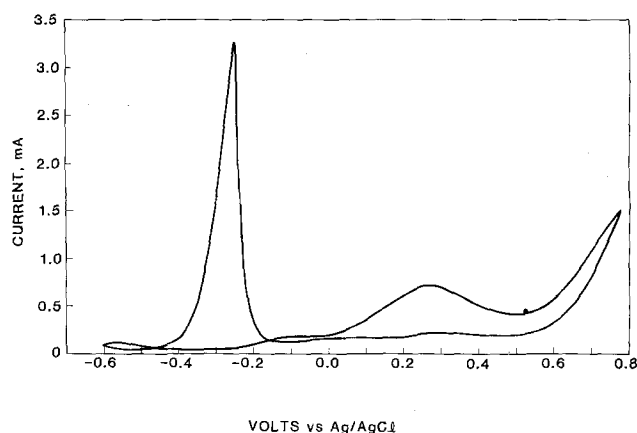


Fig. 1. Cyclic voltammogram of methylene glycolate and related copper (II) species in electroless copper solution. $[\Sigma Cu(II)] = 0.039M$; $[\Sigma CH_2O] = 0.23$; pH = 12.30. Sweep rate = 40 mV/s; rotational speed = 3000 rpm; temperature = $23^\circ \pm 1^\circ C$.

¹All voltages reported herein are with respect to Ag/AgCl reference electrode.

²Cuposit 328: (A) concentrated copper and formaldehyde solution; (S) concentrated formaldehyde solution; (Y) concentrated alkaline solution.

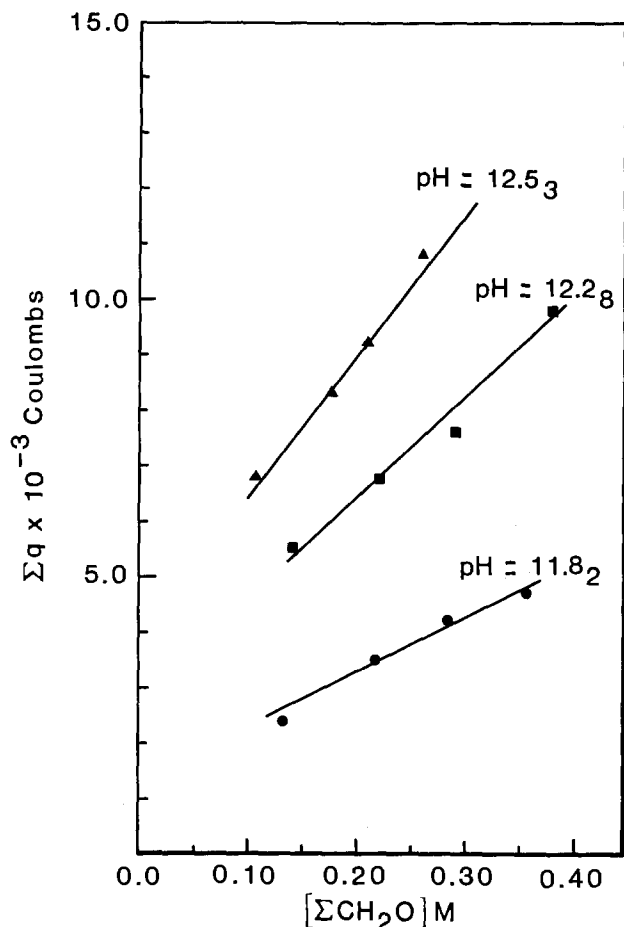
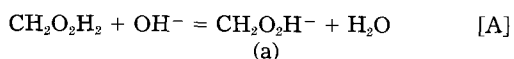


Fig. 2. Dependence of peak A's intensity of $[\Sigma \text{CH}_2\text{O}]$ and pH. Experimental conditions are given in Fig. 1.

a linear relationship is observed (see Fig. 3). These results can be represented by a general equation

$$\Sigma q = \frac{C_a Q_1 [\text{OH}^-]}{1 + Q_1 [\text{OH}^-]} [\Sigma \text{CH}_2\text{O}] + I \quad [1]$$

The principal species of formaldehyde dissolved in aqueous medium is methylene glycol, $\text{CH}_2\text{O}_2\text{H}_2$. In alkaline medium, methylene glycol will dissociate to methylene glycolate, (a) (12)



$$Q_1 = \frac{[\text{CH}_2\text{O}_2\text{H}^-]}{[\text{CH}_2\text{O}_2\text{H}_2][\text{OH}^-]} \quad [2]$$

$$[\Sigma \text{CH}_2\text{O}] = [\text{CH}_2\text{O}_2\text{H}_2] + [\text{CH}_2\text{O}_2\text{H}^-] \quad [3]$$

The value Q_1 is the equilibrium quotient for reaction [A]. Equation [3] is the mass balance equation for $[\Sigma \text{CH}_2\text{O}]$. The other terms in Eq. [2] and [3] are the equilibrium concentration of methylene glycol and methylene glycolate (a) that exist in the solution described by reaction [A]. Species a has been proposed as the electroactive

Table I. Dependence of S and I vs. $[\text{OH}^-]$.
 $[\Sigma \text{Cu(II)}] = 0.038 \pm 0.005\text{M}$. Temperature = $23^\circ \pm 1^\circ\text{C}$

$[\text{OH}^-] \times 10^{-3}\text{M}$	$S \times 10^{-2}\text{C M}^{-1}$	$I \times 10^{-3}\text{C}$
2.75	0.50	—
6.61	1.02	1.2
11.0	1.51	1.3
19.1	1.78	2.8
33.9	2.58	3.8
55.0	2.90	2.9
77.6	4.58	1.9

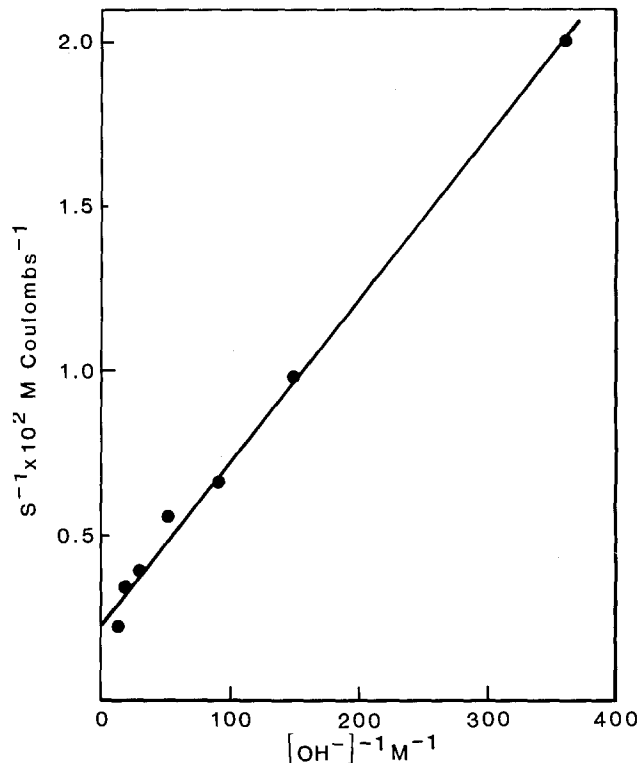


Fig. 3. Plot of S^{-1} vs. $[\text{OH}^-]^{-1}$. See Table I.

species in several other studies (4, 13). In this case, it is also proposed as one of the electroactive species that give rise to peak A. The Σq value measured can therefore be expressed by Eq. [4]

$$\Sigma q = C_a(a) + I \quad [4]$$

where C_a is the apparent proportionality constant describing the sensor parameters (*e.g.*, stirring and scan rate, surface area, etc.) and other solution matrix properties (14). In this study, these parameters were held constant. Equations [2], [3], and [4] can be used to derive Eq. [1], which describes the linear relation of Σq vs. $[\Sigma \text{CH}_2\text{O}]$ (Fig. 2) at constant $[\Sigma \text{Cu(II)}]$ and pH. The slope of the plot, $S = C_a Q_1 [\text{OH}^-] (1 + [\text{OH}^-]^{-1})^{-1}$, is pH dependent. The inverse of S gives Eq. [5], which can be used to describe the plot shown in Fig. 3

$$\frac{1}{S} = \frac{1}{C_a Q_1 [\text{OH}^-]} + \frac{1}{C_a} \quad [5]$$

From this plot, the slope $(C_a Q_1)^{-1}$ and intercept C_a^{-1} are $0.48 \text{ C}^{-1}\text{M}^2$ and $2.39 \text{ C}^{-1}\text{M}$, respectively. From these two values, the equilibrium quotients, Q_1 for reaction [A] can be calculated to be 50M^{-1} at 23°C . By using this value, the dissociation quotient for $\text{CH}_2\text{O}_2\text{H}_2$ is found to be $5.0 \times 10^{-13}\text{M}^{-1}$. Table II shows the same quotient determined by different workers.

The intercept I , from Eq. [1], first increases and passes through a maximum (pH = 12.53), then decreases as a function of pH. The change in the estimated surface concentration of formaldehyde (17) and the plating rate of electroless copper solution (18-20) with respect to pH behave in a similar fashion.

Intensity of peak A vs. $[\Sigma \text{Cu(II)}]$.—The dependence of Σq upon $[\Sigma \text{Cu(II)}]$ has also been studied. To isolate the ef-

Table II. Literature values of the dissociation quotients for the reaction $\text{CH}_2\text{O}_2\text{H}_2 = \text{CH}_2\text{O}_2\text{H}^- + \text{H}^+$

$Q_a \times 10^{-13}\text{M}^{-1}$	Ref.
0.53 (25°C)	Los (15)
2.1 (50°C)	Molenaar (16)
1.6 (23°C)	Walker (12)
5.0 (23°C)	This work

fect of $[\Sigma \text{Cu(II)}]$, Eq. [6] as used to correct the effect of $[\text{OH}^-]$, $[\Sigma \text{CH}_2\text{O}]$, and residual I value

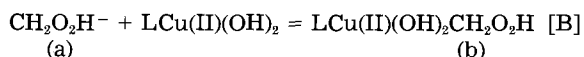
$$C_a = (\Sigma q - 1) \frac{1 + Q_1 [\text{OH}^-]}{Q_1 [\text{OH}^-] [\Sigma \text{CH}_2\text{O}]} \quad [6]$$

The values for C_a were determined with $[\Sigma \text{CH}_2\text{O}]$ maintained at 0.1M, 0.2M, and pH 12.5. The copper concentration, $[\Sigma \text{Cu(II)}]$, was varied from 0.01M to 0.10M by adding CuSO_4 and sodium tartrate salt to diluted electroless copper solutions. The value C_a decreases as $[\Sigma \text{Cu(II)}]$ increases and levels off at high $[\Sigma \text{Cu(II)}]$. A straight line is obtained by plotting $C [\Sigma \text{Cu(II)}]^{-1}$ vs. $[\Sigma \text{Cu(II)}]^{-1}$, as shown in Fig. 4. The equation that describes the plot is

$$\frac{C_a}{[\Sigma \text{Cu(II)}]} = \frac{C_1}{[\Sigma \text{Cu(II)}]} - C_2 \quad [7]$$

where $C_1 = 5.2 \times 10^{-2} \text{ C} \cdot \text{M}^{-1}$ and $C_2 = 4.6 \times 10^{-1} \text{ C} \cdot \text{M}^{-2}$. The change in shape of peak A with respect to $[\Sigma \text{Cu(II)}]$ is shown in Fig. 5. Notice that at low copper concentration, peak A is an asymmetric peak [Fig. 5(a)], which is similar to that of CH_2O in basic tartaric salt solution. But when $[\Sigma \text{Cu(II)}]$ is increased, peak A becomes more of a symmetric peak [Fig. 5(c)].

These results can be explained as follows. When copper (II) is dissolved in alkaline solution containing tartrate ion ($\text{C}_4\text{H}_2\text{O}_6^{-2} = \text{L}$), monomeric and dimeric species will form, e.g. $\text{L}_2\text{Cu(II)}$, LCu(II)(OH)_2 , and $\text{L}_2\text{Cu(II)}_2$ (21, 22). Within the pH range (11.4-12.9) of this study, the principal species is LCu(II)(OH)_2 (4, 18). The LCu(II)(OH)_2 species can react with methylene glycolate to give complex (b)



Schoenberg (18) has shown by using EPR and spectrophotometric techniques that (b) is a stable complex in the solution. Byerly has also proposed this complex as a reaction intermediate for the reduction of Cu(II) by formaldehyde (23). We are proposing that species (b) is also an electroactive species. At low $[\Sigma \text{Cu(II)}]$, the principal electroactive species is methylene glycolate, (a). As $[\Sigma \text{Cu(II)}]$ increases, (a) is being replaced by (b). The proportional constant of species (b) is smaller than that of (a). This will cause the apparent proportional constant, C_a , to decrease (Eq. [7]). This rationale is consistent with the change in shape of peak A observed Fig. 5.

Conclusion

In this report, the cyclic voltammetric technique was used to study the electroless copper solution. Quantita-

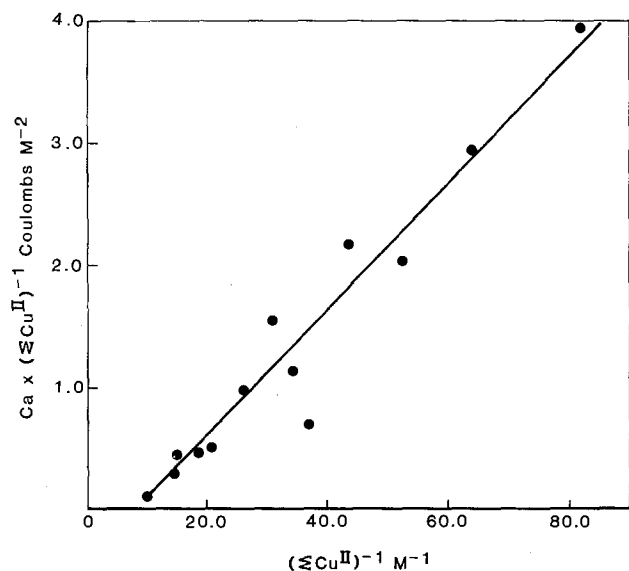


Fig. 4. $C_a [\Sigma \text{Cu(II)}]^{-1}$ vs. $[\Sigma \text{Cu(II)}]^{-1}$. $[\Sigma \text{CH}_2\text{O}] = 0.1$ or 0.2M . $\text{pH} = 12.51 \pm 0.04$. Experimental conditions are given in Fig. 1.

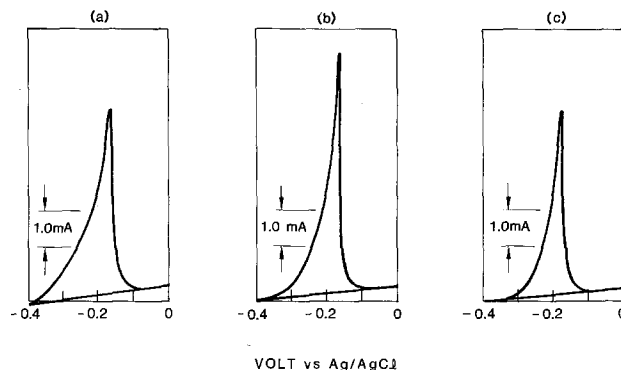


Fig. 5. Change in the shape of peak A with respect to $[\Sigma \text{Cu(II)}]$. (a) $[\Sigma \text{Cu(II)}] = 0.016\text{M}$; (b) 0.029M ; (c) 0.069M . $\text{pH} = 12.51 \pm 0.04$.

tive data have been obtained to show that the peak at -0.25V depends upon $[\Sigma \text{CH}_2\text{O}]$, $[\Sigma \text{Cu(II)}]$, and pH of the solution. For the present moment, peak A is assigned to methylene glycolate, a, and its copper (II) adduct, b. This proposal most likely is oversimplified, but, nevertheless, it is consistent with the data presented thus far.

Use of different types of electrochemical measuring systems as remote sensors have been suggested elsewhere (17, 24). The cyclic voltammetric technique used in this work is easy to operate and can be integrated into a remote monitoring system. The apparatus described has been used to measure the formaldehyde concentration in the shop solutions for more than 2 months. The only precaution required was to rinse and soak the electrodes in deionized water after they were used. The accuracy of the data is estimated to be $\pm 13\%$. Because of these advantages, this technique offers another possibility of measurements *in situ*.

Manuscript submitted Jan. 20, 1984; revised manuscript received Nov. 20, 1984.

Lockheed Missiles and Space Company, Incorporated, assisted in meeting the publication costs of this article.

REFERENCES

1. T. R. Beck, American Electroplater's Society, Sur/Fin '82, Annual Technical Conference, San Francisco, California, 1982.
2. M. Paunovic and R. Arndt, *This Journal*, **130**, 794 (1983).
3. R. Z. Acosta and T. L. Romankiw, Abstract 277, p. 736, The Electrochemical Society Extended Abstracts, Vol. 77-2, Atlanta, Georgia, Oct. 9-14, 1977.
4. M. Saito, *Met. Surf. Tech. Jpn.*, **16**, 300 (1965); *ibid.*, **17**, 15 (1965); *ibid.*, **17**, 260 (1965).
5. Shipley Inspection Procedure No. S-105, Shipley Company, Inc., Carson, CA 90745.
6. N. J. Blaedel and V. W. Meloche, "Elementary Quantitative Analysis," 2nd ed., p. 489, Harper and Row, New York (1963).
7. D. D. MacDonald, *This Journal*, **121**, 651 (1974).
8. S. Fletcher, R. G. Barrada, and J. D. Porter, *ibid.*, **127**, 1960 (1978).
9. F. M. Donahue, K. L. Wong, and R. Bhella, *ibid.*, **127**, 2340 (1980).
10. M. Paunovic, *Plating*, **55**, 1161 (1968).
11. A. Damjanovic, L. S. R. Yeh, and J. Wolf, *This Journal*, **127**, 1945 (1980).
12. J. F. Walker, "Formaldehyde," pp. 37, 107, Reinhold Publishing, Chapman and Hall Ltd., London (1974).
13. R. P. Buck and L. R. Griffith, *This Journal*, **109**, 1005 (1962).
14. A. M. Bond, "Modern Polarographic Methods in Analytical Chemistry," p. 448, Marcel Dekker Inc., New York (1980).
15. L. M. Los, A. A. M. Brinkmann, and B. J. C. Wetsma, *Electroanal. Chem. Interfacial Electrochem.*, **56**, 187 (1974).
16. A. Molenaar, M. F. E. Holdrinet, and L. K. H. VanBeek, *Plating*, **3**, 239 (1974).
17. M. Paunovic, *This Journal*, **127**, 365 (1980).
18. L. Schoenberg, *ibid.*, **119**, 1491 (1972).

19. R. F. Horn, *Plating Surf. Finishing*, **10**, 50 (1981).
 20. F. J. Nuzzi, *ibid.*, **12**, 51 (1983).
 21. E. Bottari and M. Vicedomini, *J. Inorg. Nucl. Chem.*, **33**, 1463 (1971).

22. R. L. Belford, *Chem. Commun.*, 508 (1971).
 23. J. J. Byerly and W. K. Teo, *Can. J. Chem.*, **47**, 3355 (1964).
 24. J. L. Shippey, C. U. Yu, and F. M. Donahue, *Plating*, **762** (1972).

Photoelectrochemistry of Doped and Undoped Semiconductors: A Comparison

O. E. Hüsser and H. von Känel

Laboratorium für Festkörperphysik, ETH Zürich, 8093 Zürich, Switzerland

F. Lévy

Institut de Physique Appliquée, EPF Lausanne, 1015 Lausanne, Switzerland

ABSTRACT

Recently, an experimental method was introduced which allows photoelectrochemical studies of nearly intrinsic semiconductors. In this simple technique, subbandgap illumination is used to make the bulk material photoconductive. A corresponding model explains this behavior in terms of a potential distribution which is similar to that of a doped semiconductor. The method allows one to predict whether the time consuming process of chemical doping, for applications such as photoelectrolysis, is worth undertaking. The model proposed relies heavily on the photoconductivity of the insulator. We have now been able to observe the effect even on a number of very poor photoconductors, such as layered chalcogenides SnS_2 , $\text{Sn}(\text{Se}_{0.1}\text{S}_{0.9})_2$, MnPS_3 ($M = \text{Cd}, \text{Mn}$). In the case of SnS_2 , we can compare the photoelectrochemical studies of undoped semiconductors with chemically doped semiconductors. Furthermore, we find that the response at high photon energies caused by the subbandgap illumination scales indeed with the photoconductivity of the high resistivity semiconductors, lending additional support for the model.

Photoelectrochemical investigations of undoped semiconductor electrodes are often hampered by extremely low quantum yields. The photocurrent response to monochromatic light is usually limited to a narrow spectral region near the absorption edge. For charge carriers created in the vicinity of the electrode surface by strongly absorbed photons, the internal electric fields are not sufficiently strong to provide an efficient separation of the electron-hole pairs. Recently, it has been shown (1, 2) that irradiation of the electrode with a light source providing photon energies in the range of the bandgap may drastically change the properties of the insulator-electrolyte interface. This subbandgap illumination can enlarge the spectral response due to a second monochromatic light source by several orders of magnitude, even for wavelengths much shorter than the absorption edge. A simple model (1, 2) explains this behavior as a change of the potential distribution in the electrode: the bulk of the insulator electrode gets photoconductive by irradiation with weakly absorbed light and the resulting potential distribution resembles that of a doped semiconductor.

The effect of a background illumination which induces a higher injection rate of carriers has been used for more than 10 years (3, 4). But usually only relatively highly doped semiconductors were examined.

In this paper, we show that this double-beam technique can be applied to rather poor photoconductors such as SnS_2 , $\text{Sn}(\text{Se}_{0.1}\text{S}_{0.9})_2$, MnPS_3 , and CdPS_3 . These materials crystallize in a layered crystal structure of hexagonal (SnS_2 , $\text{Sn}(\text{Se}_{0.1}\text{S}_{0.9})_2$) or rhombohedral (CdPS_3 , MnPS_3) symmetry, respectively (5, 6). The bonding between layers is weak compared to the intralayer forces, the latter being predominantly of covalent character.

Taking SnS_2 as an example, we demonstrate a close relationship between the photocurrent spectra of doubly illuminated high resistivity electrodes and chemically doped electrodes.

In addition to the photoelectrochemical measurements the bandgaps were determined by standard optical techniques.

Crystal Growth

Single crystals have been grown from the elements or from the prereacted compounds by the chemical vapor

transport reactions, with iodine as transport agent and in presence of excess chalcogen. The growth temperatures of the crystals were between 590° and 680°C and the temperature of the source material between 620° and 710°C. The temperature difference between the two ends of the crucible about 15 cm in length did not exceed 30°C. In the case of the doped sample $\text{SnS}_2\text{:Ga}$, the compound was sublimated several times from one end of the ampulla to the other before the last growth transport, in order to homogenize the impurity distribution in the crystals. Typical samples were checked by x-ray diffraction tests.

Electrode Preparation, Photoelectrochemical Cell, and Experimental Setup

All crystals were mounted on brass in Teflon cylinders with conducting silver paint. The edges of the crystal plates were protected with epoxy. In all cases, the surface perpendicular to the c-axis was exposed to the solution. The aqueous electrolytes used were 1M HCl, 1N H_2SO_4 , 1M NaOH, or 1M Na_2S , as indicated in the figure captions. The photoresponse for all electrodes was measured using a standard three-electrode cell: a working electrode, a saturated calomel electrode (SCE) as a reference, and a platinum wire as counterelectrode. For the potential control of the highly resistive electrodes an ordinary power supply was used. The doped SnS_2 electrodes were controlled potentiostatically with the disk circuit of a Tacussel bipotentiostat. The working electrode was arranged in such a way that simultaneous irradiation by two light sources was possible. Monochromatic illumination was provided by a tungsten-halogen lamp (12V, 55W) filtered through a Zeiss M4G II single prism monochromator. This radiation was chopped at 150 Hz and the photocurrent response was measured with standard lock-in techniques. Subbandgap illumination was achieved with unchopped radiation using a 150W Xe lamp and a Schott filter with an absorption edge just below that of the crystals.

Results and Discussion

Solid-state properties.—All undoped crystals have resistivities larger than $10^7 \Omega \text{ cm}$ at room temperature (7). In Table I are given the approximate values of the bandgap energies ($E_{\text{gap}} + E_{\text{phonon}}$), obtained by plotting the

Table I. Approximate value of the bandgap energy derived from optical measurements

	$E_{\text{gap}} + E_{\text{phonon}}$ (eV)
SnS_2	2.14 ± 0.02
$\text{Sn}(\text{Se}_{0.1}\text{S}_{0.9})_2$	1.98 ± 0.02
CdPSe_3	2.27 ± 0.03
MnPSe_3	1.87 ± 0.03
$\text{Sn}_{1-x}\text{Ga}_x\text{S}_2$ ($x = 0.001$ nom.)	2.19 ± 0.02

square root of the absorption coefficient α vs. the photon energy (all transitions are indirect). The expected kink in the $\sqrt{\alpha}$ curve could not be observed because all investigated layered crystals were too thin. Therefore, the phonon energy E_{phonon} could not be determined.

Photoelectrochemical measurements.—It is a characteristic feature of high resistivity semiconductor electrodes that the response to monochromatic illumination is usually limited to a small spectral region near the absorption edge.

The magnitude of the photoresponse strongly depends on the photoconductivity of a sample. In fact, it will be shown below that the photoconductivity of all our samples is rather poor. As an example, for a ternary compound exhibiting all the salient features of such a poor photoconductor we show in Fig. 1, the photocurrent-potential curves for a cathodically polarized CdPSe_3 electrode in 1M HCl. For strongly absorbed monochromatic illumination, i.e., $E_{\text{photon}} = 2.70$ eV, which is far above the adsorption edge ($E_{\text{gap}} \sim 2.27$ eV), the photocurrent remains extremely small up to the highest electrode potential (Fig. 1, lower curve). When the electrode is in addition illuminated with subbandgap light (Xe radiation, Schott filter OG530, corresponding to a cutoff around of 2.3 eV) the photocurrent increases dramatically (Fig. 1, upper curve). The magnitude of the enhancement strongly depends on the ratio of the intensities of subbandgap to monochromatic illumination. Towards high values of this ratio, a saturation of the enhancement is commonly observed (see also Fig. 4 below). The dark current was much smaller than 1 nA, just as for all other cases considered below.

With and without subbandgap illumination the photocurrent-potential curves are practically linear up to the highest applied potential (Fig. 1). The same has been found for all high resistivity materials investigated in this work. Furthermore, the photocurrent-potential curves are symmetrical for anodic and cathodic polarization. The infrared part of the subbandgap spectrum affects the enhancement very little. This is revealed most clearly by the strong dependence of the enhancement on the cutoff

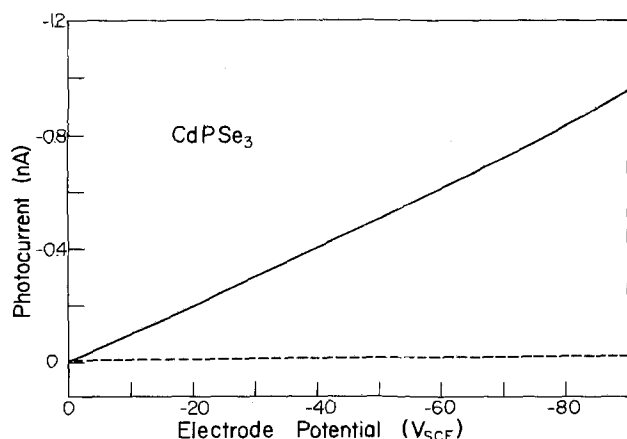


Fig. 1. Photocurrent-potential curves for a CdPSe_3 -electrode in 1M HCl, cathodic polarization. For the lower curve, the electrode was illuminated with chopped monochromatic light ($E_{\text{photon}} = 2.64$ eV) alone, whereas for the upper one both light sources (steady-state subbandgap radiation with a cutoff energy of about 2.3 eV) were used. The dark current was negligible.

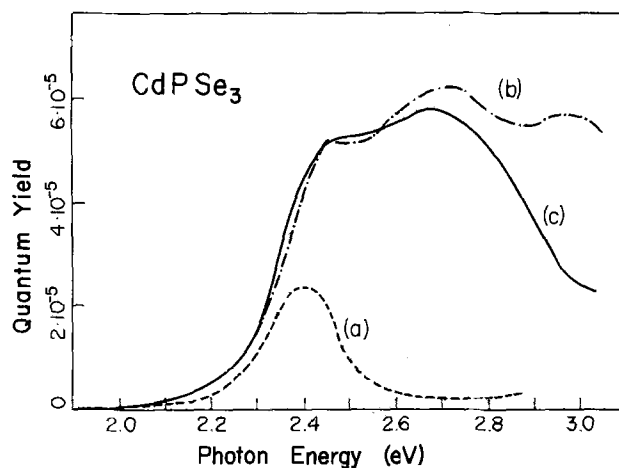


Fig. 2. Spectral dependence of the quantum yield for a CdPSe_3 electrode in 1M HCl with monochromatic illumination alone (curve a) and with additional subbandgap radiation ($E_{\text{photon}} < 2.34$ eV, curves b and c). Curve b corresponds to an anodic ($+100$ V_{SCE}) and curve c to a cathodic bias (-100 V_{SCE}). In the case of monochromatic illumination alone, the quantum yields for anodic and cathodic polarization coincide (curve a, ± 100 V_{SCE}).

filter. The use of filters with cutoff energies far below the absorption edge of the electrode does not lead to an increase of the response at high energy.

The quantum yield spectra for CdPSe_3 are shown in Fig. 2 with monochromatic illumination alone (curve a) and with additional subbandgap illumination (curves b and c). In the latter case curve b is for anodic polarization ($+100$ V_{SCE}) while curve c represents cathodic polarization (-100 V_{SCE}). For monochromatic illumination alone the curves for anodic and cathodic polarization coincide. The most remarkable feature of Fig. 2 is the huge increase of the blue response ($E_{\text{photon}} > 2.6$ eV) upon illumination of the electrode by subbandgap radiation (compare Fig. 1). In addition the photoconductivity is enhanced by roughly a factor of two at 2.4 eV. Qualitatively the behavior of CdPSe_3 is thus similar to that one of the much better photoconductor HgI_2 apart from the asymmetry between anodic and cathodic polarization for the latter (2). In fact for CdPSe_3 the symmetry is not completely achieved either when subbandgap irradiation is employed (Fig. 2, curve b and c). This might be due to increased surface recombination for short wavelengths in the cathodic case. For all other high resistivity materials considered below the symmetry is even more pronounced. This indicates that electron and hole mobilities parallel to the c-axes are of the same order of magnitude in these compounds. As an example we show the quantum yield spectra of pure SnS_2 in 1M HCl (Fig. 3). The curves are labeled in the

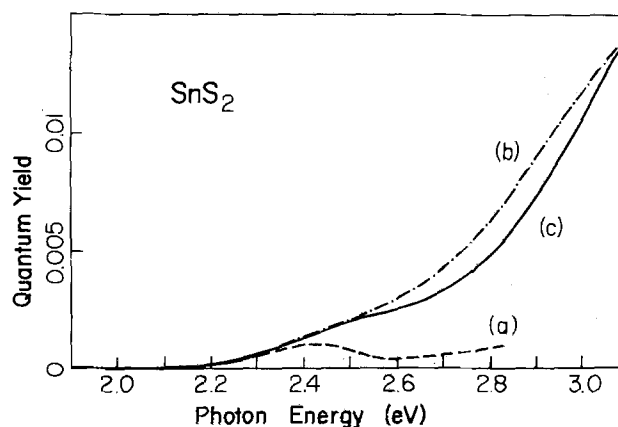


Fig. 3. Quantum yield spectra of SnS_2 in 1M HCl with monochromatic illumination alone (curve a, ± 10 V_{SCE}) and with subbandgap radiation (cutoff energy of about 2.18 eV) for anodic polarization ($+10$ V_{SCE}, curve b) and cathodic polarization (-10 V_{SCE}, curve c), respectively.

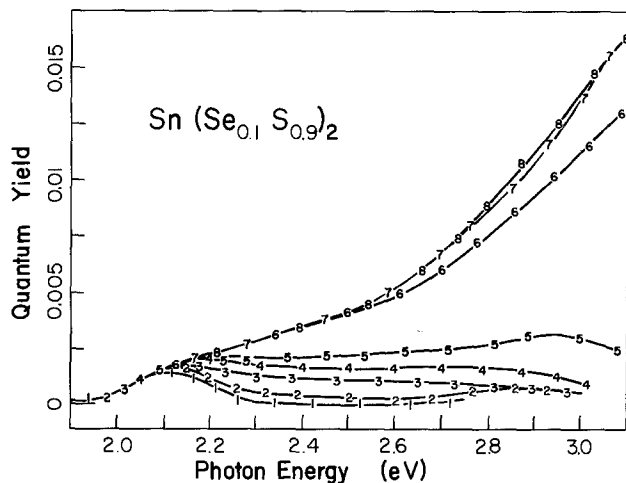


Fig. 4. Spectral dependence of the quantum yield for an $\text{Sn}(\text{Se}_{0.1}\text{S}_{0.9})_2$ electrode for various intensities of the subbandgap illumination (cutoff energy ~ 2.03 eV). Electrode potential $2 V_{\text{SCE}}$, electrolyte $1M \text{Na}_2\text{S}$. Curve 1: Monochromatic illumination alone. Curve 2: Subbandgap radiation filtered with 0.001 neutral-density filter. Curve 3: Subbandgap radiation filtered with 0.01 neutral-density filter. Curve 4: Subbandgap radiation filtered with 0.05 neutral-density filter. Curve 5: Subbandgap radiation filtered with 0.1 neutral-density filter. Curve 6: Subbandgap radiation filtered with 0.5 neutral-density filter. Curve 7: Subbandgap radiation filtered with 0.708 neutral-density filter. Curve 8: Subbandgap radiation with full Xe-lamp intensity.

same way as in Fig. 2. In contrast to the quantum yield spectra of CdPSe_3 however, the electrode potential was only $\pm 10 V_{\text{SCE}}$. It has to be borne in mind that neither Fig. 2 nor Fig. 3 represent limiting quantum yields since no saturation of the photocurrent-potential curves is observed. We believe that the lack of saturation in the photocurrent *vs.* potential is a direct consequence of the small photoconductivity encountered in these materials. The high bulk recombination rate thus prevents the establishment of a sufficient space-charge layer which would in turn lead to an efficient carrier separation. Nevertheless, it appears that the generation of charge carriers by subbandgap illumination is high enough to yield a substantial increase of the blue response, even in the poor photoconductors considered in this work. This is true only for sufficient intensities of the subbandgap radiation. Taking as an example an $\text{Sn}(\text{Se}_{0.1}\text{S}_{0.9})_2$ electrode in $1M \text{Na}_2\text{S}$, the dependence of the quantum yield spectra on the intensity of the subbandgap radiation is plotted in Fig. 4. Qualitatively, the behavior is the same as for pure SnS_2 . Intensities are given in arbitrary units. The blue response becomes larger the larger the intensity, showing saturation for the highest values of the latter. This can be seen more clearly in Fig. 5, in which the quantum yield is plotted against the intensity of the subbandgap illumination (for various photon energies of the monochromatic radiation) on a double logarithmic scale.

The behavior of MnPSe_3 is entirely similar to that one of the other materials described above.

In order to show that the spectral response of doubly illuminated high resistivity semiconductor electrodes resembles that one of chemically doped semiconductor electrodes, we compare the behavior of pure SnS_2 with that one of gallium-doped SnS_2 . Surprisingly, Ga doping (nominal 0.1%) leads to an increase of the bandgap by 0.05 eV (Table I) compared to pure SnS_2 . Furthermore, the n-type behavior (Fig. 6) indicates that Ga is not incorporated into Sn sites as a trivalent dopant. The actual donor concentration, which is not known at present, will be determined in a forthcoming publication.

In Fig. 6, the current-potential curves are represented for an SnS_2 photoanode in the dark and with monochromatic illumination ($E_{\text{photon}} = 3.1$ eV) of approximately $60 \mu\text{W}/\text{cm}^2$. The reverse dark current is negligible up to $3 V_{\text{SCE}}$. Photocurrent onset is around $0.4 V_{\text{SCE}}$. The saturation of the photocurrent for anodic potentials is relatively

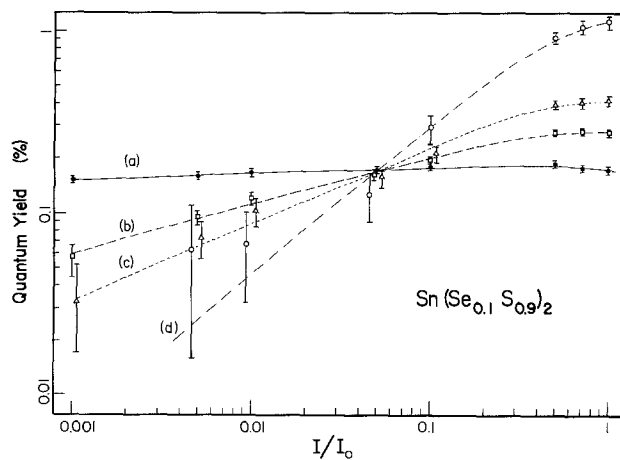


Fig. 5. $\text{Sn}(\text{Se}_{0.1}\text{S}_{0.9})_2$: Quantum yield *vs.* intensity of the dc subbandgap illumination (cutoff energy ~ 2.03 eV) for various photon energies of the chopped monochromatic beam. Intensities are given in units of the full Xe-lamp intensity I_0 . Curve a: 2.15 eV. Curve b: 2.3 eV. Curve c: 2.5 eV. Curve d: 2.9 eV. Electrode potential $2 V_{\text{SCE}}$, electrolyte: $1M \text{Na}_2\text{S}$. Plotted lines are a guide for the eye.

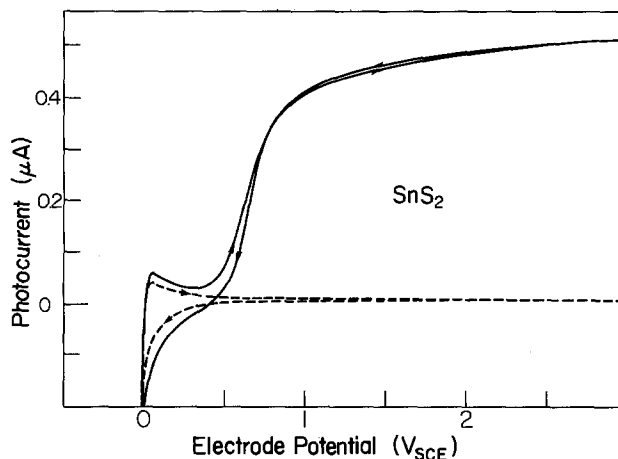


Fig. 6. Current-potential curves for a Ga (0.001 nom.) doped SnS_2 electrode in $1N \text{H}_2\text{SO}_4$. Lower curve: dark current. Upper curve: photocurrent for monochromatic illumination ($E_{\text{photon}} = 3.1$ eV, $\approx 60 \mu\text{W}/\text{cm}^2$).

slow indicating a rather low doping. The quantum yield spectrum (uncorrected for reflection) of a Ga-doped SnS_2 electrode is shown in Fig. 7. The shape of the photoresponse is virtually identical to that one of the undoped electrode in Fig. 3. The absolute magnitude of the response, however, is much larger, approaching 100% at 3.1 eV if reflection losses are taken into account. The electrolyte was $1M \text{Na}_2\text{S}$ in this case. The use of this electrolyte resulted in a much better output stability for the higher photocurrent densities at the doped electrodes (see also below). The indirect nature as well as the value of the bandgap are nicely confirmed in Fig. 8, in which both $\sqrt{\Phi \cdot h\nu}$ and $\sqrt{\alpha \cdot h\nu}$ are plotted against the photon energy. Φ and α are the quantum yield and adsorption coefficient, respectively. It should be remarked that, in accordance with Ref. (8), our data do not permit an unambiguous distinction between an indirect allowed and an indirect forbidden transition. In the latter case, a plot of the cube root of the absorption coefficient *vs.* photon energy should yield a straight line. The square root fit shown in Fig. 8 does represent our data somewhat better.

Photocorrosion.—In the dark the investigated materials were stable in all used electrolytes. The photocurrent of all investigated semiconductors was accompanied by obvious decomposition of the electrode, particularly at high irradiation intensities. For the high resistivity semiconductors [SnS_2 , $\text{Sn}(\text{Se}_{0.1}\text{S}_{0.9})_2$, CdPSe_3 , MnPSe_3] and for

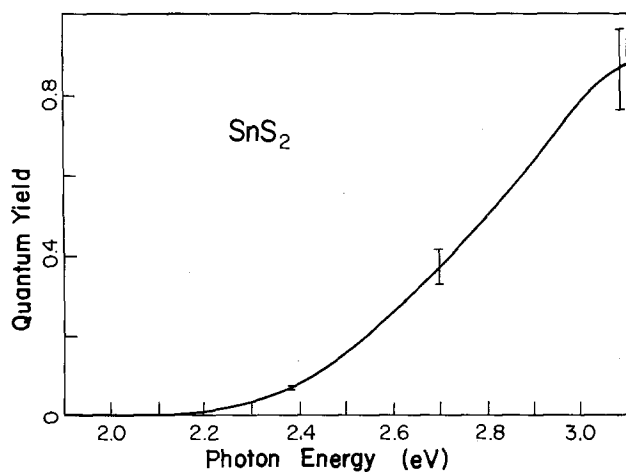


Fig. 7. Quantum yield spectrum of a doped SnS_2 electrode. Electrode potential 2 V_{SCE} . Electrolyte: $1 \text{ M Na}_2\text{S}$.

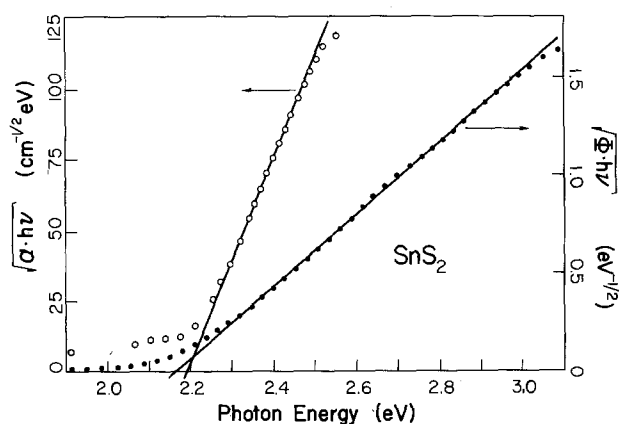


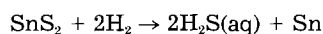
Fig. 8. Ga-doped SnS_2 : Dependence of $\sqrt{\Phi \cdot h\nu}$ (Φ = quantum yield, $h\nu$ = photon energy) and $\sqrt{\alpha \cdot h\nu}$ (α = absorption coefficient) on the photon energy. The linear behavior indicates an indirect bandgap [i.e., $\sqrt{\alpha} \propto (h\nu - E_{\text{gap}} - E_{\text{phonon}})$]. Same electrolyte and potential as in Fig. 7.

chemically doped SnS_2 the light induced decomposition was very rapid.

In the case of SnS_2 , an anodic photocurrent leads to the formation of a yellow layer (probably sulfur), accompanied by a decrease of the photocurrent. For this compound the thermodynamic data are available (9-12), assuming the reaction

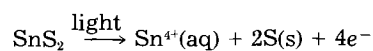


the anodic decomposition potential is calculated to be $V_{\text{dec}}^{\text{an}} \approx 0.14 \text{ V}_{\text{SCE}}$. For cathodic decomposition, we obtain $V_{\text{dec}}^{\text{cath}} \approx -0.005 \text{ V}_{\text{SCE}}$ from



at pH 0.

For anodic polarization addition of Na_2S to the electrolyte leads to a stable photocurrent for small light intensity



whereas the elemental sulfur is dissolved by the polysulfide electrolyte.

Discussion.—All high resistivity semiconductors investigated to date, appear to have the following common photoelectrochemical characteristics: (i) for monochromatic illumination alone, the photocurrent response is limited to weakly absorbed radiation, (ii) for photon energies far above the absorption edge, a significant photocurrent is obtained only when the electrode is simultaneously illuminated with a second light source,

Table II. Relation between the photoconductivity and the enhancement of the blue response due to additional subbandgap irradiation

	Φ/Φ'
SnS_2	0.1
$\text{Sn}(\text{Se}_{0.1}\text{S}_{0.9})_2$	0.1
CdPSe_3	0.3
MnPSe_3	0.1
HgI_2 (2)	0.5
GaS (1)	0.1

Φ : Maximum quantum yield at the photoconductivity peak (see, e.g., curves a and b in Fig. 2 and 3).

Φ' : Maximum quantum yield in the presence of subbandgap illumination. Average values of up to five samples were used. Individual measurements may differ by as much as a factor of 10 without a change of Φ/Φ' .

providing photon energies in the range of the bandgap, (iii) for an optimum enhancement of the blue response, a high enough intensity of the subbandgap illumination is necessary. Furthermore, the correct choice of the high energy cutoff of the latter may be crucial.

All these features are well explained by the model outlined in detail in Ref. (2). The model explains the observed enhancement of the photoresponse in terms of a change of the potential distribution in the electrode by photoexcited bulk carriers. As a consequence, the model predicts a strong dependence of the effect on the photoconductivity of a sample. This can be verified indeed by comparing the materials investigated in this work with the much better photoconductors GaS , CdS (1), and HgI_2 (2). Qualitatively, the effect of the subbandgap illumination on the photocurrent spectra is quite similar in all these cases. This has to be contrasted with the much lower absolute quantum yields of our materials, even at a bias short of electric breakdown (see, e.g., Fig. 2). There is thus an obvious correlation between the height of the photoconductivity peak Φ (curve a in Fig. 2 and 3) and the maximum quantum yield Φ' , which can be obtained for photon energies far above the absorption edge in the presence of suitable subbandgap illumination (curves b and c in Fig. 2 and 3, as well as top curves in Fig. 4). In order to put this statement in a more quantitative form, the ratio between these two quantities, Φ/Φ' , is given in Table II for several different semi-insulating electrode materials. Evidently, this number is very nearly the same for all materials. In particular, it is practically independent of the shape of the photocurrent-potential curves. However, the absolute magnitude of the quantum yields Φ' , taken at the same bias,¹ differs by as much as a factor of 2000!

These results thus give conclusive evidence that the induced photoresponse far above the absorption edge indeed scales with the photoconductivity. Another important result is the striking similarity of the photoresponse spectra for undoped, doubly illuminated SnS_2 (Fig. 3) and Ga doped SnS_2 (Fig. 7). Apart from the differences in scale, the spectra are virtually identical. This then leads to the conclusion, that the double-beam technique described above can be used to extract valuable information, such as bandgaps and spectral response curves from high resistivity electrodes, which is relevant for the doped counterparts as well. In other words, the method can be applied for a rapid scan of materials properties which are important for photoelectrochemical applications. It has been demonstrated that while the materials do have to show some photoconductive response, the method is by no means limited to good photoconductors.

¹ The quantum yields Φ' are difficult to compare in view of the gross differences of the photocurrent-potential curves for different materials. For HgI_2 (2) and CdS (1), the photocurrent-potential curves saturate at moderate potentials, while, e.g., for CdPSe_3 , a linear behavior is observed up to 100V. There is no doubt, however, that the quantum yields for the compounds listed in Table II differ enormously in the bias range accessible to the experiment.

Acknowledgments

We thank Mr. J. Müller for his reflectivity measurements. Financial support by the NEFF (Swiss Energy Research Fund) is gratefully acknowledged.

Manuscript submitted Sept. 18, 1984; revised manuscript received Dec. 5, 1984.

ETH Zürich assisted in meeting the publication costs of this article.

REFERENCES

1. H. Gerischer, M. Lübke, and B. Bressel, *This Journal*, **130**, 2112 (1983).
2. H. von Känel, E. Kaldis, P. Wachter, and H. Gerischer, *ibid.*, **131**, 77 (1984).
3. W. D. Gill and R. H. Bube, *J. Appl. Phys.*, **41**, 3731 (1970).
4. W. Siripala and M. Tomkiewicz, *This Journal*, **130**, 1062

- (1983), and references therein.
5. R. G. Wyckoff, "Crystal Structures," Interscience Publishers, Ltd., London.
6. W. Klingen, R. Ott, and H. Hahn, *Z. Anorg. Allg. Chem.*, **396**, 271 (1973).
7. S. G. Patil and R. H. Tredgold, *J. Phys. D*, **4**, 718 (1971).
8. M. J. Powell, *J. Phys. C*, **10**, 2967 (1977), and references therein.
9. K. C. Mills, "Thermodynamic Data for Inorganic Sulphides, Selenides, Tellurides," Butterworth, London (1974).
10. "Handbook of Chemistry and Physics," R. C. Weast, Editor, 57th ed. 1976-1977, CRC Press, Cleveland, OH (1976).
11. W. M. Latimer, "Oxidation Potentials," 2nd ed., Prentice-Hall, Inc., New York (1952).
12. G. W. C. Kaye and T. H. Laby, "Tables of Physical and Chemical Constants," 14th ed., Longman, London (1973).

Influence of Electrolyte Concentration on the Anodization and Breakdown Characteristics of Ta₂O₅ Films

I. Montero, J. M. Albella, and J. M. Martínez-Duart

Instituto de Física del Estado Sólido, CSIC and Departamento Física Aplicada, Universidad Autónoma Cantoblanco, 28049 Madrid, Spain

ABSTRACT

Voltage-time anodization curves, breakdown voltages, and I-V characteristics have been measured in Ta₂O₅ films grown in oxalic and phosphoric acid electrolytes. The results have been interpreted in terms of a simple avalanche model for the electronic current. The origin of the primary electrons of the avalanche is attributed to the electrolyte species incorporated into the oxide during the anodization process.

The anion incorporation from the electrolyte into the oxide during the anodization process is known to exert a strong influence on the physical and chemical properties of the films. Among others, increasing the concentration of phosphate ions into the Ta₂O₅ films lowers its density (1), permittivity (2), refractive index, and ionic conductivity (3), and, on the contrary, it increases the rate of growth and the electric field present during the anodization (4). Similarly, it is well known that the concentration of the anodization electrolyte plays a significant role in determining the breakdown voltage during the anodic oxidation (5).

In a previous paper (6), we applied a simple avalanche model, proposed by Ikonopisov (7), to explain the breakdown characteristics of the Ta₂O₅ films grown in a H₃PO₄ electrolyte at different current densities. From the results of that work, we concluded that the primary electron current of the avalanche is most likely originated in the anions incorporated into the oxide. Within the framework of this hypothesis, it was assumed that the anions act as donor levels in the oxide energy gap releasing electrons to the conduction band as a consequence of the strong anodization field. Once in the conduction band, the electrons can be accelerated and multiplied in an avalanche mechanism along the oxide thickness. The breakdown then occurs when the avalanche, and hence the thickness, reaches a critical size. Thus, in this picture, the breakdown characteristics are directly associated with the electrolyte anions incorporated into the oxide during the anodization process.

In this paper, we further investigate the influence of the incorporated anions in the electrical properties of the resulting oxide by anodizing the tantalum in electrolytes with different concentrations. We have used two kinds of electrolytes, phosphoric acid, which is known to result in a high anion incorporation into the oxide (8), and oxalic acid, which produces a negligible anion incorporation (9).

*Electrochemical Society Active Member.

Experimental

Tantalum samples of 99.96% nominal purity, supplied by Reframet Hoboken, were anodized in different electrolytes at a constant current density ($j_t = 0.85 \text{ mA cm}^{-2}$). The samples were previously cleaned and chemically polished following standard treatments (10). During the anodization, the samples were mounted in a special holder which only exposed to the electrolyte a circular area of $1.18 \pm 0.04 \text{ cm}^2$ of the sample (6). The temperature of the cell was kept constant at $20^\circ \pm 0.2^\circ\text{C}$ by means of a thermostatic bath.

The voltage-time curves during anodization, $V = V(t)$, as well as their derivatives, dV/dt , were recorded by means of a data acquisition system based on the HP 3497A digital voltmeter (input impedance $> 10^9 \Omega$) and the HP 85 microcomputer. The leakage current after anodization and the current-voltage (j-V) characteristics were measured by means of an electrometer with an input impedance of $10^9 \Omega$. Other experimental details can be found elsewhere (6).

Results

Figure 1 shows the values of the time derivative of the voltage per unit current density, j_t , as a function of the anodization voltage for different molar concentrations of the H₃PO₄ electrolyte. A slight decrease in the value of $(1/j_t)(dV/dt)$ is observed as the anodization voltage V increases. However, when the breakdown voltage is reached, the derivative abruptly decreases approaching zero (not shown in the figure). Increasing the electrolyte concentration produces a shift of the curves towards higher values of the derivative in agreement with previous observations by Amsel *et al.* (11) and Randall (2). Anodization in oxalic acid gives similar results, although in this case the influence of the electrolyte concentration on the derivative curves is much smaller than in phosphoric acid. Figure 2 presents the results of the breakdown voltage—defined by the voltage in which the anod-

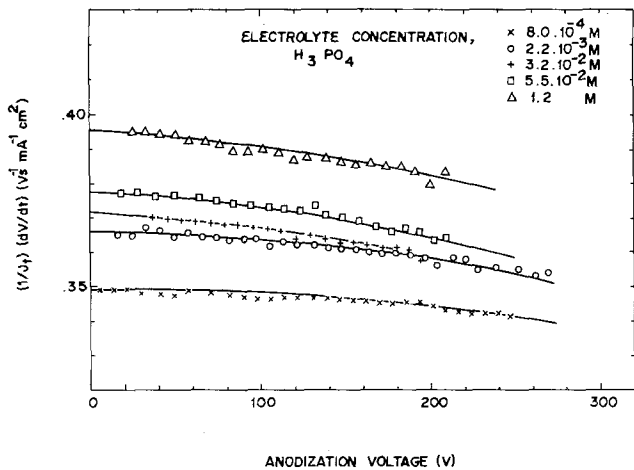


Fig. 1. Anodization rate per unit current density as a function of the anodization voltage for different molar concentrations of the H₃PO₄ electrolyte.

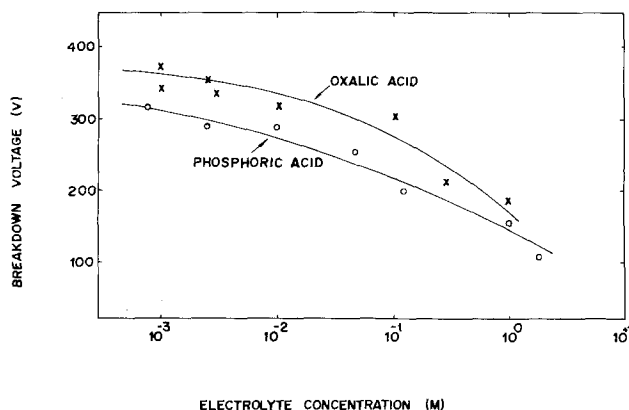


Fig. 2. Breakdown voltage during anodization as a function of the electrolyte concentration for both the oxalic acid and phosphoric acid.

ization curves of Fig. 1 abruptly change their slope—as a function of concentration of the electrolyte. It is observed that the oxalic acid, the electrolyte which incorporates the least, gives higher breakdown voltages than the phosphoric acid.

The residual leakage current after anodization, *i.e.*, the final current in the constant voltage stage at the end of the anodization, was also recorded. For this purpose, the samples were held in the electrolyte at the formation voltage, until the rate of current decrease was less than 1% in a 10 min interval. This procedure generally took more than 1h. The measured residual currents are given in Fig. 3 as a function of the formation voltage, *V_F*, for two phosphoric based electrolytes of different molarities, 1.0×10^{-2} and 2.2×10^{-3} M. Several aspects can be pointed out from these results. First, the more concentrated electrolyte gives higher currents in the whole range of the anodization voltages. Second, both curves show a linear stage in the logarithmic variation of the leakage current *vs.* the formation voltage.

The conduction mechanism dominating in these films was also investigated by measuring the *j*-*V* characteristics of the system Ta/Ta₂O₅/electrolyte. Only the more resistive samples grown in the 2.2×10^{-3} M H₃PO₄ electrolyte were studied, the measuring electrolyte and cell being the same as those used in the anodization. In that way, polarization and history effects were minimized. In the whole range of the applied fields, *E*, the current decay with time followed a law of the type $j \propto t^{-n}$ with *n* constant ($n \leq 1$), until a stationary value was reached. These values are represented in Fig. 4 in the form of a log (*j*/*E*) *vs.* *E*^{1/2} plot, for several samples grown at different formation voltages.

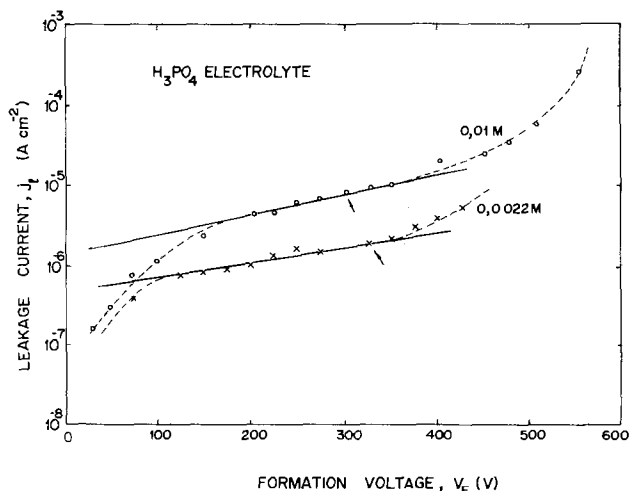


Fig. 3. Leakage current after anodization *vs.* formation voltage for samples anodized in two H₃PO₄ electrolytes of different concentrations.

Discussion

The analysis of the results has been carried out on the basis of the avalanche model proposed in a previous paper (6). According to this model, during anodization at a constant current density, *j_t*, there exists an avalanche electronic current, *j_e*, which increases exponentially along the oxide thickness, *d*, due to an impact ionization mechanism. Thus, the electronic current at the anode is

$$j_e = j_0 \exp(\alpha d) = j_0 \exp(\alpha \beta V) \quad [1]$$

where α is the impact ionization coefficient and *j₀* is the primary electron current. β is the anodization constant, *i.e.*, the angstrom per volt ratio, and it is equal to the inverse of the anodization field, *E*.

Taking into account the presence of the electronic current, the anodization ionic current, *j_i*, is given by

$$j_i = j_t - j_e = j_t - j_0 \exp(\alpha \beta V) \quad [2]$$

and the rate of voltage growth by

$$\frac{dV}{dt} = K j_i = K [j_t - j_0 \exp(\alpha \beta V)] \quad [3]$$

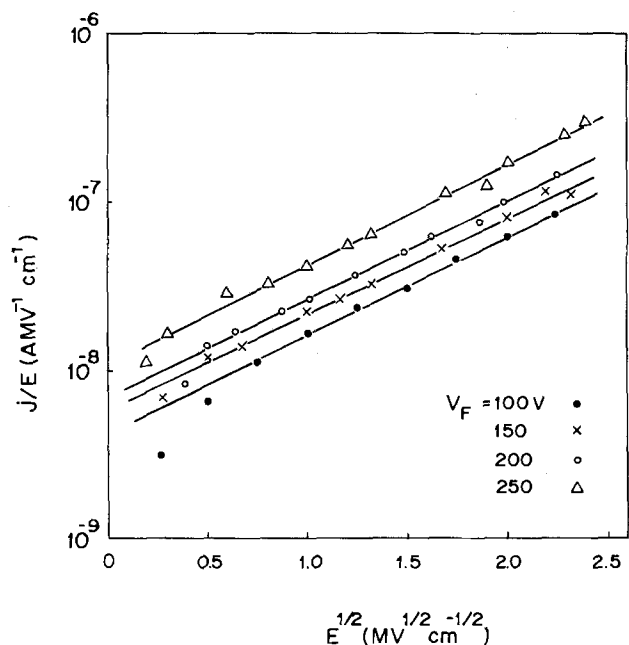


Fig. 4. Leakage current *vs.* applied field, represented in a Poole-Frenkel plot, for samples grown in a H₃PO₄ electrolyte at different formation voltages.

with K , the unitary anodization rate, expressed by

$$K = \frac{M}{10F\rho} E \quad [4]$$

M being the molecular weight, F the Faraday constant, and ρ the oxide density. By a least squares analysis, we have obtained the parameters K , j_0 , and α which best fit the experimental results of Fig. 1 to the theoretical Eq. [3]. In this way, the solid lines in Fig. 2 represent the theoretical curves obtained by this method.

The relative magnitude of the primary electron current at low voltages, j_0/j_1 , corresponding to each curve of Fig. 1, is presented in Fig. 5 as a function of the electrolyte concentration for both electrolytes, phosphoric and oxalic acids. In the above quotient, j_1 is the extrapolated ionic current density at 0 volts, *i.e.*, from the Eq. [2]: $j_1 = j_i - j_0$. It is observed in Fig. 5 that for the phosphoric acid, j_0/j_1 steadily increases with the mole concentration of the electrolyte, but, for the oxalic acid, j_0/j_1 is nearly constant. Along with these results, Fig. 5 also contains (broken line) the ratio mol P/mol Ta⁵⁺, *i.e.*, the relative phosphorous concentration in the oxide, obtained by Randall *et al.* (8) using radiotracer techniques.¹ It is evident that there exists a strong correlation between the j_0/j_1 curve for the phosphoric acid and the phosphorous concentration, which is consistent with our previous hypothesis of considering the incorporated anions as a source of the primary electrons of the avalanche. According to this mechanism, the anions act as donor levels in the forbidden band of the oxide. In contrast to the phosphoric acid, the oxalic acid is known to produce a negligible incorporation even at high electrolyte concentrations, as measured by ESCA and AES techniques (9). This fact explains the low constant value of j_0/j_1 in the whole range of the oxalic concentration (see Fig. 5).

The impact ionization coefficient of the avalanche is given in Fig. 6 for both electrolytes as a function of their mole concentration. It is observed that α is nearly constant for the oxalic acid except in the high concentration side, where the solution is near saturation. As for the phosphoric acid, the ionization coefficient slightly increases with the electrolyte concentration. Two effects can contribute to this increase in the α values. First is the anion incorporation itself, which can modify the oxide lattice, adding foreign atoms or molecules with a lower ionization potential. Second is the increase in the anodization electric field, which arises as a consequence of the electrolyte incorporation. The larger incorporation of the phosphate, as compared with the oxalate, anions also explains the differences between the corresponding values of the ionization coefficient.

The increase in the anodization field due to the electrolyte incorporation is apparent from the results of Fig. 7, where the electric field, E , has been plotted as a function of the concentration of the electrolyte for both the phosphoric acid and the oxalic acid. Here, the electric field has been obtained from the constant K in Eq. [4]. Owing to the lack of data on the variation of the oxide density with the electrolyte incorporation, it is not possible to give an accurate value of the anodization field. Therefore, a value of $\rho = 8.03 \text{ g cm}^{-3}$ has been used, which corresponds to nearly pure Ta₂O₅ films (1). However, lower values of E would be expected (within about 2% or 3% in the case of the phosphoric electrolyte) if the decrease in ρ for the films grown in the more concentrated electrolytes had been taken into account (1). The influence of the incorporated anions on the anodization electric field has been discussed in another paper and it has been attributed to increase of the energy barrier for ionic transport (12).

The results on the residual leakage current during the constant voltage stage can also be interpreted in the lines of the model, which takes into account the avalanche

¹The ratio mol P/mol Ta⁵⁺ for the whole oxide has been calculated from the reported values of the phosphorous concentration in the outer layer of the oxide.

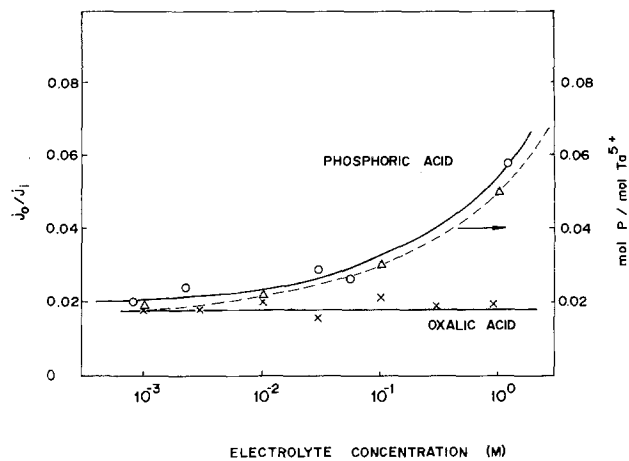


Fig. 5. Ratio of the primary electron current to the ionic current as a function of the electrolyte concentration for both the oxalic acid and the phosphoric acid. The values of the relative phosphorous concentration for films grown in H₃PO₄ electrolytes, measured by Randall *et al.* (8), are also represented.

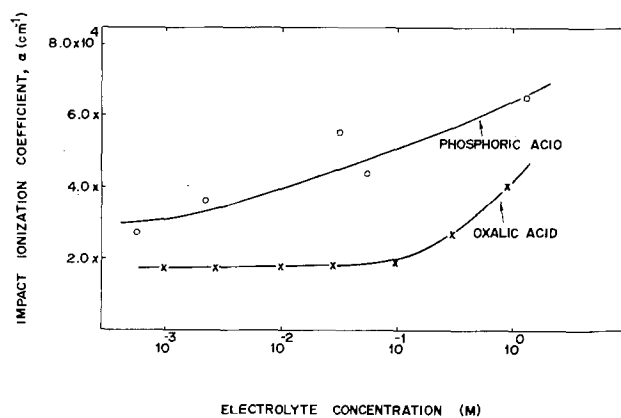


Fig. 6. Impact ionization coefficient vs. electrolyte concentration for Ta₂O₅ films grown in phosphoric and oxalic acid electrolytes.

electronic current originated at the incorporated anions. It is reasonable to expect higher electronic currents for the more concentrated electrolyte due both to a higher level of oxide doping and the higher value of the electric field found in this electrolyte. The presence of a linear stage in the curves of Fig. 3 is also in agreement with the exponential increase of the electronic current predicted by the avalanche model. In addition, the nonlinear dependence can be explained by the lower fields found in the low voltage region, as discussed by Young (13), and by the onset of breakdown processes at the side of the high voltages.

The exponential increase of the residual current, j_1 , found in the intermediate region of Fig. 3 follows the equation

$$j_1 = j_0' \exp(\alpha' V_F) \quad [5]$$

where j_0' and α' have the same meaning as the parameters of the avalanche of Eq. [1], *i.e.*, $\alpha' = \alpha\beta$. In fact, the values of j_0' and α' found from Fig. 3 are lower than the corresponding ones in the stage of constant current. Nevertheless, this is not surprising considering that, as pointed out, during the constant voltage stage the value of the electric field is much smaller than during the previous anodization at constant current.

The results of the conduction through the system Ta/Ta₂O₅/electrolyte (Fig. 4) yield straight lines in a log(j/E) vs. $E^{1/2}$ plot, which suggests a Poole-Frenkel mechanism of conduction. Other mechanisms gave a worse fitting of the results. As it can be appreciated, the experimental points follow straight parallel lines in a wide range of applied fields, E . From the slopes of these straight

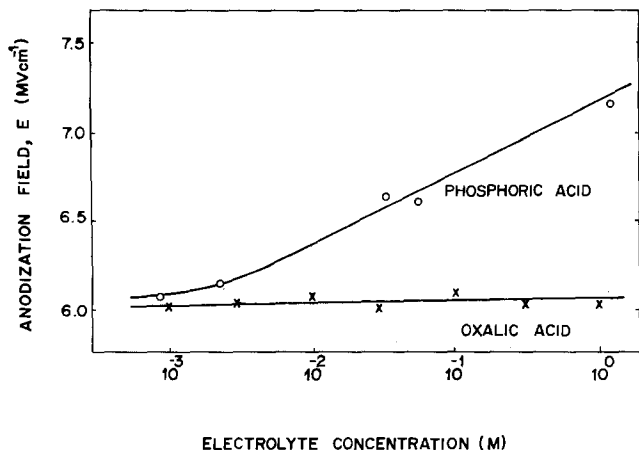


Fig. 7. Anodization electric field vs. electrolyte concentration for Ta₂O₅ films grown in phosphoric and oxalic acid electrolytes.

lines, the relative permittivity $\epsilon_r = 4.98$ (average value) has been obtained by using the well-known expression for the current density

$$j = j_c \exp(\beta_{PF} E^{1/2} / kT)$$

where $j_c = \sigma_c E$ (σ_c constant), k is Boltzmann's constant, T the absolute temperature, and β_{PF} is given by

$$\beta_{PF} = \left(\frac{e^3}{\pi \epsilon_0 \epsilon_r} \right)^{1/2}$$

e being the electronic charge and ϵ_0 the vacuum permittivity. It is worth noting that the value of ϵ_r agrees closely with that resulting from the refractive index $n = 2.2$ (2), applying the Maxwell relation, $n^2 = \epsilon_r$, thus supporting the Poole-Frenkel mechanism (14). There is a great controversy about the dominant conduction mechanism in Ta₂O₅ films (15). The majority of papers refer to the system Ta/Ta₂O₅/metal; the system Ta/Ta₂O₅/electrolyte has received comparably less attention. The general agreement is that the control of the conduction mechanism is in the bulk, while the contacting electrolyte may play a less important role (16). Taking into account the presence of the phosphate anions in the oxide, it is reasonable to associate them to the Coulomb traps of the Poole-Frenkel mechanism.

It may be observed in Fig. 4 a shift of the straight lines towards higher values of the current as the formation voltage increases. This behavior has also been displayed by samples of anodic Al₂O₃ (16) and was attributed to an avalanche mechanism of multiplication of the free carriers. This is, in turn, in agreement with our model of anodization and breakdown of the anodic Ta₂O₅ films. This view is further supported by the fact that the electronic current, j , measured at a constant field grows exponentially with the formation voltage, as is illustrated in Fig. 8. According to the results of this figure, the current j can be expressed by an equation similar to Eq. [5], with the parameters now given by $\alpha' = 0.006 \text{ V}^{-1}$ and $j_0' = 3.8 \times 10^{-7} \text{ A cm}^{-2}$, in good agreement with those obtained from Fig. 5 and 6.

In the light of the avalanche model, a lower breakdown voltage for the phosphoric acid is expected compared with the oxalic acid, as can be observed in Fig. 2. In fact, it is possible to make an estimation of the variation of the breakdown voltage V_B with the electrolyte concentration, if one assumes that the breakdown appears when the avalanche current j_e reaches a certain fraction z of the total anodization current j_t . A similar hypothesis was introduced by Ikonopisov (7). Under this condition, the breakdown voltage will satisfy the equation

$$j_0 \exp(\alpha \beta V_B) = z j_t \quad [6]$$

and hence

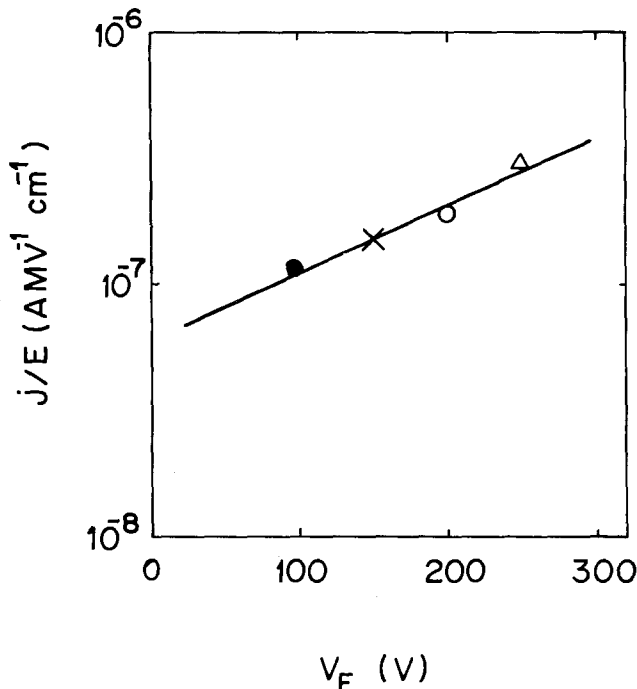


Fig. 8. Variation of the quotient j/E as a function of the formation voltage (Values taken from Fig. 4, for a value of the applied electric field of $E = 6.25 \text{ MV cm}^{-1}$).

$$V_B = \frac{1}{\alpha \beta} \ln \left(z \frac{j_t}{j_0} \right) = \frac{E}{\alpha} \ln \left(z \frac{j_t}{j_0} \right) \quad [7]$$

The parameter z is unknown; therefore, the absolute value of V_B cannot be calculated. Anyhow, Eq. [7] gives the dependence of V_B with the anodization parameters E , α , and j_0 . Thus, as it can be observed in Fig. 5, 6, and 7 for the oxalic acid, E and j_0 are nearly constant and α increases by a factor of two in the high concentration side. Probably, this is the main factor contributing to the observed decrease of V_B for the oxalic acid in this region. On the contrary, in the case of the phosphoric acid, the major contribution of the decrease of V_B comes from the increase of j_0 with the electrolyte concentration, as can be deduced from the results of Fig. 5. The differences in the values of j_0 found in the phosphoric and oxalic acid electrolytes also explain the lower breakdown voltages observed in the first electrolyte.

Conclusions

From the results presented in this paper, it can be concluded that the avalanche model is able to explain the main characteristics of the anodization curves and breakdown of anodic tantalum oxide grown in phosphoric and oxalic electrolytes at different concentrations. The close correlation between j_0/j_t and the mole concentration of incorporated phosphorous in the oxide firmly supports the hypothesis that the incorporated phosphate anions act as a source of primary electrons for the avalanche. The residual leakage current measurements as well as the j - V characteristics seem to indicate that the primary electrons are released from the impurity centers in a Poole-Frenkel mechanism. The presence of phosphorous in the anodic oxide also gives rise to an increase of the anodization electric field needed to maintain a definite current density. In contrast to the previous theories of the breakdown during anodization (8, 17) which speculate about the injecting properties of the electrolyte/oxide interface, in the present model the direct control of the breakdown is mainly attributed to the electrolyte anions incorporated into the oxide and to their ability to release electrons to the conduction band.

Manuscript submitted Aug. 3, 1984; revised manuscript received Nov. 22, 1984.

Universidad Autónoma Cantoblanco assisted in meeting the publication costs of this article.

REFERENCES

1. A. J. Schrijner and A. Middelhoeck, *This Journal*, **111**, 1167 (1964).
2. J. J. Randall, *Electrochim. Acta*, **20**, 663 (1975).
3. C. J. Dell'Oca and L. Young, *This Journal*, **117**, 1545 (1970).
4. C. J. Dell'Oca and L. Young, *ibid.*, **117**, 1548 (1970).
5. F. J. Burger and J. C. Wu, *ibid.*, **118**, 2039 (1971).
6. J. M. Albella, I. Montero, and J. M. Martínez-Duart, *ibid.*, **131**, 1101 (1984).
7. S. Ikonopisov, *Electrochim. Acta*, **22**, 1077 (1977).
8. J. J. Randall, W. J. Bernard, and R. R. Wilkinson, *ibid.*, **10**, 183 (1965).
9. S. Hofmann and J. M. Sanz, *J. Trace Microprobe Technol.*, **1**, 213 (1982).
10. J. M. Albella, I. Montero, and J. M. Martínez-Duart, *Thin Solid Films*, **58**, 307 (1979).
11. G. Amsel, C. Cherki, G. Feuillade, and J. P. Nadai, *J. Phys. Chem. Solids*, **30**, 2117 (1969).
12. I. Montero, J. M. Albella, and J. M. Martínez-Duart, *This Journal*, **132**, 976 (1985).
13. L. Young, *ibid.*, **124**, 528 (1977).
14. J. G. Simmons, *Phys. Rev.*, **155**, 657 (1967).
15. P. L. Young, *J. Appl. Phys.*, **47**, 235 (1976).
16. S. Ikonopisov, *Electrochim. Acta*, **14**, 761 (1969).
17. V. Kadary and N. Klein, *This Journal*, **127**, 139 (1980).

Using Parameter Estimation Techniques with a Simple Model of a Diaphragm-Type Electrolyzer to Predict the Electrical Energy Cost for NaOH Production

John Van Zee*

Department of Chemical Engineering, University of South Carolina, Columbia, South Carolina 29208

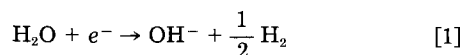
R. E. White*

Department of Chemical Engineering, Texas A&M University, College Station, Texas 77843

ABSTRACT

Predictions of the electrical energy cost for NaOH production are determined as a function of the independent operating variables and diaphragm characterizing properties. The predictions are based on data from a statistically designed experiment, a simple model of a diaphragm-type electrolyzer, a simple model of the cell voltage losses, and parameter estimation techniques. The data were obtained over a sufficiently large range of operating conditions so that the resulting design equation may be industrially useful. The simple model of the diaphragm is based on the mass transport of the hydroxyl ion, a linear potential gradient, and is presented in terms of measurable diaphragm properties. These properties are the thickness of the diaphragm (t) and a resistivity-ratio, ρ/ρ_0 , where ρ is the resistivity of the diaphragm filled with electrolyte and ρ_0 is the resistivity of the electrolyte (this ratio may come to be known as the MacMullin number, N_M). It is shown that, according to the model of the cell, the caustic yield or current efficiency of the diaphragm cell depends on the product of N_M and t and not on each separately. The simple model of the cell voltage considers the diaphragm voltage drop, anode and cathode kinetics, and the bubble-filled brine-gap voltage drop. Parameter estimation techniques are used to determine the best values of the diffusion coefficient, average specific conductivity, exchange current densities, and transfer coefficients; these parameters and the simple models provide a design equation for the electrical energy cost of NaOH production using a diaphragm cell. The design equation is used to predict a minimum electrical-energy cost at a particular $N_M t$.

In a diaphragm-type chlorine/caustic cell (see Fig.1), hydroxyl ions are produced at the cathode according to the electrochemical reaction



The energy cost for the production of hydroxyl ions depends upon the diaphragm characteristics and the operating conditions of current density and percolation velocity. That is, to prevent the loss of OH^- ions due to migration and diffusion, cell electrolyte percolates through the diaphragm from the anolyte as shown in Fig. 1. This percolation rate must not be too large, however, because the concentration of OH^- in the catholyte decreases as the percolation rate increases, which leads to a larger steam requirement if the catholyte is to be concentrated to the typical 50% by weight solution. Increasing the current density increases the concentration of OH^- ions in the catholyte, but also increases the voltage drop through the diaphragm, which increases the electrical energy cost. Also, the diaphragm characteristics affect the diffusion and migration of hydroxyl ion and the voltage drop through the diaphragm. It is desirable, therefore, to have a simple model which is consistent with industrial production cells and which can be used to predict the con-

centration of OH^- ions in the catholyte and the diaphragm voltage drop as a function of the percolation velocity, current density, and diaphragm characterizing properties. It is also desirable to combine this simple diaphragm model with a simple model of the cell voltage losses which include the thermodynamics, kinetics, and ohmic losses so that predictions of the electrical energy cost for NaOH production can be made. (A more quantitative definition of electrical energy cost is given below in the "Energy Cost" section).

These predictions are highly dependent on the transport and kinetic parameters used in the model. Consequently, it is necessary to use a set of parameters which (i) is consistent with experimental data over a large range of operating conditions and (ii) has reasonably small confidence intervals for the parameters. Here, we use the theory of nonlinear least squares regression (1-4) to obtain a suitable set of parameters for a simple model. In this sense, we do not test various models to determine the most reasonable, but, rather, we assume that the simple model presented here is reasonable and then determine the parameters which give the "best fit" of the data. In the same sense, it is not the purpose of this paper to compare the model predictions with experimental data that were not used to obtain the parameters. [See Lee (5) for a general discussion of the use of parameter estimation in electrochemical reactor design.]

* Electrochemical Society Active Member.

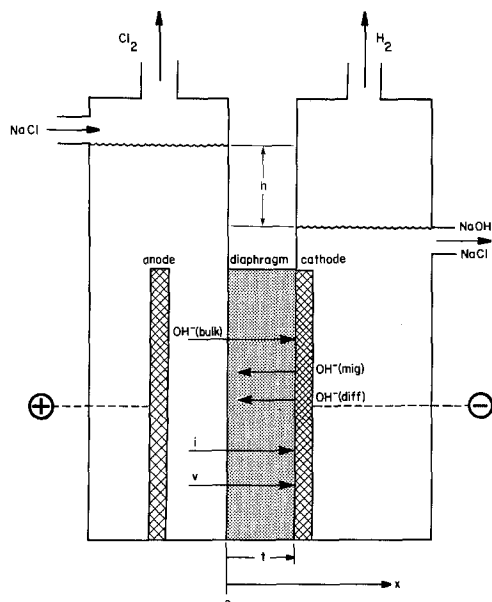


Fig. 1. A diaphragm-type chlorine/caustic cell schematic

Simple models of the diaphragm¹ have been presented before (6-10), but none have included measurable diaphragm properties as independent variables, which is required for the determination of diaphragm-independent transport parameters by regression. Also, none of the previous workers have shown the effects of these diaphragm properties and the operating conditions on the energy cost for the production of NaOH in a diaphragm-type electrolyzer. Consequently, the diaphragm characterizing properties used here will be discussed, and the previously published models will be reviewed. Then, a simple model of the diaphragm-type chlorine/caustic cell which considers OH⁻ ion only will be developed and discussed in terms of dimensionless groups. The model then will be compared in more detail to previously published models and then to experimental data using nonlinear regression to estimate the transport and kinetic parameters. Finally, predictions of the electrical energy cost per metric ton of NaOH will be discussed as a function of the independent diaphragm properties and operating conditions.

Literature Review

In a recently reported, factorially designed experiment (11), two quantities were used to characterize the diaphragm in a metal anode chlorine/NaOH electrolyzer. These two properties are the MacMullin number, N_M , and the diaphragm thickness, t . The MacMullin number is defined (12, 13) as follows

$$N_M = \frac{\tau}{\epsilon} = \frac{\rho}{\rho_0} \quad [2]$$

where ρ/ρ_0 is the ratio of the electrical resistivity of an electrolyte-saturated porous medium to the resistivity of the same thickness of electrolyte. An experimental procedure is available for measuring independently both the MacMullin number and the thickness of a diaphragm (11). It should be noted that N_M has also been referred to as the formation factor (14) and the labyrinth factor (15).

Of the simple models of the diaphragm that have been proposed (6-10), only Koh (9, 10) and Mukaibo (7) included diaphragm characterizing properties, but neither recognized that N_M can be measured directly from relatively simple experiments. Koh (9, 10) used a diaphragm characterizing parameter which was obtained from an assumed value for τ or the product τ and a presumably measured value for ϵ . Mukaibo (7) [see also Hine (14, 16, 17)] used the ratio of the diaphragm area to the area of the dia-

¹ Throughout this paper, the phrase "simple model of the diaphragm" is used to indicate a model with a linear potential gradient that can be solved by analytical integration of the governing differential equations.

phragm pores, which is not measurable directly, and, hence, this ratio was an assumed quantity when the model was compared with experimental data (16). The often-used model of Stender *et al.* (6) does not include a parameter such as N_M , but some recent modifications of this model (17, 18) have recognized the need to include diaphragm properties which are independent of the transport parameters; again, these recent modifications use assumed values for ϵ or τ , and therefore they cannot be used to determine the best values of the transport parameters for use with the model. Kubasov *et al.* (19) include the thickness of the diaphragm multiplied by a "sinuosity coefficient" as the characterizing parameter, but this coefficient was not reported as a measurable quantity.

In addition to the lack of measurable diaphragm properties, other differences exist between the previously published diaphragm models and the model presented here. For example, Gallone and Rubino (8) neglected the effect of ionic migration. Hine (14, 16, 17) does not show the difference between the solution conductivity and the effective solution conductivity in the diaphragm. Mukaibo (7) assumed that the ratio of the transference number to the concentration of hydroxyl ion is constant throughout the diaphragm.

Also, the model presented here differs from the previously reported models in the specification of the boundary condition at the catholyte/diaphragm interface. That is, the model of Stender *et al.* (6), for example, is developed with a physically unrealistic boundary condition, a fixed catholyte concentration. Consideration of Fig. 1 reveals that the concentration in the catholyte depends on the velocity and the current density as well as the diaphragm properties and therefore cannot be specified *a priori* as an independent, fixed quantity. Thus, Stender's expression for the concentration profile of hydroxyl ion {Eq [13] in Ref. (6)} does not show the correct dependence on velocity and current density because it includes the concentration at the interface.

The previously reported simple diaphragm models (6-10) have not been used to analyze the combined effects of diaphragm properties and operating conditions on the energy cost for NaOH production. That is, although Koh (9, 10) showed the effect of his diaphragm effectiveness parameter on electrolyzer energy consumption, the interaction between current density, velocity, and diaphragm properties (e.g., N_M and t) was not discussed. The contribution of the diaphragm voltage drop to energy cost and the effect of diaphragm parameters on the voltage drop were not discussed by Koh or the authors of the other simple models. Hine (14) showed diaphragm IR data for a stagnant laboratory-scale diaphragm cell, but comparison of this data to model predictions was not reported. Also, the contributions of electrode kinetics to the energy consumption have not been reported previously but are included here. A more complicated model (12) of chlorine/NaOH metal anode electrolyzer has shown the effect of the product of N_M and t on specific energy consumption; however, only the essence of the model was presented, and the details were avoided for proprietary reasons.

Model

The assumptions of the simple models are as follows.

1. Dilute solution theory (20) applies.
2. The hydroxyl ion is the only species of interest within the diaphragm, and all reactions of OH⁻ with other species (e.g., H⁺ and Cl₂) occur at the anolyte/diaphragm interface. (This assumption is reasonable because the concentrations of the other species in the diaphragm are relatively small, on the order of 2% of that of the OH⁻ ion.)
3. The spatial dimension in the direction parallel to the velocity (see Fig. 1) is the only important dimension for material balances.
4. The effective diffusion coefficient for hydroxyl ion in the porous diaphragm can be written in terms of the MacMullin number (12)

$$D_e = \frac{D_1}{N_M} \quad [3]$$

5. The current density through the diaphragm is simply related to the potential gradient through the diaphragm by an effective average specific conductivity

$$i = -\frac{\kappa_{\text{avg}}}{N_M} \frac{d\Phi}{dx} \quad [4]$$

6. Water vapor loss from the catholyte is negligible, and the generated H_2 gas mixes the catholyte so that the hydroxyl ion concentration at the diaphragm/catholyte interface equals the hydroxyl ion concentration in the electrolyzer effluent.

7. The electrochemical kinetics at the anode and cathode can be approximated by a Tafel approximation

$$\Delta V_{\text{kin},i} = \frac{RT}{\alpha_i F} \ln \left| \frac{i}{i_{0,i}} \right| \quad [5]$$

where $i = 1$ and 2 for cathode and anode, respectively.

8. The effect of temperature on ΔU^θ is negligible.

9. The Nernst concentration correction to the open-circuit or thermodynamic voltage of the electrolyzer is negligible.

10. The voltage drop between the anode and the diaphragm is given by

$$\Delta V_{\text{anolyte}} = \frac{is}{(1 - \epsilon_b)^{1.5} \kappa_{\text{anolyte}}} \quad [6]$$

where $(1 - \epsilon_b)^{1.5}$ is the Bruggeman correction for the effect of bubbles in the anolyte (21, 22) and ϵ_b is assumed to be independent of current density.

With these assumptions, the steady-state material balance for hydroxyl ion in the diaphragm is

$$\frac{dN_1}{dx} = 0 \quad [7]$$

where the expression for the flux of hydroxyl ion in the porous diaphragm can be written (12) as

$$N_1 = -\frac{D_1}{N_M} \frac{dC_1}{dx} + \frac{D_1}{N_M} \frac{F}{RT} C_1 \frac{d\Phi}{dx} + vC_1 \quad [8]$$

The boundary conditions can be obtained from the second and sixth assumptions above and by recognizing that the anolyte and catholyte approximate completely mixed reactors. That is, for a typical anolyte pH of 2, the OH^- concentration is

$$\text{at } x = 0, \quad C_1 = 0 \quad [9]$$

Since OH^- is produced at the diaphragm/catholyte interface, and since the flux in the catholyte chamber consists of only convection (*i.e.*, vC_1), the material balance is

$$\text{at } x = t \quad N_1(x = t) + \frac{i}{F} = vC_1(x = t) \quad [10]$$

Substituting Eq. [4] into Eq. [8] yields

$$N_1 = -\frac{D_1}{N_M} \frac{dC_1}{dx} - \frac{D_1}{\kappa_{\text{avg}}} \frac{Fi}{RT} C_1 + vC_1 \quad [11]$$

Substituting Eq. [11] into Eq. [7] yields the second-order differential equation which governs the concentration of hydroxyl ion throughout the diaphragm

$$\frac{D_1}{N_M} \frac{d^2C_1}{dx^2} + \left(\frac{D_1 Fi}{\kappa_{\text{avg}} RT} - v \right) \frac{dC_1}{dx} = 0 \quad [12]$$

Integration of Eq. [12] subject to the boundary conditions (Eq. [9] and [10]) is readily accomplished [see Ref. (23), for example], and the result can be written as

$$C_1(x) = \frac{\frac{i}{vF} \{1 - \exp(A_1 x)\}}{\left[\frac{FiD_1}{RT\kappa_{\text{avg}}v} - \exp(A_1 t) \right]} \quad [13]$$

where

$$A_1 = \left(\frac{-FiN_M}{RT\kappa_{\text{avg}}} + \frac{vN_M}{D_1} \right)$$

Equation [13] is plotted in Fig. 12 and 13 of Ref. (23) and can be used to obtain an expression for the hydroxyl ion concentration in the effluent

$$C_1(t) = \frac{\frac{i}{vF} \{1 - \exp(A_1 t)\}}{\left[\frac{FiD_1}{RT\kappa_{\text{avg}}v} - \exp(A_1 t) \right]} \quad [14]$$

Equation [14] shows that the effluent concentration is a dependent variable when the velocity and current density are considered independent variables. An expression for the caustic yield, η , can be obtained by using the following definition

$$\eta = \frac{vC_{1,\text{effluent}}}{i/F} = \frac{vC_1(t) F}{i} \quad [15]$$

where by the sixth assumption above, $C_{1,\text{effluent}} = C_1(t)$.

Substituting Eq. [14] into Eq. [15] yields

$$\eta = \frac{\{1 - \exp(A_1 t)\}}{\left[\frac{FiD_1}{RT\kappa_{\text{avg}}v} - \exp(A_1 t) \right]} \quad [16]$$

Note that Eq. [14] and [16] show that $C_1(t)$ and η depend on the product of N_M and t and not on either quantity separately. This should be expected, since $N_M t$ is simply the effective thickness of the diaphragm. Also, it should be emphasized that η is a derived quantity, not a parameter. That is, η is calculated according to Eq. [15] after the governing equation for $C_1(x)$ (Eq. [12]) has been solved subject to the boundary conditions (Eq. [9] and [10]). Also, note that none of Eq. [7]-[12] contain η and that this is different from the formation of Caldwell *et al.* (12) and Stender *et al.* (6).

Energy Cost

The specific electrolyzer energy cost for NaOH, EC_{el} , can be formulated as the ratio of the energy consumption rate to the mass production rate of NaOH multiplied by the electrical energy cost, CE

$$EC_{\text{el}} = \frac{iV_T}{M_1 C_1(t)v} \text{CE} \quad [17]$$

In Eq. [17], the current density, i , and the velocity, v , are considered as independent variables, while $C_1(t)$ is deter-

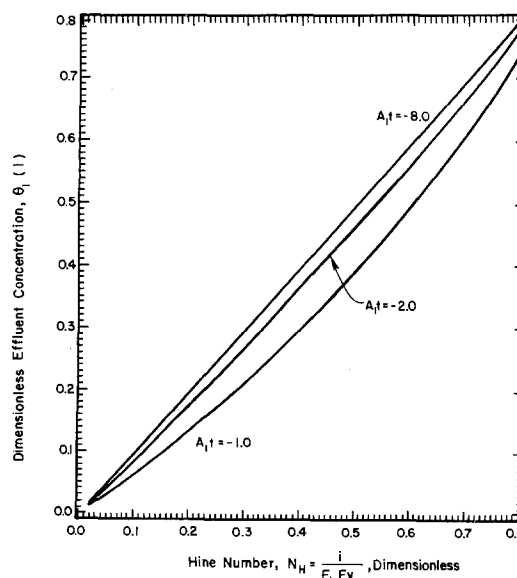


Fig. 2. Effluent concentration dependence on $A_1 t$ and N_H .

mined by Eq. [14] as a dependent variable. Also, the sum of the cell voltage drops, V_T , is a dependent variable and includes the kinetic voltage drops at each electrode, the thermodynamic voltage required for the sum of the cathodic and anodic reactions, the voltage drop in the anolyte, and the diaphragm voltage drop. The diaphragm is typically deposited onto the cathode and, hence, any voltage drop in the catholyte is negligible. Using the fifth and seventh through tenth assumptions above gives

$$V_T = \frac{iN_M t}{\kappa_{\text{avg}}} + \frac{RT}{F} \left[\left(\frac{1}{\alpha_1} + \frac{1}{\alpha_2} \right) \ln |i| - \frac{\ln(i_{0,1})}{\alpha_1} - \frac{\ln(i_{0,2})}{\alpha_2} \right] + \Delta U^\theta + \frac{iS}{(1 - \epsilon_b)^{1.5} \kappa_{\text{anolyte}}} \quad [18]$$

Other Dimensionless Groups

It is, perhaps, worth mentioning that dimensionless groups other than the ones shown in Eq. [16] can be formulated. For example, Eq. [16] can be rewritten as

$$\eta = \frac{1 - \exp(\text{Pe} + \Delta\phi)}{-\frac{\Delta\phi}{\text{Pe}} - \exp(\text{Pe} + \Delta\phi)} \quad [19]$$

where Pe is the Peclet number

$$\text{Pe} = \frac{vN_M t}{D_1} \quad [20]$$

and $-\Delta\phi$ is the dimensionless diaphragm IR drop

$$-\Delta\phi = -\frac{F}{RT} [\Phi(x=t) - \Phi(x=0)] = \frac{FiN_M t}{RT\kappa_{\text{avg}}} \quad [21]$$

The Peclet number is a measure of the effect of convection relative to diffusion and is used routinely by chemical engineers. The dimensionless diaphragm IR drop, $-\Delta\phi$, can be thought of as a measure of the importance of the effect of ionic migration.

These dimensionless groups can also be used to write in dimensionless form an expression for the concentration distribution for OH^- ions

$$\theta_1(\zeta) = \frac{C_1(x)}{F_1} = \frac{N_H \{1 - \exp[(\text{Pe} + \Delta\phi)\zeta]\}}{-\frac{\Delta\phi}{\text{Pe}} - \exp(\text{Pe} + \Delta\phi)} \quad [22]$$

where F_1 is the concentration of the NaCl in the brine feed (a constant) and N_H is the Hine number defined as

$$N_H = \frac{i}{FF_1 v} \quad [23]$$

since Hine and Yasuda (24) were apparently the first to recognize the significance of i/Fv .

Comparison of Diaphragm Model to Existing Models

Expressions similar to those given above for $C_1(x)$, $C_1(t)$, and η have been presented by Stender *et al.* (6), Koh (9), and Mukaibo (7) which with modifications or definitions of effective thickness can be shown to be consistent with the model presented here. The expressions presented by Stender *et al.* (6) for $C_1(x)$ and η are not correct because they do not contain N_M or a similar quantity. Their equations are written in terms of δ (defined to be the thickness of the diaphragm), but their expression for η can be seen to be equivalent to Eq. [16] by defining δ in terms of measurable diaphragm properties

$$\delta = N_M t \quad [24]$$

Thus, their δ should be the effective thickness and not the measured diaphragm thickness. Using Eq. [24], their dimensionless parameter $U\delta/D_1$ can be shown to be equal to $A_1 t$ of Eq. [13], [14], and [16]. In addition, their equation for $C_1(x)$ is not complete because it depends on the concentration of OH^- in the catholyte, which also depends on other variables in their expression for $C_{\text{OH}^-}(x)$. That is,

for example, both v and $C_1(t)$ cannot be set while holding i fixed because only two independent operating variables exist for the isothermal case. This point is easily overlooked when $C_1(x)$ is made dimensionless by $C_1(t)$ and the resulting expression (*i.e.*, divide Eq. [13] by Eq. [14]) is graphed as a function of distance, x , as is shown by Hine *et al.* [14] in their Fig. 12. The resulting expression, and hence Fig. 12 of Ref. (14), appears as a function of only one dimensionless variable, $U\delta/D_1$, which is misleading because the dimensionless concentration profile is described by three dimensionless groups (divide both sides of Eq. [13] by F_1 or see Eq. [22]). Furthermore, if $C_1(t)/F_1$ is held constant, then i/vFF_1 must be changed as $A_1 t$ is changed; this point is illustrated in Fig. 2, which shows that $C_1(t)/F_1$ depends on both $A_1 t$ and i/vFF_1 . Two exceptions to this dependence occur as follows

$$A_1 t < -20; \quad C_1(t) = \frac{RT\kappa_{\text{avg}}}{F^2 D_1} \quad [25]$$

$$A_1 t > 20; \quad C_1(t) = \frac{i}{vF} \quad [26]$$

Also, when $A_1 t = 0$, Eq. [13], [14], and [16] become indeterminate forms because the quantity $FiD_1/RT\kappa_{\text{avg}}v$ equals 1.0. For these indeterminate forms, application of l'Hopital's rule results in the following limit

$$C_1(x) = \frac{1.0}{\left(\frac{D_1 F}{iN_M t} + \frac{vF}{i} \right)} \quad [27]$$

when

$$A_1 t = 0$$

Next, consider the equation for η presented by Koh (9). His equation for η contains a length parameter, EL , which can be shown to be equal to $N_M t$ by considering Koh's definition of EL

$$EL = l/\epsilon \quad [28]$$

and the definitions of l (average pore length) and N_M (12)

$$l = \tau t \quad [29]$$

$$N_M = \tau/\epsilon \quad [30]$$

where τ is the tortuosity and ϵ is the porosity of the diaphragm.² Substitution of Eq. [29] and [30] into Eq. [28] shows that

$$EL = N_M t \quad [31]$$

However, even though Koh's equation for η does contain an effective thickness parameter, he did not recognize that it can be determined by measuring N_M and t . Instead, he used an assumed value for τ and a presumably measured value for ϵ to obtain $N_M t$ (his EL). Unfortunately, his $N_M t$ values are scaled for proprietary reasons, and his equation for η is difficult to use because it contains a parameter (his A) which is incorrect as written.

Mukaibo's (6, 16) expression for η is also similar to Eq. [16]; however, his equation is based on a different approach. He defined a transference number for OH^- as follows

$$n_1 = \frac{t_1(x)}{C_1(x)} \quad [32]$$

and assumed that n_1 (not t_1) is constant throughout the diaphragm. He then defined the flux of OH^- through the diaphragm to be

$$N_1 = \frac{-D_1}{A_d/A_p} \frac{dC_1}{dx} - n_1 C_1 \frac{i}{F} + vC_1 \quad [33]$$

and integrated Eq. [7] with N_1 given by Eq. [33] in a man-

² Actually, Caldwell *et al.* (12) define N_M as τ^2/ϵ , but it is immaterial whether τ is squared or not, since it is not a quantity that can be measured directly.

ner similar to that shown in Ref. (23). The equations he obtained for $C_i(t)$ and η do have the correct dependence on N_M , since N_M is related simply to his area ratio

$$N_M = A_d/A_p \quad [34]$$

as can be seen by defining (10) the porosity of the diaphragm as

$$\epsilon = lA_p/tA_d \quad [35]$$

and using Eq. [29] and [30]

$$N_M = \tau/\epsilon = \frac{l}{t} \frac{A_d/A_p}{l/t} = \frac{A_d}{A_p} \quad [36]$$

Even though Mukaibo presented equations that do have the correct dependence on N_M , he did not recognize that N_M can be measured directly and he did not present an equation for $C_i(x)$. Also, his concept of a constant transference number (n_i) is perhaps less appealing than the concept of a constant, average specific conductivity. This may be so because κ_{avg} can be measured directly by assuming that κ_{avg} is equal to the specific conductivity of an aqueous solution of NaCl and NaOH at their average concentrations over the range of effluent concentrations of interest (e.g., 2.5M of each), whereas n_i cannot. However, it is interesting to note that an average value for n_i can be obtained from κ_{avg} , if D_1 is known.

This can be seen by considering the definitions of t_i and κ . That is, according to Newman (20), the transport number for species j in an electrolyte solution is given by

$$t_j = \frac{z_j^2 u_j C_j}{\sum_i z_i^2 u_i C_i} \quad [37]$$

and the specific conductivity is given by

$$\kappa = F^2 \sum_i z_i^2 u_i C_i \quad [38]$$

Substitution of Eq. [38] into Eq. [37] written for OH⁻ yields

$$t_1 = \frac{u_1 C_1 F^2}{\kappa} \quad [39]$$

which, by assuming that the Nernst-Einstein equation (20) is valid

$$u_1 = \frac{D_1}{RT} \quad [40]$$

shows that

$$n_1 = \frac{t_1}{C_1} = \frac{F^2 D_1}{RT \kappa} \quad [41]$$

Thus, once values for D_1 and κ_{avg} are known, an average value for n_1 could be calculated according to Eq. [41].

Parameter Estimation

Diaphragm model.—The diaphragm model presented above is formulated in terms of two transport properties of the electrolyte solution within the diaphragm, D_1 and κ_{avg} . Both D_1 and κ_{avg} are average quantities which depend on temperature and the average concentration within the diaphragm. Values for these average quantities are not available in the literature.

Their values can be estimated by nonlinear least squares (LS) regression of Eq. [14] or [16] against measured values of $C_i(t)$ or η , respectively. Note that η is derived from a combination of dependent and independent variables.³ With this regression approach, the model is "fitted" to the data, and statistical theory (1-4) states that the estimates of D_1 and κ_{avg} are the best values for the data

³ For the model presented here, i and v are considered independent variables and, hence, one should obtain the same estimates for D_1 and κ_{avg} by using either $C_i(t)$ or η as the dependent variable in the regression model. That is, statistical theory specifies that the independent variables are known precisely or at least within very small error limits (2) so that all of the error in η can be attributed to $C_i(t)$.

in the sense that the estimates result in the minimum difference between the observed and predicted values of η . Then the model with these estimates can be used for interpolation. Confidence is gained in the model if the parameter estimates obtained by LS are physically realistic. If the parameter estimates are physically realistic, extrapolations beyond the experimental range could be made within the limits of the assumptions of the model. Also, if the number of data points is large, confidence intervals on the parameter estimates can be obtained in the same manner as in linear regression (3).

The estimation of D_1 and κ_{avg} by LS requires experimental data in which both N_M and t are measured quantities. The factorially designed experiments of Ref. (11) provide data in which N_M was varied from 3.3 to 7.5 and t was varied from 0.17 to 0.33 cm. Also, the current density and velocity were measured precisely and cell temperature was controlled at $70^\circ \pm 0.5^\circ\text{C}$. In addition, the brine feed concentration was set with either a high or low acid and a constant salt concentration. The diaphragm voltage drop and the concentration of OH⁻ ion in the effluent were measured simultaneously as dependent variables. Note that D_1 and κ_{avg} are independent of the diaphragm properties and, therefore, are free stream parameters rather than effective parameters of the particular diaphragm. Thus, by fixing the values of N_M and t and the independent operating variables, i and v , the only parameters of the model which can account for an inadequate model are the values of D_1 and κ_{avg} .

It should be noted that the experimental cells of Ref. (11) consisted of laboratory cells which were designed by scaling down industrial-size electrolyzers so that geometric similarity was maintained. These cells contained a diaphragm which was placed in contact with a perforated steel cathode as shown in Fig. 1. The experimental cells were therefore consistent with the majority of industrial, metal anode cells which have the diaphragm vacuum deposited on the cathode.

Also, the model presented above was formulated to be consistent with the laboratory cells of Ref. (11). These cells were run for a period of 35 days. The replicate steady-state data were obtained over the entire period (26).

The predictions of the caustic yield and the diaphragm voltage drop are coupled through the average conductivity, κ_{avg} , and thus an appropriate LS objective function is

$$G(\beta) = \sum_{l=1}^N \frac{(\eta_l^o - \eta_l^p)^2}{\hat{\sigma}_1^2} + \sum_{k=1}^M \frac{(\Delta\Phi_k^o - \Delta\Phi_k^p)^2}{\hat{\sigma}_2^2} \quad [42]$$

where η_l^p is predicted by Eq. [16] at the experimental conditions corresponding to the l th datum, $\Delta\Phi_k^p$ is predicted by integration of Eq. [4] at the experimental conditions corresponding to the k th datum, and $\hat{\sigma}_1^2$ and $\hat{\sigma}_2^2$ correspond to the estimated variance of η and $\Delta\Phi$, respectively.

The nonlinearity of Eq. [42] results from the nonlinear model equation for η , but it does not affect the theory behind LS regression (3, 4). The computations necessary to minimize this objective function become more complicated with a nonlinear function, but many computers have subroutine libraries which can perform the necessary calculations. In this work, minimization subroutines of the International Mathematical and Statistical Library (25) were used (26).

Each of the estimated variance ($\hat{\sigma}_1^2$ and $\hat{\sigma}_2^2$) in Eq. [42] correspond to the sum of the variance associated with the measurement error and the variance associated with the model error. That is, we assume (in accordance with the assumptions of LS theory) any difference between the observed and predicted values is a lumped error which is distributed randomly. Thus, $\hat{\sigma}_1^2$, for example, was calculated by dividing the minimum value of $G(\beta)$ when $\hat{\sigma}_2^2 = \infty$ by the degrees of freedom [in this case, $N - 2$, since two parameters are adjusted to minimize $G(\beta)$]. Similarly, $\hat{\sigma}_2^2$ was calculated by dividing the minimum value of $G(\beta)$ when $\hat{\sigma}_1^2 = \infty$ by $(M - 1)$ (only one parameter, κ_{avg} , is adjusted to minimize $G(\beta)$ when $\hat{\sigma}_1^2 = \infty$).

Table I. Parameter estimates for diaphragm model

Case A. Parameter estimates with $\hat{\sigma}_2^2 = \infty$; $N = 84$					
Parameter	Estimate	\pm	95% Confidence interval	Units	^a t-statistic
D_1	3.352×10^{-5}	\pm	0.275×10^{-5}	cm ² /s	24.3
κ_{avg}	0.422	\pm	0.060	$\Omega^{-1} \text{cm}^{-1}$	14.7
$\hat{\sigma}_1^2$	1.118×10^{-3}		—	none	—
Case B. Parameter estimates with $\hat{\sigma}_1^2 = \infty$; $M = 64$					
Parameter	Estimate	\pm	95% Confidence interval	Units	^a t-statistic
κ_{avg}	0.3261	+	0.0154	$\Omega^{-1} \text{cm}^{-1}$	42.3
$\hat{\sigma}_2^2$	2.688×10^{-3}		—	V ²	—
Case C. Parameter estimates with $\hat{\sigma}_1^2 = 1.118 \times 10^{-3}$ and $\hat{\sigma}_2^2 = 2.688 \times 10^{-3}$ V					
Parameter	Estimate	\pm	95% Confidence interval	Units	^a t-statistic
D_1	2.826×10^{-5}	\pm	0.112×10^{-5}	cm ² /s	49.7
κ_{avg}	0.338	\pm	0.016	$\Omega^{-1} \text{cm}^{-1}$	41.6
$G(\beta)$	1.627×10^{-2}		—	none	—

^a See Ref. (26).

The weighting of the dependent variables in the LS objective function in this fashion gives the "best values" of the parameters for Eq. [16] and [21] and the data (27). These estimated variances are shown in cases A and B of Table I. Note that $\hat{\sigma}_1$ is dimensionless, since η is dimensionless, whereas $\hat{\sigma}_2$ has the dimensions of $\Delta\Phi$. The parameter estimates for D_1 and κ_{avg} shown for cases A and B can be compared with the parameters of case C, which were estimated with the objective function weighted as described above. That is, including the data on the voltage drop through the diaphragm lowers the estimates of D_1 and κ_{avg} and narrows the confidence intervals. The narrow confidence intervals indicate a greater sensitivity of the case C objective function to changes in the parameter values.

Figures 3 and 4 compare the predicted and observed values of η and $\Delta\Phi$ at the estimates of case C in Table I. The slopes and intercepts shown on Fig. 3 and 4 indicate that the diaphragm model agrees well enough with the experimental data to be useful for approximate design purposes. The large dispersion of observed voltage drops for a given predicted voltage drop may be a result of the fifth assumption made above; that is, the potential drop is probably a nonlinear function of the operating variables.

Figures 5 and 6 show that the residuals (*i.e.*, the difference between the predicted and observed values) are independent of the dependent variables as required by LS regression theory (2, 3, 27). Similar plots of the residuals and effective thickness ($N_M t$), current density, and velocity indicate no correlation between these independent variables and residuals (26). Thus, it can be concluded that the model with the LS parameter estimates of case C in Table I can be used to predict both the caustic yield and the diaphragm voltage drop.

Also, if the diaphragm effective thickness, $N_M t$, was known to change with time (due to plugging of the diaphragm, for example), the model could be adapted for interpolation purposes by minimizing Eq. [42] by adjusting $N_M t$ with the values of D_1 and κ_{avg} held constant at the specified values of case C. This adjusting of $N_M t$ was not necessary for the experimental data used here because both the values of N_M and t were not significantly different before and after the experiments (11).

Electrode kinetics.—Calculation of the cell voltage, V_T , by Eq. [18] requires knowledge of the kinetic parameters corresponding to the Tafel equations for the anode and

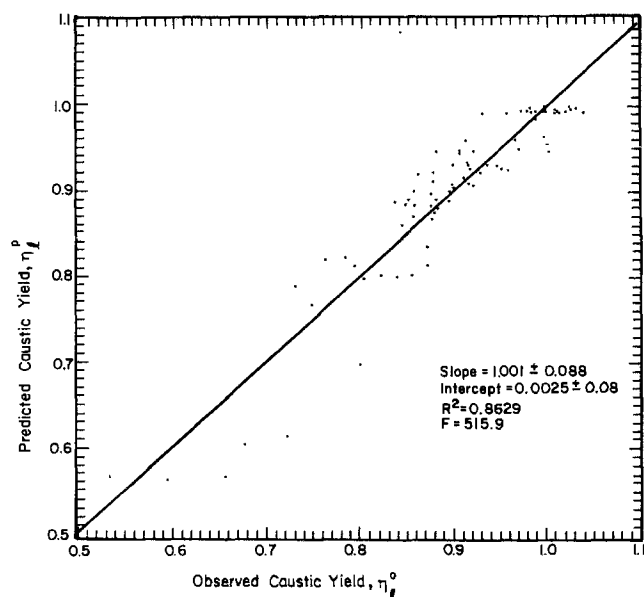


Fig. 3. Comparison of model predictions and experimental caustic yield data from Ref. (11) using the LS parameters of case C, Table I.

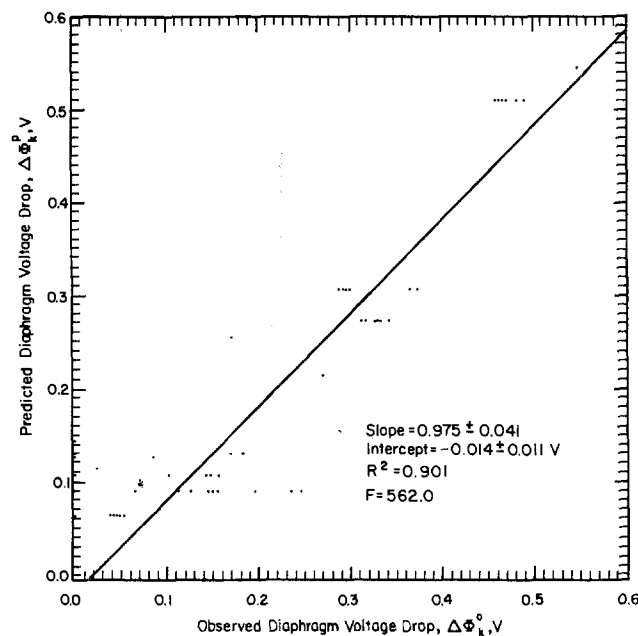


Fig. 4. Comparison of model predictions and experimental diaphragm voltage-drop data from Ref. (11) using LS parameters of case C, Table I.

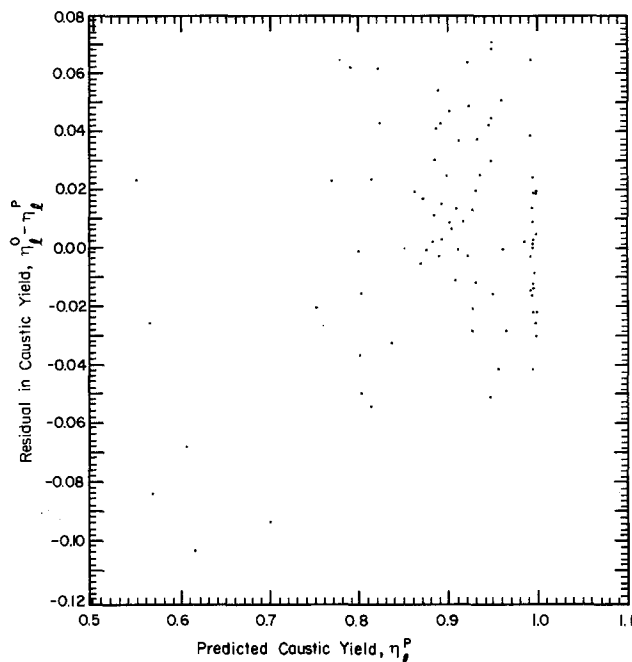


Fig. 5. Dependence of residuals on caustic yield predictions using LS parameters of case C, Table I.

cathode. The kinetic data obtained in Ref. (11) are proprietary, but for purposes of illustration, the data of Caldwell (28) can be used to estimate these kinetic parameters. That is, Caldwell reports hydrogen and chlorine overpotentials as functions of temperature and current density. By assuming that these overpotentials are independent of NaOH and NaCl concentrations, estimates of α_i and $i_{0,i}$ can be obtained by LS for use in Eq. [18] and then in Eq. [17] for prediction of the specific energy cost.

Since the overpotential data for hydrogen on low-carbon steel in 2.5M NaOH/3.01M NaCl electrolyte are large negative numbers, the Butler-Volmer expression can be inverted to give an explicit expression for V_1 , the dependent variable

$$V_1 = \frac{RT}{\alpha_1 F} \ln(i_{0,1}) - \frac{RT}{\alpha_1 F} \ln i \quad [43]$$

Thus an appropriate objective function for this data is

$$H_1(\alpha_1, i_{0,1}) = \sum_{i=1}^N (V_{1,i}^o - V_{1,i}^p)^2 \quad [44]$$

Equation [44] can be minimized easily with a hand calculator or statistical subroutines (25, 26). Unfortunately, the residuals of Eq. [44] exhibit a large correlation with temperature when all of the data (28) are used to estimate the parameters (26). Consequently, the parameter esti-

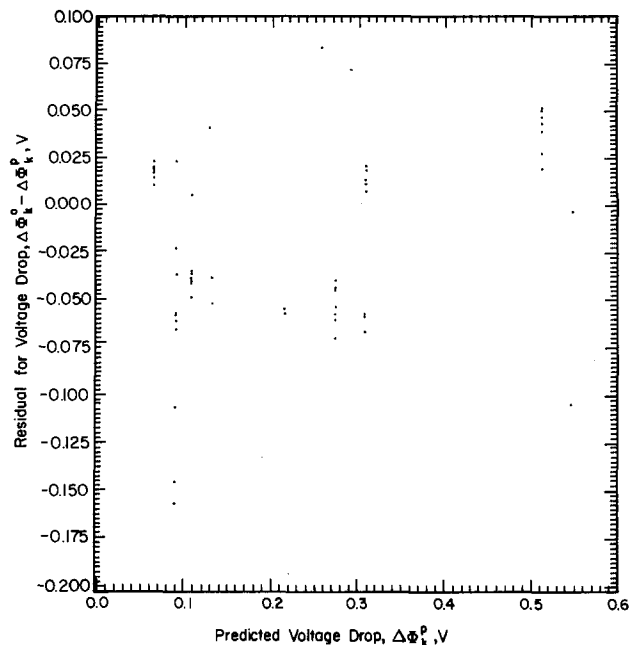


Fig. 6. Dependence of residuals on diaphragm voltage-drop predictions using LS parameters of case C, Table I.

mates (α_1 and $i_{0,1}$) were determined using only the data (28) for 343 K (*i.e.*, $N = 5$) as shown in Table II. The confidence intervals on $i_{0,1}$ and α_1 are small, even though the number of data points is small. It should be noted that even though the determination of values for α_1 and $i_{0,1}$ is simple, the determination of their confidence intervals is complicated because the Tafel equation confidence intervals correspond to $1/\alpha_1$ and $[\ln(i_{0,1})]/\alpha_1$. The confidence intervals of Table II were determined from nonlinear regression routines (26). Figure 7 compares the predictions of Eq. [43] with the data of Caldwell (28). Residual plots (26) did not show a correlation of predicted overpotentials with current density.

The overpotential data for production of chlorine on RuO₂-TiO₂ on titanium (28) should not be analyzed with a Tafel expression similar to Eq. [43] because the cathodic part of the Butler-Volmer expression is significant at small overpotentials. Instead, an implicit calculation should be performed to determine the dependent variable V_2 . This calculation is performed by forming the function, f_1

$$f_{1,j} = 0 = i_{2,j} - i_{0,2} \left\{ \exp\left(\frac{\alpha_2 F}{RT_1} V_{2,j}\right) - \exp\left[\frac{(\alpha_2 - 2) F V_{2,j}}{RT_1}\right] \right\} \quad [45]$$

Then for the given independent variables, $i_{2,j}$ and T_1 , and assumed values of α_2 and $i_{0,2}$, values of $V_{2,j}$ can be determined (by Newton's method, for example) such that $f_{1,j}$ is

Table II. Kinetic parameter estimates^a

Case A. Hydrogen on low-carbon steel in 2.5M NaOH and 3.01M NaCl electrolyte at 343.15 K					
Parameter	Estimate	±	95% Confidence Interval	Units	^b t-statistic
α_1	0.5723	±	0.0153	none	119.0
$i_{0,1}$	4.085×10^{-4}	±	0.490×10^{-4}	A/cm ²	26.5
Case B. Chlorine on RuO ₂ -TiO ₂ on titanium in 5.02M NaCl determined using Eq. [45] and [46]					
Parameter	Estimate	±	95% Confidence interval	Units	^b t-statistic
α_2	1.809	±	0.592	none	6.3
$i_{0,2}$	3.710×10^{-3}	±	3.097×10^{-3}	A/cm ²	2.5

^a Based on data presented by Caldwell (28).

^b See Ref. (26).

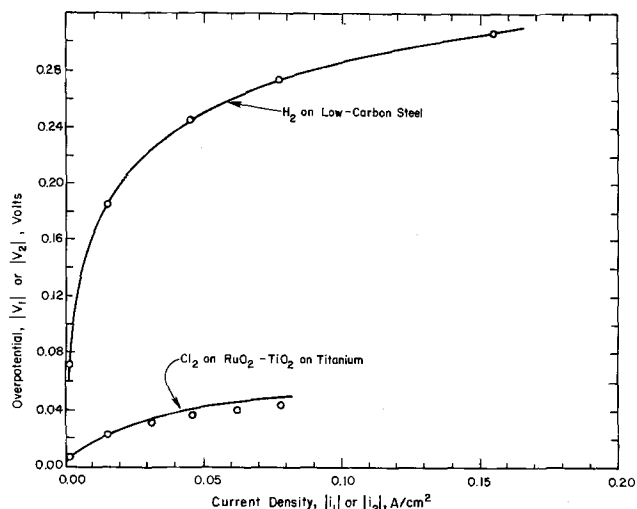


Fig. 7. Comparison of hydrogen overpotential predictions and data of Ref. (28), and comparison of chlorine overpotential data of Ref. (28) and predictions from Eq. [45] and LS parameters of case B, Table II, at 343.15 K.

approximately zero. The assumed values of α_2 and $i_{0,2}$ can be adjusted to obtain a minimized objective function which can be defined

$$H_2(\alpha_2, i_{0,2}) = \sum_{i=1}^{24} (V_{2,i}^0 - V_{2,i}^p)^2 \quad [46]$$

Nonlinear regression techniques (26) must be used to minimize Eq. [46]. It should be noted that Eq. [45] assumes that the apparent transfer coefficients sum to the number of electrons evolved in the overall oxidation of choride to chlorine (two here).

The estimated parameters using this implicit formulation for the chlorine reaction are shown in case B of Table II. The confidence intervals for these parameters are large, which indicates the need for more data at larger current densities. Figure 7 compares the experimental and predicted values at these parameter estimates. Residual plots (26) did not indicate significant correlations of the residuals with either current density or temperature, and, therefore, all of the data reported by Caldwell (28) was used.

Electrical Energy Cost Predictions

The specific electrolyzer energy cost for NaOH production (*i.e.*, Eq. [17]) can be predicted with confidence for the range of industrial conditions covered by the factorial experiment by using the parameter estimates of Tables I and II. An example of these energy cost predictions is shown in Fig. 8. The physical properties and parameters used for the calculations are shown in Table III. It should

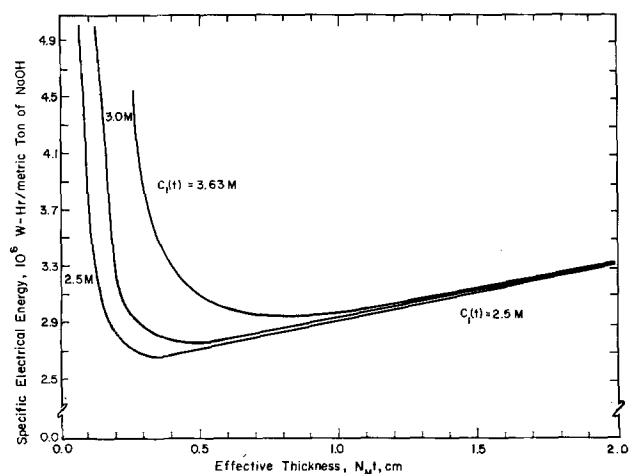


Fig. 8. Electrical energy cost predictions for NaOH production

Table III. Physical parameters for minimum energy calculation

D_1	$= 2.826 \times 10^{-5} \text{ cm}^2/\text{s}$
i	$= 0.200 \text{ A/cm}^2$
$i_{0,2}$	$= 3.710 \times 10^{-3} \text{ A/cm}^2$
$i_{0,1}$	$= 4.085 \times 10^{-4} \text{ A/cm}^2$
s	$= 0.635 \text{ cm}$
T	$= 343.15 \text{ K}$
α_1	$= 0.5723$
α_2	$= 1.809$
$ \Delta U^\theta $	$= 2.188 \text{ V}$
ϵ_b	$= 0.5$
$\kappa_{\text{anolyte}}^a$	$= 0.491 \text{ } \Omega^{-1} \text{ cm}^{-1}$
κ_{avg}	$= 0.338 \text{ } \Omega^{-1} \text{ cm}^{-1}$

^a From Caldwell (28) for 5.13M NaCl at 70°C.

be noted that the only assumed value in Table III is the void fraction of bubbles in the anolyte; all other values correspond to either parameter estimates, physically measurable properties (*i.e.*, diaphragm, electrolyte, or cell geometry properties), or operating conditions. Consideration of Fig. 8 shows that an $N_M t$ can be selected which minimizes the specific electrical energy cost for NaOH production at a specified current density and caustic effluent concentration (or effluent velocity as shown in Fig. 9). However, it is important to note that this minimum occurs at a value of $N_M t$ beyond that used in the experimental work and may, consequently, be invalid.

Conclusion

Development of a simple model of the diaphragm in terms of measurable diaphragm properties has provided a design equation which allows direct comparison of experimental data and theoretical predictions. This comparison, accomplished with parameter estimation techniques, shows that the models of the caustic yield and the voltage drop through the diaphragm are reasonable; changing the assumption of a linear potential gradient through the diaphragm may provide an improvement. The parameter estimates and the simple model provide a design equation which can be used to predict the minimum specific electrical energy required for NaOH production as a function of the effective thickness, $N_M t$, the current density, and the caustic concentration in the effluent (or the effluent velocity).

Acknowledgments

The authors acknowledge gratefully the support of this work by the Dow Chemical Company and the comments and suggestions by Mr. Donald L. Caldwell.

Manuscript submitted April 30, 1984; revised manuscript received Dec. 27, 1984.

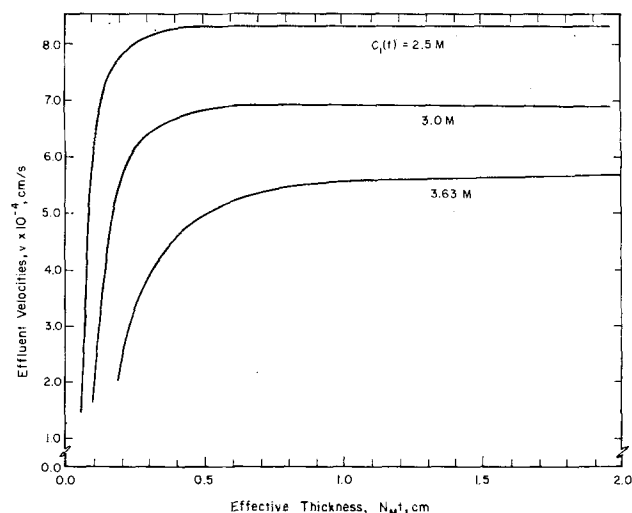


Fig. 9. Effluent velocities corresponding to energy cost predictions of Fig. 8.

LIST OF SYMBOLS

A_1	see Eq. [13] (cm^{-1})
A_d	area of diaphragm (cm^2)
A_p	area of pores within the diaphragm (cm^2)
$C_1, C_1(x)$	position dependent concentration of OH^- ion (mol/cm^3)
$C_1(x = t), C(t)$	concentration of OH^- ion at diaphragm/catholyte interface (mol/cm^3)
$C_{1,\text{effluent}}$	concentration of OH^- ion in catholyte effluent (mol/cm^3)
CE	cost of electrical energy ($\$/J$)
D_1	free stream diffusion coefficient of OH^- ion (cm^2/s)
D_e	effective diffusion coefficient of OH^- ion (cm^2/s)
EC_{e1}	specific electrical energy cost for NaOH production ($\$/g$)
EL	length parameter (see Eq. [28]) (cm)
F	Faraday's constant (96,487 C/mol)
F_1	feed concentration of NaCl (mol/cm^3)
$f_{1,l}$	functional representation of Butler-Volmer equation equal to zero at l th datum (see Eq. [45])
$G(\beta)$	least squares objective function with parameter vector β , see Eq. [42]
H_1, H_2	least squares objective function for hydrogen and chlorine electrode kinetics, respectively, see Eq. [44] and [46]
i	current density through the diaphragm (A/cm^2)
$i_{2,l}$	current density on anode corresponding to l th datum (A/cm^2)
$i_{0,1}, i_{0,2}$	exchange current density of hydrogen and chlorine electrodes, respectively (A/cm^2)
l	average pore length, see Eq. [29] (cm)
M	number of data points for diaphragm voltage drop
M_1	molecular weight of NaOH (39.99 g/mol)
N	number of data points for caustic yield or hydrogen overpotential
N_1	flux of OH^- ion in diaphragm ($\text{mol}/\text{cm}^2 \text{ s}$)
N_M	MacMullin number, see Eq. [2], dimensionless
N_H	Hine number, see Eq. [23], dimensionless
n_1	transference number of OH^- ion (cm^2/mol)
Pe	Peclet number, see Eq. [20], dimensionless
R	gas constant (8.3143 J/mol K)
s	distance between anode and diaphragm anolyte face (cm)
T	temperature (K)
t	diaphragm thickness (cm)
t_j, t_1	transport number of species j , $j = 1$ for OH^- ion
u_j, u_1	mobility of species j , $j = 1$ for OH^- ion ($\text{cm}^2 \cdot \text{mol}/J \cdot \text{s}$)
U	relative velocity expression of Stender <i>et al.</i> (6) (cm/s)
ΔU^θ	open-circuit potential for chlorine/caustic cell (2.188V)
V_T	total cell voltage, see Eq. [18] (V)
V_1, V_2	hydrogen and chlorine overpotential, respectively (V)
$V_{1,l}^o, V_{2,l}^o$	observed hydrogen and chlorine kinetic overpotential, respectively, at l th datum
$V_{1,l}^p, V_{2,l}^p$	predicted hydrogen and chlorine kinetic overpotential, respectively, at independent variables corresponding to l th datum
v	percolation velocity through the diaphragm (cm/s)
x	diaphragm dimensional coordinate (cm)
z_j, z_1	ionic charge for species j , $j = 1$ for OH^- ion

Greek

α_1, α_2	apparent transfer coefficients for hydrogen and chlorine reactions, respectively
β	vector of parameters for LS ($\beta = [D_{1,\kappa_{\text{avg}}}]^T$)
δ	diaphragm effective thickness, see Eq. [24] (cm)
ϵ	porosity of diaphragm, dimensionless
ϵ_b	void fraction of gas bubbles in anolyte, dimensionless
η	caustic yield, dimensionless
κ_{avg}	average specific conductivity of electro-

κ_{anolyte}	specific conductivity of anolyte ($\Omega^{-1} \text{cm}^{-1}$)
$\Phi(x), \Phi$	dimensional voltage in diaphragm at position x (V)
$\Delta\Phi$	dimensional voltage drop through the diaphragm (V)
$\Delta\phi$	dimensionless voltage drop through the diaphragm
ρ	resistivity of diaphragm filled with electrolyte (Ωcm)
ρ_0	resistivity of electrolyte with an equivalent thickness of the diaphragm (Ωcm)
$\hat{\sigma}_1^2$	estimated variance of caustic yield, dimensionless
$\hat{\sigma}_2^2$	estimated variance of diaphragm voltage drop (V^2)
τ	tortuosity of diaphragm, dimensionless
$\theta_1(\zeta)$	dimensionless concentration of OH^- ion at ζ dimensionless coordinate ($\zeta = x/t$)

REFERENCES

- R. J. Freund and P. D. Minton, "Regression Methods," p. 25, Marcel Dekker, Inc., New York (1979).
- B. Ostle and R. W. Mensing, "Statistics in Research," 3rd ed., pp. 166-178, Iowa State University Press, Ames, IA (1975).
- A. R. Gallant, *Am. Stat.*, **29**, 73 (1975).
- A. R. Gallant and D. W. Jorgenson, *J. Econometrics*, **11**, 275 (1979).
- J. Lee, "Identification and Estimation of Model Parameter in Electrochemical Reactor Design," Presented at AIChE Meeting, Denver, Co, August 1983.
- V. V. Stender, O. S. Ksenzhek, and V. N. Lazarev, *Zh. Prikl. Khim.*, **40**, 1293 (1967).
- T. Mukaibo, *J. Electrochem. Soc. Jpn.*, **20**, 482 (1952).
- P. Gallone and E. Rubino, *Ann. Chim.*, **66**, 103 (1976).
- W. H. Koh, *AIChE Symp. Ser.*, **77**, 213 (1981).
- W. H. Koh, Paper 391 presented at The Electrochemical Society Meeting, St. Louis, MO, May 11-16, 1980.
- K. A. Poush, D. L. Caldwell, J. W. Van Zee, and R. E. White, in "Modern Chlor-Alkali Technology," Vol. 2, C. Jackson, Editor, Ellis Horwood Limited, Chichester, West Sussex, England (1983).
- D. L. Caldwell, K. A. Poush, J. W. Van Zee, and R. E. White, in "Electrochemical Process and Plant Design," R. C. Alkire, T. R. Beck, and R. D. Varjian, Editor, p. 216, The Electrochemical Society Softbound Proceedings Series, Pennington, NJ (1983).
- R. B. MacMullin and G. A. Muccini, *AIChE J.*, **2**, 393 (1956).
- F. Hine, M. Yasuda, and K. Fujita, *This Journal*, **128**, 2314 (1981).
- L. G. Austin, "Handbook of Fuel Cell Technology," p. 160, Prentice-Hall, Inc., Englewood Cliffs, NJ (1968).
- F. Hine, M. Yasuda, and T. Tanaka, *Electrochim. Acta*, **22**, 429 (1977).
- F. Hine, *Soda To Enso*, 219 (1980).
- R. R. Chandran and D-T. Chin, Paper 562 presented at The Electrochemical Society Meeting, San Francisco, CA May 8-13, 1983.
- V. L. Kubasov, V. B. Vorbena, and L. I. Yurkov, *Sov. Electrochem.*, **15**, 1773 (1979).
- J. S. Newman, "Electrochemical Systems," Prentice-Hall, Inc., Englewood Cliffs, NJ (1973).
- D. A. G. Bruggeman, *Ann. Phys.*, **24**, 636 (1935).
- R. E. De La Rue and C. W. Tobias, *This Journal*, **106**, 827 (1959).
- R. E. White, J. S. Beckerdite, and J. Van Zee, in "Electrochemical Cell Design," R. E. White, Editor, Plenum Press, NY (1984).
- F. Hine and M. Yasuda, *This Journal*, **118**, 116 (1971).
- International Mathematical and Statistical Library subroutines ZXSSQ and ZXMIN, IMSL, Inc., Houston, TX.
- J. W. Van Zee, Ph.D. Dissertation, Texas A&M University, College Station, TX (1984).
- N. Draper and H. Smith, "Applied Regression Analysis," 2nd ed., pp. 108-112, John Wiley and Sons, Inc., NY (1981).
- D. L. Caldwell, in "Comprehensive Treatise of Electrochemistry," Vol. 2, J. O'M. Bockris, B. E. Conway, E. Yeager, and R. E. White, Editors, pp. 121-129, Plenum Press, NY (1981).

Influence of Operating Conditions on the Selectivity Factor of the Nickel/Sodium Electrodialysis Separation

Claudio Fabiani, Luigi Bimbi, Massimo De Francesco, and Bernardino Scuppa

ENEA, Divisione Chimica, Laboratorio Chimica Applicata CRE-Casaccia, Rome, Italy

ABSTRACT

The NiCl₂/NaCl separation by electrodialysis is studied as a function of several operating conditions such as current density, Na/Ni concentration ratio, and temperature. The experimental $T(\text{Ni}/\text{Na})$ separation factors are discussed, assuming a membrane-controlled process, in terms of Hittorf transport numbers and electro-osmotic coefficients for the electrically driven transport of both cations through the cationic membrane (Nafion 125 from du Pont) which is assumed to be the selective component in the cell stack. Activation energy for the separation is calculated and the obtained data are compared with the values derived from membrane resistance measurements.

Electrodialysis is a well-assessed technology in desalination and is still considered an interesting possibility in the field of valuable metal recovery and nuclear waste treatment (1-3). In this last field, the electrical power availability makes the energy requirements and costs for electrodialysis less conditioning parameters. In this work, the Ni/Na separation by electrodialysis in chloride media has been considered. Two commercially available membranes, the cation-selective Nafion 125 (from du Pont) and the anion-selective R-5035 (from RAI Corporation) were used. The former membrane was chosen because of its high performance in many electrochemical applications (fuel cells, batteries, electrolysis) and the latter because it is specifically tailored for electrodialysis.

Experimental

Membranes.—Nafion 125 membranes are homogeneous perfluorosulfonic acid polymeric films from du Pont. They have an equivalent weight of 1,200 and are 5 mil thick. Membrane specimens were treated with 0.1M HCl for 48h and boiled in bidistilled water for 72h to convert the membranes to the H⁺ form, completely wet. Membrane specimens of 37 cm² in H⁺ form were then equilibrated with the electrolyte solution until cation exchange was complete. The R-5035 Raipore membrane (from RAI Corporation) is a quaternized vinylbenzylamine-grafted anion exchange membrane 8 mil thick. Membrane specimens were equilibrated in the electrolyte solution for 72h after 48h in boiling water.

Transport parameter measurements.—The Hittorf transport numbers (t_{\pm}), the electro-osmotic coefficient (β)

(cm²F⁻¹), and the membrane area resistance ($R \Omega \text{ cm}^2$) were simultaneously measured for both membranes. The results are collected in Table I. A three-chamber plastic cell formed by a cathodic compartment bounded by two ion-exchange membranes of opposite charge and two measuring compartments separated by the membrane to be characterized (Fig. 1) was used. The current delivering electrodes were a Pt cathode and a Ag/AgCl anode, because in the anode compartment, volume changes were measured and, therefore, evolution of gaseous species should be avoided. Solutions were recirculated through a thermostated bath or, in the anode compartment, for the same reasons already mentioned, magnetically stirred. The experimental procedures used to perform such measurements are reported elsewhere (4, 5). A known electrical current, I (mA), was passed for a given time interval, Δt , across the cell, and ionic and water transports across the membrane were measured. The transport of water in the anode half-cell where the reversible Ag/AgCl electrode was placed was obtained from the change in vol-

Table I. Equilibrium and transport properties of Nafion 125 and RAI R-5035 membranes as a function of the external electrolyte concentration C (mol liter⁻¹) in NaCl and NiCl₂ aqueous solutions. $T = 30^{\circ}\text{C}$.

C (mol liter ⁻¹)	Nafion 125		RAI R-5035
	Membrane water content weight percent (w/o) (dry polymer)		
	(NaCl)	(NiCl ₂)	
0.010	17.3	—	
0.050	17.2	23.5	
0.100	17.0	22.7	
0.500	16.6	20.5	
1.00	16.1	19.7	
C (mol liter ⁻¹)	Hittorf's transport number (t)		
	$t_{+}(\text{NaCl}, 25^{\circ}\text{C})$	$t_{+}(\text{NiCl}_2, 28^{\circ}\text{C})$	$t_{-}(\text{NiCl}_2, 28^{\circ}\text{C})$
0.01	0.98	—	—
0.10	0.98	0.86	0.94
0.20	0.99	0.70	0.87
0.42	0.94	0.48	0.70
0.60	0.91	0.39	0.51
C (mol liter ⁻¹)	Electro-osmotic coefficient β (cm ² F ⁻¹) (0.1-1.0 mA cm ⁻²)		
	(NaCl)	(NiCl ₂)	(NiCl ₂)
0.10	157	225	173
0.20	143	187	151
0.40	130	131	118
0.53	—	108	105
C (mol liter ⁻¹)	Electrical resistance R ($\Omega \text{ cm}^2$)		
	(NaCl)	(NiCl ₂)	(NiCl ₂)
0.10	45.2	20.6	45.8
0.20	31.5	(7.8)	10.3
0.40	—	10.3	12.4
0.50	13.9	7.8	8.9

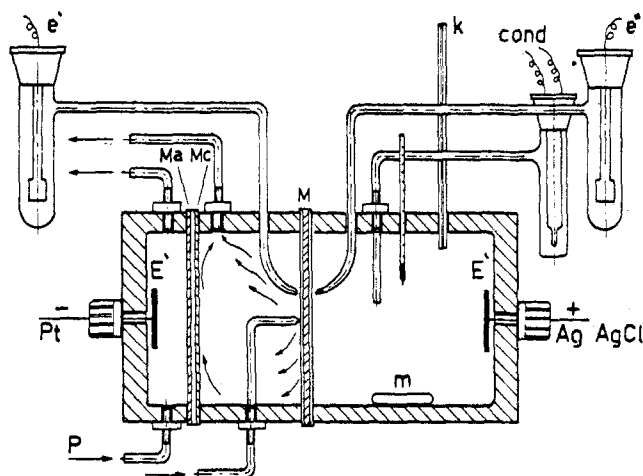


Fig. 1. Sketch of the experimental cell used for membrane transport parameter measurements. E', current bearing electrodes; P, pump; e', e'', SCE for membrane potential measurement under flowing current (membrane resistance); k, capillary for volume variation detection; cond, conductivity cell; m, stirrer; Ma, Mc, anionic and cationic ion exchange membranes; M, membrane under study.

ume solution ΔV ($\Delta V = V_f - V_i$, where V_f and V_i are the final and initial volume in cubic centimeters, respectively) observed in the capillary K (Fig. 1). This figure was corrected for the volume changes related to electrode reactions and ionic species transport. Similarly, the ionic transport used to calculate the ionic transport number was measured through the change in the electrolyte concentration ΔC (mol cm^{-3}) corrected for the contribution of the volume flow due to electro-osmosis. The electrolyte concentration changes were obtained from conductivity data (Cond, Fig. 1) by using a specific calibration curve. A two-equation system was then needed to correctly calculate the Hittorf transport number (t_+ or t_-) and the electro-osmotic coefficients β . These equations are (for the case of Ni^{2+}) (4-6)

$$2t_- = \frac{10^3 V_i}{F} (C_i - C_f) - 10^3 C_f \beta \quad [1]$$

$$\beta = \frac{\Delta V}{F} = \frac{1}{F} (V_1 + 1/2 t_+ \bar{V}_{\text{NiCl}_2} + \bar{V}_{\text{Ag}} - \bar{V}_{\text{AgCl}}) \quad [2]$$

where C_i and C_f are, respectively, the initial and final electrolyte concentrations (mol cm^{-3}), F is the number of Faraday used in the Δt time interval of the experiment, and \bar{V} are the partial molar volumes of NiCl_2 (contribution from the ionic transport), Ag , and AgCl (contributions from the electrode reaction).

The electric potential drop across the membrane was measured by means of two Luggin capillaries connected to the e' and e'' (Fig. 1) electrodes and used to calculate the membrane resistance at a given electric current.

The water content of Nafion 125 [weight percent (w/o) dry polymer] in both NaCl and NiCl_2 solutions was measured according to reported procedures (5). Membrane specimens equilibrated in a given solution were dried under vacuum in an air oven at $120^\circ\text{--}150^\circ\text{C}$ after blotting their surfaces with filter paper. Membrane dryness was checked by means of IR spectroscopy and water amount was calculated as the difference between wet and dry specimens.

Electrodialysis experiments.—A laboratory stack with five cell units 2 mm wide filled with a plastic net as turbulence promoter and delimited by membranes of 37 cm^2 area was operated with an electro dialyzer Bell II supplied by Berghof (Tubingen, Germany). The usual three solutions (200 cm^3 of electrode washing, 400 cm^3 of concentrate, and feed) were thermostated and circulated at $1400 \text{ cm}^3/\text{min}$ flow rate. For washing the electrode, a solution of the same composition as the feed solution was used in each experiment. The pH of concentrate and feed were continuously measured and recorded by using two glass electrodes inserted in the solution reservoirs. From these reservoirs, small aliquots of solutions were taken at fixed times and analyzed for Cl^- and Ni^{2+} . Chloride ions were measured potentiometrically with an Ag/AgCl electrode by using AgNO_3 for titration. The nickel concentration was obtained spectrophotometrically through the dimethylglyoxime complex. The Na^- concentration was obtained with a mass balance.

The stack resistance was also continuously measured and recorded.

Results

The loss of selectivity of charged membranes due to an increase in the concentration of the external electrolyte is a well-known effect which mainly depends on the salt uptake and decreased membrane water content (5). The first effect is a consequence of the saturation of ion-exchange sites of the membrane which reduces the Donnan coion exclusion and determines the salt invasion (with coion transport) of the membrane phase. The second effect is due to the increased osmotic pressure difference between the bathing solution and the membrane phase, which reduces the water content of the latter. The loss of selectivity can be observed from the decrease of the counterion transport number as the electrolyte con-

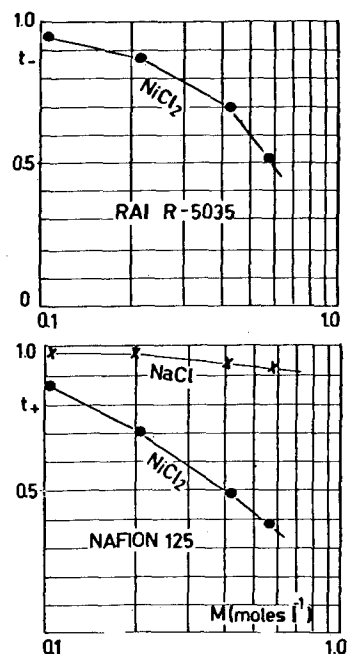


Fig. 2. Hittorf's transport numbers for Cl^- (RAI R-5035 membrane) and Na^+ , Ni^{2+} (Nafion 125) as a function of the electrolyte molar concentration.

centration increases, as shown in Fig. 2. This effect occurs at a concentration which is lower the higher the counterion valency is, as is shown from a comparison between NaCl and NiCl_2 . This is an important effect, as the decreased membrane selectivity can compensate the higher electromobility of multivalent cations. Similar effects are observed in the membrane resistance (4) and electro-osmotic coefficient which is related to the hydration of the transported ion (5). In fact, the counterion hydration also affects the membrane selectivity. It has been observed with Nafion 125 membranes exposed to alkali hydroxide (4) and chloride (7) solutions that at a given concentration in the region of low selectivity, the cation transport number decreases by increasing the hydration according to the series $\text{Cs} > \text{K} > \text{Na} > \text{Li}$. The data reported in Table I show the corresponding effect on electro-osmotic coefficients and membrane resistance. These parameters are important in determining the selective separation factor of an electro dialysis experiment. In fact, defining $T(\text{Ni}/\text{Na})$ as

$$T(\text{Ni}/\text{Na}) = [(J_{\text{Ni}}/C_{\text{Ni}})/(J_{\text{Na}}/C_{\text{Na}})] \quad [3]$$

It can be shown with some simplifying assumptions (overall membrane control, linear steady-state concentration profiles, negligible back-diffusion, ideal behavior of anion membranes, etc.) (8) that

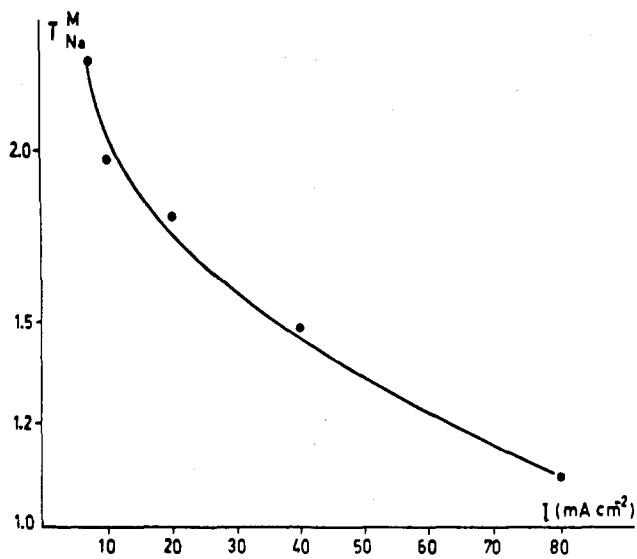
$$T(\text{Ni}/\text{Na}) = \frac{[(t_{\text{Ni}}/C_{\text{Ni}}^0) + t_w^{\text{Ni}}]}{[(t_{\text{Na}}/C_{\text{Na}}^0) + t_w^{\text{Na}}]} \quad [4]$$

where $t_w = \beta/18$ is the water transport number. Equation [4] assumes that the separation process for the $\text{NaCl}/\text{NiCl}_2$ mixture is mainly due to the cationic membrane and that polarization effects can be disregarded. This last condition was tested, in the current density range $5\text{--}80 \text{ mA cm}^{-2}$ we have used, by measuring the pH of feed and concentrate solutions during electro dialysis. The pH values remain practically constant after a small initial decrease.

For high current densities, when the electromigration is the predominant transport effect, Eq. [4] should reduce to (8)

$$T(\text{Ni}/\text{Na}) = [(t_{\text{Ni}}/C_{\text{Ni}}^0)/(t_{\text{Na}}/C_{\text{Na}}^0)] (I \rightarrow \infty) \quad [5]$$

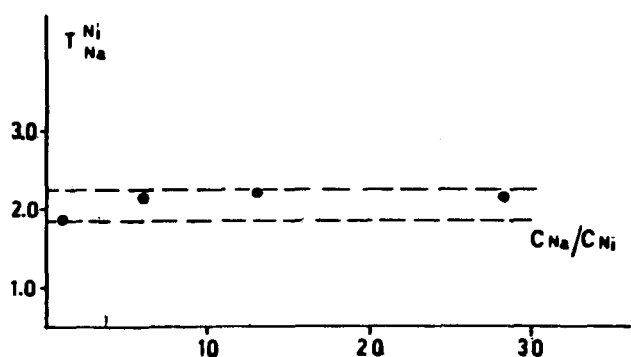
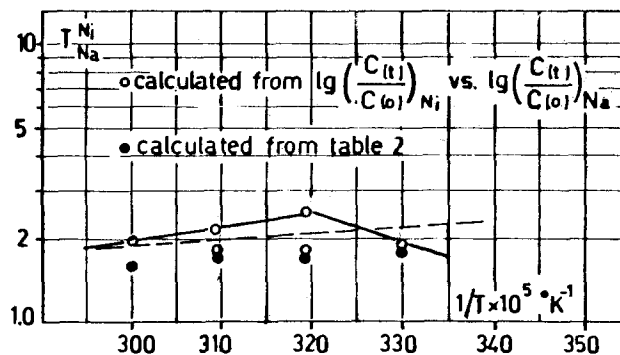
This limiting law has been tested by measuring the $T(\text{Ni}/\text{Na})$ dependence on the current density. The $T(\text{Ni}/\text{Na})$ values were obtained for NiCl_2 ($\sim 0.1 \text{ M}$) - NaCl ($\sim 0.1 \text{ M}$) mixtures from the relation (8)

Fig. 3. $T(\text{Ni}/\text{Na})$ dependence on the current density I (mA/cm^2)

$$\log [C_{\text{Ni}}^{\circ}(t)/C_{\text{Ni}}^{\circ}(0)] = T(\text{Ni}/\text{Na}) \log [C_{\text{Na}}^{\circ}(t)/C_{\text{Na}}^{\circ}(0)] \quad [6]$$

which is derived by inserting into the definition for T (Eq. [1]) the expression for the ionic fluxes and by assuming T as a constant. In Eq. [6], $C_i^{\circ}(0)$ and $C_i^{\circ}(t)$ ($i = \text{Ni}, \text{Na}$) are the bulk initial and final concentrations in the feed or concentrate solutions. The plots of $\log [C_{\text{Ni}}^{\circ}(t)/C_{\text{Ni}}^{\circ}(0)]$ vs. $\log [C_{\text{Na}}^{\circ}(t)/C_{\text{Na}}^{\circ}(0)]$ are straight lines (T constant), and from their slopes the selectivity factors can be computed. The current density was varied from 5 to 80 mA/cm^2 (Fig. 3). Equation [3] predicts a limiting value for the selectivity $T(\text{Ni}/\text{Na})$ factor, at high current densities, which is reached when the ionic transport is essentially a function of the mobilities (transport numbers) of the ionic species at a given concentration (8). From the transport numbers of Ni^{2+} and Na^+ at 0.1M concentration across a Nafion membrane (Table I), a limiting value of 0.88 is obtained.

$T(\text{Ni}/\text{Na})$ dependence on the Na/Ni ratio.—The separation factors measured at different Na/Ni ratios but at a fixed current density (10 mA/cm^2) are shown in Fig. 4. A substantial constancy is experimentally observed around a value of two corresponding to the Ni/Na valency ratio. According to the $T(\text{Ni}/\text{Na})$ definition (Eq. [1]), this result means that the Ni flux decreases by increasing the Na concentration. As a consequence, the separation yield and the current efficiency decrease. The observed constant value for $T(\text{Ni}/\text{Na})$ as the Na/Ni ratio changes may depend on the nature of the ionic couple considered, since different results have been reported for the Mg/Na couple (8). An important factor in determining the constant T value is the ion exchange constant of monovalent and divalent ions with a given membrane. The results of the hydrogen ion-divalent ion-exchange experiments reported by Steck *et al.* (9) show that the exchange selectivity is almost

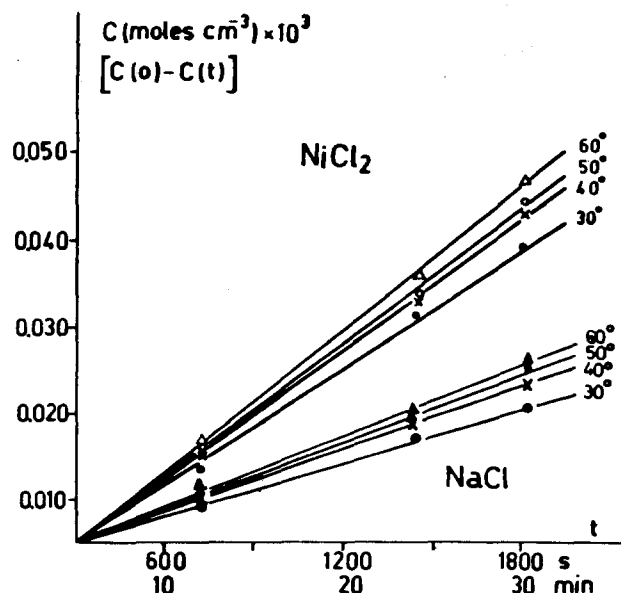
Fig. 4. $T(\text{Ni}/\text{Na})$ dependence on the Na/Ni equivalent ratio at a fixed current density 10 mA/cm^2 . C (equiv/ cm^3).Fig. 5. Experimental and calculated $T(\text{Ni}/\text{Na})$ values as a function of temperature in an Arrhenius-like plot.

equal for Na and Co, while for Mg the exchange is higher by a factor of two.

$T(\text{Ni}/\text{Na})$ temperature dependence.—The possibility of changing the separation factor with the temperature has been considered by measuring $T(\text{Ni}/\text{Na})$ at different temperatures in the 30°–60°C range. A complete equation for ionic and water transport in electrodialysis includes diffusion terms both for ions and water through the membrane couple (8). In this case, Eq. [4] does not hold any more. However, at high current densities the ionic and water transport due to the applied electrical field are predominant over diffusion and osmotic effects. Therefore, by assuming membrane control—that is, reduced film effects (polarization) at the membrane-solution interface—the simple Eq. [4] can be used. Under these conditions, the function $\tau_e = [(t_i/C^{\circ}) + t_w]$ can be considered as the “effective” transport number for the ionic species and an Arrhenius-type plot can be used to calculate the transport activation energy (Fig. 5)

$$d[\log T(\text{Ni}/\text{Na})]/d(1/T) = -(1/R)(E_{\text{Ni}} - E_{\text{Na}}) = -(1/R) \Delta E \quad [7]$$

where E_i is the activation energy for the transport of the i th ($i = \text{Ni}, \text{Na}$) cation. The experimental data in Fig. 5, however, do not allow one to reach a clear conclusion about the difference in behavior of Ni and Na fluxes with temperature. In fact, two hypotheses are possible: (i) the $T(\text{Ni}/\text{Na})$ vs. $1/T$ plot is a straight line with zero slope, which means that both Ni and Na transport processes have the same activation energy; (ii) the $t(\text{Ni}/\text{Na})$ vs. $1/T$ plot shows a discontinuity which separates two different transport conditions, $E_{\text{Ni}} \geq E_{\text{Na}}$ for $T \leq 40^{\circ}\text{C}$. In the first

Fig. 6. Evaluation of the desalting rate α of feed solutions for NaCl and NiCl_2 .

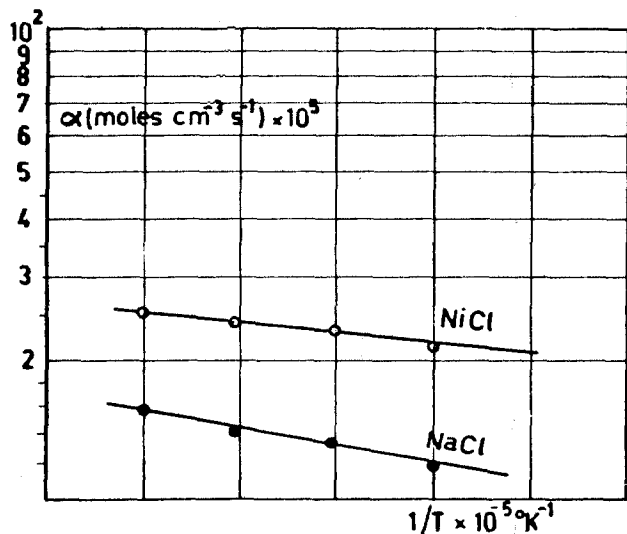


Fig. 7. Arrhenius-type plots for the α functions for NaCl and NiCl₂.

case, the overall activation energy is $\Delta E = 11.9$ kJ/mol, and in the second case $\Delta E = -9.6$ kJ/mol. In both cases, it should be possible to select a useful temperature range to optimize the separation process. A more extended investigation is needed possibly over an increased temperature range. However, a limit to this possibility is set by the thermal stability of the membranes. It is interesting to note that the reported values for the activation energies are comparable to those obtained from membrane resistance measurements on Nafion 125 membranes in alkali hydroxide solutions ($E_{Na} = 10$ -30 kJ/mol in the 0.02-10M range) (10).

Figure 5 shows also $T(Ni/Na)$ data calculated from the rate of desalting of binary NiCl₂/NaCl (feed) solutions at different temperatures. If the $C_i^{\circ}(0) - C_i^{\circ}(t)$ functions for both cations are plotted vs. time t (s), the slopes $\alpha = (nA/V)J_i$ (mol cm⁻³ s⁻¹) can be calculated (Fig. 6). According to the assumptions made to obtain Eq. [4]

$$\alpha = (nA/V)(t_i + C_i^{\circ}t_w) I/F \quad [8]$$

(where n is the number of pair units in the cell stack, A is the membrane area, and V is the solution volume) and both τ_i and $T(Ni/Na)$ values can be calculated from the desalting rate of the feed solution. The results of such calculations are given in Table II. From the Arrhenius plots of α for both counterions (Fig. 7), the activation energies for NaCl and NiCl₂ transport are obtained: $E_{NaCl} = 8.2$ kJ/mol and $E_{NiCl_2} = 4.8$ kJ/mol ($\Delta E = -3.5$ kJ/mol). This last value is very close to the figure for the activation energy, which can be calculated from the best linear plot of the experimental $T(Ni/Na)$ data reported in Fig. 5: $\Delta E = -4.2$ kJ/mol.

Table II. Evaluation of the desalting rate, α (mol cm⁻³ s⁻¹), effective transport number, τ , and separation factor $T(Ni/Na)$ for single NaCl/NiCl₂ from electrodiagnosis separation experiments. Feed solution 0.1M; NiCl₂ 0.1M.

$T(^{\circ}C)$	α_{Na} (mol cm ⁻³ s ⁻¹)	α_{Ni} (mol cm ⁻³ s ⁻¹)	τ_{Na}	τ_{Ni}	T (Ni/Na)
30	1.17×10^{-5}	2.13×10^{-5}	0.24	0.45	1.82
40	1.33×10^{-5}	2.30×10^{-5}	0.28	0.48	1.73
50	1.40×10^{-5}	2.43×10^{-5}	0.29	0.51	1.74
60	1.57×10^{-5}	2.53×10^{-5}	0.33	0.53	1.61

Conclusion

The use of Nafion 125 and RAI R-5035 membranes for electrodiagnosis of Na/Ni chloride binary solutions depends on the absolute Ni concentration because the Nafion selectivity in NiCl₂ solutions falls very sharply above 0.2M concentration. The $T(Ni/Na)$ separation factor does not substantially depend on the Na/Ni concentration ratio, and this constancy, at a given current density, shows that the current efficiency for Ni separation decreases as the Na concentration increases. The temperature effect on the $T(Ni/Na)$ separation factor is not very relevant in the 30°-60°C temperature range. However, some data indicate the possibility that the Ni yield decreases with temperature above a discontinuity point around 40°C.

Manuscript submitted Nov. 2, 1983; revised manuscript received Dec. 8, 1984. This was Paper 907RNP presented at the San Francisco, California, Meeting of the Society, May 8-13, 1983.

ENEA assisted in meeting the publication costs of this article.

REFERENCES

- J. R. Wilson, Editor, "Demineralization by Electrodiagnosis," Butterworths Scientific Pub., London (1960).
- G. S. Solt, in "Membrane Separation Processes," Ch. 6, P. Meares, Editor, Elsevier Scientific Pub. Co., Amsterdam (1976).
- R. G. Gutman, "Radioactive Waste: Advanced Management Methods for Medium Active Liquid Waste," CEN-AEPE, Ch. 4, Harwood Academic Publishers, New York (1981).
- G. Scibona, C. Fabiani, and B. Scuppa, *J. Memb. Sci.*, **16**, 37 (1983).
- C. Fabiani, G. Scibona, and B. Scuppa, *ibid.*, **16**, 51 (1983).
- N. Lakshminarayanaiah, "Transport Phenomena in Membranes," Ch. 5, Academic Press, New York (1969).
- C. Fabiani, G. Scibona, and B. Scuppa, Submitted to *Anal. Chem.*
- T.-C. Huang and T.-T. Wang, *Desalination*, **21**, 327 (1977).
- A. Steck and H. L. Yeager, *Anal. Chem.*, **52**, 1215 (1980).
- L. Bimbi, C. Fabiani, M. DeFrancesco, and B. Scuppa, Report CNEN-RT/CHI (81) 11, ENEA, Rome, Italy.

Cyclic Pulse Voltammetric Stripping Analysis of Acid Copper Plating Baths

Dennis Tench* and John White

Rockwell International Science Center, Thousand Oaks, California 91360

ABSTRACT

A pulse voltammetric stripping method is described for determining the absolute concentration of proprietary additive in acid copper baths containing contaminants derived from circuit board plating. Results are presented for both freshly prepared and production baths, and a comparison is made between the pulse and linear sweep voltammetric stripping analysis techniques.

Previous work (1, 2) has shown that the cyclic voltammetric stripping (CVS) method (3) yields the concentrations of proprietary additives and chloride ion in acid copper plating systems, but organic contaminants generated in circuit board production baths are found to interfere with the analyses. In spite of such interference, the CVS rate parameter has been demonstrated to correlate well with the deposit tensile properties (4), and, recently, improved circuit board yields attained via CVS control of acid copper baths have been documented (5). On the other hand, control of acid copper baths would be simplified if the absolute concentration of the additive were provided. One procedure is to generate a series of standard curves for each bath contaminant level, but this is tedious and valid only if the contaminants are always sufficiently similar so that their effect is constant for a given overall concentration.

In the present paper, a modification of CVS, *i.e.*, cyclic pulse voltammetric stripping (CPVS), is shown to yield the absolute additive concentration in at least one proprietary acid copper system in the presence of contaminants derived from circuit board plating.

Experimental Details

Acid copper baths used in the present work were air saturated and generally contained 75 g/liter copper sulfate pentahydrate, 10% by volume concentrated sulfuric acid, 75 mg/liter chloride, and various amounts of proprietary additive (Lea Ronal Copper Gleam PCM). The electrochemical cell was Pyrex (250 ml) with a Teflon top. Bath temperature was maintained constant ($\pm 0.1^\circ\text{C}$) via water circulated through a cell jacket.

The indicator electrode was a platinum rotating disk (0.46 cm^2) obtained commercially (Pine Instrument Company). Unless otherwise noted, the electrode rotation rate was always 500 rpm. A double-junction saturated calomel electrode (SCE) was used as the reference, and a platinum wire (99.0%) dipped directly in the cell served as the counterelectrode.

Voltammetric analyses were performed under computer control (Hewlett-Packard Model 9825). The electrode potential was controlled via a digital/analog converter and a potentiostat (Princeton Applied Research Corporation Model 173). Copper stripping charge was measured by current integration via a digital coulometer (Princeton Applied Research Corporation Model 179).

Pulse Voltammetric Method

Linear sweep cyclic voltammograms for a platinum rotating disk electrode in freshly prepared and production acid copper baths are shown in Fig. 1. Cathodic current corresponding to copper deposition is evident at potentials negative of about 0.0V, whereas the copper deposit is stripped from the inert electrode between about 0.0 and 0.2V, producing an anodic current peak. Since the sweep rate is constant (100 mV/s), the stripping peak area is proportional to the average copper deposition rate for a given voltage cycle. In conventional CVS

analysis of acid copper baths of this type, the stripping peak area determined with electrode rotation, A_T , is used as a measure of the concentration of brightening/leveling additives in the bath (2). As mentioned above, however contaminants that build up in circuit board production baths with use also affect the copper deposition rate and thus interfere with the additive analysis. Oxidation of such contaminants on platinum occurs positive of about 0.5V *vs.* SCE (Fig. 1), producing a well-defined current wave (4). Note that, for Fig. 1, data obtained at a higher electrode rotation rate (2500 rpm) than used for the analyses discussed below (500 rpm) are reported in order to accent the contaminant wave (which is partially mass-transport limited). A second anodic wave, corresponding to chloride oxidation (2), is observed positive of 1.2V; the plateau current is proportional to chloride concentration in freshly prepared baths but is generally less at the same chloride level in production baths, indicating that contaminants effectively compete with chloride for adsorption sites on the electrode in this potential region.

In the CPVS method, the effect of the contaminants, which apparently interfere with conventional CVS analysis by absorbing on the platinum electrode, is greatly mitigated by sequentially pulsing the electrode between appropriate plating, stripping, cleaning,¹ and equilibration potentials² (see Fig. 1) so that the electrode surface is maintained in a relatively clean and reproducible state. The steady-state charge density corresponding to stripping the copper deposit, plated at constant potential for a given length of time, is then proportional to the additive concentration and is unaffected by bath contaminants.

¹Note that the cleaning potential is in the oxygen evolution region, where organic contaminants are presumably oxidized or displaced by oxygen species on the platinum surface.

²Equilibration at a relatively negative potential is apparently necessary to reduce platinum oxides and to condition the electrode surface so that reproducible results are obtained.

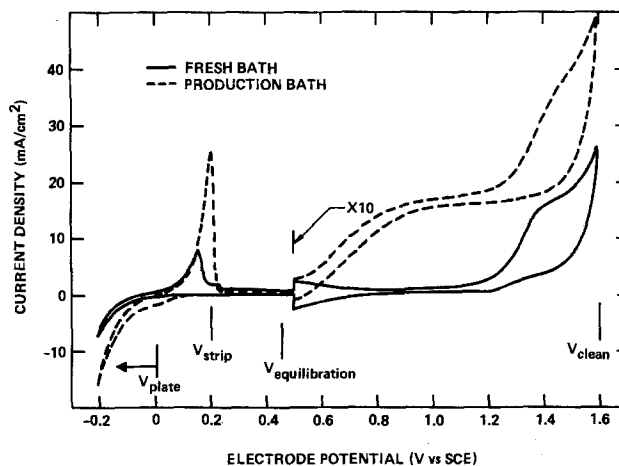


Fig. 1. Linear sweep cyclic voltammograms at 100 mV/s for a rotating platinum disk electrode (2500 rpm) in freshly prepared and production acid copper baths (22°C). Note that the current scale is an order of magnitude more sensitive positive of 0.5V.

*Electrochemical Society Active Member

The pulse sequence used in the present work was

$$V_{\text{plate}} \rightarrow V_{\text{strip}} \rightarrow V_{\text{clean}} \rightarrow V_{\text{equilibrate}}$$

This sequence was repeated (under computer control) until a steady-state copper stripping charge was obtained, *i.e.*, until two sequential values agreed within $\pm 2\%$. Steady state was generally attained within two to three cycles. It should be mentioned that the plating current also varies appreciably within a given cycle; this, coupled with the inherently greater sensitivity provided by averaging, suggests that the stripping charge should be a more reliable measure of the deposition rate than the cathodic current itself. Also, as pointed out for conventional CVS analysis (3), the copper stripping charge reflects only the copper deposition rate, whereas the cathodic current may include contributions from other reduction processes.

Results and Discussion

Preliminary studies were directed toward optimization of the measurement parameters, *i.e.*, the plating, cleaning, and equilibration potentials and times were varied to establish conditions providing good sensitivity and reproducibility. The stripping potential was always 0.2V, at which copper appears to be completely stripped from the electrode. Of course, the time required for stripping varies depending on the amount of copper previously deposited. The stripping step was terminated by the computer when the current decreased by 99.95% *i.e.*, to 0.05% of its previous value (with sampling every 100 ms).

Figure 2 shows plots of the copper stripping charge density *vs.* additive concentration for 10.0s of plating at various voltages, with cleaning at 1.6V for 5.0s and equilibration at 0.425V for 5.0s. The shape of these curves results from the opposing effects of two additive components, as discussed previously (4). Essentially, the sharp decrease at low additive levels results from high molecular weight polymeric surfactants, *e.g.*, polyethylene glycols, which suppress copper deposition by blanketing the electrode surface with polymeric film, whereas the linear increase at higher concentrations is produced by the brightener component. Since the effect of the surfactants saturates at very low additive levels (4), voltammetric stripping analysis of the undiluted bath generally reflects only the concentration of the brightener component. It should be kept in mind that additive concentrations reported here are in terms of milliliters per liter of the proprietary additive solution, which also contains the other components. Apparently, as the deposition potential is

made more negative (Fig. 2), this polymeric cathode film is broken down (presumably by reduction and/or inclusion in the deposit) so that the brightener component is increasingly effective at enhancing the copper deposition rate (slope of linear portion of curve increases). A plating voltage of -0.25V was chosen for further work because adequate sensitivity is obtained and the average current density at an intermediate additive concentration (2 ml/liter) in this case approximates that typically used for production plating processes (20 mA/cm^2), so that the data might be expected to yield more relevant mechanistic information. Also, the data for -0.3V appear to deviate slightly from linearity at the highest additive concentrations investigated.

Figure 3 shows plots of the copper stripping charge density at various additive concentrations *vs.* plating time at -0.25V , with cleaning at 1.6V for 5.0s and equilibration at 0.425V for 5.0s. The expected linearity is observed, but there is an apparent change in slope at about 5s. Since the reason for this slope change is unknown,³ it is not clear which plating time should be used. A short plating time, *i.e.*, 2s, was chosen because data scatter in this case seems to be less than observed for 10s of plating.

Note that temperature is an extremely important variable to both plating performance and voltammetric analysis of acid copper baths and should be closely controlled. For the present work, a value of 25°C was originally chosen, but it proved difficult to maintain under the prevailing ambient conditions, so the later experiments were performed at 26°C . This minor difference should not significantly affect the choice of analysis conditions, but it does appreciably affect the absolute stripping charge values.

Variations in either equilibration voltage or time were found to exert a significant effect on the stripping charge obtained under otherwise equivalent conditions, presumably because of changes in the state of the platinum surface. This suggests that complete equilibrium is not attained during the short equilibration times investigated, *i.e.*, 1-20s. Thus, it is important that the equilibration voltage and time be maintained constant; 0.425V and 5.0s were chosen for the present work because they seemed to yield somewhat more reproducible results. On the other hand, variations in the cleaning time from 1 to 10s had no discernible effect; cleaning voltage was not varied.

³Possibilities include substrate effects or residual suppression of copper deposition by the polymeric additive component at shorter plating times, or an increase in deposit surface roughness at longer times.

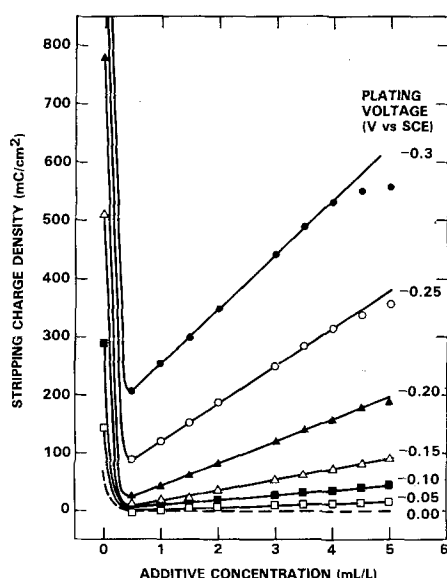


Fig. 2. Plots of CPVS copper stripping charge density for a platinum rotating disk electrode (500 rpm) at various plating voltages *vs.* additive concentration in an acid copper bath (25°C). Plating time = 10.0s; $V_{\text{clean}} = 1.6\text{V}$ (5.0s); $V_{\text{equilibrate}} = 0.425\text{V}$ (5.0s).

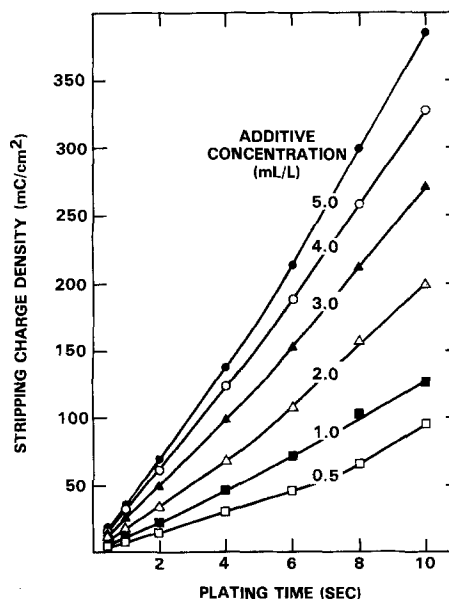


Fig. 3. Plots of CPVS copper stripping charge density for a platinum rotating disk electrode (500 rpm) *vs.* plating time (-0.25V) at various additive concentrations in an acid copper plating bath (26°C). $V_{\text{clean}} = 1.6\text{V}$ (5.0s); $V_{\text{equilibrate}} = 0.425\text{V}$ (5.0s).

It should be mentioned that one might expect the equilibration time of 5s to be sufficiently long to permit bath contaminants to reabsorb on the electrode surface and affect the additive analysis. Results presented below indicate that this is not the case, suggesting that contaminant adsorption does not occur at the equilibration voltage used (0.425V). This would be consistent with the onset of contamination oxidation at about 0.5V (Fig. 1) coinciding with contaminant adsorption, the latter not occurring at more negative voltages.

CPVS results obtained at 26°C by standard addition of a proprietary additive to a freshly prepared acid copper bath and a well-used production bath are shown in Fig. 4. Note that the production data are offset by 0.25 ml/liter to account for additive presumably already present in the bath. The data points are seen to practically coincide in the two cases, indicating that the effect of bath contaminants on the results is minimal.

For comparison, conventional linear sweep (100 mV/s) CVS results (2) for the same batch of additive are shown in Fig. 5. It is evident that contaminants in the production bath also tend to increase the stripping charge density in this case, interfering with the additive analysis.

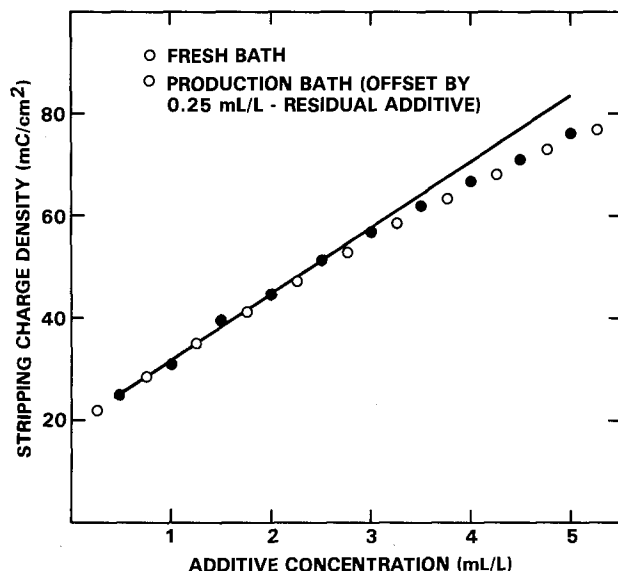


Fig. 4. CPVS results for analysis of a proprietary additive in a freshly prepared acid copper bath and a circuit board production bath (26°C).

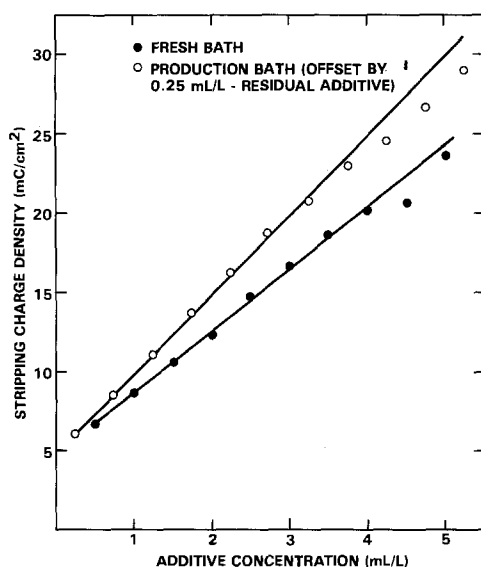


Fig. 5. Linear sweep CVS results for the same system (26°C) as for Fig. 4 (voltage swept at 100 mV/s between -0.2 and 1.6V vs. SCE; electrode rotation = 500 rpm).

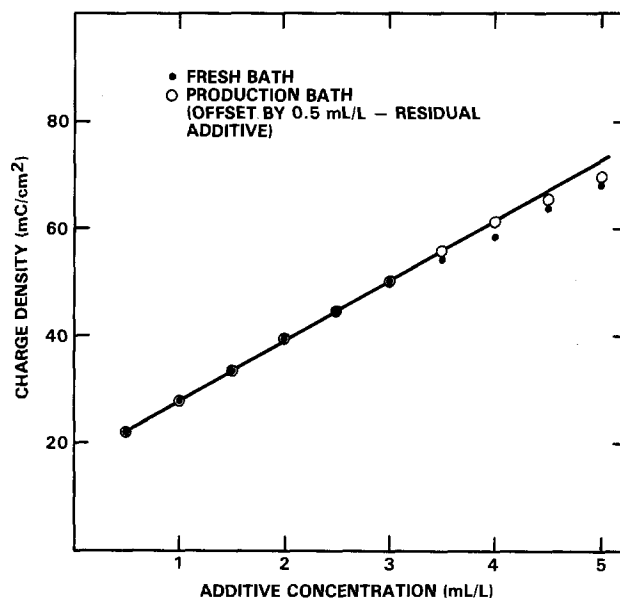


Fig. 6. CPVS results for analysis of a proprietary additive in freshly prepared acid copper bath and a circuit board production bath (26°C) from a second circuit board facility.

CPVS results obtained for a freshly prepared acid copper bath and a production bath from a different circuit board facility are given in Fig. 6. Note that the production data are offset by 0.5 ml/liter to account for additive presumably already present in the bath. Again, the data points are seen to practically coincide in the two cases. These results demonstrate decisively the effectiveness of the cyclic pulse technique in mitigating the effects of bath contaminants, at least of the types and concentrations encountered in two typical circuit board production facilities, on voltammetric stripping additive analysis.

It should be emphasized at this point that although the brightener additive component is apparently stable in freshly prepared acid copper baths, it decomposes slowly in used production baths, the decomposition rate being faster at higher additive concentrations. This phenomenon has also been observed by other workers (6). In the present case, a decrease of about 10% over one day was observed (via CPVS analysis) for additive concentrations in the 5 ml/liter range. To avoid errors associated with such effects, our analyses were always performed within a few minutes after additive additions.

Summary and Conclusions

The cyclic pulse voltammetric stripping (CPVS) method described here apparently eliminates interference of contaminants derived from circuit board plating on voltammetric analysis for additives in acid copper baths. This method involves pulsing a rotating platinum disk electrode sequentially between plating, stripping, cleaning, and equilibration voltages, and measuring the steady-state charge associated with stripping the copper deposit. Conditions used for the present work, which involved one proprietary system, were 500 rpm electrode rotation and plating at -0.25V vs. SCE for 2.0s, stripping at 0.20V until the current decreased by 99.95%, cleaning at 1.6V (oxygen evolution region) for 5.0s, and equilibration at 0.425V for 5.0s. The voltage pulse technique could most probably be used to minimize the effects of contaminants on other voltammetric analyses, e.g., chloride analyses in acid copper baths.

Acknowledgements

This work was supported by the United States Air Force Materials Laboratory, Wright-Patterson Air Force Base, under Contract no. F33615-81-C-5108. The authors thank Dr. Walter Freitag of Sperry Corporation and Dr.

Magdi Hanna of Graphic Research, Incorporated for providing the circuit board production bath specimens; the authors also thank Dr. Freitag and Dr. Peter Bratin of UPA Technology, Incorporated for useful suggestions concerning this work.

Manuscript submitted June 18, 1984; revised manuscript received Oct. 26, 1984.

Rockwell International assisted in meeting the publication costs of this article.

Electro-Oxidation of Substituted Silane High Polymers

A. Diaz* and R. D. Miller

IBM Research Laboratory, San Jose, California 95193

ABSTRACT

We report here the first electrochemical data on substituted silane high polymer films deposited on a Pt electrode. The oxidation peak potentials were measured for a series of substituted silane high polymers. The polymers oxidize irreversibly and produce soluble products which are removed from the electrode. The ease of oxidation of the polymer depends on the substituents, and polymers with the aryl groups attached directly to the silicon backbone are more easily oxidized.

The conjugative ability of the Si-Si covalent bond is well established (1, 2). The importance of this interaction is reflected in both the redox characteristics and the optical properties of a series of permethylated silane oligomers (Si₂ through Si₆) (3). These compounds have low oxidation potentials (in the range 1-2V vs. SCE) and optical excitation energies which decrease with increased catenation. In this regard, the energies for both oxidation and the electronic absorption have been shown to scale with the number of silane atoms in the chain, as may be anticipated from Huckel theory (3, 4). The cations generated by the oxidation of the silane oligomers are unstable intermediates which react to produce soluble products; for example, the oxidation of permethyldisilane leads to the formation of trimethylsilyl carbonium ions, which react further to yield solvolysis products (3).

While electro-oxidation data for high molecular weight polysilanes have not been reported, extrapolation of the solution data obtained for the permethylated oligomers indicates that they should oxidize ca. 1.0V anodic of SCE. Recent substituent studies on the electronic spectra of silane polymers suggest that the oxidation potentials might also be sensitive to the nature and the position of the substituents on the chain (9). Furthermore, these spectroscopic observations imply that the electron-transfer/chain-length correlations may not be as simple in the presence of large substituent groups as with the compact permethylsilane derivatives (see Table I).

The oxidation characteristics and the spectral properties of the oligomeric permethylsilanes resemble those properties of certain linearly coupled aromatic oligomeric materials such as the derivatives of pyrrole, thiophene, and benzene, which are also a function of the number of aromatic units in the linear chain (6). The oxidation reactions of both series are irreversible, but in the case of the aromatic oligomers polymeric films are produced which coat the electrode surface. It is the nature of the products of the oxidation that provides the biggest difference between the silane polymers and the aromatic or heteroaromatic oligomers. Whereas the permethylsilanes produce lower molecular weight soluble products when oxidized, the aromatic derivatives generate films which are electroactive and can be switched repeatedly between the neutral and the oxidized form (7, 8).

We have electrochemically oxidized a series of substituted polysilanes deposited as thin films (400-700Å) on a

* Electrochemical Society Active Member.

REFERENCES

1. R. Haak, C. Ogden, and D. Tench, *Plating Surf. Fin.*, **68**, (4), 52 (1981).
2. R. Haak, C. Ogden, and D. Tench, *ibid.*, **69**, (3), 62 (1982).
3. D. Tench and C. Ogden, *This Journal*, **125**, 194 (1978).
4. W. O. Freitag, C. Ogden, D. Tench, and J. White, *Plating Surf. Fin.*, **70**, (10), 55 (1983).
5. L. M. Flaherty, Hughes Aircraft Corp., Technology Support Div., El Segundo, CA, Unpublished results.
6. W. O. Freitag, Sperry Corp., Blue Bell, PA, Private communication.

platinum electrode, and find that the relative ease of oxidation is sensitive to the nature and position of the backbone substituents. In every case, the oxidation is irreversible, as with the lower molecular weight oligomers, and the reaction proceeds with the eventual removal of the polymer film from the electrode surface. The results of this electrochemical study are described in this paper.

Experimental

The polymers used in this study were prepared as described (*vide infra*). Thin films were cast on the platinum electrode (0.5 cm²) by spin coating a solution of the polymer. Those polymers containing aromatic substituents were spun from toluene or xylene, while a 3:1 mixture of xylene-ethylcyclohexane was found to be a more suitable solvent for the alkyl polysilane derivatives. The electrochemical measurements were carried out in a single-compartment cell equipped with the film-coated platinum working electrode, a gold counterelectrode, and a calomel reference electrode. Tetraethylammonium tetrafluoroborate/acetonitrile electrolyte solutions were employed. All ESCA analyses were performed using a Hewlett Packard 5959B ESCA spectrometer. The energy reference for the instrument is set for Au at 84.0 eV. The density of the poly(methylphenyl)silane film was determined from the weight and the thickness which was measured using a Talystep instrument.

Results and Discussion

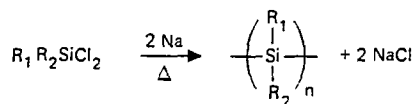
We have prepared (9) a large number of soluble, high molecular weight polysilane homopolymers by the con-

Table I. Electrochemical and absorption data for some substituted silane high polymers

Compound	Peak potential (V)	Absorption maximum (nm)
Poly(methylphenyl)silane 1	1.00	342
Poly(p-methoxyphenylmethyl)silane 2	0.69	344
Poly(methyl-β-phenethyl)silane 3	1.30	308
Poly(cyclohexylmethyl)silane 4	1.42	320
Poly(n-hexylmethyl)silane 5	1.44	303
Poly(di-n-hexyl)silane 6	1.60	317
Poly(dimethyl)silane 7	1.0 ^a	295

^a Extrapolated value obtained by plotting the values from Ref. (3) vs. 1/n.

denation of substituted dihalosilanes with sodium as shown below. These materials were purified and spectrally characterized as previously described (9). Most of these high polymers are thermally stable in nitrogen to at least 350°C, and many, particularly, but not exclusively, those with aromatic substituents, are high melting solids with glass transition temperatures in excess of 75°C. The polymers were quite soluble in aromatic solvents such as toluene but were insoluble in acetonitrile or the electrolyte solution.



- | | | | |
|----------|---|----------|---|
| <u>1</u> | $R_1 = \text{Me}; R_2 = \text{Ph}$ | <u>5</u> | $R_1 = \text{Me}; R_2 = n\text{-Hexyl}$ |
| <u>2</u> | $R_1 = \text{Me}; R_2 = p\text{-Methoxyphenyl}$ | <u>6</u> | $R_1 = R_2 = n\text{-Hexyl}$ |
| <u>3</u> | $R_1 = \text{Me}; R_2 = \beta\text{-Phenethyl}$ | | |
| <u>4</u> | $R_1 = \text{Me}; R_2 = \text{Cyclohexyl}$ | | |

The spectral properties of these polymers were quite unusual relative to related carbon polymers [see Ref. (5) and (9) for a more complete discussion of the spectral properties]. All of the sterically unencumbered alkyl derivatives display very strong electronic absorption maxima around 303-309 nm. On the other hand, those materials having aryl substituents directly bonded to the silicon backbone are characterized by a red-shifted absorption maximum in the 335-345 nm region. This strong absorption and the dramatic substituent effects are consistent with a delocalized sigma backbone, which also agrees with earlier observations made on low molecular weight model compounds (10). The response, however, is not systematic with the structural variation, indicating that the conformation of the backbone and/or the pendant groups may be a factor in determining the ultimate electronic spectrum of the polymer.

The polymers are readily oxidized in the potential range 0.7-1.6V vs. SCE. The oxidation peak potentials for the various polymeric films are summarized in Table I. Shown in Fig. 1 is the cyclic voltammogram for a thin film (420Å) of poly(methylphenyl)silane, on a platinum surface, measured in acetonitrile. The oxidation reaction is irreversible, and the shape of the peak at 1.00V is consistent with a surface localized reaction which does not involve diffusion. There is some residual oxidation on the anodic side of the peak which distorts the symmetry of the peak. For this polymer, the peak is surprisingly nar-

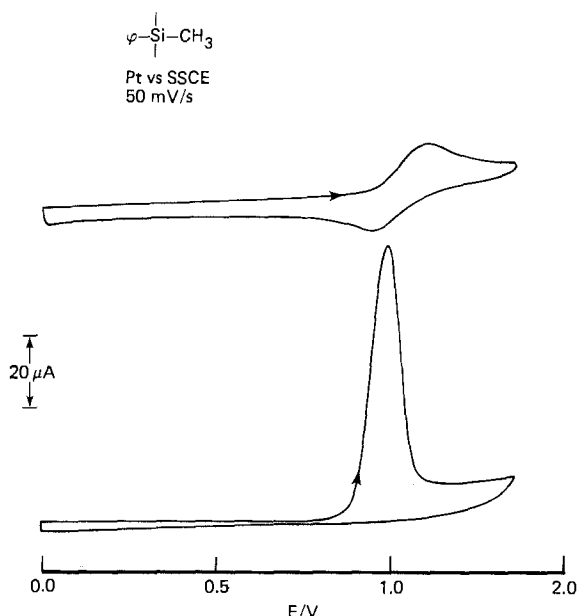


Fig. 1. Cyclic voltammogram of a poly(methylphenyl)silane film on platinum measured in acetonitrile. First (bottom) and second (top) scan.

row, with a peak width at half-height of only 100 mV. The area under the curve corresponds to 0.34 mC/cm² or 3.6 × 10⁻⁹ F/cm². For comparison, the calculated molar equivalent of the monomer units on the electrode (420Å film thickness and the film density of 1.174 g/cm³) is 40 × 10⁻⁹ mol/cm². Comparison of these numbers suggests that one electron is removed from polymer segments containing ca. 11 monomer units. With thinner films, ~120Å thick, the same symmetrical peak is observed, but at a slightly less anodic peak potential, 0.92V. The small shift in these potentials may be due to a difference in solvation of the film. The peak is also narrower, with a peak width at half-height of 90 mV. The comparison of the amount of charge involved in the oxidation reaction with the amount of polymer on the electrode indicates that one electron is removed for ca. every ten monomer units. The small change produced in the electrochemical stoichiometry by the threefold change in film thickness suggests that this number must be a close approximation of the actual value for the reaction. This stoichiometry is in the range, one electron/8-10 monomer units, which was suggested as the oligomer size range where the oxidation potentials could be used to approximate those of the corresponding high molecular weight polymer (3, 6). This stoichiometry may be an average value, and more information is needed in order to establish the precise stoichiometry.

The electrochemical stoichiometry of linear polymers, where the backbone of the chain is electroactive, is a subject which is poorly understood. This topic first emerged with the electrochemical characterization of polypyrrole, which is a linear chain of α, α' -coupled aromatic units (7). The electrochemical stoichiometry for the oxidation of this polymer is 0.25-0.30 charge/aromatic unit. Since polypyrrole, other electroactive polymers have become available and are found to have comparable stoichiometries. For example, polythiophene has 0.06 (8) to 0.25 (11) charge/aromatic unit, polypyrene has 0.31 (12), and polyazulene has 0.25 (12) charge/aromatic unit. For these polymers, the stoichiometry must reflect the length of polymer segments along the polymer chain with coplanar aromatic units which are disrupted by kinks and bends in the chain. The length of these segments must reflect a balance of the chemical stability of the delocalized cation center plus entropy considerations associated with keeping the aromatic rings coplanar.

In the case of the polysilanes, entropic considerations may be less important, since the backbone does not contain aromatic rings. For these polymers, the stoichiometry will be determined by the intrinsic coulombic interactions, which may in turn be influenced by conformational variations along the polymer backbone.

With every film, the peak is observed in the first scan only, since the integrity of the film is destroyed by the chemical irreversibility of the reaction. The electrochemical reaction produces a soluble electroactive product which is oxidized around 1.0V. Although the products of the reaction have not been identified, the reversible nature of redox reaction displayed by the electroactive product suggests that it is not simply a lower molecular weight segment of the polymer. This conclusion is based on the fact that all of the polysilane compounds studied thus far undergo chemically irreversible oxidation. Qualitatively, similar results were obtained with the films of the other polymers, except that the peaks are not so narrow and the symmetry is not as obvious because the background current anodic of the peak is significant. This can be seen with the voltammogram for poly(methyl- β -phenethyl) silane film (Fig. 2).

The films are evenly coated and featureless with no visible cracks or defects (Fig. 3). They are, however, somewhat permeable. The permeability of a poly(methylphenyl)silane film (600Å thick) coated on a platinum electrode (0.5 cm²) was estimated by measuring the cyclic voltammogram of ferrocene (10⁻⁶ mol/cm³). For this measurement, the voltage was swept between 0 and 0.7V in order to preserve the integrity of the film. With the

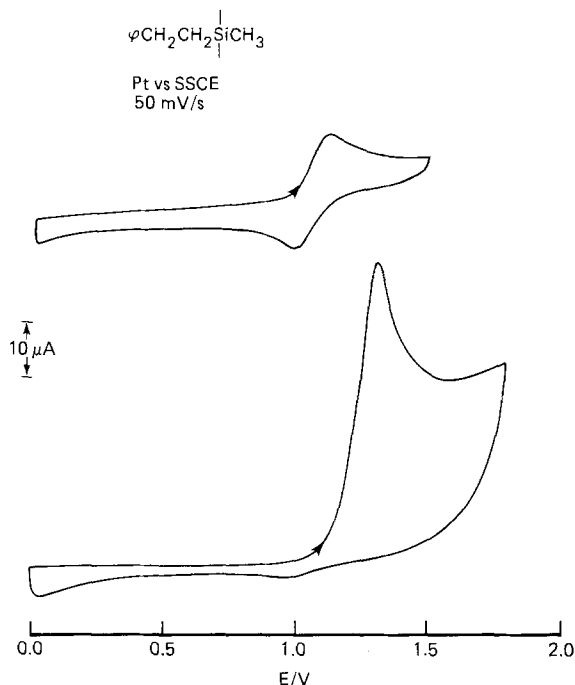


Fig. 2. Cyclic voltammogram of a poly(methyl- β -phenethyl)silane film on platinum measured in acetonitrile. First (bottom) and second (top) scan.

coated electrode, the current density for the oxidation of ferrocene is 40 times smaller than with bare platinum, and no change was observed in the E° . The shape of the resulting curve resembles a step, as is observed for reactions limited by diffusion across the film, and the size of the signal is not sensitive to sweep rate between 10 and 50 mV/s. The diffusion of ferrocene across the film was calculated using the expression, $j = nFCD/\sigma$, where D is the diffusion of ferrocene across the film and σ is the thick-



Fig. 3. Scanning electron micrograph of a thin film (2000Å) of poly(methylphenyl)silane cast on a silicon substrate.

ness of the film. The calculated values of j , D/σ , and D are 8×10^{-6} A/cm², 8×10^{-5} cm/s, and 0.5×10^{-9} cm²/s, respectively. These values are slightly lower than the values usually observed for other representative thin films. For comparison, the parameters for the diffusion of ferrocene across other thin film coatings on platinum electrodes are listed in Table II. As can be seen, the permeability of ferrocene across the polysilane film is less than for the other three films. It should be noted, however, that the method of preparation for the other films, except for the poly(vinylchloride), was different. Poly(vinylchloride) was prepared by spin coating (13), poly(2,6-dimethyl)phenol by electropolymerization (14), and polytrifluorotoluene by plasma polymerization (15).

The film is stable on the electrode in the potential range 0-0.7V; however, sweeping the potential up to 1.5V removes the film, and the size and the shape of the voltammogram for the ferrocene oxidation reaction approaches that with a clean platinum surface. For example, after three sweeps, the original size of the peak is recovered.

ESCA analysis of the platinum electrode surface indicated that the polymer film was completely removed from the surface during the brief electrolysis. These results are consistent with the electrochemical results described above. Analysis of a freshly cast film of poly(methylphenyl)silane revealed peaks for carbon 1s, silicon 2s, and oxygen 1s. The relative amounts of the elements calculated from the peak areas and corrected for the photoionization cross sections (1.0 for carbon, 0.955 for silicon, and 2.93 for oxygen) are 6.94 to 1.0 to 0.167, respectively. The carbon to silicon ratio is correct for the C_7H_9Si unit of the polymer; however, the small amount of oxygen present (ca. 2%) may be due either to moisture on the surface of the film or perhaps to the presence of small quantities of oxygen in the polymer itself. No platinum was detected. Analysis of the same electrode after electrolysis showed the presence of a small amount of residual carbon and oxygen only, in the ratio of 2.54, plus a large platinum signal. No silicon was detected on the electrode.

In the case of the aryl-substituted polysilanes, the oxidation reaction must involve the polysilane chain and not simply the aryl group because the oxidation potential of aryl groups are much more anodic. For example, the oxidation peak for alkyl- and silyl-substituted benzene derivatives appears at 2.3 and 2.5V, respectively, and that of anisole at 1.80V (16). As can be seen, aryl substituents on the polymer backbone greatly facilitate the oxidation of the polysilane polymer (Table I) and of tetramethylsilane. For example, with the introduction of a phenyl or a benzyl substituent, the oxidation peak for tetramethylsilane is shifted cathodically by 0.5 and 1.2V, respectively. This effect may be due partly to a stabilizing resonance interaction between the aryl group and the incipient silyl cation. The magnitude of this stabilizing interaction must, however, be sensitive to conformational effects in the backbone and of the aryl ring, since phenyl substituents do not facilitate the oxidation of the persubstituted cyclopentasilane derivatives listed in Table III. Thus, the conformational freedom of the phenyl ring, especially the rotational freedom, appears to be a critical factor. The stabilizing effect of the phenyl group is observed to some extent even when the phenyl group is not directly bonded to the silicon atom. In this regard, the phenyl substituent in the polysilane 3 shifts the oxidation peak cathodic of the cyclohexyl-substituted polymer by 0.1V.

Particularly striking is the large substituent effect of the methoxy group. The oxidation peak for poly(p-meth-

Table II. Data for diffusion of ferrocene across thin films on electrodes

Film	Thickness (Å)	$10^5 D/\sigma$ (cm/s)	$10^9 D$ (cm ² /s)	Ref.
Poly(methylphenyl)silane	600	8	0.5	—
Poly(vinylchloride)	30,000	12	30	(11)
Poly(2,6-dimethyl)phenol	750	1800	130	(12)
Polytrifluorotoluene	30,000	0.5	1.4	(13)

Table III. Electrochemical data for some polysilane derivatives

Compound	Half-wave potential (V)
Permethylhexasilane	1.08 ^a
Permethylpentasilane	1.18 ^a
Permethyltetrasilane	1.33 ^a
Permethyltrisilane	1.52 ^a
Permethyldisilane	1.88 ^a
Tetramethylsilane	-3.0 ^b
Phenyltrimethylsilane	2.5
Benzyltrimethylsilane	1.77
Permethylcyclopentasilane	1.35 ^c
Perphenylcyclopentasilane	1.5

^a Oxidation potentials measured using ac polarography (3).

^b Extrapolated value obtained by plotting the values from Ref. (3) vs. $1/n$.

^c A. Diaz and R. West, Unpublished results.

oxyphenylmethyl)silane (0.69V) is 0.31V less anodic than the peak for poly(methylphenyl)silane (1.00V). Although substituent effects can be large for small molecules—for example, the oxidation peak for anisole (1.80V) in acetonitrile solution is 0.5-0.7V less anodic than the peak for alkylbenzene derivatives (2.3-2.5V) (16)—they are usually small for polymers. For example, the effect of a p-methoxy group on the oxidation peak potential of N-phenylpyrrole polymer is only 0.06-0.15V (17).

The oxidation of the polymers is also somewhat sensitive to the nature of the alkyl substituents. In this regard, the permethyl-substituted polymers are more easily oxidized than the hexyl-substituted polymers. The oxidation peak for poly(dimethyl)silane (extrapolated value using the data from Table III) is shifted anodically by 0.4 and 0.6V compared to the polymer with one or two hexyl groups per silicon in the polymer. These voltage differences are only estimates because the comparison involves an extrapolated value using data from another laboratory. Nevertheless, the effect is large and in the opposite direction from what is normally observed for alkyl substituent effects. For example, simple alkyl groups shift the oxidation potential of polypyrrole (18) and thiophene (8) cathodically by 0.1-0.2V. Therefore, the effect is not electronic and may result from kinetic limitations caused by the bulky hexyl groups which provide some separation between the platinum surface and the polysilane backbone. This effect is probably not important with the poly(methylphenyl)silane because the phenyl groups provide a channel for electron transfer.

In conclusion, the substituted silane polymers which have already attracted attention because their photochemical and lithographic properties also appear to have the potential for interesting electrochemistry. Because of

the sensitivity of the oxidation potentials to the substituents, the choice of appropriate substituents may generate an interesting new class of redox polymers (19).

Manuscript submitted Aug. 3, 1984; revised manuscript received Nov. 20, 1984.

IBM Corporation assisted in meeting the publication costs of this article.

REFERENCES

- C. G. Pitt, in "Homoatomic Rings, Chains and Macromolecules of Main-Group Elements," A. L. Rheingold, Editor, Elsevier, Amsterdam (1977).
- R. West and E. Carberry, *Science*, **189**, 179 (1975).
- W. G. Boberski and A. L. Allred, *J. Organomet. Chem.*, **88**, 65 (1975).
- C. A. Coulson, *Proc. R. Soc. London, Ser. A*, **164**, 383 (1933).
- P. Trefonas, III, R. West, R. D. Miller, and D. Hofer, *J. Polym. Sci., Polym. Lett. Ed.*, **21**, 823 (1983).
- A. F. Diaz, J. I. Crowley, J. Bargon, G. P. Gardini, and J. B. Torrance, *J. Electroanal. Chem.*, **121**, 355 (1981).
- A. Diaz and K. Kanazawa, in "Extended Linear Chain Compounds," Vol. 3, J. Miller, Editor, p. 417, Plenum Press, New York (1982).
- R. J. Waltman, J. Bargon, and A. Diaz, *J. Phys. Chem.*, **87**, 1459 (1983).
- P. Trefonas, III, P. I. Djurovich, X.-H. Zhang, R. West, R. D. Miller, and D. Hofer, *J. Polym. Sci., Polym. Lett. Ed.*, **21**, 819 (1983).
- (a) C. G. Pitt, M. M. Burse, and P. F. Rogerson, *J. Am. Chem. Soc.*, **92**, 519 (1970); (b) M. Kumada and K. Tomas, *Adv. Organomet. Chem.*, **6**, 80 (1968); (c) W. G. Boberski and A. L. Allred, *J. Organomet. Chem.*, **71**, C27 (1974).
- G. Tourillon and F. Garnier, *J. Phys. Chem.*, **87**, 2289 (1983).
- J. Bargon, S. Mohmand, and R. J. Waltman, *IBM J. Res. Dev.*, **27**, 330 (1983).
- M. A. DePaoli, R. J. Waltman, A. F. Diaz, and J. Bargon, *J. Chem. Soc., Chem. Comm.*, 1015 (1984).
- P. C. Lacaze, M. C. Pham, M. Delamar, and J. E. Dubois, *J. Electroanal. Chem.*, **108**, 9 (1984).
- R. Hernandez, J. Lee, R. Waltman, J. Bargon, and A. Diaz, Paper 59 presented at the 1983 Pacific Conference on Chemistry and Spectroscopy, Pasadena, California 1983.
- "Technique of Electroorganic Synthesis," N. L. Weinberg, Editor, Pt. II, p. 690, John Wiley and Sons, Inc., New York (1975).
- A. Diaz and M. Salmon, Paper 617 presented at The Electrochemical Society Meeting, Montreal, Quebec, Canada, May 9-14, 1982.
- A. F. Diaz, A. Martinez, K. K. Kanazawa, and M. Salmon, *J. Electroanal. Chem.*, **130**, 181 (1981).
- For review of redox polymers with pendent electroactive centers, see "Oxidation-Reduction Polymers," H. G. Cassidy and K. A. Kun, Editors, Interscience Publishers, New York (1965).

Energy Density, Power Density, and Polarization Studies of the Partially Oxidized ("p-Doped") Polyacetylene Cathode

M. Maxfield,*¹ S. L. Mu,² and A. G. MacDiarmid*

Department of Chemistry, University of Pennsylvania, Philadelphia, Pennsylvania 19104

ABSTRACT

Films of polyacetylene, $(\text{CH})_x$, partially oxidized ("p-doped") to 2% and 7% having compositions $[(\text{CH})^{+0.02}(\text{ClO}_4)_{0.02}^-]_x$ and $[(\text{CH})^{+0.07}(\text{ClO}_4)_{0.07}^-]_x$, respectively, were employed as the cathode in electrochemical cells of the type $\text{Li}/1.0\text{M LiClO}_4$ (propylene carbonate)/ $[(\text{CH})^{+y}(\text{ClO}_4)_y^-]_x$. They were charged and discharged (both immediately and after a 16h delay) at constant currents ranging from 0.01 to 20.00 mA/cm² of $(\text{CH})_x$ film, and their capacities, energy densities, and average power densities were measured. The average cell voltage and coulombs released during discharges of a cell using a 7% oxidized polyacetylene cathode were relatively insensitive to an increase in discharge current of from 0.01 to 1.00 mA/cm².

Reversible electrochemical oxidation or reduction has been observed for a variety of organic polymers such as polypyrrole (1), polythiophene (2), polyazulene (3), polyparaphenylene (4), poly 2,6-(4-phenyl)quinoline (5), and polyacetylene (6-9). These polymers exhibit conductivities in the metallic regime of 10^1 - $10^3 \Omega^{-1} \text{cm}^{-1}$ when they are partly oxidized or reduced to form species such as $(\text{polymer})^{+y}\text{A}_y^-$ or $\text{M}_y^+(\text{polymer})^{-y}$, respectively, A^- and M^+ being inert monovalent counterions introduced during the electrochemical redox reactions. Experimental laboratory scale batteries have been fabricated from the oxidized and reduced forms of polyparaphenylene and polyacetylene, $(\text{CH})_x$, the most extensively studied being those using polyacetylene in its oxidized form, $[(\text{CH})^{+y}\text{A}_y^-]_x$ (6-8) or reduced form, $[\text{M}_y^+(\text{CH})^{-y}]_x$ (9). Electrochemical oxidation of polyacetylene has been reported in electrolytes consisting of salts of $(\text{ClO}_4)^-$ (6-8), $(\text{AsF}_6)^-$ (10, 11), $(\text{PF}_6)^-$ (10), $(\text{BF}_4)^-$ (10), and $(\text{CF}_3\text{SO}_3)^-$ (10) dissolved in propylene carbonate (PC) or sulfolane.

In the present study, a specific configuration of the $\text{Li}/\text{LiClO}_4(\text{PC})/[(\text{CH})^{+y}(\text{ClO}_4)_y^-]_x$ cell is further characterized by determining the dependence of the discharge voltage, V_d , average discharge voltage, \bar{V}_d , and capacity on the value of selected constant current discharge rates expressed in milliamperes per square centimeter of the $(\text{CH})_x$ film.

In order to examine the effect of different levels of oxidation (charge density) of the $(\text{CH})_x$ on its discharge characteristics, the maximum charge level of the $[(\text{CH})^{+y}(\text{ClO}_4)_y^-]_x$ electrode was varied from $y = 0.02$ to $y = 0.07$. The effect of possible nonhomogeneity of the dopant anion distribution within the $(\text{CH})_x$ film and/or fibrils was studied by varying the delay between the termination of a charge cycle and the beginning of a discharge cycle from 0 to 16h.

Experimental

The cells were constructed by pressing lithium metal foil (Alfa Ventron) onto a nickel grid (Delker Corporation, 189 mesh) and covering it with a separator, followed by a single layer of polyacetylene film, and finally by platinum gauze (A. H. Thomas, 52 mesh). Some stainless steels and nickel corrode in contact with oxidized polyacetylene; however, graphite has been shown to be a suitable current collector (11). The separator for the cell containing 2% oxidized $(\text{CH})_x$ was kiln-dried glass filter paper and that for the cell containing 7% oxidized $(\text{CH})_x$ was hydrophilic porous polypropylene (Celanese Celgard, K-5511) which had previously been treated with a plasma discharge (12). Anhydrous LiClO_4 (Alfa Ventron) was dried by melting under a dynamic vacuum.

For each cell, the assembly of current collectors (spot welded to Pt wire leads), electrodes, and separator were

*Electrochemical Society Active Member.

¹Permanent address: Allied Corporation-M.R.C., Morristown, New Jersey 07960.

²Permanent address: Department of Chemistry, Yangzhou Teacher's College, Yangzhou, China.

squeezed into rectangular glass tubing ($3 \times 9 \times 50$ mm) to which was added 0.5 ml of 1.0M LiClO_4 in propylene carbonate (Aldrich) which had been distilled in a spinning band column. No analysis of water content was made. The cell was evacuated and sealed by melting the glass around the protruding electrode leads.

The polymer electrode in both cells was free standing polyacetylene film prepared as described by Shirakawa (13), except that the catalyst was aged for only 15 min at 25°C in order to produce thinner fibrils (14). Prior to the initial electrochemical oxidation of the film, the $(\text{CH})_x$ was present as the *cis*-rich isomer having been stored at -78°C under vacuum since its preparation. The film thickness was 0.1-0.2 mm, and, according to electron micrographs of samples from the same preparation, the polymer fibrils ranged from 100 to 200Å in diameter. Since the density of the $(\text{CH})_x$ fibrils is 1.2 g/cm³ (15), and since the density of the films used in this study was 0.25 g/cm³, 80% of the undoped $(\text{CH})_x$ film was void space. The effective surface area of the $(\text{CH})_x$ fibrils in $(\text{CH})_x$ films before doping has been reported to fall in the range 60-100 m²/g (15). Before recording any electrochemical data on the cells, they were twice charged and discharged in order to convert the *cis*-rich $(\text{CH})_x$ to the more thermodynamically stable *trans*-rich isomer (16).

The amounts of film used as electrodes were 19.7 mg (4.3 cm²) for the cell in which the polyacetylene was oxidized to 2% and 6.9 mg (1.15 cm²) for the cell in which the polyacetylene was oxidized to 7%. In every charge/discharge cycle, the former cell was charged at a constant current of 0.812 mA corresponding to 2% oxidation/h of the $(\text{CH})_x$. The latter cell was always charged at a constant current of 0.142 mA, corresponding to 1% oxidation/h of the $(\text{CH})_x$. Each cell was then either immediately discharged or was permitted to stand for 16h before discharging to allow the charge distribution to reach 80% equilibrium based on a diffusion constant of 4×10^{-18} cm²/s (17) and a fibril diameter of 100-200Å. The discharges were performed at constant currents in the range of 0.01-20.00 mA/cm² of film. The discharge voltage, V_d , was recorded as a function of the coulombs released until it dropped to 2.50V, the approximate midgap potential of pristine *trans* $(\text{CH})_x$, a direct bandgap semiconductor. Because of the minute density of states in the bandgap, the reduction potential of neutral $(\text{CH})_x$ can fall anywhere between 1.75 and 3.10V vs. Li/Li^+ (18). Hence, the remaining available positive charge could be released in a 16h discharge at a constant applied potential of 2.50V without injection of negative charge.

Table I is a compilation of data for each charge/discharge cycle. It includes (i) the extent of charging expressed as a percent oxidation of the $(\text{CH})_x$ and also as the number of coulombs, $Q(\text{in})$, involved in the charge process; (ii) the average discharge voltage, \bar{V}_d ; (iii) the constant discharge current, i_d , employed; (iv) the discharge time at the applied constant current; (v) the coulombs liberated during the constant current discharge, $Q(\text{out})$; (vi)

Table I. Charge/discharge data for Li/LiClO₄(PC)/[(CH)^{+x}(ClO₄)_{0.02}]_x cells.

% Ox. ^a of (CH) _x	\bar{V}_d ^b (V)	Q(in) ^c (C)	<i>i</i> _d ^d (mA/cm ²)	Discharge time ^e (min)	Q(out) ^f (C)	Q(out, total) ^g (C)	Q _{eff} ^h (%)
² Immediate	3.44	3.00	0.10	100	2.57	2.64	88.0
² Delayed	3.37	3.00	0.10	85	2.19	2.22	74.0
² Immediate	3.41	3.00	1.00	7	1.76	2.79	93.0
² Delayed	3.25	3.00	1.00	4	1.06	2.28	76.0
² Immediate	3.37	3.00	2.00	3	1.53	2.79	93.0
² Delayed	3.06	3.00	2.00	2	0.86	2.34	78.0
² Immediate	2.96	3.00	5.00	0.6	0.81	2.76	92.0
² Delayed	2.80	3.00	5.00	0.3	0.35	2.49	83.0
⁷ Immediate	3.39	2.52	0.01	2145 ⁱ	1.48	1.62	64.3
⁷ Delayed	3.32	2.52	0.01	1623 ^j	1.12	1.51	59.9
⁷ Immediate	3.40	2.52	0.10	228	1.57	1.73	68.7
⁷ Delayed	3.33	2.52	0.10	162	1.12	1.49	59.1
⁷ Immediate	3.36	2.52	1.00	20	1.35	1.77	70.2
⁷ Delayed	3.21	2.52	1.00	13	0.910	1.56	61.9
⁷ Immediate	3.10	2.52	10.0	1.5	1.01	1.77	70.2
⁷ Delayed	2.82	2.52	10.0	0.7	0.467	1.51	59.9
⁷ Immediate	2.72	2.52	20.0	0.3	0.340	1.51	59.9

^a 2 or 7 indicates percent oxidation of the polyacetylene at the end of a charge cycle; "immediate" indicates discharge of the cell immediately after the charging cycle was completed; "delayed" indicates discharge of the cell 16h after the charge cycle was completed.

^b Average voltage during the constant current discharge.

^c Coulombs involved in a charge cycle.

^d Constant current discharge (mA/cm²) of (CH)_x film.

^e Duration of the constant current portion of the discharge.

^f Charge released during the constant current portion of the discharge cycle.

^g Sum of the charges released during the constant current and constant applied potential portions of the discharge cycles.

^h Q_{eff} = [(Q(out), total)/Q(in)]100.

ⁱ 35.75h.

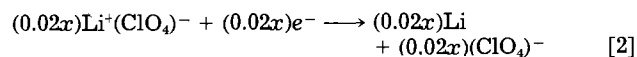
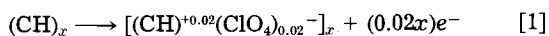
^j 27.50h.

the total number of coulombs liberated Q(out, total) during the constant current and constant applied potential discharge steps; and (vii) the coulomb efficiency, Q_{eff} = 100 [Q(out, total)/Q(in)]. The \bar{V}_d values were calculated from the area under each discharge curve divided by the number of coulombs released during the discharge.

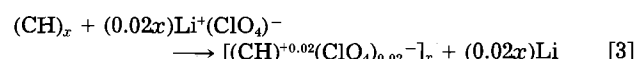
The effective resistance, R_{eff}, of a cell was determined periodically by (i) measuring the charge or discharge voltage, V; (ii) interrupting the charge or discharge cycle; (iii) measuring the open-circuit voltage, V_{oc}, within 1s; and (iv) calculating R_{eff}, by the relationship R_{eff} = (V - V_{oc})/i, where i is the constant charge or discharge current. It should be noted the R_{eff} will be larger than the internal resistance, R_i, of the cell because of charge-transfer and diffusion impedance effects; however, R_{eff} gives a qualitative indication of the change in the effective resistance of the cell at various stages during its charging and discharging.

Results and Discussion

A charge cycle of a cell from the initial uncharged open-circuit voltage of 2.75 (18) to 3.78V is given in Fig. 1. According to the value of Q(in), the polyacetylene was oxidized to 2%, i.e., to a composition of [(CH)^{+0.02}(ClO₄)_{0.02}]_x. After a 16h stand period, it was discharged at a constant current of 0.43 mA (0.10 mA/cm² of film) during 78 min. The residual charge remaining in the polyacetylene was then released by a constant potential discharge at 2.50V during ~16h, as described above. This returned the cell to its initial uncharged state. Processes occurring at the electrodes during charging are given by



resulting in the net reaction



The discharge reactions are the reverse of the above.

At the charge rate of 2%/h, the charging potential rose rapidly to 3.4V, at which stage the effective resistance of

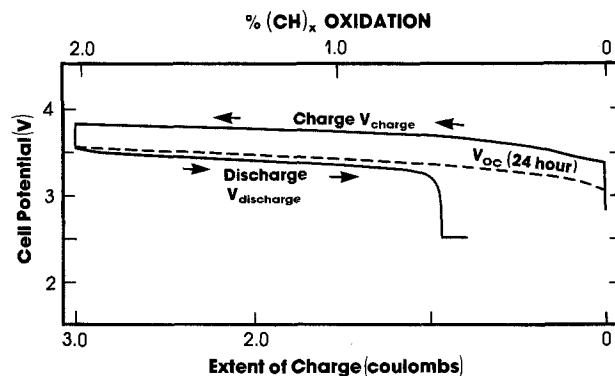


Fig. 1. Comparison of charge and discharge potentials and quasi-equilibrium cell potentials of a Li/LiClO₄(PC)/[(CH)^{+x}(ClO₄)_{0.02}]_x cell as a function of extent of charging (percent oxidation of polyacetylene).

the cell was several thousand ohms. By the time the polyacetylene was charged to 0.05%, the effective resistance was less than 200Ω and by the end of the charging process it was ~20Ω. During the following 16h stand period, the cell potential dropped from 3.78 to 3.55V (7), indicating that a quasi-equilibrium distribution of ClO₄⁻ ions throughout the (CH)_x fibrils had taken place. The dashed line gives the relationship reported previously (7) between the quasi-equilibrium values of the open-circuit voltage observed following a 24h stand period after charging, i.e., V_{oc(24h)} and the extent of charge. It can be seen that this curve and the discharge curve lie very close to each other. The rate of discharge employed was, therefore, sufficiently small to cause only very little polarization. The discharge voltage fell sharply as the charge level dropped below 0.2% based on the residual charge removed during the 16h constant potential discharge, after which only negligible charge could be recovered.

Constant current discharge cycles for the cell containing 2% oxidized polyacetylene are given in Fig. 2 for immediate and delayed discharges together with the corresponding current densities expressed as milliamperes per square centimeter of polyacetylene and as milliamperes per gram of the combined weight of the [(CH)^{+0.02}(ClO₄)_{0.02}]_x and the weight of lithium actually consumed in the discharge reaction. For the delayed discharges at 0.10 and 1.00 mA/cm², the discharge potential showed a "plateau" region before it dropped abruptly.

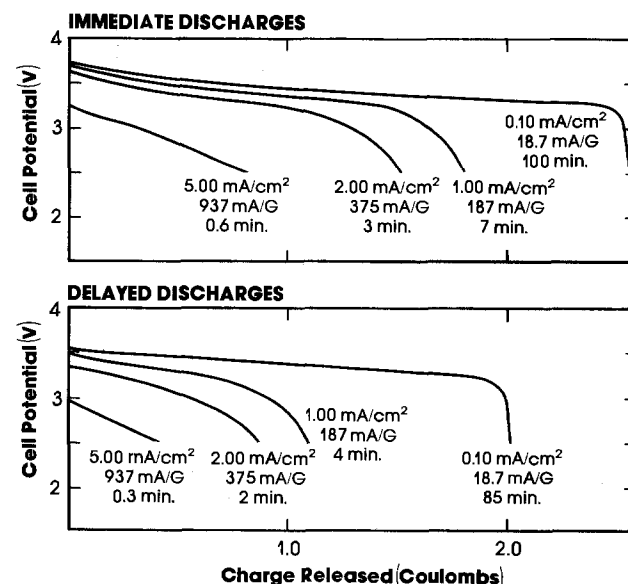


Fig. 2. Discharge characteristics of a Li/LiClO₄(PC)/[(CH)^{+0.02}(ClO₄)_{0.02}]_x cell. Upper figure: discharge immediately after a charge cycle. Lower figure: discharge following a 16h stand period after completion of the charge cycle.

The plateau regions were more apparent in the discharges performed immediately after charging. With increasing current, these plateau regions were slightly offset to lower voltage, as expected, and the number of coulombs released progressively diminished. However, both of these trends became less pronounced when the oxidation level of the polyacetylene was raised to 7%, as shown in Fig. 3. Each time the cell was discharged at currents ranging from 0.01 to 1.00 mA/cm², most of the charge was released at a discharge voltage greater than 3.0V. In fact, the plateau regions of the top three curves in the upper figure of Fig. 3 all fell at 3.4V and the charge released was only modestly affected by increasing current. It can be seen that currents as high as 10.00 mA/cm² were possible with substantial coulomb release even after the cell had been permitted to stand for 16h.

The cause of the less-than-ideal coulombic efficiency of the $[(CH)^{+y}(ClO_4)_y]_x$ cathode (see Table I) is not clear at the present time. The loss in efficiency observed immediately after the termination of a discharge cycle is undoubtedly due in large part to the diffusion of the $(ClO_4)^-$ ions from the interior to the exterior of the $(CH)_x$ fibrils (8, 19, 20). Particularly on standing or during slow charge/discharge cycles, loss of charge is also probably caused by some type of self-discharge process which regenerates undoped $(CH)_x$ and/or to irreversible chemical destruction of the cathode material by its slow reaction with the electrolyte or with impurities in the electrolyte. In addition, it has recently been shown that $[CH^{+y}(ClO_4)_y]_x$ is itself intrinsically unstable, slowly losing its conductivity on storage in an inert environment (21). The fact that the accumulated charge loss for the cell containing 7% oxidized $(CH)_x$ during the cycling experiments summarized in Table I amounts to 1 electron per 4.4 carbons without significant deterioration of the cell performance suggests that self-discharge may be the principal mechanism causing coulombic loss. Subsequent transmission infrared spectra of a similar $[CH^{+y}(ClO_4)_y]_x$ electrode revealed essentially no change in the spectrum after ten cycles to ca. 6% in 1M LiClO₄ in PC. Recent work has shown that the coulomb efficiency for immediate discharges can be at least 91%-95% for cells employing $(CH)_x$ cathodes oxidized up to 7%-10% levels (8, 11, 20).

In order to compare the discharge characteristics of the cells, the average discharge voltage, \bar{V}_d , was plotted vs. its associated current density in Fig. 4 for all the immediate and the delayed discharge cycles given in Table I and Fig. 3. The \bar{V}_d for immediate discharges of the cell containing 7% oxidized polyacetylene did not change significantly for an increase in discharge current of two orders of magnitude. At 1.00 mA/cm², it had dropped only to 3.37V. After ~80% $(ClO_4)^-$ ion equilibration had occurred within

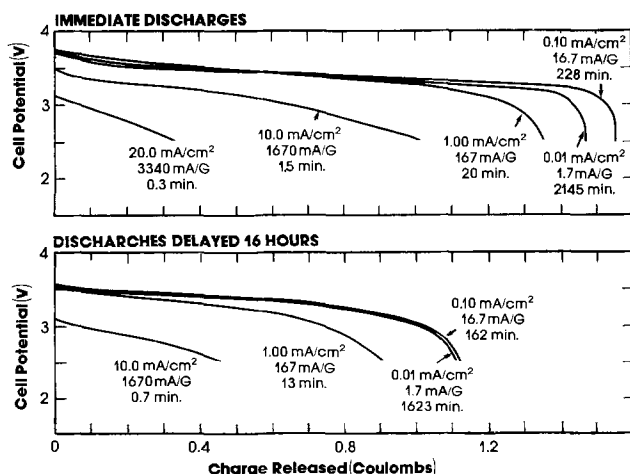


Fig. 3. Discharge characteristics of a Li/LiClO₄(PC)/[(CH)^{0.07}(ClO₄)_{0.07}]_x cell. Upper figure: discharge immediately after a charge cycle. Lower figure: discharge following a 16h stand period after completion of the charge cycle.

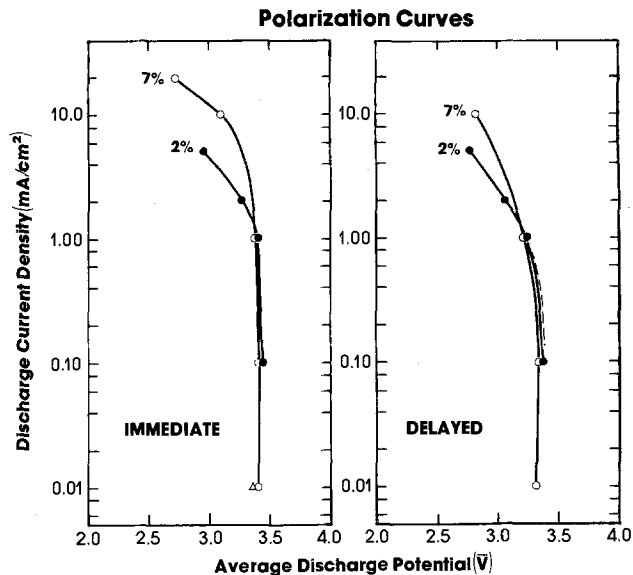


Fig. 4. Polarization curves for Li/LiClO₄(PC)/[(CH)^{0.07}(ClO₄)_{0.07}]_x cells containing cathodes consisting of polyacetylene oxidized to 2% and 7%.

the polymer fibrils as promoted by the 16h delay in discharging the cell, \bar{V}_d still decreased by only 0.5V over a current increase of three orders of magnitude. Electronic conductivity depends on the charge density within the polymer, ranging from 10⁻⁷ at zero charge density to 10² for $[CH(ClO_4)_y]_x$ at 7 charges per 100 carbons ($y = 0.07$) (16). Similarly, the rate of charge transfer increases with increasing charge density (23). The polarization at a polymer electrode might therefore be expected to depend on the overall charge density and its distribution throughout the electrode. For example, a resistive layer between the polymer bulk and the current collector could form as the charge density is depleted in that region. Replenishing the charge density at the current collector would be limited by the small diffusion coefficient of anions in the polymer [estimates as low as 4×10^{-18} cm²/s (17) and as high as 6×10^{-12} cm²/s (19) have been reported].

Since the cell voltage falls rapidly at the end of the constant current discharges, except for the higher rate discharges, the charge released, to 2.50V, $Q(\text{out})$ (see Table I), is taken to be the usable capacity of the cell for a given drain rate. Changing the voltage to which $Q(\text{out})$ was measured from 2.5 to 3.0V would substantially reduce the usable capacity at discharge rates higher than 2.0 mA/cm² but would leave the lower rate capacities essentially the same (see Fig. 5).

Energy densities are calculated using the charge released on discharge to 2.5V. Energy densities and average power densities are based on the weight of the $[(CH)^{+0.07}(ClO_4)_{0.07}]_x$ employed and the weight of the Li metal consumed in the discharge reaction.

The energy released in watt-hours (Wh) during a discharge was measured by dividing the area under the

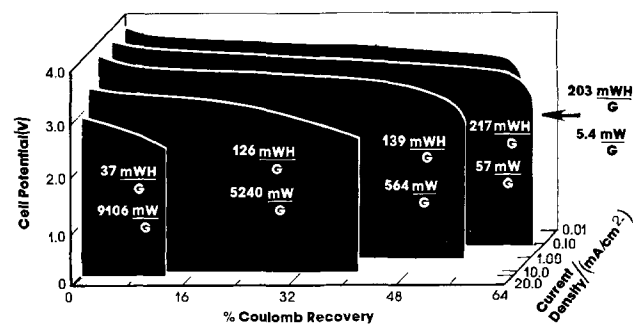


Fig. 5. Discharge characteristics of Li/LiClO₄(PC)/[(CH)^{0.07}(ClO₄)_{0.07}]_x cell. The discharge studies were performed immediately after a charge cycle was completed.

curve (volts times coulombs) by 3600 s/h. The average power in watts was calculated as the product of \bar{V}_d in volts and the current in amperes. The higher discharge rates and their associated higher average power densities result, as expected, in a decline in the energy density. The energy densities of the cell containing 2% oxidized polyacetylene are, as expected, less than those containing the 7% oxidized film; however, the average power densities are nearly the same. It might be noted that recent studies using a $\text{Li}_{0.2}\text{TiS}_2/\text{LiAsF}_6$ (acetonitrile)/ $[(\text{CH})^{+0.08}(\text{AsF}_6)_{0.08}^-]_x$ cell (24) have given 80% coulombic efficiencies at discharge currents of 5.0 mA/cm² (overall $Q_{\text{eff}} = 95\%$) (11). If similar results were attained using a Li anode instead of the $\text{Li}_{0.2}\text{TiS}_2$ anode, the energy densities and capacities would be approximately twice those given above. An increase in average power density would also be expected.

Conclusions

These studies demonstrate that cells containing 7% oxidized polyacetylene cathodes and perchlorate dopant ions, $[(\text{CH})^{+0.07}(\text{ClO}_4)_{0.07}^-]_x$, can release 40% of their charge at discharge rates up to 10.0 mA/cm² with less than a 0.5V decrease in cell potential. The effect of the nature of perchlorate dopant anion on the cell characteristics can be only determined after similar studies using other dopants have been performed. These results show that an organic polymer can act as a cathode in a rechargeable cell and that the stored charge can be delivered on demand at a surprisingly high rate.

Acknowledgments

This study was supported by the Department of Energy Contract no. DE-AC02-81-ER10832. The authors wish to thank Mr. R. B. Kaner for many useful discussions and comments.

Manuscript submitted March 19, 1984; revised manuscript received Nov. 29, 1984. This was Paper 26 presented at the Detroit, Michigan, Meeting of the Society, Oct. 17-21, 1982.

The University of Pennsylvania assisted in meeting the publication costs of this article.

REFERENCES

1. A. F. Diaz, K. K. Kanazawa, and G. P. Gardini, *J. Chem. Soc. Chem. Commun.*, 535 (1979); A. F. Diaz and K. K. Kanazawa, in "Extended Linear Chain Compounds," J. S. Miller, Editor, pp. 417-427, Plenum Press, New York (1982).
2. G. Tourillon and F. Garnier, *J. Electroanal. Chem.*, **135**, 173 (1982); K. Kaneto, K. Yoshino, and Y. Inui-shi, *Jpn. J. Appl. Phys.*, **22**, L567 (1983).
3. J. Bargon, S. Mohmand, and R. J. Waltman, *IBM J. Res. Dev.*, **27**, 330 (1983).
4. L. W. Shacklette, R. L. Elsenbaumer, R. R. Chance, J. M. Sowa, D. M. Ivory, G. G. Miller, and R. H. Baughman, *J. Chem. Soc. Chem. Commun.*, 361 (1982).
5. Y. Papir, V. P. Kurkow, and S. P. Current, Abstract 534, p.820, The Electrochemical Society Extended Abstracts, Vol. 83-1, San Francisco, CA May 8-13, 1983.
6. P. J. Nigrey, A. G. MacDiarmid, and A. J. Heeger, *J. Chem. Soc. Chem. Commun.*, 594 (1979); P. J. Nigrey, D. MacInnes, Jr., D. P. Nairns, A. G. MacDiarmid, and A. J. Heeger, *This Journal*, **128**, 1651 (1981).
7. K. Kaneto, M. Maxfield, D. P. Nairns, and A. G. MacDiarmid, *J. Chem. Soc., Faraday Trans.*, **78**, 3417 (1982).
8. G. C. Farrington, B. Scrosati, D. Frydrych and J. De-Nuzzio, *This Journal*, **131**, 7 (1984).
9. R. B. Kaner and A. G. MacDiarmid, *J. Chem. Soc. Faraday Trans.* **80**, 2109 (1984).
10. S. L. Mu, S. J. Porter, W. Q. Wu, and A. G. MacDiarmid, Submitted to *This Journal*.
11. M. Maxfield, J. F. Wolf, T. R. Jow, and L. W. Shacklette, p. 16, Abstracts of 186th American Chemical Society, National Meeting, Industrial Engineering Chemistry (1983).
12. J. J. Auburn and H. Schonhorn, in "Lithium Batteries," H. Venkatesetty, Editor, pp. 372-380, The Electrochemical Society Softbound Proceedings Series, Pennington, NJ (1981).
13. H. Shirakawa and S. Ikeda, *Polym. J.*, **2**, 231 (1971).
14. M. Aldissi, F. Schue, L. Giral, and M. Rolland, *Polymer*, **23**, 246 (1982); M. Aldissi, Ph.D. Thesis Universite des Sciences et Techniques du Languedoc, Montpellier, France (1981).
15. A. G. MacDiarmid and A. J. Heeger, *Synth. Met.*, **1**, 101 (1979/1980).
16. T.-C. Chung, A. G. MacDiarmid, A. Feldblum, and A. J. Heeger, *J. Polym. Sci. Polym. Lett.*, **20**, 427 (1982).
17. J. H. Kaufman, E. J. Mele, A. J. Heeger, R. Kaner, and A. G. MacDiarmid, *This Journal*, **130**, 571 (1983).
18. J. H. Kaufman, J. W. Kaufer, A. J. Heeger, R. B. Kaner, and A. G. MacDiarmid, *Phys. Rev. B*, **26**, 2327 (1982).
19. F. G. Will, Abstract 554, p. 838, The Electrochemical Society Extended Abstracts, Vol. 83-1, San Francisco, CA, May 8-13, 1983.
20. G. C. Farrington, B. Scrosati, and A. Padula, *Solid State Ionics*, **9**, **10**, 447 (1983).
21. M. A. Druy, S. P. Walsh, and M. F. Rubner, ICSM, Abano Terme, Italy, 1984, To be published in *Liq. Cryst. Molec. Cryst.*
22. M. Aldissi and A. G. MacDiarmid, Unpublished observations, 1983.
23. W. H. Smyrl, S. R. Kurtz, and D. S. Ginley, Abstract 551, p. 835, The Electrochemical Society Extended Abstracts, Vol. 83-1, San Francisco, CA, May 8-13, 1983.
24. M. S. Whittingham, *This Journal*, **123**, 315 (1976).

Electrochemiluminescence of Osmium Complexes

Spectral, Electrochemical, and Mechanistic Studies

Héctor D. Abruña*

Department of Chemistry, Cornell University, Ithaca, New York 14853

ABSTRACT

Electrochemical, spectral, and electrochemiluminescent (ECL) studies of bipyridine and phenanthroline complexes of osmium are presented. ECL was observed for a large number of complexes, but the emission intensity in some cases proved to be much lower than anticipated. For $[\text{Os}(\text{bpy})_2(\text{dmsO})_2]^{2+}$, this was determined to be due to an EC process taking place after oxidation of the complex to give rise to $[\text{Os}(\text{bpy})_2(\text{CH}_3\text{CN})_2]^{3+}$. Surface ECL was demonstrated for electropolymerized films of $[\text{Os}(\text{dstyr-bpy})_2 \text{diphos}]^{2+}$ (dstyr-bpy is 4,4'-distyryl 2,2' bipyridine). The phenomenon of intramolecular ECL was probed by studies on $[\text{Os}(\text{bpy})_2 \text{Fc-p}]^{2+}$ (Fc-p is 1,1' bis diphenyl phosphino ferrocene). It was found that instead of intramolecular ECL being operative, a quenching mechanism was responsible for the observed behavior. For complexes that do not exhibit complications, there was a linear correlation between the solution luminescence quantum yield and the ECL emission intensity, consistent with the direct formation of the excited state via the redox process without any intervening steps or additional relaxation pathways.

Electrogenerated chemiluminescence (ECL) is the study of the generation of emitting excited states via the electron-transfer reaction of electrogenerated reactants (1). There have been extensive studies carried out on both organic systems (1) and transition metal complexes (2, 3). In the latter category, $\text{Ru}(\text{bpy})_3^{2+}$ (bpy is 2,2'-bipyridine) has received a great deal of attention due to its high emission quantum yield and favorable electrochemical properties (3). Furthermore, ECL studies can be used to gain a better understanding of the photophysical properties of the system involved (1).

A recent report from this laboratory (4) presented a new family of electrochemiluminescent materials based on bipyridine and phenanthroline complexes of osmium. These complexes, first described by Meyer and co-workers (5), are notable in that in contrast to $\text{Os}(\text{bpy})_3^{2+}$ they exhibit high emission quantum yields. Furthermore, this new family allows for a broad range of synthetic variations.

This paper presents further electrochemical and electrochemiluminescent characterization of phenanthroline and bipyridine complexes of osmium. It is found that a large number of these complexes will give rise to ECL emission, although, in some cases, the observed ECL intensity was much lower than had been anticipated.

It is also demonstrated that surface ECL can also be observed from the films of electropolymerized complexes. Though the emission arising from these films is not as intense as that observed from electropolymerized $\text{Ru}(\text{vinylbipyridine})_3^{2+}$ films, it is much longer lived.

The phenomenon of intramolecular ECL (that is, generation of emitting excited states through intramolecular electron transfer) was addressed, and two complexes were synthesized to ascertain the feasibility of having this process take place.

Finally, in a comparison of the relative ECL intensities for a number of complexes having different solution luminescence quantum yields, it was found that, for cases with no complications, there was a linear correlation between ECL intensity and solution luminescence quantum yield, indicating the direct formation of the excited state via the redox process.

Experimental

Synthesis.— $[\text{Os}(\text{L})_2](\text{PF}_6)_2$.—L = bpy, phen (phen is 1,10 phenanthroline), v-bpy (v-bpy is 4-vinyl,4' methyl, 2,2' bipyridine). These complexes were prepared according to the procedure of Buckingham *et al.* (6).

$[\text{Os}(\text{L})_2\text{Cl}_2]$.—L = bpy, dmbpy (dmbpy is 4,4' dimethyl 2,2' bipyridine), dstyr-bpy (dstyr-bpy is 4,4'-distyryl, 2,2' bipyridine), phen. These complexes were prepared according to the procedure of Sullivan (7). Briefly, $(\text{NH}_4)_2\text{OsCl}_6$ (typically 1 mM) was heated at reflux in thoroughly

deaired ethylene glycol for 3h with 2 equivalents of L. The solution was allowed to cool, and an equivalent volume of water was added. A very large excess of sodium dithionite was added and the solution was stirred for 3h. The solution was refrigerated overnight, and $[\text{Os}(\text{L})_2\text{Cl}_2]$ precipitated. The material was collected, washed with cold water and ether, and dried under vacuum.

$[\text{Os}(\text{L})_2\text{L}'](\text{PF}_6)_2$.—L = bpy, dmbpy, dstyr-bpy, phen. L' = diphos (diphos is bis 1,2 diphenyl phosphino ethane), dpmm (dpmm is bis 1,2 diphenyl phosphino methane), dpae (dpae is bis 1,2 diphenylarsino ethane), Fc-p (Fc-p is 1,1' bis diphenylphosphino ferrocene), phen-dione (phen-dione is phenanthroline 5,6 dione). These complexes were prepared according to the procedure of Meyer *et al.* (5). Except for $[\text{Os}(\text{phen})_2(\text{phen-dione})]^{2+}$, all of the complexes were purified by recrystallization from acetonitrile/ether and by chromatography on neutral alumina. The $[\text{Os}(\text{phen})_2(\text{phen-dione})]^{2+}$ complex adhered so strongly to alumina that it could not be eluted. It, therefore, was purified by repeated (three times) recrystallizations from acetonitrile/ether.

$[\text{Os}(\text{bpy})_2(\text{CH}_3\text{CN})_2](\text{PF}_6)_2$.—This complex was synthesized by heating at reflux $[\text{Os}(\text{bpy})_2\text{Cl}_2]$ (typically, 100 mg) in thoroughly deaired ethylene glycol (15 ml) for 8h in the presence of a 100 times excess of acetonitrile. The solution was allowed to cool, and the excess acetonitrile was eliminated by evaporation. An equal volume of water was added, and the complex was precipitated with saturated aqueous NH_4PF_6 . The precipitate was collected, washed with water and ether, and dried under vacuum. The complex was purified by recrystallization from acetonitrile/ether and by chromatography on neutral alumina.

$[\text{Os}(\text{bpy})_2(\text{dmsO})_2](\text{PF}_6)_2$ (dmsO is dimethyl sulfoxide).—The dimethyl sulfoxide complex was synthesized by heating at reflux $[\text{Os}(\text{bpy})_2\text{Cl}_2]$ in thoroughly deaired dimethyl sulfoxide for 24h. The solution was allowed to cool, and the complex was precipitated with saturated aqueous NH_4PF_6 . The precipitate (brownish at this point) was collected and washed with water and ether and dried under vacuum. Purification by recrystallization proved ineffective. The complex was purified by chromatography on neutral alumina. By eluting with methanol, a brownish-green band was separated, leaving a canary yellow band at the top of the column. This material (the desired complex) was eluted with acetone. The complex was isolated by evaporating the acetone.

Except for $[\text{Os}(\text{bpy})_2(\text{Fc-P})]^{2+}$ and $[\text{Os}(\text{phen})_2(\text{phen-dione})]^{2+}$, the preparations followed literature procedures or simple extensions of these. Since the above two compounds had not been previously reported, they were characterized by elemental microanalysis. The results are consistent with the formulations $[\text{Os}(\text{bpy})_2(\text{Fc-P})]^{2+}(\text{PF}_6)_2 \cdot \text{CH}_3\text{CN}$ (calculated: 48.44% C, 5.04% N, 3.39% H, 4.02% Fe;

* Electrochemical Society Active Member.

found: 48.53% C, 4.49% N, 3.69% H, 3.83% Fe) and $[\text{Os}(\text{phen})_2(\text{phen-dione})]^{2+}(\text{PF}_6)_2 \cdot 2\text{H}_2\text{O}$ (calculated: 39.77% C, 7.74% N, 2.39% H; found: 39.82% C, 7.73% N, 2.24% H). Analyses were performed by Galbraith Laboratories, Knoxville, Tennessee.

Reagents.—Tetra-*n*-butyl ammonium perchlorate (G. F. Smith) was recrystallized three times from ethylacetate, dried *in vacuo* at 90°C for 72h, and stored in a dry box. Phen-dione was obtained from G. F. Smith Company, and Fc-p was obtained from Aldrich; all other ligands were obtained from Strem Chemical Company and were used as received. Acetonitrile (Burdick and Jackson distilled in glass) was stirred over calcium hydride for two days and distilled from it under nitrogen. It was degassed on a vacuum line and stored inside a dry box (Vacuum Atmospheres Corporation) over 4Å molecular sieves which had been previously deaerated on a vacuum line at 150°C for one week. All other reagents were of at least reagent-grade quality and were used without further purification.

Instrumentation.—Electrochemical experiments were performed with a Princeton Applied Research Model 173 Potentiostat-Galvanostat, Model 179 Digital Coulometer, and Model 175 Universal Programmer. Data were recorded on a Hewlett-Packard Model 7045-B X-Y Recorder or on a Nicolet Model 4094 Digital Oscilloscope.

ECL was detected using an Oriel Model 7240 monochromator with either an Oriel Model 7060 photomultiplier tube (operated at -700V), or a Hamamatsu Model R758 photomultiplier tube (operated at -1200V) and a Pacific Instruments Model 124 Digital Laboratory Photometer. In some cases, ECL was detected using an EG&G Electrooptics Model 450-1 Radiometer Photometer with a 550-2 Multiprobe.

Luminescence spectra were obtained on a Hitachi Perkin-Elmer Model MPF-3 Spectrofluorimeter. Neither ECL nor solution luminescence spectra were corrected for the photomultiplier response.

Procedure.—To prevent any contamination from either water or oxygen, all solutions were prepared inside the dry box. The cell used for ECL consisted of a single compartment cell with three standard tapered joints for the electrodes and provided with an optical Pyrex window. The working electrode was a platinum disk sealed in glass which was bent so as to have the surface of the electrode facing the optical window at a distance of 2-3 mm. The counterelectrode was a large area (~ 10 cm²) platinum mesh, and the reference electrode was a silver wire. Both the counter and reference electrodes were sealed through uranium glass to standard tapered joints. The working electrode was mounted on a standard tapered vacuum Teflon holder (Kontes). All solutions were prepared fresh just prior to use, and the cell was charged and sealed inside the dry box.

For obtaining ECL spectra, the potential of the working electrode was pulsed (at a frequency of 0.5 Hz) between values 100 mV positive and negative of the formal potentials for oxidation and reduction, respectively.

Obtaining reproducible ECL intensities was somewhat more complicated. However, a procedure was developed that yielded data that were reproducible to ± 6%. This deviation could arise in part from small variations in the cell positioning. In order to obtain a reproducible geometry, the same cell was used in all of the experiments, with the working electrode being aligned through markings. In addition the optical window of the cell was positioned flush with the entrance slit (fixed 10 nm bandpass) of the monochromator. For intensity measurements, the procedure used was as follows. The cell was prepared as previously described. A cyclic voltammogram at 0.2 V/s was run, and the formal potentials for oxidation and reduction were determined (in order to account for any drifts in the reference potential of the silver wire used as a reference electrode). The potential limits were set 100 mV positive and negative of the formal potentials for oxidation and reduction, respectively. Resistance compensation was used in all intensity measurements. Data were recorded on the digital oscilloscope, and both the peak value and inte-

grated intensities were recorded. The measurements presented represent averages of three different preparations with ten individual transients being averaged every time.

Other experimental conditions for ECL intensity measurements were as follows: (i) concentration of complex was $1.0 \pm 0.01 \times 10^{-3}\text{M}$, (ii) supporting electrolyte $0.100 \pm 0.005\text{M}$, (iii) pulse width of 2s, (iv) cell geometry and electrode area were strictly the same.

Electropolymerization

Two of the complexes synthesized (*i.e.*, $[\text{Os}(\text{v-bpy})_3]^{2+}$ and $[\text{Os}(\text{dstyr-bpy})_2\text{diphos}]^{2+}$) bear electropolymerizable ligands, these being vinylbipyridine and distyrylbipyridine, respectively. Electropolymerization was accomplished according to a previously reported procedure (8) where the potential of a platinum electrode in contact with a 0.5 mM solution of the complex in acetonitrile was scanned in the negative region (typically between -0.5 and -1.6V), whereupon polymerization took place. This procedure was continued until the desired coverage of electroactive material was obtained. The electrode was removed from solution, rinsed with acetone, and placed in electrolyte solution containing no dissolved complex. A cyclic voltammogram was obtained, and, from integration of the area under the voltammetric wave, surface coverages were determined. ECL spectra were determined in acetonitrile containing only supporting electrolyte.

Results and Discussion

Electrochemistry.—As mentioned in a preliminary communication (4), the electrochemical behavior of these complexes of osmium can be broadly divided into metal-localized oxidations and ligand-localized reductions. The oxidative electrochemistry of these complexes is largely metal based and as such represent formally the oxidation of Os^{II} to Os^{III}. As such, the formal potentials for oxidation are very strongly dependent on the coordination environment of the osmium. As Os(II), the complexes have a spin paired d⁶ configuration [d⁵ as Os(III)]. The presence of good sigma donors would, to a first approximation, stabilize the Os(III) oxidation state to a much higher degree than Os(II). Similarly, the presence of good π accepting ligands would stabilize the d⁶ center (through backbonding) much more than the d⁵Os(III) (10). Shifts in the formal potentials for a metal ion complex depend on the relative magnitude of the formation constants for the oxidized and reduced species. From the arguments presented above, good sigma donors would stabilize the oxidized [Os(III)] form of the complex to a greater extent than the reduced form [Os(II)] with π acceptors having the opposite effect. As such one would anticipate that good sigma donors would move the formal potentials in a negative direction, whereas good π acceptors would move them in a positive direction, consistent with the data presented.

As far as the reductive electrochemistry is concerned, a number of reduction waves, largely ligand localized, can be observed. Since the reduction is formally on the ligands, the presence of other ligands in the coordination sphere of the metal exerts only a secondary effect. As such, the formal potentials for reductions are only slightly shifted with changes in the coordination sphere of the metal. Values for the formal potentials for oxidation and reduction are presented in Table I.

Some of the complexes synthesized, however, exhibit electrochemical responses that deviate from the general trends outlined above. As such, these will be considered individually.

$[\text{Os}(\text{bpy})_2\text{Fc-p}](\text{PF}_6)_2$.—The electrochemical behavior of this complex differs from that of the others in that it exhibits two oxidation waves (Fig. 1A, 1B) in the region from 0.0 to +2.0V *vs.* SSCE. This behavior can be understood by considering the nature of the ligand and its own electrochemical characteristics. The ligand, shown structurally as an inset of Fig. 1C, consists of two diphenyl phosphino units attached to the 1,1' positions of ferrocene. Its coordinating properties are those of a

Table I. Electrochemical and luminescence data for bipyridine and phenanthroline complexes of osmium

Complex	$E_{ox}^{o' a}$	$E_{red_1}^{o' a}$	$E_{red_2}^{o' a}$	$E_{red_3}^{o' a}$	$E_{red_4}^{o' a}$	λ_{em}^b (nm)	λ_{rel}^c (nm)
[Os(dmbpy) ₂ diphos] ²⁺ d	+1.22	-1.36	-1.56	-2.27	-2.58	610	610
[Os(bpy) ₂ diars] ²⁺ e	+1.12	-1.26	-1.49	-2.18 ₅	-2.53	682	680
[Os(bpy) ₂ (dmsO) ₂] ²⁺ f	+1.79	-1.00	-1.78	-1.93	-2.21	575	575
[Os(bpy) ₂ (dppm)] ²⁺ g	+1.29	-1.25	-1.49	-2.18	-2.49	622	620
[Os(dstyr-bpy) ₂ diphos] ²⁺ h	+1.20	-1.21	-1.37	-1.52	—	655	655
[Os(dstyr-dpy) ₂ diphos] ²⁺ h	+1.29	-1.28	-1.34	-1.51	—	—	655
[Os(v-bpy) ₂] ²⁺ i	+0.73	-1.31	-1.48	-1.80	—	720	718
[Os(v-bpy) ₂] ²⁺ h	+0.76	-1.35	-1.54	-1.92	—	—	n
[Os(bpy) ₂ Fc-p] ²⁺ j	+0.87 ^k	-1.22	-1.44	—	—	622	620
[Os(phen) ₂ (phen-dione)] ²⁺ l	+0.94 ^m	-1.35	-1.60	—	—	n	n
[Os(phen) ₂ (dppm)] ²⁺	+1.32	-1.24	-1.46	p	p	610	610
[Os(phen) ₂ (diars)] ²⁺	+1.13	-1.25	-1.47	p	p	665	665

^a E in volts vs. SSCE without correction for liquid junction.

^b In acetonitrile solution.

^c In acetonitrile solution containing 0.1M TBAP.

^d dmpy is 4,4' dimethyl 2,2' bipyridine.

^e diars is 1,2 bis(dimethylarsino)benzene.

^f dppm is 1,2 bis diphenylphosphinomethane.

^g dstyr-bpy is 4,4' distyryl, 2,2' bipyridine.

^h Electropolymerized film on the surface.

ⁱ v-bpy is 4-vinyl, 4'methyl 2,2' bipyridine.

^j Fc-p is 1,1'bis diphenylphosphinoferrrocene.

^k A second oxidation is present at $E_p = +1.46V$.

^l phen-dione is 1,10 phenanthroline 5,6 dione.

^m Other waves were observed at $E_p = +0.35$ and $+0.095V$.

ⁿ Luminescence not detected.

^o Very weak luminescence detected but could not be specifically characterized.

^p Extensive adsorption precludes determination.

Note: For ECL experiments, applied voltages were 100 mV past the formal potentials for the redox processes involved, e.g., for [Os(dmbpy)₂diphos]²⁺ the potentials were +1.32 and -1.46V, respectively.

diphos-like ligand. This is evidenced by the fact that the complex [Os(bpy)₂Fc-p]²⁺ has a λ_{max} for absorption (484 nm) that is very similar to that of [Os(bpy)₂diphos]²⁺ (473 nm). The electrochemistry of the ligand [Fig. 1C, 1D (in methylene chloride solvent)] shows two oxidation waves, at +0.58 and +1.21V, respectively. The wave at +0.58V can be ascribed to oxidation of the ferrocene unit, and the one at +1.21V to oxidation of the phosphine sites. These potentials are consistent with values for substituted ferrocenes on the one hand (9) and triphenyl phosphine on the other.¹ The fact that the first oxidation wave is chemically irreversible is surprising since ferrocene derivatives generally show reversible electrochemistry. One could speculate that this irreversibility might be due in part to the presence of the phosphine groups since ferrocene derivatives with strong electron withdrawing substituents show reversible electrochemistry (e.g., diacetyl ferrocene). In fact, a cyclic voltammogram of diacetyl ferrocene in the presence of triphenyl phosphine also shows signs of chemical irreversibility. This might be due to nucleophilic attack of the phosphine on the ferricenium cation.

The complex shows a reversible oxidation at +0.87V. This wave is ascribed to oxidation of the ferrocene unit where the formal potential has been shifted, presumably by donating electron density to the osmium center through coordination. In addition, one would expect the Os^{III/II} oxidation wave to appear at more positive potentials on the basis of the ligands involved. It also appears that coordination of the diphenylphosphino units (of the ligand) to the osmium center stabilizes the ferrocene group, since once coordinated they cannot undergo the nucleophilic attack mentioned above.

Controlled potential electrolysis at +1.1V reveals that this oxidation process involves the transfer of one electron ($N \approx 0.97$) and that the process is reversible on the time scale of controlled potential electrolysis. Spectral changes upon oxidation are relatively modest (Fig. 2A, 2B) when compared to the corresponding results for [Os(bpy)₂diphos]²⁺ (Fig. 2C, 2D). Furthermore, there is the appearance of a weak absorption at about 650 nm ascribed to a ferricenium center (see Fig. 2A', 2B'), again consistent with the fact that this oxidation wave is largely localized on the ferrocene center.

¹ Triphenyl phosphine oxidizes with an E_p of about +1.3V.

A second, multiple electron (by comparing the height of this wave with that for the first oxidation) irreversible wave is observed at a peak potential value of $E_p = +1.46V$. This could represent a composite wave including not only the oxidation of Os^{II} to Os^{III}, but also the oxidation of the phosphine ligand. This again is consistent with the electrochemical behavior of the free ligand.

[Os(phen)₂(phen-dione)](PF₆)₂.—As done for the case of the Fc-p ligand, the electrochemistry of this complex (Figs. 3A, 3B) can be interpreted by considering the electrochemical behavior of the phen-dione ligand (Fig. 3C). The ligand shows reductive waves at potentials of -0.45 and -1.25V vs. SSCE (11, 12), consistent with the presence of the orthoquinone structure. The electrochemistry of the complex is, however, quite complex. On an initially positive going scan, a wave at +0.96V vs. SSCE is observed. Upon scan reversal, a wave at +0.89V vs. SSCE is observed, this being the counterpart to the wave at 0.96V. We ascribe this redox process to the Os^{III/II} couple due to the similarity in potential with [Os(phen)₃]²⁺. On continuing the negative going sweep, a second wave at $E_p = 0.27V$ vs. SSCE is observed. Further reductions are observed at $E_p = -0.2V$ and at -1.26 and -1.52V. On a second, positive going sweep, a wave at $E_p = 0.37V$ is observed. This is the anodic counterpart to the wave at $E_p = 0.27$ observed on the negative sweep. It was also found that upon scanning between 0 → -1.8V vs. SSCE the complex undergoes some type of coupling process so as to give rise to an adherent electrochemically active film of the complex on the surface of the electrode (Fig. 3B).

As mentioned before, the oxidation wave for [Os(phen)₂(phen-dione)]²⁺ (Fig. 2A) observed at $E^{o'} = +0.92V$ is ascribed to the Os^{III/II} process due to the similarity of this potential to that observed for [Os(phen)₃]²⁺ ($E^{o'} = 0.86$). Similarly, the waves at $E^{o'} = -1.26$ and $-1.52V$ are ascribed to the reduction of the phenanthroline ligands, again due to similarities in $E^{o'}$ values for [Os(phen)₃]²⁺. The fact that [Os(phen)₃]²⁺ does not exhibit any electrochemical activity between +0.70 and -1.2V indicates that the observed waves for [Os(phen)₂(phen-dione)]²⁺ in this potential region are due to the presence of the quinone center in the phen-dione ligand. The shifting of the waves in a positive direction is consistent with the effect of metal coordination to the phen-dione ligand.

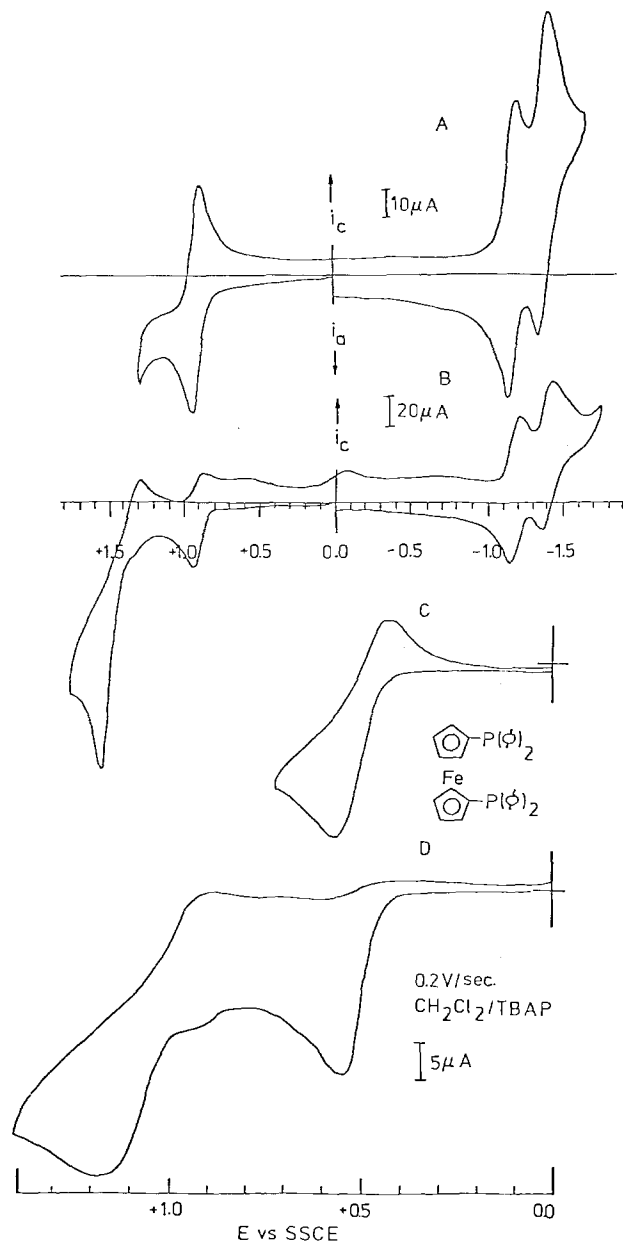


Fig. 1. A and B: Cyclic voltammograms for $[\text{Os}(\text{bpy})_2\text{Fc-P}]^{2+}$ in acetonitrile solution containing 0.1M TBAP. Sweep rate was 0.2 V/s. In A, the anodic limit was +1.3V, in B, +1.8V. C and D: Cyclic voltammograms for 1,1'-diphenyl phosphino ferrocene in methylene chloride solution containing 0.1M TBAP. Sweep rate was 0.2 V/s. In C, the anodic limit was +0.8V, in D, +1.6V.

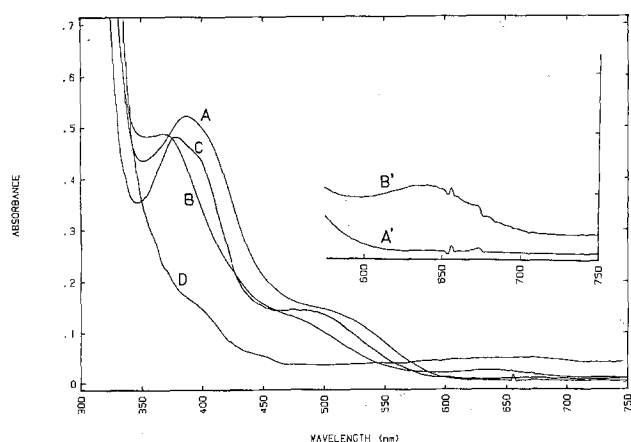


Fig. 2. Spectra in acetonitrile for $[\text{Os}(\text{bpy})_2\text{Fc-P}]^{2+}$ (A), $[\text{Os}(\text{bpy})_2\text{Fc-P}]^{3+}$ (B), (A' and B' are the spectra for the same complexes in the region from 600 to 750 nm under expanded scale to emphasize the band at 650 nm), $[\text{Os}(\text{bpy})_2\text{diphos}]^{2+}$ (C), and $[\text{Os}(\text{bpy})_2\text{diphos}]^{3+}$ (D).

$[\text{Os}(\text{bpy})_2(\text{dmsO})_2](\text{PF}_6)_2$.—A cyclic voltammogram for this complex at 0.2 V/s is shown in Fig. 4. On an initially negative going sweep, four one-electron reversible reductions can be observed (see Table I for E^0 values). As with other complexes, these reductions are ascribed to the sequential reduction of the bipyridine ligands by one and two electrons, respectively.

The oxidative electrochemistry is somewhat more complex. On an initially positive going sweep, a wave at $E_p = +1.82\text{V}$ is observed. Upon scan reversal, only a very small current is observed, indicative of decomposition of the oxidation product. Upon scanning the potential further in the negative direction, a new wave appears at $E_p = 0.89\text{V}$. Scan reversal (back in the positive direction) shows that there is an anodic counterpart to this wave and that the

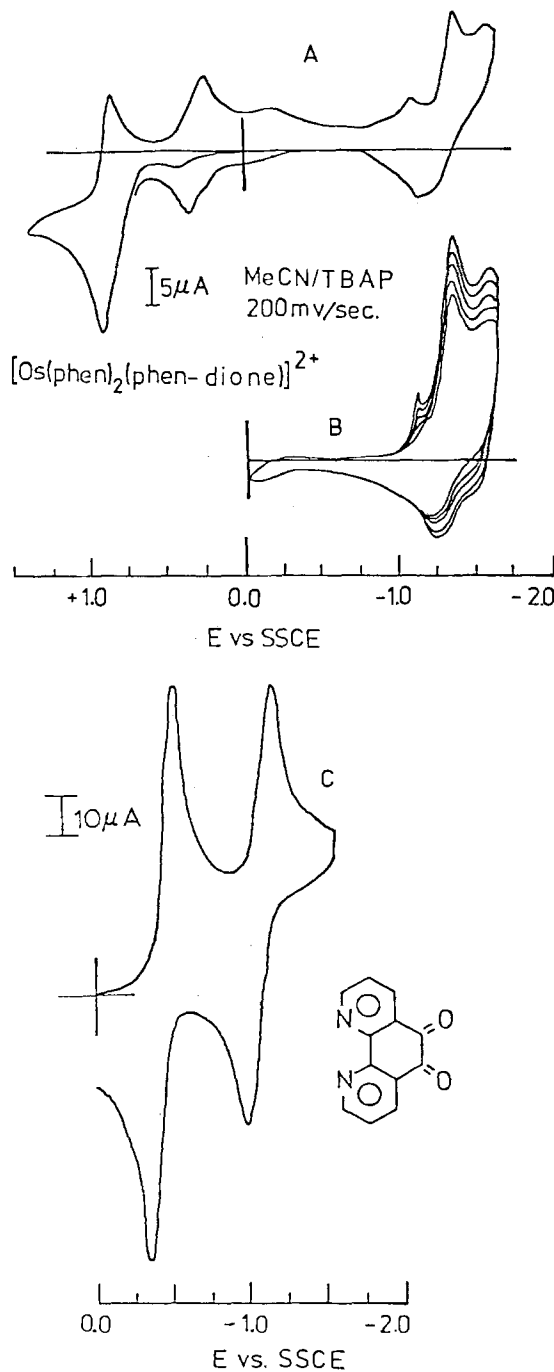


Fig. 3. A: Cyclic voltammogram for $[\text{Os}(\text{phen})_2(\text{phen-dione})]^{2+}$ in acetonitrile solution containing 0.1M TBAP. Sweep rate was 0.2 V/s. B: Consecutive voltammograms depicting surface deposition. C: Cyclic voltammogram on a glassy carbon electrode for phenanthroline 5-6 dione in acetonitrile solution containing 0.1M TBAP. Sweep rate: 0.25 V/s.

process represents a system that is both chemically and electrochemically reversible. As the rate of potential sweep is increased, the cathodic counterpart of the wave at +1.82V increases with a concomitant decrease of the wave at $E_p = +0.89V$. At sweep rates higher than 50 V/s, no decomposition is noted, and the voltammogram is that of a chemically and electrochemically reversible system with an E^0 of +1.79V. The behavior outlined is that typical of an EC-type process. In essence, upon oxidation, $[\text{Os}(\text{bpy})_2(\text{dmsO})_2]^{2+}$ undergoes rapid loss of dmsO with incorporation of 2 mol of acetonitrile (solvent) into the coordination sphere of the osmium. That the product is $[\text{Os}(\text{bpy})_2(\text{CH}_3\text{CN})_2]^{2+}$ is indicated by the fact that the additional wave that appears at slow scan rates has an E^0 value that is virtually identical to that of $[\text{Os}(\text{bpy})_2(\text{CH}_3\text{CN})_2]^{2+}$ ($E^0 = +0.91V$). Furthermore, controlled potential electrolysis at 1.9V yields an n value of 0.96. Spectral characterization of the product again confirms the fact that $[\text{Os}(\text{bpy})_2(\text{CH}_3\text{CN})_2]^{2+}$ is the reaction product.

ECL.—As reported previously (4), intense ECL could be observed from a number of these complexes (see Table I) when the potential of an electrode was pulsed between values corresponding to the oxidation and reduction plateaus of the complex. In general, the observed ECL spectrum was virtually identical to the solution luminescence spectrum obtained in acetonitrile solution.

Of particular interest was the $[\text{Os}(\text{bpy})_2(\text{dmsO})_2]^{2+}$ complex, because of its very high solution luminescence quantum yield ($\phi_2 = 0.38$). On this basis, it was expected that it would show a correspondingly high ECL intensity. This, however, did not turn out to be the case. Even though ECL was observed, and the ECL spectrum coincided with the solution luminescence spectrum in acetonitrile (Fig. 5A), the observed ECL intensity was much lower than had been anticipated. From the electrochemical study of the complex (*vide supra*), it was concluded that the low ECL intensity was due to the decomposition of the complex (loss of dmsO and solvolysis of the complex) when present in its oxidized form. In retrospect, it is not surprising that the complex is unstable in the oxidized form, particularly in light of the coordination sphere and the formal potential for oxidation. In essence, the presence of very strong π acceptors (10) such as dimethylsulfoxide shifts the value of the metal based oxidation to about 1.80V. Upon oxidation to Os^{III} , the degree of π backbonding decreases dramatically, and since the bonding of the dmsO's depends largely on this, the bonding interaction is severely weakened and there is loss of dmsO. From the electrochemical study, it was found that the decomposition could be suppressed at high sweep rates (> 50 V/s). As such, it was thought that having a short pulse width in the ECL experiment would enhance stability and increase the emission intensity. Therefore, a variety of pulse widths were examined. Though it was indeed found that shorter pulse widths

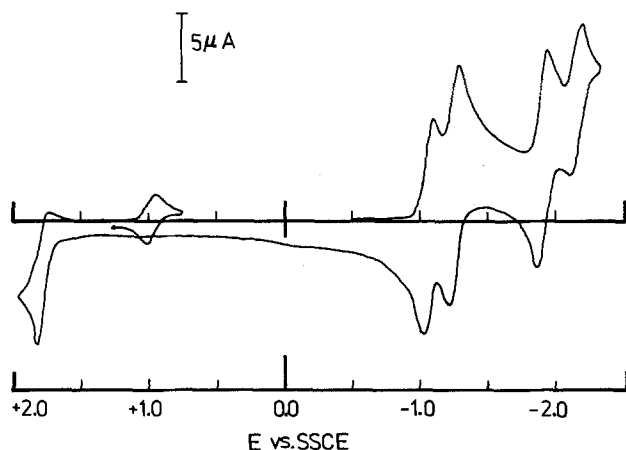


Fig. 4. Cyclic voltammogram for $[\text{Os}(\text{bpy})_2(\text{dmsO})_2]^{2+}$ in acetonitrile solution containing 0.1M TBAP. Sweep rate was 0.2 V/s, and the initial scan direction was cathodic.

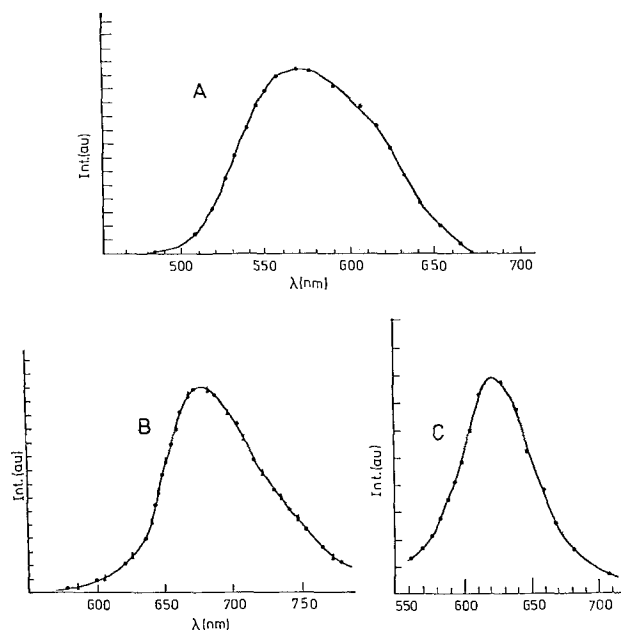
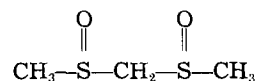


Fig. 5. A: ECL (—) and solution (·) luminescence spectra for $[\text{Os}(\text{bpy})_2(\text{dmsO})_2]^{2+}$. B: Solution luminescence (·), solution ECL (—), and surface ECL (Δ) spectra for $[\text{Os}(\text{dstyr-bpy})_2\text{diphos}]^{2+}$. C: ECL (—) and solution (·) luminescence spectra for $[\text{Os}(\text{bpy})_2\text{Fc-p}]^{2+}$.

would enhance the overall stability of the system, it was also found that ECL emission intensities did not increase to any great extent. This essentially reflects the fact that at short pulse widths the amount of electrogenerated products is small and, as such, ECL intensities are low. We are currently trying to circumvent the problem by synthesizing a chelating disulfoxide



which, by virtue of being a chelate, might impart an enhanced stability to the oxidized complex.

Intense ECL was, however, observed for a number of complexes (Table I). In conjunction with our previously reported results, this represents a very extensive series of electrochemiluminescent materials based on a transition metal.

Surface ECL.—It has been previously reported (14) that ECL can be observed from electrodes modified with electropolymerized layers of $\text{Ru}(\text{v-bpy})_3^{2+}$. The mechanism for light generation is again believed to be due to electron-transfer recombination between oxidized and reduced species within the electropolymerized film to give rise to light emission. As such, surface ECL is conceptually identical to conventional solution ECL.

The phenomenon of surface ECL was also investigated for some of the osmium complexes. Specifically, two complexes that are capable of undergoing electropolymerization were synthesized: $[\text{Os}(\text{dstyr-bpy})_2\text{diphos}]^{2+}$ and $[\text{Os}(\text{v-bpy})_3]^{2+}$. The distyryl-bipyridine and vinyl bipyridine groups can undergo electroreductive polymerization to give rise to strongly adherent and electrochemically active layers of the metal complexes. Electropolymerization was carried out from 0.5 mM solution of the monomers (further details are given in the Experimental section). After modification, the electrodes were rinsed and placed in supporting electrolyte containing no complex in solution. The electrochemical behavior of these electrodes was typical (Fig. 6) of surface immobilized redox reagents (15) with the waves being symmetrical about the potential axis, exhibiting small ΔE_p , and having peak currents that were directly proportional to the rate of potential sweep.

The conditions necessary for the observation of ECL were established by pulsing the potential of the electrode between values that were 100 mV past the formal poten-

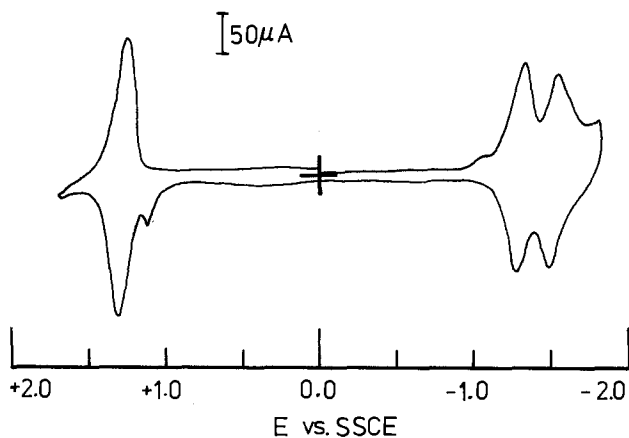


Fig. 6. Cyclic voltammogram in acetonitrile containing 0.1M TBAP for an electrode modified with an electropolymerized layer of $[\text{Os}(\text{dstyr-bpy})_2\text{diphos}]^{2+}$. Sweep rate was 0.5 V/s.

tials for oxidation and reduction. In the case of $[\text{Os}(\text{dstyr-bpy})_2\text{diphos}]^{2+}$, ECL emission was detected. The observed surface ECL spectrum corresponded closely to that obtained for homogeneous solution ECL as well as the solution luminescence spectrum (Fig. 5B). While the surface ECL intensity for $[\text{Os}(\text{dstyr-bpy})_2\text{diphos}]^{2+}$ was not as high as that for films of $[\text{Ru}(\text{v-bpy})_3]^{2+}$, it was much longer lived (~ 2 h). This material may be useful for display devices based on surface ECL. In the case of $\text{Os}(\text{v-bpy})_3^{2+}$, no surface ECL could be detected with the instrumentation available. From the value of the homogeneous solution luminescence quantum yield for $\text{Os}(\text{bpy})_3^{2+}$, one would anticipate a very weak luminescence for the immobilized layer so that the inability to detect ECL should not be very surprising.

Intramolecular quenching of ECL.—As mentioned previously, the phenomenon of ECL is generally believed to arise from the intermolecular electron-transfer recombination of electrogenerated reactants. Usually, this involves the oxidation and reduction of a single species (metal complexes in the present case). Intense ECL can be obtained with the use of external redox reagents that can serve as either oxidants or reductants. In fact, we previously reported (4) that intense ECL could also be observed for $[\text{Os}(\text{bpy})_2\text{diphos}]^{2+}$ when [n-methy phenothiazine] $^+$ or anthraquinone $^-$ were used as oxidant or reductant, respectively. The fact that external redox agents could be used suggested that it might be possible to achieve this (but in an intramolecular fashion). That is, to incorporate a second redox center into the metal complex and to try to obtain ECL by stepping the potential between this additional redox center and the appropriate redox process for the metal complex. In order to be able to demonstrate this, first one must be able to incorporate a second redox center and, second, the redox potential of this process must be such that it is straddled by the formal potentials for oxidation and reduction of the metal complex itself. Furthermore, the potential of this secondary redox center must be such that the energetic difference in formal potentials between this couple and the appropriate redox process for the metal complex is sufficient to populate the excited state. With these constraints in mind, two ligands that bear electroactive centers were identified. These are 1,1'-bis diphenylphosphino ferrocene and phenanthroline-5,6 dione.

In the first case, the ferricenium would serve as the oxidant, and, in the second, the reduced ortho-quinone group on the phenanthroline would serve as the reductant. Both of these materials fulfill the requirements outlined previously concerning the value of their redox potentials.

These systems are now considered in detail.

$[\text{Os}(\text{bpy})_2\text{Fc-p}]^{2+}$.—As mentioned previously, this complex exhibits two oxidation waves at $E_{0'} = +0.87\text{V}$ and at $E_p = +1.46\text{V}$, with the first oxidation being ascribed to the

ferrocene center. Upon pulsing the potential of an electrode, in contact with a 0.5 mM solution of the complex between +0.97 and -1.32V vs. SSCE , a weak yet perceptible luminescence is detected. More intense luminescence is obtained when the potential of the electrode is pulsed between +1.6 (corresponding to a potential past the second oxidation) and -1.32V . In both cases, the ECL spectrum was virtually identical to the solution luminescence spectrum in acetonitrile (Fig. 5C). At first, it might appear that these results are consistent with "intramolecular ECL", that is, electron transfer within the complex to yield an excited state. However, further experiments demonstrated that this was not the case. Specifically, studies on the potential dependence of the ECL intensity for $[\text{Os}(\text{bpy})_2\text{diphos}]^{2+}$ proved particularly valuable. It should first of all be mentioned that under usual ECL conditions (that is, pulsing the potential of the electrode between values that are 100 mV past the formal potentials for oxidation and reduction) the ECL intensity for $[\text{Os}(\text{bpy})_2\text{diphos}]^{2+}$ is two to three orders of magnitude higher than that for $[\text{Os}(\text{bpy})_2\text{Fc-P}]^{2+}$. This is somewhat surprising, since the solution luminescence quantum yields for these complexes do not differ by such a large factor. In addition, quite intense ECL could be observed for the $[\text{Os}(\text{bpy})_2\text{diphos}]^{2+}$ complex when the positive pulse was to only +0.9V. (This corresponds to the first oxidation wave for the $[\text{Os}(\text{bpy})_2\text{Fc-P}]^{2+}$ complex.) In fact, the ECL intensity for $[\text{Os}(\text{bpy})_2\text{diphos}]^{2+}$ under these conditions was more intense than that for $[\text{Os}(\text{bpy})_2\text{Fc-P}]^{2+}$ when pulsing between the same potential limits. These results gave an indication that perhaps what was taking place was a quenching of luminescence and not intramolecular ECL. In order to test this, both ECL and solution luminescence studies were performed in the presence of diacetyl ferrocene in its reduced and oxidized forms. Diacetyl ferrocene was chosen because its formal potential for oxidation is nearly identical to that of the first oxidation of $[\text{Os}(\text{bpy})_2\text{Fc-P}]^{2+}$.

In Fig. 7A is shown a transient of the ECL emission for $[\text{Os}(\text{bpy})_2\text{diphos}]^{2+}$ when the potential is pulsed between +1.44 and -1.33V . Figure 7B represents the experiment under identical conditions except that diacetyl ferrocene (about 0.8 eq) has been added. (It should be mentioned that the intensity scale for part A is 100 times less sensitive than that for B and C, which are on the same scale.) Also shown in Fig. 7C is an ECL transient for $[\text{Os}(\text{bpy})_2(\text{Fc-P})]^{2+}$ when the potential was pulsed between +1.6 and -1.3V . Notice that the intensity of the ECL signal is of the same order of magnitude as that for $[\text{Os}(\text{bpy})_2\text{diphos}]^{2+}$ in the presence of diacetyl ferrocene. Clearly, there is very efficient quenching by the added diacetyl ferrocene. That the quenching was due to the oxidized form (ferricenium) was demonstrated by looking at the solution luminescence of $[\text{Os}(\text{bpy})_2\text{diphos}]^{2+}$ in the absence of diacetyl ferrocene as well as in its presence in either the oxidized or reduced form. The solution emission intensity in the absence of diacetyl ferrocene as well as in its presence in the reduced form were quite comparable (a decrease of less than 10%). In the presence of ferricenium, however, the solution luminescence was almost entirely quenched. These results, then point to the fact that what is taking place in the case of $[\text{Os}(\text{bpy})_2\text{diphos}]^{2+}$ is not intramolecular ECL but rather a very effective quenching of the excited state by the ferricenium centers.

$[\text{Os}(\text{phen})_2(\text{phen-dione})]^{2+}$.—As mentioned previously, the electrochemical behavior of this material is quite complex, especially due to the fact that it undergoes some type of coupling reaction to give electrodes covered with a film of polymeric nature. Though an ECL signal was observed when pulsing between +1.4 and -1.8V , it was so weak that a spectrum could not be obtained with our current equipment. As such, the ECL behavior of the material was not pursued any further.

Correlation of ECL intensity with solution luminescence quantum yield.—It was previously reported (4) that, even though $[\text{Ru}(\text{bpy})_3]^{2+}$ and $[\text{Os}(\text{bpy})_2\text{diphos}]^{2+}$ have very sim-

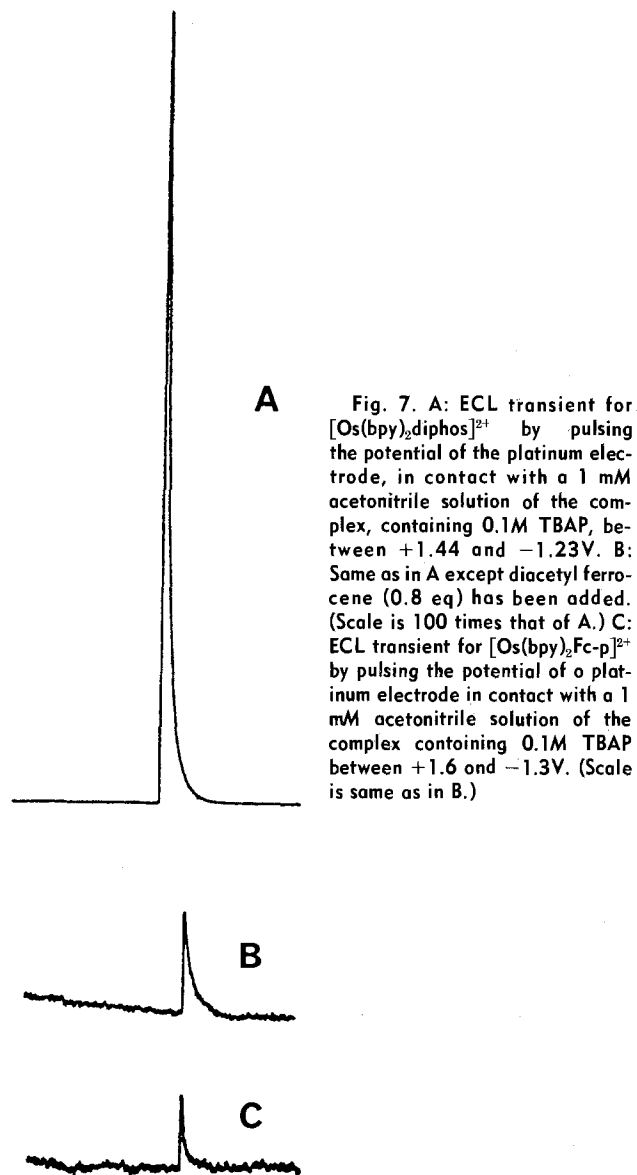


Fig. 7. A: ECL transient for $[\text{Os}(\text{bpy})_2(\text{diphos})]^{2+}$ by pulsing the potential of the platinum electrode, in contact with a 1 mM acetonitrile solution of the complex, containing 0.1M TBAP, between +1.44 and -1.23V. B: Same as in A except diacetyl ferrocene (0.8 eq) has been added. (Scale is 100 times that of A.) C: ECL transient for $[\text{Os}(\text{bpy})_2\text{Fc-p}]^{2+}$ by pulsing the potential of a platinum electrode in contact with a 1 mM acetonitrile solution of the complex containing 0.1M TBAP between +1.6 and -1.3V. (Scale is same as in B.)

ilar solution luminescence quantum yields, the ECL intensity for the osmium complex is about 30% lower than that for $[\text{Ru}(\text{bpy})_3]^{2+}$, after taking into account the differences in solution luminescence quantum yields. Two different mechanisms could be postulated as being responsible for this effect. The first is a quenching mechanism, and the second corresponds to an activation process where the energy of activation for the electron-transfer event leading to the formation of the excited state is high for the osmium complex relative to $[\text{Ru}(\text{bpy})_3]^{2+}$. Since in the experiments performed there were no intentionally added quenchers, it was speculated that the activation mechanism was perhaps responsible for the differences in ECL intensities. If this were to be the case, and if the osmium complexes follow a common mechanism giving rise to the formation of an emitting excited state, then there should be a linear correlation between solution luminescence quantum yield and ECL intensity for the osmium complexes. As such, the measurement of relative ECL intensities was pursued. These measurements, however, proved to be more difficult to perform than had been anticipated. In essence, there are a number of factors that can affect ECL intensities, and these must be recognized and reproducibly controlled.

First of all, in order to eliminate interferences from impurities, the strictest care must be exercised in the purification of the complexes, solvent, and supporting electrolyte as well as in the cleaning of the cell (see Experimental section). Since ECL intensities are known to be very sensitive to the presence of water and oxygen, a

silver wire reference electrode was used (to eliminate water contamination from an SCE) and all manipulations in the preparation of the cell were carried out inside a dry box.

Since ECL is due to the electron-transfer recombination of electrogenerated species, then the amount of oxidized and reduced material generated at the electrode surface will have a dramatic effect on the observed ECL intensity. As such, in order to be able to compare ECL intensities for different complexes, one must insure that the amount of oxidized and reduced material generated at the electrode surface is constant for all of the complexes studied. This was accomplished by measuring the formal potentials for oxidation and reduction prior to performing ECL (to account for any drifts in the silver wire reference electrode) and adjusting the pulse limits to be 100 mV past these values. Since all of the redox processes involved are electrochemically reversible and if one assumes that variations in diffusion coefficients are insignificant, then by providing the same electrode surface conditions, a constant amount of oxidized and reduced material should be generated at the electrode surface assuming a constant bulk concentration for all the complexes. This, however, presupposes that ohmic losses are small or accounted for. In fact, it was found that, in order to obtain reproducible results, the cells could not have compartments separated by sintered glass disks (frits) and iR compensation had to be employed. Under these conditions, and using the experimental procedure outlined beforehand, very reproducible ($\pm 5\text{-}7\%$) ECL intensities could be obtained. The

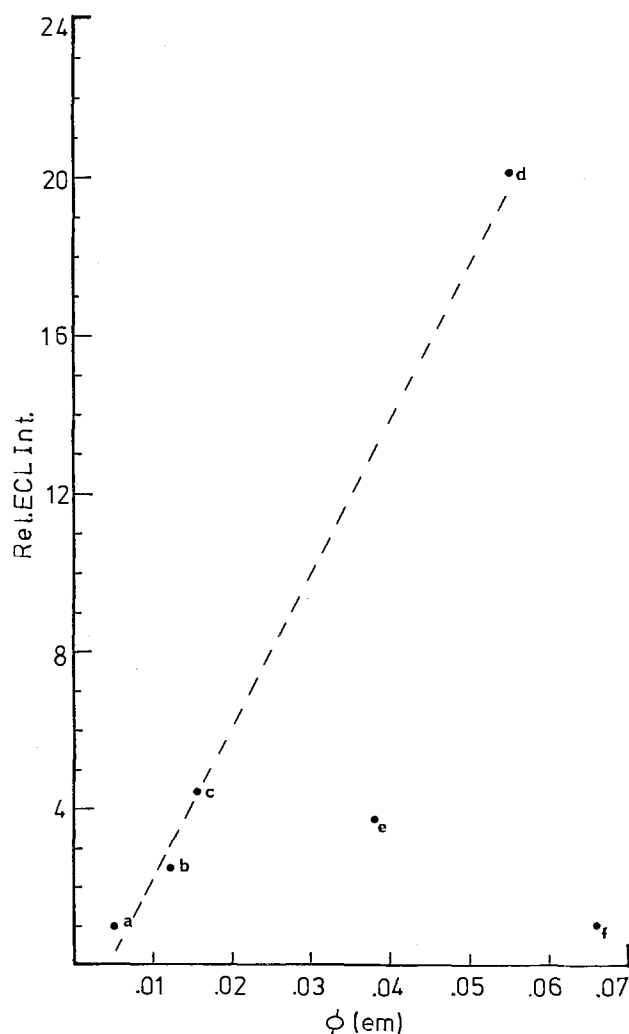


Fig. 8. Plot of relative ECL intensity vs. solution luminescence quantum yield for: $[\text{Os}(\text{bpy})_3]^{2+}$ (a), $[\text{Os}(\text{phen})_3]^{2+}$ (b), $[\text{Os}(\text{bpy})_2(\text{CH}_3\text{CN})_2]^{2+}$ (c), $[\text{Os}(\text{bpy})_2(\text{diphos})]^{2+}$ (d), $[\text{Os}(\text{bpy})_2(\text{Fc-P})]^{2+}$ (e), and $[\text{Os}(\text{bpy})_2(\text{dmsO})_2]^{2+}$ (f). Note: The quantum yield for this complex is not on scale, $\phi_e = 0.38$.

results obtained for a number of complexes are presented in Fig. 8, where relative ECL intensity is plotted against solution luminescence quantum yield. As can be seen, there is a very good correlation, and, in fact, a linear regression analysis of the data yields a correlation coefficient of 0.99. This would, then, imply the direct formation of the excited state from the redox process without other intervening pathways. ECL intensities for $[\text{Os}(\text{bpy})_2\text{Fc-p}]^{2+}$ and $[\text{Os}(\text{bpy})_2(\text{dmso})_2]^{2+}$ fall drastically off the line, consistent with these arguments and the results presented previously.

Furthermore, the ECL intensity for $[\text{Ru}(\text{bpy})_3]^{2+}$ would fall significantly above the line. These results would thus seem to indicate that $[\text{Ru}(\text{bpy})_3]^{2+}$ and $[\text{Os}(\text{bpy})_2\text{diphos}]^{2+}$ follow different pathways, leading to the formation of the emitting excited state, and that this might be reflected as a higher energy of activation in the electron-transfer event leading to the formation of the excited state.

Conclusions

Intense ECL can be observed for a large number of bipyridine and phenanthroline complexes of osmium. Surface ECL can also be observed when the complex is immobilized on the surface of the electrode. It was found that there was a good correlation between the observed ECL intensity and the solution luminescence quantum yield, implying the direct formation of the excited state via the redox process without the intervening deactivation pathways. The complexes that did not follow this correlation were shown to do so because of complicating factors such as an EC process, in the case of $[\text{Os}(\text{bpy})_2(\text{dmso})_2]^{2+}$, and intramolecular quenching, in $[\text{Os}(\text{bpy})_2(\text{Fc-P})]^{2+}$. In the last case, it had been postulated that it might exhibit intramolecular ECL, but it was shown that the observed behavior was due to the presence of intramolecular quenching.

Acknowledgments

This work was supported in part by the donors of the Petroleum Research Fund, administered by the American Chemical Society, the Research Corporation, and by the National Science Foundation through the Material Science Center at Cornell University.

Manuscript submitted July 2, 1984; revised manuscript received Dec. 7, 1984.

Cornell University assisted in meeting the publication costs of this article.

REFERENCES

1. L. R. Faulkner and A. J. Bard, *Electroanal. Chem.*, **1** (1977), and references therein.
2. N. E. Tokel-Takvoryan and A. J. Bard, *Chem. Phys. Lett.*, **25**, 235 (1974).
3. N. E. Tokel-Takvoryan and A. J. Bard, *ibid.*, **25**, 235 (1974); N. E. Tokel-Takvoryan, R. E. Hemingway, and A. J. Bard, *ibid.*, **24**, 6582 (1973); W. L. Wallace and A. J. Bard, *J. Phys. Chem.*, **83**, 1359 (1979); K. Ithoh and K. Honda, *Chem. Lett.*, **99** (1979); J. D. Luttmmer and A. J. Bard, *J. Phys. Chem.*, **85**, 1155 (1981); R. S. Glass and L. R. Faulkner, *ibid.*, **85**, 1159 (1981).
4. H. D. Abruña, *J. Electroanal. Chem. Interfacial Electrochem.*, **175**, 321 (1984).
5. E. M. Kober, B. P. Sullivan, W. J. Dressick, J. V. Caspar, and T. J. Meyer, *J. Am. Chem. Soc.*, **102**, 7583 (1980); J. V. Caspar, E. M. Kober, B. P. Sullivan, and T. J. Meyer, *ibid.*, **104**, 630 (1982).
6. D. A. Buckingham, F. P. Dwyer, H. A. Goodwin, and A. M. Sarfeson, *Aust. J. Chem.*, **17**, 325 (1964).
7. B. P. Sullivan, Unpublished results.
8. H. D. Abruña, P. Denisevich, M. Umaña, T. J. Meya, and R. W. Murray, *J. Am. Chem. Soc.*, **103**, 1 (1981).
9. H. Heing and O. Gurther, *Organomet. Chem.*, **11**, 307 (1967); J. G. Mason and N. Rosenblum, *J. Am. Chem. Soc.*, **82**, 4208 (1960); T. Kuwana, D. E. Bublitz, and G. Hoh, *ibid.*, **82**, 5811 (1960); W. F. Little, C. N. Reilley, J. D. Johnson, K. N. Lynn, and K. P. Sanders, *ibid.*, **86**, 1376 (1964); W. F. Little, C. N. Reilley, J. D. Johnson, and K. P. Sanders, *ibid.*, **86**, 1382 (1964).
10. H. Taube, "Survey of Progress in Chemistry," Vol. 6, pp. 1-46, Academic Press, New York (1973).
11. D. H. Evans and D. A. Griffith, *J. Electroanal. Chem.*, **134**, 301 (1982).
12. D. H. Evans and D. A. Griffith, *ibid.*, **136**, 149 (1982).
13. A. J. Bard and L. R. Faulkner, "Electrochemical Methods: Fundamentals and Applications," John Wiley and Sons, New York (1980).
14. H. D. Abruña and A. J. Bard, *J. Am. Chem. Soc.*, **104**, 2641 (1982).
15. R. W. Murray, in "Electroanalytical Chemistry," Vol. 13, A. J. Bard, Editor, Marcel Dekker, New York (1983).

A Theoretical Calculation of the Hydrogen Evolution Reaction Velocity at the Mercury Electrode

Zhang Lin-Shao

Department of Chemistry, Jilin University, Changchun, China

ABSTRACT

The theoretically derived expressions of the current density, the height and width of the potential barrier are presented based on the thermal activation model and Schottky effect. These expressions are suitable to the compact layer of a near-ideal polarized electrode.

On the basis of the thermal activation model the expression of the hydrogen evolution reaction velocity for compact double layer can be written as follows (1)

$$i = e \int W(E)G(E)d\nu_e \quad [1]$$

where $d\nu_e$ is the number of electrons in metal with energy between E and $E + dE$ which impinge on unit area of the metal surface in unit time. According to Fermi distribution, it is given by

$$d\nu_e = \frac{4\pi kTm}{h^3} \cdot \ln \left[1 + \exp \left(-\frac{E - E_f}{kT} \right) \right] dE \quad [2]$$

The $G(E)$ (in Eq. [1]) is the probability of having the acceptor state with energy equal to that of the electron in the metal electrode, as in the case of other workers, it can be described by using a classical distribution function (1)

$$G(E) = \exp \left(-\frac{\Delta E}{kT} \right) \quad [3]$$

Derivation of the Current Density Expression

The $W(E)$ (in Eq. [1]) is the probability of tunneling through barrier. Taking the Schottky effect into account, the potential barrier may be described by

Table I. Comparison of experimental and calculated values of current density for mercury electrode in contact with 0.1M HCl solution

Potential difference (V vs. RHE)	Electrode charge density $q^M/10^{-2}$ (cm^{-2})	H^+ - H_2O bond extension (\AA)	Current density ($\mu\text{A cm}^{-2}$)			
			Calculated	Post (2)	Bockris (1)	Conway (3)
-0.80	-11.5	2.48	5.44	5.48	5.22	3.63
-0.75	-10.7	2.67	2.20	2.19	1.90	1.40
-0.70	-10.0	2.85	0.34		0.69	0.54

$$U(x) = -\frac{e^2}{16\pi\epsilon_0\epsilon_\gamma x} - \frac{eq^M x}{\epsilon_0\epsilon_\gamma} \quad [4]$$

where q^M is the electrode charge density. This equation is suitable for the compact double layer of a near-ideal polarized electrode. Using the WKB approximation, the expression of the tunneling probability can be written as follows

$$W(E) \doteq \exp \left\{ -2\sqrt{\frac{8\pi^2 m}{h^2}} \int_{x_1}^{x_2} \sqrt{\left(|E| - \frac{e^2}{16\pi\epsilon_0\epsilon_\gamma x} - \frac{eq^M x}{\epsilon_0\epsilon_\gamma} \right)} dx \right\} \quad [5]$$

If

$$x = \frac{\epsilon_0\epsilon_\gamma E t}{eq^M}$$

Eq. [5] becomes

$$W(E) \doteq \exp \left[-\frac{8\pi\epsilon_0\epsilon_\gamma\sqrt{2m}}{3eq^M h} |E|^{3/2} \cdot \theta(E) \right] \quad [6]$$

where

$$\theta(E) = \frac{3}{2} \int_{t_1}^{t_2} \sqrt{1 - \frac{e^3 q^M}{16\pi\epsilon_0^2\epsilon_\gamma^2 E^2 t}} - t dt$$

Substituting Eq. [2], [3], and [6] into Eq. [1], we get

$$i = \frac{4\pi k T m e}{h^3} \int_{E_0}^{E_F} \exp \left(-\frac{8\pi\epsilon_0\epsilon_\gamma\sqrt{2m}}{3eq^M h} |E|^{3/2} \cdot \theta(E) \right) \cdot \exp \left(-\frac{E - E_0}{kT} \right) \cdot \ln \left[1 + \exp \left(-\frac{E - E_F}{kT} \right) \right] dE \quad [7]$$

where $E_0 = E_F - \Delta E_0 + |e\eta| + |e\Delta\phi_c|$ and ΔE_0 is the activation energy. Since the first exponential term behind the integration symbol (in Eq. [7]) is a function of E and the electrons of tunneling barrier are mainly the electrons of the level in the neighborhood of Fermi level, one may expand the exponential term into the series at $(E - E_F)$. We get

$$\frac{-8\pi\epsilon_0\epsilon_\gamma\sqrt{2m}}{3eq^M h} |E|^{3/2} \cdot \theta(E) \doteq -S + \frac{E - E_F}{P} \quad [8]$$

where

$$S = \frac{8\pi\epsilon_0\epsilon_\gamma\sqrt{2mE_F^3}}{3eq^M h} \theta(E_F)$$

and

$$\frac{1}{P} = \frac{-4\pi\epsilon_0\epsilon_\gamma\sqrt{2mE_F}}{eq^M h} \cdot \left[\theta(E_F) + \frac{2}{3} E_F \left(\frac{d\theta(E)}{dE} \right)_{E_F} \right]$$

and

$$\theta(E_F) = \frac{3}{2} \int_{t_1}^{t_2} \sqrt{1 - \frac{e^3 q^M}{16\pi\epsilon_0^2\epsilon_\gamma^2 E_F^2 t}} - t dt \quad [9]$$

The integrated limits t_1 and t_2 can be obtained by solving the equation

$$1 - \frac{e^3 q^M}{16\pi\epsilon_0^2\epsilon_\gamma^2 E_F^2 t} - t = 0 \quad [10]$$

Substituting Eq. [8] into Eq. [7] and integrating it, we get the expression of the current density

$$i = \frac{4\pi k T m e}{\left(\frac{1}{P} - \frac{1}{kT} \right) h^3} \exp \left(-S + \frac{E_0 - E_F}{kT} \right) \cdot \left\{ \ln 2 - \exp \left[\left(\frac{1}{P} - \frac{1}{kT} \right) (E_0 - E_F) \right] \cdot \ln \left[1 + \exp \left(-\frac{E_0 - E_F}{kT} \right) \right] + \int_{\exp \frac{(E_0 - E_F)}{kT}}^1 \frac{Z^{(kT/P) - 2}}{(1 + Z)} dZ \right\} \quad [11]$$

The Expressions of the Height and Width of the Potential Barrier

The barrier height (H) is defined as

$$H = \omega - |U(x_m)|$$

where ω is the work function of the metal and $U(x_m)$ is the electron energy corresponding to barrier maximum, the x_m can be obtained from Eq. [4]

$$x_m = \sqrt{\frac{e}{16\pi q^M}}$$

therefore

$$U(x_m) = -\sqrt{\frac{e^3 q^M}{4\pi\epsilon_0^2\epsilon_\gamma^2}}$$

The barrier width (d) is equal to the difference between integrating limits in Eq. [5], i.e.

$$d = x_2 - x_1 = \frac{\epsilon_0\epsilon_\gamma\omega}{eq^M} (t_2 - t_1)$$

Application of the Expression of the Current Density

We can now calculate the current density using Eq. [11] on the assumptions that Eq. [4] is suitable approximately for a mercury electrode in contact with 0.1M HCl solution (the potential difference is in the range -0.70 to -0.80V) and that the Fermi level of the metal and dielectric constant ϵ_γ are independent of the potential difference in this range. The calculated values of the current density as a function of the potential difference for the case of $\epsilon_\gamma = 6.48$ are obtained. In order that the calculated values are consistent with the experimental results, the extension of the $\text{H}^+ = \text{H}_2\text{O}$ bond ($d_{\text{H}^+ = \text{H}_2\text{O}}$) must be dependent on the electrode charge density, this relationship can be described by

$$d_{\text{H}^+ = \text{H}_2\text{O}} = \frac{0.1106115435 t_2 d}{t_2 - t_1}$$

Computed in this way, Table I gives the current density and extended values of the $\text{H}^+ = \text{H}_2\text{O}$ bond for different potentials. Table II gives the calculated values of the barrier height, barrier width, and the field strength for different potentials. The calculated formulas are in this paper.

The calculated results show that the calculated values of the height and width of the potential barrier decrease

Table II. Calculated values of barrier height, barrier width, and field strength

Potential difference (V)	Current density ($\mu\text{A cm}^{-2}$)	Field strength (V m^{-1})	X_M (Å)	Barrier height (eV)	Barrier width (Å)
-0.80	5.44	2.01×10^9	1.66	3.85	22.29
-0.75	2.20	1.87×10^9	1.73	3.88	23.98
-0.70	0.34	1.74×10^9	1.79	3.90	25.67

with increasing overpotential. It follows that the rate of successful electron transfers does depend not only on the number of particles on the solution side of the metal-

solution interface which exist in appropriate quantum states but also on the height and width of the potential barrier.

Manuscript submitted Feb. 28, 1984; revised manuscript received Sept. 4, 1984.

REFERENCES

1. J. O'M. Bockris and S. U. M. Khan, "Quantum Electrochemistry," p. 470, Plenum Press, New York (1979).
2. P. Post and C. F. Hiskey, *J. Am. Chem. Soc.*, **172**, 4203 (1950).
3. B. E. Conway, "Electrochemistry Data," p. 337, Elsevier Publishing Company, New York (1952).

Parametric Study of Zinc Deposition on Porous Carbon in a Flowing Electrolyte Cell

Charles D. Iacovangelo* and Fritz G. Will*

General Electric Company, Corporate Research and Development, Schenectady, New York 12301

ABSTRACT

X-ray radiography coupled with high resolution optical densitometry, as well as optical and scanning electron microscopy, was employed to study the effect of pivotal zinc deposition parameters on the zinc morphology within a porous C foam electrode. Deposition was carried out in zinc-bromine and zinc-zinc cells with circulating electrolyte. Results on the effects of flow rate, substrate thickness, current density, and electrolyte composition on zinc distribution in the substrate and on its surface are described. This study has shown that in the absence of organic inhibitors, very nonuniform zinc deposition occurs within the porous electrode. This zinc deposition corresponds to the nonuniform primary current distribution dominated by ohmic resistance. This study has led to the conclusions that high electrolyte flow rates, moderate current densities, and thick foams all aid in producing increasingly uniform zinc deposits. The most beneficial effects on the zinc morphology, however, were obtained by adding to the electrolyte a dendrite inhibitor-solubilizer combination consisting of certain fluorosurfactants and butyrolactone.

Commercialization of high power density secondary Zn batteries necessitates repeated uniform Zn plating at high current densities without dendrite formation or progressive Zn slumping. These problems have been addressed in state-of-the-art batteries by employing porous substrates and flowing electrolyte. Examples of such electrodes can be found in Zn-Cl₂ (1, 2), Zn-Br₂ (3-5), and Ni-Zn (6) batteries. Although the use of porous electrodes in Zn batteries has been widespread, little is known about the effects of pivotal deposition parameters on the Zn morphology within a porous substrate. Various mathematical models have been developed to explain the behavior of porous electrodes and aid the designer in development of battery systems. Newman and Tiedemann (7) recently summarized these models. Experimental verification of these models has been limited, and applied primarily to alkaline Zn cells (8). Experimental work on Zn morphology in acidic Zn cells (9, 10) has been limited to kinetic studies of nucleation on planar electrodes.

Three techniques have been reported for the experimental determination of current and reaction distribution within porous electrodes: direct measurement of potential distribution by use of multiple reference electrodes, direct measurement of current distribution among sectioned electrodes, and postmortem chemical analysis and sectioning of electrodes. Previously (11, 12), we described a novel technique of x-ray radiography coupled with high resolution optical densitometry to examine Zn morphology across and within porous C foams. This technique, along with optical and scanning electron microscopy, has now been used to optimize the effect of various electrode and process parameters on the Zn deposit morphology in terms of freedom of dendrites, small particle size, smoothness of the surface, and penetration into the substrate or utilization of the interstices of the porous substrate. The parameters examined included current density, flow

rate, electrolyte composition, substrate thickness, and substrate pore size.

Experimental

Zn was deposited in Zn-Br₂ and Zn-Zn cells on porous reticulated vitreous C (RVC) foams, cemented to graphite current-collector plates with a conductive adhesive. The dimensions of the foam and the graphite plate were $10 \times 10 \times 0.1-0.45$ cm and $13 \times 12 \times 0.64$ cm, respectively. In Zn-Br₂ cells, a Nafion 120 cation exchange membrane (E.I. du Pont de Nemours and Company) was spaced 0.2 ± 0.01 cm from the C foam, separating the Br₂ electrode from the foam. In Zn-Zn cells, the Br₂ electrode and Nafion membrane were replaced with a Zn plate to keep the concentration of Zn in the electrolyte invariant during plating. A schematic diagram of the "flow-by" cell and ancillary equipment is shown in Fig 1.

A Masterflex peristaltic pump was used to circulate the electrolyte at flow rates of 150, 395, and 730 cm³/min. Flow rates were controlled within ± 5 cm³/min. The equivalent Reynolds numbers were 100, 250, and 500, respectively,¹ defined as

$$N_{re} = \frac{2du}{\nu} \quad [1]$$

where d is the free electrolyte gap (cm), u the electrolyte velocity parallel to the face of the foam (cm/s), and ν the kinematic viscosity (cm²/s). Pressure drops due to the electrolyte flow resistance were monitored throughout plating to within 5 mm Hg. The electrolyte entered into a free electrolyte gap at the bottom of the cell, through a slotted distributor strip, flowed by the face of the porous substrate, and exited through another free electrolyte space at the top. This aided in attaining uniform electro-

¹In Ref. (12), N_{re} was defined as ul/ν , where l = length of the electrode.

*Electrochemical Society Active Member.

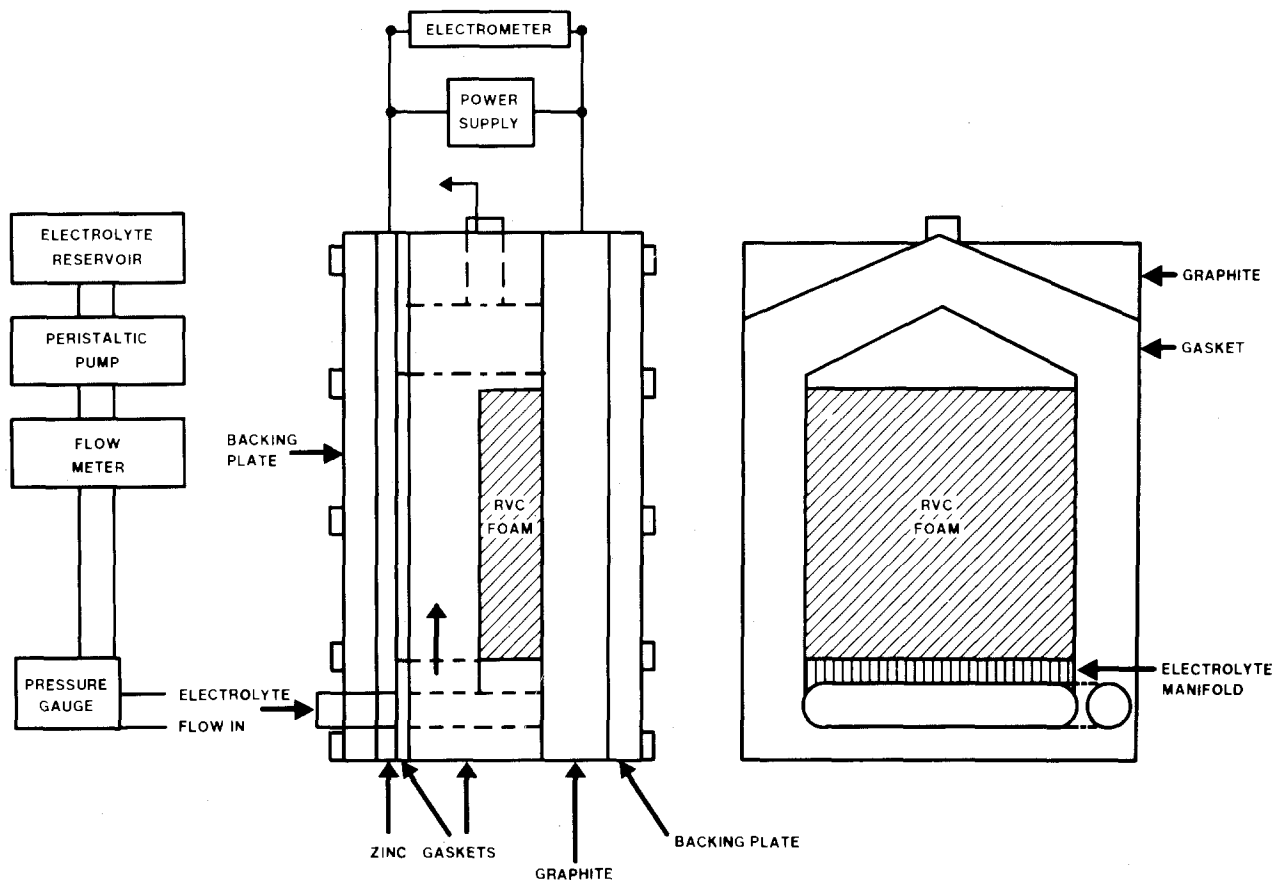


Fig. 1. Experimental cell schematic with ancillary equipment

lyte flow and Zn deposition across the electrode surface. A rubber gasket around the edges of the foam prevented the electrolyte from flowing directly through the foam. Flow of electrolyte past the foam face will cause some flow into the foam from momentum flux at the foam/electrolyte interface. As will be shown later, however, the dominant effect on zinc distribution in these platings was the ohmic resistance within the porous electrode. Substrates of two different pore sizes, namely, 0.25 and 0.55 mm (100 and 45 pores/in., respectively) were employed. The morphology of these foams has been described previously (11, 12). The void volume of each foam was about 97%. The values for surface area/volume ratio and resistivity are 26.2 cm²/cm³ and 0.5 Ω-cm for the 45 pore foam and 65.6 cm²/cm³ and 0.3 Ω-cm for the 100 pore foam, respectively. Zn deposition, corresponding to battery charging, was performed at room temperature at constant current densities from 25 to 100 mA/cm² for 1-8h. The electrolyte was an aqueous solution of 29% by weight ZnBr₂, 14% KBr, and 14% NaCl.

Reagent-grade chemicals and doubly distilled water were used in preparing the solution. Following plating, copious amounts of doubly distilled water were passed through the cell to wash the substrate free of electrolyte solution. Prior to analysis, electrodes were removed from the cell, dried, and cut into segments where applicable.

The effect of the various parameters on the Zn morphology was evaluated with optical microscopy, scanning electron microscopy, and x-ray radiography. X-ray radiographs were taken of the face and cross sections of the electrodes with a Hewlett-Packard, Faxitron series, x-ray system. Polaroid 55 positive/negative film was employed. A quantitative measure of the Zn density was obtained through densitometer measurements of the radiograph film negatives at a magnification of 20×. An automatic recording microdensitometer (Joyce-Loebel Model MKIIC) with slit dimensions 8 × 0.04 mm was employed for this purpose. The quantitative results, obtained with the densitometer, were compared with scanning electron micrographs of electrode surfaces and cross sections. The

morphology of the surface was examined over the entire 100 cm² area in one x-ray radiograph. In order to examine the Zn profile perpendicular to the foam, three 6 mm wide segments were cut from the top to the bottom of the electrode. These segments, taken from the center and each side of the electrode, were placed on edge during x-ray radiography. X-ray radiographs were taken of the bottom, middle, and top of each of the three segments, yielding nine traces for comparison of Zn distribution at different locations of the electrode. Unless otherwise stated, in comparing the effect of plating parameters, radiographs of the middle of the center segment were used. A detailed description of the x-ray radiography technique and its range of applicability has been described previously (12).

Results

Electrolyte flow rate.—The effect of electrolyte flow rate on Zn morphology and distribution within the porous substrate was examined for three flow rates of ~150, 395, and 730 cm³/min. These flow rates are equivalent to Reynolds numbers of 100, 250, and 500, and also equivalent to exchanging the electrolyte in the cell once every 15-30s. Plating was performed at 25 mA/cm² for 4h on 1.2 mm thick 100 pore foams. Scanning electron micrographs (SEM's) of the cross section of the 100 pore foam for $N_{Re} = 100$ and 500 are presented in Fig. 2. The SEM's relate to a slice taken from the center of the middle segment at a magnification of 14×. The major features of the Zn deposit evident from the SEM's are a nodular Zn growth at and near the surface of the foam with a tight Zn deposit on the internal strands of the foam. This nodular deposit is markedly different from the generally loose, mossy deposits obtained in stationary electrolyte under identical plating conditions (11). The effect of increasing flow rate is more evident in the x-ray radiographs shown in Fig. 3. Radiographs are of the entire length of the middle segment. The dark areas correspond to Zn and the light areas to voids or C foam. Plotted in Fig. 4 are densitometer traces taken from the center of the three segments shown

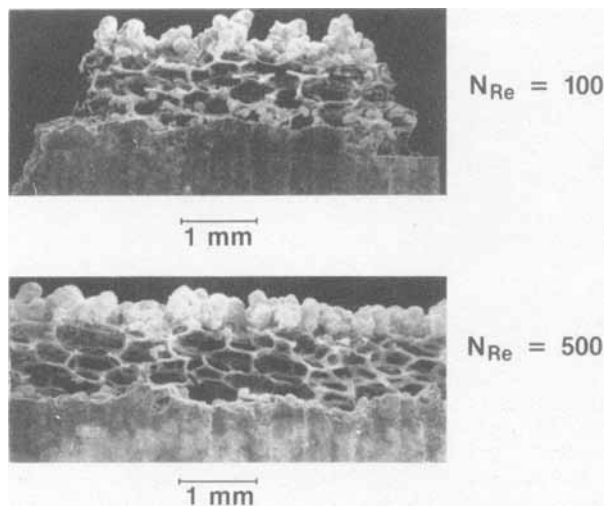


Fig. 2. SEM of 100 pore foam plated at 25 mA/cm² for 4h. Top: $N_{Re} = 100$. Bottom: $N_{Re} = 500$.

in Fig. 3. In this graph, $X = 0$ represents the foam/electrolyte interface and $X = 1.2$ mm the foam/backing plate interface. Negative values of " X " correspond to Zn extending from the foam into the free electrolyte gap. It can be seen from Fig. 3 and 4 that the pivotal effect of increasing flow rate is a decrease in Zn deposit thickness and an increase of Zn penetration into the foam. Although increasing the Reynolds number produces thinner, more compact, and smoother Zn deposits, it is obvious that Zn deposition has overwhelmingly occurred on and near the foam surface and decreased steeply within the first 0.2 mm into the foam. Listed in Table I are the amounts of Zn deposited in three relative areas of the substrate; on the surface extending into the free electrolyte gap $X/L < 0$, within the interior of the foam $0 \leq X/L \leq Y$, and near the graphite plate $Y \leq X/L \leq 1$. The dimensionless distance Y was chosen as the position at which the Zn density increased near the backing plate. As can be seen from Table I, the amount of Zn extending from the surface into the electrolyte decreased from 66% to 35% when increasing the Reynolds number, with a corresponding increase in Zn within the foam from 14% to 28%.

Substrate morphology.—The pore size of the substrate affects the specific interfacial area and the specific conductance of the electrode. The effect of two different pore sizes for constant electrode thickness (2 mm) was de-

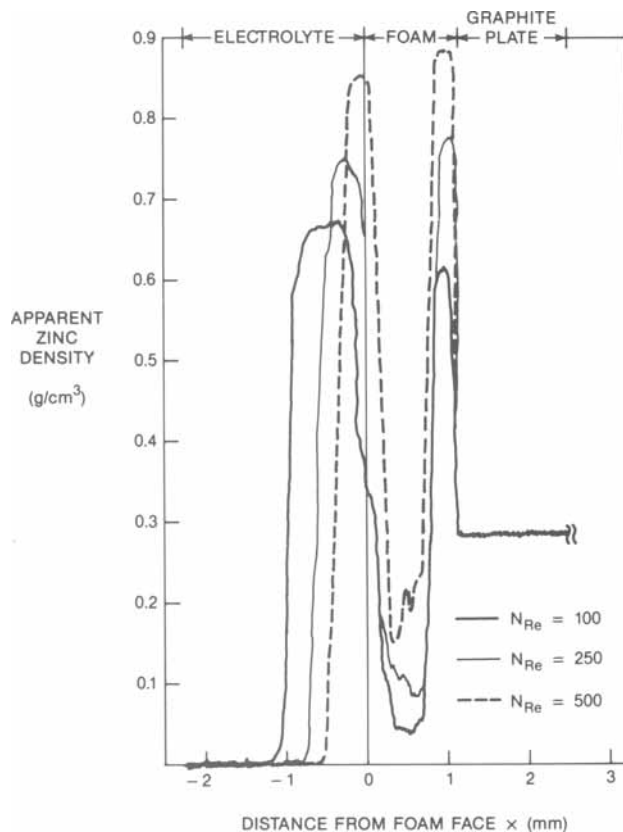


Fig. 4. Densitometer traces of 100 pore foam shown in Fig. 2 and 3. Traces taken from the center of each segment.

scribed previously (12). In Fig. 5-7, the effect of varying the electrode thickness, L , for constant pore size is shown. The electrode thicknesses were chosen to facilitate the comparison of constant pore length to pore diameter (L/D) ratios. Figure 5 shows x-ray radiographs of the cross sections for two 45 pore foams plated at 25 mA/cm² for 4h with $N_{Re} = 100$. The top radiograph represents a 2 mm thick foam; $L/D = 3.5$. The bottom three radiographs are for a 4.5 mm thick foam ($L/D = 8$), taken of the left, middle, and right segments of the electrode. Comparison of the bottom three radiographs demonstrates the uniformity of the Zn deposit across the face of the electrode. The cross-sectional radiographs of Fig. 5 were evaluated

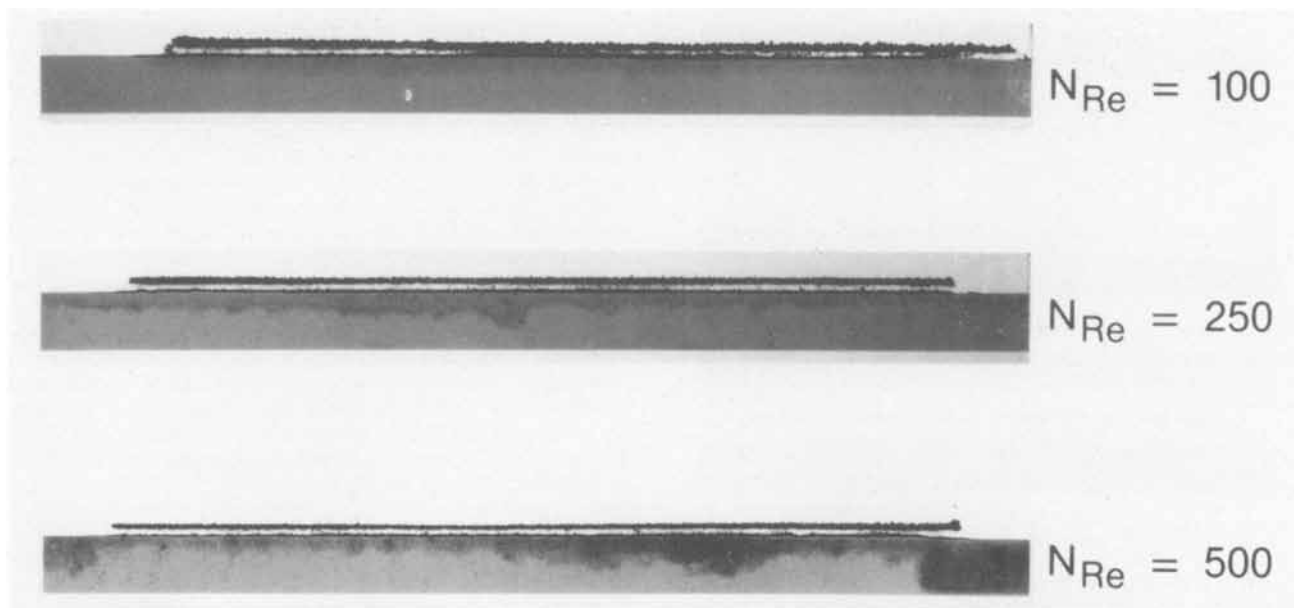


Fig. 3. Effect of flow rate with 100 pore foam. X-ray radiography of cross sections of 100 pore foam plated at 25 mA/cm² for 4h. Top: $N_{Re} = 100$. Middle: $N_{Re} = 250$. Bottom: $N_{Re} = 500$.

Table I. Fraction of zinc deposited on and in carbon foam

Foam	Thickness (mm)	L/D	N_{Re}	On surface $X/L < 0$	In interior $0 < X/L < Y$	Near plate $Y < X/L < 1$	Y
45 pore	2	3.5	100	0.52	0.12	0.36	0.6
45 pore	4.5	8	100	0.41	0.32	0.27	0.8
100 pore	2	8	100	0.37	0.38	0.30	0.63
100 pore	1.2	4.7	100	0.66	0.14	0.20	0.66
100 pore	1.2	4.7	250	0.49	0.18	0.34	0.6
100 pore	1.2	4.7	500	0.35	0.28	0.37	0.6

with the densitometer and the results are shown in Fig. 6. In this graph, $X = 0$ corresponds to the foam/electrolyte interface for each electrode, $X = 2$ mm to the foam/graphite plate interface for the 2 mm thick foam, and $X = 4.5$ mm to the foam/graphite plate interface for the 4.5 mm foam. The corresponding densitometer traces of 1.2 and 2 mm thick 100 pore foams, $L/D = 4.7$ and $L/D = 8$, are presented in Fig. 7. All four electrodes exhibited the same extremely nonuniform deposition of Zn. A predominant portion of Zn was present on the foam surface, dropping off sharply into the interior of the foam and rising sharply near the graphite backing plate. Changing the foam thickness had little effect on how far the Zn extended into the free electrolyte gap. In all four cases, Zn extended ~1 mm beyond the foam face. The extension of the Zn beyond the foam face, or dendritic nature of Zn morphology, was primarily a function of the electrolyte flow rate, as shown in Fig. 4. Increasing the substrate thickness did, however, increase the amount of Zn present within the porous substrate. This effect is clearly obvious in Fig. 7 for the 100 pore foam. Although not quite as obvious in Fig. 6 for the 45 pore foam, Table I shows a marked increase of Zn within the foam's interior from 12% to 32% of the total Zn. The corresponding increases for the 100 pore foam were from 14% to 38% of the total Zn. It is of interest to note that independent of pore size, the same L/D ratio of 8 resulted in essentially the same distribution of Zn. The 45 pore foam $L/D = 8$ resulted in a Zn distribution shown in Table I of 41%, 32%, and 27%, while the 100 pore foam $L/D = 8$ was correspondingly 37%, 33%, and 30%.

Electrolyte composition and current density.—The composition of the electrolyte, that is, the $ZnBr_2$ concentration, supporting electrolyte (inorganic salts), and organic dendrite inhibitors, plays a significant role in determining the morphology of the Zn plate in stationary electrolyte (11). The use of certain inhibitors with solubilizers produced Zn deposits which were smoother and more

uniform and reached farther into the interior of the foams than in electrolytes without inhibitor (13, 14).

Figures 3 and 4 above show that increasing electrolyte circulation, even without the use of inhibitors, produces increasingly less dendritic/nodular deposits. However, a significant fraction of the Zn is deposited on the surface of the foam. In the following experiments, the combined effects of electrolyte flow, $N_{Re} = 250$, and the use of inhibitors was examined. In these experiments, 1% by weight of FC170:L4048² (0.333 FC170 + 0.667 L4048) and 10% by weight of butyrolactone were added to the electrolyte. Platings were carried out at 25 mA/cm² for 4 and 8h, and at 100 mA/cm² for 1 and 2h, thus resulting in charge densities of 100 and 200 mAh/cm², respectively. Photomicrographs of the face and cross sections after plating at 25 mA/cm² for 4 and 8h are presented in Fig. 8 and 9. The intimate coating of the C strands with a Zn film and the lack of large nodular protrusions are clearly evident in the center micrograph of Fig. 9, referring to 4h plating and the use of 1% inhibitor. For comparison, the upper micrograph shows the pronounced nodular Zn growth and the lack of Zn penetration into the foam if no inhibitor is added to the electrolyte. Continued plating for 8h resulted in continued filling of the voids with little protrusion beyond the face of the electrode. The most salient feature in the photomicrographs for 8h plating is the greatly enhanced throwing power into the foam. The Zn extended on the average 1-1.5 mm into the 2 mm foam. The average density of this Zn layer was 1.63-2.44 g/cm³, as compared to ~0.6 g/cm³ in the absence of the inhibitor (see Fig. 3 and 4). Compared to a theoretical density of Zn equivalent to 7.14 g/cm³, the density of these Zn layers is 23%-34% of the theoretical density.

The effectiveness of the inhibitor at 25 mA/cm² shown in Fig. 8 and 9 is dramatic. For the battery designer, however, larger current densities are desirable since this results in higher power density and, hence, lower cost per unit of power and energy stored. Shown in Fig. 10 and 11 are results for identical test conditions as for Fig. 8 and 9, but at 100 mA/cm² for 1 and 2h, which corresponds to identical amounts of charge passed and Zn plated. The salient feature shown in these figures, like that of Fig. 8 and 9, is the excellent penetration of the Zn into the porous substrate. At a charge density of 100 mAh/cm², there was no discernible difference in the smoothness of the surface for plating of 100 mA/cm² compared to 25 mA/cm². However, at a charge density of 200 mAh/cm², the surface of the electrode plated at 100 mA/cm² gave evidence of increased roughness over the plating at 25 mA/cm². In addition, enhanced plating at the edges became evident when plating at 100 mA/cm² for 2h. This is shown in the three radiographs of Fig. 11, representing cross sections of the left edge, center segment, and right edge of the foam electrode. Such edge effects were absent at 25 mA/cm². The Zn penetration into the porous substrate at 100 mA/cm² was excellent. As can be seen from Fig. 11, the Zn was deposited completely into the foam with remarkably uniform density.

Discussion

It is obvious from these results that the effects and interactions of the various plating parameters are complex. For example, changing the pore size of the substrate

²These fluorinated surfactants are products of the 3M Corporation.

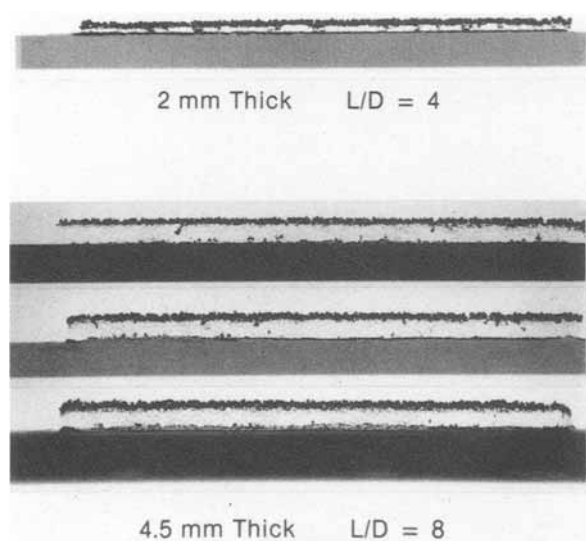


Fig. 5. Effect of foam thickness with 45 pore foam. X-ray radiography of cross sections of 45 pore foams plated at 25 mA/cm² for 4h at $N_{Re} = 100$. Top: 2 mm thick foam. Bottom three: 4.5 mm thick foam. Top: left edge. Middle: center segment. Bottom: right edge.

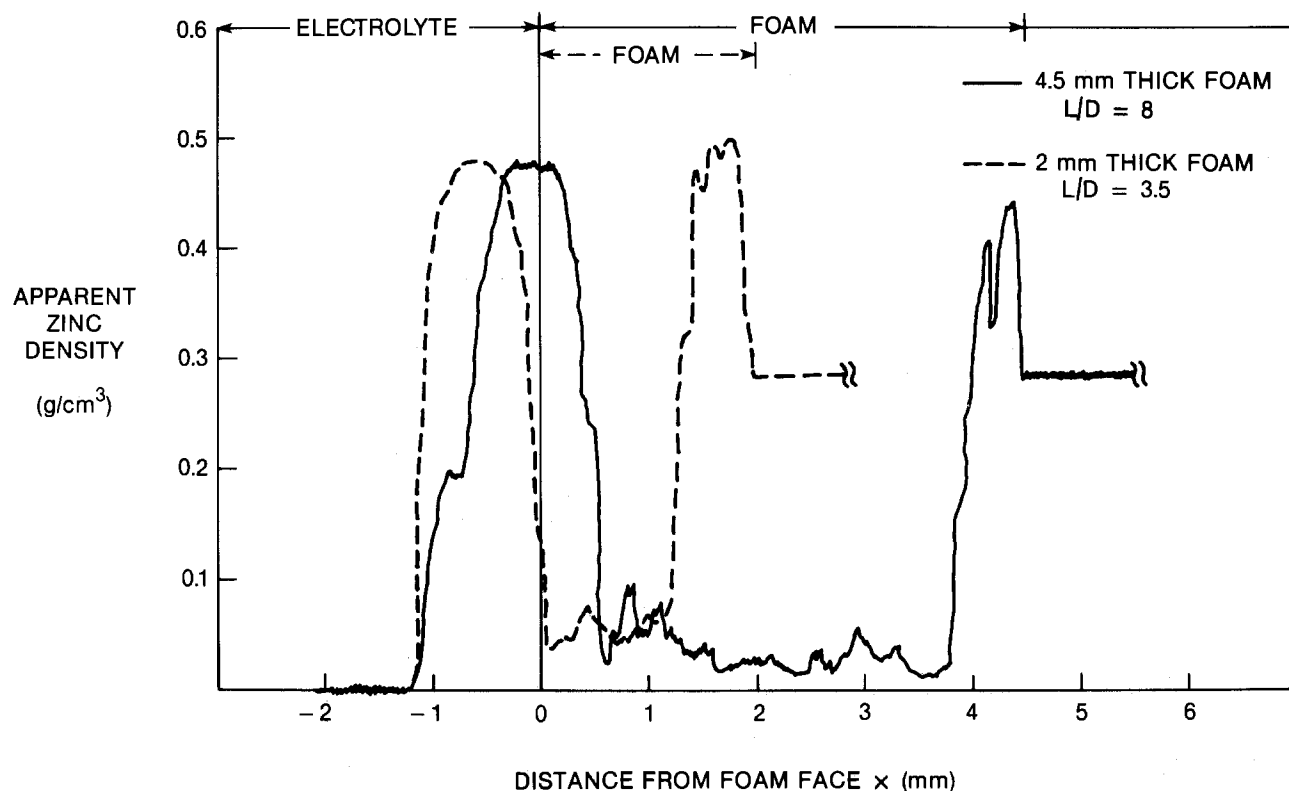


Fig. 6. Densitometer traces of 45 pore foams shown in Fig.5

changes the specific conductance of the substrate, which affects the relationship between the conductance of the matrix and the conductance of the electrolyte; this, in turn, alters the active region of the porous substrate and, hence, the true current density of plating. Additional complications arise with time during plating since Zn deposition increases the conductance of the solid matrix and decreases the conductance of the electrolyte due to increased tortuosity. Furthermore, particularly in the case of dendritic growth from the face of the substrate, the electrode thickness increased with time. Qualitative comparisons to available models on the performance of porous electrodes can, however, be made.

Newman *et al.* (7) in their review of porous electrode theory, present four dimensionless ratios which govern the current distribution within the porous substrate. The first parameter is a dimensionless current

$$\delta = \frac{\alpha_c F I L}{RT} \left[\frac{1}{\kappa} + \frac{1}{\sigma} \right] \quad [2]$$

where α_c is the charge transfer coefficient in the cathodic direction, F the Faraday constant, I the superficial current density, L the electrode thickness, R the universal gas constant, T the absolute temperature, κ the effective conductivity of the solution, and σ the effective conductivity of the substrate. For a system such as ours, with matrix conductivity much larger than the solution conductivity, the matrix potential is uniform. Under these conditions, the reaction distribution within the substrate depends on δ when Tafel kinetics predominate. For the case of linear reaction kinetics, the current distribution depends on the dimensionless exchange current

$$v = [\alpha_a + \alpha_c] \frac{F a i_0 L^2}{RT} \left[\frac{1}{\kappa} + \frac{1}{\sigma} \right] \quad [3]$$

where α_a is the transfer coefficient in the anodic direction, a the specific interfacial area, and i_0 the exchange current density. For large values of either δ or v , the current is not evenly divided between the solution and the

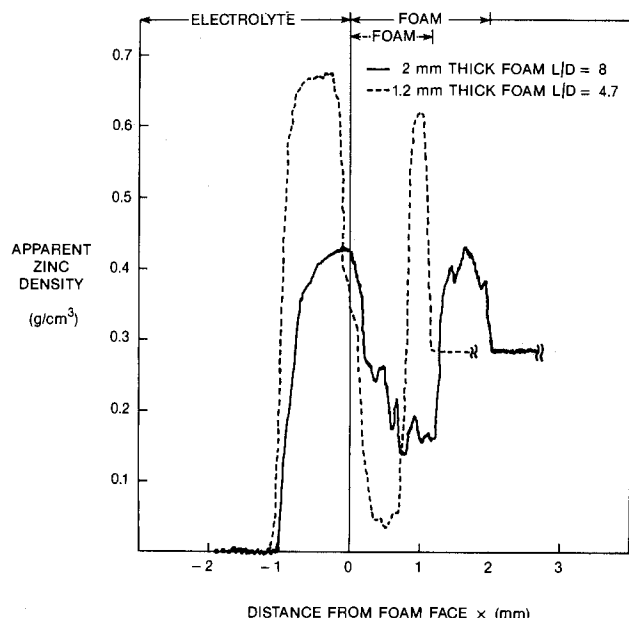


Fig. 7. Densitometer traces of 100 pore foams plated at 25 mA/cm², 4h $N_{Re} = 100$ for two thickness of 1.2 and 2.0 mm.

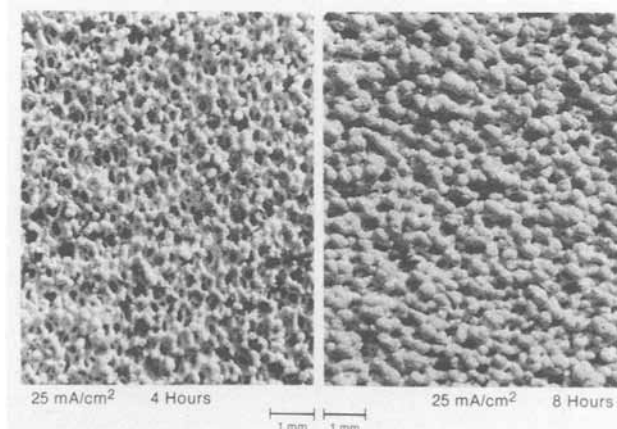


Fig. 8. SEM of the face of 100 pore foams plated at 25 mA/cm² for 4 and 8h, $N_{Re} = 250$, with 1% dendrite inhibitor added to the electrolyte.

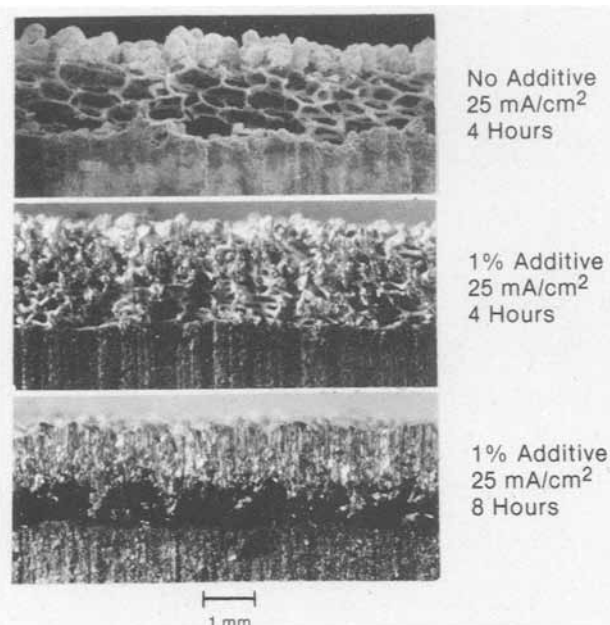


Fig. 9. Effect of FC170:L4048 additive with 100 pore foam. SEM of the cross section of 100 pore foams shown in Fig. 8 along with 100 pore foam without the dendrite inhibitor added to the electrolyte.

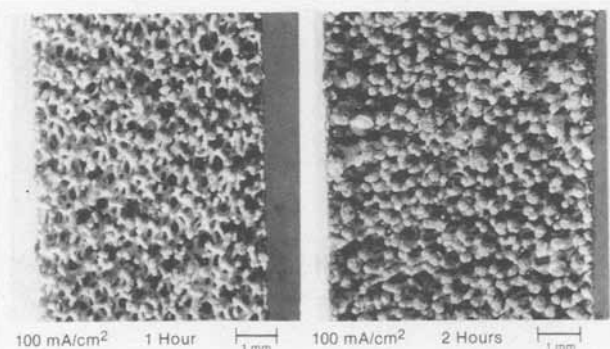


Fig. 10. SEM of the face of 100 pore foams plated at 100 mA/cm² for 1 and 2h, $N_{re} = 250$, with 1% dendrite inhibitor added to the electrolyte.

matrix and the reaction distribution is highly nonuniform, being much larger near the foam/electrolyte and foam/backing plate interfaces than in the center of the substrate. The remaining two dimensionless parameters are the ratio of transfer coefficients, α_a/α_c , and the ratio of the effective conductivities of the solution and matrix phases, κ/σ . For small values of κ/σ , the reaction occurs preferentially near the foam/electrolyte interface. The value of these four dimensionless ratios for each of the plating conditions presented earlier are listed in Table II. The numerical values for the parameters of Eq. [1] and [2] are given in the list of symbols.

Several conclusions can be drawn from the data of Table II. First, all our experimental conditions result in large values of δ and ν , i.e., > 1 . For the first four experiments, conducted at 25 mA/cm², the electrode overpotential was very small, so that linear kinetics prevailed. We would, therefore, expect the reaction distribution to depend on ν , which was very large, ranging from 6.8 to 15.9. The overpotential for the last experiment, carried out at 100 mA/cm², was considerably higher, so that Tafel kinetics were likely to dominate. The reaction distribution for this experiment would, therefore, depend on the parameter δ which was also very large: 8.31. For all plating experiments, therefore, a highly nonuniform plating distribution within the foam is expected, decreasing sharply from either foam interface into the center of the foam. Also, the ratio of κ/σ is very small due to an order of magnitude larger conductivity in the matrix compared to the electrolyte. This should result in preferential Zn deposition on

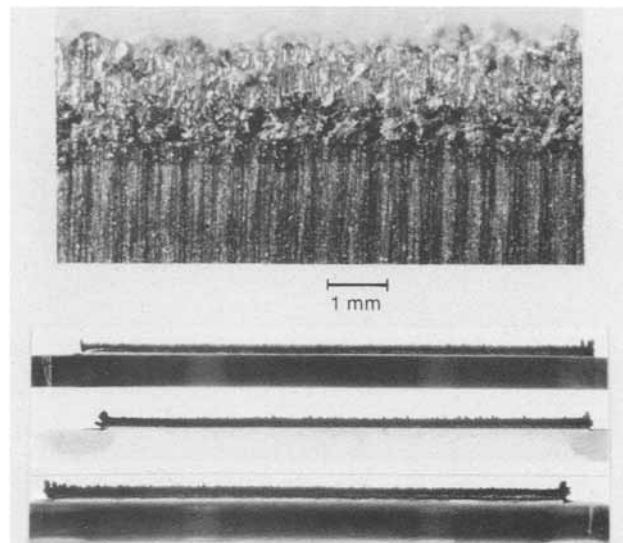


Fig. 11. SEM and x-ray radiographs of the cross section of 100 pore foam shown on the right of Fig. 10. SEM corresponds to center segment of electrode. Top radiograph taken of left edge; middle radiograph taken of center segment; bottom radiograph taken of right segment of the foam.

the foam/electrolyte interface at the expense of the foam/backing plate interface. Each of these theoretical predictions were verified experimentally, i.e., Zn deposition occurred preferentially near the foam/electrolyte interface decreasing sharply into the center of the foam. The large amount of zinc found on the backing plate is not adequately explained by the model of Newman *et al.* (7). It should be noted, however, that the zinc deposit on the solid backing plate should be denser than on the porous strand at equivalent current densities. The penetration of the Zn into the foam from the foam/electrolyte interface can be related to the ratio L/ν defined as

$$L/\nu = \frac{RT\kappa\sigma}{[\alpha_a + \alpha_c] a i_0 F [\kappa + \sigma]} \quad (\text{cm}) \quad [4]$$

Predicted values for the Zn penetration, L/ν , for the experimental conditions examined here, as listed in Table II, are very small, i.e., 0.018-0.028 cm. With the exception of 100 pore foam 0.2 cm thick, these values correlate well with penetration depths observed, namely, 0.01-0.05 cm. It is clear from these analyses that ohmic effects are dominating the utilization of porous C foams. It should be noted that, with time, the values of Table II change. As Zn is deposited on the face of the foam, σ , a , and L increase, while κ decreases due to increased tortuosity. The combined effect is to produce sharper deposits located closer to the electrolyte/foam interface. This effect is enhanced at low flow rates where a more dendritic deposit predominates the Zn morphology.

Existing theoretical models do not address the effect of dendrite inhibitors on Zn deposit morphology. We will discuss these effects qualitatively. The two major effects of the organic inhibitors are the virtual elimination of dendrite growth and greatly increased throwing power. The latter means excellent plating into the porous substrate and significantly increased Zn deposit density. Separate studies of the reductive stability of the organic inhibitor had shown unmitigated inhibitor effectiveness

Table II. Summary experimental test conditions

Substrate	L (cm)	I (A)	κ/σ	δ	ν	L/ν (cm)
45 pore	0.2	0.025	0.1	2.0	7.1	0.028
45 pore	0.45	0.025	0.1	4.5	15.9	0.028
100 pore	0.12	0.025	0.06	1.25	6.8	0.018
100 pore	0.20	0.025	0.06	2.08	11.4	0.018
100 pore	0.20	0.100	0.06	8.31	11.4	0.018

over more than 750 cyclic platings (11). These studies also demonstrated excellent stability to bromine after exposure to 1% by weight Br₂ for 6 months at 55°C. Therefore, we believe the inhibitor to be active by nondestructive adsorption on the most active growth sites during plating followed by desorption during anodic dissolution (discharge). The adsorption of the inhibitor is likely to decrease the rate of the charge-transfer reaction such that diffusion is no longer rate limiting. Under these conditions, it is generally known that dendritic growth no longer occurs and that the throwing power is increased owing to the better penetration of the electric field into the pores.

Conclusions

The application of x-ray absorption coupled with densitometry and microscopy allows quantitative analysis of Zn deposition within a porous C foam. Using these techniques, it is demonstrated that high electrolyte flow rates, high L/D ratio, and thicker foams all aid in producing more uniform Zn deposits. Overall, within the range of parameters studied, optimal results were obtained with 2 mm thick 100 pore RVC foams with electrolyte flow rates corresponding to Reynolds numbers close to 500. The Zn distributions obtained correspond to the primary current distribution modeled by Newman *et al.*, *i.e.*, highly nonuniform deposits decreasing sharply from either foam interface into the center of the foam with predominate deposition near the foam/electrolyte interface. The most striking effect on Zn morphology was obtained by adding to the electrolyte an organic dendrite inhibitor-solubilizer combination, consisting of certain fluorosurfactants and butyrolactone. The use of these inhibitors yielded dendrite-free Zn deposits well into the porous foam substrate when plating at current densities as high as 100 mA/cm² for 2h, equivalent to charge densities up to 200 mAh/cm².

Acknowledgment

This work was supported in part by the U.S. Department of Energy under Contract no. EY-76-C-02-2950. The help of Ms. A. M. Davies in performing the densitometry is gratefully acknowledged.

Manuscript submitted April 13, 1984; revised manuscript received Dec. 18, 1984.

General Electric Company assisted in meeting the publication costs of this article.

LIST OF SYMBOLS

a	specific interfacial area (cm ⁻¹); 45 pore = 26.2, 100 pore = 65.6.
d	free electrolyte gap (cm)
D	electrode pore diameter (cm)
F	Faraday's constant (2.306×10^4 cal/V-eq)
i_0	exchange current density (0.117 A/cm ²) ³
I	superficial current density to an electrode (A/cm ²)
L	electrode thickness (cm)
R	universal gas constant (1.987 cal/mol K)
T	absolute temperature (K)
α_a	transfer coefficient in anodic direction (0.5)
α_c	transfer coefficient in cathodic direction (0.5)
δ	dimensionless current density defined in Eq. [2]
κ	effective conductivity of the solution (0.202 $\Omega^{-1}\text{-cm}^{-1}$)
u	electrolyte velocity parallel to the face of the foam (cm/s)
v	square root of a dimensionless exchange current defined in Eq. [3]
σ	effective conductivity of the substrate; 45 pore = 2 $\Omega^{-1}\text{-cm}^{-1}$, 100 pore = 3.33 $\Omega^{-1}\text{-cm}^{-1}$
ν	kinematic viscosity of the electrolyte (0.005 cm ² /s)

³Unpublished results of authors conducted under contract of Ref. (11).

REFERENCES

1. P. C. Symons, U.S. Pat. 3,713,888 (1973).
2. C. H. Chi, P. Carr, and P. C. Symons, in "Proceedings 14th IECEC," Boston, MA, Aug. 1979, IECEC (1979).
3. F. G. Will, in "Proceedings 12th IECEC," Washington, DC, Aug. 1977, p. 250, IECEC (1977).
4. R. A. Putt, in "Proceedings 16th IECEC," Atlanta, GA, Aug. 1981, IECEC (1981).
5. R. J. Bellows, P. Grimes, H. Einstein, E. Kantner, T. Malachuk, and K. Newby, *IEEE Trans. Vehic. Technol.*, **vt-32**, 26 (1983).
6. A. Charkey, in "Proceedings 11th IECEC," State Line, NV, Sept. 1976, p. 452, IECEC (1976).
7. J. Newman and W. Tiedemann, *AIChE J.*, **21**, 25 (1975).
8. W. G. Sunu and D. N. Bennion, *This Journal*, **127**, 2007 (1980).
9. J. McBreen and E. Gannon, *ibid.*, **130**, 1667 (1983).
10. J. McBreen and E. Gannon, Paper 26 presented at the Electrochemical Society Meeting, Washington, DC, Oct. 9-14, 1983.
11. F. G. Will, C. D. Iacovangelo, J. J. Jackowski, and F. W. Secor, U.S. Department of Energy, Final Report C00-2950-1, March 15, 1978.
12. F. G. Will and C. D. Iacovangelo, *This Journal*, **131**, 590 (1984).
13. F. G. Will and F. F. Holub, U.S. Pat. 4,040,916 (1977).
14. F. G. Will, U.S. Pat. 4,074,028 (1978).

Electrical Conductivity and Specific Mass of the Molten LiOH-LiNO₃, NaOH-NaNO₃, and KOH-KNO₃ Mixtures

P. Claes and J. Glibert

Department of Inorganic, Analytical and Nuclear Chemistry, Catholic University of Louvain, B-1348 Louvain-la-Neuve, Belgium

ABSTRACT

The specific mass, the conductivity, and the equivalent conductance of the mixed systems LiOH-LiNO₃, NaOH-NaNO₃, and KOH-KNO₃ were determined in the whole concentration range. The specific mass isotherms present unexplained irregularities and the conductances exhibit large departures from the additivity law of the transport properties of the pure components of the mixtures. The activation energies for the equivalent conductance show, for the three investigated systems, a maximum in the vicinity of the 50 mole percent composition. These departures from additivity are explained by invoking a change of transport mechanism when the composition of the mixtures shifts from one pure component to the other.

Results reported in the literature suggest that charge transport in hydroxide melts could proceed by a mechanism other than that operating in most salts (1, 2). Shvedov and Yvanov (3) measured transference numbers

near unity for hydroxide ions in molten alkali hydroxides. Hydroxide ions take thus the largest part of charge transport in the case of molten hydroxides contrary to what happens in fused lithium, sodium, or potassium salts

where the transference numbers of the cations are larger than those of the anions (4, 5).

Furthermore, the activation energies of transport properties of molten hydroxides are significantly lower than those of fused salts (1, 6, 7).

It seemed as if it would be interesting to investigate the concentration dependence of the conductivity of molten mixtures of alkali hydroxides and alkali salts. Mixtures of alkali salts generally exhibit negative departures from an additivity law of the conductivities. It seems reasonable to expect particularly large departures when the transport mechanism in the pure components of the mixture are different.

The melting points of molten hydroxides and of molten nitrates are quite comparable; mixtures of these compounds could thus be investigated in the whole concentration range and seem to be very suitable systems for such studies.

Experimental

Materials and device.—Chemicals were analytical-grade Merck reagents. Water elimination occurred by maintaining the melt at temperatures above 673 K under a stream of dry nitrogen during at least 12h. The stream of nitrogen was maintained during the experiments.

The container was a silver crucible placed in a Pyrex cell fitted with ground glass joints. Compact alumina (Degussa Al 23), which is specially stable in neutral or slightly acidic conditions, was selected as material for the bubbling tube and for the sheath of iron-constantan thermocouple.

Conductivity measurements.—The same conductivity cell was used as in previous work (1, 2). It was composed of two compact alumina "pseudo-capillary" electrodes of 4 mm id containing platinum conductors ended by coils located at about 2 cm above the lower end of the alumina tubings. The cell factor measured by standardization in pure molten potassium nitrate was ca. 25 cm⁻¹. This value is low as far as determinations in ionic liquids are planned and requires thus the use of a multifrequency LCR meter (Hewlett-Packard 4274 A) allowing measurements up to high frequencies in order to eliminate polarization effects.

The measurements were carried out after selection of a series equivalent circuit mode. The bridge enables to use a four terminal pair wiring giving the best accuracy by minimizing any stray capacitance and residual inductance in the test leads or test fixture. The tension applied between the electrodes was of the order of 250 mV.

The measured impedance decreased when the frequency was increased, a minimum value was reached from about 20 kHz. The LCR bridge allows the determination of the resistance, of the impedance, and of the angle θ between the impedance vector and the real axes. When the minimum value is measured for the impedance, (i) the impedance equals the resistance, meaning that the capacitive factor is negligible, and (ii) θ takes a minimum value.

Specific mass measurements.—Specific mass measurements were carried out by weighing a calibrated silver

bob dipped into the melt and hung on the pan of an analytical balance (Mettler) by means of a thin platinum wire. As for conductivity, the reproducibility of the measurements was quite good.

Results

The conductivity (κ) and the specific mass (ρ) of the three binary mixtures LiOH-LiNO₃, NaOH-NaNO₃, and KOH-KNO₃ were measured as a function of temperature at compositions ranging from pure nitrate to pure hydroxide. The equivalent conductances (Λ) were calculated according to the following equation where M^{eq} is the average weight of the electrochemical equivalent

$$\Lambda = \frac{\kappa M^{eq}}{\rho}$$

taking into account the molar fractions (X) of the components

$$M^{eq} = X_{MeOH}M_{MeOH} + X_{MeNO_3}M_{MeNO_3}$$

The temperature ranges extend from a few degrees above the melting point of the investigated pure compound or mixture up to 805, 723, and 761 K, respectively, for the lithium, sodium, and potassium systems. In the case of mixtures with high nitrate contents, the higher temperature was always significantly lower in order to avoid any decomposition.

The temperature dependences of the three investigated properties (P) are correctly described by a linear relationship where b and m are constants for a given system

$$P = b + mT \text{ (K)}$$

Tables I, II, and III give the values of these coefficients as well as the corresponding correlation factors for the conductivity, the specific mass, and the equivalent conductance of the lithium, sodium, and potassium containing mixtures.

In some cases, at the highest investigated temperatures, deviations of the temperature dependence from linearity were recorded. Therefore, temperature ranges were also included in Tables I-III. The upper limit is either the temperature above which departures from linearity are observed or the last investigated temperature.

The composition dependence of the specific mass, of the conductivity, and of the equivalent conductance are shown for the three mixtures in Fig. 1-6. Because of the lack of overlapping of the temperature ranges available for the sodium containing mixtures and for the lithium containing mixtures, isotherms at 723 K are compared for the lithium and potassium systems, while experimental results recorded at 673 K are shown for the sodium and potassium systems.

Discussion

Specific mass.—The specific mass of mixtures of molten salts generally changes with the composition in a regular way; the breaks observed in the specific mass isotherms of the mixtures of alkali hydroxides and alkali nitrates are rather uncommon (Fig. 1 and 4). These irregu-

Table I. LiOH-LiNO₃ system: m and b values for the specific mass, the conductivity, and the equivalent conductance: r^2 = correlation factor. The equivalent conductances were calculated using calculated conductivities and specific mass.

X_{LiNO_3}	κ			ρ			Λ		E_A (kcal/mol)	Temperature range (K)
	$m \times 10^3$	b	r^2	$m \times 10^3$	b	r^2	m	b		
0.00	4.87	-1.2321	0.999	-0.21	1.5554	0.996	0.0894	-25.552	2.424	745-805
0.10	4.85	-1.5181	0.998	-0.33	1.6831	0.997	0.1108	-40.811	2.934	729-813
0.20	5.15	-1.9959	1	-0.38	1.7574	0.999	0.1202	-48.397	3.340	547-749
0.30	4.74	-1.9347	0.997	-0.39	1.7944	0.999	0.1251	-53.517	3.611	647-748
0.40	4.49	-1.8628	0.997	-0.38	1.8127	1	0.1277	-54.651	3.808	471-718
0.50	4.17	-1.7157	0.999	-0.47	1.8998	0.999	0.1298	-55.298	3.844	581-713
0.60	4.29	-1.7378	0.999	-0.47	1.9373	0.998	0.1433	-60.278	3.736	488-708
0.70	4.27	-1.6690	0.999	-0.40	1.9012	0.997	0.1532	-62.115	3.493	548-698
0.80	4.58	-1.7810	1	-0.43	1.9544	0.997	0.1691	-68.492	3.428	559-702
0.90	5.05	-1.9236	0.999	-0.47	2.0003	0.997	0.2056	-81.941	3.384	545-749
1.00	5.35	-2.0005	0.999	-0.44	2.0011	0.999	0.2302	-90.136	3.293	543-698

Table II. NaOH-NaNO₃ system: *m* and *b* values for the specific mass, the conductivity, and the equivalent conductance: *r*² = correlation factor. The equivalent conductances were calculated using calculated conductivities and specific mass.

<i>X</i> _{NaNO₃}	κ			ρ			Λ		<i>E</i> _Λ (kcal/mol)	Temperature range (K)
	<i>m</i> × 10 ³	<i>b</i>	<i>r</i> ²	<i>m</i> × 10 ³	<i>b</i>	<i>r</i> ²	<i>m</i>	<i>b</i>		
0.00	5.59	-1.6037	0.997	-0.42	2.0426	0.999	0.1388	-44.374	2.447	628-723
0.10	5.27	-1.7329	1	-0.46	2.0642	1	0.1431	-50.330	2.830	603-678
0.20	4.83	-1.7040	0.997	-0.51	2.1064	0.999	0.1443	-54.027	3.045	589-693
0.25	4.93	-1.8588	0.999	-0.53	2.1216	1	0.1535	-61.002	3.490	598-702
0.30	4.76	-1.8349	0.999	-0.51	2.1146	1	0.1514	-60.625	3.640	575-673
0.40	4.66	-1.8596	0.998	-0.52	2.1364	1	0.1598	-66.119	3.809	583-681
0.50	4.38	-1.7391	0.998	-0.46	2.1043	1	0.1605	-65.985	3.800	589-693
0.65	4.19	-1.6335	0.998	-0.54	2.1642	1	0.1707	-69.293	3.399	571-699
0.725	4.06	-1.5288	0.998	-0.57	2.1911	1	0.1711	-67.030	3.134	562-655
0.80	3.76	-1.3203	0.999	-0.57	2.2026	1	0.1689	-63.075	3.071	573-692
0.90	3.75	-1.2967	0.999	-0.56	2.2087	1	0.1714	-62.805	3.001	600-688
1.00	4.31	-1.5265	0.995	-0.61	2.2568	1	0.2151	-81.738	3.043	613-685

Table III. KOH-KNO₃ system: *m* and *b* values for the specific mass, the conductivity, and the equivalent conductance: *r*² = correlation factor. The equivalent conductances were calculated using calculated conductivities and specific mass.

<i>X</i> _{KNO₃}	κ			ρ			Λ		<i>E</i> _Λ (kcal/mol)	Temperature range (K)
	<i>m</i> × 10 ³	<i>b</i>	<i>r</i> ²	<i>m</i> × 10 ³	<i>b</i>	<i>r</i> ²	<i>m</i>	<i>b</i>		
0.00	4.19	-1.0759	0.995	-0.57	2.1683	0.999	0.1538	-48.751	2.747	677-761
0.10	4.71	-1.6948	0.995	-0.50	2.1045	1	0.1783	-69.460	2.934	657-741
0.20	4.73	-1.8753	0.999	-0.51	2.1052	1	0.1897	-79.211	3.358	623-740
0.30	3.98	-1.5399	0.998	-0.51	2.1076	1	0.1696	-69.190	3.630	628-718
0.40	3.93	-1.6112	0.999	-0.52	2.1179	1	0.1766	-75.553	3.744	628-708
0.45	3.91	-1.6714	0.998	-0.66	2.2215	1	0.1818	-80.996	3.934	617-703
0.54	3.60	-1.4955	0.998	-0.66	2.2231	0.998	0.1749	-75.756	4.040	592-714
0.60	3.59	-1.5284	0.998	-0.68	2.2379	1	0.1791	-79.122	3.950	599-693
0.675	3.40	-1.4415	1	-0.64	2.2201	1	0.1749	-77.020	3.970	583-713
0.70	3.20	-1.3206	0.998	-0.64	2.2183	0.998	0.1700	-73.729	3.900	608-733
0.75	3.16	-1.2970	0.999	-0.62	2.2159	1	0.1701	-72.926	3.871	593-714
0.80	3.13	-1.2871	0.998	-0.63	2.2196	1	0.1745	-75.311	3.716	608-723
0.875	3.06	-1.2537	0.999	-0.62	2.2186	1	0.1753	-75.033	3.710	613-703
1.00	2.95	-1.1693	1	-0.73	2.3173	1	0.1821	-77.172	3.643	630-720

larities, which become less apparent when the temperature is raised, suggest the occurrence of some structural event between the components of the mixture at the corresponding composition.

Distectic or transition points are observed at a mole fraction 0.5 in the phase diagrams of the three investigated systems (8-10).

The breaks occurring in the specific mass isotherms could thus be the indication of the formation of a definite compound between the components of the mixture. However, two irregularities are observed for the composition dependence of the specific mass of the potassium system when only one distectic point is found in the phase diagram (9). Furthermore, only one break appears in the

specific mass isotherm of the NaOH-NaNO₃ system, whose phase diagram exhibits two distectic points (8). These discrepancies rule out any relationship between the shape of the density isotherms and the phase diagrams of the corresponding systems.

However, the conductivity isotherms of molten salt mixtures are quite continuous, whereas anomalies in such curves are often related to the phase diagram of the investigated systems (11, 12).

Finally, it must be pointed out that the scale used for the specific mass in these graphs is largely expanded; the features of the corresponding isotherms are thus of little absolute importance.

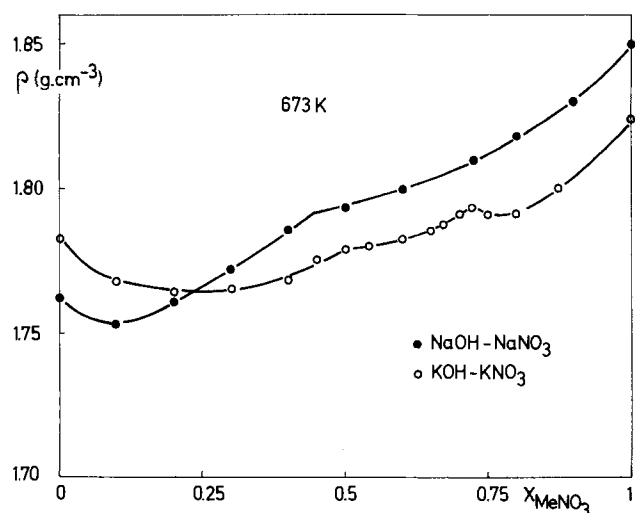


Fig. 1. Composition dependence of the specific mass of the NaOH-NaNO₃ and KOH-KNO₃ systems.

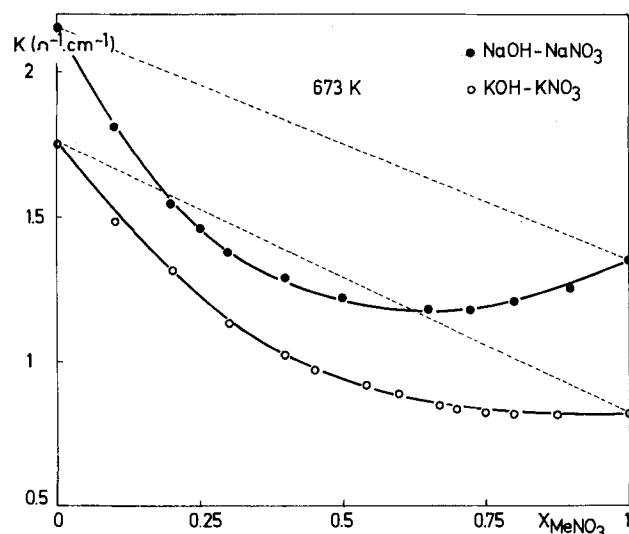


Fig. 2. Composition dependence of the conductivity of the NaOH-NaNO₃ and KOH-KNO₃ systems. Dotted line: additivity law.

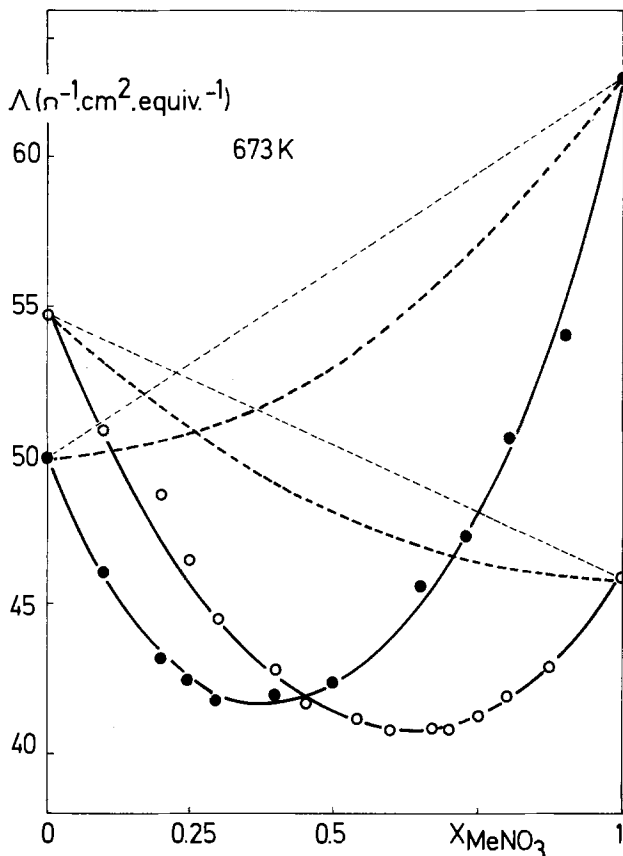


Fig. 3. Composition dependence of the equivalent conductance of the NaOH-NaNO₃ and KOH-KNO₃ systems. Dotted line: additivity law. Dotted curve: Markov law.

Nevertheless, we believe that the peculiarities of the experimental curves are significant. This opinion is supported by the following arguments.

1. As shown in Tables I, II, and III, the fits to the linear dependence of the temperature are quite good for all the

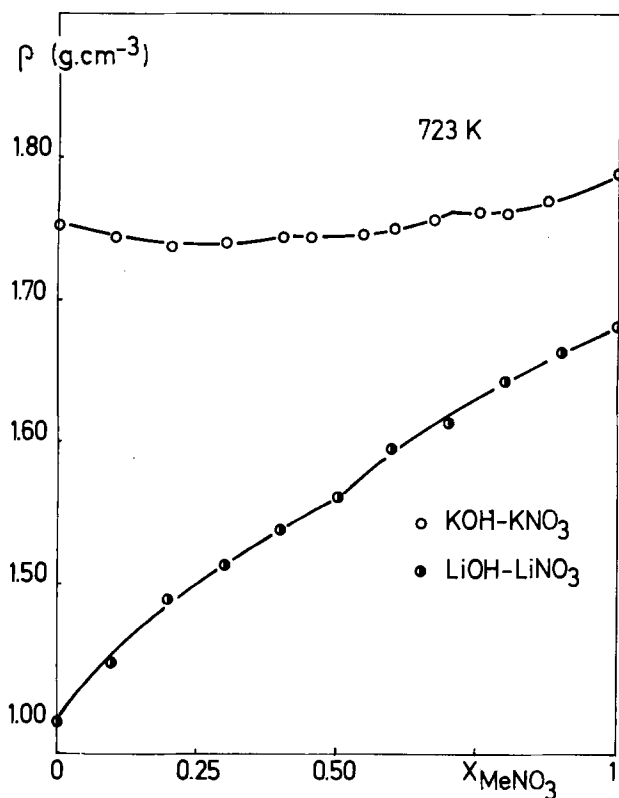


Fig. 4. Composition dependence of the specific mass of LiOH-LiNO₃ and KOH-KNO₃ systems.

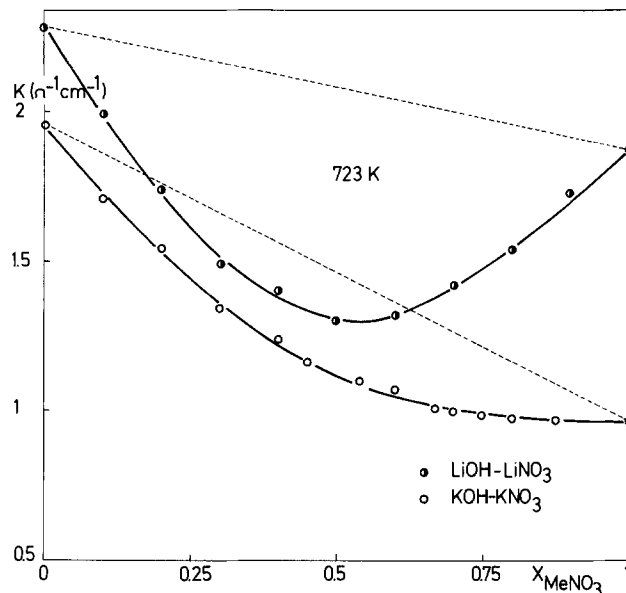


Fig. 5. Composition dependence of the conductivity of the LiOH-LiNO₃ and KOH-KNO₃ systems. Dotted line: additivity law.

investigated mixtures. A lack of accuracy of the compositions could eventually be at the origin of the discontinuities in the isotherms. However, errors as high as 10% must be invoked in order to explain the shapes of the experimental curves. Controls of the accuracy of the melt compositions have been carried out by analyzing melts prepared in the same way as those used in the reported experiments. The results of these tests are given in Table IV, which shows that the discordance between the compositions calculated from the weights of the components (A) and those determined from the titrations of the melts dissolved after cooling (B) never exceed 2%. Such departures could never explain the breaks observed in the experimental curves.

2. Errors in the composition of the melts would have the same consequences on the conductivity isotherms where such discontinuities are never observed.

3. The silver bob used for the specific mass measurements was regularly recalibrated.

4. The numerous experimental points reported on the diagrams were determined in a random sequence of compositions so that systematic errors could not be invoked in order to explain the break in the isotherms.

In the absence of any structural information about these mixtures, no grounded explanation could be provided at this time for the discontinuities in the specific mass isotherms.

Equivalent conductance of pure hydroxides in the molten state.—As shown in Fig. 3 and 6, the sequence of the equivalent conductances of the pure molten hydroxides is the following one

$$\Lambda_{\text{KOH}} > \Lambda_{\text{NaOH}} > \Lambda_{\text{LiOH}}$$

In the case of fused salts, the opposite sequence is always observed: the largest equivalent conductance is systematically measured for the lithium salt and the lowest one for the potassium salt (6). This observation strongly suggests that charge transport occurs in molten hydroxides by another mechanism than in fused salts.

In the case of molten alkali salts, the transference number of the cation is larger than that of the anion and the equivalent conductance is dictated mostly by the nature of the cation.

According to Shvedov and Yvanov, the transference numbers of the alkali cations are very low in pure fused hydroxides; they report, indeed, values of 0.1 ± 0.03 and 0.03 ± 0.03 , respectively, for sodium hydroxide and potassium hydroxide at temperatures ranging from 653 to 773 K (3). The fact that the equivalent conductances of these ionic liquids are quite different shows that the

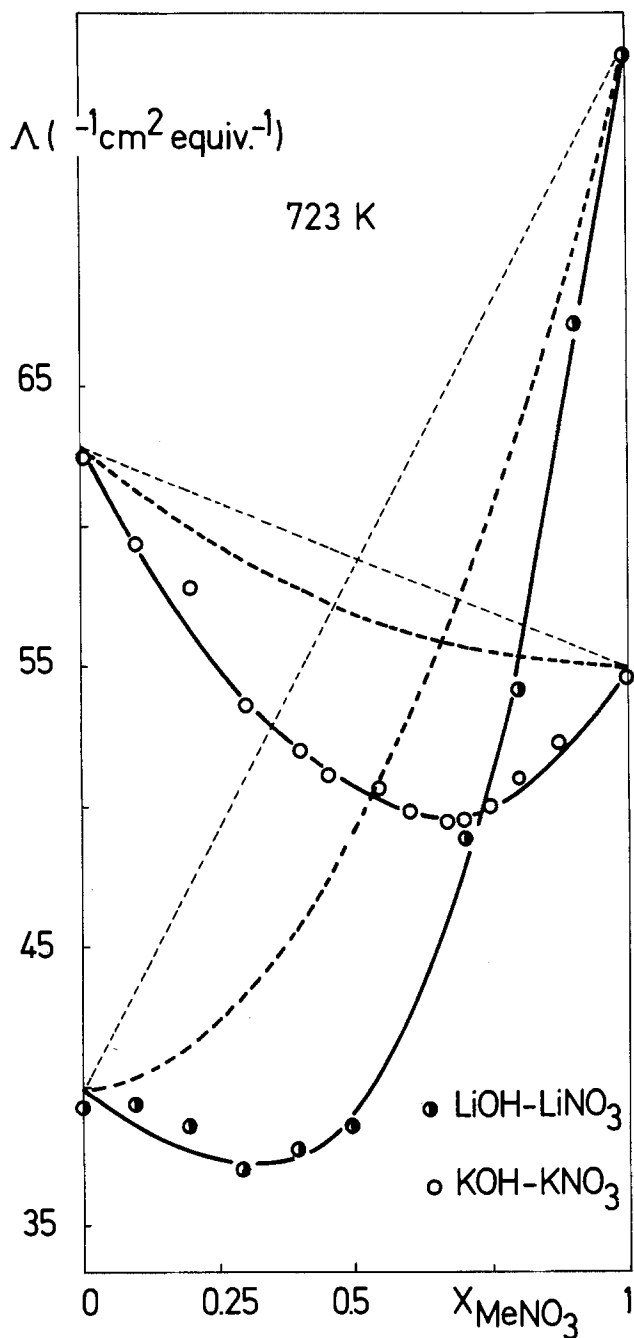


Fig. 6. Composition dependence of the equivalent conductance of the LiOH-LiNO_3 and KOH-KNO_3 systems. Dotted line: additivity law. Dashed curve: Markov law.

values of the equivalent conductances are still dictated by the nature of the cation but in an indirect way. Because of its strong polarizing electric field, the lithium cation interacts more strongly with hydroxide ions than do the other alkali ions and so hinders more effectively the reorientation and/or translation motions of hydroxide ions. Such an effect was evidenced by Duke and Owens on the mobilities of nitrate anions in alkali nitrate melts (5).

Transport properties of mixtures of nitrates and hydroxides.—As shown in Fig. 2, 3, 5, and 6, the concen-

Table IV. Controls of the accuracy of some melt compositions (648 K)

	A	B
X_{LiNO_3}	0.5	0.491
X_{NaNO_3}	0.4	0.402
X_{KNO_3}	0.4	0.407
X_{KNO_3}	0.7	0.692

tration dependence of the isotherms of conductivity and of equivalent conductance show large deviations from a linear relationship characteristic of the additivity of the properties of the pure compounds. Taking into account the fact that the conductance is a kinetic property, the Markov (13) equation is often invoked to describe the ideal behavior of mixtures of molten salts; the Markov law applied to the equivalent conductance of the investigated systems yields the dotted curves presented on the graphs of Fig. 3 and 6.

Deviations from additivity are characteristic of the mixed alkali effect; Moynihan (14) suggests using the ratios r_k and r_A in order to quantify this effect. These parameters are respectively defined as the ratios of the conductivity and of the equivalent conductance, predicted on the basis of an additivity law, to the experimental values for the mole fraction where the maximum deviation occurs. Such parameters could also be defined with respect to the Markov behavior in place of additivity; the corresponding r_A^M values would, of course, be somewhat lower since Markov law yields small negative departures from additivity.

Table V gives the values of r_k , r_A , and r_A^M for the three investigated systems. These ratios are compared with r_A values calculated from the results of Spedding (15) for the conductances of mixtures of molten alkali carbonates. Relatively strong negative deviations from additivity were indeed evidenced in this case (15-17).

The departures from a linear relationship are of the same order of magnitude for both types of mixtures and seem even to be slightly more important in the case of mixtures of nitrates and hydroxides. Furthermore, these deviations become less important when the temperature is increased.

As shown in Fig. 7, the concentration dependence of the activation energy for the equivalent conductance exhibits a well-defined maximum in the vicinity of the equimolar composition for the three investigated systems. Such a maximum is another criterion of the occurrence of a mixed alkali effect pointed out by Moynihan (14). A maximum of the activation energy is indeed found for mixtures of molten alkali carbonates (15). This effect is the largest in the case of the $\text{Li}_2\text{CO}_3\text{-K}_2\text{CO}_3$ mixture, where a positive departure 0.42 kcal/mol is found for a 50 mole percent composition.

This deviation yields, when it is compared with the value of the activation energy deduced from an additive behavior, a relative value of 9.29%.

Relative deviations of the activation energies for equivalent conductance of 24.06%, 34.15%, and 38.18% are calculated, respectively, for $\text{KNO}_3\text{-KOH}$, $\text{LiNO}_3\text{-LiOH}$, and $\text{NaNO}_3\text{-NaOH}$ equimolar mixtures. These deviations are significantly larger than those observed for molten alkali carbonate mixtures.

Despite the similarity of these results with the behavior of systems exhibiting a mixed alkali effect, the same explanation could not be invoked in this case. Indeed, in order to explain the mixed alkali effect, the polarization of the common anion by cations of different sizes or charges (18, 19) is put forward. The same transport mechanism is working in the whole concentration range, but it becomes more difficult when polarization effects become important. Such an explanation, which is satisfactory in the

Table V. Departures from additivity and from Markov behavior of transfer properties of mixtures of alkali nitrates and hydroxides and of mixtures of alkali carbonates

System	r_k	r_A	r_A^M
LiOH-LiNO_3 (723 K)	1.59	1.49	1.26
KOH-KNO_3 (723 K)	1.32	1.16	1.13
KOH-KNO_3 (673 K)	1.37	1.21	1.16
NaOH-NaNO_3 (673 K)	1.43	1.33	1.25
$\text{Na}_2\text{CO}_3\text{-K}_2\text{CO}_3$ (1203 K)		1.04	
$\text{Na}_2\text{CO}_3\text{-Li}_2\text{CO}_3$ (1153 K)		1.12	
$\text{Li}_2\text{CO}_3\text{-K}_2\text{CO}_3$ (1153 K)		1.42	

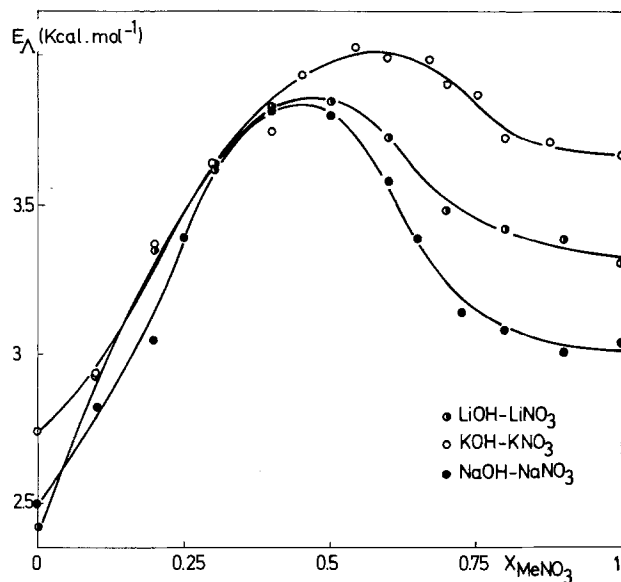


Fig. 7. Composition dependence of the activation energy for equivalent conductance of molten mixtures of alkali nitrates and alkali hydroxides.

case of mixed cation systems, could not be extended to a mixed anion effect because of the low polarizability of the cation.

It seems reasonable to refer to a real change in the transport mechanism: the charge conduction by molten nitrates and by molten hydroxides would occur by two incompatible processes. The occurrence of a proton-transfer mechanism has been suggested in order to explain the water and oxide ion dependence of the conductivity of the molten NaOH-KOH eutectic mixture (1, 2). This kind of charge transfer would be enhanced by hydrogen bridging between hydroxide ions. Greenberg and Hallgren (20) invoke indeed such interactions to explain some features of the infrared spectra of molten hydroxides. On the contrary, hydrogen bonding between hydroxide and nitrate ions would hinder the proton-transfer mechanism by reducing the interactions between hydroxide ions. However, the same interactions could provide an explanation for the hindrance of ionic rearrangements in molten alkali nitrates in the presence of hydroxide ions.

This type of explanation, which invokes a transition of transport mechanisms, even if it is not actually supported by experimental evidence, goes in the same sense as other experimental data, such as (i) the values of the transference numbers of hydroxide ions reported by

Shvedov and Yvanov, (ii) the sequence of the equivalent conductances of molten alkali hydroxides which is opposite to that found for the fused alkali salts, and (iii) the high positive departures from additivity of the activation energies for equivalent conductance.

Acknowledgments

One of the authors (J. G.) is much indebted to the Fonds National de la Recherche Scientifique de Belgique for financial assistance in this work.

Manuscript submitted Feb. 13, 1984; revised manuscript received Nov. 8, 1984.

The Catholic University of Louvain assisted in meeting the publication costs of this article.

REFERENCES

1. C. Dauby, J. Glibert, and P. Claes, *Electrochim. Acta*, **24**, 35 (1979).
2. C. Dauby, J. Glibert, and P. Claes, *ibid.*, **25**, 1077 (1980).
3. V. P. Shvedov and Y. A. Yvanov, *Russ. J. Phys. Chem.*, **39**, 396 (1965).
4. D. Topor, *Rev. Roum. Chim.*, **18**, 1311 (1973).
5. F. R. Duke and B. Owens, *This Journal*, **105**, 548 (1958).
6. G. J. Janz, F. N. Dampier, G. R. Lakshminarayanan, P. K. Lorenz, and R. P. T. Tomkins, "Molten Salts, Vol. 1, Electrical Conductance, Density and Viscosity Data," U.S. Dept. of Commerce, National Bureau of Standards, Washington, DC (1968).
7. P. Dulieu and P. Claes, *Bull. Soc. Chim. Belges*, **82**, 639 (1973).
8. E. von Jänecke, *Z. Anorg. Allg. Chem.*, **188**, 72 (1930).
9. A. G. Bergman and N. A. Reshetnikov, *Izv. Sektora Fiz. Khim. Anal. Inst. Obshchei Neorg. Khim. Akad. Nauk. S.S.S.R.*, **25**, 212 (1954).
10. E. V. Baranskaya and N. A. Reshetnikov, *Nauch. Tr. Irkutsk. Med. Inst.*, **95**, 143 (1969).
11. H. Bloom and E. Heymann, *Proc. R. Soc. London Ser. A*, **188**, 392 (1947).
12. Yu. K. Delimarskii and A. P. Samodelov, *Uch. Zap. Tsent. Nauch-Issled. Inst. Olovyan. Prom.*, **2**, 3 (1970).
13. Yu. K. Delimarskii and B. F. Markov, "Electrochemistry of Fused Salts," p. 32, Sigma, Washington, DC (1961).
14. C. T. Moynihan, *This Journal*, **126**, 2144 (1979).
15. P. L. Spedding, *ibid.*, **120**, 1049 (1973).
16. A. T. Ward and G. J. Janz, *Electrochim. Acta*, **10**, 849 (1965).
17. G. V. Vorob'ev, S. V. Karpachev, and S. F. Pal'guyev, *Fiz. Khim. Rasplavlen. Salei Shlakov Akad. Nauk SSSR Ural'sk. Filial Inst. Elektrokhim.*, *Tr. Vses. Soveshch. Sverdlovsk*, **1960**, 135 (1962).
18. C. T. Moynihan and A. V. Lesikar, *J. Am. Ceram. Soc.*, **64**, 40 (1981).
19. M. D. Ingram, C. T. Moynihan, and A. V. Lesikar, *J. Non-Cryst. Solids*, **38-39**, 371 (1980).
20. J. Greenberg and L. J. Hallgren, *J. Chem. Phys.*, **35**, 180 (1961).

Acidity and Thermochemical Stability of Molten Sodium Nitrate and Nitrite Mixtures

G. S. Picard, T. A. Flament, and B. L. Trémillon*

Laboratoire d'Electrochimie Analytique et Appliquée, associé au CNRS (LA 216), Ecole Nationale Supérieure de Chimie de Paris, F-75231 Paris Cedex 05, France

ABSTRACT

The influence of acidity on the thermochemical stability of molten sodium nitrate-nitrite mixtures used as heat-transfer fluids (as in the case of the French electrosolar power system called Thémis) has been demonstrated by considering the potential- pO^{2-} diagram relative to redox systems corresponding to these mixtures and been established from thermochemical data. The importance of fixing the pO^{2-} value with a buffer has been clarified. The couple $H_2O(g)/OH^-$, whose acid-base constant was previously determined, appears as the most efficient for this purpose. The potential- pO^{2-} diagram could be set up experimentally by studying the disproportionation of nitrite ion into nitrate and nitrogen monoxide and by determining the standard potential of the electrochemical system NO_3^-/NO_2^- by means of potentiometric measurements with a platinum electrode and with an yttria-stabilized zirconia membrane electrode indicator of pO^{2-} . This diagram has allowed us to specify, as a function of temperature, the boundary values of pO^{2-} which should not be gone beyond in order to avoid the decomposition of the mixtures as a result of the nitrite disproportionation.

Molten alkali nitrate-nitrite mixtures are known for their high heat capacities and their low melting points, which have led to their use as heat-transfer fluids at temperatures not greater than 723 K. The use of the mixture called HITEC [KNO_3 , 53- $NaNO_2$, 40- $NaNO_3$, 7 weight percent (w/o)] in the French electrosolar power system Themis, built by Electricité de France, makes necessary that this liquid can circulate in a thermal loop where the extreme working temperatures are 523 and 773 K. In view of this use, we have decided to study the chemical factors influencing the thermal stability of molten $NaNO_3$ - $NaNO_2$ mixtures.

The thermochemical decomposition of nitrates (1, 2) and nitrites (3-5) has been the subject of many studies, but the authors do not agree about the reactions which take place. It seems, nevertheless, well established that decomposition is accompanied by the release of nitrogen, nitrogen oxides, and oxygen, with the production of alkali oxide. Because of the complexity of these reactions, we have undertaken a preliminary study based on the existing thermochemical data (6). Reactions in these media put into play the redox systems of nitrogen which depend on the oxide anion activity. So, the results have been expressed in the form of a potential-(oxo)acidity diagram. This sort of presentation has already been used for alkali nitrates and for alkali nitrites by Conte and Casiadao (7), Marchiadi and Arvia (8), and by Haan and Van Der Porten (9), but not for their mixtures.

The calculated diagram has subsequently been specified by experimental determinations, and the results obtained have finally permitted the definition of the conditions which would be favorable to the thermochemical stability of the heat-transfer fluid.

We present here a part of our investigation concerning the effect of acidity, in studying especially the sodium nitrate-sodium nitrite-nitrogen monoxide systems.

Concentration units used for mixtures.—The alkali nitrate-nitrite mixtures have been shown to behave ideally (10). So, the activities of their components can be expressed by their mole fractions $N(NO_3^-)$ and $N(NO_2^-)$. The concentrations m of the dissolved (and consequently solvated) species, other than the "solvent" ones, are given in the molality scale. In particular, the acidity of the medium is defined by $pO^{2-} = -\log m(O^{2-})$ (11). The partial pressures of gases are in atmospheres.

Experimental Section

Technical

Products preparation of melts and apparatus.—After drying at 423 K, sodium nitrate and nitrite (Merck) were

mixed in the desired proportions. Dehydration of the mixtures was carried out by a progressive raising of the temperature and by maintaining for 4h at work temperature while bubbling dry nitrogen. The other products used were sodium carbonate dried at 1273 K, sodium hydroxide without any previous treatment (pure products for analysis PROLABO), and nitrogen monoxide (99% pure) supplied by COOP-LABO.

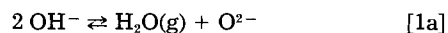
For each experiment, 100g of the nitrate-nitrite mixture thus prepared were introduced into a cylindrical platinum crucible. Platinum was chosen in order to avoid the effect of silica as an acid (12-14). The platinum crucible was itself contained in a Pyrex glass cell. The temperature was maintained at the desired value 693, 743, or 793 K at ± 1 by means of an oven thermoregulated by a Digitop (Chauvin-Arnoux) coupled to a Teledyne (Tekelec-Airtronic) relay.

Alumina tubes (reference number: Al 23) from Desmarquest were used for the different fluids and for the thermocouples. Partial pressures of water vapor were imposed above the melt by saturators at fixed temperature. The EMF's were recorded with the help of a voltmeter Tacussel Aries 20000 and a Sefram recorder (Servo-gram type).

Reference electrode.—The reference electrode used was made up of a silver wire (C.M.P.) dipped into a 0.057 mol kg^{-1} $AgNO_3$ solution in $(Na-K)NO_3$ eutectic contained in a Pyrex glass tube. All potentials are given in volts *vs.* this reference electrode (whatever the $NaNO_3$ - $NaNO_2$ mixture used).

Platinum working electrode.—The indicator electrode used was made from 1 mm diam platinum rod supplied by Johnson-Matthey.

Acidity buffer.—Previous works (15, 16) have shown that acidity can be adjusted by using the buffer effect of $H_2O(g)/OH^-$ mixtures. As a matter of fact, if we add to the melt a quantity m_0 of sodium hydroxide (per kilogram of molten mixture), the respective molalities of free O^{2-} and remaining OH^- are linked by the equilibrium



the constant K_1 of which is given as a function of temperature (and whatever the compositions of $NaNO_3$ - $NaNO_2$ mixtures may be) in Table I. The acidity level (pO^{2-}) fixed by a given $H_2O(g)/OH^-$ mixture is so deduced from the expression

$$pO^{2-}_{(at\ T)} = -\log K_{1(at\ T)} + \log \frac{P(H_2O)}{m(OH^-)^2} \quad [1b]$$

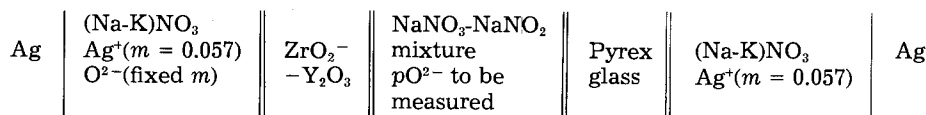
pO^{2-} measurements (description of the indicator electrode used).—In order to measure pO^{2-} in alkali nitrates,

*Electrochemical Society Active Member.

Table I. Constants K_1 of chemical equilibria

Equilibrium	Mass action law expressions	$pK_1 = A + B/1000/T$	
		A	B
(1) $2\text{OH}^- = \text{H}_2\text{O}(\text{g}) + \text{O}^{2-}$	$K_1 = P(\text{H}_2\text{O})m(\text{O}^{2-})m(\text{OH}^-)^{-2}$	-4.80	5.48
(2) $3\text{NO}_2^- = \text{NO}_3^- + 2\text{NO}(\text{g}) + \text{O}^{2-}$	$K_2 = P(\text{NO})^2 m(\text{O}^{2-})N(\text{NO}_3^-)N(\text{NO}_2^-)^{-3}$	-15.8	15.75

it has been shown (17) that an electrode with an oxide ion selective membrane is preferable to an oxygen electrode. A calcia-stabilized zirconia membrane electrode with a solid inner filling used for the first time by Eichler *et al.* (18) and by Trémillon *et al.* (19) in molten alkali chlorides, works quite well at temperatures above 873 K, but its potentiometric response becomes slow (equilibrium potential reached with difficulty) at lower temperatures. Flinn and Stern (17) for molten alkali nitrates, and Picard *et al.* (20-22) for molten alkali chlorides, have, therefore, preferred to employ a membrane of yttria-stabilized zirconia, which is twice more conductive, and a liquid inner filling. Such a device does not present the same problems as mentioned above. The galvanic chain set up to measure $p\text{O}^{2-}$ is described below



(The yttria-stabilized zirconia is supplied by Desmarquest: ZFYE tube.)

The EMF of this cell has the theoretical expression

$$E = E^\circ + \frac{2.3RT}{2F} p\text{O}^{2-}$$

Calibration.—In order to verify the potentiometric response of the yttria-stabilized zirconia membrane electrode (YSZME) and to make its calibration, we have used sodium hydroxide. When the partial pressure of water is made sufficiently low, the dissociation of OH^- according to equilibrium [1a] can be considered as practically total, and the concentration of O^{2-} ions is given by

$$m(\text{O}^{2-}) = 0.5 m_0(\text{OH}^-)$$

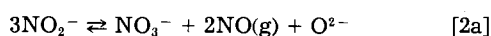
We have shown that a partial pressure of H_2O less than 10^{-3} atm is convenient for this (15).

The introduction of oxide ions by dissociation of OH^- was preferred to the direct addition of sodium oxide because this product is generally impure (presence of peroxide and superoxide).

Acidity function.—Because of the dependence of K_1 with temperature, we preferred, in order to analyze the effect of acidity on the thermochemical stability of molten nitrate-nitrite mixtures, to use the acidity function $\log [P(\text{H}_2\text{O})/m(\text{OH}^-)^2]$, the value of which, for a given temperature, is related to the $p\text{O}^{2-}$ (at T) by the above relation, Eq. [1b], and may be obtained, whatever the temperature may be, directly from the temperature-independent factors water pressure and sodium hydroxide concentration, which are experimentally set. This procedure is analogous to that employed in molten chlorides (23).

Thanks to the values of constant K_1 of equilibrium [1a] which have been determined (Table I) and which do not vary practically with the composition of the mixtures at a given temperature (15, 16), it is possible to obtain the correspondence between this acidity function and $p\text{O}^{2-}$.

Disproportionation of nitrite ions.—It has been observed that increasing acidity produces the disproportionation of NO_2^- into NO_3^- and nitrogen monoxide, according to the equilibrium

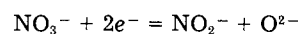


characterized by the constant K_2 , defined by

$$K_2 = N(\text{NO}_3^-) P(\text{NO})^2 m(\text{O}^{2-}) N(\text{NO}_2^-)^{-3} \quad [2b]$$

This constant has been determined by simply measuring with the YSZME the $p\text{O}^{2-}$ imposed by bubbling nitrogen monoxide (1 atm) into $\text{NaNO}_3\text{-NaNO}_2$ mixtures of given compositions. The results obtained at three different temperatures verify a straight line variation of $p\text{O}^{2-}$ with the ratio $N(\text{NO}_3^-)/N(\text{NO}_2^-)^3$ as predicted by Eq. [2b] (see Fig. 1a). The variation of $-\log K_2$ with the temperature (Fig. 1b) has been determined by regression analysis.

$\text{NO}_3^-/\text{NO}_2^-$ electrochemical system.—The melts studied contained the two components of the redox couple



So, the redox potential E of a given melt (*i.e.*, at fixed

NO_3^- and NO_2^- mole fractions) has to follow the Nernst relations

$$E = E_3^\circ + (\lambda/2) \log [N(\text{NO}_3^-)/N(\text{NO}_2^-)] + (\lambda/2) p\text{O}^{2-} \quad [3]$$

$$\left(\lambda = \frac{2.3RT}{F} \right)$$

and, consequently, only varies with the activity of oxide ion. Then, measurements of the potential of a platinum electrode immersed in molten $\text{NaNO}_3\text{-NaNO}_2$ mixtures must allow us to determine the standard potential value of the $\text{NO}_3^-/\text{NO}_2^-$ redox couple.

But, while making these determinations, we have to take care not to let $p\text{O}^{2-}$ increase beyond the value corresponding to the disproportionation of nitrite ion according to equilibrium [2a]. This limiting value of $p\text{O}^{2-}$ depends on the nitrogen monoxide partial pressure, the maximum value of $p\text{O}^{2-}$ being reached for $P(\text{NO}) = 1$ atm. This limit is represented in Fig. 2 for the three temperatures considered. We have also plotted on this figure the variations of potential *vs.* $p\text{O}^{2-}$ observed with five mixtures of sodium nitrate and sodium nitrite.

We observe in all cases that the variations of potential check very well the Nernst relation [3]. It is thus justified to determine the potential of the $\text{NO}_3^-/\text{NO}_2^-$ system at $p\text{O}^{2-} = 0$ by extrapolation. Then by plotting as a function of the ratio $N(\text{NO}_3^-)/N(\text{NO}_2^-)$, this potential at $p\text{O}^{2-} = 0$, a

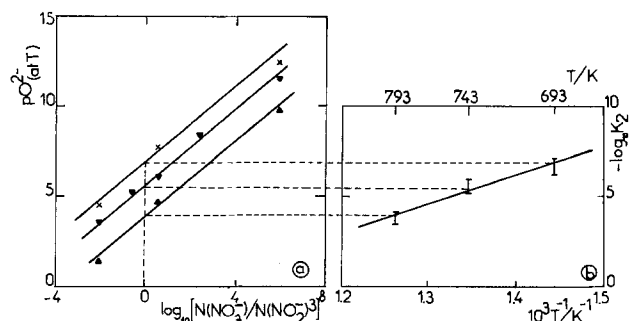


Fig. 1. Disproportionation of NO_2^- into NO_3^- and $\text{NO}(\text{g})$. a: Variation of $p\text{O}^{2-}$ (at T) for various $\text{NaNO}_3\text{-NaNO}_2$ mixtures (\blacktriangle : $T = 793$ K; \times : $T = 743$ K; \circ : $T = 693$ K). b: Variation of the logarithm of the constant K_2 corresponding to the disproportionation of NO_2^- (see text) as a function of temperature.

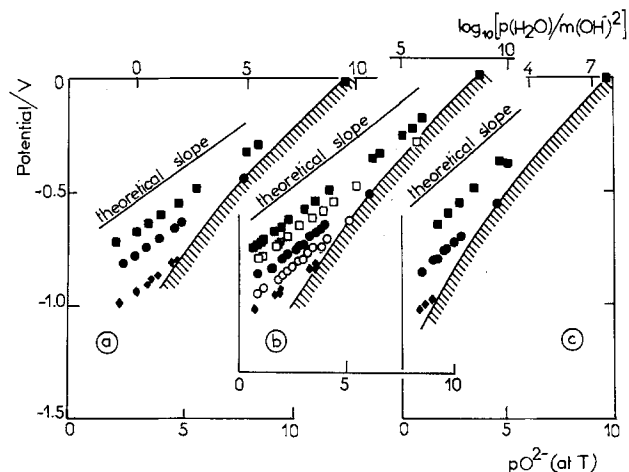
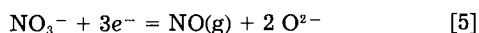
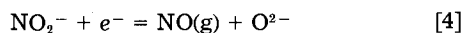


Fig. 2. Equilibrium potentials of the $\text{NO}_3^-/\text{NO}_2^-$ electrochemical system in various sodium nitrate-sodium nitrite mixtures for (a) $T = 693$ K, (b) $T = 743$ K, and (c) $T = 793$ K.

Symbol	■	□	●	○	◆
$N(\text{NO}_3^-)$	0.99	0.85	0.50	0.15	0.01
$N(\text{NO}_2^-)$	0.01	0.15	0.50	0.85	0.99

straight line agreeing with relation [3] is obtained and permits us to determine the standard potential of the $\text{NO}_3^-/\text{NO}_2^-$ electrochemical system. The results obtained according to this procedure at the three temperatures have led to the expression of the variation of the $\text{NO}_3^-/\text{NO}_2^-$ standard potential as a function of temperature given in Table II.

$\text{NO}_2^-/\text{NO}(\text{g})$ and $\text{NO}_3^-/\text{NO}(\text{g})$ electrochemical systems.—The standard potentials E_4° and E_5° of the $\text{NO}_2^-/\text{NO}(\text{g})$ and $\text{NO}_3^-/\text{NO}(\text{g})$ electrochemical systems



defined by the respective Nernst relations

$$E = E_4^\circ + \lambda \log [N(\text{NO}_2^-)/P(\text{NO})] + \lambda p\text{O}^{2-}$$

$$E = E_5^\circ + (\lambda/3) \log [N(\text{NO}_3^-)/P(\text{NO})] + (2\lambda/3)p\text{O}^{2-}$$

can be determined by combining the value of K_2 (constant of the NO_2^- disproportionation equilibrium) with the value of E_3° (standard potential of the $\text{NO}_3^-/\text{NO}_2^-$ system). We have in fact

$$E_4^\circ = E_3^\circ - (\lambda/2) pK_2$$

$$E_5^\circ = (2E_3^\circ + E_4^\circ)/3$$

The values of E_4° and E_5° are also given in Table II.

Discussion

Chemical and electrochemical properties of NaNO_3 - NaNO_2 mixtures at a given temperature.—It is possible to

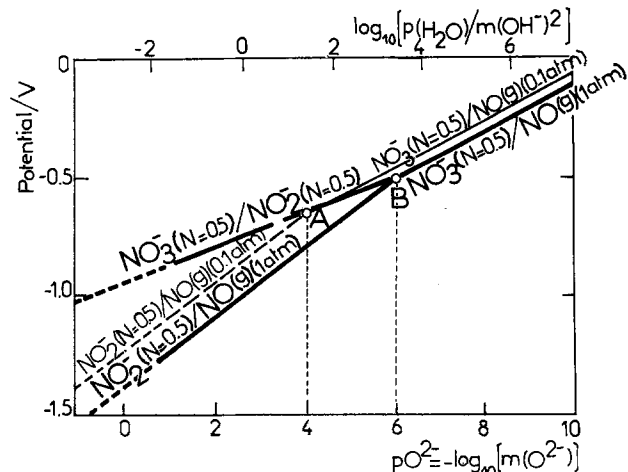
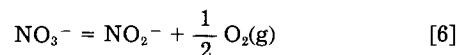


Fig. 3. Potential-acidity diagram at 743 K

summarize our experimental results in the form of potential- $p\text{O}^{2-}$ diagrams. For example, we give in Fig. 3 the diagram relative to the equimolar sodium nitrate-sodium nitrite mixture at 743 K and in the cases where the nitrogen monoxide pressure is equal to 0.1 and 1 atm. In this diagram, the value of $p\text{O}^{2-}$ corresponding to the disproportionation of nitrite is given by the abscissa of the intersection of the straight lines connected with the systems $\text{NO}_3^-/\text{NO}_2^-$, $\text{NO}_3^-/\text{NO}(\text{g})$, and $\text{NO}_2^-/\text{NO}(\text{g})$. This intersection is designated, in the following, as the "nitrite disproportionation characteristic point." For example, in the case of the equimolar mixture, this characteristic point is represented by the letter A for $P(\text{NO}) = 0.1$ atm, and by B for $P(\text{NO}) = 1$ atm.

So, we can assert that a molten NaNO_3 - NaNO_2 mixture keeps its composition only if the $p\text{O}^{2-}$ value remains less than the value of the nitrite disproportionation characteristic point.

Besides the disproportionation of nitrite, which is largely responsible for the thermal instability of NaNO_3 - NaNO_2 mixtures, another equilibrium plays an important role: the decomposition of nitrate into nitrite and oxygen according to the equilibrium



So, if we wish to explain in a complete manner the stability of NaNO_3 - NaNO_2 mixtures, we have to take into account this equilibrium, the constant of which is defined by

$$K_6 = P(\text{O}_2)^{0.5} N(\text{NO}_2^-) N(\text{NO}_3^-)^{-1}$$

Several values of K_6 are found in the literature (24-26). We have considered the value given by Sirotkin (24) which is relative to the decomposition of NaNO_3 , a value which is very close to that given by Paniccia and Zambonin for $(\text{Na}, \text{K})\text{NO}_3$ (26). The variation of the cologarithm of K_6 as a function of temperature is given in Table III.

Figure 4 represents a composition-acidity diagram which gives the variation of composition of the NaNO_3 -

Table II. Redox equilibria and standard potentials E_i° ($\lambda = 2.3RT/F$)

Electrochemical systems	Equilibrium potentials	$E_i^\circ = A + B \cdot 10^{-3}T$	
		A	B
(3) $\text{NO}_3^- + 2e^- = \text{NO}_2^- + \text{O}^{2-}$	$E = E_3^\circ + \frac{\lambda}{2} \log \frac{N(\text{NO}_3^-)}{N(\text{NO}_2^-)} + \frac{\lambda}{2} p\text{O}^{2-}$	-1.317	0.50
(4) $\text{NO}_2^- + e^- = \text{NO}(\text{g}) + \text{O}^{2-}$	$E = E_4^\circ + \lambda \log \frac{N(\text{NO}_2^-)}{P(\text{NO})} + \lambda p\text{O}^{2-}$	-2.887	2.08
(5) $\text{NO}_3^- + 3e^- = \text{NO}(\text{g}) + 2\text{O}^{2-}$	$E = E_5^\circ + \frac{\lambda}{3} \log \frac{N(\text{NO}_3^-)}{P(\text{NO})} + \frac{2\lambda}{3} p\text{O}^{2-}$	-1.840	1.03

Table III. Constants K_i of chemical equilibria

Equilibrium	Mass action law expressions	$pK_i = A + B1000/T$	
		A	B
(6) $\text{NO}_3^- = \text{NO}_2^- + \frac{1}{2} \text{O}_2(\text{g})$	$K_6 = P(\text{O}_2)^{0.5} N(\text{NO}_2^-)N(\text{NO}_3^-)^{-1}$	-5.47	5.88
(7) $2\text{NO}_2^- = 2\text{NO}(\text{g}) + \frac{1}{2} \text{O}_2(\text{g}) + \text{O}^{2-}$	$K_7 = P(\text{O}_2)^{0.5} P(\text{NO})^2 m(\text{O}^{2-})^{-2}$	-21.4	21.6
(8) $2\text{NO}_3^- = 2\text{NO}(\text{g}) + 3/2 \text{O}_2(\text{g}) + \text{O}^{2-}$	$K_8 = m(\text{O}^{2-})^2 P(\text{NO})^2 P(\text{O}_2)^{1.5} N(\text{NO}_3^-)^{-2}$	-32.3	33.4
(9) $\text{NO}(\text{g}) + \frac{1}{2} \text{O}_2(\text{g}) = \text{NO}_2(\text{g})$	$K_9 = P(\text{NO}_2) P(\text{NO})^{-1} P(\text{O}_2)^{-0.5}$	3.99	-3.06
(10) $2\text{NO}_2^- + \frac{1}{2} \text{O}_2(\text{g}) = 2\text{NO}_2(\text{g}) + \text{O}^{2-}$	$K_{10} = P(\text{NO}_2)^2 m(\text{O}^{2-}) P(\text{O}_2)^{-0.5} N(\text{NO}_2^-)^{-2}$	-13.4	15.5
(11) $2\text{NO}_3^- = 2\text{NO}_2(\text{g}) + \frac{1}{2} \text{O}_2(\text{g}) + \text{O}^{2-}$	$K_{11} = m(\text{O}^{2-}) P(\text{NO}_2)^2 P(\text{O}_2)^{0.5} N(\text{NO}_3^-)^{-2}$	-24.3	27.3
(12) $3\text{NO}_3(\text{g}) + \text{O}^{2-} = 2\text{NO}_3^- + \text{NO}(\text{g})$	$K_{12} = N(\text{NO}_3^-)^2 P(\text{NO}) P(\text{NO}_2)^{-3} m(\text{O}^{2-})^{-1}$	20.3	-24.2

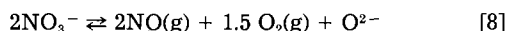
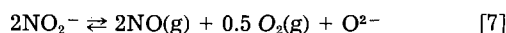
NaNO_2 mixtures [by the logarithm of $N(\text{NO}_2^-)$ vs. $p\text{O}^{2-}$ at $T = 743$ K. It was established from the constant K_2 of the disproportionation of nitrite ion (Eq. [2b]).

Partial pressures of oxygen were deduced from the constant K_6 of equilibrium [6]. From this diagram, it is possible to obtain the conditions for which a given mixture is stable under a total pressure of 1 atm. Toward the low values of $N(\text{NO}_2^-)$ (nitrate-rich mixtures), the limiting composition, due to the decomposition of nitrate ion, is given by Eq. [6] where $P(\text{O}_2)$ is equal to 1 atm. For high values of $N(\text{NO}_2^-)$, the limitation occurs from the disproportionation of nitrite ion into nitrate and nitrogen monoxide which takes place in acidic media. The limiting values (as a function of $p\text{O}^{2-}$) are given by $P(\text{NO}) = 1$ atm.

We can notice that the acidity range depends on the composition of the mixture considered. For example, the nitrate richer mixtures allow one to obtain the more acidic (and oxidant) media; on the contrary, the nitrite richer mixtures have weak acidity ranges.

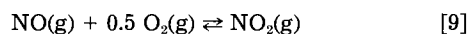
We can also observe in Fig. 4 that $\text{NO}(\text{g})$ acts as an acid in a given molten NaNO_3 - NaNO_2 mixture, because when the partial pressure of $\text{NO}(\text{g})$ increases, the $p\text{O}^{2-}$ value increases. For example, in the case of the equimolar mixture, it is possible to win two units of $p\text{O}^{2-}$ by increasing $P(\text{NO})$ from 0.1 to 1 atm (points A and B).

The acidic properties of $\text{NO}(\text{g})$ correspond to the following equilibria



because in nitrate-nitrite mixtures, $P(\text{O}_2)$ is fixed by the equilibrium [6] of the decomposition of nitrate ion. For pure NaNO_2 (Eq. [7]) or pure NaNO_3 (Eq. [8]), the acidity is fixed by a $\text{NO}(\text{g}) + \text{O}_2(\text{g})$ gaseous mixture of given composition.

If partial pressures of $\text{NO}(\text{g})$ and $\text{O}_2(\text{g})$ are fixed, the partial pressure of $\text{NO}_2(\text{g})$ is also fixed through the equilibrium



and the preceding equilibria [7] and [8] can be, respectively, rewritten

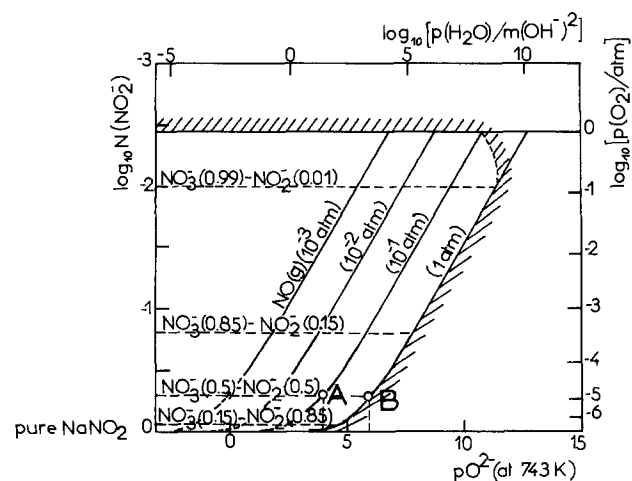
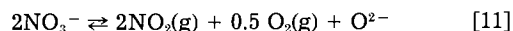
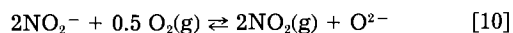


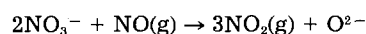
Fig. 4. Composition-acidity diagram at 743 K



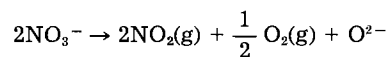
This last equilibrium, well known in molten alkali nitrate, shows that acidity can be adjusted by using $\text{NO}_2(\text{g}) + \text{O}_2(\text{g})$ gaseous mixtures. In particular, this fact was used recently by Drátovský and Havlíček for obtaining a qualitative acidity scale in molten $(\text{Na}, \text{K})\text{NO}_3$ at 533 K (27), and by Plumet *et al.* for establishing a potential-acidity diagram in molten $(\text{Na}, \text{K})\text{NO}_3$ at 748 K (28). As a consequence, if we maintain at a weak value (10^{-3} or 10^{-2} atm, for example) the partial pressure of $\text{NO}(\text{g})$ by means of bubbling argon, we see that it was not possible to modify acidity without modifying the composition of the mixture. We can also remark that it is impossible to reach media more acidic than $p\text{O}^{2-} = 6$ (point B) for the equimolar mixture and $P(\text{NO}) = 1$ atm without an increase of the nitrate ratio by disproportionation of nitrite. (The constants of the equilibria [7]-[11] were calculated from the constants K_2 and K_6 and from the literature thermodynamic data (6); they are given in Table III.)

Influence of temperature (and acidity) on the stability of NaNO_3 - NaNO_2 mixtures.—The influence of temperature on the stability of sodium nitrate-nitrite mixtures of various $p\text{O}^{2-}$ may be specified by establishing the potential-acidity diagrams of these mixtures as a function of temperature.

To obtain the stability domains of various molten sodium nitrate-nitrite mixtures, we shall conventionally consider in the following that nitrate or nitrite are "quasi-pure" if, respectively, they do not contain a proportion higher than 1 mole percent (m/o) of nitrite or nitrate. Then, we can distinguish at a given temperature (see, for example, Fig. 5, $T = 580$ K) three composition zones: those of quasi-pure nitrate and quasi-pure nitrite, and that of the NaNO_3 - NaNO_2 mixtures. The potential-acidity zone which is accessible in quasi-pure NaNO_3 is limited for high potential values by the oxidation of O^{2-} into oxygen (see Table IV) at a pressure of 1 atm (line a), and for low potential values, either by the reduction of NO_3^- ions into NO_2^- ions (line f) in the weak acidities range or by the reduction of NO_3^- into nitrogen monoxide in the high acidities range (line c), or even by the reduction of NO_3^- ions into $\text{NO}_2(\text{g})$ for very high acidity media. The characteristic points of this zone are thus, on the one hand, the reduction of NO_3^- by $\text{NO}(\text{g})$ for very high acidities (intersection of lines b and c) according to the reaction



and, on the other hand, the decomposition of nitrate into nitrogen dioxide and oxygen (intersection of lines a and b) according to



The potential-acidity zone which is accessible with the NaNO_3 - NaNO_2 mixtures whose compositions are comprised between 0.99-0.01 and 0.01-0.99 m/o is limited for high potential values by the line corresponding to the 0.99-0.01 mixture (line f), and for low potential values by the line relative to the 0.01-0.99 mixture (line h). For high acidity values, this area is limited by the disproportiona-

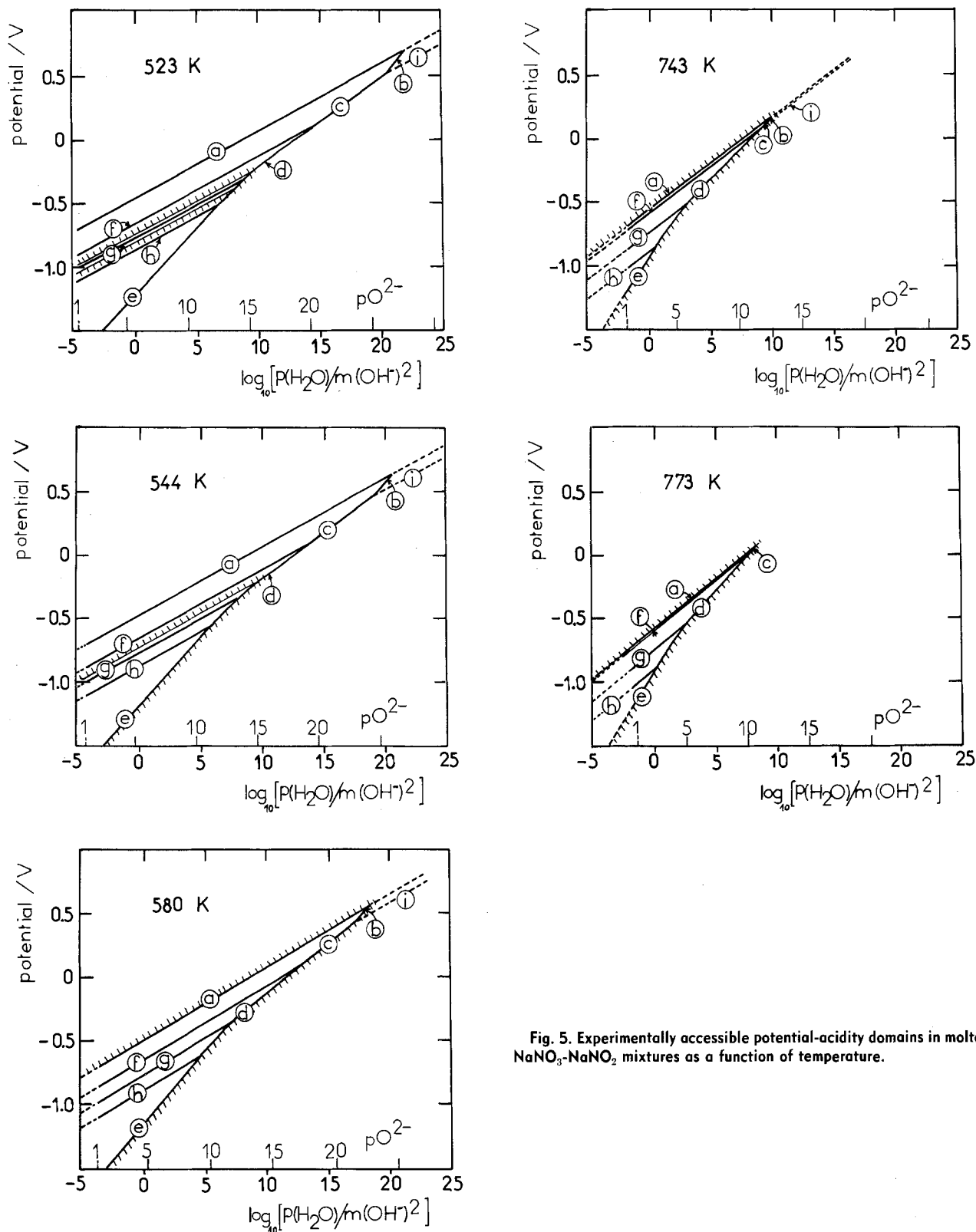


Fig. 5. Experimentally accessible potential-acidity domains in molten NaNO_3 - NaNO_2 mixtures as a function of temperature.

tion of NO_2^- into NO_3^- and $\text{NO}(\text{g})$ according to the equilibrium [2a] (line d).

At last, the potential-acidity area accessible in quasi-pure NaNO_2 is limited for high potential values by the oxidation of NO_2^- into NO_3^- (line h), and for low potential values, by the reduction of NO_2^- into nitrogen monoxide (line e). A characteristic point of this area is the intersection of lines e and h, which correspond to the beginning of the disproportionation of NO_2^- ions into NO_3^- and $\text{NO}(\text{g})$.

The whole of these three areas constitutes the accessible thermodynamical stability (potential-acidity) domain of all the NaNO_3 - NaNO_2 mixtures of every composition.

Yet at low temperatures, this domain may be limited by the melting points of pure salts or of their mixtures. Therefore, at 523 K (for which NaNO_3 and NaNO_2 are in the solid state), only the mixtures of average compositions included in the range 20 and 65 m/o NaNO_3 are melted and so can be used. At 544 K [melting point of pure NaNO_2 (29)], NaNO_2 and its mixtures with NaNO_3 till a composition of 78 w/o NaNO_3 can be used. At last, at $T > 580$ K [melting point of pure NaNO_3 (29)], the two pure salts and all their mixtures can be used.

When temperature increases, we can notice in Fig. 5 (i) an important decrease of the potential-acidity area accessible in molten NaNO_3 , which corresponds to a more im-

Table IV. Redox equilibria and standard potentials E°_i ($\lambda = 2.3 RT/F$)

Electrochemical systems	Equilibrium potentials	$E^\circ_i = A + B \cdot 10^{-3}T$	
		A	B
(13) $O_2(g) + 4e^- = 2 O^{2-}$	$E = E^\circ_{13} + \frac{\lambda}{4} \log P(O_2) + \frac{\lambda}{2} pO^{2-}$	-0.731	-0.045
(14) $NO_3^- + e^- = NO_2(g) + O^{2-}$	$E = E^\circ_{14} + \lambda \log \frac{N(NO_3^-)}{P(NO_2)} + \lambda pO^{2-}$	-3.453	2.38
(15) $NO_2(g) + 2e^- = NO(g) + O^{2-}$	$E = E^\circ_{15} + \frac{\lambda}{2} \log \frac{P(NO_2)}{P(NO)} + \frac{\lambda}{2} pO^{2-}$	-1.036	0.353

portant decomposition of NO_3^- ions into NO_2^- ions and oxygen (line a draws nearer to line f), a disappearance of the decomposition, for high acidity media, of NO_3^- into $NO_2(g)$ and $O_2(g)$ (reactions which do not take place at $T > 766$ K) and also a progressive decrease of the acidity range in which NO_3^- ions can be reduced into $NO(g)$. Contrary to the preceding area, we observe (ii) that those corresponding to the quasi-pure nitrite and to the $NaNO_3 + NaNO_2$ mixtures stay noticeable whatever the temperature may be. At last, (iii) the acidity global area which may be accessible highly decreases with the temperature: the value of the acidity function relative to the more acidic media which can be reached goes from 18.1 (which corresponds to $pO^{2-} = 22.8$ at 580 K) to 8.6 ($pO^{2-} = 10.9$ at 773 K).

These types of diagrams are important in determining the experimental conditions necessary for obtaining a maximum stability of a $NaNO_3$ - $NaNO_2$ mixture of given composition. See, for example, the equimolar mixture which is always molten in the temperature range of 523-773 K. The higher acidity value which can be reached (intersection of lines g and d) under a nitrogen monoxide pressure equal to 1 atm varies from 9.2 ($pO^{2-} = 14.9$) at 523 K to 2.9 ($pO^{2-} = 5.2$) at 773 K. From this observation, we can easily deduce that the equimolar mixture is stable between 523 and 773 K if we maintain the cologarithm of $P(H_2O)/m(OH^-)^2$ at a value less than 2.9.

Conclusion

The influence of pO^{2-} and temperature on the decomposition of molten sodium nitrite-sodium nitrate mixtures has been studied. In particular, we have specified the influence and the part played by the mixture's composition, and the partial pressures of nitrogen monoxide and water.

At the present time, this research is being completed by studying the stability of the mixtures in basic media, in which peroxide and superoxide ions can appear as it has been shown in particular by Zambonin and Jordan for low temperature melts (30).

Acknowledgments

We are grateful to Electricité de France Company for its financial support of this study. We express our thanks especially to M. P. Saint-Paul and M. P. Spiteri, of this company, for their interest in this work.

Manuscript submitted June 28, 1983; revised manuscript received Dec. 3, 1984. This was Paper 796 presented at the San Francisco, California, Meeting of the Society, May 8-13, 1983.

CNRS assisted in meeting the publication costs of this article.

REFERENCES

- J. Alexander, Jr., and S. G. Hindin, *Ind. Eng. Chem.*, **39**, 1046 (1947).
- R. F. Bartholomew, *J. Phys. Chem.*, **70**, 3442 (1966).
- J. Cases-Casanova, *Bull. Soc. Chim. Fr.*, **3**, 429, 435 (1959).
- A. Peneloux, *C.R. Acad. Sci.*, **237**, 1082 (1953).
- D. H. Kerridge, *Inorg. Chim. Acta*, **7**, 665 (1973).
- I. Barin, O. Knacke, and O. Kubaschewski, "Thermochemical Properties of Inorganic Substances," Springer Verlag, Berlin-Heidelberg-New York (1973); I. Barin, From the data bank "Thermodata."
- A. Conte and S. Casadio, *Ric. Sci.*, **36**, 488 (1966).
- S. G. Marchiano and A. J. Arvia, *Electrochim. Acta*, **17**, 25, 861 (1972).
- A. D. Haan and H. Van der Poorten, *Bull. Soc. Chim. Fr.*, **11**, 2894 (1973).
- E. Freeman, *J. Phys. Chem.*, **60**, 1487 (1956).
- B. Trémillon, *Pure Appl. Chem.*, **25**, 592 (1971).
- P. G. Zambonin, *J. Electroanal. Chem.*, **33**, 243 (1971).
- J. D. Burke and D. H. Kerridge, *Electrochim. Acta*, **19**, 251 (1974).
- G. Picard, T. Flament, J. M. Bruneau, and B. Trémillon, To be published.
- G. Picard, T. Flament, and B. Trémillon, To be published.
- B. Trémillon and G. Picard, in "Proceedings of the 1st International Symposium on Molten Salt Chemistry and Technology," Y. Ito, Editor, p. 93, Kyoto University, Kyoto, Japan (1983); G. Picard, T. Flament, and B. Trémillon, in "Proceedings of the 1st International Symposium on Molten Salt Chemistry and Technology," Y. Ito, Editor, p. 85, Kyoto University, Kyoto, Japan (1983).
- R. B. Flinn and K. H. Stern, *J. Electroanal. Chem.*, **63**, 191 (1975).
- B. Eichler, D. Naumann, and H. Ullmann, *Z. Phys. Chem.*, **236**, 372 (1967).
- R. Combes, J. Vedel, and B. Trémillon, *Electrochim. Acta*, **20**, 191 (1975).
- G. Picard, F. Séon, and B. Trémillon, *J. Electroanal. Chem.*, **102**, 65 (1979).
- G. Picard, F. Séon, B. Trémillon, and Y. Bertaud, *Electrochim. Acta*, **25**, 1453 (1980).
- G. Picard, F. Séon, and B. Trémillon, *This Journal*, **129**, 1450 (1982); *J. Electroanal. Chem.*, **138**, 315 (1982).
- B. Trémillon and G. Picard, *Anal. Chim. Acta*, **82**, 273 (1976).
- G. Sirotkin, *Russ. J. Inorg. Chem.*, **4**, 1180 (1959).
- D. A. Nissen, Sandia National Laboratories, Report 81-8007 (1981).
- F. Paniccia and P. G. Zambonin, *J. Phys. Chem.*, **77**, 1810 (1973).
- M. Drátovský and D. Havlíček, *Electrochim. Acta*, **28**, 1761 (1983).
- E. Plumet, A. Labani, and M. Ghodsi, *This Journal*, **130**, 2192 (1983).
- "C.R.C. Handbook of Chemistry and Physics," 61st ed., R. C. Weast, Editor, p. B149, CRC Press Inc., Boca Raton, FL (1980).
- P. G. Zambonin and J. Jordan, *J. Am. Chem. Soc.*, **91**, 2225 (1969).



Passive Zinc Electrodes: Application of the Effective Medium Theory

B. Aurian-Blajeni* and Micha Tomkiewicz*

Department of Physics, Brooklyn College, Brooklyn, New York 11210

Zinc has found important applications as an electrode material in batteries. The properties of zinc are the subject of numerous studies. Comprehensive reviews have been published (1-3), and many useful references to recent literature may also be found in Ref. (4).

Under anodic bias, zinc electrodes passivate with formation of zinc oxide layers (4-6). The mechanism of formation of these layers in alkaline solutions is by a solution-precipitation path. This results in a wide morphological variety, depending on the growth environment. Basically, the passive layers were described in terms of a duplex structure with a thin compact component beneath a porous one. Our aim is to characterize the passive zinc electrode by impedance measurements. Although many studies using impedance techniques were carried out for zinc electrodes, most of them involved the active regime (7, 8).

During the growth of oxide layers at the surface of zinc electrodes, electrolyte solution is also imbedded. The dielectric properties of the resulting layer are not a linear combination of the dielectric characteristics of the components (i.e., oxide and solution), but cross-term effects appear as well (9). One of the ways of describing the dielectric behavior of composites is the effective medium approximation (10, 11). Among the most used forms of this approximation are: the Maxwell-Garnett, Bruggeman, and the self-similar or differential forms. The Maxwell-Garnett approximation for a two-component system is valid whenever a distinction may be made between a "host" and a "guest" component in the composite material. This limitation is not present in the Bruggeman version, which applies for spherical inclusions in a homogeneous medium consisting from the two components. The refinement of this latter approximation, the self-similar or differential effective medium theory, allows for any form of inclusions in media in which the conductive phase remains interconnected for any ratio of the components.

The present note illustrates the application of the effective medium approximation in its differential form to electrolytically grown zinc oxide layers.

Zinc oxide layers were grown on polished surfaces of vertical electrodes (area 0.08 cm²), under vigorous stirring, in 5M KOH solutions electrolytically saturated with zinc species. Impedance measurements were performed according to the method described in Ref. (12) in the same solution in which the oxide layers were grown. The changes in the film characteristics during the measurements were minimal from the point of view of the impedance, as attested by the fact that two successive measurements resulted in almost identical values.

The form of the effective medium approximation we used was developed for sedimentary rocks (9, 10, 13). In its closed form, for a composite consisting of a porous insulator saturated with electrolyte solution, it reads

$$P = \frac{\epsilon - \epsilon_d}{\epsilon_w - \epsilon_d} \left(\frac{\epsilon_w}{\epsilon} \right)^m \quad [1]$$

* Electrochemical Society Active Member.

where P is the porosity, ϵ , ϵ_w , ϵ_d are the complex dielectric constants of the composite, solution, and insulator, respectively, and $0 < m < 1$ is a screening factor (depolarization factor) dependent on the shape of the grains in the composite (10, 11).

The complex dielectric constant for the low frequency regime ($f < 10^7$ Hz) may be written as

$$\epsilon = k - i(4\pi\sigma/\omega) = |\epsilon| \exp i\theta \quad [2]$$

where k is the dielectric constant, i the square root of -1 , σ the conductivity, and ω the angular velocity. Introducing Eq. [2] in [1] for the insulator and solution results, after some manipulation, in the values of $|\epsilon|$ and θ of the composite, as a function of the dielectric characteristics of the components and two parameters, the depolarization factor, and the porosity.

On the other hand, the frequency-dependent impedance may be expressed as

$$Z = R + iX = i l(\delta A \omega \epsilon) \quad [3]$$

where l is the thickness, δ is the roughness factor, and A the area of the sample of material under consideration (l is parallel to the electric field).

Thus the imaginary and real parts of the impedance will have the form

$$X = -(1/\delta A \omega) \operatorname{Re}(1/\epsilon) = -(l/\delta A \omega) \cos \theta/|\epsilon| \quad [4]$$

and

$$R = -(1/\delta A \omega) \operatorname{Im}(1/\epsilon) = (l/\delta A \omega) \sin \theta/|\epsilon| \quad [4']$$

respectively.

The dissipation spectrum of the impedance will be dependent on the geometric factors of the sample, the dielectric characteristics of the components, their ratio, and the microstructure.

In Fig. 1, the experimental results obtained for the impedance of a zinc oxide layer anodically grown are compared with values predicted by the relations [4] and [4']. The measured values of the impedance suggest that they are characteristic for the thin, compact layer of the duplex. Some of the parameters used were taken from the literature as: $k_w = 70$ (10), $k_d = 8.5$ (14), $\sigma_w = 0.500$ ($\Omega \text{ cm}$)⁻¹ (1).¹ The adjustable parameters are: the thickness to roughness ratio l/δ (one parameter), the conductivity of zinc oxide σ_d (depending on the nonstoichiometry of the anodically formed zinc oxide), the porosity P , and the depolarization factor m . The adjustable parameters were fit by least mean squares fitting for nonlinear models. Fitting was performed only for the imaginary part of the impedance (Fig. 1a). As a check for the consistency of the model, the values obtained for the parameters were fed into the expression for the real part of the impedance (to which 60 Ω , representing the solution resistance, were

¹ It is true that hydrous oxides often act like ion-exchange materials, so there is every reason to expect that the conductivity of the solution in the film may be different than the conductivity in the bulk of the solution. Nevertheless, the exchange of one ion for another is not expected to alter the conductivity significantly enough to affect the results.

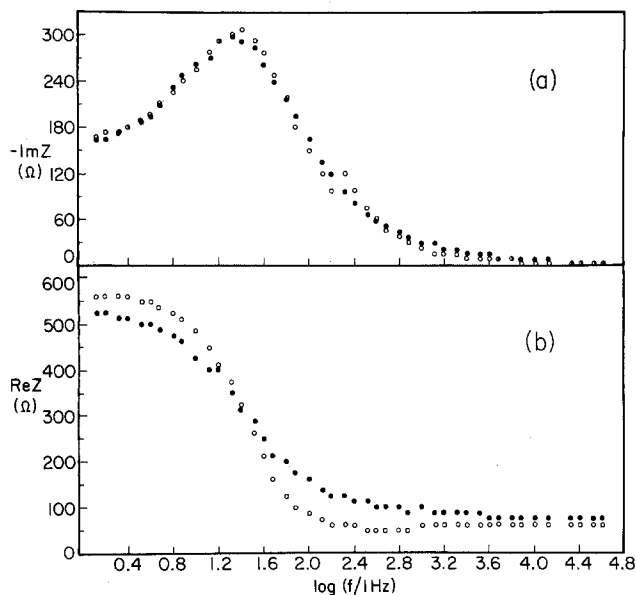


Fig. 1. Comparison between the experimental (\circ) and the predicted (\bullet) values of the impedance vs. frequency for a passive zinc electrode. a: Imaginary part. b: real part of the impedance.

added) and the results were compared with the experimental data (Fig. 1b).

The fit of the results in Fig. 1, resulted in the following set of parameters; porosity of 27.6%, depolarization factor of 0.44, conductivity of zinc oxide of $1.36 \times 10^{-11} (\Omega \text{ cm})^{-1}$, and thickness to roughness ratio of 0.8×10^{-8} cm. There is not much to say about the value obtained for the porosity, except that it is a credible figure. Work is under way focusing on its evolution as a function of the experimental conditions of growth of the oxide. The value obtained for the depolarization factor is indicative of particles shaped as prolate ellipsoids [$m = 0$ for needles, $1/3$ for spheres, $1/2$ for cylinders, and 1 for plates (10)]. Nevertheless, the value of m cannot be taken literally. Two hypotheses are involved: one is the isotropy of the dielectric constant, and the other is the parallelism of the axes of grains. In the case of electrolytic growth, the latter hypothesis is reasonable (6), while the first has to be considered with caution. From the value of σ_d an estimate of the free carrier concentration in zinc oxide of ca. 10^6 cm^{-3} is obtained, compared with ca. 10^{-11} cm^{-3} for pure zinc oxide (15) [data from Ref. (16) have been considered]. This is consistent with the coloration of the passivating layers, observed during our experiment and in the literature, which has been assigned to an excess of zinc atoms (5, 6). The apparently small value obtained for the thickness-to-

roughness ratio is deemed reasonable if the high roughness of a surface formed by a solution-precipitation mechanism and the fact that true passivation is due to a very thin layer are taken into account (4-6). Work for the elucidation of this point is currently in progress.

In conclusion, we found that the effective medium approximation is applicable to electrolytically grown zinc oxide layers. Since many of the electrolytically grown passivating layers include electrolyte, we believe that the effective medium approximation might be applied to other systems as well.

Acknowledgments

Helpful discussions with Mr. M. Kramer, from Brooklyn College, and Dr. P. Sheng, from Exxon, at various stages of this work are gratefully acknowledged. This work was supported by the Office of Naval Research.

Manuscript submitted Aug. 27, 1984; revised manuscript received Nov. 26, 1984.

Brooklyn College assisted in meeting the publication costs of this article.

REFERENCES

1. J. McBreen and E. J. Cairns, in "Advances in Electrochemistry and Electrochemical Engineering," Vol. 11, H. Gerischer and C. W. Tobias, Editors, p. 273, John Wiley and Sons, New York (1978).
2. R. D. Armstrong and M. F. Bell, in "Electrochemistry," Vol. 4, p. 1, Specialist Periodical Reports, The Chemical Society, London (1974).
3. A. Fleischer and J. J. Lander, Editors, "Zinc-Silver Oxide Batteries," John Wiley and Sons, New York (1971).
4. M. C. H. McKubre and D. D. Macdonald, *This Journal*, **128**, 524 (1981).
5. R. W. Powers and M. W. Breiter, *ibid.*, **116**, 719 (1969).
6. S. Szpak and J. C. Gabriel, *ibid.*, **126**, 1914 (1979).
7. C. Cachet, U. Stroder, and R. Wiart, *Electrochim. Acta*, **27**, 908 (1982).
8. R. D. Armstrong and M. F. Bell, *J. Electroanal. Chem.*, **55**, 201 (1974).
9. P. N. Sen, W. C. Chew, and D. Wilkinson, in "Physics and Chemistry of Porous Media," D. L. Johnson and P. N. Sen, Editors, AIP Proc. 107, p. 52, AIP, New York (1984).
10. P. N. Sen, C. Scala, and M. H. Cohen, *Geophys.*, **46**, 781 (1981).
11. D. E. Aspnes, *J. Phys.*, **44**, c10-3 (1983).
12. M. Tomkiewicz, *This Journal*, **126**, 2200 (1979).
13. P. Sheng and A. J. Callegari, in "Physics and Chemistry of Porous Media," D. L. Johnson and P. N. Sen, Editors, AIP Proc. 107, p. 144, AIP, New York (1984).
14. J. F. Dewald, *Bell Syst. Tech. J.*, **39**, 615 (1960).
15. S. M. Sze, "Physics of Semiconductor Devices," 2nd ed., Wiley Interscience, New York (1981).
16. L. E. Brus, *J. Chem. Phys.*, **79**, 5566 (1983).



Ellipsometric Study of Orientation-Dependent Etching of Silicon in Aqueous KOH

E. D. Palik, V. M. Bermudez, and O. J. Glembocki

Naval Research Laboratory, Washington, DC 20375

ABSTRACT

Ellipsometric measurements (in conjunction with observations of reflectance and cell current and voltage) have been performed in 2M aqueous KOH for Si wafers, of various crystallographic orientations and dopant types, during growth of surface films under anodic and cathodic bias and during open-circuit etch back. The optical effects have been modeled in terms of the formation and removal of thin SiO_x films ($0 \leq x \leq 2$) on the Si surface, with contributions, in some cases, from surface roughness. Changes in the thickness and stoichiometry of the surface SiO_x phase during various treatments provide a basis for a model of the Si etching chemistry and for the orientation dependence of the etch rate.

Orientation-dependent etching of Si is widely used to fabricate microstructures (1-3). Liquids such as aqueous KOH (4, 5), ethylenediamine (6), and hydrazine (7) are used. For these liquids, the etch rates follow the sequence $R\{100\} \approx R\{110\} \gg R\{111\}$, so that a variety of triangular and rectangular grooves and pyramids are made by proper masking with very slow etching SiO_2 (1, 3, 8). Etching is typically done at open-circuit potential (OCP).

In order to extend the versatility of orientation-dependent etching, we are studying the mechanisms for etching (9-12) and for control of the relative etch rates with externally applied bias (13, 14). It has proved useful to measure current and voltage and at the same time to monitor the Si/liquid interface with ellipsometry. For anodic potential, we see growth of a connective layer begin at the passivation potential (PP) and subsequent growth of SiO_2 on top of this connective layer. For cathodic potential, we see the appearance of a layer which grows for days after the potential is fixed. We have modeled these layers as forms of SiO_x in order to fit the experimental behavior of the ellipsometric parameters ψ and Δ . When the potential is released for either of these layers, they etch back slowly until the crystalline silicon interface is reached and fast etching begins. The slow etch back of the anodic-oxide layer is especially interesting, giving sharp dips in ψ and Δ when the connective layer is reached.

These experiments have been performed on n- and p-type Si of either $\{100\}$ or $\{111\}$ orientation over the doping range 10^{14} - 10^{20} cm^{-3} . The results for heavy doping ($> 10^{19}$ cm^{-3}), when all etching stops, have been discussed (15). Differences between the $\{111\}$ and $\{100\}$ surface are large in the case of etch back of anodic oxide and connective layer and small in the case of growth of connective layer and SiO_2 .

We have drawn some conclusions regarding the etching chemistry and suggest that attack of Si back bonds by H_2O and OH^- in sequence is the etching mechanism. This leads to the conclusion that the orientation dependence must depend on the shadowing of the back bonds and the ease or difficulty with which H_2O first, and OH^- second, can react with these shadowed Si-Si bonds.

Experimental Approach

We have used a spectroscopic, polarization-modulation ellipsometer (16) to study the Si/aqueous KOH interface.

A microcomputer read and printed ψ and Δ along with current (I) and potential (V) as controlled by a potentiostat. The ellipsometric parameters are defined by $\tan \psi \exp i\Delta = \tilde{r}_p/\tilde{r}_s$, where \tilde{r} is the complex amplitude reflection coefficient for polarization parallel (p) or perpendicular (s) to the plane of incidence. A standard calomel reference electrode (SCE) and platinum counterelectrode were used. Most experiments were performed at $\sim 22^\circ\text{C}$ in 2M KOH. Samples were Si wafers cleaved into $4 \times 1 \times 0.03$ cm^3 pieces with one side polished. Leads were made with InGa eutectic rubbed into the Si, followed by pressure contact with Cu wire. The liquid was contained in a BK-7 glass (angle of incidence $\theta = 60.2^\circ$) or fused quartz ($\theta = 54.6^\circ$) hollow prism. There were only small differences between data taken with the prism open to air (either with or without bubbling N_2) and the prism closed to air with bubbling N_2 to reduce CO_2 take-up. Therefore, most data were obtained in the presence of only a stream of N_2 bubbles to promote stirring. The I-V curves were obtained as the potential was slowly swept. Double peaks in I occurred in $\{111\}$ samples, the more cathodic one resulting from the $\{110\}$ and other fast etching edges. Coating the back and edges of the sample with glycol thiolate removed this "spurious" peak (15).

While a high level of accuracy is attainable in the ellipsometric measurements through application of various correction and averaging procedures (16), the present experiment requires only that changes in ψ and Δ be monitored in real-time with a high degree of precision. Therefore, we report ellipsometric parameters uncorrected (except where noted) for small systematic errors in the apparatus and stress the changes, $\delta\psi$ and $\delta\Delta$, rather than absolute magnitudes. The precision of the experiment is such that $\delta\psi$ and $\delta\Delta$ as small as 0.01° and 0.02° , respectively, are significant.

We monitored the high voltage bias on the photomultiplier which, as required for the ellipsometric measurements (16), was controlled by a programmable power supply in a feedback loop so as to maintain a constant dc anode current. The product of gain (G) and light intensity (I) impinging on the detector is a constant $GI = C$. Furthermore, G is related to bias voltage V by $\log G = \alpha + \beta V$, where α and β are constants (17). Combining these, we see that a change in unpolarized reflectance δR , leading to a change in intensity δI , corresponds to a δV given by $\log(1 + \delta R/R) = \log(1 + \delta I/I) = -\beta(\delta V)$. The calibration factor,

β , is determined using a neutral-density filter of known transmittance. The minimum detectable $\delta R/R$ was $\sim 5 \times 10^{-3}$, limited by low frequency noise and short-term drift in the light-source output.

Because light incident on the sample is focused (16) (and specularly reflected light is collected) at $\sim f/50$ to minimize the spread in the angle of incidence, the observed $\delta R/R$ is sensitive to intensity lost by scattering of light in nonspecular directions as well as to genuine changes in reflectance resulting from growth and removal of surface layers. A direct consequence of this fact is that we cannot reliably combine $\delta R/R$ with $\delta\psi$ and $\delta\Delta$ to obtain a "three-parameter" fit (n , k , and thickness) to data taken during film growth. However, useful information may be obtained from $\delta R/R$, even when surface texture is changing during film formation (16). In the present work, frequent use will be made of $\delta R/R$ as an indicator of surface roughness. The optical arrangement is such that the observed R is defined by $R = |\tilde{r}_p|^2 + |\tilde{r}_s|^2$ and, hence, represents the "unpolarized" reflectance. The calculated R at 435.8 nm for c-Si ($n = 4.88$, $k = 0.14$) in aqueous KOH at $\theta = 54.6^\circ$ is 0.322.

Model Calculations

The basis for data analysis is a model (12) consisting of a semi-infinite crystalline Si (c-Si) substrate, one or more layers of SiO_x ($0 \leq x \leq 2$), an amorphous SiO_2 (a- SiO_2) oxide film, and an aqueous KOH ambient. Different anodization and etching scenarios can be evaluated by variation of the parameters (complex indexes of refraction, $\tilde{n} = n - ik$, and/or layer thicknesses) and comparison of the observed and calculated $\delta\psi$ and $\delta\Delta$. For c-Si, a- SiO_2 , and 2M KOH, \tilde{n} was obtained from the literature, as described previously (12). For SiO_x , \tilde{n} vs. x was obtained for both the physical- and chemical-mixture models, with the results shown in Fig. 1. Here, the $x = 0$ limit corresponds to amorphous Si (a-Si) and $x = 2$ to a- SiO_2 . The physical model is based on an effective-medium microscopic mixture (18, 19) of a-Si and a- SiO_2 , while the chemical model (19) consists of a statistical distribution of $\text{Si}(\text{Si})_{4-y}(\text{O})_y$ ($0 \leq y \leq 4$) tetrahedra. Since the present experiments were carried out at only a small number of fixed wavelengths, we cannot determine which gives the better representation of the connective layer, and calculations based on either model can fit a given set of data equally well. Hence, most of the following discussion will invoke the computationally simpler (18) physical-mixture model. As noted previously (12), the connective layer is further modeled as an isotropic and homogeneous layer of composition SiO_x . Calculations (20) demonstrate that this is adequate for the present purposes. Our calculations are easily modified to include a large number of thin SiO_x

layers of varying x to represent a connective layer having a graded composition.

Figure 1 also shows \tilde{n} for c-Si at each wavelength (21) as solid circles and illustrates the reason for the high degree of sensitivity of these measurements to the thin SiO_x layer. At 435.8 nm and at 319 nm, \tilde{n} of SiO_x is very different from \tilde{n} of either c-Si or a- SiO_2 , sufficiently so that the effect of the layer on ψ and Δ is well above the precision limit of the experiment. The large variations in \tilde{n} with increasing x , in the $x = 0$ to $x \approx 1.2$ range, also account for the observed behavior of $\delta\psi$ and $\delta\Delta$ during the growth and removal of surface layers. While the experimental approach does not provide chemical information, it does afford a real-time, *in situ* probe of etching dynamics from which insight into the surface electrochemistry can be gained.

Growth of Anodic Oxide Layers

The etching of Si is drastically reduced when an anodic potential is applied. This arises from formation of a passive layer at the expense of the c-Si etching reaction. Ellipsometric results for the anodization process for p {111} Si are shown in Fig. 2 for $\lambda = 435.8$ nm. Here ψ , Δ , I , and V are plotted as functions of time. The features occurring during the first 1.5h result from etch back of the native oxide. Starting at OCP (-1.2V) at $T = 2\text{h}$ (between points d and A), there is virtually no change in ψ and Δ until about -0.7V when passivation begins. Small changes sometimes seen at OCP have been due to bubbles, roughening, or apparent growth of a "cathodic" layer at the effective OCP, which is established by the combined effects of the {111} surface, the {110} and {100} edges, and the rough back of the sample. There is a sudden decrease in Δ of $\sim 1^\circ$ from point A to B, followed by a slow change from B to C. A more rapid decrease in Δ and increase in ψ occurs from point C to D, indicating growth of SiO_2 . The p-type Si was in the dark except for the measurement light; n {111} Si behaves similarly, except that between points B and C, ψ and Δ stop changing. This confirms that holes are needed to grow oxide, but are not necessarily needed in the growth step A-B, which we term connective-layer formation. Illumination of n {111} Si with a 60W light bulb caused oxide to grow beyond B-C.

We have replotted the data in Fig. 2 as Δ vs. ψ in Fig. 3a. There are three distinct regions starting at point A, at which etching takes place and ψ and Δ change slowly as roughening gradually occurs (not shown). The regions A-B, B-C, and C-D follow. Small reverses in the direction of Δ near points B and C, clearer in Fig. 2, are lost in the linewidth of Fig. 3a. Layers grown at potentials up to $\sim 4\text{V}$ we term "soft" anodic oxides, while those formed above $\sim 6\text{V}$ are labeled "hard" anodic oxides. These two layers

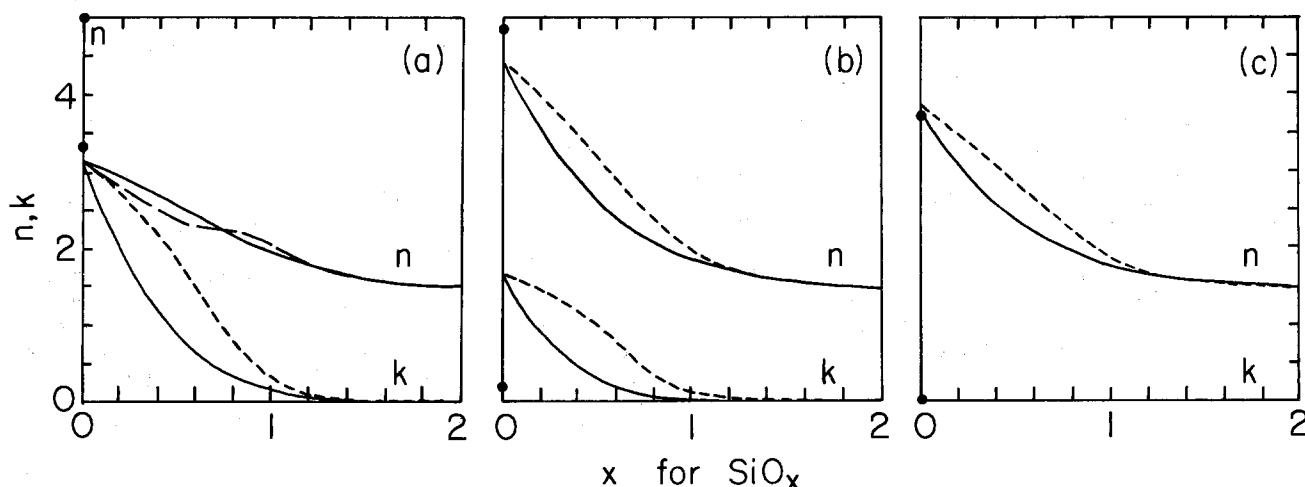


Fig. 1. Optical constants n and k for SiO_x as a function of x at three wavelengths 319.0 (a), 435.8 (b), and 800.0 (c) nm for the physical-mixture model (solid curves) and the chemical-mixture model (dashed curves). The $x = 0$ limit corresponds to amorphous Si (a-Si) and $x = 2$ to amorphous SiO_2 (a- SiO_2). The circles along $x = 0$ ordinate are n and k for c-Si.

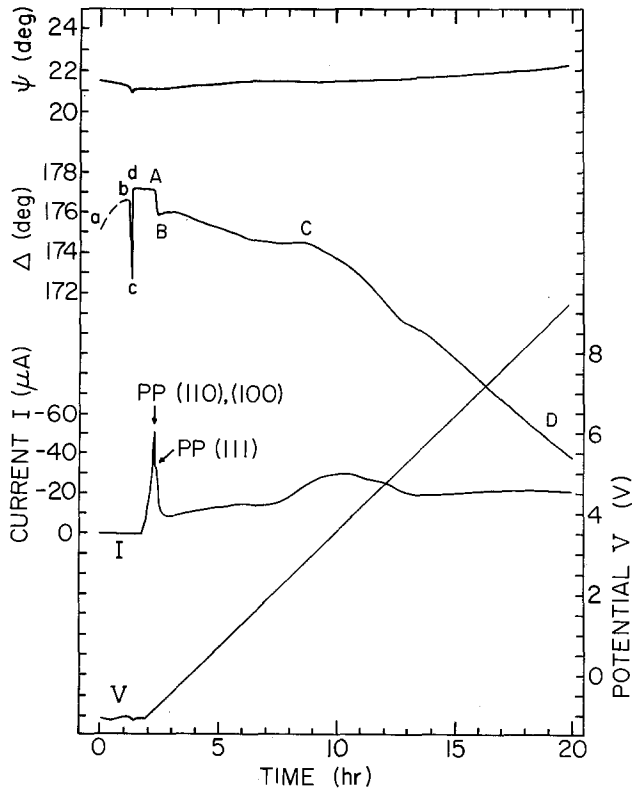


Fig. 2. The etch back and growth of anodic oxide on a p [111] Si sample with resistivity $\rho = 9 \Omega \text{ cm}$ ($1.8 \times 10^{15} \text{ cm}^{-3}$). The potential V (either open circuit or applied), current I , ψ , and Δ are displayed. $\theta = 60.2^\circ$ is the angle of incidence; $\lambda = 435.8 \text{ nm}$. Structure in ψ , Δ , and V during the initial 1.5h arises from etch back of the native oxide. Oxide grown to 1V begins to etch off at point a. Oxide begins to grow at point A.

have drastically different etch back properties when the connective layer is reached (the hard oxide resembling a thermal oxide) which will be discussed in the Etch Back of Anodic Oxides section. Oxide grown to 10V is about 200Å thick (11). Even the sweep speed in Fig. 2 (10 mV/min) is too fast for strict equilibrium, and when the sweep is stopped at 10V, the film continues to grow slowly to about 220Å before I saturates. To interpret the ψ , Δ plot, we first assume an equilibrium etching layer of 4Å of $\text{SiO}_{0.2}$ on top of c-Si at the starting point, A. We have found such a layer necessary for modeling the cathodic process, to be discussed in the Growth of Cathodic Layer section. This layer is also found to give a better fit when comparing ψ , Δ for an etching surface with ψ , Δ for a 10^{20} cm^{-3} p-Si etch-stopped surface (15). Furthermore, it is reasonable to assume that there is not a sharp $\text{H}_2\text{O}/\text{c-Si}$ interface, since the chemical reaction disrupts the crystal lattice near the surface. The exact values of x and thickness assumed for the SiO_x equilibrium etching layer are not critical.

The region A-B was modeled as shown in the inset of Fig. 3b. The $\text{SiO}_{0.2}$ layer is converted to $\text{SiO}_{0.4}$ and thickens suddenly. The region B-C is modeled as further gradation of the connective layer with some SiO_2 growing on top. Finally, at point C, the connective layer stabilizes and only further growth of SiO_2 occurs. Harvey and Kruger (22) have described the anodization process as a series of steps including slowing down of the etching process with accumulation of the soluble products, nucleation on the surface, deposition from a supersaturated solution, and stabilization of the film. Some of these steps are evident in the model in Fig. 3b. Our model also contains the salient features for a connective layer between a- SiO_2 and c-Si suggested by other experiments on thermal oxides (19, 23). The calculated results are shown in Fig. 3b with the SiO_2 thickness indicated by solid circles. The experimental ψ_e axis has been shifted by tenths of a degree with respect to the calculated ψ_c axis to emphasize the agree-

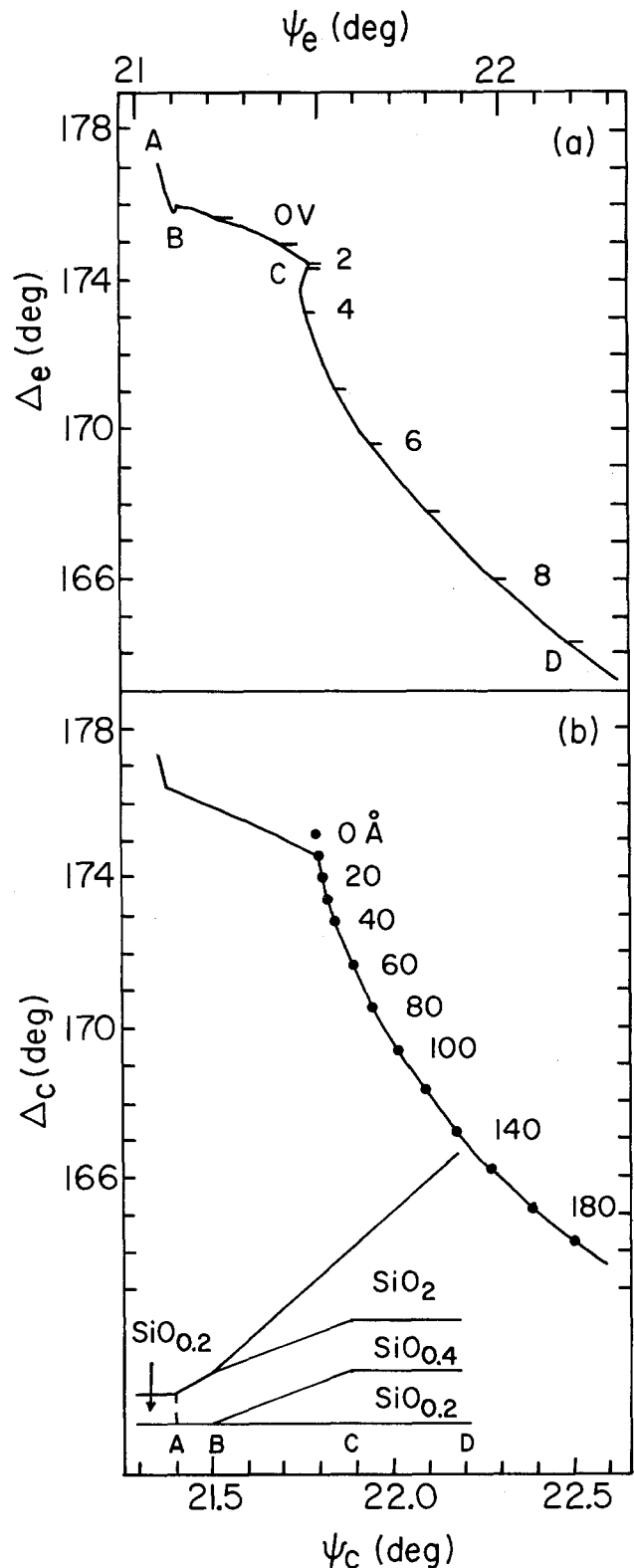


Fig. 3. a: The ψ_e , Δ_e data of Fig. 2 are replotted to show three distinct regions of growth of anodic oxide, A-B, B-C, C-D. Applied potentials are indicated by dashes along curve B-D. b: A model for growth shown in the inset gives results for Δ_c vs. ψ_c similar to the experimental Δ_e vs. ψ_e . The SiO_2 thickness is indicated by the solid circles.

ment between observed and calculated $\delta\psi$ and $\delta\Delta$. Obviously, the connective layer is changing in the region B-C, since the model does not fit the dip in Δ at B and the slight turnback of ψ after point C. On the whole, however, the observed ψ , Δ plot is well reproduced by the model calculation. This model is examined further in the Etch Back of Anodic Oxides section.

Interestingly, for B:Si with a doping density above 10^{19} cm^{-3} the anodization curve lacks with regions A-B and

B-C but shows C-D, indicating that at OCP $\approx -0.7V$ a connective layer has spontaneously formed to passivate the surface (9) and stop the etch (15).

Growth of Cathodic Layer

If at OCP (after etch back of any native oxide) we apply a cathodic bias, the changes in ψ and Δ are quite different from those in Fig. 2, as shown in Fig. 4a for n {111} Si and in Fig. 4b for p {111} Si. After about 0.3V cathodic, we stop the applied potential near $-1.5V$ which occurs within the first half-hour in Fig. 4. During this time, ψ and Δ decrease, indicating that a film is growing on the surface. Interestingly, the layer continues to grow for hours at this potential, slowing down gradually (22h in Fig. 4a and 64h in Fig. 4b). The layer begins to show a gray-tan color. The behavior of Δ vs. ψ is shown in Fig. 5 for n {111} Si and p {111} Si; the same qualitative behavior is observed. Growth of the n {111} layer is more rapid, as indicated by the initial slopes in Fig. 4a and 4b.

When the applied potential is released, the open-circuit potential is initially $-0.8V$ and then increases negatively to $-1.2V$ over 2-3h as the layer dissolves. Initially, Δ vs. ψ follows a path different from that during growth, as indicated by the dashed curves in Fig. 4a and Fig. 5. Only near $\Delta \approx 160^\circ$ does the curve begin to retrace the original path. Upon return to the equilibrium OCP, the final values of ψ and Δ differ only slightly from the initial values, and the gray-tan color has gone.

We have termed the cathodic layer, which has peculiar growth and etch-back characteristics, a "slush" layer. Since it is known (14) that n-Si stops etching for cathodic bias, we assume that the "slush" layer is composed of "incomplete" etch products (whence the term "slush") such as hydrogenated a-Si or incomplete silicates not in a soluble form of $Si(OH)_2(O^-)_2$. The "slush" layer disappears much more rapidly if slight anodic bias near PP is used. This behavior may be a consequence of an increase in OH^- concentration at the surface, which would accompany anodic potentials. The hydroxyl ions would then interact with the "slush" layer to produce "complete" silicates, thereby enhancing dissolution of the layer. It is interesting to note that an anodic current would require an interaction of $-OH$ with the surface (to provide an electron). We carried out a search for Si-H bonds in this

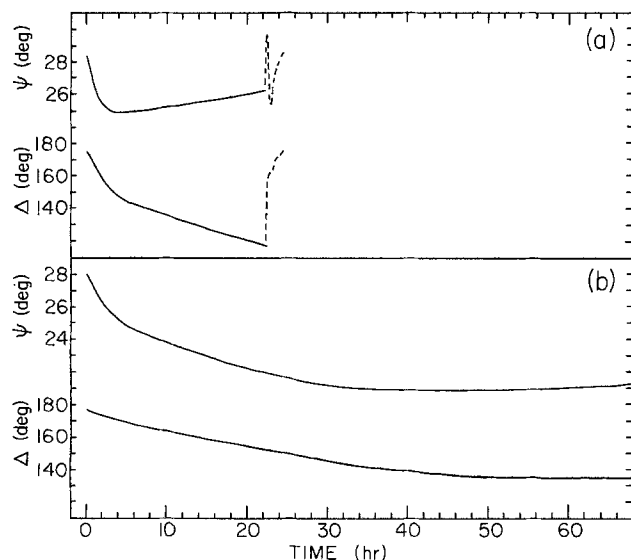


Fig. 4. a: Growth of cathodic slush layer for an n {111} Si sample with $\rho = 0.0045 \Omega \text{ cm}$ ($1.5 \times 10^{19} \text{ cm}^{-3}$) as indicated by the changes in ψ and Δ as a function of time. The cathodic potential was stopped at $-1.5V$ within the first hour, but ψ and Δ continued to change. The dashed curve represents etch back after the cathodic potential was released. Current (not shown) grew quickly as the potential was swept, but continued to grow slowly for hours finally saturating. $\theta = 54.6^\circ$; $\lambda = 435.8 \text{ nm}$. b: Growth of cathodic slush layer for a p {111} Si sample with $\rho = 0.010 \Omega \text{ cm}$ ($1.1 \times 10^{19} \text{ cm}^{-3}$) as indicated by changes in ψ and Δ as a function of time. Etch back is not shown.

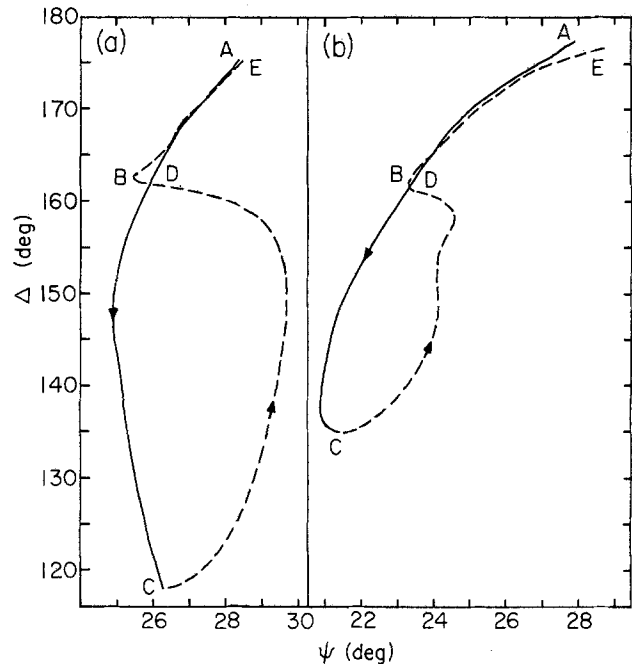


Fig. 5. a: Plot of Δ vs. ψ for growth (solid curve A-C) and etch back (dashed curve C-E) of the slush layer as obtained from the data of Fig. 4a. At A, $T = 0$; at B, $T = 95 \text{ min}$; at C, $T = 1407 \text{ min}$; at D, $T = 1492 \text{ min}$; at E, $T = 1620 \text{ min}$. b: Plot of Δ vs. ψ obtained from the data of Fig. 4b. At A, $T = 0$; at B, $T = 787 \text{ min}$; at C, $T = 2882 \text{ min}$; at D, $T = 2932 \text{ min}$; at E, $T = 4140 \text{ min}$.

layer by Raman backscattering experiments. It was not successful, probably because of the small layer thickness. For the p-Si which maintains its etch rate under cathodic bias (14), the slush layer grows more slowly, suggesting formation of some incomplete silicates but mostly soluble $Si(OH)_2(O^-)_2$. It is not possible to follow growth of the slush layer on the n or p {100} surface for very long, since fast etching of the p surface and slow etching of the n surface produce roughness making interpretation of ψ and Δ difficult.

We have attempted to model the initial growth of the slush layer at small cathodic potential over the first hour. This layer is peculiar in that both ψ and Δ decrease as the layer grows, while for a classical dielectric layer of fixed $n > 1$ and $k \approx 0$, ψ increases and Δ decreases. The simplest model which fits the data is shown in the inset of Fig. 6c. It is vital to assume an equilibrium etching layer (4 \AA of $SiO_{0.2}$) to account for the results (net decrease of both ψ and Δ). In Fig. 6, we show how ψ and Δ would vary for 0.20 \AA of several different SiO_x from $x = 0$ to $x = 0.8$ for three wavelengths. Beyond $x = 0.8$, the curves tend to reverse with the slopes decreasing again. It is not possible to account for the data simply by varying the thickness of the $SiO_{0.2}$ layer. However, if we assume an equilibrium etching layer of 4 \AA of $SiO_{0.2}$ and then allow it to change toward $SiO_{0.8}$ and thicken, then ψ and Δ both decrease, as observed. We cannot specify the exact path from $SiO_{0.2}$ to $SiO_{0.8}$ but have calculated $\delta\psi$ and $\delta\Delta$ from the values of ψ and Δ for $SiO_{0.2}$ before slush-layer growth and for the $SiO_{0.8}$ layer after growth and list them in Table I for n {111} Si and p {111} Si. At each λ the same amount of time from OCP to $-1.5V$ was used; therefore, $\delta\psi$ and $\delta\Delta$ are smaller for the slower growing p {111} layer. For n {111} Si, reasonable agreement with experiment is obtained when a 10 \AA layer of $SiO_{0.8}$ develops. Similar agreement is obtained when an 8 \AA layer of $SiO_{0.8}$ forms on the p {111} Si. Note that $\delta\psi$ is very small at 800 nm compared to 435.8 and 319 nm ; $\delta\Delta$ is only slightly smaller at 800 nm compared to the other wavelengths. This is a direct result of the λ dependence of \tilde{n} vs. x (Fig. 1). Maintaining an $SiO_{0.2}$ equilibrium etching layer under a growing SiO_x layer did not fit the observed decreases in ψ and Δ nearly as well. This model could not account for thicker slush layers.

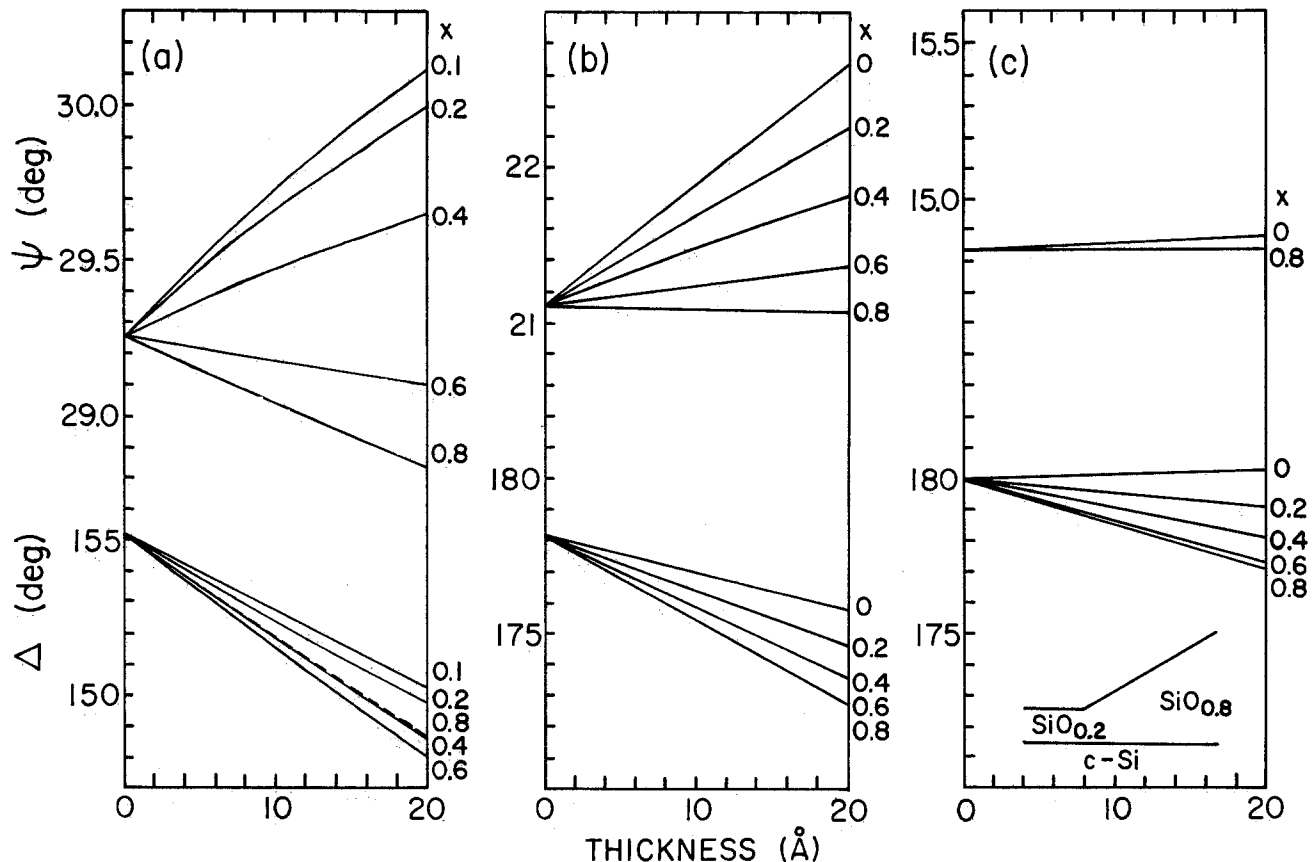


Fig. 6. Calculated changes in ψ and Δ at three wavelengths, 319.0 (a), 435.8 (b), and 800 nm (c), as function of thickness, for different SiO_x layers growing on a c-Si substrate. The curves are used to simulate the change of the 4Å $\text{SiO}_{0.2}$ equilibrium etching layer into a slush layer of $\text{SiO}_{0.8}$ as suggested by the inset in c. $\theta = 60.2^\circ$. In a, the Δ curve for $x = 0.8$ is dashed. In b, the Δ curves for $x = 0.6$ and 0.8 coincide.

Roughness

The etching of {111} and {100} surfaces at OCP produces roughness which is seen visually and in ψ , Δ , and $\delta R/R$. These effects are small on {111} wafers, since this is a slow etching surface, but are much larger on {100} and {110} surfaces. The usual effect is to decrease ψ , Δ , and R . The commercial {111} wafers are oriented to $\pm 1^\circ$. We have measured etch rates between 20 and 90 Å/min (9, 14) on various samples. As noted by Kendall (8), the {111} etch rates are pseudo-etch rates, since the ledges etch faster laterally than the {111} surface etches downward. In fact, for a $1/4^\circ$ -oriented n {111} wafer, we hardly notice H_2 bubbles and can recycle between open-circuit, anodic, and cathodic potentials for tens of hours before ψ and Δ degrade a few tenths of a degree. On the other hand, once the {100} surface is exposed to etchant after the first etch back of the oxide at OCP, roughness occurs in minutes with large changes in ψ , Δ , and $\delta R/R$, and the sample cannot be reused.

We have examined, with an optical microscope at 1000× magnification, {111}, {100}, and {110} surfaces after etching at OCP for a few minutes to hours. Some general features are noticed. After etching for ~2h, n and p {111} surfaces show triangular pits, mostly truncated as shown in

Table I. Experimental and calculated changes in ψ and Δ (in degrees) for a slush layer growing on an n {111} and a p {111} surface for the same amount of time at the same cathodic potential. The calculated values of $\delta\psi$ and $\delta\Delta$ were obtained from Fig. 6 for an initial layer of $\text{SiO}_{0.2}$ 4Å thick converting to a final layer of $\text{SiO}_{0.8}$ 10Å thick for n {111} and 8Å thick for p {111}. $\theta = 60.6^\circ$.

λ (nm)	n {111}				p {111}			
	$\delta\psi_e$	$\delta\psi_c$	$\delta\Delta_e$	$\delta\Delta_c$	$\delta\psi_e$	$\delta\psi_c$	$\delta\Delta_e$	$\delta\Delta_c$
319.0	-0.49	-0.39	-2.2	-2.2	-0.32	-0.34	-1.5	-1.4
435.8	-0.28	-0.27	-2.1	-2.0	-0.22	-0.27	-1.5	-1.5
800.0	-0.06	-0.0	-0.5	-1.3	-0.04	-0.0	-1.1	-1.0

Fig. 7a and 7c. Some samples show many pits, as indicated in Fig. 7a and 7c, while others show few; for the same time of etching, one wafer would show small triangles, and another would show large triangles. When {111} surfaces are etched for 24h or longer, the triangular pits tend to be less distinct with their corners rounded in some cases, so the surface texture appears grainy. These effects (a number of triangular pits and transition to grainy structure) are accelerated on the unpolished back side of the sample. After etching for 15 min, n and p {100} surfaces always show many dark, square pyramidal pits, some truncated, indicating very rough surfaces (Fig. 7e). An n {110} surface shows roughness in narrow bands (Fig. 7g).

When an n {111} surface is made cathodic for ~24h, producing a slush layer, and then returned to OCP until the slush layer dissolves, the surface has a cellular structure resembling triangles with their points rounded off (Fig. 7b). When a p {111} surface is made cathodic for ~24h, producing a slush layer, and returned to OCP until the slush layer dissolves, the surface has less distinct triangular pits (Fig. 7d) smaller than the triangles obtained at OCP (Fig. 7c). Remembering that the n surface stops etching while the p surface continues to etch, we might expect differences in surface textures. The results for n and p {100} surfaces both at OCP and cycled cathodically show similar roughened surfaces (Fig. 7e and 7f) with dark square pits.

The textures obtained at OCP are to be expected based on results in Ref. (24) and (25). The triangular pits for {111} wafers are either truncated or pointed with {111} planes. The {100} wafers show mostly square truncated pyramidal pits with some four-sided, pointed pyramidal pits also; the sides are various {111} planes. The {110} wafer shows boat-shaped pits with various {111} sides. Typical pits observed are drawn oversized next to the photographs for more clarity. Some planes are labeled to suggest ideal structures.

Visual observations of roughness have been augmented by measurements of ψ , Δ , and $\delta R/R$ with similar samples

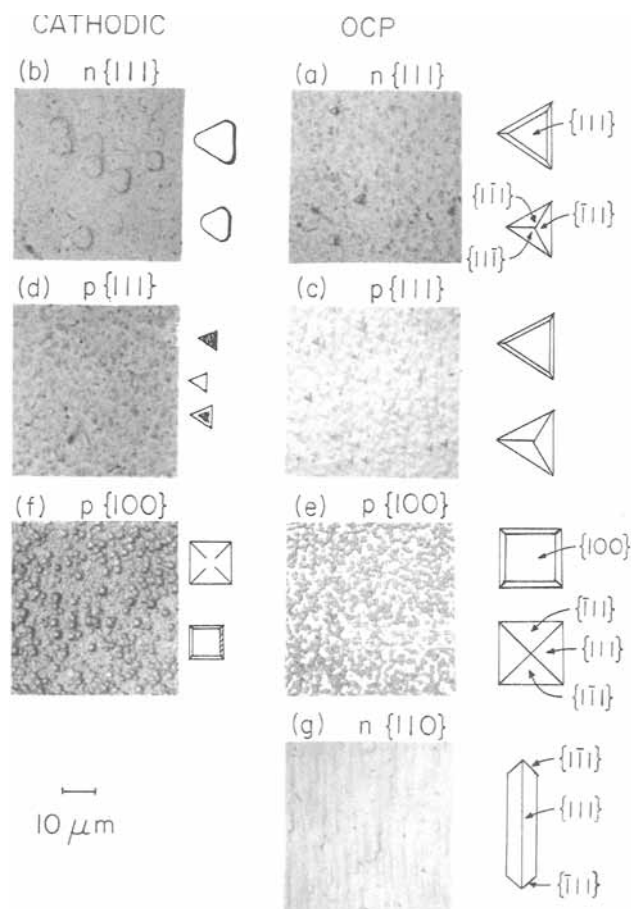


Fig. 7. Photographs of n, p {111}, {100}, {110} surfaces obtained at OCP and cathodic potential. Magnification 1000 \times . Total time of immersion; (a) 120 min, (b) 24h, (c) 120 min, (d) 36h, (e) 20 min, (f) 20h, and (g) 20 min. Typical pit shapes are drawn oversized next to each photograph with some indication of crystal planes.

and conditions. For example, for a {111} surface ψ and Δ are observed to decrease slowly ($\sim 0.1^\circ/\text{h}$) at OCP after an anodic oxide is etched back. A small portion of the decrease is due to bubbles on the surface. This effect varies from sample to sample because the pseudo-etch rate varies with the misorientation. R decreases gradually.

For a {100} surface after etch back of an anodic oxide, ψ and Δ decrease considerably, while R decreases toward zero. These results are in qualitative agreement with the results of Fig. 7a, 7c, 7e, and 7g, i.e., slight roughness for {111} surfaces and large roughness for {100} and {110} surfaces.

However, the triangular truncated pit structure on {111} surfaces suggests that considerable specular reflection still takes place. The results for ψ , Δ , and $\delta R/R$ for several {111} samples have been measured at OCP and suggest that, while ψ and Δ initially decrease by tenths of a degree, they do not decrease further, but R decreases more or less continually over hours. Then, when a connective layer is grown, eliminating bubbles, ψ and Δ tend to return toward their original values (if we take into account the changes in ψ and Δ due to the layer). R , however, does not return to anywhere near its original value. Such a phenomenon (large negative $\delta R/R$ with little effect on ψ and Δ) has been observed (26) for an n {111} Si surface treated with aqueous NaOH. The truncated triangular pits continue to give specular reflection with meaningful ψ , Δ values, while the sides scatter light out of the small collection solid angle of the ellipsometer.

Under cathodic bias the roughness appears somewhat different. The results of Fig. 5 were obtained before we began routinely to measure $\delta R/R$. Similar measurements on other samples were repeated; some are listed in Table II. From point A ($t = 0$) to point B (where the solid and dashed curves separate), there is a small negative change

Table II. Measurement of ψ , Δ , and $\delta R/R$ for slush-layer growth and etch back indicating how reflectance changed in going from point A to point E (in analogy to Fig. 5) for an n {111} sample with $\rho = 0.12 \Omega \text{ cm}$ ($n = 8 \times 10^{16} \text{ cm}^{-3}$) and a p {111} sample with $\rho = 1.4 \Omega \text{ cm}$ ($p = 9 \times 10^{15} \text{ cm}^{-3}$). $\theta = 54.2^\circ$; $\lambda = 435.8 \text{ nm}$.

	n {111}			p {111}		
	ψ	Δ	$\delta R/R$	ψ	Δ	$\delta R/R$
A	26.7	176.5	0	26.15	177.5	0
B			-0.033			0
C			-0.49			-0.19
D			-0.45			-0.087
E	26.85	176.0	-0.34	~ 26.0	~ 177.0	-0.072

in $\delta R/R$. From B to C, $\delta R/R$ increases significantly in the negative direction. This large change is probably partly absorption loss in the slush layer with some continued roughening. When the potential is released at point C, $\delta R/R$ decreases (becomes less negative) at point D, but never reaches its original value of zero. After total dissolution of the layer occurs, ψ and Δ have nearly reached their beginning values, but $\delta R/R$ is still significantly negative. We have listed values of ψ , Δ , and $\delta R/R$ at the points A-E for other samples in Table II mainly to indicate that while ψ and Δ return nearly to their original values, $\delta R/R$ is permanently different, indicating a larger decrease in R for the n {111} surface than for the p {111} surface. The slight differences in ψ and Δ from points A to E may be due to slight bubbling as well as roughness. Note that in each case, slush layer has continued to grow, faster on the n {111} surface than on the p {111} surface. While not obvious in Fig. 7b and 7d, the n {111} surface appears to have larger roughness features than the p {111} surface, in agreement with the results in Table II.

We believe that the slush layer is formed when complete etching, producing soluble $\text{Si}(\text{OH})_2(\text{O}^-)_2$, slows down. As will be discussed below, in the Etching Chemistry section, incomplete etching occurs when H_2O , but not OH^- , attacks Si-Si bonds. The incomplete silicates stick to the surface and accumulate. When complete etching is dominant, the slush layer can only grow slowly, as is observed on a p {111} surface. However, when complete etching is slowed down, the slush layer can grow more rapidly, as is observed on an n {111} surface. It is not obvious what to expect the roughness to do, although, at first glance, the p {111} surface after cathodic treatment might resemble the OCP surface since complete etching has continued. Since complete etching was reduced drastically on the n {111} surface, changes in surface texture might be expected because the etch-rate ratios of various surfaces can be altered with applied bias (14). The results of Fig. 7 and Table II indicate that $\delta R/R$ is greater for the n {111} surface than for the p {111} surface, but we have no model to account for the texture of the cathodic surfaces.

Etch Back of Anodic Oxides

Oxides easily grew on p-Si surfaces but required light to grow on n-Si surfaces. The final thickness was the same for the same potential above PP for both dopant types and both surface planes (11). The etch-back rate of these oxides was generally $\sim 0.3 \text{ \AA}/\text{min}$. However, just prior to the etching of c-Si (indicated by the appearance of H_2 bubbles), the behavior of ψ and Δ varied remarkably with {111} and {100} orientation and with the anodizing potential. Generally these etch-back effects were independent of whether the sample was n- and p-Si. Figure 8 summarizes typical etch-back results for {111} surfaces for both "soft" (Fig. 8a) and "hard" (Fig. 8b) anodic oxides. Also shown are the OCP (which generally increases negatively towards its equilibrium etching value as the anodic oxide layer etches back) and the reflectance change, $\delta R/R$.

For the {111} surface, as etch back of soft anodic oxide occurs (Fig. 8a), there is a sudden dip in ψ and Δ through points b-d, so that at point d, ψ "undershoots" (is less than) its b value and Δ "overshoots" (is greater than) its b

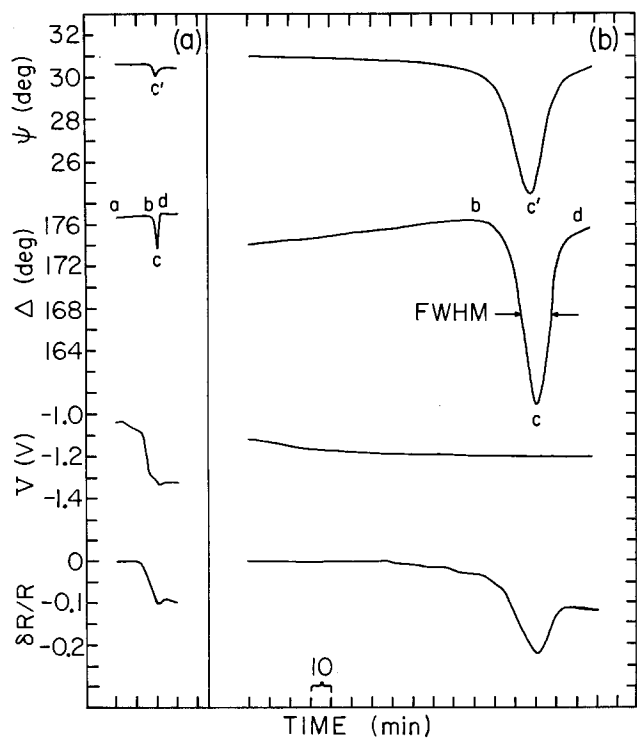


Fig. 8. a: Changes in ψ , Δ , V , and $\delta R/R$ during etch back of a soft anodic oxide on a p {111} Si sample with $\rho = 10.8 \Omega \text{ cm}$ ($1.6 \times 10^{15} \text{ cm}^{-3}$). $\theta = 54.6^\circ$; $\lambda = 435.8 \text{ nm}$. Anodizing potential was 0.3V. b: Changes in ψ , Δ , V , and $\delta R/R$ during etch back of a hard anodic oxide on the same sample. Anodizing potential was 6.5V.

value. The changes in ψ and Δ between b and c are typically $\delta\psi \approx -0.3^\circ$ and $\delta\Delta \approx -3^\circ$ with the dip feature having a full width at half maximum (FWHM) of 2-3 min. Also, point c' occurs after point c in time by a few seconds. At point d, etching of c-Si has commenced, as indicated by formation of H_2 bubbles. The reflectance R also starts to decrease slowly as roughening increases. For the hard anodic oxide in Fig. 8b, the dips in ψ and Δ are huge, with $\delta\psi \approx -6^\circ$ and $\delta\Delta \approx -17^\circ$ with a FWHM of ~ 15 min. In addition ψ and Δ usually both undershoot the respective starting values (point b), and point c' occurs before c in time by a minute or so. There is a large transient dip in R along with a slow overall decrease. Differences in the region b-c-d for the soft and hard oxides of Fig. 8 are dramatic and suggest either different connective layers or different structural effects during etching. It is evident from Fig. 3 that soft oxides are the formative stage of the connective layer, while for hard oxides, the connective layer is in its final form.

We have previously (12) modeled the observed changes in ψ and Δ for the soft oxide on a {111} surface. The model consisted of a c-Si/ $\text{SiO}_{0.4}$ /a- SiO_2 /2M KOH multilayer system. This model has been refined as shown in Fig. 9a, with the SiO_x connective layer modeled as in Fig. 3b. From point a to b, SiO_2 thins down until the graded connective layer is reached. Thereupon, the SiO_x is made more dielectric-like by increasing x to 2.0, followed by dissolution of the resulting SiO_2 and formation of the equilibrium etching layer (4Å of $\text{SiO}_{0.2}$). The horizontal axis is considered to be an arbitrary time scale which could be compressed or expanded to fit experimental results. To simulate linear time, x and d are varied linearly. The results in Fig. 9a for $\lambda = 435.8 \text{ nm}$ are in good qualitative agreement with the typical experimental results of Fig. 9b and 9c, especially as regards the overshoot of Δ

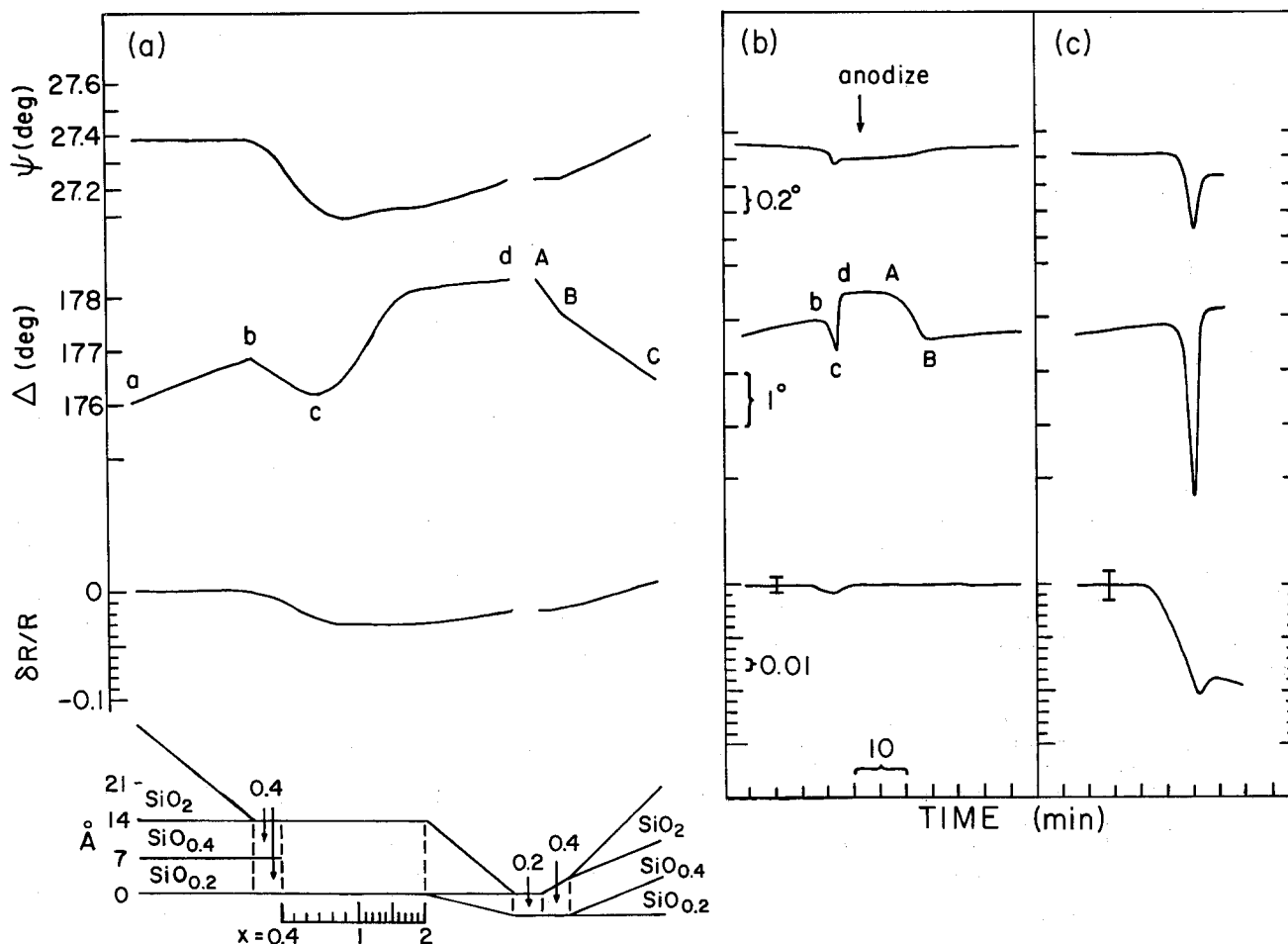


Fig. 9. a: Calculated changes in ψ , Δ , and $\delta R/R$ for the model shown in the inset, to account for the "soft" oxide etch-back results for a {111} Si sample and initial anodization. $\theta = 54.6^\circ$; $\lambda = 435.8 \text{ nm}$. b: Experimental changes in ψ , Δ , and $\delta R/R$ for an n {111} Si sample ($n \approx 1 \times 10^{15} \text{ cm}^{-3}$) with $1/4^\circ$ orientation. Anodizing potential was 0.3V. c: Experimental changes in ψ , Δ , and $\delta R/R$ for a p {111} Si sample ($p = 1.6 \times 10^{15} \text{ cm}^{-3}$). Anodizing potential was 0.3V.

and the undershoot in ψ from point b to d. Also, point c' occurs later in time than c. The reflectance change observed in going from a-b to d ($\delta R/R = -0.1$, Fig. 9c) is substantially larger than the value calculated ($\delta R/R = -0.002$) for simple removal of the SiO_x layer with no contribution from roughness-induced scattering. However, unlike the case for hard and thermal oxides (see below), the reflectance change is in the form of a step, with little or no additional time-dependent structure. The scatter in the high voltage signal before etch back has been converted into a scatter in $\delta R/R$, as indicated by the error bars. Within the scatter in $\delta R/R$ of ± 0.006 , there was hardly any change in reflection for the $\pm 1/4^\circ$ -oriented wafer (Fig. 9b).

The model described above for the removal of the exposed SiO_x connective layer is appropriate to an etching process in which voids filled with silicate material (with an index of refraction like that of SiO_2) are formed. Alternatively, the process could be described in terms of voids filled with the etching electrolyte (having an index like that of H_2O). In either case, the changing SiO_x layer is modeled within the context of an (microscopically rough) effective-medium mixture of a-Si and voids. Optically, the two models are virtually indistinguishable at the wavelengths used here, and, in reality, both probably contribute to making the exposed connective layer "dielectric-like".

The model in Fig. 9a has been extended to the anodization side to compare with the results of Fig. 9b, in analogy to Fig. 3b. While the observed magnitudes of the changes in Δ from B to C (Fig. 9b) are larger than those given by the calculation (Fig. 9a), we have not attempted detailed fits of anodization and etch back to obtain overall better fits. This might be done by using thinner connective layers and/or by changing the values of x slightly. We do not expect the connective layer at point a in Fig. 2 to be exactly the same as the connective layer at point C. These layers depend on the anodizing potential at points a and C.

Finally, we note that, in order to simplify the calculation, we have modeled the etch back as a series of discrete sequential steps; whereas one expects each new process to commence as the previous one is approaching completion. We altered this sequential approach only near point d in Fig. 9a allowing the equilibrium etching layer to develop as the " SiO_2 " layer etched back. The larger dips in ψ and Δ in Fig. 9c as compared to Fig. 9b suggest that here ψ and Δ are being affected by a slight transient roughness.

For the fast etching {100} surface, the soft anodic oxide is seen to etch back with large dips in ψ and Δ with a FWHM of 2-4 min, as Fig. 10a indicates. Then an immediate roughening of the surface occurs as ψ and Δ begin to decrease again with an accompanying large decrease in R . Some of the decrease in ψ and Δ after point d (usually less than half) is due to bubble formation. This is determined by growing the connective layer whereupon the bubbles disappear. Finally, for the hard anodic oxide on a {100} surface, we obtain a large dip in ψ and a decrease in Δ , with R decreasing towards zero within minutes. Part of the large changes in ψ and Δ results from bubble formation on the surface. Bubbles scatter light and tend to decrease ψ and Δ . For example, in Fig. 10b when the potential is changed anodic to produce the first vestige of connective layer (not shown), the dashed curves for ψ and Δ rise to $\sim 26^\circ$ and $\sim 168^\circ$, respectively, as bubbles disappear; $\delta R/R$ changes only slightly under these conditions.

An n {110} surface gave qualitatively similar results for the fast dips in ψ and Δ and decrease in $\delta R/R$ for a soft anodic oxide. A hard anodic oxide gave similar slow dips in ψ and Δ and large decrease in $\delta R/R$.

Roughening Model

The results of Fig. 8 and Fig. 10 indicated that roughening was a problem. The {111} surface can be recycled many times between anodization and etch back with little roughening. Even if left at OCP for hours, it roughens only slightly, ψ and Δ decreasing a few tenths of a degree.

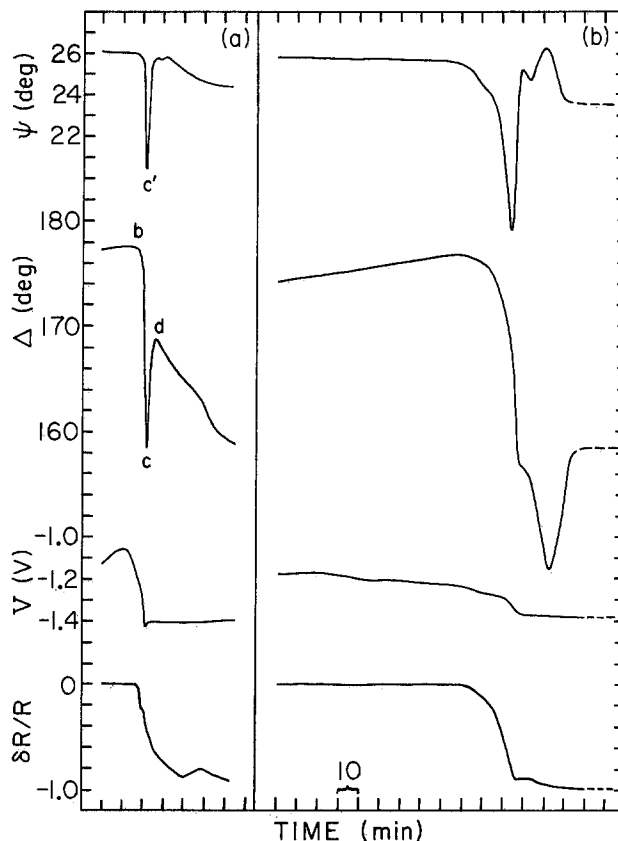


Fig. 10. a: Changes in ψ , Δ , V , and $\delta R/R$ during etch back of a soft anodic oxide on a p {100} Si sample with $\rho = 4.1 \Omega \text{ cm}$ ($4 \times 10^{15} \text{ cm}^{-3}$). $\theta = 54.6^\circ$; $\lambda = 435.8 \text{ nm}$. Anodizing potential was 0 V. b: Changes in ψ , Δ , V , and $\delta R/R$ during etch back of a hard anodic oxide on another part of the same wafer. Anodizing potential was 7.3 V.

However, the {100} surface roughens immediately, so that ψ and Δ do not return to the values at point b but continue to decrease. This problem precludes more than one experiment per {100} sample, except in the case of the soft oxide, where it is possible to reanodize immediately at point d suffering only a few tenths of a degree drop in ψ and δ each cycle.

The $\delta R/R$ data in Fig. 8b indicate a transient roughness-induced light scattering as etching progresses through the n {111} hard oxide connective layer. The value of $\delta R/R = -0.23$ at the reflectance minimum strongly suggests gross macroscopic roughness, rather than a real change in specular reflectance caused by growth of a homogeneous film. Model calculations for a wide range of film \bar{n} and thickness, including those for which the film is taken to be a microscopically rough layer [modeled in the effective-medium approximation (27)], give $\delta R/R$ smaller by an order of magnitude. An estimate of the root mean square roughness σ at the $\delta R/R$ minimum is obtained (28) from $\delta R/R = \exp[-(4\pi n \sigma \cos \theta/\lambda)^2] - 1$, yielding $\sigma \approx 230 \text{ \AA}$. Here, n is the electrolyte refractive index. The fact that σ is at least an order of magnitude greater than the connective-layer thickness provides an important clue to the source of roughness.

We have considered whether it might be useful to model the effects of this transient macroscopic roughness on ψ , Δ , and $\delta R/R$. However, we are aware of no mathematical description of the consequences of roughness, of the type encountered here, for the polarization state of specularly reflected light. Presently available theories (29) treating scattering induced depolarization in ellipsometry are restricted to the small-roughness ($\sigma \ll \lambda/10$) limit and/or the small-slope regime ($\tan \beta \ll 1$, where β is the angle between the local surface tangent and the average surface plane). We note that several studies (30-33) of macroscopically roughened Si surfaces (by chemical or thermal treatment) reported ψ and Δ decreasing with increasing roughness.

Our qualitative model for the origin of transient roughness is based on the value of $\sigma \approx 230\text{\AA}$ [compared to a connective-layer thickness of $\sim 10\text{\AA}$, similar to that observed (19) for thermal oxides] and on the larger FWHM of the etch-back structure in ψ and Δ for hard (10-15 min) vs. soft (2-3 min) oxides.

In order to understand the transient roughness observed upon etch-back of a hard oxide (Fig. 8b), we note the following order for the etch rates for several crystal planes of Si: $R_{100} \approx R_{110} \gg R_{111} \gg R_{SiO_x} > R_{SiO_2}$. We also observe that the roughness for {111} planes is primarily transient, while for the {100} and {110} planes it is permanent. There appears to be a background roughness in Fig. 8b underneath the transient roughness which is comparable to the roughness in Fig. 8a. These facts suggest that the etching of the oxide is nonuniform. This might be due to nonuniformity of the oxide layer thickness or a lateral variation in the stoichiometry of the SiO_x connective layer.

We consider a {111} plane with simple aperiodic texture of oxide due to either of the above reasons as shown in Fig. 11a. We assume SiO_2 etches back at a rate of $\sim 0.3\text{\AA}/\text{min}$. Since the rudimentary connective layer grown at PP is modeled as 7\AA of $\text{SiO}_{0.4}$ and takes $\sim 2\text{ min}$ to etch off, we assume an average etch rate of $\sim 4\text{\AA}/\text{min}$ for the completed connective layer modeled as 14\AA of SiO_x (7\AA of $\text{Si}_{0.2}$ and 7\AA of $\text{SiO}_{0.4}$). For a laterally inhomogeneous connective layer, the area of smaller x will etch faster, presumably because it resembles Si. We assume $R_{111} \approx 25\text{\AA}/\text{min}$ and $R_{100} \approx R_{110} \approx 300\text{\AA}/\text{min}$ for c-Si (14).

Regardless of which $\text{SiO}_x/\text{SiO}_2$ layer is present, the net effect will be to open pinholes, exposing c-Si, as shown in Fig. 11b. At the moment the first c-Si is exposed, the c-Si surface is smooth with $\text{SiO}_x/\text{SiO}_2$ roughness patches. The depth of these patches is D and their width is L . We have now reached the point in Fig. 8b where $\delta R/R$ is about to drop steeply.

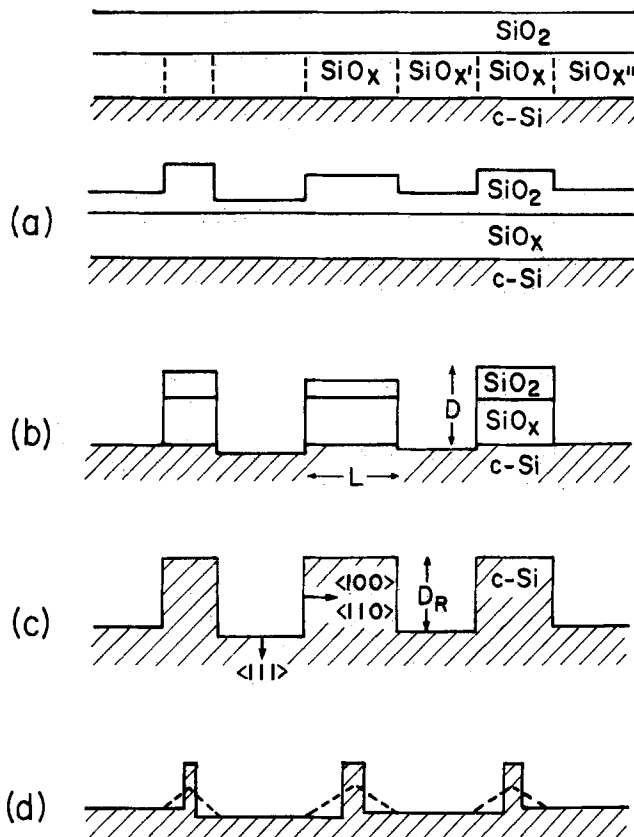


Fig. 11. a: Schematic diagram depicting two possible kinds of inhomogeneity in the $\text{SiO}_x/\text{SiO}_2$ oxide layers. b: Oxide caps remaining when etchant reaches c-Si. c: Etching of c-Si produces wells as last oxide layer etches away. d: Faster etching of c-Si walls in the lateral direction smooths out wells.

Experimentally, we observe that it requires $\sim 20\text{ min}$ to reach the minima in ψ and Δ (this time can be as short as 10 min). This number allows us to estimate the thickness D of the $\text{SiO}_x/\text{SiO}_2$ cap and the depth of the well D_R which is etched in c-Si as indicated in Fig. 11c. Using the values for R_{111} , R_{SiO_x} , and R_{SiO_2} given above, and assuming the SiO_x layer is 14\AA thick, we find that $D \approx 19\text{\AA}$, while $D_R \approx 500\text{\AA}$ in rough agreement with $\sigma \approx 230\text{\AA}$. We have now reached the extremum in $\delta R/R$ shown in Fig. 8b.

The transient effect can be accounted for by noting that the exposed walls of the wells are probably {110} and {100} planes (not necessarily vertical). Thus, the etch rate of the walls is substantially greater than that of the bottom {111} plane. This causes the walls of adjacent wells to approach each other at a rapid rate. Consequently, the thickness L is reduced toward zero. We have reached the plateau in $\delta R/R$ in Fig. 8b after the dips in ψ and Δ . Based on the observation that the dips in ψ and Δ are skewed, we assumed that 10 min (this time can be as short as 5 min) are required for this process. From $R_{100} \approx 300\text{\AA}/\text{min}$, we obtain a maximum value of $L \approx 6000\text{\AA}$ if the fast etching planes are vertical; otherwise, L will be somewhat less by a cosine factor. This characterizes the original aperiodicity in terms of average 19\AA thick $\text{SiO}_x/\text{SiO}_2$ patches which are $\sim 6000\text{\AA}$ across. Obviously, some roughness would persist, as suggested in Fig. 11d, probably as pyramidal pits, since the fast etching planes are not perpendicular to the {111} plane. This crude estimate of the roughness confirms that it is macroscopic in nature (deep, wide bumps). Independent evidence for the formation of pinholes comes from previously reported (34) ellipsometric electroreflectance (field-modulated ellipsometric) data showing that Fermi-level pinning begins just before significant penetration is made into the hard anodic-oxide connective layer.

The behavior of the {100} and {110} faces can be understood by observing that the walls of the exposed wells are probably slow etching {111} planes. Then in Fig. 11c, since $R_{100} \gg R_{111}$, D_R becomes deep and the roughness persists as Fig. 10 indicates, since the walls never etch away completely. It is most likely that random square pyramidal pits with {111} walls are formed after SiO_2 etch back on a {100} surface, as indicated in Fig. 7e.

For the fast etching {100} surface, $\delta R/R$ indicates that, even for the soft oxide, severe macroscopic roughening sets in even before the connective layer has been completely removed. Note in Fig. 7e that the lateral sizes of the pit structures are of the order of a micron.

At this point, we emphasize that the optical effects seen during etch back of the {111} soft-oxide connective layer are distinct from those for the other types of samples (Fig. 9b). First, this system exhibits little or no transient roughness effect above the $\delta R/R$ detection limit. Second, even the slightest degree of anodization (one need go no farther than point B in Fig. 2) gives the results shown in Fig. 8a and 9b during subsequent etch back at OCP. Finally, as discussed above, both the growth (Fig. 3) and etch back (Fig. 9) of the soft-oxide connective layer can be modeled successfully in terms of SiO_x .

As noted previously, based on the results in Fig. 3 and on the different etch-back characteristics of soft, hard, and thermal oxides, we identify the soft anodic oxide with a connective layer. The transition from soft to hard anodic oxide, as characterized by etch-back behavior, has been followed by monitoring the magnitude of $\delta\psi$ and $\delta\Delta$ from point b to c and the FWHM value of the dips (an indicator of the connective layer thickness-to-etch rate ratio) as shown in Fig. 12. The transition is rather abrupt around 5V. Interestingly, a plot of the maximum SiO_2 thickness vs. bias (11) shows a break at 5V, with a slope of $\sim 7\text{\AA}/\text{V}$ below and $\sim 42\text{\AA}/\text{V}$ above this critical bias. Presumably, the final stabilized connective layer is formed above 5V as the true SiO_2 oxide is growing. We have not attempted to fit the curve C-D in Fig. 3a by allowing further changes in connective layer beyond those shown in Fig. 3b.

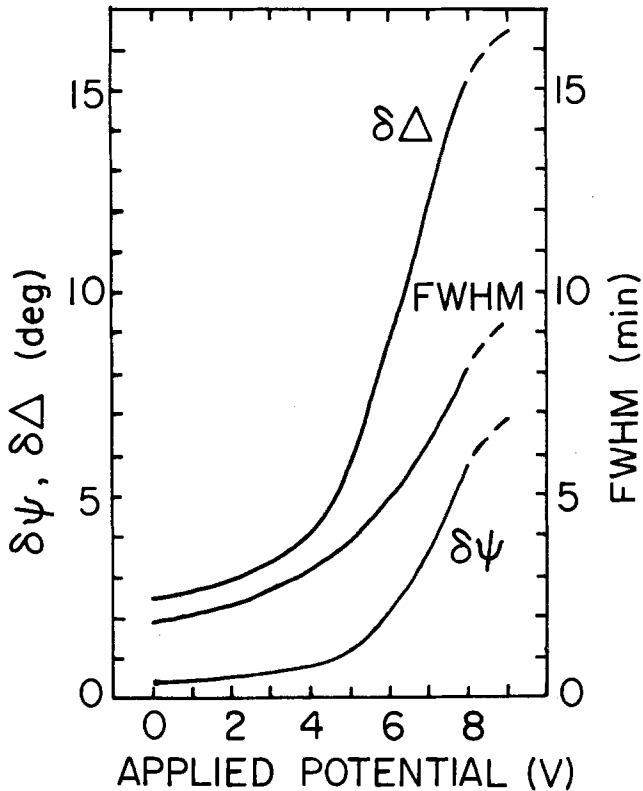


Fig. 12. Changes $\delta\psi$ and $\delta\Delta$ (from point b to c in Fig. 8) and FWHM of the dips in ψ and Δ as functions of anodization potential for several p {111} Si samples with $\rho \approx 9 \Omega \text{ cm}$ ($\sim 1.8 \times 10^{13} \text{ cm}^{-3}$). A smooth curve has been drawn through the many data points (not shown) which scatter by as much as $\pm 50\%$. A transition occurs near 5V from soft to hard anodic oxide. The dashed portions indicate a leveling off as the potential nears 10V. $\theta = 54.6^\circ$; $\lambda = 435.8 \text{ nm}$.

Spectroscopic Experiments

Several attempts were made to obtain the optical spectrum ($800 > \lambda > 250 \text{ nm}$) of a thin layer of soft anodic ox-

ide for the purpose of comparison with calculated (18, 19) results for physical- and chemical-mixture models. Such data would, in the absence of vibrational spectra, provide some insight into the chemical composition of the connective layer in the early stage of formation.

The first step is an accurate measurement of the effective dielectric function, $\langle \epsilon \rangle$, of the clean substrate, in this case taken to be a {111} n-Si wafer etching at OCP in 2M KOH (before point A in Fig. 2). A sample oriented to $1/4^\circ$ was used to minimize roughness effects over the 2h run. $\langle \epsilon \rangle$ is obtained from ψ and Δ vs. λ for the etching substrate using expressions (16) appropriate to a film-free surface. Thus, $\langle \epsilon \rangle$ will differ from the "true" $\epsilon [= \epsilon_1 - i\epsilon_2 = (n^2 - k^2) - i(2nk)]$ if the supposed clean surface actually incorporates a film, such as a thin oxide, an equilibrium etching layer, or microscopic roughness layer. Aspnes and Studna (35) have shown that the presence of such a layer is most easily detected as a reduction of $\langle \epsilon_2 \rangle$, relative to ϵ_2 , at peaks in the optical joint density of states.

Figure 13 shows $\langle \epsilon_1 \rangle$ and $\langle \epsilon_2 \rangle$ for Si obtained during 2M KOH etching. To achieve accuracy, ψ and Δ were determined using two-zone averaging (16, 36) to reduce systematic errors, and the hollow fused-silica prism serving as the sample cell had been carefully annealed after fabrication to eliminate strain-induced birefringence. In obtaining $\langle \epsilon \rangle$ vs. λ from ψ and Δ , the index of refraction of the ambient was computed using a polynomial fit to n vs. λ for H_2O , corrected for the addition of the alkali (12).

The points in Fig. 13 show the results of Aspnes and Studna (35) for an optimally smooth and clean Si surface protected by flowing dry N_2 . The agreement is quite good throughout the whole spectrum, leading us to conclude that—at least for the amount of time required for a set of spectroscopic measurements ($\sim 1.5\text{h}$)—the etching surface remains relatively free of any film sufficiently thick to degrade $\langle \epsilon \rangle$ seriously. Such a film could be an adsorbed layer, an equilibrium etching layer, or a layer of microscopic roughness. Nevertheless, there are small systematic differences between $\langle \epsilon \rangle$ for Si in KOH and the "optimum" $\langle \epsilon \rangle$. The peak value of $\langle \epsilon_2 \rangle$ at the 4.25 eV (292 nm) E_2 critical point is 45.63 vs. 47.87 (35), and $\langle \epsilon_1 \rangle$ is seen to fall slightly below Aspnes-Studna results in the 300

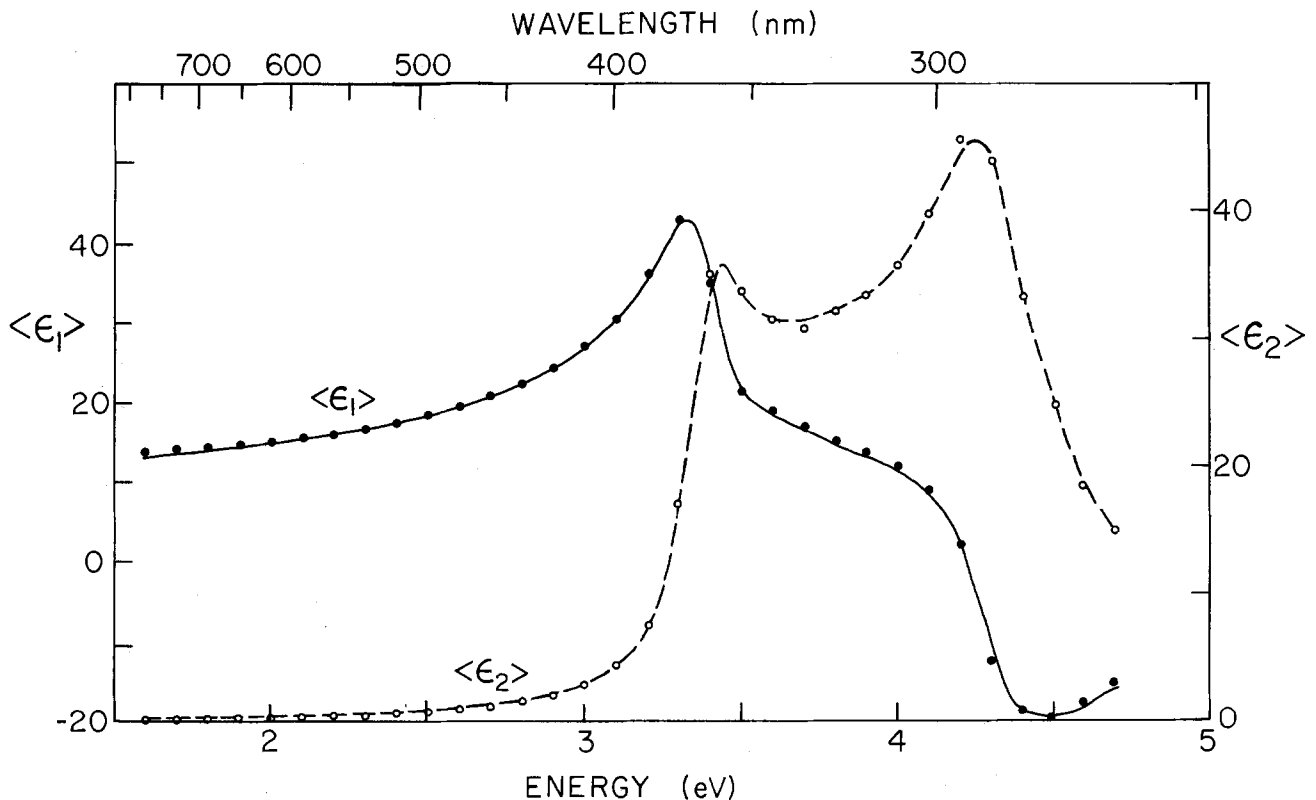


Fig. 13. Real ($\langle \epsilon_1 \rangle$, solid) and imaginary ($\langle \epsilon_2 \rangle$, dashed) effective dielectric functions for Si (n {111} wafer) obtained while etching at OCP in 2M KOH. $\theta = 54.6^\circ$. The points are the data of Aspnes and Studna (35) for a clean, smooth surface protected by dry N_2 .

$< \lambda < 350$ nm range. These discrepancies are consistent with the presence of a very thin equilibrium etching layer (modeled above as 4Å of $\text{SiO}_{0.2}$) on the Si surface in KOH.

Having obtained ψ and Δ vs. λ at OCP, we biased the sample slightly anodically to form the beginning of a connective layer (point B, Fig. 2) and obtained a second set of ψ and Δ . If the A-B process is assumed to consist of the growth of a single isotropic homogeneous film, then $\langle \epsilon \rangle$ of the film can be obtained (16) from $\langle \epsilon \rangle$ of the substrate and the observed $\delta\psi$ and $\delta\Delta$. Unfortunately, ψ and Δ at OCP (and, to a lesser extent, at point B) "drift" with time, largely as a result of slowly increasing microscopic roughness as etching continues. During the measurement time for a set of ψ and Δ vs. λ , these small changes are a significant fraction of the true $\delta\psi$ and $\delta\Delta$ observed during the A-B process at fixed λ . Thus, when $\langle \epsilon \rangle$ of the film is obtained from these data, the result resembles a somewhat broadened and distorted version of the substrate $\langle \epsilon \rangle$ shown in Fig. 13. This result is consistent with formation of a thin microscopically rough surface layer [modeled as an effective-medium mixture (27) of electrolyte-filled voids in a c-Si host].

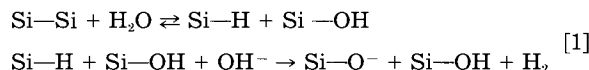
Etching Chemistry

Some possible etching reactions have been discussed previously (37, 38). We base our conclusions on several observations. After dissolution of Si in KOH, Palik *et al.* (10) observed the vibration modes of $\text{Si}(\text{OH})_2(\text{O}^-)_2$ by a Raman scattering experiment. Finne and Klein (39) have observed that 2H_2 are released for each Si dissolved by the ethylenediamine pyrocatechol etchant. We have collected the H_2 from a known amount of Si dissolved in $2M$ KOH and also find 2H_2 per Si.

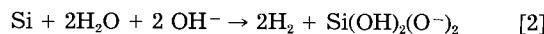
We attempted to determine the OH^- consumed in the etching reaction by titration. Four beakers were prepared, each with an identical volume (50 ml) of the same KOH solution (nominally $2M$). To each of two beakers, a known weight ($\sim 0.5\text{g}$) of $\{100\}$ p-type Si wafer was added, while the other two were left "blank." After the wafers dissolved (several days), all four solutions were titrated to the phenolphthalein end point with $1M$ HCl. Near the end of each titration of the Si solution, the mixture turned viscous with agglomerated solid matter which prevented complete mixing. The volumes of HCl needed to neutralize the two reference solutions and the two etching Si solutions were the same to within 1 ml out of 131 ml. On the assumption that the HCl reacted with both OH^- in solution and OH on the silicate $\text{Si}(\text{OH})_2(\text{O}^-)_2$, the results indicate that the total OH is conserved in the etching process. If one OH^- had been consumed per Si removed, without being replaced by a silicate OH, the difference in titration volumes between sample and blank KOH solutions would have been 18 ml. Therefore, since 2H_2 are observed for each Si which dissolved, it follows that H_2O must be a reacting species. It cannot simply be a catalyst. While this result does not conclusively prove any one mechanism, it eliminates from further consideration any scheme in which OH^- is the only reacting species. Kolbanev and Butyagin (40) ground c-Si continuously in water exposing new surface area and observed conversion of the Si into silicates, with 2H_2 released per Si dissolved. Although it is not clear whether the process of breaking Si—Si back bonds is the mechanical grinding or actual chemical etching, the experiment suggests that Si will dissolve in water if a passivating SiO_2 layer does not grow first. Other experiments (4, 38) have shown that at large OH^- concentration ($>5M$) the etch rate decreases significantly. This could be an indication that H_2O is needed for etching (3). Block (41) reports that Si does not etch in water-free alcohol/KOH solutions. Study of the dissolution of SiO_2 in aqueous hydroxides and in water-free alcohols containing NaOH indicate that water is also necessary for etching silica (42).

From such observations, we conclude that the sequence in etching is hydration of the original surface with SiOH bonds, attack of the Si—Si back bonds by H_2O to form

Si—H and Si—OH, and then attack of the SiH bond by OH^- to form Si—O $^-$ and H_2 . Thus, the etch products are 2H_2 for each Si dissolved and $\text{Si}(\text{OH})_2(\text{O}^-)_2$ as the principal silicate with some $\text{Si}(\text{OH})_3(\text{O}^-)$ and $\text{Si}(\text{OH})(\text{O}^-)_3$ also formed. Also 2 OH^- should be consumed for each Si dissolved, reappearing in the form of $\text{Si}(\text{OH})_2(\text{O}^-)_2$. This may be expressed for one Si—Si bond by the reaction



For dissolution of one Si atom, the net reaction is



These reactions are shown schematically in Fig. 14 for a $\{100\}$ surface.

It is known (43) that the SiH bond is very reactive with OH^- but not with H_2O at pH 7. Thus, while the Si—Si bond can be attacked by H_2O , the second step of attack by OH^- would hardly be present in water. The presence of OH^- in aqueous KOH continues the attack producing a soluble silicate. Note that during the reactions of Eq. [1] no net charge flows across the interface. The electron charge on OH^- "enters" the Si as anodic current in the OH^- attack of the Si—H bond, but then "leaves" as cathodic current on the O $^-$ of the soluble silicate with H_2 evolution. We suggest that OCP etching is chemical rather than electrochemical (12, 14) because it is independent of doping type and density over four orders of magnitude (9).

This model suggests that the cathodic slush layer is formed when H_2O attacks Si back bonds but then OH^- attack is inhibited. An insoluble hydrogenated silicate forms which sticks to the surface. However, subsequent H_2O attack continues and the slush layer thickens. Note that no oxide can grow at cathodic potential to protect the c-Si from H_2O "etch." This layer would be rich in SiH bonds and might resemble hydrogenated Si in a vibrational-spectroscopy experiment. We have previously discussed the bias-dependent etch rates (14, 15) and noted that slush grows faster on n $\{111\}$ surfaces than p $\{111\}$ surfaces, while etching nearly stops on n $\{111\}$ surfaces and slows down slightly on p $\{111\}$ surfaces. Thus, there is a correlation between a drop in etch rate and the growth of slush.

Orientation Dependence

Making H_2O the primary etchant species suggests a reason for the orientation dependence. It has been demonstrated (44) that H_2O adsorbs dissociatively on clean $\{100\}$ and $\{111\}$ surfaces, forming Si—H and SiOH bonds by reaction with the dangling Si bonds. The dissociation of H_2O is found to be ~ 100 times faster on the $\{100\}$ surface compared to the $\{111\}$ surface. However, these experiments, which were carried out in ultrahigh vacuum using very small exposures to H_2O vapor, gave no indication of direct attack of Si—Si bonds by H_2O .

It is not easy to say just how this attack proceeds in the liquid environment. We have built scale models of the $\{100\}$ and $\{111\}$ surfaces shown schematically in Fig. 15 using the appropriate ionic radii for Si and for H_2O and OH. The chemisorbed OH contains an H atom (not shown) which can rotate about the Si—O bond direction. The shadowing of back bonds on the $\{100\}$ surface appears less than on the $\{111\}$ surface, making it harder for an isolated H_2O molecule to bridge two Si atoms on the $\{111\}$ plane to break the Si—Si bond. Moreover, in solution, water, and surely, OH^- are enclosed within hydration spheres so the geometric constraints may be even more severe. For the $\{110\}$ plane, each Si atom has two bonds in the plane, a third pointing up, and a fourth pointing down, also suggesting less shadowing.

The contrast between orientation-dependent etching and orientation-dependent oxidation (45, 46) is interesting. While the $\{100\}$ surface etches ~ 100 times faster than the $\{111\}$ surface, the $\{111\}$ surface oxidizes about 50% faster. In fact, Kendall (7) suggests that the $\{111\}$ surface is slow etching precisely because it is faster oxidizing.

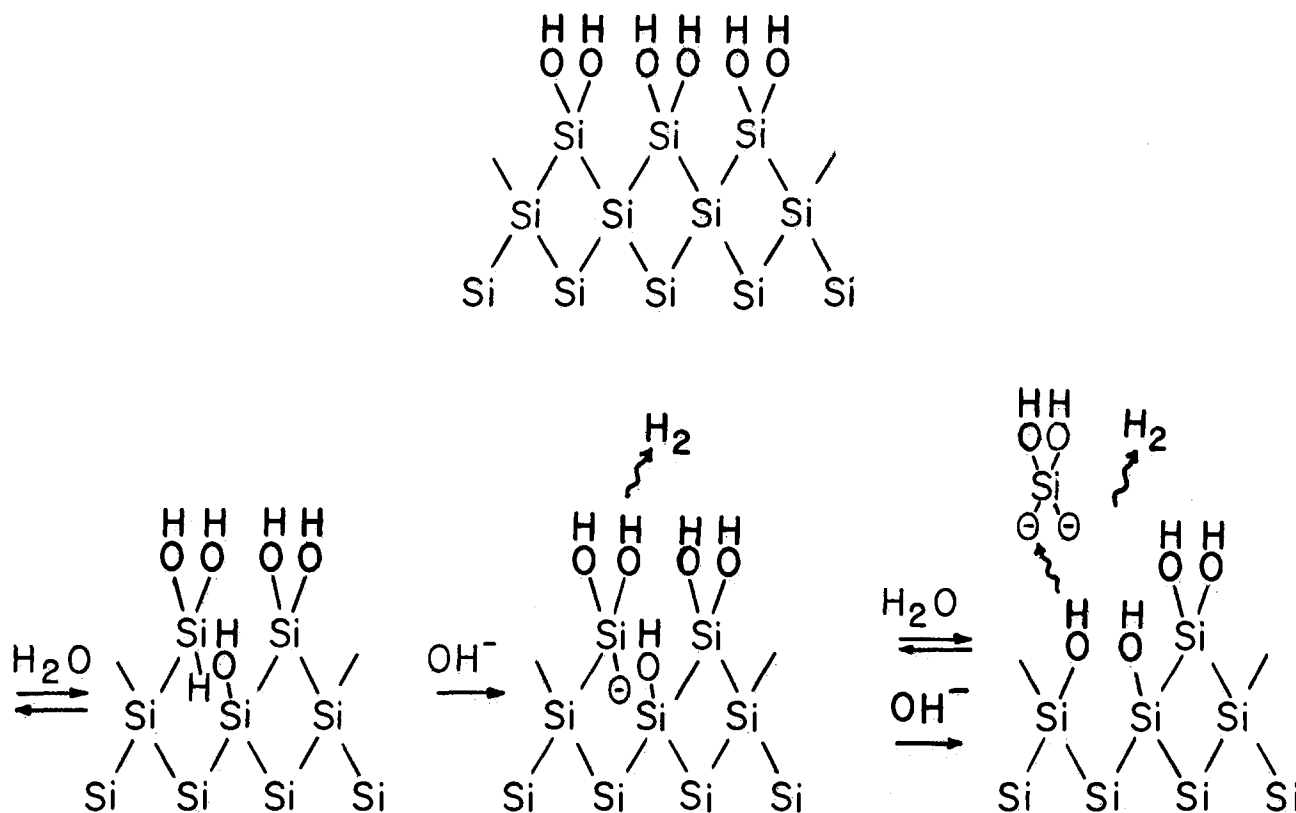


Fig. 14. Schematic diagram of the etching of a {100} surface by H_2O and OH^- in sequence with 2H_2 produced and no net consumption of OH^- for each Si dissolved, since $\text{Si}(\text{OH})_2(\text{O}^-)_2$ is produced. The initial surface is covered by chemisorbed OH which has tied up the dangling bonds, or the OH is the result of etching of the previous Si layer.

Then, "spontaneously" grown oxide effectively stops {111} etching. Since etching in aqueous OH^- solutions is quite different from oxidation with gaseous O_2 or H_2O , we do not expect a direct correlation regarding shadowing arguments, which might suggest that {100} surfaces should oxidize faster than {111} surfaces. We have not measured the anodization rate of {111} and {100} surfaces in aqueous KOH .

It has been suggested (14) that a contributing factor to the orientation dependence was the weakening of back bonds by the surface OH group, which might withdraw charge from $\text{Si}-\text{Si}$ bonds. Therefore, water attack on back bonds would proceed more readily on {100} and {110} surfaces which have two OH groups per atom as compared to one on the {111} face. This effect would manifest itself in the activation energies for the various surfaces. While the activation energies of the {100} and {111} surfaces have been measured to be 16 kcal/mol from the temperature dependence of etch rates (4), it is not clear that the {111} wafers were not misoriented enough to make the pseudo-etch rate dominant. Consequently, the nature of the orientation dependence is still not clear.

Since both H_2O and OH^- are present in aqueous solutions of ethylenediamine (39), sodium hydroxide (37), and hydrazine (7), it is probable that the etching mechanism is the same in these etchants. The control of molarity and additives like alcohols simply varies the concentration of the etching species, blocks the surface, or expedites the removal of etch products.

Summary and Conclusion

The ellipsometric parameters ψ and Δ (together with $\delta R/R$ and I and V for the electrochemical cell) have been obtained under a variety of applied potentials. These data allow us to obtain information about the $\text{Si}/\text{SiO}_x/\text{SiO}_2/\text{aqueous KOH}$ interfaces.

Under cathodic potential, we observed formation of a slush layer, which is characterized as follows: (i) there is more rapid growth on the n-Si {111} surface (etch stopped) than on the p-Si {111} surface (still etching), (ii) ellipsometric results are accounted for by an equilibrium

etching layer of $\text{SiO}_{0.2}$ changing to $\text{SiO}_{0.8}$ and thickening, (iii) measurement of $\delta\psi$, $\delta\Delta$, and $\delta R/R$ indicates that a roughness dependent on carrier type develops as the slush layer grows, and (iv) the layer probably consists of insoluble silicates containing many SiH bonds resulting from incomplete etching by H_2O and/or electrolysis.

Under anodic potentials we have observed that oxide growth occurs in two stages. The soft oxide is characterized by: (i) Growth potentials between PP and 4V anodic of PP. (ii) Ellipsometric results for n- and p-Si {111} surfaces are accounted for by an equilibrium etching layer of $\text{SiO}_{0.2}$ converting to a graded SiO_x layer topped by a beginning SiO_2 layer. We term this SiO_x a connective layer. (iii) Etch back through SiO_x produces small dips in ψ and Δ (-0.3° and -3° , respectively) and a small negative increase in $\delta R/R$ over a time of 2-3 min prior to c-Si etching. (iv) Etch back through the connective layer is modeled as oxidation or hydration of SiO_x so as to reduce the value of \bar{n} .

The hard oxide, which resembles the thermal oxide, has the following properties: (i) growth potentials greater than 6V anodic of PP, (ii) a graded SiO_x connective layer which stabilizes while SiO_2 grows on top, developing out of the connective layer, (iii) etch back produces large dips in ψ and Δ (-6° and -17° , respectively) as well as a large negative increase in $\delta R/R$ over a time of 15-25 min, similar to thermal oxides, (iv) ellipsometric and $\delta R/R$ results of etch back are explained by a transient roughness due to spatial irregularities in oxide thickness or stoichiometry which produce pinholes where rapid Si etching occurs, and (v) results for the fast etching n- and p-Si {100} surfaces could not be modeled because of large roughening effects in general.

From our results we have inferred an etching mechanism which involves H_2O attack on $\text{Si}-\text{Si}$ back bonds followed rapidly for OH^- attack. This model is consistent with the following observations: (i) the soluble etch product is a silicate of the form $\text{Si}(\text{OH})_2(\text{O}^-)_2$, (ii) for each Si atom dissolved, 2H_2 are produced, (iii) the net hydroxyl concentration is constant in the form of hydroxyl ions in solution or hydroxyl groups on silicates, (iv) Si can be

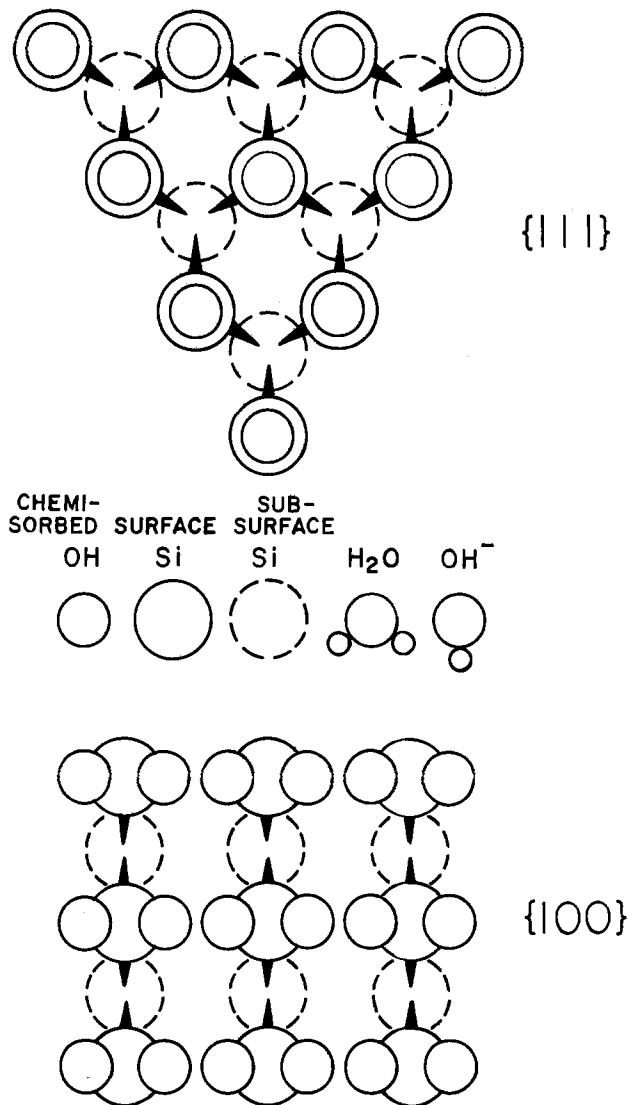


Fig. 15. Schematic diagram of the $\{111\}$ and $\{100\}$ surfaces with H_2O and OH^- molecules suggesting that more shadowing of the back bonds for the $\{111\}$ surface makes attack by H_2O and OH^- less likely with a resultant lower etch rate. Ionic radii were used in constructing the various atoms and molecules.

etched slowly by water (containing a small but finite amount of OH^-) through mechanical grinding, and (v) Si does not etch in water-free alcohol/KOH solutions.

Taking H_2O attack on Si—Si back bonds as the rate-limiting step provides an explanation for the orientation dependence. This strongly suggests that the orientation dependence is determined by a combination of different activation energies and stereoscopic effects having to do with the back-bond geometries on the different surfaces and on the relative ease of approach of the H_2O molecule in an orientation favorable for reaction.

We close by suggesting further experiments to explore some of the issues raised in the present work: (i) A vibrational-spectroscopy experiment using either Raman backscattering or infrared internal-reflection spectroscopy might identify Si—H bonds in the slush layer to help determine its chemical structure. (ii) As previously mentioned, the activation energy for etching of $\{111\}$ surfaces, as opposed to the $\{100\}$ and $\{110\}$ faces, is uncertain due to the fact that the experiments were probably done on misoriented $\{111\}$ samples. Therefore, it still remains to make this measurement on "perfect" $\{111\}$ surfaces to clarify the nature of the orientation-dependent effects. (iii) Our attempts to obtain the spectrum of the connective layer emphasize that a $\{111\}$ surface oriented to better than $1/4^\circ$ is needed. Then, there is a good chance of determining n and k and identifying the stoichiometry of this SiO_x layer and how it evolves into SiO_2 . (iv) Etching

surfaces tend to stay smoother at molarity near saturation, but the etch rate drops considerably. This suggests that repetition of some of the experiments described here would be useful to clarify roughness processes.

Acknowledgments

We thank D. E. Aspnes of Bell Communication Research for his calculated values of ϵ for the SiO_x chemical mixture. J. Freitas of NRL carried out a Raman scattering search for SiH bonds in the slush layer. G. Campisi, of NRL, and J. W. Faust, Jr., of the University of South Carolina, provided help in obtaining and interpreting the photographs of surface roughness. D. L. Kendall, of Instituto Nacional de Astrofisica, Optica y Electronica, Puebla, Mexico, participated in many discussions on etching mechanisms. One of the authors (O.J.G.) is an NRC-NRL Resident Research Associate.

Manuscript submitted July 23, 1984; revised manuscript received Jan. 3, 1985. This was Paper 578 presented at the Washington, DC, Meeting of the Society, Oct. 9-14, 1983.

Naval Research Laboratory assisted in meeting the publication costs of this article.

REFERENCES

1. K. E. Bean, *IEEE Trans. Electron. Devices*, **ed-25**, 1185 (1978).
2. J. B. Angell, S. C. Terry, and P. W. Barth, *Sci. Am.*, **248**, 44 (1983).
3. K. E. Petersen, *Proc. IEEE*, **70**, 420 (1982).
4. J. B. Price, in "Semiconductor Silicon," H. R. Huff and R. R. Burgess, Editors, p. 339, The Electrochemical Society Softbound Proceedings Series, Princeton, NJ (1973).
5. D. F. Weirauch, *J. Appl. Phys.*, **46**, 1478 (1975).
6. A. Reisman, M. Berkenblit, S. A. Chan, F. B. Kaufman, and D. C. Green, *This Journal*, **126**, 1406 (1979).
7. M. J. Declercq, L. Gerzberg, and J. D. Meindl, *ibid.*, **122**, 545 (1975).
8. D. L. Kendall, *Appl. Phys. Lett.*, **26**, 195 (1975); *Ann. Rev. Mater. Sci.*, **9**, 373 (1979).
9. E. D. Palik, J. W. Faust, Jr., H. F. Gray, and R. F. Greene, *This Journal*, **129**, 2051 (1982).
10. E. D. Palik, H. F. Gray, and P. B. Klein, *ibid.*, **130**, 956 (1983).
11. J. W. Faust, Jr., and E. D. Palik, *ibid.*, **130**, 1413 (1983).
12. E. D. Palik and V. M. Bermudez, *J. Phys. (Paris)*, **44**, C10-179 (1983).
13. H. A. Waggener and J. V. Dalton, Abstract 133, p. 450, The Electrochemical Society Extended Abstracts, Vol. 70-2, Atlantic City, NJ, Oct. 4-8, 1970.
14. O. J. Glembocki, R. E. Stahlbush, and M. Tomkiewicz, *This Journal*, **132**, 145 (1985).
15. E. D. Palik, V. M. Bermudez, and O. J. Glembocki, *ibid.*, **132**, 135 (1985).
16. V. M. Bermudez and V. H. Ritz, *Appl. Opt.*, **17**, 542 (1978); V. M. Bermudez, *Surf. Sci.*, **74**, 568 (1978).
17. R. W. Engstrom, "Photomultiplier Handbook," no. PMT-62, RCA, Lancaster, PA (1980).
18. G. Zuther, *Phys. Status Solidi A*, **59**, K109 (1980).
19. D. E. Aspnes and J. B. Theeten, *This Journal*, **127**, 1359 (1980); D. E. Aspnes and J. B. Theeten, *Phys. Rev. Lett.*, **43**, 1046 (1979).
20. G. E. Jellison, Jr., and F. A. Modine, *J. Opt. Soc. Am.*, **72**, 1253 (1982).
21. G. E. Jellison, Jr., and F. A. Modine, *J. Appl. Phys.*, **53**, 3745 (1982).
22. W. W. Harvey and J. Kruger, *Electrochim. Acta*, **16**, 2017 (1971).
23. E. Taft and L. Cordes, *This Journal*, **126**, 131 (1979).
24. J. W. Faust, Jr., in "Surface Chemistry of Metals and Semiconductors," H. C. Gatos, J. W. Faust, Jr., and W. J. LaFleur, Editors, p. 151, John Wiley and Sons, New York (1960).
25. J. W. Faust, Jr., A. Sagar, and H. F. John, *This Journal*, **109**, 824 (1962).
26. M. D. Williams and D. E. Aspnes, *Phys. Rev. Lett.*, **41**, 1667 (1978).
27. D. E. Aspnes, J. B. Theeten, and F. Hottier, *Phys. Rev. B*, **20**, 3292 (1979). D. E. Aspnes, A. A. Studna, and E. Kinsbron, *Phys. Rev. B*, **29**, 768 (1984).

28. H. E. Bennett, *J. Opt. Soc. Am.*, **53**, 1389 (1963).
29. T. V. Vorburger and K. C. Ludema, *Appl. Opt.*, **19**, 561 (1980).
30. S. Kono, L. J. Hanekamp, and A. Van Silfhout, *Surf. Sci.*, **65**, 633 (1977).
31. K. K. Svitashov, A. I. Semenenko, L. V. Semenenko, and N. L. Shvarts, *Opt. Spektrosk.*, **43**, 88 (1977); *Opt. Spectrosc. (USSR) Engl. Transl.*, **43**, 161 (1977).
32. M. A. Hopper, R. A. Clarke, and L. Young, *Surf. Sci.*, **56**, 472 (1976).
33. R. B. Bendere, R. P. Kalnynya, and I. A. Felty, *Opt. Spektrosk.*, **53**, 507 (1982); *Opt. Spectrosc. (USSR) Engl. Transl.*, **53**, 299 (1982).
34. O. J. Glembocki, in "Spectroscopic Characterization Techniques for Semiconductor Technology," p. 130, SPIE Vol. 452 (1983).
35. D. E. Aspnes and A. A. Studna, *Phys. Rev. B*, **27**, 985 (1983).
36. V. M. Bermudez, *Opt. Commun.*, **23**, 413 (1977), erratum, *ibid.*, **24**, 366 (1978); F. A. Modine, G. E. Jellison, Jr., and G. R. Gruzalski, *J. Opt. Soc. Am.*, **73**, 892 (1983).
37. S. M. Repinskii and S. V. Pershkova, *Zh. Fiz. Khim.*, **46**, 896 (1972); *Russ. J. Phys. Chem.*, **46**, 519 (1972).
38. S. O. Izidinov, *Zh. Prikl. Khim.*, **44**, 1642 (1971); *J. Appl. Chem. USSR*, **44**, 1660 (1971).
39. R. M. Finne and D. L. Klein, *This Journal*, **114**, 965 (1967).
40. I. V. Kolbanov and P. Yu. Butyagin, *Kinet. Katal.*, **23**, 327 (1982); *Kinet. Catal. (USSR) Engl. Transl.*, **23**, 271 (1982).
41. B. Block, B. Block, Inc., Los Altos, CA, Private communication.
42. J. G. Hooley, *Can. J. Chem.*, **39**, 1221 (1961).
43. F. A. Cotton and G. Wilkinson, "Advanced Inorganic Chemistry," 4th ed., Chap. 12, Wiley-Interscience, New York (1980).
44. S. Ciraci and H. Wagner, *Phys. Rev. B*, **27**, 5180 (1983); H. Ibach, H. Wagner and D. Bruckmann, *Solid State Commun.*, **42**, 457 (1982); Y. J. Chabal and S. B. Christman, *Phys. Rev. B*, **29**, 6974 (1984).
45. K. E. Bean and P. S. Gleim, *Proc. IEEE*, **57**, 1474 (1969).
46. R. L. Ligenza, *J. Phys. Chem.*, **65**, 2011 (1961).

n-Type Behavior of Chromium (III) Oxide

E. W. A. Young, P. C. M. Stiphout, and J. H. W. de Wit*

Department of Inorganic Chemistry, State University Utrecht, 3522 AD Utrecht, The Netherlands

ABSTRACT

The character of the electronic charge carriers under various conditions in chromium (III) oxide was investigated using Seebeck measurements on sintered compacts of Cr_2O_3 in the temperature range 800-1800 K. The compacts were prepared by various sintering procedures. Depending on the pretreatment of the compacts, n- or p-type materials were obtained. p-Type material resulted after sintering in an atmosphere with a high oxygen partial pressure. Sintering in an atmosphere with low oxygen partial pressure, however gave n-type material. This n-type behavior could be frozen in by cooling the compacts below 1100 K. These experimental results provide evidence for Cr interstitials being the predominating point defects in Cr_2O_3 at low oxygen partial pressure.

Chromium and many technologically important chromium containing alloys owe their high temperature oxidation resistance to the formation of protective Cr_2O_3 layers (1). The oxidation mechanism is determined by the transport properties of the formed Cr_2O_3 layer. Therefore, knowledge of the nature of the mobile species in the oxide forms the basis for the elucidation of the reaction mechanism (2, 3).

The oxidation kinetics of chromium and its alloys as well as the defect structure of bulk chromium (III) oxide have been subject to extensive studies. Considerable knowledge of the growth mechanism of Cr_2O_3 scales has accumulated. Measurements on bulk chromium (III) oxide indicated that the oxide had a metal-deficient defect structure (4). Therefore it was assumed until recently that during thermal oxidation the chromium (III) oxide layers grew by diffusion of chromium vacancies. Kofstad and Lillerud, however, concluded in a review paper on all the experimental data available that, at low oxygen partial pressures, chromium interstitials are the predominating point defects in Cr_2O_3 (3). This means that Cr_2O_3 should behave as an n-type material at low oxygen partial pressures. Kofstad and Lillerud suggest that only at relatively high oxygen partial pressures, including normal atmospheric pressure, should the material show p-type behavior. The p-type behavior of bulk Cr_2O_3 has been described in literature (5, 6). However, direct evidence for the n-type character at low oxygen partial pressures, in the form of Seebeck measurements, has not been published yet.

We have performed Seebeck coefficient measurements on sintered Cr_2O_3 compacts. Special attention was paid to the equilibration time of the samples at various temperatures and oxygen partial pressures.

Experimental

Chromium (III) oxide (Puratronic 99.999%) powder was pressed to tablets, uniaxially at a pressure of 4×10^8 Pa (0

= 8 mm, length = 15 mm). These tablets were sintered in an alumina tube furnace, in a chromium (III) oxide-coated alumina boat. Various sinter procedures were followed. A first series of samples was sintered in air at 1900 K for 3h. Only poorly sintered compacts were obtained this way (density 65%) (type A, Fig. 1A). A second series of samples was sintered at low oxygen partial pressure [after Ownby and Jungquist (7)] in a $\text{H}_2/\text{H}_2\text{O}$ (1% H_2O) mixture. Heating of the tablets up to 1770 K for 1h and cooling them in the same atmosphere resulted in moderately sintered compacts (density 85%) (type B, Fig. 1B). At 1770 K, the oxygen partial pressure of the gas mixture is 10^{-13} atm. After sintering at higher temperature, 1920 K, for 3h in $\text{H}_2/\text{H}_2\text{O}$ (1% H_2O), large grained high density samples were obtained (density 95%) (type C, Fig. 1C). At 1920 K, an oxygen partial pressure of 2×10^{-12} atm is obtained in the gas mixture.

Finally, samples sintered in CO/O_2 (0.2% oxygen) at 1770 K were prepared (p_{O_2} is 4×10^{-13} atm at 1770 K). These compacts, again, only show a moderate density (density 85%) (type D).

The sintered samples were mounted in an all-alumina Seebeck effect measuring system and pressed between two insulating alumina tablets. Only during the short period of time necessary to observe the Seebeck coefficient, Pt/Pt 10% Rh thermocouples were pressed onto the sample-ends, through a hole drilled through the two alumina tablets. The platinum leads of the thermocouples were also used for the measurement of the thermoelectric power. In this way a permanent heating of the thermocouples during equilibration of the samples could be avoided. Their lifetime was greatly enlarged, and the contamination of the samples with platinum could be kept to a minimum.

All Seebeck measurements were performed in air. Unless stated differently, the samples were given 24h equilibration time after each temperature change. The reported Seebeck coefficients are the average values from

*Electrochemical Society Active Member.

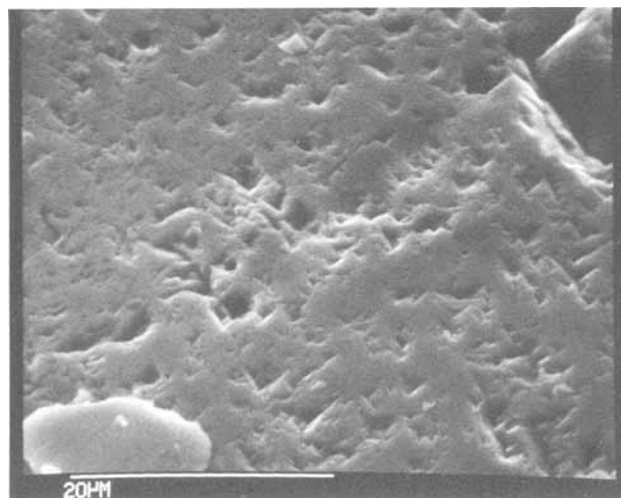
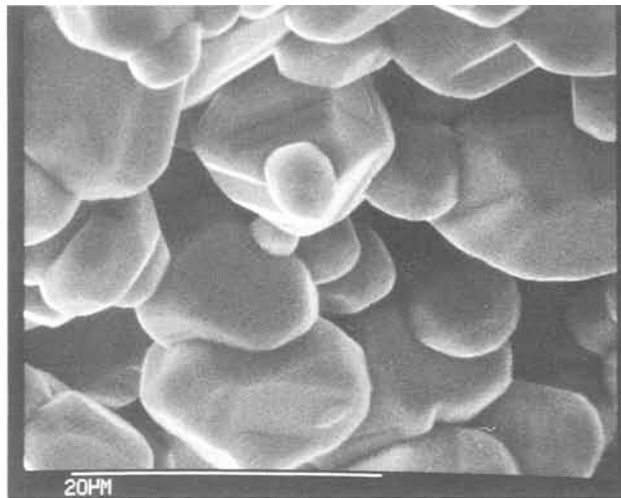
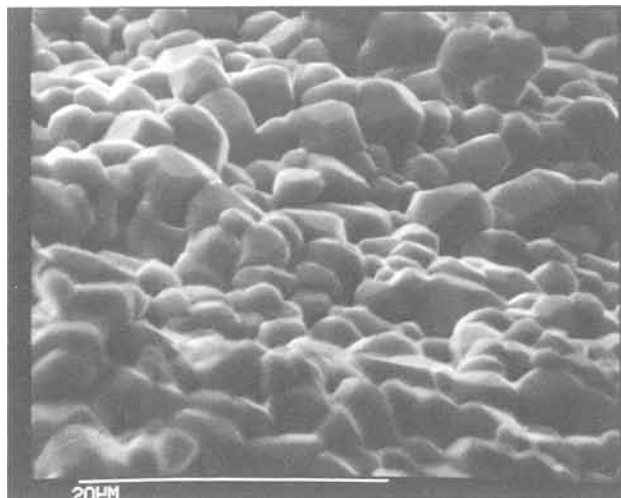


Fig. 1. A: SEM of a "porous" Cr_2O_3 compact (density 65%) sintered in air, 1920 K, 3h (type A). B: SEM of a "porous" Cr_2O_3 compact (density 85%) sintered in $\text{H}_2/\text{H}_2\text{O}$, 1770 K, 1h (type B). C: SEM of a "high density" Cr_2O_3 compact (density 95%) sintered in $\text{H}_2/\text{H}_2\text{O}$, 1920 K, 3h (type C).

measurements performed at three different temperature gradients at the same average temperature. Different temperature gradients were obtained by moving the samples in the hot zone of the furnace. The difference between the temperature at the hot and the cold end of the samples never exceeded 30° during measurements. The reproducibility of two parallel runs was within 5%.

Results

The sintering procedure turned out to have a major influence on the electronic properties of the samples.

All air-sintered samples show p-type behavior. The thermoelectric power of these air-sintered samples is independent of temperature up to 1300 K and decreases at higher temperatures from 750 to $300 \mu\text{V}/\text{K}$ at 1750 K (Fig. 2).

This is in accordance with Seebeck measurements reported by Hay *et al.* (5) and data of Fischer and Lorenz (6) for measurements at atmospheric oxygen pressures. Samples sintered in an atmosphere with a low oxygen partial pressure ($\text{H}_2/\text{H}_2\text{O}, \text{CO}/\text{O}_2$), however initially in air at temperatures below 1100 K show n-type behavior. A high temperature treatment in air alters the Seebeck coefficient of these samples.

The porous samples (Fig. 1B) rapidly shift from n- to p-type above 1300 K. Once shifted and equilibrated, the same variation of the thermoelectric power with temperature is measured for these samples as for the air-sintered samples. As can be expected, at lower temperatures more time is required for the n- to p-shift of the samples. A summary of the measured n- to p-shifts is given in Fig. 3. In Table I, a general survey of our results has been given.

Several samples already shifted from n- to p-type were given a new high temperature treatment at 1770 K in an atmosphere with a low oxygen partial pressure. These

samples, initially, at low temperatures show n-type behavior again. A new high temperature treatment in air shifts them back to p-type. These observations show that the n-to-p shift is a reversible process and that a possible contamination of the samples during the various heat-treatments cannot be the cause of the shift.

The large grained (n-type), high density samples (Fig. 1C) are not influenced by a heat-treatment in air below 1750 K. These samples simply remain n-type. However heating these compacts for several hours at 1870 K in air slightly reduces the thermoelectric power of these compacts.

Discussion

We interpret the n-type behavior as observed in air at low temperatures for the Cr_2O_3 compact (sintered in an at-

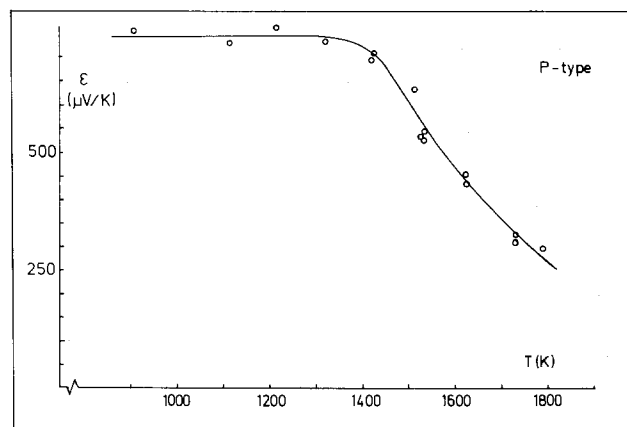


Fig. 2. Thermoelectric power of a Cr_2O_3 compact sintered in air (type A) as a function of temperature.

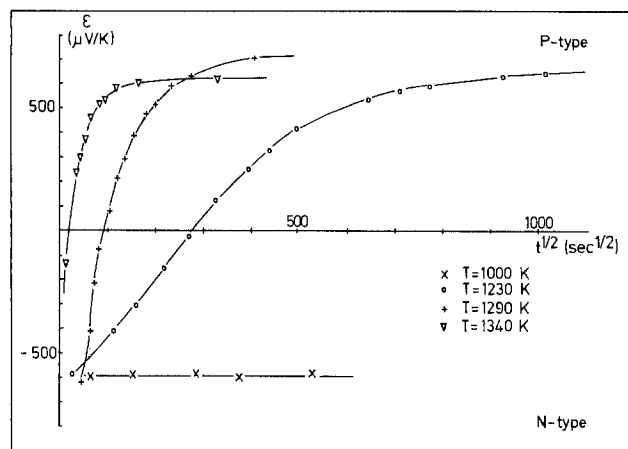


Fig. 3. Thermoelectric power of Cr_2O_3 compacts sintered in $\text{H}_2/\text{H}_2\text{O}$ (type B) measured in air as a function of time.

mosphere with a low oxygen partial pressure) as the result of a frozen in state.

At high temperatures, the compacts equilibrate with the surrounding atmosphere (air). Equilibration results in a shift from n- to p-type character of the samples.

The observed n-type behavior of chromia confirms the interstitial cation model of Kofstad and Lillerud (3). These authors based their interstitial model on an overall consideration of many defect depending properties, i.e., the sintering behavior of Cr_2O_3 while additional evidence was obtained from oxidation experiments (8, 9). Recently, high temperature oxidation experiments of Hindam and Whittle on chromium and chromium alloys provided evidence for the interstitial model (10). Various studies on the electrical behavior of Cr_2O_3 were performed, including the behavior at low oxygen partial pressures (5, 6, 11, 12). The conductivity measurements by Matsui and Naito suggest n-type behavior at low oxygen partial pressures (11). However, the n-type behavior of Cr_2O_3 at low oxygen partial pressures has never been measured directly from thermoelectric power observations. Hay *et al.* measured the thermoelectric power of Cr_2O_3 as a function of the oxygen partial pressure (5). There is a fair agreement between our experimental results and those reported by Hay *et al.* for measurements in near atmospheric oxygen partial pressures. A large discrepancy is found for the data measured at low oxygen partial pressure. Hay *et al.* observed a decreasing thermoelectric power with decreasing oxygen pressure, but they never obtained n-type material, not even in an atmosphere with a p_{O_2} of 10^{-20} atm at a temperature of 1850 K. Unfortunately, the authors do not give any experimental details concerning the density of their samples, the atmosphere nor the equilibration times that they used. Besides, the purity of the samples is not known.

Our equilibration measurements (Fig. 3) show that very long times are needed already for the equilibration of highly porous material. The large grained, high density samples we investigated (type C), in which gas-phase transport and grain boundary diffusion is reduced, even fail to equilibrate at 1870 K at all. New chromium tracer diffusion data (for single crystals), published by Hoshino and Peterson (13), show a very low self-diffusion coefficient of chromium ($10\text{--}13 \text{ cm}^2/\text{s}$ at 1770 K). Such low tracer diffusion data also predict a slow equilibration of Cr_2O_3 , as we observed ourselves. It can be assumed, therefore, that the Cr_2O_3 compacts studied by Hay *et al.* were not fully equilibrated with the low oxygen partial pressures of the atmosphere they used during measurements.

Fischer and Lorenz (6) as well as Hagel and Seybolt (9) did, in contrast with Matsui and Naito (11), not find a clear oxygen partial pressure dependence of the electrical conductivity. However, Fischer and Lorenz did not use very pure chromium oxide and nonpurified argon gas was used to control the atmosphere. This means that the atmosphere probably contained a fair amount of oxygen.

Table I. General survey of results

Sample type	Sinter conditions				Results	
	Gas	T (K)	t (h)	Density %	Sign thermoelectric power	
					After sintering	After heat-treatment in air
A	air	1920	3	65	p	p
B	$\text{H}_2/\text{H}_2\text{O}$	1770	1	85	n	p
C	$\text{H}_2/\text{H}_2\text{O}$	1920	3	95	n	n
D	CO/O_2	1770	1	85	n	p

Hagel and Seybolt used hot-pressed samples with a high density for their conductivity measurements, but short equilibration times (30 min). Thus it cannot be expected that n-type behavior would have been found by these authors.

Conclusions

From the above thermoelectric power measurements it was concluded that chromium (III) oxide equilibrated with a low oxygen partial pressure will behave as an n-type material.

Hoshino and Peterson (13), however, concluded from the increase of the chromium tracer diffusion coefficient with increasing oxygen partial pressure that Cr vacancies are the predominating defects in Cr_2O_3 even at low oxygen partial pressures. Thus the material would be p-type.

Our thermoelectric power measurements, the oxidation experiments by Hindam and Whittle (10), and the electrical conductivity data of Matsui and Naito (11) indicate that Cr interstitials are the predominating point defects at low oxygen partial pressures. Hoshino and Peterson themselves already call attention to the fact that both the temperature and the oxygen activity range for their measurements were severely limited, thus, possibly, giving misleading results. In all, one can conclude that, probably, in chromium (III) oxide, at low oxygen partial pressure, e.g., at the scale metal interface of thermally oxidized chromium and Cr alloys, Cr interstitials will be the predominating point defects.

In order to further solve the defect structure of chromium (III) oxide, additional measurements on the relation between the thermoelectric power and the oxygen partial pressure are being taken.

Manuscript submitted April 4, 1984; revised manuscript received Nov. 29, 1984.

State University Utrecht assisted in meeting the publication costs of this article.

REFERENCES

- D. P. Whittle and J. Stringer, *Philos. Trans. R. Soc. London, Ser. A*, **295**, 309 (1980).
- O. Kubaschewski and B. E. Hopkins, "Oxidation of Metals and Alloys," Butterworth, London (1962).
- P. Kofstad and K. P. Lillerud, *This Journal*, **127**, 2410 (1980).
- P. Kofstad, "Non-stoichiometry, Diffusion and Electrical Conductivity in Binary Metal Oxides," Wiley-Interscience, New York (1972).
- K. A. Hay, F. G. Hicks, and D. R. Holmes, *Werkst. Korros.*, **21**, 917 (1970).
- W. A. Fischer and G. Lorentz, *Z. Phys. Chem. NF.*, **18**, 308 (1958).
- P. D. Ownby and G. E. Jungquist, *J. Am. Ceram. Soc.*, **55**, 433 (1972).
- P. Kofstad and K. P. Lillerud, *Oxid. Met.*, **17**, 177 (1982).
- K. P. Lillerud and P. Kofstad, *ibid.*, **17**, 127 (1982).
- H. Hindam and D. P. Whittle, *This Journal*, **130**, 1519 (1983).
- T. Matsui and K. Naito, *J. Nucl. Mater.*, **120**, 115 (1984).
- W. C. Hagel and A. U. Seybolt, *This Journal*, **108**, 1146 (1961).
- K. Hoshino and N. L. Peterson, *J. Am. Ceram. Soc.*, **66**, C202 (1983).

MOS Capacitors on Cadmium Telluride

R. T. Talasek and A. J. Syllaios*

Texas Instruments, Incorporated, Equipment Group, Dallas, Texas 75266

ABSTRACT

The behavior of MOS devices on cadmium telluride is reported. The oxides were grown by anodic oxidation in 1N KOH in methanol. These devices had normal C-V behavior with definite accumulation and depletion regions; however, constant capacitance was not observed in inversion. The effects of semiconductor surface damage and thermal stability of the oxide are also reported. The effects of series substrate resistance on capacitance-voltage and conductance-voltage have been discussed and an interface trap-level density estimated.

Cadmium telluride is extensively used both as a substrate for epitaxial growth of $\text{Hg}_{1-x}\text{Cd}_x\text{Te}$ and as a material for solar cells and radiation detectors. CdTe is one of the constituents of the pseudobinary alloy $\text{Hg}_{1-x}\text{Cd}_x\text{Te}$ (1), the device processing technology of which is based on oxide growth by anodization (2). Therefore, anodic oxide growth studies and studies of the electrical behavior of metal-insulator (oxide) semiconductor devices are appropriate both as a means of evaluating CdTe material properties and device performance and as an aid in developing a complete understanding of the oxide growth of $\text{Hg}_{1-x}\text{Cd}_x\text{Te}$.

To date, several reports of MIS behavior on wide bandgap semiconductors have been made. Good C-V behavior was reported on low resistivity p-type CdTe, using Langmuir-Blodgett films of cadmium stearate as an insulator, although results were not easily reproducible (3). MIS devices on CdTe were also reported using a native oxide grown in boiling H_2O_2 , but no C-V characteristics were reported (4). The C-V behavior of MIS devices on other wide bandgap semiconductors such as GaAs (5), $\text{GaAs}_{0.6}\text{P}_{0.4}$ (6, 7), and GaP (8) using anodically grown oxides as insulators have also been reported. Low thermal generation of minority carriers was observed in all of the last three cases.

Experimental

Anodic oxide films were grown on both n- and p-type CdTe. Material resistivities were typically 10^2 - 10^4 Ω cm. All samples were single crystals of random orientation, although some crystals were oxidized on the (111) "A" face. All of the results reported here were found for as-grown crystals that were not subjected to any annealing procedures.

Back-side ohmic contacts were produced by a process similar to one described elsewhere (9) for low resistivity p-type CdTe. This process involved etching in a solution containing a $\text{K}_2\text{Cr}_2\text{O}_7$ - H_2SO_4 mixture, followed by back-side Au evaporation. Contacts on p- and n-type samples were evaluated by measuring current as a function of applied voltage and were found to be ohmic with an RA product of about 25 Ω cm^2 .

Surface preparation prior to oxidation was found to be critical to device performance, as illustrated later. Surfaces were first mechanically polished to a 0.05 μm grit finish, followed by a noncontact polishing procedure in $\text{Br}_2/\text{CH}_3\text{OH}$ solutions similar to that described elsewhere (11). Following surface preparation, samples were anodically oxidized in a 1N solution of KOH in CH_3OH . Anodization was under constant current conditions. Current densities were typically 1 mA/cm^2 and were varied as necessary to compensate for variations in substrate resistance. These current densities were much larger than those typically used for anodization of $\text{Hg}_{1-x}\text{Cd}_x\text{Te}$, and were necessary to achieve reasonable anodization rates, since a large potential was being dropped from the back-side contact to the surface in contact with the solution. Samples were anodized under strong illumination to give uniform oxide films by minimizing the voltage drop across the sample. Following anodization, oxides were

typically subjected to a voltage annealing procedure similar to one outlined for $\text{Hg}_{1-x}\text{Cd}_x\text{Te}$ (10), in which the sample was held at 80% of the final applied potential for an extended period to increase the oxide breakdown voltage. Nickel gates were deposited by vacuum evaporation. Gate area was 1×10^3 cm^2 .

Anodic passive film such as the oxide grown in this case usually follow one of two empirical rate laws

$$L = A + B \ln(t) \text{ (logarithmic law)}$$

$$1/L = C - D \ln(t) \text{ (inverse logarithmic law)}$$

to which a variety of mechanisms have been offered (12). In this case, the inverse logarithmic law was observed (Fig. 1). Oxide thicknesses were measured by ellipsom-

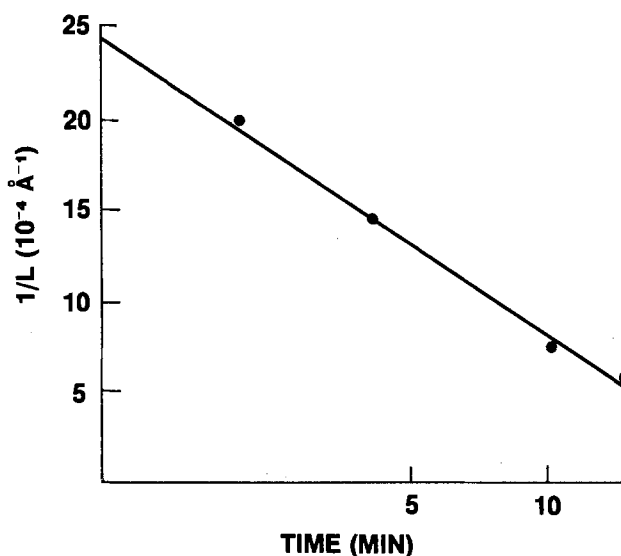


Fig. 1. Anodic oxide growth rate. Rate follows inverse logarithmic rate law.

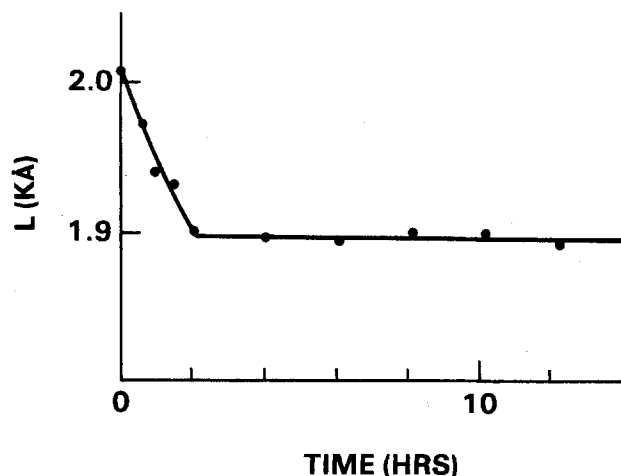


Fig. 2. Dissolution of anodic oxide in water at 20°C.

* Electrochemical Society Active Member.

etry using a Gaertner 116A automated ellipsometer. Final oxide thicknesses were approximately 2000Å. The refractive index of the oxide was found to be 2.15 ± 0.10 by ellipsometry. The breakdown field of the oxide was found to be about 2×10^6 V/cm, which approaches values reported for SiO₂. Also, in order to qualitatively determine the extent of oxide hydration (as OH⁻ from basic solution), the dissolution rate in cold (20°C) water was followed by ellipsometry, as shown in Fig. 2. From this test it was concluded that approximately the last 100Å of oxide grown was hydrated to any extent.

Electrical evaluation of the MOS capacitors were made using a Hewlett-Packard automated test system, consisting of an HP4725A multifrequency LCR meter controlled by an HP9845B desktop computer equipped with a real-time clock. This configuration allowed extremely slow scan rates (10 V/h), which proved to be necessary to minimize injection-type hysteresis. This configuration also allowed simultaneous capacitance-voltage and conductance-voltage measurements to be made and provided real-time corrections for series substrate resistance. Corrections for series resistance were made as described elsewhere (13). Samples were tested at room temperature in ambient atmosphere. All measurements were made in the dark.

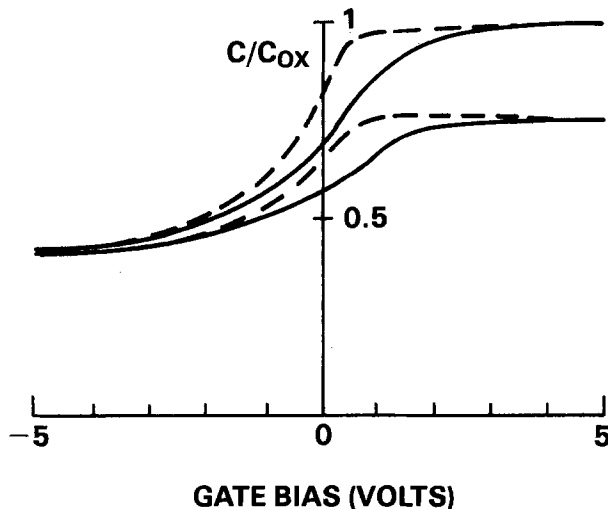


Fig. 3. Capacitance-voltage characteristics of a MOS capacitor on n-type CdTe. Top curve has been corrected for series resistance. Bottom curve is as measured. Capacitance axis is measured capacitance normalized to the oxide capacitance.

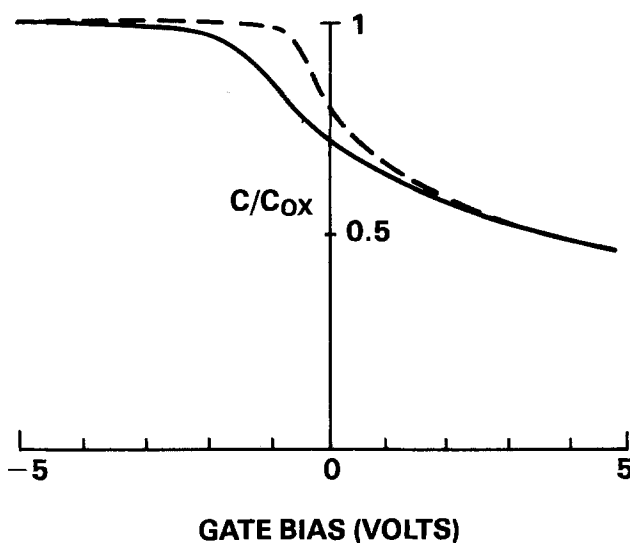


Fig. 4. Capacitance-voltage characteristic of a MOS capacitor on p-type CdTe.

Results and Discussion

Figure 3 illustrates a typical C-V plot achieved from an MOS capacitor fabricated on n-type CdTe. It shows definite accumulation and depletion regions. However, no inversion was observed due to the low thermal generation of minority carriers as is observed in other wide bandgap semiconductors. The C-V plot corrected for series resistance showed a significant capacitance correction in strong accumulation which steadily decreased in depletion until corrected and uncorrected capacitances were essentially equal. Injection-type hysteresis was typically observed and was minimized by slow voltage sweep rates. High frequency C-V's were observed down to frequencies as low as 100 Hz, also typical of low minority carrier generation. Capacitors subjected to test frequencies below 100 Hz were not well-behaved enough to observe any typical C-V behavior. Similar C-V behavior was also observed in MOS capacitors fabricated on p-type CdTe (Fig. 4). Essentially the same characteristics were observed on both n- and p-type material.

Noncontact polishing (11) was found to be an important procedure in the fabrication of MIS devices, since it removed mechanical damage better than normal chemical polishing techniques. The importance of

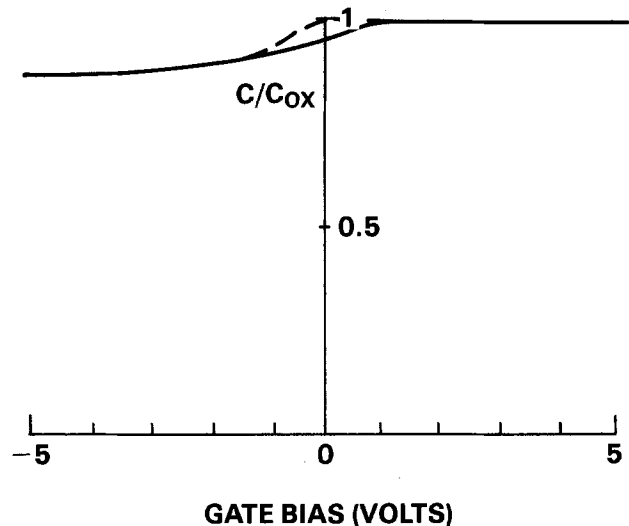


Fig. 5. Capacitance-voltage characteristic of a MOS capacitor on n-type CdTe with residual surface damage.

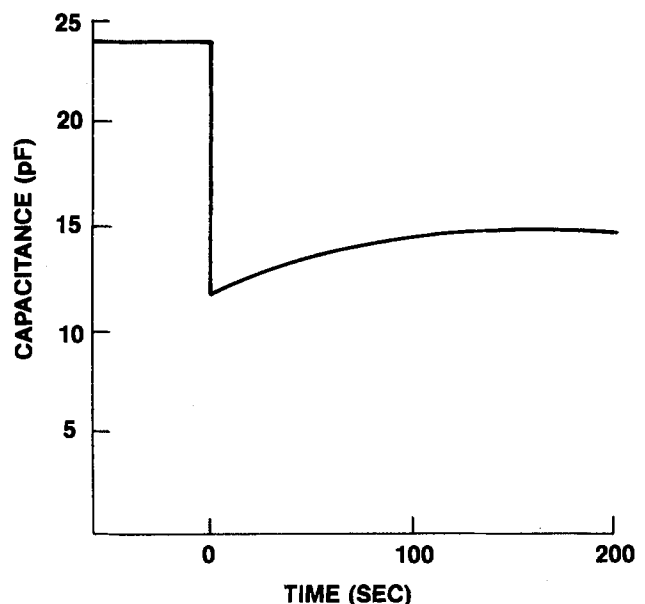


Fig. 6. Capacitance-time characteristic of a MOS capacitor on n-type CdTe. At time $T = 0$, the Ni gate is biased into depletion, and the capacitive delay is observed, as shown.

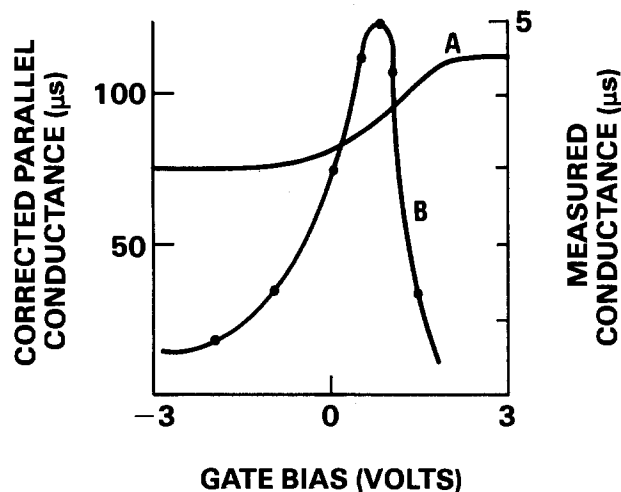


Fig. 7. (A): Measured conductance-voltage behavior. (B): Calculated parallel conductance-voltage curve corrected for series substrate resistance on n-type CdTe.

removing mechanical polishing damage is emphasized by the C-V curve shown in Fig. 5. Although chem-mechanical polishing in $\text{Br}_2\text{CH}_3\text{OH}$ followed mechanical polishing of this sample, damage removal by this method was incomplete. The effect of this damage was a drastic decrease in capacitance measured in accumulation. The samples in Fig. 3 and 4 show much better behavior than Fig. 5, due to less residual mechanical damage.

In order to determine the thermal stability of the oxide and the oxide-semiconductor interface, the C-V characteristics of a MOS capacitor were measured, then subjected to 24h at 90°C in ambient atmosphere. Subsequent retesting of the slice indicated no change in the C-V characteristics of the capacitor.

Dark storage times were also measured (Fig. 6). Average decay times of 200s were observed and were thought to be limited by leakage through the oxide.

Correction for series resistance proved to be even more important in G-V measurements than in C-V measurements. Figure 7 shows a typical example of the measured conductance and the parallel conductance corrected for series resistance. No peak was observed in the measured conductance, indicating that series resistance was the major loss. When the conductance was corrected for substrate resistance, a peak indicative of interface trap losses was observed. From such corrected conductance data, a plot of G_p/ω as a function of frequency was plotted (Fig. 8) and an interface trap density of $7 \times 10^{11} \text{ cm}^{-2} \text{ eV}^{-1}$ was estimated for a gate bias of 0.6V (approximate flatband voltage). Since no attempt was made to relate bias voltage to surface potential, the location of this trap level is not given.

Conclusion

Well-behaved MOS capacitors were fabricated on CdTe by anodic oxidation. C-V measurements yield high frequency curves with definite accumulation and depletion regions. Inversion was not observed due to low thermal generation of minority carriers. Corrections for series resistance had to be made in both C-V and G-V measurements, and corrected G-V curves were used to estimate interface trap densities.

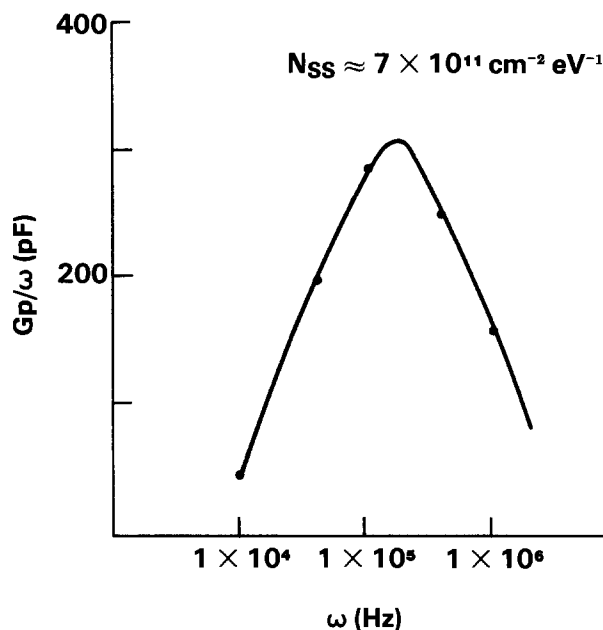


Fig. 8. Interface trap density estimated by conductance method on n-type CdTe.

Acknowledgments

The authors would like to acknowledge P. L. Anderson and D. F. Weirauch of Texas Instruments Incorporated for providing material for this study, and M. M. Lopez for noncontact surface preparation.

Manuscript submitted July 16, 1984; revised manuscript received Sept. 14, 1984. This was Paper 83 presented at the San Francisco, California, Meeting of the Society, May 8-13, 1983.

Texas Instruments, Incorporated assisted in meeting the publication costs of this article.

REFERENCES

1. K. Zanio, "Semiconductors and Semimetals," Vol. 13, pp. 164-210, Academic Press, New York (1978).
2. P. C. Catagnus and C. T. Baker, U.S. Pat. 3,977,018 (1976).
3. M. C. Petty and G. G. Roberts, "Insulating Films on Semiconductors," G. G. Roberts and M. J. Morant, Editors, p. 186, Institute of Physics, London (1979).
4. P. Stiffert, J. Berger, C. Scharager, A. Cornet, R. Stuck, R. O. Bell, H. B. Serreze, and F. V. Wald, *IEEE Trans. Nucl. Sci.*, **ns-23**, 521 (1976).
5. H. Hasegawa, K. E. Forward, and H. L. Hartnagel, *Appl. Phys. Lett.*, **26**, 567 (1975).
6. R. K. Ahrenkiel, F. Moser, T. Coburn, and S. L. Lyu, *J. Appl. Phys.*, **48**, 267 (1977).
7. L. Forbes, J. R. Yeargan, D. L. Keane, and M. G. Craford, *Solid-State Electron.*, **17**, 25 (1974).
8. T. Ikoma and H. Yokomizo, *IEEE Trans. Electron. Devices*, **ed-23**, 1720 (1976).
9. T. C. Anthony, A. L. Fahrenbruch, and R. H. Bube, *J. Electron. Mater.*, **11**, 89 (1982).
10. K. Janousek and R. C. Carscallen, *J. Appl. Phys.* **53**, (1982).
11. T. G. Magee and P. M. Raccach, in "IRIS Infrared Detector Group," Vol. I, p. 127, Environmental Research Institute of Michigan, San Diego, CA (1982).
12. C. Y. Chao, L. F. Lin, and D. D. Macdonald, *This Journal* **128**, 1187 (1981).
13. E. H. Nicollian and J. R. Brews, "MOS Physics and Technology," p. 222, John Wiley and Sons, New York (1982).

Chemical Vapor Deposition of Al_2O_3 Thin Films under Reduced Pressures

Junji Saraie, Jongho Kwon, and Yutaka Yodogawa

College of Technology, Kyoto Institute of Technology, Matsugasaki, Kyoto 606, Japan

ABSTRACT

Al_2O_3 thin films were deposited by reduced-pressure CVD using aluminum tri-isopropoxide as a source. The dependence of the growth rate on the substrate temperature and the source gas supply was determined. The activation energy of the decomposition reactions was determined to be 18 kcal/mol. The electrical resistivity and the dielectric properties are characterized. The origin of the frequency dispersion in the sample prepared under the surface reaction limited conditions are discussed.

Chemical vapor deposition of amorphous thin films of Al_2O_3 for electron device applications has been reported by Aboaf (1). He obtained dense and etchable amorphous Al_2O_3 films using aluminum tri-isopropoxide [$\text{Al}(\text{OC}_3\text{H}_7)_3$, ATI in the following] as source material at the deposition temperature of 420°C . In his deposition system, the source gas with atmospheric pressure was heated in the quartz tube furnace, so that the deposition process included homogeneous reactions.

CVD- Al_2O_3 films were studied as insulator films for MIS structures of GaAs (2, 3) and InP (4, 5). In the case of Ref. (4), Al_2O_3 films are considered to be deposited through heterogeneous reactions on the substrates, although the authors did not refer to the situation explicitly. They did not report the systematic study of deposition conditions, however.

In this report, Al_2O_3 thin films were deposited through heterogeneous reactions on the substrate under reduced pressure at substrate temperatures below 420°C . The substrate temperature and the source gas supply were varied systematically as the deposition parameters. Their electric properties such as resistivity, dielectric constant, and dielectric loss factor are studied in relation to the deposition conditions.

Experimental

Figure 1 shows the deposition apparatus. The carrier gas is N_2 gas. The bubbler containing ATI is maintained at $120^\circ \pm 0.2^\circ\text{C}$, and the stainless steel pipes and the valves are heated to $130^\circ \pm 5^\circ\text{C}$ to avoid the condensation of ATI vapor. The total flow of gases was kept 1000 ml/min throughout the study and the gas flow through the ATI bubbler (referred to as an ATI flow rate in the following) was varied mainly from 50 to 200 ml/min. The ATI bypass line was used in order to settle the bubbling condition before starting the deposition. The reaction chamber was stainless steel and vertical type. The diameter of the substrate holder was 5 cm. The gases blow down onto the heated substrates through a stainless steel mesh diffuser to obtain films with a uniform thickness. The gases were not heated to the cracking temperature before reaching the substrate surface. The reaction chamber was evacu-

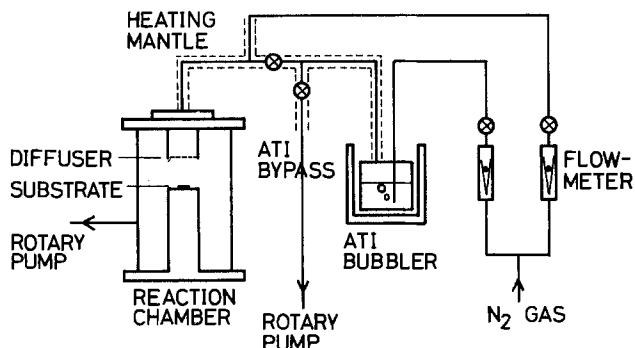


Fig. 1. Deposition apparatus

ated to a pressure of about 10 torr during deposition throughout the study. The homogeneous reactions can be minimized in the case of reduced-pressure CVD because of low concentration of gas molecules. Moreover, since the gas velocity is increased under the reduced pressure, the gas-phase heating by the substrate heater and gas convection can be largely avoided, which assures also the heterogeneous reactions and uniform gas flow as much as possible.

Silicon wafers and glass plates were used as substrates for the thickness measurement and the electrical properties measurement, respectively. Aluminum was evaporated as an electrode on the glass substrate prior to the Al_2O_3 deposition. The substrate temperature (T_{sub}) was controlled to an accuracy within 0.5°C .

ATI (Nakarai Chemicals Limited) is white, semitransparent, and brittle solid. But once melted, it does not solidify, even if the temperature is lowered to room temperature. The ATI melt is colorless and transparent. The liquid state is maintained for more than 10 days under N_2 atmosphere, but it begins to solidify in a few days if the melt is exposed to the air.

The film thickness was measured on the Si wafer sample by multi-interference microscopy. A part of Al_2O_3 films was etched off by HF, and Al was evaporated on it to obtain high reflectivity. The film thicknesses were usually 1000-2000Å.

Aluminum dots with the area of 0.025 cm^2 were evaporated on the $\text{Al}_2\text{O}_3/\text{Al}/\text{glass}$ structure. The current-voltage

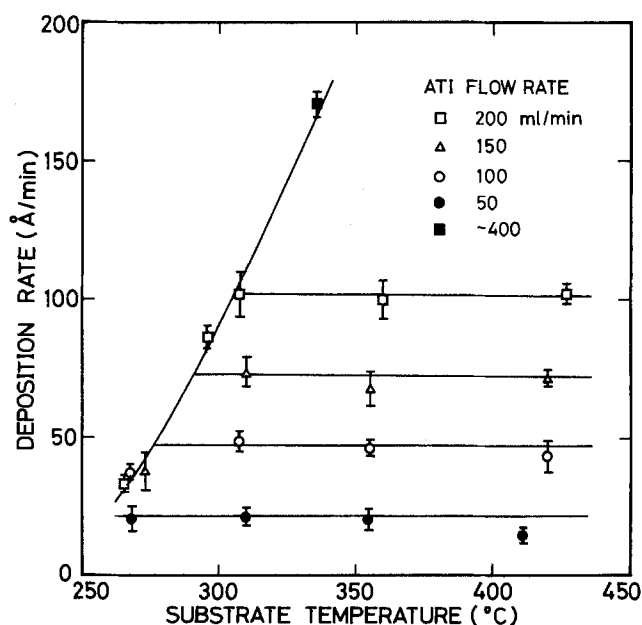


Fig. 2. Dependence of the deposition rate on the substrate temperature and the ATI flow rate. The total gas flow rate is 1000 ml/min and the pressure during deposition is about 10 torr.

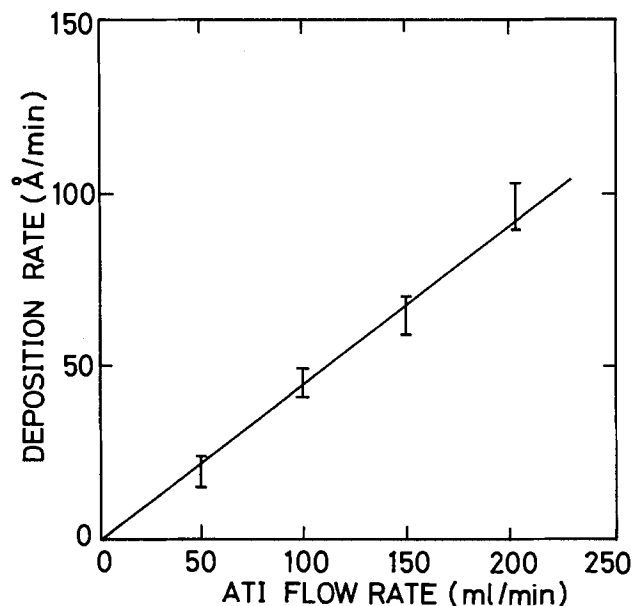


Fig. 3. ATI flow-rate dependence of the deposition rate in the mass-transfer limited region.

characteristics were measured step by step using picoammeter (Toa PM-18R), and the electrical resistivity was calculated from the slope between -0.5 and $+0.5$ V. The current was measured 1 min after applying a voltage. The dielectric properties were measured as a function of the frequency by a universal bridge (120 Hz-10 kHz, Delica 12K) and a capacitance meter (1 MHz, Boonton 72D).

Results and Discussion

Surfaces of the deposited films are mirror smooth on both thin (1000-2000Å) and thick ($\sim 1 \mu\text{m}$) films, and interference colors are observed clearly on the Si wafer substrates. Thickness was slightly larger at the periphery of the samples. The uniformity of the thickness was within 10% in the sample with dimensions of $20 \times 20 \text{ mm}^2$. X-ray diffraction experiments on the thick samples show that all the films deposited in this study are amorphous.

Figure 2 shows the dependence of the deposition rate on the substrate temperature and the ATI flow rate. The deposition rate increases and then saturates as T_{sub} increases at the same ATI flow rate. The saturation values increase with increasing the ATI flow rate. This tendency is similar to the case of usual chemical vapor deposition, that is, the deposition rate is limited by surface reaction at low T_{sub} and is limited by mass transfer (source gas supply) at high T_{sub} . The total gas flow rate and the ATI flow rate are about one order of magnitude smaller than

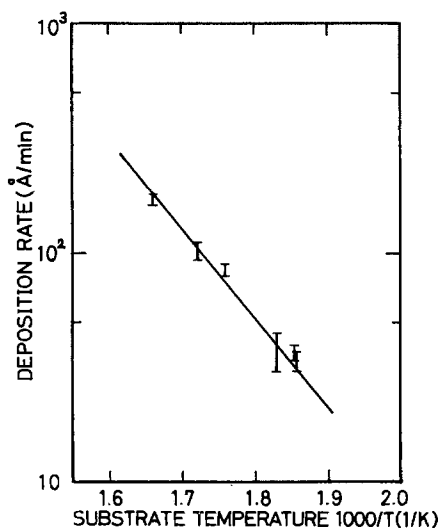


Fig. 4. Arrhenius plot of the deposition rate

those in the case of Aboaf (1). The lowest T_{sub} for Al₂O₃ deposition is found to be about 250°C. This critical temperature coincides with the results of Aboaf (1) and Tanaka *et al.* (3), but is higher than that after Kobayashi *et al.* (5).

Figure 3 shows the ATI flow rate dependence of the deposition rate in the mass-transfer limited region. The deposition rate increases linearly with the ATI flow rate, which is reasonable in the mass-transfer limited region.

Figure 4 shows the Arrhenius plot of the deposition rate in the surface-reaction limited region. The activation energy of the Al₂O₃ deposition was calculated from the slope to be 18.2 kcal/mol.

Figure 5 shows the dc electrical resistivity. The resistivity is in the range between 10^{13} and $10^{15} \Omega \text{ cm}$ and increases gradually with T_{sub} . The ATI flow-rate dependence was not so clear. These values are sufficiently high for electron device applications such as MIS structures. The time constant of the absorption current increases with decreasing T_{sub} . This fact shows that the samples prepared at low T_{sub} include slowly polarizing centers. The resistivity of these samples shown in Fig. 5 may be estimated slightly lower because the current was measured for all the samples 1 min after the application of voltages.

Figure 6 shows a typical example of the dielectric constant ϵ and the loss factor $\tan \delta$ as a function of the frequency for the samples prepared in the mass-transfer limited region. The dielectric constant is 8-9 and similar to the data of Aboaf (1). The value of $\tan \delta$ is 1-2% at low frequencies and increases to 10 kHz. These values are larger than that reported by Aboaf (1). The loss factor tends to decrease at higher T_{sub} and at a lower ATI flow rate, that is, at a slower deposition rate.

Figure 7 shows ϵ and $\tan \delta$ for the samples prepared at T_{sub} of 265°C and at the ATI flow rate of 100 ml/min, that is, prepared in the surface reaction limited region. Both ϵ

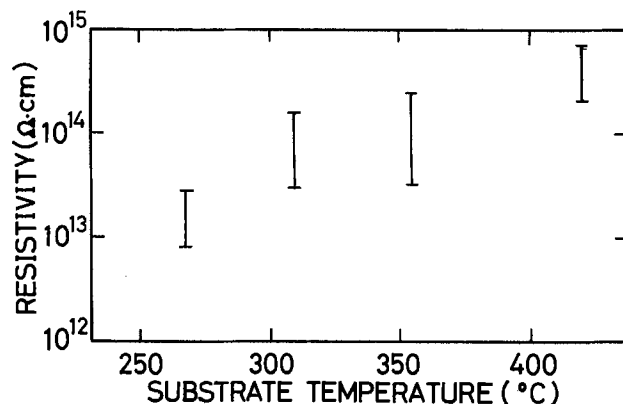


Fig. 5. DC electrical resistivity vs. the substrate temperature. The data include samples prepared at different ATI flow rates. The ATI flow rate does not affect the resistivity so much.

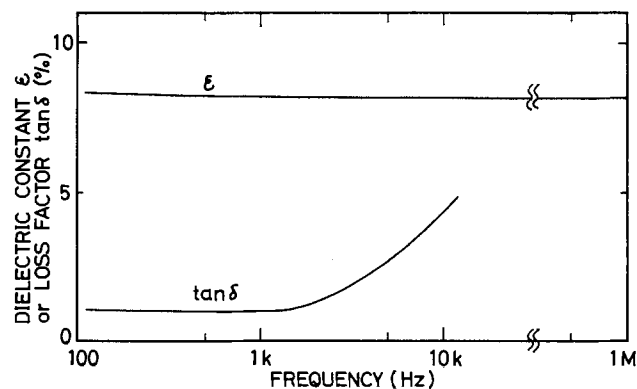


Fig. 6. Frequency dependence of the dielectric constant and the loss factor. The sample was prepared at T_{sub} of 420°C and at the ATI flow rate of 150 ml/min.

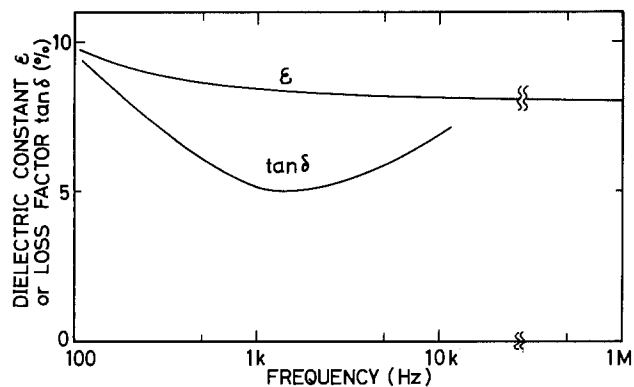


Fig. 7. Frequency dependence of the dielectric constant and the loss factor. The sample was prepared at T_{sub} of 265°C and at the ATI flow rate of 100 ml/min.

and $\tan \delta$ show a large dispersion at low frequencies, and the value of $\tan \delta$ is large. This fact shows that these samples include polarization centers whose response time is rather long, which coincides with the results in dc resistivity measurement. Such frequency dispersions have been reported also by Tanaka *et al.* (3). Similar but smaller dispersions were also found for the samples prepared at higher temperatures in the surface reaction limited region. The origin of the increase in $\tan \delta$ at 10 kHz observed in Fig. 6 and 7 is not clear at this stage.

Kobayashi *et al.* (5) have reported from Auger electron spectroscopic (AES) analysis that CVD- Al_2O_3 films prepared below T_{sub} of 300°C include carbon atoms, which were thought to form organic molecules. In our samples prepared at 265°-355°C, carbon signal was not detected by AES (signal ratio of O/Al was less than 0.015). But signal ratio differs by measuring conditions and is difficult to discuss without comparing the conditions in detail. Therefore, the possibility that such organic molecules contribute to the slow polarization cannot be excluded. And they may also be the origin of rather large values of $\tan \delta$. However, since from AES the content of carbon does not seem to increase with lowering the substrate temperature, large frequency dispersion in the samples prepared under the surface-reaction limited region should be attributed to an additional origin. In fact, these films were revealed to be weak under ion beam etching. Such

structural weakness, rather than the increase in numbers of molecular centers, seems to enhance polarization at low frequencies and contribute to the large frequency dispersions.

The low temperature deposition reported in this paper is important for III-V and II-VI compound semiconductors to avoid surface degradation at higher temperatures.

Summary

Smooth Al_2O_3 thin films were deposited reproducibly by reduced-pressure CVD through heterogeneous reactions of aluminum tri-isopropoxide. Substrate temperatures (250°-420°C) and source gas supply were systematically varied, and the dependence of the deposition rate on these parameters was determined. From the Arrhenius plot, the activation energy of the decomposition reaction was determined to be 18.2 kcal/mol. DC electrical resistivity is ranged from 10^{13} to 10^{15} Ω cm and increases gradually with the substrate temperature. The dielectric constant and the loss factor are 8-9 and 1-2%, respectively. The samples prepared under surface-reaction limited conditions show frequency dispersions at low frequency, that is, they include slowly polarizing centers. The structural weakness in these samples seems to enhance such polarizations. CVD- Al_2O_3 films reported will be useful for the combination with III-V and II-VI compound semiconductors, whose surfaces tend to degrade at higher temperatures.

Acknowledgment

The authors wish to thank Dr. T. Fuyuki of Kyoto University for AES measurements. Also, they would like to thank Mr. K. Takasugi for his assistance in the preliminary stage of this work.

Manuscript submitted Sept. 21, 1984; revised manuscript received Dec. 7, 1984.

REFERENCES

1. J. A. Aboaf, *This Journal*, **114**, 948 (1967).
2. T. Ito and Y. Sakai, *Solid-State Electron.*, **17**, 751 (1974).
3. K. Tanaka, H. Takahashi, Sh. Kuniyoshi, and H. Ohki, *ibid.*, **23**, 1093 (1980).
4. M. Okamura and T. Kobayashi, *Jpn. J. Appl. Phys.*, **19**, 2151 (1980).
5. T. Kobayashi, M. Okamura, E. Yamaguchi, Y. Shinoda, and Y. Hirata, *J. Appl. Phys.*, **52**, 6434 (1981).

Influence of Deposition Temperature, Gas Pressure, Gas Phase Composition, and RF Frequency on Composition and Mechanical Stress of Plasma Silicon Nitride Layers

W. A. P. Claassen,¹ W. G. J. N. Valkenburg, M. F. C. Willemsen, and W. M. v. d. Wijgert

Philips Research Laboratories, Eindhoven, The Netherlands

ABSTRACT

We have studied the influence of different process parameters on the composition and mechanical properties of silicon-nitride layers deposited in a $\text{SiH}_4\text{-NH}_3\text{-N}_2$ plasma. The layers were deposited at temperatures between 300° and 600°C, at total pressures between 65 and 195 Pa and RF frequencies between 0.1 and 20 MHz. The Si/N ratio and the density of the as-deposited layers were determined by means of RBS. IR spectroscopy was used to measure the hydrogen content and Si-H/N-H ratio of the plasma nitride layers. It is shown that hydrogen content, density, and mechanical stress of plasma silicon-nitride layers strongly depend on deposition conditions. To explain the experimental data, a simplified reaction model is given. With this model, differences in densities, hydrogen content, and stress can be related to cross-linking reactions and to the extent of ion bombardment which takes place at different excitation frequencies.

Plasma silicon-nitride layers are widely used in the IC technology for passivation of devices. The layers act as barriers against the diffusion of impurity ions such as sodium, and they are also used for scratch protection during mounting operations. The electrical and mechanical properties of plasma silicon-nitride layers depend strongly on composition, density, and mechanical stress and, therefore, on the deposition conditions. Composition and stress measurements of plasma silicon-nitride layers have been reported (1-4), but attempts to make a more systematic study and quantitative evaluation of the results are relatively scarce. Therefore, a systematic experimental approach was applied to study composition, density, and stress of plasma silicon-nitride layers prepared under various deposition conditions.

In this paper, we report on the influence of deposition temperature, gas pressure, gas phase composition, and RF frequency on the composition, density, and stress of plasma silicon-nitride layers. The experimental data will be described by a simplified reaction model.

Experimental

The deposition experiments were performed in a home-built parallel-plate hot-wall plasma reactor, provided with two SiC coated carbon electrodes (dimensions $0.4 \times 9 \times 50$ cm). The equipment is shown schematically in Fig. 1. Silicon substrates ($\langle 100 \rangle$, 2-5 Ω cm, p-type) were placed on the grounded bottom electrode. The RF-excited electrode is the top electrode. The electrode distance is 1.8 cm. Prior to deposition, the reactor was pumped down to a pressure of about 0.1 Pa by a two-stage rotary pump (Edwards EH 500) followed by a nitrogen flux at working pressure for at least 10 min. The latter is necessary to stabilize the temperature of the substrate wafers. The temperature setting of the reactor was calibrated with an internal thermocouple, at the same pressure and gas flow used during the deposition experiments. Due to ion bombardment and a contact conductance between wafer and electrode, the temperature of the wafer could become somewhat higher than the electrode temperature. However, as mechanical stress, composition, and etch rate in buffered HF of the as-deposited plasma nitride layers does not depend on layer thickness (or deposition time), it can be assumed that the substrate temperature is close to the temperature of the electrode. During deposition, a mixture of the gases silane (SiH_4), ammonia (NH_3), and nitrogen (N_2) was passed over the slices. By varying the flow of the input gases, layers with different composition were deposited.

Most of the deposition experiments were performed at a deposition temperature of 300°C, a total pressure of 130

¹Present address: Nederlandse Philips Bedrijven Elcoma, Processes and Materials Development Group, 6543 AE Nijmegen, The Netherlands.

Pa, a total gas flow of 1500 sccm (giving a room temperature gas velocity of about 200 cm/s), an RF frequency of 310 kHz, and a deposition rate of about 25 nm/min, which was obtained by adjusting the RF power. In some experiments, we varied deposition temperature (300°-600°C), total pressure (65-195 Pa), and frequency (0.1-20 MHz). At a deposition temperature of 300°C, a fixed distance between the electrodes of 1.8 cm, an RF frequency of 300 kHz, and a total pressure of 130 Pa, the thickness spread over five 3 in. wafers is about $\pm 3\%$, while the variation in refractive index is less than 0.01. These low values can be realized when only a small fraction of the input gases is used in the process. For this reason, we worked at a relatively high gas velocity. At higher or lower pressures within the applied pressure regime, the wafer-to-wafer reproducibility becomes worse. However, the variation in deposition rate was always less than $\pm 10\%$. Variation of deposition temperature shifts the optimum deposition conditions. At 600°C, the best wafer-to-wafer uniformity was achieved at a total pressure of 160 Pa.

For characterization of the as-deposited layer, we used the central area (~ 4 cm²) of a wafer placed in the middle of the reactor. Under all deposition conditions, the variation in film thickness over the characterization area of 4 cm was less than 1%, while the refractive index was constant within 0.005. The Si/N ratio and the density of the plasma nitride layers was measured by Rutherford backscattering.

The RBS measurements were performed using 2 MeV He^+ ions generated by a Van de Graaff accelerator (5). The hydrogen content and the Si-H/N-H ratio in the nitride layers was obtained from IR spectra, by means of the method given by Lanford and Rand (6). Due to background pressures of O_2 and H_2O , small concentrations of oxygen are incorporated in the nitride layers. Using AES, it was estimated that under the applied deposition conditions the oxygen content was about 0.4 atom percent (a/o). The thickness of the deposited layers, which value is needed to calculate the density of the nitride, was measured with an ellipsometer and with a Talystep technique. For the latter measurement, an etched step was

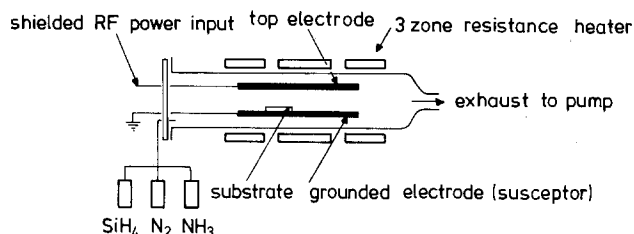


Fig. 1. Schematic view of the hot wall parallel-plate plasma reactor

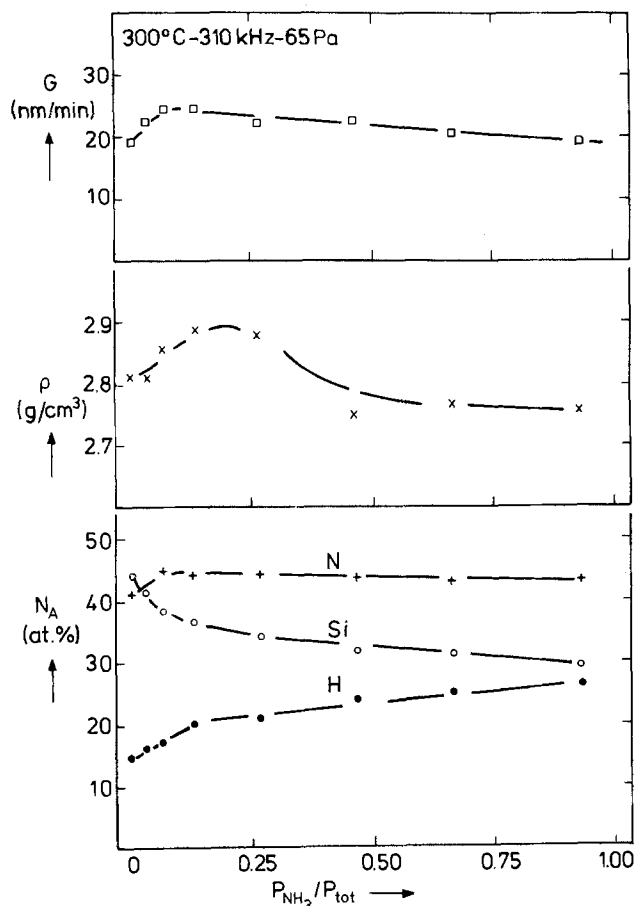


Fig. 2. Deposition rate, density, and atomic composition of layers deposited at a deposition temperature of 300°C, a RF frequency of 310 kHz, and total pressure of 65 Pa. $\phi_{\text{SiH}_4} = 100$ sccm; $\phi_{\text{N}_2+\text{NH}_3} = 1400$ sccm.

made in the middle of the wafer. Within the experimental error, the Talystep and the ellipsometrically measured thicknesses gave the same values.

The total stress in the layers was determined at room temperature by measuring the bending of nitride-coated Si <100> wafers with an x-ray diffraction topography goniometer (Lang Camera) (7). The curvature of the crystal planes (r) is directly related to the film stress

$$\sigma = \pm \frac{Ed^2}{b(1-\nu)tr} \quad [1]$$

where + and - denote tensile and compressive stresses, respectively. The stress is compressive if the wafer has a convex shape, as seen from the film side. Further, d is the substrate thickness, t the film thickness, E the Young modulus, and ν the Poisson ratio of the substrate. For Si <100>, $E/(1-\nu) = 1.8 \times 10^{11}$ Pa. Mostly layers with a thickness of 0.5 μm were used for the stress measurements. Variation of the thickness between 0.1 and 1 μm has, of course, influence on the bending of the substrates but not on the stress in the layer.

Results

The composition of plasma silicon nitride layers can be influenced by the deposition parameters: gas phase composition, deposition temperature, total gas pressure, and RF frequency. One set of experiments was performed at different values of one parameter while the other parameters were kept constant. In Fig. 2 are plotted the atomic composition (N_A), the density (ρ), and the deposition rate (G) vs. the relative ammonia pressure in the system. The deposition conditions are given in the figure caption. The ammonia concentration was changed by varying the ratio of the input gases N_2 and NH_3 while the SiH_4 flow was kept constant. The Si/N ratio of the deposited layers de-

creases with increasing ammonia partial pressure and varies between 1.08 and 0.68 for the data given in Fig. 2. At the same time, the hydrogen content varies from 14 to 26 at.%. These effects of the ammonia partial pressure are ascribed to its lower dissociation energy as compared to N_2 . A high concentration of N-H-like radicals leads to a high content of hydrogen in the plasma nitride layers. The density of the nitride layers shows a maximum which corresponds to a Si/N ratio of about 0.75. The deposition rate of silicon nitride layers depends slightly on the ammonia partial pressure. In Fig. 3 are plotted the atomic composition, the density, and the deposition rate of silicon nitride layers deposited at temperatures between 300° and 600°C. For comparison, data are also given for a layer deposited at 700°C without the presence of a glow discharge. With a glow discharge, the deposition rate increases slightly with increasing deposition temperature. With increasing deposition temperature, the hydrogen content of the layers decreases and the density increases.

Figure 4 shows the influence of total pressure on the deposition rate, density, and composition of plasma nitride layers. With increasing total pressure, the Si/N ratio and the hydrogen content increase slightly, while the density decreases. The deposition rate depends only slightly on the total pressure. In Fig. 5, the atomic composition and the density of nitride layers, deposited at different RF frequencies at 300°C, are plotted vs. the operating frequency. The deposition rates were about 25 nm/min, which was achieved by adjusting RF power. There is a large difference in the composition and the density between layers deposited below and above 4 MHz.

In Fig. 6 is given the mechanical stress for layers deposited at different temperatures, frequencies, and pressures (deposition conditions are given in the captions of Fig. 3-5). Layers deposited at low temperatures (< 550°C) and low frequencies (< 4 MHz) show a compressive stress,

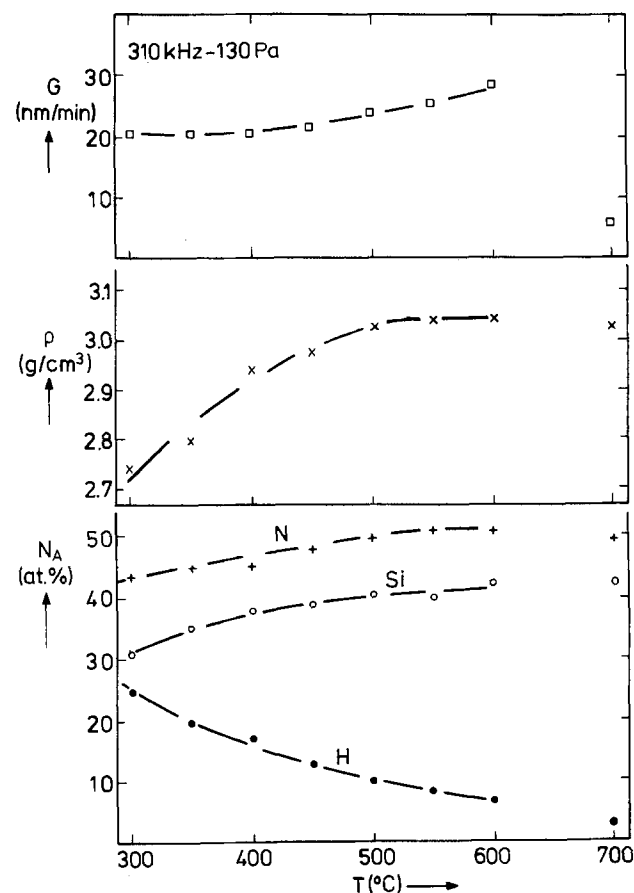


Fig. 3. Deposition rate, density, and atomic composition of layers deposited at different temperatures between 300° and 600°C with a glow discharge (310 kHz) and at 700°C without a glow discharge. $P = 130$ Pa; $\phi_{\text{SiH}_4} = 100$ sccm; $\phi_{\text{N}_2} = 200$ sccm; $\phi_{\text{NH}_3} = 1200$ sccm.

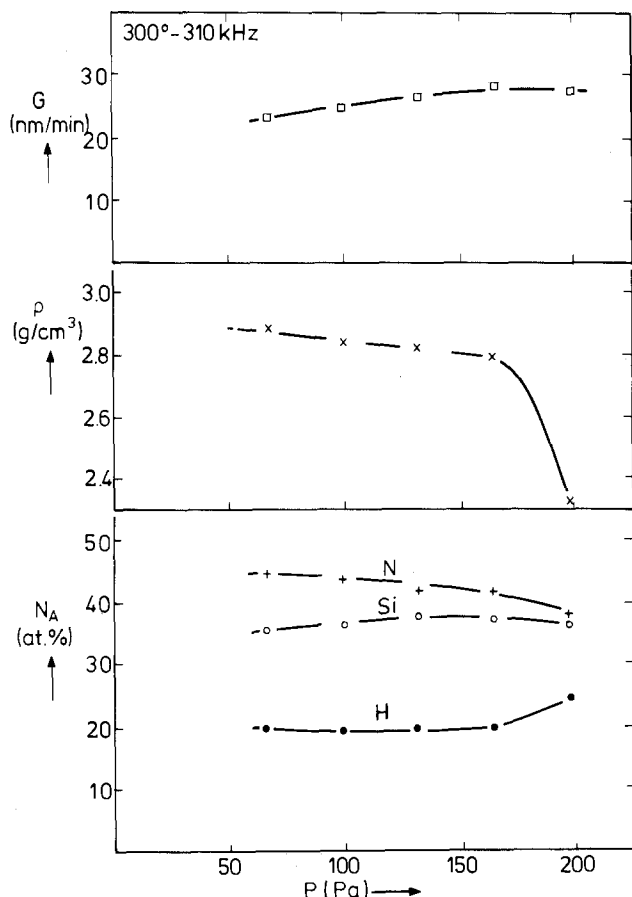


Fig. 4. The influence of total pressure on deposition rate, density, and atomic composition. $T = 300^\circ\text{C}$, $f = 310\text{ kHz}$. $\phi_{\text{SiH}_4} = 100\text{ sccm}$; $\phi_{\text{N}_2} = 300\text{ sccm}$; $\phi_{\text{NH}_3} = 1100\text{ sccm}$.

while layers deposited at higher temperatures and high frequencies ($> 4\text{ MHz}$) show a tensile stress behavior. Furthermore, the stress in the layer decreases with increasing total pressure.

The number of Si-H and N-H bonds per cubic centimeter can be calculated from the IR spectra using a method

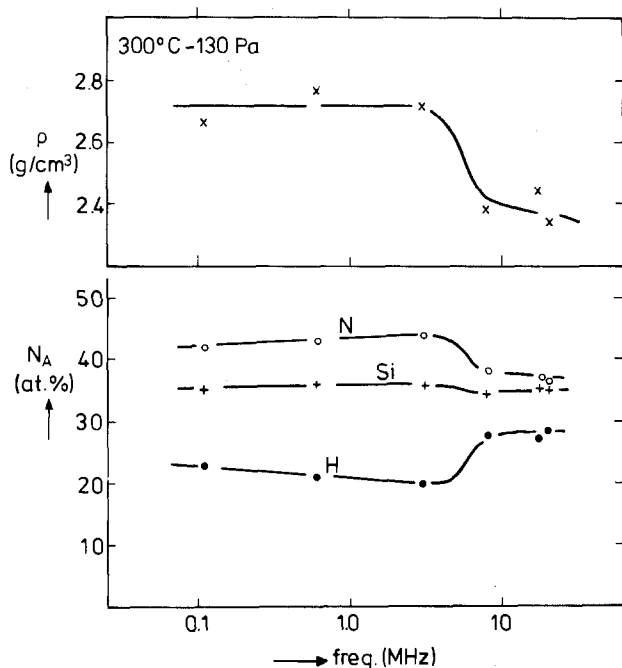


Fig. 5. Variation of composition and density of layers deposited at different RF frequencies at 300°C and a total pressure of 130 Pa. $\phi_{\text{SiH}_4} = 100\text{ sccm}$; $\phi_{\text{N}_2} = 700\text{ sccm}$; $\phi_{\text{NH}_3} = 700\text{ sccm}$.

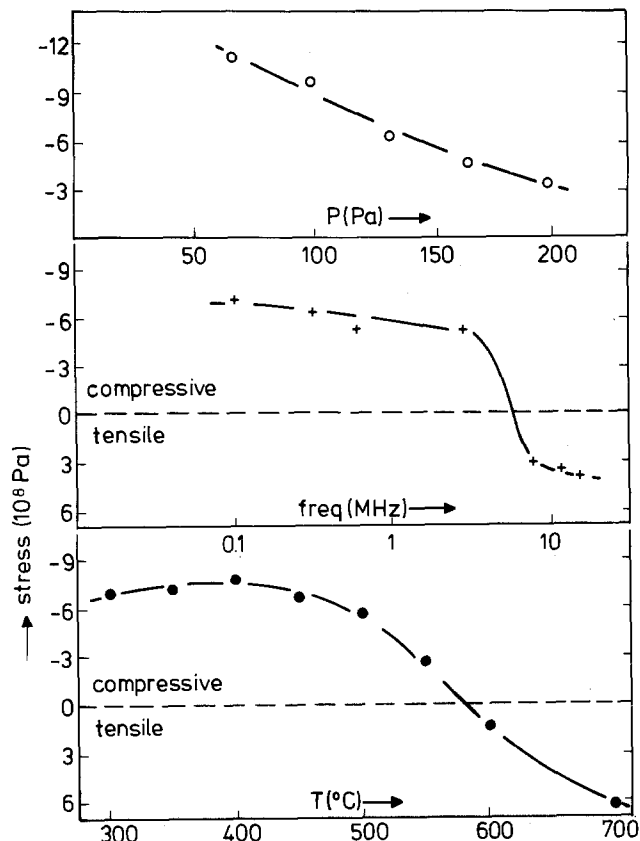


Fig. 6. Stress of plasma nitride layers vs. deposition temperature, RF frequency, and total pressure. Deposition conditions are given in the captions of Fig. 3-5.

given by Lanford and Rand (6). Figure 7 gives the fraction of Si-H bonds vs. the Si/N ratio of the layers deposited at temperatures between 300° and 600°C and an operating frequency of 300 kHz and for layers deposited at 3, 8, and 20 MHz at 300°C . At high Si/N ratios or Si-rich layers, almost all hydrogen is bonded to silicon, while at lower Si/N ratios the amount of N-H bonds increases. In a preceding paper, we reported observing the same trend for layers deposited in $\text{SiH}_4\text{-NH}_3\text{-H}_2$ or $\text{SiH}_4\text{-NH}_3\text{-Ar}$ atmospheres (1).

Discussion

Theory.—Before discussing the experimental data, we shall give some characteristics of a glow discharge which are typical for a plasma-deposition system (8). By electron impact of relatively stable molecules, active species such as ions, excited molecules, and radicals are formed. In a low pressure plasma (total pressure around 100 Pa), the mean electron energy is around 2 eV, while the electron concentration and also the positive ion concentration are about 10^{10} cm^{-3} . The electron density is determined by the mean electron energy, the electric field, the geometry of the system, the gas species, and the total pressure. Furthermore, the electron density is determined by the balance between the generation rate and the loss rate of electrons. Ionization is the most important process in sustaining the plasma, while electrons are lost by diffusion and recombination at surfaces. According to literature, at pressures around 100 Pa, the concentration of ions is two to three orders of magnitude smaller than the free radical concentration (9). The formed radicals may react via conventional pathways, but chemical reactions at the surface can also be enhanced by processes such as ion bombardment. The bombarding energy depends on the difference between the plasma potential and the substrate potential, the total pressure and the frequency of the applied field (10). At low frequencies, ions and electrons can follow the alternating RF field and, therefore, ion impingement can take place on the growing layer. Ions which leave the plasma are accelerated in the dark space

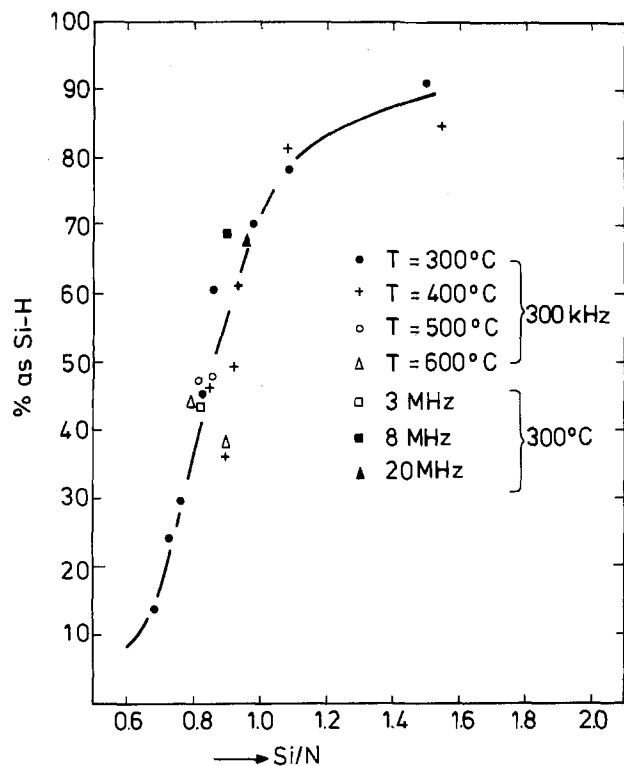
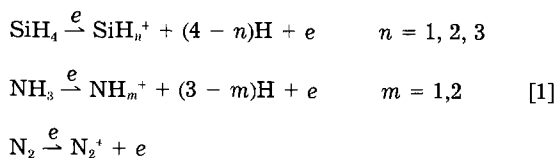


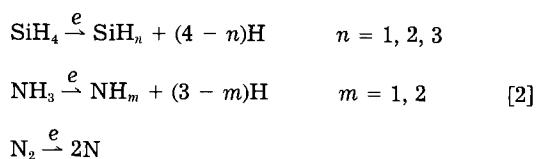
Fig. 7. Correlation between the amount of hydrogen bonded to silicon and the Si/N ratio for different deposition conditions.

and acquire a maximum energy of $V_p - V_s$, where V_p is the plasma potential and V_s the substrate potential, when they reach the substrate. In reality, collisions take place in the dark space and, therefore, the bombarding energy decreases with increasing total pressure. As the frequency of the applied field is increased, a point is reached at which the ions cannot follow the alternating field, leading to a strong reduction of the ion flux to the electrode. According to Bruce (10), who studied ion bombardment at different RF frequencies using an Ar-Kr plasma, the transition frequency at which ions cannot follow the RF field is at about 4 MHz.

Reaction scheme.—Several authors have studied the deposition of amorphous silicon from silane plasmas using mass spectrometric and optical analysis (11, 12). On the basis of these data, we propose a simplified reaction scheme for the deposition of plasma silicon-nitride from $\text{SiH}_4\text{-NH}_3\text{-N}_2$. The following reactions are taken into account: (i) gas phase ionization

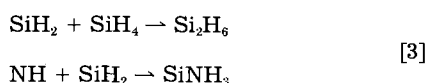


(ii) gas phase dissociation

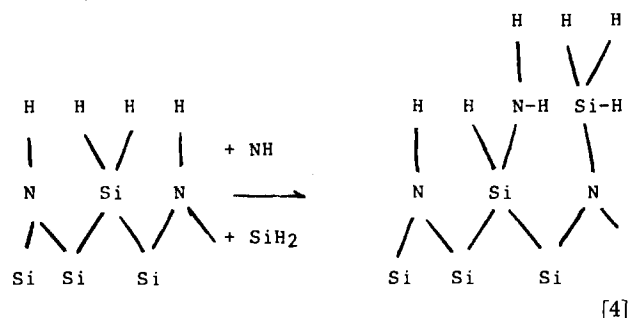


For simplicity and based on experimental data as can be found in literature (11, 13), we assume in the following that SiH_2 and NH are the most important intermediates in the gas phase.

(iii) Gas phase reactions, i.e.

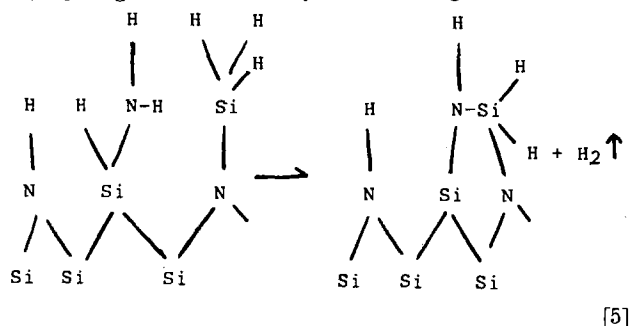


and (iv) Insertion



Adsorption on free surface sites can be neglected due to the presence of the large amounts of N-H and Si-H bonds at the surface. Formation of N-N bonds is not likely.

(v) Hydrogen elimination by cross-linking



As will be discussed below, breaking of N-H or Si-H bonds depends on temperature and on the extent of ion bombardment. This simplified reaction scheme will be used to explain the experimental data. As for CVD systems operating at low temperatures and reduced pressures, the rate-limiting step for deposition had to be found in reactions which take place at the surface. Hydrogen elimination by cross-linking (Eq. [5]) cannot be rate-limiting because the hydrogen content of the nitride layers strongly depends on deposition temperature, while the deposition rate is hardly affected by the deposition temperature (Fig. 3). In conclusion, it can, therefore, be said that hydrogen desorption takes place after the rate-limiting step for deposition being the insertion of NH or SiH_2 radicals into Si-H and N-H bonds (Eq. [4]).

According to Fig. 2-4, the deposition rate of plasma silicon nitride depends only slightly on gas phase composition, deposition temperature, and total pressure. This can be explained as follows. In a glow discharge, the rate of dissociation processes can be described by (11)

$$R = k_d [e][X] \quad [6]$$

where $[e]$ and $[X]$ are the mean concentrations of electrons and monomers, respectively, and k_d is the rate constant for dissociation. This constant depends on the average electron energy, the shape of the electron distribution function, and the cross section of the different species. As the mean electron energy or electron temperature is much higher than the substrate temperature, it can be concluded that in the experimental regime under investigation the electron impact dissociation rate is nearly independent of the deposition temperature. The rate of ionization can also be described by the expression given by Eq. [6]. However, in the pressure regime under discussion, the rate coefficient for ionization is at least two orders of magnitude smaller than the rate coefficient for dissociation (9). The formed radicals may react in the gas phase or are removed by diffusion to the electrodes where they are incorporated into Si-H or N-H bonds (Eq. [4]). The temperature dependence of these insertion reactions is small as radical-radical reactions are often either unactivated or weakly activated processes (12). Based on the discussion given above, the experimental data concerning the deposition rate vs. the deposition temperature (Fig. 3) can be described by reactions which are only slightly dependent

on or independent of the substrate temperature. Without a glow discharge, radicals can only be formed via thermal dissociation of the parent molecules, which reaction is highly dependent on temperature, leading to a deposition rate which strongly depends on temperature (15).

The small variations in deposition rate measured for different gas phase compositions (Fig. 2) can be explained by small variations in the cross sections for ionization and dissociation for the different gases. Furthermore, the mean electron energy also slightly depends on the gas phase composition. According to Fig. 4, the deposition rate of plasma silicon nitride hardly depends on pressure. This can be explained by a combined effect, as at low pressures the mean electron energy tends to be higher, while the ionization and dissociation rate are proportional to both total pressure and mean electron energy (8).

Layer-related properties.—As discussed before, the insertion reaction given by Eq. [4] can be assumed to be the rate-limiting step for the deposition process. The rate of this reaction is denoted in the following by τ_1 . The hydrogen elimination reaction, with rate τ_2 (Eq. [5]) can be much faster or much slower than τ_1 . This, however, has no influence on the deposition rate but only on the structure of the deposited layer. If $\tau_2 \gg \tau_1$, the film will contain almost no hydrogen, whereas in the opposite case a polymer is formed with a large hydrogen content. According to this model, the ratio of the rates of the two steps τ_1/τ_2 depends only on the deposition temperature, provided the Si/N ratio is constant. This is approximately the case for the experimental data given in Fig. 3. As is shown in this figure, the hydrogen content of layers deposited at different temperatures using an RF frequency of 310 kHz varies from 25 a/o at 300°C to 6 a/o at 600°C. Layers deposited at 700°C, without the presence of a glow discharge, contain about 3 a/o hydrogen, while layers deposited at room temperature under almost the same conditions are those given in Fig. 3 contain about 40 a/o hydrogen. These data are plotted in Fig. 8 in a logarithmic form vs. the reciprocal temperature. If hydrogen desorption is thermally activated, a plot of $\log [H]$ vs. $1/T$ should give a straight line. According to Fig. 8, this is approximately true at temperatures between 400° and 700°C. As discussed before, under these circumstances the hydrogen content in the plasma nitride layer is only a function of τ_1/τ_2 . At lower temperatures, the hydrogen content is lower than expected from the model. This can be explained by an enhancement of the hydrogen elimination step by ion bombardment. As discussed before, at "high" operating frequencies the extent of ion bombardment decreases, which leads in the present model to a higher hydrogen content in the layer, as is indeed observed in Fig. 5. According to Fig. 6, layers deposited at a temperatures below 550°C have a compressive stress and layers deposited at higher temperatures exhibit a tensile stress. Layers deposited at room temperature also show a compressive

stress, indicating that the stress has an intrinsic character. According to Retajczyk and Sinha (4), stress values can be corrected for thermal stress by adding a value of approximately $+2 \times 10^7$ Pa for every 100° difference between the measuring temperature (room temperature) and the deposition temperature. This leads to the conclusion that under almost all conditions applied in this study stress has intrinsic characters. As discussed before, hydrogen desorption can be enhanced by increasing the deposition temperature or, at low RF frequencies, by ion bombardment. The influence of ion bombardment on the hydrogen desorption rate can be assumed to be independent of the deposition temperature. At low temperatures, ion bombardment determines the hydrogen content in the layer, while at high temperatures this is taken over by thermal desorption. At high temperatures, the stress has a tensile character which can be explained by a hydrogen desorption rate which is not fast compared to the rate at which gas phase formed radicals are inserted into Si-H or N-H bonds. This leads to a top layer with a relatively high hydrogen content. Due to the high temperatures, hydrogen desorption and cross-linking do not stop after the actual deposition step but continue for a while, which leads to a nitride layer which shrinks at the deposition temperature, giving the tensile stress behavior. Going to lower temperatures, the stress shifts from tensile to compressive. The compressive intrinsic stress behavior at low deposition temperature is somewhat difficult to explain. From literature, it is known that tensile silicon nitride layers become compressive when they are exposed to ion bombardment (16). This is explained by expansion of the layer due to implanted atoms and broken Si-N bonds, which leads to a disturbed short-range order of the Si-N structure. In plasma CVD at "low" operating frequencies, the growing layer is exposed to ion bombardment. As ion bombardment could take place after deposition of the silicon- or nitrogen-containing radicals, the layer expands at the deposition temperature, leading to a compressive stress. According to Fig. 6, the stress shifts from compressive to tensile with increasing RF frequencies. This shift coincides with a strong variation in density and hydrogen content. According to Bruce (10), at frequencies above roughly 4 MHz the ions become slow compared to the oscillating frequency, leading to a decrease in the ion bombarding energy and of the flux of ions to the electrodes: As discussed before, in absence of ion bombardment thermal processes determine the hydrogen content and the nitride layer shrinks at the deposition temperature. This leads to a tensile stress behavior at high frequencies. According to Fig. 4, the stress in plasma nitride layers decrease with total pressure. This can also be described by the presented model, as the extent of ion bombardment decreases with increasing total pressure, due to collisions in the dark space.

We will now comment briefly on the influence of the deposition parameters on the density, the Si/N ratio, and the Si-H/N-H ratio of the deposited layers. According to the figures, the density of the deposited layers decreases with increasing hydrogen content, provided the ammonia partial pressures are constant (Fig. 3-5). This can be explained by the effect of cross-linking and hydrogen desorption (Eq. [5]) on the structure of the deposited layer. The maximum density in Fig. 2 coincides with a Si/N ratio of 0.75. At high total pressures (or silane partial pressures) (Fig. 4), the density of the deposited layers decreases enormously, possibly due to gas phase reactions such as are given by Eq. [3]. Gas phase reactions generate particulates or haze.

According to Fig. 2, the Si/N ratio of the deposited plasma-nitride layer depends on the ammonia partial pressure. This can be ascribed to the higher dissociation energy of N_2 compared to that of NH_3 . At higher frequencies, the Si/N ratio is higher than at low RF frequencies (Fig. 5). This can be explained by differences in the nature of the chemical species arriving at the substrate, due to an influence of the RF frequency on the ionization and dissociation cross sections of the different gases (Eq. [6]),

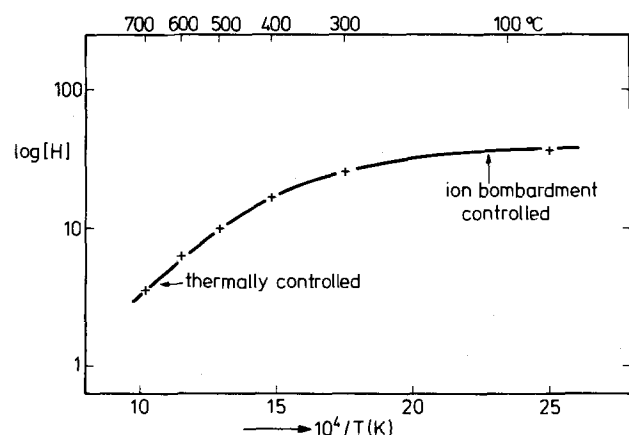


Fig. 8. $\log [H]$ vs. $1/T$ using the experimental data given in Fig. 3 and the hydrogen content of a layer deposited at room temperature using almost the same conditions as those given in Fig. 3.

or it may be attributed to a contribution of dissociative adsorption of N_2^+ ions [$N_2^+ + e \rightarrow 2N(17)$] to the deposition of nitrogen atoms, notably at low frequencies. The influence of total pressure on the Si/N ratio (Fig. 4) can be explained by a reduction in ion energy with increasing total pressure (as discussed before). This leads to higher Si/N ratios at the lower ion energies (higher pressures).

According to Fig. 7, the Si/N ratio of the deposited layers determines, in a first approximation, the way in which hydrogen is bonded. At high Si/N ratios (Si-rich layers), almost all the hydrogen is bonded to silicon. At Si/N ratios below 0.75, most of the hydrogen is bonded to nitrogen.

Conclusions

The composition and density of plasma silicon-nitride layers can be adjusted within certain limits by variation of the deposition temperature, total pressure, gas phase composition, and RF frequency. A simplified model is proposed for the deposition kinetics of plasma silicon-nitride. It is concluded that the deposition rate is determined by the insertion of silicon and nitrogen containing compounds into Si-H and N-H bonds at the surface of the growing layer. The deposition rate is almost independent of total pressure and deposition temperature. After insertion of the formed radicals into Si-H or N-H bonds, hydrogen elimination takes place by cross-linking. It is concluded that the hydrogen-elimination step can be influenced by temperature and by ion bombardment.

Layers deposited at high temperatures ($>550^\circ\text{C}$) or at high frequencies (>4 MHz) show a tensile stress behavior. This is explained by a hydrogen desorption rate which is smaller than the rate-limiting step for deposition. After deposition of silicon and nitrogen containing radicals, hydrogen desorption continues for a while, leading to a layer which shrinks at the deposition temperature and consequently to a tensile stress behavior. Layers deposited at low temperatures ($<550^\circ\text{C}$) and at low frequencies (<4 MHz) show a compressive stress. Due to ion bombardment, atoms are implanted and bonds are broken, leading to a disturbed short-range order of the Si-N structure and to an expansion of the plasma nitride layer.

Acknowledgment

The authors wish to thank Dr. A. E. T. Kuiper for valuable discussions.

Manuscript submitted June 18, 1984; revised manuscript received Dec. 20, 1984.

Philips Research Laboratories assisted in meeting the publication costs of this article.

REFERENCES

1. W. A. P. Claassen, W. G. J. N. Valkenburg, F. H. P. M. Habraken, and Y. Tamminga, *This Journal*, **130**, 2419 (1983).
2. A. K. Sinha, H. J. Levinstein, T. E. Smith, G. Quintana, and S. E. Haszko, *ibid.*, **125**, 601 (1978).
3. G. M. Samuelson and K. M. Mar, *ibid.*, **129**, 1773 (1982).
4. T. F. Retajczyk and A. K. Sinha, *Thin Solid Films*, **70**, 241 (1980).
5. F. H. P. M. Habraken, A. E. T. Kuiper, A. v. Oostrom, Y. Tamminga, and J. D. Theeten, *J. Appl. Phys.*, **53**, 404 (1982).
6. W. A. Lanford and M. J. Rand, *ibid.*, **49**, 2472 (1978).
7. E. W. Hearn, *Adv. X-Ray Anal.*, **20**, 273 (1977).
8. See, for example, B. Chapman, "Glow Discharge Processes," John Wiley and Sons, Inc., New York (1980).
9. B. Drevillion, J. Huc, A. Lloret, J. Perrin, G. de Rosny, and J. P. M. Schmitt, *Appl. Phys. Lett.*, **37**, 646 (1980).
10. R. H. Bruce, *J. Appl. Phys.*, **52**, 7064 (1981).
11. G. Turban, Y. Catherine, and B. Grolleau, *Thin Solid Films*, **67**, 309 (1980).
12. F. J. Kampas and R. W. Griffiths, *J. Appl. Phys.*, **52**, 1285 (1983).
13. S. Yokoyama, M. Hirose, and Y. Osaka, *Jpn. J. Appl. Phys.*, **20**, L117 (1981).
14. A. T. Bell, in "Topics in Current Chemistry," S. Veprek and H. Venugapalan, Editors, Chap. 2, p. 52, Plasma Chemistry III, Springer-Verlag, Berlin (1980).
15. G. Cocher, H. Mellattie, and R. Delbourgo, *This Journal*, **125**, 487 (1978).
16. E. P. Eernisse, *J. Appl. Phys.*, **48**, 3337 (1977).
17. H. F. Winters, in "Topics in Current Chemistry," S. Veprek and M. Venugopalan, Editors, Chap. 3, p. 120, Plasma Chemistry III, Springer-Verlag, Berlin (1980).

Electrical Properties, Structure, and Phase Morphology of Au-Ga Alloy Films Codeposited on GaAs Substrates

S. Leung, T. Yoshiie,¹ C. L. Bauer, and A. G. Milnes*

Center for the Joining of Materials, Carnegie-Mellon University, Pittsburgh, Pennsylvania 15213

ABSTRACT

Electrical properties, structure, and phase morphology of gold-gallium alloy films codeposited on {100} substrates of gallium arsenide have been investigated by measurement of Schottky barrier height ϕ and breakdown voltage V_b as a function of film composition and annealing conditions and comparison with corresponding structure and phase morphology, as determined by x-ray diffraction and transmission electron microscopy. Both ϕ and V_b decrease with increasing composition of gallium in the codeposited films and with increasing severity of annealing conditions. These decreases are attributed to formation of gold-gallium phases, either directly through codeposition of alloy films or through annealing of pure gold films on substrates of gallium arsenide, and localized current or field concentrations due to nonplanar phase morphologies. General behavior of electrical properties is reported and interpreted in terms of the existing structure and phase morphology near the original alloy film/gallium arsenide interface.

Certain electrical properties of metal contacts to semiconductor devices, such as Schottky barrier height ϕ and reverse voltage breakdown V_b , are known to depend on composition, structure, and phase morphology near the original interface. This dependence can be demonstrated by subjecting the metal/semiconductor couple to mild thermal treatments. For example, heating a gold film de-

posited on {100} substrates of gallium arsenide to about 350°C results in release of arsenic and formation of certain new phases, including Au_3Ga_2 , Au_5Ga , and a hexagonal gold-gallium phase (1-6). Such change, in turn, reduces ϕ from approximately 0.85-0.50 eV (7) and V_b by as much as a factor of two depending on doping concentration, film thickness, annealing time and atmosphere, and details of specimen preparation (8).

In a recent investigation, Yoshiie *et al.* (9) have characterized evolution of structure and phase morphology of

* Electrochemical Society Active Member.

¹ Present address: Faculty of Engineering, Hokkaido University, Sapporo 060, Japan.

thin films of gold deposited on {100} and {111} substrates of gallium arsenide during annealing by transmission electron microscopy, incorporating a unique cross sectioning technique. The most evident structural changes are formation of elongated pyramidal pits, bounded by {111} planes of gallium arsenide and containing gold-gallium reaction products, and formation of a continuous layer of orthorhombic Au₂Ga near the original interface, accompanied by the release of arsenic. However, concomitant changes in electrical properties were not correlated with such evolution of structure and phase morphology. An earlier investigation, however, indicates that the Schottky barrier height (0.75 eV) remains constant for a eutectic gold-gallium alloy (85 weight percent [w/o] Au) up to an annealing temperature of 400°C (10). The purpose of this investigation is to modify the aforementioned system by codeposition of gold-gallium alloys on {100} substrates of gallium arsenide and to determine concomitant electrical properties, both in the as-deposited and annealed state. In this manner, a better appreciation of how various gold-gallium phases in contact with gallium arsenide affect electrical properties can be achieved.

The remainder of this article is divided into several sections: fabrication details are described in the next section, then experimental results are presented and analyzed in the "Microstructure and Phase Morphology" and "Discussion" sections, respectively, and, last, salient features of this investigation are summarized.

Experimental Procedures

Two types of {100} gallium arsenide substrates were used throughout the course of this investigation: (i) n-type wafers doped to about $5 \times 10^{16} \text{ cm}^{-3}$ and cut from the center of 10 cm diam boules grown in boron nitride crucibles under B₂O₃ (designated LEC), obtained from Westinghouse Electric Research and Development Center, and (ii) n-type wafers doped to about $5 \times 10^{17} \text{ cm}^{-3}$ cut from boules grown by the Bridgman technique (designated BM), obtained from Morgan Semiconductor. Pure (99.999 weight percent [w/o]) gold and gallium (99.999 w/o) were simultaneously coevaporated from separate sources in an ion-pump vacuum system at a pressure of about 100 μPa and deposited to a thickness of about 200 nm on three types of substrates: (i) either {100} LEC or BM substrates of gallium arsenide with a Au-Ge/Au ohmic contact already in place on the back side, (ii) a masked glass slide for eventual electrical resistivity measurements, and (iii) a glass slide coated with photoresist for eventual x-ray diffraction measurements. Prior to metal deposition, the polished wafers were cleaned with trichloroethylene, acetone, and ethyl alcohol, etched in H₂O₂-H₂SO₄-H₂O solution for 2 min, and then soaked in HCl-H₂O solution for 5 min. After rinsing in deionized water, the wafers were loaded into an ion pump vacuum system for film deposition. The deposition rates varied from 10 to about 50 nm/min and no significant effects were found that were attributed to changes within this range. The substrate temperatures were monitored during evaporation and did not exceed 320 K. Deposition was through a molybdenum mask in contact with the specimens that defined evaporated mesas of area 1.33 mm². Composition of the deposited films was determined by independent quartz crystal monitors, precalibrated by interference microscopy. For x-ray diffraction measurements, alloy films were first produced as described above, then removed as powder by scraping, and glued on an appropriate specimen holder. In this manner, sufficient intensity could be achieved to accurately index the resulting diffraction patterns. Certain other alloy thin films, deposited on {100} substrates of gallium arsenide, were subsequently annealed in a quartz tube furnace under flowing hydrogen at temperatures ranging from 150° to 350°C.

Forward current-voltage and current-temperature (Richardson) plots were determined with the aid of a Keithley 616 digital electrometer, and capacitance-voltage characteristics were determined with the aid of a 1 MHz

Boonton 72B digital capacitance bridge. X-ray diffraction data were obtained with a Rigaku D/MAX II powder x-ray diffraction system using a scintillation counter.

Specimens were prepared for examination by transmission electron microscopy, TEM, by bonding two gallium arsenide substrates with (preannealed) alloy films face to face with an epoxy resin, curing under moderate temperature and pressure, slicing perpendicular to the alloy films with a diamond saw, thinning by mechanical grinding to approximately 50 μm , and finally thinning further with a Gatan Model 600 ion miller, using a collimated beam of argon ions accelerated by a potential difference of 6 kV. The thinned region, perpendicular to the deposited alloy film, was then examined in a JEOL JEM 120CX electron microscope. Further details concerning specimen preparation for examination by TEM are presented elsewhere (5, 9).

Experimental Results

Details of various alloy thin films of gold and gallium, codeposited on {100} substrates of gallium arsenide, are presented in Table I, where compositions of the alloy films, film thickness, and phases identified by x-ray diffraction are presented for both (a) LEC and (b) BM gallium arsenide substrates. Typical results for phase identification by x-ray diffraction are presented in Fig. 1, wherein segments of x-ray diffractometer traces (intensity vs. twice the Bragg angle 2θ) are reproduced for alloy films containing (a) 0, (b) 42, and (c) 62 atom percent (a/o) gold. In Fig. 1a, only diffraction peaks corresponding to pure gold are present. As the composition of gallium is increased, however, small amounts of hexagonal β or Au₇Ga₂ are observed (≥ 4 a/o Ga), followed by Au₂Ga (cf. Fig. 1b) and AuGa₂ (cf. Fig. 1c). In general, these results demonstrate that, as the percent of gallium is increased, compounds containing higher percentages of gallium are formed during the codeposition process. Moreover, except for specimens containing 42 and 57 a/o Ga, the observed compounds agree with those expected from the equilibrium phase diagram (11).

Electrical properties and concomitant structure and phase morphology obtained from these alloy films are presented, sequentially, in the following sections.

Electrical properties.—Typical current density (J) vs. forward voltage bias (V) plots for selected specimens are presented in Fig. 2. These data can be compared with the expression

$$J = A^*T^2 \exp(-\phi/nkT) [\exp(qV/nkT) - 1]$$

where A^* is the effective Richardson constant, n is an ideality constant, and q , k , and T denote, respectively, the electron charge, Boltzmann's constant, and absolute temperature. In order to extract ϕ , however, A^* and n must be determined by varying J as a function of T at a sufficiently large (constant) value of V . These results are presented in Table II, along with values for the doping concentration N_d , obtained from capacitance-voltage measurements, for both as-deposited and annealed specimens.

Before annealing, values of n range between 1.01 and 1.10, reflecting acceptable cleanliness of the Au/GaAs interface (13). The values for N_d range between 3 and 8 \times

Table I. The gold-gallium films deposited, composition, thicknesses, and the phases identified by x-ray diffraction

Atomic percent of Ga in the film	Film thickness (nm)	Phases identified by x-ray diffraction
0	210	Au
13	70	Au, Au ₇ Ga ₂
19	135	Au, Au ₇ Ga ₂
27	100	Au ₂ Ga ₂ , Au ₂ Ga
42	170	Au ₂ Ga
62	250	AuGa ₂
80	140	AuGa ₂ , Ga
90	270	AuGa ₂ , Ga

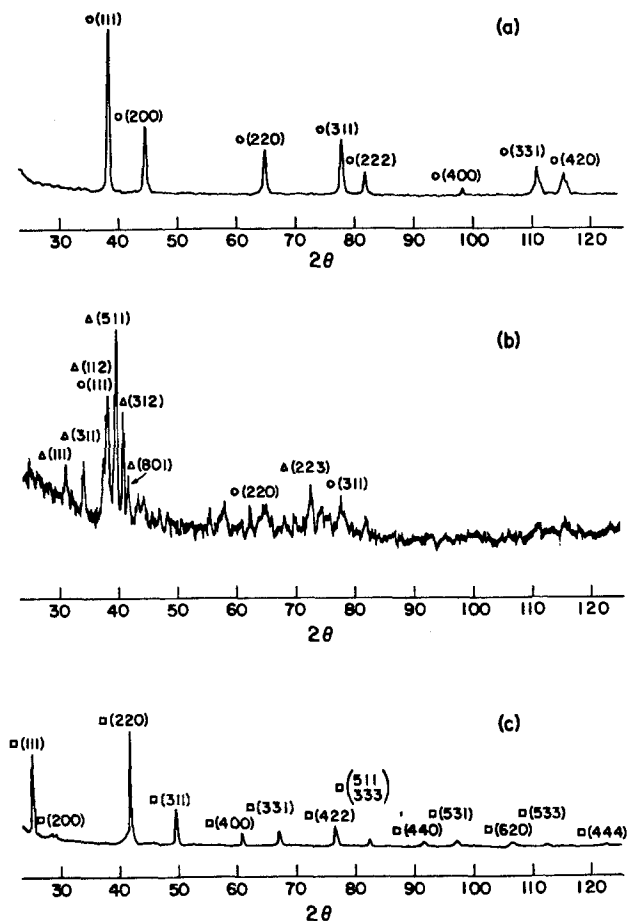


Fig. 1. X-ray powder diffraction patterns (intensity vs. $2 \times$ Bragg angle) for (a) Au, (b) Au-42 a/o Ga, and (c) Au-62 a/o Ga films (co)deposited on glass coated with photoresist. Major peaks due to diffraction from pure gold, (orthorhombic) Au_2Ga , and (Bravais lattice) AuGa_2 ore denoted by \circ , Δ , and \square , respectively.

10^{16} cm^{-3} for the LCE substrates and between 4 and $6 \times 10^{17} \text{ cm}^{-3}$ for the BM substrates used as determined by $1/C^2$ vs. V measurements. These values of N_d did not change significantly after annealing. This suggests that if doping changes were occurring in the first few micrometers of the wafer due to out-diffusion of gallium and arsenic or in-diffusion of gold, the effects were in the less than 10^{16} cm^{-3} range.

The effective Richardson constants A^* are considerably scattered in value, ranging from 2 to $100 \text{ A/cm}^2\text{K}^2$ without strong bias for either type of specimen. Such scatter is

Table II. Composition, Schottky barrier height, and ideality factor, n , for Au-Ga films codeposited on {100} gallium arsenide substrates and subsequently annealed at various temperatures

Atomic percent Ga	GaAs wafer	Unheated (eV)		Heated					
		ϕ_{bn}	n	(150°C)		(250°C)		(350°C)	
		ϕ_{bn}	n	ϕ_{bn}	n	ϕ_{bn}	n	ϕ_{bn}	n
0	LEC ^a	0.95	1.05	0.86	1.06	0.35	1.35	c	c
13	LEC ^a	0.87	1.08	0.76	1.02	0.79	1.03	0.81	1.08
19	LEC ^a	0.82	1.10	0.69	1.03	0.77	1.03	0.40	1.06
27	LEC ^a	0.79	1.04	0.76	1.03	0.76	1.04	0.73	1.08
47	LEC ^a	0.77	1.04	0.76	1.03	0.75	1.13	c	1.17
62	LEC ^a	0.68	1.05	0.77	1.04	0.73	1.03	0.74	1.04
0	BM ^b	0.87	1.08	0.85	1.10	0.31	1.8	c	c
42	BM ^b	0.68	1.03	0.64	1.03	c	1.76	c	c
80	BM ^b	0.66	1.03	0.70	1.03	0.70	1.06	0.75	1.12
90	BM ^b	0.64	1.01	0.64	1.01	c	1.04	c	c

^a Doping (average) of the LEC wafer was $0.47 \times 10^{17} \text{ cm}^{-3}$, and the A^* value measured (unheated) averaged $57 \text{ A cm}^{-2} \text{ K}^{-2}$.

^b For the BM wafer, the values were $4.7 \times 10^{17} \text{ cm}^{-3}$ and $47 \text{ A cm}^{-2} \text{ K}^{-2}$.

^c Indicates junction too conductive for measurements.

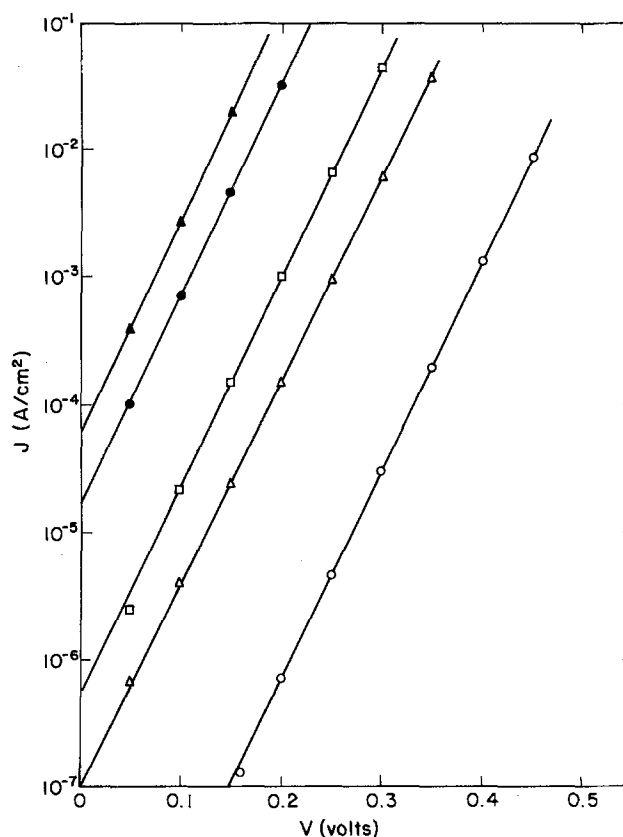


Fig. 2. Current density J vs. forward voltage bias V for various gold-gallium films deposited on {100} LEC ($0.47 \times 10^{17} \text{ cm}^{-3}$) substrates of gallium arsenide: (\circ) pure Au, (Δ) Au-13 a/o Ga, (\square) Au-47 a/o Ga, and on {100} BM substrates ($4.7 \times 10^{17} \text{ cm}^{-3}$) of gallium arsenide: (\bullet) Au-42 a/o Ga, and (\blacktriangle) Au-90 a/o Ga.

not uncommon in Schottky barrier studies (12) and reflects the limited accuracy of the measurement method and slight interface perfection problems. However, the A^* values fall within acceptable ranges, although the values tend to average somewhat larger than the theoretical value of $4.4 \text{ A/cm}^2\text{K}^2$ (12-14). After annealing, however, n increases and A^* decreases for alloy films containing less than 50 a/o Ga, whereas they remain approximately constant for alloy films containing more than 50 a/o Ga, even after annealing for 30 min at 350°C .

Schottky barrier heights obtained from forward current-voltage and current-temperature (Richardson) plots at constant forward voltage are reported in Table II, both before and after annealing for 30 min at 150° , 250° , and 350°C . These two methods of obtaining barrier heights gave very similar values (within 0.03 eV for most specimens) and the average of the two values is presented in Table II and termed ϕ_{bn} . As shown in Fig. 3, the values for the BM material are slightly smaller than for the LEC material and this is because the doping density of the Bridgman wafer is larger.

After annealing, the barrier height values ϕ_{bn} tend to decrease although this decrease is considerably more pronounced for films containing less than 50 a/o Ga and is particularly serious above 200°C for the Au films that were without Ga. The ideality factors, n , tend to remain at values of 1.03-1.08 until the barrier height has been seriously affected by the heat-treatment.

Values of Schottky barrier heights were also extracted from capacitance reverse voltage plots and termed ϕ_{bc} , and the voltage V_b was recorded at which the junction reverse current was 10^{-4} A (corresponding to a current density of 7.5 mA/cm^2). These values are presented in Table III. The barrier heights ϕ_{bc} from capacitance measurements tend to be lower by 0.06 - 0.09 eV than the ϕ_{bn} values determined by the other two methods. It is possible that the ϕ_{bc} values are being influenced by surface state (15) and/or deep level (16-18) impurity states. Some transient

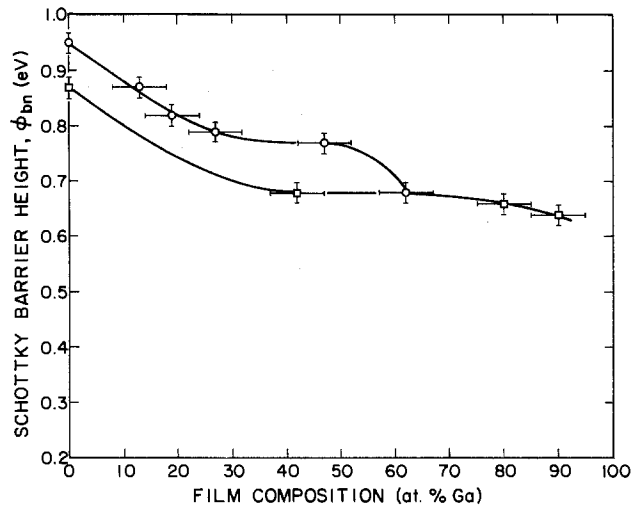


Fig. 3. Schottky barrier height ϕ_{bn} for various gold-gallium films deposited on {100} gallium arsenide substrates as a function of gallium composition, where ϕ_{bn} is the average value from forward current-voltage plots and from activation energy plots for the LEC material ($0.47 \times 10^{17} \text{ cm}^{-3}$) and the BM material $4.7 \times 10^{17} \text{ cm}^{-3}$.

capacitance measurements DLTS, were made of metal-n-GaAs junctions that had been heated to temperatures of 150° and 250°C to see if the development of electron traps could be seen as a result of the gold interaction. In the upper half of the bandgap, we could see no significant change of point defect levels down to a concentration of mid 10^{14} cm^{-3} . More extensive studies of this kind, however, need to be made.

The most important variations to be observed from Table III are those for V_b . Before annealing, the values of V_b are in reasonable agreement with those that might be expected for the doping of $0.47 \times 10^{17} \text{ cm}^{-3}$ and $4.7 \times 10^{17} \text{ cm}^{-3}$. After heat-treatment at 250°C, the values of V_b exhibit dramatic decreases, and this is especially true for the specimens with film compositions that are low in Ga.

Microstructure and Phase Morphology

In order to compare electrical properties with microstructure and phase morphology near the alloy film/gallium arsenide interface, Au/GaAs specimens were prepared and subsequently annealed at various temperatures. Typical forward current-voltage characteristics are presented in Fig. 4 for (i) an unannealed Au/GaAs specimen, and similar specimens heated for 30 min at (ii) 200°, (iii) 275°, and (iv) 345°C. In general, ϕ_b decreases and n increases with increasing annealing temperature, suggesting a degradation of the Au/GaAs interface.

Similar specimens were annealed at various temperatures and subsequently prepared for examination by TEM. Typical results are presented in Fig. 5, wherein bright-field images of the Au/GaAs interface, perpendicular to the deposited gold film, following an anneal for 30 min at (a) ambient temperature, (b) 130°, (c) 200°, (d) 275°, (e) 345°, and (f) 400°C, are pictured. No discernible reaction is evident at ambient temperature (cf. Fig. 5a); however, after annealing for 30 min at 130°C, well defined (pyramidal) pits, bounded by {111} planes in gallium arsenide are clearly visible (5, 9). After annealing for 30 min at 200°C, a new continuous phase separating the gold film and gallium arsenide substrate, in addition to the aforementioned pyramidal pits, is visible. Upon annealing for 30 min at higher temperatures, the continuous phase first becomes more evident (cf. Fig. 5d and 5e) and then appears to become more uniform and to decrease in thickness (cf. Fig. 5f). For a specimen heated for 30 min at 275°C (cf. Fig. 5d), the phase positioned between the gold film (top dark layer) and the gallium arsenide substrate has been determined, from electron diffraction patterns and corresponding dark field images, to be the orthorhombic Au_3Ga intermetallic compound. Existing crystal structures were not determined at other temperatures; however, from previous investigations, it may be assumed that a hexagonal gold-gallium compound forms in the pyramidal pits on {111} faces of gallium arsenide and the orthorhombic gold-gallium phase exists at temperatures well below 275°C (5, 9).

Table III. Schottky barrier height ϕ_{bc} from capacitance measurements and breakdown voltage V_b (reverse voltage for 10^{-4} A) for Au-Ga films on {100} GaAs with annealing for 30 min at various temperatures

Atomic percent Ga	Unheated (eV)		Heated					
	ϕ_{bc}	V_b	150°C		250°C		350°C	
	ϕ_{bc}	V_b	ϕ_{bc}	V_b	ϕ_{bc}	V_b	ϕ_{bc}	V_b
0	1.00	33	1.00	28	0.77	0.7	*	ohmic
13	0.75	49	0.70	46	0.72	16	0.74	7.7
29	0.78	52	0.70	52	0.72	12.5	0.74	1.5
27	0.69	43	0.69	43	0.67	39	0.68	2.7
47	0.69	37	0.62	33	0.69	4	*	0.9
62	0.73	21	0.73	21	0.75	22	0.70	18
0	0.86	16.5	0.85	14	0.75	1.2	*	ohmic
42	0.62	9	0.62	8.5	*	0.15	*	ohmic
80	0.59	8.1	0.61	8	0.64	7.9	0.70	4.3
90	0.55	7.1	0.57	7.1	0.63	6.5	0.70	0.6

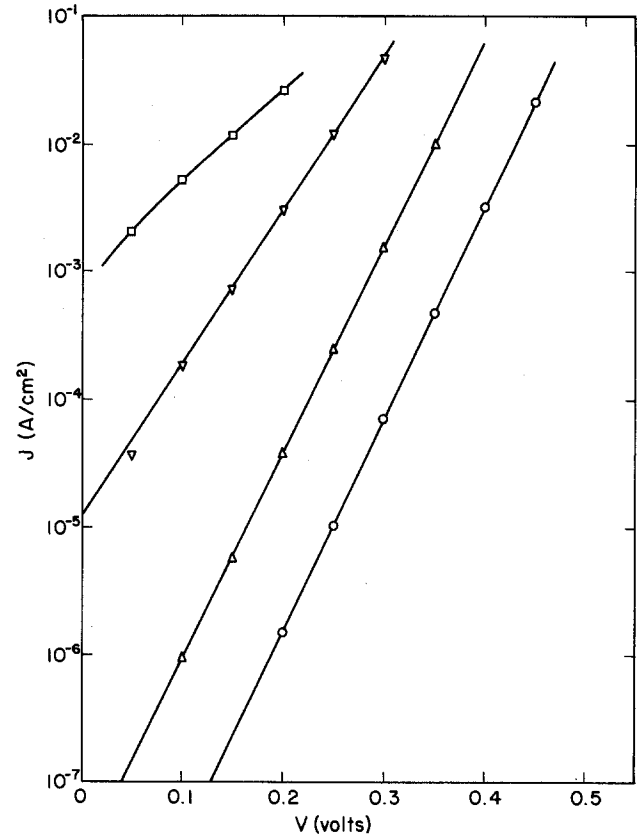


Fig. 4. Variation of current density J with forward voltage bias V for gold films deposited on {100} LCE substrates of gallium arsenide and annealed for 30 min at (○) 20°, (Δ) 200°, (▽) 275°, and (□) 345°C. Corresponding values of ϕ_{bn} decrease from 0.95 (○) to 0.76 eV (▽) at 275°C; for higher annealing temperatures, the plots become too nonlinear to extract meaningful values of ϕ .

(e) 345°, and (f) 400°C, are pictured. No discernible reaction is evident at ambient temperature (cf. Fig. 5a); however, after annealing for 30 min at 130°C, well defined (pyramidal) pits, bounded by {111} planes in gallium arsenide are clearly visible (5, 9). After annealing for 30 min at 200°C, a new continuous phase separating the gold film and gallium arsenide substrate, in addition to the aforementioned pyramidal pits, is visible. Upon annealing for 30 min at higher temperatures, the continuous phase first becomes more evident (cf. Fig. 5d and 5e) and then appears to become more uniform and to decrease in thickness (cf. Fig. 5f). For a specimen heated for 30 min at 275°C (cf. Fig. 5d), the phase positioned between the gold film (top dark layer) and the gallium arsenide substrate has been determined, from electron diffraction patterns and corresponding dark field images, to be the orthorhombic Au_3Ga intermetallic compound. Existing crystal structures were not determined at other temperatures; however, from previous investigations, it may be assumed that a hexagonal gold-gallium compound forms in the pyramidal pits on {111} faces of gallium arsenide and the orthorhombic gold-gallium phase exists at temperatures well below 275°C (5, 9).

It must be emphasized that annealing and subsequent examination by TEM were performed immediately after deposition; when specimens are maintained at room temperature for approximately 6 months and then annealed, somewhat different results are obtained. Typical results are presented in Fig. 6, where bright-field images of specimens consisting of 300 nm of gold deposited on {100} substrates of gallium arsenide, that had been stored for 6 months at room temperature, and air ambient, and then annealed for 30 min at (a) 20, (b) 130, and (c) 300°C, are pictured. In addition to the fact that reaction products form at room temperatures, slight differences in the phase morphology may be noted after annealing at elevated temperatures, such as absence of well-defined pyramidal pits

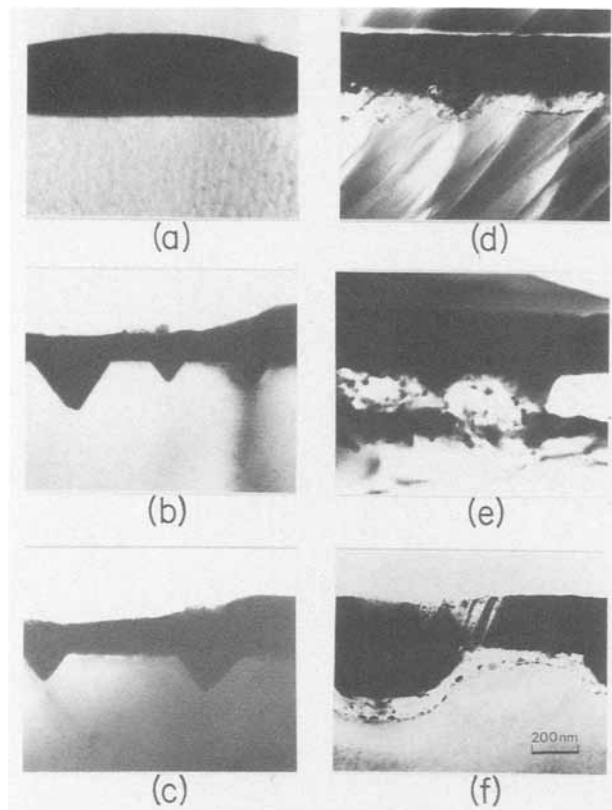


Fig. 5. Bright-field image of the cross section of a gold film deposited on {100} LEC gallium arsenide substrates and subsequently annealed for 30 min at (a) room temperature, (b) 130°, (c) 200°, (d) 275°, (e) 345°, and (f) 400°C. The phase formed between gold and gallium arsenide at 275°C has been identified by a combination of electron-diffraction and dark-field images as orthorhombic Au_2Ga .

after annealing for 39 min at 300°C (cf. Fig. 6c). Possible relationships between electrical properties and such phase morphology are considered in the discussion that follows.

Discussion of Results

Values of various electrical parameters presented in Tables II and III seem to be relatively self-consistent. Slightly lower values of ϕ are obtained with LEC than with BM substrates. Such differences are almost certainly due to the factor of ten difference in doping. In general, values of ϕ decrease with increasing composition of gallium, although this decrease is more pronounced for low compositions (< 30 a/o Ga), which corresponds approximately to the phase Au_2Ga (33 w/o Ga). Since the value and decrease in value of ϕ_b corresponds closely to those obtained after annealing in both the present and previous investigations (7), it is likely that this decrease is due to formation of new phases, especially orthorhombic Au_2Ga , at the original alloy film/gallium arsenide interface.

Composition of alloy films produced by codeposition of gold and gallium on {100} substrates of gallium arsenide and measured by independent calibrated quartz crystal monitors is self-consistent with electrical resistivity measurements. Although the complete dependence of electrical resistivity ρ on composition is unknown, values range from $8 \mu\Omega \text{ cm}$ for pure gold to a maximum of $25 \mu\Omega \text{ cm}$ for an alloy film consisting of 50 a/o Ga, which is consistent with reported bulk values of 2.4 and $40 \mu\Omega \text{ cm}$ for gold and gallium, respectively (19), since additional electron scattering (resistance) is expected for their films. Likewise, compounds identified in unannealed alloy film by x-ray diffraction correspond well with the most recent gold-gallium phase diagram. Of course, generally, any alloy film is expected to consist of a mixture of two separate phases in equilibrium with one another. These results are also consistent with results of Simc and

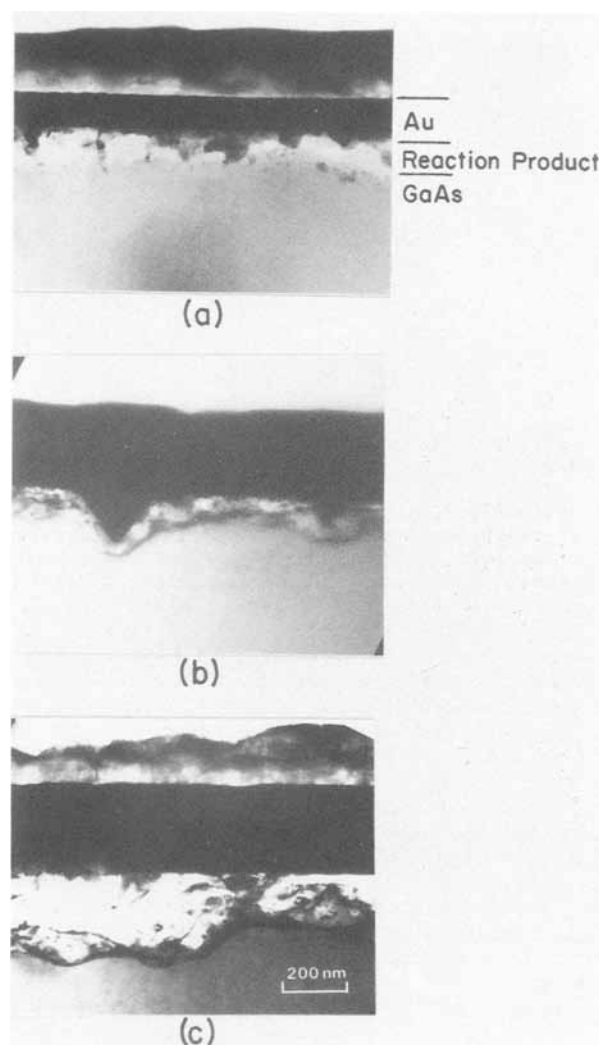


Fig. 6. Bright-field images of the cross section of a gold film deposited on {100} LEC gallium arsenide substrates and subsequently (inadvertently) annealed for approximately 6 months at room temperature and then for 30 min at (a) room temperature, (b) 130°, and (c) 300°C. A ~ 100 nm layer of reaction product is clearly evident, even without annealing above room temperature.

Marinkovic, who investigated interdiffusion between films of gold and gallium deposited on glass (19).

Results presented in Fig. 1 and Table I demonstrate clearly that several gold-gallium compounds are formed when gold and gallium are codeposited on a glass substrate coated with photoresist. Assuming that the compounds formed on gallium arsenide are equivalent to those formed on photoresist, electrical properties of the probable phases formed during codeposition can be compared with those of the phases produced by annealing. In this manner, the decrease of ϕ_b in Fig. 3 may be attributed to the presence of certain gold-gallium compounds. Such decreases, however, cannot be attributed to the presence of a specific phase because (i) generally a phase mixture is present and (ii) the distribution of phases at the alloy film/gallium arsenide interface is not uniform (cf. Fig. 5 and 6). Therefore, a weight-average value of ϕ_b for several dissimilar contacts should be used. Tu *et al.* (20, 21) have shown that, under certain conditions, it is possible to determine respective values of ϕ_b and contact area for each species. In the present investigation, however, the structures are not clearly enough defined to apply this procedure, although it does appear that, in certain cases, a continuous layer of Au_2Ga separates the metallic contact and the gallium arsenide substrate. In any event, it may be surmised that ϕ_b is reduced when phases such as Au_2Ga , Au_2Ga , and AuGa_2 are in contact with gallium arsenide in-

stead of pure gold. Annealing a pure gold/gallium arsenide contact promotes formation of these same phases, and thus concomitant reductions in ϕ_b are comparable to those of as-deposited phases.

Over and above the intrinsic interest in relationships between structure and electrical properties, evolution of structure and phase morphology at the metal/gallium arsenide interface is related to a wealth of kinetic reactions. Of special interest is the formation of pyramidal pits bonded by {111} planes in gallium arsenide and corresponding orientation relationships, as reported by Yoshiie *et al.* (5, 9). Values of V_b are especially sensitive to formation and shape of these pits, because the electric field is concentrated by the curvature of the pit apex r . Assuming a value of about 20 nm for the radius, r , it can be shown that V_b is likely to be reduced to about 40% of its original value (22). Slight differences in reaction rate between previous results of Yoshiie *et al.* (5, 9) and the present investigation stem mainly from differences in film thickness, which controls the rate of release of arsenic and, therefore, the availability of gallium to react with gold.

Surprisingly, the reactions reported herein can easily be detected after (inadvertent) annealing for about 6 months at room temperature, as clearly illustrated in Fig. 6a. This result implies mean diffusion lengths of about 100 nm and a diffusion coefficient of about 10^{-17} cm² s⁻¹. If the Au diffusion line for the range 1200°-850°C given by Kendal (23) is extrapolated (unwisely) to room temperature, this order of magnitude of diffusion coefficients might be expected. However, other high temperature data (24, 25), when extrapolated, suggest much lower diffusion coefficients, and so detailed studies of diffusion of Au in the 600°-100°C range seem desirable.

Upon annealing the aged specimens for 30 min at 130°C, pyramidal pits are formed, whereas annealing for 30 min at 300°C produces only an increasingly thick layer of reaction product. Further investigations are in progress to determine the identity of these phases.

Summary

Electrical properties and phase morphology of gold-gallium films deposited on {100} substrates of gallium arsenide have been investigated by measurement of Schottky barrier height and reverse voltage rating as a function of film composition and annealing conditions and compared with corresponding phase morphology. Either codeposition of alloy films or annealing of pure gold on gallium arsenide promotes formation of various gold-gallium compounds, the most prominent being Au₂Ga, and pyramidal pits bounded by {111} planes of gallium arsenide. Values of ϕ and V_b are reduced by the presence of Au₂Ga and, especially, by the voltage concentration at the tip of the pyramidal pits. The rate of formation of such

microstructure and phase morphology depends on deposition and annealing conditions and, therefore, affects the degradation of electrical properties and concomitant reliability of actual devices.

Acknowledgments

Support of this research by the Materials Research Laboratory Section, Division of Materials Research, National Science Foundation under Grant DMR-8119507-02 is gratefully acknowledged.

Manuscript submitted Dec. 19, 1983; revised manuscript received Sept. 24, 1984.

Carnegie-Mellon University assisted in meeting the publication costs of this article.

REFERENCES

1. S. Leung, L. K. Wong, D. D. L. Chung, and A. G. Milnes, *This Journal*, **130**, 462 (1983).
2. T. J. Magee and J. Peng, *Phys. Status Solidi A*, **32**, 695 (1975).
3. K. Kumar, *Jpn. J. Appl. Phys.*, **18**, 713 (1979).
4. X. F. Zeng and D. D. L. Chung, *This Journal*, **93**, 207 (1982).
5. T. Yoshiie and C. L. Bauer, *J. Vac. Sci. Technol.*, **111**, 149 (1984).
6. S. Leung, D. D. L. Chung, and A. G. Milnes, *Thin Solid Films*, **104**, 109 (1983).
7. J. Ohura and Y. Takeishi, *Jpn. J. Appl. Phys.*, **9**, 458 (1979).
8. H. B. Kim, G. G. Sweeney, and T. M. S. Heng, *Inst. Phys. Conf. Ser.*, **24**, 307 (1975).
9. T. Yoshiie, C. L. Bauer, and A. G. Milnes, *Thin Solid Films*, **105**, 149 (1984).
10. S. Guha, B. M. Arora, and V. P. Salvi, *Solid-State Electron.*, **20**, 431 (1977).
11. C. J. Cooke and W. Hume-Rothery, *J. Less-Common Metals*, **10**, 42 (1966).
12. A. K. Srivastava, B. V. Arora, and S. Guha, *Solid-State Electron*, **24**, 185 (1981).
13. E. H. Rhoderick, "Metal Semiconductor Contacts," p. 46, Clarendon Press, Oxford, England (1980).
14. C. R. Crowell and S. M. Sze, *Solid-State Electron*, **9**, 1035 (1966).
15. J. D. Levine, *J. Appl. Phys.*, **42**, 3991 (1971).
16. J. M. Borrego, R. J. Gutmann, and S. Ashok, *Solid-State Electron.*, **20**, 125 (1977).
17. S. F. Fonash, *J. Appl. Phys.*, **54**, 1966 (1983).
18. A. M. Goodman, *ibid.*, **34**, 329 (1963).
19. V. Simc and Z. Marinkovic, *Thin Solid Films*, **34**, 179 (1976).
20. M. Eizenberg, H. Foell, and K. N. Tu, *J. Appl. Phys.*, **52**, 861 (1981).
21. T. Okumura and K. N. Tu, *ibid.*, **52**, 922 (1983).
22. S. M. Sze and G. Gibbons, *Solid-State Electron.*, **9**, 831 (1966).
23. D. L. Kendal, in "Semiconductor and Semimetals," Vol. 4, R. K. Willardson and A. C. Beer, Editors, p. 163, Academic Press, New York (1968).
24. J. H. Crawford, Jr., and L. M. Slifkin, "Point Defects in Solids," Vol. 2, Plenum Press, New York.
25. V. L. Sokolov, *Sov. Phys. Solid State*, **6**, 265 (1964).

A New Method to Supply Solute Elements into Growth Solutions

Demonstration by Liquid-Phase Epitaxial Growth of $\text{In}_{1-x}\text{Ga}_x\text{As}$

Kazuo Nakajima and Susumu Yamazaki

Fujitsu Laboratories Limited, Atsugi Laboratories, 1677 Ono, Atsugi, 243-01 Japan

ABSTRACT

A controllable method to supply solute elements into growth solutions was developed by using a source current-controlled (SCC) method. A dc electric current was passed through a binary semiconductor compound used as the source material for solute elements. It was found that the source compound could be dissolved into even a saturated solution due to Peltier heating and Joule heating at the interface between the source compound and the solution, and that the composition of growing crystals could be controlled by the electric current passed through the source compound. The SCC method was demonstrated by the liquid-phase epitaxial growth of $\text{In}_{1-x}\text{Ga}_x\text{As}$ on InP, GaAs and InAs were used as source compounds.

Good quality epitaxial layers such as $\text{In}_{0.53}\text{Ga}_{0.47}\text{As}$ and $\text{In}_{1-x}\text{Ga}_x\text{As}_{1-y}\text{P}_y$ compounds must be lattice-matched to substrates. If bulk single crystals of the ternary or quaternary compounds were available, epitaxial layers with various lattice constants could be freely grown on bulk single crystals used as substrates, and available crystals for device fabrication would remarkably increase. $\text{In}_{1-x}\text{Ga}_x\text{As}$ (1, 2), $\text{InAs}_r\text{P}_{1-r}$ (3, 4), $\text{In}_{1-x}\text{Ga}_x\text{Sb}$ (5), $\text{GaAs}_r\text{P}_{1-r}$ (6), and $\text{In}_{1-x}\text{Ga}_x\text{As}_{1-y}\text{P}_y$ (7) bulk single crystals were prepared by liquid-encapsulated Czochralski and gradient freeze methods. However, the largest problem to prepare homogeneous bulk crystals is compositional variation during the growth due to depletion of solute elements. Similarly, it is difficult to grow thick epitaxial layers without compositional gradients by liquid-phase epitaxy (LPE) because solute elements in a finite solution are depleted during the growth.

The problem of depletion can be solved only by developing controllable methods to supply solute elements during growth. Recently, Nakajima *et al.* (8) demonstrated a controllable method to supply solute elements into a growth solution. In their work, a dc electric current was passed through a binary semiconductor compound used as the source material of the solute elements. The source compound was dissolved into the saturated growth solution because of Peltier heating and Joule heating at the interface between the source compound and the growth solution. Thus, the source compound played a dual role as the source material for solute elements and the self-heater in such a source current-controlled (SCC) method. However, their experiments were preliminary and fairly rough, and detailed experimental results on the SCC method have not been reported.

In this work, the SCC method was applied to the LPE growth of $\text{In}_{1-x}\text{Ga}_x\text{As}$ on InP substrates, and it was studied in detail to determine if the composition of LPE layers could be controlled by the SCC method. The lattice constant and wavelength of $\text{In}_{1-x}\text{Ga}_x\text{As}$ LPE layers grown from solutions in which solute elements were supplied by the electric current were measured to determine how much the composition of the LPE layers could be changed by the electric current passed through GaAs or InAs source compounds. In order to determine if enough solute elements to adjust the compositional variation in LPE layers could be supplied into growth solutions by the SCC method, the compositional variation in the thick LPE layers was studied.

Experimental Procedure and Results

Apparatus used in this work.—Figure 1 shows a schematic drawing of the parts of the boat used in this work. The boat consists of three parts, 1, 2, and 3. Part 1 is a carbon (C) boat slider with a boron nitride (BN) block as insulation. The source compound is covered by this BN block. A negative electrode (–) made of stainless steel is screwed into the carbon boat slider. Part 2 is a boron nitride (BN) slider with a cut in which a growth solution is

placed. Part 3 is a carbon (C) boat holder with a boron nitride (BN) plate and a positive electrode (+) made of stainless steel. The substrate is set in a depression in this boat holder, as shown in Fig. 1. These parts, 1, 2, and 3, were assembled into a boat, as shown in Fig. 2. Cross sections of this boat are shown in Fig. 3. When solute elements are supplied to the growth solution, the source compound and the growth solution are arranged as shown in Fig. 3-1. One side of the source compound is in contact with the growth solution, and the opposite side touches the carbon boat slider through the medium of In melt. The other four faces of the plate are covered with boron nitride (BN). The growth solution is surrounded by boron nitride. The bottom is in contact with the carbon boat holder. A dc electric current is passed through the carbon boat holder, the growth solution, the source compound, and the carbon boat slider in that order. The source compound is dissolved in the saturated growth solution because of Peltier heating and Joule heating at the interface between the source compound and the solution. When an epitaxial layer is grown, the substrate and the growth solution are arranged as shown in Fig. 3-2. The growth solution is removed from the source compound and brought over the substrate. The epitaxial layer is grown from the solution whose composition is changed by the supply of solute elements from the dissolved source compound.

LPE growth conditions for lattice matching.—The LPE growth conditions for obtaining lattice-matched $\text{In}_{0.53}\text{Ga}_{0.47}\text{As}$ layers was determined prior to performing the SCC method. $\text{In}_{1-x}\text{Ga}_x\text{As}$ ternary layers were grown from solutions with compositions on the liquidus isotherms at 790°C (9, 10). (111)A-oriented InP single crystals were used as substrates. No supersaturated solutions were used in the growth. $\text{In}_{1-x}\text{Ga}_x\text{As}$ layers were grown at a constant cooling rate of 0.5°C/min by the ramp cooling technique. The lattice constants of $\text{In}_{1-x}\text{Ga}_x\text{As}$ were measured by the double-crystal x-ray diffraction technique. The precise diffraction angle of the ternary layers were determined from the (333) $\text{Cu-K}\alpha_1$ reflection by using the

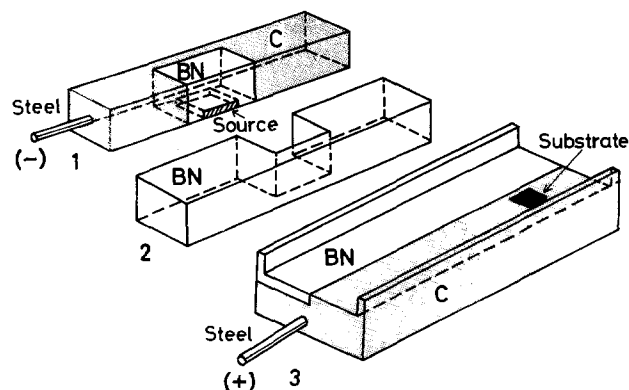


Fig. 1. A schematic drawing of the parts of the boat used in this work

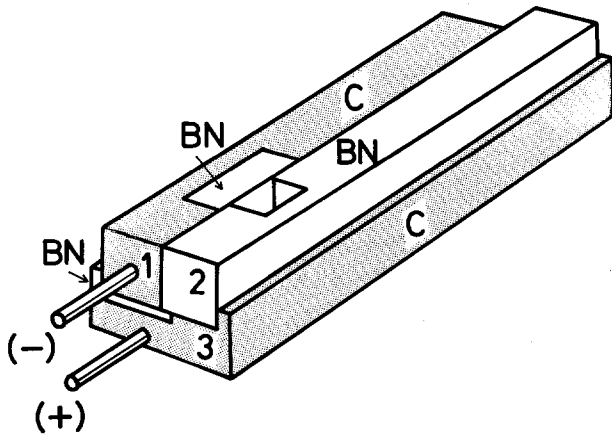


Fig. 2. A schematic drawing of the boat used in this work

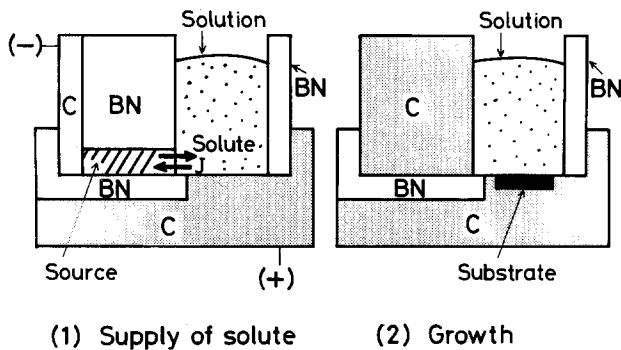


Fig. 3. Cross sections of the boat when solute elements are supplied (1) and when an LPE layer is grown (2).

substrate reflection as an internal standard (11). The lattice constant is displayed as a function of X_{Ga}^1 in Fig. 4, where X_i^1 represents the atomic fraction of an element i in the solution. The dashed line represents the lattice constant of InP. They are lattice constants of the epitaxial lattice perpendicular to the wafer surface. The solution composition for growing lattice-matched layers on InP (111)A substrates can be determined from the results.

LPE growth of thin layers using the SCC method.—In order to determine how much the composition of $In_{1-x}Ga_xAs$ LPE layers can be changed by the electric current passed through GaAs or InAs source compounds, the lattice constant and wavelength of $In_{1-x}Ga_xAs$ LPE layers grown from solutions in which solute elements, Ga, In, and As, were supplied by the electric current were measured. The apparatus employed in this experiment is

shown in Fig. 1, 2, and 3. The size of the InP substrate was $10 \times 9 \text{ mm}^2$. The thickness and weight of the solution were about 3 mm and 2.7g, respectively. The thickness of GaAs or InAs source plate was 2 mm. The area of the source plate in contact with the solution was 0.2 cm^2 , and the depth of the plate was 8 mm. The initial composition of the In-Ga-As ternary solution was $X_{Ga}^1 = 0.040$, $X_{As}^1 = 0.170$, and $X_{In}^1 = 0.790$, which was derived from Fig. 4. Pd-purified H_2 flowed through the fused-silica tube set in which the boat with the InP (111)A substrate, the GaAs or InAs source plate, and the solution were set.

Prior to passing the electric current through the source plate, the solution without contact with the source plate was rapidly heated to 20°C above the saturated temperature of 790°C and held there for about 30 min. Then, the solution was cooled to 789°C at a constant cooling rate of $1^\circ\text{C}/\text{min}$, and the solution was brought in contact with the source plate at 789°C . The electric current was passed from the solution to the source plate of GaAs or InAs for 1 min. The temperature of the solution increased by $1^\circ\text{--}5^\circ\text{C}$ due to Peltier heating and Joule heating at the interface between the source plate and the solution. When the temperature was cooled to 789°C again, the solution was brought over the InP (111)A substrate and the epitaxial growth was performed for 10s. The thickness of the epitaxial layers grown by this process was $0.7\text{--}0.9 \mu\text{m}$.

The lattice constant and wavelength of the epitaxial layers were measured to determine how much the composition of the LPE layers could be changed by the electric current passed through GaAs or InAs source compounds. Figure 5 shows the lattice constant of the $In_{1-x}Ga_xAs$ epitaxial layers as a function of the density of the electric current passed through the source compound, i_s (A/cm^2). The lattice constant of the epitaxial layer grown only by the conventional ramp cooling method, that is to say, $i_s = 0 \text{ A}/\text{cm}^2$, is 5.882\AA . When GaAs is used as a source compound, the lattice constant of the LPE layers decreases as i_s increases due to the supply of solute Ga and As from GaAs dissolved into the solutions. When InAs is used as a source compound, the lattice constant of the layers increases as i_s increases due to the supply of solute In and As from InAs dissolved into the solutions. The wavelength of the epitaxial layers was determined by the photoluminescence (PL) measurements (12). Figure 6 shows the PL wavelength of the epitaxial layers as a function of i_s . The wavelength is $1.672 \mu\text{m}$ when $i_s = 0 \text{ A}/\text{cm}^2$. When GaAs is used as a source compound, the wavelength decreases as i_s increases. When InAs is used as a source compound, the wavelength increases as i_s increases. These results show that the composition of the LPE layers can be sufficiently changed by the electric current

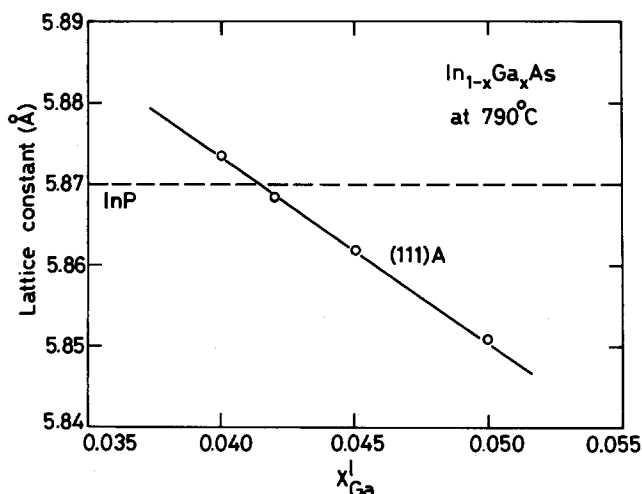


Fig. 4. The lattice constant of (111)A $In_{1-x}Ga_xAs$ LPE layers displayed as a function of X_{Ga}^1 .

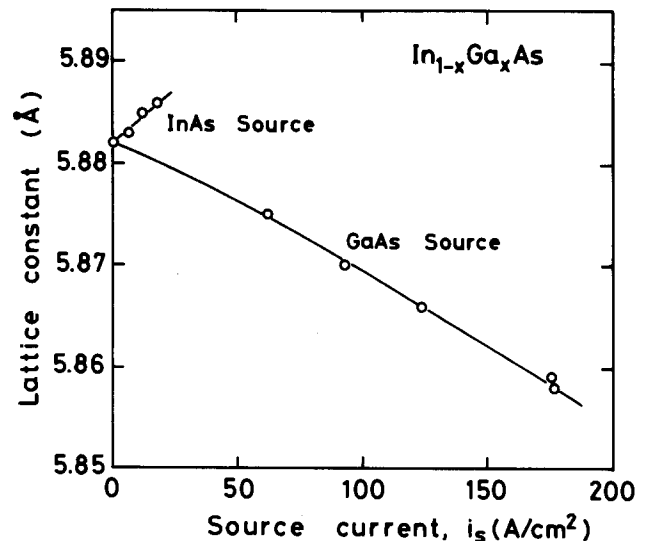


Fig. 5. The lattice constant of (111)A $In_{1-x}Ga_xAs$ LPE layers as a function of the electric current passed through the source compound, i_s (A/cm^2).

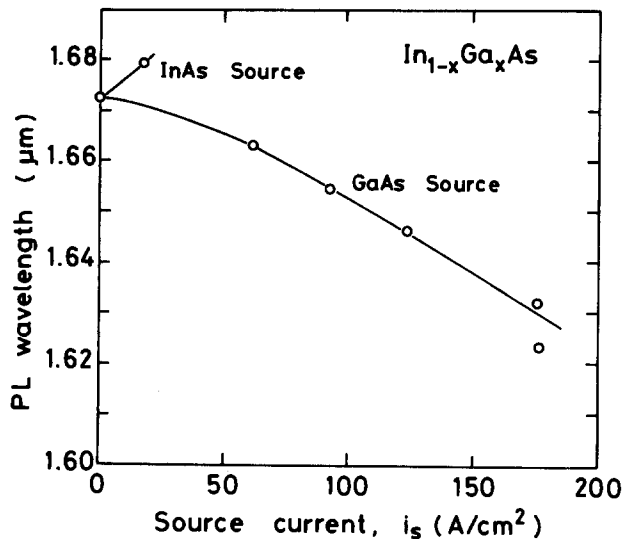


Fig. 6. The PL wavelength of (111)A In_{1-x}Ga_xAs LPE layers as a function of the electric current passed through the source compound, *i_s* (A/cm²).

passed through GaAs or InAs source compounds because enough solute Ga, In, and As can be supplied from the dissolved source compounds into the growth solutions.

In order to determine how much the composition of Ga in the ternary solution, X_{Ga}^1 , could be changed by the electric current passed through GaAs source compounds, the amount of varied X_{Ga}^1 was estimated from the experimental results shown in Fig. 4 and 5. Figure 7 shows the estimated X_{Ga}^1 at 790°C as a function of i_s . X_{Ga}^1 varies from 0.0362 to 0.0465 as i_s increases from 0 to 176 A/cm². As shown in Fig. 7, the solution composition can be controlled by the electric current. The amount of GaAs dissolved into the growth solutions was estimated by using Fig. 7. Figure 8 shows the amount of GaAs (mg) required to make 1g of an In-Ga-As ternary solution with X_{Ga}^1 shown in Fig. 7, as a function of i_s . As shown in Fig. 8, an amount of GaAs (mg) required to make 1g of the ternary solution with $X_{Ga}^1 = 0.040$, $X_{As}^1 = 0.170$, and $X_{In}^1 = 0.790$ is 24.3 mg when $i_s = 0$ A/cm². Therefore, the amount of GaAs dissolved into 1g weight of the solution by the electric current can be determined by subtracting 24.3 mg from the amount shown in Fig. 8, and it increases from 0 to 7.2 mg as i_s increases from 0 to 176 A/cm².

It was studied how the solution composition depended on the time while the electric current was being passed

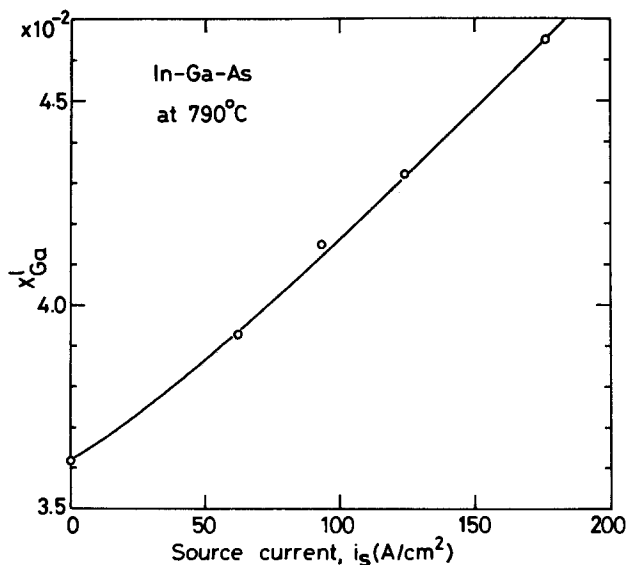


Fig. 7. Estimated amount of varied X_{Ga}^1 at 790°C as a function of the electric current passed through the source compounds, i_s (A/cm²).

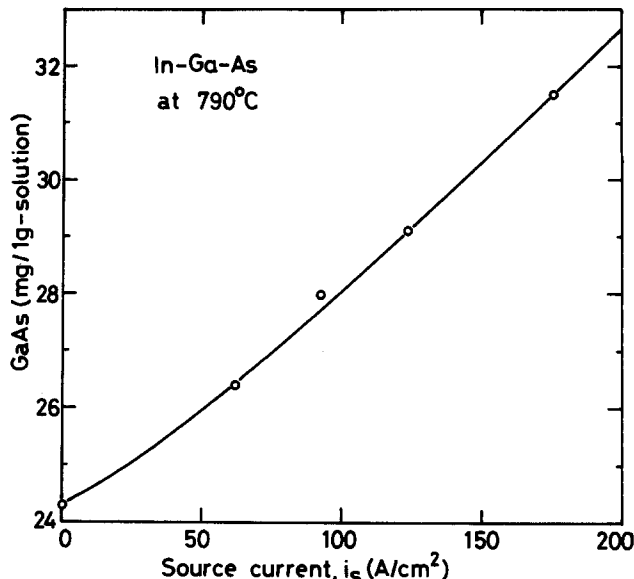


Fig. 8. Amount of GaAs (mg) required to make 1g weight of an In-Ga-As ternary solution with X_{Ga}^1 shown in Fig. 7, as a function of the electric current passed through the source compound, i_s (A/cm²).

through GaAs sources. The electric current of 88 A/cm² was passed through GaAs sources at 789°C. The epitaxial growth was performed by using the same procedure mentioned above. The epitaxial layers were grown for 10s at 789°C from the solutions in which solute Ga and As had been supplied. Figure 9 shows the lattice constant of the epitaxial layers as a function of the time (min) passing the electric current through GaAs sources. The thickness of the layers was 0.5-0.9 μm. The lattice constant varies greatly for the initial 2 min, and it varies gradually after that. The results mean that GaAs sources dissolve largely into the growth solutions for the initial 2 min because the temperature of the solution near the interface between the sources and the solutions becomes rapidly high. The results also imply that, after 2 min, GaAs sources dissolve gradually because the temperature of the solution increases slightly due to scattering of heat. Figure 10 shows the PL wavelength of the epitaxial layers as a function of the time (min) passing the electric current through GaAs sources. The wavelength varies greatly for the initial 2 min, and it varies gradually after that. As shown in Fig. 9 and 10, the solution composition varies most largely for the initial 1 min after passing the electric current.

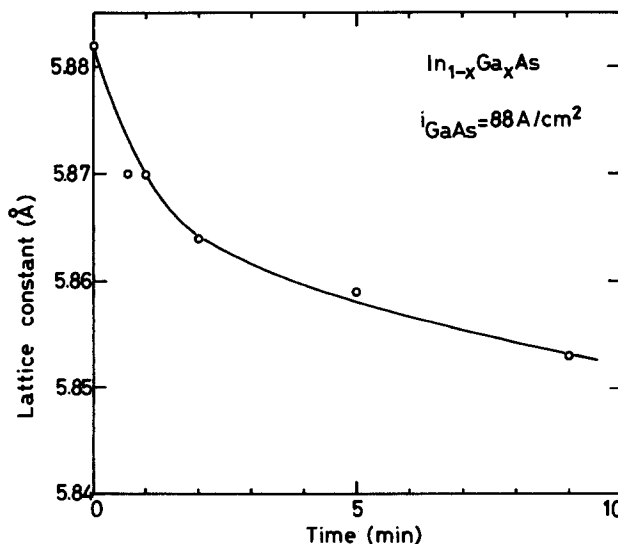


Fig. 9. The lattice constant of (111)A In_{1-x}Ga_xAs LPE layers as a function of the time (min) passing the electric current through GaAs sources.

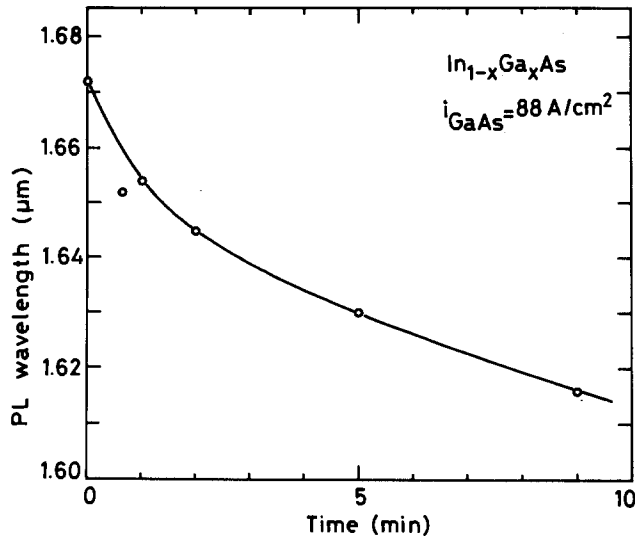


Fig. 10. The PL wavelength of (111)A $\text{In}_{1-x}\text{Ga}_x\text{As}$ LPE layers as a function of the time (min) passing the electric current through GaAs sources.

LPE growth of thick layers using the SCC method.—In order to determine if enough solute elements to adjust the compositional variation in the LPE layers could be supplied into growth solutions by the SCC method, the compositional variation in the thick LPE layers was studied. The same apparatus as shown in Fig. 1, 2, and 3 was used. Prior to the growth, the In-Ga-As solution without contact with the source plate was rapidly heated to 20°C above the saturated temperature of 790°C and held there for about 30 min. Then, the solution was cooled to 789°C at a constant cooling rate of 1°C/min, and the solution was brought over the InP (111)A substrate. The ramp cooling method was used to grow $\text{In}_{1-x}\text{Ga}_x\text{As}$ LPE layers from 789° to 760°C. The electric current was passed through the GaAs source plate after interrupting the LPE growth by removing the solution from the InP substrate and bringing the solution in contact with the source plate. The epitaxial growth was allowed again by removing the solution from the source plate and bringing it over the substrate.

Electron probe microanalysis (EPMA), employing energy dispersive x-ray detection, was used to determine the intensities of the Ga-K $_{\alpha}$ line from the sample and from the GaP standard. An electron beam energy of 25 keV

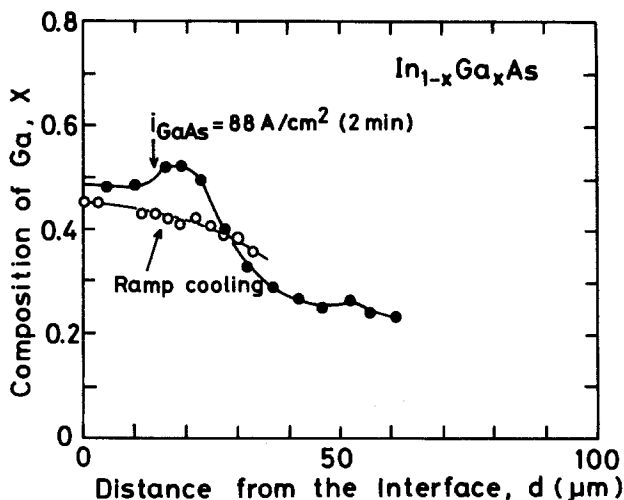


Fig. 11. Composition variation of Ga, x , in (111)A $\text{In}_{1-x}\text{Ga}_x\text{As}$ LPE layers as a function of the distance, d (μm), from the interface between the layers and the InP substrates. Open circles show the composition of the LPE layer grown only by the ramp cooling. Closed circles show the composition of the LPE layer grown from the solution in which solute Ga and As were supplied by the electric current of 88 A/cm 2 for 2 min.

was used. The measured intensities were converted to concentrations by performing the atomic number, absorption, and fluorescence corrections.

Figure 11 shows how the composition of Ga, x , in $\text{In}_{1-x}\text{Ga}_x\text{As}$ epitaxial layers varies with the distance, d (μm), from the interface between the layers and the InP substrates. The open circles show the composition of the epitaxial layer grown by only the ramp cooling. The composition varies from $x = 0.45$ at the interface to $x = 0.35$ at the surface due to the depletion of Ga in the solution. The solid dots show the composition of the epitaxial layer grown from the solution in which solute Ga and As were supplied by the electric current passed through the GaAs source plate. This epitaxial layer was grown by the ramp cooling method from 789° to 760°C at a constant cooling rate of 1°C/min. At 785°C, the epitaxial growth was interrupted by removing the solution from the substrate and bringing it in contact with the GaAs source plate. The electric current of 88 A/cm 2 was passed through the source plate for 2 min in order to dissolve the GaAs source. Then, the epitaxial growth was allowed again by bringing the solution over the substrate. As shown in Fig. 11, enough solute Ga and As to adjust the compositional gradient can be supplied into the solution by the SCC method. Figure 12 shows the composition of Ga, x , in $\text{In}_{1-x}\text{Ga}_x\text{As}$ LPE layers as a function of the distance, d (μm), from the interface between the layers and the InP substrates. The epitaxial layer was grown by the ramp cooling method from 789° to 760°C at a constant cooling rate of 1°C/min. The epitaxial growth was interrupted twice at 780° and 770°C. The electric current of 134 A/cm 2 was passed through the GaAs source plate for 2 min at 780°C and for 3 min at 770°C to supply solute Ga and As into the solution. Therefore, two humps appear on the curve of the composition variation, as shown in Fig. 12. The solid line shows the composition variation of the LPE layer grown only by the ramp cooling, and the broken line shows that of the LPE layer grown by using the SCC method, which were derived from Fig. 11.

Figures 13 and 14 show the composition of Ga, x , in $\text{In}_{1-x}\text{Ga}_x\text{As}$ LPE layers as a function of the distance, d (μm). These LPE layers were grown by the ramp cooling at 1°C/min from 789° to 730°C. The open circles show the compositions of the LPE layer grown by only the ramp cooling. The composition varies from $x = 0.45$ at the interface to $x = 0.29$ at the surface. The solid dots show the composition of LPE layers grown from the solutions in

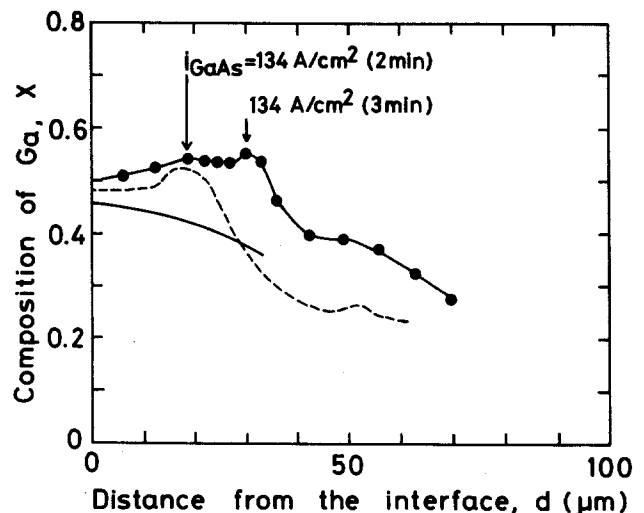


Fig. 12. Composition variation of Ga, x , in (111)A $\text{In}_{1-x}\text{Ga}_x\text{As}$ LPE layers as a function of the distance, d (μm), from the interface between the layers and the InP substrates. Closed circles show the composition of the LPE layer grown from the solution in which solute Ga and As were supplied by the electric current of 134 A/cm 2 for 2 min at 780°C and for 3 min at 770°C. The solid line shows the composition variation only by the ramp cooling. The broken line represents the composition variation shown in Fig. 11.

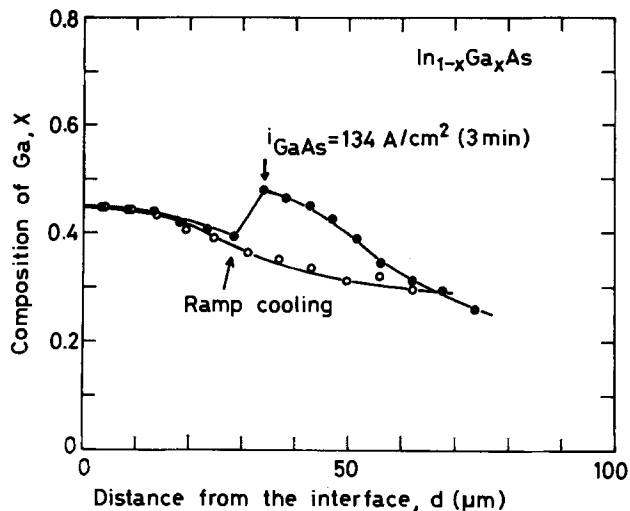


Fig. 13. Composition variation of Ga, x , in (111)A $\text{In}_{1-x}\text{Ga}_x\text{As}$ LPE layers as a function of the distance, d (μm), from the interface between the layers and the substrates. Open circles show the composition of the LPE layer grown only by the ramp cooling. Closed circles show the composition of the LPE layer grown from the solution in which solute Ga and As were supplied by the electric current of 134 A/cm^2 for 3 min at 760°C .

which solute Ga and As were supplied by the electric current passed through the GaAs source plate. For the LPE layer shown in Fig. 13, the LPE growth was interrupted at 760°C and the electric current of 134 A/cm^2 was passed through the GaAs source plate for 3 min. For the LPE layer shown in Fig. 14, the LPE growth was interrupted at 740°C and the electric current of 134 A/cm^2 was passed for 3 min. As shown in Fig. 13 and 14, enough solute Ga and As to adjust the compositional gradient can be supplied into the solution by the SCC method. The peak value of the curve shown in Fig. 13 is $x = 0.48$, and the value is larger than the value at $d = 0 \mu\text{m}$, $x = 0.45$. That is to say, the amount of supplied solute Ga into the solution by passing the electric current of 134 A/cm^2 for 3 min is larger than the amount of depleted solute Ga in the solution during the growth from 789° to 760°C . The curve shown in Fig. 14 is flatter than that in Fig. 13. This means that the amount of supplied solute Ga is almost equal to that of depleted Ga during the growth from 789° to 740°C . Although thick epitaxial layers without compositional gradients were not obtained in this work, these results

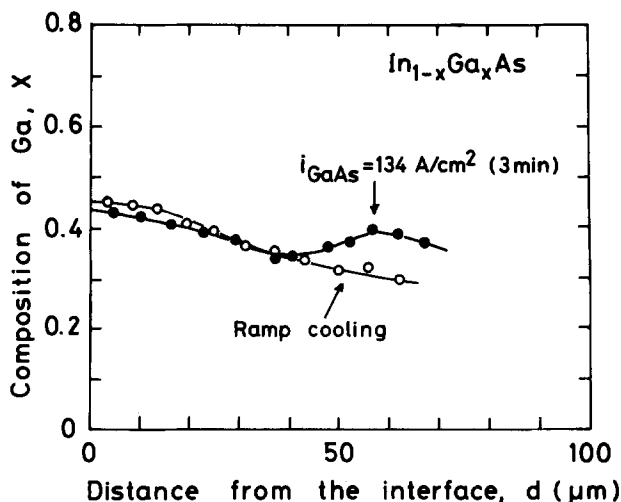


Fig. 14. Composition variation of Ga, x , in (111)A $\text{In}_{1-x}\text{Ga}_x\text{As}$ LPE layers as a function of the distance, d (μm), from the interface between the layers and the InP substrates. Open circles show the composition of the LPE layer grown only by the ramp cooling. Closed circles show the composition of the LPE layer grown from the solution in which solute Ga and As were supplied by the electric current of 134 A/cm^2 for 3 min at 740°C .

imply that thick LPE layers without compositional gradients can be obtained by controlling the electric current in proportion to the depletion of solute Ga in the solution during the growth.

Figures 15 and 16 show the cross section and surface of the $\text{In}_{1-x}\text{Ga}_x\text{As}$ epitaxial layer grown by the SCC method. The thickness of the layer is $79 \mu\text{m}$. As shown in Fig. 16, this epitaxial layer did not have a mirror-like surface and had hillocks, but cracks were not observed.

Discussion

These are preliminary results of the SCC method. Nevertheless, they show that enough solute elements to vary the composition of LPE layers can be supplied into the solutions by passing the electric current through the source compounds. Therefore, there is a possibility of the preparation of homogeneous multicomponent thick LPE layers by applying computer control of electric current during the growth to this method. There is also a possibility of the preparation of homogeneous multicomponent bulk crystals by applying the computer-controlled SCC method to the crystal pulling system.

The magnitude of Peltier heating and Joule heating in these experiments was estimated. The magnitude of the heat generated by Peltier heating, P (W/cm^2), is given (13) by

$$P = \pi_p J \quad [1]$$

where π_p (V) is the Peltier coefficient, and J (A/cm^2) is the density of the electric current. π_p of n-type GaAs is about 0.2V (14) near 800°C . The magnitude of the heat generated by Joule heating, Q (W/cm^2), is given by

$$Q = \rho J^2 l \quad [2]$$

where ρ ($\Omega\text{-cm}$) is the resistivity of the source plate and l (cm) is the depth of the source plate. ρ of Si-doped GaAs used in this work is $0.002 \Omega\text{-cm}$. l of the GaAs source plate is 0.8 cm . The area of the GaAs source plate in contact

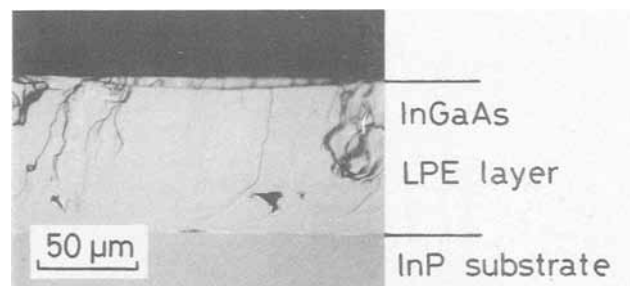


Fig. 15. The cross section of the $\text{In}_{1-x}\text{Ga}_x\text{As}$ LPE layer grown by the SCC method.

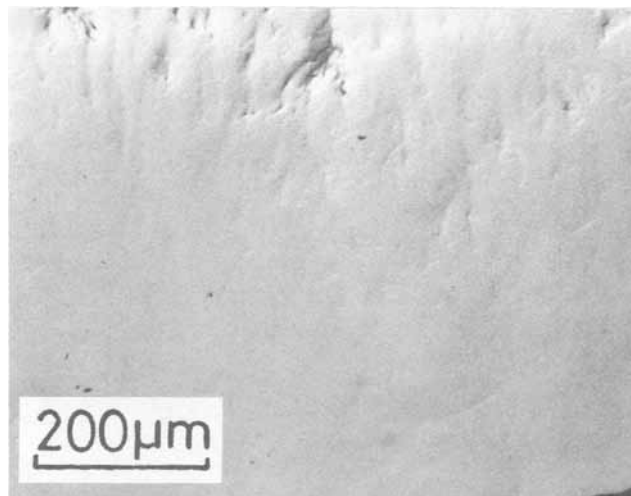


Fig. 16. The surface of the $\text{In}_{1-x}\text{Ga}_x\text{As}$ LPE layer grown by the SCC method.

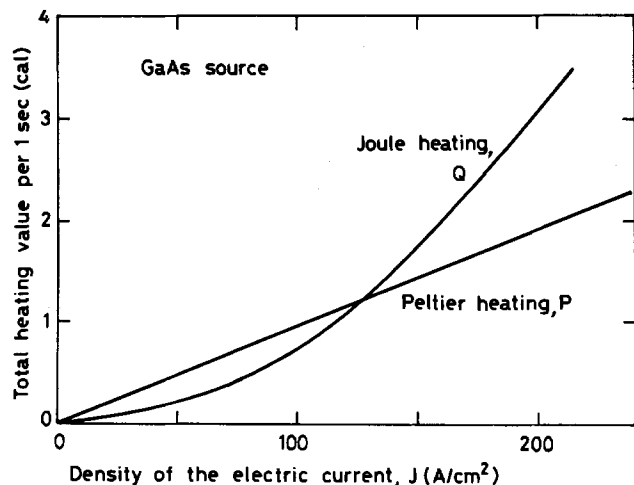


Fig. 17. Estimated Peltier heating value, P , and Joule heating value, Q , generated in the GaAs source plate as a function of the density of the electric current, J (A/cm^2).

with the solution is 0.2 cm^2 . The Peltier heating value, P , and the Joule heating value, Q , were estimated by using Eq. [1] and [2]. The estimated result is shown in Fig. 17. Figure 17 shows the total heating value per 1s as a function of J (A/cm^2). When J is smaller than 126 A/cm^2 , the Peltier heating value, P , is larger than the Joule heating value, Q . When J is larger than 126 A/cm^2 , Q is larger than P . The total heating value of P and Q at $J = 100 \text{ A/cm}^2$ is about 1.7 cal/s . In order to make P larger than Q , it is necessary to use a source plate with small ρ ($\Omega\text{-cm}$) and l (cm). In either case, enough amount of heat to dissolve a source plate into a solution can be generated by enlarging the density of the electric current, J (A/cm^2), and solute elements can be supplied into the solution in proportion to J .

Conclusions

The principle of the SCC method has been confirmed by the LPE growth of $\text{In}_{1-x}\text{Ga}_x\text{As}$ on InP . The electric current passed through the source compound (GaAs or InAs) can heat the compound due to Peltier heating and Joule heating at the interface between the compound and the solution. The composition of the solution can be changed by the electric current passed through the source compound because solute elements are supplied

from the source compound into the solution due to Peltier heating and Joule heating. The lattice constant and wavelength of $\text{In}_{1-x}\text{Ga}_x\text{As}$ LPE layers grown from solutions in which solute elements are supplied can be changed by the electric current. It was confirmed by studying the compositional variation of the thick LPE layers that enough solute elements to adjust the compositional variation in the LPE layers could be supplied into growth solutions by the SCC method.

Acknowledgments

The authors wish to acknowledge the EPMA measurements of O. Ueda. Useful discussions were held with I. Umebu and T. Kotani.

Manuscript submitted July 10, 1984; revised manuscript received Nov. 12, 1984. This was Paper 666 SOA presented at the New Orleans, Louisiana, Meeting of the Society, Oct. 7-12, 1984.

Fujitsu Laboratories Limited assisted in meeting the publication costs of this article.

REFERENCES

1. J. W. Wagner, *This Journal*, **117**, 1193 (1970).
2. Y. T. Leu, F. A. Thiel, H. Scheiber, Jr., J. J. Rubin, B. I. Miller, and K. J. Bachmann, *J. Electron. Mater.*, **8**, 663 (1979).
3. A. G. Thompson and J. W. Wagner, *J. Phys. Chem. Solids*, **32**, 2613 (1971).
4. H. Watanabe, H. Watanabe, M. Yoshida, and J. Matsui, in "Abstracts of the 15th Conference on Solid State Devices and Materials," p. 169, Tokyo (1983).
5. K. J. Bachmann, F. A. Thiel, H. Schreiber, Jr., and J. J. Rubin, *J. Electron. Mater.*, **9**, 445 (1980).
6. F. Cerrina, D. Margadonna, and P. Perfetti, *J. Cryst. Growth*, **18**, 202 (1973).
7. K. J. Bachmann, F. A. Thiel, and S. Ferris, *ibid.*, **43**, 752 (1978).
8. K. Nakajima, S. Yamazaki, and I. Umebu, *Jpn. J. Appl. Phys.*, **23**, L26 (1984).
9. T. Y. Wu and G. L. Pearson, *J. Phys. Chem. Solids*, **33**, 409 (1972).
10. M. A. Pollack, R. E. Nahory, L. V. Deas, and D. R. Wonsidler, *This Journal*, **122**, 1550 (1975).
11. K. Nakajima, S. Yamazaki, and K. Akita, *J. Cryst. Growth*, **61**, 535 (1983).
12. K. Nakajima, A. Yamaguchi, K. Akita, and T. Kotani, *J. Appl. Phys.*, **49**, 5944 (1978).
13. L. Jastrzebski, J. Lagowski, H. C. Gatos, and A. F. Witt, *ibid.*, **49**, 5909 (1978).
14. E. K. Stefanakos, A. Abul-Fadl, and M. D. Workman, *ibid.*, **46**, 3002 (1975).

A Silicon Containing Positive Photoresist (SIPR) for a Bilayer Resist System

Y. Saotome, H. Gokan, K. Saigo, M. Suzuki, and Y. Ohnishi

NEC Corporation, Fundamental Research Laboratories and Microelectronics Research Laboratories, Miyazaki 4-chome, Miyamae-ku, Kawasaki 213, Japan

ABSTRACT

A new silicon containing positive photoresist (SIPR), which has excellent durability against oxygen dry etching, was prepared and evaluated as the thin top, or resolution layer, in a bilayer resist system. SIPR, a partly trimethylsilylmethylated resorcinol-formaldehyde resin mixed with a naphthoquinonediazide, was thinly coated onto a thick layer of polyimide resin on a silicon wafer. After exposure and development, positive patterns, including $0.7 \mu\text{m}$ lines, were obtained in this thin top layer. Those patterns were transferred into the bottom layer of polyimide either by reactive oxygen ion etching ($\text{O}_2\text{-RIE}$) or oxygen ion beam etching ($\text{O}_2\text{-IBE}$) with good accuracy. No residues were observed on wafers after the transfer.

The movement of semiconductor industry toward greater integration has imposed severe requirements on photoresists. These materials have to possess not only many indispensable properties, such as film formability, adhesion without striations, and masking functions for a

wide variety of processing conditions, but also the ability to produce submicron relief images over topography.

The use of trilayer resist techniques for the production of submicron patterns was suggested by Moran and Maydan (1) to meet the above requirements, but the fabrica-

tion process is much more complex than that of the usual single-layer resist system. In order to simplify the trilayer system, a bilayer process using E-beam exposure and oxygen plasma etching was proposed by Hatzakis *et al.* (2). They indicated that the imaging (top) layer and the etch mask (middle) layer in the trilayer system can be combined into a single layer by using E-beam-sensitive poly(vinylmethylsiloxane).

We have also developed an E-beam and deep UV resist, which is a copolymer of trimethylsilylstyrene and chloromethylstyrene (3). A related copolymer of trimethylsilylstyrene and chlorostyrene (4) was reported by MacDonald *et al.* These materials showed that silicon containing polymers without siloxane linkages are also resistant to oxygen plasmas, and can be used as a top imaging layer in a bilayer resist system.

Several kinds of silicon containing resists have been reported (5-8), but there appeared only two candidates which are suitable for use in near UV region: our negative resist, TAS (7), and the positive resist containing m-trimethylsilylphenol reported by Wilkins *et al.* (8).

In this paper, a newly developed silicon containing positive photoresist (SIPR) and its application as a bilayer system is described.

Experimental

Base resin preparation.—3-Trimethylsilylmethoxyphenol (1) was prepared by the following procedure. To an ethanol (40 ml) solution of sodium ethoxide (0.1 mol) was added resorcinol (11.0g, 0.1 mol). Then, trimethylsilylchloromethane (12.3g, 0.1 mol) was added dropwise at reflux with stirring. After continuous refluxing for 48h, the solution was acidified with concentrated hydrochloric acid, filtered, evaporated, extracted with chloroform, and washed several times with water. Subsequent vacuum distillation affords pure 1 (12.0g, 61%), bp 86°C at 26 Pa, ¹H NMR (CDCl₃); δ 0.2 (s, 9H, SiCH₃), 3.5 (s, 2H, CH₂), 5.5 (br, 1H, OH), 6.2-7.3 (m, 4H, C₆H₄).

2-Methyl-3-trimethylsilylmethoxyphenol (2) and 3-(3-trimethylsilylpropoxy) phenol (3) were prepared similarly. 2: yield 65%, bp 102°-104°C at 93 Pa, ¹H NMR (CDCl₃); δ 0.1 (s, 9H, SiCH₃), 2.1 (s, 3H, CH₃), 3.5 (s, 2H, CH₂), 4.9 (s, 1H, OH), 6.2-7.1 (m, 3H, C₆H₃). 3: yield 49%, bp 115°-117°C at 13 Pa, ¹H NMR (CDCl₃); δ 0.1 (s, 9H, SiCH₃), 0.4-0.8 (m, 2H, SiCH₂), 1.5-2.1 (m, 2H, CH₂), 3.9 (t, 2H, OCH₂), 5.2 (s, 1H, OH), 6.3-7.1 (m, 4H, C₆H₄).

Subsequent addition condensation of the prepared phenols 2-methylresorcinol and formaldehyde was performed in ethanol. A typical procedure is as follows: to an ethanol (20 ml) solution of 1 (5.0g, 26 mmol), 2-methylresorcinol (2.1g, 17 mmol) and 35% formalin (3.7g, 43 mmol) was added ten drops of concentrated hydrochloric acid. The mixture was refluxed with stirring for 6h. The resin was obtained quantitatively after reprecipitation with 500 ml of water, followed by vacuum drying at 80°C for 10h.

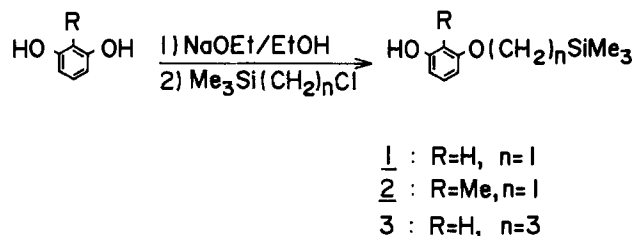
Wafer processing.—The bottom organic layer used in this study was polyimide (PI-2555, du Pont). PI-2555 was spun on silicon wafers and cured at 350°C for 1h, to yield 1.3 μm thick films. The top layer, SIPR, consisting of 10 weight percent (w/o) of the prepared base resin, 3 (w/o) of p-tolyl 1,2-naphthoquinone-2-diazide-5-sulfonate, and 87 w/o of 2-ethoxyethyl acetate, was spin-coated onto the polyimide layer, to produce 0.29 μm thick films after baking at 80°C for 30 min. Imaging was conducted with a Kasper 2001 contact printer, and development was carried out with aqueous sodium hydroxide solutions. For the image transfer into the bottom layer of polyimide, a parallel-plate reactor with a quartz etch table (DEM-451, Anelva) operating at 13.56 MHz at 1.6 Pa oxygen pressure, or an oxygen ion beam etching system with a Kaufman ion source was used. When O₂-RIE transfer was used, silicon wafers were immersed in buffered hydrofluoric acid after the transfer to remove redeposited materials from the quartz table.

Measurement technique.—¹H NMR spectra were obtained with a JEOL JNM-PMX60SI nuclear magnetic spectrometer. Gel permeation chromatograms of the res-

ins were recorded on LC-1 equipped with a polystyrene gel (Shimadzu) column. Initial resist thicknesses after baking, and residual thicknesses after development or etching, were measured by Talystep (Rank Taylor Hobson). The resist profiles were examined with a scanning electron microscope JSM-T200 (JEOL).

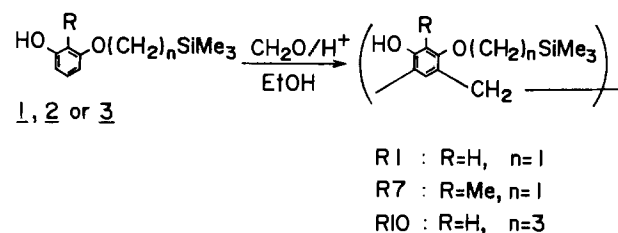
Results and Discussion

A system comprised of a combination of a novolak-type resin and naphthoquinonediazide, which works by a solution inhibition mechanism, was chosen as the positive working top layer resist. In order to introduce silicon atoms into the above combination, the preparation of a silicon containing novolak was undertaken. The acid-catalyzed condensation of p-trimethylsilylphenol with formaldehyde was unsuccessful, since p-trimethylsilylphenol is readily decomposed to phenol itself under acidic conditions, as mentioned in the literature (9). Since the silicon-aromatic carbon bond is much more easily cleaved by acid than the silicon-aliphatic carbon bond, attempts were made to prepare the novel silicon containing phenol without the former bond. In order to obtain such a phenol, silyl groups have to be connected to the phenol ring through an alkyl or alkoxy linkage. Following these considerations, three kinds of silylalkoxyphenols were synthesized by a phenoxide alkylation method. The reaction scheme is shown below



The stability of these phenols to acid was examined by ¹H NMR in a sample tube with DCl/D₂O-CD₃OD at 110°C. These results revealed the three silicon containing phenols are completely stable and, accordingly, should survive the addition condensation conditions. Furthermore, treatment with NaOD instead of DCl confirmed they are not decomposed by alkali. This suggests that the trimethylsilyloxyalkylphenolic structure is sufficiently stable to the development in an alkaline solution. Moreover, the above-mentioned stability to both acid and alkali indicates that novolak resins produced from these phenols will be stable and can be stored as ordinary novolak resins.

The addition condensation of the prepared phenols (1-3) with formaldehyde was carried out in ethanol, since the phenols are immiscible with water even at elevated temperatures



The above resins were obtained in quantitative yield. The polymer structures were confirmed by ¹H NMR. Although these polymers are soluble in most organic solvents, they are not soluble in dilute sodium hydroxide solution. This insolubility is apparently caused by the hydrophobic silylalkyl groups, and necessitated the incorporation of a hydrophilic co-monomer, 2-methylresorcinol (4)

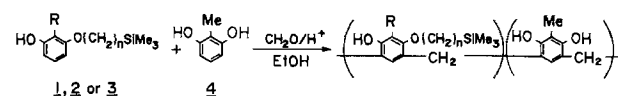


Table I. Base resins preparation

Resin	Feed (eq)			Yield (%)	Solubility in 1N NaOH	Si ^a (%)
	1	2 or 3	4			
R1	1	1.00	—	100	—	13.5
R2	1	0.75	0.25	99	—	11.1
R3	1	0.67	0.33	99	—	10.2
R4	1	0.60	0.40	100	+	9.39
R5	1	0.55	0.45	99	+	8.78
R6	1	0.50	0.50	97	+	8.15
R7	2	1.00	—	99	—	12.6
R8	2	0.60	0.40	99	+	8.97
R9	2	0.50	0.50	101	+	7.83
R10	3	1.00	—	98	—	11.9
R11	3	0.30	0.70	101	+	5.07

^a Calculated value.

As shown in Table I, the incorporation of a certain amount of 4 solubilized the resin in a sodium hydroxide solution, at the slight expense of the silicon concentration in the resin.

R4 and R8 were selected for the reasons of solubility and silicon content, and a photosensitive inhibitor, p-tolyl 1,2-naphthoquinone-2-diazide-5-sulfonate, was added. Two resist solutions, SIPR-1 containing R4 and SIPR-2 containing R8, were prepared by dissolving the above mixtures in 2-ethoxyethyl acetate. Composition of the resist solutions was described in the Experimental section.

The sensitivity characteristics of SIPR-1 and 2 were examined on silicon wafers with a Kasper 2001 contact printer. The required developer concentration for SIPR-2, defined as the minimum concentration of aqueous sodium hydroxide solution for dissolving the base resin without residue, was lower than that of SIPR-1, even though number of hydroxyl groups (phenolic OH's) in the base resin is the same in both resists. As shown in Fig. 1, the γ value for SIPR-2 was higher than that for SIPR-1.

In order to trace the difference between SIPR-1 and 2 with regard to both solubility and the γ value, the molecular weight distributions of the resins were examined. The gel permeation chromatogram for R4 (the resin used in SIPR-1) shows a discernible shoulder at the higher molecular weight side of the main distribution peak, while that for R8 (used in SIPR-2) shows a single distribution peak, as shown in Fig. 2. This difference in the molecular weight distribution might be caused by the difference in the monomer structure

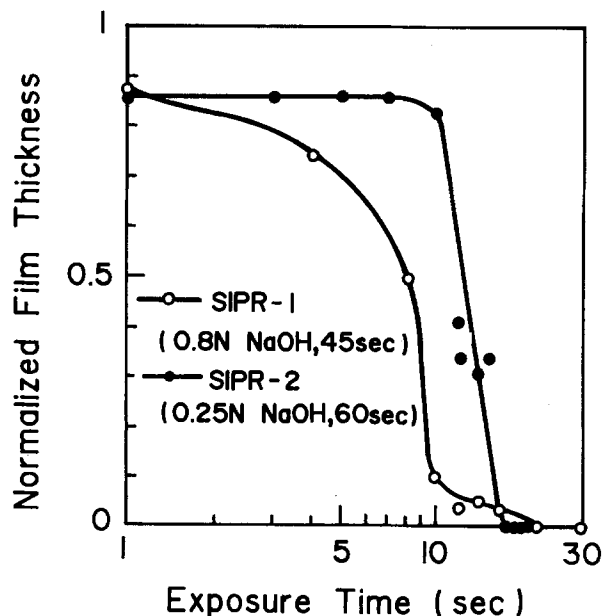
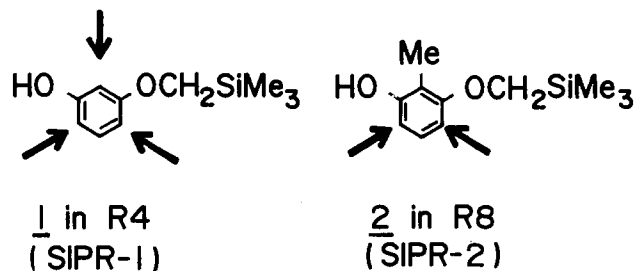


Fig. 1. Sensitivity characteristics for SIPR. The coated initial film thickness was 0.29 μm for both materials.



The arrows show the reactive positions in the addition condensation reaction with formaldehyde, 1, which has three "arrows," may cause a branched structure when polymerized to R4. Accordingly, R4 seems to have more widespread molecular weight distribution than R8 having a more linear structure. This may be responsible for the difference in the solubility and γ values.

The resistance of SIPR-2 to O_2 -RIE and O_2 -IBE was investigated in comparison with the polyimide, PI-2555. The remaining film thickness *vs.* etching time under O_2 -RIE conditions is shown in Fig. 3. Lower RF power was found to give a higher etch-rate ratio of PI-2555 to SIPR-2, although it takes longer time to etch PI-2555

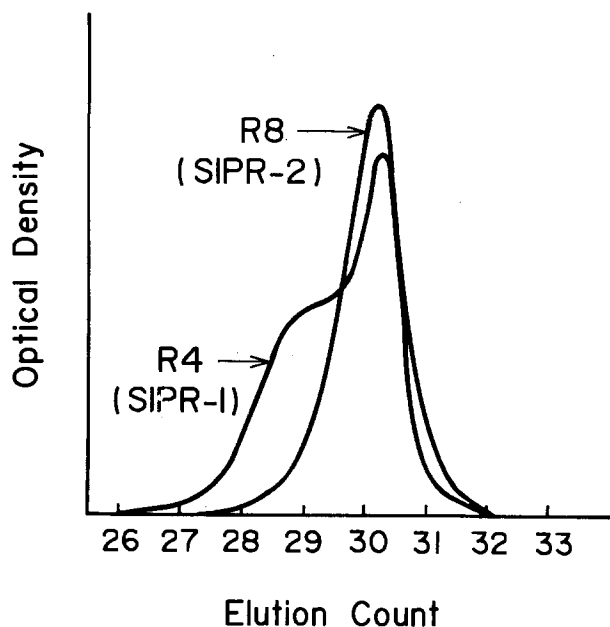


Fig. 2. Gel permeation chromatograms for R4 (SIPR-1) and R8 (SIPR-2).

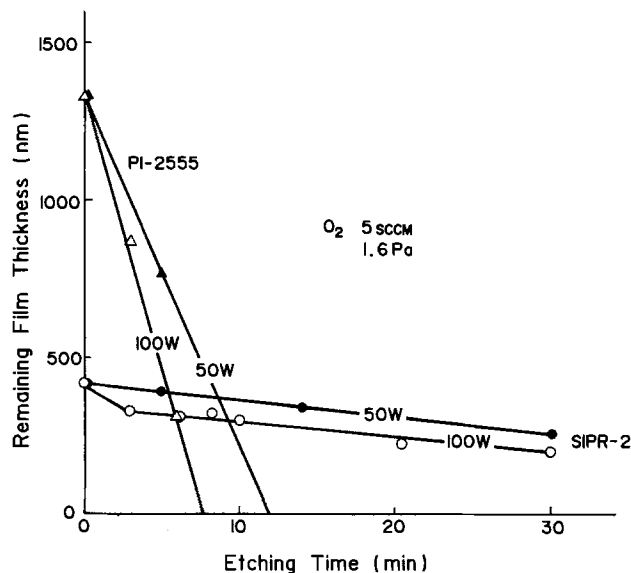


Fig. 3. O_2 -RIE characteristics for PI-2555 and SIPR-2

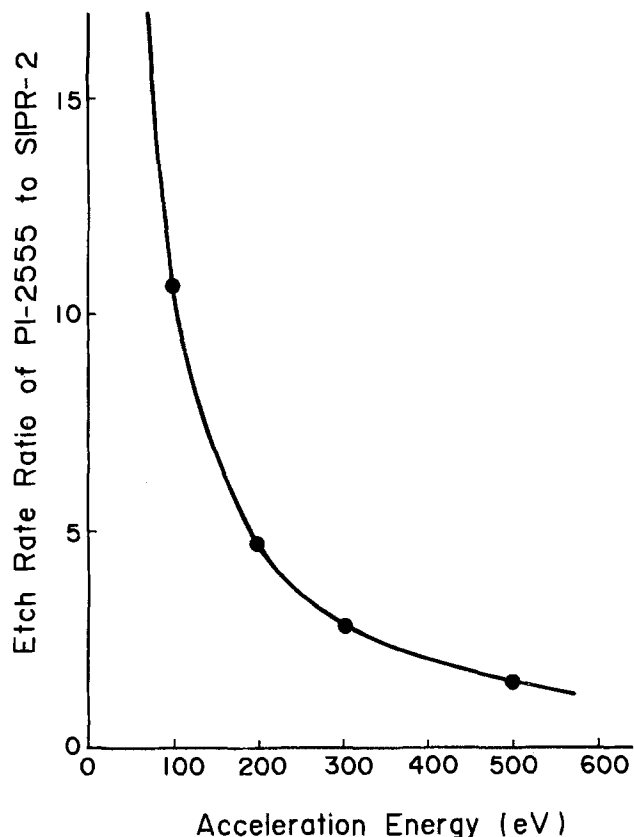


Fig. 4. Etch-rate ratio of PI-2555 to SIPR-2 vs. acceleration energy under O_2 -IBE.

away. Similarly, in ion beam etching, lower acceleration energy gave a higher etch-rate ratio, as shown in Fig. 4. The remaining film thickness vs. etching time, with 50 or 100 eV acceleration energy, is shown in Fig. 5. The etching of SIPR-2 practically stopped at 50 eV, whereas the etching of a considerable amount of PI-2555 was still observed. This is because the rate-limiting process for the

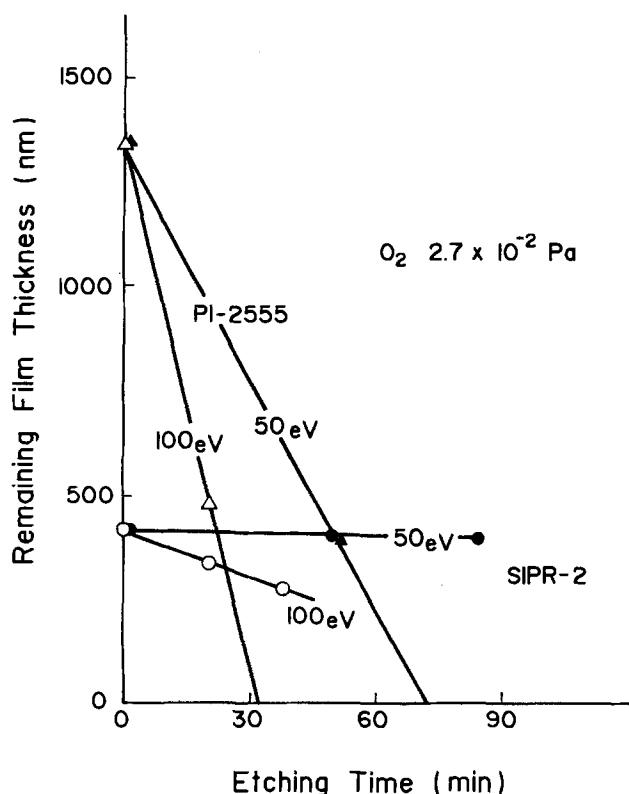


Fig. 5. O_2 -IBE characteristics for PI-2555 and SIPR-2

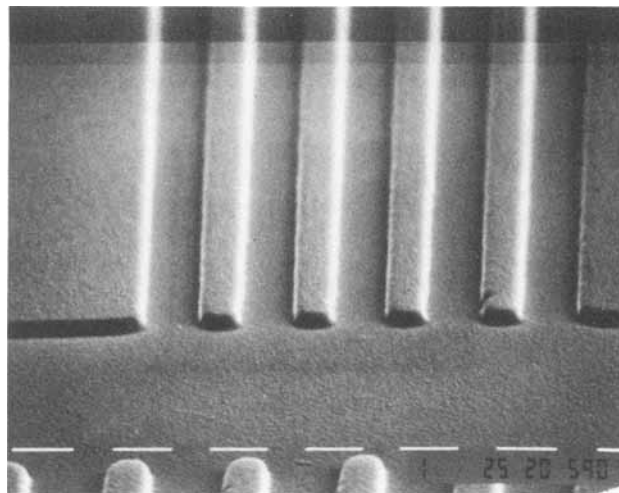


Fig. 6. SEM photograph of fabricated patterns in SIPR-2 on PI-2555. Markers $\approx 1 \mu m$.

etching of SIPR-2 is the sputtering of silicon atoms, whereas that for PI-2555 is the sputtering of carbon atoms. Generally, the sputtering yield of metals decreases significantly with decreasing acceleration energy. The threshold is observed at around 20-40 eV (10). On the contrary, the sputtering yield of carbon atoms under oxygen bombardment does not show such a strong energy dependence (11).

Typical etch-rate ratios of PI-2555 to SIPR-2 are summarized in Table II. Although the etch-rate ratio depends not only on the etching system, but also on the etching condition, it is concluded that the lower bias gives a higher etch-rate ratio.

For the bilayer resist processing, SIPR-2 was coated onto the layer of polyimide resin PI-2555, exposed for 20s ($\sim 68 \text{ mJ/cm}^2$) with Kasper 2001 and developed with 0.25N NaOH for 60s. Patterns including submicron features, 0.7 μm lines, and 0.9 μm spaces, were obtained without variance from mask patterns, as shown in Fig. 6. No adhesion promoters were necessary, and neither were intermixing inhibition techniques for coating SIPR-2 on PI-2555. Then the top layer patterns were transferred into the polyimide layer. O_2 -RIE transfer with 50 (0.08 W/cm^2) and 100W (0.16 W/cm^2) RF power gave the patterns shown in Fig. 7a and 7b, respectively. No residues were observed. A slight rounding off of the top layer patterns, observed after the etching, may be due to the temperature rise during etching. Linewidth was reduced more with 100W RF power than with 50W, as is presumed by the etch-rate ratios in Table II. In the case of the O_2 -IBE transfer, acute profiles were obtained without the top layer deformation, although longer etching time than that in O_2 -RIE is necessary. Patterns are shown in Fig. 8a and 8b, transferred with 50 and 100 eV accelerating energy, respectively. No change in linewidth was observed in the 50 eV transfer.

Judging from the transferred pattern profiles by O_2 -RIE and by O_2 -IBE, change in linewidth is mainly caused by the shrinkage in the top layer, not by the un-

Table II. Etch-rate ratios of PI-2555 to SIPR-2

Etching condition			Etch-rate ratio ^d
O_2 -RIE ^a	50W	(350V) ^c	19
	100W	(550V) ^c	12
O_2 -IBE ^b	50 eV		67
	100 eV		11

^a O_2 pressure of 1.6 Pa; O_2 flow of 5 sccm.

^b O_2 pressure: 2.7×10^{-2} Pa.

^c Induced self-bias: V_{dc} .

^d $1330/X$, where X is the etched depth of SIPR-2 while 1330 nm of PI-2555 is etched.

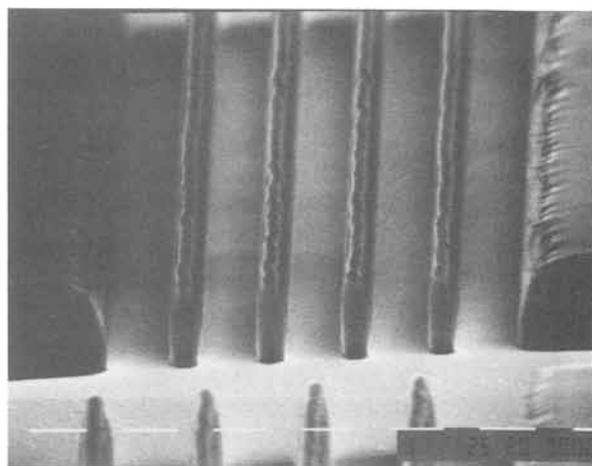
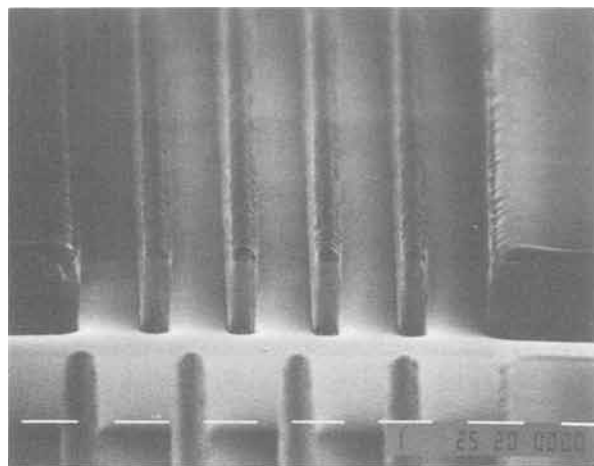


Fig. 7. SEM photographs of patterns transferred under O_2 -RIE (O_2 pressure of 1.6 Pa; O_2 flow of 5 sccm. (a, left) 50W RF power (0.08 W/cm^2). (b, right): 100W RF power (0.16 W/cm^2). Markers $\equiv 1 \mu\text{m}$.

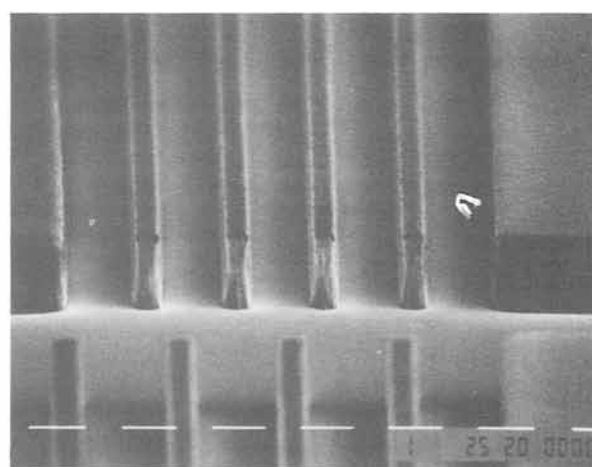
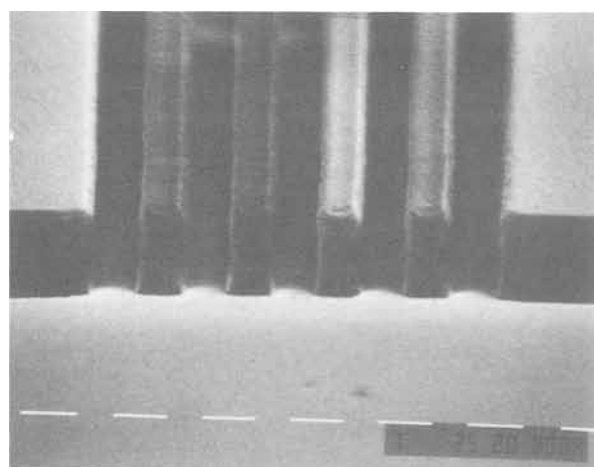


Fig. 8. SEM photographs of patterns transferred under O_2 -IBE (O_2 pressure of 2.7×10^{-2} Pa. (a, left): 50 eV acceleration energy. (b, right): 100 eV acceleration energy. Markers $\equiv 1 \mu\text{m}$.

dercut due to radical species. Since the radical contribution is not significant, the degree of ion bombardment may be estimated from the etch-rate ratio data. The etching condition for 100W in O_2 -RIE is roughly equal to that for 100 eV in O_2 -IBE. Since the self-bias voltage V_{dc} under 100W condition in O_2 -RIE was 550V, as shown in Table II, effective self-bias is estimated to be one-fifth of the V_{dc} . Similarly, effective self-bias for 50W in O_2 -RIE is also estimated to be 70V. This self-bias reduction may be caused by the cascade collisions in the plasma reactor acceleration region.

Conclusion

A new silicon containing positive photoresist (SIPR) was prepared. The etch-rate ratio of SIPR to polyimide (PI-2555) under oxygen dry etching (RIE and IBE) was less than one-tenth when a properly lower bias was employed. SIPR resolved submicron features on a layer of PI-2555 without variance from mask patterns with a near-UV exposure system. Those patterns were transferred into the layer of PI-2555 under such etching conditions and steep profiles were obtained accurately without any residues remaining on the wafers.

Acknowledgments

The authors thank S. Asanabe, D. Shinoda, S. Fujiwara, T. Matsubara, and K. Matsumi for their encouragement. They also thank K. Tanigaki and F. Watanabe for their useful discussions.

Manuscript submitted Sept. 18, 1984; revised manuscript received Dec. 27, 1984. This was Paper 375 pre-

sented at the New Orleans, Louisiana, Meeting of the Society, Oct. 7-12, 1984.

NEC Corporation assisted in meeting the publication costs of this article.

REFERENCES

1. J. M. Moran and D. Maydan, *J. Vac. Sci. Technol.*, **16**, 1620 (1979).
2. M. Hatzakis, J. Paraszczak, and J. Shaw, in "Proceedings of the International Conference on Microlithography (Microcircuit Engineering '81, Lausanne)," p. 386 (1981).
3. M. Suzuki, K. Saigo, H. Gokan, and Y. Ohnishi, *This Journal*, **130**, 1962 (1983).
4. S. A. MacDonald, F. Steinmann, H. Ito, M. Hatzakis, W. Lee, H. Hiraoka, and C. G. Willson, Paper presented at the International Symposium on Electron, Ion and Photon Beams, Los Angeles, CA, May 31-June 3, 1983.
5. M. Morita, A. Tanaka, S. Imamura, T. Tamamura, and O. Kogure, *Jpn. J. Appl. Phys.*, **22**, 659 (1983).
6. D. C. Hofer, R. D. Miller, and C. G. Willson, in "Advances in Resist Technology," Proceedings of SPIE, Vol. 469, p. 16, SPIE (1984).
7. K. Saigo, Y. Ohnishi, M. Suzuki, and H. Gokan, Paper presented at the International Symposium on Electron, Ion and Photon Beams, Tarrytown, NY, May 29-June 1, 1984.
8. C. W. Wilkins, Jr., E. Reichmanis, T. M. Wolf, and B. C. Smith, Paper presented at the International Symposium on Electron, Ion and Photon Beams, Tarrytown, NY, May 29-June 1, 1984.
9. R. G. Neville, *J. Org. Chem.*, **25**, 1063 (1960).
10. G. Carter and J. S. Colligon, "Ion Bombardment of Solids," pp. 319-322, Heinemann, London (1968).
11. H. Gokan and S. Esho, *This Journal*, **131**, 1105 (1984).

Application of Rapid Isothermal Annealing to Shallow p-n Junctions via BF₂ Implants

N. Chan Tung

Centre National d'Études des Télécommunications, Chemin du Vieux Chêne, 38243 Meylan Cedex, France

ABSTRACT

Results of rapid isothermal annealing (RIA) experiments are reported. Wafer warpage, temperature homogeneity, slip lines, and reproducibility of temperature cycles have been investigated. Sheet resistance measurements were carried out for RIA (1000°C, 10s) and for conventional furnace annealing for 30 and 50 keV BF₂ implants, the ion dose varying between 5×10^{13} and 7×10^{15} cm⁻². Spreading resistance measurements revealed that, in the case of RIA, junctions as shallow as 0.17, 0.19, and 0.21 μm have been obtained, respectively, for ion doses of 1×10^{13} , 3×10^{15} , and 5×10^{15} cm⁻² at a BF₂ energy of 50 keV. Junction depths obtained through RIA are a factor of 3-4 lower than those obtained by conventional annealing; dopant redistribution is negligible. Boron and fluorine atom concentration profiles have been equally investigated by secondary ion mass spectrometry (SIMS).

Recently, considerable research has been conducted to anneal damage and activate implanted dopants with minimal redistribution. Lasers and electron beams have been used to anneal implanted silicon samples in the milli-second time regime (1-3). Although complete dopant activation has been achieved, defects near the junctions have degraded their electrical characteristics (4). Furthermore, the implanted damaged layers are annealed by raising only the surface region of the sample to the desired temperature. The drawbacks of using these techniques are beam overlapping, low throughput, and interface problems for devices composed of thin film layers. These disadvantages can be overcome through the use of rapid isothermal techniques. In this category are included large area scanned electron beams (5), high intensity arc lamps (6), resistively heated graphite sources (7), and tungsten halogen lamps (8-9). One attractive application of rapid isothermal annealing (RIA) is the production of shallow p-n junctions required for future complementary metal-oxide-silicon (CMOS) technologies.

In this paper, we present the characteristics of the machine¹ with particular attention to wafer warpage, temperature homogeneity along an axis, slip lines, and reproducibility of the temperature cycle. Sheet resistance measurements were performed for rapid and conventional furnace anneals for BF₂ implants in the energy range of 30-50 keV and ion doses ranging from 5×10^{13} to 7×10^{15} cm⁻². Radial family sheet resistivity measurements of rapid anneals were also performed on 4 in. wafers. Profiles of the activated dopants were obtained by spreading resistance and p-n junction depths were measured for 30 and 50 keV BF₂ implants. Boron and fluorine atom concentration profiles of 50 keV implants were measured by SIMS for ion doses of 1×10^{15} and 3×10^{15} cm⁻². The redistribution of the boron atoms is negligible.

Description of the Apparatus

The RIA apparatus used for the annealing of the implants is shown schematically in Fig. 1. It consists of two banks of six tungsten infrared quartz lamps separated by a distance of ~15 cm. To avoid overheating and early failure, electrical connections of the lamps are air-cooled. Three phase-angle fired power supplies provide 30 kW to the lamps, which is sufficient to raise wafers to a temperature in excess of 1200°C.

A quartz chamber is inserted between the lamps, and annealing can be carried out in an inert atmosphere. A movable quartz plate is placed inside the chamber and supports a 4 in. wafer as well as a fixed temperature sensor. The fixed temperature sensor consists of a Chromel-Alumel thermocouple embedded inside a 2 × 2 cm² silicon piece and supported by a quartz rod. During annealing, the temperature recorded by the fixed sensor allow us to deduce the temperature of the annealed 4 in.

¹Atelier Electro Thermic, Chemin des Malacher, 38243 Meylan, France.

sample since a correlation has been previously established between the temperature of the radiation sensor and that of a 4 in. wafer inside which a thermocouple has been similarly embedded.

Temperature profiles were monitored by a movable 1 × 1 cm² sensor along the longer axis of the quartz chamber (i.e., perpendicular to the lamps). The measurements were carried out at every centimeter over a distance of 9 cm. The maximum temperature difference as measured at these different locations is ~16°C ($\sim 1.6 \times 10^{-2}$) for a 1000°C run. This good temperature uniformity allows the measurements of the wafer flatness, since it is a prerequisite for bow-free processing.

A series of measurements was conducted to determine any change in flatness on standard <100> 4 in. wafers 0.5 mm thick. The measurements were performed along two perpendicular axes before and after annealing. For a 10s anneal at a temperature of 1000°C, only negligible changes in wafer flatness were detected, namely, of ~0.5 μm. This result falls within the experimental resolution of the apparatus. Before annealing, parallel and perpendicular wafer bowings were 4.5 and 1.5 μm, respectively; after annealing, they were 5 and 2 μm, respectively. No slip lines were observed after the annealing experiments.

The reproducibility of our 1000° and 1100°C temperature heat pulse curves for 4 in. wafers is very good; only 4°-5°C separate the various 1000° or 1100°C runs. However, it must be noted that the machine does not contain any closed loop temperature monitoring. The cycle of the injected power (power value vs. time) is adjusted to obtain the desired temperature profile. For the temperature profiles of 1000° and 1100°C, the rates of temperature rise are, respectively, 150°C/s (350°-950°C in 4s) and 180°C/s (400°-1000°C in 3.3s). Such a rate of change in temperature is typical of commercially available machines that use tungsten lamps.

Sheet Resistance Measurements

In all our experiments, the wafers used were n-type and of resistivity 5-8 Ω cm. The wafers contained no oxide cap, and annealing of the implants was carried out in a nitrogen atmosphere for both the rapid and furnace an-

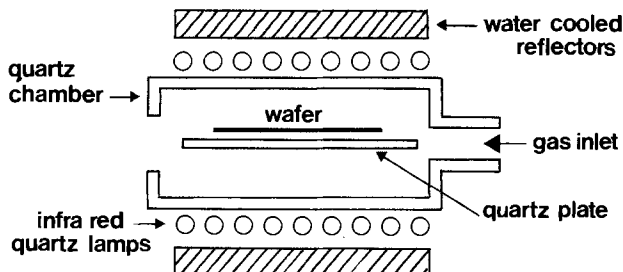


Fig. 1. Schematic cross section of the RIA apparatus

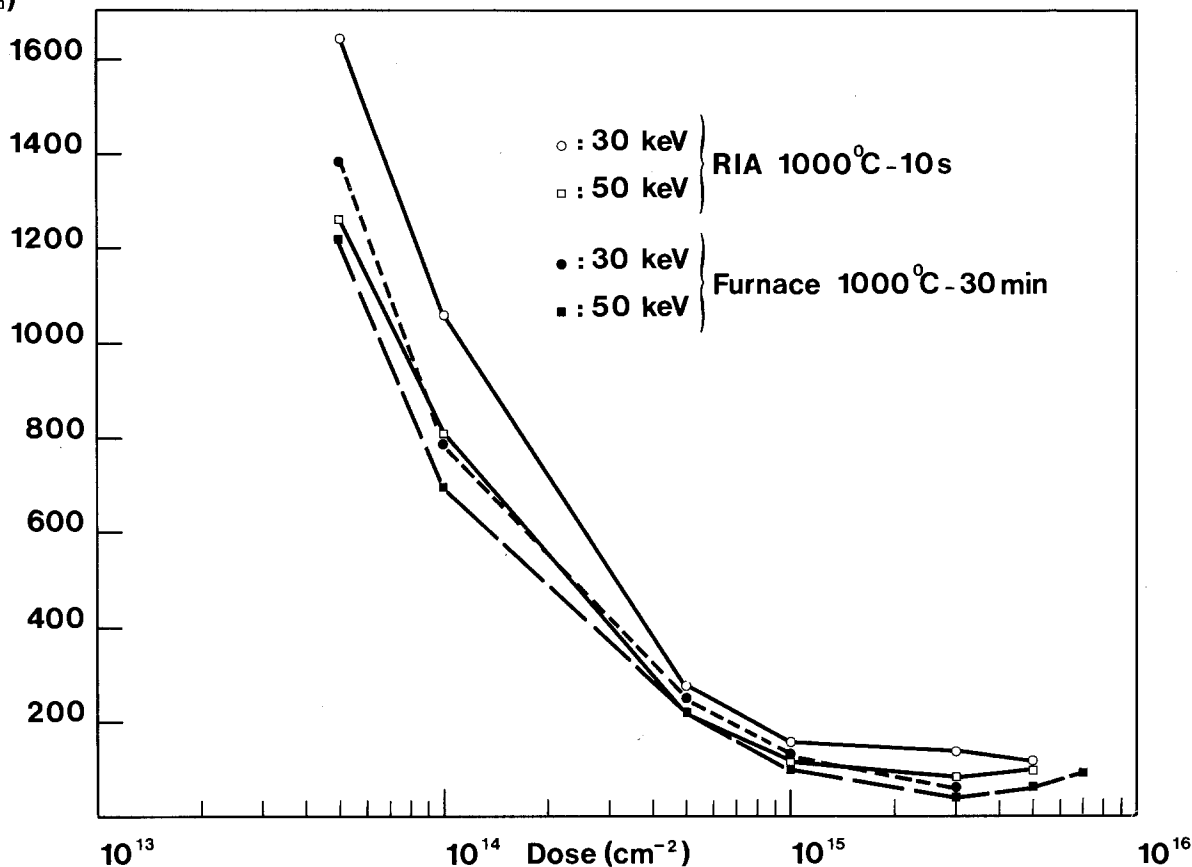
$R_{\square} (\Omega/\square)$ 

Fig. 2. Sheet resistance measurements for RIA and furnace anneals

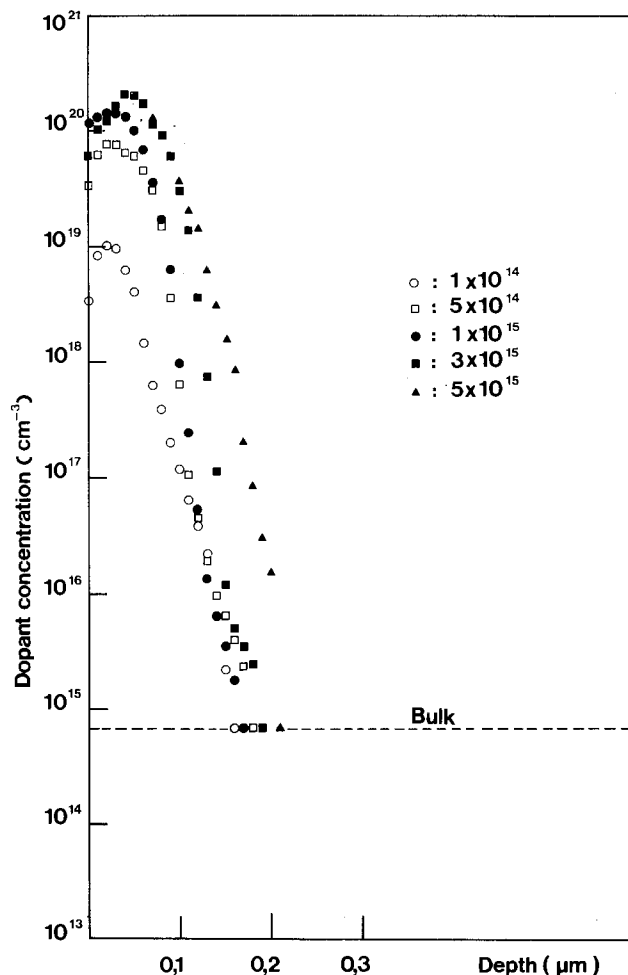
neals. The BF_2 implants were carried out in a High Voltage Engineering (H.V.E. 500) implantation machine whose main feature is that it contains two mass separating magnets. The first magnet allows the separation of the particles extracted from the ion source, while the second one, located at the opposite end of the acceleration column, filters out the undesired products of dissociation of the molecular implants, here BF_2 , in the acceleration region.

Radial family sheet resistivity measurements were carried out with a four-point probe on 4 in. wafers for 50 keV BF_2 implants and a dose of $3 \times 10^{15} \text{ cm}^{-2}$, the annealing temperature and time being 1000°C for 10s. These sheet resistance measurements were performed along eight radial axes corresponding to an angular variation of 45° . Along each axis, measurements were carried out every centimeter. The load applied to the probe was 50g. The mean value of the sheet resistivity measurements for a 4 in. wafer is $83.6 \Omega/\square$, and $\sigma = 1.3 \times 10^{-2}$.

Sheet resistivity measurements for rapid and conventional furnace anneals (1000°C , 30 min) are shown in Fig. 2 for 30 and 50 keV implants. For both rapid and furnace anneals, R_{\square} decreases when the ion energy is increased. For the 30 keV implants, R_{\square} decreases with increasing ion dose in both cases. This should be the case since an increase in the ion dose leads to an enhancement of the solid-phase epitaxy. For 50 keV molecular ions, R_{\square} measurements reached a minimum at an ion dose of $3 \times 10^{15} \text{ cm}^{-2}$ both for the rapid and furnace anneals. In the case of RIA, $R_{\square} \sim 80 \Omega/\square$. Our sheet resistivity measurements are in agreement with those published by Kato *et al.* (10), who obtained an R_{\square} value of $85 \Omega/\square$ for 60 keV BF_2 implants; the ion dose and annealing time being, respectively, $4 \times 10^{15} \text{ cm}^{-2}$ and 3s.

Spreading Resistance and SIMS Measurements

RIA activated (1000°C , 10s) dopant concentration profiles measured by spreading resistance are shown in Fig. 3 for 50 keV BF_2 implants. The measured junction depths vary from 0.16 (dose = $1 \times 10^{14} \text{ cm}^{-2}$) to $0.21 \mu\text{m}$ (dose = $5 \times 10^{15} \text{ cm}^{-2}$).

Fig. 3. Dopant concentration profiles for 50 keV BF_2^+ RIA(1000°C , 10s).

$\times 10^{15} \text{ cm}^{-2}$). These junction depths increase with the dose except for a fluence of $1 \times 10^{15} \text{ cm}^{-2}$. It must, however, be noted that, for each increase in dose, the corresponding increase in junction depth is very slight ($\sim 0.01\text{-}0.02 \mu\text{m}$) and is within the estimated accuracy of our measurements ($\sim 200\text{\AA}$). The activated dopant concentration profiles have a quasi-gaussian shape, and the maximum peak concentration increases with the ion dose. This is a natural occurrence of ion implantation process. It must, however, be noted that the concentration profile broadens slightly near its base ($\sim 0.03 \mu\text{m}$ for an ion dose of $3 \times 10^{15} \text{ cm}^{-2}$). In that region, the concentration is about five orders of magnitude lower than the peak value. This profile broadening near the base may be due to the following reasons: (i) the second magnet located at the end of the acceleration column may not have completely eliminated the dissociated BF_2 products formed in the acceleration region, (ii) slight diffusion of the dopants during the rapid anneals, or (iii) a channeling process which is not negligible for these low energy equivalent B ions. This point will be developed later on.

Our junction depth measurements [$0.19 \mu\text{m}$ for a dose of $3 \times 10^{15} \text{ cm}^{-2}$; $0.21 \mu\text{m}$ for a dose of $5 \times 10^{15} \text{ cm}^{-2}$ (50 keV implants, 1000°C , 10s anneals)] are compatible with the results of Kato *et al.* (10), who obtained a junction depth of $0.16 \mu\text{m}$ for 60 keV implants. Their ion dose and annealing conditions were $4 \times 10^{15} \text{ cm}^{-2}$ and 1000°C , 3s. It must, however, be noted that Kato's implants were performed through 400\AA SiO_2 . This may explain the slight difference between their results and ours.

Carrier concentration profiles for 50 keV ions implanted with an ion dose of $1 \times 10^{15} \text{ cm}^{-2}$ are presented in Fig. 4. For a 1000°C , 10s rapid anneal, the junction depth is $0.17 \mu\text{m}$ as compared to $0.40 \mu\text{m}$ junction depth obtained by furnace annealing (1000°C , 30 min); the increase is due to dopant diffusion. Also shown in the same figure for comparison purposes are SIMS profiles of boron

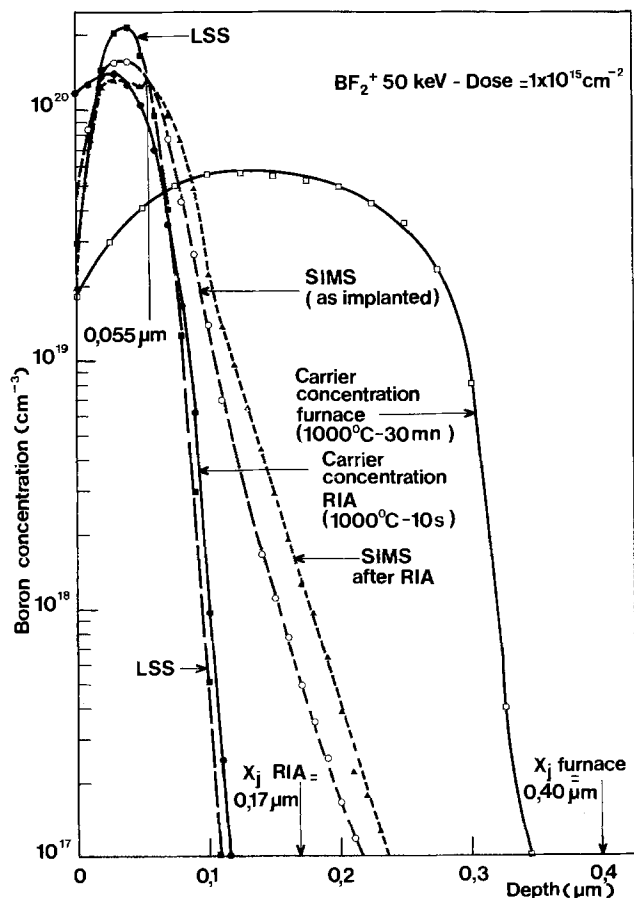


Fig. 4. Carrier profiles of electrically active dopants (BF_2^+ implants) obtained by RIA and furnace anneals, SIMS profiles of B atoms for as-implanted and annealed samples.

atoms and calculations obtained from LSS theory. These curves give rise to the following remarks.

1. The LSS theory is in good agreement with the RIA activated dopant profile.

2. The LSS theory differs from the SIMS as-implanted atomic profile. This is due to the fact that calculations from the LSS model refer to an amorphous solid (dense gas) and channeling is responsible for the broadening of the as-implanted profile. In fact, the calculated acceptance angle for channeling of 11 keV B ions in $\langle 100 \rangle$ Si, corresponding to 50 keV BF_2 , is about 10° . This angle is larger than the 7° tilt used in our experiments. Channeling processes have equally been observed by Wilson (11) for those low energy equivalent B ions (energy of $\text{BF}_2 = 45 \text{ keV}$).

3. The redistribution of the boron atomic profiles, before and after rapid annealing, is very slight ($\sim 0.025 \mu\text{m}$).

4. After rapid annealing, a second peak of same height as the first one is located at a depth of $\sim 0.055 \mu\text{m}$. The location of that peak is consistent with the region of residual damage. Such a double peak for boron atomic profiles has also been observed by Wilson (11) and Fuse *et al.* (12) for furnace annealing of 36 and 111 keV BF_2 , respectively.

The degree of activation of the 50 keV BF_2 implants with an ion dose of $1 \times 10^{15} \text{ cm}^{-2}$ is $\sim 85\%$. Fluorine atom concentration profiles are presented in Fig. 5 for 50 keV implants; the rapid annealing conditions are 1000°C , 10s. The calculated profile is in good agreement with the fluorine as-implanted atomic profile. The rapid annealed fluorine profile behaves differently. In fact, the fluorine atoms pile up in the region of damage, the transition between the amorphous and the crystalline regions. The fluorine peak is situated at $\sim 0.060 \mu\text{m}$, not far from the second boron peak ($\sim 0.055 \mu\text{m}$). The same considerations developed previously can be applied to the RIA boron and fluorine atomic profiles (Fig. 6), the ion dose being $3 \times 10^{15} \text{ cm}^{-2}$.

Spreading resistance measurements showed that for 30 keV BF_2 , junction depths are 0.10 and $0.15 \mu\text{m}$ for ion

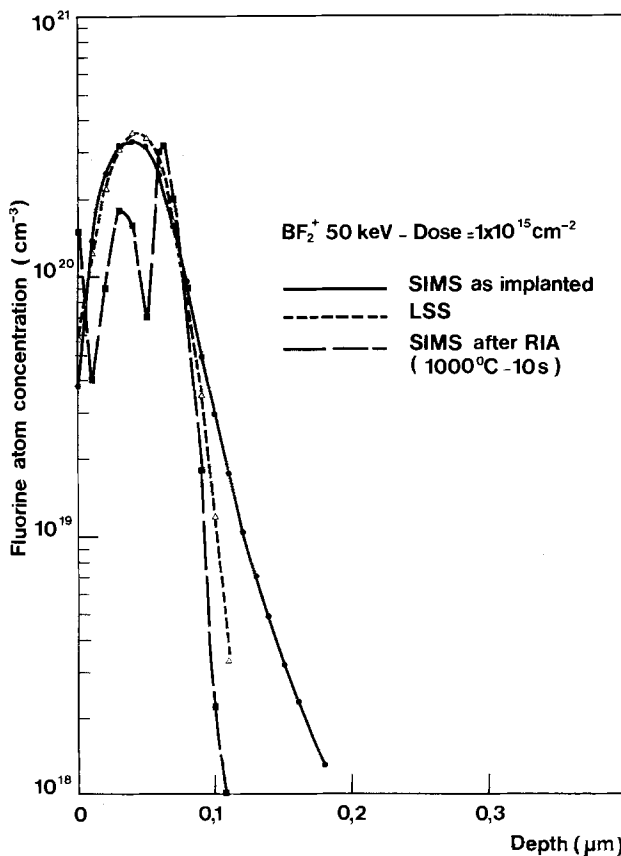


Fig. 5. Fluorine atom concentration profiles measured by SIMS before and after RIA.

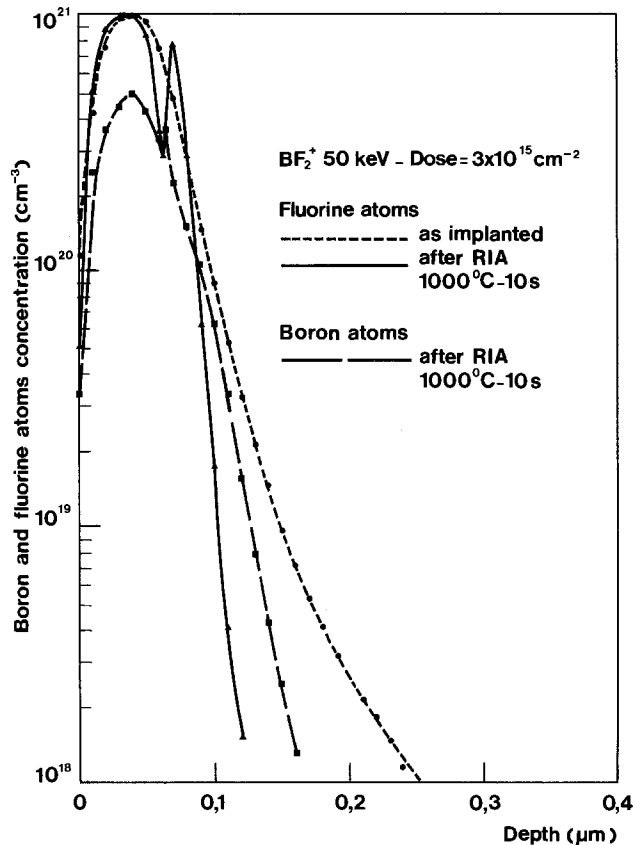


Fig. 6. Profiles of boron and fluorine atoms measured by SIMS before and after RIA.

doses of 3×10^{15} and 5×10^{15} cm^{-2} , respectively. The rapid annealed conditions are 1000°C , 10s. In the case of furnace annealing (1000°C , 30 min), the junction depth is increased to $0.30 \mu\text{m}$ for an ion dose of 3×10^{15} cm^{-2} , the ionic energy being the same (30 keV).

Conclusion

The rapid isothermal annealing experiments presented exhibit good temperature homogeneity along the axis of the chamber. Wafer warpage is $0.5 \mu\text{m}$ for a 4 in. wafer. The reproducibility of the temperature cycles is excel-

lent; only $4^\circ\text{--}5^\circ\text{C}$ separates the various runs either for the 1000° or the 1100°C annealing.

For 50 keV BF_2 RIA, junction depths exhibit ion dose dependence. Junction depths as shallow as 0.17, 0.19, and $0.21 \mu\text{m}$ have been obtained, respectively, for ion doses of 1×10^{15} , 3×10^{15} , and 5×10^{15} cm^{-2} . Junction depths obtained through rapid annealing (1000°C , 10s) are a factor of three to four lower than those obtained by conventional furnace annealing. In the case of RIA, negligible dopant redistribution has been noted.

Acknowledgments

The author wishes to thank J. C. Oberlin for the BF_2 implants, M. Gauneau for the SIMS profiles, C. Le Pen for helpful assistance, J. Dargent for critical reading of the manuscript, and J. L. Buevoz for constant interest and encouragement.

Manuscript submitted July 18, 1984; revised manuscript received Nov. 26, 1984.

Centre National d'Études des Télécommunications assisted in meeting the publication costs of this article.

REFERENCES

1. "Laser-Solid Interactions and Laser Processing," S. C. Ferris, H. L. Leamy, and J. P. Poate, Editors, American Institute of Physics Conference Proceedings 50, American Institute of Physics, New York (1979).
2. "Laser and Electron Beam Processing of Materials," C. W. White and P. S. Peercy, Editors, Academic Press, New York (1980).
3. "Laser and Electron Beam Solid Interactions and Materials Processing," J. G. Gibbons, L. D. Hess, and T. W. Sigmon, Editors, North Holland, New York (1981).
4. M. Maier, D. Bimberg, G. Fernholz, H. Baumgart, and F. Philipp, *J. Appl. Phys.*, **53**, 5904 (1982).
5. T. O. Yep, R. T. Fulks, and R. A. Powell, *Appl. Phys. Lett.*, **38**, 162 (1981).
6. R. A. Powell, T. O. Yep, and R. T. Fulks, *ibid.*, **39**, 150 (1981).
7. R. T. Fulks, C. J. Russo, P. R. Hanley, and T. I. Kamins, *ibid.*, **39**, 604 (1981).
8. D. J. Lischner and G. K. Celler, *Laser Electron Beam Interact. Solids*, 759 (1982).
9. J. L. Benton, G. K. Celler, D. C. Jacobson, L. C. Kimerling, D. J. Lischner, G. L. Miller, and McD. Robinson, *ibid.*, 765 (1982).
10. J. Kato and S. Iwamatsu, *This Journal*, **131**, 1145 (1984).
11. R. G. Wilson, *J. Appl. Phys.*, **54**, 6879 (1983).
12. G. Fuse, T. Hirao, K. Inoue, S. Takayanagi, and Y. Yaegashi, *J. Appl. Phys.*, **53**, 3650 (1982).

The Effects of Ion Beam Etching on Si, Ge, GaAs, and InP Schottky Barrier Diodes

C. S. Wu, D. M. Scott, Wei-Xi Chen, and S. S. Lau

Department of Electrical Engineering and Computer Sciences, University of California at San Diego, La Jolla, California 92093

ABSTRACT

The effects of ion beam etching (IBE) on the electrical properties of Schottky barriers on four kinds of semiconductors (Si, Ge, InP, and GaAs) were investigated. For diodes processed with IBE after metal deposition where the active device region is protected by the metal layer and only the surrounding substrate area is exposed to the beam, our results showed that the diode breakdown voltages increased 2-15 times for p-type substrates, but decreased 2-4 times for n-type substrates. The barrier heights, ϕ_B^p , on p substrates were observed to remain unchanged, while the barrier heights, ϕ_B^n , were found to decrease on n substrates. For diodes processed with IBE before metal deposition, the diode characteristics are similar to those processed with IBE after metal deposition; the only notable exception is that the barrier heights on p substrates increased for this case, while ϕ_B^p remained unchanged for diodes processed with IBE after metal deposition. The effects of IBE are observed to disappear and the diodes recover to their original characteristics upon annealing at temperatures between 300° and 375°C. These effects are consistent with the concept that ion beam processing induces donor-like defects near the surface region of the semiconductor exposed to the ions.

Ion beam etching (IBE) is becoming a commonly used processing technique in microelectronics. The properties of substrate surfaces after IBE, therefore, are of scientific and technological interests.

Fonash *et al.* (1) have found that argon ion beam etching followed by thermal deposition or ion-beam deposition alone can drastically affect the characteristics of Schottky barrier diodes made on Si, thus pointing out the importance of ion-beam-induced damage in barrier formation. They observed that ion-beam damage can lead to ohmic contacts on n-Si but does not affect Schottky barriers on p-Si for Au and Mo contacts. Chow *et al.* (2) have also observed that Schottky barrier height was increased for p-Si and decreased for n-Si when gold films were thermally deposited on reactive-ion-etched Si substrates.

Numerous other studies have found that sputter depositions of metals can also cause abnormal I-V characteristics for Schottky barrier diodes on Si (3, 4) as well as on GaAs (5-7). Electrical behavior of heterojunctions formed by RF sputtering of materials such as indium-tin-oxide (ITO) on several compound semiconductors (InP, CdTe) has been reported to change due to sputtering damage (8).

In each of these studies, either the substrate was etched prior to the metal deposition or the substrate was etched during metal deposition. The influence of ion etching on diodes after metal deposition has rarely been reported. Since ion etching to fabricate device structures after metallization is a common practice, we report here the effects of IBE on diode characteristics after the deposition of metal layers on semiconductor substrates. For comparison, diodes processed with IBE before metal deposition were also investigated for certain cases. For the case of IBE after metallization, the ion etching time was short such that the substrate area under the metallized region (circular dots) was protected from the ion beam with the remaining substrate area exposed to the beam. In this study, the I-V and breakdown characteristics of Schottky diodes on Si, Ge, InP, and GaAs were examined.

Experimental

Sample preparations.—Four different substrate materials were used in this study: Si, Ge, GaAs, and InP. For x-ray and MeV He⁺ backscattering measurements, the samples were ~ 0.5 cm in size. For electrical evaluations, diodes of 1 and 3 mm diam were formed on the wafers using mechanical masks for Si, Ge, and GaAs samples and diodes of 152 and 229 μm diam were formed using photolithography for InP samples.

Si.—Silicon substrates (n- and p-type, 1-10 $\Omega\text{-cm}$, <100> in orientation) were first cleaned ultrasonically with acetone and isopropyl alcohol, followed by the RCA cleaning process (9) and a final rinse in 10% HF:H₂O immediately

before loading into an oil-free evaporation system. On p-type Si substrates, about 500Å of Er was first deposited followed by the deposition of a Si layer (~ 750Å) from a n⁺ Si charge. The deposition rate was ~ 10 Å/s for Er and 20-30 Å/s for Si. The pressure during evaporation was ~ 10⁻⁷ torr in all cases. The samples were then annealed at 380°C for 30 min in flowing forming gas or in vacuum (~ 3 × 10⁻⁷ torr) to form the ErSi₂ contact. The deposited Si (~ 750Å) is sufficient to consume entirely the Er layer (~ 500Å) to form ErSi₂ with the excess Si removed by chemical etching after reaction. It has been shown that uniform layers of ErSi₂ can be formed on samples with this configuration with a barrier height of 0.78 eV on p-Si (10, 11). On n-type Si substrates, ~ 1000Å of Pd was thermally deposited. The deposition rate of Pd was 10Å/s at a pressure of ~ 1 × 10⁻⁷ torr. No annealing was performed on these Pd/n-Si samples. The barrier height, ϕ_B^n , is ~ 0.75 eV for as-deposited samples.

Ge.—For the Ge case, n-type, <100>-oriented Ge wafers with a resistivity of 0.8-1.5 $\Omega\text{-cm}$ were used. The wafers were first cleaned with acetone and isopropyl alcohol, followed by a rinse in a solution of H₂O:HNO₃:HF 28:3:1 at room temperature with a final rinse in 10% HF:H₂O. A layer of Er (~500Å) followed by a layer of Ge (~ 850Å of Ge at ~ 20-30 Å/s) were deposited onto the substrate. Thermal annealing at this structure at ~ 330°C has been shown to form a planar ErGe₂ layer (12).

InP.—For the InP case, the InP substrate material (10¹⁵/cm³, 0.3-0.4 $\Omega\text{-cm}$ for <n,100> and 5 × 10¹⁵/cm³, 7-8 $\Omega\text{-cm}$ for <p,100>) were cleaned with trichloroethylene, acetone, and methanol, etched in dilute HF, then etched further in a solution of H₂O:HF:HCl 4:1:1 plus one drop of H₂O₂/10ml.

Ta-Si films 1300-1500Å thick were deposited by RF sputtering (200W in Ar) from a hot-pressed Ta-Si target with a Ta to Si atomic ratio of 1:2. A pattern of Ta-Si dots was then formed from the sputtered film using a photoresist (AZ 1350) mask and dry plasma etching in a parallel plate system (CF₄ with 4% Oz, 0.4 torr, 15W, ~ 500 Å/min). The diameters of the contact dots used were 229 μm for p-InP and 152 μm for n-InP. The p-InP samples were then annealed at 350°C for 30 min in forming gas to give a ϕ_B^p of 0.97 eV and the n-InP samples were annealed at 400°C for 5 min to give a ϕ_B^n of 0.4 eV (13).

GaAs.—For the GaAs case, n-type GaAs (<100>, Si doped, 2 × 10¹⁷/cm³) wafers were used. The wafers were first cleaned with acetone and isopropyl alcohol, followed by a rinse in the diluted solution of 1:1 HCl:H₂O and a final rinse in DI water. 500Å of Er and 750Å of Si were then sequentially deposited under the same conditions as described in the p-Si case. The barrier height, ϕ_B^n ,

is ~ 0.68 eV for as-deposited samples and ~ 0.8 eV for samples annealed at 380°C for 30 min in forming gas.

Ion beam etching (IBE).—Following sample preparation, ion beam etching was carried out using a Millatron IV system.¹ This system has been described by Heath (14, 15) in detail. The system consists of a Kaufman-type (16) ion source, sample chamber, and cryogenic pump system. The ions are extracted from a gaseous plasma and accelerated to the substrate. The beam current density and ion energy can be independently controlled. In our experiment, either Ar or Freon-116 (C_2F_6) was used. The ion beam was incident normal to the substrate which was located 20 cm from the ion source and rotating during IBE. The ion energy was set at 500 eV, and the pressure of the chamber was kept at $\sim 2.3 \times 10^{-4}$ torr. The ion beam current density was set at 0.5 mA/cm^2 for this experiment.

Postannealing after IBE.—To investigate the stability of the electrical properties, certain samples were annealed between 300° and 375°C in forming gas (10% H_2 , 90% N_2) for times ranging up to 25 min after IBE.

Metal layers deposited on ion-etched substrates.—In order to compare the effects of IBE before and after metal deposition, p-Si, n-Ge, and n-GaAs substrates were first ion beam etched for 30s under the same condition as described previously and then cleaned with acetone, isopropyl alcohol and a final rinse in DI water before loading into our evaporation system. About 500\AA of Er was then deposited on each substrate to form three types of samples: Er (500\AA)/Si<p,100>, Er(500\AA)/Ge<n,100>, and Er(500\AA)/GaAs<n,100>.

Electrical measurements. The breakdown voltage (V_B) and barrier heights (ϕ_B) were determined by current-voltage measurements before and after IBE process. The samples were measured within 24h after IBE except as noted.

Experimental Results

Si.—Figure 1 shows a plot of $\log I_f$ vs. V_f for diodes of ErSi_2 on p-type Si before and after IBE for 20s. The diodes exhibit almost identical forward characteristics before and after IBE. The barrier height, ϕ_B^p , for the diodes is ~ 0.78 eV, with an n factor of 1.05. The reverse breakdown voltages, however, are quite different before and after IBE, although both types of diodes exhibit a sharp breakdown, as shown in Fig. 2. Before IBE, breakdown (V_B) takes place at $\sim 80\text{V}$ (curve A), after IBE, breakdown does not occur until about 300V (curve B). The variation in V_B vs. IBE time is shown in Fig. 3 for diodes formed either by annealing in forming gas or in vacuum. Diodes formed in vacuum initially have a much lower V_B ($\sim 22\text{V}$) values compared to those for diodes prepared in forming gas (\sim

¹ Made by Commonwealth Scientific Corporation.

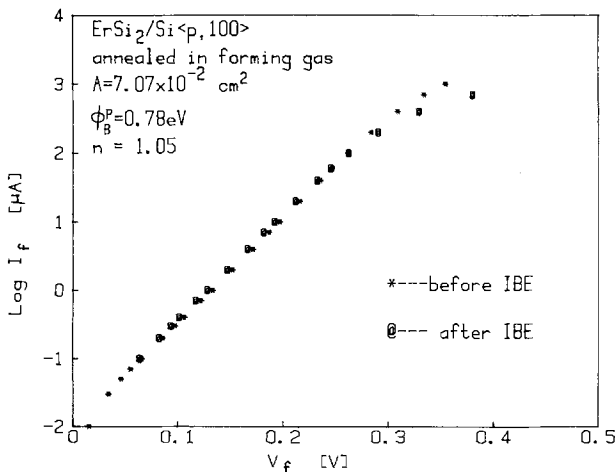


Fig. 1. $\log I_f$ vs. V_f for a $\text{ErSi}_2/\text{p-Si}$ diode (3 mm diam) before and after ion beam etching (IBE).

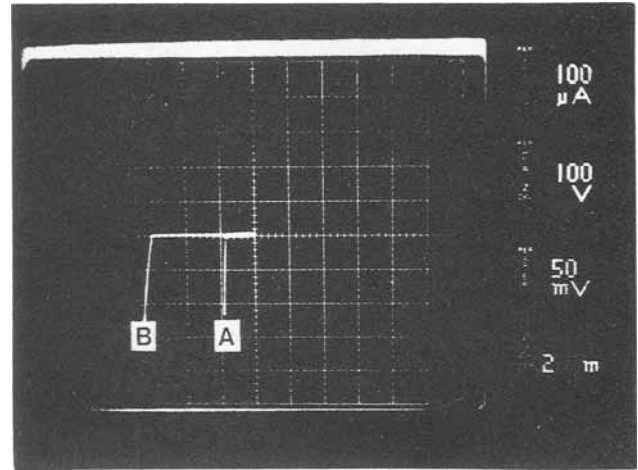


Fig. 2. I-V curves for a $\text{ErSi}_2/\text{p-Si}$ diode (1 mm diam) before (A) and after (B) IBE, indicating the effect of IBE on breakdown voltages.

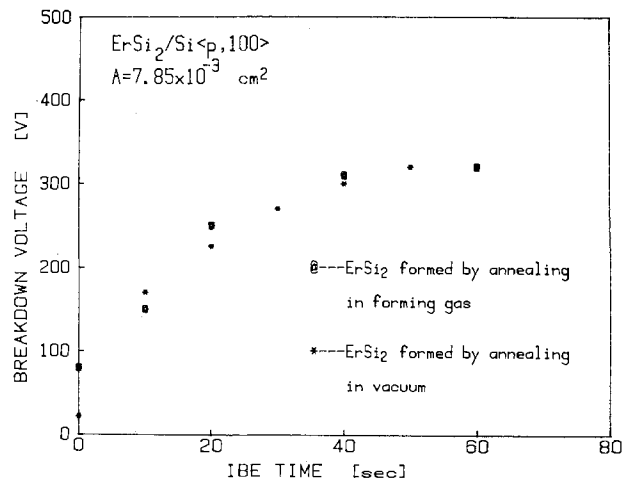


Fig. 3. Breakdown voltage as a function of ion etching time for $\text{ErSi}_2/\text{p-Si}$ diodes (1 mm diam).

80V). However, in both cases V_B rises with IBE and saturates at nearly identical breakdown voltages of $\sim 325\text{V}$.

The increase in breakdown voltage after IBE is not permanent. Annealing these p-type samples at 300°C in forming gas for only 5 min caused V_B to decrease from over 300V to $\sim 70\text{V}$, nearly equal to the initial value for the samples annealed in forming gas without IBE.

The behavior of diodes formed on n-type Si substrates is very different from those obtained with diodes on p-type Si. Figure 4 shows a plot of $\log I_f$ vs. V_f for Pd on

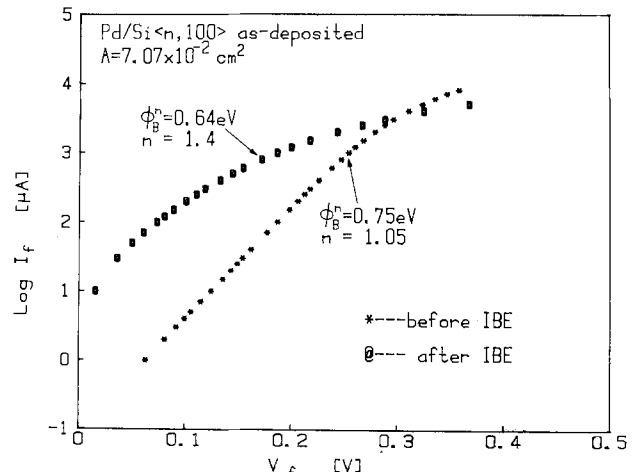


Fig. 4. $\log I_f$ vs. V_f for a Pd/n-Si diode (3 mm diam) before and after IBE.

n-type Si diodes before and after IBE for 10s. Before IBE, the diodes are nearly ideal ($n = 1.05$). ϕ_B^n is 0.75 eV, which agrees with published values (17). After IBE, the diodes no longer show ideal behavior. The $\log I$ vs. V curve is nonlinear throughout the entire range of investigation. It is not possible to deduce a unique value of ϕ_B^n from this curve. However, at forward voltage of $\sim 0.1V$, ϕ_B^n can be assigned to be ≈ 0.64 eV with $n \approx 1.4$; we can take these values to represent the change in the electrical properties after IBE. The crossover of these two curves is due to a difference between these devices in the resistance of the back contact.

Figure 5 shows the linear I-V characteristics of Pd/n-Si diodes before and after IBE for 10s. Both diodes show soft breakdowns. The reverse bias voltages measured at 1 mA decreased significantly from an initial value of 50V to about 15V after IBE for 10s. This voltage remained unchanged after further IBE up to 40s, as shown in Fig. 6. Similar breakdown voltages were observed irrespective of the gas used for IBE.

Ge.—Diodes on n-type Ge exhibited soft breakdowns similar to those on n-type Si. For the as-deposited samples with 1 mm diam dots, V_B decreased from ~ 55 to $\sim 18V$ at $I_r = 1$ mA and ϕ_B^n decreased from 0.54 to 0.51 eV after IBE for 10s. For diodes annealed at $330^\circ C$ for 1h to form a Er germanide contact, the breakdown voltage decreased from ~ 40 to $\sim 13V$ and ϕ_B^n decreased from 0.51 to 0.49 eV after 10s of IBE. Postannealing of these samples for only 5 min at $300^\circ C$ is sufficient to restore the breakdown voltage and ϕ_B^n to those initial values prior to IBE. Diodes on p-type Ge were not investigated.

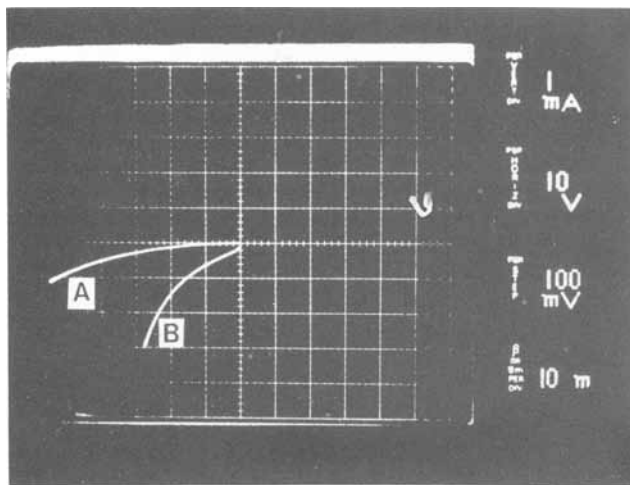


Fig. 5. I-V curves of a Pd/n-Si diode (3 mm diam) before (A) and after (B) IBE, indicating the effect of IBE on breakdown voltages.

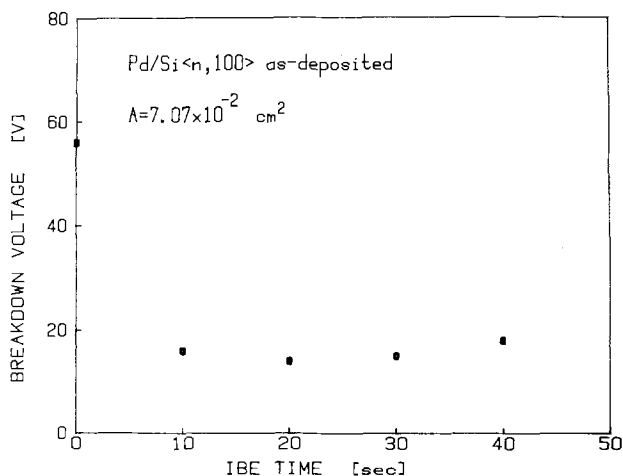


Fig. 6. Breakdown voltages of Pd/n-Si diodes (3 mm diam) as a function of ion etching time.

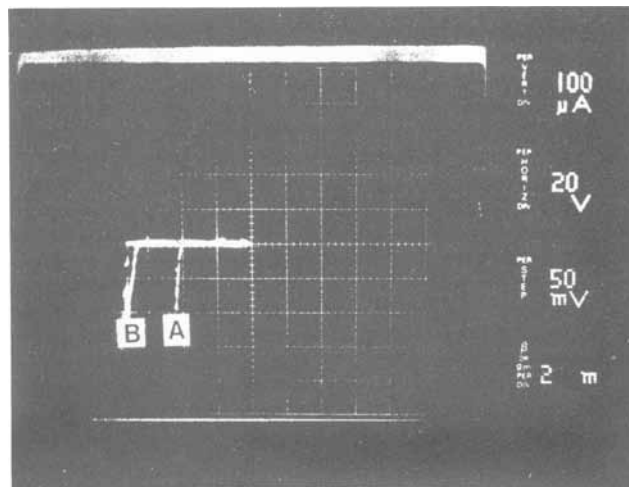


Fig. 7. I-V curves of Ta-Si/p-InP diodes ($229 \mu m$ diam) before (A) and after (B) IBE.

InP.—Figure 7 shows the reverse I-V characteristics of the diodes with Ta-Si on p-type InP. The breakdown was relatively abrupt. Initially, the breakdown voltage, V_B , was about 45V (curve A). After 10s of IBE, the V_B increased to $\sim 70V$ (curve B). After an additional 10s of IBE, V_B increased further to $\sim 90V$ (not shown in Fig. 7). The barrier height ϕ_B^n did not change significantly after IBE, although the forward currents increased slightly in the low bias region ($V_f < 0.3V$) after IBE. It is interesting to note that V_B was not altered by postannealing at $300^\circ C$ for 25 min but recovered to the original values at $375^\circ C$ for 25 min in forming gas.

The diodes ($152 \mu m$ diam) formed on n-type InP showed relatively soft breakdowns. For a reverse current of 5 mA, the corresponding reversed-biased voltage decreased from 13 to 7V after a 10s of IBE (not shown). The barrier height also decreased from 0.4 to 0.35 eV. Postannealing at $375^\circ C$ for 25 min led to the recovery of both V_B and ϕ_B^n to their original values.

GaAs.—For the ErSi₂ diodes formed on n-type GaAs, the breakdown was relatively soft, and at a reverse current of 1 mA the corresponding reverse-biased voltage decreased from 12 to $\sim 7V$ after a 10s of IBE (Fig. 8). The barrier height also decreased from 0.8 to 0.64 eV after IBE. These diodes recovered to their initial V_B of 12V and ϕ_B^n of 0.80 eV after annealing at $300^\circ C$ for 25 min.

Comparison with IBE before metal deposition—To verify some of the results reported in the literature, we checked the diode characteristics of three systems processed with IBE before metal deposition. The substrates

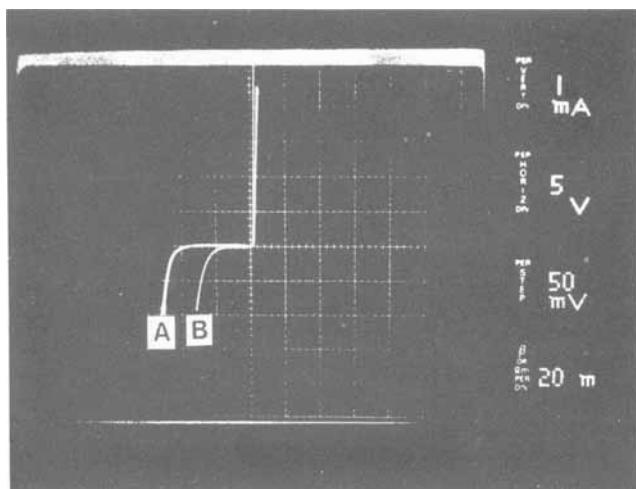


Fig. 8. I-V curves of ErSi₂/n-GaAs diodes (1 m diam) before (A) and after (B) IBE.

(p-Si, n-Ge, and n-GaAs) were IBE for 30s before a layer of Er was deposited on them. For the case of Er/p-Si, the barrier height ϕ_B^p increased from ~ 0.68 eV (as-deposited without IBE) to ~ 0.80 eV and the breakdown voltage increased from 60 to 300V. For Er on n-Ge substrates, the diodes exhibited ohmic behavior at room temperature. For the Er/n-GaAs case, ϕ_B^n was found to be ~ 0.41 eV as reduced from 0.68 eV for as-deposited samples. The breakdown voltage decreased from ~ 12 to 3V after IBE. These results are consistent with those reported in the literature and are similar to those obtained on diodes processed with IBE after metal deposition. The notable difference is that the barrier height on p-type substrates, ϕ_B^p , increases for samples processed with IBE before metal deposition, whereas ϕ_B^p remains unchanged for samples processed with IBE after metal deposition.

Discussion

It has been reported in the literature that RF (3), dc (4), and ion-beam (1) sputter deposition of metals on Si can cause anomalies in the I-V characteristics of Schottky barrier contacts, *i.e.*, a decrease in barrier heights on n-type Si and increase in barrier heights on p-type Si. To rationalize these results, Mullins *et al.* (4) have proposed a model suggesting that sputtering may induce donor-like defects at the metal-Si interface with a defect density distribution decreasing exponentially into the substrate. Assuming that the donor-like defects are ionized, this can lead to a narrowing of the depletion region on n-type substrates and an increase in apparent barrier height on p-type substrates. Ion-induced damage such as dislocation loops, small defect clusters, cavities, and embedded sputter gas as a result of sputtering of Si surfaces have been reported by Bean and his co-workers (18).

Sputter damage has also been found to cause the formation of an n-type layer on p-type InP (8). Bayliss *et al.* (19) have reported that P is preferentially depleted from the surface of InP under Ar bombardment. Temkin *et al.* (20) have reported that a P vacancy in InP behaves as a donor-like level.

For GaAs, Chiang *et al.* (21) and Jaros *et al.* (22) have reported that an As vacancy in GaAs behaves as a single donor. Yamaski *et al.* (6) and Wang *et al.* (7) have suggested the formation of donor-like defects by ion sputtering due to the depletion of As near the surface region. We believe that our experimental results can be rationalized in terms of the concept mentioned above.

Our results in this investigation show primarily two effects of ion-beam etching after metal deposition on Schottky barrier contacts.

First, on n-type semiconductors, the breakdown voltages (V_B) are lowered 2-4 times by IBE. In addition, the forward I-V characteristics (linearity, ϕ_B^n , and n) degrade as a result of IBE.

Second, on p-type semiconductors, the forward I-V characteristics remain unchanged while the breakdown voltages increase 2-15 times as a result of IBE.

These results appear to be consistent with the notion that ion beam processing induces donor-like defects near the surface region in semiconductors. In our experiments where metal dots were deposited onto the substrates before IBE, donor-like defects are expected to be present only in areas of the substrate exposed to the ion beam and not in regions of the substrates covered by metal dots. The observed IBE effects are most likely to be edge effects around the active regions of the Schottky barriers where the electric field is increased. Figure 9 shows the schematics that depict the situations before and after IBE under reverse bias. For p-type substrates, the substrate surface region around the diode is converted to n-type, thus forming a guard-ring structure around the diode, resulting in much higher breakdown voltages without changing ϕ_B^p . For n-type substrates, the substrate surface region around the diode becomes n^+ , the edge effect is intensified which leads to the tunneling of carriers resulting in lower barriers and lower breakdown voltages.

Upon annealing the samples (300°C for Si, Ge, and GaAs and 375°C for InP), the diodes recover to their original characteristics. This suggests the IBE induced defects are reduced or removed. The temperature at which recovery occurs for InP (375°C) agrees with results reported by Tsai *et al.* where n-type layer is reconverted to p-type after ion bombardment (8).

For cases where metal dots are deposited after IBE, barrier heights and breakdown voltages are raised on p-type substrates and are lowered on n-type substrates. These observations are consistent with results reported in the literature and the ion-induced donor-like defect model.

Summary

1. For the case of IBE after metal deposition, the breakdown voltages increase and the barrier heights of Schottky diodes remain unchanged on p-type substrates; on n-type substrates, both breakdown voltages and barrier heights decrease.

2. On annealing the samples at temperatures of 300°-375°C, the diode characteristics recover to their original values.

3. For the case of IBE before metal deposition, the effects of IBE are similar to those for IBE after deposition, except the barrier heights on p-type substrates are observed to increase.

4. These results are consistent with the concept of ion-beam induced donor-like defects near the surface region of the semiconductor substrates.

Acknowledgments

The financial support of DARPA (MDA-903-84-K-0002, F. Shephard and S. Roosild) is gratefully acknowledged. We also acknowledge the participation of B. Zhang in the early stage of this work.

Manuscript received Oct. 5, 1984.

The University of California assisted in meeting the publications costs of this article.

REFERENCES

1. S. J. Fonash, S. Ashok, and R. Singh, *Appl. Phys. Lett.*, **39**, 423 (1981).
2. T. P. Chow, S. Ashok, B. J. Baliga, and W. Katz, *This Journal*, **131**, 156 (1984).
3. L. P. Andersson and A. O. Ewvaraye, *Vacuum*, **28**, 5 (1977).
4. F. H. Mullins and A. Brunnsweiler, *Solid State Electron.*, **19**, 47 (1976).

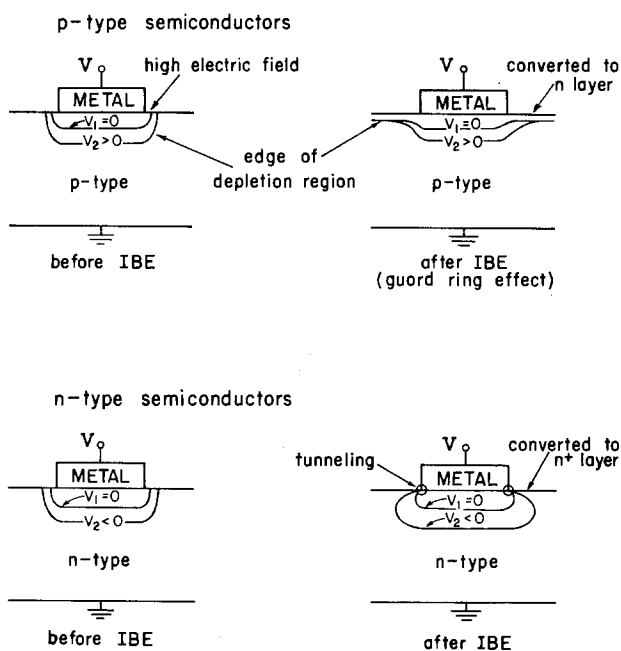


Fig. 9. Schematics showing the edge effects of diodes after IBE. For $V_1 = 0$, the diodes are under zero bias. The diodes are reverse biased at V_2 .

5. L. S. Weinman, S. A. Jamison, and M. J. Helus, *J. Vac. Sci. Technol.*, **18**, 838 (1981).
6. K. Yamaski, K. Asai, K. Shumada, and T. Makimura, *This Journal*, **129**, 2760 (1982).
7. Y. X. Wang and P. H. Holloway, *J. Vac. Sci. Technol. A*, **2**, 567 (1984).
8. M.-J. Tsai, A. L. Fahrenbruch, and R. H. Bube, *J. Appl. Phys.*, **51**, 2696 (1980).
9. W. Kern and D. A. Puotinen, *RCA Rev.*, 187 (June 1970).
10. S. S. Lau, C. S. Pai, C. S. Wu, T. F. Kuech, and B. X. Liu, *Appl. Phys. Lett.*, **41**, 77 (1982).
11. C. S. Wu, S. S. Lau, T. F. Kuech, and B. X. Liu, *Thin Solid Films*, **104**, 175 (1983).
12. C. S. Wu, To be published.
13. B. Zhang, D. M. Scott, H. H. Wieder, and S. S. Lau, *J. Appl. Phys.*, **55**, 2986 (1984).
14. B. A. Heath, *Solid State Technol.*, 75 (October 1981).
15. B. A. Heath, *This Journal*, **129**, 396 (1982).
16. H. R. Kaufman, *J. Vac. Sci. Technol.*, **15**, 272 (1978).
17. P. E. Schmid, P. S. Ho and T. Y. Tan, IBM Research Report RC9097 (no. 39777) 10/23/81, partially published in *J. Vac. Sci. Technol.*, **20**, 688 (1982).
18. J. C. Bean, G. E. Becker, P. M. Petroff, and T. E. Seidel, *J. Appl. Phys.*, **48**, 907 (1977).
19. C. R. Bayliss and D. L. Kirk, *J. Phys. D.*, **9**, 233 (1976).
20. H. Temkin, B. V. Dutt, and W. A. Bonner, *Appl. Phys. Lett.*, **38**, 431 (1981).
21. S. Y. Chiang and G. L. Pearson, *J. Appl. Phys.*, **46**, 2986 (1975).
22. M. Jaros and S. Brand, *Phys. Rev. B*, **14**, 4494 (1976).

Properties of Ion-Implanted Polycrystalline Si Layers Subjected to Rapid Thermal Annealing

S. R. Wilson, R. B. Gregory, and W. M. Paulson

Motorola, Incorporated, Semiconductor Research and Development Laboratories, Phoenix, Arizona 85008

S. J. Krause

Materials Science Group, Department of Mechanical and Aerospace Engineering, Arizona State University, Tempe, Arizona 85281

J. D. Gressett, A. H. Hamdi,¹ and F. D. McDaniel

Department of Physics, North Texas State University, Denton, Texas 76203

R. G. Downing

Center for Analytical Chemistry, National Bureau of Standards, Gaithersburg, Maryland 20899

ABSTRACT

Polycrystalline silicon films have been deposited on thermally oxidized wafers. The films have been implanted with As, B, or BF₂ and annealed with a Varian IA-200 rapid thermal annealer. The system uses infrared radiation from a resistively heated sheet of graphite to heat the entire wafer to temperatures in excess of 1000°C for times on the order of a few seconds. The effects on sheet resistance, sheet carrier concentration, and mobility due to exposure time, heater temperature, dopant species, and resultant grain size are discussed. Higher temperatures and longer exposure times produce the lowest sheet resistances. These results are compared to CW laser and conventional furnace-annealed films. A substantial loss of As occurs during the anneal unless the films are capped with SiO₂. Results on B and BF₂ implanted films indicate no boron loss has occurred during the anneal. The As and B uniformly distribute throughout the film when exposed to anneal conditions that produce very little diffusion in single-crystal Si. This implies that As and B diffusion is much faster in polycrystalline Si than in single crystal under these anneal conditions. The anneal causes both components of a bimodal grain size distribution to grow significantly until grain growth is slowed by geometrical constraints. Increased grain size results in a substantial increase in mobility. The grain growth has been modeled by an interfacial energy-driven mechanism.

Removing implantation damage and activating implanted dopants in Si with some form of transient annealing technique is becoming a very important research topic as device dimensions shrink (1-16). Transient annealing allows better control of impurity diffusion than conventional furnace annealing because of the shorter time the wafer is at an elevated temperature. This tight control of diffusion will provide for precise control in the formation of shallow junctions, narrow base width, and fine geometry devices.

Although lasers and electron beams have been successfully used to anneal implanted Si (1-5), incoherent light sources appear more applicable to device processing. Thin film interference effects are eliminated and wafer throughput is greater for the incoherent light sources. Since the entire wafer is heated and cooled uniformly, nonuniformities due to thermal gradients are reduced.

Several papers have reported using incoherent sources to anneal ion-implanted, single-crystal silicon (6-16). How-

ever, very few results have been reported for annealing polycrystalline silicon with an incoherent light source (17-20). Polycrystalline Si is used as a gate material for most metal/oxide/semiconductor (MOS) devices. Polycrystalline Si is also used as an interconnect material and as load resistors in many integrated circuits. In self-aligned implant process technology, the source, gate, and drain are all implanted in the same step and annealed in a subsequent step. Therefore, if transient annealing of source and drain implants is to be successful in MOS technology, the technique must also be useful in annealing the implanted polycrystalline Si gate material.

We report results obtained on As-, B-, and BF₂-implanted polycrystalline Si films that were deposited on 0.1 μm of SiO₂ and annealed with a Varian IA-200 rapid thermal annealer. This system uses infrared radiation from a resistively heated sheet of graphite to uniformly heat the wafers. Changes in sheet resistance (R_s), sheet carrier concentration (N_s), and mobility (μ) as a function of exposure time, heater temperature, and dopant species are presented. These effects are correlated with grain

¹ Present address: Department of Applied Physics, California Institute of Technology, Pasadena, California 91125.

growth and dopant diffusion as measured by transmission electron microscopy (TEM), Rutherford backscattering (RBS), and neutron depth profiling (NDP). The surface morphology has been examined with a scanning electron microscope (SEM) and measured with a surface profilometer. The effect of different dopants and oxide caps is discussed.

Sample Preparation and Analysis

The substrates used in these experiments were 3 in. (100) Si wafers. Silicon dioxide, 0.1 μm thick, was grown on the substrates. Undoped polycrystalline Si, 0.3 μm thick, was deposited at 630°C on the SiO_2 by low pressure chemical vapor deposition (LPCVD). The polycrystalline Si films were implanted with either As (60 keV, $5.0 \times 10^{15}/\text{cm}^2$), B (50 keV, $3.0 \times 10^{15}/\text{cm}^2$), or BF_2 (223 keV, $3.0 \times 10^{15}/\text{cm}^2$). ^{11}B was used in all cases except on samples where NDP was performed. ^{10}B was implanted into the samples where NDP was performed. A cap of sputtered SiO_2 was deposited on some of the wafers. The remaining wafers were left uncapped. Wafers from each group were subjected to rapid thermal annealing using the Varian IA-200. This system has been described previously (11-14, 16). The exposure times ranged from 10 to 30s. The nominal heater set point temperatures used were 1150° and 1200°C as measured by a thermocouple, which was located ~2 mm from the heater. This temperature is measured on the thermocouple and is estimated to be 35°-50°C lower than the actual graphite temperature based on the temperature a silicon wafer achieves for long exposure times.

Figure 1 shows a typical plot of wafer temperature *vs.* exposure time for an 1150°C heater set point. The wafer temperature is measured by an optical pyrometer located directly behind the wafer. The polycrystalline Si was implanted with ^{75}As (60 keV, $5.0 \times 10^{15}/\text{cm}^2$). The temperature measured at 0 s is indicative of the heater and not the wafer since Si is essentially transparent to infrared radiation at room temperature. As the wafer heats up the transmission decreases until only the wafer is being monitored. After 10s the wafer temperature reaches 875°C (the lowest reading on the meter) and rises to 1185°C after 20s. The wafer temperature remains nearly constant after 20s. The final wafer temperature is greater than the heater set point temperature because the heater thermocouple is located 2 mm from the heater rather than in direct contact with the heater. Therefore, the heater is actually hotter than the set point reading. The time required to reach the annealing temperature depends on the doping concentration, wafer thickness, etc. (16).

The electrical properties of the polycrystalline Si films were measured using a four-point probe and Hall effect measurements. The Hall measurements were made using van der Pauw patterns which had been etched into the films. The measurements yielded sheet resistance (R_s), sheet carrier concentrations (N_s), and mobilities (μ_n , μ_p).

The grain size in the polycrystalline film was determined by TEM. These samples were prepared by first

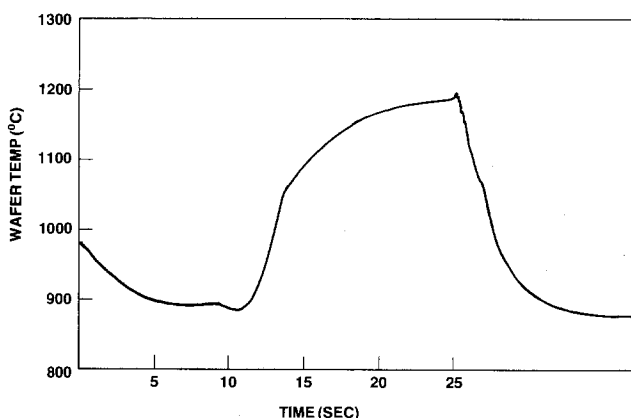


Fig. 1. Temperature *vs.* time for As-implanted Si. The anneal conditions were a heater set point of 1150°C and exposure time of 25s.

lightly ion thinning the polysilicon, floating the film off the substrate in dilute hydrofluoric acid, and finally picking the film up on a holey carbon film on a copper grid. The films were bright and dark field imaged at 200 kV in a JEOL 200CX by standard techniques. Through section images of the films were viewed in the electron microscope with no tilt of the sample holder. Cross-sectional images of many samples were viewed by tilting the sample holder to a high angle (about 60°), and examining thin edges of film fragments resting on the holey carbon film. Grain sizes were determined by counting at least 100 grains from through section views, plotting the distribution, and then choosing the peak (or peaks) in the distribution as the average grain size(s).

The As dopant profiles and the net loss of As during annealing were determined by RBS. A 2.0 MeV He beam was used with the particle detector located at a scattering angle of 154°. The samples were tilted such that the surface normal was 45° relative to the incident beam. The depth resolution for the RBS measurement was 22 nm.

The boron profiles were determined by implanting ^{10}B and performing neutron depth profiling (NDP) before and after annealing. The technique (21) and the facility used for this study (22) have been described elsewhere. The samples and standards were mounted to a mask constructed with an aperture of 7 mm diam being smaller than the neutron beam diameter in order to analyze equal and known volumes. The detector face was placed parallel to that of the surface of the sample with center points aligned and separated by a distance of 50 mm.

Results

^{75}As -implanted films.—We reported previously (18) that, unless As-implanted films were capped with SiO_2 , a substantial loss of As to the vacuum can occur during the anneal. This loss of dopant resulted in an increase in R_s with increasing exposure time. As expected, the As loss was greater for the higher heater temperature compared to the lower temperature anneal (1200° *vs.* 1150°C) (18). The loss of As from polycrystalline Si films was much greater than the loss from single-crystal silicon (12) due to the faster diffusion of As in polycrystalline Si relative to single-crystal silicon. These results are confirmed by the work of Powell and Chow (20).

Electrical results of As-doped polycrystalline Si.—To prevent As loss during annealing, an SiO_2 cap (0.05 μm) was sputter deposited on the other As-implanted films. The R_s , μ_n , and N_s *vs.* exposure time are presented in Fig. 2 for wafers annealed with a heater set point of 1150° and 1200°C. The R_s decreases and N_s and μ_n increase with increasing exposure time for both temperatures. The R_s for the 1150°C set point is always higher than the 1200°C set point. The minimum R_s of 98 Ω/\square in the 1150°C case (25s exposure) is approximately a factor of five lower than the minimum achieved on the uncapped samples where As was lost to the vacuum (18) and a factor of two lower than the R_s on a film which was furnace annealed at 950°C for 30 min (199 Ω/\square). The N_s increases rapidly for the two shortest exposure times (10-15s) regardless of set point temperatures. The N_s increases very little between 20 and 25s. The value for N_s for the 1200°C data is slightly higher than the 1150°C data. The mobility follows a similar trend of rising at the shorter times and changing very little for the two longest times. The higher μ_n and slightly higher N_s for the higher temperature anneals explains the differences in R_s as a function of temperature. The initial increase in N_s with time implies that the film must be above 1000°C (see Fig. 1) for a short time (a few seconds) in order for nearly complete activation of the dopant to occur. The increase in μ_n with exposure time implies that the average grain size in these films is increasing with exposure time. However, the R_s was a factor of about four higher and μ_n a factor of about two-and-one-half lower than films implanted with As to the same dose and CW laser annealed (23). The CW laser annealed films were thicker, but this would not account for all the differences we observed. However, the CW laser annealing caused

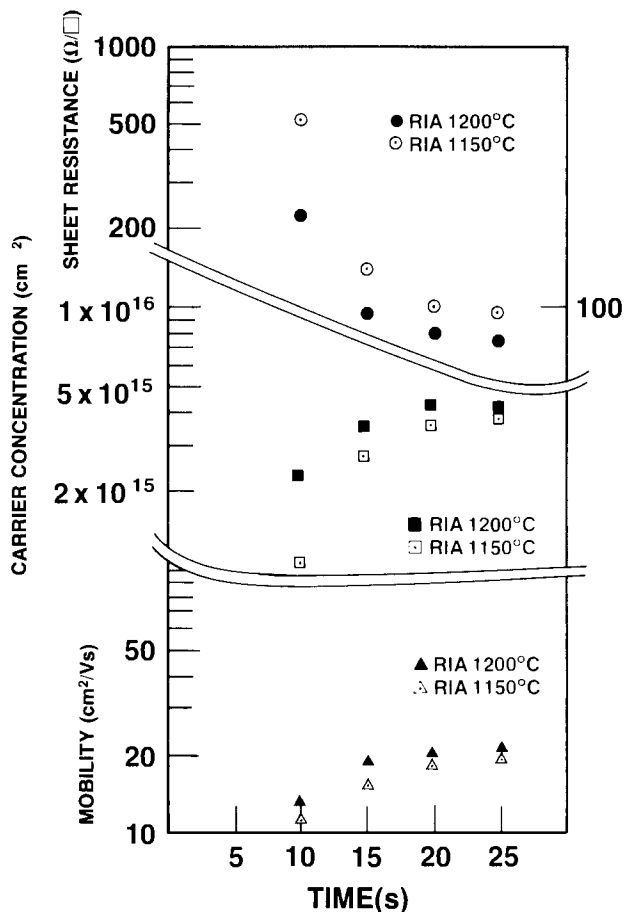


Fig. 2. Sheet resistance, carrier concentration, and mobility vs. exposure time for anneals with 1150° and 1200°C heater set point temperatures. The As implant dose was $5.0 \times 10^{15}/\text{cm}^2$.

complete melting and subsequent freezing of the polycrystalline Si film. The rapid thermal anneal is strictly a solid-phase annealing process. Differences are discussed below.

Profiles.—The As profiles for the as-implanted and 1150°C, 10 and 12.5s exposure samples are shown in Fig. 3. No loss of As was measured for the annealed samples confirming that the SiO₂ cap prevents the loss of As. The As has just begun to diffuse after 10s. There is evidence for a faster diffusion coefficient in the deep tail region ($> 0.12 \mu\text{m}$) of the wafer. In this case, the wafer reached a peak temperature of 1050°C. This faster diffusion in the tail is due to grain boundary diffusion, which is much faster than the diffusion which occurs in single-crystal silicon. Diffusion inside the grain would be similar to diffusion in single-crystal silicon and therefore much slower than grain boundary diffusion. After a 12.5s exposure, the As has uniformly distributed throughout the entire film at a concentration of $\sim 1.6 \times 10^{20}/\text{cm}^3$. The wafer reached a peak temperature of 1120°C in this case. In this case, we assume that the spreading of the dopant is dominated by grain boundary diffusion. Since these profiles were measured on films which were annealed with an oxide cap, the surfaces were smooth and the hillocks (which are discussed in the Surface morphology section) were not a problem in these profile measurements. Using an activation energy of 2.3 eV obtained by Baumgart *et al.* (24), we have calculated an effective diffusion time at the peak temperature (25). We then solved the diffusion equation numerically on a computer. To fit the 12.5s anneal profile required a diffusion coefficient for As in polycrystalline Si of $\sim 8 \times 10^{-11} \text{ cm}^2/\text{s}$ (18), which is nearly an order of magnitude greater than the diffusion coefficient reported by Baumgart *et al.* (26). Swaminathan *et al.* (26) reported an activation energy of 3.9 eV for grain boundary diffusion in polycrystalline Si. Using the same approach

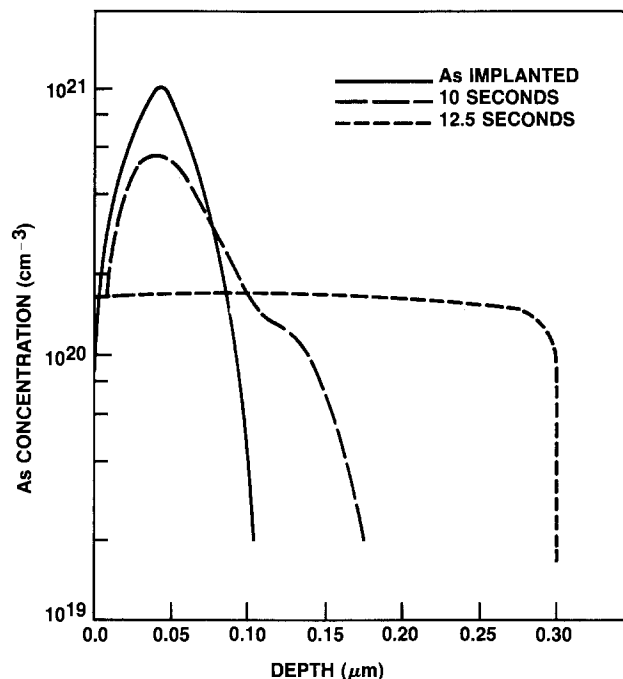


Fig. 3. As dopant profiles before annealing and after an 1150°C anneal for 10 and 12.5s.

to fit the profiles as we discussed in Ref. (18) and an activation energy of 3.9 eV requires a minimum diffusion coefficient of $\sim 2.0 \times 10^{-10} \text{ cm}^2/\text{s}$. This is a somewhat lower diffusion coefficient than the $6.7 \times 10^{-10} \text{ cm}^2/\text{s}$ that would be predicted by extrapolating the results of Swaminathan *et al.* (26) to this temperature (1120°C). The faster diffusion coefficient of Swaminathan *et al.* (26) would be consistent with the data presented here since it would produce a flat profile also. Therefore, the present results indicate a somewhat faster diffusion coefficient for As in polycrystalline silicon during rapid thermal annealing than was predicted by Baumgart *et al.* (24), but the diffusion coefficient of Swaminathan *et al.* (26) would agree with the present data.

The distribution of As throughout the film is similar to the results on CW laser annealing (23). However, there is no As spike at the surface on the graphite heater-annealed film. This spike occurs because of As segregation which occurs in the liquid-solid freezing process. The rapid thermal annealing process is a solid-phase process. The uniformly distributed As can precipitate throughout the film, especially at grain boundaries or interfaces. The furnace-annealed sample shows that As has diffused throughout the polycrystalline film. There was no loss of As detected. There was some pile-up of As at the polycrystalline Si-SiO₂ interface. This is probably due either to As segregation at the grain boundaries, as reported previously (27, 28), or to segregation at an Si-SiO₂ interface.

Although RBS indicates As is uniformly distributed throughout the film after 12.5s, the maximum in sheet carrier concentration is not obtained until after a 20s exposure (see Fig. 2). This indicates that a large amount of the As is still in the grain boundaries and inactive after the 12.5 and 15s exposure. This is due to the fact that grain boundary diffusion is much greater than diffusion inside the grains. Therefore, for the shorter exposures most of the dopant is moving in the boundaries. After longer exposure times ($\geq 20\text{s}$), the As has uniformly spread throughout the grain boundaries and there is no longer a concentration gradient to move the As through the boundaries. However, the concentration in the interior of the grains is low and now there is a gradient causing some of the dopant to move from the grain boundaries to the interior of the grains, where it can become electrically active. These data are in agreement with the work of Powell and Chow (20).

Grain size of As-doped polycrystalline Si.—The as-deposited films, prior to annealing, displayed a bimodal distribution of grain sizes. The first population is composed of elongated grains of a columnar morphology with an average diameter of 39 nm. These evidently arise from preferential growth of some grains during deposition. The second population is composed of small equiaxed grains of about 5 nm diam. The bimodal distribution is shown in Fig. 4 and 5 in cross-sectional and through section views of an as-deposited film. In the through section view, two different sets of diameters can be seen. Duffy *et al.* (29) have also reported observing a bimodal distribution of grains for polysilicon films deposited at 622°C.

In this study, the bimodal distribution of crystallite sizes was preserved in the grain-growth process during transient annealing. However, as determined from cross-sectional TEM views, both populations assumed equiaxed morphologies as grain growth progressed. Figure 6 shows a through section view of an arsenic-implanted film after 12.5s of annealing at a heater set point temperature of 1150°C. Two different sets of grain sizes with averages of about 23 and 90 nm are clearly evident in this view. At the longest times at the highest annealing temperature, the two grain size populations have grown to maximum diameters of about 160 and 330 nm. The progression of grain growth during transient annealing is shown in Fig. 7, where grain size is plotted as a function of annealing time for films subjected to treatment with an 1150°C set point heater temperature. These results are detailed in Table I, which shows annealing time, actual peak wafer temperature, and the associated grain sizes. Significant grain growth does not begin until annealing time has reached 10s. Grain growth occurs rapidly between 10 and 20s, but then slows down due to geometrical constraints to be discussed later. This is consistent with electrical measurements which show significant mobility

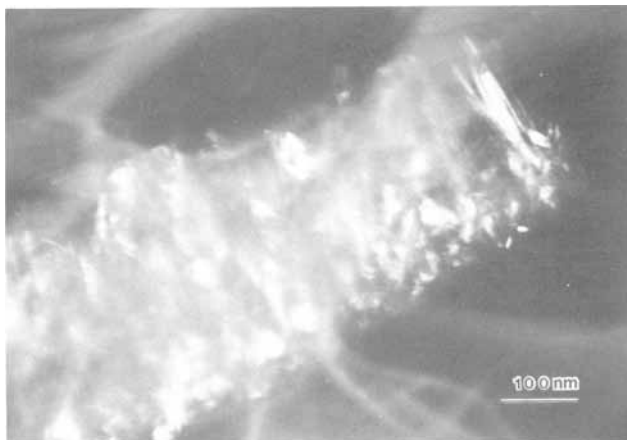


Fig. 4. Cross-sectional view of as-deposited polycrystalline Si film

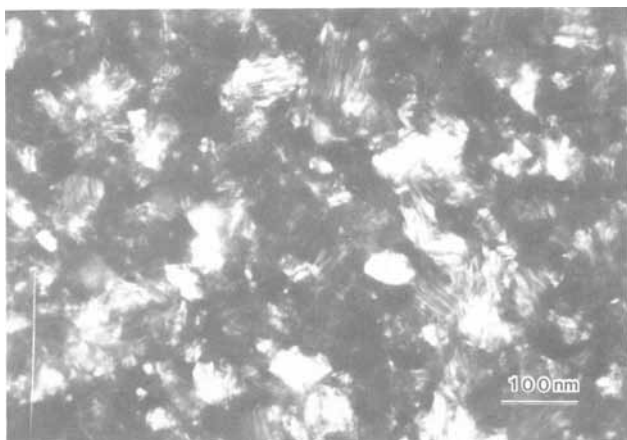


Fig. 5. Through section view of as-deposited polycrystalline Si film.

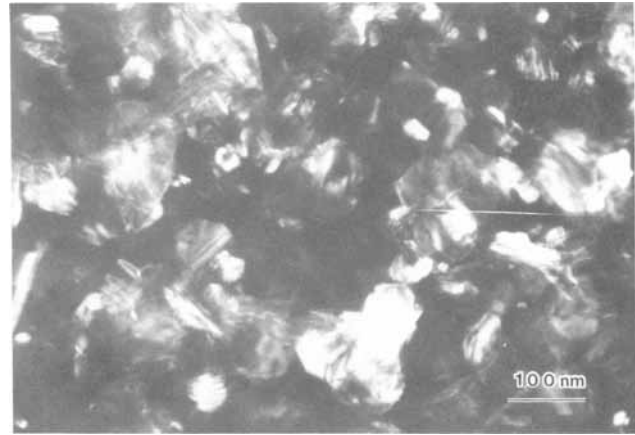


Fig. 6. Through section view of As-implanted polycrystalline Si film after 12.5s anneal at 1150°C set point heater temperature.

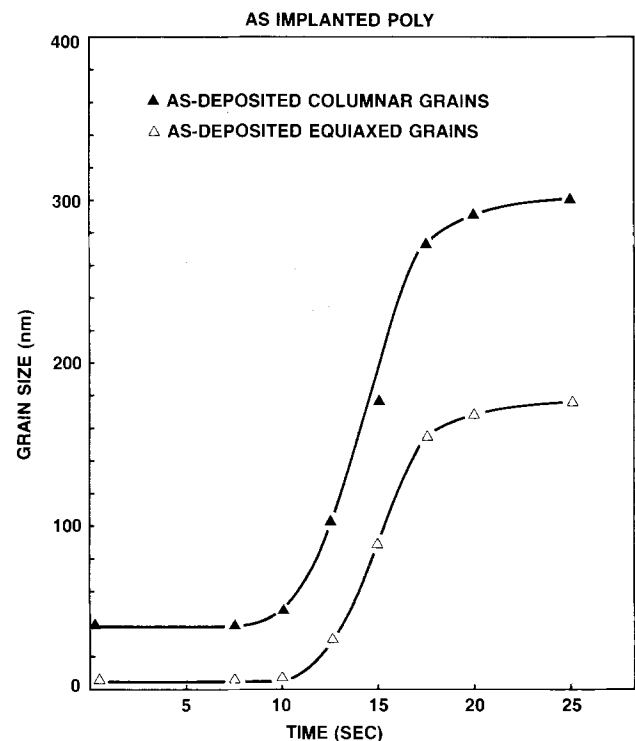


Fig. 7. Grain size as a function of annealing time for As-implanted polycrystalline Si films annealed at 1150°C set point heater temperature.

increases from 10 to 20s, but little increase after 20s (see Fig. 2). The difference in grain size between these films and films which were CW laser annealed (23, 24) explains the difference in mobility between these films and polycrystalline Si films which were CW laser annealed.

In transient annealing, significant diffusion and grain growth occur during the temperature rise and fall and must be taken into consideration. In order to account for this, we have developed a modified model for interfacial energy driven grain growth. This model successfully describes grain growth for both populations in this study and helps explain the appearance of the S-shaped curves in Fig. 7. By measuring the mean grain size (\bar{r}) and effective time (t^*) at temperature the grain boundary migration rate can be determined. In a pure material, the migration rate is equal to the grain boundary mobility times the driving force

$$G = M\bar{r} \quad [1]$$

Wada and Nishimatsu (30) have shown that the grain boundary mobility (M) is proportional to the grain bound-

Table I. Grain size and effective times for polycrystalline films annealed with a variety of heater temperatures and exposure times

Set point temperature (°C)	Peak wafer temperature (°C)	Exposure time (s)	Effective time (s)	$\sqrt{Dt^*/T}$ (cm/K ^{1/2} × 10 ⁻⁶)	Grain size (nm)	
					First population	Second population
25	—	—	—	—	39	4
1150	910	1.0	1.0	0.2	47	4
1150	1075	12.5	1.65	1.1	103	31
1150	1177	15	2.0	2.5	178	89
1150	1210	17.5	2.82	3.7	275	156
1150	1271	20	6.75	8.0	295	168
1150	1276	25	11.5	10.2	310	195
1200	1145	10	1.0	1.5	260	120
1200	1297	15	3.25	6.3	300	160
1200	1305	20	8.0	10.5	315	175
1200	1343	25	11.5	15.3	300	150

ary silicon diffusion coefficient divided by kT . If the temperature is accurately varied during grain growth, then the average grain boundary migration rate $G(T)$ can be determined from $d\bar{r}/dt(T)$. It is frequently found that the average grain size follows a time law of the form

$$r = (at)^n$$

and by determining n the recrystallization mechanism is determined. Wada and Nishimatsu (30) have shown that grain growth in doped polycrystalline Si is driven by interfacial energy, and grain size (r) is, therefore, proportional to the square root of time at constant temperature. However, we have modified the interfacial energy model in two ways to compensate for time required for heating and cooling during transient annealing. First, the effect of changing temperature has been compensated for by calculating the diffusion coefficient (D) of Si in polycrystalline Si based on the peak temperature of the wafer. Second, an effective time (t^*), as described by Shewmon (25), is calculated based on the time-temperature profile, the peak temperature (T), and the appropriate activation energy. In this study, we have used a value of 2.4 eV for activation energy of diffusion of Si in polycrystalline Si as specified by Wada and Nishimatsu (30) in their study of grain growth of doped polysilicon. Based upon a classical model for grain growth, as discussed by Wada and Nishimatsu (30), by McLean (31), and by others, a new modified model for interfacially driven grain growth can be given by the relationship: $\bar{r} \propto \sqrt{Dt^*/T}$. D may be calculated from $D = D_0 \exp(E_a/kT)$, where D_0 is the proportionality constant (and is assumed here to be 1 cm²/s for simplicity), E_a is the activation energy, and k is Boltzmann's constant.

In Fig. 8, grain size is plotted as a function of $\sqrt{Dt^*/T}$ for samples annealed at various time-temperature conditions. Both populations of grain sizes from the bimodal distributions have been plotted. The solid circles represent sizes of grains of the first population which have grown from the larger as-deposited grains with the columnar morphology. The open circles represent sizes of grains which have grown from the second population of smaller as-deposited grains with an equiaxed morphology.

A linear least squares fit was applied to the data for each population up to a value of $\sqrt{Dt^*/T}$ less than 4×10^{-6} cm/K^{1/2}, as shown by the solid line. This results in a correlation coefficient of approximately 0.98 for both grain size populations. At values of $\sqrt{Dt^*/T}$ higher than 4×10^{-6} cm/K^{1/2}, there is a break in the least squares fits due to geometrical constraints affecting grain growth. For the first population, the one with larger grains, the growth rate is lowered when the grain size reaches the thickness of the film. A similar effect has been observed for growth of polycrystalline Si films by Jain and Overstraeten (32). For the second population, the one with the smaller grains, the growth rate is reduced when the grains impinge upon one another. Similar effects for metals have been documented by McLean (31). The regions for the reduced growth rates are represented by dashed lines on the plot because the scatter of the data is high.

The reduced growth rates also explain the flattening of the S-shaped curves at longer annealing times as shown in Fig. 7. Thus, we find that, prior to geometrical interference, grain growth processes during transient annealing of doped polysilicon can be described by a modified model for interfacially driven grain growth.

B-implanted films.—Electrical results.—The R_s , N_s , and μ_p as a function of exposure time for films implanted with B (50 keV, 3.0×10^{15} /cm²) are shown in Fig. 9. The films were capped with SiO₂. However, no differences were observed between capped and uncapped films. This implies boron is not being lost during the anneal which is similar to results we obtained previously on single-crystal Si (15, 18). The N_c is essentially constant at 3.5×10^{15} /cm² for the 1150°C heater anneal. The fact that N_c is greater than the dose is not understood completely. The μ_p increases with increasing anneal time. Note that μ_p is actually higher than the μ_n obtained on the As-implanted films (Fig. 2). In single-crystal silicon with a dopant concentration of 2.0×10^{20} /cm³, μ_n would be a factor of two greater than μ_p . The reason for the higher μ_p than μ_n may be that some of the As (~30%) has segregated into the grain boundaries and acts as a barrier to electron flow, thus lowering mobility. In the case of B-implanted polycrystalline Si, no segregation to the grain boundaries occurs (33).

Profiles.—Figure 10 shows the boron profile before and after annealing as measured by neutron depth profiling. The results are analogous to those obtained from As implants (see Fig. 3) in that boron has diffused uniformly throughout the film after 12.5s anneal. The 10s anneal shows a spreading of the dopant throughout the film, but

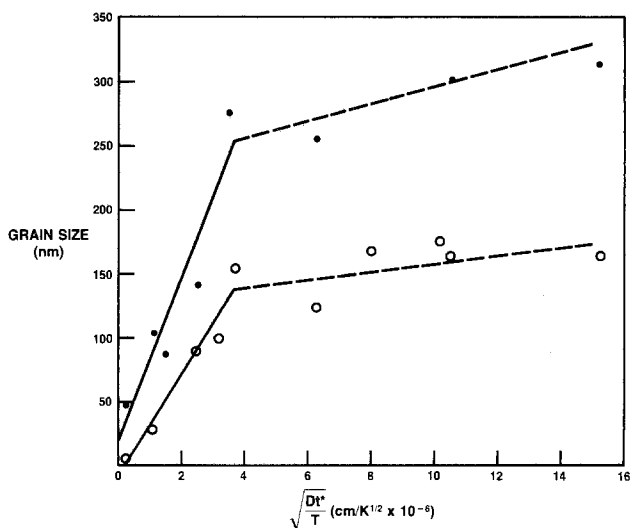


Fig. 8. Grain size as a function of $\sqrt{Dt^*/T}$ for As-implanted polycrystalline Si films annealed at 1150° and 1200°C set point heater temperatures.

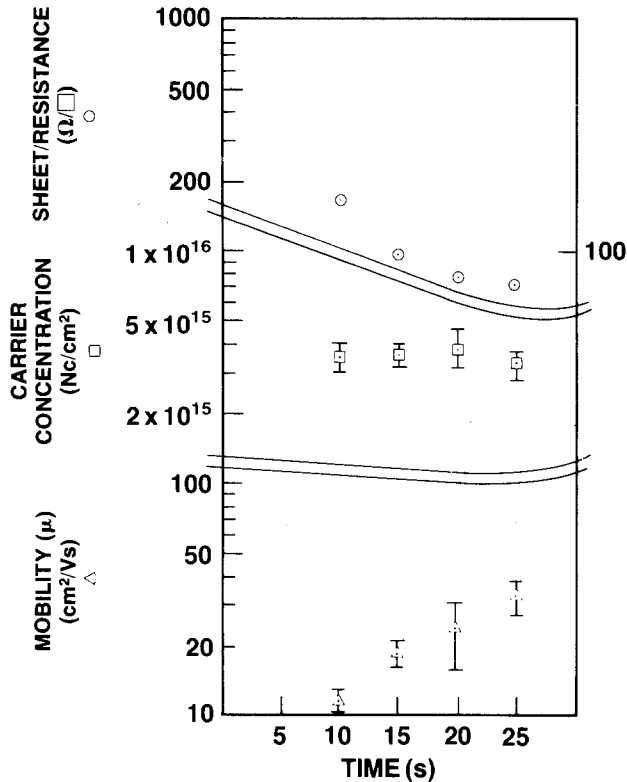


Fig. 9. Sheet resistance, carrier concentration, and mobility vs. exposure time for an anneal with an 1150°C heater set point temperature. The B implant dose was $3.0 \times 10^{15}/\text{cm}^2$.

the concentration is not yet uniform through the film. Within the repeatability of the implant doses between samples (<5%), there was no loss of boron even though the film was not capped during the anneal. This is in agreement with the previously published results on single-crystal Si (15, 18). The average thickness of the boron containing layer is $0.31 \mu\text{m}$, compared to the original deposited polysilicon thickness of $0.3 \mu\text{m}$. The apparent thickness of the film lacks sharp definition in the NDP profile as a result of averaging the various thicknesses due to hillocks in the region of the sample illuminated by the beam. In addition, the system resolution, which is not deconvolved from the data shown, adds a full width at half maximum broadening of $0.02 \mu\text{m}$. Nonetheless, there is no evidence for diffusion of boron into the underlying SiO_2 layer.

Grain size.—Results of grain growth for boron-implanted polycrystalline Si films display trends similar to those of arsenic-implanted films, but there are some differences. Similar to the As-doped films, we find significant grain growth initiates at an annealing time of about 10s. Throughout the grain growth process, the bimodal distribution continues to exist, as was observed with the arsenic-implanted films. Grain growth continues up to 20s, but does not slow down. This is because impingement of the growing grains with the film surface or with other grains does not occur because grains are not as large as in As-doped films. This is consistent with electrical measurements, which show significant mobility increases beginning at 10s of annealing and continuing through 20s of annealing. When the grain size of the population of large grains of arsenic vs. boron is compared for a 20s, 1150°C anneal, that of the arsenic is 300 nm vs. 220 nm for the boron. The larger grain size of the arsenic film is due to the well-known phenomenon of dopant-enhanced diffusion where arsenic increases the diffusivity of Si in polycrystalline Si (30). The increase is dependent on the concentration of arsenic in the Si. The dopant level in the films studied here is about $1.5 \times 10^{20} \text{ cm}^{-3}$. For this level of arsenic doping, the diffusivity of Si should be about two times that of undoped Si (30). Boron, however,

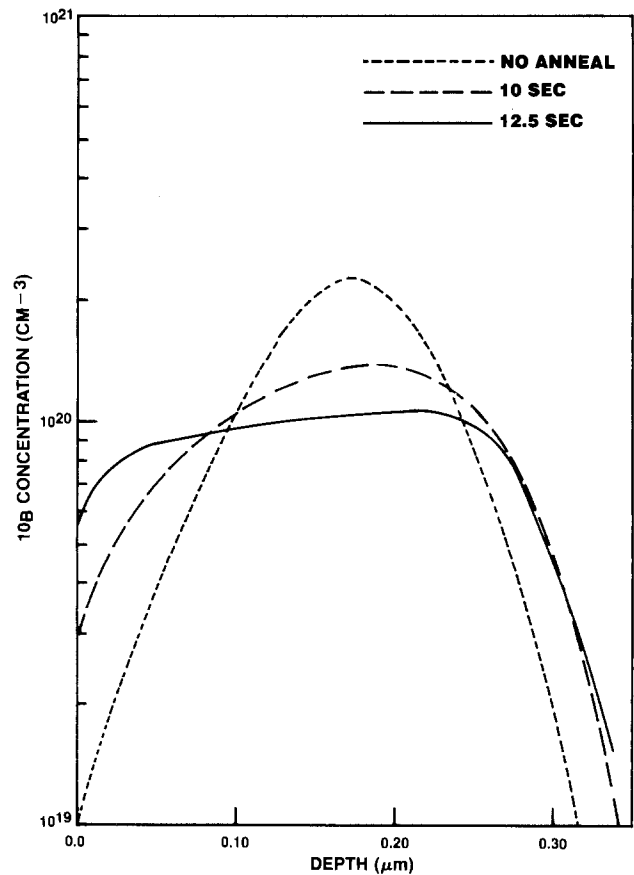


Fig. 10. B dopant profiles before annealing and after an 1150°C anneal for 10 and 12.5s.

does not significantly affect the diffusivity of Si, which would mean that the grain size would then be roughly the same grain size as for undoped silicon. Since the average grain size \bar{r} is proportional to the square root of the diffusivity (\sqrt{D}), the ratio of the grain size of the population of larger grains in the arsenic-doped polysilicon to that of the boron-doped silicon should be about $\sqrt{2}$ or about 1.41. The experimental result of $\sqrt{300/200}$ or 1.35 is in reasonable agreement with the predicted result. The ratio of the grain sizes of arsenic- and boron-doped polysilicon for the second population of smaller grains is $168/90 \text{ nm}$, and the square root of the ratio is $\sqrt{168/90}$ or 1.37. This ratio is in reasonable agreement with the ratio of 1.41 predicted by diffusivity.

Surface morphology.—Although no differences in the electrical properties or grain size were observed on the boron-implanted, capped and uncapped films, the surface was much rougher on the uncapped films. Figures 11a and 11b show SEM micrographs of capped and uncapped films. The films were annealed for a 20s exposure time with a 1200°C heater setting. Figure 11c is a surface profilometer measurement indicating the surface roughness on the uncapped film is $\sim 50 \text{ nm}$. This surface roughening on uncapped films was also observed on undoped films, but was not seen on the As-implanted films. We have not seen any relation between surface roughness and grain size or electrical properties. We believe the surface roughness is due to rapid diffusion of Si along the grain boundaries to form hillocks on the surface. We believe this rapid diffusion of Si up the boundaries is due to stress in the film. Hillock growth in metal films has been modeled by Chaudhari (34) and depends upon stresses in the film as well as mass transport along interfaces and grain boundaries. The kinetics of hillock growth for metals are inhibited by precipitation in the grain boundaries and dielectric overlayers (35). Similar characteristics were observed for transient annealing of polycrystalline Si films. The use of a SiO_2 cap layer mini-

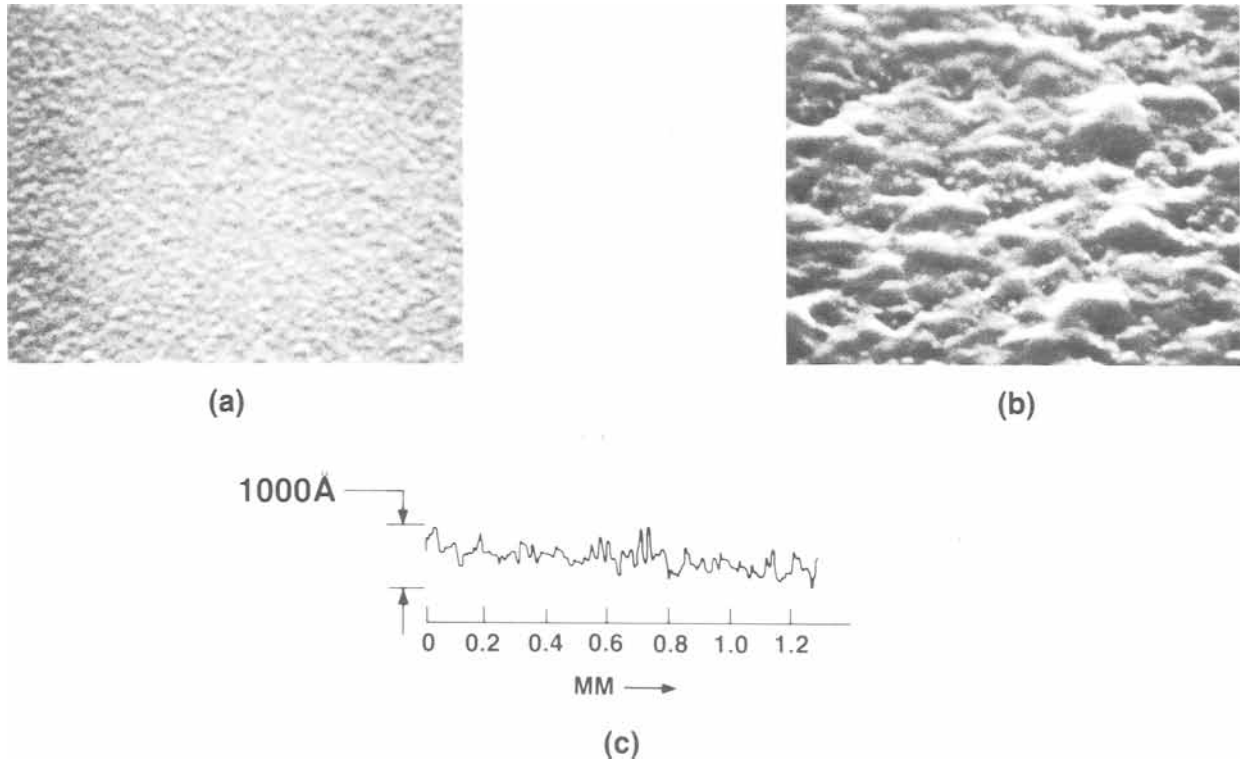


Fig. 11. B-implanted polycrystalline Si annealed at 1150°C for 25s. The figures show (a) SEM view of 50 nm SiO₂ capped film, (b) SEM view of uncapped film, and (c) surface profilometer measurement of uncapped film.

mizes hillock growth. For As-implanted films, hillocks are not observed. We believe this is due to the partial segregation of As into the grain boundaries. As segregation to the grain boundaries has been reported by Swaminathan *et al.* (27) and Batson *et al.* (28). The fact that we do not obtain 100% electrical activation for As in polysilicon (see the Electrical results of As-doped polycrystalline Si section) further supports this assumption. We believe the As in the boundaries is preventing the rapid diffusion of Si up the boundaries to the surface and thus preventing the formation of hillocks.

BF₂-implanted films.—Films were also implanted with BF₂ and annealed to determine any differences between B- and BF₂-implanted polycrystalline Si. The implant conditions for the BF₂ were adjusted to give the same range as the regular boron implant. Figure 12 presents the BF₂ sheet resistance results as a function of exposure time. The R_s is slightly higher for the 1150°C anneals as compared to the 1200°C heater set point anneals. The R_s for the B-implanted samples (see Fig. 9) are consistently lower than the BF₂ results. The TEM results indicate that the crystals in the BF₂-implanted films are not quite as large as the crystals in the boron-implanted films. The uncapped, BF₂-implanted films showed less surface roughness than the uncapped B-implanted films. However, these films were not as smooth as the uncapped As-implanted films. This suggests that some of the fluorine is moving to the grain boundaries and preventing some of the migration of Si to the surface.

Summary

We have shown that B and As ion implanted into polycrystalline Si films can be activated with a Varian IA-200 Rapid Thermal Annealer. The R_s on the As-implanted films increased with exposure time on uncapped wafers due to a loss of dopant from the film. The loss of As from the polycrystalline Si films is much greater than the loss from single-crystal Si which we reported earlier (12, 16). This greater loss is due to the faster diffusion of As in polycrystalline Si relative to single-crystal silicon. The As-implanted films which were annealed with a SiO₂ cap showed a rapid decrease in R_s and increase in N_s and

μ_n for exposure times up to 20s. Longer exposure times produced little change in these parameters.

The R_s of the B-implanted films decreased with exposure time out to 20s and then changed very slowly. The mobility of these films increased with increasing exposure time. Although B was not lost during annealing, a surface roughness due to the formation of hillocks was observed on the B- and BF₂-implanted films unless the wafers were capped. The surface roughness is due to mi-

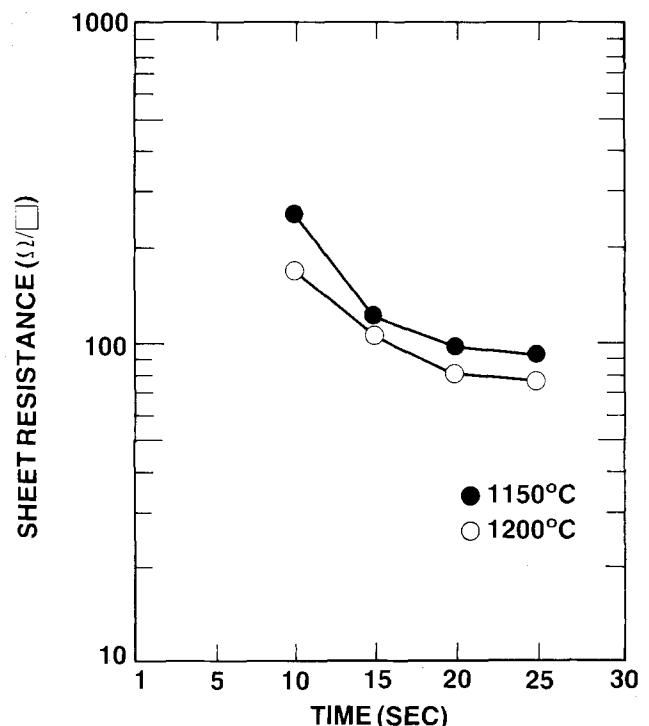


Fig. 12. Sheet resistance vs. exposure time for anneals with 1150° and 1200°C heater set point temperatures. The BF₂ implant dose was 3.0 × 10¹⁵/cm².

gration of Si up grain boundaries to the surface to form hillocks. However, in the case of As some of the dopant segregates to the grain boundaries and prevents this Si migration. This explains why we see more hillocks on B-implanted films, fewer with BF_2 implants, and no hillocks with As-implanted film.

For polycrystalline Si films in this study, a bimodal distribution of grains is present which is composed of large columnar grains and smaller equiaxed grains. The bimodal distribution of grain sizes is generally preserved in grain growth during transient annealing in both boron- and arsenic-doped polycrystalline Si films. A modified model for interfacial energy driven grain growth has been developed which describes grain growth during transient annealing of As- or B-doped polycrystalline Si. In transient annealing of arsenic doped films, dopant-enhanced diffusion increases the diffusivity and the grain growth rate for silicon in polycrystalline Si when compared to undoped or boron-doped polysilicon. Grain size increases during rapid thermal annealing for either As- or B-doped films. This grain growth increases the mobility. However, the grain size and mobility for rapid thermal annealing are less than for CW laser-annealed films.

The R_s on the rapid thermal-annealed films was lower than on the conventional furnace-annealed films. The R_s on the transient annealed films was higher than on CW laser-annealed films (23). The lower R_s on the CW laser-annealed films is due to a larger grain size and increased mobility. However, this rapid thermal anneal is a solid-phase process rather than a liquid-phase process like CW laser annealing of polycrystalline Si. Also, the present technique does not result in the large thermal gradients across a wafer that laser annealing causes. Therefore, this process will not encounter the same problems in annealing polycrystalline Si over various dielectrics that the CW laser annealing does (36). Concurrent rapid annealing of ion-implanted single-crystal silicon and polycrystalline silicon can be achieved. Anneal conditions similar to those reported here have been used to fabricate low reverse leakage diodes and functioning bipolar transistors as well as CMOS ring oscillator (37). Thin film interferences have made concurrent annealing very difficult with CW lasers.

Acknowledgments

The assistance of R. P. Lorigan and E. P. Matheson is gratefully acknowledged. The work at Arizona State University was supported in part by a grant from the University Research Fund. The research at North Texas State University is supported in part by the Robert A. Welch Foundation and the NTSU Organized Research Committee. Thanks are extended to Marlene Scott for typing the manuscript.

Manuscript submitted Aug. 16, 1984; revised manuscript received Dec. 3, 1984.

Motorola, Incorporated, assisted in meeting the publication costs of this article.

REFERENCES

- "Laser Solid Interactions and Laser Processing 1978," S. D. Ferris, H. J. Leamy, and J. M. Poate, Editors, American Institute of Physics, New York (1979).
- "Laser and Electron Beam Processing of Materials," C. W. White and P. S. Peercy, Editors, Academic Press, New York (1980).
- "Laser and Electron-Beam Solid Interactions and Materials Processing," J. F. Gibbons, L. D. Hess, and T. W. Sigmon, Editors, North-Holland, New York (1981).
- "Laser and Electron Beam Interactions with Solids," B. R. Appleton and G. K. Celler, Editors, North-Holland, New York (1982).
- "Laser-Solid Interactions and Transient Thermal Processing of Materials," J. Narayan, W. L. Brown, and R. A. Lemons, Editors, North-Holland, New York (1983).
- R. A. Powell, T. O. Yep, and R. T. Fulks, *Appl. Phys. Lett.*, **39**, 150 (1981).
- K. Nishiyama, A. Anai, and N. Watanabe, *Jpn. J. Appl. Phys.*, **19**, L563 (1980).
- R. T. Fulks, C. J. Russo, P. R. Hanley and T. I. Kamins, *Appl. Phys. Lett.*, **39**, 604 (1981).
- D. J. Lischner and G. K. Celler, in "Laser and Electron Beam Interactions with Solids," B. R. Appleton and G. K. Celler, Editors, p. 759, North-Holland, New York, (1982).
- J. L. Benton, G. K. Celler, D. C. Jacobson, L. C. Kimerling, D. J. Lischner, G. L. Miller, and Mc. D. Robinson, in "Laser and Electron Beam Interactions with Solids," B. R. Appleton and G. K. Celler, Editors, p. 765, North-Holland, New York (1982).
- D. F. Downey, C. J. Russo, and J. T. White, *Solid State Technol.*, **25**, 87 (1983).
- S. R. Wilson, R. B. Gregory, W. M. Paulson, A. H. Hamdi, and F. D. McDaniel, *Appl. Phys. Lett.*, **41**, 978 (1982).
- S. R. Wilson, R. B. Gregory, W. M. Paulson, H. T. Diehl, A. H. Hamdi, and F. D. McDaniel, *IEEE Trans. Nucl. Sci.* **ns-30**, 1734 (1983).
- S. R. Wilson, R. B. Gregory, W. M. Paulson, A. H. Hamdi, and F. D. McDaniel, in "Laser-Solid Interactions and Transient Thermal Processing of Materials," J. Narayan, W. L. Brown, and R. A. Lemons, Editors, p. 369, North-Holland, New York (1983).
- H. Baumgart, G. K. Celler, D. J. Lischner, Mc. D. Robinson, and T. T. Sheng, "Laser-Solid Interactions and Transient Thermal Processing of Materials," J. Narayan, W. L. Brown, and R. A. Lemons, Editors, p. 349, North-Holland, New York (1983).
- S. R. Wilson, W. M. Paulson, R. B. Gregory, A. H. Hamdi, and F. D. McDaniel, *J. Appl. Phys.*, **55**, 4162 (1984).
- K. Takebayashi, T. Yokoyama, M. Yoshida, and M. Inoue, *This Journal*, **130**, 2271 (1983).
- S. R. Wilson, W. M. Paulson, R. B. Gregory, J. D. Gressett, A. H. Hamdi, and F. D. McDaniel, *Appl. Phys. Lett.*, **45**, 464 (1984).
- S. J. Krause, S. R. Wilson, W. M. Paulson, and R. B. Gregory, *ibid.*, **45**, 778 (1984).
- R. A. Powell and R. Chow, Submitted to *This Journal*.
- J. F. Ziegler, G. W. Cole, and J. E. E. Baglin, *J. Appl. Phys.*, **43**, 3809 (1972).
- R. G. Downing, R. F. Fleming, J. K. Langland, and D. H. Vincent, *Nucl. Inst. Meth.*, **47**, 218 (1983).
- S. R. Wilson, W. M. Paulson, and C. W. White, *J. Electron. Mater.*, **12**, 143 (1983).
- H. Baumgart, H. J. Leamy, L. E. Trimble, C. J. Doherty, and G. K. Celler, in "Grain Boundaries in Semiconductors," H. J. Leamy, G. E. Pike, and C. H. Seager, Editors, p. 371, North-Holland, New York (1982).
- P. G. Shewmon, "Diffusion in Solids," McGraw-Hill, New York (1964).
- B. Swaminathan, K. C. Saraswat, R. W. Dutton, and T. I. Kamins, *Appl. Phys. Lett.*, **40**, 795 (1982).
- B. Swaminathan, E. Demoulin, T. W. Sigmon, R. W. Dutton, and R. Reif, *This Journal*, **127**, 2227 (1980).
- P. E. Batson, C. R. M. Grovenor, D. A. Smith, and C. Wong, in "Proceedings of the 41st Annual Meeting of the Electron Microscopy Society of America," G. W. Bailey, Editor, p. 154, San Francisco Press, San Francisco (1983).
- M. T. Duffy, J. T. McGinn, J. M. Shaw, R. T. Smith, and R. A. Soltis, *RCA Rev.* **44**, 287 (1983).
- Y. Wada and S. Nishimatsu, *This Journal*, **125**, 1499 (1978).
- D. McLean, "Grain boundaries in Metals," Oxford University Press, London (1957).
- R. K. Jain and R. J. Overstraeten, *This Journal*, **122**, 552 (1975).
- M. M. Mandurah, K. C. Saraswat, C. R. Helms, and T. I. Kamins, *J. Appl. Phys.*, **51**, 5755 (1980).
- P. Chaudhari, *ibid.*, **45**, 4339 (1974).
- E. Philofsky and E. Hall, *IEEE Trans. Parts Hybrids Packaging*, **php-11**, (1975).
- W. M. Paulson and S. R. Wilson, *J. Electron. Mater.*, **12**, 107 (1983).
- S. R. Wilson, W. M. Paulson, C. J. Varker, A. Lowe, R. B. Gregory, R. H. Reuss, S. Y. Wu, and J. D. Whitfield, in "Energy-Beam-Solid Interactions and Transient Thermal Processing," J. C. C. Fan and N. M. Johnson, Editors, p. 279, North-Holland, New York (1984).

GaAs Growth Using TMG and AsCl₃

M. Yoshida, H. Terao, and H. Watanabe

NEC Corporation, Fundamental Research Laboratories, Miyazaki 4-chome, Miyamae, Kawasaki, Kanagawa 213, Japan

ABSTRACT

A new GaAs vapor-phase epitaxial (VPE) technique using trimethylgallium (TMG) and arsenic trichloride (AsCl₃) has been developed. This VPE is free from the source instability in chloride VPE and fatally toxic arsine (AsH₃) in hydride and metalorganic VPE. The growth reaction is based on the gallium chloride transport method. Growth rates of 300-4000 Å/min were obtained at growth temperatures between 650° and 780°C. At III/V ratios below 2.3, the growth rate increased as the TMG flow rate increased and the AsCl₃ flow rate decreased. The growth rate was independent of the temperature in the gas mixing region of the reactor. High purity n-GaAs with a 77 K mobility of 36,000 cm²/Vs was obtained.

Because of its superior high frequency performance, GaAs has been used for microwave devices. As the demand for faster electronic devices increases, mass production of GaAs epitaxial layers becomes required (1). However, VPE techniques developed to date have problems in productivity. The chloride VPE has a problem of source instability (2) and, thus, the potential for scaling up of this system is limited. Both hydride VPE and metalorganic VPE have the problem of using fatally toxic arsine (AsH₃), which has hindered them from operating as a mass production system.

In this paper, a new metalorganic-chloride (MOC) VPE technique using trimethylgallium (TMG) and arsenic trichloride (AsCl₃) for GaAs growth is described. The electrical properties of GaAs layers grown in the system using triethylgallium (TEG) instead of TMG are also shown. The MOC-VPE is free of the source instability and the fatally toxic AsH₃. Since TMG and TEG decompose perfectly in a hot region (3), they act as sources for gallium which is dispersed in the vapor phase. Therefore, the MOC-VPE is also free from incomplete liquid-vapor reaction (4).

Experimental

Figure 1 shows a schematic illustration of the MOC-VPE system for GaAs growth. The TMG and the AsCl₃ were introduced separately into a hot-wall reactor together with H₂ carrier gas. An additional dilution flow of H₂ was kept at 500 standard cubic centimeter per minute (sccm) throughout the experiment. In order to prevent early decomposition of TMG, it was passed through a 30°C water-cooled quartz tube. A widely used hot-wall reactor system for chloride VPE can be used for MOC-VPE with this slight modification of the reactor inlet. It is important to complete the reaction between TMG and AsCl₃ to form gallium chloride and arsenic vapor; otherwise, epitaxy is not achieved (5). The temperature in the gas mixing region was kept high enough to eliminate wall deposition. Downstream from the mixing region, epitaxial growth proceeded on a substrate.

The temperatures of TMG, TEG, and AsCl₃ containers were 2°C (vapor pressure of 0.1 atm), 18°C (vapor pressure of 0.005 atm), and 18°C (vapor pressure of 0.01 atm), respectively. Triethylarsine (TEAs) vapor was used to pre-

vent thermal dissociation of the substrate during the heat-up. The metalorganic sources were supplied by Sumitomo Chemical Company. The substrates were 3 × 1 cm² Cr-doped 2° off (100) towards <110>. Thicknesses of the grown layers were measured in an optical microscope after 5° bevel lapping and staining with 1:1:10 HF:H₂O₂:H₂O etchant. The growth rate was related to the layer thickness at 1 cm from the front edge of the substrate. Carrier concentrations and mobilities at temperatures of 77 and 300 K were measured by the van der Pauw method with a magnetic field of 0.6T.

Results and Discussions

The dependence of the growth rate on various growth parameters was investigated. Figure 2 shows the dependence of the growth rate on the flow rate of H₂ passing through the TMG container (TMG flow rate), where that of H₂ passing through the AsCl₃ container (AsCl₃ flow rate) was 200 sccm. The mixing temperature was 850°C, and the growth temperature was 740°C. The growth rate increased linearly as the TMG flow rate increased. It reached the maximum at a TMG flow rate of 42 sccm (a III/V ratio of 2.3). At higher TMG flow rates, the growth rate decreased as the TMG flow rate increased because high supersaturation in the mixing region resulted in GaAs deposition there and caused arsenic vapor depletion in the growth region. At TMG flow rates below 25 sccm (III/V ratios below 1.4), the substrate is etched.

As shown in Fig. 3, the dependence of the growth rate on the AsCl₃ flow rate forms a contrast to Fig. 2. The TMG flow rate was 42 sccm there. At AsCl₃ flow rates below 100 sccm, no deposition occurs on the substrate.

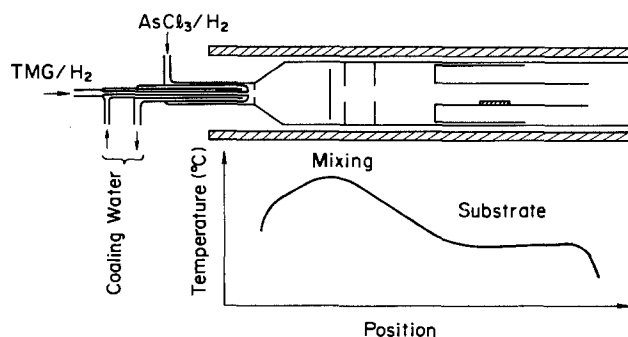


Fig. 1. Schematic illustration of growth apparatus

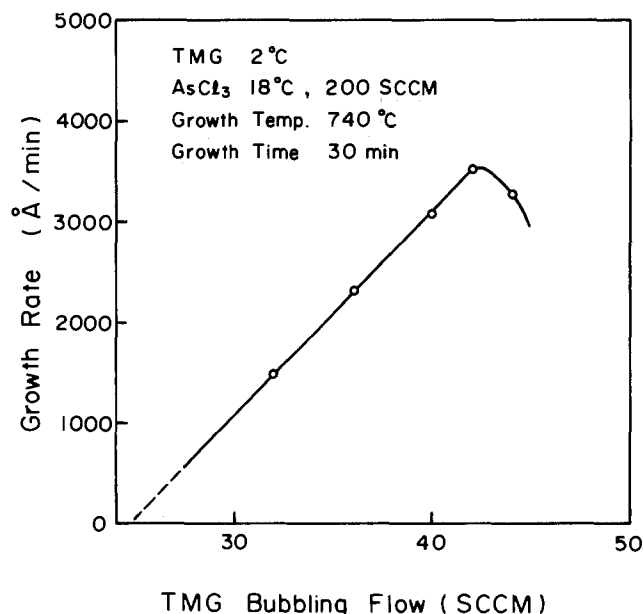


Fig. 2. Dependence of growth rate on flow rate of H₂ passing through TMG container.

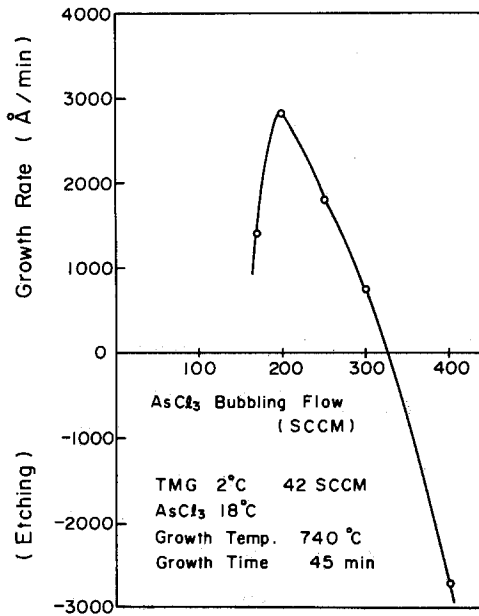


Fig. 3. Dependence of growth rate on flow rate of H₂ passing through AsCl₃ container.

The growth region is fully arsenic depleted because of unwelcome deposition in the mixing region. As the AsCl₃ flow rate increased up to 200 sccm, the growth rate abruptly increased but the surface of the grown layer was still rough due to the arsenic depletion. At higher AsCl₃ flow rates (III/V ratios below 2.3), the growth rate decreased as the AsCl₃ flow rate increased. At these AsCl₃ flow rates, the wall deposition in the mixing region disappeared. The substrate is etched at AsCl₃ flow rates above 330 sccm. The surface etched at 400 sccm was smooth. The *in situ* gas etching for making a well-controlled interface between the substrate and the epitaxial layer (6) can be carried out in the MOC-VPE system by reducing the III/V ratio.

It should be mentioned that the growth rate is independent of the mixing temperature, as shown in Fig. 4. This is a feature of MOC-VPE. Therefore, it can be said that the MOC is single-temperature VPE method like MOVPE. Figure 5 shows the variation of the growth rate with the growth temperature. The typical dependence observed in chloride VPE (7) can be seen. The growth is kinetically limited at growth temperatures below 760°C and thermodynamically limited at higher growth temperatures.

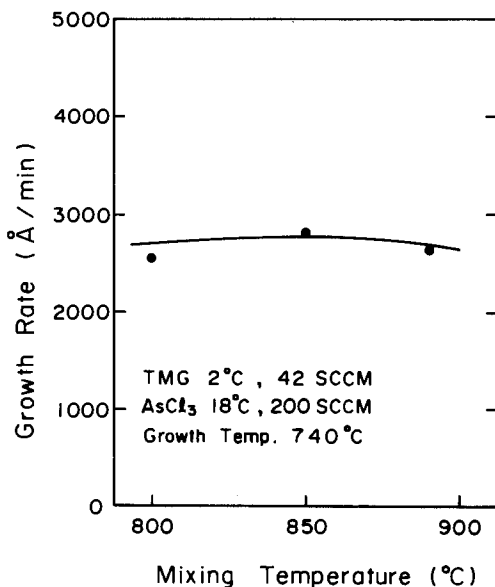


Fig. 4. Dependence of growth rate on mixing temperature

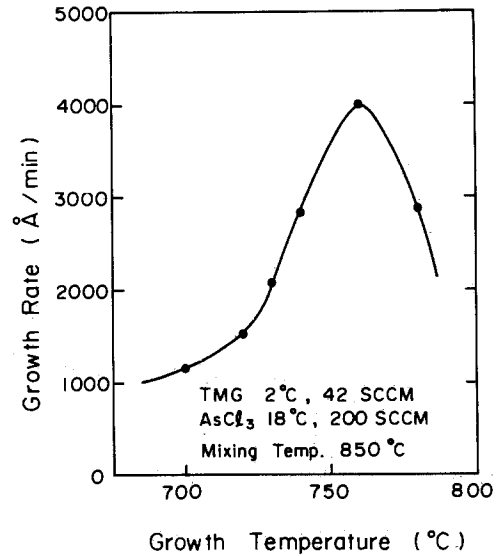


Fig. 5. Dependence of growth rate on growth temperature

Figure 6 shows the relation between the Hall mobilities and the Hall electron concentrations for nondoped GaAs layers. The electrical properties of layers grown in the TEG/AsCl₃/H₂ system are also shown. The grown layers exhibited n-type characteristics, except for some highly resistive samples grown at high III/V ratios, larger than 2.3. The epitaxial layers were grown at temperatures between 700° and 780°C in the TMG/AsCl₃/H₂ system and at temperatures between 650° and 750°C in the TEG/AsCl₃/H₂ system. The typical input concentration of TMG was 6.3×10^{-3} with an AsCl₃ input concentration of 2.7×10^{-3} in mole fraction. That of TEG was 1.4×10^{-3} with an AsCl₃ concentration 5.9×10^{-4} . The thickness varied between 0.9 and 18 μm, corresponding to growth rates of 300-4000 Å/min. The GaAs layers with lower electron concentrations were grown in the TMG/AsCl₃/H₂ system. The difference between using TMG and TEG seems to be due to the difference in the input AsCl₃ concentrations, since high purity GaAs layers with low electron concentrations are obtained at high input AsCl₃ concentrations (8).

A GaAs epitaxial layer with a thickness of 11 μm grown at a TMG flow rate of 42 sccm, and AsCl₃ flow rate of 200 sccm, a mixing temperature of 800°C, and a growth temperature of 740°C showed a mobility of 36,000 cm²/Vs with an electron concentration of 1.4×10^{14} cm⁻³ at 77 K. That compensation ratio, N_A/N_D , is 0.88 using an interpolation of the data of Walukiewicz *et al.* (9). The net impurity concentration is thus 2.2×10^{15} cm⁻³. At higher TMG and AsCl₃ concentrations, the purity of the GaAs epitaxial lay-

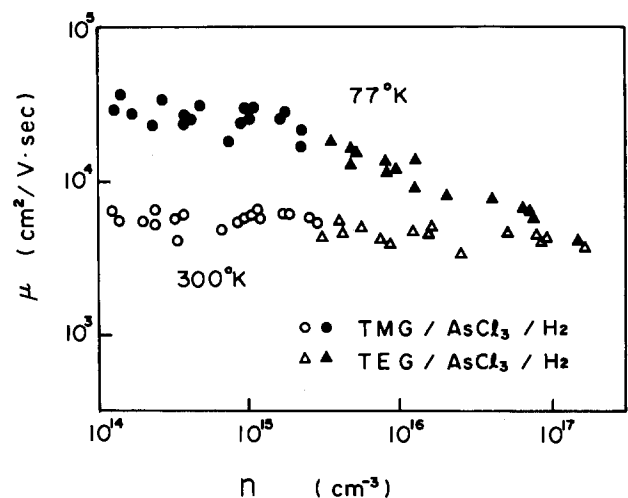


Fig. 6. Relation between electron mobility (μ) and electron concentration (n).

ers may be improved further. Since the growth reaction in MOC-VPE is similar to that in chloride and hydride VPE, it should be possible to use conventional VPE doping techniques.

To determine residual acceptors present in the layers, 11 K photoluminescence (PL) measurements with 5145Å excitation radiation from an Ar laser were performed (10). The PL spectrum of a GaAs layer grown in the TEG/AsCl₃/H₂ system with an electron concentration of $8.2 \times 10^{16} \text{ cm}^{-3}$ and a thickness of 4.62 μm showed a peak at 8300Å with a full width at half maximum (FWHM) of 66Å and a weak broad peak around 8500Å besides a main peak at 8198Å with a FWHM of 60Å. Therefore, carbon seems to be the main acceptor in this layer, since 8300Å luminescence is attributed to carbon acceptor (11).

Summary

MOC-VPE using TMG and AsCl₃ for the GaAs₃ growth shows promising features. It excludes the liquid source instability and fatally toxic AsH₃. At III/V ratios less than 2.3, the wall deposition in the mixing region was suppressed and GaAs layers with smooth surface were grown. In this III/V ratio range the growth rate increased as the TMG flow rate increased and the AsCl₃ flow rate decreased. The growth rate could be controlled over a wide range between 300 and 4000 Å/min. The growth rate is independent of the mixing temperature, which means that MOC-VPE is a single-temperature method like MOVPE. The substrate was gas etched with a smooth surface at low III/V ratios. Though carbon may have been introduced into the epitaxial layer, a high purity GaAs epitaxial layer with a 77 K mobility of 36,000 cm²/V and a 77 K electron concentration of $1.4 \times 10^{14} \text{ cm}^{-3}$ was obtained.

It should be noticed that a widely used chloride VPE system can be used for MOC-VPE with only a slight

modification of the reactor inlet. Furthermore, the *in situ* gas etching necessary for a well-controlled interface between the substrate and the epitaxial layer can be easily carried out in the MOC-VPE system by reducing the III/V ratio.

Acknowledgment

The authors wish to thank S. Asanabe, D. Shinoda, and T. Kawamura for encouragement. Useful discussions with Y. Matsumoto and A. Usui are also gratefully acknowledged.

Manuscript submitted Aug. 27, 1984; revised manuscript received Dec. 11, 1984.

NEC Corporation assisted in meeting the publication costs of this article.

REFERENCES

1. H. M. Cox, A. S. Prior, and V. G. Keramidis, "GaAs and Related Compounds, 1982," p. 133, Inst. Phys. Conf. Ser. 65, Inst. Phys., Bristol (1983).
2. D. W. Shaw, *J. Cryst. Growth*, **8**, 117 (1971).
3. M. Yoshida, F. Uesugi, and H. Watanabe, Submitted to *This Journal*.
4. V. S. Ban, *This Journal*, **118**, 1473 (1971).
5. H. M. Manasevit and W. I. Simpson, *ibid.*, **116**, 1725 (1969).
6. T. Nozaki, M. Ogawa, H. Terao, and H. Watanabe, "GaAs and Related Compounds, 1974," p.46, Inst. Phys. Conf. Ser. 24, Inst. Phys., London (1975).
7. D. W. Shaw, *This Journal*, **115**, 405 (1968).
8. J. V. DiLorenzo and G. E. Moore, Jr., *ibid.*, **118**, 1823 (1971).
9. W. Walukiewicz, J. Lagowski, and H. C. Gatos, *J. Appl. Phys.*, **53**, 769 (1982).
10. M. Yoshida, Unpublished.
11. D. J. Ashen, P. J. Dean, D. T. J. Hurle, J. B. Mullin, and A. M. White, *J. Phys. Chem. Solids*, **36**, 1041 (1975).

Effect of Annealing on Chemical State of Phosphorus in SiO₂ Films

Owen K. T. Wu*

Gould Research Center, Rolling Meadows, Illinois 60008

A. N. Saxena

Gould AMI Semiconductors, Santa Clara, California 95051

ABSTRACT

The chemical state and concentration of phosphorus in SiO₂ influence its thermal flow and etch rate. These properties of phosphorus-doped SiO₂ are quite important in both bipolar and MOS VLSI, and they influence the final yield of these circuits. In this paper, ESCA and Auger measurements were made to determine the chemical state of phosphorus in SiO₂ and its distribution through the film. Samples studied were CVD SiO₂ containing 8% phosphorus by weight, and ion-implanted phosphorus in thermal SiO₂, both annealed and unannealed. ESCA data confirmed the existence of two types of states corresponding to P-O bonds and P-Si bonds. The change in these states due to annealing is discussed.

It is well known that thermally grown SiO₂ films are absolutely essential for planar technology, and its many variations are used in the fabrication of bipolar and metal oxide semiconductor integrated circuits (MOS IC's). Almost equally important are the deposited SiO₂ films, in particular those doped with phosphorus. Today's very large scale integrated circuits (VLSIC's) cannot be fabricated without phosphorus-doped SiO₂ [such as phosphorus-doped vapox (PVX)] films, and they are expected to remain indispensable even for future VLSIC's.

PVX films are most commonly deposited by chemical vapor deposition techniques, with the weight percent (w/o) of phosphorus ranging between 4 and 8. A majority of the MOS processes use PVX as the first-layer-deposited dielectric, through which contact holes to Si

are etched and which isolates first-layer metal from the poly-Si or polycide interconnect underneath. In both MOS and bipolar processes, PVX is also used as the interlayer dielectric in the multilevel metallization schemes. Even though a few of the properties of PVX, e.g., reflow, etch rate, passivation, and their dependence on phosphorus concentration in SiO₂, are understood qualitatively, little is known about some of the basic properties like the chemical state of phosphorus and its change due to annealing (1, 2). The chemical state and concentration of phosphorus in SiO₂ influences the charge trapping centers (3), reflow, etch rate, stress, and the passivation properties. For a review of dielectric films as needed in multilevel metallizations, see Ref (4).

In this paper, ESCA and Auger measurements were made to determine the chemical state of phosphorus in SiO₂ and its distribution through the films.

*Electrochemical Society Active Member.

Experimental

Samples studied were CVD SiO₂ (PVX) containing 8% phosphorus by weight. Also, samples having ion-implanted phosphorus in thermal SiO₂, both annealed and unannealed, were used to generate P-O and P-Si states in SiO₂ and to study the effects of annealing on them. Phosphorus ions were implanted into SiO₂ with the energy of 50 keV and the dose of 1×10^{17} ion/cm². After the implantation, samples were annealed in either dry N₂ or dry O₂ at 700°-1100°C for 10-100 min. In addition, P₂O₅ powder and a phosphorus ion-implanted Si wafer were used to generate ESCA reference spectra to characterize the P-O and P-Si states.

All ESCA and Auger data were obtained using a PHI Model 548 ESCA/Auger system with computerized (PDP-11) automated data collection system. Mg K α x-rays (1253.6 eV) were used in this study, and Au foil was employed to calibrate the spectra energy. ESCA data were collected using a 25 eV pass energy and were signal averaged using 100 sweeps. Most Auger data were collected using a 5 keV electron gun and 3×10^{-6} A of electron beam current. For thick samples ($\sim 1 \mu\text{m}$), the electron gun energy was reduced to 2 keV to avoid any charging problems. The Auger phosphorus peak at 120 eV (LMM) and silicon peaks at 76 eV (LMM) and 1606 eV (KLL) were monitored for depth profiles. The ion beam used for sputter etching was Xe⁺ at 5 keV to avoid sputter artifacts (5). The total ion current for this study was 4.3×10^{-6} A. The sputter crater was 3×3 mm for Auger and 9×9 mm for ESCA studies. The sputtering rate was calibrated by Dektak IIA, which is a microprocessor-based instrument used for making measurements on the depth of a sputter crater.

Results and Discussion

Reference ESCA spectra of P-O and P-Si states.—P₂O₅ powder and a phosphorus ion-implanted Si wafer were investigated to confirm the identification of the P-O and P-Si states, respectively. Figure 1 shows the ESCA spectrum of the P₂O₅ powder which has the reference state corresponding to the P-O bond. The peak in the spectrum is phosphorus 2P characterizing the P-O bond at 134 eV. Figures 2 and 3 show the ESCA spectra of the phosphorus ion-implanted Si wafer on the surface, unannealed and annealed, respectively. Even though the P-Si state undoubtedly exists in the annealed (1100°C, 30 min, N₂) sample, the ESCA data show that the phosphorus 2P peaks are at the same energy, *viz.*, 130 eV, for both unannealed and annealed samples. The peak in the annealed sample (Fig. 3) is slightly sharper than that for the unannealed sample (Fig. 2). The difference in full width at half maximum is about 0.3 eV. This is probably due to phosphorus occupying substitutional sites in Si in the annealed sample and having a well-defined P-Si bond. In the unannealed sample (Fig. 2), phosphorus is in the interstitial as well as substitutional sites, and host Si atoms are displaced from their substitutional sites. These give rise

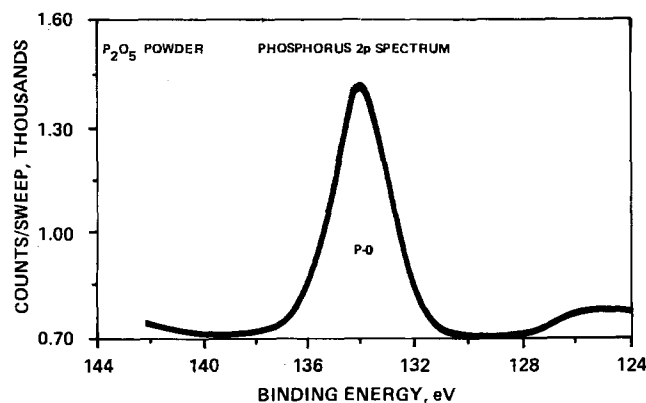


Fig. 1. The ESCA spectrum of the P₂O₅ powder which shows the reference state corresponding to the P-O bond at 134 eV.

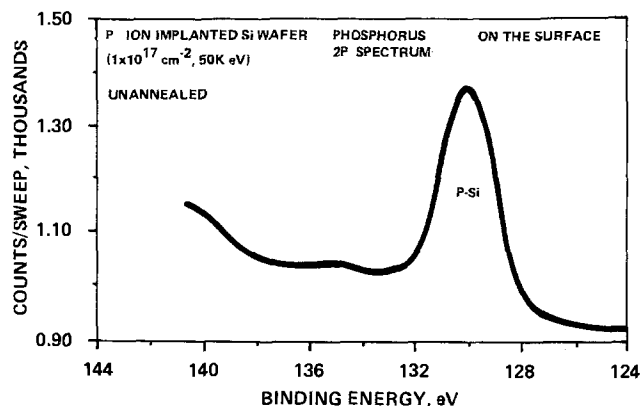


Fig. 2. The ESCA spectrum of the phosphorus ion-implanted Si wafer on the surface (unannealed) which shows the reference state corresponding to the P-Si bond at 130 eV.

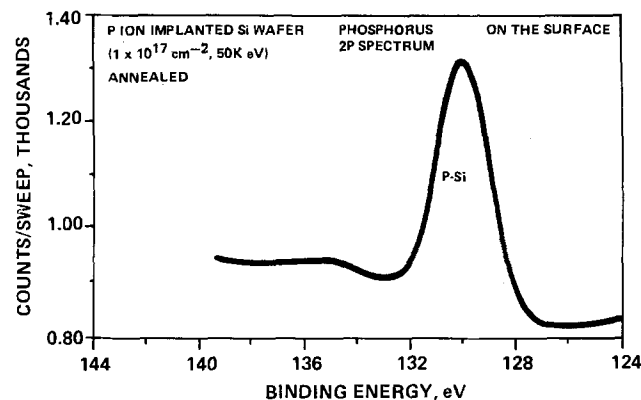


Fig. 3. The ESCA spectrum of the phosphorus ion-implanted Si wafer on the surface (annealed). Please note that the peak is slightly sharper than that for the unannealed sample in Fig. 2.

to defect states which, while still representing P-Si bonds, have a broader energy distribution. Both the unannealed and annealed samples were sputter etched to reach the peak concentration of implanted phosphorus in bulk Si. The ESCA data on these samples were identical to those in Fig. 2 and 3.

CVD SiO₂ (PVX) films.—ESCA data were taken on CVD SiO₂ (PVX) films containing 8 w/o phosphorus. The results show that there is only one phosphorus 2P peak at 134 eV on the surface (see Fig. 4). The samples were sputter etched to remove thicknesses ranging from 400 to 1000Å, and ESCA data were taken on each sample. ESCA spectra on all these samples were the same. A representative spectrum for a sputter-etched sample is shown in Fig. 5. It shows two peaks corresponding to the energies 130 and 134 eV, respectively. These two peaks are due to two different chemical states of phosphorus in the film. The high energy state at 134 eV occupied about 70% and is

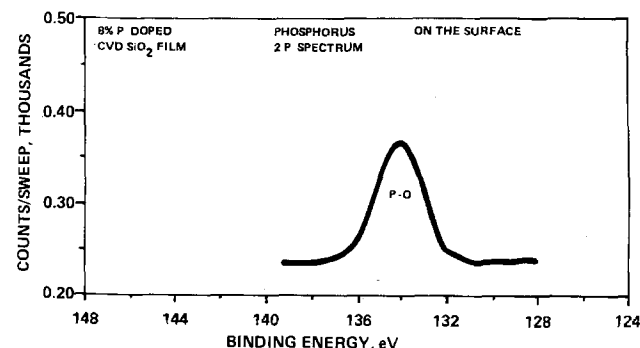


Fig. 4. The ESCA spectrum of the surface of CVD, SiO₂ (PVX) film containing 8% phosphorus which shows that there is only one phosphorus 2P peak corresponding to the P-O bond at 134 eV.

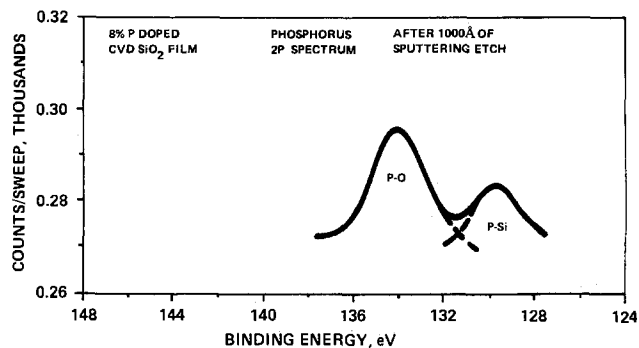


Fig. 5. A representative ESCA spectrum for a sputter-etched CVD SiO_2 (PVX) film containing 8% phosphorus which shows two peaks corresponding to the P-Si bond at 130 eV and P-O bond at 134 eV.

identified as the P-O state, and the low energy state at 130 eV occupied about 30% and is identified as the P-Si state.

The population of the P-O and P-Si states, *viz.*, 70% and 30%, respectively, in the above sputter-etched samples remained unchanged irrespective of the sputter etching condition (such as sputtering rate and time) needed to etch various thicknesses of the PVX. This suggests that the two states, P-O and P-Si, observed within the film as opposed to only one state, P-O, observed on the surface are not artifacts of the sputtering. To confirm further that sputter etching was not responsible for the creation of the P-Si state within the PVX film, chemical etching with buffered HF was used to remove 400 Å of PVX. ESCA measurements made on such a chemically etched film gave data similar to those shown in Fig. 5.

It should be noted that the peak widths of the P-O and P-Si states observed in the PVX film are slightly larger than those observed in the reference spectra shown in Fig. 1 (P-O state) and 3 (P-Si state). It is clear that a well-defined P-O state exists in the standard sample of P_2O_5 , and the P-Si state exists in the phosphorus-implanted Si sample. However, these two states are not so sharply defined in the PVX as in each of the standard samples. Instead, both the P-O and P-Si states exist simultaneously in the PVX film. It is expected that the energy distributions of the P-O and P-Si states in the PVX film are broader than those in each of the standard samples having only one state. This leads us to believe that the P-O and P-Si bonds in the PVX films are somewhat distorted and nonideal as compared to those in the reference samples.

As discussed earlier (1), the P-O state is defined to be "substitutional" corresponding to the phosphorus atom substituting for Si in the SiO_4 tetrahedron, and the formation of P_2O_5 -like agglomerates (6). The P-Si state is

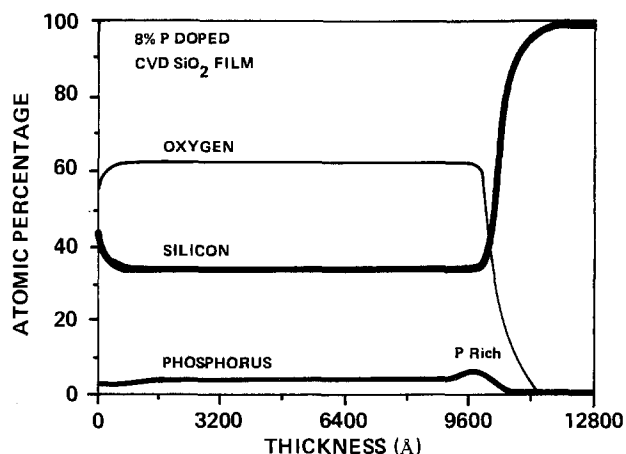


Fig. 6. The Auger depth profile of a CVD SiO_2 (PVX) film containing 8% phosphorus by weight (or 5.3% by atomic percentage) which shows that the phosphorus concentration is uniform throughout the film except at the SiO_2 -Si interface.

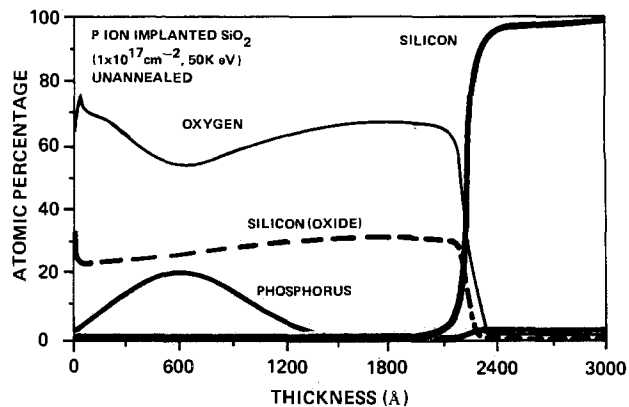


Fig. 7. The Auger depth profile of a phosphorus ion-implanted thermal SiO_2 film which shows that phosphorus has a peak concentration at about 600 Å depth.

defined to be "interstitial" corresponding to the phosphorus atom replacing oxygen atom in and interposed between the SiO_4 tetrahedra.

Auger electron spectroscopy was used along with *in situ* sputter etching to study the distribution of phosphorus in the CVD SiO_2 (PVX) films. The data are shown in Fig. 6. It can be observed that the phosphorus concentration is uniform throughout the film except at the SiO_2 -Si interface. It is approximately 30% higher at the interface as compared to the bulk of the film. Similar observations have been reported earlier (7-9). The phosphorus pile-up at the interface depends on the Si surface and deposition conditions.

Ion-implanted thermal SiO_2 films.—Unannealed.—Figure 7 shows the Auger depth profile of an unannealed phosphorus ion-implanted thermal SiO_2 film. The result indicates that phosphorus has a peak concentration at about 600 Å depth. ESCA data taken on the surface of this unannealed sample show only one state of phosphorus corresponding to P-O bond similar to that in Fig. 4. Figure 8 shows the ESCA phosphorus 2P peaks for the same unannealed phosphorus ion-implanted thermal SiO_2 film after sputter etching 600 Å. The data again show that there are two chemical states of phosphorus present in the film as in the CVD SiO_2 films. However, the P-O state occupies only 15%, and the P-Si state occupies 85%. This kind of population inversion in the unannealed sample suggests that the Si-O bonds are broken by the phosphorus implantation in thermal SiO_2 ; however, P-Si bonds are more predominant than the P-O bonds. To ensure that the Xe^+ ion beam sputter etching has no perturbation on the population of the chemical states, samples were etched by a wet chemical method such as HF etching. The data show similar results for both sputter- and chemically etched samples (see Fig. 9).

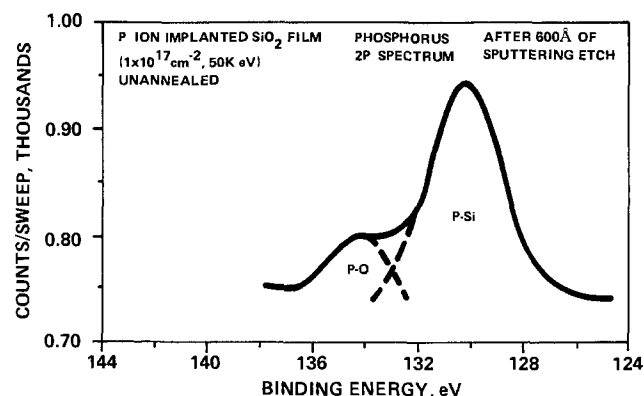


Fig. 8. The ESCA phosphorus 2P peaks for a phosphorus ion-implanted thermal SiO_2 film after sputter etching 600 Å, which shows that there are two chemical states of phosphorus present in the film.

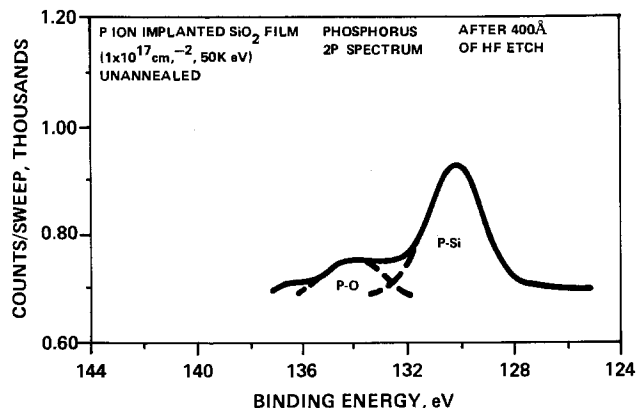


Fig. 9. The ESCA phosphorus 2P peaks for a phosphorus ion-implanted thermal SiO₂ film after 400Å of HF etch, which shows that there are two chemical states of phosphorus present in the film.

Annealing effects.—Figure 10 shows the Auger depth profile of a similar phosphorus ion-implanted thermal SiO₂ film as that used in the previous section, after annealing at 1100°C for 30 min in N₂. A comparison of Fig. 7 and 10 indicates that significant amounts (approximately 50%) of phosphorus are lost after annealing. It has been suggested by the previous study that phosphorus (probably pentoxide) is lost to the gas phase from the porous glass structure due to evaporation (10). Phosphorus leaching combined with moisture exposure is a main contributor to aluminum line corrosion (11, 12). The amount of phosphorus loss depends on annealing conditions such as annealing temperature, time, and environment. The blister formation of isolated P₂O₅ region observed under certain annealing conditions and phosphorus concentrations is important for multilevel metallizations (4). Such regions are apt to contribute to loss of yield in VLSIC's if precautions are not taken to avoid such formations. A more detailed study on the effect of annealing on the blister formation of P₂O₅ in SiO₂ will be published later (6).

Figures 11a and 11b show SEM micrographs of the ion-implanted SiO₂ film before and after annealing at 1100°C for 30 min in N₂. The results clearly show that blisters have been formed on the surface after annealing. We believe that this is due to phosphorus aggregates near the surface. The phosphorus in these aggregates exists as phosphorus oxides (probably P₂O₅) as confirmed by the ESCA studies shown later.

Figures 12 and 13 show the phosphorus 2P peak of the annealed (at 1100°C in N₂ for 30 min) ion-implanted SiO₂ film before and after sputtering. The results indicate that there is only one P-O state on the surface similar to that for unannealed implanted and CVD PVX samples. However, after 600Å of sputter etching, the P-O state occupied 68% and the P-Si state occupied 32%. The population of

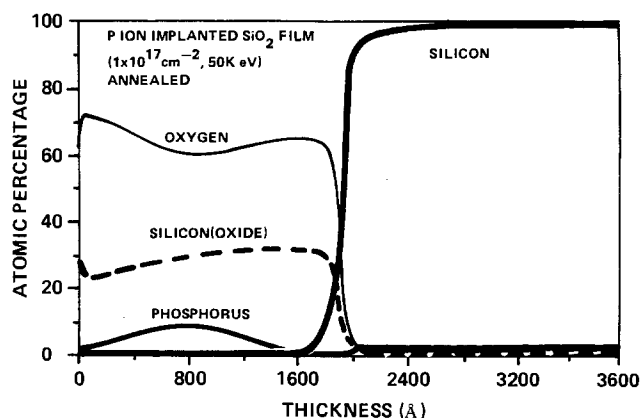


Fig. 10. The Auger depth profile of a phosphorus ion-implanted thermal SiO₂ film after annealing at 1100°C in N₂ for 30 min, which shows that about 50% of phosphorus is lost after annealing.

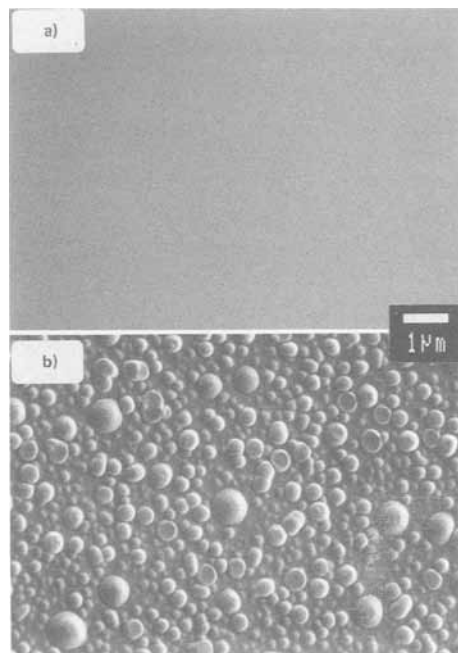


Fig. 11. SEM micrographs of the ion implanted SiO₂ film before (a) and after (b) annealing at 1100°C for 30 min in N₂.

the P-O state and P-Si state for samples annealed under different conditions was determined by ESCA measurements and summarized in Tables I and II.

Table I shows the population of the P-O and P-Si state of the ion-implanted samples annealed under dry N₂ for

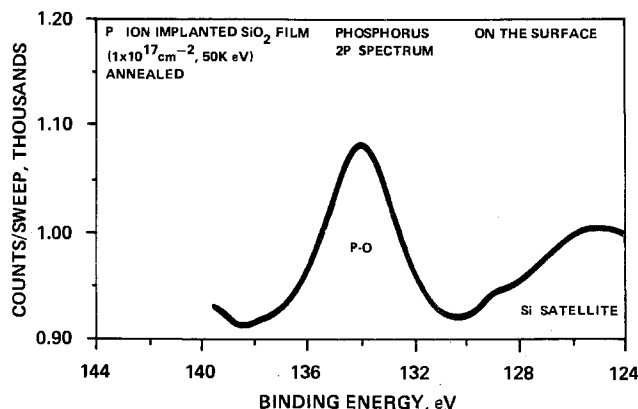


Fig. 12. The ESCA phosphorus 2P peak of the annealed (at 1100°C in N₂ for 30 min) ion-implanted SiO₂ film before sputtering, which shows that there is only one P-O state on the surface.

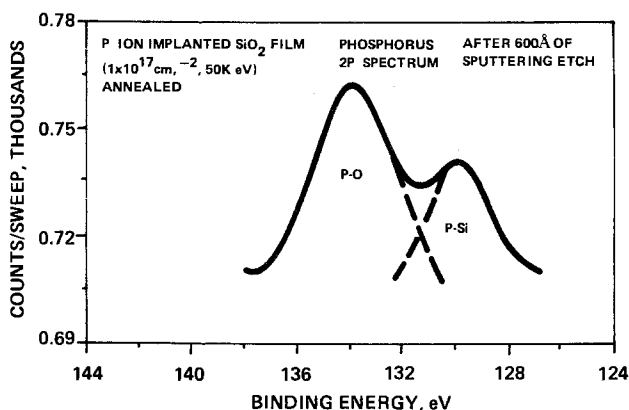


Fig. 13. The ESCA phosphorus 2P peak of the annealed (at 1100°C in N₂ for 30 min) ion-implanted SiO₂ film after sputter etching 600Å, which shows that there are two chemical states of phosphorus present in the film.

Table I. The population of the P-O and P-Si states of the phosphorus ion-implanted samples annealed under dry N₂ for 30 min at different temperatures

	P-Si state (%)	P-O state (%)
(1) As implanted	85	15
(2) 700°C	80	20
(3) 900°C	75	25
(4) 1000°C	69	31
(5) 1100°C	32	68

Table II. The population of the P-O and P-Si states of the phosphorus ion-implanted samples annealed under O₂ at 950°C for different lengths of time

	P-Si state (%)	P-O state (%)
(1) As implanted	85	15
(2) 10 min	27	73
(3) 30 min	21	79
(4) 100 min	20	80

30 min at different temperatures. The results clearly show that the sample annealed at higher temperature has more population of P-O state as compared to that annealed at lower temperature. It is interesting to note that a drastic change occurred between 1000° and 1100°C, *i.e.*, P-O state became more dominant than P-Si state, which corresponds to the reflow temperature for phosphosilicate glass (about 1050°C). It is the authors' opinion that the reflow of the phosphosilicate glass depends more on P-O state than P-Si state. Further work is underway to correlate the reflow temperatures and chemical states (5).

Table II shows the population of the P-O and P-Si state of the ion-implanted samples annealed at 950°C under O₂ for different lengths of time. The results indicate that most of the changes occurred in the first 10 min. A comparison between Tables I and II suggest that one can obtain more P-O state at lower temperature and shorter annealing time in O₂ environment. This is probably the reason why the phosphosilicate glass can be reflowed at lower temperature in oxygen or steam ambients as compared to the inert gas ambient reported previously (12, 13).

Summary

In summary, we have observed P-O and P-Si states in phosphosilicate glasses. The populations of these two

states depend upon the deposition and annealing conditions. The P-O state is observed on the surfaces of both CVD and ion-implanted SiO₂ films having phosphorus. As these films are sputter or chemically etched, both P-O and P-Si states are observed. In the CVD SiO₂ (P) film, the P-O state dominates over the P-Si state. In the P ion-implanted SiO₂ samples, the P-Si state dominates over P-O state in the unannealed samples. However, depending on the annealing conditions, the P ion-implanted samples show the conversion of the P-Si state to P-O state. It is anticipated that the reflow, stress, and etch properties of SiO₂(P) film depend on the relative population of the P-O and P-Si states. Further work to establish such a correlation is in progress.

Acknowledgments

Thanks are due to Mike Serpa and Fred Greg for their assistance in preparing samples for this study. In addition, we thank Brian Burrows and Alan Swanson for their encouragement.

Manuscript submitted Sept. 14, 1984; revised manuscript received Dec. 27, 1984. This was Paper 226 presented at the Washington, DC, Meeting of the Society, Oct. 9-14, 1983.

Gould Research Center assisted in meeting the publication costs of this article.

REFERENCES

1. A. N. Saxena and R. A. Powell, in "The Physics of SiO₂ and Its Interfaces," S. T. Pantelides, Editor, p 195, Pergamon Press, New York (1978).
2. K. Hoh, M. Saitoh, and Y. Miura, *This Journal*, **128**, 1613 (1981).
3. S. Iwamatsu and Y. Tarni, *ibid.*, **126**, 1387 (1979).
4. A. N. Saxena, in "Proceedings of First International IEEE VLSI Multilevel Interconnection Conference," pp. 1-21, IEEE, New York (1984).
5. K. S. Kim, W. E. Baitinger, and N. Winograd, *Surf. Sci.*, **55**, 285 (1976).
6. O. K. Wu and A. N. Saxena, To be published.
7. J. S. Johannessen, W. E. Spicer, J. F. Gibbons, J. D. Plummer, and N. J. Taylor, *J. Appl. Phys.*, **49**, 4453 (1978).
8. C. C. Chang, A. C. Adams, G. Quintana, and T. T. Sheng, *ibid.*, **45**, 252 (1974).
9. S. A. Schwarz, C. R. Helms, W. E. Spicer, and N. J. Taylor, *J. Vac. Sci. Technol.*, **15**, 227 (1978).
10. R. A. Bowling and G. B. Larrabee, Abstract 91, p. 140, The Electrochemical Society Extended Abstracts, Vol. 83-1, San Francisco, CA, May 8-13, 1983.
11. I. Avigal, *Solid State Technol.*, **26** (10), 217 (1983).
12. W. Kern and G. L. Schnable, *RCA Rev.*, **43**, 423 (1982).
13. W. E. Armstrong and D. L. Tolliver, *This Journal*, **121**, 307 (1974).

Submicron Silicon Epitaxial Films Deposited at Low Temperatures

C. J. Atkinson,* G. L. Wright, S. J. White, and J. D. Greenwood

GEC Research Laboratories, Hirst Research Centre, Wembley, England HA9 7PP

ABSTRACT

Submicron silicon epitaxial films have been deposited at low temperatures using only wet chemical cleans for the substrate surface preparation. The layers have been assessed by crystallographic (RHEED) techniques coupled with the electrical measurement of Schottky barrier diodes and transistors fabricated in the layers. In addition, XPS studies of the substrate surface prior to the deposition are also reported. Good quality epitaxial films have been produced at deposition temperatures of 900°C and below.

Low temperature growth of epitaxial films is of great interest to the development of many silicon technologies. Low temperature processing minimizes the diffusion of dopant atoms, whilst low temperature epitaxial growth also reduces gas phase autodoping effects. Researchers

*Electrochemical Society Active Member.

reporting direct low temperature epitaxial growth have all used an *in situ* clean prior to epitaxial growth. Typical *in situ* cleaning techniques used include heating (1), etching at high temperatures in hydrogen chloride (2), or sputter cleaning (3). The pre-epitaxial cleaning process removes native oxide which would prevent epitaxial

growth and removes some defects and surface contamination which would impair device performance. High temperature cleaning treatments reduce the advantages of lower temperature processing by increasing both the dopant diffusion and autodoping effects. *In situ* sputter cleaning requires additional expensive equipment. In this paper, a technique is described which enables device quality epitaxial films to be grown at temperatures of 900°C or lower using only wet chemical cleaning prior to loading the wafers into the reactor.

Experimental

All growth experiments were carried out in a vertically configured, RF-heated, atmospheric pressure reactor using silane in hydrogen as the deposition source. All temperature readings are derived from the in-built optical pyrometer on the reactor. Attempts to calibrate that instrument have indicated that the true substrate temperature within the reactor is somewhat lower than those readings would indicate. Substrates used were p- or n-type 100 silicon. Both float zone and Czochralski substrates were used. X-ray photoelectron spectroscopy was used to evaluate the efficiency of predeposition cleaning schedules. This method measured the thickness of native oxide present on the surface of the wafers by relating the area of the silicon peak to that of the silicon dioxide peak using the formula of Seah and Dench (4). The thickness of the deposited films was determined by including sapphire or oxidized test wafers with each growth run. Optical interferometry (or in some cases surface profilometry) was used to measure the thickness of silicon on the test wafers. Resistivity was monitored using silicon test wafers and spreading resistance measurements.

Crystal quality was largely evaluated using reflection high energy electron diffraction (RHEED). RHEED allows the observation of the top surface of the film (~50-100Å) and so gives information about crystal orientation and quality at the surface. Electrical characteristics of the films were investigated by fabricating Schottky barrier diodes (with titanium metallization) and simple structure bipolar transistors.

Results and Discussion

The effects of predeposition cleaning schedules on the thickness of native oxide grown is summarized in Table I. Immediately after a dilute hydrofluoric acid clean and brief rinse, no oxide could be detected on the surface of the wafers using XPS. Accordingly, a dilute hydrofluoric acid clean followed by a brief rinse in deionized water was used immediately prior to each epitaxial growth ex-

Table I. Thickness of native oxide on 100 silicon substrates calculated by XPS measurements

Pretreatment	Oxide thickness (Å)
Native (no preclean)	10-20
HF followed by 1:1 H ₂ SO ₄ :H ₂ O ₂	8
Dil. HF followed by 1 min DI rinse	No oxide detectable

Table II. RHEED assessment of epilayer crystallinity

Growth temperature (°C)	Layer crystallinity type
770	A
790	A
810	B
830	B
850	B
870	C
890	C
910	C
930	C
950	C

Key: A — Polycrystalline pattern and single-crystal pattern. B — No polycrystalline pattern. Single-crystal pattern with some Kikuchi lines. C — Kikuchi line pattern.

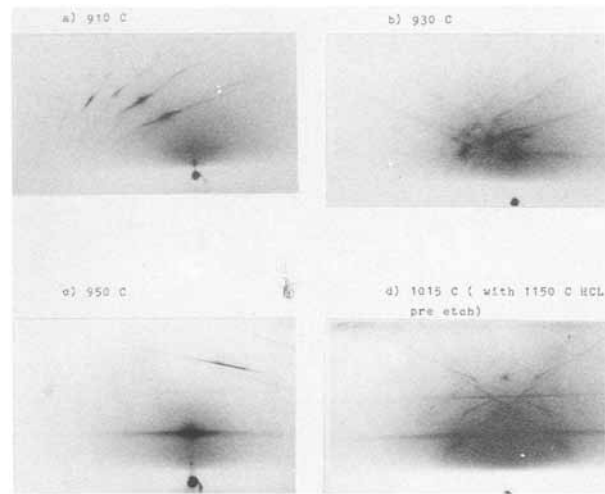


Fig. 1. RHEED photographs of epitaxial silicon grown in the epitaxy reactor.

periment. Following the cleaning procedure, the wafers were loaded quickly into the reactor and the system purged with dry nitrogen. (The actual cleaning schedule used is summarized in the Appendix). RHEED photographs of samples grown at temperatures between 770° and 950°C indicate that it is possible to grow high quality epitaxial films directly (*i.e.*, without the use of the high temperature hydrogen chloride etch) at temperatures as low as 830°C. The RHEED results are summarized in Table II, whilst Fig. 1 shows typical RHEED photographs for epitaxial films grown without an *in situ* clean at temperatures of 910°, 930°, and 950°C. A RHEED photograph of a film grown at 1015°C with an *in situ* hydrogen chloride etch at 1150°C prior to epitaxial growth is also shown for comparison. If the hydrofluoric acid clean was omitted, only polycrystalline growth was obtained, as the native oxide was sufficiently thick to mask the crystal structure of the underlying substrate. If a high temperature etch at 1150°C in hydrogen chloride was incorporated, some evidence of epitaxial growth was obtained at growth temperatures as low as 650°C, although some polycrystalline silicon was also noticeable. It is postulated that for epitaxial growth to occur, not only must the interface be largely free of contamination, but the temperature must be sufficiently high to allow some migration of the deposited atoms to lattice sites.

Schottky barrier diodes were fabricated on the epitaxial layers to obtain information about electric and crystal quality of the material. To a good approximation, the forward characteristics of Schottky barrier diodes are given by

$$I = I_0 \exp(qV/nkT)$$

where I is the forward current, V is the forward bias voltage, I_0 is the saturation current obtained by extrapolating the I vs. V plot to $V = 0$, T is the temperature, q is the charge on the electron, and n is the diode ideality factor. When $n \approx 1$, crystal quality is good and recombination in the space charge layer is small. When n approaches 2, space charge recombination is occurring, which implies

Table III. Ideality factors for diodes fabricated at various growth temperatures

Growth temperature (°C)	Ideality factor
950	1.04
930	1.05
910	1.05
890	1.1
870	1.09
850	1.11
830	1.2

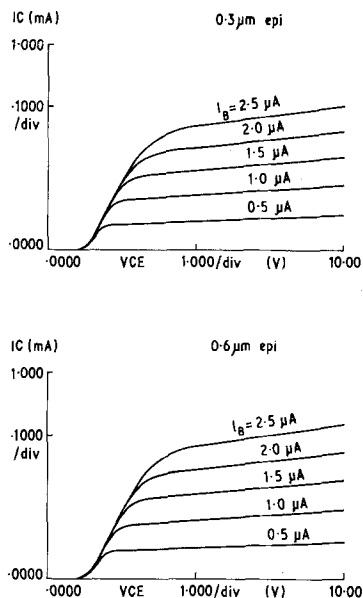


Fig. 2. Typical V_{cc} vs. I_c curves for the 0.3 and 0.6 μm films.

that crystal quality is poor. The results for test diodes fabricated in epitaxy grown directly at temperatures ranging between 830° and 950°C are summarized in Table III. The diode ideality factors tend to increase as the deposition temperature is lowered, confirming that crystal quality deteriorates as the growth temperature is decreased.

Simple bipolar transistors were fabricated in epitaxial films of thickness 0.3 and 0.6 μm grown at 900°C. For the device structure used, the collector-base junction is 0.3 μm deep, so the transistor gain is highly dependent on interfacial crystal quality. For both thicknesses of film, the transistor gain was in excess of 200, implying good elec-

trical quality. Figure 2 shows typical V_{cc} vs. I_c curves for the 0.3 and 0.6 μm films.

Conclusions

It has been shown that device quality epitaxial growth can be brought about without using *in situ* predeposition cleaning schedules. The simple cleaning technique described could produce a considerable improvement in device fabrication technologies, for example, for bipolar transistors, IMPATT diodes, and Schottky barrier diodes.

Acknowledgments

Part of this work has been carried out with the support of the Procurement Executive, Ministry of Defense, sponsored by DCVD. Our thanks are also due to Mr. I. Scobey for the RHEED measurements, Dr. P. Harris for the XPS work, and Mr. P. Burton for useful discussions.

Manuscript received Oct. 19, 1984.

APPENDIX

Cleaning Schedule Used Prior to Low Temperature Epitaxial Growth Experiments

2:1 $\text{H}_2\text{SO}_4:\text{H}_2\text{O}_2$ 120°C 5 min
 Rinse 5 min
 5:2:1 $\text{H}_2\text{O}:\text{H}_2\text{O}_2:\text{HCl}$ 85°C 10 min
 Rinse 5 min
 Rinse 30 min in recirculating water
 19:1 $\text{H}_2\text{O}:\text{HF}$ 20s
 Rinse 4 min
 Spin dry

REFERENCES

1. J. H. McFee, R. G. Schwartz, V. D. Archer, and S. N. Finnegan, *This Journal*, **130**, 214 (1983).
2. D. Richman and R. H. Arlett, *ibid.*, **116**, 872 (1969).
3. T. J. Donahue, W. R. Burger, and R. Reif, *Appl. Phys. Lett.*, **44**, 346 (1984).
4. M. P. Seah and N. A. Dench, *Surf. Interf. Anal.*, **1**, (1979).

Reduction of Radiation Damage on Silicon Substrates in Magnetron Reactive Ion Etching

Kado Hirobe and Hideaki Azuma

Hitachi Limited, Musashi Works, 1450, Josuihon-cho, Kodaira-shi, Tokyo 187, Japan

ABSTRACT

Radiation damage on silicon substrates has been reduced by decreasing the cathode dc bias in reactive ion etching (RIE). A magnetic field has been applied in the direction perpendicular to RF electric field between the parallel-plate electrodes to decrease the dc bias across the cathode dark space. Silicon substrates treated under RIE in CHF_3 and SF_6 mixed gas have been investigated by reflection high energy electron diffraction observation and lifetime measurement of the minority carrier. Low dc bias less than about 150V was found to be necessary for obtaining low damaged silicon surface.

Reactive ion etching (RIE) has been widely used to delineate fine patterns in silicon oxide films in fabrication of VLSI circuits. It is known, however, that bombardment of ions which are accelerated by the dc bias across the plasma sheath region degrades the crystal structure of the silicon substrate (1-4). Decrease in lifetime of the minority carrier (5), increase in the contact resistance between silicon substrate and metal film (6), low breakdown voltage of the oxide grown on RIE-treated silicon surface (7) are considered to be partly due to defects in the silicon crystal induced by bombardment of energetic ions. An effective method to reduce this kind of radiation damage induced by RIE is to decrease the energy of ions impinging on the silicon surface. In a conventional parallel-plate type of RIE apparatus, the decrease of RF power density, and/or the increase of operating pressure

of etch gas must be accomplished in order to reduce the cathode dc bias. Under these conditions, however, undesirable phenomena such as decrease in etch rate of silicon oxide and deposition of organic polymer films often arise. Furthermore, as the etch rate is decreased, and, consequently, as the throughput of etching apparatus is also decreased, the RIE cannot be economically operated at a low RF power density and at a high pressure.

Recently, RIE with magnetron discharge has been investigated for etching silicon oxide films at a low dc bias (8-10). Magnets are set behind the cathode to form a magnetic field perpendicular to the dc electric field over the cathode surface. These systems are called Band Magnetron (9) and planar Magnetron-HIRRIE (8). The magnetron discharge can generate highly dense radicals and ions. In the magnetron discharge system, the SiO_2 etch

rate of 500-1000 nm/min can be obtained, even if the dc bias is fairly low around 50-300V.

In the present paper, a relation between the silicon surface damage induced by RIE and the dc bias voltage across the plasma sheath is reported. Variation in dc bias voltage has been carried out using a discharge system in which a static magnetic field is applied perpendicular to the RF electric field to generate highly dense chemical species in the plasma. Radiation-induced defects on RIE-treated silicon surface have been investigated with reflection high energy electron diffraction (RHEED) and lifetime measurement of the minority carrier.

Experimental

The RIE apparatus used in this work is shown schematically in Fig. 1. Two parallel-plate electrodes of 130 mm diam are set in a cylindrical reactor made of aluminum. A sample was put on a silicon plate 1 mm thick placed on the cathode. An RF power supply at a frequency of 13.56 MHz was capacitively coupled to the cathode through a matching network. A permanent magnet system was placed in the reactor to apply a static magnetic field perpendicular to the RF electric field between the electrodes. Two magnet systems of the same external shape were used in this work. Their external shape was cylindrical, as shown in Fig. 2. The inside and outside diameters of the magnet system were about 180 and 240 mm, respectively. The height of the magnet system was 50 mm. A magnet system consists of two half-cylindrical magnets and two pole pieces made of soft steel. Their magnetic field strengths in the direction parallel to the magnetic field B were 200 ± 15 and 400 ± 50 G, over the range of 76 mm diam.

An optical emission spectrometer was attached to the reactor. The spectrometer was able to measure the light intensities of spectra emitted from any 4 mm thick layer in the discharge between the electrodes. Applying the optical system to SiO_2 RIE, light intensities of 321 nm emitted from CF_2 radical (11, 12) and of 520 nm from CO radical (13) were measured. A distribution of light intensity between the two electrodes can give a spatial distribution of relative concentration of these radicals.

A mixed gas of 99% CHF_3 and 1% SF_6 was used as an etch gas (14). The etch gas was introduced into the reactor through a hole in the top plate of the reactor and exhausted from a hole in the bottom reactor plate. No polymer deposition on silicon oxide films was detected under the conditions investigated in the work.

The silicon substrates used in this study were (100)-oriented, boron-doped single crystals of about $10 \Omega \cdot \text{cm}$ resistivity. Silicon oxide films were prepared by oxidizing the substrates at 1000°C , in dry O_2 ambient.

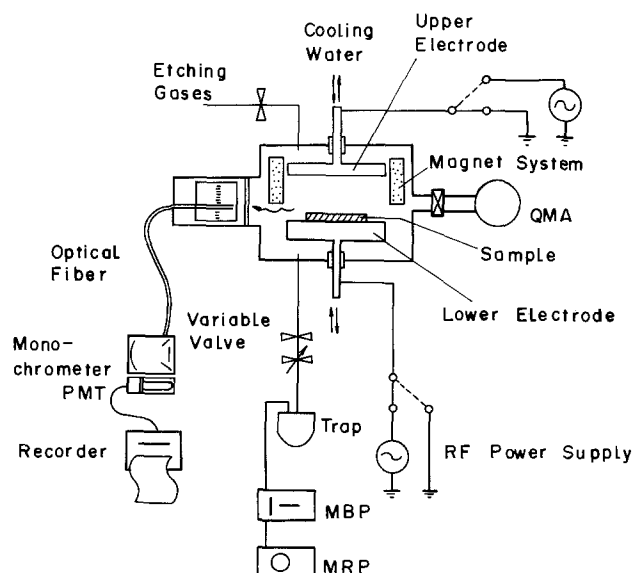


Fig. 1. Schematic drawing of experimental RIE apparatus

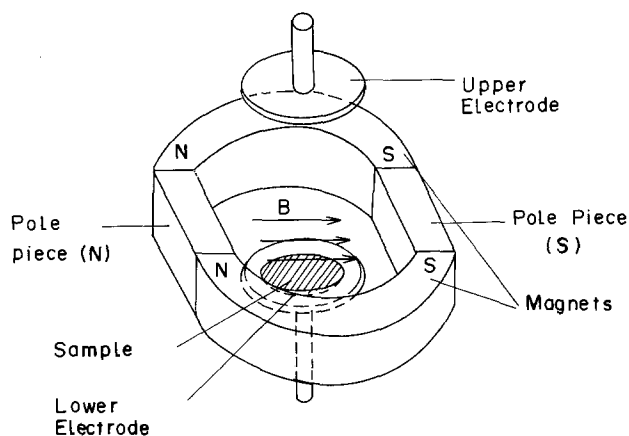


Fig. 2. Schematic drawing of permanent magnet configuration

An experimental procedure for investigating RIE-induced defects on a silicon surface was as follows: first, silicon wafers were treated under different RIE conditions, as summarized in Table I, then the silicon wafers were exposed to O_2 plasma (at 100W and 1 torr, for 10 min) to remove a trace of carbon compounds. After that, the samples were immersed into an aqueous HF solution to remove a thin silicon oxide film on the silicon surface. To investigate crystalline properties of the RIE exposed silicon surface, images of RHEED were taken. In addition, these silicon wafers were oxidized at 1000°C , in dry O_2 ambient, for 10 min to stabilize the silicon surface. After oxidation, the samples were submitted for lifetime measurement of minority carrier. An optical lifetime measurement technique was used. The measurement technique itself is published elsewhere (15). In the measurement system equipped in this study, a laser light of 904 nm wavelength used to generate hole-electron pairs in the silicon substrate can penetrate 20-30 μm deep into the silicon crystal (16). A frequency of microwave for measuring conductivity of electrons was 9.6 GHz, at which the microwave can be assumed to penetrate the silicon substrate about 500 μm deep, and so we could measure the lifetime of electrons in the region where RIE-induced defects locate.

Experimental Results and Discussion

Realization of low dc bias in magnetron RIE.—Figure 3 shows relationship between dc bias voltage across the cathode dark space and RF power density as a function of the magnetic field strength applied to the discharge. The dc bias voltage $|V_{dc}|$ was found to increase with increasing RF power density. When the magnetic field was applied perpendicular to the electric field, $|V_{dc}|$ decreased with increasing the strength of magnetic field. For example, $|V_{dc}|$ was 860V at 13 Pa (0.1 torr) and 1.5 W/cm^2 without a magnetic field. However, when the magnetic field strengths were 200 and 400G, $|V_{dc}|$ values were 340 and 120V, respectively.

Enhanced plasma discharge in the electromagnetic field, for example, in SiO_2 RIE, was indicated by in-

Table I. Summary of the RIE treatment conditions

NO.	Pressure (Torr)	Power Density (W/cm^2)	Magnetic Field (Gauss)	$ V_{dc} $ (V)	Etch Time (Second)
1	0.1	3	0	1170	50
2	0.1	1.5	0	860	83
3	0.5	1.5	0	460	300
4	0.1	1.5	200	340	60
5	0.1	0.5	200	160	300
6	0.5	3	400	150	30
7	0.5	1.5	400	80	112
8	0.1	0.5	400	60	200

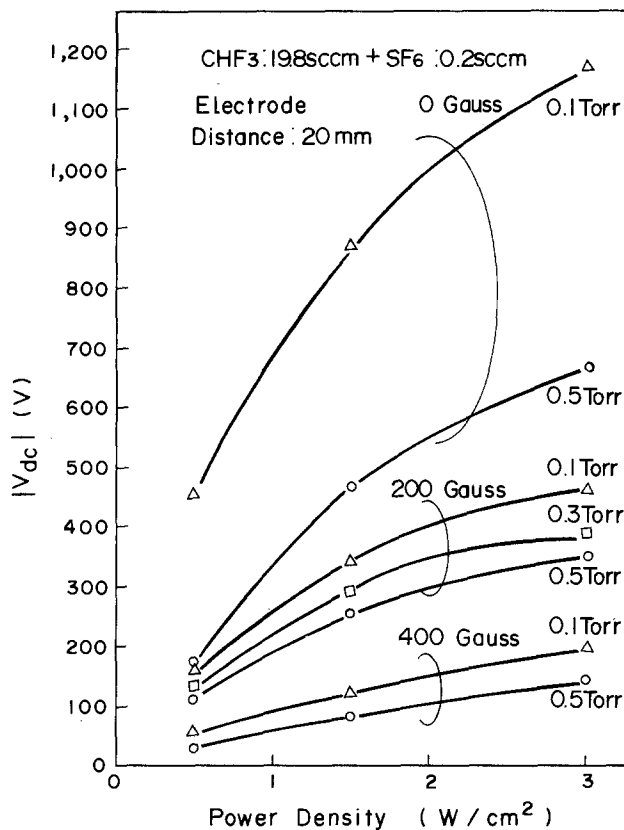


Fig. 3. Cathode dc bias $|V_{dc}|$ as a function of power density, for different pressures and magnetic field strengths.

creased emission intensities and increased SiO_2 etch rate. Figure 4 shows distributions of the emission intensity emitted from plasma discharge between two electrodes. A wavelength 321 nm is from an etchant CF_2 (Fig. 4a) and

520 nm from an etch product CO radical (Fig. 4b). In the figure, the intensity of light from CF_2 was found to be about two times stronger with a magnetic field of 400G than that without a magnetic field. In the observation of 520 nm light from CO, the light intensity was also found to be stronger with a magnetic field than that without a magnetic field. These results indicate that the application of magnetic field to the RF electric field enhances an efficiency of discharge and consequently increases a concentration of etchant radicals such as CF_2 .

In addition, the stronger light intensity of a reaction product CO suggests increased etch rate of SiO_2 in the magnetron RIE. In fact, unlike conventional RIE, high etch rates have been obtained in low $|V_{dc}|$ values by applying the magnetic field of 200 and 400G. Figure 5 shows SiO_2 etch rate as a function of $|V_{dc}|$ value and applied magnetic field strength. As shown in the figure, higher etch rates were obtained at lower $|V_{dc}|$ values by increasing the magnetic field. For example, the etch rate of SiO_2 was improved from 40 nm/min without a magnetic field to 600 nm/min with the magnetic field of 400G at 3 W/cm^2 of power density. From these results, the magnetron RIE was found to etch SiO_2 at high etch rates even with a low $|V_{dc}|$ value.

Observation of damaged silicon surface by RHEED.—Figure 6 shows RHEED patterns of the silicon surface treated under the RIE conditions summarized in Table I. In the RHEED experiment, the electron acceleration voltage was 75 kV and the incident angle of electron onto the silicon surface was about 4° . As shown in Fig. 6a, when $|V_{dc}|$ was very high such as 1170V, RHEED pattern was halo, indicating that the silicon surface is amorphous. As $|V_{dc}|$ became lower, Bragg spot patterns became stronger (Fig. 6b and 6c), and single crystalline Kikuchi line patterns were observed. At $|V_{dc}|$ of 150V, almost the same pattern as that of a control sample was observed. Polycrystalline silicon ring pattern was not observed in this study.

Deterioration in the crystal structure of the silicon surface treated under high $|V_{dc}|$ RIE is due to bombardment

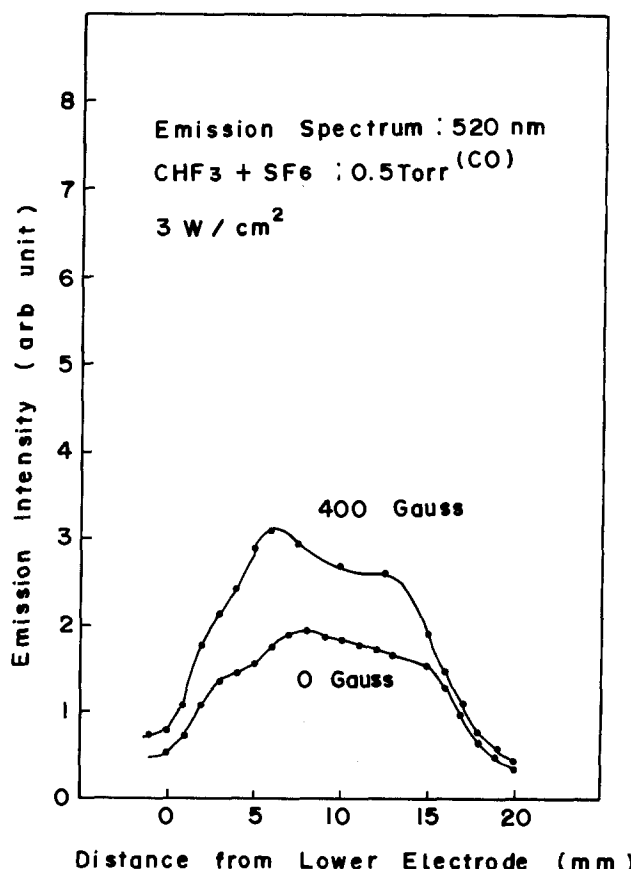
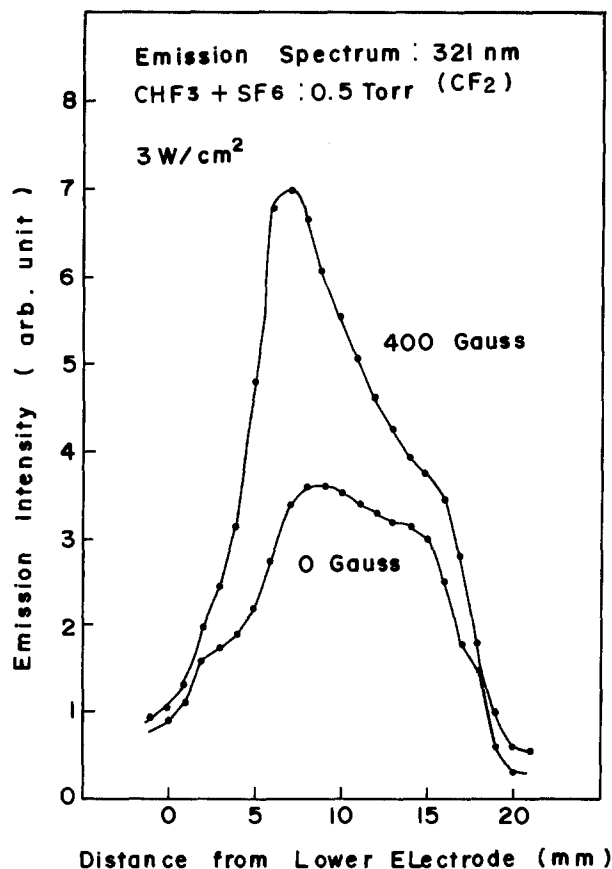


Fig. 4. Distribution of emission intensity between two parallel-plate electrodes. (a): For 321 nm from CF_2 radical; and (b) for 520 nm from CO radical.

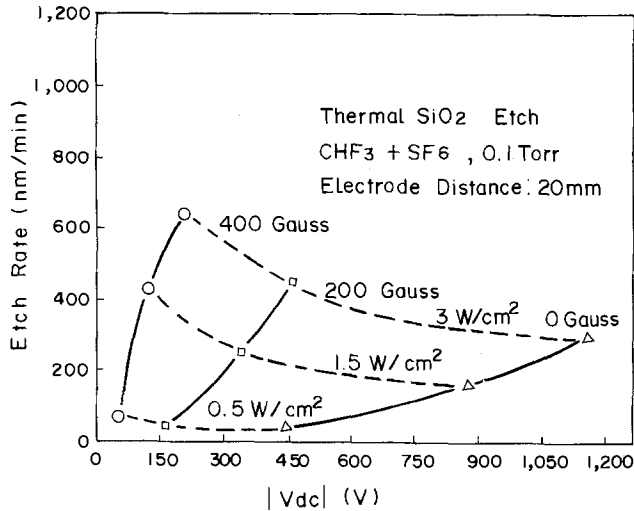


Fig. 5. Etch rate as a function of cathode dc bias $|V_{dc}|$, for different magnetic field strengths and power densities.

of energetic ions. It is considered that the kinetic energy of ions impinging onto a silicon surface is at maxima about a bias voltage $|V_{dc}|$ (17). Consequently, ions with a high kinetic energy such as 1170V disorder the crystalline structure of the surface, while ions with low energy such as 150V do not seriously deteriorate the crystal structure.

To investigate the depth of damaged surface layer at a typical $|V_{dc}|$ value of 340V in SiO₂ RIE, silicon samples were etched by 40, 80, and 120 nm with a HNO₃ and HF mixed etchant. RHEED patterns of the 40 nm deep etched sample were weak spot patterns, while single-crystalline silicon spot pattern was observed for the 80 nm deep etched sample. This result showed that the region of damaged layer was as deep as about 40 nm under the RIE condition of 340V of $|V_{dc}|$. In addition, it was

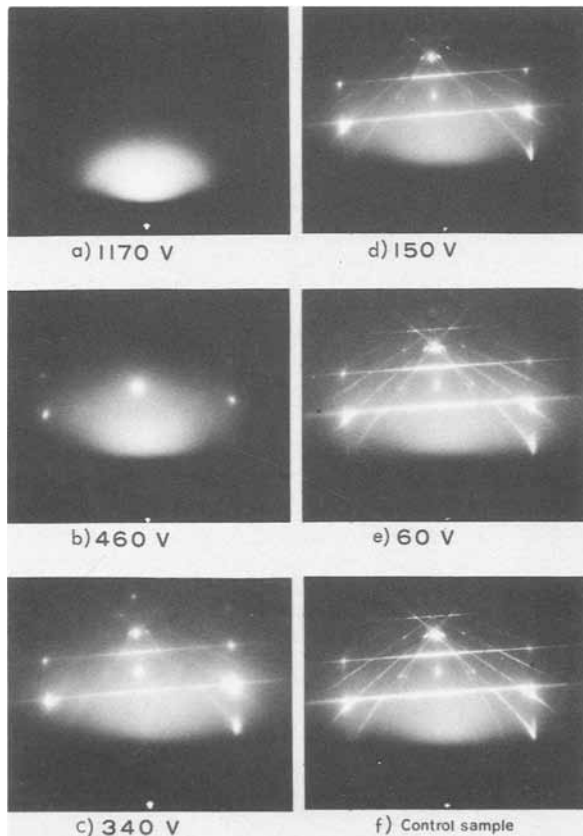


Fig. 6. RHEED patterns of silicon surface treated under RIE, for different cathode dc bias $|V_{dc}|$.

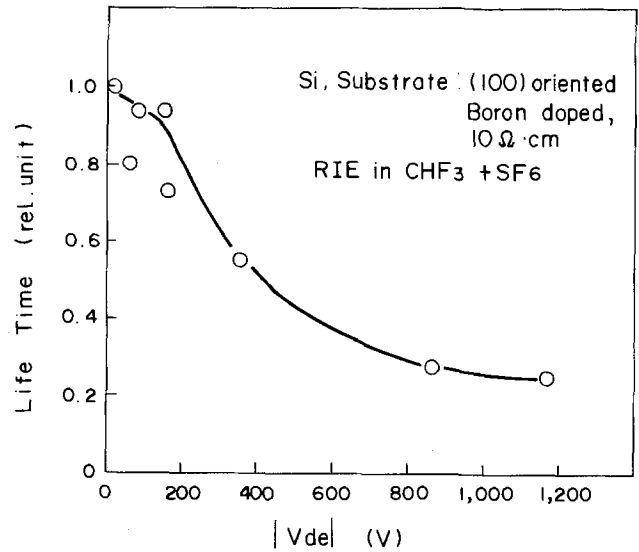


Fig. 7. Lifetime of minority carrier as a function of cathode dc bias $|V_{dc}|$.

found from RHEED patterns that the damaged layer at $|V_{dc}|$ of 340V was annealed out in dry O₂ oxidation ambient, at 1000°C, for 10 min.

From these results, the magnetron RIE which is able to obtain a low $|V_{dc}|$ such as 150V has no serious damage on the silicon surface. This is one of the advantages of the magnetron RIE over the conventional one.

Evaluation of damaged layer by lifetime measurement.—The lifetime of a minority carrier is decreased with increasing defect density in a silicon substrate. Using the phenomenon, crystalline properties of RIE-treated silicon surface were evaluated. Figure 7 shows relationship between lifetime and $|V_{dc}|$ for samples treated under the RIE conditions mentioned in Table I. The value of lifetime on the ordinate was normalized by that of a control sample. It was found that the lifetime of minority carrier (in our case, an electron) was changed from 100% to 70% of the lifetime of the control sample in the range of $|V_{dc}|$ from 0 to 150V. The lifetime was decreased sharply between 150 and 800V and leveled off at higher $|V_{dc}|$ values. In the range of $|V_{dc}|$ below 150V, plasma-exposed silicon surfaces were thought to be almost perfectly crystalline from the low decrease in the lifetime of minority carrier. However, it became clear that in the higher $|V_{dc}|$ values over 800V, RIE-treated silicon surface was not perfectly crystalline, from the low lifetime values. The results of lifetime measurement were in good agreement with RHEED observations.

Conclusions

Radiation damage on silicon substrates induced by RIE has been investigated using RHEED observation and lifetime measurement of minority carrier. RIE-induced defects could be reduced by decreasing the cathode dc bias during RIE. To decrease the dc bias across the cathode dark space, a magnetic field has been applied perpendicular to RF electric field between the parallel plate electrodes. Low dc bias less than 150V was found to be necessary for obtaining low damaged silicon surface. It was found that an advantage of the magnetron RIE over the conventional RIE is to be able to obtain high etch rates at low dc bias voltages.

Acknowledgments

The authors would like to thank Mr. Yoshifumi Kawamoto for his helpful discussion and Mr. Yoshimasa Shimizu for his RHEED observation.

Manuscript submitted July 3, 1984; revised manuscript received Nov. 30, 1984.

Hitachi Limited assisted in meeting the publication costs of this article.

REFERENCES

1. C. M. Eprath and D. J. Dimaria, *Solid State Technol.*, 182 (April 1981).
2. R. S. Frieser, F. J. Montillo, N. B. Zingerman, W. K. Chu, and S. R. Mader, *This Journal*, **130**, 2237 (1983).
3. N. Yabumoto, M. Oshima, O. Michikami, and S. Yoshii, *Jpn. J. Appl. Phys.*, **20**, 893 (1981).
4. H. R. Deppe, B. Hasler, and J. Hopfner, *Solid State Electron.*, **20**, 51 (1977).
5. S. W. Pang, C. M. Horowitz, D. D. Rathman, S. M. Cabral, D. J. Silversmith, and R. W. Mountain, in "Plasma Processing," G. S. Mathad, G. C. Schwartz, and G. Smolinsky, Editors, p. 84, The Electrochemical Society Softbound Proceedings Series, Pennington, NJ (1983).
6. J. S. Chang, Abstract 173, p. 280, The Electrochemical Society Extended Abstracts, Vol. 83-1, San Francisco, CA, May 8-13, 1983.
7. N. Lifshitz, *This Journal*, **130**, 1549 (1983).
8. H. Okano, T. Serikawa, and Y. Horiike, in "Proceedings of the Symposium on Dry Process," Tokyo, Oct. 26-27, 1981.
9. I. Lin, D. Hinson, and W. Class, Abstract 158, p. 254, The Electrochemical Society Extended Abstracts, Vol. 83-1, San Francisco, CA, May 8-13, 1983.
10. T. D. Mantei and T. Wicker, Abstract 156, p. 252, The Electrochemical Society Extended Abstracts, Vol. 83-1, San Francisco, CA, May 8-13, 1983.
11. M. M. Millard and E. Kay, *This Journal*, **129**, 160 (1982).
12. P. Venkateswarly, *Phys. Rev.*, **77**, 676 (1950).
13. "The Identification of Molecular Spectra," 4th ed., R. W. B. Pearse and A. G. Gaydon, Editors, p. 108, Chapman and Hall, London (1976).
14. E. C. Witcomb, Abstract 211, p. 339, The Electrochemical Society Extended Abstracts, Vol. 82-1, Montreal, Que., Canada, May 9-14, 1982.
15. A. Usami, Y. Fujii, and B. Kudo, *Oyo Butsuri*, **47**, 1024 (1978).
16. H. F. Wolf, "Silicon Semiconductor Data," p. 110, Pergamon Press, London (1969).
17. H. R. Koenig and C. I. Maissel, *IBM J. Res. Dev.*, **14**, 168 (1970).

Partial Pressures over the Pseudobinary Solid Solution $\text{Hg}_{1-x}\text{Cd}_x\text{Te(s)}$ for $x = 0.70$ and 0.95 and over Four Te-rich Ternary Melts

Ching-Hua Su, Pok-Kai Liao, and R. F. Brebrick*

Materials Science and Metallurgy Program, College of Engineering, Marquette University, Milwaukee, Wisconsin 53233

ABSTRACT

The partial pressures of Hg, Cd, and Te_2 have been determined between 420° and 840°C from optical absorption measurements for four Te-rich compositions and for the Te-saturated solid solution ($\text{Hg}_{1-x}\text{Cd}_x\text{Te(s)}$) with $x = 0.70$ and 0.95 . In addition to further thermodynamically characterizing the melt, the former measurements yield ternary liquidus points. They also yield tie lines when combined with the present and previous measurements on Te-saturated solid solutions. These results, from an essentially steady-state technique, agree well with those of Harman. The measurements on the solid solutions yield values for the mixing quantities which are more accurate than our previous values. These are described well in terms of a quasi-regular solution of HgTe and CdTe components with an enthalpy of mixing of 1074 cal/g-atom and an excess entropy of mixing of 0.893 cal/K-g-atom at 50 mole percent CdTe.

The partial pressures of Hg, Cd, and Te_2 have already been reported (1, 2) for a number of compositions in the Hg-Cd-Te system. Here we report measurements for additional compositions. These include four Te-rich ternary melts. The liquidus points obtained from the measurements have already been given in a thermodynamic analysis of the phase diagram and thermochemical data (3, 4), and the partial pressures fit satisfactorily with an associated solution model for the liquid phase. However, the partial pressures themselves and the tie-line data obtainable from them have not been reported. In addition, we have determined the partial pressures for Te-saturated solid solutions, $\text{Hg}_{1-x}\text{Cd}_x\text{Te(s)}$, with x values of 0.70 and 0.95, so that the partial pressures are now known over the entire composition range for Te saturation. These measurements allow another, and, we believe, more reliable, determination of the enthalpy and entropy of mixing of the solid solution from its binary compounds, HgTe(s) and CdTe(s).

Experimental

Partial pressures were determined from measurements of the optical absorbance between 200 and 800 nm of the vapor in a sealed, initially evacuated, T-shaped silica optical cell. The upper leg of the T was the optical cell proper through which the light beam passed, while the lower leg contained the solid or liquid sample. During measurements, the cell proper was held at some fixed high temperature and the sample temperature at a num-

ber of lower temperatures. Care was taken to insure the sample temperature was always the lowest in the cell. Full details of the experimental arrangement and measurement technique and accuracy have been given in Ref. (1). As described in Ref. (2), the sample portion of the sidearm was enlarged to 2.0 cm od and a heat pipe placed around the sample to reduce the temperature variation to a few tenths of a degree centigrade or less. Temperatures are conservatively estimated as accurate to within $\pm 1.5^\circ\text{C}$. The volume of each optical cell was measured as a function of distance along the sidearm by adding water from a burette with 0.05 cm³ divisions before outgassing the cell.

The starting materials were six-nine spectroscopically pure, chunk Cd and Te and High Purity Grade Hg from Cominco American, Spokane, Washington. For the solid solution samples, the elements were weighed to the nearest 0.1 mg and in stoichiometric proportions for a total of about 15g. The elements were loaded into a carbon-coated silica tube, 12 cm long and 1.6 cm od that had been previously outgassed for 16h at 1000°C and $3(10^{-7})$ torr. The loaded tube was connected to a vacuum system and sealed off after 5-10 min at about 10^{-5} torr. The loaded tube was then placed in the center of a 20 cm long, 2.2 cm id heat pipe and put into a box furnace. The temperature was raised in steps to 690°C for the 70 mole percent (m/o) CdTe sample and 680°C for the 95 m/o CdTe sample and held for 72h. The furnace was then cooled to room temperature over a period of about 50h. Each tube was opened, and all of the black, porous material collected and ground in an agate mortar to pass a 63 μm stainless

*Electrochemical Society Active Member.

steel sieve. There was no sign of elemental Hg, which would have been detectable as a smear on the agate mortar. All of the material was then loaded with a funnel into an optical cell and sealed off at about $3(10^{-7})$ torr.

The four Te-rich ternary samples were made by loading the weighed elements directly into a previously outgassed optical cell, sealing off under $3(10^{-7})$ torr, placing the cell in a T-shaped furnace centered on the sample light beam, and heating the sample for 72h at a temperature just above the estimated liquidus temperature while the optical cell proper was hotter. Table I lists the optical path length, the free volume, the total sample mass, and the starting composition x and y in the formula $(\text{Hg}_{1-x}\text{Cd}_x)_y\text{Te}_{1-y}$ for each sample cell. In Table I, the uncertainty in the free volume is ± 0.1 ml. The other numerical quantities are accurate to the number of significant figures shown.

Calibration Measurements

The quantitative relations between the characteristic absorption of the predominant vapor species in this system, Hg, Cd, and Te₂, and the respective vapor partial pressures have been determined previously by Schwartz *et al.* (1) for one optical cell temperature, 755°C. In this investigation, we repeated and extended the calibration for higher optical cell temperatures to make possible partial pressure measurements at higher sample temperatures than before. The foreign gas broadening of the Cd lines by Hg(g) was also studied more closely and the broadening parameters redetermined. A detailed description of the calibration has been given (5). Here we confine ourselves to a brief summary and give some new results of the calibration.

Mercury.—Recently, Su *et al.* (6) have measured the absorption of the red wing of the 253.7 nm Hg line between 255.4 and 330.4 nm at five optical cell temperatures between 460° and 860°C. For each optical cell temperature, the values of the optical absorbance, D_λ , for each wavelength, λ , and temperature of the liquid Hg sample, $T_s(\text{K})$, fell on a straight line on a plot of $\log D_\lambda$ vs. $1/T_s$ with a slope twice that of the vapor pressure in a similar plot. The vapor pressure is given to within 1% by (1)

$$\log_{10} P_{\text{Hg}}^\circ (\text{atm}) = -3157/T_s + 5.028; 10^{-3} < P_{\text{Hg}}^\circ < 0.1 \text{ atm} \quad [1]$$

$$\log_{10} P_{\text{Hg}}^\circ (\text{atm}) = -3099/T_s + 4.920; 0.1 < P_{\text{Hg}}^\circ < 38 \text{ atm} \quad [2]$$

Therefore, the absorption coefficient varies as the square of the concentration of Hg atoms in the vapor phase, and, from the statistical theory of broadening

$$D_\lambda \equiv \log_{10} (I_0/I_\lambda) = LA_\lambda (P_{\text{Hg}}/T)^2 \exp(-V_\lambda/kT) \quad [3]$$

where I_0 and I_λ are intensities at a given wavelength, λ , of the incident and transmitted beams, respectively, L is the optical path length, and T is the optical cell temperature, *i.e.*, the temperature of the vapor through which the light passes as opposed to the temperature, T_s , of the liquid Hg sample generating the vapor. The parameters A_λ and V_λ have been tabulated (6) for 24 wavelengths between 254.4 and 330.4 nm so that P_{Hg} can be obtained from a measurement of D_λ at any temperature of the optical cell proper between 460° and 860°C. When one uses the tabulated

values for A_λ and V_λ in Eq. [3], the standard deviation in $(D_\lambda T^2/LP_{\text{Hg}}^2)$ is less than 2% for wavelengths between 257.4 and 310.4 nm (2.8% at 300.4 nm). Thus, when Eq. [3] is inverted to solve for P_{Hg} , the standard deviation in P_{Hg} is less than 1%, assuming no error in the measured values of D_λ , T , and L .

For P_{Hg} lower than about 0.5 atm, D_λ for $\lambda \geq 254.4$ nm is about 0.01 and comparable to the ± 0.02 noise in our measurement of D_λ . In these cases, the optical absorbance was integrated over the entire 253.7 nm Hg peak. For a 755°C optical cell and a 9.83 cm optical path, a pure Hg sample gave an integrated area, A , in units of optical absorbance (\AA), that depended upon the slit width used and the pressure range. If Eq. [1] is used to eliminate the sample temperature, then the results for P_{Hg} between 10^{-2} and 10^{-1} atm are

$$\log_{10} P_{\text{Hg}}(\text{atm}) = 0.7877 \log_{10} (9.83A/L) - 1.6054; \\ 0.042 \text{ nm bandpass, } \sigma_A = 0.028$$

$$\log_{10} P_{\text{Hg}}(\text{atm}) = 0.7276 \log_{10} (9.83A/L) - 1.5689; \\ 0.083 \text{ nm, } \sigma_A = 0.018$$

$$\log_{10} P_{\text{Hg}}(\text{atm}) = 0.6975 \log_{10} (9.83A/L) - 1.5366; \\ 0.125 \text{ nm, } \sigma_A = 0.016 \quad [4]$$

If Eq. [2] is used to eliminate the sample temperature, then for P_{Hg} between 0.1 and 0.5 atm the results are

$$\log_{10} P_{\text{Hg}}(\text{atm}) = 0.8773 \log_{10} (9.83A/L) - 1.6761; \\ 0.083 \text{ nm, } \sigma_A = 0.061$$

$$\log_{10} P_{\text{Hg}}(\text{atm}) = 0.8617 \log_{10} (9.83A/L) - 1.6606; \\ 0.125 \text{ nm, } \sigma_A = 0.056 \quad [5]$$

We have assumed Lambert's law in inserting the optical path, L (cm), into these equations, which should be approximately valid for path lengths near 9.83 cm. As can be seen, the integrated optical absorbance area, A , is almost proportional to P_{Hg} . In the low pressure range, this is more nearly so the smaller the slit width and the spectral bandpass of the spectrophotometer. For the absorption lines of monatomic vapor species at low pressure, the true optical absorbance area is proportional to the concentration of absorbers in the light path and hence to the partial pressure of absorbers (7). However, these lines are extremely sharp near the line center and can attain optical absorbance values in the thousands even at low pressures. Thus the areas measured here and characterized by Eq. [4] and [5] are not the true areas as evidenced, for instance, by the fact that the observed line half-widths equal the spectrophotometer spectral bandpass used. Use of a bandpass comparable to, or greater than, the true half-width of the line reduces the observed value of the optical absorbance. The observed value is also reduced at high values, in the range 2 to 3 here, when the transmitted light intensity is so small as to produce an increase in the photomultiplier current that is smaller or comparable to that observed in the dark. Therefore, in order to establish Eq. [4] and [5] it was necessary not only to set the slit widths but to also maintain the same intensity of the incident light beam. Thus, these equations are not necessarily transferable to other experimental setups in contrast to those embodied in Eq. [3]. However, they can be used with our arrangement and serve as an empirical calibration that is valid as long as all other partial pressures are negligible compared to that of Hg.

The standard deviations σ_A , shown after Eq. [4] and [5], are those in $\log A$ as a function of $\log P_{\text{Hg}}$, if one assumes Eq. [1] and [2] for the vapor pressure of Hg are correct. When Eq. [4] and [5] are used to calculate P_{Hg} from a measured value of A , the standard deviation is that in the measured value of A plus a contribution from the uncertainty in the calibration measurements. Expressed as a

Table I. Optical path length (cm), free volume (cm³), total mass (g), and starting composition x and y in the formula $(\text{Hg}_{1-x}\text{Cd}_x)_y\text{Te}_{1-y}$

Cell	Optical path length	Free volume	Total weight	x	y
HCT-70	5.00	20.5	14.8964	0.7000	0.4966
HCT-95	9.79	25.1	14.9447	0.9500	0.4969
TER-1	9.79	25.1	10.8383	0.1046	0.1878
TER-2	9.78	25.0	12.2645	0.0605	0.2002
TER-3	9.79	24.8	10.9815	0.2110	0.0786
TER-4	9.79	25.8	14.1803	0.1280	0.2580

percentage, the latter is $c(e^{\sigma_A} - 1)$, where c is the numerical coefficient of $\log_{10}(9.83 A/L)$ in Eq. [4] and [5]. This amounts to less than 2.3% for Eq. [4] and less than 5.5% for Eq. [5].

Tellurium.—The diatomic molecule, Te_2 , exhibits a broad vibronic absorption band between 380 and 550 nm. It is observed that Beer's law holds for many of these peaks for a pure Te sample and the optical absorbance is proportional to the vapor pressure of $\text{Te}_2(\text{g})$, P_2° . The latter is given to within 2% by (1)

$$\log_{10} P_2^\circ (\text{atm}) = -5960.2/T + 4.7191; T > 450^\circ\text{C} \quad [6]$$

Thus, one can write

$$P_2 = \alpha_\lambda(D_\lambda/L) \quad [7]$$

The values of α_λ for a 755°C optical cell temperature have been given (1). Here we made measurements with optical cell temperatures of 800° and 860°C and the values of α_λ are listed in Table II. The standard deviation in α_λ given at the bottom of Table II, of course, contributes to that in P_2 when Eq. [7] is used to calculate P_2 . This contribution is generally less than 4% of the value of P_2 and always less than 6.5%.

Cadmium.—In the experiments of this investigation, the partial pressure of Cd, P_{Cd} , varied over a range of low values from 10^{-7} to 10^{-4} atm while P_{Hg} was in the 10^{-1} to 15 atm range. One expects that the optical absorbance or the area under the absorbance curve observed for the Cd lines is, therefore, broadened by $\text{Hg}(\text{g})$ and depends upon P_{Hg} as well as P_{Cd} . The calibration methods described in the Mercury section are, therefore, not applicable for Cd. Therefore, we measured the transmission as a function of wavelength and obtained the area in the transmission minimum of the Cd absorption line. Even though the transmission curve is distorted when the spectral band-pass is larger than the true line half-width, the area in the transmission minimum is approximately correct (7). If the transmission values are converted to optical absorbance, then neither the observed line shape nor its integrated area is correct. The disadvantage of transmission area measurements lies in the fact that they yield the partial pressure of the absorber only upon the assumption of a specific line shape and generally require extensive measurements in order to establish the broadening parameters. The general theory is developed in Mitchell and Zemansky (7) and has been outlined in Ref. (1) for absorption by Cd. Therefore, we summarize the minimum theoretical results required to describe our experimental measurements. A variable y' is defined as

$$y' = [(\ln 2)^{1/2}/\Delta\nu_D] \int_0^\infty (1 - I_\nu/I_0) d\nu \quad [8]$$

where I_ν/I_0 is the transmission at a given frequency, and $\Delta\nu_D$ is the Doppler half-width of the line. The integral, of course, is the area between the line for transmission equal to unity and the curve for the observed values of the transmission as a function of frequency. This integral is simply related to the experimental quantity in which the transmission is taken as a function of wavelength. If one

expresses transmission in terms of the absorption coefficient, k_ν , where

$$k_\nu = 2.303D_\lambda/L \quad [9]$$

then Eq. [8] becomes

$$y' = [(\ln 2)^{1/2}/\Delta\nu_D] \int_0^\infty (1 - \exp(-k_\nu L)) d\nu \quad [10]$$

The common assumption for low absorber partial pressures is that k_ν is given by the Voigt line shape, which is symmetrical about the line center, and that k_ν is proportional to the product of the absorber concentration, N , and the oscillator strength of the line, f . The Voigt line shape also depends upon a broadening parameter, a' . If a variable, x' , is defined as

$$x' = NfL(\ln 2)^{1/2}/\pi\Delta\nu_D \quad [11]$$

then y' depends upon x' and a' . Curves of y' vs. x' for a few fixed values of a' have been calculated and are given by Mitchell and Zemansky (7) and by Penner (8). The broadening parameter is given in terms of a natural half-width, $\Delta\nu_N$, a self-broadening half-width, $\Delta\nu_S$, and a foreign gas broadening half-width, $\Delta\nu_F$, as

$$a' = (\Delta\nu_N + \Delta\nu_S + \Delta\nu_F)(\ln 2)^{1/2}/\Delta\nu_D = a_N + a_S + a_F \quad [12]$$

The values of a_S and a_F have been determined experimentally (1) for the 228.7 and 325.7 nm Cd lines, and the values of a_N calculated from the known oscillator strengths of the lines. The results were

$$325.7 \text{ nm}; a_N = 2.69(10^{-5}), a_S = 1.50P_{\text{Cd}}(\text{atm}),$$

$$a_F = 1.18P_{\text{Hg}}(\text{atm}) \quad [13]$$

$$228.7 \text{ nm}; a_N = 0.0236, a_S = 108P_{\text{Cd}}(\text{atm}),$$

$$a_F = 4.60P_{\text{Hg}}(\text{atm}) \quad [14]$$

The foreign gas broadening coefficients were redetermined here using Hg-Cd amalgams as samples in a manner similar to that used previously (1) and described in detail elsewhere (5). The results are

$$325.7 \text{ nm}; a_F = (1.40 \pm 0.26)P_{\text{Hg}}(\text{atm}) \quad [15]$$

where 0.26 is one standard deviation and

$$228.7 \text{ nm}; a_F = 8.89P_{\text{Hg}}^{1.29} - 2.59P_{\text{Hg}}^{1.46}/P_{\text{Cd}}^{0.068} \quad [16]$$

With Eq. [16] for a_F , the standard deviation in the calculated and observed values of y' in the calibration runs is 4.6%. The new and old results are in fair agreement for the 325.7 nm line. The new result for the 228.7 nm line is not obviously interpretable from a theoretical point of view. Its form is determined largely by the results for a dilute amalgam for which the ratio of $P_{\text{Hg}}/P_{\text{Cd}}$ was about 10^7 . For the range of P_{Cd} and P_{Hg} obtained for the Hg-Cd-Te samples studied here and previously (1-3), Eq. [16] gives values for a_F that are within a factor of about two of the values calculated with Eq. [14] for a_F . However, as discussed in the next section, the new results for a_F are superior.

Table II. Values of α_λ in the equation, $P_2(\text{atm}) = \alpha_\lambda(D_\lambda/L)$ for $\text{Te}_2(\text{g})$ at 800° and 860°C optical cell temperatures. α_λ in atm-cm.

$\lambda(\text{nm})$	363.4 ^a	383.2 ^a	404.6	421.9	431.9	436.5	459.0	464.0	472.9
$\alpha_\lambda(800^\circ\text{C})$	0.0719	0.0303	0.0227 ^b	0.0228 ^b	0.0245 ^b	0.0271 ^b	0.0390	0.0451 ^b	0.0572
$\alpha_\lambda(860^\circ\text{C})$	0.0720	0.0323	0.0240 ^b	0.0245 ^b	0.0260 ^b	0.0285 ^b	0.0402	0.0463	0.0574 ^b
$\lambda(\text{nm})$	481.8	485.6	490.2	496.8	499.4	500.4 ^a	503.2	509.4	513.2
$\alpha_\lambda(800^\circ\text{C})$	0.0727	0.0865	0.0986	0.1172 ^b	0.1377 ^b	0.1557 ^b	0.1404	0.1835	0.2091
$\alpha_\lambda(860^\circ\text{C})$	0.0740	0.0850 ^b	0.0981	0.1177	0.1365	0.1500	0.1371	0.1745	0.1965
$\lambda(\text{nm})$	515.8	519.4	523.2	526.4	530.0	534.0	537.2		
$\alpha_\lambda(800^\circ\text{C})$	0.2412	0.2598	0.3105	0.3322	0.3913	0.4262	0.4963		
$\alpha_\lambda(860^\circ\text{C})$	0.2282	0.2391	0.2947	0.3140	0.3749	0.4090	0.4800		

^a Not a vibronic maximum.

^b The standard deviation in α_λ is less than 4% except for those values distinguished by a superscript "b." For the latter, the standard deviation in α_λ is between 4% and 5.5% for $\alpha_\lambda(800^\circ\text{C})$ and 4% and 6.5% for $\alpha_\lambda(860^\circ\text{C})$.

Results

General.—For mercury pressures higher than 0.30 atm, a contribution due to $\text{Te}_2(\text{g})$ to the absorbance in the 255-340 nm region was first subtracted from the net optical absorbance. This contribution was determined from the observed $\text{Te}_2(\text{g})$ absorbance in the 363-550 nm region and the assumption that the values of the $\text{Te}_2(\text{g})$ absorbance in the 255-340 nm region and the values in 363-550 nm region are in the same ratio as observed in pure $\text{Te}_2(\text{g})$ vapor. The $\text{Te}_2(\text{g})$ contribution so determined was never greater than 20% of the net optical absorbance. The value of P_{Hg} was then obtained as the average of values calculated with Eq. [3] and the corrected net optical absorbance at two to five wavelengths in the 255-340 nm region. The standard deviation of P_{Hg} was generally less than $\pm 4\%$. We estimate an uncertainty of about $\pm 5\%$ in the value of P_{Hg} .

When P_{Hg} was below about 0.5 atm, the partial pressures of Te_2 and Cd were also considerably smaller and the contribution of foreign gas broadening to the 253.7 nm Hg line was assumed to be negligible. The area obtained from a trace of optical absorbance vs. λ was used to calculate P_{Hg} with Eq. [4] and [5]. The values of P_{Hg} obtained from two methods generally agreed within the experimental error of 5% in the range between 0.3 and 0.5 atm where both could be used.

The partial pressure of $\text{Te}_2(\text{g})$ was calculated from the measured optical absorbance between 363.4 and 550.4 nm where $\text{Hg}(\text{g})$ and $\text{Cd}(\text{g})$ absorption is negligible. The values of P_2 calculated for the various wavelengths with Eq. [7], Table II and Table II of Ref. (1) generally agreed to within $\pm 2\%$. The average value was taken. Taking account of the uncertainty in the Beer law parameters we estimate an uncertainty of about $\pm 5\%$ in the value of P_2 .

The area of the transmission minima for Cd lines was measured and the quantity y' obtained for each run. The

foreign gas broadening contribution, a_f , was calculated with Eq. [15] and [16]. The self-broadening coefficient was calculated with Eq. [13] and [14] and the measured value of P_{Hg} and an initial estimate for P_{Cd} . The quantity x' (or P_{Cd}) was solved numerically for the given y' and a' . A trial and error routine (9) was used to vary P_{Cd} until the initial and final values for P_{Cd} agreed to within 1%. The 228.7 nm Cd line is stronger than the 325.7 nm line and was used to obtain P_{Cd} from its lowest values to an upper limit where the line became asymmetric. The 325.7 nm line was used to obtain P_{Cd} in its upper range. In the range where reliable measurements could be obtained for both lines, the values of P_{Cd} from each one generally agreed to within 15%. With the old values of a_f given by Eq. [13] and [14] the analogous comparison gave agreement only to within about a factor of two. Over the whole range observed, we estimate an uncertainty of about $\pm 40\%$ for P_{Cd} .

Pseudobinary.—The partial pressures along the Te-saturated three-phase curves for 70 and 95 m/o CdTe, HgTe-CdTe solid solutions are listed for representative runs and in the order of increasing sample temperature in Tables III and IV, respectively. Complete tables are given elsewhere (5). In the first column of the tables, each run is represented by a four-digit number with the first two digits indicating the date and the last two digits the sequential number of the run. It can be seen that although the sample temperature was raised and lowered several times during the run, the measured partial pressures are reproducible. The second column gives the number of hours the sample was at the temperature before measurement. The third column is the sample temperature in $10^3/T$, where T is in Kelvin. The last two columns are the calculated values for the gross composition, x and y , of the condensed phase or phases expressed by the formula $(\text{Hg}_{1-x}\text{Cd}_x)_y\text{Te}_{1-y}$. These values were obtained from the

Table III. Partial pressures (atm) over Te-saturated 70 m/o CdTe, HgTe-CdTe solid solution and composition x and y in the formula $(\text{Hg}_{1-x}\text{Cd}_x)_y\text{Te}_{1-y}$. The contribution to the uncertainty in x and y due to that in the amount of each element in the gas phase is approximately proportional to P_{Hg} . For run 2529, this contribution is $\pm 2(10^{-3})$ for x and $\pm 7(10^{-4})$ for y .

Run	Duration (h)	$10^3/T$	P_{Hg}	$10^3 \times P_2$	$10^6 \times P_{\text{Cd}}$	x	y
2830	64	1.3214	0.0476	0.6156	—	0.7002	0.4966
2831	2	1.3081	0.0561	0.6748	—	0.7002	0.4965
2833	2	1.2685	0.0822	1.194	—	0.7003	0.4965
2117	3	1.2553	0.1042	1.420	—	0.7003	0.4965
2118	2.5	1.2265	0.1568	2.100	—	0.7005	0.4964
1401	90	1.1975	0.2577	3.035	—	0.7008	0.4963
2936	2.5	1.1661	0.3645	4.314	0.415	0.7012	0.4962
1711	3.5	1.1397	0.5068	6.064	0.812	0.7016	0.4960
1712	3	1.1053	0.7821	9.059	1.620	0.7025	0.4957
2324	2	1.0862	1.0077	11.03	2.17	0.7032	0.4955
1505	2	1.0642	1.4334	13.78	3.86	0.7045	0.4950
1506	3	1.0389	2.0710	17.84	10.25	0.7065	0.4943
1815	2.5	1.0288	2.4238	19.75	15.7	0.7076	0.4940
2427	3.5	1.0092	3.2670	23.55	20.2	0.7101	0.4931
1609	3	0.9849	4.9167	28.70	52.7	0.7152	0.4913
2529	3.5	0.9639	7.0935	31.18	64.75	0.7209	0.4893

Table IV. Partial pressures (atm) over Te-saturated 95 m/o CdTe, HgTe-CdTe solid solution. For run 1311, the uncertainty in x due to those in the amount of each element in the gas phase is $\pm 10^{-4}$, while that in y is $\pm 3(10^{-5})$. For run 1519, the corresponding uncertainty in x is $\pm 10^{-3}$, that in y is $\pm 2.9(10^{-4})$.

Run	Duration (h)	$10^3/T$	P_{Hg}	$10^3 \times P_2$	$10^6 \times P_{\text{Cd}}$	x	y
1205	11	1.3015	0.0208	0.0823	—	0.9501	0.4968
1207	2.5	1.2262	0.0410	0.2384	0.472	0.9502	0.4968
1208	2	1.1927	0.0559	0.3610	0.629	0.9503	0.4968
1309	16	1.1600	0.0769	0.5622	1.04	0.9504	0.4967
1310	2	1.1286	0.1087	0.8448	1.98	0.9505	0.4967
1311	2	1.0861	0.1987	1.466	5.72	0.9510	0.4966
1103	3	1.0487	0.300	2.342	14.00	0.9515	0.4965
1104	2	1.0254	0.395	3.092	20.50	0.9519	0.4964
1720	2.5	1.0150	0.468	3.440	30.2	0.9522	0.4963
1721	1.5	0.9951	0.577	4.498	51.7	0.9527	0.4962
1722	2	0.9754	0.760	5.566	—	0.9535	0.4960
1516	1	0.9545	0.969	6.740	145	0.9543	0.4959
1723	2	0.9451	1.1908	7.868	121	0.9554	0.4956
1517	2	0.9342	1.3423	8.382	184	0.9559	0.4955
1518	1.5	0.9142	1.7537	10.12	281	0.9577	0.4951
1519	1.5	0.8974	2.2869	12.03	439	0.9600	0.4945

known weight of the starting materials, the volume profile and the corresponding temperature profile along the cell, and the assumption that Cd(g) and Te₂(g) are ideal gases while Hg(g) is a slightly imperfect gas with an equation of state given by Sugawara and Sato (10). The partial pressure of Hg was greater than that of either Te₂ or Cd in all of the measurements. Consequently the condensed phase or phases became progressively poorer in Hg with increasing reservoir temperature.

The uncertainty in the value of x or y arises from two causes. One is due to the ± 0.2 mg accuracy in the original weighing of each element. This contributes $\pm 2(10^{-5})$ or less to the uncertainty in x and y for the samples studied in this work. The other is due to the uncertainties in the number of moles of each element in the gas phase. These were taken as $\pm 10\%$ for Hg and Te and $\pm 40\%$ for Cd, allowing not only for an uncertainty in each partial pressure, but also in the sum of the volume-to-temperature ratio for the various segments of the optical cell. The resulting contribution to uncertainty in x and y from this second cause is approximately proportional to P_{Hg} and is indicated in Tables III and IV, as well as in Tables V-VIII, which are discussed later. Thus the total uncertainty in x (or y) is $[4(10^{-10}) + \delta^2]^{1/2}$, where δ is the contribution from the second cause and can be obtained by interpolation from the information in each table.

The partial pressures along the Te-saturated three phase curves are shown in Fig. 1, 2, and 3 for, respectively, P_{Hg} , P_{Te} , and P_{Cd} . Those data determined previously (1, 2, 5, 11) for CdTe of 0, 10, 20, 40, and 60 m/o are also shown for comparison. Near the 10^{-2} atm lower limit of measurement in Fig. 1, the data for 95 and 70 m/o CdTe show curvature and P_{Hg} for 60 m/o is lower than that for 70 m/o. The latter effect is probably due to experimental error. The solid curves in Fig. 1 and 2 are calculated (4) with an associated solution model for the liquid with species Hg, Cd, Te, HgTe, and CdTe. The closeness of P_{Cd} for various x values seen experimentally in Fig. 3 is also given theoretically (4).

Ternary runs.—Tables V-VIII give the partial pressures for representative runs with four Te-rich samples. Complete tables are given elsewhere (5). Figures 4 and 5 show the plot of $\log(P_{\text{Hg}})$ vs. $10^3/T$ for each sample. The liquidus temperature for each ternary composition was determined by the change of the slope on the plot (denoted by symbol X). By comparing P_{Hg} at the liquidus temperature with those for the various Te-saturated solid solutions shown in Fig. 1, the composition of the solid solution in equilibrium with that liquid was determined by interpolation. Table IX summarizes the liquidus temperature, the partial pressures of Hg, Cd, and Te₂ at that temperature, and the composition of the coexisting solid solution, for each ternary run. The least precise quantities are the liquidus temperature and the x value of the coexisting solid solution, the estimated uncertainties for these are given in Table IX.

Table V. Partial pressures (atm) over Te-rich ternary sample TER-1 and composition x and y in the formula $(\text{Hg}_{1-x}\text{Cd}_x)_y\text{Te}_{1-y}$. The contribution to the uncertainties in x and y due to those in the amounts vaporized are, respectively, $\pm 4(10^{-5})$ and $\pm 6(10^{-5})$ for run 0420 and $\pm 5(10^{-4})$ and $\pm 7(10^{-4})$ for run 0730.

Run	Duration (h)	$10^3/T$	P_{Hg}	$10^3 \times P_{\text{Te}}$	$10^7 \times P_{\text{Cd}}$	x	y
0214	2	1.3731	0.0274	0.258	—	0.1047	0.1877
0215	0.6	1.3536	0.0517	0.361	—	0.1048	0.1876
0216	1	1.3303	0.0534	0.459	—	0.1048	0.1876
0317	11	1.3018	0.0815	0.639	—	0.1048	0.1875
0318	1.3	1.2875	0.102	0.787	—	0.1049	0.1875
0319	1.5	1.2680	0.134	1.10	—	0.1049	0.1874
0936	1	1.2540	0.177	—	—	—	—
0420	11	1.2502	0.184	1.28	0.522	0.1051	0.1872
0938	1	1.2282	0.235	—	—	—	—
0522	10.5	1.2236	0.245	1.850	0.936	0.1052	0.1870
2302	11	1.2035	0.292	2.39	1.99	0.1053	0.1868
0625	4	1.1700	0.406	3.87	2.85	0.1056	0.1865
0626	4.5	1.1449	0.525	5.30	4.80	0.1058	0.1861
2305	1	1.1080	0.717	8.44	12.2	0.1062	0.1855
0729	1	1.0489	1.358	19.9	54.5	0.1077	0.1835
0730	2	1.0153	2.099	27.8	65.8	0.1094	0.1812

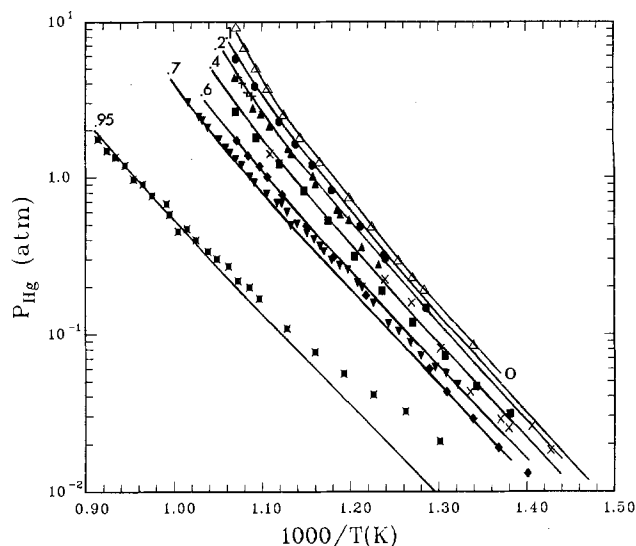


Fig. 1. Partial pressures of Hg along the Te-saturated three-phase curves for various values of x in $\text{Hg}_{1-x}\text{Cd}_x\text{Te}$ solid solutions as a function of $10^3/T$. Open triangles: $x = 0.0$ [Ref. (11)]. Circles: 0.094 [Ref. (2)]. Solid triangles: 0.196 [Ref. (5)]. Crosses: 0.197 [Ref. (2)]. Squares: 0.39 [Ref. (5)]. X's: 0.416 [Ref. (1)]. Diamonds: 0.581 [Ref. (2)]. Inverted triangles: 0.70. X's with superimposed squares: 0.95. Solid lines are the calculated results from Ref. (4) for x -values labeled adjacent to the lines.

Analysis

For a solid solution, $(\text{A}_{1-x}\text{B}_x)_y\text{C}_{1-y}(\text{s})$, with A and B atoms occupying the sites of one sublattice and C atoms occupying the sites of the other sublattice of the structure, it can be shown theoretically (12) that the sum of the chemical potentials of A and C and that of B and C in the solid are each independent of the composition y , if y is confined to values near $1/2$, *i.e.*

$$\mu_{\text{A}}^{\text{s}} + \mu_{\text{C}}^{\text{s}} = \mu_{\text{AC}}^{\text{s}}(T, x) \quad [17]$$

$$\mu_{\text{B}}^{\text{s}} + \mu_{\text{C}}^{\text{s}} = \mu_{\text{BC}}^{\text{s}}(T, x) \quad [18]$$

Thus AC and BC can be chosen as thermodynamic components of the solid solution whose chemical potentials are independent of the C to A + B atom ratio. Equations [17] and [18] hold within experimental error (1, 2) for $(\text{Hg}_{1-x}\text{Cd}_x)_y\text{Te}_{1-y}(\text{s})$. From the quantitative analysis of Tung *et al.* (2), the solid solution of HgTe and CdTe is almost ideal. We will therefore characterize this solid solution by assuming that its components mix like a quasi-regular solution, *i.e.*

$$\mu_{\text{HgTe}}^{\text{s}} = (W - VT)x^2 + RT \ln(1 - x) + \mu_{\text{HgTe}}^{\text{s}0} \quad [19]$$

$$\mu_{\text{CdTe}}^{\text{s}} = (W - VT)(1 - x)^2 + RT \ln x + \mu_{\text{CdTe}}^{\text{s}0} \quad [20]$$

where W and V are the interaction constants to be determined.

Table VI. Partial pressures (atm) over Te-rich ternary sample TER-2 and composition x and y in the formula $(\text{Hg}_{1-x}\text{Cd}_x)_y\text{Te}_{1-y}$. The uncertainties in the amount of each element vaporized contributes $\pm 4(10^{-5})$ to the uncertainty in x and $\pm (10^{-4})$ to that in y for run 2818. For run 0955, the corresponding uncertainties are $\pm 5(10^{-4})$ and $\pm 1.2(10^{-3})$

Run	Duration (h)	$10^3/T$	P_{Hg}	$10^3 \times P_2$	$10^7 \times P_{\text{Cd}}$	x	y
0742	54	1.4473	0.0125	0.090	—	0.0605	0.2001
0128	3.7	1.4012	0.0232	0.170	—	0.0605	0.2001
0229	9.5	1.3691	0.0363	0.258	—	0.0605	0.2000
3025	6	1.3436	0.0479	0.466	—	0.0605	0.2000
0440	1.5	1.3270	0.0680	0.455	—	0.0606	0.2000
0232	2.7	1.3118	0.0838	0.545	—	0.0606	0.1999
2923	1	1.3006	0.106	0.652	0.115	0.0606	0.1998
2922	1.5	1.2824	0.133	0.841	0.238	0.0606	0.1998
0334	1.3	1.2722	0.159	0.955	0.186	0.0607	0.1997
2921	1.2	1.2641	0.165	1.04	0.293	0.0607	0.1997
1906	2	1.2402	0.246	1.47	0.352	0.0607	0.1994
2818	11.5	1.1821	0.379	3.16	2.29	0.0609	0.1991
2717	1.5	1.1574	0.513	4.33	3.48	0.0610	0.1987
2008	4	1.1378	0.660	5.72	18.7	0.0612	0.1983
2715	1.5	1.0923	0.989	10.6	14.0	0.0616	0.1973
2309	60	1.0724	1.30	13.8	53.0	0.0619	0.1965
0954	1.6	0.9866	3.53	40.6	138	0.0644	0.1902
0955	2	0.9555	4.35	67.6	219	0.0652	0.1883

Table VII. Partial pressures (atm) over Te-rich ternary sample TER-3 and composition x and y in the formula $(\text{Hg}_{1-x}\text{Cd}_x)_y\text{Te}_{1-y}$. The uncertainties in the amount of each element vaporized contributes an amount to the uncertainty in x and y , that is, respectively, $\pm 6(10^{-4})$ and $\pm 2(10^{-4})$ for run 2320 and $\pm 7.6(10^{-3})$ and $\pm 1.6(10^{-3})$ for run 2426.

Run	Duration (h)	$10^3/T$	P_{Hg}	$10^3 \times P_2$	$10^7 \times P_{\text{Cd}}$	x	y
1910	13	1.3933	0.0092	0.241	—	0.2112	0.0786
2946	1	1.3739	0.0120	—	—	—	—
1911	2.5	1.3465	0.0164	0.442	—	0.2113	0.0786
1912	2.5	1.3220	0.0217	0.634	—	0.2113	0.0786
1807	10	1.3089	0.0257	—	—	—	—
2013	18	1.2907	0.0327	0.981	—	0.2114	0.0785
1706	5.5	1.2692	0.0418	1.28	0.206	0.2115	0.0785
2115	9	1.2323	0.0630	2.13	0.558	0.2117	0.0784
1704	11	1.2172	0.0766	2.58	0.816	0.2119	0.0784
1603	5	1.1662	0.138	5.35	1.72	0.2125	0.0782
2527	12	1.1333	0.208	8.16	3.15	0.2132	0.0779
1601	43	1.0804	0.345	17.2	10.6	0.2145	0.0775
2320	12	1.0455	0.552	25.3	24.7	0.2166	0.0768
2321	2.5	1.0222	0.730	34.2	32.9	0.2184	0.0762
2528	3	1.0029	1.29	45.3	28.0	0.2242	0.0744
2529	3	0.9869	2.64	55.9	60.9	0.2397	0.0699
2530	2	0.9625	3.27	77.0	81.6	0.2460	0.0683
2426	2	0.9492	5.0	92.7	—	0.2694	0.0627

It is assumed that Cd and Te_2 behave ideally in the vapor phase. It is further assumed that the fugacity of Hg, f_{Hg} , is that extracted from the equation of state for Hg(g) given by Sugawara and Sato (10), i.e.

$$\mu(\text{Hg}(g)) = RT \ln f_{\text{Hg}} = RT \ln P_{\text{Hg}} + 4857.6P_{\text{Hg}} (-1.793/T + 251/T^2 + 0.001071) \quad [21]$$

where P_{Hg} is in atmospheres and μ in calories per gram atom. One then obtains the chemical potentials of HgTe and CdTe relative to the pure gas species Hg, Cd, and Te_2 ,

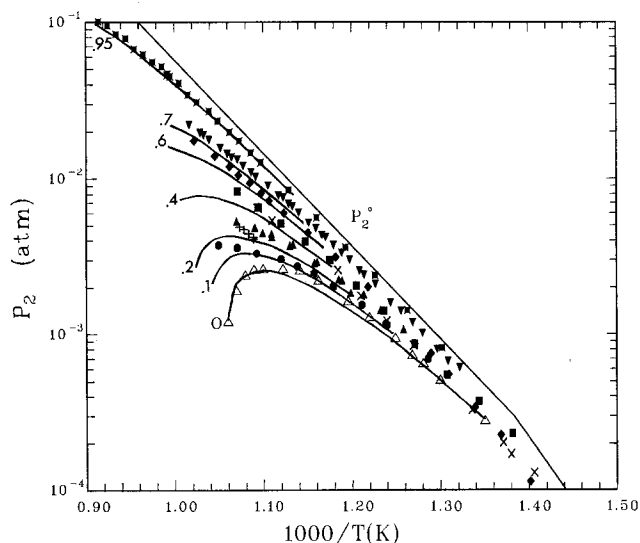


Fig. 2. Partial pressures of Te_2 along the Te-saturated three-phase curves for various x values of $\text{Hg}_{1-x}\text{Cd}_x\text{Te}(s)$. Upper solid line labeled P_2^0 represents the vapor pressure of $\text{Te}(s,l)$. Symbols have the same meaning as indicated in the caption of Fig. 1. Solid lines are the calculated results from Ref. (4) for various x values.

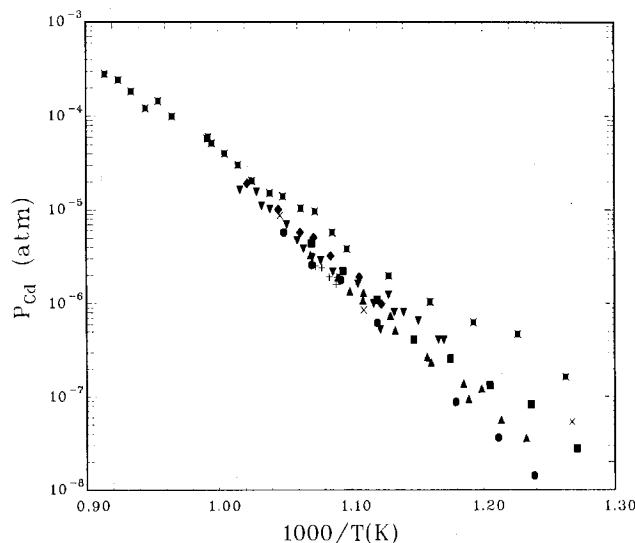


Fig. 3. Partial pressures of Cd along the Te-saturated three-phase curves for various x values of $\text{Hg}_{1-x}\text{Cd}_x\text{Te}(s)$. Symbols have the same meaning as in the caption of Fig. 1.

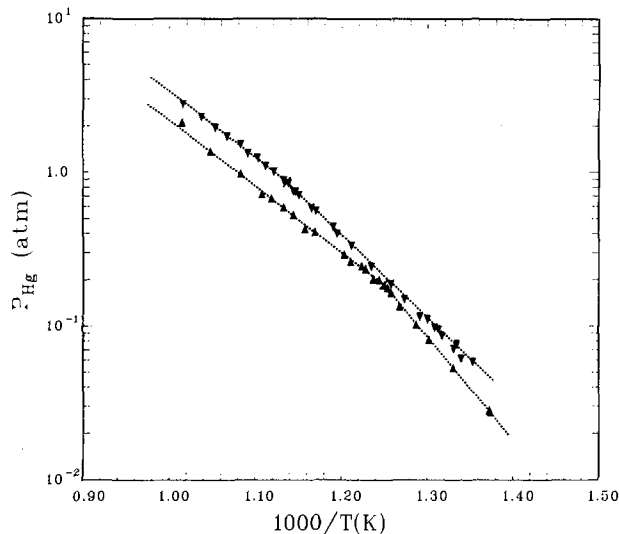


Fig. 4. Partial pressures of Hg over Te-rich ternary samples TER-1 (triangles) and TER-4 (inverted triangles) as a function of $10^3/T$. Liquidus points are indicated by X's.

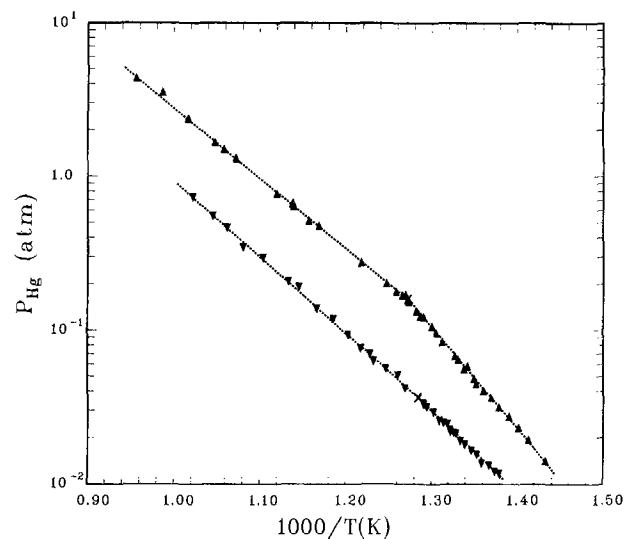


Fig. 5. Partial pressures of Hg over Te-rich ternary samples TER-2 (triangles) and TER-3 (inverted triangles). Liquid points indicated by X's.

each at 1 atm, as

$$\bar{\mu}_{\text{HgTe}}^s(x, T) = RT \ln f_{\text{Hg}} P_2^{1/2} \quad [22]$$

$$\bar{\mu}_{\text{CdTe}}^s(x, T) = RT \ln P_{\text{Cd}} P_2^{1/2} \quad [23]$$

The chemical potential of HgTe in pure HgTe(s) was taken from a recent redetermination by Su *et al.* (11) as

$$\bar{\mu}_{\text{HgTe}}^{s,0}(\text{cal}) = -40642.4 + 41.6447T \quad [24]$$

The value of this chemical potential is claimed to be accurate to ± 70 cal at the 95% confidence limit. The quantity $W - VT$ was then calculated with Eq. [19], [22], and [24] for each measurement of the partial pressures over the 70 and 95 m/o CdTe solid solutions for which the composition of the condensed phase, x , was less than 0.71 and 0.96, respectively. The results are shown in Fig. 6 in which 54 points for $x = 0.70$ and 0.95 give experimental values for $W - VT$ that are represented within a standard deviation of 117 cal by the equation

$$W - VT = 4297.1 - 3.5750T(\text{cal}) \quad [25]$$

The variables formed by calculating $W - VT$ with Eq. [25] at each temperature can be transformed so that the marginal distribution for each of the transformed variables is the Student t distribution with 52 degrees of freedom (13). Based on this, one concludes that at each temperature, the value of $W - VT$ from Eq. [25] is within ± 10 cal of the true value at the 95% confidence limit.

The chemical potential of CdTe was not used to obtain $W - VT$ because of the following facts: (i) the chemical

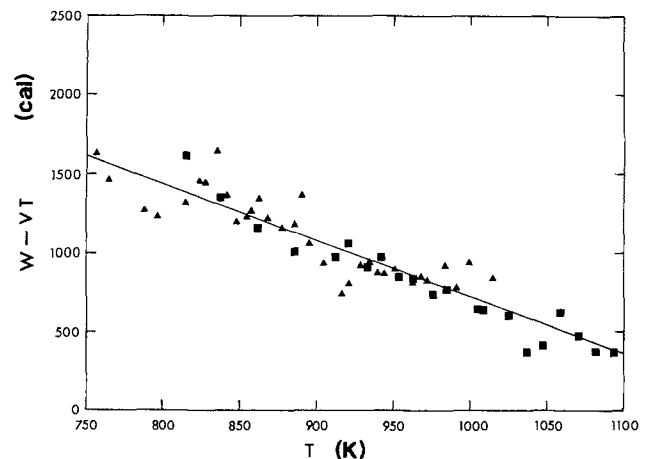


Fig. 6. The quantity, $W - VT$, calculated using Eq. [19], [22], and [24] for $x = 0.70$ (triangles) and $x = 0.95$ (squares) in the formula $\text{Hg}_{1-x}\text{Cd}_x\text{Te}(s)$, as a function of T in Kelvin. Straight line is the least squares fit to these points.

potential of CdTe for pure CdTe(s), $\mu_{\text{CdTe}}^{s,0}$, is apparently uncertain by about 1 kcal [see Ref. (2)], (ii) the values of P_{Cd} are not as accurate as those of P_{Hg} , and (iii) in the process of calculating $W - VT$ one divides a small quantity, $\bar{\mu}_{\text{CdTe}}^s - \mu_{\text{CdTe}}^{s,0}$, by another small quantity, $(1 - x)^2$, magnifying the experimental error tremendously. [For $x = 0.70$ and 0.95, $(1 - x)^2$ is 0.09 and 0.0025, respectively.] The

Table VIII. Partial pressures (atm) over Te-rich ternary sample TER-4 and composition x and y in the formula $(\text{Hg}_{1-x}\text{Cd}_x)_y\text{Te}_{1-y}$. The uncertainties in the amount of each element vaporized contributes an amount to the uncertainty in x and y , that is, respectively, $\pm 4(10^{-5})$ and $\pm 6(10^{-5})$ for run 1209 and $\pm 5(10^{-4})$ and $\pm 7(10^{-4})$ for run 1927

Run	Duration (h)	$10^3/T$	P_{Hg}	$10^3 \times P_2$	$10^7 \times P_{\text{Cd}}$	x	y
1413	18	1.3613	0.0447	0.2981	—	0.1281	0.2579
2544	1	1.3395	0.0614	—	—	0.1281	0.2579
1312	2.5	1.3250	0.0737	0.5099	—	0.1281	0.2578
1311	10	1.2918	0.1149	0.7372	—	0.1282	0.2577
1210	2.5	1.2579	0.1870	1.165	—	0.1283	0.2576
1209	4	1.2349	0.2434	1.479	—	0.1284	0.2574
1208	34	1.2117	0.3321	2.118	0.135	0.1285	0.2572
1007	3	1.1911	0.4416	2.637	0.271	0.1287	0.2569
1006	13	1.1709	0.5567	3.529	0.389	0.1289	0.2567
0905	3	1.1447	0.7477	4.676	0.656	0.1292	0.2562
1722	20	1.1331	0.8814	5.3944	0.730	0.1294	0.2559
0904	2.5	1.1217	1.0035	6.429	1.480	0.1296	0.2556
1724	2.5	1.0921	1.3160	8.9066	2.45	0.1301	0.2549
0802	3	1.0541	1.9457	14.24	9.31	0.1311	0.2534
1926	2	1.0376	2.269	17.097	11.5	0.1316	0.2527
1927	2	1.0159	2.7659	22.048	14.5	0.1324	0.2516

Table IX. Liquidus composition x_{Hg}^L , x_{Cd}^L , and x_{Te}^L , liquidus temperature, T_L , partial pressures at liquidus temperature (atm), and the compositions of the coexisting solid solution given by x_s in the formula $\text{Hg}_{1-x_s}\text{Cd}_{x_s}\text{Te}$ for Te-rich ternary samples TER-1 to TER-4

Cell	TER-1	TER-2	TER-3	TER-4
x_{Hg}^L	0.168	0.188	0.062	0.225
x_{Cd}^L	0.020	0.012	0.0166	0.033
x_{Te}^L	0.812	0.800	0.9214	0.742
T_L (°C)	527.5 ± 3	512.8 ± 5	505.7 ± 9	606.4 ± 3
P_{Hg}	0.187	0.158	3.64×10^{-2}	0.86
P_{Cd}	2.3×10^{-8}	1.15×10^{-8}	9.5×10^{-9}	3.9×10^{-7}
P_2	1.32×10^{-3}	9.6×10^{-4}	1.07×10^{-3}	5.25×10^{-3}
x_s	0.304 ± 0.03	0.19 ± 0.03	0.86 ± 0.01	0.43 ± 0.026

chemical potentials of HgTe for the lower x values were also omitted for a reason analogous to (iii) above.

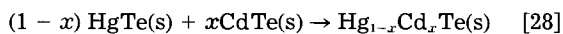
With Eq. [19], [20], and [25], one obtains

$$\Delta H_M \text{ (cal)} = (4297.1 \pm 49.9)x(1 - x) \quad [26]$$

and

$$\Delta S_M \text{ (cal/K)} = (3.5750 \pm 0.0539)x(1 - x) + 1.987 [x \ln x + (1 - x) \ln (1 - x)] \quad [27]$$

for the formation of the solid solution according to



The uncertainties given in Eq. [26] and [27] are calculated at the 95% confidence limit with a generalization of the Student t variable (13).

Discussion

The gross composition of the condensed phase or phases, x and y given in Table III-VIII, changes during the experiments due to the preferential vaporization or condensation of Hg. From the P_{Hg} and P_2 data, the 70 and 95 m/o CdTe solid solution samples appear to be Te-saturated even at the lowest sample temperatures measured. Therefore, the condensed phase was a mixture of liquid and solid phases and the partial pressures measured were those in equilibrium with a solid solution of unknown composition which can only be determined from the tie line at that temperature. However, since the value of y is very close to 1/2 for each run, the composition of the solid solution, x , coexisting with the sample should be very close to the gross x value of the condensed phases. Therefore, we set a criterion for the data and take all runs with an x value within 1% of the starting value, x_s , as acceptable data for the three-phase curve of the solid solution $\text{Hg}_{1-x_s}\text{Cd}_{x_s}\text{Te}$. Hence, those runs with $10^3/T$ lower than 1.0092 for HCT-70 and 0.8974 for HCT-95 were not accepted as the partial pressures of, respectively, $x = 0.70$ and 0.95 solid solutions and were not included in the analysis.

Numerous analyses (14) have been made to determine the interaction parameters of pseudobinary solid solutions. These were indirect in that the interaction parameters were obtained from a fit to the pseudobinary solidus and/or liquidus by assuming simple solution models for the liquid and solid phases. In this paper, these parameters are obtained more directly for $\text{Hg}_{1-x}\text{Cd}_x\text{Te(s)}$. Recently, Brebrick *et al.* (4) have fit the phase diagram and thermodynamic properties in the Hg-Cd-Te system, including the data reported here, by assuming an associated solution model for the liquid and a quasiregular model for the solid solution. Their result for $W - VT$ (cal) is given by

$$W - VT = 1385 - 0.8452T \quad [29]$$

Comparing this with Eq. [25], one finds the individual values for W and V are very different, but the value of $W - VT$ only differs 89 cal at 1100 K and 456 cal at 900 K.

The partial pressures for the ternary samples are listed in Table V-VIII. Those partial pressures with sample temperature lower than the liquidus temperature (given in Table IX) should be considered with care. They are the partial pressures over a liquid-solid, two-phase mixture, whose gross or overall composition is given by the x and y values in the tables. The individual compositions of the liquid and the solid have not been determined. For those runs with sample temperatures higher than the liquidus temperature, the composition of liquid phase is, of course, given by x and y , and these data have been used in the fit of the Hg-Cd-Te phase diagram (4).

The liquidus temperatures and tie-line data in the Te-rich portion of the phase diagram, *i.e.*, $y < 1/2$, have been determined experimentally by various techniques (15-17). The most complete and reliable liquidus temperatures were reported by Harman (15) using visual observation of the last-to-melt crystals. He also established the tie-line data by analyzing the composition of epitaxially grown films. Except for run TER-3, which is out of the composition range he covered and not so reliable as the others due to the "not so apparent" break in the slope of $\log(P_{\text{Hg}})$ vs. $10^3/T$ plot as shown in Fig. 5, our liquidus temperatures and tie-line data agree well with his results. The interested reader can make a more detailed comparison with the aid of Fig. 10 and 11 of Ref. (3). It is worth noting that the optical absorbance measurement used here is a static technique and so the possible error due to large supercooling effects for Te-rich melts is eliminated.

Acknowledgment

The authors wish to express their gratitude for support by the Air Force Office of Scientific Research, Air Force Systems Command, under Grant no. AFOSR-78-3611. In particular, they wish to acknowledge the interest and help of Dr. Max Swerdlow, AFOSR.

Manuscript submitted Sept. 4, 1984; revised manuscript received Dec. 13, 1984.

REFERENCES

1. J. P. Schwartz, T. Tung, and R. F. Brebrick, *This Journal*, **128**, 438 (1981).
2. T. Tung, L. Golonka, and R. F. Brebrick, *ibid.*, **128**, 451 (1981).
3. T. Tung, C.-H. Su, P.-K. Liao, and R. F. Brebrick, *J. Vac. Sci. Technol.*, **21**, 117 (1982).
4. R. F. Brebrick, C.-H. Su, and P.-K. Liao, in "Semiconductors and Semimetals," Vol. 19, R. K. Willardson and A. C. Beer, Editors, Academic Press, New York (1983).
5. P.-K. Liao, Thesis, Marquette University, Milwaukee, WI (1983).
6. C.-H. Su, P.-K. Liao, Y. Huang, S.-S. Liou, and R. F. Brebrick, *J. Chem. Phys.*, **81**, 11 (1984).
7. A. C. G. Mitchell and M. W. Zemansky, "Resonance Radiation and Excited Atoms," Cambridge University Press, Cambridge, England (1961).
8. J. S. Penner, "Quantitative Molecular Spectroscopy and Gas Emissivities," Addison-Wesley, Reading, MA (1959).
9. J. A. Nelder and R. Mead, *Computer J.*, **7**, 308 (1965).
10. S. Sugawara and T. Sato, *Bull. Jpn. Soc. Mech. Eng.*, **5**, 711 (1962).
11. C.-H. Su, P.-K. Liao, T. Tung, and R. F. Brebrick, *High Temp. Sci.*, **14**, 181 (1981).
12. R. F. Brebrick, *J. Phys. Chem. Solids*, **40**, 177 (1979).
13. N. Arley and K. Buch, "Introduction to the Theory of Probability and Statistics," p. 192, John Wiley and Sons, New York (1950).
14. See, for example, G. B. Stringfellow and P. E. Greene, *J. Phys. Chem. Solids*, **30**, 1779 (1969); G. M. Blom, *This Journal*, **118**, 1834 (1971).
15. T. C. Harman, *J. Electron. Mater.*, **9**, 945 (1980).
16. R. Ueda, O. Ohtsuki, K. Shinohara, and Y. Ueda, *J. Cryst. Growth*, **13/14**, 668 (1972).
17. K. L. Lawley, Texas Instruments Technical Report, Contract MDA 903-79-C-1009 (1980).

Measurements of Temperature Dependent Stress of Silicon Oxide Films Prepared by a Variety of CVD Methods

G. Smolinsky and T. P. H. F. Wendling*

AT&T Bell Laboratories, Murray Hill, New Jersey 07974

ABSTRACT

We report the stress as a function of temperature of films of undoped and doped silicon oxide. These materials were prepared by chemical vapor deposition (CVD) from a variety of chemical reactions, under different physical conditions, and include DADBS (450°, 500°, and 550°C), TEOS (500° and 685°C), silane + oxygen (400°, 410°, and 440°C), wet oxygen (950°C), and plasma-enhanced (PECVD) silane + nitrous oxide (250°C). Data from each oxide were subjected to a linear least squares analysis and the first-order equation thus obtained was used to calculate the stress at 28°C and at the deposition temperature, the so-called intrinsic stress. From the slope of the line, we found the thermal coefficient of expansion of the oxides almost always to be less than that of <100> silicon. Dopants such as phosphorus and especially the combination boron and phosphorus lower the intrinsic stress of an oxide film relative to the undoped material and cause the rate of change of stress with temperature to be relatively flat. Except for 8% P- and 2.5% B,P-glass, oxides deposited below 500°C show a thermal hysteretic effect on heating to 450°C in air. Invariably the films become more tensile stressed, which must result from a shrinking and/or an extrusion of atoms from the matrix of the oxide. In contrast, thermally grown oxide exhibits a decided compressive stress that shows no hysteresis. No doubt this results from oxygen atoms intruding into the surface of the silicon lattice as the oxide layer grows.

Films of doped or undoped silicon oxide can be deposited on surfaces from a variety of chemical reactions and under different physical conditions. For example, SiO₂ is grown on a silicon surface at 950°C in a wet oxygen ambient, while a form of silicon oxide is deposited on a wafer maintained at 200°C from a plasma of silane and nitrous oxide. Furthermore, oxide films are deposited at 400°-450°C from the reaction of silane and oxygen. In addition, the decomposition of selected organosilicon esters and anhydrides at reduced pressure in the temperature range 400°-800°C can produce oxide films. Moreover, it is often possible to dope these films with several percent boron and phosphorus. Not too surprisingly, the physical properties of the oxides prepared in these different ways differ. In this report, we will be concerned with the stress induced in a <100> silicon wafer by a silicon oxide film. We will discuss the intrinsic stress, *i.e.*, the stress of the as-deposited film at its deposition temperature, and the rate of change of stress with temperature.

Experimental Technique

Materials.—The silicon wafers were of <100> orientation, either 3 or 4 in. in diameter and between 0.021 and 0.023 in. thick. Using standard low pressure chemical vapor deposition (LPCVD) or plasma-enhanced chemical vapor deposition (PECVD) techniques, silicon oxides were deposited on silicon wafers from a variety of chemical sources at a temperature appropriate for the method employed. These sources included diacetyoxyditertiarybutoxysilane (DADBS) (1); tetraethoxysilane (TEOS); silane, phosphine, and oxygen (P-glass); steam (FOX); silane and nitrous oxide (PECVD). Phosphine and trimethyl borate were used to incorporate the dopants phosphorus (P) and boron (B), respectively, in TEOS-oxide films. Phosphine, diborane, silane, and oxygen were used to prepare B,P-glass.

Measurement of stress.—Stress of deposited oxide films was measured using an optically leveraged laser beam apparatus (2). The method involves the determination of the change in the radius of curvature of a silicon wafer caused by a thin (~ 10,000Å) film of oxide. The stress, σ , is inversely proportional to the change in this radius and can be calculated if Young's modulus and Poisson's ratio of the substrate are known (2, 3). Using the appropriate values of the various coefficients given in Ref. (2 and 3), the stress of any wafer was calculated as

$$\sigma = 1.51 \times 10^7 (D^2/t) (\Delta d) \text{ dyne cm}^{-2} \quad [1]$$

where D is the thickness of the wafer in mils, t is the film

thickness in thousands of Angstroms, and Δd is the displacement of the laser beam spot in centimeters.

The apparatus can be used to determine the stress as a function of temperature (2, 4). The stress at a particular temperature, σ_t , can be expressed as (5)

$$\sigma_t = \sigma_i + (T_t - T_d) \frac{E_f}{1 - \nu_f} (\alpha_s - \alpha_f) \quad [2]$$

where E_f is Young's modulus of the film, ν_f is Poisson's ratio of the film, α_s and α_f are the coefficients of thermal expansion of the substrate and film, respectively, T_t is the temperature of interest, T_d is the deposition temperature, and σ_i is the so-called intrinsic stress. Equation [2] implies that the temperature dependence of the stress is related to the thermal expansion coefficients of the silicon wafer and the oxide film

$$\frac{d\sigma}{dT} = \frac{E_f}{1 - \nu_f} (\alpha_s - \alpha_f) \quad [3]$$

From the sign of $d\sigma/dT$, it is possible to determine the relative magnitudes of α_s and α_f .

Usually two wafers were used to measure the stress *vs.* temperature characteristics of any given deposited silicon oxide. First, the values for the laser beam spot displacement of the uncoated wafer, d_u , were measured at six temperatures close to 28°, 100°, 200°, 300°, 400°, and 450°C. The values for the beam displacement after application of the oxide film, d_c , were remeasured, and from the difference, $d_c - d_u$, a Δd was obtained that was used in Eq. [1] to calculate the stress at the temperature of the measurement. After allowing the coated wafer to cool to room temperature, the stress was remeasured over the same temperature range to determine the extent, if any, of a hysteresis. Data from each oxide were subjected to a linear least squares analysis, and the first-order equation thus obtained was used to compute the stress at 28°C and at the deposition temperature, the intrinsic stress, σ_i , and the value of $d\sigma/dT$. The assumption that the stress *vs.* temperature curve is linear within the temperature range investigated is supported by the findings of other work (3, 5).

Film shrinkage.—DADBS-oxide (1) was deposited on silicon wafers at 410°, 450°, 500°, 550°, and 600°C, respectively. The wafers were annealed in an argon atmosphere at 900°C for 1h. Film thickness before and after annealing was determined by an optical measurement.

Etching.—An optical method was used to determine the decrease of the thickness of silicon oxide on wafers that had been immersed for 1 min in 19°C, 7:1-buffered hydrofluoric acid. The stress/temperature relation had previously been determined for each of these wafers.

* Electrochemical Society Active Member.

Table I. Stress of various silicon oxides

Oxide	Method	Deposition temp., °C	Stress, σ_i (10^9 dyne cm^{-2})		Slope, $d\sigma/dT$ (10^6 dyne cm^{-2} deg^{-1})
			σ_{28}°	σ_i	
DADBS	LPCVD	450	1.27	4.82	8.42
DADBS	LPCVD	500	1.29	4.99	7.84
DADBS	LPCVD	550	0.58	4.84	8.15
DADBS/O ₂	LPCVD	500	-0.68	3.47	8.81
4%P-DADBS	LPCVD	550	-0.60	1.98	4.94
TEOS	LPCVD	685	0.49	3.82	5.06
5%P-TEOS	LPCVD	685	-0.05	1.12	1.06
2,5%B,P-TEOS	LPCVD	685	-0.52	-0.17	0.54
5,4%B,P-TEOS	LPCVD	685	-0.27	0.23	0.77
3.5,14%B,P-TEOS	LPCVD	500	1.89	1.28	-1.30
0%P-glass	LPCVD	400	-2.85 (-2.14) ^a	1.59 (-1.43) ^a	3.41 (1.89) ^a
6%P-glass	LPCVD	400	0.03 (1.02) ^a	1.38 (1.59) ^a	3.62 (1.52) ^a
8%P-glass	LPCVD	400	0.84	1.54	1.88
8%P-glass	LPCVD	440	0.71	1.29	1.41
2,5%B,P-glass	LPCVD	410	0.43	2.59	5.64
FOX	LPCVD	950	-3.10	-1.82	1.39
SiH ₄ + N ₂ O	PECVD	200	-0.54 (1.36) ^{a,b}	0.14 (1.55) ^{a,b}	

^a These numbers were obtained from a repeated measurement of the stress. See, for example, Fig. 5.

^b See Fig. 8.

Results and Discussion

Table I lists the silicon oxides investigated and the calculated values for the stress of each material determined at 28°C and at the deposition temperature and the rate of change of stress with temperature. Table I also gives the deposition method and temperature. A discussion of each material follows.

DADBS-oxide.—Stress measurements.—Three sets of two wafers each were coated with 9000-10,000Å of silicon oxide by the thermal decomposition of DADBS in a LPCVD (~ 0.7 torr) apparatus at 450°, 500°, and 550°C, respectively. The stress induced on the wafers is listed in Table I. Plots of measured stress vs. wafer temperature for the 450° and 550°C deposited oxides are shown in Fig. 1. The film deposited on wafers held at 450°C clearly exhibits hysteresis, while the 550°C film does not; it was unclear whether the film deposited on 500°C wafers did or did not. From Table I, it is seen that all three neat DADBS-oxides possess essentially the same degree of tensile intrinsic stress, σ_i , ($\sim 4.9 \times 10^9$ dyne cm^{-2}) and show almost the same stress at room temperature. Figure 2 shows plots of stress vs. wafer temperature of 500° DADBS-oxides prepared from neat DADBS or a 1.2:1 DADBS-oxygen mixture. Clearly the addition of oxygen results in a material with a smaller tensile intrinsic stress but which shows a marked hysteresis. Note that the calculated slope, $d\sigma/dT$, of the stress vs. temperature plot for each DADBS-oxide measured the first time is nearly the same ($\sim 8.3 \times 10^6$ dyne $\text{cm}^{-2}/^\circ\text{C}$). The incorporation of ~4% phosphorus (I) into the DADBS-oxide film lowers the intrinsic stress by a factor of ~ 0.4 and reduces the slope, $d\sigma/dT$, as well. The phosphorus-doped oxide exhibits a slight hysteretic effect.

Annealing and film shrinkage.—Wafers maintained at 410°, 450°, 500°, 550°, and 600°C, respectively, were coated with a DADBS-oxide film whose thickness was measured before and after a 1h anneal at 900°C in an argon atmosphere. Percent decrease in film thickness vs. deposition temperature is plotted in Fig. 3 along with a linear fit to the data. We see that the higher the deposition temperature, the less the film shrinks on annealing. In addition, it was observed that the higher the deposition temperature, the thicker a film could be deposited before cracking: DADBS-oxide deposited in the range 410°-550°C was found to crack at ~ 6500Å at the lower temperature but could be deposited to ~ 20,000Å at the higher temperature.

Summary.—The lower the deposition temperature of a DADBS-oxide, the less dense and the weaker the resulting film. At the time of deposition, these films possess a relatively high degree of tensile stress which, however, decreases on cooling to room temperature. From Eq. [3] and the positive value of the slope, $d\sigma/dT$, it is clear that the coefficient of thermal expansion of silicon, α_s , is greater than that of the oxide α_i . The values of the room temperature and intrinsic stress, as well as the slope of the stress/temperature line, are almost independent of the deposition temperature in the range 450°-550°C. This implies that if a more dense oxide could be produced at the lower temperature, it probably would not crack even if deposited to a thickness approaching that achieved at the higher temperature. The addition of oxygen to the DADBS or incorporation of phosphorus produces an oxide film with a lower tensile intrinsic stress. These films

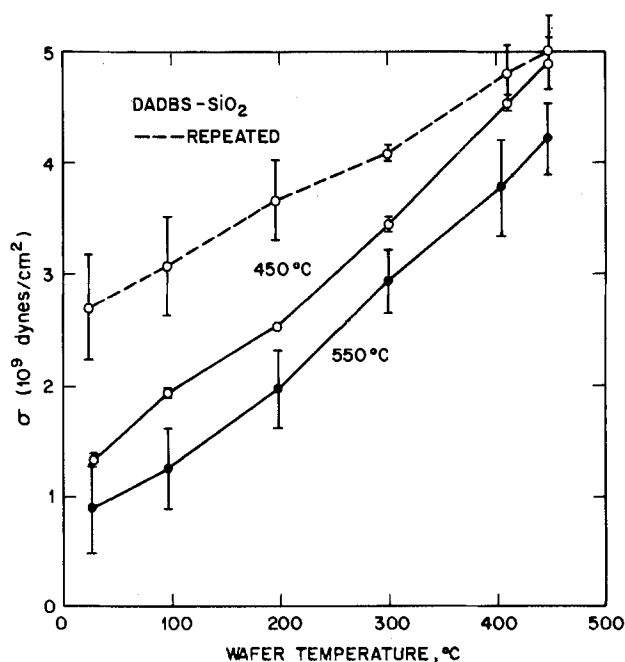


Fig. 1. Plot of the measured stress as a function of temperature of two DADBS-oxide films, one deposited at 550°C and the other at 450°C. The dotted curve was obtained from a repeated measurement of the 450°C sample.

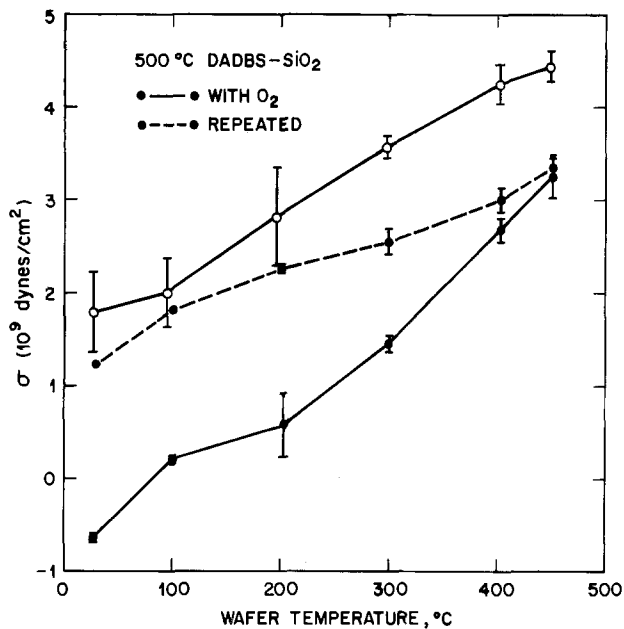


Fig. 2. Plot of the measured stress as a function of wafer temperature of two DADBS-oxide films, one prepared from neat DADBS and the other mixed with oxygen. The dotted curve is a repeated measurement.

must shrink on heating to 450°C, since the hysteretic effect results in a more tensile-stressed film at room temperature. However, note that the intrinsic stress is still less than that of the oxide prepared from neat DADBS. This may account for the observation that added oxygen enables deposition of a thicker crack-free film.

TEOS-oxide.—Stress measurements.—Duplicate 4 in. wafer were coated with about a micron of silicon oxide by the decomposition of TEOS at 685°C and a pressure of 0.3 torr, in a production facility LPCVD apparatus. Additionally, three sets of wafers were coated with an oxide doped with either phosphorus or both boron and phosphorus; a single wafer was coated at 500° with a boron-phosphorus-doped oxide. Table I lists the values for the stress and stress/temperature slope for these films. Figure 4 shows plots of the measured stress as a function of wafer tem-

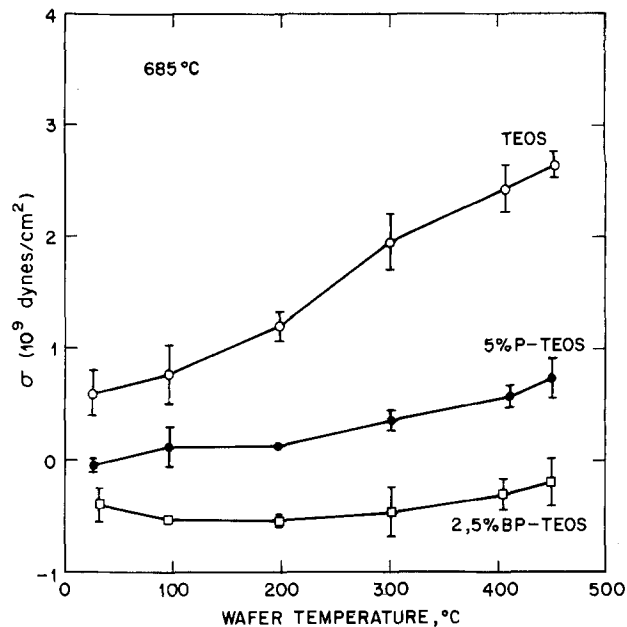


Fig. 4. Plots of the measured stress as a function of temperature of three oxide films deposited at 685°C from TEOS: undoped, 5% phosphorus-doped, and 2% boron-5% phosphorus-doped oxide films.

perature in air for TEOS-oxide, 5% P-TEOS-oxide, and 2,5% B,P-TEOS-oxide films, respectively, deposited at 685°. Clearly the incorporation of a dopant such as phosphorus, and especially the combination boron and phosphorus, lowers the intrinsic stress and also affects the slope of the stress/temperature line. The values for the stress and slope as well as the stress/temperature line for the 5,4% B,P-TEOS-oxide are similar to those found for the 2,5% B,P-TEOS-oxide. In contrast, the 500° B,P-TEOS-oxide has a much higher measured tensile intrinsic stress than the other two B,P-TEOS-oxides that, moreover, becomes even greater as the wafer cools to room temperature (a negative $d\sigma/dT$).

Summary.—Chemically, TEOS and DADBS decompose to silicon oxide by an analogous mechanism (1), yet the calculated intrinsic stress of the 685° TEOS-oxide is 80% of the tensile intrinsic stress of the DADBS-oxides, while the slope of the stress/temperature line is only about 60% of that of the DADBS-oxide lines. An explanation for these observations would seem to be related to the difference in the deposition temperature of the two processes: a higher temperature results in a lower tensile-stressed material. This argument is supported by the values for the stress listed in Table I for the 500° and 685°C B,P-TEOS-oxides.

P-glass.—Stress measurements.—Three sets of two wafers were coated at 400°C, and one set at 440°C, with silicon oxide from the reaction of silane, phosphine, and oxygen at 0.45 torr. The amount of phosphorus incorporated in the oxide was made to vary between 0% and 8%. Figure 5 shows a plot of the measured stress induced by a 400°C-deposited, 0% P-glass film as a function of wafer temperature. Clearly the repeated measurement reveals a hysteresis, which is also observed for the 6% P-glass film but not for the 400° or 440°C, 8% P-glass coatings. Table I lists the values of the calculated room temperature, and intrinsic stress, and the slope of the stress/temperature line. In addition, these same calculated values for the repeated, i.e., hysteretic, line are given in Table I. For both the 0% and 6% P-glass films, the annealed material shows an increase in tensile stress and a decrease in the value of $d\sigma/dT$. Figure 6 shows data for as-deposited and after a 685°C anneal, 2,5% B,P-glass. The marked decrease in tensile stress and the relatively flat behavior of the stress with temperature can be rationalized if the oxide is assumed to have flowed during the annealing process.

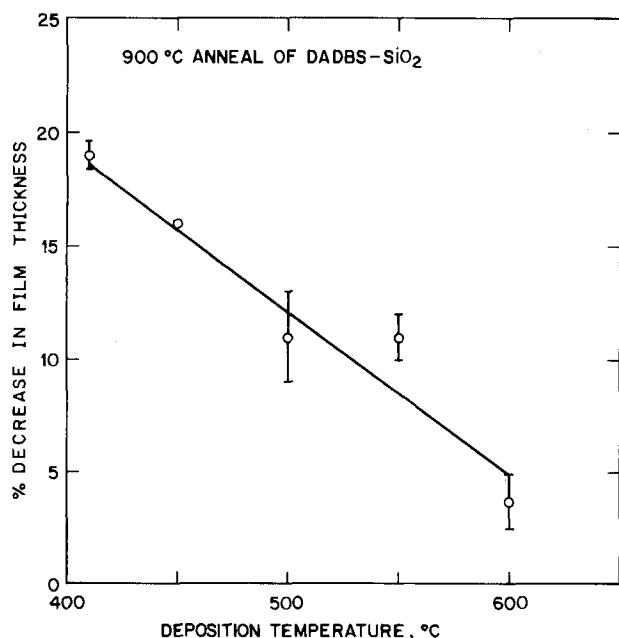


Fig. 3. Plot of the decrease in film thickness vs. deposition temperature of DADBS-oxide films after annealing for 1h at 900°C in an argon atmosphere.

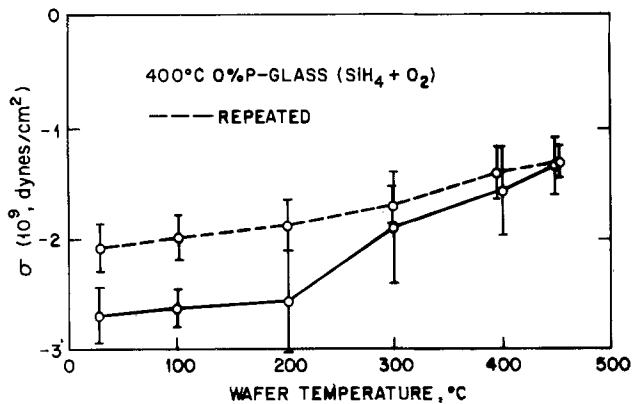


Fig. 5. Plot of the measured stress as a function of temperature of a 400°C deposited oxide from the reaction of $\text{SiH}_4 + \text{O}_2$.

Summary.—From the values listed in Table I for the two 8% P-glass oxides, the 40°C difference in their deposition temperatures is ineffectual. Surprisingly, a greater-than-6% phosphorus dopant is required in a P-glass oxide to achieve what at most a 5% phosphorus dopant does for a P-TEOS-oxide, *i.e.*, produce a material that exhibits a low tensile stress over the temperature range 28°C to the deposition temperature (compare the values listed in Table I). Again from Table I, we see that a 410°C B,P-silane glass is more tensile stressed than the B,P-TEOS glass. More provocative is the observation that the slopes of the stress/temperature lines for these two differently prepared doped oxides are disparate, indicating that the mechanical properties and/or the coefficients of expansion are markedly dissimilar. These disparities probably have their source in the 275°-285°C difference in the deposition temperatures employed to deposit the P-glass and P-TEOS, and B,P-glass and B,P-TEOS oxides, respectively. Indeed, following an anneal at 685°C, the stress/temperature curves for both B,P-doped glass and TEOS-oxide look similar (compare Fig. 4 and 6). Contrary to other oxides deposited at 450° or less, 8% P-glass and the B,P-glass show no hysteresis, indicating that these materials form an essentially homogeneous and relatively dense film.

The stress/temperature characteristics of CVD- $(\text{SiH}_4 + \text{O}_2)$ -oxide have been reported recently. In the first study

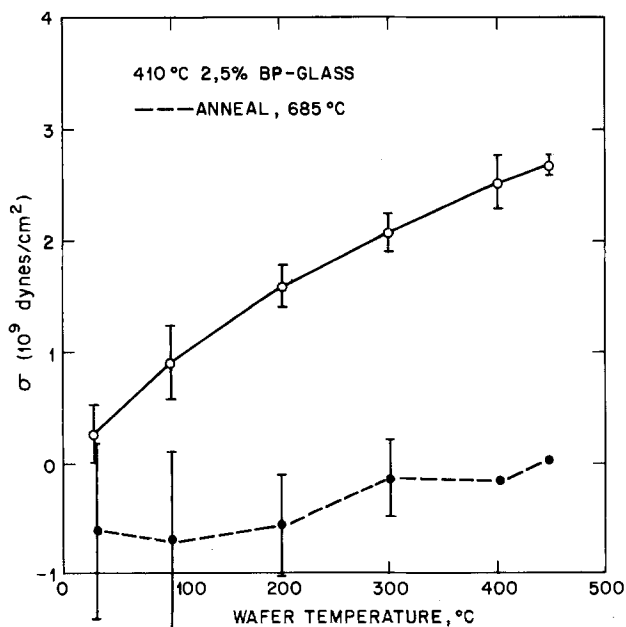


Fig. 6. Plots of the measured stress as a function of temperature of a 410°C, 2.5% B,P-glass. The solid line shows data for the as-deposited film, while the dotted line is for data from this film after a 0.5h anneal at 685°C.

(6), the oxide was deposited at a temperature of 415°C. The stress was measured in the temperature range 25°-450°C. It was decidedly compressive at 25°C ($\sim -2.8 \times 10^9$ dynes cm^{-2}) and increased steeply ($d\sigma/dT \sim 9 \times 10^6$ dynes $\text{cm}^{-2}/\text{deg}$) with temperature so that at 450°C the stress was tensile ($\sim 0.9 \times 10^9$). In the second study (7), the oxide was deposited at 250°C and found to be in tension at 20°C ($\sim 1.5 \times 10^9$ dyne cm^{-2}), which increased drastically ($d\sigma/dT = 10.7 \times 10^6$ dyne $\text{cm}^{-2}/\text{deg}$) in the temperature range 20°-125°C. Both of these silicon oxides exhibited thermal hysteresis, becoming more tensile stressed. The results from these two studies, while not in perfect agreement with each other or our work, show that a CVD- $(\text{SiH}_4 + \text{O}_2)$ -oxide deposited by three different systems exhibits similar stress/temperature behavior: a positive slope and a hysteretic effect.

FOX-oxide.—Stress measurement.—A layer of silicon dioxide was grown on two wafers that were maintained at 950°C in an ambient of wet oxygen at ~ 1 atm. Table I lists the values of the stress for this material, while Fig. 7 shows a plot of the measured stress at the indicated wafer temperatures. In addition, Fig. 7 shows the least squares linear fit to the data. The thermal oxide has a rather weak dependence of stress with temperature ($d\sigma/dT$); it deposits with a fairly high compressive stress ($= -1.82 \times 10^9$ dyne cm^{-2}) which becomes even more compressive at room temperature (-3.1×10^9).

Summary.—The compressive stress of thermal oxide no doubt results from oxygen atoms intruding into the surface of the silicon lattice as the oxide layer grows. Using Eq. [3] and the literature values for quartz (4) ($E/1 - \nu = 0.85 \times 10^{12}$ dyne cm^{-2} ; $\alpha_t = 0.55 \times 10^{-6}/\text{deg}$) and silicon (8) ($\alpha_s = 3.2 \times 10^{-6}/\text{deg}$), the slope, $d\sigma/dT$, was calculated to be $\sim 2.3 \times 10^6$ dyne $\text{cm}^{-2}/\text{deg}$. This is a factor of only 1.6 greater than that actually measured for the thermal oxide. This close agreement is a positive indication of the validity and accuracy of the method used in this study to determine the stress of the various silicon oxides.

The stress/temperature behavior of thermally grown silicon dioxide has been reported previously (6, 7). In the first study (6), the stress was measured in the temperature range 25°-900°C and was found to be in compression (from $\sim -2.2 \times 10^9$ to ~ 0 dyne cm^{-2}) with a rate of change of stress with temperature of about 0.3×10^6 dyne $\text{cm}^{-2}/\text{deg}$. The second study (7) measured the stress of the thermal oxide in the range -169°-300°C and also observed that the material was in compression (from ~ -3.8 to -3.2×10^9 dyne cm^{-2}) with a slope of about 1.7×10^6 dyne $\text{cm}^{-2}/\text{deg}$. These results are in moderately good agreement with our measurements on thermal oxide.

It should be noted that a relatively small value ($\sim 1 \times 10^6$) for the slope, $d\sigma/dT$, does not necessarily mean that the coefficient of expansion of the film, α_t , and substrate, α_s , are nearly equal. All that can be inferred is that the product $[E_f/(1 - \nu_f)] * [\alpha_s - \alpha_t]$ is a small number.

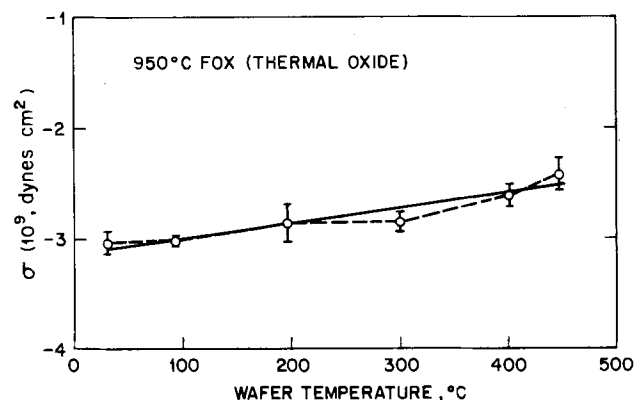


Fig. 7. Plot of the measured stress as a function of temperature of a 950°C steam-grown silicon dioxide film.

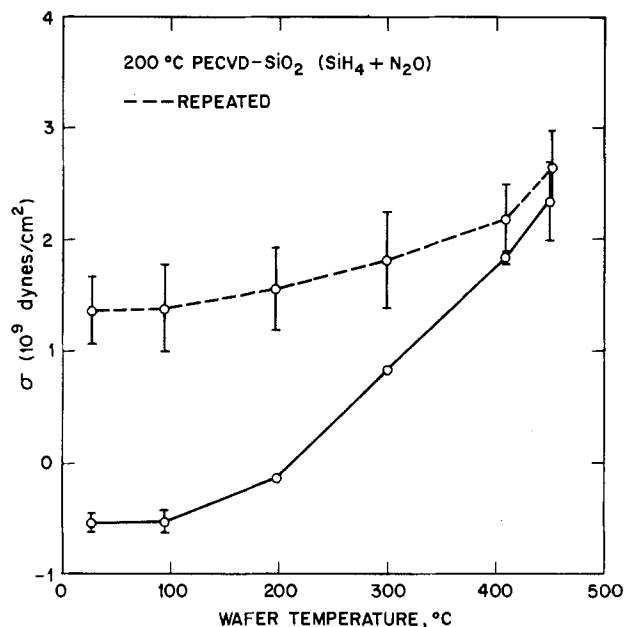


Fig. 8. Plot of the measured stress as a function of temperature of a 200°C PECVD grown oxide from the reaction of $\text{SiH}_4 + \text{N}_2\text{O}$. The dotted line is a repeated measurement.

PECVD-oxide.—Stress measurement.—Two wafers, maintained at 200°C, were coated with a silicon oxide layer by the plasma induced reaction of silane and nitrous oxide ($\text{SiH}_4 + \text{N}_2\text{O}$). The measured stress vs. temperature of this material is plotted in Fig. 8. At the deposition temperature, the stress is slightly compressive ($\sim -0.2 \times 10^9$), becoming somewhat more compressive at room temperature but remaining essentially flat in this temperature range. Heating the material above 200°C produces a decided change in the stress/temperature slope; it increases from a value of $\sim 1 \times 10^6$ to $\sim 10 \times 10^6$ dyne $\text{cm}^{-2}/\text{deg}$. In addition, this film exhibits a very pronounced hysteresis; the stress becomes tensile and increases slowly over the temperature range 28°–450°C from a value of $\sim 1.3 \times 10^9$ to $\sim 2.7 \times 10^9$ dyne $\text{cm}^{-2}/\text{deg}$.

Summary.—Properties such as etching rate (dilute HF), stress, and refractive index of PECVD-($\text{SiH}_4 - \text{N}_2\text{O}$)-oxide have been found to be a function of deposition temperature and to display a discontinuity at 200°C (9). PECVD-($\text{SiH}_4 + \text{N}_2\text{O}$)-oxide undergoes a marked change in stress on heating above 200°C in air. Because of the significant metamorphosis observed, this material would very likely change even if heated in an inert atmosphere. This marked increase in tensile stress, and its persistence on repeated measurement (see Fig. 8), a thermal hysteretic effect, can be rationalized by the loss of some material from the oxide film resulting in a decrease in volume with a concomitant increase in tension (6).

Aqueous HF etching rate.—Since both the stress and chemical reactivity of a silicon oxide should be a function of its physical and chemical nature, it was thought that there might be some correlation between hydrofluoric acid etching rate and measured stress of the various oxides. Table II lists the etching rate for several silicon ox-

Table II. HF etching rate of silicon oxides

Oxide	Deposition temp., °C	Rate ^a Å/min
DADBS	450	4460
DADBS	500	4525
DADBS	550	3532
TEOS	685	2674
5%P-TEOS	685	3857
2,5%B,P-TEOS	685	649
5,4%B,P-TEOS	685	476
0%P-glass	400	2412
8%P-glass	400	6660
8%P-glass	440	6457
FOX	950	857
($\text{SiH}_4 + \text{N}_2\text{O}$)	200	7896

^a 7:1 buffered HF at 19°C.

ides. There does not appear to be a correlation between this rate and any of the stress properties listed in Table I.

Conclusions

In general, the thermal coefficient of expansion of the various silicon oxides investigated is less than that of silicon. This results in a decrease in tension in films deposited on silicon wafers as they cool to room temperature. Dopants such as phosphorus and especially the combination boron and phosphorus lower the intrinsic stress, σ_i , of a silicon oxide film and, in addition, cause the rate of change of stress with temperature, $d\sigma/dT$, to be relatively flat. Except for the 8% P-glass and 2,5% B,P-glass, oxides deposited at temperatures less than about 500°C show a thermal hysteretic effect on heating to 450°C in air. Invariably, these oxide films become more tensile stressed. This can result from a shrinking and/or an extrusion of atoms from the matrix of the film (6, 7). A complementary study (10) to our work reached similar conclusions.

Acknowledgments

We thank D. S. Williams for many helpful discussions about stress and how it relates to silicon oxides. We thank F. B. Alexander for preparing the PECVD-($\text{SiH}_4 + \text{N}_2\text{O}$)-oxide. We are grateful to T. F. Retajczyk for allowing us to use his laboratory.

Manuscript submitted Nov. 16, 1984; revised manuscript received Jan. 7, 1985.

AT&T Bell Laboratories assisted in meeting the publication costs of this article.

REFERENCES

- G. Smolinsky and R. E. Dean, *Mater. Lett.*, In press.
- A. K. Sinha, H. J. Levinstein, and T. E. Smith, *J. Appl. Phys.*, **49**, 2423 (1978).
- D. S. Williams, Private communication.
- T. F. Retajczyk and A. K. Sinha, *Appl. Phys. Lett.*, **36**, 161 (1980).
- C. Blaauw, *J. Appl. Phys.*, **54**, 5064 (1983).
- A. Shintani, S. Sugaki, and H. Nakashima, *ibid.*, **51**, 4197 (1980).
- I. Blech and U. Cohen, *ibid.*, **53**, 4202 (1982).
- W. B. Brantley, *ibid.*, **44**, 161 (1973).
- A. C. Adams, F. B. Alexander, C. D. Capio, and T. E. Smith, *This Journal*, **128**, 1545 (1981).
- M. Shimbo and T. Matsuo, *ibid.*, **130**, 135 (1983).

Electrical Conductivity of Silicon Dioxide Thermally Grown on Silicon

J. K. Srivastava, M. Prasad, and J. B. Wagner, Jr.*

Center for Solid State Science, Departments of Physics, Chemistry, and Mechanical/Aerospace Engineering, Arizona State University, Tempe, Arizona 85281

ABSTRACT

DC and ac electrical conductivities of silicon dioxide thermally grown on p- (boron-doped) and n-type (phosphorous-doped) silicon have been measured in the temperature range of 25°-1100°C. Total dc conductivities varied from 10^{-9} to $10^{-16} \Omega^{-1}\text{cm}^{-1}$ in the temperature range of 25°-960°C. Arrhenius plots for total dc conductivities of SiO_2 grown on both the substrates exhibit two regions. Below 450°C, the conductivities were independent of temperature and are suggested to be governed by impurities. Above 450°C, the total dc conductivities increased with increase in temperature. The activation energies of conduction in the temperature range 500°-960°C were estimated to be 1.65 and 2.10 eV for SiO_2 grown on p- and n-type silicon, respectively. DC polarization measurements carried out in this temperature range suggest that conduction in SiO_2 is ionic as well as electronic. The ionic conduction is believed predominantly to be due to the transport of oxygen ions. AC conductivities were also measured in the temperature range of 550°-1100°C. The activation energies for the conduction in this temperature range were estimated to be 1.55 eV for SiO_2 on p-type silicon and 1.86 eV for SiO_2 on n-type silicon. These values are in close agreement with the values reported in the literature. AC conductivity of SiO_2 grown on n-type silicon was found to be lower than that of SiO_2 grown on p-type silicon.

In semiconductor and integrated circuit devices, silicon dioxide is grown thermally on silicon where it is used not only as an insulator, but also as a masking layer. The transport properties of SiO_2 thermally grown on silicon have therefore been studied by several investigators. Most of these studies have been restricted to a specific temperature region, depending on specific applications. Norton (1) and Sucof (2) independently studied the diffusion of oxygen in bulk fused silica. More recently, Irene (3) studied transport phenomena in thin SiO_2 films during oxidation of silicon. There is, however, considerable disagreement between the values of diffusivity determined directly and those estimated from the oxidation kinetics.

From marker studies (4-6), it is generally agreed that the inward migration of oxygen through the SiO_2 to the Si/ SiO_2 interface determines the kinetics of transport through SiO_2 . The mobile oxidant species in SiO_2 films has still not been uniquely determined. According to Revesz (7, 8), the oxygen migrating through SiO_2 during oxidation may not necessarily be a charged species. Neutral oxygen molecules may migrate through microheterogeneities, or the "channels" formed from $d\pi$ and $p\pi$ bonds (9) of silicon and lone pair electrons of the oxygen atom, respectively. Jorgensen's experiment (6) on the oxidation of silicon with and without applying an electric field, suggests that the oxygen diffusing through SiO_2 is negatively charged and that between 727° and 879°C SiO_2 is a mixed conductor with 0.4 as the value of ionic transference number (t_i). However, Raleigh (10) reported that Jorgensen's data could be equally well explained by electrolysis at each Si/ SiO_2 interface.

Mills and Kroger (11) measured electrical conductivity up to a temperature of 700°C to determine the mobile species in SiO_2 and concluded that the mobile species was charged oxygen. The extrapolated value of the total conductivity reported by Mills and Kroger (11) was several orders of magnitude higher than that reported by Raleigh (10) at 850°C and two orders of magnitude higher than the ac conductivity values of vitreous silica reported by Tripp *et al.* (12).

In spite of the large number of investigations, the exact nature of the transporting species through SiO_2 during oxidation is still unsettled. Similarly, there is considerable discrepancy between the data reported on the rate of oxidation of silicon, the diffusivities through the product layer, and the conductivity. Because of the inconsistencies in the reported data and the lack of conductivity data at higher temperatures, the present investigation was undertaken. Transport-number measurements were made

by electrical conductivity and open-circuit EMF methods on SiO_2 thermally grown on silicon substrates.

Experimental

1-5 kÅ thick SiO_2 films were grown thermally at one temperature, 1050°C, in dry oxygen on boron-doped p-type silicon <100> (14-22 $\Omega \text{ cm}$) and phosphorous-doped n-type silicon <100> (3.3 $\Omega \text{ cm}$) by Motorola, Incorporated. One side of these wafers was etched to provide a clean silicon surface. Platinum or molybdenum was sputtered thereon to provide an electrical contact. These oxidized wafers were cut into 1 × 1 cm square pieces and pressed together with oxide surface to oxide surface, to yield a symmetrical cell (A) in an oxygen activity corresponding to the Si/ SiO_2 equilibrium. For comparison, a 3 kÅ oxide thickness on p-type silicon was obtained, in this laboratory, by passing O_2 over hot water maintained at 95°C then over Si at 1100°C at a rate of 4 liter/min. AC conductivity of this SiO_2 was also measured using a cell, configuration (A). For polarization and open-circuit EMF measurements, 1 kÅ thick platinum or molybdenum was sputtered on the SiO_2 side and assembled as an asymmetrical cell (B).

The cell configurations were: for symmetrical cell (A), for total ac and dc conductivity



where M is Pt or W.

Asymmetrical cell (B) for polarization and EMF measurements



where M is Pt or W.

The apparatus consisted of a double-walled silica tube and a sample holder made of quartz with inlets and outlets for gases in each jacket, electrical circuits, and a Lindberg heavy duty furnace. Platinum or tungsten (~0.12 mm thick) in the form of disk or rectangular plate was used as electrode material. The tubular quartz furnace was electrically shielded by grounding a closely wound Kanthal wire around the tube. Shielded cables were used for external leads. Alumina disks were used in order to avoid any possible contact between the sample and the sample holder.

Each cell was positioned between platinum electrodes, and pure dry argon (oxygen less than 1 ppm) was allowed to circulate in each jacket of the silica tube. The argon in the outer jacket was used to eliminate the possible diffusion of H_2O through the quartz wall and into the sample. The samples were annealed at 600°C for about 12h prior to

*Electrochemical Society Active Member.

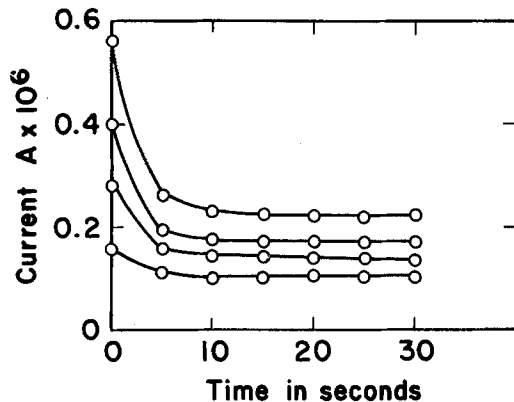


Fig. 1. Typical current vs. time curve at 860°C for SiO₂ grown on n-type Si in cell (A).

measurements. After such annealing, it was found that adjoining SiO₂ surfaces in cell (A) were bonded together.

DC conductivity was measured with cell (A) using 1000-3000Å thick SiO₂ by connecting the samples in series with a 10⁶-10¹¹Ω precision glass encapsulated standard carbon film HiMEG-Resifrom. 0.1-1.3V were applied using a Keithley 260 nV source. The voltage drop across the standard resistor was measured with a Keithley 604 differential electrometer.

Electronic conductivity was measured using the polarization technique described by Wagner (13, 14) using cell configuration (B), as suggested by Raleigh (10). In this experiment, positive potentials of 0.1-0.8V were applied on the SiO₂/Pt side using a Keithley 260 nV source and measuring the voltage drop across the standard resistor with an electrometer.

AC conductivity was measured using cell configuration (A) for different thicknesses of SiO₂ on silicon in the temperature range of 550°-1100°C, using a Wayne Kerr Model 211 conductivity bridge. The conductivities were also measured at different frequencies (50 Hz-1 kHz) at various temperatures.

Results and Discussion

Symmetrical cell (A).—The values of current (*I*) at different applied voltages (*V*) were obtained, initially in the temperature range 500°-960°C. The measurements were subsequently extended to temperatures between 500° and 25°C. At higher temperatures and higher applied voltages, the current was found to change with time for the same

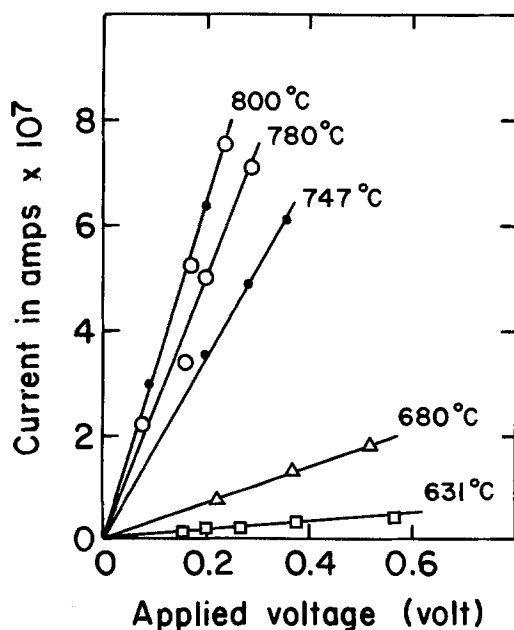


Fig. 2. I-V curves for cell (A) consisting of SiO₂ on p-type Si

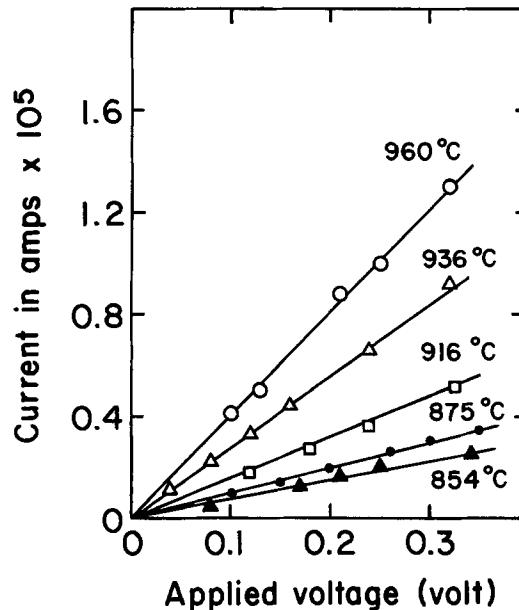


Fig. 3. I-V curves for cell (A) consisting of SiO₂ on p-type Si

applied voltage. A typical current time curve at 860°C for SiO₂ grown on n-type silicon is shown in Fig. 1. This behavior is indicative of ionic polarization. The initial current, however, varied linearly with applied voltage, exhibiting ohmic behavior, and, therefore, this was utilized to obtain the total dc conductivity. The slope of the I-V curve yielded the conductance and the total conductivity was computed from the relation $\sigma = m/lA$ where *m* is the slope of the I-V curve, *l* is the thickness, and *A* is the area of cross section of SiO₂. Because of the polarization, current reversal was not routinely carried out, but occasionally some measurements were obtained. The values thus obtained were found to be independent of the direction of the applied voltage.

Figures 2-5 show the typical current voltage plots at various temperatures. The behavior was ohmic at all the temperatures studied up to an applied EMF of ~0.3V. Higher voltages resulted in considerable damage to the platinum electrodes and the sample, probably because of

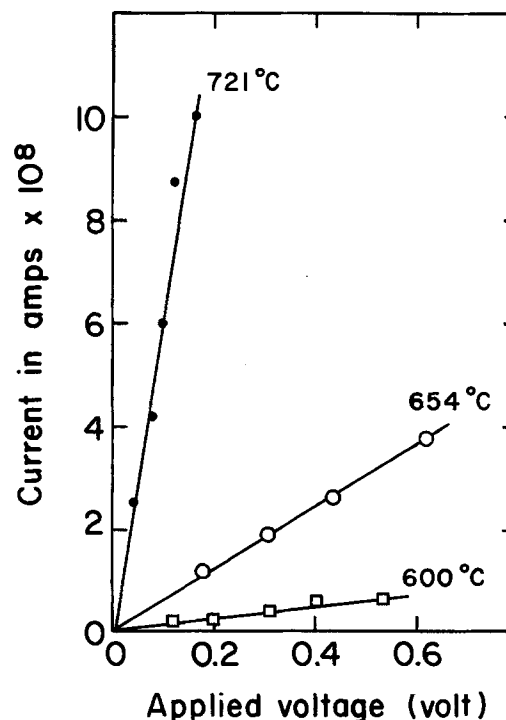


Fig. 4. I-V curves for cell (A) consisting of SiO₂ on n-type Si

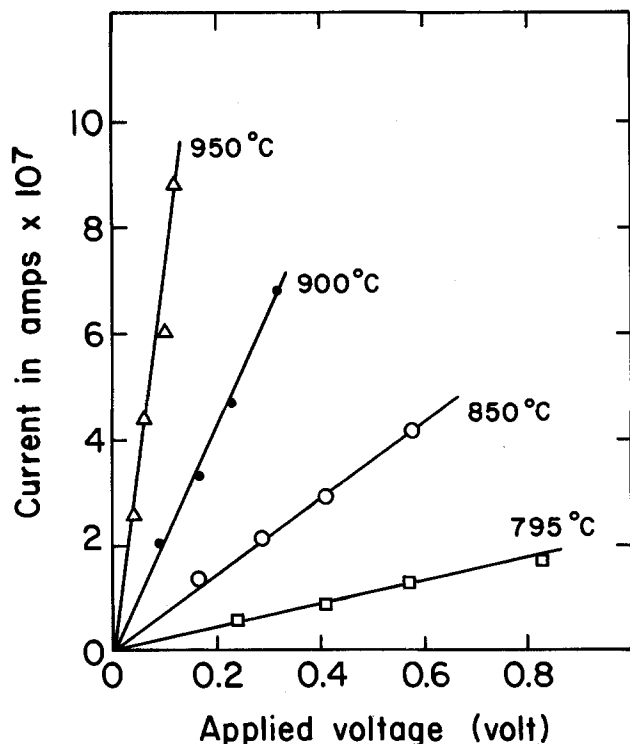


Fig. 5. I-V curves for cell (A) consisting of SiO₂ on n-type Si

the formation of platinum silicide. In a few experiments, macroscopic holes as large as 1.5 mm diam were found in the electrodes. For this reason, the applied voltages were restricted to 1V and platinum electrodes were replaced by tungsten electrodes.

Assuming that these cells are in thermal and chemical equilibrium, the measured conductivity corresponds to

silica in equilibrium with the oxygen activity equivalent to the dissociation pressures of SiO₂-Si.

Figure 6 shows the Arrhenius plots for the total dc conductivity of SiO₂ grown on p- and n-type silicon. Each plot clearly indicates two regions. Below ~450°C, the total conductivity is almost independent of temperature within the experimental scatter. Above ~450°C, the conductivity rises sharply with temperature for SiO₂ grown on both p- and n-type silicon. The activation energies were 1.65 and 2.10 eV for SiO₂ grown on p- and n-type silicon, respectively.

The ac conductivity was measured in the temperature range of 500°-1100°C initially at 1 kHz and subsequently at frequencies down to 50 Hz. Below 500°C, the conductivity was too low to be measured accurately by the conductivity bridge used. Figures 7 and 8 show the plots of log σ (1 kHz) vs. reciprocal of temperature in the temperature range 500°-1100°C for SiO₂ grown on p- and n-type silicon, respectively. Both the plots yielded straight lines. The activation energies calculated from the slopes of these lines were 1.55 and 1.86 eV for SiO₂ grown on p- and n-type silicon respectively. Conductivity vs. frequency plots are shown in Fig. 9 for various temperatures. The conductivity of SiO₂ grown on n-type silicon decreases above 1000°C. The values of ac conductivity at a fixed temperature were found to be higher than the dc conductivity. However, after extrapolating the ac conductivity data to zero frequency, the values, although slightly higher, were very close to the dc conductivity values. The variation of conductivity with frequency was more pronounced in the SiO₂ grown on p-type silicon than the one grown on n-type Si. An activation energy for conduction (extrapolated to zero frequency) of SiO₂ grown on p-type silicon was estimated to be 1.73 eV (Fig. 10). This is in close agreement to that obtained from the dc conductivity (1.65 eV).

Figure 11 shows the temperature dependence of ac conductivity at 1 kHz for different thicknesses of SiO₂. The conductivity values fall on a single straight line within ex-

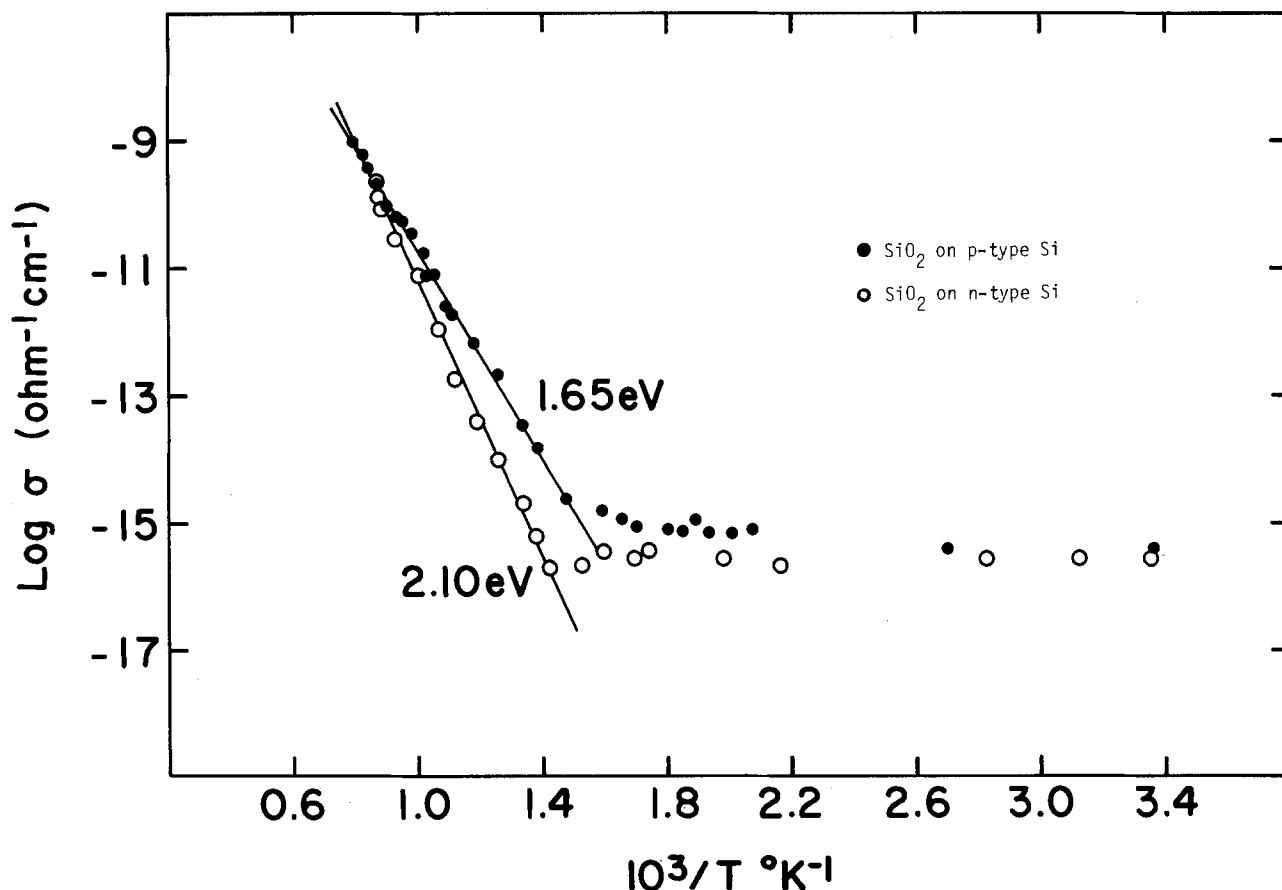


Fig. 6. Log σ vs. reciprocal temperature for cell (A) (SiO₂ on p-type Si; SiO₂ on n-type Si)

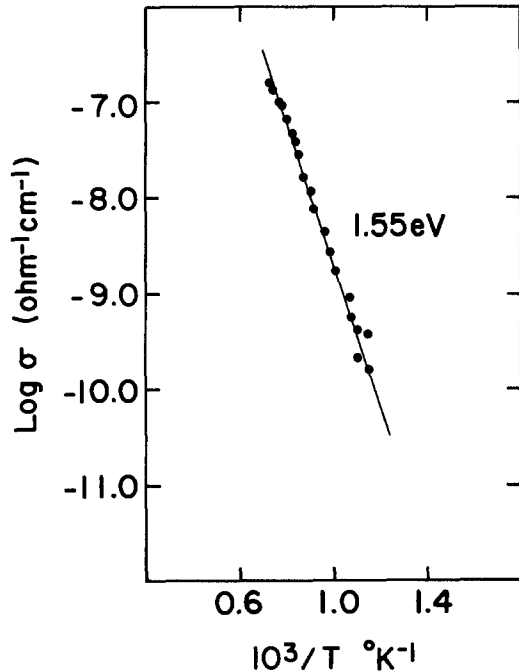


Fig. 7. Log σ vs. reciprocal temperature for SiO_2 on p-type Si measured in cell (A) (ac measurement 1 kHz).

perimental error, suggesting no dependence on oxide thickness. Figure 12 shows the Arrhenius plot for the conductivity of SiO_2 grown in wet oxygen. Analysis of this plot yields an activation energy of 1.2 eV. Comparison of this plot with that in Fig. 7 shows that the conductivity for the wet oxide is higher than for the dry oxide.

Asymmetric cell (B).—Polarization measurements.—DC polarization measurements were made using an asymmetric polarization cell configuration B. In this type of cell, the ionic conduction is blocked due to application of positive potential on SiO_2/Pt side. Under these conditions, for a mixed conductor a steady state current (I) for a given applied potential (V) is given by the following expressions (13, 14)

$$I = \frac{AkT}{Le} \sigma_n [1 - \exp(-eV/z_1kT)] + \sigma_p [\exp(eV/z_1kT) - 1] \quad [1]$$

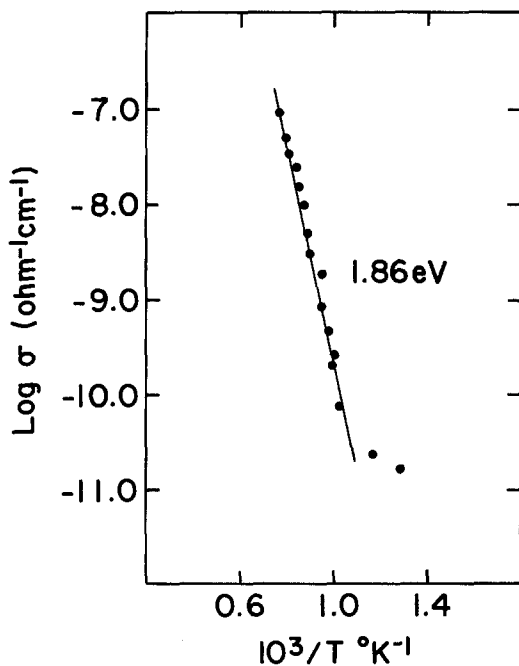


Fig. 8. Log σ vs. $10^3/T$ for SiO_2 on n-type Si measured in cell (A) (ac measurements 1 kHz).

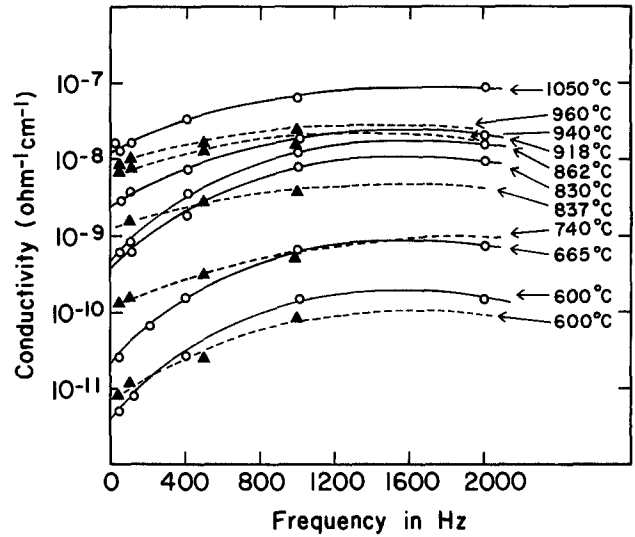


Fig. 9. σ vs. frequency for SiO_2 on p-type Si in cell (A) (solid line); and n-type Si (dashed line).

where A is the cross-sectional area, L is the thickness of the SiO_2 sample, e is the electronic charge, z_1 is the effective charge on an oxygen ion, and σ_n and σ_p are the electronic conductivities due to electrons and holes, respectively. In the limiting case when $V \gg kT/e$

$$I = \frac{AkT}{Le} [\sigma_n + \sigma_p \exp eV/kT] \quad [2]$$

thus the plot of I vs. $\exp(eV/z_1kT)$ yields a straight line. The slope and the intercept of this line gives σ_p and σ_n , respectively

$$\sigma_n = \frac{Le}{AkT} \text{ (intercept extrapolation of plateau)}$$

$$\sigma_p = \frac{Le}{AkT} \text{ (slope)}$$

Moreover, the shape of the current vs. polarization potential is indicative of the n or p character of the material (13).

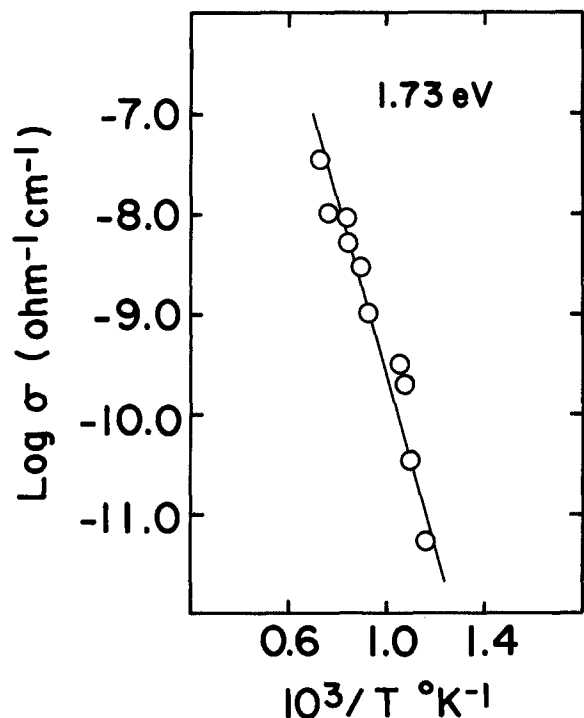


Fig. 10. Log σ vs. $10^3/T$ for the data of Fig. 9 extrapolated to zero frequency.

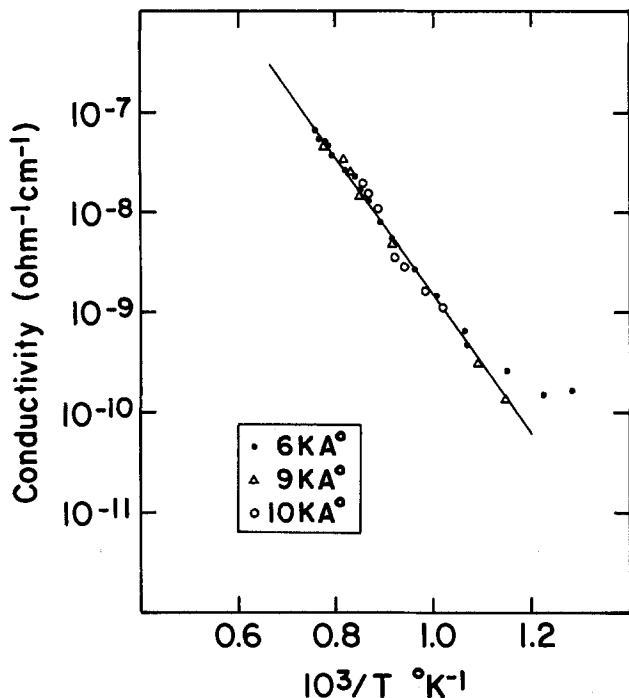


Fig. 11. Conductivity vs. reciprocal temperature for different thicknesses of SiO₂ on p-type Si cell (A) (ac measurement 1 kHz).

Figures 13-16 show the current voltage plots for SiO₂ grown on n- and p-type silicon in the temperature range 545°-960°C. These plots show a plateau, indicating that the electronic conductivity is predominantly due to electrons. The partial conductivity due to electrons can be obtained from the extrapolation to zero applied voltages of the plateau in the above curves. The electronic transference number and total conductivity for SiO₂ grown on n-type substrate is found to be higher than for SiO₂ grown on p-type at higher temperatures. An Arrhenius plot for the conductivity due to the electrons is shown in Fig. 17.

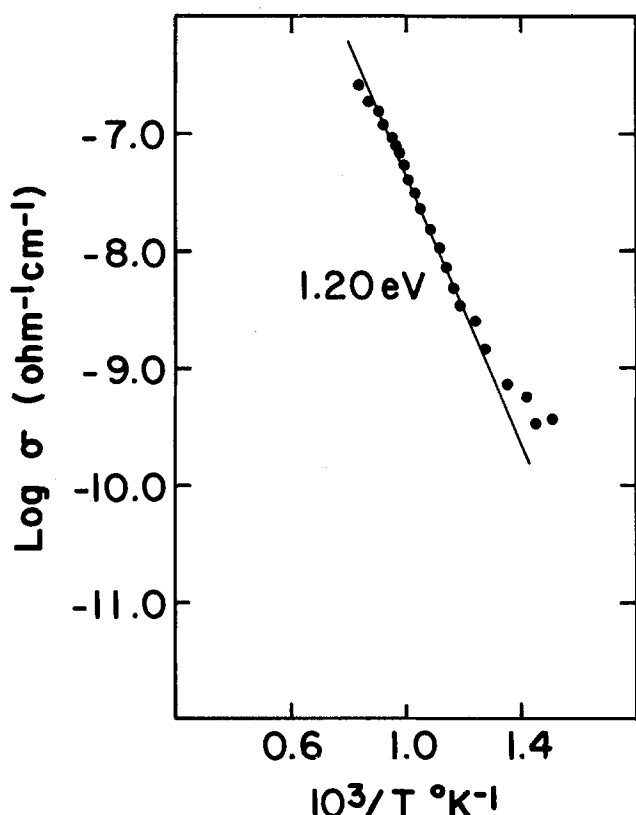


Fig. 12. Log σ vs. reciprocal temperature for SiO₂ grown under wet condition on p-type Si cell (A) (ac measurement 1 kHz).

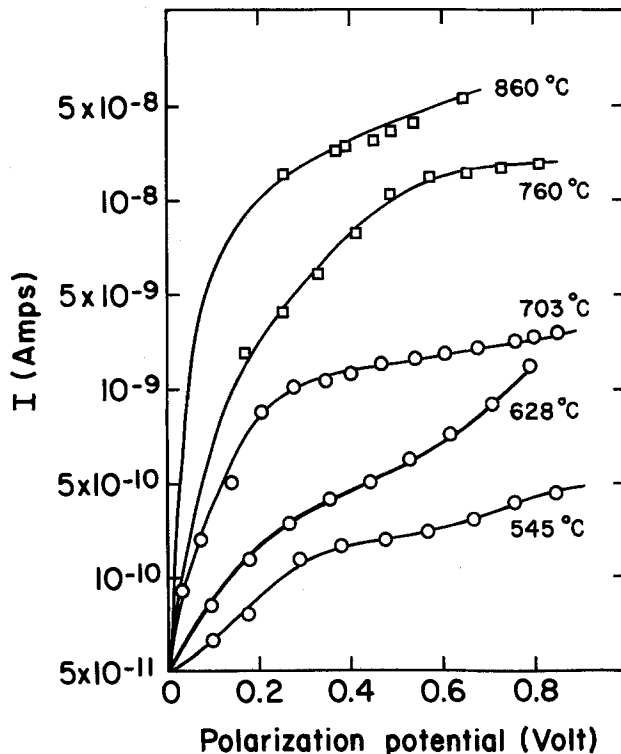


Fig. 13. Typical polarization curves for asymmetric cell (B) containing SiO₂ on p-type Si.

Open-circuit voltage measurement.—Open-circuit voltage measurements were made using cell B. In these measurements the oxygen activity varied on one side using Ar + O₂ mixtures, while oxygen activity at the other side was fixed by the Si-SiO₂ equilibrium.

The EMF of this cell is given by

$$E_{\text{theoretical}} = \frac{RT}{nF} \ln \frac{P_{\text{O}_2} \text{ (in argon)}}{P_{\text{O}_2} \text{ (Si/SiO}_2\text{)}}$$

and

$$t_i = \frac{E_{\text{measured}}}{E_{\text{theoretical}}}$$

where E is EMF in voltage, $E_{\text{theoretical}}$ is that calculated from the free energy of formation, F is Faraday, n is number of electrons per mole of oxygen involved in the transport. The partial pressure of oxygen in argon was con-

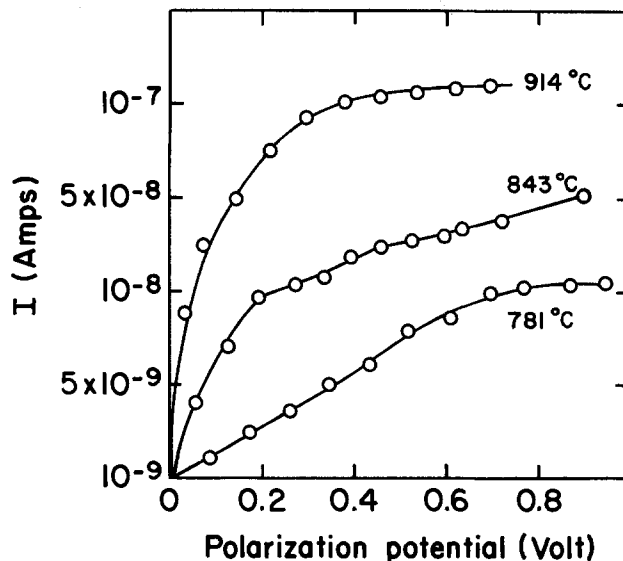


Fig. 14. Typical polarization curves for asymmetric cell (B) containing SiO₂ grown on p-type Si.

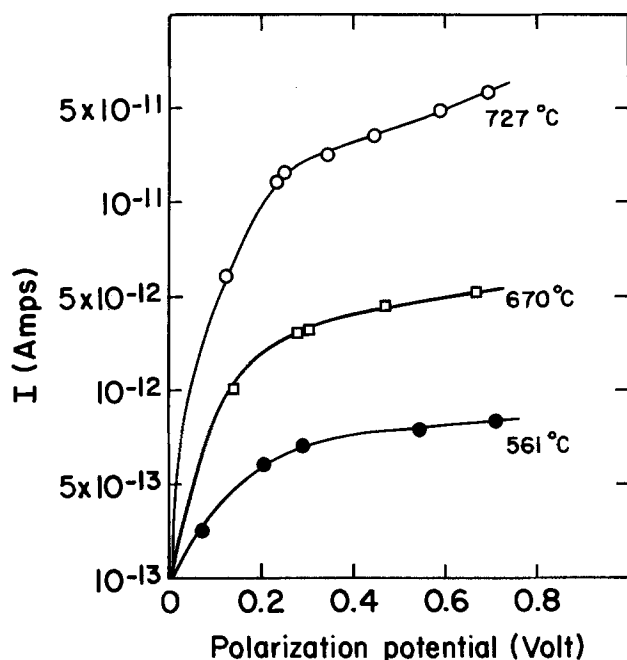


Fig. 15. Typical polarization curves for asymmetric cell (B) containing SiO_2 grown n-type Si.

trolled by passing argon over titanium chips kept at different temperatures. For higher oxygen pressures, pure Ar and oxygen were mixed in desired proportions. The oxygen pressures were measured using a zirconia probe. Figure 18 shows the plot of $\log P_{\text{O}_2}$ vs. $FE/2.303RT$. The slope of this plot yields t_i/n' over a given pressure range. The t_i for SiO_2 grown on n-type Si was calculated assuming $n = 4$ per mole of oxygen and was found to vary from 0.4 at low oxygen pressure to 0.76. These data are consistent with the observations made by Mills and Kroger (11).

The data obtained in the present investigation are compared with the data reported by other investigators in Fig. 19. It is clearly evident that below a certain critical temperature, the total conductivity is almost independent of

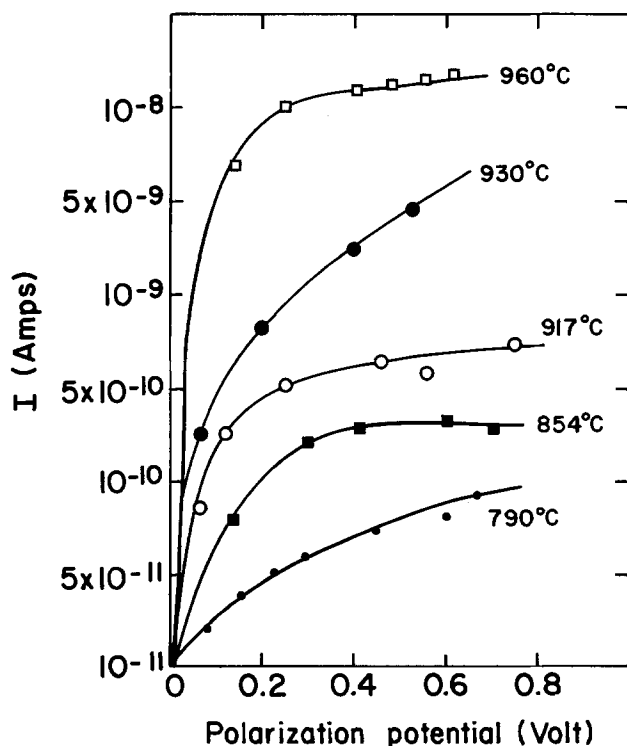


Fig. 16. Typical polarization curve for asymmetric cell (B) containing SiO_2 grown on n-type Si.

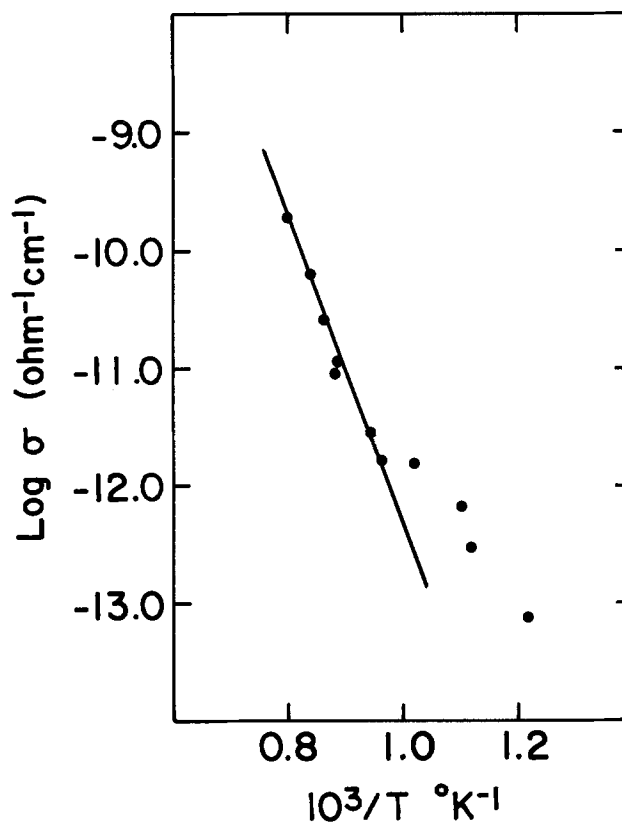


Fig. 17. $\log \sigma_n$ vs. $10^3/T$ for SiO_2 on p-type Si substrate.

temperature and above this temperature the conductivity increases in temperature with a higher activation energy. There is considerable discrepancy between various investigators regarding the temperature at which this transition occurs. Our data show a comparatively sharper transition. The temperature-independent conductivity below 450°C for our data is likely to be due to electronic contribution and is thought to be impurity controlled. Conduction in the higher temperature range $450^\circ\text{--}960^\circ\text{C}$ is mixed ionic and electronic.

Table I shows the available experimental, theoretical and extrapolated conductivity data at 850° and 25°C , and in Table II the corresponding activation energies have been summarized. The values of conductivity at 850°C calculated by Raleigh (10) from two independent ap-

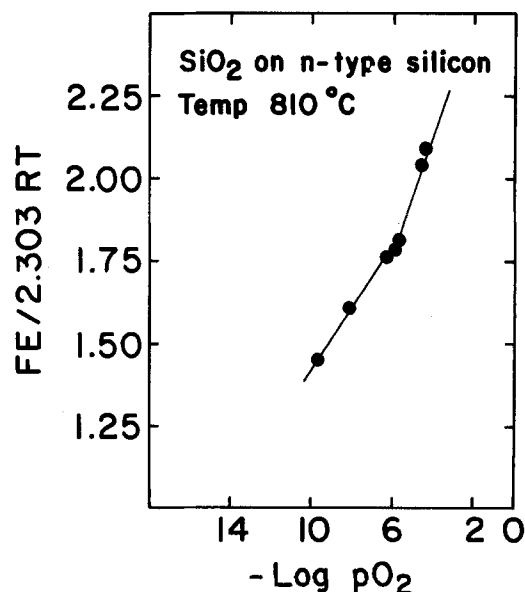


Fig. 18. Open-circuit EMF vs. $-\log P_{\text{O}_2}$ for cell (B) at 810°C . (SiO_2 on n-type Si substrate.)

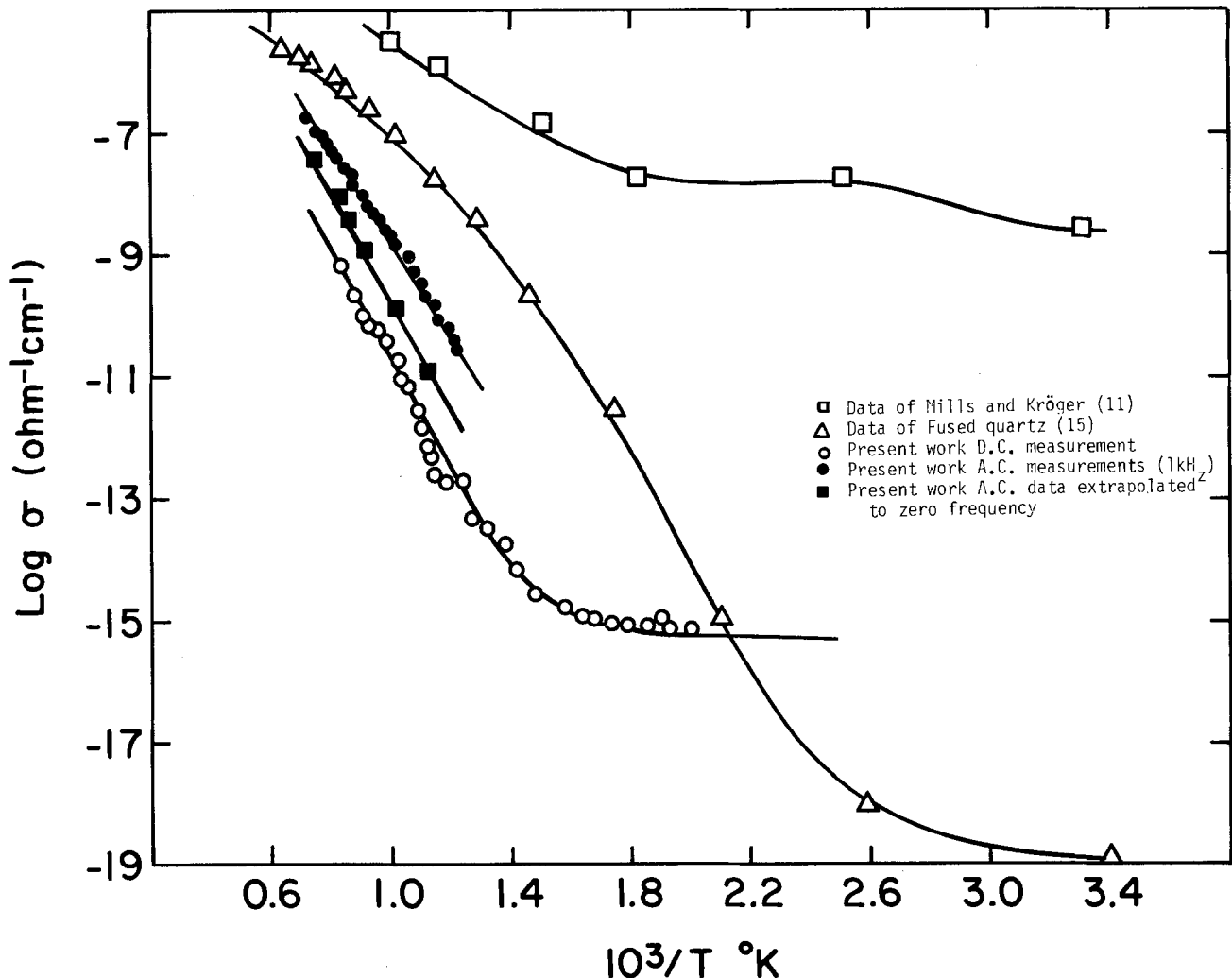


Fig. 19. Arrhenius plots of $\log \sigma$ vs. $10^3/T$ for cell (A). For our data, for fused quartz, and for the data of Mills and Kroger (11)

proaches are $3.7 \times 10^{-11} \Omega^{-1}\text{cm}^{-1}$ and $3.5 \times 10^{-11} \Omega^{-1}\text{cm}^{-1}$. The former value is obtained from the experimental data of Jorgensen (6), whereas the latter value was estimated from the diffusion of oxygen in SiO₂ as measured by Sucov (2). These values may be compared with our dc conductivity values, viz., $10 \times 10^{-11} \Omega^{-1}\text{cm}^{-1}$ and 8×10^{-11}

$\Omega^{-1}\text{cm}^{-1}$ for SiO₂ grown on p- and n-type silicon, respectively.

Our dc conductivity data obtained for different thickness of SiO₂ are reproducible within an error limit of 30%-40% and are in good agreement with Raleigh's (10) calculated values. The absolute values of conductivity dif-

Table I. Conductivity data

Ref.	Conductivity ($\Omega^{-1}\text{cm}^{-1}$)	
	850°C	25°C
(6, 10) ^a	3.7×10^{-11}	
(2, 10) ^b	3.5×10^{-11}	
(12) ^c	8.9×10^{-8}	
(11) ^d	6.3×10^{-6}	1.65×10^{-10}
(15) ^e		1.70×10^{-11}
(15) ^f		3.3×10^{-16}
		5×10^{-17}
Present work		
DC measurement	SiO ₂ on p-type Si 10×10^{-11}	5.0×10^{-16}
	SiO ₂ on n-type Si 7.8×10^{-11}	2.75×10^{-16}
AC measurement	SiO ₂ on p-type Si 10×10^{-9}	
	SiO ₂ on n-type Si 3.16×10^{-9}	
Extrapolated to zero frequency	SiO ₂ on p-type Si 6×10^{-10}	

^a Calculated by Raleigh (10) from Jorgensen's data (6).

^b Calculated by Raleigh (10) from Sucov's data (2).

^c Extrapolated from the data of Tripp *et al.* (12).

^d Extrapolated from Mills and Kroger data to 850°C.

^e Extrapolated to 25°C.

^f Data from Silicon handbook (15).

Table II. Activation energy (eV)

Ref.	Temp. range (C)	From conductivity	From diffusion		From rate constant	
(12)	1300°-1400°	0.72				
	1400°-1550°	2.93				
(11)	400°-600°	1.20				
(1)	950°-1100°		1.17			
(2)	925°-1225°		3.08			
(21)					1.29	2.05
(16)	727°-1027°				1.57	0.90
Present work	500°-960°	1.65 ^c				
	500°-960°	2.10 ^d				
	550°-1100°	1.55 ^e				
	550°-1000°	1.86 ^f				
	550°-1000°	1.73 ^g				
	550°-1000°	1.20 ^h				

^a From parabolic rate law.

^b From linear rate law.

^c For SiO₂ grown on p-type Si (dc measurement).

^d For SiO₂ grown on n-type Si (dc measurement).

^e For SiO₂ grown on p-type Si (ac measurement 1 kHz).

^f For SiO₂ grown on n-type Si (ac measurement 1 kHz).

^g For SiO₂ grown on p-type (ac measurement extrapolated to zero frequency).

^h For SiO₂ grown on p-type under wet conditions (ac measurements 1 kHz).

fer by 50%-60%, which is reasonable for such a highly insulating material. The extrapolated data of Tripp *et al.* (12) differ from our dc values by two orders of magnitude, while their data agree reasonably well with our ac values. The value of conductivity reported by Mills and Kroger (11) is greater by 4-5 orders of magnitude as compared to our dc values and 3 orders of magnitude as compared to our ac values.

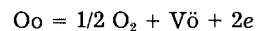
To separate out the electronic conductivity from the total conductivity, we chose the dc total conductivity values. As discussed earlier, the ac conductivity values extrapolated to zero frequency are higher than dc conductivity values. This may be because of the contribution of the dielectric loss due to variation in the capacitance with frequency and temperature. The high conductivity of SiO₂ grown in wet oxygen conditions is suggested to be due to the presence of appreciable amount of OH (18) and probably more nonbridging oxygen (19).

Examination of the activation energy data reported in Table II reveals that our data agree closely with that of Law (16), who has obtained an activation energy value of 1.57 eV from oxidation data assuming the parabolic rate law. He suggested that this represents the energy of the transport of ions during thermal oxidation of silicon.

Considering only the electronic conductivity obtained from the measurements on the asymmetric cell, the activation energy is estimated to be 2.7 eV above ~700°C (see Fig. 17). Conductivity due to electrons is lower than that due to ions by more than one order of magnitude. Further evidence of mixed conductivity is found from the results obtained from polarization measurements. From the total conductivity data and the electronic conductivity data, ionic conductivity values were determined for different temperatures. The percentage of ionic conductivity has been plotted as a function of temperature in Fig. 20. As shown in this figure, the ionic conductivity is only 40% at 545°C, and rises with temperature to a maximum of ~95% in the case of SiO₂ on p-type silicon, and ~86% for SiO₂ grown on n-type silicon between 700° and 875°C. Above this temperature, the values drop steeply. The decrease in the ac conductivity of SiO₂ on n-type silicon above 1000°C suggests that either the charge carriers experience some kind of repulsive effect in SiO₂, or that some kind of trapping of charges occurs at the Si/SiO₂ interface.

The above data suggest that conduction in SiO₂ at an oxygen pressure corresponding to Si/SiO₂ equilibrium and at temperatures above 450°C takes place via charged oxygen species as well as electrons. Transport via charged oxygen species is likely to be either because of the presence of oxygen interstitials at higher oxygen pressures or due to oxygen vacancies at lower oxygen pressures. Since the oxygen pressures surrounding SiO₂ in our investigations is very low (Si/SiO₂ equilibria), the lat-

ter seems to be more favorable. Oxygen vacancies can be generated according to the following defect equilibrium



hence

$$K = [\text{V}_o] [e']^2 P_{\text{O}_2}$$

Thus, the effect of the decrease in oxygen pressure would be to increase the electronic as well as the ionic conductivity. In SiO₂, the electronic conductivity is mainly due to electrons. At temperatures below 450°C the electrons, which are generated with increase in temperature, either pair with holes or are being trapped by the impurities, and hence the electronic conductivity in this temperature range does not increase significantly. The above defect mechanism is in agreement with the experiments made by Folkes *et al.* (17). The above equilibrium will be strongly influenced by the presence of aliovalent impurities. It has been suggested in the literature that during oxidation of silicon doped with B or P, the oxide contains detectable amounts of B or P as a result of redistribution of impurities. Segregation coefficient suggests the incorporation of boron into SiO₂, with rejection of the phosphorous back into the silicon (20). The presence of B or P would affect the above equilibrium. If the trivalent boron dissolves substitutionally into the SiO₂ lattice, additional oxygen vacancies would be generated to satisfy the condition of electroneutrality. However, the number of oxygen ion vacancies would be decreased because of the presence of pentavalent phosphorous ions in the cation lattice.

The higher values of conductivities of SiO₂ grown on silicon containing B, as compared to those containing P, seems consistent with the increased concentration of oxygen vacancies due to such a mechanism during the transport through SiO₂ in this oxygen pressure range.

At high oxygen pressures, however, the presence of oxygen interstitials is more likely. The presence of pentavalent phosphorous will then increase the number of interstitial oxygen ions and the holes associated with it, while boron will have the opposite effect. Our measurements on the oxidation of silicon in 1 atm of oxygen (unpublished) show that phosphorous-doped silicon oxidizes faster than boron-doped silicon, suggesting the presence of interstitial silicon and holes at this oxygen pressure.

The transport number measurements show that the ionic transference number is a function of oxygen pressure and temperature. There appears to be a critical oxygen pressure at which a switchover of the predominant defect from oxygen interstitials to oxygen vacancies may occur. This can only be resolved by measuring the conductivities as a function of oxygen pressures over a wider pressure range.

Acknowledgments

This research was supported by the Army Research Office under Contracts DAAG29-81-K-0109 and DAAG29-82-K-0052. The authors gratefully acknowledge the assistance of Motorola, Incorporated, in providing samples.

Manuscript submitted July 16, 1983; revised manuscript received Nov. 29, 1984. This was Paper 305 presented at the Washington, DC, Meeting of the Society, Oct. 9-14, 1983.

Arizona State University assisted in meeting the publication costs of this article.

REFERENCES

1. F. J. Norton, *Nature*, **181**, 701 (1961).
2. E. W. Sucov, *J. Am. Ceram. Soc.*, **46**, 14 (1963).
3. E. A. Irene, *This Journal*, **129**, 413 (1982).
4. J. R. Ligenza and W. G. Spitzer, *J. Phys. Chem. Solids*, **14**, 131 (1960).
5. W. A. Pliskin and R. P. Gnall, *This Journal*, **111**, 872 (1964).
6. P. J. Jorgensen, *J. Chem. Phys.*, **37**, 874 (1962).
7. A. G. Revesz, *J. Noncryst. Solids*, **4**, 347 (1970).
8. A. G. Revesz and R. J. Evans, *J. Phys. Chem. Solids*,

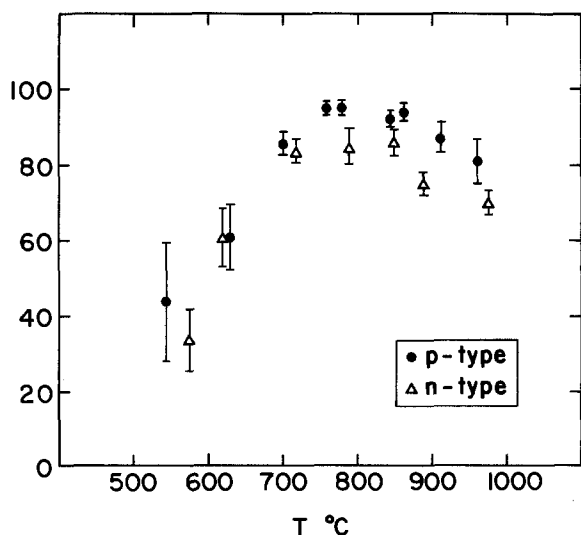


Fig. 20. Percentage ionic conductivity vs. temperature in SiO₂ grown on p-type SiO₂ and on n-type Si.

- 30, 551 (1966).
9. L. Pauling, *J. Phys. Chem.*, **56**, 361 (1962).
 10. D. O. Raleigh, *This Journal*, **113**, 782 (1966).
 11. T. Mills and F. A. Kroger, *ibid.*, **120**, 1582 (1973).
 12. W. C. Tripp *et al.*, Final Report ARL TR75-0130 June 1975.
 13. C. Wagner, in "Proceedings of the 7th Meeting of the International Committee on Electrochemistry, Thermodynamics, and Kinetics," Lindau 1955.
 14. J. B. Wagner, Jr. and C. Wagner, *J. Chem. Phys.*, **26**, 1597 (1957).
 15. H. F. Wolf, "Silicon Data Handbook," Pergamon Press, New York (1969).
 16. J. T. Law, *J. Phys. Chem.*, **61**, 1200 (1957).
 17. F. M. Folkes, Abstract 166, p. 437, The Electrochemical Society Extended Abstracts, Vol. 80-1, St. Louis, MO, May 6-11, 1980.
 18. R. Pfeffer and M. Ohring, *J. Appl. Phys.*, **52**, 777 (1981).
 19. S. K. Ghandhi, "The Theory and Practice of Microelectronics," p. 140, John Wiley and Sons, New York (1968).
 20. D. R. Lamb, *Thin Solid Films*, **5**, 247 (1970).
 21. B. E. Deal and A. S. Grove, *J. Appl. Phys.*, **36**, 3770, 1965.

Some Applications of Cold Crucible Technology for Silicon Photovoltaic Material Preparation

T. F. Cizsek*

Solar Energy Research Institute, Golden, Colorado 80401

ABSTRACT

Cold crucible melt confinement was used for four different silicon crystallization methods of interest in photovoltaic material preparation: directional solidification, Czochralski pulling, sheet growth, and continuous ingot casting. Large grained, multicrystalline ingots were directionally solidified in cold crucibles, and grain sizes up to 5 mm were observed. Dislocation-free crystals were pulled in [111] and [100] orientations, using semiconductor-grade silicon. The edge-supported pulling (ESP) growth method was employed for sheet growth. The sheets were solidified between quartz filaments. Continuous casting of square cross-sectional ingots with grain sizes of up to several millimeters was carried out. Material suitable for fabrication into solar cells was obtained by these methods. AM1 solar cell IV characteristics are presented for the different materials and for coprocessed cells made from conventional Czochralski crystals grown using quartz crucibles. Some purity and electrical property data for cold crucible crystals are also given. Dislocation-free cold crucible crystals had higher purity levels and photovoltaic conversion efficiencies than conventional Czochralski crystals.

The importance of high efficiency to viable photovoltaic systems is becoming progressively more recognized. With silicon, several researchers have already realized AM1 efficiencies above 18%. Because of its abundance, low material cost, salubrity, established technology base, and high theoretical conversion efficiency, silicon is an excellent candidate material for high efficiency PV systems. However, the minority carrier lifetime attainable in heavily doped (<0.5 Ω -cm) Czochralski-grown crystals from quartz crucibles may not be adequate for high efficiency solar cells. This paper explores some roles that cold crucible technology might play in silicon material preparation for both dislocation-free single-crystal cells and multicrystalline cells (including silicon sheets). Cold crucible growth shows a potential for less impurity incorporation than Czochralski growth because, in the former method, there are no hot reactive surfaces near the molten silicon. In addition, radio frequency (RF) repulsion tends to push the liquid silicon away from the finger-like water-cooled walls of the melt container.

Cold crucible melt confinement was used for four different silicon crystallization methods of interest in photovoltaic material preparation: directional solidification, Czochralski pulling, sheet growth, and continuous casting. Solar cells were fabricated from the crystallized silicon and compared with solar cells fabricated on conventional Czochralski-grown (CZ) wafers.

Experimental

Principles of cold crucible operation.—Heating and melt confinement with cold crucibles is provided via RF induction heating. In this study, a 65 mm diam RF coil with five turns was used at 470 kHz. The coil surrounds the cold crucible coaxially. The vertical walls of the crucible are composed of closely spaced, electrically isolated, water-cooled copper fingers that have approximately square cross sections. Each finger acts as an RF stepdown transformer, and the coil current induces RF currents to flow in the fingers. The finger currents, in

turn, induce a current to flow in the silicon charge. Heating and melting of the charge is caused by ohmic resistance to this current flow (I^2R heating). At the inside wall of the crucible, the instantaneous current directions in the fingers and in the charge are opposed (Fig. 1). Thus, a force arises due to magnetic repulsion and the silicon melt is pushed away from the fingers.

Directional solidification.—For directional solidification or Stockbarger-type growth of large grained, multicrystalline silicon, a commercial cold crucible with a 31 mm id, a 50 mm od, and a hemispherical bottom was used. The cross section of each water-cooled finger is a sector of a right cylindrical annulus, as shown in Fig. 1. The inner radii of the sectors decrease in the hemispherical bottom region until the cross section becomes a wedge at the very bottom. The crucible is made of copper with gold plating. A flared, cylindrical, fused-quartz sheath was placed between the cold crucible and the RF coil, with the flared portion extending outward over the top of the coil, to prevent arcing between the coil and crucible. The assembly was housed in a 38 cm diam, water-cooled, stainless-steel growth chamber. The crucible and coil were stationary.

A 55g charge of semiconductor-grade silicon along with sufficient boron dopant to yield approximately 2 Ω -cm resistivity was placed in the crucible. The growth chamber was evacuated before it was filled with 99.999% minimum-purity argon at 1.2 bar total pressure. The silicon charge was preheated with a graphite heater, inductively coupled to the top of the cold crucible, until it was hot enough to couple directly to the cold crucible. At this point, the preheater was moved away from the crucible region.

An RF power level of 19.5 kW (6.1 kV plate voltage and 3.2A plate current) was used to melt and stabilize the polycrystalline silicon. For directional solidification, the power was ramped down to 0 at a rate of approximately 0.5 kW/min. Figure 2 shows an etched cross section of an

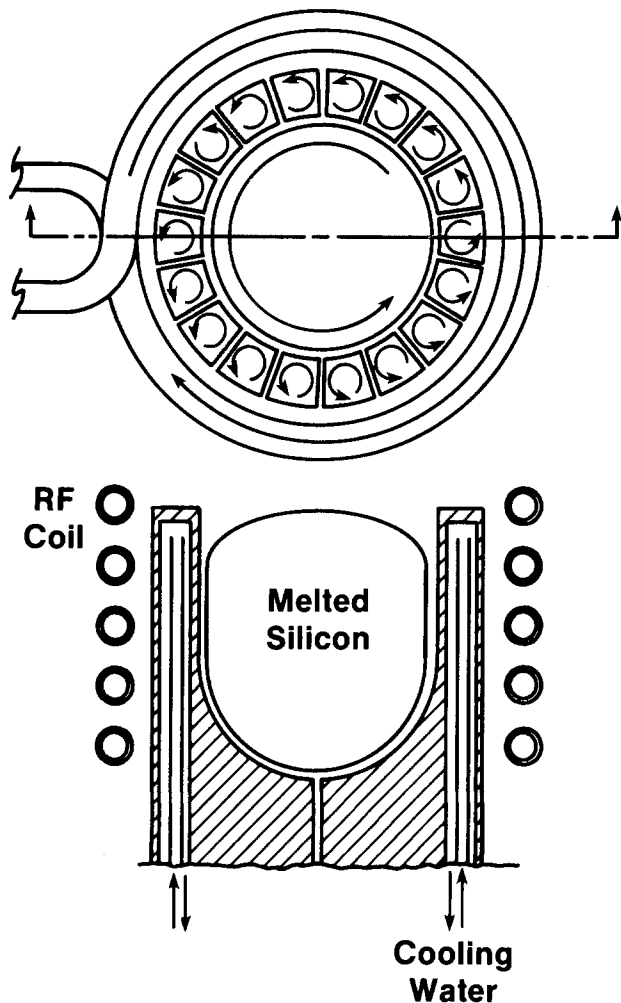


Fig. 1. Operating principle of a cold crucible showing instantaneous current flows.

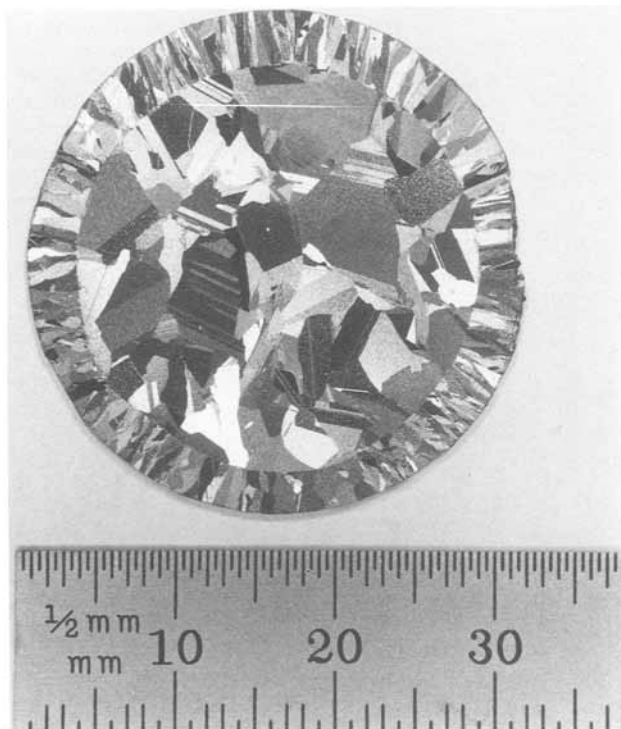


Fig. 2. Etched cross section of silicon directionally solidified in a cold crucible.

ingot solidified in this manner. Grain sizes of up to 5 mm can be seen.

Czochralski pulling.—While silicon crystals had previously been CZ pulled from a cold crucible (1), auxiliary radiant heating with a graphite heater was required for seeding. Auxiliary heating may compromise the purity of the grown crystals by increasing the carbon content, for example. In this study, both [100] and [111] dislocation-free crystals were grown without auxiliary heating from a cold crucible system similar to the one used for directional solidification of silicon.

Seeds with 4×4 mm square cross sections and either [111] or [100] orientation were used. At a generator power level of 20.5 kW (plate voltage = 6.2 kV, and plate current = 3.3A), a 60g charge of melted silicon in the cold crucible was sufficiently hot to allow good wetting on the rotating seed. When even wetting was achieved, the seed was pulled upward initially at 3 mm/min. Then the power was dropped to 19.2 kW, and the pulling speed was increased to approximately 20 mm/min in order to grow a thin-necked crystal of 1.3-2.5 mm diam and more than 2 cm long. Necks grown under these conditions were sufficient to eliminate dislocations generated in the seed attachment region and allowed subsequent growth to be dislocation-free. A rotation rate of 13 rpm was used.

After the neck was grown, the pulling speed and power were adjusted to widen the crystal to about 15 mm diam, and the rotation rate was reduced to around 5 rpm. Figure 3 shows the hot zone during the diameter transition. In addition to pushing the melt away from the cold crucible fingers, magnetic repulsion also causes the top of the melt to be nearly hemispherically domed in such a small crucible; therefore, growing crystals with diameters larger than about 15 mm is difficult. At full diameter, growth speeds from 0.2-2.8 mm/min were tried, and the power levels used ranged from 11 to 14 kW. Some crystals were doped with boron to approximately $2 \Omega\text{-cm}$ resistivity, for solar cell use.

Silicon sheet growth.—The edge-supported pulling (ESP) growth method (2-4) was employed for sheet growth, and, again, the crucible configuration was similar to that described for directional solidification. The silicon sheets were solidified between 0.5 mm diam quartz capillary filaments that had 0.02 mm wall thicknesses. The filaments were spaced 17 mm apart. Growth was initiated on a single-crystal seed sheet mounted between the filaments, and then the seed/filament assembly was moved upward at 15-30 mm/min to grow the sheet.

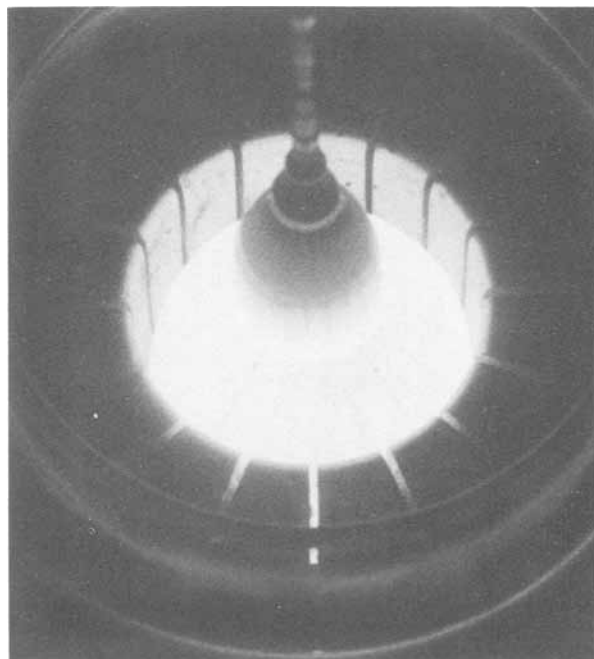


Fig. 3. Cold-crucible Czochralski pulling of dislocation-free silicon

A very high meniscus was observed, because the magnetic repulsion tends to create a mounded upper melt surface and also because there is a melt rise to the sheet's solid/liquid interface of 6-7 mm in addition to the RF effect. Under these harsh thermal gradients, the sheet quickly became multicrystalline. A larger crucible would be advantageous. Because the thin-walled quartz filaments are relatively weak, thermal expansion mismatch between them and the silicon sheet causes the filaments to break away from the sheet during cooldown and a straight sheet edge is left (Fig. 4).

Continuous casting.—The three crystallization methods described so far used a round cold crucible with a closed bottom. Continuous casting of silicon ingots was performed in an open-bottom crucible having a 26×26 mm square confinement cross section with slightly octahedral corners. The vertical water-cooled copper fingers were 6×6 mm in cross section and 104 mm high. A five-turn RF coil was used that had two outer turns with an 83 mm id and three inner turns with a 61 mm id. The coil was 38 mm high and was placed with its midplane 34 mm below the tops of the fingers. A cylindrical quartz arc shield was concentrically located between the cold crucible and the RF coil.

The casting process was started by inserting a 25×25 mm square graphite support into the bottom of the open crucible until it was at midcrucible height. 12g of silicon were placed on the support. The growth chamber was evacuated and purged with argon. Then the RF coil was energized to heat the graphite, which in turn heated the silicon, until the silicon was hot enough to couple directly to the cold crucible. An RF power level of 10.3 kW (at 464 kHz) was adequate to melt the silicon. At that point, the addition of new silicon material through the open top of the crucible was begun at a rate of 240 g/h, the RF power level was increased to 15.7 kW, and the graphite support was started downward at 2.5 mm/min. The liquid silicon solidified as it was slowly lowered out of the RF field, at a rate equal to the raw silicon addition rate. The process was operated for over an hour. Figure 5 is a schematic of the continuous casting process. Figure 6 shows a cast sili-

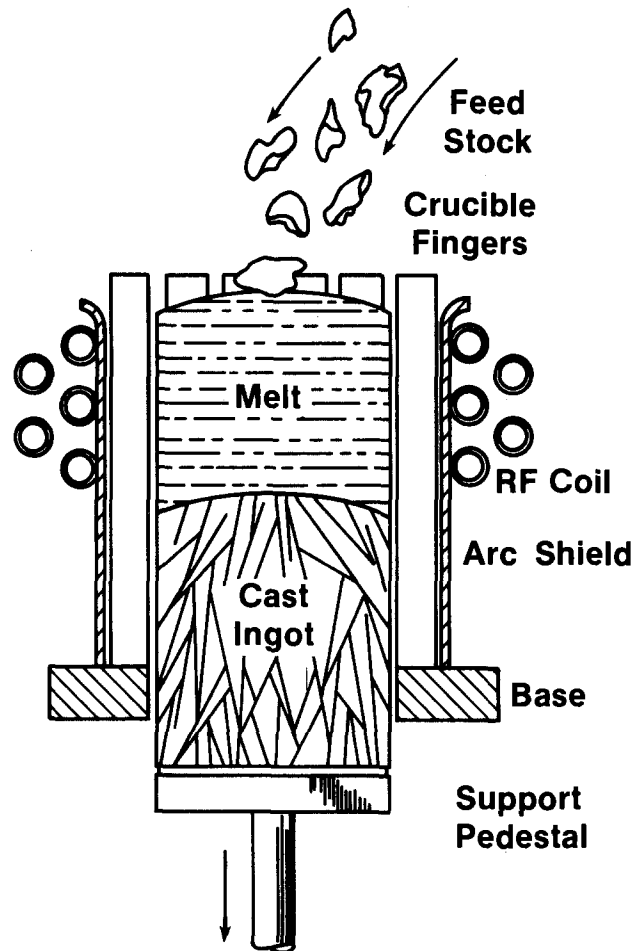


Fig. 5. Schematic diagram of a cold-crucible continuous casting process.

con ingot that is 17 cm long and has a square cross section. Grain sizes of up to several millimeters were observed.

Results

Properties measurements.—A number of characterization techniques were used to evaluate the CZ-pulled crystals. X-ray topography was used to examine the defect structure of the crystals. Molybdenum- $K_{\alpha-1}$ radiation from a line-focus tube operating at 40 kV and 30 mA was

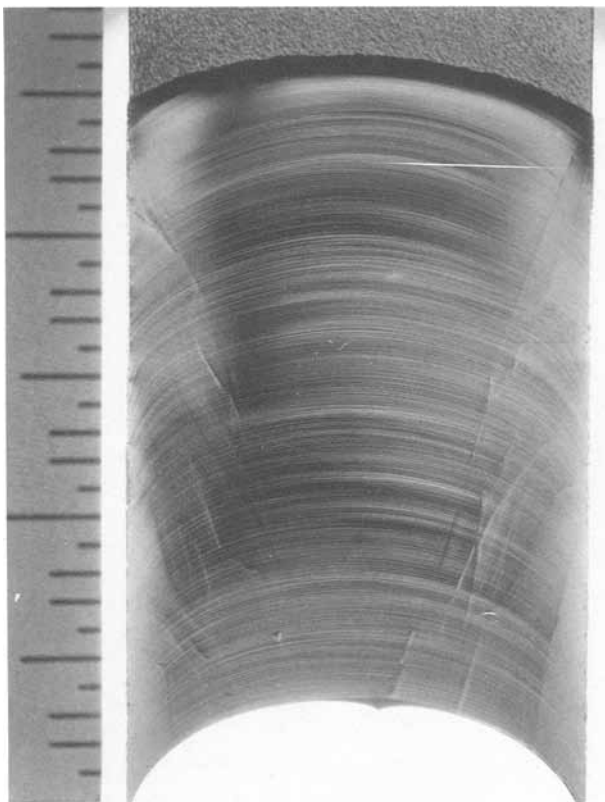


Fig. 4. An ESP silicon sheet grown from a cold crucible using quartz filaments.

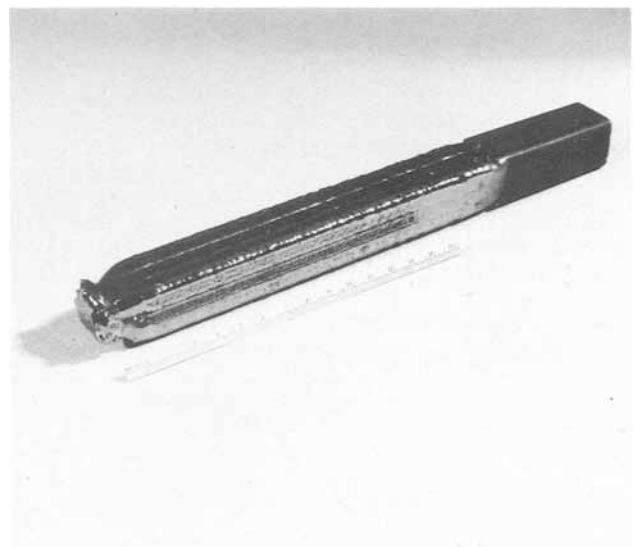


Fig. 6. A continuously cast cold crucible ingot, 17 cm long by 2.5 cm square.

used to image (220) scanning transmission topographs on Ilford L-4 photographic plates. It was verified that the neck growth procedure described in the Czochralski pulling section was sufficient to establish dislocation-free growth in both [111] and [100] orientations, and that the crystals remained dislocation-free at full diameter.

The feed-stock silicon for the cold crucible was semiconductor-grade material. An undoped [111] dislocation-free crystal was determined to be p-type with 90-200 Ω -cm resistivity, indicating an excess acceptor impurity content of approximately 1×10^{14} atom/cm³. The minority carrier bulk lifetime of this crystal, as measured by the ASTM photoconductive attenuation method, was 195 μ s. Some crystals were doped with boron, during growth, to between 2 and 3 Ω -cm p-type for solar cell evaluation. Infrared transmission spectroscopy analysis for carbon and oxygen impurities showed none above the levels in a vacuum float-zoned reference wafer. Neutron activation analysis for gold and copper in a [100], 2.5 Ω -cm, dislocation-free single crystal grown from the gold-plated copper cold crucible indicated a level of 0.14 ppb (weight) for gold and 15.0 ppb (weight) for copper.

Room temperature Hall mobility measurements were made on a polished wafer from one of the [100], dislocation-free, boron-doped crystals. Indium/tin alloy contacts were used with van der Pauw's method for disks of arbitrary shape (5). The measurements indicated a p-type carrier concentration of 8.3×10^{15} /cm³ and a resistivity of 2.55 Ω -cm. From three separate determinations, the average mobility was 295 cm²/V-s with a standard deviation of 4 cm²/V-s.

Solar cell characteristics.—Material suitable for fabrication into solar cells was obtained by three of the cold crucible methods. The continuously cast material was not doped, and no cells were fabricated. However, when properly doped, these ingots are expected to be similar in cell performance to the directionally solidified silicon.

Cold-crucible-grown silicon wafers were cut, lapped, machine polished with a colloidal silica slurry, and used to fabricate solar cells. Control cells, using commercial CZ-grown wafers of similar resistivity, were processed along with the cold-crucible-grown silicon. The cell fabrication process consisted of a phosphorus oxychloride diffusion at 850°C that created a 0.3 μ m deep junction with approximately 90 Ω/\square sheet resistance, an aluminum drive-in back contact, and photolithographically defined front metallization. A standard Ti/Pd/Ag evaporated grid deposition sequence was used for the front contact. The cell areas ranged from 0.1 to 3.0 cm². The smaller cells were mesa array cells fabricated simultaneously on a wafer. Individual cells in an array were isolated by an etched moat. Figure 7 shows the completed device array configuration. To better determine material effects on cell efficiency, antireflection (AR) coatings were generally not used.

Directionally solidified material ("Directional solidification" section, above) was large grained (see Fig. 2). Mesa-defined cells 1.61 cm² in area were cofabricated on both round directionally solidified wafers and commercial CZ controls of similar resistivity. Typical uncoated I/V characteristics under ELH lamp illumination at an intensity of 100 mW/cm² and a temperature of 25°C are shown in Fig. 8. Poorer performance in short-circuit current density (J_{sc}), open-circuit voltage (V_{oc}), and fill factor (FF) result in an efficiency of only 9.2% for the directionally solidified cell vs. 10.8% for the CZ control. AR coatings are expected to increase these values to approximately 13% and 15.4%, respectively.

Solar cell efficiencies for cold-crucible-pulled CZ crystals were observed to be higher than those of coprocessed, conventional CZ crystals. The characteristics of 0.1 cm² mesa array cells were again measured without an AR coating, so that any differences due to substrate material would not be masked by potential AR coating variations. Statistics on cell performance at 25°C under tungsten ELH lamp illumination, and at 28°C under filtered xenon solar simulator illumination, both at 100 mW/cm²

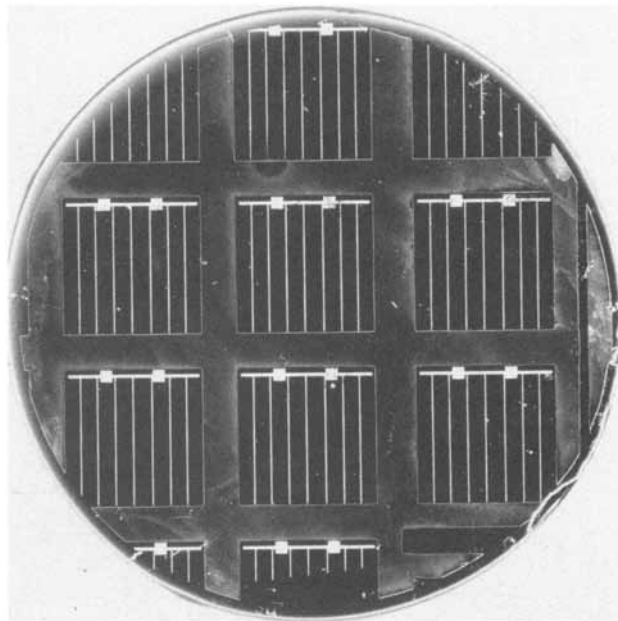


Fig. 7. An array of 0.10 cm² mesa cells on a [100] cold crucible Si wafer.

intensity, are given in Table I. Cell results from several wafers are included. In all cases, V_{oc} , J_{sc} , and cell efficiency were higher for the cold-crucible-grown material. The fill factors were nearly equal within the standard deviation (shown in parentheses) of the measurements. Under ELH illumination at 25°C, the average control efficiency was 10.9%; the cold crucible cells were 11.7% efficient. Under xenon solar simulator illumination at 28°C, the control cells were 10.2% efficient, and the cold-crucible cells had an average efficiency of 10.6%. Good AR coatings can increase the cell efficiency values by at least 43% and as much as 50% (6) if combined with surface passivation. Two larger cells were made from a CZ control wafer and a cold-crucible CZ wafer (3.04 and 0.64 cm² respective cell areas). These cells were fabricated using a relatively low efficiency base-line process, and a simple one-layer AR coating was applied. The comparative performance under 100 mW/cm² ELH illumination at 25°C is shown in Fig. 9 and indicates an 8% advantage for the cold-crucible cell under these processing and measurement conditions.

In Fig. 10, a comparison is made between several conventional CZ control cells and cold-crucible ESP sheet cells. Again, the cells are not AR-coated. In this case, a 0.1 cm² mesa array cell structure is used. The range of performance for the ESP cells correlates with the crystal structure (nearly single-crystal regions exhibit the best performance—up to 90% of the control efficiencies—while the smaller grained regions near the filaments have the lowest solar cell efficiency—as little as 68% of the control efficiencies).

Summary and Discussion

The cold-crucible method with RF heating has been successfully applied to the crystallization of silicon in

Table I. Solar cell current/voltage characteristics for some diffused-junction n/p devices of 0.10 cm² total area.

Cell Measurement Conditions	Cell Description	No. of Cells	V_{oc} (mV)	J_{sc} (mA/cm ²)	FF (%)	Eff. (%)
100 mW/cm ² , ELH lamps, 25°C, no AR coating, 0.1 cm ² cell area	Cz Control	3	573(±1)	23.8(±2)	80(±1)	10.9(±3)
	Cold Crucible	8	579(±3)	24.9(±4)	81(±1)	11.7(±2)
100 mW/cm ² SERI filtered Xenon simulator 28°C, no AR coating, 0.1-cm ² cell area	Cz Control	3	561(±4)	22.9(±1)	79.4(±3)	10.2(±1)
	Cold Crucible	4	568(±7)	23.5(±4)	78.9(±2)	10.6(±2)

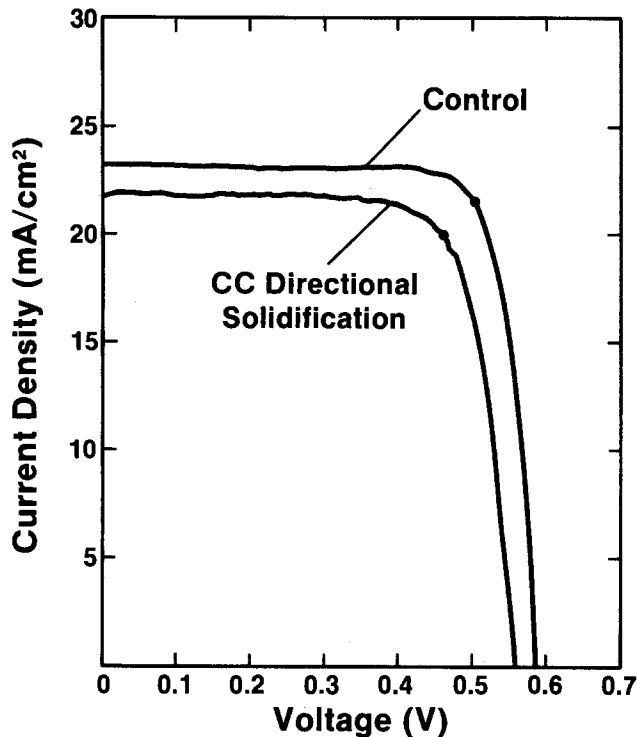


Fig. 8. I/V curves for a CZ control cell and a directionally solidified cell.

four different ways. Directional solidification yielded 30 mm diam, 55g ingots with grain sizes of up to 5 mm. This material was made into solar cells having efficiencies about 85% as good as those of conventional CZ control cells. Dislocation-free, 15 mm diam silicon crystals were pulled in both [111] and [100] orientations by a cold-crucible CZ technique. No auxiliary heating was required to grow the thin necks that are necessary to initiate dislocation-free crystals. X-ray topography verified that the crystals were dislocation-free. A number of electrical property measurements, and an analysis of solar cells made from the crystals, indicate that cold-crucible silicon may have some device efficiency advantages (4%-8%, depending on processing and illumination conditions) over conventional Czochralski-grown substrates for photovoltaic applications. Silicon sheets 17 mm wide were also pulled from a cold crucible melt using the ESP technique and quartz filaments. Pulling speeds of 15-30 mm/min were used. Solar cell efficiencies 68%-90% as good as those of conventional CZ control cells were observed. The efficiency was a function of sheet grain size, with larger grained areas having higher efficiencies.

A new continuous casting method using an open-bottom cold crucible was applied to silicon. Ingots 25 ×

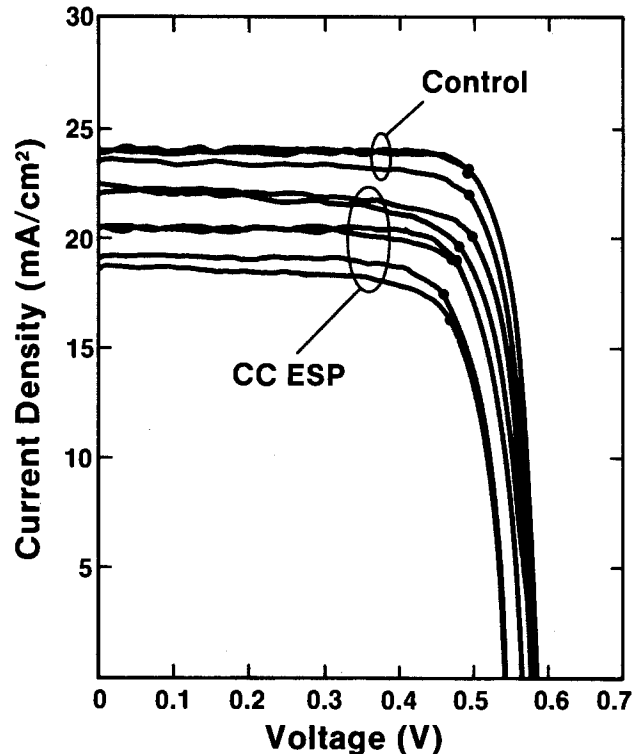


Fig. 10. I/V curves for six ESP cold crucible cells and three CZ control cells.

25 mm in cross section and 17 cm long were cast at a linear rate of 2.5 mm/min and had grain sizes of up to several millimeters. This technique should be applicable to many other materials that are electrically conductive in the molten state. A variety of feedstock geometries such as liquid melts, solid bars, pellets, and powders could be used. The solid/liquid interface is submerged and hence slag formation that occurs in some solidification processes could be kept away from the interface. Contamination levels would also be lower than those in conventional casting processes. Long ingots with tailored cross-sectional shapes can be produced.

The main advantage that cold-crucible silicon melt confinement holds over conventional crucible techniques is freedom from high levels of impurities such as oxygen and carbon. Crystal purities appear to approach those of float-zoned crystals for C and O. Neutron activation analysis indicated that no significant contamination was introduced in the silicon crystals from the copper or gold cold-crucible material.

All of the work reported here was done with relatively small cold crucibles (approximately 30 mm diam). Considerable scale-up would be necessary for commercial application. This should not be a major problem, since cold crucibles up to 45 cm diam have been used in skull melting applications.

Acknowledgments

The assistance of the following three individuals is especially appreciated: M. Schietzelt, who provided help with the crystallization experiments; J. L. Hurd, who performed the infrared analysis and helped with design detailing and fabrication of the open-bottom cold crucible; T. Schuyler, who did the solar cell fabrication and testing. In addition, the author thanks C. Osterwald for carrying out the SERI solar simulator cell measurements. Support for this work was provided by the U.S. Department of Energy under Contract DE-AC02-83CH10093 and, in part, by JPL Contract WO8746-83.

Manuscript received Oct. 1, 1984. This was Paper 336 presented at the New Orleans, Louisiana, Meeting of the Society, Oct. 7-12, 1984.

Solar Energy Research Institute assisted in meeting the publication costs of this article.

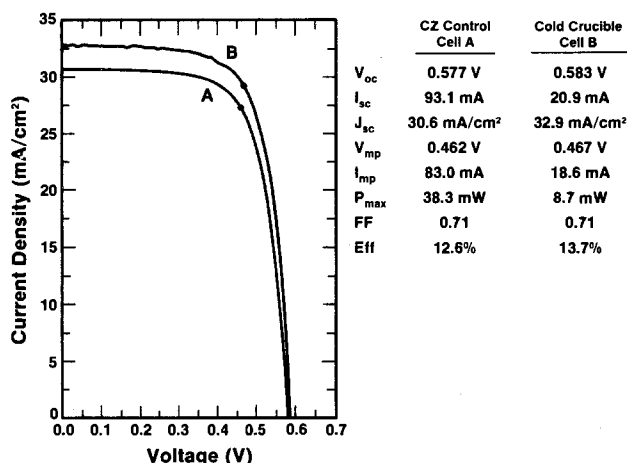


Fig. 9. I/V curves for coprocessed conventional CZ and cold crucible CZ cells.

REFERENCES

1. J. F. Wenckus and W. P. Menashi, Final Technical Report RADC-TR-82-171, Rome Air Development Center, Hanscom AFB, MA (1982).
2. T. F. Ciszek and J. L. Hurd, in "Electronic and Optical Properties of Polycrystalline or Impure Semiconductors and Novel Silicon Growth Methods," K. V. Ravi and B. O'Mara, Editors, p. 213, The Electrochemical Society Softbound Proceedings Series, Pennington, NJ (1980).
3. T. F. Ciszek, J. L. Hurd, and M. Schietzelt, *This Journal*, **129**, 2838 (1982).
4. J. L. Hurd and T. F. Ciszek, *J. Cryst. Growth*, **59**, 499 (1982).
5. L. J. van der Pauw, *Philips Res. Rpts.*, **13**, 1 (1958).
6. A. Rohatgi and P. Rai-Choudhury, Annual Report, SERI Contract XB-3-02090-4, Solar Energy Research Institute, Golden, CO (1984).

A Study of UV Absorption Spectra and Photolysis of Some Group II and Group VI Alkyls

S. J. C. Irvine, J. B. Mullin, D. J. Robbins,* and J. L. Glasper

Royal Signals and Radar Establishment, Great Malvern, Worcester, England WR14 3PS

ABSTRACT

A preliminary study has been made of the UV photolysis of metal-organic compounds of Hg, Cd, and Te which could be used for low temperature, selective area deposition of cadmium mercury telluride (CMT). High resolution UV absorption spectra have been measured for dimethylcadmium (CdMe_2), dimethylmercury (HgMe_2), and diethyltelluride (TeEt_2). Possible modes for photodissociation are discussed in light of these results. The photodissociation of these alkyls was attempted in a hydrogen stream at atmospheric pressure using a mercury-xenon lamp, deposition being onto a silica reaction tube. Yields of Cd, Hg, and Te were measured under different deposition conditions to determine the dependence on UV intensity, alkyl concentration, and flow velocity.

Recent interest in low temperature growth of the infrared detector material cadmium mercury telluride (CMT) has stimulated research into new epitaxial growth techniques (1-3). The preliminary study of UV photolysis reported here is part of an investigation to use alkyls for the growth of CMT at temperatures where they are thermally stable (4, 5) and possibly achieve selective area growth.

The alkyl sources used for metal-organic vapor phase epitaxy (MOVPE) are dimethylcadmium (CdMe_2) and diethyltelluride (TeEt_2) with Hg vapor introduced from a liquid Hg source. Pyrolysis of these alkyls enables high growth rates of CMT at substrate temperatures above 400°C. In the present study, the UV absorption spectra of CdMe_2 , HgMe_2 , and TeEt_2 have been measured. Also, photolysis experiments have been attempted at room temperature using CdMe_2 , HgMe_2 , HgEt_2 , TeMe_2 , and TeEt_2 .

Room temperature photodeposition of Cd from CdMe_2 was achieved by Jonah *et al.* (6) using a 1 kW xenon-mercury lamp, and in more recent studies Ehrlich *et al.* (7) used CdMe_2 for localized deposition of Cd using a CW laser source at 257 nm. The latter authors have also measured the UV absorption spectra of CdMe_2 in the vapor phase and as an adsorbed layer (8, 9). Multiphoton absorption of CdMe_2 has been claimed by Rytz-Froidevaux *et al.* (10), who used longer wavelength radiation (above 300 nm) to initiate Cd deposition onto a quartz window; the deposition proceeds by heat generated in the photodeposited film. This technique involves a surface selective reaction and can produce Cd deposition to a resolution better than 1 μm .

Experimental

In order to investigate the UV absorption processes leading to photodissociation, the absorption spectra of the alkyls CdMe_2 , HgMe_2 , and TeEt_2 were measured at room temperature in a stainless steel gas cell. This cell had a path length of 5.1 cm and was fitted with UV transmitting Spectrosil A quartz windows. The absorption cross section at a particular wavelength can be estimated from the absorption coefficient using the relation

$$\alpha_\lambda = N\sigma_\lambda$$

For an ideal gas at STP, $N = 2.77 \times 10^{19}$ molecules cm^{-3}

*Electrochemical Society Active Member.

$$\therefore \sigma_\lambda \sim (0.27 \times 10^{-16}) \frac{\alpha_\lambda}{p} \text{ cm}^2$$

where p is the partial pressure of the alkyl measured in torr. In all the spectra given below, the broken line represents the absorption due to H_2 carrier gas only in the cell, and the solid line represents that of carrier gas with a small pressure p of the appropriate alkyl. The absorption coefficient α (cm^{-1}) for each alkyl is then given by the difference between these curves.

The spectral region of greatest interest is 200-300 nm. At longer wavelengths, the alkyls show negligible absorption, while at shorter wavelengths the Hg lamp used for dissociation emits negligible power. Absorption data in this spectral range have previously been obtained by Thompson and Linnett (11) using photographic techniques, but these spectra do not give the necessary information on relative strengths of transitions.

The photodeposition measurements were made using a continuous stream of H_2 plus alkyl vapor at a controlled flow rate and concentration and a constant total pressure of 1 atm. High purity hydrogen is supplied via flowmeters to two lines; one is fed to the bubbler containing the alkyl, the other line acts as a dilution stream to alter the partial pressure of alkyl vapor. The mixed stream is passed at ambient temperature through a 7 mm id silica tube. Radiation from a 1 kW Oriel mercury-xenon lamp was focused onto the silica tube. Waste gases from the reaction zone, predominantly hydrogen, are passed to a combustion chamber and burnt in a continuous flame. The whole system can be pumped out to test for leaks and purged with hydrogen. There were a number of additional features which were used in some of the experiments, such as back-reflecting mirror, masking, and a power meter. A laser power meter was used, with black body absorption characteristics to measure the radiation power density passing through the silica reaction tube.

The amounts of material deposited onto the wall of the silica tube as a consequence of photolysis were dissolved in acid and determined by atomic absorption analysis. The deposits were metallic in appearance and were not expected to contain large amounts of organic impurities, as subsequent secondary ion mass spectrometer (SIMS) experiments on epitaxial thin films only show small amounts of carbon contamination (18).

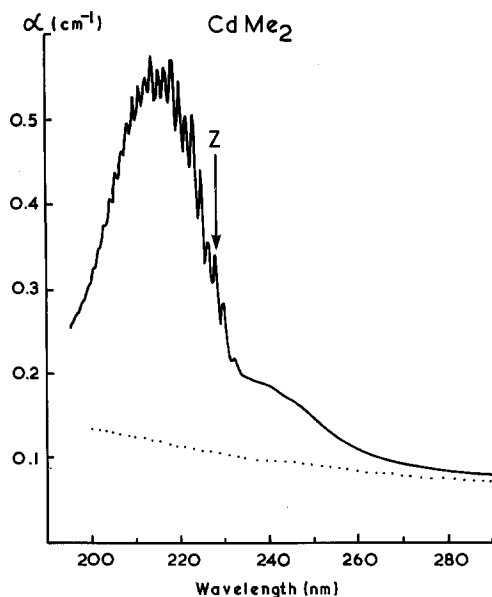


Fig. 1. Absorption coefficient vs. wavelength for CdMe_2 at a partial pressure of 0.8 torr; the zero phonon line is indicated (Z).

Absorption Spectra

The absorption spectrum of CdMe_2 at a partial pressure $p \sim 0.8$ torr is given in Fig. 1. The spectrum between 200 and 300 nm shows a discrete absorption band with well-resolved vibrational fine-structure peaking near 216 nm, together with a broad absorption continuum extending across the range of interest.

The ground state vibrational frequencies given by Bakke (12) for CdMe_2 and HgMe_2 are listed in Table I. Using these data, the vibrational progression in the CdMe_2 absorption band can be assigned as indicated in Table II, although it must be realized that there is some ambiguity in the possible assignments. Nevertheless, it seems clear from a comparison of Tables I and II that it is the totally symmetric (A_1) vibrational modes which are strongly excited in the transition. This is normally found for a strong symmetry-allowed electronic transition. We note that Thompson and Linnett (11) have discussed the fine structure in their sample of CdMe_2 as arising from CdEt_2 impurity. In view of the strength of absorption in our spectra, the known level of purity of the sample, and the agreement between hotband frequencies and Raman data for CdMe_2 , we do not consider this a credible explanation for our data.

The energies of the valence molecular orbitals (MO) in CdMe_2 have been calculated by Bancroft *et al.* (13) and compared with measured photoelectron spectra. The

Table I. Observed ground-state vibrational frequencies for CdMe_2 and HgMe_2 (12)^a

Symmetry	Mode	Energy (cm^{-1})		Type
		CdMe_2	HgMe_2	
A_1	ν_1'	2904	2910	C—H stretch
	ν_2'	465	515	C—M—C stretch
	ν_3'	1129	1182	CH_3 bend
A_2	ν_5'	(2920)	2880	C—H stretch
	ν_6'	538	550	C—M—C stretch
	ν_7'	1140	1205	CH_3 deformation
E'	ν_8'	2885	2966	C—H stretch
	ν_9'	1441	1475	CH_3 deformation
	ν_{10}'	705	787	CH_3 rocking
	ν_{11}'	150	156	C—M—C bending
E''	ν_{12}'	2963	2869	C—H stretch
	ν_{13}'	1384	1443	CH_3 deformation
	ν_{14}'	642	700	CH_3 rocking

^a Assumes eclipsed geometry of molecule with C_{3v} symmetry. Cd—C distance: 2.117 Å. C—H distance: 1.09 Å.

Table II. Vibronic progression for CdMe_2

Line energy (cm^{-1})	Proposed Assignments
42644	$-2\nu_2'$
43068	Z $-\nu_2'$
43535	Z (zero phonon line)
43867	Z $+\nu_2$
44193	$+2\nu_2$ or $+\nu_{10}$
44494	$+3\nu_2$ or $+\nu_3$
44829	$+\nu_3 + \nu_2$
45151	$+\nu_3 + (2\nu_2$ or $\nu_{10})$
45483	$+2\nu_3$
45805	$+2\nu_3 + \nu_2$
46132	$+2\nu_3 + (2\nu_2$ or $\nu_{10})$
46414	$+3\nu_3$ or $+\nu_1$
46779	
47096	
47384	
47717	
48033	
48312	
48622	
48928	

$$\nu_2' \sim 467 \text{ cm}^{-1}$$

$$\nu_2 \sim 330 \text{ cm}^{-1}$$

$$\nu_3 \sim 960 \text{ cm}^{-1}$$

$$\nu_1 \sim 2879 \text{ cm}^{-1}$$

electronic energies and orbital types are listed in Table III. The highest energy-filled MO (b_1) involves an antisymmetric linear combination of C_{σ} orbitals and is weakly bonding in the C—Cd—C chain by virtue of interaction with Cd 5p orbitals. The electronic transition giving rise to the discrete absorption band in Fig. 1 involves excitation of an electron from this b_1 MO to the first unfilled orbital, which is either nonbonding or antibonding. This electronic excitation therefore weakens the C—Cd—C bond, thereby promoting the photodissociation.

This weakening of the C—Cd bonds in the electronically excited state can be quantified from the analysis of the vibrational progression associated with the transition. The lines to low energy of the zero-phonon line (ZPL) Z in Table II are "hot bands," the transition originating from a vibrationally excited level of the ground electronic state. The ground vibrational frequency ν_2' deduced from the optical spectrum is $\nu_2' \sim 467 \text{ cm}^{-1}$, in good agreement with the Raman value listed in Table I. This mode represents a symmetric stretching of the C—Cd—C molecular chain. The lines to high energy of Z in Table II give the corresponding vibrational frequencies in the electronically excited state. From Table II, it can be seen that the C—Cd—C mode ν_2 in the excited state has a lower energy, $\nu_2 \sim 330 \text{ cm}^{-1}$, which indicates a weakening of the vibrational force constant, k . Since frequency $\propto k^{1/2}$, we obtain

$$\frac{k}{k'} \sim \left(\frac{330}{467} \right)^2 \sim 0.50$$

where k and k' are the Cd—C force constants in the excited and ground states, respectively. Thus, the UV absorption process giving rise to the discrete absorption band in Fig. 1 reduces the C—Cd—C bonding strength by a factor of ~ 2 .

Table III. Calculated orbital energies for CdMe_2 (13)^a

Symmetry	Binding energy (eV)	Orbital type
b_1	9.13	Cd—C (weakly-bonding)
a_1	10.37	Cd—C (bonding)
a_2		
b_1	13.98	C—H (bonding)
b_2	14.24	
a_1		
	20.18	
	20.71	Cd 4d orbitals

^a Assumes C_{2v} molecular symmetry.

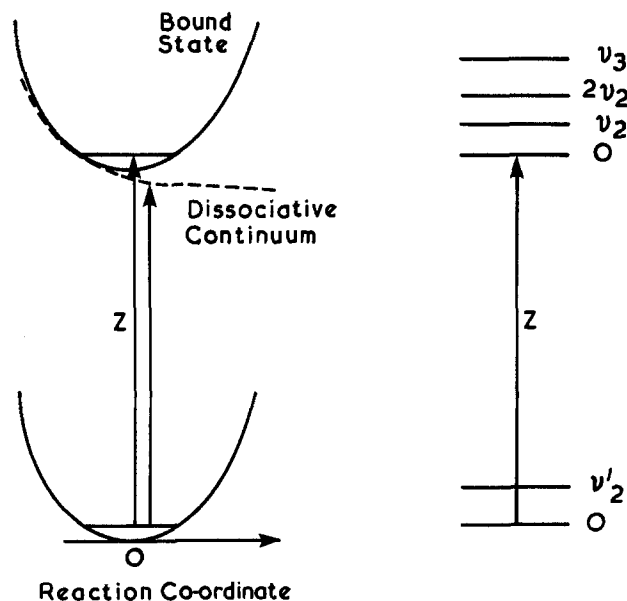


Fig. 2. Configurational coordinate model for CdMe_2

The dissociation process for CdMe_2 appears to be asymmetric, with one CH_3 radical departing first with excess kinetic energy (14). Excitation of the symmetric C-Cd-C mode ν_2 in the optical transition could lead rapidly to excitation of the corresponding antisymmetric C-Cd-C mode ν_6 , which has a similar energy. This relaxation between modes is brought about by anharmonic terms in the molecular hamiltonian and usually proceeds very rapidly; in this case, the mode ν_6 may be the reaction coordinate for the dissociation. The discrete absorption band in Fig. 1 is overlapped by a broad continuum with a relatively low energy threshold. This continuum possibly represents absorption to an unbound electronic state which is purely dissociative. The situation is represented schematically in Fig. 2. Chen and Osgood (17) have also observed a long wavelength continuum for CdMe_2 vapor at 300 K. These authors attribute this absorption to a vibrationally allowed quadrupole transition which is dissociative.

The absorption spectrum of HgMe_2 at a partial pressure $p \sim 10$ torr is given in Fig. 3. The form of this spectrum is very similar to that for CdMe_2 , except that it is slightly shifted to higher energy. The vibrational progression can

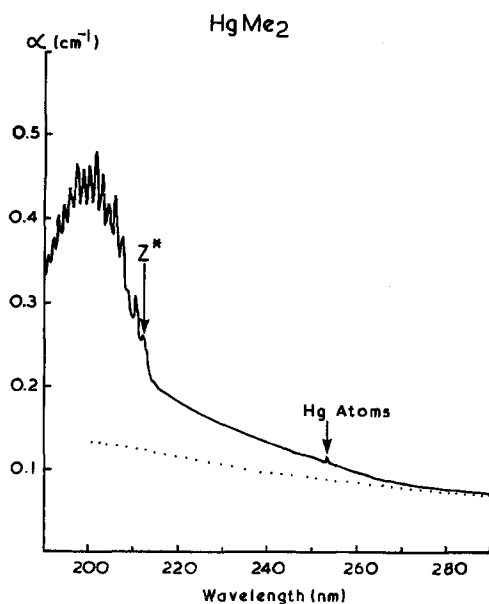


Fig. 3. Absorption coefficient vs. wavelength for HgMe_2 at a partial pressure of ~ 10 torr; the zero phonon line is indicated (Z^*).

Table IV. Vibronic progression for HgMe_2

Line energy (cm^{-1})	Proposed assignments
46533	$Z^* - \nu_2'$ (hot band)
47052	Z^* (zero phonon line)
47432	$Z^* + \nu_2$
47840	+ $2\nu_2$ or ν_{10}
48123	+ ν_3
48484	+ $\nu_3 + \nu_2$
48852	+ $\nu_3 + (2\nu_2 \text{ or } \nu_{10})$
49193	+ $2\nu_3$
49547	+ $2\nu_3 + \nu_2$
49925	+ $2\nu_3 + (2\nu_2 \text{ or } \nu_{10})$
50251	+ $3\nu_3$
50610	
50963	
51298	
51650	
51975	
52290	
52615	
51958	

$$\nu_2' \sim 519 \text{ cm}^{-1}.$$

$$\nu_2 \sim 370 \text{ cm}^{-1}.$$

$$\nu_3 \sim 1070 \text{ cm}^{-1}.$$

be analyzed as for CdMe_2 , the probable assignments being listed in Table IV. Once again the progression is dominated by the symmetric A_1 modes, and particularly by the C-Hg-C stretching mode ν_2 . The similar bonding character for CdMe_2 and HgMe_2 is also reflected in the photoelectron spectra for these compounds (15).

From a comparison of ground and excited vibrational frequencies for the mode ν_2 , we obtain as a ratio of force constants for HgMe_2

$$\frac{k}{k'} \sim \left(\frac{370}{519} \right)^2 \sim 0.51$$

This is very close to the ratio obtained for CdMe_2 , and again indicates that electronic excitation into the discrete absorption band in Fig. 3 roughly halves the C-Hg-C bond strength.

Photodissociation mechanisms in HgMe_2 and CdMe_2 are presumably quite analogous. The Hg compound again shows a broad underlying dissociative continuum, but there is also evidence for the presence of free Hg atoms in the absorption cell from the weak Hg absorption line at 253.7 nm.

The absorption spectrum of TeEt_2 at a partial pressure $p \sim 1$ torr is given in Fig. 4. The form of this spectrum is

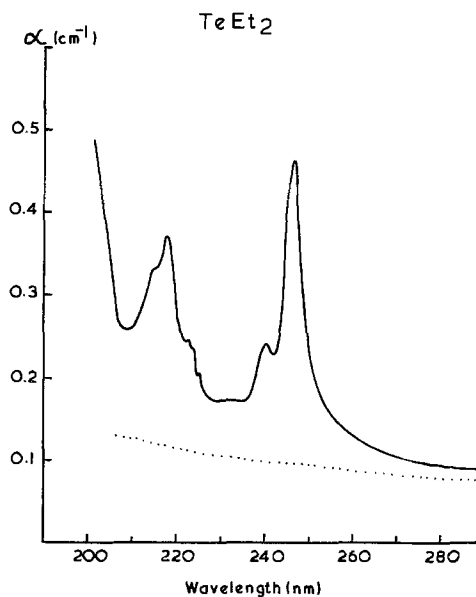


Fig. 4. Absorption coefficient vs. wavelength for TeEt_2 at a partial pressure of 1 torr.

Table V. Table of photodeposition results

Run no.	Alkyl	Exposure time (min)	Power intensity (W cm^{-2})	Partial pressure (torr)	Flow velocity (cm s^{-1})	Yield (mg)
9	CdMe_2	5	1.9	9.3	20	0.889
10	CdMe_2	5	2.0	2.3	20	0.704
11	CdMe_2	10	0.85	2.3	20	0.175 (1 cm mask)
16	HgMe_2	15	1.7	—	20	19.3
17	HgEt_2	15	1.8	—	20	<0.01
1	TeEt_2	15	—	2.3	20	0.9
4	TeEt_2	15	~0.5	2.3	20	0.668
5	TeEt_2	15	0.6	2.3	20	0.44
12	TeEt_2	15	2.3	4.2	20	0.26 (1 cm mask)
13	TeEt_2	15	2.4	4.2	20	0.36
14	TeEt_2	15	2.0	2.3	6.8	0.22 (1 cm mask)
6	TeEt_2	15	1.1	2.1	7	1.38
7	TeEt_2	15	0.6	2.3	20	0.264
8	TeEt_2	15	1.79	2.3	20	0.662

quite different from those of the metal alkyls and shows a series of discrete absorption bands without well-resolved fine structure. There is also little evidence for any strong underlying absorption continuum. At the present stage, useful analysis of this spectrum would be difficult.

Photodeposition Results and Discussion

The results of the photodeposition measurements are summarized in Table V. In run 9, a smooth mirror deposit was formed on the silica reaction tube after 1 min exposure to a beam intensity of 1.9 W cm^{-2} with a partial pressure of CdMe_2 of 9.3 torr. A photograph of this reaction tube for run 9 is shown in Fig. 5. The experiment was performed with a power meter behind the reaction tube and with no back-reflecting mirror. The beam was completely attenuated by the deposit in the high intensity region after 1 min, and this coherent deposit extended in both directions into regions of lower beam intensity. The experiment was terminated after 5 min, leaving the cadmium deposit as shown in Fig. 5 extending for 12 cm almost symmetrically about the beam axis. The weight of Cd deposited was 0.889 mg; clearly, the weight would have been larger if the beam had not been attenuated. Run 10 was conducted under similar conditions to that of run 9, except for a reduction in CdMe_2 to 2.3 torr, achieved by adjusting the ratio of bubbler flow rate to dilution flow rate. The photograph of the reaction tube for run 10 in Fig. 5 is similar to run 9, with a coherent deposit extending for about 10 cm along the reaction tube. The period of exposure to the UV beam was 5 min, yielding a total Cd deposition of 0.704 mg. Following a pattern similar to run 9, the deposit formed initially in the high inten-

sity region and extended to regions of lower beam intensity.

For run 11, a lower power, 0.85 W cm^{-2} , was used, and the reaction tube was masked, except for a 1 cm gap to allow illumination. A photograph of the reaction tube is shown in Fig. 5, where only the illuminated region has a Cd deposit.

Photolysis of HgMe_2 was attempted under flow and beam power conditions similar to those of run 9 for CdMe_2 . In order to reduce loss of Hg from the reaction tube, a liquid nitrogen trap was placed downstream of the exposed region. Atomic absorption analysis determined the weight of Hg deposited to be 19.3 mg, a significantly higher yield than Cd from CdMe_2 .

Photolysis of HgEt_2 was unsuccessful using conditions similar to HgMe_2 photolysis. No mercury was visible after 15 min, and less than 0.01 mg of Hg was measured by atomic absorption analysis. No UV absorption spectra were measured for HgEt_2 , so it is not possible at this stage to explain the absence of photolysis using a mercury lamp or to predict under what conditions photolysis would occur.

The initial diethyltelluride (TeEt_2) photolysis experiment, run 1, used a back-reflecting mirror to increase the intensity in the reaction tube. In an exposure period of 15 min, 0.9 mg of Te was deposited with a TeEt_2 partial pressure of 2.3 torr. Although, in light of later experiments, the presence of the mirror did enhance photolysis, it was removed in subsequent experiments so that a power meter could be placed behind the reaction tube.

The deposition of Te onto the silica tube was not as smooth as the Cd deposit; some of the Te formed fine particles, which were carried out of the reaction tube, causing an error in the determination of weight of deposited Te. It was also observed that deposition did not occur in the region of high UV intensity; most of the deposit was downstream of this region.

The cause of this anomalous behavior was investigated using masks so that only part of the tube could be exposed to the UV radiation. Runs 4 and 5 were performed without masks to obtain a comparison with masked tubes. In both cases, the TeEt_2 partial pressure was 2.3 torr and the flow velocity was in the region of 20 cm s^{-1} . The power intensity in the central beam region was 0.6 W cm^{-2} . Run 4 yielded 0.668 mg of Te, while run 5 yielded 0.44 mg of Te; the difference in these values probably reflects the varying amount of Te lost from the tube as a fine dust.

Using a 1 cm mask in run 12 with a higher incident power intensity of 2.3 W cm^{-2} resulted in very little deposit in the window region of the mask; only fine lines of deposit resulted at each edge, as can be seen in Fig. 6. Run 12 displayed an unexpected feature of deposition occurring 10 cm downstream from the beam axis at a point where the tube emerges from the mask and is illu-

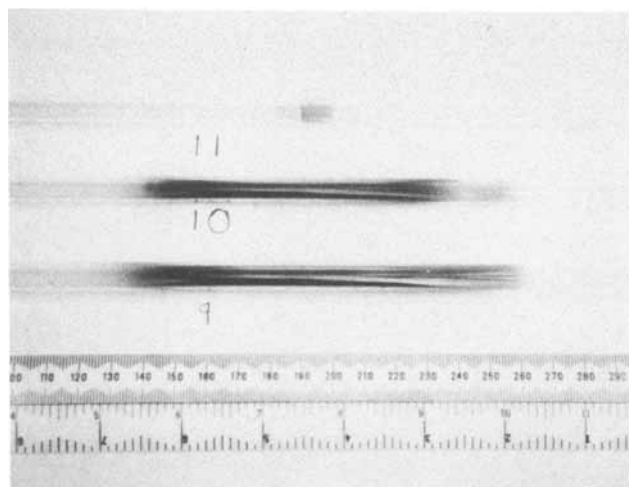


Fig. 5. Reaction tubes following photodeposition of CdMe_2 for runs 9 (1 cm mask), 10, and 11 (see text).

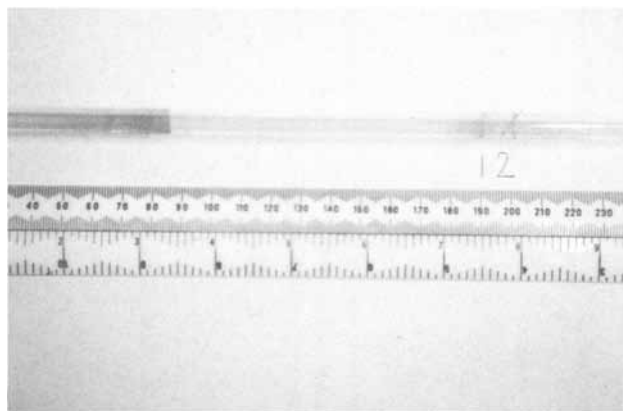


Fig. 6. Reaction tube following photodeposition of TeEt_2 ; the masked regions extend from 90 to 190 nm, and above 200 nm.

minated by a very low intensity of UV. This additional deposit can be seen in Fig. 6. It is also clear that there is little deposit within the 10 cm dark region.

In run 13, all conditions were the same except for the downstream portion of the mask being removed. A region of high intensity UV from the edge of the mask extending for about 2 cm has very little deposit, and most of the deposition is downstream of this where the UV illumination is weaker. The amount of Te deposited in run 13 was 0.36 mg, compared with 0.26 mg in run 12.

It can be concluded from these results that Te will not photodeposit onto silica in a region where the UV intensity is high, although this may not be the case for a different surface or in the presence of other species such as Cd. Te will deposit in a region where the UV intensity is lower and, as run 12 indicated, the intensity may be orders of magnitude lower than the peak intensity, but the amount of Te deposited is only a factor of 2 or 3 down from when the mask was not present. As will be discussed later, the photodeposition efficiency of TeEt_2 is a fairly simple function of the peak UV intensity. Therefore, a more complex process than simple photon absorption and dissociation of a C-Te bond is needed to explain the masking experiments. The relatively large amount of deposit occurring downstream of the mask in run 12 suggests that some TeEt_2 molecules have been pre-excited in the high intensity region. The mean time for a molecule to travel across the dark region is 0.5s, which rules out the possibility of an excited electronic state or vibrational state in the molecule. A possible mechanism is the formation of an intermediate species such as TeEt which then readily dissociates in a region of low photon flux.

The role of flow velocity of the $\text{H}_2 + \text{TeEt}_2$ stream was investigated, as it will influence the mean exposure of each TeEt_2 molecule to UV. In run 6, the flow velocity was reduced to one-third of the standard value, and the percentage yield was increased approximately three times (see Table V).

Changes in UV power intensity were investigated in runs 7 and 8, both runs being carried out without masks and flow velocities of 20 cm s^{-1} . In run 7, the beam power intensity was 0.60 W cm^{-2} , which deposited 0.264 mg of Te. In run 8, the power intensity was increased to 1.79 W cm^{-2} , depositing 0.662 mg of Te. For the concentrations used in these experiments and for photodeposition efficiencies in the region of 1%, it is likely that the weight of Te deposited would be proportional to the incident UV power intensity.

Successful photodeposition of TeMe_2 was achieved with a beam intensity of 1.3 W cm^{-2} and flow velocity around 20 cm s^{-1} . A total weight of 0.288 mg of Te was deposited in 15 min, which is approximately a factor of 2 lower than for TeEt_2 under equivalent conditions. The deposition mainly occurred downstream of the high UV intensity region, in agreement with the TeEt_2 experiments.

Conclusions

High resolution UV absorption spectra have been measured for a number of alkyl/ H_2 gas mixtures. For both CdMe_2 and HgMe_2 , there is an electronic transition from a weakly bonding to an antibonding MO in the energy range $43,000\text{--}47,000 \text{ cm}^{-1}$ which leads to significant weakening of the C-M-C molecular chain. This excitation can lead to photodissociation at room temperature. The mechanism may involve vibrational relaxation to the antisymmetric reaction coordinate of a bound state, or it may decay into the underlying continuum, which is probably dissociative. The spectrum of TeEt_2 cannot be easily analyzed to give evidence for analogous bond weakening in the excited state, although it is strongly absorbing in the part of the spectrum where the lamp emits a high UV intensity.

Photodeposition of Cd from CdMe_2 occurs readily when illuminated with a Hg lamp, although the absorption coefficient in the region of 254 nm is low ($\sim 0.05 \text{ cm}^{-1} \text{ torr}^{-1}$), in agreement with Ehrlich *et al.* (9). Similarly, HgMe_2 gives a good yield of Hg, but no significant photodissociation occurred with HgEt_2 ; the reason for this is not clear in the absence of absorption spectra for this alkyl.

The photodeposition of TeEt_2 and TeMe_2 does not appear to be first order in these experiments, as deposition did not occur in the region of high UV intensity but deposited downstream where the UV intensity was lower. Experiments by Connor *et al.* (16) on the flash photolysis of TeMe_2 indicated the formation of primary photoproducts of the type CH_3Te , although no indication was given of a delay in the production of Te photoproducts. The delay in deposition may be due to poor adsorption onto silica in a region of high UV intensity or to the formation of an intermediate compound which photodissociates further downstream in a region of low UV intensity.

Further experiments on using these alkyls for low temperature epitaxial growth are in progress.

Acknowledgments

The authors wish to thank Mr. J. S. Gough for the atomic absorption measurements and Miss G. Wooldridge for technical assistance.

Manuscript received May 7, 1984.

REFERENCES

- S. J. C. Irvine and J. B. Mullin, *J. Cryst. Growth*, **55**, 107 (1981).
- J. P. Faurie, A. Million, and J. Piagnet, *ibid.*, **59**, 10 (1982).
- R. Roussille, S. Guillot, and G. Lefeuvre, *ibid.*, **59**, 130 (1982).
- J. B. Mullin, S. J. C. Irvine, and D. J. Ashen, *ibid.*, **55**, 92 (1981).
- J. B. Mullin and S. J. C. Irvine, *J. Vac. Sci. Technol.*, **21**, 178 (1982).
- C. Jonah, P. Chandra, and R. Bersohn, *J. Chem. Phys.*, **55**, 1903 (1971).
- J. Ehrlich, R. M. Osgood, Jr., and T. F. Deutsch, *IEEE J. Quantum Electron.*, **qe-16**, 1233 (1980).
- D. J. Ehrlich and R. M. Osgood, Jr., *Chem. Phys. Lett.*, **79**, 381 (1981).
- D. J. Ehrlich, R. M. Osgood, Jr., and T. F. Deutsch, *J. Vac. Sci. Technol.*, **21**, 23 (1982).
- Y. Rytz-Froidevaux, R. P. Salathe, H. H. Gilgen, and H. P. Webber, *Appl. Phys. A*, **27**, 133 (1982).
- H. W. Thompson and J. W. L. Linnett, *Proc. R. Soc. (London) A*, **156**, 108 (1936).
- A. M. W. Bakke, *J. Mol. Spectrosc.*, **41**, 1 (1972).
- G. M. Bancroft, D. K. Creber, and H. Basch, *J. Chem. Phys.*, **67**, 4891 (1977).
- M. Tamir, U. Halavee, and R. D. Levine, *Chem. Phys. Lett.*, **25**, 38 (1974).
- D. K. Creber and G. M. Bancroft, *Inorg. Chem.*, **19**, 643 (1980).
- J. Connor, G. Greig, and O. P. Strausz, *J. Am. Chem. Soc.*, **91**, 5695 (1969).
- C. J. Chen and R. M. Osgood, *Chem. Phys. Lett.*, **98**, 363 (1983).
- S. J. C. Irvine, J. Giess, J. B. Mullin, G. W. Blackmore, and O. D. Dosser, To be published.

The Photochemical Oxidation of GaAs

P. A. Bertrand

The Aerospace Corporation, Chemistry and Physics Laboratory, El Segundo, California 90245

ABSTRACT

The vacuum ultraviolet photochemical oxidation of GaAs by N_2O (wavelengths of 2537 and 1849Å) was studied by x-ray photoelectron spectroscopy. We believe the model most consistent with our data involves (i) adsorption of molecular N_2O , (ii) dissociation of the N_2O on the surface, and (iii) oxidation of the surface by the adsorbed O atoms. The temperature dependence of the overall reaction on the stoichiometric surface is dominated by the temperature dependence of adsorption of N_2O . An As-rich surface oxidizes more slowly, and the reaction saturates; in this case, the rate-limiting step and the cause of saturation is the oxidation of the surface by adsorbed O atoms. The As-covered surface does not present the proper sites (As atoms surrounded by Ga atoms) for fast, continued oxidation of GaAs.

Thermal, plasma, and anodic oxides of gallium arsenide (GaAs) have been heavily explored as insulating and passivating layers for this important semiconductor, with relatively little success. High trap density at the interface leads to poor electrical characteristics (1-3). Certain non-native insulators, such as silicon dioxide (SiO_2) and silicon nitride (Si_3N_4) deposited by various methods, also have high interface-state densities. In this case, the interface states seem to be related to the presence of an interfacial layer of oxidized GaAs, either native oxides present before deposition or oxides created during the deposition process (4-7).

For example, in the vacuum ultraviolet irradiation (VUV) assisted chemical vapor deposition of SiO_2 on GaAs, the "Photox" process developed by Hughes Aircraft Company, a GaAs photochemical oxide is found at the GaAs- SiO_2 interface, even when no initial GaAs native oxide is present before deposition (8). Knowledge of the mechanism of photochemical oxidation of GaAs is important for reducing or eliminating this layer, and for enhancing the usefulness of the "Photox" process in GaAs passivation. In the experiments reported here, the kinetics of the VUV photochemical oxidation of GaAs by nitrous oxide (N_2O) have been observed by x-ray photoelectron spectroscopy (XPS). A probable mechanism for the reaction is suggested in which molecular N_2O adsorbs on clean, stoichiometric GaAs prior to its dissociation. This model is suggested by the temperature dependence of the reaction: the reaction is less complete as the substrate temperature is raised.

Experimental

The GaAs coupons were polished <100> faces of p-type material, zinc-doped to a carrier concentration of $5 \times 10^{18} \text{ cm}^{-3}$. To produce the native oxides, coupons were cleaned with 2% bromine (Br) in methanol for 10s, rinsed in methanol, then placed in air at room temperature for several months.

For the photochemical oxidation experiments, the photochemical reactor was enclosed in a glove bag filled with flowing N_2 . The GaAs coupons were etched in the glove bag in either 2% Br_2 in methanol for 10s (to produce a stoichiometric surface) or in concentrated HCl for 15 min (to produce an As-rich surface) (9), rinsed in ethanol, and loaded into the reactor chamber. Since this procedure was carried out in the glove bag, the cleaned samples were never exposed to air. To the sensitivity of our XPS measurements, no oxidized Ga or As is present on the surface. In the reactor, the substrate was placed on a heated copper block where it would be illuminated from above by a low-pressure mercury (Hg) lamp. The photon flux of the lamp is about $1 \times 10^{15} \text{ photon/cm}^2 \text{ s}$, equally split between the 2537 and 1849Å lines. Both lines have sufficient energy for e^-h^+ pair production in GaAs, and the 1849Å line can dissociate N_2O to produce $N_2(^1\Sigma)$ and $O(^3P, ^1D)$. N_2O was introduced into the evacuated chamber at a flow rate of 60 standard cubic centimeters per minute (sccm), and the pumping speed was adjusted to establish a pressure of 6 torr in the chamber. These

conditions are similar to those used in the photochemical deposition of SiO_2 on GaAs. The chamber has been used with a Hg sensitizer, but Hg was not intentionally added to the N_2O in these experiments. After the flow of N_2O was established, the lamp was turned on for an arbitrarily chosen period of time. As a result of the geometry of the reactor, the Hg lamp illuminates both the gas and the substrate surface.

The coupons were removed from the reactor chamber, again in a N_2 environment, and placed in a desiccator. The desiccator was transferred to a N_2 -filled glove bag attached to a modified GCA-McPherson ESCA-36 XPS spectrometer that had a spherical-sector analyzer and a position-sensitive detector (10). The coupons were loaded into the spectrometer, also in a N_2 atmosphere, and the spectrometer was evacuated to 1×10^{-7} torr. The entire procedure, from the unloading of the reactor chamber to the XPS analysis, generally took less than 30 min.

Results

GaAs native oxides.—The compositions of GaAs native oxides have been measured many times (9, 11). The results of this study are in agreement with the literature: the oxide is 80% gallium trioxide (Ga_2O_3), with 20% arsenic trioxide (As_2O_3) and occasionally a small amount of arsenic pentoxide (As_2O_5), depending on preparation conditions (see Fig. 1). The oxidized As peak, separated by 3.8-4.2 eV from the more prominent peak as a result of GaAs in this study, is assigned to As_2O_3 by comparison to binding energy values for bulk As_2O_3 (12). Some workers have found smaller values for this separation for lightly oxidized GaAs (11), values that could be due to either oxygen deficiency of the oxides or band bending effects. There is elemental As present in the native oxide. The elemental As signal is unresolvable from the GaAs As signal in these experiments because of the signals ~ 0.5 eV separation. However, the full width at half maximum

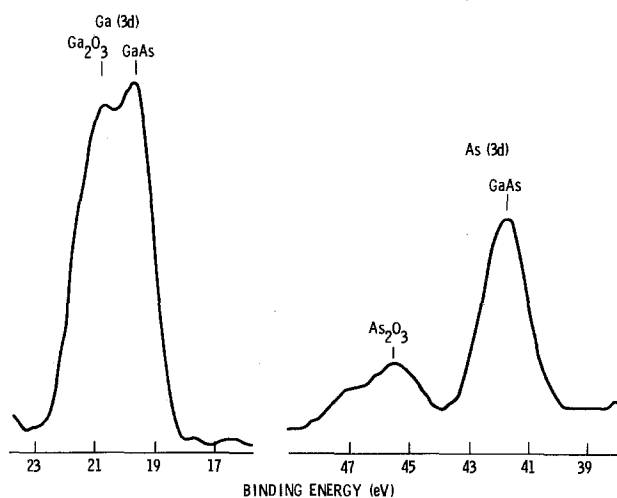


Fig. 1. XPS spectrum of native-oxide-covered GaAs

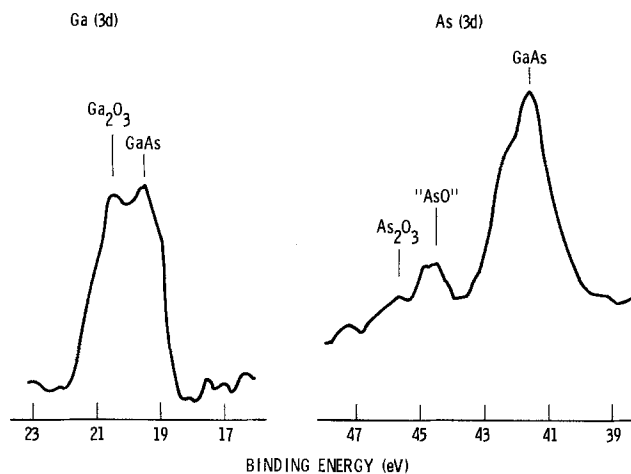


Fig. 2. XPS spectrum of native-oxide-covered GaAs after exposure to VUV radiation for 30 min at 23°C.

(FWHM) of the As XPS peak in a native-oxide-covered surface is 1.9 eV, compared to 1.4 eV for a clean surface; this clearly indicates the presence of unresolved structure.

An additional form of oxidized As is present in the native oxide after exposure to VUV radiation (see Fig. 2). It is not as highly oxidized as As_2O_3 , as shown by its XPS peak position intermediate between those of GaAs and As_2O_3 . The As(metal)- As_2O_3 separation of approximately 3.6 eV for a change of 3 in As oxidation state (12) implies that the 2.8 eV separation between GaAs and partially oxidized As corresponds to a formal As oxidation state of about +2. This should not be taken as an indication of the presence of an actual compound "AsO." The +2 oxidation state of As is not stable. Instead, this separation means that one of the As-O bonds has been broken during VUV irradiation, and the oxide is oxygen deficient. There is also a pronounced shoulder on the most intense As peak; we attribute this to elemental As.

GaAs photochemical oxide.—The photochemical oxide grown under our reaction conditions on a stoichiometric Br_2 -etched GaAs surface has equal amounts of oxidized Ga and As and is not Ga_2O_3 rich, as is the native oxide (see Table I). The Ga oxide present is Ga_2O_3 , and the As oxides are As_2O_3 and the less oxidized "AsO"-like form mentioned above (see Fig. 3). Elemental As is present, as indicated by the FWHM of the GaAs As peak of 1.7 eV. The photochemical oxide grown on an As-rich, HCl-etched surface is As rich (see Table I and Fig. 4). In fact, for short reaction times, only oxidized As (predominantly AsO) is observed, and no oxidized Ga is present. Without VUV exposures, no oxide is formed on either type of surface.

The progress of the reaction can be monitored by calculating the fraction F of the total Ga and As in the analysis volume that is oxidized (see Table I, column 5, and Fig. 5). F is calculated by taking the sum of the peak intensities for Ga as, Ga_2O_3 , and As as As_2O_3 and "AsO" and dividing that quantity by the sum of the peak intensities for Ga and As in these forms as well as in oxidized GaAs. Peak heights rather than peak areas were used because of the difficulty of uniquely resolving overlapping peaks. The O (1s) spectra were not used in the analysis because they were very broad, indicating the presence of more than one type of O environment, and could not be resolved. The peak intensities have been corrected for the spectrometer sensitivity, but not for matrix effects (which are largely unknown), molar volumes (which are not well defined, especially for the oxygen-deficient oxide "AsO"), or depth into the sample of the emitting atom (since it is not known whether the layers are smooth or island-like). If the oxides are present as islands, the signal for the oxides will not rise as rapidly as it would if the oxides were smooth layers, and the signal for the substrate will not fall as rapidly. Thus F will depend less on reac-

Table I. Photochemical oxide composition

Etch	Temperature (°C)	Reaction time (min)	As (oxides) ^a Ga_2O_3	Oxidation fraction	
Br_2	100	60	0.98	0.34	
		30	0.77	0.21	
	70	60	0.82	0.42	
		30	0.73	0.29	
		20	1.2	0.34	
		60	1.6	0.50	
	40	30	0.92	0.49	
		20	1.1	0.38	
		23	60	1.6	0.49
			30	0.77	0.40
HCl		100	20	1.0	0.35
			60	1.5	0.38
	30		1.2	0.36	
	20		^b	0.19	
	70	10	^b	0.17	
		60	1.6	0.29	
		30	1.4	0.25	
		40	60	1.2	0.35
			30	1.8	0.42
		20	^b	0.39	
	23	10	^b	0.09	
		60	2.4	0.39	
		30	0.94	0.32	
		20	^b	0.11	

^a Ratio of the amount of oxidized As to the amount of oxidized Ga observed by XPS, using the corrected XPS peak intensities as the amounts.

^b No Ga_2O_3 observed.

tion time for an island-growth mode than for a smooth-layer growth mode, but will follow the same general trends.

For the native oxide, $F \approx 0.4$, or 40% of the Ga and As in the region sampled by XPS is oxidized (as discussed below, this can be thought of as an oxide $\sim 5\text{\AA}$ thick). For a 60 min reaction time, the photochemical oxides also have $F \approx 0.4$. On the Br_2 -etched surface for reaction temperatures of 70° and 100°C, the reaction does not appear to be nearing completion; F is still increasing at 60 min. Reactions were not run for longer periods of time, so the value of F at completion is not known. For lower temperatures, the reaction appears to slow after 30 min. Except for the 23°C case, the fraction of oxidation decreases with increasing temperature. On the HCl-etched surface, the reaction is clearly slowing after 30 min; it is probably complete at 60 min for all temperatures studied, and has no obvious temperature dependence.

Discussion

The observed temperature dependence of the photochemical oxidation (a decrease in the fraction of oxidation as temperature increases) of clean, stoichiometric GaAs by N_2O and VUV irradiation indicates that a gas adsorption step could be present in the reaction mechanism.

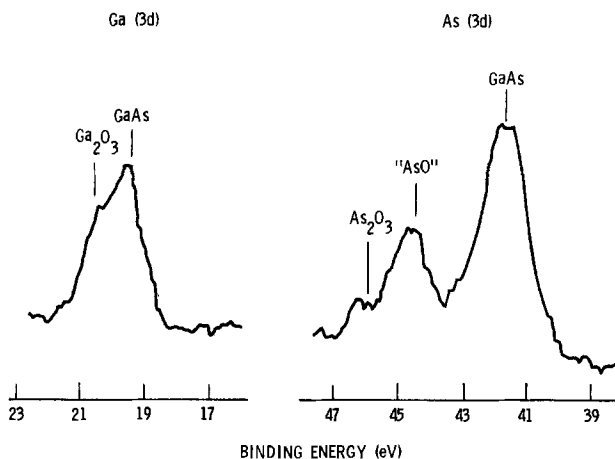


Fig. 3. XPS spectrum of Br_2 -etched GaAs after exposure to N_2O and VUV radiation for 60 min at 70°C.

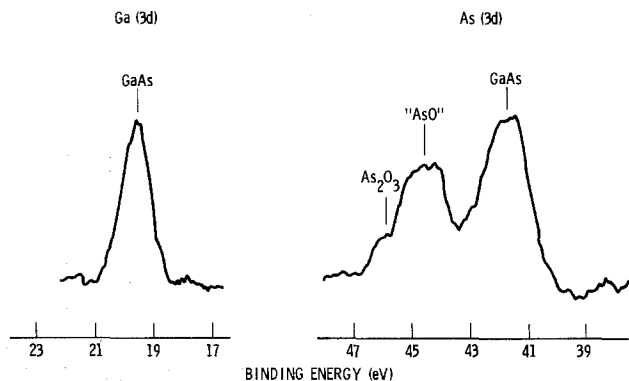


Fig. 4. XPS spectrum of HCl-etched GaAs after exposure to N_2O and VUV radiation for 30 min at $40^\circ C$.

The photodissociation of N_2O , whether in the gas phase or on the surface, is temperature independent, and the rate of oxidation of GaAs by adsorbed oxygen (O) atoms produced by the dissociation of N_2O should increase slightly with increasing temperature. An adsorption step will have its equilibrium shifted toward reactants (unadsorbed gas and the clean surface) by increased temperature. Then, since there is less gas adsorbed at higher temperature, the overall reaction will be slower. Another possibility would be diffusion of Ga or As into the oxide layer (this will be discussed later).

Given the assumption that a gas adsorption step is responsible for the temperature dependence, the adsorption energy Q can be calculated from the temperature dependence of adsorption through the equation $F \propto \exp(Q/RT)$ (see Fig. 6a), and is 2 ± 1 kcal/mol, a value typical of physical adsorption. Oxygen atoms created on the surface by electron irradiation are known to adsorb strongly to GaAs (13), and the "excited oxygen" used in many oxidation studies to produce fast, heavy oxidation may also be atomic oxygen (14). The adsorbing species in the experiments described here is only physisorbed and, therefore, is probably N_2O . The O atoms produced in the gas phase may be quenched too quickly in our experimental conditions to live long enough to react with the surface, although this seems unlikely. Another possibility is that the oxygen atoms produced in these experiments are not as reactive as those produced by electron irradiation or by interaction with an ion-gauge filament; indeed, the states of these latter two forms of "excited oxygen" have not been characterized. Therefore, the photodissociation of N_2O occurs while it is adsorbed on the surface, either directly or through mediation by the excited surface. The adsorbed O atoms produced by this step then react with the GaAs surface to produce Ga and As oxides. The overall reaction can be pictured as

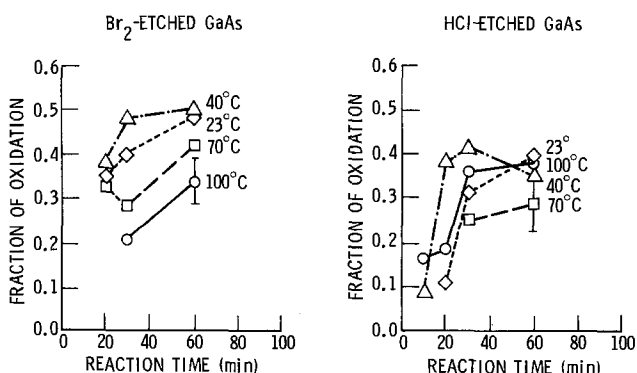
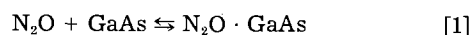


Fig. 5. Progress of photochemical oxidation of GaAs, illustrated by the fraction of oxidation as a function of time. Error bars represent the reproducibility expected in F as a result of the 15% reproducibility of XPS intensity measurements. (Left): Br_2 -etched surface. (Right): HCl-etched surface.

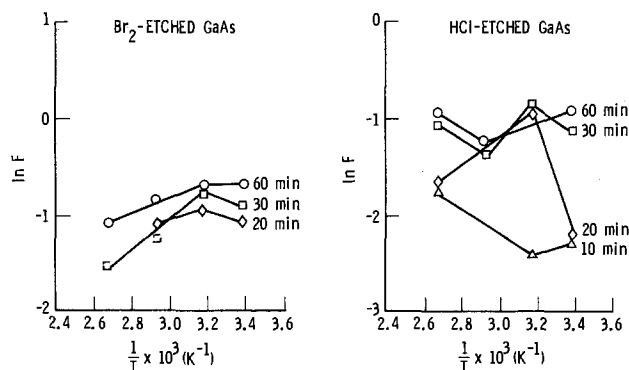
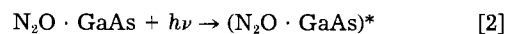


Fig. 6. Temperature dependence of photochemical oxidation of GaAs. (a, left): Br_2 -etched surface. (b, right): HCl-etched surface.



where $N_2O \cdot GaAs$ and $O \cdot GaAs$ represent adsorbed N_2O and O atoms, respectively.

Another possible explanation of the decreases in F with increasing temperature is that unoxidized Ga and/or As diffuses into the oxide layer, thus increasing the denominator of the fraction F . However, solid-state diffusion processes usually have activation energies of tens of kilocalories, many times greater than that observed here.

The thickness of the oxide layers can be calculated approximately (15) with two assumptions. First, the escape depth λ of the photoelectrons was taken to be 15\AA for both Ga and As. Second, the oxide layer is assumed to be a homogeneous film with an abrupt interface on top of the GaAs substrate. The thickness of the native oxide is calculated to be 5\AA , while the thickest photochemical oxide on a Br_2 -etched surface in these experiments is $\sim 8\text{\AA}$ thick.

The surface stoichiometry has a profound effect on the reaction. The As-covered surface does not oxidize as readily as the stoichiometric surface: the fraction of oxidation is less and saturates at ~ 30 min. The approximate thickness of the oxide layer at this point is only 6\AA . The reaction has no discernible temperature dependence, as a temperature-dependence plot shows (see Fig. 6b). The change in surface stoichiometry may eliminate or reduce the physisorption sites for N_2O , requiring gas-phase dissociation of N_2O and transport of O to the surface. The gas-phase production of O atoms and their transport to the surface is less probable than the adsorption and decomposition of N_2O for the previously considered case of a clean surface, which would account for the overall slowing of the reaction. However, it would not account for the saturation of oxidation after 30 min.

The final step of the photochemical oxidation reaction, the oxidation of GaAs by adsorbed O atoms, must be rate limiting in this case. This step should be very geometry- and composition-dependent. For example, room temperature adsorption of O_2 has been found to produce two adsorbed oxygen containing species on GaAs surfaces of various geometries and compositions: an adsorbed molecular form, bound predominantly to As, and an oxidic form, bound predominantly to Ga (13). Electron irradiation of the adsorbed molecular form converted it to the oxidic form. The mechanism of this reaction requires molecular adsorption sites in which the As atoms are surrounded by Ga atoms to enable subsequent reaction. An As-rich surface will have fewer such sites and should show reduced reaction with adsorbed O atoms. That is, the surface concentration of O in appropriate sites for reaction is rate limiting.

The limited oxidation of an As-rich surface has been used in the protection of GaAs from atmospheric effects, by creation of an As-rich layer on the surface by molecular beam epitaxy (MBE) (16) or electrochemical methods

(17). Layers of As 50-1000Å thick were found to oxidize only at their surfaces in air at room temperature and to prevent oxidation of the substrate GaAs. In the present experiments, the thickness of the As layer created by the HCl etch could not be measured, since its XPS signal was unresolvable from that of the substrate. It is probably much thinner than the MBE and electrochemical films, and may not be continuous. However, even in this case, the oxidation rate is decreased when the surface layers are As rich.

Conclusions

The photochemical oxidation of clean, stoichiometric GaAs probably proceeds by (i) adsorption of N₂O, (ii) dissociation of the N₂O on the VUV-excited surface, and (iii) oxidation of the surface by the adsorbed O atoms. The temperature dependence of the overall reaction is dominated by the temperature dependence of adsorption of N₂O. An As-rich surface oxidizes more slowly and the oxidation process saturates at 30 min. In this case, either gas-phase or surface dissociation of N₂O may occur; the rate-limiting step and cause of saturation is the oxidation of the surface by adsorbed O atoms. The As-covered surface does not present the proper sites (As atoms surrounded by Ga atoms) for fast, continued oxidation of GaAs.

Acknowledgments

The author thanks Mr. J. L. Childs for performing the XPS analyses. This work was supported by the U.S. Air Force under Space Division Contract no. F04701-83-C-0084.

Manuscript submitted Jan. 16, 1984; revised manuscript received Dec. 17, 1984.

The Aerospace Corporation assisted in meeting the publication costs of this article.

REFERENCES

1. J. Lagowski, T. E. Kazior, W. Wolukiewicz, H. C. Gatos, and J. Siejka, *J. Vac. Sci. Technol.*, **19**, 519 (1981).
2. H. Hasegawa, T. Sawada, and T. Sakai, *Surf. Sci.*, **86**, 819 (1979).
3. R. P. H. Chang, J. J. Coleman, A. J. Polak, L. C. Feldman, and C. C. Chang, *Appl. Phys. Lett.*, **34**, 237 (1979).
4. J. F. Wager and C. W. Wilmsen, *J. Appl. Phys.*, **53**, 5789 (1982).
5. J. D. Langan and C. R. Viswanathan, *J. Vac. Sci. Technol.*, **16**, 1474 (1979).
6. R. P. Vasquez and F. J. Grunthaler, *ibid.*, **19**, 431 (1981).
7. M. D. Clark and C. L. Anderson, *ibid.*, **21**, 453 (1982).
8. P. A. Bertrand, To be published.
9. P. A. Bertrand, *J. Vac. Sci. Technol.*, **18**, 28 (1981).
10. P. A. Bertrand, L. E. Tribble, W. J. Kalinowski, and L. U. Tolentino, *Rev. Sci. Instrum.*, **54**, 387 (1983).
11. H. Iwasaki, Y. Mizokawa, R. Nishitani, and S. Nakamura, *Jpn. J. Appl. Phys.*, **17**, 315, 1925 (1978); *ibid.*, **18**, 1525 (1979).
12. C. D. Wagner, W. M. Riggs, L. E. Davis, and J. F. Moulder, "Handbook of X-Ray Photoelectron Spectroscopy," p. 90, Perkin-Elmer, Eden Prairie, MN (1979); Y. Mizokawa, H. Iwasaki, R. Nishitani, and S. Nakamura, *J. Electron Spectrosc. Relat. Phenom.*, **14**, 129 (1978); L. D. Hulett and T. A. Carlson, *Appl. Spectrosc.*, **25**, 33 (1971); W. J. Stec, W. E. Morgan, R. G. Albridge, and J. R. Van Wazer, *Inorg. Chem.*, **11**, 219 (1972).
13. W. Ranke and K. Jacobi, *Surf. Sci.*, **81**, 504 (1979).
14. P. Pianetta, I. Lindau, C. M. Garner, and W. E. Spicer, *Phys. Rev. B*, **18**, 2792 (1978).
15. V. I. Nefedov, *Surf. Interf. Anal.*, **3**, 72 (1981).
16. S. P. Kowalczyk, D. L. Miller, J. R. Waldrop, P. G. Newman, and R. W. Grant, *J. Vac. Sci. Technol.*, **19**, 255 (1981).
17. J. M. Woodall, P. Oelhafen, T. N. Jackson, J. L. Freeouf, and G. D. Pettit, *J. Vac. Sci. Technol. B*, **1**, 795 (1983).

Technical Notes



High Field Ionic Conduction in Anodic Ta₂O₅ Formed in Oxalic and Phosphoric Electrolytes

I. Montero, J. M. Albella,* and J. M. Martínez-Duart

Instituto de Física del Estado Sólido, C.S.I.C. and Departamento de Física Aplicada, C-12 Universidad Autónoma, Cantoblanco, Madrid 34, Spain

In a recent paper (1), we have analyzed the anodization voltage-time curves of tantalum in terms of an avalanche model originally proposed by Ikonopisov (2). According to this analysis, the decrease of the slope of these curves during the anodization process at constant current (and hence at constant field) is brought about by the avalanche current originated in the electrolyte species incorporated into the oxide. Thus, incorporated impurities seem to play an important role in the control not only of the anodization rate but also of the avalanche electron current. This electron current turns out to be the direct cause of electrical breakdown during anodization.

Following our studies on the influence of the incorporated anions on the anodization and breakdown characteristics, new results are now presented here, concerning the anodization in oxalic acid at different current densities. They are also compared with our previous results in

*Electrochemical Society Active Member.

phosphoric acid (1). The oxalic acid is known to have low anion incorporation into the anodic Ta₂O₅ films since such cannot be detected by surface techniques such as Auger and ESCA spectroscopies (3). On the contrary, the incorporation of phosphate anions may amount up to 3% in anodization experiments in very diluted electrolytes (10⁻³M) (4). In addition, the oxalic acid along with other organic acids such as citric is widely used in the technology of tantalum thin film circuits (5).

Experimental

Tantalum samples of 99.96% nominal purity, supplied by Reframet-Hoboken, were anodized in a 0.01M solution of oxalic acid in water (1220 Ω-cm resistivity) at different constant current densities. The voltage-time curves, $V = V(t)$, as well as their time derivative, dV/dt , were recorded by means of a data acquisition system based on the HP 3497_A digital voltmeter (input impedance >10⁷ Ω) and the

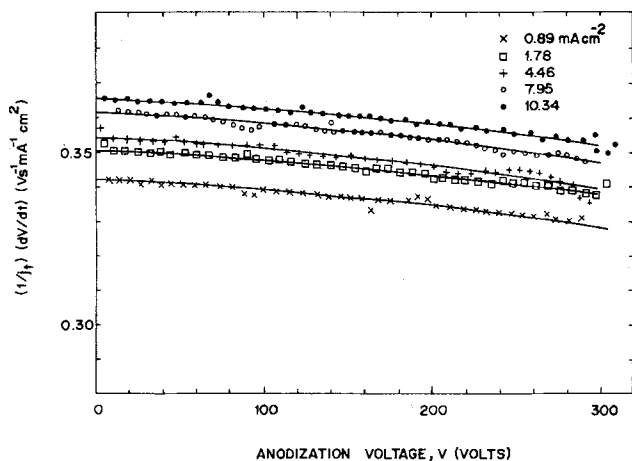


Fig. 1. Experimental values of the derivative of the voltage-time curve per unit current density as a function of the anodization voltage. Solid lines represent the computed values according to the theoretical Eq. [1] and [2].

HP 85 microcomputer. The temperature of the sample was kept constant at $20 \pm 0.2^\circ\text{C}$ by using a thermostatic bath. Other experimental details have been described elsewhere (1).

Results and Discussion

Figure 1 shows the experimental results of the anodization rate per unit current density as a function of the anodization voltage at different current densities, within the range 0.89–10.34 mA cm⁻². As compared to the results obtained in phosphoric acid (1), we have observed that, all the anodizing conditions being the same, the oxalic acid gives, in general, lower values of the derivative and a lesser decrease of it with the anodization voltage.

Following the lines of our previous analysis of the anodization curves, we have obtained by the least squares method the parameters j_e and K , which give a best fit of the theoretical equation

$$\frac{dV}{dt} = K j_i = K(j_t - j_e) \quad [1]$$

to the experimental curves. In Eq. [1], K represents the unitary anodization rate, *i.e.*, the voltage rise per unit of ionic charge, and j_i the ionic current density, which is given by the difference between the total current density j_t supplied by the source and the avalanche electronic current j_e . This last magnitude is assumed to increase exponentially along the oxide thickness d in an avalanche mechanism according to the equation

$$j_e = j_0 \exp(\alpha d) = j_0 \exp(\alpha \beta V) \quad [2]$$

where j_0 is the primary electron current, α the impact ionization coefficient, and β the anodization constant which equals the inverse of the anodization field, E . For anodization experiments performed in phosphoric acid it has been demonstrated that j_0 is closely related to the relative concentration of the phosphorous species incorporated into the oxide (1). Thus the source of the primary electrons can be ascribed to these species acting similarly to donor levels in the bandgap.

For all the anodizing currents, the oxalic acid gives a constant value of the relative primary electron current, $j_0/j_i = 0.021 \pm 0.002$, this value being lower than that obtained in a diluted solution of phosphoric acid ($2.4 \times 10^{-3}M$) (1). In addition, no oxygen evolution was observed during the experiments except at voltages close to the breakdown voltage. This observation is in agreement with the measured efficiency at low voltages for the formation of Ta₂O₅, which is very close to 100% (6). A higher concentration of oxalic acid in the electrolyte gives similar values for j_0/j_i (7). This fact could be explained taking into account the low incorporation of the oxalic acid compared with the phosphoric acid, as it has been demon-

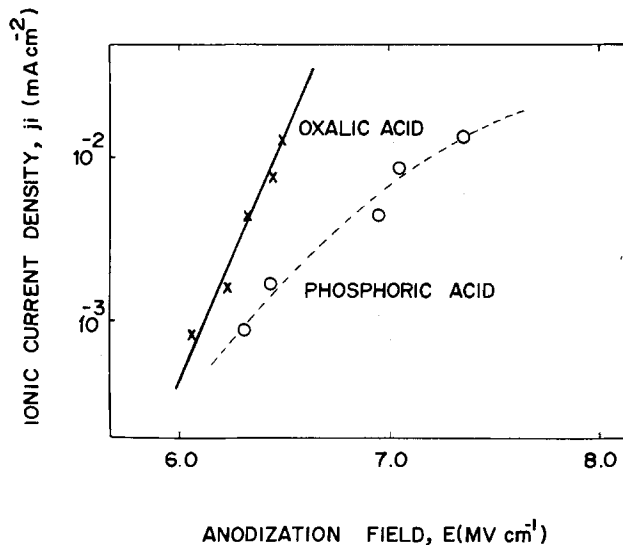


Fig. 2. Ionic current density vs. anodization field for oxalic (present work) and phosphoric acid electrolytes [previous work (1)]. The broken line has been drawn according to the work of Dell'Oca and Young (10).

strated by ESCA and AES measurements (3). The impact ionization coefficient results also in a nearly constant value, $\alpha = (1.96 \pm 0.02) \times 10^4 \text{ cm}^{-1}$. The constancy of α contrasts with its fair increase observed in phosphoric acid for increasing anodization currents (1) and can be a consequence of the different anodization fields found in each electrolyte. This effect is best appreciated in Fig. 2, where the ionic current density at low voltages, *i.e.*, $j_i \approx j_t - j_e$, has been plotted as a function of the electric field, for both the oxalic and phosphoric acid electrolytes. The value of E has been calculated from the constant K using the expression

$$K = \frac{ME}{10F\rho} \quad [3]$$

where M is the molecular weight of Ta₂O₅, F the Faraday constant, and ρ the oxide's density ($\rho = 8.03 \text{ g cm}^{-3}$).

In Fig. 2, the almost linearity of the logarithmic values of the ionic current density displayed by the oxalic acid is evident, in contrast to the curvature shown by the phosphoric acid (values taken from our previous work) (1). Also apparent in this figure are the higher electric fields needed to maintain a given ionic current for this last electrolyte. It is worth noting that the ionic conductivity values of the anodic Ta₂O₅ shown in the oxalic acid are very close to those obtained by Young and Zobel (8) in sulfuric acid, which is known to produce also a low proportion of incorporated anions. These authors measured the electric field directly from the quotient of the anodization voltage and the oxide thickness, this last magnitude being determined by ellipsometry.

The linear variation of the $\log j_i$ vs. E , within the studied range, is in agreement with the theoretical equation proposed for the ionic conduction mechanism at high fields (6)

$$j_i = j_i' \exp[-(W - qaE)/kT] \quad [4]$$

where j_i' is a constant. The exponent contains the field-dependent energy barrier in kT units found by the ions with charge q moving a distance $2a$ (the rest of the symbols have their conventional meanings). Assuming a charge of $5e$ for the ions and an energy barrier $W = 2.185 \text{ eV}$ from Young's work (9), the parameters of Eq. [4] would be $j_i' = 5.7 \times 10^{14} \text{ A cm}^{-2}$ and $a = 3.6 \text{ \AA}$.

A straightforward calculation shows that, for instance, with the above values of the parameters, a 3% change in the barrier height W results in a ten-fold variation of the current density. Thus, it seems reasonable to associate the lower ionic conductivity found for the H₃PO₄ electrolyte to a change either in the energy barrier or in the dis-

tance a as a consequence of the phosphorous incorporation. This assumption would also explain the nonlinear effects shown by the phosphoric acid in the $\log j_i$ vs. E curve. In this respect, from the work of Randall *et al.* (4) in anodization experiments with a 0.01M H_3PO_4 electrolyte, it can be inferred that the phosphorous content in the oxide may increase with current density so that it is 25% greater at 1 than at 0.1 mA cm^{-2} . More experiments in different electrolytes are now being conducted in order to obtain a deeper insight into the influence of the incorporated ions on the ionic conduction mechanism at high fields.

Manuscript submitted July 23, 1984; revised manuscript received Jan. 2, 1985.

Universidad Autónoma assisted in meeting the publication costs of this article.

The Influence of Deposition Conditions on Hydrogen Bond Configuration and Trap Sites in Sputtered Si_3N_4

H. M. Anderson*

Department of Chemical and Nuclear Engineering, University of New Mexico, Albuquerque, New Mexico 87131

P. M. Martin

Pacific Northwest Laboratory,¹ Richland, Washington 99352

Considerable effort has been spent in defining the relationship between defect structure and charge characteristics in dielectric silicon nitride films used in microelectronic devices. The gap states of silicon nitride films are important, since they regulate memory properties of metal-nitride-oxide-semiconductor (MNOS) devices and electrical properties of thin film transistors. Gap states in silicon nitride arise from defects in the film and are attributed to Si and N dangling bond ($\equiv Si$ and $\equiv N$ units) formation during the deposition process (1-3). Hydrogen is known to passivate dangling bonds and remove the gap states of amorphous silicon (a-Si), and it is thought that hydrogen plays a similarly crucial role in determining the concentration of trap states in silicon nitride (3). The configuration in which hydrogen is chemically bonded in the nitride affects the concentration of Si and N dangling bonds in the film and, consequently, the reproducibility of device memory or conductive behavior.

In this technical note, we present some results showing the influence of deposition conditions on the partition of hydrogen bonding between Si and N in sputtered Si_3N_4 films. These results may prove useful in understanding the passivation Si and N dangling bonds and the location of trap sites in nitride films. Previous theoretical calculations based on the tight binding recursion method (4) have led to the conclusion that $\equiv Si$ centers are the long-term charge storage trap in CVD-deposited nitride as well as the center responsible for charge trapping instabilities in amorphous silicon-silicon nitride thin film transistors (3). The experimental results presented in this paper provide further evidence that hydrogen acts preferentially to passivate the $\equiv N$ dangling bonds of silicon nitride films.

Experimental

The RF diode sputtering system used to deposit Si_3N_4 has been described previously (5). An RF-induced dc bias of 1000-2000V was applied to the sputtering target in this experiment. A resistive heater was embedded in the substrate electrode to provide control over substrate temper-

- ### REFERENCES
1. J. M. Albella, I. Montero, and J. M. Martínez-Duart, *This Journal*, **131**, 1101 (1984).
 2. S. Ikonopisov, *Electrochim. Acta*, **22**, 1077 (1977).
 3. S. Hofmann and J. M. Sanz, *J. Trace Micropr. Technol.*, **1**, 213 (1982).
 4. J. J. Randall, W. J. Bernard, and R. R. Wilkinson, *Electrochim. Acta*, **10**, 183 (1965).
 5. R. W. Berry, P. M. Hall, and M. T. Harris, in "Thin Film Technology," p. 280, Van Nostrand, New York (1968).
 6. C. J. Dell'Oca, D. L. Pulfrey, and L. Young, *Phys. Thin Films*, **6**, 1 (1984).
 7. J. M. Albella, I. Montero, and J. M. Martínez-Duart, To be published.
 8. L. Young and F. G. R. Zobel, *This Journal*, **113**, 277 (1966).
 9. L. Young, *ibid.*, **124**, 528 (1977).
 10. C. J. Dell'Oca and L. Young, *ibid.*, **117**, 1548 (1970).

ature. Both target and substrate RF networks were tuned by minimizing reflected power. The sputtering target was 99.999% pure Si, 15.24 cm diam. All sputtering gases were passed through a gas purifier, filtering H_2O , O_2 , and trace amounts of organics to <1 ppm. Deposition rates ranged from 120 to 260 Å/min, increasing with increased target power and decreasing with increased H_2 and N_2 . Power density to the target ranged from 1.10 to 3.30 W/cm². Substrate-target spacing was fixed at 3.18 cm.

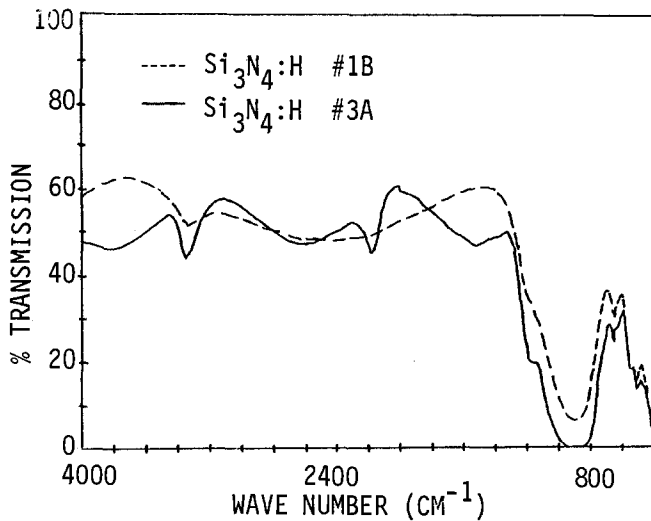
Depositions were made with premixed electronic-grade $Ar+N_2+H_2$ on either 2.54 cm diam, 0.16 cm thick fused silica substrates for ultraviolet, visible, and near-infrared spectrophotometric and electrical measurements, or 2.54 cm diam, 0.4 cm thick germanium mirror for spectrophotometric measurements in the infrared. Gas pressure and particularly the partial pressures of H_2 and N_2 were varied for each of 14 nitride depositions, as shown in Table I. Deposits were characterized by index of refraction, film thickness, and spectral dependence of the absorption coefficient. A dual monochromatic UV-visible spectrophotometer was used to measure transmission spectra of films deposited on fused silica substrates from 200 to 2500 nm. A dual-beam infrared (IR) spectrophotometer was used to obtain by transmission spectrophotometry

Table I. Sputtering gas pressure conditions.
Gas Pressure (Pa).

Sample no.	p_{Ar}	p_{N_2}	p_{H_2}	p_{total}
1A	2.13	0.80	0.13	3.07
1B	2.13	0.80	0.40	3.33
1C	2.13	0.80	1.20	4.13
2A	2.13	0.40	0.40	2.93
2B	2.13	0.40	0.80	3.33
2C	2.13	0.40	1.20	3.73
3A	2.13	0.13	0.40	2.67
3B	2.13	0.13	0.80	3.07
3C	2.13	0.13	1.20	3.47
4A	2.13	0.00	0.40	2.53
4B	2.13	0.00	1.20	3.33
5A	2.13	0.13	0.13	2.40
6A	2.13	0.80	0.00	2.93
6B	2.13	0.40	0.00	2.53

* Electrochemical Society Active Member.

¹ Operated by Battelle Memorial Institute for the U.S. Department of Energy under Contract DE-AC06-76RL0 1830.

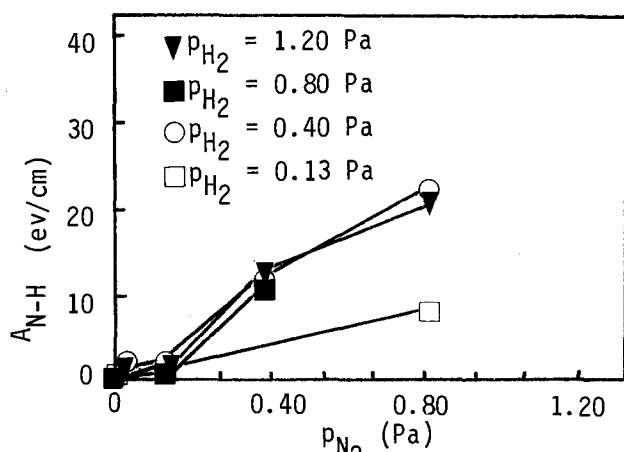
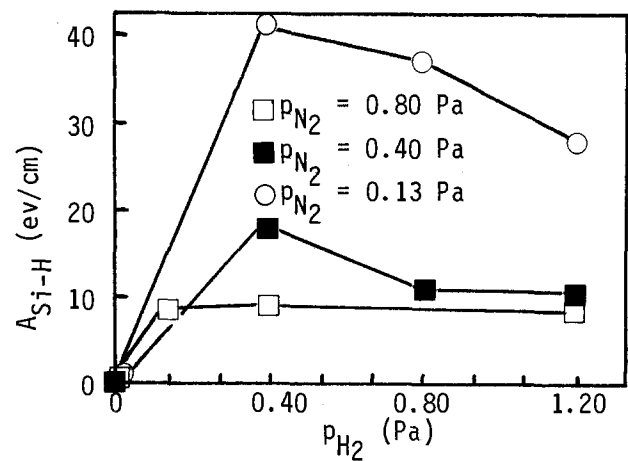
Fig. 1. Vibrational spectra of sputtered $\text{Si}_3\text{N}_4\text{:H}$

complete IR vibrational absorption spectra of films deposited on Ge substrates in the region 2500-25,000 nm.

Results and Discussion

The chemical bonding configuration of hydrogen in silicon nitride films can be determined from IR absorption in the regions corresponding to vibrational stretching frequencies of Si-H (2150 cm^{-1}) and N-H (3350 cm^{-1}) (2). Previous measurements (2, 6, 7) have shown that for both plasma and CVD nitrides, IR absorption can be used to quantitatively estimate the partition of H between Si and N through a calibration of the IR absorption to absorption cross sections for Si-H and N-H from nuclear reaction analysis.

In this study, relative values for hydrogen bond concentration and the partition of hydrogen between Si and N were obtained for reactively sputtered nitride films. Hydrogen bond configuration was determined from IR vibrational absorption spectra using a method similar to that of Lanford (6) and Percy *et al.* (7). The absorption coefficients β of the Si-H and N-H stretching modes near 2150 and 3350 cm^{-1} , respectively, were calculated as a function of photon energy using the relation $T(\omega) = T_0(\omega) \exp -\beta t$, where t is the film thickness, $T_0(\omega)$ is the transmission of a nonabsorbing film, and $T(\omega)$ is the measured transmission for a frequency ω . Integrating over the distinct Si-H and N-H stretching frequency regions according to the relation $A_s = \int_{\omega_s} \beta(\omega) d\omega$ provides a relative measure of the H content in the film (8) due to either Si-H bonding [$A_{\text{Si-H}}$ (eV/cm)] or N-H bonding [$A_{\text{N-H}}$ (eV/cm)]. Figure 1 illustrates typical vibrational spectra as a function of wave number over the stretching modes 2150 and 3350 cm^{-1} for two $\text{Si}_3\text{N}_4\text{:H}$ films.

Fig. 2. Relative N-H bonding in $\text{Si}_3\text{N}_4\text{:H}$ Fig. 3. Relative Si-H bonding in $\text{Si}_3\text{N}_4\text{:H}$

Figures 2 and 3 illustrate the results for Si-H and N-H bonding vs. the H_2 and N_2 partial pressure deposition conditions depicted in Table I. Figure 2 illustrates increased N-H bonding in the nitride films with increased N_2 partial pressures in the deposition conditions. Simultaneous increases in the H_2 partial pressure appears to contribute to increased N-H bond formation until a leveling off occurs at high H_2 partial pressures. Figure 3, on the other hand, illustrates that, at high N_2 partial pressures, the formation of Si-H bonds in the nitride film is largely suppressed, regardless of the partial pressure of H_2 . Infrared absorption indicative of Si-H bond formation in the nitride film is observed when the deposition partial pressure of N_2 is small.

The results of varying the N_2 and H_2 deposition conditions indicate a preference for N-H bond formation in nitride films. For high N_2 partial pressures, a clear trend exists in the data toward greater N-H bond formation over Si-H bonding with increases in the H_2 partial pressure. It is only when the availability of nitrogen for incorporation into the film is low that Si-H bonding dominates over N-H bonding with increases in the H_2 partial pressure. Work by Fujita (1) using ESR also suggests that preferential N-H bonding occurs over Si-H bonding in CVD nitride. Their results suggest that the ESR signal originates mainly from silicon dangling bonds in CVD films. The pattern of N-H bonding observed in this study also strongly suggests that hydrogen will preferentially act to passivate N dangling bonds in nitride films.

Acknowledgment

Support for this work was provided by the Materials Science Division, Office of Basic Energy Sciences, U.S. Department of Energy.

Manuscript submitted Sept. 4, 1984; revised manuscript received Dec. 18, 1984.

University of New Mexico assisted in meeting the publication costs of this article.

REFERENCES

1. S. Fujita, H. Sato, and A. Sasaki, Paper 122, presented at The Electrochemical Society Meeting, San Francisco, CA, May 8-13, 1983.
2. P. S. Percy and H. J. Stein, Paper 101, presented at The Electrochemical Society Meeting, San Francisco, CA, May 8-13, 1983.
3. J. Robertson and M. J. Powell, *Appl. Phys. Lett.*, **44**, 415 (1984).
4. J. Robertson, *J. Appl. Phys.*, **54**, 4490 (1983).
5. P. M. Martin and W. T. Pawlewicz, *Solar Energy Mater.*, **2**, 143 (1979/1980).
6. W. A. Lanford and M. J. Rand, *J. Appl. Phys.*, **49**, 2473 (1978).
7. P. S. Percy, H. J. Stein, B. L. Doyle, and S. T. Picraux, *J. Electron. Mater.*, **8**, 1 (1979).
8. E. C. Freeman and W. Paul, *Phys. Rev. B*, **18**, 4288 (1978).

Characterization of Boron-Implanted Silicon at Various Depths from the Surface by Raman Scattering

P. T. T. Wong

National Research Council of Canada, Division of Chemistry, Ottawa, Ontario, Canada K1A 0R6

M. Simard-Normandin

Northern Telecom Electronics Limited, Ottawa, Ontario, Canada K1Y 4H7

The preparation of a VLSI CMOS process implies the fabrication of p+n junctions with junction depths of the order of 0.25 μm . These junctions are usually fabricated by the implantation of boron or boron difluoride and annealed at high temperatures to activate the species and restore the implantation damage. Since boron diffuses very fast in silicon because of its light mass, the annealing times are shortened and new methods of annealing are implemented (laser, flashlamp, etc.). This can result in incompletely activated dopant if the annealing parameters have not been adequately chosen.

Raman scattering is an attractive method of characterizing boron-implanted silicon, allowing simultaneous measurement of the free-carrier concentration and the measurement of the number of impurities in substitutional position. It can also detect the presence of amorphous silicon, thus giving another measure of the effectiveness of the annealing cycle.

In this paper, we report Raman scattering measurements of low energy boron-implanted silicon at several depths from the surface and compare the results with the concentration profile obtained by secondary ion mass spectrometry (SIMS) techniques.

Experimental

The sample is a phosphorous-doped (3-7 $\Omega\text{ cm}$) n-type (100) CZ-grown 100 mm silicon wafer. Ions of $^{11}\text{B}^+$ with a fluence of $3 \times 10^{15}/\text{cm}^2$ were implanted at room temperature at an energy of 10 keV. The wafer subsequently received 100 nm of deposited SiO_2 at 450°C. Then furnace annealing was done in N_2 ambient at 925°C for 20 min. Finally, the wafer was coated with a 400 nm layer of deposited SiO_2 to serve as a mask for beveling.

For the Raman scattering experiment, three pieces were broken off the wafer. Half of each piece was covered with wax, and the oxide was stripped off the unmasked portion using HF. The implanted silicon was then etched in a mixture of acetic, nitric, and hydrofluoric acids using the oxide-covered side as a mask. Finally, the remaining oxide was removed to expose the surface. The height of the step was measured using an interference microscope. Samples etched 0.11, 0.18, and 0.35 μm below the surface were thus obtained. An unimplanted, unprocessed wafer of the same type was used for calibration. For the SIMS analysis, all oxide was removed from the wafer in HF. The SIMS analysis was done at the University of Western Ontario using a Cameca IMS 3-f ion microscope. A wafer implanted at the same dose and energy into bare silicon and otherwise unprocessed was used for SIMS calibration.

Raman spectra were measured with a Spex Model 14018 double monochromator equipped with 1800 line/nm holographic gratings and a cooled RCA C31034 photomultiplier. The Raman spectra, which were measured with a resolution of $\sim 2\text{ cm}^{-1}$, were excited with the 514.5 nm line with a CRL Model 12 argon-ion laser. This line had a power of 200 mW at the sample. A 90° scattering geometry was employed. The sample surface was slightly tilted with respect to the direction of the scattering so that the reflected laser beam was away from the entrance slit of the monochromator. The laser beam was linearly polarized and incident on the sample at the Brewster angle.

The absorption parameters of heavily doped silicon are given in Ref. (1). At $\lambda_0 = 514\text{ nm}$ and an angle of 75°, the penetration in the sample is of the order of 0.13 μm , which is comparable to the spacing of our data points. Using a parallel polarized beam further reduces the energy coupled into the depth of the sample, since most of this radiation is reflected. The perpendicularly polarized beam, which would normally penetrate and not be reflected, is not present in our case. Since the energy lost in the sample is exponential, we believe that only the first few molecular layers are detectable in the present experimental setup. To be precise, a small correction needs to be applied to each data point to take into account the penetration in the sample. Because the doping density is still very high ($> 10^{18}/\text{cm}^3$) at our deepest point and the absorption properties are not a very strong function of doping above that value, the correction is expected to be small and always in the same direction. In a relative analysis like the one performed here, it is safe to neglect this correction.

The data acquisition was performed by a Spex Model DM1 Datamate Processor and the resulting spectral data were transferred to a Nova IV Data General computer. Frequency and spectra sensitivity calibrations were applied to each spectrum. Frequencies, bandwidths, and integrated intensities were calculated.

Results and Discussion

Substitutional boron, with respect to its silicon neighbors, produces a local mode at a frequency higher than that of the optical phonon mode (520 cm^{-1}), i.e., at 620 cm^{-1} for boron-11. Shown in Fig. 1 are the Raman spectra of the optical phonon and the boron local mode at several depths of the sample. The top of the optical phonon

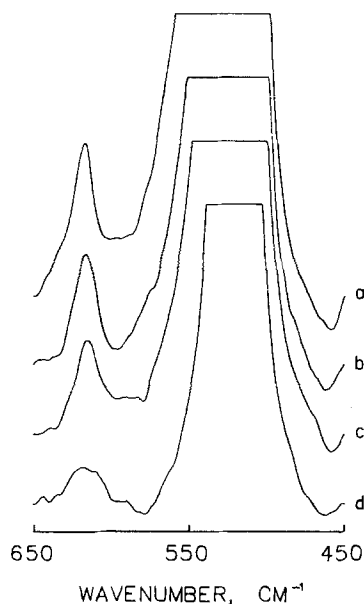


Fig. 1. Raman spectra of boron-11 implanted silicon at the depth of (a) 0.0, (b) 0.11, (c) 0.18, and (d) 0.35 μm from the surface.

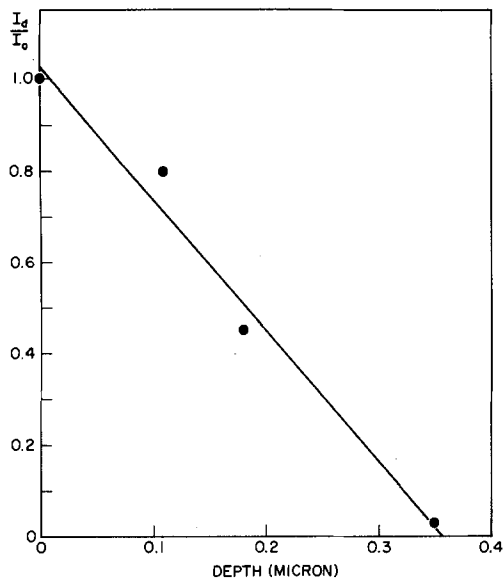


Fig. 2. Depth dependence of normalized intensity ratio of the local mode between various depths (I_d) and the surface (I_0).

height so that the intensities of the local mode measured at different depths of the silicon sample can be compared visually. It is apparent from Fig. 1 that the local mode intensity decreases with increasing depth in the sample. Moreover, the asymmetry and the intensity of the wing on the high frequency side of the optical phonon band also decreases with increasing depth. The intensity of this wing, and thus the asymmetry of the phonon band, is due to the interaction between the optical phonon and the intervalence and interconduction-band electronic transitions which are enhanced with increasing substitutional boron concentration. Consequently, the changes in the intensity of the optical phonon wing at different depths of the sample agree with the changes in the intensity of the local mode and indicate that the concentration of substitutional boron decreases with depth in the sample.

There is a very weak two-phonon Raman band in the frequency region of the boron-11 local mode which is observed in a pure silicon sample (2). The intensity of this two-phonon mode normalized against that of the optical phonon was subtracted from the normalized intensities of the local mode measured at various depths of the sample. With these normalized intensities, the percentage decrease of the local mode intensity, and thus that of the

substitutional boron concentration as a function of the depth in the sample, can be calculated and is plotted against the depth in the sample in Fig. 2. In the normalization process, the intensity of the optical phonon of pure silicon being one-third lower than that of boron-implanted silicon (3) has been taken into account. To eliminate the interference of two-phonon scattering, one may replace boron-11 by boron-10 for implantation. The local mode of boron-10 shifts to $\sim 640 \text{ cm}^{-1}$, which is about 20 cm^{-1} higher than the frequency of the two-phonon mode.

The results shown in Fig. 2 are comparable with those obtained by SIMS shown in Fig. 3. The depth dependence of the boron concentration measured by Raman scattering is consistent with that by the SIMS technique, except at the surface. For instance, if the boron concentration at the depth of $0.11 \mu\text{m}$ from the surface is taken as 1, the boron concentrations at the depths of 0.18 and $0.35 \mu\text{m}$ decrease to 0.66 and 0.26 , respectively, measured by Raman scattering, and to 0.71 and 0.21 , respectively, by SIMS.

We cannot quote the boron concentration at the surface with any certainty using SIMS. In Fig. 3, the boron concentration is shown only from the point where the silicon profile (not plotted) is constant. Close to the surface, the oxygen content in the silicon varies and the count is lower. Using the same normalization as above, the Raman intensity is 1.20 at the surface. With this factor applied to the SIMS profile, the surface concentration would be $6.5 \times 10^{19} \text{ cm}^{-3}$, which is the value of the extrapolated diffused profile. The sharp peak is due to improper annealing where dislocations getter the boron. This peak disappears at higher annealing temperatures.

As shown in Fig. 1, the top portion of the local mode band in the spectrum measured on the surface of the sample is relatively narrower than in the spectrum measured at a depth of $0.11 \mu\text{m}$, and a very broad band is underneath the narrower band. This is consistent with the fact that, for this sample, the silicon is not perfectly crystalline at, or very near, the surface.

It has been shown that free carriers cause an increase in the phonon line width and a decrease in the phonon frequency as a result of "softening" of the crystal lattice through free-carrier redistribution (4). Figures 4 and 5 show the depth dependences of the phonon line width and the phonon frequency, respectively. Except for the surface, the phonon line width decreases, while the phonon frequency increases with increasing depth of the silicon sample. These results indicate that the free-carrier concentration in the sample decreases with increasing depth. With a calibration curve between the frequency shift and the free-carrier concentration, such as that in Fig. 1 of Ref. (5), the free-carrier concentrations at various depths of the sample can be calculated by the phonon frequency shifts at various depths with respect to the frequency of the pure silicon sample. Comparison between

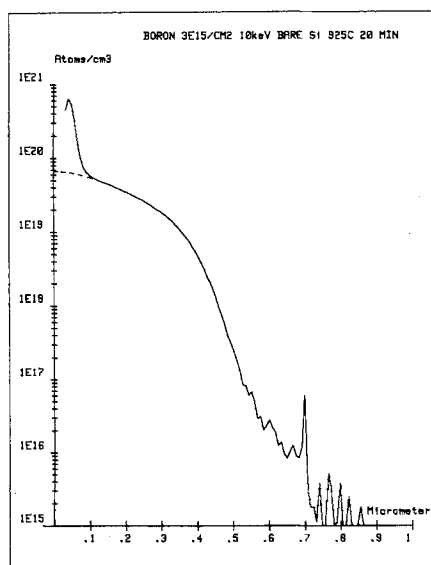


Fig. 3. Boron concentration profile obtained by SIMS technique

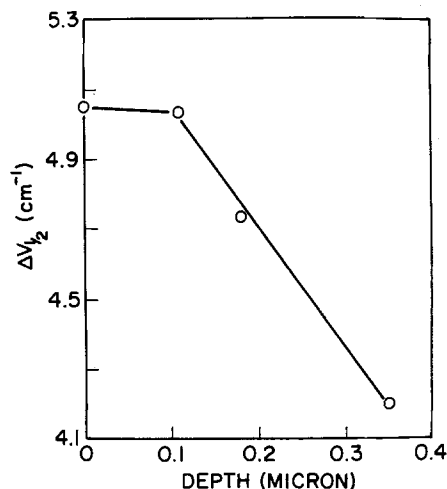


Fig. 4. Depth dependence of the phonon line width at half-height

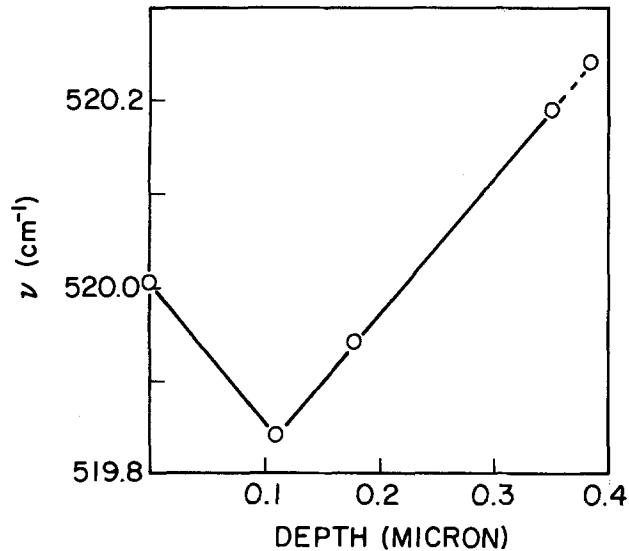


Fig. 5. Depth dependence of the phonon frequency

the depth dependence of the phonon frequency of the boron-implanted sample and the phonon frequency of a pure silicon sample is shown in Fig. 5. It indicates that the concentration of the free carrier in the boron-implanted sample reduces to 0 at the depth of about 0.39 μm from the surface.

Conclusion

The present work has demonstrated that Raman scattering is a useful technique for determining both the substitutional boron and free-carrier concentrations at different depths from the surface in boron-implanted silicon. Since Raman scattering techniques are nondestructive and do not require any electrical contact, they may be useful for industrial quality control of boron activation.

Acknowledgments

We wish to thank B. Loro for etching the samples and the Surface Science Western group for the SIMS analysis.

Manuscript submitted Aug. 6, 1984; revised manuscript received Nov. 23, 1984.

Northern Telecom Electronics Limited assisted in meeting the publication costs of this article.

REFERENCES

1. G. E. Jellison, Jr., F. A. Modine, C. W. White, R. F. Wood, and R. T. Young, *Phys. Rev. Lett.*, **46**, 1414 (1981).
2. R. A. Forman, M. I. Bell, and D. R. Myers, *J. Appl. Phys.*, **52**, 4337 (1981).
3. M. Chandrasekher, H. R. Chandrasekher, M. Grimsditch, and M. Cardona, *Phys. Rev. B*, **22**, 4825 (1980).
4. F. Cerdeira, T. A. Fjeldly, and M. Cardona, *ibid.*, **8**, 4734 (1973).
5. R. Beserman and T. Bernstein, *J. Appl. Phys.*, **48**, 1548 (1977).

A Novel Processing Technique for the Fabrication of Thick Silicon Grids by Anisotropic Etching

B. Petit and J. Pelletier

Unité de Recherche Associée au CNRS no. 844, B.P. 98, CNS-CNET, 38243 Meylan Cedex, France

R. Molins

Institut National Polytechnique de Grenoble, B.P. 75, CMTC, 38402 St. Martin d'Herès, France

Novel procedures involving the anisotropic etching of silicon by aqueous solutions of pyrocatechol ethylene diamine or hydroxides of alkali metals have been reported over the past few years. Their purpose has been to achieve high precision patterns in silicon. Applications cover such diverse fields as the fabrication of mechanical devices (1) ranging from ink nozzles (2) to ion source extraction grids (3) and fine membranes (1) such as thinned transmission electron microscopy (TEM) specimens (4) and lithography masks (5). Among the above-mentioned etching techniques, some have the disadvantage of being lengthy and tedious, e.g., ethylene diamine etching (6, 7). Others, such as those involving hydroxides of alkali metals in water, are easier to use but etch SiO_2 (2, 8-10) at a rate which rules it out as a mask in many experiments (3). Varker and Chang have found that (100) silicon wafers masked on both sides with a plasma-deposited Si_3N_4 film can be successfully etched in a KOH solution (4). The equipment required for such plasma deposition and subsequent etching, however, and the long Si etching time involved (5 or 6 h for a wafer 300 μm thick) limit the application of this technique.

Our aim was to develop a simple and relatively rapid etch process that could be used to obtain both grids of the type found in ion sources and diaphragms of extremely fine aperture. In order to realize gains in Si etch time, the etchant would be heated to the highest temperature the mask could withstand. We therefore had to find a masking material that would be chemically inert in the

heated etchant. Moreover, the masking material had to be able to withstand these temperatures without coming

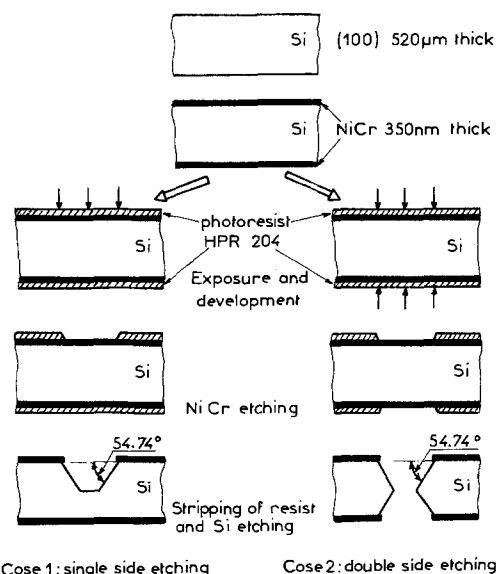


Fig. 1. Sequence of steps in the fabrication of grids using conventional photolithographic techniques and anisotropic etching of silicon substrates.

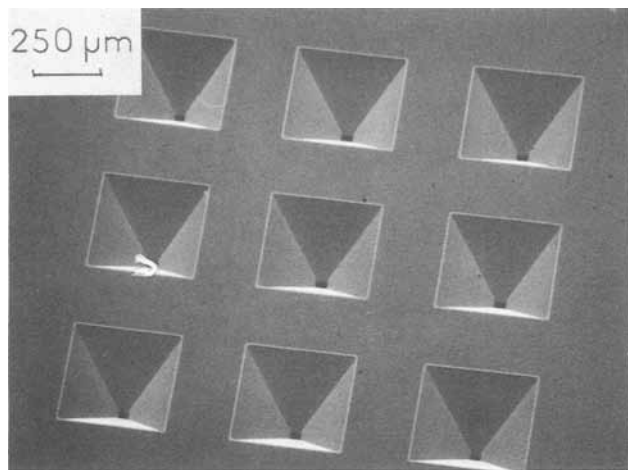


Fig. 2. SEM photomicrograph of a double-side etched grid 525 μm thick. Each base square is 390 μm on a side; and the orifices are 19 \times 19 μm^2 ; the center-to-center spacing is 740 μm .

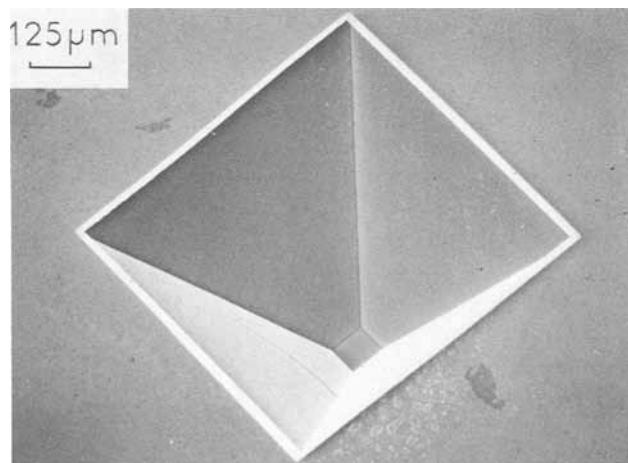


Fig. 3. Single-side etching of a 500 μm deep hole starting from a base square of 730 \times 730 μm^2 . The underetching is emphasized by the white line surrounding the base square.

away from the substrate. NiCr was found to be suitable as the masking material in a solution of 10N NaOH at 363 K (9). As seen in our experiments, raising the temperature above 363 K led to damage in the NiCr layers, *i.e.*, resulted in an overly high NiCr etch rate with respect to an only slight increase in the silicon etch rate. For example, the NiCr etch rate of about 100 nm/h at even 368 K is incompatible with the etching of relatively thick Si substrates.

Our procedure consists mainly of steps used in conventional Si processing techniques. Single-crystal, (100)-oriented, 100 mm silicon wafers 525 μm thick and polished on both sides are used. The sequence of steps is shown in Fig. 1. An NiCr film about 350 nm thick is deposited on both sides of the samples by magnetron sputtering. The required window pattern is transferred through a photoresist layer onto the NiCr film either on one (case 1) or both surfaces (case 2), care being taken not to misorient the pattern with reference to the wafer's <110> flat edge. In the case of double-side etching, the square openings on both sides of the wafer must be carefully aligned. The NiCr film is then etched for a few minutes in an aqueous oxidizing solution containing ammonium cerium nitrate and acetic acid (with no observable effect on the silicon substrate). After removal of the photoresist layers, the wafers are immersed in a well-agitated 10N NaOH bath at 363 K for a total etching time of either 4.5h for case 1 or half that time for case 2. Towards the end of the etching step, the thickness of the re-

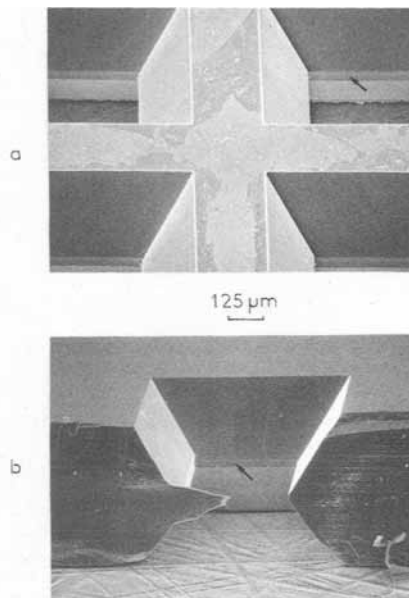


Fig. 4. SEM photomicrographs of a double-side etched grid: (a) partial view; (b) cross section of one hole of the grid shown in (a). Note the absence of the usual etch pits on the Si surface after removal of the surface masking NiCr film.

maining silicon is monitored by lowering the bath temperature a few degrees. Thus end-point detection is facilitated, especially in the more crucial case of single-side etching. At this point, the samples are ready for scanning electron microscopy (SEM) observations.

Using the technique described above, one can produce a great number of grids having orifices of only a few square micrometers, accurately defined by the pattern geometry (Fig. 2). An average etch rate of 120 $\mu\text{m}/\text{h}$ is obtained on the {100} planes at 363 K and is consistent with the results of Barycka *et al.* (9). The etch rate of the {111} planes is 3 $\mu\text{m}/\text{h}$, determined from underetching measurements of the base hole in the Si surface. Since the NiCr film remains intact, the size of the base holes after etching may only depend upon the lateral etch rate of the {111} planes. The SEM photomicrographs in Fig. 3 and 4 show the considerable depths etched, the good behavior of the masking layers even after a few hours of etching, as well as the well-defined, defect-free {111} sidewalls and (100) planes after NiCr removal. For case 2, the crystallographic planes revealed (see arrows in Fig. 4a and 4b) show a slight misorientation of the pattern from one side of the wafer to the other. The profile of the intersection of the two pyramidal shapes after anisotropic etching can also be seen.

In this very simple processing technique, the NiCr protective coating acts as a mask on both sides of the substrate; the 10N NaOH solution can thus be brought up to a temperature of 363 K, thereby allowing considerable gains in etch rates as compared to other procedures [see Table II of Ref. (1)]. Using this technique, fine mesh silicon grids suitable for mass spectrometry analysis, for instance, have been fabricated reproducibly by anisotropic etching of square-base holes through Si wafers of (100) orientation. The relatively short etching times involved, the ease of use, and good quality of the results obtained make this method an attractive tool for high precision diaphragm or grid fabrication.

Acknowledgment

We wish to thank M. Pichot for helpful discussions and support in this work.

Manuscript submitted Aug. 20, 1984; revised manuscript received Dec. 18, 1984.

CNRS assisted in meeting the publication costs of this article.

REFERENCES

1. K. E. Petersen, *Proc. IEEE*, **70**, 420 (1982).
2. E. Bassous and E. F. Baran, *This Journal*, **125**, 1321 (1978).
3. J. L. Speidell, J. M. E. Harper, J. J. Cuomo, A. W. Kleinsasser, H. R. Kaufman, and A. H. Tuttle, *J. Vac. Sci. Technol.*, **21**, 824 (1982).
4. C. J. Varker and L. H. Chang, *Solid State Technol.*, **26**, 143 (1983).
5. D. L. Spears and H. J. Smith, *Electron. Lett.*, **8**, 102 (1982).
6. R. M. Finne and D. L. Klein, *This Journal*, **114**, 965 (1967).
7. A. Reisman, M. Berkenblit, J. A. Chan, F. B. Kaufman, and D. C. Green, *ibid.*, **126**, 1406 (1979).
8. I. J. Pugacz-Muraszkiewicz, *IBM J. Res. Dev.*, **523**, (1972).
9. I. Barycka, H. Teterycz, and Z. Znamirowski, *This Journal*, **126**, 345 (1979).
10. Maah-Sango and T. Van Duzer, *IEEE Electron. Device Lett.*, **ed1-3**, 21 (1982).



Preparation and Conductivity Measurements of $\text{SiS}_2\text{-Li}_2\text{S-LiBr}$ Lithium Ion Conductive Glasses

Saeed Sahami,¹ Steven W. Shea, and John H. Kennedy*

Department of Chemistry, University of California, Santa Barbara, California 93106

We wish to report on the preparation and properties of new high lithium ion conductive glasses composed of $\text{SiS}_2\text{-Li}_2\text{S-LiBr}$. A number of conductive sulfide-based lithium glasses, which can be used as electrolytes in lithium solid state devices and batteries have been studied (1-7). The most widely studied are $\text{P}_2\text{S}_5\text{-Li}_2\text{S}$ glasses and their lithium iodide doped analogs, which show conductivity as high as $10^{-3} \text{ S-cm}^{-1}$ at 25°C . It was recently reported that since $\text{P}_2\text{S}_5\text{-Li}_2\text{S}$ (and $\text{B}_2\text{S}_3\text{-Li}_2\text{S}$) glasses require synthesis in sealed pressure quartz tubes, the $\text{SiS}_2\text{-Li}_2\text{S}$ glasses, which may be prepared under atmospheric pressure offer a viable commercial production alternative (8). The base glass, $\text{SiS}_2\text{:Li}_2\text{S}$ has a conductivity of at least $0.75 \times 10^{-4} \text{ S-cm}^{-1}$ at 25°C (8). Although the addition of LiI to $\text{SiS}_2\text{-Li}_2\text{S}$ base system increases the conductivity of these glasses up to $6.4 \times 10^{-4} \text{ S-cm}^{-1}$ (8), some oxidation of iodide to iodine may occur during synthesis (9). No investigation was reported on the effects of other lithium halides on the conductivities of these glasses.

We have investigated the effects of LiBr doping on the conductivity and the extent of glass formation of $\text{SiS}_2\text{-Li}_2\text{S}$ by varying the molar concentration of LiBr while holding the mole ratio of SiS_2 to Li_2S constant at 1:1.

The $\text{SiS}_2\text{-Li}_2\text{S}$ glasses were prepared by first mixing SiS_2 and Li_2S in a 1:1 mole ratio in a dry box with an oxygen and water level less than 2 ppm. The mixture was then placed in a vitreous carbon crucible, which in turn was positioned in a Vycor tube. The stoppered Vycor tube was taken outside the dry box and placed in a vertical furnace and heated for approximately one hour at 950°C under an argon gas blanket. The molten mixture was quickly quenched into a water bath at room temperature to form the vitreous

solid. To dope this base glass with LiBr, appropriate weights of LiBr and the vitreous glass were ground, mixed together, and the heating procedure described above was again followed. The quenched glasses were ground to a fine powder and a portion of the glass sample was uniaxially pressed into a 0.3 inch diameter rod with TiS_2 electrodes on both faces. This cell was subsequently isostatically pressed at ~ 45000 psi to achieve high density.

The ionic conductivity of each sample was measured by the complex impedance technique using a Solartron 1174 Frequency Response Analyzer interfaced to a Hewlett-Packard 9845B desktop computer and a General Radio 1435 Programmable decade resistance box. The signal applied across the sample was 25 to 100mV and the frequency varied from 0.1 to 10^5 Hz over the temperature range of 20° to 140°C .

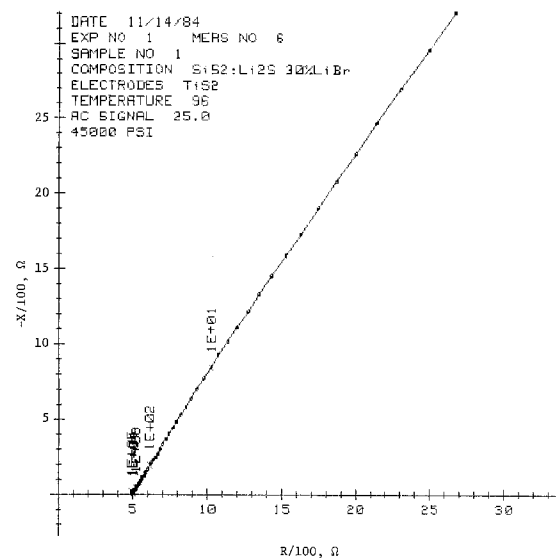


Fig. 1. Complex impedance plot for 0.3 LiBr-0.35 SiS_2 -0.35 Li_2S using TiS_2 electrodes at 96°C and applied signal of 25 mV. Frequency varied from 1 to 10^5 Hz.

As is shown in Fig. 1, the complex impedance plots of glasses consisted of a straight line intersecting the real axis at approximately a 45° angle. The bulk resistance of the glass sample was obtained from the extrapolation of the straight line portion of the complex impedance plot to the real axis. In the temperature range studied here, the ionic conductivity of all the glasses was found to obey the Arrhenius law: $\sigma = \sigma^0 \exp(-E_a/KT)$. Values of ionic conductivity (σ) measured at 25°C and the activation energies (E_a) determined from the slopes of Arrhenius plots for $\text{SiS}_2\text{-Li}_2\text{S-LiBr}$ glasses are reported in Table I. Figure 2 shows a plot of $\log \sigma$ vs. mole % of LiBr added to the base glass. Here we see that the ionic conductivity increased linearly with LiBr up to 30 mole %, then it decreased sharply with the addition of more LiBr. Table I also indicates that the activation energy in the 0 to 30 mole % LiBr range remained relatively constant, but increased rapidly with higher concentrations of LiBr.

Table I. Conductivities and Activation Energies for Silicon Sulfide Glasses.

Glass Composition	σ (S-cm ⁻¹) at 25°C	E_a (Kcal/mole)
0.5 $\text{SiS}_2\text{-0.5 Li}_2\text{S}$	1.5×10^{-4}	7.8
0.1 $\text{LiBr-0.45 SiS}_2\text{-0.45 Li}_2\text{S}$	1.9×10^{-4}	7.0
0.2 $\text{LiBr-0.4 SiS}_2\text{-0.4 Li}_2\text{S}$	2.1×10^{-4}	7.5
0.25 $\text{LiBr-0.38 SiS}_2\text{-0.38 Li}_2\text{S}$	2.4×10^{-4}	7.1
0.3 $\text{LiBr-0.35 SiS}_2\text{-0.35 Li}_2\text{S}$	3.2×10^{-4}	7.5
0.35 $\text{LiBr-0.33 SiS}_2\text{-0.33 Li}_2\text{S}$	2.3×10^{-4}	8.7
0.4 $\text{LiBr-0.3 SiS}_2\text{-0.3 Li}_2\text{S}$	1.1×10^{-4}	9.6

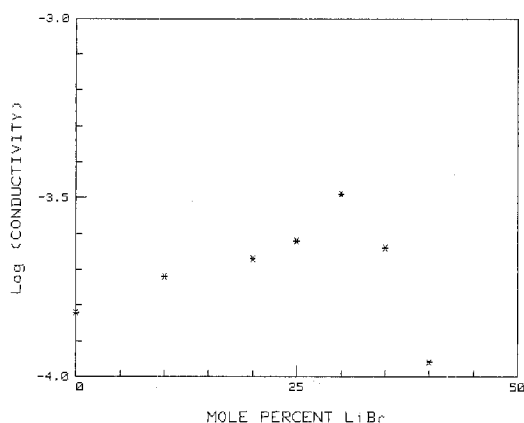


Fig. 2. Logarithm of conductivity at 25°C. as a function of LiBr mole percent in $\text{LiBr-SiS}_2\text{-Li}_2\text{S}$.

The maximum conductivity in this work was observed for the 0.3 $\text{LiBr-0.35 SiS}_2\text{-0.35 Li}_2\text{S}$ glass. X-ray diffraction analyses of LiBr doped $\text{SiS}_2\text{-Li}_2\text{S}$ glasses showed that all samples with LiBr mole% of ≤ 30 formed uniform glasses while, samples with higher LiBr content indicated traces of LiBr crystals present in the glass matrix. These observations are in good agreement with the conductivity measurements, indicating that maximum LiBr solubility is achieved with the 30% LiBr base glass at least with the quench rates used in this initial study. Upon addition of more LiBr, the extent of glass formation decreased, resulting in a drop of ionic conductivity. Further studies of these glasses, including ^7Li NMR measurements of LiBr and LiCl doped glasses are in progress in our laboratories.

REFERENCES

1. J.P. Malugani and G. Robert, *Solid State Ionics* **1**, 519 (1980)
2. R. Mercier, J.P. Malugani, B. Fahys and G. Robert, *Solid State Ionics* **5**, 663 (1981).
3. J.P. Duchange, J.P. Malugani and G. Robert, *Progress in Batteries and Solar Cells* **4**, 46 (1982).
4. B. Carette, M. Maurin, M. Ribes and M. Duclot, *Solid State Ionics* **9 & 10**, 655 (1983).
5. H. Wada, M. Menetrier, A. Levasseur and P. Hagenmuller, *Mat. Res. Bull.* **18**, 189 (1983).
6. M. Menetrier, A. Levasseur and P. Hagenmuller *J. Electrochem. Soc.*, **131**, 1971 (1984).
7. S.J. Visco, P.J. Spellane and J.H. Kennedy, Presented at Electrochemical Society Meeting, New Orleans, LA., October, 1984.
8. J.R. Akridge, US Patent 4, 465 745 (1984).
9. J.R. Akridge, Union Carbide Corporation, private communication.

* Electrochemical Society Active Member.
 † Present address: IBM, GPD, San Jose, CA 95193.

Manuscript received Dec. 12, 1984.

The Pourbaix Diagram for Cr With Fe and the Stress Corrosion Cracking of Stainless Steel

Daniel Cubicciotti*

Electric Power Research Institute, Palo Alto, California 94303

Lars Ljungberg

ASEA-ATOM, Västerås, Sweden

Hydrogen addition to the feedwater of boiling water nuclear reactors (BWR) is being used to avoid the problem of intergranular stress corrosion cracking (IGSCC) in weld sensitized regions of Type 304 stainless steel piping carrying coolant water. Hydrogen addition reduces the dissolved oxygen content of the coolant water and lowers the corrosion potential of stainless steel. The tests, mentioned below, have shown that IGSCC does not occur in sensitized stainless steel below a certain critical value of the corrosion potential. The reason for IGSCC mitigation below this critical potential has not yet been elucidated. In this note we report a correlation between the critical potential for IGSCC and the stable phase containing Cr. Above the critical potential where IGSCC can occur, the stable Cr-containing phase is Cr_2O_3 . Below the critical potential where IGSCC does not occur, the stable Cr-containing phase is FeCr_2O_4 . Our interpretation of this correlation is that a surface oxide phase of CrFe_2O_4 is protective against IGSCC while Cr_2O_3 is not. Further research is needed to define the mechanism of protection.

Thermodynamics of Cr-H₂O Systems. The equilibria for Cr between solid phases and solutions in the Cr-Fe-H₂O system at 300°C are shown in Fig. 1. Thermodynamic values for Cr were taken from Ref. 1. The only solid oxide containing both Fe and Cr, at least for which thermodynamic data are available, is FeCr_2O_4 . Its Gibbs energy of formation at 300°C was calculated from the data in Ref. 2 to be -336.5 Kcal per mole (referred to the elements at 25°C). The regions of stability of the solid Cr containing oxides depend on the activity of Fe, which in turn depends on which solid Fe compound is stable. The diagram indicates that

at the highest potentials (field A) the stable oxides are Cr_2O_3 and Fe_2O_3 and in the next lower adjacent field (B) FeCr_2O_4 and Fe_2O_3 . The change of stability of the Cr bearing oxide from Cr_2O_3 to FeCr_2O_4 is the region of interest to us.

Conditions in BWR.--During normal BWR operation the water recirculated through the reactor core contains (3) about 200 ppb (parts per billion) of dissolved oxygen and is approximately neutral (pH = 5.6). The corrosion potential of a Type 304 electrode in BWR water at about 300°C lies in the range of 0.0 to 0.1 volts, SHE, after some aging (4). This potential is still in the HCrO_4^- field, indicating that as the stainless steel recirculation piping corrodes, the Cr tends to dissolve out of the corrosion film. Examinations (5) of corrosion films on BWR piping confirm this analysis.

Mitigation of IGSCC by Low Corrosion Potential. Several series of tests (6,7) show that IGSCC of sensitized stainless steel does not occur in pure water if the potential of the steel is below a critical value in the range -0.2 to -0.3 volts SHE. In constant extension rate tests (CERT) in Ringhals-1 BWR (8) during hydrogen addition no IGSCC was observed when the corrosion potential was below -0.2 volts, when the water was pure. Tests in the Dresden-2 BWR have also shown such a critical potential.

During the tests in Ringhals-1 and in the Dresden-2 BWR with hydrogen added to the feedwater (equivalent to lowering the corrosion potential of stainless steel), it was observed that the concentration of Cr dissolved in the reactor water was decreased tenfold or more (8,9). That observation is

Manuscript submitted Nov. 26, 1984; revised manuscript received Jan. 21, 1985.

*Electrochemical Society Active member.

Keywords: Pourbaix diagrams, protective oxides, chromium oxides.

Electric Power Research Institute assisted in meeting the publication costs of this article.

in accord with the increase in stability of the Cr-containing oxide when the potential is lowered (Fig. 1).

Correlation of Critical Potential with Pourbaix Diagram. The Pourbaix diagram shows that for neutral water (pH=5.6), there is a change of phase at about -0.2 volts--i.e., at about the critical potential. Below that potential the stable Cr-containing oxide is FeCr_2O_4 and above it Cr_2O_3 . Thus, at about the critical potential for IGSCC, observed in CERT, there is a change in the stable Cr containing phase.

This correlation indicates that formation of a surface oxide of FeCr_2O_4 may be the process that provides protection against IGSCC for stainless steel. The correlation is significant in that it provides a basis for predicting the influence on IGSCC of changes in environmental conditions. Critical potentials were found to be related to the solute for 0.01 molal solution of various salts in Ref. 10.

REFERENCES

1. C. M. Chen, A. Aral, G. J. Theus, EPRI NP-3137, Vol. 2, EPRI, Palo Alto, Calif., 1983
2. O. Kubaschewski, C. B. Alcock, "Metallurgical Thermochemistry", Fifth Ed., Pergamon Press, Oxford, England, 1979.
3. B. M. Gordon, R. L. Cowan, C. W. Jewett, A. E. Pickett, Proc. Int. Symp. on Environmental Degradation of Materials in Nuclear Power Systems--water reactors, NACE, Houston, Tex., 1984.
4. M. E. Indig, J. E. Weber, EPRI NP-3362, EPRI, Palo Alto, Calif., 1983
5. L. D. Anstine, NEDO-12665, GE Co., San Jose, Calif., 1977.
6. W. E. Ruther, W. K. Soppet, G. Ayrault, T. F. Kassner, Corrosion, 40, 518 (1984).
7. A. Rosengren, B. Rosborg, in Ref. 3.
8. L. G. Ljungberg, D. Cubicciotti, M. Trolle, to be presented, Paper 100, Corrosion 85, NACE, Houston, Tex.
9. E. L. Burley, ed, DOE/ET/34203-47, GE Co., San Jose, Calif., 1982.
10. G. Cragolino, D. D. Macdonald, Int'l. Congr. on Metallic Corrosion, Vol. 2, p. 185, Nat'l. Res. Council, Ottawa, Canada, 1984.

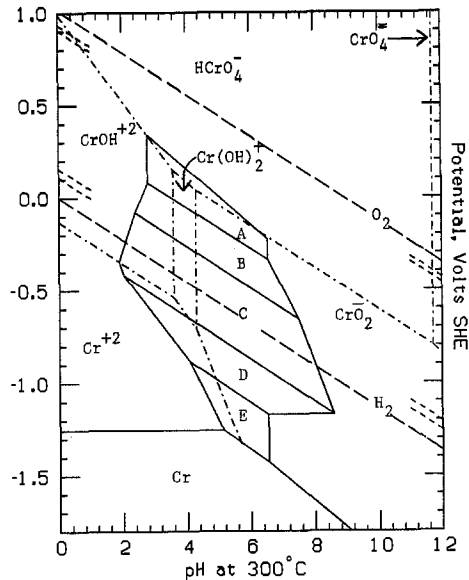


Figure 1. Pourbaix Diagram for the Cr-H₂O System with Fe at 300°C. Full lines separate regions of stability for Cr in different phases. Dissolved Cr species activities were 10⁻⁶ and metallic Cr activity 0.2 (to represent stainless steel).

Dot dash lines separate regions of stability of dissolved Cr species.

Long dashed lines represent equilibria between water and one atmosphere pressure of H₂ or O₂. Short dashed lines indicate the locations of lines for O₂ at 200 ppb and 20 ppb dissolved in water and for H₂ at 100 ppb and 10 ppb.

Letters A to E identify fields of stability of different pairs of solids, namely:

- A - $\text{Cr}_2\text{O}_3 + \text{Fe}_2\text{O}_3$
- B - $\text{FeCr}_2\text{O}_4 + \text{Fe}_2\text{O}_3$
- C - $\text{FeCr}_2\text{O}_4 + \text{Fe}_3\text{O}_4$
- D - $\text{FeCr}_2\text{O}_4 + \text{Fe}$
- E - $\text{Cr}_2\text{O}_3 + \text{Fe}$

Diffusion of Sb in (111) Silicon during N₂ Heat-Treatment

T. Kook* and R. J. Jaccodine*

Sherman Fairchild Center for Solid State Studies, Lehigh University, Bethlehem, Pennsylvania 18015

Recently thermal nitridation of silicon has been investigated and its effect on dopant diffusion has been reported(1,2). Mizuo et al. (1) found retarded B and P diffusion and enhanced Sb diffusion during N₂ and NH₃ heat treatments of the bare (100) and (111) silicon at 1100°C. They also investigated the effect of the SiO₂ capping and found that N₂ heat treatment had little effect while NH₃ heat treatment resulted in enhanced B and P diffusion and retarded Sb diffusion. Fahey et al. (2) also reported similar results. In this note we report the anomalous junction motion of Sb diffused specimens during N₂ heat treatment and the effect of the SiO₂ capping after prolonged heat treatments.

Czochralski-grown, lightly-doped, p-type (111) silicon wafers were implanted with Sb to a dose of 1.0 X 10¹⁴/cm² at 80 keV. In addition, two groups of specimens were prepared by implanting B into n-type wafers to a dose of 2.1 X 10¹⁴/cm² and P into p-type wafers to a dose of 1.0 X 10¹⁴/cm² at 100 keV and 80 keV, respectively. These were run concurrently with the Sb implanted ones. After annealing at 900°C for 30 min, all wafers were oxidized at 900°C in steam to grow 2000-Å-thick pad oxide. 1200-Å-thick silicon nitride was deposited by the low pressure chemical vapor deposition process over the oxide. Then drive-in heat treatments were performed to obtain 1-micron-deep initial junctions. P implanted specimens required 1 hr and for Sb specimens 13 h were required. B implanted specimens did not undergo the drive-in step because their junction depth was already about 1 micron after annealing and oxidation steps. Subsequent lithography and plasma etching were done to fabricate a specimen structure consisting of the SiO₂ capped silicon, the Si₃N₄ capped silicon, the SiO₂ + Si₃N₄ capped silicon, and the bare silicon. N₂ heat treatments were done in a conventional single wall quartz tube at 1100°C up to 24 h. Heat treated specimens were angle-lapped and stained to measure the

junction depths by interferometry. The junction depths after heat treatment were measured as X_{JS} in the bare silicon, X_{J0} in the SiO₂ capped silicon, X_{JN} in the Si₃N₄ capped silicon, and X_{JON} in the SiO₂ + Si₃N₄ capped silicon.

In Fig. 1, X_{JS}/X_{JON} for B, P, and Sb diffused specimens after N₂ heat treatments are plotted along with X_{J0}/X_{JON} for Sb diffused specimens. The junction motion of the Sb diffused specimens in the bare silicon is retarded after prolonged heat treatments, which is quite contradictory to the result of Mizuo et al.(1). On the other hand, the retarded junction motion of B and P diffused specimens is in good agreement with previous work(1,2). The junction motion in the SiO₂ capped silicon is enhanced after prolonged heat treatments while the Si₃N₄ capping has little effect. To rationalize the discrepancy between our study and the previous Sb studies (1,2) we made an extensive use of a precision angle-lapping and a spreading resistance probe. Fig. 2 shows the concentration profiles of Sb in the bare silicon and in the SiO₂ + Si₃N₄ capped silicon after 2 h N₂ heat treatment. It can be clearly seen that even though both regions have the same junction depths, the actual concentration profiles are quite different due to the severe out-diffusion loss

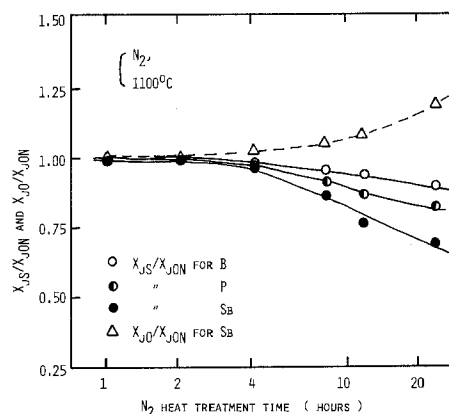


Fig. 1. X_{JS}/X_{JON} for B, P, and Sb diffused specimens and X_{J0}/X_{JON} for Sb diffused specimens after N₂ heat treatment at 1100°C.

*Electrochemical Society Active Member.

key word: thermal nitridation, Sb diffusion

of Sb atoms from the bare silicon surface during N₂ heat treatment. By integrating the concentration profiles the out-diffusion loss of Sb atoms after 2 h N₂ heat treatment was calculated to be about 25 %. Those of B and P were less than 8 %.

The concentration profiles in Fig. 2 strongly suggest that Sb diffusion is indeed enhanced during thermal nitridation of silicon in N₂. We developed a model to test the above observation by modifying the conventional drive-in model of a Gaussian distribution considering the time-averaged out-diffusion loss of dopant atoms. The time-averaged diffusivity ratio, $\langle D_S \rangle / \langle D_{ON} \rangle$ can be expressed as

$$\langle D_S \rangle / \langle D_{ON} \rangle = [(C_{SON} / C_{SS}) (\langle Q_S \rangle / \langle Q_{ON} \rangle)]^2$$

where C_{SS} and C_{SON} are the surface concentrations in the bare silicon and in the SiO₂ + Si₃N₄ capped silicon after heat treatment and $\langle Q_S \rangle$ and $\langle Q_{ON} \rangle$ are the time-averaged total dopant concentrations in each region. The changes of X_{JS}/X_{JON}, $\langle Q_S \rangle / \langle Q_{ON} \rangle$, and $\langle D_S \rangle / \langle D_{ON} \rangle$ with N₂ heat treatment time are plotted in Fig. 3. Above all, Sb diffusion was indeed enhanced by thermal nitridation of silicon. Initially $\langle Q_S \rangle / \langle Q_{ON} \rangle$ decreases rapidly but it decreases slowly as thermal nitridation proceeds. $\langle D_S \rangle / \langle D_{ON} \rangle$ increases initially up to 2 h and then decreases as thermal nitridation slows down. As a combined result of the time-dependent $\langle Q_S \rangle / \langle Q_{ON} \rangle$ and $\langle D_S \rangle / \langle D_{ON} \rangle$, X_{JS}/X_{JON} decreases after prolonged heat treatments. We also calculated $\langle D_S \rangle / \langle D_{ON} \rangle$ for B and P and found that both B and P diffusion were retarded during thermal nitridation of silicon in N₂. This favors a mechanism of silicon interstitial depletion in the surface region(2,3). The

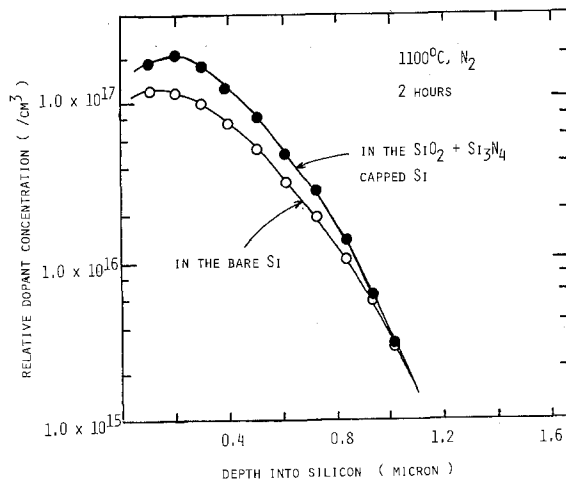


Fig. 2. Sb concentration profiles after 2 h N₂ heat treatment at 1100 °C.

undersaturation of interstitials in turn causes vacancy supersaturation and the diffusion of Sb atoms, which are considered to move almost exclusively by vacancies(4), is enhanced. The apparently retarded Sb junction motion is due to the severe out-diffusion loss of Sb atoms during N₂ heat treatment.

The SiO₂ capping resulted in enhanced Sb diffusion(see Fig. 1). This suggests a slower nitridation of substrate silicon under the oxide capping. The apparent difference from the NH₃ ambient case is the lower activity of N₂ with SiO₂. We conclude that N₂ should diffuse through SiO₂ without reaction and nitrify the substrate silicon. NH₃ is considered to react with SiO₂ and generate oxygen atoms which oxidize the substrate silicon.

In summary, the out-diffusion of Sb atoms during N₂ heat treatment and its effect upon shallow junction were investigated. It was clearly seen that the conventional angle-lapping and staining alone is not appropriate for this kind of study.

Manuscript submitted Dec. 26, 1984; revised manuscript received Jan. 18, 1985.

REFERENCES

1. S. Mizuo, T. Kusaka, A. Nanba, and H. Higuchi, J. Appl. Phys., 54, 3860(1983).
2. P. Fahey, R. W. Dutton, and M. Moslehi, Appl. Phys. Lett., 43, 683(1983).
3. H. Hayafuji and K. Kajiwara, J. Electrochem. Soc., 129, 2102(1982).
4. D. A. Antoniadis and I. Moskowitz, J. Appl. Phys., 53, 6788(1982).

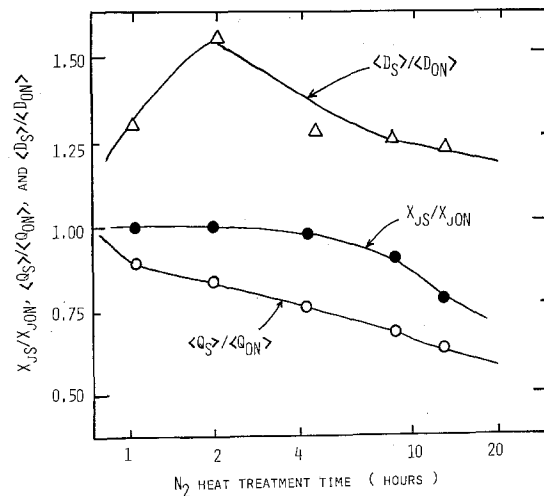


Fig. 3. X_{JS}/X_{JON}, $\langle Q_S \rangle / \langle Q_{ON} \rangle$, $\langle D_S \rangle / \langle D_{ON} \rangle$ of Sb diffused specimens after N₂ heat treatments at 1100 °C up to 24 h .

Lehigh University assisted in meeting the publication costs of this article.



Graphite Aluminum- and Silicon Carbide-Coated Current Collectors for Sodium-Sulfur Cells

M. Mikkor

Ford Motor Company, Dearborn, Michigan 48121

ABSTRACT

The electrical performance and corrosion of current collectors made from graphite foil bonded to aluminum and from stainless steel protected by silicon carbide coating are compared to current collectors protected by chromium coatings. The testing is done in corrosion cells operated under dynamic conditions in Na_2S melts at 350°C . The cells are operated under both cathodic and anodic potentials of 100-300 mV measured with respect to carbon reference electrodes. The current collectors made from graphite foil, $127\ \mu\text{m}$ thick, bonded to aluminum have lowest total impedances (ohmic plus polarization) of 2.0 and $5.4\ \Omega\text{-cm}^2$ under cathodic and anodic potential of 300 mV. The corresponding values for silicon carbide coatings, 1.8-2.0 μm thick, are 2.9 and $19.0\ \Omega\text{-cm}^2$, and, for chromium coatings $\sim 50\ \mu\text{m}$ thick, 3.2 and $10.7\ \Omega\text{-cm}^2$. No, or very little, corrosion is observed on the graphite/aluminum samples or on the silicon carbide-coated samples over a period of 2-3 months.

An open issue in developing a sodium-sulfur battery with a long life is the corrosion of the metal sulfur-electrode current collector. For load leveling application by the electric utility industry, the goal for a battery life is 10 yr.

In current development programs, chromium-plated stainless steel has been used as a sulfur container and a current collector (1). Alternative container materials with improved sodium polysulfide corrosion resistance are being explored as part of the sodium-sulfur battery development program (2-4). In the present study, the electrical performance and corrosion resistance of two new current collector materials are compared to chromium-coated steel. These materials are graphite foil bonded to aluminum- and chromium-plated stainless steel covered with sputtered silicon carbide layer.

The protective coating on the current collectors has to meet several criteria: the coating has to be electrically conductive and chemically inert to the sodium polysulfides that are formed in sodium-sulfur cells. In addition, the coating has to adhere well to the metal substrate, and be capable of withstanding thermal cycling from room temperature up to the operating temperature of the cells, $300^\circ\text{-}400^\circ\text{C}$, without peeling or flaking. The coating should also be self-healing or repairable to prevent the corrosion of the substrate from starting at pinholes or defects in the coating. Both graphite/aluminum- and silicon carbide-coated current collectors have the potential for meeting these criteria.

The composite structure of graphite layer bonded to an aluminum substrate makes a good current collector. Graphite is chemically inert to sodium polysulfides under the operating conditions of the sodium-sulfur cells (5) and is sufficiently conductive electrically ($\sigma \sim 1.0 \times 10^3\ \Omega^{-1}\text{cm}^{-1}$) to be used as a thin protective layer without introducing large ohmic losses. The use of current collectors solely made from graphite in practically sized sodium-sulfur cells results in high ohmic losses that seriously degrade the cell performance (6, 7). Aluminum is an excellent substrate. A protective nonconductive aluminum sulfide layer is formed on aluminum when it is exposed to polysulfide melt. This prevents corrosion from starting at coating defects and also allows greater flexi-

bility in current collector designs, since only selected areas need to be covered with graphite. In addition, aluminum is an excellent lightweight conductor.

Silicon carbide has an electrical conductivity of $0.001\text{-}100\ \Omega^{-1}\text{cm}^{-1}$ (8-10). It is also chemically inert to sodium polysulfide melts under the operating conditions of sodium-sulfur cells (11, 12). Sodium-sulfur cells built with sintered silicon carbide sulfur containers have shown no corrosion under testing (11). However, these containers are expensive and bulky. On the other hand, a thin conductive well-adherent silicon carbide layer applied to a steel container can protect the steel from corrosion by sodium polysulfides and, at the same time, retain the advantages of a metal container: high strength, ductility, and electrical conductivity. A system of bonding silicon carbide coatings to chromium-plated stainless steels is described in Ref. (13). The chromium forms a base to which the silicon carbide adheres well. In addition, any chromium exposed by defects within the silicon carbide layer can be protected from corrosion by the sodium polysulfides by oxidizing the exposed chromium before the current collectors are immersed into the polysulfide melt or built into the sodium-sulfur cells. The nonconductive chromium oxide formed during oxidation is inert to sodium polysulfides.

Experimental Technique

Graphite aluminum bonding.—The graphite is used in the form of foil or paper that is bonded to an aluminum substrate. In the test samples, GTA grade Grafoil, $127\ \mu\text{m}$ thick, manufactured by Union Carbide is used. The Grafoil composition is 99.9% graphite, with ash content of less than 0.1%. The nominal ash composition is 25% Al_2O_3 , 50% SiO_2 , 20% Fe_2O_3 , and 5% mixed oxides. No organic binders are used in Grafoil. The aluminum substrates, aluminum 1100 or 5 nines pure aluminum, consist of 0.5 in. wide strips, $3/2$ in. long and $\sim 1/16$ in. thick. The bonding process consists of evaporating or sputtering an aluminum layer about $1\ \mu\text{m}$ thick onto the side of Grafoil to be bonded to the aluminum substrate. This step is critical for a good bond. It allows the aluminum to come into direct contact with graphite with, at most, a very thin inter-

vening aluminum oxide layer present at the interface. The bond between the thin aluminum layer on Grafoil and the aluminum substrate is achieved by pressing the two pieces together in a hot press at 615°-620°C under a pressure of 2000 psi. The samples are kept in the hot press under argon atmosphere, at temperature, for 6-8h. During this time, a bond is formed at the aluminum/aluminum interface and the mechanical bond between the evaporated aluminum layer and graphite is strengthened by probable formation of a thin layer of aluminum carbide (Al_3C_4). Aluminum and graphite can react at temperatures as low as 400°C if no oxides are present at the interface (14, 15). The bond between aluminum and Grafoil formed by this procedure is stronger than the tear strength of Grafoil, which tends to peel off in layers. Although aluminum carbide is unstable in moist air, forming methane, no deterioration of the bond is observed in samples left in room air for weeks. Within a sodium-sulfur cell, there is little if any moisture, and the potential problem of moisture reacting with the aluminum carbide does not occur.

Slightly modified procedures from that discussed in the above for the bonding of aluminum and Grafoil were also tried. Pressing an unaluminized Grafoil sheet directly against an aluminum substrate in the hot press produced very poor bonding. The ever-present aluminum oxide on aluminum prevents the graphite from coming into direct contact with aluminum and, thus, inhibits the formation of an aluminum carbide bonding layer. However, a good bond between aluminum and Grafoil is achieved if a thin layer of cryolite/alcohol slurry is spread on the surface of aluminum before the Grafoil is hot pressed against the aluminum. The cryolite (Na_3AlF_6) is used as a wetting agent (16); it tends to break up the aluminum oxide layer and allows the chemical reaction between the aluminum and Grafoil to proceed. Cryolite can also be used to facilitate the bond formation at the aluminum/aluminum interface. This step was not found to be necessary.

Silicon carbide coating.—The silicon carbide coating is deposited on a chromium-plated stainless steel substrate. The chromium layer, 25-50 μm thick, provides a good adhesive base for the silicon carbide and allows the use of silicon carbide coatings with defects, e.g., pinholes. The chromium underlayer exposed by the defects can be oxidized to form chromium oxide, which is chemically inert in sodium polysulfide melts and thus prevents corrosion of the chromium underlayer. The silicon carbide is deposited by RF sputtering or by chemical vapor deposition (17). The adhesion of a silicon carbide layer to chromium on stainless steel can be improved by heat-treatment in an inert atmosphere above 1100°C. Through a high temperature diffusion process, tertiary compounds (13, 18) of chromium and silicon carbide can form at the interface.

The samples that are tested were not heat-treated to form tertiary compounds at the SiC/Cr interface. The silicon carbide is deposited by sputtering in a high purity argon (99%)-nitrogen (1%) gas mixture using a 6 in. sintered SiC target. Nitrogen, which acts as an n-type dopant (19) in SiC, is introduced into the system to increase the conductivity of the films. Before film deposition, the substrates are cleaned by an RF (13.6 MHz) gas discharge. The deposition rate is $\sim 60 \text{ \AA}/\text{min}$ at unheated substrate placed 52 mm from the target, at RF power of 200-300W, anode voltage of 1.3-1.6 kV, and gas pressure of 2.7×10^{-3} torr. The resistivity measurements are done on films deposited on quartz substrates, and the corrosion tests are done on films deposited on chromium-plated E-Brite (Fe-26Cr-1Mo) substrates.

Sodium polysulfide.—The sodium polysulfide (Na_2S_5) used in the tests is prepared from J. T. Baker (no. 3910) sodium monosulfide, 9 hydrate ($\text{Na}_2\text{S} \cdot 9\text{H}_2\text{O}$) crystals by drying the crystals under hydrogen/helium (1:1) gas flow at 700°-800°C to form Na_2S . The monosulfide and appropriate amount of resublimed sulfur (Mallinckrodt no. 8420) are sealed under forepump vacuum into glass ampuls, slowly heated to 450°C to form Na_2S_5 , and then

cooled to room temperature. The transfer of polysulfide to the test cell is done in a helium dry box.

Measurements.—The testing of samples is done in corrosion cells, as shown in Fig. 1, under constant cathodic and anodic potentials in sodium polysulfide (Na_2S_5) melt at 350°C. The cell consists of a Pyrex "test tube," partially filled with sodium polysulfide (Na_2S_5), usually covering only part of the sample surface to be tested. The current and reference voltage leads, either chromel or aluminum wires, are welded to the sample substrate at the top. This area is above the sodium polysulfide melt level. In a case of a chromium-plated E-Brite substrate, the sample (5/4 \times 1/2 in.) is first coated with an insulating glass on all sides except for a rectangular window left for deposition of SiC. The glass prevents the E-Brite from coming into contact with sodium polysulfides. The counter and reference electrodes are graphite rods, threaded and cemented (with alcohol-based graphite cement) to molybdenum rods above the melt level. The molybdenum rods are brought to the outside through a silicon rubber stopper. The cells are leak-tight to better than 10^{-8} standard cubic centimeters per second (sccs). Graphite leads are not brought out directly because leak-tight seals cannot be made to the porous graphite. The temperature of the cell is monitored by a thermocouple inserted into a closed-end glass tube that extends into the melt. The cells are evacuated and then backfilled with argon to a pressure of 2-3 in. of water.

The samples are tested at constant potentials with respect to a carbon reference electrode, either anodically or cathodically at 350°C. The tests are usually done at 300 mV, the maximum cathodic potential expected at the sulfur container wall. This potential corresponds to the open-circuit potential difference between Na_2S_5 and Na_2S_3 melts. Currents through the samples are monitored continuously. At periodic intervals, current-interrupt data are taken from which the change in resistance of the sample, and ohmic and polarization contributions to the resistance, are determined. The measurements are made 2 μs after the start of the current interruption pulse of 10 μs duration using an Electrosynthesis Company (East Amherst, New York) Model 800 IR interrupter. The sample surfaces are examined after the tests.

The resistivity of sputtered amorphous silicon carbide films (1.5-2 μm thick) on quartz substrates is measured by a standard four-probe method. The layout is shown in Fig. 2. Sputtered platinum contacts are used for the current and voltage leads. The resistivity measurements as function of temperature are done in an argon atmosphere.

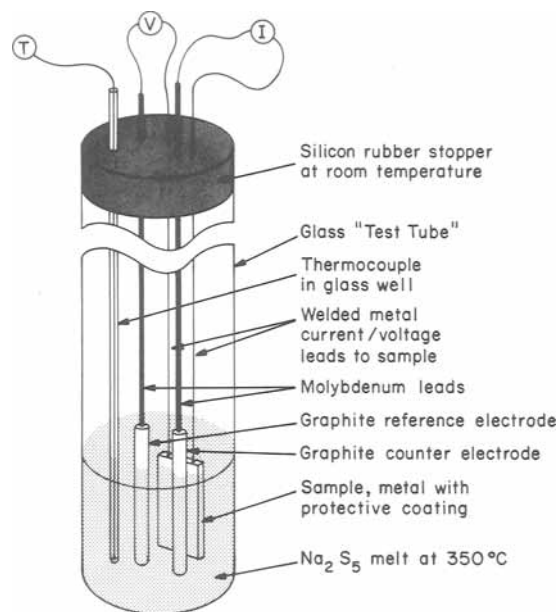


Fig. 1. Corrosion test cell using carbon reference and counterelectrodes.

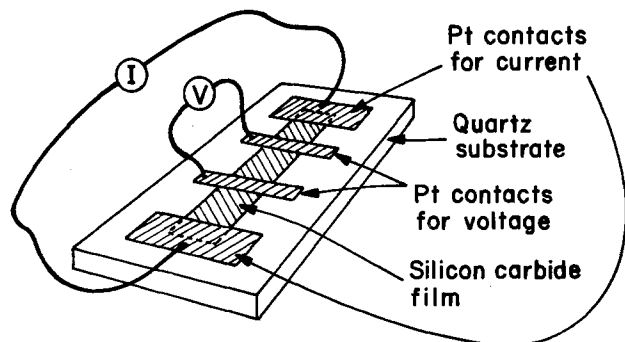
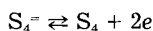


Fig. 2. Sample and electrical probe configuration for measuring resistivity of thin films.

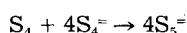
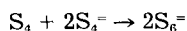
Results

Graphite/aluminum.—The current carried by a Grafoil/aluminum sample as a function of time under anodic and cathodic polarization of 200 mV is shown in Fig. 3. These polarizations correspond to the charging and discharging of a sodium-sulfur cell. In both cases, the current reached a steady state and then remained constant for approximately 70 days. The current then started to decline in a gradual and steady manner. The one sharp drop in current on sample GA-1 is unexplained. Post-test examination of the samples showed the presence of sulfur/sodium polysulfide in isolated spots at the Grafoil-aluminum interface. The steady decrease in current is most likely associated with loss of contact area between Grafoil and aluminum due to slow seepage of melt through the Grafoil.

The initial decrease of current under anodic conditions is due to the buildup of sulfur at the Grafoil-melt interface. Sulfur, which is nonconductive and immiscible in a sodium polysulfide melt, tends to block the electrode. The current decreases until an equilibrium is reached between the rate of oxidation of sulfur ions to sulfur and the rate of chemical reaction of sulfur to form soluble sulfide ions, *i.e.*

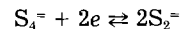


and



If the cell is left at open circuit for several days, the sulfur film at the Grafoil-melt interface is removed; if the cell is turned back on, a similar decay in current is observed as the sulfur film builds up again as shown by the data in Fig. 3 for days 87-94.

Under cathodic polarization an electrochemical reduction of sulfide ions occurs at the electrode



The initial currents are high, on the order of 130 mA/cm². The decline in current is likely caused by the partial formation of a Na₂S₂ layer at the melt-electrode interface, which partially blocks the access of Na₂S₄ and Na₂S₅ to the electrode. Steady state is reached when the electrochemical reactions reach equilibrium with the diffusion and convection of reactants at the interface. The steady-state current under cathodic polarization is higher than under anodic polarization, ~80 mA/cm² compared to 50 mA/cm², because no blocking sulfur film is formed. The voltage-current dependence is shown in Fig. 4. The data are taken under conditions where the variation of current with time has stabilized. This corresponds to days 49-50 in Fig. 3 for samples GA-1 and GA-2.

Silicon carbide.—The temperature dependence of resistivity of amorphous SiC films up to 400°C is shown in Fig. 5. A resistance change occurs during the initial heating of the films to ~400°C. On subsequent temperature cycles, the resistance changes seem to be reversible. The initial activation energy is 3.45 kcal/mol; on subsequent cycles, the activation energy is higher, 9.4 kcal/mol. The resistivity of the 1.5-2.5 μm thick films averaged around 140 Ω-cm at 350°C, the operating temperature of sodium-sulfur cells.

Similar resistance changes in amorphous SiC films have been reported by Wasa and co-workers (20). They found the resistance change with temperature to be reversible if the substrate temperature during deposition of the SiC films is higher than the temperature range of the resistivity measurements. The mechanism of resistance change in amorphous SiC films is not understood, but is thought to be associated with changes in the structure of sputtered films caused by thermally activated processes. The changes are not caused by surface oxidation of SiC films which takes place at temperatures higher than 1000°C (20, 21).

The currents carried by amorphous SiC coatings sputtered on chromium-plated E-Brite substrates as a function of time under cathodic and anodic polarizations in a sodium polysulfide melt (Na₂S₅) are shown in Fig. 6. The current under cathodic conditions across the SiC coatings is high. Initial values for the other samples ranged from 150 to 120 mA/cm² at cathodic polarization of 300 mV. The current decreases as a function of time, but tends to stabilize after ~20 days of operation. The current across sample SiC-C stabilized at ~85 mA/cm² and then slowly increased to 100 mA/cm² near the end of the test period of 84 days. The current under anodic polarization is much lower than under cathodic polarization. The current across sample SiC-B remained constant at ~32 mA/cm² until the test was terminated after 57 days.

The surfaces of the silicon carbide coatings were examined with a scanning electron microscope (SEM) before and after testing of the samples in sodium polysulfide

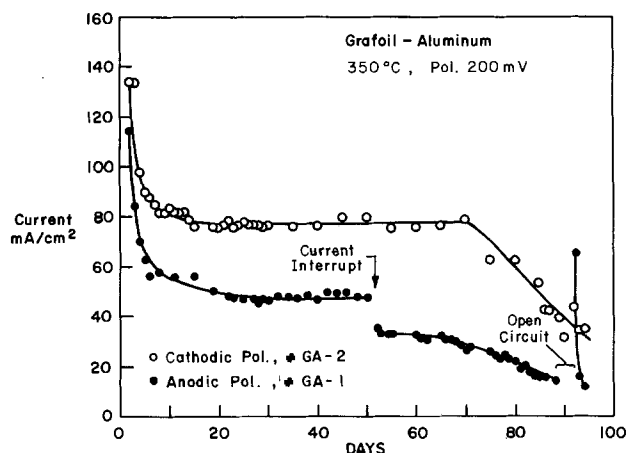


Fig. 3. Current vs. time of Grafoil/aluminum samples in Na₂S₅ melt under cathodic and anodic potentials of 200 mV.

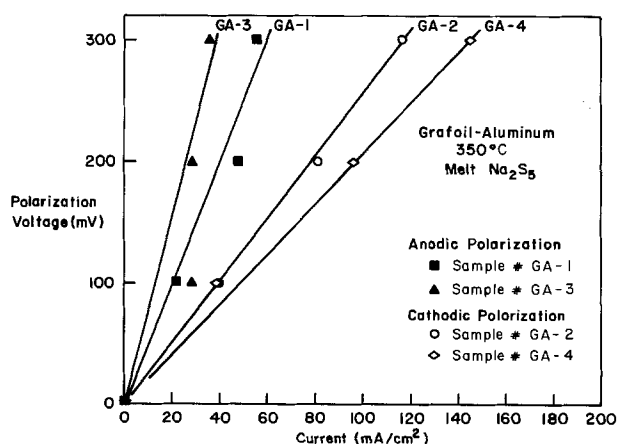


Fig. 4. Voltage vs. current of Grafoil/aluminum samples under anodic and cathodic potentials.

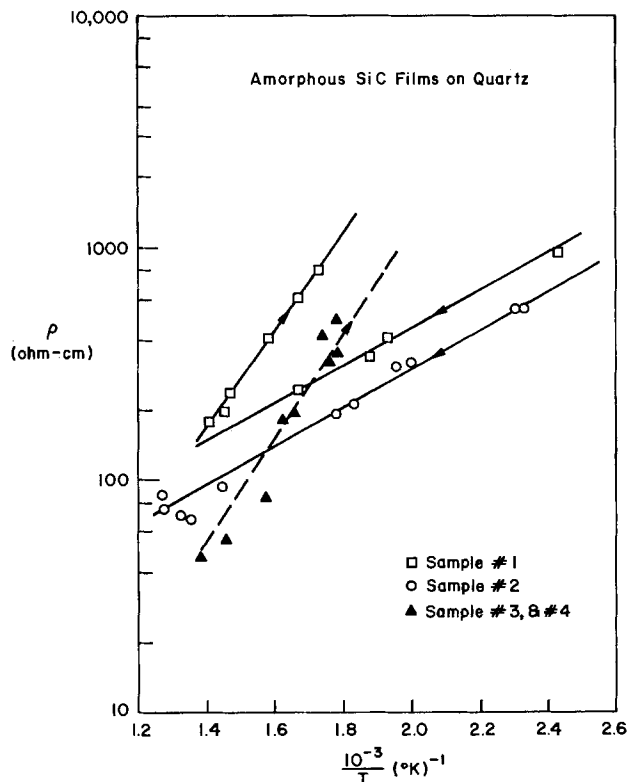


Fig. 5. Temperature dependence of resistivity of thin amorphous silicon carbide films.

melts. The surface morphology of freshly sputtered silicon carbide coating on chromium-plated E-Brite is shown in Fig. 7. The surfaces of samples tested under cathodic polarization of 300 mV for 22 days (sample SiC-A) and 84 days (sample SiC-C) are shown in Fig. 8 and 9, respectively. The surface of an anodically tested sample, SiC-B, tested for 57 days at 300 mV polarization is shown in Fig. 10.

The overall surface morphology of a sample tested cathodically for 22 days is similar to the surface of silicon carbide coating unexposed to sodium-polysulfide melt, Fig. 7. However, the exposed silicon carbide surfaces, both above (no current passing through the SiC coating) and below the sodium polysulfide melt level, Fig. 8 (current passing through the coating), are covered with small light-colored chromium sulfide crystals. More crystals are found on the coating below the melt level. Some of the crystals have a platelike hexagonal structure that is similar to Cr_2S_3 crystals found on chromium-plated sulfur containers used in sodium-sulfur cells (22). Cross-sectional analysis of samples examined with SEM showed no

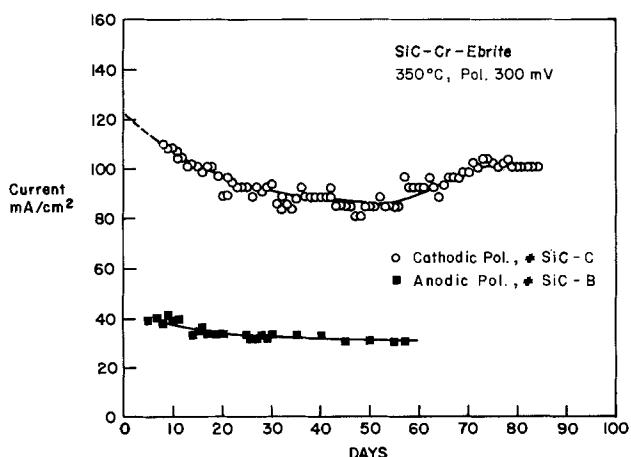


Fig. 6. Current vs. time of silicon carbide-coated samples in Na_2S_5 melt under cathodic and anodic potentials of 300 mV.

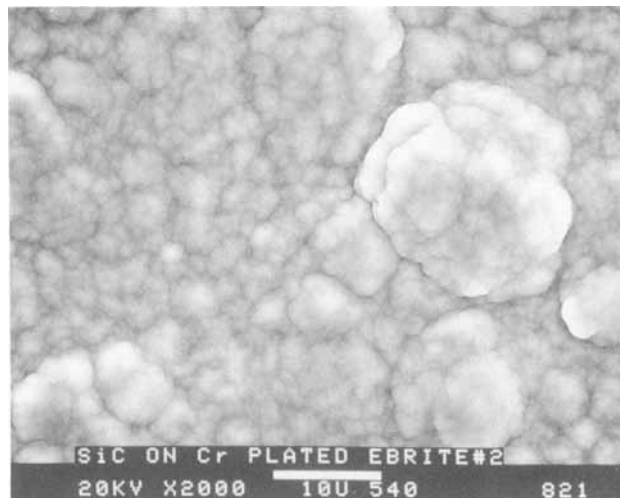


Fig. 7. Surface of sputtered amorphous silicon carbide coating before testing.

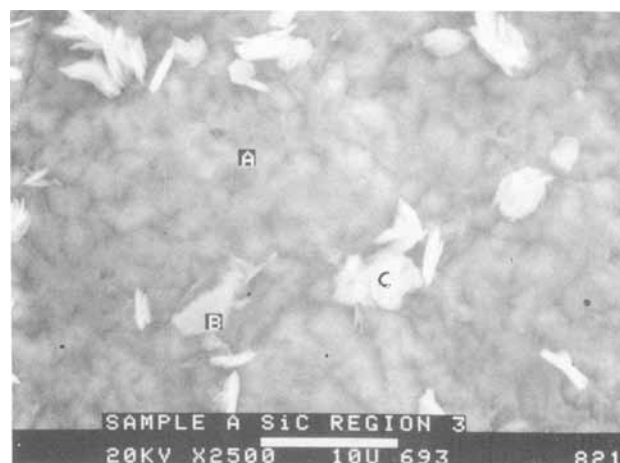


Fig. 8. Surface of SiC coating below Na_2S_5 melt level of sample SiC-A after 22 days at cathodic potential of 300 mV. Region A is amorphous SiC; region B, crystallite with very high Cr content and some S; region C, crystallite with high Cr and high S content.



Fig. 9. Surface of SiC coating below Na_2S_5 melt level of sample SiC-C after 84 days at cathodic potential of 300 mV. Region K is amorphous SiC with "worn" look; areas L are platelike chromium sulfide crystals.

indication of the presence of chromium sulfides, sulfur, or sodium polysulfides at the chromium/silicon carbide interface. The growth of chromium sulfide crystals

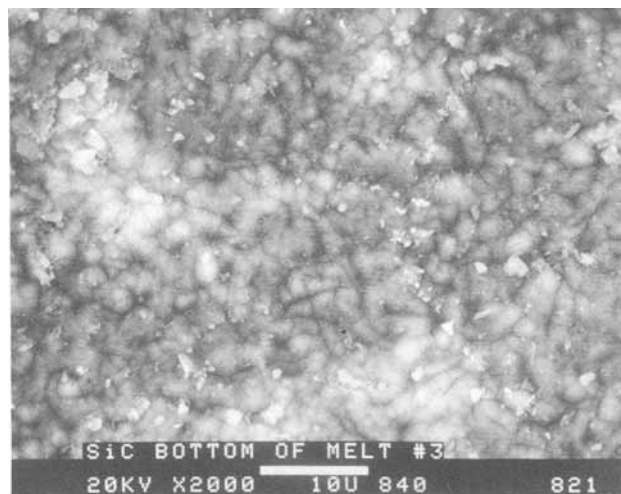


Fig. 10. Surface of SiC coating below Na_2S_3 melt level of sample SiC-B after 57 days at anodic potential of 300 mV. Small white particles are chromium sulfide crystals. Surface morphology is similar to an untested sample shown in Fig. 7.

seems to occur via transport of chromium and sulfur through the pores in the amorphous silicon carbide coating.

The amorphous silicon carbide coating exposed to the sodium polysulfide melt for 84 days shows substantial change from the initial surface morphology. The coating surface, both above and below the polysulfide melt level, is covered with numerous chromium sulfide crystals. In addition, the SiC surface morphology is no longer hilly and smooth (Fig. 7), but is "worn," especially in some areas below the sodium polysulfide melt level, Fig. 9. In other areas, the worn pattern is not as deep. The mechanism causing the changes in the morphology of the silicon carbide coating has not been determined. The changes could be due to slow chemical reactions or to dissolution, or, more likely, due to small-scale flaking at the pores within the silicon carbide coating, caused by the transport of chromium and sulfur.

The surface morphology of the sample tested anodically has not changed much from the untested sample. Figure 10 shows the surface features below the polysulfide melt level. Chromium sulfide crystals on the surfaces are still present, but are fewer in number than on the cathodically tested samples.

Comparison with chromium.—The electrical performance of Grafoil/aluminum- and silicon carbide-coated current collectors is compared to chromium-coated current collectors. The data taken under cathodic and anodic conditions are summarized in Tables I and II, respectively. The measured losses occurring at the substrate/coating/melt interface are separated into ohmic and polarization losses and are normalized to a unit area of the current collector. The summarized data are for test periods when the currents remained stable (refer to Fig. 3, 6, and 11). The electrical performance of a well-adhered Gra-

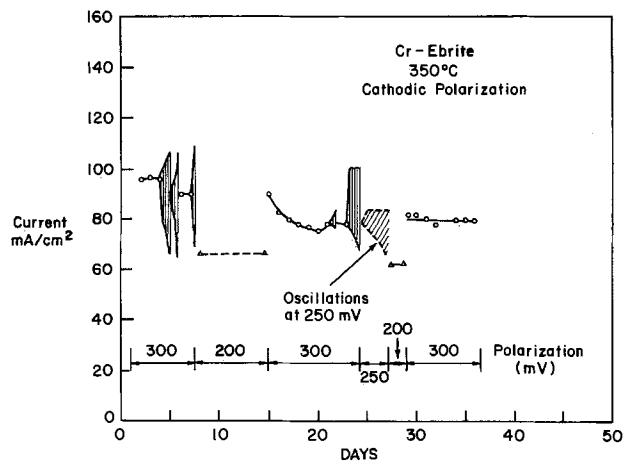


Fig. 11. Current vs. time of chromium-coated sample under different cathodic potentials. The envelope of shaded areas corresponds to the magnitude of current oscillations.

foil/aluminum current collector is superior to that of a chromium-coated current collector. It has lower overall resistance both under cathodic and anodic potentials. At a polarization of 300 mV, the resistance values are 2.0 and $5.4 \Omega\text{-cm}^2$, respectively. The comparable values for a chromium-coated current collector are 3.2 and $10.7 \Omega\text{-cm}^2$. Consequently, the Grafoil/aluminum current collectors have lower power losses and carry substantially higher currents for a given potential.

The silicon carbide-coated current collectors have comparable resistances to the chromium-coated samples under cathodic potentials. The resistances under anodic conditions are higher. However, the current carrying capability as a function of time of the silicon carbide-coated samples is better than that of chromium-coated samples; the current in the case of silicon carbide samples increased slightly during 84 days, while the current decreased from 96 to 80 mA/cm^2 in 30 days for the chromium sample (Fig. 11). Under anodic potentials, the currents are lower than under cathodic potentials because of the formation of a blocking sulfur film at the electrode surface. For the chromium- and silicon carbide-coated samples, the steady-state currents under anodic conditions are independent of potential (Table II). The current increases with voltage only for the Grafoil/aluminum samples. The polarization resistance increases rapidly with voltage, while the ohmic resistance remains constant. Under cathodic conditions, the polarization resistance is, within experimental error, also independent of voltage.

Current oscillations observed with chromium sample.—The current vs. time of the chromium-coated sample is shown in Fig. 11. Typical current oscillations and variations in cell resistance during oscillations are shown in Fig. 12 for a sample polarized cathodically at 300 mV.

The amplitude of oscillations can build up to quite high values, as indicated by the shaded regions on Fig. 11. The

Table I. Corrosion test cell data: cathodic polarization

Coating	Polarization (mV)	Current (mA/cm^2)	R-ohmic ($\Omega\text{-cm}^2$)	R-pol. ($\Omega\text{-cm}^2$)	Days on test	Sample	Remarks
Cr	300	96	0.58	2.6	2	Cr	Standard for comparison. Cr is used in Na/S cells as a protective coating on current collectors (1). Data taken before onset of current oscillations; refer to Fig. 11.
	200	60	0.58	2.7	2		
	100	33	0.58	2.4	2		
Grafoil on aluminum	300	145	0.14	1.9	26	GA-4	Data taken under stable conditions; refer to Fig. 3 for current vs. time data.
	200	96	0.13	2.0	26		
	100	39	0.16	2.4	26		
SiC	300	102	0.43	2.5	24	SiC-C	Data taken under stable conditions; refer to Fig. 6 for current vs. time data. SiC film thickness $1.8 \mu\text{m}$.
	200	69	0.55	2.3	24		
	100	41	0.53	1.9	24		

Table II. Corrosion test cell data: anodic polarization

Coating	Polarization (mV)	Current (mA/cm ²)	R-ohmic (Ω -cm ²)	R-pol. (Ω -cm ²)	Days on test	Sample	Remarks
Cr	300	28	0.85	9.8	3	Cr	Standard for comparison. Cr is used in Na/S cells as a protective coating on current collectors (1). Data taken before onset of current oscillations; refer to Fig. 11.
	200	23	0.73	7.9	3		
	100	22	0.73	3.9	3		
Grafoil on aluminum	300	55	0.59	4.8	50	GA-1	Data taken before discontinuity in current vs. time data shown in Fig. 3.
	200	48	0.50	3.7	50		
	100	22	0.45	4.0	50		
SiC	300	15.8	0.89	18.1	25	SiC-C	This sample was run under anodic conditions for short time until stable conditions were reached.
	200	15.2	0.92	12.2	25		
	100	14.1	0.85	6.2	25		

oscillations can suddenly decrease or disappear and then build up again. The onset depends on the cathodic potential and on the previous operating history of the sample. No oscillations are observed at cathodic polarization below 200 mV. The periods of oscillation are variable; at 300 mV, the period ranged from 1.9 to 2.4 min, and at 250 mV, from 3 to 9 min. During the oscillations, the ohmic contribution to the resistance remains constant, while the polarization contribution changes inversely with current (Fig. 12).

Post-test analysis of the sample shows the chromium plating to be covered with various thicknesses of chromium sulfide layers. These layers can be more than 10 μ m thick (22). Surface peeling and flaking of chromium sulfide layers are observed over large areas of a sample as shown in Fig. 13 and 14. The surface of chromium sulfide layers at higher magnification showing crystals and partially dissolved crystals are shown in Fig. 15 and 16.

The chromium sulfide layers are probably porous enough to be penetrated by the sodium polysulfide melt, yet restrictive enough to inhibit greatly the transport of the polysulfides through this layer. Under high enough cathodic potential, a concentration gradient of sodium polysulfides ranging from Na_2S_x (perhaps as low as Na_2S_2) near the chromium surface to Na_2S_5 near the outermost part of the chromium sulfide layer can be formed. This gradient gives rise to high concentration polarization. The formation of lower polysulfides within the chromium sulfide layer sets up high stresses causing the layers to flake and, thus, decreases the impedance due to polarization. As the chromium sulfide layer builds up again, the polarization impedance increases and current decreases. The rate of growth and flaking of the chromium sulfide layer is dependent on many variables, e.g., potential, porosity of the layer, and convection and diffusion near a sample surface.

Discussion

Coating processing (Grafoil/aluminum).—The mechanism of degradation of the bonding between the Grafoil and aluminum is due to the slow penetration of sodium polysulfide and sulfur through the Grafoil sheet to the Grafoil-aluminum interface. However, Grafoil can be made impervious to sodium polysulfides and sulfur by deposition of a coating of glassy or pyrolytic carbon.¹ This offers a possible method of preventing the sulfur and sodium polysulfides from reaching the carbon/aluminum interface, by modifying the bonding process, by depositing the aluminum on Grafoil coated with glassy carbon rather than on Grafoil directly. The layer of glassy carbon would not affect the bond to the aluminum.

The glassy coatings from a few mils up to 10 mil thick can be applied in a gas flow reactor using methane and inert carrier gas such as argon or nitrogen at temperatures of 2000°–2300°C (24, 25). Some reactors are up to 19 in. in diameter and 50 in. long, which would allow for batch processing of Grafoil sheets in appropriate shapes.

¹Graphite cylinders and current collectors used in glass cells have been made impervious by this process at Ford Motor Company (23).

Silicon carbide.—The amorphous coatings of silicon carbide that were tested have adequate electrical conductivity for use as a coating for the current collectors in sodium-sulfur cells. The adhesions of the coating to the substrate has been good during tests lasting up to three months. The coatings that were tested are porous; the transport of chromium and sulfur through the pores leads to the formation of chromium sulfide crystallites on the surface of a silicon carbide coating. However, the total surface area covered by these crystallites is small, and their effect on electrical performance seems to be minimal. Examination of the surface indicates some "wear" of surface, most likely due to the transport of materials through the porous coating.

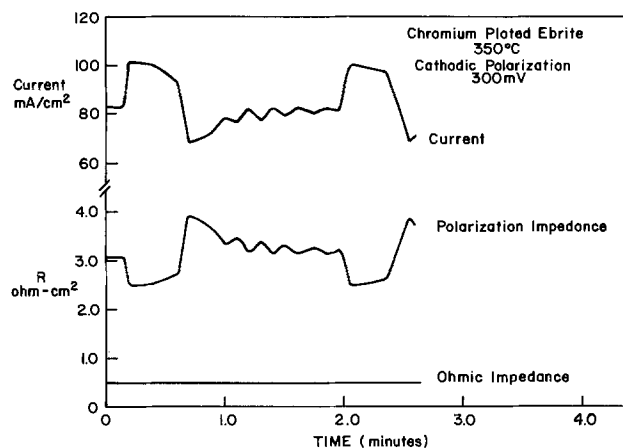


Fig. 12. Typical current oscillations and sample resistance changes observed on chromium-plated sample polarized cathodically at 300 mV. The ohmic impedance remains constant; polarization impedance is out of phase with current.

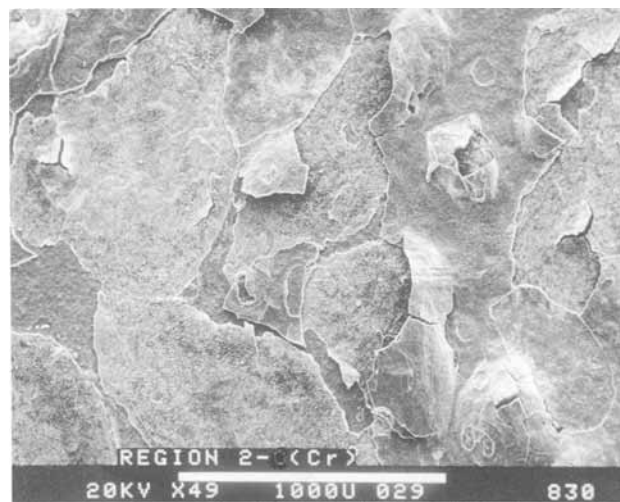


Fig. 13. Overall picture of cracked and flaking chromium sulfide layers on chromium-plated E-brite sample tested for 36 days at cathodic potential.

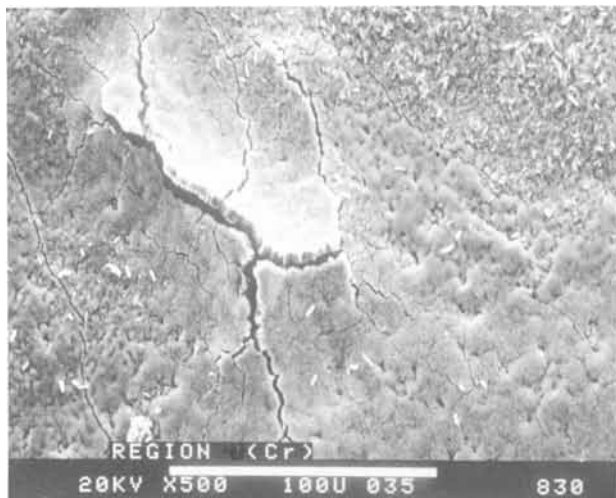


Fig. 14. A cracked and flaking chromium sulfide layer

The process parameters for depositing the silicon carbide coatings were not optimized to achieve maximum density. Although high film density is desirable, one can work with porous films by oxidizing the chromium exposed by the pores in the film (13) prior to exposure to sodium polysulfide melt. The chromium oxide is chemically inert to sodium polysulfide melts and has shown no effects of corrosion under cathodic and anodic cycling (26).

The resistivity of the tested silicon carbide films, 1.5-2.5 μm thick, of 140 $\Omega\text{-cm}$ at 350°C is adequate for coating current collectors used in sodium-sulfur cells. However, these films were not optimized to have minimum resistance. The resistivity of the films can be decreased by at least an order of magnitude by increasing the carrier concentration with optimized nitrogen doping and by crystallization of amorphous films by annealing. Crystalline films can also be formed by sputtering the silicon carbide on heated substrates. Resistivities as low as 0.13 $\Omega\text{-cm}$ have been reported at 350°C (19).

Corrosion cells and sodium-sulfur cells.—The resistance values measured in the corrosion cells, both under cathodic and anodic conditions, are much higher than the total cell resistances measured in sodium-sulfur cells. In the corrosion cells, all the current is carried by ionic conduction through the sodium polysulfide melt and all the electrochemical reactions occur at the sample surface. In sodium-sulfur cells, the current is carried from the electrolyte by electronic conduction through the graphite felt and by ionic conduction through the melt to the metal

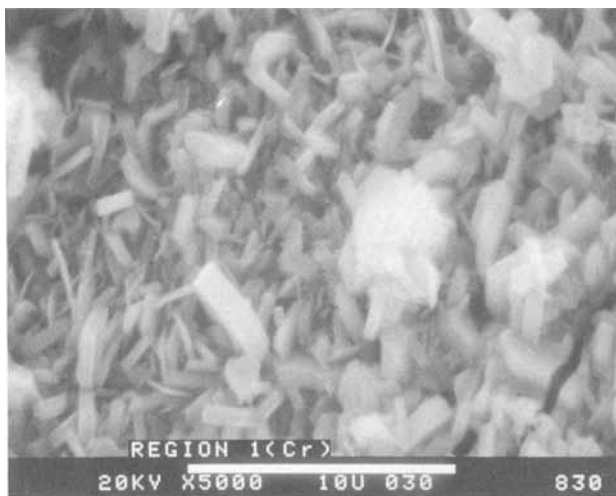


Fig. 15. Platelike chromium sulfide crystals, Cr_2S_5 , in area slightly above the Na_2S_5 melt level.

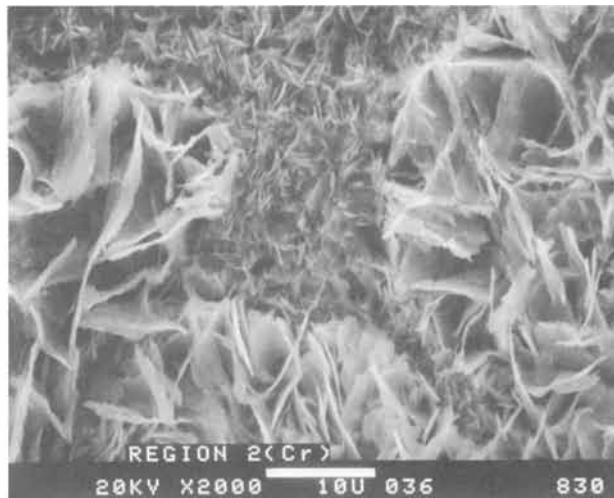


Fig. 16. Partially dissolved chromium sulfide crystals below Na_2S_5 melt level.

sulfur container. Also, most of the reactions take place at the graphite felt/electrolyte interface region and not at the sulfur container wall. For instance, during charging under an anodic potential of 300 mV, the resistance of a chromium/melt interface is 10.7 $\Omega\text{-cm}^2$ in the corrosion cell (Table II). In the sodium-sulfur cells, the total cell resistance (which includes the resistances of electrolyte, graphite felt/electrolyte contact, graphite felt electrode in a parallel circuit with ionically conductive sodium polysulfide melt, graphite felt/container contact, and the chromium sulfide/chromium layer on the sulfur container) during charging is much lower, $\sim 1.4 \Omega\text{-cm}^2$. The contact resistance at the container wall is less than one-third of cell resistance, *i.e.*, $< 0.5 \Omega\text{-cm}^2$, as compared to 10.7 $\Omega\text{-cm}^2$ measured in the corrosion cell. The resistance data obtained from corrosion cells are much higher and are not expected to correspond to values observed in sodium-sulfur cells.

The corrosion test cell offers an accelerated means, under well-controlled conditions, to test the corrosion of materials for use as sulfur-electrode current collectors in sodium-sulfur cells. The conditions in the test cell are more severe than the conditions at the sulfur container (current collector)/electrode interface in a sodium-sulfur cell. In the test cell, the 300 mV test potential is across the sample/polysulfide melt interface, while in the sodium-sulfur cell the potential across the container/electrode interface is considerably less during most of the charge-discharge cycle. Most of the chemical reactions in the sodium-sulfur cell take place away from the container wall near the graphite felt electrode/electrolyte interface. Although a direct quantitative correlation of corrosion of samples in test cells with corrosion of current collectors in sodium-sulfur cells has not been made, qualitative data indicate a much faster corrosion in the test cells. A chromium-plated E-Brite sample tested continuously for 36 days under cathodic potential of 300 mV showed severe corrosion with flaking, peeling, and some dissolution of the chromium sulfide layer that is formed on chromium (Fig. 13 and 14). In contrast, many chromium-plated E-Brite sulfur containers of sodium-sulfur cells cycled continuously for 1-2 years (1) have shown less corrosion of the chromium plate than occurred on the sample in the test cell during one month.

Summary

Both Grafoil/aluminum- and silicon carbide-coated current collectors performed well for short times. The current carrying capacity of Grafoil/aluminum collectors in sodium polysulfide melt is higher than that of chromium-plated collectors by a factor of ~ 1.5 under cathodic potentials and by a factor of ~ 2.0 under anodic potentials. The bonding between Grafoil and aluminum is stronger

than the tear strength of Grafoil. No corrosion of Grafoil was observed for samples tested for more than 90 days. A deterioration of a Grafoil/aluminum bond occurred after 70 days due to slow seepage of sodium polysulfides through the Grafoil. Presealing of the Grafoil with glassy carbon prior to aluminum bonding should alleviate this problem.

The current carrying capacity of amorphous silicon carbide covering a chromium-plated E-Brite sample is comparable to that of chromium-plated samples under cathodic potentials and lower by a factor of 0.6 under anodic conditions. No increase in resistance of the silicon carbide sample is observed over a period of 84 days, while large changes are observed with a chromium-plated sample. In addition, the adhesion of the silicon carbide coating is very good; there were no indications of peeling or flaking. The corrosion observed on the 1.8 μm thick film tested for three months is minimal and may be due to transport of reactants within the porous coating. The porosity of present coatings, while not ruling out their application in sodium-sulfur cells, can be greatly minimized by optimizing the sputtering conditions.

Manuscript submitted Oct. 31, 1984; revised manuscript received Jan. 25, 1985.

Ford Motor Company assisted in meeting the publication costs of this article.

REFERENCES

1. "Sodium-Sulfur Battery Development," Ford Interim Report no. U-6744, for period of March 1, 1980 to September 30, 1981. DOE Contract no. DE-ATM02-79CH10012, DOE Technical Information Center, Springfield, VA (1981).
2. K. R. Kinsman and W. L. Winterbottom, *Thin Solid Films*, **83**, 417 (1981).
3. G. M. Crosbie, G. J. Tennenhouse, R. P. Tischer, and H. S. Wroblowa, *J. Am. Ceram. Soc.*, **67**, 498 (1984).
4. R. P. Tischer, H. S. Wroblowa, G. M. Crosbie, and G. J. Tennenhouse, in "Molten Salts," M. Blander, D. S. Newman, M.-L. Saboungi, G. Mamantov, and K. Johnson, Editors, p. 335, The Electrochemical Society Softbound Proceedings Series, Pennington, NJ (1984).
5. Research on Electrodes and Electrolyte for Ford Sodium-Sulfur Battery, Annual Report June 30, 1975 to June 29, 1976, Contract no. NSF-C805.
6. J.-P. Pompon, "Capital Cost of Sodium-Sulfur Batteries," Laboratories de Marcoussis, Centre de Recherches de la Compagnie Generale d'Electricite, Phase II Final Report, Project 726-2, p. C1-5, Marcoussis, France, February 1978.
7. T. L. Markin, A. R. Junkin, R. J. Bones, and D. A. Teagle, in "Proceedings of the 11th International Power Sources Symposium," Brighton, Sept. 1978; in "Power Sources 7," Paper no. 48, Academic Press, New York (1978).
8. R. B. Hilborn, Jr. and H. Kang, in "Silicon Carbide, 1973," R. C. Marshall, J. W. Faust, Jr., and C. E. Ryan, Editors, p. 337, University of South Carolina Press, Columbia, SC (1974).
9. H. Kang and R. B. Hilborn, Jr., in "Silicon Carbide, 1973," p. 493, University of South Carolina Press, Columbia, SC (1974).
10. "Silicon Carbide, 1973," Appendix II, p. 673, University of South Carolina Press, Columbia, SC (1974).
11. R. R. Dubin and S. Prochazka, *This Journal*, **126**, 2156 (1979).
12. R. Dubin, *Mater. Perform.*, **20**, 13 (1981).
13. M. Mikkor and S. Shinozaki, U.S. Pat. 4,278,708 (1981).
14. S. J. Baker and W. Bonfield, *J. Mater. Sci.*, **13**, 1329 (1978).
15. L. Aggour, E. Fitzner, M. Heym, and E. Ignatowitz, *Thin Solid Films*, **40**, 97 (1977).
16. R. C. Dorward, *Met. Trans.*, **4**, 386 (1973).
17. J. Schlichting, *Powder Met. Int.*, **12**, 141, 196 (1980).
18. P. W. Pellegrini and J. M. Feldman, in "Proceedings of the Third International Conference on Silicon Carbide," p. 161, University of South Carolina Press, Columbia, SC (1973).
19. E. A. Burgemeister, W. von Muench, and E. Pettenpaul, *J. Appl. Phys.*, **50**, 5790 (1979).
20. K. Wasa, T. Tohda, Y. Kasahara, and S. Hayakawa, *Rev. Sci. Instrum.*, **50**, 1084 (1979).
21. A. Suzuki, H. Matsumami, and T. Tanaka, *This Journal*, **125**, 1896 (1978).
22. M. Mikkor, in "17th IEECEC Proceedings," p. 569, Paper no. 829098, August 8-12, 1982, Los Angeles, California.
23. "Ford Sodium-Sulfur Battery Development Program," Report for period Nov. 1977-Feb. 1979, DOE Contract no. EY-76-C-02-2566, DOE Technical Information Center, Springfield, VA (1979).
24. F. J. Szydowski, E. Peck, and B. Bax, *Appl. Spect.*, **32**, 402 (1978).
25. D. C. Manning and R. D. Ediger, *At. Absorpt. Newsl.*, **15**, 42 (1976).
26. G. M. Crosbie, G. J. Tennenhouse, R. P. Tischer, and H. S. Wroblowa, *J. Am. Ceram. Soc.*, **67**, 498 (1984).

Investigation of Li/SO₂ Cell Hazards

II. Thermal Decomposition Studies of Cell Discharge Products

William P. Kilroy*

Naval Surface Weapons Center, Silver Spring, Maryland 20903-5000

ABSTRACT

Lithium dithionite undergoes rapid adiabatic exothermic decomposition leading to large rates of self-heating and pressure generation. Lithium-lithium dithionite mixtures, which can form during overdischarge, were found to be very hazardous. Such mixtures are capable of causing explosive venting in Li/SO₂ cells. Carbon black substantially lowers the initiation temperatures required for sustained self-heating to occur and alters the mechanism of both the adiabatic and nonadiabatic dithionite decompositions. The rate of heating and the amount of electrolyte present in discharged Li/SO₂ cathodes appears to alter the overall distribution of decomposition products and the cells' thermal behavior.

In a recent paper, accelerating rate calorimetry (ARC) was used to define the thermal and pressure behavior of Li/SO₂ cells during overdischarge (1). Cells containing lithium at the end of cell life were found to undergo thermal runaway when overdischarged at ambient temperatures. The thermal runaway resulted from a series of coupled exothermic chemical reactions. Two of these reactions,

occurring in the 100°-150°C temperature region, involved the reaction of lithium with the battery electrolyte and the decomposition of lithium dithionite. These reactions are critical to Li/SO₂ safety since they provide the pathway for the propagation of a thermal runaway to the melting point of lithium. It was postulated that the initiation temperature and kinetics of each of these exothermic reactions may be interdependent and could also be affected by the amount of electrolyte present. Lithium

* Electrochemical Society Active Member.

dithionite will generate SO₂ upon decomposition (2), thereby affecting the lithium-electrolyte reaction which has been shown to be dependent on SO₂ concentration (3). In turn, the thermal stability of lithium dithionite was not fully explored, and its decomposition appeared to be a function of its degree of wetness with the electrolyte.

Other factors may influence the thermal stability of lithium dithionite. Although lithium dithionite is the product formed upon discharging a Li/SO₂ cell at 1 mA/cm² at -30° or 25°C, a more complex chemistry was observed at 71°C (4-6). Apparently, higher temperatures either change the reduction mechanism or cause some of the lithium dithionite to decompose. The question of whether the additional chemicals produced in the high temperature discharge can affect the dithionite decomposition needs to be examined.

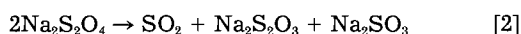
Since carbon black has been shown to be a catalyst in Li/SO₂ cells (7), it may also catalyze the decomposition of the lithium dithionite. The surface area of the carbon black was cited as the most important factor in enhancing catalytic activity. Consequently, the sample configuration, that is, the distribution of lithium dithionite on the carbon black, brought about by changes in current density, may also be a factor in the stability of the dithionite.

Previous investigations have shown that sample configuration was a factor in the thermal decomposition of the sodium salt, Na₂S₂O₄ (8). Thin layers of this salt decomposed slowly when heated isothermally, whereas large samples generally decomposed at higher temperatures and with greater rapidity. The major products that formed were attributed to the following reactions

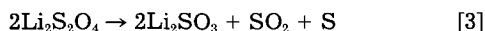
Thin layer



Thick layer



The lithium salt has been shown to undergo a different high temperature decomposition (2) according to the reaction



The objective of this investigation was to examine the thermal stability of lithium dithionite, particularly in its relation to Li/SO₂ cell components such as carbon, electrolyte, etc., and other factors that might influence its stability and ultimately lead to Li/SO₂ battery safety hazards.

Experimental

Lithium dithionite was synthesized by the method previously reported (2). Analysis confirmed it was 88% pure, containing primarily lithium sulfite as an impurity (9).

Commercial Li/SO₂ cells were discharged at constant temperature in a Tenny Jr. Environmental Chamber using constant current controlled by a PAR Model 173 or 371 galvanostat. The discharged cells were opened in a helium-filled glove box.

All differential scanning calorimetry (DSC) studies were performed under nitrogen atmosphere using a Perkin Elmer Model 2 DSC. All dry samples were weighed before and after each DSC analysis. Samples were prepared in a dry room of less than 0.4% relative humidity. All the discharged cathode samples were sealed in DSC cells under helium. After DSC analysis, the DSC cells were immediately and rapidly cooled to ambient temperature under nitrogen.

Infrared analyses were performed using Perkin Elmer Model 683 and 1500 IR spectrometers. Samples were prepared as KBr pellets in the dry room.

Mass spectroscopic studies were performed using a Finnigan Model 4000 GC chemical ionization electron impact mass spectrometer.

Samples used in the ARC studies were loaded and sealed in an 8.6 ml titanium bomb while under a helium atmosphere. The ARC analyses were performed under nitrogen in a Columbia Scientific Instruments calorimeter.

Shock sensitivity tests were performed on samples of Li₂S₂O₄ and on 1:1 mixtures of lithium and lithium dithionite using a drop-weight-impact apparatus used in U.S. Navy explosive testing. This instrument employed a microphone noise meter calibrated using the drop hammer with and without known explosive samples. The impact distance necessary to give positive tests results on 50% of the samples was determined. This distance was then compared to data giving similar results on known explosive materials.

Accelerating rate calorimetry.—The ARC is a micro-processor-controlled adiabatic calorimeter that heats a sample to a desired starting temperature, waits for thermal equilibrium to be achieved, and then checks for a self-heating rate exceeding a preselected threshold. This cycle continues in fixed temperature increments until an exotherm is detected. The instrument then maintains the sample under adiabatic conditions and continuously monitors the time, temperature, and pressure relationship until the exothermic reaction is complete.

An exothermic reaction may proceed as a slowly decelerating reaction (low activation energy) or as a rapidly self-accelerating reaction (high activation energy). In the latter case, the heat of reaction is available to continuously heat the reactants to higher temperatures and thereby increases the rate of reaction until it accelerates exponentially with temperature. Thermal runaway occurs when rapid increases in temperature and reaction rates are realized. Safety hazards occur if the temperature rise causes an uncontrolled pressure increase as a result of an increase in vapor pressure or the formation of gaseous products.

The ARC thermal data have been presented as a log rate of self-heating vs. 1/T (K) plot. The 1/T (K) temperature axis is labeled in degrees centigrade for convenience. This is essentially an Arrhenius plot of the data, and each exothermic reaction will appear as a separate peak. A heat/search mode of operation where self-heating was not observed shows up as a discontinuity in the ARC thermal curves. Additional details concerning the theory and operation of the ARC have been reported (10, 11).

Results and Discussion

Adiabatic ARC studies.—ARC studies on commercial 2/3 A and D size Li/SO₂ cells overdischarged at ambient temperature exhibited an exothermic reaction beginning near 100°C. Similar low activation energy reactions occurred near 90°C on cathodes taken from 2/3 A and D size cells discharged to 2.0V at 25°C. The D cell cathodes displayed two distinct regions of exothermicity similar to the ARC behavior found in lithium-limited cells. However, the cathodes from the 2/3 A cells had an additional exotherm starting near 116°C and exhibited coupled exothermic reactions similar to those observed on all resistively overdischarged excess lithium cells (1).

The 2/3 A and D cells were discharged to 2.0V at 1 and 10 mA/cm², respectively. Conceivably, this rate difference could alter the discharge products and in turn affect the thermal behavior. This possibility was investigated by mass spectroscopy and ARC experiments.

Portions of the cathodes from the same 2/3 A and D cells were vacuum dried and heated in turn at 3°C/min in a mass spectrometer. Both cathodes evolved sulfur and SO₂ near 100°C. Since the only product formed in 2/3 A cells under these conditions is lithium dithionite (4), the sulfur and SO₂ are attributed to the thermal decomposition of lithium dithionite. This similar chemical and temperature behavior observed for the 2/3 A and D cell cathodes indicates that the differences in their ARC behavior cannot be readily explained by differences in discharge products. This was confirmed by discharging a 2/3 A cell at 71°C where a complex array of sulfur discharge products form (5). The ion intensity vs. temperature data obtained upon heating this cathode in the mass spectrometer (Fig. 1) are similar to those obtained with the cathode containing only dithionite. Again, the major evolution of S and SO₂ begins near 110°C. The sulfur observed near

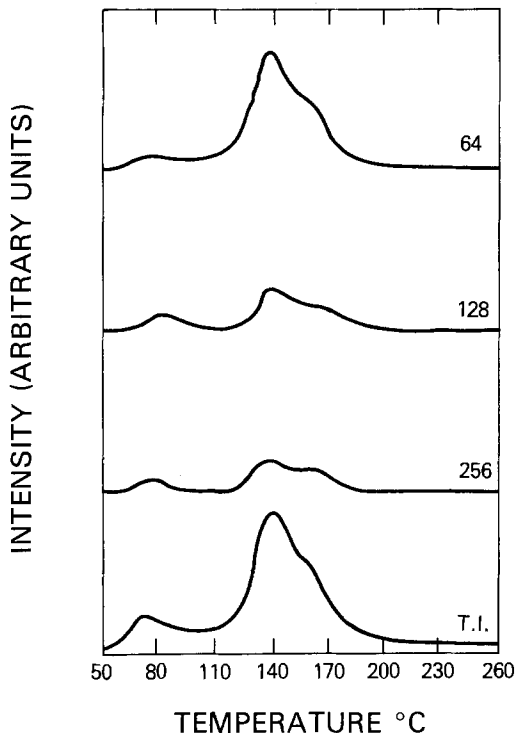


Fig. 1. Mass spectra upon heating a cathode from a 2/3 A size Li/SO₂ cell discharged at 1 mA/cm² at 71°C. Masses 64, 128, 256, total ion intensity.

60°C is consistent with the free sulfur found under these discharge conditions.

Figure 2 compares the ARC thermal and pressure data observed on cathodes taken from 2/3 A cells discharged at 1 mA/cm² at -30° and 71°C. The similar ARC behavior observed for cathodes containing only dithionite (-30°C) and cathodes with a complex discharge chemistry (71°C)

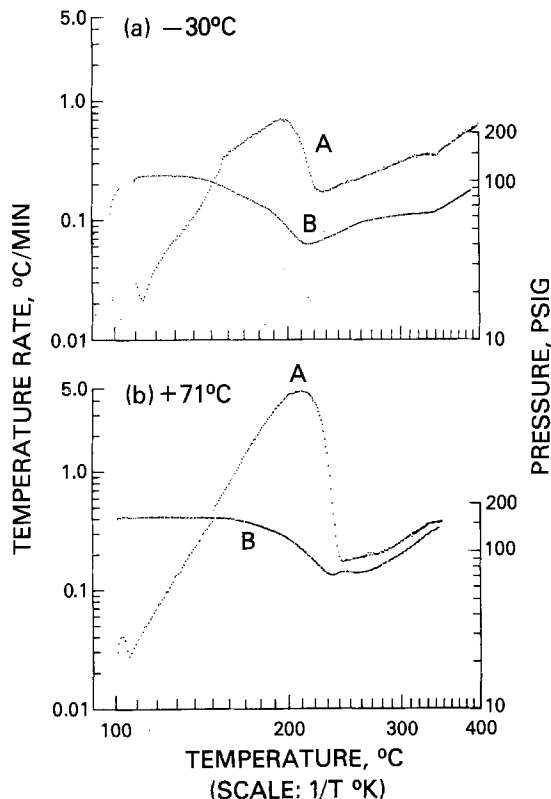


Fig. 2. ARC thermal (curve A) and pressure (curve B) behavior for cathodes from 2/3 A size Li/SO₂ cells discharged at 1 mA/cm² to 2.0V at (a) -30°C and (b) +71°C.

confirms that differences in the cathode chemistry do not account for the differences in ARC behavior reported previously (1).

Several other factors need to be considered. The D cathodes were wet with electrolyte, whereas the 2/3 A cathodes had the bulk electrolyte removed by vacuum pumping. Additionally, the differences in discharge rates alter the spatial distribution of the dithionite in the carbon black matrix. Thus, the spatial configuration of the dithionite (8) and the catalytic activity of carbon black (7) may combine to influence the ARC behavior and may account for the lower decomposition temperature of lithium dithionite than previously reported (2).

Thermal decomposition of dithionite.—ARC thermal data for samples of lithium dithionite (curve A), a mixture of lithium and lithium dithionite (curve B), and sodium dithionite (curve C) are illustrated in Fig. 3. The corresponding ARC pressure data are shown in Fig. 4.

The ARC thermal behavior of a 2.0g sample of laboratory-synthesized lithium dithionite is given in Fig. 3, curve A. Starting at about 140°C, lithium dithionite undergoes adiabatic decomposition, proceeds through two rapid exothermic reactions, and attains a self-heating rate of 85.5°C/min. The sample had an adiabatic temperature increase of 352°C to reach a final adiabatic temperature of 500°C. The corresponding ARC pressure behavior (Fig. 4, curve A) shows the sample generates 340 psig of pressure. The rate of pressure generation exceeded 60 psi/min.

ARC analysis was performed on a large sample (5.0g) of the sodium salt. The thermal behavior, illustrated by the solid line, curve C in Fig. 3, shows two distinct exotherms beginning at 122° and 230°C. During the first exotherm, the sample proceeds through a series of continuous exothermic reactions and attains a maximum self-heating rate of 137.5°C/min upon reaching a temperature of 190°C. The samples adiabatic temperature increased 250°C, reaching a final temperature of 372°C. The ARC pressure behavior is shown in Fig. 4, curve C. The sudden rise in pressure at 140°C coincides with initiation of the final reaction of the first exotherm.

These ARC data indicate the potential for safety hazards in Li/SO₂ cells. The amount of lithium dithionite used in this study was much less than that present in a fully discharged D cell. Despite this, the magnitude of the

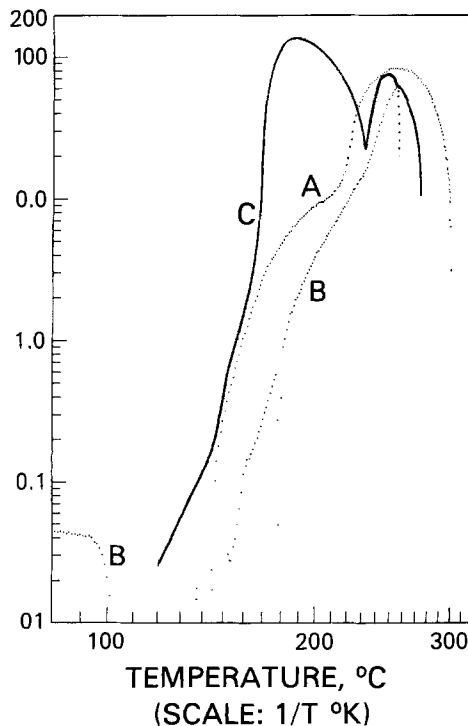


Fig. 3. ARC thermal behavior. A: Li₂S₂O₄ (2.0g). B: Li₂S₂O₄ (2.48g) + lithium metal (0.53g). C: Na₂S₂O₄ (4.9g, 98%).

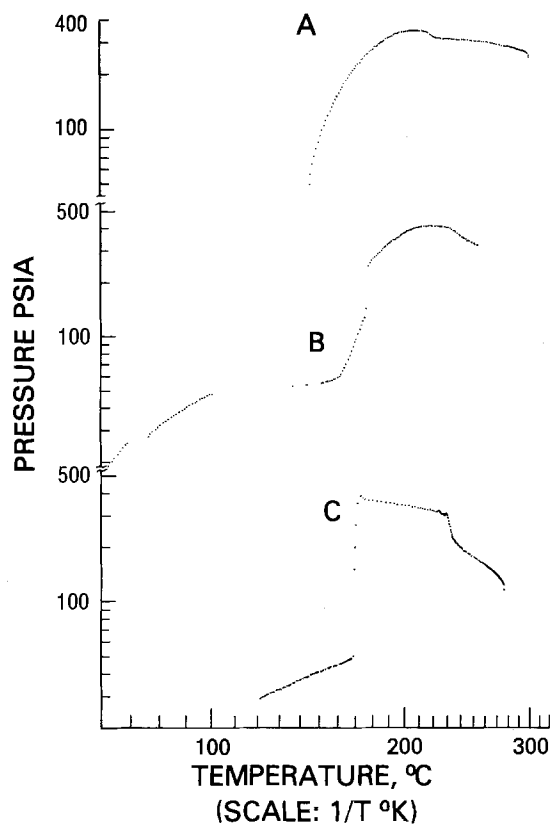


Fig. 4. ARC pressure behavior. A: Li₂S₂O₄. B: Li₂S₂O₄ + lithium. C: Na₂S₂O₄.

overall pressure rise was significant enough to cause venting in some commercial cells.

Infrared analysis on the residue from the ARC experiment on Li₂S₂O₄ is shown in Fig. 5, curve A. Several products including sulfite and sulfate can be identified. Qualitative tests with naphthol yellow S showed no dithionite remaining. Some sulfur was present.

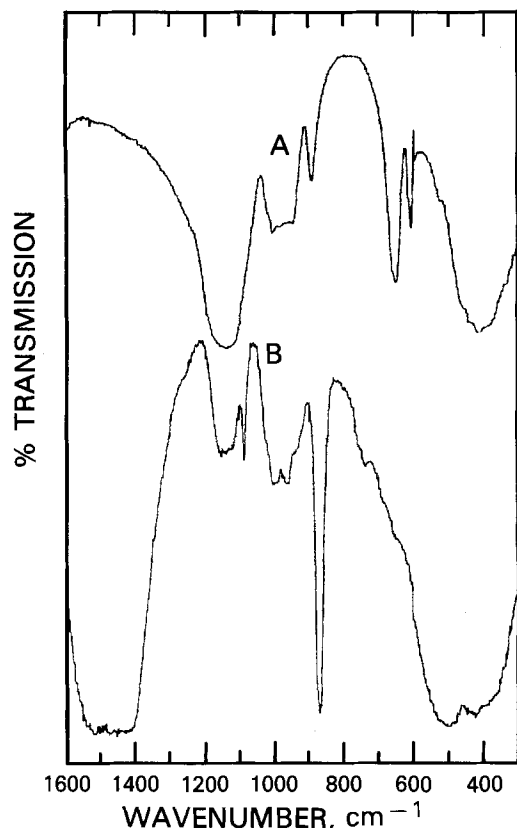
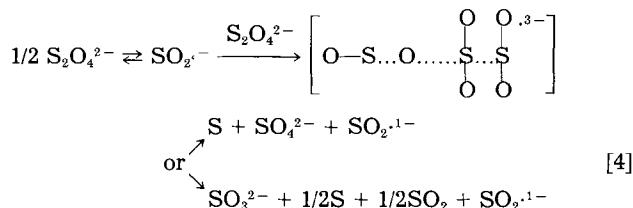


Fig. 5. Infrared spectra. A: Li₂S₂O₄ adiabatically decomposed in the ARC. B: Residue of the lithium-Li₂S₂O₄ reaction in the ARC.

Due to the rapidity of the Li₂S₂O₄ adiabatic decomposition, one plausible reaction may involve a radical chain mechanism, with one pathway given SO₃²⁻ with S and SO₂ forming through an SO intermediate



Lithium-lithium dithionite.—Safety hazards in overdischarged Li/SO₂ cells have often been attributed to the reaction of lithium with acetonitrile after depletion of the SO₂. However, even more serious hazards were observed on overdischarge at low temperatures (1) when residual SO₂ electrolyte was present. The cell capacity was limited by the saturation of the carbon current collector. The residual SO₂ passivates the lithium which deposits during overdischarge to form a lithium-carbon-lithium dithionite matrix.

The ARC thermal and pressure data for a mixture of lithium dithionite and excess lithium are illustrated by curve B in Fig. 3 and 4, respectively. A large exothermic reaction again begins near 140°C and proceeds through a series of reactions. The lithium melts at 180°C, indicated by the endotherm (dotted depression) in curve B, Fig. 3, which causes a sudden rise in the pressure, curve B, Fig. 4. This is attributed to the reaction of lithium with lithium dithionite



Heat from this reaction triggers gas producing reactions including (i) rapid decomposition of any residual dithionite to form SO₂ and (ii) reaction of the carbon with the S and SO₂ decomposition products of the dithionite. Upon reaching a self-heating rate exceeding 60°C/min and a pressure exceeding 400 psi, the calorimeter bomb shattered. A second mixture, containing a 10:1 mole ratio of 0.6g lithium and 1.2g Li₂S₂O₄, behaved similarly. The pressure was generated at a rate exceeding 340 psi/min at 200°C when the vessel again shattered.

Infrared analysis of the residue from the lithium-lithium dithionite reaction is shown in Fig. 5, curve B. Comparison of the two IR spectra in Fig. 5 reveals that lithium alters the decomposition mechanism significantly. The large broad bands at 1480, 1425, 500 cm⁻¹ and the strong sharp band at 865 cm⁻¹ correspond to the IR spectra obtained from lithium oxide. Qualitative spot tests confirmed the presence of sulfide. The additional IR bands of the spectra indicate that other products form, presumably from the reaction of SO₂ gas generated during the decomposition of the dithionite. The IR band at 1000 cm⁻¹ and shoulder at 1250 cm⁻¹ indicate some dithionate may have formed. Conceivably, the SO₂ may also react with the sulfite decomposition product to form metabisulfite, S₂O₃²⁻, giving rise to bands near 1160, 1088, 990, and shoulder near 650 cm⁻¹ (12).

Lithium dithionite-carbon.—The ARC thermal data for lithium dithionite appear appreciably different from those of the discharged cathodes. The ARC data on the discharged cathodes were characterized by the generation of pressure arising from the low temperature exotherm observed near 90°C (Fig. 2). This pressure, measured at 110°C, accounted for only 60% of that expected for complete dithionite decomposition. This was determined by using weighed cathodes, containing known amounts of carbon and dithionite determined from coulometric-iodometric analyses, placed in a fixed volume of the ARC bomb. The residual electrolyte precluded an exact determination of the percent decomposition.

After the initial decomposition of the dithionite, multiple exothermic reactions begin near 116°C, as shown by the variation in slope of the self-heating curves. The ARC

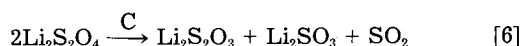
pressure data, curve B in Fig. 2, show the pressure decreasing, which indicates the SO₂ gas is consumed by a reaction during the latter part of this exothermic behavior.

A second exothermic reaction that generates additional gas pressure begins near 220°C.

The effect of carbon black on the decomposition of dithionite was investigated. A mixture, simulating the relatively moisture-laden cathodes taken from discharged D cells (1), was prepared by mixing 1.2g Li₂S₂O₄ with 0.18g undried Shawinigan carbon black under a helium atmosphere. Figure 6, curve A shows the ARC thermal behavior of this sample after two months storage in a desiccator. Sustained multiple reactions begin at 61°C. The mixture attains a self-heating rate of 11°C/min and an adiabatic temperature rise of 291°C, reaching an adiabatic temperature of 352°C.

A second mixture, simulating cathodes from the relatively moisture-free 2/3 A cells (1), was prepared under helium by grinding together lithium dithionite with Shawinigan carbon black that was vacuum dried several days at 250°C. The ARC thermal data, shown in Fig. 6, curve B, has characteristics common to both the discharged cathodes and the lithium dithionite. Although the self-heating process begins near 90°C as observed with the discharged cathodes, the rapid decomposition and pressure generation (Fig. 6, curve C) occurs near 145°C as found in the case of the lithium dithionite.

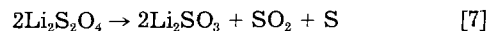
Adiabatic decomposition mechanisms.—Lithium dithionite-carbon.—Since undischarged cathodes exhibited no exothermic behavior, the low temperature exotherms are attributed to the carbon catalyzed decomposition of lithium dithionite, given by the reaction



Studies in which lithium dithionite was heated to 140°C under N₂ support this reaction. The dithionite loses mass slowly over several days, producing SO₂ gas. Infrared analysis of the residue showed only lithium sulfite and

residual dithionite. DSC analysis showed endotherms at 113° and 119°C, indicating the presence of sulfur. It should be noted that Li₂S₂O₃ undergoes endothermic decomposition into sulfur and sulfite beginning near 116°C (3).

The exotherm starting near 220°C is attributed to the decomposition of the residual dithionite according to the reaction

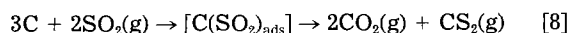


Upon completion of the ARC analysis, the residues were weighed. The mass loss was 23% consistent with the theoretical loss expected from an overall process represented by Eq. [7].

Lithium dithionite.—In the absence of carbon, the adiabatic decomposition of lithium dithionite may follow a different mechanism, as indicated by the more rapid rise in self-heating rates. Sample size may be a factor. The large samples had still higher self-heating rates and greater rates of pressure generation. The ARC data indicate two principal processes occur (with or without carbon). The proposal mechanism is given by Eq. [4], which accounts for the sulfate and sulfite products. High temperatures appear to favor formation of the sulfite, as indicated by the previous nonadiabatic studies (2). Additional studies are in progress.

Lithium-carbon-lithium dithionite.—A cathode taken from a 2/3 A size SO₂ cell overdischarged 30% at 1 mA/cm² at 25°C was vacuum dried and placed in a helium-filled combustion bomb. The bomb was evacuated and heated to 200°C. Infrared analysis on the collected gas revealed that, in addition to SO₂, some carbonaceous gases were present, primarily CS₂ and CO₂.

The ARC data indicate that the heat generated from the carbon-catalyzed Li₂S₂O₄ decomposition can trigger very exothermic reactions involving lithium. In addition to the reaction represented by Eq. [5], the lithium may also react with the sulfur present from decomposed dithionite. The heat generated apparently causes the carbon black to react according to the reaction



Mechanism for overdischarge hazards.—During forced overdischarge, especially during low temperature operation where the SO₂ electrolyte is least likely to be consumed, lithium can accumulate in the carbon cathode together with the lithium dithionite discharge product. Polarization of the carbon due to loss of some electrolyte and saturation of the carbon generates heat. Localized heating (hot spots) causes the carbon-catalyzed decomposition of Li₂S₂O₄ to generate a large adiabatic temperature increase. This heat can trigger an extremely rapid and very exothermic lithium-lithium dithionite reaction. In addition to the sudden gaseous pressure generation, the heat causes carbon to react almost synchronously with the SO₂ and S decomposition products, creating additional pressure by the formation of carbonaceous gases.

Nonadiabatic DSC-IR study of Li₂S₂O₄ decomposition.—Lithium dithionite was weighed in sealed DSC cells under nitrogen prior to heating. After heating, the DSC cell was opened and the residue was weighed and examined

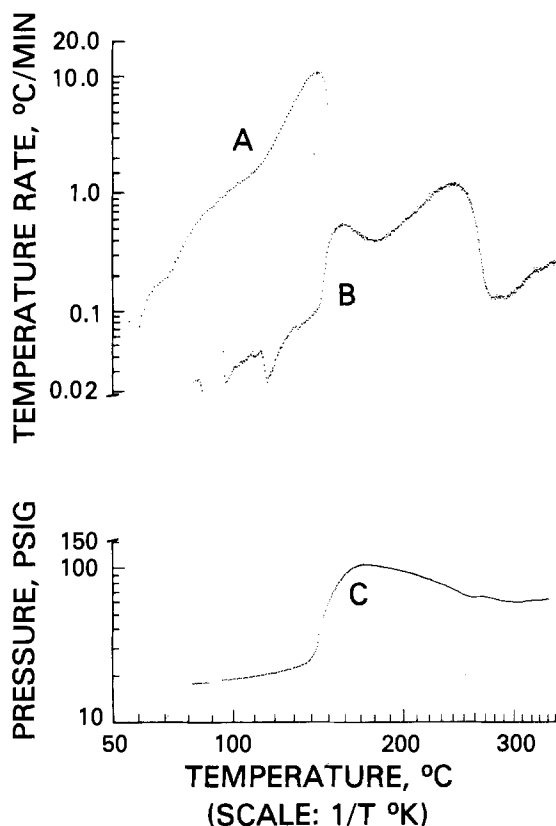


Fig. 6. ARC behavior for a mixture of Li₂S₂O₄ and carbon Shawinigan black. A: Thermal self-heating curve, Li₂S₂O₄ (0.96g) + undried carbon (0.14g). B: Thermal self-heating curve, Li₂S₂O₄ (0.6g) + dried carbon (0.10g). C: Pressure behavior of curve B.

Table I. Nonoxidative thermal decomposition study of Li₂S₂O₄

Sample number	Li ₂ S ₂ O ₄ mass ^a (mg)	Heat rate (°C/min)	Final temp. (°C)	Approximate % mass loss	IR spectra
1	5.1	20	190	0	7A
2	7.0	20	240	22	7B
3	7.0	0.62	220	25	7B
4	6.9 (12.5)	20	190	5	8A
5	7.7 (13.2)	0.62	220	—	8B
6	8.1 (13.9)	20	280	26	8B

^a Samples 4, 5, and 6 are Li₂S₂O₄-carbon black mixtures. Weight in parentheses is total mass.

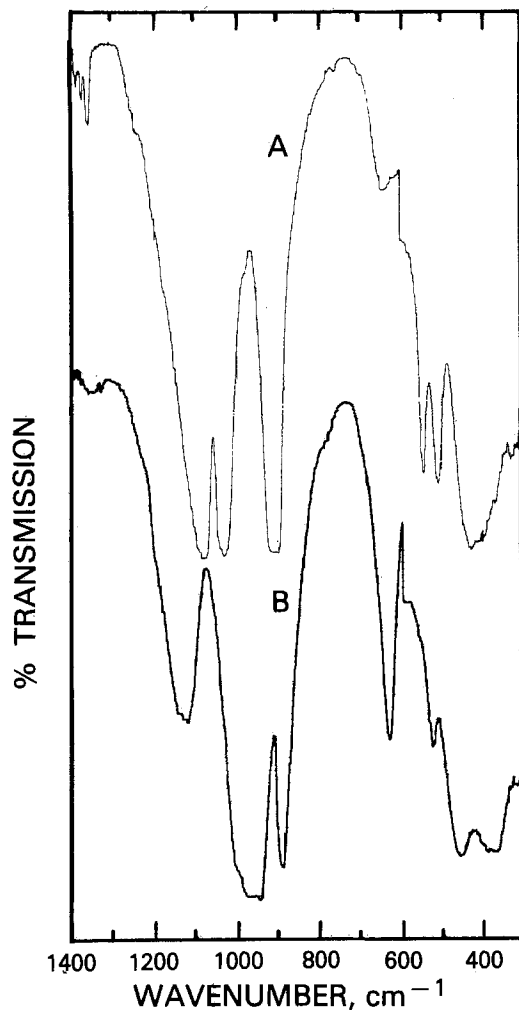


Fig. 7. Infrared spectra. A: Li₂S₂O₄ heated 20°C/min to 190°C in a DSC. B: Li₂S₂O₄ heated to 240°C at 20°C/min or at 0.62°C/min to 220°C in a DSC.

by IR analysis. Table I summarizes the DSC-IR data. The extent of dithionite decomposition was influenced by (i) the rate of heating and the final temperature and (ii) the presence of carbon black.

Infrared analysis on the residue from sample 1, shown in Fig. 7, curve A, indicates little decomposition has occurred at 190°C when the sample is heated at 20°C/min. The IR bands at 505, 545, 910, 1032, and 1082 cm⁻¹ are due to Li₂S₂O₄. Characteristic of DSC analysis, decomposition occurred sooner and to a greater degree if the sample is heated slower, 0.62°C/min. As cited earlier, isothermal heating at 140°C over several days enabled extensive decomposition to occur. The IR spectra of samples heated in the DSC to higher temperatures, as cited in Table I, resemble hydrated sulfite and are illustrated in Fig. 7, curve B. The lithium dithionite typically lost 24 ± 2% mass.

Samples 4, 5, and 6 are ground mixtures of Li₂S₂O₄ and carbon Shawinigan black. Prior to heating, such mixtures show no change in the IR spectra from that of Li₂S₂O₄. However, Fig. 8, curve A shows the IR spectra of sample 4 after heating. Comparison of samples 1 (Fig. 7, curve A) and 4 (Fig. 8, curve A) under identical heating conditions reveals that carbon black catalyzes the decomposition of Li₂S₂O₄. In the presence of carbon black, some mass loss occurs and new IR bands form. More extensive heating (samples 5 and 6) gives rise to the FTIR spectra shown in Fig. 8, curve B. Comparison of curve B in Fig. 7 and 8 reveals carbon black has altered the decomposition of dithionite as evidenced by the spectral changes, most notably at 1209 cm⁻¹ and perhaps near the 500 cm⁻¹ region.

Discharged cathodes.—A 2/3 A size commercial Li/SO₂ cell, discharge at 25°C to 2.0V at 40 mA constant current,

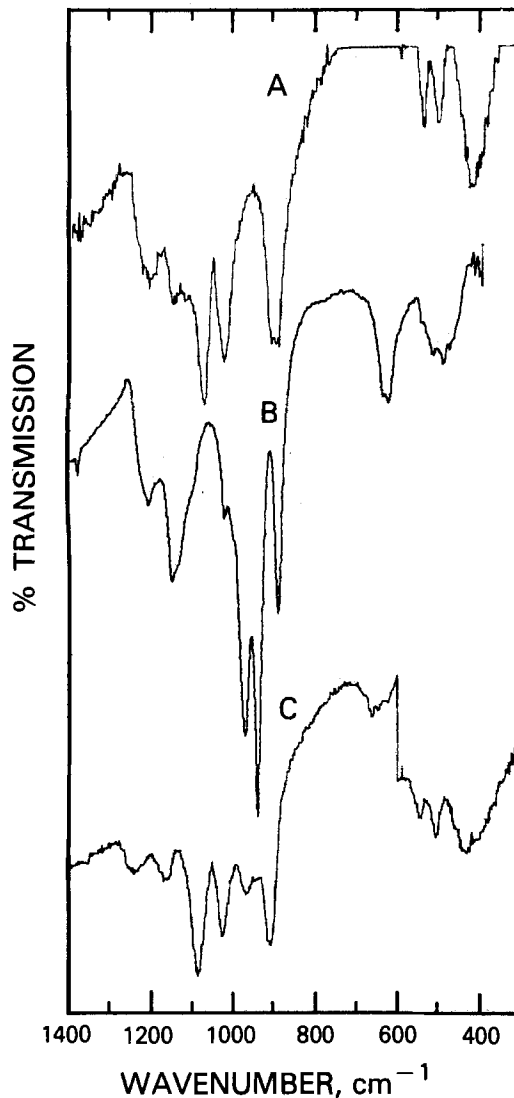


Fig. 8. A: IR spectra of a ground mixture of Li₂S₂O₄ and carbon Shawinigan black heated 20°C/min to 190°C. B: IR spectra of ground mixture of Li₂S₂O₄ and carbon Shawinigan black heated to 0.62°C/min to 220°C. C: IR spectra of a cathode from a 2/3 A size Li/SO₂ cell discharged at 25°C at 15 mA/cm² or C size cell at 71°C at 10 mA/cm².

known to contain only Li₂S₂O₄ as a discharge product (4), was opened in a helium glove box. Samples of the cathode were immediately hermetically sealed in DSC cells while still wet with electrolyte. Additional samples of this cathode were placed in a desiccator in the glove box, vacuum dried, and sealed in DSC cells. The cathode samples were analyzed by DSC at various rates of heating.

DSC and subsequent IR analyses on the residue indicated that the thermal behavior and the chemistry of discharged cathodes may be influenced by their rate of heating and to some extent their degree of wetness with electrolyte.

Figure 9 shows the temperature at the peak of the major exothermic reaction in the DSC vs. log of the DSC heating rate of the cathodes wet with electrolyte. The break in the curve indicates a change in the chemistry occurred at the higher heating rates. At slow DSC heating rates, only a single exotherm appears. A new exothermic transition begins at about 10°C/min preceding the original exotherm. As the heating rate increases, this first exotherm intensifies until, at 80°C/min, a sudden endotherm occurs between the two exotherms. Replicate analyses, performed at each heating rate, gave identical thermal behavior.

The IR spectra of the residues obtained at heating rates of 1.25° and 20°C/min are compared in Fig. 10. The 1209, 1155, and 1125 cm⁻¹ IR bands that appear at the higher heating rate confirm a change in chemistry has occurred.

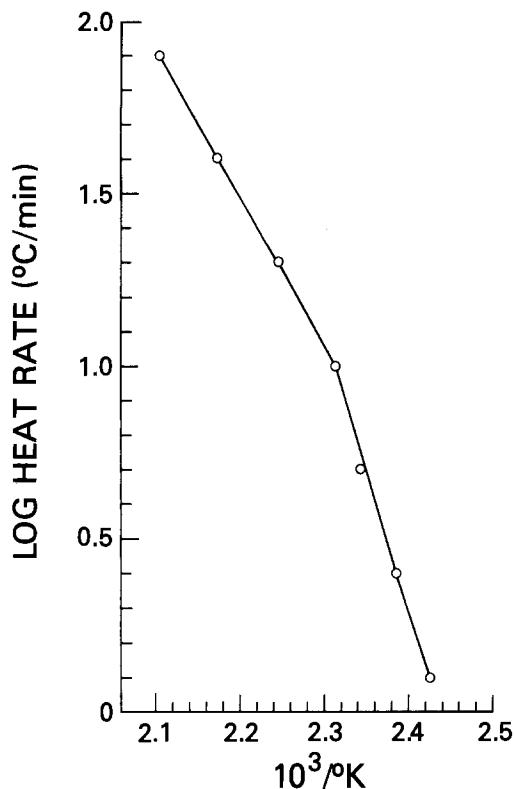


Fig. 9. Log DSC heating rate vs. peak temperature of principal exothermic reaction of a cathode still wet with electrolyte from a Li/SO₂ cell discharged at 1 mA/cm², 25°C.

DSC analyses on portions of the dried discharged cathode were performed in replicate at various rates. The samples gave rise to unexpected endothermic behavior. This generally occurred after a slowly occurring exotherm had begun.

Infrared analyses on the residues typically gave rise to the IR spectra shown in Fig. 10, curve C. The IR bands at 1209, 1153, and 1125 are similar to the IR bands observed on rapidly heating cathodes containing electrolyte (Fig. 10, curve B). The dried cathodes gave rise to a more intense 1209, 1153, and 1125 cm⁻¹ bands, relative to the other IR bands of the spectra. Whenever the 1153 and 1125 cm⁻¹ bands were prominent, endothermic behavior was consistently observed.

DSC-IR analyses permit the examination of chemical changes introduced by heating the discharged cathodes outside of the normal cell environment. To study the chemical changes induced by heat within a pressurized cell, both 2/3 A and C size cells were discharged at high rates and/or high temperatures. The cathodes were compared using IR analyses. The IR spectra for a C size cell discharged at 71°C and 10 mA/cm² is shown in Fig. 8, curve C. An identical IR spectra was obtained for a 2/3 A size cell discharged at 25°C at 15 mA/cm² where the external cell temperature reached 88°C. In addition to the five dithionite bands, new bands appear at 1240, 1165, and 970 cm⁻¹ and several small bands appear near 650 cm⁻¹. This contrasts with the 1209, 1153, and 1125 cm⁻¹ bands that form upon heating vacuum-dried cathodes or on rapidly heating the electrolyte-wet cathodes outside of the cell environment.

A 2/3 A size cell discharged at 25°C at 1 mA/cm², so as to produce only Li₂S₂O₄, was placed in an oven for two days at 71°C. Subsequently IR analysis on the cathode revealed little dithionite decomposition had occurred. This data suggests that the reduction process and/or the SO₂ electrolyte plays a role in the high rate or high temperature discharge chemistry. Additionally, the 1240 cm⁻¹ band, indicative of thionate formation, which is formed during high rate or high temperature discharges, was not found upon heating discharged cathodes in the low pressure environment of the DSC cells.

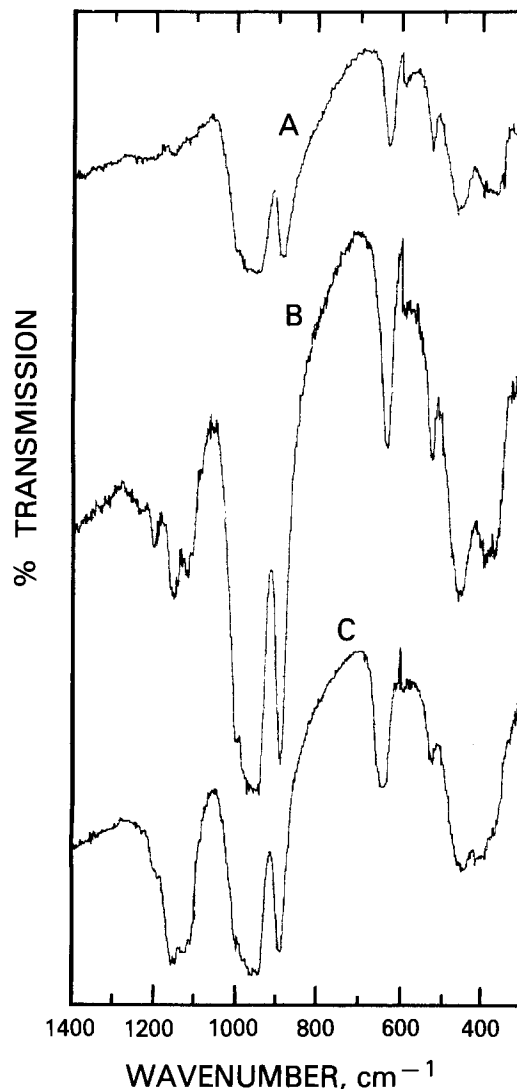


Fig. 10. IR spectra of a cathode from a 2/3 A size Li/SO₂ cell discharged at 1 mA/cm² at 25°C to 2V. A: Cathode wet with electrolyte heated 1.25°C/min to 240°C. B: Cathode wet with electrolyte heated 20°C/min to 240°C. C: Cathode vacuum dried 1 day, heated 20°C/min to 240°C.

Shock sensitivity testing.—Samples of lithium dithionite subjected to impact testing showed no evidence of any shock sensitivity. However, the tests performed on mixtures of lithium and lithium dithionite gave positive results. Sensitivity was determined from the impact distance required to give positive tests on 50% of the test samples. These data were then compared with data on known explosives that gave similar test results. The lithium-lithium dithionite samples had a sensitivity equivalent to plastic bomb explosives. During the runs when no shock sensitivity was detected, the sample ignited upon impact.

Summary and Conclusions

ARC, DSC, and IR data indicate several parameters may alter the chemistry of Li/SO₂ cells. These include the spatial distribution of products on the carbon during adiabatic heating, the amount of electrolyte at the end of cell life, and the rates of heating or discharge.

Discharged cathodes still wet with electrolyte and known to contain only dithionite gave rise to IR bands at 1209, 1153, and 1125 cm⁻¹ upon being rapidly heated in a DSC. Slow heating did not give rise to these bands. Similar but more intense bands were found after heating cathodes depleted of electrolyte in the DSC. IR studies on cathodes taken from Li/SO₂ cells discharged at high temperatures or high rates showed different IR bands at 1240, 1165, etc., cm⁻¹, indicating the effects of heat in a pressur-

Optical Etch-Rate Monitoring Using Active Device Areas: Lateral Interference Effects

P. A. Heimann*

AT&T Bell Laboratories, Murray Hill, New Jersey 07974

ABSTRACT

The technique of optical (laser) etch-rate monitoring is proving useful for integrated circuit manufacture and process development. This technique detects the change in film thickness during etching by monitoring the reflectance of the film on the integrated circuit wafer. When the reflectance is monitored over a region of the wafer containing both etched and unetched areas, the results are affected by lateral interference, which is interference between the light reflected from the different regions. This lateral interference has only a minor effect when less than 30% of the region being monitored is covered by an etch-resistant layer (typical for metal-type lithography levels), but it can cause severe distortions when a larger fraction of the region is covered by the resist. The effects of lateral interference have been examined using numerical simulations. The results are in good agreement with experimental etch-rate monitor signals from the etching of patterns with resist coverage ranging from 10 to 80% of the total area.

As integrated circuit dimensions become smaller and as the various conducting or insulating films used in these circuits become thinner, the tolerances on the etch processes for these films become more severe. The need for careful monitoring of these etch processes can be met by detecting changes in the optical reflectance of the film structures.

Originally (1, 2), the reflectance of a large area (greater than 2 mm²) was monitored while the entire area was being etched. The reflectance change was caused by the interference of light reflected from the interfaces between the various film layers ("vertical" interference), since this interference is affected by the changing thickness of the top etched layer. However, there are cases where it is undesirable or impossible to monitor the reflectance from a large area. First, a narrow beam is required, and the etch-machine operator must be able to place the beam only upon this large test area. Second, in step-and-repeat lithography, a separate reticle might be needed to produce this large area for etch-rate monitoring. Finally, etch-rate monitoring techniques have been described (3, 4) which require that the area being monitored contains both regions that are etched and regions that are covered with a photoresist or other etch-resistant layer. Therefore, it is necessary to understand what happens when this combination of etched and unetched regions is being monitored.

Whenever a patterned area is monitored, there is interference between the light reflected from the different regions (lateral interference) as well as the vertical interference described above. Lateral interference always occurs, unless the patterned wafer is imaged onto the detector. This will not happen with a simple laser system. The lateral interference is affected by the difference in height (layer thicknesses) between the etched and unetched regions. Since the light that is reflected from any one region will vary in both amplitude and phase during the etch, the resulting signal is a complicated function of the layer thicknesses, and modeling is needed to understand these signals.

Effects of Lateral Interference

As an example of the effects of lateral interference, consider the reflectance of a thermal oxide on silicon when the oxide is partially covered by resist (Fig. 1). The (complex) ratio r_e of reflected to incident amplitude of light from the etched area is given by (5)

$$r_e = \frac{r_1 + r_2 e^{-2i\delta_1}}{1 + r_1 r_2 e^{-2i\delta_1}} e^{-2i\delta_0} \quad [1]$$

where r_1 and r_2 are Fresnel reflection coefficients, computed from the oxide and silicon indexes of refraction, n_1 and n_2

* Electrochemical Society Active Member.

$$r_1 = \frac{1 - n_1}{1 + n_1}; r_2 = \frac{n_1 - n_2}{n_1 + n_2} \quad [2]$$

and δ_0 and δ_1 are phase shifts, given by

$$\delta_0 = 2\pi d_0/\lambda; \delta_1 = 2\pi n_1 d_1/\lambda \quad [3]$$

for light of wavelength λ , an oxide thickness d_1 , and a step height d_0 between the top surfaces of the oxide and the resist. The term $e^{-2i\delta_0}$ accounts for the phase change of the light as it travels down and back up the step-height distance.

If the light beam is confined only to the etched area, then the detected intensity is proportional to $|r_e|^2$, which, from Eq. [1], is equal to

$$|r_e|^2 = \frac{r_1^2 + r_2^2 + 2r_1 r_2 \cos(2\delta_1)}{1 + r_1^2 r_2^2 + 2r_1 r_2 \cos(2\delta_1)} \quad [4]$$

It can be shown that the detected intensity here is a periodic function of the oxide thickness d_1 , with a period of $\lambda/2n_1$. Note that this intensity is independent of the phase term $e^{-2i\delta_0}$ of Eq. [1]. Note also that the periodic function is not purely sinusoidal, although it can be shown that it approaches a sinusoid as n_1 approaches 1.

If the light is reflected from both etched and unetched areas, then lateral interference will cause the amplitudes, not the intensities, of the reflected light to be added together. If there is no resist erosion, then the ratio of reflected to incident amplitude of light from the unetched area will have a constant (complex) value r_u . The detected intensity I is then given by

$$I = I_0 |f_e r_e + f_u r_u|^2 \quad [5]$$

where I_0 is the incident intensity, and f_e and f_u are the

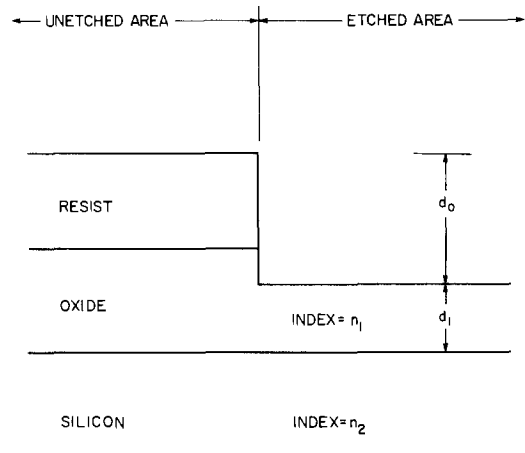


Fig. 1. Film structure partially covered by resist

etched and unetched fractions, respectively, of the total area. At this point, the algebra gets very complicated, since the amplitude and phase of r_e are oscillating, with different periods, as the oxide thickness d_i is changed. The detected intensity is no longer independent of the phase term, since the two complex reflectances are added algebraically. The resulting intensity is the sum of functions that oscillate at periods with $\lambda/2$, $\lambda/2n_i$, $(\lambda/2 + \lambda/2n_i)$, and $(\lambda/2 - \lambda/2n_i)$. This is very messy, and well suited to computer simulation (6). If there is resist erosion, then r_u is also a periodic function of resist thickness, and the resulting etch-rate monitor curves are even more complicated.

From this example, one probably gets the impression that lateral interference is undesirable. This is not necessarily so, especially for two cases of practical interest. When the etched area is a large fraction of the total area, which is typical for metal-type lithographic levels, the lateral interference causes only a minor distortion to the signal that would occur if only the etched area were being monitored, and therefore it can be ignored. Furthermore, the etch-rate monitor techniques described in Ref. (3) and (4) would not work at all without lateral interference.

Simulations and Experimental Results

For optical etch-rate monitoring of active device areas, there are two limiting cases of interest. Lithography levels such as metal and poly usually have most of the wafer area unmasked, so the optical etch-rate monitor signal for this type of level is similar to the signal for a large unpatterned area. Lithography levels such as window and polycon have only a small portion of the wafer unmasked, and therefore the signal is dominated by the resist-covered portion of the wafer. A third case of interest is the intermediate case which occurs in experimental structures such as meander patterns, in which roughly half of the wafer area is etched.

The calculated (6) etch-rate monitor curve (632.8 nm laser) for etching polysilicon on top of field oxide, with no resist present, is shown in Fig. 2. The signal is periodic, except for a slight increase in maximum reflectivity as the slightly absorbing polysilicon gets thinner. Figures 3a-3c show the calculated signals when 10, 30, and 50% of the polysilicon area is covered by resist, although it is unlikely that more than 30% of the area would be covered in a metal-type lithography level of an actual device. The solid curves correspond to the case where there is no resist erosion, and the dashed curves correspond to a resist that erodes one-fifth as fast as the polysilicon. One can see that the lateral interference does not make the curve unintelligible unless one approaches 50% coverage. In general, therefore, for a metal-type lithography levels, there is only a slight difference between the etch-rate

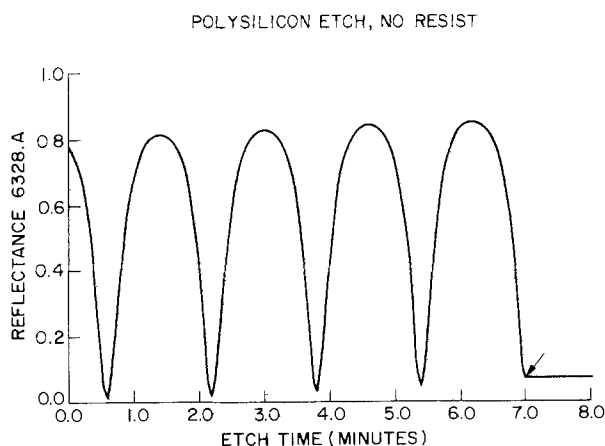


Fig. 2. Calculated etch-rate monitor curve for 3500Å polysilicon on top of 3200Å thermal oxide on silicon, for 632.8 nm light and 100% exposed area (no resist coverage). Arrow shows point of etching completely through the polysilicon layer.

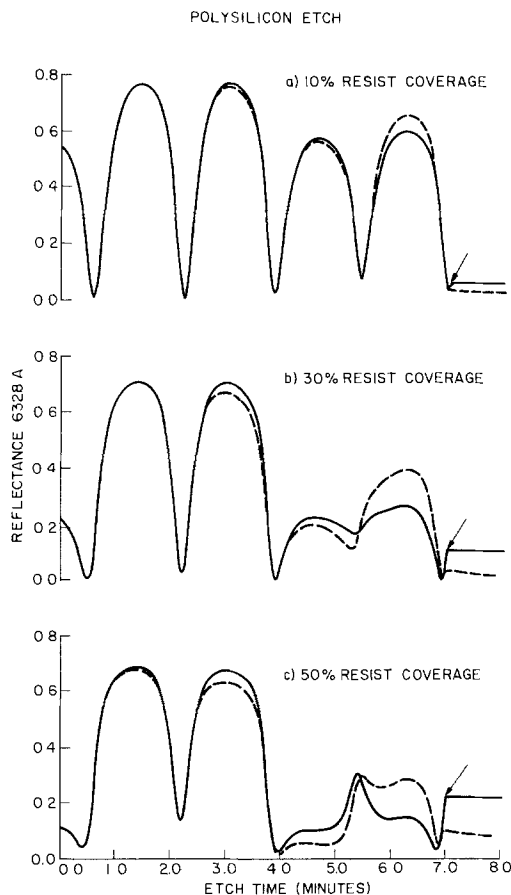


Fig. 3. Calculated etch-rate monitor curves, using 632.8 nm light, for polysilicon partially covered with resist. These fractions are typical for metal-type lithography levels. Solid curves are for no resist erosion, dashed curves are for 5:1 selectivity of polysilicon to resist. Arrows show points of etching completely through the polysilicon layer.

monitor curves from large test areas and from active device areas.

For window-type levels, the exposed area is only a small fraction, typically 1%, of the total area. Therefore, the reflectance change caused by etching these exposed areas is small, and can be masked by reflectance changes of the resist-covered areas. This effect can be minimized by selecting a light wavelength for which the resist is opaque, since then the resist reflectance will be small and constant. A 253.7 nm low pressure mercury arc is an excellent source of such light. One could also use a 632.8 nm laser and add a dye to the resist, provided that this dye does not affect the resist exposure or development, that it can withstand resist baking, and that it does not contaminate the devices below the resist. However, even when the effects of resist erosion are minimized, one is still plagued by a very low signal-to-noise ratio, since the overall reflection is quite low, and since windows, bonding pads, and "streets" between chips usually cover only about 1% of the total wafer area. Figure 4 shows simulations of window etch-rate monitor curves, using 253.7 nm light, when 95 or 99% of the area is covered with resist, along with the curve calculated for the case where there is no resist present. Again, the dashed lines indicate the curves for a 1:5 ratio of resist vs. oxide etch rates. Note that the maximum reflectance is only about 0.08, since most of the area is covered by an absorbing resist. An artifact of lateral interference is that there appears to be fewer periods of oscillation for the resist-covered samples than for the sample without resist. For instance, the dashed curve in Fig. 4b appears to have four and one-half periods, corresponding to 368 nm ($\lambda = 253.7$ nm, $n_1 = 1.55$) of oxide etched, when actually 1000 nm of oxide has been etched in this simulation. Therefore, it is impractical to determine the etch rate in real time of a window etch

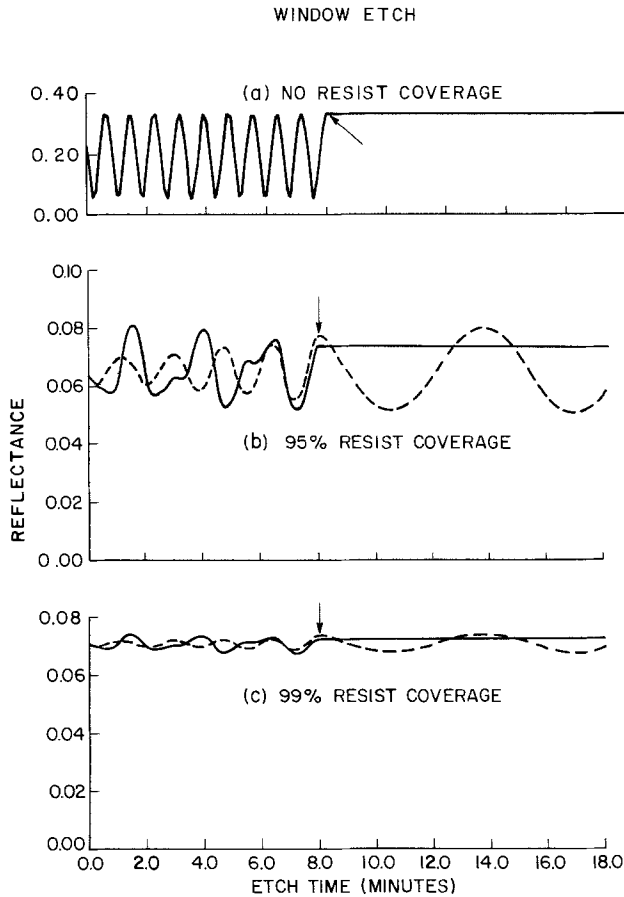


Fig. 4. Calculated etch-rate monitor curves, using 253.7 nm light, for unpatterned oxide (a) and for oxide partially covered with resist. The unetched portions cover 95% (b) and 99% (c) of the wafer area. These fractions are typical for window-type lithography levels. Solid curves are for no resist erosion; dashed curves are for 5:1 selectivity of oxide to resist. Note expanded scale for reflectance. Arrows show points of etching completely through the oxide layer.

from the structure of these curves. However, if a slight overetch can be tolerated, then the end point of the window etch can be detected easily (provided that signal-to-noise problems can be overcome) by looking for a change in the periodicity of the signal.

Experimental curves for reflectance at 632.8 and 253.7 nm from an oxide on silicon, 80% covered by resist, are shown in Fig. 5. The structure of the reflectance at 632.8 nm is determined mainly by resist erosion, which is slow. The reflectance in the ultraviolet (253.7 nm) shows a complicated structure similar to that of Fig. 4. The overall drop in intensity is believed to be caused by the buildup during etching of an ultraviolet absorbing polymer on the view port of the reactive ion-etch machine. The oxide in this sample was 1800 nm thick, which corresponds to 22 periods of oscillation. As with the simulation, there appears to be far fewer periods in the experimental curve, due to distortions caused by lateral interference. The arrow in Fig. 5 indicates the point where the structure of the curve becomes much smoother. This is the end point of the oxide etch, which is evident from the curve after only a slight overetch.

One instance where the 50% coverage is beneficial is the interferometric technique of Sternheim *et al.* (3) for monitoring either the etching of opaque layers or the etching of trenches into the silicon substrate. In these cases, there is no vertical interference because there is only one reflecting interface at any lateral position. However, if only part of the area is being etched, one can make use of lateral interference to monitor the step height between etched and unetched areas. Figures 6a and 6b show the calculated reflectance for a case presented by Sternheim *et al.*: silicon, with half of the area covered by

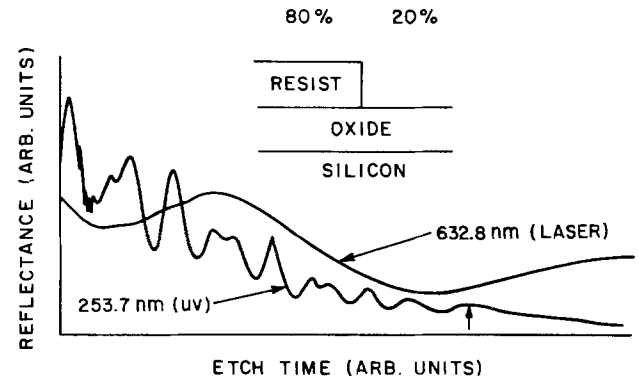


Fig. 5. Experimental etch-rate monitor curves at 253.7 nm and 632.8 nm for etching 1800 nm oxide on silicon, with 80% of the area covered by resist.

an etch-resistant thermal oxide, so that lateral interference causes the reflectance to oscillate. In Fig. 6a, the oxide is assumed to have no erosion. Using arguments similar to those of the Effects of Lateral Interference section, one can show that here a curve with N periods corresponds to an etching depth d given by

$$d = N\lambda/2 \quad [6]$$

since the index of refraction of air or vacuum is 1.0. In Fig. 6a, we have 4.1 periods using 632.8 nm light, which corresponds to 1.3 μm etching. Figure 6b models the experimental data from Sternheim *et al.*, where the oxide erodes at one-fifth of the silicon etch rate. The ampli-

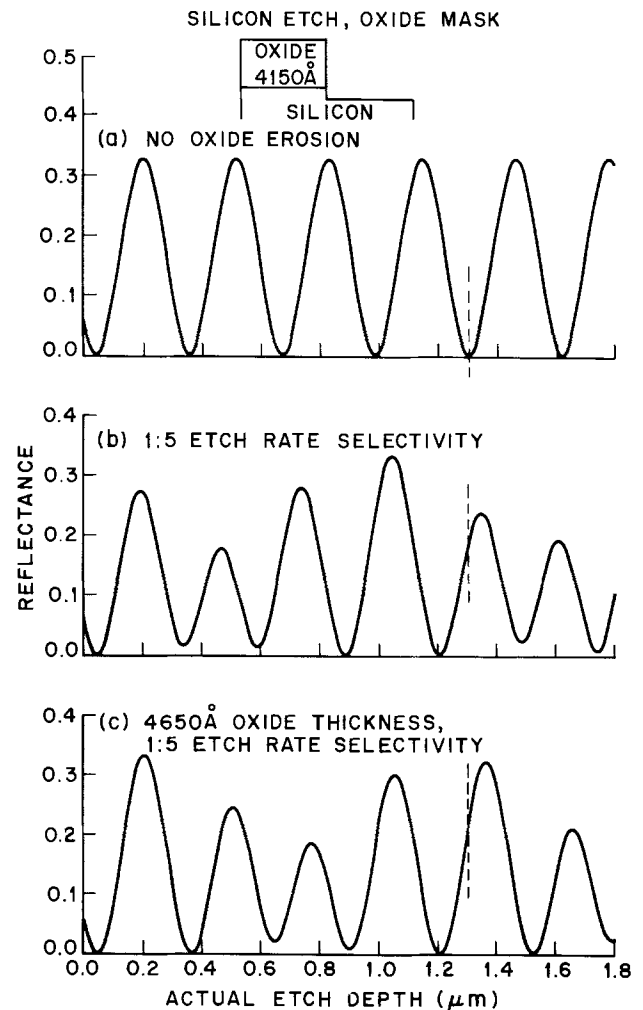


Fig. 6. Calculated etch-rate monitor curves using 632.8 nm light for etching silicon with 50% of the area covered by a masking oxide (4150Å thick). Dashed line corresponds to 1.30 μm etch depth.

tudes of the oscillation are no longer uniform. Furthermore, we now have 4.4 periods. If Eq. [6] is used for calculating the step height, one would get a value of $1.39 \mu\text{m}$, which is larger by 7% than the correct value. Sternheim *et al.* observed a 6% error for this case, with the error being in the same direction: the optical etch-rate monitor yielded a larger step than a stylus measurement. The structure of their etch-rate monitor signal [Fig. 5 of Ref. (3)] does not agree exactly with the calculated curve of Fig. 6b here. The model cannot predict the structure of the curve unless the masking oxide thickness is known precisely, but it can predict the error in step height as found by the etch-rate monitor. Figure 6c shows the calculated etch-rate monitor curve when the masking oxide is 500\AA thicker than in Fig. 6b. The structure of the curve again is different, but the $1.3 \mu\text{m}$ etch with the same erosion ratio of 1:5 still yields about 4.4 periods of oscillation. The calculated error in step height is not a simple function of oxide (or resist) erosion rate, but the calculated error is always less than 10% for erosion ratios of 1:5 or less, and always in the direction that the optical etch-rate monitor value will be too large.

Conclusions

Optical etch-rate monitor signals have been modeled for patterns that are usually found in integrated circuit manufacturing. For metal-type lithography levels, lateral interference causes a slight distortion in the shape of the etch-rate monitor curve, and may lead to a slight error in determining the etch rate. For meander-type patterns, the distortion can be serious enough to make the curves unintelligible. For window-type lithography levels, the etched area is usually too small to produce a useful etch-rate monitor signal, unless the signal from the etched

areas can be enhanced. Lateral interference can be employed for monitoring the etching of opaque or bulk materials, with a predicted error in depth value of less than about 10% for resist erosion at less than one-fifth of the film etch rate.

Acknowledgments

I would like to thank M. Feldman and A. D. White for many stimulating discussions about the lateral interference in various optical systems. The challenge of explaining experimental data supplied by R. J. Schutz and J. E. Olsen provided the inspiration and direction for this project. I would also like to thank J. M. Moran and H. J. Levinstein for their support and suggestions.

Manuscript submitted Nov. 13, 1984; revised manuscript received Feb. 15, 1985. This was Paper 387 presented at the New Orleans, Louisiana, Meeting of the Society, Oct. 7-12, 1984.

AT&T Bell Laboratories assisted in meeting the publication costs of this article.

REFERENCES

1. H. H. Busto, in "Optical Characterization Techniques for Semiconductor Technology," pp. 164-169, Society of Photo-Optical Instrument Engineers (1981).
2. P. J. Marcoux and P. D. Foo, in "Optical Characterization Techniques for Semiconductor Technology," pp. 170-177, Society of Photo-Optical Instrument Engineers (1981).
3. M. Sternheim, W. van Gelder, and A. W. Hartman, *This Journal*, **130**, 655 (1983).
4. H. P. Kleinknecht and H. Meier, *ibid.*, **125**, 798 (1978).
5. See, for instance, O. S. Heavens, "Optical Properties of Thin Films," pp. 56 ff., Academic Press, New York (1955), but watch out for algebraic errors.
6. P. A. Heimann and R. J. Schutz, *This Journal*, **131**, 881 (1984).

Drastic Changes in the Electrical Resistance of Gold-Doped Silicon Produced by a Hydrogen Plasma

A. Mogro-Campero,* R. P. Love, and R. Schubert¹

General Electric Research and Development Center, Schenectady, New York 12301

ABSTRACT

High resistivity silicon samples were prepared by gold doping and subjected to a hydrogen plasma for various times (0-4h) and temperatures (130°-450°C). Spreading resistance profiles show that the resistance decreases to values close to those of the original wafers with no gold doping up to a depth defined as the penetration depth. This behavior is consistent with the neutralization of the compensating property of gold in silicon. The derived effective diffusion coefficient $D = 9 \times 10^{-7} \exp(-0.45/kT) \text{ cm}^2\text{s}^{-1}$, with kT in electronvolts for the temperature range 130°-275°C, is in reasonable agreement with an extrapolation of the diffusion coefficient reported by others for tritium in silicon at 400°-500°C. The penetration depth seems to be related to the diffusion of hydrogen, primarily in atomic form. The implied high solubility of hydrogen in our samples ($\geq 10^{15} \text{ cm}^{-3}$) is probably determined by defects and impurities. The results of annealing experiments on plasma-treated samples are compatible with further diffusion of the neutralizing agent at the annealing temperatures. Reduced resistivities persist even after a 500°C anneal in nitrogen for 1h.

Analysis by deep-level transient spectroscopy (DLTS) has recently revealed that the concentration of the gold-related deep levels in silicon can be significantly reduced up to depths of several micrometers by exposing heated crystalline samples to a hydrogen plasma (1, 2). This paper reports on the first work on changes in resistance of gold-doped silicon samples due to exposure to hydrogen plasma. The probing depth of the DLTS technique is limited by avalanche breakdown in the silicon, whereas the depth limitation in resistance profiling is determined only by sample thickness. The changes in resistance we observe imply the neutralization of the compensating property of gold in silicon, and are consistent with obser-

vations of the reduction of the concentration of gold-related deep levels by DLTS (1, 2). Gold in silicon introduces both a donor and an acceptor deep level. When the concentration of gold becomes comparable to or greater than the shallow dopant concentration, the compensating action of the gold levels leads to drastic resistivity increases (3). Silicon wafers (n-type) had gold diffused from their back surfaces, and the resulting high resistivity samples were used in the experiments reported here. The samples were heated to various temperatures while being subjected to a hydrogen plasma for periods of 0-4h. Samples with an oxide cap and with an oxide and aluminum layer were also exposed. Spreading resistance profiles were used to measure the depths to which the neutralization of the compensating property of gold was present. The results are consistent with the diffusion of atomic hydrogen.

*Electrochemical Society Active Member.

¹Present address: Department of Physics, University of Cincinnati, Cincinnati, Ohio 45221

Procedure

The starting wafers were n-type CZ silicon, 4-10 Ω -cm, and orientation (111). Gold was evaporated onto the back of the 350 μ m thick samples, and diffused in nitrogen at 1000°C for 30 min. The solid solubility of gold in silicon at this temperature [10^{16} cm $^{-3}$ (3)] is about an order of magnitude higher than the shallow dopant (phosphorus) concentration ($\sim 10^{15}$ cm $^{-3}$) of the starting wafers. Figure 1 (curve a) shows that the resistivity of a gold-doped sample is much higher than that of the starting wafers. The resistivity gradient is consistent with a higher gold concentration near the surface, as observed also by others (4). In cases where samples were used with a thermally grown oxide layer, oxidation preceded gold diffusion; if an aluminum layer was evaporated on top of the oxide, the evaporation was performed after gold diffusion.

Samples were placed on the lower plate of a parallel-plate system, heated to a given temperature, and subjected to a hydrogen RF plasma (13.56 MHz and 100W) at 0.5 torr. The walls of the chamber are electrically grounded, and the lower plate with the sample is isolated and thus at a floating potential. Before removing the sample, the temperature was allowed to decrease to 80°C while the sample was still subjected to the plasma. A portion of the sample was angle lapped, and spreading resistance was measured vs. depth from the top silicon surface. No change in resistance profile was observed for a starting sample (prior to gold doping) subjected to a hydrogen plasma at 200°C for 1h.

Results and Discussion

Figure 1 (curves b and c) shows spreading resistance vs. depth for gold-doped samples which have been subjected to a hydrogen plasma for 1h at 200°C. We observe that the compensating property of gold has been largely neutralized in the first few micrometers from the surface, as shown by the decrease in resistance to values close to those of the starting wafers prior to gold doping. No evidence for neutralization was observed for a gold-doped sample subjected to the hydrogen ambient for 1h at 200°C, but with no RF power applied. Since curves b and c in Fig. 1 correspond to different portions of the same sample, the differences can be ascribed to experimental variability. The depth to which a substantial decrease in resistance persists is defined as x_p (penetration depth), and was evaluated graphically from the spreading resistance plots. The penetration depth was estimated by approximating the resistance curve with two straight line segments in the region of interest and finding their inter-

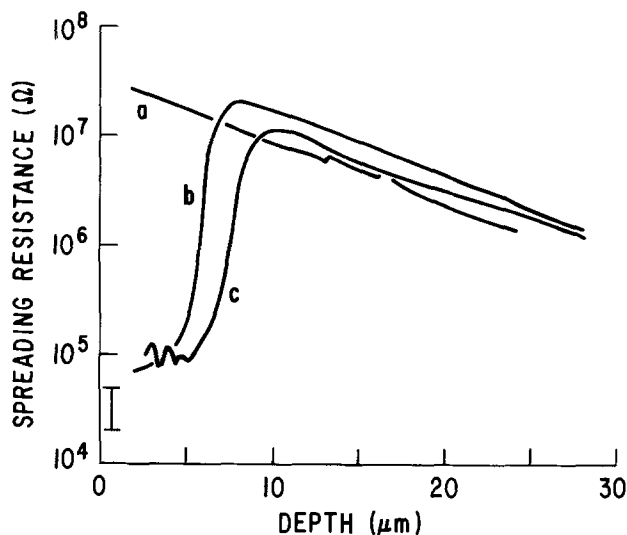


Fig. 1. Spreading resistance vs. depth; the bar indicates the range of resistance values of the starting wafers (prior to gold doping). Curve a: Gold-doped sample. Curve b: Gold-doped sample subjected to a hydrogen plasma at 200°C for 1h. Curve c: Another portion of the sample in b.

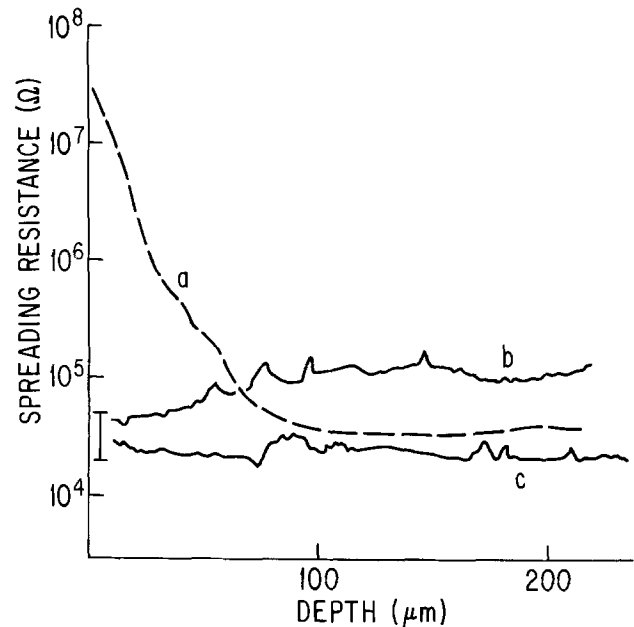


Fig. 2. Spreading resistance vs. depth. The bar indicates the range of values of the starting wafers (prior to gold doping). Curves correspond to gold-doped samples. Curve a: no plasma treatment. Curve b: hydrogen plasma for 2h at 300°C. Curve c: hydrogen plasma for 2h at 450°C.

section. One line approximates the region of rapid rise in resistance, and the other the slower decrease in resistance at greater depth. For curves b and c of Fig. 1, the values of x_p are 7 and 9 μ m, respectively. Figure 2 shows that, for high temperatures and long exposure times, the penetration depth can only be determined as a lower limit value for the gold-doped samples used here because the region of high resistance values ends at depths ≥ 60 μ m.

Figure 3 shows the penetration depth vs. the square root of time for a constant temperature of 200°C. A linear relationship is consistent with a diffusion process if the diffusion coefficient is constant with depth. Within experimental variability, a linear relationship is observed at times ≥ 1 h.

It has been usually presumed that effects similar to those reported here after hydrogen plasma exposure, such as the neutralization of gold levels in silicon (1, 2) and resistivity changes in boron-doped silicon (5), are due to the diffusion of atomic hydrogen into the sample. However, unresolved questions about the actual incorporation depth of hydrogen in silicon (6-8) have kept this an open question. The high concentration of hydrogen residing near the surface may facilitate defect generation via local strain (8), and the particular defect distribution due to hydrogen bombardment (9) may also play a role in the neutralization observed. The relative importance of these mechanisms can be expected to be different in a sample with a substantial top layer of thermal oxide. A plasma-exposure experiment for 1h at 200°C was performed on a sample with 0.1 μ m of thermal oxide. The resulting spreading resistance profile was similar to those obtained from samples without the thick oxide layer. The diffusion coefficient of deuterium molecules in vitreous silica at 200°C is 8×10^{-9} cm 2 -s $^{-1}$ (10), which is sufficiently high to make the oxide appear as an ineffective barrier to hydrogen. The experiment is, therefore, consistent with hydrogen diffusion's being the primary agent responsible for the observed neutralization. Recent indirect evidence (11, 12) also points strongly toward hydrogen diffusion, particularly results showing the neutralization of gold levels by electrolytic doping (12), in which case the effects of particle bombardment are absent.

In another experiment, we subjected a gold-doped sample with 0.1 μ m of oxide and an additional 1 μ m of evaporated aluminum to the hydrogen plasma for 2h at 200°C. There was no effect on the resistance profile com-

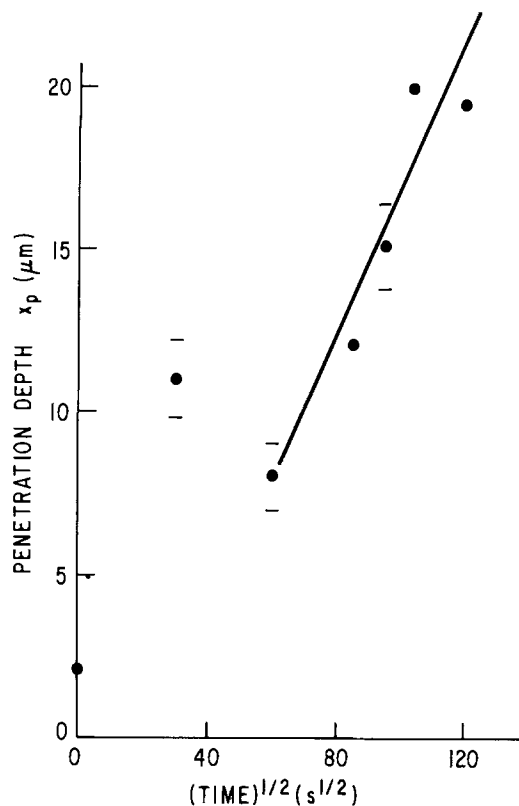


Fig. 3. Penetration depth vs. square root of time for samples subjected to a hydrogen plasma at 200°C. Dashes above and below some data points indicate values obtained on separate portions of the same sample and serve to illustrate experimental variability. A finite penetration depth is observed even for $t = 0$ because of the cooling sequence. This artifact is most significant for short times. The line shows that within experimental variability, a linear relationship is approximately obeyed for times ≥ 1 h.

pared to a gold-doped sample which had not been exposed to plasma. The diffusion coefficient of hydrogen in the aluminum layer would have to be $\leq 10^{-13} \text{ cm}^2\text{-s}^{-1}$ for the $1 \mu\text{m}$ layer to be an effective barrier. The reported values for the diffusion coefficient of hydrogen in aluminum are a strong function of purity (13, 14) and are spread over many orders of magnitude when extrapolated to the lower temperatures of our experiments. Although the starting material used in the evaporator is highly pure aluminum, we have not analyzed the purity of the deposited aluminum layer. However, the effective low diffusivity implied by our experiment may be related to the oxide layer which will inevitably form on the aluminum after exposure to air. The extrapolated diffusivity of atomic hydrogen in sapphire (15) is extremely low, so that a thin layer of, say, 10 nm would be sufficient to act as a barrier for the hydrogen at the temperature of our experiment.

In order to obtain diffusion coefficients D from the observed penetration depths x_p , we assume a constant surface concentration solution to the diffusion equation (16), from which we use the approximate expression $x_p = 5.4 (Dt)^{1/2}$, where t is time. The calculated diffusion coefficient vs. temperature is shown in Fig. 4. In terms of the simple expression $D = D_0 \exp(-E_a/kT)$, the activation energy E_a seems to increase at the higher temperatures, although we do not have sufficient data to establish this trend. By linear least squares fitting, we obtain $D = 9 \times 10^{-7} \exp(-0.45/kT) \text{ cm}^2\text{-s}^{-1}$ with kT in electronvolts. Two experimental points obtained in a similar manner by others from the neutralization of gold levels by a hydrogen plasma using deep level transient spectroscopy (17) are also shown in Fig. 4. They are in reasonable agreement with our data. Extrapolations from direct measurements of atomic hydrogen diffusion in silicon at 1100°-1200°C (18) and tritium diffusion in silicon at 400°-500°C

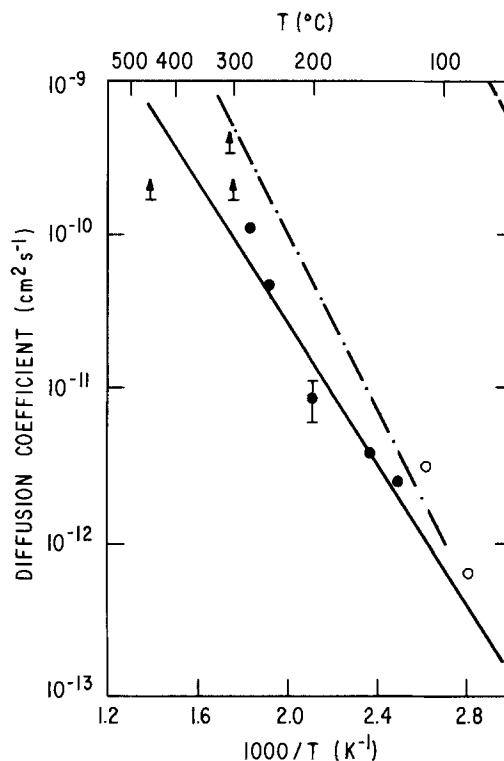


Fig. 4. Diffusion coefficient (derived from penetration depth) vs. temperature. Solid circles and lower limits are from the present work. The data point for 200°C is an average of five independent measurements. The solid line is a least squares linear fit to our data points. The open circles are data reported by others (17). The dashed line and dash-dot line are for atomic hydrogen diffusion (18) and tritium diffusion (19) in silicon.

(19) are also shown in Fig. 4. The activation energies obtained in those studies were 0.48 and 0.56 eV, respectively.

An important matter to consider is the relative roles of molecular or atomic diffusion in a given experiment. Three states of hydrogen in silicon have been suggested (20): atomic, molecular, and one in which hydrogen bonds with a silicon atom. When considering other impurities and defects, other combinations such as a gold-hydrogen association suggested by our experiment will probably come into play. The gold density being neutralized in our experiments is $\geq 10^{15} \text{ cm}^{-3}$ (the doping density before gold doping). The hydrogen solubility data at 1 atm (18) extrapolated to the temperature of our measurements (say, 250°C) is $2 \times 10^3 \text{ cm}^{-3}$. We believe this discrepancy is an indication of the importance of defects and impurities in our case.

Figure 5 shows the effect of isochromal annealing on plasma-treated samples. In general, resistance increases near the surface and decreases at depths greater than the original penetration depth with increasing temperature. This is consistent with a diffusion of the neutralizing agent both toward the surface and into the bulk. The somewhat irregular behavior, such as for the 450°C anneal, may be a measure of experimental variability.

Summary and Conclusions

Samples of high resistivity silicon prepared by gold doping were subjected to hydrogen plasma at various temperatures and times. The resistance is found to decrease to values close to those of the original wafers with no gold doping for a depth (called the penetration depth) which varies approximately as the square root of time. Results from samples covered with thermally grown oxide and with an additional aluminum layer, as well as indications from similar work by others using deep level transient spectroscopy, point to hydrogen diffusion as the mechanism most likely responsible for the observed depths of neutralization. Over the temperature range of 130°-275°C, we obtain $D = 9 \times 10^{-7} \exp(-0.45/kT) \text{ cm}^2\text{-s}^{-1}$,

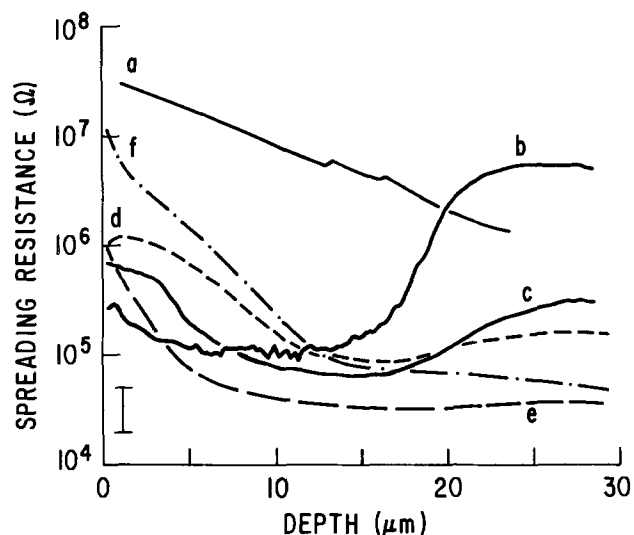


Fig. 5. Spreading resistance vs. depth. The bar indicates the range of resistance values for the starting wafers. All curves correspond to gold-doped samples. Curve a: No plasma exposure, no annealing treatment. Curve b: Exposed to a hydrogen plasma for 1h at 250°C. Curves c-f: Treated as sample in curve b, and then annealed in nitrogen for 1h at 300° c, 400° d, 450° e, and 500° f.

with kT in electronvolts. The activation energy is close to that obtained for atomic hydrogen diffusion in silicon (18) at 1100°-1200°C (0.48 eV) and to that reported for tritium diffusion in silicon (19) at 400°-500°C (0.56 eV). The activation energy for diffusion of molecular hydrogen in silicon has been estimated as 2.7 eV (20). The absolute values of diffusivity in the temperature range of our experiments can be compared with extrapolations of the higher temperature data. The extrapolation of atomic hydrogen (18) gives values a few orders of magnitude higher than ours, but the extrapolation of the tritium data results in comparable values. Extrapolation of solubility data for hydrogen in silicon (18) gives values which are significantly lower than those which our results imply. We take this as an indication that in our case solubility is dominated by defects and impurities. In conclusion, we believe that the neutralization of gold we observe is related to the diffusion of hydrogen, in which the atomic species is most likely dominant, and that the consequent effective diffusion coefficient and solubility are influenced by defects and impurities which trap hydrogen.

Annealing of samples after plasma exposure shows that the neutralizing effect is diminished near the surface, but increased at depths greater than the original penetration depth with increasing temperature, which is consistent with diffusion of the neutralizing agent in both directions.

The sample does not recover the resistivity profile which was present before plasma exposure even after an anneal of 500°C for 1h.

Acknowledgments

We thank M. Lazzeri and G. Gidley for sample preparation, P. Campbell for information and help with the plasma apparatus, and T. McGee and P. Fitzgerald for spreading resistance measurements.

Manuscript submitted Dec. 10, 1984; revised manuscript received Feb. 24, 1985. This was Paper 382 presented at the New Orleans, Louisiana, Meeting of the Society, Oct. 7-12, 1984.

General Electric Company assisted in meeting the publication costs of this article.

REFERENCES

1. S. J. Pearton and A. J. Tavendale, *Phys. Rev. B*, **26**, 7105 (1982).
2. A. J. Tavendale and S. J. Pearton, *J. Phys. C*, **16**, 1665 (1983).
3. W. M. Bullis, *Solid-State Electron.*, **9**, 143 (1966).
4. M. Hill, M. Lietz, and R. Sittig, *This Journal*, **129**, 1579 (1982).
5. J. I. Pankove, D. E. Carlson, J. E. Berkeyheiser, and R. O. Wance, *Phys. Rev. Lett.*, **51**, 2224 (1983).
6. S. J. Pearton and E. E. Haller, *J. Appl. Phys.*, **54**, 3613 (1983).
7. S. J. Pearton, J. M. Kahn, and E. E. Haller, *J. Electron. Mater.*, **12**, 1003 (1983).
8. J. M. Kahn, S. J. Pearton, and E. E. Haller, *Bull. Am. Phys. Soc.*, **29**, 208 (1984).
9. R. G. Frieser, F. J. Montillo, N. B. Zingerman, W. K. Chu, and S. R. Mader, *This Journal*, **130**, 2237 (1983).
10. J. E. Shelby, *J. Appl. Phys.*, **48**, 3387 (1977).
11. S. J. Pearton, J. M. Kahn, W. L. Hansen, and E. E. Haller, *ibid.*, **55**, 1464 (1984).
12. S. J. Pearton, W. L. Hansen, E. E. Haller, and J. M. Kahn, *ibid.*, **55**, 1221 (1984).
13. K. Papp and E. Kovacs-Csetenyi, in "Proceedings of the International Conference on Diffusion in Metals and Alloys," DIMETA 2, Tihany, Hungary, F. J. Kedves and D. L. Beke, Editors, p. 450, Trans. Tech. SA, Switzerland (1982).
14. A. Csanady, K. Papp, and K. Pasztor, *Mater. Sci. Eng.*, **48**, 35 (1981).
15. K. Hauffe and D. Hoeffgen, *Ber. Bunsenges, Phys. Chem.*, **74**, 537 (1970).
16. J. C. C. Tsai, in "VLSI Technology," S. M. Sze, Editor, p. 169, McGraw-Hill, New York (1983).
17. W. L. Hansen, S. J. Pearton, and E. E. Haller, *Appl. Phys. Lett.*, **44**, 606 (1984).
18. A. van Wieringen and N. Warmoltz, *Physica*, **22**, 849 (1956).
19. T. Ichimaya and A. Furuichi, *Int. J. Appl. Radiat. Isotopes*, **19**, 573 (1968).
20. S. Tiansheng, S. N. Sahu, J. W. Corbett, and L. C. Snyder, *Sci. Sinica A*, **27**, 98 (1984).

Ion Beam-Assisted Etching of Aluminum with Chlorine

L. Y. Tsou¹

AT&T Technologies, Incorporated, Princeton, New Jersey 08540

ABSTRACT

Ion beam-assisted etching of aluminum, in which an inert gas ion beam and a reactive gas are simultaneously applied to a substrate, was investigated for its fine line etching capability. As a result of the collimated nature of the ion beam, extremely high resolution, anisotropic etching of aluminum samples patterned with trilevel photoresist was demonstrated. Etch rates of 2000 Å/min were routinely achieved in this ion beam-assisted etching mode. In addition, etching behavior as a function of ion energy, ion flux, and reactive gas intensity was also examined.

Plasma etching and, in particular, reactive ion etching are essential to the fine line pattern transfer in current fine line semiconductor processes (1). The directionality of ions through the plasma sheath is responsible for the anisotropic profile of the etch. This ion-enhanced gas-surface interaction plays an important role in the etching process. However, it is difficult to control the behavior of the ion, its energy, or its intensity in the plasma.

On the other hand, the ion energy, current density, and the direction of the ion can be independently controlled in ion milling, in which an inert gas ion beam is employed to physically sputter off the unmasked material. The collimated ion beam has extremely high resolution. Feature sizes as small as 100 Å have been produced (2). However, the low etch rate and the lack of selectivity for different materials limit its application.

The replacement of the inert gas with a reactive gas in a conventional ion milling machine, reactive ion beam etching (RIBE) (3-6), has been recently reported to be able to enhance the etch rate and selectivity due to the chemical nature of the reactive ion, while it still preserves the inherent anisotropy. Moreover, the independent control of the process parameters will help to elucidate the basic mechanism and kinetics of the etching, and will be useful to our understanding of the complicated plasma etching process.

In another approach, a separate supply of reactive gas coupled with an inert gas ion beam (7) has an etching behavior similar to RIBE, while the corrosive attack of the ion gun is minimized. Furthermore, the reactive species and inert gas can be independently controlled in this arrangement. This setup (8) was employed to quantitatively illustrate the role that ions play in plasma etching. Here, we report the results of aluminum etching in this ion beam-assisted etching mode (IBAE). Etch rate as a function of ion flux, ion energy, and chlorine pressure was extensively investigated. The anisotropic wall profile and higher etch rate demonstrates directly that etching is enhanced by the ion bombardment. The independent control of the etching parameters, as opposed to the process parameters in the plasma etching, simplifies the interpretation of the experiment data, and quantitative information about the gas-surface interaction is derived.

Experimental

The apparatus setup is schematically shown in Fig. 1. A hot filament ion gun with permanent magnets, manufactured by Ion Tech, Incorporated, was employed as the ion beam source. This 2.5 cm diam source is capable of delivering the beam current density up to 1 mA/cm² at 500 eV. Inert gas was injected directly into the gun. The vacuum chamber equipped with a 6 in. diffusion pump and a water-cooled baffle could be pumped down to 5×10^{-7} torr. The pressure in the main chamber was 1×10^{-4} torr when a discharge was maintained with the xenon flow of 1 sccm. Both the inert gas and the reactive gas were regulated through the mass flow controllers, and the Cl₂ pressure measurement was calibrated with an MKS manometer. The beam current was measured by a Faraday cup

¹ Present address: Philips Laboratories, Briarcliff Manor, New York 10510.

that could be moved out of the way during etching. The sample was placed on a water-cooled holder, which was 10 cm from the ion extraction grid, and was electrically grounded in this study. Low energy electrons were provided by a tungsten filament to neutralize the charge on the substrate.

Results and Discussion

Etching profile.—Anisotropic etching was consistently demonstrated in this study. This indicates that the lateral etch rate of aluminum by Cl₂ alone is very slow and the vertical etching is enhanced by the directional ion beam. It has been reported (9) that Cl₂ could spontaneously react with pure aluminum at a rate independent of ion bombardment. However, anisotropic etching can also be accomplished if the sidewall of the etched feature is passivated to suppress lateral reaction (10). Since the background pressure of the system was about 1×10^{-6} torr, the rate of oxide formation was less than one monolayer per second. In this study, as the removal rate of aluminum was as high as 20 monolayers per second, the observed anisotropic etching cannot be simply described as the result of sidewall passivation by the oxide. It is conceivable that the photoresist species sputtered by the ion beam might protect the sidewall against lateral etching as well. In a separate RIE study of polysilicon with Cl₂ plasma, we found that it was more difficult to achieve an anisotropic wall profile for the wafer patterned with SiO₂ mask than that with the photoresist mask.

An SEM micrograph of a typical etched sample with 1 μm thick aluminum patterned with HPR photoresists is shown in Fig. 2. The linewidth loss measured by the Vicker's image shearing microscope is about 0.9 μm due to the erosion of the round-shaped photoresist. The high

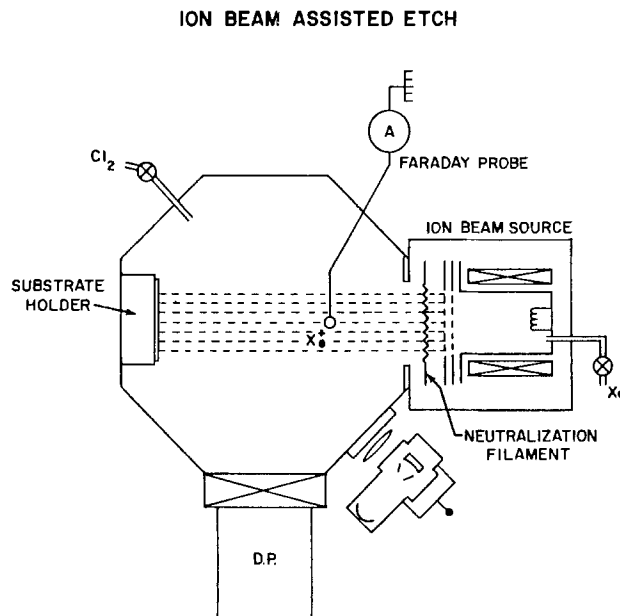


Fig. 1. Schematic diagram of the IBAE machine

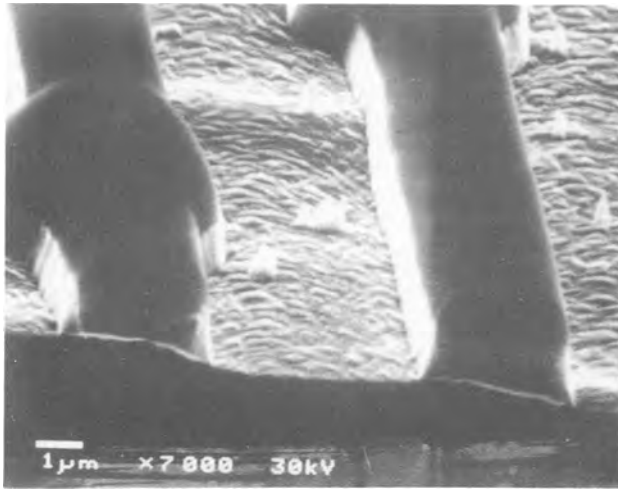


Fig. 2. SEM cross section of the etched aluminum tester patterned with single-layer resist.

resolution capability of the directed ion beam is illustrated in Fig. 3, where an aluminum sample patterned with trilevel resist was etched by IBAE. The structure consists of a 0.75 μm wide line and space with 1.5 μm thick resist on top of 1 μm thick aluminum. There is no measurable linewidth loss after etching through this hard-baked, planarizing photoresist.

Effect of reactive gas.—At a xenon ion energy of 500 eV and the beam current density of 0.75 mA/cm², the aluminum etch rate was studied as a function of Cl₂ pressure. A strong atomic aluminum optical emission line, 396 nm or 309 nm, was monitored during the run. As in reactive ion etching, this time evolution curve determines the induction period to clear the native oxide and the end point of aluminum etching. Figure 4 shows the aluminum etch rate at various Cl₂ background pressures. Etch rates up to 2000 Å/min were obtained at a Cl₂ pressure of 5 × 10⁻⁴ torr. The ion current density monitored by the Faraday cup was only increased by 10% after that amount of Cl₂ was introduced into the system, indicating some backstreaming of Cl₂ into the ion source. Pressures above this limit resulted in an unstable ion beam. A localized high flux of chlorine gas was obtained by supplying the gas through a 0.03 cm diam nozzle about 2.5 cm above the wafer at a 45° angle, while a low background pressure was still maintained in the chamber. Figure 5 illustrates the etch rate vs. gas flow through the nozzle. Etch rates of 4000 Å/min were demonstrated in this configuration. This indicates that the supply of the reactive gas is a rate-

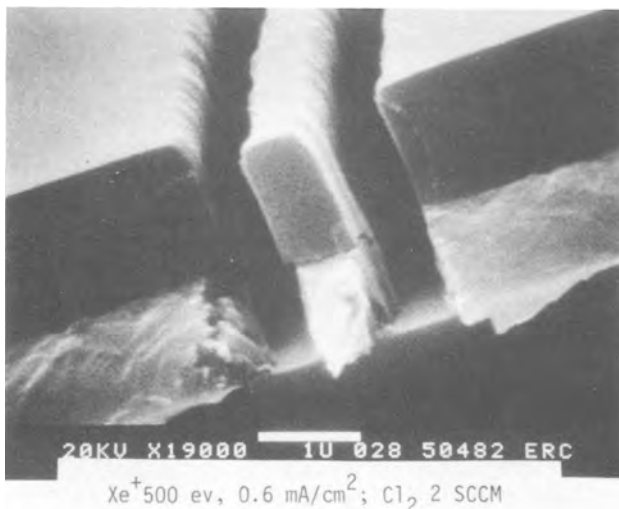


Fig. 3. SEM cross section of the etched aluminum tester patterned with trilevel resist.

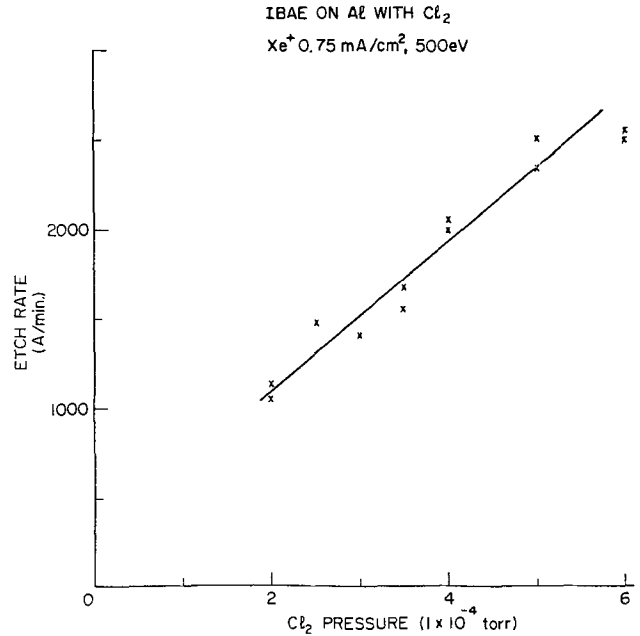


Fig. 4. Aluminum etch rate vs. chlorine pressure

determining step in ion beam-assisted etching of aluminum.

Effect of the ion beam.—The effect of the ion current density on etching was investigated with a fixed ion energy of 500 eV and a constant Cl₂ pressure of 4 × 10⁻⁴ torr. From the time evolution curve of Al optical emission, the total etch time can be divided into two parts, the induction time for native oxide etch and the real etch time for pure aluminum. Since the major mechanism to clear the oxide is by physical sputtering, it was not surprising to find that the induction time was increased as the ion density was decreased. However, the real etch rate for pure aluminum was nearly independent of the current density in the range of 0.40-0.80 mA/cm². (Note that this current

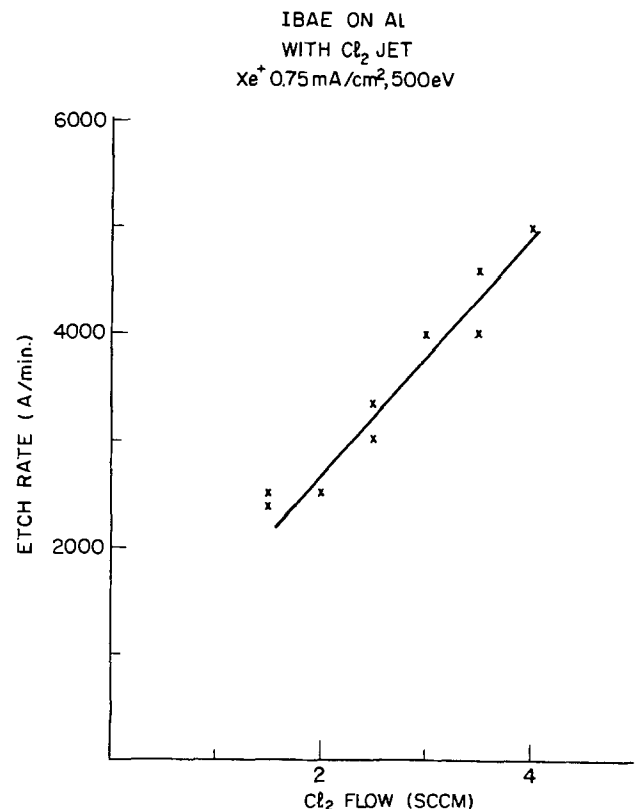


Fig. 5. Aluminum etch rate vs. chlorine flow through nozzle

density corresponds to an ion impact rate of 2-4 ions per aluminum atom per second.)

Etch rate dependence on ion energy in the range of 300-500 eV was measured at a current density of 0.40 mA/cm² and a Cl₂ pressure of 4×10^{-4} torr. Again it is interesting to observe that the etch rate of pure aluminum is insensitive to ion energy in this study. In addition, the etch rate of aluminum assisted by an argon ion is similar to that assisted by a xenon ion in our typical operating condition.

It is well established (11) in the nonreactive ion sputtering that the sputtering rate increases with ion energy initially and then reaches a plateau around 1-5 keV. A recent report (12) on the reactive ion beam etching of aluminum showed that the etch rate increases rapidly with energy in the range of 300-600 eV and starts reaching a plateau after 600 eV. Our observation that etch rate is a weak function of ion energy from 300 to 500 eV in the ion-assisted etching of aluminum may imply that 300 eV is in the plateau region of the sputtering yield curve. Future investigation to extend the ion beam capability to the lower energy side will provide more information.

Reaction probability.—The composition of the etching species in the IBAE configuration can be accurately measured. Considered in this study are the flux of the xenon ion and chlorine molecule. The actual etch rate can be obtained from the emission intensity-time curve. For an ion energy of 500 eV, a current density of 0.4 mA/cm², and a Cl₂ pressure of 4×10^{-4} torr, the aluminum removal rate is 12 monolayers per second. While in the absence of the reactive gas, Cl₂, the physical sputtering yield was measured to be 0.5 atom/ion. From the Cl₂ pressure which was measured by a capacitance manometer with an accuracy of $\pm 5 \times 10^{-5}$ torr, we can estimate the collision rate between Cl₂ and aluminum substrate, and subsequently derive the reaction probability for Al₂Cl₆ formation. The result is (23 \pm 3)% in this IBAE study. Similar value is estimated from Ref. (9), in which Cl₂ flux was low (1/20 of that in this work), but the rate was independent of the ion bombardment energy. However, it was reported recently (13) that without ion bombardment the reaction probability in the same low flux condition was only a few percent. The discrepancy among these data warrants the need of further investigation.

Conclusion

An inert gas ion beam coupled with a reactive gas, Cl₂, was applied to investigate its etching behavior on pat-

terned aluminum. Extremely high resolution, anisotropic etching of the aluminum patterned with trilevel resist was accomplished. An etch rate of 2000 Å/min has been routinely achieved. A high etch rate, 4000 Å/min, was demonstrated when a nozzle jet was employed to supply the reactive gas. As a result of the collimated nature of the ion beam, features with a high aspect ratio (0.75 μ m wide, 2.5 μ m deep) were etched.

The etch rate of aluminum was found to be independent of the ion energy and current density, in the region of 300-500 eV and 0.4-0.8 mA/cm², respectively. However, it was shown that the aluminum etch rate was increased by increasing the Cl₂ pressure. Finally, the reaction probability for AlCl₃ formation was estimated to be 23%.

Acknowledgments

The author would like to thank C. E. Chase for technical assistance and R. E. Woods for providing the SEM micrograph.

Manuscript submitted Feb. 11, 1985; revised manuscript received April 22, 1985.

Philips Laboratories assisted in meeting the publication costs of this article.

REFERENCES

1. C. M. Melliar-Smith and C. J. Mogab, in "Thin Film Processes," J. L. Vossen and W. Kern, Editors, Academic Press, New York (1978).
2. J. M. E. Harper, J. J. Cuomo, and H. R. Kaufman, *J. Vac. Sci. Technol.*, **21**, 737 (1982).
3. D. M. Brown, B. A. Heath, T. Coutumas, and G. A. Thompson, *Appl. Phys. Lett.*, **37**, 159 (1980).
4. T. M. Mayer, R. A. Barker, and L. J. Whitman, *J. Vac. Sci. Technol.*, **18**, 349 (1981).
5. M. A. Bosch, L. A. Coldren, and E. Good, *Appl. Phys. Lett.*, **38**, 264 (1981).
6. S. Matsuo and Y. Adachi, *Jpn. J. Appl. Phys.*, **21**, L4 (1982).
7. M. W. Geis, G. A. Lincoln, N. Efremow, and W. J. Piacentini, *J. Vac. Sci. Technol.*, **19**, 1390 (1981).
8. Y. Y. Tu, T. J. Chuang, and H. F. Winters, *Phys. Rev. B*, **23**, 823 (1981).
9. D. L. Smith and R. H. Bruce, *This Journal*, **129**, 2045 (1982).
10. C. J. Mogab and H. J. Levinstein, *J. Vac. Sci. Technol.*, **17**, 721 (1980).
11. H. H. Anderson and H. L. Bay, in "Sputtering by Particle Bombardment," R. Behrish, Editor, Springer-Verlag, New York (1981).
12. S. Dzioba and H. M. Naguib, *J. Appl. Phys.*, **53**, 4389 (1982).
13. H. F. Winters, *J. Vac. Sci. Technol. B*, **3**, 9 (1985).

The Composition and Properties of PECVD Silicon Oxide Films

P. Pan,* L. A. Nesbit, R. W. Douse, and R. T. Gleason

IBM General Technology Division, Essex Junction, Vermont 05452

ABSTRACT

Plasma-enhanced chemical vapor-deposited (PECVD) silicon oxide films were prepared by the reaction of SiH₄ and O₂. The deposition rate as a function of O₂ flow rate, RF power, and total pressure was obtained. The film composition and properties for samples deposited with different O₂ flow rates were measured. Si-rich films were obtained for the deposition with O₂:SiH₄ flow rate ratio of < 3.5. The refractive index increased and film thickness decreased after samples were annealed. Etch rate in a solution containing ten parts of ammonium fluoride and one part hydrofluoric acid (10:1 BHF) and refractive index decreased by increasing the Si:O ratio in samples. The SiH_n bonds were found for all Si-rich films. Both Si-OH and H-OH bonds were observed for all samples. The phases Si, SiO₂, and SiO_x were found for Si-rich films. At a constant field, the film conductivity increased with increasing Si:O ratio. Evidence of electron traps was observed for PECVD SiO₂ and Si-rich Si-O films.

The PECVD technique is widely used in the semiconductor industry for the deposition of inorganic thin films (1). The advantages of this process are good step coverage and low deposition temperature. The substrate tempera-

ture, RF power, ratio of reactant gases, and total gas pressure are the critical deposition parameters which will affect the composition and properties of the PECVD film (2, 3).

PECVD silicon oxide can be produced by the reaction of silane gas SiH₄ with an oxidizer, such as O₂, N₂O, CO₂,

* Electrochemical Society Active Member.

etc. (4, 5). The ratio of SiH_4 to oxidizer that forms a stoichiometric PECVD SiO_2 film depends on the dissociation energy of the oxidizer gas. The preparation and properties of stoichiometric PECVD SiO_2 films have been reported by many authors (4-9). The physical properties of slightly off-stoichiometric PECVD SiO_x films ($1.5 < x < 2$) also have been reported (10). The deposition and properties of PECVD SiO_2 and Si-rich SiO_x films, using SiH_4 and O_2 as reactant gases, have not been reported.

Recently, the Si-rich oxide film (*i.e.*, the so-called semi-insulating polycrystalline silicon, SIPOS), which was deposited by the conventional chemical vapor deposition (CVD) or low pressure chemical vapor deposition (LPCVD) methods, has been reported to be an excellent material for the passivation of high field transistors (10). The formation and properties of CVD or LPCVD Si-rich oxide have also been studied intensively by many authors (11-14).

The purpose of our work was to study and understand the relationship between the film composition and properties of PECVD SiO_2 and Si-rich PECVD SiO_x films ($0.48 < x < 2$) as a function of deposition parameters. In this paper, the deposition rate as a function of O_2 flow rate, RF power, and total pressure is reported. The film composition and physical and electrical properties for samples deposited with different O_2 flow rates were measured and related to the Si:O ratio in films.

Experimental

PECVD silicon oxide film was deposited in a LFE Model 301 reactor. The system was described in detail in Ref. (3). The reactant gases were SiH_4 (1.5% in Ar) and O_2 (1% in Ar). The RF frequency was 13.562 MHz. After the pressure was reduced to about 20 mtorr, the chamber was backfilled with reactant gases. The SiH_4 gas flow rate was maintained at 0.3 sccm, and samples with different compositions were obtained by varying the O_2 flow rate. Except for the results of deposition rate as a function of deposition conditions, all data reported in this paper are for samples deposited at a temperature of 350°C, with a power of 50W and a total pressure of 1.5 torr.

The Si, O, N, and C concentrations in the PECVD samples were analyzed using an electron microprobe and Auger electron spectroscopy (AES). An ~800 nm thick film was used for electron microprobe analysis. A thick (~700 nm) thermal SiO_2 film was used as the standard to determine the Si and O concentrations. A thin layer of carbon was deposited simultaneously on the standard and the unknown to reduce charging effects. Both the standard and the unknown were peaked during all measurements. The Si K_α and O K_α x-ray intensities were observed for 40s counting time. By using the MAGIC IV computer program (15), the average row counts for at least six points were corrected and converted into atomic percent. A scanning Auger microscope was used to analyze the ~50 nm thick films. The primary electron-beam voltage was 5 kV, and the beam current was 1 μA . Thin thermal SiO_2 , LPCVD Si_3N_4 ($n = 2.01$), and evaporated carbon films were used as the standards for determining the Si, O, N, and C concentrations, respectively.

For thick samples of about 800 nm deposited on bare Si, the infrared (IR) spectra were taken on a Fourier transform infrared (FTIR) spectrometer. For all measurements, the total number of scans was set at 200, and the resolution was 4 cm^{-1} for all measurements.

The refractive index and the relative film thickness, before and after annealing, were measured using an automatic ellipsometer ($\lambda = 632.8 \text{ nm}$). The etch rates in 10:1 BHF at room temperature were measured for both the as-deposited and annealed samples. In this study, all annealing was done at 1000°C in N_2 for 30 min. The film density was obtained by measuring the weight:volume ratio for a film about 800 nm thick. This film thickness was determined by using a Talystep.

Samples for transmission electron microscope (TEM) studies were prepared by etching from the back side of the silicon wafer with a nitric-hydrofluoric acid solution.

The samples were then examined with the electron beam normal to the surface plane with a TEM operated at 120 kV.

Integrated Auger spectra and x-ray photoelectron spectroscopy (XPS) data were taken in a double-pass CMA. The primary electron-beam voltage was 5 kV and the beam current was 0.5 μA . The x-ray used was the Mg K_α line of 1253.6 eV.

I-V data were measured by using a picoampere meter. Current was measured 3s after a step voltage was applied. A voltage source with linear ramping rate of 20 V/s was used for the measurements of dielectric breakdown voltage, which was defined as the applied voltage that induced a current density of $5 \times 10^{-4} \text{ A/cm}^2$ through the film.

Results and Discussion

As shown in Fig. 1, the deposition rate increased rapidly from 17.5 to 38.5 nm/min as O_2 flow rate (R) increased from 0.5 to 1.25 sccm. It also increased slowly for $R > 1.25$ sccm. This can be explained by the strong chemical reaction between Si and O radicals. The increase in O radical concentration will enhance reaction at the surface and/or in the plasma due to the formation of Si-O bonds. When the deposited film is close to the stoichiometry of SiO_2 , the enhancement of this reaction at the surface will be reduced and the deposition rate will tend to level off. The data in Fig. 1 and the film composition as a function of O_2 flow rate (Fig. 3) support this explanation. The dependence of deposition rate on RF power and total pressure is shown in Fig. 2. The increase of RF power increased the electron temperature, which results in increased concentrations of reactant radicals and in turn increases the deposition rate. The increase in total pressure increases the concentrations of reactant gases, but decreases the electron temperature. The deposition rate increased with increasing total pressure, indicating that the concentrations of reactant radicals increased with increasing total pressure. The deviation of film thickness across the wafer was found to be within 8% for samples deposited with a RF power of 50W and a total pressure of 1.5 torr. For other deposition conditions, the deviation was found to be within 15%. From data shown in Fig. 1 and Fig. 2, it is clear that the desired deposition rate can be obtained by using a proper combination of O_2 flow rate, RF power, and total pressure.

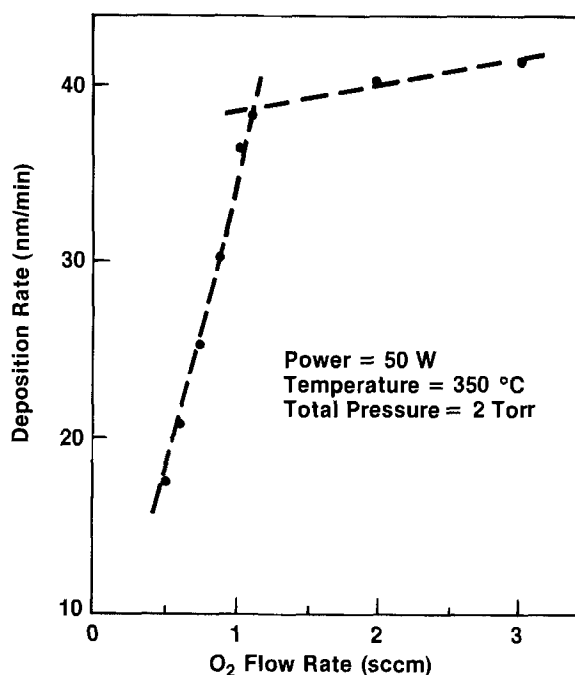


Fig. 1. Deposition rate of PECVD silicon oxide as a function of O_2 gas flow rate.

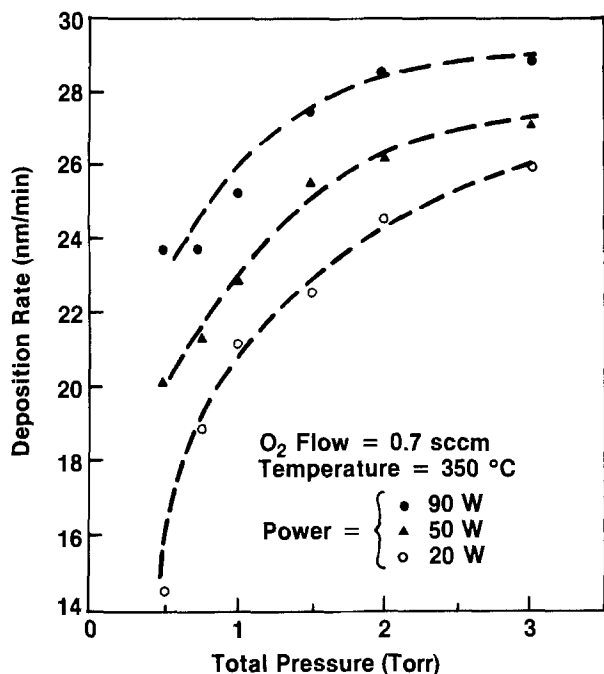


Fig. 2. Deposition rate of PECVD silicon oxide as a function of RF power and total pressure.

The Si and O concentrations in the layer as a function of O_2 gas flow rate (R) are plotted in Fig. 3. The 2σ deviation of the data is ~ 0.4 atom percent (a/o) for oxygen and ~ 0.7 a/o for silicon. Within experimental error, the Si and O concentrations for both as-deposited and annealed samples were found to be identical. From Fig. 3, it is observed that the Si and O concentrations change significantly for $R < 1$ sccm ($O_2:SiH_4 < 3.3$), and approach the stoichiometric values (Si = 33.3 a/o, O = 66.7 a/o) for $R > 1$ sccm. This indicates that a stoichiometric PECVD SiO_2 film can be obtained by using SiH_4 and O_2 as reactant gases. Films deposited on Al-coated wafers were also analyzed. No evidence of Al signal was detected, implying that the penetrating depth of the incident beam is less than the film thickness. This evidence also indicates that the observed Si concentration resulted entirely from deposited mate-

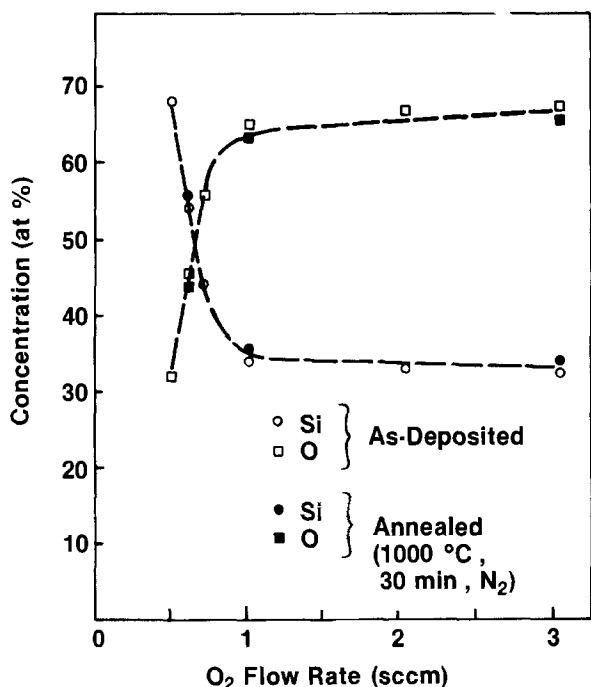


Fig. 3. Si and O atomic percent as a function of the O_2 gas flow rate (R) for both as-deposited and annealed PECVD silicon oxide films.

rial. Because of high background noise, nitrogen was not detectable in any of the samples by electron microprobe analysis.

Auger analysis for thin films, which were deposited under the same conditions as those for thick films, showed that the nitrogen and carbon concentrations are ~ 1 a/o for all Si-rich samples and are undetectable (< 0.1 a/o) in the PECVD SiO_2 samples. Because the chemical reaction between Si and O is stronger than that between Si and N or Si and C, the observation of less contamination in the stoichiometric SiO_2 film, which was deposited with a high O_2 gas flow rate, is expected. Auger depth profiling data for thin samples showed that the film composition as a function of depth is uniform. The oxygen concentration obtained by Auger analysis agrees with that obtained by electron microprobe analysis within 1.7 a/o.

The IR transmission spectra, ranging from 400 to 4000 cm^{-1} , were obtained for all samples. Typical spectra for a Si-rich sample (Si:O = 1.19) are shown in Fig. 4. The O-H ($3600-3400$ cm^{-1}), Si-H ($2250-2120$ cm^{-1}), and Si-O (~ 1053 cm^{-1}) bonds were clearly observed in the as-deposited sample. No Si-H and O-H bonds were found in the annealed sample. The wave number of the main Si-O stretching bond was found to be ~ 1080 cm^{-1} for the PECVD SiO_2 film, and between 1045 and 1060 cm^{-1} for the PECVD Si-rich films. After annealing, the wave number of the Si-O bond was found to increase to ~ 1095 cm^{-1} for all samples. For PECVD SiO_2 , the other Si-O stretching bond was found to decrease from 820 to 810 cm^{-1} and the symmetric O-Si-O bond was found to increase from 450 to 465 cm^{-1} after annealing. The full width at half maximum (FWHM) of the Si-O stretching bond was found to be ~ 100 cm^{-1} for PECVD SiO_2 , and between 120 and 150 cm^{-1} for the PECVD Si-rich sample. After annealing, the FWHM value was reduced by about 10-30 cm^{-1} . Compared with results for thermal SiO_2 (16) and CVD Si-rich SiO_x (17), we found that the wave number of Si-O stretching bonds was lower, the FWHM value was larger, and the change in both wave number and FWHM value upon annealing was larger for PECVD Si-O films. The change in degree of oxygen deficiency, film density, and/or strain in materials will result in a shift in IR stretching bonds. The presence of larger amounts of hydrogen in PECVD oxide films will result in oxygen deficiency and lower film density. The wave number and FWHM values before and after annealing are listed in Table I.

Typical IR spectra from 1700 to 4000 cm^{-1} for three Si-rich samples of different Si:O ratios are shown in Fig. 5. Two peaks in the Si-H stretching region are clearly observed. The high wave number peak is at 2250 cm^{-1} and

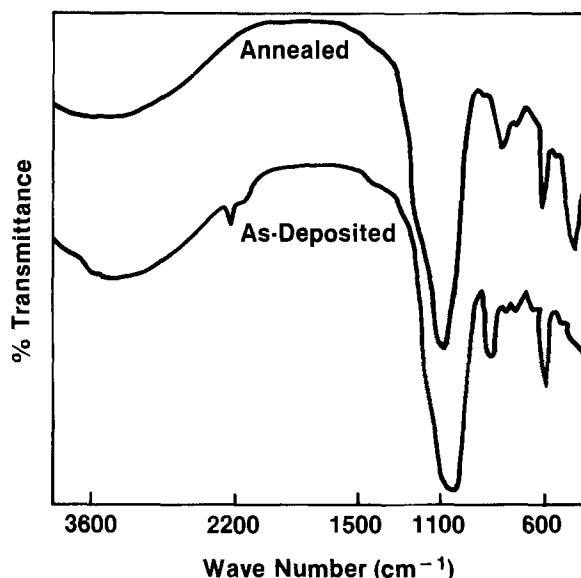


Fig. 4. Typical IR transmission spectra from 400 to 4000 cm^{-1} for sample with Si:O = 1.19.

Table I. Wave number (ν) and the full width at half maximum (FWHM) of the Si-O bond, and the ratio of the Si atomic percent to O atomic percent for samples at different O₂ gas flow rates (R)

R (sccm)	Si:O	ν (cm ⁻¹)	ν^a (cm ⁻¹)	FWHM (cm ⁻¹)	FWHM ^a (cm ⁻¹)
3	0.5	1078	1096	103	89
1	0.53	1076	1092	102	87
0.7	0.8	1057	1096	120	112
0.6	1.19	1053	1096	150	125
0.5	2.05	1046	1101	154	123

^a Annealed films.

is attributed to the Si-H group in amorphous SiO₂ (a-SiO₂). This peak is close to the SiH₂ peak with two oxygens bonded to the Si atom as reported by Lucovsky (18). The low wave number peak was found to shift from 2150 to 2120 cm⁻¹ as the Si:O ratio increased from 0.8 to 2.05. This peak is attributed to the Si-H group in amorphous Si (a-Si). Compared to the results of Brodsky *et al.* (19) on a-Si deposited by the glow discharge method one finds that the candidates attributed to these peaks are SiH₃ and SiH₂. The ratio of the intensity of the low wave number peak to that of the high wave number peak was found to increase from 0.6 to 1.2 with increasing Si:O ratio. These results also suggest that the high and low wave number peak should be attributed to the Si-H group in a-SiO₂ and a-Si, respectively. This observation of SiH_x ($x = 2$ or 3) in the deposited films suggests the deposition of major radicals in SiH₄ plasma (SiH₃ or SiH₂). Two peaks were also clearly observed in the O-H region. Following the results of Pliskin (16), the peak at 3640 cm⁻¹ was attributed to the Si-OH bond and the peak at 3400 cm⁻¹ was attributed to H-OH. The intensities per micrometer of the Si-H and O-H bonds for all samples are shown in Fig. 6. The relative concentrations of Si-H and O-H bonds from sample to sample can be obtained by comparing the relative optical densities.

As reported by Brodsky *et al.* (19), the concentration of Si-H bonds (N) can be written as

$$N = \frac{(1 + 2\epsilon_m^2)(\epsilon_m)^{1/2}}{9\epsilon_m} \cdot \frac{N_A}{(\Gamma/\xi)} \int \frac{\alpha(\omega)}{\omega} d\omega \quad [1]$$

where ϵ_m is the dielectric constant of the matrix, N_A is Avogadro's number, Γ is the absorption strength of the Si-H bond (cm²/m-mol) and ξ is the number of SiH_x bonds contributing to the absorption process. The value of (Γ/ξ) was reported (19) to be nearly equal to 3.5 for all SiH_x groups. By using Eq. [1], the Si-H concentrations in the a-SiO₂ and a-Si matrices were found to be about 3.4×10^{21} and 7×10^{21} cm⁻³, respectively, for the sample with Si:O

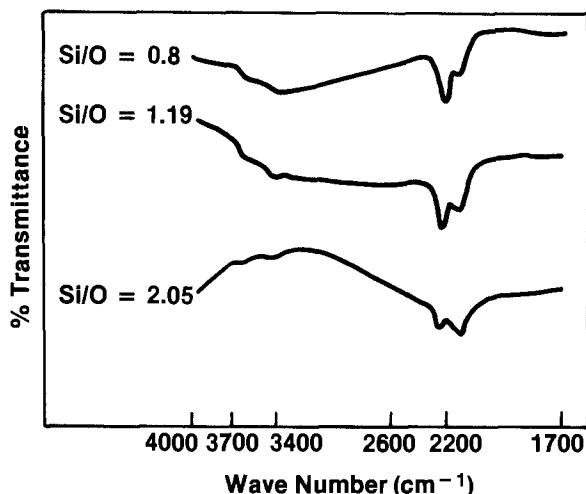


Fig. 5. IR transmission spectra from 1700 to 4000 cm⁻¹ for three samples with different film compositions.

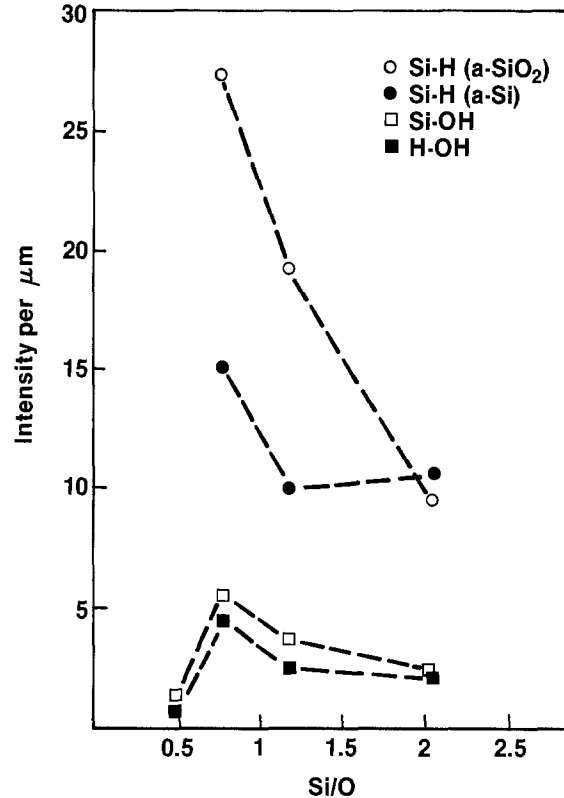


Fig. 6. Intensity per micrometer of Si-H (a-SiO₂), Si-H (a-Si), Si-OH, and H-OH peaks vs. the Si:O ratio for PECVD oxide films.

= 2.1. These values were found to be at least 100 times larger than that for CVD Si-rich oxides reported by Hartstein *et al.* (20).

Pliskin (16) showed that the concentrations of Si-OH and H-OH bonds can be written as

$$W = (-14A + 89B)(2.2/\rho) \quad [2]$$

$$S = (179A - 41B)(2.2/\rho) \quad [3]$$

where W is the weight of H-OH (including H₂O in the easily removed silanol) and S is the atom percent of OH as silanol. A and B are the optical density per micrometer for the Si-OH and H-OH bonds, respectively, and ρ is the film density. From Eq. [2] and [3], and the measured film density listed in Table II, the concentrations of H-OH and Si-OH bonds for the sample with Si:O = 1.19 were found to be 9.8×10^{19} and 4.9×10^{20} cm⁻³, respectively. These values also were found to be about 100 times larger than that for the CVD Si-rich oxide (20). An increase in deposition temperature or RF power will reduce the amount of hydrogen in as-deposited films.

Comparing the IR transmission spectra for different film thickness, one finds that Si-H and O-H bonds were clearly observed in thick samples (~800 nm), but were not detected in thin (50 nm) samples. Since the intensities of the Si-H and O-H bonds depend on the film thickness, the Si-H and O-H bonds must exist in the bulk of the film and are not a property of the film surface.

Table II. Deposition rate (r) and film density (ρ) as a function of different O₂ gas flow rates (R) for PECVD silicon oxide deposited at temperature of 350°C, with RF power of 50W, and total pressure of 1.5 torr

R (sccm)	r (nm/min)	ρ (g/cm ³)	ρ^a (g/cm ³)
3	41.2	2.09	2.22
1	36.5	2.07	2.24
0.7	25.3	2.07	2.26
0.6	20.8	2.02	2.28
0.5	17.5	1.98	2.30

^a Annealed films.

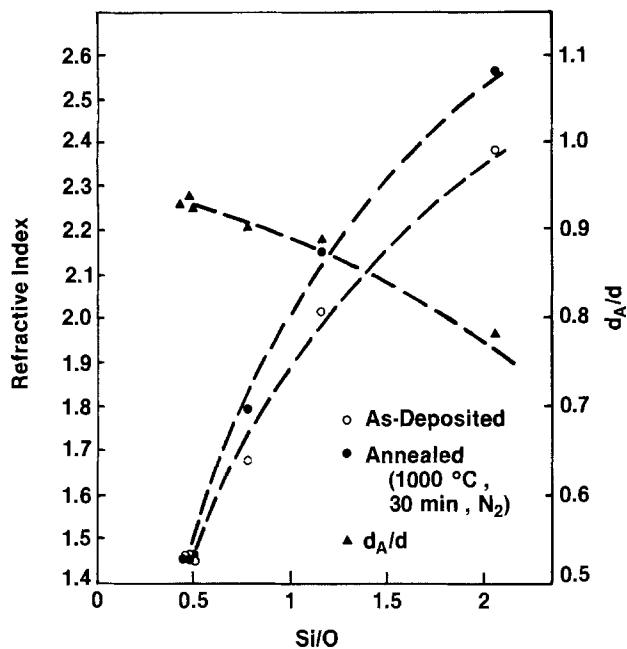


Fig. 7. Refractive index, before and after annealing, and relative film thickness (d_A/d) as a function of Si:O ratios.

The refractive index (n) of as-deposited and annealed samples and the relative film thickness (d_A/d) as a function of the Si:O ratio are shown in Fig. 7. The quantities d and d_A are the film thicknesses before and after annealing, respectively. From this figure, it is clear that d_A/d decreases with increasing Si:O ratio. Because contamination in the Si-rich films is only 1.0 a/o, and the refractive index of the CVD Si_3N_4 film is only 2.01, the observation of a higher n value for higher Si:O ratios is believed to be due mainly to the presence of excess Si in the Si-rich samples. The refractive index was also found to increase after annealing. The increase in film density after annealing could be responsible for this result. The behavior of the denser film having a higher refractive index was also reported in the literature (5, 16).

Comparing the difference in refractive index (Δn) before and after annealing, one finds that Δn of the Si-rich sample is larger than that of PECVD SiO_2 . The d_A/d values for all samples were found to be less than 0.93, which also implies a densifying effect after annealing. The observation of a larger Δn value and smaller d_A/d value for Si-rich samples strongly suggests that the change in film density before and after annealing for the Si-rich film is larger than that of the PECVD SiO_2 film. The presence of higher amounts of hydrogen discussed earlier in the as-deposited films is believed to be one of the causes of this behavior.

The etch rate as a function of Si:O ratio for as-deposited and as-annealed samples is shown in Fig. 8. The etch rate of thermal SiO_2 and annealed PECVD SiO_2 films are comparable, and the etch rate for the unannealed PECVD SiO_2 film is about 1.7 times that of thermal SiO_2 . This result indicates that the film density plays an important role in etch rate; the denser the film, the lower the etch rate. The presence of weaker Si-H bonds is another reason for the higher etch rate for the as-deposited samples. Due to the presence of excess Si in the Si-rich film, a decrease in etch rate with increasing Si:O ratio for the annealed samples is expected. The random fluctuation of the etch rate with respect to the Si:O ratio for the as-deposited films is believed to be due to the complex effects of film density and film composition.

SEM pictures for the etched surfaces of six samples are shown in Fig. 9. All of the pictures were taken after the samples had been dipped in 10:1 BHF for 1 min. It is clear from this figure that the etched surface of the unannealed Si-rich sample is much rougher than the others, possibly as a result of porosity. No roughness was

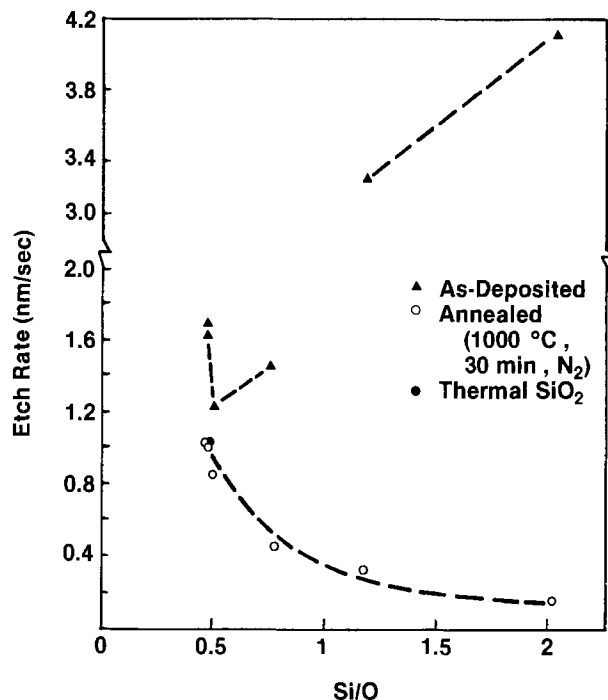


Fig. 8. Etch rate for as-deposited and for annealed samples vs. Si:O ratio.

observed on the surface of the PECVD SiO_2 films (Si:O = 0.88), and only slight roughness was found on the annealed Si-rich samples.

Two as-deposited Si-rich films of differing oxygen concentrations (~ 11.8 and 36.4 a/o) were analyzed via TEM. The film containing ~ 36.4 a/o oxygen had an electron diffraction pattern similar to, but more diffuse than, that of thermal SiO_2 , indicating a fundamental structural difference between the Si-rich film and thermal SiO_2 . By imaging a portion of the first diffuse diffraction ring near the Si (111) position, small precipitates about 1 nm in diameter were observed in dark field. Because the AES and XPS data show the presence of excess Si in this sample, the precipitates are probably clusters of amorphous Si. No such clusters or precipitates were observed in thermal SiO_2 .

The Si-rich film with an oxygen concentration of ~ 11.8 a/o yields an electron diffraction pattern similar to that of PECVD Si. For both the Si-rich oxide and PECVD Si films, the first diffuse diffraction ring is at the same position as the (111) polysilicon ring. The second diffuse ring has an intensity maxima between the (220) and (311) polysilicon ring positions. Hamasaki *et al.* (11) have demonstrated that silicon crystals with a mean diameter less than or equal to 2 nm show overlapping (220) and (311) Si diffraction peaks. Darkfield microscopy of the first dif-

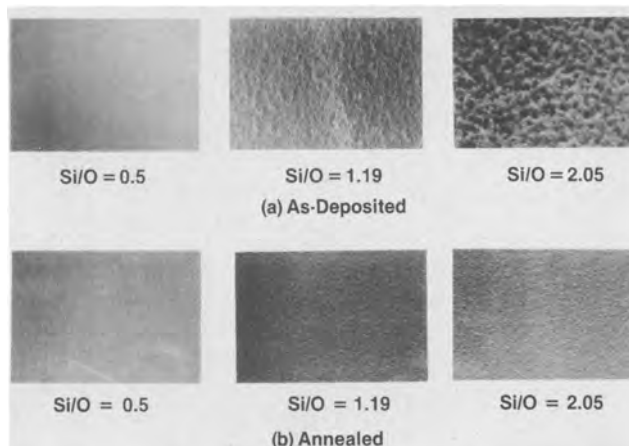


Fig. 9. SEM pictures of etched surface of six samples

fuse ring produced by the Si-rich film and by a PECVD Si film shows 1 nm precipitates, which is consistent with the calculation of Hamasaki *et al.* (11). These results indicate the presence of Si clusters in PECVD Si-rich Si-O films.

The Si grain diameters of annealed films, measured in dark field by imaging the Si (111) ring, were 10, 5, and 1 nm for samples with oxygen concentrations of 7.8, 22.8, and 36.4 at%, respectively. The two films with lower oxygen concentrations have distinct diffraction rings which are characteristic of polycrystalline silicon. However, the diffraction patterns of the film with an oxygen concentration of ~36.4 at%, before and after annealing, are nearly identical. Plots of the Si cluster size as a function of oxygen concentration for the as-deposited and annealed films are shown in Fig. 10. From this figure, one finds that the Si grain size decreases with increasing oxygen concentration for a constant annealing time and temperature, and the Si grain size for the Si-rich sample is nearly constant. These results, which are similar to those reported on CVD Si-rich oxide (11) and LPCVD Si-rich oxide (13), indicate that the presence of oxygen inhibits the growth of Si grains during annealing.

Figure 11 shows the integrated Auger Si LVV spectra for clean Si, the PECVD Si-rich oxide, and thermal SiO₂. An intermediate peak at ~83 eV, similar to those observed for the CVD Si-rich samples (21), was observed for the PECVD Si-rich oxide film. This peak has also been observed at the SiO₂/Si interface (22) and on the Si surface during the initial oxidation stage (23). Following the report of Helms (22), this intermediate peak was attributed to the presence of the transition phase SiO_r in the Si-rich film. The peak at ~90 eV for the Si-rich film corresponds to the main peak for clean Si. The AES data thus establish the presence of Si, SiO₂, and SiO_r phases in the PECVD Si-rich Si-O film.

The Si 2P XPS for a PECVD Si-rich oxide film is shown in Fig. 12. The binding energies of the two peaks are at ~103 and 99 eV attributed to the Si 2P peaks in the matrices of SiO₂ and free Si, respectively. Because of the unsymmetrical shape of the peaks, more than two gaussian curves are necessary to fit these data. This observation is similar to results reported on CVD and LPCVD Si-rich oxide (24, 25). The presence of an intermediate gaussian curve suggest the presence of the transition phase SiO_r. Based on similar observations of SiO_r at the SiO₂/Si interface (22, 26), the presence of SiO_r at the boundary of a Si cluster and the SiO₂ region is expected. The observation of Si, SiO₂, and SiO_r phases by XPS for PECVD Si-rich Si-O films is consistent with results obtained by TEM and AES analysis. No difference in the integrated Auger Si LVV spectra and the XPS data for both the PECVD SiO₂ and thermal SiO₂ samples was observed.

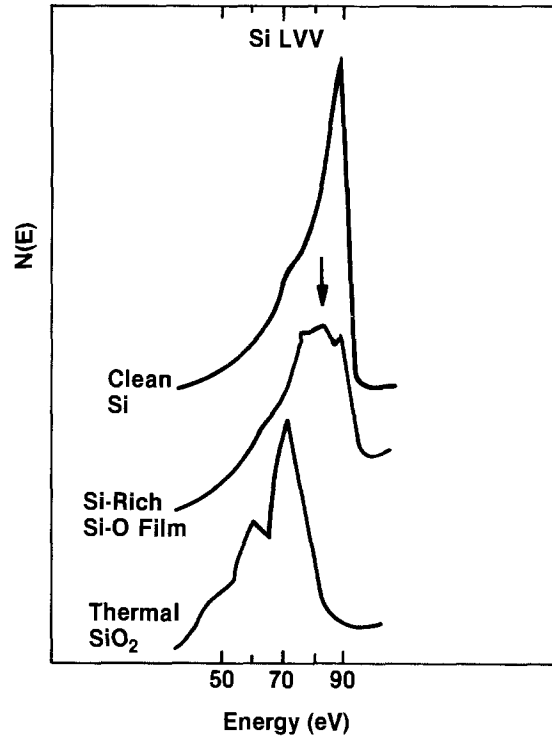


Fig. 11. Integrated Auger Si LVV spectra $N(\epsilon)$ for clean Si, PECVD Si-rich oxide, and thermal SiO₂.

I-V data for three Si-rich samples about 190 nm thick are shown in Fig. 13. The Al/Si-rich Si-O/Si structure was used. From these data, one finds that the conductivity is lower for samples deposited with high O₂ flow rate (*R*). In other words, the conductivity increases with the Si:O ratio in Si-rich films. This result is similar to that for CVD Si-rich Si-O (12) and is caused by electron tunneling between Si islands (27). The behavior of electron trapping during conduction can also be seen from these data. The applied field to reach a current of 1×10^{-9} A (current density = 2.2×10^{-7} A/cm²) across samples deposited with different *R* values is shown in Fig. 14. This field decreases sharply as the *R* value decreases from 0.95 to 0.75 and further decreases slowly as the *R* value decreases from 0.75 to 0.5. Figure 14 can be used as a guideline for the choice of deposition conditions when a PECVD Si-rich Si-O is used as an injector in EEROM applications (28, 29).

A typical distribution of dielectric breakdown strength for PECVD SiO₂ is shown in Fig. 15. Two hundred metal/SiO₂/Si (MOS) devices were tested for films depos-

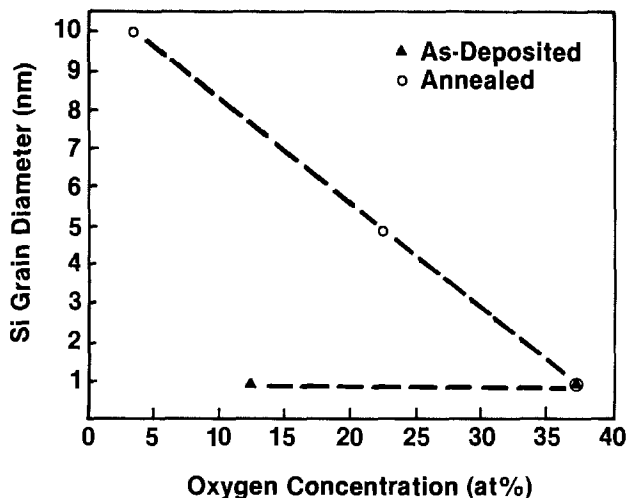


Fig. 10. Size of silicon grain as a function of oxygen atomic percent for as-deposited and annealed samples.

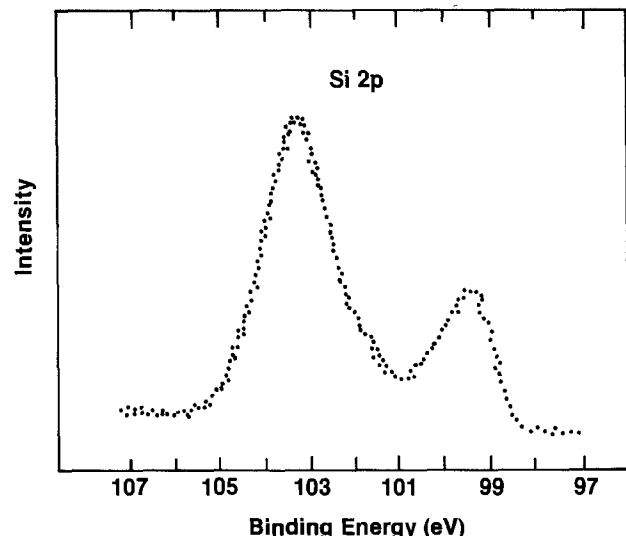


Fig. 12. Si 2P XPS data for PECVD Si-rich oxide

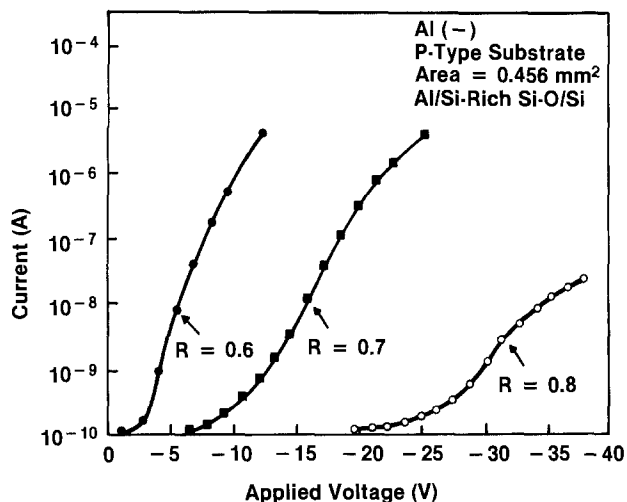


Fig. 13. I-V data for PECVD Si-rich Si-O films (190 nm) deposited with different O_2 flow rates (R).

ited with $R = 3$ sccm. About 11% of the devices have breakdown strengths of ≤ 6 MV/cm, which indicated the presence of defects in the films (e.g., pinholes). About 85% of the devices tested show catastrophic breakdown, and the rest ($\sim 15\%$) show only I-V conduction. Two typical I-V data for PECVD SiO_2 are shown in Fig. 16. The conduction of these films follows the Fowler-Nordheim (F-N) mechanism (30). The slope of the F-N plot is high, possibly due to trapping of negative charges which results in a decrease of the actual field across the SiO_2 films. A ledge on the I-V curve is observed for some samples as the result of trap generation at high fields (31). The breakdown distribution and I-V data for PECVD SiO_2 studied here, which are worse than that for thermal SiO_2 , indicate the limitations of applying PECVD SiO_2 films to an active IC device. A positive flatband voltage (~ 0.6 V) is observed for Al/PECVD SiO_2/Si devices. This is about 1.2 V higher than the flatband voltage for Al/thermal SiO_2/Si devices. The presence of negative

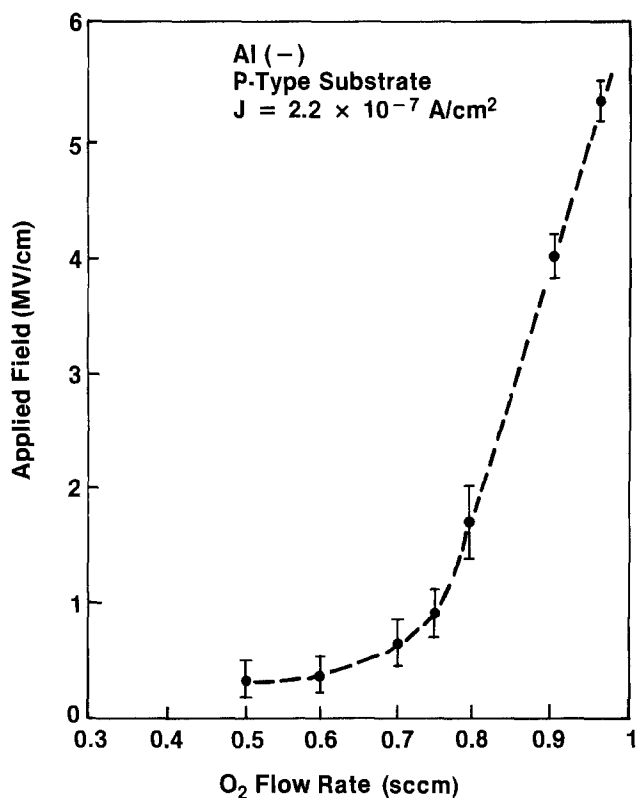


Fig. 14. Applied field, resulting in current density of 2.2×10^{-7} A/cm², across PECVD Si-rich Si-O films as a function of O_2 flow rates.

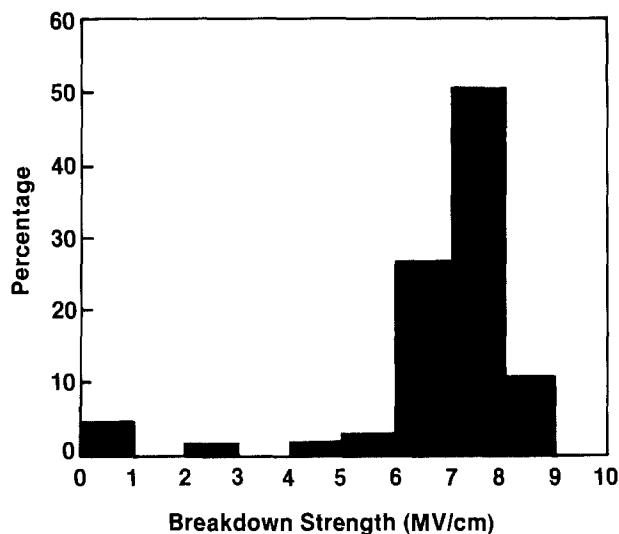


Fig. 15. Distribution of dielectric breakdown strength for PECVD SiO_2 films deposited with $R = 3$ sccm.

charges, as observed in the I-V data, is one of the causes of this positive flatband voltage.

Summary

PECVD silicon oxide films, with a range in Si:O concentration of 0.88 to 3.6, were prepared by the reaction of a constant SiH_4 gas source with varying O_2 gas flow rates. The N and C concentrations were found to be < 1.5 a/o in the Si-rich film and undetectable in the PECVD SiO_2 film. From the IR spectra of the unannealed Si-rich films, we found that the wave number of the main Si-O stretching bonds is low and their FWHM value is high. After annealing, the wave number was found to increase to ~ 1095 cm^{-1} and the FWHM values were reduced by at least 10%. These results suggest either an oxygen deficiency or porosity in the as-deposited PECVD Si-rich films. Si-H_n bonds (either in a- SiO_2 or a-Si) were found in the as-deposited Si-rich films, but were not observed in the PECVD SiO_2 film. The Si-OH and H-OH bonds were found in all unannealed films. No Si-H or O-H bonds were detected in the annealed films. The concentrations

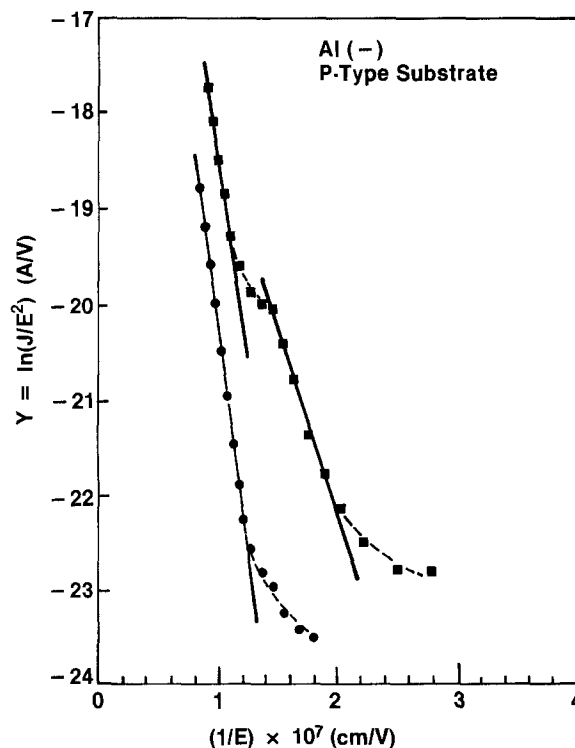


Fig. 16. Fowler-Nordheim plot for two typical PECVD SiO_2 films deposited with $R = 3$ sccm.

of Si-H and O-H bonds in the PECVD Si-rich films were found to be in the order of 10^{20} and 10^{21} cm^{-3} , respectively. These concentrations are at least 100 times greater than those in CVD Si-rich oxide films.

The refractive index was found to increase with increasing Si:O ratio, film density, or N contamination. The difference in refractive index before and after annealing was also found to be greater for the Si-rich oxide films. These results, and the smaller d_s/d value, indicate that the density of the Si-rich films is less than that of the PECVD SiO_2 film. This is consistent with the results showing higher amounts of hydrogen in Si-rich films. For the annealed films, the etch rate decreases with increasing Si:O ratio, but for the as-deposited films, the distribution of etch rate with respect to the Si:O ratio was random. This implies that the etch rate depends primarily on film composition and film density.

The presence of Si, SiO_2 , and the transition phase SiO_x was identified by TEM, AES, and XPS. The size of the Si cluster was found to be ~ 1 nm for all as-deposited samples, and was found to decrease with increasing oxygen concentration for the annealed samples. No difference in the integrated Auger Si LVV spectra and the XPS data was observed for PECVD and thermal SiO_2 .

I-V data for Si-rich Si-O films indicate that the film conductivity increases with increasing Si:O ratio. The injecting field decreases sharply as the O_2 flow rate decreases from 0.95 to 0.75 sccm. A fair dielectric breakdown distribution was observed for PECVD SiO_2 films. Trapping of negative charges and trap generation at high field for both PECVD SiO_2 and Si-rich films were found.

Based on properties studied here, we believe that the annealed PECVD Si-rich Si-O films have the potential of being used as an injector in EEROM and as passivation films for high field transistors. Annealing at low temperature ($\sim 500^\circ\text{C}$) for long times ($\sim 1\text{h}$) was found to be effective in improving the yield of PECVD SiO_2 films, which may increase the possibility of using these films as insulators in active devices.

Acknowledgments

We would like to thank H. Geipel for the critical reading of the paper. Thanks are given to E. Gardner and P. Velasquez for the encouragement given during the course of this work.

Manuscript submitted Nov. 29, 1984; revised manuscript received May 1, 1985.

IBM Corporation assisted in meeting the publication costs of this article.

REFERENCES

1. See, e.g., M. J. Rand, *J. Vac. Sci. Technol.*, **16**, 420 (1979).
2. A. K. Sinha, H. J. Levinstein, T. E. Smith, G. Quintana, and S. E. Haszko, *This Journal*, **125**, 601 (1978).
3. H. Dun, P. Pan, F. R. White, and R. W. Douse, *ibid.*, **128**, 1555 (1981).
4. J. R. Hollahan, *ibid.*, **126**, 930 (1979).
5. A. R. Reinberg, *J. Electron. Mater.*, **8**, 345 (1979).
6. E. P. G. T. van de Ven, *Solid State Technol.*, **24**, 167 (1981).
7. A. C. Adams, F. B. Alexander, C. D. Capio, and T. E. Smith, *This Journal*, **128**, 1545 (1981).
8. D. W. Hess, *J. Vac. Sci. Technol. A*, **2**, 244 (1984).
9. E. B. Priestley and P. J. Call, *Thin Solid Films*, **69**, 39 (1980).
10. T. Matsushita, T. Aoki, T. Otsu, H. Yamoto, H. Hayashi, M. Okayama, and Y. Kawana, *IEEE Trans. Electron. Devices*, **ed-23**, 826 (1976).
11. M. Hamasaki, T. Adachi, S. Wakayama, and M. Kikuchi, *J. Appl. Phys.*, **49**, 3987 (1978).
12. D. Dong, E. A. Irene, and D. R. Young, *This Journal*, **125**, 819 (1978).
13. J. T. McGuinn and Goodman, *Appl. Phys. Lett.*, **34**, 601 (1979).
14. W. R. Knolle and H. R. Maxwell, Jr., *This Journal*, **127**, 2254 (1980).
15. J. W. Colby, in "Proceedings of the 6th National Conference on Electron Probe Analysis," Paper 17, Pittsburgh, PA (1971).
16. W. A. Pliskin, *J. Vac. Sci. Technol.*, **14**, 1064 (1977).
17. H. R. Maxwell, Jr., and W. R. Knolle, *This Journal*, **128**, 576 (1981).
18. G. Lucovsky, *Solid State Commun.*, **29**, 571 (1979).
19. M. H. Brodsky, M. Cardona, and J. J. Cuomo, *Phys. Rev. B*, **16**, 3556 (1977).
20. A. Hartstein, D. J. DiMaria, D. W. Dong, and J. A. Kucza, *J. Appl. Phys.*, **51**, 3860 (1980).
21. T. Adachi and C. R. Helms, *This Journal*, **127**, 1617 (1980).
22. C. R. Helms, Y. E. Strausser, and W. E. Spicer, *Appl. Phys. Lett.*, **33**, 767 (1978).
23. P. Morgan, J. H. Onsgaard, and S. Tougaard, *ibid.*, **34**, 488 (1979).
24. J. H. Thomas III and A. M. Goodman, *This Journal*, **126**, 1766 (1979).
25. E. A. Irene, N. J. Chou, D. W. Dong, and E. Tierney, *ibid.*, **127**, 2518 (1980).
26. S. I. Raider and R. Flitsch, *IBM J. Res. Dev.*, **22**, 294 (1978).
27. J. Ni and E. Arnold, *Appl. Phys. Lett.*, **39**, 554 (1981).
28. D. J. DiMaria and D. W. Dong, *J. Appl. Phys.*, **51**, 2722 (1980).
29. D. J. DiMaria, K. M. DeMeyer, C. M. Serrano, and D. W. Dong, *ibid.*, **52**, 4825 (1981).
30. M. Lenzinger and E. H. Snow, *ibid.*, **38**, 2951 (1967).
31. P. Solomen, *ibid.*, **48**, 3843 (1977).

Copper Indium Disulfide Films by Close Spacing Chemical Transport

T. L. Chu* and Shirley S. Chu*

Southern Methodist University, Dallas, Texas 75275

C. P. Chien* and D. H. Lo

Poly Solar Incorporated, Garland, Texas 75041

ABSTRACT

Nearly stoichiometric CuInS_2 films have been deposited on alumina and graphite substrates at $650^\circ\text{--}700^\circ\text{C}$ by the close spacing chemical vapor transport technique. The source material was synthesized from the elements in a sealed fused silica tube, and a mixture of hydrogen and iodine or hydrogen and hydrogen iodide was used as the transport agent. The composition, microstructure, crystallographic, and electrical properties of the CuInS_2 films were investigated.

Ternary chalcopyrites are promising optoelectronic materials. The potential of several I-II-VI₂ compounds, such as copper indium diselenide, CuInSe_2 , for photovoltaic detectors and solar cells, light emitting diodes, etc., has been demonstrated (1-3). Similar to CuInSe_2 , copper indium disulfide, CuInS_2 , crystallizes in the chalcopyrite structure and is also a direct-gap semiconductor. CuInS_2 has a room temperature bandgap of 1.5 eV and is a promising thin film photovoltaic material.

Thin films of CuInS_2 have been deposited by several techniques: vacuum evaporation, spray pyrolysis, chemical vapor deposition, electrodeposition, etc. In the evaporation technique, the use of dual sources of CuInS_2 and S has produced p-type films with a carrier concentration of $(7\text{--}9) \times 10^{15} \text{ cm}^{-3}$ and a grain size of 1-2 μm (4). In the spray pyrolysis technique, aqueous solutions of cupric acetate, indium trichloride, and thiourea were sprayed onto substrates at $200^\circ\text{--}500^\circ\text{C}$; the electrical resistivity of the film was found to be affected strongly by the Cu/In molar ratio in the solution (5). The chemical vapor deposition technique utilizes the reaction of $\text{CuCl}(\text{NCCH}_3)_n$, $\text{InCl}_3(\text{NCCH}_3)_n$, and hydrogen sulfide on the surface of gallium phosphide substrates at 850°C or above (6). The electro-codeposition of Cu, In, and S from an aqueous solution followed by annealing in H_2S has produced CuInS_2 films on Ti substrates (7). In addition, CuInS_2 films have been prepared by treating (i) sputtered Cu-In alloy with hydrogen sulfide at $300^\circ\text{--}400^\circ\text{C}$ (8) or (ii) molecular beam deposited Cu-In alloy on glass substrates with sulfur or hydrogen sulfide at $300^\circ\text{--}400^\circ\text{C}$ (9).

In this work, CuInS_2 films have been deposited on foreign substrates by the close spacing chemical vapor transport (CSCVT) technique. Their composition, microstructure, crystallographic, and electrical properties have been investigated. The experimental procedures and results are summarized in this paper.

Close Spacing Chemical Vapor Transport of CuInS_2

The chemical transport technique has been widely used for the crystal growth and film deposition of electronic materials. This technique is applicable to solid-state materials which react reversibly with a gaseous reagent (the transport agent) to form volatile products. Since the equilibrium constant of most reactions is temperature dependent, the transport can be brought about by the presence of a temperature gradient. CuInS_2 reacts reversibly with iodine according to the equation



The chemical equilibrium of this reaction shifts to the left at lower temperatures. Iodine may thus be used to transport CuInS_2 source material from a high temperature zone to regions of lower temperatures. Hydrogen iodide

decomposes into its elements at high temperatures and may also be used as a transport agent. Hydrogen chloride and hydrogen bromide are inert toward CuInS_2 and are not suitable as transport agents. CuInS_2 crystals have been grown in a closed tube by using iodine as a transport agent (10). The conventional chemical transport technique, however, is not suitable for the deposition of CuInS_2 films on foreign substrates due to the nature of the nucleation and growth processes. Once CuInS_2 nuclei are formed on the substrate surface, further transport tends to deposit CuInS_2 on the existing crystallites rather than on the substrate surface. Thus, continuous films cannot be obtained until the crystallites coalesce, and this may require the transport of a considerable amount of CuInS_2 in the form of very thick films. The nucleation process may be greatly facilitated by using the CSCVT technique (11), where the source material and the substrates are separated by only about 1 mm. Under this condition, the deposition process is diffusion limited, and each component of the source material is directly transported across the space to the substrate.

The source material, polycrystalline plates of CuInS_2 , was synthesized from the elements (all of 99.999% purity, purchased from ASARCO, Incorporated, New York, New York) in a carbon-coated fused silica reaction tube about 30 cm long. One side of the reaction tube was of rectangular cross section ($2.5 \times 1.8 \text{ cm}$), about 15 cm long, and was attached to a circular cross section tube. Elemental copper and indium in stoichiometric quantities were placed in the rectangular cross section of the tube, evacuated, and heated to form an alloy, which adhered to the wall of the reaction tube. Sulfur, 0.2-0.4% excess over the stoichiometric ratio, was then introduced into the reaction tube, which was again evacuated and sealed while under evacuation. The reaction tube was placed in a two-zone furnace with each zone separately heated and independently controlled. Initially, the rectangular section of the tube (Cu-In) was maintained at 650°C (the mp of 1:1 Cu:In alloy is about 630°C), and the sulfur zone was heated at 450°C . The temperatures of both zones were gradually increased until all sulfur was consumed. The CuInS_2 zone was then increased to 1150°C (the mp of CuInS_2 is about 1090°C) and the reaction tube gradually pulled out of the furnace to allow the unidirectional solidification of the melt. The CuInS_2 ingots obtained in this manner are single-phase polycrystalline, p-type with room temperature resistivities of 200-500 $\Omega\text{-cm}$ as measured by the four-point probe technique.

Because of the chemical reactivity of I_2 at high temperatures, the selection of the substrates for the deposition of CuInS_2 films by CSCVT is rather limited. Alumina, graphite, and carbon-coated graphite substrates were used (carbon was deposited on graphite by the pyrolysis of propane at 1200°C in a He atmosphere, and this carbon

*Electrochemical Society Active Member.

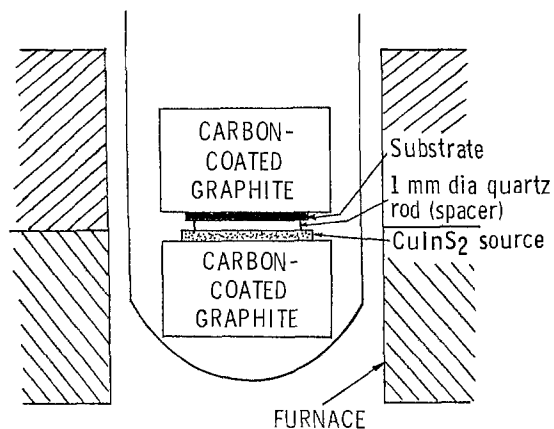


Fig. 1. Schematic diagram of the vertical apparatus for the deposition of CuInS_2 films by CSCVT.

coating eliminates the pits on the graphite surface due to its porosity). The CSCVT process was carried out in a vertical or horizontal fused silica reaction tube, as shown in Fig. 1 and 2, respectively. The heater material for maintaining the substrate and the source material at the desired temperatures is an important consideration. It should be chemically inert and introduces no impurities into the deposited films. Single-crystalline silicon was first used as heaters; however, it reacts with sulfur to form silicon sulfide which hydrolyzes in air, liberating hydrogen sulfide. Silicon dioxide- or silicon nitride-coated silicon blocks are also unsuitable because of the pinholes in the insulator. Graphite is porous, and the coating of high density graphite with about $50 \mu\text{m}$ of pyrolytic carbon is more satisfactory than that of others. Fused silica rods of 0.1 cm diam were used as spacers between the source material and the substrate. The entire assembly was enclosed in a fused silica tube provided with gas inlet and outlet tubes. Thermocouples were used to monitor the temperatures of the substrate and the source material.

The important process parameters in the CSCVT technique are the substrate temperature, the temperature difference between the source and the substrate (fixed at 0.1 cm), and the pressure of the transport agent. Many CSCVT experiments have been carried out to determine the range of process parameters required for the deposition of uniform CuInS_2 films. The use of the vertical or horizontal reaction tube and the use of iodine or hydrogen iodide as the transport agent have produced essentially the same results. The source temperature and the concentration of the transport agent are important in that they determine the reaction rate between the source material and the transport agent. Source temperatures in the range of 650°C - 700°C and an iodine or hydrogen iodide partial pressure of 200-400 torr were found to be suitable. At low source temperatures, such as 500°C , the reaction rate is too low to obtain any reasonable rates of deposition. At too high temperatures, such as 800°C , the sulfur dissociation pressure becomes appreciable. The deposited films were sulfur deficient (very high resistivity p-type or n-type). The substrate temperature determines the rate of

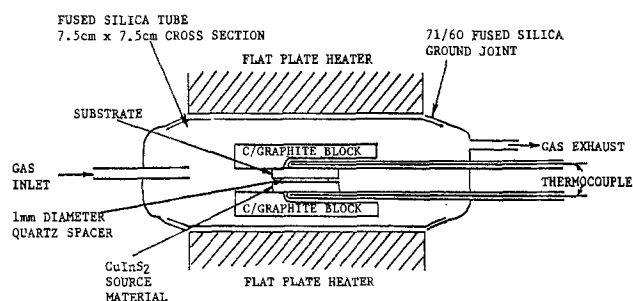


Fig. 2. Schematic diagram of the horizontal apparatus for the deposition of CuInS_2 films by CSCVT.

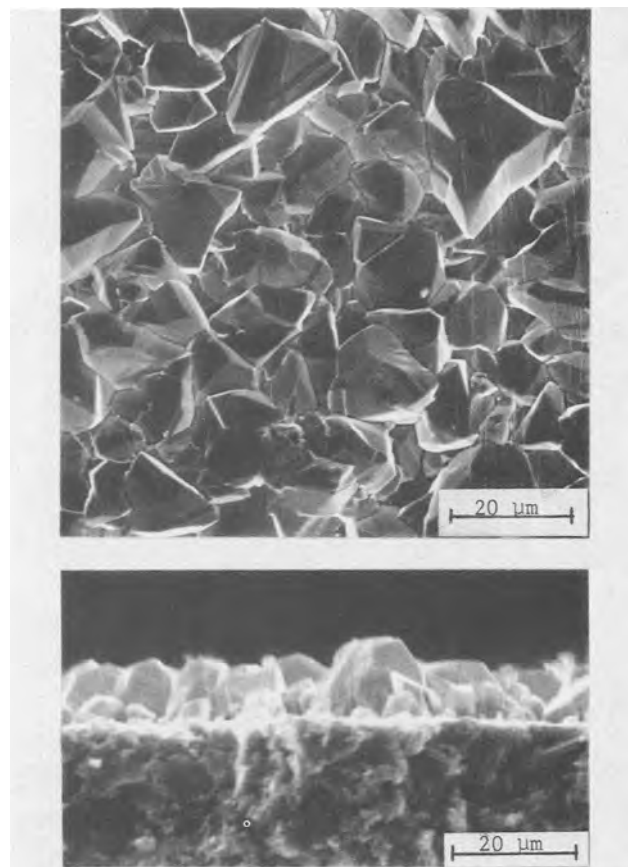


Fig. 3. Scanning electron micrographs of the surface and vertical cross section of a CuInS_2 /graphite specimen prepared at 675°C .

nucleation and the grain size in CuInS_2 films. The use of low substrate temperatures favors the nucleation process and the formation of small grains in the films. The nucleation rate is reduced and the grain size is increased at high substrate temperatures; however, the film may not become continuous until a large thickness is deposited. The temperature difference between the source and the substrate also determines the deposition rate of CuInS_2 films, and a 20°C - 30°C temperature difference was used in most experiments. By using experimental conditions in the range mentioned above, deposition rates of 10-25 $\mu\text{m}/\text{h}$ may be obtained.

Properties of CuInS_2 Films

Adherent and uniform CuInS_2 films have been deposited on alumina and graphite and carbon-coated graphite substrates over the temperature range of 650°C - 700°C by the CSCVT technique. The microstructure of the deposited films depends strongly on substrate temperature; the grain size increases with increasing temperature. An as-deposited surface of a CuInS_2 film deposited on a graphite substrate at 675°C and the vertical cross section of the specimen are shown in Fig. 3. The crystallites, though of random size ranging from $2\text{-}3 \mu\text{m}$ to larger than $10 \mu\text{m}$, show well-developed faces. Figure 4 shows the scanning electron micrograph of the surface of a CuInS_2 film on an alumina substrate. The crystallites in the CuInS_2 film on alumina substrate appear to be more densely packed than those on graphite or C/graphite substrates.

The chemical composition of several CuInS_2 films deposited on graphite substrates in the temperature range 650°C - 700°C has been analyzed by the electron microprobe technique. The results are summarized in Table I, where the data obtained by using a 20 keV electron beam of $1 \mu\text{m}$ diam indicate that the transported films are stoichiometric within the experimental error.

The crystallographic properties of transported CuInS_2 films have been determined by the x-ray diffraction tech-

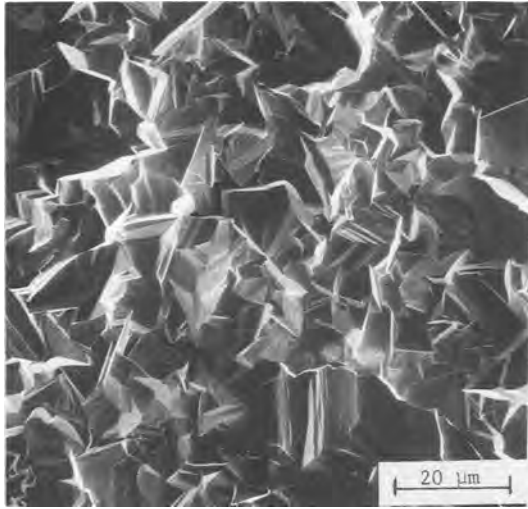


Fig. 4. Scanning electron micrograph of the surface of a CuInS_2 film on an alumina substrate.

nique using CuK_α radiation. Figure 5 shows a typical spectrum of a transported CuInS_2 film, where the " 2θ " values are in good agreement with the published structural data (12).

Using p-type CuInS_2 plates of 100-500 $\Omega\text{-cm}$ resistivity as the source material, the transported films are of p-type conductivity. The electrical resistivity of CuInS_2 films on alumina substrates, measured by the four-point probe technique, is always much higher than that of the source material. Resistivities of several thousand ohm-centimeters have frequently been observed. This high resistivity is due to sulfur deficiency in the transported CuInS_2 film, since the resistivity of the films can be reduced significantly by heating in a $\text{H}_2\text{-S}$ or $\text{H}_2\text{-H}_2\text{S}$ atmosphere at 700°-800°C. This heat-treatment may be used to control the resistivity of CuInS_2 films.

Summary

Single-phase polycrystalline CuInS_2 ingots have been synthesized from the elements of 99.999% purity in a carbon-coated, sealed, fused silica tube at about 1150°C. Using CuInS_2 ingot as the source material, adherent and nearly stoichiometric CuInSe_2 films have been deposited on alumina, graphite, and carbon-coated graphite substrates by the CSCVT technique using a hydrogen-hydrogen iodide or a hydrogen-iodine mixture as the transport agent. The substrate temperature and the partial pressure of the transport agent are the most important process parameters of the transport process. The composition of CuInS_2 films deposited at 650°-700°C has been confirmed by electron microprobe and x-ray diffraction. The electrical resistivity of CuInS_2 films is usually very high, several thousand ohm-centimeters; however, it may be reduced significantly by heating in $\text{H}_2\text{-S}$ or $\text{H}_2\text{-H}_2\text{S}$ at 700°-800°C.

Table I. Composition of transported CuInS_2 films on graphite substrates by electron microprobe analysis

Deposition temperature (°C)	Cu (a/o)	In (a/o)	S (a/o)
650	24.23 ± 1.77	24.37 ± 1.78	51.40 ± 3.75
664	24.32 ± 1.34	24.74 ± 1.36	50.94 ± 2.80
680	24.81 ± 1.19	26.74 ± 1.28	48.45 ± 2.32
695	23.97 ± 1.17	25.20 ± 1.23	50.82 ± 2.47

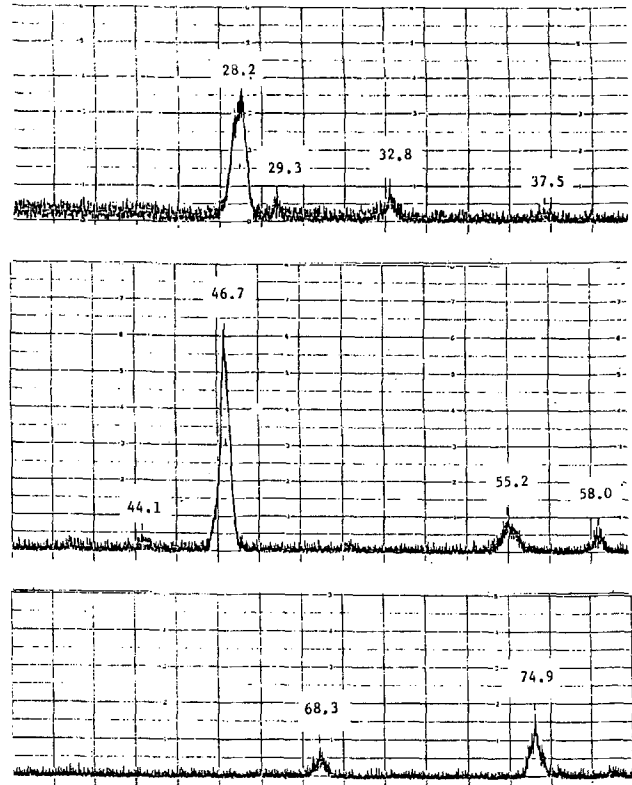


Fig. 5. X-ray diffraction spectrum of a transported CuInS_2 film.

Acknowledgments

The authors wish to thank Mr. Chuck Herrington of the Solar Energy Research Institute for the microprobe analysis of CuInS_2 films. This work was supported by the Solar Energy Research Institute under Subcontract no. XL-4-03032-5.

Manuscript submitted Jan. 8, 1985; revised manuscript received April 12, 1985.

Poly Solar, Incorporated, assisted in meeting the publication costs of this article.

REFERENCES

- J. L. Shay and J. H. Wernick, "Ternary Chalcopyrite Semiconductors: Growth, Electronic Properties, and Applications," Pergamon Press, New York (1975).
- S. Wagner, J. L. Shay, P. Migliorato, and H. M. Kasper, *Appl. Phys. Lett.*, **25**, 434 (1974).
- R. A. Mickelson and W. S. Chen, in "Conference Record of the Sixteenth IEEE Photovoltaic Specialists Conference," p. 781, IEEE, New York (1982).
- L. L. Kazmerski, in "Ternary Compounds," G. D. Holah, Editor, p. 217, Institute of Physics Conference Series 35, Institute of Physics, London (1977).
- P. Rajaram, R. Thangaraj, A. K. Sharma, A. Raza, and O. P. Agnihotri, *Thin Solid Films*, **100**, 111 (1983).
- H. L. Hwang, C. Y. Sun, C. S. Fang, S. D. Chang, C. H. Cheng, M. H. Yang, H. H. Lin, and H. Tuwan-mu, *J. Cryst. Growth*, **55**, 116 (1981).
- G. Hodes, T. Engelhard, C. R. Herrington, L. L. Kazmerski, and D. Cahen, *Prog. Cryst. Growth Charact.*, To be published.
- S. P. Grindle and C. W. Smith, *Appl. Phys. Lett.*, **35**, 24 (1979).
- J. J. M. Binsma and H. A. van der Linden, *Thin Solid Films*, **97**, 237 (1982).
- V. A. Prokhorov, E. N. Kholina, A. V. Klymkiv, and V. A. Voronin, *Izv. Akad. Nauk, SSSR, Neorg. Mater.*, **15**, 1923 (1979).
- F. H. Nicoll, *This Journal*, **110**, 1165 (1963).
- H. Hahn, G. Frank, W. Klinger, A. Meyer, and G. Storzer, *Z. Anorg. Allg. Chem.*, **271**, 153 (1953).

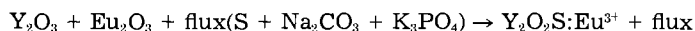
Formation Process of $Y_2O_2S:Eu^{3+}$ in a Preparation with Flux

Osam Kanehisa, Tsuyoshi Kano, and Hajime Yamamoto

Hitachi Limited, Central Research Laboratory, Kokubunji, Tokyo 185, Japan

ABSTRACT

The formation process of a red emitting phosphor, $Y_2O_2S:Eu^{3+}$, has been clarified in a reaction



Sulfuration of Y_2O_3 and Eu_2O_3 is completed at a firing temperature as low as 700°C and at a firing period of 2h. Diffusion of Eu^{3+} follows the sulfuration, and grain growth begins when lattice disorder of Y_2O_2S decreases to a minimum at 1050°C. Larger particles are obtained when a part of Y_2O_3 is replaced with YPO_4 .

A red emitting phosphor, $Y_2O_2S:Eu$, is widely used in color picture tubes because of its high efficiency and appropriate color under cathode-ray excitation. For the preparation of such rare earth oxysulfides, several methods are known: (i) reduction of rare earth sulfate by H_2 or CO (1); (ii) reduction of rare earth sulfite by CO (2); (iii) sulfuration of rare earth oxide by H_2S or CS_2 (3); (iv) sulfuration of rare earth oxide in the atmosphere of $N_2 + H_2O + H_2S$ (4); (v) reaction between an oxide and a sulfide (5); and (vi) sulfuration of rare earth oxide in the flux of $S + Na_2CO_3 + K_3PO_4$ (6).

Among these methods, the last one is most important, since it has come to be used for production of commercial phosphors. This is because the method has good productivity. As such, there have been many papers on $Y_2O_2S:Eu$ prepared in this way, mostly concerning its optical properties (7). In contrast, little has been known on the formation process of $Y_2O_2S:Eu$ in the flux method. To our best knowledge, only Ozawa reported the growth mechanism of $Y_2O_2S:Eu$ microcrystallines (8). Accordingly, in the present paper we describe the results of our investigations into the sulfuration reaction, Eu^{3+} diffusion, and grain growth using different firing times and temperatures. Examinations of the brightness and color of the phosphors prepared under the various firing conditions will be discussed.

Experimental Procedures

Samples were prepared according to the method reported by Royce *et al.* (6). A mixture of Y_2O_3 and Eu_2O_3 with a molar ratio of 0.957:0.043 was mixed with the flux, which was a mixture of S, Na_2CO_3 , and K_3PO_4 at a molar ratio of 3:1:0.1. The mixture was then charged in an alumina crucible with an alumina lid and fired. Of the starting materials, Y_2O_3 was at 99.99% purity and Eu_2O_3 at 99.9%. A small amount of Tb (14 ppm in atomic ratio) was added to the Y_2O_3 to enhance the luminescent efficiency (9). The other starting materials were of reagent grade. The standard sample was fired at 1180°C for 2h. Fired products were yellow solids with the shape of the crucible. Samples for brightness and color measurements were washed with deionized water and dil-HCl and dried at 120°C for 4h. However, samples for x-ray diffraction analysis and luminescence spectra measurements were washed only with deionized water to make the existence of Y_2O_3 in the products detectable, because Y_2O_3 is soluble in dil-HCl. Instead of Y_2O_3 , a mixture of Y_2O_3 and YPO_4 , or only YPO_4 , was also used as yttrium starting materials, because partial substitution of Y_2O_3 with YPO_4 increases grain size.

The mean particle size of the samples was obtained using the Blaine method. The principle underlying this method is to obtain the specific surface area of the sample by measuring the time it takes for air to pass through a powder bed. This method gives a better estimation of the mean size of primary particles than the sedimentation method, which tends to measure aggregated particle size.

Relative cathodoluminescence (CL) brightness was obtained using a United Detector Technology photocell de-

tektor with a photometric filter at a 10 kV accelerating voltage and $1 \mu A/cm^2$ current density. Samples were mounted on stainless steel holders having a screen weight of 100 mg/cm². Resulting data were calculated as a percentage of the value for the standard sample.

As a measure of color, the ratio between CL brightnesses with and without the use of VR-60 Toshiba filter was defined. For convenience, we call this value the red color component ratio, or R_c , which can be expressed as $R_c = (\text{CL brightness with VR-60 filter} / \text{CL brightness without VR-60 filter})$.

The value for the standard sample is 0.926. With the increase in Eu^{3+} concentration, R_c increases. CL spectra were measured with a Nikon P-250 monochromator, the dispersion of which is 6 nm/mm, and an RCA-7102 photomultiplier. Correction of spectral sensitivity was made using a data acquisition system, the Hewlett-Packard 9825A. For linewidth measurements, a Spex 1400 monochromator with a dispersion of 1 nm/mm was used.

Decay characteristics under 337 nm N_2 laser excitation were obtained using a Biomation waveform recorder, Model-1010, combined with a Toyotsusho averager, Model 1010SA. They were analyzed using the HP9825A. Scanning electron microscopy (SEM) images were obtained with a Hitachi SEM (HHS-2R) at a 25 kV accelerating voltage and $5 \times 10^{-1} \mu A$ beam current. Thermoluminescence (TL) glow curves were measured in a conventional way; a sample was irradiated by 254 nm light from a low pressure mercury lamp at 80 K for 10 min, kept at 80 K until the afterglow disappeared, and then warmed up to about 470 K at a rate of 10-15 deg/min.

Results and Discussion

Dependence on firing time.—To facilitate investigation of the sulfuration reaction, the firing time was changed from 0 to 150 min at 1180°C. When starting materials packed in an alumina crucible were set in a furnace kept at 1180°C, the furnace temperature first went down to around 900°C and then recovered to 1180°C in less than 10 min. Firing time is defined here as the period during which the sample is kept at 1180°C. Firing for 0 min means pulling the sample out of the furnace just after the furnace temperature reaches 1180°C.

The sulfuration reaction occurs very quickly for firing at 1180°C. All the samples were found to be Y_2O_2S as a result of x-ray diffraction analysis. Figure 1 shows the SEM images and Fig. 2 mean particle sizes for these samples. With a firing of 0 min, the mean particle size is 1.5 μm . However, in the SEM images, such small particles can barely be observed. The average size of a unit grain, though, is 8-10 μm , and these grains are apparently groups of coagulated primary particles. With an increase in the firing time, this aggregation decreases, primary particles grow, and the mean particle size obtained by the Blaine method comes to show good coincidence with SEM imaging unit grains.

Figure 3 shows the relative CL brightness and R_c against firing time. With firing of 0 min duration, CL brightness is only 23% of the standard sample. With an in-

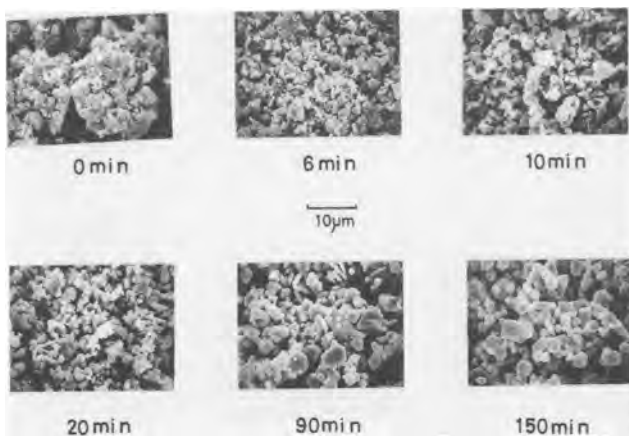


Fig. 1. SEM images of samples fired at 1180°C for different periods of time.

crease in firing time, the brightness increases drastically and reaches a standard level with 30 min firing.

For 0 min firing, R_c is already 0.900; it keeps its value for 20 min, and reaches 0.926 (= standard level) for 30 min firing. This shows that diffusion of Eu^{3+} is completed for 0 min firing, and the R_c increase from 0.900 to 0.926 is attributed to the lattice rearrangement by crystal growth.

A sample with a standard level of brightness and R_c was obtained with 30 min firing. Its mean particle size was about 2.9 μm .

Dependence on firing temperature.—As was mentioned above, the sulfuration reaction at 1180°C proceeds too fast for proper investigations of the first stage. Then firing temperature was lowered with the firing time being kept at 2h. Three starting materials for the yttrium component were examined: Y_2O_3 , YPO_4 , and Y_2O_3 (92 mole percent [m/o]) + YPO_4 (8 m/o). Each case will be described in detail below.

Y_2O_3 as a starting material.—X-ray powder diffraction analysis has shown that all products fired at 700°C and above are $\text{Y}_2\text{O}_2\text{S}$, but those fired at 500° or 600°C are a mixture of $\text{Y}_2\text{O}_2\text{S}$ and Y_2O_3 . The main-peak ratio of the x-ray diffraction between $\text{Y}_2\text{O}_2\text{S}$ and Y_2O_3 is 7:1 for firing at 600°C and 1:1 at 500°C.

In contrast to x-ray diffraction data, CL spectra show only $\text{Y}_2\text{O}_2\text{S}:\text{Eu}^{3+}$ for all samples, and not a trace of $\text{Y}_2\text{O}_3:\text{Eu}^{3+}$ was observed even for samples fired at 600°C and below. The result indicates that Eu^{3+} diffuses into $\text{Y}_2\text{O}_2\text{S}$ more easily than into Y_2O_3 . In fact, in the preparation of $\text{Y}_2\text{O}_3:\text{Eu}^{3+}$ phosphor, a higher firing temperature is needed for the diffusion than is the case for $\text{Y}_2\text{O}_2\text{S}:\text{Eu}^{3+}$.

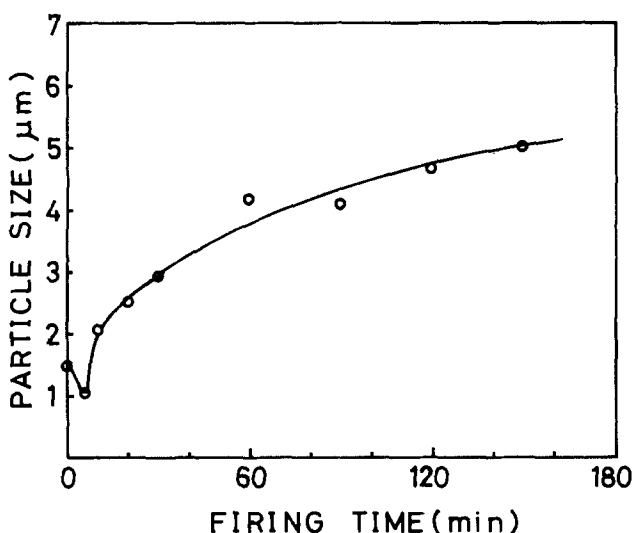


Fig. 2. Mean particle size change of samples fired at 1180°C for different periods of time.

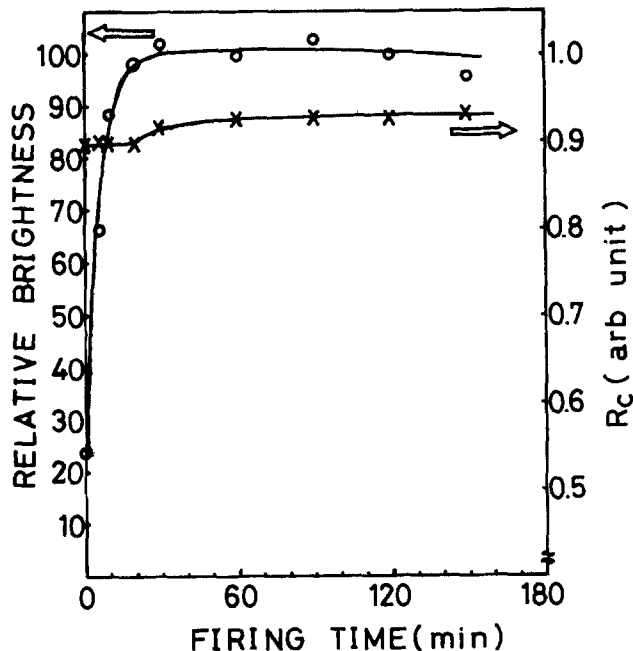


Fig. 3. CL brightness and R_c changes for samples fired at 1180°C over different periods of time.

Figure 4 shows SEM images for the Y_2O_3 starting material and fired products. Figure 5, on the other hand, presents firing temperature dependence of the mean particle size of the phosphors. Although the mean particle size of Y_2O_3 is 1.5 μm , there are no grains of this size in the SEM image, which indicates that primary Y_2O_3 particles aggregate and form coagulated grains of about 8-10 μm in size. In the initial stage of reaction, $\text{Y}_2\text{O}_2\text{S}:\text{Eu}^{3+}$ prepared at 700°C for 2h have a size and morphology similar to those for the Y_2O_3 starting material. This same similarity was also observed in $\text{Y}_2\text{O}_2\text{S}:\text{Eu}^{3+}$ prepared at 1200°C for 0 min.

This shows that mass transport is not remarkable in the initial stage of the reaction. As the sulfurizing reagent, liquid Na_2S_x or evaporated Na_2S_x , S_x gases can be assumed. Here, the melting point of Na_2S_x is 920°C, when $x = 1$. It decreases with an increase in x . It would be more difficult for liquid Na_2S_x to wet all of the fine pores and thin gaps in Y_2O_3 particles having a very low surface tension than for Na_2S_x , S_x gases. So it can be assumed that a gas-solid reaction is the predominant mechanism in the initial stage. It is confirmed that Y_2O_3 can be sulfurized into $\text{Y}_2\text{O}_2\text{S}$ with the reaction of gas components in the flux by the following experiment, though it is not direct evidence for the predominance of gas-solid reaction. Y_2O_3 in a small alumina crucible without lid was set in a larger alumina crucible with lid containing only flux component.

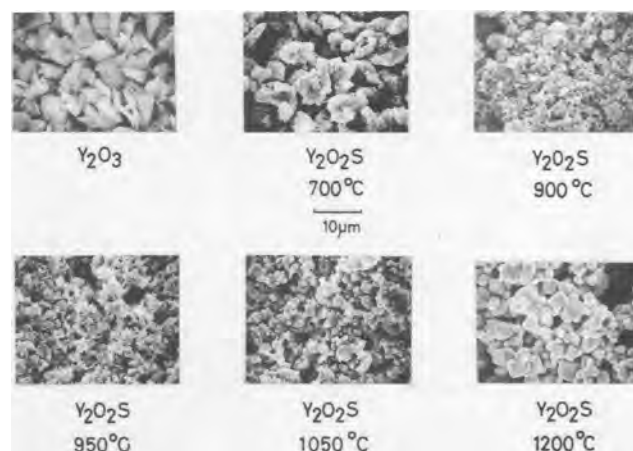


Fig. 4. SEM images of Y_2O_3 and $\text{Y}_2\text{O}_2\text{S}$ samples fired at different temperatures for 2h.

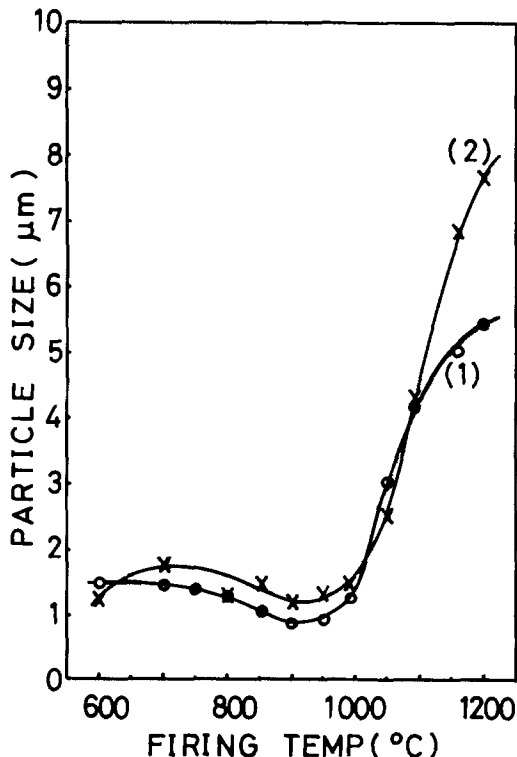


Fig. 5. Mean particle size change with increase in firing temperature. 1: Y₂O₃ was used. 2: 0.92 Y₂O₃ and 0.16 YPO₄ were used.

The ratio of the amount of charged Y₂O₃ and flux component is the same as that of the standard sample. They were fired at 900°C for 2h. In the small crucible, a certain amount of Y₂O₂S was confirmed to be prepared. Mass transport by liquid-solid contact will certainly work at high firing temperatures or over long periods, where grain growth is recognized.

The mean particle size of Y₂O₂S:Eu³⁺ fired at 900°C is about 0.9 µm, and the SEM image shows that small primary particles will most likely separate from the coagulated grains. The SEM image of Y₂O₂S:Eu³⁺ fired at 1050°C shows many small, well-crystallized particles. With firing above 1050°C, grain growth is accelerated, aggregation of particles decreases, and the unit grain size in the SEM image shows good coincidence with the mean particle size measured by the Blaine method.

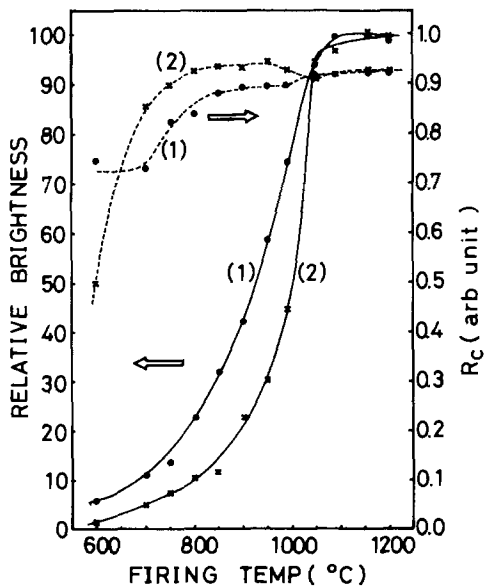


Fig. 6. Brightness and R_c changes for samples fired at different temperatures for 2h. 1: Y₂O₃ was used. 2: 0.92 Y₂O₃ and 0.16 YPO₄ were used.

Table I. Impurity analysis using atomic absorption techniques

Firing temperature (°C)	Ca (ppm)	Na (ppm)	K (ppm)
600	1.46	730	23.75
1200	0.56	8	0.70

Relative luminescence brightness and R_c under cathode ray excitation are shown in Fig. 6. As the measurement was made after treatment with dil-HCl, all Y₂O₃ was eliminated in a sample prepared at 600°C. With the increase in firing temperature from 600° to 1100°C, however, relative CL brightness increases monotonously until it reaches the standard level for firing at 1100°C. Above 1100°C, it retains the same highest value.

The red color component ratio (R_c) in the emission spectra is around 0.7 for a sample fired at 700°C. With the increase in firing temperature, R_c increases and reaches 0.900 for a sample fired at 850°C. It keeps its value for the firing in the range 850°-1000°C. These results correspond to those of firing time dependence and show that Eu³⁺ diffusion is completed for the firing at 850°C.

A sample having the standard level in brightness and R_c was obtained with firing at 1050°C. Its mean particle size was 3.0 µm and nearly equal to that of the sample fired at 1180°C for 30 min.

Table I shows the results of atomic absorption analysis of impurities in the samples fired at 600° and 1200°C. Examined elements were Ca, known as a quencher for Y₂O₂S:Eu, and the flux components Na and K. Clearly, the sample fired at 1200°C includes fewer impurities than the sample fired at 600°C. This is because impurities are segregated from the particles as lattice rearrangement proceeds with an increase in firing temperature.

The lifetime of the ⁵D₀ (Eu³⁺) emitting level and the half width for the ⁵D₀ → ⁷F₀ emission lines at LNT are shown in Fig. 7. The lifetime is analyzed as a single exponential curve. The samples fired at 1100°C and above showed a single exponential decay curve, with a lifetime of 440 µs. When the firing temperature was 1050°C and below, decay curves deviated from a single exponential form. This indicates the existence of more than one Eu³⁺ luminescence center, probably caused by the lattice disorder.

The half-width for ⁵D₀ → ⁷F₀ transition decreases monotonously with firing temperature, again showing lattice disorder at low temperatures.

The effects of lattice disorder can also be seen in the TL glow curves shown in Fig. 8. The sample fired at 1160°C

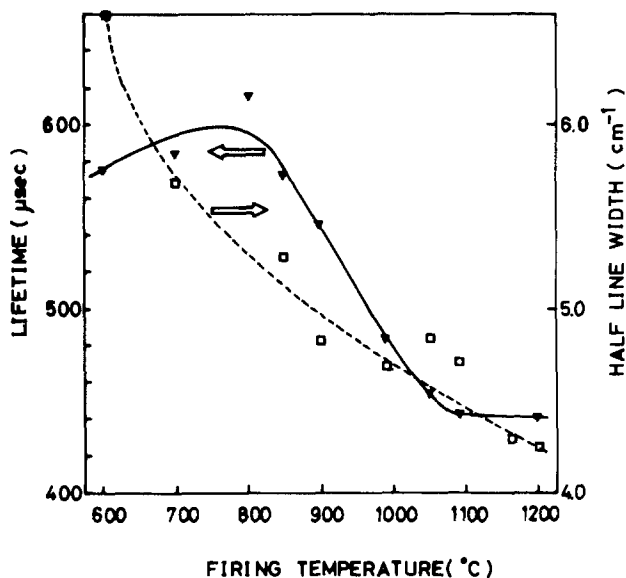


Fig. 7. Half-line width and lifetime shown in relation to firing temperature.

On the basis of the above results, formation processes can be summarized as follows.

1. Sulfuration is completed instantly for 1180°C firing and in 2h for 700°C firing. As the products of the initial stages retain the morphology of the starting material Y₂O₃, it can be considered that the sulfuration reaction is dominated by gas-solid reaction.

2. Eu³⁺ diffusion into Y₂O₂S proceeds promptly after the sulfuration reaction. When Y₂O₂S coexists with Y₂O₃ or YPO₄, Eu³⁺ diffuses into Y₂O₂S preferentially. In the Y₂O₃ and Y₂O₄ + YPO₄ cases, R_c reaches 0.900 and 0.935, respectively, for firing at 850°C. It maintains its value until brightness increases to the standard value. This R_c value of 0.900 is also obtained in the products fired at 1180°C for 0-20 min. This indicates that the diffusion of Eu³⁺ into Y₂O₂S is completed when R_c reaches 0.900 in 2h at 850°C firing or instantly at 1180°C firing. This rapid Eu³⁺ diffusion is explained by the great lattice disorder in the initial stage of the reaction.

3. Compared to Eu³⁺ diffusion, grain growth is dependent upon longer firing time and higher temperatures. Even when Eu³⁺ diffusion is completed, the product retains a morphology similar to that for starting material Y₂O₃. Nucleation can be clearly observed in Fig. 4 for firing at 900°C. It is to be emphasized that grain growth is accelerated when brightness and R_c are already at the standard level and grains are about 3 μm in size.

4. The role of YPO₄ in the grain growth is considered to be as follows. In the Y₂O₃ + YPO₄ case, R_c decreases with firing at 1050°C. This indicates that, at this temperature, YPO₄ is completely sulfurized into Y₂O₂S. As the average size of YPO₄ is smaller than that of Y₂O₃, the size of Y₂O₂S obtained from YPO₄ sulfuration is smaller than that from Y₂O₃ sulfuration. These small Y₂O₂S particles promoted grain growth in the solid-liquid reaction.

Conclusions

The formation process of Y₂O₂S:Eu in a preparation with flux has been clarified. The sulfuration reaction Y₂O₃ + Eu₂O₃ + flux(S + Na₂CO₃ + K₃PO₄) → Y₂O₂S:Eu³⁺ + flux is completed in 2h with firing at 700°C or < 10 min with firing at 1180°C firings. In this reaction, it can

be assumed that a gas-solid reaction is a predominant mechanism. Eu³⁺ diffusion proceeds promptly after the sulfuration reaction, while the host lattice still has much disorder with many impurities. Diffusion is completed in 2h with firing at 800°C or < 10 min with firing at 1180°C. When Y₂O₂S exists with Y₂O₃ or YPO₄, Eu³⁺ diffuses into Y₂O₂S preferentially. The sulfuration reaction 2YPO₄ + Na₂S_r → Y₂O₂S + flux proceeds at about 900°C, and ends at 1000°C with 2h firing. It has become clear that the grain growth is accelerated, when Eu³⁺ diffusion is completed, the brightness reaches the highest level, and the mean particle size is about 3 μm. Larger particles are obtained with partial substitution for Y₂O₃ of YPO₄. The reason for this phenomenon is not clear yet, but it may be related to the fact that YPO₄ sulfurizes into Y₂O₂S later than Y₂O₃.

Acknowledgment

The authors are grateful to Dr. Yasuhiko Uehara for his helpful discussions.

Manuscript submitted Dec. 19, 1984; revised manuscript received April 15, 1985.

Hitachi Limited assisted in meeting the publication costs of this article.

REFERENCES

1. J. J. Pitha, A. L. Smith, and R. Ward, *J. Am. Chem. Soc.*, **69**, 1870 (1947).
2. M. Koskenlinna, M. Leskela, and L. Niinisto, *This Journal*, **123**, 75 (1976).
3. J. W. Haynes and J. J. Brown, Jr., *ibid.*, **115**, 1060 (1968).
4. D. W. Ormond and E. Banks, *This Journal*, **122**, 152 (1975).
5. P. Khodadad, T. Tek, J. Flauhaut, and L. Domange, *C. R. Hung. Acad. Sci.*, **260**, 2235 (1965).
6. M. R. Royce, A. L. Smith, S. M. Thomsen, and P. N. Yocom, Abstract 86, p. 201, The Electrochemical Society Extended Abstracts, Vol. 69-1, New York, May 4-9, 1969.
7. For example, see T. Hoshina, S. Imanaga, and S. Yokono, *J. Lumin.*, **15**, 455 (1975).
8. L. Ozawa, *This Journal*, **124**, 413 (1977).
9. H. Yamamoto and T. Kano, *ibid.*, **126**, 305 (1979).

Technical Notes



Highly Selective Dry Etching of Polysilicon Using Chlorinated Gas Mixtures for VLSI Applications

E. Degenkolb,* K. O. Park,^{†1} J. B. Shorter, and M. Tabasky

GTE Laboratories, Waltham, Massachusetts 02254

With scaled-down silicon-gate MOS devices, dry etching to pattern polycrystalline silicon over thin gate oxide must meet two stringent requirements: anisotropy and high selectivity. Specifically, for gate polysilicon thicknesses of 0.6 μm, a suitable etching process should be able to produce etched gates of length 1 μm without removing more than 5 nm of underlying SiO₂. Etching of polysilicon can be made highly selective with respect to SiO₂ in plasmas of fluorine containing gases such as SF₆, but anisotropy is normally sacrificed for high selectivity (1).

*Electrochemical Society Active Member.

^{†1}Present address: Intel Corporation, Livermore, California 94550.

It was shown by Forget *et al.* (2) that the addition of Cl₂ to SF₆ improves selectivity over SF₆ alone, but in our experience this combination is not ideal because anisotropy is critically dependent on the relative concentrations of SF₆ and Cl₂. Cabral and Horwitz (3) used SiCl₄ + O₂ to etch silicon with greater than 10:1 selectivity over SiO₂. Molecular chlorine combined with argon was used for silicon etching by Schwartz and Schaible (4) and shown by Pogge *et al.* (5) to give Si:SiO₂ selectivity of approximately 20:1. Recently, Park and Rock (6) have shown that SiCl₄ + Cl₂ also gives a residue-free anisotropic silicon etch with high selectivity. In this paper, we describe the capabilities of this combination for gate polysilicon etching.

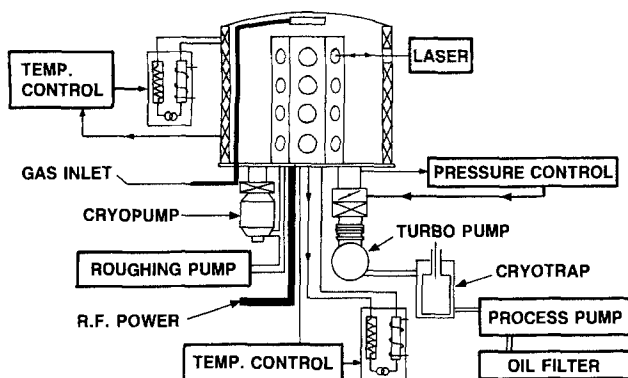


Fig. 1. Schematic of Hex-cathode reactive ion etching system

Experimental

Gate etching test samples were prepared by depositing 600 nm LPCVD polysilicon onto thermally oxidized silicon wafers. The polysilicon was implanted with 5×10^{15} cm^{-2} phosphorus at 50 keV and then cleaned by exposure to O_2 plasma. After a 15 min anneal at 800°C in O_2 , the wafers were patterned with positive AZ1400 series photoresist. Just prior to polysilicon etching, the wafers were dipped for 15s in buffered HF solution ($\text{NH}_4\text{F}:\text{HF} = 7:1$), rinsed, and baked at 90°C for 30 min.

Reactive ion etching (RIE) of polysilicon was conducted in a 24-wafer Hex-cathode reactor (Plasma-Therm 640, shown in Fig. 1), which is an asymmetric diode system using the bell jar itself as the anode (anode-to-cathode area ratio 3:1), and is equipped with a turbomolecular pump and cold trap. One to four wafers were etched at a time; bare SiO_2 -coated wafers occupied the other positions. To obtain reproducible etch rates, it was found necessary to precondition the etch chamber (before loading samples to be etched) with an O_2 plasma at 40 mtorr and 400W RF. During this treatment, the discharge color changes from blue to greenish-yellow and dc self-bias changes from -170 to -220V . The O_2 plasma may be reacting with adsorbed chlorides left from the previous etching cycle.

Polysilicon samples were loaded on Al_2O_3 -coated platens and the reactor was pumped to a background pressure of 5×10^{-5} torr before admitting reactive gases. Electrode temperature was 37°C ; chamber wall temperature was 39°C . The total flow rate of $\text{SiCl}_4 + \text{Cl}_2$ was main-

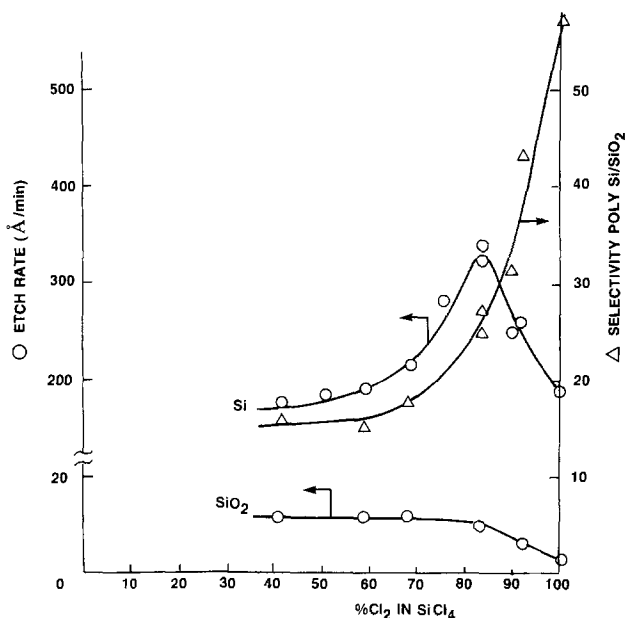


Fig. 2. Etch rate and selectivity of polysilicon to thermal oxide as a function of reactant gas composition in Hexetch 640 at 36 sccm total flow, 28 mtorr pressure, and 400W RF power.

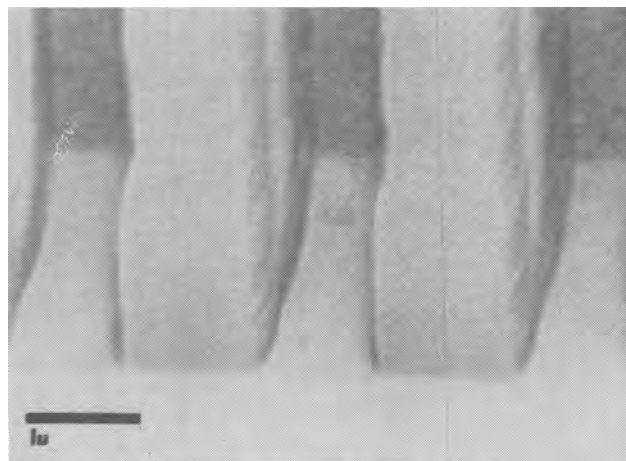


Fig. 3. Polysilicon ($0.6 \mu\text{m}$ thick) etched at 400W RF, 28 mtorr, 33 sccm Cl_2 , and 3 sccm SiCl_4 in Hexetch 640. Photoresist mask ($1.5 \mu\text{m}$ thick) is still in place.

tained at 36 sccm at a chamber pressure of 28 mtorr with RF power of 400W at 13.56 MHz. The relative concentrations of Cl_2 and SiCl_4 were controlled by varying the individual gas flows, and etch rates were measured with a Nanometrics Film Thickness Computer. Optical emission from a plasma of $\text{SiCl}_4 + \text{Cl}_2$ was recorded using an Instruments S-A scanning monochromator of focal length 0.2m and a photomultiplier of S-5 spectral sensitivity.

Results and Discussion

Figure 2 shows etch rates and Si/SiO_2 selectivity as a function of Cl_2 concentration in SiCl_4 . Since the polysilicon is covered by native SiO_2 , our measurements yield the etch rate for the composite film. From 0 to 85% Cl_2 , the polysilicon etch rate increases while the SiO_2 etch rate remains nearly constant. Beyond 85% Cl_2 , both etch rates decline, yet selectivity continues to improve and anisotropy remains high. In this region, the plasma color changes from violet to blue and the dc self-bias changes from -120 to -80V . The result of these changes is a dramatic drop in the SiO_2 etching rate, which accounts for the increase in selectivity.

Figure 3 shows polysilicon on SiO_2 which was etched with greater than 30:1 selectivity using 90% $\text{Cl}_2 + 10\%$ SiCl_4 . Anisotropy is characteristic of this gas combination, which etches without residue as long as the reactor has good vacuum integrity. Selectivity of polysilicon over photoresist is about 2:1 under these conditions and drops as RF power is increased. Anisotropic etching is also obtained using sputtered silicon nitride as a less erodible mask which can be removed with hot H_3PO_4 . Figure 4

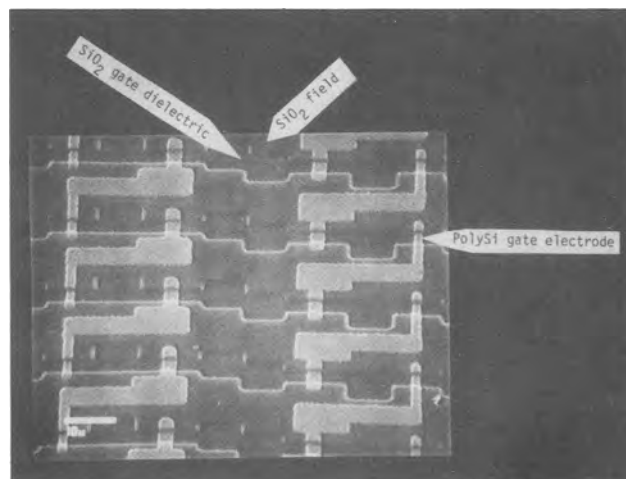


Fig. 4. Polysilicon etched as in Fig. 3, after removal of silicon nitride mask. SiO_2 step heights are $0.4 \mu\text{m}$.

POLYSILICON ETCHING WITH Cl₂ + SiCl₄

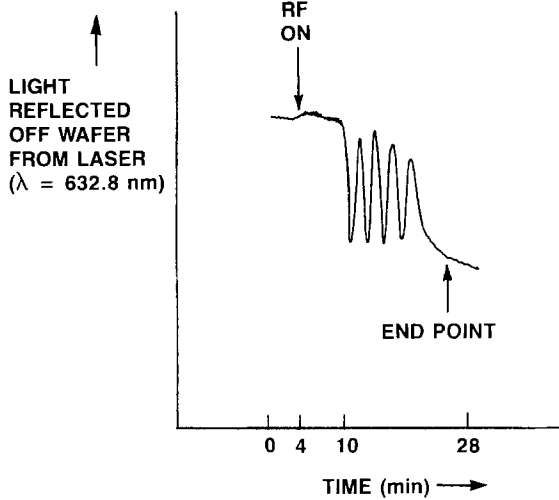


Fig. 5. Polysilicon etching signal from laser reflectometer. Arrow shows approximate end point.

shows an example of polysilicon gate structures over 0.4 μm SiO₂ steps which were etched with the same gas mixture using a 0.15 μm thick silicon nitride mask.

Polysilicon etch monitoring by laser reflectance is shown in Fig. 5 using 90% Cl₂ in SiCl₄. A delay is evident between plasma ignition and onset of polysilicon etching, which is in part due to the need to etch off native SiO₂ covering the polysilicon. The presence of residual water vapor may also contribute to the delay. Approximate end point is shown by the arrow, and the process can be terminated with less than 5 nm gate SiO₂ removal.

Alternative etch monitoring can be done using the 307 nm emission of Cl₂^{*}, as shown in Fig. 6. In this case, we see that the plasma is depleted of Cl₂^{*} until polysilicon etching is complete. The initial dip in Cl₂^{*} intensity could be due to reaction with residual water vapor. The gradual approach to end point is a reflection of slower etching near the center of the wafers. The near-ultraviolet plasma emission spectrum is shown in Fig. 7 as a function of inlet gas composition. Between the Cl₂^{*} peaks is a sharp sequence of lines due to SiCl, which disappears rapidly as

POLYSILICON ETCHING WITH Cl₂ + SiCl₄

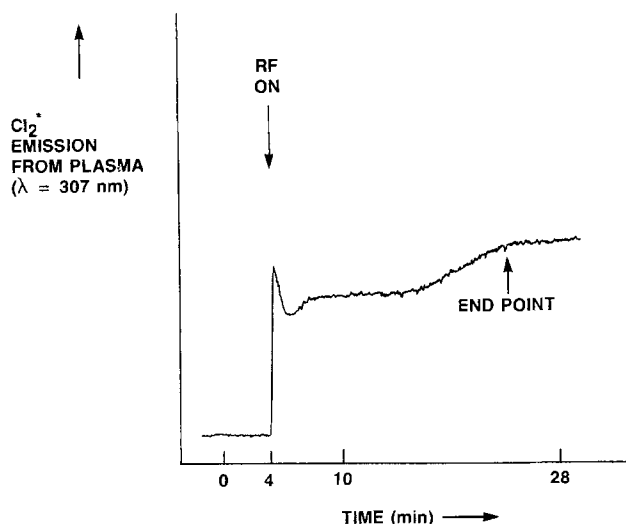


Fig. 6. Polysilicon etching signal from Cl₂^{*} optical emission. Arrow shows approximate end point.

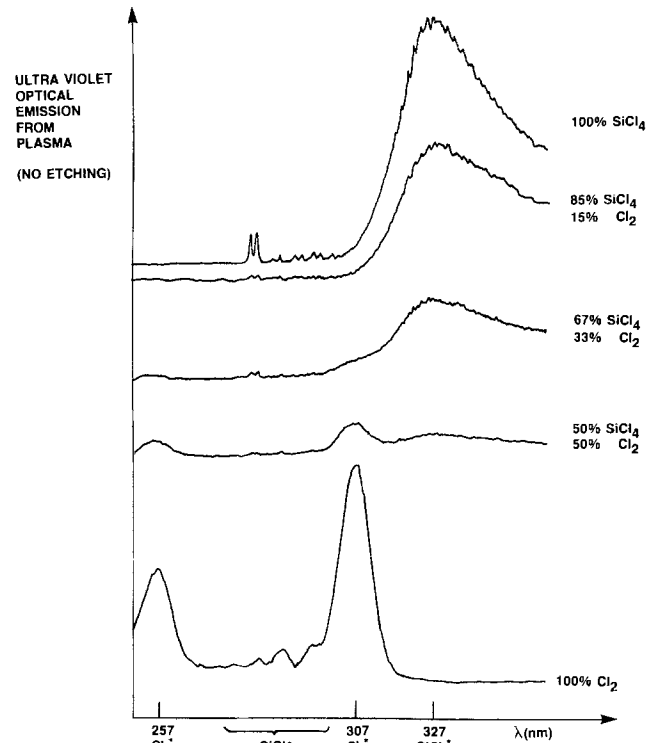


Fig. 7. Dependence of optical emission spectrum on etching gas composition.

the chlorine content is increased. A much broader emission peaked at 327 nm becomes weaker gradually as Cl₂ concentration is increased. This broad band may be due to emission from a SiCl_x species such as SiCl₂. SiCl₂ is energetically favored to form (7) and has been observed to be a major component in SiCl₄ discharges (8).

Figure 8 shows normalized emission intensities and etch rates as a function of inlet gas composition. The peak in polysilicon etch rate corresponds more closely with Cl₂^{*} than with SiCl_x^{*} or SiCl^{*} emission. From this, we conclude that Cl₂^{*} may be a primary silicon etchant species. These data are consistent with earlier results by Park and Rock (6) indicating that the function of silicon chlorides is etching SiO₂. The polysilicon etch rate decline can be interpreted by recalling that it has a native oxide, which takes longer to penetrate at higher Cl₂ content.

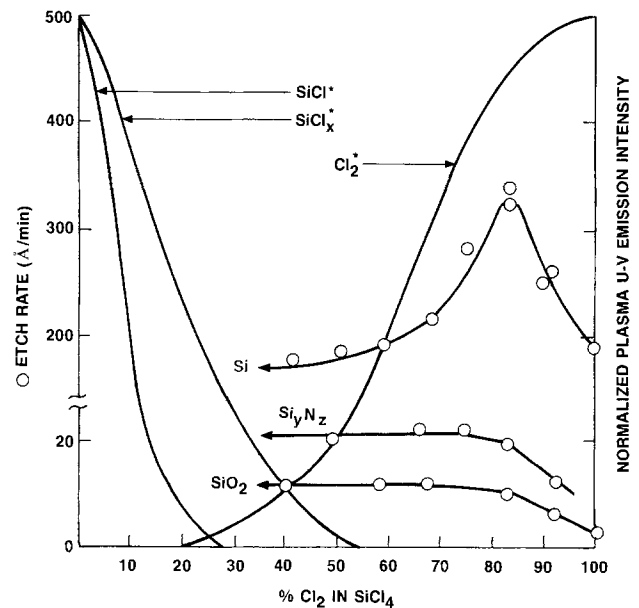


Fig. 8. Comparison of etch rates with optical emission intensities

Conclusions

Highly selective, clean and anisotropic gate polysilicon etching can be achieved in RIE reactors using a $\text{Cl}_2 + \text{SiCl}_4$ gas mixture. Sputtered silicon nitride is a more desirable etch mask than photoresist because it is less erodible and more easily removed following RIE processing. This etching process can be monitored by laser reflectance or Cl_2^* optical emission, so that less than 5 nm gate SiO_2 is removed during overetch.

Acknowledgments

Technical assistance for these experiments was provided by H. A. MacLean. We are grateful to N. J. Lewis for SEM photos, to P. E. Poppert, F. C. Rock, W. Lapatovich, and J. Kramer for helpful discussions, and to D. Casey for management support. This work is dedicated to the memory of Jeremiah McCarthy, whose fairness and courage inspired us all.

Manuscript submitted Dec. 10, 1984; revised manuscript received March 21, 1985. This was Paper 87 presented at the Cincinnati, Ohio, Meeting of the Society, May 6-11, 1984.

GTE Laboratories assisted in meeting the publication costs of this article.

REFERENCES

1. P. Parrens, *J. Vac. Sci. Technol.*, **19**, 1403 (1981).
2. L. Forget, R. Gdula, and J. Hollis, U.S. Pat. 4,214,946 (1980).
3. S. M. Cabral, D. D. Rathman, and N. P. Economou, Abstract 153, p. 246, The Electrochemical Society Extended Abstracts, Vol. 83-1, San Francisco, CA, May 8-13, 1983; C. M. Horwitz, *IEEE Trans. Electron Devices*, ed-28, 1320 (1981).
4. G. C. Schwartz and P. M. Schaible, *J. Vac. Sci. Technol.*, **16**, 410 (1979).
5. H. B. Pogge, J. A. Bondur, and P. J. Burkhardt, *This Journal*, **130**, 1592 (1983).
6. K. O. Park and F. C. Rock, Abstract 155, p. 250, The Electrochemical Society Extended Abstracts, Vol. 83-1, San Francisco, CA, May 8-13, 1984; K. O. Park, in "Plasma Processing," G. S. Mathad, G. C. Schwartz, and G. Smolinsky, Editors, p. 257, The Electrochemical Society Softbound Proceedings Series, Pennington, NJ (1983).
7. M. Farber and R. D. Srivastava, *Chem. Soc. J. Faraday Trans. 1*, **73**, 1672 (1977).
8. A. W. Kofschoten, R. A. Haring, and A. E. DeVries, *J. Appl. Phys.*, **55**, 3813 (1984).

An Anodic Oxidation Technique for the Growth of Transparent Conducting Layers of SnO_2

S. Dhar,* Susanta Sen, and Dipanker Biswas

Institute of Radiophysics and Electronics, Calcutta 700 009, India

Transparent conducting layers of SnO_2 (1, 2) are currently of interest because of their widespread use in a number of devices. Available techniques for growing this material are thermal oxidation, reactive evaporation, reactive sputtering, sputtering of oxide targets, chemical vapor deposition, and spray pyrolysis. Sputtering techniques are known for high quality yields, but their use is limited by high costs and experimental complexities. Spray pyrolysis, however, provides a comparatively simpler and cheaper method for depositing large area layers. However, this is essentially a high temperature technique, and the film quality achieved is not as good as that obtained for the sputtered layers.

For a long time, anodization has been used as a simple and efficient method for converting metals into their oxides. However, attempts to anodically oxidize tin have been only partially successful (3-6). Giany and Kelly (7) were apparently able to grow SnO_2 from tin sheet using an ethylene glycol-based bath but did not present data on the electrical conductivity and optical transparency of the grown layers. Two of the present authors (S. D. and D. B.) recently presented a preliminary report (8) on a new anodic oxidation technique for converting vacuum-deposited tin coatings to highly transparent and conducting SnO_2 . The purpose of this paper is to give a more detailed description of the process and of the results obtained.

Microscopic glass slides were used as substrates for the SnO_2 layers. They were degreased by boiling in liquid detergent, followed by 1/2h standing in chromic acid. The slides were then leached in aqua regia and finally washed in deionized water and dried in filtered air. Analytical-grade tin was then evaporated at a pressure of 2×10^{-5} torr onto the substrates to form layers of up to 1 μm thick.

The bath used for tin anodization contained 1.5g of the Na salt of EDTA in 100 ml of CH_3OH (Analar) and 100 ml of distilled water. Anodization was carried out at 30°C.

In the anodization cell, the tin layer on glass was employed as the anode, and a nickel plate as the cathode.

These electrodes were tilted such that the distance between them was smallest at the lower edges. Thus, oxide film formation was initiated at the lower edge of the anode, where the current density was highest. An average current density of 3 mA/cm^2 was found to be satisfactory for the conversion of Sn to SnO_2 , yielding a completely transparent layer. At higher current densities instead of being transparent, the tin layer is converted to a brownish mass, probably of SnO . The same effect is again observed when the concentration of EDTA in the bath is lowered. Before testing, the anodized layers were washed and dried in warm air. No heat-treatment was used.

The resistivity of the anodically grown SnO_2 layers, measured by the usual two probe technique (9), was found to be of the order of $10^{-2} \Omega\text{-cm}$. Transmittance of a 400Å thick SnO_2 layer on glass measured with a Cary 17D spectrophotometer in the automatic scan mode (bare glass sheet as reference), is presented in Fig. 1. The film is seen to be practically transparent over the wavelength range 350-700 nm.

A typical scanning electron micrograph of a 3000Å layer is presented in Fig. 2, which shows the grain structure.

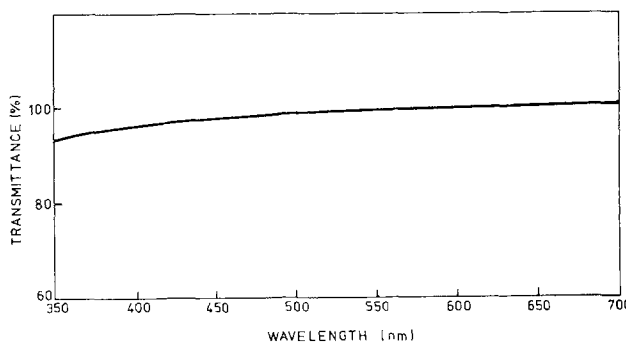


Fig. 1. Transmittance vs. incident wavelength curve for a 400Å thick anodically grown SnO_2 layer.

*Electrochemical Society Active Member.

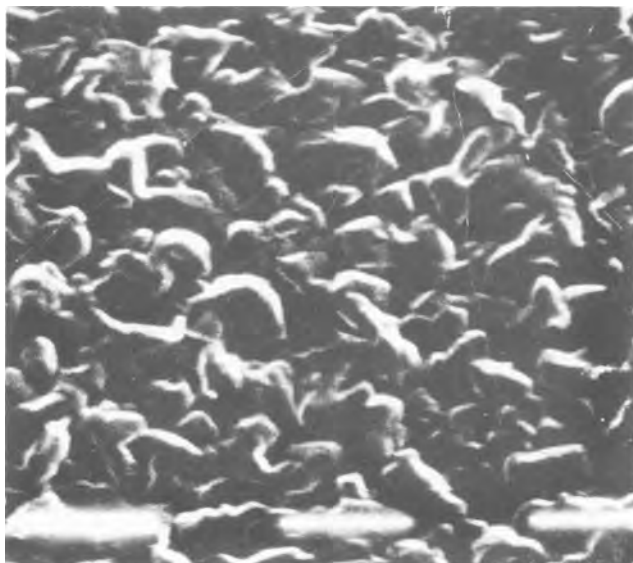


Fig. 2. Surface microstructure of an anodically grown SnO₂ layer, as revealed by scanning electron microscopy (markers correspond to 1 μm length).

An anodic oxidation procedure for growing SnO₂ layers on glass is described. Since the procedure is performed at

room temperature, it may be used to form transparent SnO₂ coatings on various substrates, including polymers. On conducting substrates, it may be possible to deposit the tin electrochemically instead of from the vacuum. Work is in progress to investigate anodic growth of SnO₂ films on substrates other than glass and to more thoroughly characterize the electrical and optical properties of such films.

Acknowledgment

The authors are indebted to Professor B. R. Nag for some valuable discussions and comments on the work.

Manuscript submitted Sept. 4, 1984; revised manuscript received Feb. 20, 1985.

REFERENCES

1. J. L. Vossen, *Phys. Thin Films*, **9**, 1 (1977).
2. K. L. Chopra, S. Major, and D. K. Pandya, *Thin Solid Films*, **102**, 1 (1983).
3. N. A. Hampson and D. Larkin, *This Journal*, **115**, 612 (1968).
4. A. Jeanne and D. Laforgue-Kantzer, *C.R. Acad. Sci. Paris*, **271C**, 1502 (1970).
5. R. Kerr, *J. Soc. Chem. Ind.*, **57**, 405 (1938).
6. G. Bianchi, *Chim. Ind.*, **29**, 295 (1947).
7. E. Giary and R. Kelly, *This Journal*, **121**, 394 (1974).
8. S. Dhar and D. Biswas, Paper presented at the Conference on Compound Semiconductors and Related Technologies, Madras, India, Sept. 21-23, 1983.
9. W. R. Runyan, "Semiconductor Measurements and Instrumentation," McGraw-Hill Kogakusha Ltd., 67 (1975).

The Role of Chlorine in the Gettering of Metallic Impurities from Silicon

Thomas A. Baginski*

Department of Electrical Engineering, Auburn University, Auburn, Alabama 36849

Joseph R. Monkowski*

Radio Semiconductor, Incorporated, State College, Pennsylvania 16801

Semiconductor device fabrication processes have been directed at developing and further refining MOS technologies. The oxides used in these devices must be of the highest quality to insure optimal device performance. Therefore, considerable effort has been devoted to improving the electrical characteristics of these oxides.

The presence of chlorine during silicon oxidation has been found many times to play a significant role in improving the minority carrier lifetime in the underlying silicon. Sometimes this improvement has been by a factor of two to three orders of magnitude (1, 2). However, at other times, very little effect has been seen. Since the lifetime improvement is believed to originate from the gettering of metallic impurities, this investigation was undertaken to determine if these discrepancies could be understood in terms of discrepancies in the gettering behavior of chlorinated oxides.

In this investigation, silicon wafers were contaminated with gold or copper. Chlorinated oxides were then grown at a variety of temperatures and HCl concentrations. Metallic impurity concentration profiles were measured. The results provide a quantitative description of the contaminant's movement during oxidation.

Experimental Procedure

Starting materials for all oxidations were (100)-oriented, 20 $\Omega\text{-cm}$, n-type, 2 in. diam. silicon wafers approximately 150 μm thick. Both before the contamination and before

* Electrochemical Society Active Member.

the subsequent oxidation, all wafers were cleaned in a standard manner using an ammonium hydroxide/hydrogen peroxide solution, a diluted hydrofluoric acid dip, a hydrochloric acid/hydrogen peroxide solution, and several deionized water rinses.

The wafers had a spin-on contamination source applied to the back side and were spun at 2000 rpm for 30s to form a source layer of uniform thickness.

The spin-on source consisted of SiO₂ plus either gold or copper in an alcohol suspension. The solution concentration exceeded 10²⁰ metal atom/g, thus insuring that the applied layer acted as an infinite source of metal atoms. After deposition of the doped oxide, the wafers were annealed for 10 min at 373 K in an N₂ ambient to bake out the alcohol, thus forming a glass layer saturated with the desired impurity.

The samples were then placed in a furnace to allow for diffusion of the metal. Copper was diffused at 1353 K. The diffusion temperature of Cu was chosen as slightly below the eutectic point in order to inhibit the formation of Cu-Si alloys while insuring a high solubility limit. The literature shows the solid solubility of Cu to be 6 $\times 10^{17}$ atom/cm³ at a temperature of 1353 K with a diffusion coefficient of 8 $\times 10^{-3}$ cm²/s. A 4h diffusion was performed in an electronic-grade nitrogen atmosphere.

Au was diffused at 1473 K for 15-30 min. Au has a solid solubility 8 $\times 10^{16}$ atom/cm³ and a diffusion coefficient of 10⁻³ cm²/s at this temperature (3). It is noted that both metals have extremely high diffusion coefficients. Setting

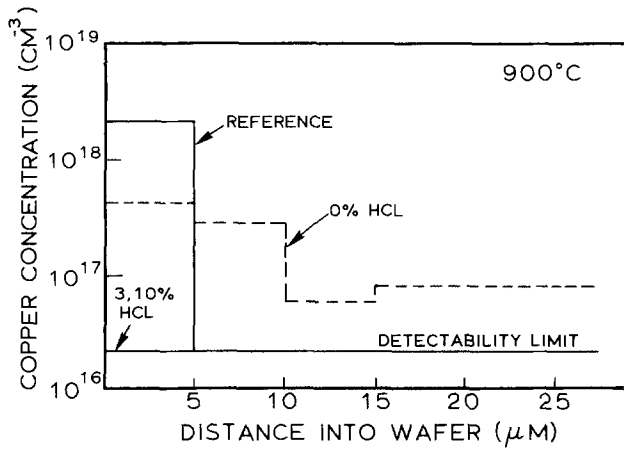


Fig. 1. Copper profiles for wafers oxidized in dry O_2 for 30 min at $900^\circ C$ with various amounts of HCl added.

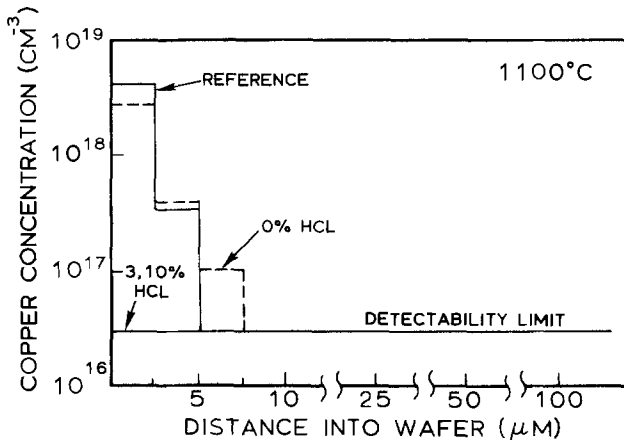


Fig. 2. Copper profiles for wafers oxidized in dry O_2 for 30 min at $1100^\circ C$ with various amounts of HCl added.

the thickness of the wafer equal to the diffusion length yields times in the range of minutes for either a copper or gold atom to travel from one side of the wafer to the other. Diffusion times were chosen between one and two orders of magnitude greater than these merely for processing convenience.

The samples were then oxidized at 1173, 1373, and 1473 K for 30 min in 0, 3, and 10% HCl/ O_2 gas mixtures.

For determination of the concentration profiles of the metals, layers of silicon were sequentially removed by etching in an ultrapure mixture of 1:20 HF:HNO₃. These solutions were then analyzed using dc plasma-excited emission spectroscopy. The layers were either 2.5 or 5 μm thick. In order to insure that only the front surface of the wafer was etched, the back side was protected with a wax inert to the etchant. In all cases, blanks were run to insure that extraneous contamination levels were below 1 ppb.

Results and Discussion

Figure 1 shows the results of oxidation at 1173 K. The reference is for a wafer profile immediately after the contamination with no further processing. Note that, in the reference profile, most of the contamination is located within several micrometers of the surface, the critical area where the device structures are located. This characteristic profile has been described elsewhere (4).

Oxidation in dry O_2 tends to redistribute the impurities to some extent, but there is clearly very little gettering. Additions of either 3 or 10% HCl to the O_2 getters the copper to below the detectability limit. Analysis of the silicon oxide grown with HCl showed no trace of copper, indicating that the copper was removed from the wafer into the HCl ambient.

The behavior of copper at 1373 K with 0, 3, 10% HCl in O_2 (Fig. 2) and at 1473 K with 0, 3, 10% HCl in O_2 (Fig. 3) is similar. In the case of $1100^\circ C$, 2.5 μm slices of Si were

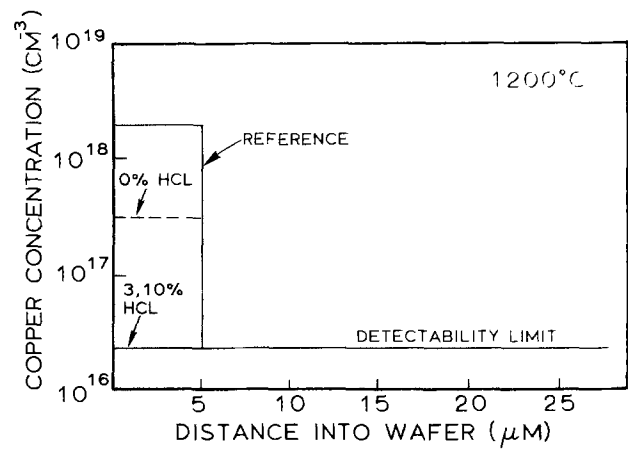


Fig. 3. Copper profiles for wafers oxidized in dry O_2 for 30 min at $1200^\circ C$ with various amounts of HCl added.

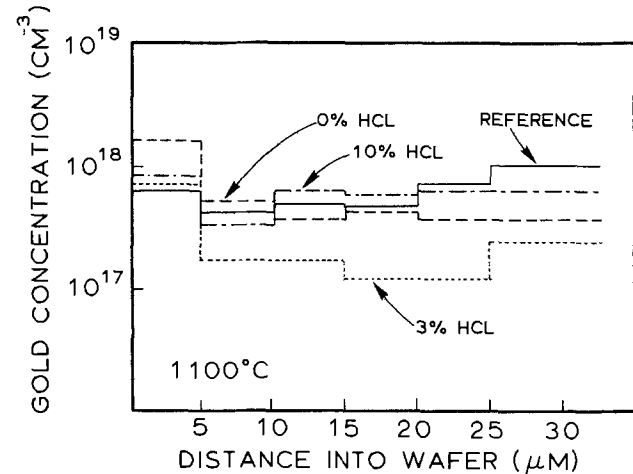


Fig. 4. Gold profiles for wafers oxidized in dry O_2 for 30 min at $1100^\circ C$ with various amounts of HCl added.

etched away to provide a finer depth resolution. The reference profile shows a high concentration of Cu within the first 2.5 μm of the wafer surface, showing clearly that the Cu segregates to the most critical region of device performance. During subsequent dry O_2 oxidation, the impurity shows little tendency to redistribute through the sample. Oxidation with 3 or 10% HCl again drops the impurity profile to below the detection limit. The oxide layer was also analyzed and was found to contain no copper. For this particular set, the wafers were etched to 50 μm from the surface, then a 2.5 μm slice was removed, and again the wafers were etched down to 100 μm and another slice removed. No Cu was detected in any part of the sample. The detection limit of the technique was approximately 10^{16} Cu atom/cm³ and 5×10^{15} Au atom/cm³.

Figure 4 shows the results with gold after the exposures. None of the treatments shows any appreciable influence on the redistribution of the gold. This behavior is in clear contrast to that of the copper, and indicates that there are indeed differences in the ability of chlorine to getter different metals. These differences are believed to stem from differences in the thermodynamic stability of the metal chloride.

For example, copper chloride is stable in a vapor phase at temperatures used during oxidation. Gold chloride decomposes at temperatures below 573 K (5).

Conclusions

In this investigation, silicon wafers were contaminated with copper and gold. Oxidations were then carried out at temperatures of 1173-1473 K using additions of 0-10% HCl to dry O_2 gas. In all cases, the metallic impurity concentration profiles were established to better than 1 ppm using atomic emission spectroscopy of solutions containing dissolved samples.

Copper is easily removed by the addition of HCl to the oxidizing ambient, but gold is not affected. The observed behavior is attributed to the existence of a volatile copper chloride and the lack of any stable gold chloride at the temperatures used.

REFERENCES

1. D. R. Young and L. M. Osburn, *This Journal*, **120**, 1578 (1973).
2. P. D. Esquenda and M. B. Das, *Solid-State Electron*, **23**, 741 (1980).
3. A. G. Milnes, "Deep Impurities in Semiconductors," p. 28, Wiley-Interscience, New York (1973).
4. F. A. Huntley and A. F. Willoughby, *Solid-State Electron*, **13**, 1231 (1970).
5. JANAF Thermochemical Tables, National Standard Reference Data Service, p. 37, National Bureau of Standards, Washington, DC (1984).

Cathodoluminescence of MgS:RE Phosphors

R. P. Rao

Materials Science Centre, Indian Institute of Technology, Kharagpur 721-302, India

Alkaline earth sulfides (AES) has been known for a long time to be excellent and versatile phosphor material (1). These are traditionally known as Lenard phosphors. Luminescence and electronic properties of sulfides like ZnS and CdS, belonging to (II-IV) group, have been widely studied (2). However, systematic investigations have not been made in detail on alkaline earth sulfides of the same group (II-VI) because of their chemical instability with atmospheric moisture and poor reproducibility. After Lehmann's extensive study (3-7), these sulfides have gained in importance as efficient phosphors, particularly in cathodoluminescence because of their low current saturation. When doped with certain impurities such as rare earths (RE), they produce emission from the UV to the near-IR regions. In the past, many workers have doped the phosphors with impurities in the presence of flux in order to reduce the doping temperature as well as to create a media for incorporation of impurities into the lattice.

Most of the earlier work on these sulfides has been carried out only on the studies of phosphorescence (8), photo-, thermo-, and electroluminescence (9-12). Recently, Kasano *et al.* (13) have reported the preparation and cathodoluminescence properties of Eu²⁺- or Ce³⁺-activated MgS and Ca_{1-x}Mg_xS phosphors. In this paper, the preparation and cathodoluminescence (CL) of MgS:RE (RE = Eu, Sm, Ce) are reported. From these results, the emissions of Eu²⁺, Ce³⁺, and Sm²⁺ are explained by considering their transitions.

Experimental

Polycrystalline MgS was prepared by reducing pure MgSO₄ (E. Merck, Germany) with pure CS₂ in an argon atmosphere. A good yield of MgS in the final product was obtained by passing CS₂ at 900°C for 1.5h. MgS phosphors were prepared by doping with different quantities of the rare earth elements Eu, Sm, and Ce. In the process of doping, MgS and MgSO₄ (4:1 by weight) were mixed with

the required amounts of respective rare earth oxides and fired at 900°C for 1.5h in the presence of CS₂. In the past, MgS:Ce films were prepared by firing MgO:Ce films in H₂S atmosphere at 950°C (14). In this investigation, films of different thicknesses were prepared by depositing fine grains of average particle sizes on well-cleaned glass substrates in an aqueous medium at room temperature (300 K) by sedimentation technique. The samples were dried and then protected from atmospheric moisture by coating with a polymer binder (Dow Corning 805). The texture of the films was studied with scanning electron microscopy.

The phosphor films were excited by 10 kV electrons at approximately 0.5 mA/cm² in a demountable cathode ray tube at 300 K. The emission from the excited samples was recorded with the help of a Bausch and Lomb monochromator and photomultiplier (PM) (XP1117) tube. All spectra presented in this paper were corrected for monochromator and PM tube response.

Results

In the process of materials preparation, the firing temperature (900°C) and the duration of firing (1.5h) were fixed at optimum values from a few trials at different temperatures and durations and from a consideration of other data such as DTA, TGA, DTC, etc. (15). To avoid the complications with residual flux left in the final product as well as the incorporation of unwanted impurities, MgS and MgSO₄ were taken as starting materials in the ratio 4:1. Moreover, MgS is highly hygroscopic, and it is difficult to separate the flux from the final product (16). As the melting temperature of MgSO₄ is well below the melting point of MgS, the firing temperature of the mixture would be reduced moderately.

X-ray diffraction spectra of these films exhibited the prominent lines of MgS, and no lines corresponding either to MgSO₄ or MgO were observed. Figure 1 shows the scanning electron micrographs of MgS doped with RE.

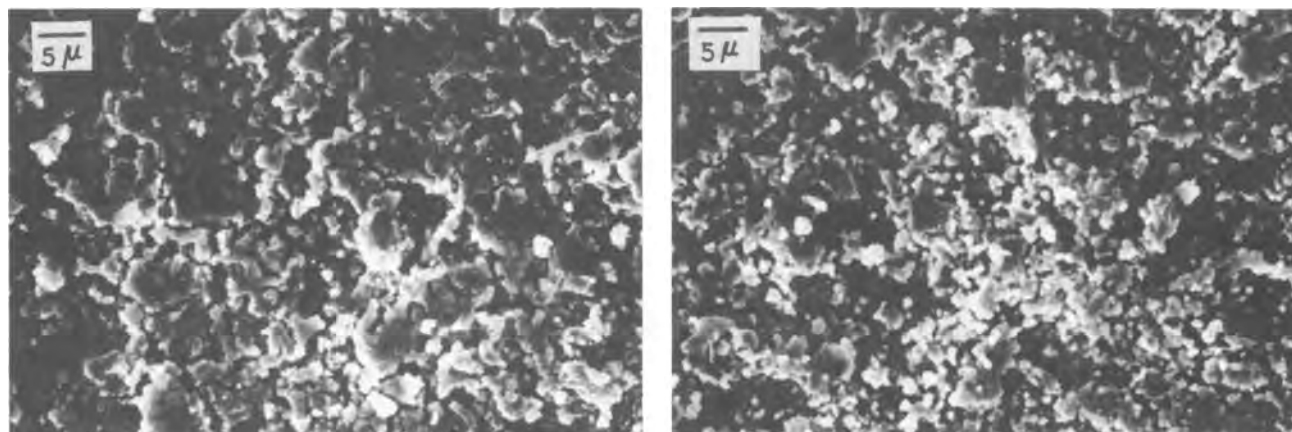


Fig. 1. Scanning electron micrographs of polycrystalline films. a (left): MgS:Eu. b (right): MgS:Ce phosphors.

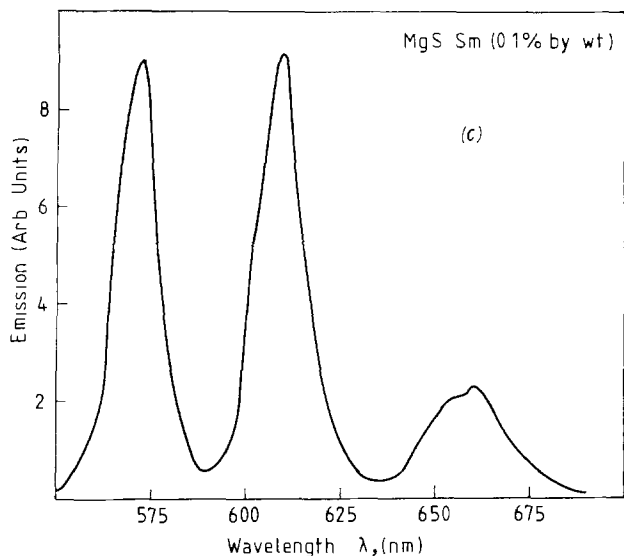


Fig. 2. Cathodoluminescence of MgS:Sm phosphor

From the photographs, it is clear that the films formed by the sedimentation technique used in this study are uniform.

Though many samples were prepared with different concentrations of impurities, only results on typical concentrations are presented in this paper. The cathodoluminescence spectrum of MgS:Eu (0.1% by weight) is observed in the red region with a band maximum at 590 nm. Two emission bands were observed in the green (525 nm) and red (590 nm) regions in the case of MgS:Ce (0.1% by weight) phosphors. As shown in Fig. 2, three emission bands are observed at 575 (green), 610 (red), and 660 nm (deep red) in the cathodoluminescence spectrum of MgS doped with Sm (0.1% by weight). The above results are explained by considering the possible transitions proposed by various workers in similar type of materials.

Discussion

The chemicals used in the preparation of MgS:RE were of 99.99% purity. The only possible activators doped were rare earths, and there was no coactivator since there was no flux material. The emission bands observed in this study are due only to rare earth ions. The Eu^{2+} ion is known as a broad-band $4f^65d \rightarrow 4f^7$ emitter. The ground state is $^6S(4f^7)$, and the lowest excited state is $4f^65d$. From the results of this investigation, the emission can also be interpreted as allowed transitions to the ground state $^6S_{7/2}$ from the excited states of $4f^65d$ configuration. Nakao (17) has observed the emission bands at 592, 652, and 594 nm for MgS, CaS, and CaSe, respectively, doped with Eu at 300 K. It was also reported (17) that sharp spiked lines (phonon lines) appeared on the shorter wavelength side at low temperatures (80 and 6 K), as observed by others in the case of alkali halides doped with Eu. From this extensive study, it was concluded that these bands are due to Eu^{2+} ion centers.

The emission of the Ce^{3+} ion corresponds to a $5d-4f$ transition. Since the configurational coordinate curves of these two levels are different, the emission has a broad-band character. The band has a doublet due to the ground-state splitting, $^2F_{5/2}$ and $^2F_{7/2}$ (18). Gilliland (14) has reported that the emission band (second peak) at 610 nm

with higher concentrations of Ce becomes dominant with the Ce to Mg ratio was 1:1 in case of MgS:Ce phosphors. The emission observed in this investigation is exactly the same as that observed by Asano *et al.* (19). They reported that the emission bands $^2T_{2g}(5d) \rightarrow ^2F_{7/2}$, $^2F_{5/2}(4f)$ originating from the intraionic transitions of Ce^{3+} . The band maxima are at 2.36 and 2.1 eV with an energy difference of 0.26 eV, which corresponds nearly to the difference between the energy levels of $^2F_{5/2}$ and $^2F_{7/2}$ of 4f electrons of Ce^{3+} ion. Lehmann has observed three bands in the yellow, red, and deep red for the same type of phosphors. Data on Sm^{3+} -doped alkaline earth sulfides are few. Also, the possible transitions are not discussed anywhere. The Sm^{3+} rare earth ion is one possessing a complex nature with a total number of 1994 levels and 306,604 possible transitions (20), it will only be speculative to propose any possible allowed transitions from the above results. However, from the bands at 17,452, 16,393, and 15,152 cm^{-1} , the transitions like $^4G_{5/2} \rightarrow ^6H_{5/2}$, $^4G_{5/2} \rightarrow ^6H_{7/2}$, and $^4G_{5/2} \rightarrow ^6H_{9/2}$ may be proposed. It needs further detailed investigations to find out the exact transitions of Sm^{3+} involved.

It is concluded from these studies that these MgS phosphors can be prepared in a simple way and used as CL phosphors. Further experiments are required to understand the role of RE impurities on the emission characteristics in these phosphors. The efficiency could be determined by comparing with standard CL phosphors.

Acknowledgments

The author expresses his gratefulness to Professor J. P. Fillard and Dr. M. De Murcia of CEM, USTL, Montpellier, for their encouragement during the course of this work. He is also indebted to the French Government for financial assistance. This is a part of the work carried out by the author at Centre d'Electronique de Montpellier, USTL, Montpellier Cedex, France, in 1982 and 1983.

Manuscript submitted Jan. 2, 1985; revised manuscript received March 1, 1985.

REFERENCES

1. P. Lenard, F. Schmidt, and R. Tomaschek, "Hand Buch der Expt. Phys.," Vol 23, Springer-Verlag, Leipzig, Germany (1928).
2. S. Shinoya, *J. Lumin.*, **1/2**, 17 (1970).
3. W. Lehmann, *This Journal*, **117**, 1389 (1970).
4. W. Lehmann, *ibid.*, **118**, 164 (1971).
5. W. Lehmann and F. M. Ryan, *ibid.*, **118**, 477 (1971).
6. W. Lehmann and F. M. Ryan, *ibid.*, **119**, 275 (1972).
7. W. Lehmann, *J. Lumin.*, **5**, 87 (1972).
8. R. P. Rao, D. R. Rao, and H. D. Banerjee, *Mater. Res. Bull.*, **13**, 409 (1978).
9. N. Yamashita, T. Ohira, H. Mizuochi, and S. Asano, *J. Phys. Soc. Jpn.*, **53**, 419 (1984).
10. R. P. Rao, *J. Lumin.*, **30**, (1984).
11. D. Thesis, *ibid.*, **23**, 191 (1981).
12. S. Bhushan and F. S. Chandra, *J. Phys. D*, **17**, 589 (1984).
13. H. Hasano, K. Megumi, and H. Yamamoto, *This Journal*, **131**, 1953 (1984).
14. J. M. Gilliland, *J. Appl. Phys.*, **38**, 2427 (1967).
15. R. P. Rao, *J. Mater. Sci. Lett.*, **2**, 106 (1983).
16. F. Okamoto and K. Kato, *This Journal*, **130**, 432 (1983).
17. Y. Nakao, *J. Phys. Soc. Jpn.*, **48**, 534 (1980).
18. G. Blasse, in "Handbook of Physics and Chemistry of Rare Earths," K. A. Gschneidner and L. R. Eyring, Editors, p. 257, North Holland, Amsterdam (1979).
19. S. Asano, N. Yamashita, and T. Ohnishi, *Physica Status Solidi B*, **99**, 661 (1980).
20. G. H. Dieke, "Spectra and Energy Levels of Rare Earth Ions in Crystals," Interscience Publishers, New York (1963).



Enhanced Diffusion in Boron Implanted Silicon

L. C. Hopkins, T. E. Seidel,¹ J. S. Williams,² and J. C. Bean*

AT&T Bell Laboratories, Murray Hill, New Jersey 07974

INTRODUCTION

When boron is implanted into crystalline silicon the dopant distribution includes a deeply penetrating tail due to ion channeling (1,2). This channeling tail is an unavoidable consequence of large angle scattering events occurring during implantation. When such samples are annealed it has been observed (3-6) that boron in the tail region diffuses anomalously fast. This occurs for both long (~30 min) furnace anneals at low temperatures (700-800°C) (3) or rapid (~10 sec) higher temperature anneals (1050-1100°C) (4-6).

The cause of this enhanced diffusion has been the subject of considerable discussion (7,8). One possibility, proposed by Fair (7), is that point defects created by the implantation (e.g., vacancies and/or self-interstitials) enhance the tail diffusivity. Because such defects are created primarily near the peak of the boron implantation distribution, this model must involve migration of such defects from the peak damaged region inward to the deeper channeling tail. In this paper we report an experimental test of this "non-local" diffusion model. Samples are annealed with and without the heavily damaged surface region and profiled by SIMS. Preliminary results show similar diffusion in both sample lots in contradiction to the Fair proposal, implying that the enhanced tail diffusion is a "local" phenomenon.

EXPERIMENTAL

Boron was implanted with two batches of 4" <100> 10 Ω cm P-type silicon wafers (#A and #B) using an Extrinsic DF4 implanter. The wafers were tilted ~7° off-normal, in an arbitrary rotational direction and implanted at room temperature. Boron energy was 40.0 keV and swept beam current was kept low (~100 μA) to avoid beam heating. After implantation wafers in each batch were divided and adjacent pieces were etched in an HF-HNO₃ solution to remove ~2000Å (as verified by Dektak profilometer measurement). This 2000Å region contained the peaks of both the boron and damage distributions. Adjacent unetched and etched portions of the B wafers were then annealed together in a rapid thermal annealing furnace at ~1100°C for ~10 sec. This yielded the following sample matrix

Table I. Sample Matrix

#	Implanted	Etched	Annealed
A	X		
A'	X	X	
B	X		X
B'	X	X	X

Boron profiles were measured using an Atomika A-DIDA-3000-30 ion microprobe. An O₂⁺ primary beam was selected to enhance boron sensitivity. The O₂⁺ beam was incident 2° off-normal at an energy of 10.0 keV. The 300 μA analysis beam was focused to ~100 μm and scanned over a 1/2 mm × 1/2 mm crater yielding an etch rate of ~1/2 μm/hr. Samples were analyzed back-to-back in a vacuum of 2 × 10⁻⁹ torr. Signal was collected only over the center 30% of the analysis crater to ensure adequate depth resolution.

Because the experiment depended on discrimination of subtle differences in diffusion profiles, two means were used to monitor and confirm stable SIMS operation. First, both boron and silicon ¹⁴Si⁺⁺ profiles were measured. Drift in the analysis beam current or detection sensitivity would then be revealed by drift of the ¹⁴Si⁺⁺ signal. Second, the depth integral of the ¹⁴Si⁺⁺ signal was compared to the measured volume of the analysis crater. Data was only used if both the ¹⁴Si⁺⁺ signal was constant during the run (within ±5%) and if the integrated silicon count to volume ratio was constant sample to sample (within ±10%).

Typical raw SIMS data is shown for samples #A in Fig. 1. Data for runs satisfying the two above tests were then converted to concentration vs depth profiles via the following processing. To generate a concentration scale, the ¹¹B⁺ count was first divided, point by point, by the ¹⁴Si⁺⁺ count. This would normalize out any residual drift in SIMS sensitivity. Second, the SIMS boron background signal (as indicated by the flat base count at the deep end of the distribution) was subtracted from the normalized boron count. Finally, the depth integral of the normalized boron count for samples A and B was compared to the stated implant dose of 2 × 10¹⁵/cm² yielding calibration constants for each sample. The calibration constants for the A and B samples were then transferred to the A' and B' samples respectively. (A and B samples were calibrated separately to account for a slight discrepancy between implantation doses to the wafers.)

Manuscript received April 22, 1985.

¹ Now at J. C. Schumacher Co., Oceanside, CA 92054.

² Permanent Address: Melbourne Institute of Technology.

* Electrochemical Society Active Member

AT&T Bell Laboratories assisted in meeting the publication costs of this article.

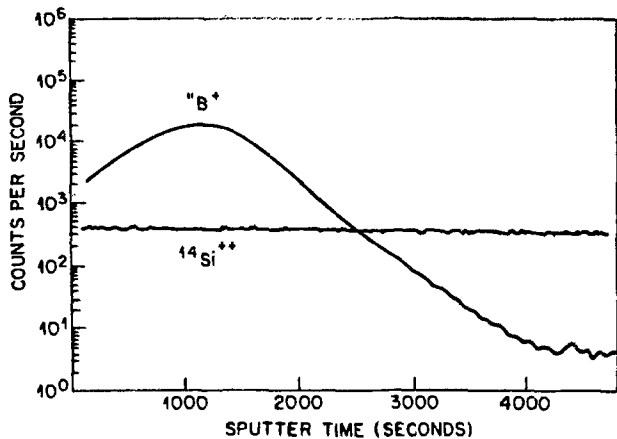


Fig. 1 Raw (unprocessed) data for control boron implanted sample (#A: unetched and unannealed).

The depth scale was established by setting the total sputter time equal to the total crater depth, sample by sample. Given that the samples were composed only of Si and trace B and that the $^{14}\text{Si}^{++}$ reference counts were constant during profiling, it can be safely assumed that the sputter rate was constant. Intermediate depth points were therefore established by linear interpolation of the total analysis depth.

RESULTS

Processed data are shown in Figs. 2 and 3. Figure 2 compares unannealed and annealed boron distributions in unetched samples (A and B). Figure 3 compares unannealed and annealed distributions in etched samples (A' and B'). In both figures the channeling tail falls at a rate of $\sim 6.1 \times 10^{15}/\text{cm}^3/\text{\AA}$ in unannealed samples vs $\sim 4.5 \times 10^{15}/\text{cm}^3/\text{\AA}$ in annealed samples. Within our experimental accuracy, the presence or absence of the maximally damaged near-surface region has no effect on the enhanced diffusion of channeled boron tail. Because samples were implanted at room temperature and subjected to no high temperature processing prior to etching, point defects created

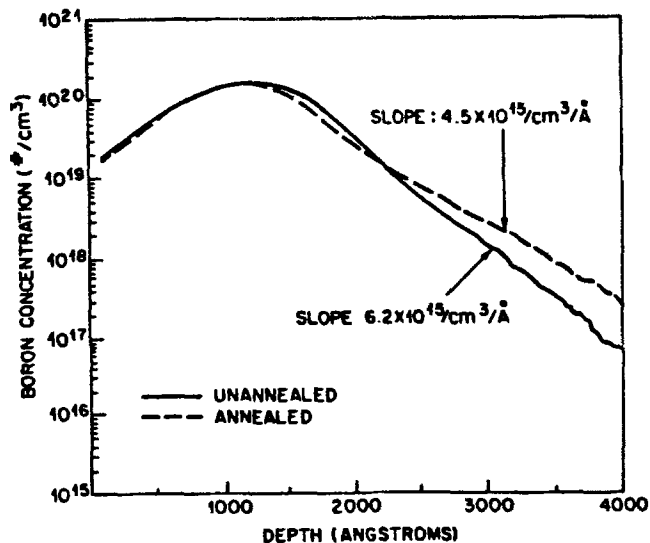


Fig. 2 Processed (calibrated) data for unetched samples with (#B) and without (#A) post implantation anneal.

near the peak of the boron distribution should have been frozen in place and thus removed by the etch. The near identical diffusion of etched and unetched samples therefore indicates that these defects are not responsible for the enhanced channeling tail diffusion.

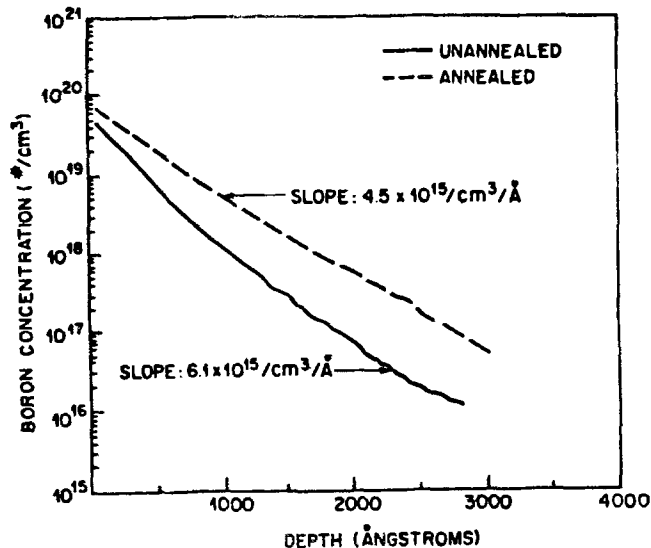


Fig. 3 Processed (calibrated) data for $\sim 2000\text{\AA}$ etched samples with (#B) and without (#A') post implantation anneal.

To summarize, SIMS profiling experiments on boron implanted silicon samples indicate that radiation damage created near the peak of the boron profile cannot be the dominant agent producing anomalous diffusion. Alternate models are therefore required to explain and predict the annealing behavior in this technologically important process.

REFERENCES

1. W. K. Chu, J. Nucl. Instr. and Meth. in Phys. Res. Sec. B: Beam Interactions with Materials and Atoms, Eds. Anderson and Picreux, March 1985.
2. D. V. Morgan, Ed. Channeling: Theory Observation and Applications, Wiley, New York, 1973.
3. W. K. Hefker, Phillips, Res. Repts. Suppl. No. 8 (1975).
4. S. R. Wilson, R. B. Gregory, W. M. Paulson, and H. T. Hichl, IEEE Trans. on Nuc. Sci. NS-30, 2, p. 1734 (1983).
5. R. T. Hodgson, V. Deline, S. M. Mader, F. F. Morehead, and J. Gelpey — in Energy Beam-Solid Interactions and Transient Thermal Processing, Eds. J. C. C. Fan and N. M. Johnson, NY, NY (1984).
6. T. E. Seidel, D. J. Lischner, C. S. Pai, R. V. Knoell, D. M. Maher and D. C. Jacobson, J. Nucl. Instr. and Meth. in Phys. Res. Sec. B: Beam Interactions with Materials and Atoms, Eds. Anderson and Picreux, March 1985.
7. R. B. Fair, J. J. Wortman, and J. Liu, J. Electrochem. Soc. 1984.
8. G. S. Oehrlein, R. Ghez, J. D. Fehriback, E. F. Gorey, T. O. Sedgwich, S. A. Cohen, and Y. R. Deline, J. Electronic Materials (Proc. 13th Int. Conf. on Defects in Semiconductors, Coronado CA 1984), to be published December 1984.

A Performance Improvement for High Temperature Stabilized-Zirconia pH Sensors

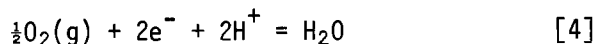
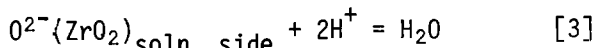
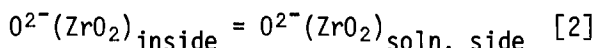
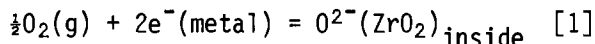
Mike J. Danielson* and Oscar H. Koski

Pacific Northwest Laboratory, Richland, Washington 99352

Jonathan Myers

Rockwell Hanford Operations, Richland, Washington 99352

In a recent paper, Danielson, Koski, and Myers (1) reviewed the literature on high temperature pH sensors constructed from yttria-stabilized zirconia. They also reported their own work in which sensors demonstrated excellent pH response in the range of 100 to 300°C. Danielson et al. (1) recognized from their potential measurements that the sensors acted reversibly to oxygen (on their internal surface) by the following equilibria:



This observation has great importance for simplifying the calibration procedure. Previously, all the metallic fills studied (Cu/Cu₂O, Ag, Au) by the authors required a preliminary autoclaving to 250 to 300°C before their potential was that predicted by Eq. [4], and this is very inconvenient for pH studies between 100 to 250°C. This note discusses a platinum fill which results in the sensors acting reversibly to oxygen at 100 to 300°C without the need for initial autoclaving at 250 to 300°C.

The metallic platinum is applied as a thin coating to the inside of the sensor (Figure 1). The Pt coated sensors will start out at 100°C being poised by oxygen from the air, and it is our experience that sensors which have good pH response at 100°C will operate even better at higher temperatures. The 8 wt% yttria sensors were evaluated in a silica-carbonate buffer (F⁻, 17.6 mg/l; Cl⁻, 335 mg/l; SO₄²⁻, 2.4 mg/l; Ca²⁺, 1.3 mg/l; K⁺, 10 mg/l; Na⁺, 399 mg/l; Si, 43.4 mg/l; CO₃²⁻, 67 mg/l; HCO₃, 32 mg/l; pH = 9.77 @ 25°C) sparged with hydrogen at

one atmosphere. A platinized-platinum hydrogen electrode and external Ag, AgCl reference electrode (0.100 M KCl) were used in the experiments carried out at 100, 150, and 200°C. Corrections were made for the thermal liquid junction potential of the external reference to place the potentials on the Standard Hydrogen Electrode scale. All the zirconia sensors had a Pt fill. Table I shows the calculated pH for the hydrogen electrode and the zirconia sensors. The old zirconia sensors had a varied autoclave history including about 30 days of autoclaving before this test. Sensor 1 is defective (doesn't give full Nernstian response at 100°C) and is included for comparison. We have observed that sensors will develop a degraded pH response (when evaluated at 100°) when subjected to 300°C conditions for a week or more.

Table I. pH Measurement Data

Sensor	Description	pH (Calculated)		
		100°C	150°C	200°C
H ₂	Hydrogen electrode	8.77	8.29	7.99
1	ZrO ₂ /old	8.39	8.36	7.71
2	ZrO ₂ /old	8.73	8.29	7.91
3	ZrO ₂ /new	8.69	8.35	7.92
4	ZrO ₂ /new	8.97	8.41	8.11

The pH values were calculated by using the E° (Table II) of Eq. [4], the measured voltage of the sensors on the hydrogen scale, and the Nernst equation (taking account that fO₂ = 0.2). This is an especially severe test of the pH performance of the zirconia sensors since pH sensors are normally standardized in a known buffer and their pH response measured relative to this value. Except for the response of Sensor 1 at 100°C, the measured pH is within 0.2 pH units of the value measured using the

* Electrochemical Society Active Member.

hydrogen electrode, and the agreement improves as the temperature increases. Though this data only goes to 200°C, it is our experience that even better performance would be expected at 250 and 300°C.

Table II. E° Data

T	E°
100°C	1.167 V
150°C	1.127 V
200°C	1.088 V
250°C	1.050 V
300°C	1.013 V

The following procedure is used to coat the sensors:

- 1) Coat inside of sensor (depth of 2.5 cm) with Englehard Pt ink (No. A-4338).
- 2) Dry at 120°C for one hour to harden the coating.
- 3) Wind piano wire around mandrel to make a spring which is a little larger in diameter than the sensor I.D. Coat spring with Pt ink and insert.

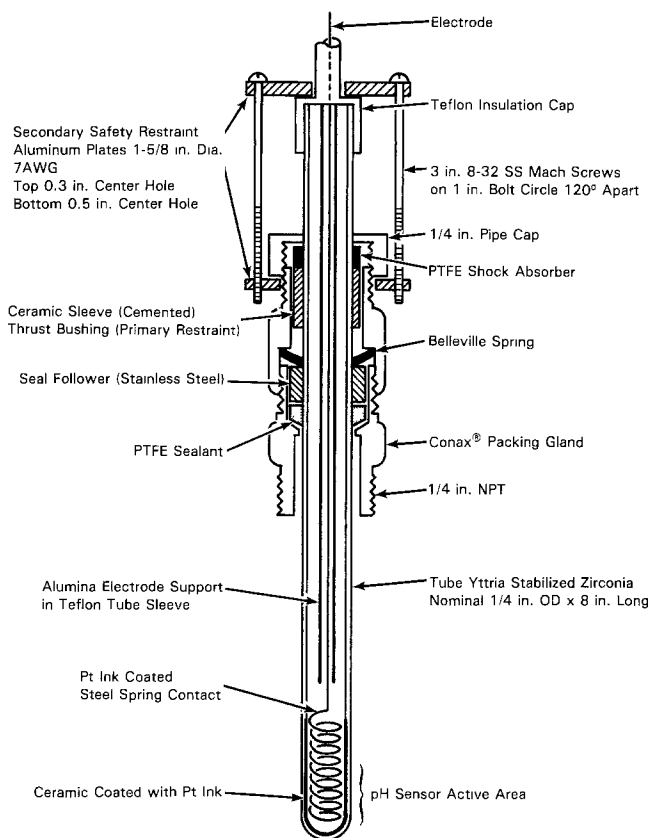


Figure 1. pH Electrode

- 4) Fire in air to 400°C for 18 hours.
- 5) Epoxy ceramic collar to upper portion of sensor after cooldown.

This development demonstrates a significant simplification in the calibration process which should assist in the practical application of the sensors for temperatures of 100 to 300°C. More accuracy can be obtained by using a buffer of known pH to standardize the sensors as is currently done with glass pH sensors at ambient conditions.

ACKNOWLEDGEMENTS

This work is supported by the Department of Energy under the Basalt Waste Isolation Project of Rockwell Hanford Operations, Richland, WA.

REFERENCES

1. Mike J. Danielson, Oscar H. Koski, and Jonathan Myers, *J. Electrochem. Soc.*, **132**, 296-301 (1985).

Manuscript submitted March 7, 1985; revised manuscript received June 3, 1985.

Battelle Pacific Northwest Laboratories assisted in meeting the publication costs of this article.



EST

A Discussion of the Mechanism of Cadmium Migration in Sealed Nickel-Cadmium Cells

David H. Fritts* and Ross E. Dueber*

Air Force Wright Aeronautical Laboratories, Wright-Patterson Air Force Base, Ohio 45433

ABSTRACT

Cadmium migration in sealed nickel-cadmium cells was studied in order to explain the occurrence of premature cell failure due to internal shorting. Time lapse microphotography of the cadmium surface revealed numerous migration regions growing during the life of a single cell. The dominant transport mechanism of the active material was hydrodynamic in nature and was due to molar volume changes occurring in the electrode. Migration occurred "en masse" with the migration regions charging and discharging with the electrode. Individual migration regions were analyzed under the SEM and were shown to consist of both crystalline and amorphous forms of active material. It was determined that the amorphous active material contained metallic cadmium which allowed for an electronic connection to the negative electrode. Growth of the migration regions occurred through a precipitation/dissolution mechanism of the active material until a short circuit developed between the two electrodes.

Failure analyses of sealed nickel-cadmium cells indicate that cadmium migration is a major cause of premature cell failure (1-4). Several theories exist explaining the mechanism by which the active material traverses the separator region from the cadmium electrode (4-6). Through the use of time-lapse microphotography, we have observed that the migration occurs "en masse" at selected positions on the surface of the electrode (7). These migration regions are not dendrites in the true sense, but are rather mound-like structures protruding into the separator. We believe the migration regions consist of both metallic cadmium and cadmium hydroxide. Our films show the regions of active material growing in size as the number of cycles increases. Eventual failure of the cell occurs by the formation of numerous "soft shorts."

Experimental

Four types of test cells were constructed for defining a mechanistic model of cadmium migration. The various cell types were fabricated to answer questions that occurred to us as the investigation progressed. The first type of test cell, cell 1, was constructed for filming under the microscope. It consisted of one cadmium and one nickel electrode, each cut $28.0 \times 18.0 \times 0.8$ mm from commercially manufactured, chemically impregnated plates, placed in a Plexiglas case equipped with a Teflon gasket and a removable Plexiglas top. One layer of nylon mat served as the separator (Fig. 1). In order to avoid interference of the electrode surface, a minimal amount of electrolyte was used (0.3 ml of 32 weight percent [w/o] KOH *vs.* a calculated 0.45 ml cell void volume). Current was drawn at the 1C rate, based on a $\text{Ni}(\text{OH})_2$ electrode capacity of 121 mAh, using a Hewlett-Packard Model 6177 dc current source. Depth of discharge progressed from 20 to 40 to 80%. Cell failure occurred at cycle 1728. All testing was performed at room temperature.

Filming of the cell was performed at $75\times$ magnification using a Bolex 16 mm movie camera attached to an Olympus Model BH10 metallurgical microscope with a time lapse control unit.

Cell 2 was designed to minimize the interactions between the nickel and cadmium electrodes by separating

the two in different compartments with a common electrolyte reservoir (Fig. 2). The electrodes were identical to those used in the first cell. Holes were drilled into the side of the cadmium electrode compartment to control electrolyte flow. A thin layer of paraffin oil was placed on the electrolyte surface to prevent the formation of carbonates in solution. The cell was given a full charge and then cycled at the 0.67C rate to a 20% depth.

In addition to the above, two other cells were also constructed for specific testing purposes. Cell 3 was constructed using nickel and cadmium electrodes cut from the above-mentioned plates without utilization of a separator. The electrodes, with dimensions $36.0 \times 12.0 \times 0.8$ mm, were placed in a Plexiglas box 6 mm apart. The space between the two electrodes was filled with 0, 10, and 20 w/o cadmium metal (Alfa-Ventron, M6N, 200

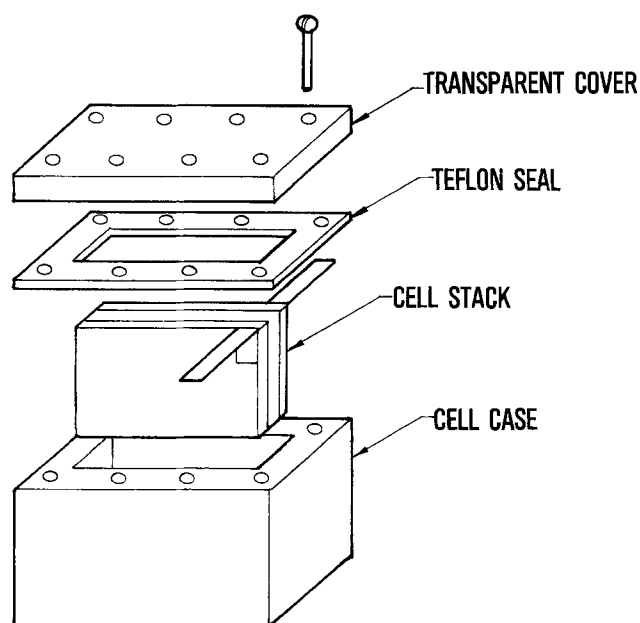


Fig. 1. Time lapse microphotography cell, cell 1

*Electrochemical Society Active Member.

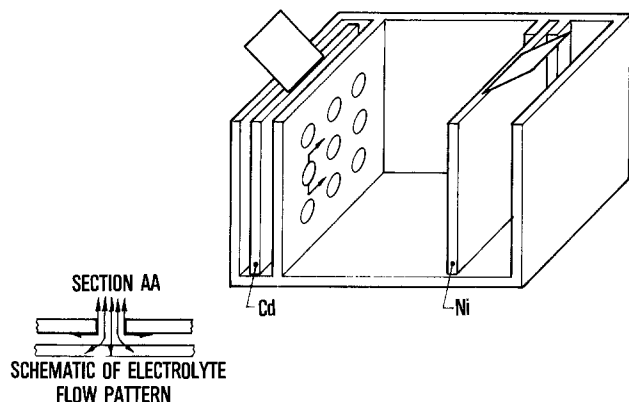


Fig. 2. Cell for isolating electrode interactions, cell 2 (inset depicts estimated electrolyte flow pattern).

mesh) with the balance of the mixture being cadmium-hydroxide (Alfa-Ventron ultrapuriss.). A constant current of 50 mA was used to charge and discharge the cell between voltage limits of 1.8 and 0.4V. The electrolyte was again 32 w/o aqueous KOH.

The fourth cell, cell 4, was constructed using a standard sintered nickel electrode with the dimensions of $15.0 \times 30.0 \times 0.8$ mm. The counterelectrode was a coiled cadmium wire of 1 mm diam. The length of the wire submerged in electrolyte was 16 cm. The cell was cycled between 1.93 (peak voltage on charge) and 0.65V. A constant current of 600 μ A was kept using the Hewlett-Packard Model 6177C dc current source. The parameters measured were cell capacity and voltage.

Analyses of the cadmium electrode surfaces and cell separators were performed with an ISI scanning electron microscope equipped with a Kevex dispersive x-ray spectrometer.

Results

Our initial viewing of the films provided us with a great deal of insight into the environment of a nickel-cadmium cell during cycling. Readily apparent from the beginning are the hydrodynamic forces present throughout the cell. In both starved and flooded cells, electrolyte could be seen constantly moving back and forth between the electrodes and the separator. Small particles of active material and sinter were detached from the electrodes by the hydrodynamic forces and subsequently distributed randomly throughout the separator region. The severity of electrolyte pumping action could be increased and decreased by proportionally varying the current rate.

Several migration regions formed on the electrode surface near the top of cell 1 and were able to be filmed. We focused upon one rather large migration region (0.63×10^{-2} cm across at base) which we found after the eight hundredth cycle. For the remainder of the cell's life, the camera filmed the behavior of this region which consisted of mossy active material. It was obvious after a few hundred cycles that the migration area indeed was growing. Measurements from the film estimated the migration region to be 1.3×10^{-2} - 2.0×10^{-2} cm at the base and 2.0×10^{-2} cm from base to peak when the cell finally failed. Another migration region similar to this one, however, was the ultimate cause of cell shorting.

A more careful viewing of the films showed other interesting phenomena occurring inside the cell. Several rather large pieces of active material, which apparently had broken off the cadmium electrode, were found moving randomly throughout the separator region. No agglomeration of these pieces was found forming a bridge between the two electrodes.

A patterned color change in the migration region was also noticed with each charge and discharge. Color changes in the migration region began at the peak and progressively moved towards the base during both charge and discharge. The color change was seen to be much faster during discharge than during charge.

In cell 2, we again observed numerous migration regions on the surface of the cadmium electrode, although they were much smaller in size than in the previous cell. Specific details of the growth of these regions was obscured due to the flooded state of the cell and the paraffin oil layer. After completing 1400 cycles, the cell was disassembled and the surface of the cadmium electrode rinsed, dried, and examined. Without the aid of magnification we were able to see four very large, distinct migration regions. The positions and size of these regions corresponded to the holes in the Plexiglas case where the electrolyte entered. Micrographs taken by the SEM revealed three distinct areas in each migration region. Figure 3 depicts an overall view of one migration region. There is the central migration area where buildup of active material is the greatest. A more detailed micrograph (Fig. 4) shows the central migration area to be a combination of both crystalline and mossy active material. Immediately surrounding the central area is a second area that is relatively clear of active material (Fig. 5). The roller tracks on the sintered substrate are even exposed. Farthest from the central area is the outer or peripheral area, which is representative of the morphology of the majority of the cadmium electrode surface (Fig. 6).

Each of the three separator mixtures used in cell 3 completed more than 100 cycles without a failure. The only change observed in the separator mixture was a gradual darkening of the originally white cadmium hydroxide with time.

The cadmium wire cell, cell 4, was deep discharged 92 cycles. The maximum capacity of the wire on discharge, between the previously stated potentials, was 1.97C. In Fig. 7, an SEM micrograph of the wire surface is shown. Generally speaking, the surface is characterized by a mossy structure which is strewn with β -Cd(OH)₂ crystals. This is very similar to our structural observations noted with sintered electrodes.

Discussion

Ordinary vented aircraft nickel-cadmium cells employ gas-impermeable separators which act as barriers to active material. Sealed nickel-cadmium cells, on the other hand, utilize nylon mat separators which allow for gas recombination to take place. Unfortunately, this permeability is a detriment to the inhibition of the migration of active material. As cycle life increases, active material from the cadmium electrode forces its way through the separator and eventually contacts the nickel electrode. These "short circuits" lead to decreased cell performance and subsequent cell failure.

Several models exist for the mechanism by which active material migrates into the separator. Mayer (8) had suggested that negatively charged Cd(OH)₂ could be transported electrophoretically away from the cadmium



Fig. 3. Migration region on cadmium electrode from cell 2



Fig. 4. Central migration area from cell 2



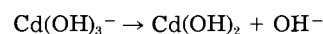
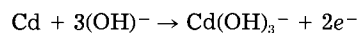
Fig. 6. Peripheral area of cadmium electrode from cell 2

electrode. Discrepancies with this model were brought forth by several other researchers in the field, including Barnard *et al.* (9) and James (10, 11); therefore, we chose not to consider it as a viable model at this time.

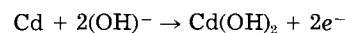
The remaining two models suppose Cd(OH)_2 is initially deposited in the separator and then converted to metallic cadmium. The difference between the two models lies in the method of reduction of Cd(OH)_2 . Several authors believe the reduction of Cd(OH)_2 occurs through a solid phase reaction (12-14). For failure to happen through such a process, Cd(OH)_2 would have to become detached from the electrode and in turn agglomerate in the separator to form a connection between the cadmium and nickel electrodes. Cadmium hydroxide would then be reduced to metallic cadmium, which results in the formation of what is termed a "soft short."

In contrast to solid-state reduction of Cd(OH)_2 , the precipitation/dissolution model advocates reduction through the formation of soluble intermediate phases (15). Rotating disk electrode studies by Okinaka (16) provided evidence for the existence of both solid and solution phase transport of cadmium species. During anodic oxidation, the mechanism appears to be a predominantly solution phase. The intermediate species formed on both charge and discharge is Cd(OH)_3^- (16-17). The Cd(OH)_3^- could, according to the model, recrystallize in the separator and provide paths for shorting to occur (18). Shorting paths could occur according to the following possible reactions as represented by McDermott (19)

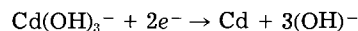
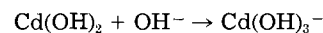
Discharge



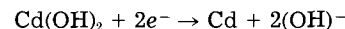
or



Charge



or



The solubility of the intermediate species is well established. Its transport is dominated by the pumping action of the electrolyte as viewed in the film of cell 1. This pumping is due to specific volume changes in the electrodes. During discharge, cadmium is converted to cadmium hydroxide, resulting in an increase in the electrode's specific volume and the accompanying displacement of electrolyte into the separator. Such convective currents as McDermott suggests (19) could carry the solvated cadmate species outwards from the electrode interior. We have found that precipitation of Cd(OH)_3^- occurs at selected nucleation sites on the cadmium electrode surface, rather than in the separator, thus forming the migration regions we observed (Fig. 8). We do not

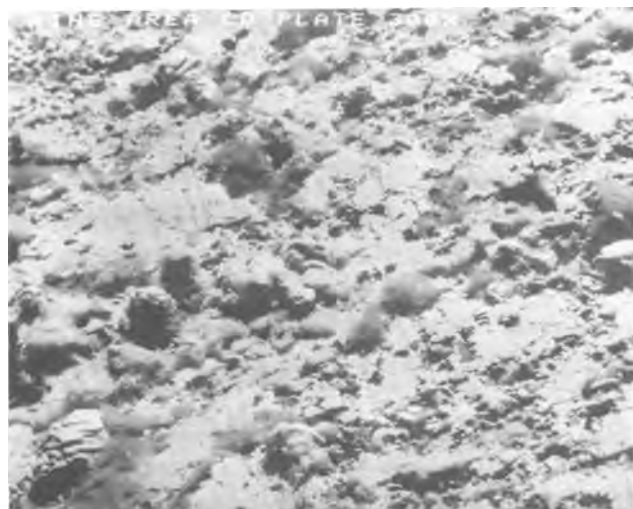


Fig. 5. Area of electrode surrounding the central migration area from cell 2.



Fig. 7. Surface of cycled cadmium wire

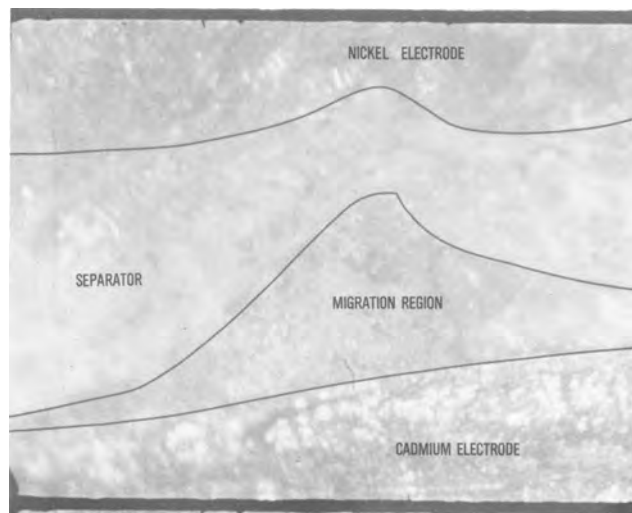


Fig. 8. Migration region filmed in cell 1 (Cd at top, Ni at bottom)

know at this time why some nucleation sites on the electrode surface are more active than others. This is quite difficult to determine in light of the fact that the micromorphology of the surface is so complex and varying. These migration regions do, however, grow in size with cycle life as increasing amounts of $\text{Cd}(\text{OH})_2$ are precipitated.

Attempts were made to study the individual migration regions in cell 1 with the SEM, but failed because of our inability to preserve an intact region upon separating the electrode and the separator. After several hundred cycles, the separator and the electrode surface meld together and become somewhat indistinguishable. We do not believe this behavior is strongly related to the degree of electrolyte starvation in our test cell. The amount of cadmate ion transported is proportional to the volume of electrolyte "pumped" from the electrodes. This pumping occurs during charge/discharge when the electrodes undergo molar volume changes. Therefore, the dominant parameter affecting migration is thought to be depth of discharge.

A micrograph was taken of a cross section of the separator (Fig. 9), and dispersive x-ray elemental mapping of the cross section verifies that active material is pushing through the separator in the form of a migration region. This would account for the presence of active material in the separator, which was previously thought to have precipitated out on nucleation sites within the separator itself. No evidence was found to support a precipitation mechanism within the separator region. Active material in the separator is the result of either intact migration re-



Fig. 9. Cross section of separator from cell 1 (Cd side at top, Ni side at bottom).

gions or pieces of migration regions detached from the electrode by the hydrodynamic forces of the electrolyte.

In order to study cadmium migration behavior without hindrance from either the separator or the nickel electrode, cell 2 was designed and built. The nickel electrode was positioned at a great enough distance from the cadmium electrode to negate the effects of gassing and specific volume change. The result was much the same as before, only this time the migration regions were smaller in size. The occurrence agrees with what Will and Hess (17) stated about the extent of migration being directly related to the rate of discharging and the number of cycles. The lower discharge rate would in fact decrease the hydrodynamic force of the electrolyte and lessen the amount of dissolved cadmium carried to the electrode surface for precipitation.

Except for the four migration regions, the dominant morphology of the electrode surface is as shown in Fig. 6. These "boulders" are $\beta\text{-Cd}(\text{OH})_2$ which have predominantly formed through the dissolution/precipitation mechanism. They have been observed by Ritterman (20), and are akin to the classical hexagonal platelets (Fig. 10).

In contrast to the well-defined $\beta\text{-Cd}(\text{OH})_2$ of the peripheral area, there are the smaller crystals and mossy material of the central migration area. Figure 4 shows the small $\beta\text{-Cd}(\text{OH})_2$ crystals covered by the mossy active material. What appears to have happened is that active material surrounding the central migration area has been swept from the substrate and deposited at its current position by the flow of electrolyte into and out of the electrode compartment. As before, the electrolyte flow is caused by specific volume changes in the cadmium electrode. The dissolved cadmate species is transported by the electrolyte flow to the central migration area, where it randomly precipitates as mossy material.

Our comparison of the structure of the mossy material to the structure of the migration region filmed in cell 1 revealed a striking similarity between the two. Others have observed the presence of this particular structure of active material as well (21, 22). Judging from the charge/discharge behavior of the migration region in cell 1 and the growth of the migration region in cell 2, we believe that this mossy active material, and not the highly crystalline structure, is responsible for the eventual short circuit. Crystalline $\text{Cd}(\text{OH})_2$, especially the large $\beta\text{-Cd}(\text{OH})_2$ crystal, is supposedly difficult to recharge (17, 20). Our films of cell 1 show the migration region is charging and discharging in unison with the cadmium electrode. The change in the color of the migration region is due to the absorption and expulsion of electrolyte caused by the specific volume change of the electrode. It is quite important to note the direction of the color change of the migration region upon current reversal. On both charge and discharge the color change begins at the



Fig. 10. Cadmium electrode from cycled cell

peak, implying that the electronic attachment to the nickel sinter is not broken.

Unlike cell 1 where the active migration regions were random throughout the electrode surface, in cell 2 we were able to select the position where migration occurs by controlling the electrolyte flow. The presence of the mossy material again implies some sort of solid-state connection to the nickel sinter. Chua found this same mossy material on the surface of cadmium electrodes which had been cycled at 1C discharge rates (22). Using the energy dispersive system, he determined the material to be cadmium. We were unable to determine the exact composition of the mossy material using the same technique owing to the elemental limitations of the instrument.

The evidence presented so far strongly suggests the growth of the migration region occurs through the precipitation of the dissolved cadmate species as $\text{Cd}(\text{OH})_2$. Electronic connection to the nickel sinter is maintained by underlying, unconvertible metallic cadmium which exists in the migration region. As the migration region grows, additional $\text{Cd}(\text{OH})_2$ is precipitated and converted to Cd until the short circuit between the two electrodes is complete.

Attempts were made to approximate both the composition and behavior of a migration region. Metallic cadmium was interspersed throughout cadmium hydroxide and placed between two electrodes in cell 3. We tried to convert the $\text{Cd}(\text{OH})_2$ to Cd with the help of the interspersed metallic Cd powder, thus creating a short circuit. Our failure to accomplish this suggests that an electronic connection with the nickel sinter begins at the electrode surface and cannot be formed through the agglomeration of migration material in the separator that comes in contact with the electrode.

The basic migration structure we have developed through the course of this paper is one that is dominated by a composite of three material forms: metallic cadmium, a finely divided $\text{Cd}(\text{OH})_2$, and $\beta\text{-Cd}(\text{OH})_2$. The $\beta\text{-Cd}(\text{OH})_2$ plays a passive role in that it is electronically isolated [continuous growth occurs through precipitation of $\text{Cd}(\text{OH})_3^-$ ions]. The portion of the structure that is capable of causing cell shorting is a mossy mixture of Cd/Cd(OH)₂. This statement implies that metallic cadmium is always present in the migration region and that it is electronically connected to the substrate. Confirming these contentions beyond a doubt is extremely difficult, and we did not develop a successful technique here, but certain questions do arise, given that the model is correct, that can be answered.

A necessary condition for the model to be correct is the migration region cannot be totally converted to $\text{Cd}(\text{OH})_2$; otherwise, it would become electronically isolated. This implies that the metallic cadmium present can only be partially converted and self-passivation by $\text{Cd}(\text{OH})_2$ occurs. To test this contention, the cadmium wire cell was built. If passivation did not occur, the wire could be discharged until it was totally converted or isolated by fracture. Our results indicate that the wire does indeed passivate. The maximum capacity achieved was 1.97C. The corresponding volume of material discharged is $1.33 \times 10^{-4} \text{ cm}^3$ as given by

$$V = CM/2\rho e$$

where C is the capacity, M the mass of cadmium atom, ρ the density of cadmium, and e an electronic charge. The value of V is approximately $8.7 \times 10^{-2}\%$ of the total wire volume.

An estimate for the thickness of the discharge layer (dr) can be obtained by dividing V by the surface area of the wire. If it is assumed that the wire surface remains smooth (area = $2\pi rl$), then the estimated discharge thickness from the capacity measurements is $3.5 \times 10^{-5} \text{ cm}$, which is three orders of magnitude smaller than a characteristic dimension of a developed migration region. It should be noted that the surface of the wire is not smooth (Fig. 7), and therefore the area is larger than the $2\pi rl$ and the dr from V is less than $3.5 \times 10^{-5} \text{ cm}$. Thus, only a small fraction of the available cadmium could be dis-

charged prior to self-passivation, making it quite possible for metallic cadmium to permanently exist in the migration region.

Conclusions

In aqueous cells with cadmium electrodes, various cadmium species are transported throughout the cells. The dominant transport mechanism is forced convection of the electrolyte caused by molar volume changes in the electrode active materials as they are charged and discharged. The species transported are soluble cadmium ions, such as $\text{Cd}(\text{OH})_3^-$ and/or particulate material such as $\beta\text{-Cd}(\text{OH})_2$ crystals.

The failure of sealed nickel-cadmium cells is often due to a phenomenon called "soft shorting." Soft-short failures are associated with the penetration of the separator by material transported from the cadmium electrode. In this paper, we have described the nature of the separator penetration that causes soft shorting.

We have chosen the terminology of migration region for these areas, as indeed they appear to be a slow migration of active material that starts from the interior of the electrode and does not terminate until it has grown through the separator and shorted the cell. Time lapse microphotography of these growth regions has shown that they are characterized by a mossy material that charges and discharges with the cadmium electrode. The structure may contain $\beta\text{-Cd}(\text{OH})_2$ crystals, but we have concluded that these are electronically inactive and do not contribute to the short. The mossy portion of the migration region consists of both metallic cadmium filaments that extend from the electrode substrate to the tip of the region and finely divided cadmium hydroxide. The metallic portion of the region can survive successive discharges, as the discharge process is self-passivating, with the average physical depth of discharge estimated to be less than $3.5 \times 10^{-5} \text{ cm}$.

We have also shown that metallic cadmium particles mixed with finely divided cadmium hydroxide will not short a cell, leading to the conclusion that random deposition of cadmium species within the separator will not cause a short. It is a necessary prerequisite for shorting that metallic cadmium filaments be grown from the electrode substrate.

Manuscript submitted Jan. 18, 1985; revised manuscript received May 3, 1985. This was Paper 6 presented at the Washington, DC, Meeting of the Society, Oct. 9-14, 1983.

Wright-Patterson Air Force Base assisted in meeting the publication costs of this article.

REFERENCES

1. S. U. Falk and A. J. Salkind, "Alkaline Storage Batteries," John Wiley and Sons, New York (1969).
2. P. Bauer, "Batteries for Space Power Systems," NASA SP-172, Washington, DC (1968).
3. S. W. Mayer and D. Taylor, SAMSO-TR-74-17, Aerospace Corporation Report No. TR-0074 (4270-10)-3, (1974).
4. K. L. Dick, T. Dickinson, R. J. Doran, S. E. A. Pomroy, and J. Thompson, in "Power Sources 7," J. Thompson, Editor, p. 195, Academic Press, London (1979).
5. S. W. Mayer, *This Journal*, **123**, 159 (1976).
6. R. W. Bramham, R. J. Doran, S. E. A. Pomroy, and J. Thompson, in "Power Sources 6," D. H. Collins, Editor, p. 129, Academic Press, London (1977).
7. R. E. Dueber and D. H. Fritts, Abstract 6, p. 9, The Electrochemical Society Extended Abstracts, Vol. 83-2, Washington, DC, Oct. 9-14, 1983.
8. S. W. Mayer, Interim Report, SAMSO-TR-74-163, Air Force Contract FO4071-74-C-0075 (1974).
9. R. Barnard, G. S. Edwards, and F. L. Tye, *J. Power Sources*, **3**, 175 (1978).
10. S. D. James, *This Journal*, **123**, 1857 (1976).
11. S. D. James and R. A. Neilhof, *ibid.*, **124**, 1057 (1977).
12. G. T. Croft, *ibid.*, **106**, 278 (1959).
13. E. J. Rubin, *ibid.*, **114**, 1980 (1967).
14. P. V. Popapat and E. J. Rubin, *ibid.*, **113**, 201C (1966).
15. Y. Okinaka and C. M. Whitehurst, *ibid.*, **117**, 583 (1970).
16. Y. Okinaka, *ibid.*, **117**, 289 (1970).
17. F. G. Will and H. J. Hess, *ibid.*, **121**, 1 (1973).
18. S. Krause, Paper presented at the 1976 Goddard

Space Flight Center Battery Workshop, X711-77-28, June 1977.

19. P. D. McDermott, Final Report NASA Grant NSG-5051, CR-14476 Goddard Space Flight Center, March 1976.
20. P. F. Ritterman, Final Report NASA Contract NAS

321253, TRW Report no. CR 167953, May 1982.

21. M. Cimino and G. Gearing, M.S. Thesis, Air Force Institute of Technology, Wright-Patterson Air Force Base, OH (1984).
22. D. Chua, Ph.D. Thesis, Rensselaer Polytechnic Institute, Troy, NY (1974).

Relationships Between Carbon Black Cathode Material Characteristics and Lithium/Oxyhalide Cell Performance

K. A. Klinedinst*

GTE Laboratories, Incorporated, Waltham, Massachusetts 02254

ABSTRACT

Nine carbon blacks with iodine surface areas ranging between 60 and 1222 m^2/gm and with dibutyl phthalate absorption numbers ranging between 125 and 420 $\text{cm}^3/100 \text{ gm}$ have been evaluated as lithium/oxyhalide cell cathode materials. Two criteria have been considered: their ability to serve as heterogeneous catalysts for the cathodic half-cell reaction (a function of both internal surface area and specific activity), and their ability to accommodate the continuous deposition of solid discharge products with minimal internal resistance losses (a function of both the porosity and pore size distribution of the agglomerated carbon particle aggregates). For carbons with surface areas of at least 250 m^2/gm , overvoltages for SOCl_2 reduction are practically independent of carbon black surface area. Furthermore, cathode porosities and Li/SOCl_2 cell discharge capacities both correlate with the DBP absorptometer numbers characteristic of the high surface area carbon blacks themselves. If the activity of a low surface area carbon is augmented via a catalytic additive (e.g., supported platinum), overvoltages similar to those obtained with high surface area carbons and complete utilization of the cathode's internal pore volume are achieved. The use of cathode "pore formers" may also lead to improved performance characteristics, particularly at very high current densities where pore former particle diameters averaging about 200 μm yield optimal performance results. Of the commercially available carbon blacks examined, Ketjenblack EC and Black Pearls 2000 function best as Li/SOCl_2 cell cathode materials, greatly outperforming the standard carbon, Shawinigan acetylene black.

Shawinigan acetylene black (containing 5-10% PTFE as a binder) is the commonly used cathode material for lithium/oxyhalide electrochemical cells. However, a variety of other carbon blacks have been examined as alternatives. Dey investigated 12 different carbon blacks as Li/SOCl_2 cell cathode materials and concluded that, overall, Shawinigan acetylene black was superior to all of the others (1). However, Gilman and Wade showed that improved $\text{Li/SO}_2\text{Cl}_2$ load voltages may be achieved with a carbon black possessing a higher surface area than that of Shawinigan black (2). More recently, this observation was confirmed by Wade *et al.*, who also showed that treating the cathode material with acetone may markedly improve $\text{Li/SO}_2\text{Cl}_2$ cell load voltages and capacities (3). Conclusions similar to those of Wade *et al.* have also been reported by Reddy and Thurston, who evaluated a variety of high surface area and chemically treated carbons as Li/SO_2 cell cathode materials (4).

All of these studies were motivated by the belief that there should be demonstrable relationships between cell performance characteristics, on the one hand, and the physical and/or chemical characteristics of the carbon black cathode materials, on the other. The work reported here was performed in order to seek broadly based experimental evidence substantiating this widely held belief (5).

Experimental

Nine carbon blacks were examined. Shawinigan acetylene black (50% compressed) was obtained from Gulf Oil Canada Limited. The furnace black specified as Conductex 40-220 was supplied by the Columbian Chemicals Company. Ketjenblack EC, another furnace-type black, was supplied by the Armak Company. Finally, several other blacks were supplied by Cabot Corporation. These included Vulcan XC-72, Black Pearls 2000, CSX 99, CSX 150A2, CSX 179B, and CSX 174. These carbons are listed in Table I along with the surface areas (by iodine adsorption, m^2/gm) and dibutyl phthalate absorptometer numbers (ASTM no. D-2414-70, $\text{cm}^3/100 \text{ gm}$) reported by the manufacturers. As indicated, of the carbons investigated, Shawinigan acetylene black possesses both the lowest

surface area (60 m^2/gm) and the highest DBP absorption (460 $\text{cm}^3/100 \text{ gm}$).

PTFE-bonded cathodes were fabricated from each of the carbons as well as from Shawinigan acetylene black containing 10% supported platinum. Each carbon was dispersed in a 50:50 water:isopropanol mixture to which was added enough du Pont TFE-30 to bring the PTFE loading to 10 weight percent (w/o). The resulting PTFE-bonded carbon mixtures were dried and subsequently applied to both sides of nickel Exmet screen current collectors so as to form 1 mm cathode sheets. Cathode porosities were determined from measured weights and volumes. Cathode-limited Li/SOCl_2 cells containing 1 $\text{cm}^2 \times 1 \text{ mm}$ cathodes (cut from these cathode sheets) were constructed within Pyrex containers with ground glass joints and glass-to-metal feedthroughs for the lead wires (6). The electrolyte was a 1.8M solution of LiAlCl_4 in SOCl_2 . The anodes, supported upon nickel Exmet screen current collectors, were cut from 0.76 mm thick lithium foil. Nonwoven glass fiber paper 0.127 mm thick was used as the separator material. These cells were discharged fully through constant loads ranging between 20 and 1000 Ω at +25°, -20°, and -40°C.

PTFE-bonded cathodes were also prepared using finely divided $(\text{NH}_4)_2\text{CO}_3$ and NH_4HCO_3 as "pore formers." $(\text{NH}_4)_2\text{CO}_3$ was mixed in equal proportions with Shawinigan acetylene black containing 10% supported platinum. In these experiments, $(\text{NH}_4)_2\text{CO}_3$ particles rang-

Table I. Carbon black properties

Carbon black	I ₂ area (m^2/gm)	DBP absorption ($\text{cm}^3/100 \text{ gm}$)
Shawinigan acetylene black (50% compressed)	60	460
Vulcan XC-72	250	180
CSX 99	425	125
Ketjenblack EC	1000	340
CSX 150A2	1025	320
Black Pearls 2000	1050	330
CSX 179B	1060	335
40-220	1100	230
CSX 174	1222	420

* Electrochemical Society Active Member.

Table II. Li/SOCl₂ cell cathode porosities and performance characteristics^a

Carbon black	Cathode porosity	I_{avg}^b (mA/cm ²)	E_{avg}^b (V)	Capacity ^c (mAh/cm ²)
Shawinigan acetylene black (50% compressed)	84.5	29.8	2.98	23.8
Vulcan XC-72	78.7	31.8	3.18	35.1
CSX 99	74.9	32.6	3.26	32.0
Ketjenblack EC	85.9	32.6	3.26	47.4
CSX 150A2	84.2	32.7	3.27	40.0
Black Pearls 2000	85.5	32.6	3.26	44.3
CSX 179B	85.8	32.8	3.28	43.3
40-220	82.9	31.8	3.18	38.8
CSX 174	88.5	32.6	3.26	52.3

^a At 25°C with 1.8M LiAlCl₄ in SOCl₂ as electrolyte. 1 cm² × 1 mm cathodes discharged through 100Ω loads.

^b Average plateau load voltage and current density.

^c Capacity per unit cathode area to 0.9E_{avg}.

ing between 18 and 30 mesh (0.59 and 0.99 mm) and >100 mesh (<0.15 mm) were used. In a second set of experiments, 60-80 mesh NH₄HCO₃ particles were mixed with carbon black, the ratio of pore former to cathode material ranging between 1:4 and 4:1. In each case, the pore former was removed from the finished cathode by heating in the air at a temperature between 100° and 200°C. Then, Li/SOCl₂ cells of the type described above containing these cathodes were discharged at 25°C through 20Ω constant loads in order to determine the relationships between high rate cell performance and pore former particle size and concentration.

Results

Correlations between carbon black characteristics and cathode performance.—The porosities of cathodes formed from the nine carbon blacks are listed in Table II along with the average plateau current densities, average load voltages, and capacities obtained with Li/SOCl₂ cells containing these cathodes discharged through 100Ω loads. The cathode porosities are plotted vs. the DBP absorptions characteristic of the carbon blacks themselves in Fig. 1. With the single exception of Shawinigan acetylene black, the porosities of the PTFE-bonded cathodes formed from the various carbon blacks correlate with the DBP absorption values. The Li/SOCl₂ cell capacities are similarly plotted vs. the DBP absorptions characteristic of the carbon blacks in Fig. 2. Again, with the single exception of Shawinigan acetylene black, the discharge capacities correlate with the DBP absorption values and, therefore, with the porosities of the PTFE-bonded carbon cathodes.

The corresponding Li/SOCl₂ cell plateau load voltages (at 30-33 mA/cm²) are plotted vs. the iodine surface areas of the carbon black cathode materials in Fig. 3. As indica-

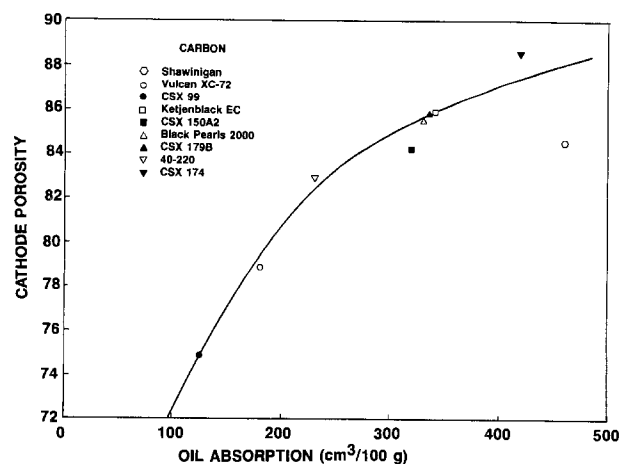


Fig. 1. Cathode porosity vs. dibutyl phthalate absorption of carbon black.

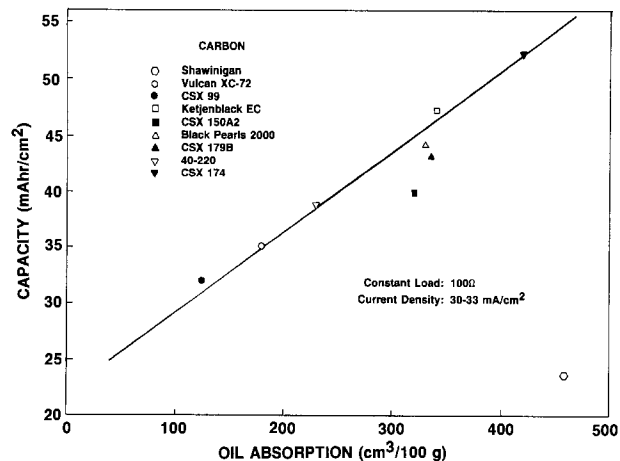


Fig. 2. Li/SOCl₂ cell capacity vs. dibutyl phthalate absorption of carbon black.

ted, with the single exception of the lowest surface area carbon (Shawinigan acetylene black), the full cell polarization data are practically independent of carbon black surface area ($E_{avg} = 3.23 \pm 0.05V$).

Of the commercially available carbon blacks examined, Ketjenblack EC and Black Pearls 2000 possess both high surface areas (1000 and 1050 m²/gm, respectively) and high DBP absorptions (340 and 330 cm³/100 gm, respectively). Furthermore, they both perform well as Li/SOCl₂ cathode materials. In fact, of the carbons examined, only CSX 174 (characterized by a 1222 m²/gm surface area and a 420 cm³/100 gm DBP absorption) outperformed Ketjenblack EC and Black Pearls 2000 in Li/SOCl₂ cell tests. Li/SOCl₂ cell polarization curves obtained at +25°C with Shawinigan black and Ketjenblack EC cathodes are compared in Fig. 4, while typical ambient temperature discharge curves are compared in Fig. 5 and 6 (corresponding to current densities of 15-16 and 30-32 mA/cm², respectively). Polarization curves obtained at -20°C are compared in Fig. 7, while typical -20°C discharge curves are compared in Fig. 8 and 9 (corresponding to current densities of 3 and 15 mA/cm², respectively). Finally, -40°C polarization curves are compared in Fig. 10, with typical discharge curves being compared in Fig. 11 and 12 (corresponding to current densities of 3 and 5.5 mA/cm², respectively). Ratios of discharge capacities achieved at +25°, -20°, and -40°C with the two cathode materials (Ketjenblack EC and Shawinigan acetylene black) are compared in Table III.

Activity enhancing additives.—It is well known that substantial improvements in Li/oxyhalide cell cathode efficiency may be achieved by incorporating various catalytic additives into the standard PTFE-bonded Shawinigan acetylene black cathode. The proven

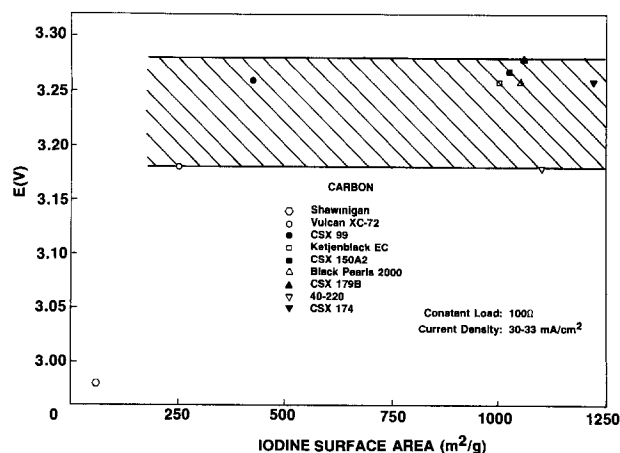
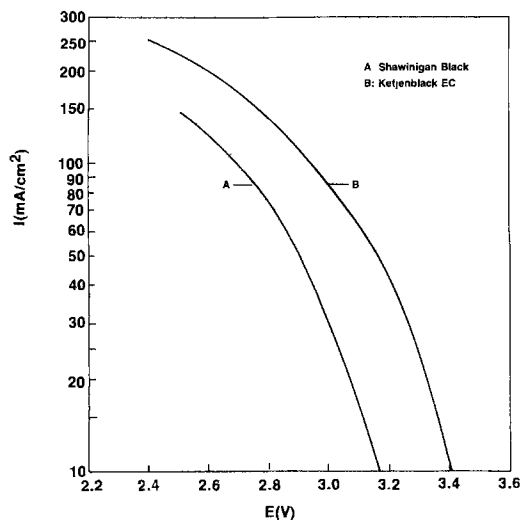
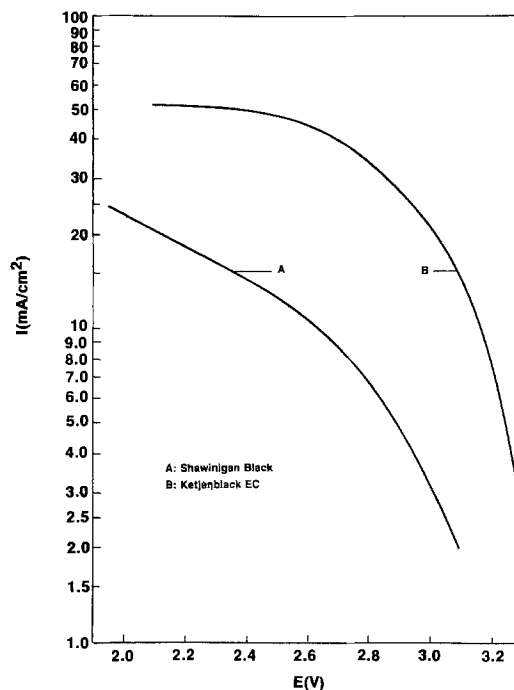
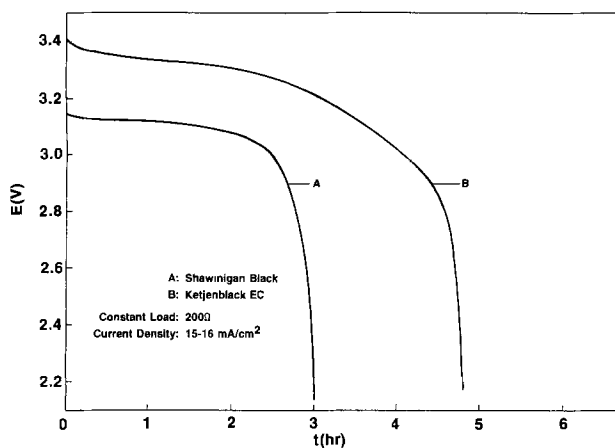
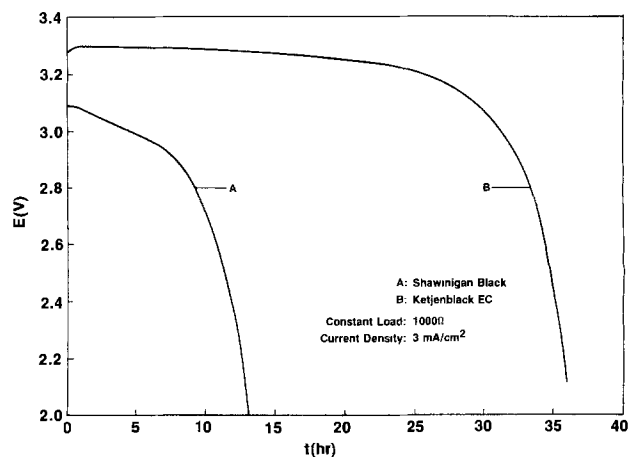
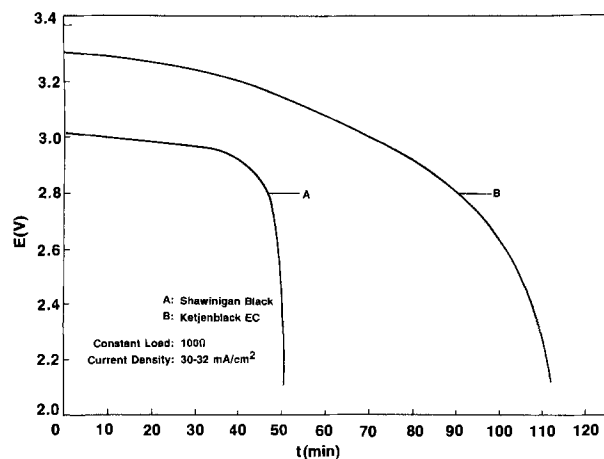


Fig. 3. Li/SOCl₂ cell load voltage vs. surface area of carbon black

Fig. 4. Li/SOCl₂ cell polarization curves at +25°CFig. 7. Li/SOCl₂ cell polarization curves at -20°CFig. 5. Li/SOCl₂ cell discharge curves at +25°C with 15-16 mA/cm² current densities.Fig. 8. Li/SOCl₂ cell discharge curves at -20°C with 3 mA/cm² current density.Fig. 6. Li/SOCl₂ cell discharge curves at +25°C with 30-32 mA/cm² current densities.

oxyhalide reduction catalysts may be classified as belonging to one of four different types: precious metals like metallic platinum (7, 8), nonprecious metals and metal halides like copper and cupric chloride (9-11), organometallics such as iron or cobalt phthalocyanine (12-15), and halogens (Cl₂ or Br₂) (16-18). In the work reported here, the Shawinigan black cathode material was modified by supporting finely divided metallic platinum upon its surface, the total platinum loading being about 10 w/o. Li/SOCl₂ cells containing PTFE-bonded cathodes fabricated from this modified acetylene black were fully

discharged through 100Ω loads. In Table IV, the resulting discharge characteristics are compared with those obtained in the absence of supported platinum (from Table II). As shown, the addition of the electrocatalyst resulted in a 240 mV reduction in cathodic overvoltage and a 140% increase in capacity.

The range of load voltages *vs.* iodine surface area determined by all of the carbon blacks examined with the exception of Shawinigan acetylene black (from Fig. 3) is

Table III. Li/SOCl₂ cell cathode capacity *vs.* temperature and discharge rate^a

T(°C)	I (mA/cm ²)	Ketjenblack capacity/ Shawinigan black capacity
+25	20	1.8
+25	100	1.5
-20	3	2.3
-20	20	1.7
-40	3	2.3
-40	20	2.0

^a With 1.8M LiAlCl₄ in SOCl₂ electrolyte and 1 cm² × 1 mm cathodes.

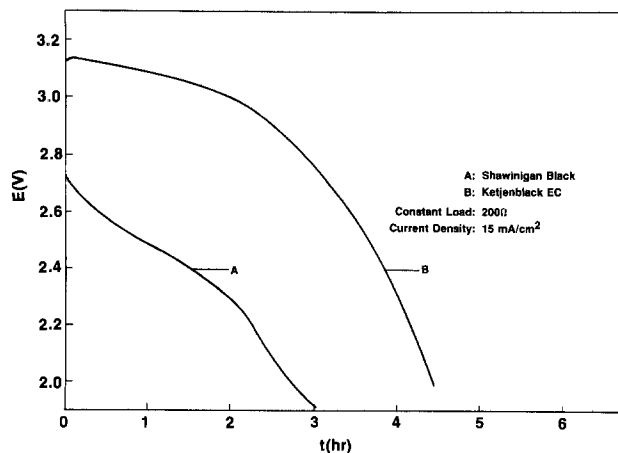


Fig. 9. Li/SOCl₂ cell discharge curves at -20°C with 15 mA/cm^2 current density.

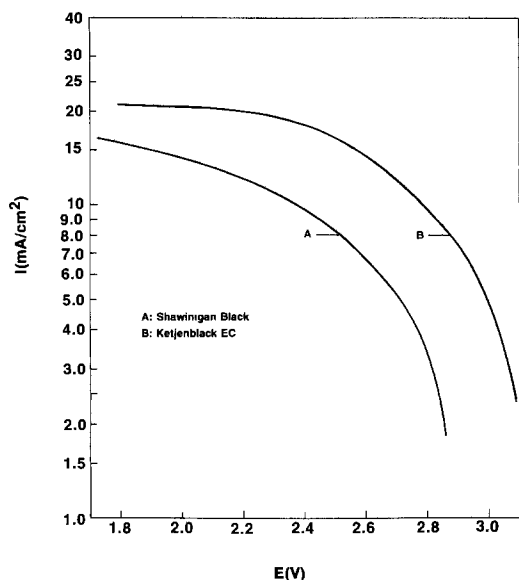


Fig. 10. Li/SOCl₂ cell polarization curves at -40°C

shown in Fig. 13. Likewise, the capacity *vs.* DBP absorption line determined by all of the carbon blacks examined with the exception of Shawinigan acetylene black (from Fig. 2) is shown in Fig. 14. Also shown in both figures are the data (from Table IV) representative of Li/SOCl₂ cells containing Shawinigan black cathodes both with and without the supported platinum electrocatalyst. With the addition of the electrocatalyst, the low surface area acetylene black exhibits polarization and capacity characteris-

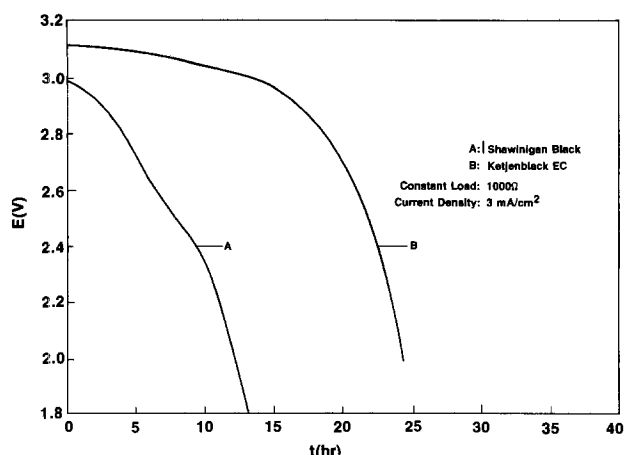


Fig. 11. Li/SOCl₂ cell discharge curves at -40°C with 3 mA/cm^2 current density.

Table IV. The effect of supported platinum upon the performance characteristics of Li/SOCl₂ cells with Shawinigan black cathodes^a

Supported catalyst	I_{avg}^b (mA/cm ²)	E_{avg}^b (V)	Capacity ^c (mAh/cm ²)
None	29.8	2.98	23.8
10% platinum	32.2	3.22	56.4

^a At 25°C with 1.8M LiAlCl_4 in SOCl₂ as electrolyte. $1\text{ cm}^2 \times 1\text{ mm}$ cathodes discharged through 100Ω loads.

^b Average plateau load voltage and current density.

^c Capacity per unit cathode area to $0.9E_{\text{avg}}$.

tics that correlate well with those of the higher surface area furnace-type blacks.

Structure enhancing additives.—There is another class of cathode additives which act to modify the structure of the PTFE-bonded carbon cathode rather than its specific activity for a particular chemical reaction. Such cathode additives, broadly classified as pore formers, have been used most successfully in the fabrication of controlled-porosity fuel cell electrodes, and they are widely used in the manufacture of porous materials (19). In the general procedure, the pore forming material, possessing a well-defined particle size distribution, is mixed with the standard electrode ingredients. The electrode is formed, and subsequently, the pore former is removed via thermal decomposition, dissolution in an appropriate solvent, etc.

In the work performed here, finely divided (NH₄)₂CO₃ and NH₄HCO₃ were used as pore forming materials in conjunction with Shawinigan acetylene black containing 10% supported platinum. Thus, PTFE-bonded electrodes

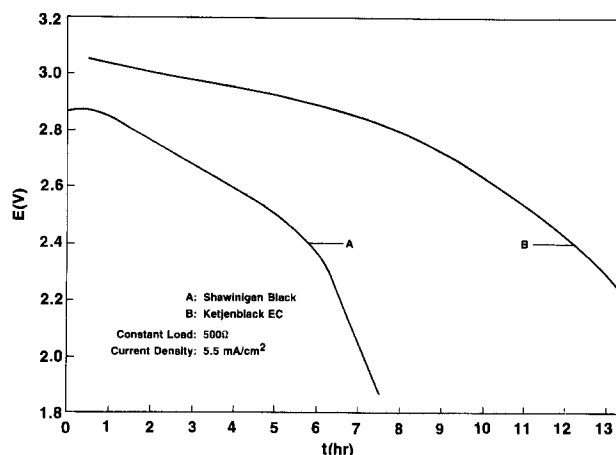


Fig. 12. Li/SOCl₂ cell discharge curves at -40°C with 5.5 mA/cm^2 current density.

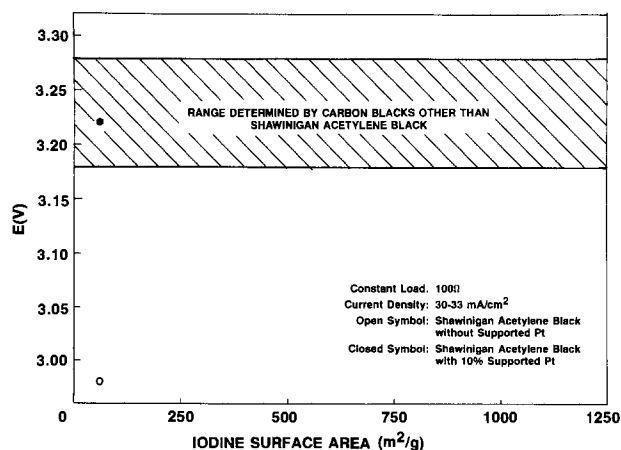


Fig. 13. Li/SOCl₂ cell load voltage vs. surface area of carbon black

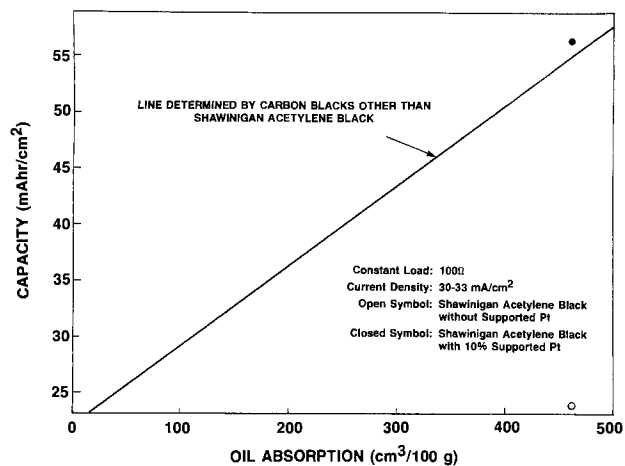


Fig. 14. Li/SOCl₂ cell capacity vs. dibutyl phthalate absorption of carbon black.

were prepared using a 50:50 mixture of (NH₄)₂CO₃ and 10% platinum on Shawinigan black, the (NH₄)₂CO₃ being subsequently removed via thermal decomposition. Prior to mixing with the carbon black, the pore former was sieved using standard mesh screens so as to produce fractions ranging in particle diameter from 0.59-0.99 mm to below 0.15 mm. Li/SOCl₂ cells containing cathodes formed from the various (NH₄)₂CO₃ fractions were discharged through 20Ω loads ($I_{avg} \approx 140$ mA/cm²) to yield the performance characteristics listed in Table V. (The high discharge rate conditions used to evaluate the pore formers are more demanding than the lower rate conditions employed elsewhere in this study and, therefore, are more likely to reveal significant performance variations that result from structurally related diffusional limitations.)

The average cell load voltages and capacities are plotted vs. (NH₄)₂CO₃ particle size (standard mesh) in Fig. 15 and 16, respectively. Optimal high rate performance characteristics are obtained with cathodes formed via the use of 60-80 mesh particles. Thus, enriching the cathode with pores approximately 200 μm in diameter [using 50% (NH₄)₂CO₃ in the cathode blend] results in a 160 mV reduction in cathodic polarization and in a 30% increase in cathode utilization efficiency at the 140 mA/cm² rate.

Next, another series of PTFE-bonded cathodes was fabricated using 60-80 mesh NH₄HCO₃ as the pore former. The amount of NH₄HCO₃ mixed with the 10% platinum on Shawinigan acetylene black cathode material ranged between 0 and 80 w/o. As before, Li/SOCl₂ cells containing these cathodes were discharged through 20Ω loads ($I_{avg} \approx 140$ mA/cm²) to yield the performance characteristics listed in Table VI. The average load voltages and capacities are plotted vs. pore former concentration in Fig. 17 and 18, respectively. Optimal high rate performance characteristics are obtained with cathodes formed from a blend containing about 40% NH₄HCO₃ (60-80

Table V. Li/SOCl₂ cell performance characteristics vs. (NH₄)₂CO₃ pore former particle size^a

Particle size range Standard mesh	(mm)	E_{avg} (V)	Capacity (mAh/cm ²)
No pore former used		2.75	21.4
>100	<0.147	2.70	19.6
80-100	0.147-0.175	2.79	22.6
60-80	0.175-0.246	2.91	28.0
30-60	0.246-0.589	2.84	25.3
18-30	0.589-0.991	2.79	21.7

^a Electrolyte = 1.8M LiAlCl₄ in SOCl₂. Cathode = 10% PTFE/90% (50% (NH₄)₂CO₃/50% of 10% Pt on Shawinigan black), 1 cm² × 1 mm. Temperature = 25°C. Constant load = 20Ω. Average current density ≈ 140 mA/cm².

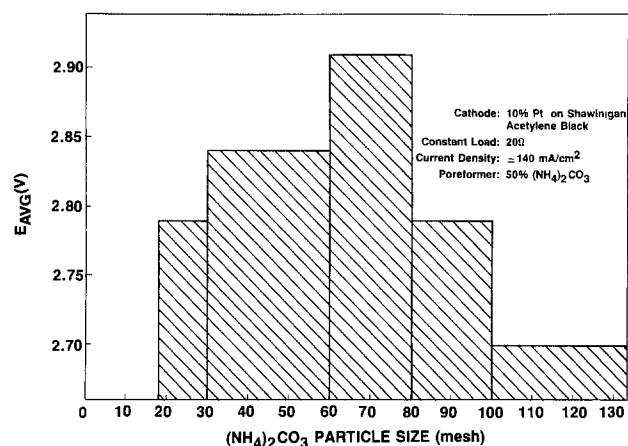


Fig. 15. Li/SOCl₂ cell load voltage vs. particle sizes of cathode pore former.

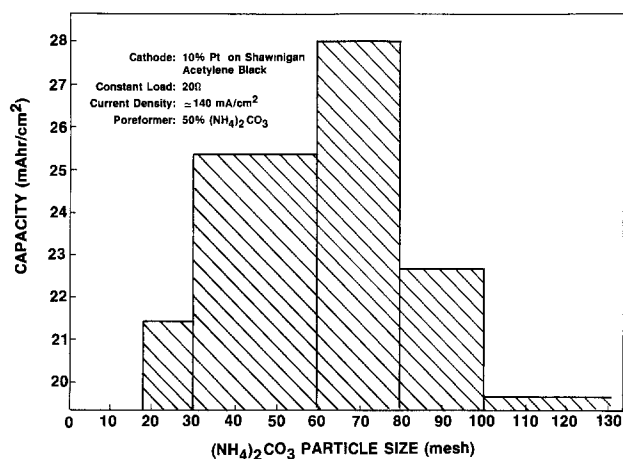


Fig. 16. Li/SOCl₂ cell capacity vs. particle sizes of cathode pore former

mesh). Thus, enriching the cathode with pores approximately 200 μm in diameter (using 40% NH₄HCO₃ in the cathode blend) results in a 45% increase in cathode utilization efficiency along with a modest reduction in cathodic overvoltage.

Discussion

Broadly speaking, the porous carbon black cathode in a lithium/oxyhalide or lithium/sulfur dioxide cell must perform two important functions in addition to its obvious role as a current collector. On the one hand, its internal surface must function as a heterogeneous catalyst for the cathodic half-cell reaction. On the other hand, its pores must be able to accommodate the continuous deposition of solid discharge products without becoming so severely narrowed that internal resistance losses lead to premature failure. In the case of the Li/SOCl₂ system, LiCl is the primary solid discharge product. Additionally, elemental

Table VI. Li/SOCl₂ cell performance characteristics vs. NH₄HCO₃ pore former concentration^a

NH ₄ HCO ₃ concentration (%)	E_{avg} (V)	Capacity (mAh/cm ²)
0	2.75	21.4
20	2.79	31.0
40	2.81	30.8
55	2.80	26.3
60	2.78	22.7
80	2.72	18.1

^a Electrolyte = 1.8M LiAlCl₄ in SOCl₂. Cathode = 10% PTFE/90% of 60-80 mesh NH₄HCO₃ blended with 10% Pt on Shawinigan black, 1 cm² × 1 mm. Temperature = 25°C. Constant load = 20Ω. Average current density ≈ 140 mA/cm².

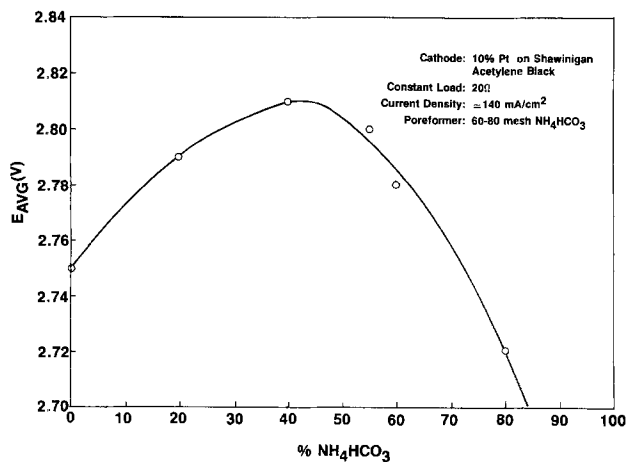


Fig. 17. Li/SOCl₂ cell load voltage vs. concentration of cathode pore former.

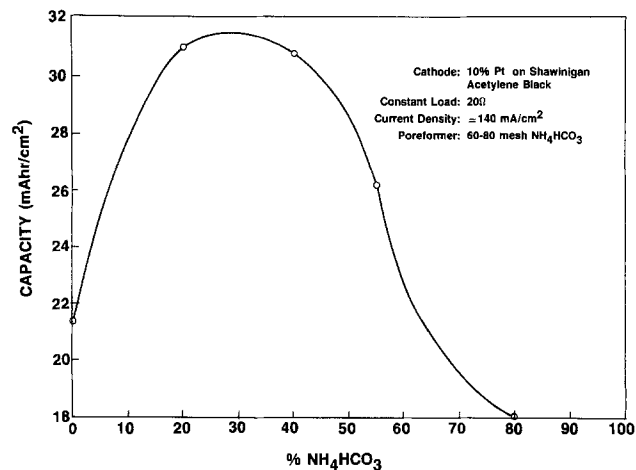
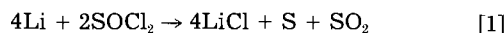


Fig. 18. Li/SOCl₂ cell capacity vs. concentration of cathode pore former.

sulfur may precipitate within the porous cathode and separator once its solubility in the oxyhalide electrolyte is exceeded (20)



The full cell polarization data (Fig. 3) obtained with the various carbons suggest that a surface area of 250 m²/gm is sufficient to effectively catalyze the electroreduction of SOCl₂ at a 30 mA/cm² rate (at ambient temperature and with a 1 mm cathode thickness). However, a 200-300 mV polarization penalty is incurred with a carbon having a surface area as low as 60 m²/gm. However, as shown in Fig. 13, when the activity of a low surface area carbon is augmented via a catalytic additive (*e.g.*, supported platinum), overvoltages similar to those achieved with high surface area carbons are obtained.

The cathode porosity and Li/SOCl₂ cell capacity data (Fig. 1 and 2) obtained with the various carbons indicate that, for carbons with surface areas of at least 250 m²/gm, the cathode utilization efficiency (capacity per unit cathode volume) increases linearly with increasing cathode porosity. Indeed, it would be surprising if this were not the case since, as shown in Eq. [1] above, insoluble LiCl is produced stoichiometrically during the discharge of a Li/SOCl₂ cell. Furthermore, virtually all of the LiCl so produced deposits within the porous cathode. Thus, the greater the cathode porosity, the longer a cathode-limited cell should be able to discharge at a given rate and at a particular operating temperature.

Equally significant, however, is the fact that both the porosity of a PTFE-bonded carbon cathode and the discharge capacity of a Li/SOCl₂ cell containing this cathode correlate with the dibutyl phthalate absorptometer number characteristic of the high surface area carbon black itself. DBP absorption is a measure of the "structure" of the carbon black, *i.e.*, the average number of particles fused together to form an aggregate. In an important paper concerning the morphology of carbon black aggregates, Medalia reported that, for eight carbon blacks of various structure levels and particle sizes, the void volume between agglomerated carbon black aggregates calculated from electron microscopic data was in good agreement with the experimentally measured DBP absorption (21). Furthermore, the analysis presented can be applied to calculate the effective volumes of carbon black aggregates in systems of arbitrary concentration from DBP absorption values. There is, therefore, ample experimental and theoretical evidence suggesting that the capacity of a cathode-limited cell should be a function of the DBP absorptometer number characteristic of the carbon black cathode material. It must be remembered, however, that the carbon black must possess a sufficiently high specific activity for the cathodic reaction in order that its full capacity may be realized in practice. As shown in Fig. 14, the activity of a low surface area/high

structure carbon may be augmented via a catalytic additive (*e.g.*, supported platinum) so as to enable the complete utilization of the porous cathode.

Finally, as noted recently by Ohsaki *et al.*, the efficiency of a given carbon black as a lithium/oxyhalide cell cathode material will be a function not only of the porosity of the PTFE-bonded cathode, but also of its pore size distribution (22). Thus, the experiments with cathode pore formers reported here were performed in order to gauge the sensitivity of Li/SOCl₂ cell high rate discharge characteristics to the distribution of pores within the PTFE-bonded cathode. Interestingly, while Ohsaki *et al.* concluded that pores having a diameter greater than 0.2 μm are not used effectively (at a 20 mA/cm² rate), the results of the present study suggest that enrichment of the cathode with pores approximately 200 μm in diameter (using 40% NH₄HCO₃ in the cathode blend) results in the most significant performance gains (at a 140 mA/cm² rate).

Summary and Conclusions

Nine carbon blacks with iodine surface areas ranging between 60 and 1222 m²/gm and with dibutyl phthalate absorptometer numbers ranging between 125 and 420 cm³/100 gm have been evaluated as lithium/oxyhalide cell cathode materials. Two criteria have been considered: their ability to serve as heterogeneous catalysts for the cathodic half-cell reaction (a function of both internal surface area and specific activity), and their ability to accommodate the continuous deposition of solid discharge products with minimal internal resistance losses (a function of both the porosity and pore size distribution of the agglomerated carbon particle aggregates).

Li/SOCl₂ cell polarization measurements indicate that a surface area of 250 m²/gm is sufficient to effectively catalyze the electroreduction of SOCl₂ at a 30 mA/cm² rate (at ambient temperature and with a 1 mm cathode thickness). However, a 200-300 mV polarization penalty is incurred with a carbon having a surface area as low as 60 m²/gm. However, if the activity of a low surface area carbon is augmented via a catalytic additive (*e.g.*, supported platinum), overvoltages similar to those characteristic of high surface area carbons may be achieved.

With carbon black cathode materials having surface areas of at least 250 m²/gm, the discharge capacities of cathode-limited Li/SOCl₂ cells increase with increasing cathode porosity. Furthermore, cathode porosity and discharge capacity both correlate with the dibutyl phthalate absorptometer number characteristic of the high surface area carbon black itself (a measure of the structure of the carbon black). In practice, however, a given high structure carbon must possess either a high surface area or a very high specific activity in order to fully utilize its internal pore volume. In general, the activity of a low surface area/high structure carbon may be augmented via a

catalytic additive so as to enable the complete utilization of a PTFE-bonded cathode formed from that carbon.

Additional experiments with cathode formers have shown that significant improvements in high rate Li/SOCl₂ cell performance may be achieved by incorporating such pore formers into the cathode blend. Thus, optimal high rate performance characteristics are obtained with cathodes formed via the use of 40% NH₄HCO₃ or (NH₄)₂CO₃ having particle sizes in the 60-80 mesh range (corresponding to a 200 μm average particle diameter).

Of the commercially available carbon blacks examined, Ketjenblack EC and Black Pearls 2000 possess both high surface areas (1000 and 1050 m²/gm, respectively) and high DBP absorptions (340 and 330 cm³/100 gm, respectively). Furthermore, as Li/SOCl₂ cell cathode materials and without the use of special catalytic additives or pore formers, they both greatly outperform the standard carbon, Shawinigan acetylene black (at temperatures between +25° and -40°C and at current densities ranging between 2 and 200 mA/cm²).

Manuscript submitted Dec. 26, 1984; revised manuscript received April 8, 1985.

GTE Laboratories, Incorporated, assisted in meeting the publication costs of this article.

REFERENCES

1. A. N. Dey, *This Journal*, **126**, 2052 (1979).
2. S. Gilman and W. Wade, Jr., *ibid.*, **127**, 1427 (1980).
3. W. Wade, Jr., C. Walker, Jr., M. Binder, and S. Gilman, in "The Electrochemistry of Carbon," S. Sarangapani, J. R. Akridge, and B. Schumm, Editors, p. 479, The Electrochemical Society Softbound Proceedings Series, Pennington, NJ (1984).
4. T. B. Reddy and E. P. Thurston, Abstract 262, p. 421, The Electrochemical Society Extended Abstracts, Vol. 82-2, Detroit, MI, Oct. 17-21, 1982.
5. K. A. Klinedinst, Abstract 136, p. 203, The Electro-

- chemical Society Extended Abstracts, Vol. 84-2, New Orleans, LA, Oct. 7-12, 1984.
6. K. A. Klinedinst and M. J. Domeniconi, *This Journal*, **127**, 539 (1980).
7. K. A. Klinedinst, U.S. Pat. 4,272,593 (1981).
8. K. A. Klinedinst, *This Journal*, **128**, 2507 (1981).
9. L. R. Giattino, U.S. Pat. 4,167,608 (1979).
10. W. K. Behl, Abstract 57, p. 12, The Electrochemical Society Extended Abstracts, Vol. 80-2, Hollywood, FL, Oct. 5-10, 1980.
11. W. K. Behl, *This Journal*, **128**, 939 (1981).
12. N. Doddapaneni, Abstract 83, p. 218, The Electrochemical Society Extended Abstracts, Vol. 81-1, Minneapolis, MN, May 10-15, 1981.
13. N. Doddapaneni, Final Report, DELET-TR-81-0381-F, ERADCOM, Fort Monmouth, NJ (1982).
14. F. Walsh and J. Hopewood, Final Report, Contract DAAK20-82-C-0379, ERADCOM, Fort Monmouth, NJ (1982).
15. F. Walsh, R. S. Morris, and M. Yaniv, Abstract 33, p. 54, The Electrochemical Society Extended Abstracts, Vol. 83-2, Washington, DC, Oct. 9-14, 1983.
16. J. C. Hall and M. Koch, Report DELET-TR-81-0420-2, ERADCOM, Fort Monmouth, NJ (1982).
17. J. C. Hall and M. Koch, Report DELET-TR-81-0420-3, ERADCOM, Fort Monmouth, NJ (1982).
18. C. C. Liang, M. E. Bolster, and R. M. Murphy, in "Proceedings of the 29th Power Sources Conference," Atlantic City, NJ, June 9-12, 1980, The Electrochemical Society, Inc., p. 144 (1981).
19. A. M. Adams, F. T. Bacon, and R. G. H. Watson, in "Fuel Cells," W. Mitchell, Jr., Editor, p. 171, Academic Press, New York (1963).
20. K. A. Klinedinst and M. L. McLaughlin, *J. Chem. Eng. Data*, **24**, 203 (1979).
21. A. I. Medalia, *J. Colloid Interface Sci.*, **32**, 115 (1970).
22. T. Ohsaki, S. Yamada, K. Mitsuyasu, Y. Sato, T. Takamura, Y. Aoki, K. Hiratsuka, and A. Matsunuma, Abstract 138, p. 207, The Electrochemical Society Extended Abstracts, Vol. 84-2, New Orleans, LA, Oct. 7-12, 1984.

Composition of Surface Layers on Li Electrodes in PC, LiClO₄ of Very Low Water Content

Gholamabbas Nazri* and Rolf H. Muller*

Materials and Molecular Research Division, Lawrence Berkeley Laboratory, University of California, Berkeley, California 94720

ABSTRACT

Surface layers formed on Li in PC, LiClO₄ with less than 1 ppm of water have been analyzed by use of IR spectroscopy, SIMS, ESCA, low angle x-ray diffraction, and SEM. Electrodeposited Li showed a highly porous micromorphology with surface layers containing primarily a partially chlorinated hydrocarbon polymer and lithium carbonate. The carbonate is mostly present in the inner film regions, the polymer in the outer. Perchlorate decomposes to chlorine compounds of lower valences, with higher-valent chlorine found in the outer film regions and lower-valent in the inner.

The electrochemistry of the alkali and alkaline earth metals in ambient temperature nonaqueous electrolytes has been reviewed by several authors (1-6). The electrolytic deposition and dissolution of Li from aprotic electrolytes with high efficiency is of interest for the operation of ambient temperature high energy-density rechargeable Li batteries. Surface layers which spontaneously form on the metal protect it to varying degrees from corrosion, but they are mainly responsible for the poor rechargeability of the lithium electrodes (7, 8).

Great efforts have been made during the last decade to prevent or minimize the formation of surface layers. Improvements have been achieved by the molecular modification of solvents (9, 10) and the use of lithium alloys as anodes (11-14), while the effectiveness of solvent purification to improve electrode performance has not been uniform. In some cases, trace amounts of water or reactive

gases such as SO₂, O₂, and N₂ have been found to improve the cycling efficiency of the lithium anodes (6). Reaction products of Li with solvent have been reported to be more detrimental to the Li morphology and cycle life than the products formed by Li-protic reactions (15). Dey and Sullivan showed that propylene carbonate (PC) decomposes on a graphite electrode below + 0.6V vs. Li (16). Rauh and Brummer claim that one of the reasons for the poor rechargeability of Li electrodes is the corrosion of the lithium anode at grain boundaries, resulting in an electrical isolation of lithium particles from the substrate by corrosion products. This isolated metal is not available for stripping during the next anodic cycle (17). Dey also showed that a lithium electrode after charge and discharge had a porous structure. Epelboin *et al.* (13) found that surface layers are formed on Li electrodes in PC, 1M LiClO₄ during charge, during discharge, and at open circuit. Yen *et al.* (18) carried out ESCA studies of the surface layer on lithium which had been cycled in a 2Me-

* Electrochemical Society Active Member.

THF, 1.5M LiAsF₆ electrolyte. They found Li, C, O, As, and F on the surface of discharged Li. A polymerization of AsOF on the surface has been proposed (13). The effect of light on the polarization on lithium electrodes in PC has been studied by Povarov and Sitnina (19). They found that the anodic current of Li decreases and the cathodic current increases during exposure of the electrode to visible light. They concluded that a passive film formed on Li in PC possesses semiconducting properties. The sign of the effect indicates a p-type semiconductor. Although the electrons and holes are formed under the influence of light, the main carrier of current through the passive film is Li ions (19).

Understanding the structure and composition of surface layers on lithium is important for further progress in the development of rechargeable ambient temperature Li batteries. The objective of this work was to elucidate the nature of the films on lithium and their role during charge and discharge of Li electrodes by use of different experimental techniques, in particular IR spectroscopy, x-ray diffraction, ESCA, SIMS, and SEM.

Experimental

Propylene carbonate (PC) (Burdick and Jackson) has been used as a solvent. After vacuum distillation, GC analysis usually showed a water content of 20-30 ppm (Propac column, 110°C injection temperature). Treatment of the distilled solvent with Li amalgam resulted in a water content which was below the detection limit of GC (1 ppm).

The LiClO₄ (G. Frederick Smith) used for the experiments has been recrystallized three times from ultrapure water and dried under vacuum at 240°C for 12h. The water content of LiClO₄ before and after vacuum drying has been measured by use of a vacuum oven with differential pressure change equipment, a digital pressure gauge, and a mass spectrometer. The sample was placed in the vacuum oven in a ceramic crucible with a thermocouple in its center. The temperature of the oven was scanned from 25° to 800°C at 3 deg/min. After each sudden change in pressure, the mass spectrum of the released gas was monitored to determine its chemical composition. Thus, the water content of vacuum-dried LiClO₄ (10⁻⁴ torr, 160°C) was found to be much below 1 ppm. Cyclic voltammetry in the PC, LiClO₄ electrolyte with Pt electrodes also showed a water content below 1 ppm.

Cyclic voltammetry with platinum electrodes of 1.0 and 1.5M LiClO₄ solutions with PC solvent prepared as described above indicated a water content of less than 1 ppm for the solutions. Before each experiment, two auxiliary electrodes of Li (2 × 2 × 0.3 cm), placed in the same cell, were used to further purify the solutions by potentiostatically cycling these electrodes between ±2V vs. a Li reference electrode at 50 mV/s for 15-20 cycles. The resulting electrolyte has been used for the experiments reported here.

Electrochemical experiments have been performed in a dry box (Vacuum Atmospheres) equipped for removal and analysis of oxygen, water, and nitrogen. The O₂ and H₂O content of the He in the inert atmosphere box was measured continuously with a calibrated O₂ fuel cell sensor (Vacuum Atmospheres A O 316-H) and a solid-state moisture sensor (Vacuum Atmospheres AM-2), both of them sensitive to < 0.1 ppm. These components, in addition to N₂, were also measured with a calibrated gas chromatograph (Vacuum Atmospheres AN-1). Concentrations of about 10 ppm of O₂ and H₂O and 50 ppm of N₂, normally achieved, were lowered to less than 1 ppm by use of a stirred pool of lithium amalgam exposed to the dry box atmosphere (He). Li sheet of 3 mm thickness (Foote Mineral 99.99%) has been used for the preparation of electrodes, unless the metal was cathodically deposited on Cu or Ni substrates. Reference and counterelectrodes were always made of solid Li.

The composition of surface layers on bulk or electrode-deposited Li has been analyzed by transmission IR spectroscopy after removal from the surface with a glass rod.

Surface layers on electrochemically deposited Li have been characterized by ESCA, SIMS, AES, and SEM. For these studies, the electrode was washed with dry PC after formation of the surface layer. The electrode was then entered into a He-filled transfer chamber which had been placed inside the dry box. After connection to the pre-evacuation chamber of the ESCA/SAM/SIMS system, the transfer chamber was purged three to four times with ultrapure Ar for removal of He, and evacuated for transfer of the specimen to the main vacuum chamber with a magnetic transfer rod. XPS spectra for Li, O, C, and Cl have been collected after different times of Ar ion bombardment. The Li and O spectra were broad and are not shown here. The sputtered area was chosen to be much (about eight times) larger than the observed area in order to minimize redeposition and surface diffusion of sputter products. X-ray diffraction also has been employed for the analysis of surface layers. The morphology of the Li deposit and the electrode after cycling has been studied by SEM.

Results and Discussion

Li amalgam (approximately 2%) has been used to investigate the behavior of PC in contact with film-free lithium before and after removal of water. The formation of a solid, black material on the amalgam surface, and a transparent material with a scale-type structure on top of it, was observed. A viscous material was present at the interface of scales and electrolyte. Spectrum C in Fig. 1 represents the scale-type material, spectrum D the dark solid material. Comparison with spectra A and B of Li₂CO₃ and PC included in Fig. 1 shows that most of the functional groups of PC, in particular covalent CO₃ (1030, 1170, 1790 cm⁻¹) and CH₃ (3000 cm⁻¹), are preserved in the precipitate. A small amount of Li₂CO₃ is possibly indicated in spectrum D by absorption at 500 and 860 cm⁻¹. The presence of residual PC in the film is not a likely cause of the observed spectral features because the procedure used for removing the solvent from the film material involved heating in vacuum. The sample chamber of the IR spectrometer was purged with Ar during the measurements.

An IR spectrum of the surface layer formed on a Li electrode in PC, 1M LiClO₄ during cathodic deposition at 1 mA/cm² on a Cu substrate is shown in Fig. 2, curve B. The spectrum of this material differs from those of the precipitate formed on the amalgam (Fig. 1) in that many of the functional groups of PC are no longer present, such as covalent CO₃ (700, 760, 1030 cm⁻¹). Comparison with the two calibration spectra for PC and Li₂CO₃ (A and C) indicates the formation of Li₂CO₃ by the presence of ionic CO₃ peaks (500, 860, 1430, and 1500 cm⁻¹). Additional peaks around 600 and 1600 cm⁻¹ and the special feature of the spectrum at around 200 cm⁻¹ show formation of other materials. The band at 620 cm⁻¹ may show the presence of a carbon-chlorine bond.

Previous studies (20) on the effect of residual water on film formation during charge and discharge of Li electrodes have shown a peak at 3560 cm⁻¹ due to lithium oxide in addition to the peaks due to Li₂CO₃ and polymer found here. The formation of oxidic and polymeric films

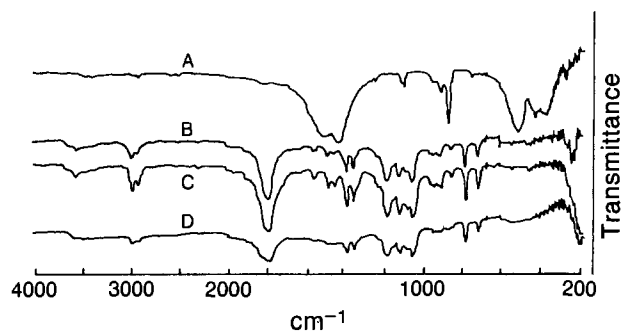


Fig. 1. Infrared transmission spectra of Li₂CO₃ (A), PC (B), scale-type transparent material near Li-Hg/PC interface (C), and precipitated dark material on Li/Hg surface (D).

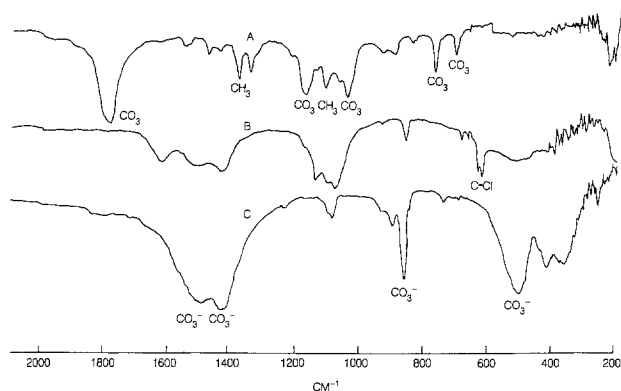


Fig. 2. IR spectra of PC (A), film formed on 1000Å thick Li (B), electrochemically deposited on Cu from PC 1M LiClO₄ and Li₂CO₃ (C).

on bulk lithium at open circuit had been postulated earlier (21). Those layers are probably too thin for observation by the present techniques.

The composition of the surface layer has also been investigated by use of ESCA with Li deposited electrochemically from PC, 1M LiClO₄ on a Cu substrate. After deposition, the electrode has been washed with dry PC and evacuated. Without exposure of the electrode to air, it was inserted in the vacuum chamber of the ESCA equipment with a transfer rod (High Vacuum Apparatus Manufacturing). Two different carbon 1s peaks have been observed, one at 290 eV related to Li₂CO₃ and another at 284 eV typical of polymeric carbon (Fig. 3). The latter peak is often seen as a result of surface contamination, and it rapidly disappears upon sputtering (after about 10Å removal). However, the depth profiling of the surface layer showed the peak at 284 eV decreasing only gradually, while that at 290 eV increased with sputter time. It can be concluded that Li₂CO₃ is mostly present in the inner film regions, polymer in the outer, although the large internal surface of the porous deposit makes it difficult to distinguish inner and outer regions and does not allow us to derive film thicknesses from sputter times. The slight shift of the peaks in Fig. 3 at different sputter times is probably due to charging of the film and change in its thickness. The ESCA spectrum for chlorine 2p (Fig. 4) showed the presence of five different chlorine compounds in the film, indicating that LiClO₄ decomposes during electrochemical deposition of Li. Literature data given in Table I have been used for identifying the peaks. Depth profiling showed that chlorine of higher valence, such as perchlorate, is mostly present in the outer regions of the film, while chloride and chlorinated polymeric compounds are present in the inner regions. The mechanism of polymer formation from PC or some of its decomposition products and the chlorination of the polymer are not clear. Since propylene had been identified as a reaction product of PC with Li (16), it is a likely participant in polymerization

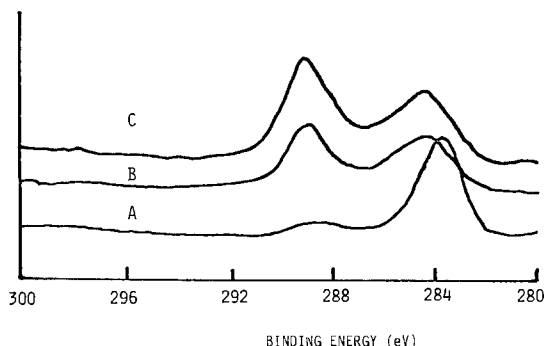


Fig. 3. XPS spectra of carbon 1s in the surface layer formed on a Li electrode, electrochemically deposited on Cu from PC, 1M LiClO₄. A: Top surface. B: After 10 min sputtering. C: After 20 min sputtering. Sputtering rate: 8 Å/min.

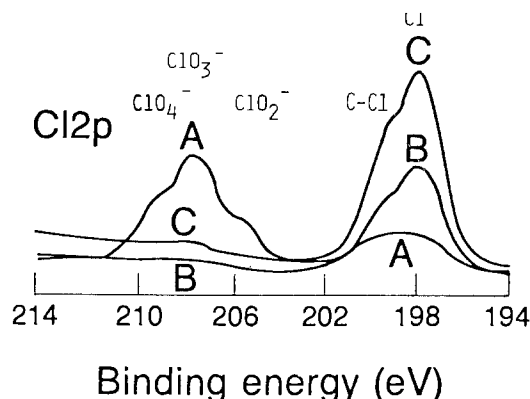


Fig. 4. XPS spectra of Cl 2p in the surface layer formed on Li, electrochemically deposited from PC, 1M LiClO₄ indicating the decomposition of ClO₄ ions. A: Top surface. B: After 10 min sputtering. C: After 20 min sputtering. Sputtering rate: 8 Å/min.

reactions. Epelboin *et al.* concluded that LiCl exists in the film (13). It is also possible that Cl ions are formed by the decomposition of ClO₄, ClO₃, ClO₂, or ClO ions due to the sputtering.

The surface layer formed on electrochemically deposited Li on Cu has been studied using SIMS. A complex spectrum was obtained, which was difficult to fully interpret. In the low mass range (Fig. 5), fragments of PC can be recognized. They include among hydrocarbons CH (13) and CH₂ (14), C₂ (24), (CH₂)₂ (28), CH₃CH₂ (29), CH₃CH₃ (30), propylene or (CH₂)₃ (42), and propane (44). Possible oxygen compounds are CO (28), CO₂ (44), and ethylene oxide (44). Chlorine appears as fragments of residual perchlorate, such as HCl (36), LiCl (42), and ClO (51), but also as chlorinated organic compounds such as CHCl (48), CH₂Cl (49), possibly CH₃Cl (51), and (not shown in the figure) CH₃CH₂Cl (64). Small amounts of water may be indicated by OH₃ (19), LiOH (24), LiO (or Na) (23), Li₃O (30), and Li₂OH (31). Other lithium compounds are possibly LiC (19) and LiCH₂CH₂ (49). After Ar ion bombardment of the surface layer, the residual gas analysis of the SIMS chamber always showed a strong Li (7) and a Li₂ (14) peak, which indicates the presence of occluded metallic Li in the film. Most of the low mass SIMS spectrum had also been observed previously from surface layers on bulk Li (21). In the high mass range (Fig. 6), fragments with mass higher than that of PC (102) were observed. These are indicative of the presence of a polymeric material in the film. Most of the mass units can be represented by fragments from a partially chlorinated hydrocarbon polymer and their Li adducts such as LiCHClCHCl (103), Li-PC (109), LiCH₂CHClCH₂Cl (118), CH₃CH₂CHClCH₂Cl (127), CH₃CH₂CHClCH₂CLi (134), and CH₃CH₂CHClCHClCH₂Li (147).

Surface layers on electrochemically deposited Li have also been studied by *in situ* x-ray diffraction. Data for galvanostatic deposition on a Ni substrate are shown in Fig. 7. The experimental procedure and the cell design used have been discussed elsewhere (22). A broad peak at low 2θ angle (14°-24°) which is characteristic of polymeric compounds has been observed, as was a narrow peak at 32° (2θ) characteristic of Li₂CO₃. In the presence of residual water, diffraction lines characteristic of the oxide have been observed (20).

Table I. Identification of Cl 2p ESCA peaks

Compound	Binding energy Cl 2p (eV)
LiCl	198
Polyvinyl chloride	200
ClO ₂ ⁻	206
ClO ₃ ⁻	208
ClO ₄ ⁻	209

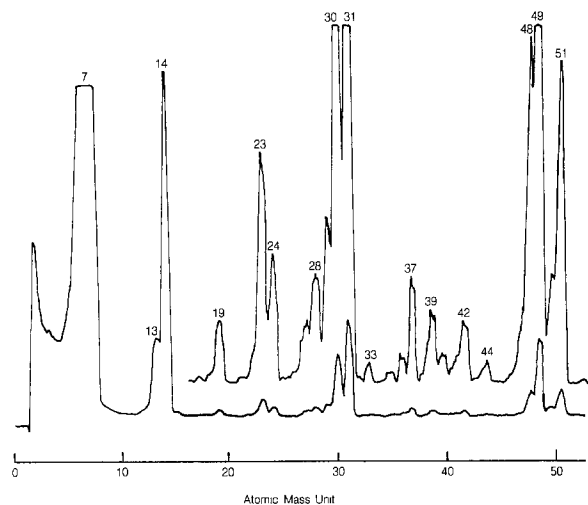


Fig. 5. SIMS spectrum of surface layer on Li electrochemically deposited from PC, 1M LiClO₄ on Cu. Two different sensitivities shown; low mass range.

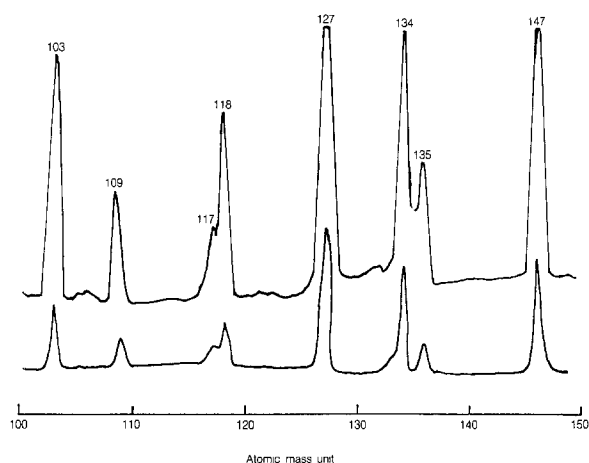


Fig. 6. As Fig. 5, but with high mass range

The morphology of electrochemically deposited Li on metallic substrates has been studied using SEM. Li deposited on a Ni substrate from PC, 1.5M LiClO₄ is shown in Fig. 8. The electrode was washed with PC and transferred to the SEM chamber by use of a He-filled transfer rod. Special care was taken not to expose the specimen to air by inserting it into the Ar-filled SEM air lock sur-

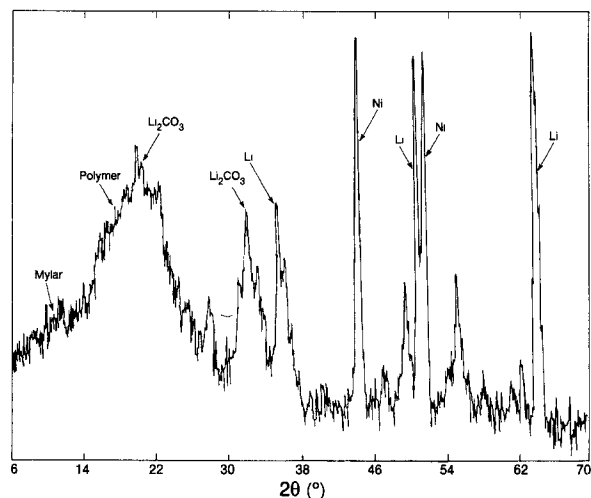


Fig. 7. *In situ* x-ray diffraction of the surface layer on electrochemically deposited Li on a Ni substrate. Li₂CO₃ and polymeric compounds are identified.

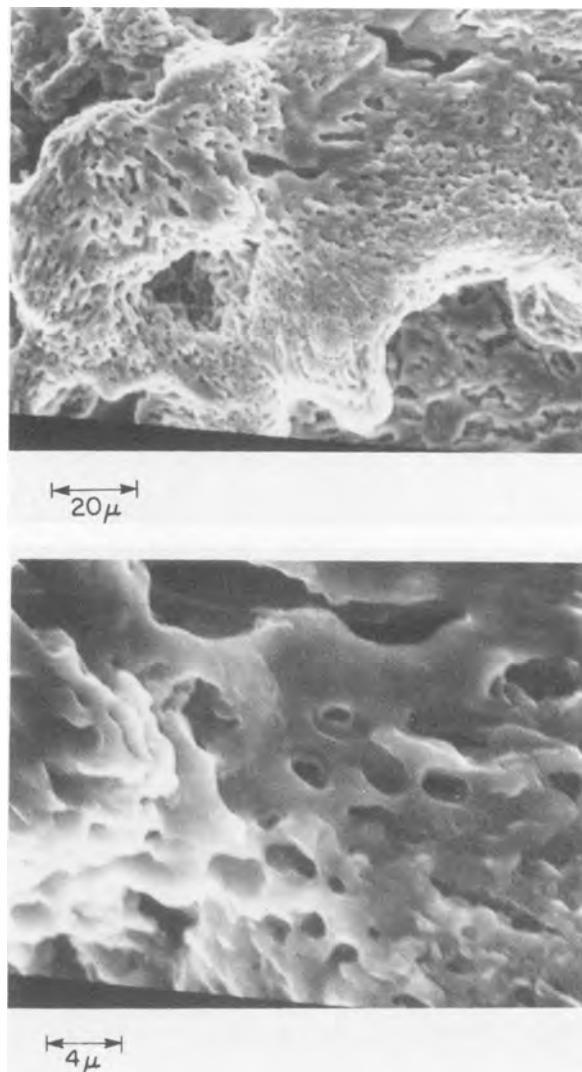


Fig. 8. SEM showing the micromorphology of Li deposited on a Cu substrate from PC, 1M LiClO₄.

rounded by an Ar-purged plastic bag. A porous structure of the deposit was observed in most cases. This porous deposit may be responsible for rapid film formation and poor rechargeability of the Li electrodes. In this structure, one can well imagine the formation of isolated regions of lithium by localized corrosion, as postulated in the literature (17).

Conclusions

In situ and *ex situ* studies of surface layers on Li electrodes in PC-based electrolytes demonstrate that PC reacts with Li under formation of several products, primarily what appears to be a chlorine containing polymer product and Li₂CO₃. When water is present, Li₂O is also formed. LiClO₄ decomposes during potential cycling of Li electrode between -2 and +2V. Surface layers are of complex composition and structure. Depth profiling of the surface layers indicates an inhomogeneous structure with concentration gradients of different components across the film. Electrodeposited Li shows a highly porous micromorphology. The use of advanced *in situ* techniques, such as x-ray diffraction with a position-sensitive detector, with its high sensitivity and short time response, promises to provide new insight into the initial step of film formation.

Acknowledgments

This work was supported by the Assistant Secretary for Conservation and Renewable Energy, Office of Energy Systems Research, Energy Storage Division of the U.S.

Department of Energy under Contract no. DE-AC03-76SF00098. We wish to thank Kenneth A. Gaugler for assistance with the ESCA and SIMS measurements.

Manuscript submitted Sept. 27, 1984; revised manuscript received April 25, 1985.

Lawrence Berkeley Laboratory assisted in meeting the publication costs of this article.

REFERENCES

1. A. Brenner, in "Advances in Electrochemistry and Electrochemical Engineering," Vol. 5, P. Delahey and C. W. Tobias, Editors, p. 205, Interscience, New York (1968).
2. J. O. Besenhard and G. Eichinger, *J. Electroanal. Chem.*, **68**, 1 (1976); G. Eichinger and J. O. Besenhard, *ibid.*, **72**, 1 (1976).
3. E. Peled, in "Lithium Batteries," J. P. Gabano, Editor, p. 43, Academic Press, New York (1983).
4. K. M. Abraham and S. B. Brummer, in "Lithium Batteries," J. P. Gabano, Editor, p. 371, Academic Press, New York (1983).
5. S. B. Brummer, V. R. Koch, and R. D. Rauh, in "Material for Advanced Batteries," D. W. Murphy, T. Broadhead, and B. C. H. Steele, Editors, p. 123, Plenum Press, New York (1980).
6. V. R. Koch, *J. Power Sources*, **6**, 357 (1981).
7. E. Peled, *ibid.*, **9**, 253 (1983).
8. S. B. Brummer, in "Lithium Nonaqueous Battery Electrochemistry," E. B. Yeager, B. Schumm, G. Blomgren, D. R. Blankenship, V. Leger, and J. Akridge, Editors, p. 130, The Electrochemical Society Softbound Proceedings Series, Princeton, NJ (1980).
9. J. L. Goldman, R. M. Mank, J. H. Young, and V. R. Koch, *This Journal*, **127**, 499 (1979).
10. V. R. Koch and J. H. Young, *Science*, **204**, 499 (1979).
11. B. M. L. Rao, R. W. Francis, and H. W. Christopher, *This Journal*, **124**, 1490 (1977).
12. J. R. Van Beek and P. J. Rommers, in "Power Sources 7," J. Thompson, Editor, p. 595, Academic Press, London (1979).
13. I. Epelboin, M. Froment, M. Garreau, J. Thevenin, and D. Warin, *This Journal*, **127**, 2100 (1980).
14. A. N. Dey, *ibid.*, **118**, 1547 (1971).
15. V. R. Koch and S. B. Brummer, *Electrochim. Acta*, **23**, 55 (1978).
16. A. N. Dey and B. P. Sullivan, *This Journal*, **117**, 222 (1970).
17. R. D. Rauh and S. B. Brummer, *Electrochim. Acta*, **22**, 75 (1977).
18. S. P. S. Yen, D. Shen, R. P. Vasquez, F. J. Grunthaner, and R. B. Somoano, *This Journal*, **128**, 1434 (1981).
19. Yu. M. Povarov and E. N. Sitnina, *Elektrokhimiya*, **17**, 633 (1981).
20. Gh. Nazri and R. H. Muller, Abstract 61, p. 98, The Electrochemical Society Extended Abstracts, Vol. 83-2, Washington, DC, Oct. 9-14, 1983; *This Journal*, **132**, 2054 (1985).
21. F. Schwager, Y. Geronov, and R. H. Muller, Abstract 37, p. 102, The Electrochemical Society Extended Abstracts, Vol. 80-2, Hollywood, FL, Oct. 5-10, 1980; *This Journal*, **132**, 285 (1985); F. Schwager and R. H. Muller, Abstract 295, p. 478, The Electrochemical Society Extended Abstracts, Vol. 82-2, Detroit, MI, Oct. 17-21, 1982.
22. Gh. Nazri and R. H. Muller, *This Journal*, **132**, 1385 (1985).

Effect of Residual Water in Propylene Carbonate on Films Formed on Lithium

Gholamabbas Nazri* and Rolf H. Muller*

Materials and Molecular Research Division, Lawrence Berkeley Laboratory, University of California, Berkeley, California 94720

ABSTRACT

Low concentrations of water in propylene carbonate solutions result in the formation of protective surface layers on lithium electrodes. Increasing concentrations of water have been found by infrared spectroscopy and x-ray diffraction to result in increasing lithium oxide and decreasing carbonate and polymer content in the layers. The oxide layers are protective and greatly reduce the rate of corrosion reactions of the metal with the electrolyte. They represent the principal resistance to current passage and can be removed by breakdown at high potential. Water-free solvent interacts differently with lithium resulting in the continuous formation of lithium carbonate and polymeric materials. Use of a thin layer cell with 10 μm electrode separation has been shown to eliminate the effect of low concentrations of water.

The structure and composition of surface layers are a major controlling factor in the dissolution and deposition of Li in ambient-temperature nonaqueous electrolytes (1-4). Peled (5) proposed migration of Li^+ in a solid electrolyte interphase as a controlling factor in the electrochemistry of lithium. The surface layers formed on Li in 1M LiClO_4 and LiAsF_6 in propylene carbonate (PC) have been investigated using potential pulse techniques and electrochemistry (6-8). Semiconductor properties of the surface layer on Li due to defects in the crystal lattice have also been reported (9). However, despite the use of various techniques, structure and composition of the surface layer formed on a Li electrode exposed to propylene carbonate (PC) containing residual water are still not definitely known. Decomposition of the PC in contact with lithium and formation of Li_2CO_3 as a surface layer has been postulated by several authors (10, 11). However, such a composition cannot fully explain the behavior and properties of the layers, and is not in agreement with optical observations (7, 8). The effect of electrolyte impurities on the performances of Li batteries, although extensively investigated, is not well understood (11, 12). Some

trace impurities such as H_2O , O_2 , and N_2 have been found to favorably affect the cycle life of lithium anodes (11, 12).

One of the major problems in electrochemical studies of Li is the purification of the electrolytes. Distillation of solvents does not remove traces of water. More than 10 ppm of residual water is often detected. Several procedures for purification of electrolytes have been established (10, 13, 14). These procedures include the pre-electrolysis of salts, recrystallization of salts and drying under vacuum, storage of solvents on molecular sieves, and distillation of solvent along with the treatments with Li amalgam or Na/K (50/50) alloy. Distillation of solvent after treatment with amalgam or NaK alloy is desirable to remove decomposition products of the solvents which may form during treatment. Purification of nonaqueous electrolytes is a tedious and time consuming process. Since most of the procedures being used today are open to questions, an effective way to minimize the effect of impurities is to use a small amount of electrolyte (less than a drop) after reasonable purification. A thin layer cell has been used for that purpose. Another difficulty in electrochemical studies of Li is the existence of an initial film on the Li electrode. Even in an inert atmosphere box with less than 1 ppm O_2 , H_2O , and N_2 , a film will form on the

*Electrochemical Society Active Member.

surface in less than 1s. Some research groups produced clean electrode surfaces *in situ* by mechanical removal of the surface layer, electrochemical pulse cleaning, or deposition of Li on metallic substrates (15-19).

The objective of this work is to understand the structure and composition of the surface layer formed on Li in PC, 1M LiClO₄ containing residual water. The effect of impurities has been minimized by use of a thin layer cell. The composition and structure of the surface layers has been analyzed using *ex situ* and *in situ* x-ray diffraction and transmission IR spectroscopy. The role of the residual water was also studied using potential cyclic voltammetry and potential pulse measurements.

Experimental Procedure

LiClO₄ has been recrystallized from water and dried under vacuum at 150°C. The dehydration of LiClO₄ has been studied by thermogravimetry. All physically and chemically adsorbed water is released below 150°C at 10⁻³ torr. After treatment with Li amalgam, the concentration of water in PC was below the detection level of the GC (1 ppm).

A cylindrical cell and a thin layer cell have been used in this work. The cylindrical cell (7, 8) contains two parallel disk electrodes of 1.9 cm diam, 3 cm apart from each other. One of these disks served as working electrode, the other as counterelectrode. The reference electrode was a Li wire with diameter of 3 mm forced into the polypropylene in such a way that only its cross section was exposed to the electrolyte. The distance between reference and working electrode was about 2 mm. The two optical win-

dows on this cell have been used in previous ellipsometric studies.

A thin layer cell has also been used. Its design is shown in Fig. 1. A pellet of lithium (Foot Mineral Company, 1.22 cm diam and 0.6 cm height) is held between two stainless steel current collectors contained in polypropylene rods. This lithium is cut in half by use of a stainless steel wire of 0.5 mm diam with the two halves serving as working and counterelectrodes. A drop of electrolyte was placed between the two electrodes and the gap between them was adjusted to 10 μm using a micrometer, which carried one of the electrodes on its nonrotating tip. Although the thin layer cell was operated inside the inert atmosphere box (Vacuum Atmospheres Company), with concentration of O₂, H₂O, and N₂ of less than 1 ppm, a polyethylene bag was placed around the cell for further isolation. This bag could be collapsed by evacuation and refilled with ultrapure He from a separate supply. This system also enabled us to expose the electrodes to any gas without contaminating the dry box atmosphere. An application of the capability will be reported separately.

The formation of surface layers on Li has been studied potentiostatically and galvanostatically using a PAR potentiostat, programmer, and coulometer. During potentiostatic pulse measurements, the results were monitored by a storage oscilloscope, then recorded by an X-Y recorder (H-P 7044B). Copper was mostly used as a substrate because of its optical properties, although alloy formation occurred with Li, as was the case for Ag, Au, and Pt and, to a lesser degree, with Ni and stainless steel. The Cu substrates were successively polished with 600 emery paper, 1 μm, and 0.25 μm diamond paste. They were then cleaned in ethanol, dried in pure He, and washed with dry PC in the glove box. Electrode potentials have been corrected for IR drop in the solution, determined at the beginning of an experiment by conventional current interruption techniques.

The composition of surface layers formed on Li in PC, 1M LiClO₄ with different water concentrations has been analyzed by transmission IR spectroscopy. The Li electrode was washed with dry PC and then evacuated for

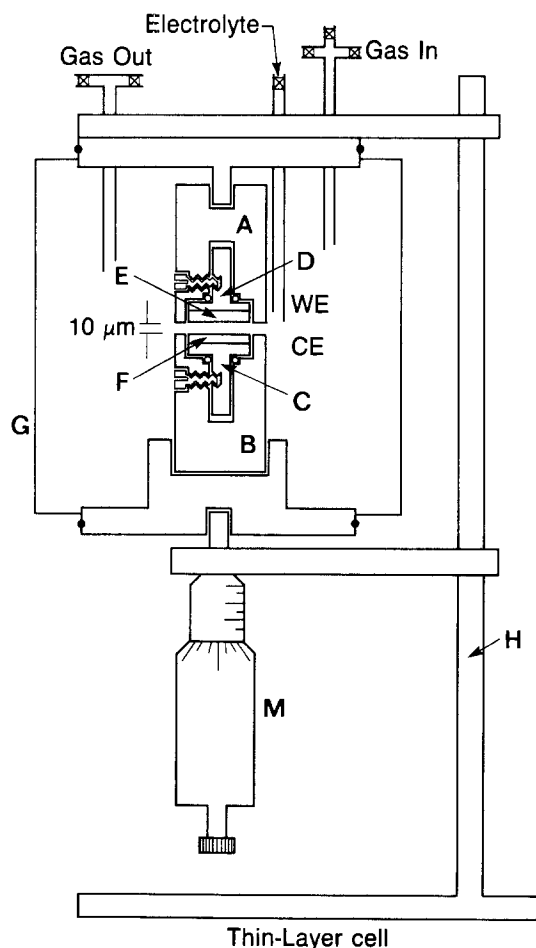


Fig. 1. Schematic of the thin layer cell for nonaqueous electrochemistry. WE: Working electrode. CE: Counterelectrode: 10 μm gap set after cutting of electrodes from single piece in inert atmosphere. M: Nonrotating tip micrometer. A and B: Polypropylene electrode holder. C and D: Stainless steel current collectors. E and F: Li electrodes. G: Polyethylene bag for control of atmosphere at the electrodes by use of gas inlet and outlet. H: Aluminum stand.

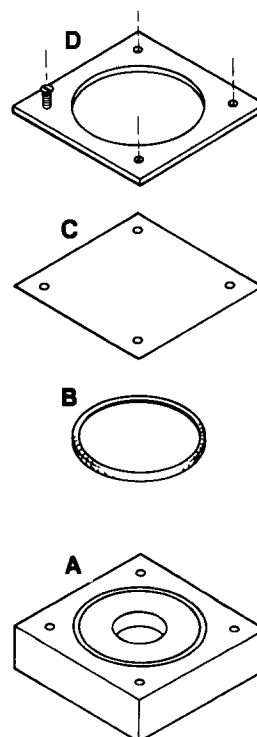


Fig. 2. Schematic of the transfer cell for x-ray diffraction analysis of surface layers on Li electrodes. A: Cell body made of polypropylene, with a cylindrical cavity in the center for the electrode and a groove around the cavity for O-ring seal. B: O-ring. C: Mylar window. D: Cu washer.

evaporating the solvent. The surface layer on the electrode was collected from the dried electrode by a glass rod and ground with KBr in the dry box. A pellet of the mixed powder was made for transmission IR spectroscopy. During the measurement, the sample chamber of the IR machine was purged with pure Ar gas. The decomposition products of the PC on Li amalgam have also been analyzed using the IR spectrometer. The IR spectrum of the surface layer was compared to the spectra of PC, Li_2CO_3 , and Li_2O . The Li electrode was potentiostatically cycled 20 times by sweeping the potential ($\pm 2\text{V}$ vs. Li) at a rate of 20 mV/s. The electrode was removed from the electrochemical cell, washed with dry PC, and isolated inside a polypropylene transfer cell with a Mylar window for the collection of x-ray diffraction data from the electrode surface. The design of the transfer cell for x-ray diffraction analysis is shown in Fig. 2.

In situ x-ray diffraction of surface layers formed on Li electrodes during anodic and cathodic polarization has been presented separately (20).

Results and Discussion

The effect of residual water in PC, 1M LiClO_4 on Li electrodes has been studied using sampled current voltammetry (21). The experiments have been performed with dry and wet PC in both the cylindrical and the thin layer cells. A potential step has been imposed on the working electrode, and the current response as a function of time has been measured for each potential step. The current observed 1s after application of the potential step is shown in Fig. 3 as a function of the potential. In these measurements, the double-layer charging does not affect the measured current. The advantage of this technique is that at the beginning of each potential step the concentration of electrolyte at the interface is the same because the bulk concentration is allowed to be reestablished before the next pulse is applied. As shown in Fig. 3, the current density observed with dry electrolyte is much higher than that in the presence of water. This result may be due to the presence of an oxide film on the electrode surface

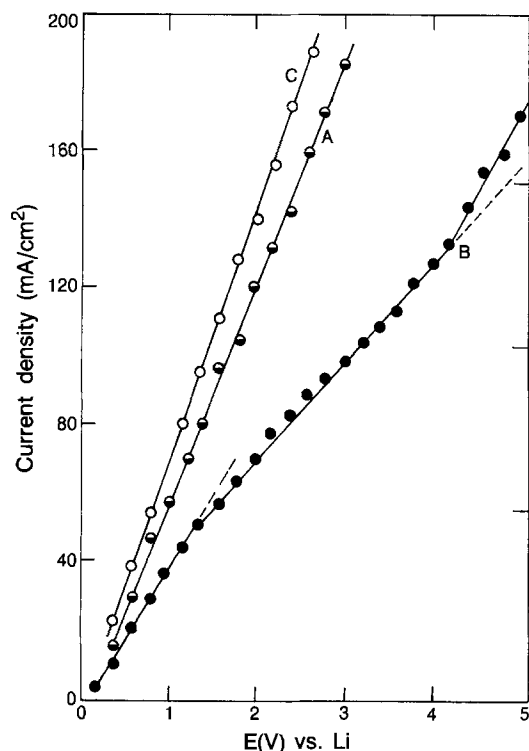


Fig. 3. Effect of water content and volume of the electrolyte on sampled-current voltammetry of Li electrodes in dry PC, 1M LiClO_4 , 20 cm^3 cylindrical cell (curve A), same solution containing 300 ppm water, 20 cm^3 cylindrical cell (curve B), same solution containing 500 ppm water, thin layer cell (curve C). Potentials for curves A and B corrected for IR drop in solution; curve C represents cell voltage.

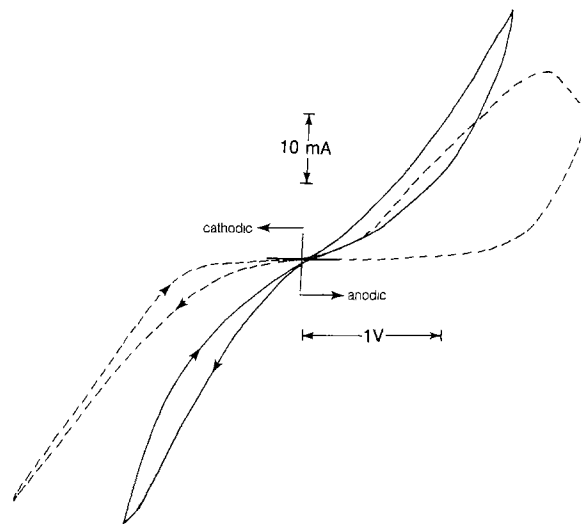


Fig. 4. Cyclic voltammetry of Li electrodes in PC, 1M LiClO_4 containing 300 ppm water using thin layer cell (solid line), and cylindrical cell containing 20 cm^3 electrolyte (broken line). The electrode surface areas were the same in both cells. IR-free electrode potential shown for cylindrical cell, cell voltage for thin layer cell.

which forms by reaction of Li with H_2O before application of the potential step. The film appears to begin to break down at higher potentials as evidenced by the change of slope at applied potentials $> 4\text{V}$. The resulting current density depends on the concentration of water in the electrolyte and the time for which the electrode has been exposed to it before the measurements are taken. The formation of an oxide layer on the electrode surface by trace amounts of water has been credited for the higher cycling efficiency of Li anodes in the presence of residual water (10).

The ability of the thin layer cell to discriminate against the effect of residual water in the electrolyte is illustrated in Fig. 4. Cyclic voltammetry of Li in PC, 1M LiClO_4 containing 300 ppm water, using thin layer cell and cylindrical cell, are compared. Higher current densities are obtained in the thin layer than in the cylindrical cell. In addition, the anodic dissolution of Li in the thin layer cell does not show the passivation seen with the cylindrical cell. Similarly, experimental results from the thin layer cell for electrolyte with 500 ppm water have been found to be almost the same as those with dry solution (< 1 ppm water) obtained in the cylindrical cell which contains 20 cm^3 of solution.

Delay-time phenomena in the passivation and activation are illustrated in Fig. 5. Four successive potential pulses of 40s duration have been applied to the Li working electrode in the cylindrical cell containing 20 ml of dry PC, 1M LiClO_4 . The current response to each subsequent potential pulse at different potential varies as

$$i_1 < i_2 < i_3 < i_4 \quad \text{for } 0.2 < E < 1.6\text{V vs. Li}$$

and

$$i_1 > i_2 > i_3 > i_4 \quad \text{for } 1.6 < E < 3.0\text{V vs. Li}$$

where i_1 , i_2 , i_3 , and i_4 are currents corresponding to the first, second, third, and fourth pulses, respectively. Up to a pulse height of 1.6V, the current increases with time and the response to the first pulse is smaller and builds up more slowly than the response to subsequent pulses. This behavior indicates that film removal (or breakdown) takes place during the first pulse and continues to a lesser degree during the succeeding pulses. These results are in agreement with a diffusion-limited migration of Li ions through the interface. For potential steps higher than 1.6V, the current decreases with time and the initial current response to the first pulse is lower than the initial response to subsequent pulses, indicative of a film-removal process, as in the low potential regime. However, after a few seconds, the current for the first pulse remains

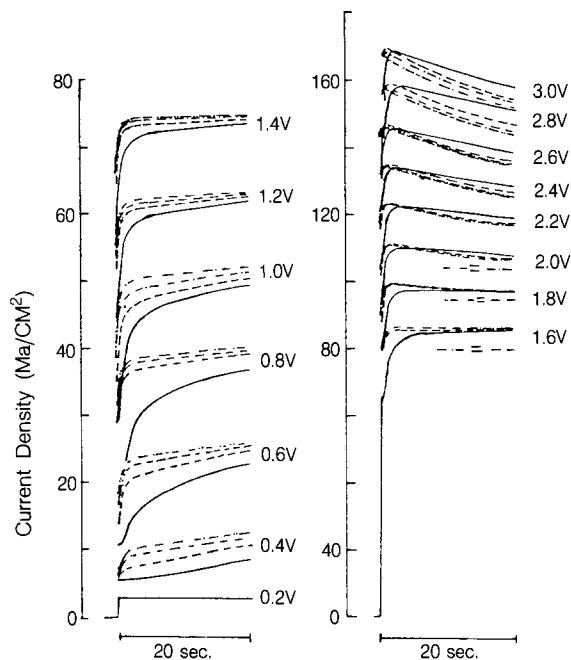


Fig. 5. Potential pulse measurements (I vs. t). Response to first pulse (—), second pulse (---), third pulse (-·-·-·-·-), and fourth pulse (-·-·-·-·-). Height of anodic pulse listed in volts; potentials corrected for IR drop in solution (dry PC < 1 ppm H_2O , 1M $LiClO_4$); pulse duration 40s; current response shown only for first 20s.

higher and declines less rapidly than that of subsequent pulses. This behavior indicates a limitation of the dissolution rate by mass transfer or film formation at high current densities. Below 0.2V, the current densities are the same for the four pulses, showing that the film remains intact and Li ions migrate through it. Removal of the film from the electrode surface by successive anodic pulses can be used for cleaning the Li surface *in situ*.

Lithium was galvanostatically deposited on a Cu substrate from PC, 1M $LiClO_4$ at 30 mA/cm² with a Li counterelectrode for a thickness of 1000Å based on Li bulk density. The formation of Li deposits on Cu with 60-70% current efficiency was determined by immersion in water and measurement of H_2 evolved. Higher current efficiencies had been found with stainless substrates. *In situ* x-ray diffraction also showed the presence of Li metal. The open-circuit potential of the Li electrode, vs. Li reference, has been monitored with electrolytes of different water content (Fig. 6). Immediately after deposition, the cell voltages were almost independent of water content. The potential of the electrodeposited Li is different from that of bulk Li (used as reference) probably because it represents a mixed potential of alloy, corrosion

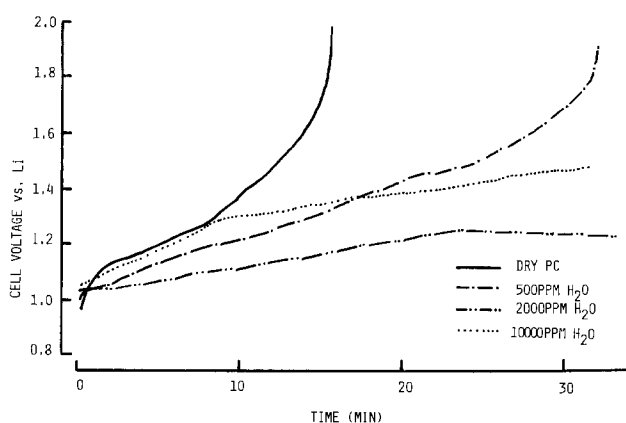


Fig. 6. Effect of water content in the electrolyte on the potential of electrochemically deposited Li (1000Å) on a Cu substrate at open circuit vs. Li reference electrode. PC, 1M $LiClO_4$ with different H_2O content.

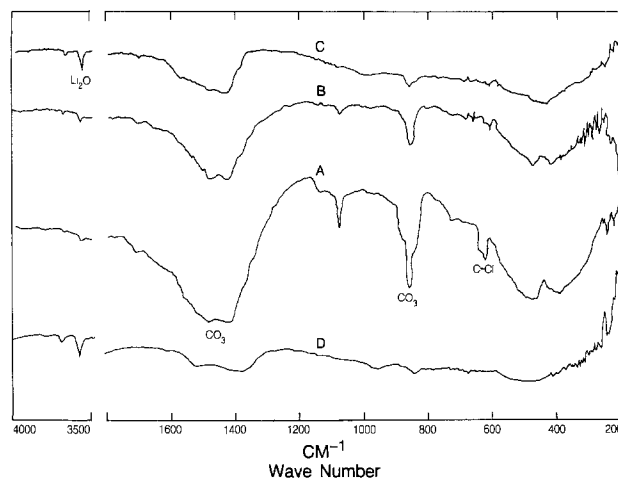


Fig. 7. IR spectra of the surface layers on a Li electrode formed after 20 cycles $\pm 2V$ vs. Li in PC, 1M $LiClO_4$ containing less than 1 ppm (curve A), 500 ppm (curve B), and 1% water (curve C). Curve D represents spectrum of the Li_2O .

products, UPD, and substrate. We have observed similar anomalous potentials for Li deposits on Cu in 2 Me-THF, $LiClO_4$. At later times, a potential characteristic of the substrate is reached much faster when no water is present. This observation shows that no protective film is formed on the electrode surface in the absence of water, allowing Li to continue to react with the electrolyte. The resistivity of the Li electrode is much higher with higher concentrations of water in the electrolyte, in agreement with the formation of a thicker, more resistive and protective oxide film. The oxide film does not fully protect the Li electrode, but greatly reduces the rate of reaction with the electrolyte.

The surface layers formed on Li in PC, 1M $LiClO_4$ containing different concentrations of water have been analyzed by transmission IR spectroscopy. Comparison to the spectra of Li_2O and Li_2CO_3 , obtained by the same procedures, shows that increasing concentrations of water result in increased Li_2O (3560 cm^{-1}), and decreased Li_2CO_3 ($860, 1430, 1500\text{ cm}^{-1}$) and C-Cl (620 cm^{-1}) content (Fig. 7). This result is consistent with the view that a partially protective oxide layer reduced the rate of lithium corrosion and solvent decomposition. Cyclic voltammetry with a Cu electrode in PC, $LiClO_4$ showed that PC decomposes anodically above 3.5V vs. Li (Fig. 8). Similar results have been obtained with Ni, Ag, and SS electrodes; with Pt, decomposition occurs at a lower anodic potential.

A Li electrode that had been cycled anodically and cathodically in PC, 1M $LiClO_4$ 20 times between $\pm 2V$ vs.

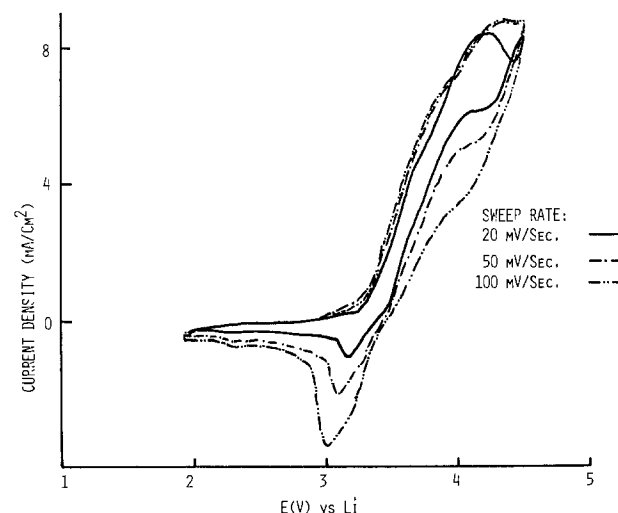


Fig. 8. Cyclic voltammetry of Cu electrode in PC, 1M $LiClO_4$ showing decomposition of PC above 3.5V vs. Li.

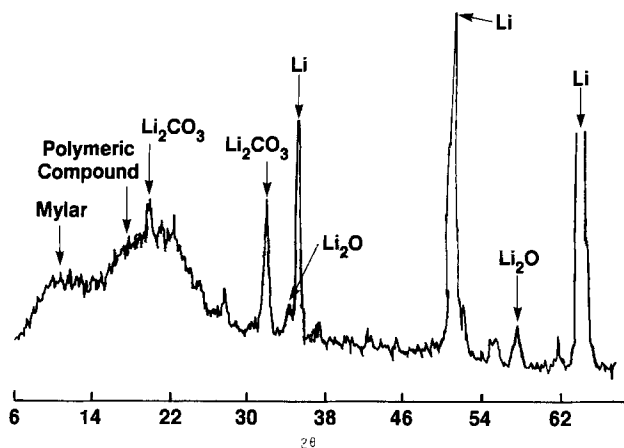


Fig. 9. X-ray diffraction of the surface layer formed on a Li electrode electrochemically cycled in PC, 1M LiClO₄ containing 700 ppm water, showing presence of Li₂CO₃, Li₂O, and a polymeric compound.

Li at a sweep rate 20 mV/s was subjected to analysis by x-ray diffraction. For this purpose, the electrode was removed from the cell, washed with dry PC, and inserted in the transfer cell with a Mylar window for placement in the diffractometer. A diffraction pattern of this electrode, shown in Fig. 9, confirms the presence of Li₂O, and Li₂CO₃ apart from Li. A noncrystalline (probably polymeric) material, which appears to result from reactions of the solvent, is indicated by a broad peak at low 2θ . The same film materials have been identified by *in situ* x-ray diffraction (20, 22). The formation of a polymeric membrane has been reported by Epelboin *et al.* (23).

Conclusions

Composition and properties of surface layers on lithium electrodes in propylene carbonate solutions, which are mainly responsible for the performance of this electrode, have been analyzed. The layers are strongly affected by small amounts of water in the solutions. The formation of an oxide in an earlier-postulated (8) inner layer in the presence of water has been confirmed. This layer greatly reduces the rate of Li corrosion, which occurs in its absence under formation of carbonate and polymer products. At low current density migration of Li ion through this film appears to control the rate of dissolution and deposition of Li. The effect of low to moderate concentrations of water (and other electrolyte impurities) on the lithium electrodes can be avoided by use of a small electrolyte volume in a thin layer cell.

Acknowledgment

This work was supported by the Assistant Secretary for Conservation and Renewable Energy, Office of Systems Research, Energy Storage Division of the U.S. Department of Energy under Contract No. DE-AC03-76SF00098.

Manuscript submitted Sept. 27, 1984; revised manuscript received April 25, 1985. Part of this article was pre-

sented as Paper 61 at the Washington, DC, Meeting of the Society, Oct. 9-16, 1983.

Lawrence Berkeley Laboratory assisted in meeting the publication costs of this article.

REFERENCES

1. E. Peled, *J. Power Sources*, **9**, 253 (1983).
2. S. B. Brummer, in "Lithium Nonaqueous Battery Electrochemistry," E. B. Yeager, B. Schumm, G. Blomgren, D. R. Blankenship, V. Legar, and J. Akridge, Editors, p. 130, The Electrochemical Society Softbound Proceedings Series, Princeton, NJ (1980).
3. G. H. Newman, in "Lithium Nonaqueous Battery Electrochemistry," E. B. Yeager, B. Schumm, G. Blomgren, D. R. Blankenship, V. Legar, and J. Akridge, Editors, p. 143, The Electrochemical Society Softbound Proceedings Series, Princeton, NJ (1980).
4. J. O. Besenhard and G. Eichinger, *J. Electroanal. Chem.*, **68**, 1 (1976); G. Eichinger and J. O. Besenhard, *ibid.*, **72**, 1 (1976).
5. E. Peled, *This Journal*, **126**, 2047 (1979).
6. Gh. Nazri and R. H. Muller, Abstract 61, p. 98, The Electrochemical Society Extended Abstracts, Vol. 83-2, Washington, DC, Oct. 9-14, 1983.
7. Y. Geronov, F. J. Schwager, and R. H. Muller, *This Journal*, **129**, 1422 (1982).
8. F. Schwager, Y. Geronov, and R. H. Muller, Abstract 37, p. 102, The Electrochemical Society Extended Abstracts, Vol. 80-2, Hollywood, FL, Oct. 5-10, 1980; *This Journal*, **132**, 285 (1985); F. J. Schwager and R. H. Muller, Abstract 295, p. 478, The Electrochemical Society Extended Abstracts, Vol. 82-2, Detroit, MI, Oct. 17-21, 1982.
9. Yu. M. Povarov and L. A. Beketaeva, *Elektrokhimiya*, **16**, 1252 (1980).
10. V. R. Koch and S. B. Brummer, *Electrochim. Acta*, **23**, 55 (1978).
11. V. R. Koch, *This Journal*, **126**, 181 (1979).
12. V. R. Koch, *J. Power Sources*, **6**, 357 (1981).
13. R. G. Selim, K. R. Hill, and M. L. B. Rao, Final Report, NASA CR-54969 (N66-35218), Mallory Inc., Burlington, MA (1965).
14. J. N. Butler, R. Jasinski, D. R. Cogley, and H. L. Jones, Report AD 718109, Tyco Labs, Inc., Waltham, MA (1970).
15. P. A. Linfors and K. M. Black, in "Microbeam Analysis," R. H. Geiss, Editor, p. 303, San Francisco Press, San Francisco, CA (1981).
16. R. N. Castellano and P. H. Schmidt, *This Journal*, **118**, 653 (1971).
17. E. J. Frazer, *J. Electroanal. Chem.*, **121**, 329 (1981).
18. A. N. Dey, *This Journal*, **118**, 1547 (1971).
19. J. O. Besenhard, *J. Electroanal. Chem.*, **94**, 77 (1978).
20. Gh. Nazri and R. H. Muller, *This Journal*, **132**, 1385 (1985).
21. W. J. Blaedel and G. A. Mabbott, *Anal. Chem.*, **53**, 2770 (1981).
22. Gh. Nazri and R. H. Muller, *This Journal*, **132**, 2050 (1985).
23. I. Epelboin, M. Froment, M. Garreau, J. Thevenin, and D. Warin, in "Power Sources for Biomedical Implantable Applications and Ambient Temperature Lithium Batteries," B. B. Owens and N. Margalit, Editors, p. 417, The Electrochemical Society Softbound Proceedings Series, Princeton, NJ (1980).

AC Impedance of the Carbon Monofluoride Electrode

Mary R. Suchanski*

Eastman Kodak Company, Research Laboratories, Rochester, New York 14650

ABSTRACT

The ac impedance of carbon monofluoride (CF) half-cells and Li/CF batteries that contain 1M LiBF₄/4-butyrolactone electrolyte was measured as a function of state of charge. The nonfaradaic components of the CF half-cell impedance were resolved with the aid of a one-dimensional macroscopic treatment of a porous electrode. The values of the nonfaradaic components and their variation with charge withdrawn provide information concerning the nature of cathode discharge products, the degree of tortuosity in the cathode and separator matrices, and the cathode failure mechanism. The CF electrode capacitance, as measured by the low frequency quadrature impedance, can serve as a semiquantitative measure of battery state of charge under certain conditions.

The electrochemical technique of ac impedance can be used, under appropriate conditions, to evaluate several important parameters of a porous electrode. The interfacial area between the electrode and the electrolyte can be obtained from the quadrature component of the impedance, provided that the double-layer capacitance of the pure electroactive component is known (1-3). Both faradaic components of the electrode impedance (charge transfer and diffusion resistances) and nonfaradaic impedance components (internal electrolyte resistance and interelectrode resistances) can be quantitatively identified from complex-plane plots (3, 4). Analysis of porous-electrode impedance data in terms of a semi-infinite cylindrical-pore model (5, 6) or, as has been done more recently, in terms of finite cylindrical pores (7), leads to values of pore radius, pore length, and pore number. Such analyses have been attempted for sintered-plate cadmium electrodes (8), gold powder and Raney gold electrodes (2), sintered nickel (2, 7), Raney nickel (4), and zinc powder (9). With Raney nickel, the impedance technique was used to obtain the pore radius, length, and number of micropores inside the catalyst grain (4).

Problems remain in characterizing the structure of porous electrodes, particularly technologically important ones, via the impedance method. Although the impedance data of simple structures, such as loosely packed metal powders, can be adequately interpreted in terms of an equivalent cylindrical-pore model (2, 9), for more complex structures, such as Raney catalysts and sintered metals, tortuosity must be introduced in the internal pore network (2, 8). Furthermore, for electrodes made of two or more materials with different particle shapes and sizes (for example, Teflon-bonded electrodes), a single pore radius cannot account for the distribution of pore sizes. Regarding pore shape, the impedance of an individual pore will reflect pore shape (7), but the impedance of an assembly of shaped pores will resemble that of cylindrical-pore electrode (2). Hence, pore shapes are better elucidated by electron microscopy. Nonetheless, the ac impedance technique can provide useful information concerning structure and mechanism in porous electrodes.

We report here the ac impedance of carbon monofluoride (CF) half-cells in 1M LiBF₄/4-butyrolactone electrolyte at different states of charge. Cognizant of the difficulties in treating the complex impedance of porous electrodes with a cylindrical-pore model, we used a macroscopic approach with two parameters, the internal electrolyte resistance and the electrode capacitance, to interpret the data. Tortuosity in the internal pore network of the electrode is related to the volume fraction solids of the electrode through an equation originally derived for ion movement in an ion-exchange membrane (10). The impedance technique can be used to resolve other nonfaradaic components of CF half-cells, including the interface resistance between the current collector and the electrode patch, the separator resistance, and the electrode capacitance. Finally, the low frequency quadrature

impedance data of both CF half-cells and commercial Li/CF batteries can be related to state of charge of the CF cathode.

Experimental

Materials.—The CF electrodes were composed of (by weight) 80% CF_{1.03} (Ozark Mahoning), 10% carbon (Vulcan XC-72, Cabot Corporation), and 10% Teflon (Teflon 30). Standard Teflon-bonded electrode fabrication techniques were used (11). The cathode current collector was Ti foil (0.013 cm thick) that has been etched in boiling 20% HCl. The lithium electrodes were made from 0.013 cm lithium foil. The electrolyte was 1M LiBF₄ (Foote Mineral Company, 97.5%) dissolved in 4-butyrolactone (Aldrich Gold Label) that had been vacuum distilled once over activated type-5A molecular sieves at 50°-55°C (1.5-2 mm Hg). The electrolyte was filtered once to remove LiF and stored in a Vacuum Atmospheres dry box in a flask containing activated type-5A molecular sieves.

The Li/CF batteries were standard 2/3A size (4300C rated capacity at 60Ω load) with a jelly-roll configuration and were manufactured by Matsushita Electric of Japan. The electrolyte in these batteries was 1M LiBF₄ in 4-butyrolactone.

Impedance vs. charge withdrawn.—Pairs of CF cathodes with various amounts of charge removed from them (0, 50, 100, 200, and 300C) were prepared by continuous discharge at a constant current density of 5 mA/cm². The cathodes were Ti foil with electrode dispersion applied to one side of the foil. The electroactive cathode patches were 2 × 2 × 0.032 cm, and the average coulombic content of the patches was 390C. One week after discharge, new cells were prepared from each pair of cathodes in which the electrode patches were positioned facing one another with one layer of nonwoven polypropylene fabric sandwiched between the two electrodes to prevent electronic contact (*cf.* Fig. 1). Fresh electrolyte was added to the cells, and the impedance of the cells was measured the next day. The cells were restrained during discharge and measurement taking to provide a minimum and uniform electrode-electrode gap.

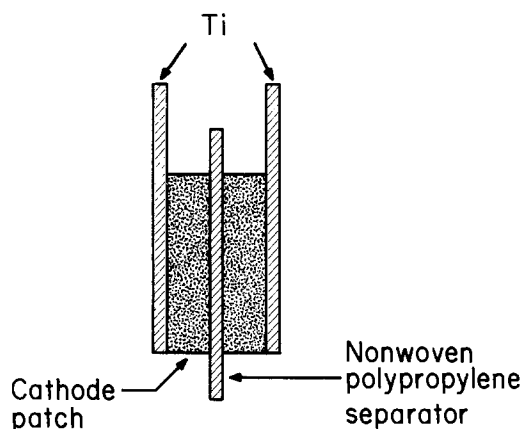


Fig. 1. Configuration of impedance cell

* Electrochemical Society Active Member.

The ac response of the CF electrodes and batteries was measured in the admittance domain by a cross-correlation technique described by Bentz *et al.* (12). A 2 mV peak-to-peak sine-wave excitation voltage with fixed frequencies in the range 0.00563-1780 Hz was generated by a Hewlett-Packard Model 203A function generator and was applied to the electrochemical cell via a PAR Model 173 potentiostat. The PAR potentiostat was used to null any voltage across the cell terminal (*i.e.*, cell held at open circuit for measurement taking) as well as to monitor the cell current via a current-to-voltage converter plug-in unit (PAR Model 176). The ac cell current was amplified 220 times and then cross correlated with an in-phase and quadrature square wave provided by the function generator. The cross-correlator output signals with frequencies > 1 Hz were integrated by a Butterworth filter, and the output signals of < 1 Hz were integrated via a gating technique. A 10Ω resistor was used to calibrate the impedance apparatus before each data collecting session. All measurements were made at room temperature.

Theory

We treated the impedance of a porous electrode by an approach similar to that of Keiser *et al.* (7) for the impedance of a cylindrical pore of finite length. Since it was unlikely that we could characterize a Teflon-bonded electrode made of three materials with different particle shapes and sizes by a single pore radius and pore length, we chose a macroscopic approach in which the geometric detail of the pore is ignored (13). The electrode with thickness l is divided (*cf.* Fig. 2) into N segments along an axis perpendicular to the plane of the electrode, and each segment is characterized by two impedance elements—a resistance R_k ($k = 0$ to N) due to the electrolyte and a corresponding capacitance, C_k , due to the electrochemical double layer. The electronic resistance of the cathode patch has been ignored in this treatment for two reasons: (i) dc resistance measurements of CF cathode patches with no coulombs withdrawn showed that the electronic patch resistance was 8-22% of the total resistance as evaluated by the ac impedance technique, and (ii) carbon is formed during CF electroreduction, which is likely to cause a decrease in patch resistance as more coulombs are withdrawn. The derivation also assumes that under the conditions of the measurements (open circuit) the contributions from any faradaic impedances are minor in comparison to the double-layer capacitance.

The network shown in Fig. 2 can be solved for using cascaded network theory in which each pair of impedance elements (R_k and C_k) is considered a two-port network (14). For a series of N such cascaded networks, calculation of the impedance becomes quite cumbersome, as it involves the multiplication of N matrices. For this circuit, it is much simpler to use the standard circuit-analysis technique of successive reduction of parallel and series impedances (15). Starting at the far right of the circuit and moving toward the left leads to the following it-

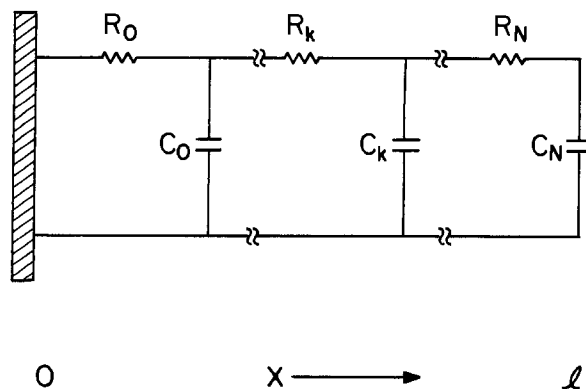


Fig. 2. Equivalent circuit of a porous electrode with thickness l . R_k is the average resistance of the electrolyte in the k th segment, and C_k is the average double-layer capacitance in the k th segment.

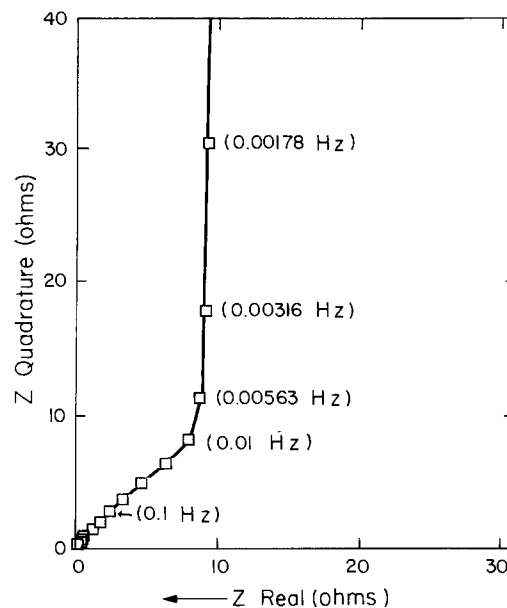


Fig. 3. Complex-plane diagram of the porous electrode impedance according to Eq. [1], with $R_k = 1\Omega$, $C_k = 0.1F$, and $N = 30$.

erative equation in which the circuit impedance from segments k to N is related to the circuit impedance from segments $(k + 1)$ to N

$$Z_k = R_k + 1/(j\omega C_k + 1/Z_{k+1}) \quad [1]$$

It is assumed that at $x = l$ the electrode is at open circuit; hence the impedance of the N th segment Z_N is infinite. By successive substitution of values of R_k and C_k into Eq. [1], the total electrode impedance Z_0 is calculated.

Figure 3 shows the Argand diagram of the complex impedance of a porous electrode according to Eq. [1], with $R_k = 1\Omega$, $C_k = 0.1F$, and $N = 30$. The Argand diagram plots the real or resistive part of the complex impedance *vs.* the imaginary or capacitive component of the electronic impedance. At higher frequencies where the current does not completely penetrate through the electrode, the phase angle between the real and the quadrature components of the impedance is 45° . At lower frequencies where the current has a chance to penetrate through the electrode, the real component approaches a constant value of $R_{sol}/3$, where R_{sol} is the total electrolyte resistance within the pores of the electrode (in this case $R_{sol} = 30\Omega$), and the quadrature component is inversely proportional to the total electrode capacitance C_T . The result shown in Fig. 3 is also obtained from the following equation derived by de Levie (6) for shallow, pores of depth l

$$Z_a = \sqrt{ZR} \cotanh lR/\sqrt{ZR} \quad [2]$$

In Eq. [2], Z_a is the impedance of a single pore of length l , Z is the pore-wall impedance per unit length ($1/j\omega C$ in our case), and R is the electrolyte resistance per unit length of pore. For an electrode consisting of n pores in parallel electrically, the relationship between the pore impedance Z_a and the electrode impedance Z_0 is as follows

$$Z_0 = Z_a/n \quad [3]$$

We used two equations to compute solution phase resistance for comparing calculated values with those obtained from impedance data via the technique outlined above. The first equation corresponds to a porous matrix in which the ions are free to travel in an unobstructed tunnel whose axis is perpendicular to the electrode face. For this case, in which ion mobility in the solution phase is assumed to be the same as in the pure solution, the resistance will be given by the equation

$$R_{sol} = l[A(1 - v_2)\kappa_0] \quad [4]$$

where l is the electrode thickness, A is the electrode face area, v_2 is the volume fraction solids of the porous matrix,

and κ_0 is the conductivity of the pure solution phase. The second equation introduces tortuosity in the diffusion pathway and was originally derived for ion diffusion through water-swollen cation-exchange resins (10). Here a cubic-lattice model was used in which each lattice site is occupied by a portion of the solid phase, an ion, or pure solvent. The increase in the length of the diffusion path over pure liquid is

$$\theta = (1 + v_2)/(1 - v_2) \quad [5]$$

According to Mackie and Meares (10), the ion mobility in a porous matrix will be reduced by the square of θ ; hence, in this case the solution phase resistance is

$$R_{\text{sol}} = l/(A\kappa_0/\theta^2) \quad [6]$$

Note that Eq. [4]-[6] can be applied to other porous phases of an electrochemical cell, for example, the nonwoven polypropylene separator.

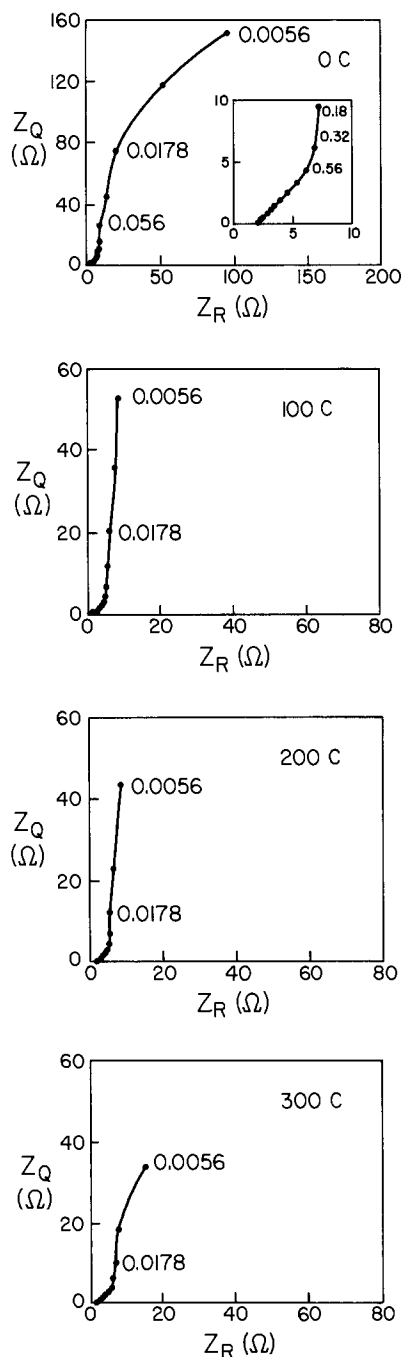


Fig. 4. Complex-plane impedance data of CF half-cells in 1M LiBF₄/4-butyrolactone electrolyte as a function of the amount of charge withdrawn.

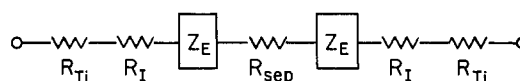


Fig. 5. Equivalent circuit of CF half-cell

Results and Discussion

Half-cell data.—Figure 4 shows the Argand diagrams of CF half-cells that have had 0, 100, 200, and 300C withdrawn per electrode patch (average is 400C stored per patch). The inset in the top diagram (0 C withdrawn) is an expansion of the high frequency portion of the Argand diagram. The high frequency portions of the Argand plots for the other CF half-cells are similar to the one in the top diagram and therefore have not been expanded. The complex-plane plots in Fig. 4 have the following features: (i) a series resistance component of $\sim 2\Omega$, (ii) a 45° angle between the impedance Z and the real axis at high frequencies, and (iii) a steeply rising quadrature impedance at low frequencies. Hence, aside from the series resistance component, which was not included in Eq. [1], there is excellent agreement between the form of the high frequency CF half-cell impedance plots and that predicted by Eq. [1]. In general, the form of the complex-plane plots at the low frequency is similar to that in Fig. 3, but in certain instances deviations occur at $f \leq 0.01$ Hz, possibly due to contributions from faradaic reactions or from diffusion. On the basis of the general good agreement between the experimental complex-plane plots and the theoretical plot in Fig. 3, we feel that analysis of the experimental data in accordance with Eq. [1] is justified.

Table I lists the impedance parameters of the CF half-cells as a function of the charge withdrawn. The series resistance is the value of Z_R at 1780 Hz (the highest frequency in the measurement) and is accurate to 0.1 Ω . The value of R_{sol} is three times the difference between Z_R at a frequency where the quadrature impedance Z_Q begins to rise steeply (0.316-0.0136 Hz) and the series resistance. The total cell capacitance is the average calculated from Z_Q at 0.01, 0.0178, and 0.0316 Hz and has a maximum deviation from the mean of ± 0.02 F. The following paragraphs treat each of these three impedance parameters separately.

Series resistance.—Initially, we thought that the series resistance was composed of the ionic resistance of the separator and the electronic resistance of the titanium current collector. Calculations of the separator resistance using Eq. [4] and [6] showed that the series resistance was too large to be composed of just these two components; therefore, to account for the series resistance, the equivalent circuit shown in Fig. 5 was used. In this equivalent circuit representation, R_{Ti} is the electronic resistance of the titanium current collector, R_I is the interface resistance between the Ti and the cathode patch, R_{sep} is the separator resistance, and Z_E is the cathode patch impedance. In this analysis, $Z_E = Z_0/2$, where Z_0 is the impedance of the two cathode patches in series. At high frequency, the series resistance is equal to $2R_{\text{Ti}} + 2R_I + R_{\text{sep}}$. R_{Ti} was determined from ac resistance measurements of bare Ti foil. Hence, this equation has two unknowns, and another equation is needed to solve for R_I and R_{sep} . For this, we built a cell with two layers of the separator, in which case the series resistance was equal to $2R_{\text{Ti}} + 2R_I + 2R_{\text{sep}}$.

Table I. Impedance parameters of CF half-cells as a function of charge withdrawn

Charge withdrawn (C)	Series resistance (Ω)	R_{sol} (Ω)	Capacitance, C_T (F)
0	2.0	14.6	0.25
50	2.4	6.6	0.54
100	2.2	8.6	0.87
200	1.9	9.5	1.43
300	2.3	12.5	1.71

Table II. Series resistance values of CF half-cell^a

Resistive component	Resistance (Ω)
R_{sep}	1.41
R_i	0.38
R_{T_1}	0.05

^a 0 C withdrawn.

Table II shows the values of the series resistance of the components of the CF half-cell in 1M LiBF₄/4-butyrolactone. The separator resistance (1.41 Ω) is in exact agreement with that calculated from Eq. [6] for a tortuous-pore network. Equation [4] predicts a value of 0.46 Ω for the separator, which is a third of that measured. Measurements of this type were also made in an electrolyte that is almost twice as conductive as the 1M LiBF₄/4-butyrolactone, and the result was the same; the separator resistance was within 10% of that calculated from Eq. [6]. Since the ion mobility in the nonwoven polypropylene separator is quantitatively linked to its volume fraction polymer per Eq. [6], it is concluded that the pore network of the separator is tortuous.

R_{sol} .—Figure 6 compares the cathode resistance R_{sol} measured via the impedance technique with those calculated via Eq. [4] and [6]. The input parameters for the calculations, *i.e.*, the electrode thickness l and the volume fraction solids v_2 , are shown in Table III. The volume fraction solid v_2 was calculated from the measured electrode dimensions and the known densities of the electrode constituents (CF, Teflon, carbon, LiF). Note that the electrode thickness approximately doubles over the course of the discharge, whereas the volume fraction solids decrease by a factor of 2.5. The measured cathode resistances do not closely match the calculated values for either the straight-pore model or the tortuous-pore model, but rather fall somewhere between the two sets of calculated data. For cathodes with 0 C withdrawn or $\geq 50\%$ of the stored coulombs withdrawn, the electrode behaves more like a tortuous network, whereas at 12.5–25% of the coulombs withdrawn the electrode behaves more like a straight-pore network. From the above comparisons, we find evidence for tortuosity in the internal pore network of Teflon-bonded CF electrodes, particularly for cathodes with 0 C or $\geq 50\%$ of the coulombs withdrawn.

Another feature of the cathode resistance data that deserves comment is the fact that as charge is withdrawn, the cathode resistance values do not increase above the original value. This result correlates with the flat discharge curve of Li/CF cells (16). If it is assumed that the impedance values reflect mainly the interparticle pore network, then it can be concluded that clogging of the

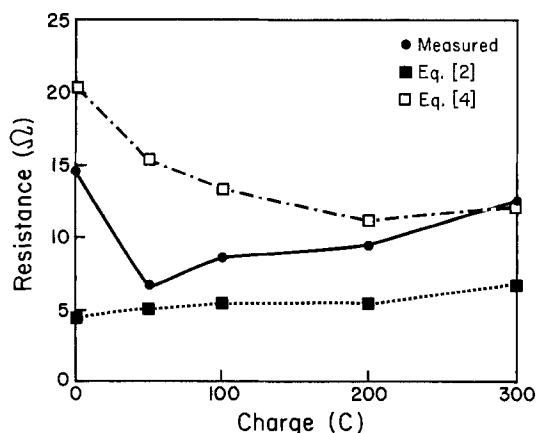


Fig. 6. Internal CF electrode resistance as a function of charge withdrawn. Circles: resistances measured via the impedance technique. Filled squares: resistances calculated for straight-pore model, Eq. [2]. Open squares: resistances calculated for tortuous-pore model, Eq. [4].

Table III. Input parameters to electrode resistance calculations

Charge withdrawn (C)	Electrode thickness (cm)	v_2
0	0.062	0.50
50	0.087	0.37
100	0.103	0.30
200	0.115	0.24
300	0.143	0.20

interparticle pore network with discharge products (*i.e.*, LiF) is an unlikely cathode failure mechanism. More likely, cathode failure mechanisms include concentration polarization or passivation of the CF particle with LiF.

Electrode capacitance.—The data in Table IV show that the CF electrode capacitance, as calculated from the low frequency impedance data, increases between 0 and 300C withdrawn. The increasing capacitance is due to the formation of carbon from the electroreduction of CF. This carbon has a high electrochemical surface area (92 F/g), which correlates with increases in the electrode's physical surface area with charge withdrawn as measured by Hg intrusion porosimetry (17). It will be shown in the following section that the CF electrode capacitance can provide limited state-of-charge information about commercial Li/CF batteries.

Battery data.—Figure 7 shows the complex-plane impedance plots for commercial Li/CF batteries with 0, 500, 1000, and 3000C removed. These measurements were arbitrarily made three months after the batteries were discharged. The high frequency arc is due to the activation resistance of the Li anode, and its variation with state of charge and time after discharge has been published elsewhere (18). It was concluded that R_{act} of Li could not be used as a measure of state of charge in commercial batteries. The low frequency battery impedance data (< 1 Hz) are assigned to the CF cathode on the basis that its capacitive component increases with charge withdrawn in a manner similar to that of the CF half-cell impedance. Table V shows that there is a semiquantitative relationship between Z_q values at 0.00563 Hz and state of charge for batteries with < 1000C withdrawn (< 25% of total stored charge) and that the low frequency Z_q values are reasonably constant from three months to four years after discharge. In a separate set of experiments in which the battery impedance was measured periodically for one year after discharge, Z_q values stabilized after two months. Thus, low frequency battery impedance data can

Table IV. Capacitance of CF half-cells as a function of charge withdrawn

Charge withdrawn (C)	Capacitance, C_T (F)	Carbon formed ^a (F/g)
0	0.25	—
50	0.54	93
100	0.87	100
200	1.43	95
300	1.71	78

^a The formula for calculating the farads per gram carbon formed is $2(C_T - 0.25)/(12C/96,484)$ where C_T is the measured capacitance of the total cell shown in Fig. 1 and C is the charge withdrawn per single electrode patch.

Table V. Low frequency impedance values of commercial batteries

Charge withdrawn (C)	Z_q (0.00563 Hz) three months after discharge	Z_q (0.00563 Hz) four years after discharge
0	18.6	17.5
150	15.0	13.4
500	8.4	—
1040	4.1	6.4
3160	4.1	4.8

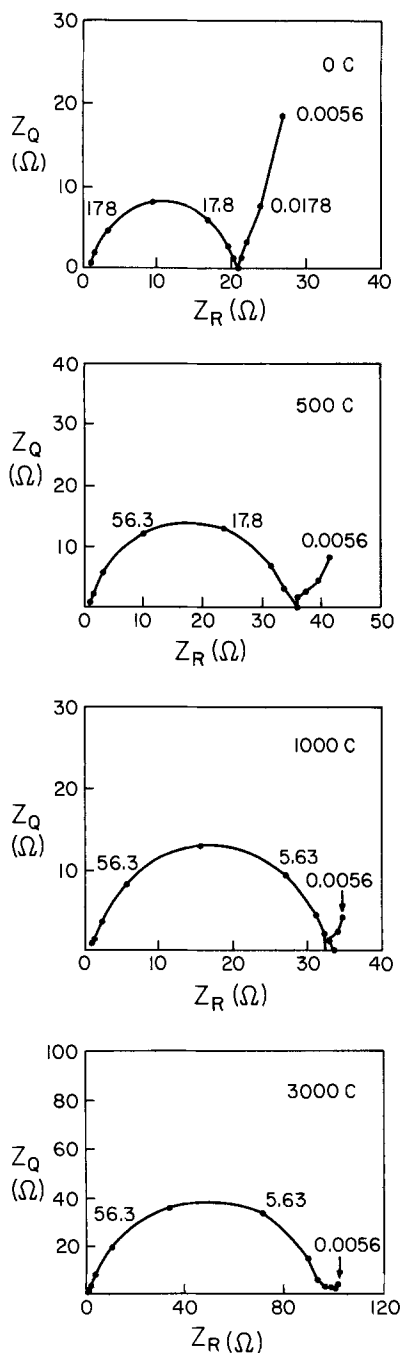


Fig. 7. Complex-plane impedance data of 2/3A Li/CF batteries as a function of the amount of charge withdrawn.

provide semiquantitative state-of-charge information for stored batteries, but would not be useful for determining the state of charge of batteries actively in service.

Summary

The following nonfaradaic components of CF half-cell impedance were resolved on the basis of a one-dimensional macroscopic treatment of a porous electrode: resistance due to electrolyte in the cathode pores, interfa-

cial resistance between current collector and cathode patch, separator resistance, and cathode capacitance. The major contributor to the ohmic resistance was the electrolyte resistance within the cathode patch. Furthermore, the impedance data provided evidence for tortuosity in the internal pore network of the nonwoven polypropylene separator and in the cathode matrix at certain states of charge (0 and $\geq 50\%$ of the coulombs withdrawn).

The mechanistic implications of the CF half-cell impedance data are as follows: (i) it is unlikely that CF cathode failure is caused by clogging of the interparticle pore network with LiF. Cathode failure may be caused by passivation of CF with LiF or by concentration polarization. (ii) Carbon with a high electrochemical surface area (92 F/g) is formed as an end product of CF electroreduction.

Finally, low frequency quadrature impedance data can serve as a semiquantitative measure of Li/CF battery state of charge, provided that the batteries have been stored for at least two months after being under load.

Acknowledgments

I thank M. A. Faust and J. R. Sandifer for the battery impedance data and H. W. Osterhoudt for bringing to my attention the theory of ion transport in swollen polymer membranes.

Manuscript submitted Jan. 23, 1985; revised manuscript received March 14, 1985.

Eastman Kodak Company assisted in meeting the publication costs of this article.

REFERENCES

1. J. McHardy, J. M. Baris, and P. Stonehart, *J. Appl. Electrochem.*, **6**, 371 (1976).
2. J. P. Candy, P. Fouilloux, M. Keddad, and H. Takenouti, *Electrochim. Acta*, **26**, 1029 (1981).
3. J. P. Candy and P. Fouilloux, *J. Chem. Soc., Faraday Trans. 1*, **79**, 823 (1983).
4. J. P. Candy, P. Fouilloux, M. Keddad, and H. Takenouti, *Electrochim. Acta*, **27**, 1585 (1982).
5. R. de Levie, *ibid.*, **8**, 751 (1963).
6. R. de Levie, *ibid.*, **9**, 1231 (1964).
7. H. Keiser, K. D. Beccu, and M. A. Gutjahr, *ibid.*, **21**, 539 (1976).
8. R. D. Armstrong, K. Edmondson, and J. A. Lee, *J. Electroanal. Chem.*, **63**, 287 (1975).
9. C. Cachet and R. Wiart, *Electrochim. Acta*, **29**, 145 (1984).
10. J. S. Mackie and P. Meares, *Proc. R. Soc. London, Ser. A*, **232**, 498 (1955).
11. R. G. Gunther, in "Power Sources 5," D. H. Collins, Editor, p. 729, Academic Press, New York (1975).
12. A. J. Bentz, J. R. Sandifer, and R. P. Buck, *Anal. Chem.*, **46**, 543 (1974).
13. J. Newman and C. W. Tobias, *This Journal*, **109**, 1183 (1962).
14. H. H. Skilling, "Electrical Engineering Circuits," p. 608, John Wiley and Sons, New York (1965).
15. H. H. Skilling, "Electrical Engineering Circuits," Chap. 5, John Wiley and Sons, New York (1965).
16. M. Fukuda and T. Iijima, in "Power Sources 5," D. H. Collins, Editor, p. 713, Academic Press, New York (1975).
17. M. R. Suchanski and P. J. Muehlbauer, in "Porous Electrodes Theory and Practice," H. C. Maru, Editor, p. 306, The Electrochemical Society Softbound Proceedings Series, Pennington, NJ (1984).
18. J. R. Sandifer and M. R. Suchanski, *J. Appl. Electrochem.*, **14**, 329 (1984).

Chemisorption and Catalysis in Polythionic/Thiosulfate Stress Corrosion Cracking

Hugh H. Horowitz*

Exxon Research and Engineering Company, Florham Park, New Jersey 07932

ABSTRACT

The stress corrosion cracking of sensitized stainless steels due to thiosulfate and tetrathionate has been associated with an increased rate of anodic dissolution in the active-passive region of voltammetric scans, via the mutual sensitivity of both phenomena to a series of anionic inhibitors. The increased anodic dissolution is caused by the adsorption of the sulfur compound and its catalysis of metal oxidation. The inhibitors function, not by competitively desorbing the corrodent, but by aiding the passivation process.

The problem of "polythionic acid stress corrosion cracking" has plagued the petroleum industry for more than forty years, and related problems have recently turned up in the nuclear industry as well. Intergranular cracks form in "sensitized" austenitic stainless steels, under stress, in the presence of air, water, and a sulfide scale on the interior walls of the vessel or pipe. "Sensitization" refers to a heat-treatment of the steel to the range of 400°-800°C, causing chromium-rich metal carbides to precipitate at the grain boundaries and depleting chromium content there to the point where corrosion resistance is lost (<12% Cr). Sensitization was first noted in the heat-affected zones around welds, but has also been caused by the process conditions themselves, as well as by fabrication heat-treatments.

The problem was first reported in a fluidized bed catalytic cracker during World War II (1). In 1956-1957, it was first ascribed to polythionic acids ($H_2S_{3-6}O_6$) by Dravnieks and Samans (2). The problem has been observed in various types of hydrodesulfurization units, in sulfur plants, catalytic crackers, cokers, and residuum-treatment units of various types. More recently, related problems have cropped up in the nuclear industry. In the Girdler process for the production of deuterium oxide, multiple fractional distillations of water are carried out in the presence of H_2S . When the equipment is opened to the atmosphere, conditions similar to those in petroleum refineries exist (3). In pressurized water reactors, solutions of sodium thiosulfate, included in auxiliary lines as quenching agents for radioactive iodine, were found in separate studies (4, 5) to be extremely potent crack promoters, acting very similarly to the closely related tetrathionate, $S_4O_6^{2-}$, which is a member of the polythionate family. A recent review summarizes both the science and the technology (6).

Dravnieks and Samans devised a method for simulating polythionic acid stress corrosion cracking in the laboratory using Wackenroder's liquid, an acidic mixture of sulfur compounds formed by the reaction of H_2S and SO_2 saturated water. Recently, workers at the University of Roorkee (7) have found that, of all the polythionic acids in this mixture, only the tetrathionate was active in promoting stress corrosion cracking. In addition, the nuclear industry work cited above showed that the strong acidity of Wackenroder's liquid (due to the strong polythionic acids as well as to free sulfuric acid) is not necessary. Cracking occurred at pH 5, where the strong acids exist exclusively as doubly charged anions $S_2O_3^{2-}$ and $S_4O_6^{2-}$.

In a previous publication (8), we reported that the above active anions did not act as sulfide did to promote hydrogen entry into a ferritic steel. They both gave rise to a pronounced anodic peak in voltammetric scans. These observations suggested that these two anions function by promotion of anodic dissolution processes within the crack rather than by promotion of hydrogen embrittlement. As to the similarity of action of the two, we noted

that the theoretical potential for the reduction of $S_4O_6^{2-}$ to $S_2O_3^{2-}$ is above the corrosion potential of steel in the absence of air and that the reduction could actually be carried out on a steel electrode. Therefore, the true corrodent at the crack tip could be $S_2O_3^{2-}$ in all cases. Thiosulfate is known to be a complexing agent for metal ions including ferric and probably ferrous ions.

The aim of this paper is to shed light on the nature of the effects of $S_2O_3^{2-}$ (and $S_4O_6^{2-}$) on the cracking process and on crack electrochemistry through stress corrosion cracking tests under electrochemical control, through adsorption studies, and through studies of the effects of added anions.

Experimental

Slow strain rate tests.—Slow strain rate tests were modeled after the work of Humphries and Parkins (9). The device used was a Model P-2000 constant extension rate tensile machine purchased from the WT Specialty Company (Orient, Ohio). It was equipped with a BLH load cell of 2000 lb capacity using a Daytronics Model 3170 signal conditioner which fed its output to a Norland 2001 digital processing oscilloscope.

The samples were 0.635 cm (1/4 in.) diam rods of stainless steel Type 304, 22.9 or 25.4 cm long, having the following compositions

Sample	Cr	Ni	Si	Mn	Mo	S	P	N	C
22.9 cm	18.0	9.5	0.67	1.89	0.36	0.003	0.010	0.021	0.056
25.4 cm	18.0	8.9	0.54	1.70	0.30	0.002	0.011	0.019	0.043

They were sensitized by holding at 1040°C under argon for 4h, cooling slowly under argon to 600°C, holding at 600°C under nitrogen for 100h, and cooling to room temperature. The 100h heat-treatment time/600°C combination lies at the center of Piehl's (10) time-temperature diagram for the sensitization of Type 304 stainless steel.

After heat-treatment, the rods were machined so as to provide a gauge length of 1.27 cm and a 0.25 cm diam (± 0.0013 cm) at the center with smooth transition regions at each end (0.38 cm long, 0.476 cm radius of curvature). The ends of the rods were threaded for attachment to the heads of the tensile device. The rods were degreased before use. For electrochemical tests, the unwaisted area was masked off with an electrically insulating paint.

The aqueous environment was maintained in a cylindrical Teflon container of 1 liter capacity which fitted on and around the sample rod via a watertight seal. This container had a closed lid with which one could maintain a nitrogen atmosphere, include a reference electrode to follow the potential of the specimen, or include a circular platinum counterelectrode to control the potential of the specimen via a potentiostat. A BC 1200 potentiostat from Stonehart Associates was used with the test piece as grounded working electrode. When the potentiostat was not used, air was sparged through the cell electrolyte to hold the potential around 0 V/SCE. A nitrogen atmosphere was maintained during potentiostat controlled

* Electrochemical Society Active Member.

runs. All experiments were conducted at room temperature.

The results of the tests were plotted in terms of percentage of elongation based on the 1.27 cm gauge length, and tensile stress based on the cross-sectional area of the gauge length. The most commonly used extension rates were 1 or 3×10^{-6} /s.

Voltammetric scans and polarization curves.—Voltammetric scans were run on end faces of 1/4 in. rods of Type 1018 carbon steel or a Type A329 steel nominally containing 7% Cr-0.5% Mo. The actual composition was

C	Mn	P	S	Si	Ni	Cr	Mo
0.10	0.41	0.021	0.025	0.58	0.33	7.9	0.6

The sides of the rod were masked either with a hardened epoxy or with Teflon tape. The electrode surface was polished on a belt sander to a 600 grit finish. Preliminary tests were also run on a 0.2 cm² disk of 4130 carbon steel mounted in a rotating disk electrode. The electrode face was immersed downward in 50 cm³ of electrolyte in a glass apparatus with a facing Pt counterelectrode and a Luggin capillary mounted to one side. The potential was controlled by a Princeton Applied Research Model 173 potentiostat with a Model 179 plug-in, for current read-out and resistance compensation, and a Model 175 programmer for ramp or pulse generation.

For pseudosteady-state polarization curve measurements, the potentiostat was controlled by a Hewlett-Packard 9836 desktop computer interfacing through a HP 3497 A data acquisition and control unit. The open-circuit potential was allowed to stabilize under nitrogen. 8 mV steps were then applied to the potential, cathodic first, and the response was measured at intervals of 0.25s for about 40 points, until a pseudosteady state was reached. Only in the voltage range where passivation occurred was a constant value not reached within this time period. The last eight current density values at each voltage were averaged and plotted on a semilogarithmic graph vs. the voltage corrected for uncompensated resistance using a HP 7470A graphics plotter. The resistance values used for ohmic drop compensation were determined early in the experiment by applying 10 mV voltage pulses around the open-circuit potential at 1000 cycle/s and determining the initial current response.

Corrosion currents were estimated by extrapolating either the anodic or cathodic Tafel slope, or both, back to the open-circuit potential. Confirmatory values were obtained from linear plots of the voltage-current density relation around the corrosion potential. The average of all these data was taken.

Adsorption experiments.—Adsorption was measured by transferring a test electrode between two electrochemical setups, each equipped with Luggin capillary, saturated calomel reference electrode, and a platinum counterelectrode. Typically a freshly polished electrode was inserted in base electrolyte solution, 0.9M sodium acetate plus 0.1 M acetic acid, and a base case scan was run. The electrode was then removed from the cell and rinsed in distilled deionized water, both with a jet of flowing liquid and with bulk water in a beaker. It was then transferred to the second solution, base electrolyte containing 0.001M sodium thiosulfate or tetrathionate, and a second scan was run, showing enhancement of the passivation peak due to the sulfur compound. After the electrode had returned to the open-circuit potential, it was removed from the cell, passed through the rinsing process, and replaced in the first cell containing the base solution, and rescanned, generally showing most of the peak enhancement due to the thiosulfate. A relatively rapid scan rate, 500 mV/s, was used during this procedure to avoid destroying the adsorbate. Several variations of the sequence, such as omitting one or both of the intermediate scans, or including inhibiting anions in the rinse water, were made as described in the text to obtain further mechanistic information.

The electrodes used were, in many cases, the same ones that were used in the voltage scan studies, including masking of the cylindrical face. However, because of the possibility of entrapment of liquid in possible crevices between the masking material and the metal, many adsorption tests were run using unmasked electrodes. Here, an exact definition of the surface area was sacrificed to unequivocally demonstrate the adsorption phenomenon.

Results and Discussion

Evidence for anodic current during the cracking process.—In the slow strain rate test on sensitized 304 stainless steel, failure occurred ductilely after 80-100% elongation in air or in acetate buffer without added corrosives. Stress-elongation curves showed a long region of plastic flow (Fig. 1). When a small amount of thiosulfate (0.01M) was added, brittle failure occurred after less than 10% elongation (Fig. 2) and the fracture surface showed the separated crystalline look typical of intergranular cracking (Fig. 3).

In a number of tests, a reference electrode was inserted in the cell and the potential of the stainless steel tensile specimen was followed as the sample was strained. Before failure occurred, the potential rested in the neighborhood of 0 vs. SCE, held at this relatively noble value by the presence of the air. Samples failing ductilely exhibited a sharp decrease in potential at the point of fracture (Fig. 1). This was undoubtedly due to the current required to restore the passive oxide layer on the freshly created surface.

When intergranular stress cracking occurred close to the point where the stress began to fall below the ductile failure levels, the potential began to decrease rapidly. It continued low until just after failure occurred (Fig. 2). This means that an active anodic center developed within the crack, causing the total electrode to take on a mixed potential wherein the anodic current issuing from the crack was equal to the cathodic current of oxygen reduction on the surface of the steel.

The anodic current was measured using a counterelectrode and a potentiostat, holding the stainless steel surface at a potential of 0 vs. SCE. Again, when cracking began and the stress fell below the expected relation, a small current was observed, rising to a peak of 250 μ A and falling to values close to zero as the cracking process was completed (Fig. 4). Similar potential and voltage excursions during stress corrosion cracking have been reported in Ref. (5), (6), and (13).

A rough integration of the current-time trace indicates that a total of about 4 μ m of metal was removed from the

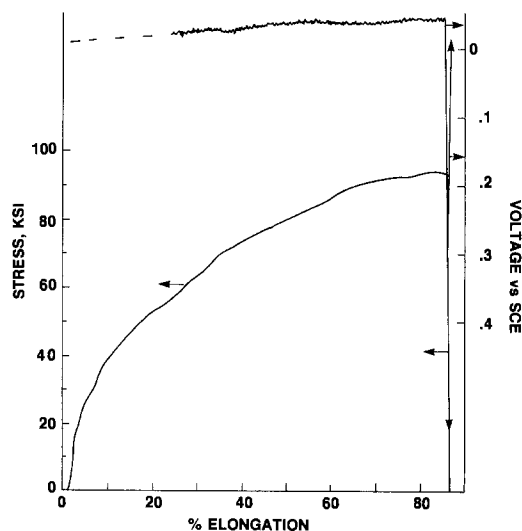


Fig. 1. Potential decrease during a ductile failure. Sensitized stainless steel, Type 304, in 0.01M Na₂S₂O₃ + 0.02M each Na₂HPO₄-NaH₂PO₄, pH 6.8; air saturated; 25°C; extension rate 3×10^{-6} /s. 1 KSI = 6.89 MPa.

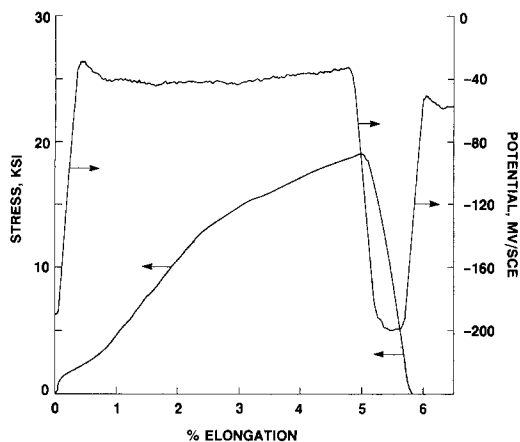


Fig. 2. Potential decrease during stress corrosion cracking. Sensitized stainless steel, Type 304, in 0.01 $\text{Na}_2\text{S}_2\text{O}_3$ in 0.02M each Na acetate-acetic acid, pH 4.8; air saturated; 25°C; extension rate 10^{-6} /s. 1 KSI = 6.89 MPa.

cross section of the waisted area. Since there are multiple cracks and many dead-end crack branches, it would appear that a large fraction of the sensitized metal in the crack area is removed.

Effect of added anions on cracking process.—A number of sodium or potassium salts were added to 0.01M $\text{Na}_2\text{S}_2\text{O}_3$ to determine if their anions would inhibit the cracking process. The results were that chloride, sulfate, nitrate, and acetate did not inhibit cracking, whereas cracking was inhibited by nitrite, various forms of phosphate at different pH's, carbonate, borate, and, to a lesser extent, hydroxide. In the presence of the first group of ions, the percentage of elongation at failure remained mostly at 20% or below, while in the presence of the second group, predominantly ductile failure occurred at 66-100% elongation (Table I).

The ability of certain anions to eliminate the action of the sulfur anions provided a variable parameter for the correlation of electrochemical phenomena with the cracking process. Also, it should be noted that the effect of the anions is not merely to make the solution basic, although the inhibitors do that in some cases. The nitrite ion leaves the solution neutral, while the phosphate was active in three different pH regions. The trisodium phosphate is strongly alkaline, while the mixed sodium monohydrogen and dihydrogen phosphate are around pH 6.5 and the dihydrogen phosphate alone is fairly acidic (pH 4.3).

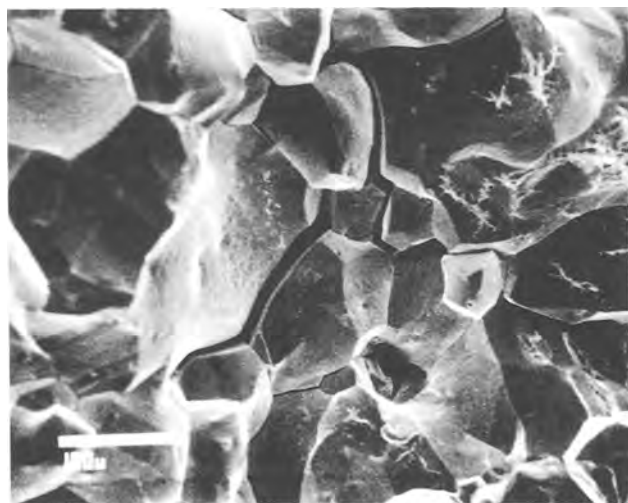


Fig. 3. Scanning electron micrograph of stress cracked surface. Sensitized stainless steel Type 304 cracked at 4.5% elongation in 0.01M $\text{Na}_2\text{S}_2\text{O}_3$ + 0.04M NaCl; air saturated; 25°C; extension rate 3×10^{-6} /s.

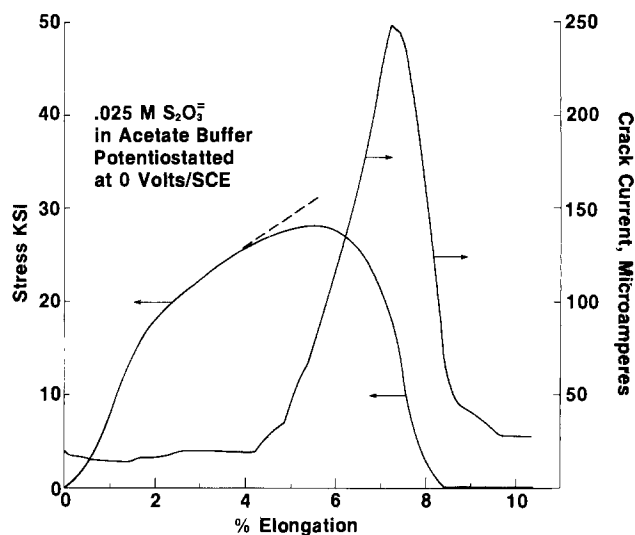


Fig. 4. Anodic current accompanying crack growth. Sensitized stainless steel, Type 304, in 0.025M $\text{Na}_2\text{S}_2\text{O}_3$ in 0.05M each Na acetate-acetic acid; N_2 saturated; 25°C; potentiostated at 0.0V vs. SCE; extension rate 3×10^{-5} /s. 1 KSI = 6.89 MPa.

Effect of thiosulfate on voltammetric scans.— Voltammetric scans were run on steel samples in thiosulfate or tetrathionate solutions to verify the enhancement of anodic activity at the crack tip as hypothesized from the cracking experiments and the previously reported hydrogen permeation studies (8). The steels used contained 0 or 7% chromium to simulate the Cr-depleted metal in the grain boundaries of the sensitized stainless. A Type 4130 steel, was used initially, followed by a 1018 carbon steel, followed by a 7% Cr, 0.5% Mo steel, and finally by a special 9% Ni-7% Cr steel. All gave similar enhancements of the anodic peak in voltammetric scans due to the addition of small concentrations of sodium thiosulfate or tetrathionate (usually 0.001M). The peak size differed from steel to steel, but the relative difference between the base case and the thiosulfate-doped solutions remained about constant. A typical case is given in Fig. 5, where it will be seen that a peak passivating current of about 1 mA/cm² in acetate buffer was increased to about 24 mA/cm² by the addition of 0.001M thiosulfate. At higher concentrations, e.g., 0.1M, corrosion was so severe that the electrode surface was not stable—corrosion products began falling rapidly from the electrode surface and clogging the space between the electrode and the Luggin capillary.

Table I. Effect of added anions on stress corrosion cracking promoted by thiosulfate^a

Concentration	Percentage elongation at failure	Concentration	Percentage elongation at failure
None	3, 13, 15, 23	0.04M NaNO_3	101
0.04M NaCl	4 ^b	0.04M NaH_2PO_4	86
0.02M Na_2SO_4	5	0.02M NaH_2PO_4	93
		+ 0.02M Na_2HPO_4	
0.04M KNO_3	6	0.02M Na_3PO_4	95
0.02M Na acetate	5, 8, 7, 20, 48	0.02M Na_2CO_3	74
+ 0.02M acetic acid		0.02M NaHCO_3	99
		+ 0.02M Na_2CO_3	
		0.02M NaOH	46
		0.01M $\text{Na}_2\text{B}_4\text{O}_7$	66

^a Conditions: 0.01M sodium thiosulfate in deionized water at room temperature. Air saturated. Stainless steel 304 sensitized at 600°C for 100h. Waisted area 0.1 in. diam, 0.5 in. long pulled at an extension rate of 3×10^{-6} /s.

^b Chloride without thiosulfate caused no cracking; ductile failure occurred at 98% elongation.

^c Some brittle failure observed in SEM. Without thiosulfate, NaOH caused ductile failure at 94% elongation.

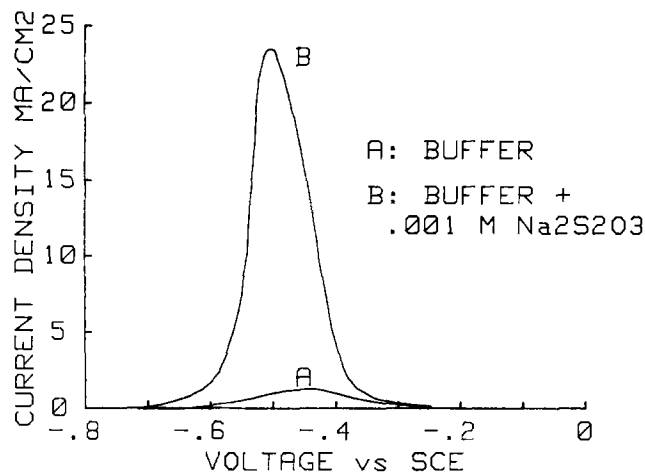


Fig. 5. Promotion of anodic dissolution by thiosulfate. 7% Cr-0.5% Mo steel in 0.9M Na acetate-0.1M acetic acid; pH 5.6; N₂ atmosphere; 25°C; scan rate 5 mV/s.

As to the effect of scan speed, it was found that the peak heights in all cases increased with scan speed, but that the greatest relative difference between the base case and the thiosulfate case was observed at low scan speeds. The data of Fig. 5, for example, were taken at a low scan speed, 5 mV/s. In the base case, the peak height increased approximately linearly with the square root of the scan speed, suggesting a diffusion-limited anodic process. This could be, for example, the formation of a partially soluble iron salt, which eventually reaches the saturation concentration and precipitates on the electrode surface to begin the passivation process. In many of the thiosulfate-promoted cases, the peak height increased less than linearly with the square root of the scan speed. Our best guess at present for the scan speed effect with thiosulfate is that the coverage with passivation oxide grows slowly with time at a given voltage, while the metal dissolution rate on the unpassivated fraction of the surface rises rapidly as the voltage is increased. Thus the faster the scan rate, the more opportunity for dissolving metal rapidly before further passivation can occur. Prior rotating disk studies (8) showing rotation speed dependence in the base case but not in the thiosulfate case support this explanation. However, no attempt to analyze the scan rate effect quantitatively was made in this work. The scan rate appropriate to the cracking process would depend on the crack velocity, but would probably be on the high side of the range studied here.

Catalytic action of thiosulfate.—While the peak height increased with the scan speed, it was possible to observe steady-state currents at various voltages around the current peak over relatively long periods of time. These were almost as high as the currents observed in the voltammetric scans at low scan rates. In one run on 1018 carbon steel, the total number of coulombs passed at constant voltage corresponded to more than all of the thiosulfate present in the solution. Yet solution analysis showed only a minor depletion of the thiosulfate. In a series of runs, the ratio of metal atoms dissolved to thiosulfate ions consumed corresponded to 100 to 400 to 1. Analysis of the solution after one of the runs showed that the amount of dissolved iron corresponded closely to that calculated from the number of coulombs of electricity passed (Table II).

In other words, the effect of the thiosulfate was catalytic. A small amount of thiosulfate catalyzed the dissolution of a large amount of iron. This may explain the results of Ref. (4) where 0.1 ppm of thiosulfate (10⁻⁶M) was sufficient to induce stress corrosion cracking. In that case, the amount of iron involved in the cracking reaction must have been much greater than the total amount of thiosulfate in the liquid in the crack or in the external liquid zone surrounding the crack.

Table II. Catalytic dissolution of steel at constant potential

Voltage vs. <i>E</i> peak (V)	Milli-Faradays passed	S ₂ O ₃ ²⁻ consumed (mM)	Ratio of Fe dissolved to S ₂ O ₃ ²⁻ consumed
0	0.427	— ^a	>4*
0	1.06	0.00501	106
0	2.51 ^b	0.0146	86
60	1.007	0.00127	395
160	0.776	0.00207	187
300	-----Current decayed to 0-----		

^a Residual S₂O₃²⁻ not analyzed. Total S₂O₃²⁻ in solution = 0.05 mM.

^b Calculated Fe concentration from charge passed: 0.0248M; measured polarographically: 0.0247M.

Effect of added anions on voltammetric scans.—It was found that the addition of certain soluble salts to solutions of thiosulfate eliminated the peak enhancement normally produced by the thiosulfate. Other salts had no effect. Figures 6 and 7 show the results obtained with both thiosulfate and tetrathionate on the 7% Cr-0.5% Mo steel. The peak heights increased with the scan speed in all cases; but nitrate, chloride, and sulfate additions did not affect the results obtained with the untreated thiosulfate, while nitrite, phosphate, borate, and carbonate reduced and peak height down to the base case levels or below. Figure 8 shows similar results in 1018 carbon steel with thiosulfate, although the NO₂⁻ is not as effective here.

The point is that the ions which decreased the anodic peak due to thiosulfate are the same ones which inhibited intergranular stress corrosion cracking in sensitized stainless steel, while the ions which did not affect the corrosion promotion affect of S₂O₃²⁻, also did not inhibit stress corrosion cracking. For both the stress cracking of the sensitized stainless steel and the stimulation of the anodic corrosion of nonstainless steels, the inhibitors were phosphate, borate, nitrite, and carbonate; noninhibitors were acetate, chloride, sulfate and nitrate.

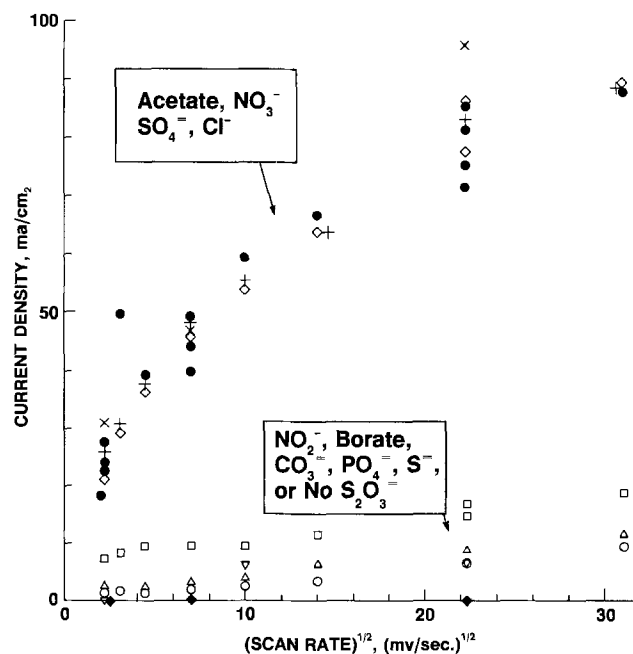


Fig. 6. Effect of inhibitors on anodic peak in voltammetric scans; 7% Cr-0.5% Mo steel in 0.001M Na₂S₂O₃; 25°C; N₂ atmosphere. ●: 0.9M Na acetate-0.1M acetic acid, pH 5.6 (= A). +: A plus 0.05M Na₂SO₄. ◇: A plus 0.05M KNO₃. X: A plus 0.05M NaCl. □: A plus 0.05M NaNO₂. ▽: A plus 0.05M Na₂S. ○: A without Na₂S₂O₃. △: 0.025M Na₂HPO₄ + 0.025M NaH₂PO₄. ◆: both 0.5M NaHCO₃ + 0.05M Na₂CO₃ and 0.1M Na₂B₄O₇.

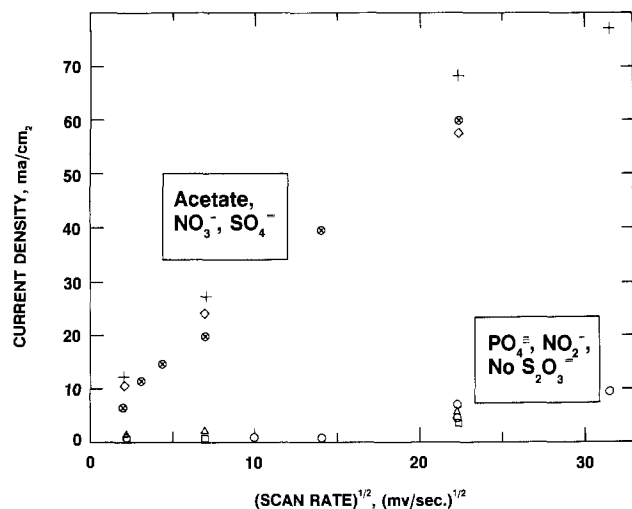


Fig. 7. Effect of inhibitors on anodic peak in voltammetric scans; 7% Cr-0.5% Mo steel in 0.001M $\text{Na}_2\text{S}_2\text{O}_3$; 25°C; N_2 atmosphere. \odot : 0.9M Na acetate/0.1M acetic acid, pH 5.6 (= A). $+$: A plus 0.05M Na_2SO_4 . \diamond : A plus 0.05M KNO_3 . \circ : A without tetrathionate. \triangle : A plus 0.025M Na_2HPO_4 -0.025M NaH_2PO_4 . \square : A plus 0.05M KNO_3 .

This is a very strong indication that the two phenomena are closely related, and led to the conclusion that enhanced anodic dissolution at or near the crack tip is the cause of the cracking.

The presence of thiosulfate also affected the anodic and cathodic branches of the polarization curve, but not nearly so dramatically as it raised the passivation current. On the 7% Cr-0.5% Mo steel, the thiosulfate increased the anodic iron dissolution current and decreased the cathodic hydrogen evolution current, thereby decreasing the corrosion potential by about 80 mV, but had a relatively small effect on the overall corrosion current (Fig. 9). The effects of thiosulfate and inhibiting and noninhibiting anions on passivation peak currents and on corrosion currents are summarized in Table III. On the 1010 carbon steel, the effect of $\text{S}_2\text{O}_3^{2-}$ on the corrosion current was very small relative to the passivation peak effect of Fig. 8 (see Fig. 10).

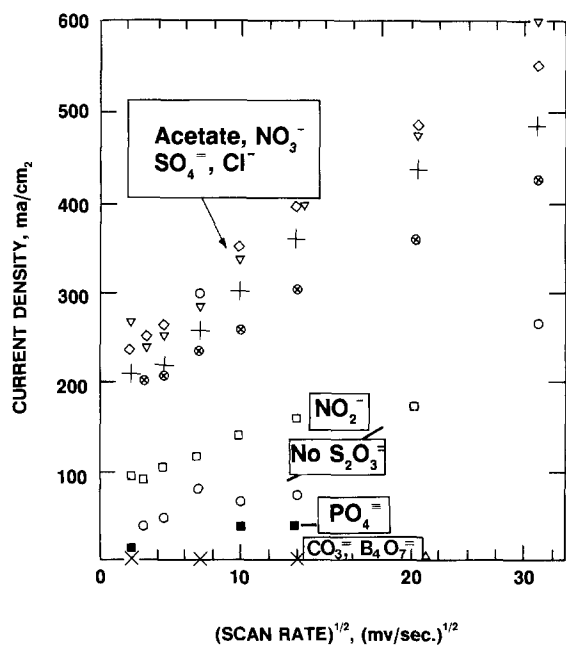


Fig. 8. Effect of inhibitors on anodic peak in voltammetric scans; Type 1018 carbon steel in 0.001M $\text{Na}_2\text{S}_2\text{O}_3$; 25°C; N_2 atmosphere. \odot : 0.9M Na acetate/0.1M acetic acid at pH 5.6 (= A). $+$: A plus 0.05M Na_2SO_4 . ∇ : A plus 0.05M NaCl. \diamond : A plus 0.05M KNO_3 . \square : A plus 0.05M NaNO_2 . \circ : A without thiosulfate. \blacksquare : A plus 0.025M Na_2HPO_4 and 0.025M NaH_2PO_4 . \times : 0.5M NaHCO_3 -0.5M Na_2CO_3 . \triangle : 0.1M $\text{Na}_2\text{B}_4\text{O}_7$.

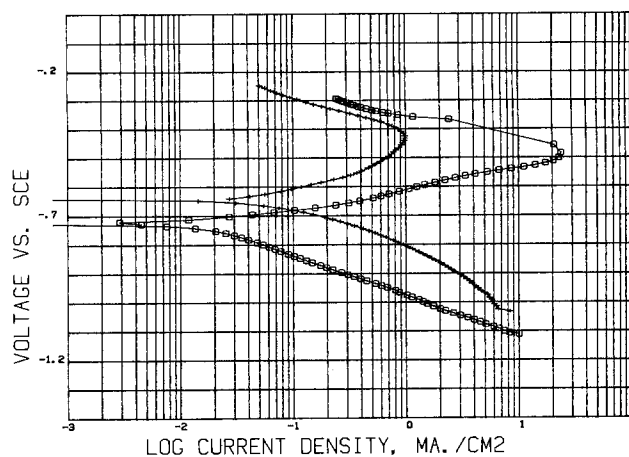


Fig. 9. Corrosion curves on 7% Cr-0.5% Mo steel + 0.9M Na acetate/0.1M acetic acid buffer at pH 5.6. Same plus 0.001M $\text{Na}_2\text{S}_2\text{O}_3$; 8 mV steps; 10s per point; corrected for solution resistance.

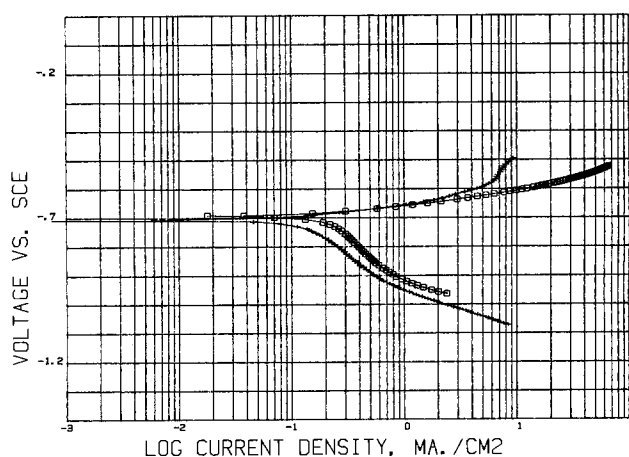


Fig. 10. Corrosion curves on 1018 carbon steel. $+$: 0.9M Na acetate/0.1M acetic acid buffer at pH 5.6. \square : Same plus 0.001M $\text{Na}_2\text{S}_2\text{O}_3$; 8 mV steps; 10s per step; corrected for solution resistance.

An interesting point is that sulfide ion acted as an inhibitor for the action of thiosulfate (Fig. 6 and Table III), again pointing to the fact that thiosulfate is not acting simply as a progenitor of an iron sulfide film. The two ions act antithetically.

Preliminary information has been obtained on the nature of the adsorbate using x-ray photoelectron spectroscopy (XPS) and Auger spectroscopy. In both analysis, the adsorbate formed on a 7% Cr-0.5% Mo steel and on a 9% Ni-7% Cr steel showed sulfur peaks corresponding to a mixture of sulfate, or SO_x , and sulfide, S^{2-} . No peaks corresponding to elemental sulfur were observed. Thiosulfate itself exhibits both an SO_x and a sulfide in XPS so that it is not possible to tell at present whether the thiosulfate has remained intact or cracked upon adsorption. Further details of this work will be given in future publications.

Demonstration of the adsorption of $\text{S}_2\text{O}_3^{2-}$ and $\text{S}_4\text{O}_6^{2-}$.—Chemisorption of thiosulfate and tetrathionate was demonstrated by means of the electrode transfer experiments described in the Experimental section. After a voltammetric scan in a thiosulfate solution, which produced considerable enhancement of the passivation peak as compared to the $\text{S}_2\text{O}_3^{2-}$ -free buffer, rinsing the electrode and transferring it back to the base solution generated a passivation peak much larger than the original base case and almost as large as the peak directly in the thiosulfate solution. This is illustrated in Fig. 11 with thiosulfate and Fig. 12 with tetrathionate.

A number of variations were made of this procedure. It was found unnecessary to run a scan in the $\text{S}_2\text{O}_3^{2-}$ solution; a simple dip would suffice. However, it was not

Table III. Effect of added ions on corrosion current and passivation peak current on 7% Cr, 0.5% Mo Steel

	Corrosion current ($\mu\text{A}/\text{cm}^2$)		Peak height (mA/cm^2) at 50 mV/s	
	No S_2O_3	0.001M S_2O_3	No S_2O_3	0.001M S_2O_3
0.9M NaOAc/0.1M HOAc (A)	60	17	2.2	47
0.05M KNO_3 in A	21	16	1.8	47
0.05M Na_2SO_4 in A	40	15	2.0	48
0.05M NaCl in A	30	25	2.4	55
0.05M KI in A	40	54	3.9	42
0.05M NaNO_2 in A	75	330	0.6	9
0.025M Na_2HPO_4 in A	24	55	3.8	2.5
0.025M Na_2HPO_4				
0.1M $\text{Na}_2\text{B}_4\text{O}_7$	0.07	0.12	0.006	0.006
0.5M Na_2CO_3	0.02	0.2	0.006	0.006
0.5M NaHCO_3				
0.05M Na_2S in A	12	57	2.4	1.6

possible to demonstrate adsorption after immersion of a freshly ground surface into thiosulfate solution without scanning at all. A scan in the base case solution or in the thiosulfate solution was necessary. Such a scan either removes impurities or generates a hydrous oxide layer with which the $\text{S}_2\text{O}_3^{2-}$ reacts.

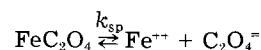
As to desorption of the adsorbed species, it was found that repeated scans in thio-ion-free electrolyte produced a gradually declining peak (Fig. 11). Holding the electrode at a potential near the passivation peak also produced a declining current, followed by a decreased anodic peak current in a subsequent scan. Both of these indicate loss of adsorbed thiosulfate at oxidizing potentials. It was for this reason that the scan rate used for the detection of adsorption was kept high, at 500 mV/s, so as to minimize the time spent at potentials where loss of adsorbate could occur. This loss could occur through the oxidation and removal of the underlying layer of steel upon which the adsorbate rests, or there could be an anodic reaction of the adsorbate-metal complex. We know from the catalytic studies that there is some loss of $\text{S}_2\text{O}_3^{2-}$, albeit small, during corrosion of the steel, which is not seen in nonreacting, stored solutions of thiosulfate in buffer electrolyte, lending credence to the reaction hypothesis.

Chemical interactions of thiosulfate and iron ions.—In an attempt to explain the effect of thiosulfate on the passivation process, its interaction with iron ions was investigated. Page reported in 1954 (11) on the existence of a soluble ferric ion-thiosulfate complex $\text{Fe}(\text{S}_2\text{O}_3)^+$ with a fairly low dissociation constant, 0.02 at 0.5 ionic strength. He also obtained indirect evidence for a weaker ferrous ion complex, FeS_2O_3 with a dissociation constant of 0.12.

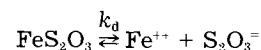
We have now verified the existence of the weak ferrous-thiosulfate complex by measuring the increase in the solubility of ferrous oxalate due to the addition of sodium thiosulfate at 25°C. The pH was held at 4.0 with acetate buffer. This reduced the free oxalate concentration by a factor of 2.64, via the formation of HC_2O_4^- , but

gave more reproducible results than at pH 7 where precipitates were observed to form. There was a definite increase in dissolved iron concentration with thiosulfate concentration.

Combination of the equilibria



and



generates the relation

$$[\text{total Fe}^{2+} \text{ dissolved}]^2 = 2.64 \times K_{sp}(1 + [\text{S}_2\text{O}_3^{2-}]/K_d)$$

From the slope of the relationship between the total dissolved iron and the thiosulfate concentration (Fig. 13), a value of K_d of 0.11 was obtained, an essential confirmation of Page's value. This high a value of the dissociation constant does not indicate strong complexation. At 0.01M of both ferrous and thiosulfate, for example, only 8% of the Fe^{2+} ions would be complexed. Only if the thiosulfate concentrations reached 1M, say at a crack tip, would 70% of the ferrous ions be complexed.

While the above soluble ferrous ion complex does not look mechanistically impressive, precipitates formed in neutral solutions were possibly more promising in explaining the crack promotion and voltage scan data. It was found that titration of a solution containing a ferrous salt (the sulfate) plus sodium thiosulfate with aqueous alkali (NaOH) produced a black precipitate. This was not simply iron hydroxide, which is green, or iron sulfide. Treatment with HCl released a mixture of elemental sulfur, SO_2 , soluble thiosulfate, and iron ions, but no H_2S . Similarly, dissolution into dilute acetic acid released thiosulfate into solution. The precipitates contained only traces of sodium as determined by inductively coupled plasma emission spectroscopy, indicating that the source of the thiosulfate released was not simply occluded sodium thiosulfate solution. It appears that

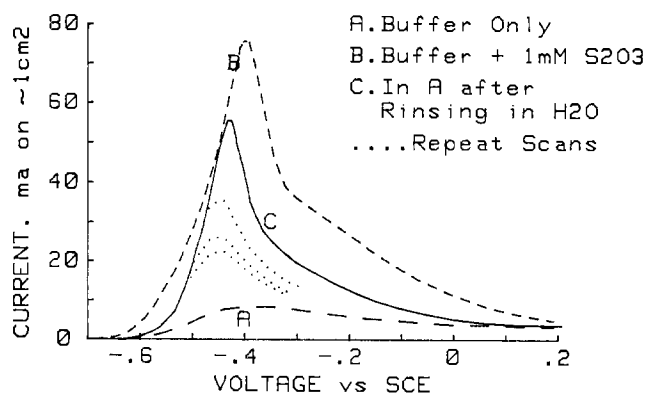


Fig. 11. Adsorption of thiosulfate on 7% Cr-0.5% Mo steel. 0.9M Na acetate/0.1M acetic acid buffer at pH 5.6; scan rate 500 mV/s; Na_2 atmosphere; 25°C.

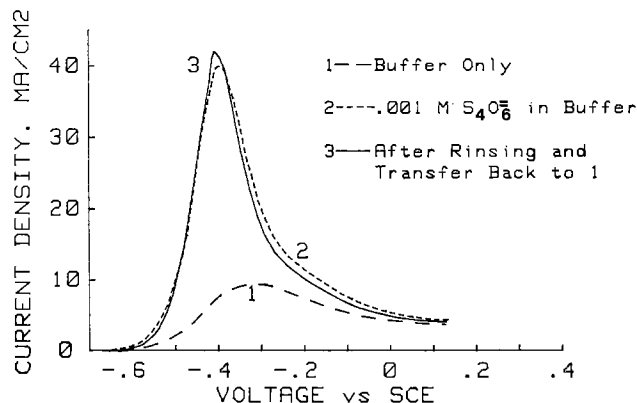


Fig. 12. Adsorption of tetrathionate on 7% Cr-0.5% Mo steel. 0.9M Na acetate/0.1M acetic acid buffer at pH 5.6; scan rate 500 mV/s; Na_2 atmosphere; 25°C.

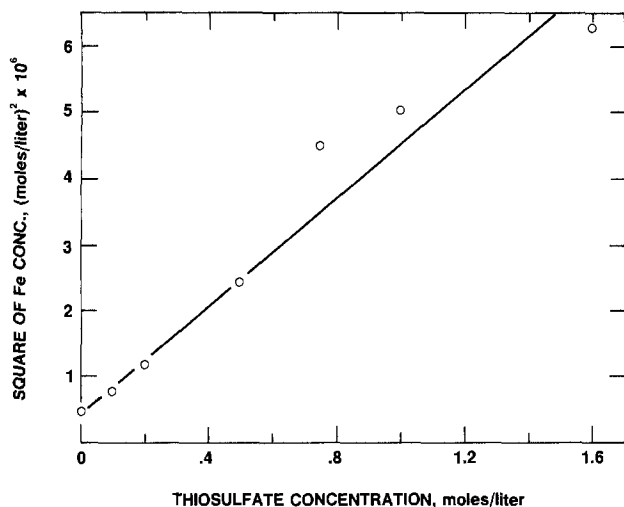


Fig. 13. Effect of added thiosulfate on ferrous oxalate solubility. Fe^{2+} ion concentration determined by atomic absorption.

ferrous ion, hydroxide, and thiosulfate form a solid complex in neutral solutions. Unfortunately, we have succeeded in obtaining neither consistent stoichiometry of this complex nor consistent x-ray diffraction spectra. The material appears to have a highly variable composition depending upon exact preparation conditions and would appear to require careful study to elucidate its structure-composition relationship. However, the existence of such a substance strongly suggests that the thiosulfate ion is able to enter into the passivating film on steel and change its composition and structure. This is probably one of the ways it may alter the passivation process, in an addition to mechanistic effects on the anodic and cathodic electrode reactions.

The role of inhibiting anions.—Experiments were run to determine whether the anions which inhibit the action of thiosulfate do so by competitively desorbing the thiosulfate. The adsorption procedure was modified to include inhibiting anions in the water used to rinse the electrode after the adsorption step. In the subsequent voltammetric scan in base electrolyte, no reduction in the $\text{S}_2\text{O}_3^{2-}$ -promoted passivation peak was observed; the inhibitor did not desorb the $\text{S}_2\text{O}_3^{2-}$ even after a 5 min soak. In contrast, when the inhibitor was included in the final test solution, then inhibition did occur, as shown by a sharp reduction in the passivation peak current (Table IV).

Thus the inhibitor does not cause the desorption of thiosulfate; it must be in solution in the presence of adsorbed thiosulfate to work. The four ions in question are known to promote the passivation of steel (12). This was observed in the present studies where carbonate and borate were observed to reduce drastically the passivation currents, relative to acetate, in the absence of thiosulfate (Table III).

Further tests were run to show that the inhibitors do not adsorb on the surface of the steel. A series of scans were run in which the 7% Cr-0.5% Mo steel was dipped alternately in buffer containing 0.001M thiosulfate and 0.001M thiosulfate plus 0.01-0.05M of the various inhibitors. In every case, the peak height was high in the thiosulfate solution and low in the thiosulfate inhibitor solution; i.e., the inhibitor effect did not carry over into the uninhibited solution. There was no evidence for adsorption of the inhibitor, as the thiosulfate was adsorbed.

The inference then is that thiosulfate or tetrathionate enters into the anodic film so as to render it less protective. Anodic dissolution is thus able to occur readily through the imperfect film. The inhibiting ions must be helping to bolster or repair the imperfect film, probably by the formation of insoluble salts or mixed oxides or hydroxides.

Summary and Conclusions

There are a number of significant findings in this work and deductions that can be made therefrom.

1. The promotion of intergranular stress corrosion cracking in sensitized stainless steel by thiosulfate and tetrathionate is accompanied by anodic current emanating from the crack. Cracking can be inhibited by the addition of certain ions to the solution, whereas other ions do not affect it.

2. Thiosulfate and tetrathionate also produce sharp increases in the passivation currents on nonstainless steels related to those which would be found on the walls of an intergranular crack in sensitized stainless steels. This has been observed with four different steels. The effect appears to be of sufficient generality that it is a virtual certainty that it will be the same in the sensitized grain boundary areas, whatever their exact composition.

3. Supporting the contention that the anodic process on the nonstainless steels is related to the intergranular cracking process is the observation that the same ions which inhibit the cracking also eliminate the high passivation currents caused by the sulfur oxyanions, while the ions which did not inhibit cracking did not reduce the high passivation currents.

4. The thiosulfate and tetrathionate promote the increased anodic currents by adsorbing on the surface of the steel and catalyzing the dissolution of iron. The adsorption step explains how extremely small concentrations of $\text{S}_2\text{O}_3^{2-}$ can promote cracking.

5. The inhibiting ions which prevent stress corrosion cracking and eliminate the anodic stimulation due to $\text{S}_2\text{O}_3^{2-}$ and $\text{S}_4\text{O}_6^{2-}$ do not desorb the adsorbed sulfur compounds from the surface, but must be present in solution to inhibit. Presumably, they function by reinforcing passive film formation by generating insoluble iron salts. Conversely, this implies that the adsorbed sulfur compounds render the surface film nonprotective either by changing the granularity or porosity of the film or by promoting ferrous ion transport.

Table IV. Comparison of inhibitors as desorbents and as solution components

Inhibitor	Peak currents in buffer (mA) ^a			Peak currents in $\text{S}_2\text{O}_3^{2-}$ (mA) ^c	
	+0.001M $\text{S}_2\text{O}_3^{2-}$	After dip and rinse ^b	Dip time (s)	Before inhibition	After inhibitor addition
0.025M Na_2HPO_4 0.025M NaH_2PO_4	46	44	10	49	8
0.05M Na_2CO_3	53	59	10	54	1
0.05M $\text{Na}_2\text{B}_4\text{O}_7$	45	52	10	53	<0.01
0.05M $\text{Na}_2\text{B}_4\text{O}_7$	45	51	60		
0.05M NaNO_2	37	40	300	55	7

^a 7% Cr-0.5% Mo steel. Exposed area: 0.32-0.5 cm² (unmasked). Base electrolyte: 1M acetate buffer, pH 5.6.

^b Dip and rinse in inhibitor solution. Rescanned in buffer without $\text{S}_2\text{O}_3^{2-}$.

^c Same steel. Base electrolyte: 0.09M Na acetate/0.01M acetic acid + 0.5M Na_2SO_4 , pH 5.6, containing 0.001M $\text{Na}_2\text{S}_2\text{O}_3$.

We now come to the question of how increased anodic dissolution promotes intergranular stress corrosion cracking. One might expect anodic dissolution to promote crack blunting. The simplest explanation seems to be that this is a case of active path dissolution or "stress-assisted intergranular corrosion." The corrodents, by delaying repassivation, keep the anodic process going within the grain boundary region until the zone of very high stress arrives at the next weak point. This could be a defect, dislocation, precipitate, or strain-induced phase transformation, etc. Metal cracking then occurs, generating fresh metal surface which reinvigorates the anodic dissolution reaction, continuing the process. This follows the observations of the Brookhaven workers (13) giving evidence for intermittent crack growth, sometimes at rates higher than can be accommodated by anodic dissolution only. Because the sides of the crack walls around the growing crack tip participate in the anodic process due to the action of the corrodent, the actual current densities are lower than that required by Faraday's law for crack tip advancement.

Manuscript received May 18, 1984; revised manuscript received May 7, 1985. This was Paper 278 presented at the New Orleans, Louisiana, Meeting of the Society, Oct. 7-12, 1984.

Exxon Research and Engineering Company assisted in meeting the publication costs of this article.

REFERENCES

1. E. L. Hildebrand, *Corrosion (Houston)*, **12**, 75 (1956).
2. A. Dravnieks and C. A. Samans, *Proc. Am. Petr. Inst.*, **37**, 100 (1957).
3. R. L. Tapping, P. A. Lavoie, and R. D. Davidson, *Mater. Perform.*, p. 43 (Sept. 1983).
4. S. Dhawale, G. Cragnolino, and D. D. MacDonald, EPRI Project RP 1166-1 (FCC 7805), pp. 26-32, Palo Alto, CA (1980).
5. H. S. Isaacs, B. Vyas, and M. W. Kendig, *Corrosion (Houston)*, **38**, 130 (1982).
6. G. Cragnolino and D. D. MacDonald, *ibid.*, **38**, 406 (1982).
7. S. Ahmad, M. L. Mehta, S. K. Saraf, and I. P. Saraswat, *ibid.*, **38**, 347 (1982).
8. H. H. Horowitz, *Corros. Sci.*, **23**, 353 (1983).
9. M. J. Humphries, Ph.D. Thesis, University of Newcastle upon Tyne, Newcastle upon Tyne, England (1966).
10. R. L. Piehl, *API Publ.*, **44**, 189 (1964).
11. F. M. Page, *Trans. Faraday Soc.*, **50**, 120 (1954).
12. L. L. Shreir, "Corrosion Control" Vol. 2, p. 18:41, Newnes-Butterworths, London (1976).
13. R. C. Newman, K. Sieradzki, and H. S. Isaacs, *Met. Trans.*, 2015 (1982).

Calculation of the Electrical Resistance of a Compact Tension Specimen for Crack-Propagation Measurements

Mark E. Orazem*

Department of Chemical Engineering, University of Virginia, Charlottesville, Virginia 22901

ABSTRACT

The electrical resistance of a notched compact specimen for determination of plane-strain fracture toughness was calculated using numerical methods coupled with the Schwarz-Christoffel transformation. Experimental measurement of this resistance is commonly used to obtain the crack length in notched specimens subjected to stress corrosion and hydrogen embrittlement tests. The results presented here predict the shape of the calibration curve for this experiment and facilitate optimal design of notched specimens for sensitivity of the resistance measurements to crack length. The electrical resistance is shown to be most sensitive to crack length for specimens containing a small starter notch. Placement of the current input leads also influences the sensitivity of the specimen resistance to the crack length. An analytic interpolation formula is presented for the primary resistance as a function of cell dimensions that reproduces the calculated results to within 5%.

The plane-strain fracture toughness of metals can be determined through tensile loading of notched specimens that have been precracked in fatigue. Common methods for this test are described in the annual book of ASTM standards (1). Measurement of crack length is an important step in the test procedure. Electrical resistance measurements have been used to monitor crack lengths in the course of hydrogen embrittlement (2), fracture toughness (3), sustained load (4), fatigue crack growth (5, 6), and stress corrosion cracking experiments (7, 8). This method has the advantages that the crack length can be monitored continuously and that the specimen is not subjected to intermittent loading and unloading of tensile stress.

The objective of this work is the calculation of the electrical resistance of a compact tension fracture specimen as a function of crack length. This calculation can be used as an aid in the selection of specimen dimensions for optimal sensitivity of electrical resistance to crack length. The results presented here can also be applied to other electrical or electrochemical systems of similar shape for which primary current and potential distributions apply.

Primary current and potential distributions apply to systems for which the surface overpotential can be neglected and the phase adjacent to the electrode has a uniform potential. These assumptions are strictly valid for

solid conductors in which the current is electronic. Calculation of the primary current and potential distributions involves solution of Laplace's equation, $\nabla^2\Phi = 0$, which is not trivial, even for simple geometries. The method of images (9), separation of variables (10), and superposition (11, 12) have been used to solve Laplace's equation for a number of systems. A review of analytic solutions has been presented by Fleck (13).

The Schwarz-Christoffel transformation (14-16) is a powerful tool for the solution of Laplace's equation in systems with planar boundaries. This method was used by Moulton (17) to derive the current and potential distribution for two electrodes placed arbitrarily on the boundaries of a rectangle. Hine *et al.* (18) used this method to describe the primary current and potential distribution for two plane electrodes of infinite length and finite width confined between two infinite insulating planes, perpendicular to but not touching the electrodes. Wagner (19) presented the primary and secondary current distribution for a two-dimensional slot in a planar electrode. Newman (20) has presented the primary current distribution for two plane electrodes opposite each other in the walls of a flow channel. These solutions made use of the Schwarz-Christoffel transformation.

Theoretical calibration curves for fracture specimens have also been obtained through application of conformal

*Electrochemical Society Active Member.

mapping for a number of simple specimen geometries, such as center- and edge-cracked plates with various starter notch or crack configurations (21-23). These are reviewed by Halliday and Beevers (24). Aronson and Ritchie (25) and Ritchie and Bathe (26) have obtained numerical solutions of Laplace's equation for the compact tension specimen considered here through application of finite element analysis. Some discrepancy was found between experimental and calculated crack lengths at long crack lengths. This discrepancy was attributed to the size of the finite-element mesh. Accurate use of finite-element solutions of Laplace's equation for this system requires a large number of nodes due to the singularities observed at the electrode edges. This difficulty is alleviated by use of the Schwarz-Christoffel transformation.

Application of the Schwarz-Christoffel transformation is generally limited, however, by the difficulty of generating solutions to the resulting integrals. Analytic solutions allow calculation of the primary current and potential distributions throughout the cell, but are possible for a limited number of system geometries. Numerical evaluation of these integrals allows calculation of both the primary current distribution along the electrodes and the cell resistance. Orazem and Newman (27) have coupled application of the Schwarz-Christoffel transformation with numerical integration to calculate the primary resistance and current distribution for a cell containing a slotted electrode. A similar approach is taken here.

Cell Geometry

The geometry of a compact tension specimen for measurement of plane-strain fracture toughness is presented in Fig. 1. The ASTM standards for specimen design are included within the figure. These standards are modified for the study of crack growth in response to fatigue. The envelope of the starter notch is typically small; Hackett *et al.* (8) used a larger notch envelope to accommodate a reference electrode. Use of a large notch may require other adjustment of the cell dimensions, e.g., use of smaller loading pinholes or wider specimens. Under the ASTM standards, the test block must be sufficiently

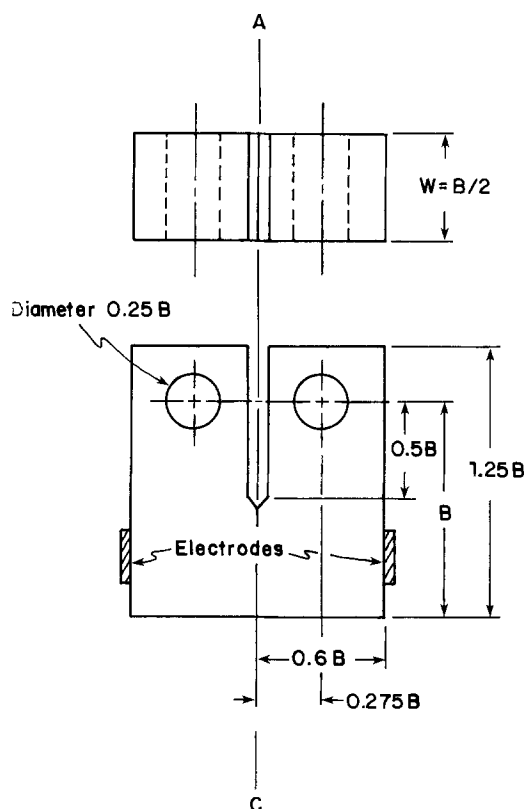


Fig. 1. Notched specimen for determination of plane-strain fracture toughness.

thick that edge effects do not influence the propagation of the crack as a plane. This requirement is consistent with analysis of the primary resistance of this system as being that of a two-dimensional specimen of the shape presented in Fig. 1 and of thickness W .

Under the assumption that electrodes for resistance measurement are placed directly opposite each other, the specimen may be bisected by a plane of symmetry represented by AC in Fig. 1. Thus the specimen will have twice the electrical resistance of the system presented in Fig. 2a, where constant potential surfaces are designated by RS and PQ and all other boundaries are considered to be insulating. The pinholes (see Fig. 1) were assumed to be filled by a close fitting pin with the conductivity of the test specimen. The specimen is placed in a complex coordinate system such that the line OA lies on the real- z axis. The coordinate system of Fig. 2a is transformed through an intermediate half-plane t (see Fig. 2b) to a coordinate system (Fig. 2c) in which Laplace's equation can be solved easily.

Theoretical Development

The primary current distribution along the electrodes and the cell resistance can be calculated through application of the Schwarz-Christoffel transformation. Complex coordinate systems are used, thus

$$z = z_r + jz_i$$

The z coordinate system is related to the t coordinate system of Fig. 2b by

$$z = \int_0^t \frac{(e-t)^{\beta/\pi}}{t^{1/2}(a-t)^{1/2}(b-t)^{1/2}(c-t)^{1/2}(d-t)^{\beta/\pi}} dt \quad [1]$$

where a , b , c , d , and e are the values of t corresponding to z values of A, B, C, D, and E, respectively. The outside angle at D is represented by β such that $\beta/\pi = 1/2$ for a right-angle corner. The electrodes PQ and CS correspond to p q and c s in the t plane.

The variable χ (see Fig. 2c) is related to the t variables by the Schwarz-Christoffel transformation

$$\chi = \int_0^t \frac{1}{(t-p)^{1/2}(q-t)^{1/2}(c-t)^{1/2}(s-t)^{1/2}} dt \quad [2]$$

Solution of Laplace's equation for the χ system yields the potential as a linear function of χ

$$\Phi = \frac{\chi_i}{\chi_{i,\max}} V \quad [3]$$

where $\chi_{i,\max}$ is the separation between electrodes cs and pq in the χ system, and V is the potential difference between the electrodes. The potential drop in the original cell of Fig. 1 is $2V$. The current density is related to the potential derivative at the electrodes. The relationships among the potential derivatives at the electrodes in the χ , t , and z coordinate systems are developed in Appendix A. These relationships are the basis for a system of nonlinear integral equations that can be solved to obtain the current density along either electrode in the z coordinate system.

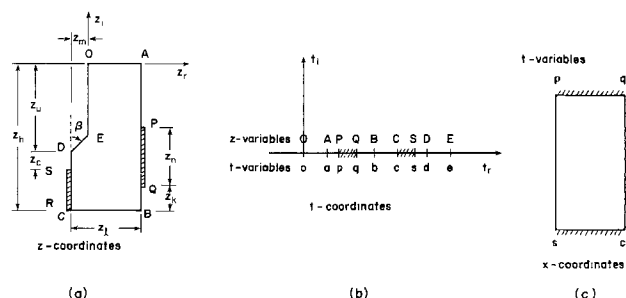


Fig. 2. Schematic diagram of the sectioned cell with coordinates. a: $z = z_r + jz_i$. b: $t = t_r + jt_i$. c: $\chi = \chi_r + j\chi_i$.

The dimensionless primary resistance, $W\kappa R$, is obtained through integration of the current density. The numerical method used in this calculation is presented in Appendix B. The primary current distribution and the dimensionless resistance are functions only of geometric ratios.

Results

The methods outlined in Appendix B were used to calculate the primary current distribution and the primary resistance of the crack-propagation test block. The calculation of the primary current distribution was used primarily to check the calculations. The quantity of greatest interest for test block design is the primary resistance, presented in the Primary resistance section.

Current distribution.—The current distribution close to the edge of an electrode adjoining an insulator with an angle α is

$$\frac{i(z_i)}{i_{avg}} = \text{const.} \frac{\pi}{2\alpha} (Q - z_i)^{\pi/2\alpha - 1} \quad [4]$$

where Q is the point of intersection of the electrode and the insulator. The calculated current distribution shows the expected asymptotic behavior, being proportional to $(Q - z_i)^{-1/2}$ at P , Q , and S , and approaching a finite value at C .

Primary resistance.—The primary resistance of the cell can be expressed as the dimensionless group $W\kappa R$. The dimensionless primary resistance is a function of the angle β , three geometric ratios associated with cell shape (e.g., z_l/z_h , z_m/z_h , and z_u/z_h), and three geometric ratios associated with electrode placement (e.g., z_1/z_h , z_2/z_h , and z_3/z_h). In the limit of the starter envelope area approaching zero, the primary resistance approaches that of a rectangle with appropriately placed electrodes. The solution for this problem has been presented by Moulton (17) in terms of tabulated elliptic functions (29) as

$$W\kappa R_m = K(1 - m_\lambda)/K(m_\lambda) \quad [5]$$

where $K(m_\lambda)$ is the complete elliptic integral of the first kind with parameter m_λ . The parameter is obtained from the geometry of the rectangle by

$$m_\lambda = \frac{\text{sn}^2(z_2|m) - \text{sn}^2(z_1|m)}{\text{sn}^2(z_3|m) - \text{sn}^2(z_1|m)} \quad [6]$$

where m is the parameter defined by $K(1 - m)/K(m) = L/h$, z_1 is the location of point Q , z_2 is the location of point P , and z_3 is the location of point S . Equation (16.23.1) in Ref. (29) was used to calculate values for the elliptic function sn .

The primary resistance of a rectangle is presented in Fig. 3 as a function of the dimensionless length of the electrode cs [$\xi = (z_h - z_u - z_c)/z_h$]. This value represents a first approximation to the primary resistance of the notched specimen and includes the influence of electrode placement and crack length. The variable ξ approaches zero as the crack grows to bisect the block, and the primary resistance approaches infinity according to

$$W\kappa R \rightarrow -2/\pi \ln(\xi) \quad [7]$$

The greatest sensitivity of primary cell resistance to crack length is shown to be for values of ξ less than 0.5. Under the ASTM standards, the maximum value for ξ is 0.4. The range of values for ξ that are of greatest interest for crack-propagation experiments extends from 0.1 to 0.4. Under the restriction of the ASTM standards for the length of the starter crack envelope, this corresponds to values of dimensionless crack length z_c/z_h of 0 to 0.3. Placement of electrodes in a manner that increases the mean path for current flow ($z_k/z_h \rightarrow \infty$) also increases the sensitivity of resistance to crack length in the region of primary importance to crack-length measurements; this advantage is offset by the disadvantage that the resistance in this region can no longer be represented by Eq. [7].

Primary resistance curves are presented in Fig. 4 for test blocks with finite crack envelope areas. The sensitiv-

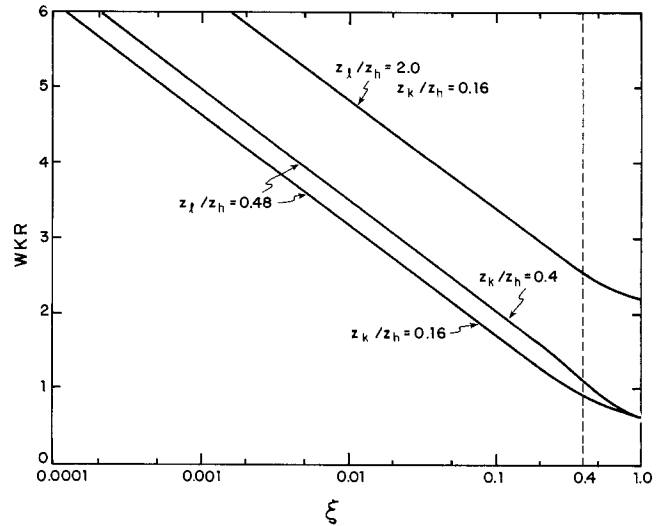


Fig. 3. Moulton's solution for the primary resistance of a rectangular conductor with $z_u/z_h = 0.4$. The resistance of the specimen shown in Fig. 1 is obtained by multiplying the resistance given above by two.

ity of resistance measurements to crack length in the region $0.1 < \xi < 0.4$ decreases with increasing envelope area. A large notch is associated with a reduced area available for conduction of electrical current. Thus, Moulton's solution for a rectangular conductor with no notch area represents a lower limit to the primary resistance of the notched specimen. The influence of the notch is greatest for z_c/z_h equal to zero ($\xi = 0.4$) and is a strong function of crack length in this region. The notch has a smaller influence on the resistance as the crack length increases and is associated with a uniform contribution to the primary resistance in the limit of $\xi \rightarrow 0$.

The primary resistance can therefore be represented by the sum of Moulton's solution and an additional resistance associated with the notch area. The additional resistance associated with notch area is presented in Fig. 5 as a function of crack length. This term is a function of notch area and electrode placement, but is relatively independent of block length. An interpolation formula for this term can be developed such that the primary resistance of the block is written

$$W\kappa R = W\kappa R_m + \Gamma + (1.4\xi + 4.24\Gamma - 0.056) e^{-(\xi_0 - \xi)/\xi} + \frac{m}{L} \left[0.5 \left(\frac{\mu}{1 - \mu} \right)^{1.5} - 0.10 \right] + \Delta_2 \quad [8]$$

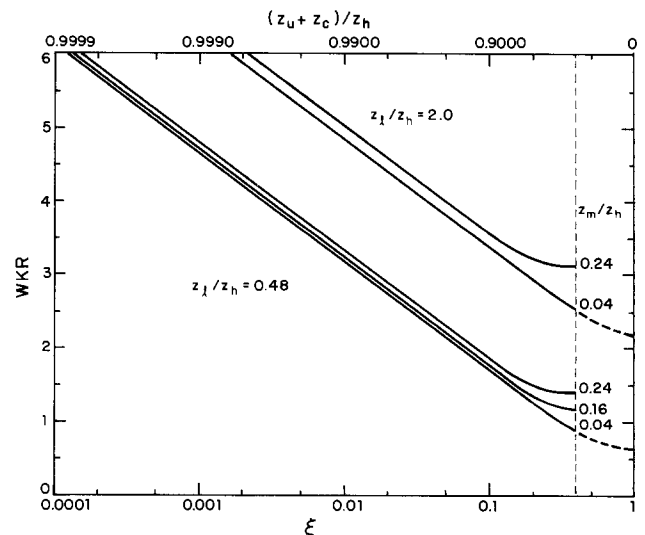


Fig. 4. Primary resistance of a sectioned cell with dimensions $z_u/z_h = 0.4$, $z_k/z_h = 0.16$, $z_u/z_h = 0.6$, and $\beta = 0.25$. Moulton's solution for a rectangular conductor is given by dashed lines. The resistance of the specimen shown in Fig. 1 is obtained by multiplying the resistance given above by two.

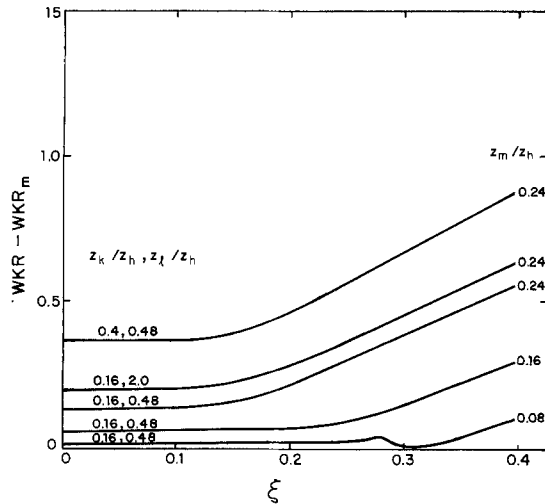


Fig. 5. Contribution to the primary resistance associated with a finite starter notch envelope. Cell dimensions are given in Fig. 4.

where $W\kappa R_m$ is the solution obtained by Moulton, Γ is a function of the notch area given by

$$\Gamma = \left\{ \frac{z_m}{0.6z_h} \left(z_u - \frac{1}{2} z_m \tan [\pi(1/2 - \beta)] \right) \right\}^{1.523} \quad [9]$$

ξ_0 is $(z_h - z_u)/z_h$, μ is z_k/z_h , and Δ_2 is a difference variable plotted in Fig. 6 as a function of ξ . Neglect of Δ_2 results in an error of less than 5% for the primary resistance of a notched test specimen with dimension close to the ASTM standards.

These results suggest that Eq. [7] provides a suitable form for calibration curves for compact tension specimens with small notch areas. This work does not address the question of potential lead placement. Aronson and Ritchie (26) state that the top surface close to the notch is the preferred location for positioning leads for measurement of potential differences across the cracked region. This location minimizes errors associated with the uncertainty of probe location. The resistance obtained as a function of crack length with leads separated from the current inputs will differ from the resistance presented in

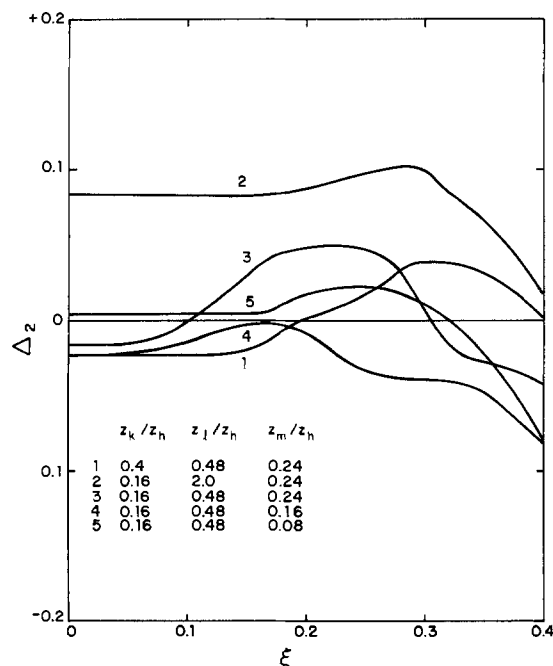


Fig. 6. Dimensionless correction to Eq. [8] for the primary resistance of a crack-propagation test specimen. Cell dimensions are given in Fig. 4.

Fig. 3 and 4 by a constant amount. The curves of Fig. 3 and 4 will be shifted in the downward direction. Electrical isolation of the pins from the test block (see Fig. 1) will result in an upward shift of these curves.

Conclusion

Application of electrical resistance methods for measurement of crack length in notched specimens is contingent upon the sensitivity of the resistance to crack length. This sensitivity is a strong function of specimen dimension and is specified by the calculations presented here. A large notch in the specimen reduces the sensitivity of the resistance method for crack length measurement; thus maximum sensitivity is found in the limit of a negligible notch area. Placement of electrodes in a manner that increases the mean path for current flow also increases the sensitivity of resistance to crack length in the region of primary importance to crack-length measurements; this advantage is offset by the disadvantage that the resistance in this region can no longer be represented by Eq. [7].

An expression is presented for the primary resistance of a notched test specimen. This expression is accurate to within 5%, and can be used to predict the resistance of such objects. This work should not be used, however, to calculate independent calibration curves for test blocks. The calculations presented here involve the assumption of a uniform specimen conductivity. A nonuniform conductivity is frequently the result of localized stress such as expected near the crack tip. This work, however, predicts the shape of the calibration curve and facilitates the optimal design of the test block for sensitivity of crack measurement.

Acknowledgment

Computation costs for this work were provided through a grant from the University of Virginia Academic Computing Center.

Manuscript submitted April 28, 1984; revised manuscript received May 7, 1985. This was Paper 280 presented at the New Orleans, Louisiana, Meeting of the Society, Oct. 7-12, 1984.

APPENDIX A

Theoretical Development

The primary current distribution along the electrodes and the cell resistance can be calculated through application of the Schwarz-Christoffel transformation. Complex coordinate systems are used, thus

$$z = z_r + jz_i$$

The z coordinate system is related to the t coordinate system of Fig. 2b by

$$z = \int_0^t \frac{(e-t)^{\beta\pi}}{t^{1/2}(a-t)^{1/2}(b-t)^{1/2}(c-t)^{1/2}(d-t)^{\beta\pi}} dt \quad [A-1]$$

where a , b , c , d , and e are the values of t corresponding to z values of A , B , C , D , and E , respectively. The outside angle at D is represented by β such that $\beta/\pi = 1/2$ for a right-angle corner. The electrodes PQ and CS correspond to pq and cs in the t plane. Along the electrode PQ, Eq. [A-1] can be expressed by

$$\frac{dz_r}{dt_i} \Big|_{pq} = jf(t_r) \quad [A-2]$$

where

$$f(t_r) = \frac{(e-t)^{\beta\pi}}{t^{1/2}(t-a)^{1/2}(b-t)^{1/2}(c-t)^{1/2}(d-t)^{\beta\pi}} \quad [A-3]$$

These equations will be used to calculate the derivative of the potential at the electrode; z_r is the direction normal to the electrode in the z plane, and t_i is the direction normal to the electrode in the t plane. Along the cs electrode, the relationship can be expressed as

$$\frac{dz_r}{dt_i} \Big|_{cs} = -jf(t_r) \quad [A-4]$$

where $f(t_r)$ is given by Eq. [A-3].

The variable χ [see Fig. 2c] is related to the t variables by the Schwarz-Christoffel transformation

$$\chi = \int_0^t \frac{1}{(t-p)^{1/2}(q-t)^{1/2}(c-t)^{1/2}(s-t)^{1/2}} dt \quad [A-5]$$

Along the electrode pq , this equation can be expressed as

$$\left. \frac{dz_r}{dt_i} \right|_{pq} = jg(t_r) \quad [A-6]$$

and along electrodes cs by

$$\left. \frac{dz_r}{dt_i} \right|_{cs} = -jg(t_r) \quad [A-7]$$

where

$$g(t_r) = \frac{1}{(t-p)^{1/2}(q-t)^{1/2}(c-t)^{1/2}(s-t)^{1/2}} \quad [A-8]$$

The variable χ_i is normal to the electrode in χ space, and t_i is normal to the electrode in t space.

The potential in the χ system is a linear function of χ

$$\Phi = \frac{\chi_i}{\chi_{i,max}} V \quad [A-9]$$

where V is the potential difference between electrodes cs and pq . The potential drop in the original cell of Fig. 1 is $2V$. The separation between electrodes in the χ system is denoted by $\chi_{i,max}$. The current density is related to the potential derivative at the electrodes. In the χ system, this derivative is given by

$$\left. \frac{\partial \Phi}{\partial \chi_i} \right|_{pq} = \frac{V}{\chi_{i,max}} \quad [A-10]$$

The potential derivative at the electrode pq in the t system is

$$\left. \frac{\partial \Phi}{\partial t_i} \right|_{pq} = \left. \frac{\partial \Phi}{\partial \chi_i} \right|_{pq} \left. \frac{\partial \chi_i}{\partial t_i} \right|_{pq} \quad [A-11]$$

and the potential derivative in the z system is given by

$$\left. \frac{\partial \Phi}{\partial z_r} \right|_{pq} = \left. \frac{\partial \Phi}{\partial t_i} \right|_{pq} \left. \frac{\partial t_i}{\partial z_r} \right|_{pq} \quad [A-12]$$

From these relationships, the potential derivatives along the electrodes in the original z coordinate system are obtained as functions of t_r

$$\left. \frac{\partial \Phi}{\partial z_r} \right|_{pq} = \frac{g(t_r) V}{f(t_r) \chi_{i,max}} \quad [A-13]$$

and

$$\left. \frac{\partial \Phi}{\partial z_r} \right|_{cs} = \frac{g(t_r) V}{f(t_r) \chi_{i,max}} \quad [A-14]$$

respectively.

The current distribution along the electrode PQ is therefore given by

$$i_{avg} = \frac{g(t_r)}{f(t_r) \int_p^q g(t_r) dt_r} \quad [A-15]$$

A similar expression results for the electrode CS . The primary cell resistance is given by

$$W\kappa R = \frac{\chi_{i,max}}{\int_p^q g(t_r) dt_r} \quad [A-16]$$

The primary current distribution and the dimensionless cell resistance $W\kappa R$ are functions only of geometric ratios.

APPENDIX B
Numerical Method

The Schwarz-Christoffel transformation is coupled here with numerical integration of the transformation equations. The solution of these equations involves two steps:

determination of t variable parameters, and integration of Eq. [A-15] and [A-16] to get the primary current distribution and cell resistance.

Determination of the t variable parameters ($a, b, c, d, e, p, q,$ and s) associated with the locations of the corners and electrode edges in the z coordinate system involves the solution of eight coupled equations of the form

$$G_i(\mathbf{x}) = \text{Re}\{A\} - \int_0^a \frac{(e-t)^{\beta_i \pi}}{t^{1/2}(a-t)^{1/2}(b-t)^{1/2}(c-t)^{1/2}(d-t)^{\beta_i \pi}} dt \quad [B-1]$$

where $G_i(\mathbf{x}) = 0$, and \mathbf{x} is a vector denoting the unknown values a through s . Through use of a Taylor series expansion about a trial solution denoted by the superscript o , the series of equations can be written in the form

$$\underline{G}^o = \underline{B}^o \Delta \mathbf{x} \quad [B-2]$$

where \underline{B}^o is related to the Jacobian of the function \underline{G}^o , i.e.

$$B_{ik}^o = -\frac{\partial G_i^o}{\partial x_k} \quad [B-3]$$

and $\Delta \mathbf{x} = \mathbf{x}^o - \mathbf{x}$. The Jacobian is a strong function of \mathbf{x} and is evaluated numerically. The inverse of the Jacobian is evaluated, and a converged solution is obtained through Newton-Raphson iteration. The amount of time associated with this computation is strongly dependent upon the value of \mathbf{x}^o . In order to reduce computation times, the inverse of the Jacobian was used to calculate a parameter sensitivity coefficient [see, e.g., Ref. (28)]

$$d_k = \underline{B}^{-1} s_k \quad [B-4]$$

where s_k is the vector $(\partial G / \partial p_k)_r$, and p_k represents a given parameter, e.g., dimensionless crack length. Thus, from the converged solution for parameters \underline{p}^o a first approximation for $\mathbf{x}(\underline{p} + d\underline{p})$ is obtained as

$$\mathbf{x}(\underline{p} + d\underline{p}) = \mathbf{x}^o + \sum_{k=1}^M d_k dp_k + O(d\underline{p}^2)$$

The predicted value for \mathbf{x} is further refined by Newton-Raphson iteration.

Once the values of $a, b, c, d, e, p, q,$ and s are obtained, the current distribution can be obtained through numerical integration of Eq. [A-15], $\chi_{i,max}$ can be obtained through integration of Eq. [A-5] from p to q , and the primary resistance can be obtained from evaluation of Eq. [A-16].

LIST OF SYMBOLS

i	current density (mA/cm ²)
j	$\sqrt{-1}$
R	half-cell resistance (Ω)
V	half-cell potential (V)
W	cell thickness (cm) (see Fig. 1)
z_c	crack length (cm) (see Fig. 2a)
z_h	cell height (cm) (see Fig. 2a)
z_k	height of electrode for resistance measurement (cm) (see Fig. 2a)
z_l	length of half-cell (cm) (see Fig. 2a)
z_m	half-width of starter-crack notch (cm) (see Fig. 2a)
z_n	width of electrode for resistance measurement (cm) (see Fig. 2a)
z_u	depth of starter-crack notch (cm) (see Fig. 2a)

Greek Characters

α	angle at corner of electrode and insulating wall
β	angle of notch (see point D in Fig. 2a)
Δ_2	error term in Eq. [26]
κ	conductivity (mho/cm)
Φ	electrical potential (V)

Subscripts

avg	average
i	imaginary
m	corresponding to Moulton's solution
r	real

REFERENCES

1. "Annual Book of ASTM Standards," Part 10, pp. 540-561, ASTM, Philadelphia (1979).
2. W. Barnett and A. R. Troiano, *J. Metals*, **9**, 486 (1957).
3. R. M. Tchorzewski and W. B. Hutchinson, *Metall. Trans. A*, **9**, 1113 (1978).
4. C. A. Stubbington and S. Pearson, *Eng. Fracture Mech.*, **10**, 723 (1978).
5. C. J. Beevers, R. J. Cooke, J. F. Knott, and R. O. Ritchie, *Metal Sci.*, **9**, 119 (1975).
6. N. A. J. Blades, W. J. Plumbridge, and D. Sidey, *Mater. Sci. Eng.*, **26**, 195 (1976).
7. H. H. Johnson and A. M. Willner, *Appl. Mater. Res.*, **4**, 35 (1965).
8. E. M. Hackett, J. R. Scully, and P. J. Moran, Paper 136 presented at the Electrochemical Society Meeting, Washington, DC, Oct. 9-14, 1983.
9. C. Kasper, *Trans. Electrochem. Soc.*, **77**, 353 (1940); *ibid.*, **78**, 131 (1940); *ibid.*, **82**, 153 (1942).
10. J. Newman, *This Journal*, **113**, 501 (1966).
11. J. J. Miksis, Jr., and J. Newman, *ibid.*, **123**, 1030 (1976).
12. P. Pierini and J. Newman, *ibid.*, **126**, 1348 (1979).
13. R. N. Fleck, M. S. Thesis, University of California, Berkeley, CA (1964).
14. R. V. Churchill, "Complex Variables and Applications," 2nd ed., McGraw-Hill, New York (1960).
15. E. T. Copson, "An Introduction to the Theory of Functions of a Complex Variable," Oxford University Press, London (1935).
16. F. Bowman, "Introduction to Elliptic Functions with Applications," John Wiley and Sons, New York (1983).
17. H. F. Moulton, *Proc. London Math. Soc., Ser. 2*, **3**, 104 (1905).
18. F. Hine, S. Yoshizawa, and S. Okada, *This Journal*, **103**, 186 (1956).
19. C. Wagner, *Plating* **48**, 997 (1961).
20. J. Newman, in "Electroanalytical Chemistry," Vol. 6, A. J. Bard, Editor, pp. 187-352, Marcel Dekker, Inc., New York (1973).
21. A. J. Carlsson, *Trans. R. Instit. Technol. Stockholm*, **189**, 1 (1962).
22. H. H. Johnson, *Mater. Res. Stand.*, **9**, 442 (1965).
23. G. Clark and J. F. Knott, *J. Mechan. Phys. Solids*, **23**, 265 (1975).
24. M. D. Halliday and C. J. Beevers, in "The Measurement of Crack Length and Shape During Fracture and Fatigue," C. J. Beevers, Editor, pp. 85-112, Chameleon Press, London (1980).
25. R. O. Ritchie and K. J. Bathe, *Int. J. Fracture*, **15**, 47 (1979).
26. G. H. Aronson and R. O. Ritchie, *J. Test. Eval.*, **7**, 208 (1979).
27. M. E. Orazem and J. Newman, *This Journal*, **131**, 2857 (1984).
28. R. A. Brown, L. E. Scrivan, and W. J. Silliman, in "New Approaches to Nonlinear Problems in Dynamics," P. J. Holmes, Editor, pp. 289-307, Society of Industrial Applied Mathematics, Philadelphia (1980).
29. L. M. Milne-Thomson, in "Handbook of Mathematical Functions," M. Abramowitz and I. A. Stegun, Editors, Chap. 16, 17, Dover, New York (1972).

An Ellipsometric Study of Electrodeposition and Electrochemical Conversion of Lead Dioxide Films

J. L. Ord,* Z. Q. Huang,^{*1} and D. J. DeSmet^{*2}

Department of Physics, University of Waterloo, Waterloo, Ontario, Canada N2L 3G1

ABSTRACT

An automated ellipsometer is used to study the galvanostatic electrodeposition of lead dioxide films onto a platinum substrate from an electrolyte containing lead acetate. The films exhibit regular optical properties over the thickness range from 0 to 600 nm. At a wavelength of 632.8 nm, the refractive index and extinction coefficient are 2.03 and 0.045, respectively. If the deposition process is assumed to require the transfer of two electrons per molecule deposited, the density of the deposited film is calculated to be 7.13 g/cm³. When the lead dioxide films are subjected to alternate anodic and cathodic galvanostatic cycles in neutral borate electrolyte, the optical data exhibit a complex but reproducible structure with inflections at points where the potential-time curve is featureless. A limited quantitative analysis of the optical cycling data can be carried out by requiring consistency between results at widely different film thicknesses. It is possible that the complex optical cycling behavior is due to the presence of two different types of sites for hydrogen within the film.

The experiments whose results are reported in this paper form part of our continuing study of electrochemical conversion in thin film systems. We have found ellipsometry to be a very effective technique for studying such processes both in electrochromic systems, where optical properties are of direct interest, and in battery systems, where they are only of indirect interest. Systems which are suitable for study by ellipsometry must remain stratified during the conversion process, *i.e.*, composition may vary with depth into the film but not with lateral displacement. We have observed homogeneous conversion in the anodic oxide of tungsten (1) and the hydroxides of nickel (2, 3) and iridium (4), and heterogeneous conversion with a sharp phase boundary between component layers in the anodic oxides of molybdenum (5) and vanadium (6). In all of these systems, the mobile ion is thought to be hydrogen, and the transport process is thought to dictate whether conversion is a homogeneous or heterogeneous process.

*Electrochemical Society Active Member.

¹Permanent address: Department of Applied Chemistry, Chongqing University, Chongqing, Sichuan, China

²Permanent address: Department of Physics, University of Alabama, University, Alabama 35486.

Although there is an extensive literature on the electrochemical conversion of lead dioxide films, ellipsometric studies are usually referenced (7, 8) as unpublished work or work to be published. One exception is the paper by Naegele and Plieth (9), who used an automated ellipsometer to study the galvanostatic deposition of PbO₂ on platinum. They present 1000 data points recorded at 0.25s intervals, but use an analysis technique which they state is not valid for thicknesses beyond 65 nm, and analyze only their first 70 points. Their analysis indicates that the refractive index varies by 20% and the extinction coefficient by a factor of 5 over the range of thickness spanned by their 70 data points, and they conclude only that the optical properties show irregular behavior below 50 nm.

The work we report in this paper has two specific objectives: (i) to study the optical properties of the deposited film to see whether they are as irregular as has been reported, and (ii) to study the optical changes associated with electrochemical conversion of the film to see what ellipsometry can add to our understanding of the processes involved. Our objectives here are similar to those in our recent study of MnO₂ films (10). *A priori*, we expect electrochemical conversion to be a more complicated process in PbO₂ than in MnO₂, but the ease with

which PbO_2 can be cycled should make it possible to get better optical data than can be obtained on MnO_2 films.

Experimental

Films were deposited onto a platinum single-crystal electrode from a buffered lead acetate solution (1M in lead acetate, sodium acetate, acetic acid) of refractive index 1.3752 under conditions which have been reported to favor the deposition of alpha lead dioxide (7, 8, 11). Electrochemical conversion of the films was studied in a neutral borate buffer of refractive index 1.3333, an electrolyte which we have used extensively in anodic oxidation studies and which Peter (8) used to study the reduction of lead dioxide. The optical cell consists of a hollow equilateral glass prism with standard-taper joints for the working-electrode holder, a platinum counterelectrode, a gas dispersion tube, and the mercury-mercurous sulfate electrode, to which all potentials quoted in this paper are referenced. The electrolyte was maintained at room temperature (22°C), and was not deaerated in these experiments since the samples are exposed to the air during transfer from the deposition cell to the cycling cell. The working electrode is in the form of a cylinder with a flat on one side for optical measurements, and when it is clamped between Teflon washers in its holder and mounted in the cell it exposes a vertical surface 1.44 cm² in the area to the electrolyte.

The self-nulling ellipsometer uses quadrature Faraday modulation decoded by a two-phase lock-in amplifier and fed back to ministeping drives through voltage-to-frequency converters. Under typical operating conditions, the instrument has a response time of a few tenths of a second and a resolution of a few thousandths of a degree. The angle of incidence is set at 60° to accommodate the equilateral cell, and refractive index values quoted here are for a wavelength of 632.8 nm, the wavelength of the helium-neon laser source.

A process-control computer operates the circuitry used with the cell and records current and potential along with polarizer and analyzer settings at specified time intervals. Potentials are digitized by a 16 bit analog-to-digital converter with a 25 μs conversion time. The operation of the ellipsometer is monitored on a four-trace oscilloscope, and progress of the experiment is followed on two storage displays and an X-Y plotter, which are updated by the computer.

Results and Discussion

Figure 1 shows the optical results from a deposition experiment carried out at a current density of 694 $\mu\text{A}/\text{cm}^2$. A polarizer *vs.* analyzer (P-A) plot of the ellipsometer null settings is shown in the upper portion of the figure, and the corresponding thickness values are plotted *vs.* accumulated charge in the lower portion. At point A, the substrate is free of film, and the null settings determine the refractive index N and extinction coefficient K for platinum. As deposition proceeds, the null settings spiral outwards in a clockwise direction on the P-A plot. P-A curves of this type are characteristic of the growth of a film which absorbs a small amount of the light passing through it. An ellipsometer measures the change in polarization resulting from interference between light reflected at the electrolyte-film and film-substrate interfaces, and the growth of a transparent film produces a "loop" on a P-A plot which closes when the product of the film thickness and the cosine of the angle of refraction is equal to half the wavelength of light in the film. If the film is slightly absorbing, the P-A locus spirals outward at a pitch which is a measure of the extinction coefficient.

The optical data trace out an essentially continuous curve, and the circles identify every third point from the set of 51 points at equal charge increments used in the optical analysis. The analysis technique, although straightforward, merits some discussion since it leads to conclusions which are quite different from those reached by Naegele and Plieth (9). Optical models assume that films

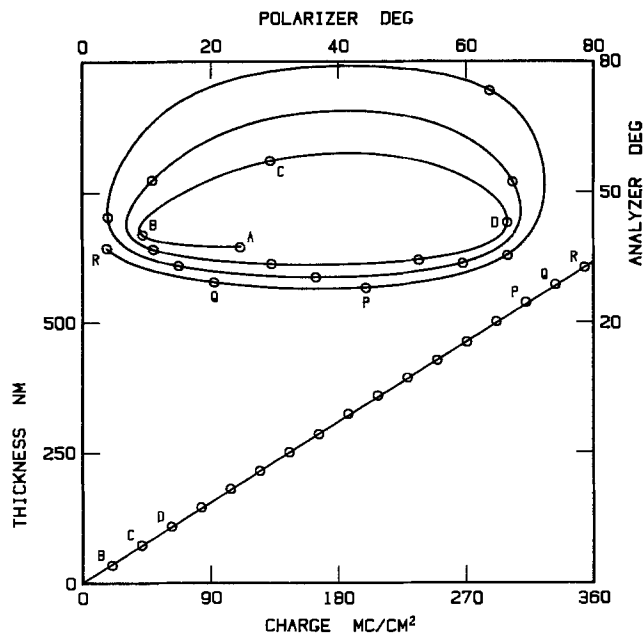


Fig. 1. Galvanostatic deposition of PbO_2 onto a platinum substrate at 694 $\mu\text{A}/\text{cm}^2$. The circles identify every third point from the set used in the optical analysis, and the calculated thicknesses are for a film with N equal to 2.03 and a mean K of 0.045.

are homogeneous in composition and uniform in thickness, but real films rarely exhibit these ideal characteristics. Anodic oxide films on valve metals owe their uniformity in thickness to the high field growth process, but electrodeposited films are bound to be somewhat nonuniform in thickness even under the best deposition conditions, and an analysis technique which is highly sensitive to film nonuniformity is not likely to give meaningful results. Naegele and Plieth use an instrument which measures an additional optical parameter, the mean reflectivity, and their analysis technique enables them to determine a unique value for N , K , and the film thickness D from a measurement at a single film thickness in an ideal system. This technique is useful when measurements cannot be performed at more than one thickness, but the conclusion that N varies by 20% and K by a factor of 5 over a relatively narrow thickness range is more likely a consequence of the limitations of the mean reflectivity analysis technique than of irregularity in the optical properties of the films themselves.

In the analysis technique used here, a set of points at equal charge increments is selected from the data, and sets of K and D values are calculated from the data for various values of N . The value of N which we judge to fit the data best is one for which both the standard deviation in K and the deviation from a linear dependence of D on Q are as small as possible. We could equally well fix the value of K and express goodness of fit in terms of the standard deviation in N , but the most meaningful measure of the standard deviation in both N and K is obtained by comparison with the values which provide the best fit to other deposition runs.

Analysis of the optical data in Fig. 1 shows the best fit is obtained when N is equal to 2.03. At this value, the mean of the fitted K values is 0.045 with a standard deviation of 0.01, and the standard deviation in the D *vs.* Q slope is 0.1%. Other deposition runs at the same current density give N values between 2.03 and 2.05, K values between 0.045 and 0.053, and D *vs.* Q slopes which differ by as much as 1.5%. The variation in K is consistent with a standard deviation of 0.01, and the run-to-run D *vs.* Q slope variation is not surprising since it is sensitive to variations in roughness factor. In the lower portion of Fig. 1, D is plotted *vs.* Q , and it can be seen that the analysis spans the thickness range from 0 to over 600 nm. If we fit only over the thickness range from 0 to 80 nm, the fit gets better, not worse (the standard deviation in K is halved),

and hence our films do not show the irregular optical properties below 50 nm which have been reported elsewhere (9).

The slope of the D vs. Q plot enables us to calculate the density of the film if we assume that the efficiency and roughness factors are unity, and that the film is entirely PbO_2 deposited by a two electron per molecule process. Under these assumptions, we get a value of 7.13 g/cm^3 for the density of the deposited film, a value which is about 75% of the value we would expect for a compact crystalline film. Peter (7) obtained a value of 6.85 g/cm^3 from interferometric data by assuming a refractive index equal to the bulk value of 2.23 at 600 nm, but this assumption is not consistent with a density which is substantially lower than the bulk value. Our measured value for the refractive index, 2.03, appears consistent with a density which is 75% of the bulk value, but there are other factors to be considered. Neutron diffraction (12-14) and inelastic scattering (15) studies indicate that electrochemically deposited films, whether alpha, beta, or amorphous in structure, undoubtedly contain some hydrogen. Further, the Pb:O ratio appears to be very close to 0.5, and if hydrogen is incorporated in crystalline material as lattice water or hydroxyl ions, the oxygens occupy normal lattice sites. The presence of hydrogen in the film, although insignificant in terms of its effect on formula weight, may lower the average number of electrons transferred per molecule deposited below the value of 2 which we assumed in the density calculation. If it does, then our calculated value of 7.13 g/cm^3 will be an underestimate of the density of the deposited film. We will return to this point when we discuss the results of the cycling experiments.

The cycling experiments are all carried out at a current density of $173 \mu\text{A/cm}^2$ in the borate buffer electrolyte. Film deposition from acetate electrolyte (at $694 \mu\text{A/cm}^2$) is followed optically, and when the desired film thickness is reached the circuit is opened. When no further optical changes are noted, a cell containing borate buffer is mounted on the ellipsometer table, the sample is transferred to this cell, and the ellipsometer is prepared to follow the optical changes associated with the galvanostatic conversion cycles. The anodic cycles extend all the way to the oxygen evolution potential, but the cathodic cycles have to be restricted to avoid damage to the sample. (The choice of the cathodic turning point is dealt with below in the discussion of Fig. 8.)

Figure 2 shows the potential-time plot from a cycling experiment on an 80 nm thick film. The as-deposited film has an anodic current applied to it at A to drive it to the anodic end point at B, then two complete cathodic-anodic cycles, B-C-D and D-E-F, are applied followed by two cycles with restricted cathodic end point, F-G-H and H-I-J. The film is then cycled to the cathodic end points so that a cycle with a restricted anodic end point, K-L-M,

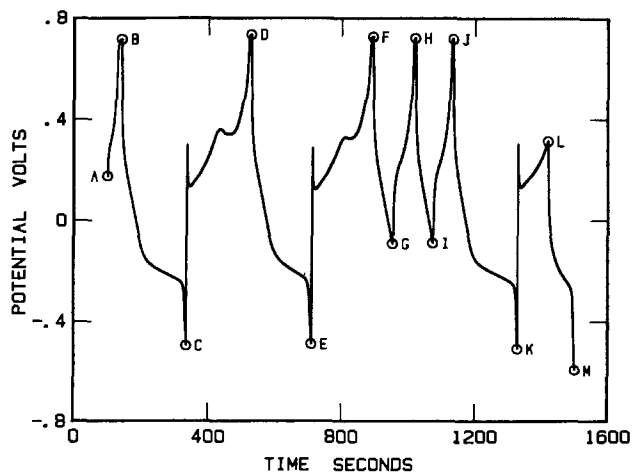


Fig. 2. Galvanostatic cycling of an 80 nm film of PbO_2 at $173 \mu\text{A/cm}^2$ in borate buffer electrolyte.

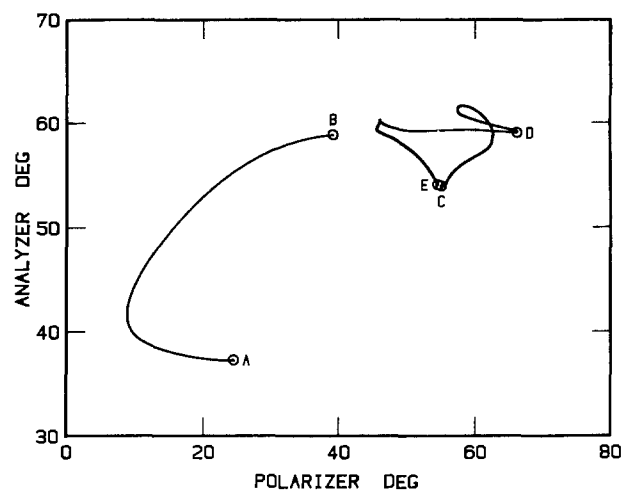


Fig. 3. Optical data on the deposition of an 80 nm film of PbO_2 (A-B) and its subsequent cycling in borate buffer (C-D-E). C-D-E indicates the same cycle in Fig. 3 as it does in Fig. 2.

can be applied. Although quantitative analysis of multiple-cycle experiments of this kind is complicated by a progressive irreversible change in the film, qualitative features change fairly slowly from cycle to cycle, and the advantages of having a complete set of measurements on the same sample outweigh the disadvantages.

Figure 3 shows the optical data obtained during deposition of the film which was subsequently subjected to the cycles shown in Fig. 2. The optical data from the first full anodic-cathodic cycle in Fig. 2, C-D-E, are also shown in the figure, and, although the change in refractive index between the deposition and cycling electrolytes introduces a small offset between the two sets of data, the magnitudes of the optical changes associated with the film growth and film conversion processes can be compared directly. The conversion curve has a complex structure with well-defined inflection points, and the irreversible optical changes which offset the final point E from the initial point C are clearly much smaller than the reversible optical changes which occur during the cycle.

Optical results from a similar experiment on a 274 nm film are shown in Fig. 4 on the same scales as used in Fig. 3. The deposition follows the curve in Fig. 1, and the conversion curve exhibits the same amount of structure as the curve in Fig. 3, and again the irreversible optical changes are small, but the detailed shape of the conversion curve reflects the fact that the film is more than three times as thick as in Fig. 3. Corresponding inflection points can easily be identified in Fig. 3 and Fig. 4, and, since the thickness ratio is known, unique N and K values

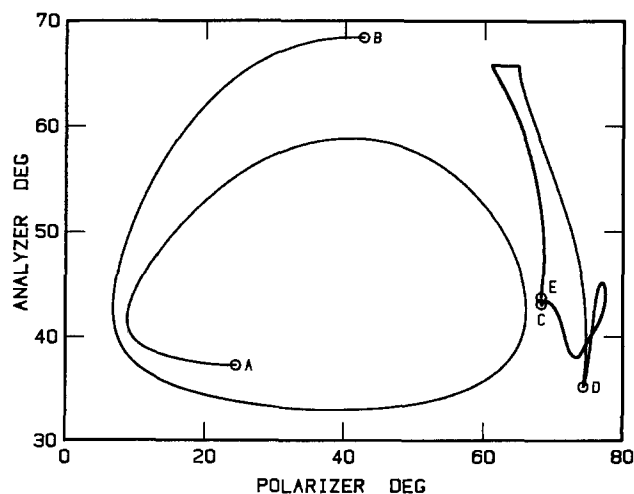


Fig. 4. Optical data on the deposition of a 274 nm film of PbO_2 (A-B) and its subsequent cycling in borate buffer (C-D-E). The cycle has the same end points as the 80 nm film cycle in Fig. 3.

can be calculated if it is assumed that the film is a single homogeneous layer at these points.

The detailed shape of the optical cycle in Fig. 3 and its correlation with the potential-time plot in Fig. 2 are shown in Fig. 5. Point X, at which the deposition was terminated (corrected for the difference in electrolyte index), and point Y, at which the cycling began, are included in the plot of the optical data in the upper portion of the figure. When the circuit is opened to terminate the deposition, optical changes continue in the X-Y direction at a decreasing rate. Although this is the direction of continued film growth, comparison with experiments at other film thicknesses shows that the magnitude of the shift is proportional to the film thickness, and hence the change in the optical properties must be due to a relaxation process of some kind involving the entire film. The curve is similar in slope and curvature to segment G-H of the cycling data in this region, and hence the processes producing the optical change in these regions may be related.

Point A, the initial point of the cycle plotted in Fig. 5, is the point which was identified as C in Fig. 2 and Fig. 3. The potential-time plot exhibits an initial overshoot between A and B when the current is made anodic, then rises progressively toward point C just past the midpoint of the cycle. Beyond C, the potential decreases slightly before rising steadily through D then increasing rapidly to the oxygen evolution potential at E. The cathodic segment of the cycle shows somewhat less structure: the potential falls rapidly at first, then at a steady rate through F and G to a plateau between G and H. The P-A locus in the upper portion of the figure is a complex curve with several sharp inflection points. The time dependence of the optical data is not plotted explicitly, but estimates can be made using the time intervals between corresponding points on the voltage-time plot. (The most notable feature of time dependence is the very rapid shift from E toward F when the current is reversed.)

Optical cycling data are expected to exhibit cusps or sharp inflections at the points where the current is reversed, but cusps at points such as F and G where the voltage-time plot is featureless are quite unexpected. These cusps add a vertex in the X-Y-F-G region to the vertices at A and E to give the P-A plot a triangular structure. The first half of the anodic cycle and the second half of the cathodic cycle both exhibit the optical behavior characteristic of film conversion by a single electrochemical process. One might expect the initial anodic and final cathodic processes to be converses of each other,

but the optical data show that this is not the case here. The second half of the anodic P-A locus traces out a tight loop with no cusp, behavior which we think is characteristic electrochemical processes operating in parallel rather than in sequence, but which we make no attempt to model here. The cusps at F and G divide the cathodic cycle into three segments, but this does not necessarily mean that three different processes are involved. The voltage-time data appear more consistent with two overlapping cathodic processes, one operating between E and G and the other between F and H. In a two-process model, X becomes the vertex toward which the first process is directed, and the locus followed between F and G is the result of superposition. (If the vertex at X can only be reached under deposition conditions, it is not surprising that the film relaxes in the direction of Y when the circuit is opened.)

We can carry out a quantitative optical analysis of the data in Fig. 5 if we make use of the data in Fig. 4 and assume that corresponding points all have the same thickness ratio. If the cusps at F and G result from the overlap of two cathodic processes, the only points likely to be identified with homogeneous films of corresponding compositions are the vertices X, E, and H (or A). The analysis of the deposition data indicates that $N = 2.03$, $K = 0.061$, and $D = 80.68$ nm at X, and analysis of corresponding points gives $N = 2.157$, $K = 0.103$, and $D = 81.97$ nm at E, and $N = 2.051$, $K = 0.033$, and $D = 85.88$ nm at H. Since only two data sets are involved in the analysis, it is difficult to assign error limits to these values, and it is safest to conclude only that at E both N and K are higher, and at H K is lower and D is higher than the corresponding values for the as-deposited film.

Quantitative optical analysis also has something to say about the nature of the film-conversion processes. In regions B-C and G-H, conversion appears to be a homogeneous rather than heterogeneous process, and takes place uniformly throughout the film rather than by working inwards from the electrolyte interface. We have attempted no quantitative modeling between C and E, and between E and F it is more the rate of change than the shape of the locus which requires explanation.

Cycles with restricted anodic and cathodic end points provide information which helps us distinguish between the effects of the various processes. Figure 6 shows a cycle (identified as F-G-H in Fig. 2) in which the anodic current is reapplied at a point which is just past G on the cycle in Fig. 5. At this point, the first cathodic process

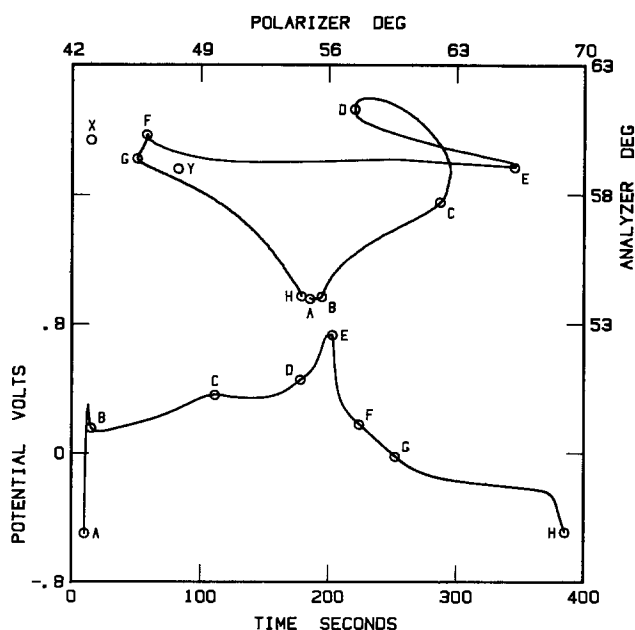


Fig. 5. Correlation of the optical cycling data from Fig. 3 with the corresponding potential-time plot from Fig. 2.

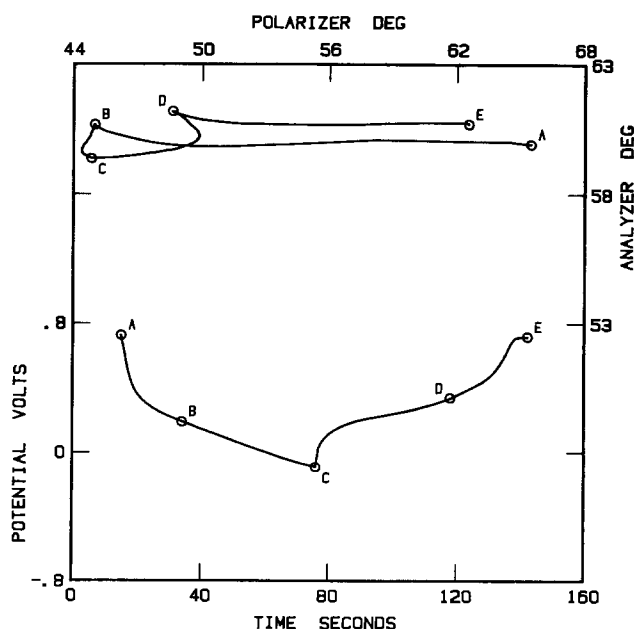


Fig. 6. A cycle with a restricted cathodic end point (cycle F-G-H from Fig. 2).

should be complete, and when the current is made anodic we see first a shift indicating partial reversal of the first cathodic process, then a hook in the optical locus as the second cathodic process begins to reverse, a cusp at D when reversal of the second cathodic process is complete, and finally a continuation of the initial shift when reversal of the first cathodic process is the only process operating. This behavior appears to indicate that the first cathodic process produces optical changes which are proportional to changes in overpotential or electric field and require very little charge transfer. The second cathodic process appears to be a more normal electrochemical process in which changes in the oxidation state of the film are proportional to the charge transferred.

A cycle with a restricted anodic end point is shown in Fig. 7. The cycle is the same one identified as K-L-M in Fig. 2. The displacement between the anodic and cathodic segments of the P-A locus provides a measure of the electrochemical irreversibility of the processes involved. The same quantitative optical analysis which indicated that A-B is characteristic of a homogeneous process shows that if a single process operates along B-C it must be an inhomogeneous process which proceeds inward in from the electrolyte interface.

The cycle in Fig. 7, the final cycle of the sequence plotted in Fig. 2, was followed by two additional cycles with restricted anodic end points, and the second of these, shown in Fig. 8, had its cathodic range extended to demonstrate the effects of film breakdown. Beyond C, the point at which cathodic cycles normally terminate, there is an additional reduction wave which reverses the curvature of the P-A locus, but beyond D the ellipsometer null signal deteriorates rapidly, and the film begins to break up at point E. C was chosen instead of D as the cathodic cycle end point in order to reduce the possibility of accidental damage to the film. The additional charge required to reach D can be estimated from Fig. 8, but it must be remembered that the cycle is the final one in an extended sequence, and the result may not be a very accurate estimate of the corresponding charge for the early cycles.

The oxidation state of lead dioxide films is usually expressed in terms of the value of x in PbO_x , but since the oxygen content of the film does not in fact vary appreciably, it might be better to define x as half of the average valence of the lead in the film. If we assume that the deposited film has $x = 2$, we find that $x = 1.17$ at point D in Fig. 8, and this is the lowest value we can reach without destroying the sample. We can lower the minimum x esti-

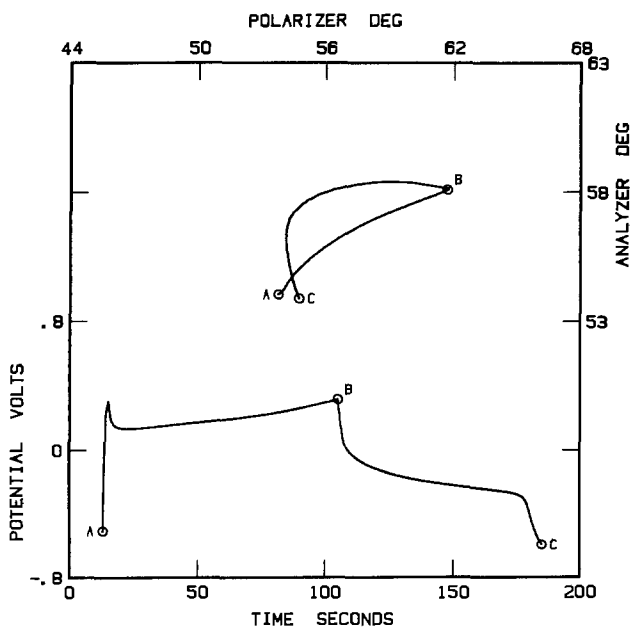


Fig. 7. A cycle with a restricted anodic end point (cycle K-L-M from Fig. 2).

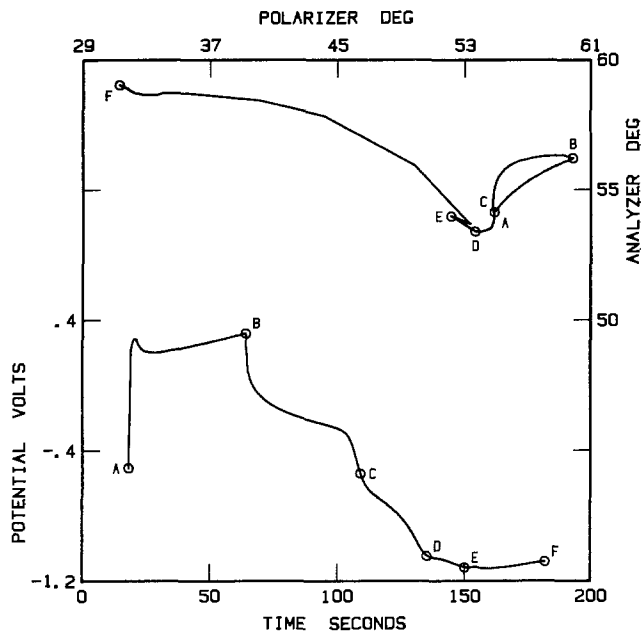


Fig. 8. A cycle with a restricted anodic end point and a cathodic end point beyond the point at which the film begins to break up (point E).

mate to a bit below 1.17 if we compensate for effect of multiple cycling on the data in Fig. 8, but even without this correction we are close to the 1.15 value where Peter (8) attributes irreversible change to nucleation of a film of lead.

We do not think it likely that the as-deposited film actually has an x value of 2. If we estimate the charge required to reach the optical end point on the initial anodic cycle in Fig. 2, and assume $x = 2$ at this point, we conclude that the deposited film has $x = 1.892$, a value which could be achieved with a hydrogen content of 0.216 atoms per PbO_2 unit. This result is in close (though perhaps fortuitous) agreement with the 0.21 hydrogen atoms per PbO_2 unit detected in beta- PbO_2 by incoherent neutron scattering (12). If we assume that the hydrogen content is a measure of the amount of the film deposited by a one electron per molecule process, we calculate the density of the film to be 8.00 g/cm^3 , a value which is somewhat higher than the value we calculated above.

If we assume for the cycle in Fig. 5 that the x value is 2.00 at the anodic end point, then it is 1.35 at the initial point on the anodic cycle, 1.93 at the first cathodic cusp, and 1.83 at the second. The values at the cathodic cusps bracket the value for the deposited film as they must in a model with two overlapping cathodic processes. The presence of hydrogen in the deposited film may explain why the optical effects associated with the two cathodic processes are so very different. If the hydrogen incorporated in the film during deposition takes part in electrochemical oxidation and reduction but is not exchanged with the electrolyte, it may produce relatively large optical effects at low concentrations, and may account for the very rapid optical changes observed during the first cathodic process. The hydrogen which enters the film during the second cathodic process must occupy a different type of site in the structure and migrate back to the electrolyte on the subsequent anodic cycle.

The discussion in the previous paragraph is both speculative and rather far removed from the ellipsometric measurements on which it is based. We are on much firmer ground when we conclude that ellipsometry provides a clear picture of the electrodeposition process and offers promise as a technique for studying the electrochemical conversion of lead dioxide films.

Acknowledgment

This work received partial support from the Natural Sciences and Engineering Research Council Canada under Grant no. A-1151.

Manuscript submitted March 28, 1985; revised manuscript received May 28, 1985.

The University of Waterloo assisted in meeting the publication costs of this article.

REFERENCES

1. J. L. Ord, *This Journal*, **129**, 767 (1982).
2. M. A. Hopper and J. L. Ord, *ibid.*, **120**, 183 (1973).
3. J. L. Ord, *Surf. Sci.*, **56**, 413 (1976).
4. J. L. Ord, *This Journal*, **129**, 335 (1982).
5. D. J. DeSmet, *Electrochim. Acta.*, **21**, 1137 (1976).
6. J. C. Clayton and D. J. DeSmet, *This Journal*, **123**, 174 (1976).
7. L. M. Peter, *Surf. Sci.*, **101**, 162 (1980).
8. L. M. Peter, *J. Electroanal. Chem.*, **144**, 315 (1983).
9. K. D. Naegele and W. J. Plieth, *Electrochim. Acta.*, **25**, 241 (1980).
10. J. L. Ord and Z. Q. Huang, *This Journal*, **132**, 1183 (1985).
11. M. Fleischmann and M. Liler, *Trans. Faraday Soc.*, **54**, 1370 (1958).
12. J. D. Jorgensen, R. Varma, F. J. Rotella, G. Cook, and N. P. Yao, *This Journal*, **129**, 1678 (1982).
13. A. Santoro, P. D'Antonio, and S. M. Caulder, *ibid.*, **130**, 1451 (1983).
14. R. J. Hill, *Mater. Res. Bull.*, **17**, 769 (1982).
15. P. T. Moseley, J. L. Hutchison, C. J. Wright, M. A. M. Bourke, R. I. Hill, and V. S. Rainey, *This Journal*, **130**, 829 (1983).

Behavior of Evaporated Palladium Catalyst for Electroless Nickel-Phosphorus Film Formation

Tetsuya Osaka* and Ichiro Koiwa

Department of Applied Chemistry, School of Science and Engineering, Waseda University, Okubo Shinjuku-ku, Tokyo 160, Japan

Leo G. Svendsen

Raychem Limited, Dorcan, Swindon, Wiltshire, England

ABSTRACT

Vacuum-evaporated palladium was used as catalyst for electroless Ni-P deposition on polyimide and alumina substrates. The effect that varying amounts of Pd had on the early stages of electroless plating was investigated by means of Rutherford backscattering spectrometry and transmission electron microscopy. No significant diffusion of the catalyst into the Ni-P film was observed; in some cases, a small amount of Pd tended to diffuse into the deposited Ni-P film, particularly on polyimide substrates. The deposition rate of the Ni-P film on polyimide was always less than that on alumina. An increased amount of catalyst decreased the deposition rate significantly without altering the stoichiometry of the plated film. When less than 10^{16} Pd at./cm² were evaporated onto the substrate, the catalyst formed clusters of palladium particles on the surface, whereas larger amounts of Pd (e.g., 2×10^{16} at./cm²) settled as a continuous film at the substrate.

The catalyst determines to a great extent the quality of the finished product of electroless plating, owing to both its influence on the adhesion of the plated layer to the substrate, and the way it controls the appearance of the film (*i.e.*, pinhole abundance, film thickness, and crystallite size). Palladium is also an expensive metal, and therefore the consumption of catalyst will be significant for the cost effectiveness of the electroless plating as a whole. The most extensively investigated catalytic systems for electroless plating have been the two-step method with a tin sensitizer and a palladium activator, and the mixed catalyst where Pd and Sn are in the same solution (1-11). The discussion about the catalyst mechanism (1, 2), improvement in sensitizer (3), and the properties of active site (4) has been done by some workers. The combination of UV ray irradiation with the catalyst (5, 6) has also been studied. There have been a few published results on the evaporated Pd catalyst (12) despite its increasing commercial importance. Recently, we have reported some new findings (13, 14) on the behavior of a commercial Pd catalyst evaporated on a polyimide substrate when used with a nickel alloy plating bath. The present communication discusses the results of our continued investigation of the evaporated Pd catalyst on polyimide and alumina.

Experimental

Preparation of catalytic substrates.—Palladium was evaporated by an electron-beam evaporator onto two types of substrates: 96% alpha-alumina ceramics from NGK Spark Plug Company Limited, and 75 μ m thick polyimide from Torey Company Limited. The conditions

were as follows: substrate temperature 25°C, pressure less than 10^{-4} torr, and target 99.99% Pd. The amount of Pd on the substrate was controlled by varying the evaporation time from 20 to 90s. For the TEM studies, evaporation times of 10 and 180s were added. For reference, substrates were prepared by the repeated two-step technique where the sample is first in a Sn sensitizer solution, then in a Pd activator solution, and repeating both dips (13).

Plating.—The prepared catalytic substrates were plated with the same ammoniacal citrate bath as the one called Ni-P(b) in Ref. (13). The bath consists of 0.027 mol/liter NiSO₄, 0.068 mol/liter (NH₄)₂SO₄, and 0.066 mol/liter NaH₂PO₂, at pH 9.0 by NaOH, and plates at 90°C. For each type of catalytic substrate, as listed in Table I, deposition periods of 10, 20, 40, and 100s were adopted. The deposition time of Ni-P film is the real time for deposition and excludes the 1 ~ 2s induction time before plating starts, *i.e.*, when the first hydrogen bubble appears.

RBS analysis.—A very brief introduction to Rutherford backscattering spectroscopic (RBS) analysis is given in Ref. (13). The RBS results were obtained by irradiating each sample with 2.0 MeV ⁴He⁺ ions to a preset beam dose

Table I. Catalysts and substrates investigated by RBS

Catalyst	Pd evaporation time (s)	Substrate used
20Pd	20	Alumina and polyimide
50Pd	50	Alumina and polyimide
90Pd	90	Alumina and polyimide
Sn/Pd	Repeated two step	Polyimide only

*Electrochemical Society Active Member.

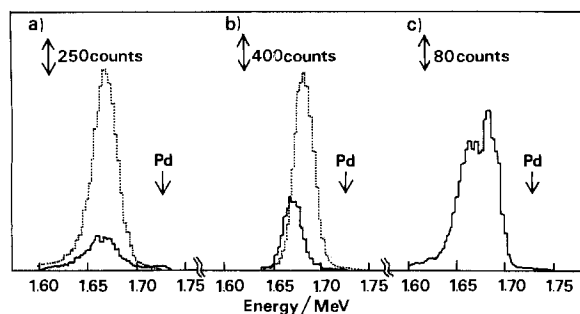


Fig. 1. Sections of RBS spectra showing the relation to the 20Pd, 90Pd, and Sn/Pd catalysts on polyimide and alumina. All samples have been plated 40s with electroless Ni-P prior to investigation. a: Alumina substrate; solid line 20Pd, dotted line 90Pd. b: Polyimide substrate; solid line 20Pd, dotted line 90Pd. c: Polyimide substrate with Sn/Pd catalyst.

and detecting the backscattered alpha particles, using a surface-barrier detector situated at an angle of 161° relative to the incoming beam. The pressure was kept below 5×10^{-7} torr.

TEM observation.—Acetylcellulose, whose surface conditions are very similar to those of polyimide, was used as substrate for the Pd-catalysts investigated by transmission electron microscopy (TEM). After having deposited Pd on acetylcellulose, carbon was evaporated on top at less than 10^{-7} torr. The substrate was then mounted on a TEM mesh after the acetylcellulose removed in a methylacetate solution.

Results and Discussion

Amount and behavior of Pd catalyst.—Figure 1 shows typical RBS spectra of the Pd catalyst on alumina and polyimide. For all the spectra shown, the integral beam dose was $20 \mu\text{C}$, but the maximum yield varies noticeably (different units on the ordinates). All the substrates shown in the figure have been plated for 40s in the Ni-P bath. Without the metal layer on top of the catalyst, the peaks would have been located opposite the respective arrows on the abscissa. In Fig. 1c, the lower energy part of the double peaks stems from Pd and the higher from Sn. In this case, the Pd shoulder would occur where the arrow indicates, and the Sn shoulder would occur at an even higher energy. The following conclusions can immediately be drawn.

1. The peaks from the same evaporating time on alumina and polyimide are always larger and narrower on polyimide (compare the yields in Fig. 1a and 1b).

2. The maxima in Fig. 1a are located at the same energy, but in Fig. 1b the maximum of the smaller peak is situated at lower energy. This finding shows that the Ni-P layers deposited on top of the catalyst both have the same thickness in Fig. 1a, but in Fig. 1b the lesser amount of Pd has a thicker Ni-P layer on top.

Table II. Amount of catalyst on various substrates

Catalyst	Substrate used	Amount of Pd or Pd + Sn measured with RBS ($\times 10^{15}$ at./cm 2)	Converted thickness (\AA)
20Pd	Polyimide	11.1 ± 0.7	16.3 ± 1.0
20Pd	Alumina	6.9 ± 0.6	10.2 ± 0.9
50Pd	Polyimide	21.2 ± 1.3	31.2 ± 2.0
50Pd	Alumina	15.4 ± 1.8	22.7 ± 2.6
90Pd	Polyimide	34.3 ± 2.2	50.4 ± 3.2
90Pd	Alumina	30.3 ± 2.0	44.5 ± 2.9
Sn/Pd	Polyimide	2.6 ± 0.3^a	
Sn/Pd	Alumina	2.6 ± 0.4^a	
Sn/Pd	Carbon	$30.0 \pm 2.2^{a,b}$	
Torey	Polyimide	2.5 ± 0.3^b	

^a Includes both the Sn and Pd signals.

^b Previous data from Ref. (13).

3. In all three cases Fig. 1a, 1b, and 1c, there is a small fraction of the catalyst giving a signal stemming from the surface, especially when using alumina as substrate. In general, the Pd peak is wider and tails off more slowly on the low energy side when originating from alumina substrates.

The results concerning the catalysts are quantified in Table II together with previous data from Ref. (13). In RBS, the thickness of a layer is measured in atoms per square centimeter as in column 2. This, however, can be converted into a more "common" linear thickness by assuming a density for the layer. In obtaining column 3, a tabulated density for Pd was used. The table only states one thickness for each combination of substrate and catalyst because it remains the same within the experimental error, irrespective of the plating period. By comparing the numbers in column 2 one finds the following.

First, within the experimental error the differences in the integral signals on polyimide and alumina are the same when comparing samples that have been evaporated for the same period of time (20, 50, and 90s), with the amount on alumina always being the lower. A highly probable explanation of this is that the rugged surface of the sintered alumina causes a certain proportion of the catalyst to be hidden from detection.

Second, the amount of catalyst is the same on both types of substrate when using the chemical route to place catalyst on polyimide and in alumina. This similarity also holds for the ratio of Sn to Pd.

Third, the amount evaporated or sputtered by Torey onto their polyimide substrates is less than one-fourth of that which we found necessary to render polyimide catalytic (20s evaporating time). Also, the behavior of the commercial Torey catalyst, as described in Ref. (13), can only be described by dissolution of Pd into the Ni-P layer. A similar statement cannot be justified on the basis of the small surface signals found in this investigation, as they might well relate to imperfections in the Ni-P layer.

Effect of evaporated Pd catalyst on deposited Ni-P film.—Two typical RBS spectra are shown in Fig. 2. The top one, 2a, relates to a polyimide substrate, and the bottom one, 2b, to alumina; both spectra are obtained with an integral beam dose of $20 \mu\text{C}$. In both cases, the evaporating time for the Pd catalyst was 20s and the precipitation time for the Ni-P layer 10s. When using alumina substrates, all the peaks (P, Ni, and Pd) are oblique towards lower energies, which suggests plating in the pores of the surface, whereas plating on polyimide forms a flat surface layer. The stoichiometry is readily obtained from such spectra. The results of the present investigation are listed in Table III together with two results from Ref. (14); there is good agreement between the stoichiometries

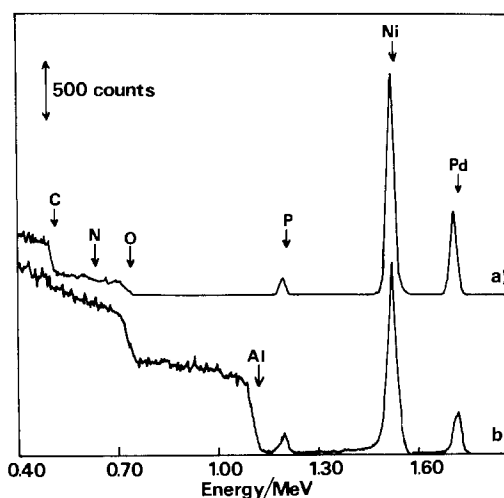


Fig. 2. Complete RBS spectra of 20Pd on alumina (a) and 20Pd on polyimide (b). Both plated 10s with electroless Ni-P prior to investigation.

Table III. Stoichiometry of Ni-P films

Catalyst	Substrate	Ni (a/o)	P (a/o)
20Pd	Polyimide	81.4 ± 1.0	18.6 ± 3.8
50Pd	Polyimide	77.9 ± 3.8	22.0 ± 3.8
90Pd	Polyimide	81.2 ± 1.1	18.8 ± 1.1
Sn/Pd	Polyimide	79.3 ± 0.5	20.7 ± 0.5
Torey	Polyimide	83.7 ± 1.1	16.3 ± 1.1 ^a
20Pd	Alumina	81.5 ± 4.6	18.5 ± 4.6
50Pd	Alumina	77.7 ± 1.9	22.3 ± 1.9
90Pd	Alumina	78.7 ± 1.6	21.3 ± 1.6
Sn/Pd	Alumina	80.1 ± 1.7	19.9 ± 1.7 ^a

^a Previous data from Ref. (14).

Table IV. Deposition rate measured by RBS on the Ni signal

Catalyst	Substrate	Deposition rate (Å/s)
20Pd	Polyimide	12.7
20Pd	Alumina	18.5
50Pd	Polyimide	8.2
50Pd	Alumina	16.3
90Pd	Polyimide	8.3
90Pd	Alumina	17.2
Sn/Pd	Polyimide	12.1
Torey	Polyimide	11.1 ^a

^a Previous data from Ref. (14).

from the two investigations, although the P content seems to be slightly higher in the present one. The same enhancement of the P content observed for the very early stages in Ref. (14) has also been registered in the present investigation. The results in Table III demonstrate finally that the stoichiometry is not affected by the amount of catalyst present.

Behavior of the deposition rate.—Nickel-phosphorus films are found to deposit faster on alumina than on polyimide, in agreement with previous results (14). Table IV summarizes the findings on deposition rate. These show nearly 50% higher deposition rate on alumina than on polyimide for the 20Pd catalyst, and approximately 100% enhancement for 50Pd and 90Pd. The deposition rate on alumina stays almost the same irrespective of the amount of Pd, but on polyimide there is a drastic change, as can be seen in Fig. 3. The results from the Pd/Sn catalytic system are also included and follow about the same slope as does the 20Pd evaporated catalyst; hence, a large amount of evaporated Pd decreases the deposition rate on polyimide.

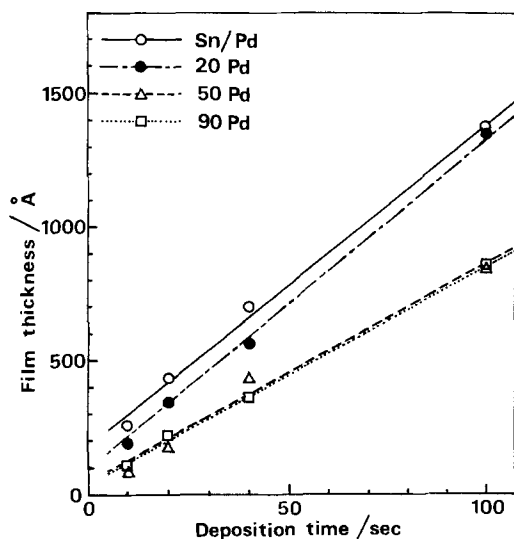


Fig. 3. The relation between type of catalyst and the initial deposition rate of Ni-P on polyimide substrates.

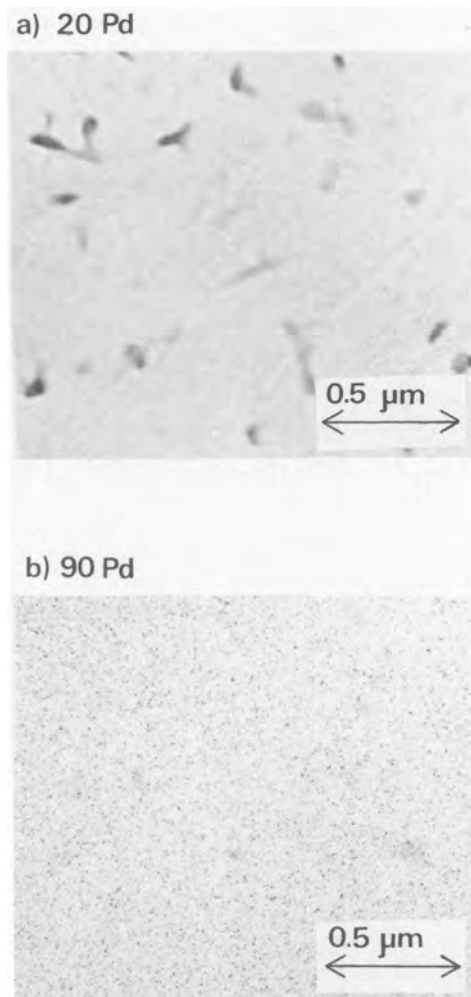


Fig. 4. TEM micrographs of 20Pd and 90Pd on acetylcellulose.

TEM observations of Pd catalyst on acetylcellulose.—A range of acetylcellulose samples with Pd evaporated onto them for 10, 20, 50, 90, and 180s were investigated under TEM. Figure 4 shows typical transmission electron micrographs of 20Pd and 90Pd samples. The surface conditions of acetylcellulose, which is adopted because it dissolves more easily than polyimide, are assumed to be almost identical for the two polymers. The 10Pd and 20Pd samples display nearly the same surface structure of clusters of particles, with a cluster size of 0.1-0.2 μm across. The remaining samples 50Pd, 90Pd, and 180Pd all appear with a continuous Pd layer. This implies that evaporating less than ca. 10¹⁶ at./cm² (from Table II) onto a polymer gives discontinuous islands of particles, but large amounts of evaporated palladium (> 2 × 10¹⁶ at./cm²) form layers of continuous film. The deposition rate of Ni-P film on polyimide correlates with the TEM results, so the Pd catalyst in the form of clusters of particles promotes the deposition rate of electroless Ni-P plating and might also have a tendency to move into the Ni-P film. For the continuous Pd catalyst, both are less pronounced.

Conclusion

The results obtained by combining RBS and TEM techniques show a clear correlation between the catalytic activity of evaporated Pd and its conditions on the surface; a particulate layer of evaporated Pd causes faster electroless plating in the early stages, as does a solid layer. Because of the rugged surface of sintered alumina, a solid layer of Pd will not form as readily on this surface as on a smooth polyimide surface; hence, one must expect the plating rate to remain approximately the same on alumina. This is indeed the case. When the evaporated Pd catalyst is in its particulate state, it is as efficient a catalyst as the Ni-P layer and the dissolution of Pd catalyst

into the bath is not affected by the state of the catalyst, but the results might suggest that a particulate Pd catalyst diffuses more easily into the Ni-P film, especially if one takes the results in Ref. (13) into account.

Manuscript received March 22, 1985.

Waseda University assisted in meeting the publication costs of this article.

REFERENCES

1. B. K. W. Baylis, A. Busuttill, N. E. Hedgecock, and M. Schlesinger, *This Journal*, **123**, 348 (1976).
2. N. Feldstein and J. A. Weiner, *ibid.*, **120**, 475 (1973).
3. N. Feldstein, S. L. Chow, and M. Schlesinger *ibid.*, **120**, 875 (1973).
4. C. H. de Minjer and P. F. J. v. d. Boom, *ibid.*, **120**, 1644 (1977).
5. B. K. W. Baylis, N. E. Hedgecock, M. Schlesinger, and A. van Wijngaarden, *ibid.*, **126**, 1671 (1979).
6. J. J. Kelly and J. K. Vonderling, *ibid.*, **122**, 1103 (1975).
7. J. P. Marton and M. Schlesinger, *ibid.*, **115**, 16 (1968).
8. S. L. Chow, N. E. Hedgecock, M. Schlesinger, and J. Rezek, *ibid.*, **119**, 1614 (1972).
9. R. Sard, *ibid.*, **117**, 864 (1970).
10. R. L. Meek, *ibid.*, **122**, 1177 (1975).
11. R. L. Meek, *ibid.*, **122**, 1478 (1975).
12. J. F. Hamilton and P. C. Logel, *J. Catal.*, **29**, 253 (1973).
13. L. G. Svendsen, T. Osaka, and H. Sawai, *This Journal*, **130**, 2252 (1983).
14. L. G. Svendsen, T. Osaka, I. Koiwa, and H. Sawai, *ibid.*, **130**, 2255 (1983).

Kinetic Investigations of the Primary Step of Electrochemical Coal Oxidation

Gerhard Kreysa* and Wolfgang Kochanek

Dechema-Institute, D-6000, Frankfurt am Main 90, Germany

ABSTRACT

Electrochemical coal oxidation in sulfuric acid has been investigated by a controlled potential coulometric technique. Both kinetic and analytical results indicate that the primary step of electrochemical coal oxidation may be considered as an indirect one in which hydroquinone groups are oxidized to quinone groups by Fe^{3+} , which is present under the experimental conditions because of the dissolution of the pyrite content of the coal.

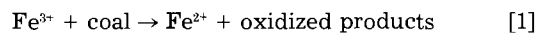
In recent years, there has been a genuine interest in the development of new processes for coal conversion. Several studies from other authors have shown that, in addition to conventional chemical methods, electrochemistry is also of interest in this regard. Presently, three main routes are discussed in the literature: (i) electrochemical coal gasification with formation of hydrogen and carbon dioxide (1-6); (ii) modification of coal structure and its composition by electrochemical oxidation (7-11) or reduction (12-24); and (iii) anodic degradation of the highly condensed coal structure under formation of lower molecular substances, which are able to undergo cathodic hydrogenation (25).

Earlier reports have stated that a coal slurry can be oxidized in the anodic compartment of an electrochemical cell under formation of CO_2 , CO, and humic acids in various yields depending on the electrolyte, electrolysis time, temperature, and electrode material (3, 4, 10, 11).

Figure 1 shows anodic polarization curves obtained with a coal slurry in sulfuric acid (curve 1). If the coal is detached from such a slurry before electrolysis, the pure electrolyte shows the polarization curve 2. Curve 3 is obtained again with an acid coal slurry; however, for this experiment, a coal was used which was carefully washed free of pyrite as long as no iron could be detected in the electrolyte by atomic absorption. A comparison between these curves indicates that the electroactive species is not the coal but the dissolved Fe^{2+} . The same conclusion was drawn by Okada *et al.* (26) and Baldwin *et al.* (27), who carried out similar polarization experiments. However, Baldwin *et al.* found a residual current density ten times higher than that of curve 3 in Fig. 1. This may be due to a small remaining iron content of the coal after the washing procedure. The general role of Fe^{2+} during anodic coal oxidation has also been shown by Coughlin and co-workers (28).

A potentiostatic current time transient with addition of Fe^{3+} obtained by a slurry electrolysis of the native coal is shown in Fig. 2. The amount of 18,500C charge which was consumed during this experiment is much higher than the 680C which would be expected if only all dissolved

iron of the coal would be oxidized. This requires the conclusion that the coal is oxidized in an indirect mechanism with $\text{Fe}^{3+}/\text{Fe}^{2+}$ as a redox mediator. According to this result, anodic coal oxidation in acid media can be described by the following reaction scheme



In this communication, we shall report on our investigations of the kinetics of this reaction. The results published here have been originally presented at CHEMA 1982 (25). However, somewhat later, but independently of our work, Dhooze *et al.* (29, 30) published their investigations about the same topic. They did employ a quite similar experimental technique and also found an indirect electrochemical mechanism of coal slurry oxidation.

Fundamentals of the Experimental Method

Considering a reaction like reaction [1], the conventional kinetic examination would be done by adding coal

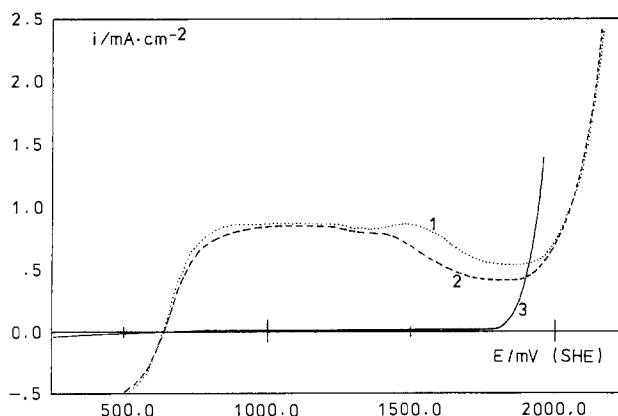


Fig. 1. Anodic polarization curves of coal slurries at a rotating glassy carbon electrode, 500 rpm. Curve 1: 20g native coal in 200 cm^3 1M H_2SO_4 at 20°C. Curve 2: detached electrolyte. Curve 3: 20g coal which was washed free of iron.

*Electrochemical Society Active Member.

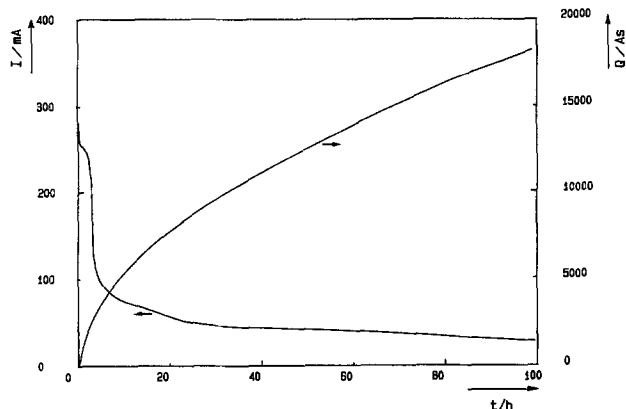


Fig. 2. Potentiostatic current time transient for anodic coal oxidation with addition of Fe^{3+} , 30g native coal and 0.3 mol Fe^{3+} in 300 cm^3 1M H_2SO_4 (β_{CO_2} was found to be less than 3%). Working electrode: expanded metal Ti/Pt with a geometric area of 256 cm^2 , 80°C, $E_{\text{SCE}} = +1250$ mV.

to a solution of Fe^{3+} and registration of the Fe^{3+} concentration with time. If a possible consecutive reaction after the primary step cannot be excluded, such a procedure has the disadvantage that in an early state the observed kinetics will be influenced by the consecutive reaction. This effect may be diminished by starting the reaction with a very small concentration of Fe^{3+} . In the controlled potential coulometry described by Bard *et al.* (31, 32) and also applied by Dhooge (29), the system is started without Fe^{3+} but with a certain amount of Fe^{2+} , which is electrochemically converted to Fe^{3+} with a current density corresponding to the actual concentration of Fe^{2+} .

The theoretical fundamentals of the method are briefly summarized in the following, since there are some modifications and generalizations compared with Bard (31, 32).

This kinetic method, which does not need any conventional analytical determination of concentrations, makes use of the circumstances that for a diffusion-controlled electrochemical reaction the current density contains simultaneously information about the actual concentration and its time derivative too. This may be expressed by the following equations

$$i = kFz_c c \quad [3]$$

$$i = \frac{VzF}{A} \frac{dc}{dt} \quad [4]$$

Considering a stirred tank reactor with a homogeneous concentration, the combination of these equations yields the well-known electrochemical batch reactor differential equation (33)

$$\frac{dc}{dt} = -A_s k c \quad [5]$$

Integration of Eq. [5] with the boundary condition $i_{t=0} = i_0$ results in the expression [4]

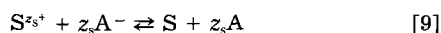
$$i = i_0 \exp(-A_s k t) \quad [6]$$

According to Eq. [6], the current time transient for a diffusion-controlled reaction, *e.g.*, a one-electron oxidation of S



can be described by an exponential function as illustrated in Fig. 3 by curve 1.

Let us now consider a more complex system with a chemical side reaction of S or S^+ with an electron acceptor or donor, respectively



In this system the reaction rate of S is given by

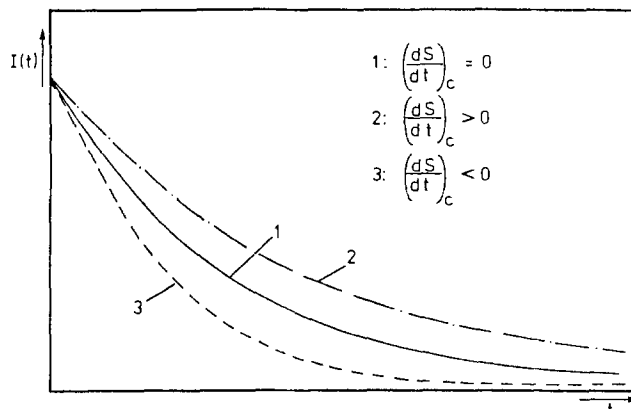


Fig. 3. Principal shapes of the $I(t)$ curves in a system with a parallel chemical side reaction of the electrochemical active species.

$$\left(\frac{dc_s}{dt}\right)_t = \left(\frac{dc_s}{dt}\right)_c + \left(\frac{dc_s}{dt}\right)_e \quad [10]$$

Contrary to Bard's treatment of the controlled potential coulometry, we do not assume $c_A \gg c_{\text{S}^{2+}}$. This seems to be more realistic and means that no steady-state current results. Therefore, the chemical rate constants cannot be derived from steady-state current and another method for evaluation of data is required.

By combining Eq. [3] and [5], the electrochemical term may be written as

$$\left(\frac{dc_s}{dt}\right)_e = -\frac{A_s}{z_s F} i(t) \quad [11]$$

whereas the total change of concentration is given by the time derivative of Eq. [3]

$$\left(\frac{dc_s}{dt}\right)_t = \frac{1}{kFz_s} \cdot \frac{di}{dt} \quad [12]$$

Inserting Eq. [11] and [12] into Eq. [10] and rearranging yields

$$\left(\frac{dc_s}{dt}\right)_c = \frac{1}{kFz_s} \frac{di}{dt} + \frac{A_s}{Fz_s} i(t) \quad [13]$$

This equation allows the determination of the reaction rate of the chemical step by the measurement of the potentiostatic current time transient in a batch reactor. Thereby it is presumed that the only electroactive species is S, and no direct electrochemical conversion of A and A^- occurs. Figure 3 illustrates the three principal shapes of the $i(t)$ curves as they may be obtained with the described system.

In general, for a reaction system consisting of n species, the complete kinetics can be described by n differential equations. This means that the concentration of m species has to be measured if $n - m$ independent balance equations are available. In the case of electrochemical or redox reactions for each elementary species which may occur in different oxidation states, one balance equation can be stated. Additionally, if electrochemical reactions are involved, a further charge balance equation is given; *e.g.*, for the reaction system [8]-[9] the following equations result

for S/S^+ mass balance

$$c_{\text{S}^0} + c_{\text{S}^+0} = c_{\text{S}}(t) + c_{\text{S}^+}(t) \quad [14]$$

for A/A^- mass balance

$$c_{\text{A}^0} + c_{\text{A}^-0} = c_{\text{A}}(t) + c_{\text{A}^-}(t) \quad [15]$$

for charge balance

$$Q(t) = z_s F V (c_{\text{S}^0} - c_{\text{S}}(t)) + z_A F V (c_{\text{A}^0} - c_{\text{A}}(t)) \quad [16]$$

Because four species are present in the reaction system [8]-[9], only the concentration of one species has to be

measured. If S is selected for this purpose, this can be done by recording the current density, which is in accordance to Eq. [3] proportional to the concentration of S.

Experimental

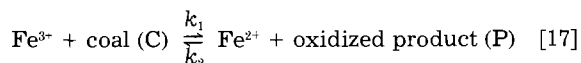
The electrochemical cell shown in Fig. 4 was employed for current time transient measurement under potentiostatic conditions. The anodic potential was kept within the diffusion-limited current density range of the Fe^{2+} -oxidation ($E_{\text{SCE}} = 1250 \text{ mV}$). The anode compartment (190 cm^3) contained a rotating platinum disk electrode (2000 rpm) with an area of 1 cm^2 . The anode compartment was separated from the cathode compartment (15 cm^3) by a ceramic diaphragm to avoid contact between the anolyte and the formed hydrogen.

The cathode was made of a 7 cm long platinum wire 0.25 mm in diameter, and the cell was thermostated by a heating jacket. In order to prevent Fe^{2+} from being oxidized by oxygen, the anode compartment was flushed with nitrogen. A suspension of coal (Westerholt Kohle, Germany; < 500 mesh) in 1M sulfuric acid containing 0.05M FeSO_4 was used as anolyte. The coal was washed free of iron by boiling under reflux in 0.1M sulfuric acid for a fortnight with daily change of the acid until no further iron could be analyzed by atomic absorption. The electrolysis was carried out using a Wenking Model POS 73 potentiostat.

Results and Discussion

Some time transients of the current density, as obtained by this method, from coal slurries and FeSO_4 at various temperatures and coal concentrations are shown in Fig. 5 and 6. The change in the initial current density with variation of the coal concentration can be only caused by a direct electrochemical reaction of the coal particles or by an enhancement of the mass-transfer coefficient of Fe^{2+} oxidation due to the presence of the particles. However, according to the polarization curves shown in Fig. 1, a direct electrochemical reaction of the coal particles can be excluded. The mass-transfer enhancement by the presence of inert particles in the electrolyte is well known (34).

Attempts were made to fit various kinetic models to the experimental data and it was found that the current-time transients can be well described by a reversible second-order reaction as the rate-determining step



Independent of the rate-determining step, in the overall reaction the primary oxidation of coal may be a z electron step. According to Eq. [17], the reaction rate of Fe^{2+} is

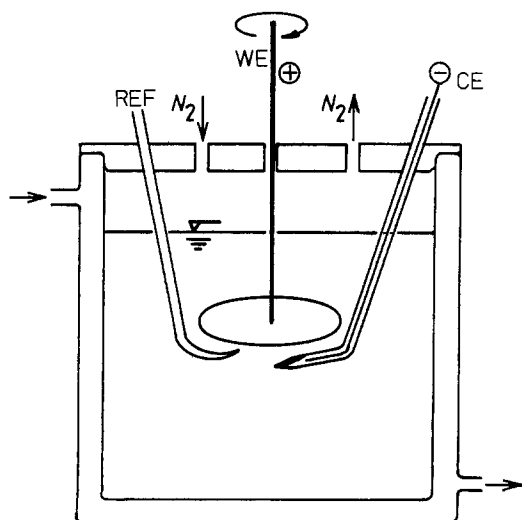


Fig. 4. Scheme of the applied electrochemical cell. REF: Reference electrode. WE: Working electrode. CE: Counterelectrode.

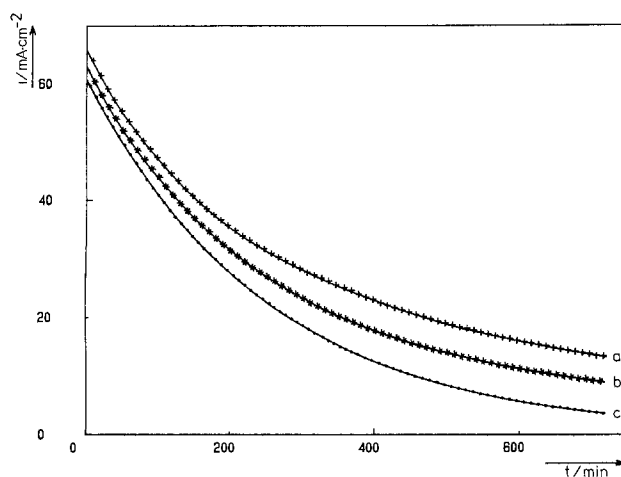


Fig. 5. Current density time curves as obtained by the transient method. a: 10g coal. b: 5g coal. c: No coal. $T = 70^\circ\text{C}$. Crosses, asterisks and dots recorded. Curves: calculated.

given by

$$\frac{dc_{\text{Fe}^{2+}}}{dt} = k_1 c_{\text{Fe}^{3+}} c_C - k_2 c_{\text{Fe}^{2+}} c_P \quad [18]$$

where c_C represents the concentration of the reactive centers at the coal, and c_P those of the oxidized product. The unknown concentrations, c_C and c_P , can be eliminated by making use of Eq. [16]. For the iron system, $z_S = 1$ is valid, whereas z_A is noted as z in the following

$$c_P = -\int_0^t \frac{i(t)A_E}{zVF} dt + (c_{\text{Fe}^{2+}}^0 - c_{\text{Fe}^{2+}}) \frac{1}{z} + c_P^0 \quad [19a]$$

$$c_C = -\int_0^t \frac{i(t)A_E}{zVF} dt + \frac{1}{kF} (i_0 - i(t)) \frac{1}{z} + c_C^0 \quad [19b]$$

With the substitution

$$-\int_0^t \frac{i(t)A_E}{zVF} dt + \frac{1}{kF} (i_0 - i(t)) = U(t) \quad [20]$$

Eq. [19] may be written as

$$c_P = \frac{U(t)}{z} + c_P^0 \quad [21]$$

Rearranging of Eq. [15] and introducing Eq. [21] results in

$$c_C = c_C^0 - \frac{U(t)}{z} \quad [22]$$

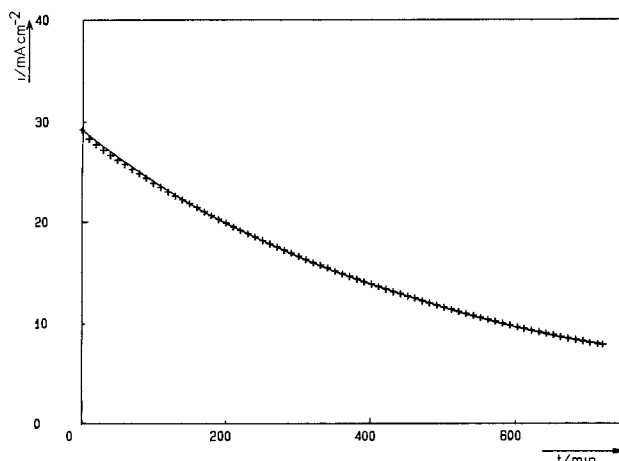


Fig. 6. Current density time curve as obtained by the transient method. 10g coal; 20°C . Crosses: recorded. Curve: calculated.

Table I. Experimentally obtained kinetic parameters of coal oxidation by Fe³⁺

Experimental conditions amount of coal (g)	T (°C)	Concentration of reactive centers at the coal (mmol/liter)	k ₁ [liter(s-mol) ⁻¹]	k ₂ [liter(s-mol) ⁻¹]
5	70	14.8	2.15 × 10 ⁻³	9.57 × 10 ⁻³
10	70	33.7	2.25 × 10 ⁻³	9.52 × 10 ⁻³
10	20	30.0 ^a	2.32 × 10 ⁻⁵	1.74 × 10 ⁻³

^a Fixed value.

In accordance with Eq. [3] and [14], $c_{Fe^{3+}}$ may be substituted by

$$c_{Fe^{3+}} = \frac{1}{kF} (i_0 - i(t)) \quad [23]$$

Introduction of Eq. [21], [22], and [23] into the kinetic rate Eq. [18] and substitution of $c_{Fe^{2+}}$ using Eq. [3] results in

$$\frac{dc_{Fe^{2+}}}{dt} = k_1 c_c^0 \left(\frac{i_0 - i(t)}{kF} \right) - k_1 \left(\frac{i_0 - i(t)}{kF} \right) \frac{U(t)}{z} - k_2 \frac{i(t)U(t)}{kFz} - k_2 c_p^0 \frac{i(t)}{kF} \quad [24]$$

Using Eq. [13] and [24] yields

$$\begin{aligned} \frac{1}{kF} \frac{di}{dt} + \frac{A_s}{F} i(t) &= k_1 c_c^0 \left(\frac{i_0 - i(t)}{kF} \right) - k_1 \left(\frac{i_0 - i(t)}{kF} \right) \frac{U(t)}{z} \\ &\quad - k_2 \frac{i(t)U(t)}{kFz} - k_2 c_p^0 \frac{i(t)}{kF} \end{aligned} \quad [25]$$

The coefficients $k_1 c_c^0$, k_1 , k_2 , and $k_2 c_p^0$ may be determined by a linear regression analysis of the experimental $i(t)$ data as given in Fig. 5 and 6, whereas $U(t)$ is defined by Eq. [20]. The charge number z of the overall oxidation of coal was set to 2 according to the mechanism suggested below. The resulting kinetic parameter values of k_1 , k_2 , and c_c^0 are summarized in Table I. At 20°C, c_c^0 was fixed at the same constant value of 30 mmol/liter as it was found for 70°C for a reasonable mathematical treatment of the experimental data. This was necessary to avoid physically unreasonable results of negative concentrations and rate constants by the fitting procedure and can be justified by the experimental conditions given in Table I. The concentration of the oxidized centers c_p^0 was found to be approximately zero.

In Fig. 7 and 8, experimental reaction rate transients as calculated by Eq. [13] are compared with the result of a

digital simulation of Eq. [18] using the kinetic parameters given in Table I.

A comparison of the simulated and experimental current density time curves in Fig. 5 and 6 shows a satisfying agreement. With the experimental rate constants of Table I, the activation energy of the reactions can be estimated by Arrhenius' law as

$$E_{Ak_1} = 18.1 \text{ kcal/mol}$$

$$E_{Ak_2} = 6.8 \text{ kcal/mol}$$

From the obtained c_c^0 values and the applied coal concentration, the molecular weight per one reactive center at the coal is estimated to be about 1700 g/mol. This value is valid for the applied particle diameter of < 500 μm.

Another experiment assists the assumption of a reversible reaction between Fe³⁺ and coal. If after a certain reaction time a further quantity of Fe²⁺ is added to the reaction system, the observed current density time curve runs below the theoretical batch reactor curve (corresponding to curve 1 in Fig. 3), as shown in Fig. 9. The actual current transient (b) after addition of Fe²⁺ shows the same behavior as curve 3 in Fig. 3. This can be well explained by the mechanism described above. In the beginning, the concentration of the reducible species P is approximately zero. This increases during reaction time. After a renewed addition of Fe²⁺, the back reaction between P and Fe²⁺ will dominate and the current density time curve runs below the theoretical batch reactor curve.

In the coal structure models as proposed by many authors (35, 36), the only group which is able to undergo a reversible redox reaction in the potential range of the Fe³⁺/Fe²⁺ system is the quinone/hydroquinone system. A possible mechanism as suggested by Vetter (37) for this system is shown in Fig. 10. The experimentally observed increase of the corresponding C=O IR bend (≈ 1600 cm⁻¹; 1100-1400 cm⁻¹) and the parallel reduction of the OH IR bend (≈ 3400 cm⁻¹) after electrochemical coal oxidation (28) is in accordance with this mechanism. Furthermore, this mechanism requires a decrease of the H:C ratio during electrolytic oxidation. For an experiment running for a longer period, the elementary analyses of the coal before and after the oxidation by Fe³⁺ are summarized in Table II. Apart from an increase of the O:C ratio

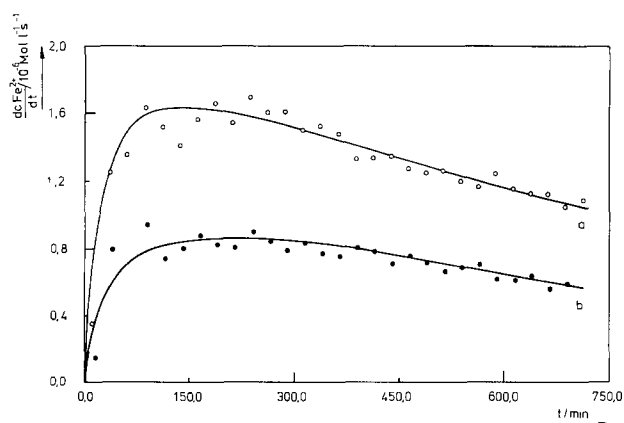


Fig. 7. Experimental (data points) and calculated (curves) time dependencies of the reaction rate. Curve a: 10g coal. Curve b: 5g coal. $T = 70^\circ\text{C}$.

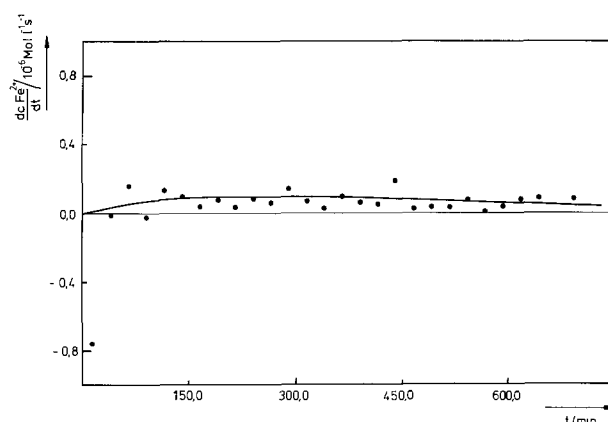


Fig. 8. Experimental (data points) and calculated (curve) time dependency of the reaction rate for 10g coal. $T = 20^\circ\text{C}$.

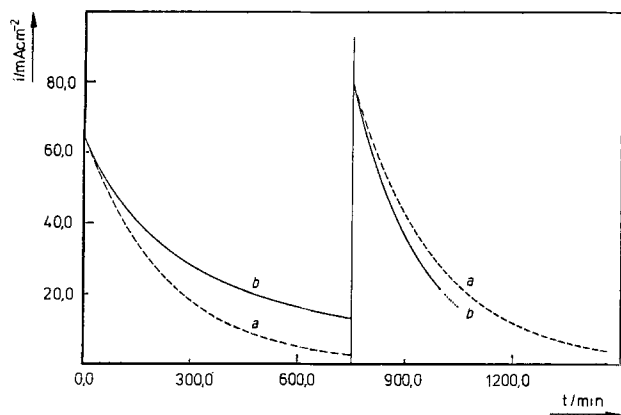


Fig. 9. Current density time curve after further addition of Fe^{2+} at $t = 750\text{s}$. Curve a: no coal. Curve b: 10g coal. 70°C .

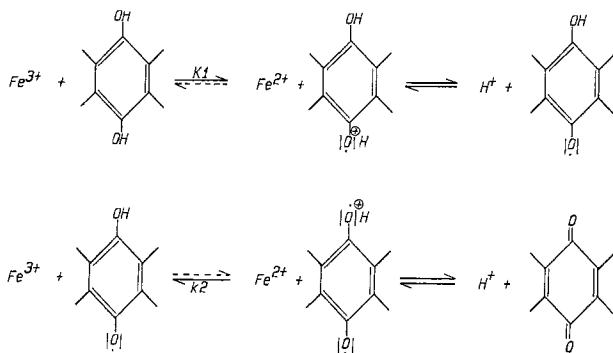


Fig. 10. Possible mechanism for the primary step of anodic coal oxidation.

due to a higher oxidation a decrease of the H:C ratio is observed. The fact that the concentration of the reducible species (quinone) is found to be approximately zero at the beginning of the reaction might be due to the washing procedure. Thereby, pyrite is partially dissolved to Fe^{2+} which can reduce all quinone groups which may be present in the native coal. An increase of the H:C ratio of about 1.7% should be expected for this reaction, if the concentration of such groups is considered to be 1 mol per 1700g of coal (see above). The observed increase given in Table II is in agreement with this value within experimental accuracy. According to the experimental results, electrochemical coal oxidation in acid media follows an indirect mechanism of charge transfer via $\text{Fe}^{2+}/\text{Fe}^{3+}$. It seems that this reaction causes no significant modification of the coal structure. More than 90% of the charge which the coal has consumed during the experiment shown in Fig. 2 may be explained by the oxidation of hydroquinone groups. Of course, also higher and other oxidized products are possible, but only a very small amount of CO_2 is formed.

The indirect mechanism of electrochemical coal oxidation offers the possibility of using other redox systems as mediator in order to get higher oxidized products or a higher reaction rate. Therefore, further experiments have

Table II. Elementary analysis of the coal after anodic oxidation by Fe^{3+}

Sample	C	H	O	N	S
Native coal	100	79.8	9.4	1.3	0.5
Coal after boiling in $1\text{M H}_2\text{SO}_4$ for 25h	100	80.9	8.6	1.7	0.8
Anodic oxidized coal	100	72.2	11.7	1.8	0.5

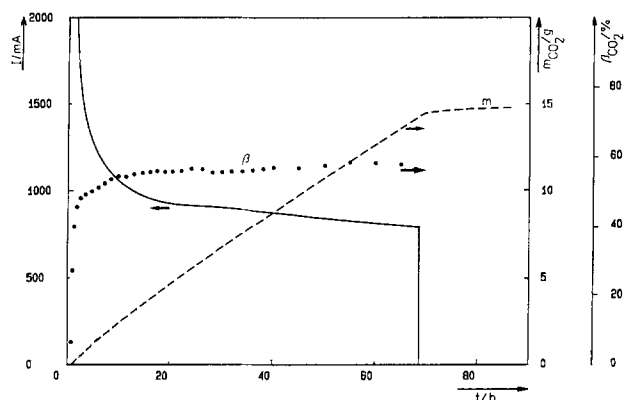


Fig. 11. Potentiostatic current time transient for anodic coal oxidation by Ce^{4+} . 30g coal and 5g $\text{Ce}(\text{SO}_4)_2 \cdot 4\text{H}_2\text{O}$ in 300cm^3 $1\text{M H}_2\text{SO}_4$. $T = 92^\circ\text{C}$. Working electrode: expanded metal Ti/Pt with a geometric area of 256cm^2 ; $E_{\text{SCE}} = +1425\text{mV}$.

been carried out also with the $\text{Ce}^{3+}/\text{Ce}^{4+}$ system, which has been investigated also by others (29, 30). The corresponding current time curve is shown in Fig. 11. In contrast to the experiments with Fe^{3+} , a comparable large amount of CO_2 is formed during electrolysis and the extraction yield in a 1:1 mixture of ethanol:toluol is increased by a factor of 2 compared with the native coal.

Conclusions

It has been shown that as the primary step of electrochemical coal oxidation the oxidation of hydroquinone groups can be considered. This reaction follows an indirect mechanism via Fe^{3+} . This result is supported by a kinetic analysis using a current transient method, results of IR spectroscopy, and elementary analysis. Due to the indirect mechanism, it is obvious that the electrochemical coal conversion is limited by the redox potential of the mediator system. On the other hand, this mechanism offers the possibility of applying other redox systems in order to change the reaction rate or of getting other products. Furthermore, the limitation in space-time yield, which is typical for any suspension electrolysis, may be overcome by a high concentration of the redox mediator system.

Acknowledgments

The authors acknowledge financial support of this work by Bundesministerium für Forschung und Technologie (BMFT) and analytical assistance by Rutgerswerke AG.

Manuscript submitted Nov. 14, 1983; revised manuscript received April 26, 1985.

DECHEMA assisted in meeting the publication costs of this article.

LIST OF SYMBOLS

A	electrode area (cm^2)
A_s	specific electrode area (cm^{-1})
c_j	concentration of the species j (mol-liter^{-1})
c_j^0	concentration of the species j at $t = 0$ (mol-liter^{-1})
$(dc_j/dt)_t$	total reaction rate of S ($\text{mol-liter}^{-1}\text{s}^{-1}$)
$(dc_j/dt)_e$	chemical reaction rate of S ($\text{mol-liter}^{-1}\text{s}^{-1}$)
$(dc_j/dt)_e$	electrochemical reaction rate of S ($\text{mol-liter}^{-1}\text{s}^{-1}$)
F	Faraday's constant (C-mol^{-1})
I	current (mA)
I_0	current at $t = 0$ (mA)
$i, i(t)$	current density (mA-cm^{-2})
i_0	current density at $t = 0$ (mA-cm^{-2})
k	electrochemical mass transfer coefficient (cm-s^{-1})
k_1, k_2	reaction rate constants ($\text{liter-sec}^{-1}\text{mol}^{-1}$)
$Q(t)$	consumed amount of charge (C)
T	temperature ($^\circ\text{C}$)
t	time (s)
V	reactor volume (cm^3)
z	number of electrons, charge number (1)
β_{CO_2}	CO_2 current efficiency assuming a $4e^-$ step (%)
$E_{\text{NHE,SCE}}$	working potential with respect to a reference electrode (mV)

REFERENCES

- G. R. Coughlin and M. Farooque, *Nature*, **279**, 301 (1979).
- M. Farooque and R. W. Coughlin, *Fuel*, **59**, 705 (1979).
- R. W. Coughlin and M. Farooque, *Ind. Eng. Chem., Process Des. Dev.*, **19**, 211 (1980).
- R. W. Coughlin and M. Farooque, *J. Appl. Electrochem.*, **10**, 729 (1980).
- V. A. Vaseen, U.S. Pat. 4,226,683 (1981).
- F. Rallo, Paper presented at the ISE Meeting, Venice, Italy, Sept. 1980.
- A. Bartoli and G. Papisogli, *Ber. Dtsch. Chem. Ges.*, **14**, 2241 (1881).
- A. Bartoli and G. Papisogli, *ibid.*, **15**, 249 (1882).
- A. Bartoli and G. Papisogli, *ibid.*, **16**, 1210 (1883).
- C. F. u. Söhne Beer, D.R.P. 380,387 (1923).
- C. S. Lynch and A. R. Collett, *Fuel*, **11**, 408 (1932).
- G. B. Willifeing, D.P.S. 946,134 (1956).
- P. H. Given and J. M. Schoen, *J. Chem. Soc.*, 2680 (1958).
- P. H. Given and M. O. Peover, *Fuel*, **39**, 463 (1960).
- P. H. Given, M. O. Peover, and J. M. Schoen, *J. Chem. Soc.*, 2674 (1958).
- P. H. Given, *ibid.*, 2684 (1958).
- P. H. Given and M. O. Peover, *Nature*, **184**, 1064 (1959).
- W. Fuchs and O. Veiser, *Erdöl Kohle*, **12**, 223 (1959).
- W. Fuchs and W. Kischio, *ibid.*, **12**, 973 (1959).
- W. Fuchs, I. Schmidt, and O. Veiser, *ibid.*, **12**, 542 (1959).
- H. W. Sternberg and I. Wender, U.S. Bureau of Mines Investigative Report 5943 (1962).
- R. E. Markby, H. W. Sternberg, and I. Wender, *Nature*, **199**, 997 (1963).
- H. W. Sternberg, C. L. Delle Donne, R. E. Markby, and I. Wender, *Fuel*, **45**, 469 (1966).
- H. W. Sternberg, C. L. Delle Donne, R. E. Markby, and I. Wender, *Adv. Chem. Ser.*, **55**, 516 (1966).
- G. Kreysa and W. Kochanek, Paper presented at the International Meeting of Chemical Engineering,ACHEMA 1982, Frankfurt am Main, Germany, June 6-12, 1982.
- G. Okada, V. Guruswamy, and J. O'M. Bockris, *This Journal*, **128**, 2097 (1981).
- R. P. Baldwin, K. F. Jones, J. T. Joseph, and J. L. Wong, *Fuel*, **60**, 739 (1981).
- R. W. Coughlin, S. Lalvani, A. Dorris, and M. Pata, Paper presented at the World Congress of Chemical Engineers, Montreal, 1981; *Fuel*, **62**, 427 (1983); Paper presented at the International Meeting of Chemical Engineering, ACHEMA, Frankfurt, Germany, June 6-12, 1982.
- P. M. Dhooge, D. E. Stilwell, and S.-M. Park, *This Journal*, **129**, 1719 (1982).
- P. M. Dhooge and S.-M. Park, *ibid.*, **130**, 1029 (1983).
- A. J. Bard and K. S. V. Santhanam, *J. Electroanal. Chem.*, **4**, 215 (1970).
- A. J. Bard and L. R. Faulkner, "Electrochemical Methods," Chap. 11, John Wiley and Sons, New York (1980).
- D. J. Pickett, "Electrochemical Reactor Design," Elsevier, Amsterdam (1977).
- G. Kreysa, S. Piontek, and E. Heitz, *J. Appl. Electrochem.*, **5**, 305 (1975).
- P. H. Given, *Fuel*, **39**, 147 (1960).
- H.-G. Franck and A. Knop, "Kohleveredlung," Springer-Verlag, Berlin (1979).
- K. J. Vetter, "Elektrochemische Kinetik," pp. 381 ff., Springer-Verlag, Berlin (1961).

Mo₆Se₆: A New Solid-State Electrode for Secondary Lithium Batteries

J. M. Tarascon

Bell Communications Research, Murray Hill, New Jersey 07974

ABSTRACT

The practical utilization of nonaqueous secondary lithium cells has never been realized, mainly because of electrode problems such as the absence of suitable cathode materials or dendritic regrowth of the lithium on the anode short circuiting the cell. Over the last few years, the cathode problem has been overcome by the discovery of new materials such as TiS₂, NbSe₃, V₆O₁₃, etc. The crystallographic structural feature that makes these compounds attractive for batteries is that they can act as "hosts," incorporating lithium atoms between the layers (TiS₂), chains (NbSe₃), or into the channels (V₆O₁₃) without an irreversible change in crystal structure. However, in spite of intensive research, the anode problem still remains. We have undertaken research in this direction. Initial results of this early work are the subject of this paper. This study reports a new solid-state electrode material (Mo₆Se₆) which can be used both as cathode and anode in secondary lithium cells. Mo₆Se₆ can take up reversibly nine lithium atoms per Mo₆Se₆ without losing its linear chain structure, leading to a theoretical volume energy density of about 1.1 Wh/cm³, compared to 1.2 for TiS₂ cathodes. Another important promising possibility which arises from this work is the use of the lithiated compounds Li₉Mo₆Se₆ as the anode instead of lithium metal in secondary lithium cells.

Over the last decade, the continuous need for high energy storage devices prompted the study of several new types of secondary rechargeable batteries. This work led to the discovery of several promising battery systems based on lithium (1, 2). However, their practical utilization has never been realized, mainly because of electrode problems such as absence of suitable cathode materials or dendritic regrowth of lithium on the anode short circuiting the cell after several cycles.

In recent years, the cathode problem has been overcome by the discovery of new solid-state electrode materials. Among them are the class of early transition metal dichalcogenides such as TiS₂ or VS₂, which, due to their open layered crystal structure, can accommodate lithium reversibly (e.g., lithium can enter into the structure and be removed easily) (3). These intercalation reactions are not limited to layer compounds, but also can occur within three-dimensional structures having large open channels such as in V₆O₁₃ (4) or in the Chevrel phases Mo₆X₈ (5-7). Another class of materials capable of intercalating lithium are the trichalcogenides of Group IVB or VB transition elements such as TiS₃ or NbSe₃. Their structures (8) can be thought of consisting of parallel chains, each only a few

atoms thick and loosely bonded to the chains around it. On discharge, three lithium ions are absorbed between the chains, giving to NbSe₃ one of the highest theoretical volume energy densities (1.6 Wh/cm³) (9-10). However, none of these materials is being used commercially because of the short cycling life of the lithium anode as alluded to above. In spite of an intensive research currently focused on decreasing the reactivity of the lithium anode by alloying it with other metals, the anode problem still remains.

In a recent study (11), we reported the synthesis of a new metastable ternary molybdenum chalcogenide of formula Li₉Mo₆Se₆, whose structure can be thought of as composed of (Mo₃Se₃)₂ chains separated by two rows of lithium atoms. The similarity of this structure to that of NbSe₃ led us to embark on a study of the chemical and electrochemical insertion of lithium into Mo₆Se₆. We found that Mo₆Se₆ is a good cathode material, and we showed that the fully lithiated compound Li₉Mo₆Se₆ can be used as an anode, replacing lithium metal.

Mo₆Se₆ was synthesized at a temperature of 420°C by oxidation of In₂Mo₆Se₆ (prepared by direct reaction of In, Mo, and Se powder in an evacuated silica tube at 1100°C)

under an HCl flow (12). The indium chloride formed during this reaction condensed at the colder part of the tube, leaving behind pure Mo_6Se_6 . The course of the reaction was followed by the weight change. The reaction was complete after 24h. This was confirmed by x-ray fluorescence analysis, which showed no trace of indium in the Mo_6Se_6 after such treatment. Prior to its use in electrochemical cells, the Mo_6Se_6 was baked at 400°C under vacuum to ensure the absence of gas molecules trapped between particles. The Mo_6Se_6 powder is composed of thin needle-like crystals which tend either to aggregate at one point more like a fan or to entangle much like a wool ball as illustrated in Fig. 1.

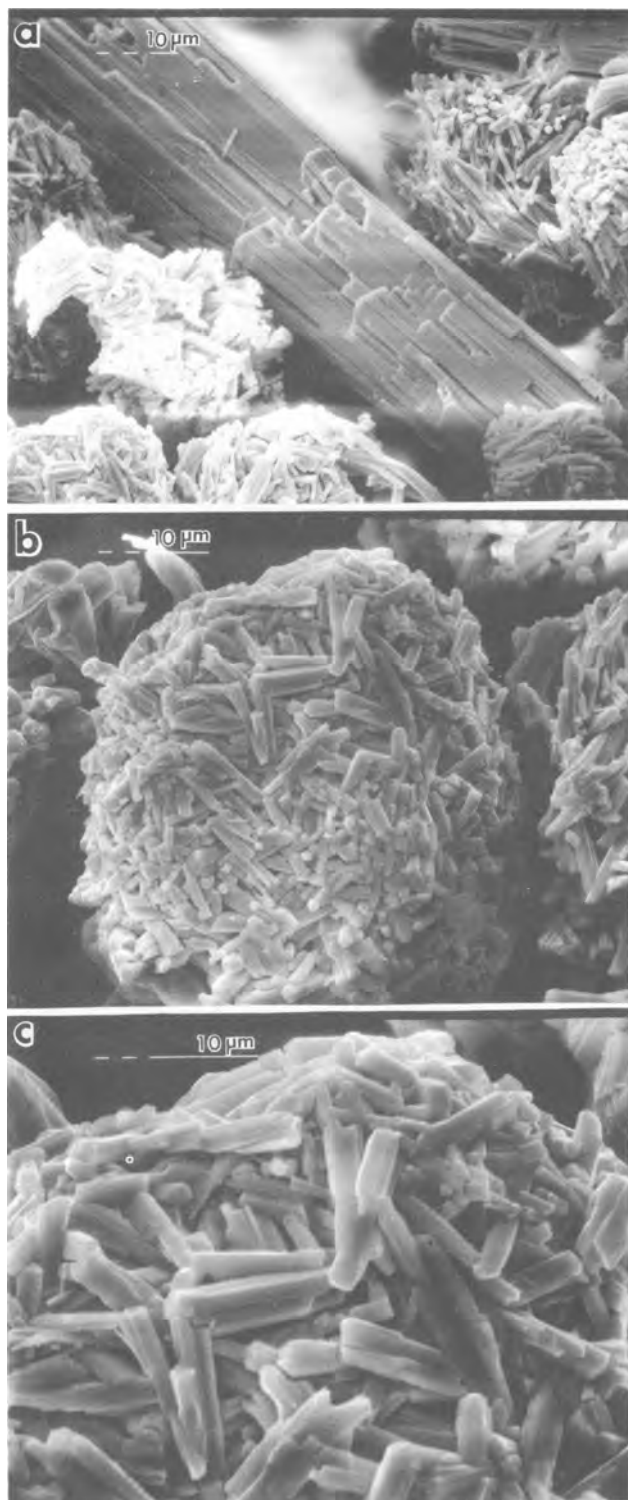


Fig. 1. Scanning electron micrographs of $53\ \mu\text{m}$ sieved Mo_6Se_6 powder prior to being used as the cathode material. a: Fanlike aggregates of Mo_6Se_6 crystals. b and c: Wool ball aggregate of Mo_6Se_6 crystals.

$\text{Li}/\text{Mo}_6\text{Se}_6$ electrochemical swagelock test cells (13) were assembled in a helium atmosphere using a lithium metal disk anode separated from the cathode (Mo_6Se_6) by porous glass paper soaked in $1\text{M LiAsF}_6/2\text{Me THF}$ electrolyte. Propylene carbonate commonly used as solvent in all secondary lithium cells was not used in this work because we previously reported (14) its ability to solvate the lithiated materials $\text{Li}_x\text{Mo}_6\text{Se}_6$.

The cells described above were cycled with a current density of $1.0\ \text{mA}/\text{cm}^2$ and with known amounts of pure Mo_6Se_6 . The preliminary cycling data summarized in Fig. 2 reveal interesting features. The discharge curves (Fig. 2a, 2c, 2d, and 2e) indicate that approximately 2.3, 3.2, 5, and 7 lithium atoms per formula unit are used on discharge to 1, 0.6, 0.49, and 0.4V, respectively. These cells are reversible and retain their capacity over many cycles. A loss of approximately 10% in capacity is observed after the first cycle, then the cells could be recharged to 100% of capacity for several cycles (15, 10, and 2 are the maximum that we have tried down to 1, 0.6, and 0.49V, respectively). Such loss in capacity after the first cycle, frequently observed in secondary lithium cells, is generally due to a small amount of intercalated lithium trapped by defects which still remain in the structure after recharging the battery. The voltage composition curves do not exhibit plateaus, but do exhibit several slopes suggesting the existence of a single phase region over the entire range of composition $0 < x < 7$. However, some caution should be exercised in so interpreting the data since the small change in potential observed in the range $0 < x < 1$ or $2.4 < x < 3.2$ may also be the result of kinetic effects (e.g., too high current densities). Another interesting feature of Fig. 2 is the rapid drop in voltage over a narrow range of composition beyond $x = 1.5$. In some cases, the voltage of a lithium insertion cell is mainly determined by the electronic energy of the charge transferred electrons (e.g., the electronic structure of the host material). A rapid decrease in voltage may then indicate the presence of an energy gap. It is important to note that the position of the voltage drop around $x = 2 \pm 0.3\ \text{Li}^+$ (e.g., 2 ± 0.3 electrons) is strongly correlated to the band structure of these materials established by Hoffman *et al.* (15). Indeed, the authors predict that Mo_6Se_6 with two extra electrons should have a closed-shell electronic structure (e.g., a semiconducting behavior). This point will be discussed in more detail elsewhere. One can also remark that the smooth voltage drop around $x = 3.2$ present in all discharge curves vanishes when the cell is recharged. The origin of such behavior remains a puzzle. Another point is the slight bending in the voltage composition curve, present in the first discharge, which vanishes on subsequent cycles. We found that the amplitude of this anomaly, which changes from sample to sample, is strongly dependent on the preparation temperature of the first $\text{In}_2\text{Mo}_6\text{Se}_6$ and the Mo_6Se_6 prepared from it.

To further probe the reversibility of the $\text{Li}/\text{Mo}_6\text{Se}_6$ system at low potential as suggested above, a cell, after being cycled ten times from 2.7 to 0.6V was discharged to 0.25V and then cycled several times. Figure 3 shows that the cell, recharged from 0.3 to 0.8V (cycle a) discharged without losing its capacity. However, over subsequent cycles between 0.25 and 0.80V one notes a loss in capacity. This behavior may result from side reactions (electrolyte decomposition or reactions with cell containers) which occur quite frequently at these low potentials as previously reported (16).

Based on the electrochemical stoichiometry, the volume energy density of the $\text{Li}/\text{Mo}_6\text{Se}_6$ cell is $1.1\ \text{Wh}/\text{cm}^3$, compared to $1.2\ \text{Wh}/\text{cm}^3$ for the Li/TiS_2 system. This makes Mo_6Se_6 a good candidate for use as a cathode material in secondary lithium cells. Furthermore, the reversibility of these cells down to 0.3V suggests the possibility of using the fully lithiated phase as the anode material instead of lithium metal. The following describes preliminary data obtained with $\text{Li}_x\text{Mo}_6\text{Se}_6/\text{Mo}_6\text{Se}_6$ cells.

Two anode materials $\text{Li}_6\text{Mo}_6\text{Se}_6$ and $\text{Li}_3\text{Mo}_6\text{Se}_6$ prepared chemically and electrochemically, respectively, were in-

vestigated. Figure 4 shows the cycling results collected for the Li₆Mo₆Se₆/Mo₆Se₆ cell, in which twice the amount of cathode than anode material was used. The cell was cycled with a current density 1 mA/cm² between 1.9 and 0.2V. One may note again the reversibility of the intercala-

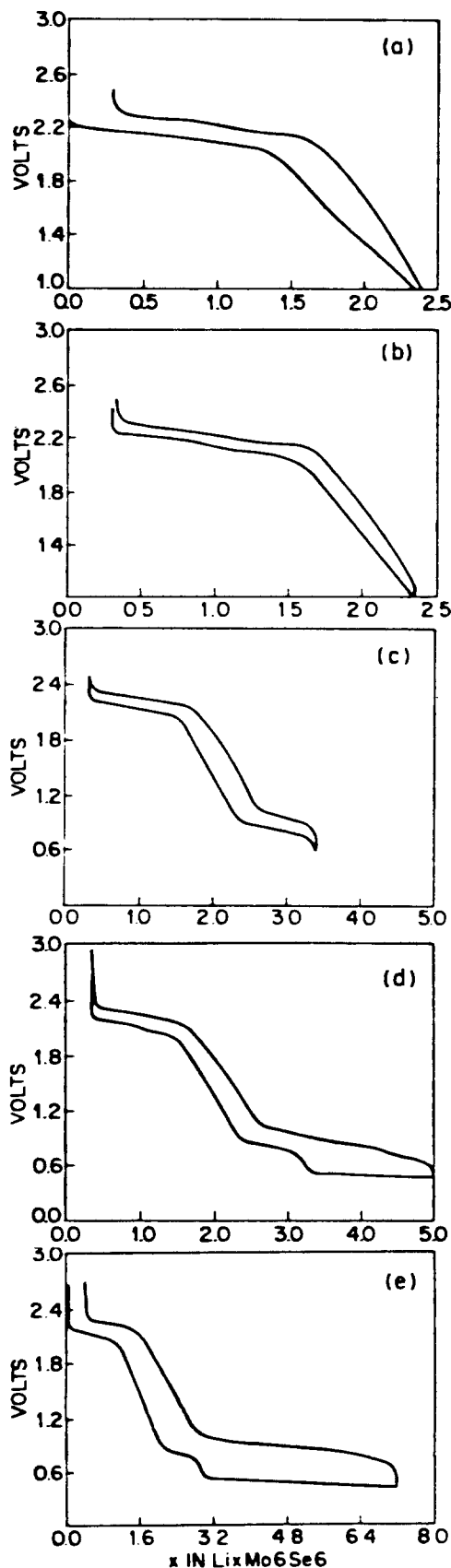


Fig. 2. Cycling data for a Li/Mo₆Se₆ cell at a current density of 1 mA/cm². 66 mg of cathode material was used. a, b, c, d, and e represent the behavior of the cell when cycled down to 1, 1, 0.6, 0.5, and 0.4V, respectively.

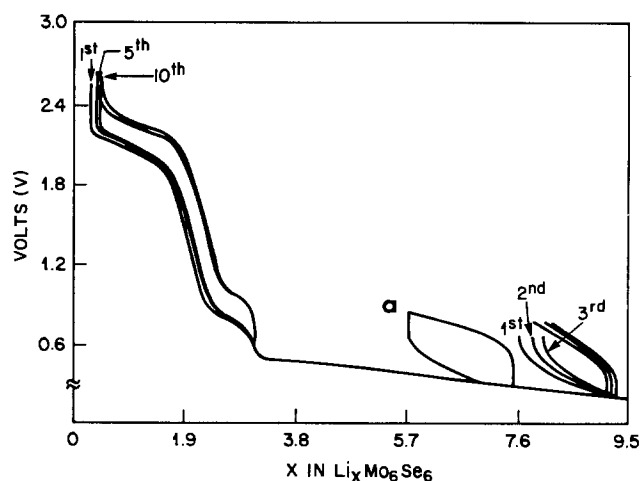


Fig. 3. The ability of an Li/Mo₆Se₆ cell to cycle over a wide range of composition and voltage is illustrated. (The cell contained 32 mg of Mo₆Se₆, and it was charged and discharged at a rate of 1.5 mA/cm².) The cell was cycled ten, one, and three times from 2.7 to 0.6, 0.8, to 0.3, and 0.8 to 0.25V, respectively.

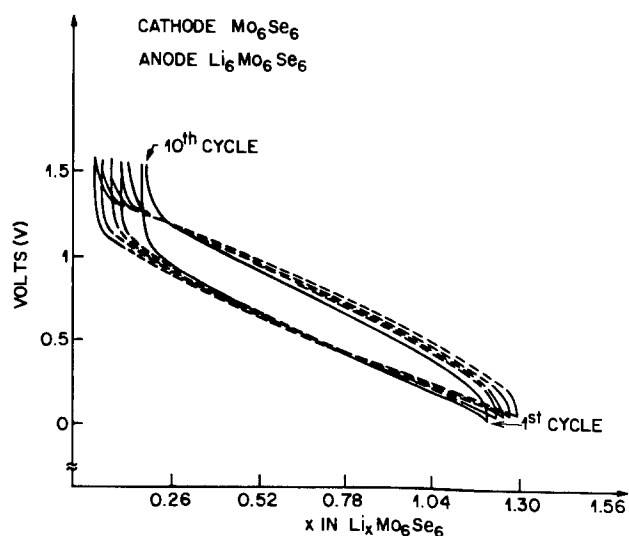


Fig. 4. The electrochemical behavior of a Li₆Mo₆Se₆/Mo₆Se₆ cell. The cell contained 41 mg of Mo₆Se₆ and 20 mg of Li₆Mo₆Se₆, and it was cycled with a current density of 1 mA/cm².

tion reaction in this system as well as the small loss in capacity after several cycles (10% after 10 cycles). However, the capacity is quite low, since with this narrow range of potential (potential limited by the potential of the anode Li_xMo₆Se₆ taken as zero), Mo₆Se₆ can take up only 1.2 lithium.

A larger potential for discharge requires a lithiated phase with a greater lithium content. Li₉Mo₆Se₆ was obtained by discharging a Li/Mo₆Se₆ cell to 0.25V. Then the cell was opened in the dry box and the lithium was replaced by fresh Mo₆Se₆. The resulting Li₉Mo₆Se₆/Mo₆Se₆ cell, containing equal amounts of cathode and anode material after charging and recharging, behaves as reported in Fig. 5. Its capacity is greater than that of the previous cell, since Mo₆Se₆ can now take up reversibly two lithiums on discharge. The reversibility of the above two cells without significant loss in capacity on cycling is quite promising and seems to confirm the possible use of Li_xMo₆Se₆ instead of lithium as anode in secondary lithium cells based on Mo₆Se₆. The loss in capacity alluded to above is less than that measured after ten cycles on identical test cells based on TiS₂ as cathode materials.

Finally, reactions of Mo₆Se₆ with n-BuLi (1.6M in hexane) and lithium in liquid ammonia were used to mimic the discharge curves, and the final material was characterized by x-ray diffraction and atomic absorption analysis to determine the lithium content in the resulting prod-

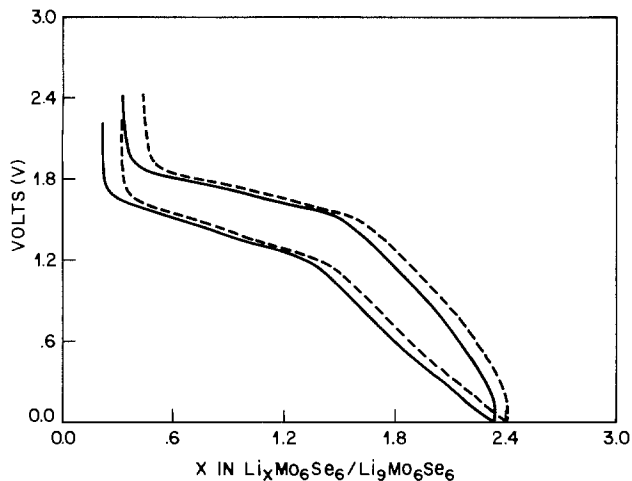


Fig. 5. Typical cycling behavior of a $\text{Li}_x\text{Mo}_6\text{Se}_6/\text{Mo}_6\text{Se}_6$ cell. Current density was 1 mA/cm^2 . 22 mg of $\text{Li}_9\text{Mo}_6\text{Se}_6$ and Mo_6Se_6 was used. The ninth (solid curve) and tenth (dashed curve) cycles are shown.

uct. We found that the lithium content does not deviate too much ($\pm 4\%$) for the nominal composition. Even with a large excess of $n\text{-BuLi}$, Mo_6Se_6 incorporates only 2.5 lithium atoms per Mo_6Se_6 . Based on the electrochemical data, using $n\text{-BuLi}$ as the reducing agent with a reduction potential of 1V , one might expect to intercalate at least 2.3 lithiums. The chemical and electrochemical results agree quite well. The lowest value obtained electrochemically is not unusual and is generally attributed to the fact that during the battery discharge some of the cathode particles are electrically isolated. Then the experimental capacity for lithium insertion is less than that expected from the total mass of the electrode and the known maximum possible lithium content. By using lithium in liquid ammonia, we lower the reduction potential and therefore insert more lithium atoms. So far, we have inserted up to six lithium atoms by this method. Further experiments in progress should confirm a greater intercalation as suggested electrochemically.

The electrochemical data suggest that stoichiometries as high as $9 \text{ Li}/\text{Mo}_6\text{Se}_6$ can be taken up reversibly without any structural change. X-ray powder diffraction patterns of the lithiated compounds were collected at room temperature using $\text{Cu K}\alpha_1$ radiation, in the hope of shedding some light on the intercalation process. Since these compounds are extremely moisture sensitive, they were always handled in a helium atmosphere, and an x-ray holder which can be evacuated was used for obtaining the x-ray data. Figure 6 shows some of these diffraction patterns. The lithiated phases exhibit very weak diffraction peaks as used as few lines. Poor quality x-ray powder patterns are not surprising since they are commonly found in solids formed near ambient temperature even if the compound is crystalline. For Mo_6Se_6 , we believe that the weak diffuse x-ray diffraction pattern results from a high degree of disorder in the structure. In the absence of the ternary element, the $(\text{Mo}_6\text{Se}_6)_x$ chains are loosely bonded (van der Waals-type forces), and, conceivably, they can move with respect to each other. Such disorder would lead to weak diffraction peaks as observed experimentally. On the basis of the hexagonal unit cell, the two stronger lines present in all patterns and situated in the range of $2\theta = 12^\circ$ and $2\theta = 40^\circ$ are the (100) and (002) reflections, respectively. They reflect directly the variation of both hexagonal a_h and c_h lattice parameters. One can note that a_h decreases when In is removed from the structure, from 8.85 to 8.37\AA , then increases when lithium is absorbed between the chains to reach values of 8.82 and 9.90\AA when $x = 2.5$ and 6 , respectively. Simultaneously, the c_h axis decreases from 4.49 to 4.45\AA , and then increases again to 4.47\AA at $x = 6$. The large interchain increase observed between $x = 2.5$ and 6 may suggest that some ammonia molecules remain trapped between the chains after the liquid ammonia reaction. Further work is

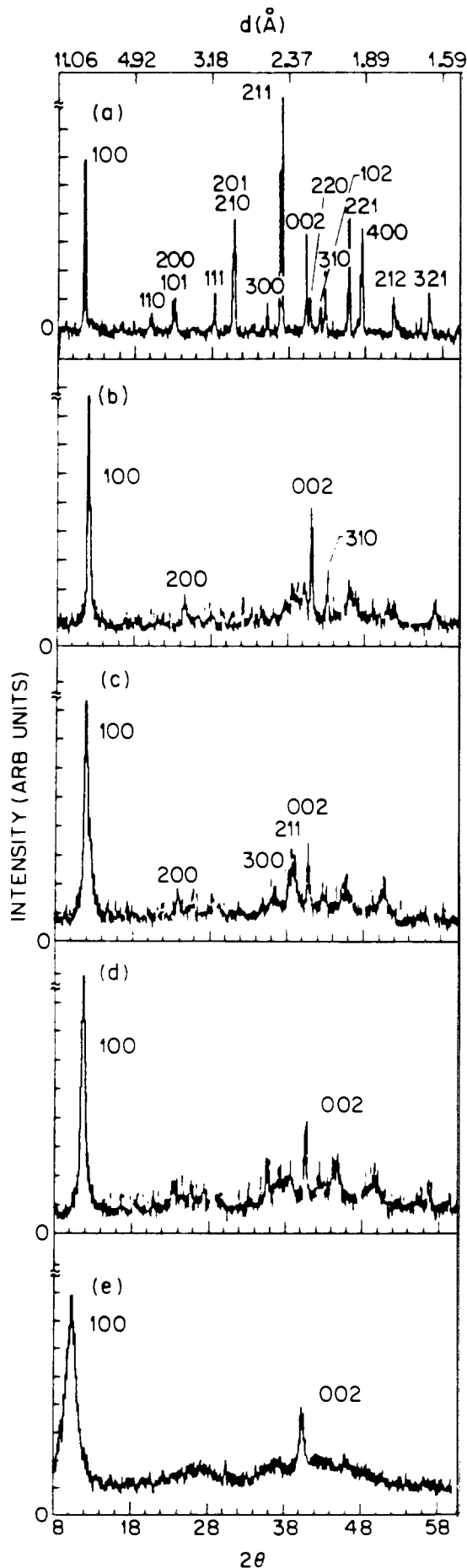


Fig. 6. X-ray powder patterns of $\text{In}_2\text{Mo}_6\text{Se}_6$ (a), Mo_6Se_6 (b), and of the lithiated phases $\text{Li}_x\text{Mo}_6\text{Se}_6$ (c-e), with x approximately equal to 1.5, 2.5, and 6, respectively. The 2θ angles are given at the bottom; d-spacings at the top.

presently directed to check this possibility. It is interesting to note that the x-ray diffraction pattern of the cathode of a Li/Mo₆Se₆ cell after being discharged to 0.3V and recharged to 2.7V is identical to that of the starting material Mo₆Se₆. Based on the above findings, although very weak, the x-ray diffraction patterns clearly indicate that Mo₆Se₆ reacts reversibly with lithium without any major structural change (e.g., the basic chain structure is maintained on lithiation). The great ability of linear chain compounds to undergo topochemical reactions with lithium, as previously shown for NbSe₃ (10) and more recently for transition metal pentachalcogenides of formula MX₅ (17), is again confirmed with Mo₆Se₆. Preliminary electrochemical experiments with Mo₆Te₆ indicate a behavior very similar to that of Mo₆Se₆.

In summary, this study reports a new solid-state electrode material (Mo₆Se₆) which can be used both as cathode and anode in secondary lithium cells. Mo₆Se₆ can take up reversibly nine lithium atoms, without losing its linear chain structure, leading to a theoretical volume energy density of about 1.1 Wh/cm³ compared to 1.2 for TiS₂ cathodes. This research also indicates another important promising possibility, namely, the use of the lithiated compounds Li₉Mo₆Se₆ as anodes instead of lithium metal in secondary lithium cells.

Acknowledgment

I would like to thank many of my colleagues for fruitful collaborations and more specially D. W. Murphy for valuable discussions and for the use of his cell cycling setup.

Manuscript submitted Feb. 20, 1985; revised manuscript received May 10, 1985.

Bell Communications Research assisted in meeting the publication costs of this article.

REFERENCES

1. J. Broadhead, in "Power Sources 4," D. H. Collins, Editor, pp. 469-481, Oriel, London (1973).
2. M. S. Whittingham, *Science*, **192**, 1126 (1976).
3. M. S. Whittingham, *Prog. Solid State Chem.*, **12**, 41 (1978).
4. D. W. Murphy, P. A. Christian, F. J. DiSalvo, and J. N. Carrides, *This Journal*, **126**, 437 (1979).
5. R. Schöllhorn, M. Kumpers, and J. O. Besenhard, *Mater. Res. Bull.*, **12**, 781 (1977).
6. J. M. Tarascon, F. J. DiSalvo, D. W. Murphy, G. W. Hull, E. A. Rietman, and J. V. Waszczak, *J. Solid State Chem.*, **54**, 204 (1984).
7. S. T. Coleman, W. R. McKinnon, and J. R. Dahn, *Phys. Rev. B*, **29**, 4147 (1984).
8. A. Meerschaut and J. Rouxel, *J. Less Common Metals*, **39**, 197 (1975).
9. R. R. Chianelli and M. B. Dines, *Inorg. Chem.*, **14**, 2417 (1975).
10. D. W. Murphy and F. A. Trumbore, *This Journal*, **123**, 960 (1976).
11. J. M. Tarascon, G. W. Hull, and F. J. DiSalvo, *Mater. Res. Bull.*, **19**, 915 (1984).
12. R. Chevrel and M. Sergent, in "Superconductivity in Ternary Compounds I," O. Fisher and M. B. Maple, Editors, p. 25, Springer-Verlag, Berlin (1982).
13. J. A. Meyer, F. J. DiSalvo, and J. J. Auburn, Unpublished work.
14. J. M. Tarascon, F. J. DiSalvo, C. H. Chen, P. J. Carroll, M. Walsh, and L. Rupp, *J. Solid State Chem.* To be published.
15. T. Hughbanks and R. Hoffman, *Inorgan. Chem.*, **21**, (1982).
16. A. J. Bard and L. R. Faulkner, "Electrochemical Methods," John Wiley & Sons, New York (1980).
17. S. Okada, H. Ohtsuka, and T. Okada, *This Journal*, **131**, 11 (1984).

Kinetics of Electrochemical Doping and Undoping of Polyacetylene

Fritz G. Will*

General Electric Company, Corporate Research and Development, Schenectady, New York, 12301

ABSTRACT

The kinetics of anodic doping and cathodic undoping of p-type doped polyacetylene electrodes is studied in organic solutions of LiBF₄ in sulfolane. The galvanostatic pulse technique is employed to obtain potential-time transients at various currents, from which the double layer capacitance and the kinetic parameters are determined. The observed capacitance shows that only the exterior surface of the microporous polyacetylene films is wetted with electrolyte. Polyacetylene is found to have rather slow kinetics, with the solid-state diffusion of the p-dopant, BF₄⁻, into and out of the polyacetylene structure controlling the rate. The rate of dopant transfer across the electrode-electrolyte interface is comparable to that of one-electron redox reactions on metals in aqueous solutions. The transfer coefficient shows considerable asymmetry of the energy barrier to charge transfer at the interface, favoring the anodic doping while impeding the cathodic undoping.

Polyacetylene is the simplest linear conjugated polymer. The first synthesis was mentioned as early as 1958 (1), but the preparation of well-characterized films was only reported in 1974 (2). Much of the intense interest in polyacetylene was stimulated by the finding that the polymer can be doped with electron donors and acceptors (3) with a concurrent rise in the room temperature conductivity of up to 12 orders of magnitude (4-6). It has been demonstrated that doping can be achieved electrochemically and reversibly (7). This opens the interesting possibility of employing polyacetylene as electrodes in rechargeable batteries (8).

Charge and discharge curves of various types of cells with at least one polyacetylene electrode (8-10) and cyclic voltammograms of polyacetylene electrodes (11) have been published. Other studies have been concerned with determining the diffusion coefficients of the p-dopants I (12-15), ClO₄⁻ (16), and BF₄⁻ (17), as well as that of the n-dopant Li (16, 18, 19) in polyacetylene. However, values reported by different authors vary by more than nine or-

ders of magnitude. Such large discrepancies appear to result from the fact that the degree of wetting of the microporous fibrillar structure of polyacetylene and, hence, the surface area active for diffusion, was unknown (17). Regarding the kinetics of the charge transfer process at the interface polyacetylene/electrolyte, this issue has apparently not been addressed in the past. Yet, a knowledge of the electrode kinetics is necessary to evaluate the inherent rate capability of polyacetylene and to provide guidance in improving the physical properties of polyacetylene electrodes with respect to improved performance in electrochemical cells and batteries.

The following study determines the rate of the charge transfer reaction at the polymer electrode/organic electrolyte interface and the diffusion coefficient of the p-dopant BF₄⁻ in polyacetylene. The wetted surface area is determined from the measured double layer capacitance; problems arising from the diffusion of dopant in the micropores between fibers (interfibrillar diffusion) are avoided by essentially eliminating electrolyte penetration of the polyacetylene interior.

* Electrochemical Society Active Member.

Experimental

Polyacetylene film had been prepared by the Rohm and Haas Company using the standard Shirakawa technique (2) at -78°C . Details regarding the synthesis conditions have been published elsewhere (20). Elemental analysis yielded 90.54% C, 7.35% H, and 1.69% O. The film had a thickness of 8.9×10^{-3} cm or 89 μm , a surface area of 40 m^2/g , and an apparent density of 0.56 g/cm^3 , as calculated from the weight and dimensions of the film. This constitutes 48% of the theoretical density of polyacetylene, as determined by x-ray diffraction measurements on *cis* polyacetylene films (21). The discrepancy is due to the known fibrillar morphology (2, 22) of polyacetylene, which results in micropores of several hundred angstroms dimensions between individual fibers. Fiber diameters are in the range from 200 to 400 \AA . Film characterization by infrared spectroscopy (20) showed the films to consist initially overwhelmingly of the *cis* isomer.

Electrodes were prepared from circular films of 1.6 cm diam (2 cm^2 area) by sputtering of an Au film of 1000 \AA thickness on the back side. Electrode contact was made by pressing a coiled Au wire against the Au film.

As air exposure at room temperature for even short periods of time has been shown to lead to oxidative degradation of polyacetylene (23-26), air exposure during polymer synthesis and subsequent handling was minimized. Samples, once prepared, were stored in dry Ar or under vacuum. Transfer into the sputtering apparatus required air exposure for a few minutes. Cell assembly and all subsequent measurements were carried out in a high quality Ar-filled dry box.

Measurements were performed at room temperature ($\sim 20^{\circ}\text{C}$) in a rectangular Teflon[®] polymer cell employing a Li counter- and a Li reference electrode. The latter was spaced from the polyacetylene electrode at a distance of approximately 3 mm. A schematic diagram of the cell is shown in Fig. 1. The electrolyte was a 30% by weight solution of LiBF_4 in sulfolane. This electrolyte has very high viscosity. Solute and solvent had been carefully purified by recrystallization and double distillation.

The galvanostatic pulse technique was employed to determine the electrode kinetics. Constant current pulses were generated with a Princeton Applied Research (PAR) Model 175 universal programmer and applied to the cell with a PAR Model 173 galvanostat/potentiostat. The pulses had a risetime of 1 μs . Potential-time transients were recorded and stored on a Nicolet Model 206 oscilloscope and, with suitable expansion of the time and voltage scales, reproduced on a Hewlett-Packard Model 7046A X-Y recorder. Pulse widths were varied from 100 μs to 100s and currents from 0.1 to 5 mA. Before applying cathodic (discharge) pulses, the electrode was doped

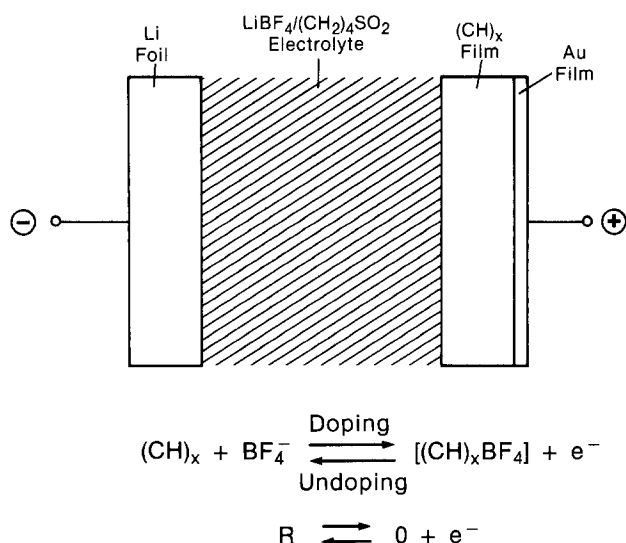


Fig. 1. Cell schematic with reaction scheme

anodically with 7 mole percent (m/o) BF_4 . Redoping was performed occasionally between discharge pulses to maintain the doping level at approximately 7 m/o. The doping level was maintained between 4 and 6 m/o during anodic (charge) pulse measurements.

Results

The overall reaction occurring during the electrochemical doping (anodic oxidation or charging) and undoping (cathodic reduction or discharging) of polyacetylene with an electron acceptor, such as BF_4 , is shown in Fig. 1.

Cathodic potential-time transients, resulting from the application of cathodic current pulses of 100 ms width and -0.1 to -3 mA amplitude, are presented in Fig. 2. The horizontal time axis is expanded by a factor of 32; and only the first 6 ms of the transients are displayed. The potentials on the ordinate are the deviations of the electrode potential E , under current flow, from its open-circuit value E_0 (both measured against the Li reference electrode) and include the ohmic voltage drop in the electrolyte between test and Li reference electrodes; E_0 for 7 m/o doping with BF_4 is approximately 3.8V. The transients exhibit a very fast initial rise followed by a gradual increase in cathodic potential with time. Application of pulses with widths of only 100 μs showed the initial rise to be of the order of microseconds and to be controlled by the risetime of the oscilloscope.

In order to evaluate the kinetics of slower steps in the electrode reaction, cathodic current pulses of 100s width were applied. Figure 3 shows the resulting cathodic potential transients over the entire pulse duration of 100s. To accommodate the transients from -0.1 to -4 mA on a single graph, the potential scale was changed from 20 mV/cm for the lower currents to 160 mV/cm for the highest currents. After the initial instantaneous potential rise, the transients exhibit steadily increasing potential over the entire time span of 100s. In fact, in longer-term experiments it was found that the potentials do not stabilize even in the course of many hours. With increasing cathodic current, the rate of potential change increases. With the exception of the -4 mA curve, all transients have concave curvature throughout the 100s observation time.

Anodic current pulses of 100 ms duration or shorter lead to anodic potential transients which are a mirror image of the cathodic transients shown in Fig. 2. Anodic transients for 100s pulse width and amplitudes from 0.1 to 5 mA are presented in Fig. 4a and 4b. While the character of cathodic and anodic transients is generally the same, closer examination reveals that the anodic transients result in smaller potential changes $E - E_0$ for identical currents. This is particularly evident for currents of 3 mA and larger. It is also noted that the anodic transients at 4 and 5 mA do not exhibit a change in curvature. In agreement with the observations made with cathodic polariza-

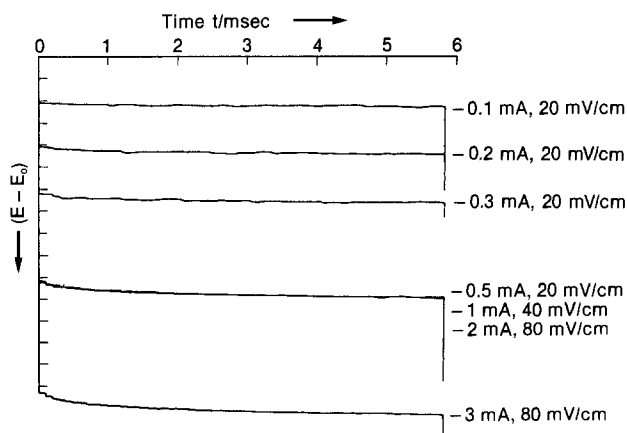


Fig. 2. Potential-time transients following cathodic current pulses (undoping) of 100 ms duration; dopant level 7 m/o.

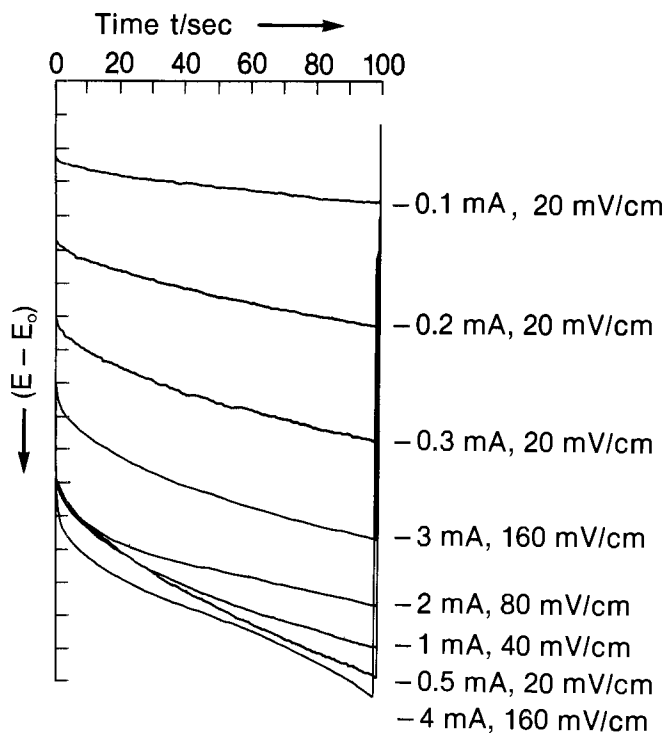


Fig. 3. Potential-time transients following cathodic current pulses (undoping) of 100s duration; dopant level 6-7 m/o.

tion, the anodic potentials continued to rise indefinitely after applying a current pulse.

Discussion

Mathematical analysis.—The potential-time transients observed in this study have the typical shape shown schematically in Fig. 5. Such transients are observed in cases of electrode reactions involving an initial ohmic voltage drop followed by charging of the double layer capacitance and simultaneous slow rate of charge transfer and diffusion.

The mathematical equations describing this case were solved by Berzins and Delahay (27) for a reaction

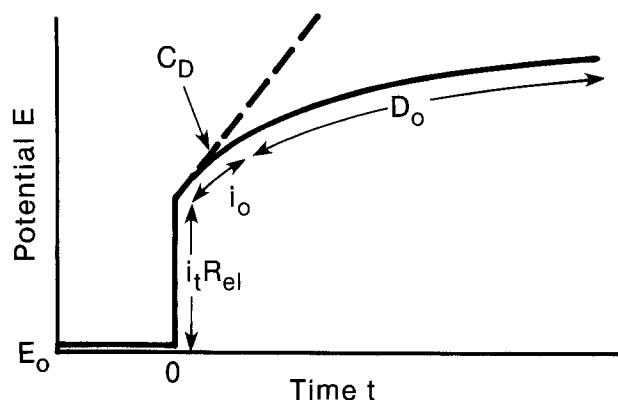


Fig. 5. Schematic of potential-time transients, showing predominant influence of ohmic voltage drop, double layer capacitance C_D , exchange current density i_0 , and diffusion coefficient D_0 .

involving a single rate-determining electron exchange of the type



The doping and undoping of polyacetylene involving the oxidation and reduction of the monovalent anions BF_4^- , AsF_6^- , and ClO_4^- are of that type. The assumptions applicable to that mathematical analysis are (i) electron transfer at the polymer/electrolyte interface across an energy barrier and (ii) the use of planar electrodes with homogeneous bulk properties in unstirred solution with diffusion as the sole mode of mass transfer. Hence, the analysis pertains to the case of semi-infinite linear diffusion. These assumptions are tantamount to nonwetting of the interfibrillar micropores with electrolyte. It will be shown that this assumption applies well to the present case of a very high viscosity electrolyte.

Only the boundary conditions and the final mathematical solution of the analysis will be presented here; for more detail, the reader is referred to the original paper (27).

At any given time, the total current density (i_t) is the sum of the faradaic (i_f) and the capacitive component (i_c)

$$i_t = i_f + i_c \quad [2]$$

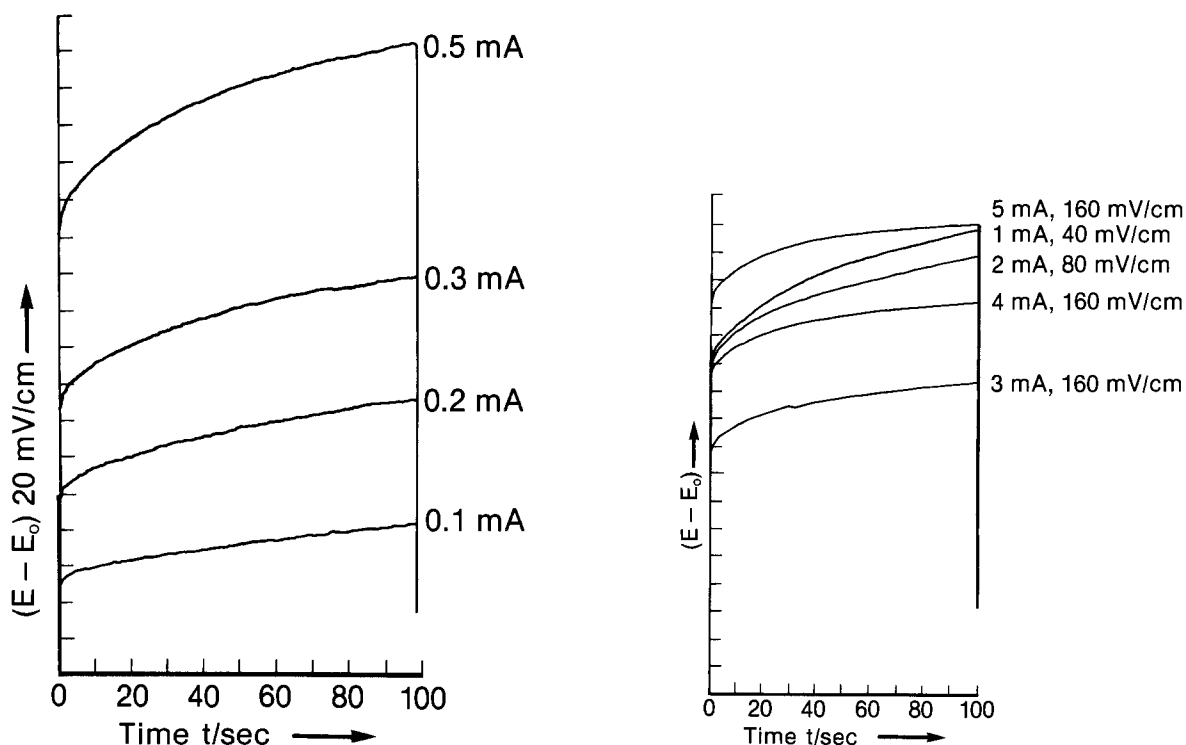


Fig. 4. Potential-time transients following anodic current pulses (doping with BF_4) of 100s duration; dopant level 4-6 m/o

The faradaic current density is given by

$$i_F = i_0 \left[\frac{c_0}{{}_0c_0} \exp(\alpha n F \eta / RT) - \frac{c_R}{{}_0c_R} \exp(-(1 - \alpha) n F \eta / RT) \right] \quad [3]$$

and the capacitive current density by

$$i_c = (C_D/A) d\eta/dt \quad [4]$$

In these equations, c_0 and ${}_0c_0$ are the concentrations of the oxidized species (BF_4 in the polymer) at the electrode surface and in the bulk polymer respectively, c_R and ${}_0c_R$ are the corresponding concentrations of the reduced species (BF_4^- in the electrolyte), α is the transfer coefficient, n the number of electrons exchanged, F the Faraday constant, η the overvoltage ($E - E_0$, with ohmic electrolyte loss subtracted out), R the gas constant, T the absolute temperature, and i_0 the exchange current density. The latter is given by

$$i_0 = n F k_0 c_0^\alpha c_R^{(1-\alpha)} \quad [5]$$

where k is the concentration-independent rate constant. The time dependence of the concentrations is given by Fick's law of diffusion

$$\delta c_0 / \delta t = -D_0 \delta^2 c_0 / \delta x^2 \quad [6a]$$

$$\delta c_R / \delta t = -D_R \delta^2 c_R / \delta x^2 \quad [6b]$$

Here x is the distance perpendicular to the electrode surface ($x = 0$) into the polymer ($x > 0$) and into the electrolyte ($x < 0$), respectively, t is the time counted from pulse initiation, and D_0 and D_R are the diffusion coefficients of the oxidized species in the polymer and of the reduced species in the electrolyte solution, respectively.

The pertinent initial and boundary conditions are

$$c_0 = {}_0c_0 \text{ for } x \geq 0 \text{ and } t = 0 \quad [7a]$$

$$c_R = {}_0c_R \text{ for } x \leq 0 \text{ and } t = 0 \quad [7b]$$

$$c_0 = {}_0c_0 \text{ for } x \rightarrow \infty \text{ and all } t \quad [8a]$$

$$c_R = {}_0c_R \text{ for } x \rightarrow -\infty \text{ and all } t \quad [8b]$$

$$i_F = n F D_0 (\delta c_0 / \delta x)_{x=0} = -n F D_R (\delta c_R / \delta x)_{x=0} \quad [9]$$

Solution of Eq. [2], [3], [4], and [6] with the initial and boundary conditions [7], [8], and [9] in closed form is not possible. For small overvoltages $\eta \ll RT/nF$, not too short times (27), and for a certain range of values of i_0 , as compared to the values of D and c (27), the following closed-form solution for the overvoltage as a function of time has been derived (27)

$$\eta(t) = \frac{(RT/nF)i_t}{\left[\frac{(2/nF\sqrt{\pi})(1/{}_0c_0\sqrt{D_0} + 1/{}_0c_R\sqrt{D_R})\sqrt{t}}{(RT/n^2F^2)(1/{}_0c_0\sqrt{D_0} + 1/{}_0c_R\sqrt{D_R})^2 C_D/A} + 1/i_0 \right]} \quad [10]$$

Determination of kinetic parameters.—An evaluation of overvoltage-time transients according to Eq. [10] allows the determination of the diffusion coefficient of the dopant BF_4 in polyacetylene and the rate constant of the discharge reaction of BF_4^- at the polymer/electrolyte interface. The dopant concentration in the polymer (${}_0c_0$), the solute concentration in the electrolyte, ${}_0c_R$, and its diffusion coefficient, D_R , must be known. The ohmic voltage drop and the double layer capacity can be determined from the transient curves at times near zero without using Eq. [10].

Ohmic voltage drop.—The trivial ohmic voltage drop in the electrolyte that results in the steep rise of the potential-time transient at time $t = 0$ (see Fig. 5) is not included in Eq. [10]. An evaluation of the initial potential rise (at $50 \mu\text{s}$) as a function of the applied current density in the short-duration transients of Fig. 2 should yield a straight line with a slope proportional to the electrolyte

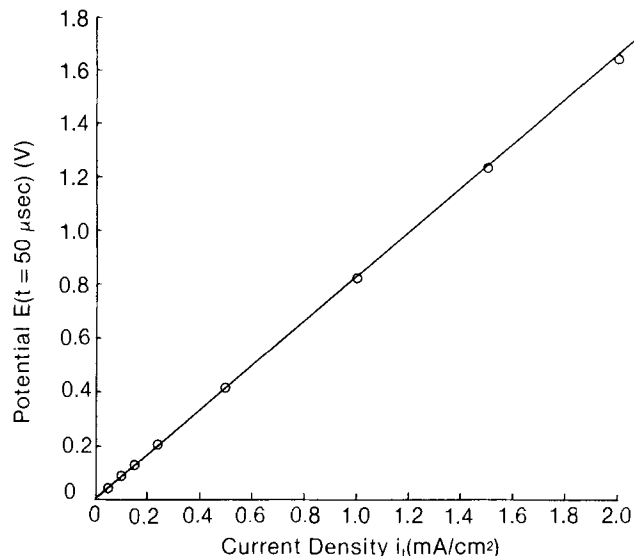


Fig. 6. Ohmic voltage drop vs. current density $50 \mu\text{s}$ after applying current pulse.

resistivity

$$\rho = d(E - E_0)/di/L \quad [11]$$

The plot in Fig. 6 shows that a straight line is obtained, and from the slope of $824 \Omega\text{-cm}^2$ and the distance $L = 0.3 \text{ cm}$ between reference and test electrode, a resistivity of $2750 \Omega\text{-cm}$ is calculated, in close agreement with conductivity cell measurements.

Double layer capacitance.—If rate of diffusion and charge transfer were infinitely fast, the initial step rise in potential would be followed by a linear rise with time, as represented by the dashed line in Fig. 5. The slope of the straight line is inversely proportional to the double layer capacitance. For finite rates of charge transfer and diffusion, the potential rises more slowly, and the double layer capacitance may be determined from the slope of the curves at $t = 0$, obtained at various current densities. According to Eq. [4], a straight line should result in a plot of $d\eta/dt$ against $i_c \cong i_t$, whose slope is inversely proportional to C_D/A . The value of $C_D/A = 11 \mu\text{F}/\text{cm}^2$ is derived from the slope of the straight line in Fig. 7, where A is the projected electrode area. This value falls within the range of

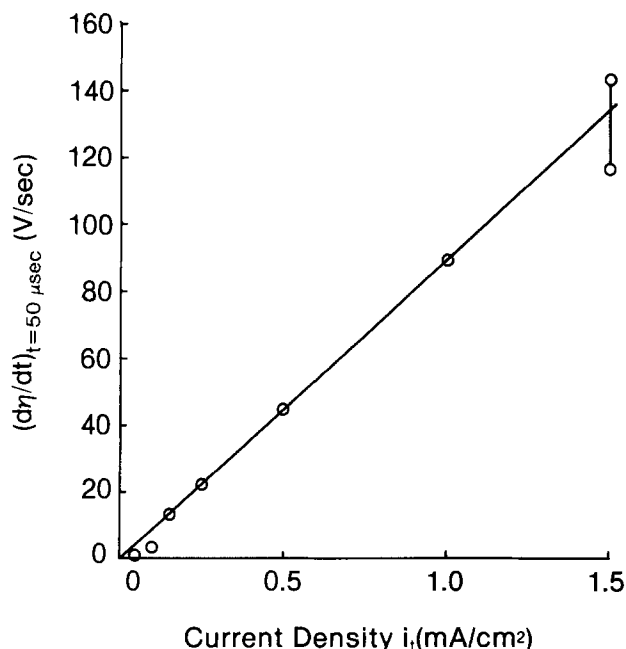


Fig. 7. Initial slope of cathodic or anodic potential-time transients at $50 \mu\text{s}$ vs. current density to determine C_D .

10-40 $\mu\text{F}/\text{cm}^2$, which are the capacitance values for the ionic double layer observed on various metal surfaces in aqueous electrolytes (28). Similar values are observed for metals in organic electrolytes. The finding of 11 $\mu\text{F}/\text{cm}^2$ of projected polyacetylene area is important evidence that in fact only the exterior surface of the microporous fibrillar polyacetylene electrode facing the electrolyte is wetted by electrolyte. Considering the high viscosity of a 30% solution of LiBF_4 in sulfolane and the very small pore size (several hundred angstroms) of the electrode, this finding is not surprising. To which extent the wetted area deviates from the projected area is uncertain. The "roughness factor," *i.e.*, wetted/projected area, is determined by the accessible surface area of the polyacetylene fibers at the exterior face of the electrode.

If the internal surface area of the microporous polyacetylene fiber structure were wetted with electrolyte, one would derive a value of only 0.0055 $\mu\text{F}/\text{cm}^2$ of true surface area. This value follows from the BET surface area of 40 m^2/g and the polyacetylene electrode weight of 0.005g, from which one determines a ratio of total true area to projected area of 2000. A value of 0.0055 $\mu\text{F}/\text{cm}^2$ is unreasonably small. It can be associated neither with the ionic double layer nor with the polyacetylene.

The capacitance associated with a charge depletion or accumulation layer in the polyacetylene is expected to have a value in excess of 10 $\mu\text{F}/\text{cm}^2$. This estimate follows from the high dopant density of $3 \times 10^{-3} \text{ mol}/\text{cm}^3$ or 1.8×10^{21} dopant molecule/per cm^3 for any dielectric constant larger than 9 and any flatband potential smaller than 1V (29). For larger dielectric constants and smaller flatband potentials, the capacitance attains values larger than 10 $\mu\text{F}/\text{cm}^2$. Such values are clearly incompatible with a value of 0.0055 $\mu\text{F}/\text{cm}^2$ resulting from complete wetting of the microporous electrode interior.

Diffusion coefficient of dopant in polyacetylene.—According to Eq. [10], straight lines should result in a plot of

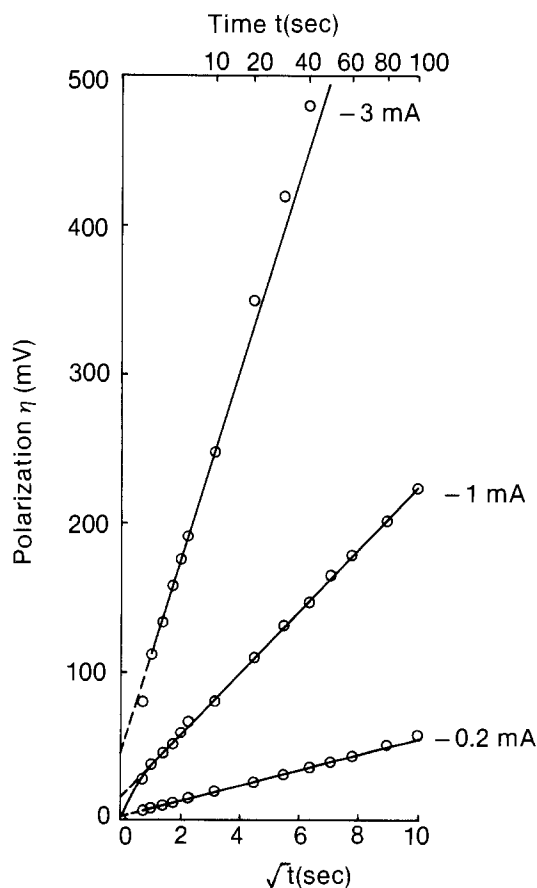


Fig. 8. Polarization (undoping) vs. \sqrt{t} for cathodic current pulses of 100s duration. Plot according to Eq. [10] to determine D_0 and i_0 . Electrode area 2 cm^2 .

the overvoltage against \sqrt{t} for not too large values of η . The slopes should be proportional to the diffusion coefficient and the applied current density. Figure 8 shows the cathodic voltage transients of Fig. 3 as a function of \sqrt{t} . Straight lines result from which a diffusion coefficient of BF_4^- in the polymer, $D_0 = 5.7 \times 10^{-12} \text{ cm}^2/\text{s}$ is determined. The following values for the other parameters were used: dopant concentration $c_0 = 3.1 \text{ mol}/\text{liter}$ or 7.1 m/o ; electrolyte concentration of BF_4^- , $c_R = 4.6 \text{ mol}/\text{liter}$; diffusion coefficient of BF_4^- in the electrolyte, $D_R = 1.2 \times 10^{-8} \text{ cm}^2/\text{s}$. The latter value was calculated from the measured conductivity, using the Nernst-Einstein relationship.

Similarly, Fig. 9 shows the anodic voltage transients of Fig. 4a in a plot of η against \sqrt{t} . The resulting straight lines yield the same value for the diffusion coefficient with the known dopant concentration of 1.8-2.7 mol/liter , corresponding to between 4.1 and 6.2 m/o .

Figure 9 shows a deviation from straight line behavior at larger values of η . This is expected since Eq. [10] is an approximation valid only for $\eta \ll RT/F$.

The good agreement between calculated and experimental curves, evidenced by Fig. 8 and 9, demonstrates the validity of a simple linear diffusion model with simultaneous charge transfer hindrance. There is no need to invoke a field-enhanced diffusion model as it has been postulated recently (16). In fact, the application of such a model to polyacetylene doped sufficiently high to be in the metallically conducting regime is questionable, as the Debye length (electronic screening length) is much smaller than the polymer fiber radius. The doping levels

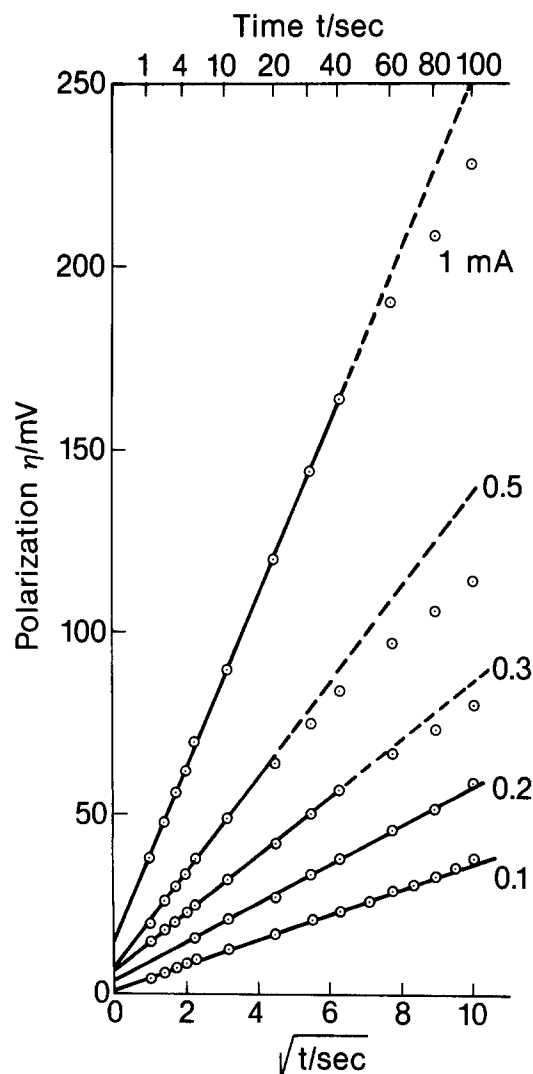


Fig. 9. Polarization (doping) vs. \sqrt{t} for anodic current pulses of 100s duration. Electrode area 2 cm^2 .

applied in the present study, namely, 7 m/o, place polyacetylene well into the metallic regime.

The value of 5.7×10^{-12} cm²/s for the diffusion coefficient follows from the η vs. \sqrt{t} transients if only the exterior surface of the electrode is wetted with electrolyte. Identical transients would have been observed if the interior were also wetted and the diffusion coefficient were correspondingly smaller, as determined by $A\sqrt{D_0} = \text{const}$. As the interior surface is 2000 times larger than the projected area, the diffusion coefficient would then have a value of only 1.4×10^{-18} cm²/s. Based upon the capacitance measurements, we regard this case as inapplicable.

The dominant influence which different degrees of wetting of the large interior surface of polyacetylene obviously have on the magnitude of the diffusion coefficients, as determined from transient measurements, make it mandatory to establish the degree of wetting independently. The fact that this has not been done in previous studies may explain the large discrepancies in the values of diffusion coefficients reported by different authors.

Several groups (12-16) have studied the diffusion of the p-dopants I and ClO₄ in polyacetylene. By measuring the I₂ absorption and desorption from very dilute solutions of I₂ in pentane, "macroscopic" diffusion coefficients in the range from 2.1×10^{-10} to 2.8×10^{-8} cm²/s were determined (12), as related to the projected polyacetylene film area. These values do not reflect the inherent diffusion coefficient of I in polyacetylene as they contain the effects of the fast diffusion (10^{-5} cm²/s) of I₂ through the solution that has penetrated between the fibers (interfibrillar diffusion) (13). In good agreement with the present study, a value of 3×10^{-12} cm²/s was later reported by the same group (15) on the basis of microwave measurements of the electrical conductivity of I-doped polyacetylene. This study pointed out the need of avoiding fast I₂ transport through the interfibrillar void space. The large value of 1.5×10^9 cm²/s reported for I diffusion in polyacetylene on the basis of short-circuit current decay measurements on a solid electrolyte cell (14) may have been affected by fast interfibrillar I₂ transport, possibly in the gas phase, as no liquid electrolyte was being used.

Kaufman *et al.* (16) estimated diffusion coefficients in the order of 4×10^{-18} cm²/s for both ClO₄ and Li, based upon open-circuit voltage decay measurements following charging in LiClO₄-propylene carbonate electrolyte. Complete wetting of the interior surface had been assumed to arrive at such low numbers. If one assumes wetting of the exterior surface only (17), then the data yield a value of 10^{-12} cm²/s, in good agreement with the value of 3×10^{-12} cm²/s determined in this paper.

Other studies of Li diffusion in polyacetylene give values of 10^{13} cm²/s at 83°C (18) and 2×10^{-17} cm²/s (19). The former value was determined from the open-circuit potential recovery of Li-doped polyacetylene after charging of a solid polymer electrolyte battery (18). ESR results of Li absorption from solutions of Li benzophenone in THF are interpreted in terms of an interfibrillar diffusion coefficient of 10^{-9} cm²/s and an intrinsic intrafibrillar diffusion coefficient of 2×10^{-17} cm²/s (19).

Kinetics of interface reaction.—Doping and undoping require the transfer of BF₄⁻ ions from the organic solution phase to the solid polyacetylene phase and vice versa. It is likely that the transfer of an electron from the ion to the polymer chain occurs at the interface. This expectation derives from the high electronic conductivity of polyacetylene when doped with dopant levels exceeding the insulator-metal transition threshold (4-6). The dopant concentrations employed in this study are well into the semimetal conduction state. The rate of the charge transfer reaction, as expressed by the exchange current density, i_0 , can be determined from the η vs. \sqrt{t} transients shown in Fig. 8 and 9. Based on Eq. [10], the intercept of the extrapolated straight lines with the axis $\sqrt{t} = 0$ is proportional to i/i_0 , so that for any applied i the exchange

current density i_0 can be determined. We find an average value of $i_0 = 8 \times 10^{-4}$ A/cm² from both cathodic and anodic transients for a BF₄⁻ concentration of 4.6×10^3 mol/cm³ and a BF₄ dopant concentration of 3.1×10^{-3} mol/cm³. The value of i_0 is referred to the projected area of the polyacetylene electrode, consistent with the double layer capacitance and the diffusion coefficient.

The observed exchange current density of the reaction $(\text{CH})_x + \text{BF}_4^- = (\text{CH})_x\text{BF}_4 + e^-$ on polyacetylene is comparable to values of i_0 for simple one-electron redox reactions on inert metal electrodes. Thus, values for the reactions $\text{Ti}^{3+} = \text{Ti}^{4+} + e^-$, $\text{Ce}^{3+} = \text{Ce}^{4+} + e^-$, and $\text{Mn}^{2+} = \text{Mn}^{3+} + e^-$ are 3×10^{-4} (30), 2×10^{-4} (31), and 2×10^{-5} A/cm² (32), respectively, for concentrations of the redox species of the order of 10^{-5} - 10^{-3} mol/cm³. Similar features between redox reactions and doping-undoping reactions of polyacetylene pertain to the diffusion of oxidized and reduced species, both present in a large possible concentration range. It is recognized, however, that the transfer of species from a liquid electrolyte into a solid polymer of crystalline nature constitutes a major difference from a true redox reaction.

The anodic transfer coefficient α of the reaction cannot be determined from the η - \sqrt{t} transients in Fig. 8 and 9 since α does not occur in Eq. [10] owing to the linearization of the exponential terms in Eq. [3]. However, α can be determined from an appropriate solution of the equations valid for large values of η ; the solution in this case (33) is

$$\eta = \frac{RT}{\alpha F} [\ln(i/i_0) + \ln(1 + \sqrt{t/\tau})] \quad [12]$$

where

$$\tau = (\pi/4)D_0F^2c^2/i_2 \quad [13]$$

The anodic transfer coefficient is determined from a plot of η vs. $\log(1 + \sqrt{t/\tau})$ which should yield a straight line with slope proportional to $1/\alpha$. Figure 10 shows that a straight line is indeed obtained, and a value of $\alpha = 0.19$ is determined from the slope. The data in Fig. 10 are the same as those in Fig. 9 for $i = 0.5$ mA/cm². In the latter figure, the data deviate from straight line behavior for large η since application of Eq. [10] is inappropriate for large η .

The anodic transfer coefficient is quite small, meaning that the energy barrier for charge transfer is quite asymmetrical, favoring the anodic doping reaction while impeding the cathodic undoping. Asymmetry of the energy barrier to the extent found here is not unusual, however. Values for $(1 - \alpha)$ of 0.25 and 0.28 have been observed in the reactions $\text{Ce}^{3+} = \text{Ce}^{4+} + e^-$ and $\text{Mn}^{2+} = \text{Mn}^{3+} + e^-$, respectively (31, 32).

The concentration-independent rate constant k can be determined from the exchange current density i_0 with a knowledge of α and of the concentrations ${}_0c_0$ and ${}_0c_R$. The value computed from Eq. [5] is 2.5×10^{-6} cm/s.

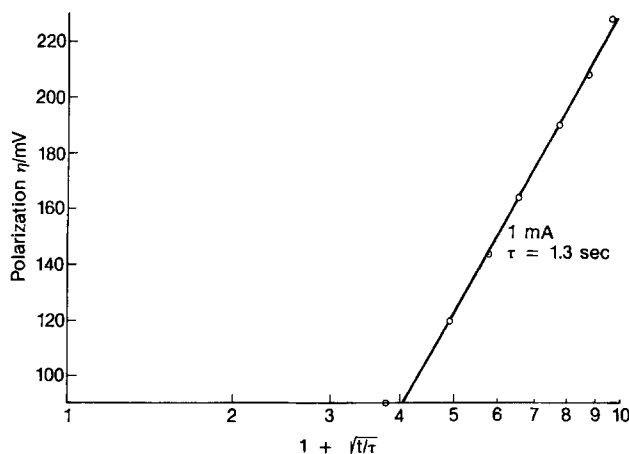


Fig. 10. Polarization (doping) vs. $\log(1 + \sqrt{t/\tau})$ for anodic current pulse of 1 mA amplitude and 100s width. Plot according to Eq. [12] for large η to determine α .

Conclusions

Application of an electrode kinetic analysis involving semi-infinite linear diffusion, double layer capacitance charging, and charge transfer at the polyacetylene/electrolyte interface has led to quantitative agreement with experimental results on the doping and undoping of polyacetylene with BF_4 using controlled current pulses. The observed double layer capacitance, $11 \mu\text{F}/\text{cm}^2$ of projected area, is a measure for the wetted surface area of the microporous fibrillar polyacetylene and shows that only the exterior surface is wetted with electrolyte. This justifies application of a semi-infinite linear diffusion model to determine the diffusion coefficient of the dopant BF_4 in polyacetylene as $5.7 \times 10^{-12} \text{ cm}^2/\text{s}$. Using studies which do not independently establish the wetted, electrochemically active surface area, one cannot arrive at a valid diffusion coefficient. Thus, if the erroneous assumption of complete wetting of the interior surface were made, the diffusion coefficient would have the exceedingly small value of $1.4 \times 10^{-18} \text{ cm}^2/\text{s}$.

Even with the observed value of $5.7 \times 10^{-12} \text{ cm}^2/\text{s}$, solid-state dopant diffusion is the rate-determining step in the charge and discharge of polyacetylene electrodes and explains the known sluggishness of polyacetylene in attaining steady-state potentials during charge, discharge, and open circuit. The rate of dopant transfer across the polyacetylene-electrolyte interface is determined as $8 \times 10^{-4} \text{ A}/\text{cm}^2$, equivalent to a rate constant of $2.5 \times 10^{-6} \text{ cm}^2/\text{s}$. Such values are comparable to those found for a variety of one-electron redox reactions on metals in aqueous solutions. The anodic transfer coefficient is 0.19, corresponding to a quite asymmetrical energy barrier that favors p-doping or charging while impeding undoping or discharging.

Acknowledgments

The author acknowledges the help of J. J. Rogers in carrying out the experiments and is indebted to the Rohm and Haas Company for the preparation of the polyacetylene films and the electrolyte.

Manuscript submitted Oct. 29, 1984; revised manuscript received May 26, 1985. This was Paper 554 presented at the San Francisco, California, Meeting of the Society, May 8-13, 1983.

General Electric Company assisted in meeting the publication costs of this article.

REFERENCES

- G. Natta, G. Mazzanti, and P. Corradini, *Att. Accad. Naz. Lincei, Cl. Sci. Fis. Mat. Nat. Rend.*, **8**, 3 (1958).
- T. Ito, H. Shirakawa, and S. Ikeda, *J. Polym. Sci.*, **12**, 11 (1974).
- D. J. Berets and D. S. Smith, *Trans. Faraday Soc.*, **64**, 823 (1968).
- C. K. Chiang, C. R. Fincher, Jr., Y. W. Park, A. J. Heeger, H. Shirakawa, E. J. Louis, S. C. Gau, and A. G. MacDiarmid, *Phys. Rev. Lett.*, **39**, 1098 (1977).
- K. Seeger, W. D. Gill, T. C. Clarke, and G. B. Street, *Solid State Commun.*, **28**, 873 (1978).
- A. J. Epstein, H. W. Gibson, P. M. Chaikin, W. G. Clark, and G. Gruner, *Phys. Rev. Lett.*, **45**, 1730 (1980).
- P. J. Nigrey, A. G. MacDiarmid, and A. J. Heeger, *J. Chem. Soc. Chem. Commun.*, 594 (1979).
- P. J. Nigrey, D. MacInnes, Jr., D. P. Nairns, and A. G. MacDiarmid, *This Journal*, **128**, 1651 (1981).
- K. Kaneto, M. R. Maxfield, D. P. Nairns, and A. G. MacDiarmid, *J. Chem. Soc., Faraday Trans.*, **78**, 3417 (1982).
- G. C. Farrington, B. Scrosati, D. Frydryk, and J. DeNuzzio, *This Journal*, **131**, 7 (1984).
- A. F. Diaz and T. C. Clarke, *J. Electroanal. Chem.*, **111**, 115 (1980).
- F. Beniere, S. Haridoss, J. P. Louboutin, H. Aldissi, and J. M. Fabre, *J. Phys. Chem. Solids*, **42**, 649 (1981).
- J. P. Louboutin and F. Beniere, *ibid.*, **43**, 233 (1982).
- F. Beniere, D. Boils, H. Canepa, J. Franco, A. LeCorre, and J. P. Louboutin, *J. Phys. C*, **44**, 567 (1983).
- S. Pekker, M. Bellec, X. LeCleach, and F. Beniere, *Syn. Met.*, **9**, 475 (1984).
- J. H. Kaufman, E. J. Mele, A. J. Heeger, R. Kaner, and A. G. MacDiarmid, *This Journal*, **130**, 571 (1983).
- F. G. Will, *ibid.*, **132**, 743 (1985).
- M. Foulletier, P. Degott, and M. B. Armand, *Solid State Ionics*, **8**, 165 (1983).
- R. Rachdi, P. Bernier, E. Faulques, S. Lefrant, and F. Schue, *J. Phys. C*, **44**, 97 (1983).
- F. G. Will, R. S. McDonald, R. D. Gleim, and M. R. Winkle, *J. Chem. Phys.*, **78**, 5847 (1983).
- R. H. Baughman, S. L. Hsu, and A. J. Signorelli, *Mol. Cryst. Liq. Cryst.*, **52**, 251 (1979).
- K. Shimamura, F. E. Karasz, J. A. Hirsch, and J. C. W. Chien, *Macromol. Chem. Rapid Commun.*, **2**, 473 (1981).
- K. Higashiura and M. Oiwa, *J. Chem. Soc. Jpn. Ind. Chem. Sec.*, **69**, 109 (1966).
- J. M. Pochan, D. F. Pochan, H. Rommelmann, and H. W. Gibson, *Macromolecules*, **14**, 110 (1981).
- M. A. Halem, D. Billaud, and A. Pron, *Polymer*, **23**, 1409 (1982).
- F. G. Will and D. W. McKee, *J. Polym. Sci., Polym. Chem. Ed.*, **21**, 3479 (1983).
- T. Berzins and P. Delahay, *J. Am. Chem. Soc.*, **77**, 6448 (1955).
- K. J. Vetter, "Electrochemische Kinetik," Springer-Verlag, Berlin (1961).
- R. H. Wilson, *Crit. Rev. Solid State Mater. Sci.*, **10**, 1 (1980).
- O. Essin, *Acta Physicochim. USSR*, **13**, 429 (1940).
- K. J. Vetter, *Z. Phys. Chem.*, **196**, 360 (1951).
- K. J. Vetter and G. Manecke, *ibid.*, **195**, 270 (1950).
- P. Delahay and T. Berzins, *J. Am. Chem. Soc.*, **75**, 2486 (1953).

Polyacetylene Solid-State Batteries

F. Benière, D. Boils, H. Cánepa, J. Franco, A. Le Corre, and J. P. Louboutin

Laboratoire de Science des Matériaux (CNRS), Université de Rennes I, 35042 Rennes, France

ABSTRACT

The present report summarizes the performances of the solid-state batteries using a superionic conductor as solid electrolyte and polyacetylene as electrode material. Two types of cells have been tested. A first class uses the mixed ionic solid RbAg_4I_5 together with a silver anode. The second one uses $\beta''\text{-Al}_2\text{O}_3$, $x\text{Na}_2\text{O}$ together with sodium-doped $(\text{CH})_x$. Both fulfill the objective of being able to discharge at room temperature. In addition to the usual performances such as voltage, current, capacity, weight, shape, etc., we give the results over 4 yr of investigations on the discharge life and storage life. Many practical problems have been encountered, especially in the case of the sodium-polyacetylene battery. They are also reported, as well as some improvements made during that period such as encapsulation, diffusion inhibitors, and separation of the components until the first charge. The conclusion is that polyacetylene is proved to be a useful electrode material in solid-state batteries at the laboratory level. The possible further development to reach the industrial stage is discussed in terms of lifetime energy, density, and cost.

The conducting organic polymers like polyacetylene (1) or polyparaphenylene (2) are attracting more and more interest from the battery, energy conversion, and energy storage industries. Such applications have been pioneered by MacDiarmid and his group with the discovery that doped polyacetylene could be used as electrode material together with an organic solvent to form an electrochemical battery (3). This followed the prior discovery by the same group (4) that $(\text{CH})_x$ presents a high electrical conductivity after suitable doping (5) by a number of possible foreign molecules (I_2 , AsF_5 , Na , K , ...). Also, after this discovery, we took interest in the doping mechanisms of polyacetylene by iodine using radioactive techniques (6) as well as proposed that the conducting organic polymers can be used also in solid-state batteries (7) working at room temperature. At the same time, Chiang (8) reported an all-polymeric solid-state battery using both polyacetylene and polyethylene-oxide which can operate above 60°C .

The doping process is essential in all those applications. In most cases, doping is even achieved during the charge of the battery. A piece of polyacetylene alone can easily be doped from a vapor source when the dopant is volatile like iodine (9) or inside a liquid solution like iodine in pentane or sodium-naphthalide in THF (10). However, electrochemical doping developed by Nigrey *et al.* (11) is more convenient for electrochemical applications as it gives a better control of the concentration. Moreover, electrochemical doping can serve as the charge itself (12, 13). This is the case in the solid-state batteries we have developed (7) and that we are describing in the present paper after 4 yr of investigation.

Basic Principles

A superionic conductor used as solid electrolyte is combined with a conducting polymer used as the cathode and/or the anode material. The polymer is doped by suitable impurities which enable the polymer to conduct electricity and which will, at the same time, be the active material(s) of the electrochemical reaction. Until now, the choice has been limited to polyacetylene as for the electrode material. Because of its fibrillar morphology, it can absorb considerable amounts of active material. As for the solid electrolyte, we have set the objective that our cells should operate around the room temperature. This requirement restricts the choice of the solid electrolytes exhibiting a high ionic conductivity with practically no electronic conductivity at room temperature to (i) RbAg_4I_5 (which can be used even somewhat below the phase transition at 27°C). The conductivity is due to the Ag^+ ions, or (ii) beta-alumina such as $\beta''\text{-Al}_2\text{O}_3$, $x\text{Na}_2\text{O}$. The carrier here is Na^+ . Both are used in the two types of cells which are considered in the present paper.

The obvious advantage of a solid-state battery is to provide a waterproof component. We found it necessary to encapsulate our cells inside a resin coating. This precaution is particularly important in the case of the sodium-

doped $(\text{CH})_x$ anode in order to prevent oxidation of sodium. Another crucial feature of our cells is possible storage in the uncharged state. The polymer remains undoped for any period of time, over years, if required. During that period, obviously, no degradation due to chemical interaction between the polyacetylene and the dopant can occur. It is the first charge which by electrolysis decomposes a part of the electrolyte into the products which dope by diffusion the conducting polymer. After this stage, the product(s) having doped the polymer form the active material of the battery, which is then ready to discharge. The storage life of the battery is greatly increased.

Materials Preparation

Polyacetylene.—We have used polyacetylene samples synthesized either by the group of Schué at the University of Montpellier (France) or in our laboratory, in both cases following Shirakawa's method.

In the case of the sodium battery, the polyacetylene film has to be synthesized upon the surface of the alumina itself. For that purpose, the alumina disks of the battery are introduced in the reactor. The catalyst $\text{AlEt}_2/\text{Ti}(\text{O}Bu)_4$ is sprayed upon one or two of the main surfaces so that a $(\text{CH})_x$ film grows on the solid electrolyte. The thickness is then a little less than $10\ \mu\text{m}$.

The $(\text{CH})_x$ cathode used in the silver or sodium battery is prepared separately. Though prepared at -70°C and therefore in the *cis* form, the further use at room temperature as well as the doping process induce the *cis-trans* isomerization (14, 15). We have tested all sorts of films of density varying from $0.1\ \text{g}\cdot\text{cm}^{-3}$ up to the almost nominal density with correspondingly largely variable thicknesses in the range $10\text{--}1000\ \mu\text{m}$. One or more films are introduced in a Pascal press and compressed to a maximum pressure of $5 \times 10^8\ \text{Pa}$.

β -Alumina.—We use the β'' -alumina doped with Na_2O synthesized at Marcoussis (France) by the Compagnie Générale d'Electricité for the experimental sodium-sulfur battery. The high ionic conductivity in this material is due to the fast motion of the Na^+ ions. In a separate study (16), the mobility and the flux of sodium ions through the alumina samples were measured by using radioactive Na-22 as a tracer and a sectioning technique. This confirmed directly the expected fast mobility of sodium which was measured. Even at room temperature, the resistance of the solid electrolyte is only $100\ \Omega$. Disks (slightly bent) of a thickness of $1\ \text{mm}$ and of $13\ \text{mm}$ diam are shaped from large β -alumina tubes.

RbAg_4I_5 .—The silver conducting electrolyte is prepared by mixing stoichiometric amounts of AgI and RbI together with a small proportion of silver powder in water. When a thick paste is obtained, the water is evaporated by heating at 120°C for 20h. The dry paste is then ground. The resulting powder is introduced in a glass tube, sealed under vacuum, heated at 350°C for 20 min and slowly

cooled down to room temperature. The electrolyte is then ground again and kept at 160°C under vacuum for 24h. After that preparation, the material is stored at 70°C under vacuum before use. The x-ray powder diffraction diagram is in excellent agreement with the data reported by Geller (17). The present mode of preparation of α -RbAg₄I₅ is intended to prevent moisture and thermal decomposition. Silver atoms are added in order to act as a getter for the iodine molecules, which tend to diffuse from the cathode to the anode through the electrolyte.

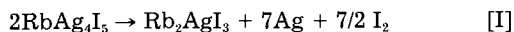
Silver anode.—Thin powder of silver is mixed with some graphite powder and pressed together as a disk of 13 mm diam at a pressure of 2×10^8 Pa. The graphite is used to improve the electrical contacts.

Silver Battery

Cell assembly.—The polyacetylene-silver battery is schematically shown in Fig. 1. It has a cylindrical form of 13 mm diam and 2 mm thickness. It is prepared in a pressure chamber of that diameter in which are successively pressed the silver powder with a little graphite (anode), the electrolyte α -RbAg₄I₅ containing silver, the polyacetylene, and finally the graphite. The electrical contacts are taken by metallic wires embedded inside the graphite. The whole element is thereafter encapsulated inside an epoxide resin coating.

Piles of, generally, three elements are prepared in the same way by successive pressing. A lead sheet separates adjacent elements to prevent iodine from diffusing from one to the next element. They deliver a voltage of 2V.

Though it is possible to start with a polyacetylene cathode already doped with iodine, the battery is generally assembled with pure polyacetylene. The polymer is later doped electrochemically *in situ* by forcing a charge of electricity which creates a partial electrolysis of RbAg₄I₅ (18) according to the reaction



and the subsequent doping of (CH)_x



The charge is proceeded at a constant current of, typically, 10⁻⁴A. The electrolysis is adjusted to reach a doping level such that $y = 0.2$. For a typical mass of 20 mg of (CH)_x, a charge of 28 Cb is needed, i.e., 8.2×10^{-3} Ah, which is reached after 82h in the experimental cells. Higher currents can be used to reduce the time of the charge. The cell becomes Ag/RbAg₄I₅/((CHI)_y)_x ready to supply electricity.

Internal resistance.—A battery is allowed to discharge on loads varying from 1 to 10⁶Ω. The current I and potential U are measured immediately before any polarization occurs. A characteristic U vs. I curve is shown in Fig. 2. The internal resistance r is derived from Pouillet's equation: $U = E - rI$, where E is the electromotive force, that is from the slope of the straight line of Fig. 2. This parameter changes from cell to cell in the range 10-40Ω. The best cells are those where r is minimum. The summation of the separate resistances of the individual components gives a much lower value: the electrolyte disk whose area

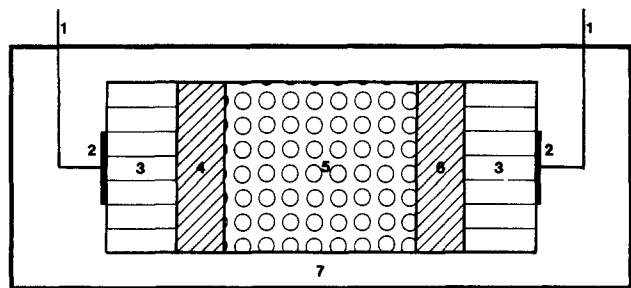


Fig. 1. Prototype of the polyacetylene-silver battery. 1: Leads. 2: Silver point. 3: Graphite. 4: Silver. 5: RbAg₄I₅. 6: CH_x. 7: Resin coating.

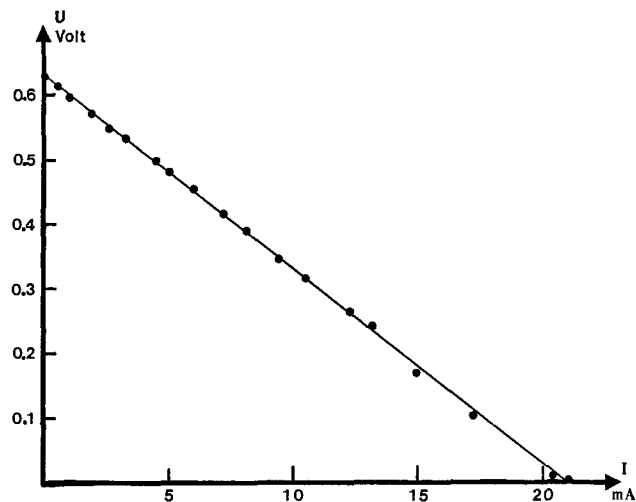


Fig. 2. Galvanostatic measurement of the voltage of a polyacetylene-silver battery. $R = 30\Omega$, $E_{oc} = 0.625\text{V}$, $I_{cc} = 21 \text{ mA}$.

and thickness are 1.3 cm² and 0.1 cm, respectively, contributes for less than 1Ω. The internal resistance of the doped (CH)_x has been measured in the same conditions, namely, inside its coating of resin. This was made possible by a microwave technique which avoids using any electrode (19). Again, this contributes for less than 1Ω. Last, when both RbAg₄I₅ and (CH)_x are removed from the battery the overall resistance of all the leads and contacts is found to be about 1Ω. To conclude, the cell resistance is mainly due to the interfacial resistance, which depends on the pressing conditions. Nevertheless, it is quite acceptable when compared to the dry batteries.

EMF at constant temperature.—The electromotive force depends on the temperature and on the iodine activity. The influence of this later parameter at the constant temperature of 30°C is shown in Fig. 3. The EMF E is measured as a function of the concentration of iodine inside (CH)_x and reported as E vs. y , y being the iodine content corresponding to the formula (CHI)_y, i.e., close to the mole fraction. E has been measured in three distinct ways: (i) in separate cells using chemically doped (CHI)_y cathodes, (ii) in separate cells using electrochemically doped (CHI)_y cathodes, and (iii) in the same cell with an original $y = 0.07$, allowed to partially discharge and measured after 24h to reach the equilibrium value.

The good agreement between the results is to be noticed, as it gives clear evidence that iodine formed by decomposition of RbAg₄I₅ smoothly diffuses into (CH)_x though it is pressed.

The experimental results on Fig. 3 also show that the EMF is $E = 0.660\text{V}$ for $y = 0.30$ at 30°C. This is quite simi-

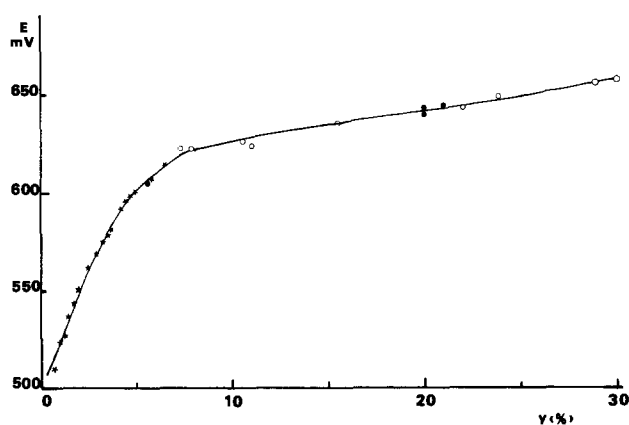


Fig. 3. Influence of the iodine content y of the (CHI)_y cathode on the electromotive force at 30°C. The data points correspond to chemically doped (CHI)_y cathodes (open circles), electrochemically doped cathodes (filled circles), and same cell after partial discharges (stars).

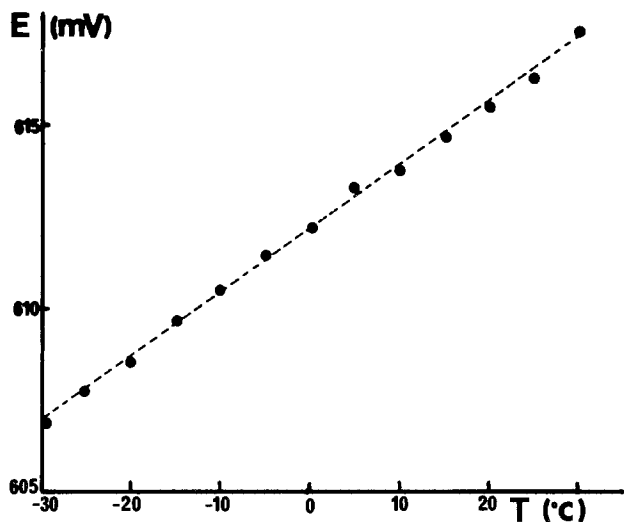


Fig. 4. Temperature dependence of the electromotive force of a polyacetylene-silver cell with $y = 0.07$.

lar to the value observed in the Owens battery (20), which used a charge transfer complex instead of the present conducting polymer. This value compares well with the EMF associated with the reaction $\text{Ag} + 1/2 \text{I}_2 \rightarrow \text{AgI}$ which would have given from Nernst equation and the standard free energy of formation of AgI: $E^0 = 0.687\text{V}$. The electrolyte would serve solely as an inert electrolyte (21). This would also mean that the effective reactant is iodine, either physically adsorbed at the surface of the fibrils of $(\text{CH})_x$ (and weakly bonded) or even as iodine gas present in the pores of the interfibrillar space and in equilibrium with the iodine of the fibrils.

However, one may consider a complete charge transfer between I_2 and $(\text{CH})_x$, which should be then written as $[(\text{CH})^{y+} (\text{I}^-)_y]_x$ or $[(\text{CH})^{y+} (\text{I}_3^-)_y]_x$. The cathodic reaction would then be the reduction $(\text{CH})_x^+ + e^- \rightarrow (\text{CH})_x$; the iodide (or polyiodide) ion would play at the same time the role of a counterion. But, taking the reduction potential of $(\text{CH})_x$ as measured by Shacklette *et al.* (22) would give a much higher EMF. It might also be supposed that, in that case, the electrolyte would be decomposed and that one would then observe the decomposition potential of RbAg_4I_5 , according to reaction [I], which is very close to the decomposition potential of AgI at 27°C.

Influence of temperature.—The influence of temperature has been carefully measured in order to determine as accurately as possible the thermodynamic parameters enthalpy, entropy, and free energy of the electrochemical reaction. As E depends both on temperature θ and iodine content y , the open-circuit voltage was measured as a function of temperature in seven cells for various y ranging from $y = 0.053$ to $y = 0.21$ in the temperature range $-30^\circ \leq \theta \leq +30^\circ\text{C}$. The data E vs. θ (Fig. 4) show the expected straight line. The enthalpy and entropy are derived from the equations

$$\Delta H = -F[E - T(\partial E/\partial T)]$$

$$\Delta S = F(\partial E/\partial T)$$

The values for ΔH and ΔS reported in Table I indicate a continuous decrease of ΔH and ΔS as y increases. They are to be compared with the parameters of the reaction

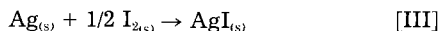
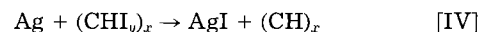


Table I. Entropy and enthalpy change in the electrochemical reaction of the polyacetylene-silver battery

y ($\times 100$)	5.3	5.7	7.09	7.78	7.85	8.02	21
ΔS ($\text{cal}\cdot\text{K}^{-1}\cdot\text{mol}^{-1}$)	5.22	4.85	3.88	3.60	2.88	2.79	1.57
ΔH ($\text{kcal}\cdot\text{mol}^{-1}$)	-12.32	-12.51	-13.07	-13.26	-13.49	-13.55	-14.44

which at 30°C are $\Delta H = -14.91 \text{ kcal}\cdot\text{mol}^{-1}$, $\Delta S = 3.14 \text{ cal}\cdot\text{K}^{-1}\cdot\text{mol}^{-1}$, $\Delta G = -15.86 \text{ kcal}\cdot\text{mol}^{-1}$, giving $E = -\Delta G/F = 0.687\text{V}$. As a matter of fact, the AgI_2 battery using pure solid iodine (in equilibrium with its vapor) at the cathode without $(\text{CH})_x$ or any other charge transfer complex does give $E = 0.687\text{V}$ (23). Making the assumption of Owens (21) that the electrolyte RbAg_4I_5 plays no electrochemical role in the discharge which should thus be written as



the difference between the reactions [III] and [IV] is the reaction of fixation of iodine on the fibrils (namely, reaction [II]). This allows estimation of the thermodynamic parameters of the absorption process. For $y = 0.07$ and $\theta = 25^\circ\text{C}$, one obtains $\Delta S = 0.74 \text{ cal}\cdot\text{K}^{-1}\cdot\text{mol}^{-1}$ and $\Delta H = -1.84 \text{ kcal}\cdot\text{mol}^{-1}$ (i.e., 0.08 eV). One would conclude that the doping by iodine is an exoenergetic process, as it might have been expected, but only slightly. In other words, the interaction seems to be quite weak.

Influence of the iodine content.—The influence of the iodine content y on E (Fig. 3) is difficult to interpret. There are no real successive steps as one would have expected from the structure studies of Baughman *et al.* (24), who assume a number of successive intercalated layers for given values of $y = 0.056$ -0.079-0.13-0.20-0.39 (first, second, and third stages with full and half-filled planes). A possible explanation would involve the experimental conditions and the fact that equilibrium is not reached so that the intercalated compound was not given enough time to be formed. To avoid this, the measurements are separated by at least two days. Such a long time was also found necessary for doping by ClO_4^- (25). This period would correspond to the time necessary for the dopant to reach the center of the fibril. Any estimation of this time requires knowledge of the diffusion coefficient. There is some discussion in the literature depending on the method of measurement. The overall diffusion coefficient assuming $(\text{CH})_x$ as a bulk material is obviously orders of magnitude larger (see *e.g.*, results shown in Fig. 18) than the microscopic diffusion coefficient. Taking a cylindrical fibril of radius $r = 100\text{\AA}$ and the microscopic diffusion coefficient $D \sim 5 \times 10^{-18} \text{ cm}^2\cdot\text{s}^{-1}$ measured with tracers (6), the diffusion time would be

$$\tau = r^2/5.78D \sim 10\text{h}$$

One can consider those fibrils homogeneously doped after approximately 5τ , which corresponds well to the time interval of 2 days between the measurements.

The experimental dependence E vs. y follows a logarithmic form shown in Fig. 5. In fact two ranges are observed. For $y < 0.08$, the results are described by the empirical equation

$$E = 0.515 \times 0.12 \log y$$

This recalls the Nernst equation $E = E^0 + 0.06 \log C$ though the coefficient is far from the theoretical value of 0.060 at 30°C. The same empirical dependence was observed for doping by ClO_4^- by Kaneto *et al.* (25) with an even higher coefficient: $E = 3.43 + 0.32 \log y$. Shacklette *et al.* (22) also observe a departure from Nernst equation (for lithium and sodium) with a plateau in the range $y = 0.01$ -0.05.

Discharge at constant current.—Cells kept in a thermostat are let to discharge with a galvanostat, while the voltage is recorded with a high impedance setup. A complete discharge at $I = 66 \times 10^{-6}\text{A}$ is shown in Fig. 6. One notices the good stability until the final drop which

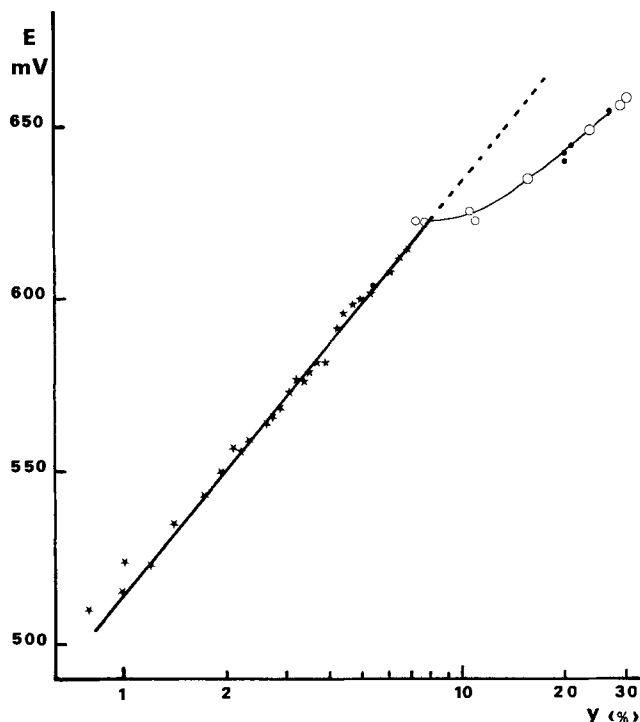


Fig. 5. Semilogarithmic representation of E vs. $\log y$

quantitatively corresponds to the full consumption of iodine. In other words, the Faraday efficiency for relatively low currents approaches unity. It seriously diminishes over $100 \mu\text{A}$. Figure 7 shows the voltage as a function of capacity in milliampere-hours. The cell is charged at the constant current $I = 0.25 \times 10^{-3}\text{A}$ (the corresponding voltage being also shown) and then let to full discharge. Results for $I = 0.4$ and $0.6 \times 10^{-3}\text{A}$ are shown. The Faraday efficiency subsequently drops down to 80 and 54%, respectively.

The energy efficiency is also calculated as the ratio W_d/W_c , with

$$W_c = I_c \int U_c dt$$

and

$$W_d = I_d \int U_d dt$$

with U_c and U_d being the voltages during the charge and discharge. The respective energy efficiencies are 60 and 43% and continuously decrease with increasing current.

Charge-discharge cycles.—We have investigated the reversibility of the cell to determine to which extent it could be considered as a rechargeable or secondary battery. Two sets of tests have been performed.

Partial discharge.—A cell having a capacity of 5 mAh was submitted to sequences of partial charges and discharges of 6 min each. This was done at the constant temperature

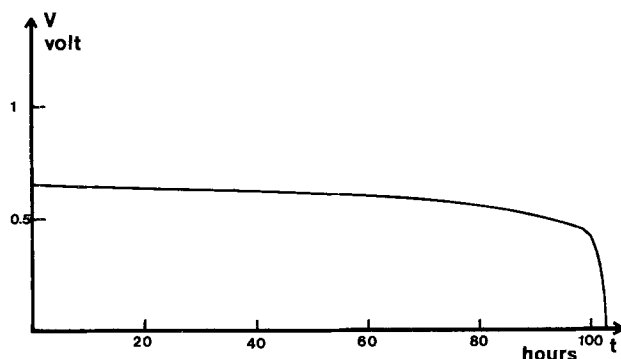


Fig. 6. Full discharge as a function of time of a polyacetylene-silver cell at $I = 66 \times 10^{-4}\text{A}$ and 30°C .

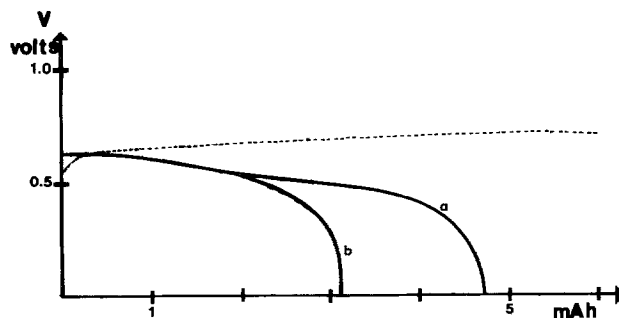


Fig. 7. Full discharges as a function of capacity of a polyacetylene-silver cell at higher currents: $4 \times 10^{-4}\text{A}$ (a) and $6 \times 10^{-4}\text{A}$ (b). The charge (dotted line) is made at $I = 2.5 \times 10^{-4}\text{A}$.

$\theta = 30^\circ\text{C}$ and for various values of the current kept constant with a galvanostat. This corresponds approximately to 2% of the capacity (full charge). This is shown on Fig. 8 for several currents (0.5, 0.76, and 1.52 mA) and two complete cycles. One observes the good behavior of the cell: reproducibility in the cycles, almost uniform voltage, and small polarization. However, for higher current, $> 3 \text{ mA}$ (Fig. 9), the voltage dramatically drops down and the cycles are no longer reproducible. We have therefore used 1 mA for the systematic tests; then, the good reproducibility is obtained over only 100 cycles. It is believed that the partial electrolysis of RbAg_4I_5 , during the charge gives Rb_2AgI_3 , which is a very poor conductor (26) and, in addition, is not fully decomposed to regenerate the electrolyte during the charge.

Full discharge.—The reversibility was also tested for complete discharge cycles using smaller currents, typically 0.1 mA. A perfect reproducibility is observed for the first cycles with an excellent efficiency. Unfortunately, this is not the case after a score of cycles. The cells contain 1g of electrolyte, and each full charge corresponds to the electrolysis of about 5% of RbAg_4I_5 . Therefore, after 20 cycles the complete amount of electrolyte would have suffered decomposition. The fact that the cell does not operate afterwards proves that the decomposition is not reversible.

To conclude these tests, the polyacetylene-iodine cathode seems to provide an efficient reversible electrode. However the duration of the cell is limited by the lifetime of the electrolyte $\text{RbAg}_4\text{I}_5 \rightarrow \text{Rb}_2\text{AgI}_3$, which prevents its use as a real secondary battery. Some other electrolytes could be better in that respect, possibly silver orthophosphate, Ag_3PO_4 or $\text{Ag}_7\text{PO}_4\text{I}_4$ (27).

Kinetics.—The kinetical study of the discharge was also performed on the same cells containing approximately 10 mg of CH_x doped by a first charge for various values of y . In fact, the kinetics depend on the doping level. The cell is thereafter let to discharge on a resistance (1Ω) much smaller than the internal resistance so that the dis-

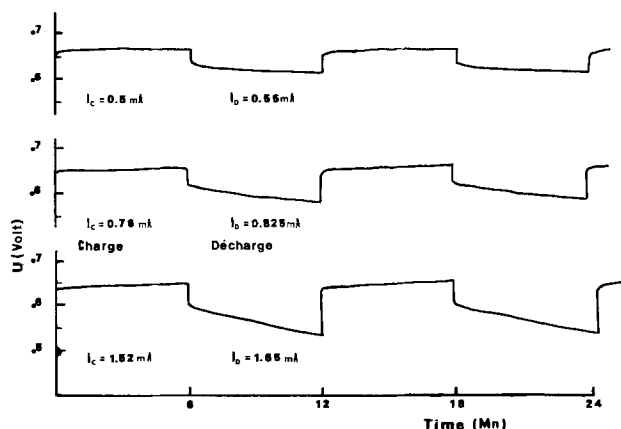


Fig. 8. Partial charge-discharge cycles of a polyacetylene-silver cell for $I = 0.5, 0.76,$ and 1.52 mA .

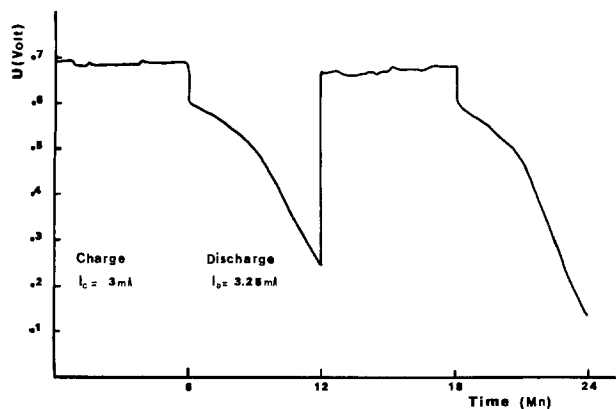


Fig. 9. Partial charge-discharge cycles for $I = 3 \text{ mA}$

charge is practically a short circuit. The current can then be recorded as a function of time (Fig. 10). The analytical form of $I = f(t)$ depends on y . For $y < 0.08$, the current varies as $1/\sqrt{t}$, as shown in Fig. 11. This behavior follows Cottrell's equation

$$I = ZFSC_0 \sqrt{d/\pi t} \quad [1]$$

where F is the Faraday, S the area of the interface, C_0 the constant concentration of iodine throughout the electrode, and D the diffusion coefficient. This indicates that the limiting process of the discharge is the diffusion of the active species (iodine) from the $(\text{CH})_x$ cathode towards the electrode/electrolyte interface, where it reacts. However, when $y > 0.08$, the current remains high for the first minute (Fig. 12) and the time variation departs from $t^{-1/2}$ (Fig. 13). Such a change for the critical value of $y = 0.08$ is to be connected with the two different regimes observed for E vs. y (Fig. 3 and 5) below and above this critical value. It favors the assumption of an intercalated compound for $y \sim 0.08$. The kinetics of the phase transformation would thus be added to the overall kinetics, accounting for the relative slowness of the kinetics observed above $y = 0.08$.

In order to derive the diffusion coefficient D from Eq. [1], we have chosen its domain of applicability, namely, $y < 0.08$. Cottrell's equation contains the initial condition that $C = C_0$ for $t = 0$ and the boundary conditions $C = C_0$ far from the interface and $C = 0$ at the interface $x = 0$. This condition can be checked by measuring the current I immediately after a preset voltage U with a potentiostat. The results I vs. U are shown on Fig. 14. Whereas for $U > 0.3\text{V}$, the current depends on the voltage, I is almost constant for $U < 0.3\text{V}$. This corresponds to a concentration of iodine $C \sim 0$ at $x = 0$. The kinetics were determined by

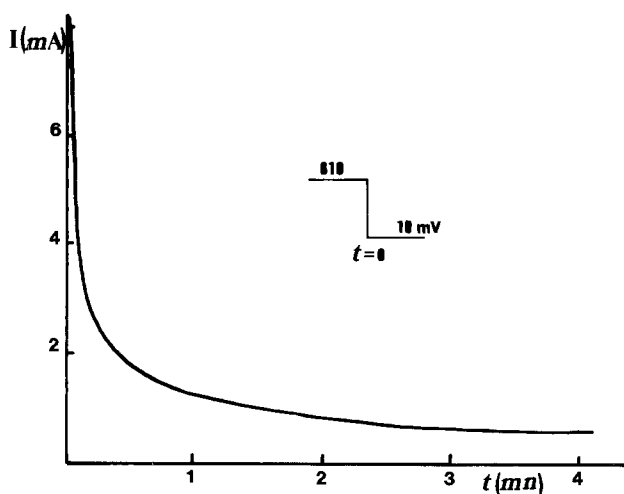


Fig. 10. Short-circuit discharge of a polyacetylene-silver cell with initial $y = 0.08$.

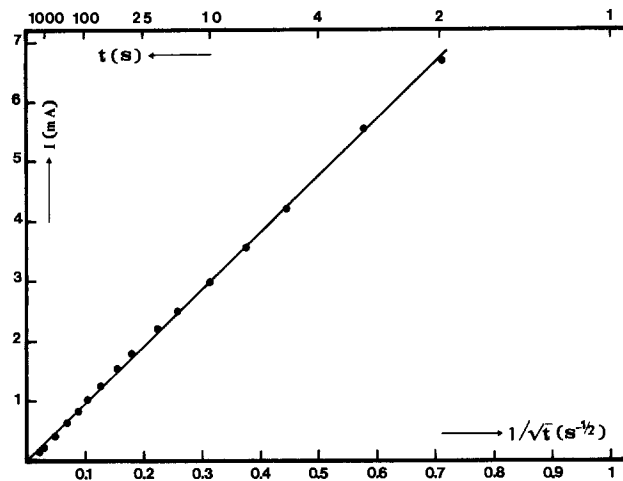


Fig. 11. Time dependence of the short-circuit current I vs. $t^{-1/2}$ with initial $y = 0.08$.

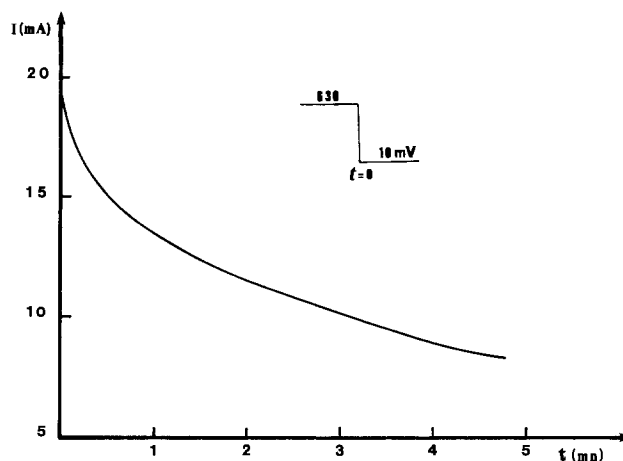


Fig. 12. Short-circuit discharge of a polyacetylene-silver cell with initial $y = 0.12$.

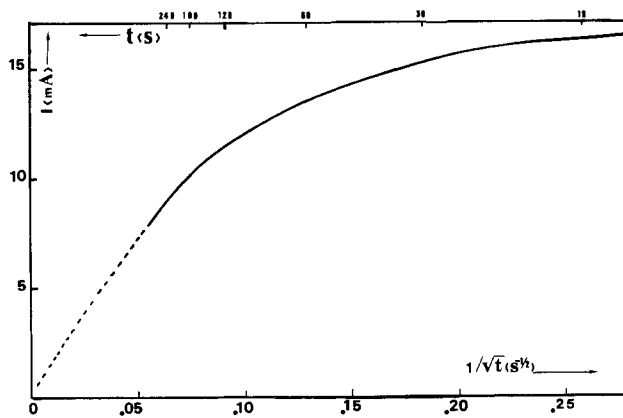


Fig. 13. Time dependence of the short-circuit current I vs. $t^{-1/2}$ with initial $y = 0.12$.

following 35 short discharges on a resistor of 1Ω . The short-circuit current (typically around 10 mA for a cross section of 1 cm^2) was measured by recording the voltage drop between the ends of that resistance. This method gives practically the same results as the potentiostatic method since the voltage remains very much smaller than 0.3V and therefore the current does not depend on the voltage.

A long time (several days) is necessary between two successive discharges to get the new homogenization of iodine inside the polymer. When the iodine content C_0 was supposed uniform, the next discharge was recorded which made C_0 (or y) to decrease. This was repeated 35

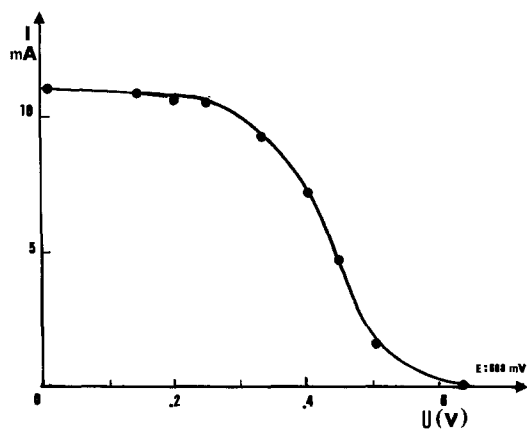


Fig. 14. Potentiostatic measurement of the current of a polyacetylene-silver battery.

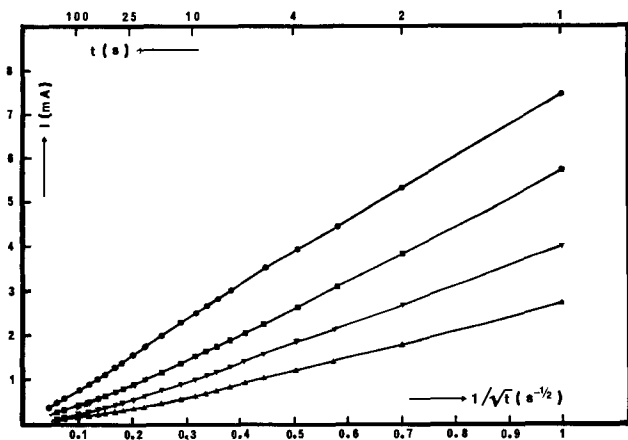


Fig. 15. Short-circuit current as a function of $t^{-1/2}$ at constant temperature (30°C) for the following iodine cathode contents: $\gamma = 0.058$ (circles), 0.047 (squares), 0.03 (filled triangles), and 0.014 (open triangles).

times until $C_0 \sim 0$. Some of the results are shown in Fig. 15. They all obey the time dependence of Eq. [1]. The slope of the straight lines should thus be equal to

$$\alpha = \frac{d(I)}{d(t^{-1/2})} = ZFSC_0 \sqrt{D/\pi} = FS \frac{y\rho}{M} \sqrt{D/\pi} \quad [2]$$

where ρ is the specific mass of pressed $(\text{CH})_x$ and M the mass of a CH unit (13g). The linear dependence of that slope α as a function of γ (Fig. 16) is in agreement with the theoretical equation. The diffusion coefficient derived from Eq. [2] is $D = 1.5 \times 10^{-9} \text{ cm}^2\text{-s}^{-1}$ for that constant temperature of 30°C .

This result compares well with the diffusion coefficient measured in the desorption of iodine out of $(\text{CHI}_y)_x$ with a radioactive technique (6). One must, however, emphasize that this coefficient is not the diffusion coefficient of I_2 into the crystalline part of $(\text{CH})_x$. It is the overall coefficient which integrates all the phenomena involved in the transfer of iodine from the polymer: intrafibrillar diffusion, diffusion in the interfibrillar spaces, desorption from the surface, etc. It is simply noteworthy that a tracer technique and an electrochemical method give independently the same result, also in agreement with the overall diffusion coefficient of profiles measured with the electron microprobe (28, 29).

Activation energy of diffusion.—The same potentiostatic measurements were performed as a function of temperature in the range -20° to $+40^{\circ}\text{C}$. A bigger cell with 33 mg of $(\text{CH})_x$ was initially charged at the level $\gamma = 0.06$. The discharge $I = f(t)$ was followed for 10s at several temperatures. Between two runs the temperature was raised at 30°C for 24h or more until equilibrium was reached again. The linear dependence of I vs. $t^{-1/2}$ is observed for all the

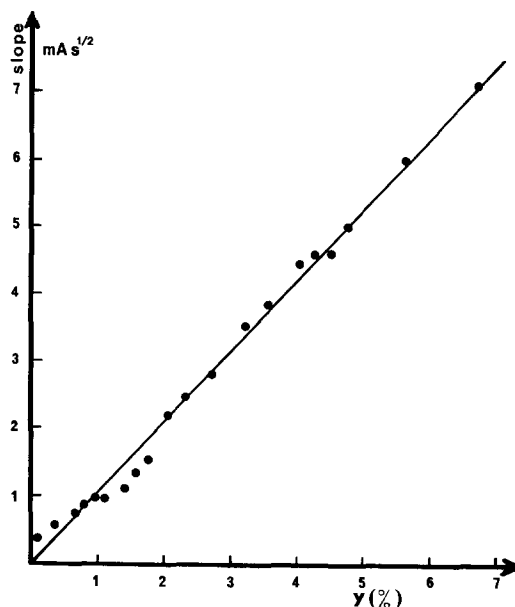


Fig. 16. Influence of the iodine cathode content on the short-circuit current (plotted as the slopes of the straight lines such as those of Fig. 15 vs. γ).

temperatures except 40°C (Fig. 17), which means that above 30°C , diffusion of iodine is no longer the only rate-controlling mechanism. The diffusion coefficient derived from Eq. [2] is plotted on Fig. 18 as $\ln D$ vs. the reciprocal temperature. It obeys the Arrhenius equation

$$D = 85 \exp(-0.607/kT) \text{ cm}^2\text{-s}^{-1}$$

The relatively large activation energy of 0.607 eV probably measures the energy of migration inside the fibrils, which would be the rate-controlling mechanism.

Self-discharge.—The main cause of self-discharge is the diffusion of molecular iodine throughout the solid electrolyte. As a matter of fact, RbAg_4I_5 is under the form of a sintered powder which allows iodine to diffuse through the pores (21, 30). We adopted the remedy proposed by Owens (20, 21), consisting in mixing a little silver powder with the electrolyte so that the escaping iodine would be trapped by the silver atoms encountered inside the electrolyte to give silver iodide. The theoretical equations of this diffusion mechanism have been established by Oldham and Owens (21). We have carried out the experimental investigation of the diffusion of iodine into RbAg_4I_5 using radioactive I-125 .

Pressed pellets of RbAg_4I_5 are prepared with the main surface of area equal to 0.75 cm^2 , accurately smoothed with a microtome. The diffusion of iodine is then let to occur at constant temperature. The iodine source is a mixture of natural and radioactive iodine in a precisely

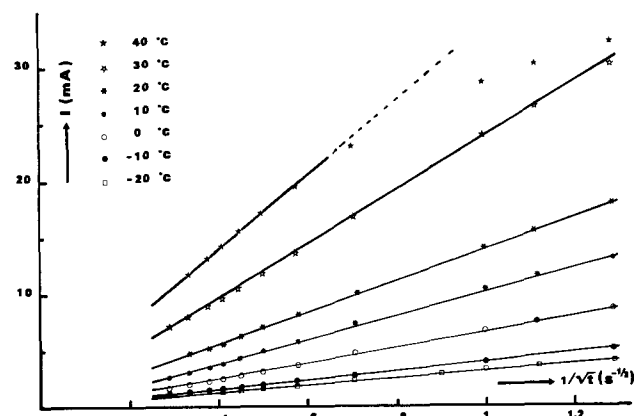


Fig. 17. Short-circuit current as a function of $t^{-1/2}$ at constant iodine content ($\gamma = 0.06$) for the several temperatures indicated.

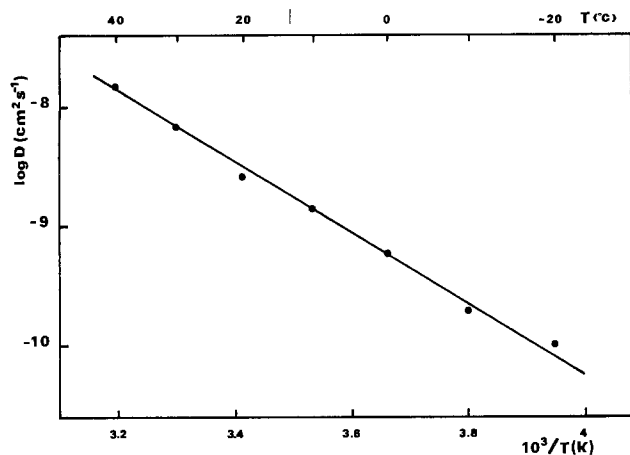


Fig. 18. Arrhenius plot of the overall diffusion coefficient of transfer of iodine in $(\text{CH})_x$.

known ratio. The concentration of iodine is thereafter readily derived from the measurement of the radioactivity. After diffusion, the sample is sectioned with a microtome in parallel sections of a thickness usually equal to 20 μm . The radioactivity due to the gamma-rays emitted by I-125 is measured in each section with an automatic counter. As an example, the diffusion profile at $\theta = -10^\circ\text{C}$ is shown in Fig. 19. The following conclusions are drawn.

1. The concentration at the origin is about $0.2 \text{ g}\cdot\text{cm}^{-3}$, and this value is found constant in the temperature range -20° to $+20^\circ\text{C}$. This quite large concentration corresponds almost exactly to the complete filling of the pores between the grains of the pressed electrolyte. The theoretical density of RbAg_4I_5 is $5.38 \text{ g}\cdot\text{cm}^{-3}$. The measured density of our samples is $5.23 \text{ g}\cdot\text{cm}^{-3}$, which gives a porosity of 3%. The pores are therefore filled at the interface with condensed iodine which diffuses further into the crystal.

2. The initial condition being $C_{i,x=0} = C_0$, one would expect the diffusion profile to follow the complementary error function $C = C_0 [1 - \text{erf}(x/2\sqrt{Dt})]$. In fact, no profile could be fitted with this equation. It was then examined whether a reaction of fixation of iodine is also occurring during the diffusion. One might think either of a

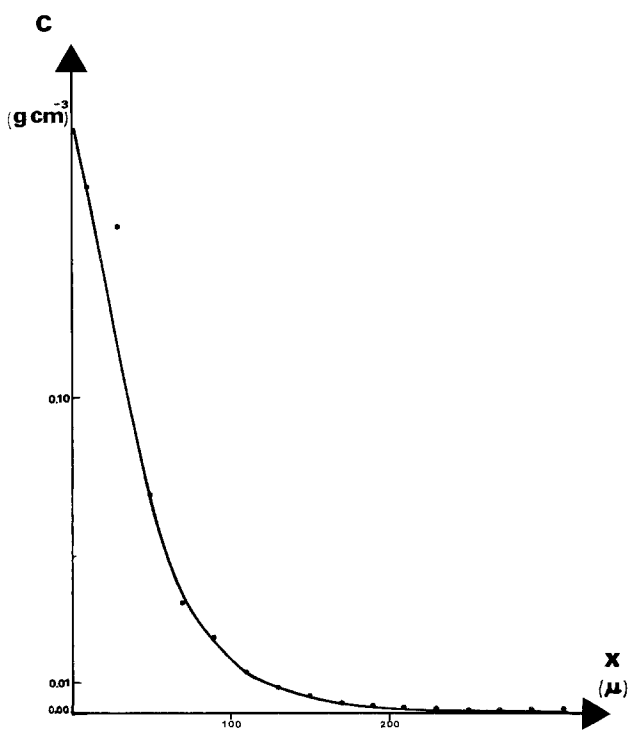
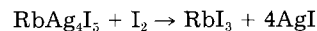


Fig. 19. Diffusion profile of I_2 into a RbAg_4I_5 pressed pellet at -10°C .

reaction of chemisorption or alternatively of a true chemical reaction like



The diffusion profile would then be given by

$$C \sim C_0 \exp(-x\sqrt{k/D})$$

where D is the diffusion coefficient and k the rate constant assuming the kinetics of the first order. Unfortunately the fitting was not improved by a large extent. The diffusion mechanism remains to be clearly elucidated.

3. Because of the poor quality of the fitting, only a rough estimation of D can be made: $10^{-9} < D < 10^{-8} \text{ cm}^2\cdot\text{s}^{-1}$. The most interesting feature is that D hardly depends on temperature. This clearly confirms that the penetration of iodine is not a solid-state diffusion mechanism. Instead, one can conclude that diffusion is controlled by diffusion of gaseous iodine through the pores, followed by some diffusion into the grains.

The general conclusion of that study was the necessity of the procedure used to prevent self-discharge, consisting in filling the pores by silver thin particles which efficiently trap the iodine molecules.

Sodium Battery

The general conclusion about the polyacetylene-silver battery is that it is a good system, at least from the electrochemical point of view. However, when compared to the other primary cells — particularly that of Leclanché — its energy cost may seem too high. It obviously comes to mind that the substitution for silver by an alkali metal would drastically cut down this cost. As a matter of fact, silver is a very heavy and very expensive metal, which enters the composition of both the anode and the electrolyte. So, another prototype polyacetylene-sodium was simultaneously studied. Sodium was chosen because of the availability of the sodium ion conducting solid electrolyte, namely beta-alumina. Chiang (8) investigated the cell $(\text{CHNa}_y)_x/\text{PEO-NaI}/(\text{CHI}_y)_x$ above 60°C . The advantage of β -alumina is its possible use at room temperature (31). Lithium would give an even higher energy density, but until now there is no satisfactory solid electrolyte conducting by the lithium ions at room temperature. Sodium has already advantages over silver as the anode (1F for 23g instead of 130g) as well as the electrolyte (a membrane of 0.2g can be used instead of 1g of RbAg_4I_5). Last, higher voltages are expected also contributing to increasing the power density.

Cell $\text{Na}/\beta\text{-Al}_2\text{O}_3/(\text{CHI}_y)_x$.—This cell was formed by assembling the cathode shown on Fig. 20 with pure sodium inside the glove box in argon atmosphere. One finds $V_{OC} = 2.76\text{V}$ and $I_{SC} = 35 \times 10^{-6}\text{A}$ at 25°C .

From the tables of thermodynamic constants, one derives the Gibbs free energy of formation of NaI at 25°C of $\Delta G_{f,\text{NaI}}^\circ = -69.99 \text{ kcal}\cdot\text{mol}^{-1}$ and hence the standard po-

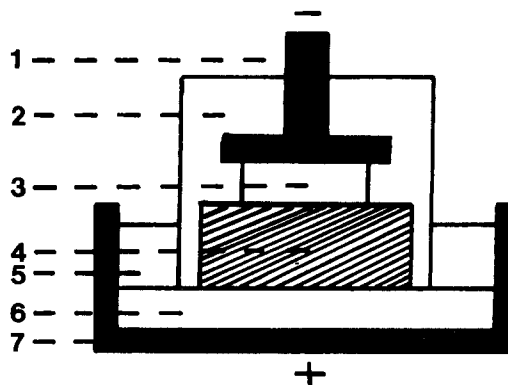


Fig. 20. Solid-state electrochemical doping of polyacetylene. 1: Cathode. 2 and 5: Waterproof coatings of resin. 3: Polyacetylene. 4: $\beta''\text{-Al}_2\text{O}_3, x\text{Na}_2\text{O}$. 6: Sodium source. 7: Anode.

tential associated with the formation of NaI: $E^\circ = 2.95\text{V}$. The electromotive force of the cell would then be $E = 2.95 \times 0.059 \log a_i$, where a_i is the activity of iodine inside $(\text{CH})_x$. Taking $a_i = 0.07$ leads to $E = 2.88\text{V}$, so that the experimental $E = 2.76\text{V}$ is well accounted for. However, the cell cannot keep the charge for more than 1h because we could not prevent oxidation of sodium. This forced us to use $(\text{CH})_x$ on both sides, *i.e.*, at the negative as well as at the positive electrode.

Preparation of the polyacetylene-sodium anode.—We have found a simple and cheap method to dope $(\text{CH})_x$ with Na inside a resin coating so that oxidation of sodium by air is prevented. Sodium is allowed to dope the film of pure $(\text{CH})_x$ by an electrochemical method through the solid electrolyte like that in Fig. 20. Several sources of sodium were tried: aqueous solution of NaOH, aqueous solution of NaNO_3 in ethanol, and solution of NaI in N-methylacetamide. Electrolysis is performed at a constant voltage. The dependence of the current on time always follows the same trend: very small current during the first hours before a sudden abrupt rise. At first, it was assumed that the current is initially limited by the high electrical resistance of the undoped $(\text{CH})_x$. After a minimum amount of sodium, the conductivity increases drastically, which accelerates the doping. The voltage must exceed 3V, which is the decomposition potential of NaI. Cracks can be observed in the alumina membrane after some use of the battery. We now think that the initial stage corresponds to the time necessary for the cracks to form, propagate, and to be filled with metallic sodium, which would eventually short-circuit the membrane.

So, the final goal is reached: $(\text{CH})_x$ can be doped by a solid-state electrochemical method, inside a protecting coating of resin, which provides an efficient and cheap method of doping. Among the various electrolytic solutions, the organic solution of NaI in N-methylacetamide gives the best results. The aqueous solutions are to be avoided because they damage the Al_2O_3 electrolyte more quickly and also the subsequent grain boundary diffusion of water molecules must be forbidden.

Study of the $(\text{CHNa}_y)_x/\beta''\text{-Al}_2\text{O}_3/(\text{CHI}_y)_x$ battery.—One more problem arose when, after assembling the cell with a sodium-doped anode and an iodine-doped cathode, it was only possible to draw a very small current. As a matter of fact, the internal resistance was $> 10^6\Omega$ instead of the $10^2\Omega$ expected with this electrolyte at 25°C . The major part of the resistance was supposed to take place in the anode/electrolyte interface. The traces of oxygen or water molecules adsorbed on the fibrils would form a highly resistive film of sodium oxide. A great improvement was found when, instead of assembling the $(\text{CH})_x$ anode and the electrolyte as separate elements, the polymer was synthesized directly upon the surface of the beta-alumina membrane. Finally, the measured internal resistance is typically $10^3\Omega$, still a large value, but providing a more acceptable current of about 10^{-5}A . The maximum short-circuit current of $\sim 10^{-3}\text{A}$ was observed in a cell which presented cracks.

Two different types of discharge curves were observed. The first one is given in Fig. 21. The initial open-circuit voltage reaches 2.94V, corresponding exactly to formation of NaI. However, it rapidly decreases down to 0.8V in a few hours without any current having been drawn. The examination of such cells revealed cracks throughout the solid electrolyte. The cracks therefore allowed metallic sodium to be formed during the charge, but at the same time gave an obvious way for the active species to diffuse and react without producing electricity. This accounts both for the high initial open-circuit voltage and fast self-discharge. The second type of discharge is more interesting (Fig. 22): the open-circuit voltage of 1.3V is lower but practically stable over several days. The short-circuit current is limited by the internal resistance of the cell. Typical values of $20\ \mu\text{A}$ are found.

In the case of the electrochemical doping in an aqueous or organic solution, the dopants transfer their charges and

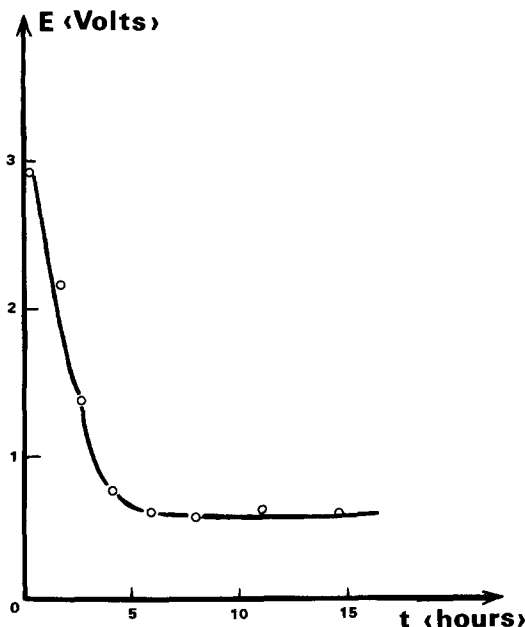
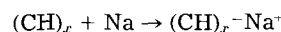
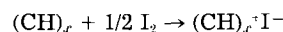


Fig. 21. Open-circuit voltage of a $\text{CHNa}_y/\beta''\text{-Al}_2\text{O}_3/\text{CHI}_y$ battery charged at high voltage.

remain in the polymer as simple counterions such as Na^+ or I_3^-



at the negative electrode, and



at the positive electrode.

The further electrochemical doping would thus be simply reduction of $(\text{CH})_x$ at the anode and oxidation of $(\text{CH})_x$ at the cathode. The free energy is the sum of the oxidation and reduction energies, which theoretically coincides with the energy gap which is 1.3V in $(\text{CH})_x$. The electromotive force should thus be equal to 1.3V (32), which is in good agreement with the present results observed when the thermodynamical equilibrium is reached. It is noteworthy that the liquid state $(\text{CH})_x$ batteries also give $E = 1.3\text{V}$ (32).

Energy density.—As an example, the battery of initial composition $(\text{CHNa}_{0.1})_x/\beta''\text{-Al}_2\text{O}_3, \text{Na}_2\text{O}/(\text{CHI}_{0.1})_x$ and a voltage of 1.3V has an energy density of 95 Wh/kg. The weight of the solid electrolyte as well as container, resin, and leads has obviously to be taken into account. All these factors make the energy density decrease down to 20 Wh/kg. This is only one-half the energy density of the lead battery. Some gain on the weight could be expected by decreasing the thickness of the electrolyte, increasing the doping level, substitution of sodium by lithium if a solid

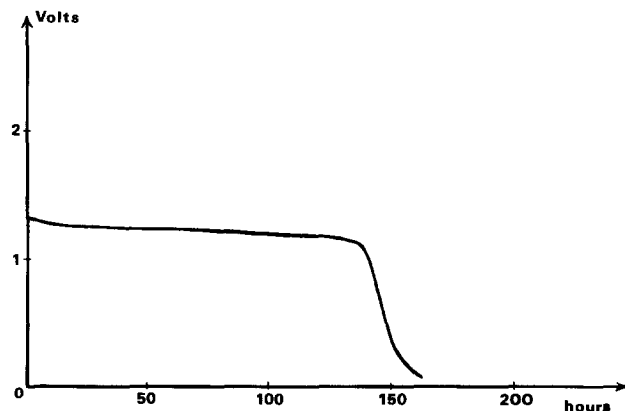


Fig. 22. Open-circuit voltage of a $\text{CHNa}_y/\beta''\text{-Al}_2\text{O}_3/\text{CHI}_y$ battery charged at low voltage.

electrolyte conducting by the lithium ions was discovered. Substitution for iodine by a lighter acceptor impurity is also desired.

Conclusion

The present study has shown that polyacetylene can be used as the electrode material in solid-state batteries working at room temperature, at least in two prototypes at the laboratory level. The obvious question is will such polyacetylene solid-state batteries ever reach the industrial level? Some important steps have been made.

1. A battery with pure $(\text{CH})_x$ and a solid electrolyte can be stored for any period of time. A partial electrolysis of the solid electrolyte leads after solid-state electrochemical doping of the polymer to making the battery ready for use only when needed. The consequence is a very long lifetime.

2. It is vital to insure a good electrical contact between the polymeric electrodes and the solid electrolyte, for instance, by synthesizing the polymer directly on the solid electrolyte.

However, there remain many improvements to achieve before one could hope to reach the commercial stage:

1. The current density $\sim 10^{-4}$ A-cm $^{-2}$ restricts the possible market to the supply of the electronic devices and liquid crystal displays.

2. The energy cost has to be reduced: both the solid electrolytes used here are quite expensive, either because of the materials (Ag and Rb in RbAg_4I_3) or because of the high technology of Al_2O_3 , $x\text{Na}_2\text{O}$.

3. The energy density has to be increased.

The final conclusion is that we have shown that polyacetylene (or any other conducting polymer) solid-state batteries are promising. However, new solid electrolytes would be desired to improve the performances.

Acknowledgments

We acknowledge the financial support of the Agence Nationale pour la Valorisation de la Recherche, Contract no. 82.4147.00, and of the Direction des Recherches, Etudes et Techniques, Contract no. 82/1014. We also thank Professor F. Schué (Université de Montpellier) for the polyacetylene samples, the Compagnie Générale d'Electricité (Laboratoires de Marcoussis) for the β' - Al_2O_3 samples and M. Frere and M. Le Guilloux (Centre National d'Etude des Télécommunications de Lannion) for the technical assistance.

Manuscript submitted Nov. 28, 1984; revised manuscript received May 10, 1985. This was Paper 890 RNP presented at the San Francisco, California, Meeting of the Society, May 8-13, 1983.

L'Université de Rennes I assisted in meeting the publication costs of this article.

REFERENCES

- H. Shirakawa, E. J. Louis, A. G. MacDiarmid, C. K. Chiang, and A. J. Heeger, *J. Chem. Soc. Chem. Commun.*, 578 (1977).
- D. M. Ivory, G. G. Miller, J. M. Sowa, L. W. Shacklette, R. R. Chance, and R. H. Baughman, *J. Chem. Phys.*, **71**, 1506 (1979).
- A. MacDiarmid, A. J. Heeger, and P. Nigrey, U.S. Pat. 4,321,114 (1982).
- A. J. Heeger, A. G. MacDiarmid, C. K. Chiang, and H. Shirakawa, U.S. Pat. 4,222,903 (1980).
- C. Wegner, *Angew. Chem. Int. Ed. Engl.*, **20**, 361 (1981).
- F. Beniere, S. Haridoss, J. P. Louboutin, M. Aldissi, and J. M. Fabre, *J. Phys. Chem. Solids*, **42**, 649 (1981); **43**, 233 (1982).
- F. Beniere, J. Franco, and J. P. Louboutin, French Pat. 81.05 568 (1981).
- C. K. Chiang, *Polym. Commun.*, **22**, 1454 (1981).
- Y. W. Park, A. J. Heeger, M. A. Druy, and A. G. MacDiarmid, *J. Chem. Phys.*, **73**, 946 (1980).
- C. K. Chiang, M. A. Druy, S. C. Gau, A. J. Heeger, E. J. Louis, A. G. MacDiarmid, and Y. W. Park, *J. Am. Chem. Soc.*, **100**, 1013 (1978).
- P. J. Nigrey, A. G. MacDiarmid, and A. J. Heeger, *J. Chem. Soc. Chem. Commun.*, 594 (1979).
- D. MacInnes, M. A. Druy, J. J. Nigrey, D. P. Nairns, A. G. MacDiarmid, and A. J. Heeger, *ibid.*, 594 (1979).
- L. W. Shacklette, R. L. Elsenbaumer, R. R. Chance, J. M. Sowa, D. M. Ivory, G. G. Miller, and R. H. Baughman, *ibid.*, 361 (1982).
- L. Mihaly, S. Pekker, and A. Janossy, *Synth. Met.*, **1**, 349 (1979/1980).
- F. Rachdi, P. Bernier, E. Faulques, S. Lefrant, and F. Schue, *J. Phys. (Paris)*, **C3**, 97 (1983).
- F. Beniere, J. Franco, and J. P. Louboutin, *Rad. Eff.*, **75**, 139 (1983).
- S. Geller, *Phys. Rev. B*, **14**, 4345 (1976).
- B. B. Owens and G. R. Argue, in "Advances in Electrochemistry and Electrochemical Engineering," Vol. 8, C. W. Tobias, Editor, New York (1971).
- S. Pekker, M. Bellec, X. Le Cleac'h, and F. Beniere, *Syn. Met.*, **9**, 475 (1984).
- B. B. Owens, J. S. Sprouse, and D. L. Warburton, in "Proceedings of the 25th Power Sources Conference," Atlantic City, NJ, May 23-25, 1972, p. 8.
- K. B. Oldham and B. B. Owens, *Electrochim. Acta*, **22**, 677 (1977).
- L. W. Shacklette, R. L. Elsenbaumer, and R. H. Baughman, *J. Phys. (Paris)*, **C3**, 559 (1983).
- D. M. Smith, *This Journal*, **106**, 635 (1959).
- R. H. Baughman, N. S. Murthy, G. G. Miller, and L. W. Shacklette, *J. Phys. (Paris)*, **C3**, 53 (1983).
- K. Kaneto, M. R. Maxfield, D. P. Nairns, A. G. MacDiarmid, and A. J. Heeger, *J. Chem. Soc., Faraday Trans.*, **78**, 3417 (1982).
- L. E. Topol and B. B. Owens, *J. Phys. Chem.*, **72**, 2106 (1968).
- T. Takahashi, S. Ikeda, and O. Yamamoto, *This Journal*, **119**, 477 (1972).
- C. Benoit, M. Rolland, M. Aldissi, A. Rossi, M. Cadene, and P. Bernier, *Phys. Status Solidi B*, **68**, 209 (1981).
- A. Janossy, L. Pogany, S. Pekker, and R. Swietlik, *Mol. Cryst. Liq. Cryst.*, **77**, 185 (1981).
- R. D. Armstrong, T. Dickinson, H. R. Thirsk, and R. Whitfield, *J. Electroanal. Chem.*, **34**, 47 (1972).
- F. Beniere, *La Recherche*, **52**, 36 (1975).
- L. W. Shacklette, R. L. Elsenbaumer, and R. H. Baughman, *J. Phys. (Paris)*, **C3**, 559 (1983).

Heterojunction Photoelectrodes

II. Electrochemistry at Tin-Doped Indium Oxide/Aqueous Electrolyte Interfaces

Oliver M.-R. Chyan and Krishnan Rajeshwar*

Department of Chemistry, The University of Texas at Arlington, Arlington, Texas 76019

ABSTRACT

Redox electrochemistry at Pt- and tin-doped indium oxide (ITO) electrodes was studied in a comparative manner in aqueous electrolytes. This study was prompted by the applicability of ITO thin films as corrosion inhibiting agents in photoelectrochemical systems. Cyclic voltammetry and steady-state polarization measurements were used to probe the relative facility of charge transfer at the two electrode/electrolyte interfaces. The candidate redox systems were $\text{Fe}(\text{CN})_6^{4-/3-}$, I^-/I_3^- , and $\text{Fe}^{2+/3+}$, the latter in the presence and absence of Cl^- ion catalysts. The key finding of this study is that differences in kinetic facility between Pt and ITO manifest to varying degrees, which depend critically on the intrinsic kinetics of the particular redox couple.

A major obstacle confronting photoelectrochemical (PEC) methods of solar energy conversion is the proclivity of most narrow bandgap semiconductor electrodes to corrosion and passivation. Corrosion is a particularly severe problem in aqueous electrolytes. Of the approaches considered thus far for protection of semiconductor surfaces, the strategy of using some type of overlayer or coating has proved to be effective. The materials comprising such overlayers have been generally of three types: polymers, wide bandgap oxides, and metals (2). Early attempts to use oxides such as TiO_2 did not yield encouraging results because of the relatively high resistivity of these materials and the consequent need to use very thin layers (3). Such layers are prone to pinhole formation and electrolyte "undercutting" problems. Problems of similar nature occur with metal coatings, whose high optical absorptivities require the use of very thin layers.

Compounds such as heavily-doped SnO_2 and In_2O_3 in thin film form, however, are unique in that they combine good optical transparency to the visible spectrum with low electrical resistivity (4). The use of these materials as coatings for PEC electrodes, therefore, is not restricted to very thin layers and associated complications as with the materials discussed above. With this rationale in mind, electrode structures comprising Si and coated with Sn-doped In_2O_3 (ITO) thin films were fabricated in previous studies in this laboratory (1). These electrodes have shown excellent stability in aqueous media, even under testing conditions typical of a Cl_2 containing ambient (1, 5).

The juxtaposition of two interfaces, namely, semiconductor/surface layer and surface layer/redox electrolyte, in a heterojunction photoelectrode structure (cf. Fig. 1), alters the picture considerably from the classical semiconductor/electrolyte case. As with the metal-film electrode structures considered by previous authors (6), the photovoltaic junction is already "built in," for example, at the Si/ITO interface¹ and the electrolyte ideally should not influence this electrostatic barrier. However, electrochemical kinetics at the ITO/redox electrolyte interface should play a key role since the two interfaces are in series (cf. Fig. 1). This expectation is realized in terms of the vastly superior photoresponse of the p-Si/ITO heterojunction photoelectrode in contact with the $\text{Fe}(\text{CN})_6^{4-/3-}$ redox system, as compared to another redox couple with a virtually identical E° , namely, the I^-/I_3^- system. Relevant data are presented in Fig. 2; they were culled from

*Electrochemical Society Active Member.

¹Note that the Si/ITO junction characteristics are dependent on the method of its fabrication. For example, neutralized Ar⁺ ion beam sputtering of ITO yields a rectifying barrier on p-Si and an ohmic contact on n-type Si. Just the opposite is observed when the ITO thin film is prepared by spray pyrolysis. This behavior has been rationalized in terms of the formation of a damaged n-type Si layer just underneath the ITO during sputtering (i.e., a "buried" homojunction is induced) (7). In spite of this subtlety, the term "heterojunction photoelectrode" is retained here regardless of whether the substrate is n- or p-type. This is done merely for the sake of brevity.

previous studies in this laboratory (1). The redox kinetics of $\text{Fe}(\text{CN})_6^{4-/3-}$ on the ITO surface are obviously much better than in the case of the polyiodide couple, as also illustrated by steady-state (polarization) measurements on ITO electrodes (cf. Fig. 2). These aspects related to the electrochemistry at the ITO/redox electrolyte interface, are probed in more detail in this study, primarily via cyclic voltammetry (CV). Three model redox couples— $\text{Fe}(\text{CN})_6^{4-/3-}$, I^-/I_3^- , and $\text{Fe}^{2+/3+}$ —in suitable supporting electrolytes were chosen for this purpose. These new measurements were prompted by the sparsity of electrochemical data on conducting and transparent oxide surfaces in general, and on ITO in particular (see below).

Electrochemistry of Conducting and Transparent Oxide Thin Films

The majority of the literature data pertain to SnO_2 and, as such, are summarized here, since these data also should be fairly indicative of the behavior to be expected from ITO. Early researchers stressed the advantages over Pt or Au in the use of thin film electrodes such as Sb: SnO_2 in terms of high O_2 overpotential and lack of surface oxidation phenomena (8). These advantages were utilized in later studies for anodic electroanalytical chemistry (9). Particularly pertinent to the present work are studies from the same group (10) on the kinetics of model redox processes at Sb: SnO_2 thin film electrodes. Interestingly enough, Pt was used as the thin film substrate for these electrochemical studies. While highly doped ($N_D \sim 10^{20} \text{ cm}^{-3}$) SnO_2 specimens exhibited reversible behavior for $\text{Fe}(\text{CN})_6^{4-/3-}$ and $\text{Fe}(\text{o-phen})_3^{2+/3+}$ (o-phen: o-phenanthroline) redox couples, the cyclic voltammograms showed pronounced asymmetry for thin films of higher resistivity. This trend was interpreted in terms of the width of the space-charge region in Sb: SnO_2 and its dependence on doping level. At high doping, the barrier becomes transparent to the flow of electrons in either direction, whereas at a value of N_D equal to ca. 10^{19} cm^{-3} , the oxidation process becomes tunnel limited. Similar trends

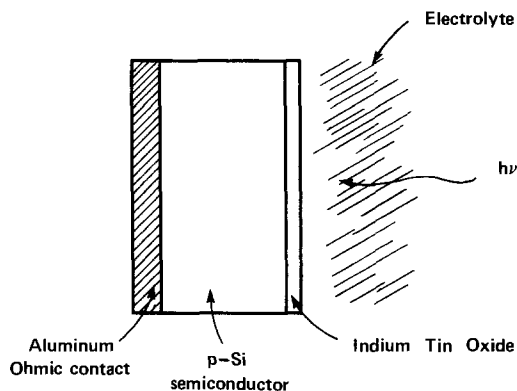


Fig. 1. Schematic of the p-Si/ITO heterojunction photoelectrode structure

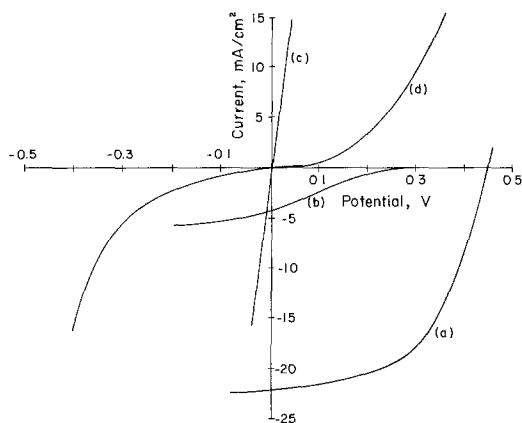


Fig. 2. Steady-state current-voltage characteristics under solar illumination for a p-Si/ITO electrode in contact with (a) 0.5M $\text{Fe}(\text{CN})_6^{4-3-}$ and (b) 1M $\text{KI}/0.05\text{M I}_2$ redox couples. The corresponding electrocatalytic activity towards the respective redox couples (curves c and d) of an ITO thin film is superimposed on the photocharacteristics [cf. Ref. (1)]. (Reprinted with permission from the Journal of American Chemical Society, 105, 324 (1983). Copyright (1983) American Chemical Society.)

are apparent for the $\text{Fe}^{2+/3+}$ redox process in a more recent study (11) on the photogalvanic applications of thin film SnO_2 electrodes.

Similar irreversibility (relative to Pt) has been observed on SnO_2 thin film electrodes in molten LiCl-KCl eutectic towards O^{2-} and Cl^- oxidation (12). In spite of this trend, however, the metal-like nature of these electrodes (in terms of their electrochemical behavior) toward a wide variety of redox reactions in molten salt electrolytes (13) was verified. The potential distribution across the SnO_2 /electrolyte interface has been analyzed via capacitance measurements both for nonaqueous (molten salt) (14) as well as for aqueous electrolyte cases (15, 16).

Other studies on the electrochemistry of conducting and transparent oxide thin films describe electrochemical platinization of SnO_2 surfaces (17a) and subsequent characterization by photoelectron spectroscopy (17). Photoelectron spectroscopy has also proved useful for probing changes in the surface composition of $\text{Sb}:\text{SnO}_2$ and ITO electrodes after electrochemistry (18). In the same study, the authors present the current-voltage (*i-E*) behavior of ITO thin film electrodes in 1N H_2SO_4 . To our knowledge, this is the only published report on the electrochemical behavior of ITO thin film electrodes.

Experimental

Instrumentation for CV and steady-state (Tafel) measurements has been described elsewhere (19). Additionally, an EG & G Model 264 electrochemistry system was also used in some cases. Standard three-electrode cell geometry with positive feedback *iR* compensation (80-90%) was employed for all measurements; these were performed at ambient temperature. The working electrode was either ITO or a Pt disk (IBM Instruments, Incorporated; geometric area: 0.20 cm^2). A Pt spiral was used as counterelectrode. Either a saturated calomel electrode or an Ag/AgCl electrode was used as reference. All potentials below, however, are quoted with respect to the latter reference. The cell contents were thoroughly purged with prepurified N_2 for ca. 10 min prior to an experiment to preclude interference from O_2 electrochemistry. All redox chemicals were reagent grade and were used as received. Triply distilled water was used for electrolyte preparation in all cases.

The ITO electrodes were fashioned out of wafers on glass slides. These thin films of ITO were deposited either by spray-pyrolysis or neutralized Ar^+ -ion beam sputtering, according to procedures described elsewhere (4, 20, 21). No differences in electrochemical behavior were observable between the films prepared by these two methods, such that further differentiation is not made for the data to be discussed below. The ITO films

utilized in this study had a nominal resistance of 7.5 Ω/\square and were ca. 0.5 μm thick. These films contained 9 mole percent (m/o) SnO_2 and had a nominal carrier concentration of ca. 10^{21} cm^{-3} . Conducting Ag epoxy (Epotek, Billerica, Massachusetts) was used for electrical connection to the ITO film surface. The requisite electrode area for voltammetric measurements (which was in the range 0.2-0.3 cm^2) was defined by careful application of insulating epoxy resin.

In electrochemical measurements employing solid electrodes, the nature of the electrode surface obviously is a key factor in controlling reproducible behavior for a given redox system (22). In preliminary survey experiments, wide variability in CV peak separation ΔE_p and values much higher than the theoretical value of 59 mV were observed for the $\text{Fe}(\text{CN})_6^{4-3-}$ system on Pt, confirming the findings of earlier authors on the extreme sensitivity of charge transfer kinetics of this redox couple to heterogeneous (surface) effects (24). A standard cleaning procedure, therefore, was established for subsequent experimentation on Pt as follows.

After the usual degreasing procedure (detergent followed by an organic solvent rinse), the Pt electrode was thoroughly washed with dichromate-sulfuric acid mixture. An electrochemical pretreatment followed in a 1M KNO_3 solution. The electrode was poised at -0.6V for ca. 10 min in this solution. Vigorous H_2 evolution at the electrode surface was noted. The potential was then moved slightly positive (ca. +0.1V) to oxidize any adsorbed hydrogen species on the electrode surface. Finally, the electrode was washed in deionized water several times.

The efficacy of the above treatment procedure was checked by monitoring ΔE_p for the particular electrode in $\text{Fe}(\text{CN})_6^{4-3-}$ redox medium. A value close to 60 mV was taken as a diagnostic criterion for the "cleanliness" of the Pt electrode surface.

For the ITO electrode, a washing sequence comprising deionized water-mild detergent-deionized water-methyl alcohol was employed followed by air-drying.

Results and Discussion

Behavior in supporting electrolyte.—Background voltammograms on ITO in neutral electrolytes (e.g., 1M KNO_3) are relatively featureless, as shown by a typical example in Fig. 3. The absence of "surface waves" at a variety of scan rates ranging from 0.001 to 0.20V/s is indicative of a relatively low degree of surface hydroxylation and oxidation of the electrode surface. High O_2 overpotentials are also typical on the ITO surface (cf. Fig. 3). (The behavior of a Pt electrode is included for comparison in the same figure). The absence of significant oxidative electrochemistry on ITO (a behavior which contrasts with that of an Au electrode, for example) is reminiscent of observations by previous authors on Sb-doped SnO_2 electrodes (8-10). The enhancement in the

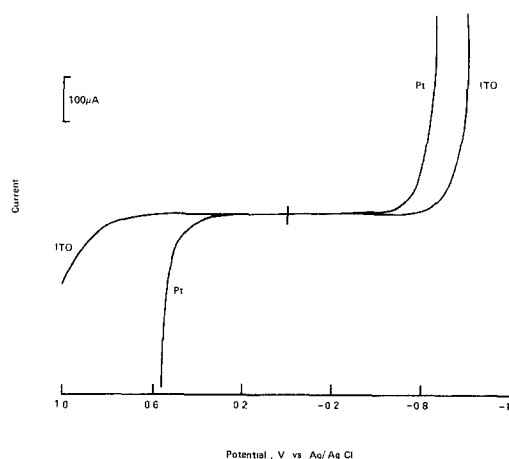


Fig. 3. Background voltammograms for Pt and ITO electrodes in 1M KNO_3 . Potential scan rate: 0.001 V/s.

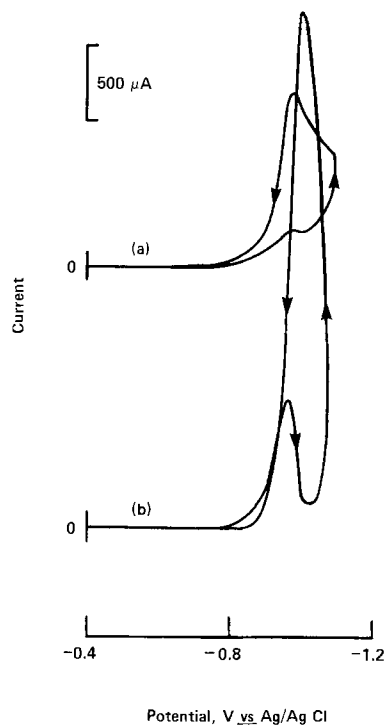


Fig. 4. Steady-state voltammograms for ITO in 1M KNO_3 . Curve a is a scan between -0.4 and -1.0V . Curve b is a scan between the same limits after holding the electrode at -1.0V for ca. 30s.

available potential window (relative to Pt or Au) on SnO_2 and ITO also has been emphasized by previous authors (8-10, 18). A mechanism based on carrier depletion in the film at positive potential excursions [cf. Ref. (10-16)] would account for the relative sluggishness of anodic charge transfer at ITO and seems particularly appropriate to the Fe^{2+} oxidation case discussed in detail below. On the cathodic side, voltammograms are characterized by hydrogen adsorption prewaves, which become particularly noticeable at moderate to high scan rates ($> 0.10\text{ V/s}$) and on holding the electrode at a potential into the H_2 evolution regime. Representative behavior is shown in Fig. 4.

As discussed by previous authors (10a, 18) and confirmed by us, prolonged use of ITO electrodes at potentials beyond the limits shown in Fig. 3 is deleterious in terms of electrode stability. Specifically, irreversible loss of Sn and O species proceeds at extreme positive and negative potential excursions, respectively. In this respect, these electrodes behave similarly to the Sb: SnO_2 system (19). Interestingly enough, changes in carrier concentration and electrode resistance should ensue as a result of these corrosion processes. Work is under way to elucidate these effects.

Behavior in $\text{Fe}(\text{CN})_6^{4-3-}$ redox electrolyte.—Figure 5 shows cyclic voltammograms on Pt (Fig. 5a) and ITO (Fig. 5b) for $\text{Fe}(\text{CN})_6^{4-3-}$ redox electrochemistry.² Relevant parameters from these data are assembled in Table I. Pertinent here is the relative magnitude of ΔE_p on Pt and ITO.

²Note that, for the comparison in Fig. 5 (as well as for the cyclic voltammograms presented in Fig. 6 and Fig. 8-10), the geometric areas of the Pt and ITO electrodes that were exposed to the electrolyte were slightly different.

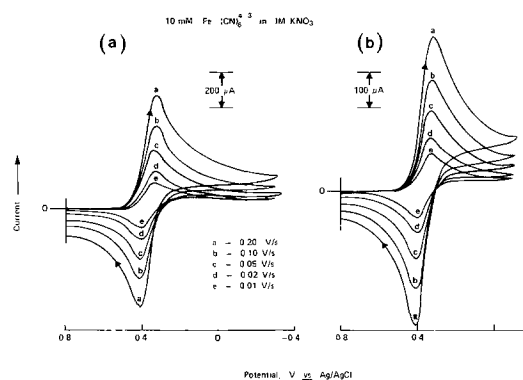


Fig. 5. Comparison of cyclic voltammograms for the $\text{Fe}(\text{CN})_6^{4-3-}$ redox couple in 1M KNO_3 at (a) Pt and (b) ITO electrodes.

In each case, ΔE_p increases with the potential scan rate, v —a trend consistent with the quasi-reversible behavior well established in the literature for the $\text{Fe}(\text{CN})_6^{4-3-}$ couple (23). But more importantly, ΔE_p is always higher for the ITO case. This difference is statistically significant in that electrode-to-electrode variations in ΔE_p on ITO ($\pm 2\text{ mV}$) is always much less than the observed difference between Pt and ITO. It should be pointed out, however, that the Pt surface exhibited wide variability in ΔE_p at a given v , unless the surface was “properly” preconditioned (cf. Experimental section). The value thus measured after optimization is very close to the theoretical value of 59 mV (at 25°C), particularly at low v . These observations with the $\text{Fe}(\text{CN})_6^{4-3-}$ couple on Pt confirm the findings of previous authors (23) on the extreme sensitivity of $\text{Fe}(\text{CN})_6^{4-3-}$ redox chemistry to surface effects.

The other CV parameters (e.g., peak current ratio) in Table I reveal fairly straightforward trends and no significant differences between Pt and ITO for the $\text{Fe}(\text{CN})_6^{4-3-}$ redox system.

Behavior in the polyiodide redox electrolyte.—Let us consider next the I^-/I_3^- redox system. Figures 6a and 6b are the counterparts of Fig. 5a and 5b for this redox system. Immediately obvious is the drastic differences in CV peak shapes in both cases relative to the $\text{Fe}(\text{CN})_6^{4-3-}$ redox system. Extensive literature (24-27) exists for adsorption effects on Pt for the I^-/I_3^- redox couple. An adsorption “spike” (the magnitude of which is dependent on v) is always present on the anodic wave on Pt and absent on ITO. The relative sharpness of the CV peaks on the latter, however, is typical of strong adsorption behavior. In both cases, the cathodic peak shapes are characteristic for reduction of strongly adsorbed species (I_2 in this case). The peak current ratios in Table II for various v values illustrate the nonideality of this redox couple in this regard. Nonzero intercepts in i_p vs. $v^{1/2}$ plots (cf. Fig. 7) are also characteristic of strong adsorption of iodine on Pt and ITO surfaces.

Notwithstanding the above similarities in I^-/I_3^- redox chemistry on Pt and ITO, important differences exist in the kinetics and symmetry of charge transfer in the two cases. The latter manifests again in the relative magnitude of ΔE_p values for the two electrodes (cf. Table II). For example, ΔE_p is as high as 1.20V (!) at $v = 0.20\text{ V/s}$ on ITO.

Behavior in the $\text{Fe}^{2+/3+}$ redox electrolyte.—Figure 8 illustrates cyclic voltammograms on Pt and ITO for the next

Table I. Cyclic voltammetry data for Pt and ITO electrodes in 1M KNO_3 containing 10 mM $\text{Fe}(\text{CN})_6^{3-}$

Scan rate v (V/s)	Pt					ITO				
	ΔE_p (V)	i_{pc} (10^6A)	i_{pa} (10^6A)	i_{pa}/i_{pc}	$i_{pa}/v^{1/2}$ ($10^3\text{A} \times \text{s}^{1/2}/\text{V}^{1/2}$)	ΔE_p (V)	i_{pc} (10^6A)	i_{pa} (10^6A)	i_{pa}/i_{pc}	$i_{pa}/v^{1/2}$ ($10^3\text{A} \times \text{s}^{1/2}/\text{V}^{1/2}$)
0.01	0.060	144	132	0.92	1.44	0.070	95	94	1.12	0.95
0.02	0.065	200	200	1.00	1.41	0.073	137	142	1.11	0.97
0.05	0.070	314	330	1.05	1.40	0.085	210	226	1.08	0.94
0.10	0.080	430	454	1.05	1.36	0.090	285	316	1.04	0.90
0.20	0.092	580	628	1.09	1.30	0.105	390	439	0.99	0.87

Table II. Cyclic voltammetry data for ITO and Pt electrodes in 1M KNO₃ containing 10 mM KI

Scan rate v (V/s)	Pt					ITO				
	ΔE_p (V)	i_{pc} (10 ⁶ A)	i_{pa} (10 ⁶ A)	i_{pa}/i_{pc}	$i_{pa}/v^{1/2}$ (10 ³ A × s ^{1/2} /V ^{1/2})	ΔE_p (V)	i_{pc} (10 ⁶ A)	i_{pa} (10 ⁶ A)	i_{pa}/i_{pc}	$i_{pa}/v^{1/2}$ (10 ³ A × s ^{1/2} /V ^{1/2})
0.01	0.095	110	19.0	0.17	1.90	a	a	a	a	a
0.02	0.105	131	21.5	0.16	1.52	1.00	410	220	0.54	1.56
0.05	0.115	177	42.0	0.24	1.88	1.08	586	360	0.61	1.61
0.10	0.130	221	59.0	0.27	1.86	1.12	740	520	0.70	1.64
0.20	0.145	279	84.0	0.30	1.88	1.20	910	730	0.80	1.64

^a Data not available.

Table III. Cyclic voltammetry data for ITO and Pt electrodes for 5 mM Fe²⁺ in 0.5M KNO₃ and 0.25M H₂SO₄

Scan rate v (V/s)	Pt					ITO				
	ΔE_p (V)	i_{pc} (10 ⁶ A)	i_{pa} (10 ⁶ A)	i_{pa}/i_{pc}	$i_{pa}/v^{1/2}$ (10 ³ A × s ^{1/2} /V ^{1/2})	ΔE_p (V)	i_{pc} (10 ⁶ A)	i_{pa} (10 ⁶ A)	i_{pa}/i_{pc}	$i_{pa}/v^{1/2}$ (10 ³ A × s ^{1/2} /V ^{1/2})
0.01	0.088	49	55	1.12	0.55	0.57	19	29	1.53	0.29
0.02	0.100	70	75	1.07	0.52	0.67	28	40	1.43	0.28
0.05	0.120	117	110	0.94	0.49	0.78	50	60	1.20	0.26
0.10	0.155	161	145	0.91	0.46	0.90	73	83	1.14	0.26
0.20	0.170	240	200	0.83	0.45	0.96	104	115	1.11	0.24

candidate system, namely Fe^{2+/3+}. Accompanying CV data may be found in Table III. Again, very high ΔE_p values on ITO (relative to Pt) demonstrate the inefficiency of charge transfer at this electrode surface for an intrinsically sluggish redox system (see below). The peak current ratios depart from unity at slow scan rates on ITO although the

ratio, $i_p/v^{1/2}$, is relatively constant, as in the Pt case (see also Fig. 7).

Kinetics in the Fe^{2+/3+} redox system are particularly amenable to improvement by "matrix" modification effects (28). Charge transfer becomes facile on adding Cl⁻ ions to the electrolyte, as illustrated in Fig. 9a and 10a for Pt. The improvement in kinetics is less dramatic on ITO, as exemplified by data in Fig. 9b, 10b, and 11. Note the systematic shift in peak potentials with v for ITO even at relatively high Cl⁻ concentrations and the "flatness" of the peak potential response on Pt (cf. Fig. 12).

The asymmetry in charge transfer at ITO, alluded to in a preceding paragraph, is particularly well typified by the cyclic voltammogram in Fig. 13, curve 1. Some degree of anodic current "recovery", however, is afforded by addition of H₂SO₄ to the electrolyte, curves 2-4, Fig. 13. Similar rectification in Fe^{2+/3+} redox chemistry has been noted by previous authors at SnO₂ electrodes in studies (11) related to photogalvanic applications.

Comparison of redox kinetics on Pt and ITO.—To couch the aforementioned differences in kinetic facility at Pt and ITO electrodes in more quantitative terms, the Nicholson method (29) was used. This method correlates the measured ΔE_p values in CV experiments with k_0 via the use of a parameter, ψ defined by Eq. [1]

$$\psi = \gamma^\alpha k_0 / \sqrt{\pi a D_0} \quad [1]$$

Here $\gamma = (D_0/D_R)^{1/2}$ and $\alpha = nFv/RT$. (Other symbols have their usual electrochemical identity.) Master plots were utilized to derive values for ψ from ΔE_p , and Eq. [1] was then used to compute k_0 . The assumption made herein, namely, that $\gamma = 1$, does not affect the results, at least in a

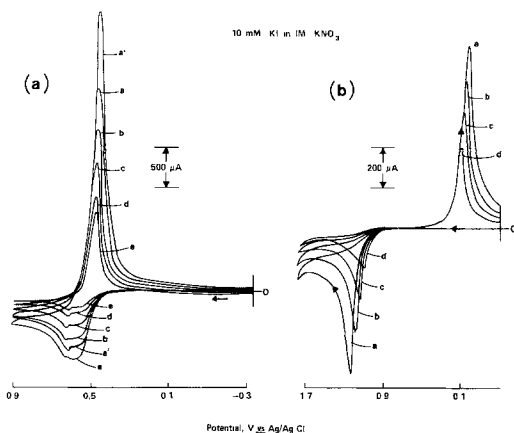


Fig. 6. Comparison of cyclic voltammograms for the I⁻/I₃⁻ redox couple in 1M KNO₃ at (a) Pt and (b) ITO electrodes. Curve notation as in Fig. 5. Curve a' in a corresponds to a scan initiated at +0.9V.

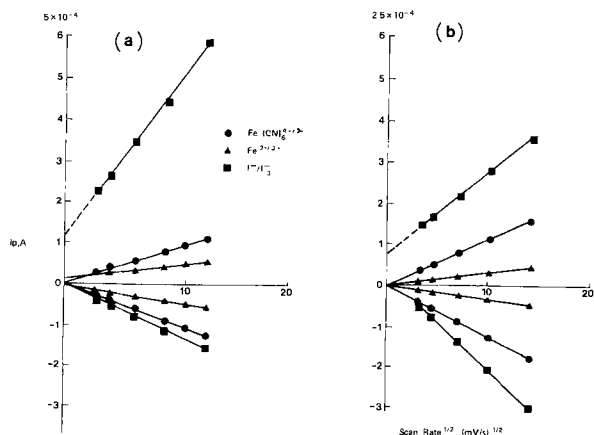


Fig. 7. Dependence of CV peak current, i_p , on $(\text{scan rate})^{1/2}$ for Fe(CN)₆^{4-/3-}, I₃⁻/I⁻, and Fe^{2+/3+} redox couples at (a) Pt and (b) ITO electrodes. Relevant data are from Fig. 5, 6, and 8.

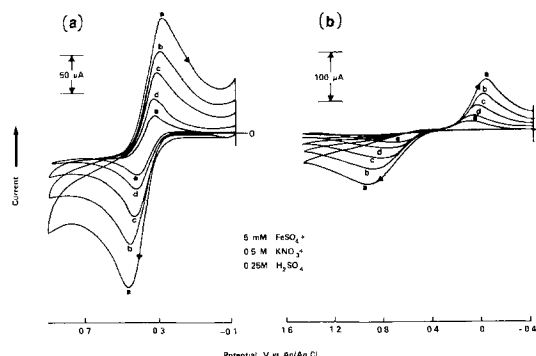


Fig. 8. Comparison of cyclic voltammograms for the Fe^{2+/3+} redox couple at (a) Pt and (b) ITO electrodes. Curve notation as in Fig. 5.

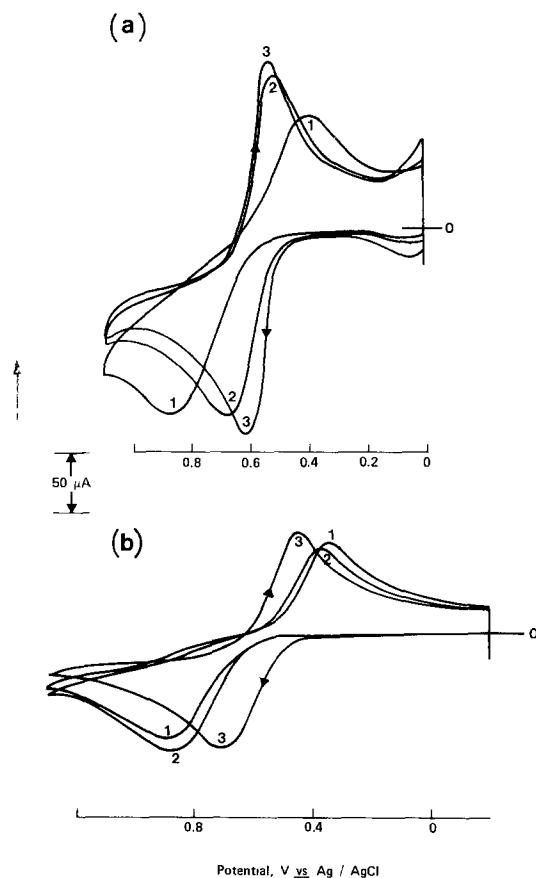


Fig. 9. Examples of chloride ion catalysis on redox chemistry of $\text{Fe}^{2+}/\text{Fe}^{3+}$ couple at (a) Pt and (b) ITO electrodes. In each case, curves 1, 2, and 3 refer to $0.5\text{M H}_2\text{SO}_4$, $0.5\text{M H}_2\text{SO}_4 + 3\text{M NaCl}$, and $1\text{M HCl} + 5\text{M LiCl}$ electrolytes, respectively. The Fe^{2+} concentration was 5 mM in all the cases.

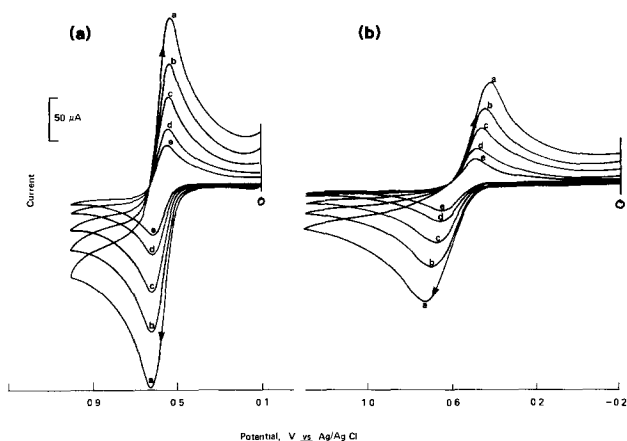


Fig. 10. Comparison of scan rate dependence of peak potentials at (a) Pt and (b) ITO electrodes for 5 mM FeSO_4 in $1\text{M HCl} + 5\text{M LiCl}$. Curve notation as in Fig. 5.

relative sense. The I^-/I_3^- redox system was excluded from these computations because of adsorption complications (see above).

The results of these calculations are assembled in Tables IV and V for $\text{Fe}(\text{CN})_6^{4-}/\text{Fe}(\text{CN})_6^{3-}$ and $\text{Fe}^{2+}/\text{Fe}^{3+}$ couples, respectively. The differences in ΔE_p values translate to an order-of-magnitude increase in k_0 values on Pt relative to ITO for the $\text{Fe}(\text{CN})_6^{4-}/\text{Fe}(\text{CN})_6^{3-}$ couple. The k_0 values on Pt accord well with those reported by previous authors for a rotating Pt disk electrode (30). For the case of $\text{Fe}^{2+}/\text{Fe}^{3+}$ in the absence of added Cl^- , computation of k_0 is precluded for ITO because the ΔE_p values lie outside the range of validity of the Nicholson method. [Note that this method applies only to a relatively restricted ΔE_p range ($65\text{--}160\text{mV}$) in the quasi-reversible charge transfer

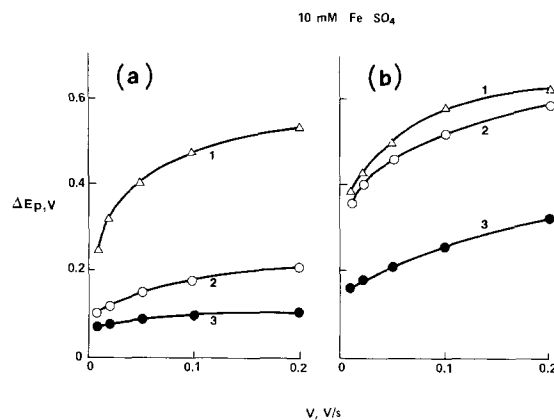


Fig. 11. Variation of peak separation, ΔE_p , with scan rate and the influence of Cl^- concentration for (a) Pt and (b) ITO electrodes. Curve notation as in Fig. 9.

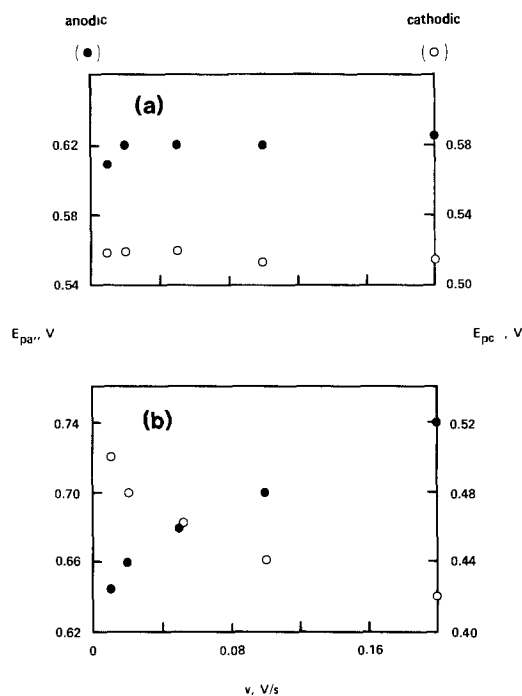


Fig. 12. Dependence of peak potentials on scan rate for the CV experiments corresponding to Fig. 10 in amplified form for (a) Pt and (b) ITO electrodes.

regime.] Even at high Cl^- concentrations (5M), k_0 values for Pt are four to five times higher than those on ITO. This has important consequences for photoelectrochemistry, as we shall attempt to show in the companion paper (31). Some overestimation is undoubtedly involved in the k_0 values corresponding to the Cl^- containing electrolytes, via the assumption that the D_0 value [$0.45 \times 10^{-5}\text{ cm}^2/\text{s}$, cf. Ref. (32)] is unchanged from the $1\text{M H}_2\text{SO}_4$ case. (The D_0 value is likely to be lower in the viscous LiCl ma-

Table IV. Kinetics parameters for $10\text{ mM Fe}(\text{CN})_6^{3-}$ (1M KNO_3) from cyclic voltammetry

Scan rate v (V/s)	Pt		ITO	
	ΔE_p (V)	k_0 ($\text{cm}\cdot\text{s}^{-1}$)	ΔE_p (V)	k_0 ($\text{cm}\cdot\text{s}^{-1}$)
0.01	0.060	^a	0.070	7.6×10^{-3}
0.02	0.065	2.2×10^{-2}	0.073	7.5×10^{-3}
0.05	0.070	1.7×10^{-2}	0.085	6.4×10^{-3}
0.10	0.080	1.0×10^{-2}	0.090	7.7×10^{-3}
0.20	0.092	1.0×10^{-2}	0.105	6.8×10^{-3}

^a Beyond the range of validity of the Nicholson method [cf. Ref. (29)].

Table V. Kinetics parameters from cyclic voltammetry for the $\text{Fe}^{2+/3+}$ redox system

Redox electrolyte	5 mM $\text{FeSO}_4/0.5\text{M H}_2\text{SO}_4/3\text{M NaCl}$					5 mM $\text{FeSO}_4/1\text{M HCl}/5\text{M LiCl}$				
	v (V/s)					v (V/s)				
Pt										
ΔE_p (V)	0.10	0.11	0.15	0.18	0.21	0.07	0.08	0.09	0.10	0.11
k_o ($10^3 \text{ cm} \cdot \text{s}^{-1}$)	1.4	1.7	1.3	1.1	1.1	6.3	4.5	5.4	5.5	5.7
ITO										
ΔE_p (V)	0.36	0.41	0.46	0.52	0.59	0.16	0.18	0.21	0.26	0.32
k_o ($10^3 \text{ cm} \cdot \text{s}^{-1}$)	a	a	a	a	a	1.2	1.1	1.1	a	a

^a Beyond the range of validity of the Nicholson method [cf. Ref. (29)].

trix). However, this difference is not of serious consequence, since we are interested here only in relative magnitudes on Pt and ITO electrodes. Again, the k_o values at Pt for the $\text{Fe}^{2+/3+}$ redox system in Table V fall within the range reported in previous studies (33).

The steady-state measurements yielded data which are consistent with the trends discussed above for CV. Thus, Tafel analyses reveal values for $j_{1,a}, j_{1,c}, j_o$, and α on ITO electrodes which were significantly lower than for Pt. Only the $\text{Fe}(\text{CN})_6^{4-/3-}$ and $\text{Fe}^{2+/3+}$ redox systems (the latter in the presence and absence of Cl^-) were included for these comparative experiments.

The aforementioned relative trends in redox electrochemistry on Pt and ITO cannot be rationalized simply in terms of difference in uncompensated resistances and other iR drop effects in the two cases. For example, analyses of CV data in terms of $(E_{p/2} - E_p)$ vs. i_p and $E_{0.8517i_p}$ vs. i_p plots, in the manner prescribed by previous authors (34), yield values for the overall resistance, R , (i.e., charge transfer plus uncompensated electrolyte resistance) which are different for $\text{Fe}(\text{CN})_6^{4-/3-}$ and $\text{Fe}^{2+/3+}$ redox systems. While values of R for a given ITO electrode agreed to within $\pm 10\Omega$ for the two types of analyses, order-of-magnitude differences (e.g. 60 vs. 920 Ω) are routinely observed for $\text{Fe}(\text{CN})_6^{4-/3-}$ and $\text{Fe}^{2+/3+}$ redox couples, respectively.

Figure 14 summarizes the important features of redox electrochemistry on Pt and ITO electrodes as revealed by CV experiments. The key finding here is that differences in kinetic facility between Pt and ITO electrodes are closely coupled with the intrinsic kinetics of the particular redox system involved (cf. Fig. 14). This finding underlies the importance of choosing a fast (preferably one-electron) redox couple in PEC regenerative systems

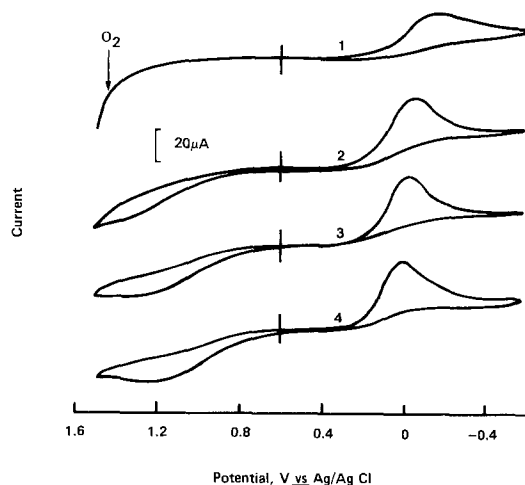


Fig. 13. Effect of acid concentration on the redox chemistry of the $\text{Fe}^{2+/3+}$ couple at ITO. In each case the redox concentration was 1 mM in 1M KNO_3 . Curves 1-4 denote H_2SO_4 of 0, 0.5, 1, and 2 mM, respectively.

based on the heterojunction photoelectrode concept. (Obviously, such a choice would be optimal for "conventional" PEC systems also, although the range of available redox candidates may be limited by electrode stability considerations in such cases). The relative trends in Fig. 14 and the data discussed in the preceding section also explain, in a quantitative manner, why the $\text{Fe}(\text{CN})_6^{4-/3-}$ redox couple was effective in the Si/ITO system while the polyiodide electrolyte was not [cf. Fig. 2 and Ref. (1)] Further detailed analyses of photoelectrochemical aspects as well as a critical examination of the heterojunction photoelectrode concept, are deferred to the companion paper (31).

Causal factors in kinetics differences between Pt and ITO and further comparisons with Sb:SnO₂ electrodes.—We now attempt to probe the causal factors for the observed differences in charge transfer kinetics at Pt and ITO electrodes (cf. Tables IV and V). It is pertinent to

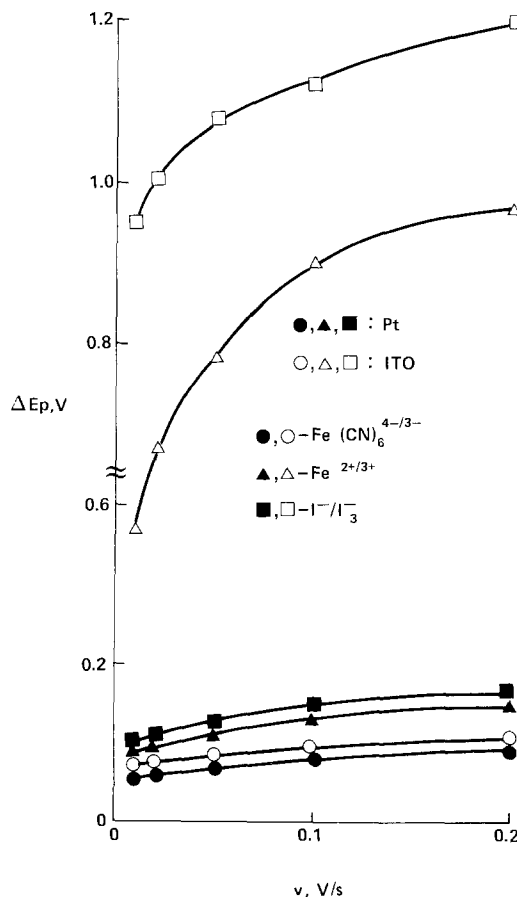


Fig. 14. Dependence of CV peak separation, E_p , on scan rate, v for $\text{Fe}(\text{CN})_6^{4-/3-}$, $\text{Fe}^{2+/3+}$, and I^-/I_3^- redox couples on Pt and ITO electrodes. In each case, the concentration of active species was 10 mM and the supporting electrolyte was 1M KNO_3 .

point out here that, aside from this work, comparisons have been previously made for Pt and Sb:SnO₂ electrodes by other authors (10b). The findings of these authors essentially parallel ours: namely, that no correlation exists between E° and electrochemical reversibility on ITO and Sb:SnO₂ for the various redox couples that were tested in these two studies. Furthermore, Fe(CN)₆^{4-/-3-} is electrochemically reversible on both ITO as well as on Sb:SnO₂. The interpretation forwarded by previous authors for their observations on the latter system is that couples which show reversible behavior "have bulky ligands which may prevent a surface interference effect" (10b). We believe, however, that by and large (*i.e.*, unless adsorption effects are present), all one-electron outer-sphere redox couples, which are intrinsically fast at Pt, will show reversible behavior at these oxide electrode surface. also. Support for our assertion is provided by our recent studies on a variety of organic and organometallic one-electron redox couples at the ITO/nonaqueous electrolyte interfaces (35) and by the comparisons of the kinetics behavior at Pt and Sb:SnO₂ electrodes that have been presented by other authors for phenothiazine and benzoquinone redox systems in acetonitrile (36).

While the above interpretation is appealing from a phenomenological viewpoint, the mechanistic aspects of electron transfer at heavily doped metal oxide/electrolyte interfaces, and the behavior of these interfaces vis-a-vis the metal case, need to be further addressed. Arguments against a "semiconductor model" (based on depletion layer effects) have been advanced by previous authors (10b, 37) for heavily doped material ($N_D = 10^{18}$ - 10^{19} cm⁻³). Instead, the redox behavior of Fe^{2+/3+} and Ce^{3+/4+} at Sb or Ru:SnO₂ has been rationalized in terms of an electron hopping mechanism from the conduction band to surface states via deep lying donor states (37). It is plausible that a similar model can be applied to the ITO system considered here. The reversible behavior observed in acetonitrile for a series of redox couples spanning a significant portion of the ITO bandgap (35), however, necessitates invoking a uniformly high density of surface states right across the ITO bandgap at the interface. In any event, further speculation is clearly not warranted by the depth of information that is currently available on this aspect.

Acknowledgment

This research was made possible by a grant from the Organized Research Fund of The University of Texas at Arlington.

Manuscript submitted Feb. 25, 1985; revised manuscript received May 6, 1985.

The University of Texas assisted in meeting the publication costs of this article.

REFERENCES

- G. Hodes, L. Thompson, J. DuBow, and K. Rajeshwar, *J. Am. Chem. Soc.*, **105**, 324 (1983).
- K. Rajeshwar, *J. Appl. Electrochem.*, **15**, 1 (1985).
- P. A. Kohl, S. N. Frank, and A. J. Bard, *This Journal*, **124**, 225 (1977).
- (a) J. L. Vossen, in "Physics of Thin Films," Vol. 9, G. Hass, Edior, p. 1, Academic Press, New York (1977); (b) G. Haake, *Ann. Rev. Mater. Sci.*, **7**, 73 (1977); (c) J. C. Manificier, *Thin Solid Films*, **90**, 297 (1982); (d) A. L. Dawar and J. C. Joshi, *J. Mater. Sci.*, **19**, 1 (1984).
- L. Thompson, J. DuBow, and K. Rajeshwar, *This Journal*, **129**, 1934 (1982).
- (a) Y. Nakato, S. Tonomura, and H. Tsubomura, *Ber. Bunsenges. Phys. Chem.*, **80**, 1289 (1976); (b) S. Meneses, A. Heller, and B. Miller, *This Journal*, **127**, 1258 (1980).
- S. Ashok, S. J. Fonash, R. Singh, and P. Wiley, *IEEE Electron Devices Lett.*, To be published.
- H. A. Laitinen and N. H. Watkins, *Anal. Chem.*, **47**, 1352 (1975).
- For example, H. A. Laitinen, and J. M. Conley, *ibid.*, **48**, 1224 (1976).
- (a) H. A. Laitinen, C. A. Vincent, and T. M. Bednarski, *This Journal*, **115**, 1024 (1968); (b) O. Elliott, D. L. Zellmer, and H. A. Laitinen, *ibid.*, **117**, 1343 (1970).
- D. E. Hall, P. D. Wilder, and N. N. Lichtin, *ibid.*, **125**, 1365 (1978).
- I. Uchida and S. Toshima, *J. Appl. Electrochem.*, **9**, 647 (1979).
- I. Uchida, K. Niki, and H. A. Laitinen, *This Journal*, **124**, 1759 (1978).
- I. Uchida, H. Urushibata, and S. Toshima, *J. Electroanal. Chem.*, **96**, 45 (1979).
- F. Mollers and R. Memming, *Ber. Bunsenges Phys. Chem.*, **76**, 469 (1972).
- J. F. McCann, S. P. S. Badwal, and J. Pezy, *J. Electroanal. Chem.*, **118**, 115 (1981).
- (a) G. B. Hoflund, D. F. Cox, and H. A. Laitinen, *Thin Solid Films*, **83**, 261 (1981); (b) G. B. Hoflund, D. F. Cox, F. Ohuchi, P. H. Holloway, and H. A. Laitinen, *Appl. Surf. Sci.*, **14**, 281 (1982-1983).
- N. R. Armstrong, A. W. C. Lin, M. Fujihira, and T. Kuwana, *Anal. Chem.*, **48**, 741 (1976).
- For example, P. Singh, K. Rajeshwar, J. DuBow, and R. Job, *J. Am. Chem. Soc.*, **102**, 4676 (1980).
- (a) J. C. Manificier, L. Szepessy, J. F. Bresse, M. Peratin, and R. Stuck, *Mater. Res. Bull.*, **14**, 109 (1979); (b) J. C. Manificier, J. P. Fillard, and J. M. Bind, *Thin Solid Films*, **77**, 67 (1981).
- (a) J. Shewshun, J. DuBow, C. Wilmsen, R. Singh, D. Burk, and J. Wager, *J. Appl. Phys.*, **50**, 2832 (1979); (b) J. C. C. Fan, *Appl. Phys., Lett.*, **34**, 515 (1979).
- R. N. Adams, "Electrochemistry at Solid Electrodes," Chap. 7, p. 187, Marcel Dekker, New York (1969).
- J. F. Rusling, *Anal. Chem.*, **56**, 578 (1984), and references therein.
- R. A. Osteryoung and F. C. Anson, *ibid.*, **36**, 975 (1964), and references therein.
- A. T. Hubbard, R. A. Osteryoung, and F. C. Anson, *ibid.*, **38**, 692 (1966).
- E. C. Toren, Jr., and C. P. Driscoll, *ibid.*, **38**, 872 (1966).
- D. C. Johnson, *This Journal*, **119**, 331 (1971), and references therein.
- F. R. Smith and C. S. Su, *J. Chem. Soc. Chem. Commun.*, 159 (1972).
- R. S. Nicholson, *Anal. Chem.*, **37**, 1351 (1965).
- F. R. van Buren, G. H. J. Broers, and T. G. M. van der Belt, *Ber. Bunsenges. Phys. Chem.*, **83**, 82 (1979).
- O. M-R. Chyan, S-I. Ho, and K. Rajeshwar, Submitted for publication.
- R. N. Adams, "Electrochemistry at Solid Electrodes," p. 220, Marcel Dekker, New York (1969).
- Y. D. Chen, K. S. V. Santhanam, and A. J. Bard, *This Journal*, **128**, 1460 (1981).
- T. Kuwana, D. K. Darlington, and D. W. Leedy, *Anal. Chem.*, **36**, 2023 (1964).
- S-I. Ho and K. Rajeshwar, To be published.
- A. F. Diaz and K. K. Kanazawa, *IBM J. Res. Dev.*, **23**, 316 (1979).
- W. Badawy, K. Doblhofer, I. Eiselt, H. Gerischer, S. Krause, and J. Melsheimer, *Electrochim. Acta.*, **29**, 1617 (1984).

Polymer Solid Electrolyte Photoelectrochemical Cells with n-Si-Polypyrrole Photoelectrodes

T. A. Skotheim

Brookhaven National Laboratory, Department of Applied Science, Upton, New York 11973

O. Inganäs

Laboratory of Applied Physics, University of Linköping, 581 83 Linköping, Sweden

ABSTRACT

We have developed photoelectrochemical cells with rectifying junctions between n-Si electrodes and thin film solvent free polymer solid electrolytes based on poly(ethylene oxide). We describe various surface modifications applied to the n-Si electrode which overcome a high activation energy barrier for efficient charge transfer to redox ions in the polymer solid electrolytes. We show that the efficiency of the present cells is limited by a high surface recombination velocity associated with surface states of the n-Si.

Solvent-free polymer solid electrolytes represent an important new class of ionically conducting materials (1). Their compatibility with thin film technology makes them potential candidates for a wide variety of technological applications.

We have developed a new type of photoelectrochemical cell (PEC) based on rectifying junctions between semiconductor electrodes and thin film polymer solid electrolytes. The absence of solvents in this system holds out the hope of being able to manufacture all thin film solid-state PEC's without the semiconductor surface corrosion problems associated with liquid electrolyte PEC's, thereby deriving the benefits both from the stability of solid-state systems and the ease of fabrication as well as the lack of susceptibility to grain barriers of electrochemical junctions. In addition, it allows for a conceptually easy construction of multispectral thin film cells based on more than one semiconductor in optical and electrical series (2).

Our present study has focused on surface modification techniques for improving the rates of charge transfer between semiconductor electrodes and redox ion couples in polymer solid electrolytes (3-5). Specifically, we have shown that surface modifications of n-Si electrodes with thin films of polypyrrole can dramatically reduce the large activation energy barrier against efficient charge transfer between bare semiconductor electrodes and polymer solid electrolytes.

Polymer Solid Electrolytes

Linear polyethers like poly(ethylene oxide) ($\text{CH}_2\text{-CH}_2\text{-O}$) (PEO) give conducting complexes with alkali metal salts (1). Such adducts are either crystalline materials or amorphous elastomers. The cations are solvated by a fraction of the ether oxygens, and a limited stoichiometry of four oxygen atoms per cation has been observed. Typically, both the cations and the anions move in the polymer matrix. The transference number of iodide, which is relevant to our study, has been measured to be in the range of 0.2-0.4 (6).

The conductivity of these electrolytes is relatively low at room temperature, typically in the 10^{-6} ($\Omega\text{-cm}$) $^{-1}$ range and increases to 10^{-4} ($\Omega\text{-cm}$) $^{-1}$ at 50°-80°C. Devices therefore require thin films.

Photoelectrochemical Cell Fabrication

The PEO electrolyte films used in the present study were solution cast from MeOH, in which were dissolved the PEO (Aldrich; molecular weight 600,000) and the complexing salt. The ion concentration, as given by the ratio of oxygen atoms in the polymer backbone to cations, was 8.

For the PEC's, we used thin films (ca. 0.5 μm) of PEO complexed with KI and I_2 to generate the iodide/triiodide redox couple. The thickness of the PEO films could be

varied by changing the viscosity of the solution and the rotation speed of the photoresist spinner. Fabrication of cells with films thinner than 0.5 μm became practically difficult. The films were spin coated onto a transparent conducting substrate, indium-tin oxide (ITO) on glass, and subsequently dried by heating under vacuum. The cell is completed by contacting the PEO with a 1 cm^2 n-Si chip by heating with light pressure under vacuum. It was found necessary to deposit 5-20Å of Pt on the ITO surface for greatly improved charge transfer between the ITO and the iodide/triiodide redox ions. Bare ITO is a highly irreversible electrode for iodide oxidation and reduction (4). Figure 1 shows a schematic cell configuration and an energy level diagram of the PEO based PEC.

Semiconductor Surface Modification

Our primary interest in this paper was to study various methods of interface modification between the semiconductor and the PEO electrolyte in order to reduce or eliminate the high activation energy barrier against efficient charge transfer of minority carriers from the n-Si to redox ions in the PEO electrolyte.

The effect of various types of Si surface modifications on the efficiency of charge transfer across the interface with the PEO electrolyte was studied by monitoring the photocurrent as a function of the surface modification under constant illumination.

The n-Si surface modifications we have studied include the following: (i) bare n-Si (etched in HF only), (ii) n-Si coated with 200-400Å polypyrrole $\cdot \text{BF}_4$, (iii) n-Si coated with 10-20Å electron beam-evaporated Pt, (iv) n-Si coated with 10-20Å Pt followed by deposition of polypyrrole $\cdot \text{BF}_4$, and (v) n-Si with 10-20Å Pt followed by deposition of polypyrrole \cdot iodide. The n-Si was always etched in HF before the surface modification. The polypyrrole films were grown on the n-Si surface with the technique of photoassisted electrochemical oxidation (7).

Figure 2 shows the effect of the surface preparations on the photocurrent density measured under constant illumination. A high activation energy barrier against charge transfer across the interface will result in a decreased photocurrent at a given light intensity.

As shown in Fig. 2, bare n-Si is a highly irreversible electrode for iodide oxidation in this medium. A similar high degree of electrochemical irreversibility has also been observed with bare semiconductor surfaces of II-VI and III-V compounds and polysulfide electrolytes (2, 8).

By polymerizing a thin coating (200-400Å) of polypyrrole $\cdot \text{BF}_4$ on the n-Si surface the charge transfer characteristics of the interface are improved by more than one order of magnitude. The addition of 10-20Å of Pt by electron beam gun evaporation onto the n-Si surface prior to the electrochemical growth of the polypyrrole $\cdot \text{BF}_4$ film

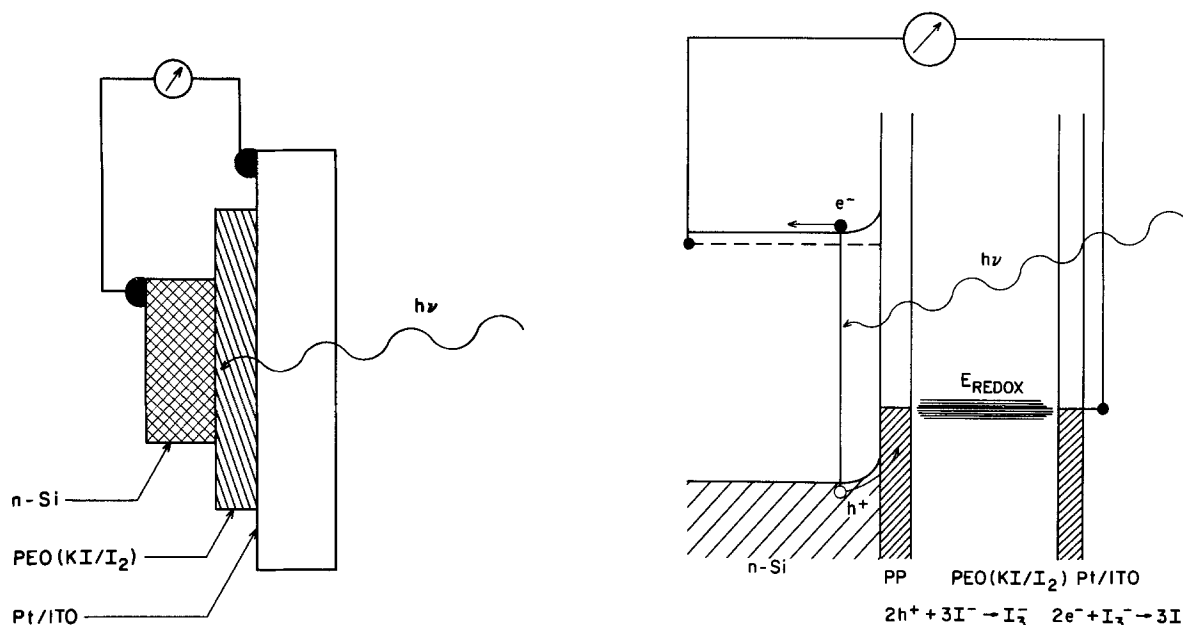
ELECTROCHEMICAL PHOTOVOLTAIC CELL
WITH SOLID POLYMER ELECTROLYTE

Fig. 1. a(left): Schematic cell configuration. b(right): Energy level diagram. Both of photoelectrochemical cell with polymer solid electrolyte and iodide/triiodide redox couple.

improves the electronic coupling between the n-Si and the polypyrrole, leading to more efficient scavenging of minority carriers from the n-Si. This has also been observed as improved junction characteristics measured in the solid state, as shown in the improvement in the quality factor of the junction from 2.2 to 1.4 (9).

As shown in Fig. 2, the most efficient interfaces incorporate iodide as the anion dopant in the polypyrrole. With the Pt-polypyrrole · iodide coating, the charge transfer characteristics relative to bare n-Si are improved by about

three orders of magnitude. The enhanced efficiency with iodide-doped polypyrrole could be due to specific iodide adsorption on the platinized Si surface. Since iodide is known to have a strong specific adsorption on Pt, this could result in efficient oxidation, or minority carrier scavenging.

Polypyrrole · iodide can be synthesized from acetonitrile solution containing tetraethylammonium iodide or KI complexed with PEO to improve solubility. Alternatively, to avoid the large parasitic currents associated with iodide oxidation, polypyrrole · iodide can be generated by ion exchange of polypyrrole · BF₄ with iodide. If iodide is the only anion in the electrolyte, it will be incorporated into the polypyrrole matrix for charge neutrality as the polypyrrole film grows in its oxidized state. The cyclic voltammogram in Fig. 3 clearly shows the signature of the iodide anion in the region where the polypyrrole is highly conductive. The iodide signal is superimposed on the capacitive charging current of the polypyrrole in its oxidized state, which is large due to the porosity and consequently large surface area of the polypyrrole film (10). The peak heights are linear with scan rate, characteristic of a surface bound species.

The cyclic voltammogram of polypyrrole · iodide is performed in an aqueous KCl electrolyte where iodide is soluble. After an initial reduction of about 40% during the first two scans, the peak heights are stable for multiple scans, indicating that besides a certain fraction of surface-bound iodide, most of the iodide is tightly bound to the polypyrrole matrix.

Current-Voltage Characteristics

The illuminated current-voltage characteristics of a PEC with PEO-iodide/triiodide electrolyte and n-Si/Pt/polypyrrole · iodide photoanode is shown in Fig. 4. The size of the Si chip was 1 cm² and the illumination was 100 mW/cm² unfiltered tungsten-halogen white light. Noticeably different I-V characteristics are observed when different size areas are illuminated. Decreasing the illuminated area by a factor of ten from 0.2 to 0.02 cm² increases both the short-circuit current density and the fill factor, defined as the fraction of the theoretical maximum efficiency with a given short-circuit current and open-circuit voltage. With an illuminated area of 0.02 cm², the fill factor was 0.5 and the energy conversion efficiency about 2%, or 3.6% corrected for absorption in the PEO/ITO.

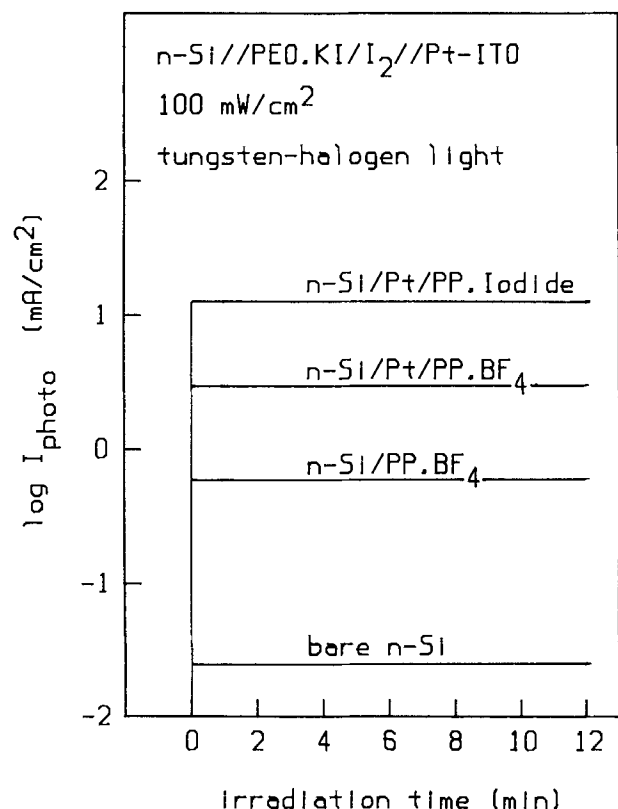


Fig. 2. Short-circuit photocurrent of PEO-iodide photoelectrochemical cells with varying surface preparation of the n-Si photoelectrodes under constant illumination of 100 mW/cm² unfiltered tungsten halogen light.

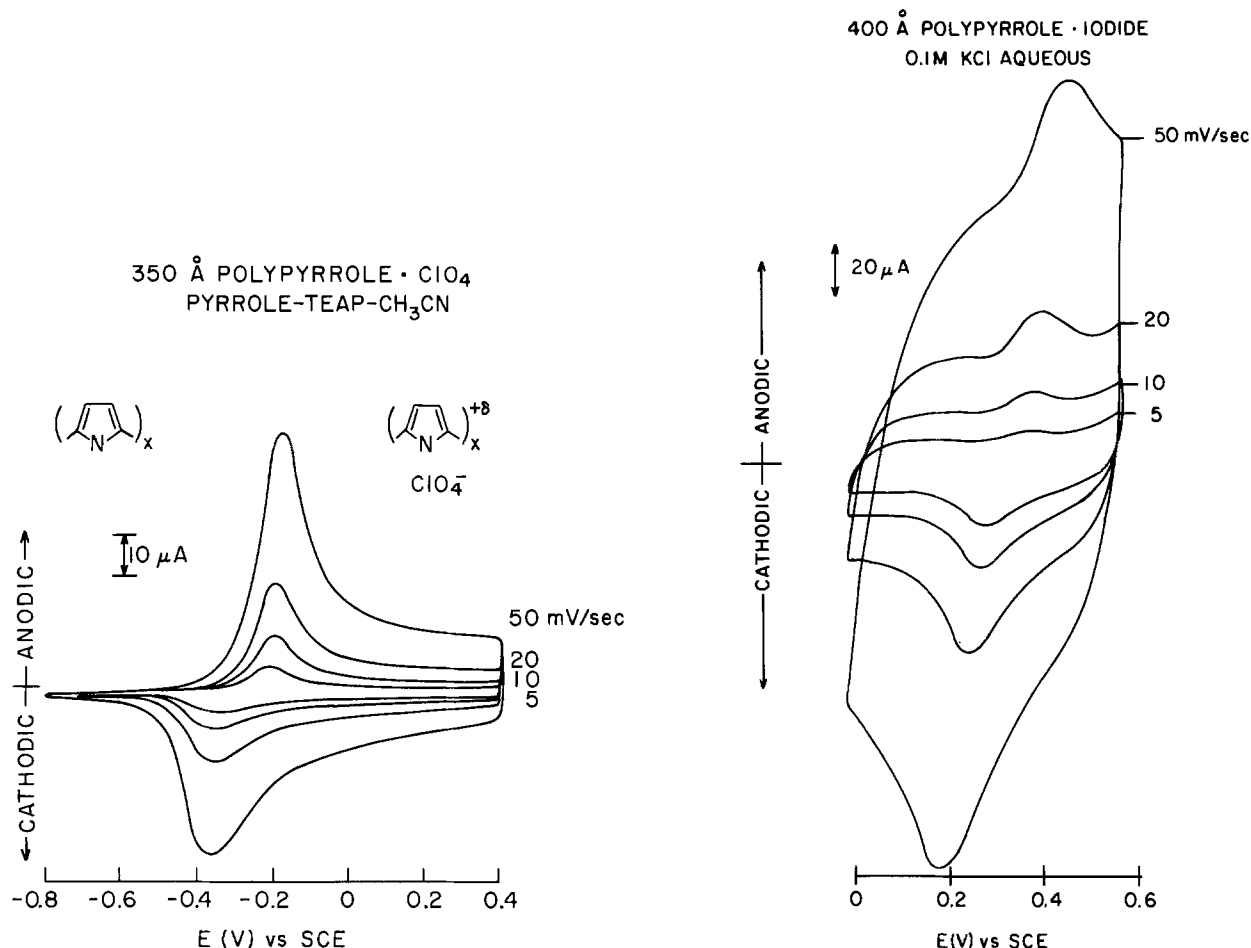


Fig. 3. Cyclic voltammogram of (a, left) polypyrrole · perchlorate in a MeCN-TEAP electrolyte containing pyrrole monomers, which are not electroactive in the region scanned, and (b, right) polypyrrole · iodide in aqueous KCl electrolyte.

The fill factor is strongly dependent on the series resistance of the cell. The forward I-V characteristics exhibit series resistance of the order of $100 \Omega/\text{cm}^2$. This is a contributing factor to the limit of the output efficiency, since photocurrents and fill factors are reduced for series resistances larger than a few ohms per square centimeter (11, 12).

The degraded response for larger illuminated areas are due to the inhomogeneities of the 1 cm^2 contact area between the Si and the PEO due to the thinness of the PEO film. Smaller illuminated areas ($< 1 \text{ mm}^2$) result in even

larger photocurrent densities, suggesting that technological optimization will lead to more efficient cells.

If the surface had been homogeneous, the fill factor would be expected to decrease upon illuminating a smaller surface area since the dark current stays the same

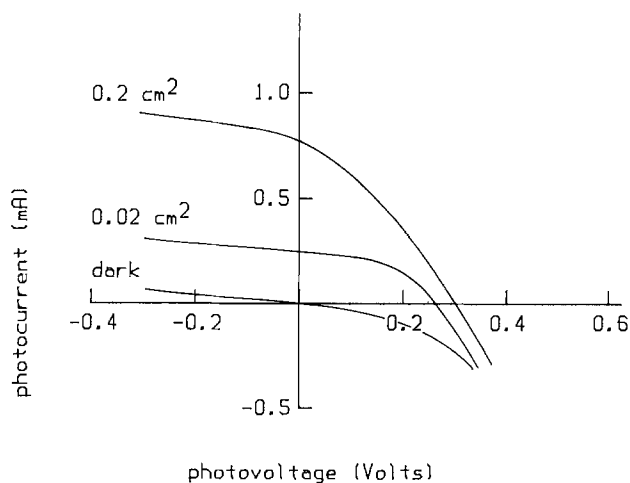


Fig. 4. Illuminated current voltage characteristics of a PEC with PEO · iodide/triiodide electrolyte and n-Si/Pt/polypyrrole · iodide photoanode. The Si chip was 1 cm^2 , and the sizes of the illuminated areas are indicated on the graph.

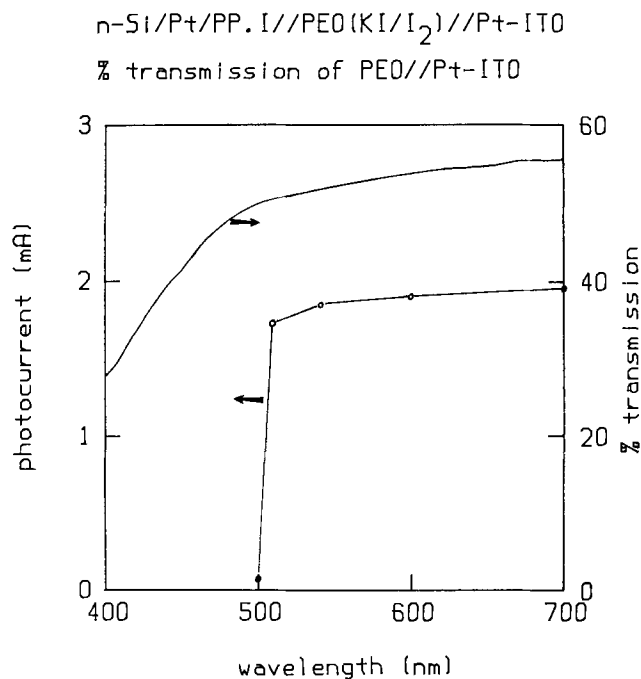


Fig. 5. Wavelength dependence of transmission of ITO/PEO · iodide and normalized spectral response of the short-circuit photocurrent of a cell with a n-Si/Pt/polypyrrole · iodide photoanode.

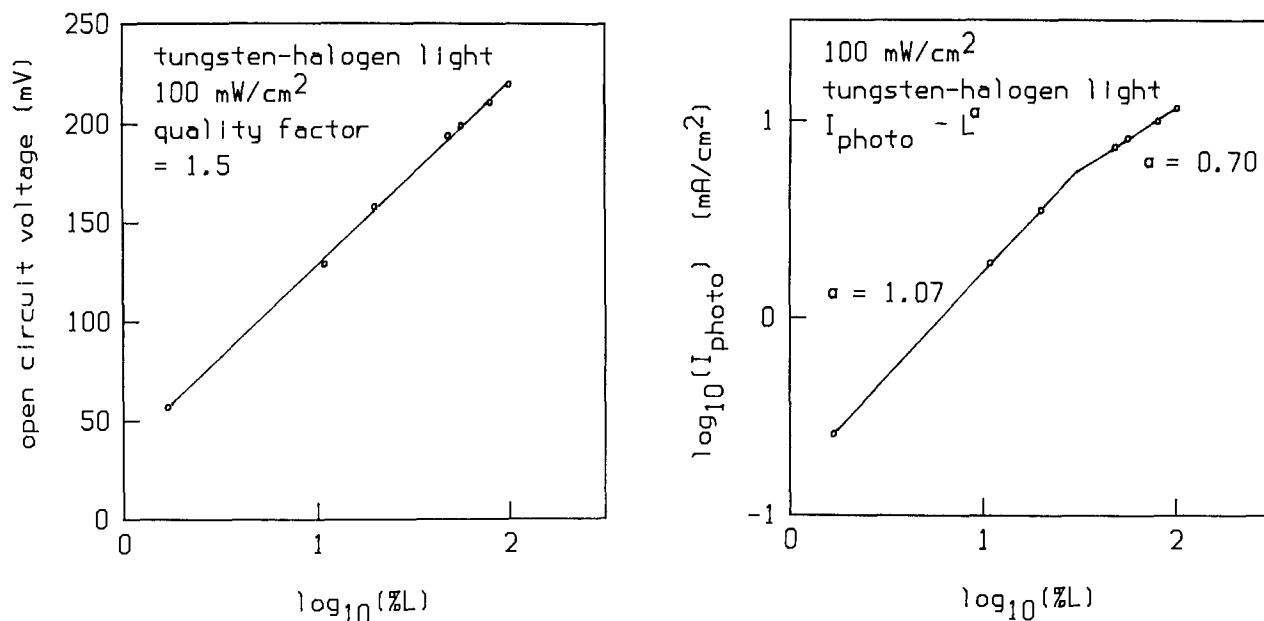


Fig. 6. Dependence on incident light intensity of the open-circuit voltage (a, left) and short-circuit photocurrent (b, right) for a cell with n-Si/Pt/polypyrrole-iodide photoanode. Maximum incident light intensity was 100 mW/cm² unfiltered tungsten halogen light, and reduced light intensity was achieved with neutral density filters.

but the photocurrent is reduced. The fact that the fill factor improves with smaller illuminated areas demonstrates that the interface is inhomogeneous.

As can also be seen from the figure, there are substantial reverse bias dark currents which are attributed to low shunting resistance due to edge effects of the Si chip. It is believed that better etching procedures will improve the shunt characteristics.

The effect of removing the PEO film is to reduce both the short-circuit current and the open-circuit voltage. The open-circuit voltages of n-Si/Pt/PP/ITO cells are consistently less than 0.2V, demonstrating the necessity of the n-Si/PEO electrochemical Schottky barrier junction for high efficiency cells.

Spectral Response

Figure 5 shows the wavelength dependence of the transmission of the PEO/ITO and the spectral response of the short-circuit photocurrent as determined by cutoff filters and normalized by the transmission of the individual filters.

The transmission of the PEO/ITO drops from about 50 to about 30% between 500 and 400 nm because of the iodide absorption in the PEO-iodide/triiodide electrolyte film. The drop in the photocurrent is much sharper than that of the transmission for wavelengths below 500 nm, or photon energies above 2.5 eV. We attribute the sharp drop in the photocurrent to high surface recombination velocities associated with a high density of surface states of the Si. Since the absorption constant of the Si increases with increasing photon energy, the higher energy photons are absorbed closer to the surface where the high recombination velocities decrease the carrier lifetimes, resulting in a decreased blue response (11).

Light Intensity Dependence of Photocurrent and Photovoltage

The dependence of the photocurrent and the photovoltage on the intensity of incident white light is shown in Fig. 6a and 6b, respectively. The open-circuit voltage increases logarithmically with light intensity over the almost two orders of magnitude studied using neutral density filters to reduce the incident light intensity from a maximum of 100 mW/cm². This is in accordance with the abrupt junction model (12). The open-circuit voltage increases by 90 mV for each decade increase in the light intensity, corresponding to a quality factor (ratio to $2.3kT/q$) of 1.5 for the barrier. A quality factor greater than 1.0 may

imply the existence of deleterious surface states acting as recombination centers (11, 12). This will reduce the open-circuit voltage by pinning the Fermi level to the surface states and limit the photocurrent by recombination of charge carriers.

The short circuit photocurrent is proportional to L^α where L is the light intensity and $\alpha = 1.07$ at low light intensities (up to 50 mW/cm²) and 0.70 at higher light intensities. The nonlinear behavior at higher light intensities indicates a decreasing quantum efficiency with increasing light intensity. The change in behavior at higher light intensities can be understood in a model where the quasi-Fermi level of the majority carriers reaches a higher density of interface states as it sweeps through the bandgap with increasing light intensity. As the Fermi level sweeps through the interface states, they are converted to recombination centers, thereby increasing the rate of recombination of charge carriers and lowering the quantum efficiency (13).

Summary

In summary, we have demonstrated techniques for derivatizing semiconductor surfaces which overcome the large activation energy barriers to efficient charge transfer between semiconductors and redox ions in PEO electrolytes. We believe these surface modification techniques represent an important advance in the control of charge transfer between semiconductor electrodes and polymer solid electrolytes.

The particular coupling of electronically and ionically conducting polymers to achieve efficient charge transfer which these techniques demonstrate is compatible with thin film technology and could, therefore, have important technological implications.

The energy conversion efficiency of the present-generation cells is limited by a high density of surface states on the n-Si electrode, and possibly by a high series resistance, and no longer by high activation energy barriers against efficient charge transfer from the semiconductor electrode to the redox ions in the PEO solid electrolyte. The continuation of this work will deal explicitly with the surface preparation of the n-Si in an attempt to eliminate the high density of surface states which degrade the behavior of the present photoelectrochemical cells.

Acknowledgments

This work was supported by the Division of Chemical Sciences, U.S. Department of Energy, under Contract no.

DE-AC02-76CH00016. O. I. received partial support from the National Swedish Board for Technical Development.

Manuscript submitted Feb. 19, 1985; revised manuscript received April 5, 1985.

Brookhaven National Laboratory assisted in meeting the publication costs of this article.

REFERENCES

1. M. Armand, *Solid State Ionics*, **9/10**, 745 (1983).
2. T. Skotheim, *Appl. Phys. Lett.*, **38**, 712 (1981).
3. T. Skotheim and I. Lundstrom, *This Journal*, **129**, 894 (1982).
4. T. Skotheim, S. W. Feldberg, and M. Armand, *J. Phys. C*, **3**, 615 (1983).
5. T. A. Skotheim and O. Inganas, *Molec. Cryst. Liq. Cryst.*, To be published.
6. D. Fauteux, J. Gauthier, A. Belanger, and M. Gauthier, Abstract 711, p. 1140, The Electrochemical Society Extended Abstracts, Vol. 82-1, Montreal, Que., Canada, May 9-14, 1982.
7. T. Skotheim, L. G. Petersson, O. Inganas, and I. Lundstrom, *This Journal*, **129**, 1737 (1982).
8. A. F. Sammels and P. G. Ang, *ibid.*, **131**, 617 (1984).
9. O. Inganas, T. Skotheim, and I. Lundstrom, *Phys. Scr.*, **25**, 863 (1982).
10. R. A. Bull, F.-R. F. Fan, and A. J. Bard, *This Journal*, **129**, 1009 (1982).
11. H. J. Hovel, "Solar Cells," Vol. 11, of *Semiconductors and Semimetals*, R. K. Willardson and A. C. Beer, Series Editors, Academic Press, New York (1975).
12. S. M. Sze, "Physics of Semiconductor Devices," John Wiley and Sons, New York (1969).
13. A. Rose, "Concepts in Photoconductivity and Allied Problems," Interscience Publishers, New York (1963).

In Situ Characterization of Redox Properties of Water-Soluble Porphyrins Irreversibly Adsorbed on Gold Electrode Using the Electroreflectance Technique

F. Bedioui and J. Devynck*

Laboratoire d'Electrochimie Analytique et Appliquée, ENSCP, 75231 Paris Cedex 05, France

C. Hinnen and A. Rouseau

Laboratoire d'Electrochimie Interfaciale du CNRS, 92190 Meudon-Bellevue, France

C. Bied-Charreton and A. Gaudemer

Laboratoire de Chimie de Coordination Bioorganique, Université Paris XI, 91405 Orsay, France

ABSTRACT

The visible electroreflectance (ER) technique coupled to capacitive and voltammetric measurements has been used to characterize the redox properties of water-soluble porphyrins [the meso-tetrakis (4-N-methylpyridyl) porphine tetrachloride (TMPyP) and the meso-tetrakis (4-N-methylpyridyl) porphine cobalt (III) pentachloride (Co(III)TMPyP)] in the potential range where they are irreversibly adsorbed on Au electrodes. The spectral features are analyzed in terms of reflectivity difference between the oxidized and reduced species and compared with optical properties of the bulk species. The ER spectra give direct evidence for the location of a reversible electron transfer reaction and allow us to determine the redox potentials of the Co(III)/Co(II) and Co(II)/Co(I) systems in their adsorbed state. The Co(III)/Co(II) couple is detected in an acidic solution (0.1M HClO₄) at $E_1 = 0.45$ V/SCE, and the Co(II)/Co(I) system is determined in neutral solution (0.02M KClO₄) at $E_2 = -0.70$ V/SCE. These potentials do not differ from the values obtained for the unadsorbed metalloporphyrin. These results provide evidence for the ability of a gold electrode covered with adsorbed porphyrin to constitute a modified electrode with well-defined redox properties.

Modified electrodes are electrochemical tools for which many methods of preparation and investigation have been described during the last years (1). Relatively few applications in the field of electrochemical catalysis have been proposed. Developments in this field necessitate extensions of the fabrication procedures to other modified surfaces or research of new catalytic reactions with the well-known modified electrodes. For this purpose, *in situ* methods of investigation are very useful. The most investigated catalytic reaction is the oxygen reduction, for which many coordination compounds have been proposed as catalysts, among them, cobalt porphyrins (1b, 5) and phthalocyanines (4). Kuwana (3), Anson (2, 6), and Murray (1b, 5) have studied the electrochemical be-

havior of adsorbed or linked porphyrins and phthalocyanines. Some *in situ* methods of investigation have been proposed for such electrode-adsorbed (or -linked) compounds (1b, 7-10).

Water-soluble porphyrins of the tetramethylpyridyl or tetraphenylsulfonate type have not been so intensively investigated as other porphyrins. Some chemical and electrochemical properties have been described (11-12), and it was shown that electrochemistry of these compounds is not as well defined as those of water-insoluble compounds and need to be completed.

In the scope of new catalytic developments of these water-soluble porphyrins, we are interested in porphyrin-modified electrode and *in situ* methods of investigation of their electrochemical properties. Recent voltammetric study of Cytochrome C (22) and electroreflectance inves-

* Electrochemical Society Active Member.

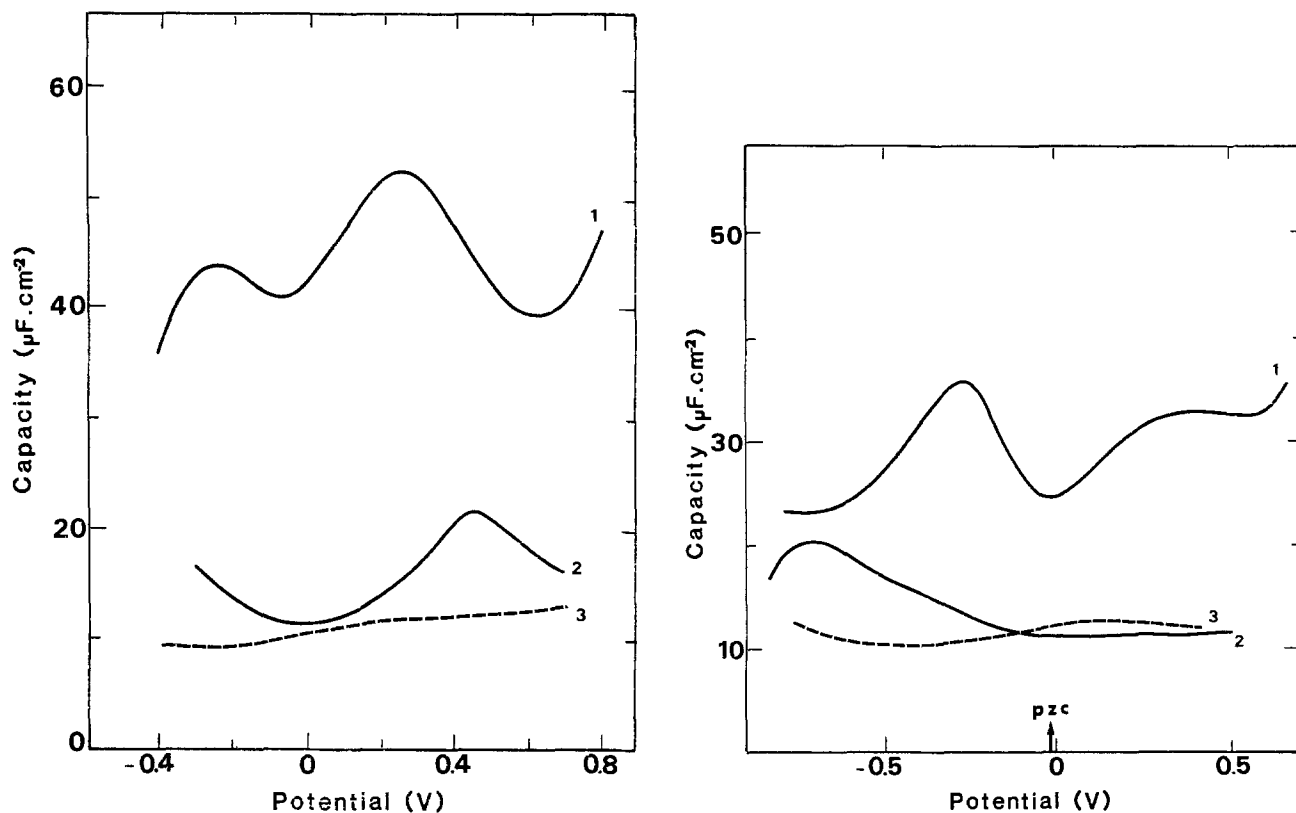


Fig. 1. Capacity-potential curves for a polycrystalline gold electrode with the influence of the pH. a(left): pH = 1 in 0.1M HClO₄. b(right): pH = 6 in 0.02M KClO₄. Curve 1: with a clean gold surface. Curve 2: with adsorbed Co(III) TMPyP. Curve 3: with adsorbed TMPyP. Frequency $f = 15$ Hz. Modulation amplitude $\delta E = 5$ mV. Voltage sweep $V = 5$ mV·s⁻¹.

tigation on gold electrode (23) have shown the interest of coupled electrochemistry and spectrochemistry.

Therefore, in this paper we examine the electrochemical behavior of some water-soluble porphyrins adsorbed on a gold electrode by electroreflectance.

Experimental

The cobalt TMPyP and free-TMPyP were prepared by a modification (24) of the published method (25, 26).

The electrodes were polycrystalline gold disks with a surface of 0.65 cm². After mechanical polishing, the electrodes were rinsed first with concentrated H₂SO₄ and then with ultrapure water.

Before each experiment, an electrochemical cleaning procedure was performed in a supporting electrolyte (0.02M KClO₄) consisting of a set of slow voltage sweeps (20 mV·s⁻¹) between two potential limits of -0.8 and +1.2 V/SCE. This procedure allows for the formation of a monolayer of oxide and its subsequent reduction of each cycle. The voltage sweep was repeated until a satisfactory cleanliness of the interface was reached as revealed by the well-known voltammogram and capacitive characteristics (27). Then the electrode was wetted with a drop of porphyrin for about 10 min, followed by thorough washing to remove the excess of porphyrin before introducing it into the experimental cell containing the electrolyte (0.02M KClO₄ or 0.1M HClO₄). The extent of the potential excursion was limited so as to maintain the porphyrin adsorbed without its undergoing chemical degradation. The potential limits depend on the pH of the solution: it ranges between -1 and +0.5V at pH = 6 and between -0.5 and +0.7V at pH = 1. At the end of each experiment, the potential limit was extended to a more positive value, +1.2V, to oxidize the adsorbed layer and regenerate a clean gold surface.

Potentials were measured vs. a mercurous sulfate electrode in order to avoid contamination of the gold surface by Cl⁻ anions, but they are quoted with respect to SCE (by adding 0.41V).

Voltammograms were recorded at a variable voltage sweep in the range of 30-300 mV·s⁻¹. Capacity and

electroreflectance measurements were made with a 15 Hz modulation voltage superimposed on a slow sweep of 3 mV·s⁻¹. Optical measurements were carried out at normal incidence with plane polarized light, in the wavelength range 300-600 nm. The procedure and apparatus for obtaining the electrical capacity and optical signals (ER) have been described (27).

All the electrochemical studies were performed in 0.02M KClO₄ or 0.1M HClO₄ solutions. Curves were obtained with a three-electrode potentiostatic system.

A visible spectrum of porphyrin solutions (0.02M KClO₄ or 0.1M HClO₄) was made from a Unicam SP 1800 ultraviolet spectrophotometer. Reduction of the Co(III) TMPyP to Co(II) TMPyP was effected by addition of sodium borohydride (NaBH₄). All the experiments were performed at 25°C.

Results

Adsorption characterization.—The presence of Co(III) TMPyP molecules at the gold electrode surface is demon-

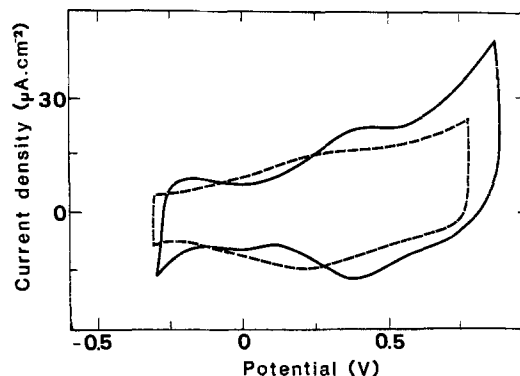


Fig. 2. Voltammogram for a modified gold electrode by adsorbed Co(III) TMPyP in aqueous solution of 0.1M HClO₄. The dashed curve indicates the behavior of a free gold surface (after desorption of porphyrin) $V = 300$ mV·s⁻¹.

strated by comparing the capacity of the gold interface after a cleaning treatment in the supporting electrolyte and after deposition of the porphyrin on the electrode surface. Capacity-potential curves in HClO_4 ($\text{pH} = 1$) and in 0.02M KClO_4 media ($\text{pH} = 6$) are presented in Fig. 1. In both media, the capacity is lowered in presence of porphyrin in a potential range larger than 1V , showing that it remains irreversibly adsorbed in this region without undergoing any chemical degradation.

Irreversible adsorption of the free-porphyrin (TMPyP) has been observed under the same conditions (Fig. 1).

In situ characterization of adsorbed Co(III) TMPyP.—0.1M HClO₄ medium.—The voltammetric curve of adsorbed Co(III) TMPyP is shown in Fig. 2. Waves that are not well defined are visible near $E = 0.45\text{ V/SCE}$ which corresponds to the peak in capacity-potential curve (see Fig. 1a).

The ER spectrum shown in Fig. 3 relative to Co(III) TMPyP is obtained in a narrow potential region near $E_p = 0.45\text{V}$ with a maximum amplitude at E_p . These structures completely disappear for any mean potential situated in more positive or negative region.

These typical spectra can be interpreted in terms of a valence change process occurring in the adsorbed layer. The ER structures displayed in the $400\text{-}500\text{ nm}$ range are relative to the simultaneous presence of both oxidized and reduced forms characterized by slightly different optical properties which are revealed by the modulation technique.

The adsorbance spectra of bulk Co TMPyP in the same acidic solution for both oxidized and reduced forms indi-

cate that the typical ER spectrum at $E_p = +0.45\text{ V/ECS}$ coincides with the differential spectrum obtained by subtracting the spectrum of oxidized, Co(III) TMPyP, from that of the reduced Co(II) TMPyP form in solution (Fig. 4). This demonstrates that the adsorbed species are probably maintained in a configuration similar to that in the solution.

The absence of any signal of adsorbed TMPyP (without metallic ion) in the same media, in the investigated potential range, indicates that the redox process concerns the cobalt ion. Thus, the capacitive, voltammetric, and electroreflectance signals are characteristics of the Co(III)/Co(II) system of the adsorbed porphyrin.

The cyclic voltammogram of the bulk Co TMPyP (Fig. 5) situates the apparent standard potential of the Co(III)/Co(II) couple at $+0.45\text{ V/ECS}$, in accordance with the value of Pasternak (19). Comparison between the electrochemical behavior of adsorbed and bulk Co TMPyP clearly shows that the redox couple Co(III)/Co(II) appears at the same potential in both adsorbed and bulk phases.

Neutral 0.02M KClO₄ medium.—Capacity and electroreflectance study of the adsorbed Co(III) TMPyP in 0.02M KClO_4 gives also one typical spectrum at a potential value of ca. -0.7 V/ECS (out of the potential range available in 0.1M HClO_4). Unexpectedly, no typical signal was observed at the redox Co(III)/Co(II) potential value previously identified in acidic solution.

The ER spectrum of Co(III) TMPyP shown in Fig. 6 was obtained in a narrow potential region near $E_p = -0.7\text{V}$. It exhibited double signed features which did not fit with the differential spectra obtained by subtracting

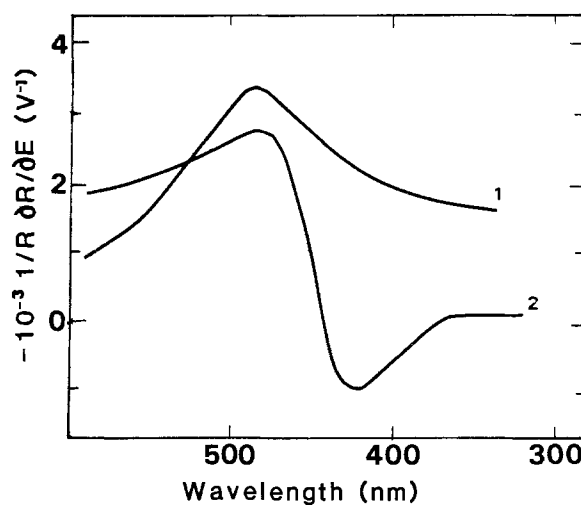
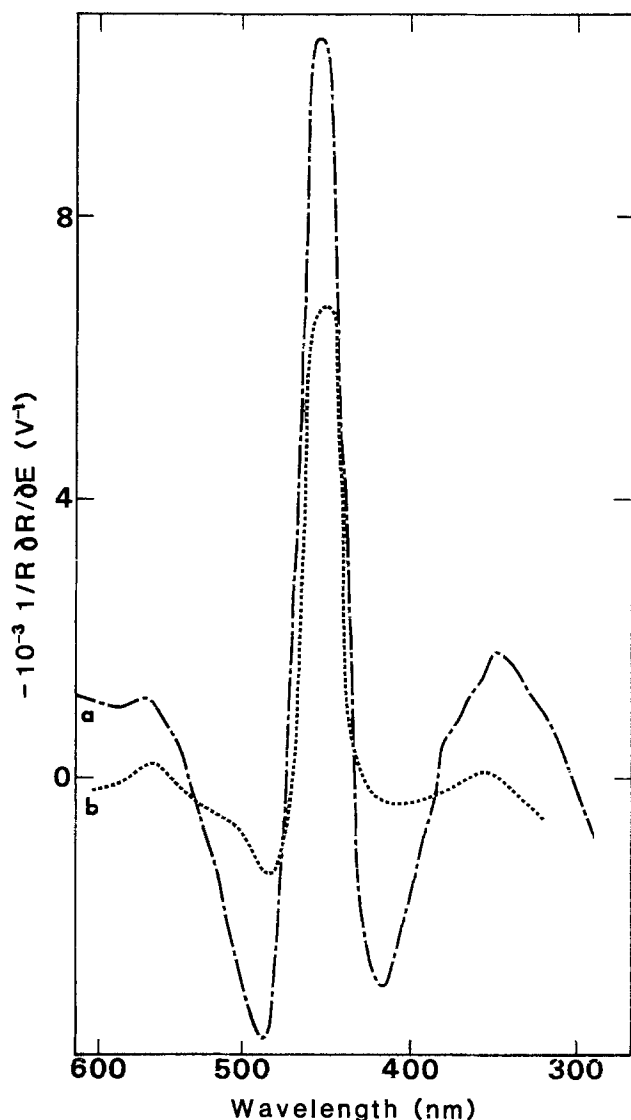


Fig. 3. a(left), curve a: Typical ER spectrum displayed at $E = +0.45\text{ V/SCE}$ for a modified gold electrode with adsorbed Co(III) TMPyP in 0.1M HClO_4 , $f = 15\text{ Hz}$, $\delta E = 100\text{ mV}$, r.m.s. Curve b: Calculated spectra obtained from the adsorption spectra of both oxidized and reduced species in the same HClO_4 solution. b(above), curve 1: Typical ER spectrum for a gold electrode surface near the potential of zero charge. Curve 2: Typical ER spectrum for the electrode covered with Co(III) TMPyP at a potential far from E_p , $E = -0.1\text{V}$.

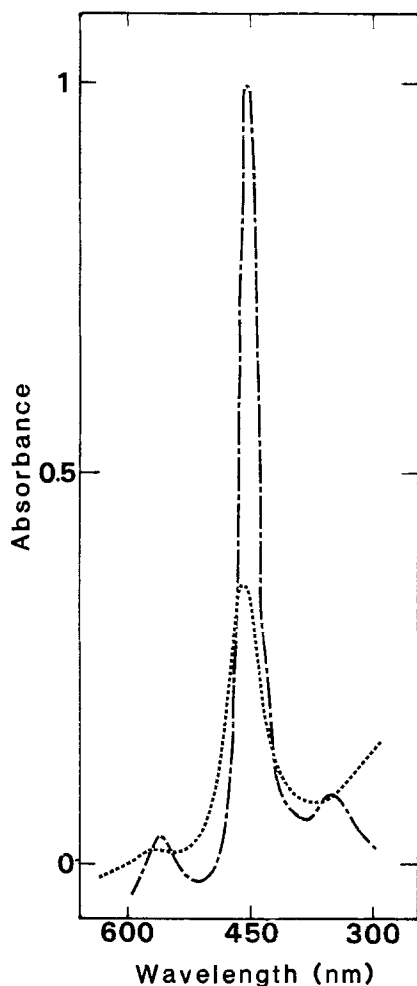


Fig. 4. Absorption spectra of a $2.2 \times 10^{-5} \text{M-liter}^{-1}$ Co(III) TMPyP solution in 0.1M HClO_4 . Dot-dashed line: reduced form. Dotted line: oxidized form.

the spectrum of the oxidized species from that of the reduced species in solution (0.02M KClO_4).¹ This confirms that the typical ER spectrum obtained at $E_p = -0.7 \text{V}$ does not stem from the Co(III)/Co(II) redox process.

¹ Absorbance properties of Co TMPy porphine (oxidized and reduced species) in 0.02M KClO_4 solution are similar to those obtained in 0.1M HClO_4 .

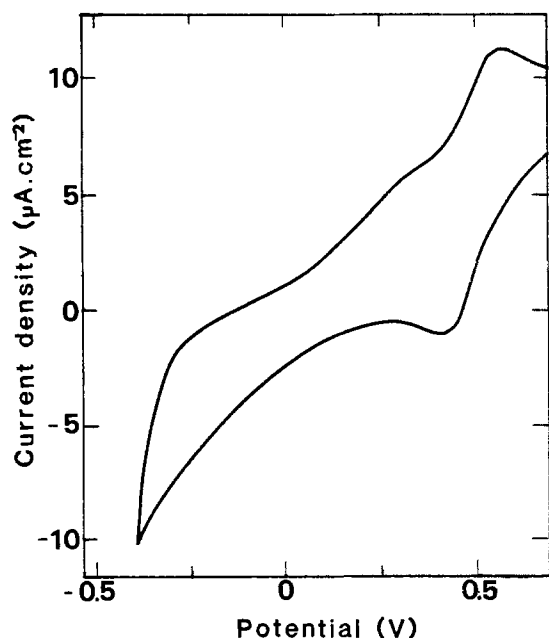


Fig. 5. Cyclic voltammogram of $10^{-4} \text{M Co(III) TMPyP}$ on micro-gold electrode in 0.1M HClO_4 . $v = 200 \text{ mV-s}^{-1}$.

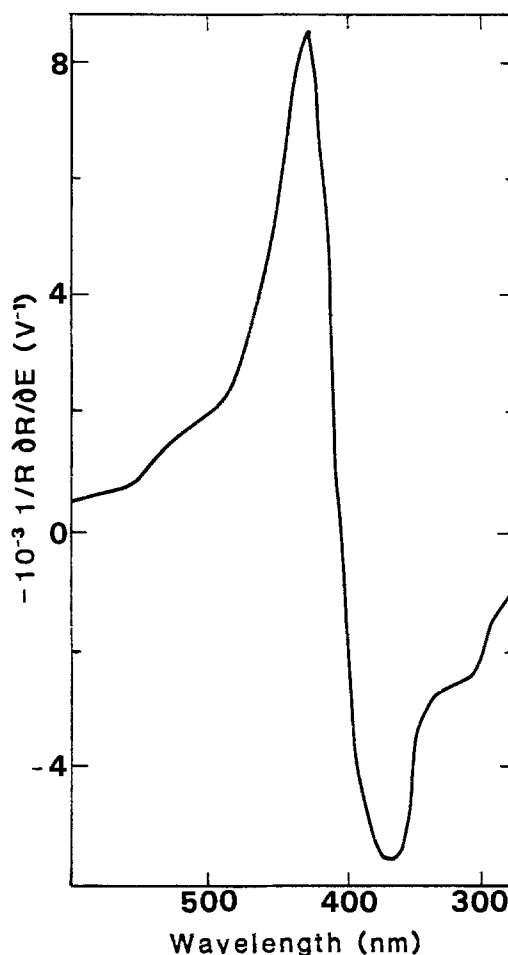


Fig. 6. Typical ER spectrum displayed at $E_p = -0.7 \text{V/SCE}$ for a modified gold electrode with adsorbed Co(III) TMPyP in neutral 0.02M KClO_4 .

Under the same conditions, the adsorbed free TMPyP does not give any signal in the capacity and electroreflectance spectra at the corresponding potential. Comparison of the results between Co TMPyP and free porphyrin indicates that the redox process at -0.7V is due to cobalt and probably to the Co(II)/Co(I) system.

Cyclic voltammograms of the Co(III) TMPyP in solution (0.02M KClO_4) present a poorly defined wave near $E = +0.45 \text{V}$ and a more well-defined one near $E = -0.7 \text{V}$ which can probably be attributed to the Co(III)/Co(II) and Co(II)/Co(I) redox systems.

Comparison of the electrochemical behavior of adsorbed Co TMPyP and that of bulk porphyrin clearly shows that a redox couple, which can be attributed to the Co(II)/Co(I) system, works at the same potential ($E_p = -0.7 \text{V}$) in both adsorbed and bulk phase. Unfortunately, ER spectra of adsorbed Co(III) TMPyP at -0.7V cannot be rigorously correlated to spectra in solution phase due to the lack of the UV-visible one of reduced (Co(I) TMPyP) form. Such a reduced form has never been described to our knowledge, probably because of the demetalation of this Co(I) porphyrin. We have observed that the characteristic voltammetric curves of Co(III) TMPyP solution were modified when the potential of the electrode was maintained at a value lower than -0.7V for a long time. The cobalt deposit confirms the demetalation process. Such a process seems to occur in the adsorbed state as observed by the disappearance of the typical ER spectra for a long negative polarization.

The absence of the ER spectra at $E_p = +0.45 \text{V}$ in neutral solution is not yet clearly understood. It should be explained by a drastic change in configuration of the Co(III) TMPyP from adsorbed form to bulk phase, or more probably by a shift of the redox potential [Co(III)/Co(II)] in a positive range out of the available do-

main. It can be noted that the positions of this couple have not been precisely characterized in solution and have never been described in this neutral media. The disappearance of a redox system in porphyrin-modified electrode has been observed by Murray (9) for a cobalt-metaleled (NH₄)₄ tetraphenylporphine attached to carbon or to platinum electrodes.

Conclusions

Co(III) TMPyP and TMPyP are strongly adsorbed on a gold electrode in a large potential range, in neutral and acidic media. A modified electrode can be easily prepared by this simple method.

Co(III) TMPyP behaves in the adsorbed form as in solution in acidic media. The Co(III)/Co(II) couple appears at +0.45V, in a potential range described by Pasternack (19) and confirmed by our experimental determinations. Thus, the catalytic applications of Co(III) TMPyP involving the Co(III)/Co(II) couple in such a medium should not be modified by linkage or adsorption on the electrode surface.

Concerning the neutral medium, our ER study gives evidence for the Co(II)/Co(I) system which has never been previously determined by bulk voltammetric studies. However, the proximity of potentials corresponding to water reduction and the possibility of demetalation reaction complicate the characterization of the bulk system.

Our results show that electroreflectance coupled with capacitance and voltammetric measurements appears to be a powerful technique in studying both spectroscopic and electrochemical properties of porphyrin derivative.

Electroreflection allows the investigation of electrode modified by adsorbed species and might be applied to other modified electrodes with good reflectance properties.

Acknowledgment

This work enters into a contract with the Centre National de la Recherche Scientifique (PIRSEM) and was supported in part by the Centre National de la Recherche Scientifique (CNRS) and by the Agence Française pour la Maîtrise de l'Énergie (AFME) (no. 980025).

Manuscript submitted Dec. 19, 1984; revised manuscript received March 6, 1985.

CNRS assisted in meeting the publication costs of this article.

REFERENCES

- (a) L. R. Faulkner, *Chem. Eng. News*, Feb. 1984; (b) R. W. Murray, in "Electroanalytical Chemistry," Vol. 13, A. J. Bard, Editor.
- R. R. Durand, Jr. and F. C. Anson, *J. Electroanal. Chem.*, **134**, 273 (1982).
- A. Bettelhum, R. J. H. Chan, and T. Kuwana, *ibid.*, **99**, 391 (1979).
- J. Zagal, R. K. Sen, and E. Yeager, *ibid.*, **83**, 207 (1977).
- R. D. Rocklin and R. W. Murray, *ibid.*, **100**, 271 (1979).
- A. P. Brown, C. Koval, and F. C. Anson, *ibid.*, **72**, 379 (1976).
- M. Itabashi, T. Masuda, and K. Itoh, *ibid.*, **165**, 265 (1984).
- B. Beden, O. Enea, F. Hahn, and C. Lamy, *ibid.*, **170**, 357 (1984).
- K. W. Willman, R. D. Rocklin, R. Nowak, K. N. Kuo, F. A. Schultz, and R. W. Murray, *J. Am. Chem. Soc.*, **102**, 7629 (1980).
- B. Z. Nikolic, R. R. Adzic, and E. B. Yeager, *J. Electroanal. Chem.*, **103**, 281 (1979).
- B. P. Neri and G. S. Wilson, *Anal. Chem.*, **44**, 1002 (1972).
- K. Kalyanasundaram and M. Neumann-Spallart, *J. Phys. Chem.*, **86**, 5163 (1982).
- A. Shamin, P. Hambright, and R. F. X. Williams, *Inorg. Nucl. Chem. Lett.*, **15**, 243 (1979).
- A. Ricci, S. Pinamonti, and V. Bellavita, *Ric. Scien.*, **12**, 2497 (1960).
- P. Worthington, P. Hambright, R. F. X. Williams, M. R. Feldman, K. M. Smith, and K. C. Langry, *Inorg. Nucl. Chem. Lett.*, **16**, 441 (1980).
- A. Harriman, M. C. Richoux, and P. Neta, *J. Phys. Chem.*, **87**, 4957 (1983).
- P. A. Forshey and T. Kuwana, *Inorg. Chem.*, **20**, 693 (1981).
- A. Harriman, *J. Chem. Soc. Dalton Trans.*, 141 (1984).
- F. Rohrbach, E. Deutch, W. R. Heinemann, and R. F. Pasternack, *Inorg. Chem.*, **16**, 2650 (1977).
- J. Chatt, C. M. Elson, and G. J. Leigh, *J. Am. Chem. Soc.*, **95**, 2408 (1973).
- D. G. Davis and L. A. Truxillo, *Anal. Chim. Acta*, **64**, 55 (1973).
- E. F. Bowden, F. M. Hawkrig, and H. N. Blount, *J. Electroanal. Chem.*, **161**, 355 (1984).
- C. Hinnen, R. Parsons, and K. Niki, *ibid.*, **147**, 329 (1983).
- J. B. Verhlac, Thesis 3ème cycle, Orsay, France (1984).
- (a) R. F. Pasternack and M. A. Cobb, *J. Inorg. Nucl. Chem.*, **35**, 4327 (1973); (b) *Biochem. Biophys. Res. Commun.*, **51**, 507 (1973).
- R. F. Pasternack, E. G. Spiro, and M. Teach, *J. Inorg. Nucl. Chem.*, **36**, 599 (1974).
- C. Hinnen, C. Nguyen Van Huong, A. Rousseau, and J. P. Dalbera, *J. Electroanal. Chem.*, **95**, 131 (1979).

Electrochemical Activity in KOH Electrolyte of Carbon-Based Air Electrodes Containing Polymeric Iron Phthalocyanine by Direct Synthesis Methods

Toshiro Hirai and Jun-ichi Yamaki*

Nippon Telegraph and Telephone Corporation, Ibaraki Electrical Communication Laboratories, Tokai, Ibaraki-ken 319-11, Japan

ABSTRACT

Polymeric iron phthalocyanine (poly-FePc) was synthesized directly onto carbon supports, and carbon-based electrodes were fabricated using the carbon supports. Three synthesis methods, melt, liquid-phase, and gas-phase, were studied. Then activity on O₂ reduction in KOH solution was compared among three electrodes. The electrode obtained by melt synthesis showed the lowest polarization and maintained the most positive potential at a 10 mA/cm² discharge. The activity of poly-FePc was in the order: melt > liquid-phase > gas-phase synthesis methods. Comparing the activity of poly-FePc for the melt synthesis electrode with that for the electrode-impregnated poly-FePc from poly-FePc/conc. H₂SO₄ solution, the former showed a lower polarization and a smaller potential drop for a 10 mA/cm² discharge.

Polymeric iron phthalocyanine (poly-FePc) is reported to be a better catalyst for oxygen reduction than monomeric FePc (1). For this reason, poly-FePc as well as monomeric FePc has been examined by many authors (2-6). In these studies, poly-FePc was supported on carbon either by *in situ* gas phase methods or by an impregnation method.

Kreja and Plewka (7, 8) examined the catalytic activity of poly-FePc directly synthesized on carbon supports by a melt method. They synthesized a poly-FePc, which had few units lacking Fe central atoms, by increasing the ratio of FeCl₃/pyromellitic dianhydride (PA). They showed that the electrochemical activity of poly-FePc increased with an increase in this ratio. However, the activity and stability of poly-FePc using this method were almost the same as those of impregnated poly-FePc from poly-FePc/conc. H₂SO₄ solution (8).

In this paper, the excellent catalytic effect of poly-FePc on the carbon supports deposited by a direct synthesis method different from that adopted by Kreja and Plewka is reported. Although several methods have been previously given for the synthesis of polymeric metal phthalocyanines (9-11), in this case 1,2,4,5-tetracyanobenzene (TCB) was used as one of the reactants instead of PA in order to increase the poly-FePc yield. We then examined the influences of different synthesis methods, optimum synthesis condition, and optimum poly-FePc loadings by polarization and discharge measurements. Furthermore, it was shown that the direct synthesis method leads to a higher electrochemical activity and stability of poly-FePc than the impregnation method.

Experimental

Catalyst preparation methods.—Catalysts were supported in two different ways.

The first way was direct synthesis, for which the following three methods were adopted. (i) The melt method, where TCB, FeCl₃ (Tokyo Chemical Industry Company), urea (Kanto Chemical Company), and carbon supports were mixed and heated in an N₂ atmosphere. TCB was prepared from PA (Tokyo Chemical Industry Company), urea, and SOCl₂ (Kanto Chemical Company) according to the method reported by Epstein *et al.* (10), except using SOCl₂ instead of COCl₂. The synthesis was carried out under all combinations of temperature (300°, 350°, 400°, 450°, and 500°C) and reaction time (18, 40, 70, and 140h). The reaction was then continued at a temperature 50°C higher for an additional 2h. The product was finally extracted with pyridine and then with methanol until the washing solvent became colorless. (ii) The liquid-phase method, where the same materials as used in the melt method were mixed with 100 ml of ethylene glycol and heated at

190°C for reaction times of 18, 40, 70, and 140h. Water (500 ml) was then added to the suspension, and the solution was filtered. The product was then washed with water until the filtrate became colorless. Finally, the product was washed with acetone. (iii) The gas-phase method, where ferrocene, TCB, and the carbon supports (14:7:24 weight ratio) were mixed and heated at 250°C for 20h in an evacuated sealed tube (3). The product was washed with pyridine and methanol as in method (i).

The second way was by impregnation, where 8g of the carbon supports were added to 200 ml of 96% H₂SO₄ containing 0.3g of poly-FePc. The poly-FePc was then precipitated onto the supports by pouring the mixture into 2 liter of ice water. After filtering, the carbon supports impregnated catalyst were washed with water until the pH of the filtrate reached 7.

Poly-FePc was synthesized from TCB, FeCl₃, and urea. The starting materials for poly-FePc synthesis were mixed and heated at 300°C for 18h in an N₂ atmosphere. The temperature was then raised to 350°C and heated for an additional 2h. The product was purified according to the method reported by Epstein *et al.* (10).

Electrode preparation.—Carbon powder (C, Nippon Carbon Company), acetylene black (AB, Denki Kagaku Kogyo Company), and Ketjen black EC (EC, Akzo Chemie Company) were used as carbon supports for the air electrodes in a 1:3:4 weight ratio (12). The catalysts were prepared on the carbon supports by the methods described above. The catalyst-prepared carbon supports were then mixed in a ratio of 9:5 with polytetrafluoroethylene (PTFE) emulsion (60 weight percent [w/o] solution, Mitsui Florochemicals Company) and kneaded with ethanol and water. The mixture was rolled into a sheet and a Ni screen (Exmet Company, 3Ni7-3/0) together with a porous PTFE sheet (Nitto Denko Company, NTF5205) was applied to one side and pressed at 82.5 kg/cm²/250°C for 30 min.

Electrochemical measurements.—**Polarization.**—The air electrode (2 cm²) was placed into a polytetrafluoroethylene (PTFE) cell with a Pt foil counterelectrode, 1N KOH (Kanto Chemical Company, $f = 1.002$) electrolyte, and a saturated calomel reference electrode (SCE). One side of the electrode was contacted with electrolyte, and another side was contacted with atmospheric air. Polarization measurements were carried out in atmospheric air at room temperature (20°-25°C). Polarization curves were recorded galvanostatically with a stepwise increasing current density up to 100 mA/cm², followed by a stepwise decrease back to zero.

Rotating ring-disk electrode measurements.—The carbon supports with poly-FePc were mixed with a spectroscopically pure paraffin wax (Uvasol, Aldrich Company) in a

*Electrochemical Society Active Member.

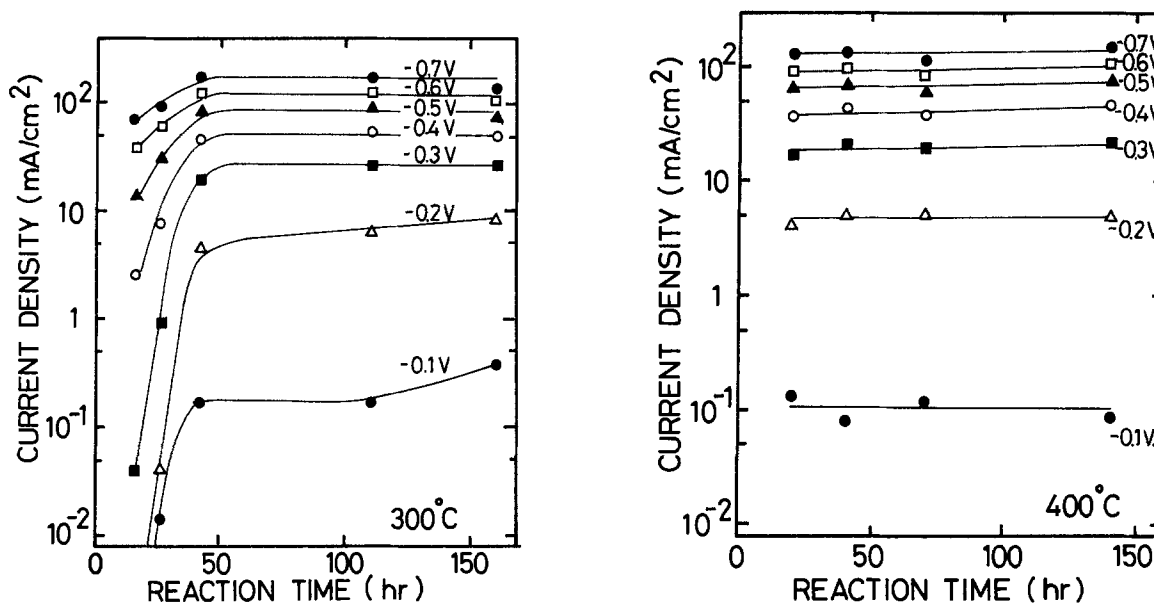


Fig. 1. Reaction time dependence on polarization characteristics of melt synthesis electrodes. Reaction temperature is 300°C (a, left) and 400°C (b, right).

2:1 weight ratio. The mixture was introduced into the disk cavity (8.00 mm diam) and was smoothed with a razor blade (13). The ring electrode consisted of gold (8.00 mm id and 12.16 mm od). A platinum sheet counterelectrode, the SCE, and a 0.1N KOH (Kanto Chemical Company, $f = 1.001$) electrolyte were used. The calculated collection efficiency of the RRDE was 0.366. Before measurements, N_2 gas was bubbled into the electrolyte to purge the O_2 in the electrolyte, and very small or no residual current for ring and disk electrodes was checked. The measurements were carried out bubbling O_2 gas into the electrolyte (O_2 concentration was 1.21×10^{-3} mol/liter). The potential of ring electrode (E_R) was maintained at +0.20V vs. SCE, where the diffusion limiting current for the oxidation of peroxide was observed (14).

All potential values for polarization and RRDE measurements were expressed in those vs. SCE.

Results and Discussion

Synthesis conditions for poly-FePc by the melt and liquid phase methods.—Direct synthesis of poly-FePc onto the carbon supports by the melt method has been examined (8). However, the poly-FePc could not be synthesized under the same conditions as those for poly-FePc synthesis alone, suggesting that the carbon supports acted as synthesis inhibitors. Therefore, the synthesizing conditions for the melt method and the liquid phase method were examined. Poly-FePc was synthesized directly onto the carbon supports using different reaction time and temperature conditions. The synthesis condition of poly-FePc was decided as a result of the cathodic polarization of the various electrodes.

Melt synthesis method.—The relationship between the reaction time and the current density at a constant potential is shown in Fig. 1. For the samples synthesized at 300°C, the current densities at constant potential increased with increasing a reaction time up to 50h (Fig. 1a). In the range 300°C/> 50h, current densities were independent of reaction time. However, when poly-FePc was synthesized at temperatures higher than 350°C, no significant difference in the activity in respect to reaction time and temperature was observed. The result at 400°C, as a typical case, is shown in Fig. 1b. Consequently, we suggest that poly-FePc should be synthesized on carbon supports by the melt method under 300°C/> 50h or 350°-500°C/> 20h conditions.

Liquid phase synthesis method.—Polarization characteristics were the same at -0.4 and -0.5V for different samples (Fig. 2). Current densities at -0.2 and -0.3V in-

creased with increasing reaction time. The current densities in the range of < 100h were larger than those at -0.2 and -0.3V in the range of < 40h in Fig. 1a. We judged this tendency was due to an increase in amount of poly-FePc synthesized onto carbon supports. The difference of current densities in the range of -0.5 to -0.7V may be due to the difference in electrode structure, for example, pore size and number of pores. In this method, it is suggested that poly-FePc should be synthesized on the carbon supports under 190°C/> 20h conditions.

Thermogravimetric measurements were carried out for the carbon supports on which the poly-FePc was synthesized by all three methods. The results are shown in Table I. The temperature where sample weight decreased rapidly was in the range of 372°-378°C, which was slightly higher than, or equal to, the decomposition temperature of the poly-FePc synthesized by the corresponding method. However, the temperature was higher than that for the monomeric FePc (335°C) and was far higher than the decomposition temperature of TCB (248°C). The results indicated that poly-FePc was the material supported on the carbon surface.

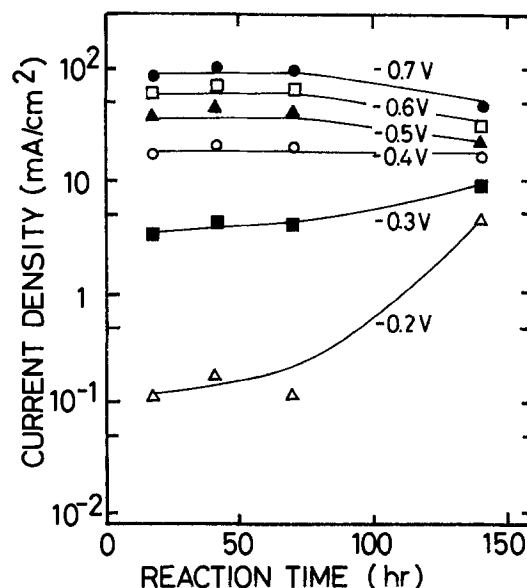


Fig. 2. Reaction time dependence on polarization characteristics of liquid phase synthesis electrodes. Reaction temperature is 190°C.

Table I. Decomposition temperature of poly-FePc

Synthesis method	Sample	
	Poly-FePc (°C)	Carbon supports containing poly-FePc (°C)
Melt	370	372
Liquid phase	372	380
Gas phase	372	378

Table II. Poly-FePc electrodes

Synthesis method	Synthesis conditions		Poly-FePc weight on carbon supports (g/m ²)
	Temperature (°C)	Time (h)	
Melt	(500 550)	(40 2)	7.88×10^{-4}
Liquid phase	190	140	1.28×10^{-3}
Gas phase	250	20	$> 4.00 \times 10^{-4}$

Electrochemical characteristics of direct synthesis electrodes.—As a result of the experiments conducted above, the electrode preparation conditions used were selected as listed in Table II. For the gas phase synthesis electrode (electrode 3), the correct amount of poly-FePc could not be evaluated because of the loss of carbon supports during the evacuation procedure. Judging from results of the dependence of amount of FePc on activity (15), the poly-FePc almost entirely covered the carbon supports.

Polarization curves are shown in Fig. 3. The poly-FePc electrode prepared by the melt method (electrode 1) exhibited the most positive potential. No polarization hysteresis of electrode 1 was observed. The hysteresis of electrode 2 was in the opposite direction. (That of curve 3 in Fig. 7 was also in the same direction.) The behavior may be rest of solvent (ethylene glycol) in micropores of carbon supports (or less wettability of bare carbon surface), although we cannot surely show that. We are now engaged in experiments about the behavior.

The potential-time curves at 10 mA/cm² discharge are shown in Fig. 4. Electrode 1 retained the most positive potential for 300h. The potential drop after a 300h discharge was as follows: for electrode 1 it was 0.01V; for the liquid phase method electrode (electrode 2) 0.08V, and for the gas phase method electrode (electrode 3) 0.067V.

As seen from the results, poly-FePc directly synthesized on the carbon supports by the melt method showed the most active catalytic effect, low polarization, and an excellent stability of activity.

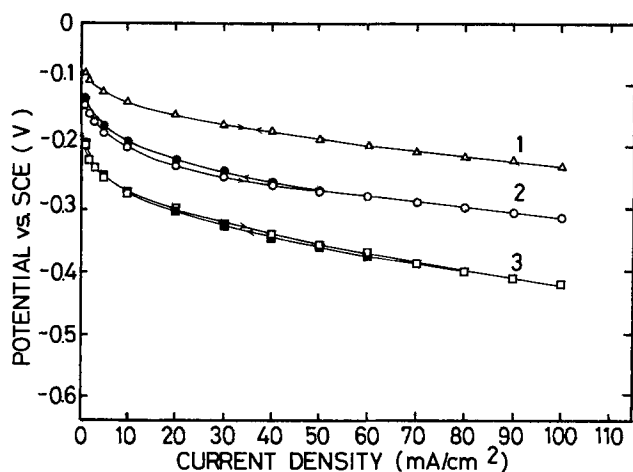


Fig. 3. Polarization curves for poly-FePc electrodes. Curve 1: melt synthesis. Curve 2: liquid-phase synthesis. Curve 3: gas phase synthesis.

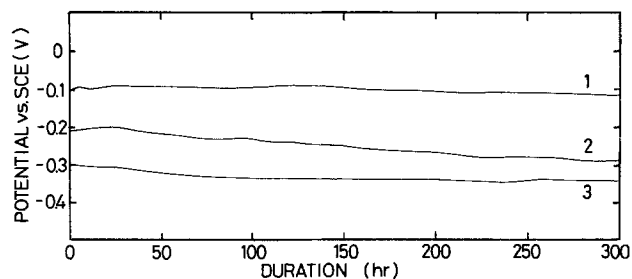


Fig. 4. Dependence of potential drop at 10 mA/cm² on time. Curve 1: melt synthesis. Curve 2: liquid phase synthesis. Curve 3: gas phase synthesis.

Elemental analysis was carried out for poly-FePc and the carbon supports deposited poly-FePc by three synthesis methods. The results are given in Tables III and IV. The N/Fe ratio of the carbon supports containing poly-FePc by melt synthesis method was 8.8. The value was close to that of poly-FePc in Table III. This suggests that the poly-FePc on the carbon supports consisted of almost all ligand units with a central Fe metal. In another study (8), a poly-FePc with few ligand units containing no Fe atoms was synthesized directly onto carbon supports using a larger amount of FeCl₃ than for the stoichiometric ratio of FeCl₃/PA. In the present work, however, poly-FePc with few Fe defect units was synthesized directly on supports by increasing reaction time and temperature with TCB and FeCl₃ in a stoichiometric ratio. Nevertheless, liquid and gas phase synthesis resulted in carbon supports containing poly-FePc with many ligands lacking Fe atoms, while the corresponding poly-FePc in Table III had a few ligands with no Fe atoms. Though the catalyst activity has correlation with conductivity (16), we believe that the excellent activity observed in the melt method mainly results from the synthesis of poly-FePc containing fewer units with no Fe metal.

The quantity of Fe atoms in poly-FePc was evaluated by atomic absorption analysis. In one treatment, the carbon supports with poly-FePc were pyrolyzed at 500°C for 2h and then placed in conc. HCl and filtered. In another treatment, they were placed in conc. H₂SO₄ for 5h, and then were filtered. The amounts of poly-FePc dissolved in conc. H₂SO₄ were evaluated from the ratio of Fe content obtained by the latter treatment to that by the former treatment. Those were 59.2 w/o for the melt method, 81.3 w/o for the liquid phase method, and 43.9 w/o for the gas phase method. This suggests that large potential drop after 300h for electrode 2 may be correlated with the solubility of liquid phase poly-FePc.

Table III. Elemental analysis of poly-FePc

Sample ^a	C (%)	H (%)	N (%)	Fe (%)	C/N	N/Fe
Melt	61.3	2.5	24.5	11.7	2.92	8.4
Liquid phase	66.1	3.2	22.6	8.0	3.41	11.3
Gas phase	65.1	5.2	19.8	9.2	3.84	8.6

^a Synthesis conditions (temperature and reaction time) are for the melt (300°C, 20h) + (350°C, 2h), for the liquid phase 190°C, 70h, and for the gas phase 250°C, 20h.

Table IV. Elemental analysis of carbon supports containing poly-FePc

Sample	C (%)	H (%)	N (%)	Fe (%)	N/Fe
Without poly-FePc	98.1	<0.2	<0.2	0.046	—
Melt	90.8	0.26	6.11	2.78	8.8
Liquid phase	94.0	1.92	3.54	0.27	52.3
Gas phase	91.5	1.01	6.32	0.15	167.9

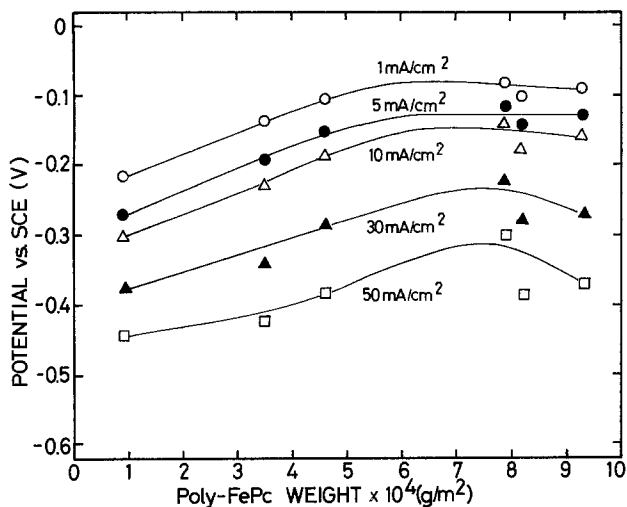


Fig. 5. Dependence of potential at constant current density on poly-FePc coverage (g/m^2) for melt synthesis electrodes.

Effect of poly-FePc amount on activity.—The dependence of the amount of poly-FePc on electrode activity for the melt synthesis method was examined. This amount was controlled by changing the ratio of the starting materials to the carbon supports. The reaction temperature was maintained at 500°C for 40h, followed by 550°C for an additional 2h. Electrode potentials at constant current density for electrodes with various amounts of poly-FePc are shown in Fig. 5. The potential became more positive with increasing coverage of poly-FePc in the range of 0.89×10^{-4} to $6 \times 10^{-4} \text{ g/m}^2$. Above this range (6×10^{-4} to $9.3 \times 10^{-4} \text{ g/m}^2$), the potentials changed little with the amount of poly-FePc present. It appears that the carbon supports were completely covered with poly-FePc molecules when more than $6 \times 10^{-4} \text{ g/m}^2$ of poly-FePc was supported. The optimum poly-FePc coverage for melt synthesis electrodes was $7.9 \times 10^{-4} \text{ g/m}^2$. Poly-FePc was supported on the carbon supports in a monolayer, based on the calculated value of $6.6 \times 10^{-4} \text{ g/m}^2$. As can be seen, the experimental optimum is close to the calculated value.

Voltammetry curves at 1000 rpm for samples with different loadings of poly-FePc are illustrated in Fig. 6. The O_2 reduction occurred in the range of $< -0.1 \text{ V vs. SCE}$ on the disk electrode with poly-FePc, while without catalyst O_2 reduction occurred in the potential range of $< -0.25 \text{ V vs. SCE}$. A ring current, I_R , was observed in the potential range of $< -0.25 \text{ V vs. SCE}$. I_R decreased with an increase in the amount of poly-FePc on the carbon supports. The

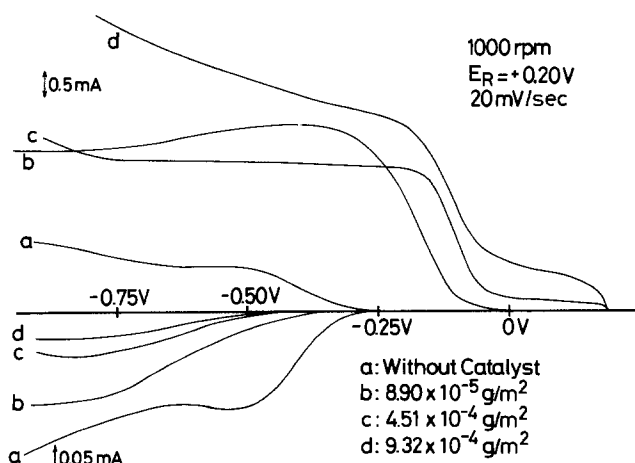


Fig. 6. Rotating ring-disk (RRDE) data for O_2 reduction on carbon supports with various amounts of poly-FePc in 1 N KOH . Scan rate: 20 mV/s . Ring potential: $+0.20 \text{ V vs. SCE}$. Rotation speed: 1000 rpm . Calculated RRDE collection efficiency: $N = 0.366$. O_2 concentration: $1.21 \times 10^{-3} \text{ mol/liter}$.

ratio of I_R to the disk current, I_D , was the smallest at a poly-FePc loading of $9.32 \times 10^{-4} \text{ g/m}^2$.

Comparison of the direct synthesis method with impregnation method on the catalytic effects of poly-FePc.—When the impregnation method was used, poly-FePc was supported on the carbon surface less uniformly because of its low solubility. Furthermore, by analogy with results for monomeric FePc (15), it is possible that the activity of poly-FePc supported by the impregnation method decreases with time. Consequently, poly-FePc supported on the carbon by the method of Kreja *et al.* showed insufficient electrochemical activity.

Polarization characteristics for O_2 reduction for poly-FePc electrodes made by the impregnation and direct synthesis (melt) methods are shown in Fig. 7. The electrode prepared by the latter method showed more negative open-circuit potential than the former electrode, although it showed more positive potential at current densities higher than 2 mA/cm^2 . In addition, the polarization hysteresis was smaller in the latter than in the former.

Discharge measurements as a function of time were carried out at 10 mA/cm^2 . Results are shown in Fig. 8. The electrode prepared by direct synthesis maintained more positive potential than that prepared by impregnation. The potential drop after discharge over 200h was -0.140 V for the latter electrode, whereas the former electrode showed no potential drop over the same period. Poly-FePc synthesized on the carbon supports therefore showed excellent stability in its electrocatalytic activity for O_2 reduction in KOH solution.

Conclusion

Poly-FePc was synthesized on carbon supports by three methods (melt, liquid phase, and gas phase) to examine

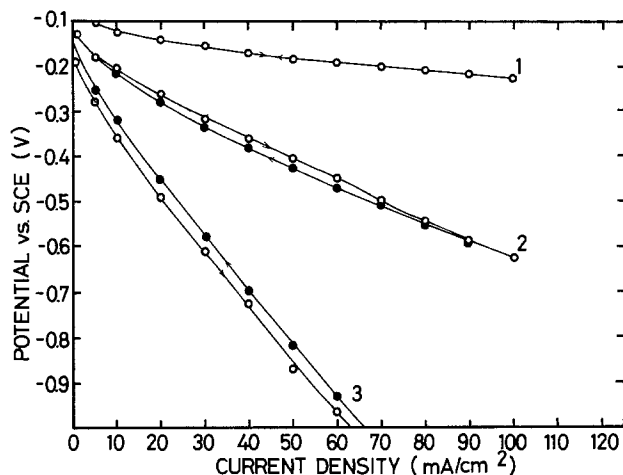


Fig. 7. Polarization curves for air electrodes. Curve 1: with poly-FePc prepared by direct synthesis. Curve 2: with poly-FePc prepared by impregnation. Curve 3: support without catalyst.

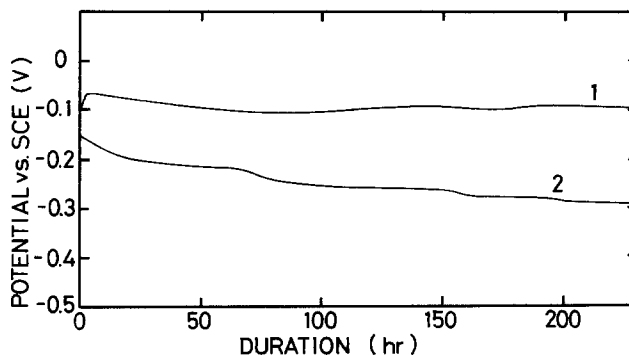


Fig. 8. Time dependence of electrode potential at 10 mA/cm^2 . Curve 1: direct synthesis poly-FePc. Curve 2: impregnation poly-FePc.

the catalytic effects on oxygen reduction in KOH solution.

Poly-FePc was successfully synthesized on the carbon supports under 300°C/> 50h or 350°-500°C/> 20h conditions for the melt method and 190°C/> 20h for the liquid phase method. From elemental analysis, the N/Fe ratio of poly-FePc supported on the carbon by the melt method was 8.8. The poly-FePc, therefore, consisted almost entirely of ligands with a central Fe metal.

The melt synthesis electrode showed the lowest polarization and maintained the most positive potential for a period of at least 300h at a 10 mA/cm² discharge. The activity of the poly-FePc was in the order of melt > liquid phase > gas phase synthesis. It is suggested that the highest activity of poly-FePc made by the melt method is due to the presence of a few monomer units with no central Fe metal. From the dependence of the poly-FePc amount on polarization, poly-FePc synthesized by the melt method entirely covered the carbon supports in the range of > 6 × 10⁻⁴ g/m². The optimum poly-FePc coverage for the activity of melt synthesis electrodes was 7.9 × 10⁻⁴ g/m², which was nearly equal to the calculated value (6.6 × 10⁻⁴ g/m²) of a poly-FePc monolayer. The RRDE results suggest that the excellent polarization characteristics obtained with this poly-FePc coverage are due to the predominant occurrence of the four-electron O₂ reduction process on poly-FePc electrodes.

The melt synthesis electrode with poly-FePc showed lower polarization in the range of 2-100 mA/cm² and a smaller potential drop over 200h during 10 mA/cm² discharge tests than that for the electrode made by impregnation. It is concluded that the poly-FePc melt synthesis electrode showed the higher electrochemical activity and stability for O₂ reduction in KOH solution.

Acknowledgments

The authors wish to express their gratitude to Mr. C. Uemura, Mr. T. Okada, and Dr. A. Yamaji for their helpful

guidance and discussions during the course of this research. The authors are also grateful to Mr. M. Fujiki for his efforts in measurements of elemental analysis.

Manuscript submitted Jan. 14, 1985; revised manuscript received ca. April 29, 1985.

Nippon Telegraph and Telephone Corporation assisted in meeting the publication costs of this article.

REFERENCES

1. A. A. Berlin and A. L. Sherle, *Inorg. Macromol. Rev.*, **1**, 235 (1971).
2. A. J. Appleby and M. Savy, *Electrochim. Acta*, **22**, 1315 (1976).
3. A. J. Appleby, J. Fleisch, and M. Savy, *J. Catal.*, **44**, 281 (1976).
4. L. Y. Johansson, J. Mrha, and R. Larsson, *Electrochim. Acta*, **18**, 255 (1973).
5. A. J. Appleby and M. Savy, *ibid.*, **21**, 567 (1976).
6. M. Savy, C. Bernard and G. Magner, *ibid.*, **20**, 383 (1975).
7. L. Kreja and A. Plewka, *Electrochim. Acta*, **25**, 1283 (1980).
8. L. Kreja and A. Plewka, *ibid.*, **27**, 251 (1982).
9. A. Epstein and B. S. Wildi, *J. Chem. Phys.*, **32**, 324 (1960).
10. D. R. Boston and J. C. Bailar, Jr., *Inorg. Chem.*, **11**, 1578 (1972).
11. T. Hara, Y. Ohkatsu and T. Osa, *Bull. Chem. Soc. Jpn.*, **48**, 85 (1975).
12. T. Hirai and A. Yamaji, Paper presented to the Technical Group on CPM, IECCE Japan, CPM82-67, 55 (1982).
13. G. Magner, M. Savy, and G. Scarbeck, *This Journal*, **127**, 1076 (1980).
14. J. Zagal, P. Bindra, and E. Yeager, *ibid.*, **127**, 1506 (1980).
15. T. Hirai, J. Yamaki, and A. Yamaji, *J. Appl. Electrochem.*, **15**, 441 (1985).
16. H. Meier, W. Albrecht, U. Tschirwitz, and E. Zimmerhackl, *Ber. Bunsenges. Phys. Chem.*, **77**, 843 (1973).

Preparation and Properties of Electrodes Modified by Polymeric Films with Pendant Anthraquinone Groups

P. M. Hoang, Steven Holdcroft, and B. Lionel Funt*

Department of Chemistry, Simon Fraser University, Burnaby, Vancouver, British Columbia, Canada V5A 1S6

ABSTRACT

Polymeric films of poly-[p-(9,10-anthraquinone-2-carbonyl)styrene]-co-styrene were deposited on Pt by evaporation of solvent from toluene solutions. The films were insolubilized and stabilized by cross-linking reactions initiated by UV irradiation. The voltammetric reduction to the radical anion is reversible in dimethylsulfoxide solution containing tetraethylammonium perchlorate. The redox peaks occur at identical potentials and show the linear current dependence on scan rate characteristic of adsorbed systems. Spectroelectrochemistry of successive reduction cycles confirmed the reversible formation of the radical anion and dianion. The electrocatalytic reduction of O₂ was conducted with these modified electrodes.

Electrodes modified with quinoid compounds have been utilized for electrocatalytic purposes. The oxidation of NADH and of ascorbic acid mediated by catechols have been described (1-4). The covalent attachment of naphthoquinone to semiconductors was utilized by Wrighton and co-workers in photoelectrochemical reductions (5, 6). Degrand employed an adsorbed film of an anthraquinone polymer with an amine backbone for electrocatalytic reduction of O₂ (7).

We previously reported the preparation of a series of polymers with pendant electroactive anthraquinone groups and investigated the electrochemical response of these polymers in solution (8). The electroactive units responded independently, and the spacing of electroactive units on the chain could be changed without affecting

*Electrochemical Society Active Member.

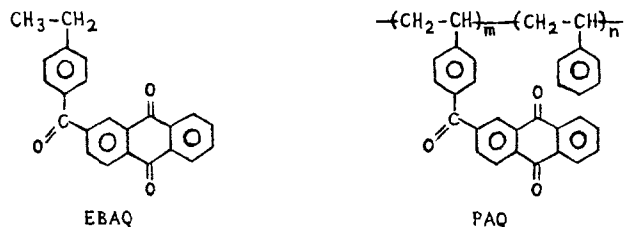
their electrochemical behavior. Previous work indicated that such systems could conform to theoretical expectations as polymeric films (9).

In this report, we describe the preparation of these films and their stabilization and insolubilization by cross-linking reactions produced by irradiation of the film. The reversibility and stability of the modified electrodes is explored by electrochemical and spectroelectrochemical techniques, and the effects of spacing of electroactive units on the backbone chain and of overall film thickness are examined. These modified electrodes are utilized for the mediated reduction of O₂ in a nonaqueous medium.

Experimental

The synthesis of a model compound 2-(p-ethyl-benzoyl)-9,10-anthraquinone (EBAQ) and of the polymer

poly-[p-(9,10-anthraquinone-2-carbonyl)styrene]-co-styrene (PAQ) was described previously (8)



Dimethyl sulfoxide (DMSO) was fractionally distilled and stored over molecular sieve 4Å, which had been activated by heating for several days at 300°C in vacuum. Tetraethylammonium perchlorate (TEAP) was recrystallized twice from distilled water and dried in vacuum.

Film preparation.—A measured volume of toluene solution of the polymer was placed on the surface of the working electrode and the solvent was allowed to evaporate slowly. The electrode was subsequently dried *in vacuo* for 5 min. The film thickness was estimated from the quantity of polymer initially present in the solution.

The films were cross-linked by irradiating the coated electrode, which was immersed in isopropanol, with light from a 100W Hg lamp (Engelhard Hanovia). The electrode was subsequently dried *in vacuo* for 10 min.

Electrochemistry.—A three-compartment cell was used which had a 5 mm ϕ Pt working electrode (Beckmann), a Pt wire counterelectrode, and a SCE reference. The working electrode was polished successively with SiC 600, 3 μm diamond paste and 2, 0.1, and 0.05 μm alumina and then sonicated in distilled water for 10 min. The reference electrode was provided with a salt bridge of 0.1M TEAP/DMSO in the Luggin capillary. The stability of the background current indicated that insignificant contamination by water occurred within the time scale of the experiments. Before each set of runs, polymer from the previous experiment was removed with tissue paper and the electrode was then cleaned chemically and electrochemically as described in the literature (10).

The solutions were flushed with Ar and an Ar atmosphere was maintained throughout the voltammetric measurements. A PAR 170 electrochemical system with IR compensation was used for stationary voltammetry, and a Pine Instrument rotating ring-disk electrode and ancillary potentiostat and controller were used for the dynamic studies. An Apple II microcomputer-based data acquisition system was employed for step function Cottrell experiments.

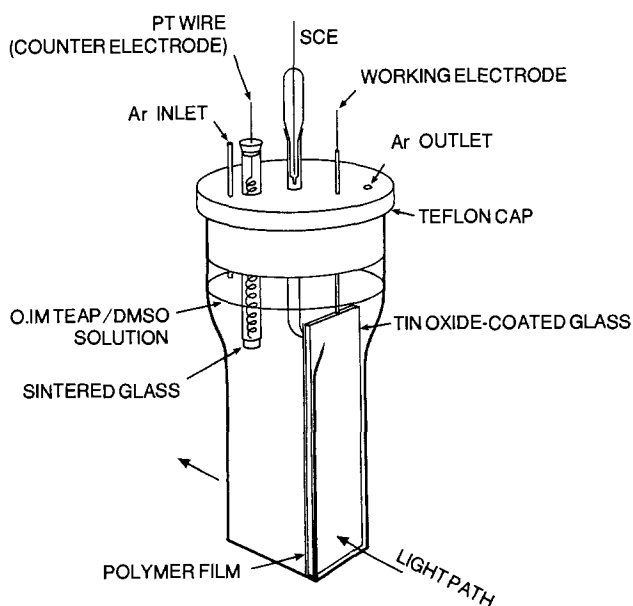


Fig. 1. Spectroelectrochemical cell

Spectroelectrochemistry.—A $1 \times 1 \times 4$ cm square cross-sectional optical cuvette, with a quartz-to-glass seal to a $1.2 \phi \times 5$ cm tube, was fitted with a Teflon cap with ports for a SCE, miniature counterelectrode, and Ar inlets, as shown in Fig. 1. The working electrode was a sheet of tin oxide-coated glass (VWR Scientific) on which the polymer sample was deposited. Electrical connections were made using silver dag, which was subsequently covered with epoxy resin. Visible spectra were recorded on a Unicam SP 8000 spectrophotometer.

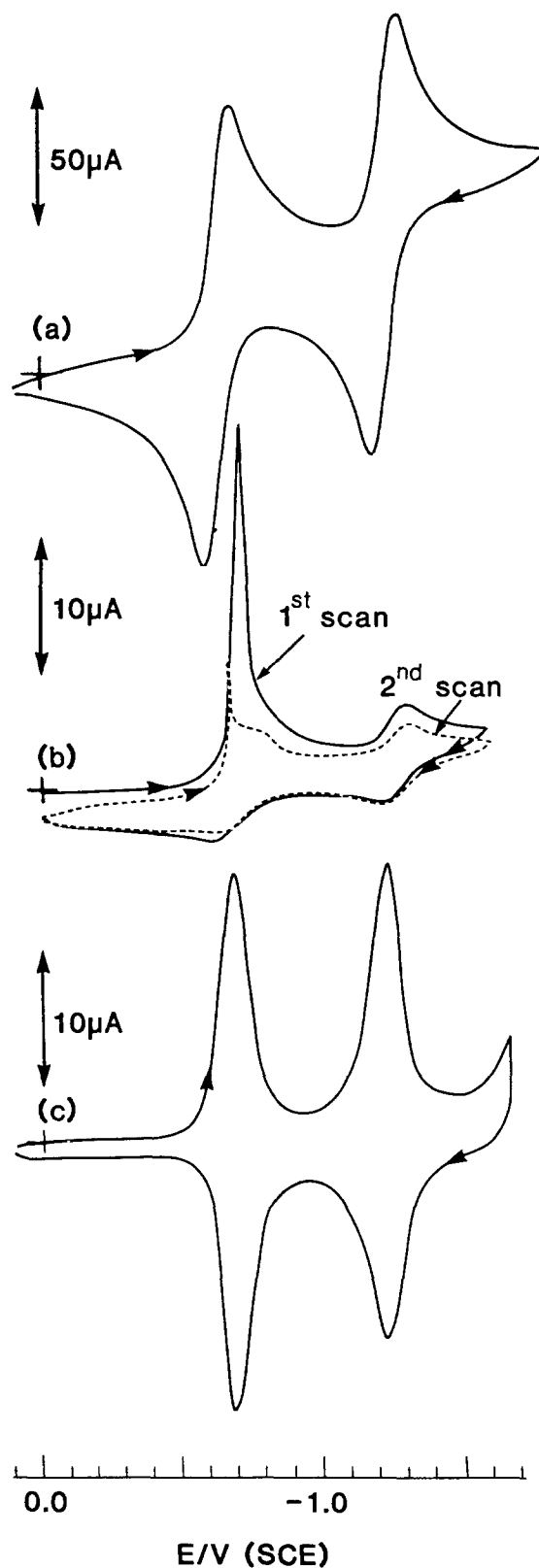


Fig. 2. Cyclic voltammograms of 3.47 mM EBAQ (a), unirradiated PAQ-coated electrode (b), and irradiated PAQ-coated electrode (1000Å thick) (c). Scan rate 50 $\text{mV}\cdot\text{s}^{-1}$; 0.1M TEAP in DMSO.

Results

The voltammetry of the polymer films and of the model compound, EBAQ, is shown in Fig. 2. A cyclic voltammogram of the model compound at a bare Pt electrode shows two well-defined nernstian peaks. An electrode coated with PAQ, which had not been cross-linked, produced successive peaks which decreased in magnitude due to desorption of the polymer, and deviations from nernstian response were also evident.

The electrode could be stabilized by cross-linking the polymer chains through exposure to UV radiation. Figure 2c shows the effect of 10 min irradiation. Only a minor decrease in peak current or in integrated charge is found after 50 cycles. The electrochemical activity was maintained for a period of many days. Moreover, the first and second reduction potentials of the AQ groups in the polymer film were essentially identical with those of the model compound, EBAQ, in solution. In contrast to our experiments with poly(vinylbenzophenone) films, where cycling above the second reduction potential leads to a loss of electroactivity, the PAQ films remain physically and chemically stable on repeat cycles to the doubly charged anion.

The effect of varying the period of UV irradiation was investigated in order to optimize film preparation. Obviously, too much irradiation will lead to destruction of electroactive centers and excessive cross-linking of chains, whereas insufficient irradiation will result in desorption from the electrode. The data in Fig. 3 show that maximum peak currents were obtained after 10 min exposure. This condition was chosen for all film preparations reported here.

Spectroelectrochemistry.—The $\text{PAQ}^{\cdot-}$ radical anion is green, and the doubly charged PAQ^{2-} is blue. The spectroelectrochemistry of successive reduction cycles was examined in order to characterize the films and to probe their stability and reversibility. Polymeric films were deposited on conducting glass in the apparatus shown in Fig. 1. The films were potentiostated at a chosen potential until maximum optical absorption was exhibited. The results are presented in Fig. 4. Below -0.7V , no effect is obtained. Between -0.7 and -1.2V , a strong absorption develops at 690 nm , which corresponds to the formation of $\text{PAQ}^{\cdot-}$ radical anions. Further increase to -1.3V and more cathodic values produces a new peak at 595 nm , (PAQ^{2-}) and a decrease in the $690, 415,$ and 392 nm peaks. The process is reversible and reproducible, and similar intensities were obtained on successive cycles.

Charge transport.—The influence of film thickness on the electrochemical performance was determined (Table I). For a 100 \AA film, the voltammogram shown in Fig. 5 was obtained. The positions of the anodic to cathodic peaks almost coincide, as expected theoretically for a

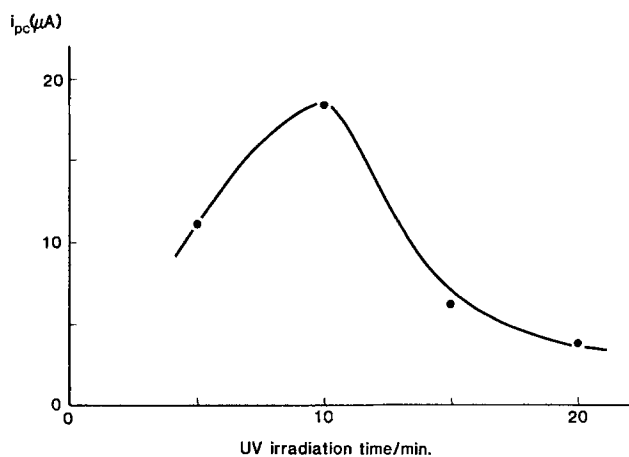


Fig. 3. Effect of time of UV irradiation on the cathodic peak current of PAQ 200(2)-coated electrodes, film thickness 1000 \AA . Scan rate $50\text{ mV}\cdot\text{s}^{-1}$; 0.1M TEAP in DMSO.

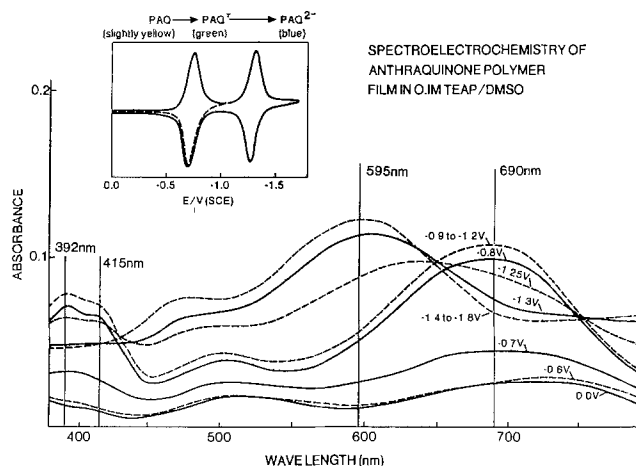


Fig. 4. Spectroelectrochemistry of film of PAQ 200(2); 0.1M TEAP in DMSO.

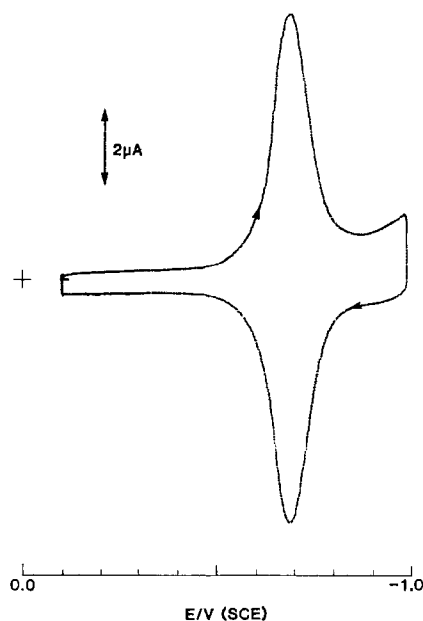


Fig. 5. Cyclic voltammogram of 100 \AA thick PAQ 200(2)-coated electrode. Scan rate $50\text{ mV}\cdot\text{s}^{-1}$; 0.1M TEAP in DMSO.

highly adsorbed substrate. The peak width at half-height is 98 mV , which is in good agreement with the theoretical value of 90.6 mV (11).

Even a 100-fold increase in film thickness to $10,000\text{ \AA}$ did not lead to major deviations. The peak separation became 16 mV and the width at half-height 112 mV for these thick films.

The dependence of peak current on thickness for the various films is shown in Fig. 6.

Table I. Voltammetric characteristics of PAQ films

Polymer	AQ%	Thickness ($\times 1000\text{ \AA}$)	ΔE (mV)	δ (mV)	i_{pc} (μA)	Γ_{obs} (nmol $\cdot\text{cm}^{-2}$)	$\frac{\Gamma_{obs}}{\Gamma_{cat}}$ %
200(2)	28.0	0.1	0	98	8.1	1.3	79
200(2)	28.0	0.5	0	110	12.2	1.9	22.6
200(2)	28.0	1	16	112	18.4	2.7	16.4
200(2)	28.0	5	16	112	72	9.7	11.8
200(2)	28.0	10	16	112	110	14.9	9.0
200(2)	28.0	15	20	112	156	21.0	8.3
200(2)	28.0	20	25	116	174	23.4	7.1
200(2)	28.0	30	32	112	184	24.8	5.0
200(1)	19.5	1	16	116	15.0	2.2	19.2
200(2)	28.0	1	16	112	18.4	2.7	16.4
200(3)	47.4	1	36	116	29.2	4.3	15.4

0.1M TEAP/DMSO ; $50\text{ mV}\cdot\text{s}^{-1}$; UV irradiation time 10 min.

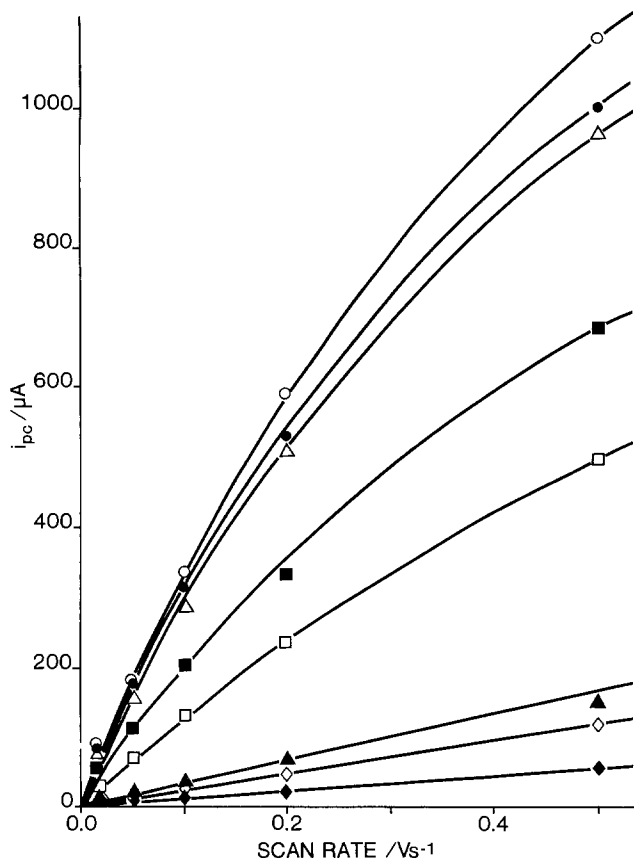


Fig. 6. Effect of scan rate for films of PAQ 200(2) of various thicknesses. Film thickness for curves from top to bottom: 3×10^4 , 2×10^4 , 1×10^4 , 5×10^3 , 1×10^3 , 5×10^2 , and $1 \times 10^2 \text{ \AA}$; 0.1M TEAP in DMSO.

The concentration of electroactive units in a unit volume is determined by the spacing of AQ groups on the backbone chain. All the PAQ polymers were prepared from a parent styrene polymer of 200 unit average chain length. The concentrations of AQ groups ranged from 19.5 to 47.4% AQ. The voltammetric characteristics obtained at a sweep rate of $50 \text{ mV}\cdot\text{s}^{-1}$ are summarized in Table I. No substantive changes in reversibility or peak shape are apparent. The ratio $\Gamma_{\text{obs}}/\Gamma_{\text{cal}}$ is the ratio of electroactive centers which undergo redox processes to that expected for the amount of polymer deposited on the electrode. This ratio remained insensitive to AQ content in the 1000 \AA film.

The process of charge transport in the film was investigated by chronoamperometry. The potential was stepped from -0.2 to -0.9 V to produce the reduction to the radical anion. A Cottrell plot (12) of the data is shown in Fig. 7. It yielded a diffusion coefficient $D_{\text{CT}} = 5.1 \times 10^{-11} \text{ cm}^2\cdot\text{s}^{-1}$ from the linear portion of the curve. Precise comparisons are not possible because of the curvature exhibited in these plots. However, similar values were obtained with cations of differing size, *i.e.*, K^+ and $(\text{C}_2\text{H}_5)_4\text{N}^+$. Closer spacing of AQ groups along the chain did not produce any detectable shift in D_{CT} . The value of this diffusion coefficient is comparable to that obtained by Murray and co-workers for cobalt porphyrin-modified electrodes (13). Table II summarizes the data obtained.

Electrocatalysis.—The catalytic reduction of O_2 to O_2^- was attempted at a PAQ-coated electrode immersed in 0.1 M tetraethylammonium perchlorate solution in DMSO. Figure 8 shows the reduction of an O_2 saturated solution (2.1 mM) at both a bare and a coated electrode. At a bare Pt electrode, a quasi-reversible curve is obtained with $E_{\text{pc}} = -0.88 \text{ V}$ and $E_{\text{pa}} = -0.66 \text{ V}$ vs. SCE. The large peak separation potential, $\Delta E = 222 \text{ mV}$, indicates that the electron transfer is not fast, and the results are consistent with those reported by Sawyer and Roberts (14).

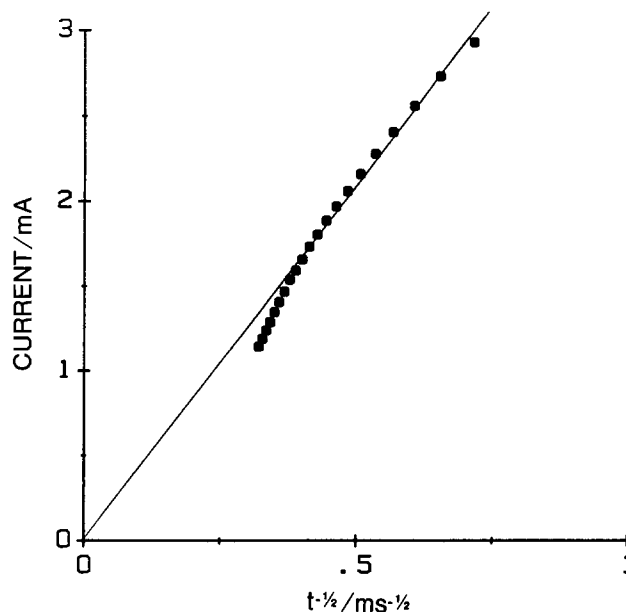


Fig. 7. Cottrell plot for PAQ 200 (2) film; 0.1M TEAP in DMSO

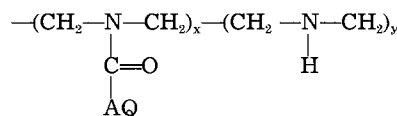
At the PAQ-coated electrode, the smaller peak separation ($\Delta E = 68 \text{ mV}$ and $E_{\text{pc}} = -0.78 \text{ V}$ and $E_{\text{pa}} = -0.71 \text{ V}$) indicates improved reversibility. Of greater interest is the 98 mV positive shift of the cathodic peak. This indicates the catalytic reduction of O_2 by PAQ and shows that the electron transfer from Pt to O_2 in solution via the PAQ film is faster than direct electron transfer from the electrode. The absence of a peak at -0.88 V in Fig. 8d shows that there is little O_2 present at the electrode surface at this potential and indicates that it has all been reduced by the PAQ film.

The presence of a single wave is consistent with a rapid electrocatalytic reduction, as found with homogeneous catalytic systems (15). A slow process should exhibit two peaks associated with the catalytic and direct reduction steps, respectively. Conversely, a very fast reduction should exhibit a precatalytic wave due to the electrocatalysis of O_2 and a second peak associated with the reduction of the polymer film.

Dynamic measurements were performed with a polymer-coated, rotating disk electrode. A shift of 60 mV in half-wave potential was observed. This compares with a shift of 98 mV in peak potential obtained with stationary cyclic voltammetry.

Discussion

Despite the similarity of the PAQ polymer and the anthraquinone polymer utilized by Degrand and Miller (16), significant differences exist. Their polymer was based on a structure



The presence of amino groups in the main chain conferred hydrophilic properties to the polymer which per-

Table II. Effect of AQ loading in 1000 \AA films

Polymer	AQ%	Supporting electrolyte (0.1M)	$D_{\text{CT}} \times 10^{11}$ ($\text{cm}^2\cdot\text{s}^{-1}$)
200(1)	19.5	TEAP	6.8
200(2)	28.0	TEAP	5.1
		KClO_4	3.6
200(3)	47.4	TEAP	5.4

In DMSO, at 25°C , UV irradiation time 10 min.

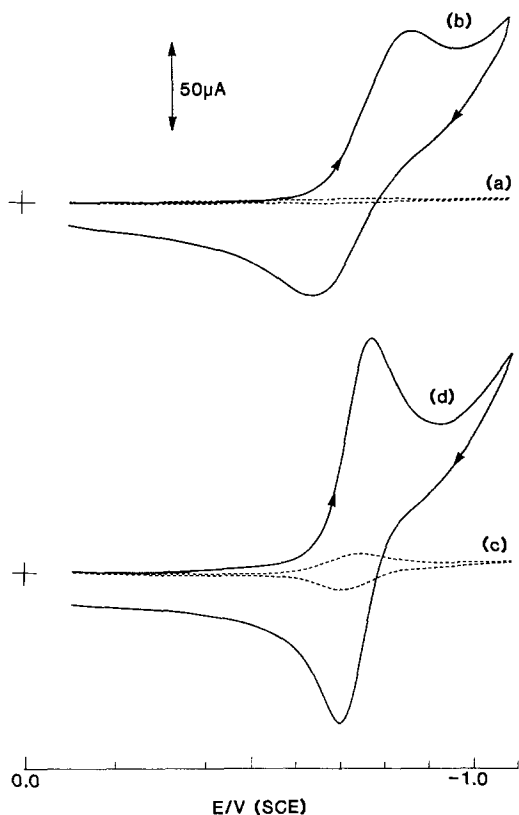


Fig. 8. Reduction of O_2 : Pt electrode under N_2 (a); as (a) but O_2 saturated (b); PAQ 200(2)-coated electrode (film thickness 100\AA), N_2 saturated (c), as (c) but O_2 saturated (d). Scan rate $50\text{ mV}\cdot\text{s}^{-1}$; 0.1M TEAP in DMSO.

mitted its utilization in aqueous media. In contrast, the PAQ polymer is inactive in water. More surprisingly, the layer-to-layer conductivity is higher, as demonstrated in the behavior of thick films of PAQ. The difference in conductivity may result from the single-electron transfer process found in this work, in contrast to the two-electron, two-proton transfer found in Miller's more complex reaction (15). Furthermore, peak broadening is not found at higher anthraquinone loadings with PAQ, but was obtained with the amino-linked polymer. These results reflect the influence of the conformation and structure of the backbone chain on ion migration and electron hopping processes.

The voltammetric results with PAQ polymers show that the 100\AA films are in accord with theoretical expectations for highly adsorbed material. The symmetry, scan rate dependence, and coulometry reflect essentially ideal behavior. For films of increased AQ content, there is little indication of deviation due to interference between neighboring groups. However, an increase in overall conductivity could be expected as electron hopping between neighboring sites is facilitated. This, as Murray has recently stated (17), is an oversimplification. To be exact, each site removed in a dilution process, or replaced in a loading process, should be comparable in size, polarity, morphology, etc., in order to ensure that distance between groups rather than chain conformation is the dominant factor. The dependence of D_{CT} on concentration has been expressed analytically (18) for Os and Ru contained in copolymer compositions. However, Buttry and Anson (19), Facci (20, 21), and Kuo (22) found D_{CT} to be independent of concentration or to decrease at high concentrations (17).

In our work, the interpretation is further complicated by an extraneous factor. The UV irradiation of the films may lead to increased cross-linking at higher AQ loadings with identical irradiation conditions. With this proviso in

mind, the failure to observe an increase in $\Gamma_{obs}/\Gamma_{calc}$ ratio in Table I may indicate that competing effects balance out the expected increase in electron transport due to smaller distances between electroactive groups.

A similar analysis applies to the effect of increase in film thickness. The change in peak current is not proportional to the total AQ content of the films. The percentage of AQ groups reduced electrochemically drops from 79 to 5.0% for a 300-fold increase in film thickness from 100 to $30,000\text{\AA}$. If reduction occurred by slow progression through successive layers, then, presumably, a limiting thickness would be encountered at which further reaction would not occur. Such a model should not show the increase of current with thickness shown in Fig. 6.

We suggest that the orientation of the polymer chains in the film leads to preferred pathways or channels for electrical conductivity. It is recognized that long chain molecules can be oriented by stretching and that such orientation results in higher crystallinity and regularity in the polymer. Thus, for films thicker than 100\AA , some regions may be completely reduced in channels from the electrode to the solution interface, while other regions may only be reduced in the first 100\AA or so layer. Such a model is consistent with the finding that films of greater thickness yield currents whose increase is not proportional to the total AQ content.

Acknowledgment

This work was performed under Contract OST8 300155 from Energy, Mines and Resources, Canada.

Manuscript submitted Dec. 3, 1984; revised manuscript received April 26, 1985. This was Paper 630 presented at the New Orleans, Louisiana, Meeting of the Society, Oct. 7-12, 1984.

Simon Fraser University assisted in meeting the publication costs of this article.

REFERENCES

- D. C-S. Tse and T. Kuwana, *Anal. Chem.*, **50**, 1315 (1978).
- C. Ueda, D. C-S. Tse, and T. Kuwana, *ibid.*, **54**, 850 (1982).
- B. W. Carlson and L. L. Miller, *J. Am. Chem. Soc.*, **107**, 479 (1985).
- K. J. Stutts and R. M. Wightman, *Anal. Chem.*, **55**, 1576 (1983).
- G. S. Calabrese, R. M. Buchanan, and M. S. Wrighton, *J. Am. Chem. Soc.*, **104**, 5786 (1982).
- G. S. Calabrese, R. M. Buchanan, and M. S. Wrighton, *ibid.*, **105**, 5594 (1983).
- C. Degrand, *J. Electroanal. Chem.*, **169**, 259 (1984).
- B. L. Funt and P. M. Hoang, *This Journal*, **131**, 2295 (1984).
- B. L. Funt and P. M. Hoang, *J. Electroanal. Chem.*, **154**, 229 (1983).
- M. Sharp, M. Peterson, and K. Edstrom, *ibid.*, **95**, 123 (1979).
- E. Laviron, L. Roullier, and C. Degrand, *ibid.*, **112**, 11 (1980).
- A. J. Bard and L. R. Faulkner, "Electrochemical Methods. Fundamentals and Applications," p. 143, John Wiley and Sons, New York (1980).
- R. D. Rocklin and R. W. Murray, *J. Phys. Chem.*, **85**, 2104 (1981).
- D. T. Sawyer and J. L. Roberts, Jr., *J. Electroanal. Chem.*, **12**, 90 (1966).
- C. P. Andrieux, C. Bloeman, J. M. Dumas-Bouchiat, F. M'Halla, and J. M. Saveant, *ibid.*, **113**, 19 (1980).
- C. Degrand and L. L. Miller, *ibid.*, **117**, 267 (1981).
- R. W. Murray, in "Electroanalytical Chemistry," Vol. 13, A. J. Bard, Editor, p. 191, Dekker, New York (1984).
- J. S. Facci, R. H. Schmehl, and R. W. Murray, *J. Am. Chem. Soc.*, **104**, 4959 (1982).
- D. A. Buttry and F. C. Anson, *J. Electroanal. Chem.*, **103**, 333 (1981).
- J. Facci and R. W. Murray, *J. Phys. Chem.*, **85**, 2870 (1981).
- J. Facci and R. W. Murray, *J. Electroanal. Chem.*, **124**, 339 (1981).
- K. N. Kuo and R. W. Murray, *ibid.*, **131**, 37 (1982).

Tri- and Tetravalent Phthalocyanine Thin Film Photoelectrodes: Comparison with Other Metal and Demetallated Phthalocyanine Systems

T. J. Klofta, P. C. Rieke,^{*1} C. A. Linkous,^{*2} W. J. Buttner, A. Nanthakumar, T. D. Mewborn, and N. R. Armstrong*

Department of Chemistry, University of Arizona, Tucson, Arizona 85721

ABSTRACT

A series of trivalent and tetravalent metal phthalocyanines (Pc) has been examined in thin film form on metal substrates by electron microscopy, UV-visible spectrophotometry, and electrochemical and photoelectrochemical techniques. These Pc's are compared with other divalent metal and demetallated phthalocyanines. The tri- and tetravalent phthalocyanines show enhanced photoresponses *vs.* the divalent metal and demetallated systems. This enhanced activity correlates with their broadened and red-shifted visible spectra and their tendency to grow as block-like or platelet-like microcrystals in the thin film. The divalent and demetallated Pc's grow as smaller, needle-like deposits with poor photoresponses. The trivalent and tetravalent Pc's have been grown in this study as thin films that act as highly doped p-type photoelectrodes or as nearly intrinsic photoconductors, exhibiting both positive and negative photopotentials, depending upon the E° of the redox couple.

There continues to be interest in the use of thin film organic materials for photovoltaic (PV) and photoelectrolytic (PE) applications (1-15). PV applications include dry cell materials, where the chromophore is sandwiched by itself or in a polymer matrix between two conductive substrates of dissimilar work functions (1-3, 16, 17). Wet cell PV and PE applications include the use of an electrolyte solution in contact with the photoactive organic material and a counterelectrode to complete the cell. Phthalocyanines (Pc) have been used in many instances as the light-sensitive, charge separating medium for these applications (5-15, 26-33). They also continue to be of interest as the primary photoreceptors in electrophotography and information processing applications, along with several other chromophores of the merocyanine, cyanine, and squarane families (34-39).

Thin film inorganic solar cells (*e.g.*, a-SiH_x) have been proposed by several researchers, which all take the same general form (Fig. 1) (16, 17, 40, 41). To the extent that organic thin film materials can be described by an energy-band model, this will apply as well to their application. Two contacting phases (labeled 1 and 3 in the figure) of dissimilar work function (or differing electrochemical potential) are sandwiched around a photoconductive material (labeled as 2 in the figure) of thickness d . This material is nearly intrinsic, but is doped to a density that must be able to support the development of a space-charge or depletion layer (of thickness δ) at both interfaces (hole blocking contacts, Fig. 1a, interface between 1 and 2; and electron blocking contacts, Fig. 1a, interface between 2 and 3). The direction of the electric field gradient within the photoconductive film depends upon the dopant density in the photoconductor (initial position of the Fermi level before contact), the thickness of the Pc film, and the relative electron affinities of the photoconductor and the two contacting phases (29-32). Two of several possible limiting cases are shown in Fig. 1a and b, both of which produce a net potential gradient which affect the photoresponse within the film and drive photogenerated holes to the interface between phases 2 and 3. These diagrams are discussed further below. Aqueous and nonaqueous electrolyte solutions are recognized to be good candidates as one of the contacting media in these cells (20-25). By changing the thermodynamic formal po-

tential, E° , of the redox couple in solution, it is possible to change the effective work function of a contacting phase (*e.g.*, phase 3) and systematically vary the sign and magnitude of the potential gradient in phase 2, and thus vary the photopotential.

Several limitations arise with the use of organic photoelectrode materials such as phthalocyanines. Rose has set forth some of the objectives for the use of any thin film photoconductor material sandwiched between two phases of dissimilar work function (16, 17); (i) the films

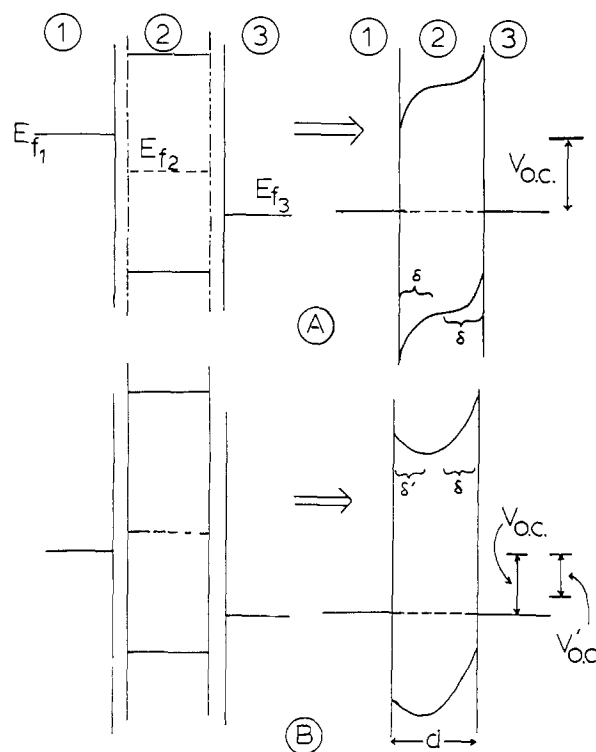


Fig. 1. Energy level schematic of an intrinsic photoconductor (phase 2) sandwiched between two contacting phases (phase 1 and phase 3). Left Side: Before contact, flatband condition. Right Side: After contact, equilibrium condition. A: Fermi levels of phases 1, 2, and 3 arranged in descending order (electron affinities increase from 1 through 3). B: Fermi level of phase 2 above either phase 1 or phase 3. Energy *vs.* electron in vacuum increases negatively in downward direction, electrochemical formal potentials increase in downward direction. V_{oc} is the maximum obtainable photopotential at open circuit.

* Electrochemical Society Active Member.

¹ Present address: Los Alamos National Laboratory, Albuquerque, New Mexico 87115.

² Present address: Brookhaven National Laboratory, Upton, New York 11973.

must possess strong light absorptivity over a large wavelength range (centered in the red), so that a thin film can capture most of the available visible wavelength light—this is generally attainable with Pc thin films; (ii) defect densities must be low enough to permit efficient transport of charge across the entire thin film in less time, τ_d , than the lifetime before recombination, τ_r —Pc films have traditionally shown excessive defect densities and inefficient charge transport; and (iii) nearly ohmic contact of the photoconductor with phases 1 and 3 (Fig. 1). This last point requires some additional modification since one of the contacts must be blocking for electrons and the other contact blocking for holes and the two contacts must have sufficiently dissimilar work functions to provide the driving force for charge separation.

Our studies of phthalocyanines have concentrated recently on chlorogallium phthalocyanine (GaPc-Cl), which exhibits unusual optical and electronic properties relative to many Pc's that have been studied previously (27-33). Films of GaPc-Cl (ca. 1 μm thick) grown very slowly on Au, and in contact with a variety of electrolyte solutions, can behave as expected for a nearly intrinsic semiconductor. The Fermi level (of several of the films studied to date) is at least 0.7 eV above the valence bandedge (29, 30). Both positive and negative photopotentials have been observed for these slowly grown films, with absorbed light photoelectrochemical quantum efficiencies of ca. 2-10%. Much thinner films of GaPc-Cl grown more rapidly on Au. (ca. 200-500 nm thickness) have shown much smaller photopotentials, but showed the same high photoconductivity and high contrast between light and dark electrochemical response (27). These films also showed an unusually red-shifted and broadened absorbance spectrum. Preliminary electron micrographs showed a high degree of long-range ordering in the microcrystalline deposits comprising each thin film. We have recently extended these studies to include several other trivalent and tetravalent metal phthalocyanines which also exhibit strong red shifting of their solution absorption spectra over most of the visible and near-IR regions. Some of these same phthalocyanines, embedded in polymer matrices, have been recently used in solid-state thin film photovoltaic cells (6-8, 42).

In this publication, we compare these tri- and tetravalent metal phthalocyanines with demetallated and divalent metal Pc's (the focus of the most previous photoelectrochemical studies) using (i) scanning electron microscopy (SEM) of both the bulk and thin film materials, (ii) UV-visible absorption spectroscopy of thin films, and (iii) electrochemical and photoelectrochemical activity of both thin (0.3-0.5 μm) and thick ($\geq 0.7 \mu\text{m}$) Pc films grown at different rates on metallized polymer substrates. Many of the tri- and tetravalent metal phthalocyanines (in comparison to phthalocyanines of divalent metals) show a superior photoresponse. We believe this is in part due to structural differences in the cofacial stacking of the Pc rings, and in part to the enhanced electrical contact with the conductive substrate.

Advantages are also observed in the use of an electrolyte solution as the third contacting phase, instead of a metal or semiconductor. Many of the defect and pore sites (short-circuit sites) of the Pc film are effectively ignored by an electrolyte with a low charge density, relative to the situation that would prevail with a contacting metal phase.

Experimental

The phthalocyanines (Pc) used, except for GaPc-Cl, were purchased commercially and purified by sublimation. Generally, two to three sublimations were required to purify the Pc to an acceptable level (with no detectable impurities found using UV-visible or infrared spectrophotometry).

Our synthesis method for GaPc-Cl has been described in detail elsewhere (43). In summary, GaCl_3 was dissolved in dry benzene while in a dry glove box. This was added dropwise to a solution of phthalonitrile dissolved in nitro-

benzene with the temperature kept at the boiling point of nitrobenzene (210°C). A bluish-black mass resulted, which was Soxhlet extracted with benzene followed by ethanol. The final product required three sublimations to obtain a very pure sample of GaPc-Cl. The absorbance spectrum in pyridine was identical to previously prepared samples and to published spectra.

The following reagents were used in this work. Electroactive species were the following: benzoquinone (BQ) (Eastman Kodak) sublimed twice at atmospheric pressure; hydroquinone (H_2Q) (Eastman Kodak) recrystallized twice from H_2O ; potassium ferricyanide $\text{K}_3\text{Fe}(\text{CN})_6$ (MCB, reagent ACS) used as obtained; potassium ferrocyanide $\text{K}_4\text{Fe}(\text{CN})_6 \cdot 3\text{H}_2\text{O}$ (Mallinckrodt, analytical reagent) used as obtained. Buffers and electrolytes were the following: potassium hydrogen phthalate (KHP) (MCB, reagent ACS) used as obtained; nitrogen N_2 (local supplier, electrochemical grade) passed through a molecular sieve and catalyst (Chemalog R3-11) to remove residual O_2 ; pyridine (Py) (Fischer, certified ACS) used as obtained; and water H_2O (TDW) triply distilled with second distillation from permanganate.

Most solutions were a pH = 4 buffer of 0.2M KHP. Redox couples were generally 1 mM in concentration. Special solutions were occasionally required for electrode surface modification. Solutions of 0.1M phenol, or a 0.1M β -naphthol, and 0.3M NaOH in methanol were used for electrochemical polymerization to give an insulating layer of polyphenol or polynaphthol. *m*-Aminophenols were electropolymerized from the normal pH = 4 aqueous electrolyte.

Oxygen was removed from the solutions before use. For stationary electrode cells, a vacuum degassing bulb was used and electrochemical-grade nitrogen used to overpressure the solutions into the cell.

Electrode preparation.—Metallized plastic optically transparent electrodes (MPOTE), gold substrates, were obtained from Sierracin Corporation. They consisted of a vapor deposited, thin (300Å), gold film on a transparent polyester sheet (Au-MPOTE) (44, 45). The platinum counterpart to this (Pt-MPOTE) was produced by a sputtering process on similar polyester sheets by Len Raymond at the Microelectronics Laboratory at the University of Arizona. The substrate electrodes were rinsed briefly in absolute ethanol, then in water, and allowed to air dry. Deposition of the Pc films occurred in a 75 mm diam glass cylinder, with several milligrams of Pc spread evenly across the bottom. The electrodes were suspended 1.75 in. above the bottom, by an aluminum (or Teflon) masking plate, held in place by indentations in the wall of the vessel. The masking plate was a 1/16 in. thick aluminum disk with seven 3/8 in. diam holes. The vessel was placed in a 500 ml heating mantle (Glas-Col), and glass wool was packed around the vessel, filling the volume of the mantle. The temperature was measured by a thermometer inserted through the glass wool to as near the base of the vessel as possible. The vessel was evacuated to ca. 10^{-7} - 10^{-6} torr and the temperature increased, at typically 10°C/min, until a steady state of about 275°C was obtained. Rapid heat-transfer to the dye at the bottom of the vessel was necessary with adequate cooling of the glass near the template to prevent excessive heating of the substrates. Sublimation took place over a period of 2-8h (Type A films, see below) or 24-100h (Type B and C films, see below). Sublimation rates of 0.3-0.5 equivalent monolayers per minute (EQM/min) resulted for the Type B and C films and rates of 1-10 EQM/min for the Type A films. The vessel was allowed to cool before opening, and the electrodes were stored covered in ambient atmosphere.

The surface coverage was obtained by dissolving the dye from the substrate with a measured volume of pyridine and comparing the peak absorbance at 670 nm to standards prepared from a fresh GaPc-Cl/Py stock solution. Film thickness is defined, in these studies, as the number of equivalent closest packed monolayers (EQM).

If each GaPc-Cl molecule is assumed to occupy a 160 \AA^2 surface when lying flat, then one EQM corresponds to $1.11 \times 10^{-10} \text{ mol/cm}^2$.

Various light sources were used, including a 450W xenon arc lamp (Oriell) powered by an Electro-Powerpacs power supply or an Oriell power supply. The output of the lamp was focused through a 4 in. IR water filter, and a long pass 470 nm filter (LP47) for polychromatic illumination (470-900 nm) in the visible region. The output of the lamp, at the point of electrode illumination, was about $100\text{-}150 \text{ mW/cm}^2$, with about half of this being heat not effectively blocked by the IR filter. Lamp output power was measured with a Coherent 210 powermeter.

Electrochemistry.—Open-circuit photopotentials were measured by two methods: (i) the potential difference (measured from the voltammograms) between the equilibrium potential of a redox couple measured at the photoelectrode and the same redox couple measured at a bare Pt or Au electrode, and (ii) the open-circuit potential was measured using a high input impedance voltmeter between the illuminated photoelectrode and bare Pt or Au electrodes in contact with the redox couple. In general, the two measurements agreed to within a few millivolts.

Electron microscopy.—Scanning electron micrographs were taken with an ISI DS-130 electron microscope, using Polaroid Type 55 positive/negative 4×5 Land film. Electrodes were mounted via double-stick tape onto the regular SEM stub and were grounded at the edge with a car-

bon cement. The electrode samples were then sputter coated with a 300\AA film of a Au-Pd alloy. This overlayer was necessary to prevent charging of the sample, which otherwise distorts the image and causes contrast problems. The Au-Pd film was sufficiently thin that it did not alter the appearance of any structure observed at the magnifications used ($10,000\text{-}34,000\times$).

Results and Discussion

Scanning electron microscopy of bulk and thin film deposits.—Table I lists all of the Pc's that have been examined for this report, and Fig. 2a-d show selected SEM's of several of the Pc's explored. Figure 2a was obtained from bulk, purified FePc, simply coated onto the SEM sample stub. Needle-like phases were formed most readily for FePc as well as for H_2Pc , CoPc, CuPc, CrPc, ZnPc, MgPc, NiPc, PdPc, and PtPc (Class II Pc's). The needles (probably representative of the α -phase form) that are obtained after a simple sublimation purification at high sublimation rates are generally long (up to $50 \mu\text{m}$) and narrow (generally $< 0.5 \mu\text{m}$). In contrast, the structures formed by bulk, tri- and tetravalent Pc's (Class I) during the purification process show a clear tendency to spontaneously form block-like or platelet-like structures. The structure of VOPc crystallites generally gives large structures with an assembly of stacked platelets. The bulk phase InPc-Cl tends to form in very large platelets whose dimensions can exceed $50 \mu\text{m}$, with several additional platelets stacked at angles and with smaller dimensions.

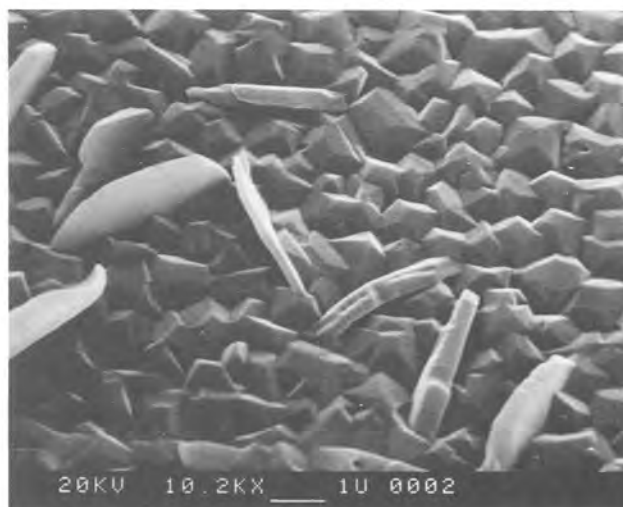
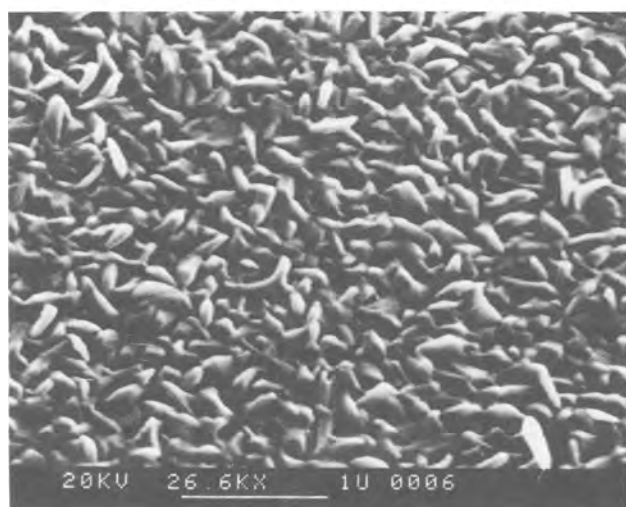
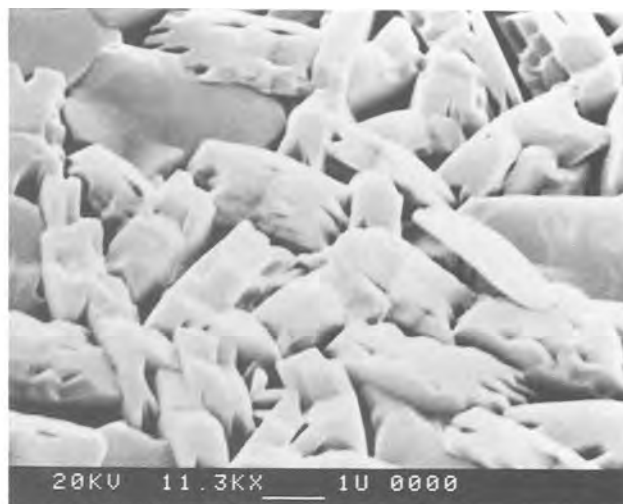
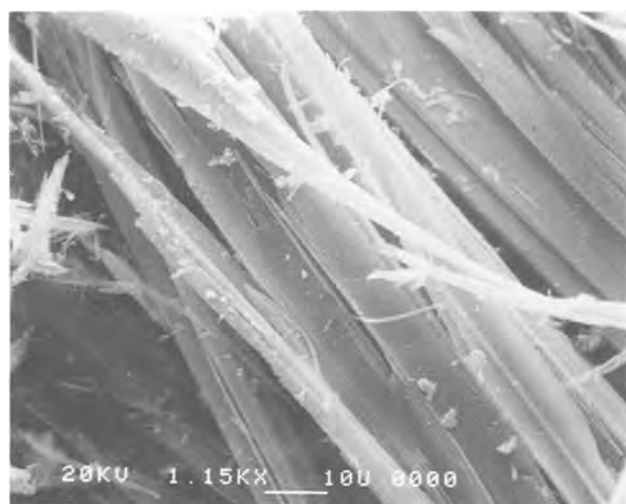


Fig. 2. Scanning electron micrographs of various phthalocyanines. a: Bulk powder of FePc. b and c: Thin films on Au-MPOTE's of InPc-Cl, in two different coverages, produced by different deposition rates (see text). d: Thin film of GaPc-Cl on a Au-MPOTE.

Table I. Classification of Pc's according to film morphology, absorbance spectra, and photoelectrochemical activity

Class I. Block-like crystallites, broadened and red-shifted visible absorbance spectra, rapid photoelectrochemical redox reaction rates, with sizable photopotentials		
AlPc-Cl ^a	InPc-Cl ^{a,c}	
GaPc-F ^a	VOPc ^{a,c}	
GaPc-Cl ^{a,b,c}	TiOPc ^a	
GaPc-I ^a		
Class II. Needle-like crystallites, broadened, blue-shifted visible spectra (or no spectral shift), poor photoelectrochemical activity		
AlPc-F ^{a,c}	CuPc ^a	PdPc ^f
SiPc ^e	H ₂ Pc ^a	PtPc ^f
FePc ^a	MgPc ^d	NiPc ^f
CoPc ^a		
CrPc ^f		

^a Type A films examined (see text).

^b Type B films examined.

^c Type C films examined.

^d Previous x-ray data predicts a structure and behavior like that of AlPc-F, Class II (57). Our studies place it in this Class I.

^e Monomer, dimer, trimer, and polymers of cofacially stacked molecules studied as thin films (60).

^f Studied by SEM only.

The GaPc-Cl and AlPc-Cl systems tend to favor a large block-like or rhombohedral structure in the bulk phase.

Many of the above Pc's were sublimed as thin films on MPOTE substrates, as well as several other substrates, with conditions known to favor formation of films designated Type A (deposition rates of ≤ 10 Å/min, 2-8h) or films designated Type C (deposition rates of ≤ 1 Å/min, 1-5 days) which are distinguished below. As discussed later, this distinction between Types A and C films can be somewhat arbitrary depending upon other vacuum deposition factors. Nevertheless, we use this notation here to designate differences in crystallite size that occur with different deposition conditions. Representative SEM's of films are shown in Fig. 2b, 2c, and 2d for the InPc-Cl and GaPc-Cl films. Other SEM examples of the Type A and Type C GaPc-Cl films have been reported previously (29, 30). The tri- and tetravalent Pc films that are formed on the MPOTE substrates consist again of block-like or platelet-like crystallites with average dimensions of 0.3-0.5 μm (Type A films, Fig. 2c) and 0.8-1.0 μm (Type C films, Fig. 2b and 2d), and appear to be tightly packed over the substrate surface. There is still occasionally a tendency to grow more than one layer of crystallites if the deposition rates are too fast (as discussed in the photoelectrochemistry section). Many of the crystallites also appear to be composed of layers of smaller units which have coalesced in the growth process. One of the targets in the growth of these films for any energy conversion application is the formation of a single layer of well-ordered crystallites.

While producing Type C films at shorter deposition times, it is possible to observe isolated crystallites on the MPOTE surface which leave exposed metal substrate between them (Type B films) (30). The problems associated with the photoelectrochemical properties of such porous films are discussed below.

Thin films of (FePc, CoPc, H₂Pc, etc.) under the growth conditions used for the tri- and tetravalent films shown above showed a much more polycrystalline thin film deposit. The individual crystallites were very difficult to observe with the SEM, having dimensions less than 500-1000Å. Where they could be observed, it was clear that the needle-like morphology had been retained. The deposits were not tightly packed crystallites, and attempts to vary the deposition conditions so as to form tightly packed deposits have been unsuccessful. There is a tendency in the tri- and tetravalent Pc systems to form a low surface to volume ratio film, with more intimate contact between the substrate and the Pc (and with fewer "short-circuit" sites).

Of particular note is that the Type C films of the quality shown above have only been grown on metallized polymer substrates (MPOTE). During the course of these studies, SEM structures of the type shown above for the Class I Pc's were obtained on both commercially available and in-house-produced MPOTE's (Au, Pt, Ag) and on indium-tin oxide (ITO) ranging in thickness from 300Å to 1 μm . Substrates such as polished glass, various metal foils and polished bulk metals, and metal oxides such as SnO₂ and ITO on glass substrates, were all unsuccessful in producing the optimum Type A or C film structure. In most cases, even with the Class I Pc's, a very polycrystalline deposit was formed on these substrates, with crystallite dimensions of <0.2 μm . In some cases, it was observed that large crystallites were formed on the substrate, but were surrounded by deposits of much smaller crystallites (43). These all led to uniformly poor photoactivity.

Previous work in this laboratory has shown that the surface composition of these metallized polymer films is not pure metal (44, 45). During the formation of the metallization layer, there is some admixture of polymer constituents with the metal film. The resultant surface has monolayer concentrations of carbon-oxygen molecules, some of which can be activated by ion-beam etching to form electrochemically active groups. Studies are currently underway to ascertain if these surface functionalities provide the initial nucleation sites for deposition of the aggregate Pc layers. The morphology of the MPOTE surface is smooth down to the level of 250-500Å. SEM studies were not able to resolve the surface roughness on this scale, in contrast to all other substrates. The degree of polycrystallinity of these Pc films is presumed to be due to the number of Pc nuclei that form per unit surface area and the growth rate of these nuclei (46, 47). There seems to be an inverse correlation between growth rates and final crystallite sizes and densities in the finished films. Nucleation theory indicates that low rates of deposition are essential for these large molecules (46, 47). Low rates of encounter between depositing Pc molecules, with high substrate temperatures, seems to insure a minimal number of nuclei will form on the smooth surface. These nuclei can grow into relatively sizable crystallites as long as they do not intersect in the process. The average maximum size we have attained thus far have length, width, and depth of 0.7-1.0 μm before they intersect.

UV-visible spectrophotometric assay of Pc thin films.—Figures 3a-3f show the visible wavelength solution and solid film spectra of several of the Pc films. The phthalocyanine chromophore has two distinct electronic transitions in the UV-visible region, the Soret band at 300-350 nm, and the Q-band region at ca. 600-700 nm. The Soret transition arises from a $\pi \rightarrow \pi^*$ excitation which is strongly localized on the Pc ring and shows little dependence on the changing environment of the molecule (48-52). The Q-band transition is a $\pi \rightarrow \pi^*$ transition of lower energy. In many instances, with the appropriate metal center, metal-to-ligand or ligand-to-metal charge transfer transitions can also be involved (57). The major band in solution is generally accompanied by one or more weaker transitions shifted to slightly higher energies corresponding to higher vibronic modes of the ground state participating in the $\pi \rightarrow \pi^*$ excitation (52). In many cases, it has been found that this Q-band region is very sensitive to the environment of the molecule, and is also more sensitive to changes in number and orientation of nearest neighbor Pc's in the solid state.

Figures 3a and 3b are representative of the visible absorbance spectra of the divalent metal phthalocyanines when prepared as thin films of thickness <0.5 μm (Type A conditions). The optical density of the Pc layer/metallized polymer substrate is <1.0 , making transmission spectra possible. Comparing these thin film spectra with the spectra in pyridine or chloronaphthalene solutions shows that the Q-band region is broadened and the maximum absorbance blue shifted. The solution spectrum of

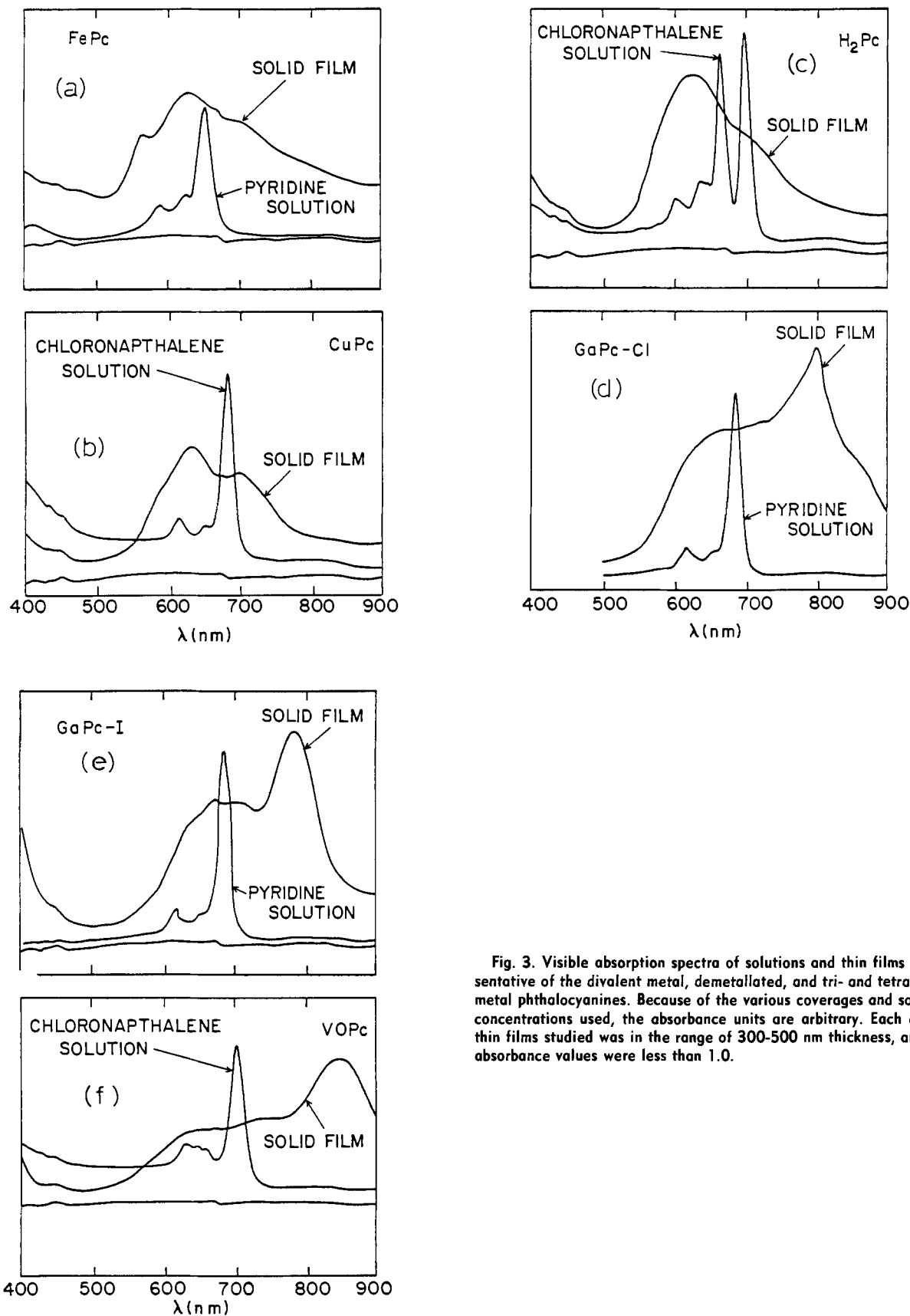


Fig. 3. Visible absorption spectra of solutions and thin films representative of the divalent metal, demetallated, and tri- and tetravalent metal phthalocyanines. Because of the various coverages and solution concentrations used, the absorbance units are arbitrary. Each of the thin films studied was in the range of 300-500 nm thickness, and the absorbance values were less than 1.0.

H₂Pc (Fig. 3c) is split in the Q-band region because of the reduction of symmetry in this molecule from D_{4h} to D_{2h} by removal of the metal center (48-52). In the thin film (Fig. 3c), the Q-band region is again broadened and the maximum absorbance blue shifted (away from the region of maximum solar flux). Recent IR studies of H₂Pc thin films in this laboratory indicate that the "α-phase" is predominantly formed under these growth conditions (53).

Figures 3d and 3e are representative of the solution and thin film spectra of the trivalent Pc's, and Fig. 3f shows the solution and thin film spectra for the tetravalent vanadyl phthalocyanine. In contrast to all of the Class II Pc's studied, these Pc systems in the solid state show strongly red shifted and broadened visible spectra. In the case of the VOPc (33) and InPc-Cl, this absorbance is shifted well into the near-IR, with high absorptivities.

Crystallographic structures have now been solved for several phthalocyanines (39, 54-59) including GaPc-Cl, VOPc, AlPc-F, AlPc-Cl, and several other Pc's in the Class II category as well as different polymorphs of H₂Pc (39, 57, 58). Several forms of silicon and germanium phthalocyanine cofacially stacked polymers have also been characterized (54-56). The polymeric SiPc and GePc species are constrained to stack in an aligned, cofacial orientation by virtue of the bond between the central silicon and the axial oxygens of each molecule. When the stacking of these adjacent Pc's is confirmed to be in this orientation, with only rotation about the central molecular axis allowed, the Q-band region of the visible spectrum appears to be blue shifted and the entire absorbance spectrum broadened. In such systems (as sublimed thin films), we have seen uniformly low photoelectrochemical activity (60).

A slip-stack orientation of adjacent Pc's has been found for several Pc's, starting first with H₂Pc and CuPc (61, 62). Other similar polymorphs were found and characterized in the VOPc system by Griffiths and co-workers (39). X-ray structures have shown that the central metal atom is displaced out of the plane of the Pc ring and that the axial oxygen counterion prevents a perfect cofacial stacking of the adjacent Pc rings. Two types of structure appear possible; those either with the oxygen double bonds oriented toward the adjacent ring, or with those bonds oriented away from the adjacent rings. Their reported visible spectra of VOPc thin films, which probably contain both of these polymorphs, agree well with the spectrum shown in Fig. 3f (33). There is little question that the typical VOPc thin films are not solely of one phase (more than one slip-stack orientation may be possible). Annealing the films at high temperature after growth causes a further red shifting of the Q-band due to phase changes in the film (39).

A crystallographic study of one of the stable configurations of the GaPc-Cl system has been recently solved by Wynne (58). As with the VOPc system, the Ga atom sits 0.439Å out of the plane of the Pc ring and the Cl counterion is not involved in cofacial stacking of the adjacent rings. The unit cell that was solved shows the adjacent Pc rings slipped so as to force overlap of the outer phenyl portions of each Pc ring. The AlPc-Cl system was also examined and appeared to align similarly (58). It is interesting to note that previous crystallographic studies of the AlPc-F and GaPc-F systems had shown them to be aligned in a cofacial fashion with the M-F bonds possessing a strong enough dipole to favor an electrostatic interaction of the type (M⁺-F⁻ . . . M⁺-F⁻ . . . M⁺-F⁻ . . .) (57). This resulted in a geometry similar to the silicon and germanium phthalocyanine polymers (54-56). For AlPc-F thin films, we have previously reported that the Q-band region was indeed broadened and slightly blue shifted from the solution spectrum, and that the photoresponse was poor (63). The GaPc-F system seemed to behave like the GaPc-Cl system, with a red-shifted visible absorbance and photoresponse comparable to that of the GaPc-Cl thin films (63).

There have been several studies on cyanine, merocyanine, and squarane-type dyes (all planar aromatic systems) that show the tendency for these systems to aggregate in slipped-stack configuration in the solid state (2, 59). Calculations have shown that the extent of overlap and the relative placement of the adjacent aromatic centers controls the direction and extent of spectral shifting observed in their absorbance spectra in the 600-850 nm region. Extensively "slipped stacks" of these planar molecules result in a "J aggregate" with a strongly red-shifted and narrowed absorbance spectrum (2, 59). By inference, we assume that the Class II Pc's belong to a similar category as the J aggregates, but are more disordered.

Photoelectrochemical studies.—The cyclic voltammetric response of the Pc thin films in contact with an electrolyte have been studied in a number of ways. The studies have been generally divided between techniques which

involve stirred solutions and rotated electrodes, or quiet solutions and stationary electrodes (29). The last technique is the most common approach and was used in the studies reported here.

Figure 4a shows the current-voltage response for the electrolysis of the hydroquinone/benzoquinone (H₂Q/BQ) redox couple (a two-electron, two-proton, chemically reversible redox process). On the bare Au electrode, there is no photoactivity and the current-voltage response is drawn out, well away from the E° for both the oxidation of H₂Q and the reduction of BQ. The E° lies roughly midway between the potentials of oxidative and reductive peak currents and is an approximate measure of the thermodynamic reactivity of the probe molecules to holes or electrons which might be produced at a photoactive surface. Figure 4a also shows the light and dark response for the same redox couple in contact with a Au/GaPc-Cl (Type A) electrode. Figure 4b shows the same responses for a Au/GaPc-I electrode (Type A). These responses are typical of our earliest Type A, Class I, Pc films (27). The dark current response in the vicinity of the E° is negligible at the current sensitivities shown, and the contrast between light and dark photoresponse is greater than 100:1.

Illumination of the Type A film with polychromatic light (470-900 nm) of ca. 100 mW/cm² produces a current response in the vicinity of the E° which is a factor of 20-50 higher than on the bare Au substrate. Surface deactivation of the bare Au (which does not occur at the Pc film) seems to be primarily responsible for the loss of electrochemical activity on Au for redox reactions of organic systems such as the quinones (43). For redox systems such as ferri/ferrocyanide, there are only small differences in maximal response, so that surface differences cannot be the cause of the above behavior for quinone systems.

Of particular note is the fact that for these Type A GaPc-Cl films under illumination only small shifts in the zero current potential (apparent E°) away from the value observed on the bare metal substrate were observed. The photocurrent response was directly dependent upon the flux of photons to the surface, only small photopotentials for the H₂Q/BQ and ferri/ferrocyanide redox couples were observed, even at the highest illumination intensities.

Figure 4c is representative of the Type A VOPc film on the same Au substrate (33). Nonporous films of VOPc show a dark oxidation of H₂O, but the reduction of BQ is suppressed. Upon illumination, the reduction of BQ is activated and the redox process appears reversible. Redox couples with the negative of E° for H₂Q/BQ are inactive in the dark. Upon illumination, the potential for photocurrent onset is shifted positively to a value very near that shown for the reduction of BQ. Redox couples positive of the E° for H₂Q/BQ show uniformly uninhibited oxidation/reduction reactions in the dark and little photoactivation (33). The Type A VOPc film is behaving like it is a highly doped p-type semiconductor electrode with a flatband potential near +0.3V vs. Ag/AgCl. Similar conclusions regarding electrochemical properties have been reported previously for other Pc films (10-14). The acceptor density in these VOPc films has been measured from Mott-Schottky capacitance plots to be ca. 6×10^{18} cm⁻³. This density is appreciably higher than our estimates for the acceptor densities in the typical Type C trivalent metal Pc films (<10¹⁷ cm⁻³; see discussion below).

Figure 4d shows the current-voltage response of a Type A H₂Pc film in contact with the same redox electrolyte. The dark current was unchanged from that of the bare gold substrate (see Fig. 4a). When the Pc films are porous, the probe molecule diffuses to the exposed metal substrates such that the peak currents and peak potentials at low scan rates are those due to the bare metal substrate (30, 64). Upon illumination, the oxidation of H₂Q remains virtually unaffected. The reduction of BQ, however, is enhanced in the region of the E° (as for the above Pc's), but the original dark current process is still observed. As the illumination intensity was changed the ratio of photocurrent current (l) to dark current (d) was also

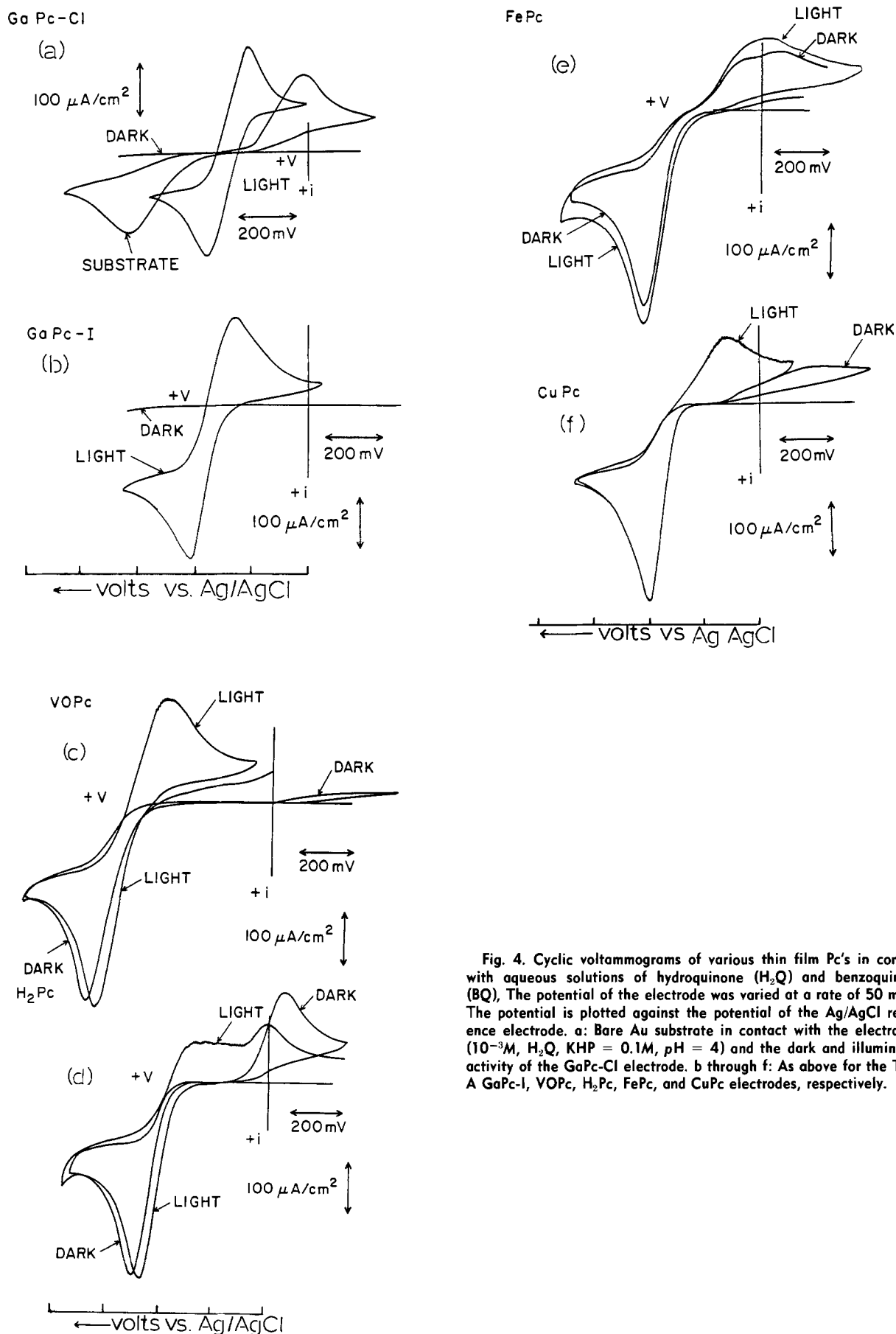


Fig. 4. Cyclic voltammograms of various thin film Pc's in contact with aqueous solutions of hydroquinone (H_2Q) and benzoquinone (BQ). The potential of the electrode was varied at a rate of 50 mV/s . The potential is plotted against the potential of the Ag/AgCl reference electrode. a: Bare Au substrate in contact with the electrolyte (10^{-3}M , H_2Q , $\text{KHP} = 0.1\text{M}$, $\text{pH} = 4$) and the dark and illuminated activity of the GaPc-Cl electrode. b through f: As above for the Type A GaPc-I, VOPc, H_2Pc , FePc, and CuPc electrodes, respectively.

proportionally changed. There is direct competition between the light-active H_2Pc sites and the exposed Au sites for the BQ molecule. When the light intensity was high

enough, it could be seen that the H_2Pc thin-film is acting as a p-type semiconductor, as seen in previous studies (5, 10). Under our conditions of Type A film formation, we

were never able to produce a truly nonporous film of H_2Pc . Because of its poor absorptivity above 650 nm, we have not pursued its use as a photoelectrode.

Figures 4c and 4f show the current voltage behavior of FePc and CuPc Type A films, typical of the remainder of the Class II Pc's. In the dark, the current voltage activity was virtually unchanged from that of the Au and showed little activation upon illumination. Films of FePc, CoPc, CuPc, etc., were quite porous and gave low photoreponses. Of the three Pc's mentioned, CuPc resembled most closely the response observed for H_2Pc when it was possible to produce a film with only partial porosity. In those cases, the voltammetric response was consistent with the notion that the CuPc film was also acting as a p-type semiconductor.

Figure 5 shows the voltammetric activity for the reduction of AQ on a recently developed Type A, nonporous InPc-Cl film (ca. 0.3 μm thick), similar in structure to that shown in the SEM of Fig. 2g. On bare gold, this redox couple has an E° of ca. -0.5V vs. Ag/AgCl . The dark current activity of the Au/InPc-Cl electrode is quite small and featureless. Upon illumination of the Pc/electrolyte interface, a sizable shift in the current-voltage curve (the apparent flatband potential for this system) is seen at $+0.2\text{V}$. In a photovoltaic device, an open-circuit photopotential (V_{oc}) of $+0.7\text{V vs. a bare Au or Pt}$ counterelectrode was observed. The electrochemical behavior of an InPc-Cl film grown under these conditions again points to p-type semiconducting properties. In the case of the InPc-Cl and VOPc films grown in this manner, we have also observed a strong directionality of the photoeffect—one dependent upon which of the interfaces is illuminated first. If the Au/Pc interface is illuminated first (back side), then the photoeffect is diminished, with a 100 mV drop in the open-circuit photovoltage (V'_{oc} vs. V_{oc}). This kind of directionality is even more evident in the VOPc films when the photocurrent is monitored as a function of wavelength (33). The reasons for this have been postulated first by Bard and co-workers (11) and appear to arise from the formation of a multiple-phase crystallite layer on the substrate, giving rise to at least two Pc layers of different photoactivity. In the InPc-Cl and VOPc films, made under these Type A conditions, the layer adjacent to the Au interface appears to be less photoactive (for transport of the photogenerated electrons). This layer absorbs some of the light that needs to reach and excite

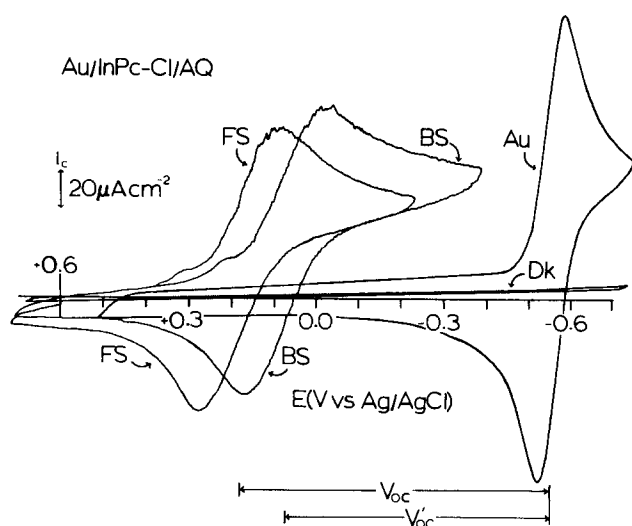


Fig. 5. Dark and illuminated current voltage activity for the Au/InPc-Cl system, in contact with 10^{-3}M aqueous, $\text{pH} = 7$ anthraquinone sulfonate (AQ) solution. The activity for the bare Au substrate is shown and forms the reference point for computation of open-circuit photopotentials. Potentials were varied at a rate of 50 mV/s. V_{oc} represents the approximate open-circuit photovoltage expected [using front side illumination (FS)] vs. a bare Au counterelectrode. V'_{oc} represents the same photopotential with illumination of the Au/InPc-Cl interface (BS) first.

the molecules at the Pc/solution interface. The metal/polymer substrate is sufficiently transparent that reflection of light from the back interface cannot be the cause of the difference in photoactivity. Recent experiments show that, if both interfaces can be illuminated simultaneously, this effect can be partially overcome and the photocurrents and photopotentials increased (65). The origin of the different layers in these films and the nature of the deposition parameters which leads to this p-type behavior is currently under exploration.

Figure 6 shows the electrochemical response typical of the Type C, GaPc-Cl films compared to a bare Au substrate. Figure 6a shows the dark current-voltage response of $\text{Fe}(\text{CN})_6^{-3}/\text{Fe}(\text{CN})_6^{-4}$ on bare Au or Pt. Figure 6a also shows the dark (d) and illuminated current-voltage responses for the Au/GaPc-Cl, Type C film. In the dark, little current is seen, indicative of the nonporous nature of the film. Upon illumination, the current-voltage response is greatly enhanced, having the same general appearance as on the Au substrate. The slope of the current-voltage response near the zero-current intercept is less steep than on bare Au and directly dependent upon the illumination intensity. The current at any potential is lower because of the lower photoconductivity of the Pc film. The entire current-voltage curve however, has been shifted negatively to ca. $+0.075\text{V}$. We have previously demonstrated that this potential shift will occur to a limit which is the approximate flatband potential of each Au/GaPc-Cl system and that this effect can be due in part to the work function of the substrate (phase 1, Fig. 1) with respect to the reference electrode potential (29, 16, 41). In a PV cell, with a Au/GaPc-Cl anode and a bare Au cathode, an open-circuit photopotential [$V_{oc}(\text{Au}) = \text{ca. } 0.3\text{V}$] is measured. The magnitude and direction of the photopotential is also varied by simply changing the redox couple and its E° (i.e., changing the work function of the contacting phase 3, Fig. 1) (29). In those cases, the Type C GaPc-Cl films behave as nearly intrinsic photoconductors. The Fermi level is apparently close enough to the middle of the bandgap to permit both positive and negative photopotential excursions.

Figures 6b and 6c show the current-voltage response of the Pt/GaPc-Cl Type C film in contact with the same electrolyte. The dark current process in Fig. 6b is en-

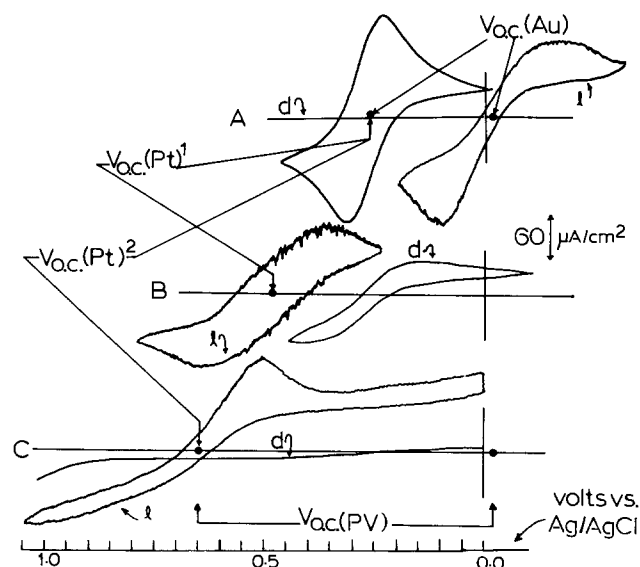


Fig. 6. Dark (d) and illuminated voltammograms for Type C GaPc-Cl electrodes on Au and Pt substrates in contact with 10^{-3}M solutions of ferricyanide and ferrocyanide, $\text{pH} = 4$ electrolyte. a: Voltammetric activity of the bare Au or Pt substrate and the dark and light activity of the Au/GaPc-Cl Type C thin film. b: Dark and light activity of the Pt/GaPc-Cl Type C thin film. c: Dark and light activity of another Pt/GaPc-Cl electrode with diminished porosity and lower dark current.

hanced over that seen on the Au/GaPc-Cl electrode (Fig. 6a). The dark current process in Fig. 6c has been diminished but at some sacrifice to the photocurrent activity. Our efforts thus far have not yielded a totally nonporous film on the Pt-MPOTE substrates. The pore sizes are small enough that the dark current activity is greatly suppressed as compared to that of the bare substrate. We estimate that the surface is greater than 90% covered with the Pc film (64).

Of particular note is that, for the same redox couple, the entire current-voltage response on the Pt/GaPc-Cl electrode is now shifted positively from the E° on the bare metal. This is consistent with the fact that the Pt substrate has a higher work function than both Au and the electrochemical potential of the electrolyte. It is understood that the Pt work function is high enough to position the Fermi level of the Pt in the valence band region for the Pc film. This may not produce a hole blocking contact that would be required to produce the current-voltage response seen (16, 17, 29, 66). The effective work function of Pt is easily changed (lowered), however, by the presence of surface impurities (67). We feel that the zero-current potential noted for the illuminated Pt/GaPc-Cl systems represents that effective work function value.

These results demonstrate the possibility of a PV cell formed by two electrodes consisting of the same photoconductor on metal substrates of different work function, immersed in an electrolyte ($M_1/Pc/Ox$, red/ Pc/M_2) (16). Under simultaneous polychromatic illumination (ca. 75-100 mW/cm²) of both electrodes with illumination of the solution interface first for the Au/GaPc-Cl electrode, and illumination of the metal/Pc interface first for the Pt/GaPc-Cl electrode, open-circuit photopotentials of ca. 0.55-0.65V were obtained. Short-circuit photocurrents of ca. 0.1-0.2 mA/cm² were observed with fill factors near 0.5, such that power conversion efficiencies of ca. 0.05% were obtained (68). The short-circuit currents, or currents at any load resistance, were limited by the photon flux, i.e., Pc-film resistance.

In the case where the projected area of the Pc microcrystals does not totally block the surface of the metal substrate to solution contact, the photoelectrochemical process, e.g., the oxidation of R to Ox at the Pc sites, is offset by the opposite reaction, Ox \rightarrow R, at the exposed metallic sites. On a Au/GaPc-Cl film, the illuminated M/Pc/solution sites are typically poised at potentials negative of the E° for the redox couple, so that if bare metal sites are nearby, the product (Ox) can move to this region and undergo back reaction. The opposite case pertains to photoassisted reduction processes. The result of this is to lower the net photocurrent at any potential and also to reduce the magnitude of the photopotential at even low current loads (30). This situation is even more of a problem when the contacting phase (phase 3 in Fig. 1) is a metal rather than an electrolyte solution. The charge density of a metal overlayer is significantly higher than the most concentrated electrolyte solutions. "Short-circuit" sites in intimate contact with a metal overlayer may prevent the formation of any photopotential under even intense illumination. We have thus far been unable to avoid serious short circuiting of metal/Pc/metal' composites (made by evaporation of another metal layer over the Au/Pc film), presumably because of the short circuiting of the two highly conductive metal phases. This is apparently due to the creation of pore sites within the Pc layer during the deposition of the second metal phase, and therefore may be ultimately remedied by modification of this step.

In electrolyte solutions, as long as the exposed substrate area is below 10% of the geometric area of the surface (estimated from voltammetric currents), the shorting reactions cannot keep up with the photoelectrochemical process, and a photopotential can be generated. Referring back to Fig. 6b and c, to the dark and illuminated current-voltage curves on Pt/GaPc-Cl electrodes of differing porosities, it can be seen that as the dark current on the exposed metal sites decreases, the illuminated i/V curves

are shifted more positively and the open-circuit photopotentials are increased [$V_{oc}(Pt)^2$ vs. $V_{oc}(Pt)^1$ in Fig. 6].

Electrochemical polymerization of easily oxidized or reduced molecules to form nonconductive surface films have been explored for some time and offer a potential solution to the problem of short circuiting (69). We have used phenol, β -naphthol, and m-aminophenol at 0.1M concentrations, electrochemically oxidized in the dark, to form insulating polymers (layers 20-40 nm thick). These polyphenoxide films have been used to seal off exposed metal sites on porous GaPc-Cl and VOPc films (30, 70). Porous Pc films treated in this fashion show significantly decreased porosity to solution components (lower dark currents), but also show a current/voltage response indicative of a more resistive film (similar to that shown in Fig. 6c). The contrast between light and dark activity is increased over the untreated films, but the overall photoactivity may be lowered. During the electropolymerization process, there is apparently some etching and/or deterioration of the Pc/metal interface which leads to this more resistive film and hence a poorer photoresponse. Postmortem visible spectroscopy of these films does not indicate loss of phthalocyanine. Electron micrographs show some smoothing of the polycrystalline material, indicating that etching of the surface layers occurred which may be paralleled by attack of the Pc/metal interfaces. It is clearly more desirable to attempt to achieve a nonporous film from the initial vacuum growth stage, such as with our best Type C GaPc-Cl films.

Conclusion

The trivalent and tetravalent phthalocyanines should give a superior photoresponse when compared to the divalent and demetallated phthalocyanines prepared under the same conditions. These new systems are distinguished by crystallites in the thin films that are larger and generally have a lower aspect ratio (ratio of length to width) than the Class II Pc's. Their spectral responses are all uniformly broadened and red shifted, which we feel correlates with their tendency to stack cofacially in orientations that cause overlap in a staggered fashion (37-39, 58, 59, 61, 62). This slip-stack configuration is apparently assisted by the presence of the central metal-counterion which does not favor direct cofacial stack of the adjacent Pc centers (39, 58). There is a clear need for the study of the electrical and photoconductivity properties of single crystals of these materials.

Within the tri- and tetravalent metal Pc series, we have observed two basic types of photoelectrochemical response. Certain film growth conditions lead to photoelectrochemistry similar to that of a p-type semiconductor, with only positive photopotentials observed in films thinner than 0.5 μ m. Other slower growth rates lead to Pc films that behave more as intrinsic semiconductors (as in Fig. 1), with both positive and negative photopotentials possible.

Under the appropriate growth conditions, the VOPc, TiOPc, InPc-Cl Type A films can behave as p-type materials with high acceptor concentrations. Recent surface analysis studies have indicated that the source of the higher acceptor concentration in VOPc films may be the presence of oxygen entrained in the Pc film for which VOPc films have a high affinity (33). The thinner versions of the GaPc-Cl and GaPc-I films, as grown under the conditions described here, are apparently nearly intrinsic and show only small photopotentials for molecules with E° values near H₂Q/BQ and ferri/ferrocyanide. For thin Pc films such as the VOPc or InPc-Cl Type A variety, the acceptor density may be high enough that a space-charge layer can form in less than the thickness of the film (30-32). However, this precludes the observation of both positive and negative photopotentials, since the material becomes strongly p-type. Work currently in progress in our laboratory indicates that the electrochemical properties of GaPc-Cl and InPc-Cl films can be further varied between the extremes of behavior shown in Fig. 5 and 6 through variation of the growth rate, sub-

strate temperature, and O₂ treatments of each film. Photoelectrochemical efficiencies have improved considerably through the use of these tri- and tetravalent Pc's. There is still an incomplete understanding, however, of the manner in which substrate chemistry, entrained dopants, and the deposition of the first layers of Pc affect the electrical properties of the entire film.

We have recently demonstrated that for the GaPc-Cl, Type C thin films, the photocurrents are limited by trapping and recombination sites, which form at the interface between the Pc and metal substrate, the bulk of the Pc crystallites, and also at the surface and intersection of the individual microcrystallites (28, 31, 32). Figure 1b shows the consequence of the deposition of an intrinsic photoconductor film on a metal surface such as Au, where the Fermi energies before contact are not arranged in descending order, as shown in Fig. 1a. Provided that sufficient charge exchange pathways exist within the film so that equilibrium can be reached, this mismatch of Au and Pc work functions leads to a potential inversion at the interface which can act as trap for photogenerated charge, accelerating the recombination rate of electron-hole pairs in that region. It must also be assumed that the surface of the Pc microcrystals are chemically distinct from the bulk (e.g., adsorbed O₂ would raise the electron affinity of the surface Pc's). It is expected that the intersection points of the Pc microcrystals will also lead to these potential inversions and regions of trapped charge.

Rose has demonstrated that the tolerable defect site density in polycrystalline thin films of this type is ca. 10¹⁷/cm³ or about 3-4 orders of magnitude above those tolerated in single-crystal materials (16, 17). Examining the average SEM of a Type C, Class I Pc film and estimating the projected surface area of the average crystal, and the number of surface Pc's per crystallite (ca. 160 Å²/molecule), we calculate that the defect site density due to chemically distinct Pc's is ca. 10¹⁹/cm³. Compared to the average Class II Pc film, this is an improvement of 2-3 orders of magnitude, consistent with the improvements noted in the photoelectrochemical responses and the decrease in surface-to-volume ratio of these films. This analysis does not account for the defects from disorder within the bulk of each of the Pc microcrystals and at the metal substrates. A decrease of at least one more order of magnitude in defect densities in these films is needed to lead to PV cells with power conversion efficiencies of 1% or higher.

Acknowledgments

This research was supported by Grants from the National Science Foundation, CHE83-17769, and IBM Corporation. We would also like to thank Ken Wynne for sharing the details of his x-ray structures of GaPc-Cl and AlPc-Cl prior to their publication.

Manuscript submitted Nov. 21, 1984; revised manuscript received April 29, 1985.

The University of Arizona assisted in meeting the publication costs of this article.

REFERENCES

- D. L. Morel, E. L. Stogryn, A. K. Ghash, T. Feng, P. E. Purwin, R. F. Shaw, C. Fishman, G. R. Bird, and A. P. Piechowski, *J. Phys. Chem.*, **88**, 923 (1984).
- A. P. Piechowski, G. R. Bird, D. L. Morel, and E. L. Stogryn, *ibid.*, **88**, 934 (1984).
- D. L. Morel, A. K. Ghash, T. Feng, E. L. Stogryn, P. E. Purwin, R. F. Shaw, and C. Fishman, *Appl. Phys. Lett.*, **32**, 495 (1978); A. K. Ghash and T. Feng, *J. Appl. Phys.*, **49**, 5982 (1982).
- G. A. Chamberlin, *ibid.*, **53**, 6262 (1982).
- F. F. R. Fan and L. R. Faulkner, *J. Am. Chem. Soc.*, **101**, 4779 (1979); *J. Chem. Phys.*, **69**, 3334 (1978).
- A. M. Hor, R. O. Loutfy, and C. K. Hsiao, *Appl. Phys. Lett.*, **42**, 165 (1983); R. O. Loutfy, *J. Phys. Chem.*, **86**, 3302 (1982).
- R. O. Loutfy and J. H. Sharp, *J. Chem. Phys.*, **71**, 1211 (1979).
- C. W. Tang and A. Albrecht, *ibid.*, **62**, 2139 (1975); *ibid.*, **63**, 953 (1975).
- F. F. Fan, B. Reichman, and A. J. Bard, *J. Am. Chem. Soc.*, **102**, 1488 (1980).
- H. Tackikawa and L. R. Faulkner, *ibid.*, **100**, 379 (1978).
- P. Leempoel, F. F. Fan, and A. J. Bard, *J. Phys. Chem.*, **87**, 2948 (1983).
- F. F. Fan and A. J. Bard, *J. Am. Chem. Soc.*, **101**, 6139 (1979).
- C. D. Jaeger, F. F. Fan, and A. J. Bard, *ibid.*, **102**, 2592 (1980).
- A. Giraudeau, F. F. Fan, and A. J. Bard, *ibid.*, **102**, 5138 (1980).
- A. M. Hor and R. O. Loutfy, *Can J. Chem.*, **61**, 901 (1983).
- A. Rose, *Phys. Status Solidi A*, **56**, 11 (1979).
- A. Rose, "Concepts in Photoconductivity and Allied Problem," R. E. Krieger, New York (1978).
- H. Gerischer, in "Physical Chemistry—An Advanced Treatise," Vol. IXA, H. Eyring, D. Henderson, and W. Jost, Editors, p. 463, Academic Press, New York (1970).
- V. A. Myamlin and Y. V. Pleskov, "Electrochemistry of Semiconductors," Plenum Press, New York (1967).
- A. Nozik, Editor, "Photoeffects at Semiconductor-Electrolyte Interfaces," ACS Symposium Series 146, American Chemical Society, Washington, DC (1981).
- M. S. Wrighton, *Acc. Chem. Res.*, **12**, 303 (1979).
- A. J. Bard, *Science*, **207**, 139 (1980).
- M. Gratzel, *Acc. Chem. Res.*, **14**, 376 (1981).
- A. J. Bard, *J. Photochem.*, **10**, 59 (1979).
- W. J. Albery, *Acc. Chem. Res.*, **15**, 142 (1982).
- T. Mezza, M. Kenney, and N. R. Armstrong, *J. Electroanal. Chem.*, To be published.
- C. L. Linkous, T. Klofta, and N. R. Armstrong, *This Journal*, **130**, 1050 (1983).
- W. Buttner, P. Rieke, and N. R. Armstrong, *ibid.*, **131**, 225 (1984).
- P. C. Rieke and N. R. Armstrong, *J. Am. Chem. Soc.*, **106**, 47 (1984).
- P. C. Rieke, C. L. Linkous, and N. R. Armstrong, *J. Phys. Chem.*, **88**, 1351 (1984).
- W. J. Buttner, P. C. Rieke, and N. R. Armstrong, *ibid.*, To be published.
- P. C. Rieke and N. R. Armstrong, *ibid.*, To be published.
- T. Klofta, C. L. Linkous, and N. R. Armstrong, *J. Electroanal. Chem.*, **185**, 73 (1985).
- V. Y. Merritt, *IBM J. Res. Dev.*, **22**, 353 (1978).
- M. Scharfe, "Electrophotography Principles and Optimization," Research Studies Press Ltd., New York (1984).
- M. H. Lee, J. E. Ayala, B. D. Grant, W. Imano, A. Jaffe, M. R. Latta, and S. L. Rice, *IBM J. Res. Dev.*, **28**, 241 (1984).
- P. S. Vincett, Z. D. Popovic, and L. McIntyre, *Thin Solid Films*, **82**, 357 (1981).
- Z. D. Popovic and J. H. Sharp, *J. Chem. Phys.*, **66**, 5076 (1977).
- C. H. Griffiths, M. S. Walker, and P. Goldstein, *Mol. Cryst. Liquid Cryst.*, **33**, 149 (1976).
- G. S. Calabrese, M.-S. Lin, J. Dresner, and M. S. Wrighton, *J. Am. Chem. Soc.*, **104**, 2412 (1982).
- D. J. Harrison, G. S. Calabrese, A. J. Ricco, J. Dresner, and M. S. Wrighton, *ibid.*, **105**, 4212 (1983).
- R. Loutfy and C. K. Hsiao, *Photo. Sci. Eng.*, **24**, 155 (1980).
- C. L. Linkous, Ph.D. Dissertation, Michigan State University, East Lansing, MI (1983).
- R. Cieslinski and N. R. Armstrong, *Anal. Chem.*, **51**, 565 (1979).
- N. R. Armstrong and J. R. White, *J. Electroanal. Chem.*, **131**, 121 (1982).
- B. Lewis and F. Cambell, *J. Vac. Sci. Technol.*, **4**, 209 (1967).
- C. A. Neugebauer, in "Handbook of Thin Film Technology," L. I. Maissel and R. Glang, Editors, Chap. 8, McGraw-Hill, New York (1970).
- A. M. Schaffer, M. Gouterman, and E. R. Davidson, *Theoret. Chim. Acta*, **30**, 9 (1973).
- A. B. P. Lever, S. R. Pickens, P. C. Minor, S. Licoccia, B. S. Ramaswamy, and K. Magnell, *J. Am. Chem. Soc.*, **103**, 6800 (1981).
- A. B. P. Lever and P. C. Minor, *Inorg. Chem.*, **20**, 4015 (1981).
- A. B. P. Lever, S. Licoccia, K. Magnell, P. C. Minor, and B. S. Ramaswamy, *Adv. Chem. Ser.*, **201**, 237 (1982).
- F. H. Moser and A. L. Thomas, "The Phthalocyanines," Reinhold, New York (1963).

53. T. D. Mewborn and N. R. Armstrong, Unpublished results.
54. K. F. Schoch, B. R. Kundalkar, and T. J. Marks, *J. Am. Chem. Soc.*, **101**, 7071 (1979).
55. C. J. Schramm, R. P. Scaringe, D. R. Stojakovic, B. M. Hoffman, J. A. Ibers, and T. J. Marks, *ibid.*, **102**, 6702 (1980).
56. J. L. Peterson, C. S. Schramm, D. R. Stojakovic, B. M. Hoffman, and T. J. Marks, **99**, 286 (1977).
57. R. S. Nohr, P. M. Kuznesof, K. J. Wynne, M. E. Kenney, and P. G. Siebenman, *ibid.*, **103**, 4371 (1981).
58. K. Wynne, Personal communication.
59. K. Norland, A. Ames, and T. Taylor, *Photo. Sci. Eng.*, **14**, 295 (1970).
60. T. Mezza, N. R. Armstrong, and M. Kenney, *J. Electroanal. Chem.*, **176**, 259 (1984).
61. J. H. Sharp and M. Lardon, *J. Phys. Chem.*, **72**, 3230 (1968).
62. J. H. Sharp and M. Abkowitz, *ibid.*, **77**, 477 (1973).
63. T. Mezza, C. L. Linkous, V. R. Shepard, N. R. Armstrong, R. Nohr, and M. Kenney, *J. Electroanal. Chem.*, **124**, 311 (1981).
64. T. Gueshi, K. Tokuda, and H. Matsuda, *ibid.*, **89**, 247 (1978).
65. T. Klofta, Unpublished results.
66. P. Rieke, Ph.D. Dissertation, University of Arizona, Tucson, AZ (1984).
67. J. C. Riviere, in "Solid State Surface Science," Vol. I, Mino Green, Editor, p. 174, Marcel Dekker, New York (1969).
68. W. Buttner, P. Rieke, and N. R. Armstrong, Submitted to *J. Am. Chem. Soc.*
69. M. C. Pham, J. C. Dubois, and P. C. LaCage, *J. Electroanal. Chem.*, **99**, 331 (1979).
70. A. Nanthakumar and N. R. Armstrong, Unpublished results.

Reversible Reduction and Reoxidation of Entire Thin Films of Octacyanophthalocyanine

B. Schumann and D. Wöhrle

Organische und Makromolekulare Chemie, Fachbereich 2-Chemie, Universität Bremen, D-2800 Bremen 33, Germany

N. I. Jaeger*

Angewandte und Physikalische Chemie, Forschungsgruppe Angewandte Katalyse, Fachbereich 2-Chemie, Universität Bremen, D-2800 Bremen 33, Germany

ABSTRACT

The electrochemical properties of solid films of Mt-2,3,9,10,16,17,23,24-octacyanophthalocyanine **2** [Mt = 2H, Zn(II), Cu(II)] were studied by cyclic voltammetry in aqueous electrolytes. The thin (10-100 nm) film electrodes show remarkably stable electrochromic redox behavior, and the charge exchanged in the cathodic and anodic waves, respectively, was found to be between 2 and 3 F/mol for scan rates up to 400 mV/s. For charge compensation, the intercalation of cations is required. At low pH values (intercalation of protons), nernstian behavior was observed, while in alkaline solutions the intercalation of the cations Li⁺, Na⁺, or K⁺ into the solid film was found to be the rate-determining step. From the half-width of the current waves, the number of electrons involved in the overall reaction was inferred and found to be different in acid and alkaline solutions. Compared to unsubstituted phthalocyanines **1**, the characteristic qualities of the electrodes are associated with the high electric conductivity of **2** and the electron accepting properties of the substituents of the ligand.

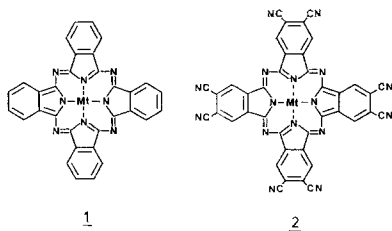
Monomeric phthalocyanines **1** and their polymeric analogues (**1**, **2**) exhibit a variety of interesting physicochemical properties. A great deal of work has been published on their semiconducting properties, and even metallic conductivity has been observed following the doping with acceptors (3-9). The properties of phthalocyanines as catalysts for the dioxygen reduction in fuel cells have been investigated intensively [(10-16), *cf.* Ref. (2)]. Titanium electrodes covered with thin layers of polymeric phthalocyanines were found to exhibit faradaic activity comparable with platinum in redox electrolytes like [Fe(CN)₆]⁴⁻/[Fe(CN)₆]³⁻ (17, 18). The effect of spectral sensitization of inorganic semiconductors by phthalocyanines on their photoelectrochemical and photovoltaic properties has been studied extensively (19-25).

Detailed investigations of the redox behavior of dissolved **1** have been reported (15, 16, 22, 26-28). As many as four reversible ligand reductions and two ligand oxidations were determined by electrochemical methods. Corresponding to the redox behavior in solution a reduction or oxidation of solid semiconducting layers of **1** can be expected. Such processes are of interest for the study of reversible charge storage and electrochromism (29-32). Cyclic voltammetric measurements of thin films of **1** (Mt = metal ion) on gold electrodes in contact with an aqueous

electrolyte resulted in the oxidation and the subsequent reduction of the films with one to two electrons per molecule under intercalation of anions (29). The charge storing capability dropped rapidly with the number of cycles. The electrode processes are impeded by the low electronic conductivity of the layers.

2,3,9,10,16,17,23,24-Octacyanophthalocyanine **2** (33) shows a high conductivity and a more positive redox potential than **1**. Depending on the central ion, *e.g.*, Mt = 2H, Zn, Cu, conductivities for the polycrystalline materials range from 10⁻¹ to 10⁻⁸ Ω⁻¹·cm⁻¹ for **2** (2) and from 10⁻⁹ to 10⁻¹⁴ Ω⁻¹·cm⁻¹ for **1** (3). In the solvent system DMF/0.1M TBAP, the first standard redox potential was found to be E° = 0.09V vs. NHE for the couple [2]/[2]⁻ (Mt = Zn) and E° = -0.62V vs. NHE for the couple [1]/[1]⁻ (Mt = Zn) in Ref. 34. In the case of **1** with other central metal ions, E° values between -0.42 and -0.65V vs. NHE have been reported (27). **2** therefore appeared to be suitable for a study of the reduction and reoxidation of solid films in contact with an aqueous electrolyte. The aim of the present work was to develop stable thin film electrodes, which could undergo reduction and reoxidation cycles not limited by diffusion processes, up to relatively fast voltage scans. The intensely studied properties of electrodes coated with redox active organic layers (35-39) are less satisfactory in these respects.

* Electrochemical Society Active Member.



Experimental

Metal free, copper(II) and zinc(II)octacyanophthalocyanine **2** were synthesized following Wöhrle *et al.* (33). All chemicals were analytical grade (Merck). All aqueous solutions were prepared from doubly distilled water. The solvent, N-methylpyrrolidone, was purified by distillation under nitrogen and reduced pressure.

The working electrodes were prepared from 0.8 cm diam gold disks (99.99%, Degussa). They were ground and polished (1200 mesh emery paper, 1 μm , 0.3 μm alumina), cleaned in chrome sulfuric acid (10 min), and then rinsed in distilled water in an ultrasonic bath. Prior to the deposition of **2**, the gold substrate was etched in aqua regia for 2s, then rinsed in distilled water and dried in air. For the film deposition, 10^{-6} mol of **2** were dissolved in 1 ml N-methylpyrrolidone. 1 to 10 μl iter containing 10^{-9} – 10^{-8} mol of **2** were spread onto the electrode surface. Upon evaporation of the solvent under vacuum (0.1 Pa), the deposited green film was tempered for 1h at 473 K within the same vessel. The electrodes were stored in vacuum until use. From the specific gravity of the bulk material (1.49 g/cm³), the film thickness was calculated to be between 10 and 100 nm. Transmission electron micrographs confirmed the formation of homogeneous films and, in contrast to evaporated layers of **1**, no microcrystallites could be observed within the resolution of the microscope (< 5 nm).

The electrodes were mounted in the window of a PTFE holder, exposing an area of 0.5 cm² to the electrolyte. Electrical contact was established by a gold wire pressed onto the back of the electrode.

Cyclic voltammetry was carried out using a Model 1003 T-NC Jaisle potentiostat and a Wenking VSG 72 voltage scan generator. The data were recorded on a HP 7004B X-Y recorder, and for fast scans on a 7623 A Tektronix storage oscilloscope. The experiments were carried out in deoxygenated solutions under nitrogen at 298 K in a two-compartment PTFE cell (80 ml), equipped with a Ag/AgCl reference electrode (205 mV *vs.* NHE), the appropriate working electrode, and a Pt counterelectrode. The reference electrode was kept at a distance less than 0.1 mm from the dye film by means of a Haber-Luggin capillary.

The color change of the film undergoing redox cycles was characterized by UV/VIS transmission spectroscopy. For this purpose, 100 nm thick films of **2** (Mt = 2H) deposited on quartz plates were chemically reduced by Sn²⁺ ions (50 mmol SnCl₂ in 1M HCl).

Results

Measurements in acid electrolyte.—A typical cyclic voltammogram for the second cycle is depicted in Fig. 1a for a 100 nm metal-free film of **2** (total amount of **2** was 10^{-8} mol) in 1M HCl. The redox cycles run between 495 and -235 mV *vs.* Ag/AgCl. Between 195 and -105 mV, the entire film is reduced, requiring the intercalation of charge compensating cations, and two peak currents can be observed at +81 and +20 mV (*vs.* Ag/AgCl) for the second cycle (Table I). Again, two peak currents appear during the reoxidation of the film at 100 and 33 mV. A broadening of the curve and the appearance of more pronounced anodic peaks can be observed following the first cycle. Up to the measured 600 cycles, no further change or loss of electrochemical activity occurs, demonstrating the high electrochemical stability of the system. The separation of the corresponding cathodic and anodic current maxima is less than 30 mV, indicating the reversi-

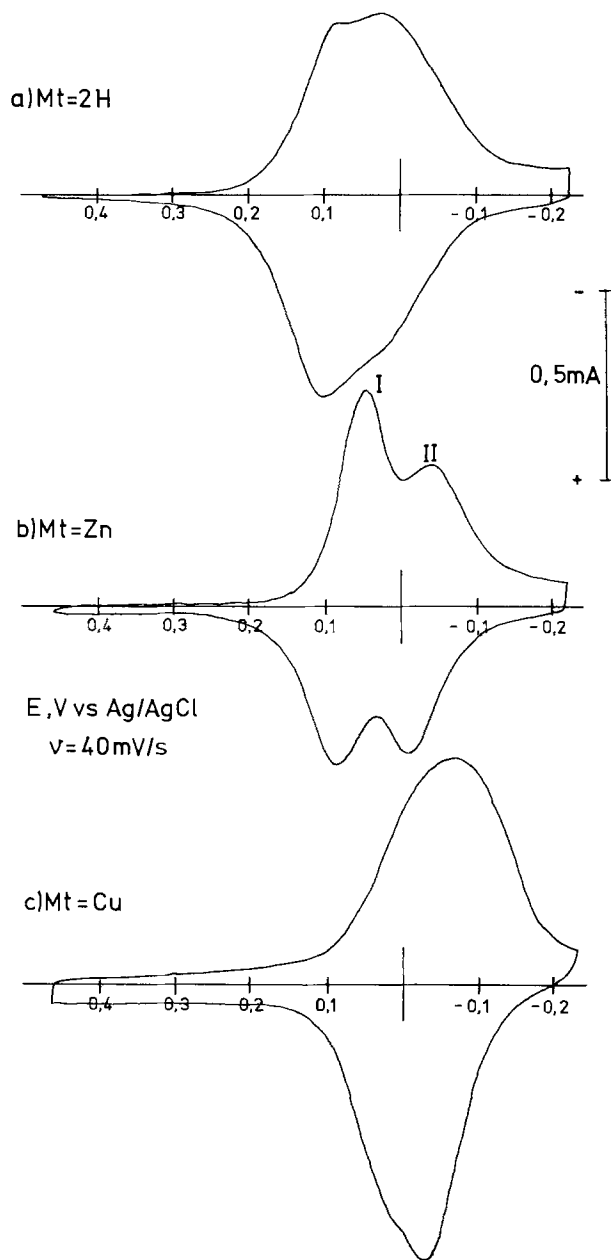


Fig. 1. Cyclic voltammograms (second cycle) of different films of octacyanophthalocyanine **2** (10^{-8} mol on 0.5 cm² gold electrodes) in acid electrolyte (1M HCl). a: **2** (Mt = 2H). b: **2** (Mt = Zn). c: **2** (Mt = Cu). Scan rate: 40 mV/s.

bility of the solid-state electrochromic redox process (Table I).

The color changes between green and dark brown during the redox cycle can also be established by chemical reduction with Sn(II) in 1M HCl. The corresponding transmission spectra are depicted in Fig. 2. The λ_{max} value of the Q band shifts from 650 to 580 nm.

The charge under the curve corresponds to 2.8 electron/molecule or to 2.8 F/mol for the cathodic as well as for the anodic branch of the second cycle, after correction for the double layer capacitance of the thin film electrode. This value was roughly estimated from the linear dependence of the constant residual current on the scan rate in the anodic region of the scan where no faradaic activity is observed. Figure 3 depicts the dependence of the stored charge on the thickness of the film of **2** (Mt = 2H). The exchanged charge of about 3 F/mol does not depend on the film thickness between 10 and 100 nm ($0.2\text{--}2 \times 10^{-8}$ mol/cm²).

Figure 4 depicts the dependence of the cathodic peak current on the scan rate v for a 100 nm film. No marked

Table I. Peak potentials of stable cycles for reduction and reoxidation of different films of 2 (10^{-8} mol; film thickness ~ 100 nm) in various electrolytes; scan rate 40 mV/s

Film of <u>2</u>	Electrolyte	Peak potentials (mV vs. Ag/AgCl)			E_{ox}^{II}	Charge storage (F/mol)
		E_{red}^I	E_{ox}^I	E_{red}^{II}		
Mt = 2H	1M HCl	81	100	20	33	2.8
	0.1M LiOH/1M LiCl	-731	-671	-846	-826	2.7
	0.1M NaOH/1M NaCl	-765	-710	-865	-830	2.7
	0.1M KOH/1M KCl	-756	-701	-866	-811	2.4
Mt = Cu	1M HCl	-63	-25			2.7
	0.1M LiOH/1M LiCl	-506	-451	-996	-916	1.5
	0.1M NaOH/1M NaCl	-681	-581	-971	-871	1.8
	0.1M KOH/1M KCl	-681	-636	-961	-906	1.75
Mt = Zn	1M HCl	50	85	-38	-10	2.7
	0.1M NaOH/1M NaCl ^a	-328	-235	-640	-575	3.0

^a $E_{red}^{III} = -905$, $E_{ox}^{III} = -845$ mV vs. Ag/AgCl.

deviation from linearity can be observed in the range from 20 to 400 mV/s. The same relationship holds for the anodic peak current. The time constant of the film reduction was estimated to be below 5 ms from potential step measurements. The charge exchanged during the cycle does not depend on the scan rate in this range. The observed separation between the cathodic and the corresponding anodic peak current remained within the IR drop between the Luggin capillary and the electrode surface for all experiments depicted in Fig. 3 and 4 and listed in Table I.

Compared to 2 (Mt = 2H), a similar voltammogram, however, with a more pronounced double peak profile, was observed for films of the Zn chelate of 2 (Fig. 1b). The reduction and reoxidation potentials are shifted into the negative direction by about 30-45 mV (Table I). The charge under the cathodic and the anodic branch was found to be 2.7 F/mol after correction for the double layer

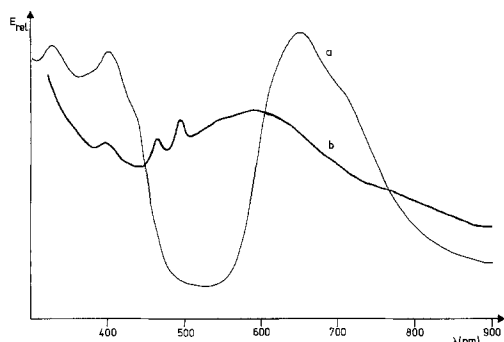


Fig. 2. Transmission spectrum of 50 μg 2 (Mt = 2H) deposited on a 3 cm^2 quartz plate (a) and following chemical reduction (5×10^{-2} M SnCl_2 in 1M HCl) (b).

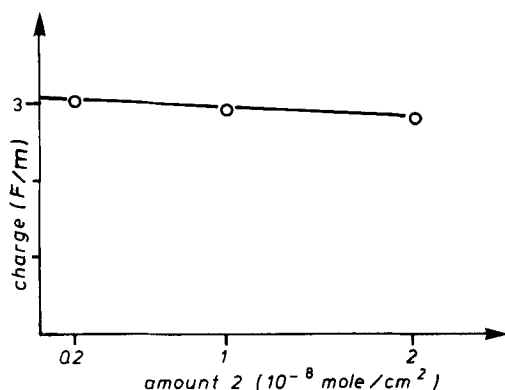


Fig. 3. Charge exchanged per mol of 2 (Mt = 2H) in either branch of the cyclic voltammogram in dependence on the amount of 2. Scan rate: 40 mV/s; acid electrolyte (1M HCl).

capacitance and irrespective of the scan rate up to $v = 400$ mV/s. Compound 2 (Mt = Zn) exhibits distinct electrochromic behavior during the redox cycle. The green color of the layer changes to intense blue (reduction peak I), and then to brown (reduction peak II).

In the case of the copper chelate of 2, no double peak can be observed in the voltammogram (Fig. 1c). The reduction peak current is shifted to a more negative potential (-63 mV vs. Ag/AgCl). Again, the stored charge during the redox cycle was found to be 2.7 F/mol and did not depend on the scan rate up to 400 mV/s.

In the range of low pH values up to $\text{pH} = 2.5$, the potential of the respective peak currents in the voltammogram shows a linear dependence on pH of about 60 mV/pH.

Measurements in alkaline electrolytes.—In order to study the dependence of the redox behavior of layers of 2 on the nature of the cation, which has to be intercalated for charge compensation, the following alkaline electrolytes were used: 0.1M LiOH/1M LiCl, 0.1M NaOH/1M NaCl, and 0.1M KOH/1M KCl. The results are depicted in Fig. 5 and 6.

In comparison to the acid electrolyte, the potentials of the cathodic and anodic peak currents are shifted negatively (Table I). In the case of metal-free films of 2, the current peaks in the cyclic voltammograms are considerably broadened (Fig. 5a and 6b). As found with acid electrolytes, the charge exchanged during the electrochromic redox process was found to be 2.7 F/mol for either branch of the cycle. The peak currents, however, do not depend linearly on the scan rate, even in the range of slow scans ($v = 40$ -160 mV/s), which indicates some hindrance of the intercalation mechanism.

Figures 5c and 6c depict representative cyclic voltammograms obtained for thin film electrodes of 2 (Mt

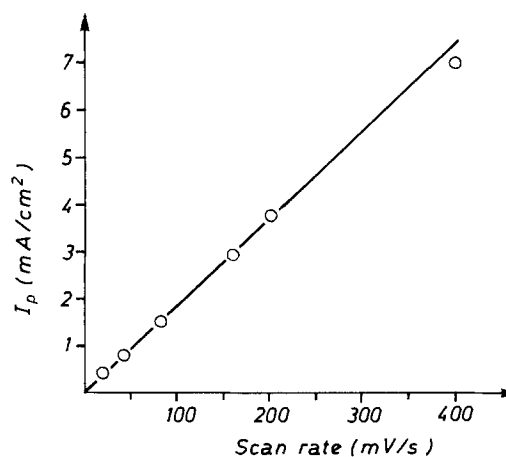


Fig. 4. Linear dependence of cathodic peak current I_p on the scan rate for a 100 nm film of 2 (Mt = 2H) $\approx 10^{-8}$ mol in acid electrolyte (1M HCl).

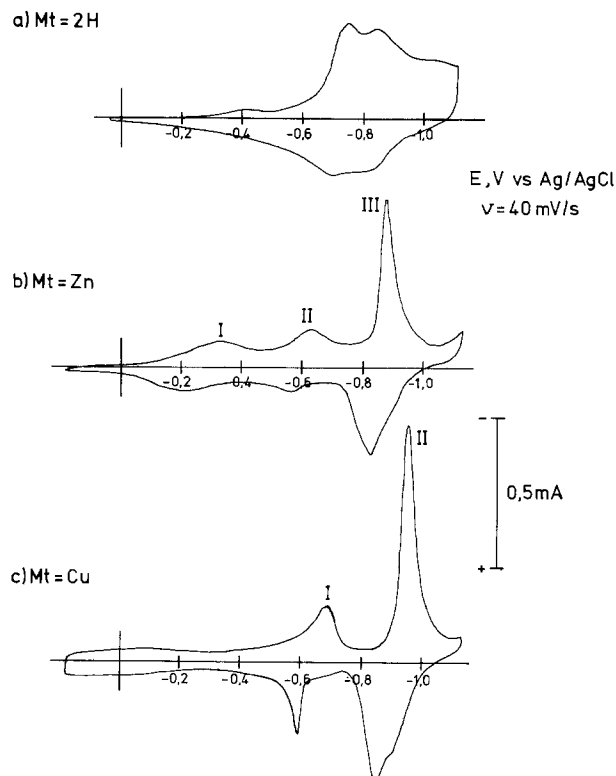


Fig. 5. Cyclic voltammograms (second cycle) of different films of octacyanophthalocyanine **2** (10^{-8} mol on 0.5 cm^2 gold electrodes) in alkaline electrolyte (0.1M NaOH/1M NaCl). a: **2** (Mt = 2H). b: **2** (Mt = Zn). c: **2** (Mt = Cu).

= Cu) in alkaline electrolytes. Compared to **2** (Mt = 2H), a tenfold increase in double layer capacitance points towards a larger real surface area of the film. In contrast to acid electrolytes, two clearly separated redox peaks, I and II, can be observed. The heights of the first cathodic (I) and of the corresponding anodic peak current are still linearly dependent on the scan rate regardless of the electrolyte. For the second cathodic (II) and corresponding anodic peak, and in the case of Li^+ the peak current is found to depend on $\nu^{1/2}$, which is indicative of a diffusion-controlled process (Fig. 6d). A deviation from linearity is also observed in alkaline electrolytes containing Na^+ or K^+ . A peak current- $\nu^{1/2}$ relationship, however, could not be established in the range of scan rates of $2.5\text{--}640 \text{ mV}\cdot\text{s}^{-1}$ in these cases. The experimental results obtained in alkaline Li^+ or K^+ containing electrolytes are summarized in Table II. For successive experiments, the scan rate was always doubled. The ratio of the corresponding peak currents $I_{p,n+1}/I_{p,n}$ was calculated and also listed in the table. The deviation from linearity is even less pronounced for the anodic wave.

The position of the first redox peak E_{red}^1 depends on the nature of the cation. A pronounced shift can be observed changing from Li^+ to Na^+ containing electrolytes (Table I). The position of the second redox peak $E_{\text{red}}^{\text{II}}$ is less affected by the choice of the cation.

After correction for the double-layer capacitance, the charge under either branch of the cyclic voltammogram is found to be less than 2 F/mol (Table I) with about 25% of the charge located under peak I and about 75% under peak II (Fig. 5c and 6c). A remarkable feature of the voltammograms obtained in Na^+ and K^+ containing electrolytes is the small half-width of the second peak, $\Delta E_{1/2} = 55 \text{ mV}$ and $\Delta E_{1/2} = 40 \text{ mV}$, respectively.

Three redox peaks, I, II, and III, can be observed in the cyclic voltammogram obtained for electrodes of **2** containing Zn as the central atom (Table I, Fig. 5b). Also in this case, the peak positions do not depend on the scan rate in the range of $40\text{--}160 \text{ mV/s}$. A total of 3 F/mol is exchanged in the electrochromic redox process in either

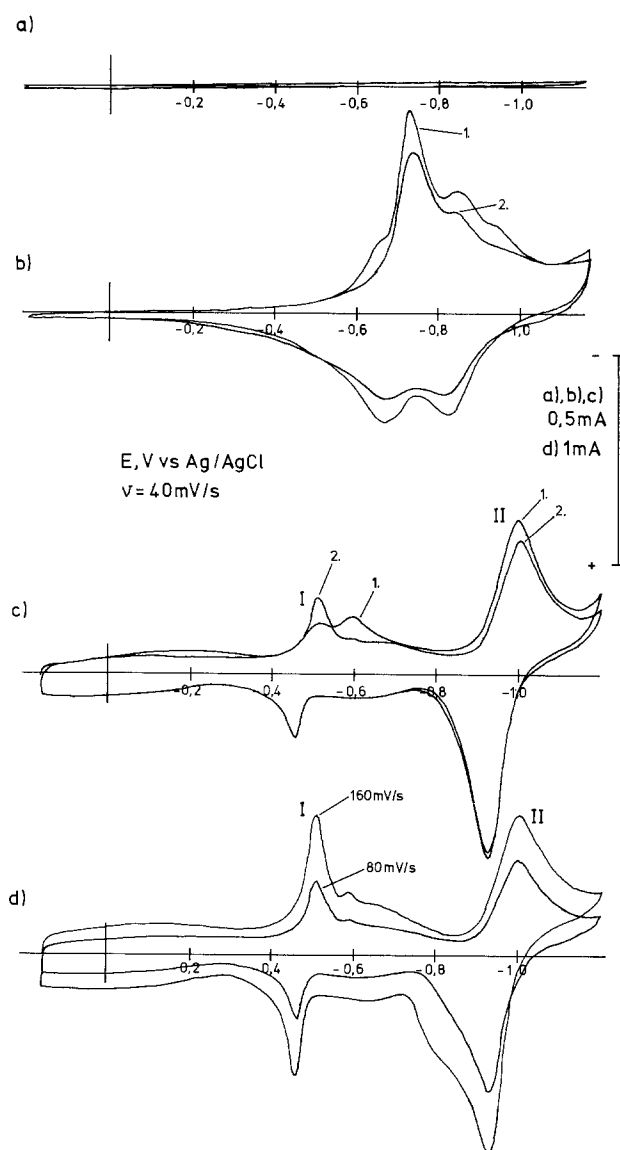


Fig. 6. Cyclic voltammograms of different films of octacyanophthalocyanine **2** (10^{-8} mol on 0.5 cm^2 gold electrodes) in alkaline electrolyte (0.1M LiOH/1M LiCl). a: Gold support. b: **2** (Mt = 2H) first and second cycle, 40 mV/s . c: **2** (Mt = Cu) first and second cycle, 40 mV/s . d: Electrode c, Different scan rates (80 and 160 mV/s).

branch of the voltammogram, with most of the charge located in peak III, which, in analogy to results obtained for **2** (Mt = Cu), shows a remarkably small half-width of $\Delta E_{1/2} \approx 50 \text{ mV}$ in a sodium hydroxide electrolyte.

There is a loss of charge of up to 10% from the first to the second cycle for all electrodes (Fig. 6b and 6c). Thereafter, the charge involved in the cathodic and the anodic waves, as well as the position of the peaks, remains unchanged and shows little dependence on the scan rate beyond the IR drop up to 160 mV/s (Fig. 6d) and on the nature of the cation involved, with the exception of Li^+ (Table I).

Discussion

The relatively good solubility of octacyanophthalocyanines **2** in organic solvents as compared to that of the unsubstituted compounds **1** allows the preparation of films from corresponding solutions by evaporation of the solvent. This is the only way for the preparation of solid-state films of **2** since sublimation would lead to partial thermal decomposition of the material. The influence of substituents on the solid-state properties of porphyrins is well known and leads to excellent electrochemical behavior in the case of films of **2**. They were found to be electrochemically and mechanically stable within the

Table II. Dependence of the second cathodic peak current I_p (Fig. 6d) on the scan rate v for films of **2 (Mt = Cu; film thickness ≈ 100 nm; electrode area 0.5 cm²) in alkaline electrolytes**

Electrolyte	n	Scan rate (mV/s)	I_p (μ A)	Ratio of peak currents $I_{p,n+1}/I_{p,n}$
0.1M LiOH/1M LiCl	1	5	88	1.56
	2	10	137	1.64
	3	20	225	1.56
	4	40	350	1.57
	5	80	550	1.49
	6	160	820	1.43
	7	320	1175	1.40
	8	640	1650	
0.1M KOH/1M KCl	1	2.5	78	1.95
	2	5	152	1.84
	3	10	280	1.73
	4	20	485	1.86
	5	40	900	1.67
	6	80	1500	1.67
	7	160	2500	1.6
	8	320	4000	1.5
	9	640	6000	

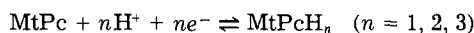
range of potentials investigated. Up to scan rates of 2×10^5 mV/s, films of **2** exhibit electrochromic reduction and reoxidation processes in acid as well as in alkaline electrolytes. Up to the scan rates of 400 mV/s and 600 cycles investigated, the exchanged charge was found to be stable in most cases for either branch of the cyclic voltammogram.

Two processes characterize the reversible reduction and reoxidation of films of **2**: injection of electrons at the Au/**2** interface, followed by the transport of the charge through the film and intercalation of charge compensating cations or their ejection during the redox cycle. The high intrinsic conductivity of **2** provides for a reversible charge transfer in acid electrolytes (intercalation of protons) up to moderate scan rates. The electron attracting nitrile groups in **2** may be responsible for reduction easier than that of **1**, which could not be reduced under the same experimental conditions.

In solution the reduction of **2** (Mt = Zn) proceeds in distinct steps at -0.15 , -0.50 , -1.10 , and -1.35 mV vs. SCE (34). In the solid state, the potentials merge. For an ideal nernstian one-electron reaction of a solid thin film on an electrode surface, the model of Anson and Brown (40) predicts a half-width of the current peak of $\Delta E_{1/2} = 90.6$ mV. $\Delta E_{1/2}$ values around 190 mV were measured for the films of **2** in acid electrolytes and might be explained by the close proximity of up to three one-electron steps. In the case of **2** (Mt = Zn), two neighboring peaks can even be distinguished (Fig. 1b). The narrow half-widths observed for the most cathodic wave for films of **2** (Mt = Zn, Cu) in alkaline Na⁺ and K⁺ containing electrolytes can be accounted for by the exchange of 1.5 F/mol in one step (Fig. 5b, peak III and Fig. 5c, peak II, respectively). The observed asymmetry of these peaks in comparison with the corresponding anodic waves could be due to the interactions between the phthalocyanine molecules combined with the observed diffusion control in the behavior of the redox system in alkaline solutions. This interpretation follows a model put forward by Laviron and Roullier (41). The shape of the wave observed for the metal-free **2** (Mt = 2H) in the same electrolytes again appears to be due to the close proximity of one-electron steps. This could be explained by the existence of distinguishable energy levels for the successive intercalation of the charge compensating cations.

At low pH values, a total charge of about 3 F/mol is consumed in the reduction and in the reoxidation of the phthalocyanine. It is well known that the nitrogen atoms in positions 6, 13, 20, 27 of the phthalocyanine can be protonated (42, 43). An acid base reaction might be the cause for the rapid intercalation of protons leading to the observed nernstian behavior of the electrodes. Up to pH

2.5 the potential of the peak current shifts 60 mV/pH (298 K) for any distinguishable peak. This pH-sensitive behavior can be expected for the exchange of protons according to the overall reaction



At high pH values, the transport of charge compensating cations other than protons may become the rate-determining step in the redox process. As a common feature of the cyclic voltammogram of **2** (Mt = Cu) in alkaline solutions, two peaks (I, II) have been established by the experiments (Fig. 6c and 6d). A dependence of the height of the cathodic peak II and the corresponding anodic peak on the square root of the scan rate is indicative of a diffusion-limited intercalation of the cation (40).

In the observed range of scan rates the $v^{1/2}$ dependence is established clearly in case of Li⁺ (ratio of successive peak currents $I_{p,n+1}/I_{p,n} \approx \sqrt{2}$). A trend towards the linear dependence of the peak current on the scan rate v can be observed in the case of electrolytes containing the larger cations Na⁺ and K⁺ at least for the low range of scan rates ($I_{p,n+1}/I_{p,n} \approx 2$). This seems to reflect decreasing electrostatic interaction with increasing size of the cation during migration through the phthalocyanine bulk.

The properties and the shape of the first cathodic (I) and the corresponding anodic wave (Fig. 5c and 6c) could be due to the reduction of a surface layer, i.e., the creation of surface states for the adsorption of the cation. The dependence of the position of the peak on the nature of the cation is therefore no surprise, even though the trend cannot be explained at the present time. From the reproducibility of the cycles with respect to the charge, and to the position of the peak currents as well as the close proximity of the anodic and the cathodic peak currents on the potential scale, nernstian behavior of the thin film electrodes without diffusion control can be inferred in the case of acid electrolytes. The pH dependence of the potential of the peak current lends additional support to this assertion. In the case of alkaline electrolytes, nernstian behavior with some diffusion limitation of the intercalation of the charge compensating cations cannot be distinguished from irreversible steps in the redox process, based on the available data.

Conclusions

Thin film electrodes of octacyanophthalocyanine **2** were found to function as reversible solid-state redox systems. The outstanding electrochemical properties appear to be due to a combination of the high intrinsic conductivity and the electron accepting properties of the substituents of **2**. The choice of the cation in the ligand of **2**, of the cation in the electrolyte, and eventually of the substituents determines the potential range for the solid-state redox processes. Applications in batteries, in redox active membranes, and in memory devices can be envisaged.

Acknowledgment

The authors are thankful for financial support from the Stiftung Volkswagenwerk (Az I 60/074).

Manuscript submitted Feb. 19, 1985; revised manuscript received May 21, 1985.

Universität Bremen assisted in meeting the publication costs of this article.

REFERENCES

1. F. H. Moser and A. L. Thomas, "The Phthalocyanines," CRC Press, Boca Raton, FL (1983).
2. D. Wöhrle, *Adv. Polym. Sci.*, **50**, 45 (1983).
3. F. Gutman and L. E. Lyons, "Organic Semiconductors," John Wiley and Sons, New York (1967).
4. H. Meier, "Organic Semiconductors," Verlag Chemie, Weinheim, Germany (1974).
5. B. M. Hoffman and J. A. Ibers, *Acc. Chem. Res.*, **16**, 15 (1983).
6. C. J. Schramm, R. R. Scaringe, D. R. Stojakovic, B. M. Hoffman, J. A. Ibers, and T. J. Marks, *J. Am. Chem. Soc.*, **102**, 6702 (1980).

7. B. N. Diehl, T. Inabe, J. W. Lyding, K. F. Schoch, C. R. Kannewurf, and T. J. Marks, *ibid.*, **105**, 1551 (1983).
8. R. S. Nohr, P. M. Kusnezof, K. J. Wynne, M. E. Kenney, and P. G. Siebenmann, *ibid.*, **103**, 4371 (1981).
9. M. Hanack, *Mol. Cryst. Liq. Cryst.*, **105**, 133 (1984).
10. H. Jahnke, *Chimia*, **34**, 58 (1980).
11. H. Meier, W. Albrecht, U. Tschirwitz, and E. Zimmerhacke, *Ber. Bunsenges. Phys. Chem.*, **77**, 843 (1973).
12. H. Behret, H. Binder, G. Sandstede, and G. G. Scherer, *J. Electroanal. Chem.*, **117**, 29 (1981).
13. S. Maroie, M. Savy, and J. J. Verbist, *Inorg. Chem.*, **18**, 2560 (1979).
14. F. Beck, *Ber. Bunsenges. Phys. Chem.*, **77**, 353 (1973).
15. J. Zagal, R. K. Sen, and E. Yeager, *J. Electroanal. Chem.*, **83**, 207 (1977).
16. J. P. Collman, P. Denisevich, Y. Konai, M. Marocco, C. Koval, and F. C. Anson, *J. Am. Chem. Soc.*, **102**, 6027 (1980).
17. D. Wöhrle, R. Bannehr, N. Jaeger, and B. Schumann, *Angew. Makromol. Chem.*, **117**, 103 (1983).
18. D. Wöhrle, R. Bannehr, B. Schumann, G. Meyer, and N. Jaeger, *J. Mol. Catal.*, **21**, 255 (1983).
19. H. Tachikawa and L. R. Faulkner, *J. Am. Chem. Soc.*, **100**, 4379 (1978).
20. C. D. Jaeger, F. R. Fan, and A. J. Bard, *ibid.*, **102**, 2592 (1980).
21. P. Leempoel, M. Castro-Acuna, F. R. Fan, and A. J. Bard, *J. Phys. Chem.*, **86**, 1396 (1982).
22. A. Giraudeau, F. R. Fan, and A. J. Bard, *J. Am. Chem. Soc.*, **102**, 5137 (1980).
23. D. Leempoel, F. R. Fan, and A. J. Bard, *J. Phys. Chem.*, **87**, 2948 (1983).
24. R. O. Loutfy, J. H. Sharp, C. K. Hsiao, and R. Ho, *J. Appl. Phys.*, **52**, 5218 (1981).
25. R. O. Loutfy and L. F. McIntyre, *Can. J. Chem.*, **61**, 72 (1983).
26. V. R. Shepard and N. R. Armstrong, *J. Phys. Chem.*, **83**, 1268 (1979).
27. A. B. P. Lever, S. Licoccia, K. Magnell, P. C. Minor, and B. S. Ramaswamy, *Adv. Chem. Ser.*, **201**, 237 (1982).
28. A. M. Schaffer, M. Goutermann, and E. R. Davidson, *Theor. Chim. Acta*, **30**, 9 (1973).
29. J. M. Green and L. R. Faulkner, *J. Am. Chem. Soc.*, **105**, 2950 (1983).
30. M. M. Nicholson and F. A. Pizzarello, *This Journal*, **128**, 1288 (1981).
31. D. Walton, B. Eley, and G. Elliot, *ibid.*, **128**, 2479 (1981).
32. V. I. Gavrillov, N. V. Butasova, E. A. Lukyanets, and I. V. Shelepin, *Elektrokhimiya*, **16**, 1611 (1980).
33. D. Wöhrle, G. Meyer, and B. Wahl, *Makromol. Chem.*, **181**, 2127 (1980).
34. A. Giraudeau, A. Louati, M. Gross, J. J. Andre, J. Simon, C. H. Su, and K. M. Kadish, *J. Am. Chem. Soc.*, **105**, 2917 (1983).
35. D. C. Bookbinder and M. S. Wrighton, *This Journal*, **130**, 1080 (1983).
36. H. Ohno, N. Hosoda, and E. Tsuchida, *Makromol. Chem.*, **184**, 1061 (1983).
37. Y.-M. Tsou and F. C. Anson, *This Journal*, **131**, 595 (1984).
38. I. Rubinstein, *ibid.*, **130**, 1506 (1983).
39. A. Skorobogaty and T. D. Smith, *Coord. Chem. Rev.*, **53**, 55 (1984).
40. A. P. Brown and F. C. Anson, *Anal. Chem.*, **49**, 1589 (1977); for details regarding the evaluation of cyclic voltammograms see also: A. J. Bard and L. R. Faulkner, "Electrochemical Methods, Fundamentals and Applications," John Wiley and Sons, New York (1980); E. Laviron and A. J. Bard, "Electroanalytical Chemistry," Vol. 12, p. 53, Marcel Dekker, New York (1982).
41. E. Laviron and L. Roullier, *J. Electroanal. Chem.*, **115**, 65 (1980).
42. S. Gaspard, M. Verdaguer, and R. Viovy, *J. Chem. Res.*, 271 (1979).
43. D. L. Ledson and M. V. Twigg, *Inorg. Chim. Acta*, **13**, 43 (1975).

Indirect Electrochemical Processes at a Rotating Disk Electrode

Oxidation of Sulfite Catalyzed by Iodide

Shi-Chern Yen and Thomas W. Chapman

Department of Chemical Engineering, University of Wisconsin-Madison, Madison, Wisconsin 53706

ABSTRACT

The anodic oxidation of sulfite in sulfuric acid solution is catalyzed by small amounts of iodide ion. The mechanism of this process is viewed as the electrochemical oxidation of iodide followed by the homogeneous oxidation of sulfite by iodine. The homogeneous reaction is too fast for its rate to be measured conveniently by cyclic voltammetry so the enhancement by sulfite of the iodide limiting current to a rotating disk electrode is used to determine the second-order rate constant ($7.5 \times 10^8 \text{ cm}^3/\text{mol}\cdot\text{s}$ at 22°C). A collocation technique is used to simulate the electrochemical-chemical process. The electrode kinetics parameters of iodide oxidation on pyrolytic graphite are also determined. The collocation model is successful in predicting anodic polarization curves in the sulfite-iodide system. The sulfite anode is depolarized by as much as 400 mV by the iodide catalyst.

The oxidation of sulfur dioxide has been investigated extensively in recent years. Most studies have been directed at direct electrochemical oxidation of SO_2 on platinum, gold, alloy, carbon, or graphite electrodes (1-17). A few investigations (18-24) were performed by using a chemical depolarizer, such as a halide ion, to facilitate the anodic oxidation of sulfur dioxide. This paper considers the anodic oxidation of SO_2 , its depolarization by iodide, and the rate of the homogeneous reaction between SO_2 and iodine.

The oxidation of SO_2 has both theoretical interest and practical applications. Besides its electroanalytical use, it offers the following potential applications: (i) anode depolarization in electrowinning of copper and other metals (25, 26), (ii) hydrogen production with SO_2 as an interme-

diating in an electrochemical-thermochemical water-splitting cycle (27-29), (iii) production of sodium hydroxide and sulfuric acid (14, 15), and (iv) electrochemical treatment for SO_2 removal from flue gas (29).

The anodic oxidation of SO_2 on platinum and many other materials in sulfuric acid solution is inhibited by the formation of a surface oxide layer or by reaction-product adsorption (9). Therefore, the electrochemical oxidation rate of SO_2 decreases with time, and at steady state the reaction is quite irreversible. If a suitable depolarizer can be added to the system, one may hope to accelerate the steady-state reaction rate. Here, we employ iodide ion because its electrode potential is close to the SO_2 oxidation potential, its electrode kinetics are nearly reversible, and its reaction product, iodine, reacts very rap-

idly with SO_2 to regenerate iodide and produce sulfuric acid.

Figure 1 shows anodic polarization curves for a vertical graphite electrode, which were obtained in a study of anode depolarization in electrowinning cells (30). Curve 1 is the potential obtained for oxygen evolution at 50°C in $0.2M$ sulfuric acid. Curve 2 is the anode potential when 0.1 sodium sulfite is added to the solution. Curve 3 is the anode polarization curve when 1.0 g/liter sodium iodide is added to the sulfite solution. It is seen that the iodide catalyzes, or depolarizes, the sulfite anode and reduces the anode potential by almost 300 mV at high current densities. Furthermore, this potential is almost 900 mV less anodic than that of the oxygen electrode. Thus, the iodide-catalyzed sulfite anode offers interesting energy saving possibilities in the applications listed above. The purpose of this paper is to examine the behavior of the sulfite-iodide electrode. A specific objective is to present methods for modeling and measuring the kinetics of a fast homogeneous reaction that is coupled with an electrode reaction.

The electrochemical oxidation of iodide has been studied by many investigators (31-43), but its mechanism has not been definitely established. Vetter (44) proposed a mechanism for the iodide-iodine redox reaction on platinum with electron transfer as the rate-determining step. This was confirmed by Newson and Riddiford (39). The anodic transfer coefficient reported by Vetter was 0.78 , but Newson and Riddiford found that the transfer coefficient depended on the concentrations of iodine and iodide and on the rotation speed of the rotating disk electrode, which they attributed to surface nonuniformity.

Swathirajan and Bruckenstein (45, 46) have recently investigated the behavior of the iodide electrode under conditions where iodine films form on a platinum anode. This phenomenon occurs when the iodide concentration exceeds 5 mM. The iodide concentrations used in this study were all $0.001M$ or lower.

In this paper, we report studies on the anodic oxidation rates of sulfite and iodide on rotating platinum and pyrolytic graphite disk electrodes. The depolarization of the sulfite anode by small concentrations of iodide is modeled as the electrochemical discharge of iodide coupled with a second-order homogeneous reaction between iodine and sulfite. The kinetics of the iodide electrode on pyrolytic graphite and of the homogeneous reaction are determined quantitatively.

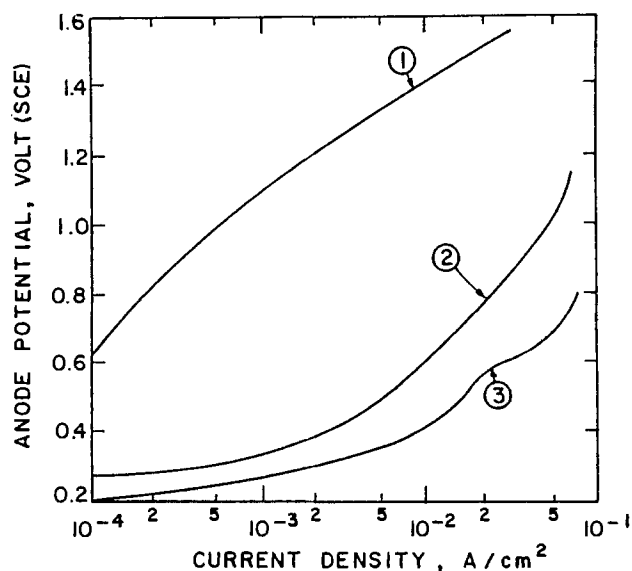


Fig. 1. Anodic polarization curves on a vertical graphite electrode in $0.2M$ sulfuric acid at 50°C . Curve 1 is oxygen evolution. Curve 2 is sulfite oxidation when sodium sulfite is present at $0.1M$. Curve 3 is obtained when 1.0 g/liter sodium iodide is added to the sulfite solution.

Experimental Methods

All chemicals were of analytical grade, and solutions were prepared with double-distilled water. Sodium sulfite was used as a source of SO_2 in solution. A saturated calomel electrode was employed as the reference electrode, and a platinum counterelectrode was used. Potentiostatic and potentiodynamic measurements were taken by using a PAR Model 170 electrochemical instrument and a PIR disk electrode rotator from Pine Instrument Company. A diagram of the apparatus is shown in Fig. 2.

Pyrolytic graphite and smooth platinum electrodes (Pine Instrument) served as working electrodes, each with an area of 0.485 cm^2 . Prior to polarization experiments, the working electrodes were prepared by the following procedure: (i) immersion in chromic acid cleaning solution for 5 min and rinsing with redistilled water, (ii) immersion in $6M$ H_2SO_4 solution for 5 min and then rinsing with redistilled water, (iii) placement of the electrode in the test solution ($1M$ H_2SO_4) and passage of nitrogen through the solution, (iv) application of potential at $-0.2V$ (SCE) for 1 min and then three cyclic scans at 10 mV/s from -0.2 to $1.2V$ (SCE), and (v) changing the potential from $-0.2V$ (SCE) to slightly anodic, $+0.4V$ (SCE), to reoxidize any absorbed hydrogen on surface, then performance of the measurements.

The temperature was approximately 22°C (room temperature), and IR compensation was applied to the rotating disk electrode measurements.

Characterization of the Iodide Electrode

Slow potentiodynamic scans were made on the rotating platinum and graphite electrodes with solutions of sodium iodide in $1.0M$ sulfuric acid. Typical results are shown in Fig. 3 and 4. Although some hysteresis was observed when the potential was scanned in the negative direction after anodic polarization because of iodine formation and possible surface oxidation, it is clear that the iodide reaction is quite reversible on both platinum and pyrolytic graphite.

Steady-state limiting currents were observed for iodide oxidation on the rotating graphite electrode at $0.6V$ (SCE) in $1.0M$ sulfuric acid solutions over a range of rotation speeds and iodide concentrations. The results shown in Fig. 5 verify that the limiting current is proportional to reactant concentration. Although iodide may be oxidized by sulfuric acid on standing, the linearity of the limiting current data seen in Fig. 5 indicates that there was negligible loss of iodide during the course of the experiments. Application of the Levich equation to the limiting currents yields an iodide diffusivity value of 1.46×10^{-5} cm^2/s . Cathodic limiting currents were also observed with

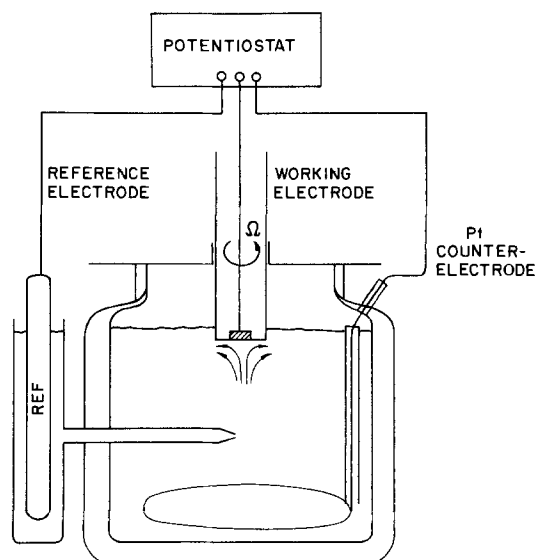


Fig. 2. The rotating disk electrode apparatus

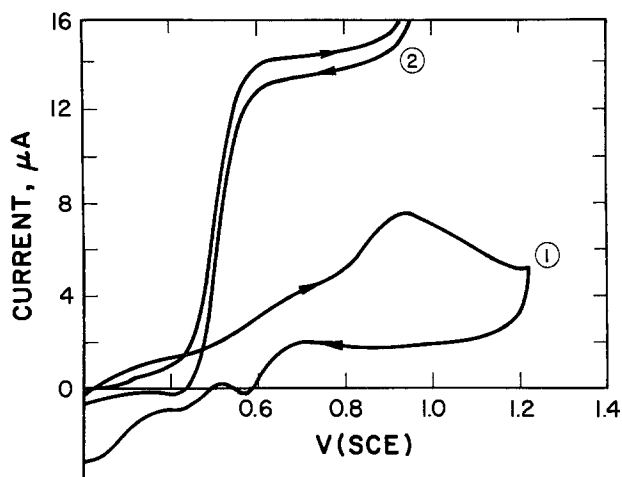


Fig. 3. Anodic polarization curves on a platinum disk electrode rotating at 1600 rpm. Area was 0.4845 cm^2 , and scan rate was 1.0 mV/s . Curve 1: $1.0M$ sulfuric acid. Curve 2: $2 \times 10^{-5}M$ sodium iodide in $1.0M$ sulfuric acid.

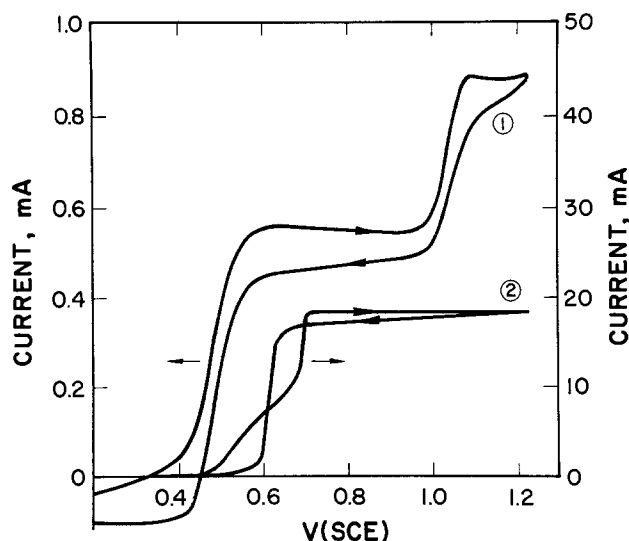


Fig. 4. Anodic polarization curves on a pyrolytic graphite disk electrode rotating at 1600 rpm. Scan rate was 1.0 mV/s , and electrode area was 0.4845 cm^2 . Curve 1: 1.0 mM sodium iodide in $1.0M$ sulfuric acid. Curve 2: 1.0 mM sodium iodide and 19 mM sodium sulfite in $1.0M$ sulfuric acid.

iodine solutions from which the iodine diffusivity was determined to be $0.93 \times 10^{-5} \text{ cm}^2/\text{s}$. These values are based on a kinematic viscosity value of $0.96 \text{ cm}^2/\text{s}$ for $1.0M$ sulfuric acid.

The kinetics of the iodide electrode on pyrolytic graphite in $1.0M$ sulfuric acid were determined quantitatively by observing the polarization curve potentiostatically at various potential values. The bulk solution contained $0.001M$ sodium iodide and $0.001M$ iodine in the sulfuric acid. For data-fitting purposes, it was assumed that the redox electrode kinetics followed a simple Butler-Volmer form, which may be written as

$$i_n = Fk_a r \left[C_{1,\infty} e^{\frac{\alpha F(E - E_0)}{RT}} - \frac{C_{1,\infty} C_{2,0}^{1/2}}{C_{2,\infty}^{1/2}} e^{\frac{-(1-\alpha)F(E - E_0)}{RT}} \right] \quad [1]$$

where E_0 is the equilibrium electrode potential for $C_{1,\infty} = C_{2,\infty} = 0.001M$ [$E_0 = 0.4535V$ (SCE)], α is the anodic transfer coefficient, and k_a^r is a specific anodic rate constant referred to the equilibrium potential E_0 .

The evaluation of the kinetic parameters was done by following the procedures outlined by Gileadi (47). The surface concentrations of iodide and iodine are expressed

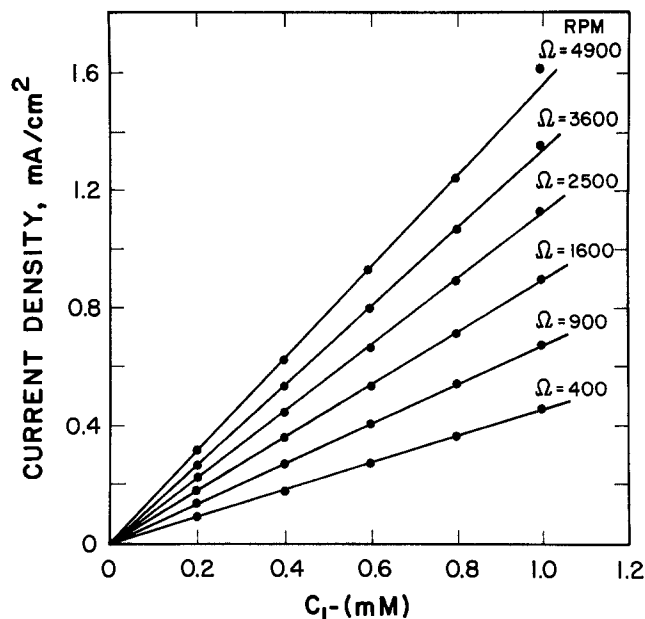


Fig. 5. Limiting anodic current density on a rotating pyrolytic-graphite disk electrode as a function of rotation speed and iodide concentration in $1.0M$ sulfuric acid.

in terms of their respective bulk values and limiting currents. For example

$$C_{1,\infty} = C_{1,\infty} \left(1 - \frac{i_n}{i_{L,a}} \right) \quad [2]$$

where $C_{1,\infty}$ is the bulk iodide concentration and $i_{L,a}$ is the anodic limiting current density for iodide oxidation. Substituting for the interfacial concentrations in this form, one may rewrite Eq. [1] as

$$\ln \left\{ F C_{1,\infty} \left[\left(\frac{1}{i_n} - \frac{1}{i_{L,a}} \right) - \frac{1}{i_n} \left(1 - \frac{i_n}{i_{L,c}} \right)^{1/2} \exp \frac{-F(E - E_0)}{RT} \right] \right\} \equiv \ln(k_a) \\ = -\frac{\alpha F}{RT} (E - E_0) - \ln(k_a^r) \quad [3]$$

where E is the electrode potential at which the current density i_n is measured.

Figure 6 is a plot vs. overpotential, $E - E_0$, of the left-hand side of Eq. [3], calculated for several levels of anodic polarization and abbreviated k_a . In agreement with Eq. [3], the data fall on a straight line. The intercept and slope indicate the values of k_a^r and α to be $6.18 \times 10^{-3} \text{ cm/s}$ and 0.80 , respectively. This rate constant value corresponds to an exchange current density of 0.6 mA/cm^2 for the iodide electrode at these bulk concentrations.

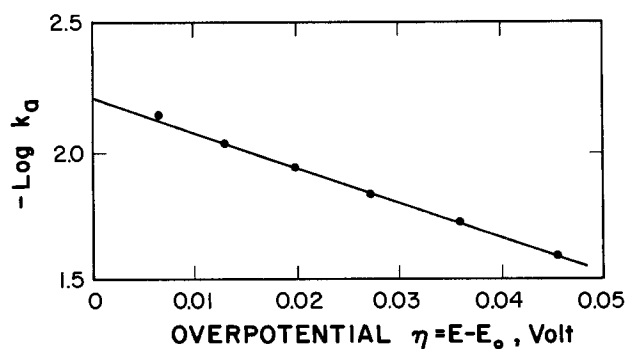


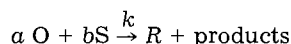
Fig. 6. Plot of anodic polarization data for iodide oxidation on pyrolytic graphite according to the form of Eq. [3].

Mathematical Model of Steady Current to a Rotating Disk Electrode with a Catalytic Chemical Reaction

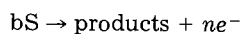
The anodic oxidation of sulfur dioxide catalyzed by iodide is called an indirect electrochemical process, an electrochemical reaction coupled with a catalytic chemical reaction, and it is represented by the following reaction scheme



on electrode surface and



in solution, where R is a reduced species, such as iodide, O is an oxidized species, such as iodine, S is an electrochemically inactive reactant, such as SO₂, k is a second-order reaction rate constant, and a, b, and n are stoichiometric coefficients. The reduced species R is regenerated in solution and then transported to the electrode surface to be oxidized. The oxidized species O is transported out to react with the reactant S in solution to achieve the overall reaction



For SO₂ + 2H₂O → H₂SO₄ + 2H⁺ + 2e⁻, the stoichiometric coefficients are a = b = 1/2 and n = 1.

In order to formulate a model of this electrochemical-chemical reaction system on a rotating disk electrode, we adopt the following assumptions: (i) the electrochemical reaction rate contributed by the direct SO₂ electrode reaction is negligible; (ii) the effect of electrical migration is negligible because of the high acid concentration; (iii) the diffusivities of all species are constant; and (iv) the homogeneous chemical reaction is of second order and irreversible. The first case to be treated is that where the applied potential is high enough to force limiting current.

The analysis of a steady-state electrochemical reaction coupled with a homogeneous catalytic chemical reaction on a rotating disk electrode has been conducted by several investigators (48-50). Levich treated first-order catalytic electrochemical processes analytically. Ulstrup (51) and Holub (52) investigated an electrochemical process with a catalytic reaction in which the electroactive reactant is regenerated by disproportionation. Pospisil (53) determined the rate constant of the reaction between the ferrous ion and hydrogen peroxide by the polarographic method. Generally, an electrochemical process coupled with a second-order catalytic reaction must be analyzed numerically.

The governing equations of the above electrochemical system at steady state are expressed as follows (48, 54)

$$v_z \frac{dC_O}{dz} = D_O \frac{d^2 C_O}{dz^2} - a k C_S C_O \quad [4]$$

$$v_z \frac{dC_R}{dz} = D_R \frac{d^2 C_R}{dz^2} + k C_S C_O \quad [5]$$

$$v_z \frac{dC_S}{dz} = D_S \frac{d^2 C_S}{dz^2} - b k C_S C_O \quad [6]$$

where $v_z = -a'\Omega(\sqrt{[\Omega/\nu]z})^2$, $a' = 0.51023$, Ω is the rotating speed, ν is the kinematic viscosity, z is the normal distance from the rotating disk electrode, C_i and D_i stand for concentrations and diffusivities of the species.

We may first consider a special case, the instantaneous homogeneous reaction.

For the case of an infinite rate constant, the reduction occurs at a plane, and an analytical solution may be obtained by modifying Eq. [4]-[6] and making them dimensionless

$$\frac{d^2 \theta_O}{dx^2} + 3x^2 \frac{d\theta_O}{dx} = 0, \text{ for } 0 \leq x \leq x_R \quad [7]$$

$$\frac{d^2 \theta_O}{dx^2} + 3\alpha_0 x^2 \frac{d\theta_O}{dx} = 0, \text{ for } 0 \leq x \leq x_R \quad [8]$$

$$\frac{d^2 \theta_S}{dx^2} + 3\alpha_s x^2 \frac{d\theta_S}{dx} = 0, \text{ for } x_R \leq x \leq \infty \quad [9]$$

where $\theta_O = (C_O/C_{R,x})$, $\theta_R = (C_R/C_{R,x})$, and $\theta_S = (C_S/C_{R,x})$ are the dimensionless concentrations, $\alpha_0 = (D_R/D_O)$ and $\alpha_s = (D_R/D_S)$ are dimensionless diffusivity ratios, $x = z/\delta$, $C_{R,x}$ is the bulk concentration of species R, x_R is the dimensionless position of the reaction plane, and δ is the thickness of the diffusion layer adjacent to the rotating electrode, which is

$$\delta = \left(\frac{3D_R}{a'\nu} \right)^{1/3} \left(\frac{\nu}{\Omega} \right)^{1/2} \quad [10]$$

The boundary conditions are

$$\text{at } x = 0, \theta_R = 0; \frac{d\theta_O}{dx} + a\alpha_0 \frac{d\theta_R}{dx} = 0 \quad [11]$$

$$\text{at } x = \infty, \theta_S = \theta_{S\infty}; \theta_{R\infty} = 1 \quad [12]$$

$$\text{at } x = x_R, \theta_S(x_R) = 0; \theta_O(x_R) = 0 \quad [13]$$

$$\left. \frac{d\theta_S}{dx} \right|_{x_R} = -\lambda \left. \frac{d\theta_O}{dx} \right|_{x_R}; \lambda = \frac{b}{a} \frac{D_O}{D_S} \quad [14]$$

Equations [7]-[9] with their boundary conditions, Eq. [10]-[14], may be solved to yield the concentration profiles for each species as

$$\theta_R = \int_0^x e^{-x^3} dx / \int_0^{x_R} e^{-x^3} dx, \text{ for } 0 \leq x \leq x_R \quad [15]$$

$$\theta_R = 1, \text{ for } x \geq x_R \quad [16]$$

$$\theta_O = a\alpha_0 \int_x^{x_R} e^{-\alpha_0 x^3} dx / \int_0^{x_R} e^{-x^3} dx, \text{ for } 0 \leq x \leq x_R \quad [17]$$

$$\theta_O = 0, \text{ for } x \geq x_R \quad [18]$$

$$\theta_S = \theta_{S\infty} \int_{x_R}^x e^{-\alpha_s x^3} dx / \int_{x_R}^{\infty} e^{-\alpha_s x^3} dx, \text{ for } x \geq x_R \quad [19]$$

$$\theta_S = 0, \text{ for } 0 \leq x \leq x_R \quad [20]$$

The position of the reaction plane, x_R , can be found by solving the following equation

$$\frac{\theta_{S\infty}(\alpha_s)^{1/3}}{a\alpha_0\lambda} = e^{(\alpha_s - \alpha_0)x_R^3} \frac{\int_{\alpha_s x_R^3}^{\infty} t^{-2/3} e^{-t} dt}{\int_0^{x_R^3} e^{-t} t^{-2/3} dt} \quad [21]$$

which is obtained from Eq. [14].

From the concentration profile of species R near the electrode, one can calculate the limiting current and show that it exceeds that expected for species R in the absence of species S. The extent of the limiting current enhancement may be expressed by defining a mass transfer enhancement factor (MTEF) as

$$\text{MTEF} = \frac{i_L(\text{with chemical reaction})}{i_L(\text{without chemical reaction})} \quad [22]$$

where the limiting current without reaction refers to that of species R alone.

The MTEF for the case of instantaneous chemical reaction can be expressed as a function of the position of the reaction plan as

$$\text{MTEF} = \frac{\Gamma(4/3)}{\int_0^{x_R} e^{-x^3} dx} = \frac{\Gamma(1/3)}{\Gamma(1/3, x_R^3)} \quad [23]$$

where $\Gamma(1/3)$ is the gamma function of $1/3$, and $\Gamma(1/3, x_R^3)$ is an incomplete gamma function. If all diffusivities are equal (i.e., $\alpha_0 = \alpha_s = 1$), then

$$\Gamma(1/3, x_R^3) = \Gamma(1/3) \left(\frac{\theta_s}{\alpha\lambda} + 1 \right) \quad [24]$$

Combining Eq. [23] and [24] gives

$$\text{MTEF} = 1.0 + \theta_{s\infty}/b \quad [25]$$

This result means that the enhanced limiting current is equivalent to that for the direct electrode reaction of species S, if it were possible, plus that of the independent limiting current of the depolarizer R itself. This special limiting case for an instantaneous chemical reaction indicates the maximum possible mass transfer enhancement provided by a homogeneous reaction.

For a finite rate of the second-order homogeneous reaction, one may make Eq. [4]-[6] dimensionless as follows

$$\frac{d^2\theta_R}{dx^2} + 3x^2 \frac{d\theta_R}{dx} + \psi\theta_s\theta_0 = 0 \quad [26]$$

$$\frac{d^2\theta_0}{dx^2} + 3\alpha_0x^2 \frac{d\theta_0}{dx} - \alpha\alpha_0\psi\theta_s\theta_0 = 0 \quad [27]$$

$$\frac{d^2\theta_s}{dx^2} + 3\alpha_sx^2 \frac{d\theta_s}{dx} - b\alpha_s\psi\theta_s\theta_0 = 0 \quad [28]$$

where ψ is a dimensionless rate constant defined as

$$\psi = \frac{kC_{R,\infty}}{D_R} \delta^2 \quad [29]$$

The boundary conditions are

$$\text{at } x = 0, \theta_R = 0 \quad [30]$$

$$\frac{d\theta_R}{dx} = 0 \quad [31]$$

and

$$\frac{d\theta_0}{dx} + \alpha\alpha_0 \frac{d\theta_R}{dx} = 0 \quad [32]$$

and

$$\text{at } x = \infty, \theta_0 = 0, \theta_R = 1, \theta_s = \theta_{s\infty} \quad [33]$$

This set of simultaneous differential equations can be solved numerically by the orthogonal collocation method (55). The first- and second-order derivatives of Eq. [26]-[32] can be represented by means of the associated $\underline{\underline{A}}$ and $\underline{\underline{B}}$ matrices, and the equations can be transformed into a set of algebraic equations

$$\sum_{j=0}^{n+1} (3x_i^2 A_{ij} + B_{ij})\theta_{R,j} + \psi\theta_{s,i}\theta_{0,i} = 0; \quad i = 1, \dots, n \quad [34]$$

$$\sum_{j=0}^{n+1} (3\alpha_0x_i^2 A_{ij} + B_{ij})\theta_{0,j} - \alpha\alpha_0\psi\theta_{s,i}\theta_{0,i} = 0; \quad i = 1, \dots, n \quad [35]$$

$$\sum_{j=0}^{n+1} (3\alpha_sx_i^2 A_{ij} + B_{ij})\theta_{s,j} - b\alpha_s\psi\theta_{s,i}\theta_{0,i} = 0; \quad i = 1, \dots, n \quad [36]$$

including the boundary conditions

$$\text{at } i = 0 \text{ (i.e., } x = 0), \theta_{R,0} = 0 \quad [37]$$

$$\sum_{j=0}^{n+1} (\theta_{0,j} + \alpha\alpha_0\theta_{R,j})A_{0,j} = 0 \quad [38]$$

and

$$\sum_{j=0}^{n+1} A_{0,j}\theta_{R,j} = 0 \quad [39]$$

and

$$\text{at } i = n + 1 \text{ (i.e., } x = \infty), \theta_{R,n+1} = 1, \theta_{0,n+1} = 0, \theta_{s,n+1} = \theta_{s\infty} \quad [40]$$

Equations [34]-[40] constitute $3n + 6$ simultaneous algebraic equations with $3n + 6$ unknowns so they can be solved numerically by standard numerical methods. The result represents an approximate solution to the original differential equations.

The mass transfer enhancement factor (MTEF), which now depends on the dimensionless rate constant ψ as well as the bulk concentration ratio $\theta_{s\infty}$, is calculated from

$$\begin{aligned} \text{MTEF} &= \frac{\left(\frac{d\theta_R}{dx} \right)_{x=0} \text{ (with reaction)}}{\left(\frac{d\theta_R}{dx} \right)_{x=0} \text{ (without reaction)}} \quad [41] \\ &= \frac{\sum_{j=0}^{n+1} A_{0,j}\theta_{R,j}}{1.1198465} \end{aligned}$$

The MTEF can be found if k (i.e., ψ) is known, and vice versa. Computed results are given in Fig. 7 for $\alpha_0 = 1.6$, $\alpha_R = 0.8$, and $a = b = 1/2$, which correspond to the properties of the iodide-iodine-sulfurous acid system. Note that the limits for large ψ correspond to the result given in Eq. [23] for an instantaneous reaction. The large ψ asymptotes in Fig. 7 do not agree exactly with Eq. [25] because the latter is obtained only for $\alpha_0 = \alpha_s = 1$.

The above case was taken to be at the limiting current where $\theta_R(0) = 0$. Below the limiting current, the zero-concentration boundary condition at the electrode surface must be replaced by the electrode kinetics of the electroactive species R. The electrode kinetics of the iodide-iodine redox reaction, as given in Eq. [1], provide the appropriate boundary condition to relate current density to electrode potential. It is assumed in this analysis that any sulfite (species S) reaching the electrode surface is not electroactive in the potential range of interest. Thus, at the electrode surface, instead of $\theta_R = 0$, the boundary condition in Eq. [30] and [37] is changed to

$$\begin{aligned} \frac{d\theta_R}{dx} \Big|_{x=0} &= \frac{k_a r \delta}{D_R} \theta_{R,0} e^{\frac{\alpha F}{RT}(E - E_0)} \\ &- \frac{\theta_{0,0}^{1/2} e^{-\frac{(1-\alpha)F}{RT}(E - E_0)}}{\theta_{0,\infty}^{1/2}} = \sum_{j=0}^{n+1} A_{0,j}\theta_{R,j} \quad [42] \end{aligned}$$

Then, in a manner similar to that used in the limiting current case, the set of differential equations can be

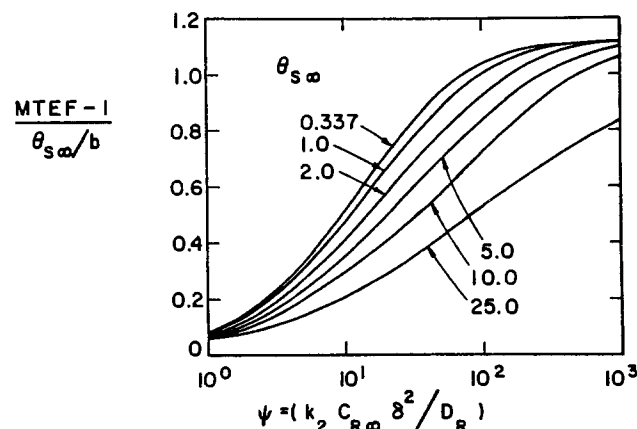


Fig. 7. Plot of the mass transfer enhancement factor (MTEF), defined by Eq. [22], for an anodic limiting current computed for the case when a second-order homogeneous reaction regenerates the reduced form of the electroactive species. Computed for $\alpha_a = 1.6$, $\alpha_R = 0.8$, and $a = b = 1/2$.

solved approximately for specified values of the chemical rate constant, the electrode rate constant, and the disk rotation speed. The current density at each applied potential can then be calculated, and the entire polarization curve may be simulated.

Determination of the Homogeneous Reaction Rate

The second-order rate constant k for the homogeneous reaction between sulfur dioxide and iodine in 1.0M sulfuric acid was determined by measuring anodic limiting currents on the rotating disk in solutions containing iodide and sulfite. Forty-five limiting current values were measured on the pyrolytic graphite electrode over a range of rotation speeds from 400 to 4900 rpm and at various concentrations of iodide (2×10^{-5} to $2 \times 10^{-4}M$) and sulfite (10^{-4} to $5 \times 10^{-4}M$). In all experiments with sulfite, a closed cell was used to prevent loss of sulfur dioxide.

For each limiting current measurement the MTEF was calculated by comparison with the limiting current of iodide in the absence of sulfite. Figure 7 was then used to determine the corresponding value of k . Some of the results are shown in Fig. 8, where the calculated value of k for various determinations is plotted vs. the disk rotation speed. It is seen that the value of the rate constant is independent of rotation speed. This indicates that the assumptions of second-order kinetics and negligible electrochemical oxidation of sulfite yield an adequate description of the electrode processes on graphite. The average value of the rate constant determinations is $7.5 \times 10^9 \text{ cm}^3/\text{mol/s}$.

Similar measurements were made on the platinum electrode. The results are shown in Fig. 9. It is seen that on platinum the apparent homogeneous rate constant falls in the same magnitude range but exhibits a dependence on rotation speed. In this case, it is likely that the sulfite does react on the electrode to some extent, enhancing the current at high rotation speed and possibly blocking the surface at lower rotation speeds.

Depolarization of the Sulfite Anode

Figure 10 shows several anodic polarization curves obtained on the rotating pyrolytic graphite electrode at 22°C and a scan rate of 1.0 mV/s. Curve 1 is that observed with only sulfuric acid in the cell. At potentials up to 1.2V (SCE), no significant current is observed because of the slow kinetics of the oxygen electrode. Curve 2 is that obtained with $19 \times 10^{-3}M$ sodium sulfite present in the solution. Significant current passes only at potentials in excess of 1.0V, although the reversible sulfite potential should be near 0.0V (SCE). These results may be compared with the higher temperature data shown in Fig. 1.

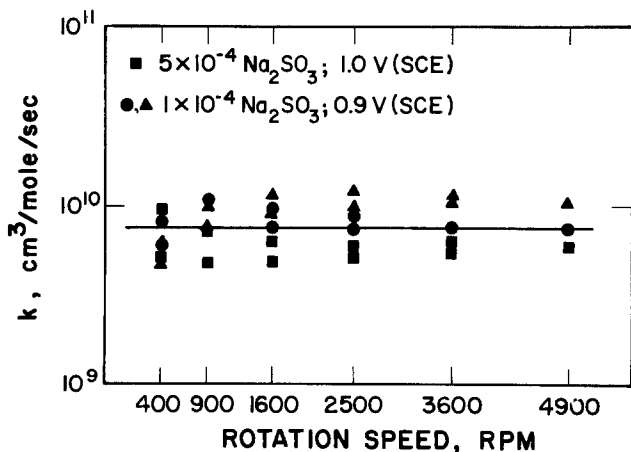


Fig. 8. The second-order rate constant for reaction of iodine with sulfite as determined from the enhancement of the anodic iodide limiting current to the rotating pyrolytic graphite disk electrode at various operating conditions.

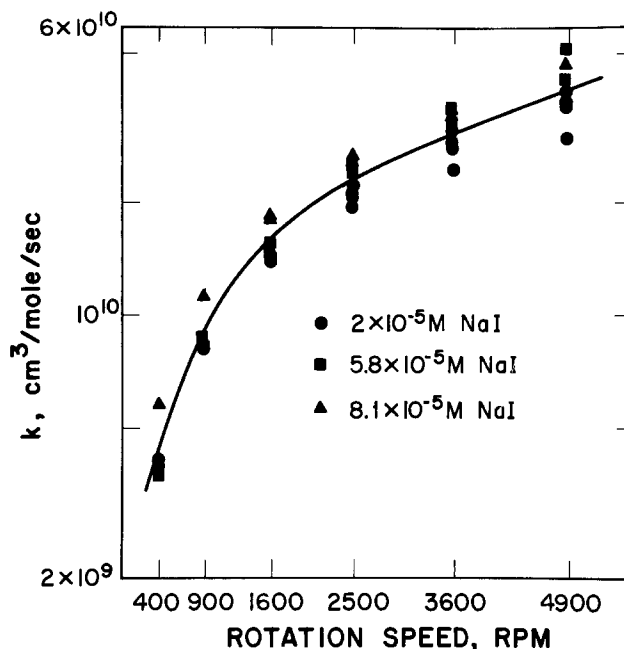


Fig. 9. The second-order rate constant for reaction of iodine with sulfite as determined from the enhancement of the anodic iodide limiting current to the rotating platinum disk electrode at various operating conditions.

Curve 3 in Fig. 10 is that obtained when $0.2 \times 10^{-3}M$ sodium iodide is added to the sulfite solution, and curve 4 is that with $10^{-3}M$ iodide. It is seen that the iodide is quite effective in catalyzing the sulfite oxidation. That sulfite is reacting is indicated by the fact that only a small fraction of the limiting current observed on curve 4 can be provided by the low concentration of iodide in the solution.

With the transport-reaction model presented in Eq. [26]-[32] and the values of relevant system parameters, one can compute the anodic polarization curve expected on the rotating disk electrode. Curve 5 shows the result of this calculation when Eq. [42], for iodide oxidation kinetics, was used as the boundary conditions on the electrode surface. This calculation used the kinetics and transport

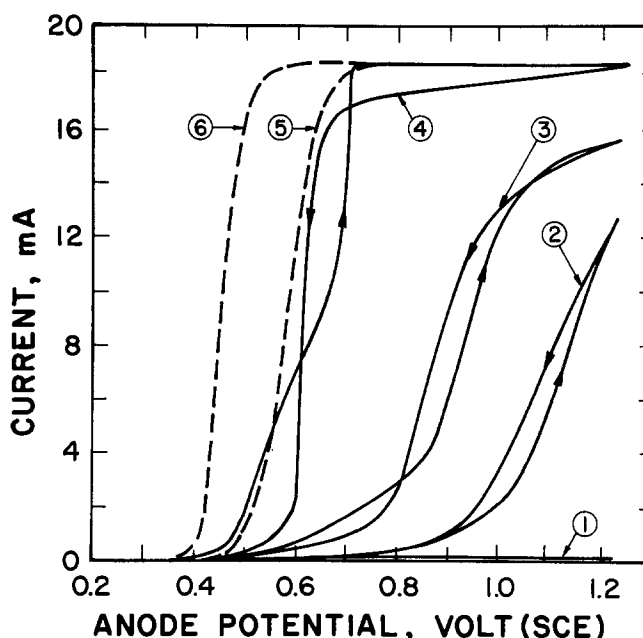


Fig. 10. Experimental and computed anodic polarization curves for the rotating pyrolytic-graphite disk electrode, area = 0.485 cm^2 . Experimental scan rate = 1.0 mV/s. Dashed curves are computed for steady-state polarization.

properties of the system as obtained in the experiments described in earlier sections. The diffusivity of sulfite was taken to be 1.8×10^{-5} cm²/s (56). It is seen that excellent agreement is obtained between the computed and experimental polarization curves.

Curve 6 shows the computed polarization curve corresponding to curve 4 obtained when an iodide-iodine equilibrium (Nernst equation) was used as a boundary condition on the electrode instead of the electrode kinetics expression. Although the iodide electrode reaction exhibits fast kinetics, they are finite and do affect the sulfite-iodide polarization at these concentrations and temperature.

In the analysis of this system, we have treated iodide, iodine, and sulfite each as single species. At the low concentrations considered, formation of triiodide should not be extensive so it has been neglected. The "sulfite," or dissolved sulfur dioxide, should be primarily in the form of undissociated sulfurous acid in these strong acid solutions. Therefore, the effective second-order rate constant that we report refers to the reaction of that species with iodine.

Conclusions

The work reported here has verified that iodide is effective in catalyzing the sulfite anode on pyrolytic graphite. Figure 10, for example, shows that a small amount of iodide reduces the sulfite anode potential by as much as 400 mV or more. The model, and its associated parameters, make possible a quantitative prediction of the effects of species concentrations and mass transfer conditions on the anode polarization. Although the parameter determinations were done at room temperature (22°C), the transport model permits extrapolation to higher temperatures. At higher temperature, the kinetics of both the electrode and the homogeneous reactions should become faster. In that case, the polarization curve should approach the potential behavior of the reversible iodide-iodine electrode and a limiting current given by Eq. [25].

The more general result of this work is the development of the collocation model for mass transfer to a rotating disk electrode accompanied by a homogeneous reaction. The model may be modified to treat various reaction stoichiometries and kinetics laws. The resulting prediction of a limiting current mass transfer enhancement factor, such as that given in Fig. 7, may be used to determine the kinetics of reactions that are too fast to measure by more conventional techniques. Use of this method requires that experimental observation of limiting currents must be possible, but if it is the method is otherwise independent of electrode kinetics behavior.

Manuscript submitted Dec. 6, 1984; revised manuscript received May 1, 1985.

LIST OF SYMBOLS

A_{ij}	collocation coefficients for first derivatives of the first-order derivatives
a, b	stoichiometric coefficient
a'	velocity profile constant ($a' = 0.51023$)
B_{ij}	collocation coefficients for second-order derivatives
C_i	concentration of species i (mol/cm ³)
D_i	diffusion coefficient of species i (cm ² /s)
E	electrode potential (V)
E_0	equilibrium electrode potential (V)
F	Faraday's constant (96,487 C/eq)
i_n	current density on electrode (anodic current is positive) (A/cm ²)
k	second-order homogeneous reaction rate constant (cm ³ /mol/s)
k_a	argument of ln on left-hand side of Eq. [3] (cm/s)
k_a^r	anodic rate constant referred to the equilibrium potential (cm/s)
MTEF	mass transfer enhancement factor
n	stoichiometric number of electrons
O	oxidized species
R	reduced species
T	temperature (K)
v_z	velocity in z direction (cm/s)

x	dimensionless distance from electrode
x_R	position of reaction plane, dimensionless
z	distance from electrode surface (cm)

Greek Symbols

α_o, α_s	ratios of diffusion coefficients
α	anodic transfer coefficient
δ	thickness of diffusion layer (cm) (see Eq. [10])
θ_i	dimensionless concentration of species i
λ	flux ratio defined in Eq. [14]
ν	kinematic viscosity (cm ² /s)
ψ	dimensionless second-order rate constant (see Eq. [29])
Ω	rotation speed (rad/s)

Subscripts

O	at electrode surface
∞	in bulk solution
L	limiting current
a	anodic
c	cathodic

REFERENCES

- A. J. Appleby and B. Pichon, *J. Electroanal. Chem.*, **95**, 59 (1979).
- V. S. Bagotskii, V. P. Bochinn, L-V. Oparim, K. A. Radyushkina, N. M. Santalova, M. R. Tarasevich, N. I. Urisson, and G. V. Shteinberg, *Elektrokhimiya*, **14**, 810 (1978).
- M. Comtat and J. Mahenc, *Bull. Soc. Chim. Fr.*, **11**, 3862 (1969).
- K. Wiesener, *Electrochim. Acta*, **18**, 185 (1973).
- F. Strafelda and J. Krofta, *Coll. Czechoslov. Chem. Commun.*, **36**, 1634 (1971).
- E. T. Seo and D. T. Sawyer, *J. Electroanal. Chem.*, **7**, 184 (1964).
- E. T. Seo and D. T. Sawyer, *Electrochim. Acta*, **10**, 239 (1965).
- A. Katagiri, Z. Takehara, and S. Yoshizawa, *Denki Kagaku*, **41**, 430 (1973).
- C. Audry and M. Voinov, *Electrochim. Acta*, **20**, 403 (1975).
- Z. Samec and J. Weber, *ibid.*, **20**, 403 (1975).
- J. Gonzalez, C. Capel-Boute, and C. Devroly, *ibid.*, **10**, 513 (1965).
- N. N. Nechiporenko, I. P. Voroshilov, A. K. Gorbachev, Kh. Voroshilov, and V. K. Beidin, *Elektrokhimiya*, **7**, 1468 (1971).
- N. N. Nechiporenko, I. P. Voroshilov, A. K. Gorbachev, P. Kh. Voroshilov, I. P. Voroshilov, S. D. Kopyl, and I. I. Vasilenko, *Z. Prikl. Khim.*, **45**, 1748 (1972).
- I. P. Voroshilov, N. N. Nechiporenko, P. Kh. Voroshilov, and V. K. Beidin, *ibid.*, **45**, 1537 (1972).
- I. P. Voroshilov, N. N. Nechiporenko, and E. P. Voroshilov, *Elektrokhimiya*, **10**, 1378 (1974).
- I. P. Voroshilov, N. N. Nechiporenko, and E. P. Voroshilova, *Z. Prikl. Khim.*, **48**, 349 (1975).
- I. P. Voroshilov, N. N. Nechiporenko, E. P. Voroshilova, and N. V. Legaza, *ibid.*, **48**, 654 (1975).
- I. M. Osadchenko, A. P. Tomilov, and V. K. Rublev, *Elektrokhimiya*, **12**, 1874 (1976).
- I. M. Osadchenko, A. P. Tomilov, and V. K. Rublev, *Zh. Obshchei Khim.*, **43**, 1654 (1973).
- M. Fremery and H. R. Buhmann, *Ger. Offen.*, 2613762 (C25B1/22) (Oct. 1977).
- R. Shulten and F. Behr, *ibid.*, 2545455 (C25B1/22) (April 1977).
- R. Shulten and F. Behr, *ibid.*, 2542935 (C25B1/22) (March 1977).
- I. P. Voroshilov, N. N. Nechiporenko, P. Kh. Voroshilov, and V. K. Beidin, *Elektrokhimiya*, **9**, 1800 (1973).
- B. D. Struck, R. Junginger, D. Boltersdorf, and J. Gehrman, Paper presented at the Seminar on Hydrogen as an Energy Vector: Its Production, Use and Transportation, Brussels, Comm. Eur. Communities, [REP] EUR 1978, EUR 6085, pp. 109-23, Oct. 1978.
- G. F. Pace and J. C. Stauter, Paper presented at the 3rd Meeting of the Hydrometallurgy Group of CIM, Edmonton, Alb., Canada, 1973.
- G. F. Pace and J. C. Stauter, *CIM Bull.*, 85 (1974).
- L. E. Brecher, S. Spewock, and C. J. Warde, Paper presented at the First World Hydrogen Energy Conference, Miami, FL, March 1-3, 1976.
- E. I. Onstott, and M. G. Bowman, Paper 232 presented at The Electrochemical Society Meeting, New York, Oct. 13-17, 1974.
- A. T. Kuhn, *J. Appl. Electrochem.*, **1**, 41 (1971).

30. S. C. Yen and T. W. Chapman, Paper presented at the Meeting of the Metallurgical Society of AIME, Las Vegas, NV, Feb. 1980.
31. I. E. Barbasheva, Yu. M. Pavarov, and P. D. Lukovtsev, *Elektrokhimiya*, **6**, 92 (1970).
32. Yu. M. Povarov, I. E. Barbashev, and P. D. Lukevtsev, *ibid.*, **6**, 306 (1970).
33. G. Dryhurst and P. J. Elving, *J. Electroanal. Chem.*, **12**, 416 (1966).
34. G. Dryhurst and P. H. Elving, *Anal. Chem.*, **39**, 606 (1967).
35. F. J. Miller and H. E. Zittel, *J. Electroanal. Chem.*, **11**, 85 (1966).
36. L. M. Dane, L. H. H. Hanssen, and J. G. Hoogland, *Electrochim. Acta*, **31**, 507 (1968).
37. P. Fan and S. Bruckenstein, *Anal. Chem.*, **40**, 1044 (1968).
38. J. D. Newson and A. C. Riddiford, *This Journal*, **108**, 695 (1961).
39. J. D. Newson and A. C. Riddiford, *ibid.*, **108**, 699 (1961).
40. G. Raspi, F. Pergola, and D. Cozzi, *J. Electroanal. Chem.*, **15**, 35 (1967).
41. F. C. Anson and J. J. Lingane, *J. Am. Chem. Soc.*, **79**, 1015 (1957).
42. W. Geissler, R. Nitzsche, and R. Landsberg, *Electrochim. Acta*, **11**, 389 (1966).
43. J. Jordan and R. A. Javick, *ibid.*, **6**, 23 (1962).
44. K. J. Vetter, *Z. Phys. Chem.*, **199**, 22 (1952).
45. S. Swathirajan and S. Bruckenstein, *J. Electroanal. Chem.*, **112**, 22 (1980).
46. S. Swathirajan and S. Bruckenstein, *ibid.*, **125**, 63 (1981).
47. E. Gileadi, E. Kirowa-Eisner, and J. Penciner, "Interfacial Electrochemistry," Addison-Wesley, Reading, MA (1975).
48. V. G. Levich, "Physicochemical Hydrodynamics," p. 345, Prentice-Hall, Englewood Cliffs, NJ (1962).
49. J. Koutecky and V. G. Levich, *Dokl. Akad. Nauk. USSR*, **117**, 441 (1957).
50. Z. Galus, "Fundamentals of Electrochemical Analysis," John Wiley and Sons, New York (1976).
51. J. Ulstrup, *Electrochim. Acta*, **13**, 1717 (1968).
52. K. Holub, *J. Electroanal. Chem.*, **30**, 71 (1971).
53. Z. Pospisil, *Coll. Czechoslov. Chem. Commun.*, **18**, 337 (1963).
54. R. Caban and T. W. Chapman, *Chem. Eng. Sci.*, **36**, 849 (1981).
55. J. S. Newman, "Electrochemical Systems," Prentice Hall, Englewood Cliffs, NJ (1973).

Transport Numbers in the Basic Aluminum Chloride-1-Methyl-3-Ethylimidazolium Chloride Ionic Liquid

Charles L. Hussey* and John R. Sanders

Department of Chemistry, University of Mississippi, University, Mississippi 38677

Harald A. Øye*

Institutt for Uorganisk Kjemi, Norges Tekniske Høgskole, N-7034 Trondheim, Norway

ABSTRACT

Transport numbers were measured for the Lewis basic aluminum chloride-1-methyl-3-ethylimidazolium chloride ionic liquid over the range of AlCl_3 mole fractions, $0.50 > x_{\text{Al}} > 0.30$. The 1-methyl-3-ethylimidazolium cation external and internal (relative to chloride) transport numbers were found to be independent of melt composition; average values for these parameters were 0.71 ± 0.02 and 0.99 ± 0.02 , respectively, at the 95% confidence level. Numerical models derived for the anionic constituents of these melts suggest that the AlCl_4^- and Cl^- ionic mobilities are approximately equal. Factors that may lead to these results are discussed.

Chloroaluminate molten salts which are liquid at room temperature have become popular solvents for electrochemical and spectroscopic studies (1, 2). The relatively high intrinsic conductivity and the variable Lewis acid-base properties of these melts have contributed significantly to their popularity. Familiar examples of these ionic liquids are mixtures of aluminum chloride with 1-n-butylpyridinium chloride (BPC) or 1-methyl-3-ethylimidazolium chloride (MEIC). Both systems have been studied with ^{27}Al NMR spectroscopy (3-5), while the former liquid was also investigated by using Raman spectroscopy (6). It was concluded from these studies that AlCl_4^- and Al_2Cl_7^- are the principal anionic components of acidic melts in the range of aluminum chloride mole fractions, $0.50 < x_{\text{Al}} < 0.67$, while AlCl_4^- and Cl^- are the extant anions in basic melt ($0 < x_{\text{Al}} < 0.50$).

Although the ionic speciation in these melts has been probed, very little is known about charge transport by the ions in these systems. In a previous paper (7), we reported the external and internal transport numbers of the organic cation in the acidic composition range of the AlCl_3 -MEIC melt and presented models for the external transport numbers of AlCl_4^- and Al_2Cl_7^- . The external transport number of the organic cation was determined to be 0.71 ± 0.03 , while the internal transport number of the cation relative to chlorine was found to be 1.01 ± 0.04 . The ionic mobilities of AlCl_4^- and Al_2Cl_7^- appeared to be

approximately equal. The present study extends the study of transport numbers in the AlCl_3 -MEIC ionic liquid to the basic composition region.

Experimental

The procedures followed for purification of chemicals, the method used to determine melt composition, and the experimental methodology employed during this study are essentially the same as those described in a previous publication (7). The transference cell used over the range of melt compositions $0.40 < x_{\text{Al}} < 0.50$ was identical to that used in acidic melts. The transference cell used with very basic melts, $x_{\text{Al}} < 0.40$, was similar to this cell except that the porous areas of the fine porosity (4-8 μm) fritted glass disk separators were slightly larger. This modification was necessary in view of the high viscosity and diminished conductivity of melts with $x_{\text{Al}} < 0.40$. The hydrostatic resistances of these separators were tested with the appropriate melt, and no correction for hydraulic flow was found necessary in the time interval which encompasses a typical experiment. As an additional precaution, the center compartment of the cell [cf. Ref. (7)] was analyzed after each experiment. The experimental results were discarded if the composition of melt in the center compartment differed from the initial melt composition by more than twice the precision of the analysis. Transference experiments were run at $25^\circ \pm 3^\circ\text{C}$. The electrolysis current density varied between 0.04 and 0.12 mA/cm^2 , depending on the melt composition.

*Electrochemical Society Active Member.

Results and Discussion

The electrochemical reaction that occurred in the cathode compartment of the transference cell imparted an orange coloration to the melt and did not result in the deposition of aluminum metal at the cathode. Since the nature of this reaction was unknown, no attempt was made to obtain information about transference from the concentration changes that took place in this cell compartment. Aluminum metal could be anodized to aluminum chloride in basic melt with no obvious side reactions. However, the aluminum anode weight loss was approximately 5% larger than predicted based on the charge passed. Similar effects were noticed in acidic melt and were attributed to corrosion of the aluminum electrode by oxidizing impurities in the melt, possibly hydrogen ion (7). This phenomenon has been observed in this melt by other workers as well (8). Also, it should be noted that the oxidation of aluminum metal by the 1-methyl-3-ethylimidazolium cation appears to be thermodynamically favorable in basic melt (9). However, trial calculations indicated that errors in the melt composition and weight that may arise from this corrosion process were negligible compared to the estimated total error associated with a transference experiment. Therefore, the effects of this corrosion process were ignored.

Experimental transference data are collected in Table I. The precision with which the aluminum chloride mole fraction, x_{Al} , could be determined is listed for each melt and expressed as the relative average deviation from the mean for triplicate samples. The superscript o denotes the conditions in the anode compartment before charge was passed, while a denotes the conditions in the same compartment after electrolysis; w and Q represent the melt weights and the charge passed, respectively.

External transport numbers.—The formal external transport numbers for the organic component, t_R , and aluminum, t_{Al} , were calculated from the data listed in Table I by using Eq. [1] and [2] (7)

$$t_R = \frac{F}{Q} \left[\frac{(1 - x_{Al}^o)w^o}{x_{Al}^o M_{AlCl_3} + (1 - x_{Al}^o)M_{RCl}} - \frac{(1 - x_{Al}^a)w^a}{x_{Al}^a M_{AlCl_3} + (1 - x_{Al}^a)M_{RCl}} \right] \quad [1]$$

$$t_{Al} = \frac{3F}{Q} \left[\frac{x_{Al}^o w^o}{x_{Al}^o M_{AlCl_3} + (1 - x_{Al}^o)M_{RCl}} - \frac{x_{Al}^a w^a}{x_{Al}^a M_{AlCl_3} + (1 - x_{Al}^a)M_{RCl}} \right] + 1 \quad [2]$$

The formal external transport number for chloride, t_{Cl} , was calculated from t_R and t_{Al} with Eq. [3]

$$t_{Cl} = 1 - t_R - t_{Al} \quad [3]$$

Table I. Experimental transference data in basic $AlCl_3$ -MEIC melt

Run no.	x_{Al}^o	x_{Al}^a	w^o (g)	w^a (g)	Q (C)
1B	0.444 ± 0.001	0.472 ± 0.001	6.886	6.823	208
2B	0.439 ± 0.003	0.470 ± 0.001	6.623	6.557	225
3B	0.483 ± 0.000	0.511 ± 0.001	7.230	7.163	206
5B	0.411 ± 0.001	0.425 ± 0.002	7.732	7.686	117
6B	0.501 ± 0.001	0.532 ± 0.001	7.284	7.217	238
7B	0.506 ± 0.001	0.533 ± 0.002	7.734	7.670	236
8B	0.403 ± 0.001	0.431 ± 0.001	7.978	7.843	255
9B	0.350 ± 0.001	0.367 ± 0.003	7.709	7.649	167
11B	0.424 ± 0.002	0.446 ± 0.000	8.241	8.168	217
14B	0.325 ± 0.001	0.343 ± 0.001	9.047	8.941	196
16B	0.300 ± 0.001	0.322 ± 0.000	9.264	9.125	263
17B	0.463 ± 0.001	0.489 ± 0.001	7.859	7.805	217
18B	0.296 ± 0.002	0.323 ± 0.001	7.504	7.377	278
19B	0.461 ± 0.001	0.504 ± 0.001	7.864	7.750	358
20B	0.308 ± 0.001	0.334 ± 0.001	8.296	8.199	263
22B	0.380 ± 0.000	0.406 ± 0.001	8.417	8.343	253
23B	0.369 ± 0.001	0.394 ± 0.001	8.360	8.270	239

The results of these calculations are recorded in Table II.

The transport numbers for the actual anionic species in the basic $AlCl_3$ -MEIC melt, i.e., $AlCl_4^-$ and Cl^- , are related to t_{Al} through the following equations

$$t_{AlCl_4^-} = -1/3 t_{Al} \quad [4]$$

$$t_{Cl^-} = 1/3(3t_{Cl} + 4t_{Al}) \quad [5]$$

The transport number for the organic cation, t_{R^+} , is synonymous with t_R , and therefore

$$t_{R^+} + t_{AlCl_4^-} + t_{Cl^-} = 1 \quad [6]$$

Figure 1 shows plots of t_{R^+} , $t_{AlCl_4^-}$, and t_{Cl^-} as a function of x_{Al}^o . From this plot, it appears that t_{R^+} is essentially independent of melt composition, while $t_{AlCl_4^-}$ and t_{Cl^-} increase and decrease, respectively, with increasing x_{Al}^o . Least squares analysis of t_{R^+} vs. x_{Al}^o yielded a slope of 0.056 ± 0.068 at the 95% confidence level. This confirms that t_{R^+} is essentially independent of melt composition with an average value of 0.71 ± 0.02 at the 95% confidence level. Similar constancy was found for t_{R^+} in acidic melt with an average value of 0.71 ± 0.03 (7). The average values of t_{R^+} measured in acidic and basic melt do not appear to be significantly different at the confidence level employed.

The large external transport numbers obtained for the organic cation over the range of compositions $0.30 < x_{Al} < 0.667$ are unexpected in view of the large ionic radius of this species compared to the radii of the extant anions. The organic cation may function as the majority charge carrier because the smaller anions are structurally constrained in the charge transport process.

Internal transport numbers.—The transport numbers for the organic component relative to chloride as the reference, t'_R , were calculated from the data listed in Table I with Eq. [7] (7)

$$t'_R = \frac{3F w^a (x_{Al}^a - x_{Al}^o)}{Q [x_{Al}^a M_{AlCl_3} + (1 - x_{Al}^a)M_{RCl}] (2x_{Al}^o + 1)} \quad [7]$$

The results of this calculation are collected in Table II. A plot of t'_R vs. x_{Al}^o is shown in Fig. 1. Least squares analysis of this plot produced a slope of 0.037 ± 0.072 at the 95% confidence level. This suggests that t'_R is independent of melt composition within the precision of the experimental data. The average value of t'_R , 0.99 ± 0.02 at the 95% confidence level, suggests that $t'_R \approx 1.00$. Therefore, the internal transport number for aluminum relative to chloride, t'_{Al} , must be essentially zero since

$$t'_R + t'_{Al} = 1 \quad [8]$$

Table II. Calculated transport numbers in basic $AlCl_3$ -MEIC melt

Experiment no.	x_{Al}^o	t_R	t_{Al}	t_{Cl}	t'_R
1B	0.444	0.714	-0.697	0.984	1.003
2B	0.439	0.701	-0.675	0.975	0.992
3B	0.483	0.755	-0.784	1.029	1.025
5B	0.411	0.753	-0.751	1.035	1.036
6B	0.501	0.716	-0.751	1.035	0.974
7B	0.506	0.688	-0.666	0.978	0.928
8B	0.403	0.773	-0.399	0.627	0.980
9B	0.350	0.656	-0.386	0.729	0.935
11B	0.424	0.670	-0.479	0.809	0.922
14B	0.325	0.770	-0.366	0.596	1.014
16B	0.300	0.734	-0.274	0.540	0.970
17B	0.463	0.703	-0.779	1.076	1.003
18B	0.296	0.671	-0.223	0.552	0.915
19B	0.461	0.727	-0.707	0.980	1.002
20B	0.308	0.687	-0.467	0.780	1.021
22B	0.380	0.675	-0.593	0.918	0.999
23B	0.369	0.717	-0.549	0.831	1.019
Mean value		0.712			0.985
Standard deviation		0.036			0.037

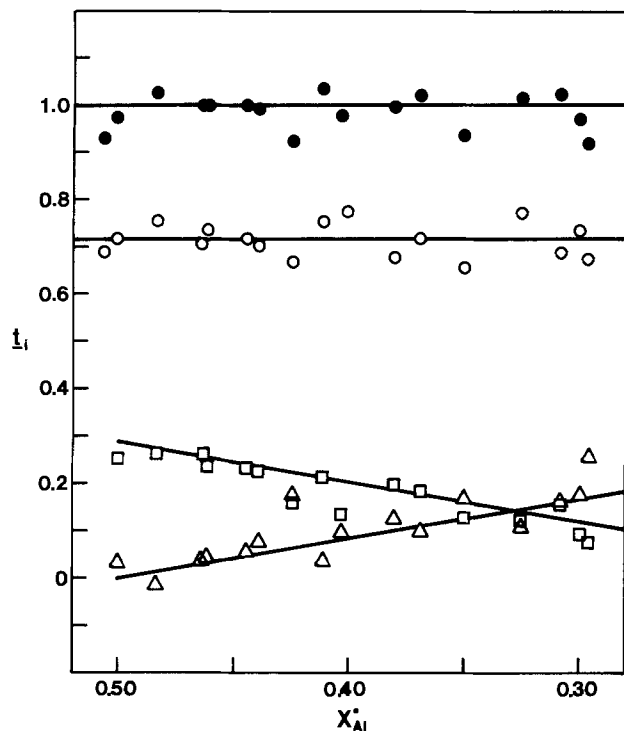


Fig. 1. Plots of t_{R^+} (filled circles), t_{R^+} (open circles), $t_{AlCl_4^-}$ (squares), and t_{Cl^-} (open triangles) as a function of x_{Al}^0 . The solid lines were calculated from Model [IIa] and $t_{R^+} = 1.00$.

and t_{Cl^-} is defined as zero. These results indicate that transport by the anions in basic melt is prescribed by the melt stoichiometry. Similar results were obtained in acid melt (7).

The result that $t_{R^+} \approx 1.00$ is also significant in that it permits the use of simplified formulas to represent the relationships between the potential of a chloroaluminate concentration cell and the chemical potential of aluminum chloride in the cell when it contains melt with a composition that is within the range spanned by this and the previous study (7). A detailed discussion of the advantage afforded by this result appears in a previous paper (7).

Numerical models for the external transport numbers.—The internal and external transport numbers for aluminum and the organic cation are related to one another through the following equations (7)

$$t_{Al} = t_{Al} + \frac{3x_{Al}^0}{2x_{Al}^0 + 1} t_{Cl} \quad [9]$$

$$t_{R^+} = t_{R^+} + \frac{1 - x_{Al}^0}{2x_{Al}^0 + 1} t_{Cl} \quad [10]$$

The results that $t_{R^+} = 0.71$, $t_{R^+} \approx 1.00$, and $t_{Al} \approx 0$ can be used with Eq. [9] and [10] to give the following models for the formal external transport numbers of the organic component, aluminum, and chloride

$$t_{R^+} = 0.71; t_{Al} = -0.29 \frac{3x_{Al}^0}{1 - x_{Al}^0}; t_{Cl} = 0.29 \frac{2x_{Al}^0 + 1}{1 - x_{Al}^0} \quad [I]$$

Models for the transport numbers of the actual component ions in basic $AlCl_3$ -MEIC melt ($0.30 < x_{Al}^0 < 0.50$) can be obtained from the models shown above by the appropriate application of Eq. [4] and [5]

$$t_{R^+} = 0.71; t_{AlCl_4^-} = 0.29 \frac{x_{Al}^0}{1 - x_{Al}^0}; t_{Cl^-} = 0.29 \frac{1 - 2x_{Al}^0}{1 - x_{Al}^0} \quad [IIa]$$

The solid lines shown in Fig. 1 were calculated from Model [IIa] and $t_{R^+} = 1.00$. It can be seen that this model provides a reasonable representation of the experimental data. Model [IIa] can be further reduced when it is considered that the anion fractions of $AlCl_4^-$ and Cl^- in basic melt are given by

$$x_{AlCl_4^-} = \frac{x_{Al}^0}{1 - x_{Al}^0} \quad [11]$$

$$x_{Cl^-} = \frac{1 - 2x_{Al}^0}{1 - x_{Al}^0} \quad [12]$$

This results in

$$t_{R^+} = 0.71; t_{AlCl_4^-} = 0.29x_{AlCl_4^-}; t_{Cl^-} = 0.29x_{Cl^-} \quad [IIb]$$

These results indicate that the mobilities of $AlCl_4^-$ and Cl^- are identical in basic melt within the precision of the experimental data. It should be noted that equal mobilities were also found for $AlCl_4^-$ and $Al_2Cl_7^-$ in acid melts (7). The equal mobilities of Cl^- , $AlCl_4^-$, and $Al_2Cl_7^-$ in the 1-methyl-3-ethylimidazolium chloroaluminate melt is surprising and of fundamental significance. This finding rules out a simple independent hopping mechanism which is dependent on the size of the anions, because a mechanism of this type would be expected to lead to mobilities in the following order $Cl^- > AlCl_4^- > Al_2Cl_7^-$.

A possible cause of the equal mobility phenomenon is ion-pair interactions. For example, strong ion-pair interactions between the organic cation and the more polarizing Cl^- ion in the basic melts may counteract the size advantage of this ion while the comparatively weaker ion-pair interactions between the cation and $AlCl_4^-$ may result in greater relative mobility for the latter. Ion-pair formation has also been proposed from proton NMR studies of cation-anion interactions in the $AlCl_3$ -MEIC melt (10, 11) and the related $AlCl_3$ -BPC system (12).

Another explanation for these results is strong coupling of the ion movements, i.e., a displacement of the cation is accompanied by a structural rearrangement of the anions in the other direction proportional to their concentrations. The movement of the anion may hence be considered a quasi-lattice movement accomplished by bridge and apical Cl^- exchange.

Acknowledgments

The authors wish to express their appreciation to Mr. E. H. Ward of the University of Mississippi for valuable assistance with the experimental portion of this study. This work was supported by the National Science Foundation through Grant no. CHE-8412730.

Manuscript submitted Feb. 11, 1985; revised manuscript received ca. March 28, 1985.

The University of Mississippi assisted in meeting the publication costs of this article.

REFERENCES

- H. L. Chum and R. A. Osteryoung, in "Ionic Liquids," D. Inman and D. G. Lovering, Editors, pp. 407-423, Plenum Press, New York (1981).
- C. L. Hussey, *Adv. Molten Salt Chem.*, **5**, 185 (1983).
- J. L. Gray and G. E. Maciel, *J. Am. Chem. Soc.*, **103**, 7147 (1981).
- J. S. Wilkes, J. S. Frye, and G. F. Reynolds, *Inorg. Chem.*, **22**, 3870 (1983).
- T. Matsumoto and K. Ichikawa, *J. Am. Chem. Soc.*, **106**, 4316 (1984).
- R. J. Gale, B. Gilbert, and R. A. Osteryoung, *Inorg. Chem.*, **17**, 2728 (1978).
- C. L. Hussey and H. A. Øye, *This Journal*, **131**, 1621 (1984).
- C. J. Dymek, J. L. Williams, and D. J. Groeger, *This Journal*, **131**, 2887 (1984).
- Z. J. Karpinski and R. A. Osteryoung, *Inorg. Chem.*, **23**, 1491 (1984).
- J. S. Wilkes, J. A. Levisky, J. L. Pflug, C. L. Hussey, and T. B. Scheffler, *Anal. Chem.*, **54**, 2379 (1982).
- A. A. Fannin, L. A. King, J. A. Levisky, and J. S. Wilkes, *J. Phys. Chem.*, **88**, 2609 (1984).
- F. Taulelle and A. I. Popov, *Polyhedron*, **2**, 889 (1983).

Film Formation and Current Oscillations in the Electrodeposition of Copper in Acidic Chloride Media

II. Mathematical Model

Arne J. Pearlstein

Department of Aerospace and Mechanical Engineering, University of Arizona, Tucson, Arizona 85721

H. P. Lee¹ and Ken Nobe*

Department and Chemical Engineering, University of California, Los Angeles, California 90024

ABSTRACT

A mathematical model of the current oscillations observed in the potentiostatic electrodeposition of a Cu rotating disk electrode is described and analyzed. The model predicts the conditions under which a CuCl film of constant thickness exists on the Cu surface, along with the conditions under which the film thickness and current density will be oscillatory (in some cases periodic) functions of time. The theoretical predictions are in excellent qualitative agreement with experimental results.

The electrodeposition of copper, iron, and other metals in acidic media is known to give rise to anodic film formation and oscillatory behavior during polarization [(1-7) and references cited by Hedges (8, 9) and Wojtowicz (10)]. Our recent potentiostatic experiments with a Cu rotating disk electrode in aqueous HCl/NaCl electrolyte show that these current oscillations can be obtained over a wide range of potential, rotation rate, and chloride ion concentration (11).

Previous efforts to model oscillatory behavior in electrochemical systems under nominally steady (*e.g.*, potentiostatic or galvanostatic) conditions include Ref. (1, 2, 4, 5, 12, 13). These and other works have been reviewed by Cooper *et al.* (2) and Wojtowicz (10). As previously discussed [Ref. (10), pp. 65-66], most models have taken as given that oscillations occur, and have then presented differential equation models that exhibit oscillatory behavior. These mathematical models tend to be ordinary differential equations that are either linear and forced, or nonlinear. The forced linear systems are completely inadequate to the task of explaining why oscillations occur under galvanostatic or potentiostatic conditions, and the nonlinear systems have had little capability to distinguish between conditions for which oscillations do or do not occur.

We propose here a detailed mechanism for the formation and dissolution of a CuCl film at the Cu electrode surface, and construct a simple mathematical model in the form of a moving boundary problem, the solution of which predicts the steady film thickness and dissolution rate under potentiostatic conditions. The model includes the kinetic scheme considered in the previous paper (11), and accounts for the diffusion of Cl⁻ through the film to the electrode. A linear stability analysis shows that the unique steady solution of the nonlinear partial differential equation system is sometimes unstable, and that a time-dependent (and, under some conditions, periodic) solution of the moving boundary problem must also exist for certain values of the parameters. The portions of the parameter space in which the steady solution is unstable are compared to the portions in which current oscillations are observed experimentally.

Mechanism and Description of Model

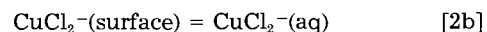
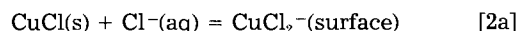
We consider the one-electron process



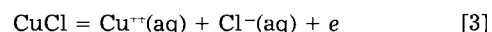
*Electrochemical Society Active Members.

¹Present address: IBM General Products Division, San Jose, California 95193.

at the electrode followed by the elementary processes



and



If the reaction product is not removed fast enough, a porous film of CuCl forms at the electrode surface (1). If further reaction of the Cu electrode via reaction [1] is to occur, chloride ions (in the electrolyte) will have to diffuse through the CuCl film to the Cu-film interface. Reaction [2a] is much faster than the desorption step [2b], and [2a] and [2b] together constitute a mass transfer-limited nonelectrochemical process, while [3] is a kinetically limited electrochemical reaction that is important only at relatively high applied potentials, as shown by rotating ring-disk electrode experiments (14).

Mathematical Model

Our one-dimensional model focuses on the diffusion of Cl⁻ through the porous film from the aqueous electrolyte phase to the Cu electrode, as shown in Fig. 1. This process is governed by the diffusion equation

$$\frac{\partial C}{\partial t} = D_1 \frac{\partial^2 C}{\partial z^2}, \quad g(t) < z < h(t) \quad [4]$$

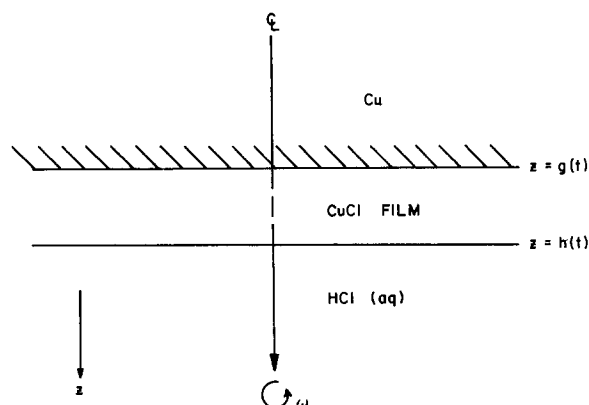


Fig. 1. One-dimensional idealization of the Cu rotating disk electrode and CuCl film.

where C is the Cl^- concentration in the film region bounded by $g(t)$ and $h(t)$. Here, D_f is the effective diffusivity of chloride ions in the porous CuCl film.

This simple model neglects all non-Fickian transport effects, assumes that the porosity, pore size distribution, and other properties of the film are uniform across its thickness, neglects the dependence of Cl^- diffusivity on porosity, neglects variations in the radial and azimuthal directions, assumes that both interfaces are planar and perpendicular to the axis of rotation, and assumes that reactions [1]-[3] occur only at the indicated interfaces and not within the film itself.

Equation [4] will be solved in the domain shown in Fig. 1; the moving locations of the Cu-film and film-electrolyte interfaces are indicated by $z = g(t)$ and $z = h(t)$, respectively. Film is produced by $z = g(t)$ by reaction [1] and is destroyed at $z = h(t)$ by reactions [2a, b] and [3]. These reactions are incorporated into the model as auxiliary conditions appended to [4].

As [4] is second order in the spatial coordinate z , two boundary conditions involving the Cl^- concentration and/or flux are needed: one at the Cu-film interface and the other at the film-electrolyte interface.

At the Cu-film interface, the Cl^- flux is related to the electrochemical reaction rate by the first boundary condition

$$D_f \frac{\partial C[g(t),t]}{\partial z} = k_1 C[g(t),t] \quad [5a]$$

where the electrochemical rate constant k_1 is that for the reaction [1] per unit area of exposed electrode.

At the film-electrolyte interface, the chloride ion concentration in the film at this boundary is assumed to be in equilibrium with its concentration C_∞ in the bulk electrolyte. This gives the second boundary condition

$$C[h(t),t] = k_H C_\infty \quad [5b]$$

where k_H is the solute distribution coefficient.

Since the two interfaces move as the Cu electrode and film dissolution processes proceed, the locations of the two interfaces, where [5a, b] are to be applied, are not known in advance but must be determined as part of the solution procedure. These two additional unknowns require two additional equations, which are obtained by performing Cu balances across the Cu-film interface

$$-\frac{\rho_{\text{Cu}}}{M_{\text{Cu}}} \frac{dg(t)}{dt} = k_1 C[g(t),t] \quad [5c]$$

and across the film itself

$$\begin{aligned} \frac{\rho_{\text{CuCl}}}{M_{\text{CuCl}}} (1 - \epsilon) \frac{d[h(t) - g(t)]}{dt} \\ = -\frac{\rho_{\text{Cu}}}{M_{\text{Cu}}} \frac{dg(t)}{dt} - [\alpha(\omega)C_\infty + k_3] \end{aligned} \quad [5d]$$

where ϵ is the void fraction of the porous film, ρ_{Cu} is the density of the Cu electrode, ρ_{CuCl} is the density of crystalline CuCl , M_{Cu} and M_{CuCl} are the molecular weights of Cu and CuCl , respectively, $\alpha(\omega)$ is the rate (depending on rotation rate ω) of the mass transfer-limited reaction [2a, b], and k_3 is the electrochemical rate constant for the film dissolution reaction [3], per unit area of film exposed to the external electrolyte phase.

The fact that the boundaries of the domain in which [4] is to be solved are moving is the reason partial differential equations of this type are known as moving boundary problems. The fact that the boundary conditions [5a, b] are to be applied at unknown locations which must be determined as part of the solution procedure, and that the rate at which the boundaries move is dependent on the solution of [4], as displayed in [5c, d], is what makes the problem [4]-[5a-d] nonlinear, and is the mathematical source of the steady solution's instability.

The functional forms of α , k_1 , and k_3 are given by

$$\alpha(\omega) \propto \omega^{1/2} \quad [6a]$$

and

$$k_i = k_{i0} \exp \left[\frac{n_i F E}{RT} \right] \quad i = 1, 3 \quad [6b]$$

where n_1 and n_3 are the numbers of electrons in [1] and [3].

Steady Film Solution

The solution of [4]-[5a-d] that corresponds to the existence of a "steady state" is steady only in the sense that the film thickness and reaction rate (and hence the current) do not vary with time. Such a steady solution corresponds to a film of constant thickness $\Delta_0 = h(t) - g(t)$ (see Fig. 1) as time increases. If u_0 denotes the constant speed at which the film moves toward the bulk Cu, then the galilean transformation (15)

$$\begin{aligned} t' &= t \\ z' &= z - u_0 t \end{aligned}$$

gives

$$\frac{\partial C}{\partial t} = \frac{\partial C}{\partial t'} \frac{dt'}{dt} + \frac{\partial C}{\partial z'} \frac{dz'}{dt} = \frac{\partial C}{\partial t'} - u_0 \frac{\partial C}{\partial z'}$$

and

$$\frac{\partial C}{\partial z} = \frac{\partial C}{\partial t'} \frac{dt'}{dz} + \frac{\partial C}{\partial z'} \frac{dz'}{dz} = \frac{\partial C}{\partial z'}$$

Under this transformation, [4]-[5a-d] become

$$\frac{\partial C}{\partial t'} - u_0 \frac{\partial C}{\partial z'} = D_f \frac{\partial^2 C}{\partial z'^2} \quad \theta'(t') < z < \Delta_0 + \Delta'(t') \quad [7]$$

$$D_f \frac{\partial C[\theta'(t'),t']}{\partial z'} = k_1 C[\theta'(t'),t'] \quad [8a]$$

$$-\gamma_{\text{Cu}} \left[\frac{d\theta'(t')}{dt'} - u_0 \right] = k_1 C[\theta'(t'),t'] \quad [8b]$$

$$\gamma_{\text{CuCl}}(1 - \epsilon) \frac{d\Delta'(t')}{dt'} = -\gamma_{\text{Cu}} \left[\frac{d\theta'(t')}{dt'} - u_0 \right] - [\alpha C_\infty + k_3] \quad [8c]$$

$$C[\Delta_0 + \Delta'(t'),t'] = C_\infty k_H \quad [8d]$$

where $\gamma_i = \rho_i/M_i$, and θ' and Δ' denote possible deviations from the steady values of the Cu-film and film-electrolyte interface locations, respectively.

For a solution that is steady in this frame, $\theta'(t') = \Delta'(t') = 0$, and the steady concentration profile $\bar{C}(z')$, film thickness Δ_0 , and dissolution rate u_0 satisfy

$$-u_0 \frac{d\bar{C}}{dz'} = D_f \frac{d^2 \bar{C}}{dz'^2} \quad 0 < z' < \Delta_0 \quad [9]$$

$$D_f \frac{d\bar{C}(0)}{dz'} = k_1 \bar{C}(0) \quad [9a]$$

$$\gamma_{\text{Cu}} u_0 = k_1 \bar{C}(0) \quad [9b]$$

$$0 = \gamma_{\text{Cu}} u_0 - [\alpha C_\infty + k_3] \quad [9c]$$

$$\bar{C}(\Delta_0) = C_\infty k_H \quad [9d]$$

Therefore, from [9]

$$\bar{C}(z') = a + b \exp(-u_0 z'/D_f) \quad [10]$$

Application of boundary condition [9c] yields the dissolution rate

$$u_0 = \frac{\alpha C_\infty + k_3}{\gamma_{\text{Cu}}} \quad [11]$$

Substitution of [10] into [9a, b, d] gives

$$a = \gamma_{\text{Cu}} + \frac{\alpha C_{\infty} + k_3}{k_1} \text{ and } b = -\gamma_{\text{Cu}}$$

and

$$\Delta_0 = \frac{D_f \gamma_{\text{Cu}}}{\alpha C_{\infty} + k_3} \ln \frac{\gamma_{\text{Cu}} k_1}{C_{\infty}(\alpha - k_1 k_{\text{H}}) + k_1 \gamma_{\text{Cu}} + k_3} \quad [12]$$

From this, it follows that there is no film if

$$\alpha(\omega) \cong (k_1 k_{\text{H}} - k_3 / C_{\infty})$$

so that for any combination of potential and $[\text{Cl}^-]$, the model predicts that the film can be eliminated by making the rotation rate ω , and hence the mass transfer coefficient α , sufficiently large.

Finally, since the coefficients a and b in [10] are uniquely determined, there is only one one-dimensional solution for which the film thickness Δ_0 , dissolution rate u_0 , and concentration distribution $\bar{C}(z')$ are steady in time.

Linear Stability Analysis of the Steady Film Solution

The stability of the steady solution [9]-[9a-9d] with respect to small disturbances to the concentration distribution, interface locations, and film thickness depends on whether small disturbances grow or decay in time. If every sufficiently small disturbance decays, then the steady solution is said to be linearly stable, whereas if some small disturbances grow, the steady solution is definitely unstable. Because of the restriction to small disturbances, these criteria are necessary for stability and sufficient for instability. The stability of the solution with respect to larger disturbances can be decided only by nonlinear methods.

Equations [7]-[8a-d] are recast in nondimensional form, taking the nominally steady film thickness Δ_0 as the length scale and defining the dimensionless variables

$$S = \frac{C}{C_{\infty}} \quad y = \frac{z'}{\Delta_0} \quad \tau = \frac{t' D_f}{\Delta_0^2}$$

$$\delta = \frac{\Delta'}{\Delta_0} \quad \chi = \frac{\theta'}{\Delta_0}$$

and dimensionless parameters

$$\beta = \frac{\alpha C_{\infty} + k_3}{k_1 C_{\infty}} \quad \Gamma = \frac{C_{\infty}}{\gamma_{\text{Cu}}} \quad \phi = \frac{\gamma_{\text{CuCl}}(1 - \epsilon)}{\gamma_{\text{Cu}}}$$

where β is a measure of the ratio of the film dissolution rate to the film formation rate, Γ is a dimensionless chloride ion concentration, and ϕ is the ratio of the film density to the density of Cu. This choice of dimensionless parameters is not unique, but has several important advantages. One of the dimensionless parameters (ϕ) depends on none of the operating variables (ω , E , C_{∞}), another (Γ) depends only on C_{∞} , and two of the operating variables (ω and E) appear only in one dimensionless parameter (β). Finally, as shown later, this nondimensionalization, which does not involve k_{H} , enables one to compute all of the results (for arbitrary k_{H}) by using $k_{\text{H}} = 1$, followed by a simple transformation. Substitution into [7]-[8a-d] yields

$$\frac{\partial S}{\partial \tau} - p\beta\Gamma \frac{\partial S}{\partial y} = \frac{\partial^2 S}{\partial y^2} \quad \chi(\tau) < y < 1 + \delta(\tau) \quad [13]$$

$$\frac{\partial S[\chi(\tau), \tau]}{\partial y} = pS[\chi(\tau), \tau] \quad [14a]$$

$$\frac{d\chi(\tau)}{d\tau} - p\beta\Gamma = -p\Gamma S[\chi(\tau), \tau] \quad [14b]$$

$$\phi \frac{d\delta(\tau)}{d\tau} = -\frac{d\chi(\tau)}{d\tau} \quad [14c]$$

$$S[1 + \delta(\tau), \tau] = k_{\text{H}} \quad [14d]$$

where the dimensionless film thickness is

$$p = \frac{\Delta_0 k_1}{D_f} \quad [15a]$$

and

$$\Delta_0 = \frac{D_f}{k_1 \beta \Gamma} \ln \frac{1}{\Gamma(\beta - k_{\text{H}}) + 1} \quad [15b]$$

A steady film solution can exist only if

$$0 < \Gamma(\beta - k_{\text{H}}) + 1 < 1 \quad [16]$$

The steady dissolution rate can be written as $u_0 = k_1 \beta \Gamma$.

By superimposing disturbances (primed quantities) on the nominally steady solution

$$S(y, \tau) = \bar{S}(y) + S'(y, \tau)$$

$$\chi(\tau) = 0 + \chi'(\tau)$$

$$\delta(\tau) = 0 + \delta'(\tau)$$

Substituting these representations into [13]-[14a-14d] and retaining only terms that are linear in the disturbance quantities gives the linear perturbation equations

$$\frac{\partial S'}{\partial \tau} - p\beta\Gamma \frac{\partial S'}{\partial y} = \frac{\partial^2 S'}{\partial y^2} \quad 0 < y < 1 \quad [17]$$

$$\frac{\partial S'(0, \tau)}{\partial y} + \chi'(\tau) \frac{d^2 \bar{S}(0)}{dy^2} = p \left[S'(0, \tau) + \chi'(\tau) \frac{d\bar{S}(0)}{dy} \right] \quad [18a]$$

$$\frac{d\chi'(\tau)}{d\tau} = -p\Gamma \left[S'(0, \tau) + \chi'(\tau) \frac{d\bar{S}(0)}{dy} \right] \quad [18b]$$

$$\phi \frac{d\delta'(\tau)}{d\tau} = -\frac{d\chi'(\tau)}{d\tau} \quad [18c]$$

$$S'(1, \tau) + \delta'(\tau) \frac{d\bar{S}(1)}{dy} = 0 \quad [18d]$$

where the nondimensional steady solution is

$$\bar{S}(y) = \frac{\bar{C}(z)}{C_{\infty}} = \beta + [1 - \exp(-p\beta\Gamma y)]/\Gamma$$

In the boundary conditions [18a, b, d], linearization results in the concentration and flux being evaluated at the nominal interface locations $y = 0, 1$.

Substitution of the expression for $\bar{S}(y)$ into [17]-[18a-d] yields a second set of linear perturbation equations

$$\frac{\partial S'}{\partial \tau} - p\beta\Gamma \frac{\partial S'}{\partial y} = \frac{\partial^2 S'}{\partial y^2} \quad 0 < y < 1 \quad [19]$$

$$\frac{\partial S'(0, \tau)}{\partial y} - p^2 \beta^2 \Gamma \chi'(\tau) = p[S'(0, \tau) + p\beta\chi'(\tau)] \quad [20a]$$

$$\frac{d\chi'(\tau)}{d\tau} = -p\Gamma[S'(0, \tau) + p\beta\chi'(\tau)] \quad [20b]$$

$$\phi \frac{d\delta'(\tau)}{d\tau} = -\frac{d\chi'(\tau)}{d\tau} \quad [20c]$$

$$S'(1, \tau) + \delta'(\tau) p\beta \exp(-p\beta\Gamma) = 0 \quad [20d]$$

involving only the previously defined dimensionless parameters. The distribution coefficient k_{H} appears in these equations (only) through p , as defined in [15a, b].

The steady solution $(S, \chi, \delta) = (\bar{S}, 0, 0)$ of [13]-[14a-d] will be linearly stable if every solution (S', χ', δ')

$$S'(y, \tau) = e^{\lambda \tau} [A_1 e^{\sigma_+ y} + A_2 e^{\sigma_- y}] \quad [21a]$$

$$\chi'(\tau) = A_3 e^{\lambda \tau} \quad [21b]$$

$$\delta'(\tau) = A_4 e^{\lambda \tau} \quad [21c]$$

of [19]-[20a-d] decays in time. That is, every temporal eigenvalue λ must lie in the left half plane. Here, σ_+ and σ_- are the two solutions

$$\sigma_{\pm} = \frac{-p\beta\Gamma \pm [p^2\beta^2\Gamma^2 + 4\lambda]^{1/2}}{2}$$

or

$$\sigma^2 + p\beta\Gamma\sigma - \lambda = 0$$

Substitution of [21a-c] into [19]-[20a-d] yields four linear equations in the unknowns $A_1, A_2, A_3,$ and A_4 . In order for the system of linear equations to have a solution, it is necessary for the determinant of the coefficient matrix to vanish, from which it follows that

$$e^{-s(1+4\eta)^{1/2}} = \phi \{ \xi \eta (r_- e^{s\tau_+} - r_+ e^{s\tau_-}) + e^{s\tau_+}(1 - \eta + r_-) - e^{s\tau_-}(1 - \eta + r_+) \} \quad [22]$$

where

$$\xi = \beta\Gamma \quad \eta = \frac{\lambda}{p^2\xi^2} \quad s = p\xi$$

and

$$r_{\pm} = \frac{-1 \pm (1 + 4\eta)^{1/2}}{2}$$

For a stable situation, all of the temporal eigenvalues must lie in the left half plane. For an unstable situation, one or more temporal eigenvalues lie in the right half plane. Thus, marginal stability corresponds to the situation where one or more eigenvalues lie on the imaginary axis, and all others are in the left half plane.

Rather than computing the denumerable infinity of solutions of [22] and deciding whether or not any of them lie in the right half plane, the D-decomposition method of Neimark (16) will be used to directly compute points on the stability boundary. The stability boundary is the locus of points that separates regions in which the steady solution [10]-[12] is stable from regions in which the steady solution is unstable. The technique actually employed is a variation of Neimark's method that has been developed to deal with problems in which the parameterized variables appear nonlinearly and implicitly, rather than in the linear fashion discussed by Neimark.

By setting $\eta = 0, r_+ = 0, r_- = 1,$ and from [22], $e^{-s} = -\phi e^{-s}$. From this, it follows that $\phi = -1$, which is not meaningful, so $\eta = 0$ is not possible and instability does not arise as a result of a temporal eigenvalue crossing into the right half plane along the real axis (as shown in Fig. 2a).

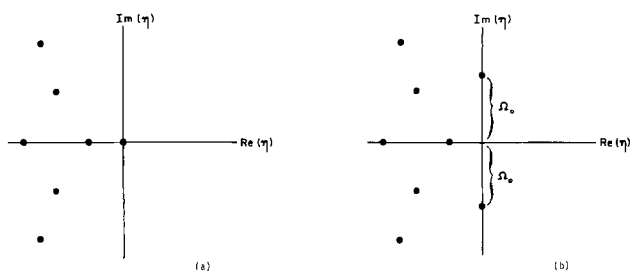


Fig. 2.(a) Instability arising as a single real eigenvalue crosses into the right half plane. (b) Instability arising as a pair of complex eigenvalues cross into the right half plane (Hopf bifurcation).

The remaining possibility is that one or more complex conjugate pairs of temporal eigenvalues cross the imaginary axis as shown in Fig. 2b [a Hopf bifurcation (17)], in which case it can be shown that the steady states lying on the unstable side of and close to the stability boundary are unstable with respect to time-periodic disturbances.

Equation [22] is rewritten as

$$f_1(s, \eta) = \phi [f_2(s, \eta)\xi + f_3(s, \eta)] \quad [23]$$

where

$$f_1(s, \eta) = e^{-s(1+4\eta)^{1/2}}$$

$$f_2(s, \eta) = \eta(r_- e^{s\tau_+} - r_+ e^{s\tau_-})$$

and

$$f_3(s, \eta) = e^{s\tau_+}(1 - \eta + r_-) - e^{s\tau_-}(1 - \eta + r_+)$$

are functions of the real variable s and the complex variable $\eta = i\Omega_0$.

Separating $f_1, f_2,$ and f_3 into real and imaginary parts, [23] can be written as two real equations

$$f_{1r} = \phi(f_{2r}\xi + f_{3r}) \quad [24a]$$

and

$$f_{1i} = \phi(f_{2i}\xi + f_{3i}) \quad [24b]$$

in the two real variables s and Ω_0 .

Therefore

$$\xi = \frac{f_{1i}f_{3r} - f_{1r}f_{3i}}{f_{2i}f_{1r} - f_{1i}f_{2r}} \quad [25]$$

and

$$\phi = \frac{f_{1r}}{f_{2r}\xi + f_{3r}} \quad [26]$$

Equations [25] and [26] can be used to find the stability boundary, for fixed ϕ , in the following manner.

After fixing ϕ , a value of Ω_0 is chosen. An initial guess is made of s , and ξ and ϕ are computed from [25] and [26]. Then s is iteratively adjusted until the desired value of ϕ is obtained.

Equations [15a] and [15b] the definitions of ξ and β give the relations

$$\Gamma = \frac{1 + \xi - e^{-s}}{k_H}$$

and

$$\beta = \xi/\Gamma$$

Therefore, once a value of s that gives the desired ϕ is obtained, Γ and β can be computed directly.

By a suitable change of variables, [19]-[20a-d] can be transformed into a form that depends only on p and the product $\beta\Gamma$. Since k_H appears only through p , it is possible to compute points on the stability boundary (for fixed ϕ) by first setting $k_H = 1$ and then expressing the results in the form shown in Fig. 3(a)-(g), where k_H appears only in the definition of the horizontal and vertical axes. Both p and $\beta\Gamma$ are invariant under the change of variables (β, Γ, k_H) \rightarrow ($\beta/k_H, \Gamma k_H, 1$).

Each point ($\beta/k_H, \Gamma k_H$) computed this way is a point on the stability boundary, and if the above process is repeated for different Ω_0 , the stability boundaries shown in Fig. 3(a)-(g) are obtained.

Results and Discussion

The results presented in Fig. 3(a)-(g) are described below and related to our experimental work (11), as well as to the instability mechanism proposed therein.

When a steady solution $(\bar{S}(y), 0, 0)$ of [13]-[14a-d] exists, it is unique, as shown in the section on steady film solution. It is well known that when a system such as [13]-

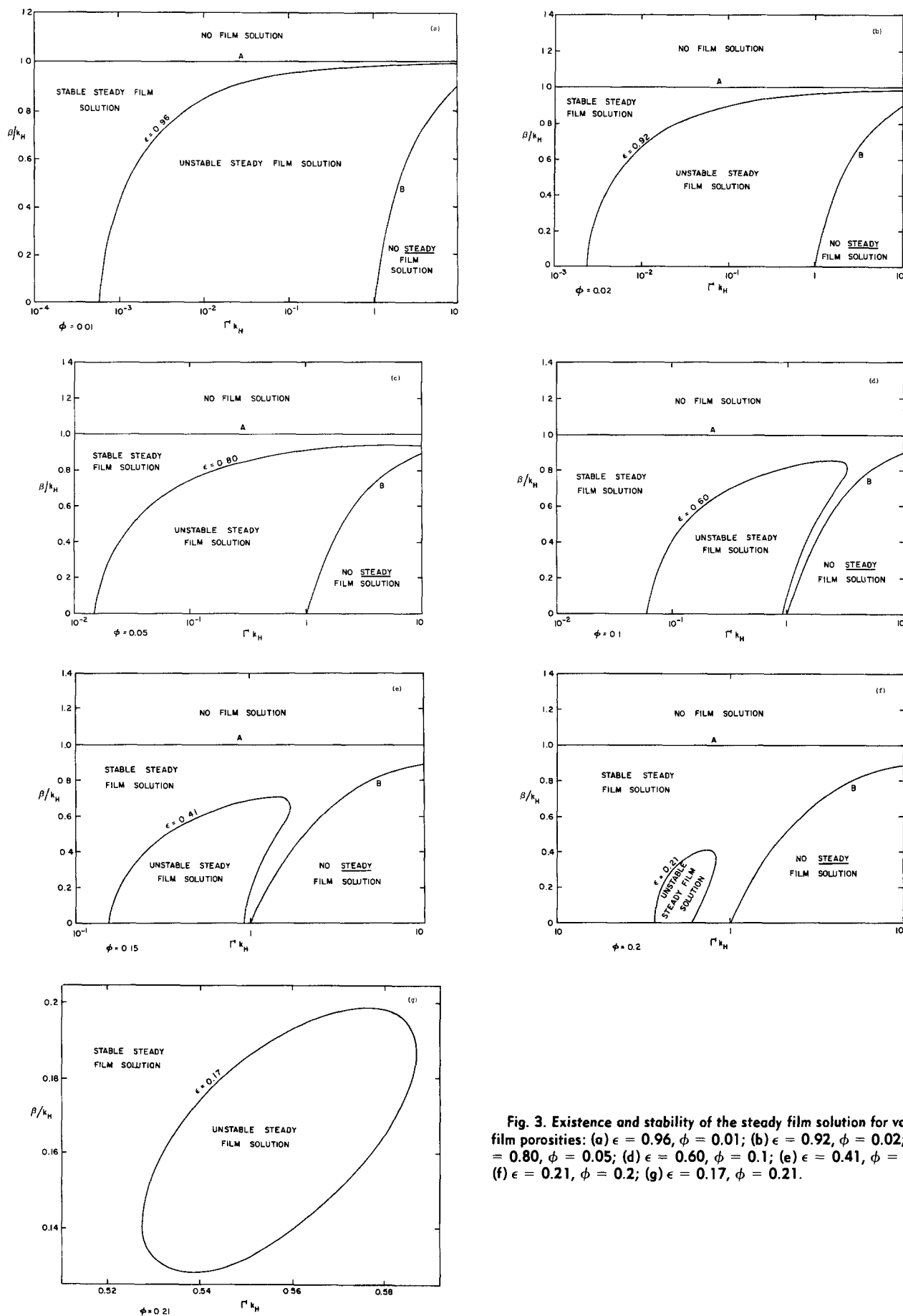


Fig. 3. Existence and stability of the steady film solution for various film porosities: (a) $\epsilon = 0.96$, $\phi = 0.01$; (b) $\epsilon = 0.92$, $\phi = 0.02$; (c) $\epsilon = 0.80$, $\phi = 0.05$; (d) $\epsilon = 0.60$, $\phi = 0.1$; (e) $\epsilon = 0.41$, $\phi = 0.15$; (f) $\epsilon = 0.21$, $\phi = 0.2$; (g) $\epsilon = 0.17$, $\phi = 0.21$.

[14a-d] has a unique steady solution that is also unstable, the full nonlinear equations must also admit at least one time-dependent solution. [For a discussion, see pp. 82-84 of Ref. (18)]. On the basis of Hopf's theorem (17), it is

known that if $(\Gamma k_H, \beta/k_H)$ is sufficiently close to the stability boundary, then the time-dependent solution is periodic for points $(\Gamma k_H, \beta/k_H)$ in the unstable region, and that the frequency and small amplitude approach Ω_0 and zero,

respectively, as $(\Gamma k_H, \beta/k_H)$ approaches the stability boundary. (Here Ω_0 is the magnitude of the imaginary parts of the two temporal eigenvalues that cross the imaginary axis in Fig. 2b as the stability boundary is traversed.)

Based on what is known about the dynamical behavior of systems like [13]-[14a-d], it is likely that as one moves farther into the unstable region the small amplitude time-periodic solution will eventually become unstable itself and will be replaced by a temporally more complicated solution. Whether the new solution will also be periodic (typically with a longer period), or whether it will be almost periodic or temporally chaotic, is a question that cannot be answered by our linear stability analysis. It is likely, however, that in the unstable region the only bounded solutions are in some sense oscillatory. "Oscillations" and "oscillatory" behavior in the unstable region are discussed below without any intent to further categorize the temporal behavior.

Above the horizontal line labeled A at $\beta = k_H$, no steady solution exists, as seen by inspection of [15]. Therefore, the steady film solution cannot be unstable, and no oscillations are predicted by our model. In fact, our model predicts that a "clean" electrode surface with no film will occur for $\beta > k_H$. Similarly, it can be seen from [16] that a solution with constant positive film thickness does not exist for $\Gamma > 1/(k_H - \beta)$ and, hence, to the right of and below the curve labeled B, our model predicts that there is no steady film solution. In this second region, the film forms faster than it can be dissolved, and no steady balance is possible. This is confirmed by Fig. 4, which shows contours of constant dimensionless film thickness p in the $(\Gamma k_H - \beta/k_H)$ plane. As curve B is approached, the steady (time-independent) film thickness increases without bound, as does the time $\tau_{0.99}$ required to achieve, say, 99% of the ultimate dimensionless steady film thickness p . As curve B is crossed, a steady film thickness is not approached asymptotically in time, and the film thickness apparently grows temporally without limit.

For each ϕ shown, the steady film solution exists and is linearly stable for values of Γk_H and β/k_H above and to the left of the indicated stability boundary but lying below the horizontal line $\beta = k_H$. In the region lying below and to the right of each stability boundary (and to the left of and above curve B), the steady film solution exists but is unstable, and oscillatory behavior is predicted.

For each ϕ shown, the appropriate value of the void fraction ϵ , based on $\rho_{Cu} = 8.96 \text{ g-cm}^{-3}$ and $\rho_{CuCl} = 3.53 \text{ g-cm}^{-3}$, is indicated. Since our experiments (11) do not provide any direct information as to the values of ϵ and k_H encountered experimentally, numerical results are presented for a range of ϵ , as shown in Fig. 3(a)-(g). Results for any value of k_H are included in each of Fig. 3(a)-(g).

Before considering the physical interpretation of these results in terms of the operating parameters (rotation rate ω , chloride ion concentration C_∞ , and potential E), it should be noted that the rate of the electrochemical film

dissolution reaction [3] depends more strongly on potential than does the rate of the electrochemical film formation reaction [1].

Thus, β/k_H is a monotonically increasing function of the rotation rate ω , and Γk_H is independent of ω , so that increasing (decreasing) ω will result simply in moving up (down) in the $\Gamma k_H - \beta/k_H$ plane. On the other hand, β/k_H is a monotonically decreasing function of C_∞ , while Γk_H increases monotonically with increasing C_∞ . Thus, increasing C_∞ results in moving down and to the right in the $\Gamma k_H - \beta/k_H$ plane, whereas an increase in C_∞ corresponds to a movement up and to the left in the $\Gamma k_H - \beta/k_H$ plane.

The dimensionless chloride ion concentration Γ is independent of potential, whereas β varies nonmonotonically with E . At low E , the nonelectrochemical film dissolution reaction [2a, b] proceeds at its potential-independent rate, whereas the rates of the Cu electrode reaction [1] and electrochemical film dissolution reaction [3] are very slow. Therefore, at low E , β is very large. At very high potentials, the electrochemical film dissolution (forming Cu^{2+}) is the fastest, and β is also very large for high E . At some intermediate potential, β reaches a minimum. Therefore, increasing E may result in going up or down in the $(\Gamma k_H - \beta/k_H)$ plane depending on the actual potential.

Beginning in the unstable region of the $\beta/k_H - \Gamma k_H$ plane (*i.e.*, the region in which the steady film solution exists and is unstable) for a given ϕ , large enough increases in the rotation rate result in vertical upward movement into the stable film region [*i.e.*, the region in which the steady film solution exists and is (linearly) stable]. Further increases in ω will eventually result in moving across the $\beta = k_H$ line and into the region in which no film exists (the filmless region). This behavior is exactly that which is shown in Fig. 2 and 4 of Ref. (11).

Decreasing the chloride ion concentration results in a move up and to the left in Fig. 3. Lowering the chloride ion concentration sufficiently (*i.e.*, reducing Γk_H to a small enough value) will result in movement far to the left of and outside of the unstable film region, into either the stable film region or the filmless region lying above curve A. In either case, the model predicts that there will be no current oscillations at sufficiently low chloride ion concentrations.

As inferred from Fig. 3(f) and (g), the present model predicts that the steady film solution (when it exists) is stable for all values of β/k_H and Γk_H if ϕ exceeds approximately 0.21, corresponding to a film void fraction of about 0.17. The existence of this "cutoff void fraction" has an explanation which is consistent with both the mathematical model of the present paper as well as with the instability mechanism proposed previously (11).

Neither the steady solution of [13]-[14a-d] nor the values of β/k_H and Γk_H for which the steady solution exists depend on ϕ , as shown in Fig. 4. The parameter ϕ (and hence the void fraction ϵ) do appear in the dynamic equations [13]-[14a-d], and hence in the linear stability analysis. In the full nonlinear equations, ϕ appears only in the boundary condition [14c], where it is the constant of proportionality that relates changes in the rate of Cu electrode dissolution to the rate of change in film thickness. In other words, if the rate of movement of the Cu-film interface ($d\chi/d\tau$) is increased by one dimensionless unit, then $1/\phi$ is the "amplification" factor that determines the magnitude of the increase in the actual film thickness ($1 + \delta - \chi$). Clearly, when the film is very porous and ϕ is very small, the dissolution of one unit of Cu electrode will be translated (by $1/\phi$) into a very large change in $(1 + \delta - \chi)$, according to [18c]. This in turn will result in a major increase in the time required for diffusional communication of information concerning the altered conditions (increased Cu electrode dissolution rate) at the Cu-film interface out to the film-electrolyte interface. According to the instability mechanism proposed previously (11), this increase in the time lag associated with diffusional communication across the suddenly thicker film will give rise to an "overshoot" type of instability. When ϵ is too small (and hence ϕ is large), $1/\phi$ will be too small, and

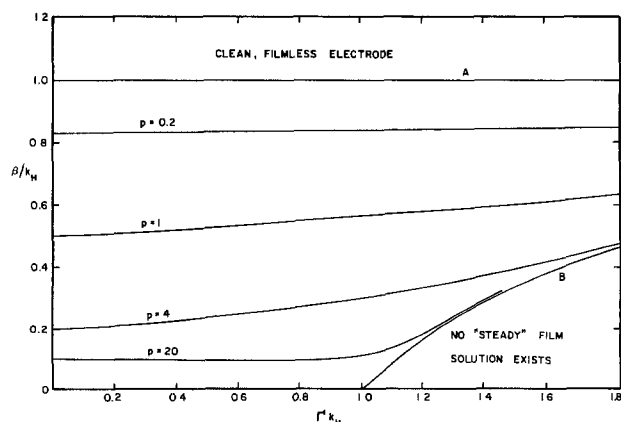


Fig. 4. Existence of the steady film solution and dimensionless thickness (p) of the steady film.

hence even relatively large disturbances to the Cu electrode dissolution rate will not be amplified by [18c] into large changes in the film thickness. Thus, large changes in the film thickness ($1 + \delta - \chi$) are not possible, major changes in the time lag associated with diffusional communication of concentration information across the film do not occur, and the overshooting instability ("overstability") proposed previously (11) is not predicted for large enough values of ϕ .

Thus, the progressive diminution, with increasing ϕ , of the unstable film region in Fig. 3(a)-(g) [note the logarithmic nature of the abscissa in Fig. 3(a)-(f) and the linear abscissa in Fig. 3(g)] is in complete agreement with the instability mechanism advanced previously (11) and is rooted in the physicochemical model described in the section on mechanism and description of the model.

We are presently unable to provide an explanation for the detailed shapes of the stability boundaries in Fig. 3(d)-(g) ($0.1 < \phi < 0.21$), other than to say that the instability mechanism and physicochemical model both predict that the steady film solution will be stabilized by increasing ϕ , and that stabilization of the steady solution implies a reduction in the size of the unstable region, which is exactly what the results show. As for the correctness of the specific value of ϕ above which instability is impossible, or the detailed shape of the unstable region for smaller values of ϕ , little can be said. However, the general features of the stability boundaries are believed to be correct, as they are in excellent qualitative agreement with our experimental results (11), as discussed above.

As for possible improvements to the model, two are suggested. The first would be to construct a model for which the porosity is treated in a more sophisticated manner. Such a model could consist of a dual porosity film with a chloride ion diffusivity D_f that is dependent on the porosity. A second improvement would be to account for the fact that both of the film dissolution reactions occur not only at the film-electrolyte interface, but also within the pores of the film itself, and that the rates per unit volume will be proportional to the surface area per unit volume, which will in turn be related to the local porosity.

Conclusions

The general form of the model considered here may be useful in the analysis of the oscillations observed in other electrodisolution processes involving the formation of anodic films. The detailed kinetics of the film formation and dissolution will, of course, be different, but the formulation of the problem as a diffusion equation (or a system of diffusion equations) with moving boundaries, followed by the investigation of the existence and stability of the steady solution(s), seems to be a promising approach to the study of these oscillations.

Acknowledgment

This work was supported in part by the University of California Water Resources Center's Saline Water Conversion program.

Manuscript submitted April 2, 1984; revised manuscript received April 23, 1985.

The University of California assisted in meeting the publication costs of this article.

LIST OF SYMBOLS

A_1, A_2, A_3, A_4 constants in Eq. [21a]-[21c]

a	$\gamma_{\text{Cu}} + \frac{\alpha C_{\infty} + k_3}{k_1}$
b	$-\gamma_{\text{Cu}}$
$\frac{C_{\infty}}{C(z')}$	chloride ion concentration in electrolyte steady concentration distribution in moving film reference frame
D_f	diffusion coefficient of Cl^- in film
f_1, f_2, f_3	$e^{-s(1+4\eta)^{1/2}} \eta (r_+ e^{sr_+} - r_- e^{sr_-}), e^{sr_+}(1-\eta+r_-) - e^{sr_-}(1-\eta+r_+)$
f_{1r}, f_{2r}, f_{3r}	real part of f_1, f_2, f_3
f_{1i}, f_{2i}, f_{3i}	imaginary part of f_1, f_2, f_3
$g(t)$	position of Cu-film interface

$h(t)$	position of film-electrolyte interface
k_H	solute distribution coefficient
k_1, k_3	electrochemical rate constants of reactions [1], [3]
$M_{\text{Cu}}, M_{\text{CuCl}}$	molecular weights of Cu, CuCl
p	dimensionless constant film thickness
τ_{\pm}	$[-1 \pm (1+4\eta)^{1/2}]/2$
s	$p\xi$
$\frac{S(y, \tau)}{\bar{S}(y)}$	dimensionless concentration variable dimensionless steady-state concentration in moving film reference frame
$S'(y, \tau)$	deviation of $S(y, \tau)$ from $\bar{S}(y)$
t	time variable
t'	time variable in moving film reference frame
u_0	steady speed of film movement
y	dimensionless position variable
z	position variable
z'	position variable in moving film reference frame

Greek Letters

$\alpha(\omega)$	rate of reaction [2a, b]
β	dimensionless constant ratio of film formation and dissolution rates
$\gamma_{\text{Cu}}, \gamma_{\text{CuCl}}$	$\rho_{\text{Cu}}/M_{\text{Cu}}$ and $\rho_{\text{CuCl}}/M_{\text{CuCl}}$
Γ	dimensionless constant chloride ion concentration
$\delta(\tau)$	dimensionless deviation of film thickness
$\delta'(\tau)$	deviation of $\delta(\tau)$ from zero
$\Delta'(t')$	deviation of film-electrolyte interface location, in moving film reference frame, from nominally steady value
Δ_0	steady film thickness
ϵ	void fraction of porous film
η	$\lambda p^{-2}\xi^{-2}$
$\theta'(t')$	deviation of Cu-film interface, in moving film reference frame, from nominally steady value
λ	temporal eigenvalue in stability analysis
ξ	$\beta\Gamma$
$\rho_{\text{Cu}}, \rho_{\text{CuCl}}$	densities of crystalline Cu, CuCl
σ_{\pm}	$\frac{-p\beta\Gamma \pm [p^2\beta^2\Gamma^2 + 4\lambda]^{1/2}}{2}$
τ	dimensionless time variable
ϕ	ratio of film and Cu densities
$\chi(\tau)$	dimensionless deviation of Cu-film interface location
$\chi'(\tau)$	deviation of $\chi(\tau)$ from zero
ω	rotation rate
Ω_0	$-i\eta$

REFERENCES

- R. S. Cooper and J. H. Bartlett, *This Journal*, **105**, 109 (1958).
- J. F. Cooper, R. H. Muller, and C. W. Tobias, *ibid.*, **127**, 1733 (1980).
- T. R. Beck, *ibid.*, **129**, 2412 (1982).
- S. Szpak and R. E. Rice, *J. Chemie u Physik*, **52**, 6336 (1970).
- K. F. Bonhoeffer and H. Gerischer, *Z. Elektrochem.*, **52**, 149 (1948).
- J. P. Joule, *Philos. Mag.*, **24**, 106 (1844).
- G. T. Fechner, *J. Chem. Phys.*, **23**, 131 (1928).
- E. S. Hedges and J. E. Myers, "The Problem of Physicochemical Periodicity," Arnold, London (1926).
- E. S. Hedges, "Protective Films on Metals," Longmans, London (1933).
- J. Wojtowicz, in "Modern Aspects of Electrochemistry," Vol. 8, J. O. Bockris and B. E. Conway, Editors, pp. 47-129, Plenum Press, New York (1972).
- H. P. Lee, K. Nobe, and A. J. Pearlstein, *This Journal*, **132**, 1031 (1985).
- U. F. Franck and R. FitzHugh, *Z. Elektrochem.*, **65**, 156 (1961).
- J. Keizer and D. Scherson, *J. Phys. Chem.*, **84**, 2025 (1980).
- P. H. Lee, Ph.D. Thesis, UCLA (1983).
- H. C. Thomas, *J. Am. Chem. Soc.*, **66**, 1664 (1944).
- Ju. I. Neimark, *Amer. Math. Soc. Trans. Ser. (2)*, **102**, 95-131 (1973); translation from *Prikl. Mat. Mekh.*, **13**, 349-380 (1949).
- G. Iooss and D. D. Joseph, "Elementary Stability and Bifurcation Theory," Springer, New York (1980).
- R. Aris, "The Mathematical Theory of Diffusion and Reaction in Permeable Catalysts," Vol. II, Clarendon Press, Oxford, England (1975).

Proton Conductivity in Mixed Solvents

Z. Stein and E. Gileadi*

Department of Chemistry, Tel Aviv University, Ramat Aviv, Israel

ABSTRACT

The equivalent conductivity at infinite dilution of an inorganic acid (HClO_4) and its salt (LiClO_4) were compared in mixtures of water with two aprotic solvents (acetonitrile and tetrahydrofuran). The variation of the ratio of equivalent conductivities with solvent composition reflects directly the anomalous conductivity of H_3O^+ , all other factors such as the changes in viscosity and dielectric friction being automatically compensated. The anomalous conductivity of the proton is not observed until the concentration of water exceeds ca. 10 volume percent which corresponds to a mole fraction of 0.24. When plotted as a function of the mole fraction of water, the ratio of equivalent conductivities at infinite dilution is almost the same for mixtures of water with AN and with THF, indicating that the aprotic solvent acts only as a diluent, increasing the distance between water molecules and destroying short-range order which may exist in water. When the same ratio is plotted as a function of the average distance between water molecules, it is found that hopping can no longer occur to a significant extent when the average distance is more than 2.2 times its value in pure water. A similar effect was observed recently in studies of the conductivity of Br^- in liquid bromine and its mixtures with nitrobenzene. The Walden product for the proton decreases significantly upon the addition of relatively small amounts of the aprotic solvent, and can decrease by a factor of two when the mole fraction of water decreases from unity to 2/3. Further studies in mixed solvents could shed light on the mechanism of proton conductivity in protic solvents and possibly on the structure of water.

The anomalous high conductivity of acids and bases has been observed over 150 years ago. According to Grotthuss, this is due to the hopping of protons from H_3O^+ ions to water molecules or from water molecules to OH^- ions. The field was reviewed by Conway (1) in 1964, by Erdey-Gruz and Lengyel (2) in 1977, and recently by Lengyel and Conway (3) in 1983. At 25°C, the equivalent conductivity at infinite dilution λ° is 349.8 for H_3O^+ and 198.1 for OH^- . This should be compared to values of 37.5, 50.1, and 73.6 for Li^+ , Na^+ , and K^+ , respectively, and to 76.4 and 68.1 for Cl^- and ClO_4^- , respectively, all in $\text{cm}^2\text{-}\Omega^{-1}\text{-eq}^{-1}$.

A smaller but still distinct effect is observed for D_3O^+ in D_2O (242.4 vs. 41.5 for Na^+ in D_2O) and in simple alcohols such as methanol and ethanol (4-6). The anomalous conductivity of H_3O^+ decreases with increasing temperature and with increasing concentration of a supporting electrolyte (7, 8). A decrease of the transference number for the positive ion with increasing concentration of HCl (which is tantamount to a decrease in the anomalous conductivity) was also observed (9). On the other hand, anomalously high conductivity was found in concentrated sulfuric (10) and phosphoric acids (11). This was associated with hopping of the proton from a protonated acid H_3SO_4^+ to a neutral acid molecule or from an acid molecule H_3PO_4 to a nearby ion H_2PO_4^- .

The anomalous conductivity was measured in mixed solvents, mostly in water and an alcohol or in water and dioxane (12-15). The product of viscosity and equivalent conductivity (the Walden product) should be independent of the composition of the solvent if simple movement of the ions through the viscous fluid is assumed. For acids, the Walden product is found to increase first with the addition of alcohols to water, then decrease below the value for pure water and increase again in pure or almost pure alcohol. The maximum observed can be associated with the maximum in viscosity of the mixture, as will be discussed below. The increase in the Walden product in pure or almost pure alcohol is due to hopping which can occur in this solvent.

The hopping of the proton has been associated in one way or another to the formation of hydrogen bonds in all the solvents discussed above. While this may be the case, it has been shown recently by Rubinstein *et al.* (16) that an anomalous conductivity occurs also in solutions of Br^- in pure bromine or in mixture of bromine and nitrobenzene.

In the present work, the anomalous conductivity of H_3O^+ in mixtures of acetonitrile and water was determined

by comparing the equivalent conductivities of LiClO_4 and HClO_4 at infinite dilution. Because acetonitrile is an aprotic solvent, its only effect should be to break up the regular structure of water and to increase the average distance between water molecules to the point that hopping can no longer occur. In pure water, the ratio of equivalent conductivities at infinite dilution is $417.9/105.6 = 3.96$, while in pure acetonitrile it is very close to unity. Thus, a moderate accuracy in the determination of the equivalent conductivities is sufficient to show the effect of solvent composition on the equivalent conductivities and particularly on their ratio.

Acetonitrile (AN) and water are completely miscible but do not form an ideal solution. This is shown by a nonzero volume of mixing and by the fact that the viscosity of mixtures of these two solvents is not a linear function of composition (17). For this reason, measurements were also taken in mixture of tetrahydrofuran (THF) and water for comparison. Although this solvent is less suitable because of its relatively low dielectric constant, the results were qualitatively the same as in AN/water mixtures, showing no major specific effect of the aprotic solvent.

Experimental

Solutions were made with deionized water which was distilled and had a conductivity of $1.0 \mu\text{mho}\text{-cm}^{-1}$ or less. Acetonitrile (Fluka AR) was distilled over molecular sieves (4Å), and the fraction boiling between 80.5° and 81.5°C was collected. Tetrahydrofuran (Merck AR) was treated with LiAlH_4 to remove peroxides and was distilled. The fraction boiling between 66.5° and 67.5°C was collected. Other chemicals, used as obtained, were LiClO_4 (Buchs SG, AR), HClO_4 70% (Merck AR), KCl (Merck AR), and LiAlH_4 (Fluka, pure). Note that the acid employed contains ca. 2.4 molecules of water per molecule of acid. Thus, even in pure AN or THF, there is always enough water to form H_3O^+ .

Conductivities were measured with a Radiometer CDM 2e conductometer which operates at 3000 Hz for conductivities above $500 \mu\text{mho}$ and at 70 Hz for lower conductivities. The accuracy of measurement was $\pm 1\%$. The cell has two flat Pt electrodes, situated about 0.3 cm apart. Temperatures were controlled to $\pm 0.1^\circ\text{C}$ above room temperature (Haake Type E52 thermostat) and to $\pm 0.2^\circ$ below room temperature (Neslab Type RTE-3 cooling thermostat). Since the conductivity changed with solvent composition by 50% for the salt and as much as 120% for the acid (*cf.* Fig. 1), this level of accuracy was considered

* Electrochemical Society Active Member.

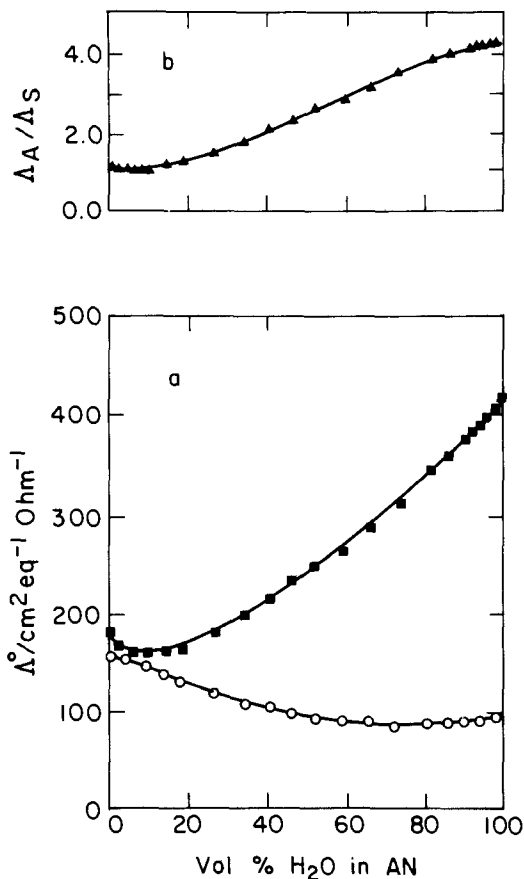


Fig. 1. The equivalent conductivities at infinite dilution (a) and their ratio (b) as a function of the v/o of water in AN. \circ : LiClO_4 , \blacksquare : HClO_4 . $C = 0.93 \text{ mM}$.

sufficient to bring out the significant features of the mixed solvents employed in this work.

Transference numbers were determined by the Hittorf method in a conventional, three-compartment cell, employing platinized Pt electrodes. The constant current was applied with an Elron Type CHG-1 galvanostat and measured with a four-digit multimeter (Data Precision). The change in acid concentration in the anode and cathode compartments was determined by following the changes in conductivity with two auxiliary electrodes in each compartment, following proper calibration. A typical experiment lasted 2-4h at a current of 1.5-3.0 mA. The data points shown in Fig. 7 are average values of four to eight experiments at each composition of the solvent.

The apparent energies of activation were determined by measuring the equivalent conductivities of 0.1 mM solutions of HClO_4 or LiClO_4 in different solvent mixtures at 5°C intervals between 5° and 50°C .

Results

The equivalent conductivity in AN/ H_2O mixtures.—The equivalent conductivity of solutions of LiClO_4 and HClO_4 in the range of concentrations of 1.0-5.0 mM was measured as a function of solvent composition in AN/water mixtures. In Fig. 1a, the values for the acid Λ°_A and for the salt Λ°_S , evaluated by plotting Λ vs. $c^{1/2}$ and extrapolating to zero, are shown as a function of the volume percent (v/o) of water in the solvent mixture. Λ°_S decreases initially from its value in pure AN as the amount of water is increased and remains constant above 60 v/o water. For HClO_4 , we find Λ°_A decreasing initially, but above ca. 10 v/o water it increases steadily to its maximum value in pure water. In Fig. 1b, the ratio $\Lambda^\circ_A/\Lambda^\circ_S$ is plotted in the same way. Note that up to about 10 v/o water (5.5M) the ratio is close to unity and independent of the amount of water present.

A plot of the viscosity η of the solvent mixture vs. composition is shown in Fig. 2 (17). For the salt, the product

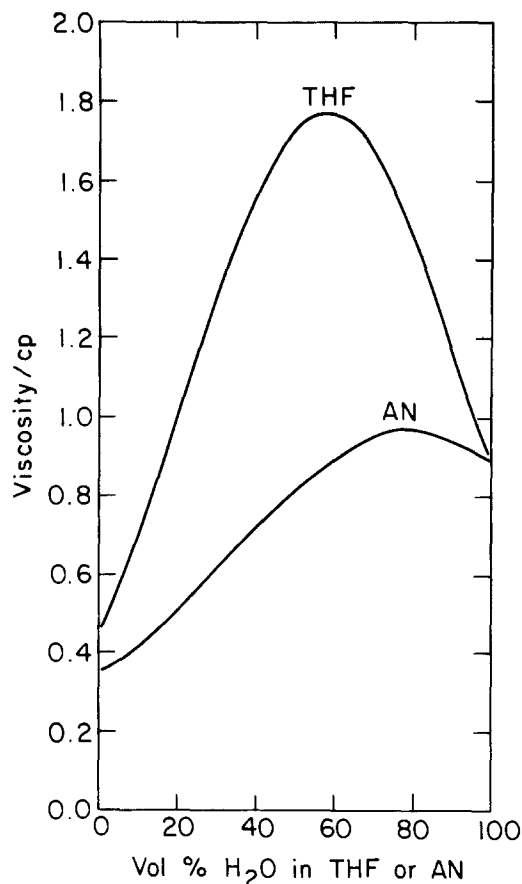


Fig. 2. The viscosity of mixtures of AN/ H_2O and THF/ H_2O as a function of the v/o of water.

$\eta\Lambda^\circ_S$ (the Walden product) should be constant to the extent that the effective Stokes radius of hydration is constant. In Fig. 3, we note a moderate increase in the Walden product for the salt in passing from pure AN to pure water, implying a 35% decrease in effective Stokes radii of the ions. For the acid, the Walden product increases by a factor of six; this is associated with the hopping mechanism of the proton in pure water or in solvent mixtures rich in water.

The equivalent conductivity in THF/ H_2O mixtures.—Since it is evident that mixtures of water and

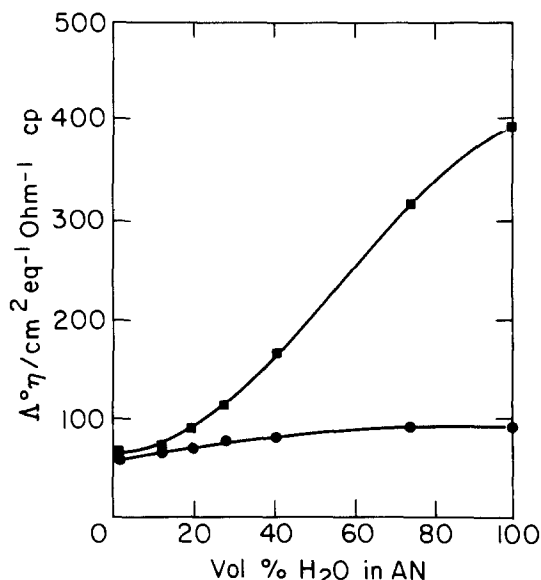


Fig. 3. The Walden product for LiClO_4 (\bullet) and for HClO_4 (\blacksquare) at infinite dilution as a function of composition in AN/water mixtures.

acetonitrile do not form ideal solutions, it is important to repeat the measurements presented above, replacing AN with another aprotic solvent which is completely miscible with water to identify features which may be due to specific interactions between water and acetonitrile. Tetrahydrofuran (THF) was chosen for this purpose. In the range of 10-100 v/o water, the equivalent conductivity was measured for concentrations of 1.0-6.0 mM and values at infinite dilution were obtained as before, by plotting Λ_A or Λ_S vs. $c^{1/2}$ and extrapolating back to zero. However, due to the relatively low value of the dielectric constant of THF (7.58), this procedure is inadequate when the concentration of water is below 10 v/o. For the range of 2-20 v/o water, the concentrations of salt and acid were 0.030-0.3 mM, respectively, and the equivalent conductivity at infinite dilution was determined employing the methods developed by Fuoss and Kraus (18, 19) for strong electrolytes in solvents of low polarity. The equivalent conductivities at infinite dilution in this range of solvent composition are shown in Fig. 4a, and the ratio Λ_A^0/Λ_S^0 is plotted in Fig. 4b. The ratio of equivalent conductivities is close to unity up to 10 v/o water as in AN/H₂O mixtures. The plots of equivalent conductivities at infinite dilution and their ratio over the full range of water composition are shown in Fig. 5.

The viscosity is plotted as a function of the composition of the solvent (20) in Fig. 2. The high maximum observed shows that this solvent mixture deviates significantly from ideality. The peak in the ratio of conductivities at infinite dilution shown in Fig. 5 is caused by the peak in viscosity, as will be discussed below. The Walden product at infinite dilution is plotted as a function of composition of the solvent in Fig. 6. For the salt, the Walden product increases by a factor of 2.5 as the water content changes from 4 to 100 v/o, while for the acid it increases by a factor of over nine in the same region.

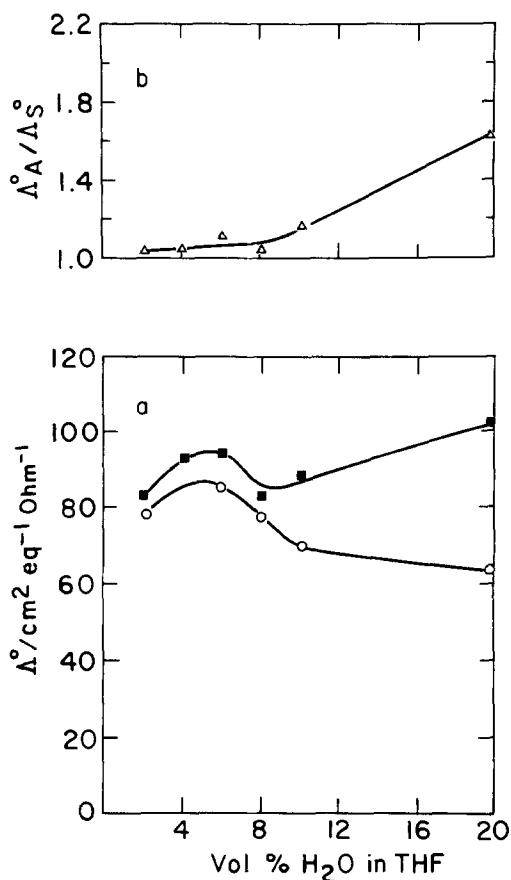


Fig. 4. The equivalent conductivity (a) and ratio of equivalent conductivities (b) as a function of the v/o of water in tetrahydrofuran (THF). ○: LiClO₄. ■: HClO₄.

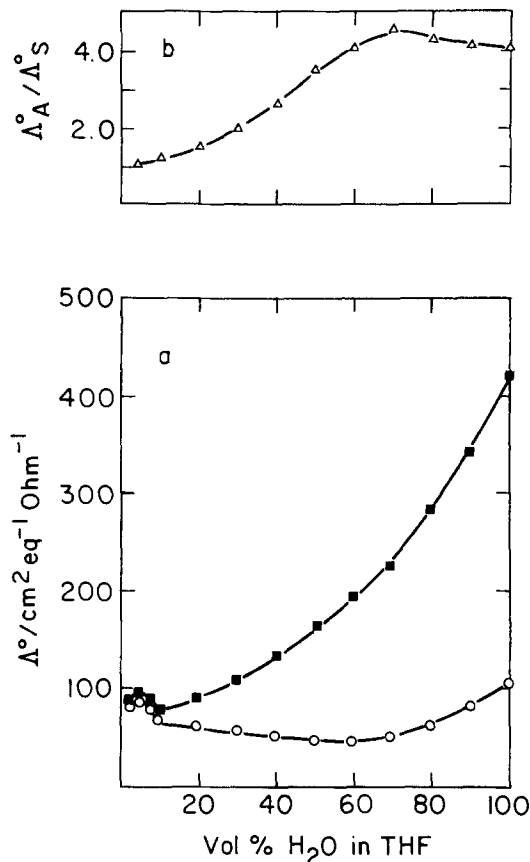


Fig. 5. Same as Fig. 4 for the whole range of solvent composition.

Measurement of transference numbers.—The transference number of ClO₄⁻ in HClO₄ was determined in 0.01M HClO₄ as a function of the composition of the solvent, in mixtures of AN/H₂O, by the Hittorf method. The results are shown in Fig. 7. The transference number for ClO₄⁻ declines from 0.56 ± 0.03 in 10% water to 0.16 ± 0.005 in pure water. Since the transference number does not change significantly with concentration of the electrolyte below 0.01M, one can use the data in Fig. 7 to calculate the equivalent conductivities of the ions ($\lambda_{\text{H}_3\text{O}^+}^0$ and $\lambda_{\text{ClO}_4^-}^0$). From $\lambda_{\text{ClO}_4^-}^0$ and Λ_S^0 , the value for $\lambda_{\text{Li}^+}^0$ is derived. The equivalent conductivities at infinite dilution for the three ions used in the above measurements, in mix-

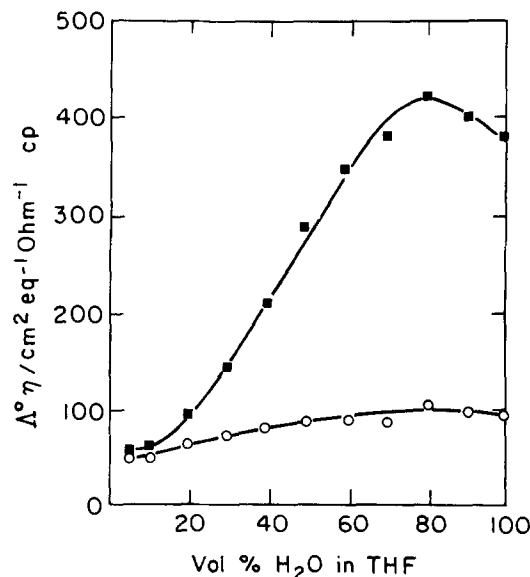


Fig. 6. The Walden product for LiClO₄ (○) and HClO₄ (■) at infinite dilution as a function of composition in THF/water mixtures.

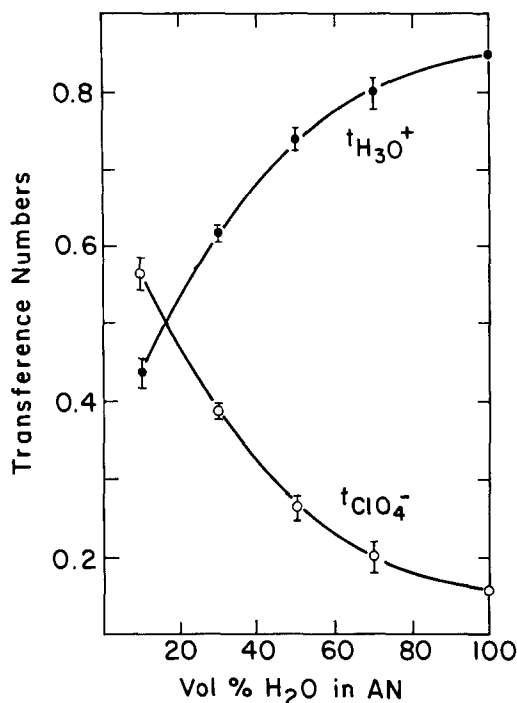


Fig. 7. Transference numbers for H_3O^+ and for ClO_4^- in 0.01M $HClO_4$ as a function of composition in AN/water mixtures.

tures of AN and water, are shown in Fig. 8. The corresponding Walden products ($\eta\lambda^\circ$) are shown in Fig. 9. Although measurements of Hittorf numbers were not conducted at concentrations of water below 10 v/o (because of the relatively high solution resistance), it is safe to assume, based on the data in Fig. 1, that the values of the Walden products shown in Fig. 9 are essentially constant from 0 to 10 v/o water.

The apparent energy of activation as a function of solvent composition.—The equivalent conductivity was measured as a function of temperature between 5° and 50°C at 5° intervals. All measurements were taken in 1.0 mM solutions of acid or salt in different mixtures of AN and water from 2 v/o to pure water. The apparent energies of activation were calculated from plots of $\log(\Lambda/T)$ vs. $(1/T)$. The change in molar concentration resulting from the change of volume of the solvent mixture with temperature was taken into account. The difference in energies of activa-

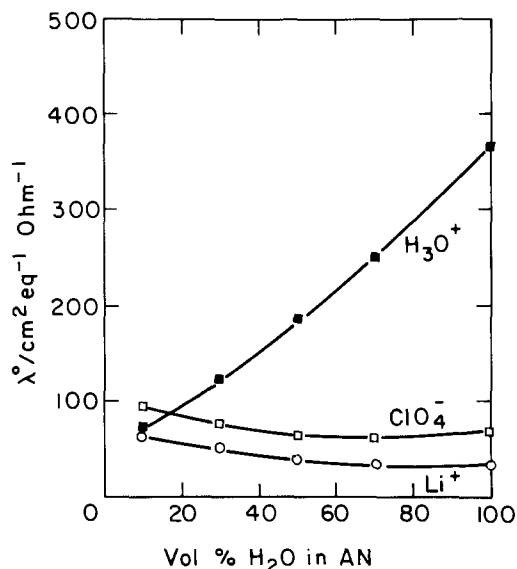


Fig. 8. Equivalent conductivity of single ionic species at infinite dilution as a function of composition in AN/water mixtures.

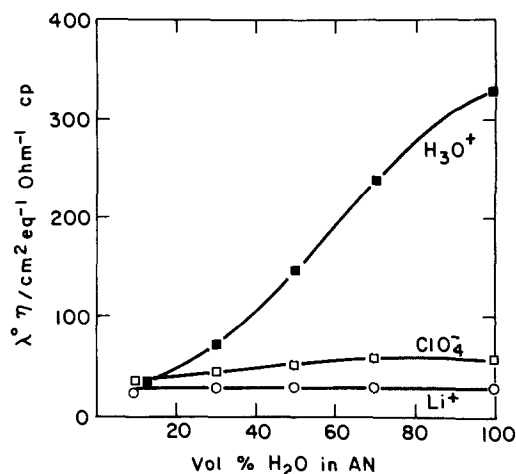


Fig. 9. The Walden product for the single ionic species at infinite dilution as a function of composition in AN/water mixtures.

tion of the salt and the acid was obtained by plotting $\log(\Lambda_A/\Lambda_S)$ vs. $(1/T)$. In this way, the effect of the change of viscosity with temperature is eliminated and the difference ($d\Delta H^\ddagger$) reflects the difference in the mechanism of conductivity of Li^+ and H_3O^+ ions, as a function of water content of the solvent. The results of these measurements are summarized in Fig. 10.

Discussion

The ratio of equivalent conductivities.—The anomalous conductivity of H_3O^+ can be represented by plotting the ratio of equivalent conductivities of an acid and its salt, or the difference between these quantities, as a function of the water content of the solvent. In the present work, the former representation was chosen. By considering the ratio of equivalent conductivities, changes of viscosity or any other factor affecting the hydrodynamic movement of ions through the solvent mixture are systematically can-

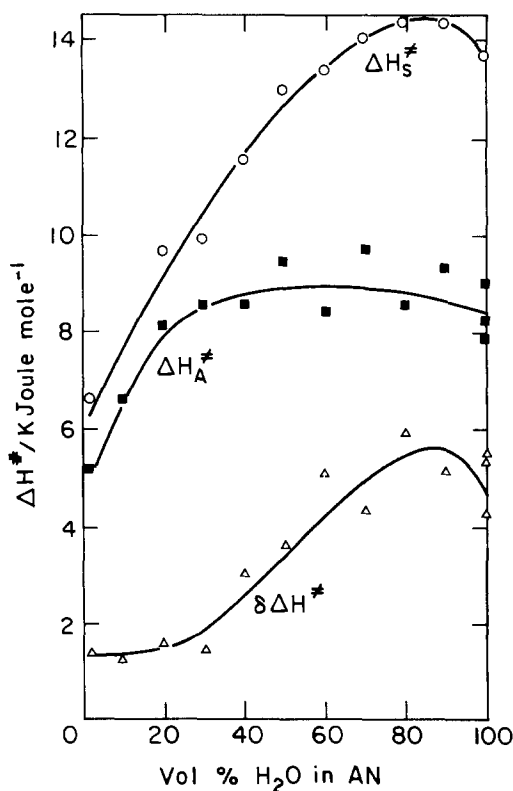


Fig. 10. The apparent heat of activation ΔH^\ddagger for conductance as a function of composition in AN/water mixtures. \circ : $LiClO_4$, \blacksquare : $HClO_4$, \triangle : Difference.

celed, and the departure of the ratio Λ_A^0/Λ_S^0 from a constant value (close to unity in an aprotic solvent) can be attributed in full to the Grotthuss-type hopping mechanism of conduction of the proton. Any artifact arising from incomplete dissociation of the electrolyte is eliminated by determining the equivalent conductivities at infinite dilution. In mixtures of H_2O/THF , the determination of equivalent conductivity at infinite dilution is less accurate at low concentrations of water due to the low dielectric constant of the medium. However, it turns out that in this region Λ_A is close to Λ_S and their ratio is quite independent of concentration below 1.0 mM at a constant composition of the solvent.

The most striking feature in Fig. 1 is that the ratio of equivalent conductivities is close to unity and is essentially independent of the concentration of water up to ca. 10 v/o, while Λ_A^0 and Λ_S^0 both vary significantly in the same region. It can be concluded that in this region the H_3O^+ ion behaves just like the Li^+ ion, moving through the solvent mixture in a simple hydrodynamic mode. This is rather surprising in view of the high molar concentration of water (at 10 v/o the mole fraction of water is ca. 0.24). If the anomalous proton conductivity is due to short-range order in liquid water, it could be argued that such structure is completely absent when water molecules constitute one out of four solvent molecules or less. Even when two out of three solvent molecules are water (40 v/o), the ratio of equivalent conductivities is only two (compared to four in pure water) showing that the anomalous conductivity is very sensitive to the structure of water.

The Walden product plotted in Fig. 3 as a function of solvent composition shows that even $LiClO_4$ does not follow the simple Walden rule and the product $\eta\Lambda_S^0$ increases from 60 to 92 $cm^2\text{-eq}^{-1}\text{-}\Omega^{-1}\text{-cP}$ from pure acetonitrile to pure water. This observation shows the advantage of considering the ratio of equivalent conductivities rather than their absolute value.

The effect of the aprotic solvent.—Replacing acetonitrile (AN) with another aprotic solvent, tetrahydrofuran (THF), should have no effect if this solvent acts only as a "spacer" diluting the water, increasing the average distance between water molecules and thus destroying the short-range order which exists in pure water. Comparing Fig. 3 to Fig. 6, we note that for the salt the Walden product is almost the same in the two solvent mixtures. For the acid, the difference is large. This difference is also evident when the ratios of equivalent conductivities in Fig. 1b and 5b are compared. Such comparison ignores, however, the differences of density and molecular weight between AN and THF. A better comparison between the effect of the two aprotic solvents is made when the ratios of equivalent conductivities are plotted as a function of the mole fraction of water, as shown in Fig. 11. Up to a mole frac-

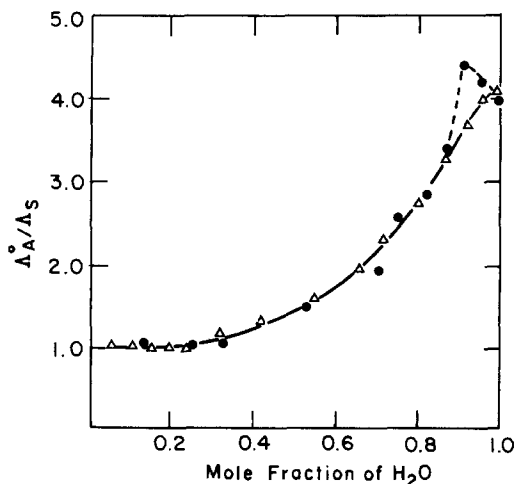


Fig. 11. The ratio of equivalent conductivities at infinite dilution as a function of the mole fraction of water in AN (Δ) and in THF (\bullet).

tion of 0.85, the two aprotic solvents have the same effect, within experimental error.

An alternative way of presenting the same data is to plot the ratio Λ_A^0/Λ_S^0 as a function of the average distance between water molecules, based on the molar concentration of water in the solvent, ignoring the properties of the other component. This is shown in Fig. 12. It is of interest to note that when the average distance between water molecules exceeds about 2.2 times its value in pure water hopping of the proton no longer occurs. In an earlier study by Rubinstein *et al.* (16), the conductivity of Br^- in liquid bromine and its mixtures with nitrobenzene were determined. A very similar phenomenon was observed. A hopping mechanism of conductivity was found for the Br^- ion in bromine-rich solvent. This mechanism became inoperative when the concentration of bromine was below ca. 2M, which corresponds to an average distance 2.2 times that in pure bromine, as in the case of AN/ H_2O and THF/ H_2O mixture.

The effect of viscosity.—The maxima observed in THF/ H_2O mixtures (Fig. 5b, 6, 11, 12) is associated with the large maximum in viscosity of this mixture, shown in Fig. 2. For the salt, the conductivity is inversely proportional to the viscosity, hence the Walden product (*cf.* Fig. 6) is not significantly dependent on the viscosity. If proton hopping depends on the structure of water and does not require movement of ionic species through the viscous fluid, it should not decrease significantly with increasing viscosity. It is indeed seen that Λ_A^0 increases steadily with water content (Fig. 5a), with no significant change in its rate of increase around 60 v/o water, where the viscosity reaches its maximum. Thus, multiplying Λ_A^0 by η constitutes an "overcorrection" and the resulting maximum in the upper curve in Fig. 6 reflects mainly the maximum in viscosity. The same applies to the maxima in the plots of Λ_A^0/Λ_S^0 vs. solvent composition. In AN/ H_2O mixtures, the maximum in viscosity is rather small and its effect is obscured by the steady increase in Λ_A^0 with water content.

The above observations indicate that anomalous proton conductivity in THF/ H_2O mixtures occurs by a mechanism in which the rate-determining step is not dependent on the viscosity of the solvent. This would probably exclude rotation of a water molecule or of aggregates of water molecules as the rds.

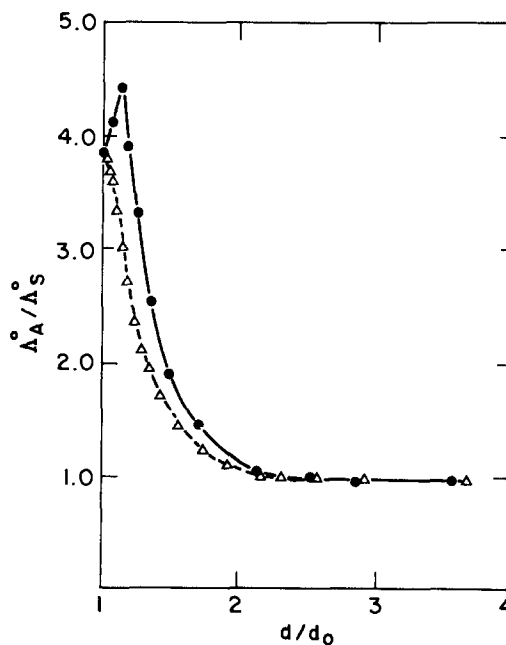


Fig. 12. Same as Fig. 11, but plotted as a function of the average distance between water molecules (d), divided by the average distance (d_0) in pure water.

The equivalent conductivity of ions at infinite dilution in pure water as a function of temperature shows a similar effect. For Na^+ and K^+ , the Walden product increases by only a factor of 1.05 and 1.24, respectively, as the temperature is decreased from 100° to 0°C. For H_3O^+ the Walden product increases by a factor of 2.4 in the same temperature range. For the OH^- ion the increase is by a factor of 1.5. It was also observed that for Br^- in Br_2 (16) and for I^- in liquid iodine (21) the Walden product increases with decreasing temperature. It can be stated that a significant increase in the Walden product with increasing viscosity (be it as a result of a decrease in temperature in a pure solvent or as a result of a change in solvent composition in a mixture of solvents) is indicative of a non-stokesian mechanism of conductivity.

In a recent study of the conductivity of solution of Al_2Br_6 and KBr in aromatic hydrocarbons (22), the Walden product was found to increase with decreasing temperature in concentrated solutions, where a hopping mechanism of conductivity prevails (23, 24).

Transference numbers and the equivalent conductivities of single ions.—Employing the transference numbers found in HClO_4 (Fig. 7), we can proceed to calculate the equivalent conductivities of each of the ions at infinite dilution (Fig. 8) and the corresponding Walden products (Fig. 9). The tendency of the Walden product to level off for H_3O^+ at high concentrations of water is due to the maximum in the viscosity, as discussed above. For lithium, the Walden product increases from 24 $\text{cm}^2\text{-eq}^{-1}\text{-}\Omega^{-1}\text{-cP}$ in 10 v/o water to 30 $\text{cm}^2\text{-eq}^{-1}\text{-}\Omega^{-1}\text{-cP}$ in pure water, and for the perchlorate ion the change is from 36 to 58 $\text{cm}^2\text{-eq}^{-1}\text{-}\Omega^{-1}\text{-cP}$ in the same range of solvent composition. In pure AN, the Walden product for most inorganic ions is reported to be significantly lower than in pure water (25, 26). This can be attributed to a higher radius of solvation. The largest effect is observed for ions such as Cs^+ , Rb^+ , I^- , Br^- , ClO_4^- which have a solvation number close to zero in pure water. Due to the higher dipole moment of AN (3.97 vs. 1.84 for water), such ions may be expected to have a higher solvation number in AN than in water. The Walden products for ClO_4^- and for Li^+ observed here in 10 v/o water in AN are equal to those reported in pure AN (25, 26).

It should be noted that the above interpretation for the variation of the Walden products with composition, which is commonly used in the literature (25), is not entirely consistent with the results obtained in this work. Thus, comparison of Fig. 3 and 6 shows that the Walden product for the salt ($\eta\Lambda^0_s$) is essentially the same in AN/ H_2O and THF/ H_2O mixtures. This would seem to render any interpretation based on specific interactions of the ions with the aprotic solvent incomplete, in view of the significant differences between AN and THF.

The heat of activation for electrolytic conductivity.—The heats of activation for conductivity (at infinite dilution) are shown for the salt and for the acid in Fig. 10. At low water content the values for the acid and the salt are almost the same (the difference is about $0.5RT$ at room temperature). Since the energy of activation for the conductivity of the salt represents approximately that for the viscosity, it may be inferred from Fig. 10 that the Walden

product for the acid will increase with decreasing temperature in solvent mixtures as well as in pure water. The extent of this increase or the difference between the values of ΔH_s^\ddagger and ΔH_v^\ddagger is a good indication of the contribution of hopping to the mechanism of electrolytic conductivity of the acid in different solvent mixtures.

Acknowledgments

The authors wish to thank Professor M. Bixon and Professor E. Kirowa-Eisner for useful discussions.

Manuscript received April 16, 1984.

REFERENCES

1. B. E. Conway, in "Modern Aspects of Electrochemistry," Vol. 3, J. O'M. Bockris and B. E. Conway, Editors, Chap. 2, Butterworths, London (1964).
2. T. Erdey-Gruz and S. Lengyel, in "Modern Aspects of Electrochemistry," Vol. 12, J. O'M. Bockris and B. E. Conway, Editors, Chap. 1, Plenum Press, New York (1977).
3. S. Lengyel and B. E. Conway, "Comprehensive Treatise of Electrochemistry," Vol. 5, Chap. 4, Plenum Press, New York (1983).
4. S. Glasstone, K. J. Laidler, and H. Eyring, "The Theory of Rate Processes," p. 570, McGraw-Hill, New York (1941).
5. W. K. La Mer and W. N. Baker, *J. Chem. Phys.*, **3**, 406 (1935).
6. G. N. Lewis and T. C. Doody, *J. Am. Chem. Soc.*, **55**, 3504 (1933).
7. N. K. Roberts and H. L. Northey, *J. Chem. Soc. Faraday Trans. 1*, **68**, 1528 (1972).
8. N. K. Roberts and H. L. Northey, *ibid.*, **70**, 253 (1974).
9. S. Lengyel, J. Giber, and J. Tamas, *Acta Chim. Acad. Sci. Hung.*, **32**, 429 (1962).
10. R. J. Gillespie and S. Wasif, *J. Chem. Soc.*, 209 (1953).
11. N. N. Greenwood and A. Thompson, *ibid.*, 3485 (1959).
12. B. E. Conway, J. O'M. Bockris, and H. Linton, *J. Chem. Phys.*, **24**, 834 (1956).
13. T. Erdey-Gruz, E. Kugler, K. Balthazar, and I. Nagy-Czako, *Acta Chim. Acad. Sci. Hung.*, **79**, 169 (1973).
14. T. Erdey-Gruz, E. Kugler, and L. Majthenyi, *Electrochim. Acta*, **13**, 947 (1968).
15. H. S. Harned and E. C. Dreby, *J. Am. Chem. Soc.*, **61**, 3113 (1939).
16. I. Rubinstein, M. Bixon, and E. Gileadi, *J. Phys. Chem.*, **84**, 715 (1980).
17. A. D'Aprano and R. M. Fuoss, *ibid.*, **73**, 400 (1969).
18. R. M. Fuoss and C. A. Kraus, *J. Am. Chem. Soc.*, **55**, 476 (1933).
19. R. M. Fuoss, *ibid.*, **57**, 488 (1935).
20. F. T. Wall, *J. Colloid. Chem.*, **54**, 979 (1950).
21. E. Kirowa-Eisner, A. Brestovisky, and E. Gileadi, *This Journal*, In press.
22. E. Peled, M. Brand, and E. Gileadi, *This Journal*, **128**, 1968 (1981).
23. A. Reger, E. Peled, and E. Gileadi, *J. Phys. Chem.*, **83**, 873 (1979).
24. E. Gileadi, in "Electrode Processes 1979," S. Bruckenstein, J. D. E. McIntyre, B. Miller, and E. Yeager, Editors, p. 366, The Electrochemical Society Softbound Proceedings Series, Princeton, NJ (1980).
25. R. L. Kay, *Adv. Chem. Ser.*, **73**, 4 (1968).
26. J. E. Desnoyers, "Comprehensive Treatise of Electrochemistry," Vol. 5, Chap. 1, Plenum Press, New York (1983).



Application of a Modified Colloid Chemical Site Binding Model to Mott-Schottky Plots Determined at Oxidic Semiconductor/Electrolyte Systems

W. Smit

Laboratory of Electrochemistry, Group Colloid Chemistry, Eindhoven University of Technology, 5600 MB Eindhoven, The Netherlands

In their note on the interpretation of Mott-Schottky plots determined at semiconductor/electrolyte systems, De Gryse *et al.* (1) demonstrated theoretically that a linear relationship between C^{-2} and V can be found experimentally even when the inequalities

$$C_{sc} \ll C_H \quad [1]$$

$$|\phi_{sc}| \gg |\phi_H| \quad [2]$$

do not hold. Here, C represents the differential capacitance of the semiconductor/electrolyte system under circumstances where a depletion layer exists at the semiconductor surface and V represents the voltage applied to the semiconductor electrode and expressed with respect to a reference electrode. C_{sc} and C_H are the differential capacitances per square centimeter of the depletion layer of the semiconductor and of the Helmholtz layer at the semiconductor surface, respectively, ϕ_{sc} is the potential drop over the depletion layer, and ϕ_H the change in Helmholtz potential drop caused by the applied voltage.

The inequalities [1] and [2] will be satisfied when the doping level of the semiconductor is low. When this is the case, $C \approx C_{sc}$, then the Mott-Schottky relationship

$$C^{-2} = (2/\epsilon_0 \epsilon q N_D)(V - V_{FB} - kT/q) \quad [3]$$

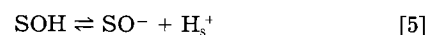
can represent the C^{-2} vs. V data. Here V_{FB} is the flatband potential, and we consider an n-type semiconductor with donor density N_D .

In this note, we discuss, like De Gryse *et al.* (1), those cases where $N_D > 10^{19} \text{ cm}^{-3}$. We also assume absence of a redox system in the electrolyte solution. Such solutions are frequently indicated as "indifferent electrolyte" solutions. In their derivation of the equation for these conditions, De Gryse *et al.* assumed that ion adsorption on semiconductor electrodes like n-TiO₂ is absent, even at the high — from a colloid chemical point of view — electrolyte concentrations usually used [0.25M K₂SO₄ + buffer (2), 0.33M phosphate buffer (3, 4)].

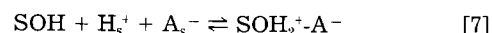
We now direct our attention to some colloid chemical aspects of the oxide/electrolyte interface. For such systems, very large surface charge densities compared to the mercury or AgI surface are found accompanied by quite modest values of the electrokinetic potential (5). The very large surface charges, obtained from titration data, can be explained by the porous gel model (6) of the oxide-solution interface. This model, however, cannot be applied when such a gel layer is absent, as was proved for TiO₂ surfaces by Yates *et al.* (7) by tritium exchange studies. An alternative model for such cases is the site-dissociation site binding model (8-10) which involves a direct binding of counterions to the surface charges. This model compromises the notion of "indifferent electrolyte." Experimental evidence for the adsorption of sodium ions in the compact layer of vitreous silica and of α -Al₂O₃ single

crystals, in absence of a gel layer, was given by Smit *et al.* (11-13). The adsorption of anions in dependence on solution pH and adsorbate concentration was measured by the radiotracer method on TiO₂ electrode (14) and for Br⁻ ions on α -Al₂O₃ (12, 13).

In the site-dissociation site binding model, the following amphoteric ionization reactions of surface sites



are considered together, following Davis *et al.* (9), with the surface complex ionization reactions



Here, s refers to surface values, K⁺ is a cation, and A⁻ an anion. SO⁻-K⁺ is a neutralized SO⁻ site, and SOH₂⁺-A⁻ a neutralized SOH₂⁺ site. The surface charge density, as measured by titration, is given by

$$\sigma_o = F\{[\text{SOH}_2^+] + [\text{SOH}_2^+ \text{-A}^-] - [\text{SO}^-] - [\text{SO}^- \text{-K}^+]\} \quad [8]$$

The charge density of the adsorbed ions, which are located in the inner Helmholtz plane, is given by

$$\sigma_B = F\{[\text{SO}^- \text{-K}^+] - [\text{SOH}_2^+ \text{-A}^-]\} \quad [9]$$

In the original idealized planar surface model (9), the inner C_1 and outer C_2 capacitances of the compact layer and the diffuse layer capacitance are put in series. Values of around 20 $\mu\text{F}\cdot\text{cm}^{-2}$ for C_2 are generally found to be satisfactory for the site-dissociation site binding model. Since C_1 is much larger than C_2 , the apparent compact layer capacitance C_H will also be around 20 $\mu\text{F}\cdot\text{cm}^{-2}$. However, from capacity measurements on semiconductor electrodes an unexpectedly low value of the Helmholtz layer capacitance (3-6 $\mu\text{F}\cdot\text{cm}^{-2}$) was found as a common feature (15, 16). Dewald (16) questioned the use of a C_H value taken from work with the mercury electrode, for ZnO.

In our laboratory, we performed coulometric pulse relaxation experiments on oxidized Ti/electrolyte interfaces [see Van Leeuwen (17, 18) for a discussion of the method]. The potential transients can be transformed to complex impedance values $Z(j\omega)$. These impedance data are fitted to equivalent circuits containing frequency independent elements [aperiodic equivalent circuit (19, 20)] by analysis with complex nonlinear least squares (21, 22).

In the experiments on oxidized Ti, where more than 80% of the relaxation signal came from the electrolyte side of the interface, we found at least six relaxation times, among them a diffusional relaxation in the electrolyte. The equivalent circuits to be considered are rather complicated. We have not yet finished the evaluation of our data, but two facts have already been established.

First, the equivalent circuit on the electrolyte side is composed of at least two impedances in parallel. This is in agreement with circuits proposed by Gerischer (23) and Bousse and Bergveld (24), and with the aperiodic equivalent circuit for adsorption of electroinactive species with slow adsorption step and negligible charge transfer, as deduced theoretically by Pilla (20). Second, the value of the Helmholtz layer capacitance is much lower than $20 \mu\text{F}\cdot\text{cm}^{-2}$.

We proposed a modification of the site binding model (25) in order to reconcile this model with these experimental facts. When this model is applied with σ_0 and electrokinetic potential data obtained on $\alpha\text{-Al}_2\text{O}_3$ single crystals (13), lower (outer) compact layer capacitances are indeed required to fit the data.

We now return to the Mott-Schottky plots. In the following sections, we propose our modification of the treatment by De Gryse *et al.* (1). This modification is based on our modified site binding model.

We consider a surface area of 1 cm^2 . The total surface charge density σ_0 is given by Eq. [8]. Two kinds of charged surface sites can be recognized: (i) sites SOH_2^+ and SO^- , which can influence the charge in the diffuse layer directly, and (ii) sites $\text{SOH}_2^+\text{-A}^-$ and $\text{SO}^-\text{-K}^+$, in which charges are shielded by the adsorbed ions. This also holds for the charges in the semiconductor.

For calculation purposes, we think the shielded sites moved to one part of the surface and the other sites, mainly SOH_2^+ , SO^- , and SOH , to the remaining part. In this way, we obtain two parallel capacitance branches. The fraction of the total surface occupied by incomplected sites is given by

$$f \approx ([\text{SOH}_2^+] + [\text{SOH}] + [\text{SO}^-])/N_s \quad [10]$$

where N_s = surface site density ($\text{mol}\cdot\text{cm}^{-2}$).

The capacitance between the surface area f of the uncomplexed sites and the outer Helmholtz plane is the real Helmholtz capacitance C_H ($\mu\text{F}/f\cdot\text{cm}^2$ of the 1 cm^2 considered).

We introduce the following assumptions: (i) the surface potential at the semiconductor surface is the same everywhere. Thus, the potential drop ϕ_{sc} over the depletion layer is also the same everywhere; (ii) the potential drop in the Gouy layer can be neglected; (iii) the variation of C_H as a function of the change of the potential drop ϕ_H over this capacitance is negligible. (Experimentally, we found some potential dependency, see Fig. 2); and (iv) the fraction f does not depend on the variation of the applied potential.

The last assumption is supported by the work of Kazarinov *et al.* (14), who found that the potential variation has virtually no effect on the amount of adsorbed anions.

The applied voltage (with respect to the flatband situation) can follow two pathways: over the complexed sites and over the uncomplexed sites. We follow the latter path

$$V - V_{FB} = \phi_{sc} + \phi_H \quad [11]$$

In the case considered, one has $V > V_{FB}$, $\phi_{sc} > 0$, and $\phi_H > 0$. In the Mott-Schottky approximation [$\exp(-q\phi_{sc}/kT) \ll 1$], the space charge q_{sc} in the semiconductor is given by

$$q_{sc} = (2\epsilon\epsilon_0 N_D)^{1/2} (\phi_{sc} - kT/q)^{1/2} \quad [12]$$

per square centimeter.

However, behind the surface area f , this charge is $f q_{sc}$. We take the charge in surface states $q_{ss,f}$ in the surface area f and the charge in the uncomplexed sites $\sigma_{o,f}$ together

$$Q_{ss} = q_{ss,f} + \sigma_{o,f} \quad [13]$$

Since we have now based the charges and the capacitance on the same surface area f , we can write

$$\phi_H = (f q_{sc} + Q_{ss})/C_H \quad [14]$$

From Eq. [13] and [14], the following relationship between ϕ_H and ϕ_{sc} follows

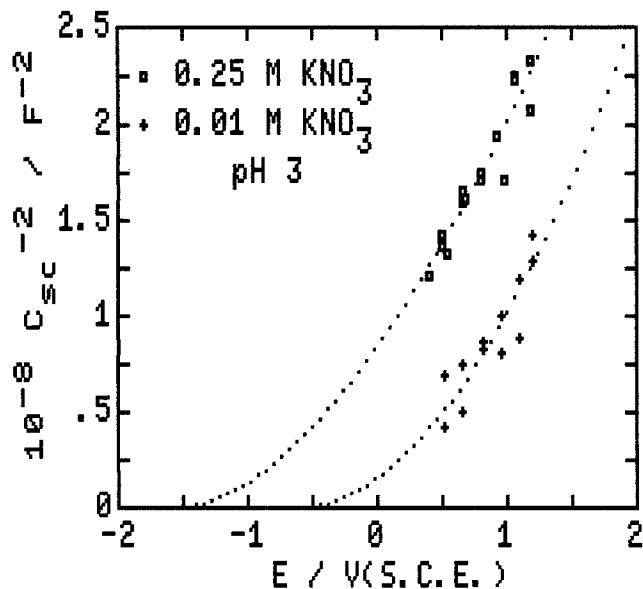


Fig. 1. Fit of Eq. [22] to C_{sc}^{-2} vs. applied potential data. Oxidized and activated Ti; $A = 4 \text{ cm}^2$; in 0.01M (crosses) and 0.25M (squares) KNO_3 at pH 3.0.

$$\phi_H = 2fa(\phi_{sc} - kT/q)^{1/2} + Q_{ss}/C_H \quad [15]$$

where

$$a = (\epsilon\epsilon_0 q N_D / 2C_H^2) \quad [16]$$

Inserting Eq. [15] into Eq. [11] and subtracting kT/q from both sides, the following quadratic equation in $(\phi_{sc} - kT/q)^{1/2}$ is obtained

$$V - V_{FB} - kT/q = \phi_{sc} - kT/q + 2fa(\phi_{sc} - kT/q)^{1/2} + Q_{ss}/C_H \quad [17]$$

Hence

$$(\phi_{sc} - kT/q)^{1/2} = -fa + [(fa)^2 + (V - V_{FB} - kT/q - Q_{ss}/C_H)]^{1/2} \quad [18]$$

Since ϕ_{sc} is assumed constant over the whole surface of the semiconductor, the ϕ_{sc} calculated with Eq. [18] can be inserted in the Mott-Schottky relationship

$$C_{sc}^{-2} = (2/\epsilon\epsilon_0 q N_D A^2) (\phi_{sc} - kT/q) \quad [19]$$

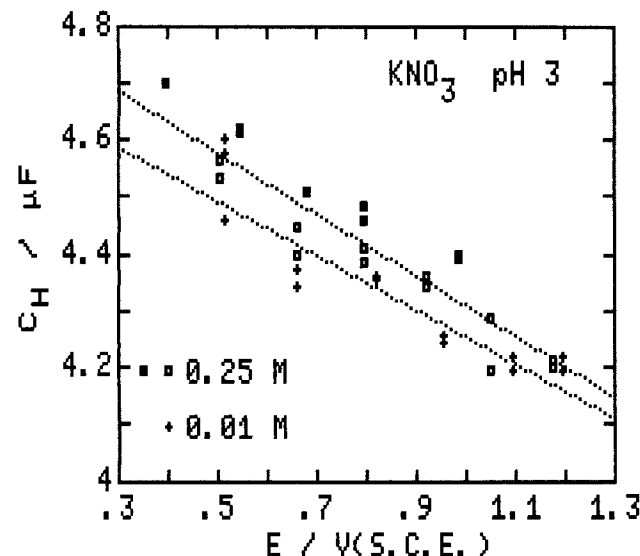


Fig. 2. Helmholtz capacitance vs. applied potential plots obtained by pulse relaxation experiments on oxidized and activated Ti. $A = 4 \text{ cm}^2$, in 0.01M (crosses) and 0.25M (squares; two runs) KNO_3 at pH 3.0.

Table I. Parameters and estimated uncertainties found by least squares fitting of Eq. [22] to C_{sc} data
Oxidized and activated Ti; $A = 4 \text{ cm}^2$; $\epsilon = 100$; KNO_3 at pH 3

M	Fit	V_{FB} (V vs. SCE)	$10^{-19} N_D$ (cm^{-3})	C_H (μF) ^a	Q_{ss}^0 (C) ^a	P (V^{-1})	f
0.25	1	-1.58 ± 0.67	6.1 ± 1.6	1.58 ± 0.48	-0.3 ± 1.0	-2.9 ± 24	0.81 ± 0.24
0.25	2	-1.22 ± 0.66	5.8 ± 1.6	1.29 ± 0.44	-0.5 ± 0.8	-4.4 ± 12	0.62 ± 0.20
0.01	1	-0.52 ± 0.66	6.1 ± 2.8	1.52 ± 0.80	-0.3 ± 0.9	5.1 ± 10	0.71 ± 0.34
0.01	2	-0.71 ± 0.62	5.3 ± 2.8	1.34 ± 0.72	0.03 ± 0.6	-30 ± 175	0.72 ± 0.40

^a Refers to fraction f of 1 cm^2 surface area.

where we introduced the surface area A of the electrode exposed to the solution.

Introduction of Eq. [18] in Eq. [19] yields

$$C_{sc}^{-2} = (2/\epsilon_0 \epsilon q N_D A^2) \{ (V - V_{FB} - kT/q - Q_{ss}^0/C_H + 2(af)^2 - 2af[(af)^2 + (V - V_{FB} - kT/q - Q_{ss}^0/C_H)]^{1/2} \} \quad [20]$$

Q_{sc} can be dependent on ϕ_{sc} . In order to keep the calculations manageable, we introduced a linear dependency of Q_{ss} on ϕ_{sc}

$$Q_{ss} = Q_{ss}^0 + P Q_{ss}^0 (\phi_{sc} - kT/q) \quad [21]$$

With this Q_{ss} introduced in Eq. [14], we arrive at

$$C_{sc}^{-2} = (2/\epsilon_0 \epsilon q N_D A^2 B^2) \{ B(V - V_{FB} - kT/q - Q_{ss}^0/C_H) + 2(af)^2 - 2af[(af)^2 + B(V - V_{FB} - kT/q - Q_{ss}^0/C_H)]^{1/2} \} \quad [22]$$

where

$$B = (C_H + P Q_{ss}^0)/C_H$$

For our experiments with the pulse relaxation method, it is not necessary to combine C_{sc} with a compact layer capacitance into a capacitance C , as done by De Gryse *et al.* (1). Two of the relaxations can be attributed to the semiconductor side. We turned the two RC circuits in series (Voigt circuit) into the Maxwell circuit as used by Tomkiewicz (3, 4). One of the two capacitances shows Mott-Schottky behavior and is C_{sc} ; the other capacitance is presumably C_{ss} . From our circuit analysis, we also find a value for C_H as used in the equations above.

However, we fitted Eq. [22] with V_{FB} , C_H , N_D , f , Q_{ss}^0 , and P as parameters to the experimental data by a nonlinear least squares computer program, using a Marquardt algorithm (26). Then we can compare the predicted C_H values with the experimental ones.

We shall now apply Eq. [22] to C_{sc} vs. $V(\text{SCE})$ data obtained on oxidized Ti [30 min in O_2 at 700°C , followed by activation at 600°C for 30 min in 1:7 $\text{H}_2\text{O}/\text{N}_2$ (27)] in KNO_3 solutions at pH 3. Figure 1 shows C_{sc}^{-2} vs. $V(\text{SCE})$ plots. The potential region accessible to measurement was limited by breakdown. The C_{sc} data are moderately accurate because less than 20% of the relaxation signal in these experiments originated from the semiconductor side of the interface. This is related to the low C_H capacitance and the high donor concentration in the semiconducting oxide layer. The values of C_H as found by analysis of the pulse relaxation data are shown in Fig. 2. Full details of these experiments will be presented elsewhere. In Fig. 1, fits of Eq. [22] to the experimental data are shown. The exposed surface area $A = 4 \text{ cm}^2$ and $\epsilon = 100$ was used in the calculations. The final values of the parameters found by the least squares fitting procedure, starting from two different sets of initial values, are shown in Table I, together with the uncertainty of these values. In the correlation matrix, the correlation coefficient between the V_{FB} and Q_{ss}^0 parameters is highest (> 0.6). With these parameters, ϕ_{sc} can be solved from Eq. [17] or Eq. [18]. In Fig. 3, the C_{sc}^{-2} data are plotted vs. these ϕ_{sc} values. The extrapolated linear least squares lines intersect the horizontal axis at $\phi_{sc} = kT/q$, conform Eq. [19]. The differences in slope are related to the uncertainties in N_D . According to these calculations, less than 10% of the

voltage applied to the electrode is found back as a change in ϕ_{sc} .

From Fig. 2, one can see that C_H varies from 1.17 to $1.03 \mu\text{F}\cdot\text{cm}^{-2}$ ($A = 4 \text{ cm}^2$) in the applied voltage interval. The mean value, $1.1 \mu\text{F}\cdot\text{cm}^{-2}$, is within the estimated uncertainties equal to the C_H values of Table I. Thus, the model is with respect to C_H consistent with the experimental facts. As the parameter f concerns, it is a support for the model to see that the values found by the curve-fitting are indeed fractions, although with the uncertainties unity can be exceeded. These uncertainties, unfortunately, make it impossible to draw conclusions about the extent of adsorption from these parameters. We attribute the shift of V_{FB} to more negative potentials on an increase of the KNO_3 concentration to a higher adsorption of NO_3^- ions. Approximately the same shift was found in KCl solutions at pH 3. This increase of adsorption of electrolyte ions with increasing bulk electrolyte concentration can also be derived from the circuit elements on the electrolyte side of the total equivalent circuit of the interface.

The Q_{ss} values calculated with Eq. [21] are negative, setting aside their uncertainties. From our zeta potential measurements on the same oxidized Ti plates, we found that pH 3 is below the isoelectric point (28). On isolator oxides like $\alpha\text{-Al}_2\text{O}_3$, $\sigma_{o,f}$ is equal to minus the charge in the diffuse layer and is of the order of $\mu\text{C}\cdot\text{cm}^{-2}$. Below the isoelectric point, $\sigma_{o,f}$ is positive for such oxides. If this remains true for the TiO_2 electrodes, then the negative Q_{ss} values would point to negatively charged surface states.

Conclusions

The model used is an extension of the treatment by De Gryse *et al.* (1). The model predicts from the C_{sc}^{-2} vs. applied voltage curves C_H values which are consistent with experimentally found C_H values. The model is based on a

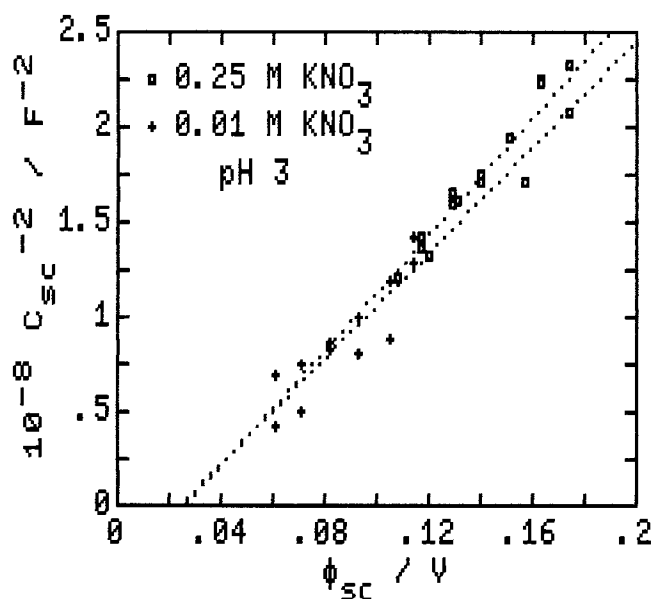


Fig. 3. Mott-Schottky plots of the C_{sc}^{-2} data from Fig. 1 vs. ϕ_{sc} calculated with Eq. [17] and parameter values of Table I.

modified colloid chemical site-dissociation site binding model. This modification was introduced to reconcile the original model with experimental facts found at semiconductor/electrolyte electrodes: low values of the Helmholtz layer capacitance and at least two parallel impedance branches on the electrolyte side.

Manuscript received Jan. 2, 1985.

Eindhoven University of Technology assisted in meeting the publication costs of this article.

REFERENCES

1. R. De Gryse, W. P. Gomes, F. Cardon, and J. Vennik, *This Journal*, **122**, 711 (1975).
2. E. C. Dutoit, F. Cardon, and W. P. Gomes, *Ber. Bunsenges. Phys. Chem.*, **80**, 475 (1976).
3. M. Tomkiewicz, *This Journal*, **126**, 1505 (1979).
4. W. Siripala and M. Tomkiewicz, *ibid.*, **129**, 1240 (1982).
5. R. J. Hunter, "Zeta Potential in Colloid Science," Chap. 7, Academic Press, London (1981).
6. J. Lyklema, *J. Electroanal. Chem.*, **18**, 341 (1968).
7. D. E. Yates, R. O. James, and T. W. Healy, *J. Chem. Soc. Faraday Trans. 1*, **76**, 1 (1980).
8. D. E. Yates, S. Levine, and T. W. Healy, *ibid.*, **70**, 1807 (1974).
9. J. A. Davis, R. O. James, and J. O. Leckie, *J. Colloid Interface Sci.*, **63**, 480 (1978).
10. R. O. James, J. A. Davis, and J. O. Leckie, *ibid.*, **65**, 311 (1978).
11. W. Smit, C. L. M. Holten, H. N. Stein, J. J. M. de Goey, and H. M. J. Theelen, *ibid.*, **63**, 120 (1978).
12. W. Smit and H. N. Stein, *J. Electroanal. Chem.*, **91**, 393 (1978).
13. W. Smit and C. L. M. Holten, *J. Colloid Interface Sci.*, **78**, 1 (1980).
14. V. E. Kazarinov, V. N. Andreev, and A. P. Mayorov, *J. Electroanal. Chem.*, **130**, 277 (1981).
15. Yu. V. Pleskov, in "Comprehensive Treatise of Electrochemistry," Vol. 1, J. O'M. Bockris, B. E. Conway, and E. Yeager, Editors, p. 291, Plenum Press, New York (1980).
16. J. F. Dewald, *Bell Syst. Tech. J.*, **39**, 615 (1960).
17. H. P. Van Leeuwen, *Electrochim. Acta*, **23**, 207 (1978).
18. H. P. Van Leeuwen, in "Electroanalytical Chemistry," Vol. 12, A. J. Bard, Editor, p. 159, Marcel Dekker, New York (1982).
19. A. A. Pilla, *This Journal*, **117**, 467 (1970).
20. A. A. Pilla, *ibid.*, **118**, 1295 (1971).
21. J. R. Macdonald and J. A. Garber, *ibid.*, **124**, 1022 (1977).
22. J. R. Macdonald, J. Schoonman, and A. P. Lehnen, *J. Electroanal. Chem.*, **131**, 77 (1982).
23. H. Gerischer, in "Physical Chemistry," Vol. 9A, H. Eyring, D. Henderson, and W. Jost, Editors, p. 463, Academic Press, New York (1970).
24. L. Bousse and P. Bergveld, *J. Electroanal. Chem.*, **152**, 25 (1983).
25. W. Smit, Submitted to *J. Colloid Interface Sci.*
26. P. R. Bevington, "Data Reduction and Error Analysis for the Physical Sciences," Chap. 11, McGraw-Hill, New York (1969).
27. P. Carlsson and B. Holmstrom, *This Journal*, **129**, 1851 (1982).
28. W. Smit and C. L. M. Holten, To be published.

Economic Optimization of Electrolyzers by an Extension of Ibl's Formula

Thomas Z. Fahidy*

Department of Chemical Engineering, University of Waterloo, Waterloo, Ontario, Canada, N2L 3G1

The well-known optimization formula of Ibl (1)

$$i^* = \left(\frac{a}{bR} \right)^{1/2} \quad [1]$$

is based on the assumptions that (i) a linear relationship between cell potential V and current density i exists

$$V = V_1 + Ri \quad [2]$$

(ii) the variable investment cost and time are linearly related

$$K = \alpha At \quad [3]$$

and (iii) the current efficiency (at the cathode) is independent of current density. In an electrorefining process where V_1 may be negligible, the sum of the investment cost and the cost of electricity may be written, in consequence, as

$$C_T \cong At(Rbi^2 + \alpha)$$

or, removing time as an explicit variable

$$C_T = \frac{zFm}{e_c M} \left[\frac{\alpha}{i} + Rbi \right] \quad [4]$$

If $e_c = \text{const.}$, Eq. [1] immediately follows by setting $dC_T/di = 0$.

The third condition, independence of current efficiency of current density, is obeyed only in a limited number of electrodeposition processes; in fact, e_c may be a distinct function of i , all other parameters being constant (e.g., in the electrowinning of zinc). Under such circumstances, Eq. [1] either underestimates or overestimates the true optimum, as illustrated in Fig. 1. The

optimum current density is found by differentiating Eq. [4] and setting it to zero

$$\frac{dC_T}{di} = \left(\frac{\partial C_T}{\partial i} \right)_{e_c} + \left(\frac{\partial C_T}{\partial e_c} \right)_i \frac{de_c}{di} = 0 \quad [5]$$

Upon rearrangement, the expression

$$\left(-\frac{\alpha}{i^2} + Rb \right) e_c = \left(\frac{\alpha}{i} + Rbi \right) \frac{de_c}{di}$$

is obtained; the final form of the optimization formula

$$\frac{d \log e_c}{d \log i} \equiv \mathbf{F}(i) = \frac{Rbi^2 - \alpha}{Rbi^2 + \alpha} \quad [6]$$

replaces Eq. [1]. As shown in Fig. 1, the intersection of the experimental $d \log e_c/d \log i$ curve with $\mathbf{F}(i)$ yields the optimal current density. The procedure is simpler if the current efficiency is a power function of the current density of the form $e_c = A/i^m$ or $e_c = Ai^m$ where A and m are empirical parameters. Then, $d \log e_c/d \log i$ equals $-m$ or $+m$, respectively, and defines a straight line parallel to the i -axis. In fact, the analytical solution

$$i^* = \left(\frac{1 \pm m}{1 \mp m} \right)^{1/2} \left(\frac{\alpha}{bR} \right)^{1/2} \quad [7]$$

in such cases obviates a graphical solution.

To illustrate the magnitude of error introduced by using Eq. [1] instead of Eq. [6] when the latter is warranted, consider a copper electrorefining process where the mild dependence

$$e_c = 95.94 - 6.25i\% \quad [8]$$

$$[i]: \text{kA/m}^2$$

*Electrochemical Society Active Member.

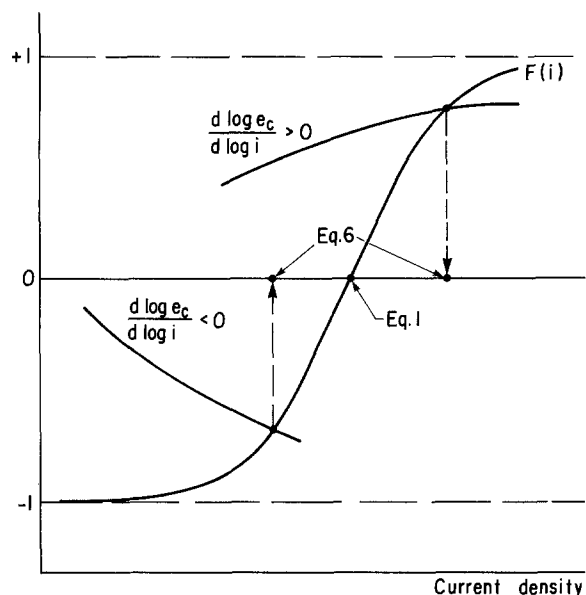


Fig. 1. Optimal current density via Ibl's formula (Eq. [1]) and its extension (Eq. [6]).

is assumed to be empirically known. Using Ibl's estimates (1) of $a = 6.29 \times 10^{-3} \text{ \$/m}^2\text{-h}$, $b = 1 \times 10^{-5} \text{ \$/Wh}$, and $R = 9 \times 10^{-4} \text{ \Omega-m}$, the expressions

$$d \log e_c / d \log i = -6.25i / (95.94 - 6.25i)$$

and

$$F(i) = (9i^2 - 6.29) / (9i^2 + 6.29)$$

are obtained. Then, a graphical construction yields $i^* \cong 792 \text{ A/m}^2$, which is 44 A/m^2 less than the estimate via Eq. [1]. If e_c is a sharper function of i , the error could be much larger. The extended Ibl formula is recommended for optimization problems where the $e_c(i)$ relationship cannot be ignored and the optimum is narrow, but more sophisticated optimization procedures (e.g., 2, 3) are not warranted.

Manuscript submitted Oct. 22, 1984; revised manuscript received Feb. 4, 1985. This was Paper 411 presented at the Toronto, Ontario, Canada, Meeting of the Society, May 12-17, 1985.

The University of Waterloo assisted in meeting the publication costs of this article.

LIST OF SYMBOLS

A	total electrode area
a	investment cost per unit electrode area and unit time
b	specific energy price
C_T	sum of the variable investment cost and the cost of electricity
e_c	current efficiency
i	current density; i^* is its optimal value
K	variable investment cost
M	molar mass of electrolytic product
m	amount of electrolytic product
R	cell resistance per unit electrode area
V	cell potential; V_1 is its zero-current value
t	time

REFERENCES

1. N. Ibl, *Electrochim. Acta*, **22**, 465 (1977).
2. M. J. Jaskula, *ibid.*, **28**, 1395 (1983).
3. T. R. Beck, in "Techniques of Electrochemistry," E. Yeager and A. J. Salkind, Editors, Chap. 1, John Wiley and Sons, New York (1978).

Visible Absorption Spectra of Solid Thionine on an SnO_2 Substrate

T. I. Quickenden and I. R. Harrison

Department of Physical and Inorganic Chemistry, University of Western Australia, Nedlands, Western Australia 6009, Australia

J. M. Austin

Department of Chemistry, University of Canterbury, Christchurch, 1, New Zealand

Thionine-coated electrodes have received some attention (1-3) because of their possible use as converters of solar energy to electricity. Thionine has been electrochemically deposited on conducting electrodes held at static (1, 4) or cycled (2, 3) potentials. Unfortunately, little is known of the structure of the stable thionine layers deposited by these methods.

It has been suggested (2) that the layers consist of thionine molecules linked by carbon-nitrogen bonds; however, surprisingly little spectroscopic information is available to substantiate this suggestion. Albery *et al.* (1) have reported a broad absorption between 400 and 600 nm for layers deposited on SnO_2 at a fixed potential. This spectrum is largely unresolved, but it does indicate a general maximum between about 560 and 640 nm.

Thionine in aqueous solution absorbs with a relatively narrow peak centered at 600 nm with a shoulder absorption at 575 nm due to the presence of a labile dimer (5). It is clearly important to obtain more highly resolved absorption spectra for the electrochemically deposited thionine and to ascertain whether there are spectral differences between the layers deposited at static and cycled potentials. No absorption spectra have been previously reported for layers deposited by the latter method.

The purpose of the present paper was to obtain absorp-

tion spectra for both types of electrochemically deposited layers and to compare these with the spectra of solid thionine layers deposited by several different methods.

Materials and Methods

All reagents used in the present study were of analytical reagent grade, except for SbCl_5 , which was of reagent grade, ethanol, which was of spectroscopic quality (Ajax Chemicals, Spectrosil grade), and thionine, which was of biological grade (Gurr). The method of purification of the thionine and the purity checks carried out have been described previously (3). All solutions were prepared with water which had been redistilled once after distillation from alkaline permanganate. Argon gas was ICI Special Grade and contained less than 7 ppm of O_2 . Conducting SnO_2 electrodes were prepared by the method described previously (3).

Visible absorption spectra were determined with a Hewlett-Packard 8450A absorption spectrophotometer and fluorescence spectra were determined with a Perkin Elmer 650-40 fluorescence spectrophotometer. The cycled-potential deposition of thionine layers was carried out with the cyclic voltammetry equipment described previously (3), except that the working electrode comprised an $8 \times 5 \text{ cm}$ plate of conducting SnO_2 glass and the

counterelectrode was a polymethylmethacrylate plate of the same size coated with a thick layer of vacuum-deposited gold. The potential was cycled between 0.05 and 1.40V (NHE) during the deposition. A potential of 1.40V (NHE) was maintained for the static-potential depositions. Solutions for the electrochemical deposition of thionine contained $0.050 \text{ mol-dm}^{-3} \text{ H}_2\text{SO}_4$ and $6 \times 10^{-5} \text{ mol-dm}^{-3}$ thionine in water.

In order to enable the subtraction of the background absorbance of the uncoated SnO_2 plate, only half of the electrode was immersed in the deposition solution.

Absorption spectra were then measured at a minimum of five positions across the coated portion of the plate and at the same number of positions across the uncoated portion. The coated plates were washed in distilled water and dried in a vacuum desiccator before the spectra were measured.

Oxygen-free thionine depositions were carried out under an argon atmosphere inside a glove bag which was maintained under a positive pressure of argon during the deposition (ca. 12h). All solutions were thoroughly deoxygenated prior to use. Thionine was evaporated from aqueous solution in a polymethylmethacrylate "boat" constructed with an SnO_2 base. The evaporation process was carried out at 333 K inside the glove bag. Absorption measurements were also carried out in an argon atmosphere in these cases.

Results and Discussion

Figure 1 shows the progressive growth of the absorption spectrum of the SnO_2 electrode as thionine is deposited thereon by the cycled-potential method. Figure 2A shows the absorption spectra after 7h of deposition by the cycled-potential (curves 1-3 in Fig. 2A) and static-potential (curve 4 in Fig. 2A) methods. The differences between the spectra for the two modes of electrochemical deposition are not significant and are about the same order of magnitude as the reproducibility of the spectra.

The electrochemically deposited layers of thionine are compared with the layers of thionine deposited by evaporation of an aqueous thionine solution in Fig. 2C. The layers deposited by bulk evaporation did not differ significantly from layers obtained by spraying the electrode with an aqueous or ethanolic solution of thionine, and the spectra were not significantly different when the depositions were carried out in the absence of oxygen.

The electrochemically deposited layers in Fig. 2A mainly differ from the evaporated layers in the 490-500 nm region, where the electrochemical deposition has produced a prominent peak. Extensive leaching of the electrochemical layers with water, ethanol, dimethylene chloride, n-hexane, and toluene did not substantially reduce the peak at 495 nm, whereas the solid thionine peaks at longer wavelengths were largely removed after ethanol

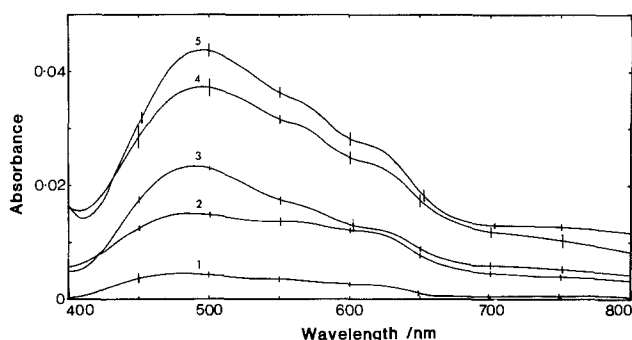


Fig. 1. Absorption spectra showing the progressive growth of layers of solid thionine deposited on SnO_2 by the cycled-potential method. Deposition potential = 0.05-1.40V (NHE). Sweep rate = 100 mV-s^{-1} . Spectra were recorded after 20, 60, 120, 240, and 420 min of cycling (curves 1, 2, 3, 4, and 5 respectively). Each error bar represents the 50% confidence interval associated with the mean of five absorbances determined at different positions on the SnO_2 electrode.

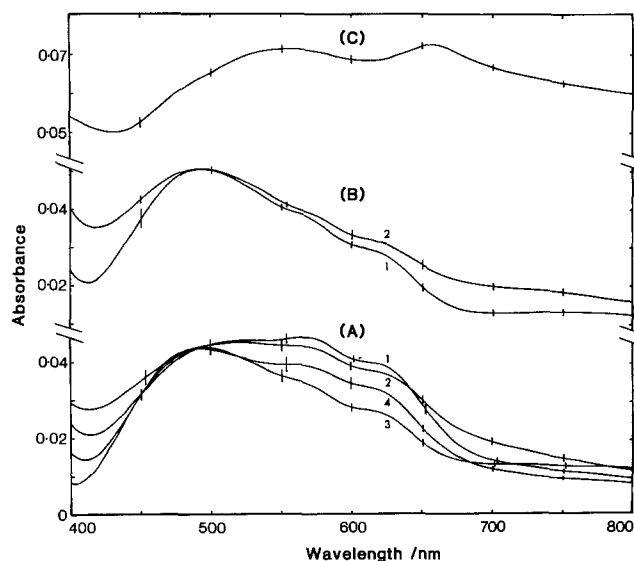


Fig. 2. Region A: Absorption spectra of thionine electrochemically deposited on SnO_2 by the cycled-potential method (curves 1-3) and by the static-potential method (curve 4). Spectra were recorded after 420 min of deposition and have been normalized to the same absorbance at 495 nm. Region B: Absorption spectra of solid thionine deposited on SnO_2 by the cycled-potential method (420 min) after two types of extractive treatment. Curve 1: by solvent extraction in ethanol of the layer in Fig. 2A, curve 1. Curve 2: by voltage cycling of the layer in Fig. 2A, curve 2 in $0.050 \text{ mol-dm}^{-3} \text{ H}_2\text{SO}_4$ for 26h between 0.05 and 1.40V (NHE) at 100 mV-s^{-1} . Each error bar in regions A and B represents the 50% confidence interval associated with the mean of five absorbances determined at different positions on the SnO_2 electrode. Region C: Absorption spectrum of solid thionine deposited on SnO_2 by the evaporation of aqueous thionine in air at 333 K. The spectrum is the mean of the spectra of four different evaporated samples normalized to the same average absorbance, and the error bars represent 50% confidence intervals in the means.

leaching (Fig. 2B, curve 1). The eluent from the ethanol extraction had the same fluorescence excitation spectrum and fluorescence emission spectrum as thionine solution. The amount of fluorescent solute removed from the layer was in the vicinity of $4 \times 10^{-11} \text{ mol-cm}^{-2}$, which suggests that about 45% of the layer is soluble when one obtains an estimate of the layer thickness (45-50 monolayers) by cyclic voltammetry. Thionine deposited by evaporation from bulk solution or by spraying an SnO_2 glass surface was completely removed by ethanol.

Repeated voltage cycling (0.05 to 1.40V (NHE) at 100 mV-s^{-1}) of the electrochemically deposited layers in $0.050 \text{ mol-dm}^{-3} \text{ H}_2\text{SO}_4$ almost completely removed the solid thionine peaks in the 550-650 nm region, while the peak at around 495 nm was not substantially decreased, even after 26h of voltage cycling (Fig. 2B, curve 2).

The above observations indicate that the electrochemically deposited thionine layers contain a solvent extractable component which is probably occluded thionine and a strongly bonded component with a prominent absorption peak around 495 nm.

The variability of the solvent extractable thionine region (550-650 nm) in the layers in Fig. 2A suggests that electrochemical deposition causes the occlusion of varying amounts of loosely bonded thionine.

The strongly bonded material absorbing around 495 nm has an extinction coefficient of $(1.7 \pm 0.1) \times 10^3 \text{ m}^2\text{-mol}^{-1}$. This determination required the layer thickness, which was measured by cyclic voltammetry on the coated electrode in a background electrolyte comprising $0.050 \text{ mol-dm}^{-3} \text{ H}_2\text{SO}_4$. The layer thickness was obtained using the background-corrected charge enclosed by the cyclic voltammogram. It was assumed that the reduction and oxidation of the layer occurred by a process involving two electrons per monomer unit and that all the material in the layer was electrochemically active. If these assumptions do not hold, then the replication error shown for the

extinction coefficient may be an underestimate of the actual error.

The solvent-resistant material absorbing around 495 nm appears only in the electrochemically deposited layers and does not appear in the spectrum of evaporated thionine layers. This material is probably the thionine polymer, which Bauldrey and Archer (2) suggest is deposited by the electrochemical process.

Acknowledgment

I. R. H. gratefully acknowledges support by a University of Western Australia Research Studentship.

Experimental Determination of the Collection Efficiency of a Metal/n-Type Semiconductor Rotating Ring-Disk Electrode

E. Verney, J. R. Martin, and P. Clechet*

Laboratoire de Physicochimie des Interfaces, Unité associée du CNRS no. 404, Ecole Centrale de Lyon, 69131 Ecully Cedex, France

The rotating ring-disk electrode (RRDE) is a very useful tool for studying chemical corrosion in the dark and light-stimulated corrosion of semiconductor materials immersed in liquid media (1-3). This method is most often used to evaluate the extent to which the capture of photogenerated minority carriers by soluble redox species competes with surface corrosion. The resolution of this problem is critical to the development of photoelectrochemical solar cells, especially for readily corrodable low bandgap n-type covalent materials (4-10). In this case, the efficiency of the protective reductant is measured by the stabilization factor, S , defined as the ratio of the current resulting from the oxidation of the reducing agent, i_{ox} , to the total photocurrent $i_{photo} = i_D$, obtained at the semiconductor disk electrode. The value of i_{ox} is calculated by dividing the ring current i_R by the collection efficiency N of the RRDE. Therefore, we must know the latter quantity accurately.

For a metal-metal RRDE, the evaluation of N is easily obtained from the geometric parameters of the electrode (11) or from the slope of the i_R vs. i_D curve. With a semiconductor disk, the problem is more complex. The first method is often inconvenient because of the low geometrical definition of round hand-machined semiconductor disks. The second method requires the use of a fully protective fast redox couple ($S = 1$) whose existence has to be proved beforehand, for example, by RRDE. There is therefore an obvious need for a method which does not imply the existence of such a couple. In this paper, we suggest a new method which consists in an *in situ* provisional metallization of the n-type semiconductor disk and the use of this Schottky diode, forward biased in the dark, to monitor the reduction of an oxidant. The value of N is then obtained by measuring the ring electrode current used in collection (oxidation) or shielding (reduction) of the oxidant being reduced at the metallized disk electrode. The thin metal layer deposited on the semiconductor protects its surface from possible chemical corrosion, by hole injection, from the dissolved acceptor species. Additionally, it can also protect it against reductive decomposition under the negative biases used here. Thus, the n-type semiconductor, being in the dark and cathodically polarized, is protected against any kind of corrosion.

To check this method, we have considered a corrodable n-type semiconductor material, n-GaAs, the photoprotection of which involved the use of strong air-sensitive reductants (8-12). The oxidizing agent was an aqueous solution of ferricyanide, and the deposited metal was gold. The ring electrode was also made from gold in order to avoid masking steps during plating.

*Electrochemical Society Active Member.

Manuscript submitted Feb. 8, 1985; revised manuscript received ca. April 19, 1985.

REFERENCES

1. W. J. Albery, W. R. Bowen, F. S. Fisher, A. W. Foulds, K. J. Hall, A. R. Hillman, R. G. Egdell, and A. F. Orchard, *J. Electroanal. Chem.*, **107**, 37 (1980).
2. J. M. Bauldrey and M. D. Archer, *Electrochim. Acta*, **28**, 1515 (1983).
3. T. I. Quickenden and I. R. Harrison, *This Journal*, **132**, 81 (1984).
4. W. R. Bowen, *Acta Chem. Scand. A*, **34**, 437 (1980).

The experimental data presented here lead to a collection factor which tallies well with that calculated on a carefully and geometrically well-defined electrode. As the deposited metal can be eliminated later by polishing and etching, the checked electrode can then be used for further experiments. This technique can evidently be adapted to other semiconductor materials.

Experimental

Our rotating ring-disk electrode consists of a demountable setup as first conceived by Menezes *et al.* (9). The semiconductor disk is cut from n-GaAs <100> single-crystal slices (MCP Electronic Materials Limited; thickness = 500 μm ; $N_D = 2 \times 10^{16} \text{ cm}^{-3}$).

Rear-side ohmic contacts are formed by melting a Sn and NH_4Cl mixture at 350°C under N_2 flow. The semiconductor is carefully centered in the system and threaded to planarity to the ring. The remaining gap between the disk and the ring is then filled with a cyanoacrylate (Loctite IS 430). Excess adhesive is removed with dimethylformamide (DMF), and the ring and disk made coplanar by polishing with 3 and 1 μm diamond pastes before each experiment. Samples are etched twice with $\text{H}_3\text{PO}_4\text{:H}_2\text{O}_2\text{:H}_2\text{O}$ (1:1:18 volume ratio, 15°C) solutions and then dipped for a few seconds in $\text{HCl:CH}_3\text{OH}$ (1:1 volume ratio) mixture. To dismount the disk, the adhesive is dissolved in an ultrasonically agitated bath containing DMF at 40°C.

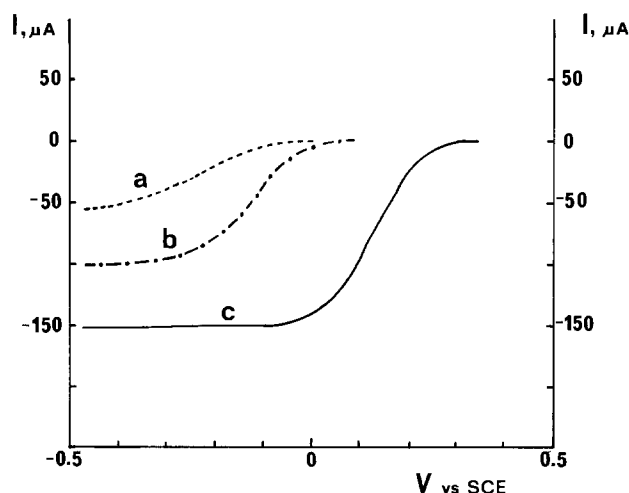


Fig. 1. I-E curves at rotating disk electrodes in $\text{Fe}(\text{CN})_6^{3-}$, 10^{-3}M , pH 5 (acetate buffer), $\omega = 600 \text{ rpm}$. Curve a: n-GaAs/Au (photoassisted metallization). Curve b: n-GaAs/Au (electrolytic deposition). Curve c: gold electrode.

Electrolytic solutions are prepared from reagent-grade chemicals (Merck and Prolabo) and distilled water. The ferricyanide solution is $10^{-3}M$ at pH 5 (acetate buffer). We use a two-compartment cell containing 80 cm^3 of solution.

This cell is fitted with a saturated calomel electrode (SCE), a platinum counterelectrode, and an optical flat window at the bottom to allow the disk to be illuminated by light conducted by an optical fibre. The electrode is driven by an Oxford variable rotation speed motor. Current-voltage curves are obtained with a Tacussel bipotentiostat and an HP plotter monitored by an Apple IIe microcomputer.

Nominal dimensions are $(r_3/r_1) = 1,467$ and $(r_2/r_1) = 1,195$. The corresponding theoretical collection factor is $N = 0.328$.

Photoassisted deposition of gold is realized by illumination of the electrode immersed in a $3 \times 10^{-3}M$ $\text{AuCl}_3/0.1N$ HClO_4 solution for a few minutes. The surface is then rinsed with distilled water and blown dry. The thin film obtained does not seem to be uniform, and, following the statement of Frese *et al.*, the estimated gold thickness is around 200 \AA (14).

For electrolytic gold deposition, we use a 20 g-liter^{-1} KAu(CN)_2 , 100 g-liter^{-1} sodium citrate aqueous solution at pH 5 maintained at 70°C . The density of current is 10 mA-cm^{-2} , and the duration 15s. The electrode is then washed and dried as above. With a faradaic efficiency of 100%, the metal thickness should be close to 1500 \AA . The deposit is adherent and quite uniform.

Results and Discussion

The behavior of n-GaAs in ferricyanide solutions, at various pH values, has been studied in prior works (1, 2, 13-15). This redox system is pH independent above pH 4, and its Fermi level is located below the valence bandedge of GaAs at pH 14 and within its forbidden bandgap at pH 6 (1, 2). In an alkaline medium, hole injection is thus possible, and we do observe corrosion in such conditions in the dark. At pH 6, corrosion apparently stops. These results, as well as the general features of the current-voltage curves (not reported here), are in full accord with the experimental results of the above-cited works. After gold deposition, chemical corrosion is no longer observed. Such improvement in the stability of gold-covered GaAs has been previously noted by Frese *et al.* with other redox couples, even under illumination (14). These interfaces behave like Schottky diodes with a barrier height of several hundred millivolts (16) in series with the solution, as proved by Menezes *et al.* (15). The dark current-voltage curves obtained in $10^{-3}M$ Fe(CN)_6^{3-} at pH 5 with the gold-

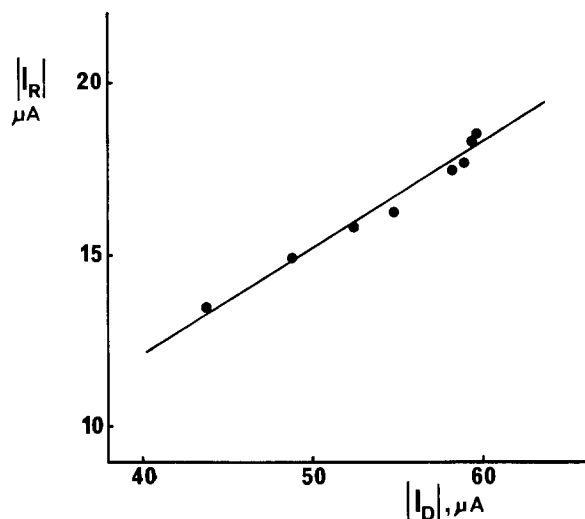


Fig. 2. i_R - i_D curve in Fe(CN)_6^{3-} $10^{-3}M$, pH 5 (acetate buffer) at n-GaAs/Au electrode (photoassisted metallization). $E_D = -0.4V$ vs. SCE, $E_R = 0.6V$ vs. SCE, $\omega =$ from 0 to 1600 rpm collection efficiency, $N = 0.310$.

plated GaAs electrodes are compared with the curves obtained on a pure gold electrode in Fig. 1. With GaAs/Au electrodes, the curves normally shift toward negative voltages due to the solid-state Schottky barrier formed. The better barrier is clearly obtained with the electrolytic deposition of gold. As the shape of these curves has no influence on the precision of the S calculation, we do not try to optimize them.

Figure 2 shows the i_R vs. i_D plot obtained for the first type of metallization (photoassisted deposition). The slope yields a collection efficiency of 0.310, close to its estimated nominal value. The i_R vs. i_D curve obtained with the second method of metallization is represented in Fig. 3. The slope of this straight line gives a collection factor equal to 0.320, which seems very reliable.

After removing the protective thin gold layer by successive polishing and etching of the surface, the bare electrode can again be used for classical electro- or photoelectrochemical studies. The provisional gold deposition appears to have no remaining influence on the subsequent electrode behavior. This is proved by the i_D - E_D and i_R - E_D curves obtained with our electrode, in $7M$ NaI, $10^{-2}M$ HI under photon flux-limited conditions, (Fig. 4), as these curves are absolutely the same before and after gold treatment and subsequent cleaning. The highly concentrated iodide solution is used to suppress the semiconductor photocorrosion process by promoting hole transfer to the solution (17, 18). In the dark, the reverse disk

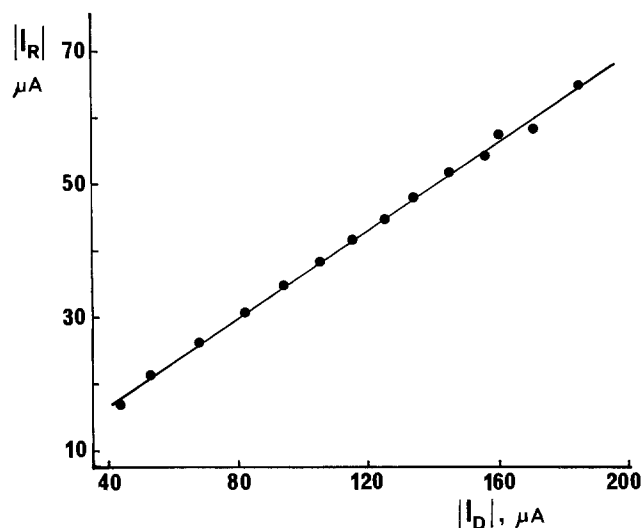


Fig. 3. i_R - i_D curve in Fe(CN)_6^{3-} $10^{-3}M$, pH 5 (acetate buffer) at n-GaAs/Au electrode (electrolytic metallization). $E_D = -0.4V$ vs. SCE, $E_R = 0.6V$ vs. SCE, $\omega =$ from 0 to 2400 rpm collection efficiency, $N = 0.320$.

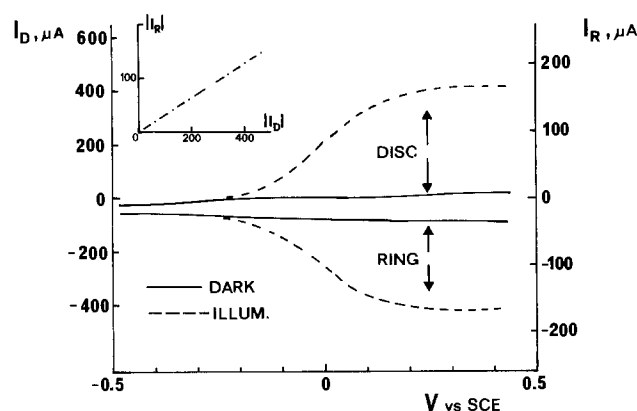


Fig. 4. i_D - E_D and i_R - E_D curves at RRDE (recovered disk) in $7M$ NaI, $10^{-2}M$ HI under photon flux-limited conditions. $\omega = 600$ rpm. $E_R = -0.2V$ vs. SCE. The insert shows the corresponding i_R - i_D curve for this electrode, under illumination, in the same medium.

current is negligible (good Schottky barrier at the semiconductor/electrolyte interface). The residual ring current corresponds to the reduction of the iodine quickly formed in such highly concentrated iodide solution. The i_R vs. i_D plot in the insert of Fig. 4 is linear with slope $N = 0.317$, agreeing with the above. Inversely, this conformity proves that a good photo stabilization of GaAs is obtained in such media. These results will be discussed elsewhere.

Conclusion

The analysis of the reduction dark current generated at the metallized n-type semiconductor disk of a RRDE allows its collection efficiency to be determined reliably. The salient point is that this provisional gold metallization can be easily and completely removed when the measurement of the collection factor has been made. The recovered electrode can thus be successfully used for further photoelectrochemical quantitative experiments requiring knowledge of the collection efficiency.

Acknowledgment

This work was supported by the GRECO 130061 of CNRS.

Manuscript submitted Feb. 12, 1985; revised manuscript received April 22, 1985.

CNRS assisted in meeting the publication costs of this article.

REFERENCES

1. S. Menezes and B. Miller, *This Journal*, **130**, 517 (1983).
2. F. Decker, B. Pettinger, and H. Gerischer, *ibid.*, **130**, 1335 (1983).
3. J. J. Kelly and P. H. L. Van Notten, *Electrochim. Acta*, **29**, 589 (1984).
4. T. Inoue, T. Watanabe, A. Fujishama, K. Honda, and K. Kohayakawa, *This Journal*, **124**, 719 (1977).
5. R. Menning, *Ber. Bunsengen. Phys. Chem.*, **81**, 732 (1977).
6. T. Kobayashi, H. Yoneyama, and H. Tamura, *Chem. Lett.*, 457 (1979).
7. F. Van Overmeire, F. Van Den Kerchove, W. P. Gomes, and F. Cardon, *Bull. Soc. Chem. Belg.*, **89**, 181 (1980).
8. K. W. Frese, Jr., M. J. Madou, and S. R. Morrison, *J. Phys. Chem.*, **84**, 3172 (1980).
9. S. Menezes, L. F. Schneemeyer, and B. Miller, *This Journal*, **128**, 2167 (1981).
10. J. R. Wilson and S. M. Park, *ibid.*, **129**, 149 (1982).
11. W. J. Albery and S. Bruckenstein, *Trans. Faraday Soc.*, **62**, 1920 (1966).
12. B. A. Parkinson, A. Heller, and B. Miller, *This Journal*, **126**, 954 (1979).
13. R. Memming, *ibid.*, **125**, 117 (1978).
14. K. W. Frese, Jr., M. J. Madou, and S. R. Morrison, *ibid.*, **128**, 1939 (1981).
15. S. Menezes, A. Heller, and B. Miller, *ibid.*, **127**, 1269 (1980).
16. G. Horowitz, P. Allongue, and H. Cachet, *ibid.*, **131**, 2653 (1984).
17. L. F. Schneemeyer and B. Miller, *ibid.*, **129**, 1977 (1982).
18. P. Allongue, H. Cachet, P. Clechet, J. R. Martin, and E. Verney, Paper presented at the 5th International Conference of Photochemical Conversion and Storage of Solar Energy, Osaka, Japan, 1984.



Photoelectrochemical and Corrosion Study of n-Type SnS_xSe

B. Fotouhi, A. Katty, and O. Gorochov

Laboratoire de Physique des Solides, CNRS, 92195 Meudon Principal Cedex, France

ABSTRACT

Single crystals of n-type SnS_xSe_{2-x} ($x = 1.04$) obtained both by transport and Bridgman methods exhibit an energy gap of 1.53 eV. The flatband potential is pH dependent, and its values in acidic and alkaline solutions are, respectively, 0.06 and -0.6 V (SCE). In the dark, SnS_xSe is stable in acidic medium, but the stability decreases as pH increases. It is also unstable in acidic solutions containing the oxidizing form of a redox reagent with a sufficiently positive redox potential (ca. more positive than 0.8V/SCE). The presence of an oxidizing form of a redox couple in alkaline medium enhances the already existing corrosion reaction. The corrosion reaction is accompanied with an anodic current. The corrosion rate as well as the magnitude of the anodic current depends on pH and the concentration of the oxidizing state of the couple. Light-driven reactions in both acidic and alkaline media are corrosion reactions. However, decomposition may be avoided in acidic solution containing potassium iodide.

The solid solution SnS_xSe_{2-x} can be prepared over the entire composition range from SnS₂ to SnSe₂. Compounds obtained are layered semiconductor with CdI₂-type structure. Optical properties of the mixed series SnS_xSe_{2-x} (where $0 < x < 2$) have already been studied (1). Indirect energy gaps obtained vary linearly between SnSe₂ (1.09 eV) and SnS_{1.5}Se_{0.5} (1.75 eV). A deviation from linearity is observed between SnS_{1.5}Se_{0.5} and SnS₂ (2.22 eV). Photoelectrochemical properties of SnS₂ have already been studied (2), and it seems interesting to consider the ternary compound.

Although this ternary compound could present a particular interest in solar energy conversion because of its adjustable energy gap, it has not yet received attention in photoelectrochemistry. SnS_xSe, whose reported energy gap is 1.52 eV (1), which is an optimum value for solar spectrum, could be an interesting candidate for solar energy conversion into electrical or chemical energy.

Experimental

SnS_xSe_{2-x} single crystals were obtained both by transport and Bridgman methods. In both cases, stoichiometric amounts of purified tin sulfide and selenium were used. In the transport method, iodine and bromine were the transporting agents. The charge zone was at 630°C and the transport zone at 580°C. Single crystals of SnS_xSe_{2-x} ($3 \times 3 \times 0.1$ mm) were obtained within a week. In the Bridgman method, the transport zone was fixed at 780°C and the temperature gradient was 70°C. Ingots of 10 cm length with 1 cm diam were obtained. Microprobe analysis indicated that the composition of the samples prepared by transport was $x = 1.04$. For those prepared by Bridgman technique, the same composition was found for the higher part of the tube ($x = 1.05$). The composition for the lower and the central parts of the tube was approximately $x = 1.2$. Hall measurements gave a carrier concentration of 6×10^{17} cm⁻³ and a resistivity of 0.36 Ω-cm at room temperature for samples prepared by transport method, and a carrier concentration of 2×10^{16} cm⁻³ and a resistivity of 200 Ω-cm for those prepared by Bridgman method. Electrical contact was achieved using In-Ga eutectic and silver paste. Samples were mounted on a copper plate cleaved and insulated with Dow Corning glue. Only the van der Waals surface was exposed to the solution. Electrochemical experiments were performed using classical methods. Capacitance-voltage

measurements were performed using 5206 E.G.E. lock-in amplifier with an incorporated frequency generator. A 250W tungsten halogen lamp was used as light source. Samples were illuminated by monochromatic light ($\lambda = 600$ nm, $100 \mu\text{W}\cdot\text{cm}^{-2}$), using a JOBIN-YVON, monochromator. For the light-driven corrosion studies and photo-potential determination, white light was used ($200 \text{ mW}/\text{cm}^2$). Analytical-grade chemicals and deionized water were used for the preparation of the solutions. Results in this paper correspond to the crystal with a composition $x = 1.04$ grown by Bridgman technique designated as SnS_xSe in the text.

All potentials are referred to the saturated calomel electrode.

Results

Electrode reactions in the dark.—SnS_xSe has a diode-like blocking behavior in acidic solutions (the dark current being equal to 4×10^{-7} A-cm⁻² at anodic potentials); however, the dark current increases with increasing pH, and at pH = 14 a substantial increase in anodic current is observed. Figures 1 and 2 demonstrate the behavior of SnS_xSe in acidic and alkaline media. The variation of anodic current at 1.0V (SCE as a function of pH is shown in Fig. 3). A sharp increase in current is observed at pH values greater than 7. The anodic current is accompanied with the corrosion of the sample. The corrosion in alkaline solution is enhanced upon addition of the oxidized state of a redox reagent such as Fe(CN)₆³⁻. The corrosion, as well as the dark current, depends on the concentration of the oxidized form of the redox couple. The dark current and the corrosion intensity increase with increasing concentration of Fe(CN)₆³⁻. Figure 4 demonstrates the variation of anodic current as a function of Fe(CN)₆³⁻ concentration in KOH (pH = 14). In acidic medium, Fe(CN)₆³⁻ contributes very little to the increase of anodic current (8×10^{-7} A-cm⁻²) and corrosion of the electrode, whereas Ce⁴⁺ decomposes the electrode with a higher rate and an anodic current is established upon addition of Ce⁴⁺. The current is a function of the concentration of cerium ion (Fig. 5). The corrosion product in alkaline medium containing Fe(CN)₆³⁻ and acidic medium containing Ce⁴⁺ is a yellow-brown layer which deposits on the surface.

Cathodic polarization of SnS_xSe leads also to a decomposition reaction. Hydrogen evolution does not take place due to the energetic position of the conduction band. The

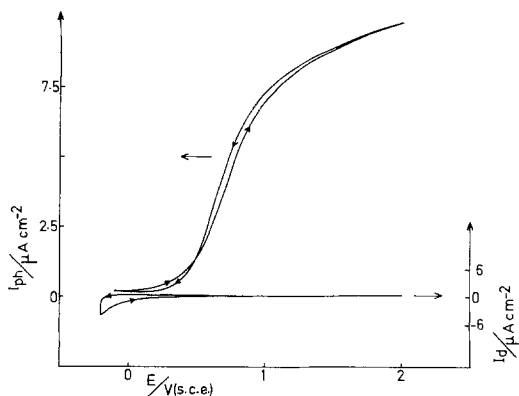


Fig. 1. Photocurrent and dark current vs. electrode potential in H_2SO_4 0.5M.

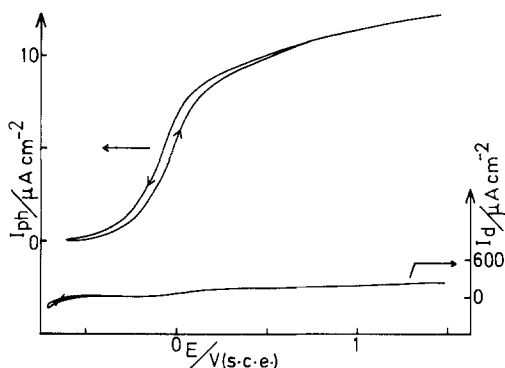


Fig. 2. Photocurrent and dark current vs. electrode potential in KOH 1M. Incident light intensity $\sim 100 \mu\text{W}\cdot\text{cm}^{-2}$ at 600 nm.

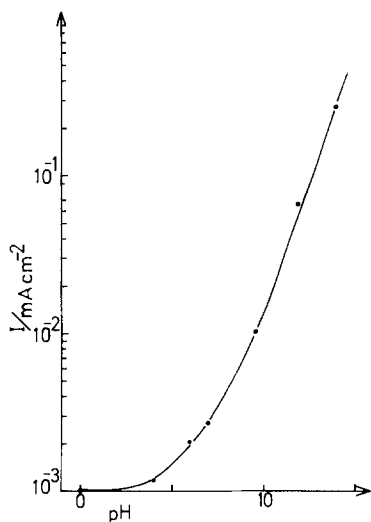


Fig. 3. Logarithmic variation of dark current as a function of solution's pH ($V = +1V$).

decomposition product which covers the electrode surface was proved to be the lower oxide of tin (SnO) by x-ray analysis.

Figures 6 and 7 demonstrate the Mott-Schottky plots for samples prepared by Bridgman and transport methods, respectively, flatband potential shifts to more negative value as pH increases. The slopes (assuming $\epsilon = 10$) gave a carrier concentration of 1.3×10^{16} and $4.6 \times 10^{17} \text{ cm}^{-3}$ for Bridgman and transport samples, respectively. These values are in agreement with those determined by Hall measurements.

Electrode reactions under illumination.— $I(V)$ curves are demonstrated in Fig. 1 and 2. A negative displacement of photocurrent onset in alkaline medium is observed. The flatband potential values are confirmed by a plot of square of photocurrent as a function of potential at 760

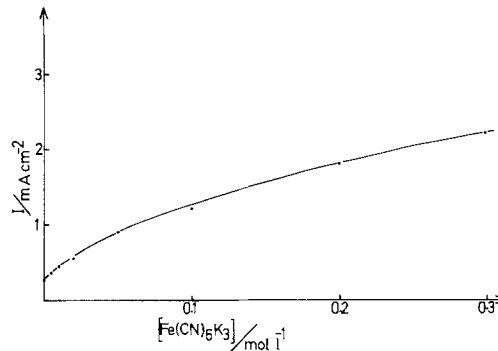


Fig. 4. Variation of dark current as a function of potassium ferricyanide concentration at pH 14 ($V = +1V$).

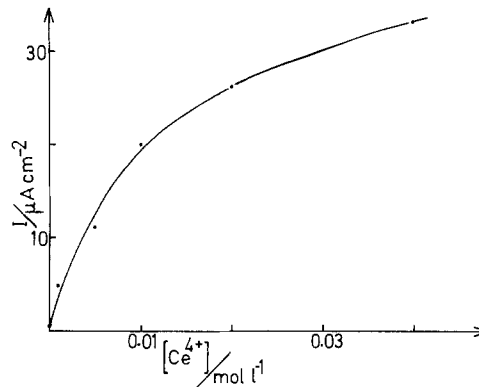


Fig. 5. Variation of dark current as a function of Ce^{4+} concentration in H_2SO_4 0.5M ($V = +1V$).

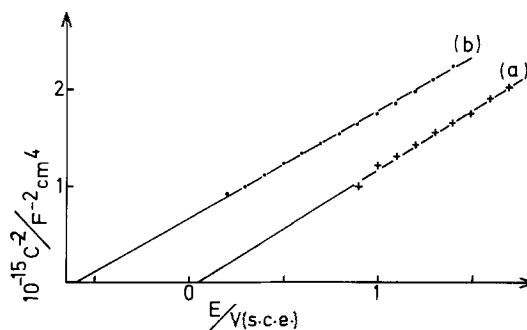


Fig. 6. Mott Schottky plots. a: in H_2SO_4 0.5M. b: in KOH 1M

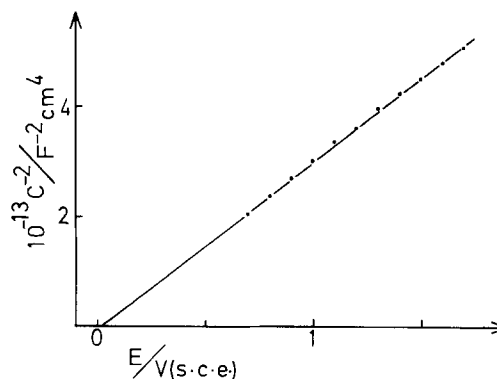


Fig. 7. Mott Schottky plot in H_2SO_4 0.5M

nm where the condition $\alpha\omega \ll 1$ and $\alpha L_p \ll 1$ is satisfied, Fig. 8.

The spectral dependence of the photocurrent at constant photon flux is shown in Fig. 9. A plot of $(I_{ph}/h\nu)^{1/2}$ as a function of $h\nu$ yields the value of 1.53 eV as the first indirect transition, which is in agreement with the value found in the literature (1). When electrodes were illuminated under white light ($200 \text{ mW}/\text{cm}^2$) at 0.5-1V polariza-

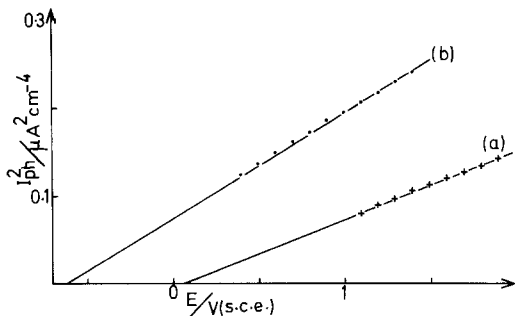


Fig. 8. Square of photocurrent at 760 nm vs. applied voltage. a: H₂SO₄ 0.5M. b: KOH 1M.

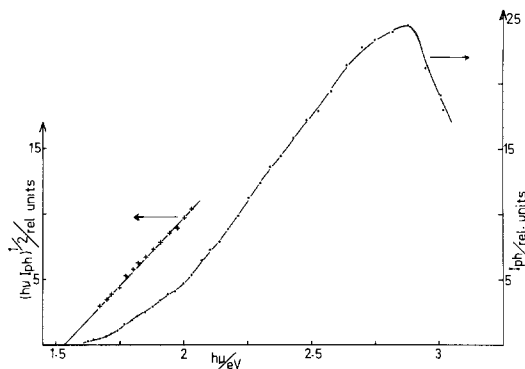


Fig. 9. Spectral response of SnSSe in H₂SO₄ 0.5M. a: I_{ph} vs. light energy. b: (hν I_{ph})^{1/2} vs. light energy.

tion in either acidic or basic solution, a brown layer was formed after approximately 30 min. Therefore, the light-induced reactions in acidic and alkaline solutions are corrosion reactions. The same corrosion layer was found in the dark in the presence of the oxidized form of a redox couple. The stability of the electrode can be substantially improved in acidic solution containing 2M potassium iodide. The presence of I₃⁻ in acidic medium shifts the flatband potential and the photocurrent onset to more negative values as in the case of some other dichalcogenides. The negative shift depends on the concentration of I₃⁻. The shift has been considered to be due to I₃⁻ adsorption (2-5). Photopotentials (Table I) are small and do not vary with redox couples' potential as theoretically predicted.

The energy diagram of SnSSe and the position of different redox reagents with respect to energy bands is demonstrated in Fig. 10. It can be seen that the redox potentials of all couples used in this experiment are situated in the bandgap region.

Discussion

Corrosion reaction in the dark in the presence of redox reagents has already been reported in the case of CdS, CdSe, and SnS₂ (3, 6, 7). In the case of CdSe, the corrosion is independent of pH and redox couple concentration, and it depends primarily on the redox couple's potential, which should be sufficiently positive. The dark anodic current was not affected for CdSe or for CdS. Corrosion of SnS₂ is independent of pH in solutions not containing redox couples, but it depends on the concentration of redox reagents used and it is accompanied with an anodic

Table I. Difference between light and dark steady-state V_{oc}.

Medium	Photopotential (mV)
0.5M H ₂ SO ₄ + I ⁻ /I ₃ ⁻	210
0.5M H ₂ SO ₄ + Fe(CN) ₆ ⁴⁻³⁻	260
0.5M H ₂ SO ₄ + Fe ^{2+/3+}	220
0.5M H ₂ SO ₄ + Br ⁻ /Br ₂	250
0.5M H ₂ SO ₄ + Ce ^{3+/4+}	240

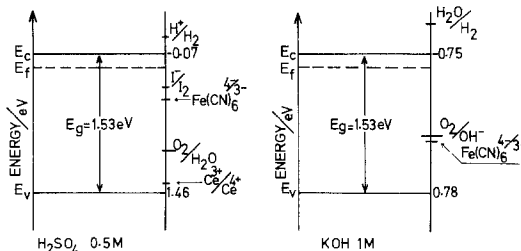
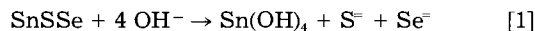
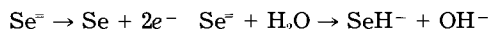
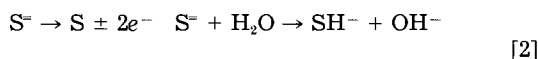


Fig. 10. Energy scheme of SnSSe in H₂SO₄ 0.5M and in KOH 1M (pH = 14).

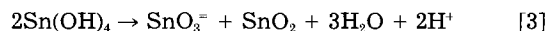
current. Corrosion of SnSSe, however, depends on the pH, and a substantial increase in the dark current is observed when pH is increased. At pH = 14, the analysis of the solution indicates that selenium, sulfur, and tin diffuse out into the solution. The corrosion product which stays back on the surface was also dissolved in KOH and the analysis indicated that it was constituted of a mixture of selenium, sulfur, and tin. It seems that in alkaline medium, hydroxide ions react with the semiconductor in such a way that selenium and sulfur are substituted by these ions in a reaction such as



From the fact that the corrosion reaction is accompanied with an anodic current, it is reasonable to assume that a part of S⁻ and Se⁻ formed according to reaction [1] whose energies are sufficiently high can inject electrons into the conduction band and a part diffuse out into the solution according to the following reactions

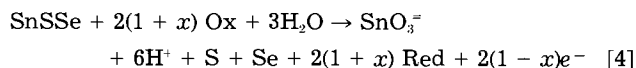


On the other hand, thermodynamic consideration indicates that Sn(OH)₄ dissolves partly to SnO₃²⁻ in alkaline medium (8)



The presence of sulfur, selenium, and tin, both in the solution and in the layer which deposits on the surface, and the fact that the total charge consumed during the electrolysis is six times smaller than the concentration of dissolved tin, would support this interpretation. The addition of Fe(CN)₆³⁻ to the alkaline solution increases the anodic current and the corrosion rate. The magnitude of the anodic current and the corrosion rate depend on the concentration of Fe(CN)₆³⁻. Corrosion leads to the formation of a yellow-brown layer on the surface, and in this case it primarily consists of sulfur and selenium.

The amount of tin found in the surface layer was very small, and the analysis of the solution indicated that it diffuses out into the solution. As in the preceding case, the total charge produced during the overall reaction was six times smaller than the concentration of SnO₃²⁻ found in the solution. The same phenomenon was observed in the case of SnS₂ (3), and it seems that the same mechanism for the corrosion reaction in the dark can be considered



According to reaction [4], (Ox) injects a hole in the surface states situated in the bandgap region (Fig. 11), breaking a chemical bond in a first step. In a second step, a part of the intermediate product formed injects an electron into the conduction band. 2(1-x)e⁻ would correspond to the anodic current observed. The corrosion product in this case is identical to that under illumination and tin is completely dissolved and passes into the solution, in contrast to corrosion in pure KOH. This may be due to the fact that (Ox) can inject a hole which is equivalent to a photo-induced hole.

In acidic solution, Fe(CN)₆³⁻ contributes very little to the increase of anodic current and to the corrosion reac-

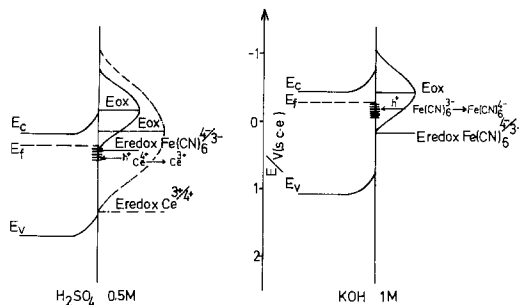
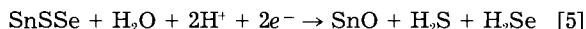


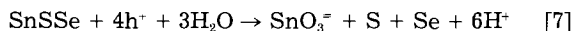
Fig. 11. Redox potential of $\text{Ce}^{3+/4+}$ and $\text{Fe}(\text{CN})_6^{4-/3-}$ relative to the bandedges in H_2SO_4 0.5M and KOH 1M. The values of λ have been taken from Ref. (10).

tion. This may be due to the positive shift of the flatband potential so that a proper overlap does not exist between surface states and the energy level of the oxidized form of this couple for which $\lambda = 0.6$ eV (Fig. 11). However, the oxidized form of a couple with a more positive potential, such as Ce^{4+} , produces a corrosion reaction and increases substantially the anodic current in acidic solution. It can be seen from Fig. 11 that an overlap exists between surface states and the oxidized form of cerium for which $\lambda = 1.25$ eV. Note that only distribution functions of oxidized species ($\text{Fe}(\text{CN})_6^{3-}$ and Ce^{4+}) are plotted in Fig. 11.

As was mentioned, the electrode undergoes a cathodic decomposition reaction at cathodic potentials; the reaction product is the lower oxide of tin (SnO) which deposits on the electrode and has been identified by x-ray analysis. The following reaction can be considered for cathodic decomposition in acidic medium.



We shall now discuss the electrode reactions under illumination. These reactions are decomposition reactions in both acidic and alkaline media. In both cases, tin diffuses out into the solution and a mixture of sulfur and selenium stays on the surface according to the reactions



As previously mentioned, corrosion products are identical to those found during the electrode decomposition in the dark in the presence of redox reagents. Substantial improvement can be achieved in the stability in acidic solution containing potassium iodide. The anodic polarization (+1V) under white light ($200 \text{ mW}\cdot\text{cm}^{-2}$) for 4h in a 2M I^- , 0.05M I_2 , and 0.5M H_2SO_4 solution did not lead to corrosion. The analysis of the solution did not show any trace of tin, and current stayed stable at $7 \text{ mA}\cdot\text{cm}^{-2}$.

Shifts in photopotentials do not follow the redox couple's potential. This is due to the existence of dark cathodic current at potentials positive to the flatband position. Surface states should be at the origin of the dark current onset at potentials positive to V_{FB} . On the other hand, in the case of Ce^{4+} and Br_3^- , the anodic current, due to corrosion, limits the band bending; therefore, in the presence of $\text{Ce}^{3+/4+}$ and $\text{Br}^-/\text{Br}_3^-$, the band bending in the dark is much smaller than expected, leading to approximately the same photopotential as in the presence of $\text{Fe}^{2+/3+}$ and $\text{Fe}(\text{CN})_6^{4-/3-}$. The same phenomenon has been observed previously in the case of SnS_2 and ZrS_3 (1, 9). As the anodic and cathodic dark currents depend on the concentration of the redox species in the solution, it is worth mentioning that photopotential, particularly in the presence of $\text{Ce}^{3+/4+}$ and $\text{Br}^-/\text{Br}_3^-$, decreases with increasing concentration of the above reagents.

Conclusion

It has been shown that SnSSe , a layered-type semiconductor with an energy gap of 1.53 eV, has a diode-like behavior. Although light-driven reactions are corrosion reactions, the stability can be improved substantially in the presence of an acidic solution containing potassium iodide.

Acknowledgment

Thanks are due to Mrs. Rommeluere and Service Central d'Analyse CNRS (Vernaison) for microprobe and solution analysis. B. F. would like to thank the Center International des Etudiants et Stagiaires for financial support. We would also like to thank Dr. Jonathan Foise for critical reading of the paper.

Manuscript submitted Dec. 12, 1984; revised manuscript received May 20, 1985.

CNRS assisted in meeting the publication costs of this article.

REFERENCES

1. P. A. Lee, G. Said, R. Davis, and T. H. Lim, *J. Phys. Chem. Solids*, **30**, 2719 (1969).
2. A. Katty, B. Fotouhi, and O. Gorochov, *This Journal*, **131**, 2806 (1984).
3. B. Fotouhi, A. Katty, and R. Parsons, *J. Electroanal. Chem.*, To be published.
4. W. Kautek and H. Gerischer, *Electrochim. Acta*, **12**, 1771 (1981).
5. J. A. Turner and B. A. Parkinson, *J. Electroanal. Chem.*, **150**, 611 (1983).
6. V. A. Tyagi and G. Ya Kolbasov, *Surf. Sci.*, **28**, 423 (1971).
7. K. W. Frese, Jr., *J. Appl. Phys.*, **53**, 1571 (1982).
8. M. Pourbaix, "Atlas d'équilibres électrochimiques," p. 475, Gauthier-Villars, Paris (1963).
9. O. Gorochov, A. Katty, N. le Nagard, G. Levy-Clement, A. Redon, and H. Tributsch, *This Journal*, **130**, 1301 (1983).
10. K. W. Frese, Jr., *J. Phys. Chem.*, **85**, 3911 (1981).

Reduction in Polysilicon Oxide Leakage Current by Annealing prior to Oxidation

K. Shinada, S. Mori, and Y. Mikata

Toshiba Corporation, Semiconductor Device Engineering Laboratory, Saiwai-ku, Kawasaki, Japan

ABSTRACT

The mechanism of leakage current reduction in phosphorus-doped polysilicon oxide by high temperature annealing prior to low temperature oxidation was investigated by bias polarity dependence of oxide leakage current, polysilicon grain size measurement, and polysilicon surface observation. Increased phosphorus concentration in polysilicon makes the grains larger and smoothens the surface roughness; consequently, the highest electric field is obtained at the phosphorus concentration of about $6 \times 10^{20} \text{ cm}^{-3}$. Even at the optimum concentration, leakage current due to field enhancement at the interface between polysilicon oxide and polysilicon is still high. Leakage current can be reduced remarkably by high temperature annealing prior to oxidation, especially at the optimum concentration. The annealing effect is explained by interface flatness improvement due to grain growth during annealing and increase of phosphorus atoms in grains. Phosphorus atom migration from the grain boundaries inside the grains is considered to enhance the grain growth.

Thermal oxide grown on heavily doped polysilicon is commonly used as the dielectric of MOS LSI's. Particularly, in a floating polysilicon gate EPROM's and EEPROM cells polysilicon oxide (poly-oxide) hardness to the electric field plays an important role in determining data retention characteristics. However, poly-oxide is well known to be more conductive than bulk silicon oxide, which has been attributed mainly to surface roughness at the poly-oxide/polysilicon interface.

A smoother interface is obtained by oxidizing polysilicon at higher temperatures (1), where the viscous flow of the oxide and the small dependence of oxidation rate on polysilicon orientation can moderate the surface roughness generated by oxidation. A similar improvement in the surface roughness is attained by using polysilicon with amorphous structure (2). Also, high temperature annealing just after polysilicon oxidation improves the breakdown field (3). This improvement is explained by the release of stress in the structure, which prevents further flawing induced after the oxidation and thermal cycling.

In this paper, the role and mechanism of high temperature annealing prior to oxidation of phosphorus-doped polysilicon is investigated as an effective means of improving the reliability of low temperature oxidized poly-oxide. The bias polarity dependence of Fowler-Nordheim tunneling current through poly-oxide, measurement of the polysilicon grain size, and observation of the oxidized polysilicon surface using TEM and replica techniques are reported.

Experimental

Polysilicon films with thickness of $0.40 \mu\text{m}$ were deposited by low pressure chemical vapor deposition (LPCVD) at 620°C onto thermally oxidized Si substrates and were doped with phosphorus by diffusion at 900°C from a POCl_3 source. Prior to oxidation, $0.30 \mu\text{m}$ thick CVD oxide films were deposited onto the doped polysilicon films, and annealing was performed at 950° and 1100°C for 10 min in N_2 atmosphere. Some of the Si substrates remained unannealed, as shown in the experimental procedure of Fig. 1. High temperature annealing without CVD film in inert gas atmosphere causes the outdiffusion of phosphorus and sometimes results in grain growth in the vertical direction, which enhances the surface roughness. After annealing, CVD oxide film was removed and $400\text{-}500\text{\AA}$ thick poly-oxide was formed at 950° and 1000°C in dry O_2 atmosphere. The upper doped polysilicon electrodes were formed to fabricate polysilicon/poly-oxide/polysilicon capacitors. The capacitor area was $250 \times 400 \mu\text{m}^2$.

The Fowler-Nordheim current through poly-oxide was measured by applying positive and negative bias voltage to the upper polysilicon electrodes, and effective barrier

height ($\phi_{B, \text{eff}}$) for the poly-oxide was calculated from Fowler-Nordheim plots, using the well-known equation [1] (4)

$$J/E^2 \propto \exp\left(-\frac{4(2m)^{1/2}(\phi_{B, \text{eff}})^{3/2}}{3e\hbar} \cdot \frac{1}{E}\right); m = 0.4m_0 \quad [1]$$

It is said, based on photocurrent measurements, that the barrier height for poly-oxide is comparable to that for oxide grown on single Si substrate (5), but it is speculated that the electrical barrier height is lowered by field enhancement at the poly-oxide/polysilicon interface.

The critical electric field for the poly-oxide was estimated from the applied positive voltage to provide 10^{-9} A/mm^2 low level leakage current. Grain size and surface roughness of the oxidized polysilicon were investigated

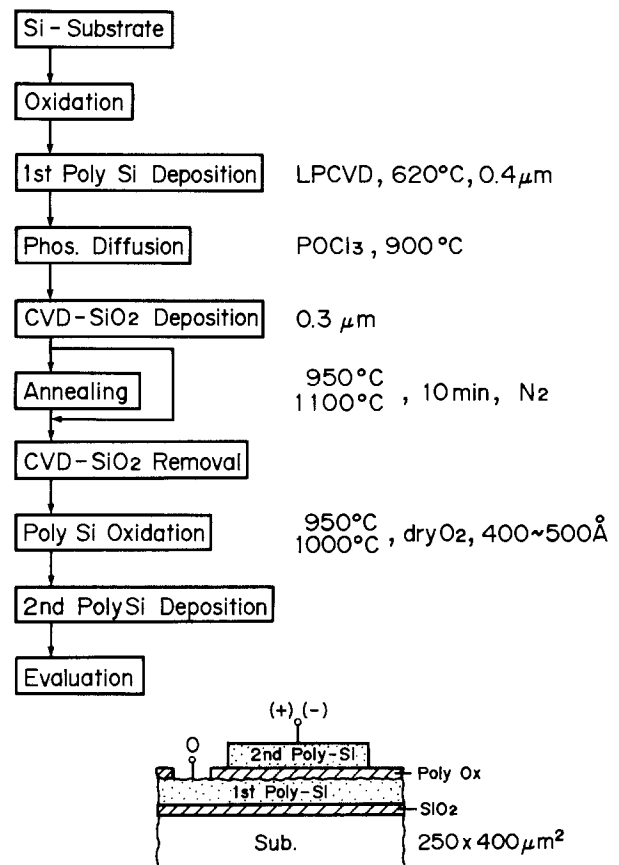


Fig. 1. Experimental procedures and capacitor structure

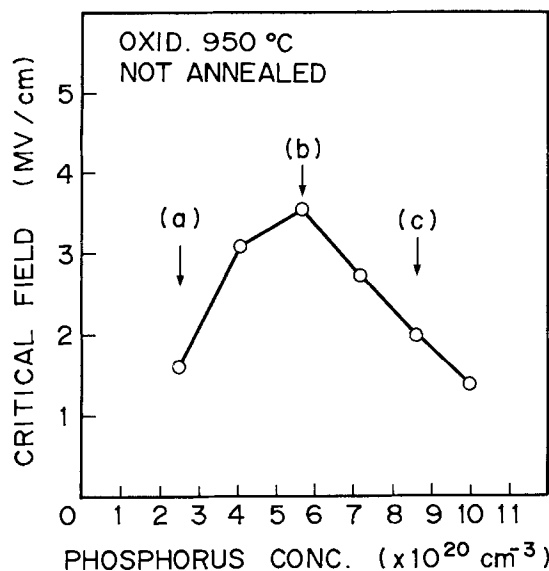


Fig. 2. Relation between critical field and phosphorus concentration in polysilicon. Critical field is defined as applied positive voltage, which provides 10^{-9} A/mm², divided by poly-oxide thickness.

by means of TEM and replica observations. The poly-oxide thickness was obtained by capacitance measurement. The phosphorus concentration in polysilicon was analyzed by AES. In these experimental conditions, the concentration profiles are nearly uniform in the polysilicon films even after phosphorus diffusion from a POCl_3 source, because of the high diffusivity along grain boundaries.

Results and Discussion

A critical electric field depends upon phosphorus concentration in the polysilicon. An optimum concentration exists at about 6×10^{20} cm⁻³, and the critical field decreases in regions of both lower and higher concentration, as shown in Fig. 2. This result agrees with the data of previous reports (6, 7). Oxidation was performed at 950°C.

Fowler-Nordheim plots for the poly-oxide leakage current at 2.5×10^{20} cm⁻³ and a photograph of the oxidized polysilicon surface obtained by replica technique are shown in Fig. 3. Poly-oxide is first removed in NH_4F in order to observe the interface between poly-oxide and polysilicon by this technique. When a positive bias is applied to the upper polysilicon electrode, the poly-oxide is more conductive, owing to electron emission from the lower polysilicon. This phenomenon can be explained by surface roughness at the poly-oxide/polysilicon interface, as indicated by the polysilicon surface photograph. Thus, the Fowler-Nordheim current is determined by low effective barrier height induced by local field enhancement at the asperity.

The grain size is larger and the surface roughness becomes smoother with increasing phosphorus concentra-

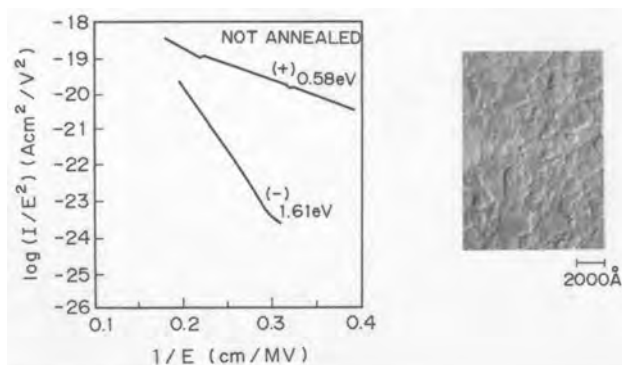


Fig. 3. Fowler-Nordheim plots for poly-oxide leakage current and photograph of oxidized polysilicon surface. Oxidation at 950°C. Phosphorus concentration: 2.5×10^{20} cm⁻³.

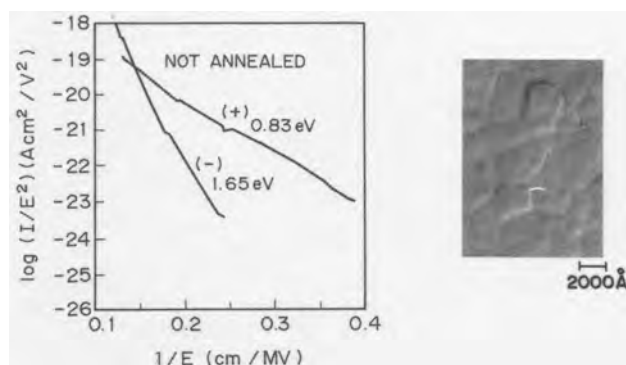


Fig. 4. Fowler-Nordheim plots for poly-oxide leakage current and photograph of oxidized polysilicon surface. Oxidation at 950°C. Phosphorus concentration: 5.7×10^{20} cm⁻³.

tion in polysilicon, as clearly shown in Fig. 4. The grain and grain boundary are clearly distinguished in the polysilicon surface photograph. This surface flatness improvement is based on grain growth due to incorporation of more phosphorus atoms into the grains during the period of phosphorus diffusion from POCl_3 . As a result, the critical electric field increases and the maximum value of 3.5 MV/cm is obtained at the optimum concentration of about 6×10^{20} cm⁻³. However, electron emission from the lower polysilicon is still higher than that from the upper polysilicon, even at the optimum concentration. On the other hand, in the case of oxidation at 1000°C, effective barrier heights at (+) and (-) bias are 1.14 and 1.63 eV, respectively, and the bias polarity dependence of Fowler-Nordheim current is small compared to that at 950°C oxidation, because high temperature oxidation improves the surface flatness.

At concentrations higher than about 6×10^{20} cm⁻³, the critical electric field decreases with phosphorus concentration, in spite of better surface flatness. There is no bias polarity dependence of leakage current through poly-oxide, as shown in Fig. 5. This means that the critical electric field is not necessarily determined by the surface roughness. A possible interpretation of the phenomenon is poly-oxide degradation, caused by phosphorus and/or others clusters in the poly-oxide. Precipitation of a large number of phosphorus atoms at the grain boundary, which exceeds the solid solubility of about 6×10^{20} cm⁻³ at 950°C (8), must play an important role in forming such clusters.

The critical electric field becomes higher when the sample is annealed at temperatures higher than the phosphorus doping temperature prior to oxidation, as shown in Fig. 6. Phosphorus concentration is 5.7×10^{20} cm⁻³. Figure 7 shows the relation between the critical electric field and phosphorus concentration, for 1100°C annealing and no annealing. Solid and dashed lines represent the relations with and without annealing, respectively. Im-

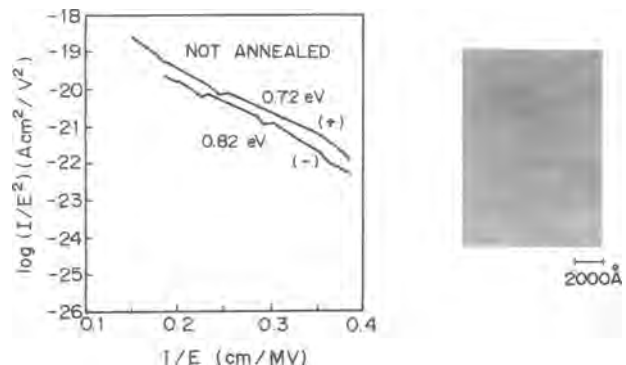


Fig. 5. Fowler-Nordheim plots for poly-oxide leakage current and photograph of oxidized polysilicon surface. Oxidation at 950°C. Phosphorus concentration 8.6×10^{20} cm⁻³.

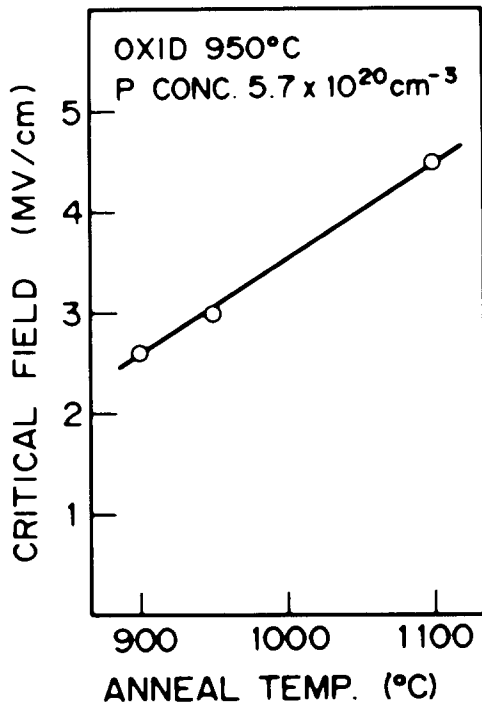


Fig. 6. Relation between critical field and annealing temperature

provement in the critical electric field is attained independent of the phosphorus concentration. In particular, poly-oxide leakage current drastically decreases at the optimum concentration and the critical field of 4.6 MV/cm is obtained, which approaches the critical field of ~7 MV/cm for oxide grown on single-crystal silicon.

Fowler-Nordheim plots for poly-oxide leakage current at the optimum concentration for 1100°C annealing and no annealing are shown in Fig. 8. The leakage current of the annealed sample is almost independent of the polarity of the applied bias voltage. By this annealing, the effective barrier height increases from 0.83 to 1.21 eV. This phenomenon can be understood by more reduction of surface roughness of the grain due to grain growth during high temperature annealing, as clearly indicated in polysilicon surface photographs of Fig. 4 and 8. The relation between the critical electric field and average grain size of samples with and without 1100°C annealing is shown in Fig. 9. It is clearly seen that the critical electric field correlates with the grain size in the phosphorus con-

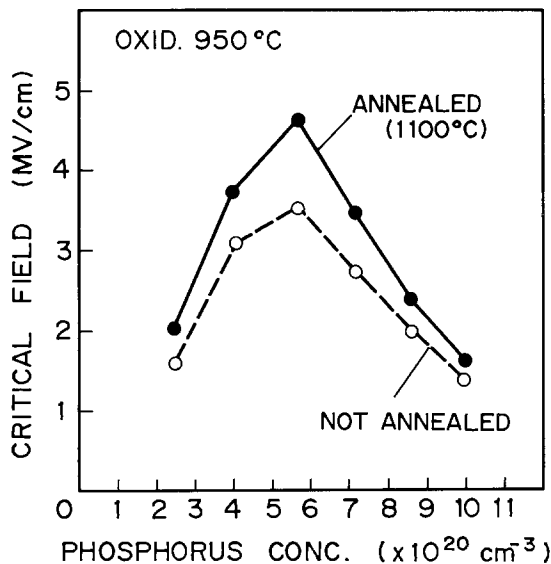


Fig. 7. Relation between critical field and phosphorus concentration in polysilicon. Solid line is for 1100°C annealing, and dashed line is for no annealing.

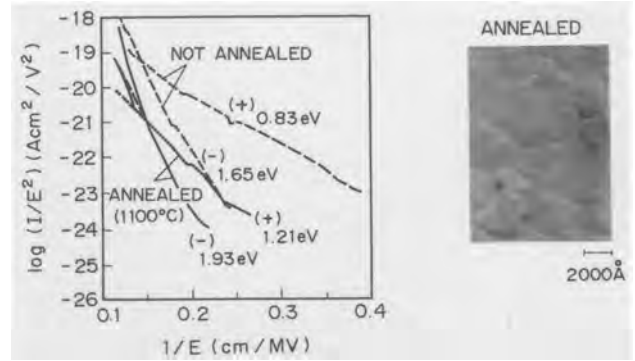


Fig. 8. Fowler-Nordheim plots for poly-oxide leakage current and photograph of oxidized polysilicon surface. Solid line is for 1100°C annealing, and dashed line is for no annealing.

centration region below about $6 \times 10^{20} \text{ cm}^{-3}$ and high temperature annealing plays an important role in increasing the grain size. The ratio of phosphorus atoms in the grains to the total phosphorus atoms in polysilicon, N_G/N is represented by solid and open circles for 1100°C annealing and no annealing in Fig. 10. N_G is defined as the number of carriers estimated from the polysilicon sheet resistivity and Hall mobility, and N is the number of phosphorus atoms obtained from AES analysis. Values of N_G/N for the samples with and without 1100°C annealing are 0.87 and 0.74, respectively, at a phosphorus concentration of $5.7 \times 10^{20} \text{ cm}^{-3}$. In the case of $2.5 \times 10^{20} \text{ cm}^{-3}$, values of N_G/N are 0.80 and 0.41 for the samples with and without 1100°C annealing, respectively. These values are in good agreement with calculated values as a function of annealing temperature for experimental grain size, using Mandurah's segregation model (9). The calculated values are represented by solid and dashed lines in Fig. 10. Entropy factor of 1.5 and heat of segregation of 10 kcal/mol are used in this calculation. From these results, phosphorus atom migration from the grain boundaries inside the grains is considered to enhance the grain growth during high temperature annealing. It is concluded that high temperature annealing prior to oxidation can make phosphorus atoms doped into the polysilicon efficiently contribute to the surface flatness improvement.

Figure 11 shows critical electric field histograms for the samples oxidized at 950° and 1000°C. In the case of 950°C oxidation, the distribution peak for the annealed samples clearly moves toward higher electric field and the critical electric field for this annealed sample is higher than that for unannealed samples oxidized at 1000°C.

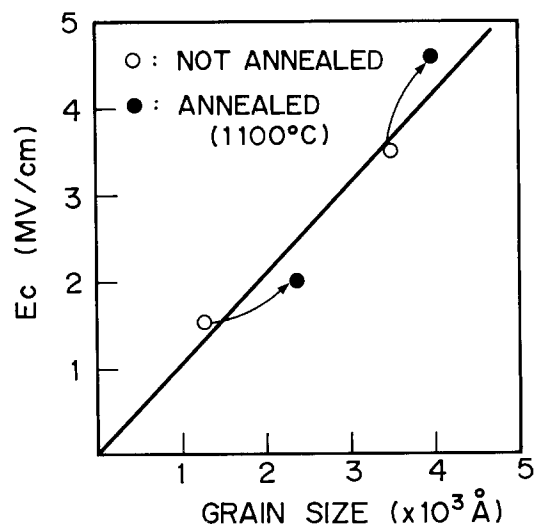


Fig. 9. Relation between critical field and grain size of samples. Solid circles represent relation for 1100°C annealing, and open circles represent that for no annealing.

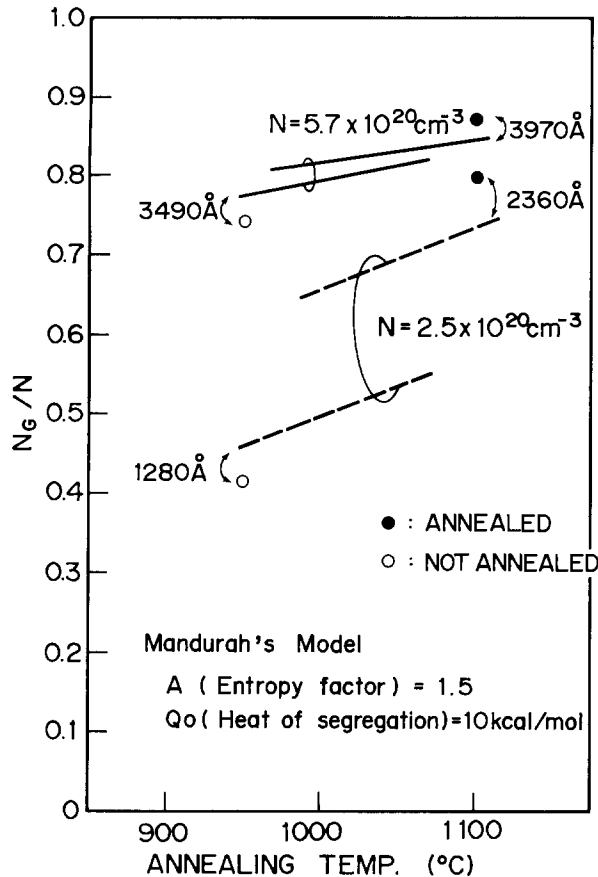


Fig. 10. N_c/N as a function of annealing temperature. Solid and open circles represent experimental values of N_c/N for annealed and unannealed samples, respectively. Solid and dashed lines represent calculated results for $N = 5.7$ and $2.5 \times 10^{20} \text{ cm}^{-3}$, respectively.

Conclusion

Leakage current characteristics of the phosphorus-doped polysilicon oxide formed at low temperature are studied by bias polarity dependence of leakage current, polysilicon grain size measurement, and polysilicon surface observation.

Increased phosphorus concentration in polysilicon makes the grains larger and smoothens the surface roughness. Simultaneously, the leakage current decreases in the concentration region below about $6 \times 10^{20} \text{ cm}^{-3}$. The highest electric field is obtained at about $6 \times 10^{20} \text{ cm}^{-3}$. However, leakage current due to field enhancement at the interface between poly-oxide and polysilicon is still high. At concentrations of greater than about $6 \times 10^{20} \text{ cm}^{-3}$, leakage current is not determined by the surface roughness but presumably is due to poly-oxide degradation. Leakage current can be reduced remarkably by high

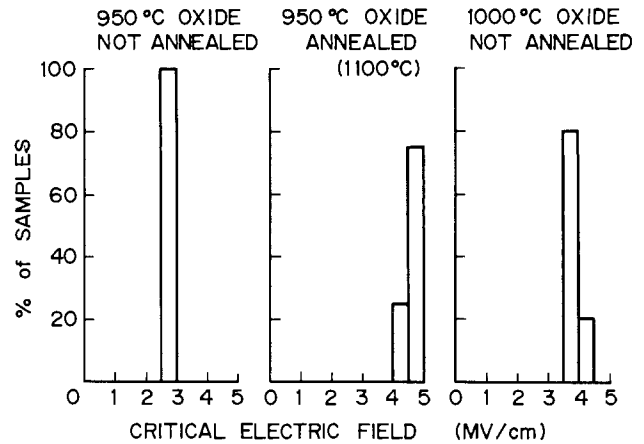


Fig. 11. Critical field histograms for samples oxidized at 950° and 1000°C.

temperature annealing prior to oxidation, especially at about $6 \times 10^{20} \text{ cm}^{-3}$. This annealing effect is explained by surface flatness improvement due to grain growth during annealing and increase of phosphorus atoms in grains. Phosphorus atom migration from the grain boundaries inside the grains is considered to enhance this grain growth.

Acknowledgment

We would like to thank K. Yoshikawa, K. Kanzaki, and M. Sato for helpful suggestion and discussion.

Manuscript submitted Feb. 19, 1985; revised manuscript received May 20, 1985. This was Paper 348 presented at the New Orleans, Louisiana, Meeting of the Society, Oct. 7-12, 1984.

Toshiba Corporation assisted in meeting the publication costs of this article.

REFERENCES

1. R. M. Anderson and D. R. Kerr, *J. Appl. Phys.*, **48**, 4834 (1977).
2. L. Faraone, in "Symposium on VLSI Technical Digest," p. 110 (1983).
3. D. K. Brown and C. A. Barile, *This Journal*, **130**, 1597 (1983).
4. M. Lenzlinger and E. H. Snow, *J. Appl. Phys.*, **40**, 278 (1969).
5. D. J. DiMaria and D. R. Kerr, *Appl. Phys. Lett.*, **27**, 504 (1975).
6. F. Kiyosumi, M. Ino, and Y. Mizokami, Abstract 198, p. 316, The Electrochemical Society Extended Abstracts, Vol. 82-1, Montreal, Que., Canada, May 9-14, 1982.
7. K. Shinada, S. Mori, Y. Mikata, K. Yoshikawa, and F. Kanzaki, Abstract 348, p. 484, The Electrochemical Society Extended Abstracts, Vol. 84-2, New Orleans, Louisiana, Oct. 7-12, 1984.
8. E. Kooi, *This Journal*, **111**, 1383 (1964).
9. M. M. Mandurah, K. C. Saraswat, and C. R. Helms, *J. Appl. Phys.*, **51**, 5755 (1980).

Compositional Studies of Thermally Nitrided Silicon Dioxide (Nitroxide)

M. M. Moslehi, C. J. Han, K. C. Saraswat,* C. R. Helms,* and S. Shatas¹

Integrated Circuits and Solid State Laboratories, Department of Electrical Engineering, Stanford University, Stanford, California 94305

ABSTRACT

The kinetics of thermal nitridation of silicon dioxide in ammonia ambient has been studied. SiO₂ films of 100-1000Å thick were thermally nitrided at 950°-1100°C for times from 15s to 2h. Our experimental results based on etch rate and Auger electron spectroscopy measurements clearly indicate the multilayer structure of nitrided-oxide films. Nitrogen-rich layers are formed at the surface and interface regions at a very early stage of the nitridation process. After a few minutes, the nitridation reaction mainly goes on in the bulk region, with the surface and interface nitrogen content remaining fairly constant. The Auger depth profiles show that the interface moves away from the nitrogen-rich layer as the nitridation proceeds. In addition, our results indicate the formation of an oxygen-rich layer underneath the nitrogen-rich layer whose thickness increases with nitridation time. The formation of this oxide-like layer can be attributed to a slow oxidation of the silicon substrate at the nitroxide/silicon interface by the oxygen which is a by-product of the bulk exchange reaction between NH₃ (or nitrogen containing species) and SiO₂. The results of this work can be qualitatively used to explain effects such as enhanced boron and phosphorus diffusion and growth of stacking faults in the silicon substrate during nitridation of oxide.

Thermally grown silicon dioxide films have many obvious applications in silicon devices and technology including gate insulators of IGFET's and tunnel insulators for nonvolatile memories such as E²PROM. In VLSI, the trend towards smaller device dimensions and higher integration density implies that very thin ($\leq 100\text{\AA}$) gate and tunnel insulators will be required in future devices. For instance, megabit DRAM and high density FLOTOX E²PROM devices will need gate or tunnel insulators in the subhundred angstrom region. There are, however, several technological and reliability problems with silicon dioxide in the very thin regime. The fact that very thin layers of thermal SiO₂ are poor masks against impurity diffusion places additional constraints on processing steps following the growth of gate or tunnel oxides. Moreover, the growth of high quality very thin layers of SiO₂ is rather difficult due to defect density, integrity, and yield problems. It is also known that high energy radiation can generate a high density of interface states in the oxide, resulting in degradation of device performance.

Thermal nitridation of silicon and silicon dioxide is an alternative approach for growing very thin gate and tunnel insulators. It has been observed that thermal nitridation of silicon dioxide films results in the formation of a nitrided-oxide or nitroxide layer with a composition profile that varies with depth. It has also been reported that both thickness and refractive index of thin oxide films are increased after high temperature nitridation in ammonia (1, 2). The changes in composition of the initial oxide film after nitridation in ammonia have been studied using several techniques such as Auger electron spectroscopy (AES), etch rate, Rutherford backscattering spectroscopy, infrared transmittance spectroscopy, and oxidation resistance measurements (1, 3-6, 11, 13-16). Ito *et al.* observed that, after nitridation of a 500Å oxide at 1200°C, a nitrogen-rich layer is formed at the surface and nitrogen gradually decreases moving farther from the surface of the film (3). However, their AES data did not show the presence of significant amounts of nitrogen near the silicon interface. Therefore, Ito *et al.* concluded that direct nitridation occurs predominantly at the surface of SiO₂ rather than at Si/SiO₂ interface.

Their conclusion that there is no pile-up of nitrogen close to the silicon interface is surprising, since we have evidence for the presence of nitrogen-rich layers both at the surface and interface regions for films nitrided under a wide range of nitridation conditions, consistent with the findings of several other investigators. Since their AES data were for 500Å thick oxides nitrided at 1200°C for 1h, a

possible reason for their conclusion was the relatively high temperature used for nitridation. At 1200°C for 1h, the amount of nitrogen incorporated into the bulk is quite significant, and therefore the level of the bulk signal and Auger broadening effects associated with the interface could easily mask the interface nitrogen.

Wong *et al.* performed nitridation of 100Å oxides at relatively low temperatures (925°C) and low pressures in ammonia and an ammonia plasma ambient (4). Their AES data for 100Å SiO₂ nitrided at 925°C show nitrogen peaks at the surface and the interface regions, with negligible nitrogen in the bulk. Their data also indicated that more nitrogen was present at the interface than at the surface and that the interface nitrogen belongs to a more stoichiometric Si₃N₄ layer as opposed to the surface layer. The fact that after nitridation of oxide there is a relatively high concentration of nitrogen at the outer surface and interface regions with a smaller concentration in the bulk of the film now is well established and confirmed (5, 6). Aucoin *et al.* attributed the enhanced nitridation of oxide at the surface to reconstruction of the SiO₂ surface by ammonia (7). Their work indicates that the equivalent nitride thickness at the surface is fairly independent of nitridation time and is saturated after a short time. This is also confirmed by the results of this work.

It has also been observed that the ammonia partial pressure has a significant effect on composition of nitrided-oxide films (1). Higher ammonia partial pressure results in an increase in the nitrogen content of the films, as shown by the etch rate and oxidation resistance data of Hayafuji and Kajiwara (1). Their AES data for 100Å oxide nitrided at 1000°C for 5h did not show however any peak nitrogen concentration at the surface. This nitrogen peak at the interface was not observed, possibly because of the high level of bulk nitrogen and broadening effects.

The influence of nitridation of SiO₂ on impurity diffusion and stacking fault growth in the silicon substrate have also been studied, and it has been observed that the length of preexisting stacking faults increased during nitridation of oxidized silicon (2). The growth was observed to be linear with nitridation time even after 10h of nitridation. Moreover, for a given set of nitridation conditions, an increase in the thickness of the initial oxide increased the growth rate of the stacking faults.

Consistent with stacking fault data, nitridation of SiO₂ films thermally grown on Si substrate enhances diffusion of P and B and retards the diffusion of Sb dopant profiles located in the Si substrate underneath the nitroxide film (8, 9). These phenomena are similar to those observed during oxidation processes (oxidation-enhanced diffusion or OED) and have been attributed to injection of silicon interstitials into the Si substrate during nitridation

¹Present address: AG Associates, Palo Alto, California 94303.

*Electrochemical Society Active Member.

of oxide (8, 9). However, the actual physical mechanism responsible for these phenomena has not yet been firmly established. The results of this work indicate that the most possible physical mechanism responsible for these phenomena is the liberation of oxygen species in the bulk of the oxide, which reoxidizes the interface to the silicon similar to what occurs during oxidation of silicon.

Vasquez *et al.* (10) used x-ray photoelectron spectroscopy (XPS or ESCA) to study the composition of 100Å thermal SiO₂ nitrided in pure ammonia at atmospheric pressure at 1000°C for 4h. In order to preserve the original chemical composition, they used depth profiling by chemical etching instead of ion sputtering. Back-side etch of the Si bulk by XeF₂ was used to verify the structure of the film at the interface. It was observed that nitrogen was distributed throughout the film with a higher concentration at the surface and interface regions. XPS results show that the peak nitrogen concentration close to the interface was about 25Å away from the silicon/film interface. The results indicated the presence of a relatively oxygen-rich layer within 15Å of the interface. However, they found that, while the interface is oxygen-rich relative to the rest of the film, a significant amount of nitrogen is incorporated in this interfacial layer. They suggested that the strained interfacial SiO₂ is more reactive to ammonia than the bulk oxide, resulting in the formation of a nitrogen-rich layer. They also suggested that the formation of the relatively oxygen-rich layer at the interface is due either to the reaction of a nitrogen species with the top layer of the strained region or to reaction of the nitridation by-products with the silicon substrate. The results of our kinetics studies are in favor of the latter and rule out the reaction with top strained region as the only cause of the presence of an oxygen-rich interfacial layer.

Yoriume has also studied the distribution of nitrogen in thermally nitrided SiO₂, using AES and other techniques (11). For 100Å oxide nitrided at 1100°C for 2h, the nitrogen-to-oxygen concentration ratio at the surface was estimated to be about 1. The data showed that the maximum nitrogen Auger signal strength at the interface was relatively temperature independent and that a highly nitrided layer was formed at the interface. The surface nitrogen concentration decreases slightly with the film thickness, and the temperature dependence was observed to be rather small. For nitridation at 900°C, the bulk nitrogen concentration was negligible even after 2h of nitridation. The results also indicated that the surface nitrogen pile-up occurs in the early stages of nitridation (≤ 30 min) and nitrogen permeates through the oxide films even as thick as 1000Å at 900°-1100°C. However, his calculation of the diffusion coefficient of the nitrogen species from the profile near the surface assuming a complementary error function distribution may be erroneous since the effect of AES broadening on the nitrogen profile was not taken into account.

This paper follows our earlier published letter on time-dependent compositional variation in SiO₂ films nitrided in ammonia (12). Two of the major new results reported in that letter were the quantitative observation of oxygen depletion in the nitroxide "bulk" region and the reoxidation of the interface by oxygen presumably liberated by the bulk exchange reaction. In this study, we have investigated the time evolution of the nitridation process of SiO₂ in atmospheric ammonia at temperatures from 950° to 1200°C. The SiO₂ thickness varied from 100 to 1000Å. Special attention has been given to the interfacial oxygen-rich layer observed by Vasquez *et al.* A model for the nitridation process will be given based on the findings.

Experimental

The oxide films used in this work were thermally grown in dry O₂ at 900°C to a thickness of 95Å and at 1000°C to thicknesses of 270, 405, and 1021Å, on 5-10 Ω -cm (100) silicon wafers. The thermal nitridation experiments were performed for times from 15s to 2h at 950° and 1100°C in pure ammonia at atmospheric pressure. All the short-time nitridations (15s-4 min) were performed in a

lamp-heated rapid thermal annealing (Heatpulse 210) system manufactured by AG Associates (Palo Alto, California). In each of the rapid thermal nitridation (RTN) experiments, the system was thermal, first in pure argon and then in pure ammonia after loading the wafer. After establishing a pure flowing ammonia ambient in the quartz chamber, the temperature was ramped up to the desired process temperature in pure ammonia. At the end of all rapid thermal nitridation experiments, the temperature was ramped down while ammonia was still flowing. Finally, the wafer was unloaded after purging the system in argon flow. The ramp-up and ramp-down times at the beginning and at the end of each rapid thermal nitridation cycle were usually very fast (≤ 10 s) and much shorter than the actual nitridation time. As a result, the effects of ramp-up and ramp-down times on rapid nitridation kinetics were expected to be insignificant. The longer nitridation experiments were carried out in a cold-wall RF-heated reactor which has been described elsewhere (5). After loading the wafers, the system was purged first in pure nitrogen and then in pure ammonia. Temperature was then ramped up to the nitridation temperature while ammonia was flowing, and at the end of the nitridation, the temperature was ramped down while ammonia was still flowing. The wafers were unloaded after purging the system in nitrogen. The ramp-up and ramp-down times for nitridation experiments performed in the RF-heated reactor were relatively fast (≤ 2 min) and usually much shorter than the minimum nitridation time (the shortest nitridation time in the RF-heated reactor was 15 min) for the experiments in the reactor. Therefore, the effects of ramp-up and ramp-down times on the kinetics data including those for 15 min nitridation were expected to be negligible, similar to the rapid thermal nitridation experiments.

The nitrided oxide films were investigated using step-by-step etch rate measurements and Auger electron spectroscopy. In the etch-rate measurements, the thickness of the remaining film was measured using single-wavelength ellipsometry after step-by-step etching in 50:1 DI H₂O:HF. The wavelength of the laser was 6328Å incident at 70° from the normal to the surface of the film. In all the ellipsometry measurements the refractive index used for the single-crystal Si substrate was 3.85-0.02i.

The system for the Auger sputter profiling analyses was a Varian 2730 spectrometer, which uses an integral electron source located coaxially with a single-pass cylindrical mirror analyzer (CMA). The electron gun was operated at 4.5 keV and at 3 μ A rastered over a 900 \times 900 μ m area. These conditions were chosen to reduce any electron-beam damage, stimulated desorption, and electron-beam-induced diffusion to the surface. The samples to be analyzed were located at the focus of the CMA and tilted 30° from the normal surface of the electron beam. The resolution of the CMA was set to 1.2% for these studies and a 2V peak-to-peak modulation voltage with lock-in detection was used. The concentrations of elements were obtained by comparing the peak-to-peak heights of the derivative Auger spectra with those of a standard sample. This standard calibration sample consisted of 500Å of LPCVD stoichiometric silicon nitride deposited on oxidized silicon with 100 and 1000Å initial thermal oxides. Depth profiles of the samples were obtained by sputter etching with Ne⁺ ions during the Auger analyses. The ion beam was operated at 1 keV, 49° incidence, and rastered over a 0.5 \times 0.5 cm² area. The effective current density of the ion beam was 36 μ A/cm², which provided a sputtering rate of nearly 20 Å/min for SiO₂. In addition to the standard and samples investigated using these two techniques, selected nitroxide samples were studied using a hybrid wet etch/sputter etch technique to assess the effects of sputter-induced artifacts in the profiles.

Results and Interpretation

Auger electron spectroscopy.—To calibrate the relative sensitivity factors, a Si₃N₄/SiO₂ standard was used. It was a 500Å thick CVD Si₃N₄ film on a layer of 1000Å thick

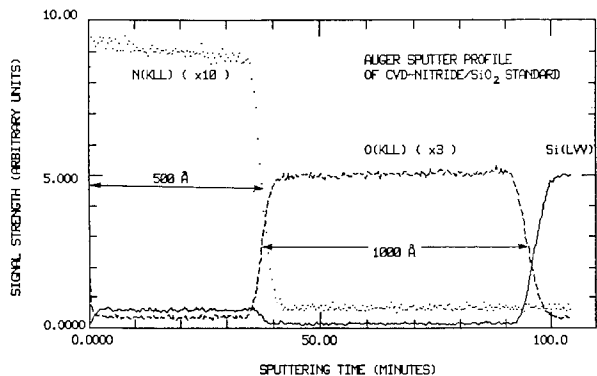


Fig. 1. The AES depth profile for a 500Å CVD Si_3N_4 on 1000Å SiO_2 on Si. This was used as a standard to calibrate the relative sensitivity factors for oxygen and nitrogen.

SiO_2 thermally grown on Si. The profile we obtained for this sample is shown in Fig. 1. Since both the nitride and the oxide are of known stoichiometry and hence of known oxygen and nitrogen concentrations, we were able to calibrate the concentrations of elements in the nitride samples using this result. The horizontal axis of the profile is the sputtering time of the analysis. Assuming a uniform sputtering rate in each region of the sample, this axis can easily be converted to the depth from the surface. The sputtering rate for each material was calculated by specifying the location of interfaces from the 50% transition positions in the Auger depth profiles (and the corresponding sputtering times) and the nitride and oxide thicknesses measured by ellipsometry. For our conditions, the sputtering rate in the SiO_2 (depth/time) is about 30% faster than the rate in Si_3N_4 . The sputtering rate is proportional to the ion flux of the incident ions; hence, various factors such as the Ne pressure inside the chamber, the contamination on the surface of the ion gun filament, and the warmup time of the ion gun may affect the current density of the ion beam. Our experience has shown that this sputtering rate may vary by 10% over a typical run. Similarly, the vertical scale may fluctuate by as much as 15% because of varying electron-beam intensities and sample charging which may affect the energy analyzer collection efficiency. In the presentation of the data below, all of our profiles were normalized such that the samples with the same insulator film thickness have the Si_{LVV} (92 eV) transition 50% point located at the same point. Also, the peak intensities of the Si_{LVV} (92 eV) transition are normalized to the same value.

Figure 2 shows the results from three nitroxide samples with different starting SiO_2 thicknesses all nitrided in NH_3 for 15 min. We identify three obviously distinct regions in the profiles of 405 and 270Å samples. (These are the initial oxide thicknesses, not necessarily the total thickness.) Two of these regions originate from rapid thermal nitridation at the SiO_2 surface and at the Si/ SiO_2 interface. Similar results have been observed by other investigators (10). In addition, nitridation at a much slower rate is observed in the bulk of the SiO_2 . This nitrogen concentration remains approximately constant with depth in the bulk. The 95Å sample, however, shows a merging of the surface and the interface peak, and the bulk region is not clearly observed. The apparent loss of this bulk region is probably an artifact of instrumental broadening rather than a real physical effect, as will be shown below. In principle, by measuring the sputtering time to the interface the film thickness can be determined. However, the difference in sputtering rate between Si_3N_4 and SiO_2 (30%) and the normal experimental uncertainty in the ion flux (5%) makes this determination difficult. Within these limits, the film thickness does not appear to change significantly after nitridation; however, other experimental evidences (5, 1, 2) from ellipsometry measurements (with single wavelength 6328Å laser) and etch rates suggest some increase in the thickness and effective refractive index, specially for the thinner initial oxides, which

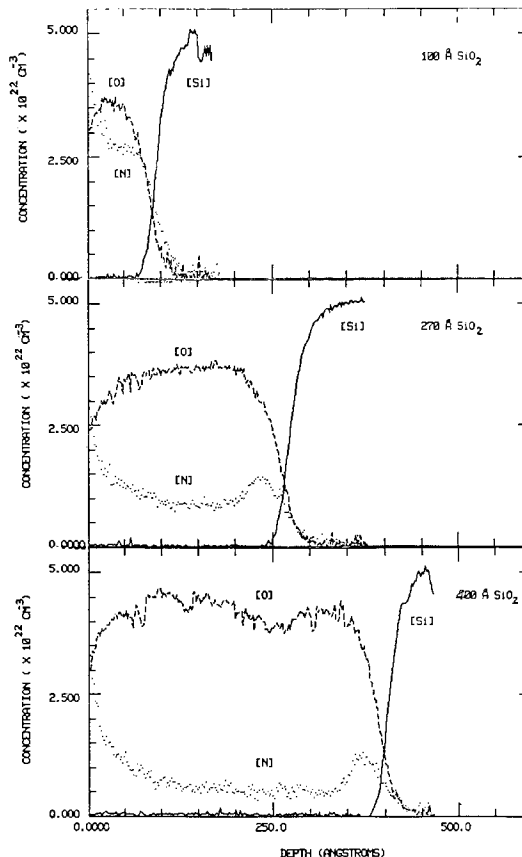


Fig. 2. The AES data for different SiO_2 thicknesses (95, 270, and 405Å) all nitrided at 1100°C for 15 min.

would be within the limits of the sputter time measurements. Considering the fact that nitroxide has an inhomogeneous structure, ellipsometry measurements yield values for effective refractive index and thickness calculated from measured values of ellipsometry parameters ψ and Δ . In single-wavelength ellipsometry, the mapping from ψ - Δ plane to thickness-refractive index plane is done based on the assumption that the film has a homogeneous structure. This could introduce some error into the calculated values; however, the error is expected to be rather small for nitroxide films because they have a fairly homogeneous structure throughout most of the bulk region in the dielectric (as will be described later). Some numerical calculations are being performed to study the errors introduced into the thickness and refractive index measurements in single-wavelength ellipsometry of inhomogeneous materials such as nitroxide. Meanwhile, the data obtained from high resolution cross-sectional TEM results have been in fairly good agreement with our ellipsometry results. As a check for other sputter-induced artifacts in our profiles, we examined several samples that were chemically etched back before the Auger sputter profile analysis. The results from these etched-back samples were consistent with the profiles in Fig. 2, indicating negligible sputter-induced distortion in the Auger depth profiles.

Since the three regions were best separated in the 405Å sample, we will describe a detailed study of these samples. Three samples from each nitridation condition were analyzed to improve the reliability of the collected Auger data and give a fair statistical average. The results from these samples are shown in Fig. 3. The Auger profiles were each calibrated with respect to the standard sample of Fig. 1. The profiles for each element are plotted separately with the nitridation time as the parameter for each curve. Initially, the nitrogen peaks at the surface and at the interface grow rapidly. As will be discussed, the surface peak and the interface peak both saturate before 15 min of nitridation. The bulk nitrogen level also increases with nitridation time, but at a much

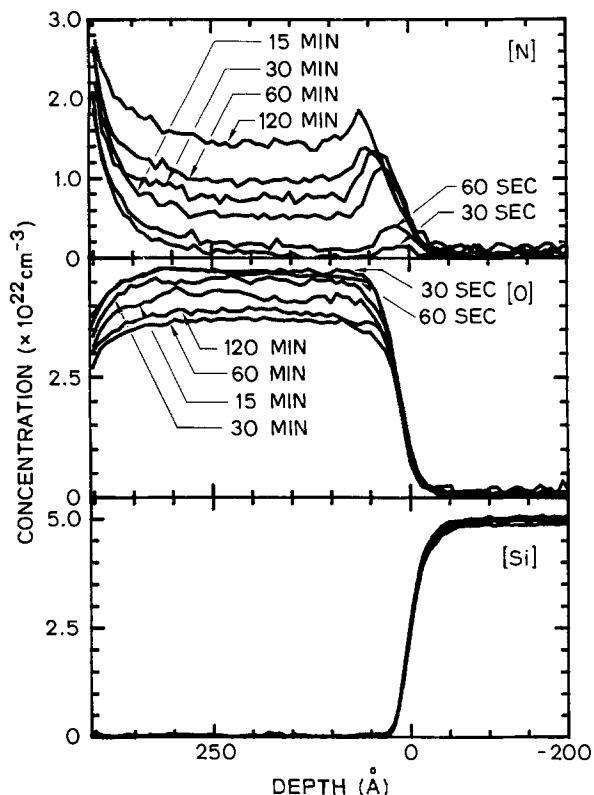


Fig. 3. The AES data for 405 Å initial SiO_2 samples nitrided at 1100°C for various nitridation times (30s-2h). The Auger profiles were each calibrated with respect to the standard sample of Fig. 1.

slower rate than at the surface or interface. Even after 2h of nitridation at 1100°C, the nitrogen level is still increasing and no apparent saturation of the nitrogen concentration is observed. This bulk nitrogen increase is also accompanied by a decrease of the oxygen concentration in the same region. The apparent increase in the oxygen level in Fig. 3 for the 2h sample is probably due to uncertainties in the normalization. Another interesting feature in the profile is the observed shift of the nitrogen profiles at the interface. The instrumental broadening effects make quantifying the physical effect in this region difficult. An attempt was made to model the interfacial nitrogen profile by assuming a superposition of a step function profile and a narrow high concentration peak at the interface, as to be discussed in the next section.

Figure 4 shows the ratio of the nitrogen to oxygen concentrations at the surface vs. nitridation time from 30s to 2h calculated from AES data. There is a rapid increase in the ratio for very short nitridation times, as shown by the data points for 30 and 60s of nitridation. However, the data for 15 min or longer nitridation times show that the surface nitrogen concentration saturates very rapidly. Also shown are two data points for 95 and 270 Å oxide nitrided at 1100°C for 15 min. Data indicate that at a given nitridation temperature the surface nitrogen concentration is almost independent of the initial oxide thickness and saturates rapidly with nitridation time.

Using the data from AES, the nitrogen to oxygen concentration ratio in the bulk was calculated vs. nitridation time for 405 Å thick oxide samples nitrided at 1100°C. The results are illustrated in Fig. 5. It shows that the bulk nitrogen concentration increases monotonically with nitridation time. After 2h of nitridation, the ratio is about 0.30. The rate of increase in the ratio in the bulk decreases with nitridation time; however, there is no saturation after 2h. The dependence of bulk oxygen concentration on nitridation time is shown in Fig. 6 for 405 Å oxide nitrided at 1100°C. For comparison, this figure also illustrates the dependence of the bulk nitrogen ($[\text{N}]$) on nitridation time. It indicates a monotonic decrease in oxygen content of the bulk due to continuing exchange reaction of bulk oxide

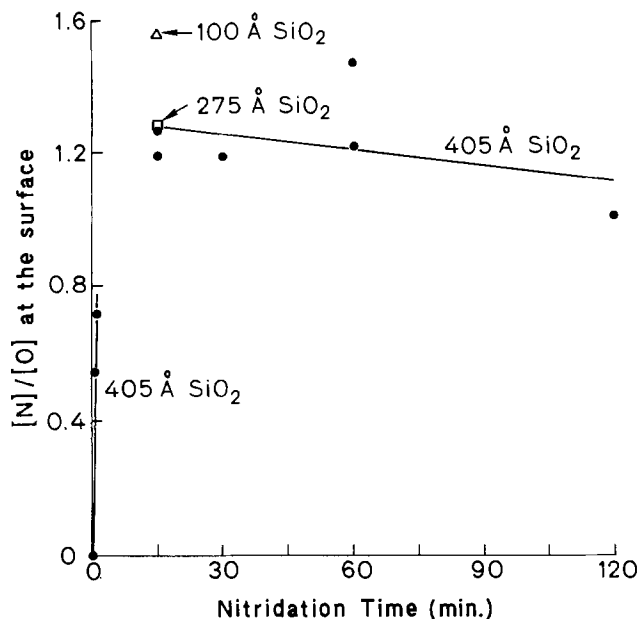


Fig. 4. The ratio of the nitrogen to oxygen concentrations at the surface of nitride vs. nitridation time, from 30s to 2h for 405 Å initial oxide nitrided at 1100°C for various nitridation times.

with nitridation species, similar to what is observed from Fig. 5. Another interesting feature in the nitrogen Auger profiles shown in Fig. 3 is the shift observed in the peaks of nitrogen profiles at the interface. As the nitridation time increases, the peaks shift farther away from the interface toward the surface. Instrumental broadening effects make quantifying this behavior difficult. However, as we show below, this effect cannot be completely explained by instrumental broadening and appears to correspond to the growth of an oxygen-rich layer right at the interface to the Si substrate.

Etch profile.—Precision etch profiling is an accurate measurement tool for studying the composition of the nitroxide films without significant measurement artifacts such as ion knock-on and broadening effects in AES. The etch profiles were obtained by measuring both refractive index and thickness independently until the thickness was below about 100 Å, for which the refractive index was fixed at 1.46. Our experimental ellipsometry data for subhundred angstrom nitride and nitroxide films and also some preliminary calculations based on

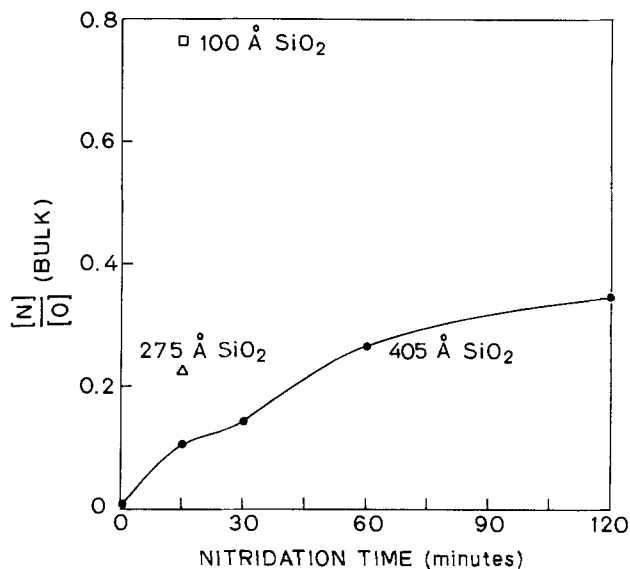


Fig. 5. The nitrogen-to-oxygen concentration ratio in the bulk of nitroxide vs. nitridation time. The solid curve is for 405 Å oxide nitrided at 1100°C.

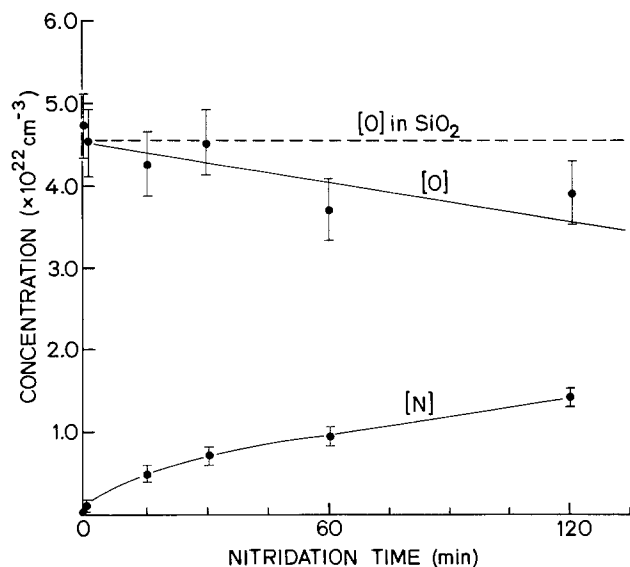


Fig. 6. The bulk oxygen concentration in nitroxide vs. nitridation time. The data are for 405 \AA oxide nitrided at 1100°C for various nitridation times. The nitrogen concentration in the bulk is also shown for comparison with the oxygen concentration.

the fundamental ellipsometry equations indicate that the error introduced in the measured thickness due to varia-

tions in the refractive index is rather small, and that the thickness measurement sensitivity to refractive index becomes less as the insulator thickness is reduced. The thickness measurement based on a measured or prefixed average value for effective refractive index seems to work fairly well for the purpose of this work. The results are in close agreement with the thickness measurement with high resolution cross-sectional TEM. The original purpose of chemical etch profiling in this work was a qualitative study of the compositional changes in the nitroxide insulators; therefore, some possible small errors introduced into the ellipsometry measurement results due to the inhomogeneous nature of the films will not have any effect on our fundamental conclusions regarding the kinetics of nitridation of oxide.

Figure 7a shows a typical step-by-step etch profile for an oxide film of 405 \AA thick nitrided at 1100°C for 2h. This etch profile was obtained by a precision step-by-step etch and thickness measurement which enables us to detect the details of changes in composition of the nitroxide layer. Six different regions are observed in the nitroxide etch profile shown in Fig. 7a. The data indicate that for over 320 \AA in the bulk of the film the etch profile is fairly uniform and the etch rate is nearly constant. Figure 7b illustrates an expanded picture of the surface etch profile from the surface to the point where about 100 \AA of the film has been removed. This figure shows the three different regions including the bulk. The etch rate at the top

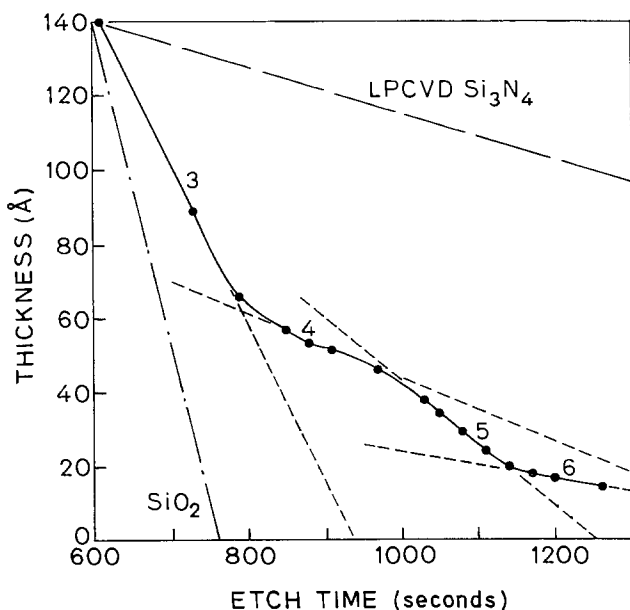
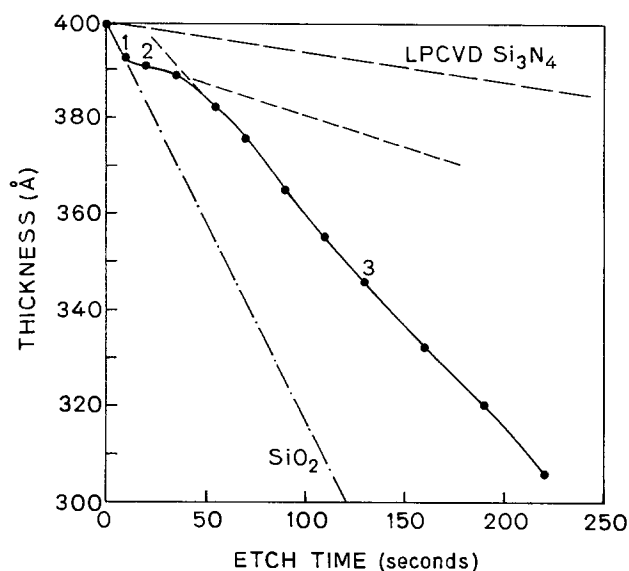
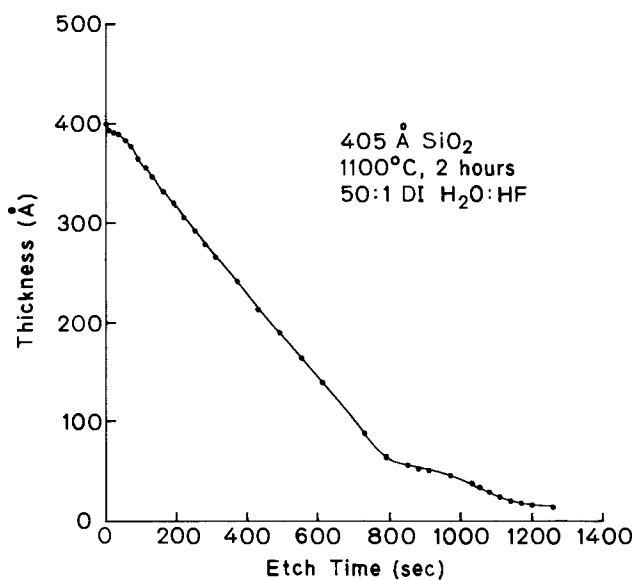


Fig. 7. The etch profile for the 405 \AA SiO_2 nitrided at 1100°C for 2h. a(top left): Complete profile. b(above): Expanded surface etch profile. c(left): Expanded interface etch profile. The data were obtained by step-by-step etching of the film in 50:1 DI H_2O :HF etchant and ellipsometry thickness measurement.

surface is relatively fast and is close to that for pure SiO_2 . The two dashed lines are the experimental reference etch profiles for pure thermal oxide and CVD nitride. The fast etch rate at the top surface can be due to adsorption of moisture and oxygen at the surface after unloading the wafers from the nitridation reactor and during the storage time.

Following the top layer, there is a thin layer whose etch rate is between the etch rates for pure SiO_2 and deposited silicon nitride. For this surface nitrogen-rich layer, the actual thickness is very small and just a few ($\approx 5\text{\AA}$) angstroms, as illustrated in the etch profile. The fact that the surface nitrogen-rich layer is very thin implies that the surface reaction is a result of surface reaction only on the top atomic layer, as proposed by Aucoin *et al.* (7). Finally, the expanded surface etch profile in Fig. 7b shows a transition from the surface nitrogen-rich layer to the bulk region, in which the etch rate is almost constant.

The etch profile experimental measurement results indicate that the etch rate throughout most of the bulk region is constant. For the 405\AA oxide nitrided at 1100°C for 2h, the bulk etch rate is somewhat slower than that for oxide and much faster than that for stoichiometric nitride. The change in chemical etch rate is clearly an indication of change in composition. However, the relationship between etch rate and fractional nitrogen concentration is not linear and not exactly known for nitrided oxide, and, therefore, no quantitative data regarding exact values of nitrogen concentration may be extracted from the etch-profile data. The etch-profile data can be used to estimate the thicknesses of various layers in the film.

Figure 7c shows the expanded picture of the etch profile close to the interface region for the sample with the same etch profile as that in Fig. 7a. As shown in this figure, following the relatively thick bulk region there is a thin layer ($\leq 20\text{\AA}$) whose etch rate is much slower than that for oxide and is very close to the etch rate for stoichiometric nitride. The etch profiles for pure thermal oxide and LPCVD nitride are shown in the picture for reference. The fact that the etch rate in this thin layer is very close to that for stoichiometric nitride implies that this layer is nearly stoichiometric nitride. Underneath this thin, nearly stoichiometric nitride, there is another thin layer whose etch rate is faster than that for nearly stoichiometric nitride layer but slower than that in the bulk region. The fact that the etch rate of this interfacial layer is faster than that of the top nitride layer implies that it has more oxygen. Therefore, we call this an oxide-rich layer. Finally, the etch profile ends with a region whose etch rate is somewhat slower than that of the stoichiometric nitride. The slow etch rate in this final layer may be due to high nitrogen content or high amorphous silicon content in that layer or an artifact of ellipsometry measurements. The bulk etch rate is fairly constant in more than 320\AA of nitroxide. Therefore, the bulk nitrogen concentration is fairly uniform and constant. The etch rates measured for control oxide samples grown at 900° and 1000°C was about 0.83 \AA/s and for LPCVD nitride was 0.063 \AA/s . The average bulk etch rate of this nitroxide sample is more than seven times of that for CVD nitride and about half of that for oxide.

The six different regions detected from etch-profile data are shown schematically in the insert of Fig. 8. Correspondingly, the etch-rate profile which is the derivative of the step-by-step etch profile with respect to etch time *vs.* the thickness of film remained is shown in Fig. 8. This etch-rate profile was calculated from the etch profile of Fig. 7a. Based on a nearly constant etch rate in each region, we might assume a uniform composition in each region, which is a reasonable assumption for simplified modeling of the kinetics of oxide nitridation.

Calculated according to the etch-rate profile, the approximate thicknesses of the different layers in the nitroxide sample prepared by nitridation of a 405\AA oxide at 1100°C for 2h are shown in Table I. For comparison, the thicknesses of various layers obtained from the AES data

Table I. Layer thicknesses

Layer	(Etch profile data) Etch rate (\AA/s)	Thickness (\AA)	(AES data) Thickness (\AA)
Adsorbed layer	0.69	7	—
Surface nitrogen rich	0.15	5	10
Bulk region	0.45	324	—
Interface nitrogen rich	0.09	18	9
Interface oxygen rich	0.17	27	30
Transition region	0.04	19 ^a	—

^a This thickness is partially due to the measurement offset introduced by ellipsometry.

(as will be described later) are also shown in the table. The agreement between these two sets of data is fair and reasonable.

Owing to the multilayer structure of the nitroxide, the refractive index measured by ellipsometry is an effective refractive index of the multilayer structure. For the 405\AA oxide nitrided at 1100°C , the effective refractive index was fairly constant and equal to 1.55 for all the refractive index measurement range ($400\text{--}140\text{\AA}$). However, as Fig. 9 illustrates, the effective refractive index of the 270\AA oxide sample nitrided at 1100°C for 2h is more than that of oxide. Its value depends on the thickness of the top layer removed by etching. Below about 150\AA , accurate independent measurement of refractive index was not possible. Using the simplified multilayer model and ellipsometry equations, it should be possible to simulate the dependence of the effective refractive index on thickness of the film after step-by-step etching and compare it to the experimental results. This may be another approach to verify the composition and thickness of various layers in a given model. However, because of the inhomogeneity of the nitroxide films, it would seem hazardous to draw major conclusions from effective refractive index profiles such as that shown in Fig. 9, unless all the inhomogeneity effects on single-wavelength ellipsometry measurement results are carefully taken into account.

Discussion

From the results presented, it is clear that the structure resulting from the nitridation of SiO_2 is a complicated one. In this section, we will present a comparison of the etch-rate and Auger profiling results and discuss how these relate to the findings of other investigators. Our discussion will center on the model shown in the insert of

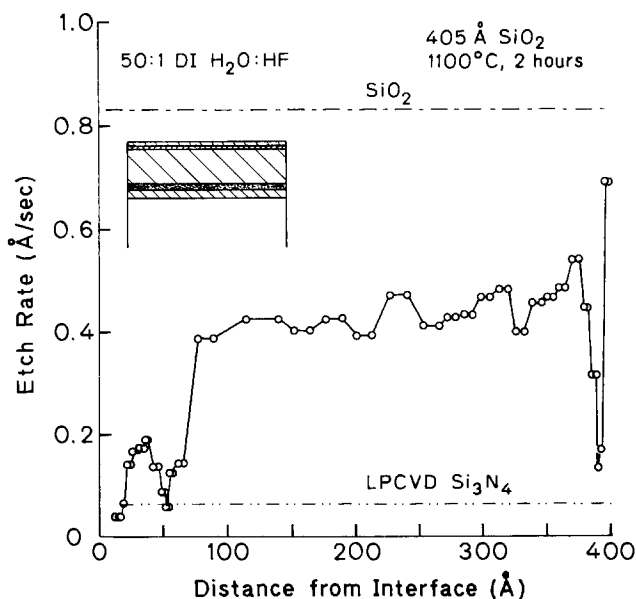


Fig. 8. The derivative etch-rate profile of the 405\AA SiO_2 nitrided at 1100°C for 2h.

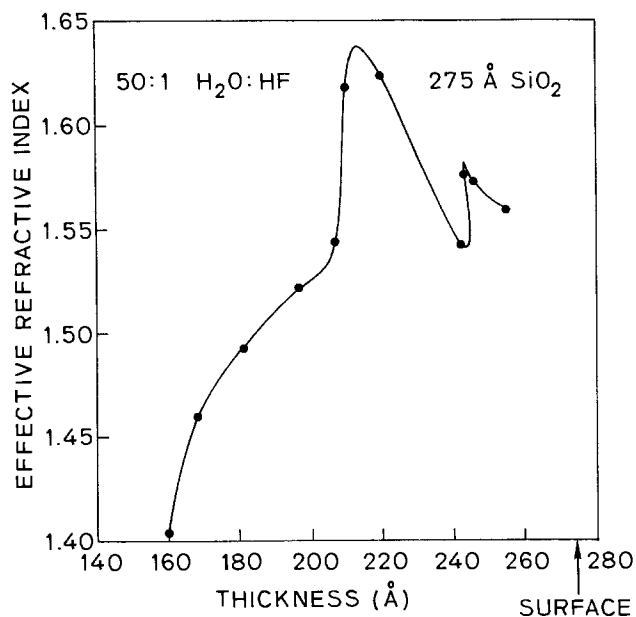


Fig. 9. The effective refractive index of the 270 Å SiO₂ nitrided at 1100°C for 2h as a function of the thickness remained after step-by-step etching.

Fig. 8. Five distinct regions plus a very thin interfacial region right at the Si substrate surface are observed. In addition, the outer region with the higher etch rate on the surface after the nitridation was completed and the sample exposed to air. This leaves four regions of interest: the surface nitrogen-rich region, the bulk, the near-interface nitrogen-rich region, and the interface oxygen-rich region. All of these regions are observed in the etch-rate data, whereas only the first three are observed in the Auger profiling results. In addition, for the thinnest sample investigated, the bulk region could not be distinctly separated. As we will show, this is due to broadening inherent in the sputter profiling experiments; when this is accounted for, agreement between the two techniques is obtained.

As a first approximation to the instrumental broadening due mainly to the sputtering process, the actual concentration profiles appear convolved with a gaussian to yield the measured profiles. Within this approximation, a step function profile produces an error function profile after the broadening, and a thin layer produces a gaussian profile. As a starting point for modeling the nitrogen profiles, we assume that the bulk nitrogen concentration is constant, and that near the interface there is a thin region of stoichiometric Si₃N₄. Although this latter assumption is clearly an idealization, it provides a lower limit on the thickness of this region. We are interested in the interface region, so the surface nitrogen peak has been neglected in this analysis. The model is shown in Fig. 10a. This profile can then be convolved with a gaussian to fit the measured profiles. A typical fit is shown in Fig. 10b for the 15 min nitrided sample. The full width at half maximum of the gaussian broadening function was 47 Å. In the fits to the other profiles, this was kept constant and the thickness of the thin nitride layer and the distance away from the interface were adjusted. A plot of the interfacial nitride thickness and the separation of the thin layer from the Si interface is shown in Fig. 11. The error bars are not shown in Fig. 11 because the curve-fittings were performed on the averaged nitrogen and oxygen profiles for each nitridation condition and as a result single values of interfacial nitride and oxide thicknesses were calculated for each nitridation condition (instead of performing three separate curve fittings for Auger depth profiles obtained from three Auger measurements of nitroxide samples having the same nitridation conditions); however, these error bars are estimated

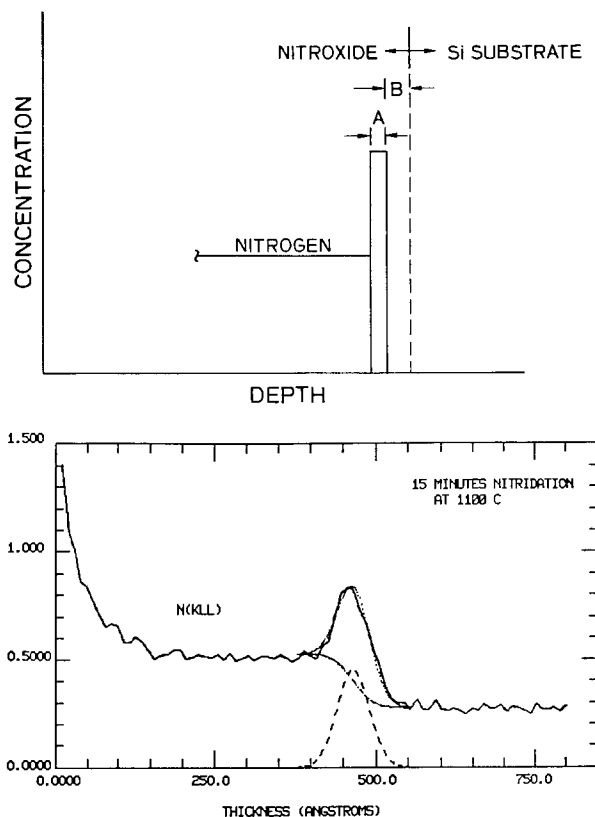


Fig. 10. a(top): A simplified model for the structure of nitroxide. b(bottom): The fitting results for the 405 Å SiO₂ nitrided at 1100°C for 15 min.

to be a small fraction of the absolute thickness values of the interfacial oxide and nitride layers. From this figure, we see that the interfacial nitrogen-rich layer saturates (in terms of the product of the nitrogen concentration and the thickness) very quickly. However, the separation between this region and the Si interface increases monotonically with time up to 30 Å after 2h at 1100°C. These results, although somewhat ambiguous in themselves, are consistent with the etch-rate data, which give an 18 Å thickness for the nitrogen-rich region compared to 9 Å from the Auger data and a 27 Å thickness for the interfacial oxygen-rich layer compared to 30 Å for the Auger data. The discrepancy of interfacial nitride thickness values obtained from Auger and chemical-etch data may be attributed to the combination of various experimental uncertainties present in both techniques. High resolution cross-sectional TEM is being employed to study the thicknesses of these various layers in nitroxide and correlate them to those from Auger and etch-rate data. Similar fits to the oxygen profiles are also consistent with the in-

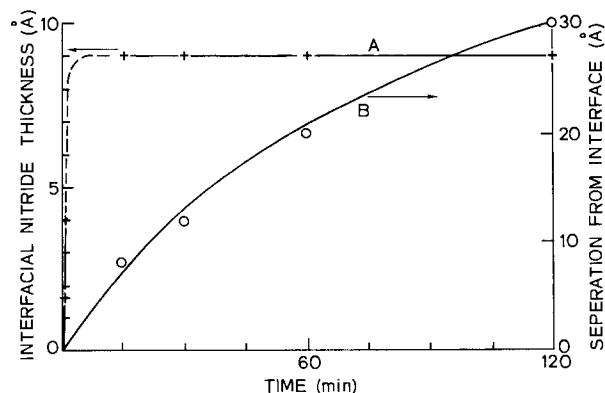


Fig. 11. The interfacial nitride thickness and its distance or the thickness of interfacial oxide layer from the Si interface vs. nitridation time.

terpretation that the region right next to the Si interface is oxygen rich.

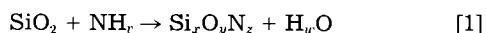
Our findings indicate that the SiO₂ nitridation occurs by three processes. Upon exposure to NH₃, the SiO₂ surface is nitrided very rapidly (see Fig. 4). The etch rate profile in Fig. 7b indicates that the surface layer with slow etch rate is very thin, about 5Å thick. This suggests that the enhanced surface reaction occurs just on an atomic scale and is restricted to the top surface. Although the interface nitridation reaction occurs more slowly, it is clearly due to rapid diffusion of the nitrogen containing species through the SiO₂ and reaction at the interface. The average concentration of the nitrogen in this interfacial region saturates at $1.7 \times 10^{16} \text{ cm}^{-2}$ for the 1100°C case in less than 15 min.

From the etch-rate as well as Auger data it is clear that another layer between the high nitrogen concentration region and silicon grows slowly with nitridation time. If we look at the comparison of this growth rate and the rate of exchange between nitrogen and oxygen in the bulk, we see the time scales are identical (Fig. 5 and 11). Moreover, it is clear that this region is oxygen rich. These findings give strong evidence for a mechanism whereby oxygen liberated by the bulk reaction diffuses to the interface where the silicon there is oxidized.

The AES data for the nitroxide samples prepared by short-time nitridation indicate that the nitrogen peak is not located in the oxide and is in between the oxide and the silicon substrate. This is due to the fact that the interfacial nitrogen peak location is observed to be well after the position of the 50% point on the falling edge of the oxygen profile and next to the substrate Si signal. The AES data also indicate that for very short-time nitridation of oxide (≤ 60 s) there is a very thin layer of nearly stoichiometric silicon nitride at the interface. There are several reasons to believe that the interfacial nitride layer is actually "nearly stoichiometric." The obvious evidence comes from our etch-rate data that show that the etch rate for the interfacial thin nitride layer is very close to that of stoichiometric LPCVD silicon nitride. The strong possibility that the interfacial nitride layer is formed by initial reaction of ammonia (and/or nitrogen containing species) with the silicon substrate under the thin SiO₂ also suggests that this layer should be nearly stoichiometric silicon nitride (with low oxygen content). Based on oxidation resistance experiments on etched back nitroxide samples, Wong *et al.* (4) suggested that the interfacial nitride layer resembles stoichiometric Si₃N₄, which is known to be more resistant to oxidation than oxide or oxynitride layers.

For the samples nitrided at 1100°C for very short times (≤ 60 s), the AES data indicate that the bulk nitrogen content is almost negligible. This implies that the bulk reaction rate is much slower than that for interface and surface nitrogen-rich layers. In fact, at temperatures below 950°C or so the bulk reaction is not activated even for long nitridation times (4).

Figure 3 shows the AES data for 405Å oxide nitrided for 30s, 15 min, 30 min, 1h, and 2h superimposed. It can be observed that as the nitridation goes on for longer nitridation times the bulk nitrogen concentration is increased so that, for instance, after 2h of nitridation at 1100°C, more than 30% of the oxygen in the bulk has been exchanged with nitrogen. Moreover, as the nitridation goes on, the amount of oxygen in the bulk is reduced. This implies that the increase in nitrogen content of the bulk is responsible for the decrease of the oxygen concentration in the bulk. Therefore, this is a strong evidence for the exchange nature of the reaction in the bulk region which was also suggested by Ito *et al.* (3) and Habraken *et al.* (13)



where v , w , x , y , and z depend on the nitridation process. After 2h of nitridation, the bulk has acquired a nitrogen concentration of $1.42 \times 10^{22} \text{ cm}^{-3}$ vs. a loss of $0.81 \times 10^{22} \text{ cm}^{-3}$ of oxygen. This result indicates that the gain of ni-

trogen in the bulk seems to be greater than the loss of oxygen. This implies that the replacement of oxygen with nitrogen is not quite one to one. Since the Auger measurement uncertainty for the bulk oxygen loss is much greater than the uncertainty observed for the nitrogen gain in the bulk (as shown by the arrow bars in Fig. 6), more exact measurement of oxygen loss is needed to draw any firm conclusion regarding the ratio of oxygen loss to nitrogen gain in the bulk. If the nitrogen gain is actually greater than oxygen loss, it could be attributed to additional incorporation of nitrogen into the bulk of the film in addition to the replacement reaction.

Another important phenomenon observed in the AES data is that, as the nitridation proceeds for longer times, the silicon-film interface moves away from the nitrogen peak inside the oxide. A nitridation reaction at the oxide-nitride interface cannot be the reason for this phenomenon because it is fairly well known that the interfacial nitride is very thin. However, the data indicate the growth of an oxide-rich layer underneath the originally formed nitride-rich layer. The shift of the nitrogen peak implies that the thickness of this interfacial oxygen-rich layer increases slowly with nitridation time. Throughout these experiments, we tried to eliminate any possible source of oxygen or water contamination in the nitridation ambient. Because of the ultrahigh purity of the gases used for purging and nitridation, and also the fact that the reactor is closed tube and cold wall (resulting in negligible contamination from outside the quartz tube), the oxygen and water contamination of the nitridation ambient were estimated to be well below 1 ppm. Considering the fact that the nitridation ambient is very pure and oxidant free, the only source that can provide oxygen for the oxidation of the silicon substrate is the original oxide. Some of the reaction by-products of the bulk exchange reaction with the nitridation species, diffuse into the film, and further oxidize the silicon substrate. It seems that the interfacial nearly stoichiometric nitride is so thin ($\leq 20\text{Å}$) that it does not block the diffusion of these exchange reaction by-products. It is also suggested that some of the exchange reaction by-products diffuse away and go into the nitridation ambient.

Figure 12 summarizes the nitridation sequence from very short times to long nitridation times (from seconds to hours). The sequence illustrates the fast reaction of ammonia with the top surface of the oxide and also the rapid diffusion of the ammonia (and/or other nitrogen containing species such as NH and NH₃) through the oxide and the formation of a nearly stoichiometric nitride layer at the interface. For longer nitridation times, the surface nitrogen concentration saturates and the exchange bulk reaction and the oxidation of the silicon substrate by the exchange reaction by-products continue. Auger electron spectroscopy does not allow detection and measurement of the hydrogen content of nitroxide. Habraken *et al.* (17) measured the hydrogen content of nitroxide films by means of resonant nuclear reaction. Their results indicated that the hydrogen concentration amounts to less than 1-3 atom percent in the bulk of nitroxide. Hydrogen has an essential role in the bulk exchange reaction. This is also supported by the fact that, in contrast to ammonia, N₂ does not react with SiO₂ in the typical temperature range of thermal nitridation processes. Ito *et al.* (3) and Habraken *et al.* (13) suggested that the rupture of Si-O bonds in the bulk of nitroxide occurs under the action of hydrogen. Rupture of Si-O bonds results in subsequent incorporation of nitrogen atoms in the bulk of nitroxide.

Our model for the kinetics of nitridation of oxides can explain the physical mechanisms responsible for oxynitridation-enhanced diffusion of boron and phosphorus and also the growth of stacking faults. The mechanism responsible for the injection of silicon interstitials into the silicon substrate during the nitridation of oxide should be closely related to the oxidation of the silicon substrate by the exchange reaction by-products. However, according to the etch-rate data and the AES profile for the 405Å oxide nitrided at 1100°C, the thickness of the interfacial

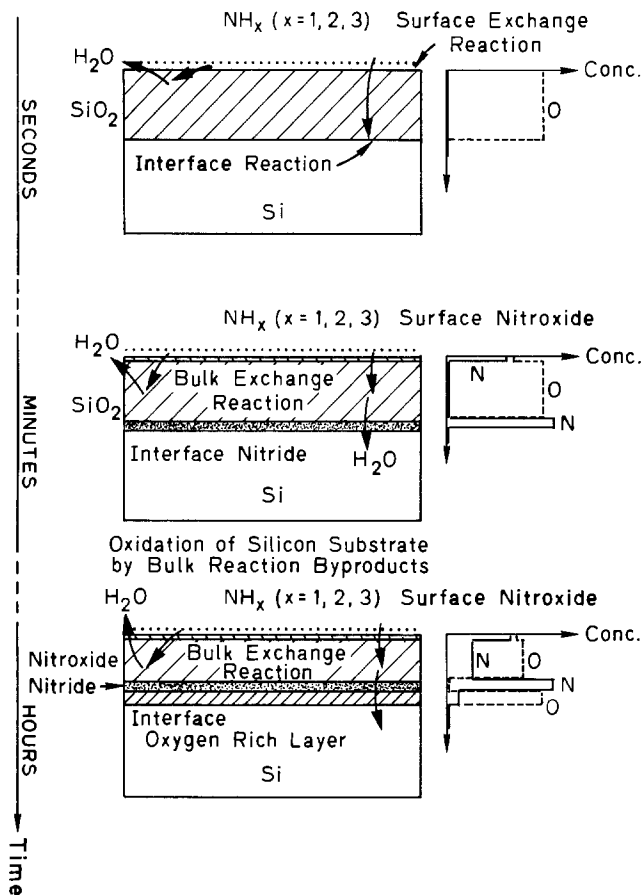


Fig. 12. The simplified model for the nitridation sequence from very short to long nitridation times.

oxide-rich layer grew to 30Å after 2h of nitridation. A comparable oxidation process for the growth of a thermal oxide with the same thickness has much less influence on impurity diffusion or stacking faults. As a result, the growth of the interfacial oxygen-rich layer during the nitridation of oxide is much more efficient in injecting interstitials into the substrate than a comparable normal oxidation process. The thickness of the interfacial oxide obtained from the position of the nitrogen peak with respect to the silicon interface and from the etch-rate data increases slowly and monotonically with nitridation time. There is no indication of saturation after 2h of nitridation.

Summary

In summary, the kinetics of thermal nitridation of SiO₂ and the composition of nitroxides have been studied. The results clearly indicated the multilayer structure of nitroxide films. The formation of the nitrogen-rich layers at the surface and interface regions occurs at the very early stage of the nitridation process. The nitrogen contents of the surface and interface regions saturate in the first few

minutes of the nitridation. Then the nitridation reaction slowly goes on in the bulk region. The movement of the interface away from the interfacial nitrogen-rich layer indicated the slow growth of an oxygen-rich layer underneath the nitrogen-rich layer. The formation of this oxygen-rich layer is due to the slow oxidation of the silicon substrate by a fraction of the oxygen containing species which are liberated in the bulk of nitroxide by the exchange reaction. The results can have important implications for understanding the effects of thermal nitridation processes on bulk and interfacial electrical characteristics of oxides and subsequent nitroxides.

Acknowledgments

The authors would like to acknowledge the support of DARPA under the Contracts MDA903-80-C-0432 and MDA903-79-C-0257. They are grateful to J. D. Meindl and J. D. Plummer for their encouragement and support during the course of this research.

Manuscript submitted Nov. 13, 1984; revised manuscript received March 21, 1985.

AG Associates assisted in meeting the publication costs of this article.

REFERENCES

1. Y. Hayafuji and K. Kajiwara, *This Journal*, **129**, 2102 (1982).
2. Y. Hayafuji, K. Kajiwara, and S. Usui, *J. Appl. Phys.*, **53**, 8639 (1982).
3. T. Ito, T. Nozaki, and H. Ishikawa, *This Journal*, **127**, 2053 (1980).
4. S. Wong, C. Sodini, T. Ekstedt, H. Grinolds, K. Jackson, and S. Kwan, *ibid.*, **130**, 1139 (1983).
5. M. M. Moslehi and K. C. Saraswat, in "Silicon Nitride Thin Insulating Films," V. J. Kapoor and H. J. Stein, Editors, pp. 324-345, The Electrochemical Society Softbound Proceedings Series, Pennington, NJ (1983).
6. T. Ekstedt, S. Wong, Y. Strausser, J. Amano, S. Kwan, and H. Grinolds, in "Insulating Films on Semiconductors," J. F. Verweij and D. R. Wolters, Editors, p. 189, Elsevier Science Publishers B. V. (1983).
7. R. Aucoin, C. Kirk, M. Naiman, F. Terry, R. Reif, and S. Senturia, Paper 377 presented at the Electrochemical Society Meeting, Denver, CO, Oct. 11-16, 1981.
8. S. Mizuo, T. Kusaka, A. Shintani, M. Nanba, and H. Higuchi, *J. Appl. Phys.*, **54**, 3860 (1983).
9. P. Fahey, R. W. Dutton, and M. M. Moslehi, *Appl. Phys. Lett.*, **43**, 683 (1983).
10. R. Vasquez, M. Hecht, F. Grunthner, and M. Naiman, *Appl. Phys. Lett.*, **44**, 969 (1984).
11. Y. Yoriume, *J. Vac. Sci. Technol. B*, **1**, 67 (1983).
12. C. J. Han, M. M. Moslehi, C. R. Helms, and K. C. Saraswat, *Appl. Phys. Lett.*, **46**, 641 (1985).
13. F. Habraken, A. Kuiper, Y. Tamminga, and J. Theeten, *J. Appl. Phys.*, **53**, 6996 (1982).
14. J. Amano and T. Ekstedt, *Appl. Phys. Lett.*, **41**, 816 (1982).
15. S. Wong, S. Kwan, H. Grinolds, and W. Oldham, Paper 127 presented at the Electrochemical Society Meeting, San Francisco, CA, May 8-13, 1983.
16. T. Ito, T. Nakamura, and H. Ishikawa, *IEEE Trans. Electron Devices*, **ed-29**, 498 (1982).
17. F. Habraken, E. Evers, and A. Kuiper, *Appl. Phys. Lett.*, **44**, 62 (1984).

Investigation of Leakage Currents in a Zinc Borosilicate Glass Passivated p-n Junction Using a Gate-Controlled Diode

S. Murakami, Y. Misawa, and N. Momma

Hitachi Limited, Hitachi Research Laboratory, Hitachi Ibaraki, Japan

ABSTRACT

A new type of gate-controlled diode to investigate the leakage currents of a thick zinc-borosilicate glass passivated p-n junction is described. Using this diode, temperature dependencies of surface and bulk components of the leakage current were measured at different values of the reverse voltage. It was revealed that the surface generation current component cannot be ignored, as compared with bulk current component, even at temperatures above 100°C. The surface recombination velocity at room temperature in glass/silicon system calculated from surface generation current component exhibited a larger value of 300-400 cm/s than did the SiO₂/silicon system, and it tended to decrease with decreases in reverse voltage or with increases in junction temperature.

Surface passivation techniques using glasses (1, 2) have been applied to the fabrication of a wide variety of power semiconductor devices. These techniques can offer such advantages as resistance against the entry of moisture and ionic impurities that affect electrical performance. Among the various glass materials, zinc borosilicate glass have been widely used because of its electrical stability at high temperatures and in high electric fields (3, 4). Properties of the silicon/glass interface have been investigated for zinc-borosilicate glasses by using metal-glass-semiconductor capacitors (5, 6). Although there have been many reports concerning those materials themselves and applications to raise breakdown voltage of p⁺-n junctions, little has been done with leakage currents and their temperature dependence. In the case of planar-diffused p-n junction having a silicon dioxide/silicon system, several types of gate-controlled diode (GCD) have been extensively used to investigate surface leakage currents (7-9). As for zinc borosilicate glass passivated p-n junctions, a GCD was applied to investigate the surface stability from the viewpoint of operational stress (3). The present work seeks to offer a suitable GCD structure with a thick glass/silicon system, which allows a more detailed examination of temperature dependence of separated surface and bulk leakage current components in a zinc borosilicate glass passivated p⁺-n junction.

Experimental

Device preparation.—A cross-sectional view of the GCD is shown in Fig. 1. This GCD was designed with the following considerations. (i) Surface depletion layer spreading would occur at the n-type silicon surface on application of a reverse voltage or a negative gate voltage. In estimating the surface recombination velocity, the surface depleted area must be defined as constant. The lateral depletion layer stopper n⁺ region shown in Fig. 1 served to hold the surface depleted area constant, thereby making it easy to measure the characteristics of the GCD without use of a guard ring voltage as was necessary in previous work (7). (ii) The deep groove structure made it possible to fabricate a GCD having a thick glass/silicon system. By controlling the amount of glass powder, the surface of the fired glass could be flattened, which made it easier to form both gate and anode electrodes using a conventional lift-off process. (iii) The gate electrode was arranged on the glass surface so as to overlap the p⁺-n and n-n⁺ junctions.

The GCD was fabricated by using 68 Ω-cm, 475 μm thick, phosphorous-doped n-type substrate with (111) orientation. The wafers were first oxidized and patterned to give a circular 70 μm selective boron diffusion, which served as the anode region. A second thermal oxidation was then performed and patterned to give an annular 40 μm selective phosphorous diffusion which served as the stopper for lateral depletion layer spreading at the surface. The back (cathode n⁺ region) was diffused simultaneously with this phosphorous diffusion. After formation

of the p⁺ region and n⁺ region mentioned above, the thermal silicon dioxide formed during the diffusion process was selectively removed. Then the exposed silicon surface was etched by U01 etchant [200 cm³ HF:800 cm³ HNO₃:19g, CO(NH₂)₂] to obtain a deep groove (20 ± 2 μm) for 45s at 10°C. An electrophoretic method was used to place glass powders of ZnO (65 weight percent [w/o]), B₂O₃ (25 w/o), and SiO₂ (10 w/o) composition into the groove. Firing was then carried out in a nitrogen atmosphere at 700°C for 30 min. The aluminum electrodes of gate and anode were formed by evaporating and subsequent patterning using the conventional lift-off process in a nitrogen atmosphere for 20 min at 470°C. The cathode electrode was formed by evaporating chromium-nickel-silver, in that order.

Measurements.—All leakage current measurements were carried out by placing the gate-controlled diode in an electrically shielded light-tight box. The currents were measured using a Takeda Riken Industry Company Limited electronic picoammeter Type TR 8641, which is capable of detecting currents as small as 5 × 10⁻¹⁴A.

Results and Discussion

Leakage current—Gate voltage characteristics at room temperature.—Figure 2 shows typical leakage current-gate voltage characteristics measured at a fixed reverse voltage, V_R = 1V. The characteristic of the SiO₂-passivated GCD in which SiO₂ was formed in the junction diffusion process is also shown. The latter structure is planar, having no groove. The fundamental leakage current I_R-gate voltage V_G characteristics have three current regions according to the values of the carrier densities at the n layer surface. General expressions of the leakage currents I_R are as follows.

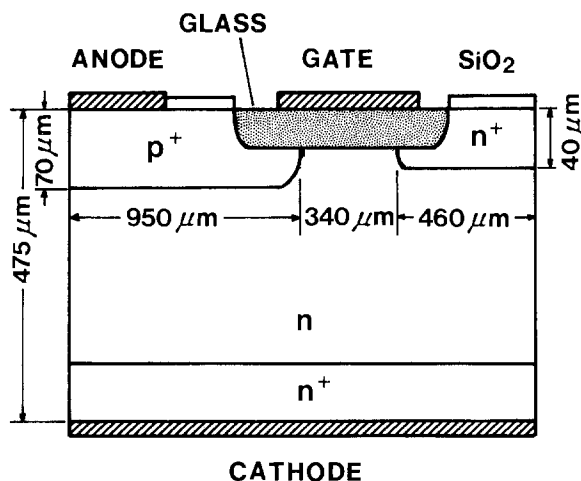


Fig. 1. Cross-sectional view of the gate-controlled diode with a groove structure and n region to repress spreading of the surface depletion layer.

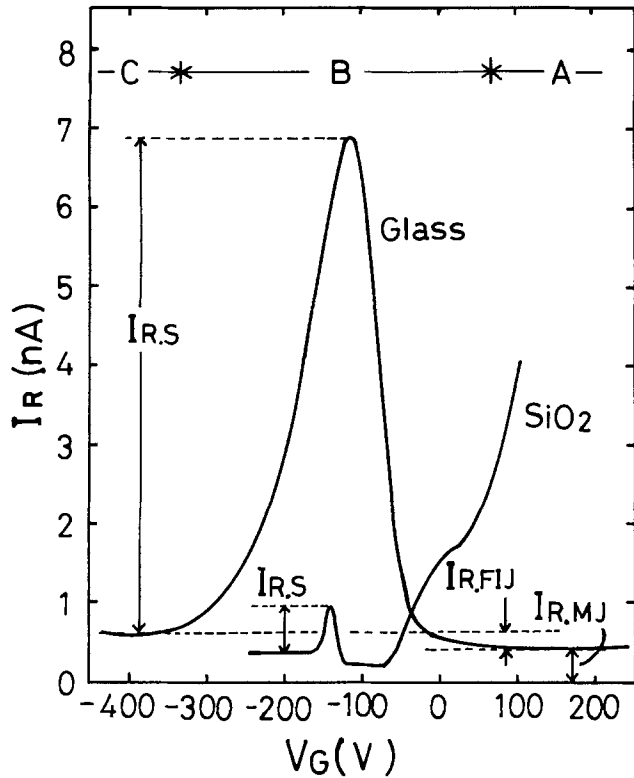


Fig. 2. I_R - V_G characteristics for gate-controlled diodes passivated by zinc-borosilicate glass and SiO_2 ($V_R = 1\text{V}$).

Region A: accumulation

$$I_R = I_{R,MJ} \quad [1]$$

Region B: depletion or weak inversion

$$I_R = I_{R,MJ} + I_{R,FJ}(x_d) + I_{R,S} \quad [2]$$

Region C: strong inversion

$$I_R = I_{R,MJ} + I_{R,FJ}(x_{dmax}) \quad [3]$$

In these equations, $I_{R,MJ}$ is the current flowing across the metallurgical junction, which consists of the generation current $I_{gen,MJ}$ due to electron-hole pairs generated within the junction depletion region and diffusion current $I_{diff,MJ}$ due to minority carriers generated within the neutral n and p regions. Assuming that the amount of minority carrier is negligibly small within the p⁺ region, $I_{R,MJ}$ can be expressed as follows (10)

$$I_{R,MJ} = I_{gen,MJ} + I_{diff,MJ} \\ = \frac{1}{2} q \frac{n_i}{\tau_{0,MJ}} W A_{MJ} + q \sqrt{\frac{D_p}{\tau_p}} \times \frac{n_i^2}{N_D} A_{MJ} \quad [4]$$

where $\bar{\tau}_{0,MJ}$ is the effective lifetime within a reverse biased metallurgical p⁺-n junction, W the depletion layer width of metallurgical p⁺-n junction, D_p , τ_p the diffusion constant and lifetime of minority carrier within the neutral n region, respectively, N_D the impurity concentration of n region, and n_i the intrinsic carrier density. The intrinsic carrier density n_i is expressed as following function of absolute temperature T (11)

$$n_i = 3.87 \times 10^{16} T^{3/2} \exp\left(-\frac{7.02 \times 10^{13}}{T}\right) \quad [5]$$

If the bulk generation-recombination centers are indeed located near the intrinsic Fermi level, the temperature dependence of $I_{R,MJ}$ is mainly proportional to n_i (first term) and n_i^2 (second term). When the surface under the gate electrode is inverted, the field-induced junction is formed between inverted p region and underlying substrate. Based on $I_{R,MJ}$, we obtain the following equation for the field-induced junction

$$I_{R,FIJ} = I_{gen,FIJ} + I_{diff,FIJ} \\ = \frac{1}{2} q \frac{n_i}{\tau_{0,FIJ}} x_d A_s + q \sqrt{\frac{D_p}{\tau_p}} \times \frac{n_i^2}{N_D} A_s \quad [6]$$

where $\bar{\tau}_{0,FIJ}$ is the effective lifetime within the surface depletion layer, x_d the surface depletion layer depth, and A_s the surface area of the n substrate under the gate electrode. The first term is the generation component which arises from generation carriers within the surface depletion layer. The second term is diffusion component due to minority carriers being diffused from the neutral n substrate to the surface depletion layer edge. If the surface is depleted, surface generation is caused by surface states, resulting in the flow of surface generation current $I_{gen,s}$. If the surface generation-recombination centers are located near the intrinsic Fermi level, the surface generation current is usually defined (10) as

$$I_{gen,s} = 1/2 q n_i s_0 A_s \quad [7]$$

where s_0 is the surface recombination velocity.

At the completely depleted surface, the surface leakage current $I_{R,S}$ (third term of Eq. [2]) is mainly due to $I_{gen,s}$. In the I_R - V_G curve of the GCD, the maximum leakage current is observed when the surface is depleted and the surface carrier density reaches the intrinsic. This means that the surface generation current begins to decrease as soon as the surface potential exceeds the Fermi level. Generally diffusion components of leakage currents at room temperature can be neglected as very small in comparison with generation currents. As is shown in Fig. 2, surface generation current $I_{gen,s}$ of the glass passivation is one order of magnitude larger than that of SiO_2 passivation. From the definition of s (Eq. [6]), its values are 320 cm/s for the glass passivation, and 38 cm/s for SiO_2 passivation. Although the latter system has a smaller s value, an anomalous current increase is observed with increase in positive gate voltage. This phenomenon was described previously and was attributed to inversion layer and surface crystal imperfections on the p layer surface (12).

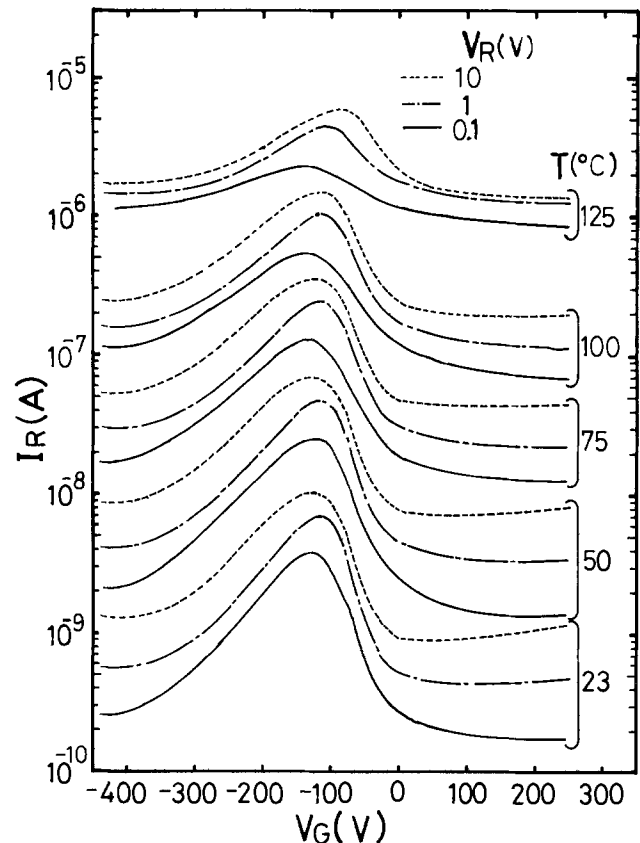


Fig. 3. I_R - V_G characteristics at different temperatures and reverse voltages.

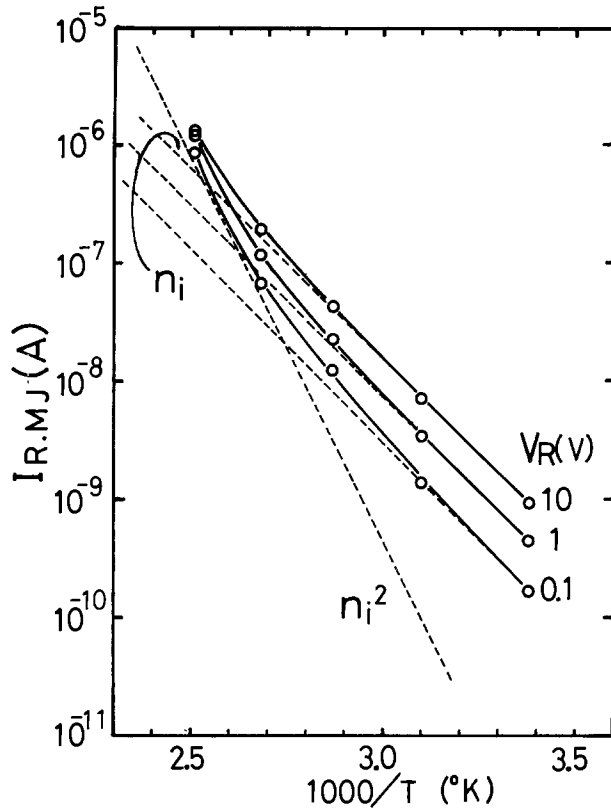


Fig. 4. Temperature dependence of $I_{R,MJ}$ at different reverse voltages

Temperature dependence of I_{R-V_G} characteristics.—The I_{R-V_G} measurements at various temperatures are described next. As shown in Fig. 3, leakage current in the range of the positive gate voltage exhibits the $I_{R,MJ}$ component. Leakage current begins to include the surface generation component with increasing negative gate voltages, and has its maximum value in the vicinity of $V_G =$

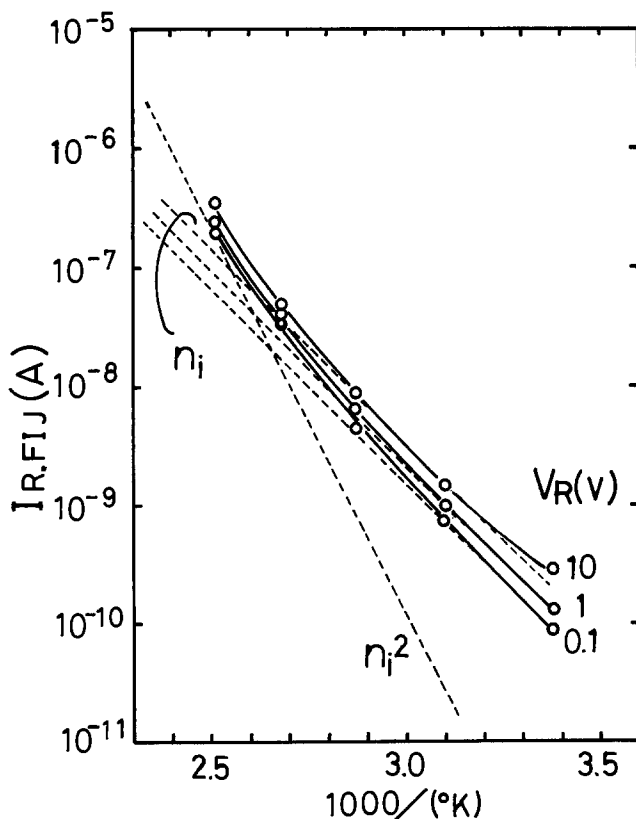


Fig. 5. Temperature dependence of $I_{R,FIJ}$ at different reverse voltages

–120V. This surface current component cannot be ignored as compared with bulk current component, even at temperatures above 100°C. The gate voltage value which shows the maximum leakage current does not vary significantly with the temperature and reverse voltage. This indicates that the values of the gate voltage needed to induce the inversion layer should be invariable for the temperature ranges studied.

Separated leakage currents and their temperature dependence.—Figure 4 shows the temperature dependence of $I_{R,MJ}$, which is derived from the accumulation region A of I_{R-V_G} curve shown in Fig. 3. According to Eq. [4], the currents flowing across the metallurgical junction $I_{R,MJ}$ can be separated into two components. One is the generation component in the depletion region, which shows the same temperature dependence as n_i . The other is the diffusion component, which has the same temperature dependence as n_i^2 . At low temperatures, the generation component is dominant, while the diffusion component becomes dominant at temperatures above 100°C.

$I_{gen,MJ}$ is approximately proportional to the depletion layer width W , assuming a one-sided abrupt junction

$$W = \sqrt{\frac{2\epsilon_s(V_{bi} + V_R)}{qN_D}} \quad [8]$$

where V_{bi} is the built-in voltage and ϵ_s the permittivity of silicon.

At room temperature, the value of $I_{gen,MJ}$ for each reverse voltage is approximately proportional to the square root of V_R , except for $V_R = 0.1V$. This value is 40% less than the extrapolated value from the data at $V_R = 1$ and 10V. This is attributed to the decrease in carrier generation rate within the depletion layer (13). However, since $I_{diff,MJ}$ is independent of the reverse voltage, these three curves should possess the same diffusion component as dotted line for n_i in Fig. 4. By combining the first term of Eq. [4] with Eq. [8], we estimate the effective lifetime $\tau_{0,MJ} = 33 \mu s$. However, using the second term of Eq. [4] and employing $D_p = 11.1 \text{ cm}^2/\text{s}$ (11), a value of $\tau_p = 164s$ is found.

Figure 5 shows the temperature dependence of $I_{R,FIJ}$, for data derived from the leakage currents in the strong inversion region, subtracted by $I_{R,MJ}$. The temperature dependence of $I_{R,FIJ}$ is similar to that of $I_{R,MJ}$. That is, at low temperatures the generation component is dominant, while the diffusion component becomes dominant at tem-

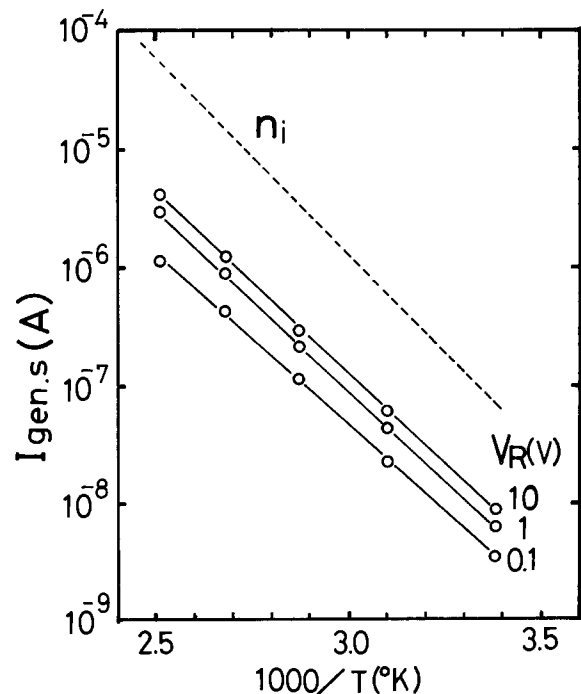


Fig. 6. Temperature dependence of $I_{gen,s}$ at different reverse voltages

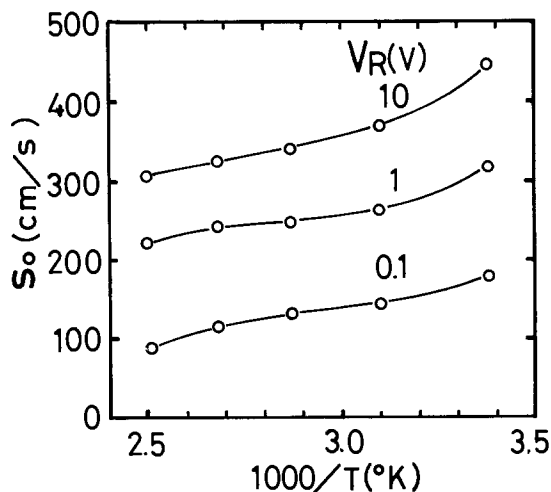


Fig. 7. Temperature dependence of surface recombination velocity at different reverse voltages.

peratures above 100°C. Estimation of $I_{\text{gen},s}$ in conjunction with $I_{R,FIJ}$ is as follows. As we mentioned in the previous section, the maximum leakage current can be observed when the surface begins to invert. Therefore, the maximum current, which shows the peak value in the I_R-I_G curve, involves the sum of $I_{R,FIJ}$ (weak inversion), $I_{R,FIJ}$, and $I_{R,FIJ}$ (maximum). Supposing $I_{R,FIJ}$ (weak inversion) is approximately equal to $I_{R,FIJ}$ (strong inversion), $I_{\text{gen},s}$ is defined as the subtraction of the sum of $I_{R,MJ}$ and $I_{R,FIJ}$ (strong inversion) from the peak value. Figure 6 shows the temperature dependence of $I_{\text{gen},s}$ which has approximately the same temperature dependence as n_i . Using Eq. [6], surface recombination velocity s_0 is estimated as shown in Fig. 7. It tends to decrease with increases in temperature. A possible explanation is that the energy level E_i of the main surface generation-recombination center is not located exactly at the intrinsic Fermi level. Also, as is shown in Fig. 7, s_0 tends to decrease with decreases in reverse voltage. This reverse voltage dependence suggests that surface recombination velocity is subjected to a decrease in surface potential under the reverse biased nonequilibrium condition.

Conclusions

A new type of gate-controlled diode (GCD) was proposed to investigate the leakage currents of a thick zinc

borosilicate glass passivated p⁺-n junction. In this GCD, the n layer of the p⁺-n junction was surrounded by the highly doped n region which repressed lateral depletion layer spreading. Moreover, a semiplanar structure having a deep groove made possible the easy fabrication of the GCD. Using this diode, it was revealed that the surface generation current component cannot be ignored as compared with bulk current component even at temperatures above 100°C. The surface recombination velocity in the glass/silicon system, calculated from surface generation current component exhibited a larger value of 300-400 cm/s, in comparison with that of a SiO₂/Si system, and was dependent on temperature and reverse voltage.

Acknowledgments

The authors would like to thank Mr. Y. Ikeda, Mr. H. Yagi, Dr. M. Okamura, and Mr. K. Miyata for their helpful suggestions and encouragement throughout this work.

Manuscript submitted Oct. 22, 1984; revised manuscript received April 11, 1985.

Hitachi Limited assisted in meeting the publication costs of this article.

REFERENCES

1. A. M. Goodman, *IEEE Trans. Electron Devices*, **ed-21**, 753 (1974).
2. D. L. Flowers and H. G. Hughes, *This Journal*, **129**, 154 (1982).
3. K. Miwa, K. Ikeda, and K. Aoki, *NEC Rev. Dev.*, **42**, 1 (1976).
4. C. A. Goodwin, Paper 353 presented at The Electrochemical Society Meeting, Las Vegas, NV, Oct. 17-22, 1976.
5. Y. Misawa, H. Hachino, S. Hara, T. Ogawa, and H. Yagi, *This Journal*, **128**, 614 (1981).
6. Y. Misawa, H. Hachino, S. Hara, and M. Hanazono, *ibid.*, **131**, 359 (1984).
7. A. S. Grove and D. J. Fitzgerald, *Solid-State Electron.*, **9**, 783 (1966).
8. P. C. T. Roberts and J. D. E. Beynon, *ibid.*, **16**, 221 (1973).
9. R. F. Pierret and R. J. Grossman, *ibid.*, **20**, 373 (1977).
10. A. S. Grove, "Physics and Technology of Semiconductor Devices," p. 172, John Wiley and Sons, New York (1967).
11. F. J. Morin and J. P. Maita, *Phys. Rev.*, **96**, 28 (1954).
12. T. Tokuyama, "MOS Devices," p. 302, Kogyo Chosakai, Tokyo (1973).
13. C. T. Sah, R. N. Noyce, and W. Shockley, *Proc. IRE*, **45**, 1228 (1957).

Process-Induced Interface and Bulk States in MOS Structures

K. Hofmann and M. Schulz*

Institute of Applied Physics, University of Erlangen-Nürnberg, D-8520 Erlangen, Germany

ABSTRACT

The effect of processing on the generation of interface states and bulk states is analyzed in MOS structures. Simple process steps are simulated by postoxidation annealing in nitrogen ambient at temperatures in the range $T_A = 600^\circ\text{C}$ - 1150°C . Interface-state and bulk-trap densities are measured by constant capacitance DLTS. Interface and bulk states are strongly generated at anneal temperatures below 900°C . The interface-state density changes from a distribution showing a gradual decrease from the conduction bandedge to a distribution having a broad maximum near midgap. For the bulk traps at energy $E_c - E_T \approx 0.5$ eV, the density steeply increases within 100 nm from the interface. Densities up to $N_T = 10^{16}$ cm⁻³ are measured after 600°C annealing.

Adequate control of electronic traps in the SiO₂-Si interface region, e.g., interface states and bulk states in the silicon substrate, is an essential requirement for the production of MOS integrated circuits. Many studies have shown (1-4) that oxidation and postoxidation annealing conditions strongly affect the trap densities at the SiO₂-Si inter-

*Electrochemical Society Active Member.

face. Annealing in a H₂ containing atmosphere (1, 3-5) or other annealing procedures (6, 7) are employed for interface-state density reduction. Although the fabrication technology could be improved to achieve interface-state densities at a concentration below $D_{it} = 10^{10}$ cm⁻²eV⁻¹, the current understanding of the structure of these electronic defects and their generation kinetics is still specu-

lative, because too many interacting parameters exist in device processing. Less well studied are the interface-state and bulk-trap generation kinetics for growth and annealing sequences of the SiO₂-Si system at low temperatures as required for VLSI technology. This domain will be especially characterized in this paper.

Several models have been proposed for the microscopic structure of SiO₂-Si interface defects (1, 5, 9-11) to explain various aspects of observed annealing effects and electrical properties. For the perfect SiO₂-Si interface, *i.e.*, when all the Si surface bonds are saturated, no intrinsic defects should appear within the silicon bandgap (12, 13). At present, it is widely accepted that interface states are due to imperfections in the SiO₂-Si interface, *i.e.*, to bonding defects, such as dangling bonds or strained bonds, or to impurity atoms. In all the cases, a strong dependence of the interface-state density on different process variables is expected.

In this paper, we report a detailed experimental study of the interface-state density distribution and the bulk-state density in n-type MOS structures subjected to a postoxidation anneal (POA) in N₂ ambient at temperatures in the range 600°-1150°C to simulate simple device processing steps. Simple MOS capacitors have been employed in this investigation rather than complex devices in order to reduce the number of process steps for sample preparation.

The electronic properties of the SiO₂-Si interface have been characterized by constant capacitance deep level transient spectroscopy (CC-DLTS) (14, 15). Compared to the quasistatic capacitance voltage (CV) method (16), commonly used in MOS interface-state analysis, CC-DLTS is advantageous because of its sensitivity and ability to distinguish between interface states and bulk traps in the silicon substrate. The experimental results presented in the following sections show that interface states and bulk states of intrinsic origin are generated during POA treatment, especially at temperatures below 900°C. It appears that the annealing behavior of interface states in the vicinity of the conduction band edge is different than that of states in the midgap region.

Experimental

Sample preparation.—MOS capacitors were fabricated on (100) silicon wafers (Czochralski-grown or epitaxial) of both n- and p-conductivity type and different resistivity. The standard preoxidation cleaning sequence consists of hot NH₃/H₂O₂, hot HCl/H₂O₂, and HF with rinses in deionized water. The wafers were thermally oxidized in nominally dry oxygen atmosphere at temperatures of 920°, 1020°, and 1120°C to film thicknesses of 60-70 nm and annealed in argon for 15 min at the same temperature. The samples were pulled from the furnace and cooled in argon ambient. The gases were used as delivered by the supplier (< 5 ppm H₂O), without intentionally increasing the H₂O content. The sample and oxidation data are summarized in Table I. The other process parameters were comparable to standard MOS fabrication.

Isochronal postoxidation annealing was performed for 30 min in N₂ atmosphere at temperatures in the range of

Table I. Sample and oxidation data

Material	Oxidation temperature T _{ox} (°C)	Oxidation time t _{ox} (min)	Oxide thickness d _{ox} (nm)
n-Type Epi (1-2 Ω-cm)	920	270	70
p-Type CZ (3-6 Ω-cm)	920	270	67
n-Type CZ (0.2-0.3 Ω-cm)	1020	80	61
p-Type CZ (3-6 Ω-cm)	1020	80	58
n-Type CZ (0.2-0.3 Ω-cm)	1120	15	57.5
p-Type Epi (5-7 Ω-cm)	1120	15	58.5

600°-1150°C. The annealing time was chosen to be comparable with heat-treatments commonly used in implantation damage annealing. After annealing, the samples were pulled from the furnace at cooling rates of greater than 300 K/min. Rapid cooling was used to avoid generation or annealing of defects at intermediate temperatures.

Subsequently, gate electrodes were fabricated by E-gun evaporation of aluminum dots, 200 nm thick and of approximately 0.6 mm diam. As a substrate contact, an aluminum layer was uniformly deposited on the back surface. Finally, the Al contacts were baked at 450°C in N₂ atmosphere for 30 min. On the wafer oxidized at 920°C, additional capacitors having a guard ring with approximately 5 μm spacing from the gate electrode were fabricated.

The gate oxide was removed after metallization in an HF etch on a portion of the wafers to form Schottky diodes by Au or Al evaporation on n- or p-type substrate material, respectively, for the measurements of bulk levels and doping.

Evaluation procedure.—The density of interface states and bulk states in the SiO₂-Si interface region is determined by CC-DLTS. The measurement technique is described in detail elsewhere (14, 15, 17, 18). The basic principle is explained in Fig. 1. Interface states and bulk states are filled with majority carriers (electrons in Fig. 1), when the gate is pulsed to accumulation. After the filling pulse, the SiO₂-Si interface is biased into depletion and the initially occupied states reemit the trapped charge with a time constant, τ (19). For n-type material

$$\frac{1}{\tau} = \sigma_n v_n N_c \exp \left[-\frac{E_c - E_t}{kT} \right] \quad [1]$$

where σ_n is the capture cross section, v_n is the thermal velocity of electrons, N_c is the effective density of states in the conduction band, E_c - E_t is the trap energy in the silicon bandgap, k is the Boltzmann constant, and T the sample temperature.

In the CC-DLTS technique, the depletion capacitance, *i.e.*, the band bending is kept constant during the emission period by adjusting the gate voltage. The gate voltage transient measured at two delay times t₁ and t₂ after the filling pulse comprises the contribution of the continuously distributed interface-state density D_{it} and the bulk-trap density N_T. The CC-DLTS signal ΔV_g is given by

$$\Delta V_g(E_{FS}, T, \tau) = q \int_0^{y_x} \left(\frac{d_{ox}}{\epsilon_{ox}} + \frac{x}{\epsilon_s} \right) N_T [\exp(-t_1/\tau) - \exp(-t_2/\tau)] dx + \frac{q d_{ox}}{\epsilon_{ox}} \int_{E_{FS}}^{E_c} D_{it}(E) [\exp(-t_1/\tau) - \exp(-t_2/\tau)] dE$$

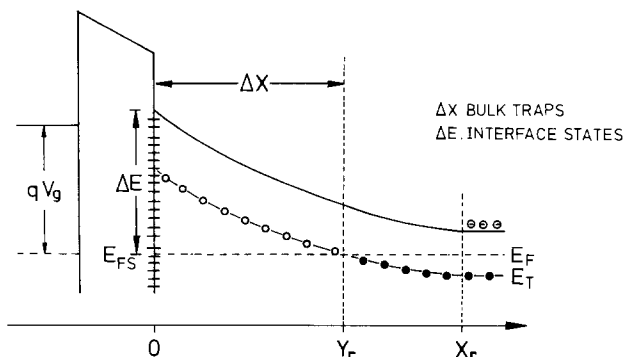


Fig. 1. Schematic band diagram of an MOS structure (n-type) in depletion, illustrating the principle of the CC-DLTS measurement. For a filling pulse to accumulation, the emission of carriers from interface states in the energy interval ΔE and from bulk states in the depth range ΔX contribute to the CC-DLTS signal. The intervals ΔE and ΔX are defined by the interface Fermi level E_{FS} and the Fermi level cross point Y_r. The width of the space charge region X_r varies with the gate voltage V_g applied to the MOS structure.

where q is the electronic charge, d_{ox} is the oxide thickness, ϵ_{ox} and ϵ_s are the oxide and substrate permittivities. For the other abbreviations, refer to Fig. 1.

In the measurement of the spectrum, the CC-DLTS signal is recorded at fixed delay times t_1, t_2 as a function of temperature. Interface states are observed in the CC-DLTS spectra as a continuum and bulk states occurring at discrete energy positions in the gap are observed as peaks. The energy position $E_0 = E_c - E_t$ of trap levels measured at temperature T_0 is calculated from Eq. [1], where the emission time constant is defined by the DLTS delay times (19)

$$E_0 = kT_0 \ln \left(\frac{\sigma_n v_n N_c}{\ln(t_2/t_1)} \right) \quad [3]$$

The interface-state density and the bulk-trap concentration can be evaluated from the CC-DLTS signal by

$$D_{it}(E_0) = \frac{\epsilon_{ox}}{d_{ox}} \frac{\Delta V_g(T_0)}{qkT_0 \ln(t_2/t_1)} \quad [4]$$

$$N_T(E_0) = \frac{2\epsilon_s C_{ox}}{q} \frac{\Delta V_{max}(T_0)}{[\exp(-t_1/\tau) - \exp(t_2/\tau)] (2\epsilon_s A y_r + C_{ox} y_r^2)} \quad [5]$$

where C_{ox} is the oxide capacitance and A is the capacitor area. ΔV_{max} is the peak maximum attributed to bulk states. In order to convert the CC-DLTS spectra recorded as a function of temperature into an energy spectrum, a constant capture cross section $\sigma_p = \sigma_n = 10^{-15} \text{ cm}^2$ is assumed in the evaluations of Eq. [3] and [4].

Results

Interface-state density distribution.—The interface-state density distribution in the silicon bandgap is shown in Fig. 2 for as-oxidized samples. States in the upper half of the bandgap are measured on n-type samples, and states below midgap on p-type samples. The peaks near midgap superimposed on the continuous spectra of interface states are caused by bulk states in the SiO_2 -Si interface space charge region. These peaks will be further discussed in the following section.

The interface-state distribution varies significantly with the oxidation temperature. For MOS capacitors oxidized at 920°C , the interface-state density decreases continuously from the conduction bandedge to the valence bandedge, while for the higher oxidation temperature of

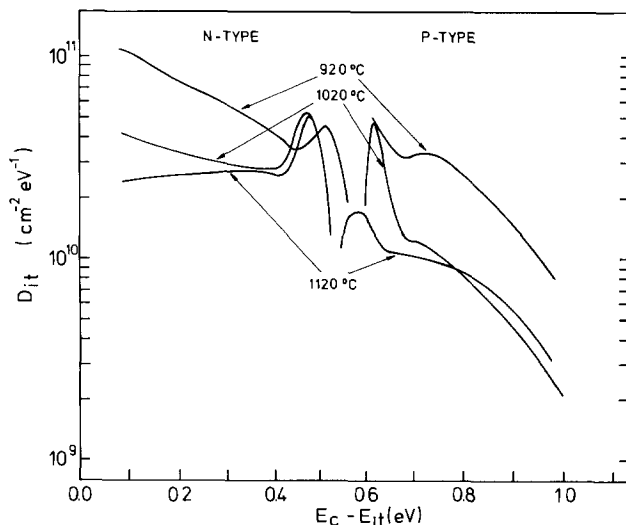


Fig. 2. Interface-state densities in the silicon bandgap for MOS structures oxidized at 920°C , 1020°C , and 1120°C . States in the upper half of the bandgap were observed on n-type MOS capacitors, and those below midgap on p-type samples.

1120°C a broad maximum in the midgap region appears. The decrease in interface-state density towards the valence bandedge visible in Fig. 2 is frequently observed in DLTS experiments (5, 20-22). This decrease is in contrast to the U-shaped interface-state distribution observed in quasi-static CV data for the as-oxidized SiO_2 -Si interface (3). In quasi-static CV measurements taken on the samples of Fig. 2, we obtain a flat interface-state distribution in the midgap region ($E_t \pm 0.3 \text{ eV}$) at densities of $D_{it} = 1.4 \times 10^{10} \text{ cm}^{-2} \text{ eV}^{-1}$. A decrease in density below midgap is not observed. The reason for this discrepancy is still not clear. It may be caused by the limited accuracy of the CV technique or by the presence of slow states near the valence bandedge as reported by Sher *et al.* (23).

Slow states which do not emit the trapped charge at time constants of less than 100 ms do not contribute to the CC-DLTS signal, but they can still be measured by the quasi-static CV method. Near the conduction bandedge, slow states are not reported. The annealing data are therefore only presented for n-type samples.

The interface-state density distribution for MOS capacitors oxidized at $T_{ox} = 920^\circ\text{C}$ and annealed at various temperatures prior to metallization are shown in Fig. 3. The spectra were recorded at DLTS delay times of $t_1/t_2 = 2/4 \text{ ms}$ and $t_1/t_2 = 20/40 \text{ ms}$, respectively. Peaks appearing near midgap are attributed to bulk traps as mentioned above. Compared to the unannealed reference sample, the interface-state density is reduced by a postoxidation anneal in nitrogen at a temperature $T_A = 1075^\circ\text{C}$, higher than the oxidation temperature. Only a slight slope towards higher values at the conduction bandedge is observed. For annealing temperature $T_A = 600^\circ\text{C}$, POA results in an increased trap density near midgap; however, near the conduction bandedge, the interface-state density is the same as before annealing. It is noted that the shape of the

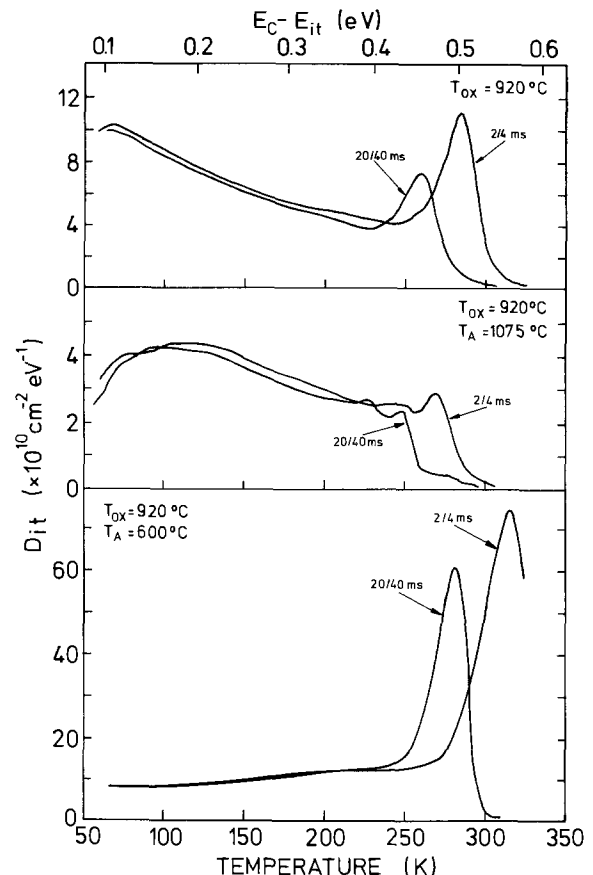


Fig. 3. Interface-state density distribution for MOS capacitors oxidized at $T_{ox} = 920^\circ\text{C}$ and subjected to different POA treatments: without POA (top), POA at 1075°C (middle), and POA at 600°C (bottom). The CC-DLTS spectra were recorded at delay times of $t_1/t_2 = 2/4$ and $20/40 \text{ ms}$, respectively. An approximate energy scale is given at the top.

energy distribution of interface-state density changes considerably with the POA temperature from a decreasing to an increasing distribution.

In order to characterize the annealing effects, we have plotted in Fig. 4-6 the interface-state density at two energy positions of $E_c - 0.4$ eV and $E_c - 0.15$ eV as a function of the POA temperature for samples oxidized at 920°, 1020°, and 1120°C, respectively.

The CC-DLTS spectra of all the samples indicate a smooth continuous interface-state distribution without any distinct structure. Independent of oxidation conditions, the lowest midgap values of D_{it} are measured for samples which received a POA at temperatures of 900°-1000°C and an increased density is observed for POA temperatures of less than 800°C and higher than 1000°C. A similar temperature dependence is observed for the shallow interface states ($E_c - 0.15$ eV) on MOS structures oxidized at 920° and 1120°C. The shallow interface states in samples oxidized at 1020°C are not affected by POA. However, in all the cases the interface-state density is lower near the conduction bandedge than near midgap after 600°C annealing. In general, the effect of a POA treatment on shallow interface states is weaker than that on deep interface states.

Midgap interface-state density and oxide charge.—Interface-state densities and flatband voltages evaluated from standard high frequency and quasi-static CV curves are shown in Fig. 7 and 8, respectively. Since reliable interface-state densities near the bandedges cannot be determined by this technique, only midgap values of D_{it} are presented in Fig. 7 for samples oxidized and annealed at various temperatures as indicated. The trap densities deduced from CV measurement agree quite well with the CC-DLTS results of Fig. 4-6 for midgap states. In the temperature range $T_A < 900^\circ\text{C}$, where the interface-state density increases, a large shift in flatband voltage up to -10V is observed. A shift in flatband voltage of $\Delta V_{FB} = -1\text{V}$ corresponds to an increase in oxide charge of approximately $Q_{ox} = -C_{ox}/A \Delta V_{FB} = 3 \times 10^{11} \text{ cm}^{-2}$, assuming that the charge centroid is located in the vicinity of the SiO_2 -Si interface (2). The CV curves taken at room tem-

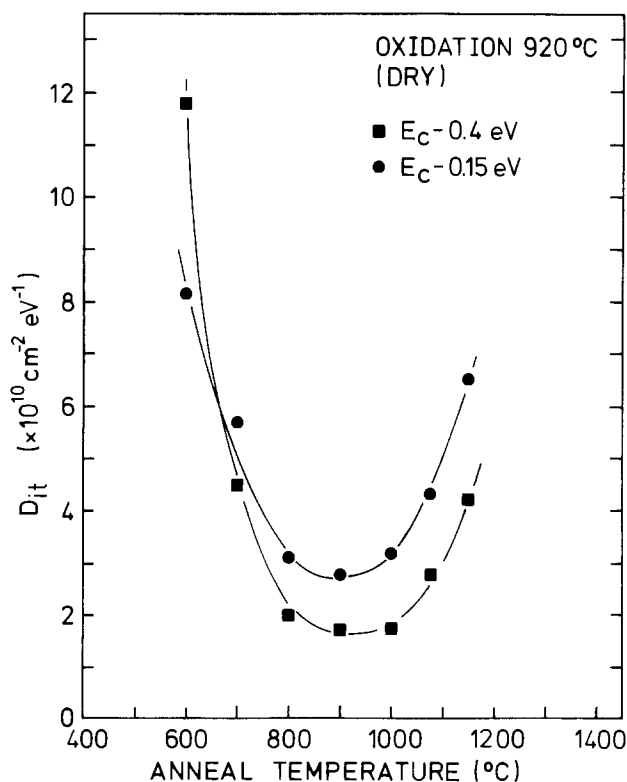


Fig. 4. Interface-state densities at energy positions of $E_c - E_{it} = 0.4$ eV and $E_c - E_{it} = 0.15$ eV for samples oxidized at 920°C and annealed at temperatures $T_A = 600^\circ\text{C}$ -1150°C.

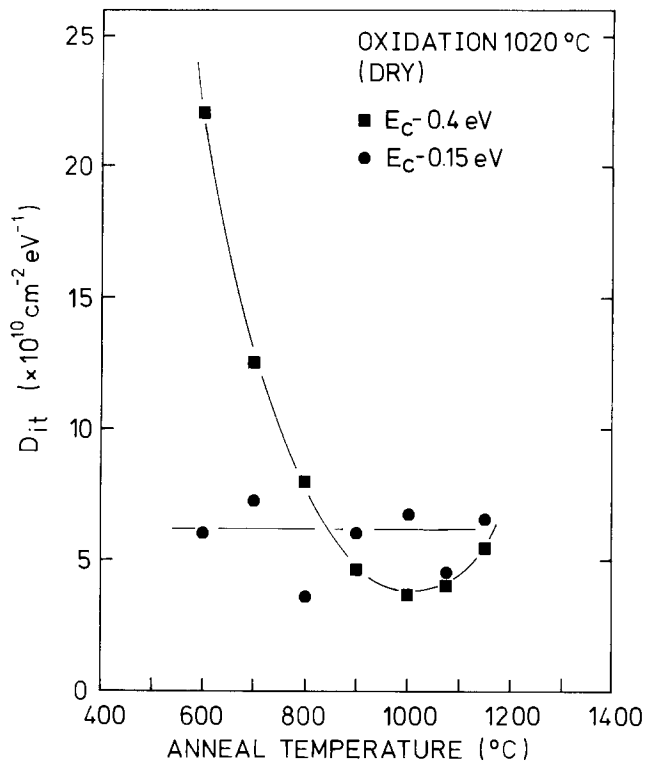


Fig. 5. Interface-state density as a function of POA temperature for MOS capacitors oxidized at 1020°C.

perature show no hysteresis and no shift in flatband voltage during bias stressing, thus indicating that only a negligible amount of mobile oxide charge is present at this temperature. A mobile oxide charge caused by sodium or hydrogen ions (2) can therefore be ruled out.

Bulk states.—Bulk states in the space charge region of the silicon substrate of MOS structures cause discrete energy levels in the bandgap and are therefore observed as peaks in the CC-DLTS spectra. The peak height of bulk levels is proportional to the measurement volume, i.e., the width of the space charge region (see Fig. 1). The peak height is therefore dependent on the surface potential ψ_s or the sample capacitance C_r . The CC-DLTS spectra shown in Fig. 9 are obtained on an MOS structure having

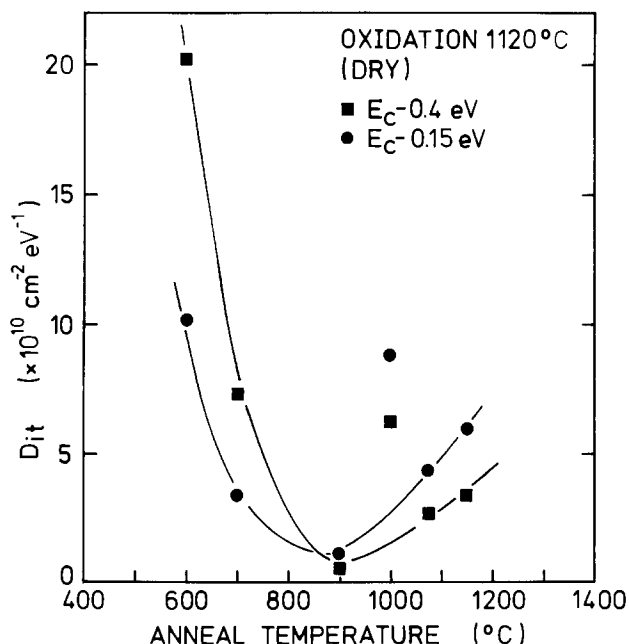


Fig. 6. Interface-state density as a function of POA temperature for MOS capacitors oxidized at 1120°C.

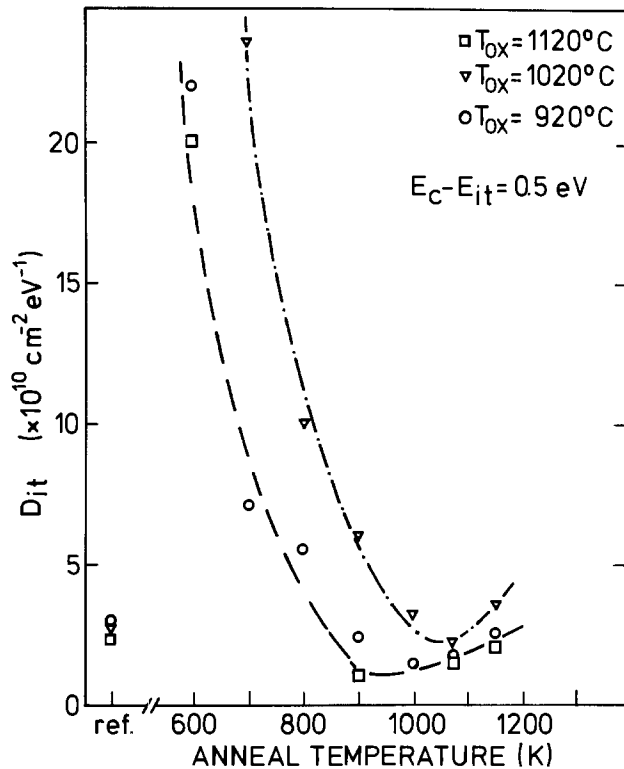


Fig. 7. Midgap interface densities measured by the quasi-static CV method for the samples of Fig. 4-6.

a guard electrode. Surface potentials are determined by high frequency CV measurements. By applying a guard electrode voltage $V_1 = -8V$, the inversion capacitance is reduced from 105 to 89 pF, thus indicating that deep depletion is achieved at the interface and that minority carrier buildup in an inversion layer can be neglected. The peak of bulk traps appearing at approximately 270 K is very sensitive to the variation of the quiescent capacitance C_i in the CC-DLTS measurement. The peak temper-

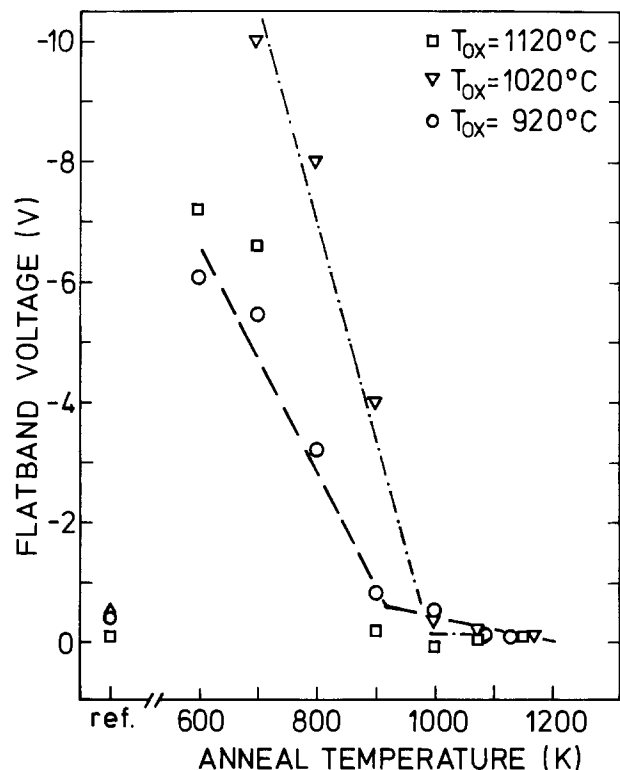


Fig. 8. Flatband voltages derived from high frequency CV measurements for the samples oxidized and annealed at different temperatures as indicated.

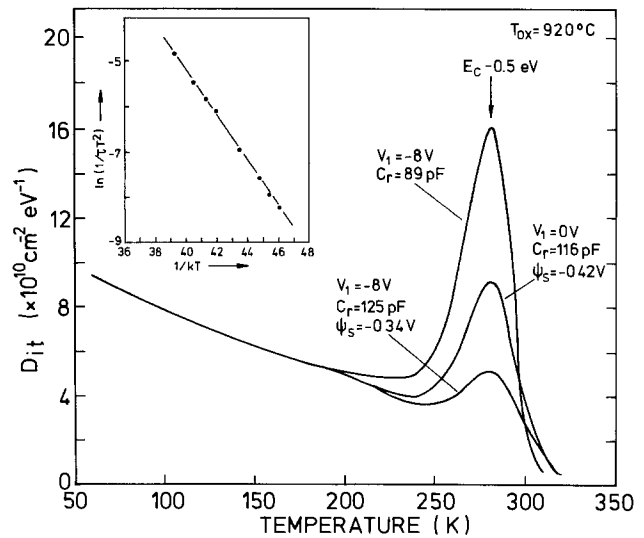


Fig. 9. CC-DLTS spectra for a MOS capacitor ($T_{ox} = 920^\circ C$) having a guard ring. Measurements are obtained at different sample capacitances C_i (i.e., different surface potentials). V_1 is the voltage applied to the guard electrode. The peak appearing in the spectra is due to a deep bulk trap. The energy position of the bulk trap ($E_c - E_T = 0.5$ eV) is derived from the Arrhenius plot of the emission time τ shown in the insert. The emission time τ is determined from DLTS results by the relation $\tau = (t_2 - t_1) / \ln(t_2/t_1)$.

ature position, however, is independent of the capacitance in all the three spectra, thus indicating the absence of recombination effects in the DLTS spectra. The Arrhenius plot of the peak temperature *vs.* the emission time constant is shown in the insert. A trap energy of $E_c - E_T = 0.5$ eV and a capture cross section $\sigma_n = 6 \times 10^{-14}$ cm² is derived from the slope. The bulk-trap density calculated by Eq. [5] is $N_T = 6 \times 10^{14}$ cm⁻³. A detailed analysis of the peaks observed in the CC-DLTS spectra (see Fig. 2 and 3) shows that bulk traps are present in nearly all the MOS structures used in this study. These bulk traps are located deep in the bandgap except in two samples, where two additional shallow traps are observed.

The trap level energies and the corresponding trap densities are summarized in Fig. 10 and 11. The deep bulk traps have identical energy position ($E_c - E_T = 0.5 \pm 0.03$ eV) within the overall error independent of oxidation and POA conditions. We therefore conclude that the origin of the deep traps is identical. A correlation between a special process parameter and a specific trap level could not be observed.

In MOS capacitors annealed at 900°C, no bulk traps were resolved by CC-DLTS. The detection limit for deep

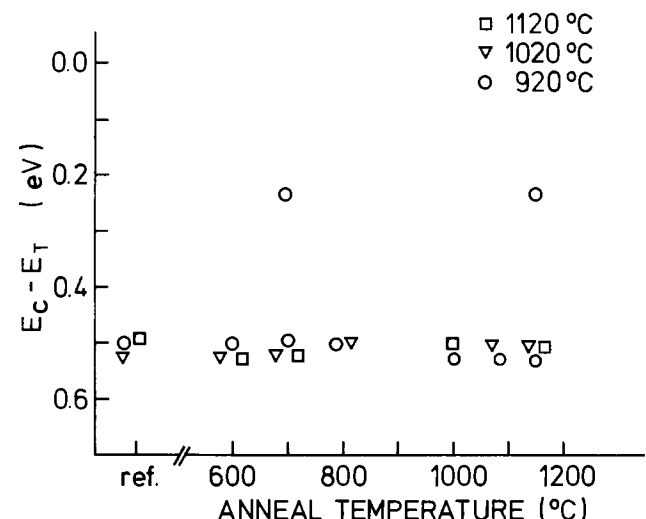


Fig. 10. Energy position of the bulk traps observed in the MOS structures after various oxidation and anneal treatments.

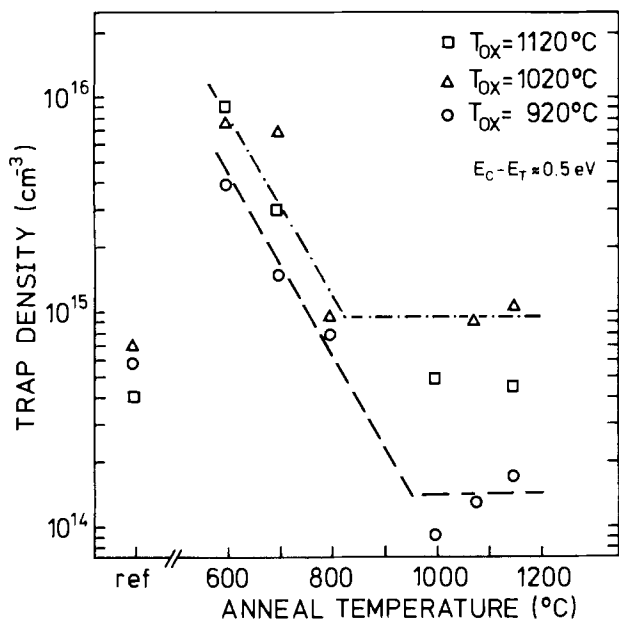


Fig. 11. Bulk-trap density in the immediate vicinity of the SiO_2 -Si interface (< 100 nm). Only the density of the deep states ($E_c - E_T = 0.5$ eV) in Fig. 10 are depicted.

bulk traps is rather high, approximately $N_T = 5 \times 10^{13}$ cm^{-3} , because of the narrow depletion region in MOS structures. The density values in Fig. 11 represent traps located in the immediate vicinity (< 0.1 μm) of the SiO_2 -Si interface. In order to measure concentrations of bulk traps deeper in the substrate, CC-DLTS measurements were performed on Schottky diodes. These spectra show no bulk-trap densities larger than $N_T = 5 \times 10^{12}$ cm^{-3} in a depth range of 0.2-1 μm from the metal electrode. The deep traps observed in MOS structures seem to appear only in the immediate SiO_2 -Si interface region. The trap density decreases by more than three orders of magnitude within the first 2000Å from the interface in samples annealed at 600°C.

Discussion

Annealing of interface states.—Data reported in the literature show that there is still a controversial discussion on the annealing behavior of trap states at the SiO_2 -Si interface in contrast to annealing effects for oxide charges where better agreement is established. It has been emphasized by Razouk *et al.* (3, 24) that the final interface-state density distribution in the SiO_2 -Si system depends on a variety of process variables, such as oxidation and pull/cool conditions, *in situ* POA, POA in argon or nitrogen ambient, anneal time, metallization procedure, and postmetallization anneal (PMA).

The interface-state density distributions presented in this paper as shown in Fig. 2 do not represent the properties of a simple as-oxidized SiO_2 -Si interface. The 15 min *in situ* POA included in the oxidation process is believed to considerably reduce the interface-state density in the upper half of the bandgap (25), compared to that of the as-oxidized cases. Various hydrogen species needed for interface-state annihilation by complexing at low temperatures (500°C) (6) are generated by the reaction of aluminum with water vapor absorbed in the oxide (4). This assumption is supported by the observation of the flat interface-state distribution detected on samples oxidized at 1020°C (see Fig. 2). The interface-state spectra are in agreement with results published in Ref. (3) for MOS structures after a hydrogen anneal.

An oxidation temperature effect visible in Fig. 2 indicates that the PMA process is not completely controlling the interface-state distribution and that the oxidation conditions prior to the annealing affect the density. In particular, for samples oxidized at temperatures below 1000°C, an interface-state density increasing towards the conduc-

tion bandedges was also found in previous investigations of MOS structures annealed in forming gas (27) or subjected to hydrogen "layer" annealing (5, 8).

Nitrogen POA at elevated temperatures is commonly applied in device processing to reduce fixed oxide charges (Q_{ox}). However, for prolonged N_2 anneal an increase in the values of Q_{ox} after an initial decrease has been reported (24, 28-30), which is explained by the formation of Si_3N_4 at the interface. For our samples, a serious effect of such nitrogen reaction is not expected because a thick oxide layer (60-70 nm) is used and because only short annealing times (30 min) are applied.

Recently, it has been shown by Akinwande *et al.* (31) that long anneal times of up to several hours have to be used to reach steady-state values of Q_{ox} for argon annealing at temperatures below 800°C. The results presented in Fig. 8 for the flatband voltage, although showing a similar temperature dependence as the data in Ref. (31), may therefore still deviate from that for the equilibrated SiO_2 -Si interface. We believe that the same argument is probably valid for the interface-state density values of the samples annealed at temperatures $T_A < 900^\circ\text{C}$, because a strong correlation between interface-state density and oxide charges is established in Fig. 4-8. For nitrogen POA, a correlation of D_{it} and Q_{ox} values is, however, not generally observed by other authors (4, 24). We do not know the differences in the material and processing data that cause the differing behavior, and thus we cannot comment on this discrepancy.

Our results show that POA affects the residual interface-state density, even when PMA is applied. This observation is confirmed by two-step annealing experiments, where the annealing sequence consists of an initial anneal at 1150° or 700°C followed by an anneal at the oxidation temperature of 920°C. The CC-DLTS spectra of samples without POA, with one-step annealing, and with two-step annealing clearly show variations due to the various process steps. The residual interface-state density distribution is therefore determined by the entire processing history and not only by the final high temperature process. The annealing behavior of interface states illustrated in Fig. 4-6 is mainly caused by the nitrogen POA.

The essential result of our study is the difference in annealing behavior for interface states near midgap and those near the conduction bandedge. For low POA temperatures ($T_A = 600^\circ\text{C}$) the interface-state density decreases towards the conduction bandedge independent of oxidation conditions, while after high temperature POA ($T_A > 900^\circ\text{C}$) the interface-state density increases. The lowest density values were observed after POA at 900°-1000°C in accordance with observations of Yeow *et al.* (26).

Origin of interface states.—It is clear that microscopic models for the origin of interface states cannot be deduced unambiguously from electrical measurements such as CC-DLTS. We can only give some arguments to rule out unintentional impurities introduced during oxidation and annealing as an origin for the observed effects.

Contamination with alkali ions, especially Na^+ , cannot explain the large negative shift of the flatband voltage observed after low temperature annealing ($T_A < 900^\circ\text{C}$). Although there is some evidence for the presence of electrically inactive Na^+ ions in the SiO_2 -Si system (24), we do not believe that complete passivation of Na^+ occurs after annealing at high temperatures, where low negative flatband voltages are observed. Na^+ ions are also assumed to cause a band tail of interface states near the conduction bandedge (14, 32), which is not observed in our measurements. We therefore conclude that the alkali-ion contamination level is sufficiently low in our samples not to affect the interface-state density.

Other possible contaminations are metallic impurities which may act as charges in the oxide (24) or as electronic traps in the SiO_2 -Si interface region (33-35). For impurities introduced during processing, we expect an increased contamination level at elevated temperatures and diffusion of the contaminant into the substrate. If impurities

are present, the well-known trap levels related to metallic impurities should be detected in the CC-DLTS spectra of the Schottky diodes. Such trap levels were not resolved at concentrations exceeding the detection limit of $N_T = 5 \times 10^{12} \text{ cm}^{-3}$. Metallic impurities are therefore believed to cause only a negligible distortion in the interface-state distribution. The MOS structures studied in this work are assumed to exhibit the properties of the intrinsic SiO_2 -Si interface.

It is widely accepted that interface states of intrinsic type are associated with structural defects in a disordered interfacial transition layer (24, 36). The presence of interfacial layers has been demonstrated with various analytical techniques by several authors (37-39). Structural defects, e.g., strained bonds or dangling bonds residing in the interfacial region, may cause electronic traps as well as fixed oxide charges. The correlation of interface-state density and oxide charge observed during POA supports an interpretation by the same origin. According to Akinwande *et al.* (31), the distinct breakpoint at annealing temperature of $T_A \approx 900^\circ\text{C}$ for interface-state density and oxide charge observed indicates a change in the generation process, e.g., by the formation of mechanical stress. This breakpoint at about 900°C nearly coincides with the viscous flow threshold of thermal oxides $T_c \approx 965^\circ\text{C}$ (40). Stress in the oxide and interface defects related to it is not removed by elastic flow when annealing is carried out at temperatures below 900°C . It is also possible that defects are generated during annealing in the presence of mechanical stress. A direct correlation between stress distribution at the SiO_2 -Si interface and generation has been reported for radiation-induced interface states (41).

Bulk states.—We also observe a steep increase in bulk-trap density in the same temperature range ($< 900^\circ\text{C}$) where interface states and oxide charges are generated during POA. All the three types of defects, oxide charge, interface traps, and bulk traps are therefore correlated. The trap density profiles measured depict a maximum in trap density right at the interface, thus indicating that the deep trap levels ($E_c - E_t \approx 0.5 \text{ eV}$) may be attributed to a specific interface defect. At an energy position near midgap, oxidation-induced defects (42) and interface defects in MOS structures (18, 43) are frequently reported. Interstitial silicon atoms generated during oxidation may also cause a deep trap level at the SiO_2 -Si interface (44). The concentration of interstitial silicon in the interface region increases with oxidation rate (45), i.e., higher oxidation temperature. Because this dependence on oxidation temperature was not observed in Fig. 11, we conclude that the deep traps detected at energy $E_c - E_t = 0.5 \text{ eV}$ are not directly related to interstitial silicon atoms. A possible origin for the deep bulk traps associated with structural defects in the SiO_2 -Si interface region are silicon dangling bonds (12). This assumption would easily explain the strong correlation between interface states and bulk states mentioned above. At present, we can only speculate on the exact nature of bulk traps because the data are insufficient for the drawing of further conclusions.

Summary

The CC-DLTS technique was applied to study the interface-state distribution and the bulk-state density in MOS structures after oxidation and postoxidation nitrogen annealing. Oxidations were performed in dry oxygen ambient at temperatures of 920°C - 1120°C . The interface-state distribution was not found to be U-shaped in the silicon bandgap. Instead, for 920°C oxidation, the interface-state density decreases monotonically from the conduction bandedge to the valence bandedge, and, for 1120°C oxidation, a flat maximum was observed near midgap.

The postoxidation annealing behavior of interface states and bulk states in the upper half of the bandgap was investigated in the temperature range of 600°C - 1150°C . Annealing at temperatures $T_A < 900^\circ\text{C}$ generates both interface states and bulk states. The increase in interface-state density is more pronounced for states near midgap

than for states near the conduction bandedge. After a 600°C temperature treatment, the interface-state density decreases towards the conduction bandedge. For annealing at elevated temperatures $T_A > 1000^\circ\text{C}$, the slope in the energy distribution is reversed.

Deep bulk traps at an energy of $E_c - E_t \approx 0.5 \text{ eV}$ are detected in the immediate vicinity of the SiO_2 -Si interface by CC-DLTS. Specific process parameters which cause these trap levels could not be identified. The bulk-trap densities up to $N_T = 10^{16} \text{ cm}^{-3}$ have been measured in the region within 1000\AA of the interface after 600°C annealing. A strong correlation in the annealing effects of fixed oxide charges, interface-state density, and bulk-trap density has been established.

Acknowledgment

Financial support of this work by the Bundesministerium für Forschung und Technologie is gratefully acknowledged. Portions of this work were also sponsored by the ERO Contract no. DAJA 37-81-C0002.

Manuscript submitted Jan. 28, 1985; revised manuscript received March 27, 1985.

Universität Erlangen-Nürnberg assisted in meeting the publication costs of this article.

REFERENCES

1. Y. C. Cheng, *Prog. Surf. Sci.*, **8**, 181 (1977).
2. B. E. Deal, *This Journal*, **121**, 198C (1974).
3. R. R. Razouk and B. E. Deal, *ibid.*, **126**, 1573 (1979).
4. F. Montillo and P. Balk, *ibid.*, **118**, 1463 (1971).
5. M. Schulz, *Surf. Sci.*, **132**, 422 (1983).
6. T. W. Hickmott, *J. Appl. Phys.*, **48**, 723 (1977).
7. N. Saks, *Appl. Phys. Lett.*, **41**, 737 (1982).
8. L. Risch, E. Pammer, and K. Friedrich, *Inst. Phys. Conf. Ser.*, **50**, 114 (1979).
9. C. M. Svensson, in "Physics of SiO_2 and Its Interfaces," S. T. Pantelides, Editor, p. 328, Pergamon, New York (1978).
10. M. Schulz, *Inst. Phys. Conf. Ser.*, **50**, 93 (1979).
11. K. L. Nagi and C. T. White, *J. Appl. Phys.*, **52**, 820 (1981).
12. R. B. Laughlin and J. D. Joannopoulos, in "Physics of SiO_2 and Its Interfaces," S. T. Pantelides, Editor, p. 321, Pergamon, New York (1978).
13. T. Sugano, in "Insulating Films on Semiconductors," J. F. Verweij and D. R. Wolters, Editors, p. 1, North Holland, Amsterdam (1983).
14. M. Schulz and E. Klausmann, *Appl. Phys.*, **18**, 196 (1979).
15. N. M. Johnson, *J. Vac. Sci. Technol.*, **21**, 303 (1982).
16. A. Goetzberger, E. Klausmann, and M. Schulz, *CRC Crit. Rev. Solid State Sci.*, **6**, 1 (1976).
17. K. Yamasaki, M. Yoshida, and T. Sugano, *Jpn. J. Appl. Phys.*, **18**, 113 (1979).
18. K. L. Wang, *IEEE Trans. Electron Devices*, **ed-27**, 2231 (1980).
19. D. V. Lang, in "Thermally Stimulated Relaxations in Solids," p. 93, Topics in Applied Physics 37, Springer Verlag, New York (1983).
20. C. Jörgensen and C. Svensson, *J. Appl. Phys.*, **56**, 1093 (1984).
21. N. M. Johnson, D. K. Biegelsen, and M. D. Moyer, in "Insulating Films on Semiconductors," M. Schulz and G. Pensl, Editors, p. 35, Springer Series in Electrophysics 7, Springer-Verlag, Berlin (1981).
22. M. Schulz and N. M. Johnson, *Appl. Phys. Lett.*, **31**, 622 (1977).
23. A. Sher, H. L. Hoffmann, P. Su, and Y. H. Tson, *J. Appl. Phys.*, **54**, 5183 (1983).
24. B. E. Deal, in "Semiconductor Silicon 1977," H. R. Huff and E. Sirtl, Editors, p. 276, The Electrochemical Society Softbound Proceedings Series, Princeton, NJ (1977).
25. M. Hamasaki, *J. Appl. Phys.*, **52**, 3484 (1981).
26. Y. T. Yeow, D. R. Lamb, and S. D. Brotherton, *J. Phys. D*, **8**, 1495 (1975).
27. K. Hofmann, Unpublished results.
28. D. W. Hess and B. E. Deal, *This Journal*, **122**, 1123 (1975).
29. H. P. Vyas, G. D. Kirchner, and S. J. Lee, *ibid.*, **129**, 1757 (1982).
30. M. Revitz, S. I. Raider, and R. A. Gulda, *J. Vac. Sci. Technol.*, **16**, 345 (1979).
31. A. I. Akinwande, C. P. Ho, and J. D. Plummer, *Appl. Phys. Lett.*, **45**, 263 (1984).
32. E. Rosencher and R. Coppard, *J. Appl. Phys.*, **55**, 971 (1984).

33. J. W. Chen and A. G. Milnes, *Ann. Rev. Mat. Sci.*, **10**, 157 (1980).
34. E. R. Weber, *Appl. Phys. A*, **30**, 1 (1983).
35. K. Graff and H. Pieper, in "Semiconductor Silicon 1981," H. R. Huff and R. J. Kriegler, Editors, p. 331, The Electrochemical Society Softbound Proceedings Series, Pennington, NJ (1981).
36. J. Maserjian and N. Zamani, *J. Appl. Phys.*, **53**, 559 (1982).
37. S. I. Raider and R. Flitsch, in "Physics of SiO₂ and Its Interfaces," S. T. Pantelides, Editor, p. 384, Pergamon, New York (1978).
38. F. J. Grunthaler and J. Maserjian, in "Physics of SiO₂ and Its Interfaces," S. T. Pantelides, Editor, p. 389, Pergamon, New York (1978).
39. E. Taft and L. Cordes, *This Journal*, **126**, 131 (1979).
40. E. P. EerNisse, *Appl. Phys. Lett.*, **35**, 8 (1979).
41. V. Zekeriya and T. P. Ma, *ibid.*, **45**, 249 (1984).
42. L. E. Katz and L. C. Kimerling, *This Journal*, **125**, 1680 (1978).
43. K. Hübner, H. Käster, B. Derlich, and W. Ecke, *Phys. Status Solidi B*, **118**, K133 (1983).
44. H. Lefevre, *Appl. Phys.*, **22**, 15 (1980).
45. S. M. Hu, *Appl. Phys. Lett.*, **43**, 449 (1983).

An Analysis of Particle Adhesion on Semiconductor Surfaces

R. Allen Bowling*

Texas Instruments Incorporated, Materials Science Laboratory, Dallas, Texas 75265

ABSTRACT

This paper constitutes an analysis of the forces of adhesion of small particles to surfaces, most specifically as applied to semiconductor surfaces. The primary forces of adhesion of small, less than 50 μm diam particles on a dry surface are van der Waals forces. These van der Waals forces of adhesion can increase as a function of time due to particle and/or surface deformation which increases the contact area; micron-size particles can be held to surfaces by forces exceeding 100 dyn, which corresponds to pressures of 10⁹ dyn/cm² or more. Total forces of adhesion for micron-size particles exceed the gravitational force on that particle by factors greater than 10⁶. Electrostatic forces only become important and predominate for particles larger than 50 μm diam. Immersion of the adhered particle system can, in some cases, greatly reduce the total adhesion force, first by shielding of the electrostatic and van der Waals attractions, and also by adding double layer repulsion because of dipolar alignment of liquid molecules or dissolved ions at the surfaces. Double layer interactions may, however, also add to the attractive forces if dipoles align properly for attraction. An important consideration is the possibility that if the particles are not removed by the liquid immersion, then a liquid bridge can be formed by capillary action between the particle and surface upon removal from the liquid. This would add a very large capillary force to the total force of adhesion. This capillary force has been shown to remain, in some cases, even when the system is baked at above the liquid boiling point for more than 24h. Removal of these small particles from surfaces is in theory possible but is in practice extremely difficult. It is clear that emphasis should be placed on prevention of particle deposition rather than on counting on achieving subsequent removal.

A basic understanding of particle adhesion is vital to the search for ways to insure the particle-free semiconductor processing needs of the future. It may be very important in increasing our understanding of how to better remove particulates from wafer and IC surfaces. Particles are known to have, even at present, a very dramatic effect on the manufacture of IC's and are a major yield loss factor. Particles will only become more important as the size of individual semiconductor operational units decreases (1). The present analysis was undertaken with those thoughts in mind, principally to try to understand ways of most effective particle removal from silicon wafers. As will become apparent from the presentation of the findings, it is probable that the most effective efforts may be to prevent particle adhesion in the first place. Information about particle adhesion mechanisms can also aid one in more effective particle prevention. A general summary of some basic concepts about particles is given below, followed by discussions of the forces which control basic particle adhesion to surfaces.

General particle information.—Particles are present all around us in the atmosphere in great abundance. They include, for example, pollens, dusts, fibers, metals, metal oxides, hydrocarbons, and organic matter. They are generated by several means, including mechanical abrasion, chemical reactions, and combustion processes. People are large sources of particles in a semiconductor production facility, e.g., from their clothes, from their skin and hair, and from their breath, particularly if they smoke. Particles adhere to surfaces with great tenacity. One needs only to invert a surface with adhered particles to realize that, even for particles that are quite large, the adhesion force is greater than the gravitational force on those particles. Similarly, vigorous blowing of the surface only manages to dislodge relatively few of the largest particles

(2, 3). The total adhesion force on a particle, as will be shown later in this paper, decreases approximately linearly as a function of the diameter of the particle. On the other hand, the weight of a particle decreases as a function of the diameter cubed, i.e., volume reduction. This means that, for most particles, the adhesive force is about equal to the weight of the particle for particles with diameters ranging from about 0.01 to 1 mm. For a 1 μm diam particle, the force of adhesion easily exceeds the force due to gravity by a factor greater than 10⁶ (4).

The term adhesion describes particle attachment to a surface, and general particle-particle attachment is called agglomeration. Due to adhesion of particles to each other, agglomerates are more frequently encountered than individual particles. Smaller particles, less than 0.5 μm diam, exhibit more violent Brownian motion in air and thus have greater opportunity to collide to form an agglomerate or flocculated mass (5). Particle deposition and removal are also distinctly different. Removal is further complicated over the original deposition because of deformation of the particle at the point of contact, which causes increased contact area and allows chemical bond formation (6).

Typical particles are also not spherical. They are more often agglomerated chains or flocculates of nonuniform shapes. Mechanically generated particles from abrasion processes tend to be quite large, usually greater than 1 μm diam. Vaporization generated particles, e.g., from chemical reactions and combustion processes, are generally very small, typically less than 0.5 μm diam. The distribution of particles in the atmosphere typically reflects these facts by being bimodal with a large number of particles peaking in the range 0.2-0.3 μm diam and a large number of particles peaking at 10-20 μm diam. Also, in general, the smaller the particle, the greater the number of particles of that size in the atmosphere; the number of particles increases as particle sizes decrease as a function

*Electrochemical Society Active Member.

of the reciprocal diameter cubed, d^{-3} . This increase in number of particles as particle size decreases, however, probably begins to turn down at diameters ranging from 0.01 to 0.1 μm due to agglomeration (7, 8).

Filtration of gases and liquids is very important in semiconductor production. Filtration removal of particles from gases is achieved as the result of three basic mechanisms, interception in which the particle is larger than the filter "pore" sizes, inertial impaction of particles into the filter material or strands, and diffusion, *i.e.*, Brownian statistical movement, with subsequent adhesion to the filter material. This differs drastically from fluid filtration which is achieved only by particle interception. Thus the filtration of gases is generally most effective for very small particles with high diffusive movement, and for larger particles that can be easily intercepted or impacted. The particle diameter region of least efficiency for standard HEPA¹ filters is typically around 0.3 μm or less (9, 10). Also, constant point-of-use recirculating filtration of process liquids can be vital to the reduction of particles on devices as a result of liquid processing. We already seem to realize the need for constant air refiltration and constant downward air flow in the reduction of particles from the atmosphere in clean rooms. These are both best understood by considering the gravitational settling rates of particles in solutions and in air. A typical 1 μm -diam particle would require about 50 min to settle 1 ft in air and would require over 5000 min to settle 1 ft in water. Thus, one can see that natural removal of particles by their own gravitational fall does not work. Conscious efforts must be made to remove them and to continue to remove them as new particles are being added to the processing medium.

Particle adhesion mechanisms.—There are, to date, practically no physical models of adhesion which relate adhesive strength to established fields of physics. The difficulties arise from the fact that adhesion strength is a mixture of physical and chemical forces and mechanical strains and stresses, all at and around the adhesive interface. Also, adhesion forces can only be measured destructively. Therefore, an adhesion measurement does not represent an equilibrium situation, so that a kinetic model of adhesion is required. Adhesion must thus usually be approximated geometrically by a sphere on a flat surface (11). The discussions below on adhesion mechanisms all initially assume a spherical particle on a flat surface. The effects of nonspherical particles and rough surfaces are discussed and quantified when possible. The discussions are also primarily theoretical because of the problems in making measurements of adhesive force for very small particles. A typical measurement method is to apply a force for removal by spinning the surface with the attached particles and monitoring the rotation rate at which particles are removed. Removal of 1 μm diam particles, however, are impossible by this method; they would require forces greater than 10^7g , which corresponds to rotation rates greater than 10^6 rotations per minute, a rate not obtainable for known materials. This fact emphasizes the magnitude of adhesive forces, which can be quite large for particles even as large as 10-50 μm in diameter.

Total forces of adhesion of small particles to surfaces can range from a total of 10^{-5} to 10^2 dyn. This total force can correspond to a tremendous force per unit area of up to $>10^9$ dyn/cm² for micron-size particles. Interactions between solids which bring about adhesion can be classed into several groups. Group I includes long-range attractive interactions which act to bring the particle to the surface and establish the adhesive contact area. These include van der Waals forces, electrostatic forces, and magnetic attractions. Electrostatic attractions include both bulk excess charge image forces and electrostatic contact potentials, also known as electrical double layer forces. Group II includes other forces which, along with group I forces, establish the adhesive area. This group of interfacial reactions includes sintering effects such as dif-

fusion and condensation, diffusive mixing, and mutual dissolution and alloying at the interface. This category also includes the establishment of liquid and solid bridges between particle and surface, and the consequential capillary forces associated with these phenomena. Group III includes very short range interactions which can add to adhesion only after the establishment of an adhesive contact area. It includes chemical bonds of all types and intermediate bonds such as hydrogen bonds (11, 12).

In general, the quantitative treatment of group II and III adhesive forces are very difficult because they are primarily specific to each case, being dependent upon the particle and surface materials. The sections below will thus primarily treat group I only. The effects of capillary forces, from group II, will also be discussed and quantitatively treated. This essentially ignores a general treatment of complex chemical bonding to surfaces. We do know, however, that chemical bonds play an important role in particle adhesion on silicon surfaces. For example, it has been shown that silicon particles on a silicon surface can oxidize along with the surface and effectively become entrapped in the oxide; HF cleaning can be important to the removal of the oxide, thus allowing the particle to be removed by other means. The outer surface of silicon is also known to have a large number of "dangling" —OH groups, called a silanol surface. Molecules which themselves have —OH groups can form strong estersil bonds with this silanol surface. The remaining Si—O—Si surface of silicon can also hold many species by hydrogen bonding at the electronegative oxygen atoms. All these effects must be considered when trying to remove particles, but none of these bonding factors are general enough to be treated in a quantitative manner as a function of particle size. One important factor in ignoring these in a general treatment is that bonding and interfacial reactions are not generally very active at room temperature. Higher temperatures are required for most materials before these become significant.

The primary forces which act to bring particles to a surface and then hold them there are van der Waals forces and electrostatic forces. Electrostatic forces predominate for large particles, *i.e.*, greater than about 50 μm diam. Van der Waals forces, however, predominate for smaller particles. Electrostatic forces are comprised of two types of forces, excess charge image forces and electrostatic contact potentials, also known as electrical double layer forces. For dry uncharged particles on a dry uncharged surface, only van der Waals and electrical double layer forces will act to hold the particles on the surface, *i.e.*, specifically if no bonding or other interfacial reactions can occur for the materials. Charged particles and/or charged surfaces then add an additional electrostatic image force. Wet systems can then have an additional capillary force acting to hold the particles, and immersed systems may experience a shielding of each of these forces so that the total force holding the particles is reduced. As follows, the individual forces for dry particle systems will be described followed by a treatment of wet and immersed systems.

Van der Waals Forces.—Van der Waals forces can be understood as follows. Even at absolute zero temperature, solids can contain local electric fields which originate from polarizations of the constituent atoms and molecules. Above zero degrees, additional contributions come from thermal excitations of the atoms and molecules. As explained by quantum theory, the electrons of an electrically neutral solid do not occupy fixed states of a sharply defined minimum energy which results in spontaneous electric and magnetic polarizations varying quickly with time (11). Van der Waals forces thus include forces between molecules possessing dipoles and quadrupoles caused by the polarizations of the atoms and molecules in the material. This can include both natural as well as induced instantaneous dipoles and quadrupoles. The nonpolar van der Waals forces are also referred to as London-

¹High efficiency particulate air filter.

van der Waals dispersion forces because London associated these forces with the cause of optical dispersion, *i.e.*, spontaneous polarizations (5, 13, 14). This dispersion force will make the major contribution to the intermolecular force, except in the case where the polarizability is small and the dipole moment is large. These forces are postulated by some to be additive for assemblies of atoms and molecules. This assumption has been used to calculate the van der Waals force using a microscopic approach which starts from interactions between individual atoms or molecules and calculates the attraction between larger bodies as an integration over all pairs of atoms and molecules (2, 3, 5). This method has been used by Hamaker (15). His method uses the so-called Hamaker constant, A , whose value is not measurable and is definable by order of magnitude only. This approach has severe shortcomings because linear additivity is actually not correct, as it does not consider cross correlation of charge (11, 16). One author has stated that the Hamaker approach is in certain cases "not only inaccurate but also downright misleading as to the laws of force" (6). A more satisfactory macroscopic approach was developed by Lifshitz, who started directly from the bulk optical properties of the interacting bodies (17). In this approach, the decisive material value is the Lifshitz-van der Waals constant, h , which is defined as an integral function of the imaginary parts of the dielectric constants of the adhering materials (6, 11, 16, 18).

This constant, h , depends only on the materials involved, provided the separation distance is very small. Under some conditions, the Lifshitz-van der Waals constant may be related to the Hamaker constant by the equation, $h = 4\pi A/3$ (4). This Lifshitz-van der Waals constant generally ranges from about 0.6 to 9.0 eV, depending on the materials combination (16). Qualitatively, since this constant is related to the optical absorptivity of a material, materials with strong optical absorption have strong spontaneous fields and thus should be bound by greater forces of adhesion due to van der Waals (vdW) attractions. The force per unit area between two parallel flat surfaces in contact can be exactly calculated to be

$$\frac{F(\text{vdW})}{\text{cm}^2} = \frac{h}{8\pi^2 z^3}$$

where z is the atomic separation between the surfaces (11, 16, 12). The van der Waals adhesion force between a spherical particle and a flat surface reduces in approximation to

$$F(\text{vdW}) = \frac{hr}{8\pi z^2}$$

where r is the particle radius. This formula treats the force of adhesion as the force necessary to remove the particle, and as such it is a maximum force under ideal conditions for a perfectly spherical particle on a flat surface. This formula can be further reduced by substituting $d/2$ for r , and assuming an adhesion distance, z , of about 4Å. The formula becomes

$$F(\text{vdW}) = 2hd \text{ mdyn}$$

where d is the particle diameter in microns. The constant, h , ranges from about 0.6 eV for polymers to about 9.0 eV for metals such as silver and gold. In Table I are shown some typical particle/surface van der Waals constants.

From a 1 μm-diam particle with a constant of 0.6 eV to a 100 μm-diam particle with a constant of 9.0 eV, the van der Waals force can range from about 1 mdyn to 1800 mdyn. This corresponds to a force per unit area of from about 0.2×10^9 to 3.0×10^9 dyn/cm². These are tremendous pressures, and most particles and/or surfaces can be deformed by such forces. The amount of deformation depends on the hardness of the particle and surface, and this deformation can increase with length of time that the force acts on the particle and surface. From this, it can be readily seen that the time to remove particles is as soon as possible after they are deposited. A time delay can allow

Table I. Empirically determined Lifshitz-van der Waals constants [data from Ref. (4) and (11)]

Particle	Surface	h (eV)
polymer	polymer	0.6-0.9
KBr	KBr	2.0
Al ₂ O ₃	Al ₂ O ₃	4.0
Ge	Ge	6.8-7.6
Si	Si	6.8-7.2
Ge	Si	7.5
graphite	graphite	7.2
graphite	Si	6.8
Cu	Cu	8.5
Ag	Ag	9.0

the force of adhesion to increase dramatically. The additional van der Waals force due to deformation is a function of the increased contact area caused by this deformation and is given by

$$F(\text{vdW deform.}) = \frac{h\rho^2}{8\pi z^3}$$

where ρ is the radius of the adhesive surface area. This reduces, for z of 4Å, to

$$F(\text{vdW deform.}) = 9.96 \times 10^3 h\rho^2 \text{ mdyn}$$

for ρ in microns. The total van der Waals force is then

$$F(\text{vdW total}) = F(\text{vdW}) + F(\text{vdW deform.})$$

If the contact of a 5 μm-diam particle is increased from point contact to a 0.05 μm radius area by deformation, and assuming h is 7 eV, the $F(\text{vdW deform.})$ can be 174 mdyn, which is much greater than the 70 mdyn normal $F(\text{vdW})$ of the system. This is only a 2% deformation of the particle, *i.e.*, the 5 μm-diam particle is flattened only to the point of having a 0.1 μm-diam contact area. The $F(\text{vdW deform.})$ would increase by a factor of five if the deformation were increased to a 0.5 μm-diam area, or 10%. This new contact area, and thus the $F(\text{vdW deform.})$, depends on the hardness of the particle and surface materials. Softer materials yield to greater deformations and thus greater forces of adhesion. In general, the constant, h , is also much smaller for soft materials. This means that the greatest forces of adhesion are generally for soft materials bound to a metal. The metal gives the combination a greater h and the soft material gives greatest added deformation. A hard oxide layer on a metal surface, on the other hand, tends to reduce adhesion of hard particles to that surface. Figure 1 is a graph of $F(\text{vdW})$ and $F(\text{vdW deform.})$

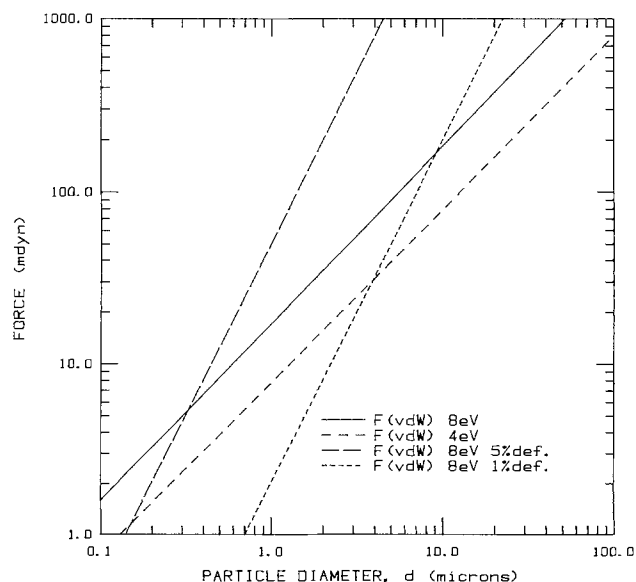


Fig. 1. $F(\text{vdW})$ and $F(\text{vdW deform.})$ as a function of particle diameter

form.) *vs.* particle diameter for materials combinations of 4 eV and 8 eV and 1% and 5% deformation. It shows the $F(\text{vdW})$ without deformation for h equal to 4 eV and 8 eV, plus the additional force due to deformation of 1% and 5% for h equal to 8 eV. It clearly shows that deformation can add tremendously to the total force of adhesion. A first look at these plots should not be incorrectly interpreted that the forces of adhesion simply decrease with decreasing particle diameter. Although the total force does decrease, the force per unit area increases with decreasing particle size, and the force of adhesion also increases relative to the gravitational force acting on the particle. These relationships will be further discussed later.

Electrostatic forces.—Two types of electrostatic forces may act to hold particles to surfaces. The first is due to bulk excess charges present on the surface and/or particle which produce a classical coulombic attraction known as an electrostatic image force. This attractive force is given by the equation

$$F(i) = \frac{q^2}{4\pi\epsilon_0 E l^2}$$

where E is the dielectric constant of the medium between the particle and surface, E_0 is the permittivity of free space, q is the charge, and l is the distance between charge centers. The distance between charge centers is in this case approximately equal to $2r$, where r is the particle radius, and q can be expressed as a function of the particle radius by the expression

$$q = CU = 4\pi\epsilon_0 rU$$

where C is capacitance, and U is the potential in volts. The capacitance has been expressed as a function of r via an approximation of the Euler equation. The expression for total image force then reduces as a function of particle diameter, d , in approximation to

$$F(i) = 3 \times 10^{-2} d^2 \text{ mdyn}$$

where d is the particle diameter in microns. This equation assumes a charge density of 10 electronic charges per square micron, what might be considered a typical large charge. The maximum charge density normally possible is about 100 electronic charges per square micron, which corresponds to a flashover potential of about 20,000 V/cm. It is important to note that for conductors, these excess charges are balanced by contact charge flow so that adhesive forces by electrostatics is small. On the other hand, for nonconductors, electrostatic attraction is significant.

The more important electrostatic force for very small particles is electrostatic contact potential induced electrical double layer forces. Two different materials in contact develop a contact potential caused by differences in the local energy states and electron work functions. Electrons are transferred from one solid to another until an equilibrium is reached where the current flow in both directions is equal. The resulting potential difference is called a contact potential difference, U , which generally ranges from 0 to about 0.5V. It sets up a so-called double layer charge region. In the case of two metals in contact, only the surface layer carries contact charges. For semiconductors and insulators, these regions may extend into the bulk up to 1 μm or deeper. For a particle on a surface, this double layer force can be calculated as

$$F(\text{el}) = \frac{\pi E_0 r U^2}{z} \text{ dyn}$$

which reduces to

$$F(\text{el}) = 4dU^2 \text{ mdyn}$$

where d is in microns and U is in volts. For a maximum of potential difference of 0.5V, $F(\text{el})$ is approximately equal to d mdyn (4, 11 19). Figure 2 is a comparison of the van der Waals forces and electrostatic forces of particle adhe-

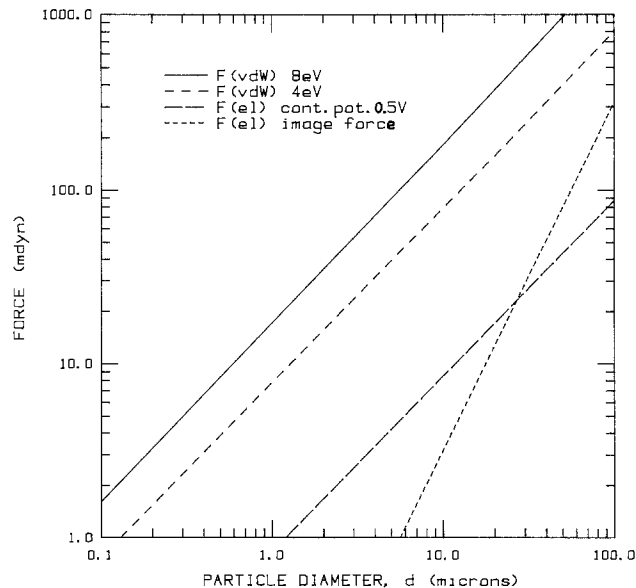


Fig. 2. $F(\text{vdW})$ in comparison to electrostatic forces of adhesion as a function of particle diameter.

sion *vs.* particle diameter. It is clear, at least for these ideal calculations, that the van der Waals forces predominate over electrostatic forces for very small particles. Double layer electrostatic forces also generally predominate over electrostatic image forces for small particles. Materials that can carry charges high enough to allow electrostatic forces to contribute significantly to the total force of adhesion are generally polymers of poor conductivity or other extreme insulators.

It is very important in this case to point out again that these first considerations have been for spheres on flat surfaces. Electrostatic forces can in fact predominate over van der Waals forces in the case where surface asperities of the particles are significant enough to remove the bulk of the particle from the contact point. This is due to the rapid decrease in $F(\text{vdW})$ with increasing distance between the adherents. In the presence of surface asperities, calculation of the van der Waals force should not be based on the full radius of the particle, but rather on the radius of curvature of the surface elevation at which the adherents are in contact. Conversely, electrostatic forces do not change much with asperities; at not too large deviations from spherical, the effective radius for electrostatic forces is approximately equal to the true radius. This comparison can be quite complex, especially when considering that multiple asperities may be present and thus multiple contact point may be formed so that $F(\text{vdW})$ once again predominates. Also, deformation of particles and/or surfaces after a period of time may change these asperities at the contact point so that $F(\text{vdW})$ again also predominates (4, 11, 19).

For a dry system, the total forces of adhesion are thus a combination of van der Waals forces and electrostatic forces. As stated before, for particles less than 50 μm diam, this total adhesion force greatly exceeds the force due to gravity for a given particle size. For a 1 μm -diam silicon particle on a dry silicon surface, the total force of adhesion exceeds the gravitational force by a factor of greater than 10^7 . A comparison of the total force of adhesion for a dry system *vs.* the ratio of total force of adhesion to gravitational force is made in Fig. 3. The total force of adhesion line is calculated for a van der Waals constant of 8 eV and 1% particle deformation, assuming a contact potential of 0.5V and an image force from Fig. 2. The gravitational attraction is calculated for a particle density of silicon (2.33 g/cm^3) based on the equation

$$F(\text{grav.}) = 4/3\pi r^3 \rho$$

where ρ is the density and r is the particle radius. For particles less than about 20 μm diam it can be seen that

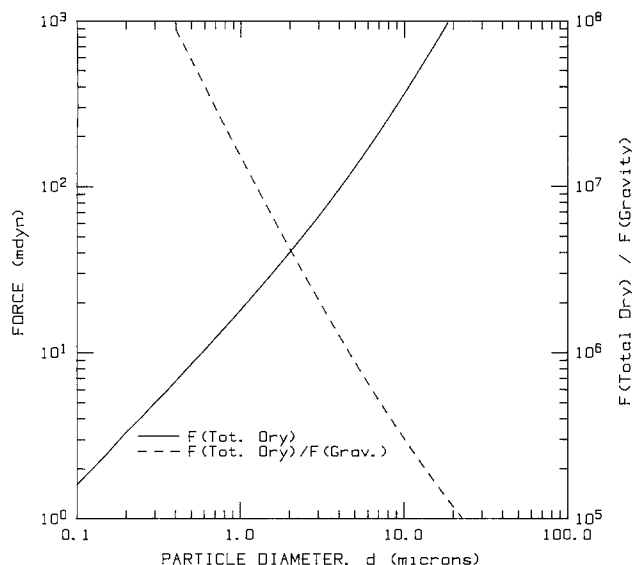


Fig. 3. Total force of adhesion of particles on a dry surface as compared to the ratio of total force to gravitational force as a function of particle diameter.

the total force of adhesion exceeds the gravitational force by a factor of at least 10^5 .

Effects of humidity and liquids on adhesion.—Due to high humidity or to an adhered particle/surface system having been immersed and then withdrawn from a liquid, a liquid film can be formed by capillary condensation or capillary action between the particle and surface. The resulting capillary force can make a large contribution to the total force of adhesion. The capillary force is a function of the particle radius and liquid surface tension (surface tension of water at 18°C is 73.0) as shown by the formula

$$F(\text{cap.}) = 4\pi r\gamma \text{ dyn}$$

where r is the particle radius, and γ is the liquid surface tension. This reduces to

$$F(\text{cap.}) = 0.63d\gamma \text{ mdyn}$$

where d is the particle diameter. There is evidence that a capillary force may remain even after baking at above the boiling point of the liquid, even for as long as 24h. If the liquid contains substances that can crystallize upon evaporation, a solid crystalline bridge might also form during

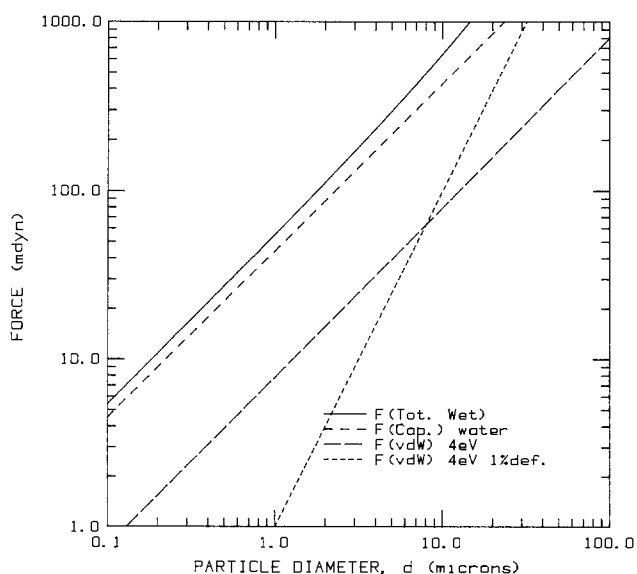


Fig. 4. Capillary force and total wet force of adhesion as a function of particle diameter.

drying. It should be pointed out that hydrophobic surfaces are not generally affected by capillary forces. Figure 4 shows the magnitude of a capillary force, for water as the liquid, in comparison to the van der Waals forces for h equal to 4 eV and for 1% deformation of the particle. It can be seen that the capillary force can be predominant over other forces for small particles. A comparison of the total wet force of adhesion, as a combination of reduced van der Waals force and capillary force, to the gravitational force is given in Fig. 5. As will be discussed later, particle forces may be reduced by immersion in liquids, particularly for large particles, but if the particles are not removed in the liquid, then the added capillary forces which remain upon removal from the liquid can increase the total adhesion force by an order of magnitude or more.

Immersion effects on adhesion.—By immersion of adherent particles in a liquid, the van der Waals force can be reduced by, in most cases, about a factor of two, since the liquid partially shields the attraction. For calculation purposes, the van der Waals constant, h , must be replaced by an immersed van der Waals constant, $h(\text{im.})$. Table II shows some typical $h(\text{im.})$ values as compared to h values (11). Electrostatic image forces are more or less eliminated by immersion, and electrostatic contact potential forces are greatly reduced. The electrostatic forces generally tend to become negligible because of the enhanced static dielectric constant of the liquid, as compared to a gaseous or vacuum environment, and because of the sorption phenomena which tend to shield the charges.

Immersion does not necessarily always cause a reduction in adhesion purely because of its shielding effect of charges. The liquid molecules and/or ionic impurities in the liquid can actually add to the total adhesive force. Likewise, in some cases, the reduction in total adhesion force by immersion is greater than predicted by shielding alone. To understand these possibilities, one must consider the interactive forces between the boundary layers present at all solid-liquid interfaces of the adherents (these same discussions can apply to the humid and wet situations described above). Molecules of a liquid are often adsorbed at the solid surfaces and are polarized and/or oriented in a certain direction so that an electrical double layer is formed at each solid-liquid interface. If the processes occur in the same way on all surfaces, dipole layers can cause repulsive forces, thus adding to the reduction in adhesive force, and in some cases actually cause removal. If the liquid itself is dissociable into ions and/or if the liquid contains dissolved species which are present as ions, again dipolar alignments on surfaces can occur to cause double layer attractions or repulsions.

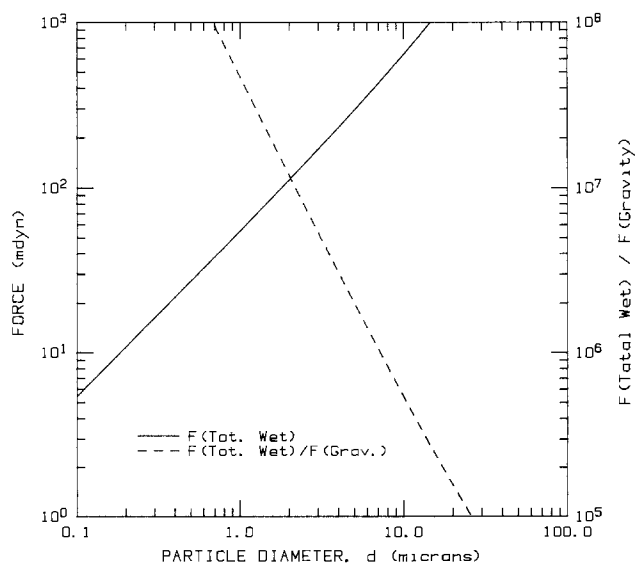


Fig. 5. Comparison of the total wet force of adhesion to the gravitational force as a function of particle diameter.

Table II. Comparison of immersed and nonimmersed van der Waals constants [from Ref. (11)]

Particle-liquid-surface	h (eV)	h (im.) (eV)
polystyrene-water-polystyrene	0.6	0.1
silicon-water-silicon	6.8-7.2	3.49
copper-water-copper	8.5	4.9
silver-water-silver	9.0	7.76

These forces can be approximated by the formula for electrostatic contact potentials if the contact potential difference is determinable. For a particle on a surface, the repulsive or attractive force due to these charge double layers, for a certain charge density in solution, can be alternatively approximated by the formula

$$F = \pm 64\pi r N k T \delta$$

where r is the particle radius, T is the temperature in degrees Kelvin, N is the charge density in charges per cubic centimeter, and δ is the double layer thickness, which is typically about 50Å. This reduces to approximately

$$F = \pm 7 \times 10^{-25} d T N$$

For 0.1 g/liter NaCl, N is 2×10^{18} charges/cm³. The charge density depends on the charge of the ions as well as on the number of ions produced. Whether the force is attractive or repulsive is completely system dependent. For particles which are the same materials as the surface, charges generally form double layers the same on both surfaces so that the double layer interactions are repulsive. Different ions may, however, collect differently at unlike surfaces so that either attractive or repulsive forces are possible depending on their alignment.

Figure 6 is a comparison of the total wet and total dry adhesion forces, as given in Fig. 3 and 5, to the possible repulsive forces from double layer formation. (Although these are described as repulsive forces, they should also be considered as potentially attractive forces which would add to the total force of adhesion.) First, assuming a very large contact potential of 5V, using the contact potential force equation, the possible repulsive force exceeds either of the two total adhesion forces. This potential, however, exceeds the normal maximum possible potential difference by a factor of ten, so that this possibility is totally unreasonable, but it does effectively point out the difficulty in removal of particle by charging. In principle it would be possible to charge the particle

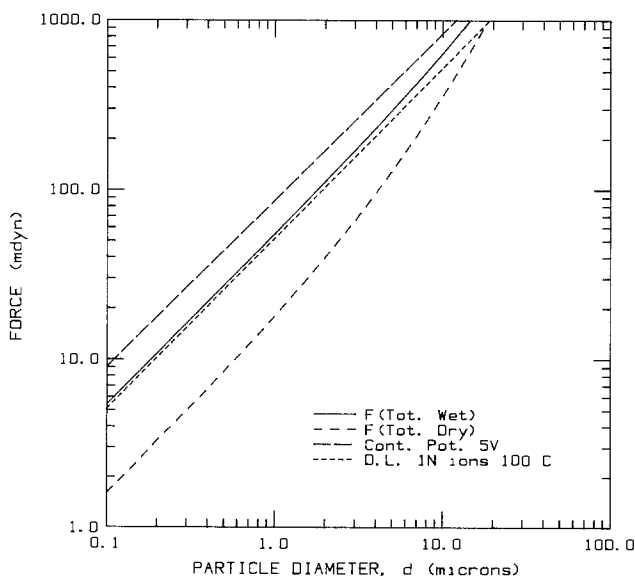


Fig. 6. Total wet and dry forces of adhesion compared to the calculated possible repulsive forces from double layer formation for the specified parameters.

and/or surface, unimmersed, so that repulsion would cause particle removal, so-called electrostatic removal. This is, however, quite difficult because of the large charges which must be placed on the small particles. Second, a solution with 1N ions, in which the ions align themselves correctly for repulsion, at 373 K is needed to balance the total wet force of adhesion. This is a concentrated solution which itself may cause more problems than it solves by particle removal. Also, because the solution is so concentrated, it is highly unlikely that large potential differences will result, so that this calculation is probably not valid at such high concentrations. Although unrealistic, it again points out the extremes needed for removal of small particles.

Detergency.—One final topic for consideration is aqueous and nonaqueous detergency. It is known that adhered colloidal particles below about 0.2 μ m diam are virtually impossible to remove and that removal is difficult even for particles as large as 10 μ m diam or more. One paper has reported that significant detachment of small particles can occur in nonaqueous surfactant media by polymeric detergency (20). The exact mechanism of this action is not known, but it has been referred to as an endropic repulsion mechanism where it has been hypothesized that the polymeric detergent may act as a "molecular wedge." Endropic action implies that the source of repulsion which counteracts particle adhesion is the reduction in configurational entropy of the adsorbed polymer chains when they are compressed in the space between particle and surface. The detergent molecule must not only be small enough to be able to be adsorbed between the adhered particle and solid surface, but also must be large enough to exert an effective entropic repulsion. Therefore, the size of the detergent molecule is very critical (20). These considerations imply that each particle size will be most effectively removed by a different detergent molecule size which is optimized for that particle size. Also, deformed systems in which the particle and/or surface have an extended contact area may not be so affected by this detergency, so that the longer the deformable particles are left on the surface, the less effective detergency may be.

Conclusion

It has been determined that small particles on a dry surface are primarily held by strong van der Waals forces which can increase in magnitude with time due to deformation of the particle and/or surface which increases the total contact area. Immersion generally significantly reduces the total force of adhesion while the particle/surface system is still immersed. Upon removal from the liquid, however, predominating capillary forces of adhesion may be added due to the formation of liquid bridges between particle and surface. The same phenomenon of capillary action may also occur in high humidity. The total forces of adhesion for small particles are so large that they exceed the gravitational force on those particles by many orders of magnitude. Emphasis should be placed on prevention of particle deposition rather than counting on their subsequent removal. All specific considerations of particle adhesion could not have been treated in a review such as this; however, hopefully this treatment has conveyed a general overview of the major considerations of particle adhesion. Additional references on particle adhesion not already cited in this paper appear in Ref. (21-26).

Acknowledgments

The author would like to express special thanks to Olga Paradis for much technical library assistance in the compilation of this information, and to Graydon Larrabee for his helpful assistance in completing this work.

Manuscript received Oct. 31, 1984.

Texas Instruments Incorporated assisted in meeting the publication costs of this article.

REFERENCES

- J. M. Duffalo and J. R. Monkowski, *Solid State Technol.*, **27**, 109 (1984).
- M. Corn, *J. Air Pollut. Control Assoc.*, **11**, 523 (1961).
- M. Corn, *ibid.*, **11**, 566 (1961).
- J. Visser, *Surf. Colloid Sci.*, **8**, 3 (1975).
- M. Corn, in "Aerosol Science," C. N. Davies, Editor, p. 359, Academic Press, New York (1966).
- J. A. Kitchener, *J. Soc. Cosmet. Chem.*, **24**, 709 (1973).
- "Fine Particles," B. Y. H. Liu, Editor, Academic Press, New York (1976).
- N. A. Fuchs, "The Mechanics of Aerosols," MacMillan Co., New York (1964).
- "Air Filtration," C. N. Davies, Editor, Academic Press, London (1973).
- R. G. Dorman, in "Aerosol Science," C. N. Davies, Editor, p. 195, Academic Press, New York (1966).
- H. Krupp, *Adv. Colloid Interface Sci.*, **1**, 111 (1967).
- S. Bhattacharya and K. L. Mittal, *Surf. Technol.*, **7**, 413 (1978).
- F. London, *Z. Phys.*, **63**, 245 (1930).
- F. London, *Trans. Faraday Soc.*, **33**, 8 (1937).
- H. C. Hamaker, *Physica*, **4**, 1058 (1937).
- H. Rumpf, in "Proceedings of the Second International Symposium on Agglomeration," Vol. 1, K. V. S. Sastry, Editor, p. 97, American Institute of Mining, Metallurgical, and Petroleum Engineers, Inc., New York (1977).
- E. M. Lifshitz, *Sov. Phys. JETP*, **2**, 73 (1956).
- B. B. Morgan, *Br. Coal Util. Res. Assoc., Mon. Bull.*, **25**, 125 (1961).
- B. V. Deryagin and A. D. Zimon, *Colloid. J. USSR (Engl. Transl.)*, **23**, 454 (1961).
- E. J. Clayfield and E. C. Lumb, *Discuss. Faraday Soc.*, **42**, 285 (1966).
- S. N. Omenyi, J. Chappuis, and A. W. Neumann, *J. Adhes.*, **13**, 131 (1981).
- D. Bargema and F. Van Voorst Vader, *J. Electroanal. Chem. Interfacial Electrochem.*, **37**, 45 (1972).
- A. D. Zimon, "Adhesion of Dust and Powders," 2nd ed., Consultants Bureau, New York (1982).
- B. V. Deryagin, N. A. Krotova, and V. P. Smilga, "Adhesion of Solids," Consultants Bureau, New York (1978).
- "Surface Contamination: Genesis, Detection, and Control," Vol. I and II, K. L. Mittal, Editor, Plenum Press, New York (1979).
- R. K. Iler, "The Colloid Chemistry of Silica and Silicates," p. 95-259, Cornell University Press, Ithaca, NY (1955).

Anomalous Diffusion of Tin in GaAs

H. H. Erkaya* and R. J. Roedel

Department of Electrical and Computer Engineering, Arizona State University, Tempe, Arizona 85287

R. Lareau and P. Williams

Department of Chemistry, Arizona State University, Tempe, Arizona 85287

J. Leavitt

Department of Physics, University of Arizona, Tucson, Arizona 85720

A. Von Neida

AT&T Bell Laboratories, Murray Hill, New Jersey 07794

ABSTRACT

We have used a "leaky tube" diffusion system to carry out tin diffusion in p-type GaAs substrates in an attempt to produce n-p junctions with a low temperature processing technique. Solid SnS was used as the source for the tin, and the diffusions were carried out in the temperature range 650°-750°C for times varying from 2 to 24h. Both secondary ion mass spectrometry (SIMS) and Rutherford backscattering spectrometry (RBS) showed that tin had been introduced into the substrates in concentrations as high as $3.3E + 19 \text{ cm}^{-3}$ and to depths as large as $2 \mu\text{m}$. However, electrochemical carrier concentration profiling revealed that the diffused region remained p-type with net carrier concentration barely altered by the diffusion process. The reason for this anomalous behavior is not understood, but pairing or some other compensation may be taking place.

The fabrication of local p-type regions in III-V semiconductor materials is readily carried out with zinc or cadmium diffusion (1, 2) or ion implantation (3). On the other hand, a similar fabrication of local n-type areas in III-V's can only be done with ion implantation. Localized n-type diffusion in compound semiconductors has always been a difficult procedure and the development of a viable n-type diffusion technology for III-V's would be most valuable. This technology could be used to generate shallow n layers for ohmic contact formation, in self-aligned gate FET fabrication, for isolation regions in III-V bipolar circuits, and so on. The purpose of this work was to establish a low temperature n-type diffusion process for GaAs using a solid tin source in a novel diffusion system.

Various workers have carried out tin diffusion into GaAs in the past. Goldstein and Keller (4) performed tin diffusions into GaAs in closed tubes at 1060°-1260°C. Paint-on radioactive ^{113}Sn was used as the impurity source. The distribution profile was found to satisfy

Fick's equation with fixed source boundary conditions. Fane and Goss (5) also carried out closed tube tin diffusions into GaAs from an elemental tin source at 1100°-1150°C. "Slow" and "fast" components of the diffusion were observed with only the former being electrically active. Von Muench (6) used tin-doped oxides as a source of the impurity and as a protection layer for the surface. Open-tube oxide deposition and closed-tube diffusion temperatures were 700° and 1000°C, respectively. The diffusion profiles satisfied the infinite source solutions of Fick's equation. Average carrier concentrations of $3.0E + 18 \text{ cm}^{-3}$ were obtained. Gibbon and Ketchow (7) used doped-oxides and an open-tube diffusion system at 850°-1050°C. Average carrier concentrations of $6.0\text{-}8.0E + 18 \text{ cm}^{-3}$ were obtained.

More recent work has been carried out by Baligha and Ghandhi (8), who obtained planar selective diffusions from tin-doped oxides with phosphosilicate glass film masks. Diffusions were carried out in closed tubes at 1010°C. Arnold *et al.* (9) obtained step-like doping pro-

* Electrochemical Society Student Member.

files from unexhausted spin-on emulsion source layers. The diffusion coefficient was found to be a parabolic function of the concentration. Nissim *et al.* (10) also used spin-on source layers for tin diffusion. The majority of the tin was found to be electrically inactive until a further anneal was performed. Arnold and Heime (11) have employed spin-on tin emulsions and have measured surface concentrations to be $2.0E + 18 \text{ cm}^{-3}$.

In this work, we have attempted to produce n-p junctions using a so-called "leaky tube" diffusion furnace. This system has been shown to be extremely reliable for the diffusion of zinc into GaAs; details about this system have been published previously (12). A series of diffusions into p-type GaAs substrates were carried out using solid SnS as the source of tin, and the diffused wafers were characterized by optical inspection, electrochemical profiling, secondary ion mass spectrometry (SIMS), and Rutherford backscattering spectrometry (RBS). Both SIMS and RBS demonstrated that large concentrations of tin were introduced into the substrates during the diffusion, but curiously, the electrical examination revealed that no n-p junctions were formed. Further details about these experiments and speculations about the results constitute the rest of this paper.

Experimental Technique

One of the reasons why zinc diffusion into III-V's is now routine is that zinc has a large vapor pressure at relatively low temperatures. In leaky tube diffusion, elemental zinc is used as the source, and at a furnace temperature of 600°C , the zinc vapor pressure is nearly 10 torr. On the other hand, it is a well-noted property of tin that even though its melting point is rather low, its vapor pressure is miniscule at temperatures below 1600°C . Consequently, elemental tin is a poor choice for a source with this diffusion technique. There are a variety of tin compounds with high vapor pressures at temperatures in the 500°C - 700°C range which have been used as tin sources for ion implantation (13). Tin halides possess substantial vapor pressures at low temperatures, but were rejected because of the possibility of halogen etching of the substrates. Solid SnS was chosen because of its adequate vapor pressure [approximately 1 torr at 750°C (14)] and manageable toxicology.

P-type substrates with both (100) and (111) orientation were used in these experiments. They were doped with zinc to a concentration of $5.0E + 16$ - $2.0E + 17 \text{ cm}^{-3}$. After bromine-methanol polishing and degreasing, the wafers were coated with SiO_2 deposited by RF glow discharge sputtering. It has been observed that dielectric protection of the GaAs surface is required to prevent thermal decomposition in the leaky tube system. In the case of zinc diffusion at 600°C , 50 - 75\AA of SiO_2 is adequate (15). However, for the tin diffusion it was discovered that thin dielectric layers would not suffice: there was drastic etching of the wafer surface, presumably due to the formation of volatile gallium and arsenic sulfides, probably enhanced by gas convection effects. Relatively thick (1000 - 3500\AA) SiO_2 layers were deposited to prevent the decomposition of the substrate surfaces. It is interesting to note that the thick SiO_2 films did not act as diffusion masks; the tin did indeed reach the GaAs surface. As may be expected, the penetration depth of the tin into the substrates diminished with increasing SiO_2 thickness, but the tin surface concentration was not affected by the thickness. Some deterioration of the SiO_2 during diffusion was noticed, but this was inconsequential, as the dielectric films were stripped off before further testing.

After an additional cleaning step, the wafers and SnS crucible were loaded into the cold end of the furnace. Purging of the furnace in ultrapure helium was carried out for 2h, after which the boat holding the wafers and source was pushed into the hot zone of the furnace. Diffusions were performed for times varying from 2 to 24h at the temperatures of 650° , 700° , and 750°C . At the end of the diffusion, the boat was pulled back to the cold end of the

furnace and the wafers were allowed to cool for several hours before unloading.

Results

After the samples were removed from the diffusion furnace and the SiO_2 layers stripped in buffered HF, they were cleaved and stained for optical inspection. The staining fluid was a dilute solution of KOH and $\text{K}_3\text{Fe}(\text{CN})_6$ in water. The cleaved and stained (110) surface of sample LT096-B [24h, 700°C diffusion, (100) orientation] is shown in Fig. 1. The stain clearly reveals a line approximately $1.4 \mu\text{m}$ below the surface; this type of line is generally associated with a junction or a diffusion front. All of the samples in this work showed similar stain lines, and most were as regular and uniform as that displayed in Fig. 1.

The net carrier concentration ($N_A - N_D$) of each sample was measured as a function of depth with a modified Polaron electrochemical profiler. This apparatus can measure concentrations in the range $4.0E + 13$ - $4.0E + 21 \text{ cm}^{-3}$ with a depth resolution as small as 35\AA . Figures 2a, 2b, and 2c show the carrier profiles for samples LT095-A, LT096-B, and LT097-B, which were diffused at 650°C (12h), 700°C (24h), and 750°C (12h), respectively. In all three cases, the samples remained p-type. In fact, every diffused GaAs wafer (approximately thirty samples in total) remained p-type. Each of the three representative samples displayed here do show some minor alteration in the net concentration near the surface, but there are no indications of the formation of an n-type layer. These alterations, however, are related to the tin diffusion in some manner, because control samples subjected to the same heat-treatment without the tin source showed no alterations in the carrier profile whatsoever.

The atomic concentration profiles for these same samples were then measured using a secondary ion mass spectrometer (Cameca IMS3f). The primary beam consisted of positively-charged oxygen ions accelerated to 12.5 keV ; the secondary ions were accelerated to 4.5 keV . Depth profiles were obtained for arsenic (mass, 75), zinc (mass 64), and tin (mass 120). Figures 3a, 3b, and 3c are the SIMS profiles for the samples whose carrier concentrations were plotted in Fig. 2a, 2b, and 2c, respectively. The distance scale was calibrated by using a Dektak surface profilometer to measure the depth of the SIMS crater. No tin-implanted sample was available for exact calibration of the atomic concentration scale, but an approximate calibration was performed by using ratios of the dopant signals to the arsenic signal and by referring to the Rutherford backscattering spectrometry (RBS) data (to be discussed later).

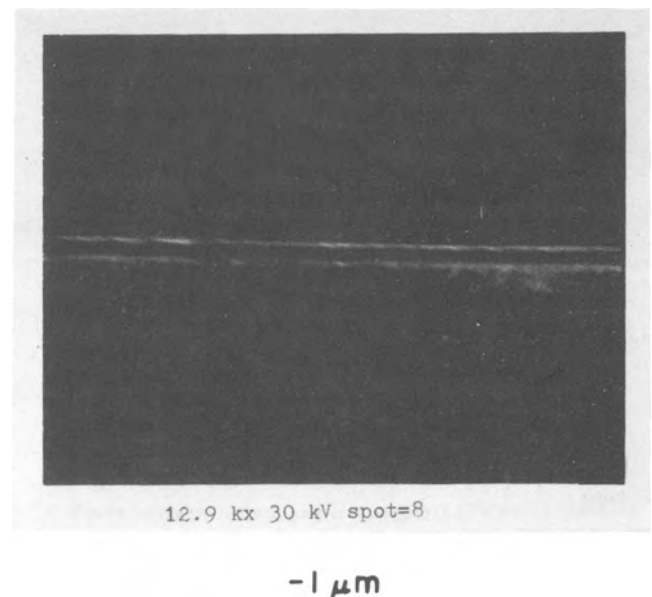


Fig. 1. A photomicrograph of the cleaved and stained edge of a tin-diffused wafer (sample LT096-B).

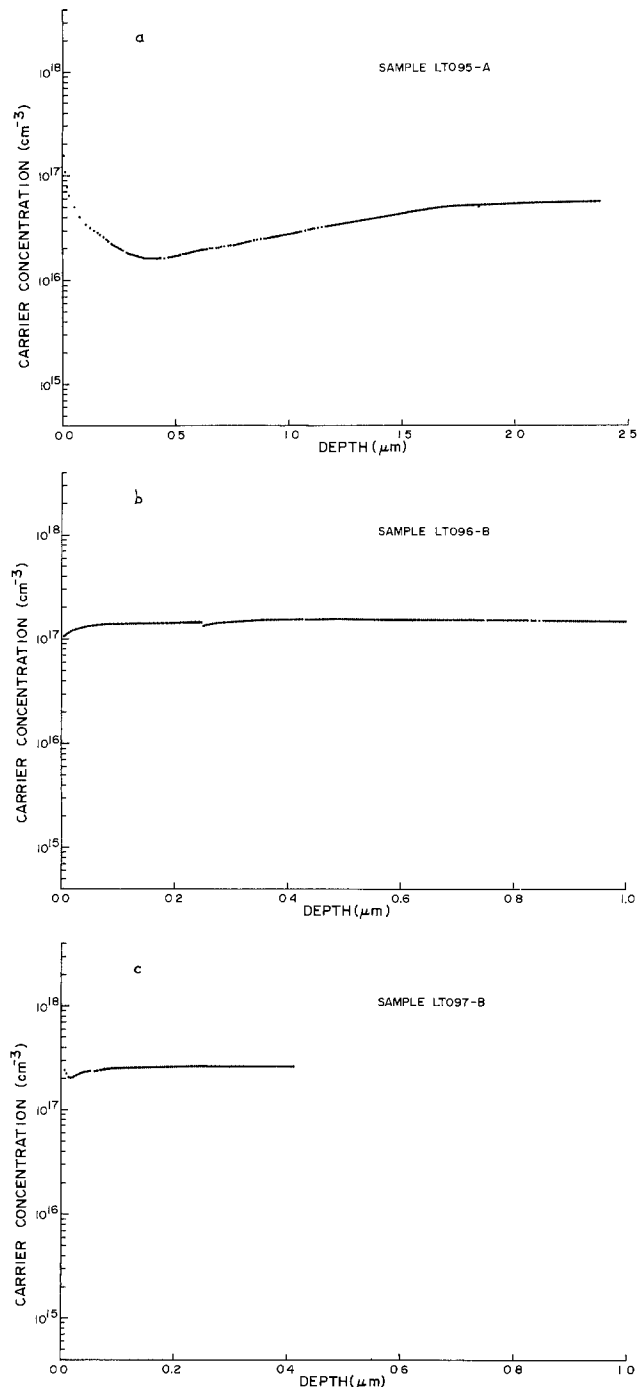


Fig. 2. Doping profiles from three tin-diffused samples as measured with electrochemical profiling. a: 12h, 650°C. b: 24h, 700°C. c: 12h, 750°C.

The SIMS analysis clearly demonstrates that the diffusion introduced tin into the GaAs substrates, with concentrations perhaps as high as $3.0E + 19 \text{ cm}^{-3}$. The tin concentrations were significantly larger than the zinc background concentrations, and the tin penetration was as deep as $2.2 \mu\text{m}$. In addition, the shape of the tin profile (most readily observed in Fig. 3a and 3c) is quite reminiscent of the profile of zinc introduced into GaAs with the leaky tube system (12). That is, the profile has a relatively flat plateau region followed by a very steep drop-off at the diffusion front; this suggests that the tin diffusion coefficient is a function of the tin concentration and that the tin may also diffuse by means of the interstitial-substitution mechanism.

Rutherford backscattering spectrometry was also employed in the characterization of these samples. RBS was used to corroborate the SIMS measurements and to obtain an estimate of the tin concentration near the surface.

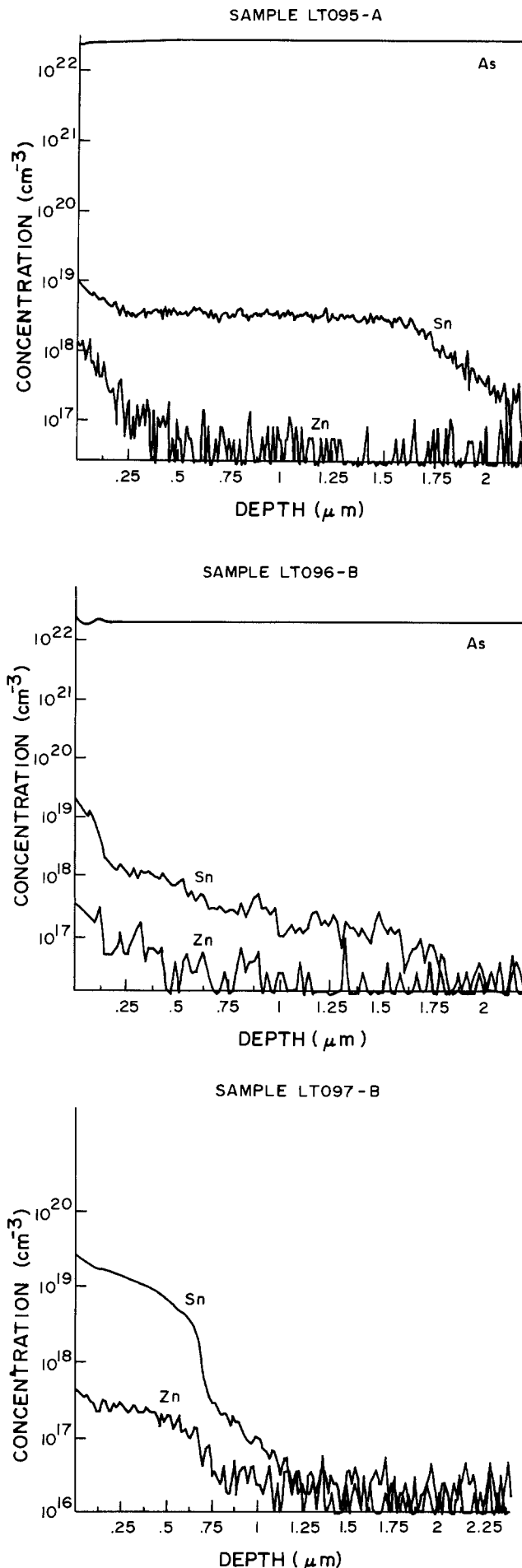


Fig. 3. Atomic concentration profiles as measured by SIMS for the three samples whose doping profiles were shown in Fig. 2.

Table I.

Sample	Diffusion conditions	N_A	t_{SiO_2} (Å)	[Sn] _{max} (cm ⁻³)	Penetration (μm)	
					Optical	SIMS
LT095-A	12h 650°C	5.2×10^{16} cm ⁻³ (111)	1100	$\sim 1 \times 10^{19}$ a	—	2.2
LT096-B	24h 700°C	1.6×10^{17} cm ⁻³ (100)	1500	$\sim 3 \times 10^{19}$ a	1.4	1.8
LT097-B	12h 750°C	2.6×10^{17} cm ⁻³ (100)	3500	3.3×10^{19} b	1.1	1.3

^a Estimated from SIMS.

^b RBS measurement.

Although RBS is not generally applied in trace element detection, these particular samples are well suited for the technique because of the large difference in mass between the trace element and the matrix. Helium ions with energies of 3.78 MeV were utilized, and signal-to-noise figures were enhanced by employing long counting times (~30 min), large doses (~100 μC), and pulse pile-up rejection techniques. Figure 4 shows the RBS spectrum for sample LT097-B (750°C, 12h), plotted to emphasize the tin signal. By using standard RBS analysis procedures (16), it was determined that the concentration of tin at the surface was approximately 0.15 (±0.03) atomic percent (a/o), or, $N_{Sn} \approx 3.3E + cm^{-3}$. This number was utilized in quantifying the SIMS results shown earlier.

The results of the characterization of these samples are summarized in Table I. As mentioned previously, the surface concentration was in the vicinity of $1.3.E + 19 cm^{-3}$ for each sample, and is apparently insensitive to the SiO₂ thickness. On the other hand, the tin penetration depth decreased with increasing SiO₂ thickness.

Discussion

It is clear from the above presentation that the leaky tube diffusion system does indeed introduce tin into the p-type GaAs wafers. The tin concentration is quite high and the penetration is substantial. Yet it is also just as clear that the tin has a negligible effect on the electrical properties of the diffused samples. No n-p junctions have been produced with this low temperature processing scheme. What is not clear is the reason for the discrepancy between the atomic concentration and the electrically active concentration of the tin. Figures 3a-3c demonstrated that the background dopant, zinc, was redistributed by the heat-treatment. The zinc concentration was increased at the surface by perhaps 1-2 orders of magnitude above that in the bulk. But this increase is not substantial enough to compensate the tin introduced by the diffusion.

As pointed out in the introduction, various workers have successfully diffused tin into GaAs to produce n-type layers. It is interesting to note, however, that virtually all of these diffusions have been carried out at temperatures exceeding 1000°C. In fact, Nissim *et al.* (10)

demonstrated that tin can be introduced into GaAs from a spin-on dopant source at temperatures as low as 700°C, but at low temperatures, most of the tin is electrically inactive. Furthermore, it remains inactive until a high temperature (900°C) annealing step is performed. Our results also demonstrate that a low temperature processing cycle can introduce tin, but tin that is electrically inactive. Due to equipment limitations, we did not attempt any high temperature anneals.

It appears that tin doping to produce n-type layers in GaAs is viable only at high processing temperatures. Why this is the case is not understood, but a number of scenarios are possible. (i) The tin may reside predominantly on interstitial sites and may remain electrically neutral until a high temperature step is employed to move the interstitial tin atoms to donor sites. (ii) The tin may behave in an amphoteric manner and produce self-compensation by the formation of an equal number of donors and acceptors. A high temperature step may readjust the donor/acceptor ratio in favor of the donors, as in the case of silicon in GaAs. (iii) Perhaps tin complexes are formed at low temperatures which are electrically inactive. (iv) Or perhaps the tin is being compensated by some unknown deep center that is active only at relatively low processing temperatures.

One last interesting point in this diffusion process is the behavior of sulfur. Stannous sulfide was the source in these experiments and it was expected that if sulfur were to diffuse into the wafers along with the tin, it would also contribute to the formation of an n-type layer. With the absence of n-p junctions, it was initially believed that sulfur was not introduced into the substrates during the diffusion. However, SIMS depth profiling, employing a cesium beam, revealed that sulfur was present in a very shallow surface layer, with a maximum depth not exceeding 100Å. Apparently, the dissociation of the SnS in the furnace is nearly complete, and the volatile sulfur collects at the cold end of the furnace and is unavailable for extensive diffusion.

Summary

We have endeavored to develop a low temperature n-type diffusion process for GaAs. A leaky tube diffusion system was employed using solid SnS as the source for the tin dopant. Although both SIMS and RBS demonstrated that tin did indeed diffuse into the GaAs samples, with concentrations as high as $3.3E + 19 cm^{-3}$ and to depths as large as 2.2 μm, electrical testing revealed that no n-p junctions were produced. It is suspected that the tin forms electrically active donors only when the diffusion temperature (or a subsequent annealing temperature) exceeds 1000°C (9-11). We are presently pursuing TEM and photoluminescence characterization of the diffused samples in an attempt to shed more light on this phenomenon.

Acknowledgments

The authors would like to thank J. L. Edwards and S. Ageno for their assistance with the diffusion and profiling measurements, and P. Stoss and D. Cooper for their assistance with the RBS measurements. HHE and

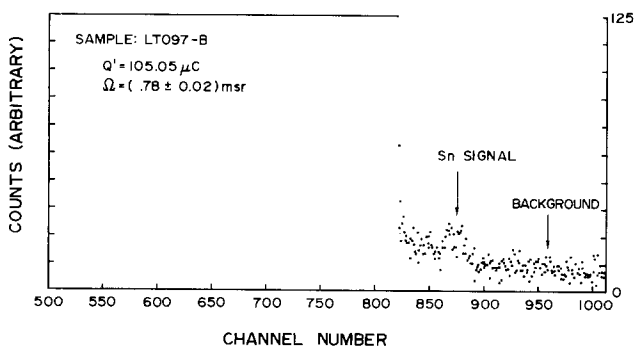


Fig. 4. Backscattering profile for sample LT097-B as measured with RBS.

RJR acknowledge support from Arizona State University Faculty grant-in-aid, RTL and PW acknowledge support by NSF Grant DMR-8206028, and JAL acknowledges financial support for the IBM/UA Ion Beam Analysis Facility from IBM General Products Division, Tucson, Arizona, and from the Arizona Research Laboratories.

Manuscript submitted Oct. 26, 1984; revised manuscript received April 25, 1985.

Arizona State University assisted in meeting the publication costs of this article.

REFERENCES

1. See for example, C. S. Hong, Y. Z. Liu, P. D. Dapkus, and J. J. Coleman, *IEEE El. Dev. Lett.*, **ed1-2**, 225 (1981).
2. See for example, H. Ando, N. Susa, and H. Kanbe, *IEEE Trans. El. Dev.*, **ed-29**, 1408 (1982).
3. F. H. Eisen, in "Ion Implantation in Semiconductors," S. Namba, Editor, Plenum Press, New York (1975).
4. B. Goldstein and H. Keller, *J. Appl. Phys.*, **32**, 1180 (1961).
5. R. W. Fane and A. J. Goss, *Solid State Electron.*, **6**, 383 (1963).
6. W. Von Muench, *ibid.*, **9**, 619 (1966).
7. C. F. Gibbon and D. R. Ketchow, *This Journal*, **118**, 975 (1971).
8. B. J. Baliga and S. K. Ghandhi, *ibid.*, **126**, 135 (1979).
9. N. Arnold, H. Daembkes, and K. Heime, *Jpn. J. Appl. Phys.*, **19**, 361 (1980).
10. Y. I. Nissim, J. F. Gibbons, C. A. Evans, V. R. Deline, and J. C. Norberg, *Appl. Phys. Lett.*, **37**, 89 (1980).
11. N. Arnold and K. Heime, in "Gallium Arsenide and Related Compounds 1981," T. Sugano, Editor, p. 371, Institute of Physics, London (1982).
12. R. Roedel, J. L. Edwards, A. Righter, P. Holm, and H. Erkaya, *This Journal*, **131**, 1726 (1984).
13. D. R. Stull, *Ind. Eng. Chem.*, **39**, 4 (1947).
14. C. M. Hsiao and A. W. Schlichten, *J. Met.*, **4**, 65 (1952).
15. J. L. Edwards and R. J. Roedel, *Electron. Lett.*, **19**, 962 (1983).
16. W. K. Chu, J. W. Mayer, and M-A. Nicolet, "Backscattering Spectrometry," Academic Press, New York (1978).
17. W. G. Spitzer and W. Allred, *J. Appl. Phys.*, **39**, 4999 (1968).

Empirical Modeling of Low Energy Boron Implants in Silicon

M. Simard-Normandin and C. Slaby

Northern Telecom Electronics Limited, Ottawa, Ontario, Canada K1Y 4H7

ABSTRACT

The depth distribution of low energy boron implants in silicon are analyzed using secondary ion mass spectroscopy. The profiles for equivalent energy implants of B^+ (10-30 keV) and BF_2^+ (50-120 keV) are compared. Fluorine trapping in BF_2^+ implants is also investigated. New range parameters are extracted from the measured profiles using a least squares fitting technique. The Pearson IV distribution provides an excellent representation of the doping profile in B^+ implants, while for BF_2^+ implants the profiles are better represented using a gaussian distribution with an attached exponential tail.

The formation of shallow junctions in semiconductors using ion implantation is a well-established technique. Most process modeling aids use the results of LSS theory (1) to predict the dopant depth distribution. This technique is strictly valid for implantation into amorphous media, even though in most applications implantation is carried out into crystalline substrates. For low implantation energies, the conventional method of simulating an amorphous substrate by tilting the wafer a few degrees off normal is not sufficient and the doping profiles measured are markedly different from theoretical profiles. More sophisticated theoretical distributions are required in these cases, with parameters fitted to carefully measured experimental data. In this paper, we report on a detailed study of B^+ and BF_2^+ implants in crystalline silicon at various doses and energies of interest in VLSI applications. Similar work has already been reported by Wilson (2) and by us in a previous paper (3, 4), but for a smaller range of dose and energies, and only for Pearson IV distributions.

The doping profiles after implantation are measured using secondary ion mass spectroscopy (SIMS). Empirical range statistics are extracted from these profiles for the Pearson IV distribution and for the gaussian distribution with an attached exponential tail.

We also investigate quantitatively the problem of fluorine trapping in the damaged layer produced by BF_2^+ implants for various rapid thermal annealing (RTA) and furnace annealing conditions.

Sample Fabrication

The starting wafers were 3-7 Ω -cm n-type (phosphorus-doped) (100) CZ-grown silicon. Some wafers were oxidized in dry O_2 at 1000°C to form approximately 40 nm of SiO_2 . Implants were carried out either into bare Si or

through the 40 nm SiO_2 . The wafers that were to be annealed further received 100 nm of deposited SiO_2 at 450°C before the annealing.

The $^{11}B^+$ was implanted at 10, 15, 20, 25, and 30 keV, and the $^{10}BF_2^+$ was implanted at 25, 50, 75, 100, and 120 keV. The implant doses were between 5×10^{14} and 5×10^{15} cm^{-2} . There is a 5:1 ratio of implant energy between the BF_2^+ and the B^+ implants since the ratio of the masses is very close to 5. All implants were done using a 7° tilt angle at room temperature. The BF_2^+ implants and the B^+ implants for energies greater than or equal to 20 keV were performed in a high current implanter using postacceleration mass analysis. The remaining B^+ implants were done in a medium current implanter. In the case of the high current implanter, the wafer rotation was controlled and the rotation angle was 0° for all implants. In case of the medium current implanter, initially the rotation angle was set to 0° but it was randomly disturbed during the loading operation. No significant discrepancies in the results due to this disturbance were observed. The ion current in case of BF_2^+ implants was 1-5 mA. For B^+ implants done on the high current implanter, the current was 500-700 μA , and for those done on the medium current machine it was approximately 40 μA .

The slice temperature as determined through the use of thermal stickers attached to the back of the wafers did not rise significantly during implantation. It is estimated that the maximum temperature rise for the highest current implantations did not exceed 20°-30°C.

The wafers implanted at 3×10^{15} cm^{-2} were annealed either in a conventional furnace tube or in a tungsten halogen lamp rapid thermal annealer. Furnace anneals lasted 20 min and took place at 925°, 1000°, or 1100°C. Lamp anneals lasted 12s and were carried out at 1050° or 1150°C using a Heatpulse 210T rapid annealing system.

Measurements

For each sample, the depth distribution profile was obtained by SIMS using a Cameca IMS 3-f ion microscope with 8 keV O_2^+ as the bombarding species. The sputtering beam angle of incidence was 30° . The crater depth was measured using a Dektak stylus, and the depth scale was calibrated by assuming a constant sputtering rate. The conversion from ion counts to concentration was made by integrating the profile and equating the result to the total implant dose. There are, however, several effects which may cause deviations of the measured profile from the original dopant distribution. Wittmaack (5) points out that a depth correction of about 1.4 nm/(keV/O atom) should be applied to the profile because of the reduction in erosion rate which occurs as the sample becomes loaded with oxygen. In our case, this correction amounts to 4.85 nm. We have analyzed one sample of $3 \times 10^{15} B^+/cm^2$ at 10 keV implanted into silicon preamorphized with an implant of ^{28}Si . We found that the measured profile can be described accurately with LSS range parameters. Since the correction is small and is of the order of the accuracy to which we can measure crater depths, we have not applied it to the range parameters quoted in this paper for implantation into crystalline silicon.

For sufficiently high dose and energy BF_2^+ implantation, an amorphous region is produced. Since amorphous silicon etches slowly in concentrated HF , we can measure the thickness of the amorphous layer, $X_{amorphous}$, by soaking the samples in 49% HF for 2 days and then measuring the height of the resulting step with an interference microscope. We can also infer this quantity from SIMS measurement as described in the next section.

Results of measurements of $X_{amorphous}$, the junction depth X_j as determined from the SIMS profile, and the position of the maximum concentration X_{peak} are listed in Table I.

Results

The advantage of using BF_2^+ is that it amorphizes the surface of the silicon during implantation (at doses and energies of interest to VLSI device fabrication). This amorphous region is claimed to anneal at a lower temperature than does a heavily damaged crystalline structure (6, 7). The extent of the amorphous region can be measured before annealing by etching in HF as described previously. It can also be inferred from the SIMS profile

Table I. X_{peak} and $X_{amorphous}$

Sample Designation	X_{peak} (μm) SIMS	$X_{amorphous}$ (μm) SIMS	HF	X_j (μm) SIMS
BF5E14-50C	0.029	—	—	0.25
BF5E14-75C	0.032	—	0.050	0.30
BF5E14-100C	0.052	—	0.075	0.35
BF5E14-50UC	0.041	—	0.070	0.25
BF5E14-75UC	0.059	—	0.110	0.40
BF5E14-100UC	0.081	—	0.110	0.45
BF1E15-50C	0.031	—	0.030	0.20
BF1E15-75C	0.033	—	0.045	0.35
BF1E15-100C	0.041	—	0.090	0.40
BF1E15-50UC	0.045	—	0.060	0.25
BF1E15-75UC	0.065	—	0.100	0.40
BF1E15-100UC	0.084	—	0.140	0.45
BF3E15-50C	0.024	0.025	0.025	0.25
BF3E15-75C	0.023	0.060	0.050	0.40
BF3E15-100C	0.055	0.090	0.090	0.45
BF3E15-50UC	0.050	0.070	0.060	0.35
BF3E15-75UC	0.074	0.105	0.095	0.35
BF3E15-100UC	0.090	0.130	0.130	0.45

Note: A mnemonic has been used to describe the samples. B and BF mean a B^+ and a BF_2^+ implant, respectively. Next comes the dose (e.g., 3E15). Following the dash is the implant energy. C means implantation through a 40 nm oxide (cap), UC means implantation into bare silicon (uncapped).

after annealing. The fluorine distribution is double peaked after annealing, and the minimum corresponds to the depth of the amorphous region after implantation (Fig. 1). The peak of the as-implanted dopant distribution is always shallower than the amorphous region. After annealing, one peak corresponds approximately to the range of the implant, and one is located deeper than the depth of amorphization. This has been attributed to a plane of damage, which acts as a getter site (8). In BF_2^+ -implanted samples, both boron and fluorine show a double-peak structure after annealing. The position of these peaks is fixed with respect to the silicon surface for a given implant and does not depend on the annealing. We have investigated five very different annealing conditions, and the two maxima and the minimum are always coincident, although their amplitudes may vary.

Using the etching method, we have observed a well-delineated step in samples implanted with as little as $5 \times 10^{14} BF_2^+$ ion/cm², indicating that this low dose is sufficient to produce amorphization. Table I compares the HF and the SIMS methods of evaluating the depth of the amorphous layer; agreement is excellent.

In Fig. 2, we compare implantation of BF_2^+ into bare silicon with implantation through a 40 nm layer SiO_2 . The oxide layer was left on the sample for the SIMS analysis. The samples were not annealed. Both profiles were analyzed under the same conditions, and the silicon profiles match exactly, far from the regions very close to the surface or the Si- SiO_2 interface. The boron profiles show similar agreement. However, the fluorine count is lower for implantation through the oxide layer at every point in the silicon wafer. The evidence presented in Fig. 2 implies that the presence of SiO_2 on top of the Si substrate does not have a significant effect on the amount of boron channeling, at least at the oxide thickness used in this study, and that the range statistics presented for boron in this paper can be used for implantation through a thin layer of SiO_2 . It also suggests that in the case of BF_2^+ implants through SiO_2 a measurable fraction of the fluorine is missing from the silicon wafer. We have not attempted to calibrate the profiles in the SiO_2 layer to see whether the fluorine was trapped there or had escaped.

After annealing, the fluorine and the boron redistribute themselves differently in the wafer (2, 8). If the fluorine profile after annealing is integrated, using the unannealed profile as calibration, we find for the 925° and $1000^\circ C$ 20 min furnace anneals and the 1050° and $1150^\circ C$ 0.2 min rapid anneals that 20-100% of the fluorine is still present in the silicon. For the $1100^\circ C$ 20 min anneal, the fluorine has decreased by two orders of magnitude, leaving a fluorine dose of the order of $5 \times 10^{13} cm^{-2}$ in the crystal. The nature of the chemical bond which binds the fluorine to the silicon and the boron is currently under investigation. Depending on the annealing conditions, the

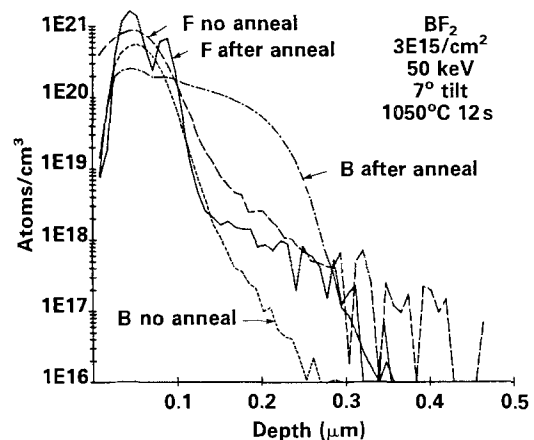


Fig. 1. Depth distribution profiles for boron and fluorine before and after annealing. The implant dose was $3 \times 10^{15} BF_2^+ cm^{-2}$ at 50 keV and annealing was carried out at $1050^\circ C$ for 12s. The fluorine dose after annealing is $6.2 \times 10^{15} cm^{-2}$.

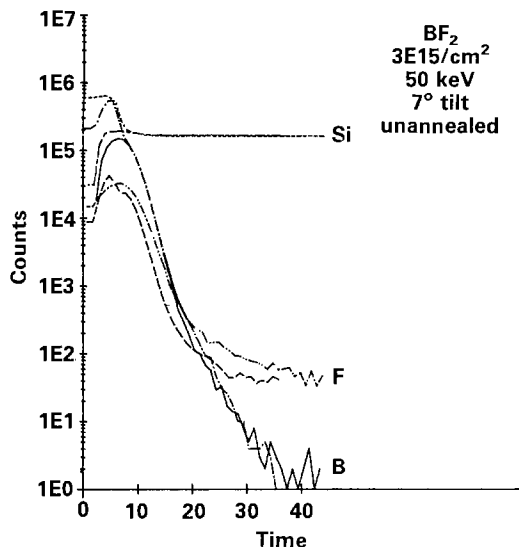


Fig. 2. Uncalibrated SIMS results showing the comparison of boron and fluorine distribution profiles for implantation of BF_2^+ into bare silicon and through a 40 nm SiO_2 layer. Solid line: Boron into bare silicon. Dot-dash line: Boron through SiO_2 . Dot-dot-dash line: Fluorine into bare silicon. Broken line: Fluorine through SiO_2 .

deeper peak sometimes has a larger intensity than the first one. For boron, the second peak is always the lower one for the annealing conditions that we have studied.

Modeling

Because of the channeling tails in low energy boron implants, modeling of as-implanted profiles requires special attention. Figure 3 shows a typical SIMS profile for a low energy boron implant ($3 \times 10^{15} \text{ cm}^{-2}$, 10 keV) together with different theoretical profiles. Profiles calculated using LSS range statistics are clearly in disagreement with measurements. It is also obvious that even a gaussian distribution fitted to the measured profile cannot account for the "tail" region. Another modeling technique applied, for example, in SUPREM-II, uses a Pearson distribution with an exponential tail. Although this technique could describe the profile correctly, the current SUPREM-II model does not give good results.

A comparison of equivalent energy implantation of B^+ and BF_2^+ is presented in Fig. 4. The ranges of the distributions can be matched by adjusting the ratio of the implant energies for the two species (the factor 5:1 that we have used is not exact; therefore, the top of the profiles do not match exactly), but the shapes of the doping profiles are markedly different for B^+ and for BF_2^+ . We have found the Pearson IV distribution (9) can describe correctly B^+ and

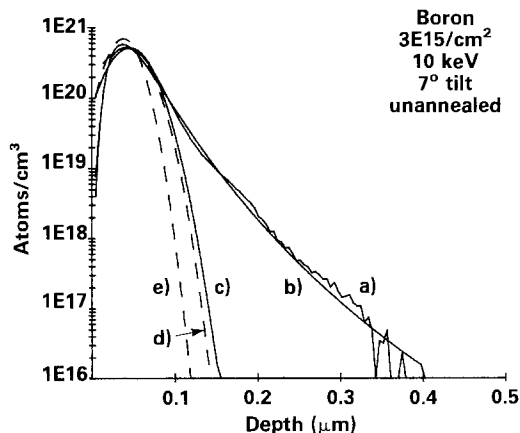


Fig. 3. As-implanted profile of $3 \times 10^{15} \text{ cm}^{-2} \text{ B}^+$ at 10 keV (a), superimposed with the best-fit Pearson IV profile (b), the best-fit gaussian profile (c), the Pearson IV profile in SUPREM-3 (d), and the LSS gaussian profile (e).

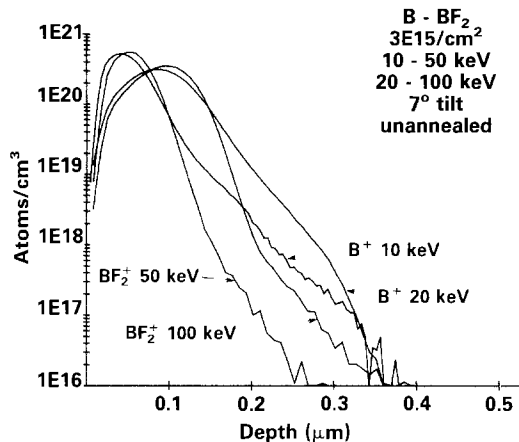


Fig. 4. Comparison of equivalent-energy B^+ and BF_2^+ implants. The dose is $3 \times 10^{15} \text{ cm}^{-2}$ in all cases. The samples have not been annealed.

BF_2^+ profiles provided that empirically determined range parameters are used, but the parameters are different for B^+ and BF_2^+ implants of equivalent energies. We have also found that BF_2^+ implants can be modeled even better by a gaussian distribution with an attached exponential tail.

Pearson IV parameters for boron implants.—Parameters of the Pearson IV distribution for boron implants were extracted from the measured profiles through a least squares fitting procedure. The quality and accuracy of these plots are discussed in Ref. (3) and are found to be very satisfactory. Table II contains a complete set of data for 10-30 keV boron implants with doses varying from 5×10^{14} to $5 \times 10^{15} \text{ cm}^{-2}$. The data for each of the four moments of Pearson distribution are plotted separately in Fig. 5-8, together with the corresponding values currently used in SUPREM-3.

Comparing the data for the projected range (Fig. 5) and the standard deviation (Fig. 6), we observe that the empirical parameters parallel theoretical data having consistently higher values. The important difference between empirical and theoretical data is in the third distribution moment, skewness (Fig. 7), which must be positive to fit the experimental data. This results in profiles that are tilted towards the bulk and therefore properly account for

Table II. Boron Pearson IV distribution parameters

Dose Energy	5E14	1E15	2E15	3E15	5E15	Mean
R_p (μm)						
10	0.03940	0.04840	0.04052	0.04887	0.04232	0.04390
15	0.05971	0.05964		0.06617		0.06184
20	0.07878	0.07892		0.08673 ^a		0.08148
25	0.09400			0.09746		0.09573
30	0.11792			0.11481		0.11637
ΔR_p (μm)						
10	0.02589	0.02709	0.02576	0.02489	0.02486	0.02570
15	0.03128	0.03160		0.02973		0.03087
20	0.03908	0.03731		0.03957 ^a		0.03865
25	0.04292			0.04146		0.04219
30	0.05221			0.04499		0.04860
Skewness						
10	0.99515	0.80580	0.82332	1.18048	0.81259	0.92347
15	0.87658	0.94349		1.00287		0.94098
20	0.75461	0.76618		0.57269 ^a		0.69783
25	0.55395			0.37232		0.46314
30	0.43368			0.35588		0.39478
Kurtosis						
10	4.95270	4.27255	4.37026	6.62917	4.76621	4.99864
15	4.83110	4.74503		4.98230		4.85281
20	4.10034	4.15459		4.02233 ^a		4.09242
25	3.89490			3.77105		3.83298
30	3.62604			3.56133		3.59369

^a Mean of 11 profiles.

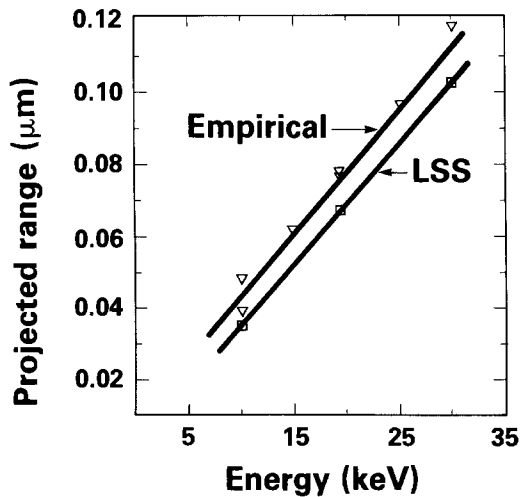


Fig. 5. The range parameter R_p of the Pearson IV distribution for boron implants compared with the LSS values.

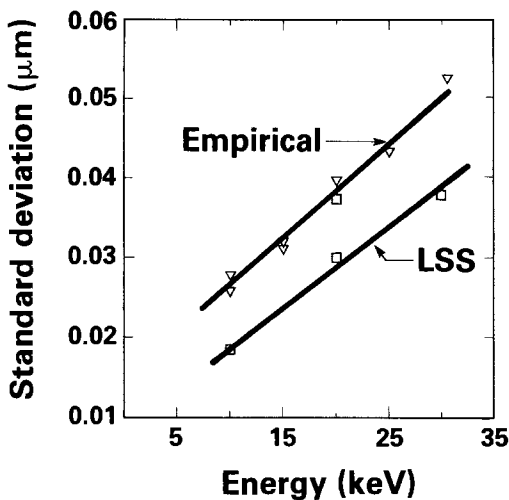


Fig. 6. The straggle ΔR_p of the Pearson IV distribution for boron implants compared with the LSS values.

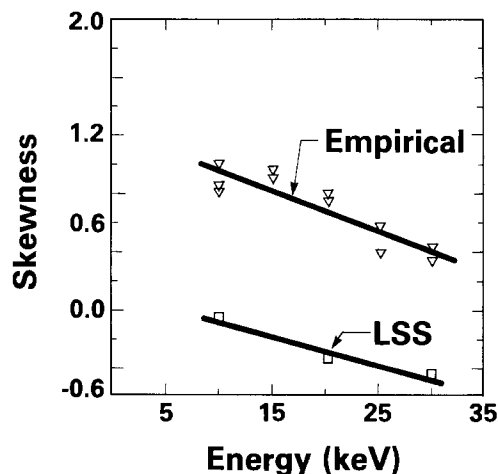


Fig. 7. The skewness of the Pearson IV distribution for boron implants compared with the LSS values.

the distribution tails. As a consequence of this difference, we also observed a different behavior for the fourth moment, kurtosis (Fig. 8).

Pearson IV parameters for BF_2^- implants.—Modeling of BF_2^+ implants proved to be more complicated. Although it was possible to obtain good fits in each individual case for the Pearson IV distribution, a considerable scatter in the parameters was obtained, in particular, for skewness and kurtosis. This is because the BF_2^+ implant profiles

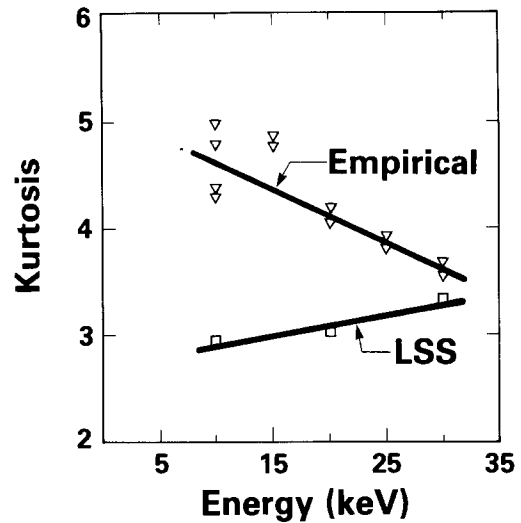


Fig. 8. The kurtosis of the Pearson IV distribution for boron implants compared with the LSS values.

tend to be concave towards the bulk, while the Pearson IV distribution is convex. The fitted parameters are summarized in Table III. We can reasonably describe BF_2^+ implants with this set of data which are much more accurate than the LSS data. Once R_p , ΔR_p , and skewness are determined, the shape of the profile is very insensitive to variations of the kurtosis; therefore, the high values obtained for the 75 keV implants can be replaced by an average value between the 50 and 100 keV values and the quality of the fit remains excellent.

Gaussian distribution with an exponential tail for BF_2^+ implants.—Another modeling technique used, for example, in process simulation programs such as SUPREM, uses a simple gaussian distribution with an exponential tail attached somewhere on the distribution shoulder. The drawback of this approach in SUPREM-II is the use of a fixed tail with its parameters independent of the implant energy. Our approach is to generalize the distribution which is now characterized by the projected range R_p , the standard deviation ΔR_p , the characteristic length of the tail L , and the fraction parameter F , which is the fraction of the peak concentration where the exponential tail is attached.

The following mathematical expression describes the profile used, where x_{int} is the interception point where

Table III. BF_2^+ Pearson IV distribution parameters

Dose Energy	5E14	1E15	3E15	Mean
R_p (μm)				
25			0.02583	0.02583
50	0.04751	0.03793	0.05286	0.04610
75	0.05656	0.05598	0.06448	0.05901
100	0.07757	0.06891	0.08019	0.07556
120			0.08207	0.08207
ΔR_p (μm)				
25			0.01446	0.01446
50	0.02442	0.02397	0.02519	0.02453
75	0.03155	0.03197	0.03036	0.03129
100	0.04026	0.03710	0.03372	0.03703
120			0.03490	0.03490
Skewness				
25			-0.65139	-0.65139
50	0.29530	-0.06825	-0.57686	-0.11660
75	0.01694	-0.15746	-0.57125	-0.23726
100	-0.04293	-0.14657	-0.38061	-0.19004
120			-0.36106	-0.36106
Kurtosis				
25			11.96689	11.96689
50	4.52633	6.21693	8.06505	6.26944
75	16.87185	18.26434	11.29269	15.47629
100	7.62934	9.95231	5.64738	7.74301
120			7.15967	7.15967

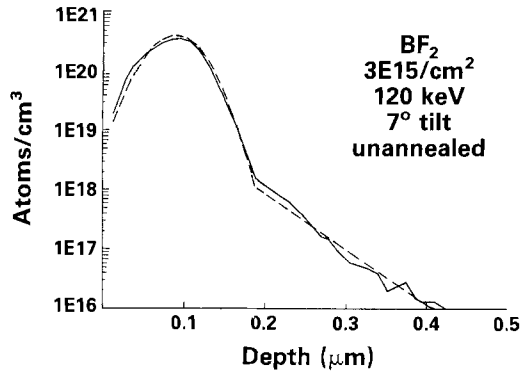


Fig. 9. Profile of an implant of $3 \times 10^{15} \text{ BF}_2^+ \text{ cm}^{-2}$ at 120 keV compared with a fitted gaussian distribution and attached exponential tail.

the exponential tail is attached to the gaussian distribution

$$y(x) = \begin{cases} \frac{A}{\sqrt{2\pi} \Delta R_p} \exp[-(x - R_p)^2/2\Delta R_p^2]; & 0 \leq x \leq x_{\text{int}} \\ \frac{A}{\sqrt{2\pi} \Delta R_p} \exp[-(x_{\text{int}} - R_p)^2/2\Delta R_p^2] \exp[-(x - x_{\text{int}})/L]; & x > x_{\text{int}} \end{cases} \quad [1]$$

and where L is the characteristic length of the exponential.

The coefficient A is determined by integrating the profile and equating the result to the implant dose. The fraction F of the peak concentration where the exponential tail is attached is given by

$$F = y(x_{\text{int}})/y_{\text{max}} \quad [2]$$

We have found that this technique is particularly useful in the case of BF_2^+ implants. Figure 9 illustrates the quality of fits obtained with this approach. The extracted parameters for this distribution are shown in Table IV, while

Table IV. BF_2^+ gaussian distribution with exponential tail parameters

Dose Energy	5E14	1E15	3E15	Mean
	R_p (μm)			
25			0.02191	0.02191
50	0.04345	0.03998	0.05284	0.04542
75	0.05990	0.05941	0.07085	0.06339
100	0.08113	0.06969	0.09086	0.08056
120			0.08732	0.08732
	ΔR_p (μm)			
25			0.01538	0.01538
50	0.02435	0.02141	0.02410	0.02329
75	0.02578	0.02845	0.02459	0.02627
100	0.03722	0.03071	0.03166	0.03320
120			0.02925	0.02925
	x_{int} (μm)			
25			0.07393	0.07393
50	0.11221	0.09700	0.11792	0.10904
75	0.12217	0.13968	0.14381	0.13522
100	0.19583	0.16565	0.20110	0.18753
120			0.18728	0.18728
	L (μm)			
25			0.01815	0.01815
50	0.02444	0.02502	0.02408	0.02451
75	0.03717	0.03891	0.03853	0.03822
100	0.04499	0.04792	0.03569	0.04287
120			0.04590	0.04590
	Fraction of peak			
25			0.00224	0.00224
50	0.01629	0.01504	0.00894	0.01342
75	0.02421	0.01142	0.00598	0.01387
100	0.00814	0.00784	0.00252	0.00617
120			0.00316	0.00316

the energy dependence of these parameters is illustrated in Fig. 10 to 13.

Double gaussian profiles for BF_2^+ implants.—Dissociation of the BF_2^+ molecule causing abnormal boron distribution profiles has been observed previously (10). Although dissociation problems in the beam are negligible in a postacceleration mass analysis type of implanter, like the one used in this study, dissociation has been claimed to occur upon impact with the silicon wafer (6, 8). We have investigated this possibility to explain the tail of the BF_2^+ profiles. The model assumes that some BF_2^+ molecules dissociate to form an ionic form of BF . Under these conditions, boron penetrates with 11/49 and 11/30 of the implantation energy. To represent this condition, two gaussian distributions with $R_{p2} = (49/30)R_{p1}$ have been used. The standard deviations and the fraction of the dose in the second peak are left as fitting parameters. Excellent agreement with measured profiles can be obtained, as displayed in Fig. 14. This observation is in contradiction with the complete dissociation of the BF_2^+ molecule at the silicon surface. If this were the case, all the boron should have 11/49 of the implant energy.

For higher energy implants, the second profile does not match the "hump" exactly. It may be that further dis-

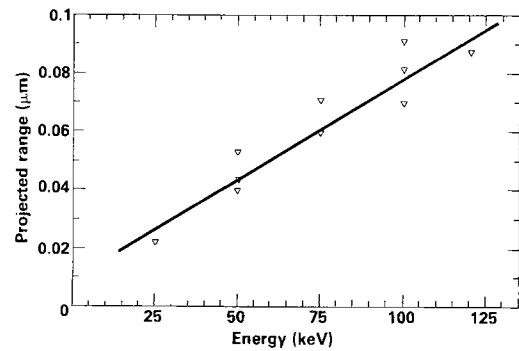


Fig. 10. The range parameter R_p of the gaussian distribution for BF_2^+ implants.

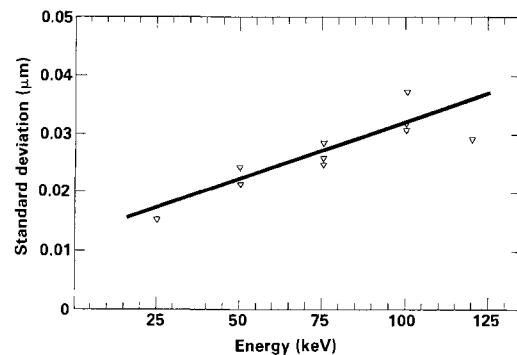


Fig. 11. The straggle ΔR_p of the gaussian distribution for BF_2^+ implants.

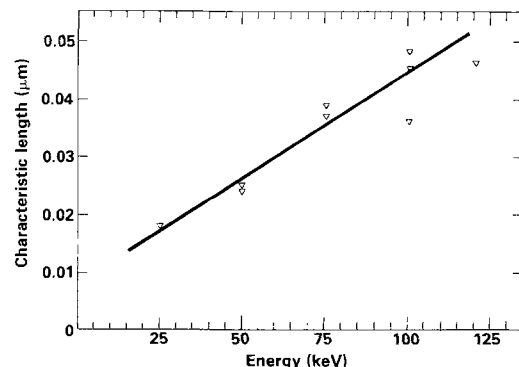


Fig. 12. The characteristic length of the exponential tail attached to the gaussian distribution for BF_2^+ implants.

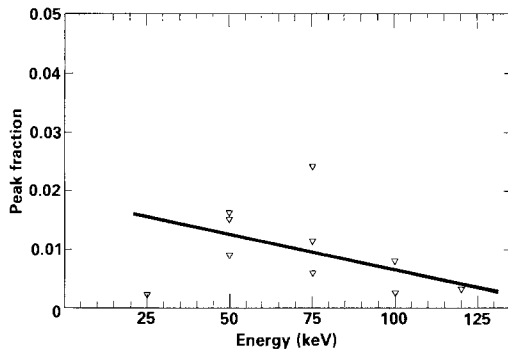


Fig. 13. The fraction of the peak concentration where the exponential tail is attached for BF_2^+ implants.

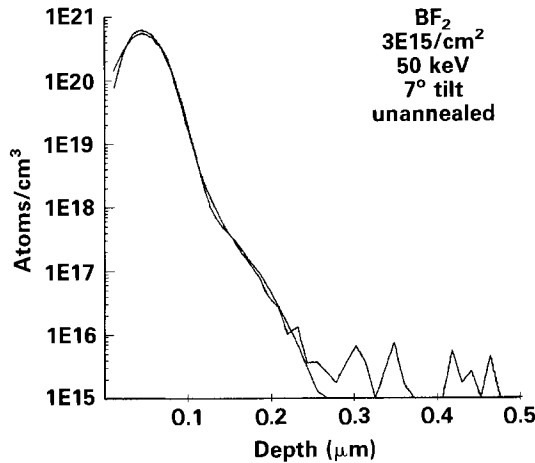


Fig. 14. Profile for an implant of $3 \times 10^{15} \text{BF}_2^+ \text{cm}^{-2}$ at 50 keV superimposed with a distribution consisting of 2 gaussian profiles, with parameters $R_{p1} = 0.04645 \mu\text{m}$, $\Delta R_{p1} = 0.02105 \mu\text{m}$, $R_{p2} = (49/30)R_{p1}$, $\Delta R_{p2} = 0.04835 \mu\text{m}$, and F , the fraction of the dose in the second peak, = 0.00462.

sociation into B and F occurs, but we have not taken this process into account as it would greatly increase the number of adjustable parameters. In all cases, the fraction of the dose in the second peak is between 0.1 and 0.5%.

Conclusion

We have compared B^+ and BF_2^+ implants in silicon at equivalent energies. Fluorine is trapped in the silicon after BF_2^+ implants, and very long anneals at high temperatures are required to drive it out. These conditions are incompatible with VLSI processing techniques.

The Pearson IV distribution fits B^+ implants into crystalline silicon at a 7° tilt angle, but range parameters different from those of LSS theory must be used. BF_2^+ implants are adequately fitted with a Pearson IV distribution, although the shape of the distribution does not match the profile exactly. A gaussian distribution to which an exponential tail is attached gives a better fit to the profile. Two gaussian profiles corresponding to BF_2^+ and ionic forms of BF can reproduce the lower energy profiles extremely well, indicating that complex dissociations are likely to happen on impact with the silicon surface.

These results significantly improve the accuracy of process simulation and are of special value when applied to such novel process techniques as rapid thermal annealing, where limited diffusion means that a precise description of the as-implanted profile is of particular importance.

Acknowledgments

We wish to thank the group at Surface Science Western for their excellent work in making the SIMS measurements. We also wish to thank B. Loro, who etched the amorphized samples in HF, I. Calder, who provided the preamorphized sample, and F. Shepherd and M. King for many stimulating discussions.

Manuscript submitted Dec. 20, 1984; revised manuscript received April 23, 1985. This was Paper 702 RNP presented at the New Orleans, Louisiana, Meeting of the Society, Oct. 7-12, 1984.

Northern Telecom Electronics Limited assisted in meeting the publication costs of this article.

REFERENCES

1. J. Lindhard, M. Sharff, and H. E. Schiott, *K. Dan. Vidensk. Selsk., Mat. Fys. Medd.*, **33**, (14) (1963).
2. R. G. Wilson, *J. Appl. Phys.*, **54**, 6879 (1983).
3. M. Simard-Normandin and C. Slaby, *Can. J. Phys.*, **63**, 890 (1985).
4. C. Slaby and M. Simard-Normandin, Paper 702, RNP presented at The Electrochemical Society Meeting, New Orleans, LA, Oct. 7-12, 1984.
5. K. Wittmaack, *Rad. Eff.*, **63**, 205 (1982).
6. H. Müller, H. Ryssel, and I. Ruge, in "Second International Conference on Ion Implantation in Semiconductors," I. Ruge and J. Graul, Editors, Springer-Verlag, Berlin (1971).
7. B. A. MacIver and E. Greenstein, *This Journal*, **124**, 273 (1977).
8. M. Y. Tsai, B. Streetman, P. Williams, and C. A. Evans, Jr., *Appl. Phys. Lett.*, **32**, (3), 144 (1978).
9. W. K. Hofker, *Philips Res. Rpt.*, Suppl. 8 (1975).
10. T. W. Sigmon, V. R. Deline, C. A. Evans, Jr., and W. M. Katz, *This Journal*, **127**, 981 (1980).

Angle-Resolved X-Ray Photoelectron Spectroscopy Study for Reactive-Sputter-Etched GaAs Surface

Norikuni Yabumoto and Masaharu Oshima

Nippon Telegraph and Telephone Public Corporation, Musashino Electrical Communication Laboratories, Musashino-shi, Tokyo 180, Japan

ABSTRACT

The chemical state and oxide layer structure of the GaAs surface after reactive sputter etching (RSE) with CCl_2F_2 gas were investigated by angle resolved x-ray photoelectron spectroscopy (XPS). From the XPS results taken at a low take-off angle, an As-depleted layer exists in the top surface. The RSE-GaAs surface oxide is found to be composed of two layers consisting of a Ga_2O_3 first layer and a $\text{Ga}_2\text{O}_3 + \text{As}_2\text{O}_3$ mixed second layer. The thickness of the top Ga_2O_3 layer increases with increasing bias voltage from 0 to 7Å, while the mixed layer thickness is rather likely to be reduced. The total oxide layer thickness of the RSE-GaAs surface grows gradually thicker with increasing bias voltage over the 0.2-0.8 kV region and is nearly equal to that of the native oxide before etching unless the mirror gloss of the surface is destroyed by RSE.

Dry etching technology for GaAs devices has been widely developed, *e.g.*, ion beam etching for gate formation in GaAs MESFET's (1), selective dry etching of the AlGaAs-GaAs heterojunction (2), and plasma etching of Si_3N_4 films on GaAs substrates (3). However, plasma surface treatment might cause damage to the GaAs surface as well as the Si surface (4). Various kinds of damage such as contamination, crystalline defects, and variations of the surface composition are observed on the GaAs surface after reactive sputter etching (RSE) (5) which is representative of dry etching technology.

The damage of the GaAs surface assessed by Auger electron spectroscopy (AES) was found to depend on RSE conditions, especially on the gas species and bias voltage (5). The surface stoichiometry changes from Ga-rich to As-rich with different etching gas species, and the degree of damage is affected by bias voltage. However, the extreme surface chemical state was not understood from AES study.

Many studies of GaAs surface oxides and metal-semiconductor interfaces have been reported using x-ray photoelectron spectroscopy (XPS). Since a surface oxide study is important for the MOS structure and other devices, not only the initial oxidation state of the cleaved surface in ultrahigh vacuum (6, 7), but also the oxidation states of real surfaces such as native, thermal, and plasma oxides (8-10) have been studied. Although the damage caused by RSE may affect the surface oxide state, very few studies on the reactive-sputter-etched GaAs (RSE-GaAs) surface have been reported.

The purpose of this paper is to clarify the extreme surface composition variation of the RSE-GaAs and the oxide layer structure which is formed by contact with air after RSE. It is desirable to establish the GaAs surface chemical state after contact with air because the usual device fabrication processes are carried out in an air atmosphere. Angle-resolved XPS (ARXPS) was adopted as a very surface-sensitive technique, in addition to usual XPS. The oxidation state of the RSE-GaAs surface was compared with the native oxide in order to distinguish the RSE-GaAs surface from the non-RSE-GaAs surface.

Experimental

The RSE-GaAs (100) surface was investigated with XPS and ARXPS. RSE experiments were carried out using a diode RF sputter etching apparatus with a 100 mm diam target. CCl_2F_2 gas was used as an etching gas. This gas was found to selectively remove As atoms to make the GaAs surface Ga-rich (5). Our intent is to understand the oxide structure on this reactively etched surface which is formed by contact with air. The gas pressure was set at 0.04 torr. The bias voltage was varied from 0.2 to 0.8 kV. Etching duration was 3 min, and the target material which was selected was fused quartz. After RSE, the

samples were placed in the XPS apparatus through air atmosphere.

The XPS measurements were performed using monochromatized Al $K\alpha$ x-ray from a rotating anode. For Ag $3d_{5/2}$, the signal intensity of 3000 cps was obtained with an energy resolution of 0.9 eV full width at half maximum (FWHM). The samples were rotated from a take-off angle of $\theta = 90^\circ - 25^\circ$, while the x-ray source and analyzer were fixed. Peak separation of the XPS spectra was accomplished after smoothing and subtracting the background in order to determine the Ga 3d and As 3d intensities from the surface oxide and underlying substrate.

Results and Discussion

Dependence of surface composition variation on RSE bias voltage.—The XPS spectra, as shown in Fig. 1, revealed that the oxygen content on GaAs etched with CCl_2F_2 gas was larger than for the native oxide before RSE based on the relative intensity of the O 1s to the Ga 3d and As 3d bands. This indicates that the damaged surface of RSE-GaAs is more active toward oxidation. Since the chemical state of the surface oxide formed after RSE is thought to reflect that of the RSE-GaAs surface, the Ga 3d and As 3d core levels were measured on the oxide to estimate the RSE-GaAs surface variation.

The XPS spectra of Ga 3d and As 3d core levels in the GaAs substrate were obtained at 18.5 and 40.7 eV, respectively, in binding energy. Chemical shifts of Ga 3d (+1.0 eV) and As 3d (+3.0 eV) were also observed, which corresponded to Ga_2O_3 and As_2O_3 , respectively (11), but the As 3d chemical shift of +5.0 eV corresponding to As_2O_5 (11) was not observed in this study.

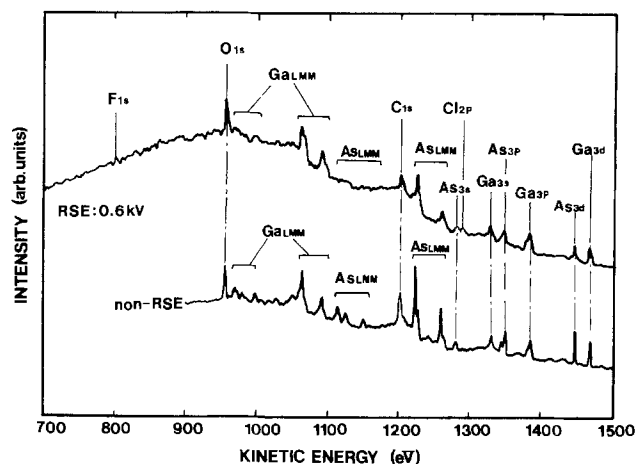


Fig. 1. XPS spectra of GaAs surface before and after RSE with bias voltage at 0.6 kV.

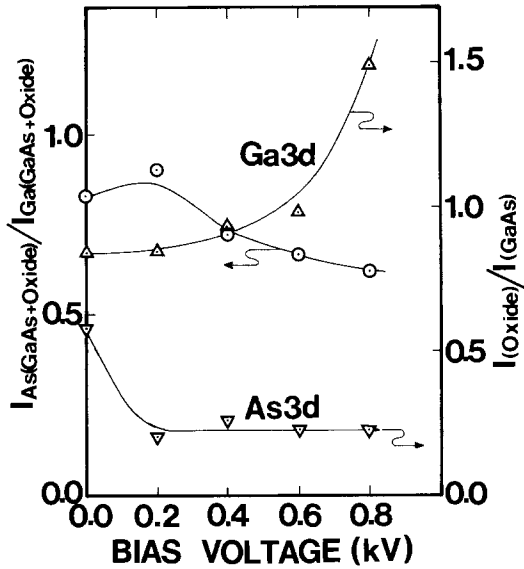


Fig. 2. The intensity ratio of As 3d/Ga 3d which involves both GaAs and oxide states, and the intensity ratio of oxide/GaAs of As 3d and Ga 3d as a function of RSE bias voltage.

The total intensity ratio $I_{As(GaAs - Oxide)}/I_{Ga(GaAs + Oxide)}$ as well as the oxide-to-GaAs intensity ratios $I_{Ga(Oxide)}/I_{Ga(GaAs)}$ and $I_{As(Oxide)}/I_{As(GaAs)}$ were plotted as a function of RSE bias voltage in Fig. 2. The former intensity ratio indicates the intensity ratio of the sum of the As 3d photopeaks in GaAs and oxide states to that of the Ga 3d photopeaks in GaAs and oxide states. These measurements were carried out at $\theta = 90^\circ$, because the deep region was desired to be examined. $I_{As(GaAs + Oxide)}/I_{Ga(GaAs + Oxide)}$ decreases from about 0.8 to 0.6 with an increasing bias voltage, indicating that As is easily removed from the surface subjected to RSE with an ion energy higher than 0.4 keV. This energy might be the critical point at which the GaAs crystal was destroyed.

As bias voltage increases, $I_{As(Oxide)}/I_{As(GaAs)}$ drops rapidly and remains constant. On the other hand, $I_{Ga(Oxide)}/I_{Ga(GaAs)}$ increases from about 0.8 to 1.5. These results suggest that the RSE-GaAs surface oxide might consist of both an As containing oxide and an As-free oxide whose thicknesses should increase with bias voltage.

Chemical states of RSE-GaAs surface.—ARXPS was used in order to examine the oxidation state of the RSE-GaAs extreme surface region. Figure 3 shows ARXPS spectra of Ga 3d and As 3d from $\theta = 90^\circ$ – 25° where the

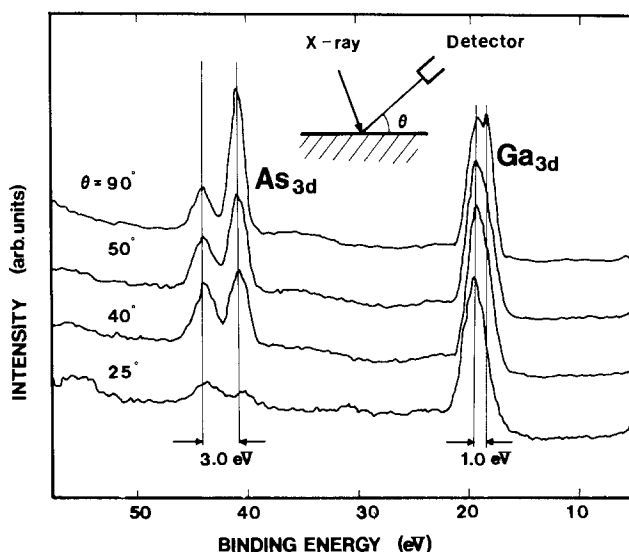


Fig. 3. Angle-resolved XPS spectra of Ga 3d and As 3d from 90° to 25° ; RSE bias voltage was at 0.6 kV.

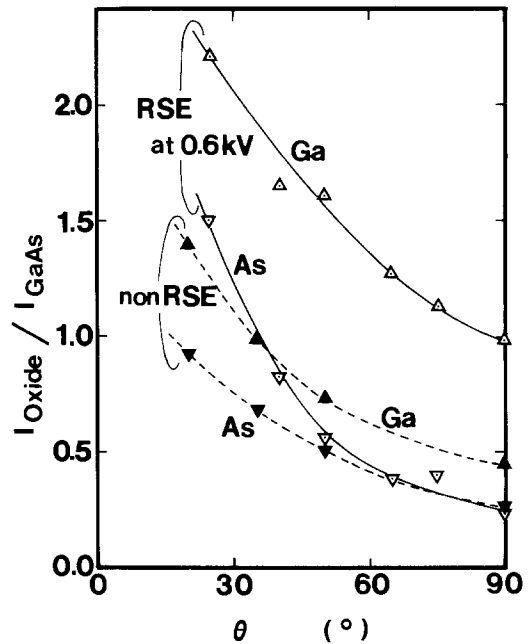
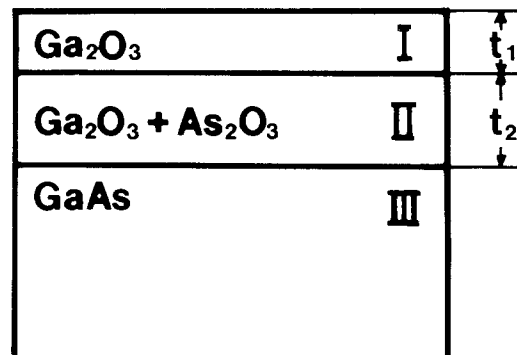
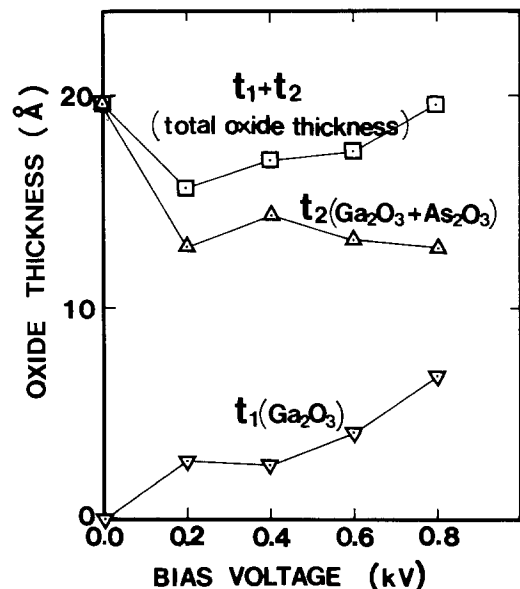


Fig. 4. Dependence of the intensity ratio of oxide for GaAs of Ga 3d and As 3d on detected angle; RSE bias voltage was at 0.6 kV. The dotted lines are from Kohiki et al. (8).



(a)



(b)

Fig. 5. a: Two-layer structure model of reactive-sputter-etched GaAs surface oxide. b: Calculated oxide thickness of RSE GaAs based on the two-layer structure model as a function of RSE bias voltage.

RSE bias voltage was set at 0.6 kV. No crystalline defects are found by transmission electron microscope observation, but a stoichiometric variation is observed on RSE-GaAs at this bias voltage. By increasing the bias voltage, the As 3d intensity weakens compared with Ga 3d, and the oxide photopeaks grow stronger relative to the substrate signals. This indicates that oxides cover most of the available surface area and that As_2O_3 is depleted relative to Ga_2O_3 at the extreme surface.

Both oxide and substrate As 3d photopeaks are barely

$$\frac{I_{\text{Ga(Oxide)}}}{I_{\text{Ga(GaAs)}}} = \frac{n_{\text{Ga}}^{\text{I}} \lambda_{\text{Ga}}^{\text{I}} \left[1 - \exp\left(-\frac{t_1}{\lambda_{\text{Ga}}^{\text{I}} \sin \theta}\right) \right] + n_{\text{Ga}}^{\text{II}} \lambda_{\text{Ga}}^{\text{II}} \left[1 - \exp\left(-\frac{t_2}{\lambda_{\text{Ga}}^{\text{II}} \sin \theta}\right) \right] \exp\left(-\frac{t_1}{\lambda_{\text{Ga}}^{\text{I}} \sin \theta}\right)}{n_{\text{Ga}}^{\text{III}} \lambda_{\text{Ga}}^{\text{III}} \exp\left(-\frac{t_2}{\lambda_{\text{Ga}}^{\text{II}} \sin \theta}\right) \exp\left(-\frac{t_1}{\lambda_{\text{Ga}}^{\text{I}} \sin \theta}\right)} \quad [2]$$

observable at $\theta = 25^\circ$, where the escape depth of As 3d photoelectrons is calculated to be about 5Å and surface-sensitive XPS spectra can be obtained. Therefore, the extreme surface region is found to abound with Ga_2O_3 and be very scarce in As_2O_3 and GaAs components. It is expected that the surface oxide layer after RSE splits into two layers with Ga_2O_3 in the first layer and $\text{Ga}_2\text{O}_3 + \text{As}_2\text{O}_3$ in the second layer. The fact that the As 3d substrate signal is found in a very small amount of $\theta = 25^\circ$ also suggests that GaAs patches remain even in the second oxide layer, and that the interface between the second layer and the GaAs substrate is not flat, or that the $\text{As}_2\text{O}_3/\text{Ga}_2\text{O}_3$ ratio in the second layer changes from 1 at the interface between the second layer and the substrate to 0 at the interface between the first and the second layer.

Figure 4 shows the dependence of the Ga 3d and As 3d intensity ratios of the oxide to the GaAs substrate on take-off angle, comparing the oxidation state of the RSE-GaAs surface with the native oxide before RSE in order to distinguish the RSE-GaAs surface from the non-RSE-GaAs surface. The solid line is from the present work and indicates the oxidation state on the GaAs surface after RSE with CCl_2F_2 at 0.6 kV, and the dotted line is from Kohiki *et al.*, who reported on the native oxide of the GaAs (100) surface (8). At $\theta = 90^\circ$, $I_{\text{Ga(Oxide)}}/I_{\text{Ga(GaAs)}}$ of RSE-GaAs is twice as strong as that of native oxide, while $I_{\text{As(Oxide)}}/I_{\text{As(GaAs)}}$ is almost the same value in both RSE-GaAs and native oxide. This indicates that the oxide layer of RSE-GaAs differs from the native oxide on two points, *i.e.*, that the oxide thickness on the etched wafer is thicker than that of the latter and that it also contains a higher mole fraction of Ga_2O_3 .

The comparison of RSE-GaAs surface oxide with the native oxide at the small θ region shows that the former is more easily oxidized than the latter. Because the GaAs surface is attacked by ions and radicals derived from CCl_2F_2 during RSE, and As atoms are removed selectively from the surface region, many As-removed holes surrounding the Ga atoms exist in the surface region. This results in the surface becoming an active state, where oxygen molecules are easily dissociated and adsorbed.

Although the $I_{\text{As(Oxide)}}/I_{\text{As(GaAs)}}$ of RSE-GaAs is almost the same as that of native oxide at $\theta = 60^\circ$ - 90° , it begins to increase more than the $I_{\text{As(Oxide)}}/I_{\text{As(GaAs)}}$ of native oxide with a decreasing θ from about 40° . This result implies that As atoms are also easily oxidized because a small amount of Ga atoms are also removed and O atoms intrude the neighborhood of As atoms.

Oxide layer structure.—The oxide layer thickness of the RSE-GaAs surface was estimated from the model as shown in Fig. 5a. Here we assumed that a Ga_2O_3 homogeneous layer exists in the first layer and a mixed layer of Ga_2O_3 and As_2O_3 exists in the second layer. The RSE-GaAs surface and the interface between the two layers are supposed to be flat. The intensity of photoelectrons I is given by Eq. [1] as

$$I = C \int_0^\infty n(x) \exp[-x/\lambda(x) \sin \theta] dx \quad [1]$$

where C is a proportional constant, $n(x)$ is the number of atoms per unit volume at a depth x , σ is the ionization cross section, $\lambda(x)$ is the photoelectron escape depth of each layer, and θ is the take-off angle. The λ of both Ga 3d and As 3d in Ga_2O_3 are 13Å and that in As_2O_3 is 21Å; they are calculated by the method of Penn (12). For the λ of Ga 3d and As 3d in GaAs, 16 and 19Å were adopted, respectively (8).

The intensity ratio equations of oxide to GaAs concerning Ga 3d and As 3d were made from Eq. [1] as

$$\frac{I_{\text{As(Oxide)}}}{I_{\text{As(GaAs)}}} = \frac{n_{\text{As}}^{\text{II}} \lambda_{\text{As}}^{\text{II}} \left(1 - \exp\left(-\frac{t_2}{\lambda_{\text{As}}^{\text{II}} \sin \theta}\right) \right)}{n_{\text{As}}^{\text{III}} \lambda_{\text{As}}^{\text{III}} \exp\left(-\frac{t_2}{\lambda_{\text{As}}^{\text{II}} \sin \theta}\right)} \quad [3]$$

Here, t_1 and t_2 are the thicknesses of the first and second layers, and Roman numbers I, II, and III mean the first layer, second layer, and substrate, respectively. The t_1 and t_2 were calculated by the least squares method using Eq. [2] and [3] and the measured values.

Figure 5b shows the calculated oxide thickness of RSE-GaAs based on the two-layer structure model as a function of bias voltage. The Ga_2O_3 top layer enlarges to about a 7Å thickness with bias voltage, though it is apparent that an As-free oxide top layer does not exist on the native oxide before RSE. On the other hand, the mixed layer thickness of Ga_2O_3 and As_2O_3 is reduced from 20 to 13Å by 0.2 kV RSE, and remains about 13Å for the bias voltage increase.

The total oxide thickness on the RSE-GaAs surface becomes slightly thinner at 0.2 kV than the native oxide, growing gradually thicker with a bias voltage of more than 0.4 kV. This tendency will accelerate with increasing bias voltage above 0.8 kV, because the damaged layer spreads deeper and the mirror gloss of the surface is lost. The reason the total oxide thickness becomes thinner at 0.2 kV may be explained by the fact that only the native oxide on the GaAs wafer is etched by 3 min RSE at 0.2 kV.

The GaAs surface after RSE was oxidized immediately by contact with air because of its activity. The oxide layer thickness was equal to that of the natural oxide layer before RSE if the mirror gloss of the surface was maintained under RSE conditions. However, the oxide layer after RSE with CCl_2F_2 split into two layers, which were composed of the Ga_2O_3 top layer without As atoms and the $\text{Ga}_2\text{O}_3 + \text{As}_2\text{O}_3$ mixed underlying layer. This suggests that during RSE of GaAs using CCl_2F_2 , As atoms break away first and then the remaining Ga atoms are released.

Here the layers I and II were assumed to be homogeneous and flat. However, in the real surface, the interface between the layers I and II, or the layers II and III, may not be flat. The $\text{As}_2\text{O}_3/\text{Ga}_2\text{O}_3$ ratio in the layer II may not be constant, and the layer II may contain bare GaAs patches.

In this paper, the chemical states of GaAs surfaces etched with CCl_2F_2 and air oxidized were determined. These results imply that the oxide layer structure of the RSE-GaAs surface etched with CF_4 and CCl_4 (which makes the GaAs surface Ga rich) as well as CCl_2F_2 is $\text{Ga}_2\text{O}_3/\text{Ga}_2\text{O}_3 + \text{As}_2\text{O}_3$, and that the surface etched with CHCl_3 (which makes the GaAs surface As rich) is $\text{As}_2\text{O}_3/\text{Ga}_2\text{O}_3 + \text{As}_2\text{O}_3$.

Conclusion

The air-exposed GaAs surface following RSE with CCl_2F_2 gas was investigated using angle-resolved XPS. The surface oxide layers split into a two-layer structure consisting of a Ga_2O_3 top layer and a mixed layer of $\text{Ga}_2\text{O}_3 + \text{As}_2\text{O}_3$, *i.e.*, no As atoms are found to exist in the top layer. The thicknesses of these layers were calculated by means of photoelectron intensity ratios and estimated es-

cape depths of Ga 3d and As 3d. The top Ga₂O₃ layer thickness enlarges with bias voltage, whereas the mixed layer thickness of Ga₂O₃ + As₂O₃ diminishes somewhat. The total oxide thickness grows gradually thicker with a bias voltage over 0.4 kV, and is nearly equal to that of the native oxide before etching unless the mirror gloss of the GaAs surface is lost by RSE.

When GaAs is reactive-sputter-etched with CCl₂F₂ gas, Ga and As do not break away at the same time, but rather Ga is released later following the release of As from the surface, which is exposed to a CCl₂F₂ plasma. Consequently, many As vacancies exist in the surface region and the RSE-GaAs surface becomes active to oxygen uptake.

Acknowledgments

The authors wish to thank Seiji Hattori and Mineharu Suzuki for their useful discussion.

Manuscript submitted Jan. 16, 1985; revised manuscript received May 6, 1985.

Nippon Telegraph and Telephone Public Corporation assisted in meeting the publication costs of this article.

REFERENCES

1. C. L. Chen and K. D. Wise, *IEEE Trans. Electron Devices*, **ed-29**, 1522 (1982).
2. K. Hikosaka, T. Mimura, and K. Joshin, *Proc. 3rd Symp. Dry Processes*, 97 (1981).
3. H. Saganara and M. Suzuki, *Proc. 5th Symp. Dry Processes*, 67 (1983).
4. N. Yabumoto, M. Oshima, O. Michikami, and S. Yoshii, *Jpn. J. Appl. Phys.*, **20**, 893 (1981).
5. N. Yabumoto, M. Oshima, and S. Maeyama, *Proc. 4th Symp. Dry Processes*, 73 (1982).
6. C. W. Wilmsen, R. W. Kee, and K. M. Geib, *J. Vac. Sci. Technol.*, **16**, 1434 (1979).
7. Z. M. Lu, W. G. Petro, P. H. Mahowald, M. Oshima, I. Lindau, and W. E. Spicer, *ibid.*, **B1**, 598 (1983).
8. S. Kohiki, K. Oki, T. Ohmura, H. Tsuji, and T. Onuma, *Jpn. J. Appl. Phys.*, **23**, L15 (1984).
9. G. P. Schwartz, G. J. Gaultieri, G. W. Kammlott, and B. Schwartz, *This Journal*, **126**, 1737 (1979).
10. G. P. Schwartz, B. Schwartz, and J. E. Griffiths, *ibid.*, **127**, 2269 (1980).
11. G. M. Muilenbery, "Handbook of X-Ray Photoelectron Spectroscopy," Perkin-Elmer Corporation (1979).
12. D. R. Penn, *Phys. Rev. B*, **13**, 5248 (1976).

Silicon Layers Grown by Differential Molecular Beam Epitaxy

H.-J. Herzog and E. Kasper

AEG-TELEFUNKEN Forschungsinstitut, D-7900 Ulm, Germany

ABSTRACT

We report on molecular beam epitaxy (MBE) of Si layers at 750° and 550°C onto (100) Si substrates covered with a patterned oxide mask. Within the exposed substrate windows epitaxial growth and on the oxide-covered areas polycrystalline growth take place at both temperatures. Different ratios of MBE film thickness to oxide thickness have been realized. The lattice perfection of the epitaxial layers, the grain size of the poly-Si, and the boundary between the single-crystalline and the polycrystalline Si at the oxide edges were investigated by scanning and transmission electron microscopy complemented by Nomarski microscopy and Secco etching. These differential MBE layers reproduce the oxide pattern and, with MBE films thinner than the oxide, the layer on top of the oxide can be removed by a lift-off step. The electrical conductivity of Sb-doped differential MBE layers is measured by means of spreading resistance. As an example of device application, a molybdenum Schottky diode is prepared and electrically characterized.

At present, the molecular beam epitaxy of silicon (Si-MBE) is capable of growing uniform layers on large area substrates (1, 2) with high crystal quality and, in particular, with arbitrary doping profiles (3, 4). However, in integrated device fabrication, the uniform planar epitaxy is a very early step and subsequent high temperature processes for preparation of lateral device dimensions limit or even destroy the advantage of the low temperature MBE process. Therefore, and also with respect to novel devices it may be promising to define lateral structures by the epitaxy process itself (5). This can be achieved by Si-MBE on a suitable prepatterned substrate surface without any change in growth parameters compared to uniform MBE layers. With VPE, for example, selective growth on a substrate with a SiO₂ pattern can be attained when the growth conditions are balanced near equilibrium by adding an etching gas such as SiCl₄ (6). Near-equilibrium nucleation takes place only on the Si; it does not on the SiO₂. With MBE, the situation is completely different because growth always takes place under heavy supersaturation. At the usual Si-MBE temperatures, the growth rate is temperature independent, the desorption is negligible, and the condensation coefficient is near unity (7, 8). On the SiO₂ surface, two reactions are possible: (i) impinging Si atoms react with SiO₂, forming volatile SiO, and the velocity of this oxide consuming reaction being strongly dependent (9); and (ii) above a critical growth rate, the nonconsumed Si condenses on the SiO₂ surface and suppresses reaction (i) by growing a polycrystalline layer on top of the oxide. A sketch of the possible results is given in Fig. 1.

At high substrate temperatures (Fig. 1a) reaction (i) dominates up to growth rates ranging from 0.03 nm/s at

850°C to 2 nm/s at 1000°C. An epitaxial layer grows on the Si surface, whereas the oxide thickness decreases. Depending on the initial oxide height, the resulting surface can be flat or the oxide layer can be consumed completely.

At the usual MBE temperature, reaction (i) is slow (Fig. 1b and 1c). On the oxide surface, a polycrystalline layer forms, whereas on the substrate an epitaxial layer grows (10-12). For this growth mode of uniform deposition on SiO₂ and Si but selective epitaxy on Si, the terms differential epitaxy (10) or patterned epitaxy (11) are used. Here, two cases can be distinguished: with thick oxides (oxide layer thicker than epitaxial layer, Fig. 1b) the poly- and single-crystalline layers are separated and, if necessary, the poly-Si can be removed by a lift-off procedure (11). With thin oxides (Fig. 1a), there is an interface between the epitaxial layer and the poly-Si film. Employing additional technological steps (etching, ion implantation), the poly-Si layer can be utilized for structures such as resistors and contact connections.

In the present study, differential epitaxial growth of undoped and Sb-doped films was carried out at growth temperatures of 750° and 550°C onto Si substrates provided with a patterned mask of SiO₂. Particular attention was directed to the two cases: MBE layer thinner than the SiO₂ and MBE layer thicker than the SiO₂.

The lattice perfection of the epitaxial layers, the grain size of the polycrystalline Si, the boundary between the single- and polycrystalline films, and the pattern distortion, *i.e.*, change of lateral dimensions of the mask pattern after layer deposition, were investigated by scanning electron microscopy (SEM) and transmission electron microscopy (TEM) assisted by Nomarski interference micros-

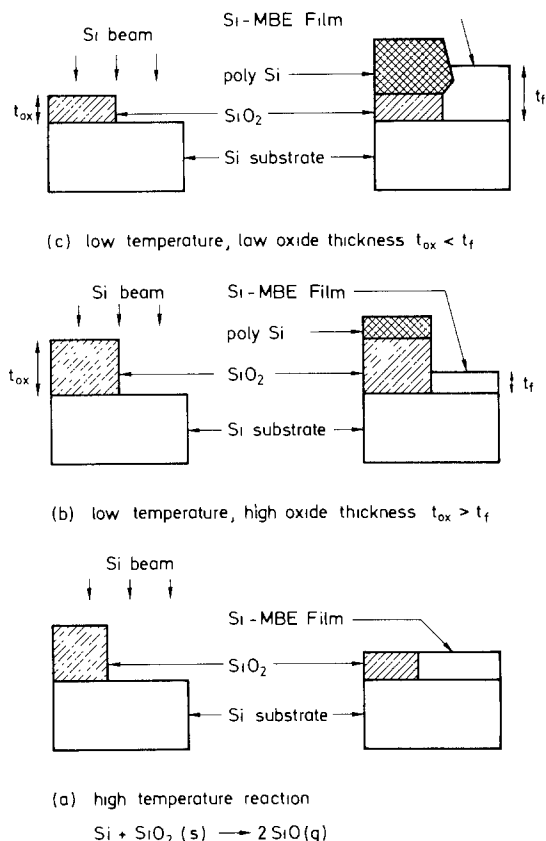


Fig. 1. Sketch of different cases of Si MBE deposition on a patterned Si substrate. a: High temperature case marked by SiO_2 consuming reaction. b: Low temperature case with SiO_2 thickness $t_{ox} >$ MBE film thickness t_f . c: Low temperature case with $t_{ox} < t_f$.

copy and Secco etching. The strain of a poly-Si film was determined by means of x-ray diffraction. The electrical conductivity of Sb-doped layers was examined by spreading resistance measurement. As an example of device applications, a molybdenum Schottky diode was prepared.

Sample Preparation

Standard 3 in. diam (100) silicon substrates of 1000 $\Omega\text{-cm}$ p-type and 1 $\text{m}\Omega\text{-cm}$ n-type resistivity were used. Thermally grown SiO_2 with thicknesses ranging from 0.1 to 0.5 μm was chosen as masking material. Two different mask patterns, one consisting of a simple layout of circles ranging from 3 to 10 μm in diameter and another more complex memory-test layout, were transferred by optical lithography. The 0.1 μm thick SiO_2 was only wet chemically etched. In contrast, the 0.5 μm thick SiO_2 was reactive ion etched in a fluorine plasma to achieve oxide walls as vertical as possible. The plasma etching was stopped 30-50 nm before reaching the oxide-substrate interface. Thus, any contamination and damage caused by the reactive etch was avoided. A final wet chemical etching step using buffered HF was performed to completely open the windows. Before loading into the MBE apparatus, all wafers were subjected to a conventional cleaning procedure [RCA etch (13)].

The high throughput MBE apparatus used for these experiments is described in detail elsewhere (2). A brief description is as follows. A separately UHV-pumped storage chamber with a ten-wafer cassette for 3 in. standard substrates is connected with the growth chamber by a pneumatic gate valve. The main elements of the epitaxy chamber are a UHV-pump system, a radiation-heated substrate heater, an electron gun for silicon, effusion cells for dopant evaporation (all beam sources provided with shutters), and *in situ* control facilities such as a thickness monitor, a quadrupole mass spectrometer, charged particle detectors, and temperature sensors. After loading a

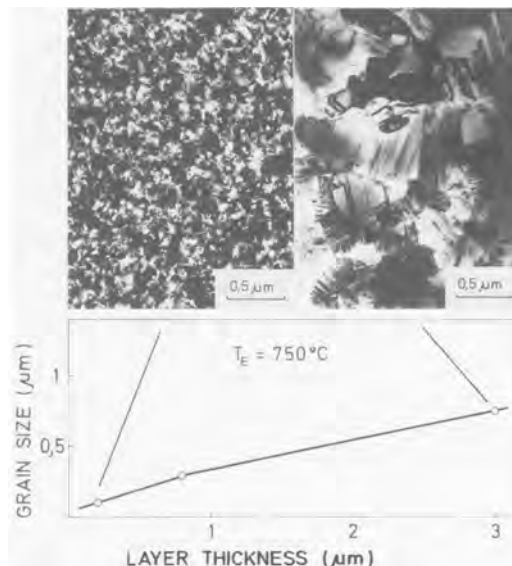


Fig. 2. Grain size dependency on the layer thickness of poly-Si in different MBE layers grown at 750°C . Two typical TEM micrographs are inset.

substrate from the cassette into the substrate heater, the epitaxy process starts at a total pressure in the 10^{-8} Pa range with an annealing step (5 min at 900°C). The substrate temperature is then reduced to the desired epitaxy temperature and the shutters above the preadjusted molecular beam sources are opened.

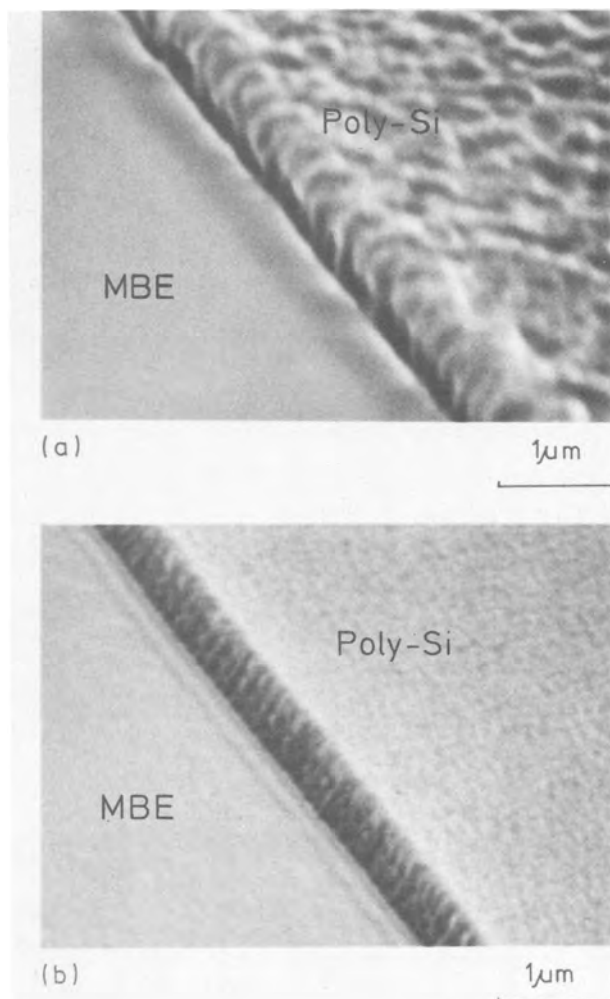


Fig. 3. Top view SEM micrographs of differential MBE layers around an oxide step with layer thickness (0.2 μm) smaller than oxide thickness (0.5 μm). Epitaxy temperatures are 750° (a) and 550°C (b).

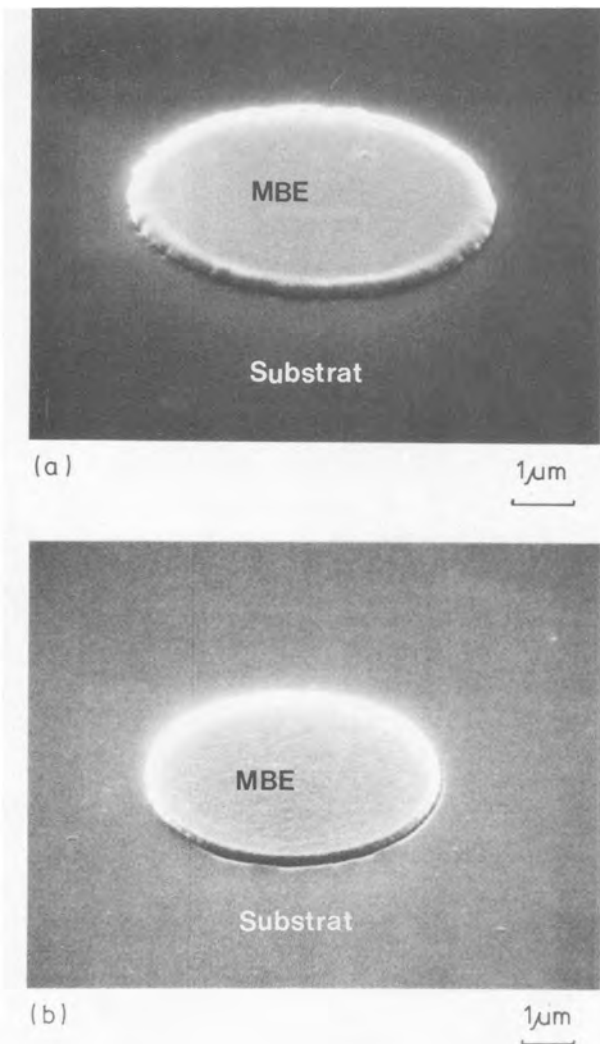


Fig. 4. Mesa-like epitaxial islands of $0.2 \mu\text{m}$ height onto the substrates after lift-off of the surrounding layer parts. Epitaxy temperatures are 750° (a) and 550°C (b).

Results

MBE layers were grown at epitaxy temperatures of 750° and 550°C and with different ratios of layer thickness to oxide thickness. As an essential result, it is found that at both epitaxy temperatures single-crystalline growth takes place onto the exposed substrate areas. The layers on top of the oxide exhibit polycrystalline growth, as shown by TEM analysis. The grain size was found to depend on epitaxy temperature and layer thickness as well. In Fig. 2, typical TEM micrographs of layers grown at 750°C are inset in the diagram showing an almost linear increase of the average grain size from $0.1 \mu\text{m}$ at a layer thickness of $0.2 \mu\text{m}$ to $0.75 \mu\text{m}$ at a thickness of $3 \mu\text{m}$. At 550°C , the average grain sizes range from 30 nm at a layer thickness of $0.2 \mu\text{m}$ to 40 nm at $0.7 \mu\text{m}$. A similar dependency of grain size on film thickness was reported recently by Lu and co-workers (14) for LPCVD poly-Si layers grown at 620°C on thermal oxide. On fused quartz, Matsui *et al.* (15) reported growth of polycrystalline films by molecular beam deposition (MBD) down to 400°C .

One goal of this work was to study the transition regions between the single-crystalline layer in the windows and the polycrystalline layer on top of the oxide. In Fig. 3, two top-view SEM micrographs of differential MBE layers are shown with an oxide thickness of $0.5 \mu\text{m}$ and a layer thickness of $0.2 \mu\text{m}$ grown at epitaxy temperatures of 750° (Fig. 3a) and 550°C (Fig. 3b) representing the case of layer thickness smaller than the oxide thickness. Both single-crystalline films are completely smooth and, as revealed by Secco etching, free of detectable crystal de-

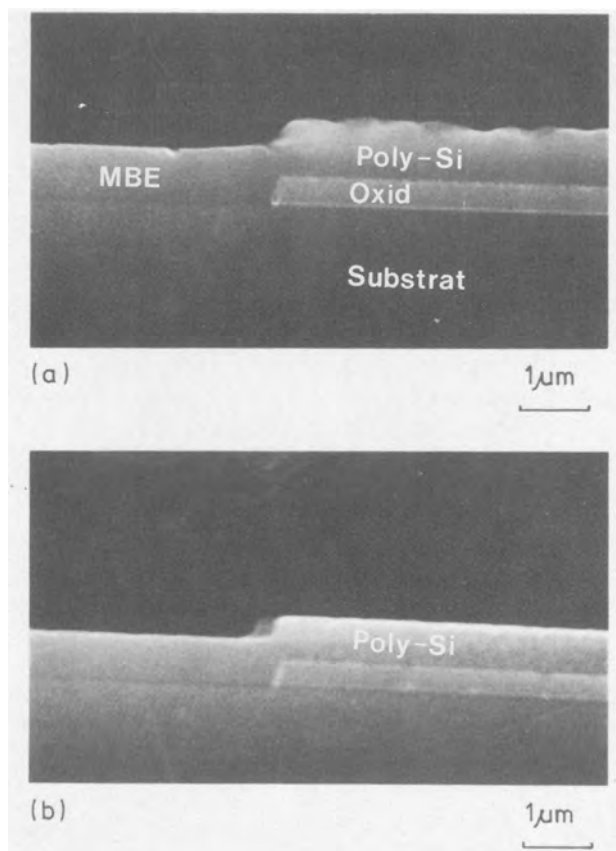


Fig. 5. Cross-sectional SEM micrographs of differential MBE layers around an oxide step with layer thickness ($0.8 \mu\text{m}$) larger than oxide thickness ($0.5 \mu\text{m}$). Epitaxy temperatures are 750° (a) and 550°C (b).

fects. Owing to the difference in grain sizes the poly-Si in Fig. 3a exhibits a rather grainy surface structure, whereas the poly-Si in Fig. 3b shows a fine roughness only. A subsequent treatment in an ultrasonic HF acid bath for 10-20 min completely lifts off the poly-Si layer parts by dissolving the SiO_2 and produces mesa-like single-crystalline islands on the substrate. The lift-off with the circular patterned SiO_2 is shown in Fig. 4a and Fig. 4b for layers grown at 750° and 550°C , respectively. The mask pattern is exactly reproduced leaving epitaxial disks of $3 \mu\text{m}$ diam and $0.2 \mu\text{m}$ height on the substrate surface. The notches at the rim of the mesa in Fig. 4a may be due to a shadowing effect during the growth by overhanging grains.

As a second important case, we prepared samples with oxide thickness smaller than the MBE layer thickness. In Fig. 5, SEM micrographs of the cross section of MBE layers grown at 750° (Fig. 5a) and 550°C (Fig. 5b) are given. The thicknesses of the masking oxide and the MBE layer amount to 0.5 and $0.8 \mu\text{m}$, respectively. That means that above the oxide edge the single-crystalline film comes in contact with the polycrystalline layer. After polishing the cross section, the samples were treated by Secco etch for 5s to intensify the contrast in the micrographs. The MBE layers reveal on the surfaces an exact replica of the oxide step without any significant pattern distortion equally in the lateral direction and in the vertical direction. The microscopic structure of the transition region polycrystalline/single-crystalline layer is demonstrated by the top-view TEM micrograph in Fig. 6. The layer sequences are $0.1 \mu\text{m}$ thick oxide and $0.2 \mu\text{m}$ thick MBE film grown at 750°C . There is a sharp transition between the polycrystalline and the single-crystalline Si. With exception of some small stacking faults or twin faults at the boundary, no crystal defects were found within the crystalline film. By preparing a sample with a patterned oxide layer of $0.14 \mu\text{m}$ followed by a $3 \mu\text{m}$ thick MBE layer grown at 750°C , it is illustrated that the pattern distortion is by far smaller than the film height. In Fig. 7 a top-view Nomarski micrograph of this differential MBE layer and a correspond-

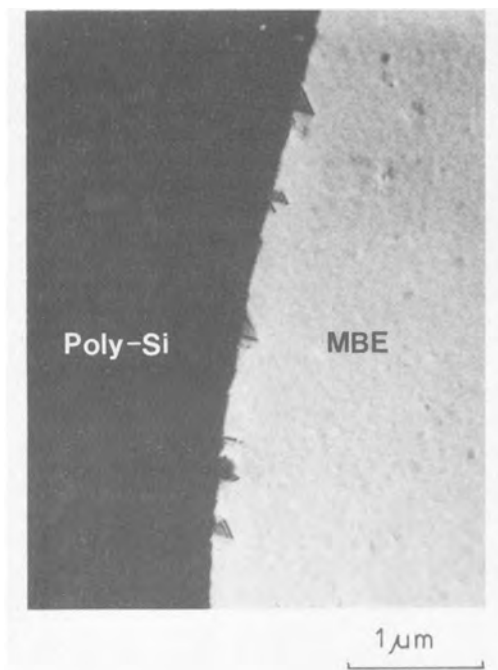


Fig. 6. Top-view TEM micrograph showing some stacking faults or twin faults at the single-crystalline/polycrystalline boundary. Layer thickness: $0.2 \mu\text{m}$. Oxide thickness: $0.1 \mu\text{m}$. Epitaxy temperature: 750°C .

ing cross-sectional SEM micrograph are given. The cross-sectional sample has been etched for 5s in Secco etch. Of course, there is a strong interlocking between the single-crystalline and polycrystalline layer, but the boundary runs almost vertically from the oxide edge to the layer surface. From the SEM micrograph, the pattern distortion on the layer surface can be estimated to be about $0.5 \mu\text{m}$.

With a wafer having the same thickness sequence as in Fig. 7, but an unpatterned oxide, an analysis of the strain in the layer was performed. Since a strained layer causes a bending of the substrate-overgrowth structure, the curvature k of the sample was measured by means of x-ray diffraction (16, 17) before and after Si-MBE. The film strains ϵ_f were calculated in terms of substrate thickness t_s and film thickness t_f using the relation (18)

$$\epsilon_f = \frac{kt_s^2}{6t_f}$$

It is found that both the SiO_2 film and the polycrystalline layer are under compressive strain of -2.85×10^{-3} and -0.5×10^{-3} , respectively. Accordingly, the strain in the poly-Si layer is more than a factor five smaller than in the oxide film.

With respect to the preparation of Schottky diodes as an example for device application of this differential growth technique, Sb-doped layers with thicknesses ranging from 0.2 to $0.8 \mu\text{m}$ were grown at 550°C on n^+ substrates. The pattern in the $0.5 \mu\text{m}$ thick masking oxide consisted of circular windows. The conductivity of these layers was measured using a spreading resistance probe. The resistivity within the single-crystalline parts amounts to $6.5 \times 10^{-2} \Omega\text{-cm}$ corresponding to a doping level of $1.5 \times 10^{17} \text{cm}^{-3}$. In contrast, the spreading resistance of the poly-Si layers on top of the oxide was found to be beyond the measuring range ($10^9 \Omega$) of the apparatus used. Hence it follows that the resistivity of the poly-Si is as much as five orders of magnitude higher than that of the adjoining single-crystalline Si. This considerably deviates from the result of differential MBE given by Ota (10), who reported a change in resistivity of about two magnitudes. However, this may be due to the higher epitaxy temperature of 800°C and/or the other dopant type and doping technique, namely, B doping by ion implantation. The doping profile as calculated from the spreading resist-

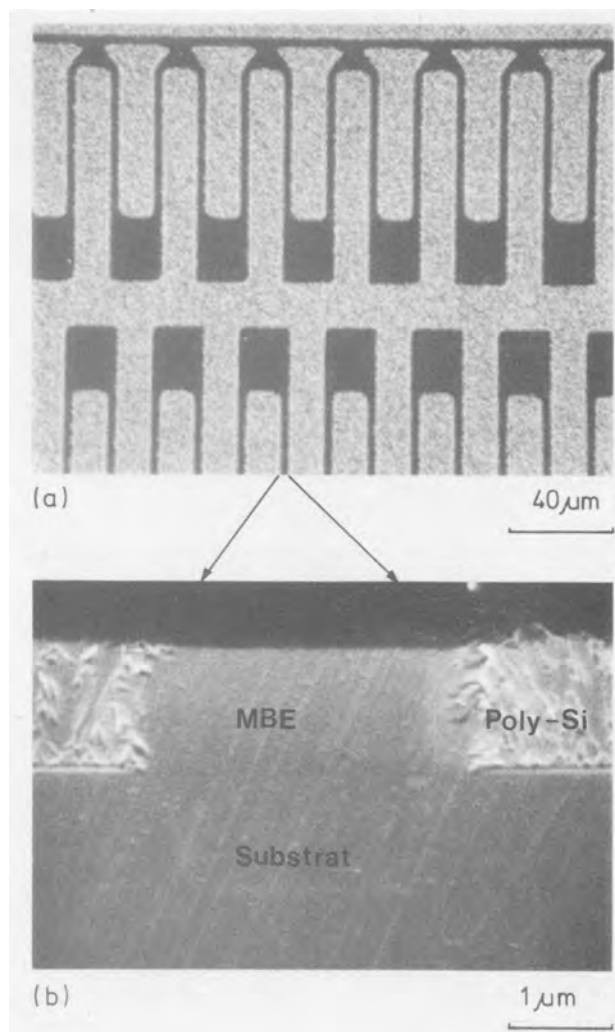


Fig. 7. Comparison of a Nomarski micrograph (a) with a corresponding cross-sectional SEM micrograph (b) of a differential MBE layer grown at 750°C . MBE layer thickness: $3 \mu\text{m}$. Oxide thickness: $0.14 \mu\text{m}$. The pattern distortion is estimated from Fig. 7b to be about $0.5 \mu\text{m}$.

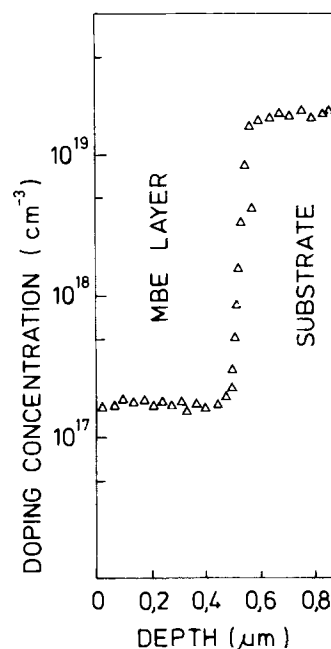


Fig. 8. Sb doping profile in the epitaxial area of a differential MBE layer grown at 550°C . A sharp transition from the n^+ substrate to the layer and a flat profile of $n = 1.5 \times 10^{17} \text{cm}^{-3}$ within the $0.5 \mu\text{m}$ thick MBE layer are obtained.

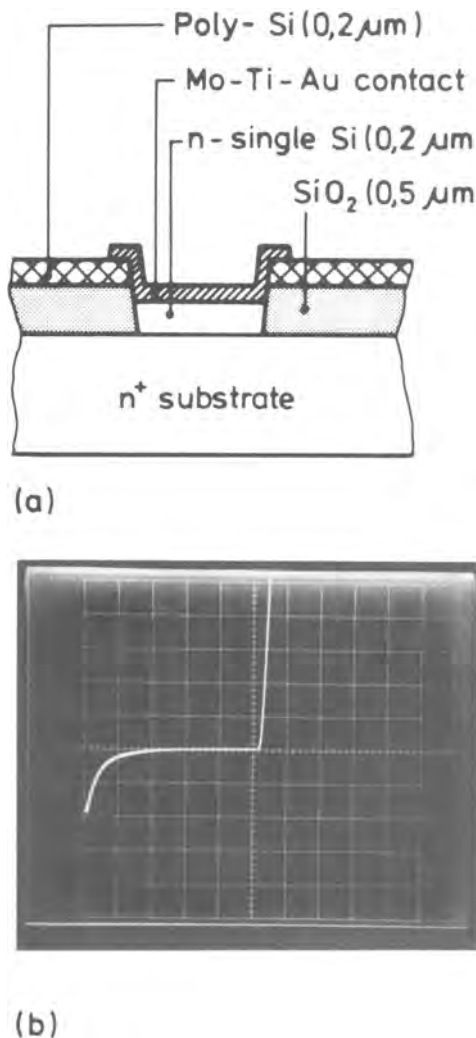


Fig. 9. a: Schematic setup of the Schottky diodes using differential Si-MBE. b: Current-voltage characteristic of a diode (horizontal scale: 2V-division⁻¹; vertical scale: 2 mA-division⁻¹).

ance in the single-crystalline areas is shown in Fig. 8, demonstrating that an abrupt transition occurs at the interface between substrate and MBE layer followed by a flat Sb profile of $n = 1.5 \times 10^{17} \text{ cm}^{-3}$ within the layer.

As Schottky barrier material, a Mo-Ti-Au metallization was deposited onto differential MBE layers and structured by optical lithography and chemical etching. A cross-sectional view of a Schottky diode with a 0.2 μm thick MBE film grown at 550°C is sketched in Fig. 9a. The I-V curve of such a Schottky diode is shown in Fig. 9b, clearly revealing forward and reverse characteristics. The reverse breakdown voltage is typical for the film thickness and doping density.

Conclusion

Si-MBE layers were grown at two different temperatures on Si substrates covered with a mask oxide. Thicknesses of the Si and SiO₂ films ranged from 0.2 to 3 μm and from 0.14 to 0.5 μm , respectively. The following results are obtained from these differential MBE layers.

At both epitaxy temperatures of 750° and 550°C epitaxial growth with good crystal perfection takes place on the exposed substrate areas.

On the oxide polycrystalline growth is obtained. The grain sizes of layers grown at 750°C are found to increase almost linearly from 0.1 μm at 0.2 μm film thickness to

0.75 μm at 3 μm film thickness. At 550°C, the grain sizes amount to 30 nm at 0.2 μm film thickness and 40 nm at 0.7 μm , respectively.

With layer thickness smaller than the oxide thickness, the single-crystalline film is separated from the surrounding polycrystalline layer provided that the oxide walls are nearly vertical. If desired, the poly-Si can be lifted off by dissolving the oxide. By that means mesa-like epitaxial layers are obtained which exactly reproduce the pattern of the oxide.

With layer thickness larger than the oxide thickness, the single-crystalline film is interlocked with the surrounding oxide overlayer. However, the boundary proceeds almost vertically from the oxide edge to the layer surface. Hence, the pattern distortion is by far smaller than the film height even if the thickness ratio between MBE and oxide is 3-0.14 μm .

The poly-Si is under compressive strain. This strain for 3 μm thick layers grown at 750°C amounts to 5×10^{-4} , which is more than five times smaller than the compressive strain in the underlying oxide.

Differential Si-MBE layers intentionally doped with Sb to $n = 1.5 \times 10^{17} \text{ cm}^{-3}$ were analyzed by spreading resistance. A sharp transition and a flat profile are obtained in the single-crystalline regions. On the other hand, in the polycrystalline films up to a thickness of 0.8 μm the resistivity is found to be as much as five decades higher in comparison to the adjoining single crystal.

Acknowledgments

The authors wish to thank H. Kibbel for MBE work. They would also like to thank H. Jorke, S. Lindenmaier, D. Gruchmann, Dr. K. Strohm, C. Adamek, A. Schaub, and W. Pilz for technical assistance. Support by the Ministry of Research and Technology of Germany is acknowledged.

Manuscript submitted Feb. 20, 1985; revised manuscript received June 3, 1985.

AEG-TELEFUNKEN assisted in meeting the publication costs of this article.

REFERENCES

- U. König, H. Kibbel, and E. Kasper, *J. Vac. Sci. Technol.*, **16**, 985 (1979).
- U. König, H.-J. Herzog, H. Jorke, E. Kasper, and H. Kibbel, in "Collected Paper of MBE-CST-2," p. 193, Tokyo (1982).
- F. G. Allen, S. S. Iyer, and R. A. Metzger, in "Proceedings of the SPIE Technical Symposium, Los Angeles," p. 2 (1982).
- J. C. Bean, *J. Vac. Sci. Technol. A*, **1**, 540 (1983).
- H. M. Liaw, I. Rose, and P. L. Fejes, *Solid State Technol.*, **5**, 140 (1984).
- See, for example, K. E. Bean, *Thin Solid Films*, **83**, 173 (1981).
- E. Kasper, *Appl. Phys. A*, **28**, 129 (1982).
- T. de Jong, Ph.D. Thesis, University of Amsterdam, Amsterdam (1983).
- A. Ishizaka, K. Nakagawa, and Y. Shiraki, in "Collected Paper of MBE-CST-2," p. 183, Tokyo (1982).
- Y. Ota, *Thin Solid Films*, **1**, 104 (1983).
- J. C. Bean and G. A. Rozgonyi, *Appl. Phys. Lett.*, **41**, 752 (1982).
- E. Kasper and K. Wörner, in "VLSI Sciences and Technology/1984," K. E. Bean and G. A. Rozgonyi, Editors, p. 429, The Electrochemical Society Softbound Proceedings Series, Pennington, NJ (1984).
- W. Kern, *Semicond. Int.*, **4**, 94 (1984).
- N. C. C. Lu, C. Y. Lu, M. K. Lee, C. C. Shih, C. S. Wang, W. Reuter, and T. T. Sheng, *This Journal*, **131**, 897 (1984).
- M. Matsui, Y. Shiraki, and E. Maruyama, *J. Appl. Phys.*, **53**, 995 (1982).
- G. A. Rozgonyi and D. C. Miller, *Thin Solid Films*, **31**, 185 (1976).
- E. Kasper and H.-J. Herzog, *ibid.*, **44**, 357 (1977).
- A. Brenner and S. Senderoff, *J. Res. NBS*, **42**, 105 (1949).

Instrumental Neutron Activation Analysis of Processed Silicon

Joseph A. Keenan,* Bruce E. Gnade, and John B. White

Texas Instruments, Incorporated, Materials Science Laboratory, Dallas, Texas 75265

ABSTRACT

Instrumental neutron activation analysis has been applied to the surfaces of processed silicon wafers with analytical sensitivity down to parts per million of a monolayer. Residual contamination with gold, copper, and sodium has been shown to be consistently present in the range 4-500 ppm of a monolayer. Copper and sodium are added to the surface from oxidation furnaces.

The electrical properties of Si, and, therefore, the yield of usable devices fabricated from Si, are dependent upon impurity concentrations in the range of subparts-per-billion to parts-per-million. In order to determine impurity concentrations at these levels in small samples, it is necessary to use a very sensitive analytical technique. Instrumental neutron activation analysis (INAA) fulfills most of the requirements necessary for this analysis. The present work is an application of INAA as a monitor for silicon device processing.

The sensitivity of INAA for key elements such as gold, copper, and sodium allows detection at concentration levels which are too low to distinctly impact device performance. Therefore, it is desirable to determine an acceptable base line of impurity levels in manufacturing. This base line was established by collecting data over a 2.5 yr period, incorporating data from a wide range of cleanup and oxidation process steps. The great sensitivity of INAA allows for the realization of changes in impurity concentrations before they cause measurable yield loss in a monitored process. As might be expected, there is a great deal of scatter in the data when very low concentrations are measured. Nevertheless, enough data have been acquired to justify a statistical analysis. This provides a basis for understanding when a contamination level is out of control as well as a means of determining when trends arise or when significant changes in contamination levels have occurred.

Neutron activation is especially applicable for samples in which the matrix does not become highly activated, such as high purity Si or graphite. More than 40 elements undergo neutron capture to produce radioactive products which are readily detectable by gamma-ray spectroscopy. Quantitation in INAA requires a knowledge of the neutron flux to which the samples are exposed. The flux can be determined using one of several single-flux monitor procedures (1-4). In the present work, the average flux was initially derived from the use of a single Au and Co monitor (2). This method of flux determination, in conjunction with the Westcott formalism (5) for obtaining effective (thermal/epithermal) neutron cross sections, has been shown to be a valid quantitative technique (2), if the energy distribution of the reactor's neutron flux is stable.

Experimental

The utilization of INAA as a monitor for wafer processing is done best using relative measurements to compare unprocessed wafers (as controls) with processed wafers. Both N<111> and P<100> 3 in. wafers were monitored. Pilot wafers were processed in several different types of equipment for each procedure so that individual oxidation furnaces and cleanup apparatus could be compared.

It is important to remember that any contamination introduced after the irradiation will not affect the analysis, since it is not radioactive. Handling through completion of the test up to the irradiation is the critical step. A set of pilot wafers was selected from N<111> and P<100> unprocessed starting material, with controls for each group being set aside at this point. The pilot wafers were prepared for testing in a class 100 clean room. Some of these

wafers were used to test the effectiveness of the various clean-up procedures and apparatus. The remaining wafers were then subjected to the standard preoxidation cleanup, which is described below, and used to test oxidation furnaces. The flow of test wafers is depicted in Fig. 1.

Upon completion of the tests, the wafers were scribed, broken, and placed in a clean 2 in. quartz dish. This work was done in an area with less than 1500 particle/ft³. Prior to use, the quartz dish was cleaned by (i) soaking in H₂SO₄:H₂O₂ (7:4) mixture for 10 min, (ii) rinsing with de-ionized (DI) water for 10 min, (iii) soaking in 10% HF for 1 min, (iv) rinsing with DI water for 10 min, (v) soaking in HCl:H₂O₂:H₂O (4:1:5) for 2 min, and (vi) finally rinsing for 10 min in DI water. The individual wafers were separated by clean 2 in. Si slices. The wafers were held in place by a piece of compressed Zr foil to minimize breakage. The quartz dish was then wrapped in Al foil and placed inside an Al irradiation container. The Al container was sealed with epoxy to avoid leakage of reactor cooling water onto the samples.

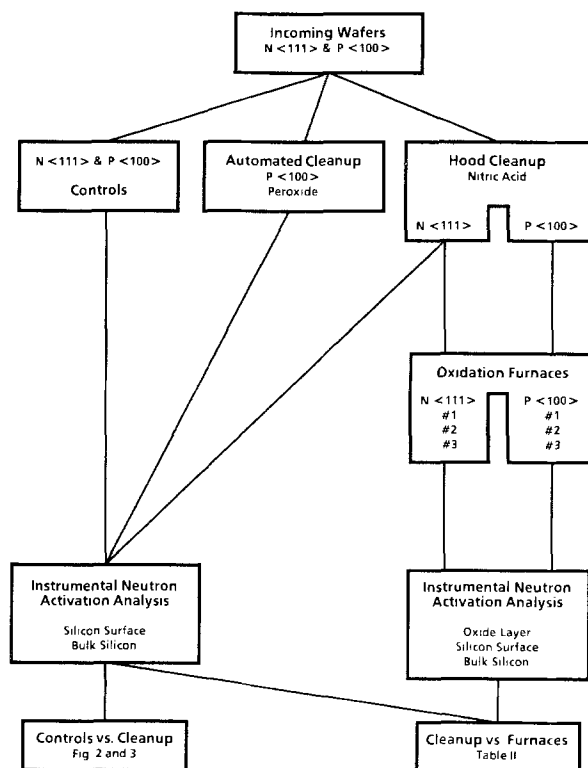


Fig. 1. A diagram of the materials flow for INAA testing. Incoming N<111> and P<100> wafers were sampled as controls. P<100> wafers went through an automated cleanup using peroxide-based chemicals. N<111> and P<100> wafers went through a conventional cleanup hood in which nitric acid served as the inorganic cleanup step, and then went on to test oxidation furnaces. Some N<111>, but no P<100>, wafers were tested by INAA following the hood cleanup, but the control wafers are compared to cleaned wafers in Fig. 2 and 3. Cleaned wafers are compared to wafers from oxidation furnaces in Table II.

*Electrochemical Society Active Member.

The samples were irradiated at the Texas A&M Nuclear Science Center research reactor for 14h at a nominal flux of 1.5×10^{13} neutron/cm²-s. The maximum sample size is a cylinder approximately 5 cm in diameter by 2.5 cm in height. Analysis begins about 12h after irradiation, allowing the detection of short-lived isotopes such as ⁶⁴Cu and ²⁴Na in the oxide and surface layers. This decay time allows the activity of the ³¹Si ($t_{1/2} = 2.62$ h) matrix and ²⁸Al ($t_{1/2} = 2.24$ min), which is formed from ²⁸Si, to decay to a safe level. Once the samples are received, they are rinsed three times with an HCl/CH₃OH mixture to remove any surface contamination that may have inadvertently been introduced during the packaging procedure. If the surface of the sample is to be analyzed, the back of the sample is protected with acid-resistant tape. The oxide layer, if any, is removed with 50% HF, and the etch solution is analyzed to determine contamination levels in the oxide. Next, approximately 2 μm of material is removed by etching the sample for 30s in planar etch (2HF:15HNO₃:5 acetic acid). This etch solution, which represents a sample of the surface contamination, is then analyzed. The remainder of the sample is etched three times in an HF:HNO₃ (1:3) solution, and then in a warm Aura etch solution (1% NaOH, 1% EDTA, 2.5% p-nitrobenzoic acid, and 1% NaCN) to remove and complex any further surface contaminants. The etched wafer is then analyzed as a solid, giving a good measure of the quality of the bulk material.

The oxide and surface solutions are counted at approximately 15h after the end of irradiation, while the bulk samples are counted at 30h and again at 60h after the end of irradiation. The bulk samples are counted at two different times to give maximum sensitivity for both short- (⁶⁴Cu, ²⁴Na, etc.) and long-lived (⁵⁹Fe, ⁶⁰Co, etc.) species, as well as to ensure that the elemental identification is correct. (Elements are identified by both half-life and gamma-ray energy.)

The samples are counted for periods of 8000s each on each of three large volume Ge(HP) detectors. These detectors have > 20% relative efficiency at 1.3 MeV, with an energy resolution of 1.8 keV FWHM at 1332 keV. The solutions are counted in a standard geometry, which is directly against the face of the detector. Each detector is housed inside a graded Pb shield to minimize background radiation. The systems are calibrated for energy and efficiency with an absolutely calibrated mixed-radionuclide source of the same geometry as the etch solutions. The data are acquired with a computer-based multichannel analyzer, and stored on local floppy disk. Once acquisition is complete, the spectral data are transferred from the multichannel analyzer to a VAX 11-750, where the data reduction is performed.

Concentrations of contaminants are determined by calculating the volume of Si present from the amount of ³¹Si activity (4). This eliminates the need to precisely determine the neutron flux for each irradiation, since everything is measured relative to the counting rate of the 1266 keV gamma ray from the decay of ³¹Si. The drawback to this technique is that the absolute accuracy of contamination levels is only as good as the accuracy of the ³⁰Si

thermal cross section and resonance integral, as well as the Cd ratio. We feel these errors are constant and insignificantly larger than the errors encountered in measuring the flux with external monitors (2). For bulk silicon samples, this method also avoids the experimental errors generated in determining the absolute counting efficiency for each different sample shape. Surface contaminations in units of atoms per square centimeter were computed using the concentrations derived from INAA (atoms per cubic centimeter) and the measured weight and thickness of the sample, assuming a density of 2.32 g/cm³ for silicon. Contamination levels measured in these units were found to be independent of the thickness of "surface sample" removed by etching.

Results and Discussion

Surface contaminants can be broadly classified as either organic or inorganic. Most organic contaminants are residual materials such as waxes, resins, oils, and trace residues from solvents. Layers of such organic impurities are usually chemisorbed to the surface. However, inorganic contaminants such as sulfate ion, sodium, copper, and gold are either physically adsorbed, electrochemically deposited on the surface or entrapped in the oxide film (6).

The sequence of surface cleaning must follow a logical course: (i) organic contaminants must be removed before subsequent reagents can contact the underlying surface; (ii) next, the native oxide on bare silicon or the outer 100-200Å of oxide on an oxide film must be removed; (iii) then it is possible to remove inorganic contaminants (7).

In the processes tested here, a mixture of sulfuric acid and hydrogen peroxide was routinely used for the removal of organic contaminants. Oxide removal was done with hydrofluoric acid diluted 10:1 with deionized water. Inorganic removal was done with one of two alternate methods. The first method used nitric acid preceded and followed with extensive rinses in deionized water. The second method used a sequence of ammonium hydroxide with hydrogen peroxide and hydrochloric acid with hydrogen peroxide (7).

All N<111> wafers and all P<100> wafers being prepared for furnace tests received the first method for removal of inorganic contamination. This process is identified in Fig. 1 as the "hood cleanup" since all of these cleanups were performed manually in traditional cleanup hoods. The P<100> wafers tested after cleanup received the second method for removal of inorganic contamination. This step was carried out in automated equipment manufactured by FSI Incorporated and is identified in Fig. 1 as the automated cleanup.

In order to place the levels of contamination being measured in perspective, consider that one atomic layer on a <100> silicon surface should ideally consist of 6.8×10^{14} at./cm², while one atomic layer on a <111> silicon surface should consist of 7.8×10^{14} at./cm² on the basis of a purely geometric argument. Normalizing to units of monolayers shows that the surface concentrations measured in INAA are ppm of a monolayer. The following discussion will make use of these units.

The bulk contamination levels for Cu, Au, As, and Sb ranged from a low of 1×10^{10} at./cm³ for Au to a high of 6×10^{13} at./cm³ for As. The bulk detection limits for Fe and Zn are 1×10^{16} and 2×10^{14} at./cm³, respectively. These levels of contamination in the bulk are consistent with the reported concentration gradient (13) between surface and bulk material which is maintained during high temperature processing. Since the purpose of this work was to study the introduction and removal of surface contamination, only the oxide and surface data will be discussed here. Eight elements, listed in Table I, were detected in these samples. Table I lists the frequency with which these elements were detected and the maximum and minimum surface concentration detected. Based on Table I, gold, copper, and sodium were selected for statistical analysis. Chromium, cobalt, arsenic, and tungsten were detected far too inconsistently for statis-

Table I. The frequency of detection of eight elements in silicon surfaces (times detected/times analyzed). The top two rows list the maximum and minimum level detected in parts per million of a monolayer

	Au	Cu	Na	As	Sb	Cr	Co ^a	W
Maximum	430	4410	1920	200	2560	2310	370	13
Minimum	1.2	14	20	0.9	0.7	1540	49	1.4
N-control	21/21	21/21	20/21	13/21	19/21	1/21	3/21	6/21
N-cleaned	22/22	20/22	22/22	9/22	19/22	1/22	3/22	1/22
P-control	23/23	21/23	22/23	12/23	14/23	0/23	0/23	0/23
P-cleaned	22/22	21/22	22/22	8/22	15/22	0/22	2/22	1/22

^a The detection limit for iron under these conditions for INAA is approximately 700 times worse than for cobalt.

tical analysis. Antimony was usually detected near the minimum value given in Table I, with the stated upper limit being an isolated occurrence.

An important dimension of any trace element analysis technique is the determination of a detection limit when an element is not observed. The formulation of Currie (8, 9) is used to calculate both a limit of qualitative detection, as well as a limit of quantitative determination. Detection limits were not entered into the data sets for statistical analysis. The number of data points analyzed for any particular set, therefore, is less than or equal to the total number of irradiations carried out during the test period. The statistical interpretation and presentation of the INAA data are based on the methods presented in Ref. (10).

Figure 2 compares the N<111> control wafers with the N<111> wafers after water-nitric-water inorganic cleanup with respect to the elements, sodium, copper, and gold. For both the long- and the short-term t-test, no significant difference is observed for the levels of copper and gold before and after cleanup. A significant improvement after cleanup is observed for sodium in the long term. The short-term difference is less clearly established. Figure 3 presents the same comparison for P<100> material. For these wafers, the peroxide-based inorganic cleanup was used in an automated system. Again, the elements sodium, copper, and gold are presented. Over both the short and the long term, significant improvement after cleanup is seen for sodium and gold. The short-term difference for copper is also significant.

With respect to the initial points, the last few points are "out of control" for all three elements on the P<100> control wafers (Fig. 3). These last points reflect a change in polishing procedures by the wafer supplier which appears to have had a favorable impact. Both the N<111> wafers and the P<100> wafers report points out of control for copper. The loss of control over copper is especially important for the P<100> process since it is this which casts doubt upon the long-term difference between control and post-cleanup samples.

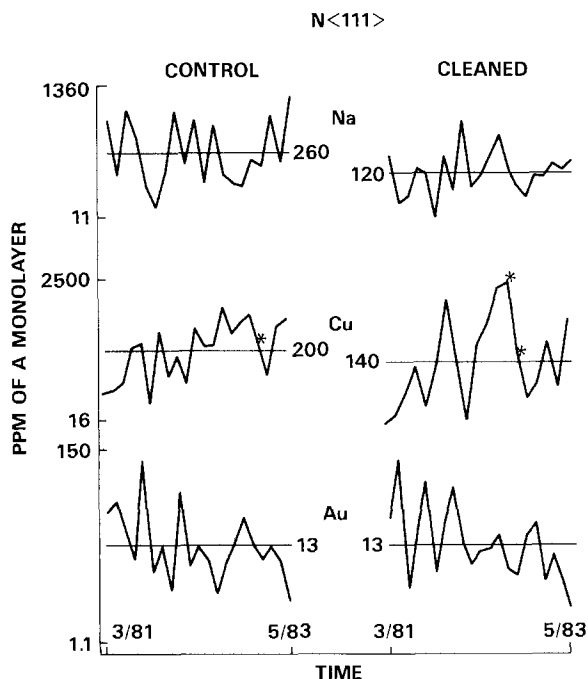


Fig. 2. A comparison of surface contamination on cleaned N<111> wafers with "as-received" control wafers. The vertical scale is logarithmic with the labels in units of parts per million of a monolayer. The horizontal scale is linear in time. Asterisks indicate points which are "out of control" on a statistical basis. For sodium, a t-test shows an 80% probability of a true difference between the control wafers and cleaned wafers in the short term and 90% probability of a true difference in the long term. For copper and gold, the same test shows no significant difference.

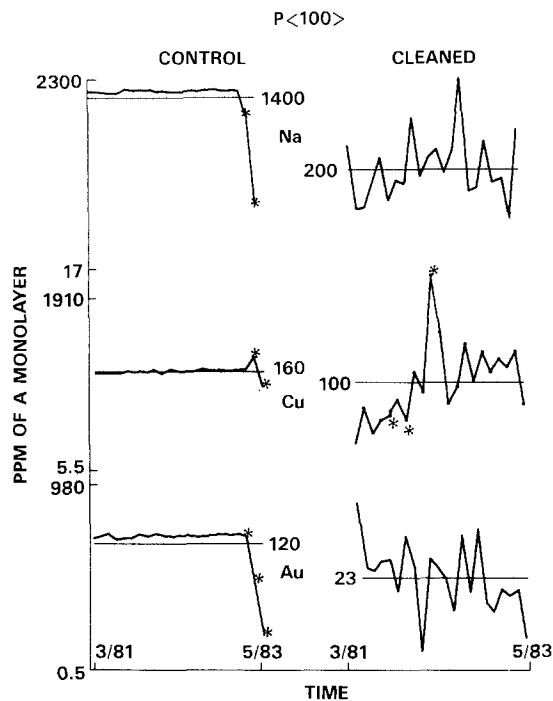


Fig. 3. A comparison of surface contamination on cleaned P<100> wafers with "as-received" control wafers. The vertical scale is logarithmic. Asterisks indicate points which are "out of control" on a statistical basis. The points out of control for the control wafers reflect a change in polishing procedure by the wafer supplier. For sodium and gold, a t-test shows 99.9% probability of a true difference between the cleaned wafers and the control wafers in both the short and the long term. For copper, the significance of the difference is 90% in the short term and 80% in the long term.

A comparison of the N<111> control wafers (Fig. 2) and the P<100> control wafers (Fig. 3) suggests that the P<100> wafers were consistently more contaminated up until the change in polishing procedures. Schmidt *et al.* (11) observed that P<100> wafers are most prone to contamination during polishing, while N<111> wafers appeared to be the less readily contaminated. That trend is reflected here. Since the chemicals used in the cleanups and the method of applying those chemicals (manual *vs.* automated) differs, the impact of orientation or type upon ease of cleanup cannot be determined. In general, the cleanups were successful. The impurity levels observed on cleaned <111> and <100> slices are comparable and appear to represent very clean silicon surfaces.

Table II compares average results over the test period from the monitoring of three furnaces used to process

Table II. Surface impurity concentrations in parts per million of a monolayer for gold, copper, and sodium in cleaned wafers, and for test wafers from six oxidation furnaces

Wafer type process step	Gold	Copper	Sodium
N<111> hood cleanup	13	140	120
P<100> automated cleanup	23	100	200
Average cleaned wafer	18	120	160
Furnace N-type 1 oxide	0.2	19	180
Surface	3.5	86	81
Total	3.7	105	261
Furnace N-type 2 oxide	0.3	15	280
Surface	5.0	100	70
Total	5.3	115	350
Furnace N-type 3 oxide	0.3	27	380
Surface	16	420	120
Total	16.3	447	500
Furnace P-type 1 oxide	0.2	27	220
Surface	8.0	260	86
Total	8.2	287	306
Furnace P-type 2 oxide	0.2	30	140
Surface	5.0	190	66
Total	5.2	220	206
Furnace P-type 3 oxide	0.1	22	200
Surface	8.0	190	86
Total	8.1	212	286

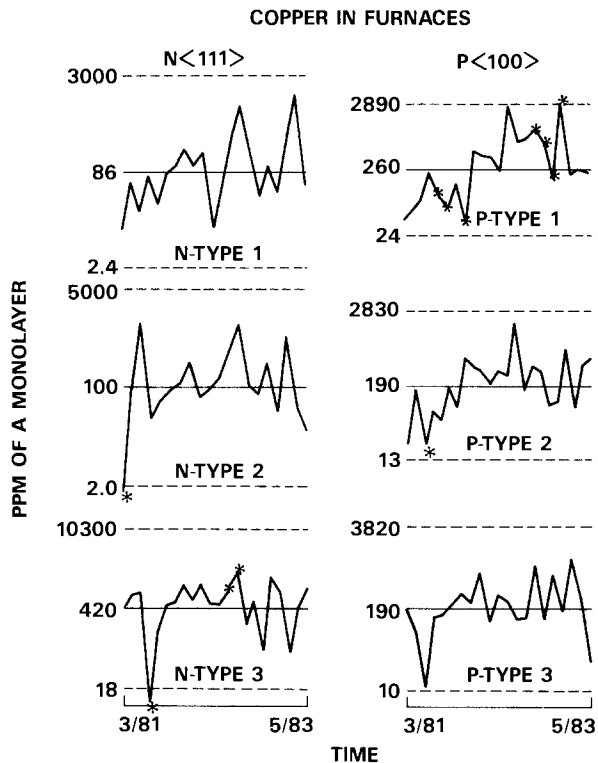


Fig. 4. Variations in time of copper contamination on pilot wafers processed in six furnaces. The data are for the silicon surface under the oxide layer. Three furnaces were used to process N<111> wafers, and three processed P<100> wafers. The vertical scale is logarithmic. Asterisks indicate points which are "out of control" on a statistical basis.

N-type <111> wafers and three furnaces used to process P-type <100> wafers with cleaned wafers. The results for cleaned wafers are the data from Fig. 2 and 3. P-type <100> wafers were cleaned along with the N-type <111> material for furnace tests (Fig. 1). However, no P-type wafers were set aside after cleanup.

After irradiation, the oxide layers and the silicon under the oxide were separated by etching and individually analyzed. Both results are included in Table II. Sodium appears mostly in the oxide sample, while copper and gold appear to a greater extent in the silicon surface sample. This result is produced during the oxide removal step by the tendency of copper and gold to deposit on a silicon surface from acid solution (6, 11). Sodium, being readily water soluble, is effectively removed with the oxide. Non-radioactive copper and gold carriers added to the planar etch used for silicon removal helped reduce this "plate-back" effect during the surface sampling. Nevertheless, the measured copper and gold levels are probably consistently underestimated due to this effect. Since the comparison here is between cleaned surfaces and processed surfaces, which were all analyzed in a consistent manner, any error due to "plate back" or sample preparation prior to irradiation should be systematic.

One would usually expect surface contamination carried into the furnace on the wafers or deposited on the wafers during the furnace step to appear in the oxide sample. Because of the sampling problem during oxide removal, it is preferable to compare the cleaned surfaces with the sum of impurities in the oxide and the surface samples. This is done in rows labeled "total" in Table II.

After oxidation, the level of gold contamination is consistent with cleaned wafers. Sodium is clearly high compared to cleaned wafers for N-type 3 and N-type 2. Two furnaces used for N-type <111> wafers, N-type 1 and 2 in Table II, maintain copper levels similar to cleaned wafers. The remaining four furnaces give evidence of copper contamination. The variations in copper contamination with time for the six furnaces are shown in Fig. 4. The time dependence of sodium contamination is shown in Fig. 5.

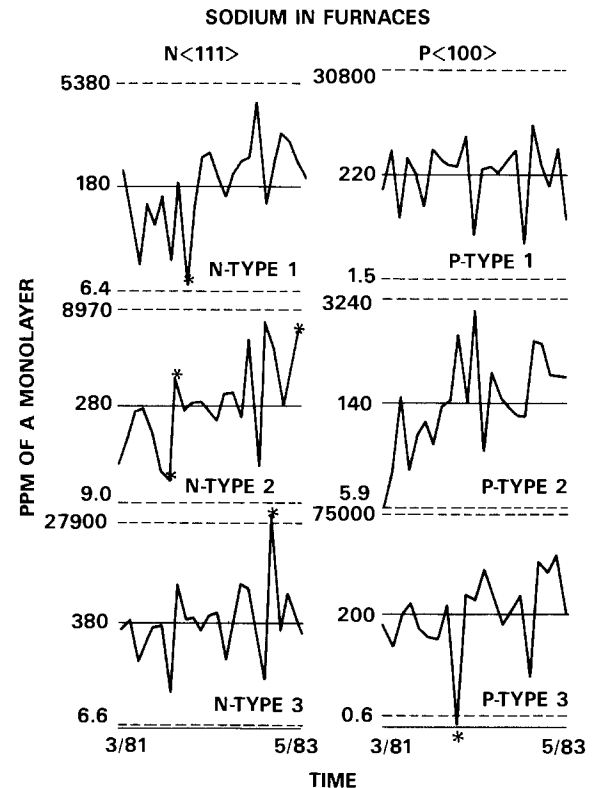


Fig. 5. Variations in time of sodium contamination on pilot wafers processed in six furnaces. The data are for the oxide layer. Three furnaces were used to process N<111> wafers, and three processed P<100> wafers. The vertical scale is logarithmic. Asterisks indicate points which are "out of control" on a statistical basis.

Changes over the test period such as copper in P-type 1 are readily seen, but the t-test used on Fig. 2-3 provides a firm basis for determining when there is a real difference. Figure 6 compares copper observed on the silicon surface for P-type 1 and sodium observed in the oxide layer from P-type 2 in the period March-November 1981 and December 1981-May 1983. The exact month in which

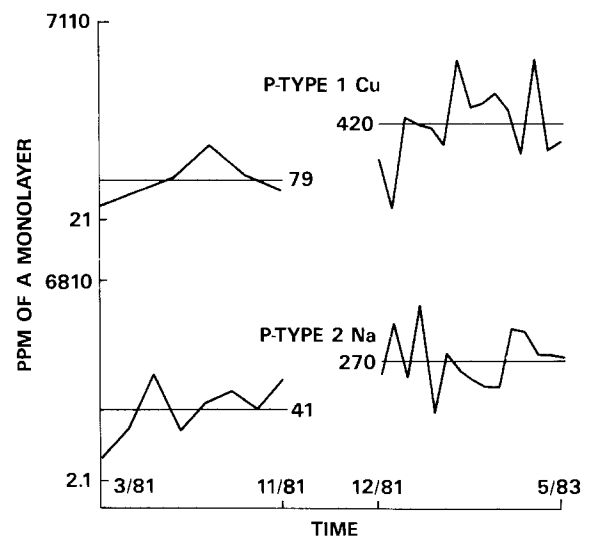


Fig. 6. A comparison of copper and sodium contamination on pilot wafers processed in furnace P-type 1 and P-type 2. The left-hand side represents the period from May 1981 to November 1981. The right-hand side represents the period from December 1981 to May 1983. The date chosen to define subsets of the test period is not exact. The t-test indicates that the level of copper is different for the two time periods with a 90% significance in the short term and 80% significance in the long term. The difference for sodium is 99.9% certain in the short term and 98% certain in the long term. The vertical scale is logarithmic.

Table III. Operating conditions for the six furnaces tested by INAA. Column 1 lists the furnaces. Column 2 lists the gas flowing between the inner and outer quartz liner. Column 3 lists the maximum operating temperature in the center zone in degrees C. Columns 4-7 list the sequence of gasses used in each oxidation

1	2	3	4	5	6	7
N-type 1	Oxygen-HCl	1100	Oxygen	Oxygen-HCl	Nitrogen	Oxygen
N-type 2	Oxygen-HCl	1100	Oxygen	Oxygen-HCl	Nitrogen	Oxygen
N-type 3	Oxygen-HCl	950	Oxygen	Steam	Nitrogen	Oxygen
P-type 1	Nitrogen	900	Oxygen	Steam	Nitrogen	
P-type 2	Oxygen-HCl	1100	Oxygen	^a	Nitrogen	
P-type 3	Oxygen-HCl	1100	Oxygen	^a	Nitrogen	

^a Occasional use of POCl₃.

one period ends and another begins is not clear. The t-test confirms that there is a real difference between the average values for the selected periods. While differences with time were seen for several furnaces, the differences of greatest significance are shown in Fig. 6. The t-tests also show that copper levels in P-type 2 increased between March-November 1981 and December 1981-May 1983 and sodium increased in N-type 1 between March 1981-January 1982 and February 1982-May 1983. None of these changes marked a clear transition from "clean" (as compared to cleaned wafer) to contaminated, as is the case with P-type 1 and P-type 2.

Contamination could arise from the quartz furnace liners, the heating elements (by diffusion through the quartz liners), boats, or rods introduced into the furnace, or ambient gases. INAA tests indicate that the cleanups are not at fault. There is no strong evidence to indicate that the quartz furnace liners are at fault. INAA of quartz confirms this belief (11).

The operating conditions for the six furnaces are listed in Table III. If a diffusion mechanism is the cause of contamination, the furnaces operating at higher temperatures should be most effected. As can be seen in Table III, this is not the case. An oxygen-HCl gas ambient between the inner and outer liner is often used to block such diffusion (12). A comparison of N-type 3 and P-type 1 shows that more contamination resulted when an oxygen-HCl barrier was in use than when it was omitted. This is true for sodium throughout the test period and for copper during the early portion of the test period. The observed trends are opposite of what might be expected if impurity diffusion from sources outside the quartz liner were a major source of contamination for these furnaces.

If ambient gases are a factor, trends in contamination should correlate with column five of Table III, which lists the differences in gases used. With respect to sodium, the most contaminated furnace is N-type 3, followed by N-type 2, and P-type 1. From Table III, the best results for sodium contamination were obtained in furnaces using POCl₃ and oxygen-HCl. Results not so good were obtained in furnaces using oxygen-HCl and steam. For copper, the most contaminated furnace is N-type 3. The next worst is P-type 1, but only for the latter portion of the test period. P-type 2 and 3 show slight copper contamination, and N-type 1 and 2 are consistently clean. Again from Table III, the lowest copper contamination was seen in furnaces using oxygen-HCl and steam. The highest levels of copper contamination occur where steam is used. Slight copper contamination appears where POCl₃ is used.

Summary and Conclusion

Table I indicates that gold, copper, and sodium are the most consistently occurring contaminants, as seen by INAA, followed by antimony and arsenic. Other transition metals such as chromium and cobalt were detected, but not as consistently as copper. It is reasonable to assume that iron and zinc are also present below the detection limit for INAA in these experiments. The levels re-

ported here constitute a base line which production of 2.5-5.0 μm geometry NMOS and PMOS devices tolerated.

The worst results for both copper and sodium correspond to the use of steam. The best results with respect to copper correspond with the use of oxygen-HCl. The removal of copper from a silicon surface requires oxidation and a complexing agent (7). Therefore, oxygen-HCl would be expected to show cleaning action, as these data suggest.

The ambient gases may impact contamination as corrodors, transporters, or cleaners. There is evidence for all three processes in this case. Surface contamination from sodium is water soluble and therefore readily transportable by steam. These results suggest that steam introduces sodium rather than removes it. POCl₃ is not a likely cleaning agent. There is no evidence that it introduces sodium. The mixed results for sodium in furnaces using oxygen-HCl suggests that there was no casual connection with sodium contamination. In the presence of water vapor, either HCl or POCl₃ should initiate corrosion of metals such as brass or steel, or even stainless steel. The corrosion products could then be transported, perhaps as very fine particles by the more common gases such as nitrogen and oxygen.

Acknowledgments

The authors wish to thank R. Martin for the sample preparation, and S. Halfacre and C. Blackburn for the analysis of the activation data. A special debt of gratitude is owed to G. Larrabee for valuable comments and discussion.

Manuscript submitted July 2, 1984; revised manuscript received March 19, 1985.

Texas Instruments, Incorporated, assisted in meeting the publication costs of this article.

REFERENCES

1. F. Girardi, G. Guzzi, and J. Pauly, *Anal. Chem.*, **37**, 1085 (1965).
2. J. A. Keenan and G. B. Larrabee, *Chem. Instrum.*, **3**, 125 (1971).
3. F. DeCorte, A. Speeke, and J. Hoste, *J. Radioanal. Chem.*, **3**, 205 (1969).
4. P. F. Schmidt and D. J. McMillan, *Anal. Chem.*, **48**, 1962 (1976).
5. C. H. Westcott, W. H. Walker, and T. K. Alexander, in "Proceedings of the Second International Conference on Peaceful Uses of Atomic Energy," Geneva 1958, p. 202, United Nations, New York (1959).
6. P. F. Kane and G. B. Larrabee, "Characterization of Semiconductor Materials," pp. 202-209, McGraw-Hill, New York (1970).
7. W. Kern, *RCA Rev.*, **31**, 234 (1970).
8. L. A. Currie, *Anal. Chem.*, **40**, 586 (1968).
9. V. C. Rogers, *ibid.*, **42**, 807 (1970).
10. "Statistical Quality Control Handbook," Western Electric Corp., Indianapolis, IN (1956).
11. P. F. Schmidt and C. W. Pearce, *This Journal*, **128**, 630 (1981).
12. D. R. Fewer, W. L. Gill, H. G. Carlsen, G. A. Brown, and V. Harrap, Contract Report AS30 (602)-3723 RADC (March 1967).
13. A. Ohsawa, K. Honda, and N. Toyokura, *This Journal*, **131**, 2964 (1984).

Self-Compensation in Rapid Thermal Annealed Silicon-Implanted Gallium Arsenide

S. K. Tiku and W. M. Duncan

Texas Instruments, Incorporated, Central Research Laboratories, Dallas Texas 75265

ABSTRACT

This paper describes the regrowth and activation characteristics of Si-implanted GaAs resulting from rapid thermal annealing (RTA) using optical radiation heating. Activation of Si in GaAs by RTA is observed to increase with temperature up to a maximum value, then decrease sharply for additional increases in temperature. The optimum annealing temperature is dependent on both implant dose and annealing time. This activation behavior in RTA time regimes is explained by the competition between kinetic and thermodynamic factors. From Arrhenius plots of the activation data, regrowth under these conditions is shown to be a thermally activated process. Electrical and photoluminescence measurements demonstrate that Si self-compensation limits activation at high annealing temperatures.

Ion implantation has become the most viable method available for controllably and reproducibly introducing shallow conductive layers into GaAs for application to digital and monolithic microwave integrated circuit fabrication. A requisite step in ion implantation processing is a high temperature anneal to reduce the ion damage produced in the crystal during implantation and to activate the implanted dopant. Furnace annealing at about 850°C for 15-20 min with the use of arsenic overpressure or encapsulating layers is normally employed for activating implants. Rapid thermal annealing (RTA) has been shown to yield higher peak carrier concentrations and sharper dopant profiles than furnace annealing (1). More importantly, RTA has greater application for annealing self-aligned n^+ implants in MESFET and HEMT devices and for implanted contact layer activation in other structures where long duration furnace anneals can cause degradation. Silicon has been studied here, as it is the most commonly employed n-type species for GaAs implantation. Because of the amphoteric nature of Si in GaAs, its activation behavior can be strongly dependent on the parameters of the annealing process. In this work, the regrowth and activation characteristics of Si-implanted GaAs and the carrier loss due to self-compensation under RTA conditions are studied and discussed.

Experimental

In the present work, a tungsten halogen lamp system (HEATPULSE, A.G. Associates) was used to activate $^{29}\text{Si}^+$ in semi-insulating LEC GaAs. Figure 1 shows a schematic diagram of the rapid annealing system. An extra quartz plate has been introduced in the system for better uniformity and to collect As lost from slice backsurfaces during anneal. The GaAs wafers were placed face up on a 4 in. Si wafer during the anneal. The temperature was measured using a thermocouple attached to a small Si wafer placed near the substrate. The thermocouple was calibrated using glasses of known melting point (Omegalag, Omega Engineering, Incorporated). Plasma-deposited silicon nitride and reactively sputtered aluminum nitride encapsulants were used; both were about 500Å thick. Both materials had excellent adhesion to GaAs and retained their integrity during anneal. After annealing, the encapsulants were stripped using HF or phosphoric acid to yield undamaged mirror surfaces.

A RF cold cathode discharge source was employed for $^{29}\text{Si}^+$ ion generation from implantation-grade SiF_4 . Diagnostic mass scans of the SiF_4 source plasma were examined to assure ion beam purity. The implants were carried out in a random equivalent orientation to avoid axial channeling. All implants were performed at room temperature. Implant activations were determined using a contactless sheet conductivity probe (Model 1200XR, Lehighton Electronics, Incorporated). For some samples, contactless conductivity values were checked using transmission line (2) and van der Pauw Hall effect (3) measurements. Reported mobility values were also determined

using Hall effect measurements. Photoluminescence (PL) measurements were carried out at 4.2 K using an argon ion laser at 488 nm as the excitation source. Spectra were recorded at 10 W/cm² excitation power densities using a 1m Czerny-Turner monochromator at 0.3 nm resolution. A S-1 photocathode photomultiplier tube and synchronous demodulation electronics were used for signal detection.

Results and Discussion

Figure 2 shows the sheet conductivity vs. temperature behavior of samples implanted over a range of doses, after RTA for 10s. From the figure it can be seen that the Si activation increases to a maximum value and then decreases sharply on the high temperature side of the maximum. The optimum annealing temperature is seen to shift to higher temperature with increasing dose. As lattice damage increases with increasing dose, the optimum anneal time-temperature product is expected to increase with increasing dose. The decrease in activation observed at temperatures above the optimum is more abrupt than is found for furnace anneals where Si activation remains constant or decreases slightly at temperatures above 850°C. Similar behavior is seen in uncapped anneals. However, very high temperatures are not generally used in uncapped anneals for fear of arsenic loss; therefore, the effect is less prominent. This decrease in activation above the optimum temperature in thermal pulse anneals has been attributed to As loss by some authors (1). However, Auger measurements on these samples do not show As in the encapsulant after RTA. Furthermore, photoluminescence measurements do not show any evidence of arsenic vacancies in the RTA samples. The absence of As loss from the front sample surface has been confirmed in both Si_3N_4 - and AlN-encapsulated annealed samples. Activation results are nearly identical for the two encapsulants.

From thermodynamic considerations, the decrease in activation at temperatures above the optimum annealing temperature can be explained due to an increase in Si self-compensation. Under equilibrium conditions, the concentration of Si on Ga, Si(Ga), and Si on As sites, Si(As), is related to the corresponding vacancy concentrations. Thus the ratio, R , of Si on As sites to those on Ga sites is directly related to the ratio of As vacancy, $V(\text{As})$, to Ga vacancy, $V(\text{Ga})$, concentration

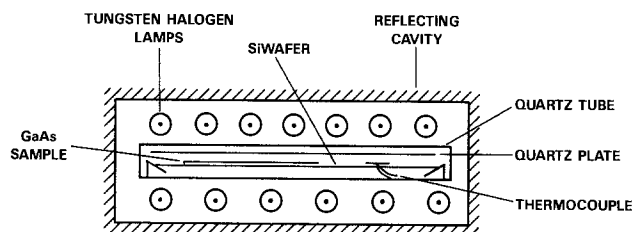


Fig. 1. Schematic diagram of the HEATPULSE annealing system

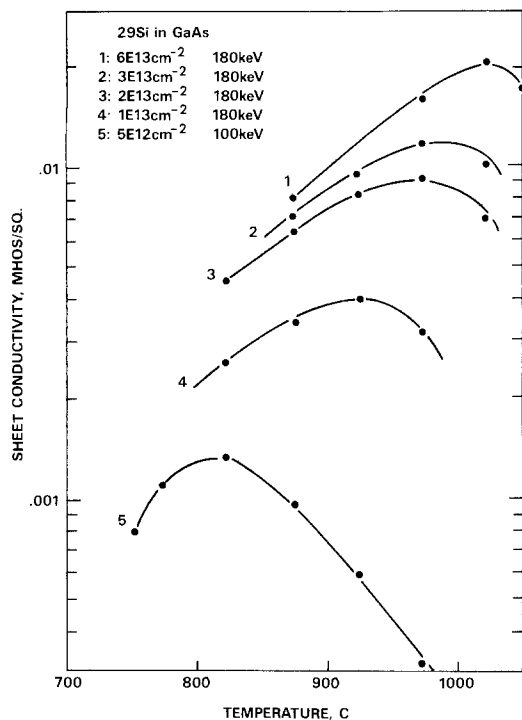


Fig. 2. Sheet conductivity of ²⁹Si implants as a function of anneal for 10s anneals.

$$R = \frac{[Si(As)]}{[Si(Ga)]} \times \frac{[V(As)]}{[V(Ga)]}$$

As excess As vapor pressure is not involved in these anneals, it is assumed that the vacancy concentrations at equilibrium are for the Ga-rich side of the liquidus line. The concentrations of V(Ga) and V(As) under these conditions are given by (4)

$$[V(Ga)] = 3.33 \times 10^{18} \exp(-0.4/kT)$$

$$[V(As)] = 2.22 \times 10^{20} \exp(-0.7/kT)$$

or

$$R = [Si(As)]/[Si(Ga)] = 66 \exp(-0.3/kT)$$

Therefore, at equilibrium, the ratio R increases exponentially as a function of temperature. Regrowth is expected to drive the lattice toward the equilibrium vacancy concentrations. At high temperatures, Si should have an increasing tendency to occupy As sites, and at very high Si concentrations the material should be almost

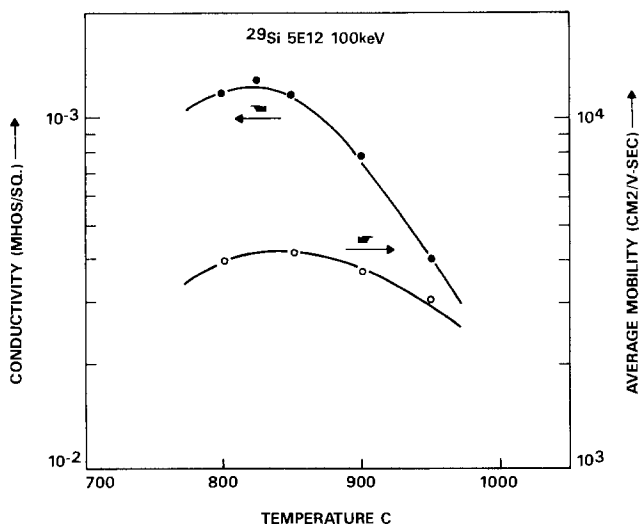


Fig. 3. Conductivity and mobility as a function of annealing temperature for 10s anneals.

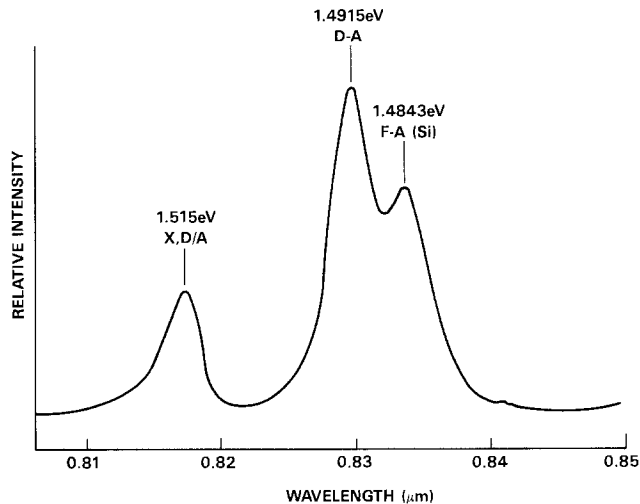


Fig. 4. Photoluminescence spectrum of a sample Si implanted at 180 and 50 keV with doses of 1.25×10^{12} and $0.35 \times 10^{12} \text{ cm}^{-2}$, respectively, after 10s anneals.

fully compensated (5, 6). Transport and photoluminescence measurements demonstrate conclusively that self-compensation is responsible for the decrease in activation on the high temperature side of maximum activation. Figure 3 shows the sheet conductivity and average mobility of a sample after annealing over a range of temperatures. The drop in average mobility which tracks the drop in conductivity confirms an increase in compensation, although the compensation ratio cannot be computed from these data alone (7). Additional confirmation of self-compensation comes from photoluminescence measurements. Figure 4 shows a characteristic PL spectrum of a Si-implanted, RTA sample. The free electron-to-Si acceptor band [F-A(Si)] at 1.4843 eV is of primary interest in the current analysis. The band at 1.515 eV is an envelope of bound exciton states which are not resolvable under these conditions, and the band at 1.4915 eV is donor to acceptor in nature. The Si acceptor band is found to increase monotonically with annealing temperature for a given dose under RTA conditions. This behavior of the F-A(Si) band with RTA temperature is shown in Fig. 5 for two implant conditions.

Figure 6 shows an Arrhenius plot of donor activation vs. anneal temperature for three Si doses. The data fit the Arrhenius form at low temperatures, indicating that silicon activation under RTA conditions is kinetically limited on the low temperature side of the maximum activa-

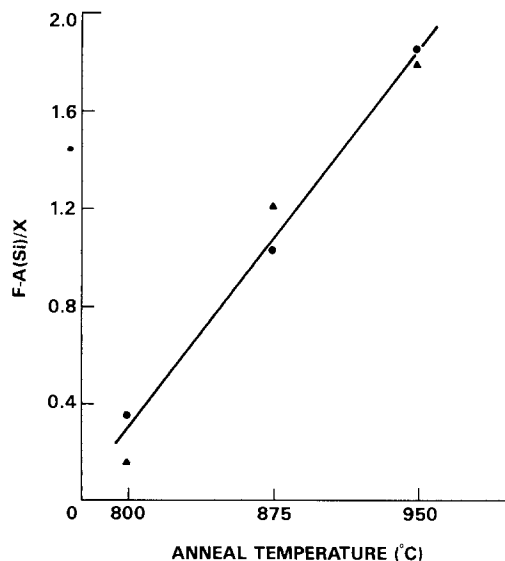


Fig. 5. Free-to-silicon acceptor [F-A(Si)] normalized to bound exciton (X) band intensity vs. annealing temperature for 10s anneals.

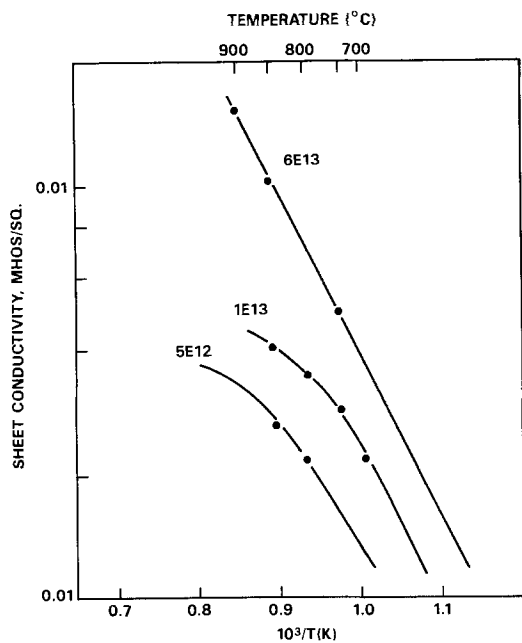


Fig. 6. Arrhenius plot of donor activation vs. anneal temperature for 10s anneals.

tion temperature. The activation energy for the rate-limiting step as determined from Fig. 6 is 0.76 eV. This activation energy cannot correspond to vacancy generation, as the value is too low, and vacancies are present in large numbers in ion-implanted material. Diffusion in the damaged material may be important for maximizing Si donor activation; however, the contribution of enhanced diffusion in damaged material containing local stoichiometric disturbances (8, 9) cannot be assessed, as these activation barriers are not known. Activation energies for self-diffusion and vacancy diffusion in single-crystal GaAs (10, 11) are, however, clearly too large for these processes to contribute to the rate-determining step. The activation energy of 0.76 eV may therefore correspond to local reordering needed for regrowth. In summary, at low temperatures, Si activation is kinetically limited, as is shown by the Arrhenius activation behavior. At high temperatures Si activation does not show Arrhenius behavior, as the Si starts to prefer As sites, because of thermodynamic reasons described earlier. The overall activation behavior of Si in GaAs is a competition between kinetic and thermodynamic factors.

Shown in Fig. 7 is the optimum anneal time needed for maximum donor activation as a function of anneal temperature for a range of Si doses. Also included in the figure are literature data points plotted in the same format. It is interesting that the slope of these lines is nearly equal over the large range of schedules shown in Fig. 6. This is evidence that the activation process is independent of dose and is not affected by damage and stoichiometric disturbances.

Conclusions

This paper provides the first mechanistic explanation of the activation behavior of Si in GaAs as a competition between kinetic and thermodynamic factors. Arrhenius fits of the activation data provide information about the

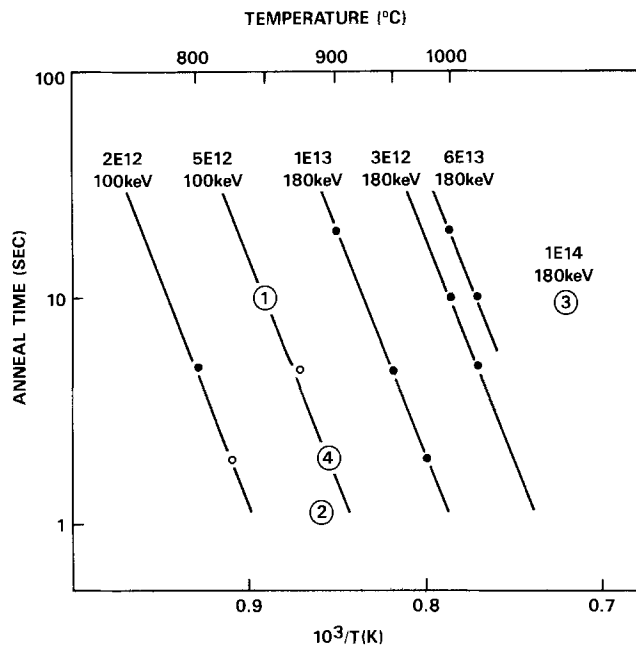


Fig. 7. Optimum anneal times as a function of optimum anneal temperature for a range of Si doses. Numbers enclosed by circles are literature data points.

kinetics of the activation process. Also, guidelines for annealing conditions over a range of implant conditions are presented. Finally, electrical and photoluminescence measurements demonstrate that Si self-compensation limits activation at high annealing temperatures.

Acknowledgment

Discussions with S. E. Matteson, W. V. McLivage, G. H. Westphal, and H. T. Yuan are gratefully acknowledged.

Manuscript submitted Feb. 7, 1985; revised manuscript received June 1, 1985. This was Paper 451 presented at the New Orleans, Louisiana, Meeting of the Society, Oct. 7-12, 1984.

Texas Instruments, Incorporated, assisted in meeting the publication costs of this article.

REFERENCES

1. H. Kohzu, M. Kuzuhara, and Y. Takayama, *J. Appl. Phys.*, **54**, 6998 (1983).
2. J. L. Freehuf, T. N. Jackson, S. E. Laux, and J. M. Woodall, *J. Vac. Sci. Technol.*, **21**, 570 (1982).
3. L. J. van der Pauw, *Philips Res. Rep.*, **13**, 1 (1958).
4. S. Y. Chiang and G. L. Pearson, *J. Appl. Phys.*, **46**, 2986 (1975).
5. F. A. Kroger, "The Chemistry of Imperfect Crystals," Vol. 2, p. 755, North Holland, New York (1974).
6. T. C. Banwell, M. Maenpaa, M-A. Nicolet, and J. L. Tandon, *J. Phys. Chem. Solids*, **44**, 507 (1983).
7. J. S. Blakemore, *J. Appl. Phys.*, **53**, R174 (1982).
8. C. W. Farley and B. G. Streetman, *J. Electron. Mater.*, **13**, 401 (1984).
9. L. A. Christel and J. F. Gibbons, *J. Appl. Phys.*, **52**, 5050 (1981).
10. D. L. Kendall, in "Semiconductors and Semimetals," Vol. 4, R. K. Willardson and A. C. Beer, Editors, p. 163, Academic Press, New York (1968).
11. H. D. Palfrey, M. Brown, and A. F. W. Willoughby, *This Journal*, **128**, 2225 (1981).

Ambient Gas Effects on the Reaction of Titanium with Silicon

Subramanian S. Iyer,* Chung-Yu Ting, and Peter M. Fryer

IBM T. J. Watson Research Center, Yorktown Heights, New York 10598

ABSTRACT

Because of its low resistivity and excellent thermal stability, TiSi_2 is finding widespread application as an interconnect material in novel schemes such as the salicide structure. The Ti-Si reaction is complex and has been studied previously in certain regimes. This investigation shows that the ambience in which the reaction is conducted influences the reaction considerably. We show that after the commencement of the interfacial reaction, *i.e.*, after reduction of interfacial oxides, the initial stage of the reaction proceeds rapidly. The extent to which it proceeds depends on the nature of the Ti ambient gas interaction. A final stage of the reaction begins when the silicide phase and the ambient species phase interfere; the reaction then proceeds relatively slowly at a rate depending on the nature of the ambient species. Some important implications of these observations for device processing applications are pointed out.

Scaling of VLSI devices into the submicron domain, puts increased demands on the contact and interconnect technologies. In MOS devices, one needs to simultaneously reduce the sheet resistance of the polysilicon gate and areas of the single-crystal source and drain diffusions, as well as the contact resistance associated with the source and drain. One method that has been proposed (1) is the self-aligned silicide (salicide) technology. In this method, metal deposited over a FET structure with oxide sidewall insulation along the gate, is reacted with the exposed silicon areas on the source and drain, as well as the exposed polysilicon areas on the gate, to form a silicide. The unreacted metal is then selectively etched away. TiSi_2 proposed by Ting *et al.* (2) and also pursued by Lau *et al.* (3) and Park *et al.* (4), is by far the most promising material for this technology. This is due to its low resistivity, high thermal stability, a demonstrated contact metallurgy, and compatibility with submicron processing technology. We have, therefore, investigated the Ti-Si interaction in more detail in order to determine the important parameters that govern the reaction.

The Ti-Si reaction has been studied in various aspects. Bower and Mayer (5) concluded that the Ti-Si reaction followed diffusion-limited kinetics. Chu *et al.* (6) showed that silicon was the dominant moving species. Recently, Hung *et al.* (7) investigated the reaction with both amorphous and single-crystal silicon in vacuum, and confirmed the diffusion-limited reaction. Bene and Yang (8) and Kato and Nakamura (9) have reported on the phases that are nucleated during the interaction including some metastable phases observed at low film thickness. Butz *et al.* (10) have also reported on the initial stages of silicide formation and silicon motion to the surface in UHV conditions.

It is clear from the above work that the Ti-Si interaction is very complex. This, to a major extent, is due to the extreme reactivity of Ti. As a result, it not only readily absorbs various gases, but can also reduce other compounds (11). Furthermore, analysis of the Ti-Si reaction by conventional means is often rendered difficult because of the nonuniformity of the interface.

This study was undertaken to examine the influence of the ambient gas on the Ti-Si reaction. As is recognized by all workers in the field, the purity of the reacting gas is very important. Impurities such as oxygen have been observed to cause an increase in resistivity of the TiSi_2 film and also reduced thermal stability. However, we have found that the influence of the ambient gas is much more far reaching and subtle. Even so-called inert gases like He appear to exert considerable influence on the nature, rate, and extent of the Ti-Si interaction. The extent of the reaction both in the growth direction and laterally, the dependence on film thickness, and the effect of the ambience on the resistivity discussed in terms of the three-stage reaction model we propose.

Experimental

P-type silicon wafers with a (100) orientation and a resistivity between 2 and 10 $\Omega\text{-cm}$ were used in this study.

*Electrochemical Society Active Member.

The wafers were cleaned using standard processes and dipped in buffered hydrofluoric acid prior to loading in the evaporator. High purity Ti was then evaporated onto the wafers. The base pressure used was about 25 μPa . The substrates were held at 150°C during evaporation. The evaporation was done by resistive heating, the deposition rate was between 0.8 and 1.2 nm/s. Film thickness between 30 and 400 nm were used in this experiment.

The Ti-Si samples were then annealed in an ultraclean furnace. Different ambient gases were used. He that was purified by passing over heated Ti granules, 99.999% pure argon also purified by passing over Ti granules, and house nitrogen were used in this study. The samples were annealed in these ambiences for times between 30 and 120 min at temperatures between 600° and 800°C. In addition, some samples were soaked in nitrogen at 500°C and subsequently annealed in helium. Some general comments regarding the purity of the ambient gas are in order here. Using a residual gas analyzer (mass spectrometer type) it is observed that at high enough flow rates, as used in these experiments, no oxygen is detectable. This translates to less than 10^{-1} Pa partial pressure of oxygen. Clearly, therefore, we cannot exclude the effect of these impurities.

The reacted films were analyzed by Rutherford backscattering spectroscopy, and the amount of silicide phase formed was determined using standard techniques. In the Ti-Si reaction, the various interfaces, which are used to determine the amount of silicide and of unreacted Ti are not easily delineable because of the nonuniformity of the interfaces and the consequent smearing of the backscattering spectra. The nonuniformity of the silicide-silicon interface, easily seen by stripping off the TiSi_2 and also in cross-sectional transmission electron spectroscopy, is believed to arise because of the importance of the nucleation mechanism in the process of silicide formation (16). In order to increase the accuracy of the RBS analysis, we have developed a novel technique of selective etching of the unreacted Ti. In this method, the films are reacted and first analyzed by RBS in the conventional manner,

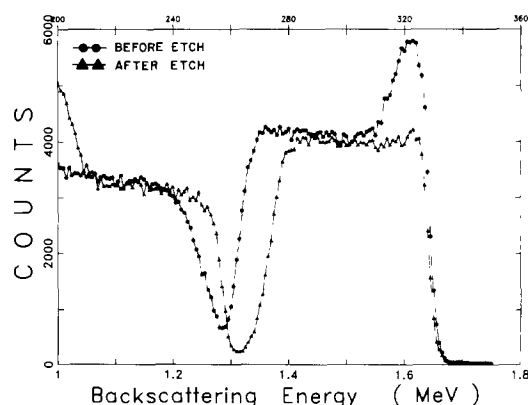


Fig. 1. RBS spectra of 200 nm Ti on Si annealed at 600°C for 120 min.

i.e., the total amount of Ti present is estimated from the number of counts under the Ti peak. The sample is then etched in a selective etch described previously (2) which dissolves all the unreacted Ti, leaving behind only the reacted phase. This is analyzed by RBS again, and the counts under the Ti peak now represent the reacted Ti. Figure 1 shows the RBS spectra for a 200 nm Ti film reacted with Si at 600°C for 120 min, both before and after etching. The clean etching of the unreacted Ti is clearly seen. The etching procedure takes off the nitride phases of Ti (when present) as well.

In addition, we have also monitored the sheet resistance of the reacted films after annealing in various ambient gases at different temperatures and for various spans of time.

Finally, the ambience also influences the lateral formation of silicide which is examined by electron microscopy.

Results and Discussion

On the basis of our studies, we have formulated a model for the Ti-Si interaction in the presence of an ambient species. We shall first present this model and point out the consequences. We shall then present experimental results to support the model including some kinetic data. The effect on resistivity of the film will also be discussed. Finally, the effects of the ambient gas on the lateral formation of TiSi_2 will be discussed.

The model.—We propose that the Ti-Si reaction proceeds in three stages. The first stage is the initiation of the reaction. Since the silicon surface is usually covered with a native oxide, typically 1-2 nm thick, this has to be reduced prior to the direct silicide formation. Generally, the reduction can take place at temperatures below the silicide formation temperature. At the silicide formation temperature, the thin native oxide is consumed quite swiftly; the oxide reduction time depends on the nature of the surface treatment prior to the deposition of the metal.

The second stage of the titanium silicide reaction begins now. Here, we recognize that there are actually two interfaces to consider. This is shown in Fig. 2a. At the bottom, we have the Ti-Si interface, and at the top we have the Ti-A interface, where A refers to the ambient species. At this point, the entire Ti film is substantially free from any ambient gas impurities (other than those which were incorporated during the evaporation of the film and those which diffused in during the first stage). As time proceeds, however, two interactions progress. One, of course, is the Ti-Si interaction at the bottom interface resulting in the formation of the silicide phase. Simultaneously, the ambient gas species interacts with the Ti film at the top interface. The nature and extent of this top interface interaction depends on the species A. We shall discuss this in more detail below. Thus, we have two interactions proceeding from opposite directions towards each other. The final stage of the reaction is when the Ti-Si and the Ti-A phase interact. Of course, the interac-

tion depends on the A species and we recognize that one of three possibilities may occur: (i) the silicide phase grows at the expense of the Ti-A phase; (ii) the Ti-A phase grows at the expense of the silicide phase; or (iii) the two phases interact to form a third new phase. This is shown schematically in Fig. 2d.

The outcome depends on both thermodynamic and kinetic considerations. Our interest here is primarily those situations where the silicide phase grows. The details of this third stage of the reaction depend on the nature of the species A and how well it is bound to the Ti. In the third stage, one needs to recognize that the ambient species may have reacted physically; for instance, it may be in solution. Thus, for example, in the case of nitrogen, which not only dissolves in Ti but also reacts with it to form a variety of phases, the third stage would be much more complex.

We now discuss in more detail the second and third stages of the reaction with the help of our experimental results. This is shown in Fig. 2b, where the pure Ti is bounded by the Ti-A phase on the top and the Ti-Si phase at the bottom. The important characteristic of this second stage of the reaction is that the silicon is reacting with a relatively pure Ti film.

The extent to which this stage of the reaction proceeds depends on how fast the Ti-A interface advances. When the two interfaces meet, as shown in Fig. 2c, this stage of the reaction is terminated.

Helium anneals.—In Fig. 3, we have shown the RBS spectra for a 100 nm film annealed in helium at 600°C for 30, 60, and 90 min, respectively. It is clearly seen that the reaction is not complete even at 90 min. Using backscattered counts under the Ti peak to determine the total amount of Ti and our selective etching method to determine the amount of reacted Ti, we have plotted in Fig. 4 for two different initial Ti thicknesses, the equivalent thickness squared of Ti reacted (which is proportional to the silicide thickness squared) vs. the reaction time. This type of scaling (rather than linear scaling) provides the best fit to our data and indicates a diffusion-controlled reaction. More interesting is the fact that the reaction rate is almost twice as fast for the 200 nm film as for the 100 nm film.

Nitrogen and argon anneals.—In Fig. 5, we show the RBS spectra for a 100 nm film annealed in N_2 at 600°C for 30, 60, and 90 min. In Fig. 6, we show the spectra for annealing at 650°C for the same thickness and times. In this figure, we clearly see a distinct surface phase which was identified by Auger spectra to be nitridized. In the case of argon anneals, we see results very similar to the N_2 case.

The influence of a noble gas species on the Ti-Si reaction is, indeed, quite surprising. It is well known (12) that the noble gas species are unstable in most metals. In fact, the equilibrium concentration of He in Ti at these temperatures is not expected to be significant, although the

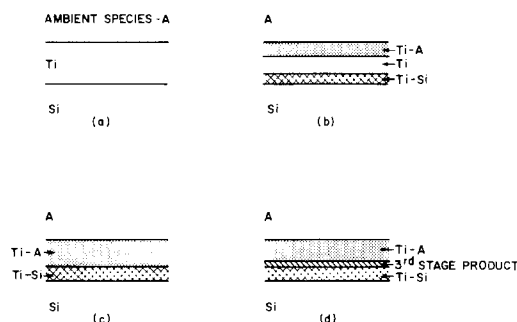


Fig. 2. Schematic diagram of the different stages in the Ti-Si interaction in the presence of an ambient gas. a: Prior to reaction. b: Ti-A interaction and Ti-Si interaction proceed towards each other. c: Ti-A interface meets Ti-Si interface. d: Third stage of reaction.

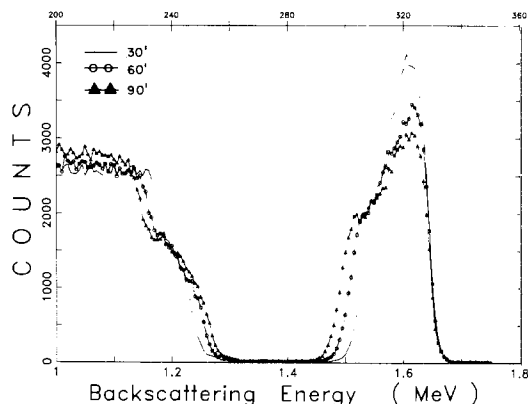


Fig. 3. RBS spectra for 100 nm Ti on Si annealed at 600°C for indicated times (min) in He.

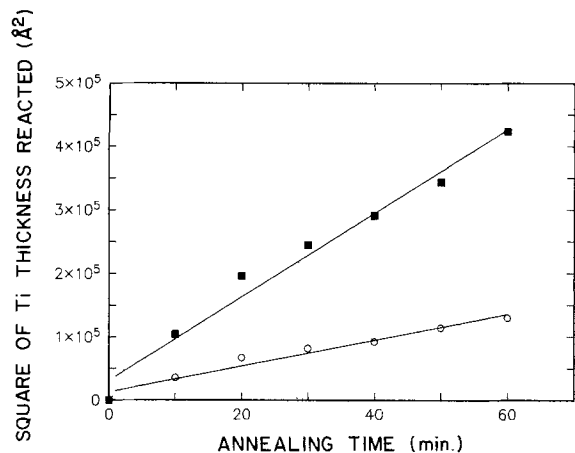


Fig. 4. Square of the amount of reacted Ti plotted as a function of the time, indicating a regime where diffusion-limited kinetics prevail. Squares: 2000Å. Circles: 1000Å.

diffusivity of He through the film may be quite high. Furthermore, it is known (12) that the He atom binds very strongly to vacancies with energies of several electronvolts. Therefore, we can only speculate on the reason for our results. Since the silicide reaction is diffusion limited, the ambient species obviously interferes with Si diffusion through the already formed TiSi_2 , perhaps by tying up vacancy sites. We must not exclude the possibility of unknown impurities causing the observed effects. For example, hydrogen, which can occur in He, has significant solubility (~8%) in Ti (12) and may also produce similar results. Certainly, more experiments are needed to verify the details of the mechanisms involved.

The dependence on thickness in the helium case suggests that the top surface plays an important role. We believe that the top surface is sealed, perhaps by impurities that, unfortunately, always occur in the ambience, in a short time. Thus, the impurity that affects the reaction is trapped in the film and occurs in different concentrations in films of different thicknesses. Thus, thicker films with a lower impurity concentration may react faster. This implies that the Ti-Si reaction in this case occurs predominantly during the third stage.

What is more important is that argon, another inert gas, behaves quite differently. Size differences may play a role here. Although nominally of the same purity, we cannot exclude the probability that argon may contain higher concentration of nitrogen.

The behavior of nitrogen is perhaps most logical. Diffusion of N_2 into the film occurs rapidly to solid solubility limits ~19% (12). Simultaneously, a nitridized phase grows at the surface. Nitrogen occupies interstitial sites in Ti and has been observed to segregate outside the silicide phase (15), similar to the observations of Berti *et al.* (14)

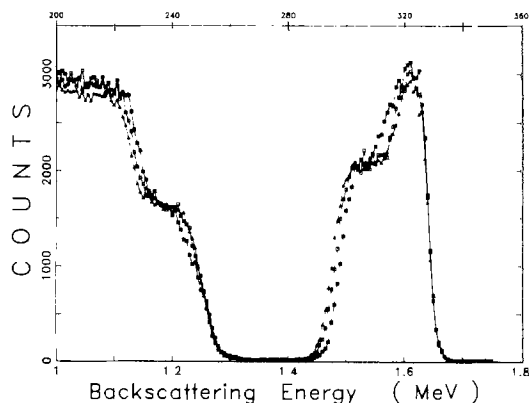


Fig. 5. RBS spectra for 100 nm Ti on Si annealed at 600°C for 30 min (filled squares), 60 min (open squares), and 90 min (triangles) min, respectively, in N_2 .

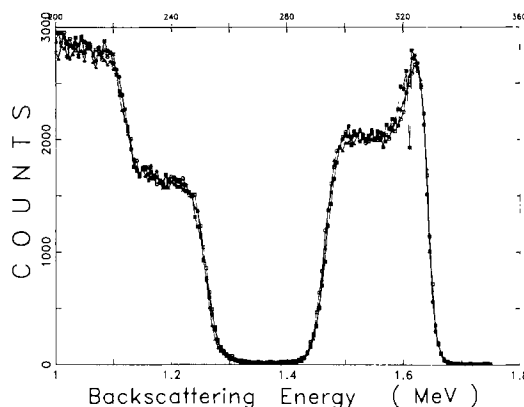


Fig. 6. RBS spectra for 100 nm Ti on Si annealed at 650°C for 30 min (closed squares), 60 (open squares), and 90 (triangles) min, respectively, in N_2 .

for oxygen. The reaction occurs extremely fast until the interface reaches the nitridized phase. Thereafter, the reaction does not proceed at all; in fact, thermodynamic considerations favor the growth of the nitride phase.

Comparison of different ambiances.—Figure 7 shows the RBS spectra for a 100 nm film annealed at 600°C for 30 min in He, N_2 , and Ar. The tremendous impact of the two types of ambiances is clearly seen. In the case of He, the silicide/Ti interface is less clearly defined. The reaction in the case of N_2 and Ar is more uniform. The silicide reaction in the N_2 and Ar cases has also proceeded to a much greater extent. Figure 8 shows the results of an interesting annealing sequence. We first soak the samples at 500°C in nitrogen for 60 min. Figure 8a shows for a 100 nm thick Ti film that the effect of the soak is to convert the top Ti layer into a nitridized phase. This is seen from the decrease in the surface peak of the Ti spectrum. No noticeable silicide phase has formed. In Fig. 8b is shown the RBS spectrum of a 200 nm film annealed in He at 600°C for 30 min and also one when the sample is first soaked in N_2 at 500°C for 60 min and then annealed in He at 600°C for 30 min. It is seen that the soaked sample shows signs of silicide reaction to a greater extent than does the unsoaked one. This is understood from the fact that the nitridized surface layer screens the rest of the Ti layer from the ambient gas (in this case He) and thus extended the second-stage reaction. In Fig. 8c and 8d are shown the spectra after 60 and 90 min annealing, respectively, in He. It is seen that the reaction has proceeded into the third stage. In the case of the nitrogen soak, the reaction has slowed down much more (as would be expected with a strong Ti-N bond) than in the case of the pure He anneals. The reaction continues, until at 90 min the two cases are almost identical.

Effect of film thickness.—The effect of the ambience also introduces a dependence of the extent of the reaction

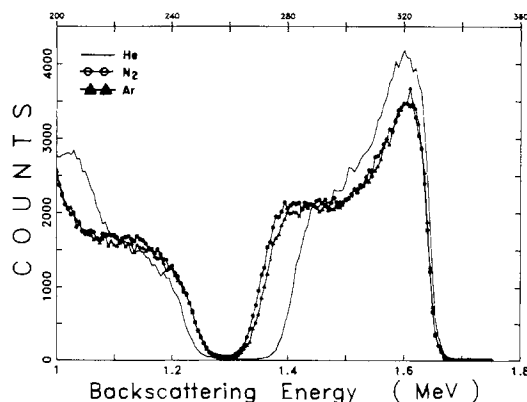


Fig. 7. RBS spectra for 100 nm Ti on Si annealed at 600°C for 30 min in various gases.

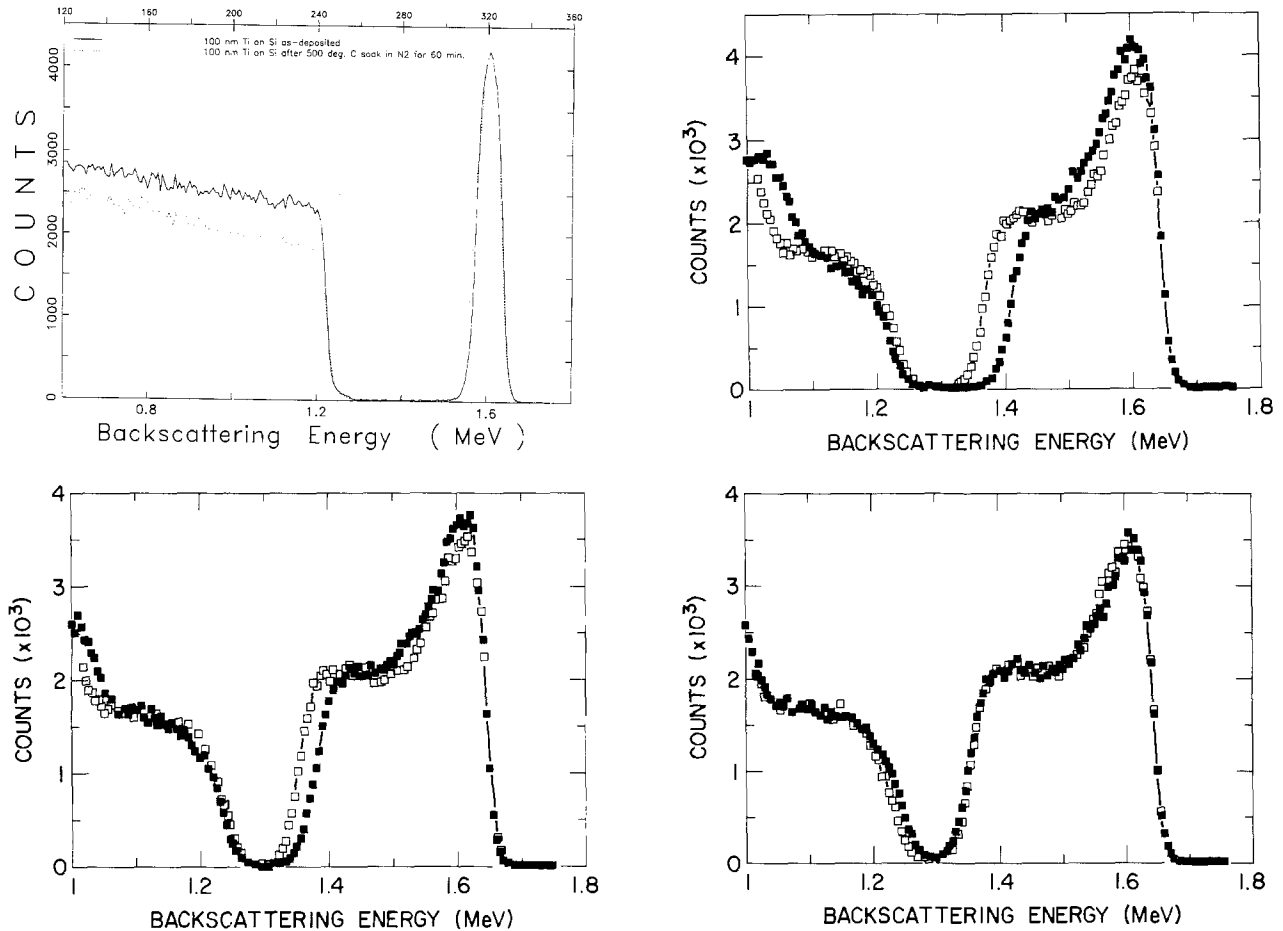


Fig. 8. a: RBS spectra showing as-deposited 100 nm Ti film and after 500°C soak for 60 min in N₂. Note surface nitridation and that no significant silicide phase is formed. b, c, and d: Comparisons of RBS spectra for 200 nm samples annealed in He with (open squares) and without (filled squares) N₂ presoak for 30 min (b), 60 min (c), and 90 min (d) at 600°C. Spectra for the presoaked samples are shifted left by three channels.

on the thickness of the film. This is clearly seen in Fig. 9, where the RBS spectra for 100 and 200 nm thick films annealed in N₂ at 600°C for 30 min are shown. Note that the surface nitridized layer is about the same in both cases. Thus the pure Ti layer is much greater in the case of the thicker film than in the case of the thinner one. In the thermal cycles considered here, we find that the amount of silicide formed is limited only by the nitridized surface phase. We have already mentioned that in the case of He the reaction rate depends on the film thickness which is also the case for films annealed in Ar. Figure 10 shows that by using the selective etching technique of analysis and plotting the Ti counts representing the reacted Ti with film thickness for different thermal cycles. An almost linear increase of reacted Ti on film thickness is seen in the regime investigated. A temperature depen-

dence is also noted, indicating that at higher temperatures thicker films react to a greater extent.

Effect on resistivity.—The sheet resistance of the reacted films is also expected to reflect the effects of the ambience. However, interpretation of the sheet resistance data is not a reliable method of studying the reaction. The aggregate sheet resistivity is sensitive to (i) the amount of the silicide phase, (ii) the extent of the Ti-A phase, (iii) the free Ti, (iv) defects in all of these films, and (v) other unaccounted impurities. Figure 11 shows the sheet resistivity behavior for different thermal cycles and different ambiances for a 200 nm Ti film on Si.

The 600°C data are considered here. In the case of He anneals, a slow but steady drop in sheet resistivity after a slight initial increase is seen. In the case of Ar, the initial increase is not significant and the subsequent drop oc-

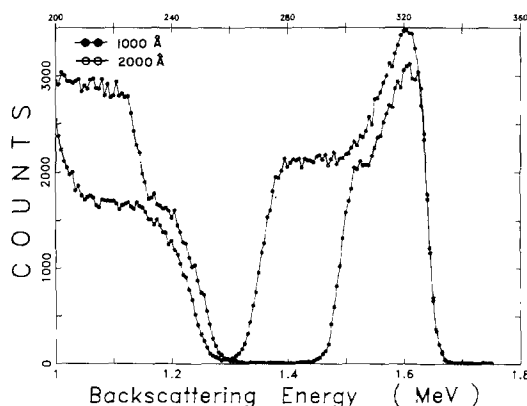


Fig. 9. RBS spectra for Ti films of different thicknesses on Si after annealing at 600°C for 30 min in N₂.

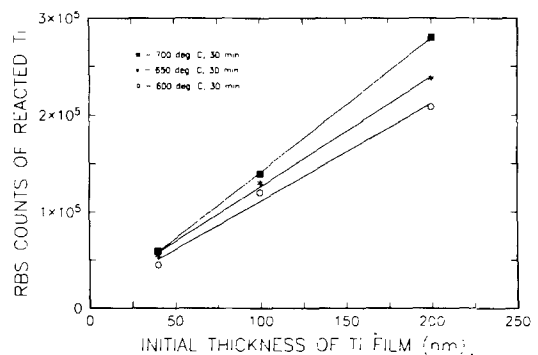


Fig. 10. RBS counts representing reacted Ti plotted against film thickness. Squares: 700°C, 30 min. Asterisks: 650°C, 30 min. Circles: 600°C, 30 min. All anneals were done in argon.

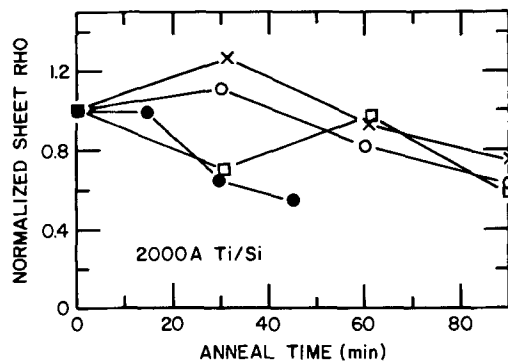


Fig. 11. Resistivity behavior for samples annealed in argon (filled circles), helium (open circles), nitrogen (crosses), and helium after a 60 min soak in nitrogen at 500°C (squares). Final anneals were done at 600°C for 30 min.

curs fairly rapidly. In the case of nitrogen anneals, the initial increase is not seen in the time resolution here. There is first a rapid decrease in sheet resistivity, and then a slower decrease. In the case of He anneals with a pre-anneal nitrogen soak the results are similar qualitatively to that of the nitrogen anneals, as discussed earlier.

The effect on lateral diffusion.—In IC processing, it is necessary to limit the extent of silicide formation to a certain exposed silicon area. This is true in the case of Schottky or ohmic contacts as well as in the silicide case, where lateral diffusion must be minimized to prevent bridging (short circuiting) of the gate with the source or drain areas. The ambience in which the reaction proceeds plays an important role in determining the lateral extent of the reaction.

Consider the situation shown in Fig. 12a, where we have a window in the oxide exposing silicon. Ti is then evaporated over this structure and reacted. While most of the reaction occurs in the window, since the reaction proceeds predominantly by silicon motion, the silicon may diffuse through the already formed silicide laterally onto the oxide, leading to silicide formation there. As we have seen, the diffusivity of silicon as well as the reactivity between Si and Ti is dependent on the nature of the impurity in the Ti film. On the SiO₂, the reaction of silicon is different; the ambient species does not have to compete with free silicon for the Ti. Hence, the Ti film contains much more of the ambient species, and that is well bound. The Ti film on the oxide is thus either stuffed with nitrogen or forms tin on the top and no longer reacts with silicon easily. Consequently, lateral silicide formation is inhibited.

In the case of inert species such as He, we observe that lateral diffusion proceeds fairly rapidly. The presence of impurities such as O₂ in the helium has the effect of slowing the lateral extent of the reaction somewhat, and the conductivity of the TiSi₂ formed is poor. Reactive species have an inhibiting effect on the lateral extent of the reaction.

In this case, a 400 nm film of Ti was used. After reaction, the unreacted Ti was selectively etched away and the samples examined in an electron microscope. This reaction was done at 600°C for 8h. Clearly, there is significantly less lateral diffusion in the case of the N₂ anneals. The inhibiting effect of N₂ over He is also seen in electrical data, and the beneficial effect of N₂ in localizing the reactions has been reported in other laboratories as well (3, 4).

Summary and Conclusions

We have shown that the gas ambience plays a subtle and important role on the Ti-Si interaction. This is due to the extreme reactivity of Ti and also the ability of the interacting ambient species to alter the properties of the film. This results in a reduction of the number of diffusion paths in the Ti, surface passivation of the Ti film as some of the effects of ambience. Consequently, these effects affect reaction rate and extent both in the film and

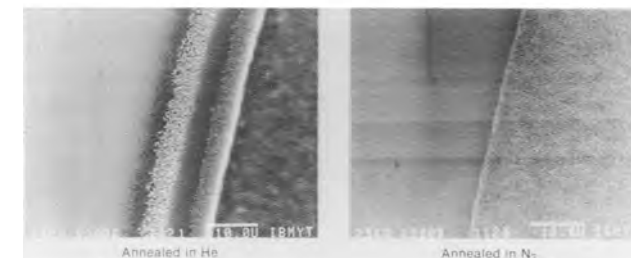
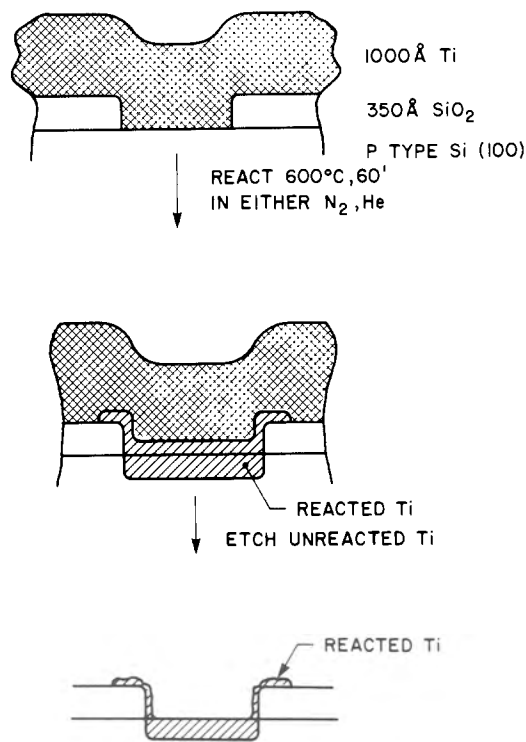


Fig. 12. Lateral formation of TiSi₂. a: Structure. b: SEM micrographs for 4000Å Ti on a 1000Å thick SiO₂ window after 8h at 600°C and Ti etch. The N₂ annealing arrests lateral migration completely, as compared to He annealing. Note that the N₂ annealed surface exhibits a rough surface morphology.

lateral formation as well. They also introduce a thickness dependence.

The effect of oxygen impurities on our interpretations needs to be evaluated more carefully. Our analysis shows that oxygen if present occurs only in trace quantities. Its effect is qualitatively at least, similar to that of nitrogen. We have also observed that oxygen contamination in more than trace amounts results in silicide films with very poor electrical characteristics. The films used in our analysis had excellent electrical characteristics, and the ambient effects we have observed are certainly not attributable to any significant level to inadvertent impurities.

The above effects have an effect on the film quality, resistivity, and thermal stability. For silicide applications, N₂ or N₂-based forming gas are attractive annealing ambiances. They offer the advantage of greater process reproducibility, small sensitivity to impurities in the gas, besides being crucial in preventing lateral diffusion. They also allow for the reaction of a greater part of the film in a given time than helium leading to lower sheet resistivity.

In addition, the above work also stresses the importance of the initial purity of the film and the deposition methods. Silicides formed from films deposited by sputtering usually loaded with the sputtering gas, often Ar, and therefore to have different properties from silicides formed from films deposited by evaporation (sputter deposition are usually preceded by an energetic surface cleaning step, and this must be taken into account). The choice of the gas ambience will be dictated by the considerations discussed in this paper, and proper control of the

ambience is crucial to process reproducibility and reliability.

Acknowledgments

Useful discussions with F. M. d'Heurle are acknowledged with pleasure. The authors would like to thank the Yorktown Silicon Facility, especially S. Brodsky for processing of the films, P. Saunders for the RBS data and R. Savoy for the x-ray microprobe data, and T. Ross for the electron micrographs.

Manuscript submitted March 4, 1985; revised manuscript received June 10, 1985. This was Paper 56 presented at the Cincinnati, Ohio, Meeting of the Society, May 6-11, 1984.

IBM Corporation assisted in meeting the publication costs of this article.

REFERENCES

1. C. M. Osburn, M. Y. Tsai, S. Roberts, C. J. Lucchese, and C. Y. Ting, in "VLSI Science and Technology," C. J. Dell'Oca and W. M. Bullis, Editors, p. 213, The Electrochemical Society Softbound Proceedings Series, Pennington, NJ (1982).
2. C. Y. Ting, S. S. Iyer, C. M. Osburn, G. J. Hu, and A. M. Schweighart, in "VLSI Science and Technology," C. J. Dell'Oca and W. M. Bullis, Editors, p. 224, The Electrochemical Society Softbound Proceedings Series, Pennington, NJ (1982).
3. C. K. Lau, Y. C. Lee, D. B. Scott, J. M. Bridges, J. M. Perma, and R. D. Davies, *IEDM Tech. Dig.*, 714 (1982).
4. H. K. Park, J. Sachitano, G. Eiden, E. Lane, and T. Yamaguchi, *J. Vac. Sci. Technol. A*, **2**, 259 (1984).
5. R. W. Bower and J. W. Mayer, *Appl. Phys. Lett.*, **20**, 369 (1972).
6. W. K. Chu, S. S. Lau, J. Mayer, H. Muller, and K. N. Tu, *Thin Solid Films*, **25**, 393 (1975).
7. L. S. Hung, J. Gyulai, J. W. Mayer, S. S. Lau, and M-A. Nicolet, *J. Appl. Phys.*, **54**, 5076 (1983).
8. R. W. Bene and M. Y. Yang, *J. Electron. Mater.*, **12**, 1 (1983).
9. H. Kato and Y. Nakamura, *Thin Solid Films*, **34**, 135 (1976).
10. R. Butz, G. W. Rubloff, T. Y. Tan, and P. S. Ho, *Phys. Rev. B*, **30**, 5421 (1984).
11. C. Y. Ting, M. Wittmer, S. S. Iyer, and S. Brodsky, in "VLSI Science and Technology/1984," K. E. Bean and G. A. Rozgonyi, Editors, p. 397, The Electrochemical Society Softbound Proceedings Series, Pennington, NJ (1984).
12. A. R. Miedema, *Solid-State Commun.*, **39**, 1337 (1981).
13. H. Conrad, *Prog. Mater. Sci.*, **26**, 131 (1981).
14. M. Berti, A. V. Drigo, C. Cohen, J. Siejka, G. G. Bentini, R. Nipoti, and S. Guerri, *J. Appl. Phys.*, **55**, 3558 (1984).
15. C. Y. Ting, Unpublished data.
16. F. M. d'Heurle, Submitted to *J. Appl. Phys.*

Properties of Tungsten Film Deposited on GaAs by RF Magnetron Sputtering

Nobuhiko Susa, Seigo Ando, and Sadao Adachi

Nippon Telegraph and Telephone Corporation, Musashino Electrical Communication Laboratory, Musashino-shi, Tokyo 180, Japan

ABSTRACT

The crystalline and electrical properties of W films are studied with regard to their relation to Ar sputtering pressure. An α -W phase is formed at a pressure below 5×10^{-2} torr, and its density is 19.2 g/cm^3 , independent of the pressure. Above 5×10^{-2} torr, the β -W phase and WO_3 are detected by x-ray diffraction, and the oxygen and carbon are detected by SIMS. The RIE etching rate is found to be independent of the pressure for the α -W phase. This rate increases with Ar pressure after β -W phase formation, and the etching characteristic suffers from aging after deposition. Resistivity is found to be related to density rather than grain size. The W-GaAs Schottky characteristics are somewhat influenced by the pressure. Degradation in carrier density, barrier height, and dark current caused by sputtering damage can be recovered by annealing.

Refractory metals such as tungsten are attractive for use as interconnections in VLSI's because of their low resistivity and fine patternability (1-4). Recently, W films have also been used as bases embedded in a GaAs epitaxial layer, thus facilitating the fabrication of GaAs permeable base transistors (PBT) (5, 6). In these papers, no changes in W Schottky characteristics were observed at MO-CVD growth temperatures of $600^\circ\text{--}800^\circ\text{C}$ (7). Although W films have received much attention as interconnections for LSI's, only a few studies have been carried out on their electrical properties when applied as Schottky contacts deposited on GaAs (8, 9).

Tungsten films have been fabricated by CVD (10, 11), electron-beam evaporation (12), and sputtering (13, 14). The properties of W films deposited by sputtering are known to depend on the sputtering pressure. In the present experiment, the crystalline and electrical properties of W films prepared by RF magnetron sputtering were studied, especially the characteristics of W Schottky contacts. The observed characteristics were then analyzed in terms of their relations to the Ar sputtering pressure.

Film Deposition and Crystalline Properties

Film deposition.—The W films were prepared by RF magnetron sputtering (ULVAC, SBR-1304E) at an Ar pressure ranging from 1×10^{-2} to 2×10^{-1} torr. Prior to

Ar gas introduction, the chamber was evacuated on the order of 10^{-7} torr with a He cryogenic pump. The W target was cleaned by presputtering for 30 min at 200W. During deposition, the RF power was set at 50W. The substrate bias was 0 V, and no substrate was intentionally heated.

At a 50W input, however, the substrate temperature increased to about 100°C during the deposition. Film thicknesses were measured with a mechanical stylus. The W films on the substrates were partially lifted off by photolithography in order to measure the thickness. Film thicknesses were in the range of $500\text{--}6000\text{\AA}$.

The deposition rate increased with Ar pressure, as shown in Fig. 1a. When the Ar pressure exceeded 1×10^{-1} torr, the deposition rate increased sharply. This is primarily due to the increase in the ion flux rather than the reduction in density, because the films deposited above 1×10^{-1} torr were heavier than those prepared at low pressures for an identical deposition time.

It is well known that stress in W films is compressive at low Ar pressures, while being tensile at high pressures (4). Cracks are sometimes observed in thick W films deposited on GaAs substrates due to this stress. The use of thick films, however, is required to control the device characteristics of a PBT, which has a W Schottky electrode embedded in the GaAs as described before. The existence of cracks was examined in relation to Ar pressure

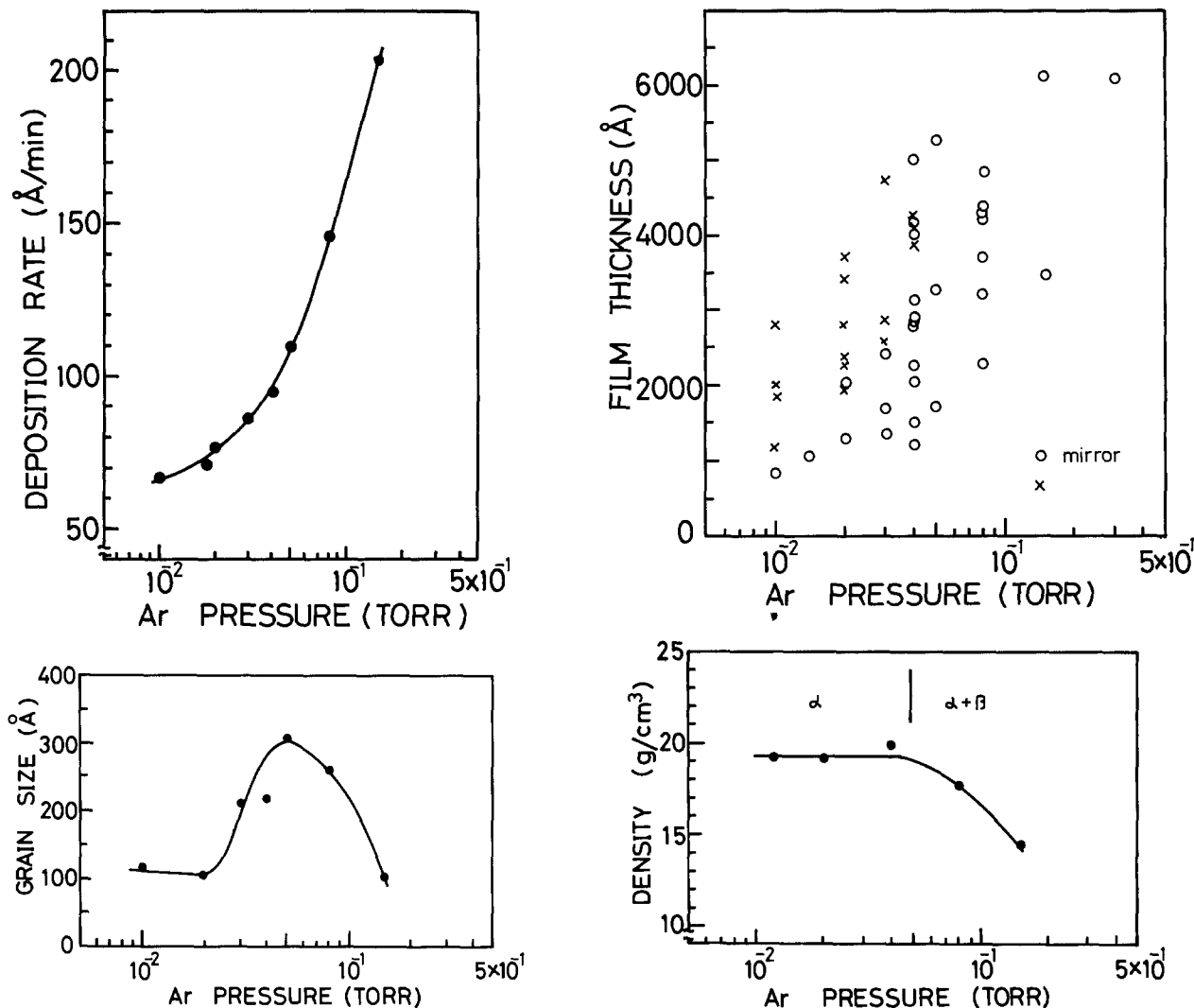


Fig. 1. Deposition rate (a, top left), existence of cracks (b, top right) density (c, bottom left), and grain size (d, bottom right), as functions of sputtering pressure.

and film thickness, and the results are shown in Fig. 1b. Films thicker than 1000 \AA cannot be obtained at low Ar pressures, while thick films containing no cracks can be deposited at higher pressures.

The reason for this is not clear. The substrate temperature rose to about 100°C, even when the substrate was not intentionally heated. Thermal expansion coefficients are 4.2×10^{-6} and $6.0 \times 10^{-6} \text{ } ^\circ\text{C}^{-1}$ for W (15) and GaAs (16), respectively. Since the temperature of the substrate is cooled from 100°C to room temperature after deposition, compressive stress, caused by the difference in thermal expansion coefficients between W and GaAs, is induced in the W films. The compression initially existing in the W film deposited at a low Ar pressure, due to the peening effect, increases during this cooling period. However, tension in the films prepared at the higher pressure was reduced after deposition. The W films deposited at the lower pressures suffer from larger compressive stress and may contain cracks. The densities of the films deposited at the higher pressures were smaller than those for the lower pressure, as will be described in the following section. Films prepared at higher pressures may be porous and may withstand greater stress than films prepared at the lower pressures.

Density and grain size.—Densities of the W films deposited on glass plates are shown in Fig. 1c as a function of the sputtering pressure. The density was obtained from the weight increase and film volume after W deposition. Densities were 19.2 g/cm^3 and were independent of the Ar pressure in the range of 1.5×10^{-2} torr; however, they decreased above this range. The W films were revealed to be in the α -W phase for the Ar pressure of 1.5×10^{-2} torr,

while the β -W phase was formed above 5×10^{-2} torr, as shown in Fig. 2.

The smaller density obtained for the high Ar pressure is related to the existence of the β phase rather than the grain size. This is because the W films having the α phase and prepared at 1.2×10^{-2} torr showed a large density of 19.2 g/cm^3 even when the grain size was small, as shown in Fig. 1d. However, the existence of the β phase alone cannot explain the lower density, as described below. The α -W phase has a body-centered cubic structure with a 3.16 \AA lattice constant. The β -W phase structure is an A-15-type structure having a 5.04 \AA lattice constant, and is body-centered cubic having two atoms on each of its {100} planes (17). Densities calculated from the above parameters for the α and β phases are quite similar: 19.4 and 19.1 g/cm^3 , respectively. Thus, the presence of the β phase alone cannot cause the lower density.

Since WO_3 has a lower density than that of metal, it is possible that the WO_3 , which was always detected by x-ray diffraction for samples consisting mainly of the β -W phase, is responsible for the low density. The larger deposition rate may also cause the low density by making the deposited film porous.

The grain sizes of the W films were determined from x-ray line broadening analysis and are plotted in Fig. 1c. The (110) α phase diffraction patterns were used for analysis. The grain size became small when the β -W phase was formed, as reported in a previous paper (14). Grain size, however, was also small for the films prepared at 1.2×10^{-2} torr, in spite of the presence of the α -W phase. The influence of grain size on resistivity will be discussed later.

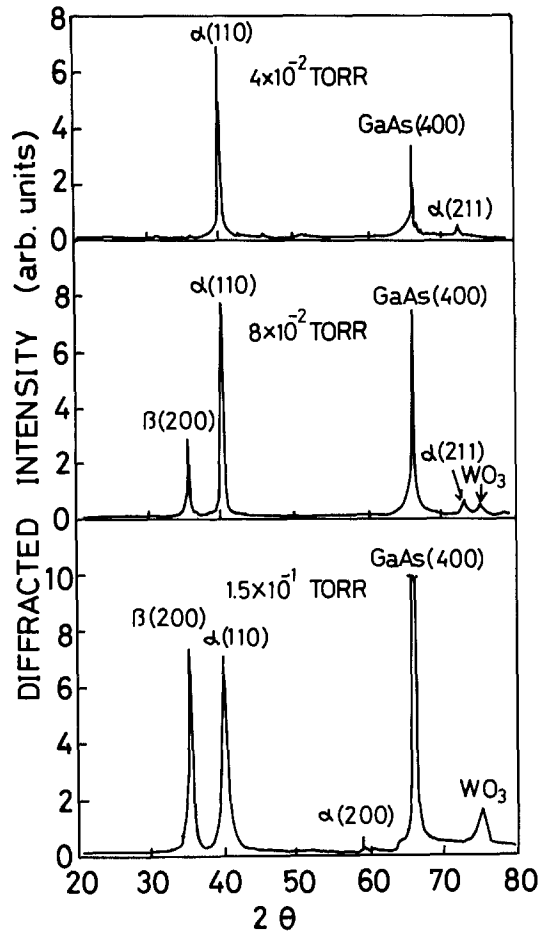


Fig. 2. X-ray diffraction patterns for W films deposited on GaAs at 4×10^{-2} , 8×10^{-2} , and 1.5×10^{-1} torr.

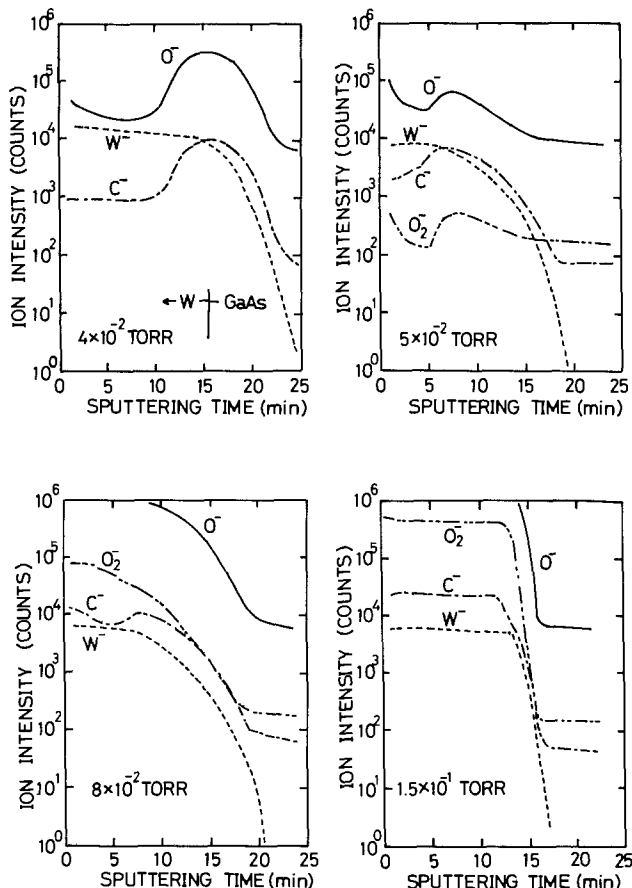


Fig. 3. Impurity profiles measured by SIMS for W films prepared on GaAs at 4×10^{-2} , 5×10^{-2} , 8×10^{-2} , and 1.5×10^{-2} torr.

Orientation and impurity. The x-ray diffraction pattern for the W films deposited on GaAs changed when the Ar sputtering pressure was varied, as shown in Fig. 2. Below a 5×10^{-2} torr Ar pressure, diffraction from the $\alpha(110)$, $\alpha(211)$ planes was observed. The intensity ratios of $\alpha(211)$ to $\alpha(110)$ x-ray diffractions were 0.08 and 0.2 for the present experiment and for the ASTM data on W powder, respectively. This implies that the films deposited at below 5×10^{-2} torr were well oriented in the $\langle 110 \rangle$ direction.

The $\beta(200)$ diffraction was observed for films prepared at above 5×10^{-2} torr, and WO_3 diffraction also was observed. The WO_3 was always detected when the β -W phase was formed. These results are consistent with previous reports suggesting that oxygen stabilizes the β phase (12, 13, 18). Etching characteristics, density, grain size, and impurity content changed owing to the existence of the β -W phase, as will be described below.

Impurities in the W films deposited on the GaAs such as oxygen and carbon were analyzed by secondary ion mass spectroscopy (SIMS), and the films were bombarded by a Cs^+ ion beam. The bombarded area was $60 \mu\text{m}$ in diameter. The results are shown in Fig. 3. The W films with a $2000\text{-}6000\text{\AA}$ thickness were sputtered by Cs^+ ions. Data on the W-GaAs interface were not very accurate, because the W film surface, sputtered by the Cs^+ ions, became rough during the sputter etching. When the W film was deposited at a high Ar pressure, oxygen and carbon contents increased. In particular, oxygen increased rapidly with an increase in the Ar pressure. The existence of oxygen was also detected by the x-ray diffraction as a part of the WO_3 .

At the W-GaAs interface, C and O concentrations were large, as in the case for GaAs epitaxial layers grown on a GaAs substrate. They are probably due to the existence of the GaAs surface oxide layer and also due to C contamination before W deposition.

For the application to device fabrication, the etching rate for reactive ion etching (RIE) using CF_4 was studied with respect to the W deposition pressure dependence. The etching rate for RIE is shown in Fig. 4 as a function of pressure. The W films were etched under the conditions of 50W and 10 Pa (7.5×10^{-2} torr). The etching rate was constant for the W films deposited at below 5×10^{-2} torr Ar pressure and was independent of time after deposition. On the other hand, the etching rate increased with an increase in the sputtering pressure above 5×10^{-2} torr. This etching rate, however, decreased after 2 months. The etching rate increased when the β -W phase was formed and the film density decreased. Although the reason for the reduction in the etching rate after 2 months is not clear, it seems to be related to the existence of the β -W phase.

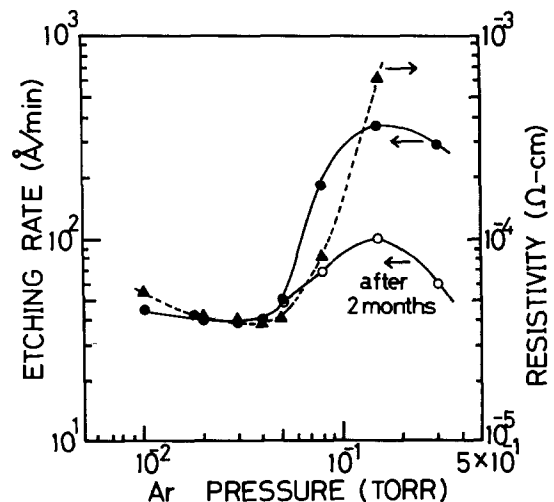


Fig. 4. Etching rates of RIE measured immediately after and 2 months after W deposition and resistivity, as functions of sputtering pressure.

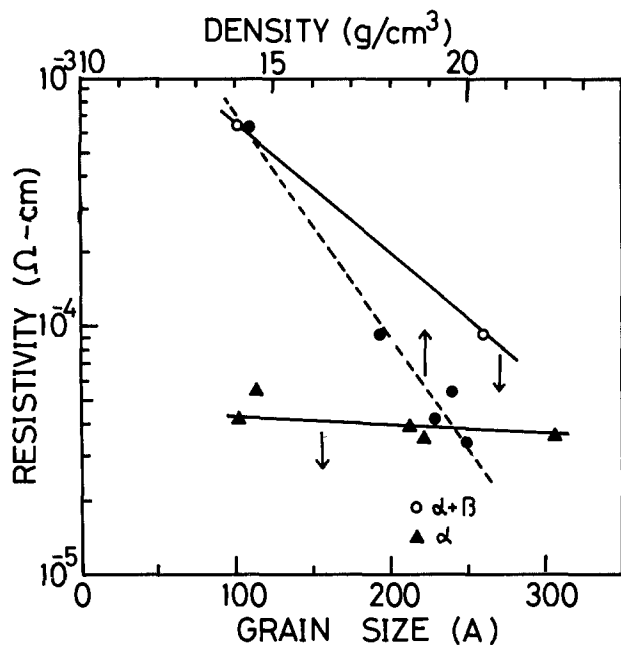


Fig. 5. Resistivity as a function of density and grain size

Electrical Properties

Resistivity.—The resistivity of W films deposited on semi-insulating GaAs is also shown in Fig. 4. A four-point probe was used for the measurement. These results were similar to those for W films prepared on glass plates. The α -W films exhibited lower resistivity than those in the β -W phase (14, 19). Resistivity decreased slightly when the deposition pressure increased in the range of $1\text{--}2 \times 10^{-2}$ torr. This was probably due to the smaller grain size as shown in Fig. 1c.

Resistivity is plotted in Fig. 5 as a function of W film density. It can be seen that resistivity is related to the film density as well as volume fractions of β - and α -W phases.

Figure 5 shows resistivity as a function of grain size calculated from the x-ray diffraction pattern. Data for the α -W phase are somewhat influenced by the grain size, contrary to a previous report (14). The resistivity is $5 \times 10^{-5} \Omega\text{-cm}$ when grain size is extrapolated to zero. Since this value is larger by about one order of magnitude than that for the bulk, it is concluded that scattering resulting from impurities and defects is larger than that caused by the grain boundary.

Schottky characteristics.—When the W film is applied to devices such as a PBT, Schottky characteristics are important for realizing good device performance. Tungsten film was deposited on a GaAs epitaxial layer grown on a

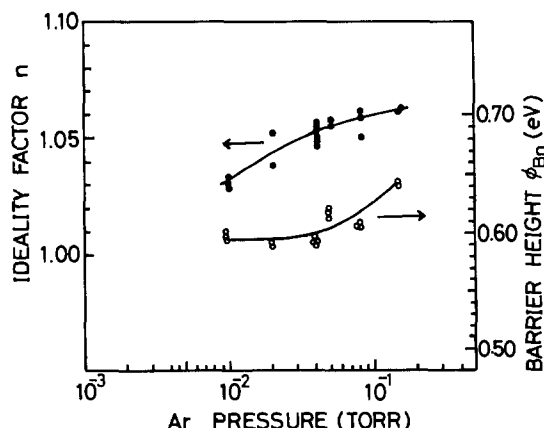


Fig. 6. Ideality factor and barrier height as a function of sputtering pressure.

n^+ -GaAs substrate. The epitaxial layer was $2.6 \mu\text{m}$ thick, and its carrier concentration was $1 \times 10^{17} \text{cm}^{-3}$. Ohmic contacts (alloyed Au-Ge-Ni) were formed on the n^+ -GaAs substrates. A W Schottky contact of $200 \mu\text{m}$ diam was deposited through metal mask. Ideality factor, n , and barrier height, ϕ_{Bn} , obtained from the forward current and voltage characteristics (20), are shown in Fig. 6. The ideality factor increased from 1.03 to 1.06 when the sputtering pressure was varied from 1×10^{-2} to 2×10^{-1} torr. However, the barrier height was 0.6 eV, and was constant in the range of $1\text{--}5 \times 10^{-2}$ torr, where the α -W phase existed. The barrier height increased to 0.64 eV for a 2×10^{-1} torr Ar pressure.

Leakage currents for diodes were larger at a reverse bias voltage by several orders of magnitude than those for diodes with a Au Schottky contact prepared by Au vacuum evaporation. The carrier concentration profile, calculated from the C-V characteristics, showed that the carrier density decreased at the W-GaAs interface as a result of sputtering damage to the epitaxial layer surface during the deposition. In order to improve the crystal quality, an attempt to anneal GaAs deposited with W film was carried out at 430°C .

Annealing.—The GaAs diodes having W Schottky contacts were annealed at 430°C in a 10% H_2 -90% He gas flow.

Carrier concentration profiles obtained from the C-V characteristics are shown in Fig. 7. A sample was annealed for 3 min at 430°C . The carrier density was reduced at the W-GaAs interface by sputtering damage for the as-deposited diodes. After annealing, the reduction in the carrier was recovered by performing a relatively short annealing process.

Dark currents for diodes with as-deposited and annealed (2 min) W contacts as well as a reference (Au Schottky) contact are shown in Fig. 8a as a function of reverse bias voltage. The dark current can be reduced by about one order of magnitude as a result of annealing. However, no further dark current reduction was observed for annealing of over 2 min. The dark currents for annealed diodes, however, were still larger than those for the reference.

Forward currents for diodes with as-sputtered and annealed W contacts are shown in Fig. 8b. The W film was prepared at 4×10^{-2} torr. Data for the diode having the Au evaporated Schottky contact are also shown for reference. The barrier height increased from 0.55 to 0.61 eV owing to annealing. A similar improvement in barrier height has been reported by Sinha (9). The barrier height obtained from the I-V characteristics agreed with that calculated from the C-V characteristics. However, barrier height for as-deposited diodes calculated from the C-V characteristics (0.66 eV) was higher than that obtained from the I-V characteristics (0.55 eV). The values obtained

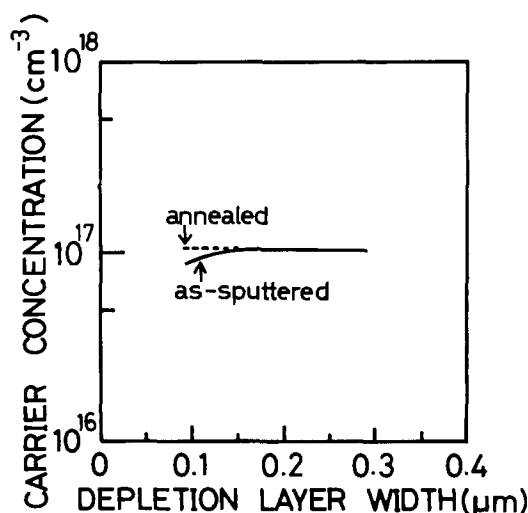


Fig. 7. Carrier concentration profiles for GaAs diodes with as-sputtered and annealed W contacts.

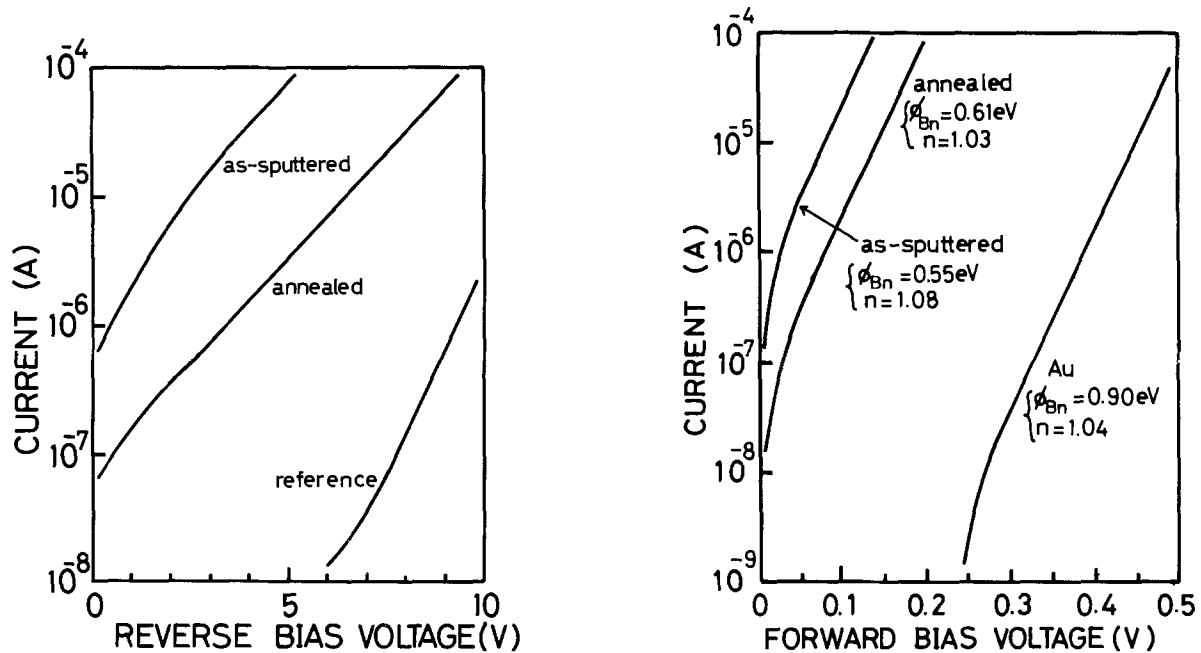


Fig. 8. Reverse (a, left) and forward (b, right) currents for diodes with as-sputtered and annealed W Schottky contacts as functions of bias voltage. Currents for diode having Au evaporated Schottky contact are shown for reference.

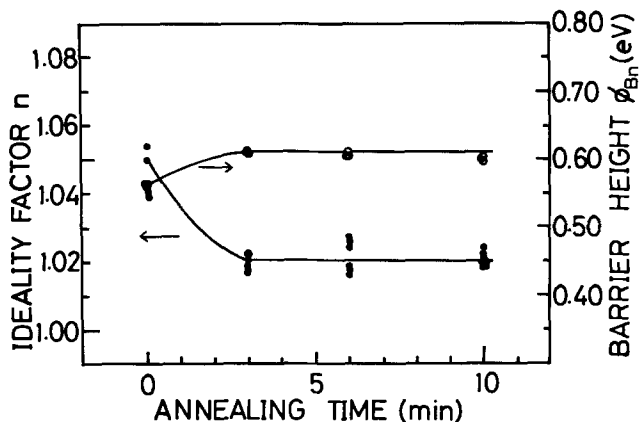


Fig. 9. Ideality factor and barrier height as a function of annealing time.

from the C-V measurement became much larger than those for the C-V characteristics when the damage was seriously increased. This suggests that an insulator layer was formed by sputtering deposition (21).

The ideality factor decreased slightly from 1.08 to 1.04 owing to annealing. No further improvement in the ideality factor or barrier height was observed for a heat-treatment of longer than 3 min, as shown in Fig. 9.

Conclusion

Properties of W films deposited by RF magnetron sputtering were investigated in terms of their relation to Ar sputtering pressure, which ranged from 1×10^{-2} to 3×10^{-1} torr. Below 5×10^{-2} torr, an α -W phase was formed and the density was 19.2 g/cm^3 , independent of the Ar pressure. The β -W phase and WO_3 were detected by x-ray diffraction for films prepared at pressures above 5×10^{-2} torr. Oxygen and carbon contained in the W films as impurities increased with the pressure. The RIE etching rate was found to be independent of the pressure for the α -W film. This rate increased with an increase in β -W phase content in W films and was dependent on time after deposition.

Resistivity increased sharply when the volume fractions for the β -W phase and WO_3 were increased. Density rather than grain size was found to affect the resistivity.

The Schottky characteristics of W-GaAs diodes were studied. The barrier height and ideality factor were in-

fluenced somewhat by the sputtering pressure. Degradation of barrier height, carrier concentration, as well as the increase in dark current due to sputtering damage, can be recovered by carrying out annealing at 430°C for 2-3 min.

Acknowledgments

The authors would like to express their gratitude to Dr. Kenji Kamabe, Dr. Hideo Sugiura, and Dr. Yoshifumi Takanashi for their helpful discussions. They are also grateful to Hiromitsu Asai for the x-ray diffraction measurements and Yoshikazu Homma for the SIMS measurements.

Manuscript submitted Dec. 27, 1984; revised manuscript received May 22, 1985.

Nippon Telegraph and Telephone Corporation assisted in meeting the publication costs of this article.

REFERENCES

1. P. L. Shah, *IEEE Trans. Electron Devices*, ed-26, 631 (1979).
2. A. K. Sinha, *Jpn. J. Appl. Phys.*, Suppl. 2, 487 (1974).
3. S. Iwata, N. Yamamoto, N. Kobayashi, T. Terada, and T. Mizutani, *IEEE Trans. Electron Devices*, ed-31, 1174 (1984).
4. R. S. Wagner, A. K. Sinha, T. T. Sheng, H. J. Levinstein, and F. B. Alexander, *J. Vac. Sci. Technol.*, 11, 582 (1974).
5. C. O. Bozler and G. D. Alley, *IEEE Trans. Electron Devices*, ed-27, 1128 (1980).
6. H. Asai, S. Adachi, S. Ando, and K. Oe, *J. Appl. Phys.*, 55, 3868 (1984).
7. K. Matsumoto, N. Hashizume, H. Tanoue, and T. Kanayama, *Jpn. J. Appl. Phys.*, 21, L393 (1982).
8. P. M. Batev, M. D. Ivanovitch, E. I. Kafediiska, and S. S. Simeonov, *Phys. Status Solidi A*, 45, 671 (1978).
9. A. K. Sinha, *Appl. Phys. Lett.*, 26, 171 (1975).
10. W. A. Metz, J. E. Mahan, V. Malhotra, and T. L. Martin, *ibid.*, 44, 1139 (1984).
11. C. M. Melliar-Smith, A. C. Adams, R. H. Kaiser, and R. A. Kushner, *This Journal*, 121, 298 (1974).
12. B. Basavaiah and S. R. Pollach, *J. Appl. Phys.*, 39, 5548 (1968).
13. P. M. Petroff and W. A. Reed, *Thin Solid Films*, 21, 73 (1974).
14. P. Petroff, T. T. Sheng, A. K. Sinha, G. A. Rozgonyi, and F. B. Alexander, *J. Appl. Phys.*, 44, 2545 (1973).
15. "Metal Handbook," American Society for Metals, Metals Park, OH (1948).
16. M. E. Straumanis and C. D. Kim, *Acta. Crystallogr.*, 19, 256 (1965).
17. W. R. Morcom, W. L. Worrell, H. G. Sell, and H. I.

- Kaplan, *Metall. Trans.*, **5**, 155 (1974).
 18. C. C. Tang and D. W. Hess, *Appl. Phys. Lett.*, **45**, 633 (1984).
 19. D. W. Hoffman and J. A. Thornton, *Thin Solid Films*, **45**, 387 (1977).
 20. S. M. Sze, "Physics of Semiconductor Devices," pp. 279-284, Wiley-Interscience, New York (1981).
 21. J. R. Waldrop, *Appl. Phys. Lett.*, **41**, 350 (1982).

An Experimental and Theoretical Study of the Infrared Reflectance of Thin Oxide Films on Metals

David K. Ottesen

Sandia National Laboratories, Livermore, California 94550

ABSTRACT

External reflectance infrared spectroscopy has been used to study the formation of oxide films on chromium and iron alloys. Experimental data have been acquired with an FTIR spectrometer using a polarized beam at high angles of incidence to the surface normal. Theoretical calculations have been made for these systems and are compared with the experimental results. Particular attention is given to the quantitative calculation of film thickness. Complications which arise from distortions in band shape, frequency shifts, the appearance of additional reflectance minima, and beam divergence and state of polarization are discussed in detail.

This paper presents an experimental and theoretical study on the applicability of Fourier transform infrared (FTIR) reflectance spectroscopy for the study of oxide films formed on binary iron-chromium alloys. A thorough understanding of these results is a vital step leading to the study of more complex ferrous alloys, such as the stainless steels. The quantitative study of metal alloy oxidation and corrosion using this technique requires a detailed understanding of the physical processes governing the optical properties of such layered systems. We have also sought to determine the effect of nonidealities, such as the roughness of films and substrate, and variations in experimental parameters, such as the angle of incidence, beam divergence, and state of polarization.

Infrared spectroscopy has played an increasingly important role over the past few years in the chemical characterization of surfaces. In particular, external reflection spectroscopy at large angles of incidence has been of special value in examining thin, dielectric films on metallic substrates. The usefulness of this technique was first noted by Berreman (1) and later popularized by Greenler under the name "reflection-absorption spectroscopy" (2,4).

Reflection-absorption spectroscopy has much in common with ellipsometry, another surface-sensitive optical technique. While both approaches utilize linearly polarized light, visible wavelength ellipsometry has generally been acknowledged to be the more sensitive technique to small changes in surface coverage. This is due to the clearly observed changes in phase angle of light reflected from a substrate covered by a dielectric film only a few angstroms thick. This advantage, however, has been offset somewhat by recent developments in double-modulation FTIR reflectance spectroscopy (5).

The outstanding advantage of reflection-absorption spectroscopy lies in the positive identification of chemical species in surface films through the spectral structure in the observed reflectance. In general, ellipsometry suffers from the lack of spectral data in single wavelength measurements, with the consequent assumption of surface species and their optical constants. Even scanning ellipsometric measurements in the visible region can be relatively featureless, resulting in unavoidable ambiguities in the determination of surface species (6).

Reflection-absorption spectroscopy has been successful in a large number of recent qualitative investigations. Interest has centered primarily on the characterization of chemisorbed gases (5, 7) and thin layers of organic compounds deposited on metals (7-13). Reference (7) is a particularly useful review article of results up to 1976.

Investigations of inorganic thin films on metallic substrates have also been numerous (1, 4, 14-24). These results are qualitatively quite different from the studies of chemisorption and thin organic films. The interpretation of the resulting reflectance spectra for these systems is complicated by distorted band shapes and frequency shifts for thin films when compared to absorption spectra of the pure, bulk material. This behavior is generally caused by the large values of refractive index and absorption coefficient associated with the absorbing film and the metallic substrate and the complex interaction of these optical properties with the electric field of the incident infrared beam. In addition to our own experimental work on metal oxides, we will draw on earlier spectroscopic studies of the high temperature oxidation of iron (14, 18) and chromium (24).

Theoretical

We will adopt the nomenclature of Heavens (25) in our treatment of the interaction of light with a thin film on a bulk substrate. This is shown for an n -layer film in Fig. 1. Here n_m and k_m are the refractive index and absorption coefficient, respectively, d_m is the thickness of the layer, and Φ_0 is the angle of incidence, while Φ_m ($m > 0$) is the angle of refraction within a layer, m . For absorbing media, we also note that the refractive index and angle of refraction are in general complex. In this case, the so-called complex refractive index is defined as

$$\hat{n}_m = n_m - ik_m \quad [1]$$

The amplitude of the electric field both incident and reflected from this system of layers can be expressed by solving Maxwell's equations in terms of these quantities. Using the boundary conditions that the tangential components of both the electric and magnetic vectors be continuous at each layer interface, we arrive at the expression shown in Eq. [2] and [3] for the ratio of the electric field amplitudes in the plane where layer m is in contact with layer $m + 1$

$$E^-_{mp}/E^+_{mp} = [(\hat{n}_m \cos \Phi_{m+1}) - (\hat{n}_{m+1} \cos \Phi_m)] / [(\hat{n}_m \cos \Phi_{m+1}) + (\hat{n}_{m+1} \cos \Phi_m)] \quad [2]$$

$$E^-_{ms}/E^+_{ms} = [(\hat{n}_m \cos \Phi_m) - (\hat{n}_{m+1} \cos \Phi_{m+1})] / [(\hat{n}_m \cos \Phi_m) + (\hat{n}_{m+1} \cos \Phi_{m+1})] \quad [3]$$

These ratios are more commonly known as the Fresnel reflection coefficients, r_{mp} and r_{ms} , where P and S refer to the polarization of the light. The change in phase of the

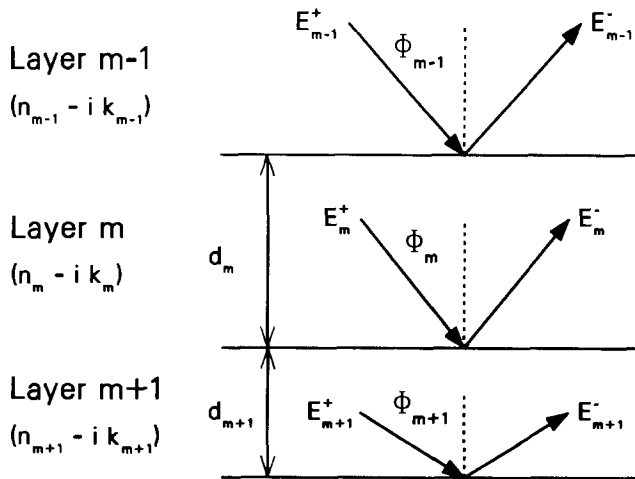


Fig. 1. Nomenclature for reflectance in a multilayer system

light, δ_m , within layer m as a function of wavelength, λ , is defined as

$$\delta_m = (2\pi/\lambda)\hat{n}_m d_m \cos(\Phi_m) \quad [4]$$

For a single absorbing layer on a substrate, the reflected electric field amplitude can then be expressed

$$\mathcal{R} = [r_1 + (r_2 e^{-2i\delta_1})]/[1 + (r_1 r_2 e^{-2i\delta_1})] \quad [5]$$

where it is understood that \mathcal{R} will be appropriate for either P- or S-polarized light, depending upon the values of the Fresnel coefficients used in Eq. [5].

The experimentally measured reflectance is the energy of the reflected beam, and this is related to \mathcal{R} by

$$R = \mathcal{R}\mathcal{R}^* \quad [6]$$

We have written a computer program to calculate the reflectance as a function of optical constants for up to three absorbing dielectric layers on an absorbing substrate. The method can be easily extended to additional layers, since Eq. [5] is evaluated from a product of matrices, each matrix corresponding to one layer in the film. Values for the refractive index and absorption coefficient are supplied for each layer and the substrate. The films may be either optically isotropic or anisotropic. In the case of an anisotropic medium, however, the Fresnel coefficients must be redefined (Eq. [2] and [3]). These relations are given in Ref. (25) and they are, as that author states, "complex and depressingly complicated." Other input data are the angle of incidence and state of polarization of the infrared beam. These are determined by the experimental conditions which are discussed below.

We have also included the capability of averaging the calculated reflectance over a number of angles of incidence to simulate an incident beam which has been focused to a small image on the sample surface. In these calculations, we assume that our experimental infrared source is a lambertian emitter. This implies that the intensity of the light incident on a sample at an angle θ from the principal optical axis will be attenuated by a factor equal to $\cos \theta$. The divergence of the infrared beam from the optical axis is determined experimentally for each set of auxiliary reflectance optics.

A provision has been made to model losses in the reflected light due to scattering on a rough surface by including a frequency dependent term. The effect of scattering is especially noticeable in the decrease of reflectance with increasing wave number. Our data are fit well by multiplying the calculated reflectance at a given frequency by a term which is proportional to $1/[1 + (c\nu)^2]$, where c is a constant. Since the size of the crystallites formed on the metal surfaces is, at most, on the order of a few micrometers in our study, this behavior of the scattering coefficient is in good agreement with previous studies of diffuse reflectance (26). This approach is simi-

lar to that taken by Allen and Swallow in their study of oxide films on Cr substrates (24).

Another characteristic of real thin films is a variability in the layer thicknesses. Our model takes this into account by performing a weighted average of calculations for a given distribution of layer thickness. The general effect of this refinement is to broaden and shift the position of reflection minima. Particularly striking changes may occur for various spectral features, and this is discussed in some detail for iron oxide films.

The calculated reflectance is optimized with respect to the experimental data by varying the order of the layers, their thicknesses, and the coefficient in the scattering term. For situations where good data were available for the optical constants of the absorbing layers, the use of experimental measurements at different angles of incidence and polarization produced rapid and unambiguous fits of the observed spectra.

Experimental

Specular reflectance of oxidized metals and alloys was measured using a Digilab FTS-14 spectrometer equipped with a CsI/Ge beamsplitter, TGS detector, and wire grid polarizers. This arrangement permitted a usable bandwidth of 250-1500 cm^{-1} . Two auxiliary optical attachments were used to provide a single reflection at angles of incidence of 22° and 73° relative to the surface normal. Mounting the sample holder on translation stages allowed the precise centering and focusing of the incident beam on the sample. The minimum dimension of the beam on the sample was 4-6 mm, depending on the focusing optics. Half-angles of divergence for the two attachments were 20° and 12°, respectively (21). All data presented here were acquired with a spectral resolution of 4 cm^{-1} .

Samples were prepared from the following high purity metals and metal alloys [all percentages are given as weight percent (w/o)]: Cr, Fe-10% Cr, and Fe-15% Cr. After being cut to a typical 12 mm square size, the samples were polished to at least 600 grit finish and ultrasonically cleaned in acetone. Pure chromium substrates were oxidized in air at 700°C, while the Fe-10% Cr and Fe-15% Cr binary alloys were oxidized in air at 850°C. Oxidation times varied from a few minutes to several hours.

Reference reflectance spectra were obtained using either unoxidized metal samples polished to a 600 grit finish, or first surface mirrors of gold or aluminum. The use of gold or aluminum reference mirrors is preferable for calibration purposes, since the reflectance values for these materials are well known and are very close to 1. However, this approach sometimes produced a residue of uncompensated curvature and structure in the base line due to nonlinear aberrations in the reflectance attachment optics. In those cases, ratioing sample spectra to that of an unoxidized substrate gave relative reflectance values in which the spectrometer instrument function was largely eliminated.

The experimental reflectance values we present in this paper are those data which exhibited the least uncompensated instrument function. They have been scaled linearly so that nonabsorbing regions of the spectrum at low wave number yield reflectance values in agreement with our theoretical calculations. This normalization procedure may produce a systematic offset of the base line by a few percent, but should have little or no effect on the relative behavior of the absorbing regions of the spectrum.

Results and Discussion

Theoretical calculations for single-phase thin films.— Before considering the complexities of real thin films with many absorption modes, it is profitable to note the effect of angle of incidence, film thickness, and state of polarization on the reflectance of a simple, single-phase thin film. It is important to be aware of these relationships since the resulting reflectance of a highly absorbing oxide film may result in rather bizarre "distortions" of band shape and position.

For the purposes of illustration, we consider a hypothetical material having two active infrared modes with

Table I

Resonance center (cm^{-1})	Damping constant (cm^{-1})	Band strength
400	15	0.30
600	25	0.05

the optical properties shown in Table I. These values are representative of many metal oxides. We calculate n and k values as a function of wave number using the classical dispersion equation

$$e = e_1 - ie_2 = e_\infty + \sum_j \frac{4\pi\rho_j\nu_j^2}{(\nu_j^2 - \nu^2) + i\gamma_j} \quad [7]$$

and the relation of the refractive index and absorption coefficient to the dielectric constants

$$\hat{n} = n - ik = (e_1 - ie_2)^{1/2} \quad [8]$$

In this formulation, e_∞ is the value of the high frequency dielectric constant, ν_j is the frequency at the band center, ρ_j is a dimensionless band strength, and γ_j is a constant damping coefficient associated with mode j . Values of n and k used for the substrate are those of metallic chromium (27). This is perhaps the simplest model for deriving values of n and k from the optical constants, and it has the advantage that the damping constants can be related to bandwidths at half-height for the imaginary portion of the dielectric constant, e_2 . Calculated values for n and k are shown in Fig. 2.

We calculate the reflectance for a P-polarized beam at normal incidence for three different thicknesses as shown in Fig. 3. The two thinner films produce reflection minima near the mode centers, as one would intuitively expect. We do observe a shift in the band centers toward lower energy as the thickness increases from 0.5 to 1.0 μm . The film of 2.0 μm thickness, however, produces additional minima which have no apparent connection with the two specified vibrational modes. In addition, no reflectance minimum is observed at the 600 cm^{-1} mode center of the second band. This situation becomes more confusing and complex as the thickness of the layer increases.

As pointed out by Swallow and Allen (23), this phenomenon is caused by the rapidly changing values of n and k in the region of the mode centers. As the value of n increases, interference due to multiple reflections occurs, and for sufficiently thick films one or more fringes may be observed near the band centers. This effect should always be considered as a possibility when complex spectral features appear as surface films increase in thickness. The assumption that additional observed bands are due to different chemical species may not be warranted in many cases.

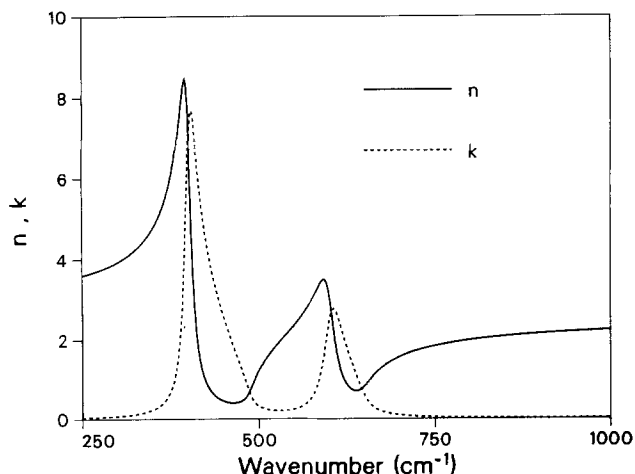


Fig. 2. Calculated values of n and k for a hypothetical material with two infrared active modes.

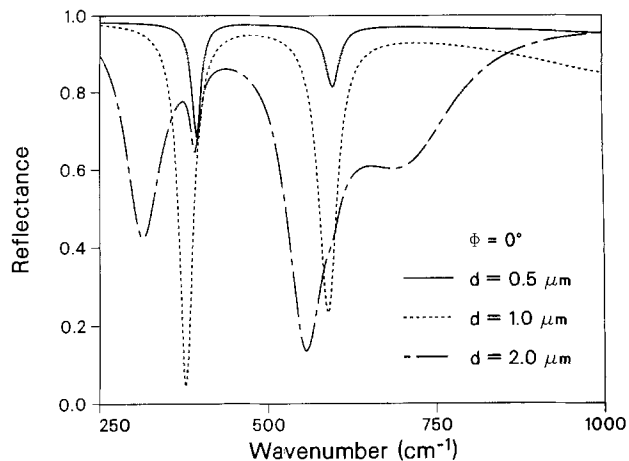


Fig. 3. Calculated P-polarized reflectance of a thin film showing the effect of layer thickness.

Swallow and Allen present a detailed and lucid examination of these effects and their dependence on mode frequency, band strength, and damping coefficient, and the reader is referred to their article (23). Their treatment is based on approximate equations for normal incidence, however, and they did not consider the effects of angle of incidence and state of polarization. These variables profoundly influence the resulting reflectance, and they are examined below.

The effect of angle of incidence is shown in Fig. 4. We consider here films of 0.5 μm thickness and a P-polarized beam incident at angles of 0° , 22° , and 73° (the latter two values corresponding to our experimental conditions). Two additional reflection minima appear and grow in intensity as the angle increases from normal incidence. Berreman (1) has shown that these features are coincident with the longitudinal optic (LO) phonon modes which are infrared forbidden for bulk crystalline material at any angle of incidence. The boundary conditions imposed by the thin film-substrate geometry on Maxwell's equations allow these modes to be observed as reflection minima for P-polarized light when the angle of incidence is greater than zero.

These additional modes are not predicted to occur for either polarization at normal incidence. Hence, some authors who have used simpler, approximate equations for reflectance at normal incidence (23, 24) have found it necessary to postulate a scattering effect in order to produce these minima. This is not necessary, since they are a natural consequence of reflectance calculations at non-normal incidence for P-polarized light at even rather small angles of incidence. Thus the straightforward re-

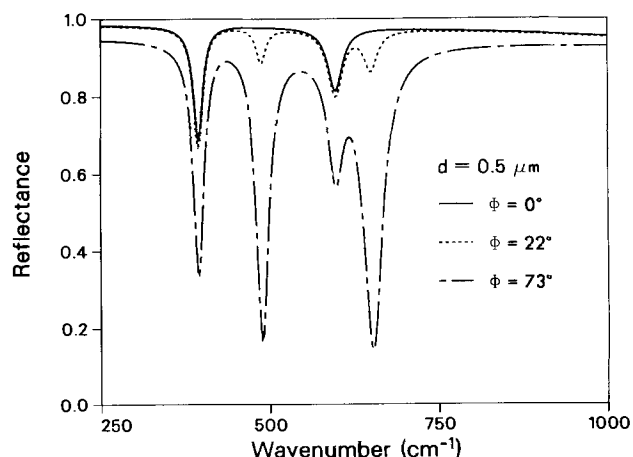


Fig. 4. Calculated P-polarized reflectance of a thin film showing the effect of angle of incidence.

flectivity equations for normal incidence are not adequate to interpret all features of the experimental results.

Experimental measurements for chromium oxide forming alloys.—Accurate determinations of optical constants are available for several transition metal single-phase oxides. We have used previous work on metal oxides for our calculations on Cr_2O_3 (28) and Fe_2O_3 (29), and data for chromium and iron metals (27).

Reflectance spectra at near-normal incidence for Cr_2O_3 grown on bulk chromium substrates by thermal oxidation in air have been reported by Allen and Swallow (24) for relatively thick films (0.3–7.5 μm), and by Mertens (18) for films between 0.05 and 0.4 μm thick. In fitting their experimental data, Allen and Swallow found it necessary to modify the literature values of optical constants for chromium oxide given by Renneke and Lynch (27). These changes were quite small and resulted in a set of constants which effectively assumed that the oxide was isotropic in its optical properties. We have also measured the reflectance of thermally grown oxide films on chromium substrates in the same thickness range as Mertens. Estimates of thickness were made by weight-gain measurements and ranged from 0.04 to 0.40 μm .

Reflectance measurements for these very thin films were made using P-polarized light at an angle of incidence of 73° . Agreement with Allen and Swallow's results for films of 0.4 μm thickness at near normal incidence is relatively good, with the exception of the intensity of the band at 735 cm^{-1} . Since this band is coincident with an LO optical phonon, its intensity is expected to greatly increase with increasing angle of incidence as shown above. Our data agree more closely with those of Mertens, and this is expected since he utilized an experimental angle of incidence similar to ours.

The set of optical constants used by Allen and Swallow also fit our observed data very well over the entire range of thickness, and a plot of experimental and calculated spectra are shown in Fig. 5 for a thickness of 0.39 μm . Optical constants for metallic chromium (27) were used for the substrate. Agreement between calculated and measured frequencies and their relative intensities is quite good for these films. The observed bands, however, are generally broader than their calculated counterparts and are asymmetric. Broadening reduces the observed splitting between bands near 415 and 600 cm^{-1} , and the 735 cm^{-1} band is noticeably asymmetric on the low energy side.

Other investigators have pointed out (25) that this broadening probably stems from large anharmonicities in the thin film lattice modes in contrast to bulk crystals from which the optical constants were taken. These differences tend to arise from imperfections in the oxide structure and may broaden the lattice phonons considerably. Band asymmetry has been shown (1) to result from the use of a frequency-dependent damping term, $\gamma(\nu)$, in

contrast to the constant term used in Eq. [7] above. This results from the rapid fluctuation in the value of γ near the mode center. Furthermore, large changes of γ in regions not near lattice mode frequencies resulted in the observation of weak reflection minima for a thin film of LiF on silver (1). This may be an additional cause of the pronounced asymmetry in the 735 cm^{-1} band for our thin Cr_2O_3 films.

The calculated thickness for a given film may be obtained in a straightforward manner by the comparison of the theoretical and experimental minimum reflectance for several bands. This is a rather simple process for very thin films where the base line is well defined. However, for increasingly thicker layers it becomes more difficult to precisely locate the base line in the region of the strong bands (for instance, see Fig. 5). Our experimental data for the thicker chromium oxide films generally possess a rather flat character in the transparent regions below 400 and above 800 cm^{-1} , and linear base lines were drawn connecting these two regions.

Some authors (18) suggest that a logarithmic relation (analogous to absorbance) in some cases would offer a linear correlation with film thickness. In Fig. 6, we show a plot of calculated $-\log R_{\min}$ values for the band near 735 cm^{-1} . Evidently, a linear increase in this function does exist for films thinner than 0.1 μm . This reflectance function goes through a maximum for films near 0.18 μm , and gradually rolls off with increasing thickness.

We also present experimental data for oxide films grown on bulk chromium in air at 700°C . These are given in Fig. 6 as circles, and they also exhibit an initial linear region with a slope identical to that of the theoretical plot. A positive linear offset in the measured film thickness from the theoretical curve is clearly observable. The thicknesses for these films were calculated from weight gain measurements, and it is quite probable that enhanced growth at the sample edges caused an overestimation of the average thickness on the flat surface. This seems especially likely in that the experimental values do not extrapolate to 0.03 (the value for bare chromium) at thickness equal to zero. We therefore attribute the systematic positive offset in experimental points from the theoretical curve to this cause.

In performing these calculations for thin films, it is of crucial importance to include the effects of infrared beam divergence. Most experimentalists use a highly focused beam in order to improve sensitivity and minimize sample dimensions by reducing the spot size to a few millimeters in cross section. This means, however, that the infrared radiation will be incident on the sample over a range of angles rather than a single value. The theoretical curve presented in Fig. 6 was evaluated using an angle of incidence of 73° and a half-angle of divergence of 12° . The effects of disregarding beam divergence are shown in Fig. 7. The reflectance minimum is extremely sensitive to the

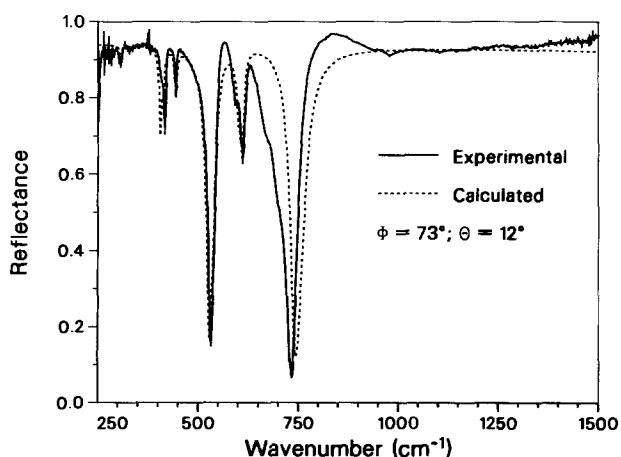


Fig. 5. Experimental and calculated P-polarized reflectance of 0.39 μm film of Cr_2O_3 on Cr.

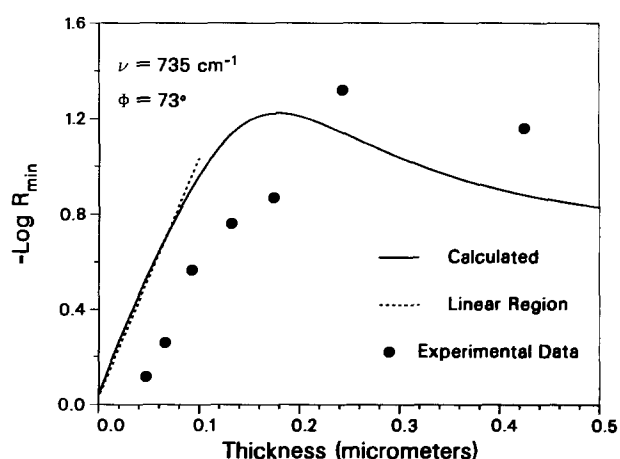


Fig. 6. Experimental and calculated P-polarized reflectance for the 735 cm^{-1} band of Cr_2O_3 on Cr.

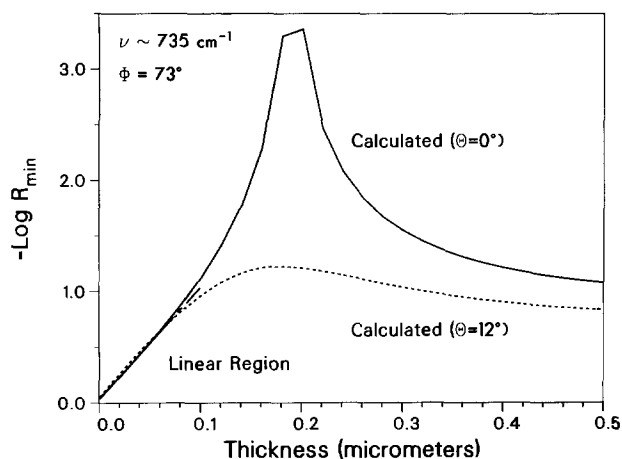


Fig. 7. Calculated P-polarized reflectance for the 735 cm^{-1} band of Cr_2O_3 films on Cr showing the effect of beam divergence.

angle of incidence, and the value of $-\log R_{\min}$ is shown to strongly increase around a thickness of $0.18\ \mu\text{m}$ for a beam which is collimated at 73° angle of incidence.

Other bands in the reflectance spectrum also exhibit characteristic increases in intensity with film growth, and they may also be used to calculate film thicknesses. In Fig. 8, we show the composite theoretical and experimental behavior for three vibrational modes: the mode coincident with the bulk LO phonon discussed above, and two transverse optic (TO) modes near 530 and 415 cm^{-1} .

The 530 cm^{-1} mode seems to be especially well suited for thickness determinations. Indeed, the scatter in experimental data for films greater than $0.2\ \mu\text{m}$ thick is considerably less than that for the much more intense 735 cm^{-1} band discussed above. We note, however, that this band exhibits a very different characteristic behavior and shows no linear region of growth for $-\log R_{\min}$. Although the data for the band near 415 cm^{-1} also seem to agree well with theory, its use is more problematic for two reasons. First, it is of quite low intensity, and, second, it is a "forbidden" mode (27) and shows a considerable intensity variation in relation to the other bands depending on the conditions of film preparation.

Finally we observe that for layers thinner than $0.05\ \mu\text{m}$, only the band at 735 cm^{-1} is observed with any substantial intensity. Thus any departure of the film's optical constants from the input values will have a serious effect on calculated thicknesses since only one band is being fit.

Air oxidation of Fe-15% Cr alloys at high temperatures tends to form an oxide scale which is predominantly Cr_2O_3 . The P-polarized reflectance spectrum of the sample heated for 3h is shown in Fig. 9. The resemblance

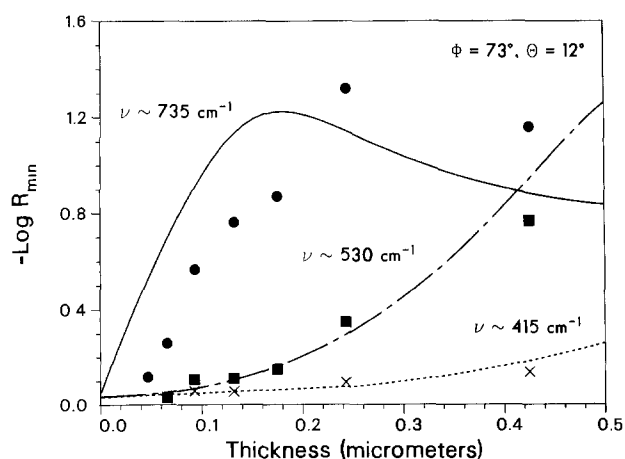


Fig. 8. Calculated P-polarized reflectance for three bands of Cr_2O_3 films on Cr.

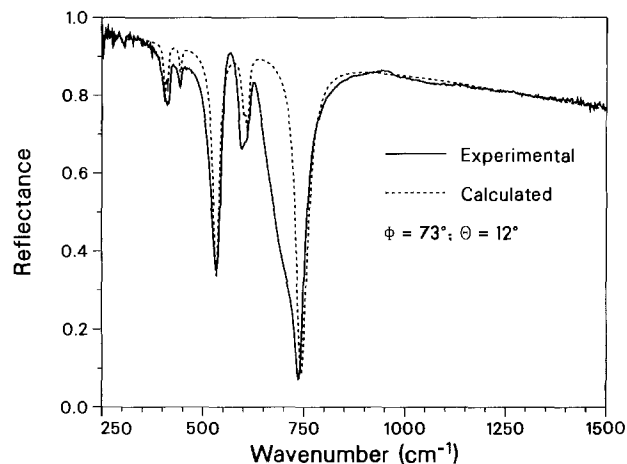


Fig. 9. Experimental and calculated P-polarized reflectance for a $0.31\ \mu\text{m}$ film of Cr_2O_3 on Fe-15% Cr.

to the films grown on pure chromium substrates is obvious, and we fit the observed spectrum to the calculated reflectance for a $0.31\ \mu\text{m}$ thick layer of Cr_2O_3 . The principal deviation of the calculated curves from the measured spectra is again the breadth of the bands and the asymmetry of the 735 cm^{-1} band. We note, however, that the degree of asymmetry for this band is far more pronounced than in the spectra of the oxides grown on the pure chromium substrates.

An additional mechanism for producing absorbance in the region between 660 and 735 cm^{-1} is the substitution of Fe for Cr in the Cr_2O_3 layer. Chang and Mitra (30) have studied the behavior of optic mode frequencies in certain classes of mixed crystals. They have shown that these frequencies vary continuously and approximately linearly with concentration from the frequency characteristic of one end member to that of the other end member for several mixed oxides. Unpublished work by Ottesen and Nagelberg at this laboratory has confirmed that the mixed oxide, $(\text{Fe}, \text{Cr})_2\text{O}_3$, exhibits this behavior. The presence of a small amount of iron in our thin chromium oxide films would be expected to produce absorptions precisely in the region between 660 and 735 cm^{-1} . The exact nature of the resulting reflectance spectrum would depend on the manner in which the iron atoms were distributed throughout the predominantly Cr_2O_3 thin film.

We now wish to determine layer thicknesses for these films grown on Fe-15% Cr alloys and to fit the calculated thicknesses to an experimental kinetic rate law plot. While optimum fits of theoretical calculations to experimental data are obtained by using a nonlinear least squares analysis, an approach based on minimum band reflectance has much to recommend it in terms of both simplicity and speed. Provided that the limits of applicability can be accurately quantified, this method of determining film thicknesses is of great potential value to a variety of users.

Using the theoretical curves for $-\log R_{\min}$ determined above for bands near 735 and 530 cm^{-1} , we calculate thicknesses for our six samples. Assuming that the oxidation process is diffusion controlled, the calculated thickness data are plotted vs. the square root of oxidation time in Fig. 10.

Initially the fit to a parabolic rate law is reasonably good (indicated by the straight line). However, as the film thickness increases, this interpretation becomes less clear. This is primarily due to the scatter of the data points for the four greatest thicknesses determined using the 735 cm^{-1} band. This scatter is not unexpected. Traditional analytical methods (31) have shown that the maximum accuracy in spectroscopic measurements is obtained for linear absorbance measurements in the vicinity of 0.43 . Accuracy for our $-\log R_{\min}$ measurements is expected to degrade seriously below 0.2 and above 0.7 , and the four points mentioned above all have values above 0.8 .

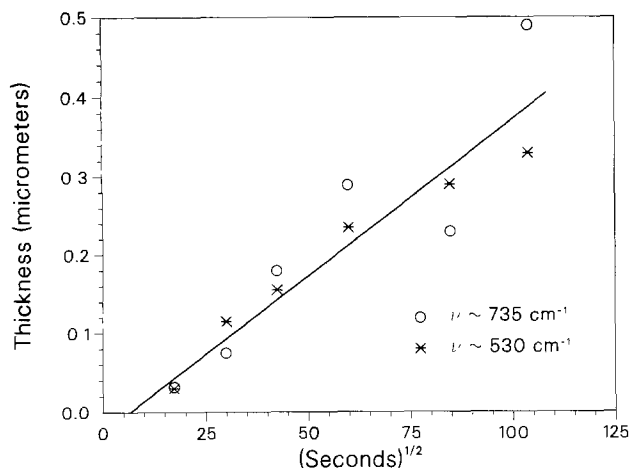


Fig. 10. Parabolic rate law plot for Cr_2O_3 film thickness as formed during air oxidation of Fe-15% Cr in air at 850°C .

Using this criteria for accuracy, acceptable limits for determining film thickness using the 735 cm^{-1} band are $0.01\text{--}0.07\text{ }\mu\text{m}$. For the 530 cm^{-1} band, these limits are $0.20\text{--}0.38\text{ }\mu\text{m}$. This also avoids the major uncertainty in the determination of the experimental base line discussed above. The area of greatest uncertainty lies in the vicinity of the 530 cm^{-1} band when it is quite weak and therefore unreliable for thickness determinations.

Thus we may expect a reasonably accurate determination of Cr_2O_3 film thicknesses using these two bands over a range of $0.01\text{--}0.38\text{ }\mu\text{m}$ with somewhat greater uncertainty in the intermediate range of $0.07\text{--}0.20\text{ }\mu\text{m}$.

For thicker films, it may be best to use the interference fringes in the transparent region for thickness determinations. These become more closely spaced and increase in intensity as the oxide film grows in thickness, and their use in such determinations has been demonstrated elsewhere for chromium oxide (24), and will be described below for iron oxide forming alloys. For layers thinner than $0.01\text{ }\mu\text{m}$, considerable care must be taken in determining thicknesses using infrared reflectance data. Our approach is predicated on the underlying assumption of uniform surface coverage and optical constants which do not change with film thickness. Both of these criteria become increasingly debatable for such thin layers, and the quantitative use of external reflectance must be buttressed by careful calibration and independent measurements by other surface science methods.

Experimental measurements for iron oxide forming alloys.—Binary alloys containing smaller amounts of chromium exhibit strikingly different behavior during thermal oxidation. Previous work has shown that the oxidation mechanism and oxide film composition for a given alloy depend strongly on the chromium content of the substrate, the temperature, and the oxygen partial pressure (32).

We have studied the oxidation of an Fe-10% Cr alloy in air from 700° to 850°C . At 850°C , much thicker films are grown on this alloy compared to Fe-15% Cr. The reflectance spectra of a coupon oxidized for 1h are shown in Fig. 11 and 12. Note the strong features in the S-polarized spectrum as compared to the flat, featureless curves which occur for very thin films (2). The oscillations in both S- and P-polarized spectra above 700 cm^{-1} are due to interference fringes. The spacing between the fringes decreases in the vicinity of 700 cm^{-1} due to the rapid variation in the film's refractive index.

These experimental spectra were fit using calculated data for hematite ($\alpha\text{-Fe}_2\text{O}_3$). Optical constants of iron were used for the substrate (27), and optical constants for hematite were obtained from the literature (29). Since this material is strongly anisotropic, we were not able to construct a set of "average" optical constants, as was the case for Cr_2O_3 . Our computer program accommodates anisotropic, uniaxial absorbing media as long as the symmetry

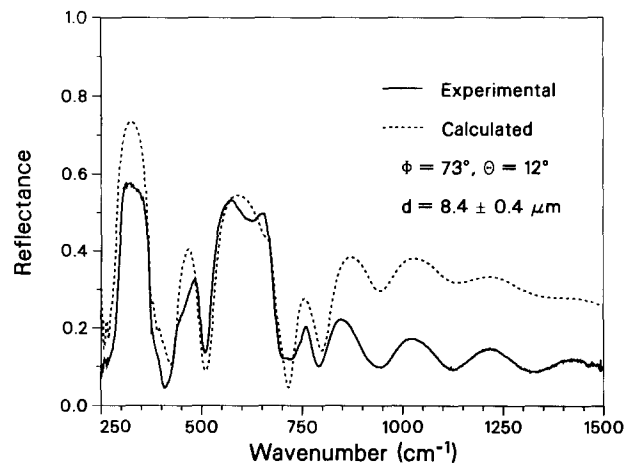


Fig. 11. Experimental and calculated P-polarized reflectance for an $8.4\text{ }\mu\text{m}$ film of $\alpha\text{-Fe}_2\text{O}_3$ on an Fe-10% Cr substrate.

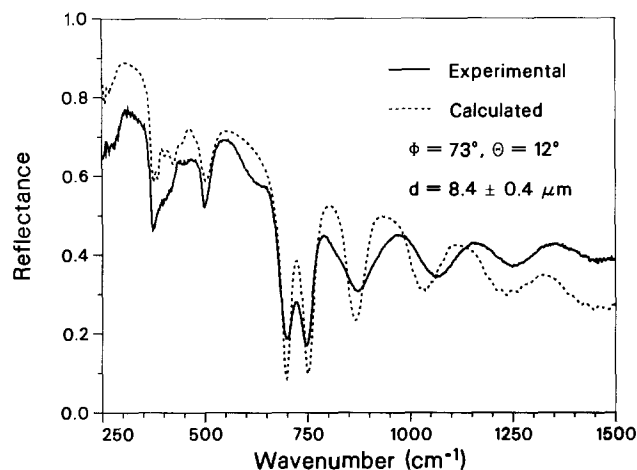


Fig. 12. Experimental and calculated S-polarized reflectance for an $8.4\text{ }\mu\text{m}$ film of $\alpha\text{-Fe}_2\text{O}_3$ on an Fe-10% Cr substrate.

axes of the crystal are aligned normal or parallel to the surface. Since hematite possesses trigonal crystal symmetry, we approximated a random orientation of microcrystals on the surface by averaging calculations for layers with the crystal c axis parallel and perpendicular to the surface (shown schematically in Fig. 13).

If the two conditions with the crystal c axis parallel to the surface are equivalent, then the interaction of the incident infrared radiation would result in the electric vector's being perpendicular to the c axis twice as often as it would be parallel to the c axis. Accordingly, we cal-

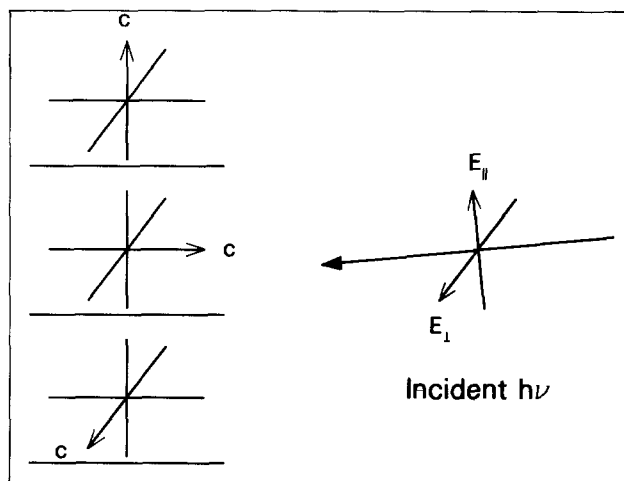


Fig. 13. Schematic orientation of $\alpha\text{-Fe}_2\text{O}_3$ crystal symmetry axis with respect to the substrate and incident infrared beam.

culated reflectance spectra for these different orientations and performed a weighted average in our comparison with experimental results.

The calculations for P- and S-polarizations for a 0.67/0.33 mixture of the orientations given above are also shown in Fig. 11 and 12. The agreement between calculated and experimental data in the absorption region is extremely good with two exceptions. A weak, broad band in the experimental spectra at 620 cm^{-1} is not present in the calculated curves. Also, the detailed structure of the strong doublet centered at 710 cm^{-1} in the P-polarized experimental spectrum is calculated as a slightly narrower singlet. We attribute these differences primarily to a small amount of $(\text{Fe}_{3-x}\text{Cr}_x)\text{O}_4$ oxide phase in the experimentally grown oxide film. Previous work (32) suggests that this phase should be present as a thin layer between the hematite film and the substrate.

Earlier experimental studies of similar oxide films (21) noted the lack of reliable optical constants in the reference literature for complex oxide phases, and the present theoretical treatment of these systems serves to emphasize this deficiency. This situation prevents a complete interpretation of our external reflectance measurements.

The calculated spectra presented in Fig. 11 and 12 also include an assumption of $\pm 0.4\text{ }\mu\text{m}$ standard deviation in film thickness. This was modeled by assuming a gaussian distribution of layer thicknesses about the mean, and performing a weighted average of five calculations in which the layer thickness was varied in equal increments from 7.9 to $8.9\text{ }\mu\text{m}$. The assumption of surface roughness was necessary to adequately fit the shape of the experimentally observed interference fringe region. This was particularly important for the S-polarized component, and a comparison of the rough surface calculation and a smooth surface calculation is shown in Fig. 14. This shows that the assumption of a uniformly thick oxide layer would be seriously in error for this system.

We find, however, that the assumption of a single angle of incidence of the infrared beam results in a very good approximation to the observed data in contrast to the results for thin chromium oxide films discussed above. Calculated spectra for a P-polarized spectrum taken at 73° angle of incidence assuming no angular spread and $\pm 12^\circ$ half-angle of divergence show no significant difference.

Finally, we note that although the correct spacings and shapes of the interference fringes are calculated by our present model, their relative intensities and the treatment of the base line leave something to be desired. The principal cause for this is most likely our simple approach to modeling scattering phenomena with a single ν^2 term. While this may be satisfactory for the thinner chromium oxide films presented earlier, electron micrographs for these thicker films clearly show a complex microcrystalline morphology which might be expected to exhibit behavior intermediate between specular and diffuse reflection.

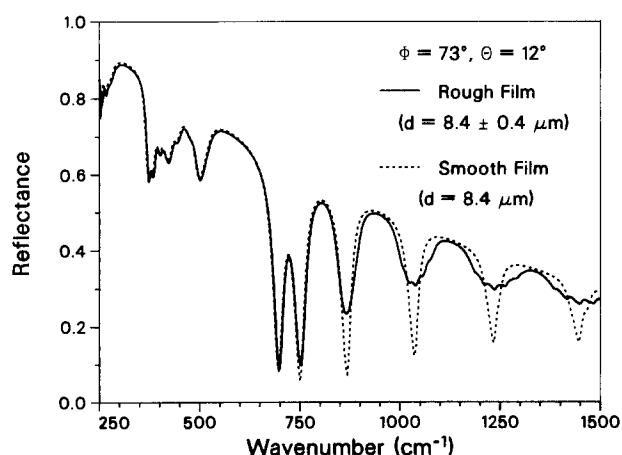


Fig. 14. Calculated S-polarized reflectance for $\alpha\text{-Fe}_2\text{O}_3$ on an Fe-10% Cr substrate showing the effect of surface roughness.

Quantitative film thickness determination.—One of the most significant uses of external infrared reflectance would seem to be the monitoring of film thickness during an industrial process. In a previous paper, Mertens (18) addressed precisely this feature of the method, and a set of calibration factors was derived for four transition metal oxides which related thickness to the measured negative logarithm of reflectance for the most intense band in the spectrum. As we noted above, this band corresponds to the position of the highest LO mode in the bulk oxide, and its $-\log R_{\min}$ function exhibits roughly linear behavior for very thin layers.

We derive analogous calibration factors from our experimental data and calculated spectra for chromium oxide and from a theoretical treatment for the oxides of iron and nickel. The calculations for chromium and iron have been discussed in detail above; optical constants for NiO and Ni metal have been taken from the literature for similar calculations (33, 27). The results for each oxide's highest energy mode are shown in Fig. 15 for films between 0.001 and $0.5\text{ }\mu\text{m}$ in thickness. All three of these modes show similar qualitative behavior: linearly increasing $-\log R_{\min}$ for thin films with a gradually increasing negative deviation from this straight line behavior. Slopes of the initial portion of the curve are taken, and calibration factors analogous to those of Ref. (18) in units of angstroms per $-\log R_{\min}$ are derived. Those values are expressed in units of angstrom/absorbance/reflection, where the term "reflection" refers to the number of external reflections in a multiple-pass experimental apparatus.

These values are compared in Table II, and we see that there is a very large discrepancy between the two sets. The disagreement becomes progressively less as the linear region for $-\log R_{\min}$ increases. Thus the values for chromium oxide differ by a factor of 10, those for nickel oxide by a factor of 2.7, and those for iron oxide by a factor of 3. One factor which complicates the earlier results (18) is the calculation of intensity factors using data from films whose thicknesses have entered the nonlinear region for $-\log R_{\min}$. This is especially the case for chromium oxide and may account for the astounding degree of difference between the two approaches.

This may account for much of the disagreement for nickel oxide and iron oxide calibration factors as well. It is not a simple matter to quantitatively reconcile this previous study with our present investigation, however. The principal obstacle to this lies in Mertens' use of multiple reflectance sampling optics which were designed to maximize optical sensitivity for extremely thin films (18, 19). That experimental arrangement consists of two rectangular sample (or reference) surfaces which are arranged parallel and very close to each other. The infrared beam is then focused on the space between the two surfaces, and the resultant reflected light is collected at

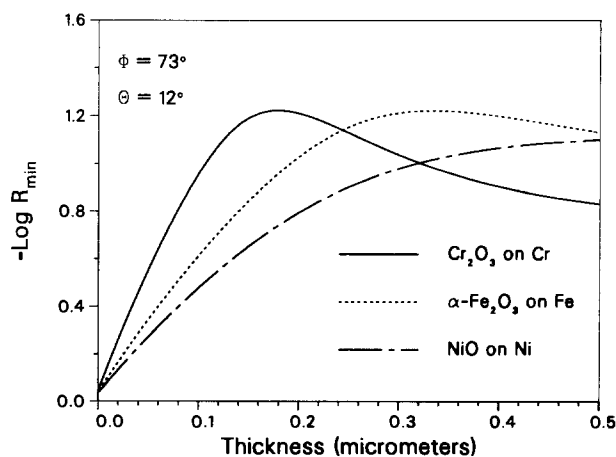


Fig. 15. Calculated P-polarized $-\log R_{\min}$ of the highest energy infrared active mode for thin films of transition metal oxides on metallic substrates.

Table II

Metal oxide	Infrared band (cm ⁻¹)	Calibration factor (Å/-log R _{min})	
		Ref. (18)	This work
α-Fe ₂ O ₃	655	5000	1695
NiO	582	5900	2200
Cr ₂ O ₃	733	9800	1030

the other end. Since the beam is incident on the sample surface over a range of angles, the number of reflections at the sample surface depends on both the angle of incidence and the spacing between the surfaces.

The angles of incidence used in that experiment thus range about 72° for the initial reflection. The net effect is to accentuate the lower angles of incidence which experience more reflections for a given sample length than the higher angles of incidence. We noted above that the incorporation of a range for the angle of incidence generally results in a lowering of the peak -log R_{min} values (see Fig. 7). We assume that the effective skewing of this distribution to lower angles, as would be the case for the multiple reflectance apparatus, would lower the resulting peak values even more.

Whatever the specific behavior of the measured "absorbance" might be, the lower values of -log R_{min} would certainly result in correspondingly higher values for the calibration factors than those which we obtain from the strictly linear region of -log R_{min} and a complete reflection calculation. The present work thus serves as a warning to experimentalists using multiple reflectance optics. Although these sampling attachments do indeed enhance the sensitivity of the technique, the resulting measurements are not simply related to single reflectance measurements, and they will certainly have a depressingly complicated dependence on the beam angular divergence.

Potential users should keep in mind that linear calibration factors derived from external reflectance studies will be transferrable to other measurements only when precisely similar sampling optics are used. This is true of our single reflection measurements as well, although in this case theoretical confirmation is much more straightforward.

Conclusions

External reflectance infrared spectroscopy has been shown to be a reliable technique for the study of thin oxide films formed on air oxidized Fe-Cr alloys. A computer program has been written to calculate the external reflectance for these films using optical constants from the reference literature for the oxides. This method is useful in the determination of both composition and film thickness of simple oxide films, and extends over a wide range of layer thickness (0.01-10 μm for Cr₂O₃).

Many of the features observed in the reflectance spectra of these thin films can be misleading when compared to absorption spectra. These complications arise primarily from the large (and rapidly varying) indexes of refraction for metal oxides, the rough nature of the oxide films, the presence of complex oxide phases, and several experimental parameters (angle of incidence, angle of divergence, beam polarization).

Finally, theoretical calibration factors for the determination of film thickness have been derived for three transition metal oxides. These factors utilize the most intense oxide reflectance band and are useful in a region where the negative logarithm of the reflectance band increases

linearly with film thickness. These values are in marked contrast to those of an earlier study (18), and this discrepancy is attributed to differences in the experimental reflectance optics used in the two investigations.

Acknowledgments

I would like to thank Karen Siegfried, who prepared many of the experimental samples for this investigation, and who also collected some of the experimental data in addition to incorporating several modifications in the reflectance optics. I would also like to thank John Hamilton for kindly providing the thin chromium oxide films grown on bulk chromium substrates, and Alan Nagelberg for his helpful discussion of metal oxidation. This work is supported by the U.S. Department of Energy under Contract DE-AC04-76DP00789.

Manuscript submitted Jan. 21, 1985; revised manuscript received April 22, 1985.

Sandia National Laboratories assisted in meeting the publication costs of this article.

REFERENCES

- W. D. Berreman, *Phys. Rev.*, **130**, 2193 (1963).
- R. G. Greenler, *J. Chem. Phys.*, **44**, 310 (1966).
- R. G. Greenler, *ibid.*, **50**, 1963 (1969).
- R. G. Greenler, *J. Catal.*, **23**, 42 (1971).
- W. G. Golden, *J. Phys. Chem.*, **82**, 843 (1978).
- R. M. A. Azzam and N. M. Bashara, "Ellipsometry and Polarized Light," North Holland, Amsterdam (1977).
- J. Pritchard and T. Catterick, "Experimental Methods in Catalytic Research," Vol. 3, p. 281, Academic Press, New York (1976).
- G. W. Poling, *This Journal*, **114**, 1209 (1967).
- M. Ito and W. Suetaka, *J. Catal.*, **54**, 13 (1978).
- J. F. Blanke, *Spectrochim. Acta*, **32A**, 163 (1976).
- F. J. Boerio and S. L. Chen, *Appl. Spectrosc.*, **33**, 121 (1979).
- D. L. Allara, *Macromolecules*, **11**, 1215 (1978).
- A. E. Dowrey and C. Marcott, *Appl. Spectrosc.*, **36**, 414 (1982).
- G. W. Poling, *This Journal*, **116**, 958 (1969).
- C. M. Phillippi and S. R. Lyon, *Phys. Rev. B*, **3**, 2086 (1971).
- A. J. Maeland, *Thin Solid Films*, **21**, 67 (1974).
- F. J. Boerio and L. Armogan, *Appl. Spectrosc.*, **32**, 509 (1978).
- F. P. Mertens, *Corrosion*, **34**, 359 (1978).
- F. P. Mertens, *Surf. Sci.*, **71**, 161 (1978).
- R. J. Thibeau, *Appl. Spectrosc.*, **32**, 532 (1978); R. J. Thibeau, *This Journal*, **127**, 37 (1980).
- D. K. Ottesen and A. S. Nagelberg, *Thin Solid Films*, **73**, 347 (1980).
- M. Handke, *Mater. Chem.*, **5**, 199 (1980); M. Handke, *J. Mater. Sci.*, **16**, 307 (1981); M. Handke and J. Dziedzic, *J. Mol. Struct.*, **79**, 43 (1982).
- G. A. Swallow and G. C. Allen, *Oxid. Met.*, **17**, 141 (1982).
- G. C. Allen and G. A. Swallow, *ibid.*, **17**, 157 (1982).
- O. S. Heavens, "Optical Properties of Thin Solid Films," pp. 46-95, Dover Publications, New York (1965).
- W. W. Wendlandt and H. G. Hecht, "Reflectance Spectroscopy," p. 67, Interscience Publishers, New York (1966).
- A. S. Siddiqui and D. M. Treherne, *Infrared Phys.*, **17**, 33 (1977).
- D. R. Renneke and D. W. Lynch, *Phys. Rev.*, **138**, A530 (1965).
- S. Onari, *Phys. Rev. B*, **16**, 1717 (1977).
- I. F. Chang and S. S. Mitra, *Phys. Rev.*, **172**, 924 (1968).
- F. Twyman and C. B. Allsopp, "Practice of Absorption Spectrophotometry," A. Hilger, London (1934).
- N. Birks and G. H. Meier, "Introduction to High Temperature Oxidation of Metals," Edward Arnold Publ., London (1983).
- P. J. Gielisse, *J. Appl. Phys.*, **36**, 2446 (1965).

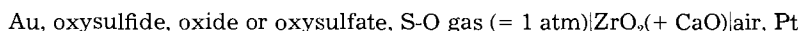
Electrochemical Determination of Standard Gibbs Energies of Formation of Rare-Earth Oxysulfides and Oxysulfates

Norihiko Fukatsu,¹ Noriyuki Shidawara,² and Zensaku Kozuka

Department of Metallurgical Engineering, Faculty of Engineering, Osaka University, Suita, Osaka 565, Japan

ABSTRACT

The oxygen chemical potentials established by the equilibrium reactions between the rare-earth (La, Ce, Nd, Gd, and Y) oxysulfide and the corresponding rare-earth oxide or oxysulfate were measured in the temperature range 1200-1500 K using the cell



where S-O gas represents the gas mixture whose species consist of only sulfur and oxygen. The sulfur chemical potentials were determined by calculations on the complex equilibrium reactions among gas species under the restriction of the constant total pressure. The standard Gibbs energy changes for the reactions were calculated from these results regarding that the activities of the participating solid components were unity. The standard Gibbs energies of formation of $\text{Ce}_2\text{O}_3\text{S}$, $\text{Nd}_2\text{O}_3\text{S}$, $\text{Gd}_2\text{O}_3\text{S}$, $\text{Y}_2\text{O}_3\text{S}$, $\text{Nd}_2\text{O}_2\text{SO}_4$, and $\text{Gd}_2\text{O}_2\text{SO}_4$ were determined from these data. The standard Gibbs energies of formation of $\text{Ce}_2\text{O}_3\text{S}$ obtained in this study were slightly more negative than that determined with gas equilibrium method by Fruehan. The Gibbs energies of formation of oxysulfides estimated by Gschneidner *et al.* were found to agree fairly well with the present experimental results.

Rare-earth elements have been widely used in the industrial material production processes as additives to improve the properties of the product. In these applications, rare-earth elements are sometimes used in the environment where the oxygen and sulfur are both contained as the components. For example, they are used as deoxidizer, desulfurizer, and modifier of the morphology of inclusions in the steel production, are used to control the graphite morphology in the production of cast iron, and are used as the additives to improve the high temperature corrosion resistance properties. To use them efficiently in these applications, it is important to understand the thermodynamic aspects of the system containing both sulfur and oxygen. However, thermodynamic data of rare-earth compounds with sulfur and oxygen are very limited. Especially, the temperature dependence of the Gibbs energies of formation of rare-earth oxysulfides are not known except for $\text{Ce}_2\text{O}_3\text{S}$ (1), in spite of those industrially important as rare-earth-doped phosphors.

It has been ascertained that the EMF method employing the stabilized zirconia solid electrolyte is a useful tool for investigating the thermodynamic properties of the systems containing both sulfur and oxygen as the components. The present authors have utilized this method on the thermodynamic studies of the system Bi-S-O (2, 3), Ag-S-O (4), and Pb-S-O (5) and have gotten satisfactory results. In the present work, the same method was applied to RE-S-O systems (RE = La, Ce, Nd, Gd, and Y) to determine the Gibbs energies of formation of oxysulfides and oxysulfates of these elements.

Recently, Dwivedi and Kay (6) measured the oxygen partial pressures corresponding to the oxysulfide/oxysulfate equilibrium using a similar EMF method; they determined the Gibbs energy changes for the reactions between the oxysulfides and the respective oxysulfates. However, the Gibbs energies of formation of either compound could not be determined. For Ce and Y, they also measured the oxygen partial pressures corresponding to the oxide/oxysulfide equilibrium in the condition that Ag and Ag_2S coexisted (7); the Gibbs energies of formation of $\text{Ce}_2\text{O}_3\text{S}$ and $\text{Y}_2\text{O}_3\text{S}$ were determined based on those of oxides, but their temperature dependences could not be obtained because the cells operated successfully over a very limited temperature range.

In the present experiment, the oxygen partial pressures corresponding to the oxide/oxysulfide equilibrium were

¹Present address: Department of Material Engineering, Nagoya Institute of Technology, Gokiso-cho, Showa-ku, Nagoya 466, Japan.

²Present address: Nippon Steel Corporation, Tokai, Nagoya 476, Japan.

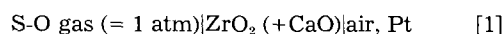
measured in "quasi isobaric closed" conditions. The equilibrium sulfur pressures were determined by calculations on the complex equilibrium reactions among gas species. The Gibbs energies of formation of oxysulfides, therefore, could be determined directly from those of oxides for more wide temperature range. The Gibbs energies of formation of oxysulfates were also determined from these data.

Theory

A metal-sulfur-oxygen system at a constant temperature may be thermodynamically characterized by the equilibrium oxygen and sulfur partial pressures. In these two variables, the oxygen partial pressure may be measured preferentially with the coexisting sulfur partial pressure by using oxygen galvanic cell employing stabilized zirconia as solid electrolyte (8). When the equilibrium oxygen partial pressure is known, the equilibrium sulfur partial pressure may be determined by calculation if the gas phase consists of the species made only from oxygen and sulfur atoms and if its total pressure was known. Since this method was first used by Larson and Elliott (9) to determine the Gibbs energies of formation of several sulfides, it has been used to measure the Gibbs energies of formation of sulfates (10-13), to measure the activities of sulfur in liquid melts (2, 4), and to study the phase equilibria in metal-sulfur-oxygen systems (5, 14, 15). In those experiments, it was most of the cases that the gas phase may be substantially regarded to be pure SO_2 or S_2 . Even if this condition is not satisfied, sulfur partial pressure can be determined by calculation when the thermodynamic data of all coexisting gas species is known, as is explained below.

According to the phase rule, the degree of freedom is two when three phases are contained in a system which is composed of three elements, RE, S, and O (RE = La, Ce, Nd, Gd, and Y). In these systems, the unique oxygen partial pressure is, therefore, established when the two condensed phases and a gas phase coexist in the equilibrium state at a given temperature and a given total pressure. The oxygen partial pressure established over the two condensed phases may be measured by the following galvanic cell

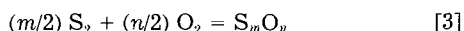
Pt, Au, oxysulfide, oxide or oxysulfate,



When the ionic transport number of the solid electrolyte may be considered to be 1—and this condition is satisfied in the present experiment (16)—EMF of the above cell is given as

$$E = -(1/4F) RT \ln (P_{O_2}/0.21) \quad [2]$$

where, E is the reversible cell, EMF, R is the gas constant, T is the temperature of the cell, and P_{O_2} is the equilibrium oxygen partial pressure of the left electrode (17). Therefore, the oxygen partial pressure at the left electrode may be determined by measuring the EMF of the cell. The partial pressures of other gas species, S_mO_n , (e.g., SO_2 , SO_3 , etc.) may be represented in a function of sulfur partial pressure and oxygen partial pressure using the following equilibrium relations



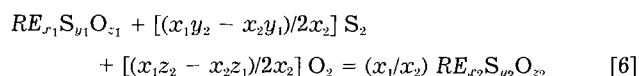
$$P_{S_mO_n}/(P_{S_2})^{m/2}(P_{O_2})^{n/2} = \exp(-\Delta G^0_3/RT) \quad [4]$$

where, ΔG^0_3 is the standard Gibbs energy of formation of S_mO_n . On the other hand, from the condition that the total pressure is kept constant

$$\sum P_{S_mO_n} = P_{total} \quad [5]$$

The sulfur pressure may, therefore, be calculated by solving Eq. [4] and [5] simultaneously. The detail of this calculation was already reported elsewhere (2).

When pure condensed phases $RE_{x_1}S_{y_1}O_{z_1}$ and $RE_{x_2}S_{y_2}O_{z_2}$ are in equilibrium with gas phase of the total pressure P_{total} , the equilibrium reaction may be represented by



The Gibbs energy change of this reaction may be given in terms of the chemical potential of oxygen and the chemical potential of sulfur by

$$\Delta G^0 = [(x_1y_2 - x_2y_1)/2x_2] RT \ln (P_{S_2}/P_{total}) + [(x_1z_2 - x_2z_1)/2x_2] RT \ln (P_{O_2}/P_{total}) \quad [7]$$

In the present calculations, SO_2 , S_2O , SO_3 , S , S_2 , S_3 , S_4 , S_5 , S_6 , S_7 , S_8 , O , O_2 , and O_3 are considered as the coexisting gas species. The Gibbs energies of formation of these gas components, except that of SO_2 , were adopted from the compiled data of Barin and Knacke (18). For the free energy of formation of SO_2 , the calculated values based on the CODATA key values ΔH^0_{298} and ΔS^0_{298} (19) and the data of ΔC_p compiled by TPRC (20) were used. These data are shown in Table I.

Experimental

Materials.—Rare-earth oxides (La_2O_3 , CeO_2 , Nd_2O_3 , Gd_2O_3 , and Y_2O_3) were all supplied from Shinetsukagaku Company Limited. The purities of these oxides are 99.99% for La and Y and 99.9% for Ce, Nd, and Gd. Main impurities were the other rare-earth oxides. All rare-earth oxysulfides except La_2O_2S were prepared by holding the respective oxide powders in the alumina crucible at 1473 K for 10,800s under flowing H_2S atmosphere. The product phases are identified by x-ray diffraction analysis. For lanthanum, oxysulfide phase was not formed by the above conditions, but La_2S_3 was obtained by holding at 913 K for 3600s with the same procedure. Therefore, for

Table I. Standard Gibbs energy changes of the reactions used in the calculation

Reactions	ΔG^0 (J)	Ref.
$(1/2)S_2 + O_2 = SO_2$	$-361,540 + 72.92 \cdot T$	(19, 20)
$(1/2)S_2 + (1/2)O_2 = SO$	$-57,550 - 5.32 \cdot T$	(18)
$S_2 + (1/2)O_2 = S_2O$	$-168,600 + 63.19 \cdot T$	(18)
$(1/2)S_2 + (3/2)O_2 = SO_3$	$-457,900 + 164.10 \cdot T$	(18)
$(1/2)S_2 = S$	$218,800 + 60.15 \cdot T$	(18)
$(3/2)S_2 = S_3$	$-44,570 + 63.02 \cdot T$	(18)
$2S_2 = S_4$	$-58,850 + 114.6 \cdot T$	(18)
$(5/2)S_2 = S_5$	$-199,000 + 231.9 \cdot T$	(18)
$3S_2 = S_6$	$-269,200 + 302.9 \cdot T$	(18)
$(7/2)S_2 = S_7$	$-324,900 + 370.4 \cdot T$	(18)
$4S_2 = S_8$	$-388,500 + 444.6 \cdot T$	(18)

the La-S-O system, oxide and sulfide phases were used as the charging materials.

Apparatus.—The schematic diagram of the apparatus and the cell assembly are illustrated in Fig. 1. An 11 mole percent (m/o) CaO stabilized zirconia tube (5 mm id, 8 mm od, and 300 mm length) closed at one end supplied from Nippon Kagaku Togyo Company Limited was used as the solid electrolyte of the cell. Air-Pt reference electrode was prepared on the outside of the closed end of the tube by painting platinum paste and heating it in air at 1300 K. Air was flowed at the rate 0.8 cm³/s over the reference electrode. Gold, which is virtually inactive to both sulfur and oxygen, was used for the material of the working electrode because the electric conductivities of these samples are very low. Iridium wire spot-welded to Kanthal wire was used as the lead wire to the working electrode, which was protected from corrosion by sulfur and oxygen using alumina sheath and alumina cement. Temperature was measured by the Pt-Pt 13% Rh thermocouple in the protecting tube which is touched to the bottom of the zirconia tube. A Kanthal-wound furnace and an electronic controller were used to maintain the temperature of the cell within ± 1 K to the selected values.

Procedure.—In the present work, all measurements are on the two-condensed phase equilibria. It is not necessary that the ratio of the amounts of charge materials be chosen rigidly to a certain value. The ratio of oxysulfide to oxide is selected to be about 2:1, because the sulfur is transferred to gas phase by sublimation or the reaction with the oxygen permeated through the zirconia electrolyte owing to its small electronic conduction. A slight amount of pure sulfur was added to them in the several systems exhibiting the relative high partial pressure of sulfur to check the reliability of the EMF data. They were well mixed in a mortar, and 0.6g of them were used as the charge material. About 1g of pure gold bead was loaded at the bottom of the zirconia tube, and the lead wire was set to touch it. The sample was then charged over the gold and the zirconia crucible was well tapped to ensure the dense packing.

The reaction compartment of the cell was first evacuated at 473 K to a vacuum of 0.1 Pa, and then purified SO_2 was introduced. SO_2 was allowed to overflow

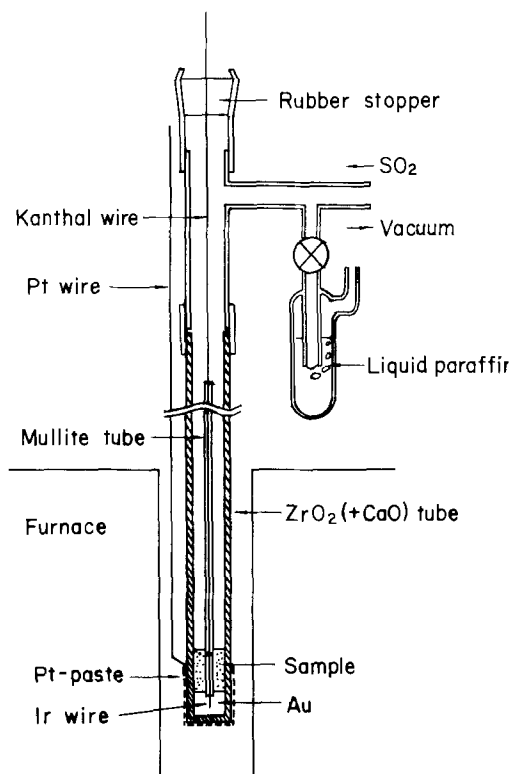


Fig. 1. Schematic diagram of cell assembly

through the liquid paraffine bubbler located near the gas inlet of the apparatus as shown in Fig. 1 to keep the total pressure equal to the atmospheric pressure. In such "quasi isobaric closed" conditions, the cell was heated to the temperatures to be studied. The condition mentioned in the theoretical section, *i.e.*, gas phase must be made from the species which consist of only sulfur and oxygen and the total pressure must be kept constant, could be satisfied by this method. This is ascertained in other works of the authors by comparing the data by this method with those by other methods (2-5). The cell should first be heated to the temperature over the melting point of gold to establish the good contact between gold and zirconia solid electrolyte; the lead wire was lowered until it touched the liquid gold electrode; the temperature was changed to the preselected one; and the EMF measurement was started. The EMF was recorded with time, and, when at a given temperature EMF maintained a constant value within 0.2 mV for at least 1800s, the value was adopted as a data. The measurement was performed within the temperature range 1200-1500 K. Thermoelectromotive force between Kanthal and platinum lead wires was measured beforehand, and the EMF of the cell was corrected according to the data. All EMF values in this paper are these corrected values. The atmospheric pressure was measured by a mercury manometer. The total pressure of the reaction compartment of the cell was taken to be equal to the atmospheric pressure. The effect of the daily change of atmospheric pressure on the EMF of the cell was found to be negligibly small. After the measurement was completed, the cell was pulled out from the furnace at appropriate temperature and cooled swiftly in air. The quenched samples were subjected to the x-ray analysis for the identification of the phases at each equilibrium.

Results and Discussion

Cell performance.—When the cell was first heated from the room temperature to the preselected one about 1350 K, it took approximately 12,000s to get a stable EMF after the cell temperature was stabilized. Afterwards, the equilibrium time was about 2000s for the subsequent change of temperature by about 30 K in either ascending or descending direction. The inner resistance of the cell was evaluated by measuring the EMF change when a small current was impressed from an external power source through it. Most of the cells had the inner resistances below 1 k Ω ; stable values of EMF were obtained using these cells. A few cells exhibit the inner resistance more than 100 k Ω ; stable EMF's were not obtained with these cells, and the resulting data were discarded. The reversibility of the cell was checked by passing a current for a short time through the cells exhibiting the stable EMF; the EMF was observed to return to the original value in a short time.

The whole gas phase does not come to the equilibrium in this measurement because it extends to the room temperature zone. The condition of the measurement is satisfied when the gas phase around the condensed phase comes to equilibrium. To confirm it was the case, the flow rate of the overflowing SO₂ was varied and the location of the gas outlet was changed; the EMF's were not affected by these matters. Furthermore, in some experiments, the quantities of the pure sulfur added to the specimens were varied in separate runs; the resulting data did not exhibit the significant differences among these runs. The measurements were performed with both ascending and descending temperatures; the overall reproducibility of the EMF values was excellent. From these facts, it was concluded that the equilibrium between the specimen and the gas phase around it were established under 1 atm total pressure.

The gas composition around the specimen may be estimated by calculations on the complex equilibrium reactions. Typical examples of the result are indicated in Table II. Case 1 is for the measurement on Ce-S-O at 1191 K; it is the most reduced state among the present ex-

Table II. Typical examples of calculated gas composition

Species	Case 1 (%)	Case 2 (%)
SO ₂	5.9991	99.6020
SO	0.0158	0.0985
S ₂ O	0.2939	0.0191
SO ₃	Trace	0.0006
S	0.00003	0.00005
S ₂	89.7096	0.2795
S ₃	3.9108	0.0003
S ₄	0.0382	Trace
S ₅	0.0312	Trace
S ₆	0.0070	Trace
S ₇	0.0005	Trace
S ₈	0.00004	Trace
O	Trace	Trace
O ₂	Trace	Trace
O ₃	Trace	Trace

Table III. Least squares analysis of cell EMF data

Equilibrium condensed phases	EMF (mV) = A + BT		Standard deviation (mV)	Temperature range (K)
	A (mV)	B (mV/K)		
La ₂ O ₂ SO ₄ , La ₂ O ₂ S	1173.5	-0.4442	2.4	1190-1510
CeO ₂ , Ce ₂ O ₂ S	1087.8	-0.2945	1.2	1180-1530
Nd ₂ O ₂ SO ₄ , Nd ₂ O ₂ S	1134.0	-0.4314	1.2	1170-1400
Nd ₂ O ₃ , Nd ₂ O ₂ S	728.3	-0.1413	0.4	1400-1510
Gd ₂ O ₃ , Gd ₂ O ₂ S	710.5	-0.0795	2.0	1250-1510
Y ₂ O ₃ , Y ₂ O ₂ S	747.9	-0.1351	1.8	1190-1500

periments; the main gas species is S₂. Case 2 is for the measurement on Nd-S-O at 1400 K; it is a more oxidized state; SO₂ is the most predominant species.

The specimens of the quenched cells were easily separated from its electrolyte; careful inspection of them showed that no reactions between the specimen and the electrolyte occurred. For all the related compounds, the x-ray patterns obtained from the specimens after the measurements corresponded closely to the standard ASTM Index patterns noted. This evidence indicates that the activities of the condensed phases did not deviate so greatly from unit ones after the reactions in the measurements. In view of the fact that the errors introduced from the contamination of the condensed phase are relatively small, all the compounds were regarded to be at unit activity in the calculation of the Gibbs energy change for the reactions.

The results for the individual system will be stated separately below.

La-S-O system.—Powdered La₂S₃ and La₂O₃ were used as the charge materials. The EMF measured is shown in Fig. 2 and the equation of least square regression analysis is given in Table III. It was ascertained from x-ray analysis that the phases existing at the equilibria were La₂O₂S and La₂O₂SO₄. The equilibrium reaction may be represented by

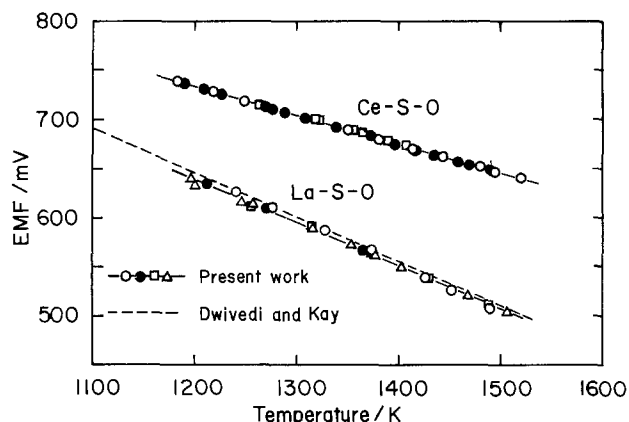
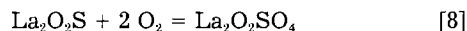


Fig. 2. Variations of EMF with temperature for the cells [Pt, CeO₂, Ce₂O₂S][ZrO₂(+CaO)]air, Pt and [Pt, La₂O₂SO₄, La₂O₂S][ZrO₂(+CaO)]air, Pt. The different symbols represent the separate runs of experiments.



When both phases were considered to be pure, the Gibbs energy change may be represented by

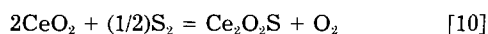
$$\Delta G^\circ_8 = 2RT \ln P_{\text{O}_2} \quad [9]$$

These values were calculated from the measured oxygen partial pressures and are represented as a function of temperature in Table IV.

This system was recently studied by Dwivedi and Kay (6) based on the method similar to ours. They measured the equilibrium oxygen partial pressures of reaction [8] under the coexistence of La_2O_3 . The total pressure of S_mO_n in their experimental condition must be very low as compared with the present measurement. Their data are also shown with a dashed line in Fig. 2. As is seen in the figure, the agreement between two measurements is very good, which shows that the "quasi isobaric closed" conditions mentioned in the Theory section are satisfied in the present measurement.

In the temperature range studied, La_2O_3 was not in equilibrium with oxysulfide phase. The Gibbs energies of formation of either $\text{La}_2\text{O}_2\text{S}$ or $\text{La}_2\text{O}_2\text{SO}_4$, therefore, could not be determined in this study.

Ce-O-S system.— CeO_2 and $\text{Ce}_2\text{O}_2\text{S}$ were used as the charge materials. The measured EMF's are shown in Fig. 2; the result of the regression analysis is given in Table III. The x-ray analysis of the quenched specimen showed that the coexisting phases were CeO_2 and $\text{Ce}_2\text{O}_2\text{S}$. The equilibrium reaction is represented as³



As both condensed phases may be considered to be pure, the Gibbs energy change of the reaction may be represented by

$$\Delta G^\circ_{10} = -RT \ln (P_{\text{O}_2}/P_{\text{S}_2}^{1/2}) \quad [11]$$

The values of ΔG°_{10} were evaluated using the measured oxygen partial pressure and the sulfur partial pressure calculated by the method mentioned earlier. The least squares analysis gave the equation as a function of temperature listed in Table IV. The standard Gibbs energy of formation of $\text{Ce}_2\text{O}_2\text{S}$ was calculated from these results using the Gibbs energy of formation of CeO_2 recom-

³Strictly speaking, cerium oxide must be represented by CeO_{2-x} , where x is a function of the equilibrium oxygen partial pressure. It was ascertained, however, that the error introduced from neglecting this effect is so small that CeO_2 was assumed in this study.

Table IV. Standard Gibbs energy changes of the reactions determined in the present work

Reaction	ΔG° (J)	Estimated uncertainty (J)	Temperature range (K)
$\text{La}_2\text{O}_2\text{S} + 2 \text{O}_2 = \text{La}_2\text{O}_2\text{SO}_4$	$-905,880 + 317.2 \cdot T$	± 3800	1190-1510
$2\text{CeO}_2 + (1/2)\text{S}_2 = \text{Ce}_2\text{O}_2\text{S} + \text{O}_2$	$423,910 - 104.5 \cdot T$	± 2300	1180-1530
$\text{Nd}_2\text{O}_3 + (1/2)\text{S}_2 = \text{Nd}_2\text{O}_2\text{S} + (1/2)\text{O}_2$	$60,800 + 10.10 \cdot T$	± 4600	1400-1510
$\text{Nd}_2\text{O}_2\text{S} + 2 \text{O}_2 = \text{Nd}_2\text{O}_2\text{SO}_4$	$-875,400 + 307.4 \cdot T$	± 600	1170-1400
$\text{Gd}_2\text{O}_3 + (1/2)\text{S}_2 = \text{Gd}_2\text{O}_2\text{S} + (1/2)\text{O}_2$	$73,060 + 12.89 \cdot T$	± 6500	1250-1510
$\text{Y}_2\text{O}_3 + (1/2)\text{S}_2 = \text{Y}_2\text{O}_2\text{S} + (1/2)\text{O}_2$	$65,330 + 33.87 \cdot T$	± 5800	1190-1500

Table V. Standard Gibbs energy changes of formation for oxysulfides and oxysulfates

Reaction	ΔG° (J)	Estimated uncertainty (J)	Temperature range (K)
$2\text{Ce(l)} + \text{O}_2(\text{g}) + (1/2)\text{S}_2(\text{g}) = \text{Ce}_2\text{O}_2\text{S(s)}$	$-1,753,500 + 311.4 \cdot T$	$\pm 25,000$	1180-1530
$2\text{Nd(l)} + \text{O}_2(\text{g}) + (1/2)\text{S}_2(\text{g}) = \text{Nd}_2\text{O}_2\text{S(s)}$	$-1,753,400 + 300.0 \cdot T$	$\pm 14,000$	1400-1510
$2\text{Gd(s)} + \text{O}_2(\text{g}) + (1/2)\text{S}_2(\text{g}) = \text{Gd}_2\text{O}_2\text{S(s)}$	$-1,741,000 + 288.7 \cdot T$	$\pm 19,000$	1250-1510
$2\text{Y(s)} + \text{O}_2(\text{g}) + (1/2)\text{S}_2(\text{g}) = \text{Y}_2\text{O}_2\text{S(s)}$	$-1,828,000 + 312.5 \cdot T$	$\pm 16,000$	1190-1500
$2\text{Nd(s)} + 3 \text{O}_2(\text{g}) + (1/2)\text{S}_2(\text{g}) = \text{Nd}_2\text{O}_2\text{SO}_4(\text{s})^a$	$-2,616,300 + 599.5 \cdot T$	$\pm 15,000$	1170-1289
$2\text{Nd(l)} + 3 \text{O}_2(\text{g}) + (1/2)\text{S}_2(\text{g}) = \text{Nd}_2\text{O}_2\text{SO}_4(\text{s})^a$	$-2,629,500 + 609.7 \cdot T$	$\pm 15,000$	1289-1400
$2\text{Gd(l)} + 3 \text{O}_2(\text{g}) + (1/2)\text{S}_2(\text{g}) = \text{Gd}_2\text{O}_2\text{SO}_4(\text{s})^a$	$-2,631,700 + 615.6 \cdot T$	$\pm 21,000$	1000-1250 ^b

^a Phase transformations observed in solid Nd_2O_3 , Nd, and Y_2O_3 are ignored because the accompanied enthalpy changes are too small compared with the experimental errors.

^b Based on the standard Gibbs energy change for the reaction $\text{Gd}_2\text{O}_2\text{S} + 2 \text{O}_2 = \text{Gd}_2\text{O}_2\text{SO}_4$ measured by Dwivedi and Kay.

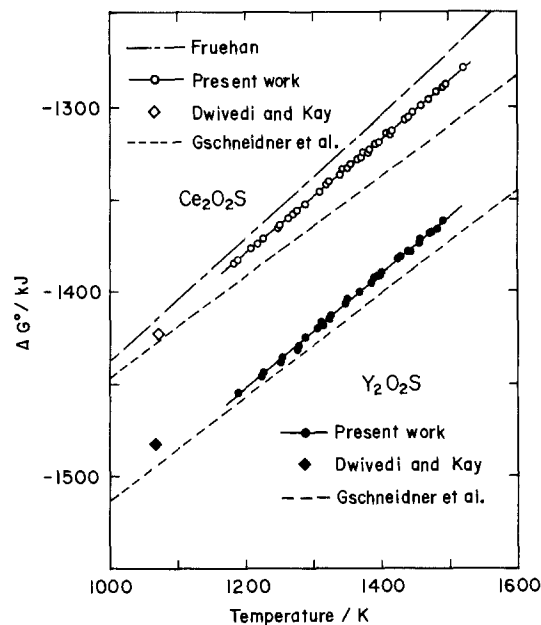


Fig. 3. Standard Gibbs energies of formation of $\text{Ce}_2\text{O}_2\text{S}$ and $\text{Y}_2\text{O}_2\text{S}$ as a function of temperature.

mended by Gschneidner *et al.*; the results are shown in Fig. 3, and the least squares equation is listed in Table V. In the figure, the measured value by Fruehan (1), who used gas-equilibrium method, is also shown with a dot-dashed line. The present results are 7.5 kJ negative than theirs. The dotted line shows the estimated value by Gschneidner *et al.* (21). Agreement with the present result is fairly good in view of the large estimated uncertainty (60 kJ) given to their values. In Fig. 3, the value reported by Dwivedi and Kay (7) is also shown. They used the reaction between Ag and Ag_2S to fix the partial pressure of sulfur. The reliability of the value, therefore, depends on the data of the Gibbs energy of formation of Ag_2S . However, the extrapolated value of the present result agrees with it very well within the error of only 4 kJ.

Nd-S-O system.—The charge materials were Nd_2O_3 and $\text{Nd}_2\text{O}_2\text{S}$. The measured EMF's are shown in Fig. 4; the result of the regression analysis is given in Table III. As can be seen from this figure, there is found a marked break in the temperature dependence of EMF around 1400 K. One may infer that one of the equilibrium phases is trans-

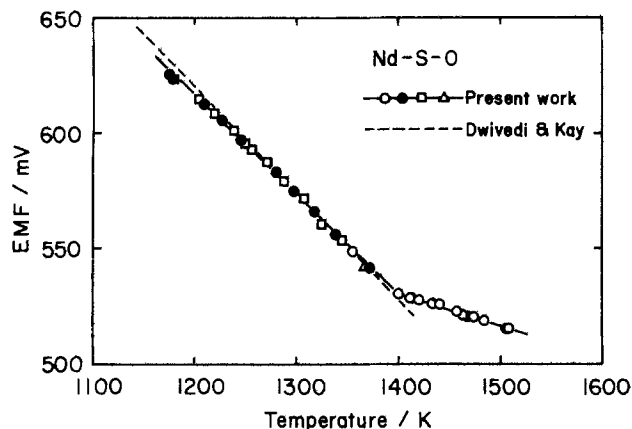
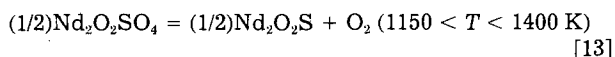
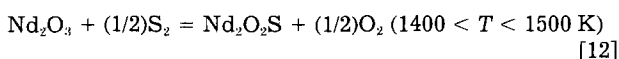


Fig. 4. Variations of EMF with temperature for the cell [Pt, $\text{Nd}_2\text{O}_2\text{SO}_4$] or $[\text{Nd}_2\text{O}_3, \text{Nd}_2\text{O}_2\text{S}/\text{ZrO}_2(+\text{CaO})/\text{air}, \text{Pt}]$. The different symbols represent the separate runs of experiments.

formed to another at the temperature. The x-ray analysis was performed for the specimens quenched from higher and lower temperatures than this point; it was found that the equilibrium phases were Nd_2O_3 and $\text{Nd}_2\text{O}_2\text{S}$ for higher temperature and $\text{Nd}_2\text{O}_2\text{SO}_4$ and $\text{Nd}_2\text{O}_2\text{S}$ for lower temperature, respectively. The equilibrium reactions may, therefore, be represented by



The Gibbs energy changes for reactions [12] and [13] were calculated from the measured oxygen partial pressures and the calculated sulfur partial pressures and are listed in Table IV as a function of temperature. The Gibbs energy of formation of $\text{Nd}_2\text{O}_2\text{S}$ was calculated using the data of Gibbs energy of formation of Nd_2O_3 , recommended by Gschneidner *et al.* and is shown in Table V. By extrapolating this value to lower temperature, the Gibbs energy of formation of $\text{Nd}_2\text{O}_2\text{SO}_4$ was also determined by combining the measured value for reaction [13] and is listed in Table V.

The EMF values measured by Dwivedi and Kay on the reaction between the oxysulfide and the oxysulfate with the coexistence of the oxide (6) are shown in Fig. 4. The good agreement between two measurements shows also that the conditions mentioned in the Theory section were satisfied in the present experiments.

Gd-S-O and Y-S-O system.—The oxides and the oxysulfides were used as the charge materials in both systems. The measured EMF's for Gd-O-S system and Y-S-O system are shown in Fig. 5. The results of regression analysis

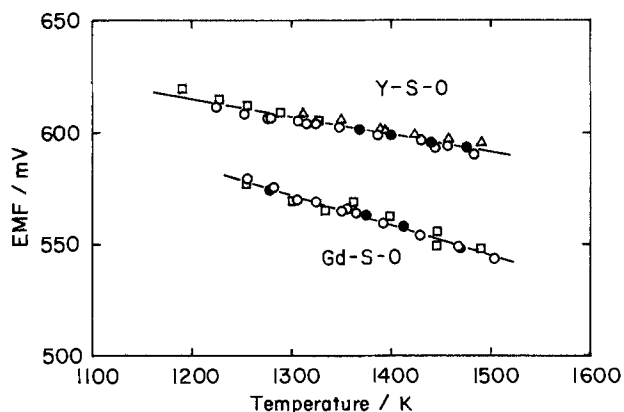
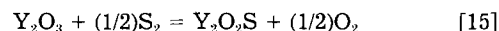
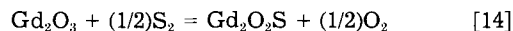
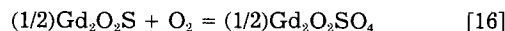


Fig. 5. Variations of EMF with temperature for the cells $[\text{Pt}, \text{Gd}_2\text{O}_3, \text{Gd}_2\text{O}_2\text{S}/\text{ZrO}_2(+\text{CaO})/\text{air}, \text{Pt}]$ and $[\text{Pt}, \text{Y}_2\text{O}_3, \text{Y}_2\text{O}_2\text{S}/\text{ZrO}_2(+\text{CaO})/\text{air}, \text{Pt}]$. The different symbols represent the separate runs of experiments.

are given in Table III. In the measured temperature range, the experimental points show the linear dependence on temperature. It was ascertained from the x-ray analysis of the quenched samples that the equilibrium phases were the oxysulfide and the sesquioxide of each element for both systems. The equilibrium reactions may be written, respectively, as



The Gibbs energy changes for these reactions were calculated from the measured oxygen partial pressures. The calculated sulfur partial pressures are listed in Table IV. The Gibbs energies of formation of oxysulfides of these elements were calculated based on the Gschneidner's recommended values for the Gibbs energies of formation of oxides and are shown in Table V. For the Gd-S-O system, Dwivedi and Kay (6) have reported the data of the Gibbs energy change for the reaction



Based on their value and the present results, the Gibbs energy of formation of $\text{Gd}_2\text{O}_2\text{SO}_4$ was determined. The calculated value is shown in Table V.

The Gibbs energy of formation of $\text{Y}_2\text{O}_2\text{S}$ is shown in Fig. 3. The data of Dwivedi and Kay (7) are 9.4 kJ more positive than ours. The broken line indicates the estimated value by Gschneidner *et al.*, which agrees fairly well with the present result in view of the large uncertainty given in their report.

Estimated uncertainty.—In the present measurements of the Gibbs energy changes of the reactions, some errors are introduced from the uncertainties of the thermodynamic data used in the calculation of sulfur chemical potentials. These errors are estimated as follows. First, we assumed the errors of the formation energies of SO_2 , S_2O , and S, which are considered to have the most serious effect on the result of the calculations, to be ± 4200 , ± 2100 , and ± 2100 J, respectively. Then, the uncertainties of the calculated results were evaluated. The typical values introduced from this effect were ± 4150 J for Nd (reaction [12]) and ± 450 J for Ce (reaction [10]). The uncertainties introduced from the EMF measurement were added to these values and the total uncertainties are shown in Table IV. The uncertainties of the free energies of formation of oxysulfide and oxysulfate given in Table V are considerably large. The main reason for this large uncertainty comes from the low accuracy of the Gibbs energy

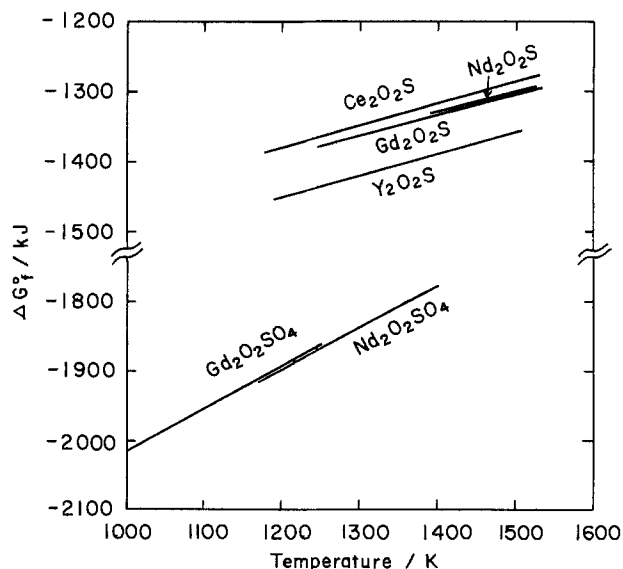


Fig. 6. Standard Gibbs energies of formation of $\text{Ce}_2\text{O}_2\text{S}$, $\text{Gd}_2\text{O}_2\text{S}$, $\text{Nd}_2\text{O}_2\text{S}$, $\text{Y}_2\text{O}_2\text{S}$, $\text{Gd}_2\text{O}_2\text{SO}_4$, and $\text{Nd}_2\text{O}_2\text{SO}_4$ as a function of temperature.

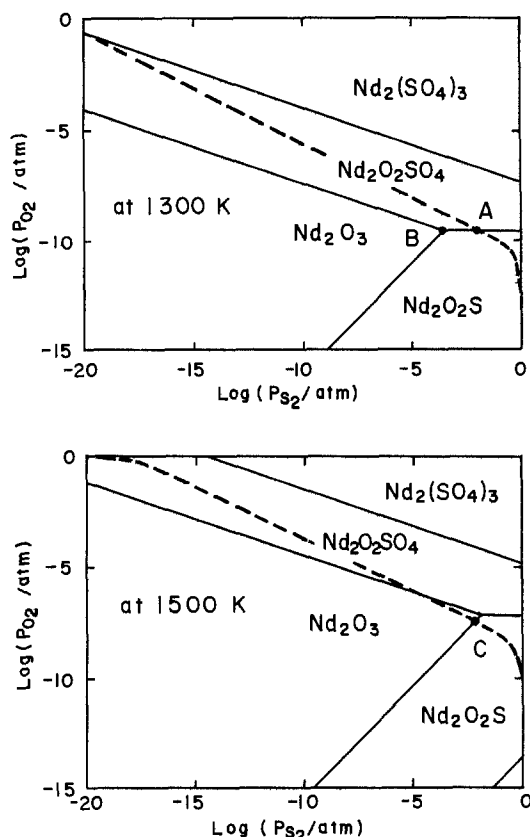


Fig. 7. P_{S_2} - P_{O_2} potential diagrams of the system Nd-O-S for 1300 and 1500 K. The broken lines represent the condition of $P_{total} = 1$ atm.

of formation of oxides used as the basis of the calculations.

The thermodynamic stabilities of oxysulfides and oxysulfates.—The Gibbs energies of formation of oxysulfides and oxysulfates determined in this study are summarized in Fig. 6. The standard entropies of formation of oxysulfide and oxysulfate do not vary significantly from one rare-earth element to another, and have values of about -300 and -610 J/K-mol, respectively. Gschneidner *et al.* estimated that the stability of oxysulfide increases as the atomic number of the constituent rare-earth element increases. The present data also may show essentially a similar trend, but it is not much clearer. On the other hand, the stability of $Nd_2O_2SO_4$ is almost the same or a little larger than that of the heavier rare-earth oxysulfate $Gd_2O_2SO_4$. Considering that the oxysulfate of lanthanum did not decompose at the highest temperature of the present measurement, it appears that the stability of oxysulfate decreases as the atomic number of the constituent rare-earth element increases. These considerations explain the fact that the stability of the oxysulfate with respect to the oxysulfide shows the more obvious dependence on the atomic number of the constituent, which was reported by Dwivedi and Kay (6).

The phase equilibrium relations.—The P_{S_2} - P_{O_2} potential diagrams for Nd-S-O system, in which the free energies of formation of oxysulfide and oxysulfate were determined

in the present work, were made for 1300 and 1500 K, as shown in Fig. 7. The thermodynamic data for normal sulfate are based on the recommended value by Kellogg (22). In Fig. 7, the condition of $P_{total} = 1$ atm is shown by the dashed line. The present experimental condition is represented by point A for 1300 K and by point C for 1500 K. The experiment of Dwivedi and Kay (6) is of the three condensed phase equilibria. Their experimental condition for 1300 K may be represented by point B. At 1500 K, the condition represented by point D is located at the total pressure of more than 1 atm. The decomposition of oxysulfate observed by Dwivedi and Kay (6) may be explained by the above considerations.

Acknowledgments

The authors would like to thank Dr. S. Otsuka for the helpful advice and Mr. K. Utata for his help in the experimental work.

Manuscript submitted Feb. 5, 1985; revised manuscript received May 17, 1985.

Osaka University assisted in meeting the publication costs of this article.

REFERENCES

1. R. J. Fruehan, *Met. Trans.*, **10B**, 143 (1979).
2. N. Fukatsu, H. Mukai, and Z. Kozuka, *J. Jpn. Inst. Metal.*, **44**, 412 (1980).
3. N. Fukatsu and Z. Kozuka, *J. Min. Metall. Inst. Jpn.*, **99**, 49 (1983).
4. N. Fukatsu and Z. Kozuka, *J. Jpn. Inst. Metal.*, **45**, 1263 (1981).
5. N. Fukatsu and Z. Kozuka, *Metall. Rev. MMIJ*, **1**, 27 (1984).
6. R. K. Dwivedi and D. A. R. Kay, *Met. Trans.*, **15B**, 523 (1984).
7. R. K. Dwivedi and D. A. R. Kay, *J. Less-Common Metals*, **102**, 1 (1984).
8. N. Fukatsu, S. Tokumoto, and Z. Kozuka, *J. Min. Metall. Inst. Jpn.*, **91**, 785 (1975).
9. H. R. Larson and J. F. Elliott, *Trans. Metall. Soc. AIME*, **239**, 1713 (1967).
10. A. W. Espelund and S. N. Flengas, *Can. J. Chem.*, **49**, 1545 (1971).
11. J. M. Skeaff and A. W. Espelund, *Can. Metall. Quart.*, **12**, 445 (1973).
12. L. Wittung, *Chem. Scr.*, **10**, 21 (1976).
13. K. Sadakane, M. Kawakami, and K. Goto, *Tetsu-to-Hagane*, **63** (1977).
14. A. W. Espelund and H. Jynge, *Scan. J. Metall.*, **6**, 256 (1977).
15. T. Rosenqvist, *Met. Trans.*, **9B**, 337 (1978).
16. J. W. Patterson, *This Journal*, **118**, 1033 (1971).
17. H. Schmalzried, *Z. Electrochem.*, **66**, 572 (1962).
18. I. Barin and O. Knacke, "Thermochemical Properties of Inorganic Substances," Springer-Verlag, New York (1973); I. Barin, O. Knacke, and O. Kubaschewski, "Thermochemical Properties of Inorganic Substances," Supplement, Springer-Verlag, New York (1977).
19. CODATA key values, *J. Chem. Thermodynamics*, **10**, 903 (1978).
20. Y. S. Touloukian and T. Makita, "Thermophysical Properties of Matter," Vol. 6 and 6s, The TPRC Data Series, IFI/Plenum, New York-Washington (1970).
21. K. A. Gschneidner, N. Kippenham, and O. D. McMasters, "Thermochemistry of Rare Earths," Rep. IS-RIC, Institute for Atomic Research, Iowa State University, Ames, IA (1973).
22. H. H. Kellogg, *Trans. Metall. Soc. AIME*, **230**, 1622 (1964).

Hot Corrosion of Nickel in Na₂SO₄-CaSO₄ Mixtures

M. Arbab and S. R. Shatynski¹

Department of Materials Engineering, Rensselaer Polytechnic Institute, Troy, New York 12181

ABSTRACT

The hot corrosion of pure nickel was studied in Na₂SO₄-CaSO₄ salt mixtures at 900°C in purified oxygen. The kinetics of the reactions and the microstructures of the reaction products were examined. The effect of pure CaSO₄ was shown to be only slightly different than simple oxidation. The addition of Na₂SO₄, which resulted in lower melting deposits, significantly enhanced the corrosion. Both V₂O₅ and PbO additions to the salt resulted in reduced corrosion compared with the Na₂SO₄ salt. These results are correlated with existing models for hot corrosion.

Nickel-based superalloys have been proposed as candidate materials for heat-transfer tubes in fluidized bed coal combustors (fbcc) (1). Sulfur emissions in fbcc's can be minimized by adding limestone, which reacts with sulfur impurities to form the stable solid CaSO₄, which condenses on the heat-transfer tubes and forms a dense, adherent deposit. In one test fbcc, a 50 μm thick deposit was formed after only 500h of operation (2). Accelerated corrosion of heat-transfer tubes has been observed in some test fbcc's. In one test fbcc, nickel-based superalloy and stainless steel tubes were found to corrode with a linear rate (3). Significant amounts of CaSO₄ deposit were found above the corrosion product. The extent to which CaSO₄ itself is responsible for the observed corrosion in fbcc's is not clear. Also contributing may be a reducing/sulfidizing environment, which is thought to result from a low oxygen potential at the deposit/scale interface or from high carbon concentration due to uneven coal/air distributions in the fbcc (4). The reducing/sulfidizing environment may be solely responsible for the observed corrosion or may increase the corrosive activity of the CaSO₄ deposit. Other corrosive impurities found in coal itself, such as sodium, potassium, lead, and vanadium may also play a role (5).

The study of high temperature corrosion of transition metals in the presence of molten salts, particularly Na₂SO₄, has been the subject of many investigations (1, 6, 7). A variety of different models have been proposed, among which the acid-basic fluxing model of Goebel *et al.* (12) that was extended later by Rapp and Goto (7) appears the most promising. Goebel *et al.* (12) have proposed a model based upon the fluxing or dissolution of the protective scale by the basic or acidic component of Na₂SO₄. Basic fluxing is associated with the generation of a high concentration of oxide anions (O⁻²), whereas acidic fluxing is generally achieved by the dissolution of MoO₃, WO₃, or other acidic oxide from the corrosion products on the alloy. Rapp and Goto (7) suggested that fluxing of an oxide can only be self-sustained by the establishment of a negative solubility gradient at the oxide/salt interface. Localized electrochemical half-reactions spatially separated are used to describe the corrosion reactions.

This study compares the corrosion due to CaSO₄ and Na₂SO₄-CaSO₄ mixtures with that due to Na₂SO₄. Pure nickel was chosen as the test alloy for a number of reasons. First, nickel is the base metal of most superalloys. A complex superalloy B-1900 was also studied for a comparison; the results are reported in a separate publication (17). Second, nickel is an excellent model system, because only a limited number of reaction products (NiO, Ni₃S₂, and NiS) are possible.

Experimental Procedure

Standard thermogravimetric analysis (TGA) supplemented with scanning electron microscopy (SEM) and energy dispersive x-ray analysis (EDAX) were employed in the experiments. Samples were prepared from high purity nickel rods (Table I). The rods were cut into disks of 0.5 cm diam and of approximately 0.22 cm thickness.

¹Deceased.

Each sample had a 0.16 cm hole drilled for suspending in the TGA rig. Typical total area of each sample was 0.80 cm²/g. Samples were then annealed at 900°C for 1h (in static air) to remove the residual stresses. They were subsequently ground to 600 grit and degreased. Samples were finally preheated to 300°C and sprayed with an aqueous salt mixture, producing a salt coating layer corresponding to 2 mg/cm².

The effects of four chemical compounds, *i.e.*, Na₂SO₄, CaSO₄, V₂O₅, PbO, and mixtures thereof, on the corrosion of nickel were studied. Among the four, only Na₂SO₄ is highly soluble in distilled water. The solubility of CaSO₄ is only about 2.09 g/liter of H₂O. In order to obtain a homogeneous solution, the ratio of CaSO₄ to water was closely controlled. Solubilities of PbO and V₂O₅ in water are very low. Therefore, a solution of the former in acetone was used and the mixture of the latter in water was carefully homogenized prior to each application.

Since the first few minutes of high temperature exposure of samples to an oxidizing atmosphere were found to be extremely critical in these experiments, all samples were kept out of the hot zone of furnace (at 300°C) and in 1 atm of purified argon during the elementary steps of preparing the system for a run. After a run was completed, corroded samples mounted and cross sections through the corrosion product were polished to 3 μm grit for morphological studies. All samples were oxidized in 1 atm of oxygen.

Results and Discussion

For pure Na₂SO₄-coated samples, extensive corrosion was noticed when the samples were exposed to 1 atm oxygen at 900°C. The melting point of Na₂SO₄ is 884°C. Samples coated with 2 mg/cm² had weight gains in excess of 20 mg/cm² before the accelerated growth came to an end (Fig. 1). Goebel *et al.* (6) have obtained similar results for the hot corrosion of Ni in the presence of 0.5 mg/cm² Na₂SO₄ at 1000°C. That study shows a similar termination after a weight gain of only 4 mg/cm². This significant difference emphasizes the role of salt quantity in determining the extent of hot corrosion (6). It was also noticed that when a sample was exposed to additional Na₂SO₄ coating after the termination of the first accelerated growth and initiation of stage three (after 70 min), rapid linear growth was again observed. These results are in agreement with the point of view expressed by Stringer (1), who noted that even though the basic fluxing model is not self-sustaining, it should not be excluded as a possible explanation for catastrophic hot corrosion of alloys.

Table I. Concentration of impurities in the nickel samples

Element	ppm
Iron	<3
Aluminum	<1
Calcium	<1
Chromium	<1
Copper	<1
Magnesium	<1
Silicon	<1
Silver	<1

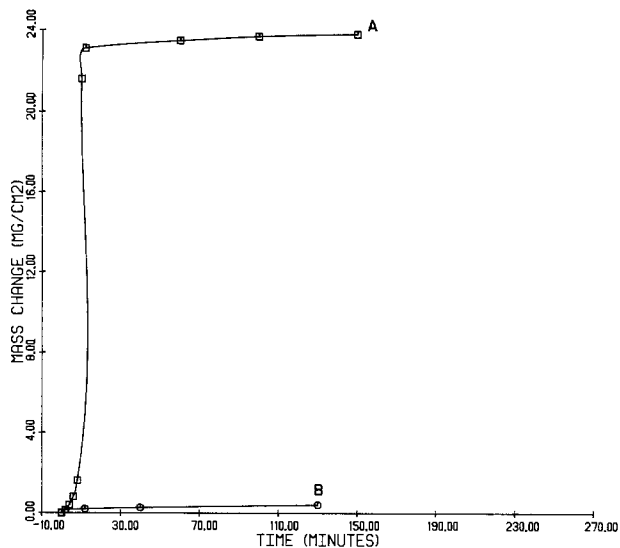


Fig. 1. Variations of weight gain with time for nickel samples exposed to 1 atm of oxygen at 900°C. A: coated with 2 mg/cm² of Na₂SO₄. B: simple oxidation.

Samples coated with 2 mg/cm² of CaSO₄ and in 1 atm of oxygen did not experience any considerable hot corrosion attack. The TGA results in this case were comparable to that of simple oxidation, which is shown as curve B in Fig. 1. The crucible experiments with 2g of CaSO₄ produced similar results. The melting point of this salt is 1450°C, *i.e.*, considerably above the experimental temperature of 900°C, and molten salt was not observed at any time in these experiments. Thus, according to any of the fluxing models, the occurrence of extended hot corrosion is not expected at 900°C.

The TGA results for nickel coated with 2 mg/cm² of Na₂SO₄-CaSO₄ mixtures are shown in Fig. 2 and 3. The curves indicate that as the CaSO₄ content in the mixture increases, the extent of weight gain decreases. For 40% CaSO₄-60% Na₂SO₄,² however, the extent of weight gain compared to the immediate curves is higher, *i.e.*, for this mixture, a relative maximum of attack exists. Beyond the above mixture, the degree of attack decreases uniformly, and for mixtures containing 80% or more of CaSO₄, the TGA results correspond to that of simple oxidation. According to the CaSO₄-Na₂SO₄ phase diagram (16), for compositions greater than 3% CaSO₄, a liquid phase does not

²Unless otherwise specified, numbers preceding a compound indicate its weight percentage in the mixture.

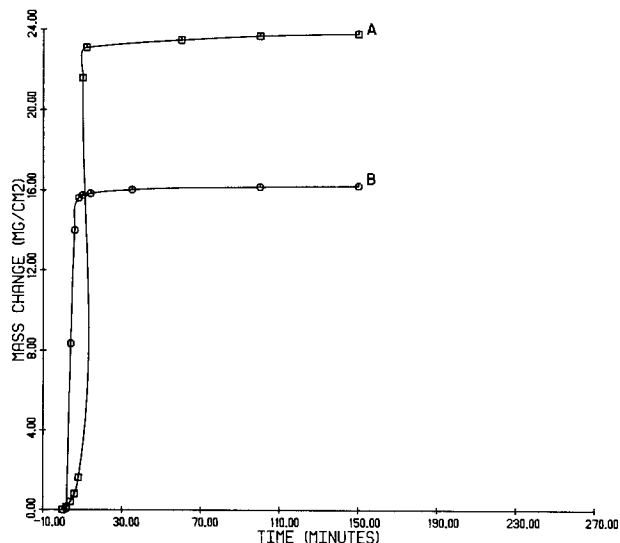


Fig. 2. Variations of weight gain with time for nickel samples exposed to 1 atm of oxygen at 900°C and coated with 2 mg/cm² of 100% Na₂SO₄ (A) and 90% Na₂SO₄-10% CaSO₄ (B).

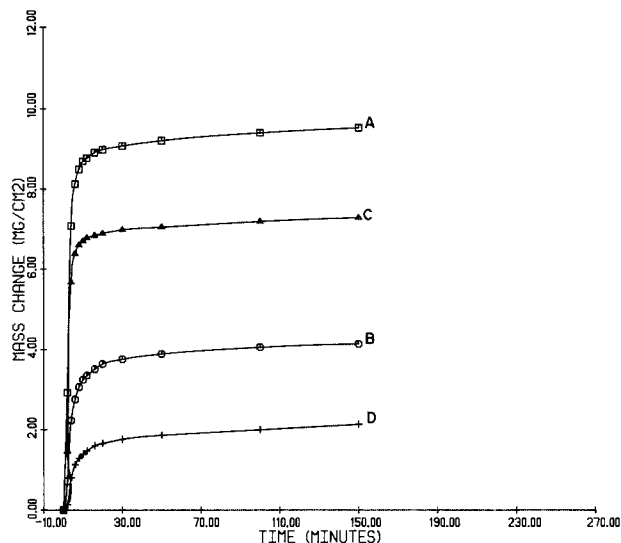


Fig. 3. Variation of weight gain with time for nickel samples exposed to 1 atm of oxygen at 900°C and coated with 2 mg/cm² of: A, 80% Na₂SO₄-20% CaSO₄; B, 70% Na₂SO₄-30% CaSO₄; C, 60% Na₂SO₄-40% CaSO₄; D, 50% Na₂SO₄-50% CaSO₄. Note the existence of a relative maximum weight gain for the eutectic salt composition.

exist at 900°C. The eutectic composition of this system is a 39% CaSO₄-61% Na₂SO₄ mixture which melts at 913°C. Therefore, the phase diagram indicates that the salt deposit should have remained solid and that hot corrosion of nickel beyond 3% CaSO₄-Na₂SO₄ should have been quite low. However, the possibility of the presence of other compounds has not been included in the above analysis.

If the salt does not melt at 900°C, then the high temperature oxidation of the sample will proceed initially and the formation of NiO will introduce a third compound in addition to Na₂SO₄ and CaSO₄. Gupta and Rapp (13) have shown that there is a high degree of solubility of NiO in Na₂SO₄ when $\alpha_{\text{NiO}} > 10^{-4}$ at 927°C. These basic conditions have been shown to exist in Na₂SO₄ melts at 900°C under certain conditions (6, 7). The dissolution of NiO in the salt may lead to a decrease in the melting point of the Na₂SO₄-CaSO₄ mixture, which in turn will result in the accelerated attack to the sample. Considering that most CaSO₄-Na₂SO₄ mixtures are solid salt layers at 900°C, in contrast to pure Na₂SO₄, Ni transport must occur in the solid layer or at local regions where there is melting of Na₂SO₄ for the above argument to be valid.

Even though a simple binary phase diagram did not suggest the presence of a liquid phase, molten salt was observed both in the crucible experiments and on the surface of those samples coated with a variety of Na₂SO₄-CaSO₄ mixtures, including those containing more than 40% CaSO₄. An EDAX analysis of the latter samples showed that the solid salt remaining on the surface of the samples did not contain any detectable amount of Na₂SO₄. This suggests that the presence of CaSO₄, only increases the melting temperature of the salt mixture, but otherwise it does not influence the hot corrosion mechanism at 900°C.

A relative maximum weight gain was recorded for a nearly eutectic salt mixture (Fig. 1-3), while at all other experimental salt compositions there was a uniform decrease of weight gain as the ratio of CaSO₄ to Na₂SO₄ increased. Therefore, the extent of attack is an increasing function of the concentration of Na₂SO₄ mixture and is enhanced if a liquid phase is formed.

The weight gain *vs.* time curves are generally composed of three distinct regions: (i) the incubation period, (ii) the linear accelerated period, and (iii) the plateau. It was not possible to determine a common equation which could fit all three regions. It was concluded that the mechanism of scale growth differs from one period to another.

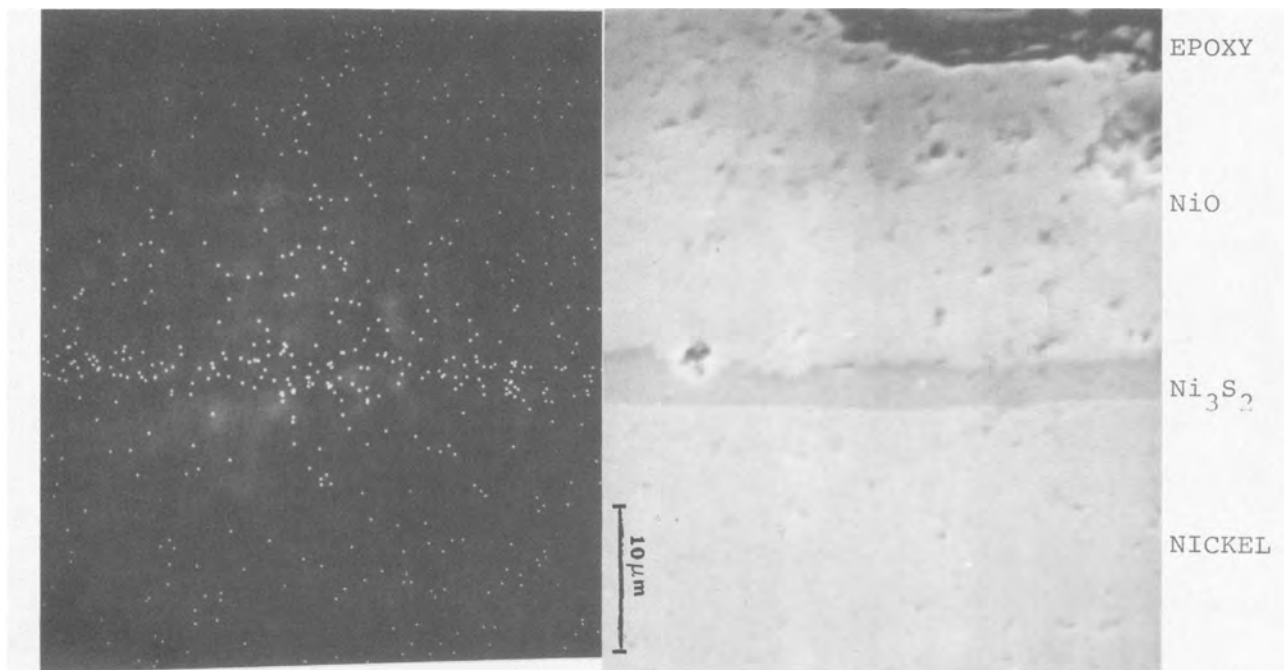


Fig. 4. Micrograph of a nickel coated with Na_2SO_4 and exposed to 1 atm of oxygen at 900°C for 24h (SEM secondary electron image) (right). Sulfur $K\alpha$ plot illustrating the sulfur distribution in the area shown (left).

The incubation stage was most pronounced in the case of pure Na_2SO_4 , while in the case of 100% CaSO_4 its absence is compatible with the attribution of the observed corrosion to simple oxidation. In most cases, the incubation period lasts up to 2 min, while for pure Na_2SO_4 an average incubation period of 10 min was observed. The linear accelerated period occurs for $2 \leq t \leq 4.5$ min of the experiment, with an exception for the case of pure Na_2SO_4 , where the longer incubation period shifts it to $10 \leq t \leq 16$ min. The rate of oxygen uptake in this stage is in the range of 1.3×10^{-3} to 3.6×10^{-3} $\text{mg}/\text{cm}^2\text{-s}$. This region becomes less distinct as the CaSO_4 content of the salt mixture increases. The rate of weight gain in the accelerated stage continuously decreases until a plateau is reached. This transition shows a parabolic behavior, and it continues for up to 14-16 min. The slopes of the plateaus for different curves are between 3.3×10^{-5} and 4.5×10^{-5} $\text{mg}/\text{cm}^2\text{-s}$. The behavior of the attack after the accelerated stage resembles that of simple oxidation. It is observed that simple oxidation of nickel consists of two stages:³ an initial parabolic growth and a plateau. The parabolic stage lasted for 13 min (comparable to 14-16 min of the former situation) and the slope of the plateau was 2.5×10^{-5} $\text{mg}/\text{cm}^2\text{-s}$. Thus, it may be concluded that the termination of the accelerated stage corresponds to the onset of simple oxidation of the corroded sample, *i.e.*, a protective scale forms beneath the nonprotective scale. However, a considerable difference between the slopes of the parabolic regions of the transition period in the presence of salt and simple oxidation of salt-free samples is noticed. In the former case, the slopes assume an average value of $0.4 \text{ mg}/\text{cm}^2\text{-s}^{1/2}$, while in the latter it is as low as $0.04 \text{ mg}/\text{cm}^2\text{-s}^{1/2}$.

The slope of the plateaus remained constant for a period of 48h except for a few instances when it slightly increased. This increase was found to be due to the cracking of the scale, as determined by the optical analysis.

Metallographic analyses indicated that a protective and coherent oxide layer (NiO) is formed adjacent to the nickel substrate during high temperature simple oxidation and its thickness is nearly uniform everywhere. The results of corrosion in pure Na_2SO_4 are shown by Fig. 4, where a typical portion of the corroded sample has been

photographed. A layer of nickel sulfide formed immediately adjacent to the nickel substrate. The physical formation of the layer, *i.e.*, its coherent contact with both the substrate and the oxide layer above it, as well as its ability to fill all gaps, suggests that at 900°C the sulfide is melted. Based on this observation and EDAX results, the sulfide layer is thought to be essentially Ni_3S_2 .

Above the sulfide layer, a thick layer of NiO has been formed. The porosity of this layer is less than what is expected from the literature (6), and its thickness increases at certain limited areas. These areas of higher corrosion differ morphologically from other parts of the scale (Fig. 5). The outer NiO is layered and porous, and further inward a more uniform and compact oxide similar to that found in the rest of the scale exists. Goebel and Pettit (6) have reported this latter type of scale to be dominant for

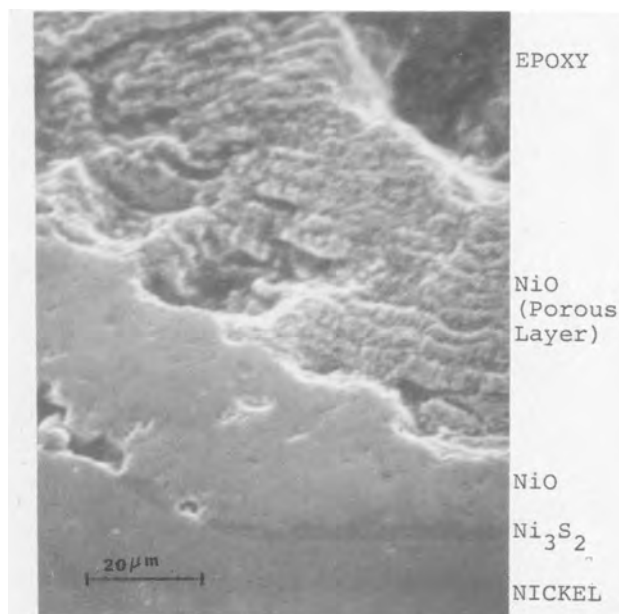


Fig. 5. Area of higher corrosion on a nickel sample coated with Na_2SO_4 and exposed to 1 atm of oxygen at 900°C for 24h (SEM secondary electron image). This morphology is typical of high corrosion areas on different samples.

³A completely parabolic growth of the scale in the case of simple oxidation was not registered owing to the lack of apparatus precision for small weight gains. However, since both cases are affected equally, a comparison of the results is possible.

Na_2SO_4 corroded nickel base alloys, and their theory of basic fluxing is partly based on similar observations. As in the case of pure Na_2SO_4 , the scale for any of the salt mixtures with a CaSO_4 content of less than 80% consists of a sulfide and an oxide layer. The uniformity of the scale generally increases as the amount of Na_2SO_4 in the salt decreases. The NiO regions closer to the nickel substrate are less porous than the outer sections. This is in accordance with our earlier discussion, where a comparison with the TGA results for simple oxidation of nickel showed that after the accelerated attack, which results in the formation of a porous oxide, a more protective thick oxide layer similar to the scale on the salt-free samples is formed. Also, the scale includes some sulfide particles, which are nonuniformly dispersed. This indicates that the oxygen partial pressure in the oxide layer can be low enough to permit the formation of intermixed scales (14, 15).

For those salt mixtures containing 80% or more CaSO_4 , the sulfide layer was virtually absent and sulfide particles were dispersed in the oxide layer. Therefore, we concluded that for such salt mixtures the sulfur diffusing through the initial oxide was totally consumed by nickel sulfide (Ni_3S_2) formation within the oxide layer and did not reach the Ni-NiO interface. This suggests that the initial formation of Ni_3S_2 occurs in the oxide layer, probably creating an easy path for sulfur diffusion, as pointed out by Giggins and Pettit (14) and Birks (15), in previous cases where a sulfide layer was formed. The extent of corrosion for high CaSO_4 salts and especially in the case of pure CaSO_4 resembles simple oxidation of nickel except for some sulfidation, which implies limited solid-state decomposition of CaSO_4 at the salt/scale interface.

The occurrence of the local areas of higher attack may be due to one or more of the following reasons.

1. During the coating of the sample with a salt mixture, it was noted that upon the complete evaporation of water more salt remained in the hole drilled through the sample than any other place. The extent of corrosion in this region was high and the overall morphology resembled that of Fig. 5 and 6. Therefore, some geometrical variation on the surface, caused during the sample preparation (such as a pit), may lead to a region of high salt buildup and eventually into a region of more extensive hot corrosion.

2. Since Na_2SO_4 is soluble in water and CaSO_4 is not, the latter will precipitate on the surface of the preheated sample before the complete evaporation of water. This

can result in the local segregation of the two compounds; local regions rich in Na_2SO_4 may suffer enhanced attack. However, the uniform thickness of the salt layers left on the corroded sample, the absence of such areas of higher corrosion on samples coated with salt mixtures containing V_2O_5 and PbO (see below), and the increase in the uniformity of the scale with increasing the CaSO_4 concentration as mentioned above indicate that additional factors may be involved.

3. Finally, sample variations such as different grain structures can have a strong effect on the extent of hot corrosion attack and on the final corrosion morphology.

The general morphology of the samples contradicts certain aspects of the theory of simple basic fluxing based on sulfidation. This theory assumes that sulfur is generated from the melt and is transported to the metal where sulfidation occurs. As a consequence, the melt increases in oxygen anion activity and attacks the protective NiO. An examination of the areas of higher corrosion shows that the thickness of the sulfide layer is either less than or equal to that of other regions where the attack was uniform and slower (Fig. 6). However, according to simple basic fluxing, the contrary is expected; *i.e.*, higher corrosion rates should be accompanied by higher sulfidation. Thus, sulfidation is one of the reduction reactions, but not the only one. This view is consistent with the treatment of Rapp and Goto (7).

The effects of V_2O_5 and PbO impurities.—A CaSO_4 : Na_2SO_4 ratio of 1.5, which is close to the eutectic composition, was selected for this part of the study. Other mixtures were shown to produce similar results.

V_2O_5 .—In order to preserve a Na_2SO_4 : CaSO_4 ratio of 1.5 in the presence of the impurity, mixtures of 57% Na_2SO_4 -38% CaSO_4 -5% V_2O_5 and 59% Na_2SO_4 -39% CaSO_4 -2% V_2O_5 were used. For 2% V_2O_5 , no differences in the TGA or the metallographic analysis were noticed compared with the vanadium-free mixture. With 5% V_2O_5 , the extent of attack was reduced to a level comparable to simple oxidation (Fig. 7). The micrographs of such samples also indicated a very limited attack. Immediately above the substrate, a thin layer of NiO was formed. This scale was coherent and compact and consisted of three regions. The interior layer, adjacent to the substrate, was pure NiO. Above it was a second layer containing Ni, V, and O, presumably nickel vanadate. The third layer, adjacent to the salt phase, was again NiO, but it contained considerable amounts of calcium and sulfur as solid solutions. The V_2O_5 -NiO phase diagram (16) indicates that at 900°C for more than 75% NiO a solid nickel vanadate

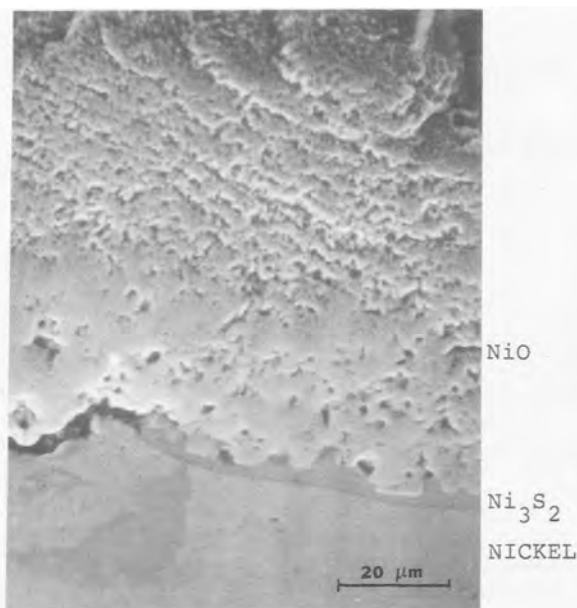


Fig. 6. Area of higher corrosion on a nickel sample coated with 85% Na_2SO_4 -15% CaSO_4 and exposed to 1 atm of oxygen at 900°C for 24h (SEM secondary electron image). The thickness of Ni_3S_2 layer in such areas is either less or equal to that of the same layer in less corroded areas.

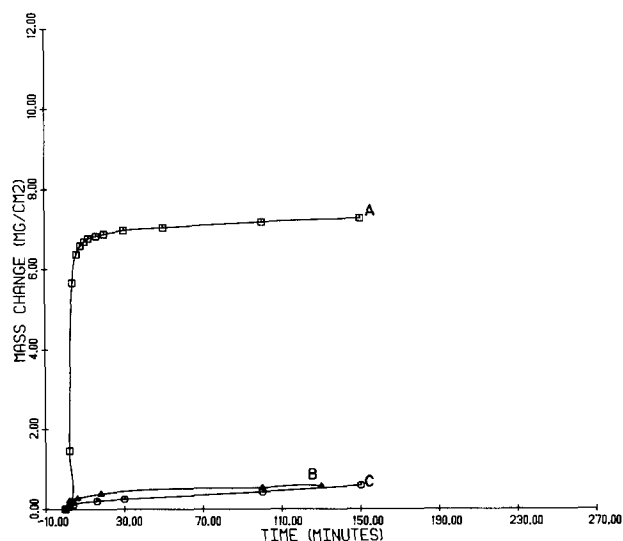


Fig. 7. Variations of weight gain with time for nickel samples exposed to 1 atm of oxygen at 900°C and coated with 2 mg/cm² of: A, 60% Na_2SO_4 -40% CaSO_4 ; B, 57% Na_2SO_4 -38% CaSO_4 -5% V_2O_5 ; C, 59% Na_2SO_4 -39% CaSO_4 -2% PbO .

$\text{Ni}_3(\text{VO}_4)_2$ and nickel oxide phase exists. Also, based on a study of the effects of V_2O_5 on the high temperature oxidation of nickel, Bornstein and DeCresente (10) have reported that in 1 atm of oxygen the formation of a nickel-vanadium oxide on nickel samples coated with V_2O_5 , considerably decreased the extent of oxidation. Therefore, in the case of the present study, the formation of a solid and compact $\text{Ni}_3(\text{VO}_4)_2 + \text{NiO}$ layer is considered to be similarly responsible for the protection of the sample from an otherwise accelerated attack. No localized areas of enhanced corrosion were detected.

Finally, it must be noted that even though the presence of 2% V_2O_5 also results in the formation of $\text{Ni}_3(\text{VO}_4)_2$, the quantity of the product is not high enough to form a protective layer.

PbO.—A mixture of 59% Na_2SO_4 -39% CaSO_4 -2% PbO was used for this experiment. According to the TGA results (Fig. 7) and the SEM analysis, the extent of corrosion is reduced to that of simple oxidation in the presence of a 2% PbO mixture. The reasons for an inhibiting effect have not been understood yet, especially since it was observed that pure PbO enhances the high temperature oxidation of nickel, both in the present study and elsewhere (11). On the other hand, Chatterji *et al.* (9) have noticed the same inhibitory effect of PbO when they studied the hot corrosion of nickel samples coated with 1% PbO-99% Na_2SO_4 (mole percentages are indicated). The morphology reported from their investigation resembles the morphology observed in the present study, *i.e.*, the presence of a sulfide-free, dense oxide layer.

Summary

The high temperature corrosion of nickel induced by various salt deposits was studied at 900°C in an environment of pure oxygen by the use of TGA and metallographic techniques. The salt deposits were Na_2SO_4 , CaSO_4 , various mixtures of Na_2SO_4 - CaSO_4 , and mixtures of the Na_2SO_4 - CaSO_4 eutectic to which small amounts of V_2O_5 or PbO were added. Enhanced attack relative to simple oxidation was observed when the deposit, or a portion of it, melted. Thus, fast attack was observed for pure Na_2SO_4 and mixtures containing up to 50% CaSO_4 . Pure CaSO_4 and 80% CaSO_4 -20% Na_2SO_4 did not melt and did not exhibit enhanced attack. The addition of 2% PbO or 5% V_2O_5 to the eutectic Na_2SO_4 - CaSO_4 mixture greatly inhibited the rate of attack. In the case of the V_2O_5 addition,

a protective layer of nickel vanadate formed. PbO apparently plays a different, but as yet not understood, inhibitory role.

Manuscript submitted Feb. 16, 1983; revised manuscript received Feb. 26, 1985.

Rensselaer Polytechnic Institute assisted in meeting the publication costs of this article.

REFERENCES

1. J. Stringer, *Ann. Rev. Mater. Sci.*, **7**, 477 (1977).
2. R. H. Cooper and J. H. DeVan, in "Ash Deposits and Corrosion Due to Impurities In Combustion Gases," R. W. Bryers, Editor, pp. 561-579, Hemisphere Publication Corporation, Washington DC (1978).
3. J. W. Clark and C. J. Spengler, Proceedings of 4th Annual Conference on Materials for Coal Conversion and Utilization, 5-11 (1979).
4. J. Stringer and S. Ehrlich, ASME Paper 76-WA/CS-4, Ann. of Soc. of Mech. Eng., NY (1976).
5. W. F. Wigton, in "Ash Deposits and Corrosion Due to Impurities in Combustion Gases," R. W. Bryers, Editor, pp. 537-555, Hemisphere Publication Corporation, Washington, DC (1978).
6. J. A. Goebel and F. S. Pettit, *Met. Trans.*, **1**, 1943 (1970).
7. R. A. Rapp and K. S. Goto, Abstract 350, p. 947, The Electrochemical Society Extended Abstracts, Vol. 78-2, Pittsburgh, PA, Oct. 15-20, 1978.
8. T. Huang, E. A. Gulbransen, and G. H. Meier, *J. Metals*, **31**, 25 (1979).
9. D. Chatterji, D. W. McKee, G. Romeo, and H. S. Spacil, *This Journal*, **122**, 941 (1975).
10. N. S. Bornstein and M. A. DeCresente, in "Properties of High Temperature Alloys," Z. A. Foroulis and F. S. Pettit, Editors, p. 626, The Electrochemical Society Softbound Proceedings Series, Princeton, NJ (1977).
11. M. Obayashi, *J. Jpn. Inst. Metals*, **38**, 518 (1974).
12. J. A. Goebel, F. S. Pettit, and G. W. Goward, *Met. Trans.*, **4**, 261 (1973).
13. D. K. Gupta and R. A. Rapp, *This Journal*, **127**, 2194 (1980).
14. C. S. Giggins and F. S. Pettit, *Oxid. Metals*, **14**, 363 (1980).
15. N. Birks, M. C. Pope, and P. Singh, "Proceedings of the International Symposium on the Reactivity of Solids," Cracow, Poland (1980).
16. E. M. Levin, C. R. Robbins, and H. W. McMurdie, "Phase Diagrams for Ceramists," The American Ceramic Society, Columbus, OH (1969).
17. S. F. C. Stewart and S. R. Shatynski, *Oxid. Metals*, **18**, 163 (1982).

Carburization Mechanisms of High Chromium Alloys

T. A. Ramanarayanan* and D. J. Srolovitz¹

Exxon Research and Engineering Company, Corporate Research Science Laboratories, Annandale, New Jersey 08801

ABSTRACT

Carburization is a major mode of corrosive degradation of high chromium alloy materials in many high temperature processes. The process generally involves the transfer of carbon from the gas phase onto the alloy surface followed by diffusion of carbon to the alloy interior with concurrent precipitation of chromium-rich carbide phases. The kinetics of this overall process has been determined by thermogravimetry in the temperature range 1173-1373 K using Fe-20 Cr and Ni-30 Cr model alloy systems and H_2 - CH_4 gas mixtures to provide the carburizing medium. Mathematical expressions for the overall kinetics have been developed in terms of surface reaction and diffusion steps. Both processes contribute to carburization, the influence of the surface reaction step increasing with increase in temperature. Additions of sulfur as H_2S to the gas phase slows down the surface reaction step sufficiently so that the whole carburization process can become surface reaction controlled.

High chromium alloys used in high temperature service are susceptible to carburization in environments with high carbon activity. This form of corrosion leads to the precipitation of chromium-rich carbide phases, M_{23}C_6 and M_7C_3 , in the alloy interior with resultant degradation of

the high temperature mechanical properties of the alloy (1, 2). Schnaas and Grabke (3-5) have described the carburization process in H_2 - CH_4 gas mixtures, in the absence of a surface oxide layer, as being controlled by the diffusion of carbon in the alloy, the kinetics obeying a parabolic rate law.

Grabke and co-workers (6-11) have also investigated the kinetics of decomposition of CH_4 on iron surfaces at ele-

*Electrochemical Society Active Member.

¹Present address: Los Alamos National Laboratory, Los Alamos, New Mexico 87545.

vated temperatures using extremely thin foils so as to avoid diffusion as a rate limiting step. Additions of small amounts of sulfur as H_2S to CH_4 - H_2 gas mixtures had a retarding effect on the methane decomposition kinetics.

In the present work, the kinetics of carburization of model Fe-20 Cr and Ni-30Cr alloys have been determined in the 900°-1100°C temperature range, using H_2 - CH_4 gas mixture as the carburizing medium. Further, the effect of adding small quantities of H_2S below the stability limit of CrS was investigated. The aim of the study is to develop an understanding of the contribution from surface reaction and diffusion to the overall corrosion.

Experimental Procedure

The investigations were conducted on two model alloys, Fe-20 Cr and Ni-30 Cr. The former has a body-centered cubic structure, while the latter is face-centered cubic. Further, the tendencies of Fe and Ni to partition between the metal matrix and the carbide precipitates is expected to be different. The alloys were obtained in the cast form; Fe-20 Cr alloy samples were cut from a region having an average grain size of $\sim 100 \mu m$. In the Ni-30 Cr alloy samples, the grain size varied from about $50 \mu m$ near the sample surface to $\sim 250 \mu m$ in the sample center. The samples had rectangular geometry with dimensions of $2 \text{ cm} \times 1 \text{ cm} \times 2 \text{ mm}$. The samples were ground to a 600 grit SiC finish and cleaned ultrasonically in acetone.

The procedure used in the study was to first establish the kinetics of carburization of the selected alloys in a purely carburizing environment and then add predetermined amounts of sulfur as H_2S and redetermine the carburization kinetics. The investigations were carried out in the temperature range, 1173-1373 K. Since small amounts of oxygen in the environment can lead to the formation of Cr_2O_3 on the surface of high chromium alloys, it was essential to remove trace oxygen impurity from the carburizing gas. This was done by passing the gas over an activated copper catalyst at $\sim 200^\circ C$ and subsequently drying by passing through a column of anhydrous calcium sulfate. The H_2 -2000 ppm H_2S stream was dried only and then mixed with the carburizing gas. The formation of a chromia layer would decrease the carburization rate of the alloy and would make it difficult to separate the influence of sulfur on the carburization rate from that of chromium oxide.

A H_2 - CH_4 gas mixture was used as the carburizing medium. The carbon activity in this gas mixture is fixed by the equilibrium

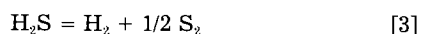


whereby

$$a_C = K_1 p_{CH_4} / p_{H_2}^2 \quad [2]$$

where K_1 is the equilibrium constant for reaction [1]. The gas mixtures used in this investigation had a carbon activity of 0.9 relative to pure graphite as the standard state.

When it was desired to fix a partial pressure of sulfur in the carburizing gas mixture, a preselected amount of H_2S was added. The sulfur pressure is then fixed by the H_2 - H_2S equilibrium



whereby

$$p_{S_2} = K_2^2 p_{H_2S}^2 / p_{H_2} \quad [4]$$

Precisely controlled gas mixture compositions were obtained by controlled flow of H_2 -10% CH_4 , H_2 -2000 ppm H_2S and H_2 through Tylan mass flow controllers.

The kinetics of carburization in the presence and absence of sulfur were determined thermogravimetrically in a Cahn 1000 thermogravimetric unit shown in Fig. 1. The alloy sample was hung from the Cahn Electrobalance by a Pt suspension wire. A vertical quartz reactor tube surrounded the sample. A preheated platinum resistance furnace could be moved up to surround the quartz reactor tube and bring the specimen to the reaction temperature

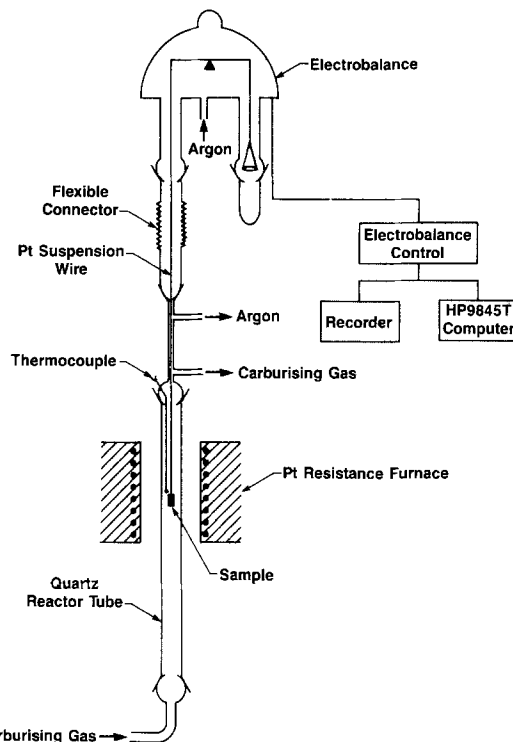


Fig. 1. Thermogravimetric assembly used for the determination of carburization kinetics.

in minutes. The reactive gases entered the quartz reactor at the bottom and exited at the top along with an argon stream used to provide an inert environment within the electrobalance. At the start of an experiment, the sample was suspended from the electrobalance and an argon stream was introduced into the quartz reactor tube. When the furnace temperature reached the desired value, the argon stream was replaced by the carburizing gas stream and after an interval of ~ 30 min the furnace was raised to heat the sample. Sample weight gain data were collected and analyzed using a Hewlett Packard 9845 T computer.

Results

Investigations on Ni-30 Cr alloys.—Most investigations of Ni-30 Cr alloys were carried out at 1173 K at a carbon activity of 0.9. The carburization kinetics in the absence of H_2S , and for three different H_2S levels, are shown in Fig. 2.

The carburized microstructure corresponding to the sulfur-free case in Fig. 2 is shown in Fig. 3. The attack is internal; carbide precipitates can be seen both within alloy grains and at alloy grain boundaries. The grain boundary carbides have penetrated much deeper into the alloy. The grain boundaries can act both as preferred nucleation

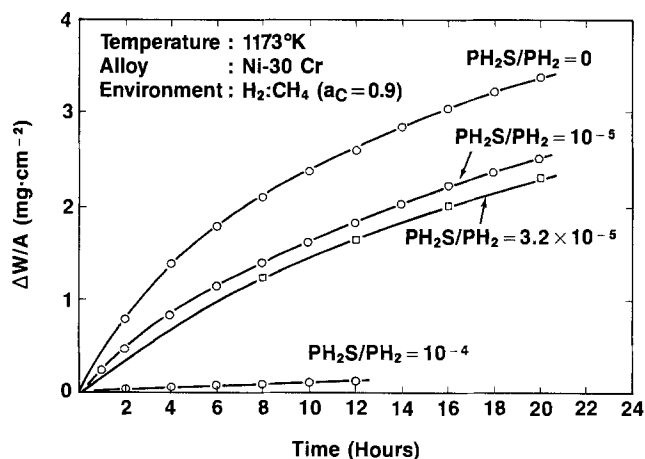


Fig. 2. Carburization data for Ni-30 Cr at 1173 K and $a_C = 0.9$ as a function of p_{H_2S}/p_{H_2} .

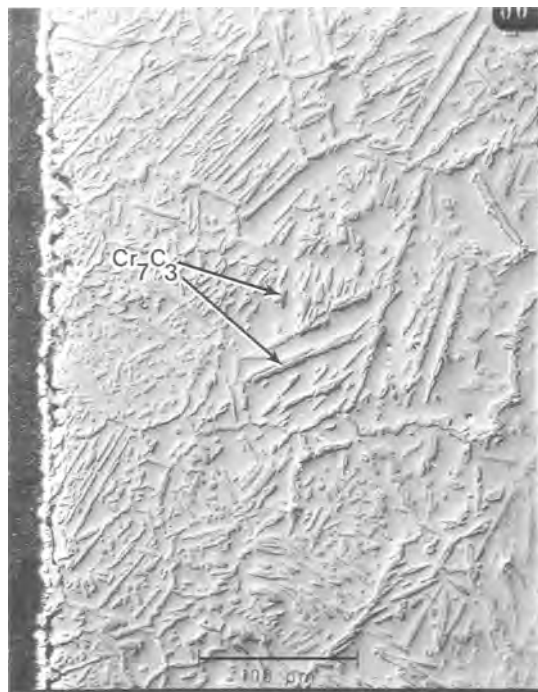


Fig. 3. Typical carburized microstructure of Ni-30 Cr

sites for carbides and high diffusivity paths for carbon transport.

The composition of the carbide phase at various depths was determined using a scanning Auger analyzer. The carbide composition was found to be independent of depth within the sample; a typical Auger spectrum is shown in Fig. 4. The carbon-to-chromium ratio as determined from the Auger spectrum corresponds to Cr_7C_3 .

Upon adding H_2S to the carburizing gas medium, the rate of carburization weight gain (Fig. 2) decreased, which is also reflected as a decrease in the depth of carburization. In Fig. 2, the kinetic carburization curves changed from a nearly parabolic time dependence in the absence of sulfur to a linear rate at higher levels of sulfur. At a $p_{\text{H}_2\text{S}}/p_{\text{H}_2}$ ratio of $\sim 9 \times 10^{-5}$ in the gas, a thin layer of chromium sulfide, CrS , precipitated on the alloy surface as detected by energy dispersive x-ray analysis. Thus the line in Fig. 2, corresponding to a $p_{\text{H}_2\text{S}}/p_{\text{H}_2}$ ratio of 9.4×10^{-5} does not describe carburization alone. For the kinetics plot for $p_{\text{H}_2\text{S}}/p_{\text{H}_2} = 5 \times 10^{-5}$ in Fig. 5, no CrS formation occurred; the extremely small linear weight gain in this case only resulted from carburization. For a ratio of 7.5×10^{-5} (Fig. 5), which is also below the stability limit of CrS ,

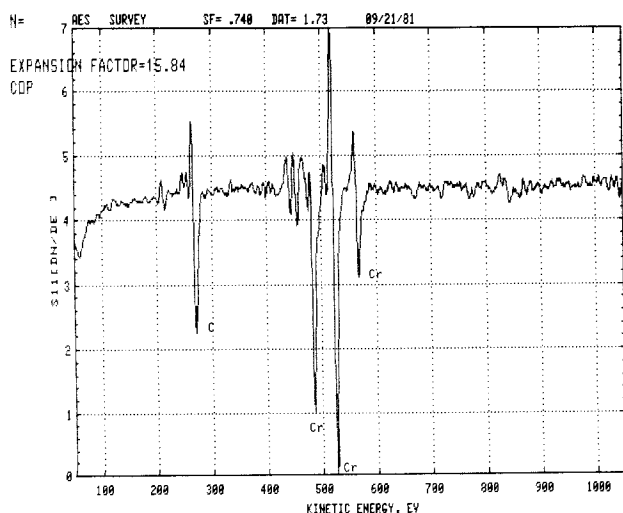


Fig. 4. Auger spectrum of Cr_7C_3 carbide

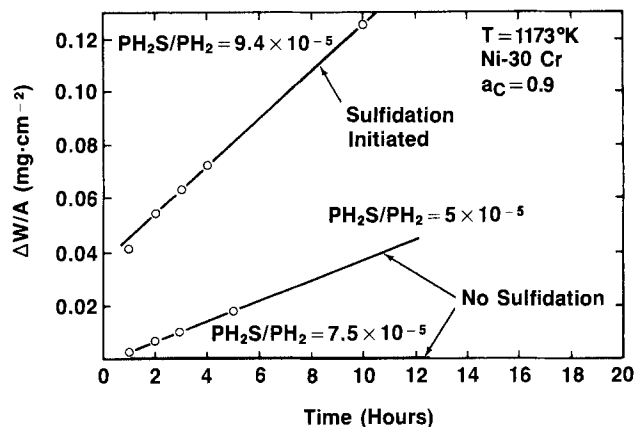


Fig. 5. Carburization kinetics of Ni-30 Cr alloy at 1173 K at higher $p_{\text{H}_2\text{S}}/p_{\text{H}_2}$ values.

no carburization weight gain could be detected. Upon exceeding a $p_{\text{H}_2\text{S}}/p_{\text{H}_2}$ ratio of 10^{-4} , the alloy corroded by sulfidation (Fig. 6). Kinetic curves for carburization of Ni-30 Cr at 1273 K are shown in Fig. 7; only one $\text{H}_2\text{S}/\text{H}_2$ ratio was investigated at this temperature.

Investigations of Fe-20 Cr alloys.—The experiments on Fe-20 Cr alloys covered three different temperatures, namely 1173, 1273, and 1373 K. Carburization kinetics at 1173 K in sulfur-free and sulfur containing environments are presented in Fig. 8. Figure 8 bears some similarities to Fig. 2 in the sense that at higher sulfur levels, the carburization weight gain approaches a linear rate law. At $p_{\text{H}_2\text{S}}/p_{\text{H}_2} = 7.5 \times 10^{-5}$ some carburization was observed in the Fe-20 Cr alloy, but none for Ni-30 Cr (Fig. 2). The car-

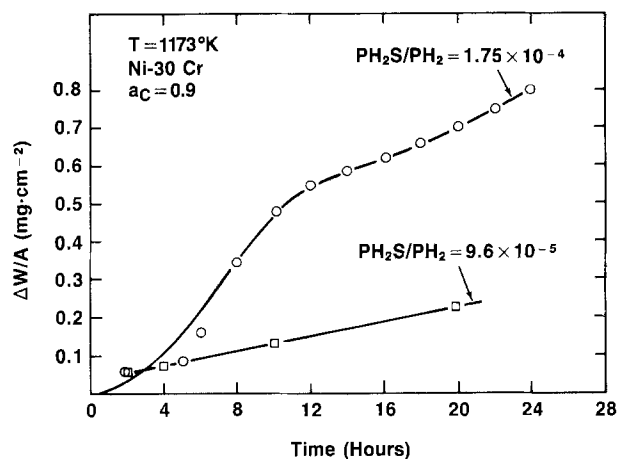


Fig. 6. Sulfidation of Ni-30 Cr alloy at 1173 K at $p_{\text{H}_2\text{S}}/p_{\text{H}_2} = 1.75 \times 10^{-4}$.

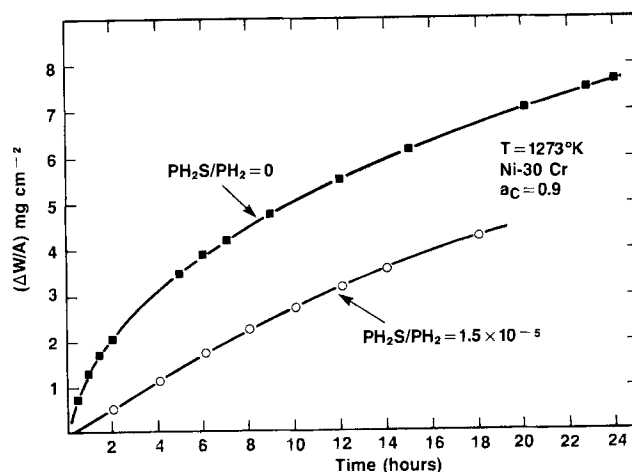


Fig. 7. Carburization kinetics of Ni-30 Cr at $a_C = 0.9$ at 1273 K

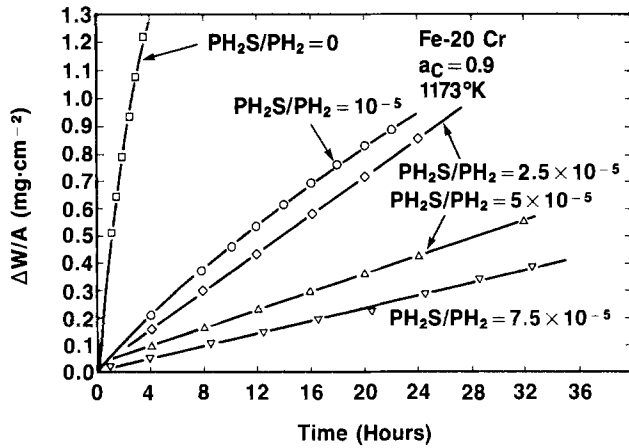


Fig. 8. Carburization kinetics of Fe-20 Cr alloy at 1173 K at various p_{H_2S}/p_{H_2} ratios.

burized microstructure for Fe-20 Cr, Fig. 9, was similar to that for the Ni-30 Cr except that the carbide was of the $M_{23}C_6$ type, M comprised of ~75% Cr and ~25% Fe. The carbide particles at the surface (Fig. 9), however, were M_7C_3 type. Upon introducing a gas mixture with $p_{H_2S}/p_{H_2} = 1.5 \times 10^{-4}$, CrS was formed at the alloy surface (Fig. 10).

When the temperature was raised to 1273 K, the kinetic curves obtained were similar to those at 1173 K, but higher H_2S levels were required to limit carburization to the same level as shown in Fig. 11. Again, the approach to a linear kinetics at higher H_2S levels is evident. Upon exceeding a H_2S/H_2 partial pressure ratio of 1.5×10^{-4} at 1273 K, sulfidation occurred in addition to carburization, leading to larger weight gains. The effect of sulfur on carburization becomes less pronounced upon increasing the reaction temperature to 1373 K (Fig. 12).

A comparison of the kinetic curves at 1173, 1273, and 1373 K for the sulfur-free experiments (Fig. 8, 11, 12) shows that there is a deviation from parabolic kinetics with increase in temperature even in the absence of sulfur.

Discussion

In the high temperature carburization of an alloy, three distinct kinetic steps are involved. 1. The transfer of car-

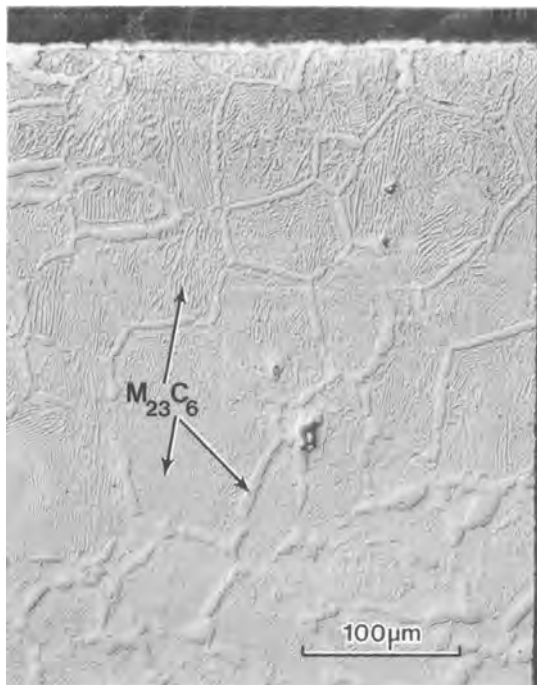


Fig. 9. Typical carburized microstructure of Fe-20 Cr alloy

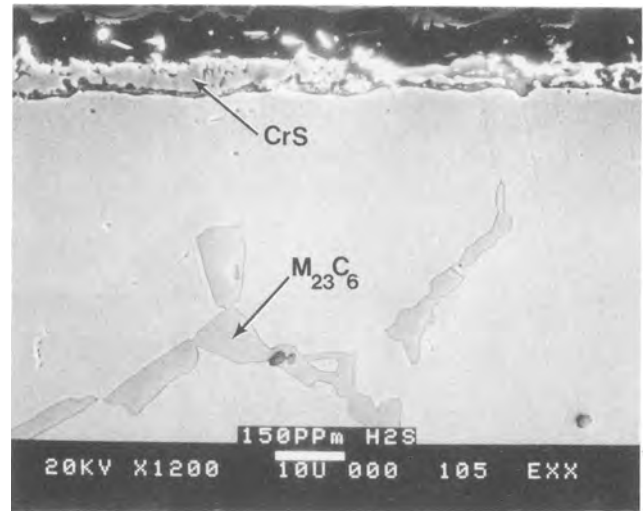


Fig. 10. Formation of chromium sulfide phase on Fe-20 Cr alloy at $p_{H_2S}/p_{H_2} = 1.5 \times 10^{-4}$ at 1173 K.

bon from the gas phase to the alloy surface and the formation of an adsorbed, carbon containing complex. 2. The diffusion of carbon from the alloy surface into the alloy interior. 3. The reaction of carbon with chromium to form chromium carbide phases in the alloy interior.

Kinetics controlled by diffusional processes with time independent boundary concentrations have a parabolic time dependence, whereas kinetics controlled by a surface reaction obey a linear rate law. The parabolic nature of the carburization weight gain *vs.* time curves in the absence of sulfur at the lower temperatures (Fig. 2 and 8) suggests that under these conditions carbon diffusion into the alloy controls the rate of carburization. The gradual approach to linear kinetics upon sulfur additions (Fig. 2, 7, 8, and 11) or increase in carburization temperature (Fig. 12) indicates that step 1 in the aforementioned sequence of steps becomes increasingly important. Thus, sulfur tends to retard the kinetics of step 1 sufficiently so that it becomes the slowest step in the sequence. Sulfur cannot penetrate the alloy rapidly enough to influence the kinetics of step 3. Further, one can conclude that an increase in temperature has a larger influence on the diffusion step as compared with the surface reaction step.

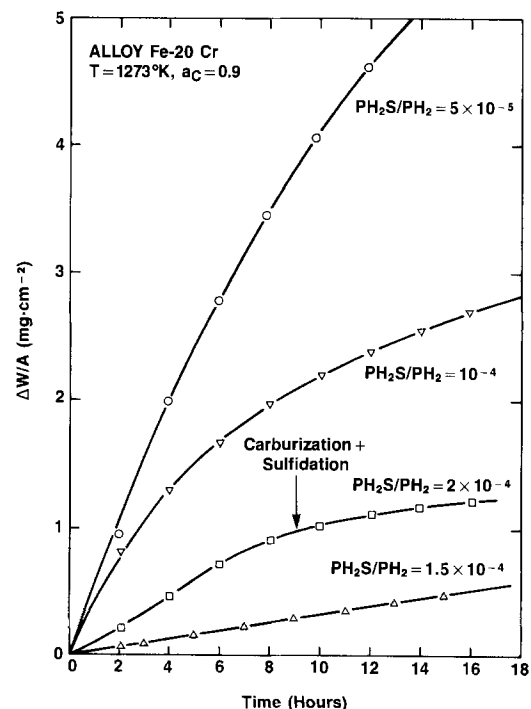


Fig. 11. Carburization kinetic data for Fe-20 Cr alloy at 1273 K

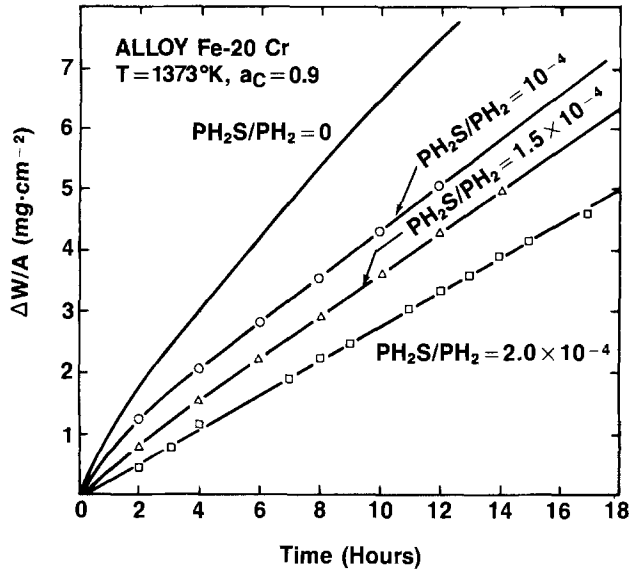
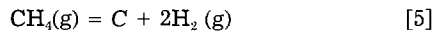


Fig. 12. Carburization kinetic data for Fe-20 Cr alloy at 1373 K

It is assumed in the discussion below that the overall process of carburization is controlled by the carbon transfer reaction at the alloy surface and carbon diffusion into the alloy bulk, step 3 being relatively rapid. The overall surface reaction transferring carbon onto the alloy surface can be represented as



where C represents carbon dissolved in the alloy. The kinetics of reaction [5] can be represented by the expression (7)

$$\frac{dn_c}{dt} = A(k_1 p_{\text{CH}_4} \cdot p_{\text{H}_2}^{-\nu} - k_2 p_{\text{H}_2}^{2-\nu} \cdot a_c^e) \quad [6]$$

where k_1 and k_2 denote the forward and backward rate constants for reaction [1], a_c^e is the activity of carbon on the alloy surface, dn_c/dt is the number of moles of carbon transferred to the alloy from the gas phase per unit time, A is the surface area, and the value of ν depends upon which of several possible rate limiting steps is controlling. Under conditions of thermodynamic equilibrium, $dn_c/dt = 0$, so that

$$k_1 p_{\text{CH}_4} p_{\text{H}_2}^{-\nu} = k_2 p_{\text{H}_2}^{2-\nu} a_c^e \quad [7]$$

where a_c^e is the equilibrium activity of carbon on the alloy surface. Substituting Eq. [7] into Eq. [6]

$$\frac{1}{A} \frac{dn_c}{dt} = k(a_c^e - a_c^s) \quad [8]$$

where k equals $k_2 p_{\text{H}_2}^{2-\nu}$.

The differential equation describing carbon diffusion into the alloy can be expressed in terms of Fick's second law as

$$\frac{\partial c_c}{\partial t} = D_c \left(\frac{\partial^2 c_c}{\partial x^2} \right) \quad [9a]$$

where D_c is the diffusivity of carbon in the alloy and x is the distance coordinate perpendicular to the surface. Equation [9a] assumes a concentration-independent diffusion coefficient, D_c . Further, if a concentration-independent activity coefficient, γ_c , is assumed, Eq. [9a] can be rewritten

$$\frac{\partial a_c}{\partial t} = D_c \left(\frac{\partial^2 a_c}{\partial x^2} \right) \quad [9b]$$

During carburization, the carbon furnished by the surface reaction in accordance with Eq. [8] must diffuse into the alloy interior. Mathematically stated

$$\frac{1}{A} \frac{dn_c}{dt} = k(a_c^e - a_c^s) = -\frac{D_c}{\gamma_c} \left(\frac{\partial a_c}{\partial x} \right)_{x=0}$$

or

$$\left(\frac{\partial a_c}{\partial x} \right)_{x=0} = \frac{-k\gamma_c}{D_c} (a_c^e - a_c^s) \quad [10]$$

where $x = 0$ represents the surface of the alloy. Additionally, one has the initial condition

$$a_c = 0 \text{ at } x \geq 0, t = 0 \quad [11]$$

The solution which satisfies Eq. [9-11] is given by

$$a_c = a_c^e \left\{ \operatorname{erfc} \left(\frac{x}{2\sqrt{D_c t}} \right) - \exp \left(\frac{k\gamma_c x}{D_c} + \frac{k^2\gamma_c^2 t}{D_c} \right) \left[\operatorname{erfc} \left(\frac{x}{2\sqrt{D_c t}} + k\gamma_c \sqrt{\frac{t}{D_c}} \right) \right] \right\} \quad [12]$$

where erfc is the complementary error function. The activity of carbon at the surface is obtained by setting $x = 0$ in Eq. [12]. Thus

$$a_c^s = a_c^e \left\{ 1 - \exp \left(\frac{k^2\gamma_c^2 t}{D_c} \right) \operatorname{erfc} \left(k\gamma_c \sqrt{\frac{t}{D_c}} \right) \right\} \quad [13]$$

Upon combining Eq. [10], [12], and [13]

$$\frac{1}{A} \frac{dn_c}{dt} = k a_c^e \exp \left(\frac{k^2\gamma_c^2 t}{D_c} \right) \operatorname{erfc} \left(k\gamma_c \sqrt{\frac{t}{D_c}} \right) \quad [14]$$

Equation [14] can be transformed into an expression for carburization weight gain per unit area using the relation

$$\frac{\Delta W}{A} = \frac{12}{A} \int_0^t \frac{dn_c}{dt} dt \quad [15]$$

where $\Delta W/A$ is the weight gain by carburization per unit area of the specimen. On combining Eq. [14] and [15] and performing the necessary integration

$$\frac{\Delta W}{A} = \frac{12 D_c}{k\gamma_c^2} a_c^e \left[\exp \left(\frac{k^2\gamma_c^2 t}{D_c} \right) \operatorname{erfc} \left(k\gamma_c \sqrt{\frac{t}{D_c}} \right) + (2/\sqrt{\pi}) k\gamma_c \sqrt{\frac{t}{D_c}} - 1 \right] \quad [16]$$

Two limiting cases of Eq. [16] can now be examined. When the rate of carbon transfer reaction at the alloy surface is extremely fast, i.e., $k^2\gamma_c^2 t \gg D_c$, one has diffusion-controlled carburization and Eq. [16] simplifies to

$$\frac{\Delta W}{A} = \frac{24}{\pi} \frac{a_c^e}{\gamma_c} \sqrt{D_c t} \quad [17]$$

When the surface reaction is slow compared with diffusion, i.e., $k^2\gamma_c^2 t \ll D_c$, then

$$\frac{\Delta W}{A} = 12 k a_c^e t \quad [18]$$

Equation [17] applies to the situation where, in the absence of sulfur in the environment, and at the lower temperatures, parabolic kinetics have been observed. At relatively high sulfur levels where linear kinetics have been observed, Eq. [18] applies. At intermediate levels of sulfur or higher carburization temperatures, one must take into account both surface reaction and carbon diffusion in describing the kinetics of carburization and Eq. [16] must be used. Figure 13 shows the carburization weight gain vs. time plot for such a "mixed control" situation at a $p_{\text{H}_2\text{S}}/p_{\text{H}_2}$ ratio of 10^{-5} for Fe-20% Cr carburized at 1173 K. Also shown in Fig. 13 are the calculated points using Eq. [16]; the agreement is very good. A similar situation for the carburization of Ni-30% Cr at 1173 K is shown in Fig. 14.

It was pointed out earlier that sulfur retards carburization as long as the level of sulfur in the gas is below that at which chromium sulfide forms as a surface phase.

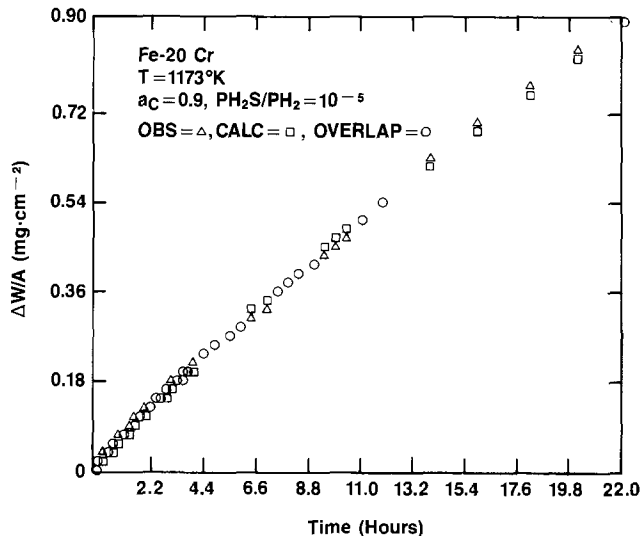


Fig. 13. Comparison of experimental carburization data with prediction based on mathematical model for Fe-20 Cr at 1173 K.

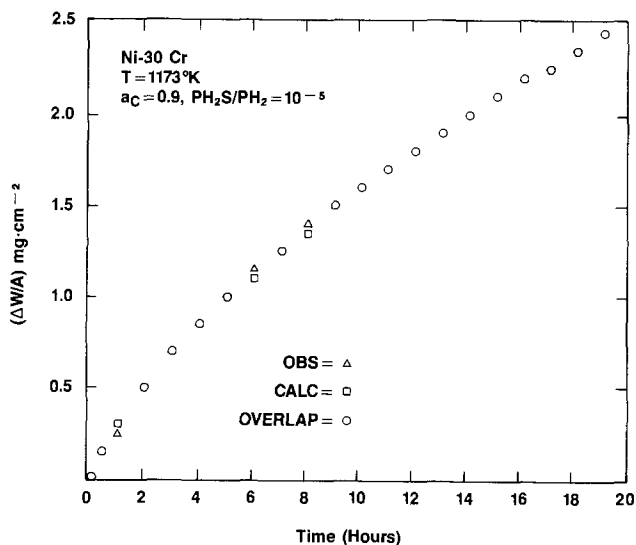


Fig. 14. Comparison of experimental carburization data with prediction based on mathematical model for Ni-30 Cr at 1173 K.

Above this critical sulfur level, rapid sulfidation can occur since chromium sulfide does not form a protective scale. Based on thermodynamic grounds, the critical sulfur activity at which chromium sulfide formation is initiated increases with temperature.

The surface of alloys exposed to carburizing environments at sulfur concentrations below the critical level was examined using Auger spectroscopy. The Auger spectrum indicated the presence of adsorbed sulfur in all the cases. A typical example is shown in Fig. 15.

The above findings lead to the hypothesis that adsorbed sulfur on the alloy surface blocks potential sites where the carbon transfer reaction occurs, thereby reducing the speed of this reaction. A similar conclusion was reached by Grabke and co-workers (10, 11), who studied CH_4 decomposition on thin foils of iron in the presence of H_2S . A schematic representation of the sulfur effect is shown in Fig. 16. In the absence of sulfur (Fig. 16a) there is a high concentration of carbon in the adsorption layer; thus carburization is controlled by the rate at which carbon diffuses from the alloy surface into the bulk. At sulfur concentrations just below the level at which chromium sulfide formation is possible, there is a high concentration of sulfur in the adsorption layer (Fig. 16b). The concentration of carbon in this layer is therefore extremely small and is limited by the rate of the carbon transfer reaction at the surface. No significant gradient in

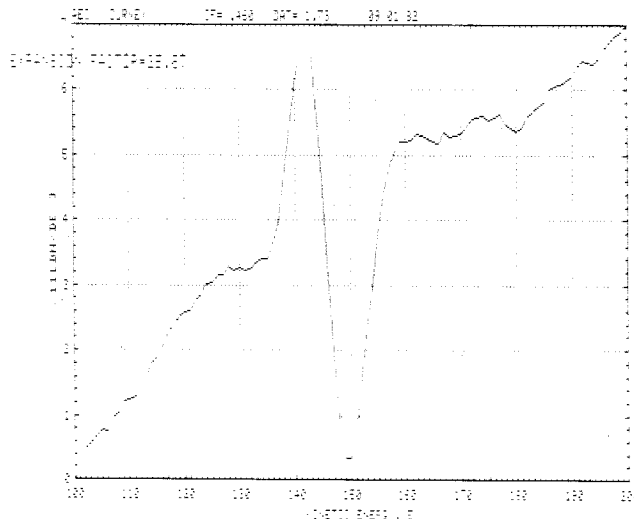


Fig. 15. Auger spectrum for adsorbed sulfur on Fe-20 Cr alloy exposed to carburizing environment containing sulfur.

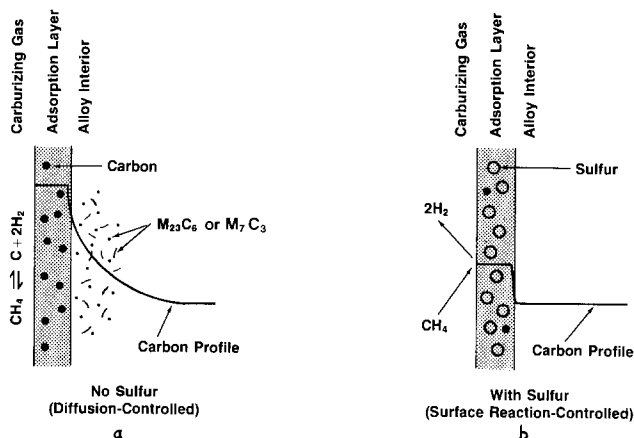


Fig. 16. Schematic mechanism of inhibition of carburization by sulfur

carbon concentration exists between the surface and the bulk and the overall carburization process is surface reaction limited.

Summary

The influence of sulfur on the carburization of high temperature alloys has been investigated by exposing model Ni-30 Cr and Fe-20 Cr alloys to high carbon activity (~ 0.9) environments in the temperature range 1173-1373 K at predetermined levels of sulfur as H_2S . The following conclusions are reached from the present study. 1. Sulfur inhibits the carburization of high temperature alloys; this effect becomes less pronounced at higher temperatures. 2. The extent of inhibition increases with increase in the amount of sulfur added until the thermodynamic stability limit of chromium sulfide, CrS , is reached. At higher concentrations of sulfur, sulfidation attack is initiated. 3. Sulfur inhibits carburization by decreasing the kinetics of the reaction which transfers carbon from the gas phase into the alloy surface.

Manuscript submitted Jan. 28, 1985; revised manuscript received May 30, 1985.

Exxon Research and Engineering Company assisted in meeting the publication costs of this article.

REFERENCES

1. T. A. Ramanarayanan and R. Petkovic-Luton, *Corrosion (Houston)*, **37**, 712 (1981).
2. T. A. Ramanarayanan and R. Petkovic-Luton, in "High Temperature Corrosion," R. Rapp, Editor, p. 430, NACE (1983).
3. H. J. Grabke and A. Schnaas, in "Alloy 800, Proceed-

- ings of the Petten International Conference," p. 195, North Holland Publishing Company, Amsterdam (1978).
4. A. Schnaas and H. J. Grabke, *Oxid. Met.*, **12**, 387 (1978).
 5. A. Schnaas and H. J. Grabke, *Werkst. Korros.*, **29**, 635 (1978).
 6. H. J. Grabke and E. Martin, *Arch. Eisenhuettenwes.*, **44**, 837 (1973).
 7. H. J. Grabke, *Ber. Bunsenges. Phys. Chem.*, **69**, 409 (1965).
 8. H. J. Grabke, *Met. Trans.*, **1**, 2972 (1970).
 9. H. J. Grabke, in "Chemical Metallurgy of Iron and Steel, Proceedings of the Sheffield Conference, 1971," p. 363, The Iron and Steel Institute, London (1973).
 10. H. J. Grabke, W. Paulitschke, and S. R. Srinivasan, in "Proceedings of the 8th International Symposium on the Reactivity of Solids," J. Wood, Editor, p. 55, Plenum Press, New York (1977).
 11. H. J. Grabke, E. M. Peterson, and S. R. Srinivasan, *Surf. Sci.*, **67**, 501 (1977).

Chemical Vapor Deposition of Erosion-Resistant TiB₂ Coatings

A. J. Caputo, W. J. Lackey, I. G. Wright,¹ and P. Angelini

Oak Ridge National Laboratory, Metals and Ceramics Division, Oak Ridge, Tennessee 38731

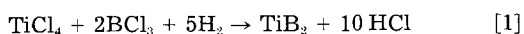
ABSTRACT

Erosion- and wear-resistant coatings are needed for numerous applications, including valve and pump components for coal liquefaction and gasification plants. Titanium diboride is unusually hard and stable and offers considerable promise for use in highly erosive and corrosive environments. We deposited TiB₂ coatings by hydrogen reduction of TiCl₄ and BCl₃. Our objective was to correlate process variables with coating structure and properties, with emphasis on obtaining coatings having high erosion resistance. We varied deposition temperatures from 750° to 1050°C and the TiCl₄ and BCl₃ flow rates. Commercial cemented carbides and experimental nickel-bonded TiB₂ were used as substrates. After structural characterization, the resistance of the deposited coatings to erosion was determined by a hot coal-oil slurry impingement test. The deposition rate was very temperature dependent, ranging from 0.1 to 2.9 μm/min between 750° and 950°C. The surface of the coatings showed nodules increasing in size with temperature. The coatings were dense and adherent. The grain size varied with deposition conditions. Often, the grains were too small to resolve optically, but transmission electron microscopy showed the grain size to be very small (2-300 nm) and to increase with distance from the substrate. Electron microscopy and x-ray diffraction showed only single-phase TiB₂, and ion microprobe analysis revealed a constant Ti:B ratio across the coating thickness. Energy-dispersive fluorescence analyses showed more chlorine in coatings deposited at 800°C than in coatings deposited at higher temperatures. The Knoop microhardnesses of coatings deposited at 800° and 900°C were 15 and 33 GPa, respectively. Coatings deposited at 850°C or below eroded extensively (up to 30 μm deep craters during a 1h test), while those deposited at 900°C showed very little or no erosion (0-3 μm).

In the past several years there has been an increasing interest in the use of titanium diboride (TiB₂), in the form of both ceramic bodies (1) and coatings prepared by chemical vapor deposition (CVD) (2-4). This interest is the result of favorable properties: high hardness; moderate strength, toughness, and electrical conductivity; and excellent resistance to erosion, wear, and corrosion. These desirable properties are retained by TiB₂ even at high temperature. Such properties make the application of TiB₂ desirable in several areas of coal conversion plants, but especially so in coal liquefaction plants, where erosion of letdown valves is still one of the most serious materials problems. In this case, a high flow of a coal-oil slurry must pass through a small orifice to produce the required 10-15 MPa (1500-2000 psi) pressure drop. In this application, the life of valve trim and seat material may be hours, days, or a few weeks. Their high hardness, wear resistance, and chemical stability also make TiB₂ coatings attractive for use as metal cutting tools and other applications.

Previously, hot-pressed nickel-bonded TiB₂ substrates produced at Oak Ridge National Laboratory (Oak Ridge, Tennessee) were coated with CVD TiB₂ at Sandia National Laboratories (Albuquerque, New Mexico) (5). In erosion tests of these coatings, some samples eroded rapidly, while others experienced essentially no erosion. The low erosion results were extremely encouraging, but the inconsistency of the results (all specimens were coated in the same run) indicated the need for further development.

The TiB₂ coatings were deposited according to the reaction



This reaction has been used by various researchers (2-4, 6) to deposit TiB₂. The thermodynamics and kinetics of the reaction have been studied extensively (7, 8). Lower depo-

sition temperatures are possible by use of TiCl₄ and diborane as reactants (9), but diborane is very toxic and can burn explosively in air. The lower deposition temperatures were not judged to be a sufficient advantage for this study to offset the safety hazard.

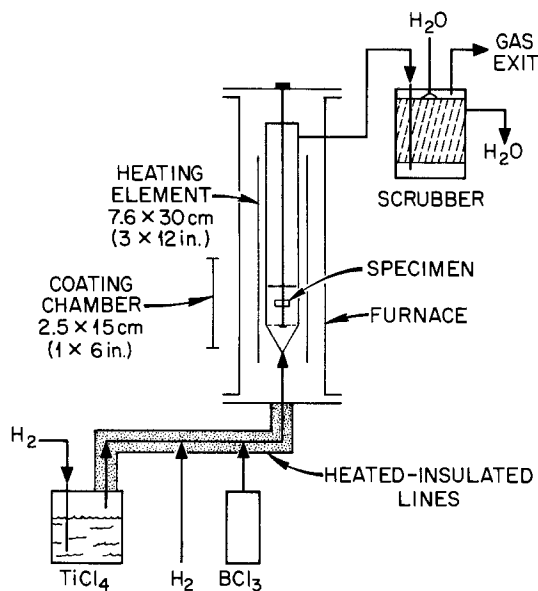
The purpose of our work was to investigate by use of a statistically designed experiment the influence of deposition conditions and substrate type on the structure and properties, particularly erosion resistance, of the TiB₂ coatings.

Materials, Experimental Apparatus, and Procedure

The coating runs were made with the equipment shown schematically in Fig. 1. The graphite coating chamber was heated with a graphite resistance heating element within a water-cooled, metal-wall furnace. The substrate was held by a support rod in the center of the coating chamber. The temperature of the outside surface of the coating chamber wall at the same elevation as the specimen was measured with an optical pyrometer sighted through a silica glass window. Because blackbody conditions were closely approximated (viewing the graphite chamber through a slot in the graphite heating element), no emissivity correction was made. The flow of TiCl₄ out of a heated reservoir was controlled by the flow rate of hydrogen carrier gas and the temperature of a reflux condenser on the exit line from the reservoir. Hydrogen in excess of that needed for the TiCl₄ flow was added separately. The heated BCl₃ flow was controlled by a flowmeter, and the header of mixed inlet gases was heated to prevent condensation until entry into the coating chamber.

This study was divided into three sets of coating runs. The first set of 18 runs was a statistically designed experiment as shown schematically in Fig. 2 and Table I. From prior work and several exploratory coating runs, the "center point" process gas flow rates (cm³/min) for this design were established: TiCl₄, 40; BCl₃, 240; and total H₂, 2200.

¹Battelle Columbus Laboratories, Columbus, Ohio 43201

Fig. 1. Equipment for TiB₂ deposition

Variables in the experimental design were temperature (800° and 900°C), TiCl₄ flow rate (20, 40, and 60 cm³/min), and BCl₃ flow rate (120, 240, and 360 cm³/min). These process conditions result in boron-to-titanium ratios for the reactants ranging from 2 to 18 and hydrogen-to-titanium ratios of 34 to 117, which prior work had indicated would be worthy of investigation. Erosion testing of selected samples of this series (see Table I) indicated the deposition temperature to be the most significant variable affecting the erosion performance. Thus, a second series of eight runs was made, in which the deposition temperature was varied in 50°C increments from 750° to 1050°C. The data for this temperature series are shown in Table II. The substrate type for each coating run in the first and second set of runs was a commercially available² cemented carbide (WC-TaC-TiC-Co) machining tool insert. These inserts are square in cross section (12.7 mm edge length and 4.8 mm height). A third set of three coating runs was made at 900°C to study the effect of substrate type. The data are shown in Table III.

²Grade GE-370, General Electric Company.

Table I. Deposition conditions and erosion results of TiB₂ coatings^a from the first series

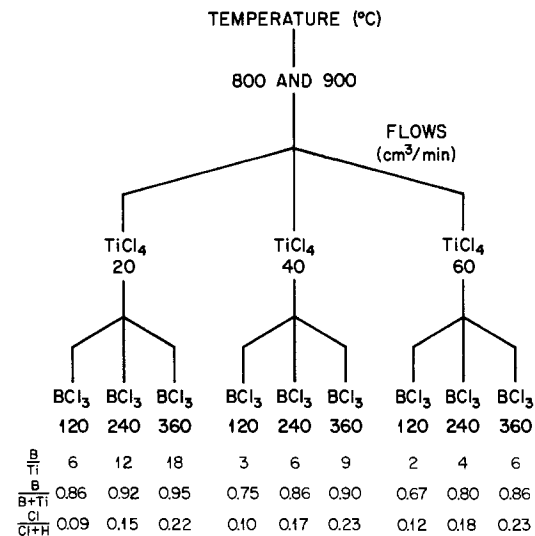
Run	Flow (cm ³ /min)			Flow ratio		Weight gain (mg)	Coating thickness ^b (μm)	Erosion crater depth (μm)
	TiCl ₄	BCl ₃	H ₂	B/Ti	H ₂ /Ti			
Deposited at 800°C								
399	20	120	2340	6	117	20	8	
406	20	240	2220	12	111	20	8	
400	20	360	2100	18	105	18	7	
401	40	120	2320	3	58	11	4	5.2
394	40	240	2200	6	55	18	7	11.4 ^c
402	40	360	2080	9	52	12	5	8.7
397	60	120	2300	2	38	8	3	
405	60	240	2180	4	36	12	5	
403	60	360	2060	6	34	12	5	
Deposited at 900°C								
407	20	120	2340	6	117	64	26	
409	20	240	2220	12	111	69	28	
398	20	360	2100	18	105	115	46	
411	40	120	2320	3	58	54	22	~0 ^d
391	40	240	2200	6	55	73	29	~0 ^d
404	40	360	2080	9	52	60	25	~0 ^d
412	60	120	2300	2	38	66	26	
408	60	240	2180	4	36	78	31	
410	60	360	2060	6	34	89	36	

^a For each coating run, the substrate was Type GE-370 cemented carbide, and the run time was 20 min.

^b Calculated from weight gain.

^c Three additional runs (one of which used a nickel-bonded TiB₂ substrate) were made at this condition, except longer run times were used to produce thicker coatings. Erosion crater depths ranged from 23 to 33 μm, comparable to the coating thicknesses.

^d Crater depths were of the same order of magnitude as surface roughness, so the detection limit is in the range of 0-2 μm.

Fig. 2. Statistically designed experiment for TiB₂ deposition

The substrates studied are described in Table III and included various grades of commercially available cemented carbides and two experimental formulations of hot-pressed, nickel-bonded TiB₂. These substrates permitted investigation of the influence of substrate thermal expansion coefficient and composition on coating structure and properties.

The erosion test procedure and equipment are more fully described elsewhere (10). In summary, it is a 1h test in which a hot (315°C) high velocity (100 m/s) coal-oil slurry (8% solids in anthracene oil) is impacted on the test specimen at an angle of 20° (Fig. 3). Erosion resistance was determined by measuring (using profilometer traces) the depth of the erosion crater. For those coatings that exhibit very little wear, distinguishing the crater depth from the normal fluctuations of the as-deposited coating surface was difficult, and distinguishing between crater depths in the range of 0-2 μm was sometimes difficult.

Results and Discussion

Deposition rate.—The deposition rate of TiB₂ was most dependent on the temperature. The change in deposition rate as a function of temperature is shown in Fig. 4. The

EROSION BEHAVIOR OF TiB_2 COATINGS WAS DETERMINED BY HIGH-VELOCITY COAL-OIL SLURRY EXPOSURE (350°C, 1 h, 100 m/s, 20° INCIDENCE ANGLE)

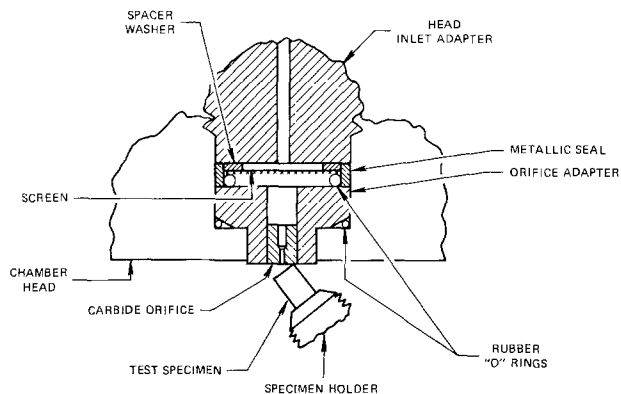


Fig. 3. Schematic diagram of the specimen fixturing for the slurry erosion test.

data points represent runs in which the centerpoint $TiCl_4$ and BCl_3 flow rates were used, i.e., 40 and 240 cm^3/min , respectively. The bars represent the variation in deposition rate for the runs using other flows of $TiCl_4$ and BCl_3 (see Table I). Although the gas flow rate affects the deposition rate at a given temperature, the dominant effect is that of temperature. The deposition rate increased with increasing temperature up to 950°C and then decreased. The decrease in deposition rate above 950°C was probably caused by deposition on the hot wall of the reaction chamber and gas phase reactions which depleted the $TiCl_4$ and BCl_3 contents of the gas mixture before contact with the substrate. Indeed, a considerable amount of TiB_2 powder was formed in these runs, especially at 1050°C.

Table II. Deposition conditions^a and erosion results of second series of TiB_2 coatings—temperature variation

Run	Deposition temperature (°C)	Deposition time (min)	Weight gain (mg)	Coating ^b thickness (μm)	Erosion crater depth (μm)
449	750	40	9	4	6.6
443	800	20	20	8	7.0
447	850	20	22	9	9.7
450	850	30	36	14	17.4
442	900	10	37	15	5.5
445	950	10	72	29	8.3
446	1000	10	59	24	5.1
451	1050	10	37	15	5.1

^a Reactant flows (cm^3/min): $TiCl_4$, 40; BCl_3 , 240; H_2 , 2200. Substrate for all runs: WC-TaC-TiC-Co (GE-370).

^b Calculated from weight gain.

Table III. Deposition conditions^a and erosion results of third series of TiB_2 coatings—temperature variation

Specimen	Grade	Source	Substrate ^b		Erosion crater depth (μm)
			Composition (w/o)	Thermal expansion coefficient (K^{-1})	
452A	K-701	Kennametal	WC-10Co-4Cr	6.5×10^{-6}	2.8
452B	GE-883	GE	WC-6Co	4.5	2.9
452C	GE-370	GE	WC-11TaC-8TiC-9Co	5.8	0.1 ^c
453A	K-703	Kennametal	WC-5.5(Co, Cr)	4.5	7.6
453B	NT-90AD	ORNL	TiB_2-Ni	8.8	2.0
453C	GE-370	GE	WC-11TaC-8TiC-9Co	5.8	0.2 ^c
454A	K-151A	Kennametal	TiC-Ni	8.3	21.0
454B	NT-80K	ORNL	TiB_2-Ni	8.8	0 ^c
454C	GE-370	GE	WC-11TaC-8TiC-9Co	5.8	17.8

^a Reactant flows (cm^3/min): $TiCl_4$, 40; BCl_3 , 240; H_2 , 2200. Deposition time, 20 min; deposition temperature, 900°C. Coating thicknesses were in the range 15-20 μm .

^b For comparison, the thermal expansion coefficient of chemically vapor-deposited TiB_2 is $8.0 \times 10^{-6} K^{-1}$.

^c Crater depths were of the same order of magnitude as surface roughness, so the detection limit is in the range of 0.2 μm .

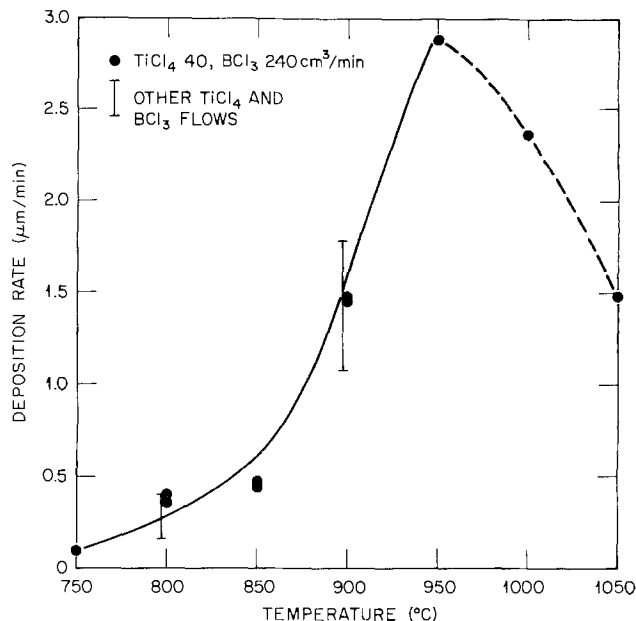


Fig. 4. Influence of temperature on the TiB_2 deposition rate

Surface morphology.—The coatings deposited at and below 850°C were bright and smooth, while those deposited at 900°C and above tended to be dull and rough, especially, the 1000° and 1050°C coatings. Scanning electron microscopy clearly showed the surface morphology to depend on temperature. Figure 5 shows the surface nodules to be small (2-3 μm) at 800°C, somewhat larger (5-10 μm) at 900°C, and large (20-40 μm) platelets at 1000°C. Reactant gas flow rates had less effect on surface morphology, as shown in Fig. 6. At 900°C and a $TiCl_4$ flow rate of 40 cm^3/min , the surface morphology became finer textured as the BCl_3 flow rate increased.

Microstructure.—Optical microscopy showed the coatings to be dense and well bonded³ to the substrate, as shown in Fig. 7. Coating thickness was surprisingly uniform at sharp corners but sometimes varied from one side of a specimen to another.

The TiB_2 grains were typically columnar and generally small (<2 μm in width). The grain size, however, varied considerably from one specimen to another (Fig. 8) and was not correlated with deposition temperature or reactant gas flow rates. The grain size for the finer grained material was in the range 2-300 nm. Generally, the

Coating adherence was not evaluated quantitatively, but debonding was neither observed in the metallography specimens nor experienced during handling, erosion testing, or reheating to 1000°C. Debonding was, however, sometimes observed during attempts to use the coated specimens as machine tool inserts.

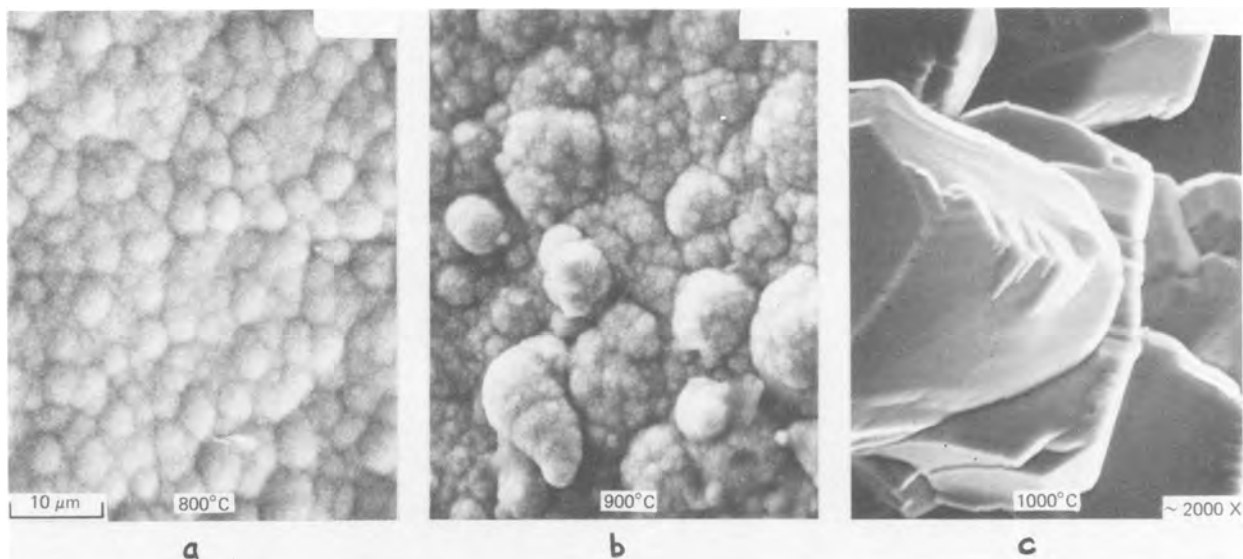


Fig. 5. Surface morphology of TiB₂ coatings are temperature dependent. Flow rates (cm³/min): TiCl₄, 40; BCl₃, 240; and H₂, 2200. (a) 800°C. (b) 900°C. (c) 1000°C.

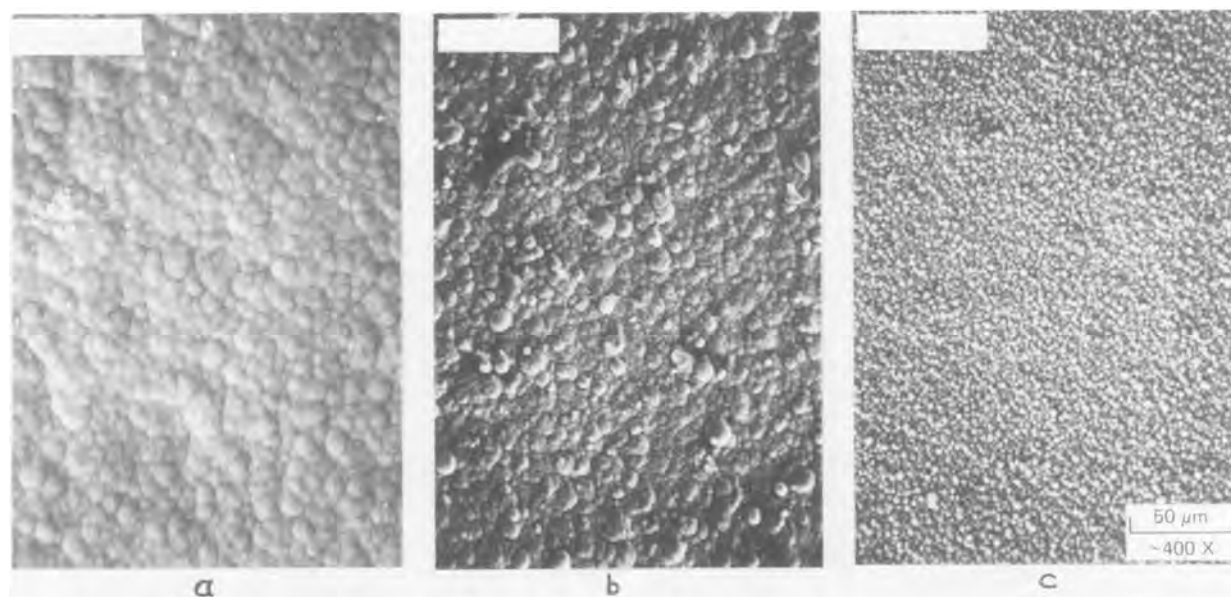


Fig. 6. The BCl₃ flow rate influences coating surface texture. Deposition temperature, 900°C; TiCl₄ flow rate, 40 cm³/min. BCl₃ flow rate (a) 120, (b) 240, (c) 360 cm³/min.

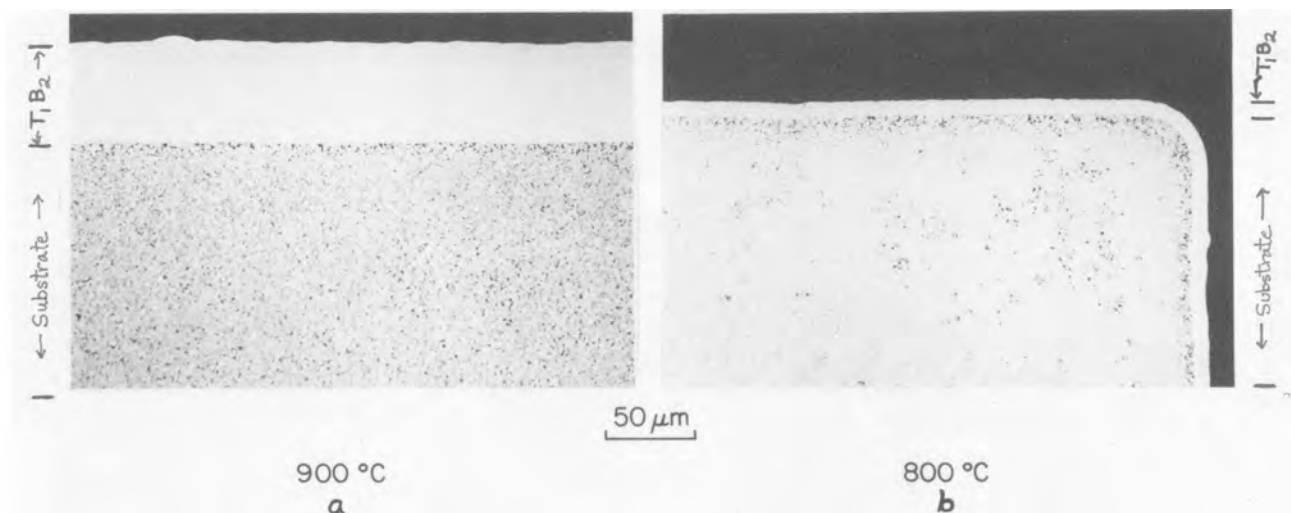


Fig. 7. The TiB₂ coatings were dense, adherent, and of uniform thickness. Deposited at (a) 900°C, (b) 800°C

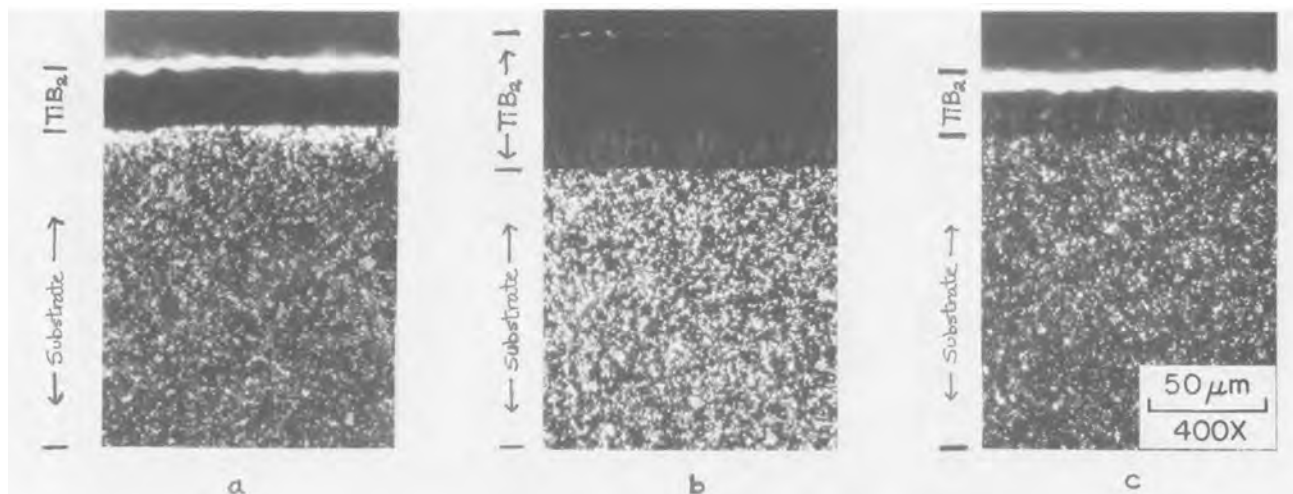


Fig. 8. Polarized light shows (a) no grain structure, (b) some structure, and (c) structure throughout the TiB_2 coatings

grain size increased with distance from the substrate (Fig. 9). Sometimes, however, the grain size changed abruptly (either decreased or increased) across the thickness of the coating, producing a banded or striated structure (Fig. 8). Fortunately, as will be apparent later, these variations in grain size did not appear to influence the erosion resistance of the coatings.

X-ray diffraction and transmission electron microscopy results showed only single-phase crystalline TiB_2 to be present. Preferred orientation occurred in most specimens, but the preferred plane and the degree to which a given crystallographic plane was preferred varied with deposition conditions.

Selected-area electron diffraction patterns of thin sections parallel to the substrate of a fine-grained specimen deposited at 800°C (Fig. 10) showed preferred orientation of the grains. The extent of preferred orientation and grain size increased with distance from the substrate. The diffraction patterns also showed the TiB_2 to be highly crystalline and rather defect free.

Chemical homogeneity, composition, and impurity content.—Ion microprobe analyses indicated a constant titanium-to-boron ratio across the coating thickness. The only impurity detected by energy-dispersive x-ray fluorescence analysis was chlorine. Although actual concentrations were not obtained, the chlorine-to-titanium intensity ratio for coatings deposited at 800° , 900° , and 1000°C were 0.187, 0.021, and 0.008, respectively. We do not know if this is free chlorine or a subchloride of the reactants in a concentration too low for x-ray diffraction to detect. This is one of the few differences in the coatings deposited at 800° and 900°C , and the possible influence of chlorine content on hardness and erosion results is discussed in a later section.

Microhardness.—Knoop microhardness data for the first set of coatings deposited at 900°C (coatings deposited at 800°C were too thin for measurement) are shown in Fig. 11. The data show that the TiB_2 coatings at the center point process condition (TiCl_4 and BCl_3 flow rates of 40 and $240\text{ cm}^3/\text{min}$) had a hardness of 33 GPa, as compared

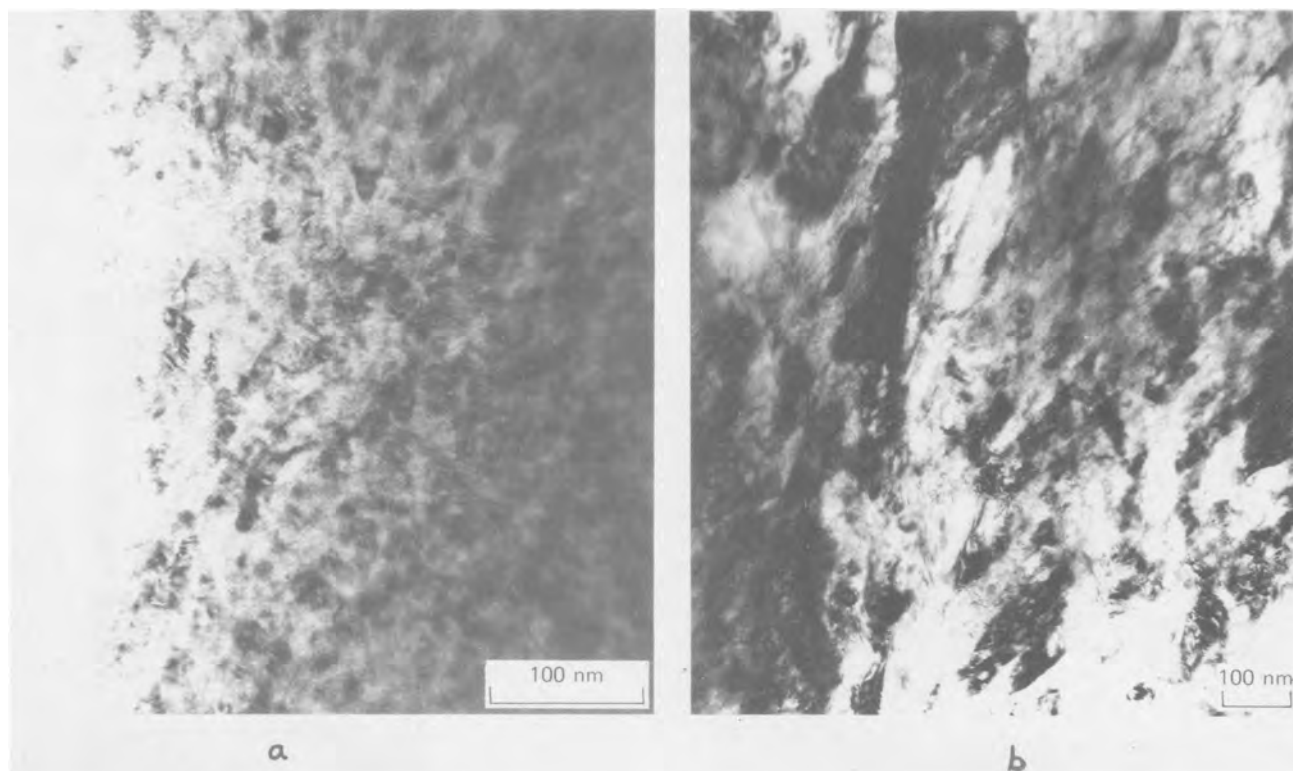


Fig. 9. Transmission electron microscopy shows that the grains are small and increase in size with distance from the substrate. (a) Grain size 2-20 nm, $0.2\text{ }\mu\text{m}$ from substrate. (b) 20-30 nm at $3\text{ }\mu\text{m}$.

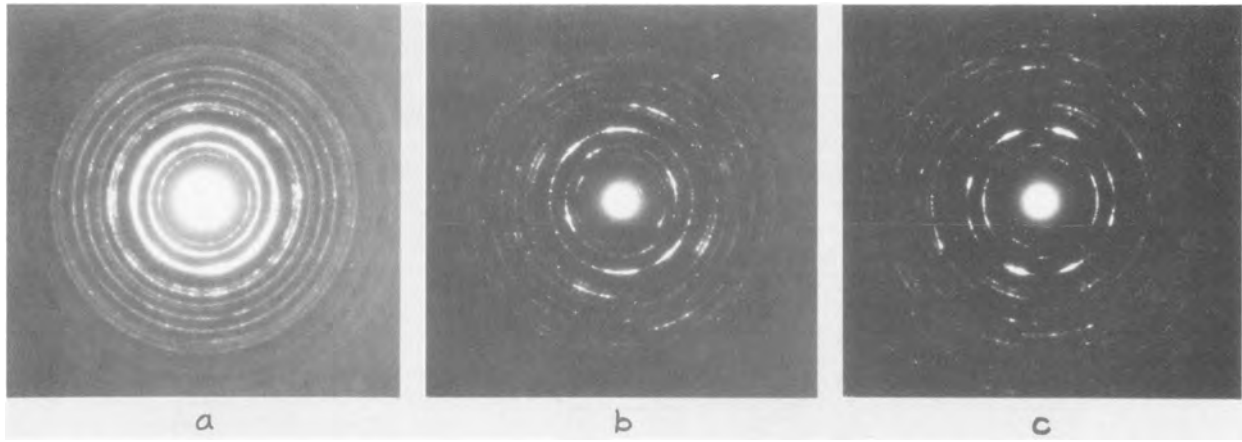


Fig. 10. Selected-area diffraction patterns show increasing grain size and preferred grain orientation with distance from substrate: (a) 0.2, (b) 2, and (c) 3 μm .

with the cemented carbide substrate of 19 GPa at the same indenter load of 100g. The data in Fig. 11 also show the following.

1. The maximum hardness values occurred at the centerpoint process conditions.
2. At a TiCl₄ flow of 40 cm³/min changing the BCl₃ flow from 240 to either 120 or 360 cm³/min had little effect on hardness.
3. At TiCl₄ flows of 20 or 60 cm³/min, the hardness values were lower and were significantly affected by the BCl₃ flow.
4. As expected, the hardness values were influenced by the load on the hardness indenter. The hardness values at the 25 and 50g load are higher than normally reported but are shown to emphasize the fact that the indenter load must be known before hardness values can be compared and to show the general trend of hardness at the various flow conditions.

Additional measurements indicated that coatings deposited at 800°C were not nearly as hard as those deposited at 900°C (15 vs. 33 GPa for a 100g indenter load). The hardness data for the second set of runs (the temperature series) again showed that deposition temperature affects hardness. Coatings deposited at 850°C and below were not as hard as those deposited at the above 900°C. For deposition temperature in the range 900°-1000°C, hardness values are in the range 32-44 GPa for a 50g indenter load. It is not clear whether 900° or 1000°C yields the harder coatings, but it should be noted that all coatings deposited in the 900° to 1000°C range were very hard. However, coatings deposited at 900°C are preferred because they are smoother.

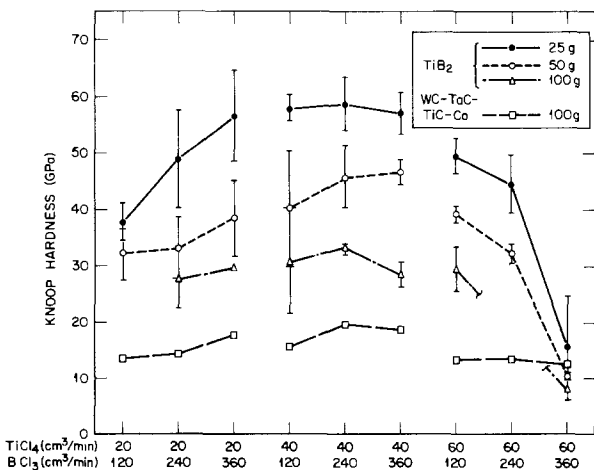


Fig. 11. Microhardness of TiB₂ coatings deposited at 900°C as a function of reactant gas flow rates and indenter load. For comparison, the curve labeled WC-TaC-TiC-Co shows data for the GE-370 substrate.

Erosion resistance.—Six specimens from the first series were chosen for erosion testing. These were the three samples coated with a TiCl₄ flow rate of 40 cm³/min at 800°C and the three with the same flow rate at 900°C (see Fig. 2 and Table I). However, the 800°C samples had a coating thickness of only 4-7 μm as compared with 20-30 μm for the 900°C samples. Therefore, three more runs were made at 800°C with the centerpoint flow rates, but the run time was increased from 20 min to 2 to 4h. This provided samples coated at 800°C with coating thickness in the same range as the 900°C coatings. Also, one of these runs was made with a hot-pressed, nickel-bonded TiB₂ substrate.

As shown in Table I, all the coatings deposited at 800°C were completely penetrated during the test, regardless of the coating thickness (4-25 μm), gas flow rate, or substrate type. In contrast, none of the coatings deposited at 900°C showed up appreciable erosion for the coating thicknesses (22-29 μm) or gas flow rates investigated.

The second series of coating runs was made to permit further investigation of the influence of deposition temperature. The deposition conditions and erosion results for this set of samples are shown in Table II. These results again indicate an effect of deposition temperature on coating erosion resistance. Coatings deposited at 850°C or lower (4-14 μm thick) were essentially completely penetrated, but coatings deposited at 900°C and above were only partially penetrated. For coatings deposited at 900°C and above, the crater depths were greater than expected from the first set of results. However, some of the discrepancy is probably due to the measurement technique, in which crater depths are determined from profilometer traces. Coatings deposited at the higher temperatures are erosion resistant but have rougher surfaces, so the crater depth to be measured is small and close to the magnitude of the variation in the surface of the as-deposited coating. This increases the uncertainty of the crater depth measurement.

The third series of coatings was made to investigate the effect of substrate on coating erosion resistance. The substrates tested were five commercially available grades of cemented carbides and two experimental formulations of nickel-bonded TiB₂ (see Table III). The coating conditions, substrates, and erosion results are summarized in Table III. Note that in each of the coating runs 452, 453, and 454 three substrates were simultaneously coated and that, for each of these runs, one of the substrates was the GE-370 grade of cemented carbide, which served as a standard. The erosion results for the coatings deposited on the standard GE-370 substrate indicated that coating runs 452 and 453 were normal, good runs, but run 454 was somewhat suspect. Substrate type does not appear to strongly influence erosion resistance, although this conclusion is clouded by scatter in the data. There is some indication that the GE-370 grade of cemented carbide and the nickel-bonded TiB₂ may be preferable. Examination

of the data in Table III leads to the conclusion that erosion resistance does not appear to correlate with how closely the thermal expansion coefficient of the substrate matches that of TiB_2 .

Summary and Conclusions

The most significant conclusion that can be reached from this investigation is that properly deposited CVD coatings of TiB_2 have shown little or no erosion during accelerated testing. Thus TiB_2 coatings appear to be very promising for highly erosive environments such as those encountered by valve trim material and pump components in coal liquefaction processes. Low erosion rates were demonstrated for TiB_2 coatings deposited on different substrates (various grades of cemented carbides and nickel-bonded TiB_2) for a range of temperatures and flow rates of reactants.

Deposition temperature is the most important process variable in determining the erosion performance of the coatings. Coatings deposited at 900°C or higher exhibit very low erosion rates, but coatings deposited at 850°C or lower exhibit very high erosion rates. The property that most obviously correlates with the deposition temperature and therefore with erosion resistance is hardness. Coating hardness increased with increasing deposition temperature, at least up to 900°C and perhaps to 1000°C. Coatings deposited at 900°C had hardness values of about 33 GPa, whereas coatings deposited at 800°C had hardness values of about 15 GPa for a 100g indenter load.

Another significant difference between the 800° and 900°C coatings was the chlorine content. Raising the deposition temperature from 800° to 900°C lowered the chlorine content by a factor of 9. Increasing the temperature from 900° to 1000°C further lowered the chlorine content by a factor of 2.6. Whether or not the chlorine content is a significant factor affecting the erosion performance of the coating is not yet known.

Other conclusions follow.

1. The deposition rate increased as the temperature increased from 750° to 950°C, but then decreased as the temperature continued to increase to 1050°C.

2. The surface morphology of the coatings was strongly temperature dependent. The coating surface had small nodules at the lower temperatures (800°C), somewhat larger nodules at the intermediate temperatures (900°C), and a platelet structure at the higher temperatures. Changing the gas flows had only slight effect on the surface morphology.

3. The coatings were fine-grained, adherent, and of uniform thickness. Varying degrees of preferred grain orientation were observed. The grain size did not appear to correlate with any of the process variables. Both fine-grained and coarser-grained specimens exhibited excellent erosion resistance.

4. X-ray diffraction indicated the presence of only TiB_2 , with no unidentified peaks, and ion microprobe analyses

indicated a constant titanium-to-boron ratio across the coating thickness.

Acknowledgments

The authors wish to acknowledge the assistance of others in the performance of this work: D. P. Stinton for assistance in designing the statistical experiment, P. F. Becher for fabrication of the Ni- TiB_2 substrates, W. B. Stines and G. A. Cerny for performing the deposition runs, N. M. Atchley for metallography and hardness measurements, H. W. Dunn for scanning electron microscopy and energy-dispersive x-ray fluorescence, O. B. Cavin for x-ray diffraction, J. I. Federer for review of the manuscript, Gail Gollhofer for typing the draft, and Sigfred Peterson for editing.

This research was sponsored by the Fossil Energy Office of Coal Liquefaction Technology and the Pittsburgh Energy Technology Center Coal Liquefaction Instrument and Component Project Office, U.S. Department of Energy, under Contract DE-AC05-84OR21400 with Martin Marietta Energy Systems, Incorporated.

Manuscript submitted June 15, 1984; revised manuscript received June 3, 1985. This was Paper 198 presented at the Cincinnati, Ohio, Meeting of the Society, May 6-11, 1984.

Oak Ridge National Laboratory assisted in meeting the publication costs of this article.

REFERENCES

1. V. J. Tennery, C. B. Finch, C. S. Yust, and G. W. Clark, in "Science of Hard Materials," R. K. Viswanadham, Editor, pp. 891-909, Plenum Publishing Corp., New York (1983).
2. H. O. Pierson, E. Randich, and D. M. Mattox, *J. Less-Common Met.*, **67**, 381 (1979).
3. H. O. Pierson and E. Randich, *Thin Solid Films*, **54**, 119 (1978).
4. H. O. Pierson and A. W. Mullendore, *ibid.*, **95**, 99 (1982).
5. I. G. Wright *et al.*, in "Fossil Energy Materials Program Quarterly Progress Report," ORNL/FMP-82/2, Oak Ridge National Laboratory, Oak Ridge, TN, March 31, 1982.
6. T. M. Besman and K. E. Spear, *J. Cryst. Growth*, **31**, 60 (1975).
7. K. E. Spear, in "Chemical Vapor Deposition," T. O. Sedgwick and Hans Lydtin, Editors, pp. 1-16, The Electrochemical Society Softbound Proceedings Series, Princeton, NJ (1979).
8. T. M. Besman and K. E. Spear, *This Journal*, **124**, 786 (1977).
9. H. O. Pierson and A. W. Mullendore, *Thin Solid Films*, **72**, 511 (1980).
10. I. G. Wright, A. H. Clauer, D. K. Shetty, T. R. Tucker, and J. T. Stropki, "Evaluation of Advanced Materials for Slurry Erosion Service," DOE/NBM-3007365, U.S. DOE, Fossil Energy Materials Program, Nov. 1982. Available from National Technical Information Service, U.S. Department of Commerce, Springfield, VA 22161.

Optical Properties of CuInSe_2 and Related Compounds

P. Lange, H. Neff, M. Fearheiley, and K. J. Bachmann*

Department of Chemistry, North Carolina State University, Raleigh, North Carolina 27695-8204

ABSTRACT

Reflectivity and photoluminescence (PL) spectra of stoichiometric CuInSe_2 and of two nonmolecular defect structures tied to the liquidus composition $\text{Cu}_3\text{In}_3\text{Se}_9$ and $\text{Cu}_2\text{In}_4\text{Se}_7$ are presented. At room temperature the fundamental gap and high energy features in the reflectivity spectra show only a very weak dependence on the stoichiometry of the compounds, while the PL spectra exhibit distinct differences. The PL of the stoichiometric material is dominated by free exciton emission, but the defect structures are characterized by broad deep luminescence bands of currently unknown origin.

The ternary compound semiconductor CuInSe_2 has attracted attention in the context of photovoltaic devices, optical detectors, and light emitting diodes (1, 2). In particular, CuInSe_2 -based solar cells with power conversion efficiencies in excess of 10% at AM1 and excellent resistance against degradation under operating conditions have been reported (3-5). Conflicting experimental data and analyses of the experimental results have been published (6-10) concerning the relation between the optical properties of copper indium diselenide and point defects in this material that is characterized by a wide homogeneity range. In the opinion of the authors, the primary cause for this confusion is a lack of control over the point defect chemistry and surface preparation conditions. In this paper, we report on the reflectivity and photoluminescence (PL) of stoichiometric CuInSe_2 and of related defect structures of well-defined composition.

Experimental Procedure

Bulk single crystals of stoichiometric CuInSe_2 , which is an incongruently melting material, were grown from the appropriate liquidus composition as described elsewhere (11). In addition, single crystals of the defect structures tying to the liquidus compositions $\text{Cu}_3\text{In}_3\text{Se}_9$ and $\text{Cu}_2\text{In}_4\text{Se}_7$ were prepared. Crystals prepared from these liquidus compositions were previously described as separate solid phases of same composition (12, 13). This contention is certainly wrong, since detailed phase diagram studies (11) show no evidence for the existence of a solid phase $\text{Cu}_3\text{In}_3\text{Se}_9$. As determined by electron microprobe analyses, both liquidus compositions tie to different solidus compositions, *i.e.*, $\text{Cu}_3\text{In}_4\text{Se}_7(\text{l})$ to $\text{Cu}_{0.19}\text{In}_{0.29}\text{Se}_{0.52}(\text{s})$ and $\text{Cu}_3\text{In}_5\text{Se}_9(\text{l})$ to $\text{Cu}_{0.21}\text{In}_{0.29}\text{Se}_{0.51}(\text{s})$ corresponding to atom ratios $\text{Cu}:\text{In} = 0.66$ and 0.72 and $(\text{Cu} + \text{In}):\text{Se} = 0.92$ and 1.00 , respectively.

Samples for the optical measurements were prepared by cleaving on (110) for the stoichiometric CuInSe_2 . As-grown natural (112) faces were used for the evaluation of the defect structures. Cutting, mechanical polishing, and chemical etching significantly alter the surface composition and optical response of the samples and was avoided in our work. The PL spectra were recorded in the temperature range $9 \text{ K} \leq T \leq 60 \text{ K}$ using a closed cycle He cryostat. The 514.5 nm Ar ion laser line at 150 mW incident power was used as excitation source and the emitted PL radiation was analyzed by means of an Instruments SA Model HR 320 monochromator. A 1200 g/mm holographic grating affording a spectral resolution of $\approx 3 \text{ \AA}$ was utilized in conjunction with either a Ge photodiode or a S1 photomultiplier tube. The data acquisition/signal processing system consisted of a PAR Model 192 chopper, a PAR Model 5206 lock-in analyzer, and a Tek 4052 computer. A similar setup was used for the reflectivity measurements using a Xe lamp as light source and, in the UV region, an alternative holographic grating with 1800 g/mm plus a R955 photomultiplier tube.

Results and Discussion

Figure 1 shows the reflectivity of CuInSe_2 and of the defect structure materials. The fundamental gap and the

*Electrochemical Society Active Member.

transitions at 3.9 and 4.5 eV do not show significant shifts for all samples, while the feature near 2.9 eV exhibits a dependence on composition. The nature of the high energy transitions is presently not understood. In Ref. (14) and (15), they are characterized as transitions from Cu d levels to the conduction band or E_1 -like transitions from the upper valence band or pseudodirect transitions. The above result indicates that the bandgap at room temperature is not significantly affected by deviations from molecularly. This finding is corroborated by the location of the low energy cutoff in the spectral response of liquid junction solar cells of the defect structure materials tied to liquidus compositions $\text{Cu}_3\text{In}_3\text{Se}_9$ and $\text{Cu}_2\text{In}_4\text{Se}_7$, respectively, shown in Fig. 2.

Figure 3 shows the PL spectra of stoichiometric CuInSe_2 at four different temperatures. A dominant peak at 1.03 eV and four additional peaks at 1.02, 0.97, 0.94, and 0.90 eV are observed. Note that the FWHM for the peak at 1.03 eV decreases upon increase of the temperature from 10 to 30 K. This shows that the 1.02 eV transition visible as a shoulder on the low energy side of the peak at 1.03 eV is strongly quenched. The 9 meV FWHM peak at 1.03 eV is assigned to the free exciton that is located 20 meV below the conduction band edge (CBE) (17). The bandgap is 1.05 eV in agreement with the previous data of Ref. (7) and (8). The absence of significant deep emission features in the PL spectrum of the stoichiometric CuInSe_2 sample of this study shows that it has substantially lower concentration of point defects than the heretofore reported CuInSe_2 crystals. For such high purity material, the transition probability for the free exciton is much higher than for band-to-band transition, which could be

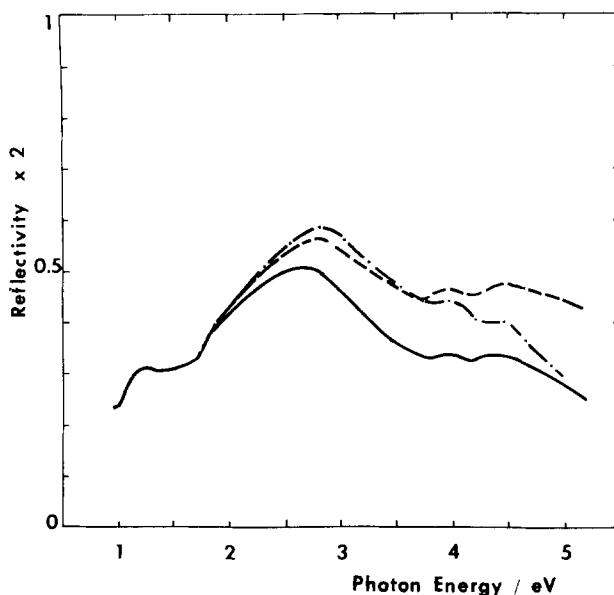


Fig. 1. Reflectivity vs. photon energy of CuInSe_2 (solid line) and related compounds tied to the liquidus composition $\text{Cu}_3\text{In}_3\text{Se}_9$ (dashed line) and $\text{Cu}_2\text{In}_4\text{Se}_7$ (dot-dash line).

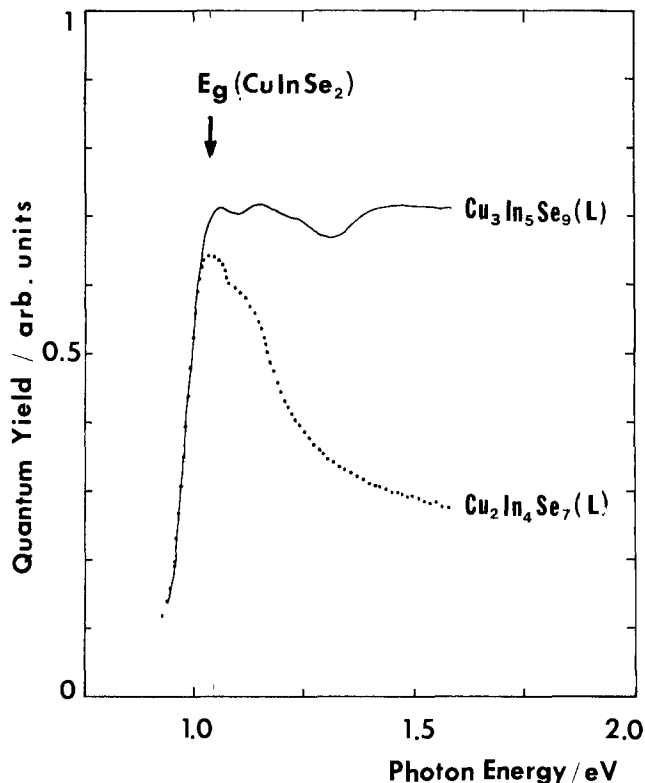


Fig. 2. Spectral response of defect structure materials tied to $\text{Cu}_2\text{In}_4\text{Se}_7(\text{l})$ and $\text{Cu}_3\text{In}_5\text{Se}_9(\text{l})$ in a $\text{V}^{++}/\text{V}^{+++}$, HCl, aqueous redox system. The position of the fundamental gap of CuInSe_2 is denoted by an arrow.

observed in the high energy region (16), but is not resolved in Fig. 2. A temperature increase by 50 K shifts the free exciton peak position by 5 meV, which is in good agreement with the previous results of Won Yu (8).

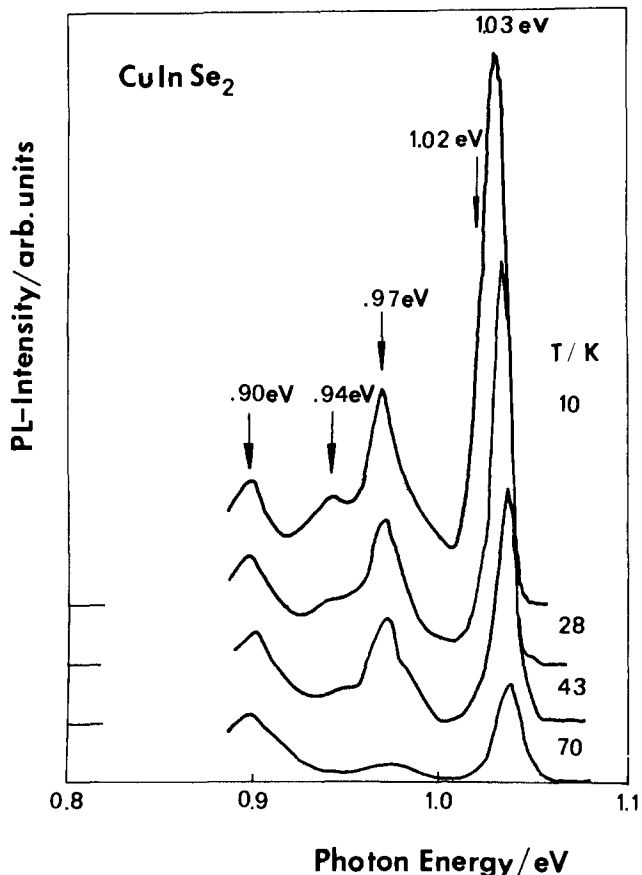


Fig. 3. Photoluminescence spectra for CuInSe_2 from a cleaved (110) surface for different temperatures showing five transitions.

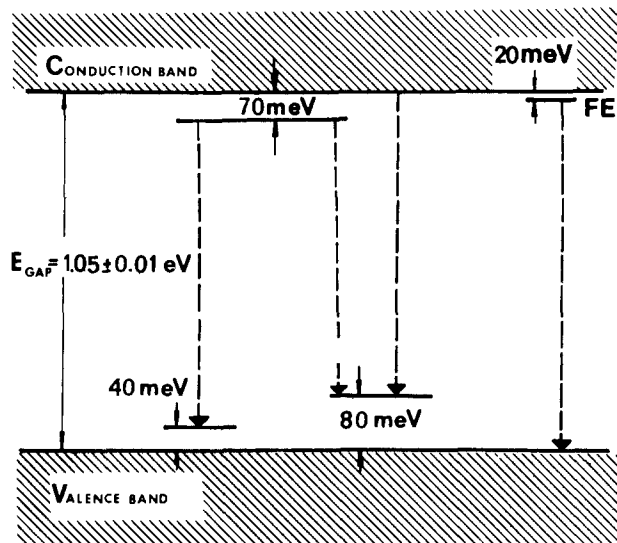


Fig. 4. Energy level diagram for CuInSe_2 indicating the acceptor and donor levels, the position of free exciton level (FE), and the fundamental gap.

In a previous communication (19), we reported complementary features in the PL and photoconductivity spectra of a sample of atom ratios $\text{Cu}:\text{In} = 1.01$ and $(\text{Cu} + \text{In}):\text{Se} = 1.04$ that were explained by the presence of two acceptor states at 40 and 80 meV above the valence bandedge (VBE) and one donor state at 70 meV below the CBE. These states were related to Cu on In antisites, In vacancies, and Se vacancies, respectively. In accord with this model, the 0.94 and 0.90 eV transitions observed for the stoichiometric compound are interpreted as D-A transitions between the Se vacancy level and the Cu_{In} antisite and the In vacancy levels, respectively. The small peaks at 0.90 and 0.94 in Fig. 1 are probably of the same origin. The additional peak at 0.97 eV is interpreted as a CBE to the 80 meV acceptor level as indicated in the energy level diagram, Fig. 4. It has been observed in other samples of CuInSe_2 previously and has been characterized as a D-A transition by others (8, 18).

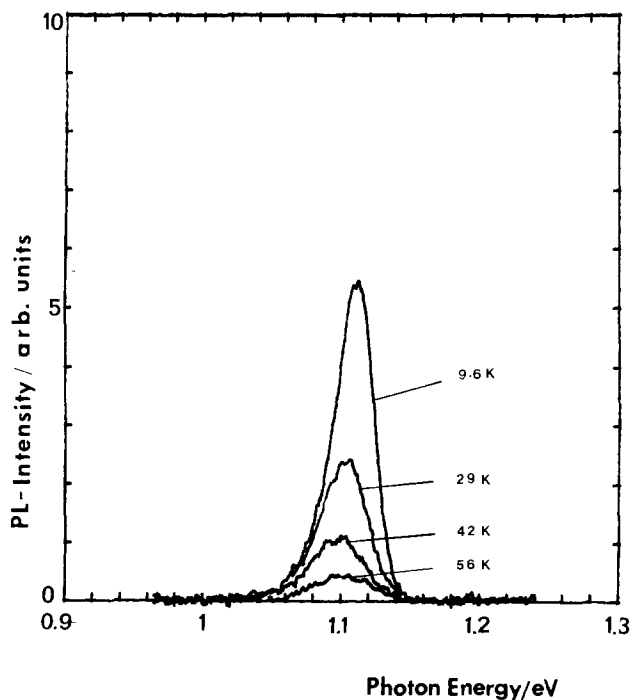


Fig. 5. Photoluminescence spectra of nonstoichiometric crystals tied to $\text{Cu}_3\text{In}_5\text{Se}_9$ liquid from the free (112) surface for different temperatures showing broad-band emission.

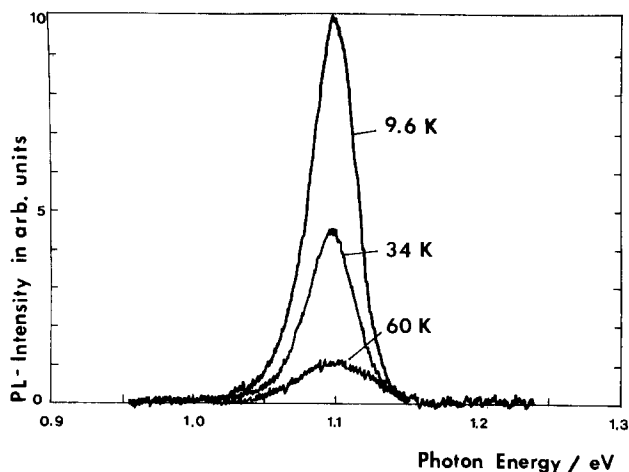


Fig. 6. Photoluminescence spectra of nonstoichiometric crystals tied to $\text{Cu}_2\text{In}_4\text{Se}_7$, liquid from the (112) surface for different temperatures showing broad emission.

Figures 5 and 6 show the PL spectra for the nonmolecular samples grown from $\text{Cu}_3\text{In}_3\text{Se}_8$ and $\text{Cu}_2\text{In}_4\text{Se}_7$, liquidus compositions, respectively. In both cases, the PL is dominated by broad deep emission, the location of which with regard to the bandedges cannot be assigned at this time. Since the solidus composition of the two cases considered correspond to Cu:In ratios < 1 and to metal:selenium ratios ≤ 1 , other defects are likely to dominate the recombination in this case than those considered in the discussion of Fig. 1. Both Cu-vacancy acceptors and In on Cu antisite donors are likely contributing defects, but need positive identification. Clearly, at low temperature the bandgaps of the two nonmolecular crystals are shifted to significantly higher energy than observed for stoichiometric CuInSe_2 , which is consistent with the observations of others who reported larger energy gaps for crystals of nominal composition CuInSe_2 grown from melt compositions that could have tied into In-rich material (11, 20).

Summary

Reflectivity and photoluminescence data have been reported for stoichiometric CuInSe_2 and for nonmolecular defect structures tied to the liquidus compositions $\text{Cu}_3\text{In}_3\text{Se}_8$ and $\text{Cu}_2\text{In}_4\text{Se}_7$. At room temperature, the location of the critical points corresponding to high energy transitions at 3.9 and 4.5 eV and the fundamental gap are not significantly affected by the point defect chemistry. However, substantial differences in both the bandgaps

and the dominant PL features are observed for stoichiometric CuInSe_2 and nonmolecular defect structures at low temperature.

Acknowledgments

This work has been partially supported by SERI Subcontract XL-4-04041-1 and a grant by ARCO Solar, Incorporated.

Manuscript submitted Jan. 25, 1985; revised manuscript received April 2, 1985.

North Carolina State University assisted in meeting the publication costs of this article.

REFERENCES

1. J. L. Shay and J. H. Wernick, "Ternary Chalcopyrite Semiconductors," Pergamon, New York (1975).
2. "Ternary Compounds," G. D. Holah and L. L. Kazmerski, Editors, Institute of Physics, London (1977).
3. S. Menezes, H. J. Lewerenz, and K. J. Bachmann, *Nature*, **305**, 615 (1983).
4. J. L. Shay, S. Wagner, and H. M. Kasper, *Appl. Phys. Lett.*, **27**, 89 (1975).
5. L. L. Kazmerski, F. R. White, and G. K. Morgan, *ibid.*, **29**, 268 (1976).
6. F. Abou-Elfotouh, D. J. Dunlavy, D. Cahen, R. Noufi, L. L. Kazmerski, and K. J. Bachmann, "VI International Conference on Ternary and Multinary Compounds," Caracas, Venezuela (1984); *Prog. Cryst. Growth Charact.*, To be published.
7. G. Masse and E. Redjai, *J. Appl. Phys.*, **56**, 1154 (1984).
8. P. Won Yu, *ibid.*, **47**, 667 (1976).
9. P. Migliorato, J. L. Shay, H. M. Kasper, and S. Wagner, *ibid.*, **46**, 1777 (1975).
10. W. E. DeVaney, R. A. Mickelsen, W. S. Chen, Y. R. Hsiao, J. M. Stewart, L. C. Olson, and A. Ruthwarf, Semiannual Report, Boeing Engineering and Construction Company, Seattle, WA, May 1984.
11. M. Fearheiley, C. Herrington, and K. J. Bachmann, Submitted to *This Journal*.
12. V. I. Tagirov, N. F. Gakhramanov, A. G. Guseinov, F. M. Aliev, and G. G. Guseinov, *Sov. Phys. Crystallogr.*, **25**, 237 (1980).
13. R. Lesueur, C. Djega-Mariadassou, P. Charpin, and J. H. Albany, *Inst. Phys. Conf. Ser. No. 35*, 15 (1977).
14. J. Austinat, H. Nelkowski, and W. Schrittenlacher, *Solid State Commun.*, **37**, 285 (1981).
15. W. Horig, H. Neumann, and I. Godmanis, *ibid.*, **36**, 181 (1980).
16. M. A. Gilleo, P. T. Bailey, and D. E. Hill, *Phys. Rev.*, **174**, 898 (1968).
17. J. J. M. Binsma, L. J. Giling, and J. Bloem, *J. Lumin.*, **27**, 55 (1982).
18. C. Rincon, J. Gonzales, and G. Sanches Perez, *J. Appl. Phys.*, **54**, 6634 (1983).
19. P. Lange, H. Neff, M. Fearheiley, and K. J. Bachmann, *Phys. Rev. B*, **31**, 4074 (1985).
20. H. Neumann, B. Perlt, B. Schumann, and G. Kuhn, *Phys. Status Solidi B*, **111**, K133 (1982).

Photoelectrochemical Defect Delineation in GaAs Using Hydrochloric Acid

R. Bhat*

Bell Communications Research, Murray Hill, New Jersey 07974

A number of different defect delineation techniques — chemical (1, 2), electrochemical (3), and photoelectrochemical (PEC) (4) — have been reported for gallium arsenide. The advantage of an electrochemical and PEC etch over a chemical etch is that the depth of etching is easily monitored and controlled. This enables one to evaluate thin layers and also specific layers in a multilayer structure. In this note, we report on a PEC technique using dilute hydrochloric acid and illumination. Hydrochloric acid was chosen as the electrolyte because (i) it is commonly available, (ii) the anodic oxide which is formed continuously dissolves in it, and (iii) it does not attack gallium arsenide appreciably.

Experimental

A Polaron profile plotter¹ (Model PN4100) was used to monitor the current-voltage behavior of an n⁺-GaAs electrode in 1HCl:10H₂O electrolyte. The same instrument was also used for defect delineation. The sample was held against a sealing ring mounted on one side of an electrochemical cell made of Teflon by a spring-loaded plunger. The sealing ring exposed approximately 0.1 cm² of the sample surface to the electrolyte. Ohmic contacts were formed on the back of the sample by applying a 40V, 60 Hz supply, through a current limiting resistor, for 150 ms to two tin-plated probes contained within the plunger. The cell contained a saturated calomel reference electrode and a carbon cathode. Light from a 150W tungsten lamp was filtered using a short pass filter with a cutoff wavelength of about 550 nm and then focused on to the sample through a Plexiglas window on the cell. The optics were adjusted to give uniform illumination over an area with a diameter of approximately 1 cm. The arrangement is similar to that reported in Ref. (5). Some experiments were also done using a 250W high pressure mercury arc lamp from a photoresist exposure system and a larger cell. This enabled defect characterization of entire wafers as large as 50 mm in diameter.

A typical plot of current-voltage characteristics is shown in Fig. 1. For defect revelation, we selected a bias point such as A in Fig. 1. The etching was more selective when it was done with an unsaturated photocurrent (point A) rather than with a saturated photocurrent (point B). This result is similar to that reported by Faktor and Stevenson (3) for PEC etching of GaAs using 0.5M Tiron. A Nomarski interference contrast photomicrograph of an etched, Si-doped ($N \approx 2 \times 10^{18} \text{ cm}^{-3}$) GaAs substrate oriented 6° off the (100) toward the (111)A is shown in Fig. 2. The etching was done under conditions similar to point A in Fig. 1 by appropriately choosing the bias and light intensity. The etching time was 30-35 min, resulting in an etched depth of approximately 0.6 μm of GaAs. Figures 3a and 3b show the same region of the wafer etched using molten KOH (2) and PEC etches, respectively. A one-to-one correlation between the hexagonal and conical pits in Fig. 3a and the raised features in Fig. 3b is seen. However,

*Electrochemical Society Active Member.

¹Polaron Equipment Limited, England.

some linear features such as the rectangular-shaped one located close to the left-hand edge of the photograph (Fig. 3b) appear only as two hexagonal pits in Fig. 3a. The reason for this difference is not clear at present. In addition, it is seen that the PEC technique not only reveals dislocations but also reveals bands or striations. Finally, we have found that work damage such as that caused by chemi-

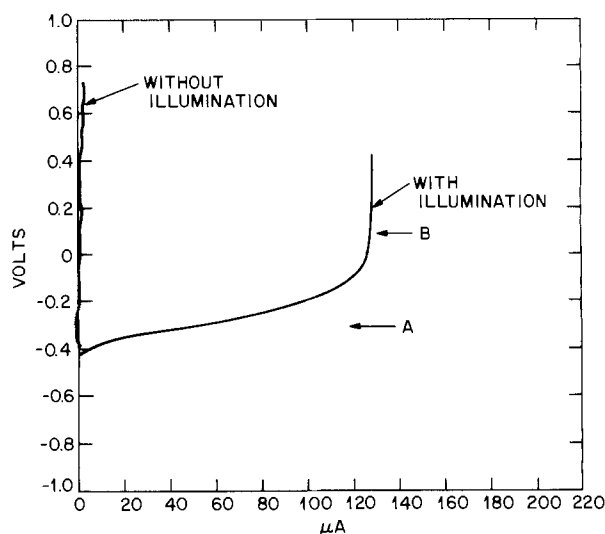


Fig. 1. Typical current-voltage characteristics of an n⁺-GaAs electrode in 1 HCl:10 H₂O electrolyte. Voltages are measured with respect to a saturated calomel electrode.

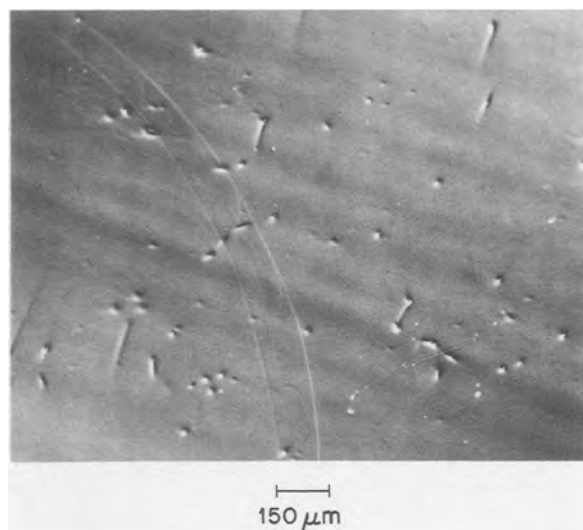


Fig. 2. A Nomarski interference contrast photomicrograph of a photoelectrochemically etched n⁺ GaAs substrate (approximately 0.6 μm of GaAs has been etched).

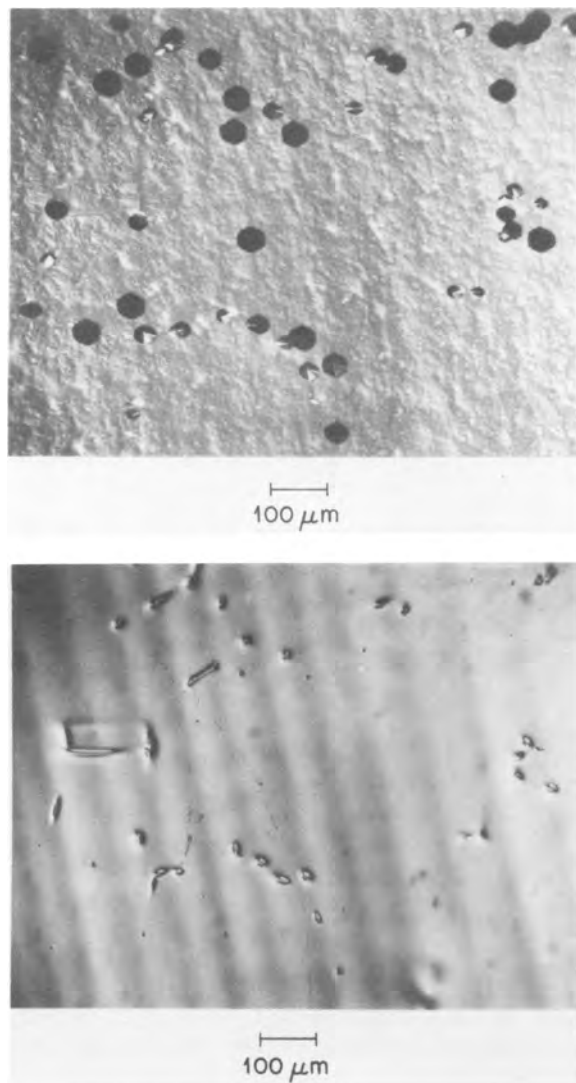


Fig. 3. Nomarski interference contrast photomicrographs of the same region of an n^+ GaAs substrate showing defects revealed by molten KOH etching (top) and photoelectrochemical etching (approximately $0.5 \mu\text{m}$ of GaAs has been removed) (bottom).

mechanical polishing can also be revealed. This damage shows up as a network of raised, criss-crossed lines, al-

though no such pattern is visible prior to etching even with a Nomarski interference contrast microscope.

The PEC technique is sensitive to all hole traps and recombination centers (4) regardless of their origin. These regions are not etched as rapidly as the rest of the region, since the holes needed for the reaction are not readily available at these centers due to recombination or trapping of holes. Hence, the PEC technique delineates dislocations and work damage as raised features. Further, the variation in hole lifetime caused by a fluctuation in the impurity incorporation during crystal growth is also revealed, and this appears as bands or striations as seen in Fig. 3b (4). In contrast, the molten KOH etch reveals dislocations only as pits. Further, the electrochemical technique also reveals dislocations as pits because etching occurs primarily at defect sites where holes are generated by impact ionization. This technique, however, has been shown not to be as sensitive as the PEC technique (4). Therefore, the PEC etch is preferred to the molten KOH and electrochemical etches.

Conclusions

In summary, a simple defect delineation technique using dilute hydrochloric acid has been shown to be a sensitive technique to evaluate n-type GaAs wafers. A correlation between the commonly used molten KOH etch and the electrochemical technique has been established.

Acknowledgments

The author wishes to thank V. G. Keramidis for his support and encouragement. This work was partially done at General Electric Company, Electronics Park, Syracuse, New York.

Manuscript submitted Jan. 18, 1985; revised manuscript received April 5, 1985.

Bell Communications Research assisted in meeting the publication costs of this article.

REFERENCES

1. M. S. Abrahams and C. J. Buiocchi, *J. Appl. Phys.*, **36**, 2855 (1965).
2. J. G. Grabmaier and C. B. Watson, *Phys. Status Solidi*, **32**, K13 (1969).
3. L. I. Greene, *J. Appl. Phys.*, **48**, 3739 (1977).
4. M. M. Faktor and J. L. Stevenson, *This Journal*, **125**, 621 (1978).
5. T. Ambridge, J. L. Stevenson, and R. M. Redstall, *ibid.*, **127**, 222 (1980).

Dry Cleaning of Contact Holes Using Ultraviolet (UV) Generated Ozone

H. Norström, M. Östling,* R. Buchta, and C. S. Petersson*

Institute of Microwave Technology, Stockholm, Sweden

The reduction in minimum feature size of circuit elements to below $2 \mu\text{m}$ in modern IC technology has made dry etching a well-established technique for pattern transference. However, to further exploit the inherent potential of dry processing, many of the presently used wet cleaning steps must be replaced or completed with gas phase cleaning techniques, because a high surface tension together with a tendency to bubble formation within liquid agents will result in an ineffective cleaning of narrow openings. Consequently, immersion of silicon wafers in an oxygen glow discharge has been used for removing polymer formations as well as for photoresist trimming (decumming) and removal (ashing).

*Electrochemical Society Active Member.

In the following, we will show that UV-ozone equipment can be a versatile complement or replacement for the more expensive and "muscular" plasma ashers.

Experiments and Results

Two types of commercially available UV-ozone systems¹ were evaluated. Both were equipped with low pressure mercury UV lamps. No significant differences in performance could be observed for the two systems under identical conditions.

Ozone was generated by the mercury lamps through the

¹Model TO306, UVOCS, Incorporated, Montgomeryville, Pennsylvania 18936; Model 88-9660-02, BHK, Incorporated, Monrovia, California 91016.

interaction of 185 nm radiation and oxygen in the air (1-4). As shown by Vig (1), the UV intensity on a surface positioned at a distance d from the lamp is related to the source intensity (I_0) according to the expression

$$I = I_0 \exp(-130pd) \quad [1]$$

where p equals the average partial pressure of ozone between the lamp and the substrate. Consequently, a low power UV source can be used, presuming the samples to be cleaned are positioned in close vicinity to the lamp.

In view of the foregoing, all wafers to be ozone treated were placed at a fixed distance of 5 mm from the lamp. Prior to any wafer cleaning, the interior of the enclosure, fixtures, etc., were ozone cleaned in a "dry run" for 15 min to remove any possible organic contamination.

Reactive sputter etching (RSE) was performed in a homemade system equipped with a 150 mm diam quartz covered cathode, capacitively coupled to a 13.56 MHz RF power supply (5). Before admission of the CHF_3 gas, the system was evacuated to below 10^{-6} torr, using a 750 liter/s diffusion pump. All experiments were performed at a constant flow rate of 20 sccm, a partial pressure of 20 mtorr, and a power density of 0.5 W/cm^2 .

Two sets of samples were used in the experiment. For the initially performed nuclear resonance measurements, bare p-type, 16-24 $\Omega\text{-cm}$ (100)-oriented silicon wafers were reactively sputter etched for 10 min in CHF_3 .

Immediately after reactive sputter etching, the reference samples were sputter coated with a thin layer of titanium (800Å) to seal the interfacial carbon from any further contamination (6) during transportation to the accelerator. The same procedure was repeated for the ozone-treated specimens.

The carbon analysis was carried out in a tandem van de Graaff accelerator using the $^{12}\text{C}(\alpha, \alpha)^{12}\text{C}$ resonance at 4.26 MeV. A thorough description of the technique has been the subject of a paper by Ostling *et al.* (7). This technique increases the relative sensitivity for a light element, such as carbon, in a heavier matrix by a factor of 200 compared to conventional Coulomb scattering.

The results of the carbon analysis for two typical samples, *viz.*, one reference and one for 15 min treated specimen, are depicted in Fig. 1a and 1b. The energy of the α -particles was increased to 4.28 MeV to compensate for an energy loss caused by the surface titanium layer, thereby fulfilling the conditions of resonance at the silicon-titanium interface. The labeled arrows included in the graphs indicate the surface position of the respective elements, and the inset shows the analyzed structure. As the scattering cross section no longer follows the simple relation of Coulomb scattering, an irregular behavior of the silicon signal can be observed.

In Fig. 1a, two carbon peaks are easily distinguished. The one with a slightly lower intensity at higher energy is due to surface carbon on the titanium film. A lower detected intensity for the surface carbon film does not necessarily indicate a lower content, but is solely due to a lower scattering cross section, as resonance occurred for interfacial carbon. A similar peak belonging to surface carbon is also seen on the second sample, Fig. 1b; it results from contamination during transportation and installation into the accelerator as well as carbon buildup by the beam during analysis.

As pointed out above, the resonance scattering cross section no longer follows the relation of Coulomb scattering (*i.e.*, is inversely proportional to the energy square); instead, its dependence on the energy of the incoming α -particles is much more complex. A calibration procedure, similar to the one described in Ref. (7) — using plasma-deposited amorphous carbon films (8, 9) with various thicknesses as an internal standard — was therefore performed to render it possible to estimate the carbon film thickness.

The low energy carbon signal (Fig. 1a) possessing a larger intensity originates from carbon at the silicon titanium interface. The thickness of this carbon layer was estimated to be roughly 40Å. As verified by Fig. 1b, this low

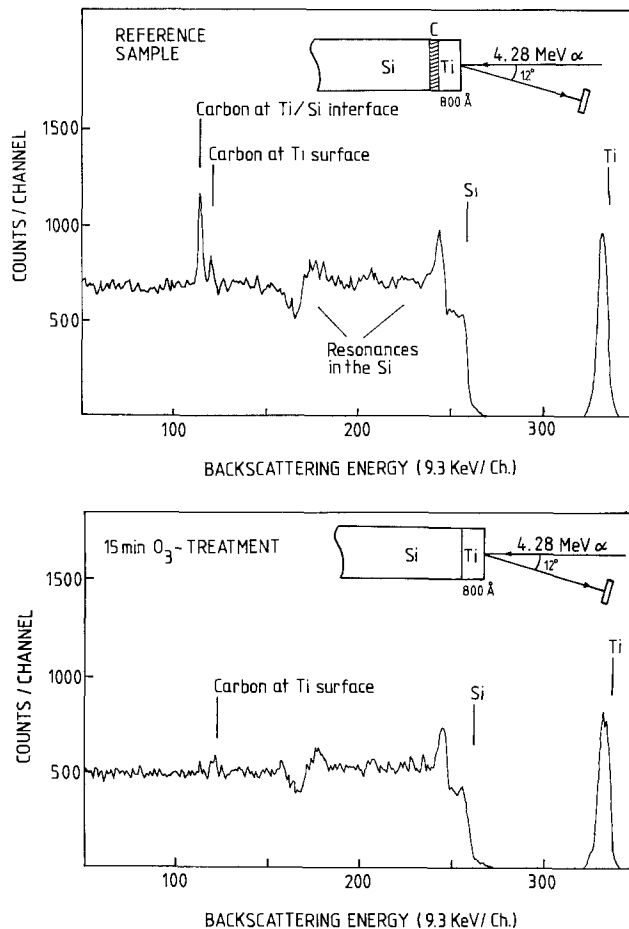


Fig. 1. a (top): Backscattering spectrum of a reference sample, *i.e.*, sample without ozone treatment. The energy of the alpha particles was 4.28 MeV. This corresponds to a carbon resonance energy of 4.26 MeV at the titanium-silicon interface. b (bottom): Backscattering spectrum of a sample after a 15 min ozone treatment. The alpha particle energy was the same as in 1a. Only surface carbon on the titanium film can be observed.

energy peak has vanished after a 15 min ozone treatment. However, similar results were obtained for a shorter (10 min) ozone treatment. It is therefore anticipated that if this technique results in the removal of roughly 40Å of carbon within 10 min, the longer time (15 min) would produce a practically clean surface.

To further evaluate the effectiveness of ozone cleaning of carbon residues, holes were patterned with a photoresist mask and defined by RSE through a 6000Å SiO_2 layer. Two sets of samples were compared: one set received only the standard wet cleaning (10), whereas the other was completed with a 15 min O_3 cycle. After the cleaning, both sets were metallized in parallel with a titanium/titanium nitride layer (300/1000Å) (11). The samples were then examined under a light microscope. The results are shown in Fig. 2a and 2b. It is evident that the samples which did not receive the ozone treatment exhibited a weak metal-to-silicon bond, whereas the ozone-treated ones showed an excellent adhesion. This shows that the originally present polymer film in the contact openings was removed by the O_3 treatment.

Considering device operation, it is essential that the resultant oxide layer subsequent to the ozone treatment should not be too thick, as this would result in a poor metal-semiconductor contact with high intrinsic series resistance.

To confirm that no embarrassing oxide growth occurred as a result of the ozone treatment, the SiO_2 film thickness was monitored with an automatic ellipsometer using a program with fixed refractive indexes. The recorded data are presented in Fig. 3 in the form of differences. These were obtained by subtracting the previously measured native oxide thickness from the one recorded

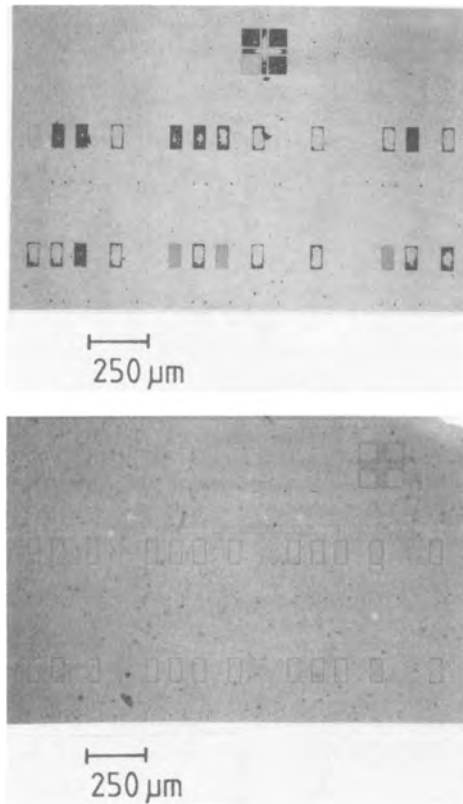


Fig. 2. a (top): Optical micrograph of a Ti/TiN (300/1000Å) metallized water following RSE in CHF_3 and standard wet cleaning. The marker is equal to 250 μm . b (bottom): The same preparation and scale as in the previous figure, but cleaning completed with a 15 min ozone treatment.

after ozone cleaning. It should be pointed out that the presented data are limited by the accuracy in the measurements, but the tendency was justified by several repetitive measurements.

For short cleaning times, up to 10 min, a decreasing thickness can be observed. This is due to the removal of a thin organic layer originally present on the silicon surface. However, after a prolonged treatment, a positive difference, indicating a minute oxide growth, is observed. It is therefore concluded that even an extensive ozone treatment will cause only vanishingly small oxide thickening, which should be of no harm if a proper metallization scheme is selected. This is, however, not always true for the much more intensive plasma strippers, where a significant oxidation can occur.

Conclusion

It is shown that ozone, generated via the interaction of 185 nm UV radiation with oxygen in the air, is an effective carbon scavenger and therefore can be used to clean narrow contact holes defined by RSE in CHF_3 .

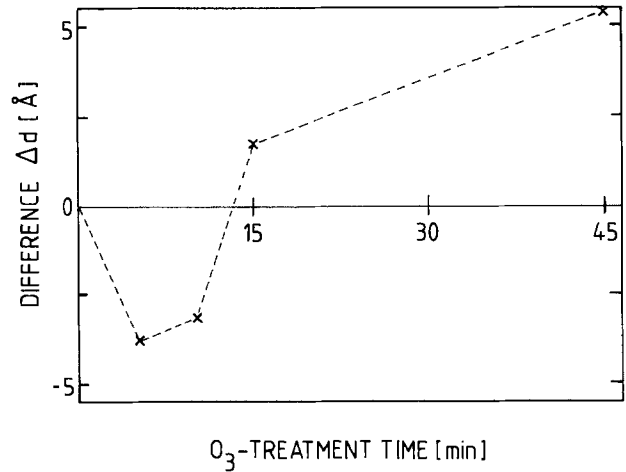


Fig. 3. The difference in oxide film thickness as a function of the ozone cleaning time.

The oxidation of silicon caused by the ozone treatment was found to be very small and is therefore anticipated not to cause any contact resistance problems. An improved metal-to-silicon adhesion was observed if the standard wet cleaning technique was completed with a 15 min ozone treatment. We have, however, not examined whether the UV radiation will have any detrimental effects on the properties of the MOS system, not being annealed out during subsequent processing. Neither have any contact resistance measurements comparing plasma- and UV-O₃-cleaned contact openings been performed. Further investigations regarding this eventual problem should therefore be undertaken.

Manuscript submitted Feb. 8, 1985; revised manuscript received June 11, 1985.

Institute of Microwave Technology assisted in meeting the publication costs of this article.

REFERENCES

1. J. Vig, *J. Vac. Sci. Technol.*, To be published (May 1985), and references therein.
2. J. Vig and J. W. LeBus, *IEEE Trans. Parts, Hybrids, Packag.*, **12**, 365 (1976).
3. D. M. Mattox, *Thin Solid Films*, **53**, 81 (1978).
4. J. A. McClintock, R. A. Wilson, and N. E. Byer, *J. Vac. Sci. Technol.*, **20**, 241 (1982).
5. H. Norström, R. Buchta, F. Runovc, and P. Wiklund, *Vacuum*, **32**, 737 (1982).
6. R. R. Sowell, R. E. Cuthrell, D. M. Mattox, and R. D. Bland, *J. Vac. Sci. Technol.*, **11**, 474 (1974).
7. M. Ostling, C. S. Petersson, and G. Possnert, *Nucl. Instr. Meth.*, **218**, 439 (1983).
8. L. Holland and S. M. Ojha, *Thin Solid Films*, **38**, L17 (1976).
9. L. P. Andersson, S. Berg, H. Norström, R. Olaison, and S. Towta, *ibid.*, **63**, 155 (1979).
10. W. Kern and D. Puotinen, *RCA Rev.*, **31**, 187 (1970).
11. H. Norström, T. Donchev, M. Ostling, and C. S. Petersson, *Phys. Scr.*, **28**, 633 (1983).

Boron Diffusion Profile in Silicon and Data Analysis

F. Găiseanu

Research and Development Center for Semiconductors (CCSIT-S), R-72996 Bucharest, Romania

On the basis of the assumption that a vacancy mechanism should operate during the boron diffusion in silicon, it has been suggested (1) that the diffusion coefficient D would depend linearly on the boron concentration C , for $C > n_i$ (n_i being the intrinsic carrier concentration). How-

ever, it has been shown recently that the high concentration profile (2), the diffusion depth, and the boron amount after the diffusion from a liquid BBr_3 source (3) is well described if $D \sim C^{1/2}$. In this paper, an analysis of the boron profile obtained after diffusion from a solid source

(BN) by the H_2 injection technique is presented. The results are compared with those of the diffusion from a BBr_3 source.

Experimental

Dislocation-free, (111)-oriented, phosphorus-doped, 5 Ω -cm silicon wafers were used. The wafers were polished on both sides and underwent the following deposition cycle: 5 min $O_2 + N_2$, 2 min $H_2 + O_2 + N_2$, and 120 min flowing N_2 , at 1100°C. After the removal of the borosilicate glass (BSG), successive sectionings by chemical etching in a mixture of HF, HNO_3 , and CH_3COOH suitable to maintain the luster of the silicon surfaces were made. The sheet resistivity was measured each time by the four-point method and converted afterward into a corresponding concentration value (4).

A chemical method consisting of dosing of the boron amounts from the etching solutions by emission spectrography (5) was also applied for the profile determination.

Data Analysis and Discussion

Diffusion profile.—The measured concentration profile is shown in Fig. 1. The agreement (within $\pm 7\%$ error limits) between the two data sets allows a unique representation of the curve. One may, consequently, consider that within the experimental error limits the whole boron amount present in silicon is electrically active.

The Boltzmann-Matano analysis was applied to the diffusion profile. This proved to be, in this case, sufficiently accurate because of the particular shape of the profile. The result is presented in Fig. 2, showing a linear variation of D in the concentration range of about $(6 \times 10^{19} - 2 \times 10^{20}) \text{ cm}^{-3}$. This result experimentally supports Fair's earlier assumption (1), *i.e.*, $D \sim C$, and is characteristic of a diffusion mechanism by single charged monovacancies (1).

An approximate solution of the diffusion equation in this case is (6)

$$1 - 1.25y = 0.78(C/C_0) + 0.152(C/C_0)^2 \quad [1]$$

where $y = z/2(D_0t)^{1/2}$, $D_0 = D(x=0)$, and t is the diffusion time, allowing an easy determination of the depth x of an isoconcentration plane.

A deviation of the boron concentration profile near the silicon surface with respect to the boron diffusion profile

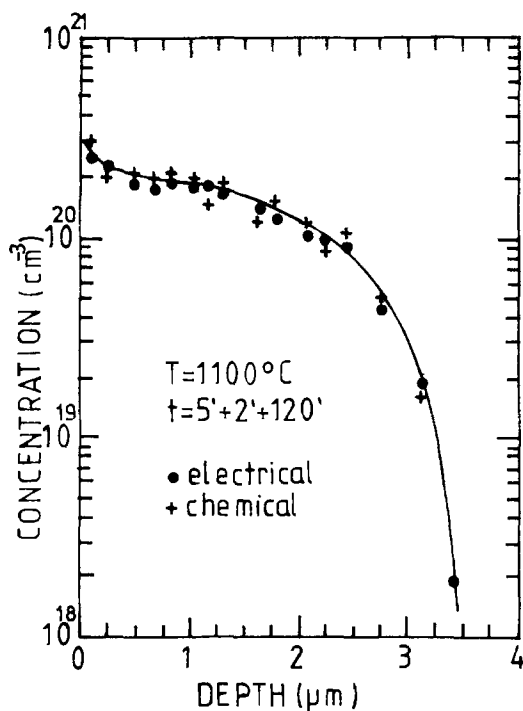


Fig. 1. Experimental boron profile obtained by sheet resistivity (dots) and emission spectrography (crosses) measurements.

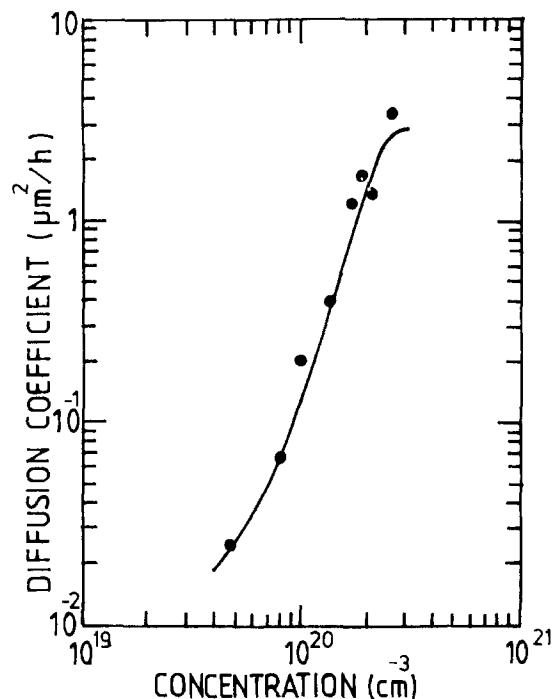


Fig. 2. Dependence of the boron diffusion coefficient on the boron concentration deduced from the Boltzmann-Matano analysis of the experimental diffusion profile.

in the silicon bulk region may be noticed (Fig. 1), showing a rapid increase of the boron concentration to the silicon surface. This increase is correlated with a corresponding decrease of the boron diffusion coefficient (Fig. 2).

Comparative data analysis.—In spite of the two different results — (i) $D \sim C^{1/2}$ (2, 3), and (ii) $D \sim C$ (in this analysis) — the boron diffusion into the silicon bulk should be described by a single dominant mechanism, independent of the doping source and of the ambient atmosphere of the deposition process. This point may be discussed as follows.

In the analysis leading to result (i), the measured surface concentration was considered as a reference value (2, 3). For the discussion of result (ii), we dispose of two types of experimental data: some of them obtained after diffusion from the BN source by different techniques [that of this paper and, for instance, that of Ref. (7), where it clearly appears that the boron diffusion depends on the ambient atmosphere in the furnace tube], and others obtained by diffusion from BBr_3 source. Whereas, for some experimental data belonging to the first type, a diffusion "kink" near the silicon surface may be observed [Fig. 1 and Fig. 1 of Ref. (7)] that for the second type is not evident. Therefore, considering that the specific properties of the BSG-Si system perturb the boron diffusion near the silicon surface in both cases (*i.e.*, the profile near the surface is a product of this perturbation) then an analysis of all these data in terms of solid solubility of boron in silicon may be done.

In Fig. 3, some collected experimental data (8) and our own are represented as C/C_0 vs. x/x_0 , where $C_0 = C(x=0)$ and x_0 is depth for which $C = 10^{18} \text{ cm}^{-3}$. If one considers that C_0 would be the measured surface value, then the collected data may be represented by the dashed curve plotted in Fig. 3. This curve was deduced from Fair's universal curve [relation [5] in Ref. (1)], and it is close to the curve obtained after a proper solving of the diffusion equation (2), by using the result (i) [see Fig. 1 of Ref. (2)]. Considering now that C_0 would be the solid solubility of boron in silicon at the diffusion temperature, then both the collected and our experimental data are this time well described by the curve plotted as a full line in Fig. 3. This curve was deduced from Eq. [1] by using the result (ii), and it is very close to the curve obtained from Guo's computed curve [Eq. [16] of Ref. (9)].

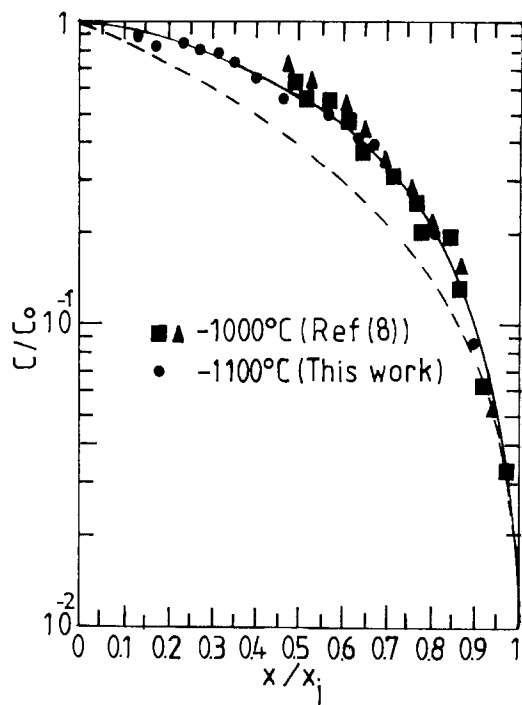


Fig. 3. Normalized boron diffusion profile for Co representing: the measured surface value (broken line) and the solid solubility (solid line). The experimental conditions of the collected data (8) were: 7.2% O_2 , 0.04% BBr_3 (squares), and 1.8% O_2 , 0.04% BBr_3 (triangles).

The solid solubility $C_0 = 1.2 \times 10^{20} \text{ cm}^{-3}$ of boron in silicon at the diffusion temperature $T = 1000^\circ\text{C}$ previously reported (8) was taken into account as a reference value to represent in Fig. 3 the collected experimental data. These data resulted from successive sheet resistivity measurements after the boron diffusion from a liquid BBr_3 source, carried out under two different ambient conditions (see the legend of Fig. 3). The reference value $C_0 = 2.2 \times 10^{20} \text{ cm}^{-3}$ obtained by the best fitting of the curve deduced from Eq. [1] with our experimental data represented as C/C_0 vs. x/x_j as in Fig. 3 considered as solid solubility of boron in silicon at the temperature $T = 1100^\circ\text{C}$.

The result of this analysis brings into accord Fair's previous assumption (*i.e.*, $D \sim C$) with the experimental data exhibiting the boron diffusion profile in silicon bulk.

Summary and Conclusions

A chemical dosing method was applied as a technique for the boron profile determination after the boron diffusion in silicon from a BN solid source by H_2 injection. Direct comparison between the experimental results and those obtained by electrical measurements shows that the boron atoms in silicon might be considered as wholly ionized.

From the analysis of the experimental diffusion profile, a dependence, $D \sim C$, characteristic to a diffusion mechanism by monocharged vacancies for $C > n_i$ was emphasized in a silicon bulk region. An approximate solution of the diffusion equation under these conditions is given, allowing the estimation of the boron diffusion profile. An increase of the boron concentration and a corresponding decrease of the boron diffusion coefficient near the silicon surface with respect to their behavior in the silicon bulk were also pointed out.

The comparative analysis of the data resulting from the boron diffusion from the BN solid source and those obtained after the boron diffusion from a liquid BBr_3 source under different ambient conditions shows that the boron diffusion in the silicon bulk may be described considering that $D \sim C$, irrespective of the doping source and/or of the atmosphere of the deposition process, if one admits that the specific properties of the BSG-Si system perturb the diffusion near the silicon surface in all these cases.

Manuscript submitted Jan. 14, 1985; revised manuscript received April 4, 1985.

REFERENCES

1. R. B. Fair, *This Journal*, **122**, 800 (1975).
2. P. Găiseanu, *Phys. Status Solidi A*, **77**, K59 (1983).
3. F. Găiseanu, Abstract 491 RNP, *This Journal*, **131**, 318C (1984).
4. R. A. Evans and R. P. Donovan, *Solid State Electron.*, **10**, 155 (1968).
5. F. Găiseanu, V. Loghin, and I. Dima, Paper 330 presented at the Electrochemical Society Meeting, Washington, DC, Oct. 9-14, 1983.
6. F. Găiseanu, Paper presented at the National Physics Conference, Bucharest, Oct. 21-23, 1982.
7. J. Stach and A. Turley, *This Journal*, **121**, 722 (1974).
8. P. Negrini, A. Ravaglia, and S. Solmi, *ibid.*, **125**, 609 (1978).
9. S. F. Guo, *ibid.*, **127**, 2506 (1980).



Each issue of the **Journal** will have a section of "Comments." In this section, we provide a means via short pieces, *i.e.*, one column or less, to applaud, dispute, or otherwise discuss the papers published in the **Journal**. Space will be provided for one response by the paper's author(s) to each comment.

Since space available in each issue for the "Comments" section is limited, it is important to be concise.

Comments should be sent to the Editor, Dr. Norman Hackerman, President's Office, Rice University, P.O. Box 1892, Houston, TX 77251.

Norman Hackerman
Editor

Electrochemical Intercalation of Lithium in an Active Carbon

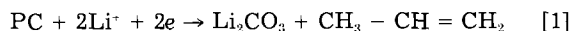
Yoshio Takasu, Masao Shiinoki, and Yoshiharu Matsuda

(pp. 959-960, Vol. 131, no. 4)

A. N. Dey:¹ In this paper, the authors suggested that the cathodic electrolysis of 1.0 mol-dm⁻³ of LiClO₄ in an equivolume mixture of propylene carbonate (PC) and 1,2 dimethoxyethane produces an intercalation compound of lithium and carbon, LiC₅, when "active carbon" is used as a cathode. The experimental evidences provided in the paper are (i) x-ray diffraction spectra of the active carbon electrode before and after discharge and (ii) the relation between the amount of Li⁺ detected in the cathode and the charge passed.

Let us first consider the x-ray diffraction spectra of the discharged carbon. A critical examination of the spectra indicates that all the new peaks that appeared as a result of discharge coincide with the major peaks of Li₂CO₃. We found earlier² that cathodic electrolysis of LiClO₄ in PC on graphite resulted in the decomposition of PC to form Li₂CO₃ and CH₃-CH=CH₂ quantitatively. Therefore, we suspect that the same reaction is occurring in this case as well and that the reaction product is Li₂CO₃ and not LiC₅. I recommend that the authors test their discharged cathode for evolution of CO₂ on acidification in order to confirm this possibility.

The evidence in regard to the relationship between the amount of Li detected in the cathode and the charge passed may be fortuitous, since the authors used Pt disk for establishing electrical contact with the carbon pellet. We discovered earlier³ that Pt formed intermetallic compound with Li when subjected to cathodic electrolysis in organic electrolyte. It is quite possible that the linear region of Fig. 3 of this paper corresponds to the decomposition of PC according to



and the subsequent nonlinearity is due to the loss of Li as Li₃Pt₂ intermetallic compound which has not been analyzed for Li. I recommend that the authors immerse their Pt disk in water after the discharge and test the aqueous solution for alkalinity in order to verify the possible formation of Li₃Pt₂ intermetallic compound.

Y. Takasu, M. Shiinoki, and Y. Matsuda:⁴ Dr. Dey has attempted to explain our result on the cathodic behavior of the active carbon electrode⁵ based on his investiga-

¹Duracell Incorporated, Duracell Research Center, Needham, Massachusetts 02194.

²A. N. Dey and B. P. Sullivan, *This Journal*, **117**, 222 (1970).

³A. N. Dey, *ibid.*, **118**, 1547 (1971).

⁴Faculty of Engineering, Yamaguchi University, 2557 Tokiwadai, Ube 755, Japan.

⁵Y. Takasu, M. Shiinoki, and Y. Matsuda, *This Journal*, **131**, 959 (1984).

tions using a graphite cathode.^{6,7} However, his explanations are not in conformity with the findings in our study.

When we used a graphite cathode for comparison, the electrode potential dropped rapidly and showed *ca.* -1.94V (*vs.* SCE) with the discharge as shown in Fig. 2, curve b, in the previous paper.⁵ During the galvanostatic discharge, a substantial evolution of gas was also observed on the graphite cathode. Both the cathodic performance of the graphite electrode and the gas evolution correspond to the result reported by Dey and his co-workers.⁶ But, we found no indications of gas evolution on the active carbon cathode. Moreover, the potential dropped gradually with discharge to *ca.* 0.3 Ah-g⁻¹ of discharge (Fig. 2) curve b.⁵ It must also be noted that the potential did not drop below -1.4V. To check the influence of carbonate ions, we performed the galvanostatic discharge of the active carbon electrode in various electrolyte solutions, *i.e.*, DME (1,2-dimethoxyethane), THF (tetrahydrofuran), PC, and PC · DME (1:1), each of which contained 1.0 mol-dm⁻³ of LiClO₄. The cathodic performance of the active carbon electrode in the THF-LiClO₄ was not much inferior to those of PC-LiClO₄ and PC · DME (1:1)-LiClO₄; moreover, that in the DME-LiClO₄ was also much better than that of the graphite electrode in PC · DME(1:1)-LiClO₄. It is difficult to assume that carbonate ions are formed easily by decomposition of either THF and DME. These findings show that the main cathodic reaction of the active carbon cathode was not the formation of Li₂CO₃. As pointed out by Dey, the new peaks on the x-ray diffraction spectrum of the discharged active carbon electrode⁵ coincide with the major peaks of Li₂CO₃. We think that such Li₂CO₃ must be formed either by a side reaction at the cathode or by the reaction of the intercalated (or adsorbed) lithium with carbon dioxide in air because the discharged cathode was analyzed by the x-ray diffractometry in air.

As to the lack of evident increase in lithium detected in the discharged cathode beyond *ca.* 0.3 Ah-g⁻¹, we have confirmed that this phenomenon was caused by decomposition of the electrolyte solution at the platinum anode as described in the previous paper.⁵ That is, the gradual increase of the cathode potential beyond *ca.* 0.3 Ah-g⁻¹ discharge⁵ could not be found when we used a lithium plate as the anode. In order to reveal the effect of some organic species, which might be formed at the platinum anode, the following experiment was made. The electrolyte solution of PC · DME(1:1)-LiClO₄ (1.0 mol-dm⁻³) was pre-electrolyzed with an H-type cell having a nickel net cathode and a platinum plate anode separated by a cation exchange membrane. The quantity of electricity passed corresponded to that passed before the potential of the active carbon cathode began to increase, *i.e.*, *ca.* 0.4 Ah-g⁻¹ discharge. Then only the pre-electrolyzed anolyte was used as the electrolyte solution

⁶A. N. Dey and B. P. Sullivan, *ibid.*, **117**, 222 (1970).

⁷A. N. Dey, *ibid.*, **118**, 1547 (1971).

of the galvanostatic discharge of the active carbon electrode. On discharge, the cathode potential immediately dropped to -0.5V and then increased to *ca.* -0.2V after $3.0\text{ Ah}\cdot\text{g}^{-1}$ discharge. The x-ray diffraction spectrum of this discharged cathode ($3.1\text{ Ah}\cdot\text{g}^{-1}$) gave no evident new peaks, and the amount of lithium detected in the discharged cathode was only $4.7 \times 10^{-3}\text{ mol}\cdot\text{g}^{-1}$ (active carbon). These findings strongly suggest that some organic ions formed by the decomposition of the electrolyte solution at the platinum anode mainly took part in the reaction on the cathode after the intercalation of lithium (or adsorption) into the active carbon reached saturation ($Q \approx 0.3 - 0.4\text{ Ah}\cdot\text{g}^{-1}$). The UV spectrum of PC · DME(1:1)-LiClO₄ electrolyte solution after the electrolysis using the active carbon cathode and platinum anode showed that PC was partly decomposed; *i.e.*, the peak at 243 nm , which is characteristic peak of PC, was reduced after the electrolysis. On the other hand, the used electrolyte solution using the active carbon cathode and the lithium anode gave little evidence of decomposition. The formation of Li₃Pt₂ on the platinum disk, which was used for the electrical contact with the active carbon pellet, was not confirmed by our experiment.

Electrochemical Conversion of CrO₂

D. Fousse, V. Jovancicevic, and F. Tissier

(pp. 2734-2736, Vol. 131, no. 11)

F. Beck:⁸ The cyclovoltammograms Fig. 1 and 2 have been performed with pressed powder layers 0.1 mm thick on platinum in phosphate buffer of pH 7. This corresponds to about $0.5\text{ mmol CrO}_2/\text{cm}^2$, and, with a total $1\text{ e}^-/\text{mol}$ conversion, about $50\text{ As}/\text{cm}^2$. The measured reduction charges have been $5 \times 10^{-7}\text{ As}/\text{cm}^2$, if the ordi-

⁸Gesamthochschule Universität, Duisburg, D-4100 Duisburg 1, Germany.

nate reads in $0.01\text{ }\mu\text{A}/\text{cm}^2$ units, or $5 \times 10^{-3}\text{ As}/\text{cm}^2$ if $100\text{ }\mu\text{A}/\text{cm}^2$ is the correct scale. Nevertheless, in both cases conversion of oxide is extremely low, *i.e.*, 10^{-6} or $10^{-2}\%$. By this way, an impurity effect seems to be reasonable.

I do not know what SSE-standard electrode means. If it means "standard silver chloride electrode" or "saturated silver chloride electrode," then the oxidation potential for $\text{Cr}_2\text{CO}_3 \rightarrow \text{CrO}_3$ follows from Fig. 1 and 2 to be about $+0.3\text{V vs. SHE}$. However, we have found at pH 7 $+0.93$ and $+1.58\text{V}$.⁹

D. Fousse,¹⁰ V. Jovancicevic,¹¹ and F. Tissier:¹⁰ CrO₂ is a quite new material from an electrochemical point of view, and its behavior is not yet fully understood. Nevertheless, the evidence for electrochemical stability and oxidation-reduction processes taking place at the oxide surface seem to be very convincing.

The calculations given by Beck concerning the amount of charge for the conversion of 0.1 mm thick CrO₂ is correct. However, we disagree with his interpretation to account for a small conversion of oxide where the impurity effect is put forward. On the one hand, it is highly unlikely that impurity effects are the same in CrO₂ and Cr₂O₃. It is also improbable that impurity is responsible for the two-step reversible oxidation-reduction process observed in voltammograms. On the other hand, the conversion is ascribed as a surface and not bulk reaction and, consequently, the participation of only $10^{-2}\%$ of CrO₂ in the reaction seems to be reasonable. The consecutive oxidations of reduced CrO₂ back to Cr(IV) and Cr(VI) are consistent with observed results.

The reference electrode SSE means "Saturated mercurous sulfate electrode."

⁹F. Beck and H. Schulz, *Ber. Bunsenges. Phys. Chem.*, **88**, 155 (1984), especially Table 1.

¹⁰Centre de Recherches du Fer Blanc, 57103 Thionville, France.

¹¹Department of Chemistry, Texas A&M University, College Station, Texas 77843.



On the Preferred Dissolution of Iron from Thin Films of Permalloy

M. Köhler, A. Wiegand, and A. Lerm

Akademie der Wissenschaften der DDR, Physikalisch-Technisches Institut, 6900 Jena, Germany

The spontaneous dissolution behaviour of alloys is of importance in corrosion processes and etching technology. Electrochemical investigations show that selective dissolution of single components is possible. The enrichment of Mo at the surface was observed in electrochemical dissolution experiments with steel (1). Zn is selectively dissolved at the beginning of the anodic dissolution of a copper/zinc alloy in a chloride containing bath (2). Studies on rotating ring disk electrodes of a Cu-Ni alloy show selective dissolution of Ni at low potentials (3).

Preferred dissolution is observed when dissolving Fe-Ni-alloy thin layers in an etching bath under open circuit conditions. The dissolution behaviour of such films is characterised by a typical time dependence of the open circuit potential. Alterations in the open circuit potential are caused by inhomogeneous dissolution of components of the alloy. The etching process was interrupted after different time intervals in order to investigate the dissolution behaviour. The resulting etching solutions were analyzed polarographically. The relative concentrations of iron and nickel in these etching solutions differ considerably from the composition of the alloy (Fig. 1a). The measurements show that at the beginning of the dissolution process iron is the component which is dissolved preferentially (stage I). In the second stage (II) the rates of dissolution of iron and nickel remain nearly constant, but a somewhat higher dissolution rate of iron is observed. During the last stage (III) only nickel is dissolved, because all iron

had been dissolved during stages I and II.

The analytical data of the etching solutions correlate with the observed open circuit potentials (Fig. 1b). At the beginning of the first stage the potential decreases. This decrease is connected with a preferred dissolution of iron. In this way nickel is enriched at the surface. The dissolution of nickel begins after a fifth of the etching time, whereby the potential increases slowly. The following constant potential is caused by constant dissolution rates of iron and nickel, respectively. Probably, the ratio of iron and nickel at the surface remains constant in this stage. This means that the enriched nickel is dissolved with a slower specific rate than iron. The rapidly increasing potential at the end of the etching process is caused by the complete consumption of iron. The increasing potential causes an increasing rate of dissolution of the remaining nickel.

Measurements of the open circuit potential during the etching of thin permalloy films of various thickness are shown in Fig. 2. As may be seen the duration of stage I is nearly independent of the film thickness. In contrast, the length of stages II and III increases with the thickness. Stage II is missing when 0.3 μm thick films are etched. Thus, we can conclude that the enrichment of nickel is a surface effect. Obviously, the preferred dissolution of iron takes place in the upper 0.2 to 0.3 μm of the film.

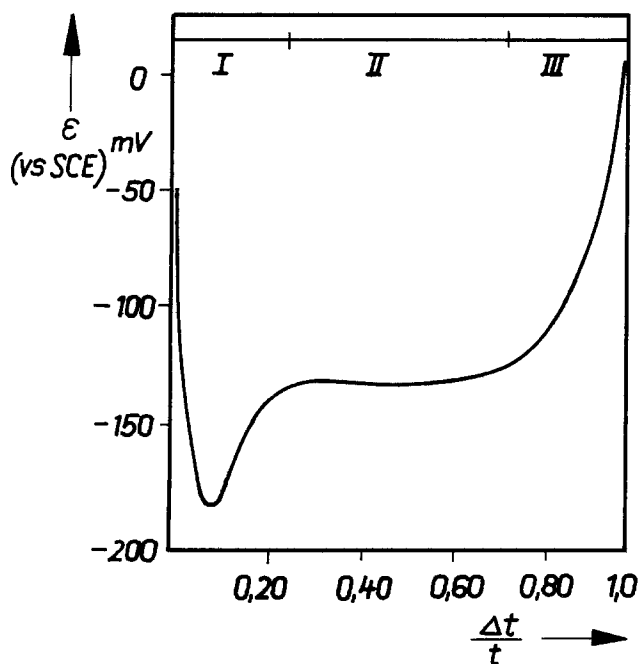
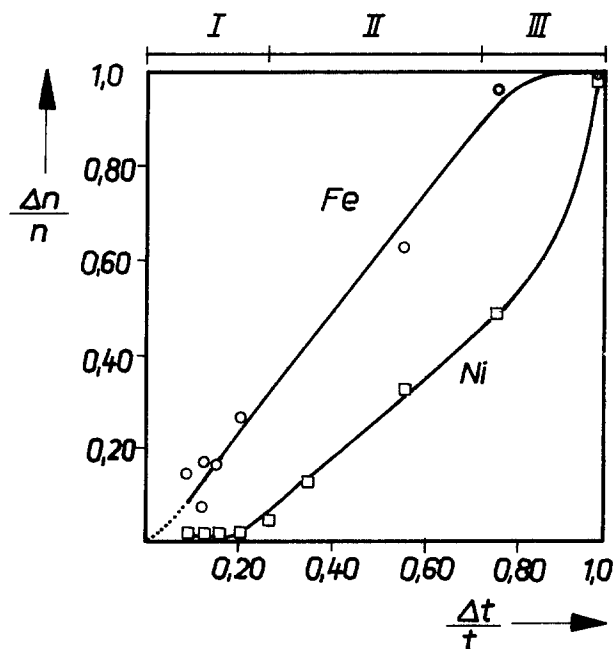


Fig. 1a. Relative amount of dissolved iron and nickel, respectively, in dependence on the normalized etching time. $\Delta t/t = 1$ is equivalent to a completely dissolved permalloy film.

Fig. 1b. Open circuit potential versus normalized etching time $\Delta t/t$.

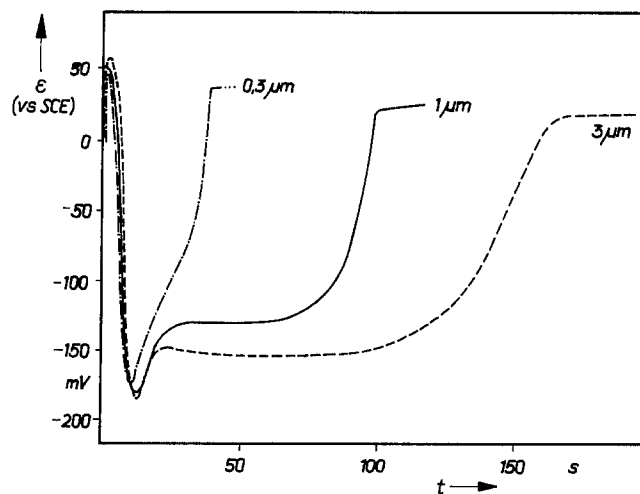


Fig. 2. Open circuit potential ϵ in dependence on the etching time t for three permalloy films of different thickness.

It is possible to estimate the amount of nickel at the surface during stage II by comparison of the open circuit potential with the current-voltage dependence of bulk pure iron or nickel, respectively. From such measurements a nickel concentration of about 80% was estimated.

EXPERIMENTAL

The thin FeNi-films (50/50 wt %) on copper coated glass substrates were prepared by high rate sputtering. The open circuit potential was measured in aqueous solutions containing 0.1 M NH_4F and 0.45 M $(\text{NH}_4)_2\text{S}_2\text{O}_8$ at room temperature. The concentrations of the dissolved metals were determined by means of the polarograph OH 105 (Radelkis). Cyclovoltammograms for the estimation of the nickel enrichment were recorded by means of the potentiostat PS 4 (Meinsberg).

REFERENCES

1. Ya. M. Kolotyarkin, *Br. Corros. J.*, **15**, 102 (1980).
2. A. I. Marshakov, A. P. Pchel'nikov, and V. V. Losev, *Elektrokhimiya*, **19**, 356 (1983).
3. H. P. Lee and K. Nobe, *J. electrochem. Soc.*, **131**, 1236 (1984).

Loading Effect of Ashing Rate Observed in Cr Mask Fabrication

Fumio Mizuno, Yoshihiko Okamoto, Makoto Kato, and Katsuro Sugawara*

Hitachi Limited, Device Development Center, Kodaira, Tokyo 187, Japan

INTRODUCTION

For LSI's with higher density and higher performance, precise control of mask making has been required in addition to that of wafer processing. One problem is how to control the etching of Cr masks. An accurate "in process" method was reported in the case of the mask making using spray etching (1). Another problem is how to remove the residue of the resist which is often observed after developing the resist film. An ashing treatment is used to remove this kind of the residue. It gives influence on the thickness of the resist film and also on dimension of the mask through thinning the resist. In this treatment, a new phenomenon was observed which showed that Cr film on the mask acted as a load for the ashing rate in the case of Cr mask making. In this note, this novel effect and experimental results will be reported in the following.

RESULTS AND DISCUSSION

Specimens used in this experiment were low expansion glass substrates of 5 inches in square with electron-beam negative resist, PGMA, polycidylmethacrylate (2) of 4000Å in thickness and with or without Cr film of 800Å in thickness. Ashing conditions were as follows. Ashing was carried out in a reactor of parallel plate type which consisted of 200mm diameter stainless steel watercooled electrodes run at 13.56MHz and RF power of 40W. The reactor was evacuated, ashing gas, O₂ was fed in and the pressure was kept at 67 Pa (0.5 Torr). Ashing was done for 2 min. Ashing rate was determined as a difference of the resist film before and after the ashing treatment, measured by using an automatic thin film thickness measurement system for selected small area, NANOSPEC/AFT.

*Electrochemical Society Active Member.
Keywords: photo-mask, ashing of resist film, precise control of dimension, electron beam technology.
Manuscript received June 3, 1985.

Figure 1 is the ashing rate of the resist film coated on Cr mask. It shows the ashing rate increased as area ratio of the resist pattern on the mask increased. This tendency was also observed under different ashing conditions such as moistured air instead of O₂ and a barrel type reactor instead of the parallel reactor. This trend is quite contrary to the usual loading effect observed in plasma etching (3).

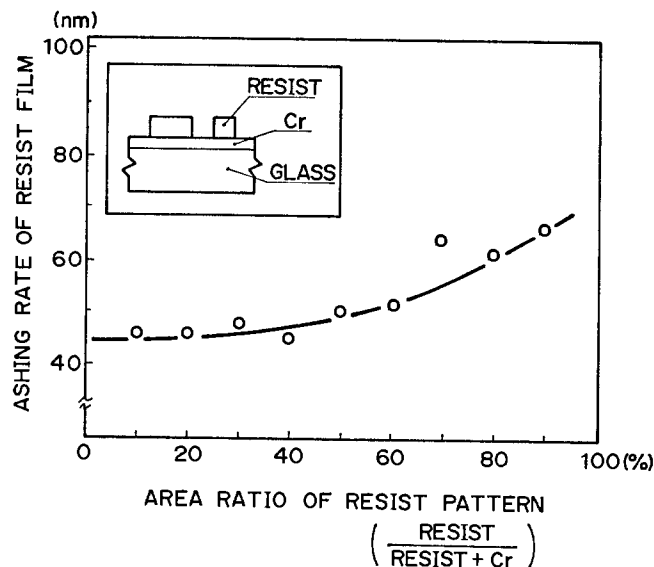


Fig. 1 Dependence of ashing rate to area ratio of resist pattern in the case of Cr mask.

To explain this new phenomenon, following experiments were tried. At first, the difference between Cr mask and glass substrate of the mask was examined. Fig. 2 is the result of the ashing rate in the case of the glass substrate of the mask done under the same ashing condition. As the area of the resist pattern on the glass substrate increased, the ashing rate decreased. This tendency was quite similar to that of the conventional plasma etching (3). The second evidence was the result of Auger electron spectroscopy analysis.

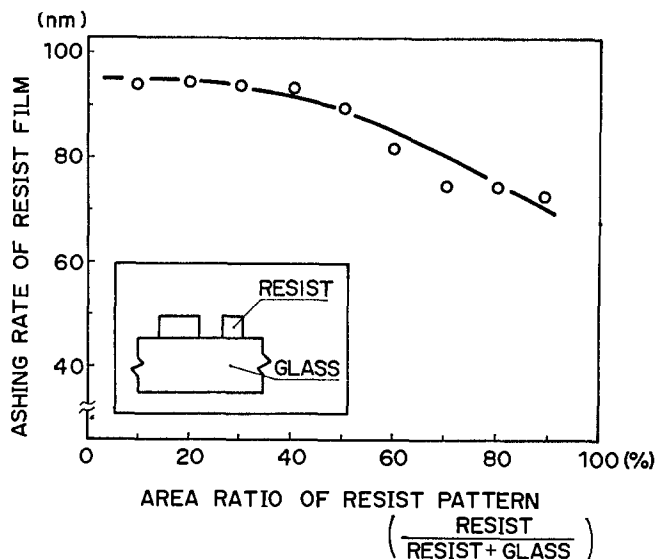
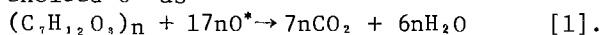
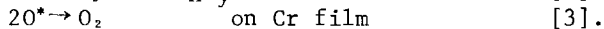
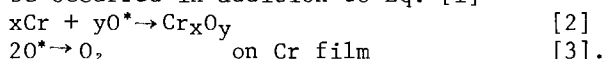


Fig. 2 Dependence of ashing rate to area ratio of resist pattern in the case of glass substrate.

Fig. 3 shows sputter profiles of chromium and oxygen measured with Ar sputtering. There was a remarkable difference of the oxygen distribution before and after the ashing treatment; Fig. 3(a) and 3(b) are the profiles before and after the ashing, respectively. After the ashing, oxygen content increased at the surface of the Cr mask. This phenomenon may be explained as follows. In the case of the glass substrate, PGMA, $(C_7H_{12}O_4)_n$ may be reacted by the excited O^* as



As the area of the resist patterns increases the ashing rate becomes decreased as the result of consuming larger amount of the excited O^* . In the case of the Cr mask, following reactions may be occurred in addition to Eq. [1]



At the large ratio of the Cr pattern = the small ratio of the resist pattern, the excited O may be more reacted by Eq. [2] and Eq. [3] than by Eq. [1], therefore, the increasing tendency of the ashing rate may be brought about.

SUMMARY

In Cr mask fabrication, an ashing process was adapted to remove the residue of the resist and novel loading effect was observed, which showed Cr film acted as the load. This may be explained by a stronger reaction between Cr and oxygen radical than the conventional reaction between the resist film and oxygen radical.

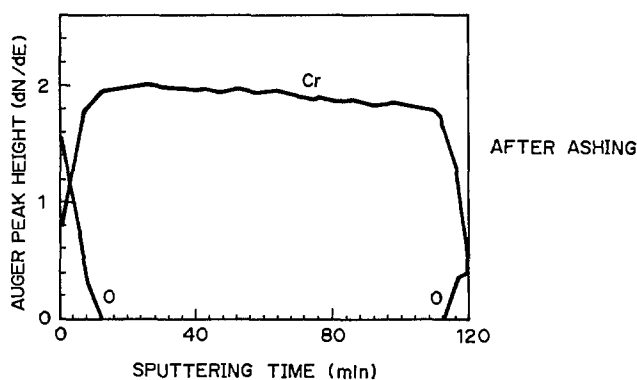
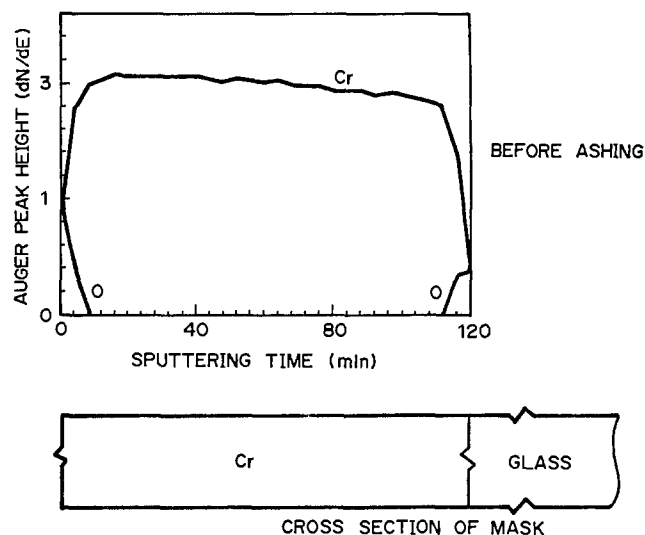


Fig. 3 Component sputter profiles of Cr mask measured by Auger electron spectroscopy.

(2) Before ashing

(b) After ashing

Hitachi Limited assisted in meeting the publication costs of this article.

ACKNOWLEDGEMENT

The authors express their sincere gratitude to Dr. Y. Ohya for his encouragement, to Mr. Y. Takehana and Mr. K. Hirobe for helpful discussions, to Mr. S. Mori, Mr. H. Nakaune and Mr. K. Kamiyama for their assistance in the experimental work, and to Mr. M. Tamura for his analysis of Auger electron microscopy.

REFERENCES

1. F. Mizuno, M. Kato, T. Koizumi, Y. Takehana, K. Sugawara, and K. Mori, *This Journal*, **132**, 1495 (1985).
2. Y. Taniguchi, Y. Hatano, H. Shiraishi, S. Horigome, S. Nonogaki and K. Naraoka, *Japan. J. Appl. Phys.*, **18**, 1143 (1979).
3. C.J. Mogab, *This Journal*, **124**, 1262 (1977).

Transient Photoconductivity Profiles of Electrochemical Interfaces: The α -Si:H Aqueous Electrolyte Contact

R. Könenkamp and H. J. Lewerenz

Hahn-Meitner-Institut für Kernforschung Berlin, Bereich Strahlenchemie, D-1000 Berlin 39, Germany

Transient photoconductivity measurements using the technique of the time-of-flight (TOF) method¹ are demonstrated for the hydrogenated amorphous silicon (α -Si:H)/aqueous electrolyte junction. Our results indicate that local surface variation achieved by in situ alteration of the interfacial oxide by solution composition is clearly reflected in the time dependence of the photoconductivity.

A block diagram of the experimental arrangement is shown in fig.1. A voltage pulse (typical duration $t_V=300\mu s$) is applied to the working electrode via a pulse generator. Within a period considerably shorter than the dielectric relaxation time of the α -Si:H films (here typically 1ms) a nanosecond laser pulse (Excimer Laser, Lambda Physics) of 8ns duration with $\lambda=308nm$ falls onto the sample. The generation of electron-hole pairs occurs in the surface near region due to the high absorption of the semiconductor at that wavelength. One type of carrier (electrons when the working electrode is positive) then drifts in the applied field to the back contact giving rise to a photocurrent which is recorded using a Tektronix 7912AD digitizer. The photogenerated charge is not greater than $\sim 10^{-10} Ccm^{-2}$ per pulse which is low enough to avoid space charge effects.

The electrochemical cell, especially designed for photocurrent transient measurements², consists of the α -Si:H working electrode, a carbon counterelectrode ring and a saturated calomel electrode (SCE). Solutions were prepared from analytical grade chemicals and distilled water. The α -Si:H films were prepared in a conventional rf glow discharge in SiH_4 ³ onto stainless steel; substrates were held at $T=270^\circ C$. The films were undoped but were provided with a 200Å thick n^+ layer to establish an ohmic contact. The film thickness ranged between 2.5 and $3\mu m$.

Manuscript submitted April 9, 1985; revised manuscript received June 11, 1985.

Hahn-Meitner-Institut für Kernforschung Berlin assisted in meeting the publication costs of this article.

The time dependence of the photocurrents in a solution made of 1M NH_4F in H_2O ⁴ is displayed in fig.2 for a series of bias voltages. Similar results have been obtained in a solution made of 5M LiCl and 1M NH_4F . We note that a distinct voltage dependence of the photocurrent transients is observed. The general shape of the $\log I$ vs. $\log t$ plots is characterized by a constant current, a bend and a pronounced current decrease at larger t . The time regime of constant photocurrent is interpreted as the collection of the drifting photogenerated excess carriers in the applied field. The bend indicates the termination of the primary carrier drift and the tail at larger t is considered to arise from detrapping and subsequent drift. Up to $\sim 4V$, a linear increase of I with bias voltage is observed. For $V_b > 4V$ the photocurrent saturates. The transit times, t_T , show the expected behavior, i.e. faster drift at higher fields. The changes of I with V_b and the differences in t_T indicate that the external voltage drops across the semiconductor bulk. The existence of a current at 0V bias can be attributed to an internal electric field at the interface most likely due to trapped charge. From the transient behavior at high voltages the drift mobility of electrons can be determined. With $\mu_D = l^2 / V t_T$ where l denotes the semiconductor thickness we obtain $\mu_D \approx 3 cm^2 / Vs$ in accordance with measurements using evaporated metal contacts¹.

A pronounced change in transient behavior is noted in the absence of NH_4F . Fig.3 shows measurements equivalent to those in fig.2 but performed in supporting electrolyte (5M LiCl) only. Here, photocurrent saturation occurs already at external voltages of $\sim 1V$ and no transit time dependence is observed. The comparison with fig.2 shows that the transit time for 1V in fig.3 corresponds to the expected value in fig.2 but beyond that voltage no decrease in t_T is achieved in fig.3.

In a first tentative interpretation, these results indicate different electric fields to be effective at the surface and in the bulk of the sample, depending on solution composi-

tion. Electrochemical measurements on single crystalline and amorphous silicon show pronounced differences in electrode behavior in the presence or absence of NH_4F 4,5. In particular, a dark current is observed in NH_4F after immersion of the electrode, whose magnitude and time dependence is linked to the thickness of interfacial $\text{SiO}_2\text{-SiO}_x$ species. In a separate combined electrochemical and XPS experiment⁴ it was found that a-Si:H in supporting electrolyte LiCl is covered by SiO_2 mainly. In NH_4F , however, the surface appears to be free of oxygen and fluorine within the XPS resolution limit. We therefore attribute the differences observed with TOF to the different surface conditions with and without oxide. Although the determination of the actual field distribution has to await further detailed investigation, we have shown the applicability of TOF for analysis of microscopic interfacial changes. The applicability appears, however, to be restricted to intrinsic or almost intrinsic material and, in the case of monitoring surface or interface changes, to effects of these surface conditions on the internal field distribution in the intrinsic semiconductor. Since the field distribution in semiconductors is sensitive to even small changes in the surface, the TOF method in this form might be successfully applied in situ in a variety of suitable systems.

Acknowledgements

The authors thank H.Gerischer for stimulating discussions and H.Tributsch for very encouraging support. Support from the BMFT (No.03E-8375A) is also gratefully acknowledged.

References

1. R.A. Street, Phys. Rev. B27, 4924 (1983)
2. W. Jaegermann, J. Phys. Chem. 88, 5309 (1984)
3. SERI Annual Report 1983, SERI/PR-212-2172, DE840004494
4. R. Könenkamp, H. Gerischer, M. Lübke, D.Schmeißer and H.J.Lewerenz, to be published
5. M. Matsomura and R. Morrison, J. Electroanal. Chem. 147, 157 (1983)

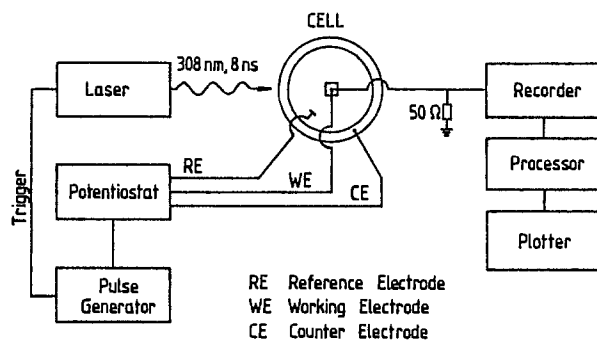


Fig.1: Block diagram of the experimental arrangement

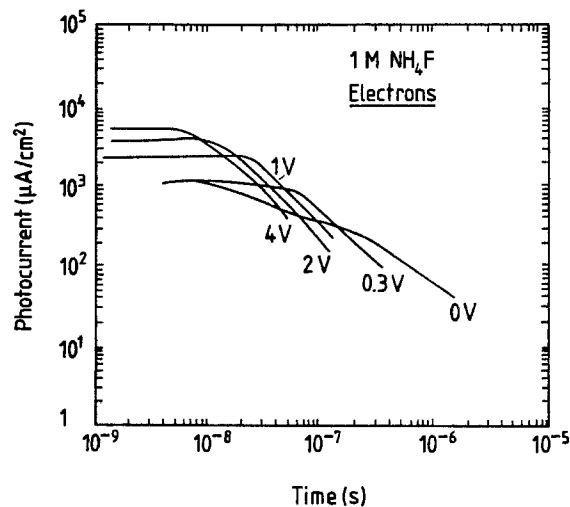


Fig.2: Photocurrent transients obtained in an aqueous solution of 1M NH_4F . The bias voltage is measured between working electrode and reference electrode.

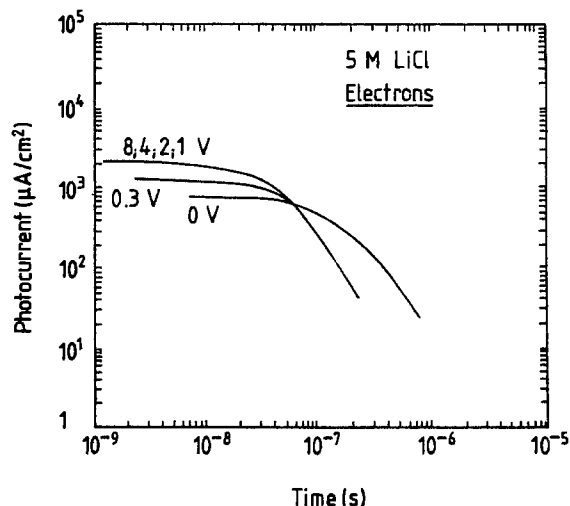


Fig.3: Photocurrent transients in 5M LiCl for the same samples as in fig.2.

Indium Oxide, Oxygen Photoanode of High Quantum Efficiency

Lynn C. Schumacher, Susanne Mamiche-Afara, and Michael J. Dignam*

Lash Miller Chemical Laboratories, University of Toronto, Toronto, Ontario, Canada M5S 1A1

To date, high quantum efficiencies ($\sim 100\%$) for transition-metal-oxide oxygen-photoanodes have been reported only for TiO_2 (1), WO_3 (2), SrTiO_3 (3) and SnO_2 (4). To this list we now add a thin film form of In_2O_3 .

We have formed thin films of indium oxide by thermal oxidation of thin indium metal films which reproducibly display quantum efficiencies close to 100% at the absorption maximum of 310 nm (4.0eV). The technique used for making these thin oxide electrodes involves depositing indium metal films by sputtering from a 6" diameter indium metal target. The films are deposited in 1.0×10^{-2} torr of argon to an average thickness of about 800Å onto indium tin oxide (ITO) substrates held at 350°C. Following deposition of the metal, the plasma is shut off, the argon flow stopped and oxygen bled into the bell jar. The substrates are then left in 1.0×10^{-2} torr of oxygen for 30 minutes at 350°C after which the oxygen flow is stopped, the bell jar evacuated, and the substrates cooled down to room temperature over 4 hours. An indium metal-film of mean thickness of about 800Å will oxidize to form an In_2O_3 film of mean thickness $\sim 1000\text{Å}$. However, SEM studies show that the resulting oxide is not flat but consists of a series of hemispherical structures of mean radius $\sim 3.0 \times 10^{-5}$ cm. Transmission studies of these films deposited directly onto quartz showed less than 10% transmission of the incident light for $\lambda < 325\text{nm}$.

Photoelectrochemical and impedance properties of these films have been determined using a PAR model 170 Electrochemical System along with a focused xenon lamp carefully calibrated using the iron oxalate actinometer system. The experimental arrangement has already been described in some detail (5,6). The quantum efficiency, (ϕ), was calculated using the expression $\phi = 1.2408 J / I_0$, where J is the photocurrent density in $\mu\text{A}/\text{cm}^2$, 1.2408 a conversion

*Electrochemical Society Active Member.

factor relating photon flux density to power flux density and I_0 is the power flux density in mW/cm^2 at wavelength λ (expressed in nm) incident upon the photoelectrode surface. No corrections were made for reflection and transmission losses at the electrode. As a further check on the accuracy of our quantum efficiencies, such measurements were made for a thin film TiO_2 electrode which had previously been compared to a single crystal electrode (7). Our present calibration places the maximum TiO_2 single crystal quantum efficiency at 80%, in good agreement with the value of 81% obtained by Mavroides et. al. (1).

Figure 1 shows the measured quantum efficiency for a thermally oxidized indium metal layer at a bias potential of + 0.50 V(SCE) in 0.10 M NaOH. Figure 2 shows the d.c. photocurrent response at 310 nm of this same electrode. The photocurrent onset of -0.25 V(SCE) agrees very well with that reported for single crystal n- In_2O_3 (8), -0.20 V(SCE) in 1.0M NaOH. While the maximum in the quantum efficiency for these thermally oxidized metal films occurs at the same wavelength (310 nm) as that for the only single crystal studied (8), the increase in quantum efficiency from 25% for the single crystal to 90% for these thermally oxidized films is quite dramatic. The electrode response was stable under constant illumination for 3 days at +0.5 V(SCE) bias in 0.10 M NaOH. Measurements on a blank ITO substrate showed no photocurrent indicating that the observed photoresponse is due entirely to the thermally oxidized In_2O_3 . They were checked periodically over several weeks and no sign of corrosion or instability was detected. The poor behaviour of the single crystal has been attributed by Bockris et. al. (8) to high recombination rates due to the presence of a high density of impurity centres incorporated

into the crystal lattice during crystal growth. The technique used to produce these thin $n\text{-In}_2\text{O}_3$ films, has advantages over single crystal growth. These oxide films can be formed within at most 30 minutes of metal deposition, compared to several days, and at the much lower temperature of 350°C , compared to 950°C for single crystal growth. Furthermore, the fabrication procedure minimises contamination. Further studies are underway to characterise the photoelectrochemical, optical, morphological and impedance properties of indium oxide films produced in this way.

ACKNOWLEDGEMENTS

The authors wish to express their appreciation to the Natural Science and Engineering Research Council of Canada for supporting this research.

REFERENCES

1. J.G. Mavroides, D.I. Ichernev, J.A. Kafalas and D.F. Kolesar, Mat. Res. Bull. **10**, 1023 (1975).
2. G. Hodes, O. Cahan and J. Manassen, Nature, **260**, 312 (1976).
3. M.S. Wrighton, A.B. Ellis, P.T. Wolczanski, D.L. Morse, H.B. Abrahamson and D.S. Ginley, J. Am. Chem. Soc., **98**, 2774 (1976).
4. M.S. Wrighton, D.L. Morse, A.B. Ellis, D.S. Ginley and H.B. Abrahamson, J. Am. Chem. Soc., **98**, 44 (1976).
5. M.F. Weber, L.C. Schumacher and M.J. Dignam, This Journal, **129**, 2022 (1982).
6. L.C. Schumacher, S. Mamiche-Afara, M.F. Weber and M.J. Dignam, submitted This Journal.
7. R.L. Sasseville, S. Mamiche-Afara, M.F. Weber and M.J. Dignam, Proceedings of the 5th World Hydrogen Energy Conference, Hydrogen Energy Progress V, Vol. 3, 1047 (1984).
8. J.F. McCann and J.O'M. Bockris, This Journal, **128**, 1719 (1981).

Manuscript submitted May 20, 1985; revised manuscript received July 8, 1985.

The University of Toronto assisted in meeting the publication costs of this article.

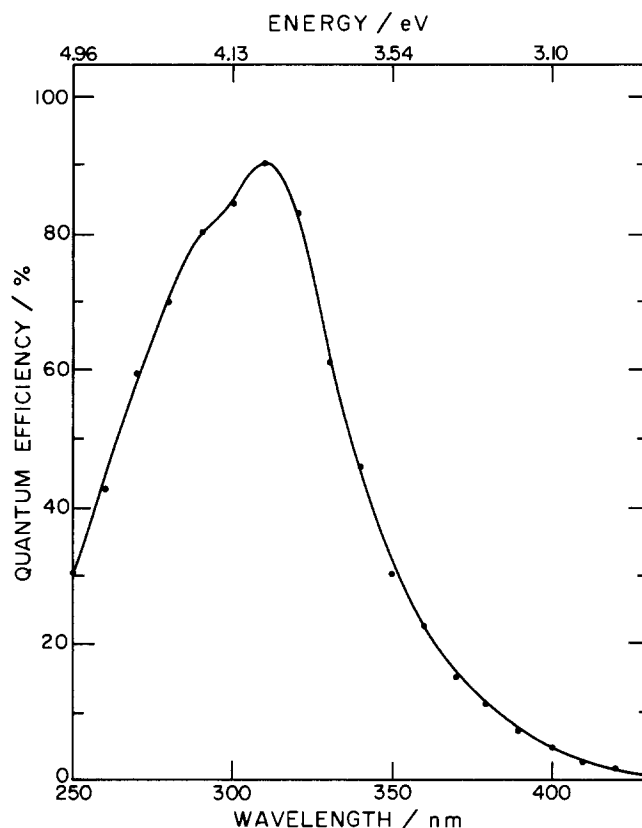


Figure 1: Quantum efficiency of thermally oxidized indium metal film at 350°C , measured in nitrogen purged 0.10 M NaOH .

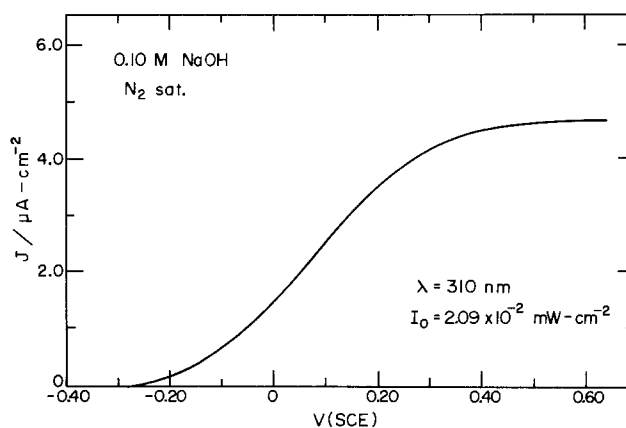


Figure 2: D.C. photocurrent response at the maximum in the quantum efficiency ($\lambda = 310\text{ nm}$) curve.



EST

Physical and Chemical Characteristics of Hermetically Sealed High Rate Li/SOCl₂ C-Cells

K. M. Abraham* and L. Pitts

EIC Laboratories, Incorporated, Norwood, Massachusetts 02062

William P. Kilroy*

Naval Surface Weapons Center, White Oak Laboratory, Silver Spring, Maryland 20903-5000

ABSTRACT

Pressure-temperature-voltage relationships in hermetically sealed high rate Li/SOCl₂ cells have been studied using specially instrumented C-size cells. The cells generated considerably lower pressures than those expected on the basis of established discharge reactions. This is believed to be due to the SO₂ generated being complexed by LiAlCl₄ and/or absorbed by the carbon cathode. Li-limited cells produced lower internal temperatures and pressures towards the end of discharge and during voltage reversal than cathode-limited cells. In high rate discharge involving >10 mA/cm², Co-TAA-catalyzed cathode cells exhibited higher capacities and lower IR heating than uncatalyzed cells. Li-limited Co-TAA catalyzed cathode cells appear to be a desirable design for high rate applications.

The Li/SOCl₂ battery is a very attractive high energy density system for many high power applications since it can provide load voltages near 3.0V under high current drains. However, high rate applications are generally limited by safety hazards that occur under certain conditions of operation such as forced overdischarge or by poor cathode performance. Several recent papers have examined some of the factors that can affect cell performance and safety in SOCl₂ cells. Cell design is one such factor. Early studies with spirally wound cells revealed that some anode-limited cells exhibited hazardous behavior during forced overdischarge at low rates (1, 2). These cells were considered anode limited rather than Li limited since substantial amounts of Li remained on the anode despite anode potentials greater than 4.0V. This was attributed to poor electrical contact between the Li and the anode grid. Recent studies confirm that during high rate cell reversal, cathode-limited cells were more hazardous than those of Li-limited design (3).

A great deal of work has also been devoted to improving cell performance via the use of catalysts. Studies show that both organic macrocyclic (4) and inorganic (5) additives substantially improve cathode performance, especially at low temperatures. Recently, the use of cobalt tetraazaannulene complexes as catalysts has been proposed to enhance the safety of the SOCl₂ system by altering the discharge mechanism so that no pressure building SO₂ product is generated (6).

The presence of water as a safety factor in SOCl₂ cells has received little attention. Studies have primarily addressed the effect of water on voltage delay or hydrolysis reactions that produce HCl or H₂ gas (7-9). Water has been shown to increase cell capacity of reverse polarity SOCl₂ cells following storage at room temperature (10).

Despite the fact that no energetic products capable of causing detonations have been found, occasionally SOCl₂ cells have exhibited explosive behavior. Indeed the mechanism of generating safety hazards is still not well understood.

*Electrochemical Society Active Member.

To date, very little has been reported on the physicochemical characteristics of Li/SOCl₂ cells discharged under high rate regimes. In particular, a detailed knowledge of the cell's internal pressure-temperature-electrode potential behavior and its dependence on discharge rates, depth of discharge, and environmental temperatures are extremely important for the ultimate description of safe cells.

By using specially instrumented cells, we have reexamined the effects of cell design, catalysis, and water on the performance-chemistry-safety relationship of Li/SOCl₂ cells.

Experimental

Cell construction.—Specially instrumented, spirally wound C-size Li/SOCl₂ cells, manufactured by Hellekens Battery Engineering, Incorporated (Hyde Park, Massachusetts), were used in this study. Each cell contained a vent mechanism designed to vent at ~250 psig. A stainless steel threaded bushing fitted with a removable plug was incorporated into the cell top. This allowed electrolyte sampling and the installation of a pressure transducer (Precise Sensor, Incorporated, Monrovia, California) capable of measuring the internal pressure of the cell in the 0-500 psig range. The temperatures at two different points on a horizontal plane perpendicular to the cell wall were measured using internal and external iron-constantan thermocouples. The internal thermocouple was 0.010 in. diam with a 304 stainless steel sheath placed in a 0.020 in. id-0.040 in. od closed tube positioned at the core of the spiral electrode package halfway down the electrode length. This permitted the thermocouple to be isolated from the electrolyte yet provided rapid response to temperature changes. The cell skin temperature was measured by an external thermocouple held in place at the middle of the cell height by the heat-shrinkable cell jacket. Each cell contained a Li reference electrode to enable measurements of individual electrode potentials during discharge. All other components had conventional characteristics of commercial cells.

Cell specifications.—Cells were designed as cathode and Li limited. The specifications of the cathode-limited cells were as follows: dimensions of the Li anode were $0.058 \times 29.2 \times 3.8$ cm; Li weight of 2.4 ± 0.2 g. The dimensions of the cathode were $0.064 \times 25.4 \times 3.8$ cm; the carbon weight was 3.3 ± 0.5 g. The electrolyte was $1.8M$ $LiAlCl_4$ in $SOCl_2$; its weight was 19.5-20g. The void volume was 1.5-1.8 ml based on electrolyte deletion. The average weight of the cathode-limited cell was 63g. The cell volume was 29.5 cm^3 .

The specifications of the Li-limited cells were as follows. The dimensions of the Li anode were $0.023 \times 37.5 \times 3.8$ cm; the Li weight was 1.10 ± 0.15 g. The dimensions of the cathode were $0.064 \times 33 \times 3.8$ cm; the carbon weight was 4.3 ± 0.5 g. The electrolyte was $1.8M$ $LiAlCl_4$ in $SOCl_2$, and its weight was 24.5-25g. The void volume was 1.5-1.8 ml based on electrolyte deletion. The average weight of the Li-limited cell was 68g, and the cell volume 29.5 cm^3 .

Dry electrolyte, containing less than 10 ppm of water, was used for all cells. The "dry" cells contained ~ 50 ppm water. "Wet" cells containing ~ 500 ppm of water were prepared by adding water to the dry electrolyte in a controlled manner.

Catalyst.—Cathodes were prepared from Shawinigan acetylene black. In addition to the regular cathodes, those containing 5 weight percent of dibenzotetraazaannulene complex of cobalt (Co-TAA) as a catalyst additive were used. The catalyzed cathodes were prepared by mixing the carbon with the catalyst and then heat-treating the mixture at $500^\circ C$ under inert gas. After cooling, this mixture was made into a paste with water, isopropanol, and Teflon binder, and then dried below $100^\circ C$. The mixture was cured by heating to $\sim 275^\circ C$ under inert gas. At no time was the catalyst heated above $100^\circ C$ in air. The possibility exists that the catalyst undergoes structural perturbations during the heat-treatment at $500^\circ C$; however, we did not investigate this.

Testing and analysis.—Prior to electrochemical experiments, the cell was housed inside a specially designed test chamber (11) provided with feedthroughs for electrical connections and ports for collecting gases and liquid. A stainless steel capillary tubing with 0.5 cm^3 of void volume connected the pressure transducer located on the outside of the chamber to the cell inside. The chamber was housed in a constant temperature environmental chamber prior to electrochemical tests. Standard electrochemical equipment was used. Data collection and retrieval were done with Bascom-Turner Instruments Series 8000 recorders equipped with microprocessor accessories.

Cell postmortem and sample collection for analyses were done in a Vacuum Atmospheres dry box maintained with an Ar atmosphere. Infrared (IR) spectra were recorded on a Beckman Acculab-5 double-beam spectrometer. X-ray data were obtained by the Debye-Scherrer technique. Gas chromatographic (GC) analysis of volatile materials from the cells were performed on a Varian 920 Gas Chromatograph equipped with a thermal conductivity detector and a 6 ft chromosorb Analabs column.

The water content of the cells was measured by removing electrolyte samples from cells stored one week. The hydrolysis products present were analyzed using infrared spectroscopy and quantitatively measured against IR calibration curves prepared from samples of the dry electrolyte containing known amounts of water.

Results and Discussion

The discharge and overdischarge data and the related pressure-temperature behavior for cathode-limited cells containing uncatalyzed cathodes are given in Fig. 1 and 2. The temperature and pressure changes which accompany the discharge and overdischarge at $0.2A$ (~ 1 mA/cm^2) are rather minor. The temperature and pressure increase slightly at the end of discharge when the cell potential approaches 0 V. The internal pressure after the voltage reversal remains at a slightly higher value than that during

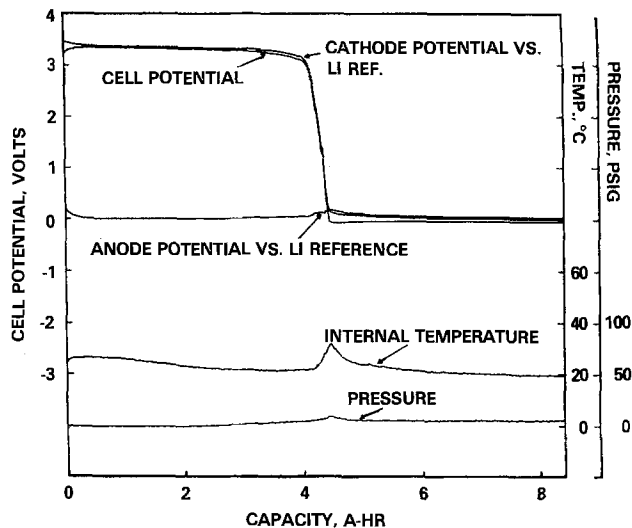
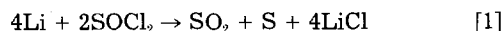


Fig. 1. Temperature, pressure, and voltage data for an uncatalyzed cathode-limited $Li/SOCl_2$ cell discharged at $0.20A$ at room temperature.

normal discharge. The data in Fig. 2 for the discharge and overdischarge at $2A$ (~ 10 mA/cm^2) show that the internal temperature increased to $\sim 50^\circ C$ during the course of the first 15% of discharge and remained at this value until the end of the normal discharge. The internal pressure increased slightly during the course of the normal discharge, but attained a maximum of only ~ 25 pounds per square inch (psi) at the 100% depth-of-discharge stage to a $2.0V$ limit.

By using the following information and the cell geometry and specifications given in the Experimental section, we have calculated the internal pressure of the cells on the basis of the generally accepted cell discharge reaction given below



The vapor pressure of SO_2 at $50^\circ C$ is about 130 psi (12). The solubilities of SO_2 in $SOCl_2$ and $SOCl_2/LiAlCl_4$ are given in Ref. (13). The calculated volume reduction which accompanies the $Li/SOCl_2$ cell discharge is 0.56 ml/Ah (14).

The pressure of the cell discharged at $2A$ was calculated to be at least 130 psi from the 75% depth-of-discharge stage onwards. The observed pressures were much lower. In addition, the internal temperature increases to $\sim 115^\circ C$ during the early stages of voltage reversal. At this temperature, an amount of SO_2 produced according to Eq. [1] would have generated a pressure of at least 500 psi. The measured maximum pressure is only ~ 140 psi, slightly lower than the cell venting pressure of ~ 250 psi. As the data in Table I show, the internal pressures are significantly lower than that expected on the basis of the

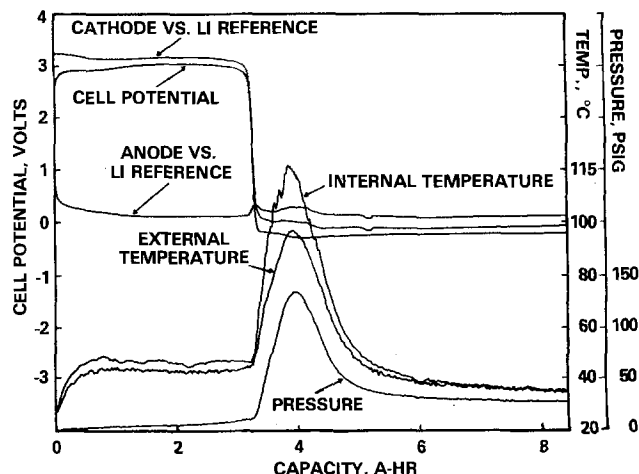


Fig. 2. Temperature, pressure, and voltage data for an uncatalyzed cathode-limited $Li/SOCl_2$ discharged at $2.0A$ at room temperature.

Table I. Averaged pressure-temperature behavior and safety characteristics of uncatalyzed Li/SOCl₂ C-cells

Cell type ^a	Discharge current (A)	Environmental temperature (°C)	Capacity (Ah) ^c		Extent of overdischarge (Ah)	Maximum internal temp. (°C) ^e	Maximum internal pressure (psig) ^f
			2.0V	0.0 V			
A-W	2.0	20	2.54	2.63	>5	79	73
A-W	2.0	-12	2.20	2.37	>5	54	^b 73
A-D	0.2	20	2.90	3.0	>5	30	^b 70
A-D	2.0	20	2.66	2.95	>5	73	70
A-D	2.0	-12	2.63	2.90	>5	53	^b 70
A-D ^d	3.0	20	2.61	2.90	>5	95	72
C-D	0.2	20	4.75	4.85	>7	30	7
C-D	0.2	-12	2.70	2.88	>5	^b 30	^b 7
C-D	2.0	20	3.45	3.59	>7	102	138
C-D	2.0	-12	1.60	2.16	>7	58	^b 138
C-D	3.0	20	2.25	2.4	>7	130	153
C-W	2.0	20	3.26	3.42	>7	117	158
C-W	2.0	-12	1.74	2.10	>7	71	^b 158

^a A-W: Li-limited wet cells containing 500 ppm added H₂O. A-D: Li-limited dry cells. C-D: cathode-limited dry cells. C-W: cathode-limited wet cells containing 500 ppm added H₂O.

^b Pressure transducer response at -12°C was poor, so pressure data were unreliable.

^c Average of five cells for each test current. No cells vented.

^d At a 3.0A rate, cell became cathode limited and vented after ~3 Ah overdischarge.

SO₂ stoichiometry of Eq. [1]. Complexation of the SO₂ by LiAlCl₄ (15), the absorption of SO₂ by carbon (10), and/or the presence of a significant amount of the low volatile (SO)_x rather than its decomposition products S and SO₂ may be occurring (16). The minimum amount of LiAlCl₄ in our cells is ~0.02 mol, which is sufficient to complex all the SO₂ produced at the 2.0A rate according to Eq. [1] to form an adduct of the composition [Li⁺(SO)₂AlCl₄⁻]. Raman spectroscopic studies have revealed the existence of such complexes in LiAlCl₄ solutions in SO₂ (15). However, there is strong evidence for significant absorption of SO₂ by Shawinigan carbon (10). The desorption of this SO₂ gas is reflected in the rapid pressure rise accompanying the temperature increase seen in the early stages of overdischarge. If it were not for a built-in SO₂ scavenging mechanism, the Li/SOCl₂ cell would produce excessive internal pressures capable of potentially violent venting, especially during early stages of cell reversal. If the scavenging mechanism involves the formation of SO₂ adducts with LiAlCl₄, then the salt concentration is critical: cells with higher salt concentrations should be safer. However, a lower salt concentration is a widely recognized remedy for alleviating voltage delays in the Li/SOCl₂ cell (16).

Some typical data for uncatalyzed cells are given in Table I. The temperature and pressure maxima reached in the Li-limited cells were considerably lower than the cathode-limited cells as illustrated by a comparison of the data in Fig. 2 and 3. A substantial fraction of the internal

heating at the end of cell life in cathode-limited cells at both 20° and -12°C was associated with cathode polarization. Very little cathode polarization occurred in Li-limited cells.

The effects of environmental temperature and the addition of 500 ppm H₂O on uncatalyzed cell performance are also tabulated in Table I. The data are averaged over five discharges for each type of cell. Some of the observations follow.

1. Addition of water showed no adverse affect on voltage delay at either 20° or -12°C. Cells with and without the added water showed substantial voltage delays when discharged at >10 mA/cm² at -12°C. In both types of cells, the voltage delay exceeded 60s of time to recover to 2.0V. Previous studies have examined the effects of smaller additions of water on voltage delay after storage at 23° and 55°C. Subsequent to room temperature storage for 1 month, cells containing an additional 100 ppm water displayed a decreased delay and attained their running potentials faster (10). Interestingly, partially discharged and stored cells behaved as well as fresh cells. Thus cells discharged for 1 Ah at 2.0A and stored 4 months at ambient room temperature experienced no voltage delay on redischarge at 2.0A (14 mA/cm² Li) at room temperature. The same type of cells redischarged at 3.0A (27 mA/cm² Li) did exhibit a voltage delay.

2. The internal temperature and pressure maxima at 2A at -12°C were substantially lower than that found at 20°C. The internal temperature of cathode-limited cells was always higher in the presence of added water. Data for a cathode-limited cell overdischarged at -12°C are illustrated in Fig. 4.

3. As seen in Table I, the capacity of the Li-limited cells was decreased ~11% at 20°C and ~18% at -12°C by addition of the water.

4. Two cells each from the four types of uncatalyzed cells were stored 4 months after having been discharged for 1 Ah at 2.0A current. The pressure generated after 4 months storage was 42% greater in the "wet" cells.

In general, the uncatalyzed cathode- and Li-limited cells exhibited safe behavior during extended periods of forced overdischarge at both the 0.2 and 2.0A rates. No cells vented.

Effect of Co-TAA catalyst.—The benefits of Co-TAA catalysis in 1/2 AA Li/SOCl₂ cells have been recently cited. These include superior cell performance, significant reduction in voltage delay, and a new SO₂-free reduction mechanism (6, 17). Our studies revealed that the addition of Co-TAA affected the behavior of Li/SOCl₂ cells in the following manner.

1. *Increased voltages.*—The catalyst gives rise to higher load voltages at the 2.0A and higher discharge rates. Typical discharge and overdischarge data at 2.0A at 20°C for

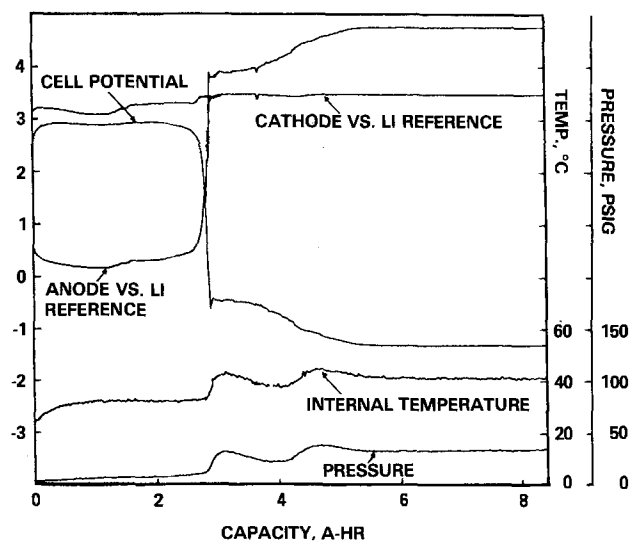


Fig. 3. Temperature, pressure, and voltage data for an uncatalyzed Li-limited Li/SOCl₂ cell discharged at 2.0A at room temperature.

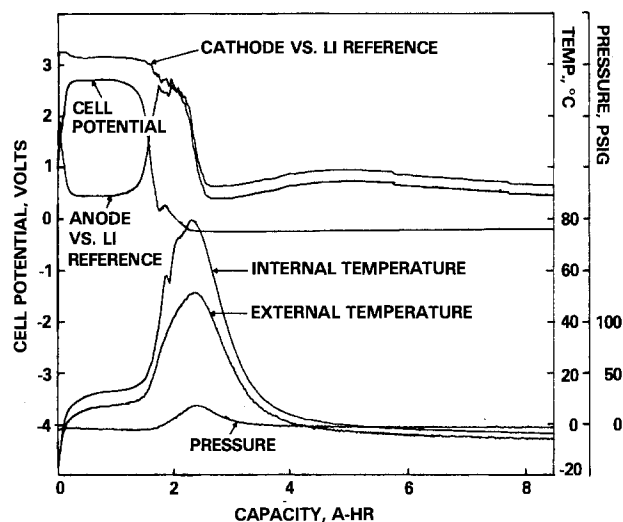


Fig. 4. Temperature, pressure, and voltage data for an uncatalyzed cathode-limited Li/SOCl₂ cell containing 500 ppm H₂O discharged at 2.0A at -12°C. Because of the poor response of the transducer, the pressure reading may not be accurate.

cathode and Li-limited cells are depicted in Fig. 5 and 6, respectively. The cathode potential profiles vs. the lithium reference electrode indicate that the higher voltage results largely from improvements in cathode load voltages—polarization of the catalyzed cathodes at the higher currents is considerably lower than in the uncatalyzed cells. In general, for both wet and dry cells discharged at -12° and 20°C, the average mid-discharge voltage was ~10 and 20% higher in cathode- and Li-limited cells, respectively, when the catalyst was present.

2. Increased performance.—The effect of catalyst on increasing the average cell capacity is shown in Table III. The data indicate that wet cathode-limited cells discharged at high rates and low temperatures benefit most from the catalyst.

The cells discharged at low temperatures exhibited the most pronounced effect of the catalyst. Even at low rates, where no beneficial effect was expected, cathode-limited cells discharged at -12°C at 0.2A (0.8 mA/cm²) showed a 55% improvement in cell capacity. As Table III indicates,

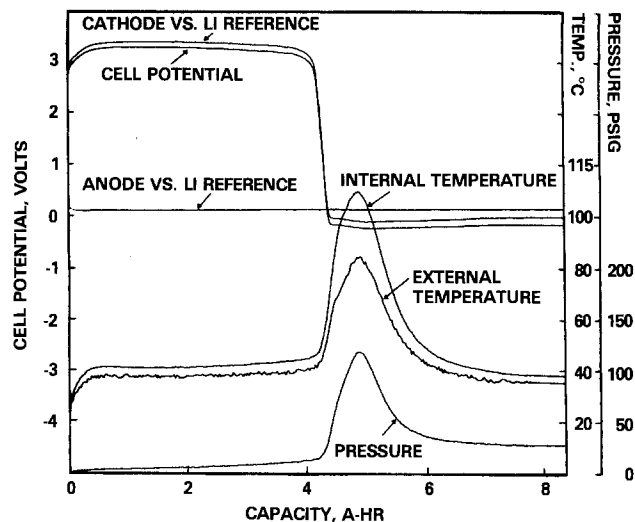


Fig. 5. Temperature, pressure, and voltage data for a catalyzed cathode-limited Li/SOCl₂ cell discharged at 2.0A at room temperature.

at the 2.0A rate at -12°C these cells had approximately a 74% average increase in cell capacity. At double the rate, 4.0A, the same cells containing catalyst had a 28% larger average capacity at -12°C than uncatalyzed cells discharged at only a 2.0A rate. Indeed, the catalyst was most effective at higher discharge rates. Dry cathode-limited cells discharged at 20°C at 0.2, 2.0, and 3.0A rates showed a 8.6, 20.3, and 61.2% increase, respectively, in cell capacity with added catalyst.

Interestingly, as Table III indicates, the catalyst was most effective in enhancing the capacity of cells containing 500 ppm H₂O. In Li-limited cells, the catalyst appears to have negated the detrimental effect of water, perhaps by inhibiting corrosion of the anode. The water or hydrolysis products may play a role in the catalysis mechanism to increase the capacity of cathode-limited cells.

3. Lower internal temperatures and pressures.—Catalyzed cells exhibited lower average internal temperatures (~40°C) during discharge compared with uncatalyzed cells (~50°C). This difference was also reflected in the temperature maximum accompanying cell reversal. The

Table II. Pressure-temperature behavior and safety characteristics of catalyzed Li/SOCl₂ C-cells

Cell type ^a	Discharge current (A)	Environmental temp. (°C)	Capacity (Ah) ^c		Extent of overdischarge (Ah)	Maximum internal temp. (°C) ^c	Maximum internal pressure (psig) ^f
			2.0V	0.0 V			
C-A-D	0.2	20	3.20	3.24	>5	31	20
C-A-D	2	20	2.92	2.98	>5	65	57
C-A-D	2	-12	2.94	2.90	>5	43	^b
C-A-W	2	20	3.05	3.15	>5	65	55
C-A-W	2	-12	2.91	3.17	>5	45	^b
C-A-D ^d	3	20	2.86	2.92	>5	74	^b
C-A-D ^d	4	20	2.93	3.06	>5	131	140
C-A-W ^e	4	20	2.98	3.02	>5	145	^b
C-A-W ^e	5	20	2.99	3.02	2	>200	190
C-C-D	0.2	20	5.15	5.20	>7	37	20
C-C-D	0.2	-12	4.60	4.72	>7	4	^b
C-C-D	2	20	4.16	4.32	>7	102	74
C-C-D ^e	3	20	3.80	3.95	>7	150	236
C-C-D ^d	4	20	3.14	3.53	>7	150	350
C-C-D	2	-12	3.23	3.51	>7	69	^b
C-C-D	3	-12	3.12	3.40	>7	130	^b
C-C-W	2	-12	3.52	3.87	>7	68	^b
C-C-W	2	20	4.39	4.52	>7	84	76
C-C-W ^e	3	20	3.82	3.97	>7	146	218
C-C-W ^f	4	20	3.38	3.53	2	>200	>300

^a C-A-D: catalyzed Li-limited dry cells. C-A-W: catalyzed Li-limited wet cells. C-C-D: catalyzed cathode-limited dry cells. C-C-W: catalyzed cathode-limited wet cells.

^b Pressure transducer response at -12°C was too poor to obtain reliable data.

^c Average of three or four cells for each current.

^d Only one or two cells used in this category.

^e One cell vented.

^f Two out of two cells vented.

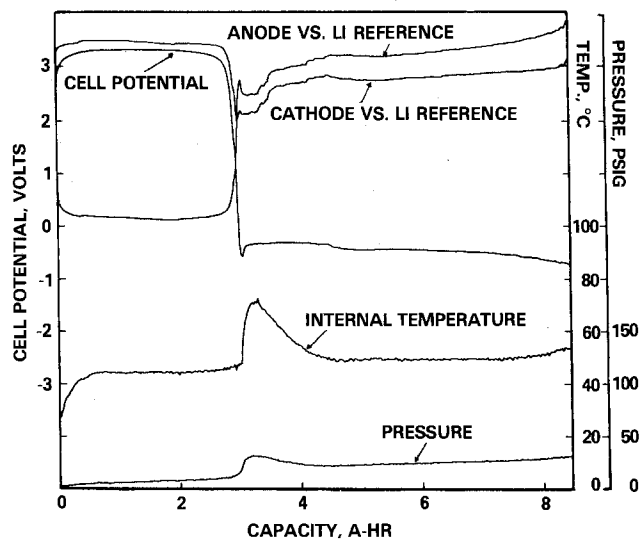


Fig. 6. Temperature, pressure, and voltage data for a catalyzed Li-limited Li/SOCl₂ cell discharged at 2.0A at room temperature.

data in Tables I and II reveal that addition of catalyst to cathode-limited wet cells reduced the average internal temperature ~28% during overdischarge at room temperature.

Cells which experienced lower internal temperatures also displayed lower pressure maxima. Upon addition of the Co-TAA catalyst, the average pressure maxima in type A-D, A-W, C-D, and C-W cells were reduced 19, 25, 46, and 52%, respectively.

Our results so far indicate that the catalyst is ineffective in reducing the resistive heating which accompanies the steep drop in cell voltages at the end of discharge and during early stages of cell reversal. On the other hand, the catalyst appears to be effective in lowering cell polarizations during high rate discharge. As a result, the catalyzed cells maintain an overall lower internal temperature profile relative to uncatalyzed cells.

Indeed, the pressure-temperature profiles which accompany cell reversal at high rates were significantly better in the Li-limited cells. Since Co-TAA catalyzed cells exhibited lower cathode polarizations and higher capacities, Li-limited catalyzed cells are a highly desirable design for high rate applications with practically attractive capacities. It should be noted that our Li-limited test cells were not optimized. Larger anodes would have provided additional capacity.

Discharge data for one of the lithium-limited catalyzed cells tested at a constant current of 4.0A are given in Fig. 7. None of the dry Li-limited cells vented at the 4.0A rate. Similar cells have been discharged and forced overdischarged at currents up to 5.0A to monitor their pressure-temperature profiles and safety characteristics.

Co-TAA catalyzed cathode-limited cells have also shown higher useful capacities and lower polarizations at the 3.0 and 4.0A discharge rates. However, in this design, the internal temperature during reversal at 4.0A rises to very high values, approaching the melting point of Li. One of the catalyzed cathode-limited cells tested at 3.0A

Table III. Effect of catalyst on increasing the average cell capacity

Temp. (°C)	Discharge rate (A)	Cell balance ^a	Increase in average cell capacity (%)	
			Dry	Wet
20	2.0	A	1	20
20	2.0	C	20	32
20	3.0	C	61	—
-12	2.0	A	0	34
-12	2.0	C	63	84

^a A = Li limited. C = cathode limited.

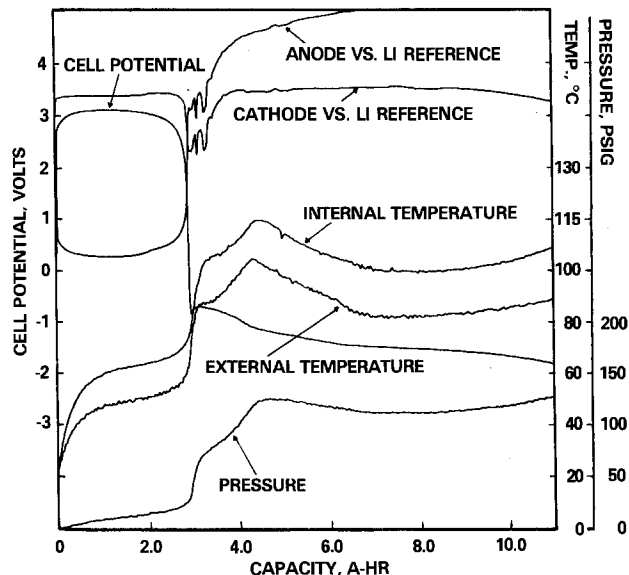


Fig. 7. Temperature, pressure, and voltage data for a catalyzed Li-limited Li/SOCl₂ cell discharged at 4.0A at room temperature.

and two cells tested at 4.0A vented following reversal. The venting occurred during the high temperature excursion. Typically, the cells first vented relieving the internal pressure. Soon after, a second highly exothermic reaction seemed to take place increasing the internal temperatures to excessively high values (Fig. 8). A number of products have been identified in the gases collected from vented cells (*vide infra*).

Constant current vs. constant load discharge.—The pressure-temperature behavior observed at the end of cell discharge would be different in constant current and constant load discharges. Since the current decreases substantially as the voltage falls towards 0.0 V in a constant load discharge, cell heating would be much less compared to a constant current discharge. This is illustrated in Fig. 9 for a catalyzed cell discharged through a 1.0Ω load. The constant current data are most relevant to cells in series connected batteries.

Cell chemistry.—Gas analysis.—Vapor phase IR spectra and GC analysis were performed on collected gases. The results indicate: (i) SO₂ is a discharge product of catalyzed cells; (ii) HCl gas was most often found in wet cells with high internal temperatures; and (iii) cells exhibiting the largest temperature rise generated the largest amount of the carbonaceous gases, COS, CO₂, and CS₂; specifically, they were cells discharged at high rates, cathode-limited

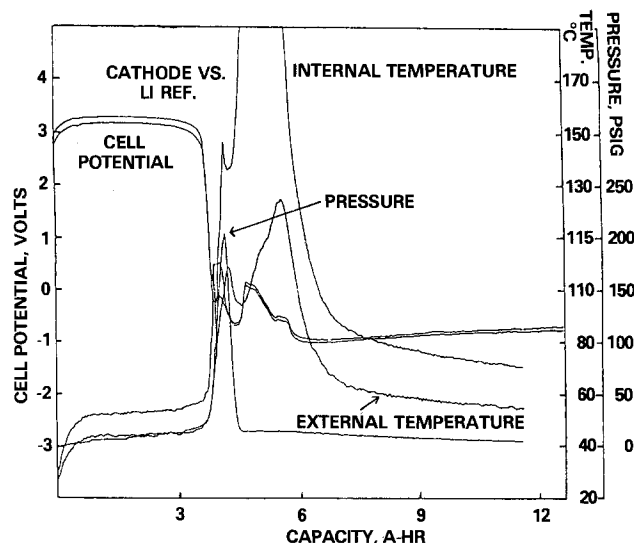


Fig. 8. Temperature, pressure, and voltage data for a catalyzed cathode-limited cell discharged at 3.0A at room temperature.

Table IV. X-ray diffraction data for cathodes from uncatalyzed cells at 2.0A at 20°C

Cell discharged 50%		Cathode-limited cell ^a		Li-limited cell ^a		LiCl ^b		S (rhombohedral) ^b		LiAlCl ₄ ^b		Li ₂ O ^b	
d (Å)	I/I ₀	d (Å)	I/I ₀	d (Å)	I/I ₀	d (Å)	I/I ₀	d (Å)	I/I ₀	d (Å)	I/I ₀	d (Å)	I/I ₀
5.71	40	9.98	Diffuse ^c							5.82	50		
5.09	40	8.44	Diffuse ^c							4.88	40		
3.78	60	5.90	Diffuse ^c					5.40	60	4.76	50		
3.61	60	5.06								4.60	50		
3.21	100	3.82	30	3.87	80			3.89	100	3.25	75		
		3.39	10	3.45	30			3.42	80	3.00	60		
3.05	10	2.99	10	3.21	10					2.89	100		
2.92	20	2.95	100	2.96	40	2.97	100			2.86	75	2.66	100
2.72	10	2.70	40	2.72	100					2.83	75		
2.52	40	2.56	100	2.56	60	2.57	86			2.73	20		
2.27	70			2.49	20								
				2.28	10								
				2.21	50								
2.16	30												
2.03	60												
1.95	20			2.11	5			2.21	40	2.22	25		
1.92	50			2.03	10			2.08	20	2.19	35		
1.80	20	1.90	20	1.92	80			2.02	80				
		1.81	90	1.86	10			1.95	40				
1.74	50	1.55	80	1.81	30	1.82	58	1.92	80			1.63	40
1.65	10	1.48	70	1.71	20			1.82	80				
1.63	10	1.28	50	1.68	10			1.72	40				
1.50	20	1.21	30	1.57	90			1.65	80				
1.47	30	1.17	60	1.54	10	1.55	29	1.56	80				
		1.15	70	1.48	10	1.48	16	1.49	80			1.39	16
1.40	10			1.42	5								
1.37	10			1.36	60			1.35	60				
1.35	10			1.33	10			1.32	20				
1.31	20			1.28	20	1.28	4						
1.22	40			1.21	70			1.23	10				
				1.18	10	1.18	10	1.19	20				
				1.15	10	1.15	12	1.17	20				

^a Forced overdischarged > 150% of the discharge capacity.

^b Literature data from the ASTM files. In contrast to rhombohedral sulfur, the monoclinic form has primarily three strong lines at 6.6 (25), 3.74 (20), and 3.29 Å (100%).

^c The diffuse lines at high d values are carbon background lines.

cells, and cells that vented. Comparison of Fig. 7 and 8 reveals cathode-limited cells have higher internal temperatures.

Gases collected from cathode-limited cells forced overdischarged at > 3A showed small amounts of COS and CO₂, in addition to SOCl₂ and SO₂. Appreciable quantities of these carbon containing gases and some CS₂ were found in all cells that vented during forced overdischarge. The cells that vented at high discharge rates generally were those containing the 500 ppm of water. These cells displayed the greatest amounts of HCl.

The formation of these gases typically accompanied or followed the large temperature increase which occurred in the early stages of voltage reversal. It appears the carbonaceous gases are produced in thermally initiated reac-

tions of carbon with S and SO₂. Evidently, rather high temperatures are required for the formation of these materials. Hence, the carbon cathode seems to play a major role in the safety hazards.

Analysis of solids.—Tables IV and V summarize x-ray data on cathodes taken from various discharged and overdischarged uncatalyzed and catalyzed cells. Recent x-ray studies on overdischarged (19) and 100% discharged (20) cells have been interpreted to involve the formation of Li₂O₂ under those circumstances. It should be noted that the x-ray data for Li₂O₂ can be accounted for by the combined x-ray powder patterns of LiCl and rhombohedral sulfur. It has been proposed that the Co-TAA catalyst alters the mechanism of SOCl₂ reduction to form Li₂O (6).

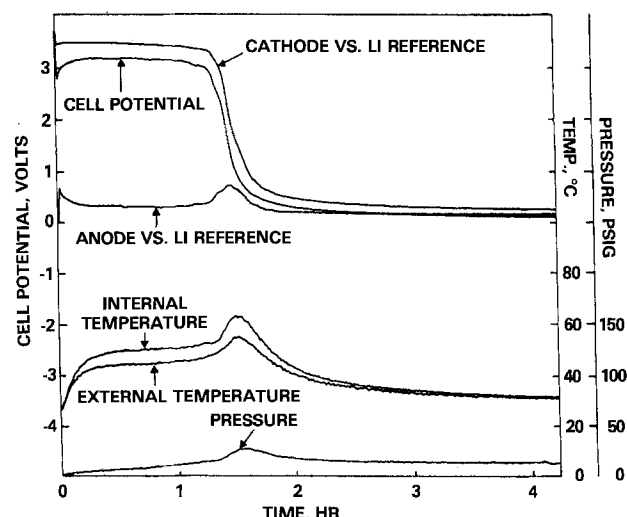


Fig. 9. Temperature, pressure, and voltage data for a catalyzed cathode-limited cell discharged through a 1Ω load at room temperature.

Table V. X-ray diffraction data of cathodes from catalyzed cathode-limited cells

Discharged at 3A to 0.0V at room temperature		Forced overdischarged at 2A at room temperature	
d (Å)	I/I ₀	d (Å)	I/I ₀
9.38	Diffuse	9.94	Diffuse
8.09	Diffuse	8.53	Diffuse
5.61	Diffuse	5.67	Diffuse
4.88	Diffuse	5.13	Diffuse
3.87	20	3.82	30
3.40	10	2.96	100
3.17	10	2.70	90
3.04	5	2.56	100
2.93	100	2.20	10
2.81	5	1.91	10
2.53	100	1.81	80
2.09	5	1.56	20
1.80	90	1.54	50
1.54	80	1.48	50
1.47	60	1.36	40
1.28	50	1.28	10
1.17	60	1.21	10
1.15	70	1.17	50
		1.09	50

The x-ray data in Table V give little evidence for this and are generally in good agreement with the x-ray patterns for LiCl and S.

In general, the catalyzed and uncatalyzed cells exhibit the same discharge products. While the relative intensities of the LiCl peaks show good agreement to the literature data, the sulfur peaks do not. This may be due to poor crystallinity of the sulfur and/or the existence of more than one allotropic form of S. Furthermore, S exhibits substantial solubility in SOCl₂ and, as a result, only small amounts would probably be present in the solid state in partially discharged cells.

Additional x-ray lines are present in the cathodes of partially discharged cells. These may arise from crystallized solvates of LiAlCl₄ containing SO₂, SOCl₂, or SO₂Cl₂. Evidence for solvates in overdischarged Li-limited cells comes from both the x-ray data and IR spectra.

When the electrolyte solution from overdischarged cells was collected and dried by pumping off the volatiles under vacuum, a glassy solid formed. These extracted salts were examined by IR analysis. Catalyzed and uncatalyzed cells gave identical spectra. However, as observed with the x-ray data, the Li-limited cells displayed a more complex spectral pattern than cathode-limited cells. The IR spectrum of the salt extracted from an overdischarged Li-limited cell is given in Fig. 10. The major absorptions at 1330 and 1070 cm⁻¹ are attributed to the complex Li⁺[(SO₂)_x(SO₂Cl₂)_yAlCl₄]⁻. Such a complex has recently been proposed (18). The peak at 1195 cm⁻¹ may be the S—O absorption associated with Li⁺(SOCl₂)_rAlCl₄⁻ and agrees with the strong band reported for LiAlCl₄ · 2SOCl₂ (21). The fact that SO₂Cl₂ is commonly reported in overdischarged Li-limited cells supports the proposed first complex. Additionally, the 1070 and 1195 cm⁻¹ bands were not present in the IR spectra of the salts extracted from the overdischarged cathode-limited cells. The peaks at 825 and 695 cm⁻¹ are probably due to an oxychloroaluminate salt (18, 22). Studies indicate that the relative amounts of the various materials formed during anode-limited reversal depend on a number of factors including the amount of electrolyte (*i.e.*, flooded or starved cells), the extent of overdischarge, and current density (2, 18, 23).

We also identified Li₂S₂O₄ in the cathodes of some overdischarged cathode-limited cells via qualitative tests with naphthol yellow-S (24). IR spectra of the cathode did not show the characteristic absorptions of Li₂S₂O₄ (11, 25), indicating it was a minor product. A band at 1015 cm⁻¹ appeared only in catalyzed overdischarged cathode-limited cells and may be associated with the catalyst.

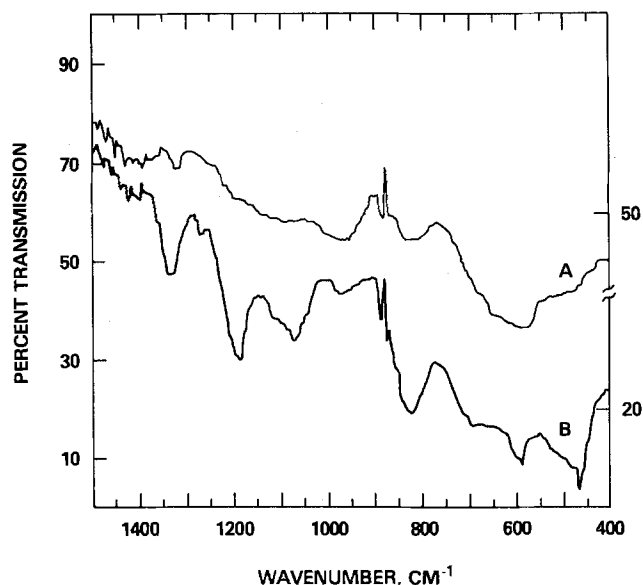


Fig. 10. Infrared spectrum of the glassy solid obtained by evaporating the liquid products from forced overdischarged "dry" cells. Curve A: cathode limited. Curve B: Li limited.

Infrared spectra of the liquid collected from extensively overdischarged cells, with or without catalyst, did not differ from the spectra obtained prior to the overdischarge. SO₂ was the only product in the liquid. Previous studies on electrolyte flooded cathode-limited cells showed evidence for LiAlSCl₂ formation (2).

The ability of Li-limited cells to sustain extensive periods of overdischarge, as evidenced by their overdischarge voltage profiles, seem to indicate regenerative processes similar to those previously characterized (2).

Cathode-limited cells that were forced overdischarged for extended periods exceeding the amount of Li originally present in the cell suggests cell short-circuiting accompanying plating of lithium onto the cathode. The short-circuited cell apparently shunts current as if it were a resistor. The fact that a substantial amount of Li remains on the anodes of extensively overdischarged cells supports this hypothesis.

Several cathode-limited cells experienced premature anode polarization during discharge. A typical pattern of behavior can be seen in Fig. 4. Polarization of the anode begins after achieving ~1 Ah capacity, initiates a corresponding temperature rise, and appears to trigger the onset of cathodic polarization. This phenomenon was unpredictable, and most frequently occurred in uncatalyzed cells discharged at low temperatures (-12°C) and usually at 2.0A rates or higher. Occasionally, the anode polarized at low rates as shown in Fig. 11. This event was frequently characterized by a subsequent (ganging) or possibly simultaneous (mimicking) failure of the cathode and by the unexplained recovery of the anode to 0 V. It appears that a continuously growing LiCl anode film during discharge or crystallized LiAlCl₄ on the surface of the anode as a result of ionic concentration gradients in the cell increases the resistance to Li⁺ transport across the anode/solution interphase. Higher current densities and low temperature increase the associated resistance polarization of the anode. Eventually, the voltage of the Li anode recovers, indicating that a disruption or dissolution of the film has occurred. However, the mechanism of this interesting process is not well understood. Lithium has been recently shown to undergo anodic passivation in research cells (26). It has also been shown that a greater passivation occurs when LiCl films are grown quickly (27). A temporary film has been recently shown to exist during anodization of lithium in the SO₂ system (28). Additional studies are warranted to characterize this interesting phenomenon.

Conclusions

The pressure generated in Li/SOCl₂ cells has been found to be significantly less than that predicted on the

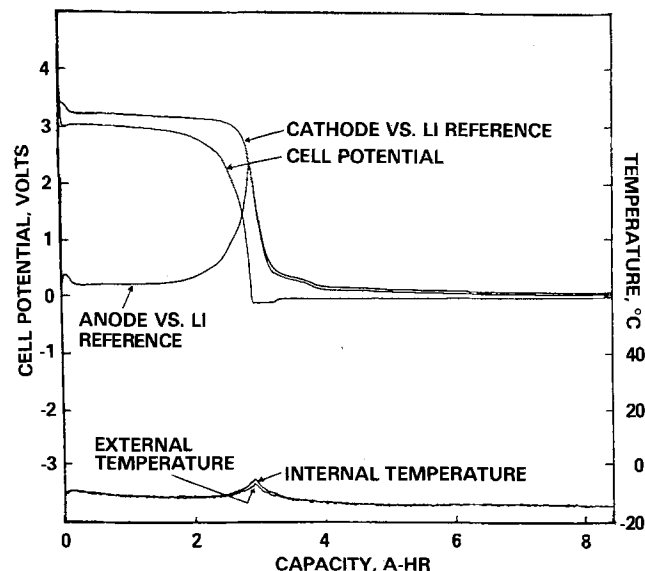


Fig. 11. Temperature and voltage data for an uncatalyzed cell discharged at 0.2A at -12°C.

basis of the accepted discharge reaction. This is believed to be due to the complexation of the generated SO_2 by LiAlCl_4 and/or the absorption of SO_2 by the carbon cathode. The highest internal heating was observed towards the end of constant current discharge and during early stages of cell reversal. Cathode polarization was identified as the major contributing factor to this type of internal heating. Runaway reactions and venting were observed in some cathode-limited cells in which the heating caused the internal temperature to exceed the melting point of Li. The generation of CO_2 , COS, and CS_2 appeared to be a function of internal temperature—the higher the temperature, the greater the amount of the carbonaceous gases that were produced. Li-limited cells show very little or no cathode polarization towards the end of cell discharge, and they produce considerably less heat than cathode-limited cells. Premature anode polarization has also been observed. This is proposed to be due to a growing anode film or ionic concentration gradients which increases the resistance of Li^+ transport across the anode-solution interface. The addition of water appeared to have no significant effect in voltage delay but generally lowered the capacity of uncatalyzed Li-limited cells, generated greater pressures in stored cells, increased the temperature of cathode-limited cells, and enhanced venting at high rates. Cells incorporating Co-TAA catalyzed cathodes exhibited higher capacities and less internal heating than uncatalyzed cells, especially at low temperatures. Li-limited cells with Co-TAA-catalyzed cathodes appear to be highly desirable for high rate applications.

Acknowledgment

We wish to express our appreciation to N. Marincic and his associates at Hellesens Battery Engineering for the preparation of the Co-TAA catalyst. We are grateful for the continued financial support provided by the Independent Research Program at NSWC and for the High Energy Batteries for Weapons Block Program.

Manuscript received April 22, 1985.

The Naval Surface Weapons Center assisted in meeting the publication costs of this article.

REFERENCES

1. K. M. Abraham, P. G. Gudrais, G. L. Holleck, and S. B. Brummer, in "Proceedings of the 28th Power Sources Symposium," June 12-15, 1978, Atlantic City, NJ, The Electrochemical Society, Inc., p. 251 (1979).
2. K. M. Abraham and R. M. Mank, *This Journal*, **127**, 2091 (1980).
3. N. Doddapaneni, Abstract 47, p. 77, The Electrochemical Society Extended Abstracts, Vol. 83-2, Washington, DC, Oct. 9-14, 1983.

4. N. Doddapaneni, ERADCOM Technical Report, DELET-TR-83-0379-F, Fort Monmouth, NJ (April 1984).
5. G. J. DiMasi, M. Brundage, and L. Jarvis, in "Lithium Batteries," A. N. Dey, Editor, p. 111, The Electrochemical Society, Softbound Proceedings Series, Pennington, NJ (1984).
6. F. Walsh and M. Yaniv, ERADCOM Technical Report, DELET-TR-83-0386-F, Fort Monmouth, NJ (May 1984).
7. K. French, P. Cukor, C. Persiani, and J. Auburn, *This Journal*, **121**, 1045 (1974).
8. R. Staniewicz and R. A. Gary, *ibid.*, **126**, 981 (1979).
9. R. C. McDonald, *ibid.*, **129**, 2453 (1982).
10. W. Clark, F. Dampier, L. Lombardi, and T. Cole, Air Force Report no. AFWAL-TR-83-2083 (Dec. 1983).
11. M. W. Rupich, L. Pitts, and K. M. Abraham, *This Journal*, **129**, 1857 (1982).
12. D. R. Stull, *Ind. Eng. Chem.*, **39**, 517 (1947).
13. K. L. Klinedinst and M. L. McLaughlin, *J. Chem. Eng. Data*, **24**, 203 (1979).
14. N. Marincic, *J. Appl. Electrochem.*, **6**, 51 (1976).
15. Y. Bedfer, J. Corset, M. C. Dhameincourt, and F. Wallart, *J. Power Sources*, **9**, 267 (1983).
16. A. N. Dey, *ibid.*, **5**, 57 (1980).
17. F. Walsh, R. S. Morris, and M. Yaniv, Abstract 33, p. 54, The Electrochemical Society Extended Abstracts, Vol. 83-2, Washington, DC, Oct. 9-14, 1983.
18. A. I. Attia, C. Sarrazin, K. A. Gabriel, and R. P. Burns, *This Journal*, **131**, 2523 (1984).
19. F. W. Dampier and R. C. McDonald, in "Lithium Batteries," A. N. Dey, Editor, p. 154, The Electrochemical Society Softbound Proceedings Series, Pennington, NJ (1984).
20. B. J. Carter, M. Evans, S. Rao, and R. M. Williams, Abstract 149, p. 228, The Electrochemical Society Extended Abstracts, Vol. 84-2, New Orleans, LA, Oct. 7-12, 1984.
21. R. C. McDonald, F. W. Dampier, P. Wang, and T. Bennett, GTE Final Report NSWC N60921-81-C-0229 (Jan. 1983).
22. J. C. Bailey and G. E. Blomgren, in "Electrocatalysis," W. E. O'Grady, P. N. Ross, Jr., and F. G. Will, Editors, The Electrochemical Society Softbound Proceedings Series, Pennington, NJ (1982).
23. B. J. Carter, R. M. Williams, M. Evans, Q. Kim, S. Kim, F. D. Tsay, and H. Frank, Abstract 38, p. 61, The Electrochemical Society Softbound Proceedings Series, Vol. 83-2, Washington, DC, Oct. 9-14, 1984.
24. L. V. Haff, in "The Analytical Chemistry of Sulfur and Its Compounds," Part 1, J. H. Karchmer, Editor, p. 245, Interscience Publishers, New York (1970).
25. D. M. Oglesby, R. L. Ake, and W. P. Kilroy, in "Proceedings of the 30th Power Sources Symposium," June 7-10, 1982, Atlantic City, NJ, The Electrochemical Society, Inc., p. 127 (1982).
26. S. D. James, *J. Power Sources*, **10**, 105 (1983).
27. A. N. Dey and C. R. Schlaikjer, in "Proceedings of the 26th Power Sources Symposium," Atlantic City, NJ, April 29-30, May 1-2, 1974, p. 47 (1974).
28. P. Zlatilova, Y. Geronov, and R. Moshtev, *J. Power Sources*, **13**, 327 (1984).

Electronmicroscopic Examination of Corroded Aluminum-Copper Alloy Foils

D. Y. Jung,* I. Dumler, and M. Metzger*

Department of Metallurgy and Mining Engineering and Materials Research Laboratory, University of Illinois at Urbana-Champaign, Urbana, Illinois 61801

ABSTRACT

The formation of particles of copper through selective dissolution of dilute Al-Cu solid solutions in sulfuric acid was studied by transmission electron microscopy of foils prethinned before corrosion. A technique was employed for prethinning without surface enrichment. At -500 mV vs. SCE, a significant fraction of the copper made available by selective dissolution appeared as particles, but not at -100 mV vs. SCE. The results are discussed with reference to concurrent AES observations on the Cu-enriched solid solution beneath the anodic film over the main body of the electrode.

Selective dissolution during corrosion of Al-Cu alloys may lead to the formation of metallic copper on the surface and a large enhancement of the cathode reaction rate

* Electrochemical Society Active Member.

(1). In HCl solutions, this is displayed through rapid and accelerating pitting corrosion (2, 3). One of the surface reactions in the selective dissolution was recently identified by Strehblow and co-workers (4, 5), who showed by

Rutherford backscattering and ion scattering spectrometry that anodic sweeps of Al-Cu alloys in buffer solutions of pH 5.0-9.2 produced an undoped alumina film with enrichment in Cu of the substrate beneath the film. The observations reported in this paper, which are part of a study that included electrochemical and AES measurements, were concerned with the formation of particles of copper metal on the surface. The identification, distribution, and crystallography of these particles can be examined by TEM with high spatial resolution. The corrosion was performed in sulfuric acid in order to maintain passive conditions and with the intent to employ the body of information on anodic films as an aid in interpreting film behavior. Specimens were thinned to near electron transparency and then exposed to corrosion to a small depth. A problem of specimen preparation arises with these alloys in that electropolishing, which is required to thin specimens properly for microscopy, itself produces surface enrichment in Cu. A procedure was devised to deal with this.

Experimental

The high purity binary alloys, in the form of 1 or 0.1 mm sheet, contained 0.06, 0.20, 0.60, or 2.0% Cu. They were given a final anneal at 580°C to yield solid solutions of grain size >2 mm and water quenched. Testing was done in 2.4M H₂SO₄ at 25.0° ± 0.2°C, without deaeration or stirring, at -500 or -100 mV vs. SCE. Before switching on the control potential, the rest potential was monitored for a few minutes as a check on specimen surface cleanliness. In all cases, the initial rest potential was ≈ -950 mV vs. SCE and near that of 99.999% Al, there being negligible corrosion in this interval. Specimens for electrochemical testing were polished mechanically to avoid initial surface copper enrichment. Mechanical polishing cannot be employed to thin specimens for TEM. Several electropolishing baths were tested and all produced severe surface enrichment in Cu. It was found that the enriched region could be removed by sputtering. This was possible because of the apparent absence of preferential sputtering under the conditions employed, as seen in the AES work. A procedure for thinning from one side, as diagrammed in Fig. 1, was developed. After dishing a 0.12 mm sheet just to perforation by electropolishing in a

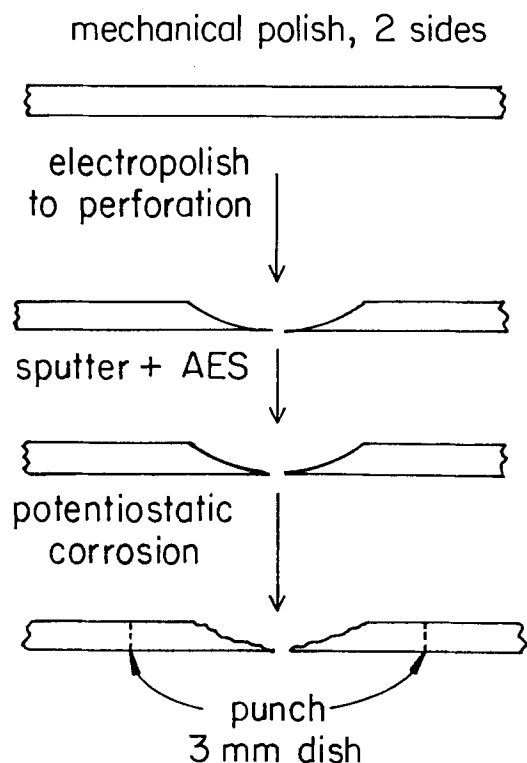


Fig. 1. Preparation of aluminum-copper corrosion specimens for transmission electron microscopy.

HNO₃-H₂O bath, the specimen was inserted into the Physical Electronics 545 Auger unit and sputtered with 1 keV Xe⁺ over a region larger than the dish. The Cu peak at 918 eV was monitored, and the sputtering continued until the Cu signal was indistinguishable from the bulk value as determined on a mechanically polished specimen. After sputtering, both sides of the sheet were exposed in sulfuric acid for a period which would make the equivalent of a few monolayers of Cu available by selective corrosion of the solid solution. In the 0.60% Cu alloy, on which most of the work was done, this required only a fraction of a micrometer depth of corrosion. This, being small and relatively uniform, enlarged the original hole but usually left sufficient thin region for examination.

Observations were made either on a Phillips 400 microscope at 120 kV or a JSEM 200B microscope at 200 kV, both equipped with EDS capability for chemical analysis.

It was confirmed by electron diffraction of the matrix material that a single-phase solid solution was retained by quenching in all the alloys. Even the 2.0% Cu alloy aged one week at room temperature showed a diffraction pattern in the [100] orientation with no streaking indicative of the formation of Guinier-Preston zones. With this alloy, difficulties were anticipated in completely removing severe surface enrichment without metallurgical changes in the foil corrosion specimens, and it was not examined.

Results and Discussion

-500 mV vs. SCE.—At this potential, no loss of Cu from the solid solution by direct dissolution would be expected. Cu particles or rounded patches were visible in the thinner regions of the corroded foil as dark areas 4-35 nm across (Fig. 2a and 2b). These remained visible during tilting, i.e., they were visible by mass thickness contrast even in the absence of diffraction contrast and thus had thicknesses substantial fractions of their diameters. The particle density was relatively uniform from one field to another and from one foil to another though showing local variations within one field (Fig. 2). There was a tendency for alignment or clustering of particles in the walls of a topographic cell structure.

Figure 3a is a micrograph of the alloy of Fig. 2b after twice as much corrosion. It is seen that the particle density increased but the range of particle diameters remained about the same.

EDS observations in the thinner regions of the foil, employing the ratio of the Cu K α peak height to that of the Al, readily confirmed the presence of Cu in excess of the bulk value. Observations with selected areas of 0.1 μ m diam (Fig. 3) confirmed that local regions of higher particle density gave higher Cu/Al ratios (Fig. 3b and 3c).

The micrographs of copper particles were similar in general appearance to micrographs shown by Tomashov *et al.* (6) of palladium particles in extraction replicas from a steel containing 25% Cr and 0.5% Pd. These were, however, produced under different conditions, i.e., by a few minutes of active dissolution in sulfuric acid.

Selected-area diffraction in regions containing a number of particles (Fig. 4) showed full rings of very fine

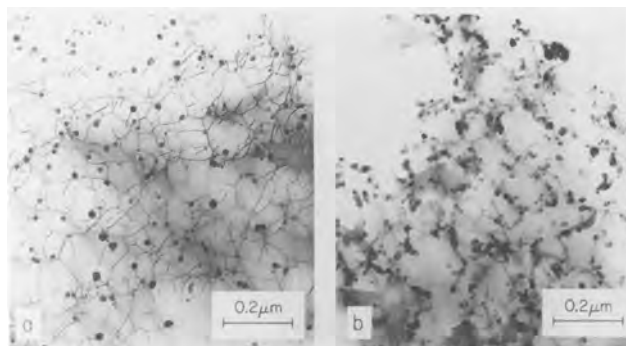


Fig. 2. Transmission micrographs showing copper particles in Al-Cu foils after corrosion at -500 mV vs. SCE. a: 0.06% Cu, 12h. b: 0.60% Cu, 2h.

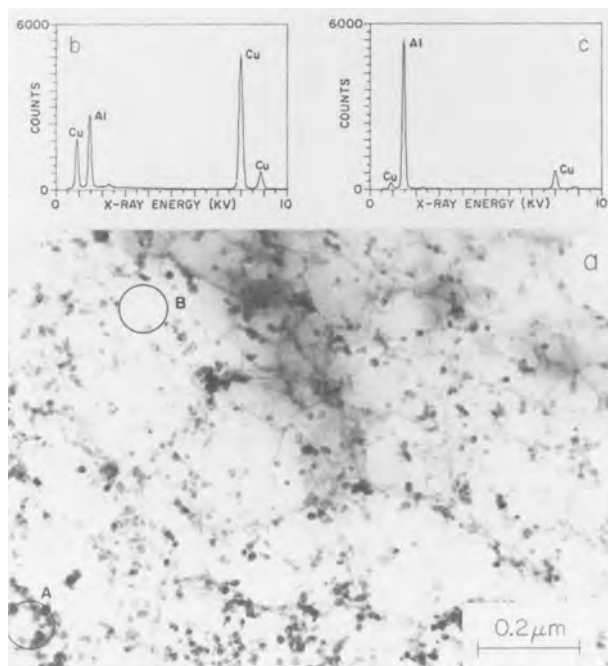


Fig. 3. Analytical examination of 0.60% Cu foil after 4h at -500 mV vs. SCE. a: Transmission electron micrograph. b: EDS spectrum of region A. c: EDS spectrum of Region B.

grained Cu_2O and spotty rings of Cu together with the single-crystal spot pattern (incomplete cross grating) from the selected grain of the aluminum substrate. A layer of Cu_2O would have formed on the surface of the Cu when the specimen was removed from the acid bath and rinsed with water. Al_2Cu was not observed. Darkfield micrographs employing portions of Cu rings imaged the particles. All diffraction patterns represented regions well within a single grain of the substrate so that the observation of closely spaced spots on the Cu rings indicated that a large number of Cu particle orientations arose from a single orientation of the Al-Cu solid solution substrate.

-100 mV vs. SCE.—A second test potential of -100 mV vs. SCE was chosen as one at which there is a small corro-

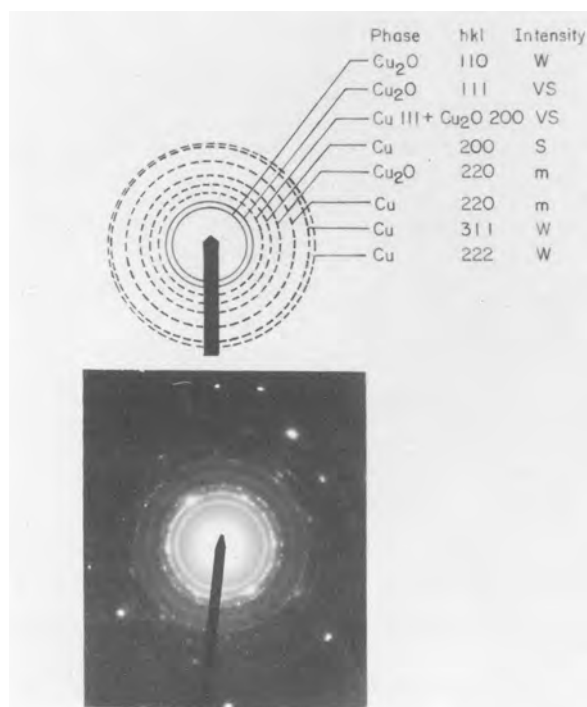


Fig. 4. Diffraction pattern in an area containing many particles and indexing of the rings as Cu and Cu_2O . 0.60% Cu, -500 mV vs. SCE, 4h.

sion current for pure Cu, i.e., $\approx 80 \mu\text{A}/\text{cm}^2$ as indicated by data of Ghandehari *et al.* (7). Thus, any metallic Cu exposed to the acid would suffer some corrosion and would be removed unless it grew faster than it dissolved. The severest case examined was that of the 0.60% Cu alloy exposed 4h at -100 mV vs. SCE with a depth of corrosion $0.66 \mu\text{m}$ and with the amount of Cu which would have been made available by selective corrosion of the Al equivalent to a 1.2 nm thick layer, far greater than in Fig. 2b or 3a. No Cu particles were detected in electron micrographs (Fig. 5a), and an intensive search of thin regions of the foils failed to reveal any Cu or Cu_2O rings in the diffraction pattern.

The topographic cell structure seen in Fig. 5a for 0.60% Cu is characteristic of the potential rather than the copper content since it appeared also with 99.999% Al (Fig. 5b). Impedance data showed that the presence of this structure did not indicate severe surface roughening, as may accompany selective dissolution in some cases (8).

Further Discussion

Quantity of copper in particles.—In many of the micrographs, particles were visible down to projected diameters of about 4 nm. Examination of the micrographs indicated that any smaller particles present probably would have been indistinguishable from the faint phase contrast background, owing to the presence of the amorphous alumina surface film. The distribution of particle diameters had a maximum at 11-14 nm and fell more or less sharply for smaller diameters. It was concluded that in any case only a small fraction of the volume of copper would have been in undetected particles below 4 nm diam.

An estimate of the amount of copper appearing as particles was made from the measured distribution in bright field images. The particles being mainly noncircular in section, a diameter was assigned to each particle to give an equal area. For purposes of estimation, the particles were assumed to be hemispheres and the volume of particles in each size class was calculated and summed. The results for three specimens are compared in Table I with the total copper which would have been made available by selective dissolution. The latter was obtained by integrating the partial anode current during the exposure at -500 mV vs. SCE. The estimates show that under the conditions of these experiments a significant fraction up to perhaps one-half of the available copper appeared as particles. It may be noted that an analogous calculation was made for the total surface area of the copper particles in the micrographs. The results were in rough agreement with copper area figures deduced from capacitance measurements and from cathodic polarization data, thus supporting the validity of the TEM data.

An additional portion of the copper made available by selective corrosion should be in the Cu-enriched solid solution beneath the film over the main body of the electrode, according to the results of Strehblow *et al.* (4). To discuss this point, some pertinent results are cited below from the companion AES study, which will be reported separately.

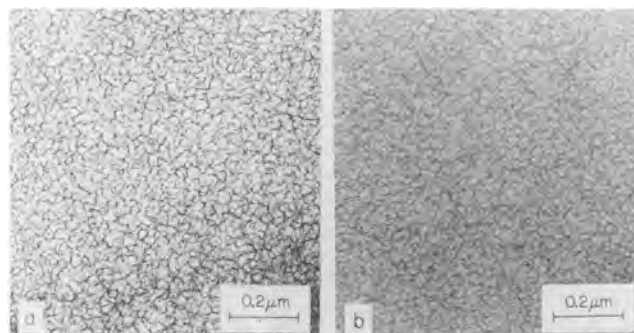


Fig. 5. Transmission electron micrographs of foils after corrosion at -100 mV vs. SCE. a: 0.60% Cu, 4h. b: 99.999% Al, 12h.

Table I. Quantity of copper metal produced by selective corrosion at -500 mV vs. SCE

Cu content (w/o)	Time (h)	Calculated weight loss (g/cm^2)	Available Cu (g/cm^2)	Estimated Cu as particles, TEM data ^a (g/cm^2)	Fraction Cu in particles
0.06	12	3.9×10^{-4}	2.4×10^{-7}	9×10^{-8}	0.4
0.60	2	4.9×10^{-5}	3.0×10^{-7}	1.6×10^{-7}	0.5
0.60	4	9.0×10^{-5}	5.4×10^{-7}	2.3×10^{-7}	0.4

^a Particles assumed hemispherical.

AES observations.—Figure 6 presents for illustration some AES depth profiles for the 0.60% Cu alloy. The enrichment in Cu of surfaces of Al-Cu alloys prepared by electropolishing, which has been noted previously for an alloy of higher copper content (9), is shown in Fig. 6a. This enrichment appears greater than that of the mechanically polished specimen exposed to sulfuric acid at -500 mV vs. SCE (Fig. 6b), but the efficiency of enrichment was actually much greater in the latter case, which was produced by corrosion to a depth two orders of magnitude smaller. The depth profiles in Fig. 6 show a maximum in the copper signal at the oxide-metal interface, indicative of an enriched zone beneath the film. These data do not reveal the lateral distribution of copper or the phases present. In interpreting these depth profiles, it must be borne in mind that the enriched zone will appear thicker than it actually is. The mixing effect of ion bombardment (i) causes the enriched zone to be sensed before the nominal sputtered depth has actually reached the outer limit of the zone, and (ii) drives some of the excess copper inward so that an excess copper signal persists beyond the original maximum depth of the enriched zone.

Surface at -500 mV vs. SCE.—The Cu particles formed at this potential were up to 25 nm across and thus were too large to be covered by the alumina film (estimated as ≥ 4 nm thick). Even if they had originally formed beneath it, the overlying film would disappear by slow chemical dissolution in the acid since the copper blocks its renewal. The exposed copper metal would be stable at this immune potential. The alloy surface at a particular exposure time is then modeled, as shown schematically in Fig. 7a, as isolated patches of copper covering a few percent of

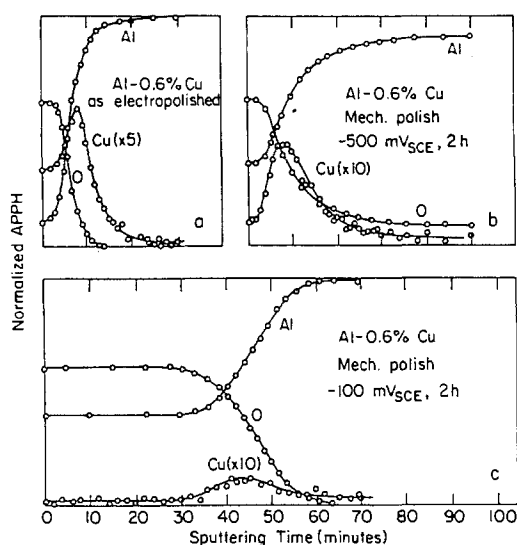


Fig. 6. Auger depth profiles of 0.60% Cu alloy after various treatments. Sputtering was performed with 0.5 keV Xe^+ . a: Electropolished in 20% perchloric acid in ethanol. b: Mechanically polished and exposed in 2.4M H_2SO_4 , -500 mV vs. SCE, 2h. c: Mechanically polished and exposed in 2.4M H_2SO_4 , -100 mV vs. SCE, 2h.

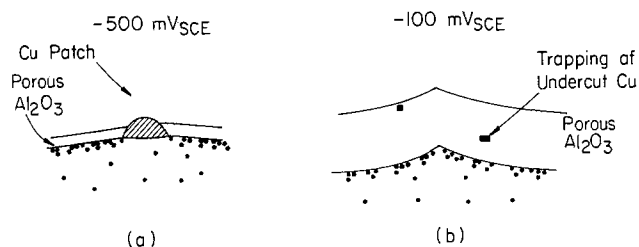


Fig. 7. Schematics of proposed surface conditions after exposure at -500 mV vs. SCE (a) and -100 mV vs. SCE (b).

the surface with the remainder, in line with Strehblow's model, consisting of an undoped alumina film overlying a few layers of enriched solid solution. An AES depth profile of such a surface with a 0.03 mm² electron-beam sampling many particles would show a copper concentration of a few percent at the external surface concurrent with the oxide film signals and there would be a maximum at the film-substrate interface, consistent with Fig. 6b. The copper depth profile does not yield a separation of the contributions from particles and enriched zone. Estimates of the total excess copper in these profiles are subject to some uncertainty, but do suggest that a substantial or large fraction of the copper made available by corrosion remains on the electrode at this potential.

Although the copper metal particles are immune at this potential, there would be a tendency for them to be undercut and released in the course of continued corrosion. The smallest particles would be most susceptible to undercutting, the ones which achieve larger diameters surviving longer. This could explain why the particle size frequency decreases at the smaller diameters.

Surface at -100 mV vs. SCE.—The processes occurring at this potential are considered to be the same as at -500 mV vs. SCE, except for the presence of a significant dissolution current for copper. The cell current was higher and the film thicker.

Consideration is given first to the special case of the 0.60% Cu alloy. The AES depth profile in Fig. 6c shows a Cu-enriched zone beneath the film, but also shows a small copper signal concurrent with the oxygen signal through the film region. The latter would be contrary to Strehblow's model if such signified doping of the film structure with copper ions. The copper signal from within the film cannot be attributed simply to copper metal particles of the size and nature discussed in the previous section because no Cu or Cu_2O was detected in the TEM observations and the cathode polarization data were also not consistent with this. The behaviors of 99.999% Al and 99.999% Cu in this acid are such that an area fraction of exposed copper of only 10^{-5} would produce cathode currents an order of magnitude greater than those of the pure aluminum. It is conceivable that the film formed on this alloy contains fragments of copper, or of copper-aluminum alloy from the enriched zone, which have been undercut from the substrate and trapped in the film, which at this potential is ≥ 20 nm thick. Such fragments are presumably suffering slow corrosion in the porous film. The model is represented schematically in Fig. 7b. Some small particles or clusters yielding the small ($\leq 0.6\%$) Cu signal in Fig. 6c could be undetected by electron microscopy, and, being isolated from the substrate by an alumina film of low electronic conductivity, they would not be effective cathodes.

In the 0.20 and 0.06% Cu alloys exposed at -100 mV vs. SCE, the AES depth profiles showed no detectable copper signal from within the film (0.20% Cu still showed copper enrichment beneath the film). This is interpreted as a consequence of a lower rate of particle formation and growth in these alloys so that any copper or copper-containing patches exposed at the surface would have dissolved before they could be undercut. Overall, it is concluded that the presence of a Cu signal from within the film may arise from processes other than doping of the

film structure with copper ions and that the present AES observations are not necessarily inconsistent with Strehblow's model.

Orientation relationships.—The dissolution in this system is highly selective at -500 mV vs. SCE and it would be expected that the nucleus of a particle of copper metal would have to form by a solid-state process from copper atoms in the alloy and would thus tend to be coherent with the substrate and of the same crystal orientation. This is expected whether the nucleation occurs through aggregation of copper atoms in the enriched zone under the film or if it occurs in conjunction with film breakdown and transient pitting processes. The orientation would persist during growth although misfit dislocations would form. Forty and Durkin (10) made a TEM study of selective dissolution in (111) orientation thin foils of Ag-Au solid solutions and found the substrate orientation retained in the gold-enriched regions; it may be noted that this is a system with minimal coherency strains because the lattice parameter varies by less than 0.2%. However, in the well-formed copper particles noted in the present work, many orientations were present within a single grain of the alloy. Also, in many cases (e.g., Fig. 2b), the particle images showed internal structure indicating that they were not generally monocrystalline. Multiple orientations could have come from nuclei forming in twin relation to the substrate and from growth twinning. The copper requires a strain of 12% to remain coherent with the substrate. It is conceivable that the copper particles do not necessarily nucleate as thin coherent plates but may nucleate in the enriched solid solution beneath the film as incoherent entities too thick to be coherent. The distribution of orientations of the copper particles and its origin needs further study. It is thought unlikely that nucleation at this potential involves transport through the electrolyte. Mechanisms of particle growth will be discussed elsewhere.

Acknowledgments

This work was supported by the National Science Foundation through the Materials Research Laboratory under Contract DMR 80-20250. The authors are indebted to J. A. Eades for advice on contrast questions and particle detectability.

Manuscript submitted April 6, 1984; revised manuscript received July 10, 1985. Part of this article was presented as Paper 80 at the Detroit, Michigan, Meeting of the Society, Oct. 17-21, 1982.

The University of Illinois assisted in meeting the publication costs of this article.

REFERENCES

1. D. Kuhlmann-Wilsdorf and G. Masing, *Z. Metallkd.*, **41**, 497 (1950).
2. G. Tammann and W. Boehme, *Z. Anorg. Allgem. Chem.*, **226**, 82 (1935).
3. M. Metzger and O. P. Arora, *Trans. Met. Soc. AIME*, **227**, 1305 (1963).
4. H. H. Strehblow, C. M. Melliar-Smith, and W. M. Augustyniak, *This Journal*, **125**, 915 (1978).
5. H. H. Strehblow and D. L. Malm, *Corros. Sci.*, **19**, 469 (1979).
6. N. D. Tomashov, G. P. Chernova, V. N. Modestova, T. V. Chukalovskaya, L. N. Volkov, and R. P. Vasilyeva, in "Proceedings of the 4th International Congress on Metallic Corrosion," p. 642, NACE, Houston, TX (1972).
7. M. S. Ghandehari, T. N. Andersen, and H. Eyring, *Corros. Sci.*, **16**, 123 (1976).
8. H. W. Pickering, *This Journal*, **115**, 690 (1968).
9. J. M. Pountney and M. H. Loretto, in "Electron Microscopy 1980," Vol. 3, P. Brederoo and V. E. Cosslett, Editors, p. 180, 7th European Congress on Electron Microscopy, Leiden, The Netherlands (1980).
10. A. J. Forty and P. Durkin, *Philos. Mag. A*, **42**, 295 (1980).

Anodic Oxide Films on CrSi₂

A. J. Barcz,¹ M. Bartur,* T. Banwell, and M-A. Nicolet*

California Institute of Technology, Pasadena, California 91125

ABSTRACT

Oxide layers on chromium disilicide of thicknesses up to several thousand angstroms are formed by constant current anodization in ethylene glycol containing different amounts of water. For low H₂O concentrations (1-10%), the films have essentially uniform composition of about 92% SiO₂ and 8% Cr₂O₃; the chromium being dissolved in the electrolyte during the anodic oxidation at a rate of one Cr atom per seven oxygen atoms incorporated. Greater H₂O content leads to increased current efficiency and higher angstrom per volt values for the anodization. In a 50% H₂O electrolyte, Cr-free SiO₂ films can be grown up to a limited thickness. These results are compared with the anodic oxidation of Si and the thermal oxidation of CrSi₂.

It is expected that silicides will be applied to interconnection lines in VLSI technology due to silicides, low resistivity relative to the commonly used polysilicon (1) as well as their ability to form insulating layers upon thermal oxidation (2). An exciting feature of the oxidation of most silicides is that the growing oxide appears to be pure SiO₂ while the integrity of the silicide is being preserved. From a purely thermodynamic point of view, assuming equilibrium and unlimited supply of the reactants, one might expect that both silicon and the metal will oxidize since the heat of formation of the silicides is small compared to those of the respective metal oxides [see, for example, the data tabulated per metal atom in Ref. (1)]. The calculations fall closer to the experimentally observed results when the corresponding heats of reaction are taken per one oxygen atom (3). Neverthe-

less, it seems that kinetic factors such as oxygen transport through the oxide and the rapid migration of Si and metal atoms through the silicide at the temperature of oxidation play a key role in the mechanism which leads to the formation of the metal-free oxide. Several possibilities concerning the mass transport across the silicide layer are discussed in Ref. (2).

In this paper, we report on a study of the formation of anodic oxides on CrSi₂ grown in an ethylene glycol containing small quantities of KNO₃ and H₂O, an electrolyte known to produce high quality, compact SiO₂ films when applied to silicon (4). This study gives an interesting opportunity to verify concepts adopted to explain the thermal oxidation processes and, specifically, to identify what is common and what is different in the thermal vs. electrochemical mechanism of the oxidation of silicides. First, in anodic oxidation carried out at room temperature any atomic transport across the remaining silicide can be ignored. Second, ionic movement in the high electric

* Electrochemical Society Active Member.

¹ Present address: Institute of Electrical Technology, 02-668 Warsaw, Poland.

field within the oxide includes usually both cationic and anionic components (5), in contrast to the thermal oxidation of Si, in which the mobile species in the oxide is an oxygen containing molecule.

Finally, we point out that the potential advantages of using anodic *vs.* thermal oxides of a silicide could be (i) a higher dielectric constant results if the metal oxide is present in the SiO₂ film, and (ii) that the silicon-silicide interface is not being affected by the high temperature treatment.

Experimental Procedure

Chromium films about 750Å thick were deposited in an oil-free vacuum of $\sim 10^{-7}$ torr by electron-beam evaporation onto Si <111> substrates. The wafers were then heat-treated in a vacuum furnace (600°C, 20 min, 10^{-7} torr range) to form $\sim 2300\text{\AA}$ of the stoichiometric chromium disilicide. The samples to be oxidized were degreased with trichloroethylene, rinsed in deionized water, and blown dry prior to being placed as anodes in an electrolytic cell. The samples were masked so that a limited area (0.3 cm²) was in contact with the electrolyte. A platinum cathode was positioned about 2 cm from the anode, and the electrolyte was stirred. The solution used in the present experiment was anhydrous ethylene glycol containing 0.5 weight percent (w/o) KNO₃ with different quantities of water: 1, 2, 10, 20, and 50 w/o. Oxidations were performed at a constant anode current density of 3 mA/cm² up to a predetermined voltage (V_{\max}) followed by a current decay at the maintained voltage V_{\max} down to one-quarter of its initial value. After the oxidations, the samples were rinsed in acetone and high resistivity water. Also, some oxidations were made using either 2 atom percent KNO₃ in the electrolyte or 0.5 mA/cm² current density. No detectable influence of these parameters changes on the composition of the films was found. Complementary thermal oxidations of CrSi₂ were performed in an open-tube furnace at 900°C by steam oxidation. The samples were introduced into the furnace with high N₂ flow to minimize oxidation during the temperature rise of the sample. After the sample had reached the desired temperature, O₂ bubbled through 96°C water was introduced.

It is important to note that the as-evaporated Cr contains about 7 a/o oxygen (6). Also, after thermal oxidation a thin layer of Cr oxide was always observed on the sample surface.

Elemental analysis of the oxidized layers was performed using 2 MeV ⁴He⁺ backscattering spectrometry (BS). Samples were positioned normal to the primary beam, and backscattered ions were detected at an angle of 170°. The backscatter analysis provides full information about the composition of the films, since, owing to a large mass difference, signals corresponding to the three components Si, Cr, and O can be independently observed. From these, we derive such quantities as stoichiometric ratios and overall oxygen content. Also, owing to the existing reference plane at the Si-CrSi₂ interface, it is possible to detect the loss of Si or Cr atoms by comparing the respective count integrals before and after the anodic processing. The masked edge enables reliable comparison of oxidized and unoxidized CrSi₂ at adjacent spots on the sample.

Results

Most oxidations were performed with either 1 or 10 w/o H₂O electrolytes. In these conditions, laterally uniform anodic films were reproducibly grown up to cell voltages of about 125V. Occasionally, it was possible to obtain V_{\max} as high as 200V (1% H₂O) before the initial reaction ceased. Typical voltage-time curves for CrSi₂ and pure Si substrates oxidized in the above electrolytes are shown in Fig. 1. There is a pronounced difference in the slope of the two curves corresponding to CrSi₂, while the curves for Si seem to overlap except for the initial potential rise. Figure 2 depicts the BS spectra of the CrSi₂ oxide resulting from the oxidation in the 10% H₂O glycol to $V_{\max} = 50\text{V}$; the solid line represents the spectrum of the initial silicide. First, we noticed that the surface film contains

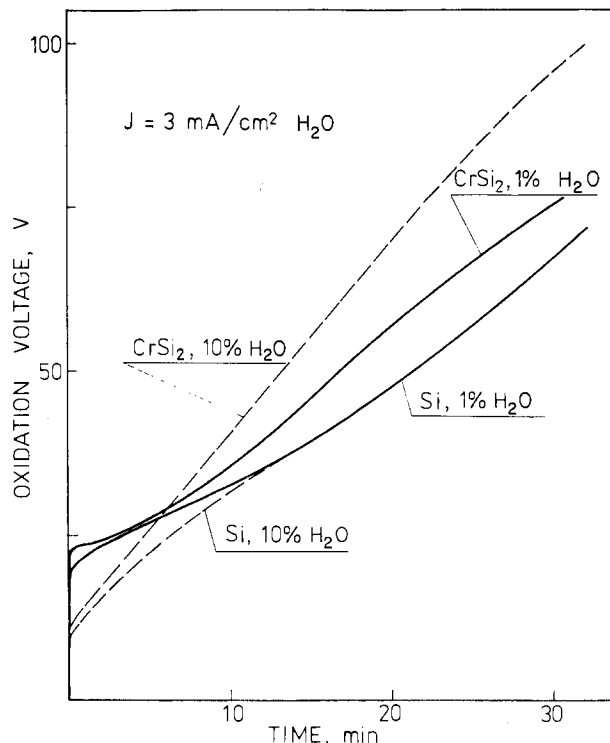


Fig. 1. Voltage-time curves for CrSi₂ and Si anodization in glycol with water percentage of either 1 or 10% at constant current density of 3 mA/cm².

oxygen, silicon, as well as chromium atoms. The integral over the O peak yields 1.2×10^{18} at./cm² of incorporated oxygen. Furthermore, the stoichiometry ratios calculated on the basis of the signal heights give O/Si = 2.27 and Cr/Si = 0.17. It is thus clear that the oxide grows deficient in chromium with regard to the elemental proportions in the silicide (Cr/Si = 0.5). The difference in the Cr integrals confirms the net loss of chromium atoms equal to 1.8×10^{17} at./cm², *i.e.*, one Cr atom lost per seven O atoms incorporated. No loss of silicon atoms is detected. We also note that the composition profile is uniform and that the oxide-silicide interface is, and Si-silicide interface remains, sharp. A similar picture presented in Fig. 3 concerns the anodization to $V_{\max} = 75\text{V}$ in a solution containing smaller amounts of water (1 w/o). Here, the resultant oxygen content is 4.9×10^{17} at./cm² with a stoichiometry profile comparable to the previous case. A slight Cr enrichment at the surface becomes more evident for the anodic runs in which the electrolyte was not stirred (broken line in the figure). Without

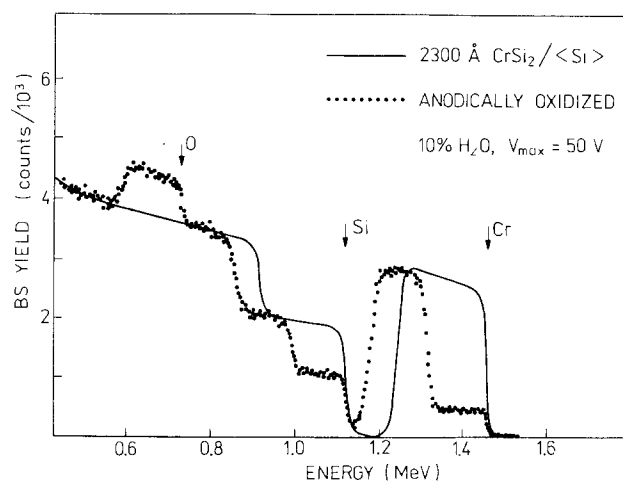


Fig. 2. 2 MeV ⁴He⁺ backscattering spectra of CrSi₂ on Si before (solid line) and after anodically oxidized in 10% H₂O electrolyte to a voltage of 50V (full dots).

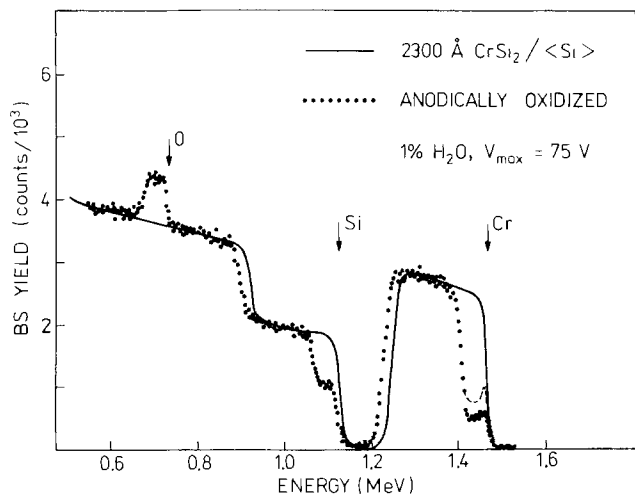


Fig. 3. Backscattering spectrum corresponding to CrSi_2 oxide obtained by oxidation in glycol containing 1% water to $V_{\text{max}} = 75\text{V}$ (dots), when no stirring was applied to the electrolyte (broken line), and with CrSi_2/Si substrate (solid line).

stirring, the current decay stage proceeded down to one-tenth (instead of one-quarter) of its nominal 3 mA/cm^2 , and the Cr appeared at even higher concentrations reaching the ratio of $\text{Cr/Si} = 0.5$.

Considering the above two figures, it is evident that the water content has a large effect on the outcome of the anodization: the sample oxidized in 10% H_2O to a lower voltage contains 2.4 times more oxygen than the one oxidized to the higher voltage in the 1% H_2O electrolyte. This trend is clearly appreciable in Fig. 4, where the oxygen content in atoms per square centimeter is plotted against the maximum effective potential drop ΔV in the oxide ($\Delta V = V_{\text{max}}$ minus initial potential rise). For comparison, data for pure Si are also shown. In all cases, the dependence appears to be linear; for CrSi_2 , the slope for oxidations carried out at 10% H_2O is significantly higher than that for the 1% H_2O electrolyte. Both slopes for CrSi_2 are greater than that of Si, which oxidizes at a rate which is nearly independent of the H_2O content. These slopes can be expressed in terms of convenient "electrochemical" units of angstroms per volt by assuming atomic concentration of the oxygen atoms equal to that of pure SiO_2 which is justified by a relatively small contribution of the Cr oxide. The corresponding values are 5.2 \AA/V for Si, 18.5 \AA/V for CrSi_2 (1% H_2O), and 65 \AA/V for CrSi_2 (10% H_2O).

Anodization in solutions of increasingly aqueous character leads to further increase in the angstroms per volt value and to a more efficient Cr dissolution. At the same

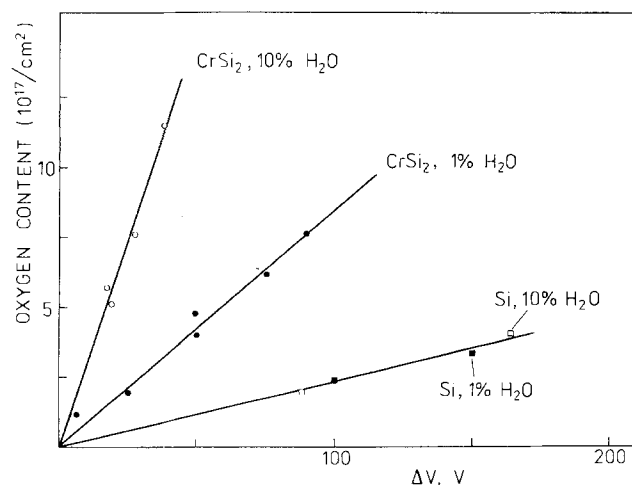


Fig. 4. Amount of oxygen incorporated during oxidation vs. effective potential drop in the film for CrSi_2 and Si, processed at constant current density of 3 mA/cm^2 in 1 and 10% H_2O glycol.

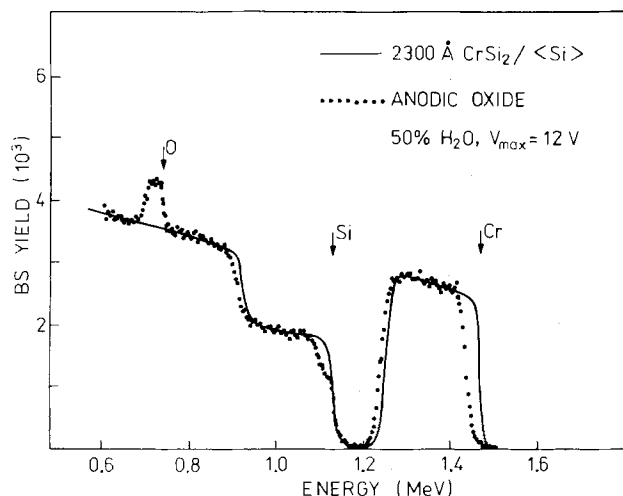


Fig. 5. Backscattering spectra of CrSi_2 (solid line) and CrSi_2 oxide (dots) produced in 50% H_2O glycol; $V_{\text{max}} = 12\text{V}$.

time, the maximum voltage that the film can sustain is reduced to 10-20V. An example of this type of behavior is shown in Fig. 5, where the anodic growth proceeded only to $V_{\text{max}} = 12\text{V}$ (from the starting potential of 7.5V , $V = 4.5\text{V}$). The oxide layer is practically free of Cr and constitutes a pure SiO_2 of a thickness of about 850 \AA . This result is thus similar to thermally grown oxides except that the silicide is not preserved as a whole, and Cr is lost into the solution.

Additional information about the growth mechanism can be acquired by analyzing an oxide layer produced by anodic followed by thermal oxidation. In Fig. 6, backscatter spectra are shown for the individual oxidations of CrSi_2 : anodic oxidation (10% H_2O , $V_{\text{max}} = 30\text{V}$ producing incorporation of $5 \times 10^{17}\text{ O at./cm}^2$), thermal oxidation (900°C , wet, 30 min) resulting in an oxide with $8.5 \times 10^{17}\text{ O at./cm}^2$, together with the spectrum resulting from thermal oxidation of the already preformed anodic

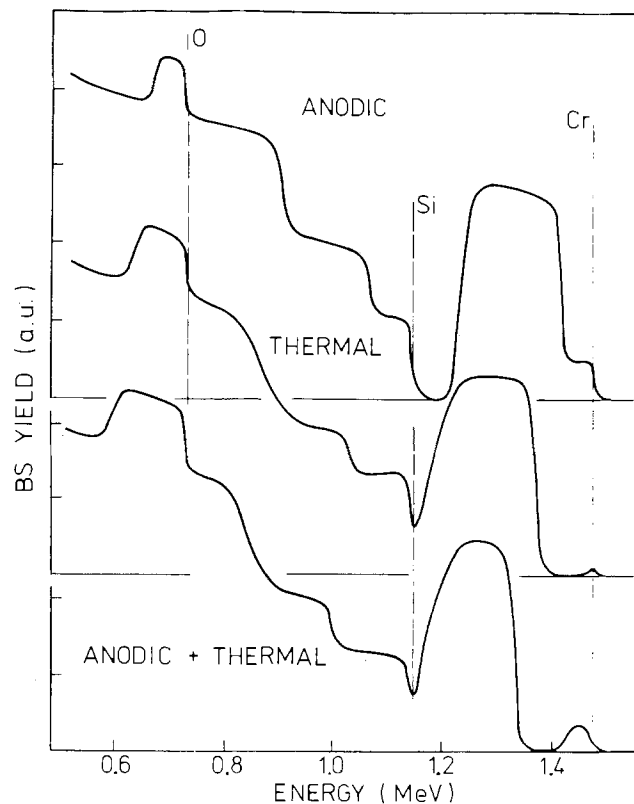


Fig. 6. Schematic BS spectra of chromium disilicide oxides. Anodic: 10% H_2O ; $V_{\text{max}} = 30\text{V}$. Thermal: 90°C , wet, 30 min. Anodic followed by thermal.

oxide (11.5×10^{17} O at./cm² incorporated). A most interesting feature in these spectra is the observation of the Cr exclusion within the films. As far as the concentration level of Cr in the anodic oxide is concerned, only a trace amount is detected at the surface in the thermal case. In the double-oxidized sample, the Cr profile in the oxide seems to be divided into two regions: a surface region (1.4-1.45 MeV) with similar Cr concentration as in the anodic oxide, and a chromium-free layer underneath (1.35-1.4 MeV). The deleterious effect of the heat-treatment on the Si-CrSi₂ interface is also visible in the bottom spectra as broadening of the step at 0.85 MeV.

For a sample that was initially oxidized thermally, followed by anodic oxidation and finally thermal oxidation again, Cr was not detected in the oxide layer.

Discussion and Conclusion

The experiment described in this paper gives evidence that thick uniform oxides can be grown on chromium disilicide by anodic oxidation in ethylene glycol + potassium nitrate + water electrolyte. This may be regarded as the main result of this work. In view of a still inadequate understanding of the anodic processes, it is not possible to rigorously predict whether a given material in a given oxidizing medium will yield substantial oxide films (7, 8). Apart from valve metals such as Al, Hf, or Ta that oxidize with 100% current efficiency to voltages of at least 200V and sustain high electric fields ($>10^6$ V/cm), there exist many other materials that only partially fulfill these criteria. Such behavior is exhibited by silicon, which in organic electrolytes can be oxidized to several hundreds volts, though exhibiting a poor current efficiency suggesting the evolution of an appreciable amount of oxygen (9). On the other hand, chromium, which passivates to form Cr₂O₃ (10), has not been reported to produce thick oxides. In the electrolytes employed here, anodization of a pure Cr film does not induce any potential buildup, and creates a black spot on the Cr film surface containing no oxygen detectable by He backscatter spectrometry. Consequently, the CrSi₂ compound seems to be a rather complicated system as far as its anodic behavior is concerned. It is known that compounds or single phase alloys composed of valve or near-valve metals oxidize easily (11). The general situation becomes more complicated. Extensive studies on the anodization of GaAs (12), for example, show that several factors (*e.g.*, current density, oxide thickness) determine the composition and quality of the compound oxide formed. As for silicides, data on anodic oxidation are not available; the corrosion study of Cu, Co, and Ni silicides published in Ref. (13) was oriented primarily toward electrorefining and electrowinning from ores.

Summarizing the oxidation of CrSi₂ in glycol with a water content ranging from 1 to 10%, it can be concluded that the oxide has a fixed composition with a relative concentration of the constituents given by O/Si = 2.27 and Cr/Si = 0.17. Assuming that the film is composed of SiO₂ and Cr₂O₃ molecules, these numbers are consistent with a composition of 92% SiO₂ and 8% Cr₂O₃. This indicates that during the film formation, a substantial segregation takes place; preservation of the Cr/Si proportion in the silicide would require an oxide composition of 83% SiO₂, and 17% Cr₂O₃. Undoubtedly, the excess Cr is dissolved in the electrolyte. From the corrosion behavior of chromium, it is known that at higher potentials Cr atoms enter the electrolyte as CrO₄²⁻ anions (14). Also, chromium tends to lose its passivity rather easily in the presence of certain contaminants, especially chloride ions (9). The accumulation of Cr at the oxide surface observed when the 1% H₂O electrolyte was not stirred during the anodization suggests that the dissolution could be further reduced by saturating the solution with Cr ions. Alternatively, more Cr atoms are leached out of the film for electrolytes with greater water content. Hence, the Cr-to-Si ratio in the oxide can be controlled by choosing adequate experimental conditions.

The current efficiency for oxide formation on CrSi₂ increases from 3 to 16% when the H₂O content of the electrolyte is raised from 1 to 10%. This is probably associated with enhanced field-assisted ionic transport across the (porous) oxide. It is unlikely that there is suppression of the current contribution from parasitic reactions and/or electronic conduction, since the oxide breakdown voltage dropped with increasing H₂O content as one might anticipate (15). The ionic current associated with Cr dissolution also degrades the current efficiency.

Anodic vs. Thermal

Comparison between anodic and thermal oxidation gives further insight to the prevailing processes.

1. In both cases, the silicide dissociates readily. In thermal oxidation, the excess Cr diffuses through the silicide to the Si substrate, where it reacts and reforms silicide, hence preserving the silicide (16). But, during anodic oxidation, Cr diffuses through the growing oxide and a fraction of the dissociated Cr oxidizes while the rest is dissolved in the electrolyte.

2. Increasing the water content in the oxygen gas during thermal oxidation increases the oxidation rate. In anodic oxidation, a higher water content also results in a higher oxide formation rate. Possibly, it has to do with the oxygen containing molecule that diffuses through the oxide. In the thermal oxidation case, the effective diffusion coefficient changes, while in anodic oxidation it may be only the boundary condition at the oxide/electrolyte interface.

3. With the assumption that the heat capacity of the reactants and products are similar, the heat of the reaction ΔH at room temperature and at high temperatures (for thermal oxidation) never exceeds 3 kcal/gatom (17). So the thermodynamic predictions (3) are the same by definition for anodic and thermal oxidation. The observed different results are due to different kinetic limitations.

4. From the sequential thermal/anodic oxidation results, we conclude that (i) chromium cannot diffuse through thermal SiO₂ (see Fig. 6 and also the results of thermal/anodic/thermal), and (ii) an oxygen containing molecule diffuses through the anodic oxide driving wet oxidation faster than through thermal oxide. This conclusion is reached with the assumption that the thermal oxidation is parabolic rate limited. The predicted oxygen content of anodic and thermal oxides, assuming the same diffusion coefficient in anodic and thermal oxides, is $10^{17} (5^2 + 8.5^2)^{1/2} = 9.9 \times 10^{17}$ O at./cm²; while we get 11.5×10^{17} O at./cm², which is indicative of a faster diffusion rate in the anodic oxide.

Since no electrical characterization of the layers was conducted and no data on insulating properties of anodic Cr₂O₃ have been published, it is difficult to predict dielectric constant ϵ or breakdown voltage of the films. There are indications, however (9), that the anodic oxide of Cr, having a low formation field, should have a high ϵ value (> 40), as it is known that low ϵ values (*e.g.*, SiO₂) tend to be associated with high anodization fields and vice versa. Additionally, the breakdown voltage can be roughly estimated from the angstrom per volt values because they are nearly linearly correlated (18). (However, it is uncertain how the individual properties of SiO₂ and Cr₂O₃ will contribute in the mixed oxide.)

Acknowledgment

The authors would like to thank Dr. M. Croset (Thomson-CSF) and J. Siejka (Ecole Normale Supérieure) for fruitful discussions and final comments.

Manuscript submitted Dec. 26, 1984; revised manuscript received June 23, 1985.

The California Institute of Technology assisted in meeting the publication costs of this article.

REFERENCES

1. F. M. d'Heurle, in "VLSI Science and Technology/1982," C. Dell'Oca and W. M. Bullis, Editors, p. 194, The Electrochemical Society Softbound Pro-

- ceedings Series, Pennington, NJ (1982).
2. M. Bartur and M-A. Nicolet, *This Journal*, **131**, 1118 (1984).
 3. M. Bartur, *Thin Solid Films*, **107**, 55 (1983).
 4. M. Croset, E. Petreanu, D. Samuel, G. Amsel, and J. P. Nadai, *This Journal*, **118**, 717 (1971).
 5. A. Damjanovic and A. T. Ward, in "Electrochemistry," Vol. 6, J. O'M. Bockris, Editor, pp. 105-106, Butterworths, Boston (1976).
 6. C.-D. Lien, L. S. Wielunski, and M-A. Nicolet, *Thin Solid Films*, **104**, 235 (1983).
 7. L. Young, "Anodic Oxide Films," Academic Press, New York (1961).
 8. S. P. Maminova and L. L. Odynets, *Elektrokhimiya*, **2**, 346 (1966).
 9. A. K. Vijh, in "Oxides and Oxide Films," Vol. 2, J. W. Diggle, Editor, p. 1, Marcel Dekker, New York (1972).
 10. N. Hackerman, *Z. Electrochem.*, **62**, 632 (1958).
 11. G. C. Wood and S. W. Khoo, *J. Appl. Electrochem.*, **1**, 189 (1971).
 12. M. Croset, J. Diaz, D. Dieumegard, and L. M. Mercandalli, *This Journal*, **126**, 1543 (1979).
 13. A. T. Kuhn, H. Shalaby, and D. W. Wakeman, *Corros. Sci.*, **17**, 833 (1977).
 14. T. P. Hoar, *Corros. Sci.*, **7**, 341 (1967).
 15. S. Ikonopisov, *Electrochim. Acta*, **22**, 1077 (1977).
 16. M. Bartur and M-A. Nicolet, *This Journal*, **131**, 371 (1984).
 17. R. Pretorius, J. M. Harris, and M-A. Nicolet, *Solid State Electron.*, **21**, 667 (1978).
 18. P. J. Harrop and D. S. Campbell, *Thin Solid Films*, **2**, 273 (1968).

Application of Kramers-Kronig Transforms in the Analysis of Electrochemical Systems

I. Polarization Resistance

Digby D. Macdonald* and Mirna Urquidi-Macdonald

Chemistry Laboratory, SRI International, Menlo Park, California 94025

ABSTRACT

A Kramers-Kronig transform that is useful for validating electrochemical and corrosion impedance data is employed to calculate the polarization resistance from the frequency-dependent imaginary component. Applications of the transform in the analysis of experimental impedance data for TiO₂-coated carbon steel in HCl/KCl solution at ambient temperature and for aluminum and Al-0.1P-0.1In-0.2Ga-0.01Ti alloy in 4M KOH solution at 25°C are discussed.

Electrochemical techniques are now used extensively for investigating the mechanisms of electrochemical and corrosion processes, and for the measurement of corrosion rates (1-4). With respect to the latter, the advantages offered by electrochemical methods are that they can be applied *in situ* in hostile environments and that they require minimal manipulation of samples or post-test analyses. In all electrochemical methods for estimating corrosion rates, the objective is to measure the polarization resistance (R_p), from which the corrosion current and corrosion rate may be calculated using the Stern-Geary relationship (5, 6), provided that the Tafel constants are known.

A widely used technique for measuring R_p is impedance spectroscopy (1-3), in which the impedance of the corroding interface is measured over an effectively infinite bandwidth. The polarization resistance is therefore given by

$$R_p = |Z(j\omega)|_{\omega \rightarrow 0} - |Z(j\omega)|_{\omega \rightarrow \infty} \quad [1]$$

$$= \text{Re} [Z(j\omega)]_{\omega \rightarrow 0} - \text{Re} [Z(j\omega)]_{\omega \rightarrow \infty} \quad [2]$$

where Re denotes the real part of the complex impedance $Z(j\omega)$. In other words, the polarization resistance may be obtained from only the real component of the impedance, provided that it is measured over a sufficiently wide frequency range.

A critical problem in any impedance analysis involves validation of the data. This is particularly true because of the need to employ low amplitude excitations, and when working with inherently "noisy" systems. In this paper, we describe how Kramers-Kronig transforms may be used to estimate R_p from the imaginary component of the impedance. We also argue that comparison of the R_p value computed from the imaginary component via the K-K transforms with that derived directly from Eq. [2] represents a simple and convenient test of the validity of corrosion impedance data.

*Electrochemical Society Active Member.

Kramers-Kronig Transforms

Derivation of the Kramers-Kronig transforms (7-11) is based upon four quite general conditions of the system being fulfilled.

Causality.—the response of the system is due only to the perturbation applied, and does not contain significant components from spurious sources.

Linearity.—the perturbation/response of the system is described by a set of linear differential laws. Practically, this condition requires that the impedance be independent of the magnitude of the perturbation.

Stability.—the system must be stable, in the sense that it returns to its original state after the perturbation is removed.

Impedance values.—the impedance must be finite valued at $\omega \rightarrow 0$ and $\omega \rightarrow \infty$, and must be a continuous and finite valued function at all intermediate frequencies.

Provided that the above conditions are satisfied, the K-K transforms are purely a mathematical result, and do not reflect any other physical property or condition of the system. The transforms have been used extensively in the analysis of electrical circuits (9), but only rarely in the case of electrochemical systems (10-14).

Two of the more important transforms may be stated as follows (9, 11)

$$Z'(\omega) - Z'(\infty) = \left(\frac{2}{\pi}\right) \int_0^{\infty} \frac{xZ''(x) - \omega Z''(\omega)}{x^2 - \omega^2} dx \quad [3]$$

$$Z'(\omega) - Z'(0) = \left(\frac{2\omega}{\pi}\right) \int_0^{\infty} \left[\left(\frac{\omega}{x}\right) Z''(x) - Z''(\omega)\right] \cdot \frac{1}{x^2 - \omega^2} dx \quad [4]$$

where Z' and Z'' are the real and imaginary components of the impedance, respectively. Therefore, according to Eq. [2], the polarization resistance simply becomes

$$R_p = \left(\frac{2}{\pi}\right) \int_0^{\infty} \left[\frac{Z''(x)}{x}\right] dx \approx \left(\frac{2}{\pi}\right) \int_{x_{\min}}^{x_{\max}} \left[\frac{Z''(x)}{x}\right] dx \quad [5]$$

The forms of Eq. [3]-[5] deserve brief comment. First, it is evident that if the integral in Eq. [5] is to be convergent and finite, then $Z''(x)/x \rightarrow 0$ as $x \rightarrow x_{\min} \rightarrow 0$ and $x \rightarrow x_{\max} \rightarrow \infty$. The approximation is valid when the integrals from $x = 0$ to x_{\min} and from x_{\max} to ∞ are negligible compared with the integral from x_{\min} to x_{\max} . Second, it appears that the functions beneath the integrals in Eq. [3] and [4] contain singularities at $x = \omega$. However, as we show later (16), expansion of $(x^2 - \omega^2)^{-1}$ reveals that no singularity actually exists, and hence that the precision of integration is not compromised on passing through $x = \omega$, as is sometimes claimed.

In this study, we evaluate the integral in Eq. [5] in a piece-wise fashion by fitting a fifth-order polynomial to experimental Z'' vs. frequency (x) data using a least squares technique

$$Z''(x) = a_0 + a_1x + a_2x^2 + a_3x^3 + a_4x^4 + a_5x^5 \quad [6]$$

The segments over which the integral is evaluated are chosen to coincide with changes in the sign of $Z''(x)$ and/or with changes in the gradient of $Z''(x)$ vs. frequency. The total integral is then evaluated as

$$R_p \approx \left(\frac{2}{\pi}\right) \sum \left[a_0 \ln x + a_1x + \frac{a_2x^2}{2} + \frac{a_3x^3}{3} + \frac{a_4x^4}{4} + \frac{a_5x^5}{5} \right]_{x_i}^{x_{i+1}} \quad [7]$$

where i is the segment number. The limitation on the size of the segment is that the number of data points must exceed the highest order of the polynomial; we have found that a fifth-order polynomial is well suited for the cases discussed later in this paper.

The use of Eq. [5] in the analysis of impedance data for corroding systems has also been proposed by Kendig and Mansfeld (12) and was subsequently used by Mansfeld *et al.* (13). However, these workers propose that this equation is a basis for estimating polarization resistance data from the imaginary component of the interfacial impedance at high frequencies, thus avoiding the need to obtain impedance data at time consuming low frequencies. As noted by Kendig and Mansfeld (12), this approach is valid only if the plot of Z'' vs. $\log \omega$ (e.g., see Fig. 2) is symmetrical. This is true only for those systems that exhibit single semicircles in the complex plane that are either depressed or centered on the real axis; it is generally not valid for systems that exhibit multiple resistive/capacitive or resistive/inductive relaxations or for those systems that are best described in terms of a diffusional impedance or a transmission line. Accordingly, the method described by these workers is not expected to be generally applicable to experimental impedance data, except in those cases for which the condition noted above holds.

In this work, we adopt a more general approach in the application of Eq. [5], in that the integration is carried out over the entire frequency range and not just over the high frequency arm of the Z'' vs. $\log \omega$ region, as proposed by Kendig and Mansfeld (12). Accordingly, our analysis is not restricted by the shape of the Z'' vs. $\log \omega$ correlation, but should be applicable to all impedance data, provided that the four general conditions for a valid impedance are fulfilled and that the integral in Eq. [5] can be evaluated. This then forms the basis for using Eq. [5] as a diagnostic criterion for determining the validity of impedance data.

Analysis of Experimental Data

In order to illustrate the application of the K-K transformation method for validating polarization resistance measurements in particular and for verifying impedance data in general, we consider three systems: TiO_2 -coated steel in a HCl/KCl solution of pH = 2 at 25°C, Al-0.1P-0.1In-0.2Ga-0.01Tl alloy in 4M KOH at 25°C, and pure aluminum (99.99%) also in 4M KOH at 25°C. The first system was

chosen because it is characterized by an extensive (Z' , Z'') vs. frequency data set that appears to satisfy the four conditions listed previously for a valid impedance. The second and third systems are included because aluminum corrodes rapidly in KOH solution, so that the condition of stability may not be satisfied. Furthermore, the third system exhibits characteristics that suggest the presence of experimental artifacts in the experimental impedance data. Accordingly, this system affords an opportunity to examine the sensitivity of the transform currently being considered to apparently "bad" data.

The complex plane plot for TiO_2 -coated carbon steel in HCl/KCl solution, pH = 2, at 25°C is shown in Fig. 1. The high frequency region exhibits a slope of $\sim \pi/4$, indicating that the interfacial properties are dominated by a mass-transfer process. At lower frequencies, the locus of data points curls over and ultimately intercepts the real axis at a frequency of less than 0.01 Hz. The measured polarization resistance is readily computed from the high frequency and low frequency intercepts as $R_p = 158.48 - 1.35 = 157.13 \Omega$. The experimental Z'' vs. $\log_{10} x$ (x = frequency in hertz) data are plotted in Fig. 2, and demonstrate that this system exhibits a single dispersed relaxation centered about $x = 0.58$ Hz. Also plotted on this figure are data calculated from the least squares piecewise fit of Eq. [6] to the experimental data. In this case, five segments were used, corresponding to one for $x < 0.58$ Hz and four for $x > 0.58$ Hz. The value of R_p calculated from the integral (Eq. [7]) was found to be 158.20 Ω which differs from the experimental value noted above by less than 0.7%. This error is of the same order (1-1.5%) as that found by transforming data calculated from equivalent electrical circuits; systems that we know *a priori* satisfy the conditions for a valid impedance. Thus, the observed error may be attributed principally to the algorithm itself.

In the second case Al-0.1P-0.1In-0.2Ga-0.01Tl alloy in 4M KOH at 25°C, (Fig. 3 and 4), both the complex plane and the Z'' vs. $\log_{10} x$ plots demonstrate the existence of resistive/capacitive and resistive/inductive relaxations at high and low frequencies, respectively. The data plotted in Fig. 4 were analyzed in three segments: A-B, B-C, and C-D. Agreement between the experimental data and that recalculated from Eq. [6] is clearly less exact in this case than in the previous one. Also, it was necessary to use much wider segments in the evaluation of the integral in Eq. [5]. The calculated R_p value was found to be 82.4 Ω compared with $90 \pm 5 \Omega$ obtained by extrapolating the

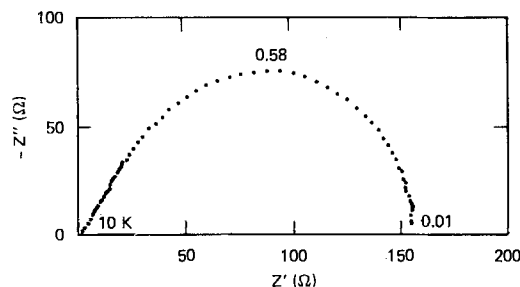


Fig. 1. Complex plane impedance plot for TiO_2 -coated carbon steel in HCl/KCl solution. pH = 2. $T = 25^\circ\text{C}$. The numbers refer to frequencies in hertz.

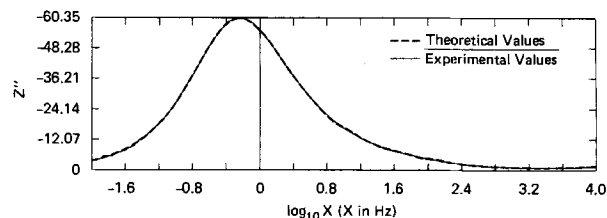


Fig. 2. Plot of Z'' vs. $\log_{10} x$ (x in hertz) for TiO_2 -coated carbon steel in HCl/KCl solution. pH = 2. $T = 25^\circ\text{C}$. Dashed line: polynomial fit (Eq. [6]). Solid-line: experimental data.

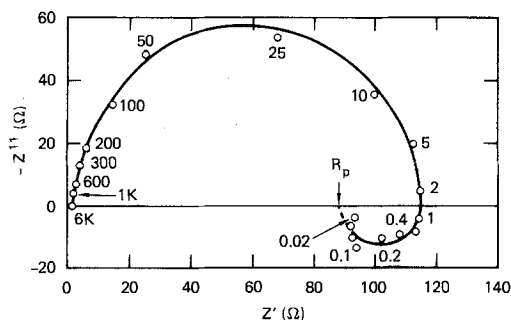


Fig. 3. Impedance diagram for Al-0.1P-0.1In-0.2Ga-0.01Ti alloy in 4M KOH at 25°C and at the open-circuit potential (-1.760V vs. Hg/HgO). Numbers next to the experimental points are frequencies in hertz.

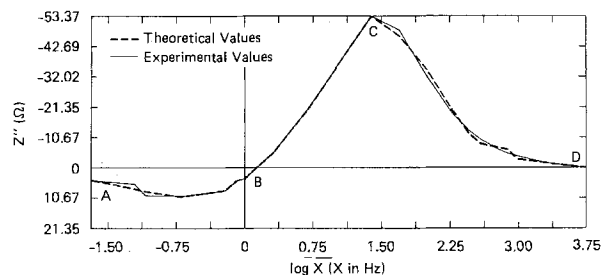


Fig. 4. Plot of Z'' vs. $\log x$ (x in hertz) for Al-0.1P-0.1In-0.2Ga-0.01Ti alloy in 4M KOH at 25°C under open-circuit conditions ($E = -1.76V$ vs. Hg/HgO). Dashed line: polynomial fit (Eq. [6]). Solid line: experimental data.

measured impedance to intercept the real axis in the limit of zero frequency. We believe that the difference is significant, and that it reflects not only an overall lower quality of data, as expected for a rapidly corroding system, but also a less extensive data set, particularly in the critically low frequency region. Nevertheless, the transform is quite satisfactory, considering the dubious fulfillment of the stability condition.

The final case considered in this paper (Fig. 5 and 6) was chosen because the system apparently exhibits a negative resistance at high frequencies and multiple intersecting loops at low frequencies. This latter characteristic is frequently observed experimentally, and is predicted

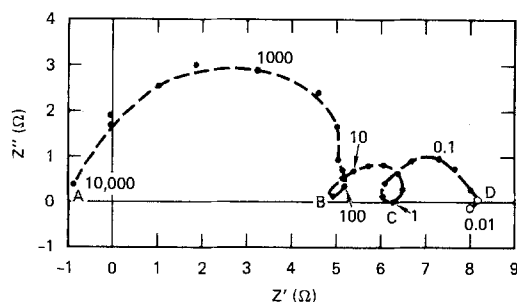


Fig. 5. Complex plane impedance plot for pure Al (99.99%) in 4M KOH at 25°C. $E = -1.56V$ vs. Hg/HgO. Numbers next to the experimental points are frequencies in hertz.

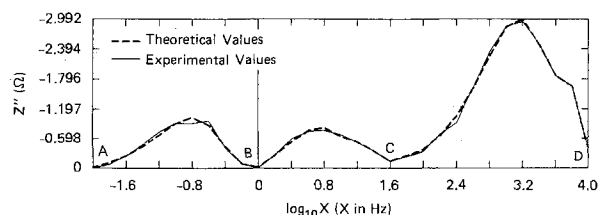


Fig. 6. Plot of Z'' vs. $\log_{10} x$ (x in hertz) for Al in 4M KOH at 25°C. $E = -1.56V$ vs. Hg/HgO. Dashed line: polynomial fit (Eq. [6]). Solid line: experimental data.

theoretically for certain dissolution reactions (12), so that verification that data of this type correctly transform is a matter of considerable interest. The negative resistance at high frequencies is almost certainly an experimental artifact, presumably arising from poor cell design. In carrying out the transformation, a three-segment (A-B, B-C, C-D, Fig. 6) integration was used to yield an R_p value of 7.55Ω. This value is significantly lower (by 18%) than the value of 9.2Ω obtained by extrapolating the high and low frequency arms to the real axis. Part of the difference may be due to the fact that the data were not obtained at a sufficiently low frequency to detect an inductive loop; note that the data point at 0.01 Hz does in fact lie below the real axis. However, a more likely explanation is that the real component of the impedance is distorted by some cause that results in the appearance of an apparent negative resistance at high frequency. Indeed, if it is assumed that the high frequency data intersects the real axis at the origin, then an experimental value for R_p of $8.2 \pm 0.5\Omega$ is obtained. This value is in much better agreement with that calculated above using the K-K transform.

Discussion

The analyses described above demonstrate that the Kramers-Kronig transform, as embodied in Eq. [5], is an accurate and convenient tool for assessing the validity of electrochemical impedance data.

From the present analysis, it is evident that the quality of electrochemical impedance studies depends heavily upon the size and accuracy of the experimental data set, as exemplified by the first example analyzed in this study. It is also apparent that pseudoinductive impedances (second case), and possibly those exhibiting intersecting loops (third case), also transform correctly, and hence may be regarded as valid characteristics of an observed impedance function. Finally, the transform apparently is sensitive to experimental artifacts that may, for example, lead to the distortion of one component; in the third case analyzed here, the distortion results in negative resistance at high frequencies. It is important to note, however, that the entire weight of the validation test afforded by Eq. [5] is placed on a knowledge of the real and imaginary components of the impedance over an effectively infinite frequency bandwidth. Since reliable impedance data for the low frequency region are not always available, considerable care must be exercised in applying Eq. [5] as a quantitative validity test. It is possible that more accurate and convenient validation analyses might be developed by considering the full set of K-K transforms, including Eq. [3] and [4], in order to de-emphasize the importance of the low frequency region. This possibility is currently being explored, and will be discussed in the second part of this series (16).

Acknowledgments

Financial support of this work from the Department of Energy and Eltech Systems, Incorporated, through Contract LNL-1806205, is greatly appreciated. The authors also thank Dr. M. C. H. McKubre for supplying data on TiO₂-coated carbon steel and Ms. Silvia Real for some of the experimental data for aluminum.

Manuscript submitted Feb. 8, 1985; revised manuscript received June 10, 1985.

SRI International assisted in meeting the publication costs of the article.

REFERENCES

1. D. D. Macdonald and M. C. H. McKubre, in "Modern Aspects of Electrochemistry," Vol. 14, J. O'M. Bockris, B. E. Conway, and R. E. White, Editors, p. 61, Plenum Press, New York (1982).
2. D. D. Macdonald and M. C. H. McKubre, in "Electrochemical Corrosion Testing," STP727, ASTM, Philadelphia (1981).
3. D. D. Macdonald, "Transient Techniques in Electrochemistry," Plenum Press, New York (1977).
4. A. J. Bard and L. R. Faulkner, "Electrochemical Methods," John Wiley and Sons, New York (1980).

5. M. Stern and A. L. Geary, *This Journal*, **104**, 56 (1957).
6. F. Mansfeld, *Adv. Corr. Sci. Technol.*, **6**, 163 (1976).
7. H. A. Kramers, *Physiol. Zool.*, **30**, 522 (1929).
8. R. de L. Kronig, *J. Opt. Soc. Am.*, **12**, 547 (1926).
9. H. W. Bode, "Network Analysis and Feedback Amplifier Design," Chap. 14, Nostrand, New York (1945).
10. V. A. Tyagai and G. Ya. Kolbasov, *Elektrokhimiya*, **8**, 59 (1972).
11. R. L. Van Meirhaeghe, E. C. Dutoit, F. Cardon, and W. P. Gomes, *Electrochim. Acta*, **21**, 39 (1976).
12. M. Kendig and F. Mansfeld, *Corrosion*, **39**, 466 (1983).
13. F. Mansfeld, M. W. Kendig, and W. J. Lorenz, *This Journal*, **132**, 290 (1985).
14. C. D. S. Tuck, Abstract 191, p. 276, The Electrochemical Society Extended Abstracts, Vol. 84-2, New Orleans, LA, Oct. 7-12, 1984.
15. M. Keddani, O. R. Mattos, and H. Takemouti, *This Journal*, **128**, 257 (1981); *ibid.*, **128**, 266 (1981).
16. M. Urquidi and D. D. Macdonald, To be submitted to *This Journal*.

Anodic Oxide Growth on Aluminum in the Presence of a Thin Thermal Oxide Layer

Walter J. Bernard* and Steven M. Florio

Sprague Electric Company, North Adams, Massachusetts 01247

ABSTRACT

The presence of a thin film of thermal oxide on the surface of aluminum promotes the growth of additional crystalline (γ' - Al_2O_3) oxide during subsequent anodization in an aqueous phosphate solution. It was shown through the use of phosphorus-32 tracer and chemical thinning procedures that the anodic crystalline oxide is formed beneath a discrete, continuous layer of amorphous oxide, and that the original thermal oxide is incorporated in the anodic crystalline film. The concentration of phosphorus in the amorphous layer is greater than that which occurs in the absence of crystalline oxide. Evidence is given that the occluded phosphorus species has some ionic mobility in both oxides.

The anodic oxidation of aluminum in aqueous borate or phosphate solutions generally results in the growth of oxide films that appear amorphous by x-ray or electron diffraction. Under some conditions, however, these dielectric films may display some degree of crystallinity. For example, if the metal is treated with hot water before anodic oxidation to a high voltage in aqueous borate, a portion of the dielectric contains crystals of γ' - Al_2O_3 (1, 2). This has been studied in some detail. Low voltage films grown in citric acid after a boiling water treatment have also been shown to have a partial crystalline character (3).

Crystalline oxide growth may also be promoted by the use of a brief thermal oxidation prior to the anodic oxidation (4, 5). The thermal oxide, identified as γ - Al_2O_3 (6), has been shown (7, 8) to consist of small crystallites that nucleate below the pre-existing amorphous oxide, spreading laterally to cover the entire metal surface.

The presence of the thermal oxide modifies the mechanism of anodic oxidation so that the growth of additional crystalline oxide is promoted, and it may also affect the composition of the layers of oxide that comprise the overall complex film structure. That such compositional modification can be brought about by the presence of an existing film was shown (9) in the case of anodic oxidation of aluminum in an aqueous phosphate solution. When the surface is free of oxide the dielectric contains substantial amounts of phosphorus (10, 11), but when the foil is first covered with a hydrous oxide layer the subsequently formed anodic oxide is essentially free of phosphorus. One purpose of this study was to see if the thermal oxide behaves analogously.

The location of the thermal oxide during anodization may be conveniently observed by the use of a pretreatment of the foil in hot phosphoric acid containing ^{32}P . As a result of this treatment, the aluminum surface becomes covered with a monolayer of the acid (or other phosphate species). This phosphorus is retained during thermal oxidation, becoming incorporated into the thin thermal film and thereby acts as a marker during the following anodization. The location of the tagged thermal oxide may be determined by measuring the amount of residual ^{32}P during chemical sectioning of the composite films.

Further information on the mechanism of the reaction was obtained by carrying out the foil pretreatment in non-

radioactive phosphoric acid; in this case, the thermal step was followed by anodization in a radioactive solution of ammonium dihydrogen phosphate.

Experimental

The aluminum specimens were cut from 76 μm thick Alcoa foil of 99.99% purity. Prior to phosphoric acid treatment, the specimens were electropolished in a perchloric acid/acetic anhydride mixture for 150s at 10 mA/cm^2 , and then rinsed with distilled water and dried with acetone. This electropolishing procedure produces a smooth metal surface covered with a very thin ($<20\text{\AA}$) oxide film (12).

Carrier-free ^{32}P isotope was obtained from New England Nuclear as H_3PO_4 in water. A 2.0 mCi portion of this acid was incorporated into a 0.01M solution of H_3PO_4 ; a similar 0.01M H_3PO_4 solution without tracer was also prepared. A second 2.0 mCi portion of the radiolabeled acid was incorporated into a 0.01M solution of ammonium dihydrogen phosphate (ADP); a similar 0.01M ADP solution without tracer was also prepared.

Standards for determining activity were prepared by the uniform distribution of an aliquot (either 50 or 100 μliter) of the active solutions, in small droplets, over an area of aluminum equivalent to that used for counting experimental specimens. The phosphoric acid for these standards was neutralized with 0.01N NaOH before use. The foils were then dried at 60°C before counting.

For all radioactive specimens, a circular area of 7.9 cm^2 was measured with a Geiger-Müller counter. A tantalum mask, 0.76 mm thick, served to define the counting area. The aluminum foil itself was transparent to β -radiation emitted by ^{32}P , and hence both sides of the experimental samples were counted simultaneously.

Acid pretreatment was carried out in vigorously boiling solutions of 0.01M H_3PO_4 for 90s. These foils were then thoroughly washed with distilled water, dried with acetone, weighed, and counted when applicable. The weight changes for this step and all subsequent operations were determined with a digital microbalance. Specimens were oxidized in air at 600°C for 5 min, and then reweighed and counted.

After thermal oxidation, the active specimens were anodized in nonactive 0.01M ADP solution; foils that had been pretreated with nonradioactive H_3PO_4 , on the other hand, were anodized in ADP solutions containing the ^{32}P tracer.

*Electrochemical Society Active Member.

Anodizations were performed in glass-jacketed cells, using Teflon supports for platinized-platinum counter-electrodes. Stirring of the electrolyte was accomplished with a magnetically driven stirring bar. A constant-temperature liquid pumped through the cell jacket maintained the anodizing solution at $85^\circ \pm 0.2^\circ\text{C}$. The current density was 1.0 mA/cm^2 , and during the constant-voltage period it was allowed to decay to 0.05 mA/cm^2 .

Measurements of series capacitance, at 120 Hz, were made in a similar cell using aqueous ammonium borate at 25°C .

The distribution of radiotracer in the films was determined by dissolving the films stepwise in a stirred solution of 2% $\text{CrO}_3/5\% \text{H}_3\text{PO}_4$ at 65°C . This solution has been shown to attack amorphous Al_2O_3 uniformly at a moderately fast rate, with extremely little attack on the metal (13). However, the rate of attack on crystalline Al_2O_3 has been shown to be much slower (14, 15). As such, this procedure is effective for discriminating between the two types of oxide.

In addition to the determination of weight loss and residual radioactivity following the chemical sectioning steps, capacitance and remaining barrier voltage were obtained to give a measure of the film thickness. The barrier voltage was determined by applying a small constant current (i.e., 10% of the formation current density) in the original anodizing electrolyte, and observing the knee of the V-t curve. The point which is taken as V_b is the beginning of the constant slope corresponding to the calculated rate of new film growth. This is found by extrapolation of the straight line to the point of curvature, and is indicated by vertical lines on the tracings in Fig. 3. For short chemical treatment times, the break in the curve is satisfactorily sharp, and observations were reproducible to a volt or two. For longer periods, where film undercutting may occur, there is correspondingly less certainty in the value.

Results and Discussions

The amount of thermal oxide grown on aluminum depends on both the temperature and the reaction time. Crystalline oxide can be formed at temperatures as low as 450°C (6), but more complete coverage of the foil is achieved under more vigorous conditions; this, in turn, increases the amount of crystalline anodic oxide. Five minutes at 600°C gave satisfactory results for the work reported here.

Under the experimental conditions used, it is believed that after thermal treatment the oxide present on the metal surface is almost entirely crystalline. The exposure to dilute phosphoric acid serves to dissolve the natural amorphous oxide as well as to create an adsorbed layer of phosphate. The oxide-free aluminum is thus largely protected from regrowth of oxide until exposure to temperatures which permit the growth of crystalline oxide. This sequence of events is supported by weight measurements showing that the loss in weight during exposure to phosphoric acid corresponds to the removal of the original amorphous film; no substantial weight gain occurs until high temperature oxidation takes place. Only a small fraction of the resulting film is soluble in phosphoric acid. Details will be given in a future publication.

In the first series of experiments foil samples were treated with active H_3PO_4 , thermally oxidized, and then anodized in nonactive ADP. When these foils were subjected to the chemical sectioning procedure, the ^{32}P activity and oxide weight varied with time, as shown in Fig. 1.

The duplex nature of the anodic films can be deduced from these results. It is apparent from the weight loss curve that a soluble oxide is positioned above an insoluble layer, as shown by the abrupt reduction in weight loss after 2 min. The insoluble layer was identified by electron diffraction as $\gamma'\text{-Al}_2\text{O}_3$, confirming earlier reports (14, 16). In addition, the fact that only about 10% of the original activity is lost during chemical stripping shows that the bulk of the original adsorbed species has become a constituent of the insoluble crystalline oxide. This can only have come about by nearly complete incorporation

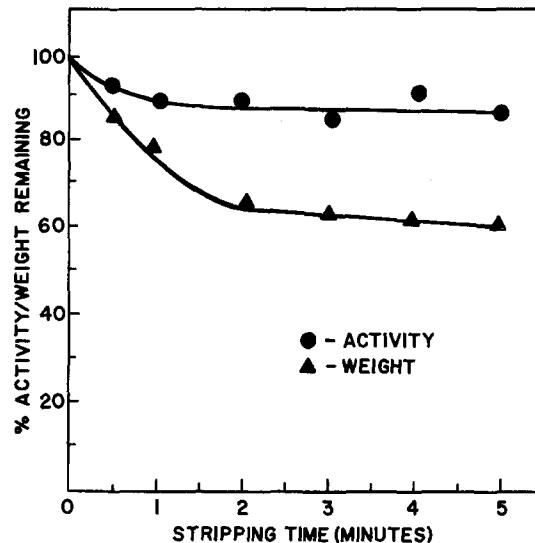


Fig. 1. Loss of activity and weight during chemical sectioning of 100V ADP films. Pretreated with active H_3PO_4 and then thermally oxidized.

of phosphorus in the thermal oxide that was grown at 600°C ; upon anodization this thermal oxide, which enhances the anodic growth of $\gamma'\text{-Al}_2\text{O}_3$, occupies the same location in the complex film as the thicker crystalline film.

It is not clear why the thermal oxide failed to tie up the entire layer of adsorbed phosphoric acid, allowing about 10% of the phosphorus to be removed during the early stage of the chemical sectioning. It might have been reasonable to expect the $\gamma'\text{-Al}_2\text{O}_3$ film to have sufficient mass to accommodate all the phosphorus available; using a density of 3.6 g/cm^3 (5) and an oxide weight of $5.7 \mu\text{g/cm}^2$, the film thickness is estimated to be about 160\AA .

The very small amount of phosphorus introduced as a marker has apparently no significant effect on the mechanism. From activity data, it was calculated that only about $0.035 \mu\text{g/cm}^2$ was present before thermal treatment, and that about $0.030 \mu\text{g/cm}^2$ remained in the final duplex oxide before chemical sectioning. These figures were essentially independent of the anodization voltage, as shown in Table I.

The curves of weight loss and residual activity do not show the limiting horizontal lines which would be anticipated for ideal behavior. This is most likely a result of the incompletely continuous nature of the crystalline oxide, which permits some degree of penetration and undercutting of the crystalline particles, followed by mechanical dislodging of these grains.

The curves in Fig. 2 provide further evidence for the layered structure of the dielectric film. Separate foil specimens were chemically stripped and reanodized to determine the amount of barrier remaining (V_b), as well as the capacitance of the remaining film. The shape of the V_b curve is similar to that of the weight loss curve of Fig. 1, and for a 100V film it indicates that about 35% of the original barrier consists of the easily soluble amorphous oxide. The remainder of the film appears to be largely crystalline, although the presence of an additional thin amorphous layer at the metal/oxide interface is likely (3), and is supported by the manner in which the crystalline

Table I. Weight of phosphorus on aluminum surface (ng/cm^2)

	Anodization voltage		
	50V	100V	150V
Before 600°C treatment	38	35	33
After 600°C treatment	34	36	35
Final weight in oxide	30	29	27

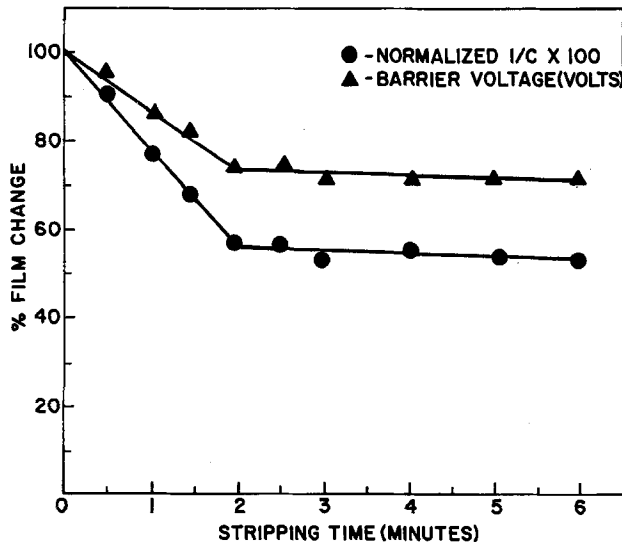


Fig. 2. Change in barrier voltage and reciprocal capacitance during chemical sectioning of 100V ADP films. Pretreatment as in Fig. 1.

film may be undercut after extended chemical stripping. When carried out for sufficiently long periods, it was possible to observe minute particles of insoluble oxide suspended in the stripping solution.

Reanodization curves also demonstrate that the crystalline layer is not a completely impenetrable barrier, but consists, in part at least, of some defects and channels in which amorphous film is grown. A typical reanodization curve, shown in Fig. 3, demonstrates that a small but significant charge is required to refill gaps in the crystalline layer when chemical sectioning approaches the amorphous/crystalline interface. A 30s stripping (curve I) required only 6.8 mC/cm² to recharge the film to 97V, corresponding to 3.6% of the charge passed during the original formation to that voltage. A longer reaction time of 120s,

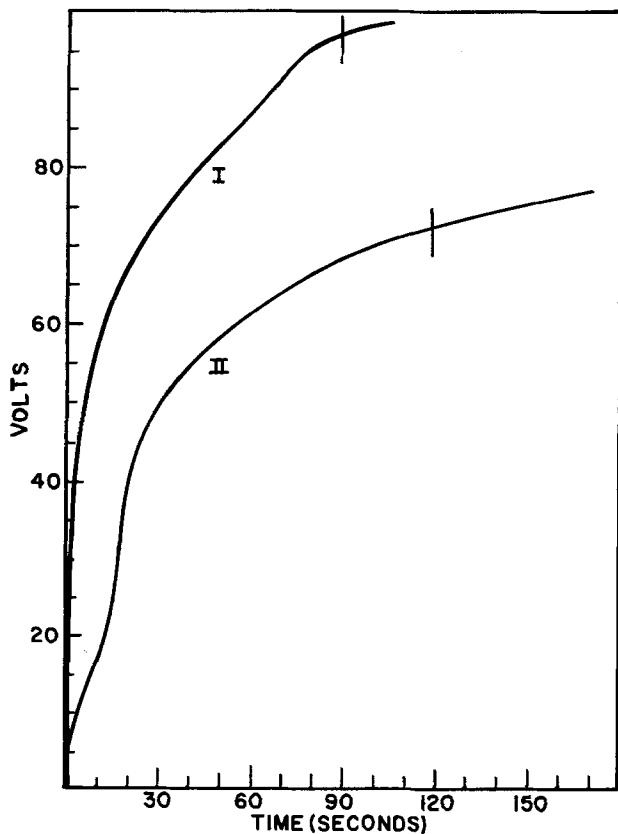


Fig. 3. Recorder tracings of reanodization of 100V ADP films chemically stripped for 30s (curve I) and 120s (curve II). Foils pretreated as in previous figures.

on the other hand, required the passage of 9.3 mC/cm² to reach the residual barrier level of 71V (curve II); in terms of anodization charge, this amounts to 6.6% of that needed to form a 71V film.

Figure 2 also shows the dependence of reciprocal capacitance on stripping time; a constant value of 1/C is reached after about 120s, the same point at which V_B becomes constant. The data in this plot represent measurements made immediately after reanodization, which gave stable reproducible values. If measured before reanodization, however, capacitances were unstable and fictitiously high, either through the dissolution of intergranular amorphous oxide, or because of some degree of dielectric instability revealed by the chemical treatment. This type of dielectric relaxation is commonly observed in high voltage films that have been formed in the presence of a hydrous oxide layer, but has also been observed with low voltage films of the type described here (2, 17).

The two forms of anodic oxide differ not only in their degree of crystallinity, but also in other properties. The growth constant (reciprocal field strength) of the crystalline layer is obviously greater than that of the amorphous film, and it should be possible to estimate its value from the curves in Fig. 2 and from the appropriate physical constants of the amorphous oxide, i.e., 14.8 Å/V¹ and ε = 8.5 (18).

The voltage across the crystalline film is 71V (assuming that there is only a negligible amount of amorphous oxide at the metal interface), while its reciprocal capacitance is only 54% of the total film. If its dielectric constant is 8.6, as reported (5), its growth rate is calculated as 7.2 Å/V. This suggests that the field in the crystalline oxide is much higher than has been reported previously; weight measurements, on the other hand, lead to different results. From the curve in Fig. 1, and using an oxide density of 3.61 g/cm³ (5) for the crystalline layer, the growth rate is calculated to be 9.2 Å/V, in good agreement with Alwitt and Takei (5).

These discrepant results could perhaps be reconciled if a higher value of ε for γ'-Al₂O₃ were used. In view of the relatively high values that have been published for polycrystalline aluminas—10.5 and higher (19)—it would not be surprising to find the value for γ'-Al₂O₃ to be somewhat greater than 8.6.

The second set of experiments involved the use of active phosphorus in ADP solution to tag the growing anodic film. The amount of phosphorus take-up (Fig. 4) was constant with formation voltage up to 150V, as was ob-

¹The cited paper reported 12.3 Å/V at a current density of 0.05 mA/cm² at 25°C. From this value, we have made an estimate of the thickness of the amorphous film at 85°C.

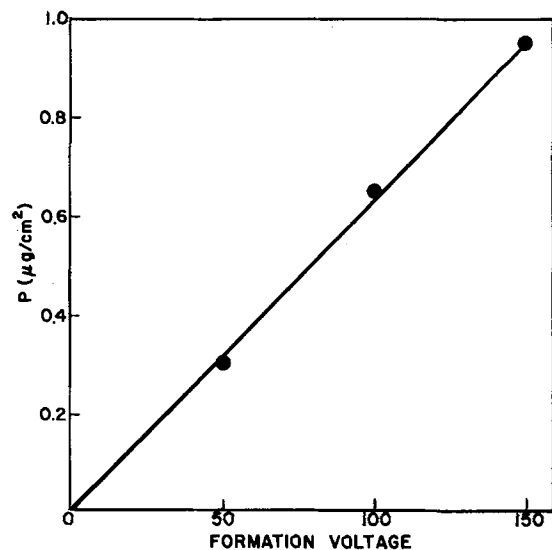


Fig. 4. Weight of phosphorus incorporated into films during anodization in active ADP. Foils previously treated with inactive H₃PO₄, followed by thermal oxidation.

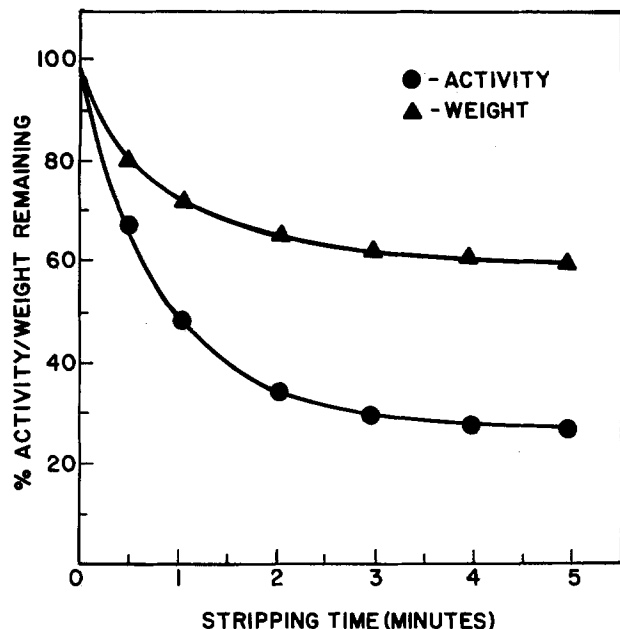


Fig. 5. Loss of activity and weight during chemical sectioning of 100V films anodized in active ADP. Foils pretreated as in Fig. 4.

served earlier in films formed in the absence of a thermal oxide (10), but the distribution was quite different. Figure 5 shows the rate at which activity was lost in the chemical stripping solution; the rate of weight loss is also depicted, in good agreement with the previous independent set of measurements. The bulk of the phosphorus (about 65%) is in the outer amorphous layer, but a significant amount is incorporated in the crystalline film.

The concentration of phosphorus in the amorphous layer is influenced by the presence of the underlying crystalline material. When anodization conditions are chosen so that a fully amorphous oxide is grown, a 100V film has a [P] of 640 ng/cm² (20, 21). But since phosphorus is found only in the outer 70% of the film, where it is homogeneously distributed (10), the concentration may be better expressed as 9.1 ng/cm² for each volt of film. In the case of the duplex film described in the paper, however, the outer amorphous layer does not appear to be as homogeneous, judging from the absence of a sharp transition in the rate of activity lost during chemical sectioning, and the phosphorus concentration is much greater. From the activity data, it was calculated to be 19 ng/cm²-V or about twice that found in the conventional film. The crystalline portion of the film, on the other hand, has a [P] of only 4.4 ng/cm²-V.

These data suggest that the crystalline oxide acts as a conductor not only for aluminum ions during film growth, but also for oxygen and phosphate ions. The presence of phosphorus in that portion of the dielectric cannot come about by direct occlusion from solution as it does for the outer amorphous film, since the crystalline layer is never in contact with the solution once the first contribution to film growth by metal ion migration takes place. The results cannot therefore be reconciled to the picture of P as an inert marker, but rather as a film component with ionic mobility.

The difference in the phosphorus concentration in the amorphous and crystalline oxide forms can thus be attributed to its lower mobility in the γ' -modification. In the case of a wholly amorphous film, it was found (10) that

the rate of phosphorus incorporation from the advancing oxide/solution interface is constant at constant current density; the rate of phosphorus diffusion into the phosphorus-free region grown at the metal/oxide interface is such that a uniform distribution results in the outer layer of the duplex film. In the present case, however, because the diffusing ions encounter the environment of γ' -Al₂O₃ in which mobility is sharply reduced, the concentration in the amorphous layer is increased.

It is also significant that the total amount of phosphorus in the overall film structure is greater than the parallel case with an all-amorphous film, the figures being 950 and 640 ng/cm², respectively. This can be accounted for if the contribution to film growth by aluminum ion motion is greater in the presence of the crystalline film, since this would lead to greater growth at the electrolyte interface and increased inclusion of phosphate ion.

A more detailed description of the process—in particular, the transport numbers of the ions—is not justified by the available data. If the P species is not an immobile marker, the measurement of its profile in the outer layer alone cannot be used to estimate transport numbers. A concentration profile of P in the crystalline films by means other than chemical sectioning might do much to throw more light on the overall process.

Manuscript submitted April 3, 1985; revised manuscript received May 27, 1985. This was Paper 54 presented at the Toronto, Ontario, Canada, Meeting of the Society, May 12-17, 1985.

Sprague Electric Company assisted in meeting the publication costs of this article.

REFERENCES

1. R. S. Alwitt, *This Journal*, **114**, 843 (1967).
2. R. S. Alwitt and C. K. Dyer, *Electrochim. Acta*, **23**, 355 (1978).
3. C. Crevecoeur and H. J. deWit, Abstract 174, p. 413, The Electrochemical Society Extended Abstracts, Vol. 78-1, Seattle, Washington, May 21-26, 1978.
4. C. Crevecoeur and H. J. DeWit, Paper 132 presented at the 27th Meeting of the International Society of Electrochemistry, Zurich (1976).
5. R. S. Alwitt and H. Takei, in "Passivity of Metals and Semiconductors," M. Froment, Editor, p. 741, Elsevier, Amsterdam (1983).
6. A. F. Beck, M. A. Heine, E. J. Caule, and M. J. Pryor, *Corros. Sci.*, **7**, 1 (1967).
7. P. E. Doherty and R. S. Davis, *J. Appl. Phys.*, **34**, 619 (1963).
8. J. J. Randall, Jr., and W. J. Bernard, *ibid.*, **35**, 1317 (1964).
9. R. S. Alwitt and W. J. Bernard, *This Journal*, **121**, 1019 (1974).
10. J. J. Randall, Jr., and W. J. Bernard, *Electrochim. Acta*, **20**, 653 (1975).
11. M. F. Abd Rabbo, J. A. Richardson, and G. C. Wood, *Corros. Sci.*, **16**, 689 (1976).
12. Z. Fujimura, *J. Electrochem. Soc. Jpn.*, **31**, 7 (1963).
13. J. E. Lewis and R. C. Plumb, *This Journal*, **105**, 496 (1958).
14. D. J. Stirland and R. W. Bicknell, *ibid.*, **106**, 482 (1959).
15. K. Shimizu, S. Tajima, G. E. Thompson, and G. C. Wood, *Electrochim. Acta*, **25**, 1481 (1980).
16. N. F. Jackson and P. D. S. Waddell, *J. Appl. Electrochem.*, **2**, 345 (1972).
17. W. J. Bernard and P. G. Russell, *This Journal*, **127**, 1256 (1980).
18. W. J. Bernard and J. W. Cook, *ibid.*, **106**, 643 (1959).
19. "Alumina as a Ceramic Material," W. H. Gitzen, Editor, p. 78, The American Ceramic Society, Columbus, OH (1970).
20. R. C. Plumb, *This Journal*, **105**, 498 (1958).
21. H. Takahashi, K. Fujimoto, H. Konno, and M. Nagayama, *ibid.*, **131**, 1856 (1984).

Anodic Oxidation of Reductants in Electroless Plating

Izumi Ohno,¹ Osamu Wakabayashi,² and Shiro Haruyama

Tokyo Institute of Technology, Faculty of Engineering, O-okayama, Meguro-ku, Tokyo 152, Japan

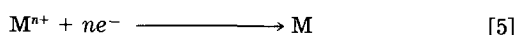
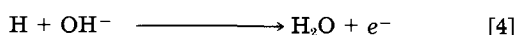
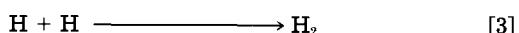
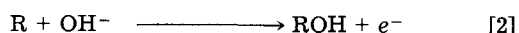
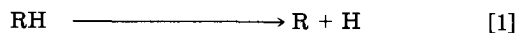
ABSTRACT

The anodic oxidation of reductants (hypophosphite, formaldehyde, borohydride, dimethylamine borane, and hydrazine) was studied on different metal electrodes (Au, Pt, Pd, Ag, Cu, Ni, and Co) at various temperatures, with special interest in the catalytic aspect of electroless plating. The rate of the anodic oxidation strongly depended on the pH value, the concentration of reductants, and the nature of the metal electrode. The catalytic activities of the metals for the anodic oxidation of different reductants were evaluated by the potentials at a reference current density. The order of the catalytic activity with metal varied depending on the nature of the reductants. The catalytic activity series thus obtained can be utilized for choosing the reductant suitable for the metal to be deposited. Arrhenius plots of the anodic currents on different metals at a reference potential yielded their respective straight lines. Some correlations were observed between the catalytic activity and the activation energy. The catalytic activity series was discussed in connection with that for hydrogen electrode reaction.

It is widely accepted that electroless plating proceeds along the electrochemical mechanism as the simultaneous reaction of cathodic metal deposition and anodic oxidation of reductant (1-5). The electrochemical conditions for electroless plating taking place are, first, the oxidation potential of the reductant's being less noble to the reversible potential of the metal to be deposited, and, second, the metal's having enough catalytic activity for the anodic oxidation taking place with reasonable rate. The first condition can be readily provided by simple thermodynamic consideration. Therefore, the rate of anodic oxidation of the reductant is, in some sense, a dominant factor in electroless plating.

The reductants used in electroless plating have a special feature. A limited variety of reductants is used in an electroless process, e.g., hypophosphite, formaldehyde, borohydride, dialkylamine borane, and hydrazine. Electroless plating usually accompanies hydrogen evolution, the rate of which is not directly related to that of metal deposition. Different reaction mechanisms have been proposed to account for the hydrogen evolution during electroless plating: (i) the proton discharge mechanism (6, 7), (ii) the hydroxide mechanism (8, 9), and (iii) the hydride ion mechanism (10, 11) and atomic hydrogen mechanism (12, 13). It was found by Gorbunova *et al.* (14) and Holbrook *et al.* (15) that the hydrogen evolved during electroless plating was originated mainly from the reductant molecule. Electroless plating proceeds mostly on certain metals that are known to be hydrogenation-dehydrogenation catalysts. It was reported by Gorbunova *et al.* (16) and Pearlstein *et al.* (17) that the poison for hydrogenation catalysts such as thiourea and mercaptobenzothiazole functions as stabilizer in an electroless process.

Various reaction mechanisms were presented for respective electroless processes (18-25). It was suggested by several workers that the key step in the reaction is the dissociative chemisorption to form adsorbed atomic hydrogen and an adsorbed anion radical. Van der Meerakker (26) claimed that all the electroless plating processes can be explained by a universal mechanism with the dehydrogenation of the reductant as the first step, thus



where RH represents the reductants. Reactions [3] and [4] represent the recombination and ionization of adsorbed atomic hydrogen, respectively, which can occur in paral-

¹Permanent address: Tokyo Institute of Technology, Graduate School at Nagatsuta, Midori-ku, Yokohama 227, Japan.

²Present address: Komatsu Limited, Technical Research Center, 2597, Shinomiya, Hiratsuka 254, Japan.

lel. Van den Meerakker also advocated that the catalytic aspect in electroless plating is originated from the catalytic property of the metal for reaction [3]. There are, however, only a few works on the anodic oxidation of the reductant in connection with the catalytic activity of the metal.

The aim of this paper is to establish the anodic oxidation behavior of the reductants on different metal electrodes with special interest in the catalytic activities of the metals in electroless plating.

Experimental Details

Polarization experiments were carried out on gold, platinum, palladium, silver, copper, nickel, and cobalt electrodes in the appropriate complex solutions containing sodium hypophosphite, formaldehyde, sodium borohydride, dimethylamine borane, and hydrazine, respectively. The standard compositions of the baths and the experimental conditions are summarized in Table I. Platinum, gold, and silver plates of surface area 0.4 cm² were used as the working electrodes. A platinum plate of the same surface area plated with the metal under investigation was also used as the working electrode. The counter-

Table I. Electrolytic solutions and experimental conditions for anodic oxidation of reductants

Reductant	Electrolyte	
NaH ₂ PO ₂	NaH ₂ PO ₂	0 ~ 0.4M
	Na-citrate	0.2M
	H ₃ BO ₃	0.5M
	pH	7.0 ~ 9.5
	Temperature	290.2 ~ 350.2 K
HCHO	HCHO	0 ~ 1M
	EDTA · 2Na	0.175M
	pH	11.0 ~ 13.2
	Temperature	278.2 ~ 330.2 K
	Nitrogen atmosphere	
NaBH ₄	NaBH ₄	0.01 ~ 0.1M
	EDTA · 2Na	0.175M
	pH	11.5 ~ 13.8
	Temperature	277.2 ~ 320.2 K
	Nitrogen atmosphere	
DMAB*	DMAB	0 ~ 8 g/liter
	Na-citrate	0.2M
	H ₃ BO ₃	0.5M
	CH ₃ OH	2 ml/liter
	pH	6.0 ~ 8.0
	Temperature	287.2 ~ 329.2 K
	Nitrogen atmosphere	
NH ₂ NH ₂	NH ₂ NH ₂ · H ₂ O	0 ~ 2M
	EDTA · 2Na	0.175M
	pH	11.0 ~ 13.0
	Temperature	298.2 ~ 339.2 K
	Nitrogen atmosphere	

* Dimethylamine borane.

electrode was a platinum plate of surface area 18 cm². The electrolytic cell was a Pyrex cylinder 5 cm in diameter and 8.5 cm in height. The potential of the working electrode was measured against a saturated calomel electrode (SCE) via a Luggin capillary and a salt bridge. Polarization measurements were made in potentiodynamic mode with a sweep rate of 0.002 V/s using an electronic potentiostat and a function generator. The experiments were carried out without agitation at 298.2 K unless otherwise noted. Some of the experiments were performed by using a rotating disk electrode. The rotating electrode was a platinum disk 0.3 cm in diameter plated with the metal under investigation. It was found, however, that the rotation of the electrode had no significant effect on the polarization behavior.

Results and Discussions

The anodic and cathodic reactions in electroless plating are more or less interdependent when they occur simultaneously (27, 28). The rate of the anodic oxidation of the reductant is in many cases accelerated in the presence of the cathodic deposition of the metal. As a first approximation, however, it can be assumed that the anodic polarization curve obtained in the absence of the metallic ion represents the true partial anodic reaction that would occur in the complete baths. In order to understand the catalytic aspect in electroless plating, the anodic polarization experiments were carried out on gold, platinum, palladium, silver, copper, nickel, and cobalt electrodes in the baths containing the reductants as listed in Table I. Similar polarization experiments were carried out in the baths in the absence of the reductant to distinguish the anodic current attributable to the dissolution of the metal.

Effect of pH and the concentration of reductant.—The rate of the anodic oxidation of the reductants increases with increasing either pH value or the concentration of the reductant. As the examples, the effects of the concentration on the anodic polarization curve of nickel in the solution containing hypophosphite are shown in Fig. 1. The polarization curves exhibit a maximum in current

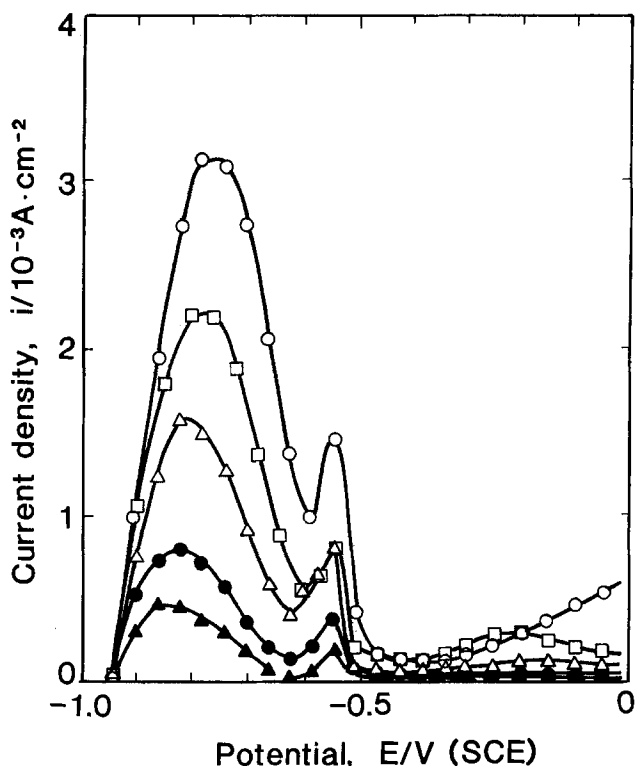


Fig. 1. Current-potential curves of anodic oxidation of hypophosphite on nickel at different concentrations. Bath composition: 0.2M Na-citrate + 0.5M H₃BO₃ + NaH₂PO₂ (varied), pH 9.0, 343 K. Concentration of NaH₂PO₂ (mol/dm³): open circles, 0.40; open squares, 0.20; open triangles, 0.10; solid circles, 0.06; solid triangles, 0.03.

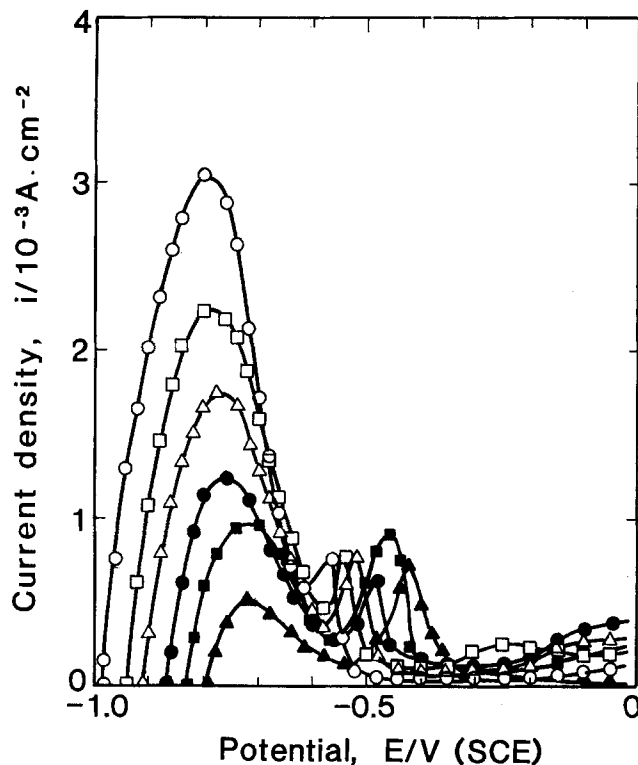


Fig. 2. Current-potential curves of anodic oxidation of hypophosphite on nickel at different pH values. Bath composition: 0.2M NaH₂PO₂ + 0.2M Na-citrate + 0.5M H₃BO₃, 343 K. pH: open circles, 9.5; open squares, 9.0; open triangles, 8.5; solid circles, 8.0; solid squares, 7.5; solid triangles, 7.0.

which increases with increasing the concentration. Although the depression of current after the maximum has been often attributed to the formation of an oxide film on surface, it occurs sometimes on noble metals and the depression potentials are mostly less noble compared to the reversible potentials for the oxide formation of the metals.

Figure 2 shows the effect of pH value on the anodic oxidation of hypophosphite on nickel. The current increases with increasing the pH value, shifting the current maximum to less noble potentials. The effects of the concentration of hypophosphite and the pH value on the anodic current at a fixed potential are summarized on logarithmic diagrams in Fig. 3 and 4, respectively. The slopes of the current-concentration diagram in Fig. 3 scattered between 0.44 and 0.80, depending on the nature of metal. The reaction orders with respect to hydroxyl ion were obtained from Fig. 3 to be approximately 0.25, except that for platinum (29).

Polarization experiments similar to those described above were carried out in the other baths shown in Table I. The dependencies of the current on pH value and the concentration of reductant in the other baths were very complicated, and the logarithmic plots of the relation similar to Fig. 3 and 4 did not exhibit a straight line (30, 31). Summarizing all the results, the reaction orders with respect to the reductants seem to scatter between 0.4 and 0.8, regardless of the natures of metal and reductant. The reaction orders regarding hydroxyl ion ranged from 0.2 to 0.4. Since the anodic oxidation of the reductants in the complex solutions is affected by pH in various ways, however, the apparent reaction orders may not be so helpful for the diagnosis of the reaction mechanism.

Effect of the nature of metals.—The polarization curves for the anodic oxidation of hypophosphite on different metals in sodium citrate solution are shown in Fig. 5. Anodic current attributable to the oxidation of hypophosphite was not observed on copper and silver electrodes, which simply dissolved anodically as indicated by the dotted line in Fig. 5. The polarization curve on palladium electrode exhibits a monotonous increase in current with

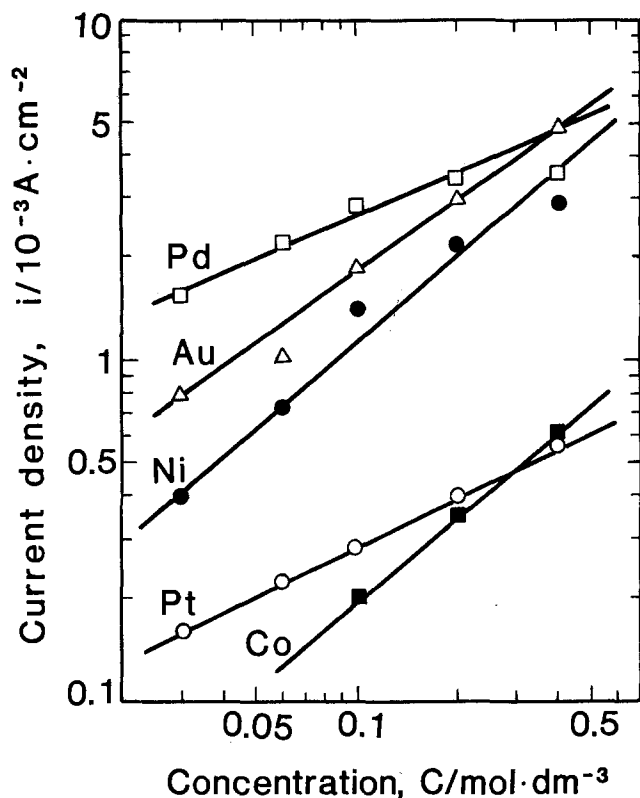


Fig. 3. Dependency of the anodic oxidation current at constant potential on the concentration of hypophosphite. Bath composition: 0.2M Na-citrate + 0.5M H_3BO_3 + NaH_2PO_2 (varied), pH 9.0, 343 K. Potentials (vs. SCE): $-0.80V$ (for Pd, Au, Ni, Co), $+0.20V$ (for Pt).

shifting the potential to noble direction. The polarization curve on gold shows three maxima of current, and the current falls off finally at around 0 V. The current on nickel electrode reaches a maximum at $-0.7V$ and falls off at $-0.4V$. Cobalt electrode dissolved anodically at the potentials noble to the current maximum. It is readily seen in Fig. 5 that platinum is less active for the anodic oxidation of hypophosphite.

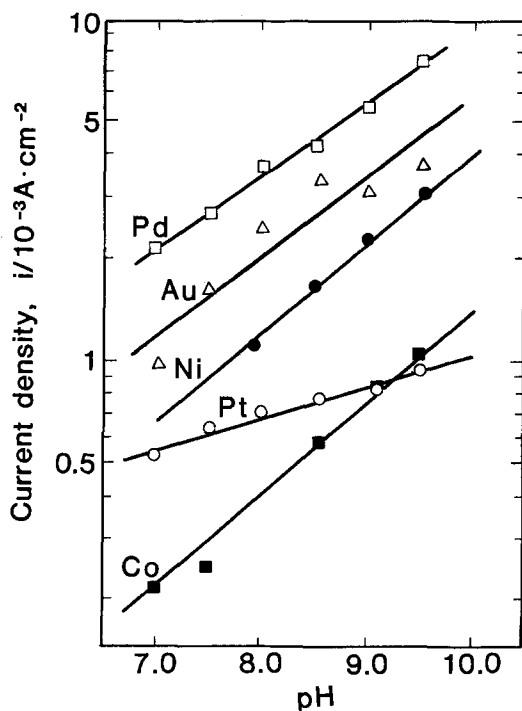


Fig. 4. Dependency of the anodic oxidation current of hypophosphite on pH value. Bath composition: 0.2M NaH_2PO_2 + 0.2M Na-citrate + 0.5M H_3BO_3 , 343 K. Potential (vs. SCE): $-0.80V$ (for Au, Ni), $-0.70V$ (for Pd, Co), $+0.20V$ (for Pt).

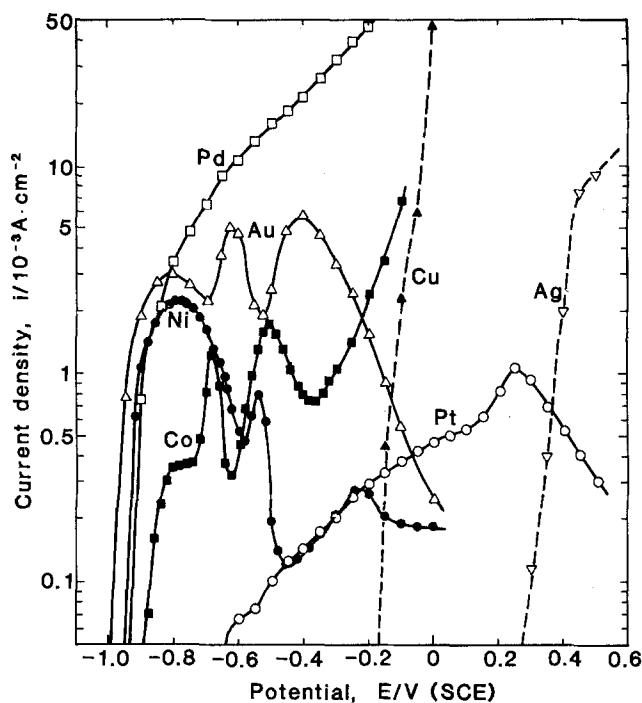


Fig. 5. Polarization curves for the anodic oxidation of hypophosphite on different metals. Bath composition: 0.2M NaH_2PO_2 + 0.2M Na-citrate + 0.5M H_3BO_3 , pH 9.0, 343 K. Dotted line: current attributable to the anodic dissolution of Ag and Cu electrodes.

The polarization curves for the anodic oxidation of formaldehyde on different metals in a EDTA solution are shown in Fig. 6. Cobalt and nickel electrodes exhibit the anodic current attributable to oxidation of formaldehyde only at the potentials noble to 0.3V. The anodic current on copper starts to rise at $-0.95V$ and falls off at $-0.3V$, exhibiting a maximum in current. The polarization curves on gold, silver, platinum, and palladium electrodes obey the Tafel relation at less noble potentials, exhibiting a limiting current at noble potentials. The limiting current was scarcely affected by the rotation of the electrode.

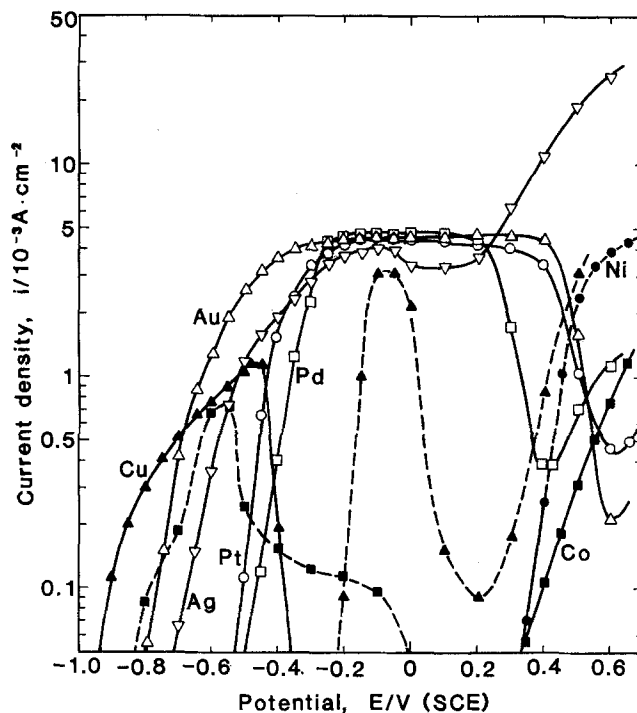


Fig. 6. Polarization curves for the anodic oxidation of formaldehyde on different metals. Bath composition: 0.1M HCHO + 0.175M EDTA, 2Na, pH 12.5, 298 K. Dotted line: current attributable to the anodic dissolution of Cu and Co electrodes.

It is seen in Fig. 6 that the apparent oxidation potential of formaldehyde on copper is less noble than that on the other metals.

The polarization curves for the anodic oxidation of borohydride on different metals are shown in Fig. 7. Most of the polarization curves obey the Tafel relation exhibiting an asymptotic behavior at noble potentials, whereas those on cobalt and nickel electrodes show a current maximum.

Figure 8 shows the polarization curves for the anodic oxidation of dimethylamine borane on different metals. Copper electrode simply dissolved without exhibiting the current attributable to anodic oxidation of dimethylamine borane. The current maximum behavior was observed on nickel, cobalt, and platinum electrodes.

The polarization curves for the anodic oxidation of hydrazine on different metals are shown in Fig. 9. The polarization curves on cobalt and nickel show a maximum current behavior, whereas those on platinum, palladium, copper, gold, and silver exhibit well-defined Tafel lines.

Referring to the results shown in Fig. 5-9, it is seen that the shapes of the polarization curves can be classified into three categories: the Tafel type, the Tafel type with limiting current, and the volcano type. The limiting current has been attributed to a limited diffusion of reactant in solution, whereas it is less sensitive to agitation of solution. Occurrence of the volcano type of polarization curve has been often attributed to the formation of anodic oxide film on surface, although the potential of falling off of current is usually less noble than the reversible potential of oxide formation. It is highly probable that these polarization behaviors reflect the mechanism of anodic oxidation of reductants as such. It is also noted that electroless plating usually takes place at the potentials corresponding to the less noble branch of the polarization curves.

Effect of temperature.—The anodic polarization experiments similar to those described above are carried out on various metals and reductants at different temperatures. The Arrhenius plots of the currents on different metals at appropriate potentials for the anodic oxidation of hypophosphite, formaldehyde, borohydride, dimethylamine borane, and hydrazine are shown in Fig. 10, 11, 12, 13, and

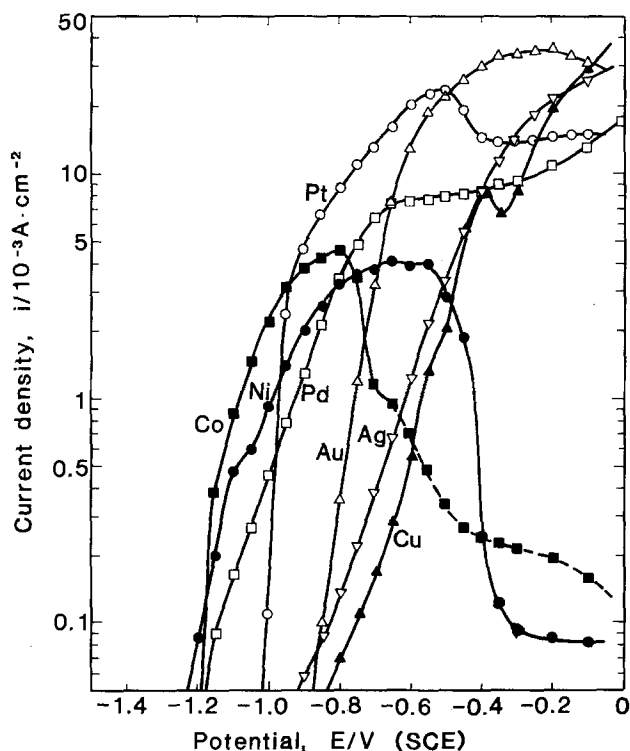


Fig. 7. Polarization curves for the anodic oxidation of borohydride on different metals. Bath composition: 0.03M NaBH_4 + 0.175M EDTA.2Na, pH 12.5, 298 K. Dotted line: current attributable to the anodic dissolution of Co electrode.

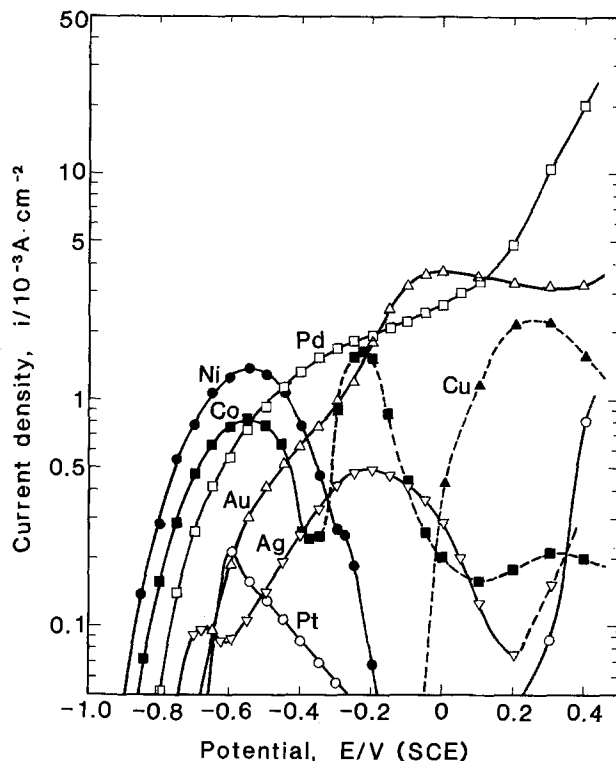


Fig. 8. Polarization curves for the anodic oxidation of dimethylamine borane (DMAB) on different metals. Bath composition: 2.0 g/dm³ DMAB + 0.2M Na-citrate + 0.5M H_3BO_3 , pH 7.0, 298 K. Dotted line: current attributable to the anodic dissolution of Cu and Co electrodes.

14, respectively. The reference potential was so selected in the Tafel region at less noble potentials in Fig. 5-9 that the temperature dependency of the current on different metals could be evaluated on the basis of a common potential. Because of difference in the shape of polarization curves and in its temperature dependency, however, all the data on different metals could not be covered by

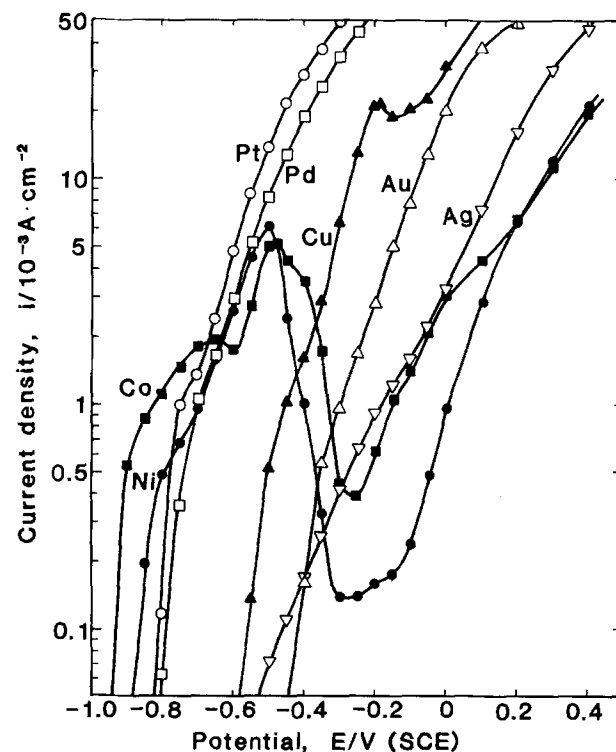


Fig. 9. Polarization curves for the anodic oxidation of hydrazine on different metals. Bath composition: 1.0M N_2H_4 + 0.175M EDTA.2Na, pH 12.0, 298 K.

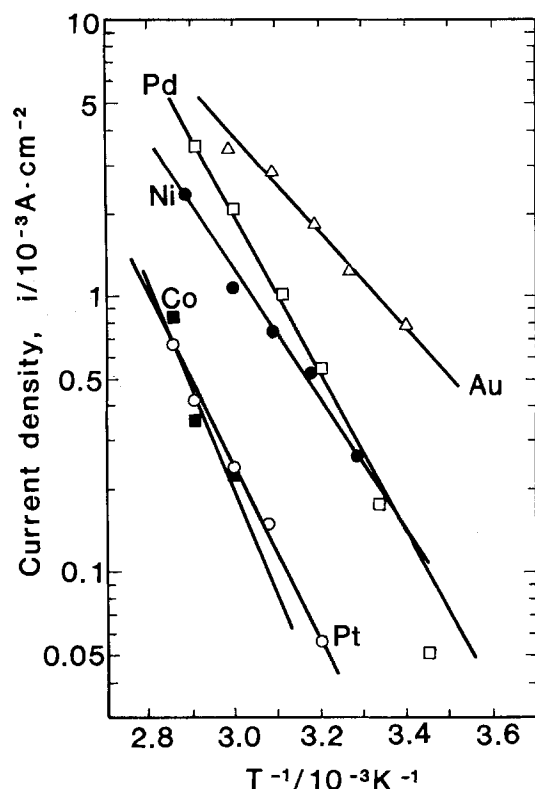


Fig. 10. Arrhenius plots of the anodic oxidation current of hypophosphite at a reference potential. Bath composition: 0.2M NaH_2PO_2 + 0.2M Na-citrate + 0.5M H_3BO_3 , pH 9.0. Reference potential (vs. SCE): -0.80V (for Au, Pd, Ni, Co), $+0.20\text{V}$ (for Pt).

single reference potential. The apparent activation energies and the frequency factors obtained from Fig. 10-14 are summarized in Table II, together with the reference potentials. The activation energies (kJ/mol) hitherto published on the rate of electroless plating in the net electroless baths are 74.1 for NiP-hypophosphite (18), 49.0 for

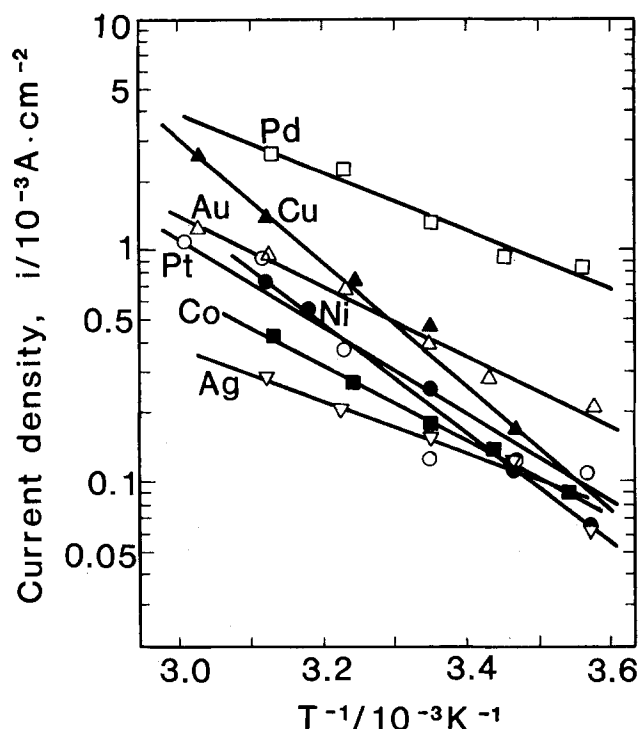


Fig. 11. Arrhenius plots of the anodic oxidation current of formaldehyde at a reference potential. Bath composition: 0.1M HCHO + 0.175M EDTA.2Na, pH 12.5. Reference potential (vs. SCE): -0.70V (for Au, Cu), -0.65V (for Ag), -0.50V (for Pt), -0.35V (for Pd), 0.40V (for Ni), 0.45V (for Co).

Cu-formaldehyde (32), 44.4-64.0 for NiB-dimethylamine borane (33), 80 for Au-borohydride (22), and 66.5 for Co-hydrazine (34). The activation energies for the anodic oxidation of reductants shown in Table II seem to be appreciably low in comparison with those for the rate of electroless plating in the net electroless baths, probably because the latter values involve the temperature depend-

Table II. Potentials at $1.0 \times 10^{-4} \text{ A/cm}^2$ (E^*), apparent activation energies (E_a), and frequency factors ($\log i^*$) for the anodic oxidation of reductants on different metals. For conditions, see the captions of Fig. 10-14

Reductants	Metal	E^* (V vs. SCE)	E_a (kJ/mol)	$\log i^*$ (10^{-3} A/cm^2)	Reference potential (V vs. SCE)
NaH ₂ PO ₂	Au	-0.982	33	5.7	-0.80
	Ni	-0.935	46	9.2	-0.80
	Pd	-0.910	54	8.9	-0.80
	Co	-0.854	88	11	-0.80
	Pt	-0.300	59	8.8	0.20
HCHO	Cu	-0.906	50	8.5	-0.70
	Au	-0.770	29	4.7	-0.70
	Ag	-0.675	29	4.3	-0.65
	Pt	-0.508	38	6.1	-0.50
	Pd	-0.464	24	4.4	-0.35
	Ni	0.366	46	7.3	0.40
	Co	0.450	31	4.8	0.45
NaBH ₄	Ni	-1.190	40	7.2	-0.95
	Co	-1.180	40	8.2	-0.95
	Pd	-1.136	54	10	-0.95
	Pt	-0.983	46	8.4	-0.95
	Au	-0.850	39	7.4	-0.70
	Ag	-0.832	46	7.4	-0.70
	Cu	-0.761	46	7.3	-0.70
DMAB	Ni	-0.866	35	6.2	-0.55
	Co	-0.832	37	6.3	-0.55
	Pd	-0.766	41	7.1	-0.55
	Au	-0.650	42	6.8	-0.55
	Pt	-0.633	14	1.6	-0.55
	Ag	-0.565	50	8.0	-0.55
NH ₂ NH ₂	Co	-0.940	31	5.7	-0.75
	Ni	-0.871	33	5.5	-0.75
	Pt	-0.800	17	3.0	-0.75
	Pd	-0.797	38	6.1	-0.75
	Cu	-0.556	33	5.3	-0.50
	Ag	-0.460	42	6.3	-0.50
	Au	-0.413	59	8.1	-0.50

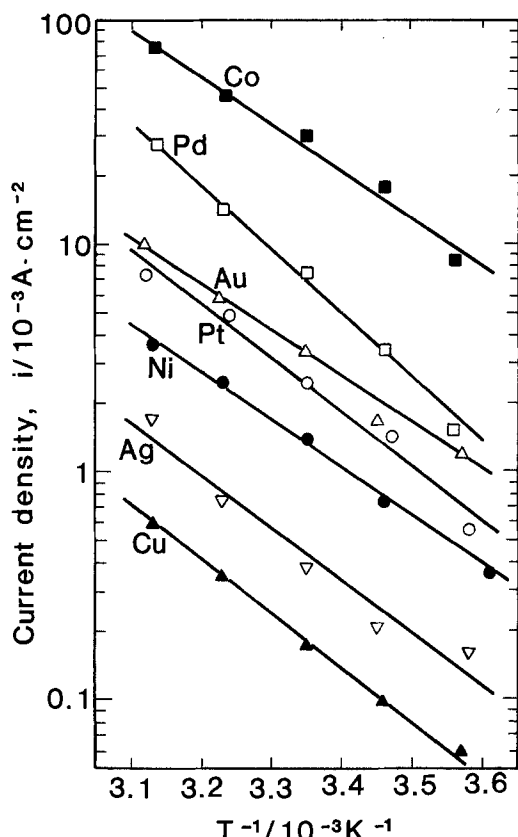
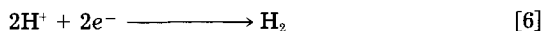


Fig. 12. Arrhenius plots of the anodic oxidation current of borohydride at a reference potential. Bath composition: 0.03M NaBH₃ + 0.175M EDTA.2Na, pH 12.5. Reference potential (vs. SCE): -0.95V (for Pt, Pd, Ni, Co), -0.70V (for Au, Ag, Cu).

encies of the rate of cathodic metal deposition and of the dissolution equilibrium of complex ion.

Hydrogen evolution during anodic oxidation of reductant.—Before the polarization experiments start, evolution of hydrogen gas was observed on some electrodes at open-circuit condition, especially in the solutions containing either hypophosphite or borohydride or dimethylamine borane. With shifting the potential to noble potentials, however, hydrogen evolution on cobalt, nickel, palladium, and platinum electrodes decreased and finally ceased. Therefore, it is probable that the hydrogen evolution in open circuit is attributable to the cathodic proton discharge under mixed potential control, thus



On the other hand, the rate of hydrogen evolution on copper, silver, and gold electrodes increased with shifting the potential to noble direction, regardless of the nature of the reductant. This means that the reductants are anodically oxidized on copper, silver, and gold electrodes accompanied by evolution of hydrogen gas that is originated from the reductant molecule. Accordingly, it is likely that the anodic oxidation of the reductants proceeds mainly along the hydrogen evolution mechanism on copper, silver, and gold, and the hydrogen ionization mechanism predominates on cobalt, nickel, palladium, and platinum.

Catalytic activity of the metal.—As is shown in Fig. 5-9, the shape of the polarization curves of anodic oxidation of the reductants varies in a complicated way depending on the natures of metals and reductants, probably because of complexity in reaction mechanism. Therefore, it seems difficult to evaluate the catalytic activity of the metal for respective reductants on the basis of a unified theoretical standard. As a first approximation, however, it can be assumed that the catalytic activities of the metals are char-

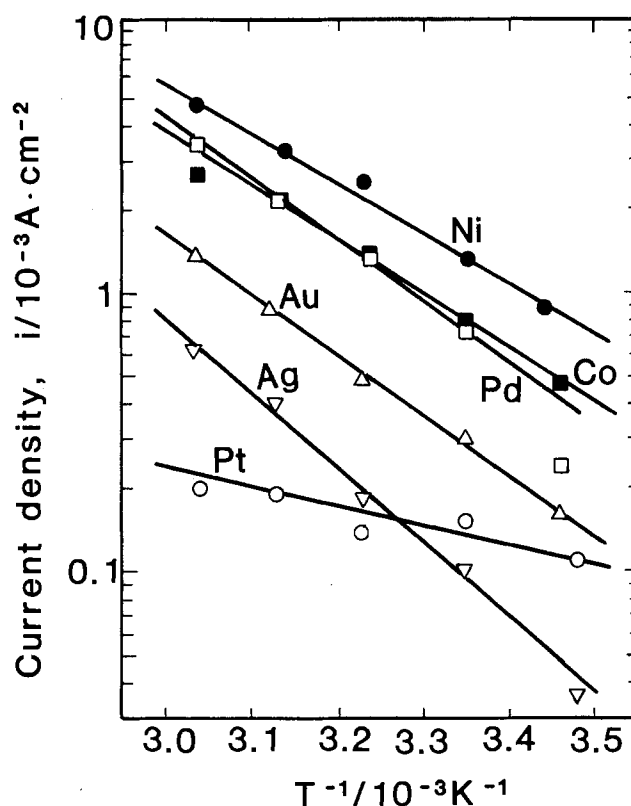


Fig. 13. Arrhenius plots of the anodic current of dimethylamine borane (DMAB) at -0.55V (vs. SCE). Bath composition: 2.0 g/dm³ DMAB + 0.2M Na-citrate + 0.5M H₃BO₃, pH 7.0.

acterized by the potential at a reference current density on the polarization curves shown in Fig. 5-9. The characteristic potentials at 1.0×10^{-4} A/cm² are summarized in Fig. 15. The oxidation-reduction potentials of the reductants and the reversible hydrogen potentials in respective solutions are also indicated in Fig. 15.

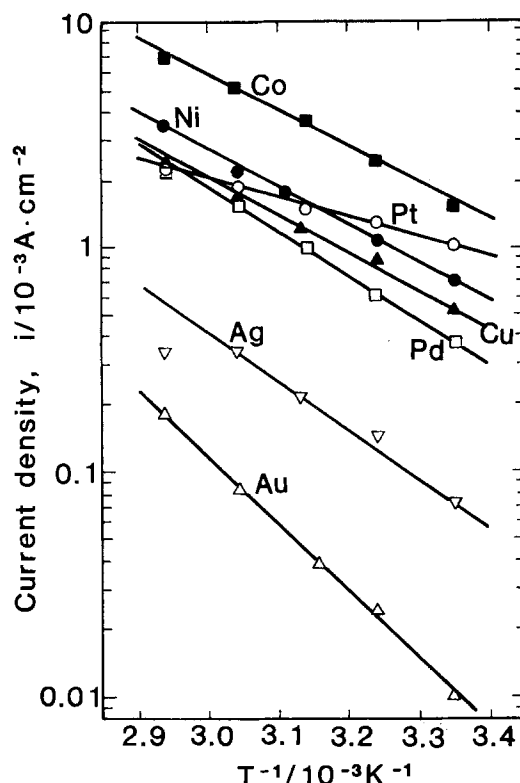


Fig. 14. Arrhenius plots of the anodic oxidation current of hydrazine at a reference potential. Bath composition: 1.0M N₂H₄ + 0.175M EDTA.2Na, pH 12.0. Reference potentials (vs. SCE): -0.75V (for Pt, Pd, Ni, Co), -0.50V (for Au, Ag, Cu).

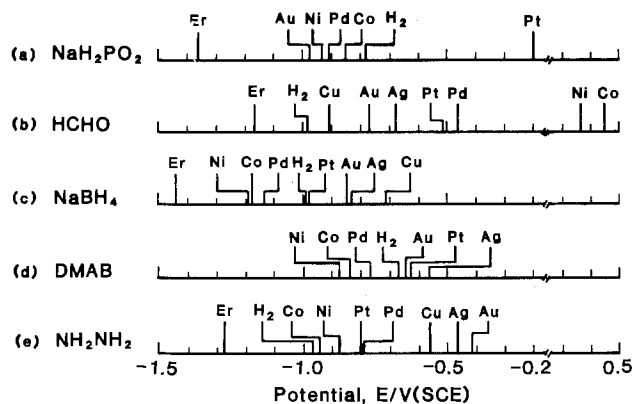


Fig. 15. Catalytic activities of metals (the potentials at 10^{-4} A \cdot cm $^{-2}$), for anodic oxidation of different reductants. E_r : oxidation-reduction potentials of reductants. H_2 : reversible hydrogen potentials. Conditions: (a) 0.2M NaH $_2$ PO $_2$ + 0.2M Na-citrate + 0.5M H $_3$ BO $_3$, pH 9.0, 343 K; (b) 0.1M HCHO + 0.175M EDTA.2Na, pH 12.5, 298 K; (c) 0.03M NaBH $_4$ + 0.175M EDTA.2Na, pH 12.5, 298 K; (d) 2.0 g/dm 3 DMAB + 0.2M Na-citrate + 0.5M H $_3$ BO $_3$, pH 7.0, 298 K; (e) 1.0M N $_2$ H $_4$ + 0.175M EDTA.2Na, pH 12.0, 298 K.

It can be seen in Fig. 15 that the catalytic activity of the metals for the anodic oxidation of different reductants decreases in the following order, respectively: Au, Ni, Pd, Co, and Pt for hypophosphite, Cu, Au, Ag, Pt, Pd, Ni, and Co for formaldehyde, Ni, Co, Pd, Pt, Au, Ag, and Cu for borohydride, Ni, Co, Pd, Au, Pt, and Ag for dimethylamine borane, Co, Ni, Pt, Pd, Cu, Ag, and Au for hydrazine. Although there is no simple rule governing these orders, it is noted that the order of the catalytic activity for borohydride is almost the same as that for dimethylamine borane. This fact seems to imply that the anodic oxidation of these two boron containing reductants involve the same adsorbed intermediate in the rate determining step as was suggested by Okinaka (3). It must be also pointed out that copper, silver, and gold are very active for the anodic oxidation of formaldehyde, whereas they are less active for the other reductants.

The requisite kinetic condition for the electroless plating taking place with a reasonable rate is the characteristic potentials being less noble to the reversible potential of the metal to be deposited. According to this approach, Fig. 15 can be utilized for choosing the reductant suitable for electroless process of respective metals. Since the reversible potentials of metals in the complex solutions that are utilized in electroless processes are mostly in the range from -0.65 to -0.45 V (SCE) (35, 36), it is said that the reductants available for depositing the metals are hypophosphite for Au, Ni, Pd, and Co, formaldehyde for Cu, Au, Ag, (Pt), and (Pd), borohydride for Ni, Co, Pd, Pt, Au, Ag, and (Cu), dimethylamine borane for Ni, Co, Pd, and (Pt), and hydrazine for Co, Ni, Pt, Pd, and (Cu). It can be seen that borohydride can be utilized for the electroless process of most metals and formaldehyde is substantially the only reductant which can be used in high speed electroless copper process. Such speculations based on Fig. 15 are in accord with the conventional usage of the reductant in electroless process.

The characteristic potentials at 1.0×10^{-4} A/cm 2 are listed in Table II, together with the activation energies. The activation energies are plotted against the characteristic potentials in Fig. 16. For the anodic oxidation of hypophosphite and dimethylamine borane, the characteristic potential shifts, except for platinum, to noble potentials with increasing the activation energy. Somewhat similar correlation is observed on hydrazine. Although the physical meaning of the activation energy is not clarified yet, the observed parallelism between the catalytic activity and the activation energy is quite acceptable from the usual understanding of chemical reaction. On the other hand, the correlation as described above is not observed for borohydride and formaldehyde. The activation energies for borohydride and formalde-

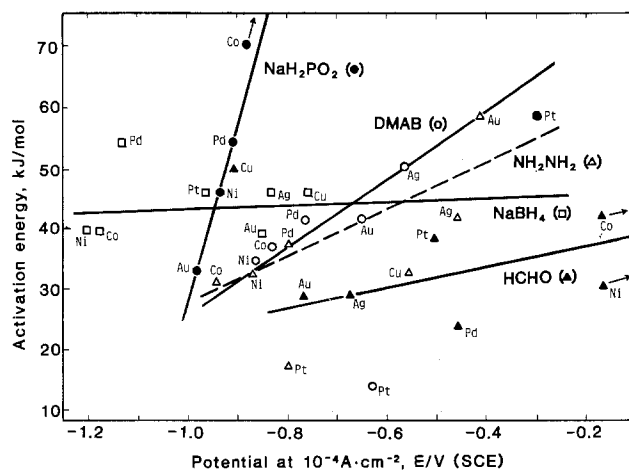


Fig. 16. Relation between activation energies and the potentials at 10^{-4} A \cdot cm $^{-2}$.

hyde scatters around 42 and 30 kJ/mol, respectively, regardless of the nature of metal.

Since the electroless plating accompanies hydrogen evolution originated from the reductant molecule, the catalytic nature in electroless plating has been often discussed in connection with that in hydrogen electrode reaction (12, 13, 16). According to Van den Meerakker (26), the anodic oxidation of the reductant proceeds along four elementary steps: dissociative adsorption, anodic oxidation of adsorbed radical, and recombination and/or ionization of adsorbed hydrogen. Namely, the adsorbed atomic hydrogen formed by dissociative adsorption of reductant is removed by either recombination or ionization, as similar with that in hydrogen electrode reaction. It is known (37) that the exchange current density of hydrogen electrode reaction decreases in the following order with metal: Pt, Pd, Ni, Co, Cu, Ag, and Au. It is probable that the anodic oxidation of the reductants proceeds mainly along the hydrogen evolution mechanism on copper, silver, and gold electrodes which are less active for hydrogen electrode reaction. Thus, it seems likely that the preferential reaction path for removing the adsorbed atomic hydrogen is related to the activity of metal for hydrogen electrode reaction. However, there is no simple correlation between the order of catalytic activity with metal for hydrogen electrode reaction and that for the anodic oxidation of the reductants. Therefore, it is not likely that the rate of anodic oxidation of the reductants is controlled by the removal of the adsorbed hydrogen. Much attention should be focused on the electrochemical step for removing the adsorbed anion radical.

Summary

The catalytic activity of metals for the anodic oxidation of different reductants in electroless plating was evaluated by the potentials at a reference current density. The catalytic activity series thus obtained serve to choose the reductant suitable to the metal to be deposited. Some correlations were observed between the catalytic activity and the apparent activation energy.

It is suggested that the anodic oxidation of the reductants proceeds mainly along hydrogen evolution mechanism on copper, silver, and platinum, whereas the hydrogen ionization mechanism predominates on cobalt, nickel, palladium, and platinum. It is found, however, that the catalytic activity series of metal for anodic oxidation of reductants does not coincide with that for hydrogen electrode reaction.

Manuscript submitted Dec. 10, 1984; revised manuscript received May 9, 1985. This was Paper 444 presented at the New Orleans, Louisiana, Meeting of the Society, May 12-17, 1985.

Tokyo Institute of Technology assisted in meeting the publication costs of this article.

REFERENCES

- M. Saito, *J. Met. Finish. Soc. Jpn.*, **16**, 300 (1965); **17**, 14 (1966).
- M. Paunovic, *Plating*, **55**, 1161 (1968).
- Y. Okinaka, *This Journal*, **120**, 739 (1973).
- M. Matsuoka and T. Hayashi, *Denki Kagaku*, **41**, 211 (1973).
- I. Ohno, *Surf. Technol.*, **4**, 515 (1976).
- W. Machu and S. El-Gendi, *Metalloberflaeche*, **13**, 97 (1959).
- C. H. de Minjer, *Electrodeposition Surf. Treat.*, **3**, 261 (1975).
- P. L. Gavallotti and G. Salvago, *Electrochim. Met.*, **3**, 239 (1968).
- G. Salvago and P. L. Gavallotti, *Plating*, **59**, 665 (1972).
- P. Hersh, *Trans. Inst. Met. Finish.*, **33**, 417 (1955-1956).
- R. M. Lukes, *Plating*, **51**, 969 (1964).
- A. Brenner and G. E. Riddell, *J. Res. Nat. Bur. Stand.*, **37**, 1 (1946).
- F. M. Donahue, *Oberflaeche*, **13**, 301 (1972).
- K. M. Gorbunova, M. V. Ivanov, and V. P. Moiseev, *This Journal*, **120**, 613 (1973).
- K. A. Holbrook and P. J. Twist, *J. Chem. Soc. A.*, 890 (1971).
- K. M. Gorbunova, M. V. Ivanov, and A. A. Nikiforova, *Prot. Met.*, **6**, 470 (1970).
- F. Pearlstein and R. F. Weightman, *Plating*, **61**, 154 (1974).
- G. Gutzeit, *ibid.*, **46**, 1158 (1959).
- J. P. Elder and A. Hickling, *Trans. Faraday Soc.*, **58**, 1852 (1962).
- D. J. Levy, *Electrochem. Technol.*, **1**, 38 (1963).
- J. W. Dini and P. R. Coronado, *Plating*, **54**, 385 (1967).
- Y. Okinaka, *ibid.*, **57**, 914 (1970).
- J. P. Randin and R. F. Weightman, *ibid.*, **54**, 523 (1967).
- A. Molenaar, M. F. E. Holdrinet, and L. K. H. van Beek, *ibid.*, **61**, 238 (1974).
- J. Dumesic, J. A. Koutsky, and T. W. Chapman, *This Journal*, **121**, 1405 (1974).
- J. E. A. M. Van den Meerakker, *J. Appl. Electrochem.*, **11**, 395 (1981).
- I. Ohno and S. Haruyama, *Surf. Technol.*, **13**, 1 (1981).
- I. Ohno, M. Suzuki, and S. Haruyama, "Proceedings of the First AES Electroless Plating Symposium," American Electroplaters' Society, Winter Park, FL (1982).
- I. Ohno, O. Wakabayashi, and S. Haruyama, *J. Met. Finish. Soc., Jpn.*, **34**, 594 (1983).
- I. Ohno, O. Wakabayashi, and S. Haruyama, *Denki Kagaku*, **53**, 190 (1985).
- I. Ohno, O. Wakabayashi, and S. Haruyama, *ibid.*, **53**, 196 (1985).
- F. L. Shippey and F. M. Donahue, *Plating*, **60**, 43 (1973).
- A. F. Schmeckenbecher, *ibid.*, **58**, 905 (1971).
- D. J. Levy, *ibid.*, **50**, 29 (1963).
- C. Milazzo and S. Caroli, "Tables of Standard Electrode Potentials," Project of the IUPAC Electrochemistry Commission, John Wiley and Sons, New York (1978).
- I. Ohno and S. Haruyama, *Bull. Jpn. Inst. Met.*, **20**, 979 (1981).
- H. Kita, *This Journal*, **113**, 1095 (1966).

Copper Electrodeposition onto Moving High Resistance Electroless Films

J. F. D'Amico* and M. A. DeAngelo

AT&T Technologies, Incorporated, Princeton, New Jersey 08540

F. R. McLarnon*

Applied Science Division, Lawrence Berkeley Laboratory, Berkeley, California 94720

ABSTRACT

The electrodeposition of Cu from aqueous $\text{CuSO}_4\text{-H}_2\text{SO}_4$ electrolyte onto a high resistance moving substrate has been studied. Substrate speeds of 0.5-2.0 cm/s, average current densities of 12-50 mA/cm², input Cu thicknesses of 0.1-0.5 μm , and cell depths of 30-74 cm were employed. Measured Cu metal thickness distributions showed good agreement with those predicted by a steady-state "terminal effect" model.

The production of printed circuits by additive methods (1) is initiated by the electroless deposition of a thin (0.1 μm) conductive coating of Cu onto an insulating substrate. This coating may be patterned (1) or may be a uniform deposit over the dielectric. The thickness of this coating can then be increased to practical values (ca. 35 μm) by electrodeposition of Cu. The patterned electroless coating may be built up by electrodeposition (if the pattern is continuous) or by high speed electroless plating. The unpatterned electroless deposit will most often be used as a cathodic connection for pattern electrodeposition through a plating mask. The latter process is usually referred to as "semiadditive" plating.

Additive production methods permit an inventory of Cu metal which is smaller than that required by standard printed-circuit production methods, where the starting material is (typically) an insulating substrate clad with 35 μm thick Cu foil. The additive printed-circuit production method minimizes reliance on etching processes, which thereby enhances the process capability for definition of fine-line patterns.

Continuous or semicontinuous production of flexible printed circuits may be carried out by passing a sheet of substrate material through a series of processing tanks, using rollers to guide the substrate along its desired path.

*Electrochemical Society Active Member.

A schematic diagram of the electrodeposition portion of such a continuous processing machine is illustrated in Fig. 1. Electrodeposition apparatus similar to that shown might be expected to increase the thickness of the Cu deposit from 0.1 to 5 μm . The apparatus, with dimensions as shown in Fig. 1, accommodates substrate speeds of 1-5 cm/s in order to be compatible with the remainder of the additive process. Economic constraints dictate that the apparatus should be compact and have the capability of operating at high current densities.

Previous studies by D'Amico *et al.* (2) showed that practical current densities in the electrodeposition apparatus (Fig. 1) were well below mass-transfer-limited values. Measurements of Cu thickness distributions indicated that this limitation was a consequence of highly nonuniform current distributions; the local current density was a strong function of axial position of the substrate in the apparatus. This highly nonuniform current density distribution was attributed to the so-called "terminal effect" (3), caused by the relatively high resistance (small Cu thickness) of the substrate on which the Cu metal is electrodeposited. Another source of nonuniform current distribution is the uneven division of current between different loops of Cu-clad substrate connected to one or more metallic rollers that are held at the same cathodic potential. Proportionately more current is distributed to sub-

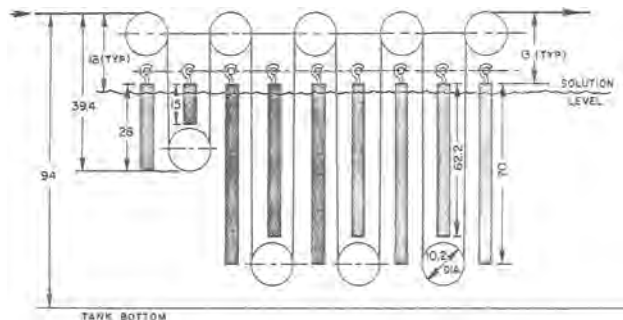


Fig. 1. Schematic diagram of a continuous, multipass electrodeposition apparatus. The five top rollers (stainless steel) are parallel-connected cathodes. The (hanging) copper bars are parallel-connected anodes. A side view of the complete apparatus is shown. A plan view of a single section is similar to that presented in Fig. 2. All dimensions are in centimeters.

strate loops with thicker Cu deposits; *i.e.*, higher currents are observed closer to the location where the substrate exits the electrodeposition apparatus. D'Amico *et al.* evaluated several designs that provided more even current density distributions, including "field shields," additional cathode connections located within the electrolyte phase, and shorter loops near the location where the substrate enters the electrodeposition apparatus.

The purpose of the present work is to apply basic models of current density distribution to evaluate measured Cu deposit thickness variations in a pilot-scale continuous electrodeposition apparatus. It is expected that these models can be used as a predictive basis for the design of full-scale electrodeposition equipment employed in the production of printed circuits by additive methods.

Other investigators have studied the problem of non-uniform current density distribution during electrodeposition onto a substrate of high ohmic resistance. Both steady-state (3) and transient (4) analyses of the current density distribution on resistive, stationary plane-parallel electrodes have been performed, and the transient current density distribution on a resistive, stationary wire electrode has been studied (5). The problem of nonuniform current density distribution during electrodeposition onto a moving wire electrode of high ohmic resistance has been analyzed (6, 7). Both steady-state (8) and transient (9) analyses of forced-convection mass transfer to a moving sheet electrode of negligible resistance have been performed. None of these investigations has studied the problem of nonuniform current density distribution along resistive, moving plane-parallel electrodes.

Experimental

Electrodeposition apparatus.—Copper electrodeposition was carried out in the "single-pass" cell shown in Fig. 2. This cell is intended to model a single loop of a "multipass" apparatus, such as that shown in Fig. 1. The anodes were 0.64 cm thick, 15.2 cm wide oxygen-free, high conductivity Cu sheets of various lengths. The 6.5 cm wide, 0.05 mm thick polyimide (du Pont Kapton®) flexible substrate material, initially coated with a 0.1-2.5 μm layer of Cu (unpatterned), passed over 3.5 cm diam stainless steel rollers, which served not only to guide the substrate through the cell, but also to make electrical contact to the substrate. Electrical connection to the substrate on the side not in contact with these rollers was made through numerous Cu-plated through-holes in the

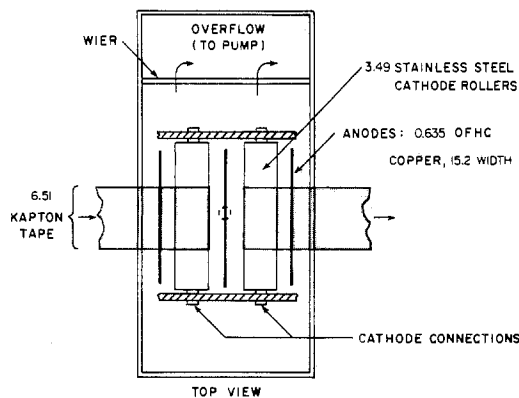


Fig. 2. Schematic diagram of electrodeposition cell. A side view of the cell is shown in the lower portion of the figure, and a plan view of the cell is shown in the upper portion of the figure. All dimensions are in centimeters.

substrate, as described previously in Ref. (2). Anode/cathode spacings were 1.9 and 5.7 cm, as shown in Fig. 2. A mean electrode separation of 3.8 cm was employed in the subsequent analysis. Average electrolyte flow velocities were 2.8-3.8 cm/s.

Electrolyte.—The electrolytes used were acid copper sulfates, having compositions and conductivities as listed in Table I. Electrolytes I and II were proprietary compositions, Cubath I® and Cubath II® supplied by Sel-Rex Company (Nutley, New Jersey). Electrolyte III was a 50-50 (volume percent) mixture of I and II. In addition to the sulfate ingredients listed, these baths contained trace amounts of electroplating additives, including 30 ppm Cl^- . These additives are expected to have little effect on the electrolyte conductivity.

The conductivities reported in Table I were measured with a direct reading conductance bridge (Industrial Instruments, Incorporated) at 1 kHz. The conductance cell was platinum-glass, with a cell constant of 1.0 cm^{-1} . Measurements were made at 22°-24°C in reagent-grade $\text{CuSO}_4 \cdot \text{H}_2\text{SO}_4$ mixtures. The conductivity of electrolyte III was not measured, so an interpolated value $\kappa = 0.319$ was used in subsequent calculations.

Table I. Electrolyte properties

Electrolyte	Concentrations (mol/liter)		Conductivity ($\Omega^{-1}\text{-cm}^{-1}$)
	CuSO_4	H_2SO_4	
I	0.27	1.76	0.475
II	0.90	0.57	0.162
III	0.59	1.17	—

The electrolyte temperature was maintained at 22°–25°C, and it was continuously pumped through polypropylene and carbon filters in a recirculation loop. The electrolyte composition was monitored by periodic measurement of Cu^{2+} , pH, and Cl^- . Electrolyte losses due to water evaporation and mechanical loss (*i.e.*, the small amount of electrolyte that adhered to the substrate) were compensated for by periodic additions of H_2O , CuSO_4 , H_2SO_4 , and/or HCl, as necessary.

Electrodeposition experiments.—Electroless Cu-clad substrate was passed through the electrodeposition cell shown in Fig. 2. After setting the substrate speed and cell current, the cell was operated for an interval corresponding to three to four times the substrate residence time within the electrolyte, in order to assure that steady-state conditions were reached. The cell circuit was then opened and the substrate movement was simultaneously halted. The two locations where the substrate rested at the top of the stainless-steel rollers were marked on the substrate, and the substrate was then fed out of the cell at 3 cm/s. This procedure resulted in an open-circuit residence time within the electrolyte of not more than 1 min. Other experiments showed that during a 1 min interval, not more than 0.01 μm of Cu would be etched by the $\text{CuSO}_4/\text{H}_2\text{SO}_4$ electrolyte. This amount of etching could create errors as high as 10% (near the entrance to the cell) in subsequent determinations of Cu thickness.

Copper thicknesses were determined by weighing the deposited metal. The substrate was cut in to 3.2 cm long specimens, which were then weighed on a Mettler H-15 balance (accuracy of approximately 0.1 mg). The specimens were then dipped in dilute HNO_3 solution to remove the Cu metal, and the substrate was dried and reweighed to arrive at the net weight of Cu metal. The weight of the 3.2 cm long Cu-free substrate was 135 mg. The standard bulk Cu density of 8.93 g/cm^3 and the measured specimen area of 40 cm^2 (both sides) was used to calculate the average Cu metal thickness on the specimen.

Analysis

A complete analysis of the electrodeposition cell used in this study would necessarily consider the interrelated electric-field, kinetic, hydrodynamic, and mass-transfer effects, as well as the spatially and temporally variable ohmic resistance of the cathode substrate. However, consideration of the conditions that exist in a continuous electrodeposition cell suggests that the following approximations may be made (refer to the cell geometry shown in Fig. 3). (i) The anode/cathode separation is typically much smaller than the depth and width of electrodes, so the primary current density distribution (in the limiting case where the cathode substrate resistance is zero) is fairly uniform. (ii) The electrolyte is continuously agitated by pumping, so that concentration and temperature gradients within the cell are relatively small. Mass-transfer limiting conditions are not approached anywhere in the cell. (iii) The net thickness change ($\leq 35 \mu\text{m}$) of electrodeposited metal in a multiloop electrodeposition apparatus (Fig. 1) is much smaller than the anode/cathode separation. Therefore, provided that electrodeposition conditions lead to a uniformly smooth metal deposit, the anode/cathode separation is constant. (iv) The net Cu electrodeposit thickness change (0.5–5 μm) over the cathode substrate length L (which corresponds to one-half of a loop in a multiloop electrodeposition apparatus) is small relative to the local electrodeposit thickness (0.1–35 μm). This approximation is most likely to be valid near the exit of the electrodeposition apparatus where the metal deposit is relatively thick, and it is least likely to be valid near the entrance to the device where the metal deposit is relatively thin. However, it has been shown (2) that it is appropriate to use lower currents and shorter loops (smaller values of L) where the metal deposit is relatively thin, which leads to a smaller net Cu electrodeposit thickness change per loop near the entrance to the device. This approximation permits the effective resistance of the

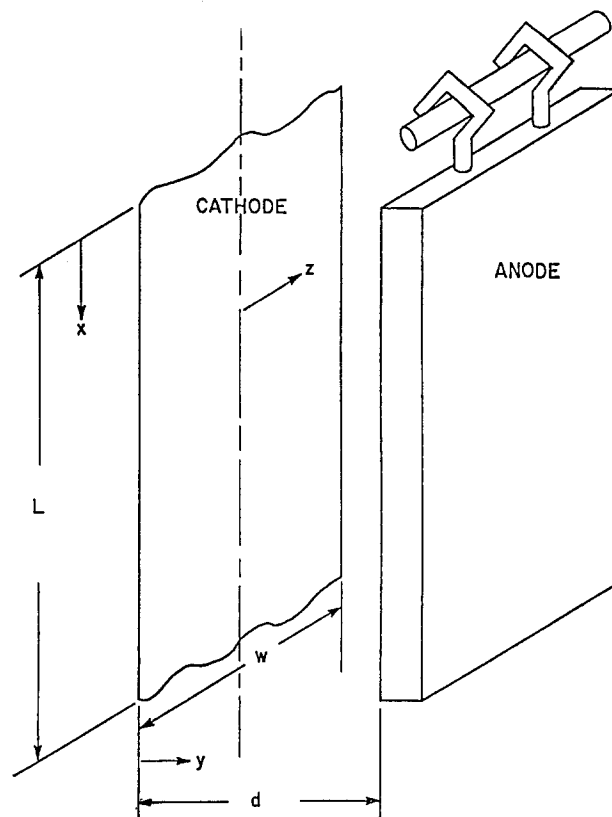


Fig. 3. Cell coordinate system

cathode substrate to be defined by a single value that is characteristic of the average (*i.e.*, averaged over the Z-direction) thickness of the Cu deposit at some location $0 \leq x \leq L$. (v) Because the Cu metal is either shielded (upward facing side of the cathode substrate) or remote (downward facing side of the cathode substrate) from the anodes, little metal deposition (or dissolution) occurs as the cathode substrate passes around the lower guide roller ($x > L$). (vi) Negligible rates of metal deposition (or dissolution) occur after the cathode substrate leaves the electrolyte phase and enters air. (vii) The electrode kinetics for Cu electrodeposition on the cathode substrate and Cu electrodisolution from the anode may be described by linear expressions. This should be a good approximation if the cell design leads to a fairly uniform current density distribution, because even if the levels of current density correspond to operation in the Tafel region, the Tafel expression can be linearized if there are only small excursions from average current density values. (viii) The electrodeposition process is 100% efficient, *i.e.*, there are no side reactions such as H_2 evolution. (ix) Steady-state conditions prevail.

By making the nine approximations listed above, it is possible to treat each half-cell as a classical steady-state "terminal effect" problem, solved by Tobias and Wijnsman (3). They found the current density distribution to be a strong function of a single parameter ϕ (defined in Eq. [2]), that represents the ratio of the electrode resistance to the electrolyte resistance, and identified conditions under which a simplified model could be applied. Their results show that the simplified model can be used when $d/L < 0.1$, $(\lambda_o + \lambda_a)$ is not $\gg 1$, and $(\mu_o + \mu_a)$ is not $\gg 1$. For the conditions employed in the present work, $0.05 < d/L < 0.12$, $0.04 < (\lambda_o + \lambda_a) < 4.0$, and $0.02 < (\mu_o + \mu_a) < 0.06$. Even when $d/L = 0.12$, the computed results shown in Fig. 10 of Ref. (3) suggest that the simplified model will predict values of local current densities that fall within about 2% of those calculated for the exact solution, $0.05 < x/L < 1$. The simplified model is easier to apply than the exact model, and it thereby permits rapid estimation of the current density distributions that will result from various designs of the electrodeposition apparatus. The simplified Tobias-Wijnsman model can now be ap-

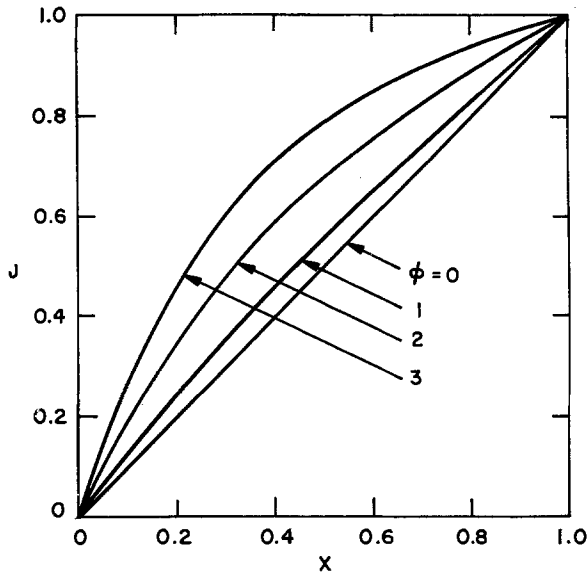


Fig. 4. Dimensionless current per unit cathode substrate width for various values of the parameter ϕ .

plied directly. The dimensionless current J per unit width (in the Z -direction) of Cu is given by

$$J(X) = 1 - \frac{\sinh[\phi(1 - X)]}{\sinh \phi} \quad [1]$$

where

$$\phi^2 = \frac{\rho_e \kappa L^2}{T(d + 2\kappa b)} \quad [2]$$

is a parameter related to the ratio of the X -direction potential gradient in the resistive cathode substrate to the potential gradient in the electrolyte phase. The corresponding local current density distribution is given by

$$\frac{i(X)}{i_{avg}} = \phi \frac{\cosh[\phi(1 - X)]}{\sinh \phi} \quad [3]$$

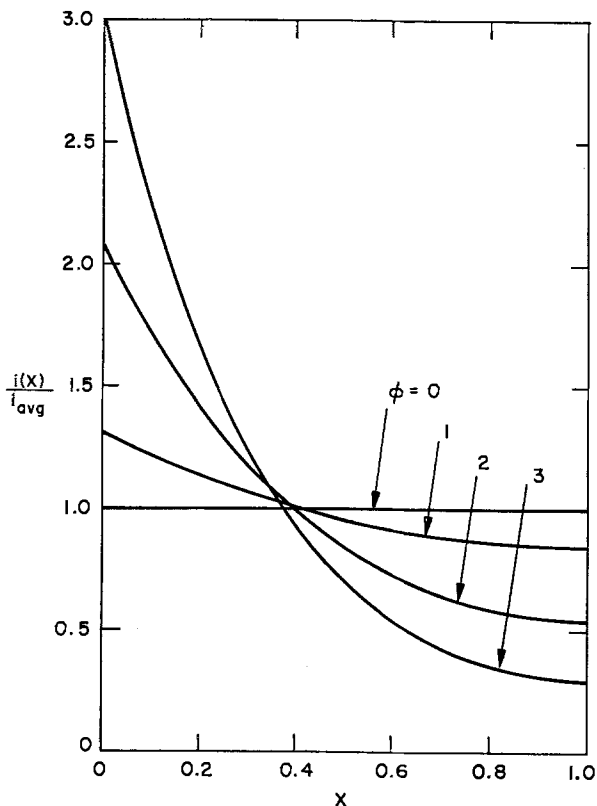


Fig. 5. Dimensionless current density distributions for various values of the parameter ϕ .

Equations [1] and [3] are plotted in Fig. 4 and 5, respectively, for various values of the parameter ϕ . Small values of ϕ correspond to uniform local current densities and a linear variation of J vs. X . Large values of ϕ correspond to nonuniform local current densities and a nonlinear variation of J vs. X .

The local Cu metal thickness can be related to the local current density through Faraday's law

$$T(x) = T(0) + \frac{M}{nF\rho v} \int_0^x i(x) dx \quad [4]$$

or it may be equivalently related to the current per unit width (in the Z -direction) of Cu

$$T(x) = T(0) + \frac{M}{nF\rho v} j(x) \quad [5]$$

Equations [1] and [5] can be combined to predict the axial distribution of Cu metal thickness in the electrodeposition cell.

Results and Discussion

Electrolyte composition, loop depth, substrate speed, cell current, average cathodic current density, and entering Cu deposit thickness are listed for ten separate experiments in Table II. The measured steady-state axial Cu thickness distributions are shown as the filled circles in Fig. 6-10.

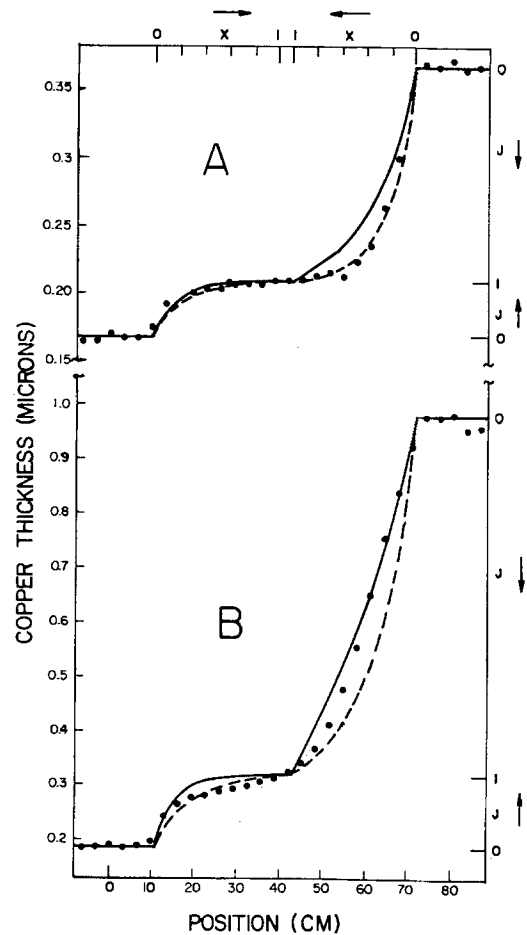


Fig. 6. Axial Cu thickness distributions. Lower abscissa: distance along cathode substrate (cm). Upper abscissa: dimensionless axial distance x/L . Left ordinate: Cu thickness (μm). Right ordinate: dimensionless Cu thickness $J(X)$. Dashed line: dimensionless thickness distribution $J(X)$, computed using the Cu thickness at the lower guide roller location $x = L$ to calculate the effective substrate resistivity ρ_e . Solid line: dimensionless thickness distribution $J(X)$, computed using the Cu thickness where the substrate enters the electrolyte (for the portion of the solid curve to the left of the inflection point), or where the substrate leaves the electrolyte (for the portion of the solid curve to the right of the inflection point). Solid circles: measured axial Cu thickness distributions. The experimental parameters employed for the data shown in the upper half (A) and lower half (B) of the figure are listed in Table II.

Table II. Experimental conditions

Figure	Electrolyte ^a	L (cm)	v (cm/s)	I (A)	i_{av} (mA/cm ²)	T(0) (μ m)
6A	I	30.5	1.45	9.3	11.7	0.17
6B	I	30.5	0.55	14.7	18.5	0.19
7A	I	30.5	1.93	23.2	29.2	0.51
7B	I	30.5	1.09	23.0	29.2	0.50
8A	I	30.5	0.53	23.2	29.2	0.41
8B	I	30.5	0.54	32.9	41.5	0.44
9A	II	30.5	0.78	11.5	14.5	0.08
9B	II	30.5	0.78	40.1	50.5	0.08
10A	III	74.1	1.94	45.3	23.5	0.54
10B	III	74.1	1.06	45.5	23.6	0.51

^a See Table I.

The Cu deposit resistivities were measured using the standard four-point probe method. Strips 1.27 cm wide and 15.2 cm long were cut from sections of the plated substrate, and their resistances were measured on a special fixture designed to accommodate these specimens. The copper thickness of the same specimens was then determined using the weighing method previously described. This method requires that the deposit density be known, and the literature value for electrolytic copper was used for both electroless and electroplated Cu. The density of electroless Cu is reported (10) to be only a few percent lower than that of electrolytic Cu.

Electroplated Cu deposit resistivity ρ_e was 2.0×10^{-6} Ω -cm, which is close to the literature value of 1.8×10^{-6} Ω -cm. Electroless Cu deposit resistivity was three times higher, 6.0×10^{-6} Ω -cm. The linear polarization parameter $b = 1.3$ Ω -cm² was estimated by linearizing Cu electrode kinetic data, reported by Turner and Johnson (11), about the average cathode current density. The use of a single polarization parameter will not account for asymmetry of the anodic and cathodic polarization curves, nor will it apply when there are large variations in local current density [see approximation (*vi*) above]. However, the effect

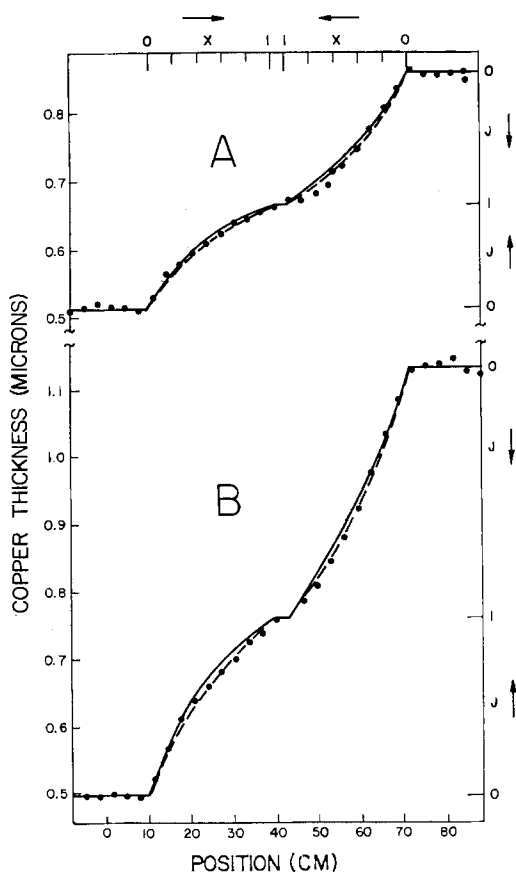


Fig. 7. Axial Cu thickness distributions. Designations are identical to those listed in the caption for Fig. 6.

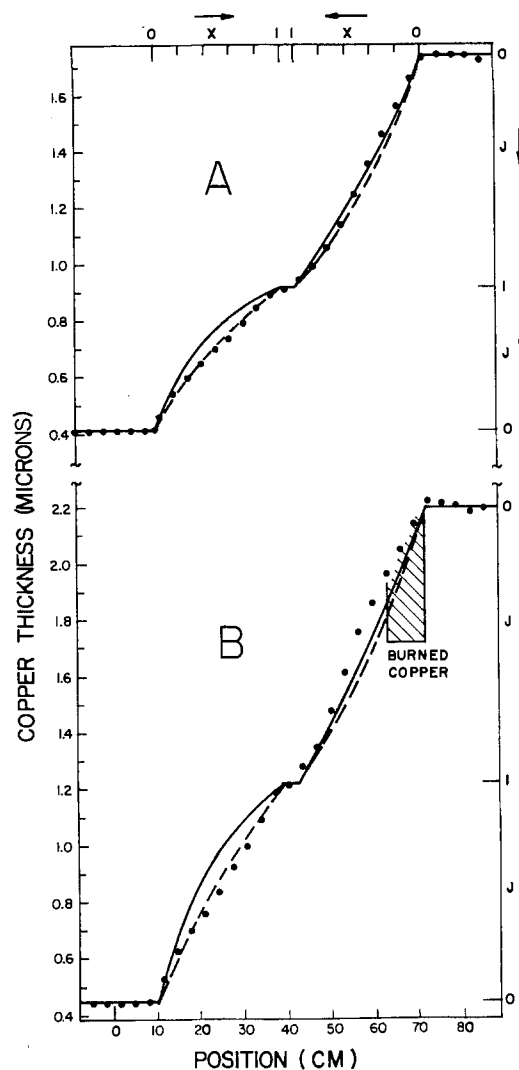


Fig. 8. Axial Cu thickness distributions. Designations are identical to those listed in the caption for Fig. 6.

of electrode kinetics on the current density distribution is expected to be relatively small. This effect can be estimated from the magnitude of the last term in the denominator of Eq. [2]; even if this term is neglected, there results only a 5-15% error in the value of ϕ , which corresponds to a similar error in the associated current density distribution Eq. [3]. The assumption that both the anode and cathode exhibit the same linear electrode kinetic behavior, which is consistent with the assumptions made in the derivation of Eq. [2], is therefore expected to lead to small errors in calculated current density distributions and metal thickness distributions. Values of the computed dimensionless parameter ϕ ranged from 0.7 to 6.0.

Computed dimensionless thickness distributions $J(X)$ are plotted as the dashed and solid curves in Fig. 6-10. The dashed curves correspond to the value of ϕ calculated using the measured Cu deposit thickness at the bottom guide roller. The solid curves to the left of the inflection points correspond to the value of ϕ calculated using the measured Cu deposit thickness on the substrate as it enters the electrolyte [*i.e.*, $T(0)$ listed in Table II]. The solid curves to the right of the inflection points correspond to the value of ϕ calculated using the measured Cu deposit thickness on the substrate as it leaves the electrolyte. The solid and dashed curves therefore represent extremes of effective cathode substrate resistivity along a single half-loop. The spread between the solid and dashed curves indicates the uncertainty associated with employing a single value of Cu deposit thickness to characterize the effective resistance of the cathode substrate.

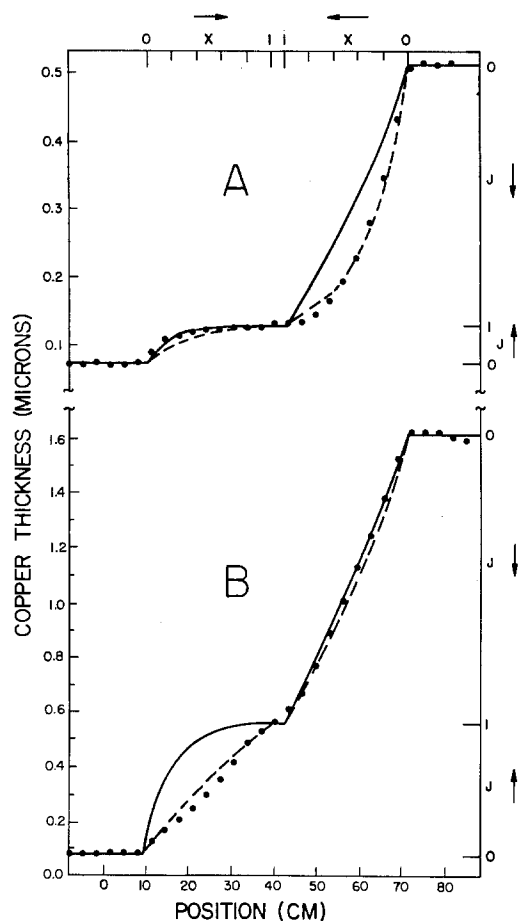


Fig. 9. Axial Cu thickness distributions. Designations are identical to those listed in the caption for Fig. 6.

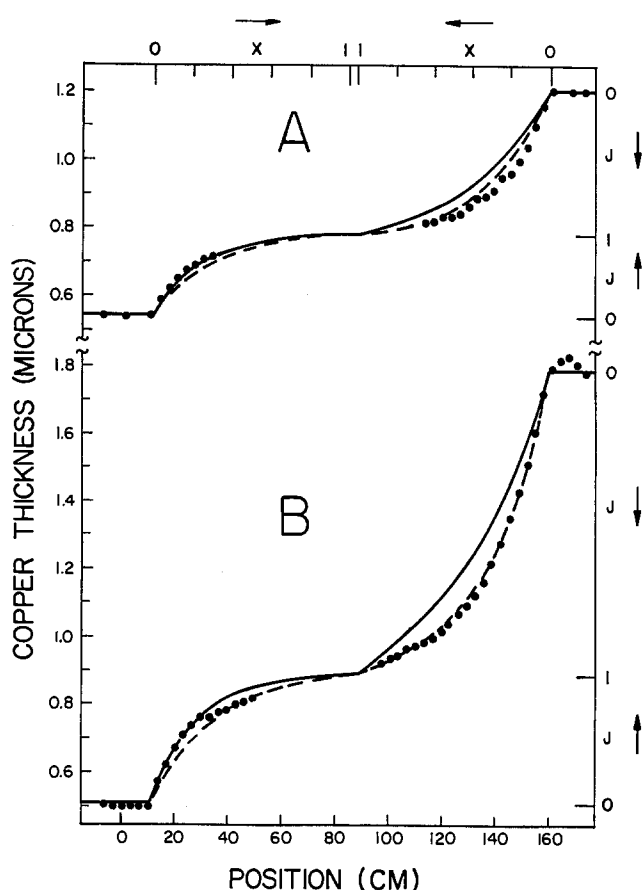


Fig. 10. Axial Cu thickness distributions. Designations are identical to those listed in the caption for Fig. 6.

For example, the large spread between the solid and dashed curves to the left of the inflection point on Fig. 9B suggests that the use of a single value of Cu deposit thickness to compute a characteristic value of ϕ may lead to considerable error. In this case, the experimental parameters give rise to an increase in Cu deposit thickness from 0.08 to 0.55 μm , which violates the conditions leading to approximation (iv). The failure of the present analysis to accurately predict the measured axial Cu thickness distribution to the left of the inflection point in Fig. 9B is, therefore, not unexpected.

Another case where the predicted axial thickness distributions do not agree well with the measured distributions is in Fig. 8B, where the measured thickness distribution is more uniform than that predicted. Note that a relatively high average current density of 41.5 mA/cm^2 was employed with the low Cu^{++} -concentration electrolyte, and a discolored ("burned") Cu electrodeposit was observed near the location where the substrate exits the cell. These observations suggest that mass-transfer limiting conditions were approached, which violates approximation (ii). Again, therefore, it is not surprising that in Fig. 8B the measured axial thickness distributions do not agree well with those predicted.

Figures 6-10 show that the "terminal-effect" model provides a good basis for predicting axial metal thickness distributions (and the associated current density distributions Eq. [4]) under a range of electrolyte compositions, cell depths, substrate velocities, average current densities, and initial Cu thicknesses. The uniformity of current density distribution (linearity of Cu thickness distribution) is enhanced by: (i) more shallow loops (cf. Fig. 7A and 10A), (ii) thicker initial Cu deposits (cf. Fig. 6B and 7B), (iii) slower substrate speeds (which leads to thicker Cu electrodeposits) (cf. Fig. 7A and 7B), (iv) higher average current densities (which leads to thicker Cu deposits) (cf. Fig. 9A and 9B), and (v) lower electrolyte conductivity (see Eq. [2]).

Conclusions

The steady-state "terminal effect" model has been shown to provide a good basis for the prediction of axial metal thickness distributions along a resistive cathode substrate in a continuous electrodeposition cell. Good agreement between predicted and measured thickness distributions is found for a wide range of experimental parameters; for example, the dimensionless parameter ϕ ranged from 0.7 to 6.0. These results indicate that the current density distribution is typically determined by the value of ϕ , which includes several factors: ohmic potential drop in the resistive cathode, ohmic potential drop in the electrolyte, kinetic overpotential at the electrodes, and cell geometry. Other factors, such as the concentration overpotential, are of secondary importance. Conditions leading to cases where the model may not apply have been identified; these conditions can correspond to cell designs and operating parameters (e.g., those leading to local mass-transfer limiting currents) that can produce electrodeposited metal exhibiting undesirable properties.

Acknowledgment

Manuscript submitted March 15, 1985; revised manuscript received June 26, 1985. This was Paper 270 presented at the Washington, DC, Meeting of the Society, May 2-7, 1976.

AT&T Technologies, Incorporated, assisted in meeting the publication costs of this article.

LIST OF SYMBOLS

b	kinetic polarization parameter ($\Omega\text{-cm}^2$)
d	anode/cathode separation (cm)
F	Faraday constant (C/eq)
i	local current density (A/cm^2)
i_{avg}	average current density (A/cm^2)
I	cell current (A)
j	current per unit substrate width (A/cm)
J	$j(x)/j(L)$

L	electrode length (cm)
M	molecular weight of electrodeposited metal (g/mol)
n	cation valence (eq/mol)
T	metal deposit thickness (cm)
v	substrate speed (cm/s)
w	electrode width (cm)
x	axial coordinate (cm)
X	x/L
z	horizontal coordinate (cm)
κ	electrolyte conductivity ($\Omega^{-1}\text{-cm}^{-1}$)
λ_0, λ_d	dimensionless parameter $\rho_e \kappa L/T$ for the electrodes at $y = 0$ and $y = d$, respectively
μ_0, μ_d	dimensionless parameter $\kappa b/L$ for the electrodes at $y = 0$ and $y = d$, respectively
ρ	density of electrodeposited metal (g/cm^3)
ρ_e	resistivity of electrodeposited metal ($\Omega\text{-cm}$)
ϕ	dimensionless parameter (Eq. [2])

REFERENCES

1. J. F. D'Amico, M. A. DeAngelo, J. F. Henrickson, J. T. Kenney, and D. J. Sharp, *This Journal*, **118**, 1695 (1971).
2. J. F. D'Amico, M. A. DeAngelo, and L. D. Noble, *ibid.*, **123**, 478 (1976).
3. C. Tobias and R. Wijsman, *ibid.*, **100**, 459 (1953).
4. R. Alkire, *ibid.*, **118**, 1935 (1971).
5. R. Alkire and A. Tvarusko, *ibid.*, **119**, 340 (1972).
6. R. Alkire and R. Varjian, *ibid.*, **124**, 388 (1977).
7. R. Alkire and R. Varjian, *ibid.*, **121**, 622 (1974).
8. D. T. Chin, *ibid.*, **122**, 643 (1975).
9. R. S. R. Gorla, *ibid.*, **125**, 865 (1978).
10. J. Hajdu and J. Wynschenk, Abstract 211, p. 530, The Electrochemical Society Extended Abstracts, Miami, FL, Oct. 8-13, 1972.
11. D. R. Turner and G. R. Johnson, *This Journal*, **109**, 798 (1962).

Electrochemical Production of Potassium Carbonate

F. Hine,* M. Yasuda,* Y. Ogata, and T. Kojima

Nagoya Institute of Technology, Nagoya 466, Japan

Yang Weiyi*¹

Jinxi Research Institute of Chemical Industry, China

ABSTRACT

Direct production of potassium carbonate by electrolysis of potassium chloride solution with the membrane cell was studied. The current efficiency was high since the hydroxyl ion concentration in the cathode compartment was low, resulting in minimum back-migration of OH^- through the membrane. The reduction of the cell voltage is discussed in some detail. The anode and cathode materials having low overvoltages were studied, and Nafion 423 was used as the separator. The operation of a separate reactor for carbonating the catholyte liquor is also described briefly.

Although the production capacity and the market of caustic and carbonate potash are small in comparison with the soda products, they are still important chemicals. Potassium carbonate is produced only by absorption of carbon dioxide with caustic potash, and there is no direct route from chloride such as the Solvay process for making soda ash because of the large solubility of potassium carbonate: 127g/100g H_2O compared to 46g/100g H_2O of Na_2CO_3 at 60°C (1).

Caustic potash is produced by electrolysis of potassium chloride solution. However, the current efficiency of the membrane cell is said to be low somewhat caused by small transport number of K^+ in the membrane compared to the case of NaCl electrolysis (2).

There are several publications on the electrolytic production of sodium carbonate where the caustic catholyte is carbonated to keep the OH^- concentration low, resulting in high current efficiency (3, 4). In fact, it is troublesome since sodium carbonate and bicarbonate deposit in the cathode compartment.

In the case of potassium salts, on the other hand, this process would be desirable because of no unwanted deposition (5). This paper deals with a small cell experiment and a pilot test for the direct electrolytic production of potassium carbonate from potassium chloride solution with a membrane cell followed by absorption of carbon dioxide with the catholyte effluent.

Flowsheet and Reaction Sequence

A proposed flowsheet is illustrated in Fig. 1. Concentrated and purified KCl solution is pumped to the anode compartment of the membrane cell, and its effluent is sent back to the reservoir through the gas-solution separator where chlorine gas is recovered. Polishing of the feed brine with the chelating resin column is of great importance in eliminating a trace of hardness ions so as to keep the cell performance high and in extending the membrane service life (6, 7). The depleted brine is sent to the brine treatment yard. It is not shown in this figure.

* Electrochemical Society Active Member.

¹ Exchange scholar at Nagoya Institute of Technology (1981-1982).

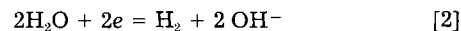
The catholyte liquor flows down from the top of the CO_2 absorption tower packed with the Raschig rings to carbonate caustic solution into carbonate, then bicarbonate after separation of hydrogen. A part of the catholyte liquor is bypassed to the second stage of the absorption tower, where carbonate is converted into bicarbonate.

Water is supplied to the catholyte reservoir to adjust the water balance and the solution concentration.

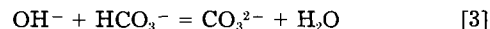
The reaction sequence is simple. In the electrolytic cell, chlorine and hydrogen are liberated at the anode and the cathode, respectively



and



Since the catholyte contains bicarbonate ions, reaction [3] takes place in the bulk of solution



The catholyte effluent is further carbonated in the absorption tower to keep the OH^- concentration low, but the bicarbonate content in the product should also be controlled.

An excess solution absorbs more CO_2 to convert into bicarbonate in the second stage of the tower

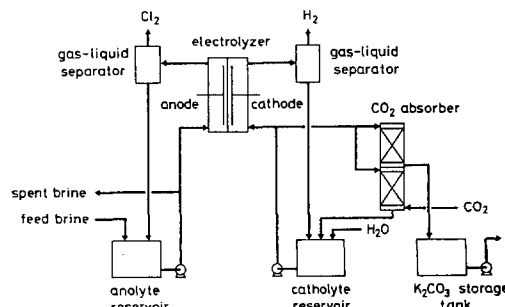
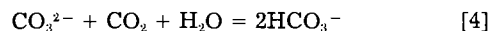


Fig. 1. Flowsheet for the electrolytic production of potassium carbonate

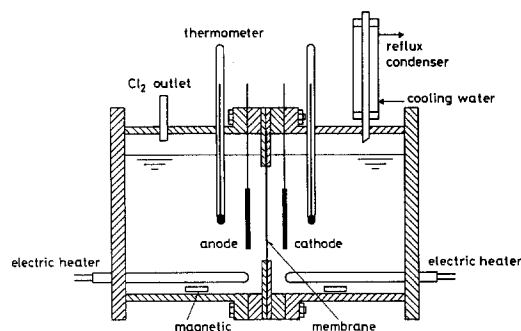


Fig. 2. A small Lucite cell

Experimental Procedure

A small Lucite cell, shown in Fig. 2, was fabricated to determine the electrode polarization, the IR drop through the membrane, and the cathode current efficiency in the batch-wise system. That is, four Luggin-Haber probes were positioned on the front of the anode and cathode, and both sides of the membrane. The Luggin probes located at the cathode compartment were connected with respective reference electrodes composed of $Hg/HgO/1M$ KOH, while the probes in the anode side were referred to the saturated calomel electrodes (SCE).

The solution gaps in both the anode and cathode compartments were large enough for the convenience of experiment.

The DSA-type ($RuO_2 + TiO_2$) anode was prepared by a conventional manner, and another material—named MODE—was also used. The MODE is a platinized Ti mesh loaded with IrO_2 as the electrode catalyst (8). A nickel sheet was used as the cathode.

The solutions, 0.2 liter each in volume at the anode and cathode sides, were agitated by the magnetically driven stirrer, and the temperature was controlled at $60^\circ C$ by electric heater.

The flowsheet of the pilot experiment was almost the same as shown in Fig. 1, with some exceptions. A major difference was the separate operation of the electrolyzer from the gas absorber.

A vertical and rectangular-type electrolytic cell, also made of Lucite resin, is illustrated in Fig. 3. The Nafion membrane of 5 cm wide and 40 cm long was flanged by two frames, and supported by the anode mesh. The

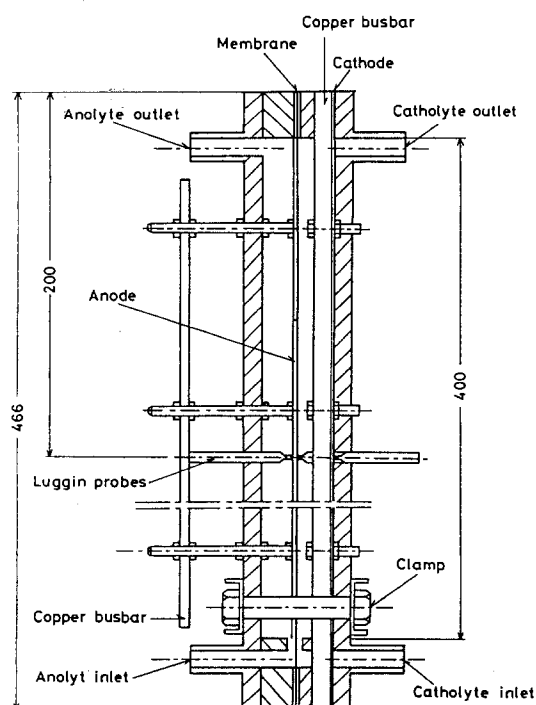


Fig. 3. A vertical cell

membrane-to-cathode gap was adjusted by a frame of a certain thickness. A MODE mesh was employed with this cell. A plain Ni sheet was mostly used as the cathode, and some experiments were conducted with an activated mesh cathode consisting of a steel coated with the Raney nickel. An alloy composed of 50% Ni and 50% Al was plasma-sprayed on a steel mesh substrate, then aluminum was leached out with hot concentrated caustic soda for a day. The apparent electrode area was about the same as of the membrane, so that the current density on both electrode and membrane was *ca.* $40 A/dm^2$ at 80A in total amperage. The current density presented in this paper is referred to the membrane surface.

Nafion membranes 315, 417, and 423 were employed. Most experiments were conducted with 423. These membranes were treated with boiling water for about an hour prior to experiment.

The temperature was controlled by the electric heater immersed in the reservoir. The solution volume was 8 liters each side. The anolyte flow was kept constant at 3 liter/min, and was large enough to keep the solution composition to be unchanged during experiment. On the other hand, the catholyte flow rate was varied in a wide range, 0.04-3.0 liter/min. All the catholyte flows through the gap between the membrane and the flat plate cathode. On the other hand, a part of the catholyte and hydrogen bubbles evolved may pass through the back-space when the mesh cathode is provided.

Potassium chloride of 4.2M in concentration was fed to the anode compartment. The catholyte was composed of a mixture of $KHCO_3$ and K_2CO_3 . The total molarity was kept constant at 2.0M, and the concentration ratio of the constituents was varied in a wide range. Its composition and concentration are not optimum, but it is just for the convenience of experiment. In practice, the higher the catholyte concentration, the higher is the performance of the cell. Potassium hydroxide was also added to the catholyte if necessary. These electrolytes were prepared with reagent-grade chemicals and deionized water. Also, the anolyte was further treated by passing through the chelating resin column when the hardness content reached unacceptable levels.

The catholyte was titrated with HCl solution and the indicator composed of methyl red and bromocresol green before and after electrolysis to evaluate the current efficiency for the cathode products. The solution composition was determined by pH titration.

A vertical cell was normally operated continuously for 30 Ah at various current densities, while a small batch cell was operated for 2.1 Ah.

Results and Discussion

As is shown in Eq. [3] and [4], the reaction of KOH with $KHCO_3$ is just a neutralization, so that OH^- and CO_3^{2-} may exist in alkaline solution. On the other hand, the solution containing excess CO_2 or HCO_3^- is composed of $KHCO_3$ plus K_2CO_3 , but no KOH. In consequence, a parameter α shown by Eq. [5] is used to represent a nature of the mixed solution or the $KOH-K_2CO_3-KHCO_3$ system instead of the molar concentration C of the components

$$\alpha = \frac{C_{CO_3^{2-}} + C_{OH^-}}{C_{HCO_3^-} + C_{CO_3^{2-}}} \quad [5]$$

At $\alpha = 1$, neither OH^- nor HCO_3^- exist in the solution; that is, the solution contains only K_2CO_3 . If $\alpha < 1$, the solution contains excess $KHCO_3$, but no KOH. On the other hand, OH^- remains in the solution, but there is no $KHCO_3$ when $\alpha > 1$. It is useful to compare the electrolyte of different composition and concentration.

Figure 4 shows an example of the current efficiency and the terminal voltage of a small cell shown in Fig. 2 as functions of α . It is clear that the current efficiency decreases when α increases, especially in the region larger than unity of α caused by a significant migration of OH^- from the cathode compartment to the anode side through the membrane. On the other hand, the cell voltage goes down with the increase of α because the IR drop between

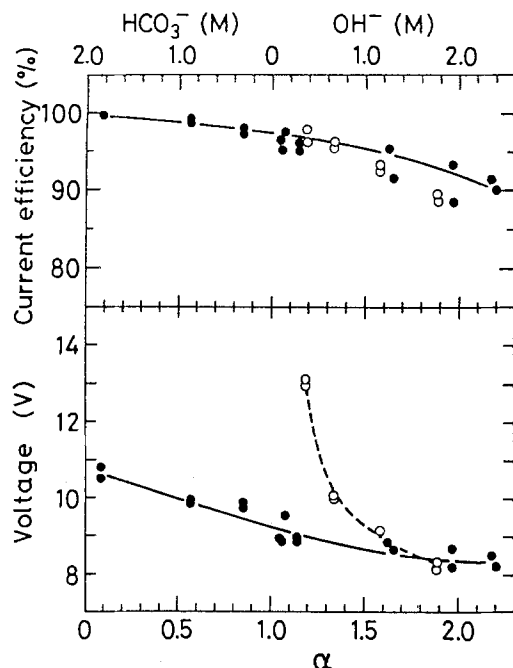


Fig. 4. Current efficiency and voltage of the small cell as functions of the solution composition. Closed points: solution containing carbonate. Open points: solution free of carbonate. Anode: DSA. Cathode: plain Ni. Membrane: Nafion 423. Anode-to-membrane gap: 27 mm. Cathode-to-membrane gap: 27 mm. Current density: 20 A/dm². Temperature: 60°C.

the cathode and the membrane decreases with the increase of the ionic strength and/or the KOH concentration. The cell voltage in this figure is very large and is shown as reference because the solution gaps in both the anode and cathode sides are large.

This figure also shows the current efficiency and the cell voltage obtained with the KOH catholyte free of carbonate. The current efficiency is almost equal to that of the cell operated with mixed solutions. It represents that the back-migration of OH⁻ through the membrane is not affected significantly by carbonate ions. The cell voltage was, of course, very high in weak solutions whereas it was almost the same as of the cell filled with mixed solutions in the concentration range of OH⁻ more than 1.5M.

The current efficiency and the voltage of the vertical cell equipped with Nafion 423 as functions of the catholyte composition are shown in Fig. 5. The current density was 20 A/dm², and the solution temperature was kept constant at 60°C. The catholyte flow was 3 liter/min or ca. 16.7 cm/s in a 6 mm gap between the flat plate cathode and the membrane. As is shown by the top draft in this figure, the current efficiency of the vertical cell was almost equal to that of the small cell described above. The cell voltage in this case is relatively low in comparison with that of the small cell because the membrane touches on the anode mesh and the cathode gap is small, but is still insufficient. The flow rate was a small factor on the current efficiency as shown in Fig. 6. Of course, electrolytic hydrogen bubbles associate with forced circulation to agitate the catholyte and to keep the solution composition uniform across the vertical cell.

At the flow rate lower than 0.1 liter/min or 0.6 cm/s, the OH⁻ concentration in the cathode compartment increases and causes the current inefficiency.

Figure 7 illustrates that the current efficiency is almost independent of the current density in the range 10-40 A/dm² if α does not exceed unity. Also, the current efficiency did not change in the temperature range 40°-70°C. The cell voltage is almost linear with the current density in the range 10-40 A/dm² (see bottom of the figure), which represents that the major factor of the cell voltage is the ohmic component, either membrane or electrolyte, rather than the overvoltage.

From the viewpoint of product quality, potassium carbonate is contaminated by either caustic potash or bicar-

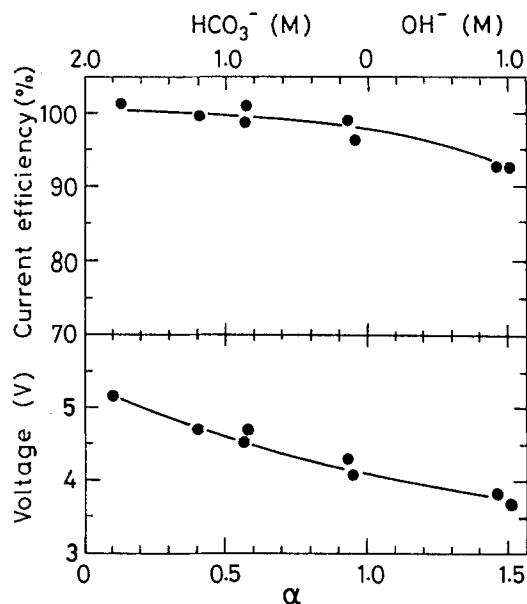


Fig. 5. Current efficiency and voltage of the vertical cell as functions of the solution composition. Anode: MODE. Cathode: plain Ni. Membrane: Nafion 423. Cathode-to-membrane gap: 6 mm. Current density: 20 A/dm². Temperature: 60°C. Catholyte flow rate: 3 liter/min.

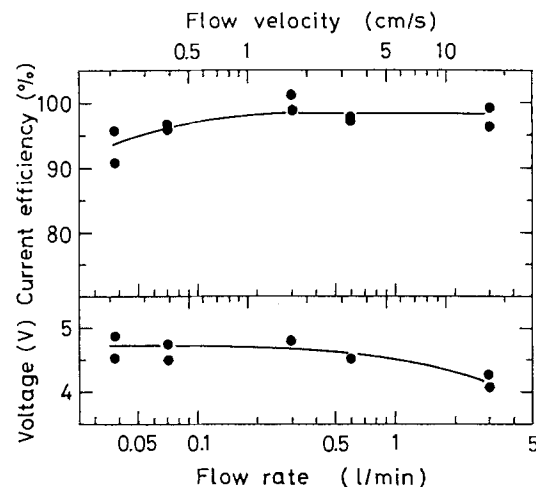


Fig. 6. Current efficiency and voltage of the vertical cell as functions of the catholyte flow. Operating conditions were the same as in Fig. 5, except $\alpha = 0.9-1.0$.

bonate depending on α , and hence α must be controlled as exactly as possible.

Table I shows the breakdown of the terminal voltage of the small cell and the vertical cell at a given current density (20 A/dm²) and temperature (60°C). The figures for the small cell were obtained by experiment with the exception of the catholyte IR drop. Its IR drop was calculated with an assumption of 6 mm for the electrolysis gap to compare the voltage drop in two cells under the same conditions. The solution conductivity was measured with a separate cell for this treatment. The anolyte IR drop of the small cell was dropped from the list for the same reason. Both cells were equipped with a mesh-type MODE anode, a plain Ni cathode, and Nafion 423. As shown in Fig. 2, since the solution gaps in both the anode and cathode compartments of the small cell are large enough, the gas voidage is small, and hence it is concluded that the experimental results do not contain any bubble effect of hydrogen and chlorine in this case.

In the vertical cell, on the other hand, Nafion membrane is supported by the anode mesh while the cathode plate is located at 6 mm from the membrane, and the catholyte is circulated in between at a constant rate (3 liter/min). Therefore, detachment of chlorine bubbles from the anode-membrane structure is delayed, and the

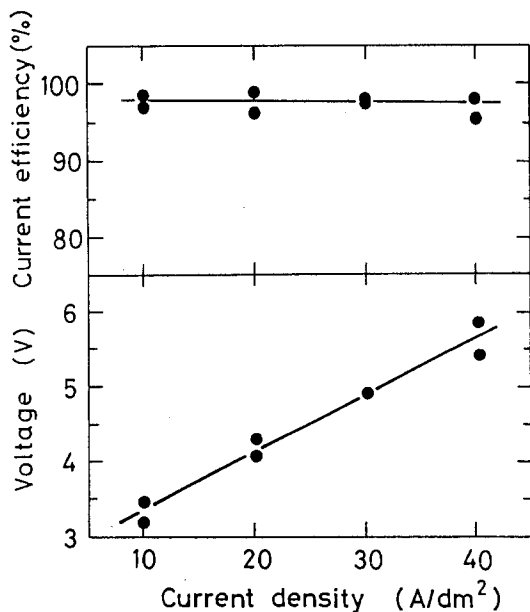


Fig. 7. Current efficiency and voltage of the vertical cell as functions of the current density. Operating conditions were the same as in Fig. 5, except for $\alpha = 0.9-1.0$.

catholyte in the electrolysis zone is crowded by hydrogen bubbles to some extent. As a result, the overvoltages at the anode and the cathode, and also the membrane IR drop, increase considerably depending on the blinding of these surfaces.

The reversible potentials for the hydrogen and chlorine electrode processes under operating conditions of solution composition and temperature were measured with the small cell and agreed with theory. These results were used to break down the cell voltage shown in Table I.

The overvoltages obtained with the small cell are also shown in Fig. 8. In this case, the IR drop between the working electrode and the Luggin probe was calibrated by the current interruption technique. However, the anode potential of the vertical cell in Table I contains some IR drops between the anode and the Luggin probe.

The membrane IR drop in the small cell was some 0.6V, as shown in Table I, and did not contain any disturbance as the vertical cell was affected. However, it is still very large in comparison to the IR drop of similar Nafion employed in the NaCl cell: ca. 0.3V at 80°C with Nafion 427 (9) due to different conductivity in both cases.

As is shown in Table IIA as example with Nafion 315, the resistance of Nafion membranes immersed in potassium electrolyte is larger than that in sodium salt solution due to different permeability of K^+ and Na^+ . Also, the specific resistance in carbonate solution is large compared to hydroxide solution. These factors reflect directly the IR drop through the membrane in potassium

Table I. Breakdown of the cell voltage at 20 A/dm². Membrane: Nafion 423. Anode: MODE mesh. Cathode: plain Ni plate. Cathode-to-membrane gap: 6 mm. Flow rate: 3 liter/min. $\alpha = 1$. Temperature: 60°C

	Small cell (V)	Vertical cell (V)
Anode potential	1.350	1.563
Reversible potential	1.300	1.300
Overvoltage	0.050	0.263
Cathode potential	-1.315	-1.321
Reversible potential	-0.735	-0.735
Overvoltage	-0.580	-0.586
Catholyte IR drop	0.348	0.363
Membrane IR drop	0.662	1.130
Membrane potential	-0.010	-0.025
(Sum) Terminal voltage	3.665	4.357

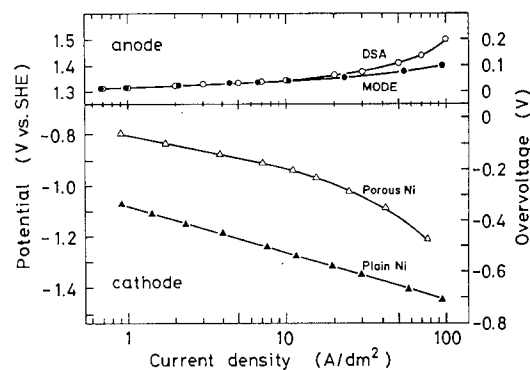


Fig. 8. Polarization curves of various electrodes. Analyte: 4.2M KCl. Catholyte: 2.0M K_2CO_3 . Temperature: 60°C.

carbonate cell under discussion. Table IIB lists the nominal resistance of Nafion membranes in a dilute KCl solution (0.6N KCl at 25°C, reported by du Pont) and the test results obtained in the small cell under operating conditions.

On the other hand, very large IR drop through the membrane positioned in the vertical cell was recorded as shown in Table I. Because the membrane was supported by the anode mesh, chlorine bubbles liberated from the anode were disturbed to escape, and hence the membrane surface was covered by gas bubbles to a great extent. This causes large IR drop through the membrane, and also the anode overvoltage. It is known that gas bubbles can detach from the membrane if the surface is hydrophilic.

Uneven current distribution in the membrane attached to the mesh electrode is also a factor on high voltage drop; that is, the effective area for passing electrolytic current reduces to some extent, which is a common problem for the membrane cell technology. Consequently, an adequately designed electrode must be employed to eliminate, or minimize at least, these troubles.

The cathode overvoltage is the second largest factor of the terminal voltage after the membrane IR drop when the plain Ni cathode is used. Several cathode materials showing low hydrogen overvoltage are available in the market. The hydrogen overvoltage of a Raney-type porous Ni cathode is very low (see Fig. 8), and its Tafel slope is somewhat small, ca. 110 mV/decade, in comparison with 142 mV/decade of a plain Ni cathode.

The solid line labeled 423 in Fig. 9 shows the volt-ampere curve of the cell equipped with Nafion 423 and a porous Ni-coated mesh cathode attached with Nafion. The voltage saving from the cell with a plain Ni cathode (see dotted line) is ca. 0.6V at 20 A/dm². The experimental

Table II. Resistance of Nafion membranes

A. Nafion 315 in various solutions at 60°C

Anolyte	Catholyte	Resistance ($\Omega\text{-cm}^2$)
4.2M KCl	2M K_2CO_3	4.0
	1M K_2CO_3 + 2M KOH	3.2
	4M KOH	2.7
5.4M NaCl	2M Na_2CO_3	2.7
	1M Na_2CO_3 + 2M NaOH	2.0
	4M NaOH	1.6

B. Nafion 423, 417, and 315

Type of Nafion membranes		Resistance ($\Omega\text{-cm}^2$)	
		Nominal ^a	Measured ^b
423	5-1200/T-12	5.4	3.3
417	7-1100/T-12	4.1	2.3
315	2-1500/4-1100/T-12	5.5	4.0

^a In 0.6N KCl at 25°C, quoted from du Pont's brochure.

^b Anolyte: 4.2M KCl. Catholyte: 2.0M K_2CO_3 at 60°C.

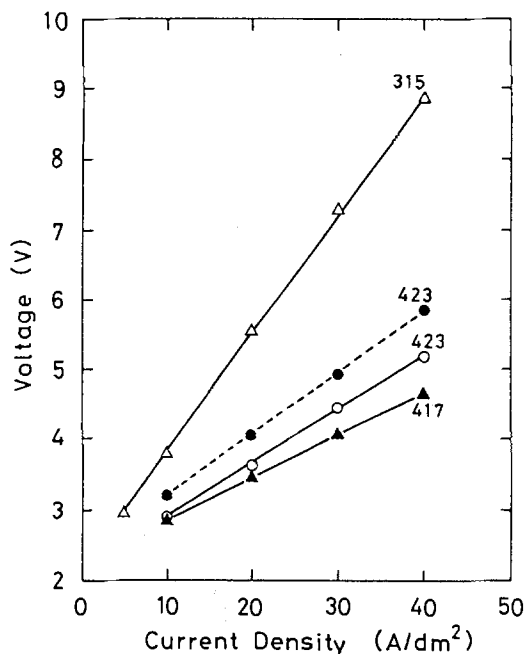


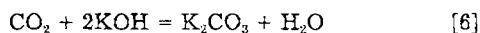
Fig. 9. Voltage vs. current density curves (solid line) of the vertical cell equipped with MODE and a porous Ni cathode attached with Nafion membrane at 60°C. Dotted line shows the results with a plain Ni cathode located at 6 mm for the membrane (see Fig. 8). Catholyte flow: 3 liter/min. $\alpha = 0.9-1.0$.

results with other membranes are also shown. The cathode current efficiency at 20 A/dm² was, of course higher than 95% in all cases.

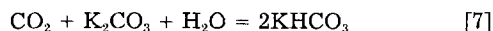
The solution temperature is an important factor for cell operation. The higher the temperature, the lower is the cell voltage. The cell voltage could be reduced further by 0.2V when the operating temperature is raised from 60° to 90°C, whereas only few experiments were conducted under such conditions since the plastic cell was affected by chemical attack.

Most experiments described here were conducted with the catholyte of 2M total concentration and at the current density of 20 A/dm² for the convenience of experiment. Of course, the higher the concentration, the lower was the cell voltage. The current efficiency was almost independent of the total catholyte concentration. Therefore, the concentration must be kept as high as possible. Also, we estimate that an optimum current density may exist at higher levels than 20 A/dm², so that the investment or the fixed charge is lowered while further experiment and engineering considerations are required for evaluating the economy of this process.

Absorption of carbon dioxide with potassium hydroxide solution (reaction [6]) followed by reaction [4] or [7] is a typical process of gas absorption accompanied with chemical reaction (10-12), and is very fast, especially at high temperatures



and



The catholyte can be carbonated by introducing CO₂ gas into the cathode compartment, while the cell configuration is complicated somewhat (4). However, use of a sepa-

rate reactor in parallel with the electrolyzer is preferable for easy operation and reduction of the energy consumption, as is illustrated in Fig. 1.

Excess caustic in the catholyte effluent is neutralized in the upper column of the absorption tower (see Fig. 1), and a part of solution is recovered as an intermediate of the product, which is concentrated or evaporated, depending on the market. Remains flow down to the second stage of the tower where the solution absorbs more CO₂ to obtain bicarbonate (reaction [4A]) to prepare the catholyte liquor.

In conclusion, electrochemical production of potassium carbonate with a membrane cell was studied. The cathode current efficiency was high at almost 100% in a wide range of the operating conditions since the OH⁻ concentration in the cathode compartment was low. The IR drop through the membrane was the largest factor of the terminal voltage. Although Nafion 423 was employed most often in this experiment, any membrane having lowest resistivity is preferable since the OH⁻ concentration in the catholyte liquor is sufficiently low, and further reduction of the cell voltage is thus anticipated. The flowsheet shown in Fig. 1 is applicable to practice because of easy operation of the whole process of interest.

Acknowledgments

The Nafion membranes were supplied by the Experimental Station of E. I. du Pont de Nemours and Company, Wilmington, Delaware, by arrangements of Mr. S. Higuchi of du Pont Japan, Tokyo. The Raney-type Ni-coated cathode was prepared by Showa Company, Nara, Japan. The authors wish to thank Y. Ishida, A. Kuroyanagi, and N. Yamauchi for their laboratory efforts.

Manuscript submitted March 19, 1985; revised manuscript received ca. June 28, 1985. This was Paper 423 presented at the Toronto, Ontario, Canada, Meeting of the Society, May 12-17, 1985.

Nagoya Institute of Technology assisted in meeting the publication costs of this article.

REFERENCES

1. "Lange's Handbook of Chemistry," 12th ed., J. A. Dean, Editor, Section 10, McGraw-Hill, New York (1979).
2. W. Yang, K. Hara, and F. Hine, *Soda to Enso*, **33**, 123 (1982).
3. H. Kaden, P. Volland, K. Zimmermann, and H. Hofmann, *Chem. Technol.*, **27**, 356 (1975).
4. D. L. DeRespiris and T. J. Gilligan, Abstract 451, p. 1130, The Electrochemical Society Extended Abstracts, Vol. 78-1, Seattle, WA, May 21-26, 1978.
5. W. Yang and F. Hine, *Soda to Enso* **33**, 192 (1982).
6. K. Sekine and C. Motohashi, *ibid.*, **33**, 66 (1982).
7. C. Motohashi, *ibid.*, **34**, 516 (1983).
8. T. Asaki, Y. Kamegaya, and K. Takayasu, in "Advances in the Chlor-Alkali and Chlorate Industry," M. M. Silver and E. M. Spore, Editors, p. 165, The Electrochemical Society Softbound Proceedings Series, Pennington, NJ (1984).
9. T. Berzins, Abstract 437, p. 1137, The Electrochemical Society Extended Abstracts, Vol. 77-2, Atlanta, GA, Oct. 9-14, 1977.
10. "Chemical Engineers' Handbook," 5th ed., R. H. Perry and C. H. Chilton, Editors, Section 14, McGraw-Hill, New York (1973).
11. S. Hatta, *Kogyo Kagaku Zasshi*, **31**, 869 (1928); *ibid.*, **32**, 809 (1929).
12. S. Hatta, *ibid.*, **35**, 1397 (1932); *ibid.*, **36**, 7 (1933).

Analysis of Laboratory Data in Early Stages of Evaluation of Electro-Organic Reactions

Edward K. Yung^{*,1} and Richard C. Alkire^{*}

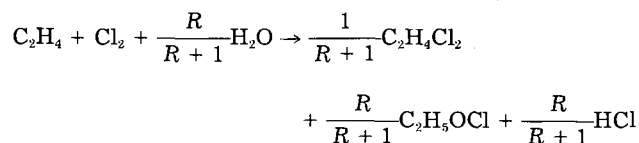
Department of Chemical Engineering, University of Illinois, Urbana, Illinois 61801

ABSTRACT

The production of 1,2-dichloroethane and ethylene chlorohydrin by electrolysis of ethylene containing hydrochloric acid solutions was studied with a bench-scale continuous-flow undivided parallel-plate cell. The product distribution was independent of electrolyte flow rate and current density, but was significantly influenced by the chloride ion concentration. The cell current-voltage curves were found to be independent of electrolyte flow rate. Engineering models which included consideration of the chemical environment in the electrolysis zone were developed from fundamental principles of mass transport, ohmic resistance, and reaction kinetics. The models were verified by comparison with experimental findings, and were subsequently used to explore engineering aspects of scale-up and optimization. These models were incorporated with economic analyses to study the influence of design and operating parameters on the cost of 1,2-dichloroethane. A successive quadratic programming method was used to identify optimal operating conditions as well as the most sensitive parameters of the system.

Development of new electro-organic synthesis processes depends on knowledge of chemical mechanism as well as on engineering design trade-offs. The unification of these perspectives at an early stage of development can promote a more cost-effective exploration of those factors which control the candidate process. The purpose of the present study was to provide methodology by which small-scale experiments can be exploited to evaluate process limitations at an early stage. The emphasis of the work was on a methodology which is simple and portable to other applications, and not on development of a specific candidate process.

The process chosen for study was the production of 1,2-dichloroethane (DCE) and ethylene chlorohydrin (EC) by electrolysis of hydrochloric acid solutions containing ethylene. The synthesis was an indirect electrochemical process in which chlorine was produced at the anode, and products were generated by electrophilic addition of chlorine to ethylene



where R is the product ratio defined as $R = [\text{EC}]/[\text{DCE}]$. The reaction mechanism consists of formation of a chloronium ion intermediate followed by attack from nucleophiles (1).

A series of feasibility studies for electrochemical chlorination of ethylene was carried out by Tedoradze *et al.* (2-5). Experiments were carried out in ethylene-sparged beaker cells with planar electrodes. Parameters investigated included purity and concentration of HCl solutions, temperature, current density, electrode materials, and ethylene feed rate. The dependence of yield and product spectrum upon these parameters was reported. These studies made their contribution in demonstrating feasibility and identifying the proper chemical environment for the process.

Early aspects of process evaluation also require quantitative data obtained in well-characterized experimental systems. The scope of the present work included bench-scale experiments, formulation of models of the reaction chemistry and of the electrolytic cell, scale-up, cost evaluation, optimization, and sensitivity analysis.

Fundamental analyses of the parallel-plate cell geometry have been reported (6). For the system under study, however, gas evolution on both electrodes complicated

the mass transfer and ohmic resistance aspects. The influence of gas bubbles on the current distribution in electrolytic cells has been reported (7, 8) for situations where the population distribution of bubbles was uniform. A review of gas evolving electrodes has been provided by Vogt (9).

The scale-up of electrochemical processes has recently been reviewed (10) with emphasis on the value of engineering models to exploit limited bench-scale laboratory data. Capital costs for electrochemical cells have become available (11), and examples of economic evaluations have been reported (12).

Methods for optimization of electrochemical processes (13) are beginning to emerge for analysis of individual cells (14, 15) as well as entire electrolytic processes (16). In general, optimization considerations should be based on the entire flowsheet, since in some cases it is worthwhile to accept cell modifications in order to achieve better downstream operations.

Experimental

Apparatus.—The electrochemical cell was of undivided parallel-plate geometry and consisted of two cell housing pieces and a spacer, all of polypropylene. The electrodes were mounted flush with the flow channel surfaces, opposite each other, and were held in place by the spacer which also served to establish the gap distance between electrodes. The anode material was Karbate[®] no. 22 (Union Carbide), a graphite material impregnated with a standard phenolic resin, impervious to liquids. [Results of auxiliary limiting current experiments (17) for chlorine reduction with a Karbate[®] rotating disk electrode indicated that deviation of the active surface area from the apparent surface area was less than 5%.] The cathode was platinized graphite (17) on a substrate of Poco AXF-5Q (Union Oil) graphite. The exposed electrode surface had a dimension of 10.2 × 2.54 cm. A hydrodynamic entrance length (43.2 cm) was provided for flow development upstream from the electrodes. For a typical cell gap of 0.635 cm, this hydrodynamic entrance length was adequate up to a Reynolds number of 1700, where the Reynolds number was based on the cell gap (18). The downstream calming region was 10.2 cm long. Current feeders consisted of threaded oxygen-free copper rods (1/8 in. diam) connected to the back side of the electrodes.

The flow system is shown schematically in Fig. 1. A bubble column (4 ft length) was included for ethylene (Air Products, C.P. Grade, 99.8%) absorption. The ethylene stream eventually passed through a Dry Ice cold trap for recovery of residual 1,2-dichloroethane. The liquid stream passed through flow measurement devices (Gilmont, F1500 and F1300), flow stabilizer, the electrochemical cell, and then returned to the reservoir. The function of the flow stabilizer was to collect the gradually released

*Electrochemical Society Active Member.

¹Present address: International Business Machines Corporation, Thomas J. Watson Research Center, Yorktown Heights, New York 10598.

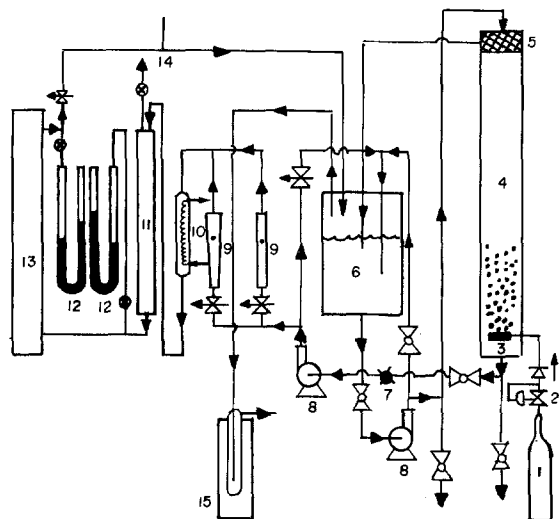


Fig. 1. Flow system. 1: Ethylene cylinder. 2: Regulator. 3: Gas sparger. 4: Bubble column. 5: Rasching ring packing. 6: Reservoir. 7: Sampling port. 8: Pump. 9: Rotameter. 10: Condenser. 11: Flow stabilizer. 12: Manometer. 13: Cell. 14: Thermometer. 15: Dry ice cold trap.

ethylene gas so that a steady, bubble-free electrolyte would enter the cell. For electrolysis experiments, the cell pressure was monitored at 1.2 atm, for which release of ethylene gas was found to be sufficiently slow. Tubing and piping were of 1/2 in. polypropylene.

Flow electrolysis experiments were carried out in constant current mode. A current controlling resistor (Koolohm®, 10W, 1Ω) was connected to the power supply (PAR, 371) for cell current monitoring. Current readout was given by a digital multimeter (Keithley, 179A). For cell current-voltage measurements, a function generator was connected to the potentiostat to provide the voltage scan, and the cell current was recorded by an X-Y recorder (Houston Instrument, 2000). HCl (Mallinckrodt, AR) and deionized water were used in electrolyte preparation.

A rotating disk (Pine Instrument, AFDD 20) was used to determine charge transfer parameters. A Karbate® disk (0.318 cm diam) was used for chlorine evolution, and a platinized graphite disk (0.159 cm diam) for hydrogen evolution. The disk sizes were chosen so that the current distribution would be uniform to within 20% up to a current density of 100 mA/cm² (25).

Procedures.—Prior to each electrolysis experiment, ethylene was bubbled for at least 20 min with electrolyte circulation. The period of electrolysis was typically 2h, following which the bulk solution and cold trap were sampled and analyzed by gas chromatography (Varian 3740 Chromatograph and Vista 401 Data Station). The combinations of operating parameters which were investigated included three electrolyte flow rates (95, 328, 1380 ml/min) and four current levels (200, 400, 800, 1600 mA). Four electrolyte concentrations (1, 2, 4, 8M HCl) were used to study the effect of chloride ion concentration on the product spectrum. Temperature range was (25 ± 4)°C.

No organic impurities were found in the electrolyte that would interfere with the chemical analysis. The column was 2 mm glass, 6 ft length, and packed with 1% SP-1000 on 60/80 Carboxpack (Supelco, Incorporated). A prepacking of sodium bicarbonate was used to retard attack of HCl on the packing. Helium was the carrier gas; the flow rate was 30 ml/min at an inlet pressure of 50 psig. The flame ionization detector was held at 210°C, while the flash injector was held at 180°C. For analysis, the column was held at 50°C for 2 min and then subjected to temperature programming at a ramp rate of 10°C/min to a final temperature of 150°C. Ethanol was used as the internal standard.

Cell current-voltage curves were recorded for various combinations of cell gap and flow rate. Voltage sweep

rate was 10 mV/s, which appeared to be slow enough to minimize double-layer charging effects as well as to allow the cell to operate at pseudo-steady state.

Results and Discussion

The amount of the two major products, 1,2-dichloroethane (DCE) and ethylene chlorohydrin (EC), was a linear function of the electrolysis period. For most experimental runs, the material yield (*Y*)

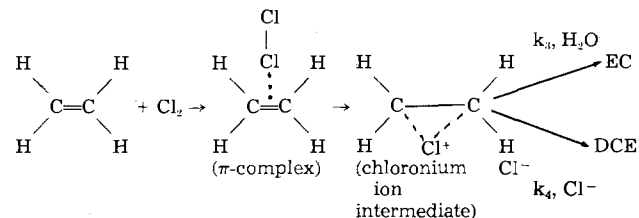
$$Y = \frac{\text{sum of the amount of EC and DCE}}{\text{total amount of chlorine generated at 100\% current efficiency}}$$

was in the range of (100 ± 5)%. Therefore, the current efficiency for chlorine evolution was 100% at all current densities investigated. Electrolyte flow rate and cell current were found to have little influence on the product spectrum.

Chloride ion concentration was found to have significant influence on the product distribution. As the chloride ion concentration was increased, the product spectrum shifted towards 1,2-dichloroethane. Supplementary experiments for the study of solution phase reaction between ethylene and chlorine were carried out with a chemical flow reactor having no electrodes. To within experimental error, it was found that the product distribution was practically identical to that from the electrolysis experiments. It was concluded that, even in the presence of electrodes, the reaction was still occurring in the solution phase. Figure 2 shows the dependence of the product distribution upon the ratio $[H_2O]/[HCl]$. The equation which fits these data is

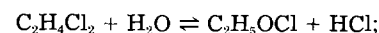
$$R = \frac{[EC]}{[DCE]} = -0.102 + 0.132 \frac{[H_2O]}{[HCl]} \quad [1]$$

The product distribution results in Fig. 2 agree with the commonly accepted mechanism of chlorination of olefins (1)



According to this mechanism, the slope of the straight line would be the ratio (k_3/k_4) of the two rate constants leading to the formation of the two major products. Evidence given by Serguchev and Konyushenko (19, 20) indicated that the ratio k_3/k_4 was relatively independent of the reactivity of the unsaturated compounds. The number obtained in our experiments (0.132) compares favorably with that for chlorination of styrene in aqueous system (0.133) as well as that for chlorination of allyltrimethylammonium perchlorate (0.156). The activity of styrene has been estimated to be 1.2×10^5 times that of allyltrimethylammonium perchlorate. However, there was evidence (20) that the ratio depended upon the solvent composition. Therefore, extension of the experimental finding to systems other than aqueous hydrochloric acid would not be recommended.

The product ratio resulting from thermodynamic equilibrium between the two products following the reaction



$$K_{eq} = \frac{[C_2H_5OCl][HCl]}{[C_2H_4Cl_2][H_2O]}$$

would be expected to be pH dependent. However, supplementary experiments with mixed electrolytes of HCl and NaCl showed that the product distribution depended upon total chloride ion concentration but not upon HCl concentration. It was therefore concluded that the product distribution was controlled by the kinetics of the homogeneous reaction.

It was found that the same I-V curve was recorded for both 1M HCl and for ethylene-saturated 1M HCl as long as

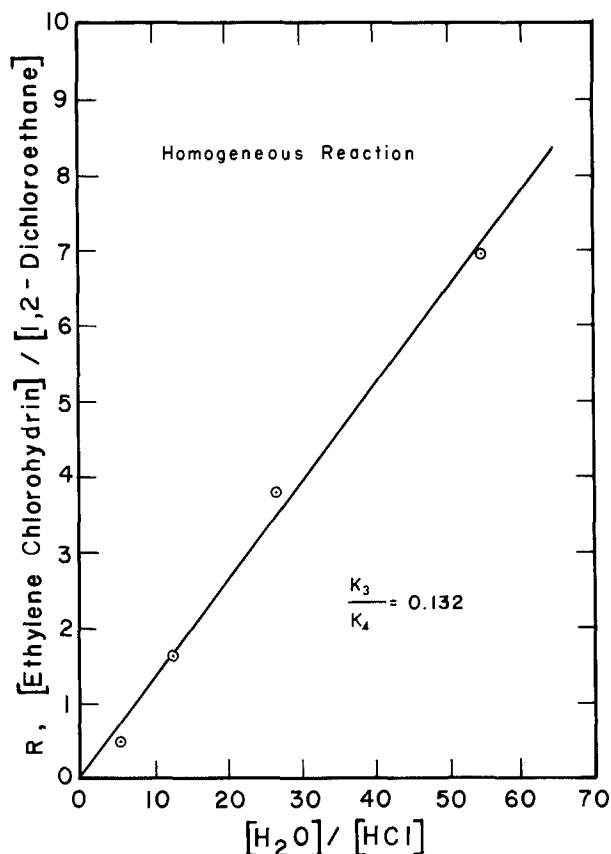


Fig. 2. Determination of the ratio of rate constants (k_3/k_4)

the cell was kept continuously active. If the power was turned off, the I-V curve from the first subsequent voltage scan would then be different, but subsequent scans eventually reverted to the curve found in ethylene-free electrolyte. These observations suggest that as long as the cell is continuously activated, there will be no possibility for the adsorption of ethylene to occur and the electrode will not respond to the presence of ethylene. These results support the interpretation that rapid reaction between ethylene and chlorine occurs in the solution phase and that the cell plays only the role of a chlorine source.

For a fixed cell gap, the I-V curves were found to be independent of the electrolyte flow rate over a range from 50 to 2000 ml/min. The I-V curves recorded for various cell gaps ranging from 0.323 to 1.892 cm are shown in Fig. 3. It can be seen from the slope of the high current portion of the curves that at the same cell voltage the cell current is smaller for larger cell gap, owing to larger ohmic loss in solution phase. Also, the cell gap influences the overall shape of the curves; the curves become straight lines at lower current levels for larger cell gaps. These measurements were clarified by visual observations described in the following paragraphs.

For visual observation of flow pattern in the electrolysis region, a transparent Plexiglas® spacer 1.224 cm thick was used. While the results are qualitative in nature, the phenomena which were observed were essential for resolution of I-V data.

Gas evolution was observed at both electrodes. Three distinct regions were seen. Next to the anode surface, a thin layer containing a chlorine bubble swarm was observed. All bubbles seemed to move at the same velocity. Coalescence of bubbles was not apparent. A similar bubble layer containing hydrogen bubbles was seen adjacent to the cathode. The central portion of the flow channel was free of bubbles. The diameter of hydrogen bubbles was estimated to be 200 μm and that of chlorine bubbles was estimated to be 100 μm . Bubble size distribution seemed to be narrow. Neither cell current nor electrolyte flow rate seemed to influence the bubble sizes. The thickness of the moving bubble layers was not uniform

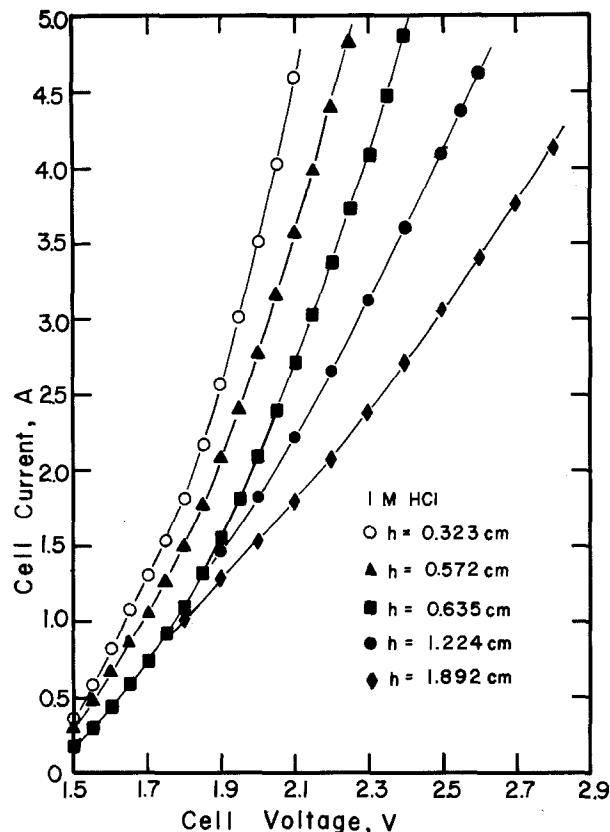


Fig. 3. Experimental cell current-voltage curves for different cell gaps

over the entire electrode length; it increased with the distance from the leading edge. The thickness of the moving bubble layers increased slightly with decreasing electrolyte flow rate. The current level was found to have little influence on the thickness. The hydrogen layer was thicker than the chlorine layer. For a flow rate of 1560 ml/min, hydrogen layer thickness at the center of the electrode was estimated to be 0.05 cm, while the corresponding chlorine layer thickness was estimated to be 0.02 cm. The thickness of the moving bubble layers, δ_{avg} , is represented by

$$\delta_{\text{avg},a} = 0.02(Q/26.0)^{-0.5} \quad [2]$$

$$\delta_{\text{avg},c} = 0.05(Q/26.0)^{-0.5} \quad [3]$$

The rise velocity of bubble swarms was not influenced by the change of electrolyte flow rate for a fixed cell current. Over the cell current range under study (1-3A), the rise velocity varied nearly proportionally with the cell current for fixed electrolyte flow rate, while the layer thickness did not change. For a cell current of 1A, the rise velocity of hydrogen bubble swarm was estimated to be 6 cm/s. The corresponding value for chlorine bubbles was 2 cm/s. These values were in reasonably good agreement with values calculated on the assumption of Stoke's law (21) for an isolated bubble without internal circulation. The rise velocity of bubble swarms was therefore represented as

$$u_{g,\text{Cl}_2} = 2I_{\text{cell}} \quad [4]$$

$$u_{g,\text{H}_2} = 6I_{\text{cell}} \quad [5]$$

According to observation of others on bubble formation at solid surfaces (9), it is reasonable to expect that a layer of small stationary bubbles exists underneath each moving bubble layer. This immobile layer would not be expected to be affected by liquid flow, owing to its thinness and the attachment of the bubbles to the electrode surfaces.

A schematic of the flow pattern in the electrolysis region, based on visual observation, is summarized in Fig. 4. This flow pattern will play a central role in formulation of the cell model which follows.

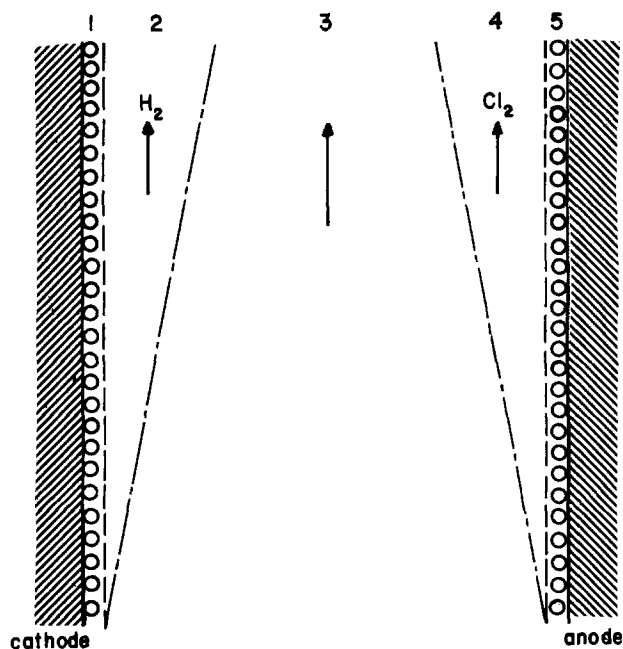


Fig. 4. Schematic of the flow pattern in the experimental cell. Layer 1: Fixed hydrogen layer. Layer 2: Moving hydrogen layer. Layer 3: Bubble-free liquid layer. Layer 4: Moving chlorine bubble layer. Layer 5: Fixed chlorine bubble layer.

Charge transfer measurements with the rotating disk electrode were carried out at four concentrations (1, 2, 4, and 8M HCl), and were corrected for the ohmic component by assuming that the reference electrode was infinitely far away. The data for both reactions followed the Tafel equation

$$i_c(x) = i_{c0} \left\{ \frac{[H^+]_s(x)}{C^*} \right\}^2 \exp \left\{ \frac{-\alpha_c n_c F}{RT} [-E_{eq,c} - \phi_{s,c}(x)] \right\} \quad [6]$$

$$i_a(x) = i_{a0} \left\{ \frac{[Cl^-]_s(x)}{C^*} \right\} \exp \left\{ \frac{\alpha_a n_a F}{RT} [V_{cell} - E_{eq,a} - \phi_{s,a}(x)] \right\} \quad [7]$$

By examination of the data represented by Eq. [7], a value of 1.05V vs. SCE was assigned to $E_{eq,a}$, and the exchange current density (i_{a0}) was therefore evaluated at a reference concentration ($[Cl_2]_0$) for each electrolyte such that the combination of $[Cl^-]$ and $[Cl_2]_0$ yielded a value of 1.05V for $E_{eq,a}$. By examination of the data represented by Eq. [6], a value of -0.123V vs. SCE was assigned to $E_{eq,c}$; the exchange current density (i_{c0}) was then evaluated at a reference concentration ($[H_2]_0$) which yielded a value of -0.123V for $E_{eq,c}$. These data are listed in Table I.

Theoretical

Reaction chemistry near the anode.—Chlorine produced at the anode reacts homogeneously with ethylene which is dissolved in the solution. The concentration profiles near the electrode were investigated theoretically with use of a transport model, described in the Appendix. Calculations were carried out for combinations of flow rates (3, 10, 20 ml/s) and current densities (8, 16, 32, 64, and 128 mA/cm²). A rate constant of 2×10^5 cm³/mol-s was used since this value had been reported for the uncatalyzed reaction (23); the actual overall rate constant is probably larger since the HCl-catalyzed reaction path would also be available. Details on computation aspects are available in Ref. (17).

Results of these calculations indicated that the homogeneous reaction takes place in a very sharply defined zone

at a distance from the anode. At this reaction plane, the chloride ion concentration is essentially identical to that in the bulk solution. Therefore, the product distribution would be expected to be the same as if the chlorine had been bubbled directly into the solution, in agreement with experimental findings. Also, it was computed that the product distribution varied by less than 0.5% for all combinations of flow rates and current densities. These results supported the experimental finding that the product distribution was not affected by either flow rate or current density. Also, the calculations demonstrated that the ethylene concentration between the reaction plane and the anode would be zero, supporting the view that ethylene is not adsorbed on the anode as long as the electrode is maintained in the active state.

The discussion in the first paragraph of the Appendix suggests that the effect of gas bubbles is to increase the rate of transport in comparison with the rate of homogeneous reaction. One simple way to achieve such alteration in relative rates in the present model is to decrease the reaction rate constant (or to increase the diffusion coefficient). When calculations were carried out with rate constants which were 10⁶-fold smaller (that is, a value of 2×10^{-1} cm³/mol-s), it was found that the qualitative features of behavior described in the previous paragraph remained valid. It was therefore concluded that the general features described above would not be qualitatively different had a more detailed treatment of bubble evolution been carried out.

Analysis of the electrolytic cell.—An undivided parallel-plate reactor was modeled. The present analysis differs from previous treatments of parallel-plate flow cells owing to the presence of gas bubbles which requires consideration of flow pattern in the formulation of effective electrolyte conductivity. Phenomena under consideration included charge transfer, ohmic resistance, and mass transfer. Parameters for each phenomena were determined experimentally or were obtained from the literature for use in model calculations; these parameters are compiled in Table I. The mathematical articulation of these components into a unified representation of the entire cell constitutes an important task. While each element of the following overall model could be represented in a more sophisticated manner, it is rarely cost effective to do so in early stages of process evaluation. By the method described below, the most sensitive features of an optimized simple model can be identified. In turn, these components can then be upgraded in order to improve in a selective manner the most important features of the cell model.

The charge transfer characteristics of the chlorine and hydrogen evolution reactions on the electrode materials used in this study were obtained experimentally as discussed in the presentation of Eq. [6] and [7] above.

The solution phase ohmic resistance was assumed to be the sum of the resistance of each layer represented in the flow pattern depicted in Fig. 4. The effective conductivity of the bubble curtains was assumed to be 1/5 of the bulk value (27). A thickness of 50 μm was assigned to the chlorine bubble curtain, and a value of 60 μm was assigned to the hydrogen bubble curtain (27).

Bruggeman's equation (28) was used to describe the effective conductivity of the moving bubble layers on each electrode

$$\kappa_{avg,a} = \kappa_0 \left[1 - \frac{RT(I_{cell}/2)}{2FP_{cell}\delta_{avg,a}u_{g,Cl_2}W} \right]^{3/2} \quad [8]$$

$$\kappa_{avg,c} = \kappa_0 \left[1 - \frac{RT(I_{cell}/2)}{2FP_{cell}\delta_{avg,c}u_{g,H_2}W} \right]^{3/2} \quad [9]$$

The total solution phase ohmic resistance was expressed as

$$R_s = 5(0.005)/A\kappa_0 + 5(0.006)/A\kappa_0 + \delta_{avg,a}/A\kappa_{avg,a} + \delta_{avg,c}/A\kappa_{avg,c} + (h - 0.005 - 0.006 - \delta_{avg,a} - \delta_{avg,c})/A\kappa_0 \quad [10]$$

Table I. System parameters used in the modeling of the experimental cell

Parameter	Physical meaning	Value or functional	Ref.
C	HCl concentration	Variable (M), normally $1M$	
h	Cell gap	Variable (cm)	
L	Cell length	10.16 cm	
W	Cell width	2.54 cm	
Q	Flow rate	Variable (ml/s)	
V_{cell}	Cell voltage	Variable (V)	
C_0	C_2H_4 concentration	$5.0 \times 10^{-3}M$	
T	Temperature	298.15 K	
P_{cell}	Cell pressure	1 atm	
i_{a0}	Exchange current density for Cl^-/Cl_2 redox pair	4.78×10^{-4} A/cm ² for $1M$ HCl	(17)
i_{e0}	Exchange current density for H_2/H^+ redox pair	4.523×10^{-5} A/cm ² for $1M$ HCl	(17)
i'_{a0}	Exchange current density for H_2O/O_2 redox pair	1.0×10^{-6} A/cm ²	(17)
$\alpha_a n_a$	Anodic transfer coefficient for chlorine evolution	0.2779 for $1M$ HCl	(17)
$\alpha_c n_c$	Cathodic transfer coefficient for hydrogen evolution	1.2986 for $1M$ HCl	(17)
$\alpha'_a n'_a$	Anodic transfer coefficient for oxygen evolution	0.30	(17)
$E_{\text{eq. a}}$	Equilibrium potential for Cl^-/Cl_2	$1.05V$	(17)
$E_{\text{eq. c}}$	Equilibrium potential for H_2/H^+	$-0.123V$	(17)
$E'_{\text{eq. a}}$	Equilibrium potential for H_2O/O_2	$1.01V$	(17)
d_{b, Cl_2}	Chlorine bubble departure diameter	50 μm	(27)
d_{b, H_2}	Hydrogen bubble departure diameter	60 μm	(27)
κ_0	Electrolyte conductivity	$\kappa_0 = 0.0126143 + 0.380292C - 0.0591346C^2 + 0.00365068C^3 - 0.0000842448C^4$ (mho/cm)	(35)
D_{HCl}	Diffusion coefficient of HCl	$D_{\text{HCl}} = (2.87445 + 0.58244C) \times 10^{-5}$ (cm ² /s)	(35)
ρ	Density	$\rho = 0.999802 + 0.0159094C$ (g/ml)	(35)
η	Viscosity	$\eta = (0.896375 + 0.0393314C + 0.00251171C^2) \times 10^{-2}$ (g/cm-s)	(36)
t_{H^+}	Transference number of H^+	$t_{H^+} = 0.811794 + 0.0302287C - 0.00525897C^2 - 0.000472662C^3 + 0.0000514969C^4$	(35)
D_{Cl_2}	Diffusion coefficient of chlorine	$D_{Cl_2} = 1.44T/(293.15\eta) \times 10^{-7}$ (cm ² /s)	(17)

Note: Range of applicability: 1-8M HCl.

A correlation for mass transfer in the presence of microconvection owing to bubble growth on an electrode surface (24) was used

$$Sh = 0.93 Re^{0.5} Sc^{0.487} \quad [11]$$

The equations governing mass transfer were

$$i_a(x) = Fk_{\text{mt,a}}[C_b(x) - [Cl^-]_s(x)] \quad [12]$$

$$i_c(x) = Fk_{\text{mt,c}}[C_b(x) - [H^+]_s(x)] \quad [13]$$

Variation of bulk concentration of HCl was obtained from a differential mass balance

$$C_b(x) = C^* - \frac{W}{2FQ} \left(\frac{R_0 + 2}{R_0 + 1} \right) \int_0^x i_a(x') dx' \quad [14]$$

The solution phase potential on both electrode surfaces were related by the following equations

$$\phi_{s,a}(x) = \phi_{s,c}(x) + i_c(x)AR_s + \eta_{c,c}(x) + \eta_{c,a}(x) \quad [15]$$

The concentration overpotentials were formulated on the assumption of dilute solution theory as well as linear concentration profile in the mass-transfer boundary layer (29)

$$\eta_{c,c}(x) = \frac{2RT}{F} \ln \left[\frac{C^*}{[H^+]_s} - t_{H^+} \left(1 - \frac{[H^+]_s}{C^*} \right) \right] \quad [16]$$

$$\eta_{c,a}(x) = \frac{2RT}{F} \ln \left[\frac{C^*}{[Cl^-]_s} - t_{Cl^-} \left(1 - \frac{[Cl^-]_s}{C^*} \right) \right] \quad [17]$$

The last equation needed is for current balance

$$i_c(x) = i_a(x) \quad [18]$$

Equations [1]-[18] constitute a system of 18 independent equations for 18 variables at each location of the cell. The variables are i_a , i_c , $k_{\text{mt,a}}$, $k_{\text{mt,c}}$, $[Cl^-]_s$, $[H^+]_s$, $\phi_{s,a}$, $\phi_{s,c}$, $\eta_{c,a}$, $\eta_{c,c}$,

$\delta_{\text{avg,a}}$, $\delta_{\text{avg,c}}$, u_{g,Cl_2} , u_{g,H_2} , $\kappa_{\text{avg,a}}$, $\kappa_{\text{avg,c}}$, R_s , and C_b . This set of equations contains parameters the values of which are set according to literature sources or laboratory measurement as well as estimations when literature values were unavailable. Table I lists the values used in the present study.

Method of solution.—It is convenient to arrange the integral in Eq. (14) by approximating it as

$$\int_0^x i_a(x') dx' \cong \sum_{j=1}^{m-1} i_a(j) \frac{L}{N} + \left(x - \frac{L}{N}(m-1) \right) i_a(m) \cong \sum_{j=1}^{m-1} i_a(j) \frac{L}{N} \quad [19]$$

where

$$(m-1) \frac{L}{N} < x \leq m \frac{L}{N}$$

since no iterations were then required for the solution of the equations. Integration was carried out by dividing the cell into N sections along the flow direction, and proceeding section-wise starting from the upstream end of the cell. The set of equations was combined into two nonlinear algebraic equations, and IMSL subroutine ZSPOW was used on the Cyber 175 computer to solve them. Subsequently, the cell current was evaluated by

$$I_{\text{cell}} = W \int_0^L i_c(x) dx = W \sum_{j=1}^N i_c(j) \frac{L}{N} \quad [20]$$

Results

The calculated cell current-voltage curves for various cell gaps and flow rates are listed in Table II and their comparison with experimental curves is shown in Fig. 5. The discrepancy at low current densities is probably the result of errors in evaluation of kinetic parameters. However, for current densities above 100 mA/cm² ($I_{\text{cell}} > 2.6A$),

Table II. Calculated I-V curves based on the actual flow pattern

h (in.)	0.127		0.225		0.250		0.482		0.745		
	Q (ml/s)	3.6	15.7	3.6	15.7	3.6	15.7	3.6	15.7	3.6	15.7
V (V)	I (mA)										
1.4	58.3	58.3	57.5	57.5	57.3	57.3	55.5	55.5	53.7	53.6	
1.5	135.4	135.1	131.3	131.0	130.3	130.0	122.0	121.8	114.2	114.0	
1.6	300.8	299.5	282.6	281.5	278.5	277.4	246.7	245.9	220.5	220.0	
1.7	621.2	616.3	556.8	553.2	543.1	539.8	448.4	446.4	381.0	379.6	
1.8	1162	1148	984.8	975.6	950.0	941.6	730.6	726.2	592.7	590.1	
1.9	1951	1919	1567	1548	1497	1480	1083	1075	846.7	842.5	
2.0	2970	2910	2281	2249	2161	2133	1491	1479	1133	1127	
2.1	4178	4082	3099	3051	2918	2875	1941	1925	1444	1436	
2.2	5533	5394	3996	3929	3744	3686	2424	2402	1774	1763	
2.3	6999	6812	4953	4866	4625	4550	2931	2903	2119	2105	
2.4	8551	8313	5957	5848	5546	5453	3457	3423	2474	2458	
2.5	10170	9878	6998	6866	6501	6388	3998	3958	2839	2820	
2.6	11841	11493	8067	7913	7481	7349	4552	4506	3211	3189	

the error between experimental and calculated curves was less than 30 mV. The model also indicated that the cell current-voltage curves will be insensitive to the flow rate change (see Table II), a phenomenon also observed during the experiments. Reasonable variation in the choice of values of δ_{avg} and u_g (Eq. [2]-[5]) did not affect this conclusion. For a comparison, formulation of the cell model based on a commonly used flow pattern, namely, homogeneous gas-liquid mixture with no slip between phases, was done; the results showed strong dependence of I-V curves on flow rate. The comparison demonstrates that understanding of flow pattern, which in turn can vary with design considerations and operating conditions, is essential for predicting cell behavior of gas evolving systems.

Scale-up and cost analysis.—The application of the cell model to scale-up was made with the following modifications to the foregoing model.

1. The flow pattern was assumed to be a homogeneous gas-liquid mixture over the entire cell domain because of the merging of bubble layers in cells of very large length/gap ratio.

2. Pumping power requirement was included in the scale-up. A correlation proposed by Vogt (30) was used for pressure drop estimation for gas-liquid mixture.

3. The mass-transfer rate was described by a correlation proposed by Vogt (31) which considered the mass transfer to be jointly controlled by gas evolution and hydrodynamic flow.

4. Oxygen evolution following Tafel kinetics was included as an anodic side reaction.

Analyses were carried out for a hypothetical production facility operating at 10^4 metric tons of DCE per year. The overall cost was composed of three components: capital cost, operating cost, and raw material cost. The capital cost was evaluated to the cell battery limit, i.e., cell banks together with their peripheries including rectifiers and bus bars, pumps, piping, instrumentation, etc. Equipment cost of upstream feed preparation and downstream product recovery operations was not included. Operating cost, which included energy cost, labor, and maintenance, was also considered to cell battery limit. Economic information by Keating and Sutlic (11) and supplementary data by Danly (32) for electrochemical cells was used. All cost information was corrected to March 1983 prices. Electricity cost was assumed to be 5 ¢/kWh.

The raw material cost included reactant cost and credit for useful by-products. A price (12 ¢/lb), or half the market price for ethylene glycol, was arbitrarily assigned for ethylene chlorohydrin credit. Credit was also given to hydrogen based on its heat of combustion at an assumed thermal efficiency of 90%. A payback time of seven years was selected. The production cost of DCE was determined so that the total revenue would be equal to the total cost at the end of the payback period.

Calculations were carried out initially for 1M HCl to investigate the influence of design and operating parameters on DCE cost. Two parameters, cell gap and flow rate, showed pronounced effects. The variation of DCE cost with cell gap is shown in Fig. 6. A sharp minimum can be seen. For smaller cell gaps, unit cell production rate was higher at a fixed cell voltage, which would lead to smaller capital investment. However, pumping power, as a fraction of operating cost, was strongly influenced by the cell gap ($\Delta P \sim h^{-3}$, approximately) so that pumping cost dominated the operating cost and outweighed gains in capital investment. For larger cell gaps, unit cell production rate was lower at fixed cell voltage due to larger ohmic loss in the solution phase.

The variation of DCE cost with flow rate is shown in Fig. 7. Since over the range under investigation mass-transfer rate was mainly dominated by gas evolution phenomenon, increase of electrolyte flow rate would not substantially increase the production rate. Instead, operating cost would be significantly increased owing to pumping power. For very low flow rate, ohmic loss in the solution phase owing to the high gas content lowered the unit cell production rate which resulted in higher capital investment. However, the effect of high gas content was not very strong and, therefore, the minimum seen in Fig. 7 is not very sharp.

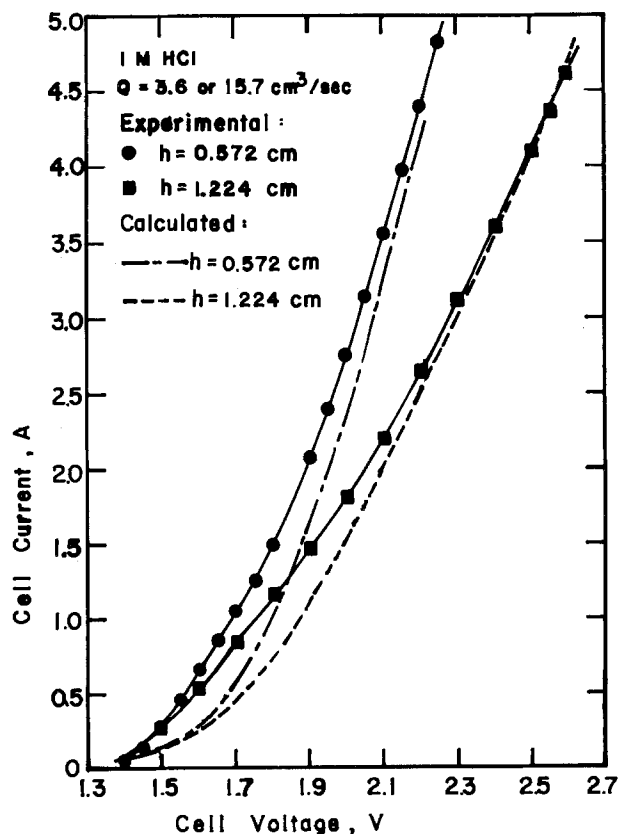


Fig. 5. Comparison of experimental and calculated cell current-voltage curves.

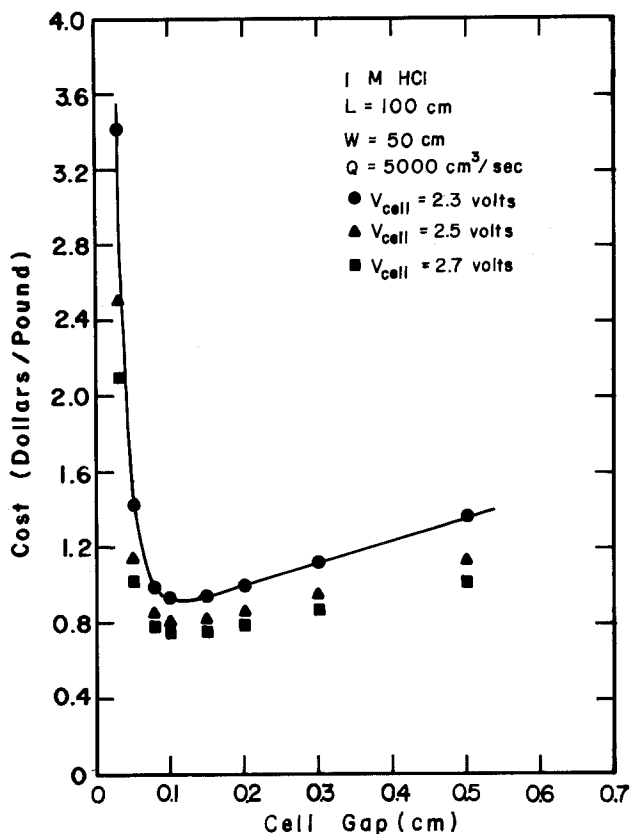


Fig. 6. Influence of cell gap on 1,2-dichloroethane cost

Results shown in Fig. 6 and 7 were carried out for 1M HCl because of the more distinct variation with the parameters under study.

The market price of DCE was 17 ¢/lb (July 1983 price) which is substantially lower than these calculated costs. It has been shown in Fig. 2 that the product distribution depends on $[Cl^-]/[H_2O]$. In particular, DCE cost will de-

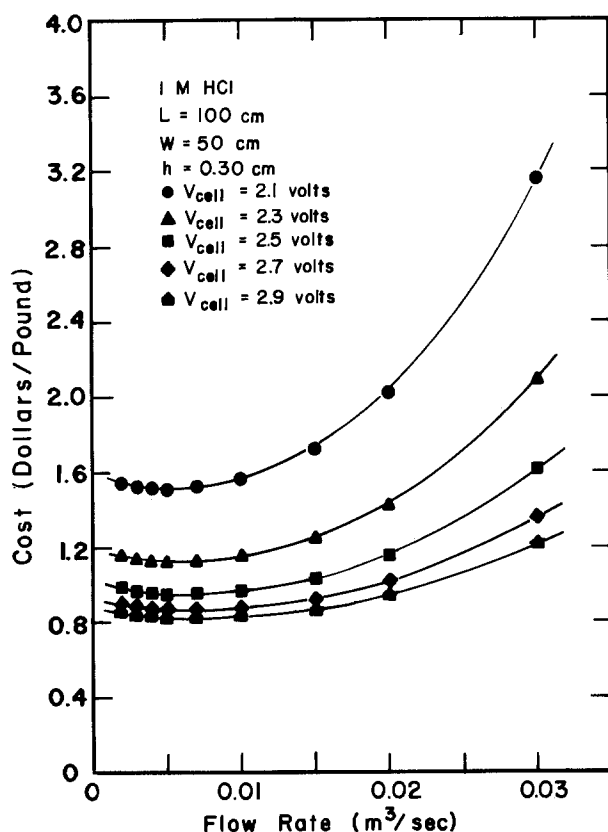


Fig. 7. Influence of electrolyte flow rate on 1,2-dichloroethane cost

crease as HCl concentration increases. For example, when 8M HCl is used as the electrolyte, a calculated cost of 22 ¢/lb for DCE is obtained at a current density less than 1 A/cm².

Optimization.—An enhanced successive quadratic programming (SQP) method (14) was applied to the cost model described in the previous section in order to locate the optimal design parameters and operating conditions. The SQP method was chosen because it is known to be successful in situations where a large number of function and derivative evaluations are required, a category to which our system belongs. The SQP method has only recently been reported for electrochemical applications (15), and the present study represents the first known application of its use in directing bench-scale studies.

Starting with an initial set of values for the independent variables, a quadratic programming problem was formulated by taking a quadratic approximation of the objective function as well as linearization of the constraint functions. Solution of this problem by the Han-Powell algorithm (33) produced a search direction. Improvement of the objective function value was attempted along this search direction, and a new set of values was thereby obtained. The same procedure repeated itself until no further improvement was made. Five independent variables (cell gap, cell length, electrolyte flow rate, cell voltage, and cell width) were considered in the present analysis. The objective was minimization of DCE cost. Other more sophisticated objectives could be chosen for evaluation, but the general method would be the same. Three constraint functions were implemented: an upper limit was set on the maximum current density for anode protection, an upper limit (0.40) was also set for gas volume fraction at the outlet of the cell to prevent development of hot spots, and the maximum electrode area was set to be 0.8 m².

The software package SQPHP for solving nonlinear programming problems using an enhanced version of the Han-Powell method for successive quadratic programming was developed by Chen (33, 34), and is available commercially.² The program requires 41.4K words of core on the CDC Cyber 175 computer.

Results of optimization calculations for 1M HCl are summarized in Table III. It was found that the major fraction of computer time was consumed in function and derivative evaluations, not in the optimization procedure. For example, in Run no. 10, 120.526 CP seconds were consumed, of which only 0.154 CP seconds were used for 19 calls of SQPHP. Most runs terminated when there was lack of improvement of objective function value along the final search direction. In these cases, the final solution is believed to be very close to a local minimum. The results of Runs 1-4 suggest the possibility of local minima since different initial guesses ended up with different sets of optimal values for the variables.

Sensitivity analysis was carried out by finite difference evaluation of the cost change for small changes in each independent variable at the optimal condition. The strong influence of cell gap and cell voltage on the economy was demonstrated by the sensitivity analysis results shown in the footnote of Table III.

A simplified method for determining which phenomenon controls the cell resistance is to calculate the cell current that would pass if the entire driving force (cell voltage) were consumed by the particular phenomenon under consideration. That phenomenon which gives the smallest current is the limiting process. When such calculations were done for the optimal conditions corresponding to a maximum current density of 0.5 A/cm² (Run no. 4 of Table III), values of 2.12, 20.73, and 1.84 for dimensionless cell current were obtained in response to charge transfer, mass transfer, and ohmic resistance-controlled system, respectively. Therefore, it was concluded that mass transfer will not control the cell; measures towards

²M. Stadtherr, Department of Chemical Engineering, University of Illinois, Urbana, Illinois 61801.

Table III. Results of optimization calculations for 1M HCl

Run no.	Initial guess set no. ^a	Scaling factor set no. ^b	Stop mode ^c	Optimal cost (\$/lb)	Maximum c.d., x_1 i_{\max} (A/cm ²)	Cell gap, x_1 (cm)	Cell length, x_2 (cm)	Electrolyte flow rate, x_3 (ml/s)	Cell voltage, x_4 (V)	Cell width, x_5 (cm)	Y ^d
1	1	1	B	89.26	0.5	0.790 E - 1	0.718 E + 2	0.287 E + 4	0.221 E + 1	100	0.324 E - 1
2	2	1	A	89.98	0.5	0.426 E - 1	0.540 E + 2	0.157 E + 4	0.215 E + 1	100	0.625 E - 3
3	3	1	B	89.18	0.5	0.862 E - 1	0.769 E + 2	0.334 E + 4	0.222 E + 1	100	0.244 E - 1
4	4	1	B	89.19	0.5	0.883 E - 1	0.800 E + 2	0.343 E + 4	0.222 E + 1	100	0.299 E - 2
5	5	1	B	89.72	0.5	0.529 E - 1	0.563 E + 2	0.171 E + 4	0.217 E + 1	100	0.423 E - 1
6	4	2	B	89.16	0.5	0.931 E - 1	0.794 E + 2	0.348 E + 4	0.223 E + 1	100	0.984 E - 2
7	4	3	B	89.26	0.5	0.912 E - 1	0.688 E + 2	0.318 E + 4	0.223 E + 1	100	0.269 E - 1
8	5	1	B	142.4	0.2	0.889 E - 1	0.800 E + 2	0.233 E + 4	0.199 E + 1	100	0.920 E - 2
9	4	1	A	98.05	0.4	0.640 E - 1	0.687 E + 2	0.224 E + 4	0.213 E + 1	100	0.705 E - 3
10	4	1	A	83.65	0.6	0.905 E - 1	0.791 E + 2	0.372 E + 4	0.229 E + 1	100	0.472 E - 3
11	4	1	B	76.83	0.8	0.656 E - 1	0.534 E + 2	0.270 E + 4	0.235 E + 1	100	0.344 E - 2
12	4	1	A	72.98	1.0	0.549 E - 1	0.500 E + 2	0.245 E + 4	0.242 E + 1	100	0.349 E - 3
13	4	1	A	67.40	5.0	0.558 E - 1	0.500 E + 2	0.347 E + 4	0.290 E + 1	100	0.475 E - 3

^a Initial guessSet no. 1: $x_1 = 0.1$, $x_2 = 80$, $x_3 = 4000$, $x_4 = 2.2$, $x_5 = 100$.Set no. 2: $x_1 = 0.03$, $x_2 = 100$, $x_3 = 20,000$, $x_4 = 2.0$, $x_5 = 50$.Set no. 3: $x_1 = 0.3$, $x_2 = 60$, $x_3 = 2500$, $x_4 = 2.5$, $x_5 = 90$.Set no. 4: $x_1 = 0.1$, $x_2 = 80$, $x_3 = 4000$, $x_4 = 2.1$, $x_5 = 100$.Set no. 5: $x_1 = 0.2$, $x_2 = 75$, $x_3 = 5000$, $x_4 = 1.95$, $x_5 = 100$.^b Scaling factorSet no. 1: $\delta_1 = 10$, $\delta_2 = 100$, $\delta_3 = 100,000$, $\delta_4 = 0.1$, $\delta_5 = 1000$, $\delta_6 = 2.0$.Set no. 2: $\delta_1 = 100$, $\delta_2 = 100$, $\delta_3 = 10,000$, $\delta_4 = 1$, $\delta_5 = 1000$, $\delta_6 = 2.0$.Set no. 3: $\delta_1 = 1$, $\delta_2 = 100$, $\delta_3 = 100,000$, $\delta_4 = 0.01$, $\delta_5 = 100$, $\delta_6 = 5.0$.^c Stop mode

A Convergence criteria are satisfied.

B Five calls of SQPHP are required.

Sensitivity analysis for run no. 9

 $s_1 = 0.239E + 2$ \$/cm. $s_2 = -0.444E - 3$ \$/cm. $s_3 = -0.995E - 4$ \$/(ml/s). $s_4 = -0.167E + 2$ \$/V. $s_5 = -0.202E - 2$ \$/cm.^d Sum in convergence test.

enhancement of mass-transfer rate, such as implementation of turbulence promoters, would not be expected to improve the cell economic performance. The present system is controlled primarily by ohmic resistance and, to a lesser degree, by a charge transfer resistance. Increasing the solution conductivity with a different electrolyte seems unlikely since the most mobile cation, H⁺, is already present in the electrolyte. Development of a more active electrode surface for enhancement of charge transfer rate would represent only a limited contribution to process improvement. Further improvement in yield would be achieved by increasing the total chloride ion concentration beyond that obtainable with pure HCl electrolyte, such as by addition of chloride ion containing salts.

Conclusions

Because electrochemical processes can be complex, early stages of process evaluation must be guided so that efficient use is made of development efforts. Simple methods need to be used for modeling cells, their scale-up properties, and their economic features, and for predicting their optimal configuration. The incorporation of such methods along with bench-scale laboratory data can be carried out with numerical software available commercially on most mainframe systems.

In the present investigation, the most sophisticated numerical computations were those used to clarify the chemical reaction sequence which occurred near the electrode surface, summarized in the Appendix. The development of a model of an entire cell involved a few dozen equations, primarily nonlinear algebraic equations, which in the present study were easily solved by commercial software. Optimization and identification of the most sensitive parameters were also found to be readily accomplished with successive quadratic programming methods. While the present study did not include aspects of the process flow sheet other than the electrolytic cell, methods for flowsheet simulation and optimization represent an area of active research where rapid advances may be anticipated in the near future.

As a model system for the investigation of these methods, the electrochemical process for 1,2-dichloroethane production by electrolysis of ethylene containing hydrochloric acid solutions was studied with a bench-scale continuous-flow undivided parallel-plate cell. Ethylene chlorohydrin was the only by-product. The product spectrum was found to be independent of both electrolyte flow rate and cell current, but was found to be significantly influenced by the chloride ion concentration. Product distribution data supported the reaction mecha-

nism involving a chloronium ion intermediate and subsequent attack by nucleophiles (chloride ion and water molecule).

An approximate model which considered the chemical environment in the electrolysis zone was developed from fundamental principles of mass transport and reaction kinetics. The calculations supported the view that the cell served to generate chlorine, and that reaction of ethylene occurred solely by homogeneous chemical reaction.

The cell current-voltage curves were found to be independent of electrolyte flow rate. The flow patterns arising from gas evolution in the cell were observed experimentally and were used to establish a mathematical model of the cell. The cell model took into account mass transfer, charge transfer, and solution phase ohmic resistance. When a correlation was constructed for solution phase ohmic resistance based on the observed gas bubble flow pattern, the model characterized the experimental cell accurately, particularly the observation that the I-V curve was independent of flow rate.

Economic analyses were carried out for a hypothetical production facility. Influence of key operating and design parameters on the balance of capital cost and operating cost was demonstrated. An enhanced successive quadratic programming code was applied to locate the optimal operating conditions and to identify the most sensitive variables. The methods developed in this study are portable and can be applied to a wide variety of electrolytic processes.

Acknowledgments

Financial support of this work was provided by the American Chemical Society Petroleum Research Fund (13402-AC7). Computer costs were partially supported by the University of Illinois Research Board.

Manuscript submitted March 22, 1985; revised manuscript received May 28, 1985. This was Paper 318 presented at the Cincinnati, Ohio, Meeting of the Society, May 6-11, 1984.

The University of Illinois assisted in meeting the publication costs of this article.

APPENDIX

Reaction Chemistry Near the Anode

A two-dimensional representation of the reaction zone, illustrated in Fig. A-1, was used to calculate concentration profiles near the anode. Reference (17) contains a complete discussion of the summary which follows. The primary assumptions were (i) constant physical properties, (ii) well-developed laminar flow with a linear velocity field in the thin reaction region, (iii) homogeneous reaction which is first order in both chlorine and ethylene concentrations, (iv) 100% current efficiency for chlorine evolution, and (v) transport by convection along the electrode and by diffusion normal to the electrode. The last assumption represents a limiting case of behavior which does not include the effect of gas bubbles. The presence of such bubbles would serve to increase mass transfer of Cl^- and ethylene toward the anode, and to transport Cl_2 into the bulk at rates faster than given by the model. That is, the consequence of gas bubbles would be to increase rates of transport with respect to rates of chemical reaction, a point to which discussion will return.

The differential mass balances for chlorine and ethylene

$$D_{\text{Cl}_2} \frac{\partial^2 [\text{Cl}_2]}{\partial y^2} - u_x(y) \frac{\partial [\text{Cl}_2]}{\partial x} = k[\text{Cl}_2][\text{C}_2\text{H}_4] \quad [\text{A-1}]$$

$$D_{\text{C}_2\text{H}_4} \frac{\partial^2 [\text{C}_2\text{H}_4]}{\partial y^2} - u_x(y) \frac{\partial [\text{C}_2\text{H}_4]}{\partial x} = k[\text{Cl}_2][\text{C}_2\text{H}_4] \quad [\text{A-2}]$$

where the linear velocity field is represented by

$$u_x(y) = 6\langle u \rangle \left(\frac{y}{h} - \frac{y^2}{h^2} \right) = 6\langle u \rangle \frac{y}{h} \quad [\text{A-3}]$$

The six boundary conditions are

$$[\text{Cl}_2] = 0 \text{ at } y = \delta_R \text{ for all } x \quad [\text{A-4}]$$

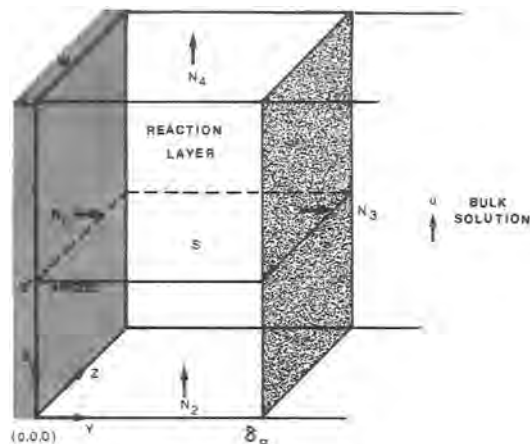


Fig. A-1. Basis of the reaction chemistry model. N_1 : chlorine flux at anode. N_2 : convective flux of chlorine into the reaction zone. N_3 : diffusive flux of chlorine into bulk solution. N_4 : convective flux of chlorine out of the reaction zone. S : rate of consumption of chlorine in the reaction zone.

$$[\text{C}_2\text{H}_4] = C_0 \text{ at } y = \delta_R \text{ for all } x \quad [\text{A-5}]$$

$$-D_{\text{Cl}_2} \frac{\partial [\text{Cl}_2]}{\partial y} = \frac{i}{2F} \text{ at } y = 0 \text{ for all } x \quad [\text{A-6}]$$

$$\frac{\partial [\text{C}_2\text{H}_4]}{\partial y} = 0 \text{ at } y = 0 \text{ for all } x \quad [\text{A-7}]$$

$$[\text{C}_2\text{H}_4] = C_0 \text{ at } x = 0 \text{ for all } y \quad [\text{A-8}]$$

$$[\text{Cl}_2] = 0 \text{ at } x = 0 \text{ for all } y \quad [\text{A-9}]$$

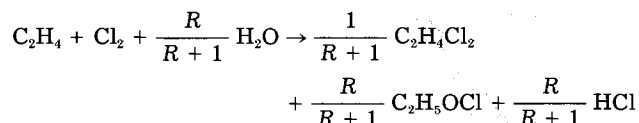
Different concentration profiles will be obtained for different values of reaction layer thickness δ_R . The value of δ_R must be chosen so that it satisfied a chlorine mass balance

$$\frac{iWL}{2F} = W \int_0^{\delta_R} [\text{Cl}_2](y) \Big|_{x=0}^{x=L} u_x(y) dy + W \int_0^L \int_0^{\delta_R} r(x, y) dy dx \quad [\text{A-10}]$$

The differential mass balance for chloride ion is

$$D_{\text{HCl}} \frac{\partial^2 [\text{Cl}^-]}{\partial y^2} - u_x(y) \frac{\partial [\text{Cl}^-]}{\partial x} + \frac{R}{R+1} r = 0 \quad [\text{A-11}]$$

where r is the local reaction rate, which can be calculated after the concentration profiles for both chlorine and ethylene have been obtained. Diffusion coefficient of HCl molecule, D_{HCl} , is used in Eq. [A-11] because of the binary nature of the electrolyte (22). The last term accounts for chloride generation following the stoichiometric reaction



The local product ratio was

$$R(x, y) = \frac{[\text{EC}]}{[\text{DCE}]}(x, y) = -0.102 + 0.132 [\text{H}_2\text{O}][\text{Cl}^-](x, y) \quad [\text{A-12}]$$

The boundary conditions associated with Eq. [A-11] are

$$D_{\text{HCl}} \frac{\partial [\text{Cl}^-]}{\partial y} = \frac{i}{F} \text{ at } y = 0 \quad [\text{A-13}]$$

$$[\text{Cl}^-] = [\text{Cl}^-]_0 \text{ at } y = \delta_R \quad [\text{A-14}]$$

$$[\text{Cl}^-] = [\text{Cl}^-]_0 \text{ at } x = 0 \quad [\text{A-15}]$$

where $[\text{Cl}^-]_0$ is the chloride ion concentration in the bulk solution.

The overall product ratio can be calculated by

$$R_{\text{overall}} = \left(\frac{[\text{EC}]}{[\text{DCE}]} \right)_{\text{overall}} = \frac{\frac{iLfR_0}{2F(R_0 + 1)} + \int_0^L \int_0^{\delta_R} \frac{r(x, y)R(x, y)}{R(x, y) + 1} dy dx}{\frac{iLf}{2F(R_0 + 1)} + \int_0^L \int_0^{\delta_R} \frac{r(x, y)}{R(x, y) + 1} dy dx} \quad [\text{A-16}]$$

where R_0 is the ratio obtained from reaction in the bulk solution and f is the fraction of chlorine being carried out of the reaction layer by convection

$$f = \int_0^{\delta_R} u_x(y)[\text{Cl}_2](y)|_{x=L} dy / \left(\frac{iL}{2F} \right) \quad [\text{A-17}]$$

Concentration profiles were computed by a finite difference method (IMSL subroutine ZSPOW) implemented on a Cyber 175 computer. Additional details are available in Ref. (17).

LIST OF SYMBOLS

A	electrode area (cm^2)
C_b	bulk concentration of HCl (mol/cm^3)
C_0	ethylene concentration in electrolyte (mol/cm^3)
C^*	bulk concentration of HCl at cell inlet (mol/cm^3)
d_b	bubble departure diameter (cm)
D_i	diffusion coefficient of species i (cm^2/s)
E_{eq}	equilibrium potential (V)
f	fraction of chlorine flux out of the reaction layer
F	Faraday's constant (96,487 C/eq)
h	cell gap (cm)
i	current density (A/cm^2)
i_0	exchange current density (A/cm^2)
I_{cell}	cell current (A)
k	reaction rate constant for chlorination of ethylene ($\text{cm}^3/\text{mol}\cdot\text{s}$)
k_3	rate constant for ethylene chlorohydrin formation ($\text{cm}^3/\text{mol}\cdot\text{s}$)
k_4	rate constant for 1,2-dichloroethane formation ($\text{cm}^3/\text{mol}\cdot\text{s}$)
k_{mt}	mass transfer coefficient (cm/s)
L	cell length (cm)
n	number of electrons involved in the electrochemical reaction
$N_1 - N_4$	chlorine fluxes in Fig. A-1 ($\text{mol}/\text{cm}^2\cdot\text{s}$)
P_{cell}	cell pressure (atm)
Q	electrolyte flow rate (cm^3/s)
R	product ratio ($[\text{EC}]/[\text{DCE}]$); gas constant (8.3144 J/g-mol-K), when appearing as RT
R_0	product ratio in bulk electrolyte
R_s	solution phase ohmic resistance (Ω)
Re	$V_g d_b / A \nu$, Reynolds number (dimensionless)
S	amount of chlorine reacted in the reaction layer per unit time (mol/s)
Sc	ν / D_{HCl} , Schmidt number (dimensionless)
Sh	$\kappa_{\text{mt}} d_b / D_{\text{HCl}}$, Sherwood number (dimensionless)
t_i	transference number of ionic species i
T	temperature (K)
$\langle u \rangle$	average velocity of electrolyte flow, (cm/s)
u_g	rise velocity of bubble swarm, (cm/s)
V_{cell}	cell voltage (V)
V_g	volume rate of gas bubble formation (cm^3/s)
W	cell width (cm)

Greek Symbols

α	symmetry factor in Butler-Volmer equation
δ_{avk}	average thickness of moving bubble layer (cm)
δ_R	reaction layer thickness (cm)
η_c	concentration overpotential (V)
κ_{avk}	effective conductivity of moving bubble layer (mho/cm)
κ_0	conductivity of gas bubble-free electrolyte (mho/cm)
ν	kinematic viscosity (cm^2/s)
ϕ_s	solution phase potential (V)

Subscripts

a	anodic
c	cathodic
s	surface

REFERENCES

- R. C. Fahey and H.-J. Schneider, *J. Am. Chem. Soc.*, **90**, 4429 (1968).
- G. A. Tedoradze, V. A. Paprotskaya, and A. P. Tomilov, *Elektrokhimiya*, **10**, 1103 (1974).
- V. A. Paprotskaya, G. A. Tedoradze, and A. P. Tomilov, *ibid.*, **12**, 206 (1976).
- G. A. Tedoradze, V. A. Paprotskaya, and A. P. Tomilov, *ibid.*, **10**, 1612 (1974).
- G. A. Tedoradze Yu.M. Sokolov, E. A. Panomarenko, V. A. Paprotskaya, and A. P. Tomilov, *PCT Int. Appl.* **80** 01,686, Aug. 21, 1980 (C.A.:93:247451).
- W. R. Parrish and J. Newman, *This Journal*, **117**, 43 (1970).
- C. W. Tobias, *ibid.*, **106**, 833 (1959).
- I. Rousar, *ibid.*, **116**, 676 (1969).
- H. Vogt, "Comprehensive Treatise of Electrochemistry," Vol. 6, E. Yeager *et al.*, Editors, p. 445, Plenum Press, New York (1983).
- J. R. Selman, in "Tutorial Lectures in Electrochemical Engineering and Technology," Part II, R. Alkire and D. Chin, Editors, p. 101, AIChE Symposium Series 229, AIChE, New York (1983).
- K. B. Keating and V. D. Suttic, in "Electro-Organic Synthesis Technology," M. Krumpett, E. Weismann, and R. Alkire, Editors, p. 119, AIChE Symposium Series 185, AIChE, New York (1979).
- R. E. W. Jansson, in "Tutorial Lectures in Electrochemical Engineering and Technology," Part II, R. Alkire and D. Chin, Editors, p. 119, AIChE Symposium Series 229, AIChE, New York (1983).
- T. R. Beck, in "Techniques of Electrochemistry," Vol. 3, E. Yeager and A. J. Salkind, Editors, Wiley-Interscience, New York (1978).
- R. C. Alkire, G. D. Cera, and M. A. Stadtherr, *This Journal*, **129**, 1225 (1982).
- R. Alkire, S.-A. Soon, and M. A. Stadtherr, *ibid.*, **132**, 1105 (1985).
- R. C. Alkire, R. D. La Roche, G. D. Cera, and M. A. Stadtherr, Paper 410 presented at the Toronto, Ont., Canada Meeting of the Society, May 12-17, 1985.
- E. K. Yung, Ph.D. Thesis, University of Illinois, Urbana, IL (1985).
- H. Schlichting, "Boundary-Layer Theory," 7th ed., p. 185, McGraw-Hill, New York (1979).
- V. P. Konyushenko, Yu. A. Serguchev, and V. I. Staninets, *Khim. Prom.*, 146 (1979).
- Yu. Serguchev and V. P. Konyushenko, *Ukr. Khim. Zhurn.*, **42**, 100 (1976).
- R. B. Bird, W. E. Stewart, and E. N. Lightfoot, "Transport Phenomena," p. 59, John Wiley and Sons, New York (1960).
- J. Newman, "Electrochemical Systems," p. 223, Prentice-Hall, Englewood Cliffs, NJ (1973).
- P. W. Dun and T. Wood, *J. Appl. Chem. Lond.*, **17**, 53 (1967).
- K. Stephan and H. Vogt, *Electrochim. Acta*, **24**, 11 (1979).
- J. Newman, *This Journal*, **113**, 1235 (1966).
- J. Newman, *ibid.*, **113**, 501 (1966).
- H. Vogt, *Electrochim. Acta*, **26**, 1311 (1981).
- D. A. G. Bruggeman, *Ann. Phys.*, **24**, 659 (1935).
- J. Newman, "Electrochemical Systems," p. 383, Prentice-Hall, Englewood Cliffs, NJ (1973).
- H. Vogt, *J. Appl. Electrochem.*, **12**, 261 (1982).
- H. Vogt, *Electrochim. Acta*, **23**, 203 (1978).
- Kirk-Othmer, "Encyclopedia of Chemical Technology," Vol. 8, p. 704, John Wiley and Sons, New York (1979).
- H. S. Chen, Ph.D. Thesis, University of Illinois, Urbana, IL (1982).
- H. S. Chen and M. A. Stadtherr, *Comp. Chem. Eng.*, **8**, 229 (1984).
- T. W. Chapman and J. Newman, "A Compilation of Selected Thermodynamic and Transport Properties of Binary Electrolytes in Aqueous Solution," AEC Contract w-7405-eng-48 (1968).
- "CRC" Handbook of Chemistry and Physics," 63rd ed., R. C. Weast and M. J. Astle, Editors, p. D-240, CRC Press, Boca Raton, FL (1982).

Charge-Discharge Behavior of Polyacetylene Electrodes

Fritz G. Will*

General Electric Company, Corporate Research and Development, Schenectady, New York 12301

ABSTRACT

The charge-discharge and open-circuit behavior of polyacetylene electrodes, p-doped with BF_4 , is examined. Discharge curves for controlled current are interpreted quantitatively in terms of a model involving slow dopant diffusion and slow discharge at the polymer/electrolyte interface. The open-circuit potential is measured as a function of mean dopant level. It is shown that, due to the slow dopant diffusion, no steady-state potentials are attained. The coulombic efficiency of pristine polyacetylene electrodes in identical states of doping is determined as a function of discharge current. Discrepancies among results of different authors are related to different dopant states near the polymer surface. A quantitative relationship between efficiency and current is derived which is shown to be valid for small polarizations and short discharge times.

Polyacetylene $(\text{CH})_x$ can be doped and undoped electrochemically (1) with a variety of ions and can, therefore, principally be used as novel electrode material in rechargeable batteries. Certain aspects of repetitively charging (p-doping or anion incorporation) and discharging (undoping) polyacetylene electrodes have been described in the literature. Nigrey *et al.* (1) applied controlled current charges and discharges of short duration to polyacetylene films in solutions of LiClO_4 in propylene carbonate. This resulted in ClO_4 dopant level changes of the order of 0.5 mole percent (m/o). Kaneto *et al.* (2) described the open-circuit voltage behavior following consecutive controlled potential charge and discharge pulses and determined the coulombic and energy efficiency of ClO_4 -doped polyacetylene at various constant current discharges. They observed an unexplained increase in coulombic efficiency from 74 to 87% for a ten-fold increase in discharge current. Farrington *et al.* (3) found quite different open-circuit voltage behavior after p-doping with ClO_4 or AsF_6 , characterized by a pronounced voltage step at 2 m/o doping level and a linear increase in voltage at higher doping levels. Furthermore, coulombic efficiencies reported in Ref. (3) for controlled current discharge from identical dopant levels as in Ref. (2) are only approximately half of the values reported in Ref. (2), that is, only 41-51%.

In the present paper, we study the open-circuit voltage behavior of polyacetylene electrodes p-doped with BF_4 , following consecutive controlled current charges and discharges of 0.1-100s duration. Furthermore, we establish the coulombic efficiency of pristine polyacetylene film electrodes for various controlled current charges and discharges of typically 1h duration. We show that the coulombic efficiency is determined by slow dopant diffusion (4, 5) in the polyacetylene structure. The anomalies of efficiency *vs.* discharge current observed by others (2) and the discrepancies among the efficiency values reported by different groups (2, 3) can be reconciled by the nonsteady-state nature of dopant diffusion and concentration in polyacetylene.

Experimental

Polyacetylene films had been prepared by the Rohm and Haas Company and shipped in sealed glass vials, filled with inert gas. Prior to electrochemical experiments, films were predominantly in the *cis* form as evidenced by infrared spectroscopy (6). They had an apparent density of 0.56 g/cm^3 , corresponding to 48% of the theoretical density and a true surface area of 40-50 m^2/g . The internal void space of 52% consists of interconnected micropores of a few hundred to a few thousand angstroms diameter between individual polyacetylene fibers of a few hundred angstroms diameter. This microfibrillar structure of polyacetylene is well established (7, 8).

Details of the film preparation and characterization have been described elsewhere (6). Circular electrodes A of 2 cm^2 area with 89 μm thickness and B of 1.25 cm^2 area

with 68 μm thickness were cut from the films. The former corresponds to 2.7 m/o dopant per $\text{A-s}/\text{cm}^2$ charge, the latter to 3.5 m/o/ $\text{A-s}/\text{cm}^2$. Electrodes were provided with 1000 \AA sputtered Au films on the back side. Contact was made by attaching Au wires with Au-epoxy cement. Experiments were carried out in PTFE cells using Li counter and reference electrodes. Approximately 1 cm^3 electrolyte was employed, consisting of 30% by weight solutions of LiBF_4 in sulfolane for electrodes A and 10% solution for electrodes B. These electrolytes have very high viscosity. Handling of and experimentation with the polyacetylene were carried out in a high quality dry box.

Coulombic efficiency studies were performed for each different discharge current on a pristine polyacetylene electrode, charged with identical current density of 0.24 mA/cm^2 .

Controlled currents were generated with a PAR Model 175 Universal Programmer and applied with a PAR Model 175 Galvanostat/Potentiostat equipped with Digital Coulometer Model 179. Voltage-time traces were recorded on a Nicolet Model 206 Storage Oscilloscope or a Hewlett-Packard Model 17501A Recorder, depending on pulse duration.

Results

Nonsteady-state polarization behavior.—Figure 1 shows polarization-time transients for electrode A, subjected to short-duration discharge and charge pulses separated by open-circuit periods. Electrode A had been previously charged to 7 m/o BF_4 dopant level. The polarization data are corrected for the ohmic voltage drop between test and reference electrode and are referred to the open-circuit potential of 3.8V obtained after 7 m/o doping. It is seen from Fig. 1 that discharge and charge with current densities as small as 0.05 and 0.5 mA/cm^2 yield low polarizations which do not appear to change significantly after the first few hundredths of a second.¹ Open-circuit stand for 0.1s following discharge or charge with 0.05 mA/cm^2 for 0.1s results in negligible remaining polarization, whereas a current density of 0.5 mA/cm^2 for 0.1s al-

¹ Closer examination of the curves and charging or discharging for longer periods of time, however, reveals that the polarizations do not attain steady-state values.

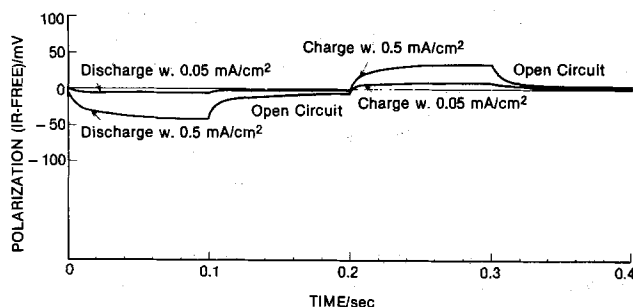


Fig. 1. Short-term charge, discharge, and open-circuit behavior of BF_4 -doped polyacetylene electrodes; doping and undoping with 0.1s current pulses.

* Electrochemical Society Active Member.

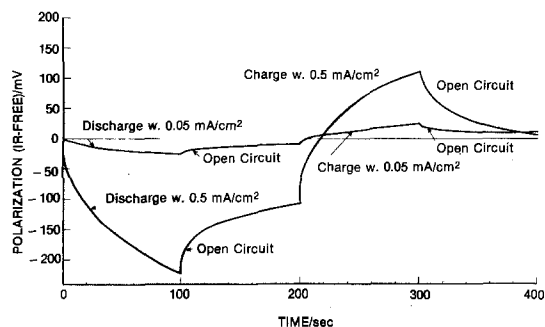


Fig. 2. Short-term polarization behavior of BF_4 -doped polyacetylene electrodes; doping and undoping with 100s current pulses.

ready produces a perturbation which does not dissipate completely on open circuit in 0.1s. Charge or discharge with 0.5 mA/cm^2 for 0.1s corresponds to a dopant injection or removal of $3.1 \times 10^{14} \text{ BF}_4$ molecule/ cm^2 .

Figure 2 shows polarization-time transients for pulse lengths and open-circuit periods of 100s each. Thus, dopant injection or removal corresponds to 3.1×10^{16} and $3.1 \times 10^{17}/\text{cm}^2$ in a single 0.05 and 0.5 mA/cm^2 pulse. It is seen that even for the small current density of 0.05 mA/cm^2 steady-state polarizations are never attained. This is even more pronounced for the 0.5 mA/cm^2 pulse. During the 100s open-circuit periods following current pulses, the perturbations caused by the charge injection or removal do not relax. Slow diffusion (4, 5) prevents steady state from being attained.

Open-circuit potential-dopant level relationship.—Prior to establishing the open-circuit potential-dopant level relationship, electrode A had been cycled several times, discharged to 1.3V, and left on open circuit for 1h, which led to recovery of the potential to 3.33V. The electrode was then p-doped in a series of 100s charging pulses of 0.25 mA/cm^2 , each followed by an open-circuit period of 100s (part a of curve). In part b of the curve, the open-circuit period was increased from 100 to 500s. The potential-time transients were equivalent to those shown in Fig. 2. The charge input and the open-circuit potential were both recorded and the potential at the end of the open-circuit stand plotted in Fig. 3 against the incremental charge input. The upper abscissa shows the incremental dopant level if the dopant were uniformly distributed throughout the entire polyacetylene film.² It is appreciated from the discussion in the preceding paragraph that the potentials plotted in Fig. 3 are nonsteady-state values. The open-circuit potential increases monotonically from 3.35 to 3.72V for a mean dopant level change of 1.5 m/o. The decrease at 3.62V is due to the change of open-circuit stand from 100 to 500s. Discharge in a series of 100s pulses of 0.25 mA/cm^2 with 500s stand after pulses results in decreasing open-circuit potentials as shown in Fig. 3. The relevant curve exhibits considerable hysteresis such that the open-circuit potentials on discharge are by an average of 0.2V lower than those on charging at identical mean dopant levels. Under the conditions applied, namely, charging with 100s pulses of 0.25 mA/cm^2 followed by open circuit for 500s and discharging with the same pulse regime, polyacetylene electrodes do not behave reversibly, and no unique relationship between open-circuit potential and mean dopant level is established.

Charge-discharge cycling simulating battery applications.—The charge-discharge curves of Fig. 1 and 2 are of little interest to practical battery operation as the discharge times are too short and the doping level changes too small to yield energy densities competitive with other batteries. Figure 4 shows the results of three consecutive charges and discharges of longer duration. Pristine film was charged initially at controlled potentials of 3.5, 4, and 4.5V for a total of 2h. A charge of 1.5 A-s/cm^2 was thus injected over a time period of 2h, corresponding to a mean

² Referred to as mean dopant level or mean concentration from here on.

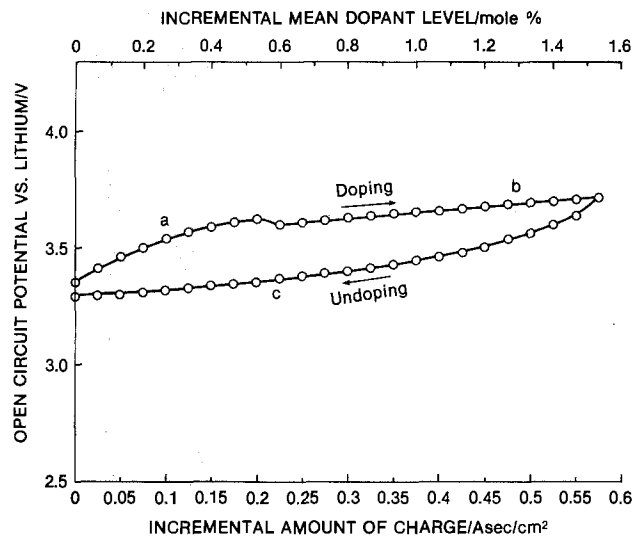


Fig. 3. Open-circuit potential of BF_4 -doped polyacetylene vs. incremental state of charge or mean dopant level. a: 100s on open circuit after $0.25 \text{ mA/cm}^2 \times 100\text{s}$ charging pulses (doping). b: 500s on open circuit after doping. c: 500s on open circuit after $0.25 \text{ mA/cm}^2 \times 100\text{s}$ discharge pulses (undoping).

dopant level of 4 m/o. Subsequent discharges were performed at 0.25 mA/cm^2 to a lower voltage limit of 1.3V and alternate charges at 0.25 mA/cm^2 for 1-2.5h. The charging, discharging, and open-circuit conditions are summarized in Table I, as are the coulombic efficiencies. The latter values vary greatly, from 19 to 55%, in spite of identical current densities during charge and discharge in these three cycles. It appears from Table I that a short open-circuit period between charge and discharge leads to high coulombic efficiencies and vice versa.

Coulombic efficiency of pristine polyacetylene.—The nonreproducibility of consecutive charge-discharge curves of polyacetylene films subjected to different open-circuit periods prior to discharge suggests that the film is in different dopant states. This makes an evalua-

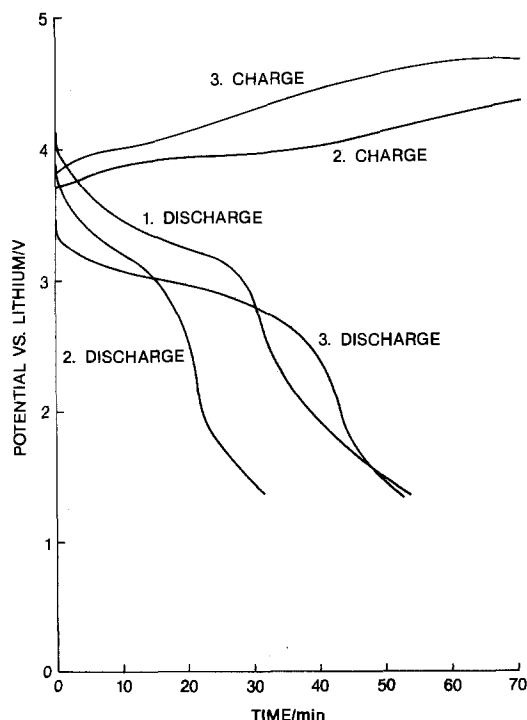


Fig. 4. Consecutive charge-discharge curves of BF_4 -doped polyacetylene. First charge potentiostatically at 3.5, 4, and 4.5V; subsequent charges and discharges galvanostatically at 0.25 mA/cm^2 . Additional details in Table I.

Table I. Coulombic efficiencies in consecutive cycling

Charging			Open circuit <i>t</i> (min)	Discharging			Open circuit <i>t</i> (min)	Efficiency Q_{out}/Q_{in}
<i>i</i> (mA/cm ²)	<i>t</i> (min)	Q_{in} (A-s/cm ²)		<i>i</i> (mA/cm ²)	<i>t</i> (min)	Q_{out} (A-s/cm ²)		
Const. V	120	1.45	10	0.25	54	0.80	30	0.55
0.25	160	2.39	50	0.25	31	0.46	60	0.19
0.25	120	1.75	10	0.25	54	0.82	60	0.47

tion of the effect of current density on discharge performance difficult or impossible.

Therefore, a comparative study of the very first charge and discharge on pristine polyacetylene films was undertaken with discharges performed at different current densities. This enables determination of the coulombic efficiency as a function of current density for polyacetylene identically pretreated and hence presumably in identical initial dopant states. Figure 5 shows charge-discharge curves for three pristine film electrodes B. Charging was carried out with 0.24 mA/cm² for 70 min, equivalent to 1 A-s/cm² or a dopant level of 3.5 m/o. The charging curves for all three films were identical. Discharging was performed after 1h open-circuit stand with current densities of 0.08, 0.24, and 1.2 mA/cm², respectively. A voltage plateau occurs with inflection points at 3.5, 3.45, and 3.03V, respectively. The coulombic efficiencies for discharge to 2.5V decrease from 70% at 0.08 mA/cm² to 64% at 0.24 mA/cm² and to 30% at 1.2 mA/cm².

Reproducibility of the charge-discharge curves was ascertained at 0.24 mA/cm² by employing a fourth pristine film. A charge-discharge curve identical to the relevant curve in Fig. 5 was obtained.

Discussion

Nonsteady-state polarization behavior.—Polarization-time transients of short duration such as those shown in Fig. 1 and 2 are quantitatively interpreted (4) in terms of a semi-infinite linear diffusion model with charge transfer through the polyacetylene/solution interface superimposed on the very slow diffusion (5) of dopant in the polyacetylene. Applicability of semi-infinite linear diffusion to the microporous structure of polyacetylene films is tantamount to the assumption that only the exterior surface of the film is wetted by the electrolyte and that the large interior surface (2000 times larger than the projected area) remains essentially electrolyte free. This assumption is justified by the fact that the observed

double-layer capacitance (4, 5) is 14 and 22 μ F for electrodes B and A, respectively. Such values yield 11 μ F/cm² if only the exterior surface is wetted and 0.005 μ F/cm² if the large interior surface is also wetted. Clearly, only the former value is in agreement with generally accepted double-layer capacitance values. Considering the high viscosity of the electrolytes used in this study, the nonpenetration of the micropores is not surprising. This condition may not apply to electrolytes with low viscosities, especially if the electrodes are carefully vacuum impregnated. Vacuum impregnation, however, has not been applied in this study or, apparently, in other studies (1-3).

The mathematical model further assumes a solid slab of homogeneous physical properties. This means that the fibrous structure is neglected and that an isotropic diffusion coefficient is assumed. In fact, however, the diffusion coefficient is expected to be different parallel and perpendicular to the fiber axis. More complex future models may take these features into account and future experiments may establish the diffusion coefficients parallel and perpendicular to the fiber axis.

The effect of charging the double-layer capacitance is only significant in the first few milliseconds of the transient and can be neglected thereafter. For times short compared to the time constant for diffusion through the entire film and for small polarizations η , the transient is given (9) by

$$\eta = (RT/F) (i/i_0 + 2i \sqrt{t}/\sqrt{\pi D} F c_0) \quad [1]$$

where i is the applied current density, i_0 the exchange current density, t the time, c_0 the initial dopant concentration, D the dopant diffusion coefficient, R the gas constant, T the temperature, and F the Faraday constant. The current densities are related to the wetted exterior (or projected) surface area where ion charge and discharge is thought to occur.³

Validity of Eq. [1] assumes that the dopant concentration is nearly constant (c_0) over a distance from the exterior surface into the interior comparable to the diffusion depth relevant to the subsequent transient. Whether or not this is the case depends on the duration of the pulses and open-circuit periods. Figure 6 shows the polarization transients of Fig. 2 for both charge and discharge at 0.5 mA/cm² in a plot of η against \sqrt{t} . The curves exhibit the straight line behavior required by Eq. [1]. The slope of the straight line yields the diffusion coefficient, and the intercept with the axis $\sqrt{t} = 0$ yields the exchange current density. It is, therefore, clear that the nonsteady-state behavior of polyacetylene electrodes results from the very slow diffusion of dopants into and out of the polymer.

The concentration gradients relevant to a pulse sequence are qualitatively shown in Fig. 7. Figure 7a corresponds to charging (doping) of a pristine or well-equilibrated film. The constant value of dc/dx is dictated by the constant applied current density. Figure 7b shows the partial relaxation of the concentration profile during open circuit. At the interface, $dc/dx = 0$ as the current is zero. Figure 7c shows commencement of discharge with concentration gradients from the preceding charging event still present. Figure 7d shows the relaxation on open circuit of the concentration gradients left from the previous discharge. For comparison with Fig. 7c, Fig. 7e shows the concentration profile for discharge of a well-equilibrated film, kept on open circuit for a long time.

³ It is for this reason that we refer to doping and diffusion of BF_4^- rather than BF_4^- ions in the polyacetylene structure.

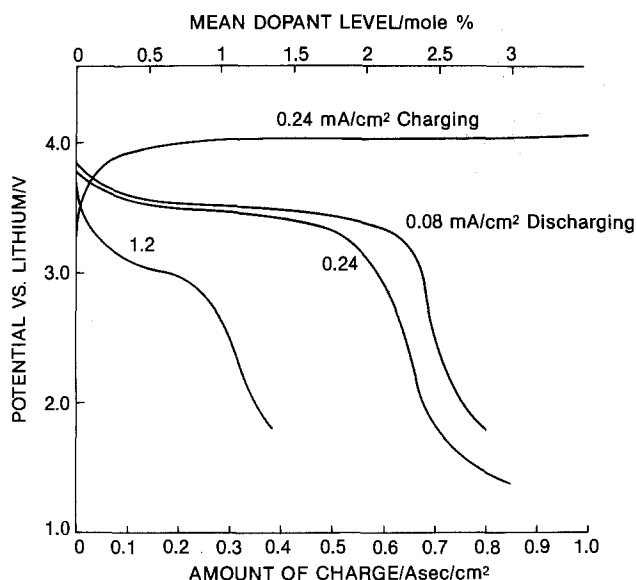


Fig. 5. First charge-discharge curves of pristine BF_4^- -doped polyacetylene at various discharge currents; 1h on open circuit following charging to 3.5 m/o.

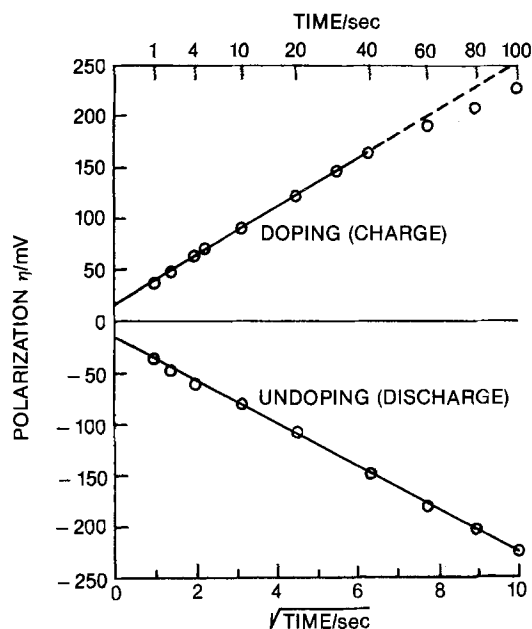


Fig. 6. Polarization-time transients of polyacetylene, BF_4 -doped to 7 m/o, during charging and discharging with $0.5 \text{ mA/cm}^2 \times 100\text{s}$ current pulses; η plotted against \sqrt{t} according to Eq. [1].

Open-circuit potential-dopant level relationship.—The open-circuit potential is dependent on the activity or concentration of dopant at the polyacetylene/solution interface. In view of the small diffusion coefficients of dopants in polyacetylene, very long times of equilibration are required after charging or discharging before steady-state open-circuit potentials are obtained which correspond to uniform dopant concentration throughout the polyacetylene. For a $70 \mu\text{m}$ thick film, equilibration times are in excess of 300h, and for a $7 \mu\text{m}$ film, in excess of 8h. The open-circuit potential vs. charge data in Fig. 3 are thus nonsteady-state data, and the dopant levels near the surface deviate considerably from the mean levels in Fig. 3. The surface values decrease or increase toward the in-

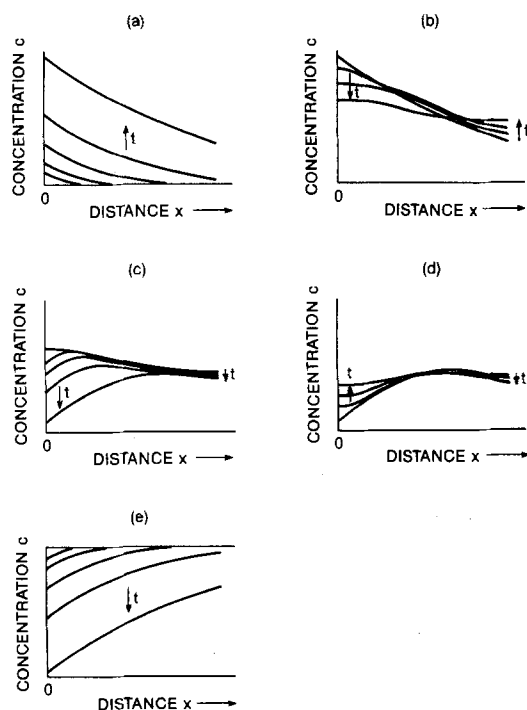


Fig. 7. Dopant concentration profiles in polyacetylene electrodes (qualitatively) at different times during consecutive (a) charging, (b) 1. open circuit, (c) discharging, and (d) 2. open circuit; (e) discharge of previously equilibrated charged film.

terior after charge or discharge, respectively, in a way qualitatively shown in Fig. 7. The decrease in open-circuit potential with longer open-circuit time and the hysteresis of the curves on charge and discharge, as shown in Fig. 3, are thus explained in terms of nonsteady-state diffusion.

Kaneto *et al.* (2) determined the open-circuit potential as a function of dopant level at different times after charging with a series of potential steps. Their results after 2s and 24h open-circuit stand are plotted in Fig. 8 together with the present results. Straight lines result in a semilog plot with slopes between 300 and 400 mV/decade. The open-circuit potentials are highest after the consecutive $0.25 \text{ mA/cm}^2 \times 100\text{s}$ current pulses and 100s open-circuit times employed in this study, since the surface concentration of dopants is highest. The consecutive voltage pulses applied by Kaneto *et al.* allowed more time for the dopant to diffuse into the interior. Hence, the open-circuit potentials are lower after only 2s open-circuit time. The values after 24h open-circuit time are lower yet, but still cannot be regarded as steady-state values. Farrington *et al.* (3) employed 0.05 mA/cm^2 current pulse charges of various durations. Discharge for more than 16h had preceded charging. Open-circuit potentials were observed at unspecified time after charging. The data are also shown in Fig. 8. The high mean dopant levels employed in this study correspond to exceedingly large dopant levels near the surface. Such high dopant levels, in the region of 10-50 m/o, may result in formation of a second phase which would explain the step change in open-circuit potential at 3 m/o mean dopant level.

The large observed slopes of 300-400 mV/decade in Fig. 8 are not readily explained in terms of simple solution behavior as it applies, for example, to the alkali intercalates of graphite (10). Such large changes in open-circuit potential with doping have, however, been observed (11) in other intercalation compounds, such as Li_xTiS_2 and Na_xTaS_2 ; they are consistent with a salt-like model, requiring lattice rearrangement energy, and may also be associated with shifts in the Fermi level energy brought about by the donation of p-type charge carriers from the dopant molecules to the conduction band.

It appears that the slow diffusion of dopants in polyacetylene is responsible for the different behaviors observed by different authors. The boundary conditions established at the surface depend on the previous history of the polyacetylene, such as potentiostatic vs. galvanostatic conditions, applied current density, duration of open-circuit periods, etc. The open-circuit potential, in turn, depends only on the surface concentration. In all studies to date, open-circuit times have been too short to establish the true steady-state relationship between open-circuit potential and dopant level.

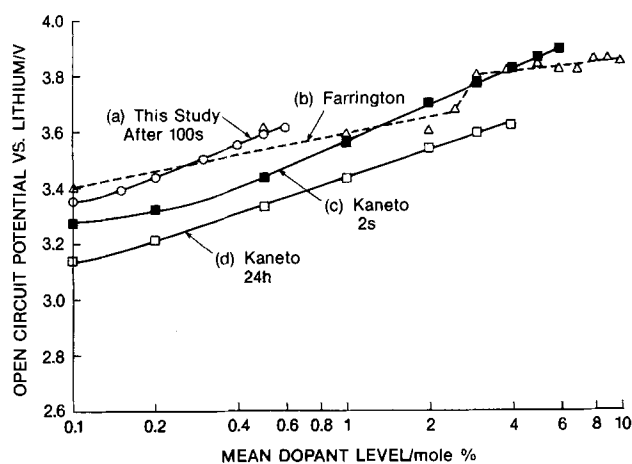


Fig. 8. Open-circuit potential of p-doped polyacetylene vs. logarithm of mean dopant level at specified times after charging. (a) 100s after BF_4 doping with 0.25 mA/cm^2 pulses; (b) unspecified time after ClO_4 doping with 0.05 mA/cm^2 ; (c) 2s after ClO_4 doping with increasing voltage pulses; (d) 24h after ClO_4 doping with voltage pulses.

Charge-discharge cycling.—Short-duration charge and discharge curves such as those shown in Fig. 1 and 2 can be readily interpreted in terms of the simple Eq. [1]. For such short times, the polarization η remains small and the linearization of the exponential terms in the discharge equation leads to cancellation of the terms containing the transfer coefficient α .

However, for longer charge and discharge times, as they are of interest to battery applications, the polarization becomes large enough so that the expression

$$\eta = -[RT/(1 - \alpha)F] [\ln(-i/i_0) - \ln(1 - \sqrt{t/\tau})] \quad [2]$$

must be used (12). The transition time τ is given by

$$\tau = \pi D F^2 c_0^2 / 4 i^2 \quad [3]$$

and signifies the time at which the dopant concentration at the polyacetylene surface has become zero; τ must not be confused with the time constant for dopant diffusion through the entire film.

When τ has been reached, η increases rapidly; this is the case for $\tau = 7200$ s for the discharge curve at 0.08 mA/cm^2 on pristine polyacetylene, shown in Fig. 5. From Eq. [3] with $D = 5.7 \times 10^{12} \text{ cm}^2/\text{s}$, we calculate a dopant concentration of $3.1 \times 10^{-2} \text{ mol/cm}^3$. This corresponds to 34.8 m/o doping when averaged over the penetration depth \sqrt{Dt} of approximately $3 \mu\text{m}$ during 1h charging and 1h on open circuit. Figure 9 shows the discharge curve for 0.08 mA/cm^2 of Fig. 5 in a plot of η vs. $-\log(1 - \sqrt{t/\tau})$. A straight line results at large η as required by Eq. [2]. The slope yields an α value of 0.77 and the intercept with the ordinate at $\sqrt{t/\tau} = 0$ results in an i_0 value of $3.6 \times 10^{-5} \text{ A/cm}^2$. Discharge curves published by Kaneto *et al.* (2) for discharge of polyacetylene doped with 7 m/o ClO_4 also yield straight lines for large η when plotted in terms of η vs. $-\log(1 - \sqrt{t/\tau})$. As an example, the lower curve in Fig. 9 corresponds to discharge at approximately 0.5 mA/cm^2 with $\tau = 2400$ s. The slope yields $\alpha = 0.93$, and the intercept $i_0 = 2.1 \times 10^{-4} \text{ A/cm}^2$. To arrive at these numbers, we have made the reasonable assumption that the diffusion coefficients of BF_4 and ClO_4 are approximately the same. Hence, the model of slow diffusion and discharge explains the present data and those of Kaneto *et al.* equally well. We find no support for the recent model of field-enhanced diffusion of Kaufman *et al.* (13), which they employ to explain a perceived three orders of magnitude discrepancy between observed discharge currents and currents predicted on the basis of a standard diffusion model. The perceived discrepancy is based upon an estimate of the diffusion coefficient which is six orders of magnitude in error [see Ref. (5)]; in addition, the model of field-enhanced diffusion which has been applied to O_2

diffusion in thin SiO_2 films on Si (14) is not applicable to highly doped polyacetylene, as the Debye length for such high charge-carrier densities is far too small.

Coulombic efficiency as function of discharge current.—In consecutive cycling of polyacetylene electrodes with 0.25 mA/cm^2 , we have observed variations of the coulombic efficiency from 19 to 55% (Table I) and have found that long open circuit results in low efficiencies and vice versa. This behavior is due to a larger fraction of the dopant diffusing into the bulk of the polyacetylene during longer open-circuit stand. Figure 7 shows the relevant time-dependent concentration profiles.

Farrington *et al.* (3) observed variations in efficiency from 21 to 46% in three consecutive cycles with approximately identical mean dopant levels of 3 m/o and charge/discharge currents of $0.05/0.5 \text{ mA/cm}^2$. The open-circuit time between charge and discharge was not specified, and we speculate that the variations in their efficiency values too may have been caused by different open-circuit periods.

A study of the effect of current density on coulombic efficiency also requires identical previous history and, hence, identical states of doping. This was assured in the present study by employing pristine polyacetylene and identical charging conditions and open-circuit times prior to discharge. According to the results in Fig. 4, the coulombic efficiency of pristine film, charged and discharged once, decreases significantly with increasing discharge current density. Such behavior may be suspected again to result from the slow diffusion of dopants in polyacetylene. The effect of slow diffusion and simultaneous slow discharge on the coulombic efficiency can be predicted from Eq. [1] or [2], for small or large values of η , respectively. For discharge performed at various current densities i_d to small fixed polarization η_F , the relevant discharge times t_d follow from Eq. [1] as

$$\sqrt{t_d} = (\sqrt{\pi D} F c_0 / 2) (F \eta_F / RT i_d - 1/i_0) \quad [4]$$

The mean dopant concentration c_0 is related to the input charge $q_{in} = i_c t_c$ by

$$c_0 = q_{in} / F \delta \quad [5]$$

where i_c , t_c are charge current density and time, respectively, and δ the film thickness. The coulombic efficiency $e_{\text{coul}} = q_{\text{out}}/q_{\text{in}}$ then follows from Eq. [4] as

$$e_{\text{coul}} = (\pi D q_{in} i_d 4 \delta^2) (F \eta_F / RT i_d - 1/i_0)^2 \quad [6]$$

According to Eq. [4], for discharge to a fixed small polarization η_F , a plot of $\sqrt{t_d}$ vs. the reciprocal discharge current ($1/i_d$) should yield a straight line. Figure 10 shows a plot of this type for $\eta_F = 50 \text{ mV}$ and 100s discharge pulses applied to electrode A. A straight line is indeed obtained, and the observed discharge times are predicted very well for a doping concentration near the surface of 5 m/o, which is somewhat smaller than the 7% derived from the charge input under the assumption of a flat concentration profile throughout the polyacetylene.

No quantitative agreement between observed and predicted coulombic efficiencies is obtained for large polarizations as they apply to the discharge curves in Fig. 4 and 5. Only the general trend is predicted correctly; namely, that for polyacetylene in identical dopant state just prior to discharge, the efficiency decreases significantly (70, 64, and 30%) with increasing current density (0.08, 0.24, and 1.2 mA/cm^2).

On polyacetylene in different dopant states prior to discharge, Kaneto *et al.* (2) observed an unexplained increase in coulombic efficiency (74, 79.3, and 86.7%) with increasing current (0.1, 0.55, and 1.0 mA). Charging in all three cases had been carried out to a mean dopant level of 7 m/o but for times of 12, 7, and 5.5h, respectively. The results of the present study provide a ready explanation for the anomalous observed behavior: during longer charging time, a larger fraction of the total amount of dopant diffuses into the polyacetylene, thus leaving a smaller dopant concentration near the surface for reduction dur-

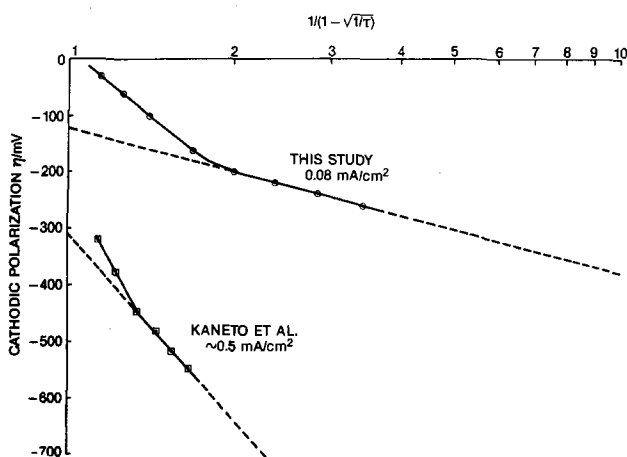


Fig. 9. Cathodic polarization or discharge curves during undoping vs. $-\log(1 - \sqrt{t/\tau})$ according to Eq. [2]. (a) 1h discharge of pristine 3.5 m/o BF_4 -doped polyacetylene with 0.08 mA/cm^2 (see Fig. 5); $\tau = 7200$ s; (b) 0.7h discharge of 7 m/o ClO_4 -doped polyacetylene with $\sim 0.5 \text{ mA/cm}^2$, $\tau = 2400$ s.

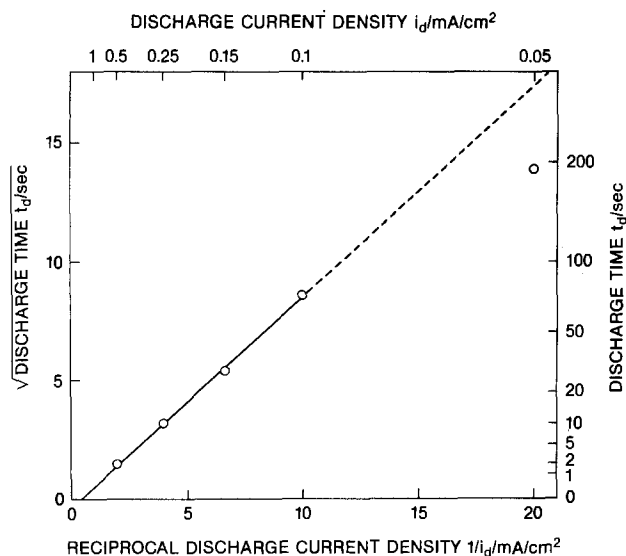


Fig. 10. Discharge time $\sqrt{t_d}$ vs. reciprocal discharge current density to fixed polarization of -50 mV according to Eq. [4]; evaluation of transients from 0.05 to 0.5 mA/cm² shown in Fig. 2.

ing subsequent discharge. This behavior is evident from the time-dependent concentration profiles shown in Fig. 7.

Conclusions

The behavior of BF₄-doped polyacetylene electrodes during charge, discharge, and open circuit is controlled by slow solid-state diffusion of the dopant in the polymer. Steady-state potentials are therefore usually not attained, unless the amount of charge (dopant) injected or removed is of the order of only 0.01 mA-s/cm² or open-circuit times between charges or discharges are exceedingly long, *i.e.*, in excess of 300h for a 70 μ m thick film. Since such long times have not been employed in this or other studies, no unique relationship between open-circuit potential and state of charge or dopant level has been established as yet.

Discharge curves of BF₄-doped polyacetylene reported here and of ClO₄-doped polymer obtained by others are interpreted quantitatively by a model involving slow diffusion and discharge. There appears to be no need to invoke a field-enhanced diffusion model.

Coulombic efficiencies observed on pristine polyacetylene electrodes, identically BF₄-doped for 1h with

0.24 mA/cm² to 3.5 m/o followed by 1h on open circuit, are 70, 64, and 30% for discharge with 0.08, 0.24, and 1.2 mA/cm², respectively. The dependency of efficiency on current is predicted quantitatively by a semi-infinite diffusion model if the discharge polarizations and times are small. The anomalous increase in efficiency with increasing discharge current observed by other authors is readily explained by different dopant concentrations near the surface caused by very different charging times.

Acknowledgments

The preparation of the polyacetylene films and the electrolytes by the Rohm and Haas Company, and the help of J. J. Rogers in the experimentation, are gratefully acknowledged.

Manuscript submitted Dec. 26, 1984; revised manuscript received May 24, 1985. This was Paper 616 presented at the New Orleans, Louisiana, Meeting of the Society, Oct. 7-12, 1984.

General Electric Company assisted in meeting the publication costs of this article.

REFERENCES

1. P. J. Nigrey, D. MacInnes, Jr., D. P. Nairns, and A. G. MacDiarmid, *This Journal*, **128**, 1651 (1981).
2. K. Kaneto, M. R. Maxfield, D. P. Nairns, and A. G. MacDiarmid, *J. Chem. Soc., Faraday Trans.*, **78**, 3417 (1982).
3. G. C. Farrington, B. Scrosati, D. Frydryk, and J. DeNuzzio, *This Journal*, **131**, 7 (1984).
4. F. G. Will, *ibid.*, **132**, 2093 (1985).
5. F. G. Will, *ibid.*, **132**, 743 (1985).
6. F. G. Will, R. S. McDonald, R. D. Gleim, and M. R. Winkle, *J. Chem. Phys.*, **78**, 5847 (1983).
7. T. Ito, H. Shirakawa, and S. Ikeda, *J. Polym. Sci.*, **12**, 11 (1974).
8. K. Shimamura, F. E. Karasz, J. A. Hirsch, and J. C. W. Chien, *Macromol. Chem. Rapid Commun.*, **2**, 473 (1981).
9. T. Berzins and P. Delahay, *Z. Elektrochem.*, **59**, 792 (1955).
10. S. Aronson, F. J. Salzano, and D. Ballafiore, *J. Chem. Phys.*, **49**, 434 (1968).
11. M. S. Whittingham, in "Progress in Solid State Chemistry," Vol. 12, G. M. Rosenblatt and W. L. Worrell, Editors, pp. 41-100, Pergamon Press, Elmsford, NY (1980).
12. T. Berzins and P. Delahay, *J. Am. Chem. Soc.*, **77**, 6448 (1955).
13. J. H. Kaufman, E. J. Mele, A. J. Heeger, R. Kaner, and A. G. MacDiarmid, *This Journal*, **130**, 571 (1983).
14. W. A. Tiller, *ibid.*, **127**, 625 (1980).

Kinetic Investigation on the Mechanism of the Photoelectrochemical Oxidation of Water and of Competing Hole Processes at the TiO₂(Rutile) Semiconductor Electrode

F. Vanden Kerchove, A. Praet, and W. P. Gomes*

Rijksuniversiteit Gent, Laboratorium voor Fysische Scheikunde, B-9000 Gent, Belgium

ABSTRACT

The competition between the oxidation of H₂O and that of Br⁻ ions at the illuminated surface of the semiconducting rutile anode was studied as a function of the Br⁻ concentration at the surface, the light intensity, the electrode potential, and the surface pretreatment by means of the rotating ring-disk electrode (RRDE) technique. The results allow one to propose a mechanism for the multistep oxidation of H₂O to O₂ as well as for the oxidation of Br⁻, the latter reaction being assumed to occur with the surface intermediate H₂O₂ of the former. The data also indicate the occurrence of a surface electron-hole recombination process involving intermediates of the H₂O oxidation, and demonstrate the influence of surface imperfections upon the competition studied.

The anodic oxidation of water to oxygen by photo-generated holes at the semiconducting TiO₂ (rutile) electrode is the reaction which led, more than a decade ago, to the concept of solar-to-chemical energy conversion in photoelectrochemical cells (1). However, the mechanism of this important reaction is not known in detail yet. Indeed, the saturation photocurrent density only depends on the light intensity. Therefore, data on the reactivity of water for holes and on the different steps of this oxidation are not directly accessible by kinetics, and can only be obtained by studying the competition between different reagents for the holes at the electrode surface. One possible method, which was formerly used for TiO₂ (2) and SrTiO₃ (3), consists of the measurement of the photocurrent under the addition of so-called current doubling reagents to the photoelectrochemical cell. A more recent technique uses the rotating ring-disk electrode (RRDE): the reaction product of one of the competitive photoreactions at the semiconductor disk electrode is detected specifically at the metal ring electrode. A competitive reagent, which is well suited for this study, is the bromide ion. Its oxidation product, Br₂, is stable in acid solutions and can be easily detected at the ring electrode.

Other investigators have already presented results, obtained by means of this method at monocrystalline TiO₂ electrodes, where Br⁻ competed with water for holes. Kobayashi *et al.* (4) observed at pH = 2 that Br⁻ was very reactive as compared to water. At high concentrations of Br⁻ ($c \geq 10^{-2}$ mol-dm⁻³), the fraction n of the photocurrent that oxidizes Br⁻ appeared to be independent of the light intensity. At lower bromide concentrations, n decreased when the light intensity increased, apparently because of the diffusion limitation of the bromide transport to the electrode. Also, Fujishima *et al.* (5) studied the competition between Br⁻ and H₂O. They also stated that n was independent of the light intensity, without mentioning, however, at which values of pH and c this observation was made. Both groups of investigators found that the reactivity of Br⁻ decreases with respect to that of water when the pH of the solution is increased. Hence, higher concentrations of bromide can be used for competition studies in less acid solutions, so that the oxidation of Br⁻ at the anode is no longer limited by the diffusion rate. However, at higher pH, several complications must be taken into account: dismutation of Br₂ to hypobromite and bromide is possible (6); in unbuffered solutions, the pH at the photoanode changes because of the photo-oxidation of water; and in buffered solutions, the buffer (*e.g.*, acetate) may react with the holes (7).

Therefore, we preferred to confine our measurements to solutions of a pH less than 2, so that the addition of buffers could be avoided and nevertheless changes in pH could be neglected. At these pH values, the range of bro-

mid concentrations, in which changes of n can be observed without the influence of diffusion limitation, is rather small; however, the concentration range can be considerably extended by exploiting the properties of the RRDE. By varying the rotation speed of the RRDE, the flux of bromide to the disk can be monitored. By application of the diffusion laws, c_s (the concentration of bromide at the disk surface) can be calculated (see results). Thus, n can be measured as a function of c_s under different circumstances of light intensity, electrode potential, and surface pretreatment. Such measurement may yield interesting indications on reaction mechanisms, as was recently shown in the case of III-V semiconductor electrodes [see, *e.g.*, Ref. (8) and (9)]. By measuring n at different stages of the photoetching procedure, the influence of the surface pretreatment on the photoelectrochemical behavior of TiO₂ can be studied.

Experimental

All TiO₂ electrodes were cut from one monocrystalline sample, purchased from NL Industries (South Amboy, New Jersey). The sample was doped with 0.05 weight percent (w/o) Nb₂O₅. The electrodes were worked to a cylinder with a height of 5.0 mm and a diameter of 5.0 mm. The front side was the (001) face. Before the TiO₂ sample was mounted as the disk electrode, indium was evaporated on the back and then it was heated in a nitrogen flow during 20 min at 400°C. After cooling, the disk was fitted in a Teflon® tube, which was in turn fitted in a copper tube, on top of which a platinum ring was soldered. Around the ring and the copper tube, a PVC shaft of a suitable shape was mounted. In order to avoid leaks to the back of the electrodes, Cyanolit® 202, a cyanoacrylate ester, was applied between the electrodes and the Teflon and solidified there. Before any measurement, the electrode surface was successively polished with abrasive papers and Al₂O₃ powders of decreasing grain size (0.3 μm final polish) and the previously described photoetching procedure (10) was applied.

Six electrodes were assembled in this way. All but one, exhibiting an inhomogeneous surface, showed very similar behavior. The results reported below were all obtained on two of them, indicated by A and B, respectively. The dimensions of the RRDE r_1 , r_2 , r_3 (being the radius of the disk, and the inner and the outer radius of the ring, respectively), and the theoretical collection efficiency N are given in Table I. For the calculation of N from the dimensions of the RRDE, the theoretical treatment of Albery and Bruckenstein (11) was followed.

The combined ring-disk electrode was fixed in the cover of the perspex electrochemical cell. In the cell, an auxiliary electrode made of platinized platinum gauze was present; a saturated K₂SO₄-Hg₂SO₄ reference electrode (Radiometer K601) was connected to the cell

* Electrochemical Society Active Member.

Table I. Characteristics of the electrodes used

Specimen	r_1 (mm)	r_2 (mm)	r_3 (mm)	N
A	2.37	3.47	3.88	0.213
B	2.40	3.45	3.92	0.232

through a saturated K_2SO_4 salt bridge. The four electrodes were connected to a bipotentiostat (Bipad Tacussel). The potential of the disk or the ring could be swept by a homemade voltage programmer. All electrode potentials will be expressed in volts vs. the saturated sulfate electrode (SSE). The cell was installed in an earthed metal case. The ring-disk electrode could be rotated by means of an electric motor (Tacussel); the rotation speed could be varied between 0 and 2400 rpm. The speed was measured by means of an opto-digital tachometer.

The disk was illuminated by a 450W xenon arc lamp with a stabilized power supply (Oriol). The light was entering the electrochemical cell through a Pyrex window. By placing neutral density filters (Balzers) in the light beam, different light intensities were obtained. No absolute measurement of the light intensity was performed. The saturation photocurrent was always proportional to the light intensity for each state of the electrode surface and was hence considered as a measure of the light intensity for the electrode state considered. All electrodes were mounted in the same position relative to the lamp; thus, the saturation photocurrent under full light intensity can be used as a reference for the measurement of the light intensity at the different states (damaged or etched) of the surface.

All solutions were prepared with reagent-grade chemicals (Merck) in deionized water. During the measurements, pure N_2 (99.98%) was bubbled through the electrolyte solution in order to remove the dissolved and formed oxygen.

The value of N was checked experimentally by dark reduction of $Fe(CN)_6^{3-}$ at the disk and reoxidation of the resulting $Fe(CN)_6^{4-}$ at the ring. The mean experimental value of N differed from the calculated one by less than 0.2% for electrode A and by less than 0.1% for electrode B.

Results on the competition between Br^- and H_2O are expressed by the competition ratio n . The value of n is calculated from the currents at the ring-disk electrode

$$n = I_{Br}/I_D = |I_R|/NI_D \quad [1]$$

where I_{Br} is the photocurrent associated with the oxidation of bromide, and $|I_R|$ and I_D the absolute increase of the (negative) ring and the (positive) disk current, respectively, resulting from the illumination of the disk. Unless otherwise stated, the disk was kept at +1.00V, i.e., in the saturation region of the photocurrent, and the ring at -0.20V, i.e., in the saturation region of the bromine reduction.

Results

Fully etched electrodes.—Influence of the light intensity and of the bromide concentration on n .—In accordance with the results of Kobayashi *et al.* (4) and Fujishima *et al.* (5), it is a general observation that, for relatively high concentrations of Br^- , n is independent of the light intensity, while for lower concentrations a strong dependence of n on the light intensity is observed. This is illustrated in Fig. 1, when n is given as a logarithmic function of the saturation photocurrent density i for three different concentrations of Br^- . These curves are very similar to those presented by Kobayashi *et al.* (4). As part of these curves are influenced by diffusion limitation of Br^- , we will, in order to isolate the effect of the light intensity, consider in what follows the concentration of Br^- ions at the surface, c_s . Under circumstances of diffusion control, c_s is smaller than the bromide concentration in the bulk, c . In the steady state, the flux of material reacting at the electrode surface must equal the flux being transported through the diffusion layer. Hence

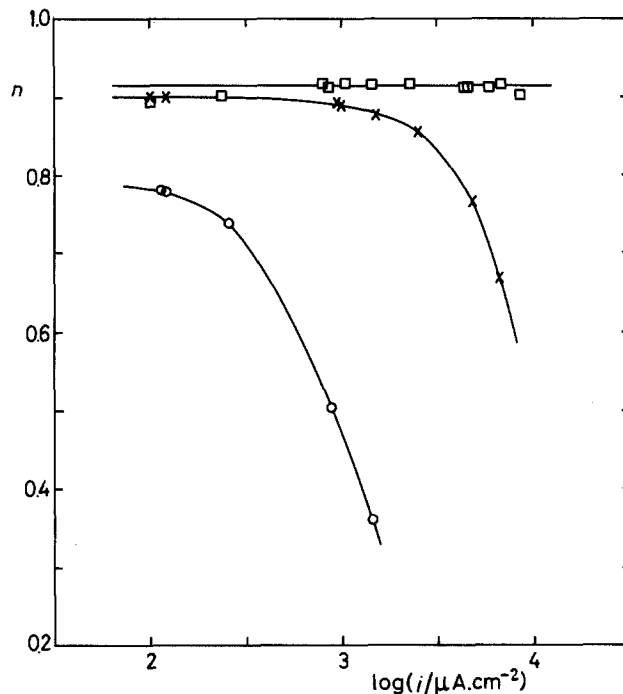


Fig. 1. The competition ratio n as a function of the logarithm of the total photocurrent density i at different concentrations c of bromide. $n-TiO_2$ (specimen A), surface area 17.6 mm^2 , disk potential +1.0V vs. SSE, ring potential -0.2V vs. SSE, rotation speed 600 rpm, supporting electrolyte $0.33 \text{ mol}\cdot\text{dm}^{-3} \text{ HClO}_4$. Bromide concentration $c/\text{mol}\cdot\text{dm}^{-3}$: (□) 0.1; (×) 0.01; (○) 0.001.

$$i_{Br} = \frac{I_{Br}}{A} = \frac{FD(c - c_s)}{x_D} \quad [2]$$

i_{Br} being the part of the photocurrent density corresponding to the oxidation of Br^- , A the surface area of the disk, F the Faraday constant, x_D the thickness of the diffusion layer, and D the diffusion constant of Br^- . The value of x_D (in SI units) is given by (12)

$$x_D = 0.643 W^{-1/2} \nu^{1/6} D^{1/3} \quad [3]$$

with W the rotation speed of the RRDE (in revolutions per second) and ν the kinematic viscosity of the solution ($\nu = 0.9 \times 10^{-6} \text{ m}^2\cdot\text{s}^{-1}$).

The value of D can be calculated from the slope of the plot of I_{Br} vs. $W^{1/2}$ under circumstances of pure diffusion control. Indeed, when $c_s = 0$ and c is kept constant, I_{Br} is a function of the rotation speed only (see Eq. [2] and [3]). A value of $D = 1.56 \times 10^{-9} \text{ m}^2\cdot\text{s}^{-1}$ was obtained in $0.33 \text{ mol}\cdot\text{dm}^{-3} \text{ HClO}_4$ as the supporting electrolyte, which is in good agreement with that measured by Johnson and Bruckenstein (13) in $1 \text{ mol}\cdot\text{dm}^{-3} \text{ H}_2\text{SO}_4$ ($D = 1.58 \times 10^{-9} \text{ m}^2\cdot\text{s}^{-1}$).

From Eq. [1]-[3], Eq. [4] can be derived, which shows that c_s can be varied by varying the rotation rate and the bulk concentration of Br^- , and can be determined by measuring $|I_R|$ at given c and W , the values of N , A , ν , and D being known

$$c_s = c - \frac{0.643\nu^{1/6}}{NFAD^{2/3}} \cdot \frac{|I_R|}{W^{1/2}} \quad [4]$$

Values of n were measured at three different light intensities as a function of c_s . The results for the etched electrode A are plotted in Fig. 2(a). At high values of c_s , n tends to a constant value, but at lower values of c_s , n appears to be a function of both c_s and of the light intensity and, hence, of the total photocurrent density i .

Influence of the electrode potential on n .—The photocurrent at the disk remains nearly unaffected by variations of the disk potential, if larger than +0.25V. However, when the potential is decreased gradually to -0.5V, the photo-

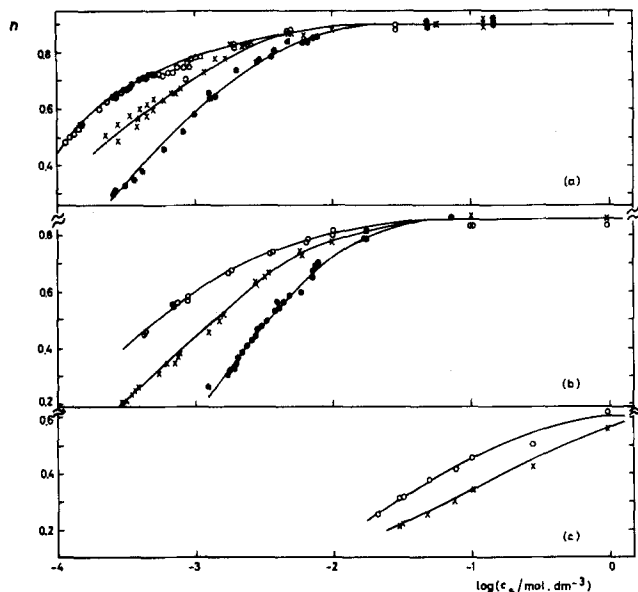


Fig. 2. The competition ratio n as a function of the logarithm of the bromide concentration at the surface c_s at different light intensities corresponding to three values of the disk current density $i/\mu\text{A}\cdot\text{cm}^{-2}$: (○) 142; (×) 568; (●) 2840. Surface pretreatment: (a) photoelectrochemically etched; (b) damaged by polishing on Al_2O_3 powder of $0.3\ \mu\text{m}$ grain size; (c) as in (b), but $1.0\ \mu\text{m}$ grain size. $n\text{-TiO}_2$ (specimen A), disk potential $+1.0\ \text{V}$ vs. SSE, ring potential $-0.2\ \text{V}$ vs. SSE, supporting electrolyte $0.33\ \text{mol}\cdot\text{dm}^{-3}\ \text{HClO}_4$.

current declines to almost zero because of the recombination of holes with electrons, and simultaneously n is observed to increase. In Fig. 3, the top curve represents results obtained at a fully etched electrode. In order to avoid complications by diffusion limitation, the light intensities were kept low enough. It can be noticed that the photocurrent can be decreased by decreasing either the light intensity or the disk potential, the effect on n being generally more pronounced in the latter case. This phenomenon is illustrated clearly in Fig. 4, by plotting n as a

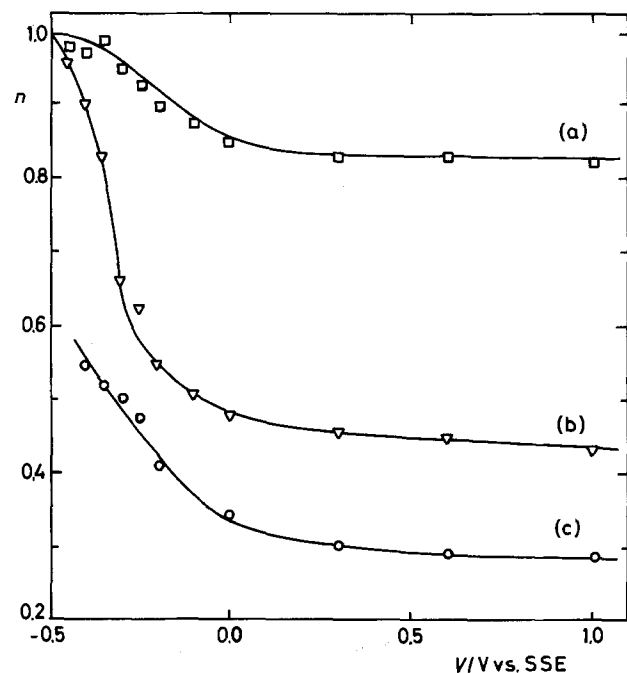


Fig. 3. The competition ratio n as a function of the disk potential V , with a limiting photocurrent density (at $V = +1.0\ \text{V}$ vs. SSE) of $616\ \mu\text{A}\cdot\text{cm}^{-2}$, after different periods of photoetching: (a) 20h (fully etched); (b) 13h; (c) 6.5h. $n\text{-TiO}_2$ (specimen B), ring potential $-0.2\ \text{V}$ vs. SSE, rotation speed 600 rpm, supporting electrolyte $0.33\ \text{mol}\cdot\text{dm}^{-3}\ \text{HClO}_4$, bromide concentration $0.01\ \text{mol}\cdot\text{dm}^{-3}$.

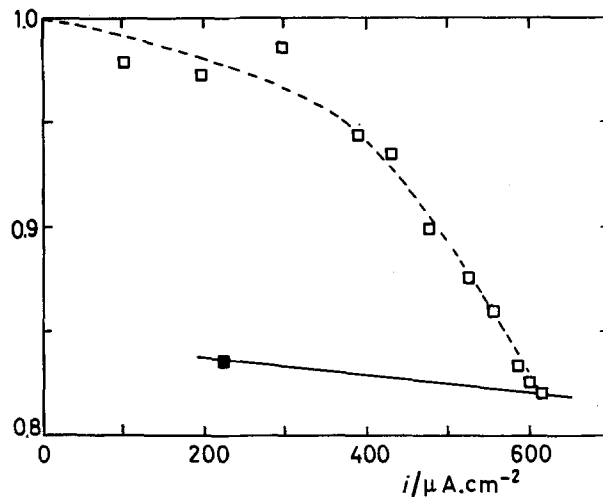


Fig. 4. Plot of n vs. the total photocurrent density i , changed by either varying the electrode potential (□) (same data as in curve (a) of Fig. 3) or the light intensity (■).

function of the photocurrent density. The full line shows the change of n when the photocurrent is varied by a change of the light intensity. As the broken line indicates, the variations of the photocurrent, due to changes of the disk potential, are by far more considerable; in that case, n can rise to its maximum value of 1.

Damaged electrodes.—Influence of the light intensity and of the bromide concentration on n .—After the measurements represented in Fig. 2(a), the electrode was polished with Al_2O_3 powder of $0.3\ \mu\text{m}$ so that damage was induced to the surface and to the underlying region. As a consequence of the ensuing enhanced electron-hole recombination (10), the light intensities had to be increased by a factor of 2.1 in order to obtain nearly the same photocurrents as in Fig. 2a. Then the dependence of n on the light intensity and on c_s was studied again [see Fig. 2b]. Finally, the polishing was repeated with Al_2O_3 powder of $1\ \mu\text{m}$. As a result of the larger degree of damaging, the light intensities had to be increased again, now by a factor of about 5 relative to those used for Fig. 2(b). Even with full illumination, it was no longer possible to produce a photocurrent of $500\ \mu\text{A}$ in this case. The results obtained after the final polish are plotted in Fig. 2(c).

For damaged surfaces, the concentration range where the influence of the light intensity on n is observed, is extending to higher values of c_s ; this effect is very pronounced in Fig. 2c. By comparing parts a, b, and c of Fig. 2, it is obvious that the more the surface has been damaged, the lower the value of n is for each pair of parameters (i and c_s).

Influence of the electrode potential on n .—Similarly, as with fully etched electrodes, it is observed with damaged disks that in the onset region of the photocurrent-voltage curve, n increases significantly as the potential is decreased. In Fig. 3, below curve a representing data for the fully etched electrode B, two other curves (b and c) are given, representing data, obtained before the photoelectrochemical etching of the electrode was completed. The values of n , corresponding with curve c were measured after about 6.5h of photoetching (the limiting photocurrent was at that moment $100\ \mu\text{A}$ with full illumination). The values of curve b were measured after another 6.5h of etching; the limiting photocurrent had risen to $300\ \mu\text{A}$, while the complete etching lasted 20h and led to a maximum photocurrent of $400\ \mu\text{A}$.

In all cases, n decreases with increasing V to reach a constant value in the voltage region where, also, the photocurrent is almost constant.

Discussion

Other investigators (4) obtained results, similar to those shown in Fig. 1, but ascribed the decrease of n at increas-

ing light intensity in dilute bromide solutions fully to the diffusion limitation of Br^- transport. The measurements reported here, however, reveal a clear influence of the light intensity and hence of the total photocurrent density on n , at given concentration of Br^- at the surface, for etched as well as for damaged electrodes. Such influence shows that the competing anodic oxidation reactions, *i.e.*, those of H_2O and Br^- , do not occur through parallel pathways involving consecutive one-hole steps, since in that case n should be independent of the light intensity.

In several recent publications by our research group, the kinetics of competing hole processes at semiconductor photoanodes have been analysed (8, 9, 14, 15). Although stabilization of photocorroding n-type III-V semiconductor electrodes is particularly stressed, the kinetic models developed there can be easily adapted to the treatment of the competition between the oxidation of H_2O and that of Br^- at the TiO_2 surface. With III-V compounds as well as with TiO_2 , one reagent is always present in large excess (*i.e.*, the electrode material itself in the case of III-V compounds and H_2O in the case of TiO_2) and is oxidized in a multistep reaction, whereas another reducing agent is added to the solution, oxidized in a relatively simple reaction, and detected in a quantitative way. The analysis of competing electrode reactions mentioned leads to the conclusion that those mechanisms, which lead to a light-intensity-dependent competition ratio, are grouped kinetically into two classes, in which n is either a function of the single variable c_s/i or of c_s^2/i . The present experimental results were found to belong to the latter class, as is illustrated by Fig. 5, where the data of Fig. 2a have been replotted as n vs. $\log(c_s^2/i)$, leading to one single curve. All but one (a chemically improbable one) of the previously derived kinetic relationships in which n is a function of (c_s^2/i) are of the type $n^2/(1-n) \sim c_s^2/i$. This relationship appears not to be obeyed in the present case, however.

Therefore, in order to account for the experimental kinetics of the H_2O vs. Br^- competition on the TiO_2 electrode, we propose a reaction mechanism which is to a certain extent analogous to mechanisms devised earlier for cases in which the competition ratio is a function of c_s^2/i and which is furthermore based upon various literature data on the photooxidation of H_2O on TiO_2 . By spin trapping and electron spin resonance techniques, Jaeger and Bard (16) revealed the existence of adsorbed hydroxyl and perhydroxyl radicals on illuminated TiO_2 powder, which were dispersed in aqueous solutions. Wilson (17) proposed associating intermediates of the O_2 evolution process with surface states within the bandgap of TiO_2 . It is presently accepted that OH^\cdot radicals and adsorbed H_2O_2 molecules are involved as intermediates and as surface states in the photo-oxidation of H_2O on TiO_2 ; in a number of recent papers, Salvador and Gutierrez dealt with this subject (18-20). These authors proposed the following mechanism for the photo-oxidation of H_2O to H_2O_2 : (i) capture of a photogenerated hole by a Ti-OH -surface group, creating a surface OH^\cdot radical; (ii) electron transfer from an OH^- ion, physisorbed from solution, to a

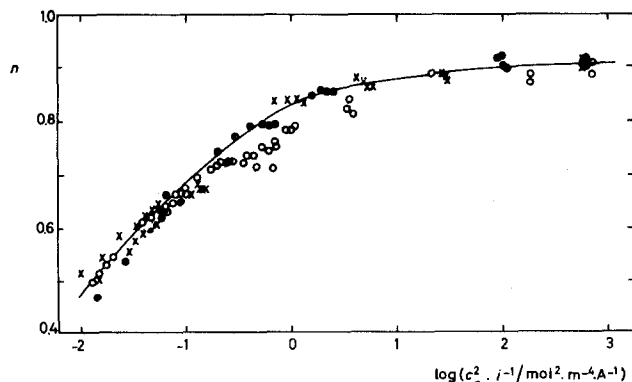
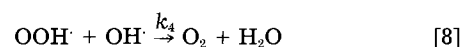
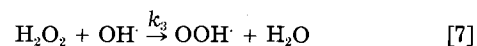
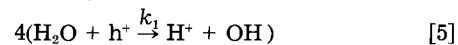


Fig. 5. Plot of n vs. $\log(c_s^2/i)$. Same data as in Fig. 2(a).

surface OH^\cdot radical; (iii) formation of H_2O_2 from two OH^\cdot radicals. Oxygen is then suggested to be formed either by decomposition of H_2O_2 or by further capture of two holes. Details about these eventual reactions are not given in the references cited. Neither of both these proposed pathways for further reaction of H_2O_2 can account for the n vs. c_s^2/i relationship describing the competition between H_2O and Br^- (see below), so that we propose the following mechanism for the photoanodic oxidation of H_2O



Hence, the overall reaction is



Reaction [7] was already considered by Jaeger and Bard (16) as a possible source of the observed OOH^\cdot at TiO_2 surfaces. Reactions [7] and [8] are assumed to occur during the gas phase decomposition of H_2O_2 (21).

The general kinetic analysis mentioned above (8) suggests consideration of the reaction of Br^- with the surface intermediate H_2O_2 , which is known to proceed in the case of a homogeneous liquid phase and to take place according to (22)



followed by the much faster reaction



Note that in this mechanism (reactions [5]-[8], [10], and [11]), the competition between the formation of O_2 and that of Br_2 is actually a competition for H_2O_2 between OH^\cdot radicals and Br^- ions, as expressed in Eq. [7] and [10], and that the light-intensity dependence originates from the fact that the OH^\cdot radicals are formed by holes (Eq. [5]) and hence by light. The intermediates OH^\cdot , H_2O_2 , and OOH^\cdot are assumed to be adsorbed to the surface. The OH^\cdot radical is considered as being mobile along the surface (a layer of adsorbed H_2O can be conceived in which the OH^\cdot radical captures an electron from a neighboring H_2O molecule). The adsorbed H_2O_2 is assumed to react with a bromide ion from the adjacent solution layer (reaction [10]).

Under steady-state conditions, the concentrations of the intermediates OH^\cdot , H_2O_2 , and OOH^\cdot are constant, resulting in Eq. [12]-[14]

$$\frac{dx_1}{dt} = k_1 p_s - 2k_2 x_1^2 - k_3 x_1 x_2 - k_4 x_1 x_3 = 0 \quad [12]$$

$$\frac{dx_2}{dt} = k_2 x_1^2 - k_3 x_1 x_2 - k_{\text{Br}} x_2 c_s = 0 \quad [13]$$

$$\frac{dx_3}{dt} = k_3 x_1 x_2 - k_4 x_1 x_3 = 0 \quad [14]$$

Here x_1 , x_2 , and x_3 represent the surface concentrations of OH^\cdot , H_2O_2 , and OOH^\cdot , respectively, and p_s the concentration of holes at the electrode surface.

The total steady-state current density is proportional to the light intensity and is given by the following expression, in view of Eq. [5] and considering the surface H_2O concentration to be constant

$$i = ek_1 p_s \quad [15]$$

where e is the absolute value of the elementary charge. According to Eq. [10] and [11], the part of i corresponding to the oxidation of Br^- is given by

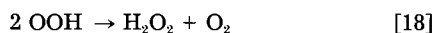
$$ni = i_{\text{Br}} = 2ek_{\text{Br}} x_2 c_s \quad [16]$$

Elimination of the unknown quantities p_s , x_1 , x_2 , and x_3 from Eq. [12]-[16] leads to the expression

$$\frac{n^2(1+n)}{(1-n)^2} = \frac{ek_2k_{Br}^2}{k_s^2} \cdot \frac{c_s^2}{i} \quad [17]$$

which conforms to the experimental result that n is a function of the single variable c_s^2/i (Fig. 5).

It should be remarked that, in this equation, k_1 and k_4 are absent: only reactions [6], [7], and [10] determine the competition. It has been found that the shape of the function (Eq. [17]) is not changed if reaction [5] is assumed to be reversible. Neither is it changed when reaction [8] is replaced by another plausible reaction (21)



Under the latter assumption, only the ratio of the reaction constants in Eq. [17] must be adapted. On the other hand, if further oxidation of H₂O₂ by a hole instead of reaction [7] were assumed, an expression would result in which n is a function of (c_s/i) instead of (c_s^2/i) ; if decomposition of H₂O₂ were assumed, an i -independent expression for n would be obtained.

When the experimental results are plotted as $n^2(1+n)/(1-n)^2$ vs. c_s^2/i , the linearity is not completely satisfactory. However, it can be improved by inserting, instead of n , a quantity n' defined by

$$n' = n/n_{\max} \quad [19]$$

and in which n_{\max} represents the observed maximum value of n (in Fig. 2, n_{\max} is equal to 0.90, 0.86, and 0.59 for parts a, b, and c, respectively). In Fig. 6, the data of Fig. 2 have been replotted as $\log[n'^2(1+n')/(1-n')^2]$ vs. $\log(c_s^2/i)$. It is seen that the sets of data a, b, and c can be represented in a very satisfactory way by linear plots with slope 1, demonstrating that Eq. [17] holds for n' and hence indicating that the proposed competing reaction mechanism (Eq. [5]-[7], [10], and [11]) is valid.

Kobayashi *et al.* (23) already remarked that, at damaged TiO₂-electrodes, n does not tend to 1 when the concentration of bromide is increased. This was explained by the assumption that polishing results in the creation of special surface sites (*e.g.*, Ti³⁺-Ti³⁺ pairs), where the formation of O₂ (and surface electron-hole recombination) would occur by preference. Hence, the surface might be conceived as being composed of two parts, *i.e.*, a nondamaged one, where the competition between the formation of Br₂ and that of O₂ proceeds according to reactions [5]-[11], and a damaged one, where only O₂ is formed. This reasoning would be compatible with the correction of n by the factor $(1/n_{\max})$. Also, with the fully etched electrode, the limiting value of n remains less than 1. It is therefore supposed that even after prolonged etching, a certain fraction of the surface consists of special Ti³⁺-Ti³⁺ sites.

The foregoing considerations refer to situations in which surface electron-hole recombination can be excluded because of the large band bending. Recombination mechanisms, in which conduction band electrons are captured in surface states, associated with intermediates of the anodic decomposition of the semiconductor, have

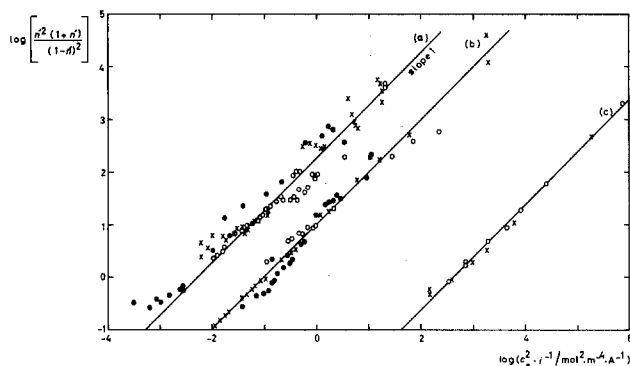
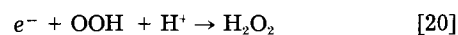


Fig. 6. Plot of $\log [n'^2(1+n')/(1-n')^2]$ vs. $\log(c_s^2/i)$. Same data as in Fig. 2 (a, b, and c).

been treated kinetically in a recent paper (9). Specifically it was shown that, if the intermediate involved in recombination corresponds to a higher degree of oxidation than that involved in the competing reaction with the solved reducing agent, then decreasing the voltage in the photocurrent onset (*i.e.*, increasing the conduction band electron concentration at the surface) should result in a change in the competing rates in favor of the solved reducing agent. This conclusion has very recently been verified experimentally on the system n-GaAs/Fe²⁺ (24). In an analogous way, the results presented in Fig. 4 may be interpreted by assuming the occurrence, not only of ordinary electron-hole surface recombination, but also of a recombination step in which conduction band electrons are captured by OOH[•] radicals according to



It can be easily seen from a simplified reaction scheme (Fig. 7, in which protons and ordinary surface recombination have been omitted) that this recombination step prevents the oxidation of H₂O₂ to O₂ and hence leads to the enhancement of the competition ratio n . Reaction [20] is conceivable to occur in view of the energetic position of the OOH[•]/H₂O₂ redox couple [$U^0 = 1.5\text{V vs. SHE at pH} = 0$ (16), corresponding to an energy level at -1.5 eV vs. SHE , *i.e.*, about midgap].

Another recombination step, in which conduction band electrons are captured by H₂O₂, adsorbed at the TiO₂ surface, has been suggested in the literature (19). The occurrence of this step is in principle not excluded by the present results, but may contribute to a minor extent only when H₂O₂ is much more reactive with respect to bromide ions than to conduction band electrons.

It should be remarked that, also, Kobayashi's concept (23) of special sites for preferential H₂O oxidation and surface recombination may explain the influence of the electrode potential upon V : when V is decreased and hence the conduction band electron concentration at the surface increased, surface recombination competes in these sites only with the H₂O oxidation, resulting in an increase in the observed value of n .

Conclusions

The present study on competing hole processes has allowed us to propose a mechanism for the oxidation of water molecules at the TiO₂ photoanode, in which hydroxyl radicals are assumed to be involved in at least three of the subsequent reaction steps. The results also indicate that the hole processes occurring simultaneously with the H₂O oxidation reaction, *i.e.*, oxidation of Br⁻ and to a certain extent also surface electron-hole recombination, do not occur in parallel with the water oxidation, but that these three processes are linked through the intermediates of the latter, analogously to what has previously been observed on n-type III-V electrodes. In particular, the oxidation of Br⁻ ions appears to occur by reaction with the surface intermediate H₂O₂ of the H₂O oxidation. If this type of oxidation mechanism for reducing agents at the TiO₂ photoanode were general, this would evidently have important implications as to the factors which determine the reactivity and selectivity behavior of this electrode: these factors would then be connected with the thermodynamics and kinetics of reactions between solved reducing agents and adsorbed hydrogen

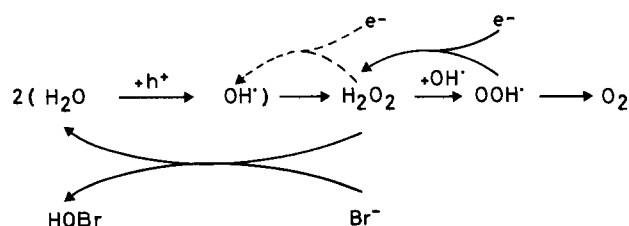


Fig. 7. Reaction scheme for processes occurring at the illuminated TiO₂ electrode.

peroxide. Experimental work with reducing agents different from bromide will be needed in order to clarify this point.

Acknowledgments

One of the authors (F. V. K.) wishes to thank the Nationaal Fonds voor Wetenschappelijk Onderzoek (N.F.W.O.) for a research grant. Acknowledgment is made to Lic. J. Willaert for performing part of the experiments.

Manuscript submitted Nov. 14, 1984.

REFERENCES

1. A. Fujishima and K. Honda, *Nature*, **238**, 37 (1972).
2. E. C. Dutoit, F. Cardon, and W. P. Gomes, *Ber. Bunsenges. Phys. Chem.*, **80**, 1285 (1976).
3. F. Vanden Kerchove, J. Vandermolen, W. P. Gomes, and F. Cardon, *ibid.*, **83**, 230 (1979).
4. T. Kobayashi, H. Yoneyama, and H. Tamura, *J. Electroanal. Chem.*, **122**, 133 (1981).
5. A. Fujishima, T. Inoue, and K. Honda, *J. Am. Chem. Soc.*, **101**, 5582 (1979).
6. F. A. Cotton and G. Wilkinson, "Advanced Inorganic Chemistry," p. 477, Interscience, New York (1972).
7. K. Hirano and A. J. Bard, *This Journal*, **127**, 1056 (1980).
8. F. Cardon, W. P. Gomes, F. Vanden Kerchove, D. Vanmaekelbergh, and F. Van Overmeire, *Faraday Disc.*, **70**, 153 (1980).
9. D. Vanmaekelbergh, W. P. Gomes, and F. Cardon, *J. Chem. Soc., Faraday Trans. 1*, **79**, 1391 (1983).
10. A. Praet, F. Vanden Kerchove, W. P. Gomes, and F. Cardon, *Solar Energy Mater.*, **7**, 481 (1983).
11. W. J. Albery and S. Bruckenstein, *Trans. Faraday Soc.*, **62**, 1920 (1966).
12. W. J. Albery, "Electrode Kinetics," p. 53, Clarendon Press, Oxford (1975).
13. D. C. Johnson and S. Bruckenstein, *This Journal*, **117**, 460 (1970).
14. D. Vanmaekelbergh, W. P. Gomes, and F. Cardon, *ibid.*, **129**, 546 (1982).
15. D. Vanmaekelbergh, W. Rigole, W. P. Gomes, and F. Cardon, *J. Chem. Soc., Faraday Trans. 1*, **79**, 2813 (1983).
16. C. J. Jaeger and A. J. Bard, *J. Phys. Chem.*, **83**, 3146 (1979).
17. R. H. Wilson, *This Journal*, **127**, 228 (1980).
18. C. Gutierrez and P. Salvador, *J. Electroanal. Chem.*, **138**, 457 (1982).
19. P. Salvador and C. Gutierrez, *Surf. Sci.*, **124**, 398 (1983).
20. P. Salvador and C. Gutierrez, *J. Phys. Chem.*, **88**, 3696 (1984).
21. A. Tessier and W. Forst, *Can. J. Chem.*, **52**, 794 (1974).
22. A. A. Frost and R. G. Pearson, "Kinetics and Mechanism," 2nd ed., p. 207, John Wiley, New York (1961).
23. T. Kobayashi, H. Yoneyama, and H. Tamura, *J. Electroanal. Chem.*, **138**, 105 (1982).
24. D. Vanmaekelbergh, W. P. Gomes, and F. Cardon, *Ber. Bunsenges. Phys. Chem.*, To be published.

Ellipsometry of the Growth and Dissolution of Anodic Oxide Films on Aluminum in Alkaline Solution

R. Greef* and C. F. W. Norman**

Department of Chemistry, The University, Southampton, England SO9 5NH

ABSTRACT

Ellipsometry has been used to study the growth of anodic films on superpure aluminum in sodium hydroxide of concentration range 0.1-4M. The ellipsometer used was a self-nulling type, and all experiments were performed *in situ* at a constant wavelength of 632.8 nm. The results are explained by the growth and dissolution of anodic films that are duplex in nature. During the dissolution process, at certain potentials, a highly reproducible transient effect in the optical signal is seen. This effect has been related to roughening of the underlying aluminum substrate, followed by subsequent smoothing upon completion of the dissolution process. The latter is indicated by the optical signal returning close to its initial value prior to film growth.

Until comparatively recently, interest in oxygen containing films on aluminum has focused largely on their protective and decorative properties. Newer applications for aluminum and aluminum alloys include their use in corrosion control as sacrificial anodes, and as primary battery anodes (1-3). In the latter role, the presence of passivating oxide films is detrimental to the primary function of the substrate, which is to dissolve electrochemically at the lowest possible overpotential.

Aluminum used in these applications is alloyed with such elements as zinc, tin, indium, and gallium, the effect of which is to improve reactivity (4-7). The full reasons for the effect of alloying with these metals is not yet clear, and recent work (8) with zinc-tin and zinc-indium alloys in 0.1M NaOH has shown the system to be complex. To help understand the mechanisms involved, it was acknowledged that investigation with super-pure aluminum would be of fundamental importance.

A method of monitoring the surface condition of the metal under working conditions with the metal *in situ* in the electrolyte was required. Ellipsometry provides such a technique (9, 10) and allows precise monitoring of the electrode surface by measuring the change in the state of polarization of a beam of light specularly reflected from the surface. These changes can be interpreted in terms of

the thickness and refractive index of overlayers on the metal surface.

Previous ellipsometric studies of pure aluminum are available and are concerned with anodic film growth in acidic or buffered solutions (11-14) or in hot water (15). This paper describes an ellipsometric study of aluminum in sodium hydroxide solutions, in which aluminum oxide is soluble, and which for this reason is a medium of importance in battery applications.

Ellipsometry is shown to be capable of monitoring the growth and dissolution of surface films over a range of potentials and alkali concentrations, and the results can be interpreted in terms of the porosity of the films. The results are explained with a detailed model of changes in density profile through the thickness of the film as a function of time.

When the surface film dissolves, it does so finally to leave a smooth aluminum surface, but an unexpected and large transient optical signal is observed just before the last of the porous film disappears. This is explained by the short-lived presence of a microrough metal surface formed by exposure and corrosion of the substrate as the overlying layer becomes discontinuous. When all the protective layer dissolves, the peaks of the rough metal surface are preferentially attacked and dissolve, and the substrate again becomes smooth, as is shown by a return of the optical signal to a point closely corresponding to its starting point before the initiation of anodic film growth.

*Electrochemical Society Active Member.

**Electrochemical Society Student Member.

Experimental Method

Materials.—Aluminum rods (99.999% Al) were cut into cylindrical electrodes of 6 mm diam. Electrical connection was made with a copper wire attached with thermosetting silver-loaded epoxy resin. The samples were mounted in epoxy resin.

Smoothing.—The electrodes were ground on 400 grit, then mechanically polished for 6 min on 6 μm diamond, and finished on alumina (0.05 μm). The powder was mixed with distilled water.

Cell.—The electrodes were mounted in a polypropylene cell, designed to support the surface horizontally at the optical center of the ellipsometer. The cell contained a platinum counterelectrode and a reversible hydrogen reference electrode. The reference electrode consisted of a platinized platinum electrode sealed into a tube with a closed upper end and an open lower end immersed in the electrolyte. It was prepared by passing a cathodic current of approximately 10 $\text{mA}\cdot\text{cm}^{-2}$ until a bubble of hydrogen formed enveloping half of the platinum. Electrode potentials are reported throughout *vs.* this reversible hydrogen electrode in the same solution. The electrolyte was air-saturated, AR-grade sodium hydroxide solution.

Electrochemical measurement.—The electrode potential was controlled by a Wenking potentiostat (70TS1) coupled to a Wenking voltage scan generator (VSG72). Cyclic voltammograms were recorded on an analog X-Y recorder.

Optical measurements.—The ellipsometer is a self-nulling fully automated type, employing Faraday modulation

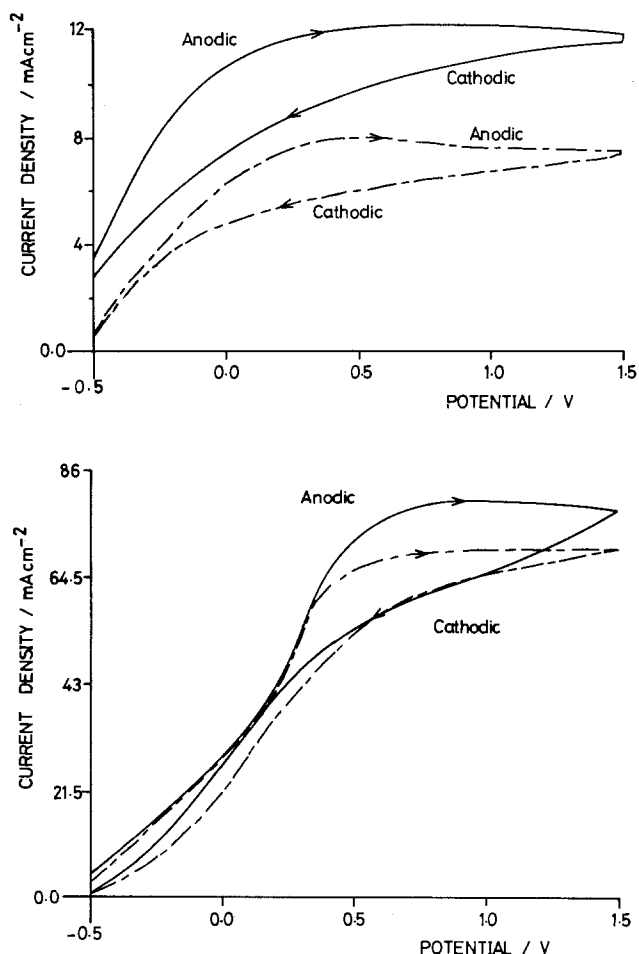


Fig. 1. a, top: Cyclic voltammetry of super pure aluminum in 0.1M NaOH, sweep rates 40 $\text{mV}\cdot\text{s}^{-1}$ (bold line) and 25 $\text{mV}\cdot\text{s}^{-1}$ (dashed line). Potentials throughout are against the reversible hydrogen electrode in the same solution. b, bottom: Cyclic voltammetry as in 1a in 1.0M NaOH.

and compensation. The optical and mechanical parts of the ellipsometer have been described elsewhere (16).

The ellipsometer was used in the monochromatic mode, the source being a He-Ne laser of wavelength 633 nm. The time constant for the self-nulling process is of the order of 0.1s.

The ellipsometer is linked to a SWTPC M6809 micro-computer which controls the operation and data acquisition. The computer is interfaced with a Hewlett-Packard Type 7470A plotter, which enables direct monitoring of the results while the experiment is running. Data points consisting of readings of time, the ellipsometric parameters Δ and ψ , and the working electrode potential and cell current were recorded on diskette.

Electrochemical results.—Cyclic voltammograms for super-pure aluminum in 0.1 and 1.0M NaOH are given Fig. 1a and 1b.

On the forward anodic sweep, at a potential close to -0.5V there is a region where little hydrogen evolution occurs together with no film growth. Here we have a small net anodic current and, ellipsometrically, an almost steady signal.

At higher anodic potentials there is an increase of current and the resulting broad plateau is characteristic of film growth. Currents are slightly lower on the reverse sweep and indicate a continuation of film growth.

Current time transients were recorded by stepping the potential from -0.5V to other more anodic potentials. The resultant transients shown in Fig. 2 show a fall of current with respect to time indicative of the growth of a porous film. Hurlen and Haug (17) have recently obtained transients that are similar in structure, but the potential steps are much smaller than in our experiments.

When the potential is stepped back to -0.5V , the current becomes zero very quickly and after several seconds rises to the small anodic value it had prior to the anodic pulse. This time period is known as the recovery time, and previous accounts of similar phenomena in acidic electrolytes are available (18-21).

The recovery time depends upon the electrolytic concentration and the height of the anodic peak. The recovery time is longer for more dilute concentrations and higher anodic pulses.

Optical terminology.—Ellipsometry measures the quantity ρ , which is the ratio of the reflection coefficients parallel to (p component) and perpendicular to (s component) the plane of incidence. Each of these reflection coefficients is a complex quantity which is an expression of the fact that it contains both amplitude and phase information. The ellipsometer measures two angular quantities Δ and ψ which are related to ρ by the equation

$$\rho = \tan \psi e^{i\Delta}$$

The possible range of Δ is 0° - 360° , and of ψ is 0° - 90° . Oxide films on aluminum are transparent, and the theory

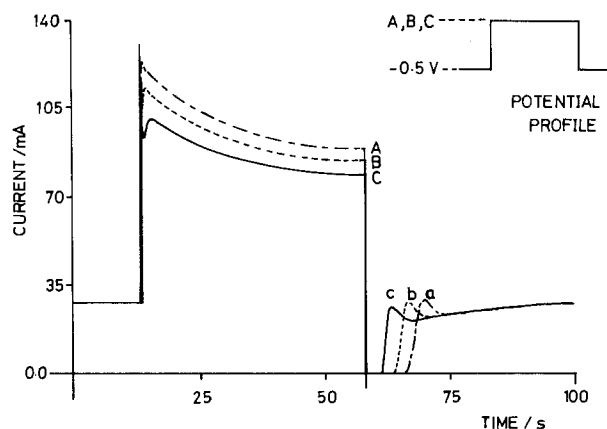


Fig. 2. Current-time transients for the potential program shown. Anodic potentials +1.5V (A), +1.0V (B), and +0.5V (C). a, b, and c are recovery currents corresponding to A, B, and C, respectively.

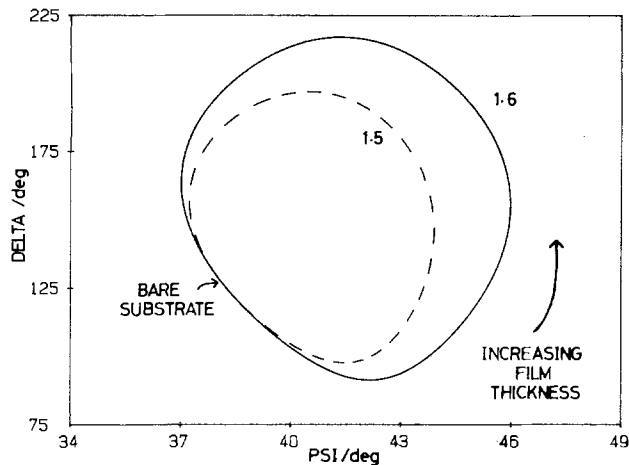


Fig. 3. Optical signals Δ and ψ for an idealized uniform film growth model on a smooth substrate. The refractive index is indicated for each curve.

for an idealized uniform film model shows that as the film grows, a cyclic change in both Δ and ψ is traced, (see Fig. 3) the size of which depends upon the refractive index of the oxide.

Pretreatment and growth potentials.—On immersing the electrode in the electrolyte, the potential was quickly adjusted to -1.0V in the hydrogen evolution region to cathodically protect the polished surface. After 10s, the potential was shifted to -0.5V , where the optical signal is steady. A pipette was used to disperse the remaining hydrogen bubbles before the potential was stepped to the higher anodic growth potential. A diagram of this potential cycle is shown in Fig. 4.

Optical measurements during cyclic voltammetry.—Figure 5 shows the Δ - ψ signature obtained during a cyclic sweep of potential at 25 mV/s in 0.1M NaOH . The starting point A is at -0.5V , where the optical signal is stable. As the potential was scanned positive, a distorted egg-shaped curve was produced, as shown in section A-B. Point B represents a potential of 2.0V , and section B-D is the return scan to -0.5V .

Only a qualitative interpretation of this result was attempted. The anodic sweep A-B evidently results in the formation of a film, but because of the distorted egg shape of the curve, this cannot be a layer of constant optical properties increasing in thickness. During the negative sweep the film continues to grow for a time, but then as point C is approached the Δ - ψ curve turns back on itself and traverses around an inner curve until a position near the starting point is reached.

The optical signal at A did not move appreciably until a potential of 0.1V was reached. The signal at C corresponds to 1.3V . It is possible that the general shape of the Δ - ψ signature in Fig. 5 could be attributed to two entirely different processes: film growth, which accelerates as the

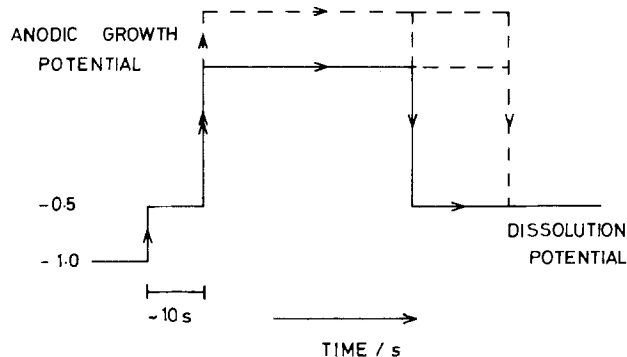


Fig. 4. Potential profile for anodic growth and dissolution of oxide layers.

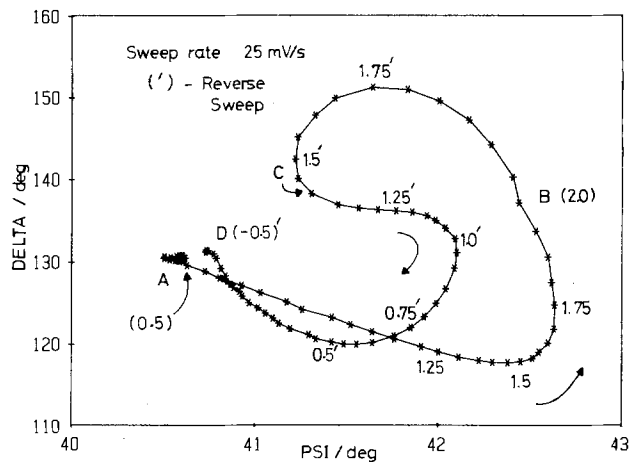


Fig. 5. Optical signals Δ and ψ during cyclic voltammetry as shown in Fig. 1a, covering potential range -0.5V (point A) to $+2.0\text{V}$ (point B) and returning to -0.5V (point D). The time interval between each data point is 2s.

potential increases, and chemical dissolution of the film as the potential is reduced.

This experiment suggests that the refractive index of the film is dependent on potential, so the effect of the formation potential was explored in detail.

Constant potential experiments.—A series of films was formed using the potential profile already described (see Fig. 4), in which the pretreatment at -1.0 and -0.5V was held constant, while formation potentials between 1.5 and 3.5V were applied, until approximately one whole Δ - ψ "egg" had been traced.

The eggs traced out at high potentials tended to form nearly closed curves, characteristic of a uniform transparent film. When plotted on common axes (see Fig. 6), the formation curves form a very striking set or "nest" of eggs, which is strongly suggestive of an oxide film increasing in refractive index very regularly with formation potential. The smoothly variable composition of the film implied by this increasing refractive index is most plausibly explained by a film of varying porosity, which fits well with the electrochemical results of Fig. 2.

Another series of eggs (see Fig. 7) was obtained by keeping the anodic growth potential constant ($+2.5\text{V}$) and varying the concentration of the sodium hydroxide. Increasing the concentration decreased the size of the egg, and this implies that the refractive index of the transparent film also decreases, corresponding to the increasing solubility of Al oxides and hydroxides at higher pH's.

Dissolution at open circuit.—In Fig. 8, two curves are shown for growth at $+2.5\text{V}$ in 0.1M NaOH . The maximum

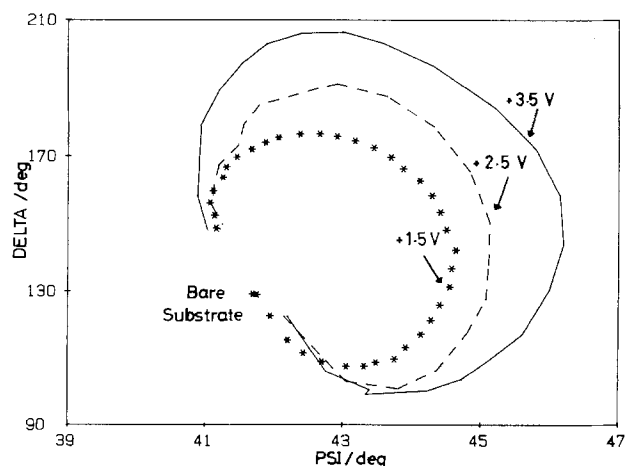


Fig. 6. Family of anodization curves at the indicated growth potentials with data points every 5s. Each run was carried out with a freshly polished electrode.

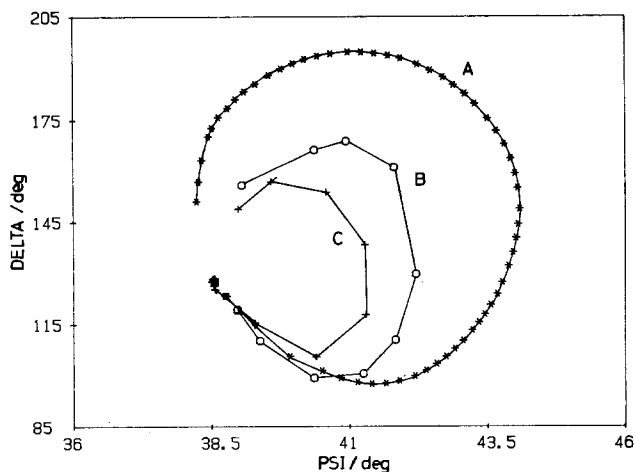


Fig. 7. A family of growth curves at +2.5V, for NaOH concentrations of 0.1M (A), 1.0M (B), and 4.0M (C). Curves B and C have points at intervals of 1s; the time interval between points for curve A is 2s.

current density for this electrolyte is about 50 mA/cm². When a certain film thickness was obtained, the film was allowed to dissolve at open circuit. The potential decreased quickly at first until it reached -0.9V at a position close to the starting position. The potential approached E_{corr} , but in the duration of the experiment never completely stabilized.

During the dissolution phase, the optical signal did not even begin to retrace the formation curve but departed immediately on a totally different path, which nevertheless brought the curve back closely to the starting point.

Dissolution at -0.5V.—A family of curves is shown in Fig. 9 for growth at 2.5V but with interruption of the growth at different stages to show the dissolution signal at -0.5V. All of these curves were obtained with the same electrode, the oxidation potential being reapplied as soon as the dissolution process had brought the $\Delta\psi$ values closely to the starting position. Each point was recorded at a time interval of 1s.

It is convenient to reduce this rather complex picture into three main regions: (i) the film growth region, (ii) the dissolution pathway until the point D_L (D_L = dissolution limit) is reached, and (iii) the remaining part, which we will call the "loop," which finally returns the optical signal to the starting point.

The corresponding current-time transients are identical in structure compared with those in Fig. 2. Examination in three stages shows, first, the falling transient after the anodic pulse which indicates porous film formation; second, a region where after stepping the potential back to

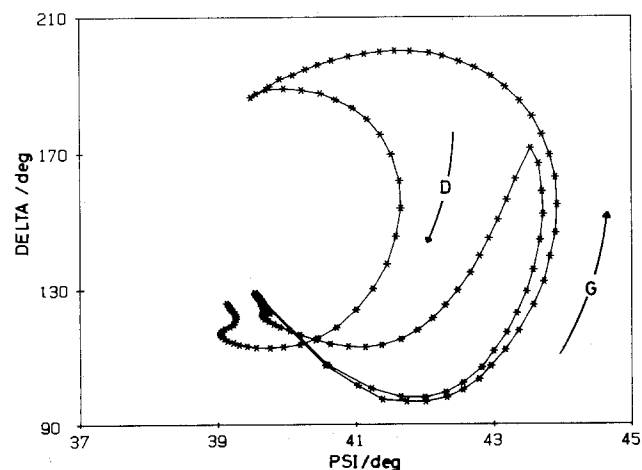


Fig. 8. Growth curves for +2.5V in 0.1M NaOH interrupted at different film thicknesses (G), and their resultant dissolution curves at open circuit (D). The time interval between points is 4.5s.

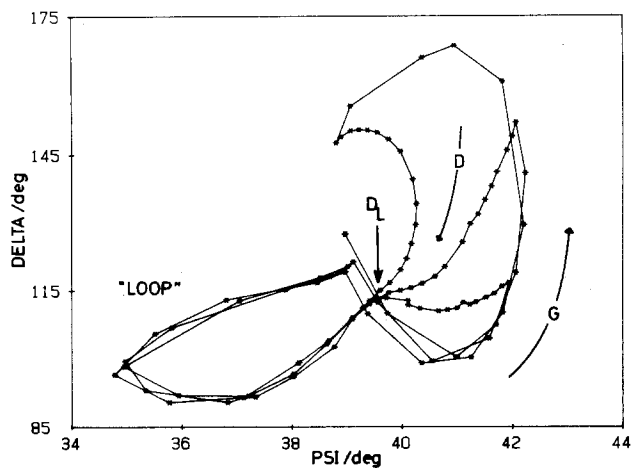


Fig. 9. A family of curves for growth +2.5V (G), interrupted at different stages to show the dissolution signal at -0.5V (D). D_L corresponds to the dissolution limit in the text. The time interval between points is 1s.

-0.5V negligible current flows and the process occurring is attributed to chemical dissolution of the film by the electrolyte; and last, the rising current when the recovery time is complete, the onset of which coincides with the point marked D_L in Fig. 9. The return of the net anodic current accompanies the optical signal which traverses the loop before returning to the starting position.

The formation of the loop is very reproducible even after three growth-dissolution cycles and is fast, taking only about 8s from the point marked D_L to the starting position.

Dissolution at other potentials.—The result of the open-circuit dissolution and the dissolution at -0.5V seem to indicate that the behavior of the loop region of the dissolution process is potential controlled. Further experiments where the dissolution potential was varied can be seen in Fig. 10 and 11. In Fig. 10, the potentials -1.0 and -0.8V were very close to the open-circuit potential (see Fig. 8) and the dissolution behaviors are very similar. Increasing the dissolution potential (Fig. 11) to more anodic potentials than -0.8V leads to the appearance of the loop, which increases in size with an increase of dissolution potential up to about 0.0V where, as seen in Fig. 5, at this potential the rate of film growth exceeds that of film dissolution. Therefore, at this potential no net film dissolution would be expected.

Discussion

It is possible to make qualitative conclusions based purely upon the general shape of the $\Delta\psi$ signatures. It is

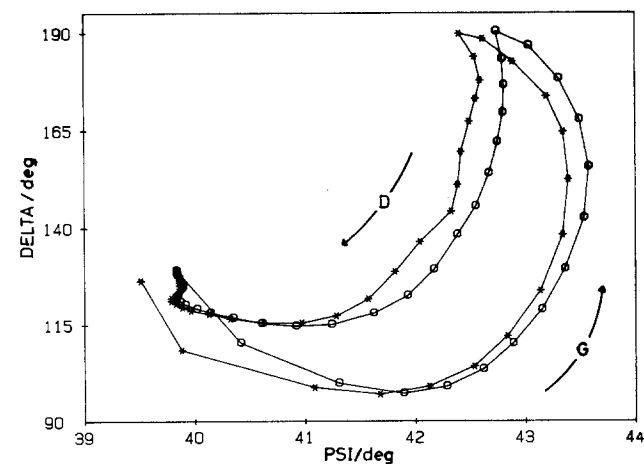


Fig. 10. Optical signal for film growth at +2.5V (G), with dissolution at -1.0V (asterisks) and -0.8V (open circles) (D). The time interval between points is 5.5s.

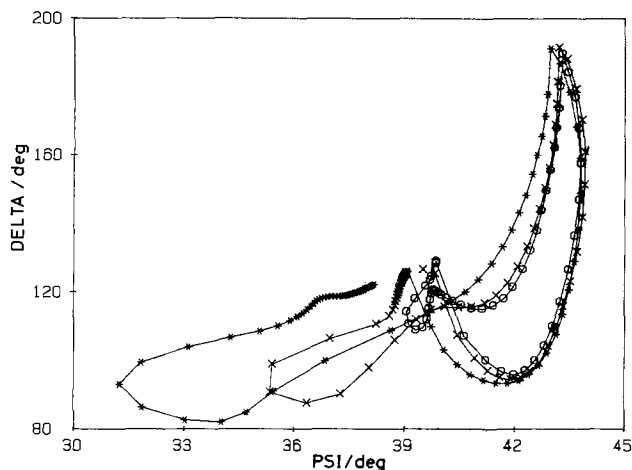


Fig. 11. Growth curves as in Fig. 10, with dissolution at -0.6V (open circles), -0.4V (X's) and -0.2V (asterisks). The time interval between points is 5.5s.

clear that a porous film grows (see Fig. 5) on the aluminum substrate above potentials of about 0.1V and that the refractive index of the film, and hence its density, increases regularly with increasing formation potential and decreasing electrolytic concentration. Films formed in this way dissolve to leave a clean surface which is still smooth even after several growth-dissolution cycles.

The conclusions can be tested in a quantitative way by calculating the $\Delta\psi$ response, using a single-film or multi-film model, measured or estimated values of the various optical constants, and a computer program such as that of McCrackin and Colson (22).

Optical constants of the substrate.—The condition of the surface at -0.5V before anodization is stable and has been used as a reference state. It is not a film-free surface, however, as a film of oxide formed in air during the polishing process is not removed even at -1.0V . Values of n and k for bare, pure aluminum surfaces are available (11, 12, 15, 23, 25), but not for the polished aluminum substrate immersed in a caustic electrolyte. The values of the bare surface optical constants were therefore estimated by assuming that a thin layer (0.5 nm) of oxide of refractive index 1.65 exists initially on the aluminum. The effect of "removing" this layer in the calculations is to increase Δ and decrease ψ . Using this new starting point in the film calculation does give a noticeable change in the $\Delta\psi$ signatures predicted, but none of the conclusions is changed by using the initial measured $\Delta\psi$ values as if they represented a clean surface. Using this and the fact that the surfaces are mechanically polished and are never exactly reproducible, approximate optical constants of the aluminum used were $n = 1.5 \pm 0.15$ and $k = 5.5 \pm 0.4$. These values can be compared with those for aluminum deposited under UHV conditions (23) of $n = 1.43$ and $k = 7.28$. Under our conditions these values correspond to "bare surface" Δ and ψ values of 131.08° and 40.90° , which lie close to the observed starting points.

Film growth models.—The simplest model is the single-film model Fig. 3, in which a uniform oxide film lies between the alloy substrate and the immersion medium. This model suffices for films grown on pure aluminum under certain conditions (14, 15). When the model is applied to these results, however, it is obvious from Fig. 12 that a uniform film model is inadequate (25). Initially, the experimental data indicate a constant refractive index, but as the film thickens the refractive index seems to decrease, implying that the film is increasing in porosity.

Two multilayer models were therefore explored (26), having a linear and an exponential fall in the refractive index with distance from the electrode. Neither model yielded $\Delta\psi$ signatures that fitted any substantial part of the experimental curves.

A two-film model similar to that used by Dell'Oca and Fleming(11) was then tried in which there was a dense ox-

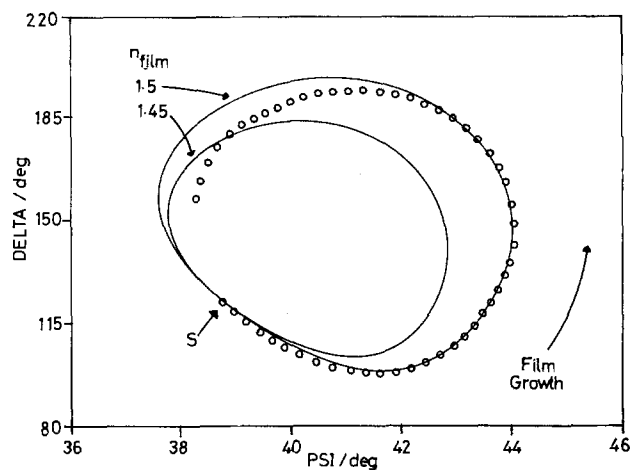


Fig. 12. Comparison of calculated uniform film models (value for the oxide refractive index as indicated), with an experimental growth curve $+2.0\text{V}$ in 0.1M NaOH (open circles). S corresponds to the initial experimental point, with further points taken at 2s intervals.

ide layer next to the electrode and a more porous layer in contact with the electrolyte. The model was refined by proposing a smooth transition between the two refractive indexes rather than a sudden step (see Fig. 13). This was done by dividing the film up into many thin slices and generating a function with which to define the refractive index of each slice. The function used was

$$n = n_{\min} + (n_{\max} - n_{\min}) \exp(-x) / [\exp(-x) + \exp(-x_{\max}/f)]$$

where n_{\min} and n_{\max} are the values of refractive index in contact with the electrolyte and metal, respectively, and x_{\max} is an arbitrary number which controls the sharpness of the refractive index transition between the two extreme values. The value of x varies from 0 to x_{\max} in equal increments for each slice from the metal to the outer film boundary. The fraction $1/f$ determines the distance at which the step from n_{\max} to n_{\min} is half complete. So for Fig.13, the theoretical parameters are film thickness = 420 nm, slice thickness = 4 nm, $n_{\min} = 1.45$, $n_{\max} = 1.50$, $x_{\max} = 60$, and $f = 2.2$, which implies the dense part of the film is 190 nm thick.

The calculation of the $\Delta\psi$ response is started with a bare surface, and the slices are added one at a time until the total film has been assembled. The result shown in Fig. 13 is a set of $\Delta\psi$ points tracing out the simulated characteristics.

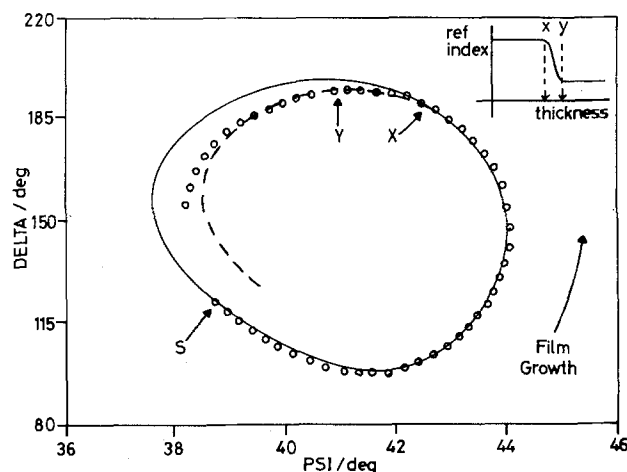


Fig. 13. Comparison of the refined duplex model for film growth (dashed line) superimposed upon the experimental curve from Fig. 12 (open circles) and the uniform film model curve in Fig. 12 (bold line). Theoretical parameters: film thickness = 420 nm, $n_{\min} = 1.45$, $n_{\max} = 1.50$, $x_{\max} = 60$, and $f = 2.2$. The inset shows the smooth transition for the refined model; the start and end of the transition between the two layers are indicated by X and Y, respectively.

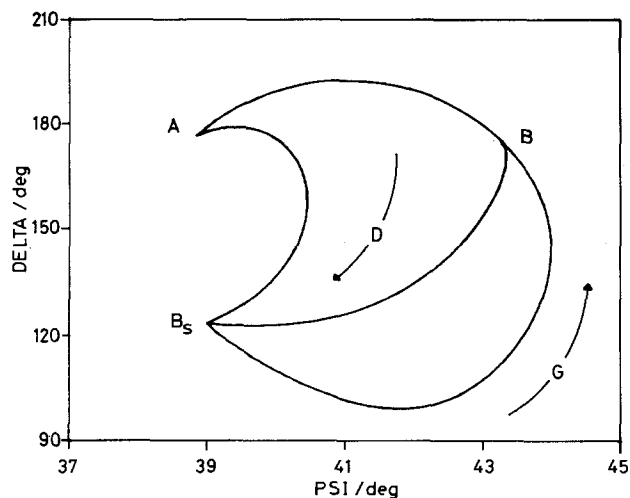


Fig. 14. A calculated anodization curve (G) with two dissolution curves (D), $x_{\max} = 60$, film thicknesses 320 nm (point A) and 210 nm (point B). B_s corresponds to the bare surface.

Film dissolution models.—Accepting that the growth curves can only be explained by a graded-film model, it is clear that a dissolution process quite different from the reverse of the formation process is needed to explain the dissolution trajectory in the Δ - ψ plane. A model in which all of the oxide layers begin to relax toward a lower refractive index at the end of the growth phase was found to give the correct kind of shape. Out of many curves produced by trial and error, Fig. 14 shows the main features seen in the open-circuit dissolution experiment (see Fig. 8).

It therefore seems clear that the outer layers of the oxide are porous enough to allow attack of the inner, dense layers to start immediately upon cessation of the anodization process.

Figure 15 shows a three-dimensional plot indicating how the refractive index of the film changes with thickness and time. At the point marked A, the potential is pulsed anodically and a film of uniform refractive index starts to form. At B, the film becomes duplex in nature and as the thickness increases so the refractive index profile through the film changes until the lower refractive index limit is reached. At C, the potential is stepped back to its initial value and the film chemically dissolves. Note that the thickness remains constant but the refractive index diminishes until at D the whole of the film reaches a predetermined refractive index which represents the point D_L in Fig. 9.

This simple dissolution model is capable of reproducing qualitatively the open-circuit dissolution curve in Fig.

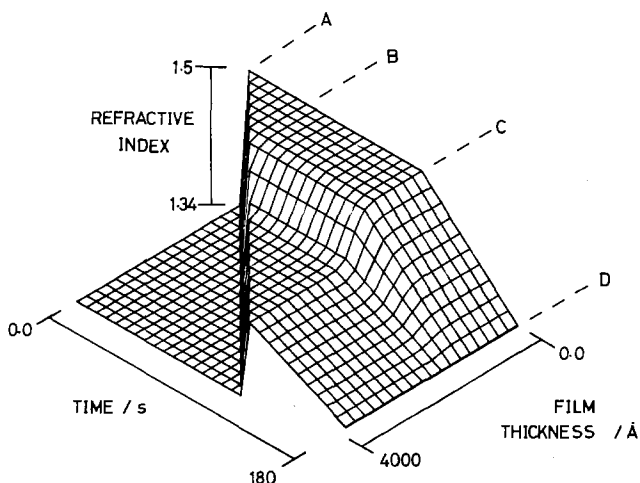


Fig. 15. A three-dimensional plot indicating how the refractive index of the film varies from A (the initial anodic pulse) to D (the dissolution limit D_L in Fig. 9), with both time and film thickness.

8. However, from Fig. 9 and 11 it is obvious that the model is insufficient in explaining the complete dissolution process which contains the loop phenomenon. A more complex model is therefore required.

At the position D_L (see Fig. 9), the Δ - ψ value(s) corresponding to this portion clearly indicates that a film of finite thickness still remains on the substrate. At this position, subsequent dissolution causes the current to rise (see Fig. 2) and the Δ - ψ response to depart from the dissolution curve and traverse the loop before returning close to the starting position.

The net anodic recovery current must be due to the chemical breakdown of the film at random sites, thus exposing bare metal and allowing preferential metal dissolution. The metal dissolution process would result in appreciable roughening of the metal surface.

The large Δ - ψ excursion from the dissolution curve cannot be explained by a continuation of the dissolution process alone, nor by the growth of another transparent film or by a mixture of both. The optical constants of the transparent system cannot produce any Δ - ψ values for any film thickness in this region of the Δ - ψ plane, where $\Delta < \Delta_{\text{starting position}}$ and $\psi < \psi_{\text{starting position}}$, assuming reasonable values for the refractive index of the film ($1.4 \leq n \leq 4.0$). This region is therefore "out of bounds" for a transparent film on a smooth aluminum substrate. It very quickly becomes obvious that we must introduce a k (extinction coefficient) value into the optical constants of the system to force the Δ - ψ response into this region. The appreciable roughening caused by the aluminum dissolution reaction must now be taken into account.

The model used so far has assumed a perfectly smooth interface between the substrate and the film (9), such that the reflection from which can be described by the Fresnel complex reflection coefficients and the Drude equation. The problem of microscopically rough surfaces can be treated however by using simple models to characterize the roughness of the surface. The simplest optical model that approximates to a rough substrate is to represent the rough layer as an effective medium of intermediate optical properties, sandwiched between a perfect substrate and a perfect ambient (27). There are several effective-medium models that represent a heterogeneous dielectric mixture by a single parameter. The Maxwell-Garnett (MG) and the Bruggeman effective-medium approximation (EMA) are two of the most popular theories used.

Aspnes *et al.* (27) have shown that the MG treatment is inconsistent in its definition of the volume fractions of the substrate and ambient media, and they recommend as being self-consistent the Bruggeman theory (EMA). The equation that relates the volume fraction of the inclusions (V_2) in the ambient medium (film) (1) can be written as

$$(1 - V_2) \frac{\epsilon_1 - \langle \epsilon \rangle}{\epsilon_1 + 2\langle \epsilon \rangle} = -V_2 \frac{\epsilon_2 - \langle \epsilon \rangle}{\epsilon_2 + 2\langle \epsilon \rangle}$$

where $\langle \epsilon \rangle$ is the effective dielectric function of the rough layer and ϵ_1 and ϵ_2 are the dielectric functions of the film material and bulk substrate, respectively. The effective dielectric function is a complex quantity.

The rough layer was divided into a number of slices of equal thickness, and various structural models (27) describing the inclusion of the substrate into the film were employed. These models were triangular ridges (model 1), close-packed cones (model 2), hemispheres (model 3), inverse cones (model 4), and inverse hemispheres (model 5). Figure 16 shows a section through a rough layer structure using model 1 as the geometric shape with the layer divided into equal slices. From this geometric shape, it is easy to calculate the volume fraction of the base material in each slice of the rough layer. The EMA theory allows the calculation of the optical constants of each slice, knowing the volume fraction of the inclusions, and from these values a new curve is produced in the Δ - ψ plane.

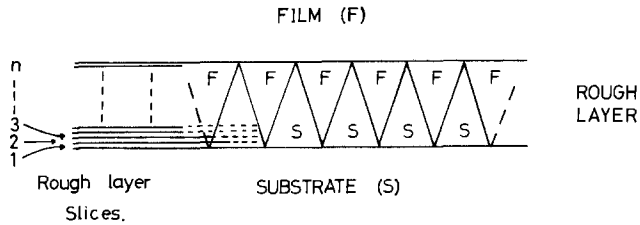


Fig. 16. A schematic diagram showing the rough layer section using rough model 1 (triangular ridges) to describe the inclusion of substrate into the film, and the division of the rough layer into slices of equal thickness.

In Figure 17, the simulated dissolution reaction is stopped at D_L and the rough layer for model 1 is grown for two different rough layer thicknesses. Both curves move into the out-of-bounds region, and increasing the thickness of the rough layer causes the curve to deviate further from the point D_L .

From the $\Delta\psi$ curves in Fig. 9, the $\Delta\psi$ response, having traversed the loop, returns very close to the starting position. Here the film will be very thin, and the optical constants of the system will approach the initial values of the substrate before the first anodic pulse. This can only be explained by the roughened substrate becoming smooth again. With the chemical dissolution of the film near completion, a preferential "leveling off" process of the rough layer, via the aluminum dissolution reaction, would seem to occur. This process may be akin to the leveling and brightening effects observed in electropolishing (28).

The leveling-off process is a simple process to model, as one slice at a time in the rough layer starting from the film boundary has its optical constants changed to those of the medium (1.34, 0) until the underlying substrate boundary is reached. Figure 18 shows how the extinction coefficient varies with time and the rough layer thickness. Initially $k = 5.5$ and is representative of the substrate, whereas at B, when the rough layer is completely grown, k tends to 0, representing the transparent film. From B, the removal shows k progressively made equal to 0 from the outermost slices at the film boundary until at C the removal of the rough layer is complete.

To allow the film dissolution to continue while the roughening process is occurring, the computer program was adapted so that a suitable constant could be included which represents the ratio of roughening to dissolution in the system. So for example, if the constant was equal to 3, the computer simulation would represent the growth of three slices in the rough layer for every one small reduction in the refractive index of the film (representing film

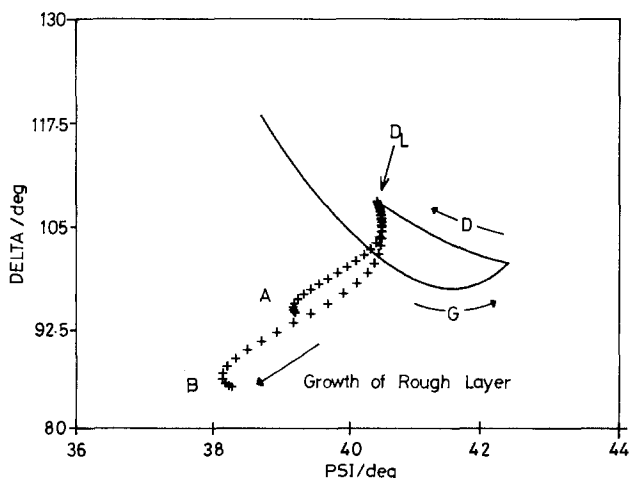


Fig. 17. A calculated growth (G) and dissolution curve (D); parameters are refractive index of film = 1.5, film thickness = 100 nm, and slice thickness = 10 nm. The calculation is stopped when the film refractive index reaches 1.4 (D_L). Simulated roughening using model 1 is then calculated with different rough layer thickness, 10 nm (A) and 20 nm (B).

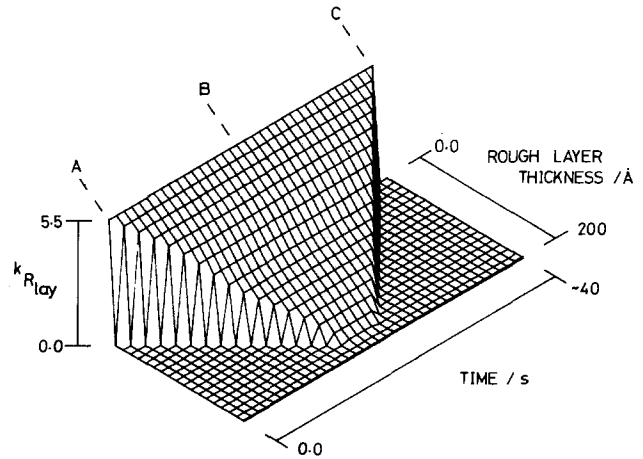


Fig. 18. A three-dimensional plot showing how the extinction coefficient varies with time and the rough layer thickness during the processes of growth (A to B) and dissolution (B to C) of the rough layer.

dissolution). When the rough layer was completely grown, its removal via the leveling-off process was simulated. The initial rate was still used, and three rough layer slices were removed for every one step in the reduction in the refractive index of the film. The best results for all five models used were found when the roughening occurs quickly compared to the film dissolution.

Figure 19 shows a theoretical response for model 1. The saw tooth appearance to the shape of the loop is present to show the two separate parts of the calculation, although this curve could be made smooth by modeling both processes in the same step of the calculation.

All five of the models have a theoretical $\Delta\psi$ response which moved into the out-of-bounds region when the rough layer was grown and produced a loop when coupled to the film dissolution and the smoothing process. However, models 1 and 2 produced loops that showed the greater resemblance to the experimental curves in Fig. 9. Experimentally, film breakdown leading to the substrate roughening would occur at random sites across the substrate and the highly structured rough layer models used here would only be an approximation to the real system.

Finally, another result that can now be explained is the dependence of the loop size upon potential (see Fig. 11). In Fig. 1a and 1b the cyclic voltammograms show that as the potential is raised from -1.0 to -0.2 V the current also increases. Therefore, when film breakdown occurs at a more anodic potential in this range, the aluminum disso-

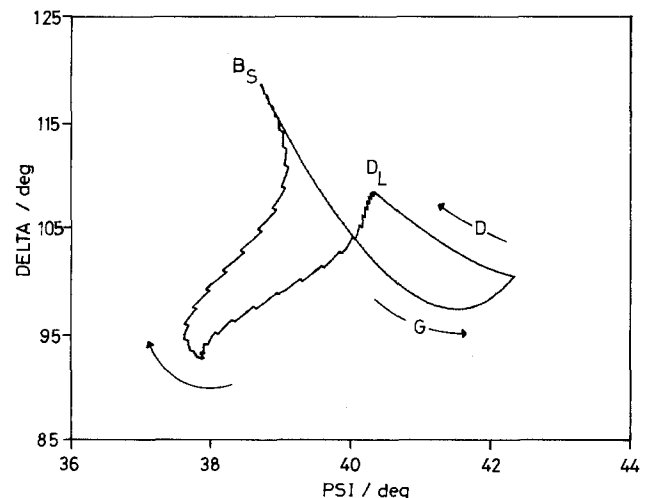


Fig. 19. The complete theoretical model depicting film growth and dissolution to D_L , and the growth and dissolution of the rough layer together with the continued dissolution of the film until point B_S is reached (bare surface). Parameters for the film as in Fig. 17, with rough layer parameters of model = 1, thickness = 20 nm, slice thickness = 0.33 nm.

lution reaction can occur at a faster rate and the effect of the roughening will be greater. Figure 17 shows that an increase in the rough layer thickness, possibly caused by more vigorous aluminum dissolution reaction at higher anodic potentials, would lead to an increase in the size of the loop.

Conclusions

1. The density of anodic oxide films on aluminum in alkaline conditions depends upon the potential of formation and the electrolyte concentration. The films increase in porosity toward low formation potentials and high electrolytic concentrations.

2. The films are not of uniform density throughout their thickness, being denser at the metal surface. A model consisting of a duplex film with a smooth transition in refractive index between the two layers produced a good fit with the experimental results.

3. The dissolution process is not the reverse of the formation process. The oxide layer begins to dissolve throughout its thickness upon cessation of anodization until a critical point is reached where the underlying metal is preferentially dissolved due to film breakdown.

4. Dissolution of the underlying metal and the incomplete oxide layer proceed in parallel, giving a $\Delta\psi$ signal that departs from the dissolution curve and moves into a region in the $\Delta\psi$ plane that is "forbidden" for any reasonable transparent film system.

5. The preferential dissolution of the underlying metal leads to appreciable roughening which has been modeled by constructing a layer between the substrate and the film where inclusions of metal into the film (and vice versa) are used to represent the rough layer.

6. Having now moved into this forbidden region, the $\Delta\psi$ response traverses a loop and returns close to the starting position. The optical constants of the system are now very similar to those before the initial anodic pulse. This implies that the anodic oxide film has been removed and that the rough substrate has become smooth again via some form of leveling-off process.

Acknowledgments

We thank S.E.R.C. and Alcan International Limited for financial support.

Manuscript submitted Feb. 5, 1985; revised manuscript received June 24, 1985.

REFERENCES

1. A. R. Despic and P. D. Milanovic, *Recueil Des Travaux de l'institut des sciences techniques de*

- l'academie serbe des sciences et arts*, **12**, 1 (1979).
2. J. Ruch, *Prog. Batt. Solar Cells*, **3**, 227 (1980).
3. T. Valand, O. Mollestad, and G. Nilsson, Paper 34 presented at the 12th International Power Sources Symposium, Brighton, England (1980).
4. A. R. Despic, D. M. Drazic, M. M. Purenovic, and N. Cikovic, *J. Appl. Electrochem.*, **6**, 527 (1976).
5. D. S. Keir, M. J. Pryor, and P. R. Sperry, *This Journal*, **114**, 777 (1967).
6. D. S. Keir, M. J. Pryor, and P. R. Sperry, *ibid.*, **116**, 319 (1969).
7. W. Bohnstedt, *J. Power Sources*, **5**, 245 (1980).
8. R. Greef and C. Norman, "Control and Exploitation of the Corrosion of Aluminium Alloys," Cranfield, England, April 1983. To be published by Alcan Aluminium, Banbury, England.
9. R. H. Muller, in "Advanced Electrochemistry and Electrochemical Engineering," Vol. 9, R. H. Muller, Editor, p. 167, Wiley, New York (1973).
10. W. E. J. Neal, *Appl. Surf. Sci.*, **2**, 445 (1979).
11. C. J. Dell'Oca and P. J. Fleming, *This Journal*, **123**, 1487 (1976).
12. C. J. Dell'Oca, *Thin Solid Films*, **26**, 371 (1975).
13. C. K. Dyer and R. S. Alwitt, *Electrochim. Acta*, **23**, 347 (1978).
14. R. M. Goldstein, R. J. Lederich, and F. W. Leonhard, *This Journal*, **117**, 503 (1970).
15. M. A. Barrett and A. B. Winterbottom, in "First International Congress on Metallic Corrosion," p. 657, Butterworths, London (1961).
16. A. C. Lowe, *Surf. Sci.*, **56**, 134 (1976).
17. T. Hurlen and A. T. Haug, *Electrochim. Acta.*, **29**, 1133 (1984).
18. J. F. Murphy and C. E. Michelson, in "Proceedings of the Symposium on Aluminium Anodizing," Nottingham, 1961, p. 83, Aluminium Development Association, London (1961).
19. J. F. Murphy, in "Proceedings of the Symposium of Aluminium Anodizing," Birmingham, 1967, p. 3, Aluminium Development Association, London (1967).
20. J. P. O'Sullivan and G. C. Wood, *Proc. R. Soc. London, Ser. A*, **317**, 511 (1970).
21. H. Takahashi, M. Nagayama, H. Akahori, and A. Kitahara, *J. Electron Microsc.*, **22**, 149 (1973).
22. F. L. McCrackin and J. P. Colson, National Bureau of Standards Technical Note 479, Washington, DC, April 1969.
23. A. C. Nyce and L. P. Skolnick, *J. Opt. Soc. Am.*, **65**, 792 (1975).
24. J. E. Norman, *Corros. Sci.*, **17**, 39 (1975).
25. C. J. Dell'Oca and L. Young, *Surf. Sci.*, **16**, 331 (1969).
26. F. L. McCrackin and J. P. Colson, National Bureau of Standards Miscellaneous Publication 256, p. 61, Washington, DC (1963).
27. D. E. Aspnes, J. B. Theeten, and F. Hottier, *Phys. Rev. B*, **20**, 3292 (1979).
28. A. K. Vijh, "Electrochemistry of Metals and Semiconductors," p. 200, Marcel Dekker Inc., New York (1973).

Electrochemical Formation of Graphite-Sulfuric Acid Intercalation Compounds on Carbon Fibers

Yasuhisa Maeda,* Yasuo Okemoto, and Michio Inagaki

Department of Materials Science, Toyohashi University of Technology, Tempaku-cho, Toyohashi 440, Japan

ABSTRACT

The cyclic voltammograms in 98% H₂SO₄ were measured on the mesophase-pitch-based carbon fibers heat-treated at various temperatures. They showed a marked dependence on the heat-treatment temperature of the carbon fibers. The electrochemical formation of graphite-sulfuric acid intercalation compounds was confirmed by x-ray diffraction. The change of graphite layer planes in the carbon fibers due to electrolysis was examined by Raman spectra.

Graphite forms intercalation compounds by the insertion of various ions, atoms, and molecules into its interplanar space. Recently, graphite intercalation compounds (GIC's) have attracted attention because of their unique properties. For a number of new GIC's synthe-

* Electrochemical Society Active Member.

sized by different methods, their structure, physicochemical properties, and applications have been studied actively (1-3).

Graphite is electrochemically oxidized in a concentrated sulfuric acid to form graphite-sulfuric acid intercalation compounds as follows



A bisulfate ion and sulfuric acid molecules are inserted between graphite layers. The positive charge of the oxidized graphite network is balanced by the negative charge of the intercalated ions. In this case, intercalation occurs in the anodic process and deintercalation in the cathodic process.

There are several papers (4-8) reporting electrochemical formation of graphite-sulfuric acid intercalation compounds on the graphite electrodes with high crystallinity, natural graphite, and highly oriented pyrolytic graphite. However, extensive studies on carbon electrodes are uncommon, although carbon materials have wide varieties in structure, in texture, and in shape. Carbon fibers have different textures and different degrees of perfection in structure according to their precursor and heat-treatment (9-11). Therefore, carbon fibers are interesting host materials of GIC because they may give much information on the GIC formation behavior in relation to crystallinity of host materials and also on the development of applications.

In this paper, the electrochemical formation behavior of graphite-sulfuric acid intercalation compounds was examined on the mesophase-pitch-based carbon fibers (11) heat-treated at various temperatures.

Experimental

The electrode materials were the mesophase-pitch-based carbon fibers (Kureha Chemical Industry Company) heat-treated at temperatures of 1800°, 2100°, 2400°, 2700°, and 3000°C for 30 min in argon atmosphere. Figure 1 shows the SEM micrograph of a cross section of the 3000°C treated carbon fibers. It is well known that the degree of graphitization of carbon materials is higher with the rise of heat-treatment temperature (HTT). The average interlayer spacing $\bar{d}(002)$ determined from 002 x-ray diffraction line by using inner standard of silicon is usually used as graphitization degree. The $\bar{d}(002)$ values of the heat-treated carbon fibers are summarized in Table I. The value decreases to the value for the natural graphite, 3.354Å, with the rise of HTT as has been found in various carbon materials.

A bundle of carbon fibers (weight of about 40 mg) attached to a copper lead wire with conducting silver epoxy was prepared as a working electrode. A platinum wire



Fig. 1. SEM micrograph of cross section of the 3000°C treated mesophase-pitch-based carbon fiber.

Table I. Interlayer spacing of the mesophase-pitch-based carbon fibers heat-treated at various temperatures

HTT (°C)	$\bar{d}(002)$ (Å)
3000	3.361
2700	3.362
2400	3.383
2100	3.405
1800	3.426

and a saturated calomel electrode were used as a counter and a reference electrode, respectively. An electrolyte was 98% sulfuric acid. Cyclic voltammograms were measured by using a potentiostat (Hokuto Denko, Model HA-501) and a function generator (same company, Model HB-104).

The x-ray diffraction pattern of the carbon fibers electrolyzed at a certain potential was measured in order to confirm the formation of graphite-sulfuric acid intercalation compounds. Because of instability of intercalation compounds in air, the electrolyzed carbon fibers were taken out from the electrolyte in nitrogen atmosphere and mounted to the x-ray sample holder with a cover of 0.5 mm thick polyethylene film. The x-ray diffraction measurement was made with a diffractometer (Rigaku Denki, Model Geigerflex-2028).

Raman spectra were measured in order to examine the change of graphite layer planes in the carbon fibers due to electrolysis. In this case, the electrolyzed carbon fibers were taken out from the electrolyte, rinsed repeatedly with pure water, and dried in air. The Raman measurement was made with a Raman spectrometer (JRS, Model 400D) using 4880Å line (150 mW) of Ar-ion laser (NEC, Model GLG-3200). The angle between the incident beam and the fiber axis was 45°, and the scattered light was collected under 90° with the fiber axis. The slit widths at entrance, intermediate, and exit were 500, 600, and 500 μm , respectively.

Results and Discussion

Figure 2 shows the cyclic voltammograms (CV's) on the mesophase-pitch-based carbon fibers heat-treated at

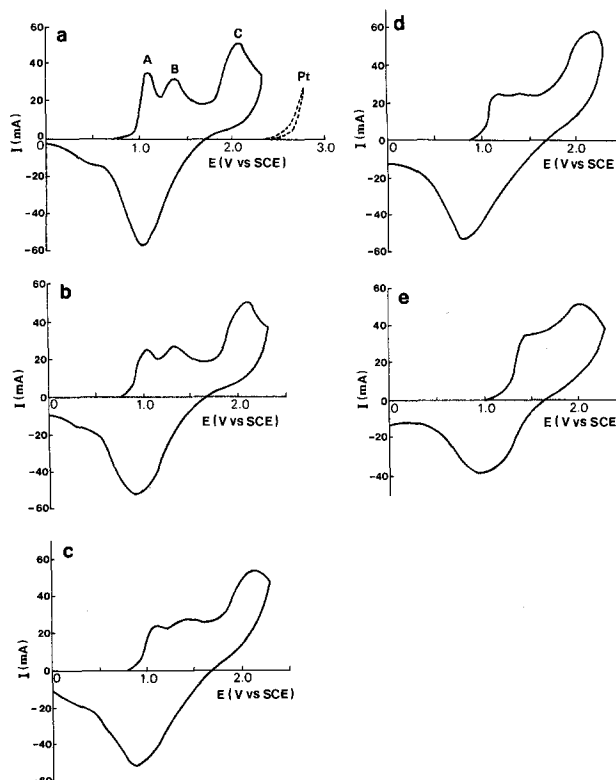


Fig. 2. Cyclic voltammograms (first scan) on the mesophase-pitch-based carbon fibers in 98% H_2SO_4 . a, b, c, d, and e: The carbon fibers heat-treated at 3000°, 2700°, 2400°, 2100°, and 1800°C, respectively. Scan rate: 10 $\text{mV}\cdot\text{s}^{-1}$. Pt: Platinum.

3000°, 2700°, 2400°, 2100°, and 1800°C. The CV's in a concentrated sulfuric acid showed a remarkable dependence on HTT. In Fig. 2a on the 3000°C treated carbon fibers, three anodic current peaks A, B, and C were observed at potentials of about 1.1, 1.4, and 2.1V, respectively. A cathodic peak appeared at about 1.0V. A platinum working electrode gave no anodic and cathodic peaks in the potential range of 0.0-2.3V in 98% H₂SO₄. The CV on the 2700°C treated carbon fibers (Fig. 2b) is similar to that on the 3000°C treated carbon fibers. From the CV's on the 2400°C and the 2100°C treated carbon fibers (Fig. 2c and 2d), it is indicated that both the anodic current peaks corresponding to A and B peaks in Fig. 2a become broad with the decrease in HTT. In contrast with peaks A and B, peak C seems to be almost independent of HTT. In the CV on the 1800°C treated carbon fibers (Fig. 2e), only two anodic current peaks were observed.

Figure 3 shows the x-ray diffraction patterns of the 3000°C treated carbon fibers for original (a) and 60 min electrolysis at the potential of 1.1, 1.4, and 2.1V (b, c, and d, respectively). On the electrolyzed carbon fibers, 001 diffraction lines from graphite layer planes disappear and new lines due to the formation of GIC are observed. The diffraction lines in Fig. 3b can be indexed by the stage 2 graphite-sulfuric acid intercalation compound with the identity period along the c-axis I_c of 11.33Å, as shown in the figure, and those in Fig. 3c by the stage 1 compound with I_c of 7.98Å. Therefore, anodic current peaks A at the potential of 1.1V and B at 1.4V observed in the CV (Fig. 2a) are attributed to the formation of the stage 2 and the stage 1 compounds, respectively. As shown in Fig. 3d, the product obtained by the anodic oxidation up to the potential of 2.1V has two diffraction lines at almost the same

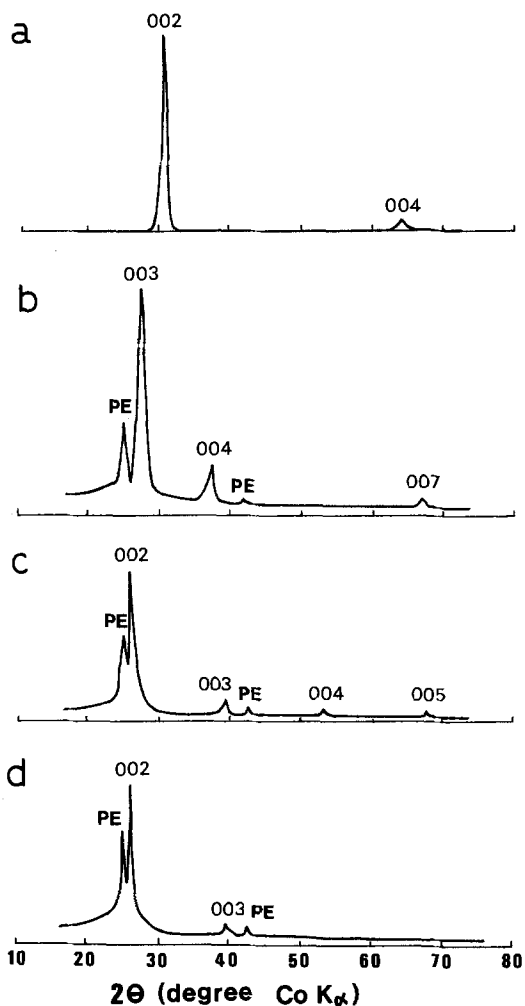


Fig. 3. X-ray diffraction patterns of the 3000°C treated carbon fibers. a: Original. b, c, and d: After electrolysis for 60 min at the potential of 1.1, 1.4, and 2.1V, respectively. PE: Polyethylene.

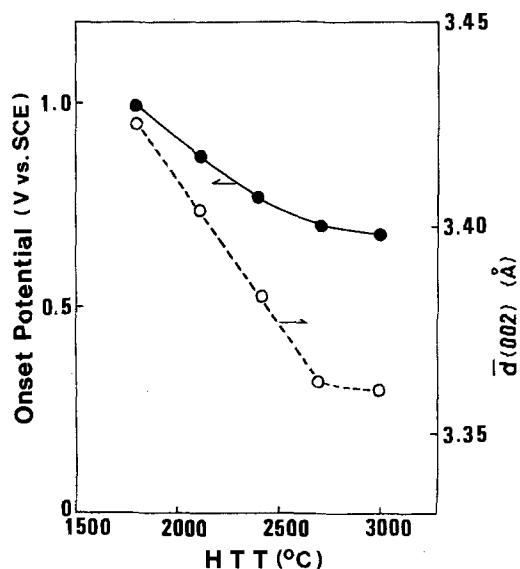


Fig. 4. Dependences of onset potential and of interlayer spacing $\bar{d}(002)$ on heat-treatment temperature.

diffraction angles as the stage 1, but two higher-order diffraction lines are missing. Since the stage 1 GIC which has the maximum content of intercalant is already formed at the potential of 1.4V, anodic current peak C is supposed to be due to the formation of graphite oxide (12, 13). Besenhard *et al.* (8) mentioned the formation of graphite oxide following that of the stage 1 compound on the highly oriented pyrolytic graphite electrode in 96% H₂SO₄. In the CV's on the carbon fibers, the anodic current peak C is quite different from the peaks A and B with regard to HTT dependence. The broadening of the peaks A and B with the decrease in HTT suggests that a distinction in staging of GIC formed gets obscure on the carbon fibers with lower degree of graphitization.

Figure 4 shows the dependences of the onset potential (OP) and of the interlayer spacing $\bar{d}(002)$ on HTT of the carbon fibers. The OP is denoted as the threshold potential which shows the beginning of the anodic current flow in the first scan. The OP value of the carbon fibers treated at the higher HTT is less positive. A striking similarity between the HTT dependences of OP value and $\bar{d}(002)$ suggests that the OP value is closely related to the crystallinity of the host carbon fibers, the higher degree of graphitization facilitating the formation of GIC.

Figure 5 shows the CV on the 3000°C treated carbon fibers in the range of 0.0-1.4V. In this potential range, only the formation of GIC occurs, as shown by two anodic current peaks at 1.1 and 1.4V, but not the forma-

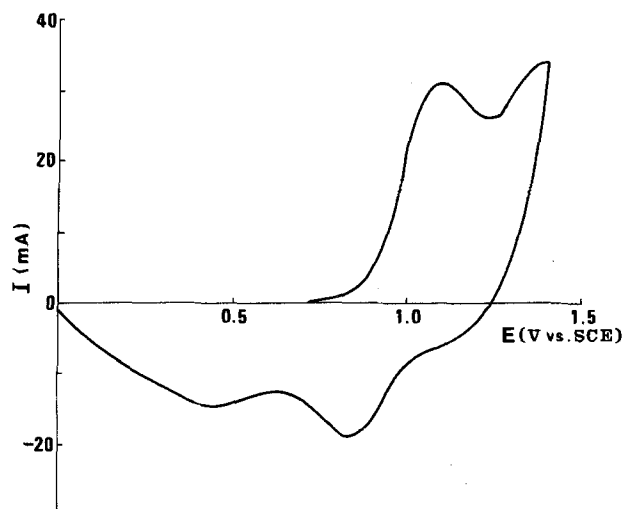


Fig. 5. Cyclic voltammogram (first scan) on the 3000°C treated carbon fibers in 98% H₂SO₄. Scan rate: 10 mV·s⁻¹.

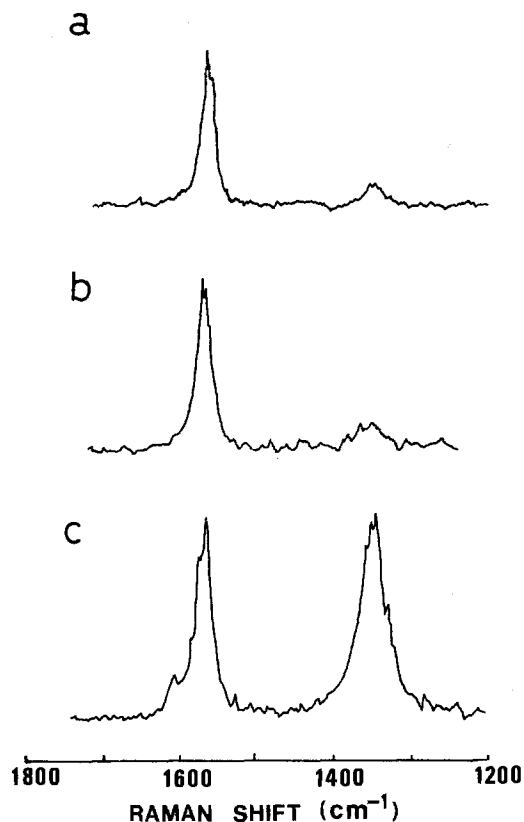


Fig. 6. Raman spectra of the 3000°C treated carbon fibers. a: Original. b and c: After ten times cyclic electrolysis in the range of 0.0-1.4V and 0.0-2.3V, respectively.

tion of graphite oxide. This CV characteristically shows two cathodic peaks at the potential of about 0.4 and 0.8V, which correspond to the reduction of the stage 2 and the stage 1 graphite-sulfuric acid intercalation compounds, respectively. These waves are not clearly detected with scans up to the potential of 2.3V, as shown in Fig. 2a. The CV's (0.0-1.4V range) on the 2700°, 2400°, and 2100°C treated carbon fibers also showed two cathodic current peaks. The potential of these peaks shifted to less positive values with the decrease in HTT. This dependency seems to imply a relation between the deintercalation process and the crystallinity of the carbon fibers.

Figure 6 shows Raman spectra of the 3000°C treated carbon fibers before and after electrolysis. It has been known that carbon materials have two Raman bands at 1580 and 1360 cm^{-1} (14-16), the former being due to the in-plane motion of carbon atoms in the hexagonal graphite layers, and the latter being related to the presence of structural defects in the graphite layer planes. As shown in Fig. 6a, the original carbon fibers without electrolysis give a strong sharp band at 1580 cm^{-1} but only a weak one at 1360 cm^{-1} . The ten times cyclic electrolysis in the range of 0.0-1.4V did not affect the spectrum (Fig. 6b). This suggests that graphite layer planes of the original carbon fibers retain their perfection after the electrochemical formation of the stage 1 graphite-sulfuric acid intercalation compound. In the spectrum of the carbon fibers after the ten times cyclic electrolysis in the range of 0.0-2.3V (Fig. 6c), however, a marked increase in the relative intensity of 1360 cm^{-1} band is observed. Thus the formation of graphite oxide seems to give rise to various

defects in graphite layer planes, which may be related to puckering of layer planes due to the carbon-oxygen bond in graphite oxide (12, 13). The introduction of the defects in layer planes by the formation of graphite oxide may cause the disappearance of the higher-order diffraction lines of the stage 1 intercalation compound, as shown in Fig. 3d.

Summary

The results obtained can be summarized as follows. The CV's in 98% H_2SO_4 were measured on the mesophase-pitch-based carbon fibers heat-treated at the various temperatures. Three anodic current peaks at the potential of about 1.1, 1.4, and 2.1V in the CV's were attributed to the formation of the stage 2 and the stage 1 graphite-sulfuric acid intercalation compounds and of the graphite oxide from the measurements of x-ray diffraction patterns and Raman spectra. The CV depended strongly on HTT of the carbon fibers; the onset potential shifting to the positive value, and the anodic current peaks due to the formation of GIC becoming broad with the decrease in HTT. Thus the electrochemical behavior showed a marked dependence of the GIC formation on the crystallinity of the host carbon fibers. For the Raman spectra of the 3000°C treated carbon fibers, the graphite layer planes of the original fibers were found to retain their perfection even after ten times cyclic electrolysis up to 1.4V, that is, ten times repetition of formation and decomposition of the stage 1 compound, but various defects were introduced in the layer planes by the formation of graphite oxide.

Acknowledgment

The authors wish to thank Dr. M. Nakamizo of Government Industrial Research Institute, Kyushu, for Raman spectra measurement. A part of this work was supported by Grant-in-Aid for Scientific Research (A) of the Ministry of Education, Science and Culture, Japan.

Manuscript submitted Feb. 12, 1985; revised manuscript received June 3, 1985.

Toyohashi University of Technology assisted in meeting the publication costs of this article.

REFERENCES

1. L. B. Ebert, *Ann. Rev. Mater. Sci.*, **6**, 181 (1976).
2. M. S. Dresselhouse and G. Dresselhouse, *Adv. Phys.*, **30**, 139 (1981).
3. M. Inagaki, *Hyomen*, **20**, 130 (1982).
4. M. J. Bottomley, G. S. Parry, A. R. Ubbelohde, and D. A. Young, *J. Chem. Soc.*, 5674 (1963).
5. S. Aronson, S. Lemont, and J. Weiner, *Inorg. Chem.*, **10**, 1296 (1971).
6. R. Fujii, *Denki Kagaku*, **41**, 52 (1973).
7. F. Beck, H. Junge, and H. Krohn, *Electrochim. Acta*, **26**, 799 (1981).
8. J. O. Besenhard, E. Wudy, H. Möhwald, J. J. Nickl, W. Biberacher, and W. Foag, *Synth. Met.*, **7**, 185 (1983).
9. S. C. Bennett and D. J. Johnson, *Carbon*, **17**, 25 (1979).
10. D. J. Johnson, I. Tomizuka, and O. Watanabe, *ibid.*, **13**, 321 (1975).
11. M. Inagaki, M. Endo, A. Oberlin, S. Kimura, M. Nakamizo, Y. Hishiyama, and H. Fujimaki, *Tanso*, **99**, 130 (1979).
12. W. Rüdorff, *Adv. Inorg. Chem. Radiochem.*, **1**, 223 (1959).
13. R. C. Croft, *Quat. Rev.*, **14**, 1 (1960).
14. F. Tuinstra and J. L. Koenig, *J. Chem. Phys.*, **53**, 1126 (1970).
15. M. Nakamizo, R. Kammereck, and P. L. Walker, Jr., *Carbon*, **12**, 259 (1974).
16. M. Nakamizo, H. Honda, M. Inagaki, and Y. Hishiyama, *ibid.*, **15**, 295 (1977).

Open-Circuit Reduction of Oxygen Coverage on Au by Allyl Alcohol in Aqueous Electrolytes

R. Celdrán and J. González-Velasco

Departamento de Electroquímica, Facultad de Ciencias, Universidad Autónoma de Madrid, 28049 Madrid, Spain

ABSTRACT

An open-circuit study of the reduction of oxygen coverage on Au by allyl alcohol was made. The experimental results have been interpreted using Christov's scheme (15). The gold oxide coverage appears to be removed via a chemical, an electrochemical, or a mixed mechanism, depending on different potential values which characterize the diverse zones appearing in the $E-t$ curves. Gold oxide reduction seems to take place through two steps in acidic electrolytes and through three in neutral ones. The first step appears to be the reduction of Au_2O_3 to Au_2O , the second a reduction of Au_2O to Au, while the third has been interpreted as a reduction of an aged form of Au_2O .

In previous papers, (1, 2), we have reported on the oxidation mechanism of allyl alcohol on gold in aqueous solutions. The oxidation of the organic substance would interfere with that of the electrode itself. The oxide coverage can then interact with the organic molecules giving rise to a fairly rapid oxygen coverage removal, depending on oxidation level, structure, and stability of the oxide layers. The aim of the present study is to clarify the mechanism of the interaction between the organic reducing agent and the oxide coverage. The study could also provide indirect evidence for the composition and structure of superficial oxygen coverage on gold.

The open-circuit potential decay technique was applied. In this way, it is possible to follow the changes in potential under null net current conditions. The $E-t$ curves recorded after anodic polarization of a gold electrode in the bulk electrolyte and in the presence of allyl alcohol give information on the interaction mechanism between electrolyte and oxide layer.

Various authors have used this method to study the development and evolution of oxide coverage on metal electrodes (3-10). The influence of stirring (6, 7) and of diverse reducing agents (6-12) was also investigated. Few papers have appeared on the reduction of oxygen coverage on gold by organic reducing agents (13, 14).

Experimental

Procedures.—Cell, electrodes, apparatus, and activation method have been described elsewhere (1, 2). The reactants were NaOH, K_2SO_4 , H_2SO_4 (Merck, P.A.). Allyl alcohol (Fluka, P.A.), was also used. Experiments were carried out under N_2 atmosphere and in unstirred solutions. Temperature (except in experiments for determination of the activation energy) was kept constant at $25.0^\circ \pm 0.1^\circ C$. Two series of experiments were carried out under the following conditions.

In the first series, a potential $E_a = 1.15 V_{SCE}$ was applied to the working electrode (WE) in the bulk solution for a given time t_a . The circuit was then opened and the $E-t$ curve recorded. The electrode was then activated (1) in the bulk solution and the I/E curve was recorded and compared with a standard I/E curve in order to check its catalytic activity. Thereafter, the electrode was polarized at E_a and allyl alcohol was added in N_2 atmosphere, immediately prior to opening the circuit. The resulting $E-t$ relationship was recorded. Measurements were made in unbuffered solutions (H_2SO_4 , NaOH, and $10^{-1}M$ and $5 \times 10^{-1}M$ K_2SO_4), and in buffer solutions (Britton-Robinson) for the complete pH range. The allyl alcohol concentration was varied from $c = 10^{-2}$ to $5 \times 10^{-2}M$. The time during which the polarization was applied, t_a , was changed from 5 to 20 min.

In the second series, the WE was activated in the bulk solution ($0.1M$ H_2SO_4 ; $\mu = 1$ with K_2SO_4) then introduced into a second, previously deoxygenated cell containing a solution of allyl alcohol. The solution was stirred with N_2 for 2 min and then left for 30s. Finally, a potential E_a was applied to the WE for a time, t_a , before opening the circuit

and recording the $E-t$ curve. For this series, the allyl alcohol concentration, c , was varied from 10^{-3} to $10^{-1}M$, and t_a was varied from 4 to 45s. The catalytic activity of the WE was checked after each experiment as described (1). All potential values are expressed *vs.* SCE.

Both series of experiments gave rise to similar $E-t$ responses. In acidic medium, the different values of the transition times which can be deduced from Fig. 2 and 5 are due to the different t_a and E_a applied.

The experimental determination of τ according to Ref. (15) was made, either as the time corresponding to the intersection of the tangents to AB and CD (Fig. 1) or as the time at which characteristic potential is reached. This po-

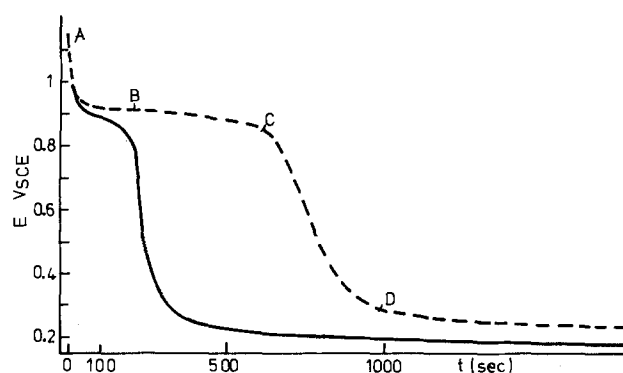
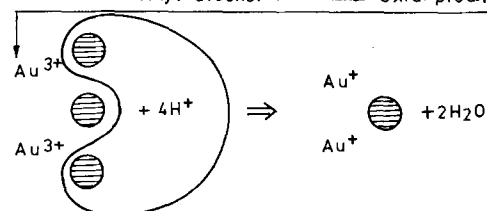


Fig. 1 b

Section A-B) Chemical interaction between allyl alcohol and Au_xO_y coverage. (see Eq. 1)

Section B-C) Electrochemical interaction
Allyl alcohol + bare Au \rightarrow Oxid. prod. + ne



Section C-D) Electrochemical interaction
Allyl alcohol + bare Au \rightarrow Oxid. prod. + ne

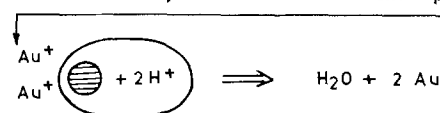


Fig. 1. Open-circuit $E-t$ curve of $0.1M$ H_2SO_4 + 10^{-2} allyl alcohol. ($E_a = 1.16 V_{SCE}$, $t_a = 5$ seconds, $T = 25^\circ C$) showing the different gold oxide reduction zones (9), and a description of the processes supposed to be implied in every section (b).

tential, which corresponds to zero oxygen coverage is given by $E = 0.62 V_{SCE}$ for Au in acidic medium (1, 18, 26). In this case, the potential value corresponding to the tangent intersection point is $0.86 \pm 0.01 V_{SCE}$ and the values of τ obtained from both methods do not differ by more than 5%.

Results.—Figures 2, 3, and 4 show $E-t$ curves obtained in different media: acid, neutral, and basic (18). In all media, a marked decrease in τ is brought about by the presence of allyl alcohol. The decrease is larger in unbuffered than buffered solutions for all pH values. In alkaline medium, at $t = \tau$ the potential drops sharply to values close to that for H_2 evolution and then increases. Similar behavior is observed for allyl alcohol on other metals (1).

The theoretical treatment (15-17) was applied to the $E-t$ curves obtained in the second series of experiments. Table I summarizes the results for the different sections of the $E-t$ curves (see Fig. 1) in the second series of experi-

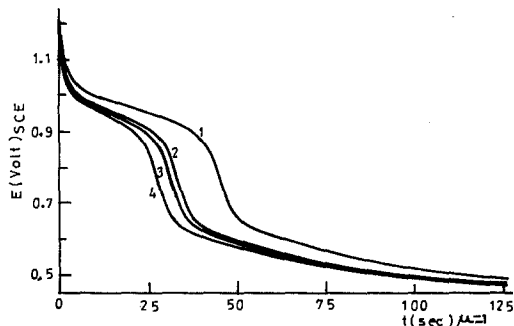


Fig. 2. Open-circuit $E-t$ curves in acidic medium at different adsorption times (t_a). Solution = $0.1M H_2SO_4$ ($\mu = 1$) + $10^{-2}M$ allyl alcohol. 1: $t_a = 45s$. 2: $t_a = 30s$. 3: $t_a = 25s$. 4: $t_a = 20s$; $E_a = 1.20 V_{SCE}$.

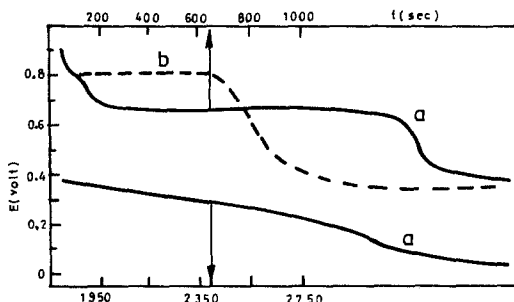


Fig. 3. Open-circuit $E-t$ curve in (a) $0.1M K_2SO_4$ + $10^{-2}M$ allyl alcohol ($t_a = 5$ min, $E_a = 0.91 V_{SCE}$), (b) $0.1M K_2SO_4$ and the values for t_a and E_a given in (a).

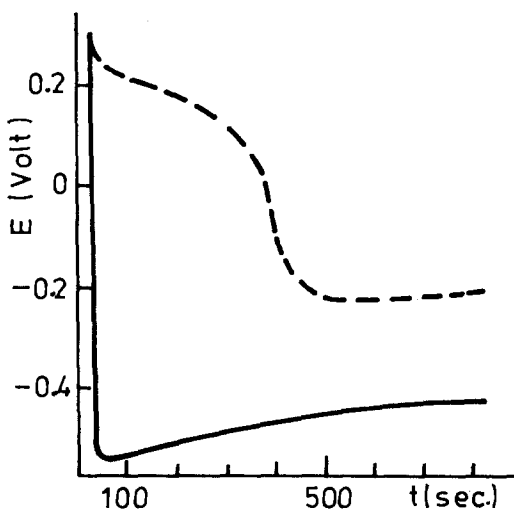


Fig. 4. Open-circuit $E-t$ curves in (1) $0.1M OHNa$, (2) $0.1M NaOH$ + $10^{-2}M$ allyl alcohol. $t_a = 20$ min. $E_a = 0.3 V_{SCE}$.

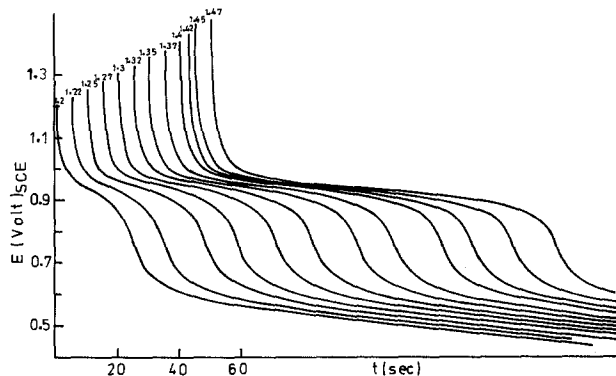


Fig. 5. Open-circuit $E-t$ curves for different E_a values. Solution: $0.1M H_2SO_4$ + $10^{-2}M$ allyl alcohol. $EdS = 10s$. $T = 25^\circ C$.

ments. In addition to the results summarized in Table I, the following were determined. The dependence of τ on the different experimental parameters is as follows. τ decreases with increasing allyl alcohol concentration [plots of $(\log \tau / \log c)_{E_a, t_a}$ are linear and show a slope value of $b' = -0.48 \pm 0.02$ ($E_a = 1.22 V_{SCE}$, $t_a = 45s$, and an intercept of $+0.90$). τ shows an exponential increase with increasing E_a and a linear increase with increasing intermediate values of t_a (Fig. 6). τ decreases with increasing temperature values. From the slope of the $(\log \tau / T^{-1})_{t_a, E_a}$ plot, the value of the apparent activation energy (E_A) of the overall process can be obtained: $E_A = 73.6 kJ \cdot mol^{-1}$ (Fig. 6).

In general, it can be said that the results are similar to those obtained by Christov (15) for the interaction between organic substances and the platinum oxides.

Theoretical Treatment of Data

Christov *et al.* (15-17) have proposed a general mechanism to interpret the complete open-circuit reduction of oxygen coverage on Pt by organic reducing agents. It was assumed that two parallel processes take place at the electrodes, and this assumption can be essentially kept for the case of the gold oxides, considering the following equations for the interaction between allyl alcohol and the gold oxides

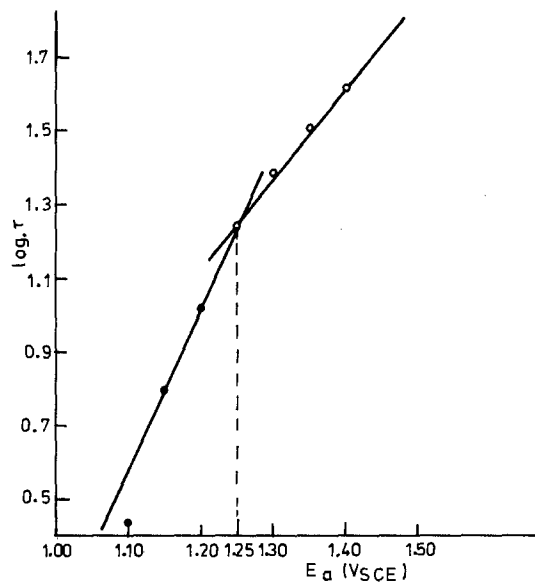
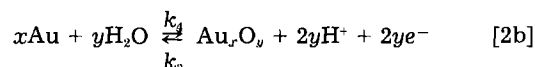
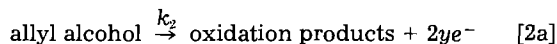
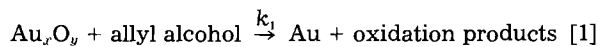


Fig. 6. Plot of $\log \tau$ vs. E_a . $T = 39.8^\circ C$; $t_a = 10s$. $0.1M H_2SO_4$ + $10^{-2}M$ allyl alcohol. (E_a) critical = $1.25 V_{SCE}$.

Table I. Results obtained for the second series of experiments

Section A-B	c_{allyl} (mol-liter ⁻¹)	a ($\delta E/\delta \log t$) _c	b ($\delta \log t/\delta \log c$) _E	
	10^{-2} - 10^{-2}	-0.120 ± 0.002	-0.30 ± 0.02	
	5×10^{-2} - 10^{-1}	-0.138 ± 0.002	-0.50 ± 0.02	
Section B-C	c_{allyl} (mol-liter ⁻¹)	$E_f/\log c$	$[\log(-dE/dt)/\log \tau]_{E=E_i}$	$[\log(dE/dt)/\log c]_{E=E_i}$
	10^{-2} - 10^{-1}	0.95 ± 0.02	-1.10 ± 0.05 (slope) -0.72 ± 0.05 (intercept)	0.42 ± 0.02
Section C-D	c_{allyl} (mol-liter ⁻¹)	$m[\partial \log(\tau - t)/\partial \log c]$	$(\partial E/\partial \log(\tau - t))_c$	α
	5×10^{-2} - 10^{-1}	$-1/2$	0.244 ± 0.005	0.48 ± 0.01

The partial reactions [1], [2a], and [2b] correspond to chemical oxidation of the reducing agent by the oxygen coverage, electro-oxidation of the reducing agent on the free electrode surface, and electrochemical oxidation and reduction of the electrode, respectively. The e^- produced in reaction [2a] take part in reaction [2b]. k_1 , k_2 , k_3 , and k_4 represent the rate constants of the respective processes.

Although both the structure and the composition of the oxide layers are different for Au and Pt, the kinetic assumptions upon which Cristov (15) based his theory apply to both metals.

The dependence of E on t in every region of Fig. 1 can be theoretically deduced on the assumption that the chemical interaction of the reducing agent and the oxygen coverage is rate determining and the adsorption can be described by a Temkin isotherm. On this basis, a general analytical $E-t$ dependence is derived for the overall process. In order to achieve the direct determination of the kinetic parameters, some particular cases are examined.

High coverage (section A-B of Fig. 1).—The theoretical treatment (16) gives rise to the following relations for a chemical mechanism

$$(\partial E/\partial \log t)_c = \frac{-2 \times 2.303}{f} \approx 0.12V \quad [3]$$

$$(\partial t/\partial \log c)_E = -1 \quad [4]$$

where $f = F/RT$, t = time after opening the circuit, E the electrode potential, c the bulk concentration of reducing agent (allyl alcohol), and α the transfer coefficient

$$(\partial E/\partial \log t)_c = -2 \times 2.303/f(1 - \alpha) \approx 0.24V \quad [5]$$

$$(\partial t/\partial \log c)_E = -3/2 \quad [6]$$

For high coverage and an electrochemical mechanism, the following values should be obtained

$$(\partial E/\partial \log t)_c = -2.303/\alpha f \approx 0.12V \quad [7]$$

$$(\partial t/\partial \log c)_E = 0 \quad [8]$$

Low coverage (section C-D of Fig. 1).—The resulting equations (16) take the form

$$(\partial E/\partial \log(\tau - t))_c = 2 \times 2.3/(1 - \alpha)f \approx 0.24V \text{ when } k_2c \gg k_4 \exp(\alpha FE) \quad [9]$$

$$(\partial E/\partial \log(\tau - t))_c = 2 \times 2.3/f \approx 0.12V \text{ when } k_2c \ll k_4 \exp(\alpha FE) \quad [10]$$

where τ = time required for the complete reduction of oxygen coverage. The concentration interval over which [9] or [10] is valid, is determined by the slope of the plot $(\log(\tau - t)/\log c)_E$. This slope gives values of $-1/2$ and -1 for Eq. [9] and Eq. [10], respectively.

Medium coverage (section B-C of Fig. 1).—According to Ref. (17), the mathematical analysis predicts the appear-

ance of one or more inflections in the $E-t$ curves, depending on the value of α . This case can be characterized by the concentration dependency of the potential in the region of the inflection

$$E_i = (2.3/f) \log(k_2k_3/k_1k_4) \text{ when } (1 - \alpha)k_2c \ll k_4 \exp(\alpha E_i) \quad [11]$$

$$E_i = (2.3/(1 - \alpha)f) \log(k_3/k_1) - (2.3/(1 - \alpha)f) \log c \text{ when } (1 - \alpha)k_2c \gg k_4 \exp(\alpha FE_i) \quad [12]$$

and by the slope of the plateau in the $E-t$ curve

$$\log(-dE/dt)_{E=E_i} = \log[4g(k_1k_2)^{1/2}/qf] + \log c \text{ when } (1 - \alpha)k_2c \ll k_4 \exp(\alpha FE_i) \quad [13]$$

$$\log(-dE/dt)_{E=E_i} = \log[4g(k_1k_2)^{1/2}/(1 - \alpha)qf] + \log c \text{ if } (1 - \alpha)k_2c \gg k_4 \exp(\alpha FE_i) \quad [14]$$

where g is inhomogeneity factor from Temkin's isotherm and q the charge required for the formation of a monolayer of oxygen coverage on gold. An additional relation between $(-dE/dt)_{E=E_i}$ and $\log \tau$ can be obtained. The re-

$$\left. \begin{aligned} (\partial E/\partial \log t)_c &= \frac{-2 \times 2.303}{f} \approx 0.12V \\ (\partial t/\partial \log c)_E &= -1 \end{aligned} \right\} \text{for } k_2c \ll k_4 \exp(\alpha FE) \quad [3]$$

sulting slope and intercept are predicted to be independent of the kinetic parameters. The effect of various factors (t_a , E_a , c , ...) on τ is also considered (17).

Discussion

The results obtained in the first series of experiments confirm the existence of alcohol-gold oxide interaction observed in other studies (1, 2). Under experimental conditions that differ slightly from those described before, the $E-t$ curves show that the reduction occurs in more than one step (more than one plateau from which more than one transition time can be measured) or show the co-existence of more than one type of adsorbed species. In alkaline medium, results suggest that only one type of oxide [possibly $\text{Au}(\text{OH})_3$] is present at sufficiently high anodic potentials.

As said above, the second series of experiments leads to results similar to the first. This can be explained on the basis of the results (1, 2) obtained for the direct oxidation of allyl alcohol on gold. In that case, an inhibition of the oxidation of the organic substance at the potentials at

which gold oxides were formed was observed (E_p , peak potential for the allyl alcohol oxidation appears at 1.03 V_{SCE} and E_p for gold oxide at 1.15 V_{SCE}). It could be argued that a part of allyl alcohol can be oxidized and reduced by electron tunneling through the Au oxide film, analogous to electron tunneling in the case of oxygen evolution at Pt oxide covered Pt electrodes. This contribution could take place at more anodic potentials (E_a) than those applied in this work. At these potentials the electron tunneling contribution should be too small to be considered. A chemical interaction between allyl alcohol and the gold oxides can take place during anodic polarization, but the initial conditions at the moment of open circuit seem to be similar to those obtained for the first series.

The results for this second series show a slow change in the slope in the section C-D of the $E-t$ curve (Fig. 1). This suggests that the removal of the oxide layer occurs in steps. This has also been observed by other authors (4), and attributed to changes occurring in the nature of the adsorbed species. At $E = 0.86 V_{SCE}$ the same oxygen coverage is achieved for any value of c , while at $E = 0.62V$, the whole oxide layer is removed.

In order to evaluate the $E-t$ curves, the diagnostic criteria derived from Christov's treatment (15, 17) were used.

The first section (A-B) of the $E-t$ curve is characterized by high potential values and high oxygen coverages. High anodic potentials would enhance the electro-oxidation of the alcohol. High oxygen coverages would hinder its adsorption on the bare metal surface, and hence electro-oxidation, while it would facilitate the chemical interaction between the oxide layer and the alcohol in solution.

The values of the slope $\alpha = (\partial E / \partial \log t)_c$ (Table I) tend to increase with increasing c and this result, similar to that for Pt (20), suggests a chemical interaction between the gold oxide and the alcohol which requires that $k_2c \ll k_4 \exp(\alpha f E)$ be satisfied (Eq. [3]). This condition does appear to hold, since at high anodic potentials the electro-oxidation of the electrode surface predominates over that of the alcohol. Moreover, Eq. [11] predicts that for low c values, $E_i \neq f(c)$, while for higher c , E_i would decrease with increasing c , according to Eq. [12]. The E_i values obtained from the experimental $E-t$ curves, show that for $c < 10^{-2}M$, $E_i \neq f(c)$, while a slight decrease in E_i is observed for $c > 5 \times 10^{-2}M$. Moreover, the value of the slope α is the same as that obtained for a purely electrochemical mechanism (Eq. [7]). To choose between chemical or electrochemical interaction, it is necessary to resort to the value of b (Table I). A purely electrochemical mechanism would give $b = 0$ (Eq. [8]), while a chemical one would give $b = -1$ (Eq. [4]).

Table I gives two values of b for section A-B of the curve, depending on the c concentration range. For $c \approx 10^{-3}$ - $10^{-2}M$ $b = -0.30$, but -0.50 when c varies between 5×10^{-2} and $10^{-1}M$. Both values are intermediate between 0 and -1 , which suggests that the reduction proceeds through a mixed mechanism with approximately 30% of the reduction being chemical. The higher relative contribution of chemical reduction with increasing c could be expected. The above interpretation is in agreement with previously observed potentiodynamic curves (1, 2). These show that, if c is increased, the electroreduction oxide peak decreases until it disappears at sufficiently high c . At the same time, the allyl alcohol oxidation peak in the cathodic sweep increases with c . This is due not only to its direct oxidation but also to the faster appearance of bare gold surface enhanced by the direct chemical reaction between alcohol (in higher concentrations) and the most oxidizing oxide form. It can be seen in Ref. (21) that a species possibly implied in the process, Au_2O_3 , can chemically oxidize the alcohols.

When the section B-C is reached, the oxygen coverage on the electrode has decreased. Thus, chemical oxidation of the alcohol is expected to be slower than in section A-B. Also, the allyl alcohol might encounter a larger bare metal surface, which would increase its electro-oxidation rate. The theory predicts the appearance of an inflection

point when both chemical and electrochemical oxidation rates become of the same order.

The experimental potential, E_i , corresponding to the inflection point is independent of c (Table I), for low c values. Equation [11]-[12] predict that, for low values of c , $E_i \neq f(c)$ (Eq. [11] is followed), while for higher values of c , E_i decreases with increasing c according to Eq. [12]. A slight decrease in E_i is observed for $c > 5 \times 10^{-2}M$.

The electro-oxidation of the alcohol should make the electrode potential more negative. The potential value, however, shows only a very slight decrease in this section of the decay curve.

Thus, another mechanism for the elimination of negative charge from the electrode must accompany e^- transfer from the alcohol. The only negative species on the electrode would be the O^- ions, which can react with the H^+ ions in solution. This elimination would yield zero net current and explains why the potential value remains almost unchanged.

The proposed electrochemical mechanism should be responsible for the elimination of the oxide coverage, as suggested by the similarity between the experimental values in Table I— -1.10 and -0.72 (slope and intercept, respectively, of the $\log [(-dE/dt)/\log \tau]_{E=E_i}$ plot—and the theoretically predicted— -1.00 (slope) and -0.81 (intercept) (20).

Furthermore, if this mechanism is correct, influence of H^+ concentration on the reaction rate and, consequently on the $E-t$ curves, should be observed. It is to be expected that the elimination rate of O^- would decrease with decreasing H^+ concentration, giving rise to an increase in τ . This is the result obtained (Fig. 3) for $E-t$ curves recorded at near-neutral pH values.

There is a disagreement between the theoretically (20) predicted slope of the plot of $(-dE/dt)$ vs. $\log c$ (at $E = E_i$) and the experimental ones (1.00 and 0.42, respectively).

It should be pointed out that for oxygen coverage reduction of PtO by organic substances it has been assumed (22) that both chemical and electrochemical reactions follow the same path, i.e., via dehydrogenation of α -H atoms. For gold oxide-alcohol interaction (1, 2), the reaction may follow different paths, giving rise to different reaction rates.

In the section C-D, the theoretical treatment supposes that the electro-oxidation of the organic substance is much faster than its chemical oxidation. The low oxygen coverage makes the chemical oxidation rate too low to be considered. The decreasing potential values in this section are due to electrochemical oxidation of the alcohol.

The experimental values for this section are summarized in Table I. The experimental value for $(\partial \log(\tau - t) / \partial \log c)_E$ coincides with the theoretically predicted (-0.5) when $C_{allyl} \gg 5 \times 10^{-2}M$, and shows that Eq. [9] should be valid. The plot of Eq. [9] gives in fact a value for $(\partial E / \partial \log(\tau - t))_c$ of $0.224 \pm 0.005V$, in a very good agreement with the theoretical value $0.220V$. The derived value of α should be 0.48 ± 0.01 .

The observed discrepancy between experimental and theoretical values for low values of c is similar to that obtained for the reduction of PtO by organic substances (20). This fact could be explained if the condition $k_2c \gg k_4 \exp(\alpha f E)$ in Eq. [9] is no longer satisfied due to the decrease of c .

The variation of τ with the different experimental parameters (c , t_a , E_a , T , ...) is similar to that for Pt and agrees with the proposed interaction mechanism. The decrease in τ with increasing c implies an alcohol-gold oxide interaction whose rate increases with c , according to potentiodynamic studies (1, 2). This decrease of c cannot be attributed to a smaller oxygen coverage due to the presence of the alcohol during anodic polarization (in the second series of experiments), because the same result is obtained in the first series of experiments, in which the WE was polarized before the addition of the alcohol. The linear relation between $\log \tau$ and E , as well as between τ and t_a , can be deduced by supposing a mixed chemical and electrochemical reduction mechanism of the oxygen cov-

erage. At sufficiently positive potentials but not too high coverage, the rate of oxygen coverage formation will be much greater than the reduction rate. Assuming that the oxygen coverage increase can be described by means of a Temkin isotherm, the linear terms in θ can be neglected. In this way the following equation (17) can be derived

$$[1 - 2g(k_1 k_2)^{1/2} c \tau / \pi q]^{-1} = 1 + (k_1 / k_2)^{1/2} (\pi g k_4 t_a / 2q) \exp(\alpha f E_a) \quad [15]$$

where g represents the interaction coefficient in the Temkin isotherm and q is the charge required for the formation of a monolayer of oxygen coverage.

In order to obtain an idea about the value of the $2g(k_1 k_2)^{1/2}$ factor, plots of Eq. [13] and [14] were made. From the slope value it was deduced that $4g(k_1 k_2)^{1/2} / qf = 0.01778$, and taking (27, 28) $q = 850 \mu\text{C}\cdot\text{cm}^{-2}$, gives $g(k_1 k_2)^{1/2} = 1.47 \times 10^{-4}$. This value is very similar to that deduced from the intercept of the $(\log \tau / \log c)_E$ plot (17). In this case, $\log(\pi q / 2(k_1 k_2)^{1/2} g) = \text{intercept} = 0.9$, and $g(k_1 k_2)^{1/2} = 1.68 \times 10^{-4}$. [Incidentally, this value provides an additional test for the validity of Christov's treatment for the case of gold oxides, since it is very similar to that obtained for that case (15).]

A rearrangement of Eq. [15] can be easily made by supposing that $\pi q \gg 2g(k_1 k_2)^{1/2} c \tau$, as is obtained from the value for $2g(k_1 k_2)^{1/2}$ formerly deduced. Finally, the following expression can be obtained for the relation between τ and t_a and E_a

$$\tau = (\pi^2 k_d / 2ck_2) \exp(\alpha f E_a) t_a \quad [16]$$

Plots of $\log \tau$ vs. E_a at different temperatures were made (Fig. 6). At 25.2°C and $t_a = 10\text{s}$ the intercept¹ value leads to a k_d/k_2 ratio of 7×10^{-6} , i.e., the oxidation reaction of allyl alcohol is faster than the gold oxide formation. At 39.8°C , the intercept gives a value of 3.5×10^{-6} for this ratio. It seems that with an increase in the temperature k_2 increases more rapidly than k_d . The exponential increase of τ with E_a could be in agreement with the idea of the differential characteristics of the adsorbed species, supposedly formed at different potential values.

Figure 7 gives the τ vs. t_a plots at $T = 25.0^\circ\text{C}$ and $E_a = 1.22 \text{ V}_{\text{SCE}}$. The result indicates that, the higher the allyl alcohol concentration, the faster would be the oxide layer elimination. The rate of change of τ with t_a is also dependent on c and can be attributed to a change in the value of α in Ref. (16) induced by the different participation of chemical and electrochemical reactions in the mixed mechanism proposed. These changes of α can be followed by substituting the k_d/k_2 values obtained from the plots of Fig. 6.

Substituting the k_d/k_2 ratio obtained in Eq. [11], ($E_1 = 0.95 \text{ V}_{\text{SCE}}$), one obtains a value of $k_3/k_1 = 5.86 \times 10^{12}$, the same order of magnitude as found in the PtO study (15). This would mean that the chemical interaction [1] between allyl alcohol and gold oxide would be much slower than the electrochemical one (Eq. [2a] and [2b]).

The decrease of τ with stirring for $c < 10^{-2} \text{ M}$ (Fig. 10) shows the influence of convective diffusion on the process. Faster transport of the alcohol to the surface would accelerate the chemical and electrochemical reduction rates. For $c > 10^{-2} \text{ M}$, the slightly higher values of τ can be explained supposing the formation of adsorbed intermediates, which would be partly eliminated by stirring, thus making slower the rate of production of electrons (by oxidation of the allyl alcohol molecules initially present). This fact is reflected in potentiodynamic curves taken in almost neutral solutions (Fig. 10). Under stirring, a second reduction peak is recorded which can be attributed to the reduction of a gold oxide produced in a first reduction step. When stirring is stopped, only a reduction peak (Fig. 11b) is obtained. The allyl alcohol molecules keep in contact with the electrode surface and supply electrons for the complete reduction of the oxide layer in a single step.

¹We take the intercept as the value of $\log \tau$ at the critical potential point in which the oxygen coverage takes intermediate values ($E = 1.2 \text{ V}_{\text{SCE}}$).

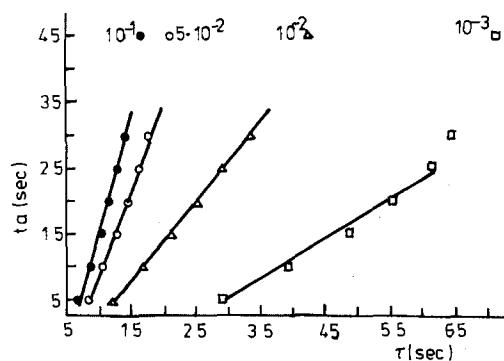


Fig. 7. Plots of t_a vs. τ in $0.1 \text{ M H}_2\text{SO}_4$ at different allyl alcohol concentrations. $E_a = 1.20 \text{ V}$. $T = 25^\circ\text{C}$.

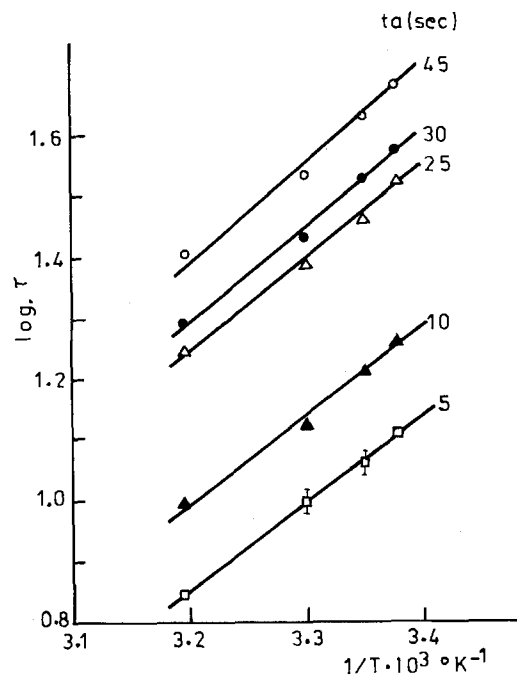


Fig. 8. Plots of $\log \tau$ vs. $1/T$ at different t_a values. $0.1 \text{ M H}_2\text{SO}_4 + 10^{-2} \text{ M allyl alcohol}$. $E_a = 1.20 \text{ V}_{\text{SCE}}$.

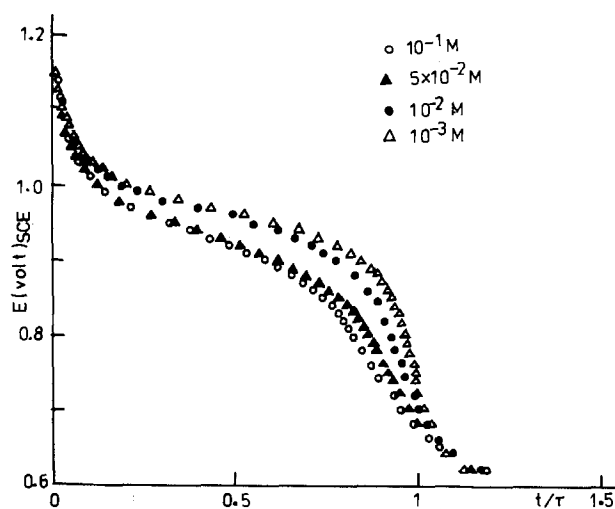


Fig. 9. Plots of E vs. t/τ in $0.1 \text{ M H}_2\text{SO}_4$ at different allyl alcohol concentrations. $t_a = 45\text{s}$. $E_a = 1.20 \text{ V}_{\text{SCE}}$.

Section A-B is hardly influenced by stirring. This suggests that the chemical process is not transport dependent. In this range, the rate-determining step should be the adsorption of the organic substance as predicted by the assumed mechanism.

Finally, an interpretation of the Au-electrode open-circuit potential decay in absence of alcohol can also be given.

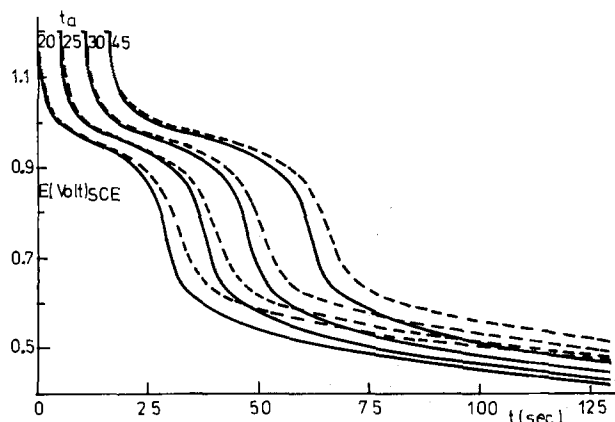
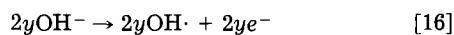
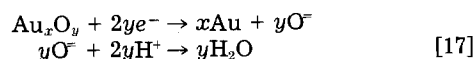


Fig. 10. Influence of stirring on the $E-t$ curves taken after different t_a values. $E_a = 1.20 \text{ V}_{\text{SCE}}$. $0.1\text{M H}_2\text{SO}_4 + 10^{-2}\text{M}$ allyl alcohol. Dashed line: without stirring. Solid line: with stirring.

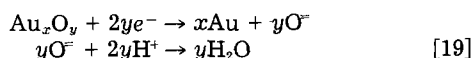
In basic medium the reaction mechanism would be initiated by the oxidation of OH^- species



and



The $\text{OH}\cdot$ radicals can then react with each other and produce H_2O_2 . In acidic medium, the H_2O molecules could play the role of the reduced species which can be oxidized and induce the reduction of the oxides

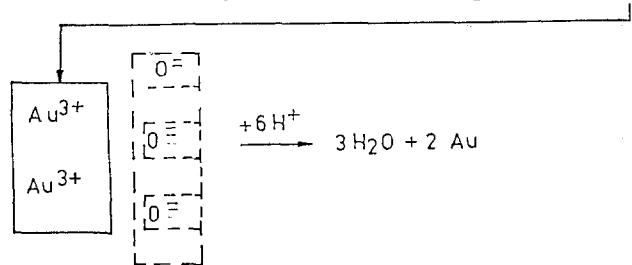
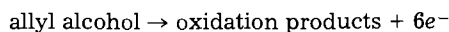


giving rise to $\text{OH}\cdot$ radicals which can produce H_2O_2 .

The fact that $\tau_{\text{basic medium}} < \tau_{\text{acid medium}}$ seems to predict a reaction [18] slower than reaction [16]. It can be said that the transition times in acid as well as in basic solutions are much longer without, than with, allyl alcohol present in the solution.

Conclusions

On the basis of the experimental data, a mixed mechanism (chemical-electrochemical) can be postulated for the reduction of gold oxide layers (23-26). The following equations give a summarized view of the process described in Fig. 1



On the surface, after reduction of Au^{3+} ions, the uncompensated charges of O^- make them to repel each other. If the proposed mechanism should take place, the rate of the third step would be dependent on the $(\text{H}^+)_{\text{aq}}$ according to



and

$$v = -\frac{d\theta_{\text{O}^-}}{dt} = K(\theta_{\text{O}^-})^a \cdot (\text{H}^+)_{\text{aq}}^b \cdot f(E)$$

where $K = (1/\tau)$, and $f(E)$ is a function of the potential

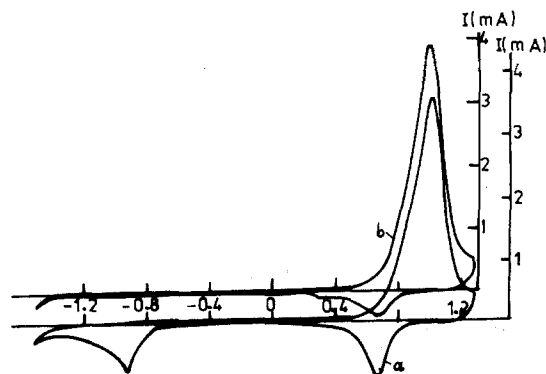


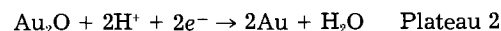
Fig. 11. Voltammograms of $0.1\text{M K}_2\text{SO}_4 + 10^{-2}\text{M}$ allyl alcohol solutions. a: Without stirring. b: With stirring.

value, decreasing from the first to the third step. Thus, at $(\text{H}^+)_{\text{aq}} = 10^{-7}\text{M}$, the third step could become rate determining. Both $E-t$ curves and $i-E$ potentiodynamic diagrams seem to agree with such supposition: The $E-t$ curves obtained in neutral electrolytes show three different plateaus (Fig. 3). The first one corresponds to the peak potential value obtained for the oxide reduction in voltammograms taken in acidic electrolytes. This process is then attributed to the reduction of Au_2O_3 . The second one appears at a potential value similar to the one of a second reduction peak obtained maintaining the electrode at oxide formation potentials values for a given time. This peak is attributed to the reduction of Au_2O , formed by reduction of Au_2O_3 . The third one is attributed to the reduction of a more stable form of Au_2O , directly formed during the gold oxidation, and after having undergone the so-called aging process (23-25). This process seems to stabilize such oxide species and that can explain why its reduction occurs only at more negative potentials. In summary, the following equations could describe the processes supposed to be taking place at the potentials of the different plateaus

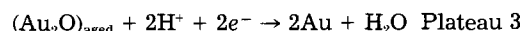
Step 1:



Step 2:



Step 3:



Thus, the Au_2O coverage would be formed in the following way

$$(\theta_{\text{Au}_2\text{O}})_{\text{total}} = (\theta_{\text{Au}_2\text{O}})_{\text{initial}} + (\theta_{\text{Au}_2\text{O}})_{\text{(from step 1)}}$$

supposing

$$(\theta_{\text{Au}_2\text{O}})_{\text{initial}} \ll \theta_{\text{Au}_2\text{O}_3}, \text{ then } (\theta_{\text{Au}_2\text{O}})_{\text{step 1}} \approx \theta_{\text{Au}_2\text{O}_3}$$

The higher values of τ for the second and the third plateaus reflect not only the higher stability of both Au_2O species, but also the lower electro-oxidation rate of allyl alcohol with decreasingly positive potentials. The decrease of θ_{O^-} gives rise to a lower electrostatic repulsion between neighboring O^- , influencing in this way also, the rate of the third step. The influence of $(\text{H}^+)_{\text{aq}}$ is confirmed since in very acidic solutions, the second plateau almost disappears.

Likewise, the potentiodynamic $i-E$ curves in the same neutral solutions (Fig. 8) show two cathodic reduction peaks. Only the second one appears under stirring. Stirring carries away from the electrode the intermediates produced in the allyl alcohol oxidation before that process occurs completely. Thus, a partial reduction of Au^{3+} would take place, giving rise to Au_2O , which, in turn, reduces, giving a second peak. Without stirring the alcohol, oxidation continues and produces the e^- for the direct reduction from Au^{3+} to Au (one single peak).

In summary, it has been shown that an interaction between gold oxides and organic substances takes place and that the interaction follows a similar pattern to the process occurring between the same type of substances and Pt-oxides. The differences observed must be a consequence of the more complex oxidation processes occurring on gold electrodes.

Acknowledgment

This study was supported by the Comision Asesora de Investigación Científica y Técnica (Madrid).

Manuscript submitted Jan. 7, 1985; revised manuscript received June 17, 1985.

REFERENCES

1. R. Celdrán and J. González-Velasco, *Electrochim. Acta*, **26**, 525 (1981); *ibid.*, **26**, 763 (1981).
2. R. Celdrán and J. González-Velasco, *Ann. Quim.*, **77**, 88 (1981); *ibid.*, **77**, 328 (1981).
3. D. W. Shoesmith, T. E. Rummery, and D. Owen, *Electrochim. Acta*, **22**, 1403 (1977).
4. H. Dietz and H. Göhr, *Electrochim. Acta*, **8**, 343 (1963).
5. B. MacDougall and M. Cohen, *ibid.*, **23**, 145 (1978).
6. J. E. Oxley, G. K. Johnson, and B. T. Buzalski, *ibid.*, **9**, 89 (1964).
7. M. D. Drazic and V. Drazic, *ibid.*, **11**, 1235 (1966).
8. M. W. Breiter, *This Journal*, **109**, 425 (1962).
9. E. I. Sokolova, *Izv. Otd. Him. Nauki Ban*, **8**, 524 (1975).
10. G. Vertés, G. Horanyi, and F. Nagy, *Acta Chim. Acad. Sci. Hung.*, **67**, 145 (1971); *ibid.*, **68**, 217 (1971).
11. L. D. Burke and A. Moynihan, *Electrochim. Acta*, **16**, 167 (1971); *ibid.*, **15**, 1437 (1970).
12. G. Bianchi and P. Longhi, *Chim. Ind.*, **46**, 1286 (1964).
13. M. Betowska-Brescinska, *Electrochim. Acta*, **24**, 409 (1979).
14. W. Hauffe and J. Heitbaum, *Ber. Bunsenges. Phys. Chem.*, **82**, 487 (1978).
15. M. V. Christov and S. N. Raicheva, *J. Electroanal. Chem.*, **73**, 43 (1976).
16. M. V. Christov and S. N. Raicheva, *ibid.*, **73**, 55 (1976).
17. M. V. Christov, *ibid.*, **73**, 63 (1976).
18. R. Celdrán, Tesis Doctoral, Universidad Autónoma de Madrid, Madrid, Spain (1979).
19. G. A. Bogdanovskii, *Elektrokimiya*, **4**, 1196 (1968); *ibid.*, **5**, 472 (1969); *ibid.*, **6**, 909 (1970).
20. M. V. Christov and S. N. Raicheva, *J. Electroanal. Chem.*, **73**, 71 (1976).
21. M. P. Pourbaix, "Atlas of Electrochemical Equilibria in Aqueous Solutions," Pergamon Press, New York (1966).
22. M. V. Christov, *J. Electroanal. Chem.*, **76**, 147 (1977).
23. C. M. Ferro, A. J. Calandra, and A. J. Arvia, *ibid.*, **65**, 963 (1975).
24. J. W. Schultze and M. M. Lohrengel, *Ber. Bunsenges. Phys. Chem.*, **80**, 552 (1976).
25. M. M. Lohrengel and J. W. Schultze, *Electrochim. Acta*, **21**, 957 (1976).
26. A. C. Chialvo, W. E. Triaca, and A. J. Arvia, *J. Electroanal. Chem.*, **171**, 303 (1984).
27. R. C. Newman and G. T. Burstein, *ibid.*, **129**, 343 (1981).
28. J. Ganon, G. Nguyen van Huong, and J. Clavilier, *Surf. Sci.*, **79**, 245 (1979).

Electron-Transfer Rates on Chemically Modified Conducting Polypyrrole Film Electrodes

Miguel Saloma and Martha Aguilar

Facultad de Química, Universidad Nacional Autónoma de México, Ciudad Universitaria, Coyoacán 04510, México, D.F.

Manuel Salmón*

Instituto de Química, Universidad Nacional Autónoma de México, Circuito Exterior, Ciudad Universitaria, Coyoacán 04510, México, D.F.

ABSTRACT

A cyclic voltammetric study of the ferrocene redox reaction was used to evaluate the substituent effect in various *para*-substituted poly-*N*-phenylpyrrole films used as electrodes. To determine the film electrode substituent effect on the ferrocene couple reaction, the heterogeneous standard rate constant values were determined. The observed changes in the film electron-transport rate are the result of the structure monomer variation. Electronic interaction between the polypyrrole nucleus and the *para* substituents on the *N*-phenyl ring affects the electron-transfer rate of polymer electrodes.

A new class of organic electrodes has become available through the electropolymerization of aromatic compounds such as pyrrole (1). Electrochemically grown thin films of highly conductive polypyrrole, doped with BF_4^- , are insoluble and have long-term stability.

Conductive films of polypyrrole can be modified by introducing substituents into the cationic pyrrole polymer or varying the accompanying anion (2). The fact that the polypyrrole films are prepared electrochemically facilitates these modifications since the variations are made in the selection of the electrolyte or the monomer. We have now made a study of polypyrrole films modified by placing phenyl substituents in the *N* position of the pyrrole ring; the phenyl substituent assumes a particularly important role because it provides a means of introducing a wide selection of functional groups into the polymer structure as substituents on the phenyl ring.

In polymeric coatings on electrodes, the rate of charge and electron transport across the layer defines the usefulness of these films in devices. This paper deals with a cy-

clic voltammetric study of the quasi-reversible redox behavior of ferrocene on some poly-*N-para*-substituted phenylpyrrole films used as electrodes. We found that the electron transfer rate constant (k_s) of the ferrocene couple reaction depends on the film electrodes.

Experimental

The polymeric films of poly-*N-para*-substituted phenylpyrrole were prepared by electropolymerization of the corresponding *N-para*-substituted phenylpyrrole monomer with *p*-H, *p*-CH₃, *p*-OCH₃, *p*-Cl, *p*-Br, and *p*-NO₂.

All *N-para*-substituted phenylpyrroles were synthesized from 2,5-dimethoxytetrahydrofuran and the appropriate amine (3). The pure pyrrole monomers were identified by ¹H-NMR, IR, and MS and compared with reported data (4).

The film preparations were performed in a one-compartment cell using Pt as the working electrode, a similar counterelectrode, and a saturated calomel reference electrode (SCE). Each electrolytic solution contained 10⁻³M of the corresponding pyrrole monomer, plus 0.1M of tetra-

* Electrochemical Society Active Member.

ethylammonium tetrafluoroborate in distilled acetonitrile. The films were grown on 0.5 cm² Pt electrode surface, passing 20 mC·cm⁻² of charge to control the film thickness, estimated as *ca.* 50 nm considering the area of the electrode, density of the film, and the apparent *n* value for the reaction (5).

The electro-oxidation of the *N*-*para*-substituted phenylpyrroles conducted at a constant potential of 1.50V for *p*-H and *p*-NO₂, 1.12V for *p*-CH₃ and *p*-OCH₃, and 1.19V for *p*-Cl and *p*-Br, proceeds with the formation of insoluble polymer film on the electrode, as was previously reported (6). Films of these polymers, when mounted in acetonitrile/Et₄NBF₄ solution, can be electrochemically driven between the oxidized and the neutral forms. The films are stable to this reaction and can be cycled repeatedly without evidence of decomposition.

The cyclic voltammetric study of ferrocene (1 × 10⁻³M in acetonitrile/Et₄NBF₄ solution) was accomplished using thin films of *N*-phenyl-pyrroles on a Pt working electrode. All the measurements were prepared with IR compensation.

Electrochemical measurements were performed with a Princeton Applied Research Model 173 Potentiostat, a Model 175 Programmer, and a Hewlett-Packard 7004B X-Y recorder.

Results and Discussion

As can be seen in Table I, the formal potentials, E° , for the redox reaction of the dissolved ferrocene using [Pt] poly-*N*-*para*-substituted-phenylpyrrole-BF₄ electrodes are not significantly different from those measured with a Pt bare electrode. Peak heights vary linearly with the square root of the sweep rate, $\nu^{1/2}$, from 10 to 100 mV/s, as expected for a diffusion-limited process, and the ratio of the peak heights i_{pa}/i_{pc} is always close to unity. There is no evidence of absorption or adsorption on the polymer surface, indicated by the fact that $i/AC\nu^{1/2}$ values (A is the electrode area, C , mol/cm³) remains constant in the potential sweep range tested. The cyclic voltammograms produced using thicker films (70 nm) provide the same $i/AC\nu^{1/2}$ values, indicating that the signal amplitudes do not depend on film thickness. Moreover, the E° for ferrocene do not superimpose on the E° of the polymer films (6). Representative cyclic voltammograms are displayed in Fig. 1.

The potential difference between the peaks E_{pa} and E_{pc} (ΔE) is greater than 59 mV and increases with the sweep rate. Nicholson's treatment (7) for determining k_s values was used to evaluate the effect of the electrode on the redox reaction. Values for the Ψ parameter were obtained from the ΔE values. For a quasi-reversible reaction, Nicholson's empirical equation is

$$\Psi = k_s (RT/nF\pi D\nu)^{1/2}$$

where $n = 1$ electron/molecule for this reaction, D is the diffusion coefficient [$D = 2.76 \times 10^{-5}$ cm²/s, ferrocene in CH₃CN, measured chronocoulometrically (8)], F the Faraday, R gas constant, and T absolute temperature.

Table I. Electrochemical data activity from cyclic voltammetry of [Pt] poly-*N*-*para*-substituted phenylpyrrole film electrodes. Redox electrolyte: 10⁻³M ferrocene in acetonitrile/Et₄NBF₄

Poly- <i>N</i> - <i>para</i> -substituted phenylpyrrole electrode	Peak separation ΔE (mV) ^a	E° (mV) ^b	10 ³ k_s (cm·s ⁻¹)
-NO ₂	90	400	14.70
-Br	92	417	13.14
-Cl	95	412	12.35
-H	95	412	12.35
-CH ₃	97	410	11.16
-OCH ₃	100	408	10.47
Bare platinum electrode	60	440	—

^a Scan rate 100 mV·s⁻¹.

^b vs. SCE.

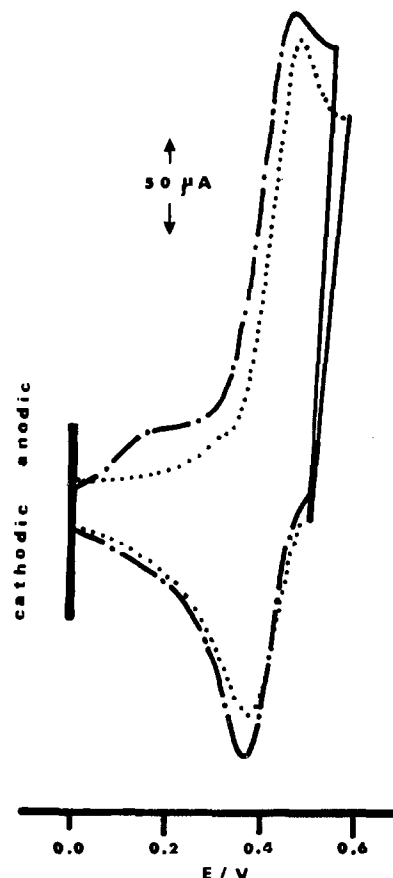


Fig. 1. Cyclic voltammograms of 1 × 10⁻³M ferrocene using 20 mC of [Pt]-coated electrodes with poly-*N*-*para*-methylpyrrole (dot-dash line) and poly-*N*-*para*-chlorophenylpyrrole (dotted line) at 100 mV/s in CH₃CN containing 0.1M Et₄NBF₄.

All these polypyrroles, PPy, polymers, are produced by an electrochemical oxidative coupling process which yields an acceptor-doped conducting complex directly, such as PPy⁺BF₄⁻ (9, 11). With acceptor doping, Hall coefficient measurements (12) clearly showed that the conduction is *p*-type, *i.e.*, positively charged carriers. It demonstrates that the majority of the carriers move through the organic material and not through the dopant array (13). Then the modification of the monomer should affect the charge transfer rate of the polymer, as can be observed in Table I.

In an earlier communication (14), it was proposed, on a qualitative basis, that a poor interaction between the pyrrole and the phenyl ring was produced by an orthogonal conformation through both rings. Further studies showed that in the *N*-*ortho*phenylpyrrole series electroactive substituents exhibit electronic and steric effects (15), whereas in the *N*-*para*-phenylpyrroles only electromeric effects were observed (6). Therefore, the electron-attractive or electron-repulsive induction of *para* groups involve interannular conjugation as well as inductive effects.

In the first study of this series (14), the electroactive behavior of the nitro phenyl group in the poly-*N*-*para*-nitrophenylpyrrole was analyzed by cyclic voltammetry. Although the nitrophenyl group is independently electroactive, the electron-transfer process between the platinum and the film for the reduction reaction involves an electron exchange between the unsaturated pyrrole matrix and the pendent nitrophenyl groups rather than a hopping process between the groups.

Consequently, the electronic interaction between the polypyrrole nucleus and *para*-substituents on the *N*-phenyl ring affects the electron-transfer rate of polymer electrodes (16). In effect, when the log of k_s are plotted against their respective Hammett-Brown substituent constants, a linear correlation is obtained (Fig. 2); the resonance and inductive interaction effects are undoubtedly

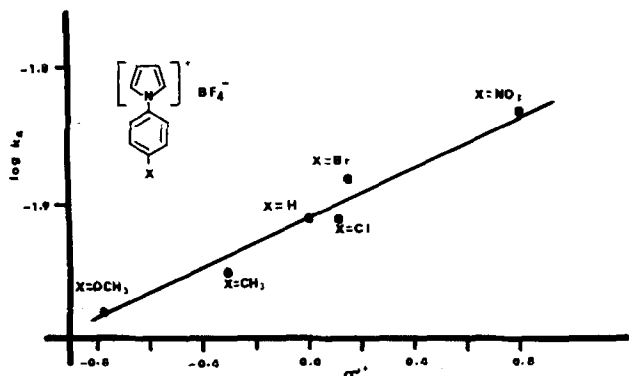


Fig. 2. Electron-transfer rate constant of the ferrocene couple reaction on the poly-N-*para*-substituted phenylpyrrole vs. their respective Hammett-Brown substituent constants.

the principal effects involved in the $\rho_{\pi}\sigma^+$ relationship. The positive sign for the substituent constant ρ_{π} reveals that as the substituents take on more electrophilic character the electron-transfer rate becomes faster.

We can conclude that changes in the electron-transfer rate of the series of polypyrroles is dependent on electronic interaction between the electroactive pyrrole ring of the polymer and the *para*-substituent through the phenyl ring. This electronic interaction has also been observed in the oxidation of the corresponding monomer, due to the fact that, as the substituent takes on more electrophilic character, the oxidation of the N-substituted phenylpyrrole proceeds with more difficulty (6). The mobility of the carriers will be determined by a variety of effects, including chain perfection, crystallinity, etc. (17); however, a delocalized π -system with relatively broad energy bands is certainly an advantage for effective electron transport.

Acknowledgment

The authors would like to thank M. Rosales Hoz for critically reviewing the manuscript.

Manuscript submitted Feb. 25, 1985; revised manuscript received June 10, 1985.

Universidad Nacional Autónoma de México assisted in meeting the publication costs of this article.

REFERENCES

1. A. F. Diaz, K. K. Kanazawa, and G. P. Gardini, *J. Chem. Soc., Chem. Commun.*, 635 (1979); A. F. Diaz and J. I. Castillo, *ibid.*, 397 (1980).
2. M. Salmón, A. F. Diaz, A. J. Logan, M. Krounbi, and J. Bargon, *Mol. Cryst. Liq. Cryst.*, **83**, 265 (1982).
3. H. Gross, *Chem. Ber.*, **95**, 2270 (1962).
4. N. Clauson-Kass and Z. Tyle, *Acta Chim. Scand.*, **6**, 67 (1952); M. Elming and N. Clauson-Kass, *ibid.*, **6**, 867 (1952).
5. A. F. Diaz, J. I. Castillo, J. A. Logan, and W. Y. Lee, *J. Electroanal. Chem.*, **129**, 115 (1981).
6. M. Salmón, Ma. E. Carbajal, J. C. Juárez, A. Diaz, and M. C. Rock, *This Journal*, **131**, 1802 (1984).
7. R. S. Nicholson, *Anal. Chem.*, **37**, 1351 (1965).
8. A. F. Diaz, F. A. Orosco Rosales, J. Paredón Rosales, and K. K. Kanazawa, *J. Electroanal. Chem.*, **103**, 233 (1979).
9. K. K. Kanazawa, A. F. Diaz, G. P. Gardini, W. O. Gill, P. M. Grant, J. F. Kwak, and G. B. Street, *Synth. Met.*, **1**, 329 (1980).
10. W. R. Salaneck, R. Erlandsson, J. Prejza, I. Lundström, and O. Inganas, *ibid.*, **5**, 125 (1983).
11. J. Prejza, I. Lundström, and T. Skotheim, *This Journal*, **129**, 1685 (1982).
12. L. W. Shacklette, R. R. Chance, D. M. Ivory, G. G. Miller, and R. H. Baughman, *Synth. Met.*, **1**, 307 (1979).
13. R. R. Chance, D. S. Boudreaux, H. Eckhardt, R. L. Elsenbaumer, J. E. Frommer, J. L. Bredas, and R. Silbey in "Quantum Chemistry of Polymers—Solid State Aspects," J. Ladik *et al.*, Editors, D. Reidel (1984).
14. M. Salmón, A. Diaz, and J. Goitia, in "Chemically Modified Surfaces in Catalysis and Electrocatalysis," J. S. Miller, Editor, p. 65, ACS Symposium Series 192, American Chemical Society, Washington, DC (1982).
15. M. Salmón, Ma. E. Carbajal, M. Aguilar, M. Saloma, and J. C. Juárez, *J. Chem. Soc., Chem. Commun.*, 1532 (1983).
16. M. Salmón, M. Aguilar, and M. Saloma, *ibid.*, 570 (1983).
17. W. Dietz, P. Cukor, M. F. Rubnes, and H. Jonson, *J. Electron Mater.*, **10**, 683 (1981).

Oxygen Reduction in Tetrafluoroethane-1,2-Disulfonic Acid

K. A. Striebel, P. C. Andricacos,^{*1} E. J. Cairns,* P. N. Ross,* and F. R. McLarnon*

Lawrence Berkeley Laboratory, University of California, Berkeley, California 94720

ABSTRACT

The kinetics of oxygen reduction on platinum in tetrafluoroethane-1,2-disulfonic acid (TFEDSA) and trifluoromethane sulfonic acid (TFMSA) have been studied with the rotating disk electrode technique at pH 1. The resulting Tafel plots coincide within the error of the experiment, indicating similar kinetics in the two electrolytes. The reaction order with respect to oxygen concentration was studied by varying the partial pressure of oxygen above the electrolyte. The rotation-independent currents at 0.90V vs. DHE were used to calculate a reaction order equal to one. A first-order analysis of the rotation-dependent currents was then used to extract kinetic currents at lower potentials. These kinetic currents also exhibited first-order dependence on oxygen concentration.

Trifluoromethane sulfonic acid (TFMSA) has been considered for low temperature (< 110°C) fuel cell applications due to the favorable oxygen reduction rate observed in this electrolyte compared with phosphoric acid (1). The use of the less-volatile, higher homolog of TFMSA, tetrafluoroethane-1,2-disulfonic acid (TFEDSA), was suggested by Baker *et al.* (2) to overcome the problems of high acid vapor pressure and low contact angle with PTFE observed with concentrated TFMSA. Preliminary investigations with TFEDSA (3) show insignificant acid vapor pressure and acceptable water vapor pressure at

*Electrochemical Society Active Member.

¹Present address: IBM Thomas J. Watson Research Center, Yorktown Heights, New York 10598.

60-70 weight percent acid, as well as high (nonwetting) contact angles with PTFE. In this work, the kinetics of oxygen reduction in TFEDSA and TFMSA on smooth Pt have been studied with the rotating disk electrode (RDE) technique. Kinetic measurements were made in each of the acids at pH = 1. The dependence of the reduction current on oxygen concentration was determined by varying the partial pressure of oxygen in contact with the electrolyte. This reaction order has been shown to be unity in perchloric, sulfuric, and phosphoric acid electrolytes (4-6). However, in "superacid" electrolytes (TFEDSA and TFMSA) the analysis of RDE data according to a first-order model has not been conclusive. Deviations from first-order analysis have previously been attributed to

impurity effects (7, 8) and a nonunity reaction order with respect to oxygen (9). We varied the bulk concentration of oxygen in the electrolyte in order to have an independent method for determining reaction order.

Experimental

Experiments were performed in a Pyrex cell with a surrounding water jacket. Circulation of thermostatically controlled water was used to maintain the cell temperature of $25^\circ \pm 0.5^\circ\text{C}$. The rotating disk platinum working electrode had an area of 0.458 cm^2 and was polished with a succession of alumina papers, followed by $6\text{ }\mu\text{m}$ and then $1\text{ }\mu\text{m}$ diamond paste. Rotation was achieved with a Pine Instruments analytical rotator. A dynamic hydrogen electrode (DHE) (10) was held in a separate compartment which was connected to the main cell through a Luggin capillary. The DHE held a constant potential of 3 mV negative of an RHE at the same pH. A 1 cm^2 Pt-foil counterelectrode was used directly in the cell, placed as shown in Fig. 1. Premixed cylinders of oxygen and nitrogen ($4.31\text{-}58.66\% \pm 0.01\%$ oxygen), pure oxygen, and pure nitrogen were further purified by passing through three molecular-sieve beds (9). All gases were humidified by bubbling through doubly distilled water at room temperature before entering the cell.

The potential of the working electrode was controlled with a PAR Model 173 potentiostat and a PAR Model 175 universal programmer. Current-potential data could be recorded simultaneously with a Nicolet digital oscilloscope and an HP7046B X-Y recorder.

All glassware and electrodes (except the DHE) were cleaned by soaking in a mixture of concentrated sulfuric and 70% nitric acids for two days. This was followed by rinsing and soaking in freshly distilled water at least four times.

TFMSA (from 3M Corporation) was purified by distillation and hydrogen peroxide treatment as reported earlier (8). Tetrafluoroethane-disulfonate was received as the potassium salt from KOR, and it was converted to the acid via ion exchange with prepurified resin (11). Complete conversion to the acid was checked by titration. Water was removed by vacuum distillation, leaving the acid dihydrate. The hygroscopic nature of this solid prevented exact knowledge of the water content. Solutions were prepared by dilution with ultrapure water² to pH 1. TFMSA solutions were prepared in a similar manner. Both solutions were pre-electrolyzed in the cell for at least 72h at a current of 1 mA .

Results and Discussion

Two single-sweep cyclic voltammograms recorded in TFEDSA at pH = 1 are shown in Fig. 2. Curve A was recorded for the stationary disk following the pretreatment potential profile shown in the inset of Fig. 2. For an indication of electrolyte purity, curve B was recorded following the same pretreatment profile with the addition of a

²Harleco Company, Gibbstown, New Jersey.

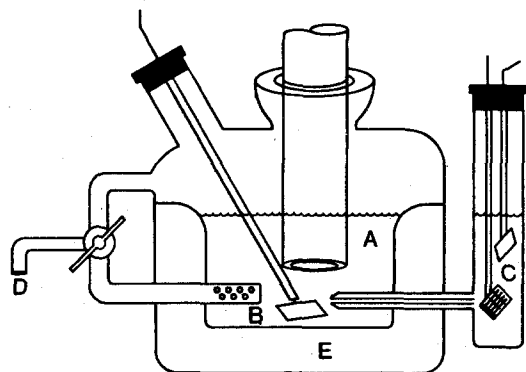


Fig. 1. Electrochemical cell. A: Rotating disk electrode. B: Counterelectrode. C: Dynamic hydrogen reference electrode. D: Gas inlet. E: Water jacket.

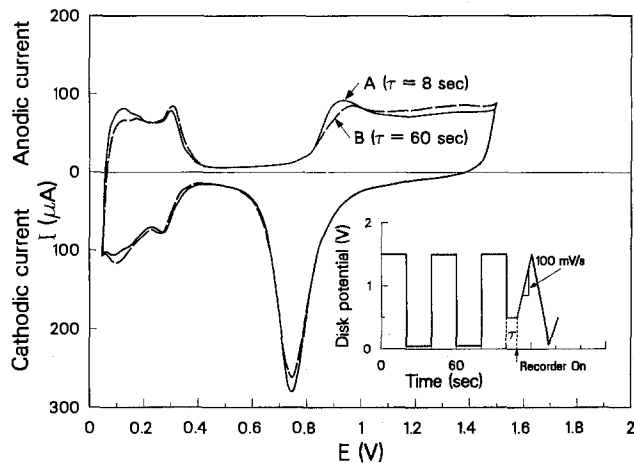


Fig. 2. First-sweep cyclic voltammetry in TFEDSA, pH = 1, 25°C , Ar atmosphere. A: Recorded after pretreatment. B: Recorded after pretreatment and holding 60s at 0.4 V while rotating at 1600 rpm .

min hold at 0.4 V vs. DHE while rotating the working electrode at 1600 rpm before recording the voltammogram on the stationary electrode.

Several voltammograms were recorded in both electrolytes without repolishing the working electrode. The charge associated with the hydrogen adsorption region of the curves increased chronologically. The relative increase in this charge was used to quantify the increase in active electrode area caused by repeated cycling (roughening). All kinetic currents were adjusted downward to an effective roughness factor of 1.5. However, current densities were computed using the projected electrode area.

Similar voltammograms were recorded at a sweep rate of 10 mV/s in order to quantify the anodic currents associated with platinum oxidation. These anodic currents were added to the reduction currents recorded with low pressures of oxygen to adjust for the nonzero base line observed in those experiments.

Current-potential sweeps at rotation speeds of $100\text{-}1600\text{ rpm}$ for TFEDSA in contact with pure oxygen are shown in Fig. 3. The potential profile used for electrode pretreatment is shown in the inset in Fig. 3. The reduction currents were found to depend somewhat on sweep rate and sweep direction because of the changing oxidation state of the electrode. Therefore, for the purpose of comparing TFEDSA and TFMSA, positive going sweeps at 10 mV/s were used in all cases. Uncompensated solution resistances of $15\text{-}20\Omega$ were accounted for by reading constant-potential data along lines of constant surface potential (with slopes of $1/R_s$), as is indicated in Fig. 3.

The current-potential relationship

$$I = nFAk_c (C_{\text{O}_2}^{\circ})^m \exp\left(\frac{-\alpha VF}{RT}\right) \quad [1]$$

where A is the electrode area, k_c is the reaction rate constant for the cathodic reaction and includes the pH dependence, $C_{\text{O}_2}^{\circ}$ is the concentration of oxygen at the electrode surface, m is the reaction order for oxygen, α is the fraction of the overvoltage aiding the reduction reaction, and V is the electrode potential, is expected to apply for oxygen reduction on platinum. Because of the large overpotentials in this reaction, the anodic term has been neglected.

During cathodic reduction, the concentration of oxygen at the electrode surface is lower than that in the bulk. For transport to the rotating disk, it can be shown that

$$C_{\text{O}_2}^{\circ} = \left(\frac{I_L - I}{I_L}\right) C_{\text{O}_2}^{\infty} \quad [2]$$

where I_L is the limiting current and $C_{\text{O}_2}^{\infty}$ is the bulk concentration of oxygen in the electrolyte. Since, in general,

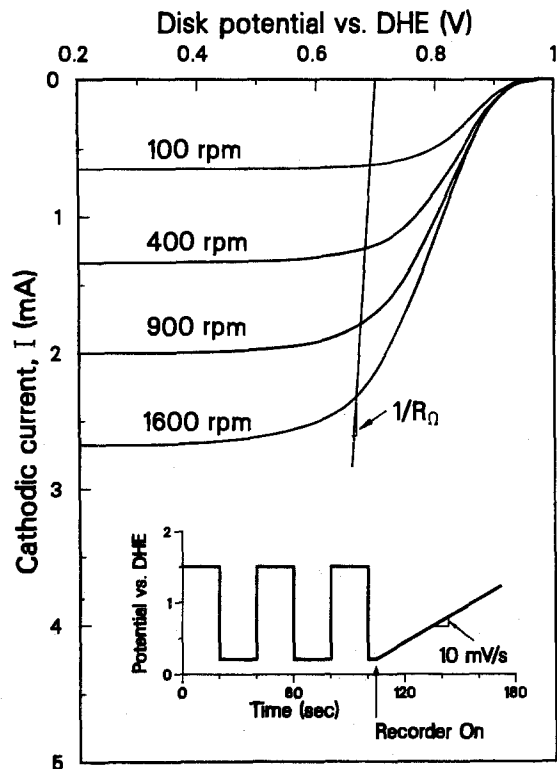


Fig. 3. Current-potential sweeps in TFEDSA, pH = 1, 25°C

$C_{O_2}^\circ$ is not known, but $C_{O_2}^\infty$ can be known or controlled, a more useful expression is obtained by substitution of Eq. [2] into Eq. [1], dropping the last term of Eq. [1], with the result

$$I = nFAk_c (C_{O_2}^\infty)^m \left(\frac{I_L - I}{I_L} \right)^m \exp \left(\frac{-\alpha FV}{RT} \right) \quad [3]$$

When I is small compared to I_L , then the reaction order m can be determined from the slope of a plot of $\log I$ vs. $\log C_{O_2}^\infty$ for constant V . For other conditions, the determination of m is more complicated.

Before reaction order m can be determined, it is necessary to establish the relationship between p_{O_2} , the controlled variable, and $C_{O_2}^\infty$. This was done by use of the Levich equation

$$I_L = 0.62nFC_{O_2}^\infty D^{2/3} \nu^{-1/6} \omega^{1/2} \quad [4]$$

The slope of a plot of I_L vs. $\omega^{1/2}$ is therefore proportional to $C_{O_2}^\infty$. If Henry's law is obeyed

$$C_{O_2}^\infty = K_H p_{O_2} \quad [5]$$

the Levich slope $B = 0.62nFC_{O_2}^\infty D^{2/3} \nu^{-1/6}$ should be proportional to p_{O_2} .

The applicability of Eq. [4] to the results of Fig. 3 is shown in Fig. 4. All of the lines are straight and pass through the origin, as they should. Figure 5 shows a plot of $\log B$ vs. $\log p_{O_2}$, which has a slope of unity, demonstrating that Henry's law holds for O_2 in both TFMSA and TFEDSA at pH = 1 and 25°C.

Equation [5] now may be substituted into Eq. [3], yielding

$$I = nFAk_c K_H^m p_{O_2}^m \left(\frac{I_L - I}{I_L} \right)^m \exp \left(\frac{-\alpha FV}{RT} \right) \quad [6]$$

For potentials near 0.9V, the currents are insensitive to rotation speed above about 400 rpm, as shown in Fig. 3. Under these conditions $I \ll I_L$, so that $(I_L - I/I_L)$ approaches unity, and, according to Eq. [6], a plot of $\log I$ vs. $\log p_{O_2}$ for constant V should be a straight line of slope m . This plot for TFMSA and TFEDSA (see Fig. 6, part A) indicates that the reaction order m is 1.0 ± 0.05 .

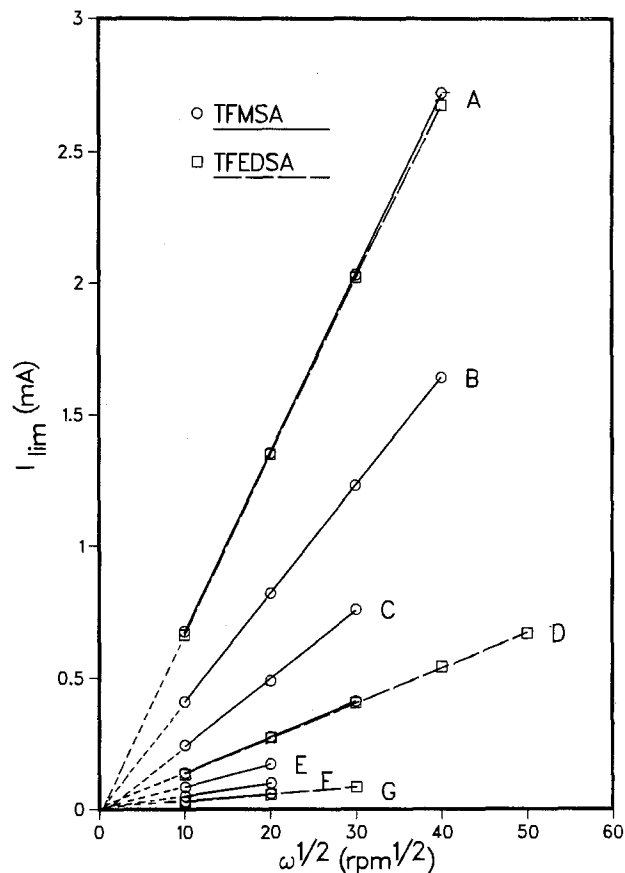


Fig. 4. Levich plots for TFEDSA and TFMSA at various oxygen partial pressures. A: 1.0 atm. B: 0.5866 atm. C: 0.3503 atm. D: 0.2028 atm. E: 0.1258 atm. F: 0.0753 atm. G: 0.043 atm.

The result that m is unity (at 0.90V) allows a simplification of further analysis for higher currents and overvoltages. Even though Eq. [6] is difficult to apply when I is not very small relative to I_L , it can be rearranged as follows. First, define the kinetic current I_k (for $m = 1$)

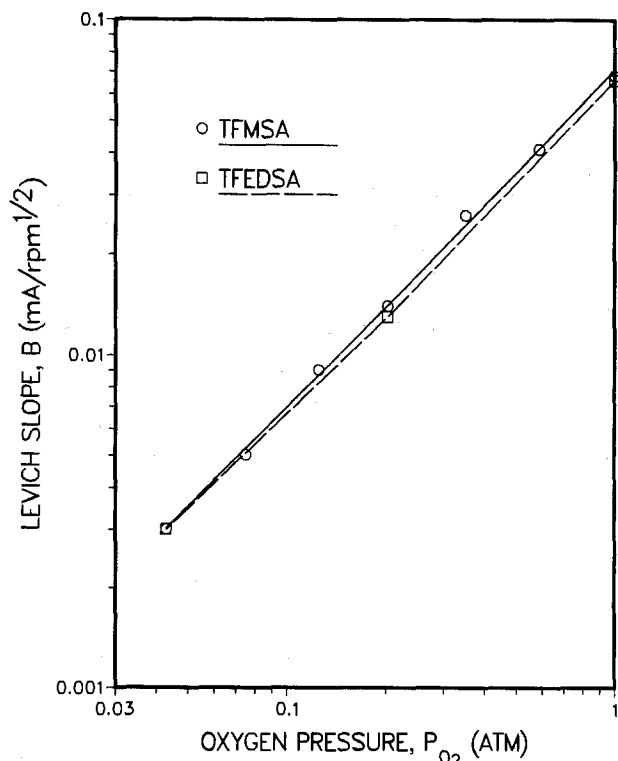


Fig. 5. Levich slopes from Fig. 4

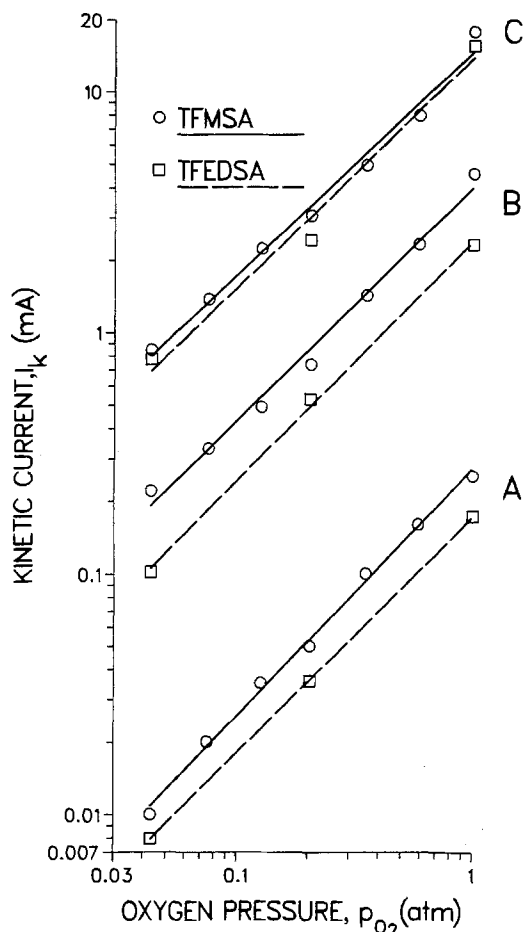


Fig. 6. Kinetic current dependence on oxygen pressure in TFEDSA and TFMSA. A: 0.90V vs. DHE. B: 0.80V vs. DHE. C: 0.70V vs. DHE.

$$I_k = nFAk_c C_{O_2}^m \exp\left(\frac{-\alpha FV}{RT}\right) \quad [7]$$

Substituting Eq. [7] into Eq. [6], setting $m = 1$, and rearranging yields the familiar relation (11)

$$\frac{1}{I} = \frac{1}{I_k} + \frac{1}{I_L} \quad [8]$$

Equation [8] shows that I_k may be obtained from a plot of I^{-1} vs. I_L^{-1} , or since $I_L = B\omega^{1/2}$, a plot of I^{-1} vs. $\omega^{-1/2}$ for constant V and p_{O_2} yields I_k from the intercept. The values of I_k may then be used with Eq. [5] and [7] to test the value of m , by plotting $\log I_k$ vs. $\log p_{O_2}$ for a given voltage. This is shown in Fig. 6 for 0.8 (lines B) and 0.7V (lines C), and m is seen to be unity within experimental error.

A direct comparison of the kinetic current densities for TFEDSA and TFMSA was made by first multiplying the currents in TFEDSA by the ratio of the roughness factors (calculated from the hydrogen oxidation peaks observed in the voltage-sweep experiments of the type shown in Fig. 2): $[(RF)_{TFMSA}]/[(RF)_{TFEDSA}] = 0.83$. These currents were then divided by the geometric area of the rotating disk electrode, 0.458 cm^2 . No correction for solubility or diffusivity differences was made, since $B = 0.46$ and $0.44 \text{ mA/cm}^2\text{-s}^{1/2}$ for TFMSA and TFEDSA, respectively, at $p_{O_2} = 1.0$. The potential-log current density curves for 1 atm oxygen pressure are shown in Fig. 7. Over the potential range 0.67-1.0V vs. DHE, the kinetic currents are very similar. The familiar change of slope is observed at 0.8V, as is the case in other acids. This change in Tafel slope occurs at the potential below which the electrode surface is oxide free. Exchange current densities calculated by extrapolation of the results obtained at higher potentials are 4×10^{-6} and $6 \times 10^{-6} \text{ mA/cm}^2$ for TFMSA and TFEDSA, respectively. These can be compared with the exchange current density of $9 \times 10^{-8} \text{ mA/cm}^2$ reported for 1.1N TFMSA, 25°C, by Appleby and Baker (7).

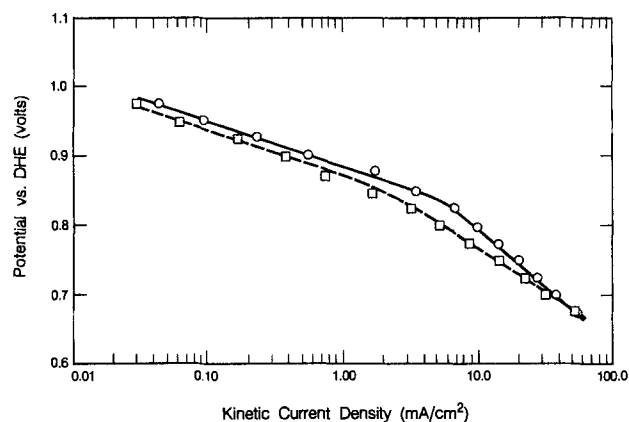


Fig. 7. Tafel plot for oxygen reduction in TFEDSA (squares) and TFMSA (circles) at 1 atm oxygen; pH = 1.0; 25°C.

Conclusions

From the experiments reported above and the analysis of the data, it is concluded that the reaction order of the electrochemical reduction of oxygen on platinum in TFEDSA and TFMSA with respect to oxygen concentration is unity, over the full potential range studied (1.0-0.65V vs. DHE). The kinetics of oxygen reduction on platinum in TFEDSA are very similar to those for TFMSA, the currents being very closely comparable at pH = 1 for identical overvoltages.

These results offer some promise for the use of fluorinated organic acids in high performance fuel cells, while avoiding the high vapor pressure of TFMSA and its undesirable wetting of PTFE. Furthermore, pressurization is expected to improve significantly the performance of cathodes in fuel cells using TFEDSA and TFMSA.

Acknowledgments

This work was supported by the Assistant Secretary for Conservation and Renewable Energy, Office of Energy Systems Research, Energy Storage Division of the U.S. Department of Energy under Contract no. DE-AC03-76SF00098.

Manuscript submitted Jan. 26, 1985; revised manuscript received May 21, 1985. This was Paper 410 presented at the Cincinnati, Ohio, Meeting of the Society, May 6-11, 1984.

The University of California assisted in meeting the publication costs of this article.

REFERENCES

1. A. J. Appleby, in "Proceedings of the Symposium on Renewable Fuels and Advanced Power Sources for Transportation Workshop," H. L. Chum and S. Srinivasan, Editors, p. 55, Solar Energy Research Institute, Golden, CO (1982).
2. B. Baker, Final Technical Report, U.S. Army Mobility Equipment Research and Development Command, Contract no. DAAK02-73-C-0084 (1975).
3. P. N. Ross, *This Journal*, **130**, 882 (1983).
4. A. Damjanovic and V. Brusic, *Electrochim. Acta*, **12**, 615 (1967).
5. A. J. Appleby, *This Journal*, **117**, 328 (1970).
6. Y. Ya. Shepelev, M. R. Tarasevich, and R. L. Burshstein, *Elektrokhimiya*, **7**, 999 (1971).
7. A. J. Appleby and B. S. Baker, *This Journal*, **125**, 404 (1978).
8. P. N. Ross and P. C. Andricacos, *J. Electroanal. Chem.*, **154**, 205 (1983).
9. K-L. Hseuh, H. H. Chang, D-T. Chin, and S. Srinivasan, Abstract 730, p. 1074, The Electrochemical Society Extended Abstracts, Vol. 83-1, San Francisco, CA, May 8-13, 1983.
10. J. Giner, *This Journal*, **111**, 376 (1964).
11. P. C. Andricacos and P. N. Ross, EPRI Report no. 1676-02, Palo Alto, CA, June 1982.
12. Yu. V. Pleskov and V. Yu. Filinovskii, "The Rotating Disk Electrode," p. 90, Consultants Bureau, New York (1976).

Irreversible Voltammetric Behavior of the (100) IrO₂ Single-Crystal Electrodes in Sulfuric Acid Medium

Tadeusz Hepel^{*,1}

Department of Physics, Brooklyn College, City University of New York, Brooklyn, New York 11210

Fred H. Pollak^{*}

Department of Physics, Brooklyn College, City University of New York, Brooklyn, New York 11210 and Department of Physics, Graduate School and University Center of City University of New York, New York, New York 10036

William E. O'Grady^{*}

Brookhaven National Laboratory, Department of Applied Science, Upton, New York 11973

ABSTRACT

The electrochemical behavior of (100) IrO₂ single-crystal electrodes in 0.5 mol/dm³ H₂SO₄ has been studied using linear potential scan cyclic voltammetry. A highly irreversible behavior of the main electrochemical process of hydrogen or hydronium ion injection/ejection has been found in the potential range 360-580 mV (*vs.* Ag/AgCl reference). The obtained voltammograms have been compared with those for RuO₂ single crystals possessing similar electrocatalytic properties and the same crystallographic structure and also with the behavior of sputtered and anodic IrO₂ films. It has been found that the energy of major interaction of hydrogen species with the IrO₂ single-crystal structure is close to that observed for sputtered IrO₂ films but differs by *ca.* 29 kJ/mol (corresponding to 300 mV in the potential scale) from that for the anodic IrO₂ films. The penetration depth for hydrogen is highly minimized in the case of single-crystal IrO₂ electrodes and involves at most one or two monolayers. Thus, the coloration/bleaching process described for the IROX films cannot develop on nonhydrated single-crystal IrO₂ electrodes unless their crystallographic structure is damaged by cycling in a wide potential range.

Anodic films of iridium dioxide have recently been the subject of numerous studies on account of their interesting electrocatalytic and electrochromic behavior. Both the oxygen and chlorine evolution reaction proceed on the IrO₂ electrodes with extremely low overvoltages (1-5). In contrast to RuO₂ possessing similar electrocatalytic properties (6-10), the IrO₂ films undergo dissolution at higher positive potentials ($E > 1600$ mV *vs.* Ag/AgCl) and can be removed from the electrode surface (2, 11-13). The hydrous, amorphous IrO₂ films on Ir metal electrodes show electrochromic properties (13-22) sensitive to the change in the electrode potential. The mechanism proposed for the rapid coloration/bleaching process (about 40 ms) is based on the proton injection/ejection mechanism (13). It has been found that the electrochemical processes of anodic formation and cathodic reduction of a thick porous IrO₂ film are highly reversible (12-14).

The initial stages of IrO₂ film growth on Ir electrodes have recently been studied by Mozota and Conway (11), Capon and Parsons (23), and other authors (24-26). The mechanism of interaction of the IrO₂ surface with aqueous solutions has also been discussed from the point of view of the surface acid-base properties (27-31). The latter works have been done using thermal IrO₂ powders.

The behavior of the anodic oxide on Ir electrodes during oxygen evolution in acidic solutions has also been studied by *ex situ*, x-ray photoelectron spectroscopy (XPS) by Kotz *et al.* (32). These authors demonstrate conclusively that a thin oxide (or hydroxide) is formed on iridium surface during O₂ evolution and no higher than IV oxidation states of Ir are present in the film. The composition profiles within the amorphous anodic IrO₂ films have been determined by McIntyre and co-workers (13) using nuclear reactions. The thickness of the hydrated IrO₂ films has been measured by Kim *et al.* (33) using XPS technique.

As regards single crystals, the electrical-transport properties of IrO₂ have been reported by Ryden *et al.* (34) and conduction electron screening effects have been demon-

strated in IrO₂ by Wertheim and Guggenheim (35). The optical properties of a single-crystal IrO₂ have been described by Goel *et al.* (36). The latter authors, measuring a near-normal incidence reflectivity in the photon energy range 0.5-9.5 eV, have determined the spectral dependence of the complex dielectric function and refractive index. This in turn allowed making a direct comparison with recent band structure and density-of-states calculations performed by Mattheiss (37).

In this paper, the voltammetric characteristics of the IrO₂ single-crystal electrodes with the exposed (100) surface are presented and discussed in terms of the hydrogen and hydronium ion injection/ejection processes. The observed significant differences between the electrochemical behavior of the IrO₂ (100) electrodes and that of the anodic IrO₂ films on Ir substrates (IROX films) are discussed in detail. A comparison is also made with the RuO₂ and TiO₂ single-crystal electrodes having the same crystallographic structure.

Experimental

The electrochemical cell was of a conventional three electrode design. A coiled Pt wire counterelectrode was separated from the working electrode compartment by a sintered glass joint. A double-junction Ag/AgCl electrode with a saturated KCl internal solution was used as a reference electrode.

The working electrodes were prepared from the oriented IrO₂ single crystals using silver epoxy resin for low resistance contacts and Epoxide (Buehler) for body insulating. The IrO₂ single crystals were grown in this laboratory by a chemical vapor transport in a flowing gas system at 1300°C under 2 atm of the oxygen partial pressure. This procedure was similar to the growth of large RuO₂ single crystals (38, 39). The source materials were the Ir powder of the electronic-grade purity and oxygen. The exposed surface area of the IrO₂ (100) electrode was approximately 0.01 cm². The crystal was oriented by x-ray Laue backscattering to within 1°.

A PAR Model 173 potentiostat and PAR Model 175 universal programmer were used for cyclic voltammetry (CV) measurements. The experimental curves were recorded using a Hewlett-Packard 7044 X-Y recorder.

^{*}Electrochemical Society Active Member.

¹Present address: Department of Chemistry and Institute of Colloid and Surface Science, Clarkson University, Potsdam, New York 13676.

Results

Typical cyclic voltammetry characteristics for the IrO_2 single-crystal electrode with the exposed crystallographic face (100) are shown in Fig. 1 and 2. One major pair of anodic/cathodic peaks is observed in the potential range 360-600 mV vs. Ag/AgCl in 0.5 mol/dm³ H_2SO_4 at 298 K. Several other small features are clearly seen or can be inferred both on the anodic and cathodic half-cycles. They are labeled from A_1 to A_4 for anodic processes and C_2 to C_4 for cathodic ones. The sharp current increase A_5 at $E = 1300$ mV is due to the oxygen evolution reaction. The hydrogen evolution reaction C_0 starts at $E = -370$ mV.

It is informative to discuss the voltammetric behavior of the IrO_2 (100) electrodes comparing the obtained characteristics with published voltammograms for another transition metal dioxide RuO_2 [single crystals with several orientations (9)] and for iridium metal electrodes covered with anodic IrO_2 films (11, 13, 23-26). There are significant differences in CV characteristics for these electrodes in the whole accessible "structure" window from HER (hydrogen evolution reaction) to OER (oxygen evolution reaction). They are discussed separately for the hydrogen deposition/ionization region and the oxide rearrangement region, although, in case of the IrO_2 single-crystal electrodes, presumably all the processes are based on the injection/ejection of hydrogen or hydronium ions (13). The observed results are reported in the same order.

Hydrogen deposition/ionization region.—In the cathodic half-cycle of the voltammograms for the IrO_2 (100) electrodes, two small features C'_2 and C''_2 are resolvable on the expanded scale curves as illustrated in Fig. 3. The peak potentials are -70 and $+25$ mV, respectively. On the anodic side of the voltammograms a peak A_2 is observed at $E = +170$ mV and may be considered as a counterpart of one or both the cathodic peaks C'_2 and C''_2 . Another anodic peak A_1 appears at $E = -180$ mV (Fig. 2), when the cathodic inversion potential is well shifted into HER region.

The oxide rearrangement region.—The anodic IrO_2 films formed on Ir electrodes contain large amounts of water, and they are porous and amorphous (11-26). These properties result in a high degree of reversibility of the process involved in the oxide rearrangement region.

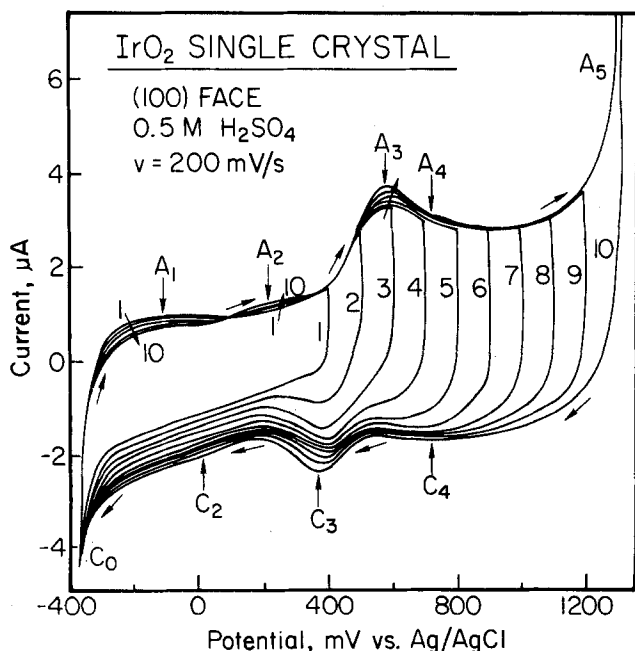


Fig. 1. Dependence of the CV characteristics for the IrO_2 (100) electrode in 0.5 mol/dm³ H_2SO_4 upon the anodic inversion potential $E_{i,a}$ [mV]: (1) 400, (2) 500, (3) 600, (4) 700, (5) 800, (6) 900, (7) 1000, (8) 1100, (9) 1200, (10) 1300. Potential scan rate $v = 200$ mV/s.

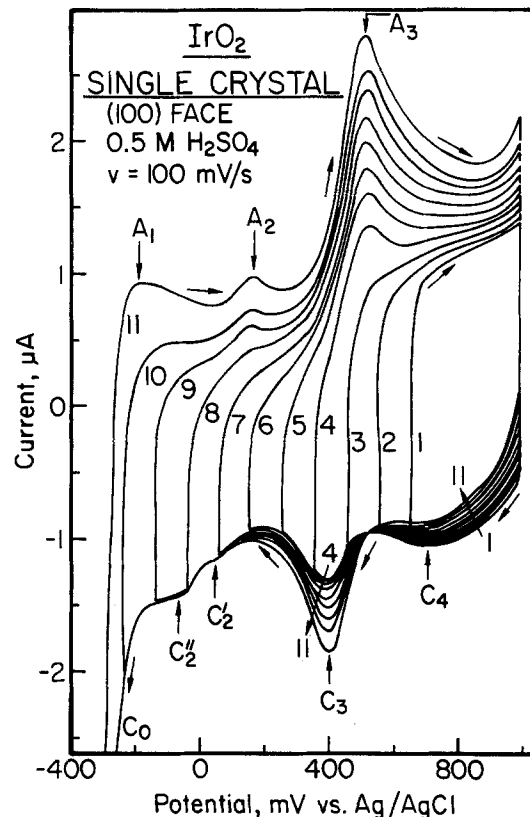


Fig. 2. Dependence of the CV characteristics for the IrO_2 (100) electrode in 0.5 mol/dm³ H_2SO_4 upon the cathodic inversion potential $E_{i,c}$ [mV]: (1) 650, (2) 550, (3) 450, (4) 350, (5) 250, (6) 150, (7) 50, (8) -50 , (9) -150 , (10) -250 , (11) -350 . Potential scan rate $v = 100$ mV/s.

However, the oxide rearrangement processes we observed on the well-defined, water-free IrO_2 (100) substrates exhibit significant retardation due to the compact structure of the electrode material. The appearance of the main pair of peaks A_3 - C_3 is illustrated in Fig. 1 and 2 and in a narrow potential scale in Fig. 4. The peak potentials at scan rate $v = 200$ mV/s are 580 and 350 mV for the peaks A_3 and C_3 , respectively. A small increase in the peak height is observed after prolonged cycling in the po-

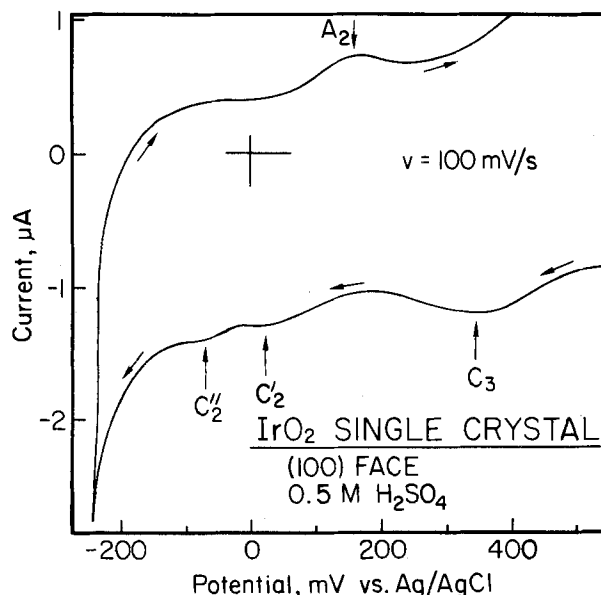


Fig. 3. Part of a cyclic voltammogram for the IrO_2 (100) electrode in 0.5 mol/dm³ H_2SO_4 , showing cathodic features C'_2 and C''_2 . Cycling between -250 and $+1300$ mV. Scan rate $v = 100$ mV/s.

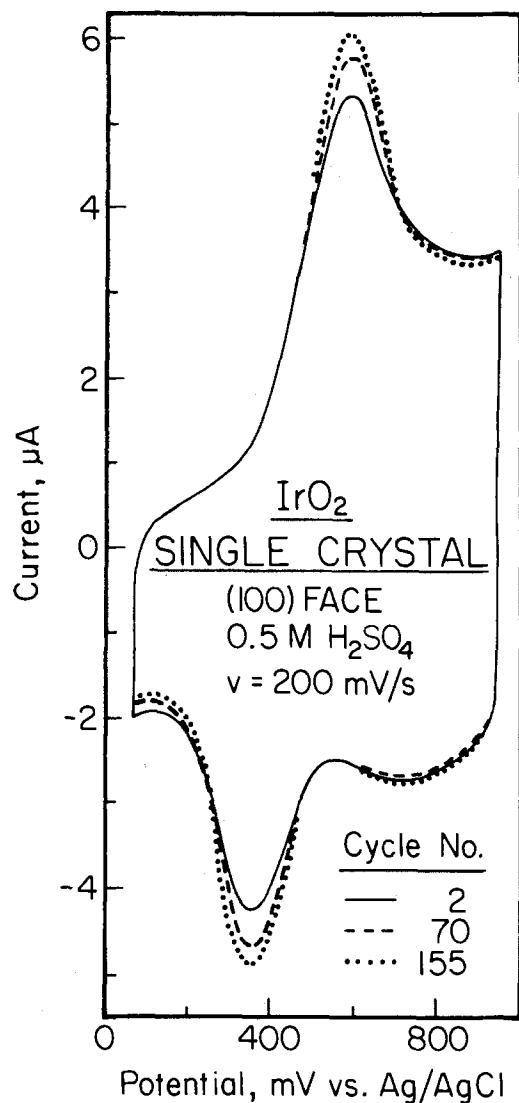


Fig. 4. Cyclic voltammograms for the IrO₂ (100) electrode in 0.5 mol/dm³ H₂SO₄ solution. Effect of the prolonged cycling between +50 and +950 mV at $v = 200$ mV/s. Cycle numbers are indicated in figure.

tential range 50-950 mV. In Fig. 4, curves are presented for cycles number 2, 70, and 155. The electrode was previously used in cycling experiments, so that some amount of disordered surface monolayers could eventually exist on the electrode surface. However, the pronounced observed irreversibility, as evidenced by the peak separation, remains all the time unchanged. At more positive potentials, there is seen a second pair of peaks labeled A₄-C₄ (the peak A₄ is seen in Fig. 1 when the anodic inversion potential does not exceed 1100 mV). The peak potentials are both equal to 715 mV and are independent of the scan rate v . In contrast to the process A₃-C₃, this is a reversible reaction. The broadness of the peak C₄ suggests repulsive interactions in the presumably hydrated monolayer of the rearranged oxide.

Another pair of peaks labeled A'₃-C'₃ in Fig. 5 appears rather unexpectedly during the long term experiments with changing scan rates from 1 up to 200 mV/s. The peak potentials of this irreversible process change with v and at $v = 110$ mV/s are 740 and 160 mV for A'₃ and C'₃, respectively. The peaks are situated on the falling branches of the main peaks, A₃ and C₃. The peaks A'₃ and C'₃ disappear after 15 min conditioning of the electrode at $E = 550$ mV, as shown in Fig. 6. Note that the peaks A'₃-C'₃ were not observed after prolonged cycling in the range 50-950 mV (Fig. 4). Therefore, the only possible reason for the observed change in voltammetric behavior of the IrO₂ electrode is a difference (300 mV) in the cathodic inver-

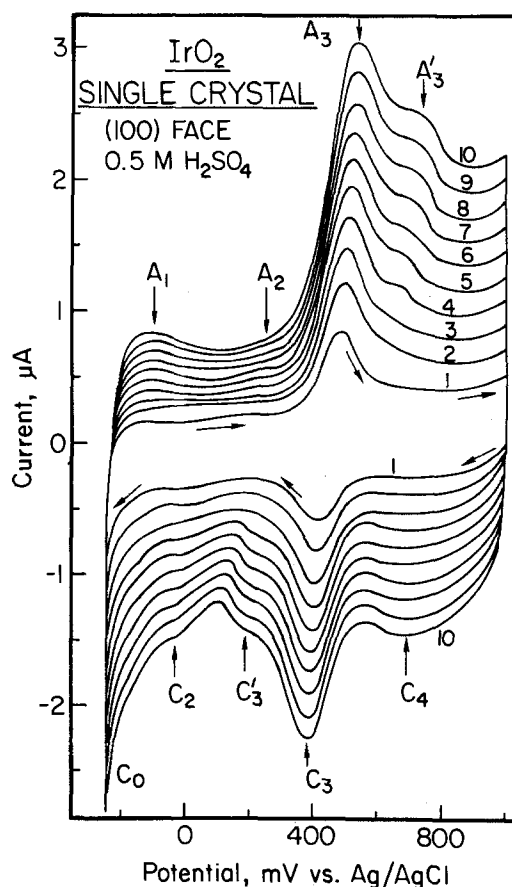
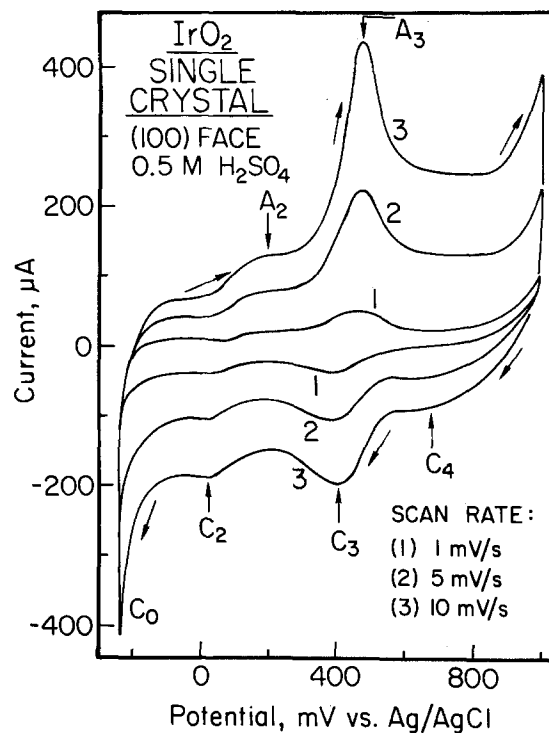


Fig. 5. Scan rate dependence of the CV characteristics for the IrO₂ (100) electrode in 0.5 mol/dm³ H₂SO₄ for slower (a, top) and faster (b, bottom) scan rates. v [mV/s]: (1) 1, (2) 5, (3) 10, (4) 20, (5) 30, (6) 40, (7) 50, (8) 60, (9) 70, (10) 80, (11) 90, (12) 100, (13) 110.

sion potential ($E_c^1 = -250$ mV in the reported slow scan rate experiments (see also Fig. 5). A possible explanation of this behavior and a comparison with the behavior of the anodic oxides on the Ir electrodes are given in the next section.

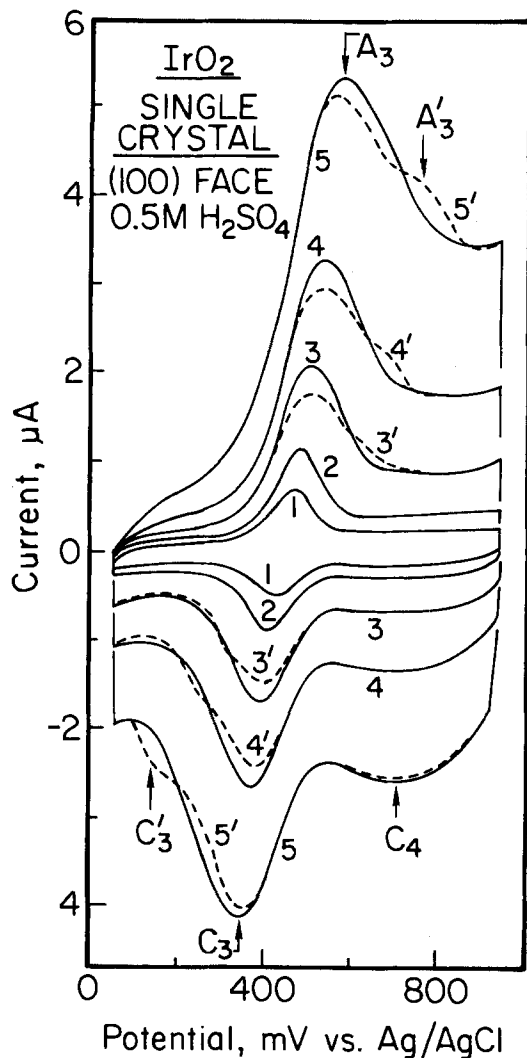
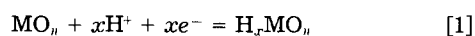


Fig. 6. The CV characteristics for the IrO_2 (100) electrode in $0.5 \text{ mol/dm}^3 \text{ H}_2\text{SO}_4$ solution obtained after prolonged experiments at very slow scan rates (dashed curves) and after additional stirring deoxygenation and conditioning at $+550 \text{ mV}$ (solid curves). v [mV/s]: (1) 10, (2) 20, (3,3') 50, (4,4') 100, (5,5') 200.

Discussion

Most of the 4d and 5d transition-metal dioxides crystallize with a distorted rutile-type structure with a monoclinic or orthorhombic symmetry (37). Among the almost undistorted materials are IrO_2 , RuO_2 , and OsO_2 . The lattice parameters, a , c , and c/a for IrO_2 are as follows: $a = 4.4983\text{\AA}$, $c = 3.1544\text{\AA}$, and $c/a = 0.701$, which can be compared with data for the RuO_2 single crystals whose voltammetric behavior for several crystallographic orientations we have presented elsewhere (9): $a = 4.4919\text{\AA}$, $c = 3.1066\text{\AA}$, and $c/a = 0.696$. The parameter c/a serves as a measure of the distortion from the ideal rutile structure, which has $(c/a)_{\text{ideal}} = 0.586$. We see that the lattice parameters for both the IrO_2 and RuO_2 crystals are almost identical. However, the Fermi surface cross sections as calculated (37) or derived from the experimental magneto-thermal-oscillation data obtained by Graebner *et al.* (40) are entirely different for IrO_2 and RuO_2 since the Ir atoms are in a $5d^5$ state while the Ru atoms are in $4d^5$ state. It is of a considerable interest to compare the electrochemical characteristics for these two oxides, and also for the n-TiO₂ semiconductor electrode, to gain our understanding of the electrocatalytic properties of these materials. The generalized electrode reaction which can be considered for the above materials is the reduction-oxidation process involving injection/ejection of hydrogen and change in the apparent oxidation state of the metal M



There are many possible ways for hydrogen to interact with MO_n structure. In the limiting case, the hydration water can be formed. However, hydrogen can also penetrate through the lattice channels and create intercalation structures. The apparent oxidation state of the metal changes, but charge is not localized at any particular metal atom because of the electron band structure, which in the case of IrO_2 and RuO_2 consists of a partially filled E_g band. The oxidation state of the trapped hydrogen may be different. In TiO_2 , hydrogen can be considered as a highly ionized neutral donor (41). In anodic IrO_2 films, hydrogen is mainly in the form of hydronium ions near the electrode/electrolyte interface (13), so the net reduction process can be expressed as follows



where $n = 2$. The energy of interaction between the hydrogen and the rutile-type oxide structure may also vary with the hydrogen uptake. This is observed, for example, in some lithium intercalation materials. The multiple peak structure in cyclic voltammetry characteristics for transition metal oxide electrodes is therefore not unexpected. At the present stage of our knowledge, we cannot derive any conclusive correlations between the voltammetric peak structure and the localization of the hydrogen interactions. However, it is interesting to compare voltammetric characteristics for different transition metal oxide single crystals having similar crystallographic structure but different electron-band structure and chemical activity. On the other hand, we would like to emphasize significant differences we observed in voltammetric behavior of the same basic compound (IrO_2) synthesized in a different way. Thus, we compare our data for IrO_2 (100) single-crystal electrodes with literature data for anodic IrO_2 films (11-27) and those for IrO_2 sputtered layers (42).

By analyzing voltammograms for the IrO_2 (100) electrode and those for the RuO_2 single crystals with exposed surfaces (110), (001), (111), (101), and (100), we find differences rather than similarities. The behavior of the RuO_2 electrodes is highly reversible in the oxide rearrangement region, and the suggested penetration depth for hydrogen does not exceed one monolayer. In the case of the IrO_2 single crystal, the irreversible character of the major pair of peaks (A_3 - C_3) for hydrogen injection/ejection processes [2] remains even at $v = 1 \text{ mV/s}$. Moreover, the penetration depth increases upon cycling, especially when cathodic limit is below 0 mV and anodic limit exceeds 1300 mV (OER region).

In the hydrogen region, the voltammetric behavior of the IrO_2 (100) electrode shows some similarities with that of the RuO_2 (100) surface and the n-TiO₂ (001) electrode [there are no electrochemical data for TiO₂ (100) surface]. For all the three crystals, IrO_2 (100), RuO_2 (100), and n-TiO₂ (001), there are seen two cathodic adsorption peaks and only one anodic desorption peak.

In comparison with other single-crystal electrodes, the overvoltage for hydrogen evolution is very low for the IrO_2 (100) electrodes. If the "bleaching" process as described for the hydrated anodic IrO_2 films on the Ir electrodes (13) would take place efficiently on our nonhydrated compact IrO_2 crystals, one would not expect as sharp a current increase at HER potential as we observed. Certainly, the decrease in conductivity and hydrogen diffusion into the crystal bulk is rather inefficient in the case of the IrO_2 (100) electrode. This observation may be compared with the effect of cathodization of the n-TiO₂ single-crystal electrodes (41) resulting in the modification of the doping level by the hydrogen injection into the crystal lattice. An increase in conductivity and the majority carrier concentration is observed in this latter case.

On the basis of the crystallographic structure of IrO_2 single crystals and the experimental observations, we propose a model of the ideal (100) surface being in contact with an aqueous solution. In this model illustrated in Fig. 7, we attempt to correlate the findings of previous authors (12-14) concerning changes in the composition of

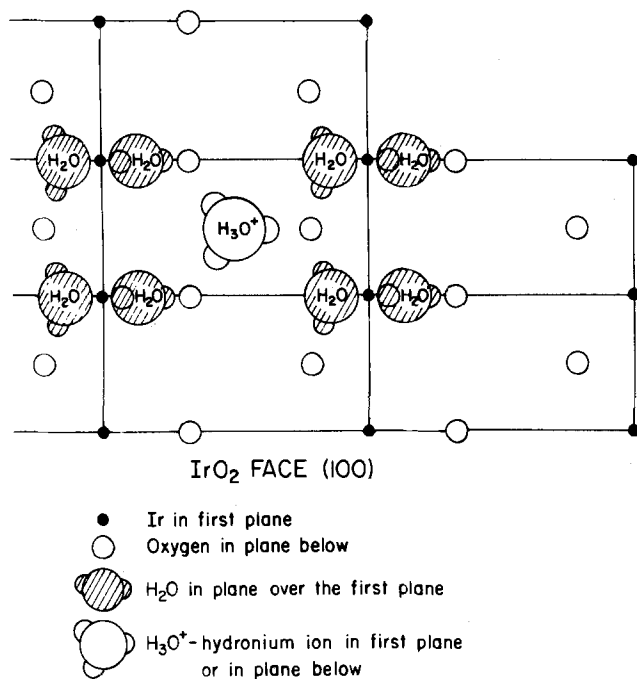


Fig. 7. Schematic representation of the IrO₂ (100) ideal surface after hydration and hydrogenation in first monolayer.

the IROX films upon cathodization ("bleaching") and anodization ("coloration"). The iridium atoms present on the ideal (100) surface have broken bonds with oxygens caused by crystal termination. On contact with an aqueous electrolyte, the iridium atoms will form active centers for the adsorption of water molecules that take an orientation with hydrogens directed toward the electrolyte phase. A dissociation of the hydrogen-oxygen bonds is very probable. It has been found by Trasatti and co-workers (31) that the IrO₂ powders in aqueous solutions are highly negatively charged. The XPS studies revealed (43) that the dissociative adsorption of water molecules always takes place on the iridium metal samples. A negatively charged IrO₂ surface should lead immediately to the attraction of hydronium ions from the solution. The most stable arrangement of the H₃O⁺ ion, in the center of the unit cell, is shown in Fig. 7. The composition of the unit cell (two first plane plus surface water) is then HIrO₂ · 3H₂O, the same as found by McIntyre *et al.* (13, 14) for "bleached" IROX films. On anodization, this composition should change to IrO₂ · H₂O, what can be achieved by withdrawal of H₃O⁺ ion. We feel that it would be difficult for hydration and hydrogenation of the next monolayers of a nonhydrated IrO₂ single crystal to proceed without reconstruction of the unit cell. This in turn requires large energies due to the high activation barriers associated with reconstructing process. The single protons can eventually penetrate into the crystal bulk. Cycling in a wide potential range may result in a distortion of the surface lattice and a formation of the next monolayer of the hydrated form of IrO₂ with the expanded unit cell. This process could possibly be manifested by an additional pair of peaks like A₃-C₃ in Fig. 5b with a high degree of irreversibility.

Comparing the electrochemical behavior of the anodic hydrated IrO₂ films on the Ir electrodes described by previous workers (11-27) with that of the IrO₂ (100) electrodes presented in this paper, one observes good reversibility of the main, hydrogen injection/ejection process [2] represented by a couple of peaks at 720 mV in the former case and a high degree of irreversibility of this process (peaks A₃-C₃) in the latter case. Also, the reversible potential for this process is lower for single-crystal electrode ($E = 410$ mV). In the hydrogen region, CV characteristics for the anodic IrO₂ films become sluggish because of the re-

duced conductivity in the bleached material. This phenomenon is not observed in case of the IrO₂ (100) electrode as the hydrogen penetration depth is highly minimized in the single crystal and does not involve more than perhaps one or two monolayers.

It is characteristic that the sputtered IrO₂ films (42) exhibit a reversible voltammetric behavior similar to the IROX (anodic) films, but in contrast to them the reversible potential for the major process [2] is equal $E = 450$ mV, *i.e.*, very close to the value $E = 410$ mV we observed for our single-crystal IrO₂ (100) electrode. Note that the density of the sputtered films decreases on operating in aqueous electrolytes from 10 to 7.8 g/cm³ due to water uptake. These numbers can be compared with the density for crystalline IrO₂, which is equal to 11.68 g/cm³ and resembles compact structure of the latter material. On the other hand, the electric conductivity of the IROX films changes by four orders of magnitude during the bleaching/coloration process (from 100 to 0.01 Ω-cm), while that of the sputtered layers changes only by one order of magnitude (from 0.01 to 0.001 Ω-cm). The specific resistivity for crystalline IrO₂ is 10⁻⁴ Ω-cm, and we did not observe in voltammetric characteristics any significant changes in resistivity of our single-crystal IrO₂ electrodes. Thus, the interatomic distances and water content in IrO₂ samples which are determined by the method of synthesis and pretreatment procedure are directly responsible for both the energy of interaction of hydrogen with IrO₂ structure and the degree of reversibility of the hydrogen injection/ejection process [2]. Also, the electric conductivity and the penetration depth of hydrogen species into the electrode material are directly related to the structural changes caused by preparation conditions.

Conclusion

A highly irreversible behavior of the main electrochemical process of the hydrogen injection/ejection corresponding to Eq. [2] at single-crystal IrO₂ electrodes has been described for the (100) surface. It is manifested by a difference between the voltammetric peak-potentials for the anodic and cathodic half-reactions which approaches 220 mV at $v = 200$ mV/s. This behavior can be opposed to that of the sputtered and anodic IrO₂ films on the Ir substrates which is reversible. Also, we did not observe characteristic ceasing of the current in the hydrogen region caused in case of the IROX films by a decrease in electrical conductivity associated with the "bleaching" process. Instead, a low overvoltage for the hydrogen evolution reaction has been observed on the IrO₂ (100) electrodes. All these differences can be interpreted by a strong retardation of the hydration and hydrogenation of the compact IrO₂ single crystals in comparison with the favorable compositional changes of the amorphous anodic IrO₂ films. These changes can involve layers 100-200 nm thick in the latter case, while the hydrogen penetration depth for the IrO₂ single crystal electrodes does not exceed one or two monolayers.

Thus, the coloration/bleaching process as described for the IROX films cannot develop on nonhydrated single-crystal IrO₂ electrodes unless their crystallographic structure is damaged by cycling in a wide potential range.

The energy of major interaction of hydrogen species with the IrO₂ single-crystal structure is close to that observed for sputtered IrO₂ films but differs by *ca.* 29 kJ/mol (corresponding to 300 mV difference in the reversible potential for reaction [2]) from that for the anodic IrO₂ films.

Acknowledgment

This work was supported by the United States Department of Energy under Contract no. DE-AC02-80ER10654.

Manuscript submitted April 3, 1984; revised manuscript received *ca.* March 25, 1985.

Brooklyn College assisted in meeting the publication costs of this article.

REFERENCES

- S. Trasatti and G. Lodi, in "Electrodes of Conductive Metallic Oxides, Part B," S. Trasatti, Editor, Elsevier, Amsterdam (1981).
- S. Gottesfeld and S. Srinivasan, *J. Electroanal. Chem.*, **86**, 89 (1978).
- J. Mozota and B. E. Conway, *This Journal*, **128**, 2141 (1981).
- J. P. Hoare, "The Electrochemistry of Oxygen," Interscience, New York (1968).
- J. Horkans and M. W. Shafer, *This Journal*, **124**, 1201 (1977).
- S. Trasatti and W. E. O'Grady, in "Advances in Electrochemistry and Electrochemical Engineering," Vol. 12, H. Gerischer and C. W. Tobias, Editors, pp. 177-261, Wiley and Sons, New York (1981).
- D. M. Novak, B. V. Tilak, and B. E. Conway, in "Modern Aspects of Electrochemistry," Vol. 14, J. O'M. Bockris and B. E. Conway, Editors, pp. 195-318, Plenum Press, New York (1982).
- S. Trasatti and G. Buzzanca, *J. Electroanal. Chem.*, **29**, Appl. 1 (1971).
- T. Hepel, F. H. Pollak, and W. E. O'Grady, in "The Chemistry and Physics of Electrocatalysis," J. D. E. McIntyre, M. J. Weaver, and E. B. Yeager, Editors, p. 512, The Electrochemical Society Softbound Proceedings Series, Pennington, NJ (1985).
- A. T. Kuhn and C. J. Mortimer, *This Journal*, **120**, 231 (1973).
- J. Mozota and B. E. Conway, *Electrochim. Acta*, **28**, 1 (1983).
- B. E. Conway and J. Mozota, *This Journal*, **28**, 9 (1983).
- J. D. McIntyre, S. Basu, W. F. Peck, W. L. Brown, and W. M. Augustyniak, *Phys. Rev. B*, **25**, 7242 (1982).
- S. Gottesfeld, J. D. E. McIntyre, G. Beni, and J. L. Shay, *Appl. Phys. Lett.*, **33**, 208 (1978).
- S. Gottesfeld and J. D. E. McIntyre, *This Journal*, **126**, 742 (1979).
- G. Beni and J. L. Shay, *Appl. Phys. Lett.*, **33**, 567 (1978).
- J. D. E. McIntyre, W. F. Peck, and S. Nakahara, *This Journal*, **127**, 1264 (1980).
- G. Beni, C. E. Rice, and J. L. Shay, *Phys. Rev. B*, **21**, 364 (1980).
- G. Beni, C. E. Rice, and J. L. Shay, *This Journal*, **127**, 1342 (1980).
- C. E. Rice and P. M. Bridenbaugh, *Appl. Phys. Lett.*, **38**, 59 (1981).
- C. E. Rice, *ibid.*, **35**, 563 (1979).
- J. L. Shay, G. Beni, and L. M. Schiavone, *ibid.*, **32**, 942 (1978).
- A. Capon and R. Parsons, *J. Electroanal. Chem.*, **39**, 275 (1972).
- J. M. Otten and W. Visscher, *ibid.*, **55**, 1 (1974).
- J. M. Otten and W. Visscher, *ibid.*, **55**, 13 (1974).
- D. A. J. Rand and R. Woods, *ibid.*, **55**, 375 (1974).
- L. D. Burke, M. E. Lyons, E. J. M. O'Sullivan, and D. P. Whelan, *ibid.*, **122**, 403 (1981).
- S. Ardizzone, A. Carugati, and S. Trasatti, *ibid.*, **126**, 287 (1981).
- G. A. Kokarev, V. A. Kolesnikov, A. F. Gubin, and A. A. Korobanov, *Elektrokhimiya*, **18**, 466 (1982).
- M. A. Butler and D. S. Ginley, *This Journal*, **125**, 228 (1978).
- S. Ardizzone, D. Lettieri, and S. Trasatti, *J. Electroanal. Chem.*, **146**, 431 (1983).
- R. Kotz, H. J. Lewerenz, P. Bruesch, and S. Stucki, *ibid.*, **150**, 209 (1983).
- K. S. Kim, C. D. Sell, and N. Winograd, *Electrocatal.*, **242**.
- W. D. Ryden, A. W. Lawson, and C. C. Sartain, *Phys. Rev. B*, **1**, 1494 (1970).
- G. K. Wertheim and H. J. Guggenheim, *ibid.*, **22**, 4680 (1980).
- A. K. Goel, G. Skorinko, and F. H. Pollak, *ibid.*, **24**, 7342 (1981).
- L. F. Mattheiss, *ibid.*, **13**, 2433 (1976).
- Y. S. Huang and F. H. Pollak, Private communication.
- Y. S. Huang, H. L. Park, and F. H. Pollak, *Mater. Res. Bull.*, **17**, 1305 (1982).
- J. E. Graebner, E. S. Greiner, and W. R. Ryden, *Phys. Rev. B*, **13**, 2426 (1976).
- T. Hepel, M. Hepel, and R. A. Osteryoung, *This Journal*, **129**, 2132 (1982).
- W. C. Dautremont-Smith, L. M. Schiavone, S. Hackwood, G. Beni, and J. L. Shay, *Solid State Ionics*, **2**, 13 (1981).
- T. S. Wittig, D. E. Ibbotson, and W. H. Weinberg, *Surf. Sci.*, **102**, 506 (1981).

Finite-Element Method Approach to the Problem of the IR-Potential Drop and Overpotential Measurements by Means of a Luggin-Haber Capillary

Koichi Tokuda,* Tatsuro Gueshi,¹ Koichi Aoki, and Hiroaki Matsuda*

Department of Electronic Chemistry, Graduate School at Nagatsuta, Tokyo Institute of Technology, Nagatsuta, Midori-ku, Yokohama 227, Japan

ABSTRACT

A finite-element method is applied to the problem of potential distribution around a Luggin-Haber capillary placed perpendicularly to the planar working electrode for the cases when overpotential is absent and when there is overpotential which is linear to current density. Approximate equations are presented for the IR-potential drop between the working electrode and the Luggin-Haber capillary as functions of the outer and inner radii of the capillary tip, the distance from the capillary tip to the working electrode, conductivity of the solution, and average current density. Approximate equations which relate the measured overpotential to the true overpotential, the IR-potential drop, and the relevant parameters are also presented. In the presence of overpotential or polarization, it has been shown that the measured potential can be regarded as a sum of the true overpotential and the IR-potential drop, provided that the tip of the Luggin-Haber capillary is placed no closer from the electrode surface than a distance equal to the outer diameter of the capillary tip.

Measurement or control of the potential of a working electrode under current flow is of great importance not only in the studies on electrode kinetics, but also in practical electrolysis. For this purpose, a Luggin-Haber capillary connected to a reference electrode is usually employed. The cell voltage of a galvanic cell composed of

the working and reference electrodes is measured or controlled. Minimization of the ohmic potential drop included in the measured or controlled voltage will be achieved by placing the tip of the Luggin-Haber capillary as close to the surface of the working electrode as possible. When the capillary tip is placed very close to the electrode, however, it shields the latter, causing a decrease in current density and distortion of equipotential surfaces near the capillary tip, so that the potential measured or controlled by the capillary corresponds to a spot of the

*Electrochemical Society Active Member.

¹Present address: Sanyo Electric Company, Limited, Research Center, Hirakata, Osaka 573, Japan.

electrode at which the current density is much lower than that in the region of electrode surface sufficiently remote from the capillary tip.

Piontelli and co-workers (1, 2) and Barnartt (3, 4) performed potential mapping studies using rather large model electrolysis cells and obtained equipotential maps around the electrode and capillary tip. Barnartt (3, 4) concluded that the potential inside a capillary of diameter $2r_0$ placed $4r_0$ from one of a pair of parallel-plate electrodes is equal to that in the undistorted field a distance $2r_0/3$ closer than the capillary tip position.

From a theoretical viewpoint, the solution of the Laplace equation with appropriate boundary conditions is required in order to obtain the potential or primary and secondary current distributions in electrolytic cells. Since Kasper's work (5), there have been a number of papers on the potential and current distributions in electrolysis cells. Although it is highly desirable to have analytical solutions, they can be given only for simple geometries by the use of conformal or imaging transformations (6-12). The recent development of high speed computers has made it possible to apply various numerical methods to the problems for more complicated electrode geometries. A finite difference method was utilized by Klingert *et al.* (13) for the computation of the primary and secondary current distribution in an L-shaped region. Pierini and Newman (14) employed the superposition technique to calculate the potential distribution around a disk electrode in axisymmetric cylindrical cells. Fedkiw (15) applied a perturbation method to the calculation of the primary current distribution at an electrode with a sinusoidal profile. An orthogonal collocation technique (16) and a variational method (17) have also been applied to current distribution problems. In recent years, the finite-element method (FEM) has been used in various fields of engineering (18-20). It is a powerful numerical procedure for solving the differential equations of physics and engineering. To our knowledge, the first application of FEM to electrochemistry was done by Kawai and co-workers (21-23) for the solution of Fick's equation and that coupled with chemical reaction terms. One of the advantageous properties of FEM is that it allows us to treat boundary value problems for two- or three-dimensional regions with irregularly shaped boundaries to which an analytical approach is usually very difficult. From this viewpoint, the application of FEM to many problems in electrochemistry is expected. Recently, Alkire *et al.* (24) used FEM to predict the shape changes at a cathode during electrodeposition. Sautebin *et al.* (25) applied FEM to the simulation of the leveling of triangular surface during anodic dissolution in electrochemical machining. In our laboratory, FEM has been used for the calculation of primary current distribution in a two-dimensional model cell composed of an electrode with holes (26) and for the calculation of chronopotentiometric $i-t$ curves at the electrodes coated with polymer of uneven thickness (27).

The present paper describes the application of FEM to the calculation of the potential distribution around the Luggin-Haber capillary placed perpendicularly to the working electrode in the cases (i) where overpotential is absent and (ii) where there is overpotential which is assumed to be linear to current density. This assumption may be justified if the current densities do not deviate much from the average current density. Approximate equations with reasonable accuracies are presented for the IR-potential drop as functions of the outer and inner radii of the capillary tip, the distance between the capillary tip and the working electrode, conductivity of the solution, and average current density. Furthermore, approximate equations which relate the measured overpotential to the true overpotential, the IR-potential drop, and the relevant parameters are presented. It has been shown that in the presence of overpotential or polarization the measured potential can be regarded as a sum of true overpotential and the IR-potential drop when the distance between the capillary tip and the electrode surface is no closer than the outer diameter of the capillary tip. A part

of this work has been published as a preliminary note (28).

Formulation of the Problem

The electrochemical problem.—Consider an electrolysis cell composed of three electrodes: a working, an auxiliary, and a reference electrode. The variation of electrical potentials in the cell is schematically shown in Fig. 1. For convenience, we assume in what follows that the working electrode acts as a cathode and the auxiliary as an anode. Since the electrode potential is defined as the difference between the inner potential of the electrode phase and that of the solution adjacent to the electrode surface, we have

$$E^c = \psi^c - \phi^c \quad [1]$$

We can assume without any loss of generality that there is no polarization at the auxiliary electrode and the potential of the electrode is constant

$$E^a = \psi^a - \phi^a = \text{const.} \quad [2]$$

We can also assume that the potential of the reference electrode is constant since current passing through it is negligibly small and polarization at the electrode can be ignored. Thus we have

$$E^{\text{ref}} = \psi^{\text{ref}} - \phi^{\text{ref}} = \text{const.} \quad [3]$$

In Fig. 1, the variation of potentials is depicted in reference to the inner potential of the electrolyte solution adjacent to the auxiliary electrode, ϕ^a , which is also assumed to be constant. Under the equilibrium condition where no current flows through the cell, the inner potential of the electrolyte solution is uniform throughout the cell

$$\phi_{\text{eq}}^c = \phi_{\text{eq}}^{\text{ref}} = \phi^a \quad [4]$$

Since the cell voltage is defined as

$$V = \psi^a - \psi^c \quad [5]$$

the cell voltage under the equilibrium condition is given by

$$V_{\text{eq}} = \psi^a - \psi_{\text{eq}}^c = (\psi^a - \phi^a) - (\psi_{\text{eq}}^c - \phi_{\text{eq}}^c) = E^a - E_{\text{eq}}^c \quad [6]$$

When current flows without any overpotential at the working electrode (cathode), the electrode potential at the

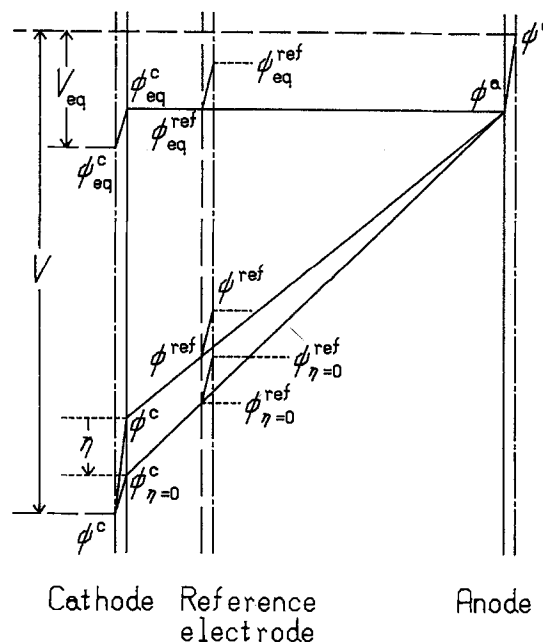


Fig. 1. Schematic diagram of variation of electrical potentials in an electrolysis cell.

cathode is equal to that under the equilibrium condition $E_{\eta=0^c} = E_{\text{eq}}^c$, i.e.

$$\psi^c - \phi_{\eta=0^c} = \psi_{\text{eq}}^c - \phi_{\text{eq}}^c \quad [7]$$

If the electrode reaction occurs at the cathode with overpotential, η , then we have

$$\eta = E^c - E_{\eta=0^c} = E^c - E_{\text{eq}}^c = (\psi^c - \phi^c) - (\psi_{\text{eq}}^c - \phi_{\text{eq}}^c) = (\psi^c - \psi_{\text{eq}}^c) + (\phi_{\text{eq}}^c - \phi^c) \quad [8]$$

In terms of Eq. [4]-[6], Eq. [8] can be rewritten as

$$\eta = -(V - V_{\text{eq}}) + \phi^a - \phi^c \quad [9]$$

As stated above, the measured or controlled electrode potential is the potential difference between the terminals of a galvanic cell composed of the working and the reference electrodes; that is, the inner potential of the working electrode against that of the reference electrode

$$(E^c)_m = \psi^c - \psi^{\text{ref}} \quad [10]$$

Thus, the equilibrium potential of the working electrode is given by

$$(E_{\text{eq}}^c)_m = \psi_{\text{eq}}^c - \psi_{\text{eq}}^{\text{ref}} = E_{\text{eq}}^c - E^{\text{ref}} \quad [11]$$

The IR-potential drop, ΔV_{IR} , due to the solution resistance can be given as the difference between the measured potential of the working electrode when current flows without any overpotential and that at equilibrium

$$-\Delta V_{\text{IR}} = (E_{\eta=0^c})_m - (E_{\text{eq}}^c)_m \quad [12]$$

where ΔV_{IR} is taken to be positive. Equation [12] can be written as

$$\begin{aligned} -\Delta V_{\text{IR}} &= (\psi^c - \psi_{\eta=0^c}^{\text{ref}}) - (E_{\text{eq}}^c - E^{\text{ref}}) \\ &= \psi^c - \phi_{\eta=0^c} + \phi_{\eta=0^c}^{\text{ref}} - \psi_{\eta=0^c}^{\text{ref}} - (E_{\text{eq}}^c - E^{\text{ref}}) + \phi_{\eta=0^c} - \phi_{\eta=0^c}^{\text{ref}} \\ &= \phi_{\eta=0^c} - \phi_{\eta=0^c}^{\text{ref}} \quad [13] \end{aligned}$$

where the last expression is obvious from Fig. 1. On the other hand, the measurable overpotential is given by

$$\begin{aligned} (\eta)_m &= (E^c)_m - (E_{\text{eq}}^c)_m = \psi^c - \psi^{\text{ref}} - (\psi_{\text{eq}}^c - \psi_{\text{eq}}^{\text{ref}}) \\ &= (\psi^a - \psi_{\text{eq}}^c) - (\psi^a - \psi^c) + (\psi_{\text{eq}}^{\text{ref}} - \psi^{\text{ref}}) \\ &= -(V - V_{\text{eq}}) + (\phi^a - \phi^{\text{ref}}) \quad [14] \end{aligned}$$

The electrolytic cell model.—Figure 2 shows the schematic diagram of the axisymmetric cylindrical cell together with the cylindrical coordinates employed for the analysis. The cathode (working electrode) and the anode, facing each other, are located in the planes $z = 0$ and $z = 25r_0$, respectively, where r_0 denotes the outer radius of the Luggin capillary. The cell has a cylindrical insulator wall at $r = 15r_0$. The following two cases are treated: (i) the Luggin capillary is placed in front of the cathode, the tip of the capillary is at $z = d$, and (ii) the capillary is placed through the back of the cathode, its tip being flush with the front surface of the cathode. In either case, z -axis is taken as the center axis of the capillary. Although the choice of the distance between the cathode and the anode ($25r_0$) and the position of the insulator wall ($15r_0$) is arbitrary, these are chosen so that the presence of the capillary does not affect the potential or current distributions in the vicinities of the anode or the insulator wall. It has been confirmed that the use of the values larger than $25r_0$ and $15r_0$ has little effect on the calculated results.

The boundary value problem.—Inner potential in the solution satisfies the Laplace equation

$$\nabla^2\phi = \partial^2\phi/\partial r^2 + r^{-1}\partial\phi/\partial r + \partial^2\phi/\partial z^2 = 0 \quad [15]$$

The boundary conditions are as follows: at anode (Γ^a)

$$\phi = \phi^a \quad [16]$$

at cathode (Γ^c)

$$\phi = 0 \quad [17]$$

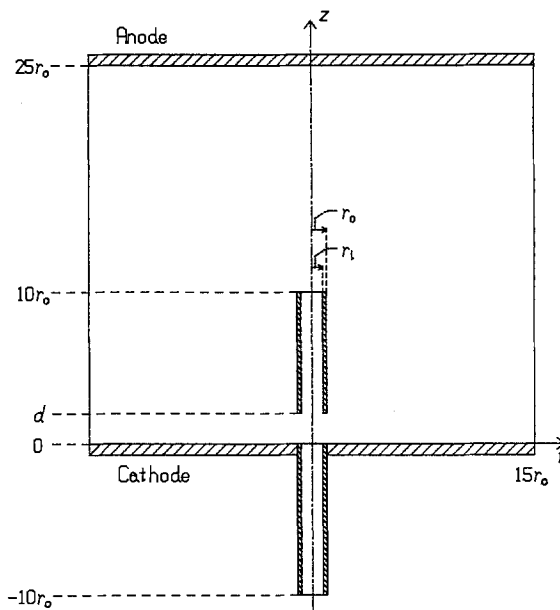


Fig. 2. Schematic diagram of axisymmetric cylindrical model cell and the cylindrical coordinates employed for the analysis. The Luggin-Haber capillary is placed along the center axis either in front of the cathode or through the back of the cathode.

when there is no overpotential, or

$$f(\phi_{\text{re}}, [\partial\phi/\partial n]_{\text{re}}) = 0 \quad [18]$$

when there is overpotential, and at insulator surface or symmetric axis (Γ^i)

$$\partial\phi/\partial n = 0 \quad [19]$$

where n is the outward normal and the function f defines the potential-current density relationship.

In this paper, we assume that the overpotential is given as a linear function of current density (29)

$$\eta = \eta_0 + hj \quad [20]$$

where η_0 and h are constants. Although, in general, such a relation does not hold over a wide range of current densities, this approximation may be adequate so far as the current densities do not deviate too much from the average current density. Since the current density at the cathode is given by

$$j = -\kappa(\partial\phi/\partial z)_{z=0} \quad [21]$$

where the sign of cathodic current is taken to be negative and κ is conductivity of the solution, we have in place of Eq. [18]

$$\eta = \eta_0 - h\kappa(\partial\phi/\partial z)_{z=0} \quad [22]$$

or, by the use of Eq. [9]

$$\phi^a - \phi^c - (V - V_{\text{eq}}) = \eta_0 - h\kappa(\partial\phi/\partial z)_{z=0} \quad [23]$$

With the transformation of the variables

$$\Phi = \Phi^a[1 - (\phi^a - \phi)/(V - V_{\text{eq}} + \eta_0)] \quad [24]$$

$$R = r/r_0 \quad [25]$$

$$Z = z/r_0 \quad [26]$$

and

$$n^* = n/r_0 \quad [27]$$

our boundary value problem is given as

$$\partial^2\Phi/\partial R^2 + R^{-1}\partial\Phi/\partial R + \partial^2\Phi/\partial Z^2 = 0 \quad [28]$$

at Γ^a

$$\Phi = \Phi^a \quad [29]$$

at Γ^c

$$\Phi = 0 \text{ or } \Phi = (hk/r_0)(\partial\Phi/\partial Z) \quad [30]$$

at Γ^i

$$\partial\Phi/\partial n^* = 0 \quad [31]$$

The FEM representation of the problem.—Now divide the domain Ω to be analyzed into a number of finite elements and let the potential Φ at any point within a finite element (e) be approximated by

$$\Phi = [N^{(e)}]\{\Phi^{(e)}\} \quad [32]$$

where $[N^{(e)}]$ is a row vector of interpolation (or shape) function of element (e), and $\{\Phi^{(e)}\}$ is a column vector composed of nodal values. Using $[N^{(e)}]$ as weighting functions, applying the Galerkin method to Eq. [28], we have

$$\int_{\Omega} [N^{(e)T}] (\partial^2\Phi^{(e)}/\partial R^2 + R^{-1}\partial\Phi^{(e)}/\partial R + \partial^2\Phi^{(e)}/\partial Z^2) d\Omega = 0 \quad [33]$$

where superscript T denotes a transpose and $d\Omega = R d\theta dR dZ$ because of axisymmetry. Performing the integration in Eq. [33] by parts and using the Green Gauss theorem yields local finite-element equations

$$[k^{(e)}]\{\Phi^{(e)}\} = \{f^{(e)}\} \quad [34]$$

where

$$[k^{(e)}] = 2\pi \int_{\Omega^e} \{ (\partial[N^{(e)T}]/\partial R)(\partial[N^{(e)}]/\partial R) + (\partial[N^{(e)T}]/\partial Z)(\partial[N^{(e)}]/\partial Z) \} R dR dZ + 2\pi (r_0/hk) \int_{\Gamma^c} [N^{(e)T}][N^{(e)}] R dR \quad [35]$$

$$\{f^{(e)}\} = 2\pi \int_{(\Gamma^c+\Gamma^i)} [N^{(e)T}](\partial[N^{(e)}]/\partial Z) R dR \quad [36]$$

In the derivation of Eq. [35] and [36], boundary conditions [30] and [31] have been taken into account. The global finite-element equations are obtained by assembling the contributions of each element equation

$$[K]\{\Phi\} = \{F\} \quad [37]$$

where

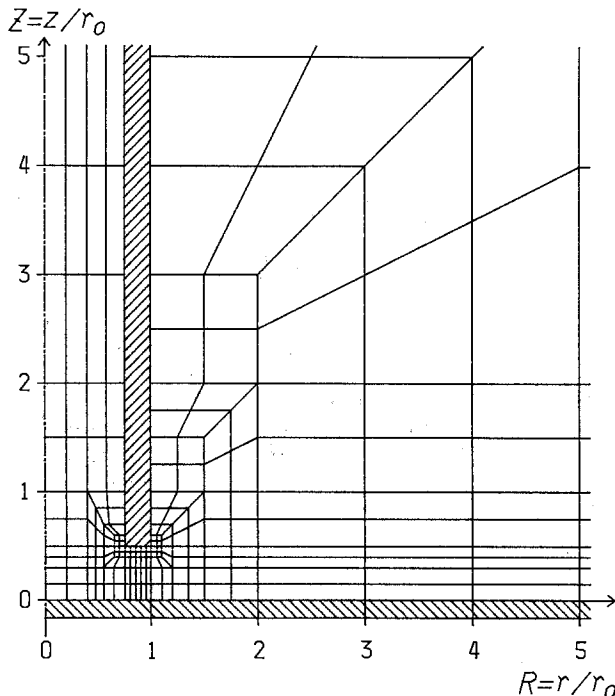


Fig. 3. Example of quadrilateral element grid used in the analysis for the geometry $d/r_0 = 0.5$ and $r_1/r_0 = 0.75$. Shaded part for $Z \geq 0.5$ indicates the cross section of the capillary wall, and that for $Z \leq 0$ denotes the cathode.

$$\{\Phi\} = \sum_e \{\Phi^{(e)}\}; [K] = \sum_e [k^{(e)}]; \{F\} = \sum_e \{f^{(e)}\} \quad [38]$$

Procedure of computation.—Since our problem is axisymmetric, the region Ω was divided into a number of ring elements obtained by revolving quadrilaterals. Quadratic elements were employed. Division of Ω into isoparametric quadratic quadrilateral elements and numbering of nodes were carried out semiautomatically by use of a FORTRAN program which is a modified version of one proposed by Cohen (30). The region Ω was usually divided into ca. 200 elements and thus had 1000 ~ 1200 nodes. Automatic renumbering of nodes was employed to minimize the bandwidth of the global matrix $[K]$ (31). Examples of the parts of element grid thus divided are shown in Fig. 3 and 7. The region where sharp potential change is considered to occur was divided into smaller elements than other region. It is well known that the boundary between the electrode and the insulator wall (e.g., the point at $Z = 0$ and $R = 1$ in Fig. 7) is a mathematical singular boundary where the derivative of potential is discontinuous. For the elements including such a singular point, singular elements introduced by Henshell and Shaw were employed (32). The global matrix was assembled by the stiffness method and then altered according to the boundary conditions given by Eq. [29] and [30]. The set of simultaneous equations was solved by the Gauss elimination method.

Calculations were carried out for various values of parameters, r_1/r_0 (0.0 ~ 1.0), d/r_0 (0.1 ~ 4.0), and hk/r_0 (0.0 ~ 20.0). Φ^a was taken to be 25.0.

Results and Discussion

Primary potential distribution and the IR potential drop.—Figure 4 shows, as an example, the potential distribution around the Luggin-Haber capillary calculated for geometry $d/r_0 = 0.5$ and $r_1/r_0 = 0.75$ based on the element grid, part of which is shown in Fig. 3, and for $h = 0$ and $\eta_0 = 0$, i.e., when there is no overpotential. It can be seen that the presence of the capillary causes distortion of equipotential surfaces only in the vicinity of the capillary tip and that the potential distribution in the solution region farther than $2r_0$ from the capillary tip is almost equal to that in the absence of the capillary. The value of potential in the capillary becomes constant in the region about

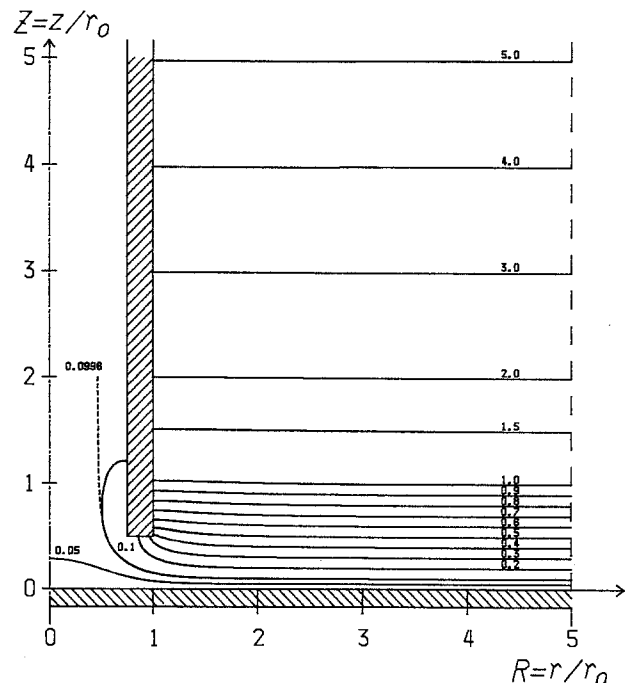


Fig. 4. Primary potential distribution around the capillary tip for the electrode geometry shown in Fig. 3. Numerals on the curves indicate values of function Φ .

$2r_0$ inside from the tip. The difference between this potential and that of the working electrode surface corresponds to the IR-drop involved in the measured electrode potential. Although the equipotential surfaces in Fig. 4 are given not in ϕ but in Φ , it can be seen from Eq. [24] that the real potential distribution is similar to that in Fig. 4.

The current density at the cathode is given by Eq. [21]. By use of Eq. [21], [24], and [26] and condition $\eta_0 = 0$, we have

$$j = -(V - V_{eq})(\kappa/r_0\Phi^a)(\partial\Phi/\partial Z)_{Z=0} \quad [39]$$

Thus the current density at the place sufficiently remote from the capillary is given by

$$j^\infty = -(V - V_{eq})(\kappa/r_0\Phi^a)(\partial\Phi/\partial Z)_{Z=0, R \rightarrow \infty} \quad [40]$$

Then we have

$$j/j^\infty = (\partial\Phi/\partial Z)_{Z=0}/(\partial\Phi/\partial Z)_{Z=0, R \rightarrow \infty} \quad [41]$$

Variations of relative current distribution j/j^∞ near the capillary tip with the distance from the center axis are shown in Fig. 5 for $r_i/r_0 = 0.75$ when d/r_0 is changed. As a matter of fact, one can see that the more remotely the capillary tip is placed from the electrode surface, the less distortion of the current distribution there is. This figure also reveals that only the part of the electrode just below the capillary tip is shielded and that the current density becomes almost uniform in the region $r \geq 3r_0$. In addition, it has been found that the thinner the capillary wall, the less the distortion of the current distribution, although this is not shown in the figure.

Now we consider the IR-potential drop, ΔV_{IR} , due to the solution resistance under the effect of the presence of the capillary. This can be given by Eq. [13]. Eliminating ϕ from Eq. [13] and [24] and using the condition, $\Phi_{\eta=0} = 0$ yields

$$\Delta V_{IR} = (V - V_{eq})\Phi_{\eta=0}^{ref}/\Phi^a \quad [42]$$

Dividing Eq. [42] by Eq. [40] and rearranging the resulting equation gives

$$\Delta V_{IR} = (-j^\infty r_0/\kappa)\Phi_{\eta=0}^{ref}/(\partial\Phi/\partial Z)_{Z=0, R \rightarrow \infty} \quad [43]$$

Values of $(-j^\infty r_0/\kappa)\Delta V_{IR}$ are plotted in Fig. 6 against d/r_0 for several values of r_i/r_0 . The straight dot-dashed line corresponds to the uniform potential distribution when there is no capillary. It can be seen from Fig. 6 that the IR-potential drop measured with the capillary is a function of both d/r_0 and r_i/r_0 and that when d/r_0 is larger than 2, the measured value of ΔV_{IR} is smaller by a constant value than the value which would be observed in the absence of the capillary. We tried to express this dependence of ΔV_{IR}

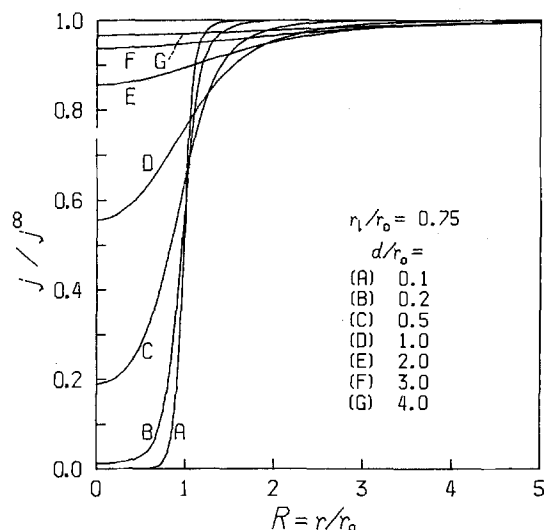


Fig. 5. Effect of the distance between the capillary tip and the cathode on the relative primary current density distribution at the cathode near the capillary tip.

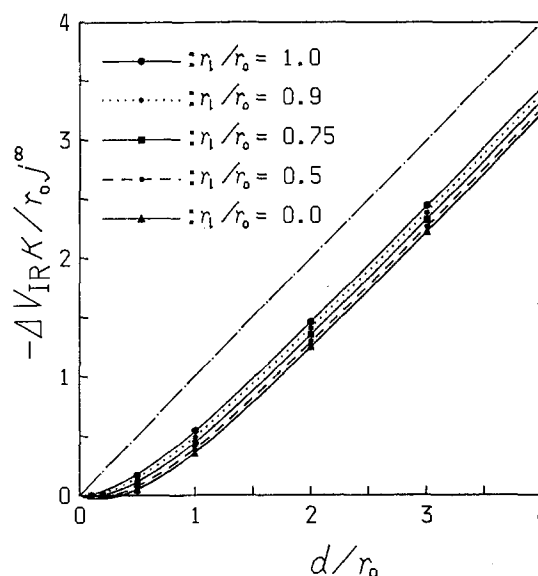


Fig. 6. Dependence of IR-potential drop measured with Luggin-Haber capillary on the distance between capillary tip and the cathode and on the thickness of capillary wall.

on d/r_0 and r_i/r_0 in terms of elementary functions and obtained the following approximate equation with reasonable accuracy

$$\Delta V_{IR} = (-j^\infty/\kappa)[d - r_0\sigma\{1 - 0.1898 \exp(-1.51d/r_0) - 0.8102 \exp(-1.757d/r_0)\}] \quad [44]$$

where σ is a function of r_i/r_0 given by

$$\sigma = 0.780\{1 - 0.01896(r_i/r_0) - 0.08812(r_i/r_0)^2 - 0.1739(r_i/r_0)^3\} \quad [45]$$

The curved lines in Fig. 6 are those calculated from Eq. [44] and [45]. Equation [45] indicates that the effect of the thickness of the capillary wall is rather small since the value of σ changes only from 0.78 to 0.56 when r_i is changed from 0 to r_0 . If the value of d/r_0 exceeds 2.8, then the exponential terms in Eq. [44] are negligible within an error of 1%, and hence Eq. [44] reduces to

$$\Delta V_{IR} = (-j^\infty/\kappa)(d - r_0\sigma) \quad [46]$$

Barnartt (3) proposed $2/3$ as a value of σ for $d/r_0 \geq 4$ from his experiment using a model capillary of $r_i/r_0 = 2/3$. Introducing this value into Eq. [45] yields $\sigma = 0.699$, which is 5% higher than the value $2/3$ proposed by Barnartt. It can be said that these values are in good agreement if we consider that the experimental value might have some contribution of polarization. Piontelli *et al.* (2) concluded from the experiment with capillaries of varied wall thickness from $r_i/r_0 = 0.08$ -1 that $\sigma = 0.6$ for $d/r_0 \geq 6$ and that the approximate equation can be used practically even for $d/r_0 \geq 2$. They also demonstrated that σ is dependent on the ratio r_i/r_0 and varies from 0.714 to 0.476 when r_i/r_0 changes from 0.08 to 1 for $d/r_0 \gg 1$. The discrepancy between these values and those calculated from Eq. [45] may result from their semicylindrical model cell, the diameter of which is 200 mm, being too small for the model capillary of 63 mm diam.

The primary potential and current distributions were also calculated for the electrode geometry where the capillary is placed through the back of the working electrode. Figure 7 shows an example of the element grid for the geometry $r_i/r_0 = 0.75$ employed in the FEM calculation. The primary potential distribution is depicted in Fig. 8, which reveals that the equipotential surfaces are almost parallel to the cathode surface if $r \leq 2r_0$ or $z \leq 2.5r_0$. The potential measured by the Luggin-Haber capillary depends on the inner radius of the capillary; the thinner the capillary wall, the higher the measured potential value. The relative primary current density distribution at such an elec-

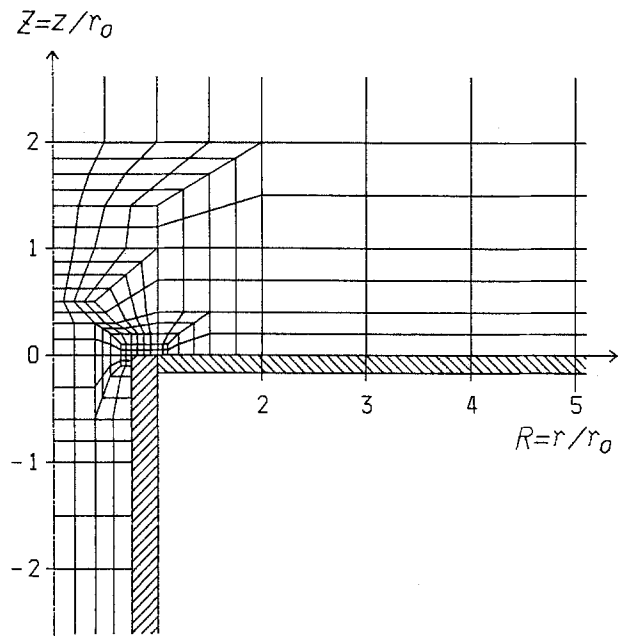


Fig. 7. Part of the quadrilateral element grid used in the analysis for the electrode geometry where the capillary is placed through the back of the cathode. $r_1/r_0 = 0.75$. Shaded part for $0.5 \leq R \leq 1.0$ indicates the cross section of the capillary, and that for $R \geq 1.0$ does the cathode.

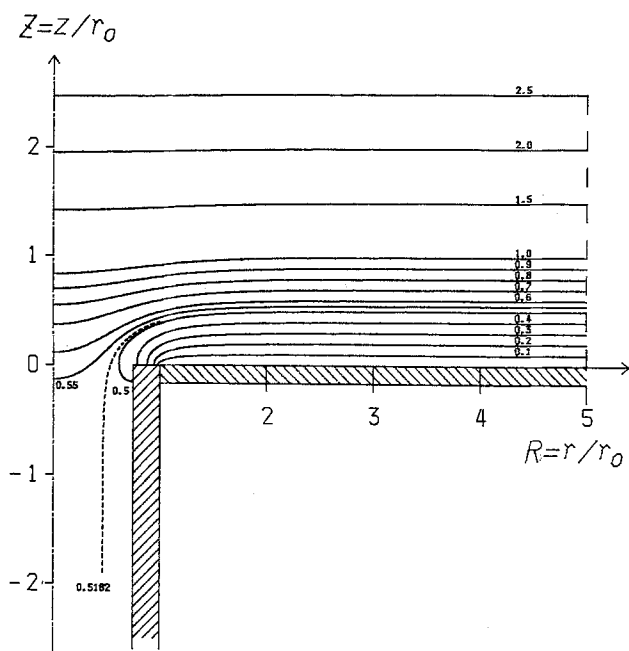


Fig. 8. Primary potential distribution around the capillary tip for the electrode geometry shown in Fig. 7. Numerals on the curves indicate values of function Φ .

trode geometry is shown in Fig. 9. It will be seen that the current density becomes infinity at the boundary between the cathode and the Luggin-Haber capillary wall. Variation of the IR-potential drop calculated from Eq. [41] with the ratio r_1/r_0 is depicted in Fig. 10. It was found that the potential drop ΔV_{IR} can be approximated as a function of r_1/r_0 by

$$\Delta V_{IR}(\kappa/r_0 | j^\infty) = 0.64 \exp[-0.018(r_1/r_0) - 0.159(r_1/r_0)^2 - 0.24(r_1/r_0)^3 - 0.082(r_1/r_0)^{10}] \quad [47]$$

This equation is valid within an error of 0.01 or a relative error of 2.2%.

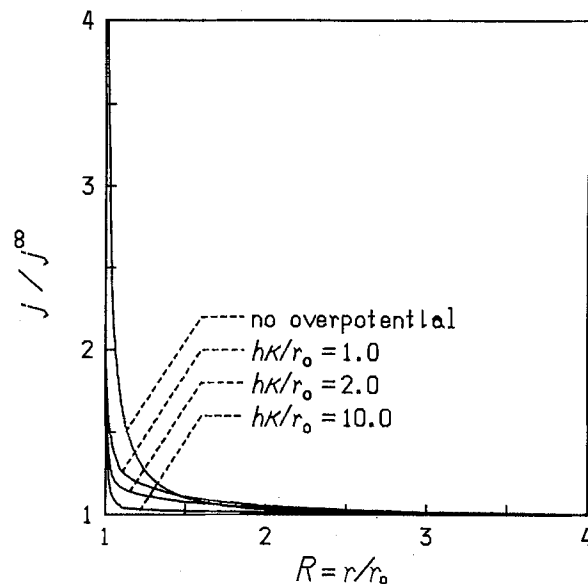


Fig. 9. Relative primary and secondary current density distributions at the cathode for the geometry shown in Fig. 7.

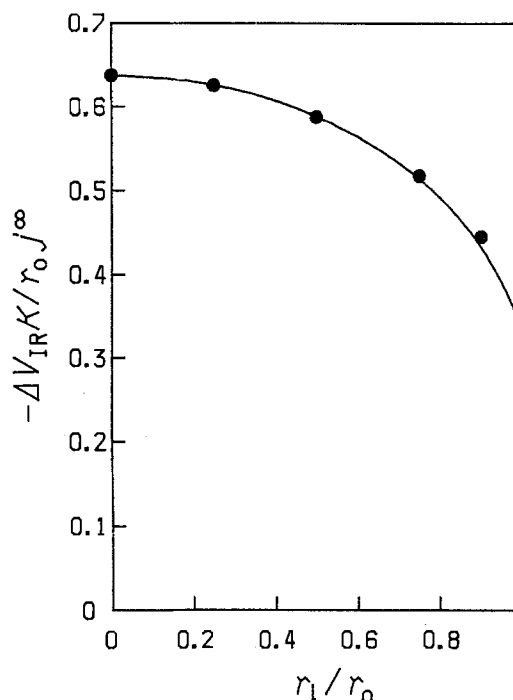


Fig. 10. IR-potential drop measured with the capillary placed through the back of the electrode as a function of r_1/r_0 .

Secondary potential distribution and overpotential measured by Luggin-Haber capillary.—In the presence of overpotential, the electrode potential of the cathode is a function of position or $R = r/r_0$. On the assumption of the linear relation between the overpotential and the current density given by Eq. [22], we can use a quantity $h\kappa/r_0$ as a single parameter expressing the effect of overpotential on the potential distribution in the electrolytic cell as can be seen from the foregoing derivation in the Theoretical section. The parameter is known as the Wagner number (12), and is defined by

$$Wa = (d\eta/dj)(\kappa/L) = h\kappa/r_0 \quad [48]$$

where L is the characteristic length and is taken to be equal to r_0 . If the current density-overpotential relation is given by the Tafel equation and is approximated by the linear relation [20], then h is given by b/j^∞ , where b is the Tafel coefficient.

The potential distributions for the electrode geometries shown in Fig. 3 and 7 are depicted in Fig. 11 and 12, respectively, for $h\kappa/r_0 = 1.0$. Contrary to the case in the absence of overpotential shown in Fig. 4 and 8, the potential at the cathode surface is a function of position in the presence of overpotential, which is manifested in Fig. 11 and 12 by the equipotential surfaces intersecting with the cathode surface. One can see, however, that the distortion of equipotential surfaces are confined only to the region close to the capillary tip. Current density in the presence of overpotential is written in terms of Φ by

$$j = -(V - V_{eq} + \eta_0)(\kappa/r_0\Phi^a)(\partial\Phi/\partial Z)_{Z=0} \quad [49]$$

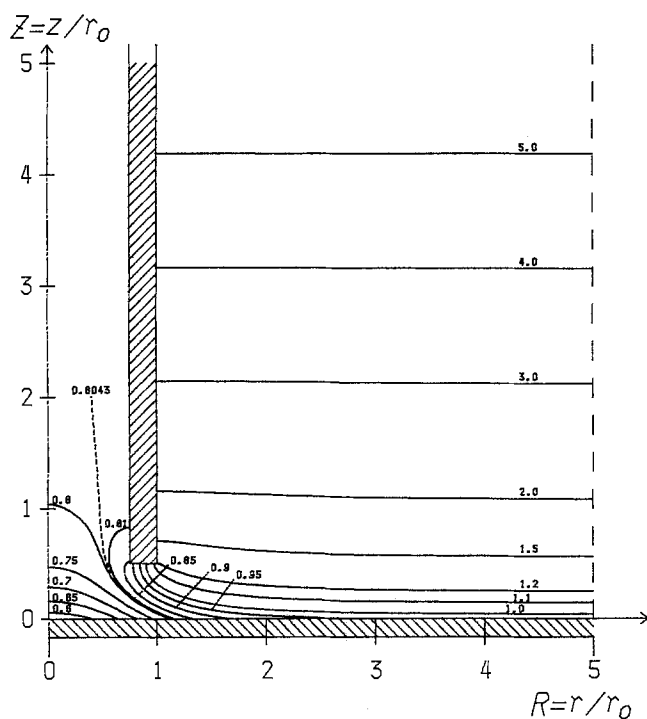


Fig. 11. Secondary potential distribution around the capillary tip for the electrode geometry shown in Fig. 3 for $h\kappa/r_0 = 1.0$. Numerals on the curves show values of function Φ .

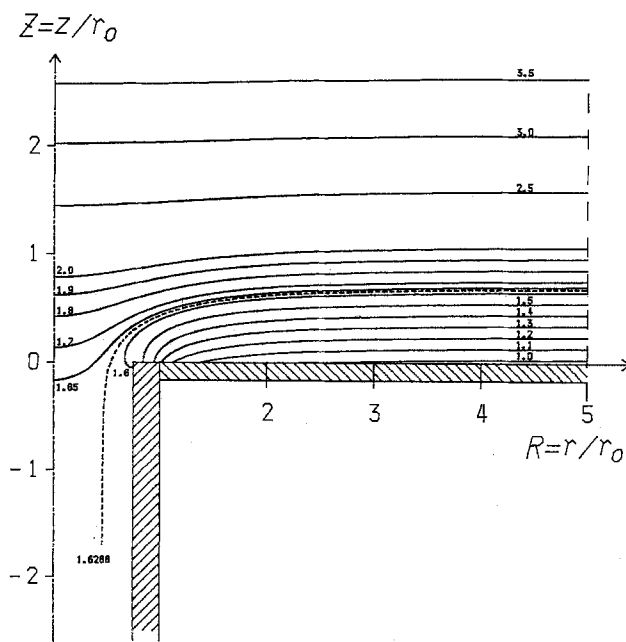


Fig. 12. Secondary potential distribution around the capillary tip for the electrode geometry shown in Fig. 7 for $h\kappa/r_0 = 1.0$. Numerals on the curves show values of function Φ .

The relative current density distribution is calculated from Eq. [41] which is also obtained from Eq. [49] or directly from

$$j/j^\infty = \Phi_{Z=0}/\Phi_{Z=0, R \rightarrow \infty} \quad [50]$$

This equation is obtained from Eq. [41] and [30]. In Fig. 13, variations of the relative current density distribution with the distance from the center axis are shown for the geometry of $r_1/r_0 = 0.75$ and $d/r_0 = 1.0$ and for the various values of the Wagner number $h\kappa/r_0$. For the electrode geometry depicted in Fig. 7, the effect of $h\kappa/r_0$ on the current density distribution is shown in Fig. 9. Figures 13 and 9 indicate that the more uniform current density distribution is obtained as the $h\kappa/r_0$ value becomes higher, i.e., the higher the overpotential or the conductivity of the solution, and that the presence of the capillary has little effect on the current density distribution of the electrode region $r \geq 3r_0$.

Evaluation of true overpotential.—It is of interest to examine the significance of the measured overpotential, $(\eta)_m$. We have, from Eq. [14], [24], and [49]

$$(\eta)_m = \eta_0 + (j^\infty r_0 / \kappa) \Phi^{\text{ref}} (\partial\Phi/\partial Z)_{Z=0, R \rightarrow \infty} \quad [51]$$

From Eq. [51] and [43] it follows

$$\begin{aligned} (\kappa/j^\infty r_0) \{ (\eta)_m + \Delta V_{\text{IR}} - \eta_0 \} \\ = \Phi^{\text{ref}} (\partial\Phi/\partial Z)_{Z=0, R \rightarrow \infty} - \Phi_{\eta_0}^{\text{ref}} (\partial\Phi/\partial Z)_{Z=0, R \rightarrow \infty} \end{aligned} \quad [52]$$

Values of $(\kappa/j^\infty r_0) \{ (\eta)_m + \Delta V_{\text{IR}} - \eta_0 \}$ calculated from the right-hand side of Eq. [52] are plotted against $h\kappa/r_0$ in Fig. 14 for varied values of d/r_0 . One can see the plot is almost linear and has unity slope when $d/r_0 \geq 2$. We tried to find an approximate equation which expresses the term $\{ (\eta)_m - (\eta_0 + hj^\infty) + \Delta V_{\text{IR}} \}$ as a simple function of $h\kappa/r_0$ and obtained the following relation

$$(\eta)_m = (\eta_0 + hj^\infty) - \Delta V_{\text{IR}} - (j^\infty r_0 / \kappa) \{ c_1 (h\kappa/r_0) / (c_2 + h\kappa/r_0) \} \quad [53]$$

where c_1 and c_2 are coefficients which depend on d/r_0 and r_1/r_0 and can be expressed by

$$\begin{aligned} c_1 = 0.402 \exp[-0.709(d/r_0)] \\ + [2.5 - 1.3(r_1/r_0)] \exp[-2.8(d/r_0)] \end{aligned} \quad [54]$$

and

$$c_2 = -0.963 + 2.93(d/r_0)^{0.278} \quad [55]$$

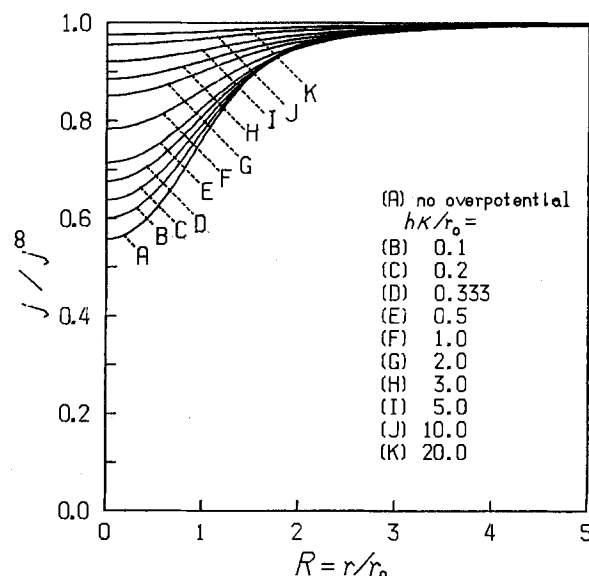


Fig. 13. Dependence of relative current density distribution around the capillary tip upon the parameter $h\kappa/r_0$ for the electrode geometry of $r_1/r_0 = 0.75$ and $d/r_0 = 1.0$. Curve A is identical with curve D in Fig. 5.

respectively. Equations [53]-[55] are valid for $d/r_0 \geq 0.5$ and $0.5 \leq r_i/r_0 < 1.0$ within the relative error of 2%. Although the error involved in Eq. [53]-[55] becomes larger for values of d/r_0 less than 0.5 and these equations cannot be used, it is not recommended that one place the tip of the Luggin-Haber capillary closer than $0.5r_0$ from the electrode surface as will be seen from the discussion below. Figure 15 shows the plots of $(\kappa/r_0 j^\infty) \{(\eta)_m - (\eta_0 + hj^\infty) + \Delta V_{IR}\}$, which is equivalent to $-c_1(h\kappa/r_0)/(c_2 + h\kappa/r_0)$, against d/r_0 for three values of $h\kappa/r_0$. One can see from Eq. [54] that the values of c_1 are small when $d/r_0 \geq 2$, and also see from Fig. 15 that the values of $(\kappa/r_0 j^\infty) \{(\eta)_m - (\eta_0 + hj^\infty) + \Delta V_{IR}\}$ are very small irrespective of the value of $h\kappa/r_0$ when $d/r_0 \geq 2$. It has also been found that values of $(\kappa/r_0 j^\infty) \{(\eta)_m - (\eta_0 + hj^\infty) + \Delta V_{IR}\}$ scarcely depend on r_i/r_0 . These facts indicate that the last term on the right-hand side of Eq. [53] can be neglected and the following approximate equation

$$(\eta)_m = (\eta_0 + hj^\infty) - \Delta V_{IR} \quad [56]$$

is valid under the condition $d \geq 2r_0$. This means that as far as the distance between the capillary tip and the electrode surface is larger than the outer diameter of the capillary tip, the measured overpotential can be regarded as a sum of the true overpotential $(\eta_0 + hj^\infty)$ and the potential

drop due to the solution resistance, $(-\Delta V_{IR})$. In other words, if the capillary tip is located at a distance from the electrode surface closer than its diameter, the effect of the shielding of the electrode surface by the capillary can no more be neglected. One can see from Fig. 15 that the measured overpotential is always equal to or larger than the sum of the true overpotential and the IR-potential drop.

For the electrode geometry where the capillary is placed through the back of cathode, Fig. 16 shows plots similar to those in Fig. 14 and 15. It has been established that the following approximate equation holds

$$(\eta)_m = (\eta_0 + hj^\infty) - \Delta V_{IR} + (j^\infty r_0 / \kappa) [c_3 (h\kappa/r_0)^p / (c_4 + (h\kappa/r_0)^p)] \quad [57]$$

where c_3 , c_4 , and p are coefficients which are functions of r_i/r_0 . We obtained simple approximate equations for these coefficients

$$c_3 = 0.338 + 0.0691(r_i/r_0)^4 + 0.0377(r_i/r_0)^8 \quad [58]$$

$$c_4 = 1.138 + 0.229(r_i/r_0)^4 - 0.633(r_i/r_0)^8 \quad [59]$$

$$p = 0.719 - 0.0281(r_i/r_0) \quad [60]$$

Using Eq. [57]-[60], $(\eta)_m$ can be calculated within 3% relative error. Although there occurs no shielding of the electrode surface in this case, one can note that the absolute value of the measured potential is always larger than the sum of the values of true overpotential and the IR-potential drop. It can be said that although this electrode geometry looks sophisticated, it is not recommended for practical use in view of the above fact and the difficulty in fabrication except for the case where the disturbance of electrolyte solution flow due to the presence of the Luggin-Haber capillary should be avoided.

Conclusion

Potential and current distributions around the Luggin-Haber capillary placed perpendicularly to the plane electrode surface have been obtained by solving Laplace equation with a finite element method. Approximate equations with reasonable accuracy have been presented for the IR-potential drop as functions of the outer and inner radii of the capillary tip, distance between the capillary tip and the working electrode, conductivity of the solution, and average current density. Approximate equations which relate the measured overpotential to the true overpotential, the IR-potential drop, and the relevant parameters have also been presented. In the presence of overpotential, it has been confirmed that the measured potential can be regarded as a sum of the true overpoten-

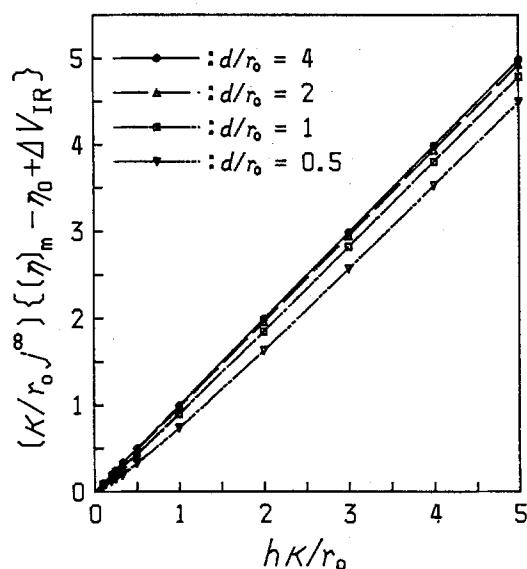


Fig. 14. Variation of the difference between the measured overpotential and IR-potential drop with the value of the parameter $h\kappa/r_0$ for the electrode geometries of $r_i/r_0 = 0.75$ and varied values of d/r_0 .

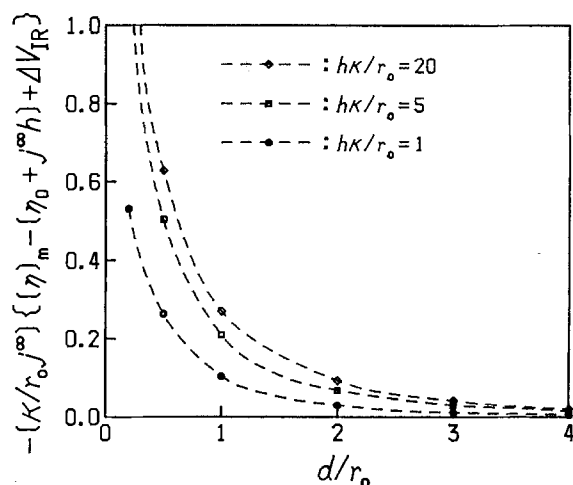


Fig. 15. Dependence of the difference between the measured overpotential and the sum of true overpotential and IR-potential drop on the position of the capillary tip.

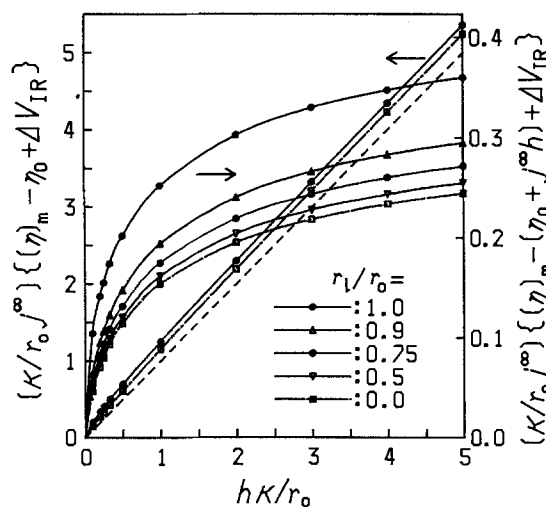


Fig. 16. Plots of the difference between the measured overpotential and IR-potential drop, and the difference between the measured overpotential and the sum of true overpotential and IR-potential drop against the parameter $h\kappa/r_0$ for the electrode geometry where the Luggin capillary is placed through the back of the electrode.

tial and the IR-potential drop provided that the tip of the capillary is placed not closer from the electrode surface than the distance equal to the diameter of the capillary tip.

Manuscript submitted Dec. 26, 1984; revised manuscript received ca. March 28, 1985.

Tokyo Institute of Technology assisted in meeting the publication costs of this article.

LIST OF SYMBOLS

c_1, c_2, c_3, c_4	coefficients in Eq. [53] and [57]
d	distance between the capillary tip and the cathode (m)
E	electrode potential (V)
$\{f^{(e)}\}$	element flux vector
$\{F\}$	global flux vector
h	constant (see Eq. [18]) ($\Omega\text{-m}^2$)
j	current density ($\text{A}\cdot\text{m}^{-2}$)
j^∞	current density at the place sufficiently distant from the capillary ($\text{A}\cdot\text{m}^{-2}$)
$[k^{(e)}]$	element coefficient matrix
$[K]$	global coefficient matrix
L	characteristic length (m)
n	normal boundary coordinate (m)
n^*	transformed normal boundary coordinate
$[N^{(e)}]$	row matrix of interpolation functions
p	coefficient in Eq. [57]
r	radial coordinate (m)
r_i	inner radius of the Luggin-Haber capillary (m)
r_o	outer radius of the Luggin-Haber capillary (m)
R	transformed radial coordinate
V	cell voltage (V)
ΔV_{IR}	IR-potential drop (V)
W_a	Wagner number
z	axial coordinate (m)
Z	transformed axial coordinate

Greek characters

Γ	boundary or surface of the region analyzed
η	overpotential (V)
η_0	constant (see Eq. [18]) (V)
θ	angular coordinate
κ	conductivity of solution ($\text{S}\cdot\text{m}^{-1}$)
ϕ	inner potential of solution (V)
Φ	transformed potential function
ψ	inner potential of electrode (V)
Ω	region to be analyzed

Superscripts

a	anode
c	cathode
(e)	element
i	insulator
ref	reference electrode
T	transpose of matrix

Subscripts

eq	at equilibrium
$\eta=0$	without overpotential
m	measured or measurable

REFERENCES

1. R. Piontelli, G. Bianchi, and R. Aletti, *Z. Elektrochem.*, **56**, 86 (1952).
2. R. Piontelli, G. Bianchi, U. Bertocci, C. Guerci, and B. Rivolta, *ibid.*, **58**, 54 (1954).
3. S. Barnartt, *This Journal*, **99**, 549 (1952).
4. S. Barnartt, *ibid.*, **108**, 102 (1961).
5. C. Kasper, *Trans. Electrochem. Soc.*, **77**, 353 (1940); *ibid.*, **78**, 131 (1940); *ibid.*, **82**, 153 (1942).
6. C. Wagner, *Plating*, **48**, 997 (1961).
7. S. Ishizaka and H. Matsuda, *Denki Kagaku*, **19**, 89 (1951); *ibid.*, **20**, 38 (1952); *ibid.*, **20**, 84 (1952); *ibid.*, **22**, 420 (1954).
8. F. Hine, S. Yoshizawa, and S. Okada, *This Journal*, **103**, 186 (1959).
9. J. Newman, *ibid.*, **113**, 501, 1235 (1966).
10. J. Newman, in "Electroanalytical Chemistry," Vol. 6, A. J. Bard, Editor, p. 187, Marcel Dekker, New York (1973).
11. J. Newman, "Electrochemical Systems," Chap. 18, Prentice-Hall, Englewood Cliffs, NJ (1973).
12. N. Ibl, in "Comprehensive Treatise of Electrochemistry," Vol. 6, E. Yeager, J. O'M. Bockris, B. E. Conway, and S. Sarangapani, Editors, Chap. 4, Plenum Press, New York (1983).
13. J. A. Klingert, S. Lynn, and C. W. Tobias, *Electrochim. Acta*, **9**, 297 (1964).
14. P. Pierini and J. Newman, *This Journal*, **126**, 1348 (1979).
15. P. Fedkiw, *ibid.*, **127**, 1304 (1980).
16. R. Caban and T. W. Chapman, *ibid.*, **123**, 1036 (1976).
17. S. H. Glarum, *ibid.*, **124**, 518 (1977).
18. O. C. Zienkiewicz, "The Finite Element Method," McGraw-Hill (UK), London (1977).
19. L. J. Segerlind, "Applied Finite Element Analysis," John Wiley and Sons, New York (1976).
20. T. J. Chung, "Finite Element Analysis in Fluid Dynamics," McGraw-Hill, New York (1978).
21. Y. Fujitani, T. Kihara, K. Honda, and T. Kawai, *Seisan Kenkyu*, **24**, 248 (1972).
22. K. Honda, T. Kihara, T. Watanabe, T. Kawai, Y. Fujitani, and S. Shiina, *ibid.*, **24**, 410 (1972).
23. T. Kawai, Y. Fujitani, K. Honda, T. Kihara, and T. Watanabe, *ibid.*, **25**, 113 (1973).
24. R. Alkire, T. Bergh, and R. L. Sani, *This Journal*, **125**, 1981 (1978).
25. R. Sautebin, H. Froidevaux, and D. Landolt, *ibid.*, **127**, 1096 (1980).
26. Y. Nishiki, K. Aoki, K. Tokuda, and H. Matsuda, *J. Appl. Electrochem.*, **14**, 653 (1984).
27. K. Aoki, K. Tokuda, H. Matsuda, and N. Oyama, *J. Electroanal. Chem.*, **176**, 139 (1984).
28. T. Gueshi, K. Tokuda, and H. Matsuda, *Denki Kagaku*, **51**, 107 (1983).
29. C. Wagner, *This Journal*, **98**, 116 (1951).
30. H. D. Cohen, *Int. J. Num. Meth. Eng.*, **15**, 470 (1980).
31. R. J. Collins, *ibid.*, **6**, 345 (1973).
32. R. D. Henshell and K. G. Show, *ibid.*, **11**, 180 (1977).

Electrochemistry of Molten Calcium Nitrate Tetrahydrate

Keith E. Johnson* and F. Wayne Yerhoff

Department of Chemistry, University of Regina, Regina, Saskatchewan, Canada S4S 0A2

ABSTRACT

The electrochemical properties of calcium nitrate tetrahydrate were studied by voltammetry, coulometry, and chemical analysis. The electrolyte anode reaction was oxidation of water to oxygen on either gold or platinum. The major reaction at a gold cathode was reduction of nitrate to nitrite and a solid calcium hydroxide electrode film. Small amounts of oxygen and more than the theoretically predicted quantity of nitrite were detected, suggesting a secondary chemical reaction. The reduction reaction at platinum gave 50-75% of the theoretical yield of nitrite. The voltammetric behavior of OH^- , NO_2^- , and HNO_3 in this system were studied.

Molten calcium nitrate tetrahydrate and similar molten hydrates are of considerable interest as solvents with properties intermediate between those of aqueous solutions and ionic melts. Conductance measurements (1), additivity of molar volumes (2), PMR studies (3), entropies of solution (4), diffusion coefficients [(5, 6) but see Ref. (7)], acoustic velocity measurements (8), and x-ray diffraction measurements (9) all indicate that the water molecules in calcium nitrate tetrahydrate melts are strongly coordinated to the calcium ion. The result is a liquid with the properties of an ionic melt composed of bulky $(\text{Ca}(\text{H}_2\text{O})_4)^{+2}$ cations and nitrate anions. The low melting point of this compound (42.7°C), together with a metastable supercooled phase extending to room temperature, thus allows the direct comparison of an "ionic" solvent with dilute aqueous solutions.

Calcium nitrate tetrahydrate has been used as a supporting electrolyte in the electrochemical investigation of a number of cations (5-7, 10-15). Courgnaud and Tremillion (16) have investigated the electrochemistry of the molten hydrate itself at gold and platinum electrodes using bulk electrolysis followed by chemical analysis and single sweep voltammetry. The anode reaction was found to give oxygen and protons, as expected for water electrolysis, but at a potential almost 0.7V more negative for Au than for Pt. The authors concluded, on the basis of their finding no detectable concentration of nitrite ion after electrolysis with a platinum cathode, that the electrolytic reduction of this melt also involved only water. Like the anode reaction, reduction appeared to occur at a more negative potential (by 0.3V) at gold than at platinum.

These solvent electrolysis properties, as described, appeared useful for a coal electrogasification study we had undertaken, since only water was electrolyzed and some control over initial decomposition potentials appeared to be available simply by changing electrode materials. Our preliminary results, however, did not correspond to those reported, and we therefore reexamined in detail the electrochemical properties of calcium nitrate tetrahydrate.

Experimental

Calcium nitrate tetrahydrate (Fisher certified ACS or BDH analytical reagent) was used without further purification. Dehydration *in vacuo* at room temperature, then at 150°C, gave a hydration number of 4.00 ± 0.01 . Certified ACS sodium nitrite (Fisher), calcium hydroxide (Fisher), and nitric acid (CIL) were also used without purification. Electrodes were of 99.999% Pt or Au (Johnson, Matthey, and Mallory) sealed in soft glass. Microelectrodes were ground to a flat surface with a Bethlehem 7a7 CW12 glass grinding wheel; electrode areas, measured by optical micrometry, were 0.018 mm² for Pt and 0.066 mm² for Au.

Cyclic voltammograms were obtained using a Metrohm E626 Polarecord and E612 VA Scanner plus a Houston Instruments RE0074 X-Y recorder. All electrochemical measurements were made relative to a 0.05M Ag^+/Ag in $\text{Ca}(\text{NO}_3)_2 \cdot 4\text{H}_2\text{O}$ reference electrode consisting of a 0.8 mm

diam silver wire dipped in the silver ion solution contained in a narrow glass tube ending in a porous ceramic plug. This system has been shown to be well behaved in calcium nitrate tetrahydrate melts (4). The microelectrode, reference electrode, and a spiral Pt wire counterelectrode were mounted in a rubber stopper which was fitted tightly into the cell containing the solution in $\text{Ca}(\text{NO}_3)_2 \cdot 4\text{H}_2\text{O}$ to prevent loss of water. Voltammograms of electrolytes in this solvent were made first upon a weighed amount of the most concentrated solution. Weighed amounts of pure solvent were then added with thorough mixing to give the lower concentrations measured. Solutions were maintained at $70.0 \pm 0.1^\circ\text{C}$ using a Polyscience Polytemp bath thermostat. No inert gasses were passed through the solution once it had been confirmed that oxygen was too insoluble to be detected in this system (6, 16).

Bulk electrolysis was performed using a Fisher controlled potential electroanalyzer; current was measured using a Weston Instruments milliammeter, and total charge calculated by graphical analysis of the current-time curve. The cell was equipped with a cathode compartment, consisting of a 2.5 cm diam glass tube ending in a fine sintered glass frit, which was suspended from the rubber cell cover so as to be easily removed. After electrolysis, the cathode compartment plus the Au (16 cm²) or Pt (19 cm²) plate cathode was removed, rinsed off with water, dried, and weighed. The catholyte was thoroughly mixed, and then weighed samples taken for analysis. Finally, the cathode cell components were washed, dried, and weighed to give the total weight of catholyte (25-30g). After the longer electrolyses, nitrite was also detectable in the anolyte, presumably because of leakage through the fritted disk; this quantity was included in the nitrite total.

A weighed sample of electrolyzed material in aqueous solution was tested for nitrite by addition of sulfanilamide and N(1-naphthyl)-ethylenediamine dihydrochloride (Marshall's reagent), followed by comparison of the 550 nm absorption of the diazo compound thus formed with external standards. The total concentration of reducing agents formed by electrolysis was measured by adding a weighed sample of electrolyzed melt to water or cold saturated H_3BO_3 solution, adding a measured quantity of standard Ce(IV) solution sufficient to oxidize all reducing agents, and backtitrating with standard Fe(II) using "ferroin" indicator.

Gas analysis was run in cells with a sealed anode or cathode compartment connected to a "Tedlar" gas sampling bag and arranged to allow flushing of the system with purified nitrogen. Two plates were arranged to allow complete emptying of the gas bag by squeezing. The system was flushed with nitrogen, and the gas bag was emptied, after which the electrolysis was run. After electrolysis, gas was transferred from the sampling bag to a gas measuring apparatus to give the total quantity of gas produced. Gas analysis was performed using a Carle AGC-311 gas chromatograph, with a thermistor detector calibrated to allow quantitative determination of the gas composition.

* Electrochemical Society Active Member.

Results

The products of oxidation of pure calcium nitrate tetrahydrate (90°-95°C, +1.3V vs. Ag/Ag⁺ reference) at a platinum anode were oxygen and nitric acid, as reported (16). The nitric acid concentration in the gases above the electrolyte was substantial, and resulted in chemical attack on the gas sampling bag used in the apparatus, as well as any rubber or tygon seals or connectors used. The measured quantity of oxygen produced in such cases was somewhat variable. In a glass apparatus plus sampling bag with relatively short contact times or in runs where the theoretical amount of Ca(OH)₂ had been added to neutralize HNO₃, oxygen production was 100 ± 5% of theoretical.

The major product of reduction at a gold cathode (90°-95°C, -1.2 to -1.3V) was nitrite, detected both by specific analysis for nitrite and by quantitative analysis for reducing agents (methods agreed within 1%). Figure 1 shows the total amount of NO₂⁻ as a percentage of the theoretical yield relative to the total number of coulombs passed. The amount of nitrite detected in excess of 100% (8% at 68C) was well above the total estimated error. The only significant gaseous cathode product was a small amount of oxygen observed after extensive electrolysis (100-350C), amounting to 5-10% of the theoretical nitrite value. After the most extensive electrolysis, traces of hydrogen and nitrous oxide were also detected by GC.

The major product of reduction of calcium nitrate tetrahydrate at a platinum cathode (90°-95°C, -1.2 to -1.3V) was again nitrite ion, although in considerably lower yield. Figure 1 shows nitrite produced at a Pt electrode, cleaned in concentrated nitric acid before each run, as a function of total coulombs passed. Electrodes not cleaned in a systematic manner before use gave less regular nitrite/coulomb relationships. A white, water-insoluble film was again formed on the electrode. Gas bubble formation on the electrode was sometimes observed to a slight extent. No measurable volume of gaseous products could be detected. Electrolysis under a propane atmosphere showed no significant production of nitrogen. The possibility that water was being reduced at the cath-

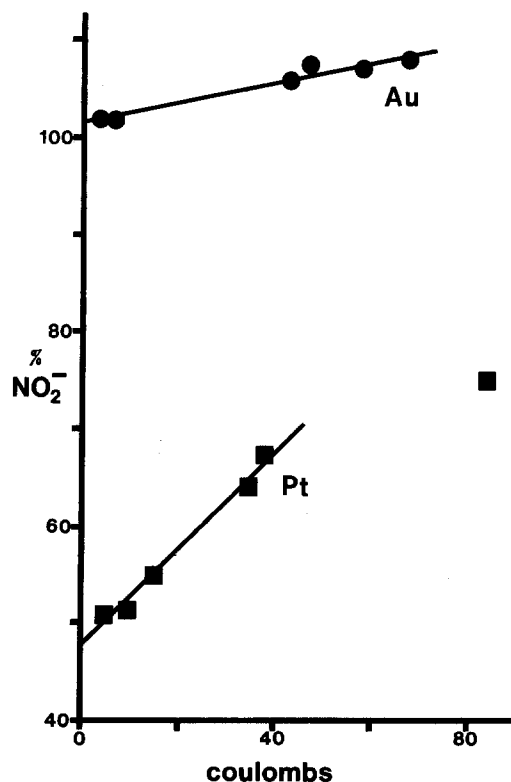


Fig. 1. Total amount of nitrite produced as a percentage of the theoretical yield by electrolysis of calcium nitrate tetrahydrate melt at 90°-95°C using a platinum (19 cm²) or a gold (16 cm²) plate cathode.

ode to hydrogen, which then reacted chemically with nitrate or nitrite, was tested: no sign of reaction between hydrogen gas and calcium nitrate tetrahydrate with or without added nitrite ion could be detected after contact with stirring at 95°C for 3 days. The possibility of further reduction of nitrite ion at the electrode was also considered: no significant quantities of the gaseous reduction products NO, N₂O, or N₂ were detected by GC, nor was any trace of the characteristic color of NO₂ or the characteristic smell of NH₃ observed at any time. In two cases the catholyte was analyzed both for reducing substances [by Ce(IV)/Fe(II) redox titration] and spectrophotometrically for nitrite. The reducing capacity of the catholyte was found to be equivalent to the quantity of nitrite present, indicating that no other soluble oxidizable products of NO₃⁻ reduction had been formed.

Calcium nitrate tetrahydrate electrochemistry was also examined by means of linear sweep and cyclic voltammetry. Figure 2 shows full range (+2.0 to -2.5V) and partial range (+1.4 to -1.2V) cyclic voltammograms obtained for this electrolyte using both gold and platinum electrodes relative to 0.05M Ag⁺/Ag in calcium nitrate tetrahydrate. Table I summarizes the peak current potentials observed, along with the reactions represented and the symbols identifying these peaks in Fig. 2. The electrolyte oxidation potentials were found to be similar (1.1-1.3V) for both Au and Pt, in contrast to the previously reported (16) difference of 0.7V. The major cathodic process was attributed, from the chemical evidence, to reduction of nitrate to nitrite with concomitant formation of an insulating film on the electrode. The apparent peak A in Fig. 2, which occurred consistently at -1.5V with both Au and Pt electrodes at 50 mV/s, was an artifact of film formation. If the reverse sweep potential was not taken above 0.7-0.8V, all current flow ceased. Increasing the sweep rate resulted in large cathodic shifts in the "peak" position as well as large increases in the maximum current.

The electrode film produced during reduction of nitrate was removed by the oxidative process giving rise to

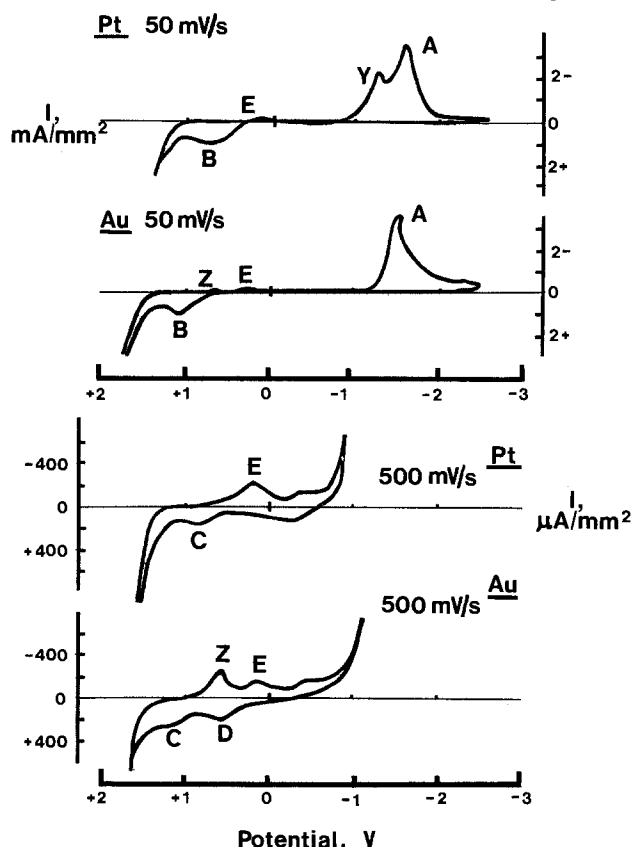


Fig. 2. Cyclic voltammograms of calcium nitrate tetrahydrate at 70.0°C using a platinum or a gold microelectrode. a: +2.0 to -2.5V b: +1.5 to -1.1V.

Table I. Cyclic voltammetry peak potential values vs. Ag^+/Ag for $\text{Ca}(\text{NO}_3)_2 \cdot 4\text{H}_2\text{O}$ melt

Electrode reaction	Peak potential (V)		$[E_p - E_p/2]$ (V)		Fig. 2 Symbol
	Au	Pt	Au	Pt	
Anodic sweep					
NO_2^- oxidation	+0.4	+0.5	0.15	0.15	Peak D
OH^- oxidation	+1.0	+0.9	0.10	0.14	Peak C
$\text{Ca}(\text{OH})_2$ solid film	$\approx +0.9$	$\approx +0.8$	≈ 0.5	≈ 0.3	Peak B
H_2O oxidation	$> +1.2$	$> +1.2$	—	—	—
Cathodic sweep					
Oxide film reduction	+0.6	—	0.03	—	Peak Z
HNO_3 reduction	+0.1	+0.1	0.07	0.08	Peak E
Unidentified reduction	—	-1.2	—	0.1	Peak X
NO_3^- reduction	"-1.5"	"-1.5"	—	—	Peak A

anodic peak B of Fig. 2 in the area of 0.8-1.3V. This peak was not observed where the cathodic sweep did not go beyond -1.0V. The cyclic voltammogram of calcium hydroxide solution in calcium nitrate tetrahydrate between +0.5 and +1.3V showed a single broad anodic peak with no cathodic peak, rapidly decreasing on subsequent cycles. Peak voltages were similar for Au and Pt electrodes (Table II). The single sweep peak current varied linearly with concentration for both electrodes up to approximately 0.02*m*, giving lines with similar slopes. A linear relationship between peak current and the square root of scan rate was found for scan rates from 10 to 300 mV/s for both metals, with a similar slope and small negative current intercept for each. A corresponding peak (peak C, Fig. 2) is observed for pure solvent only in the limited range sweeps, where film formation is not extensive enough to block all current flow.

Voltammetry cycles between +1.3 and -1.3V in the pure melt gave rise to an additional anodic peak at approximately +0.5V on a gold electrode (peak D, Fig. 2). This was identified as the oxidation peak of nitrite ion by studies of dilute solutions of sodium nitrite. Cyclic voltammograms of such solutions showed a broad peak near +0.5V (Table II) with both Au and Pt electrodes; peak currents decreased rapidly on subsequent cycles. Both metals also gave a small shoulder about 0.2V less anodic, which disappeared on subsequent cycles. The gold electrode gave a small additional anodic peak near +0.75V. Single-sweep voltammetry anodic peak currents were shown to vary linearly with concentration for both metals (similar slopes, intercepts near 0) up to about 0.015*m* NaNO_2 . The peak current *vs.* (sweep rate)^{1/2} relationship was linear from 10 to 300 mV/s, with a small positive intercept and a slope slightly greater for Au than Pt. This relationship was also roughly linear for the small +0.75V peak on gold.

Cyclic voltammetry of NaNO_2 solutions with either Au or Pt gave, on the cathodic sweep, a broad cathodic peak at 0.1-0.3V, also seen in the voltammograms of pure calcium nitrate tetrahydrate (peak E, Fig. 2), and identified as characteristic of nitric acid (below). An additional sharp cathodic peak was also seen with a gold electrode (peak Z, Fig. 2), and was investigated further. Cyclic sweeps in 0.01*m* NaNO_2 at 100 mV/s were run from -0.2V to positive potentials beginning at +0.6V and incremented by +0.1V. The sharp cathodic peak Z was just detectable (at +0.66V) on the return from a sweep to +0.8V. The peak grew and shifted to +0.56V over the next three cycles (to +1.1V), after which it stayed approximately constant. A similar experiment run with pure calcium nitrate tetrahydrate, however, showed no trace of this peak until anodic sweeps to 1.3-1.4V were run, *i.e.*, until some nitric acid had been generated by solvent electrolysis. In addition, cycles run as far as +1.3V in circumstances where an oxidizable species (NO_2^- , OH^- , film) was present but nitric acid could not persist [*e.g.*, sat. $\text{Ca}(\text{OH})_2$] did not produce a +0.56V peak on the cathodic return, but rather led to a new cathodic peak at -0.2V. This indicated that the formation of the electroactive species responsible for the +0.56V peak required both a potential greater than +0.7V and the presence of nitric acid.

The electrochemistry of nitric acid in calcium nitrate tetrahydrate gave considerably different voltammograms with gold and platinum microelectrodes. With gold, a sweep from +1.0 to -0.5V gave two cathodic peaks (Fig. 3, Table II), one at about +0.2V and a sharp peak at about +0.6V. The first, at +0.2V, gave a peak current varying linearly with added HNO_3 concentrations up to 0.025*m* at a sweep rate of 50 mV/s (Fig. 4). The second, corresponding to peak Z in Fig. 2, showed an approximately constant current at all HNO_3 concentrations. The peak current *vs.* (sweep rate)^{1/2} relationship for the +0.2V peak due to 0.010*m* HNO_3 was composed of two linear portions with a distinct break between 100 and 150 mV/s, also observable in the peak potential values (Fig. 5). The anodic sweep of the cycle was consistent with nitrite oxidation.

The shape of the voltammetric curve due to nitric acid on a platinum electrode (Fig. 3) was dependent upon both the nitric acid concentration and the sweep rate. At low concentrations or high sweep rates the cathodic sweep gave a single peak near 0.0 V (Table II). The return anodic sweep gave a broad peak at +0.6V characteristic of nitrite oxidation. At low sweep rates or high concentrations the voltammograms had the complex form shown in Fig. 3. The anodic return sweep, starting from 0 current, produced a strong cathodic current. The relationship observed between cathodic peak currents and HNO_3 concentration at a 50 mV/s sweep rate is shown in Fig. 4; the transition between simple peaks and the type shown in Fig. 3 occurred between 0.005 and 0.010*m*. Figure 5 shows the dependence of cathodic peak currents on (sweep rate)^{1/2} for 0.010*m* HNO_3 . Voltammograms of the type shown in Fig. 3 occurred at sweep rates of 50 mV/s or less, simple voltammograms were observed at 200 mV/s or greater, and transitional shapes were observed at intermediate sweep rates. This transition was a function of both sweep rate and concentration.

Aside from nitric acid reduction, the most marked difference between calcium nitrate tetrahydrate voltammograms using Au and Pt microelectrodes was the appearance of a large cathodic peak at -1.25V (peak Y, Fig. 2) only with platinum. This peak, which partly overlapped the nitrate reduction "peak," was presumed to represent the process which did not lead to nitrite production during coulometric analysis using a Pt cathode at -1.2 to 1.3V. Cyclic voltammograms were run from various positive potentials to -1.35V. Those run from +0.7V or less deteriorated rapidly to 0 current flow. However, cycles from +1.25 to -1.35V gave a stable system which showed the -1.25V peak on the cathodic sweep. On the anodic sweep, a cathodic current peak appeared at approximately the same potential (Fig. 6). The only other current observed was an anodic peak at +1.0V, as expected for hydroxide film removal. Table III shows the results obtained from cyclic voltammetry at various sweep rates; as rate increased the cathodic peak current stayed almost constant, while the anodic sweep cathodic current increased until it was the greater of the two. Peak potentials were almost constant throughout. In order to determine if the reaction producing peak Y was responsible for film formation on Pt, 500 mV/s cyclic voltammograms were run from 0.0 V to negative potentials starting at -1.20V

Table II. Peak potential values of electroactive solutes in $\text{Ca}(\text{NO}_3)_2 \cdot 4\text{H}_2\text{O}$, 70°C

Solute	I variable concentration 50 mV/s				II variable scan rate, 0.010M			
	0.005M		0.025M		25 mV/s		300 mV/s	
	Au	Pt	Au	Pt	Au	Pt	Au	Pt
$\text{Ca}(\text{OH})_2$	+1.03	+0.84	+0.99	+0.88	+1.01	+0.83	+1.08	+0.86
NaNO_2	+0.42	+0.55	+0.44	+0.47	+0.44	+0.45	+0.45	+0.55
HNO_3	+0.17	+0.03	+0.31	+0.28 ^a	+0.23	+0.23 ^a	-0.03	+0.05

^a Leading peak.

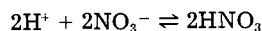
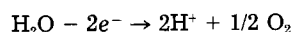
and incremented by -0.05V. Runs to -1.20 and -1.25V showed no significant change in the maximum (edge) current after ten cycles. Runs to -1.30, -1.35, and -1.40V showed a drop in maximum current of 10, 20, and 40%, respectively, after ten cycles. Thus, film formation appeared much more closely related to the nitrate reduction "peak" A than to peak Y.

Full +2.0 to -2.5V cycles at 50 mV/s with a gold electrode and added water (1-10M) showed no additional peaks. A general increase in peak current beyond -1.5V was observed. The platinum electrode behaved similarly, but the unique peak Y appeared to decrease slightly in size and shift to a slightly more anodic value. Peak current values for Y obtained from 50 mV/s cyclic voltammetry between +1.4 and -1.4V are shown in Table IV as a function of added water concentration. The cathodic peak potential became slightly more positive with increasing water content, while the anodic sweep cathodic current increased. These peak current changes may be related to electrode film dissolution by water.

Attempts to detect a number of other species in calcium nitrate tetrahydrate solution by voltammetry were not successful. Bubbling of oxygen, hydrogen, or nitrous oxide for up to 1/2 h gave no detectable peaks in this solvent or in solvent saturated with $\text{Ca}(\text{OH})_2$. The lack of reactivity of oxygen had been observed previously (6, 16) and attributed to the low solubility of oxygen in the melt.

Discussion

The solvent oxidation reaction in calcium nitrate tetrahydrate appears to be a straightforward oxidation of water



We have not been able to reproduce the 0.7V difference in oxidation potential previously observed (16) between

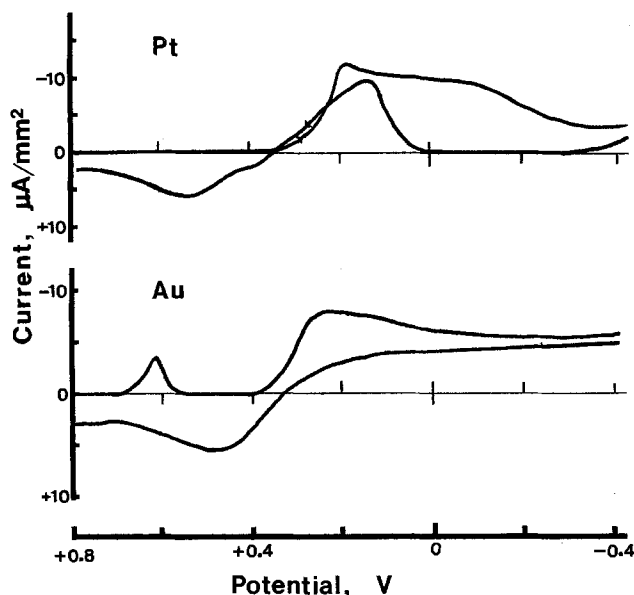
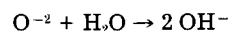
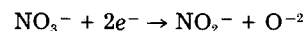


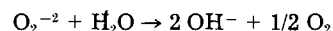
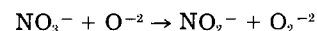
Fig. 3. Cyclic voltammograms of 0.01M nitric acid in calcium nitrate tetrahydrate at 70.0°C using a platinum or a gold microelectrode.

gold and platinum electrodes in this electrolyte. Both voltammetry and the potentials observed during bulk electrolysis indicate similar oxidation potentials at both electrode materials.

The major solvent reaction at a gold cathode is clearly reduction of nitrate to nitrite ion



The excess of nitrite observed coupled with the observation of oxygen as a cathode product suggests the results observed in the reduction of alkali nitrate melts (17), where oxide dianions produced in the electrochemical reduction of nitrate react chemically with nitrate ion to give additional nitrite and peroxide ions



The existence of oxide ions in a hydrate melt appears unlikely, but in this system an insoluble basic film, as shown by cyclic voltammetry, forms rapidly on the cathode. Similar films occur at the cathode during the reduction of $\text{Ca}(\text{NO}_3)_2/\text{KNO}_3$ melts (18). Local depletion of water could occur near the electrode surface, allowing oxide ions to exist long enough to react with nitrate. The concentration of free water in this system is low, and the rate of diffusion of bulky $(\text{Ca}(\text{H}_2\text{O})_4)^{2+}$ into the film should be

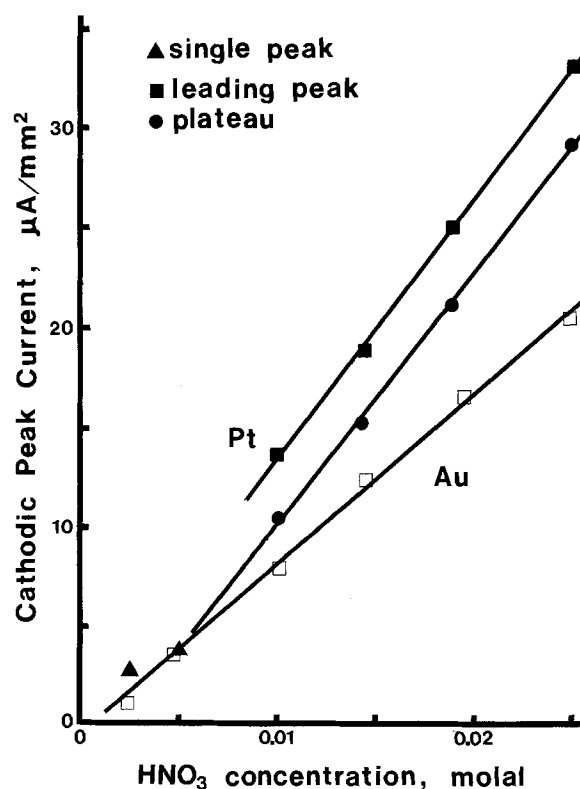


Fig. 4. Cyclic voltammetric cathodic peak current as a function of concentration of nitric acid in calcium nitrate tetrahydrate at 70.0°C and 50 mV/s using a platinum or a gold microelectrode.

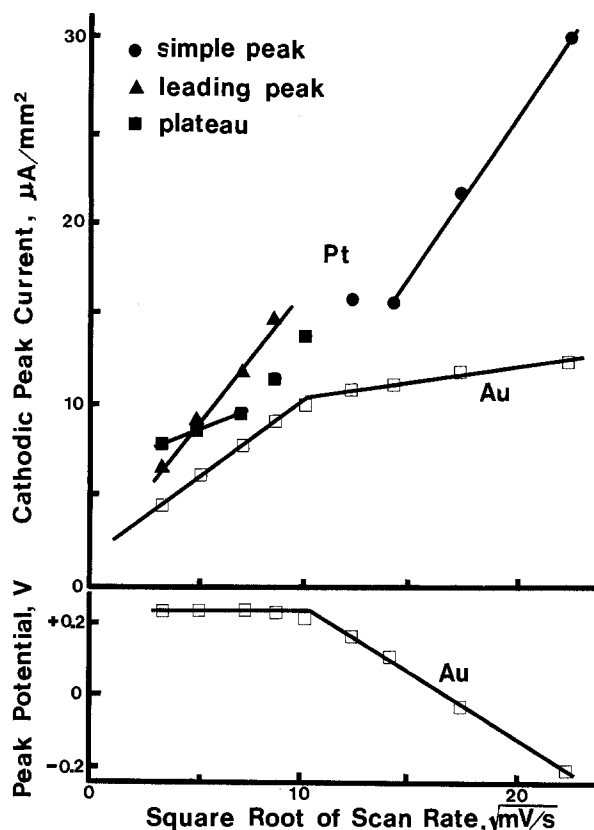


Fig. 5. Cyclic voltammetric cathodic peak current and peak potential as a function of the square root of scan rate for 0.01M nitric acid in calcium nitrate tetrahydrate at 70.0°C using a platinum or a gold microelectrode.

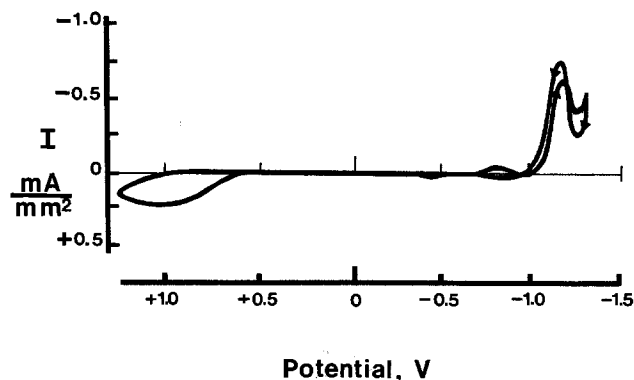


Fig. 6. Cyclic voltammogram of calcium nitrate tetrahydrate at 70.0°C and 50 mV/s using a platinum electrode.

relatively slow. Peroxide ions produced by the oxide/nitrate reaction would diffuse out and produce oxygen after reaction with water. This evidence for the production of oxide dianion suggests that water is not involved in the initial electrochemical reduction reaction on gold.

The previously reported 0.3V difference in solvent reduction potential between Au and Pt appears to be due to the identification of the slope of peak Y (Fig. 2) as due to solvent reduction; a peak in this position was in fact observed in voltammetry of the 2.6 H₂O hydrate melt (16). The fact that the reaction represented by peak Y does not give nitrite as a reduction product explains why the authors concluded that water reduction was the major solvent reaction in this system.

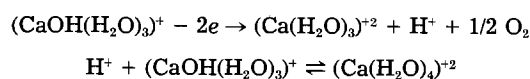
The reaction represented by peak Y appears, both from the chemical evidence and from the absence of nitrite oxidation peaks in the anodic sweep (Fig. 2 and 6), to produce a product other than nitrite. This peak may represent reduction of water to hydrogen, but if so then all the

hydrogen must be adsorbed on the electrode, since none is detected by GC and hydrogen has been shown to be neither reactive nor soluble in the melt. A second possibility is reduction of a previously formed platinum oxide film. The possibility that peak Y represents a further reduction of nitrite cannot be excluded, although no plausible products of such a reaction could be detected.

We have observed that a cyclic voltammogram of Ca(NO₃)₂·4H₂O run using a freshly ground Pt microelectrode surface does not show peak Y, although it appears as soon as an electrochemical reaction occurs at the electrode or if the electrode is soaked in concentrated nitric acid. This result supports the "PtO" reduction hypothesis, since concentrated HNO₃ is known to produce such films (23-25). The observed reaction, however, represents a very large quantity of material. If one assumes that the roughly linear increase in bulk nitrite production represents a linear decrease in peak Y material, the percentage NO₂⁻/coulomb data in Fig. 1 can be used to estimate that 0.65 C/cm² are required for complete reduction of this material. The surface area of bright platinum has been estimated to be 1.5-2.5 times the theoretical value by hydrogen charging experiments, which imply that the total charge required to reduce one "monolayer" of "PtO" will be 400-650 μC/cm² (19-21). It has been demonstrated that more than one monolayer may be deposited on a Pt electrode, but, although the exact nature of this oxide/oxygen film was controversial, there was a general belief that it amounted to no more than two to five additional "monolayers," whether deposited by anodization (19-22) or chemically (23-25). This gives an estimated charge required for complete film removal of 1-3 mC/cm², or approximately 300 times less than the estimated charge consumed here. The large charge capacity of the reaction is confirmed by the peak current observed in voltammetry, where the estimated area of peak Y in Fig. 2 represents a value of about 0.7 C/cm².

The reaction represented by peak Y also exhibits unusual behavior during cyclic voltammetry, in that a cathodic peak is observed during the anodic sweep of the cycle (Fig. 6). This type of anomaly has been reported in a few other cases (11-13, 26-28) and attributed to adsorption or other surface phenomena. The observation of an adsorption/desorption phenomenon is more easily associated with the hypothesis that this peak is due to production of adsorbed hydrogen, since a similar result is reported for the neutral molecule N₂O in alkaline aqueous solution (26). There was, however, no detectable effect on the electrochemistry of this system resulting from hydrogen (or N₂O or O₂) being bubbled through the melt. Water did cause both a change in peak current and a small positive shift in peak potential, but this may be attributable to a solvent effect on the electrode film. An important difference in the *I* vs. (scan rate)^{1/2} relationship was also observed: with the N₂O reduction peak, these values were found to be directly proportional, while in this work such a relation was not found. The explanation involving trace organic impurities (28) may be relevant to this system: reagent-grade calcium nitrate tetrahydrate shipped in plastic bottles was used without further purification and may well have contained trace organics.

The overall cyclic voltammogram of calcium nitrate tetrahydrate indicates no reversible electrochemical reactions for any of the solvent oxidation or reduction products. Of the three major products, soluble hydroxide, presumably in the form (CaOH(H₂O)₃)⁺, behaves in the simplest manner on both gold and platinum electrodes



Linear relationships with near-zero intercepts are seen for both metals between peak current values and both the concentration up to 15-20 mM and the square root of scan rate up to 300 mV/s. Peak potentials show a small increase with increasing scan rate. The peak potential on Pt

Table III. Peak current and potential values, $\text{Ca}(\text{NO}_3)_2 \cdot 4\text{H}_2\text{O}$, 70°C, Pt electrode +1.25 to -1.35V, variable scan rate

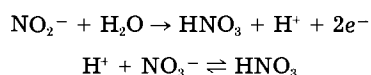
Scan rate (mV/s)	Cathodic scan			Anodic scan		
	V_p (V)	I (mA/mm ²)	V_p (V)	I (mA/mm ²)	V_p (V)	I (mA/mm ²)
50	-1.21	-0.94	-1.17	-0.31	+0.9	0.19
100	-1.22	-1.25	-1.20	-0.86	+1.0	0.31
250	-1.22	-1.31	-1.21	-1.42	+1.0	0.47
500	-1.22	-1.31	-1.20	-1.53	+1.0	0.58
1000	-1.21	-1.31	-1.20	-1.53	+1.0	0.69

Table IV. Peak current and potential values, $\text{H}_2\text{O}/\text{Ca}(\text{NO}_3)_2 \cdot 4\text{H}_2\text{O}$, 70°C, Pt electrode +1.4 to -1.4V, 50 mV/s

$[\text{H}_2\text{O}]$ (<i>m</i>)	Cathodic scan			Anodic scan		
	V_p (V)	I (mA/mm ²)	V_p (V)	I (mA/mm ²)	V_p (V)	I (mA/mm ²)
0	-1.27	-3.05	-1.22	-1.35	+1.12	0.75
1	-1.24	-2.80	-1.21	-1.35	+1.05	0.95
2.5	-1.23	-2.55	-1.20	-1.40	+1.00	0.65
5	-1.20	-2.25	-1.19	-1.45	+0.95	1.05
7.5	-1.19	-2.15	-1.17	-1.70	+0.90	0.85
10	-1.19	-2.35	-1.19	-2.35	+0.86	1.15

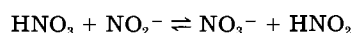
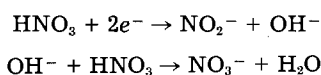
is in reasonable agreement with a single-scan value derived previously (16).

The oxidation of nitrite also appears reasonably straightforward. Variations of peak current with concentration are again linear up to 15-20 *mM*, as is the relationship with (scan rate)^{1/2} up to 300 mV/s. The detection of HNO_3 on the reverse sweep indicates the overall reaction



An additional cathodic peak (peak Z) is seen only with a gold electrode, and appears to be a gold oxide film reduction peak. It is observed only in the presence of nitric acid and when the potential is more positive than +0.7V, but the peak current is independent of nitric acid concentration. The peak is narrow ($E_p - E_p/2 = 30$ mV) and symmetrical; there is no detectable diffusion current due to this peak. A small secondary peak on the nitrite diffusion current is also observed at +0.75V at high nitrite concentrations. In the absence of nitric acid but in the presence of oxidizable substances, this peak is not observed; rather, a peak with similar characteristics appears at -0.2V.

The reduction mechanism of nitric acid appears complex, with substantial differences between gold and platinum electrodes. The reduction peak shape on gold is simple (Fig. 3), and the relationship between peak height and concentration is linear at 50 mV/s to at least 25 *mM* (Fig. 4). The I vs. (scan rate)^{1/2} relationship, however, shows a sharp break to a lower slope at approximately 100 mV/s (Fig. 5). Changes in slope of this kind are characteristic of a change from reversible (fast electrode kinetics) to irreversible (slow electrode kinetics) systems, as is the simultaneous change from constant peak potential to decreasing peak potential observed here. In simple cases of this kind, however, there is a substantial, nonlinear, "quasi-reversible" zone not seen here. Additionally, the low slope and high slope linear portions of the relationship both extrapolate to the origin in the simple system (29), whereas in this case the low slope line extrapolates to a large positive current. Behavior of this type implies a more complex reduction mechanism. Switches from high to low slope roughly similar to that observed are predicted in systems where reversible or quasi-reversible electrode kinetics are followed by irreversible chemical reaction. The present system will be still more complex since reduction here will produce two molecules, one of which will be a basic anion which should react irreversibly with an additional molecule of the starting material, HNO_3



The situation at the platinum electrode appears even more complex. Two entirely different peak shapes are observed, depending upon both HNO_3 concentration and scan rate. The low sweep rate/high concentration form (Fig. 3) features, on the cathodic sweep, a leading peak which trails into a level plateau region terminating in a drop to near zero current over only 150 mV. This is accompanied on the reverse anodic sweep by a cathodic current peak, also of complex shape. Other instances of reverse current peaks have already been described with reference to peak Y. In this case, the observation that continuation of the sweep beyond -0.6V gives rise to a new peak with concomitant loss of the return cathodic current suggests that an adsorbed insulating film is responsible for the current drop at -0.2V in the anodic sweep. Presumably, the anodic sweep cathodic current results from desorption of the film allowing further reduction, while the -0.6V peak represents reductive destruction of the film and renewed reduction of HNO_3 . The correlation of this peak system with HNO_3 concentration suggests that the adsorbed material is a product of HNO_3 reduction (or chemical reaction). The shape of the cathodic peak/plateau is of a type predicted for either a reversible chemical reaction followed by reversible reduction or reversible reduction followed by irreversible catalytic chemical reaction (29). Neither of these simple situations is likely to describe the system fully.

At high sweep rates or low concentrations, the peak shapes simplify to a single cathodic peak on the cathodic sweep with no detectable cathodic peak on the anodic return sweep. The simple cathodic peak has, however, an exceptionally low trailing diffusion current relative to that observed with a gold electrode, while the I_p vs. (scan rate)^{1/2} relationship (Fig. 5), although apparently linear, has a large negative current intercept. Both observations suggest a continuing effect due to adsorbed material. The reason for the change in peak shape with scan rate, which is not of the type predicted for simple systems, is unclear. The disappearance of the cathodic peak on the anodic sweep shows that the role of adsorption has changed; the rate of formation of adsorbable material, the total quantity of adsorbable material, and the rate of desorption at potentials less than -0.2V may all be involved. A complex equilibrium network involving NO_3^- , NO_2^- , HNO_3 , HNO_2 , and H_2O is likely associated with reductions at both Pt and Au electrodes.

Acknowledgment

The authors wish to thank the National Science and Engineering Research Council of Canada for financial support of this work.

Manuscript submitted Jan. 24, 1984; revised manuscript received June 7, 1985. This was paper 794 presented at the

San Francisco, California, Meeting of the Society, May 8-13, 1983.

The University of Regina assisted in meeting the publication costs of this article.

REFERENCES

1. C. A. Angell, *This Journal*, **112**, 1224, (1965); C. A. Angell, *J. Chem. Phys.*, **70**, 3988 (1966).
2. J. Braunstein, L. Orr, and W. MacDonald, *J. Chem. Eng. Data*, **12**, 415 (1967).
3. C. T. Moynihan and A. Fratiello, *J. Am. Chem. Soc.*, **89**, 5546 (1967).
4. B. Burrows and S. Noersjamsi, *J. Phys. Chem.*, **76**, 2759 (1972).
5. J. Braunstein et al., *J. Electroanal. Chem.*, **15**, 337 (1968).
6. C. T. Moynihan and C. A. Angell, *J. Phys. Chem.*, **74**, 736 (1970).
7. D. G. Lovering, *J. Electroanal. Chem.*, **50**, 91 (1974).
8. R. Carpio, M. Mehmed, F. Borsay, C. Petrovic, and E. Yeager, *J. Phys. Chem.*, **86**, 4980 (1982).
9. R. Caminiti, A. Musinu, G. Paschina, G. Piccaluga, and G. Pinna, *Z. Naturforsch.*, **36A**, 831 (1981).
10. D. G. Lovering, *Collect. Czech. Chem. Commun.*, **37**, 3697 (1972); *ibid.*, **38**, 1719 (1973).
11. C. Nanjundiah and R. Narayan, *Electrochim. Acta*, **26**, 203 (1981); *ibid.*, **26**, 367 (1981).
12. R. Narayan and K. T. Valsaraj, *ibid.*, **27**, 153 (1982).
13. R. Narayan and C. Nanjundiah, *J. Electroanal. Chem.*, **136**, 159 (1982).
14. N. P. Bansal and J. A. Plambeck, *This Journal*, **124**, 1036 (1977).
15. N. P. Bansal and J. A. Plambeck, *Electrochim. Acta.*, **23**, 1053 (1978).
16. R. P. Courgnaud and B. Tremillion, *Bull. Soc. Chim. Fr.*, 758 (1965).
17. P. G. Zamboni, *J. Electroanal. Chem.*, **24**, 365 (1970); K. E. Johnson and P. Zacharias, *This Journal*, **124**, 448 (1977).
18. V. D. Prisyazhnyi, D. A. Tkalenko, and N. A. Chmilenko, *Elektrokhimiya*, **16**, 115 (1980).
19. D. Gilroy and B. E. Conway, *Can. J. Chem.*, **46**, 875 (1968).
20. R. Thacker and J. P. Hoare, *J. Electroanal. Chem.*, **30**, 1 (1971).
21. A. J. Appleby, *ibid.*, **24**, 97 (1970).
22. T. Biegler and R. Woods, *ibid.*, **20**, 73 (1969).
23. J. P. Hoare, *This Journal*, **110**, 1019 (1963).
24. J. P. Hoare, R. Thacker, and C. R. Wise, *J. Electroanal. Chem.*, **30**, 15 (1971).
25. J. P. Hoare, *This Journal*, **126**, 1502 (1979).
26. K. E. Jonson and D. T. Sawyer, *J. Electroanal. Chem.*, **49**, 95 (1974).
27. P. Margaretha and P. Tissot, *ibid.*, **99**, 127 (1979).
28. A. Damjanovic, M. A. Genshaw, and J. O'M. Bockris, *This Journal*, **114**, 446 (1967).
29. D. D. MacDonald, "Transient Techniques in Electrochemistry," Chap. 6, Plenum Press, New York (1977).

A Capacitance and Electrolyte Electroreflectance Study of the ZnSe/Electrolyte Interface

P. Lemasson,* C. Hinnen, N. R. de Tacconi,¹ and C. Nguyen Van Huong

Laboratoire d'Electrochimie Interfaciale du CNRS, 92195 Meudon Principal Cedex, France

ABSTRACT

The semiconductor-electrolyte junction is studied in the particular case of n-ZnSe/indifferent electrolytes by means of capacitance and electrolyte electroreflectance measurements. In comparing both kinds of results obtained for two extreme pH conditions (pH = 0 and 14), we need to define a reference state for the clean electrode in each medium. A basic solution acts as a more able etching solution than an acidic one creating fast acceptor interface states in the vicinity of the valence band maximum tending to fix the Fermi level. The evolution of these reference states with controlled perturbations of the interface confirm that the characteristics of the junction remains governed mainly by the presence of interface states at the semiconductor electrode. Such an analysis of combined electrical and spectroscopic data constitutes a promising way for a better understanding of the semiconductor/electrolyte junction in connection with the physical models developed for metal/semiconductor junctions.

During the last 30 years, the semiconductor-electrolyte junction has received much attention. This attraction was mainly due to the simple preparation procedure and the versatility of this junction as compared to the classical solid Schottky barriers, although such an important parameter as temperature cannot be easily varied in a large range.

The models used in the description of the semiconductor-electrolyte interface (1) are generally based on those already elaborated for solid-state junctions, especially metal-semiconductor junction (2). However, this analogy necessitates the definition of a proper Fermi level in the electrolyte. Such a requirement can be easily fulfilled in the case of a redox electrolyte, but it presents much more difficulty for an electrolyte without an explicit redox couple (3). Due to its fundamental interest as well as its use in physical measurements (electroreflectance) and semiconductor technology, the latter case necessitates more insight, and it is the aim of the present article to deal with some physical and electrochemical aspects of semiconductor-indifferent electrolyte junctions.

The semiconductor used as an electrode in such investigations must fulfill two requirements: (i) its physical properties are clearly established and can be accounted for unambiguously by a band model; (ii) its electrochemical behavior has already received attention and can be considered as simple. For this purpose, we selected n-ZnSe, a II-VI compound with wide energy gap (2.7 eV) whose electrochemical behavior (5, 6) and EER investigations have been previously described (6c).

By analyzing mainly two types of measurements, capacitance and electrolyte electroreflectance (EER), which bring complementary information, we attempt in this article to give more insight into the formation of the semiconductor-electrolyte (indifferent) junction. The description of such a junction necessitates the use of many different physical parameters. The various data obtained can then be accounted for by a model similar to that of metal-semiconductor junctions, provided that the existence of different types of interface states is taken into account.

Experimental

The zinc selenide single crystals were grown and donated by Professor Lozykowski.² They were In doped

²H. Lozykowski, Institute of Physics, Nicholas Copernicus University, Torun, Poland

*Electrochemical Society Active Member

¹Permanent address: Instituto de Investigaciones Fisicoquimicas Teoricas y Aplicadas (INIFTA), 1900 LaPlata, Argentina.

with a free carrier density of $\sim 2 \times 10^{17} \text{ cm}^{-3}$ as determined by Hall effect measurement. Prior to their mounting as electrodes, an ohmic contact was realized with In-Hg amalgam by heating at $\sim 300^\circ\text{C}$ in argon atmosphere for 1-2 min. A gold wire was then soldered to these contacts. The back and sides of the crystals were insulated from the electrolyte by means of an epoxy resin (Scotch Cast, 3M Company) and then mounted on the electrode holder. The exposed face was carefully polished with diamond paste ($0.25 \mu\text{m}$) and, when necessary, etched in a 1% bromine in methanol solution at $\sim 5^\circ\text{C}$. The best etching time was found to be 20s (see Discussion section).

The cell was of the classical three-electrode type with quartz windows for light passage and a gold counterelectrode. The reference electrode was a mercury-mercurous sulfate immersed in saturated potassium sulfate aqueous solution (0 V vs. MSE = +0.65V vs. NHE).

Electrolytes were prepared by dissolving Merck-Suprapur grade chemicals in Millipore purified water. The following solutions were used: 1M HClO_4 , 1M NaOH, and 10^{-2}M $\text{K}_3\text{Fe}(\text{CN})_6$ + 1M HClO_4 , and 10^{-2}M $\text{K}_3\text{Fe}(\text{CN})_6$ + 1M NaOH. In order to saturate or to eliminate oxygen, either an oxygen or an argon bubbling of the electrolytes was undertaken prior to electrochemical experiments.

As a light source, a 400W tungsten-halogen lamp was used together with electrochemical and electroreflectance equipment which have been described previously (6a, 7).

The capacity measurements are achieved at 15 Hz and 100 kHz. The EER spectra are recorded at almost normal incidence for the light beam, and with an electrical perturbation whose characteristics are 15 Hz and $0.5V_{\text{eff}}$.

Results

Etched Electrode Surface and Definition of a Reference State

The changes in voltammograms, capacity curves, and EER spectra are studied simultaneously as a function of the semiconductor surface preparation. The characteristics are reported in Fig. 1 in the case of 1M NaOH electrolyte. During the electrochemical investigations, the potential range was limited negatively to hydrogen evolution and positively at +2.0V vs. MSE, *i.e.*, in a range where no anodic current is detectable within the limit of $10^{-9} \text{ A}\cdot\text{cm}^{-2}$. The EER spectra are reported for a dc potential of 0 V vs. MSE; thus, the possibility of anodic current even for large ac modulation ($1V_{\text{eff}}$) can be excluded.

In the case of a freshly polished electrode surface, without etching treatment (Fig. 1) the Mott-Schottky plot (C^{-2} vs. V, where C is capacity and V is potential) is far from linear and the EER signal is small and without distinct structure in the vicinity of the fundamental transition E_0 at about 2.72 eV.

The influence of a further chemical etching in bromine-methanol solution is clearly evidenced in Fig. 1 for two different etching times (10 and 20s). In both cases, the C^{-2} -V plots now present an acceptable linearity, but the flatband potential V_{FB} as well as the free carrier density N_D deduced from these plots differ noticeably ($V_{\text{FB}} = -2.6\text{V}$ vs. MSE and $N_D = 3.6 \times 10^{17} \text{ cm}^{-3}$ for 10s; $V_{\text{FB}} = -3.1\text{V}$ and $N_D = 8 \times 10^{17} \text{ cm}^{-3}$ for 20s). We have to emphasize that these values are deduced from measurements with a 15 Hz perturbation. At 100 kHz, in the second case (etching time 20s) we obtain $V_{\text{FB}} = -3.1\text{V}$ vs. MSE and $N_D = 2.7 \times 10^{17} \text{ cm}^{-3}$. The EER spectrum shows more clearly the influence of the etching (Fig. 1b), and it is only in the second case that it becomes acceptable, with a large signal enabling a precise determination of the peak energies. This typical spectrum and the corresponding capacity values being reproducible are proposed to characterize the reference state for this junction.

Equivalent observations are made in acidic medium (1M HClO_4 , pH 0) (Fig. 2). We notice, however, that the C^{-2} -V plots as well as the EER spectra differ in some aspects, when the so-called reference state is reached. Excluding the variation of V_{FB} with pH, the slopes of the C^{-2} -V plots are larger and lead to a unique value of $N_D \approx 2 \times 10^{17} \text{ cm}^{-3}$ at 15 Hz and 100 kHz; the EER spectrum pres-

ents oscillations of slightly lower amplitude. As will be discussed in the Discussion section, these observations may certainly be correlated with physical differences during the formation of the semiconductor-electrolyte interface.

At both pH values, there was no noticeable influence of the presence of oxygen in the electrolyte.

Modifications of the Reference State

Influence of a positive polarization.—The electrochemical treatment is achieved in order to induce a modification of the semiconductor-electrolyte interface when studied under the same conditions as described in the previous section, allowing a comparison with the reference state. The treatment is strictly dependent on the pH of the solution.

pH 0.—In this case, a positive polarization at a potential value where a detectable current crosses the junction induces a remanent effect only if the solution is saturated in oxygen and if the electrode is illuminated during the process. The particular conditions used here are (i) polarization value of +8.0V vs. MSE, (ii) electrolyte saturated in oxygen, and (iii) illumination with white light.

The main results obtained in capacity and EER measurements are reported in Fig. 3. During the whole treatment, the current density is small ($\sim 1.5 \mu\text{A}\cdot\text{cm}^{-2}$) and constant. We observe that at 15 Hz, the C^{-2} -V plot differs from that obtained in the reference state (the slope and the linear portion decrease), whereas at 100 kHz the C^{-2} -V plot remains identical to that of the reference state. The EER spectra at a dc voltage of 0 V diminish in amplitude, mainly for the negative part of the oscillation, and after 1h of such a treatment present the perturbed shape indicated in the lower part of Fig. 3b.

pH 14.—In that case, the perturbation of the junction is obtained with a positive polarization only (no noticeable influence of either oxygen or light). Our experimental conditions are then (i) polarization at +4.0V vs. MSE up to 15 min, and (ii) presence of oxygen and illumination or not.

We already noticed that a treatment lasting more than 15 min does not further influence the behavior of the semiconductor-electrolyte interface. The net result of the electrochemical treatment on both C^{-2} vs. V plot and EER spectra is presented in Fig. 4. Whereas an enhancement of the EER signal together with an improvement of the signal/noise ratio is noticeable, the C^{-2} -V plots at 15 Hz are strongly modified: the linearity range and the slope decrease together.

Influence of oxidizing species.—The Ox species is $\text{K}_3\text{Fe}(\text{CN})_6$. The treatment is achieved in an electrochemical cell devoted exclusively to this purpose; the characterization is then realized in a separate cell containing the supporting electrolyte.

pH 0.—The electrode treatment is achieved in a 1M HClO_4 solution containing 10^{-2}M $\text{K}_3\text{Fe}(\text{CN})_6$. The complete cycle is eight voltage sweeps between -2.0 and $+2.0\text{V}$ vs. MSE at a sweep rate of $50 \text{ mV}\cdot\text{s}^{-1}$.

The result of this treatment is presented in Fig. 5. We notice that the C^{-2} -V plot is slightly modified at high frequency as well as at low frequency, whereas the EER signal decreases progressively in a way analogous to that observed with an electrochemical treatment (see the positive polarization pH 0 section).

Furthermore, we mention that at the end of the treatment the electrode surface presents a slightly modified aspect (green-gray) easily detectable with naked eye.

pH 14.—During the treatment, which consists of six voltage sweeps between -2.0 and $+2.0\text{V}$ vs. MSE at a sweep rate of $50 \text{ mV}\cdot\text{s}^{-1}$, the electrolyte is 1M NaOH + 10^{-2}M $\text{K}_3\text{Fe}(\text{CN})_6$ solution.

Under further investigation in 1M NaOH electrolyte, the behavior of the ZnSe-electrolyte interface changes slightly for Mott-Schottky plots (at high and low frequency) but drastically for the EER spectra, which pres-

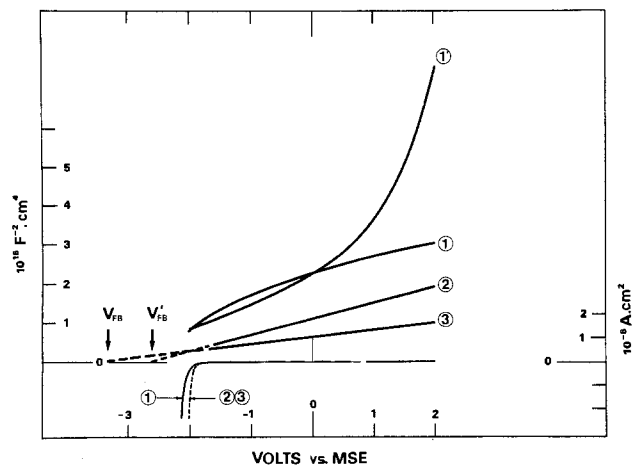
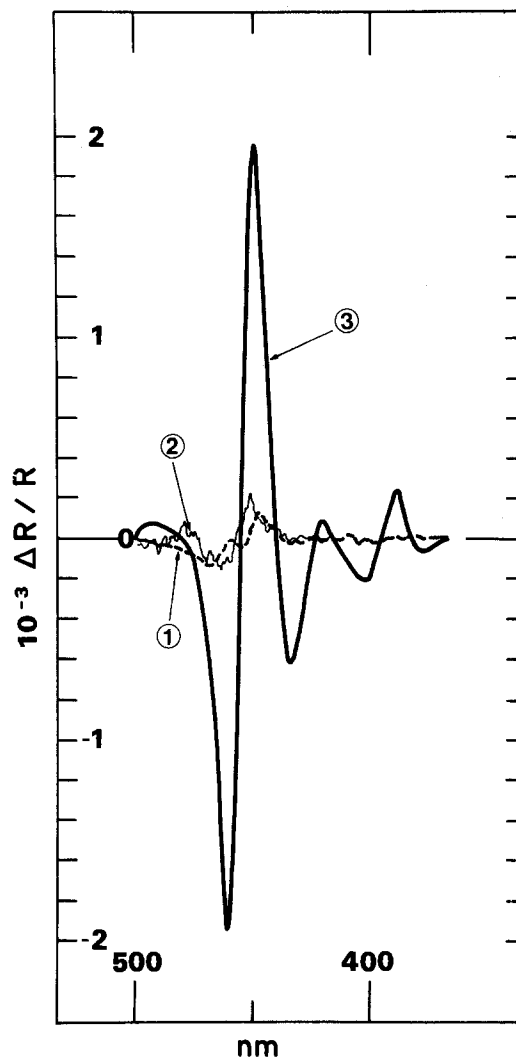


Fig. 1. Electrical and electro-optical characteristics of the n-ZnSe-1M NaOH junction for different semiconductor surface preparations. 1 and 1': Just polished with $0.25 \mu\text{m}$ diamond paste. 2: Etched 10s in 1% bromine-methanol solution. 3: Etched 20s in 1% bromine-methanol solution. a(above): Dark current and C^{-2} vs. V characteristics. In the latter case, the perturbation frequency is 15 Hz. For clarity's sake, the Schottky plot at 100 kHz is not represented. b(right): EER spectra.



ent a complete rotation of phase together with an important attenuation (Fig. 6).

The semiconductor surface becomes reddish as the treatment is completed. The red layer formed is dissolved easily in CS_2 , thus indicating that it is a selenium layer.

Discussion

Reference State: Electrical and Electro-optical Characterization

Prior to electrochemical investigations, the semiconductor electrode is mechanically polished and chemically etched. Such a preparation plays a major role in the subsequent electrode behavior. Results presented in the Results section allow a definition of quality for the semiconductor surface, based upon electrical (capacity) and electro-optical (electroreflectance) measurements. More precisely, the criteria are twofold.

First, the differential capacity *vs.* potential measurement must lead to linear Mott-Schottky plots (C^{-2} - V) for high as well as low frequency perturbation. Furthermore, in a large potential range ($\geq 1\text{V}$), a correct Mott-Schottky plot enables calculation of free carrier density analogous to that determined by physical techniques such as Hall effect measurement. This requirement is generally obeyed only at high frequency, but, in some cases, it can be verified even at low frequency (a few hertz).

Second, the electroreflectance signal must be sufficiently large in the vicinity of the fundamental E_0 transition ($\sim 10^{-3}$ in absolute value in our case).

Third, nevertheless, this latter criterion must be adequately adapted due to the influence of the free carrier density on the amplitude of the EER signal as outlined by Aspnes (8).

In addition to the large signal amplitude, the broadening parameter, Γ , must be sufficiently small ($\sim 50 \text{ meV}$ in the present case).

When the first two conditions are fulfilled, it becomes possible to (i) fix the energy position of the semiconductor Fermi level in an electrochemical scale by means of the flatband potential value V_{FB} and (ii) determine a precise value of the fundamental transition energy E_0 (and of the higher transition energies).

Results reported in Fig. 1 indicate that the damaged layer produced by the mechanical polishing must be removed by an adequate chemical etching which depends on the semiconductor. Thus, in the case of ZnSe, a satisfying surface preparation consists in a mechanical polishing with diamond paste $1/4 \mu\text{m}$ followed by a chemical etching in 1% bromine in methanol solution at $\sim 5^\circ\text{C}$ for $\sim 15\text{s}$.

The parameter values corresponding to the reference state are reported in Table I. We must notice first that an open-circuit barrier height or band bending, V_s , can be deduced from rest and flatband potentials. The rest potential is accurately determined using an electrometer. From one experiment to another, fluctuations are very small and V_R can be considered as really fixed. This band bending is pH dependent

$$V_s = 1.65\text{V at pH} = 0$$

$$V_s = 2.3\text{V at pH} = 14$$

Such values are large as compared to those obtained for ZnSe in the metal-semiconductor configuration (9). However, they seem to be fairly explained by the existence of acceptor interface states, located in the range 0.5-1.0 eV

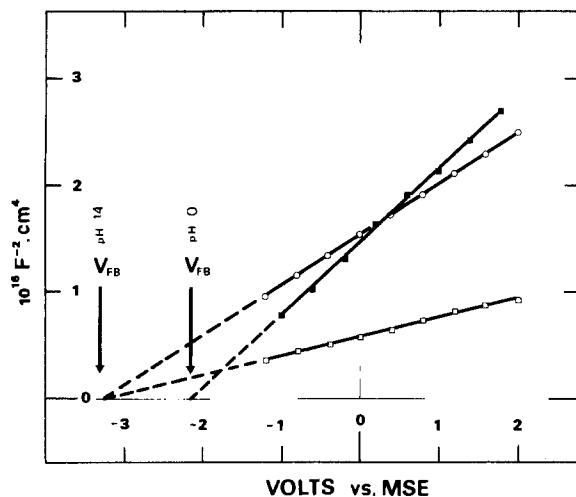
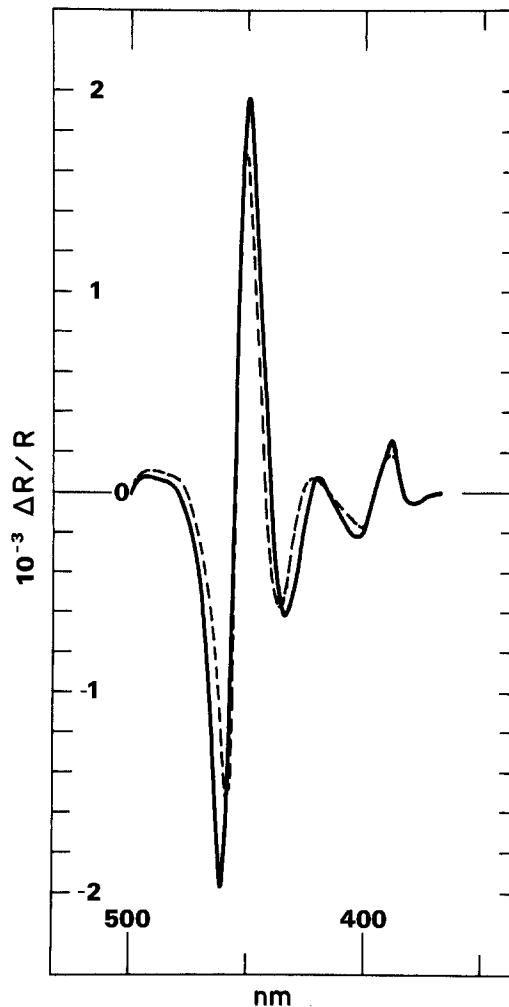


Fig. 2. Comparison of electrical and electro-optical characteristics of the n-ZnSe-indifferent electrolyte junction in the reference states (see the text for the definition) at pH 0 and 14. a(above): C^{-2} vs. V . Filled squares: pH 0, 15 Hz, and 100 kHz. Open squares: pH 14, 15 Hz. Circles: pH 14, 100 kHz. b(right): EER spectra. Solid line: pH 14. Dashed line: pH 0.



higher than the valence-band maximum, which tend to fix the Fermi level. The existence of such acceptor states has already been demonstrated for semiconductor-vacuum interfaces by photoemission measurements, especially in the case of n-GaAs, which is isoelectronic to ZnSe (10), and also for ZnSe (11). They may be explained by the penetration in the gap of the empty surface-state band associated with Se atoms upon removal of the "clean" surface reconstruction. In contact with an electrolyte this removal is more pronounced when the solution is an etchant for ZnSe, which is the case for NaOH. The higher value of V_s at pH 14 agrees well with these considerations. Further discussion is possible together with an analysis of capacity and EER measurements in the reference state of the electrode.

Differential capacity.—At high frequency (100 kHz), the reference states are slightly different at pH 0 and 14 (N_D calculated from the Mott-Schottky slope changes from $2 \times 10^{17} \text{ cm}^{-3}$ to $2.7 \times 10^{17} \text{ cm}^{-3}$) and differ noticeably at low frequency (N_D changes from 2×10^{17} to $8 \times 10^{17} \text{ cm}^{-3}$). The flatband potential value is here insensitive to the perturbation frequency (Table I). These observations may likely be correlated with the above considerations on the existence of acceptor surface states in the vicinity of the valence-band maximum.

We attempt now to estimate the density of surface states analyzing the capacity measurements. This estimation is made assuming that the models established in the case of the metal-semiconductor junctions can be used for electrolyte-semiconductor junctions and the analysis is different according to the possibility or impossibility for the interface states to follow the perturbation (2a, 12).

At 100 kHz, we may assume that the interface states do not follow the perturbation. This hypothesis corresponds to a linear C^{-2} - V plot in a large potential range for band bendings greater than 2V. If the interface states followed the ac perturbation at 100 kHz, no such linear plots could exist. In that case and provided that the occupation of

these states is governed by the semiconductor Fermi level, the slope of the Mott-Schottky plot is no longer proportional to N_D^{-1} but to $[(1 + \alpha)N_D]^{-1}$ (12), where

$$\alpha = \frac{e\delta D_{sa}}{\epsilon_1} \quad [1]$$

and δ is the thickness of the interfacial layer, D_{sa} the density of states per surface unit, ϵ_1 the dielectric constant of the interfacial layer, and e the electron charge. Therefore, due to the similarity between $(N_D)_{\text{Hall}}$ and $(N_D)_{\text{Schottky}}$ at pH 0, we may assume that D_{sa} is smaller than that at pH 14, a statement which matches well the etching character of basic solutions. From the slope value at 100 kHz in the electrolyte of pH 14, we calculate

$$\alpha = 0.35 \quad [2]$$

It seems reasonable to assume δ of the order of some angstroms and ϵ_1 slightly lower than ϵ_s ($8.7\epsilon_0$). This leads to the estimation of D_{sa}

$$D_{sa} \sim 5 \times 10^{13} \text{ cm}^{-2} \quad [3]$$

a value which is compatible with the barrier height of 2.3 eV.

At low frequency, it is no longer valid to assume that the interface states do not follow the perturbation and the above analysis is no longer possible. However, Fonash (12) has recently proposed a detailed treatment of that case, and we applied it to our results. Without giving more details, it is sufficient to say that the amount of very slow surface states, as deduced from this treatment, is low, on the order of 10^{11} cm^{-2} .

The D_{sa} value, as computed from relation [1], seems to be in the limits for Fermi level pinning, as established re-

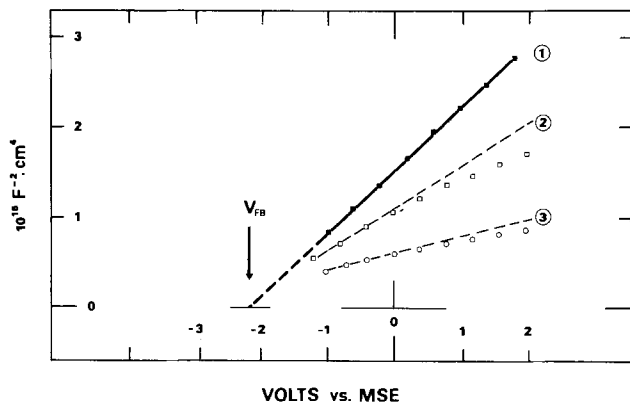
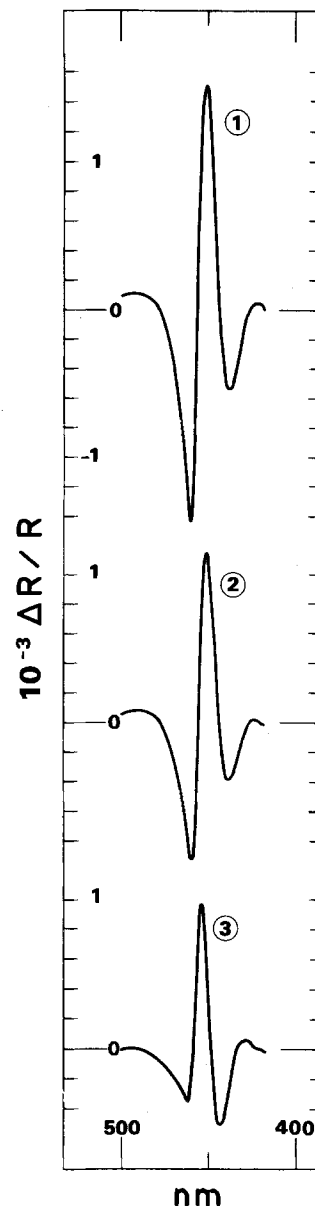


Fig. 3. Characteristics of the n-ZnSe-1M HClO₄ junction before and after electrochemical perturbation (positive polarization + 8V vs. MSE and illumination in the presence of oxygen). 1. Reference state. 2 and 3: After, respectively, 30 min and 1h of perturbation. a(above): C⁻² vs. V (15 Hz). b(right): EER spectra.



cently by Zur *et al.* (13), in the case of submonolayer metal coverage. The influence of the very slow surface states is therefore negligible on this phenomenon irrespective of their influence on the frequency dispersion of Mott-Schottky plots.

Electrolyte electroreflectance.—Provided that the low field approximation can be made, the EER spectra can be fairly analyzed using the three-point method (14). The validity of this method depends on the existence of a fully depleted layer at the surface of the semiconductor and on the assumption that the electro-optical energy $\hbar\Omega$ and the broadening parameter obey the relation

$$3\hbar\Omega < \Gamma \quad [4]$$

Consequences of relation [4] are (i) the proportionality between the EER signal amplitude and that of the alternating modulation and (ii) the constancy of the transition energy when the dc potential changes.

In the present case, we have

$$\hbar\Omega = 24 \text{ meV}$$

$$\Gamma = 50 \text{ meV}$$

and condition [4] is clearly not fulfilled. However, the two main consequences are verified and it seems reasonable to assume that the low field limit approximation is valid. The E_0 and Γ values deduced are reported in Table I

and we remark that they differ slightly between pH 0 and 14. The smaller value of Γ at pH = 0 seems to be consistent with the above remarks about the lower density of interface states at this pH than at pH 14. Another feature, not reported in Table I, consists in the larger signal amplitude at pH 14 than at pH 0. If we follow a treatment proposed recently by Tomkiewicz *et al.* (15), the general expression for $\Delta R/R$ (8)

$$\frac{\Delta R}{R} = - \frac{2eN_D V_{ac}}{\epsilon_s} L(\hbar\omega) \quad [5]$$

[where $L(\hbar\omega)$ is the spectral lineshape function] can be rewritten

$$\frac{\Delta R}{R} = A \left(1 - \frac{e}{C_H} \frac{dD_{sa}}{dV} \right) dV \quad [6]$$

with $A = - \frac{2eN_D}{\epsilon_s} L(\hbar\omega)$ and C_H the capacity of the

electrolyte Helmholtz layer. Changing expression [5] to expression [6] is possible assuming that the variations in potential are divided between the space-charge layer and the Helmholtz layer by means of interface states. If the dc potential is fixed, an interface which presents acceptor states must correspond to larger signals than an interface

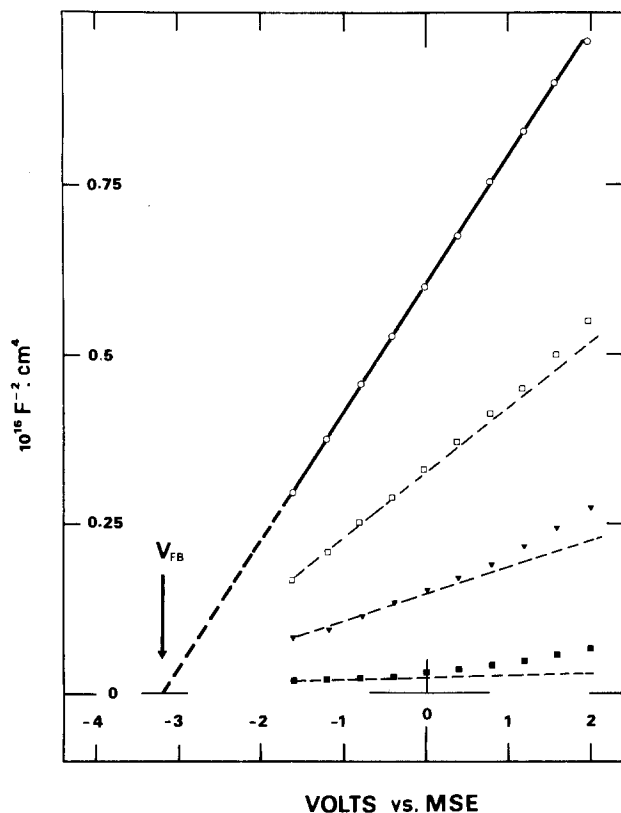


Fig. 4. Characteristics of the n-ZnSe-1M NaOH junction before and after electrochemical perturbation (polarization + 4V vs. MSE). a(above): C^{-2} vs. V (15 Hz). Circles: Reference state. Open squares: 5 mn treatment. Triangles: 10 mn treatment. Closed squares: 15 mn treatment. The C vs. V (100 kHz) plots do not differ noticeably and are not represented. b(right): EER spectra. Solid line: Reference state. Dashed line: After 15 min electrochemical perturbation.

without states: in the first case dD_{sa}/dV is negative and in the second $dD_{sa}/dV = 0$. We have to notice that the treatment which leads to expression [6] is independent of the nature of the interface states, and will be used in the following when the existence of donor interface states can be assumed.

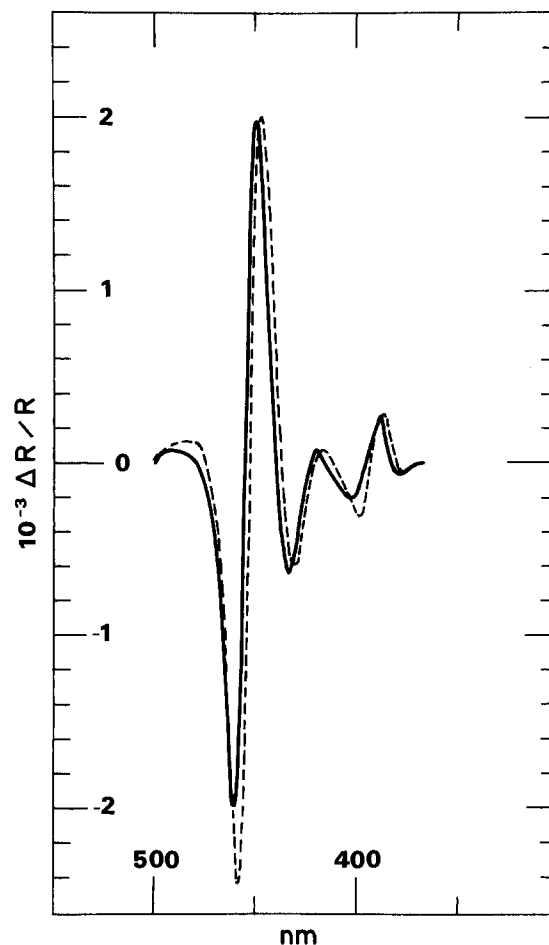
Expression [6] accounts for the difference observed in $\Delta R/R$ amplitude between pH 0 and 14 and is consistent with the existence of acceptor interface states in greater amount at pH 14.

A conclusion deduced from both capacity and EER data analysis concerning the reference state can already be pointed out: the interface ZnSe-electrolyte (and this is certainly not limited to ZnSe) behaves more ideally at pH 0 than at pH 14.

The Perturbed Reference State

Electrochemical perturbation.—This type of perturbation corresponds to that induced by the various treatments achieved in supporting electrolyte under positive polarization of the electrode. According to the remarks about the experimental results (Results section), we can ascertain that the charge transfer mechanism at pH 14 differs from that at pH 0. In the former case, there is no influence of both dissolved oxygen and illumination, whereas in the latter the situation is completely reversed. It appears that at pH 14 the transfer step must be associated with majority carriers (electrons) and at pH 0 with minority carriers generated by illumination. Such an analysis has already been proposed by one of us (6b), but, nevertheless, needs to be made more precise. The main results are reported in Table I.

pH 0.—At pH 0, the transfer step is associated with holes and induces a modification of the electrode behavior only in the presence of oxygen. Therefore, the complete



reaction is not specifically limited by the potential value, provided that the electric field in the space-charge layer is large enough to confine the holes in the immediate vicinity of the semiconductor surface. The exact reaction occurring is difficult to determine, but a comparison with results obtained about the oxidation of ZnSe exposed to oxygen and light (16) allows the assumptions of (i) the formation of both Zn excess and ZnO and (ii) the transformation of Se into soluble products (H_2SeO_3 , presumably).

After such a treatment, the differential capacity measured at 100 kHz remains unchanged, whereas at 15 Hz it leads to noticeably different apparent values of N_D ($8.6 \times 10^{17} \text{ cm}^{-3}$) and to a diminution of the potential range where a Mott-Schottky behavior is observed. This observation may be accounted for by the statement that the fast interface states remain unaffected, whereas new slow states are created in an amount of approximately 10^{11} cm^{-2} (this result is obtained by arguments similar to those developed in the Differential capacity section).

More striking are the variations with respect to the reference state observed in the EER oscillations in the vicinity of E_0 . In this energy range, the absorption coefficient, α , is $10^3 < \alpha < 10^4 \text{ cm}^{-1}$ (17) and the penetration depth of light is at least one order of magnitude larger than the space-charge layer thickness. We conclude from this observation that EER spectra would account mainly for the bulk properties of the semiconductor. Such a statement contradicts clearly our experimental results. We observe an important spectrum shape modification, a slight shift of E_0 towards lower values, and an important attenuation of the spectrum amplitude. By reference to Eq. [6], these results imply the formation of new interface states (already deduced from capacity measurements) and we can ascertain that these states are of the donor type ($dD_{sa}/dV > 0$). Such observations may be correlated with those made by photoemission during the formation of metal-semiconductor junctions where such donor states have been evidenced (18, 19).

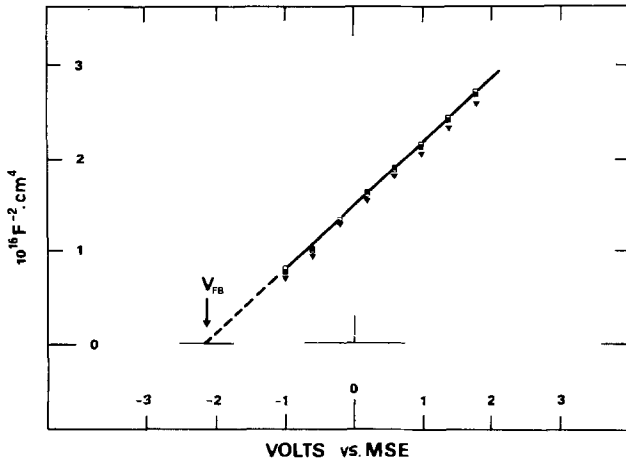
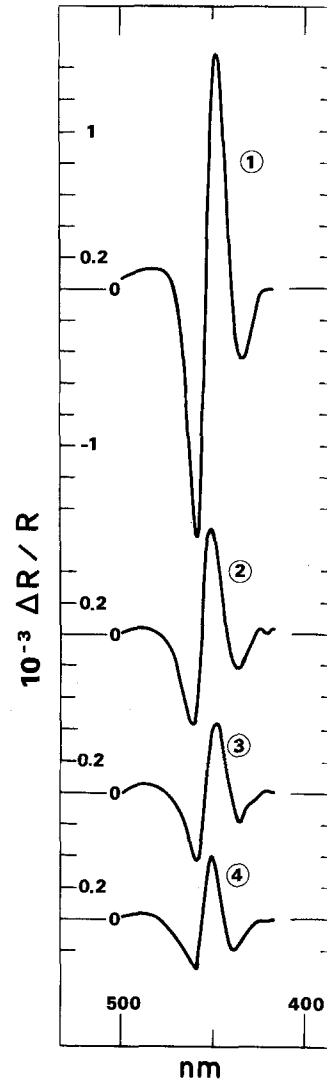


Fig. 5. Behavior of the n-ZnSe-1M HClO₄ junction before and after chemical perturbation [cycling between -2.0 and +2.0V vs. MSE in 1M HClO₄ + 10⁻²M Fe(CN)₆³⁻ for eight cycles at a sweep rate of 50 mV·s⁻¹]. a(above): C⁻² vs. V plots. Closed squares: Reference state at 15 Hz and 100 kHz. Triangles: Perturbed state at 15 Hz. Open squares: Perturbed at 100 kHz. b(right): EER spectra. 1: Reference state. 2: After two cycles. 3: After four cycles. 4: After eight cycles.



pH 14.—The transfer step is associated with electrons, and the resulting modifications to the reference state are independent of both oxygen and light. It seems reasonable to assume that electrons are injected by OH⁻ adsorbed at the electrode surface into the semiconductor conduction band. The control of this process by the electrode potential indicates that the transfer occurs via a tunneling process. By analogy with the metal-semiconductor case, we can attempt to determine the present transfer mechanism more precisely.

Calculating the probability *P* of a triangular barrier being penetrated by an electron with energy ΔE less than the height of the barrier, it is found that

$$P = \exp \left[-\frac{2}{3} (\Delta E)^{3/2} / E_{00} V_s^{1/2} \right] \quad [7]$$

where the parameter

$$E_{00} = \frac{\hbar}{2} \left[\frac{N_D}{m_e^* \epsilon_s} \right]^{1/2} \quad [8]$$

(m_e^* is the effective mass of the electron in the semiconductor) plays a major role. In the present case ($m_e^* = 0.17 m_0$; $\epsilon_s = 8.7\epsilon_0$, and $N_D = 2 \times 10^{17} \text{ cm}^{-3}$), we have

$$E_{00} = 6.8 \times 10^{-3} \text{ eV}$$

Using the expression developed by Padovani and Stratton (20), we can define the band bending values delimiting the various charge transfer processes: thermionic, thermionic-field, and field emission (the two latter refer

to tunneling processes). Details of the calculations are beyond the scope of the present paper, and the results are

$$\begin{aligned} V_s \leq 0.6V & \quad \text{thermionic emission} \\ 0.6 < V_s \leq 29.4V & \quad \text{thermionic-field emission} \\ V_s > 29.4V & \quad \text{field emission} \end{aligned}$$

Obviously, the band bending value during the electrochemical treatment ($\sim 10 \text{ eV}$) implies that the transfer process we observe is analogous to thermionic-field emission. A consequence of these considerations is that ΔE must be rather small (ca. 0.1 eV), thus leading to the location of the OH⁻ adsorbed groups which donate their electrons in the vicinity of the conduction bandedge ($-3.1V$ vs. MSE) in an energy position very different from that they occupy in the electrolyte bulk.

The electrochemical treatment analyzed above induces some particular features in the differential capacity as well as the EER signal. The high frequency capacity remains unchanged, whereas the low frequency capacity is strongly modified and the "pseudo" Mott-Schottky slope increases up to 2×10^{19} (Table II). This variation can be interpreted in terms of slow interfacial energy states (cf. the Differential capacity section) and leads to a density of states of ca. $2 \times 10^{12} \text{ cm}^{-2}$. This density of states can be related to the increase of the EER signal, which, by means of relation [6], indicates that dD_{sa}/dV is more negative than in the reference state at pH 14.

The electrochemical treatment can then be considered as a strong etching process which, like the etching by

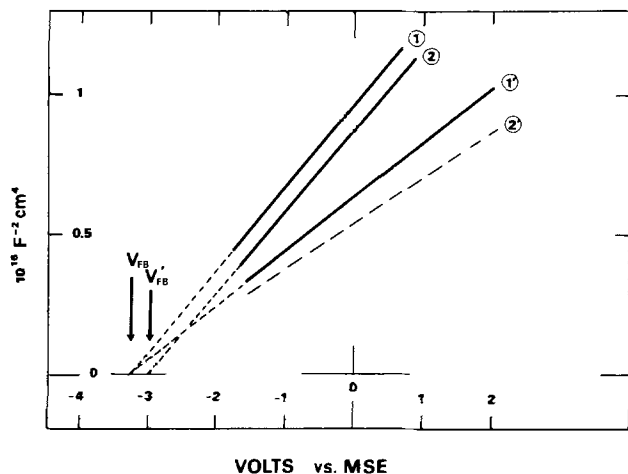
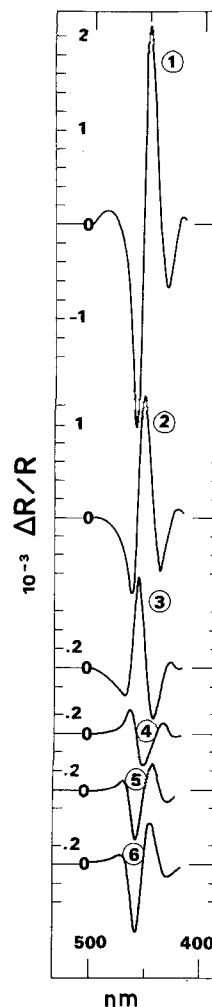


Fig. 6. Characteristics of the ZnSe-1M NaOH junction before and after chemical perturbation [cycling between -2.0 and $+2.0$ V vs. MSE in $1\text{M NaOH} + 10^{-2}\text{M Fe(CN)}_6^{3-}$ for six cycles at a sweep rate of $50\text{ mV}\cdot\text{s}^{-1}$]. a(above): C^{-2} vs. V plots. 1 and 1': Reference states at 100 kHz and 15 Hz , respectively. 2 and 2': Perturbed states at 100 kHz and 15 Hz , respectively, at the end of the six cycles. b(right): EER spectra. 1: Reference state. 2: After two cycles. 3: After three cycles. 4: After four cycles. 5: After five cycles. 6: After six cycles. Notice that the phase rotation appears to be complete after four cycles and after six cycles, and that the spectrum is restored in phase but strongly attenuated as compared to the reference state.



NaOH, preserves the surface stoichiometry (Zn and Se are involved in final soluble products) and increases the density of interfacial acceptor energy states.

Chemical perturbation.—By chemical perturbation, we mean that the chemical composition of the semiconductor surface is severely perturbed. The use of the oxidizing species Fe(CN)_6^{3-} seems especially adequate for this purpose (6b). The exact process by which this species produces the modified semiconductor surface is not yet clear and depends on the pH of the solution. At pH 0, the reaction seems to be chemical, whereas at pH 14 it seems to be a mixture of electrochemical and chemical processes. At each pH value, the resulting surface is different and behaves specifically when studied in supporting electrolyte of equivalent pH value.

pH 0.—The modified interface behaves like that produced by electrochemical perturbation at pH 0 both in capacity and EER.

It seems reasonable to assume that the semiconductor surface produced by the ferricyanide treatment is similar

to that produced by the former electrochemical treatment and, therefore, we do not emphasize it.

pH 14.—The final result of the treatment is to create a selenium layer on the top of the ZnSe electrode. This layer induces a specific behavior of the modified electrode when immersed further in an electrolyte of pH 14. The EER signal is strongly attenuated and rotates in phase. The slope of the Mott-Schottky plot changes at low frequency, but does not at high frequency. In the latter case, in addition, the flatband potential shifts towards a slightly more positive value. This observation seems in good agreement with that already made on CdSe electrodes upon deposition of a Se layer (21). By analogy with the observation made during the formation of Ge-GaAs interfaces (22), it seems appropriate to assume the creation of donor interface states with large relaxation time due to the interaction between Se atoms and the ZnSe surface. The strong attenuation of the EER signal is in part accounted for by the absorption of light in the Se layer, whose fundamental energy gap is ca. 2 eV, and the absorption coefficient larger than 10^5 cm^{-1} in the region

Table I. The reference state parameters at pH 0 and 14. The steady-state barrier height V_s (open circuit) can be deduced from V_R and V_{FB} determinations using the relation $V_s = |V_{FB} - V_R|$. The free carrier density as determined by Hall effect is $\sim 2 \times 10^{17}\text{ cm}^{-3}$ and serves as a reference value

Electrolyte	Rest potential V_R (V vs. MSE)	Capacity				N_D (cm^{-3}) Hall effect	Electroreflectance	
		V_{FB} (V vs. MSE)		N_D (cm^{-3})			E_0 (eV)	Γ (meV)
HClO_4 (pH = 0)	-0.65	15 Hz	100 kHz	15 Hz	100 kHz	2×10^{17}	2.724	43
		-2.2	-2.3	2×10^{17}	2×10^{17}			
NaOH (pH = 14)	-0.8	-3.2	-3.1	8×10^{17}	2.7×10^{17}	2×10^{17}	2.711	57

Table II. The question mark indicates that the experimental results cannot be interpreted using a simple model. The Schottky plots are not clearly linear in a large potential range, and the phase rotation of the EER signals excludes the use of the three-point method

Electrolyte	Treatment	Capacity				EER	
		V_{FB} (V)		N_D (cm ⁻³)		E_0 (eV)	(meV)
HClO ₄	Positive polarization + Oxygen } + Light }	15 Hz	100 kHz	15 Hz	100 kHz	2.714	35
		?	-2.3	8.6×10^{17}	2×10^{17}		
	Fe(CN) ₆ ³⁻	?	-2.2	2.4×10^{17}	2.1×10^{17}	2.728 (?)	43
NaOH	Positive polarization	-3.1	-3.1	2×10^{19}	3.0×10^{17}	2.732	61
		(?)					
	Fe(CN) ₆ ³⁻	-3.2	-3.0	1.5×10^{18}	2.8×10^{17}	?	?
		(?)			(?)		

of 2.7 eV (23). The phenomenon of phase rotation of the EER signal has already been described by other authors and has been accounted for similarly by the existence of interface energy states induced by an electrochemical treatment (15) and by the formation of a heterojunction (24).

Conclusion

By coupling electrochemical and *in situ* electroreflectance measurements and by applying controlled perturbations at the interface, we tried to infer a description of the ZnSe-electrolyte interface by analogy with the models used for the metal-semiconductor junctions.

The above discussion establishes that the ZnSe-supporting electrolyte junction behaves like a metal-semiconductor junction. However, the main interface properties are governed not by the bulk properties of the semiconductor-electrode, but by its surface states. These surface states can be either intrinsic to the semiconductor surface or resulting from a specific interaction with the electrolyte.

Summing up, we can say that an electrolyte with no etching properties (acidic medium) leads to the formation of an interface with a low density of interface states, whereas a basic electrolyte with etchant character leads to a pinning of the semiconductor Fermi level by acceptor surface states located ca. 0.5 eV above the valence band maximum.

Perturbing the reference state defined above induces particular effects which differ according to the nature and intensity of the perturbation. The simple model with acceptor interface states governing the junction properties must be made more sophisticated to incorporate a relatively large density of donor interface states located in the upper part of the semiconductor gap.

Provided that these considerations are taken into account, an electrolyte-semiconductor junction can be described, at least qualitatively, like a metal-semiconductor interface.

Manuscript submitted Jan. 22, 1985, revised manuscript received April 25, 1985.

REFERENCES

- See, e.g., J. F. Dewald, *Bell Syst. Tech. J.*, **39**, 615 (1960); H. Gerischer, *Z. Phys. Chem. (N. F.)*, **26**, 223

- (1960); V. A. Myamlin and Yu. V. Pleskov, "Electrochemistry of Semiconductors," Plenum Press, New York (1967); S. R. Morrison, "Electrochemistry at Semiconductor and Oxidized Metal Electrodes," Plenum Press, New York (1981).
- See, e.g., (a) E. H. Rhoderick, "Metal-semiconductor contacts," Oxford University Press, Oxford, England (1978); (b) L. J. Brillson, *Surf. Sci. Rpt.*, **2**, (2) (1982).
- D. Haneman, *Surf. Sci.*, **86**, 462 (1979).
- See, e.g., A. J. Bard, A. B. Bocarsly, F-R. F. Fan, E. G. Walton, and M. S. Wrighton, *J. Am. Chem. Soc.*, **102**, 3671 (1980).
- R. Williams, *This Journal*, **114**, 1173 (1967); P. M. Smiley, R. N. Biagioni, and A. B. Ellis, *ibid.*, **131**, 1068 (1984).
- (a) J. Gautron, P. Lemasson, F. Rabago, and R. Triboulet, *ibid.*, **126**, 1868 (1979); (b) P. Lemasson and J. Gautron, *J. Electroanal. Chem.*, **119**, 289 (1981); (c) P. Lemasson, J. Gautron, and J. P. Dalbéra, *Ber. Bunsenges. Phys. Chem.*, **84**, 796 (1980).
- J. P. Dalbéra, C. Hinnen, and A. Rousseau, *J. Phys. C (Paris)*, **38**, 185 (1977).
- D. E. Aspnes, *Phys. Rev. Lett.*, **28**, 913 (1972).
- S. G. Lorrie, J. R. Chelikowsky, and M. L. Cohen, *Phys. Rev. B*, **15**, 2154 (1977).
- D. Bolmont, V. Mercier, P. Chen, H. Lüth, and C. A. Sébenne, *Surf. Sci.*, **126**, 509 (1983).
- A. Ebina, T. Anno, Y. Suda, H. Koinuma, and T. Takahashi, *J. Vac. Sci. Technol.*, **19**, 301 (1981).
- S. J. Fonash, *J. Appl. Phys.*, **54**, 1966 (1983).
- A. Zur, T. C. McGill, and D. L. Smith, *Phys. Rev. B*, **28**, 2060 (1983).
- D. E. Aspnes and J. E. Rowe, *Phys. Rev. Lett.*, **27**, 188 (1971).
- M. Tomkiewicz, W. Siripala, and R. Tenne, *This Journal*, **131**, 736 (1984).
- A. Ebina, K. Asano, Y. Suda, and T. Takahashi, *J. Vac. Sci. Technol.*, **17**, 1074 (1980).
- J. Gautron, C. Raisin, and P. Lemasson, *J. Phys. D: Appl. Phys.*, **15**, 153 (1982).
- D. Bolmont, P. Chen, and C. A. Sébenne, *Surf. Sci.*, **117**, 417 (1982).
- W. E. Spicer, P. W. Chye, P. R. Skeath, C. Y. Su, and I. Lindau, *J. Vac. Sci. Technol.*, **16**, 1422 (1979).
- F. A. Padovani and R. Stratton, *Solid-State Electron.*, **9**, 695 (1966).
- K. W. Frese, Jr., *J. Appl. Phys.*, **53**, 1571 (1982).
- P. Chen, D. Bolmont, and C. A. Sébenne, *J. Phys. C: Solid State Phys.*, **15**, 6101 (1982).
- J. Stuke, *J. Non-Cryst. Solids*, **4**, 1 (1970).
- R. L. Brown, L. Schoonveld, L. L. Abels, S. Sundaram, and P. M. Raccach, *J. Appl. Phys.*, **52**, 2950 (1981).

Photoelectrochromic Properties of Polypyrrole-Coated Silicon Electrodes

Hiroshi Yoneyama,* Koichi Wakamoto, and Hideo Tamura

Department of Applied Chemistry, Faculty of Engineering, Osaka University, Yamada-oka 2-1, Suita, Osaka 565, Japan

ABSTRACT

Photoelectrochromic properties of polypyrrole-coated Si electrodes in propylene carbonate solutions were investigated to obtain fundamental information on optical image formation. It took about 1 s or more for a coated film ca. 90 nm thick to complete its color change when the entire surface of the film was illuminated with a 500 W xenon lamp, an observation of which indicates diffusion limitation of electrolyte anions in the film. In contrast, different image forming behaviors were seen when the film was illuminated with a He-Ne laser. Illumination of the film on n-type Si substrates with the laser for 1 s gave an optical image of about ten times of the illuminated area, while an optical image comparable with the illuminated area was obtained for p-type Si substrates for the same illumination time. In either case, continuous irradiation caused peripheral growth of the optical image in the film.

One of recent interests in polymer-coated electrodes concerns their electrochromic properties (1-14). A polymer film is usually deposited on a metallic conductive substrate, such as a thin Pt film, and highly conducting SnO_2 and In_2O_3 . A color change of the coated film occurs when it is stimulated by a large current pulse that causes oxidation of a reduced film or reduction of an oxidized film. If a semiconductor is used in place of the metallic conductive substrates, different features in electrochromism will appear with the assistance of illumination. Since semiconductor electrodes have a photosensitized action, illumination of polymer-coated semiconductor electrodes should spontaneously cause the color change without a change in the applied bias if the electrodes are properly biased in advance. Several interesting features of photoelectrochromism have recently been reported by Inganaes and Lundström for polymethylpyrrole-coated n-type Si (15). In this paper, we wish to report detailed characteristic features concerned with optical image formation and its storage. The polymer chosen was electropolymerized polypyrrole, which was deposited onto n- and p-type single-crystal wafers. It will be shown that behavior of the color change caused by illumination shows little difference between the conductivity type of the semiconductor substrate.

Experimental

Silicon single-crystal wafers manufactured by Osaka Titanium Company were used. They were polished with 0.06 μm alumina to give a mirror finish, then etched in 46% HF for 15 min, and finally rinsed with methanol. Electrodeposition of polypyrrole was made at 0.3 $\text{mA}\cdot\text{cm}^{-2}$ in 0.1M pyrrole dissolved in propylene carbonate. The electrolysis charge usually employed was 36 $\text{mC}\cdot\text{cm}^{-2}$, which gave ca. 90 nm thickness (14).

The polymer deposition on n-type Si electrodes was carried out by illuminating the electrode with light of wavelengths longer than 390 nm, obtained from a 500 W xenon lamp in combination with a colored glass filter (Toshiba UV-390), while the deposition onto p-type Si was conducted without illumination. The illumination intensity was ca. 2.3 W, as determined by a power meter (Coherent Radiation, Model 201).

For *in situ* measurements of the color change associated with the redox reaction of the polymer film, the electrode was set in an electrolytic cell in such a way that the incident light path was ca. 45° with respect to the perpendicular from the surface. The illuminating light in this case was the same as that described above. The light reflected from the electrode surface was passed through a monochromator (JASCO, Model CT-25), a chopper (Nikon, Model M205), and introduced to a PbS detector (Hamamatsu Photonics, Model P397). The signal from the detector was measured by an electrophotometer (Nikon, Model SP 104). The monochromator was used to isolate

*Electrochemical Society Active Member.

the 400 nm light from the reflected light. According to the published optical properties of oxidized and neutral polypyrrole films (14, 16, 17), the latter film has large absorptivity at this wavelength, but this is not so for the oxidized film. In order to obtain optical image formation, a 1.3 mm diam area of the film on Si was illuminated with a He-Ne laser (NEC, Model GLG 5700). The intensity of the laser beam was 24.5 mW.

A potentiogalvanostat (Hokuto Denko, Model HA 101), a function generator (Hokuto Denko, Model HB 104), and a X-Y recorder (Yokogawa Electric, Model 3077) were used for conventional electrochemical measurements. A saturated calomel electrode (SCE) served as a reference electrode, and the counterelectrode was a Pt plate. The potential cited in this paper is referred to this reference electrode. Polypropylene carbonate was purified by distillation (18), and lithium perchlorate was dried *in vacuo* at 150°C overnight. Other chemicals were reagent grade.

Results and Discussion

Current-potential curves taken under illumination of polypyrrole-coated Si at 100 $\text{mV}\cdot\text{s}^{-1}$ are shown in Fig. 1 and 2 for the cases of n- and p-type Si substrates, respectively, together with the reflectance change associated with photoelectrochemical reactions of the coated elec-

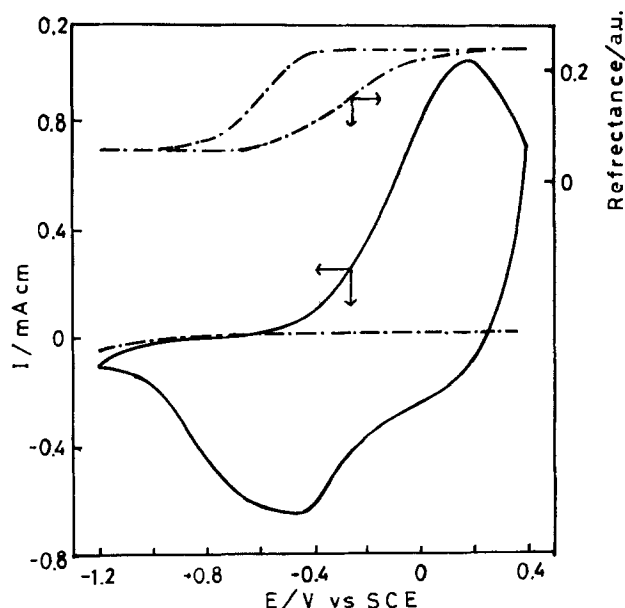


Fig. 1. Steady current-potential curves of a polypyrrole-coated n-type Si electrode under illumination (solid line) and in the dark (dot-dash line), and the top curve is for reflectance of the film measured *in situ*. Film thickness: ca. 90 nm. Solution: 0.1M LiClO_4 in propylene carbonate. $dE/dt = 100 \text{ mV}\cdot\text{s}^{-1}$.

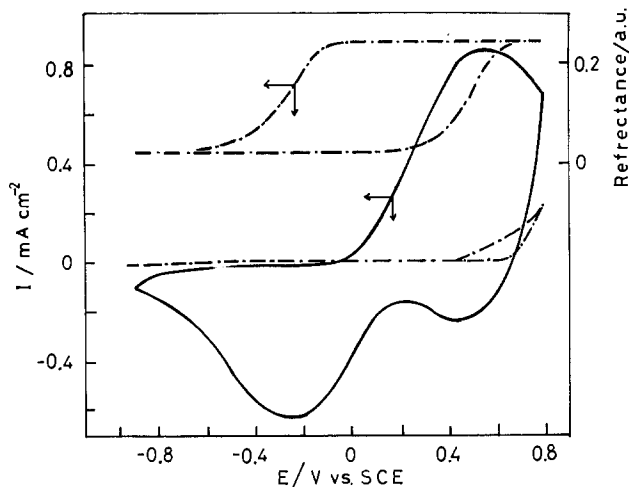


Fig. 2. As in Fig. 1, but for a p-type Si substrate.

trodes. Also given in the figures are the dark currents. In the case of using the n-type Si substrate, some reduction of the oxidized polymer occurred in the dark at 0.4V (not shown in the figure). This potential was chosen as the anodic limit of the potential sweep in Fig. 1, since the oxidized polymer on Pt is reduced a little at this potential. Appreciable reduction of the oxidized polymer in the dark occurred, however, at potentials where a large cathodic wave appeared under illumination. The polymer-coated p-type Si did not show appreciable reactivities in the dark unless the film was in a neutral state. The neutral film shows voltammograms similar to those shown in Fig. 2 during the anodic scan.

The color of polypyrrole in the neutral state is yellow. In the oxidized state it is dark brown. The film on Si electrodes was, however, green in the neutral state and dark brown in the oxidized state to the naked eye, owing to interference of the black Si substrate.

The oxidized film on p-type Si was not reduced in the dark, and, similarly, the neutral film on n-type Si was not oxidized in the dark at potentials similar to those shown in Fig. 1 and 2. Thus, the electrode potentials of -0.9V for p-type Si and 0.4V for n-type Si were chosen in the following experiments to cause photosensitized reactions of the coated polymer film. As Fig. 1 and 2 demonstrate, these potentials are sufficiently large to reduce the film on p-type Si and to oxidize the film on n-type Si electrodes, respectively.

The transient photocurrent behavior and reflectance change of the film-coated electrode are shown in Fig. 3 together with the imposed electrode potential profiles; in each case, the entire electrode surfaces were illuminated. Upon illumination of the neutral film-coated n-type Si electrode at 0.4V , anodic photocurrents flowed until the film was completely oxidized, as seen in the reflectance change (Fig. 3a). Additional illumination had no significant effect. When the electrode potential was switched to -1.2V , cathodic currents flowed, as shown in the figure, and simultaneously the film was reduced to give the original reflectance. The reduction behavior of the film at -1.2V was not greatly affected by the illumination. Similar results were obtained for the p-type Si substrate except that illumination was required to reduce the film. A long time was required to complete the color change of the films for both n- and p-type Si electrodes; it took about 1s or more. The diffusion of electrolyte anions in the polymer film seems to control the rate of the color change (6).

The film color at p-type Si produced by photosensitized reduction of the oxidized film was stable after interruption of illumination, provided that the electrode bias was not interrupted (Fig. 4a). Under open-circuit condition, however, the color of the reduced film gradually changed, indicating that oxidation occurred. Residual oxygen in the electrolyte solution must be responsible for

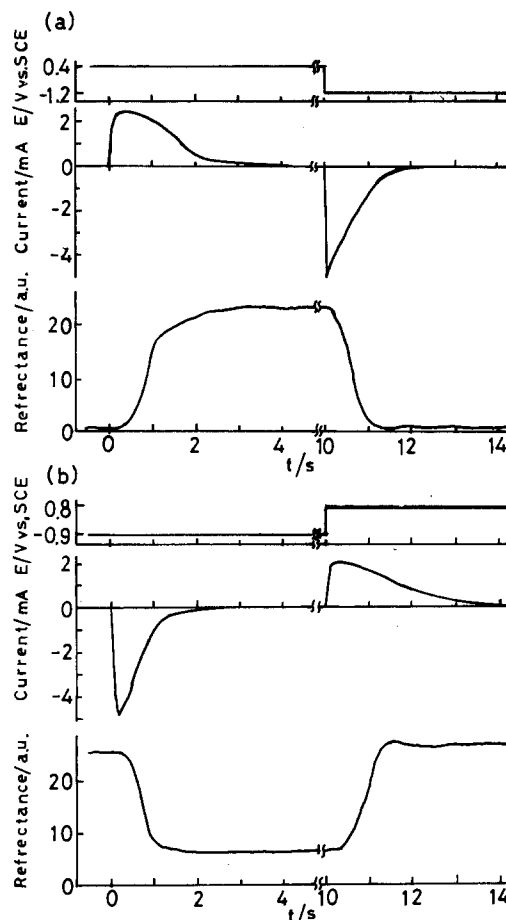


Fig. 3. Transient behavior of current and reflectance at 400 nm of polypyrrole-coated Si electrodes during an imposed potential step. a: n-Type Si electrode coated initially with neutral polypyrrole film. b: p-Type Si electrode coated initially with oxidized polypyrrole film. The entire surfaces of the electrodes were illuminated during the measurements.

the observed color change. In the case of the oxidized film on n-type Si, the interruption of illumination at 0.4V caused small instantaneous cathodic current flow, as described above. The initial value of this cathodic current was ca. $1/15$ of the initial current observed when the electrode potential was switched from 0.4 to -1.2V under illumination (Fig. 3a).

This current, however, soon decayed to zero. As a result, the cathodic charge due to this dark current did not result in any significant fading of the film color. The color produced by the photosensitized oxidation of the neutral film was stable irrespective of whether or not the electrode bias was interrupted, possibly because the residual oxygen has no effect on the oxidized state of the film.

The durability of the color change to repeated potential step pulses was investigated under illumination of the

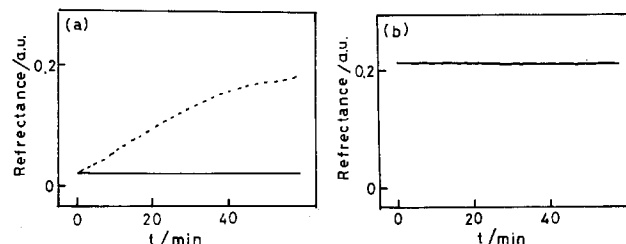


Fig. 4. Stability of the film color produced by illumination during its interruption. a: Polymer-coated p-type Si polarized at -0.9V in the dark (solid line) and under open circuit (dashed line). b: Polymer-coated n-type Si in the dark with and without polarization at 0.4V .

coated film. The voltage pulse chosen had a 10s interval and ranged from 0.8 to -0.9 V for p-type Si and from -1.2 to 0.4 V for n-type Si. The response characteristics during the initial stage are those shown in Fig. 3. It was found that with repeated potential step cycles, reduction of the film decreased. If the ratio of the difference in reflectance of the film between the oxidized and the reduced state at extended potential pulse cycles (ΔR) to that at the first cycle ($\Delta R_{\text{initial}}$) is plotted as a function of the cycle number, Fig. 5 is obtained.

We speculated that the decrease of $\Delta R/\Delta R_{\text{initial}}$ with the cycles might have been brought about by oxidative decomposition of the coated film (19). The effect of the anodic potential on the durability of the film was then investigated. The results showed, however, that the decrease in the anodic potential from 0.4 to 0 V for the case of n-type Si and from 0.8 to 0.3 V for p-type Si did not make any appreciable improvements. Furthermore, the decrease in the anodic potential also produced a slow-down in the response of the color change. Additional studies are required to clarify detailed chemistry related to the decrease of $\Delta R/\Delta R_{\text{initial}}$ with the potential step cycles.

In order to obtain information on optical image formation, the film was irradiated with a laser beam to produce an image pattern in a spot on the coated film. The same anodic potential was used as that employed in obtaining Fig. 3: 0.4 V for n-type Si and -0.9 V for p-type Si. While an image could be formed, the area of the spot gradually increased on continuous irradiation of the film. The peripheral growth of the image occurred more rapidly at the n-type Si electrode than at the p-type one. Photographs of image patterns were taken at different illumination time, and the patterned area of the spot to the total filmed area was determined. This ratio was compared with the ratio of the charge consumed in the image formation to that required in the conversion of all the film to the same color as the image. The results are shown in Table I. The area of the laser beam was 0.013 cm², and the total area of the electrode surface was 0.95 cm².

As may be seen in Table I, the illumination for 1s of p-type Si coated with the oxidized polymer produced an image of the laser beam. In the case of the n-type material, the image pattern was ten times larger than the area of the laser beam. The charge consumed during the image formation was larger for all illumination times for the p-type electrode compared to that at the n-type one. As described below, such difference in the image formation behavior must be closely related to the mechanism by which the color change initially propagates.

When the image is formed in the film on the n-type Si electrodes, electrolyte anions are incorporated into the illuminated part of the film in its outermost part, to change there from a reduced state of high electrical resistivity to an oxidized state of low electrical resistivity.

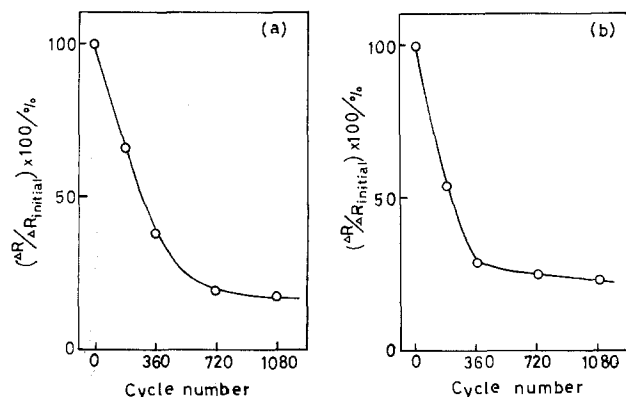


Fig. 5. The ratio of the difference in reflectance between the oxidized and neutral states at extended potential pulse cycles to that at the first cycle vs. the cycle number of the potential pulse. a: n-Type Si substrate. b: p-Type substrate. Potential pulse: -0.9 to 0.8 V for a, and -1.2 to 0.4 V for b. The interval of the pulse: 10s.

Table I. Growth of the optical image pattern with continuous irradiation of a fixed area of the electrode surface^a

Illumination time (s)	n-Type Si		p-Type Si	
	Colored area ^b (%)	Fraction of charge consumed ^c (%)	Colored area (%)	Fraction of charge consumed (%)
1	15	0.92	1.2	4.2
2	22	1.8	4.9	16
3	35	2.7	7.7	19
4	42	3.5	15	27
5	68	4.3	31	31

^a The semiconductor electrodes coated with polypyrrole of ca. 90 nm thickness were illuminated with a He-Ne laser beam of 24.5 mW. The n-type Si coated initially with a neutral film was polarized at 0.4 V, and the p-type one with an oxidized film was polarized at -0.9 V.

^b The colored area to the entire electrode surface is given.

^c The ratio of charge consumed in the formation of the colored image to that required for the complete coloring of the entire surfaces.

Once the outermost part of the film becomes highly conductive, the peripheral growth of the optical image pattern will easily occur at the film/solution interface, as illustrated in Fig. 6a. However, the growth of the optical image in the p-type Si electrode is associated with exclusion of the incorporated anions to give an insulating polymer film. The image pattern formation in this case must occur initially from the film/semiconductor interface as a result of diffusion of the incorporated anions towards the solution side of the film, as illustrated in Fig. 6b.

As already reported (20-23), adhesion of the polymer to Si is rather poor, so that the existence of electrolyte solu-

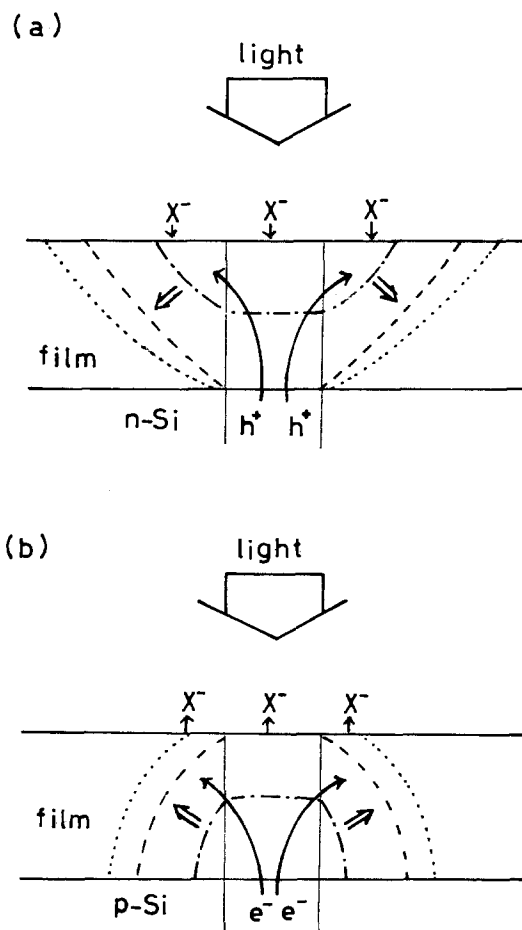


Fig. 6. Schematic illustration of the growth of the domain where the color change of the coated film occurs. a: n-Type Si substrate. b: p-Type substrate. X⁻ denotes an electrolyte anion.

tions in the film as well as at the film/Si interface is highly probable. If so, the distance for photogenerated charge carriers to travel an insulating layer zone will be short compared with the apparent film thickness, and the real situations encountered in the image forming process will be more complicated than that discussed above. Nevertheless, the different behavior of the propagation of the image pattern with illumination time between the n-type and p-type S substrate (Table I) can be explained well by the above described discussion with use of Fig. 6.

Conclusion

In this study, we employed polypyrrole films as photoelectrochromic material. The durability of the coated film and its response behavior are unsatisfactory from the view point of practical application, but improvements in the properties might be made by suitable choice of another kind of electrically conductive polymer. The resolution of the optical image formed, however, will be controlled by similar manner, as shown in Table I and schematically illustrated in Fig. 6. In this sense, the exposure of patterned light for well-controlled time is said to be important for the formation of good optical images.

Manuscript submitted Dec. 26, 1984; revised manuscript received May 1, 1985.

Osaka University assisted in meeting the publication costs of this article.

REFERENCES

1. F. B. Kaufman, A. H. Schraeder, M. Edward, and V. V. Patel, *Appl. Phys. Lett.*, **36**, 422 (1980).
2. H. Akaboshi, S. Toshima, and K. Itaya, *J. Phys. Chem.*, **85**, 818 (1981).
3. G. C. S. Collins and D. J. Schiffrin, *J. Electroanal. Chem. Interfacial Electrochem.*, **139**, 335 (1982).
4. K. Itaya, H. Akaboshi, and S. Toshima, *This Journal*, **129**, 762 (1982).
5. P. C. Bookbinder and M. S. Wrighton, *ibid.*, **130**, 1080 (1982).
6. A. F. Diaz, J. I. Castillo, J. A. Logan, and E.-Y. Lee, *J. Electroanal. Chem. Interfacial Electrochem.*, **129**, 389 (1983).
7. P. C. Lacaze, J. E. Dubois, A. Desebene-Monvernay, P. L. Desbene, J. J. Bassetier, and D. Richard, *ibid.*, **147**, 107 (1983).
8. F. Garnier, G. Tourillon, M. Gazard, and J. E. Dubois, *ibid.*, **148**, 299 (1983).
9. A. Desbene-Monvernay, P. C. Lacaze, J. E. Dubois, and P. L. Desbene, *ibid.*, **152**, 87 (1983).
10. R. N. Dominey, T. J. Lewis, and M. S. Wrighton, *J. Phys. Chem.*, **87**, 5345 (1983).
11. K. Kaneto, S. Ura, K. Yoshino, and Y. Inuishi, *Jpn. J. Appl. Phys.*, **23**, L189 (1984).
12. G. Tourillon and F. Gardiner, *J. Phys. Chem.*, **87**, 2289 (1983).
13. T. Kobayashi, H. Yoneyama, and H. Tamura, *J. Electroanal. Chem. Interfacial Electrochem.*, **161**, 419 (1984).
14. S. Kuwabata, H. Yoneyama, and H. Tamura, *Bull. Chem. Soc. Jpn.*, **57**, 2247 (1984).
15. O. Ingnaes and I. Lundström, *This Journal*, **131**, 1129 (1984).
16. K. Yakushi, L. J. Lauchlan, T. C. Clarke, and G. B. Street, *J. Chem. Phys.*, **79**, 4774 (1983).
17. J. L. Bredas, J. C. Scott, K. Yakushi, and G. B. Street, *Phys. Rev. B.*, **30**, 1023 (1984).
18. C. K. Mann, in "Electroanalytical Chemistry," Vol. 3, A. J. Bard, Editor, p. 119, Dekker, New York (1968).
19. R. A. Bull, F.-R. F. Fan, and A. J. Bard, *This Journal*, **127**, 1009 (1982).
20. R. N. Noufi, A. J. Frank, and A. J. Nozik, *J. Am. Chem. Soc.*, **103**, 1849 (1981).
21. T. Skotheim, I. Lundström, and J. Prejza, *This Journal*, **128**, 1625 (1981).
22. F.-R. F. Fan, B. L. Wheeler, A. J. Bard, and R. N. Noufi, *ibid.*, **128**, 2042 (1981).
23. T. Skotheim, L.-G. Petersen, O. Inganäs, and I. Lundström, *ibid.*, **129**, 1737 (1982).

Technical Notes



Performance of Suspension-Impregnated Sintered Nickel Composite Electrodes

W. A. Ferrando*

Naval Surface Weapons Center, Materials Division, White Oak, Silver Spring, Maryland 20903-5000

Low cost, high performance nickel electrodes will be required for improved Ni-H₂, Ni-Zn, Ni-Fe cells. Several years of effort have been directed to the development of a porous sintered, nickel-plated graphite fiber plaque impregnated by the electrochemical method (1, 2). Plaques were successfully fabricated by compression sintering of electroless nickel-plated graphite mat (3). In the course of optimization, it was found that plaques produced using chopped electroplated graphite fiber exhibited more uniform porosity, durability, and other properties.

Concurrently, an effort was undertaken to find an alternative method of active material [Ni(OH)₂] impregnation suitable for these composite plaques. The electrochemical method had been observed to produce good results. Although simpler and quicker than the older chemical methods, the electrochemical method requires batch processing in tanks with temperature, pH, time, and current

control, as well as time-consuming rinsing. There is also some concern over bath concentration depletion and chemical attack on the plaque.

The Suspension Impregnation Method

It was found that the pore size (~50 μm) and open pore structure of the composite plaque allowed it to accept direct impregnation by fine particulate Ni(OH)₂. To accomplish this, commercial battery-grade Ni(OH)₂ was ground by ball milling to particle diameters (~1-20 μm). The powder was mixed with ethylene glycol (b.p. 198°C) to the consistency of a heavy cream (about 1:2 by weight). The inert semiviscous glycol fluid served to hold the fine active material particles in suspension and provided the lubrication necessary for direct infiltration into the pores.

The impregnation procedure consists of several simple steps. The plaque is placed on a level, nonporous surface. A quantity of the freshly mixed suspension fluid is ap-

*Electrochemical Society Active Member.

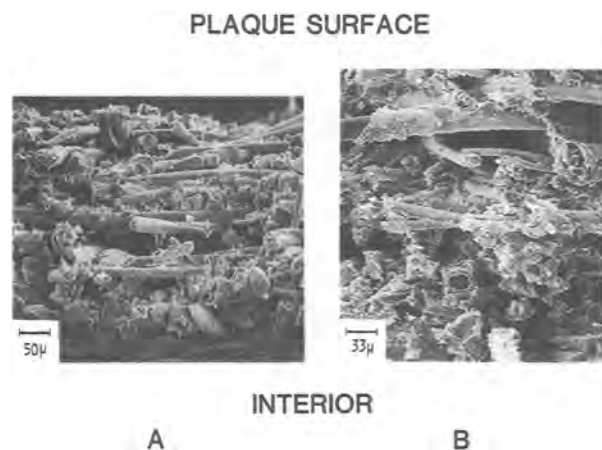


Fig. 1. SEM micrographs, composite plaque cross sections (as cut surfaces). Active material deposition by electrochemical impregnation (A), and by suspension impregnation (B).

plied on and gently rubbed into the plaque surface. The operation is repeated from the reverse side. The plaque is heated ($\sim 150^{\circ}\text{C}$) to evaporate the glycol carrier fluid. Finally, it is brushed lightly to remove surface material and weighed to determine electrode capacity. The operation is repeated, if necessary, to achieve the desired loading level. The entire process can be carried out in a few minutes. Figure 1 shows SEM photographs of the cut edges of suspension-impregnated (A) and electrochemically impregnated (B) composite plaques. Cut ends of the nickel-plated graphite fibers are visible. The pictures enable one to make a rough visual comparison of the initial active material distribution through the cross section by the two methods.

Cobalt Additive Addition

Cobalt additive has long been used to improve utilization and cycle life of nickel electrodes. Recent investigation (4) has revealed that cobalt additive is most efficiently utilized when it is applied to the active material surfaces within the pores, rather than as a volume constituent. The cobalt apparently facilitates proton charge transfer across the active material-electrolyte interface. This addition may be accomplished chemically by soaking the impregnated plaque in an aqueous cobalt compound solution followed by conversion to $\text{Co}(\text{OH})_2$. Cobalt may be added also by a very brief electrochemical deposition from a cobalt impregnation bath. Cobalt added by either method constitutes about 1-4 weight percent of the active mass. Surface deposition of the additive allows the suspension-impregnated electrode to achieve 90% utilization within five to ten discharge cycles.

Test cells were fabricated using a single composite nickel electrode sandwiched between two commercial negatives in 31% KOH with no electrolyte additives and under flooded conditions. Electrochemically impregnated electrode capacities were determined from the postformation weight gain of active material. Capacities of the suspension-impregnated electrodes were determined by the total weight increase measured after cobalt treatment.

Results

Continuous cycling tests were performed on the cells. The imposed regime included charging at the C rate (125%), 10 min rest, followed by discharge at the $C/2$ rate to 0.75V cutoff ($> 95\%$ DOD). Table I lists several important parameters for representative composite electrodes tested according to this regime. The reported utilizations were measured after the initial rise in capacity. Since an objective of this effort was to maximize the usable energy density, several electrodes (no. 83, 85, 95) were electrochemically reimpregnated after initial formation in order to augment loading levels. The high theoretical loadings achieved were of little advantage, however, since reduced utilizations were observed for these electrodes. Working energy densities of 150-170 Ah/kg ($0.27\text{-}0.35\text{ Ah/cm}^2$) were realized generally for the electrochemically impregnated electrodes. The inability to effect a usable increase in energy density by repeated electrochemical impregnation was due probably to the difficulty of maintaining proper conditions within the pores for compact deposition at high loading levels.

Suspension-impregnated electrodes did not suffer this drawback to high loading levels. Entries to Table I indicate that a combination of high active material loading and good utilization could be attained. Operating energy densities in the range of 175-192 Ah/kg ($0.24\text{-}0.325\text{ Ah/cm}^2$) were observed in the cycling tests. Utilization of active material rarely failed to achieve 90% and sometimes exceeded 100% of theoretical capacity. Table I includes several 2.5 mm thick electrodes, which were rapidly and efficiently impregnated by the suspension method. Thick plaques normally present a challenge for any impregnation method. Microgrinding or special precipitation techniques might be able to produce a finer $\text{Ni}(\text{OH})_2$ powder for use in the suspension. In such case, better filling of small pores might allow somewhat higher useful energy densities to be attained.

Several electrodes without current collector grids were fabricated and tested. These are represented by entry no. 44 of Table I and in the data of Fig. 2. The limited test (80 cycles) yielded good utilization and verified the inherent integrity and electrical conductivity of the composite structure. This result indicates that successful composite electrodes might be fabricated without a current collector grid.

Table I. Test electrode parameters

Electrode ^a	Plaque porosity (%)	Nominal thickness (mm)	Theoretical capacity (Ah/kg)	Theoretical capacity (Ah/cm ²)	Ultimate utilization (%)
83-A ^b	89	1.0	190	0.345	82
85-A	85	1.0	191	0.380	83
95-A	82	1.0	208	0.448	78
97-A	82	1.0	205	0.410	74
101-A	71	1.0	169	0.363	86
44-B	83	1.0	183	0.321	95
65-B	91	1.5	189	0.248	93
73-B	73	2.5	193	0.256	95
74-B	73	2.5	208	0.327	91
70-B	73	2.5	169	0.219	113
75-B	82	1.0	183	0.308	105
Powder sinter (commercial) 8/81	—	0.84	86	0.323	—

^a Electrode dimensions: $2.4 \times 4.5\text{ cm}$.

^b A indicates electrochemical impregnation; B indicates for suspension impregnation.

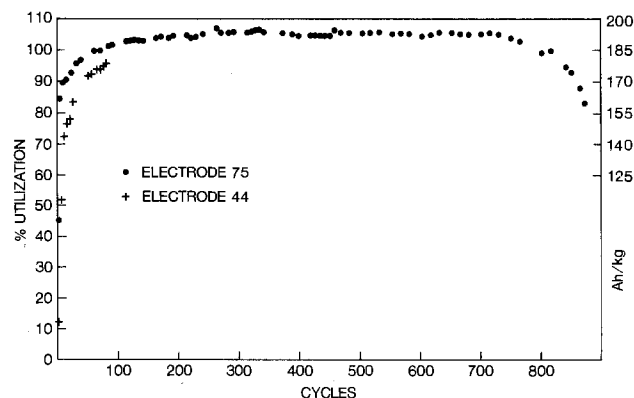


Fig. 2. Active material utilization and volumetric energy density vs. charge-discharge cycles for suspension-impregnated electrodes. No. 75 with current collection grid. No. 44 without current collection grid.

Figure 2 shows the excellent life-cycle durability results obtained with the suspension-impregnated composite electrode. Electrode no. 75 yielded very constant utilization in excess of 100% throughout its lifetime of 800 cycles under the aforementioned test regime. This performance level was typical of the test electrodes with cobalt surface treatment, although most tests were not carried beyond 80-100 cycles.

In order to provide a meaningful life-cycle base line, a commercial positive was tested under substantially identical conditions. Its capacity was determined from the manufacturer's specified cell rating. This capacity, however, apparently underestimated its true capacity somewhat from the observed extended discharge period. This, in turn, implied correspondingly lighter cycling conditions than the specified charge (C) and discharge (C/2). Figure 3 shows the test results. The utilization, normalized here to the maximum observed value, remained reasonably constant over most of the test period. A (gravimetric) energy density of about 115 Ah/kg was achieved. A useful life of about 900 cycles was observed. Cycle-life durability is a major consideration in any secondary battery system. Thus, the main intention in presenting Fig. 2 and 3 is to show the comparability of cycle life between the composite electrode and a powder sintered electrode under the same demanding cycling regime.

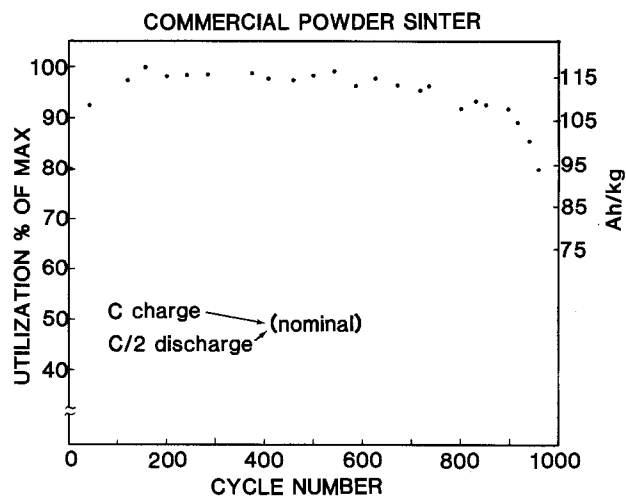


Fig. 3. Normalized active material utilization and volumetric energy density vs. charge-discharge cycles for commercial powder sintered electrode.

In conclusion, this work shows the potential for a successful high energy density, electrically durable, lightweight nickel composite electrode fabricated by a relatively simple suspension method of active material impregnation.

Manuscript received Jan. 18, 1985.

The Naval Surface Weapons Center assisted in meeting the publication costs of this article.

REFERENCES

1. D. F. Pickett, "Fabrication and Investigation of Nickel-Alkaline Cells. Part I: Fabrication of Nickel Hydroxide Electrodes Using Electrochemical Impregnation Techniques," AFAPL-TR-75-34, Air Force Wright Aeronautical Laboratories, WPAFB, OH (1975).
2. W. A. Ferrando and R. A. Sutula, in "The Nickel Electrode," R. G. Gunther and S. Gross, Editors, pp. 271-285, The Electrochemical Society Softbound Proceedings Series, Pennington, NJ (1982).
3. W. Ferrando, W. W. Lee, and R. A. Sutula, *J. Power Sources*, **12**, 249 (1984).
4. W. W. Lee and W. A. Ferrando, NSWC Technical Report, TR 84-122, Naval Surface Weapons Center, White Oak, MD, Defence Technical Information Center, Alexandria, VA.

Electroless and Immersion Plating of Palladium on Zirconium

Cheazone Hsu and Robert E. Buxbaum

Department of Chemical Engineering, Michigan State University, East Lansing, Michigan 48824-1226

Zirconium is an important metal which is widely used in nuclear and chemical industries. In some applications, the zirconium surface is coated with a thin metal film to prevent corrosion or to change the surface properties. A thin coating of copper, nickel, or iron on zirconium is reported to prevent corrosion of cladding material in nuclear reactors (1, 2). Also, Dini *et al.* (3) studied plating nickel, silver, or chromium on zirconium in order to join zirconium to stainless steel.

Palladium is a particularly attractive coating for zirconium. Buxbaum (4) describes the advantages of using a coated palladium window of zirconium for separating tritium from the breeder blanket of a fusion reactor. Also, Stokes and Buxbaum (5) have suggested using a palladium coating to allow the removal of H isotopes from zirconium pressure tubes in CANDU-PHW reactors.

Currently, the following metals can be plated on zirconium: Ni, Fe, Cu, Sn, Cr, and Ag. Schicker *et al.* (6, 7) describe nickel and iron electrodeposition on zirconium following pretreatment by mechanical descaling, alkaline

cleaning, and chemical etching. After electrodeposition, the sample is baked at 200°C to prevent blistering. Kohan (8) describes immersion plating of nickel, copper, and tin on Zircaloy 2 using a pretreatment of vapor blasting, cathodic alkaline cleaning, and pickling. Thicknesses up to 7 μm are deposited by this method. Saubestre (9) describes nickel and copper electroplating on zirconium using a cathodic pretreatment in a suitable electrolyte. Wax *et al.* (10) describe the electroplating of copper, nickel, and chromium on zirconium using an activation solution of ammonium bifluoride and sulfuric acid; and Donaghy (1, 2) holds two patents on processes for electroplating and electroless plating of these same metals. Recently, Dini *et al.* (3) described electroplating nickel, silver, and chromium on zirconium, and showed that adhesion was improved by a postplating heat-treatment at 700°C in constrained geometry or by mechanical treatments such as surface threading or knurling.

At least two dozen formulations for palladium plating baths have been suggested or patented. However, no

technique has been published for either electroplating or nonelectrolytic plating palladium on zirconium.

Experiments

The following two palladium bath formulations were selected for this study. First, we used the immersion plating solution that Johnson (11) used to plate palladium on copper, brass, beryllium-copper, phosphor-bronze, and nickel-silver. The composition was PdCl₂, 5 g/liter; HCl (38%), 200 ml/liter. The temperature was 25°C. Second, we used the electroless palladium bath solution of Pearlstein and Weightman (12). The composition was PdCl₂, 2 g/liter; HCl (38%), 4 ml/liter; NH₄OH (28%), 160 ml/liter; NH₄Cl, 27 g/liter; NaH₂PO₄ · H₂O, 10 g/liter. The temperature was 50°C. The pH was 9.8.

The surface pretreatment was as follows.

1. The sample, zirconium disk with surface area of 10 cm², was machined from a zirconium bar of 99.8% purity.
2. Surface grinding and polishing were used to remove some surface scale and oxide.
3. Detergent washing and solvent cleaning with trichloroethylene were used to remove surface oil and grease.
4. The sample was given a cathodic alkaline cleaning. (Composition: NaOH, 35 g/liter; Na₃PO₄, 10 g/liter. pH: 12. Temperature: 90°C. Time: 3 min. Cathodic current density: 0.1 A/cm². Voltage: 4V.)
5. The sample was given a water rinse.
6. The sample was given an "acid pickling" (13). (Composition: HNO₃ 70%, 10 parts; HF 49%, 1 part; H₂O, 10 parts. Temperature: 25°C. Time: 0.5 min.)
7. Another water rinse was given.
8. The sample was given an activation etching. (Composition: NH₄HF₂, 15 g/liter; H₂SO₄, 1 g/liter. Temperature: 25°C. Time: 1, 2, 3, 6, or 10 min.)
9. A final water rinse was applied.
10. Then, the palladium plating was applied. Immersion plating was tried with and without activation etching step in the surface pretreatment.

Immersion Plating Results

Because the positive potential of zirconium is higher than that of palladium, the palladium ions can theoretically replace atoms of the zirconium substrate in solution by immersion plating. For this process, zirconium atoms must be simultaneously oxidized and dissolved as ions into the solution while palladium ions in solution deposit onto the zirconium substrate. We find, however, that immersion plating (using a PdCl₂-HCl solution) does not give good results: the palladium did not coat the zirconium surface. Without the activation etching prior to immersion plating, a possible explanation is that an oxide film stopped the replacement reaction. Zirconium, being a reactive metal, quickly forms a stable film of surface oxide when the pickled surface is exposed to air or water. Although the thickness of surface oxide is less than 0.0025 μm (14), it may be thick enough to stop atomic replacement. With activation etching in the surface pretreatment, a thin film of zirconium hydride was formed

on the surface and there was still no replacement reaction.

Electroless Plating Results

The surface was activated for electroless plating of palladium on zirconium by forming an adherent, electrically conducting film of black zirconium hydride using a solution containing 15 g/liter NH₄HF₂ and 1 g/liter H₂SO₄. Zirconium hydride provides an improved surface for palladium deposition because it, like palladium, is a face-centered cubic structure (15). Activation etching times of 1, 2, 3, 6, and 10 min were tested at 25°C, and it was found that at least 3 min is necessary to form an adherent palladium deposit. About 9 μm of zirconium was etched off after 3 min of activation at 25°C.

Adhesion was determined by scratching through the coating with a sharp blade; the surface showed no lifting or peeling when viewed under a microscope. Adhesion was also evaluated by a heat quenching test (16): the sample was heated in a vacuum oven to 200°C at a rate of 30°C/h, and was then immersed in room temperature water. No flaking, peeling, or blistering was observed. An adherent palladium coating 5 μm thick was achieved after 3h plating at 50°C.

Acknowledgment

The authors are grateful to the National Science Foundation, who supported this research through Grant no. CPE 8205021.

Manuscript submitted Feb. 4, 1985; revised manuscript received June 10, 1985.

Michigan State University assisted in meeting the publication costs of this article.

REFERENCES

1. R. E. Donaghy, U.S. Pat. 4,093,756 (1978).
2. R. E. Donaghy, U.S. Pat. 4,137,131 (1979).
3. J. W. Dini, H. R. Johnson, and A. Jones, *J. Less-Common Met.*, **79**, 261 (1981).
4. R. E. Buxbaum, *Sep. Sci. Technol.*, **18**, 1251 (1983).
5. C. L. Stokes and R. E. Buxbaum, "Paper presented at the AIChE North Central Student Conference, April, 1984.
6. W. C. Schickner, J. G. Beach, and C. L. Faust, *This Journal*, **100**, 289 (1953).
7. W. C. Schickner, J. G. Beach, and C. L. Faust, *Met. Finish.*, **52** (7), 57 (1954).
8. L. R. Kohan, *ibid.*, **57** (11), 68 (1959).
9. J. B. Saubestre, *This Journal*, **106**, 305 (1959).
10. D. E. Wax and R. L. Cowan, U.S. Pat. 4,017,368 (1977).
11. R. W. Johnson, *This Journal*, **108**, 632 (1961).
12. F. Pearlstein and R. F. Weightman, *Plating*, **56**, 1151 (1969).
13. "Metal Finishing Guidebook Directory," p. 168, Metals and Plastics Publications, Hackensack, NJ (1984).
14. T. L. Barr, *J. Vac. Sci. Technol.*, **14**, 660 (1977).
15. F. Fitzwilliam, A. Kaufmann, and C. Squire, *J. Chem. Phys.*, **9**, 678 (1941).
16. Standard Test Methods for Adhesion of Metallic Coatings, ASTM B571-79, American Society for Testing and Materials, Philadelphia (1984).

Effect of Active Layer Composition on the Service Life of (SnO₂ and RuO₂)-Coated Ti Electrodes in Sulfuric Acid Solution

Chiaki Iwakura and Kenji Sakamoto

Department of Applied Chemistry, Faculty of Engineering, Osaka University, Suita, Osaka, Japan

Although RuO₂- and IrO₂-coated Ti electrodes (Ti/RuO₂ and Ti/IrO₂) have been known to possess high catalytic activity, not only for chlorine evolution, but also for oxygen evolution, they lack the stability required for practical

use as an oxygen anode, and therefore many researchers have been trying to prolong their service lives by different means (1). In general, the addition of ca. 70 mole percent (m/o) TiO₂ to the RuO₂ layer produces the bene-

ficial properties for chlorine evolution (2), but the service life as well as catalytic activity of the (TiO₂ and RuO₂)-coated Ti electrodes (Ti/TiO₂-RuO₂) for oxygen evolution decreases monotonously with increasing TiO₂ content (3). Recently, Burke and McCarthy (4) have reported that the addition of 20 m/o ZrO₂ to the RuO₂ layer increased the service life of the Ti/RuO₂ electrode for oxygen evolution in 6M KOH at 80°C by a factor of 5.3. Noguchi *et al.* (5) have also reported that the addition of ca. 33 m/o Co oxide to the IrO₂ layer increased the service life of the Ti/IrO₂ electrode for oxygen evolution in 4M H₂SO₄ at 60°C by a factor of 12.5. In both cases, however, it is not clear why such compositions are optimum for the active layers.

In this work, the effect of active layer composition on the service life of (SnO₂ and RuO₂)-coated Ti electrodes (Ti/SnO₂-RuO₂) in sulfuric acid solution was investigated in connection with the electrodes physicochemical properties from a fundamental viewpoint rather than a practical viewpoint. Both fundamental and practical investigations on the Ti/SnO₂-RuO₂ and related electrodes are still active, as can be seen from recent papers (6-9), although the idea of the use of SnO₂ in RuO₂-based anodes for industrial brine electrolysis goes back to earlier patents (10-12). The electrocatalysis of such electrodes for oxygen and chlorine has already been studied by Chertykovtseva *et al.* (13) and the present authors (14).

Experimental

The test electrodes (Ti/SnO₂-RuO₂) were prepared by a thermal decomposition method in the following way. First, a Ti plate (2.5 cm²) was mechanically polished with emery paper (~ no. 1000) and then chemically etched with a boiling aqueous solution of 0.2M oxalic acid for 10 min. Next, an appropriate amount of a mixture of 0.1M SnCl₄ and 0.1M RuCl₃-20 weight percent (w/o) HCl aqueous solution was applied to one side of the cleaned Ti plate. It was dried at 50°C and then placed in a preheated furnace at 350°C for 10 min. Such operations were repeated four times. Finally, the fifth coating was made and then the plate was dried at 50°C, followed by heating at 450°C for 1h to complete the thermal decomposition. The total loading amount of SnO₂ and RuO₂ was kept constant at 1×10^{-5} mol/cm². The amount of each metal oxide will be indicated in parentheses in mole percent.

All the electrochemical measurements were done in 0.5M H₂SO₄ at 30°C by conventional means. An all-Pyrex glass H-type cell with Teflon stoppers was used as an electrolytic cell and a Pt sheet as a counterelectrode. The reference electrode used was a mercury (I) sulfate electrode (Hg/Hg₂SO₄, 0.5M H₂SO₄).

The other experimental procedures and conditions will be given in the next section when necessary.

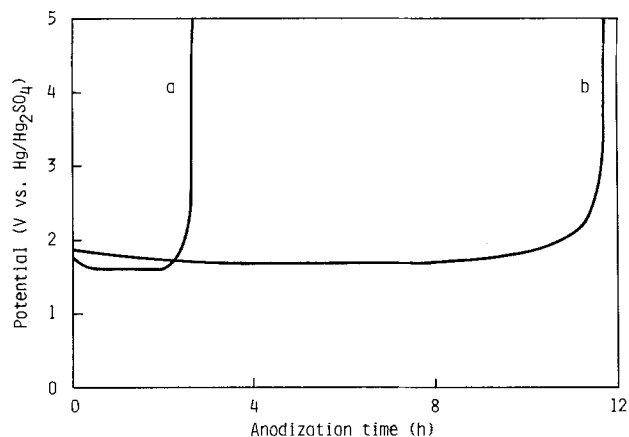


Fig. 1. Typical potential-time curves for Ti/RuO₂ (a) and Ti/SnO₂(70)-RuO₂(30) (b) electrodes under anodization at 500 mA/cm² in 0.5M H₂SO₄.

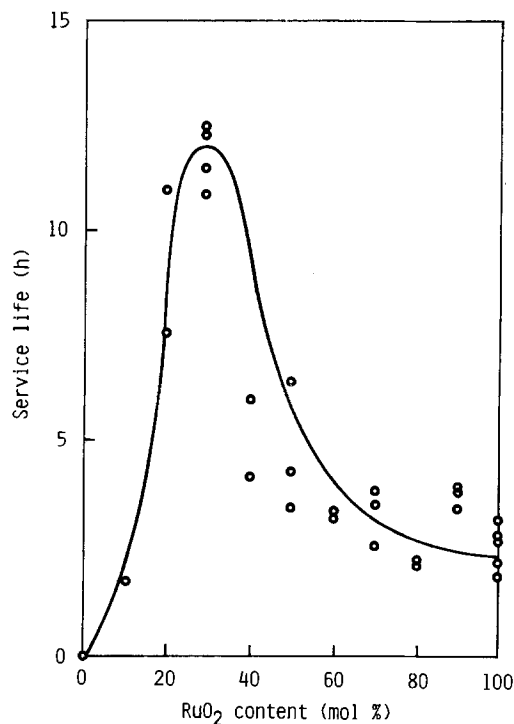


Fig. 2. Plot of service life against RuO₂ content for Ti/SnO₂-RuO₂ electrodes.

Results and Discussion

The accelerated life tests of the Ti/SnO₂-RuO₂ electrodes with different RuO₂ contents were carried out by anodization at 500 mA/cm². Typical potential-time curves are shown in Fig. 1. In any case, the potential remains almost unchanged for a certain time and then increases rapidly. Hereinafter, the service life will be defined as the time of operation before the anode potential increases significantly, say 5V vs. Hg/Hg₂SO₄ (iR included). Figure 2 shows the plot of service life against RuO₂ content. It is clear that the service life vs. RuO₂ content plot has a maximum at around 30 m/o RuO₂. This happened to coincide in Sn/Ru ratio with the reported Sn-Ru binary alloys, *i.e.*, Ru₃Sn₇, RuSn₃, and Ru₂Sn₅ (15). The service life of the Ti/SnO₂(70)-RuO₂(30) electrode is longer than that of the Ti/RuO₂ electrode by a factor of 4.5-5. This is in a marked contrast to the result obtained with a series of Ti/TiO₂-RuO₂ electrodes for oxygen evolution (3).

The anodic polarization curves of some Ti/SnO₂-RuO₂ electrodes are shown in Fig. 3. All the electrodes shown, except for the Ti/SnO₂(90)-RuO₂(10) electrode, have the dual Tafel slopes of 0.06 and 0.12 V/decade, suggesting that the mechanism of the oxygen evolution reaction is

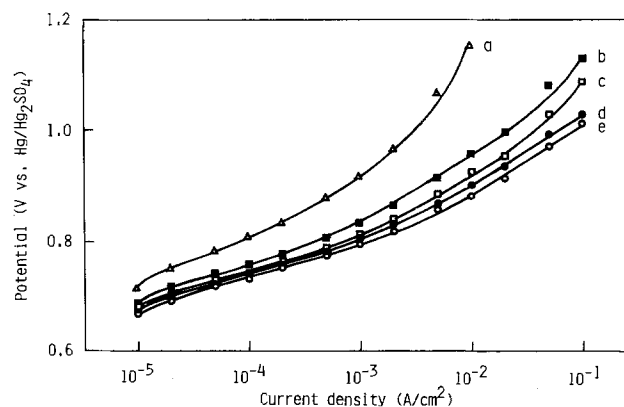


Fig. 3. Galvanostatic polarization curves of Ti/SnO₂(90)-RuO₂(10) (a), Ti/SnO₂(70)-RuO₂(30) (b), Ti/SnO₂(50)-RuO₂(50) (c), Ti/SnO₂(30)-RuO₂(70) (d), and Ti/RuO₂ (e) electrodes.

unchanged. Furthermore, the current-potential curves of these electrodes can almost completely be superposed upon each other when they are replotted on the basis of the current density per given amount of RuO_2 (e.g., 1×10^{-5} mol/cm²). This indicates that the active center for the oxygen evolution reaction is on the Ru sites, which is in agreement with the view reported previously (14).

Figure 4 shows SEM microphotographs of the surfaces of the Ti/RuO_2 and $\text{Ti/SnO}_2(70)\text{-RuO}_2(30)$ electrodes. Evidently, the surface of the latter electrode is much more smooth and compact, with smaller cracks and pores than those of the former electrode. Thus, the result of Fig. 2 cannot be explained simply on the basis of an increase of effective surface area in the usual way (8). The increased smoothness and compactness of the electrode surface are considered to lead to the prolonged service life because they depress the penetration of electrolyte through cracks or pores in the active layer and thereby the formation of a resistive TiO_2 film on the Ti substrate (3).

The coloring of the solution straw-yellow during the life tests indicates clearly the occurrence of the anodic dissolution of the active layer, which can also lead to the formation of a resistive TiO_2 film on the Ti substrate (3). So, the dissolution rate of the active layer during anodization was determined by fluorescent x-ray analysis for both the Ti/RuO_2 and $\text{Ti/SnO}_2(70)\text{-RuO}_2(30)$ electrodes. Many test electrodes were used in the measurements, so that one electrode corresponds to each point in Fig. 5 as well as in Fig. 2. Figure 5 shows the variation of the normalized residual amounts of Ru and Sn species with the anodization time. In either case, the Ru species dissolve fast at the first stage, quite slowly in the middle period, and again rapidly at the final stage. From a detailed comparison of these data with the data shown in Fig. 1, one can notice that the potential change is almost paralleled by the dissolution of RuO_2 . In addition, the charges, de-

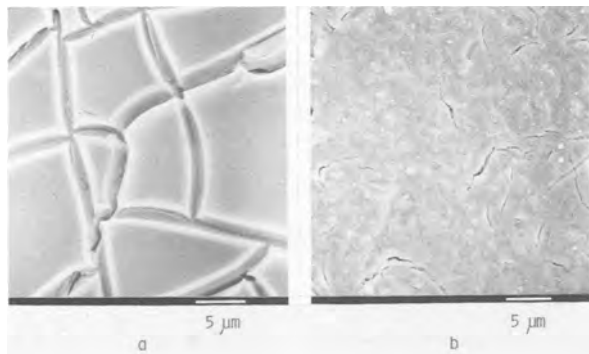


Fig. 4. Microphotographs taken by SEM of the surfaces of Ti/RuO_2 (a) and $\text{Ti/SnO}_2(70)\text{-RuO}_2(30)$ (b) electrodes.

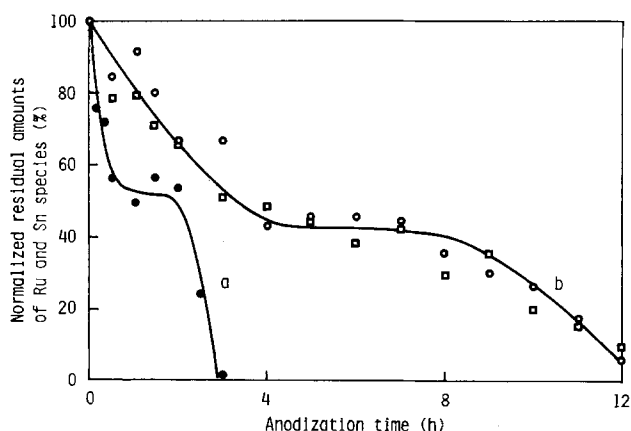


Fig. 5. Variation of normalized residual amounts of Ru (circle) and Sn (square) species with anodization time for Ti/RuO_2 (a) and $\text{Ti/SnO}_2(70)\text{-RuO}_2(30)$ (b) electrodes.

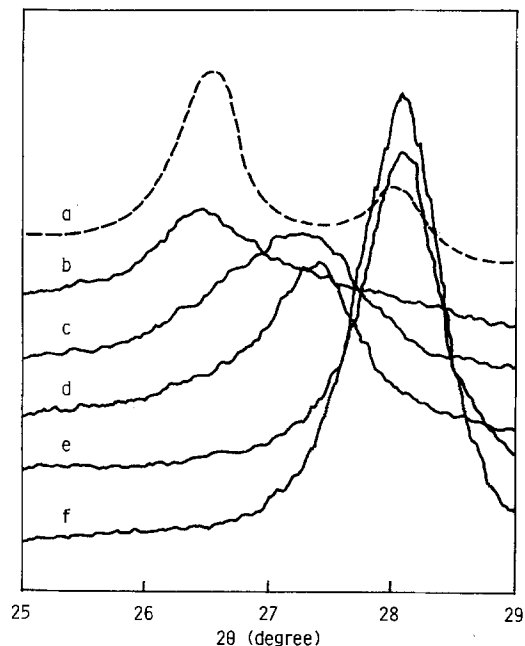


Fig. 6. X-ray diffraction patterns of $\text{SnO}_2(70)\text{-RuO}_2(30)$ mixed powders (a), Ti/SnO_2 (b), $\text{Ti/SnO}_2(90)\text{-RuO}_2(10)$ (c), $\text{Ti/SnO}_2(70)\text{-RuO}_2(30)$ (d), $\text{Ti/SnO}_2(50)\text{-RuO}_2(50)$ (e), and Ti/RuO_2 (f) electrodes.

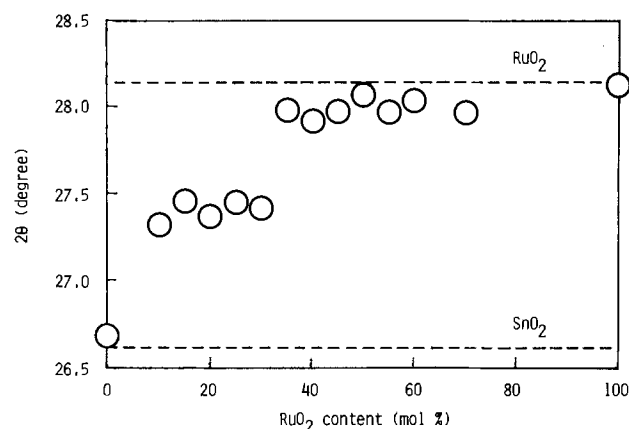


Fig. 7. Plot of x-ray diffraction angle against RuO_2 content for $\text{Ti/SnO}_2\text{-RuO}_2$ electrodes.

termined by cyclic voltammetry between 0.1 and 0.3V vs. $\text{Hg/Hg}_2\text{SO}_4$, was also found to change correspondingly with the anodization time; i.e., it increased and decreased at the first and final stages, respectively. Though the reason why a period of constancy in overpotential, as well as charges, with no dissolution exists is unclear at the present stage, it is evident from Fig. 5 that the RuO_2 dissolution is depressed to a great extent by the coexistence of SnO_2 and RuO_2 and that not only RuO_2 but also SnO_2 dissolve anodically, as was already confirmed by means of SIMS (14). Besides these facts, it is worth noting that both RuO_2 and SnO_2 dissolve almost in the same manner, suggesting the interaction between them.

The x-ray diffraction measurement was carried out for different electrode samples under the following conditions: a counterelectrode of Cu; tube voltage of 30 kV; tube current of 10 mA, time constant of 4s, scan rate of $0.5^\circ(2\theta)/\text{min}$; and a slit width of 0.3 mm. Figure 6 shows the x-ray diffraction patterns of some $\text{Ti/SnO}_2\text{-RuO}_2$ electrodes together with the mixed powders of $\text{SnO}_2(70)$ and $\text{RuO}_2(30)$. In this figure, only the patterns for each main peak in a (110) plane are shown since the patterns for the subpeaks in the other planes such as (101) and (211) were quite similar to those for the main peaks. As shown typically for the $\text{Ti/SnO}_2(50)\text{-RuO}_2(50)$ electrode, the peaks of the electrodes with relatively high RuO_2 contents coin-

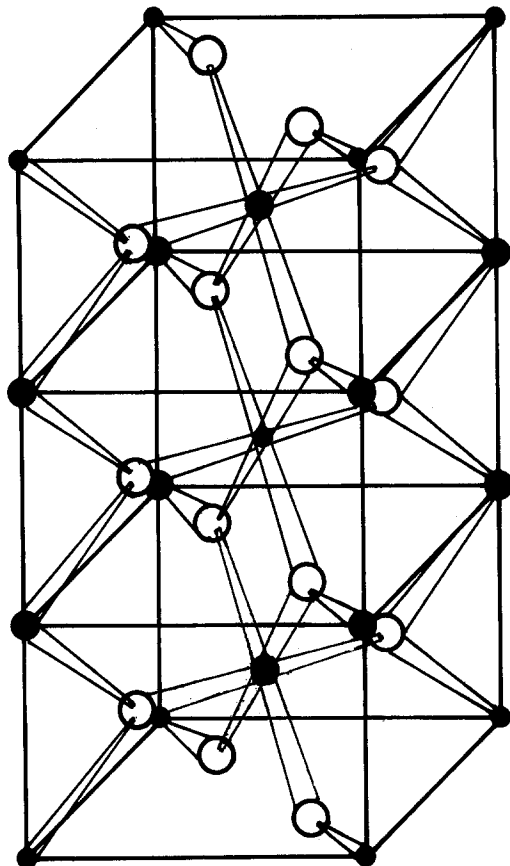


Fig. 8. Probable triple-rutile structure of RuSn_2O_6 . Small filled circles: Ru. Large filled circles: Sn. Open circles: O.

cided in diffraction angle with the peak of the Ti/RuO₂ electrode though they were somewhat broader, probably because of the replacement of Ru site by Sn species without change of the RuO₂ crystal structure. However, the Ti/SnO₂(70)-RuO₂(30) electrode exhibits a specific diffraction peak which lies between the two peaks of SnO₂ and RuO₂. The change of the diffraction angle of the main peak with the composition is more clearly shown in Fig. 7. No diffraction peak was observed for the Ti/SnO₂(95)-RuO₂(5) electrode, indicating the destruction of the SnO₂ crystal structure. The alternative broad diffraction peaks appeared at the Ti/SnO₂(90)-RuO₂(10) electrode, and they became sharp gradually with increasing RuO₂ content up to 30 m/o. These suggest strongly that a new, somewhat distorted, crystalline structure, probably RuSn_2O_6 , is formed at the electrode with the composition of around SnO₂(70)-RuO₂(30) during the electrode preparation. From the analogy to triple-rutile structure of mossaite FeNb_2O_6 (16), the new crystal may be represented by the structure shown in Fig. 8, though further detailed studies are necessary.

In conclusion, the service life of the Ti/RuO₂ electrode can be prolonged by the presence of SnO₂ in the active layer with the optimal composition of around 70 m/o SnO₂ and 30 m/o RuO₂. This is probably due to the formation of a new crystalline but somewhat disordered RuSn_2O_6 , which leads to the depression of the anodic dissolution of the active layer, in addition to the increased smoothness and compactness of the active layer.

Acknowledgments

Financial support of a part of this work by Toyo Soda Manufacturing Company, Limited, is gratefully acknowledged. The authors are greatly indebted to Professor Nobutami Kasai, Osaka University, for helpful comments on the interpretation of the x-ray diffraction data.

Manuscript submitted Feb. 20, 1985; revised manuscript received June 4, 1985.

Osaka University assisted in meeting the publication costs of this article.

REFERENCES

1. A. Nidola, in "Electrodes of Conductive Metallic Oxides," S. Trasatti, Editor, Part B, 627, Elsevier, Amsterdam (1981).
2. F. Hine, M. Yasuda, and T. Yoshida, *This Journal*, **124**, 500 (1977); F. Hine, M. Yasuda, T. Noda, T. Yoshida, and J. Okuda, *ibid.*, **126**, 1439 (1979).
3. C. Iwakura, M. Inai, M. Manabe, and H. Tamura, *Denki Kagaku*, **48**, 91 (1980).
4. L. D. Burke and M. McCarthy, *Electrochim. Acta*, **29**, 211 (1984).
5. F. Noguchi, S. Matsumura, T. Iida, T. Mitamura, Y. Arai, and Y. Kamegaya, *Denki Kagaku*, **51**, 713 (1983).
6. W. Badawy, K. Doblhofer, I. Eiselt, H. Gerischer, S. Krause, and J. Melsheimer, *Electrochim. Acta*, **29**, 1617 (1984).
7. N. Krastajic, M. Spasojevic, and M. Jaksic, *J. Res. Inst. Catal. Hokkaido Univ.*, **32**, 19, 29 (1984).
8. A. Bandi, I. Vartires, A. Mihelis, and C. Hainarosie, *J. Electroanal. Chem.*, **157**, 241 (1983).
9. R. U. Bondar, E. A. Kalinovskii, I. V. Kunpan, and V. S. Sorokendya, *Elektrokhimiya*, **19**, 1104 (1983).
10. G. Bianchi, V. De Nora, P. Gallone, and A. Nidola, South African Pat. 68/7371, 68/7482 (1968).
11. J. H. Etwisle, D. Lee, and A. Scrutton, Ger. Offen. 1,952,484 (1970); *C.A.*, **73**, 491 (1970).
12. K. J. O'Leary, U.S. Pat. 3,776,834 (1983); *C.A.*, **80**, 450 (1974).
13. T. A. Chertykovtseva, D. M. Shub, and V. I. Veselovskii, *Elektrokhimiya*, **14**, 275, 1260 (1978); T. A. Chertykovtseva, Z. D. Skuridina, D. M. Shub, and V. I. Veselovskii, *ibid.*, **14**, 1412 (1978).
14. C. Iwakura, M. Inai, and H. Tamura, *Chem. Lett.*, 225 (1979); C. Iwakura, M. Inai, T. Uemura, and H. Tamura, *Electrochim. Acta*, **26**, 579 (1981); C. Iwakura, Y. Taniguchi, and H. Tamura, *Chem. Lett.*, 689 (1981).
15. F. A. Shunk, "Constitution of Binary Alloys, Second Supplement," p. 650, McGraw-Hill, New York (1969).
16. R. Kiriya, in "Kessho Kogaku Handobukku," Henshu Iinkai, Editor, p. 57, Kyoritsu Shuppan, Tokyo (1975).

Application of Electrochemical Fluorination to the Synthesis of Perfluoroalkane Sulfonic Acid Electrolytes

Preparation of $F_2C(SO_3H)_2$

E. J. M. O'Sullivan*,¹

Department of Chemistry, Case Center for Electrochemical Sciences, Case Western Reserve University, Cleveland, Ohio 44106

F. W. Klink,** C. C. Liu,* and E. B. Yeager*

Department of Chemical Engineering, Case Center for Electrochemical Sciences, Case Western Reserve University, Cleveland, Ohio 44106

Perfluorinated alkane sulfonic acids have been receiving attention in the last few years as potential fuel cell electrolytes (1, 2). However, except for trifluoromethane sulfonic acid, acids of this class are not widely available, particularly the multifunctional compounds. Consequently, progress in the evaluation of the electrolyte properties of these acids has been impeded. Effective methods for the synthesis of attractive perfluorinated sulfonic acids are therefore needed which can generate appreciable quantities of these acids in a highly pure form.

Synthetic routes based on electrochemical fluorination (ECF) (3-7) in anhydrous hydrogen fluoride (AHF) are attractive for the preparation of perfluoroalkane sulfonic acids. Although the fluorination of alkane sulfonic acids cannot be carried out directly by ECF (3), Brice and Trott (8) and Gramstad and Haszeldine (9) showed that alkane sulfonyl halides (chlorides and fluorides) could be successfully fluorinated by this method to give perfluoroalkane sulfonyl fluoride products in fairly high yields. The perfluorinated sulfonyl fluoride products were converted to the corresponding acid salt by alkaline hydrolysis, the free acid then being obtained either by distillation from a solution of concentrated sulfuric acid and sulfonic acid salt, or by ion exchanging solutions of the salt (10).

In this paper, the electrochemical fluorination of methanedisulfonyl fluoride, $H_2C(SO_2F)_2$, to produce difluoromethanedisulfonyl fluoride, $F_2C(SO_2F)_2$, in high yields is described, along with the conversion of the latter compound to the disulfonic acid form. The formation of $F_2C(SO_2F)_2$ from $H_2C(SO_2F)_2$ via ECF has been reported previously (11). Methanedisulfonyl fluoride was selected as a substrate for ECF rather than the corresponding disulfonyl chloride since it has been established (9) that substrates containing the $-SO_2F$ group rather than the $-SO_2Cl$ group give higher yields of the perfluoroalkane sulfonyl fluoride compounds. Also, in the case of substrates containing a high ratio of $-SO_2Cl$ groups to C-H bonds there is the possibility of formation of undesirable C-Cl bonds in the course of electrolysis.

Experimental

The methanedisulfonyl fluoride reactant used in the electrochemical fluorination reaction was synthesized via a two-step process. In the first step, methanedisulfonyl chloride, $H_2C(SO_2Cl)_2$, was synthesized by a reaction involving acetic acid (Fisher, Reagent), chlorosulfonic acid (Pfaltz and Bauer, 99%), and phosphorous oxychloride (Fisher, Purified) as described by Fild and Rieck (12). In the second step, the $H_2C(SO_2Cl)_2$ was converted to $H_2C(SO_2F)_2$ by the action of potassium bifluoride (Harshaw, 97%) in acetonitrile (Fisher, 99%). Following removal of the precipitated KCl product by filtration, the $H_2C(SO_2F)_2$ was recovered by vacuum distillation. Typically, chemical yields of 70-75% were obtained by each of

these two reactions. Elemental analysis and proton and fluorine NMR confirmed the identification of $H_2C(SO_2F)_2$. This material was purified by further vacuum distillation, and its purity was found to be in excess of 98% by gas chromatography. The major impurities in the $H_2C(SO_2F)_2$ were $H_2C(SO_2Cl)_2$ and $H_2C(SO_2Cl)SO_2F$.

The electrochemical fluorination reaction was conducted in a Simon-type reactor (3) with a volume of 500 ml. The details of the cell design and support system have been reported previously (13). In a typical experiment, the reactor temperature was maintained at $10^\circ \pm 1^\circ C$ with the condenser kept at -50° to $-60^\circ C$. A 20 ml/min flow rate of nitrogen was maintained throughout the experiment in order to sweep away hazardous gaseous products. Typically, 450 ml of anhydrous hydrogen fluoride (AHF) was added directly to the cell and purified by pre-electrolysis at a constant cell voltage at 5.5V until the current decayed to a constant base-line value of $\sim 0.2 A/dm^2$. The purpose of this pre-electrolysis step, which was typically conducted for 12-18h, was to form the anodic nickel fluoride film and remove any water present in the AHF.

After the pre-electrolysis of the AHF, approximately 30g of $H_2C(SO_2F)_2$ was added to the cell, bringing the reactant concentration to 5% by weight. The cell was operated at a constant cell voltage of 5.5V with an average current density of $\sim 0.5 A/dm^2$. The electrolysis current remained relatively constant as long as the reactant was present and rapidly decayed when the last amount of reactant was consumed. New reactant was then added when the current decayed to the base-line value. A typical run duration was 150h. The fluorination product formed a separate heavy phase, which could be observed along with some solid corrosion products, at the bottom of the reactor when the agitation was turned off. A greenish-white corrosion product, presumably nickel difluoride (9), could also be observed loosely coating the anodes.

One of the methods employed for carrying out salt-to-acid conversions in the present work was electrodiolysis. A three-compartment PTFE cell was employed which used Nafion 117 membranes as separators. The Nafion membranes (proton version, 1100 eq weight, 0.007 in. thick) were cleaned in hot water, which was frequently changed, for at least two weeks prior to use. A solution of the sulfonate salt, $F_2C(SO_3Li)_2$, rather than the Ba salt, was placed in the central compartment. Solutions of LiOH (0.5M) and trifluoromethane sulfonic acid (1.0M) were placed in the cathode and anode compartments, respectively. Platinum gauze was used for the anode and cathode. Current densities of $10 A/dm^2$ with respect to the Nafion membranes were employed. In view of the rather high electric fields present across the membrane at such high current densities, diffusion of the bulky $F_3CSO_3^-$ ion from the anode compartment should be negligible. Similarly, back-diffusion of Li^+ ion from the cathode compartment should also be minimal.

Results and Discussion

At the completion of the electrolysis experiment, the cell and cell condenser were warmed to room tempera-

*Electrochemical Society Active Member.

**Electrochemical Society Student Member.

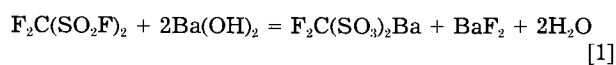
¹Present address: IBM Thomas J. Watson Research Center, Yorktown Heights, New York 10598.

ture. To facilitate recovery of volatile products from the cell, which included the $F_2C(SO_2F)_2$, a cold trap consisting of coiled Monel tubing immersed in a Dry Ice/isopropanol mixture (temperature $\sim -73^\circ C$) was incorporated in the outlet gas stream from the condenser. HF and product material were simultaneously carried over from the warmed cell and condenser in a stream of N_2 gas and were collected in a flask of ice water placed at the outlet of the cold trap. The HF dissolved in the water, while the $F_2C(SO_2F)_2$ product was insoluble, forming a second, transparent layer at the bottom of the flask. Only a trace quantity of organic material remained with the corrosion products in the cell. The product recovered in the ice water trap was separated from the aqueous phase and washed further with water to remove traces of HF. No traces of color were exhibited by this product at any time.

Fractional distillation of the ECF product initiated at $56.5^\circ C$ and rose rapidly to a steady temperature of $57.2^\circ C$. A 250 ml round-bottom glass distillation flask was employed and operated at ambient pressure. In order to avoid any introduction of contaminants, no stopcock grease was used for the glass joints. Thermometers with ground glass joints were placed in both the still flask and at the entrance of the condenser. Only the product recovered at $57.2^\circ C$ was employed for the conversion to $F_2C(SO_3H)_2$. Fluorine NMR confirmed the structure of $F_2C(SO_2F)_2$ showing two triplets, one centered at -36.6 ppm relative to $CFCl_3$ and the other at 96.8 ppm. Proton NMR confirmed the absence of C-H bonds in the product, indicating the maximum C-H material presented was less than 5%.

The chemical yield of the ECF step was approximately 70%, with a product-recovered-based current efficiency averaging 44%.

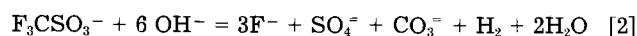
Preparation of $F_2C(SO_3H)_2$ from $F_2C(SO_2F)_2$.—Various methods were explored for converting $F_2C(SO_2F)_2$ to the acid form. In general, perfluorinated alkane sulfonyl fluorides are readily hydrolyzed under alkaline conditions only (9). The hydrolysis of $F_2C(SO_2F)_2$ was found to be most effectively carried out using concentrated aqueous solutions of either $Ba(OH)_2$ or $LiOH$ since the relatively insoluble fluoride salt by-products, BaF_2 and LiF , respectively, could be separated from the hydrolysis mixtures by filtration. The stoichiometric equation for the $Ba(OH)_2$ hydrolysis reaction, for example, may be written as follows



The hydrolysis reactions were conducted at room temperature over periods of 1-2 days. In this step, the $F_2C(SO_2F)_2$ was added in a batchwise manner to the alkali solutions in FEP bottles. The additions were carried out in such a manner that the reaction temperature did not exceed $35^\circ C$. A slight excess of alkali was employed in order to insure complete conversion of sulfonyl fluoride functional groups to sulfonate groups. At the completion of the reaction, the insoluble fluoride salts were removed by filtration. The Ba or Li disulfonic acid salts were recovered from the filtrate after removal of the water using an aspirator.

Sulfate anion was detected in the hydrolysis solutions utilizing $LiOH$ as the hydrolyzing base. The odor of sulfur dioxide from the hydrolysis solutions has also been detected at the completion of the hydrolysis reaction. The sulfate was removed as $BaSO_4$ by the addition of barium hydroxide. The amount of sulfate formed during the hydrolysis reaction has been found to be 0.001-0.002 mol per mole of $F_2C(SO_2F)_2$. Sulfate was not present in the original $F_2C(SO_2F)_2$ and only to a very minor extent as an impurity in the $LiOH$. The sulfate is evidently generated by hydrolysis of the $F_2C(SO_3^-)_2$ anion.

Fabes and Swaddl (14) have reported that $F_3CSO_3^-$ oxidatively hydrolyzes quantitatively in alkaline solutions at $297^\circ C$, and suggested the following equation for the process



Perhaps a process similar to reaction [2] leads to the instability of the difluoromethane disulfonate even though the temperature did not exceed $35^\circ C$. A more likely process, however, is the oxidation of the disulfonate in alkaline solution by O_2 from the air. The disulfonate may be more susceptible to oxidative hydrolysis than the monosulfonate because the presence of two $-SO_3^-$ groups on one carbon leads to lower stability.

Various methods were explored for converting the disulfonic acid salts to the acid form, principally ion exchange and electro dialysis. A disadvantage of the electro dialysis method is the relatively long periods required (several days) to reduce the Li^+ content to very low levels (e.g., 2-3%) in the disulfonic acid material. Furthermore, despite extensive cleaning of the Nafion 117 membranes employed in the cell, cyclic voltammograms of smooth Pt electrodes recorded in $F_2C(SO_3H)_2$ solutions (e.g., 1.0M) prepared by this method indicated the presence of impurities, particularly in the hydrogen adsorption/desorption region. These impurities were also found to interfere severely with rotating ring-disk electrode measurements of O_2 reduction in these electrolytes. These impurities were not removed by pre-electrolysis methods or by treatment with hydrogen peroxide. Since the $F_2C(SO_2F)_2$ was highly purified prior to hydrolysis by multiple fractional distillations, it seems likely that a major portion of these impurities were generated during the further hydrolysis of $F_2C(SO_3^-)_2$. The $F_2C(SO_3Li)_2$ salt cannot be purified readily by recrystallization from aqueous solutions prior to being submitted to electro dialysis owing to its extremely high solubility. In general, the most effective method for purifying the newly prepared $F_2C(SO_3H)_2$ was found to be distillation of its dihydrate under reduced pressure (~ 0.3 torr air). Distillation also served to remove traces of salt remaining after electro dialysis.

Ion exchange was also investigated as a convenient method for converting $F_2C(SO_3Li)_2$ to the acid form. Amberlite IR 120 resin was employed after being washed extensively with ultrapure water. The ion exchange resin did not appear to degrade while it was in contact with the disulfonic acid, and essentially quantitative conversion of the salt to the acid was achieved. The disulfonic acid prepared by ion exchange was also subsequently purified by vacuum distillation of its dihydrate, and its composition was confirmed by elemental analysis. In the case of perfluoroalkane sulfonic acid salts, which can be purified by recrystallization, e.g., the potassium salts of tetrafluoroethane-1,2- and hexafluoropropane-1,3-disulfonic acids, the method of electro dialysis would be one of the methods which should produce purer acid than ion exchange methods (15), since the resin is a potential source of organic impurities.

Voltammetry of platinum.—Linear potential sweep voltammetry of smooth Pt in a N_2 (Matheson, 99.9995%) saturated solution provides a convenient qualitative check of electrolyte purity. Cyclic voltammograms of 0.5M $F_2C(SO_3H)_2$ and 1.0M H_3PO_4 are shown in Fig. 1. The disulfonic acid was purified by twice distilling the dihydrate under reduced pressure, while the phosphoric acid was carefully purified as described elsewhere (16). The voltammogram of the $F_2C(SO_3H)_2$ exhibits reasonably well-defined hydrogen and oxide film regions. The minor peak present at $\sim 0.75V$ vs. RHE (1 atm) in the anodic sweep increases slightly with sweep rate and becomes less pronounced at lower concentrations. It is probably an impurity peak. Overall, however, the voltammogram of $F_2C(SO_3H)_2$ indicates that this acid is reasonably pure.

There are some differences between the hydrogen and oxide regions of the voltammetric profiles of Pt recorded in the 0.5M $F_2C(SO_3H)_2$ and H_3PO_4 electrolytes. The onset of oxide formation in the anodic sweep occurs at ~ 70 mV more negative in the case of the sulfonic acid electrolyte relative to phosphoric acid. This is an indication of weaker adsorption on Pt by the sulfonic acid electrolyte relative to phosphoric acid. Also, as observed in the case

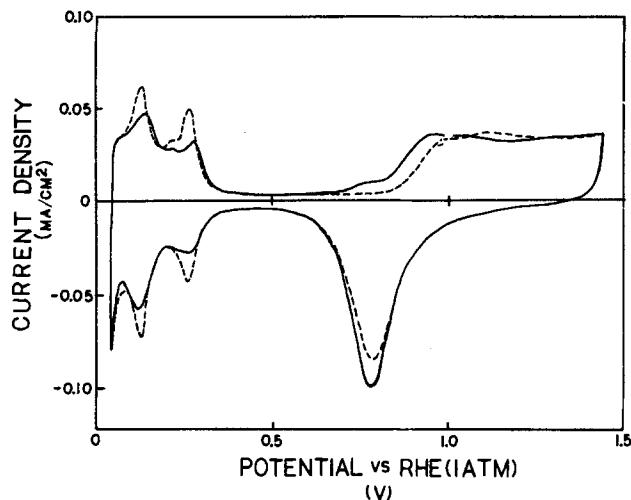


Fig. 1. Voltammograms of platinum in purified 0.5M $F_2C(SO_3H)_2$ (solid line) 1.0M H_3PO_4 (dashed line) at 25°C, N_2 saturated, sweep rate = 25 mV/s.

of weakly adsorbing acids (17), e.g., $HClO_4$, the peak current for the strongly adsorbed form of hydrogen on Pt at ca. 0.25V is lower for the $F_2C(SO_3H)_2$ than for the H_3PO_4 . The absence of significant adsorption behavior on electrode surfaces such as platinum is a desirable property for acid fuel cell electrolytes.

Conclusions and Future Works

Electrochemical fluorination of methanedisulfonyl fluoride in AHF is a viable route for the production of difluoromethanedisulfonyl fluoride. High yields are obtained by this method, and it is anticipated that a variety of other perfluoroalkane sulfonyl fluorides may be prepared in this manner. We have recently constructed a new electrochemical reactor system with a three-electrode configuration, improved agitation, and a more uniform current density distribution. We believe these improvements will increase the yield and permit use of higher current densities.

The physicochemical properties of $F_2C(SO_3H)_2$, e.g., conductivity and vapor pressure, are being characterized. The dihydrate does not wet Teflon above its melting point ($\sim 70^\circ C$). Studies of O_2 electroreduction on platinum using rotating ring-disk and gas-diffusion electrode tech-

niques are also in progress and will be reported. The stability of $F_2C(SO_3H)_2$ will also be checked, particularly at elevated temperatures.

Acknowledgments

This research has been supported by NSF, by NASA through a fellowship to one of the authors (F. W. K.), and by the Electric Power Research Institute.

Manuscript submitted Feb. 18, 1985; revised manuscript received May 13, 1985.

Case Western Reserve University assisted in meeting the publication costs of this article.

REFERENCES

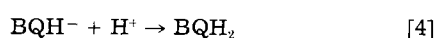
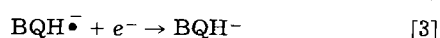
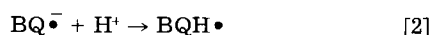
1. A. J. Appleby and B. S. Baker, *This Journal*, **125**, 404 (1978).
2. P. N. Ross, *ibid.*, **130**, 882 (1983).
3. J. H. Simons, "Fluorine Chemistry," Academic Press, New York (1950).
4. J. Burdon and J. C. Tatlow, in "Advances in Fluorine Chemistry," Vol. 1, M. Stacey, J. C. Tatlow and A. G. Sharpe, Editors, pp. 129-165, Butterworth's Scientific Publications, London (1960).
5. S. Nagase, in "Industrial Electrochemical Processes," A. T. Kuhn, Editor, pp. 71-88, Marcel Dekker, New York (1967).
6. A. P. Tomilov, S. G. Mairanovskii, M. Y. Fioshin, and V. A. Smirnov, "Electrochemistry of Organic Compounds," J. Schmorak, Translator, pp. 417-441, Wiley, New York (1972).
7. N. L. Weinburg, in "Technique of Electroorganic Synthesis," N. L. Weinburg, Editor, pp. 1-82, in "Techniques of Chemistry," John Wiley and Sons, New York (1975).
8. T. J. Brice and P. W. Trott, U.S. Pat. 2,732,398 (1956).
9. T. Gramstad and R. N. Haszeldine, *J. Chem. Soc.*, 173 (1956); *ibid.*, 2460 (1957).
10. F. E. Behr, U.S. Pat. 4,329,478 (1982).
11. F. E. Behr and R. J. Koslar, Paper 5 presented at the Fifth Winter Fluorine Conference, Daytona Beach, FL, Feb. 1-6, 1981.
12. V. M. Fild and H. Rieck, *Chem. Z.*, **100**, 391 (1976).
13. C. Polisen, C. C. Liu, and R. F. Savinell, *This Journal*, **129**, 2720 (1982).
14. L. Fabes and T. W. Swaddle, *Can. J. Chem.*, **53**, 3053 (1975).
15. B. E. Conway, H. Angerstein-Kozlowska, W. B. A. Sharp, and E. E. Criddle, *Anal. Chem.*, **45**, 1331 (1973).
16. J. C. Huang, R. K. Sen, and E. Yeager, *This Journal*, **126**, 786 (1979).
17. J. C. Huang, W. E. O'Grady, and E. Yeager, *ibid.*, **124**, 1732 (1977).

In Situ Spectra of Intermediate Species Recorded during Electrochemical Reduction of p-Benzoquinone

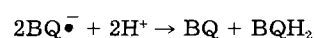
Chong-Hong Pyun* and Su-Moon Park**

Department of Chemistry, University of New Mexico, Albuquerque, NM 87131

p-Benzoquinone has been studied extensively photochemically and/or electrochemically due to its importance as an electron acceptor in many chemical as well as biological reactions. It is generally recognized to undergo an electrochemical-chemical-electrochemical (ECE) reaction when reduced in nonaqueous media (1-6), i.e.



where BQ represents p-benzoquinone. Rates of chemical steps, i.e., reactions [2] and [4] have not been reported in nonaqueous solutions, but are slow enough for a nearly complete reoxidation peak for the anion radical to be observed on cyclic voltammetric scales. The apparent decay rate of $BQ^{\bullet -}$ was reported by Fukuzumi *et al.* (7) to be $5.7 \times 10^{-3} \text{ min}^{-1}$ in neutral water at room temperature with first-order kinetics. The second-order disproportionation rate of $BQ^{\bullet -}$, i.e.



is, however, reported to be 1.7×10^8 and $1.1 \times 10^9 \text{ M}^{-1}\text{s}^{-1}$ at pH = 7.2 and 2, respectively, in water by Adams and Michael (8). This disparity indicates the complexity of the

* Electrochemical Society Student Member.

** Electrochemical Society Active Member.

chemistry of p-benzoquinone anion radicals. We believed that a half-life of about 2h for $BQ^{\bullet-}$ in water as reported by Fujuzumi *et al.* (7) was excessively long.

Spectra of intermediate species including $BQ^{\bullet-}$ and BQH^{\bullet} have been studied using either pulse radiolysis (8-12) or by oxidation of hydroquinone (BQH_2) with solid oxidants such as MnO_2 in water (7). The medium was either water (pure or buffered) or a water-isopropylalcohol (up to 3M) mixture. These media are often saturated with N_2O to scavenge radical species produced upon pulse radiolysis, which may lead to some unknown side reactions. Iso-propylalcohol was used to remove any intermediate radical species other than OH^{\bullet} . Attempts at recording transient spectra *in situ* in an electrochemical cell under well-controlled conditions have been made (5, 6), but to the best of our knowledge no such spectra have been recorded using spectroelectrochemical methods with controlled amounts of proton donors.

In this communication, we report the spectra of intermediate species electrogenerated in dimethylsulfoxide (DMSO) solution using near-normal incidence reflectance spectroelectrochemistry (NMIRS). We believe we recorded spectra for all the intermediate species, *i.e.*, $BQ^{\bullet-}$, BQH^{\bullet} , and BQH^- .

Eastman Organic's reagent-grade p-benzoquinone was used after recrystallization from water. Mallinckrodt's reagent-grade DMSO was used after fractional distillation with a reflux ratio of 5:1 under the reduced pressure. Tetra-n-butylammonium perchlorate (TBAP; Southwestern Analytical, Incorporated, Austin, Texas) was used as a supporting electrolyte after drying for 24h at about 100°C. The spectra were recorded at a reflective platinum disk electrode (Sargent Welch S-30101-20A) using a bifurcated optical fiber probe. The spectroelectrochemical system was controlled by an Apple II+ microcomputer. Details of the instrumentation are described elsewhere (13). Cyclic voltammograms were recorded with a Princeton Applied Research (PAR) Model 173 potentiostat-galvanostat along with a PAR Model 175 universal programmer.

Cyclic voltammograms (CV's) shown in Fig. 1 indicate that the anion radical produced upon negative potential sweep is very stable. When water is added to this electrochemical system, practically the same reversible CV is obtained with a prewave due to the enhanced adsorption at the electrode surface. The adsorbed species is stripped off with one scan, leaving the following electron transfer practically reversible (Fig. 1b). This illustrates that the electrogenerated anion radical is fairly stable, even at a reasonably high concentration of the proton donor. Similarly, one can conclude from the CV's shown that the rate of protonation is fairly slow even in solutions containing water.

The spectrum of the anion radical, $BQ^{\bullet-}$, recorded after 11 min of electrolysis in "dry" DMSO, is shown in Fig. 2a. This spectrum was recorded while electrolysis was proceeding. To compensate the amount of the $BQ^{\bullet-}$ building up in the probe path, the wavelengths were scanned up and down, and the average value of the two was used. The data acquisition time was approximately 5 min.

The spectrum shown in Fig. 2a has exactly the same features as in those recorded in water (7-12), except that the absorption bands are red shifted by about 30 nm in DMSO. We believe that the spectral blue shift observed in the aqueous medium is due to the hydrogen bonding to the benzoquinone carbonyl groups, as was observed in the 9,10-anthraquinone system (14). To confirm this, we ran an experiment in water with 0.20M $NaClO_4$ as a supporting electrolyte; exactly the same spectrum as shown in Fig. 2a was observed. The spectrum in water, however, showed about 32 nm of blue shifts. Furthermore, the anion radical was reasonably stable. To our surprise, the anion radical spectra were observed even after more than 30 min after its generation by controlled potential electrolysis. The absorption maxima are believed to arise from the $\pi-\pi^*$ transition, and spectral features are due to the C—O stretching vibration in the excited state (15).

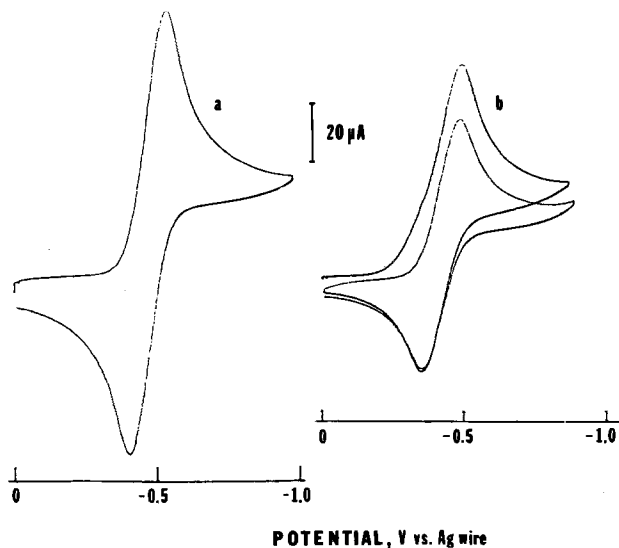


Fig. 1a: Cyclic voltammogram (CV) recorded in a solution containing 1.87 mM p-benzoquinone and 0.10M TBAP in "dry" DMSO. b: CV recorded in a solution containing 1.21 mM p-benzoquinone, 0.10M TBAP, and 10.0% H_2O in DMSO. The reference electrode was a Ag wire, and the scan rate was 100 mV/s for both experiments.

When further electrolysis is performed under the same condition, the spectrum shown in Fig. 2b is obtained. One can notice in this spectrum that the absorption bands at 427 nm and at about 670 nm are growing. This effect is more pronounced when the electrolysis is carried out in DMSO containing 10.0% H_2O even at a much shorter electrolysis time. Note also that the spectral bands show 4 ~ 5

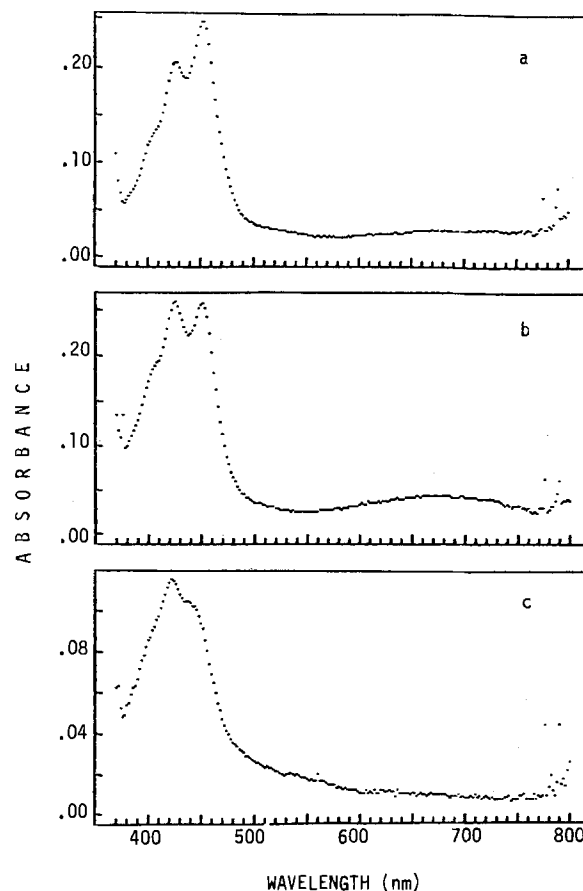


Fig. 2a: Absorption spectrum recorded after 11 min of electrolysis for the solution containing 1.87 mM p-benzoquinone at $-0.68V$ vs. Ag wire electrode. b: Absorption spectrum recorded after 36 min of electrolysis for the same solution as in a. c: Absorption spectrum recorded after 3 min of electrolysis for the solution containing 1.21 mM p-benzoquinone and 10.0% H_2O at $-0.62V$.

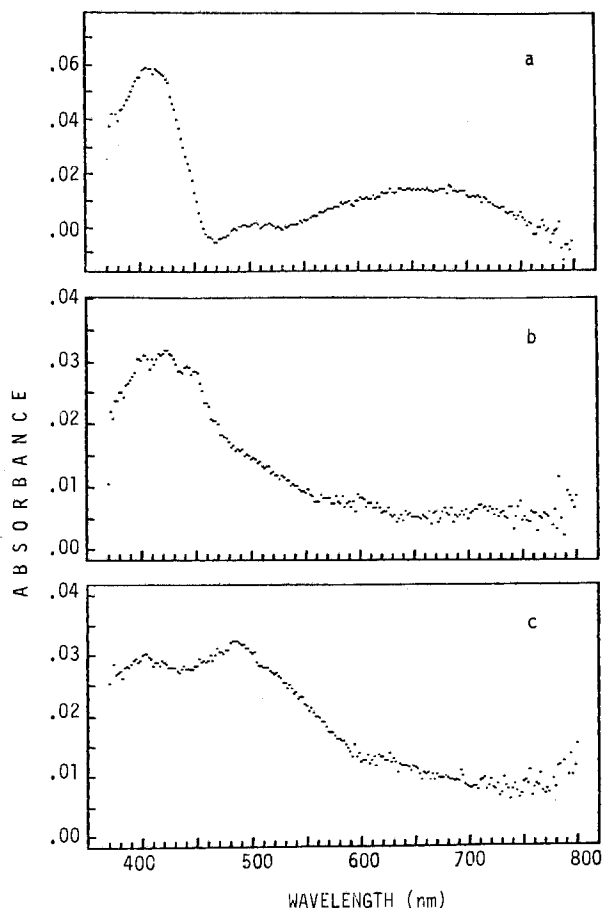


Fig. 3a: Difference spectrum obtained from those shown in Fig. 2b and 2a. b: Difference spectrum obtained from the solution containing 1.21 mM p-benzoquinone and 10.0% H₂O for electrolysis times of 8 and 19 min, respectively. c: Spectrum recorded with the circuit open after 30 min of electrolysis for the solution used in Fig. 3b.

nm blue shifts in Fig. 2c compared to those shown in Fig. 2a due to the addition of water. When the difference between the spectra shown in Fig. 2b and 2a is taken, a spectrum shown in Fig. 3a is obtained. The same spectra as in Fig. 3a are also obtained when differences are calculated from those shown in Fig. 2c and 2a. This indicates that the process producing a species responsible for the spectrum in Fig. 3a is facilitated by the presence of water. Note that this process is already occurring in "dry" DMSO but the rate is much slower. Thus, we attribute the spectrum in Fig. 3a to the free radical generated upon protonation of the anion radical, which is formed at the top of the diffusion layer. We believe that the broad band at about 670 nm is perhaps also from the free radical. For several spectra that we obtained, almost constant ratios of the absorbance at 410 nm to that at 670 nm were observed, indicating that both absorption peaks came from the same source. One may speculate, however, that the absorption band at 670 nm may have resulted from the intermediate dimer formed from the free radical. The presence of such a dimer was speculated by Eggins and Chambers from their cyclic voltammetric studies (5).

The absorption spectrum of the free radical, BQH•, was reported by Adams and Michael (8). They produced this species by generating anion radicals in water of pH = 2.0. The assumption was that anion radicals produced protonate quickly to produce free radicals at low pH's. The spectrum recorded at pH = 2.0 had similar spectral features to the one recorded at a neutral pH, but had its absorption maximum at about 410 nm. In our spectrum,

the blue shift of the free radical with respect to that of the anion radical is more extensive than in Adams and Michael's observation. This could perhaps be due to the solvent/supporting electrolyte effects. The transition of the benzoquinone anion radical should be affected by the solvent polarity more than that of the free radical, which does not carry any charges on it.

Also noticed in this spectrum (Fig. 3a) is the presence of an absorption band at about 500 nm. This band grows significantly enough to give a band broadening as shown in Fig. 3b, when the water content becomes high. When the electrical circuit is open, we notice that the absorption peak at about 500 nm grows at the expense of the one at 410 nm, as shown in Fig. 3c. Eventually, all the transient absorption peaks disappear, and the final solution is dominated by the absorption peaks attributable to the final product, hydroquinone (BQH₂). Of course, this happens only when the exhaustive electrolysis is performed. This series of spectroscopic observations indicate that there are no final products detectable other than hydroquinone. Thus, we believe that the absorption band observed at about 500 nm is due to the protonated anion (BQH⁻) in reaction [3]. An attempt to obtain the spectrum of BQH⁻ by deprotonating BQH₂ in strong alkaline medium was not successful; the deprotonation reaction was accompanied by the oxidation of BQH₂ as well. Although the spectra of intermediate species were assigned mostly from the sequence of reactions summarized by [1]-[4], they are in good agreement with those reported for BQ• and BQH• obtained under quite different experimental conditions. The spectrum for BQH⁻ has not been reported to the best of our knowledge.

We conclude from the current spectroelectrochemical study that we observed transient spectra corresponding to the anion radical (BQ•), protonated free radical (BQH•), and protonated anion (BQH⁻) species. Surprisingly, as already pointed out, the electrogenerated BQ• is reasonably stable even in neutral water as was originally observed by Fukuzumi *et al.* (7). Perhaps the benzoquinone anion radical generated by pulse radiolysis (8-12) may not be stable due to the host of other reactive intermediate species produced along with the desired product. Particles of very high energies are employed in pulse radiolysis. Further work on the solvent effect on the spectra, effect of water, and the rate of decay of each intermediate species is in progress in our laboratory.

Manuscript submitted March 11, 1985; revised manuscript received May 8, 1985.

REFERENCES

1. S. Wawzonek, R. Berkey, E. W. Blaha, and M. E. Runner, *This Journal*, **103**, 456 (1956).
2. I. M. Kolthoff and T. B. Reddy, *ibid.*, **108**, 980 (1961).
3. R. Jones and T. M. Spotswood, *Aust. J. Chem.*, **15**, 492 (1962).
4. W. R. Turner and P. J. Elving, *This Journal*, **112**, 1215 (1965).
5. B. R. Eggins and J. Q. Chambers, *ibid.*, **117**, 186 (1970).
6. V. J. Koshy, V. Sawayambunathan, and N. Periasamy, *ibid.*, **127**, 2761 (1980).
7. S.-I. Fukuzumi, Y. Ono, and T. Keii, *Bull. Chem. Soc. Jpn.*, **46**, 3353 (1973).
8. G. E. Adams and B. D. Michael, *Trans. Faraday Soc.*, **63**, 1171 (1967).
9. P. S. Rao and E. Hayon, *J. Phys. Chem.*, **19**, 2274 (1973).
10. G. N. R. Tripathi, *J. Chem. Phys.*, **74**, 6044 (1981).
11. G. N. R. Tripathi and R. H. Schuler, *ibid.*, **76**, 2139 (1982).
12. G. N. R. Tripathi and R. H. Schuler, *J. Phys. Chem.*, **87**, 3101 (1983).
13. C.-H. Pyun and S.-M. Park, *Anal. Chem.*, To be published.
14. M. Fujihara and S. Hayano, *Bull. Chem. Soc. Jpn.*, **45**, 644 (1972).
15. Y. Harada, *Molec. Phys.*, **8**, 273 (1964).

Investigation of Photoelectrode Redox Polymer Junctions

Ronald L. Cook* and Anthony F. Sammells*

Eltron Research, Incorporated, Aurora, Illinois 60505

There are several incentives for the characterization of semiconductor junctions with redox containing solid polymer electrolytes (SPE). An understanding of such junctions can be expected to have important implications on the design of solid-state photoelectrochemically rechargeable galvanic devices possessing charge capacity. In addition, the presence of polymer-incorporated redox species in close proximity to the semiconductor surface may act as an antenna probe for measuring perturbations in interbandgap surface states when the junction is exposed to selected chemical species.

We have previously shown the viability of such junctions for the storage of photogenerated electrochemical energy (1, 2). Here, solid-state cells based upon both poly(ethylene oxide) and Nafion¹ as SPE's have been shown to be potentially attractive for energy storage. A recent example discussed by us is the two photoelectrode cell

$p/\text{InP}/\text{Fe}^{+3}$ porphine/Nafion 117/ Ru^{2+} (bpy)₃/ $n\text{-CdS}$

which has been shown to generate photopotentials in excess of 1V upon simultaneous AM1 illumination of both photoelectrodes, using the above electrochemically reversible redox couples (2). In addition, semiconductor films deposited onto appropriate substrates have been found promising, via the use of impedance techniques, for the detection of gases such as CO (3-5).

For electrochemical energy storage, the redox polymer phase should, in principal, possess the following properties: (i) the redox species must be fixed into a relatively immobile polymer site so that any self-diffusion resulting in spontaneous self-discharge would be eliminated; (ii) the immobilized redox species must retain some electrochemical reversibility; and (iii) an excess concentration of mobile conducting species should be present in the vicinity of the redox couple, over and above that normally necessary for ionic conduction, to preserve electroneutrality in the proximity of the immobilized redox species during redox electrochemistry. The perfluorinated cation exchange material Nafion was selected as a candidate SPE material whose properties may address these criteria (6-9).

Photoelectrochemical (PEC) cells using $n\text{-CdS}$ as a photoanode and Nafion 117 as the SPE were prepared and doped with a variety of transition metal complexes of varying redox potentials and overall molecular charge (+2, 0, -1). The role of such introduced redox species for perturbing photoelectrode properties was of interest both for understanding conditions which promote electron transfer for charge (or discharge) in solid-state PEC storage devices, and also for understanding their role in changing semiconductor properties which might facilitate the use of this junction for various detector applications.

Experimental

$n\text{-CdS}$ single crystals were obtained from Cleveland Crystals, Incorporated, and were initially polished with 600 grit emery paper, followed by 5 μm alumina on a Texmet polishing cloth and finally with 0.3 μm alumina on a Microcloth polishing cloth. The ohmic contact area was initially etched with a solution of $\text{HNO}_3:\text{H}_2\text{SO}_4:\text{HOAc}:\text{HCl}$ (30:20:10:0.1) for 20s. Ohmic contact was achieved by introduction of a gallium-indium eutectic onto the etched CdS face. Current collection was achieved via a Nichrome wire using a silver epoxy, which was cured at 150°C for 1h. Immediately prior to fabrica-

* Electrochemical Society Active Member.

¹ Nafion is the registered trademark for a family of perfluor-sulfonic acid ion-exchange membranes manufactured by E. I. du Pont de Nemours and Company.

tion of the cell, the front face was polished with 5 and 0.3 μm alumina, rinsed, and the face etched with $\text{HNO}_3:\text{H}_2\text{SO}_4:\text{HOAc}:\text{HCl}$ solution as above.

Electrochemical measurements were performed using potentiostatic control provided by either a Stonehart Associates BC 1200 or a Wenking LT 78 potentiostat. Differential capacitance measurements for Mott-Schottky plots were performed using a H-P 4276A digital LCZ meter at 1000 and 10,000 Hz. Thin film coatings of gold and silver were vacuum-deposited on glass slides with an Edwards 306A evaporator. Photoelectrode illumination was achieved via a Sylvania 300W ELH bulb. Light intensities were measured with an Eppley 8-48 pyranometer. Cyclic voltammograms on the redox couples were run in acetonitrile (Burdick and Jackson) with tetrabutylammonium hexafluorophosphate (Southwestern Analytical Chemicals, Incorporated) as supporting electrolyte. A three-electrode configuration consisting of a platinum working electrode, a platinum counterelectrode, and a Ag/Ag^+ reference electrode was used for the cyclic voltammetry scans.

Results and Discussion

Cell preparation.—Solid-state PEC cells were fabricated by introducing 0.05 ml of a solution containing 50 mg/ml of Nafion 117 and 0.5 mg/ml of the appropriate redox couple in a solution of lower aliphatic alcohols onto the surface of a $n\text{-CdS}$ photoanode and a glass slide possessing both an evaporated gold counterelectrode and silver quasi-reference electrode. The Nafion was allowed to dry partially for 15 min on each of these surfaces, after which the two half-cells were pressed together and allowed to dry for an additional 2h. The cell configuration used in this work is shown in Fig. 1. The transition metal complexes selected for introduction into the Nafion polymer included FeCp_2 , $\text{Ru}(\text{bpy})_3^{2+}$, $\text{Fe}(\text{bpy})_3^{2+}$, $\text{Fe}(\text{CN})_6^{4-}$, and $\text{Fe}(\text{acac})_3$. These complexes were selected to provide for both a variation in overall molecular charge and chemical potential at localized sites within the Nafion polymer. Several films were initially cast onto Teflon substrates and allowed to dry. Upon removal and visual examination of these films (40 \times magnification), the polymer con-

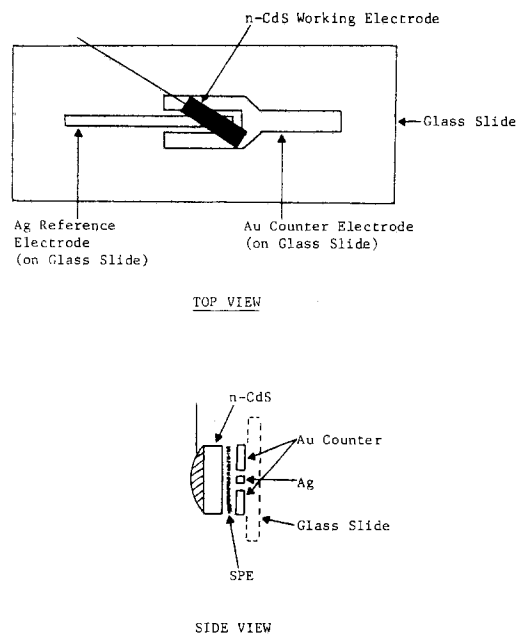


Fig. 1. Schematic diagram of cell configuration used in this work

taining $\text{Ru}(\text{bpy})_3^{2+}$ was yellow and homogeneous. For concentrations of $\text{Ru}(\text{bpy})_3^{2+}$ up to 20 mg/ml SPE, the polymer remained homogeneous in appearance. Similar observations were made when $\text{Fe}(\text{bpy})_3^{2+}$ was introduced into the polymer.

In comparison, ferrocene, was in fact insoluble at concentrations greater than 1 mg/ml of the SPE, as manifested by its appearance as microcrystalline needles upon solvent removal from the polymer. Similar observations were made when $\text{Fe}(\text{acac})_3$ was introduced into the polymer. The anionic complex $\text{Fe}(\text{CN})_6^{4-}$ remained homogeneous at concentrations up to 2 mg/ml SPE.

Photoelectrochemical measurements.—To gain some preliminary insight into the respective PEC characteristics of the SPE cell when the redox species FeCp_2 , $\text{Ru}(\text{bpy})_3^{2+}$, $\text{Fe}(\text{CN})_6^{4-}$, and $\text{Fe}(\text{acac})_3$ are present in the proximity of semiconductor/SPE junctions, cells possessing the general configuration n-CdS/SPE + redox species/Au were prepared using the procedures discussed above. The initial photopotentials realized from these cells under simulated AM1 illumination conditions are compared in Table I. As can be seen, these photopotentials (which are mainly around 200 mV) appear to be relatively invariant when compared to, for example, $E_{1/2}$ values for the same redox species in acetonitrile using a platinum electrode, e.g., FeCp_2 (0.285V vs. Ag/Ag^+), $\text{Ru}(\text{bpy})_3^{2+/3+}$ (1.25V vs. Ag/Ag^+).

Although this was initially thought explainable by the presence of Fermi level pinning by the n-CdS, it was later observed that photopotentials for $\text{Ru}(\text{bpy})_3^{2+}$ -modified SPE-PEC cells were in the -500 to -600 mV range when SnO_2 conducting glass was used as the counterelectrode. This result suggests that the photopotentials observed in the CdS/Nafion + redox couple/Au system may have been limited by inadequate interfacial contact between the Nafion polymer and the gold counterelectrode. Such interfacial contact limitations have previously been reported using Nafion/ WO_3 -based SPE electrochromic devices (10). SnO_2 , however, shows significant adhesive strength attributable to covalent bonding between the sulfonic acid groups in the SPE and receptive functional groups on the SnO_2 substrate electrode (11). Thus, the increased photopotentials observed for n-CdS/SPE cells using SnO_2 conducting glass counterelectrodes can, in part, be explained by improved interfacial contact with the Nafion polymer at the counterelectrode.

In order to determine the dependency of the SPE-incorporated redox species concentration on the photopotential of n-CdS/Nafion + $\text{Ru}(\text{bpy})_3^{2+}$ /conducting glass, SPE cells, $\text{Ru}(\text{bpy})_3^{2+}$ concentrations were varied between 0.0004g and 0.006 g/ml/SPE and their photopotentials under 100 mW/cm² illumination compared. As can be seen from Table II, the photopotentials for this system were not dependent on the concentration of the incorporated redox species over the concentration range studied, thereby indicating that the double layer present at the semiconductor/SPE junction was invariant under these experimental conditions. If significant perturbation of the double-layer region were to have occurred, however, this might have influenced the photopotential observed by changing the space charge region width and the corresponding barrier height.

For cells based upon the proton conducting SPE, generally low currents were observed which were attributed

Table I. Photopotential values for the PEC cells CdS/Nafion + redox species/Au

Redox species introduced into H ⁺ conducting Nafion 117	Photopotential under AM1 illumination at n-CdS (mV)
$\text{Ru}(\text{bpy})_3^{2+}$	-200
$\text{Fe}(\text{bpy})_3^{2+}$	-190
$\text{Fe}(\text{CN})_6^{4-}$	-220
FeCp_2	-270
H ⁺ conducting Nafion	-200

Table II. Photopotential measurements on n-CdS/Nafion 117 + $\text{Ru}(\text{bpy})_3^{2+}$ /conducting glass as a function of $\text{Ru}(\text{bpy})_3^{2+}$ concentration

$\text{Ru}(\text{bpy})_3^{2+}$ (mg/ml/SPE ^a)	Photopotential (mV)
0.375	-485
0.75	-488
1.5	-490
3.0	-480
6.3	-500

^a 1 ml SPE solution contains 50 mg/ml Nafion 117.

to the poor conductivity of this polymer when used in solid-state cells. However, substitution of Na^+ for H^+ conductivity in the SPE/alcohol mixture before polymer formation on the semiconductor substrate was found to enhance overall ionic conductivity of the final solid-state cell. Figure 2 shows a current-voltage PEC curve for the cell n-CdS/SPE: FeCp_2 : NaCl/Au . Overall cell resistance was found to be 14 k Ω , and a current density of 25 $\mu\text{A}/\text{cm}^2$ could be obtained by applying a 300 mV anodic overpotential to the photoanode.

Capacitance measurements.—For cells prepared in this work, differential capacitance measurements were performed on n-CdS/redox SPE junctions, to determine if there was any sensitivity of the measured n-CdS flatband potential to the redox species introduced into the Nafion polymer. Figure 3 compares differential capacitance measurements performed on n-CdS junctions with the proton conducting SPE, (i.e., no introduced redox species) and the SPE's containing $\text{Ru}(\text{bpy})_3^{2+}$ and $\text{Ru}(\text{bpy})_3^{2+} + \text{FeCp}_2$, performed at 1000 Hz. These C_{sc}^{-2} vs. V plots show good linearity even though some of the cells possessed a relatively high resistance. Some frequency dispersion was noted at higher frequencies. Deviations from linearity for such plots might be expected if there is a high electrolyte resistance in series with the semiconductor space charge region or if a high population of surface states is present at the semiconductor/electrolyte interface (12). Results obtained from both current-voltage curves and the application of an ac signal to the cell suggested that some degree of rectification may be present at the semiconductor/SPE interface. Here, the ac signal from a signal generator was introduced through the cell and a measuring resistor. The output current as measured across the resistor was fed into an oscilloscope. The negative half of the sine wave was only two thirds the height of the positive half of the sine wave. This suggested that

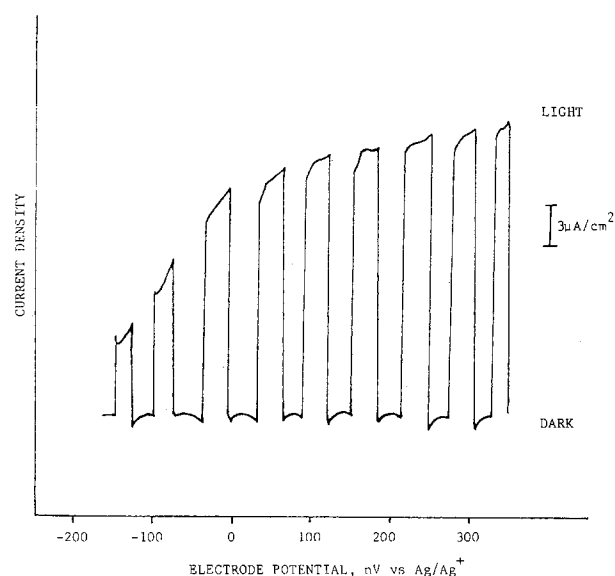


Fig. 2. Current-voltage relationship for the cell n-CdS/Nafion: FeCp_2 : NaCl/Au

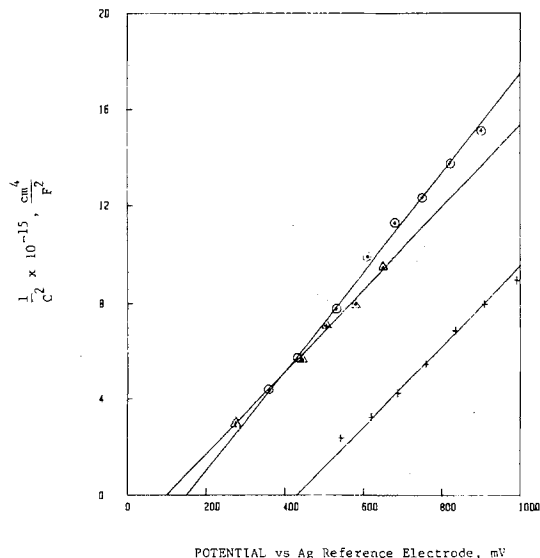


Fig. 3. Mott-Schottky plots for CdS/SPE/Au (crosses), CdS/SPE + Ru(bpy)₃²⁺/Au (circles), and CdS/SPE + Ru(bpy)₃²⁺ + FeCp₂/Au (triangles).

about 30% rectification was present in the cell. It should be noted that for semiconductor/metal oxide solid-state junctions where current rectification is seen, linear Mott-Schottky plots have been obtained (12).

Since good linearity and reproducibility were obtained from C_{sc}^{-2} vs. V plots in work reported here, it was of interest to compare measured n-CdS flatband potentials (V_{FB}) as a function of the introduced redox species. For the undoped proton, conducting SPE, V_{FB} was $-0.43V$ vs. the silver reference electrode. Upon the introduction of Ru(bpy)₃²⁺ or FeCp₂ into the SPE, the n-CdS flatband potential was shifted progressively in a cathodic direction [$V_{FB} = 0.151V$, Ru(bpy)₃²⁺, $V_{FB} = 0.097V$, (FeCp)₂]. This cathodic shift is consistent with that for the oxidation potentials seen for Ru(bpy)₃²⁺ ($E_{1/2} = 1.25V$ vs. SCE) and FeCp₂ ($0.285V$ vs. SCE) in acetonitrile. Similar cathodic shifts have also been observed in the cells n-TiO₂/Nafion + redox couple/SnO₂ conducting glass and n-TiO₂/polyamps² + redox couple/SnO₂ conducting glass.

Such changes in V_{FB} may be due to modifications at the electrode surface induced either by direct adsorption of the redox couple or to variations in the capacitance associated with the polymer itself upon changing the redox species. Currently experiments are being performed by us to identify the origin of such observed V_{FB} shifts upon varying the introduced redox couple. If, in fact, the shift in V_{FB} is directly dependent in part on the redox potential of the introduced redox couple, then such semiconductor/SPE junctions might form the basis of a detector technology. For example, an introduced gas or chemical species might be expected to modify the immediate chemical environment of the SPE-incorporated redox couple and thus give detectable parametric changes (e.g., V_{FB}) at the semiconductor surface.

For the n-CdS/redox SPE solid-state junctions considered here, changes occurring in the Helmholtz double-layer voltage V_H as a result of varying redox species can result in perturbation of the semiconductor bandedge en-

ergy. This can be expected by consideration of the relationship

$$V_{FB} = E_{sc}^0 - \mu + V_H$$

where μ is the difference in energy between the bulk conduction bandedge and the Fermi level, and V_H is the Helmholtz double-layer voltage. When a redox-containing surface is introduced onto a semiconductor, three possibilities can be envisioned for perturbing V_H : (i) the presence of interface states at the junction may induce a voltage drop across the polymer that may be indistinguishable from a Helmholtz voltage; (ii) if the polymer is insulating, the point of zero charge (PZC) will be different than that for the bare semiconductor resulting in perturbation of V_H ; and (iii) if electron exchange can occur between semiconductor surface states and polymer-incorporated redox species, then the former will define V_H and thus V_{FB} .

Donor surface states are expected near the valence band and acceptor states near the conduction band. If the E_{redox} for a redox species is below the donor state, or above the acceptor state, then the energetics will promote charging of surface states and thus change V_{FB} . Work is currently being performed directed towards clarifying which of these effects influences V_{FB} at n-CdS/SPE interface. It is not clear at this time, however, which of these mechanisms is responsible for the observed shift in the n-CdS flatband potential.

In conclusion, (i) it has been observed that the measured flatband potential in the described cells can be modified by introduction of selected redox species into the SPE, (ii) photopotentials in the range 500-600 mV can be obtained if good interfacial contact is maintained at both the working and counterelectrode, and (iii) the photopotentials obtained in the n-CdS/Nafion 117 + Ru(bpy)₃²⁺ conducting glass SPE cells are not dependent on the concentration of the incorporated redox species.

Acknowledgment

This work was supported in part by the Office of Naval Research.

Manuscript submitted Jan. 8, 1985; revised manuscript received ca. March 15, 1985.

Eltron Research, Incorporated, assisted in meeting the publication costs of this article.

REFERENCES

1. A. F. Sammells and P. G. P. Ang, *This Journal*, **131**, 617 (1984).
2. A. F. Sammells and S. K. Schmidt, *ibid.*, **132**, 520 (1985).
3. R. R. Hooker, U.S. Pat. 3,933,433 (1974).
4. V. W. Brown, in "Proceedings of the Second West Virginia University Conference on Coal Mine Electrotechnology, 22-1/22-17 (1974).
5. J. G. Firth, A. Jones, and T. A. Jones, *Ann. Occup. Hyg.*, **18**, 63 (1975).
6. R. S. Yeo, *This Journal*, **130**, 533 (1983).
7. H. L. Yeager, B. Kipling, and R. L. Dotson, *ibid.*, **127**, 303 (1980).
8. H. L. Yeager, Z. Twardowski, and L. Miclarke, *ibid.*, **129**, 324 (1982).
9. N. E. Prieto and C. R. Martin, *ibid.*, **131**, 751 (1984).
10. J. P. Randin, *ibid.*, **129**, 1215 (1982).
11. D. A. Buttry and F. C. Anson, *J. Am. Chem. Soc.*, **104**, 4824 (1982).
12. S. R. Morrison, "Electrochemistry at Semiconductor and Oxidized Metal Electrode," Chap. 8, Plenum Press, New York (1980).

² Polyamps is poly(2-acrylamido-2-methyl-propane sulfonic acid).



Rapid Isothermal Fusion of PSG Films

J. S. Mercier,* I. D. Calder, R. P. Beerkens,¹ and H. M. Naguib*²

Northern Telecom Electronics Limited, Semiconductor Components Group, Ottawa, Ontario, Canada K1Y 4H7

ABSTRACT

This paper presents results on rapid isothermal fusion (RIF) characteristics of phosphosilicate glass (PSG) obtained using an incoherent lamp annealer in a N_2 ambient. The effects of varying the temperature (1000°-1200°C), the cycle duration (10-60s), and the phosphorus concentration in the glass (2.5-8.0 w/o) were investigated. The out-diffusion of phosphorus from the PSG films during RIF cycles were also studied. In conjunction with these experiments, dopant redistribution induced by typical RIF cycles in a boron-implanted silicon substrate was measured to assess the practicality of the RIF technique for VLSI applications and to identify a process window. The results for the boron profile redistribution were used as a basis of comparison between RIF and conventional furnace treatments. Although restricted to VLSI applications where a relatively high phosphorus content of approximately 8 w/o is acceptable in PSG films, it is concluded that RIF in a N_2 ambient is nevertheless much more effective for the fusion of PSG films than conventional furnace processing and thus much more compatible with VLSI processing.

As a part of the fabrication sequence for integrated circuits, a layer of phosphosilicate glass (PSG) is deposited to provide passivation and electrical insulation between metal interconnects and underlying structures. Before the subsequent deposition of metal takes place, it is necessary to smooth the surface topography to ensure continuity of the overlying metallization. At present, this treatment is typically a furnace glass fusion cycle at 1000°C for 30 min or more (1-5) and is the last high temperature process step in the fabrication of LSIC's. This heavy thermal load will be unacceptable for processing new generations of VLSI circuits because it will induce appreciative lateral and vertical dopant redistribution in small geometry devices.

Thermal processing requirements can be eased by using different materials or ambients during the fusion cycle. Although increasing the phosphorus concentration does lead to a lower fusion temperature for PSG films, excessive concentrations eventually promote the formation of phosphoric acid in the presence of moisture (2, 4), thereby causing reliability problems due to corrosion of overlying aluminum interconnect lines. As an alternative solution, rapid isothermal fusion (RIF) has been shown in limited studies to improve PSG step coverage, while causing less junction diffusion than conventional furnace processing cycles because of its lower time-temperature product (6-9).

In this work, we have studied the effect of RIF on PSG films having a practical range of phosphorus concentrations, namely, 2.5, 4.0, 6.6, and 8.0 w/o. The RIF experiments were performed in a N_2 ambient using a tungsten halogen lamp system.³ In addition, the out-diffusion of phosphorus from the PSG films during RIF was examined.

The amount of dopant diffusion induced by RIF in underlying device junction areas will largely determine its range of usefulness for VLSI applications (6-12). There-

fore, boron-implanted silicon wafers were also processed separately and junction depths were measured after undergoing typical RIF cycles. Finally, fusion and dopant redistribution experiments were carried out in a conventional furnace and the results were compared with the RIF data to assess the relative applicability of each technique to VLSI processing.

Experimental Procedures

Sample preparation.—The test structure used to observe PSG fusion is illustrated in Fig. 1. A thermal SiO_2 layer was first grown on a Si(100) substrate to a thickness of 100 nm, at a temperature of 1000°C. A 1.0 μm LPCVD polysilicon film was deposited at 625°C and phosphorus-doped with a $POCl_3$ cycle at 900°C. The polysilicon was then patterned into sharp steps using a dry etching technique. Finally, 1.0 μm thick PSG films were deposited in a horizontal, hot-wall LPCVD system at a temperature of 410°C using the silane and phosphine oxidation process.

Samples for studying dopant redistribution in silicon were formed by first growing a 40 nm thermal oxide on (100) n-type Si substrates. Boron was then implanted through this oxide layer with a dose of $3 \times 10^{15} B/cm^2$ at an energy of 25 keV.

Rapid isothermal fusion.—The fusion cycles were carried out in a commercially available tungsten halogen lamp systems. Cycle durations were varied from 10 to 60s and temperatures from 1000° to 1200°C. The RIF experi-

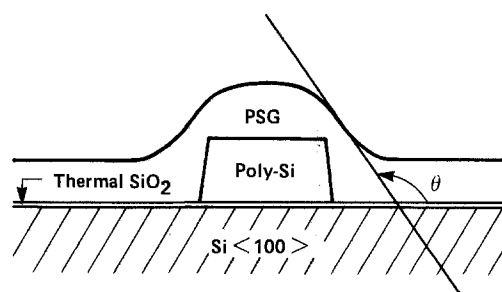


Fig. 1. Test structure for RIF studies, showing the step coverage angle θ . The PSG film is 1.0 μm thick, the polysilicon step is 1.0 μm high, and the thermal oxide thickness is 100 nm.

* Electrochemical Society Active Member.

¹ Present address: Department of Electrical Engineering, University of Waterloo, Waterloo, Ontario, Canada N2L 3G1.

² Present address: Fairchild Camera and Instrument Corporation, Mountain View, California 94039.

³ A Heatpulse 210T[®] tungsten halogen lamp annealing system was used. It was manufactured by A. G. Associates, Palo Alto, California.

ments were performed in a N_2 ambient. The temperature was controlled using feedback from a Chromel-Alumel thermocouple attached to a silicon test piece situated to the side of the wafer.

Junction dopant redistribution.—Boron-implanted silicon wafers were subjected separately to rapid isothermal annealing (RIA) cycles identical to some of those used in the RIF experiments. Other implanted samples were subjected to an 80 min, 900°C annealing cycle in 1 atm of N_2 , performed in a conventional furnace.

Analysis.—To quantify the extent of the fusion, SEM cross-sectional micrographs were used to measure the change in the PSG step coverage angle θ , with an accuracy of $\pm 5^\circ$. In order to measure the angle θ with the SEM, the samples were cleaved and given a decorative etch for 1 min in 50:1 buffered HF to delineate the underlying polysilicon/PSG interface. The phosphorus concentration of the PSG films was determined with energy dispersive x-ray (EDX) electron microprobe analysis to within ± 0.2 w/o.⁴ For an electron-beam energy of 6 keV, a value of 600 (± 60) nm was calculated for the probing depth.

The dopant redistribution in the implanted silicon samples was evaluated using secondary ion mass spectroscopy (SIMS) and a "bevel-and-etch" (B&E) technique. The B&E method relies on the larger etch rate of doped silicon relative to undoped silicon in certain etchants. By using this property on a beveled ($\sim 1^\circ$ - 2°) implanted silicon substrate, the junction area can be delineated interferometrically and related back to the actual junction depth. SIMS measures both active and inactive impurity concentrations, *i.e.*, the metallurgical junction depth, while the B&E technique yields a measure of the depth of active dopants, *i.e.*, the electrical junction depth.

Results and Discussions

Rapid isothermal fusion.—A summary of the complete RIF results is given in Table I. For all phosphorus concentrations investigated, the control (*i.e.*, as-deposited) PSG samples showed a typical step coverage angle θ of approximately 80° . Representative results obtained after RIF for a range of initial phosphorus concentrations $[P]_0$ are shown in the SEM micrographs of Fig. 2. For all but the 8.0 w/o PSG films, a temperature of 1200°C and/or a 60s cycle duration is needed to obtain substantial PSG fusion (*i.e.*, $\theta \geq 110^\circ$).

Results for 8.0 and 6.6 w/o PSG films are shown in Fig. 3 and 4, respectively. For these films, an 1100°C/10s RIF cycle is sufficient to obtain a value of 113° for θ (Fig. 3c). It would seem quite plausible that by increasing either the RIF cycle duration to 60s or the temperature to 1200°C, further fusion will be obtained. Unfortunately, the SEM micrograph of Fig. 3d shows that large voids form on each side of the step as a consequence of these extreme RIF treatments. For the 6.6 w/o films, the SEM micrographs of Fig. 4 show similar results, except under more severe RIF conditions.

The formation of voids has been observed previously, although their presence was largely attributed to the use

⁴ Calibration was obtained using colorimetric analysis performed at Balazs Laboratory, Mountain View, California.

Table I. Summary of RIF results listing, for given temperatures, the minimum cycle duration for which fusion occurs and eventually voids form

P content (w/o)	Onset of fusion		Void formation	
	T (°C)	t (s)	T (°C)	t (s)
2.5	1200	≈ 40	—	—
3.9	1150	≈ 60	—	—
3.9	1200	≈ 20	—	—
6.6	1100	≈ 20	—	—
6.6	1150	≈ 10	1200	≈ 40
8.0	1050	≈ 60	1100	≈ 60
8.0	1100	≈ 10	1200	≈ 10

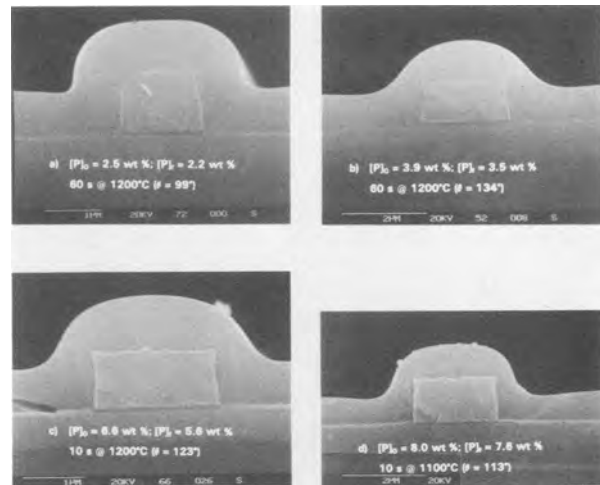


Fig. 2. SEM micrographs showing the best RIF results obtained at four different phosphorus concentrations. $[P]_0$ and $[P]_x$ are the initial and the final phosphorus concentrations, respectively.

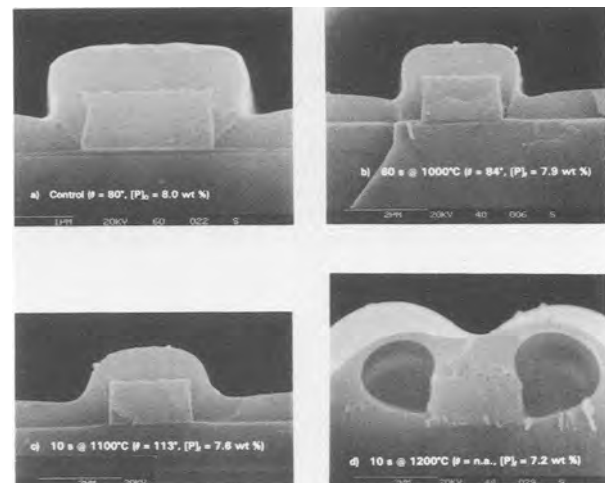


Fig. 3. SEM micrographs showing $[P]_0$ and $[P]_x$ fusion results for 8.0 w/o PSG films. The phosphorus concentrations given under micrographs 3b and 3d were measured after the RIF cycles.

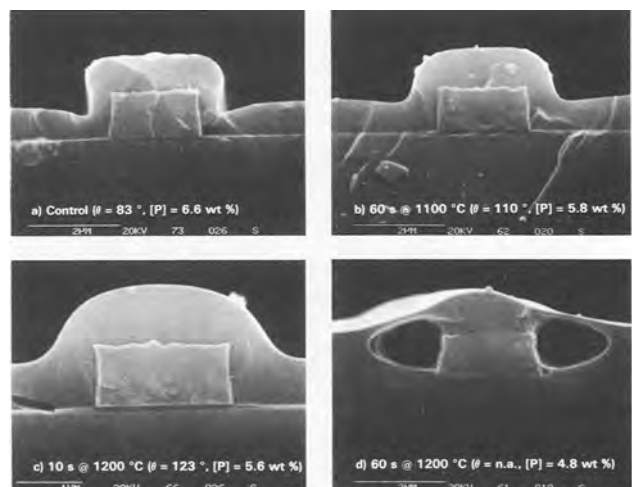


Fig. 4. SEM micrographs showing fusion results for 6.6 w/o PSG films. The phosphorus concentrations given under micrographs 3b to 3d were measured after the RIF cycles.

of a H_2 ambient (13). In that study, it is argued that the presence of phosphorus in the glass, in the form of phosphorus pentoxide (P_2O_5), is also directly responsible for

the formation of voids. This conclusion is supported by our findings, since an enhancement in void formation was observed with an increase in the phosphorus content of the PSG films.

Because P_2O_5 sublimates at a temperature of about 300°C , a sufficient local concentration of P_2O_5 could, under the right conditions, lead to the formation of cavities in the glass. In the case of RIF, accelerated sublimation of the P_2O_5 may result from the rapid heat-treatment which would not allow sufficient time for the P_2O_5 to diffuse slowly out of the film without creating a permanent deformation of the softened PSG. The reasons for which the conditions favoring the formation of voids are found only on the sides of steps are not clear. To our knowledge, the only experimental evidence suggesting different glass properties in these regions comes from the faster etch rate observed on each side of steps for as-deposited oxide films, after the cross-sectional decorative etch of cleaved samples has been performed for the SEM examination. As a result, diagonal etch lines, visible in the SEM micrograph of Fig. 3a, are formed in the glass on each side of the polysilicon steps. RIF inhibit the occurrence of these etch lines, as seen in the micrographs of Fig. 3. Although the severity of these etch lines is observed to decrease proportionally with the nominal phosphorus content in the layer, they still remain for undoped glass films. Therefore, a localized structural property which does not depend entirely on the presence of phosphorus, such as a different glass density or stress level, could also be involved in the formation of voids. More work is needed to understand the mechanisms of such localized void formation.

Phosphorus out-diffusion.—Some loss of phosphorus from the PSG films occurs during RIF treatments, as can be inferred from the initial phosphorus concentrations $[P]_0$ and the final concentrations $[P]_t$ detailed in Fig. 2 and 3. Since only the top half of each PSG film was probed with EDX during the phosphorus analysis, it can be concluded that the observed changes in phosphorus concentration were likely caused by out-diffusion to the ambient. These results can be plotted to extract useful information on the diffusion of phosphorus in PSG during RIF.

If we assume that the probing depth d_p (600 ± 60 nm) for the EDX electron microprobe analysis of phosphorus in the PSG films is much larger than the diffusion length $(Dt)^{1/2}$, the reduction in phosphorus concentration $\Delta[P]$, lost to the ambient out of the original concentration $[P]_0$, is given by (14)

$$\Delta[P]/[P]_0 \approx (2/d_p)(Dt/\pi)^{1/2} \quad (1)$$

where D is the diffusion coefficient for phosphorus in SiO_2 and t is the time. In Fig. 5, we plot the expression $\Delta[P]/[P]_0 t^{1/2}$ against $1/T$, which should also vary with $D^{1/2}$, to find an Arrhenius relationship, described by $D = D_0 \exp(-E_D/kT)$. Only data for $[P]_0 = 6.6$ and 8.0 w/o were used, since for these cases alone was the loss $\Delta[P]$ sufficiently greater than the experimental error. An activation energy $E_D = 2.24 \pm 0.28$ eV, which is twice the slope of the line fit in the plot shown in Fig. 5, was determined. For example, a value of $D = 8.5 \pm 2.3 \times 10^{-13}$ cm^2/s is calculated at 1100°C . These values obtained for both E_D and D are comparable to results reported elsewhere (15, 16) for studies performed in a conventional furnace at similar phosphorus concentrations ($\sim 10^{21}$ cm^{-3}). Values for D which are several orders of magnitude lower than the above result have also been published, although lower phosphorus concentrations were involved (15, 17).

Dopant redistribution.—Figure 6 shows the effect of various RIA cycles on the diffusion of boron in implanted silicon test samples, as determined by SIMS (closed symbols) and by the B&E techniques (open symbols). The as-implanted values of junction depth measured with these two techniques were 0.35 and 0.20 μm , respectively. It must be noted that, although the absolute results obtained from the two measurement techniques

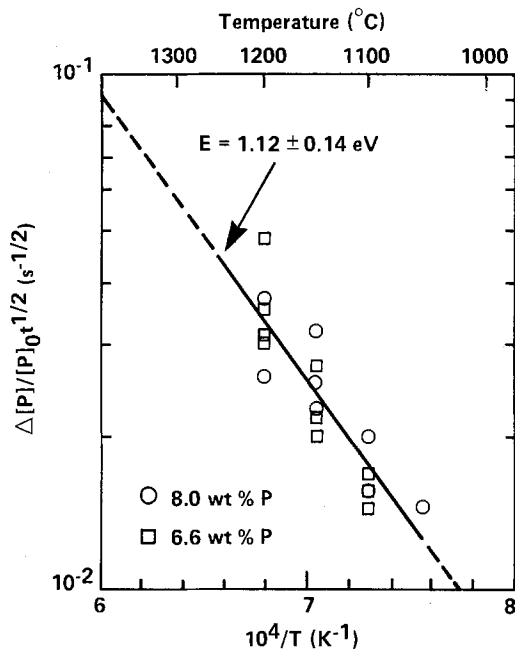


Fig. 5. Arrhenius plot for the out-diffusion of phosphorus during RIF treatments, for two concentrations and various RIF conditions. $\Delta[P] = [P]_t - [P]_0$ is the amount of phosphorus lost to the ambient during RIF. The slope of the linear fit yields $E_D/2$, where E_D is the activation energy for phosphorus diffusion in glass.

are different, the measurements of the junction depth increases Δx_j agree quite closely. The SIMS results from the 900°C , 80 min furnace annealing cycle in N_2 are also included in Fig. 6.

Example of VLSI process window for RIF.—In order to establish the upper bound of a process window for the application of RIF of PSG films to VLSI processing, the issue of dopant redistribution induced by rapid isothermal processing in underlying device shallow junctions must be addressed (7-12). For VLSI applications, a somewhat arbitrary upper limit of 0.1 μm could be placed on the acceptable junction depth increase resulting from a fusion cycle. This would correspond to, for example, a 50% displacement of a typical 0.2 μm shallow junction. As a consequence, the results from Fig. 6 indicate upper limits to RIF conditions of $1000^\circ\text{C}/60\text{s}$ or $1100^\circ\text{C}/10\text{s}$.

The dopant redistribution results also show that any 1200°C RIF cycle would be too extreme. Also, on the basis of the RIF results alone (Table I), a 1200°C cycle should be

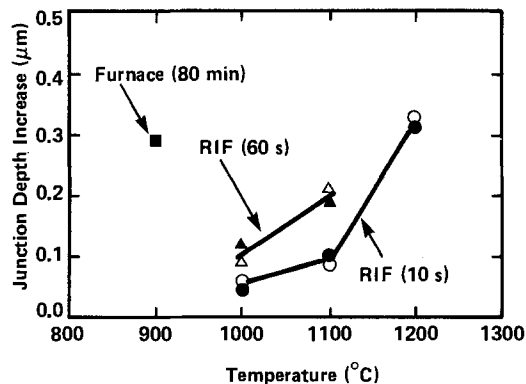


Fig. 6. Graph showing the temperature dependence of the junction depth increase in a boron-implanted Si substrate induced by various heating cycles. The results shown were obtained with both the B&E method (open symbols) and SIMS (closed symbols). The implantation conditions are given in the text. The junction depth for the as-implanted Si samples was 0.20 μm , as measured with the B&E method, and 0.35 μm , as measured with SIMS. The result for the $60\text{s}/1200^\circ\text{C}$ was $\Delta x_j = 1.4$ μm (B&E) and thus was not included in the figure.

avoided in any case since undesirable fusion characteristics are observed, namely, void formation in high phosphorus content PSG and insufficient fusion in low phosphorus content PSG. In addition, the use of a long fusion period (> 20 s) could be economically impractical in a serial processing system.

It must be emphasized that the discussion for the given example applies to silicon substrates implanted with boron, which is one of the fastest diffusing species of the commonly used dopants in IC fabrication (18). If a slower diffusing species is used, such as arsenic, larger and/or hotter RIF cycles could be acceptable. However, if even shallower junctions are required, more stringent restrictions would be imposed on the RIF conditions.

The RIF results summarized in Table I can be used to determine the lower bound for the process window which is defined as the point when the reentrant profile is eliminated (i.e., $\theta > 90^\circ$). From Table I, it is clear that the 1100°C/10s RIF cycle can only induce acceptable fusion in 8.0 w/o PSG films. It has also been reported that an 1100°C/10s RIA cycle would be sufficient for the dopant activation of shallow junctions (10). Furthermore, experiments conducted in our laboratories and elsewhere (19) have shown that wafer warpage induced by RIA cycles of up to 1100°C is negligible; in some cases, wafer flatness is even improved. For the 1000°C/60s case, which is really too long for practical applications, as discussed above, satisfactory fusion was not obtained for any of the phosphorus concentrations investigated.

RIF vs. conventional furnace processing.—A comparison between RIF results and conventional furnace fusion (FF) results in a N_2 ambient is shown in Table II. In this experiment, the same boron implant used above to define a process window was the basis of comparison between RIF and FF. The results for the optimum 1100°C/10s RIF cycle ($\Delta x_j \approx 0.1 \mu\text{m}$ and $\theta \approx 113^\circ$) are compared with FF results obtained with the 900°C, 80 min furnace annealing cycle. The dopant redistribution result for the boron-implanted silicon substrate during the FF cycle ($\Delta x_j = 0.3 \mu\text{m}$) is much larger than for the RIF result ($\Delta x_j \approx 0.1 \mu\text{m}$), as also shown in Fig. 6. Nevertheless, absolutely no fusion was obtained during the FF cycle, for all phosphorus concentrations investigated. Similar fusion results were also obtained elsewhere (1). This comparison demonstrates quite convincingly that, for equivalent redistribution of a typical boron dopant profile in silicon, RIF is much more effective than FF for the fusion of PSG films.

Table II. Comparison of rapid isothermal processing and conventional furnace processing, giving the increase in junction depth Δx_j in an implanted silicon substrate, for a dose of $3 \times 10^{15} \text{ B}^+/\text{cm}^2$ implanted at 25 keV through a 40 nm thermal SiO_2 layer, and the change in step coverage angle θ (initially at 80°) of a reflowed PSG film

Process (N_2 ambient)	Heating cycle	Δx_j (μm)	Fusion for 8 w/o PSG
Furnace	80 min at 900°C	0.3	None
RIF	10s at 1100°C	0.1	$\theta = 113^\circ$

Conclusion

We have proved that, for equivalent dopant redistribution of junction profiles in silicon, rapid isothermal processing in a N_2 ambient is much more effective than conventional furnace processing for the fusion of PSG films.

A process window has been identified for typical VLSI applications. It consists of an 1100°C/10s RIF treatment of PSG films containing approximately 8 w/o phosphorus. These conditions increased an initial reentrant step coverage angle of 80° to a final value of more than 110° . A typical boron profile implanted in a silicon substrate and subjected to the same conditions underwent only a 0.1 μm increase in junction depth, making RIF compatible with VLSI applications where a relatively high phosphorus content is acceptable in PSG films.

Acknowledgments

The authors would like to thank B. Tait, J. Saeki, M. Brown, T. Abraham, A. Loro, and B. Theriault for their technical assistance and V. Ho for helpful discussions.

Manuscript submitted Feb. 26, 1985; revised manuscript received June 12, 1985. This was Paper 420 presented at the New Orleans, Louisiana, Meeting of the Society, Oct. 7-12, 1984.

Northern Telecom Electronics Limited assisted in meeting the publication costs of this article.

REFERENCES

1. J. B. Price and E. Reed, Abstract 372, p. 571, The Electrochemical Society Extended Abstracts, Vol. 83-1, San Francisco, CA, May 8-13, 1983.
2. R. A. Bowling and G. B. Larrabee, *This Journal*, **132**, 141 (1985).
3. N. Hashimoto, Y. Yatsuda, and S. Mutoh, *Jpn. J. Appl. Phys.*, **16**, 73 (1977).
4. W. E. Armstrong and D. L. Tolliver, *This Journal*, **121**, 307 (1974).
5. A. Naumaan and J. T. Boyd, *J. Vac. Sci. Technol.*, **17**, 529 (1980).
6. D. F. Downey, C. F. Russo, and J. T. White, *Solid State Technol.*, **25**, 87 (1982).
7. J. Kato and S. Iwamatsu, *This Journal*, **131**, 1145 (1984).
8. H. Nishimura, Y. Suizu, and T. Tsujimaru, Abstract 519, p. 760, The Electrochemical Society Extended Abstracts, Vol. 84-2, New Orleans, LA, Oct. 7-12, 1984.
9. T. Hara, H. Suzuki, and M. Furukawa, *Jpn. J. Appl. Phys.*, **23**, L453 (1984).
10. J. Narayan, O. W. Holland, R. E. Eby, J. J. Wortman, V. Ozguz, and G. A. Rozgonyi, *Appl. Phys. Lett.*, **43**, 957 (1983).
11. R. B. Fair, J. J. Wortman, and J. Liu, *IEDM Tech. Dig.*, 658 (1983).
12. T. E. Seidel, *IEEE Electron Dev. Lett.*, **ed1-4**, 354 (1983).
13. H. Takeuchi and J. Murota, *This Journal*, **131**, 403 (1984).
14. B. I. Boltaks, "Diffusion in Semiconductors," Chap. IV, Academic Press, New York (1963).
15. M. Ghezzi and D. M. Brown, *This Journal*, **120**, 146 (1973).
16. C. T. Sah, H. Sello, and D. A. Tremere, *J. Phys. Chem. Solids*, **11**, 288 (1959).
17. R. N. Ghoshtagore, *Thin Solid Films*, **25**, 501 (1975).
18. R. B. Fair in "Impurity Doping Processes in Silicon," F. F. Y. Wang, Editor, Chap. 7, Elsevier, North-Holland, New York (1981).
19. M. Current and A. Yee, *Solid State Technol.*, **26**, 197 (1983).

Effects of Wet Cleaning on Si Contaminated with Heavy Metals during Reactive Ion Etching

Tetsuo Hosoya, Yoshiharu Ozaki, and Kazuo Hirata

Nippon Telegraph and Telephone Corporation, Atsugi Electrical Communication Laboratory, 1839, Ono, Atsugi-shi, Kanagawa Prefecture 243-01, Japan

ABSTRACT

Heavy metal removal from Si wafers contaminated during reactive ion etching (RIE) is studied using wet cleaning techniques. Si wafers are intentionally contaminated during RIE with Fe, Cr, or Ni, which are atomic components of stainless steel, the material used in dry etching apparatus. The Si wafers are washed with several reagents, and heavy metal removal results are estimated using secondary ion mass spectrometry and stacking fault observation. The results show that Fe and Cr are removed by wet etching the Si wafers to approximately a 30 nm depth but that Ni cannot be removed. The results indicate that to protect Si wafers against heavy metal contamination during RIE, Ni-free materials should be used for fixtures in the dry etching chamber.

In fabrication processes for high density LSI's, dry etching techniques are essential in producing fine patterns with high accuracy. Reactive ion etching (RIE) is especially useful in etching fine patterns because of its anisotropic etching features. However, RIE results in more contamination and damage to etched Si wafers than plasma etching. This is due to the sputtering and bombardment action of energetic ions generated during RIE. Many studies have been done on relationships between RIE conditions and device characteristics (1-3). It has been found that heavy metal contamination in a reactor during RIE causes a decrease in Si wafer minority carrier lifetime in silicon wafers subsequently subjected to high temperature heat-treatment.

To avoid heavy metal contamination in Si wafers, RIE reactor design improvement is required to prevent stainless steel used in the etching chamber from coming into contact with the plasma, or materials containing heavy metals should not be used in the etching chamber. Another approach, to eliminate the influence of heavy metal contamination, is to develop effective methods for removing the contaminated layer in the LSI fabrication process. This paper concerns Si wafer heavy metal-contaminated layer removal by wet cleaning methods, focusing on the behavior of Fe, Cr, and Ni, stainless steel's constituent elements.

In this study, Si wafers were intentionally contaminated with heavy metals during RIE. Pure metals, Fe, Cr, and Ni, are used as contamination sources, and wet cleaning procedures are developed so as to be applicable to LSI processes. The Fe and Cr removal and Ni nonremoval results are obtained through examination using secondary ion mass spectrometry (SIMS) and stacking fault (SF) observation.

The following sections describe the experimental procedures and results, the reason for Ni nonremoval, and application of findings to RIE apparatus design.

Experimental

Si wafer heavy metal contamination was carried out using RIE. The RIE reactor used in this work is shown schematically in Fig. 1. The RF power (13.56 MHz) was applied to the cathode electrode. Si wafers, which were 3 Ω -cm boron-doped (100) slices with a diameter of 3 in., were loaded on a stainless steel cathode electrode (Fe 74%, Cr 18%, Ni 18%). CF_4 was used as the etching gas at a pressure of 2 Pa. The RF power density and the etching time were set to 0.18 W/cm² and 30 min, respectively. Etching rates for Si were 9 ~ 13 nm/min. The wafers were contaminated with heavy metals sputtered from the cathode electrode. When using pure metals as a source of contamination, metal plates with a high purity (99.9%), i.e., Fe, Cr, and Ni, were set on the cathode electrode. The wafers were then placed on the plates. A 50 μ m thick Teflon sheet was placed between the plates and the cathode electrode. This sheet was replaced with a new sheet after ev-

ery plate change to avoid Si wafer contamination from other plate metals which may have adhered to the sheet.

Cleaning procedures following the contamination step in RIE consisted of the following steps: (i) ashing in O_2 glow discharge, (ii) washing in $H_2SO_4 + H_2O_2$ solution and rinsing in deionized water, (iii) cleaning by RCA treatment (4) (washing in $NH_4OH + H_2O_2$ and $HCl + H_2O_2$ solution) followed by diluted HF washing after each step. The reagents used were IC-grade EL-class reagents. In this paper, the authors call these three treatment steps the basic cleaning procedure. Steps i and ii are for removal of the plasma polymerized film and resists after dry etching, and step iii is for final Si wafer cleaning. As a result, the Si surface was etched off to an 8 nm depth in the basic cleaning procedure. When heavy metal contamination was not sufficiently removed from the Si wafers by the basic cleaning procedure, additional cleaning treatments using various liquid reagents were tried between steps ii and iii.

SIMS and SF observation were used to evaluate the degree of heavy metal removal. SIMS analysis was carried out using both Hitachi IMA-2 for estimating the heavy metal amounts remaining on the Si surface and Cameca ims-3f for the depth profile analysis. Hitachi IMA-2 was used under 10 kV Ar^+ ion beam acceleration voltage conditions with a 1300 μ m spot diameter. Cameca ims-3 was used under 15 kV O_2^+ ion beam acceleration voltage conditions with a 150 μ m spot diameter. Evaluation was carried out using the peak height ratio of each secondary ion spectrum intensity to that of $^{28}Si^+$. It is desirable to detect isotopes with the highest existence ratio for each metal in order to detect the secondary ions in high sensitivities. In this work, $^{54}Fe^+$, $^{52}Cr^+$, and $^{60}Ni^+$ were picked to detect each heavy metal. This was done to avoid an S/N ratio reduction due to the secondary ion settling on Si. The SF occurrence was observed as follows. Contaminated Si wafers were treated using the above-mentioned cleaning procedure. Next, they were oxidized at 1100°C in a wet O_2 atmosphere for 2h. After the SiO_2 was etched off with an HF solution, SF was visualized by etching the wafers to a

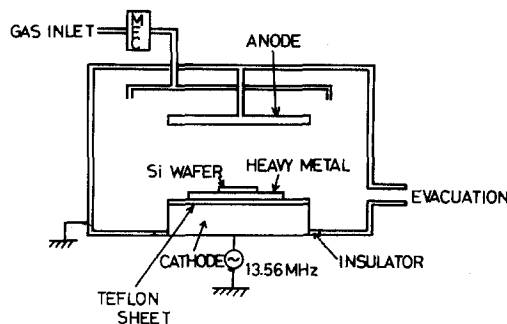


Fig. 1. RIE reactor diagram

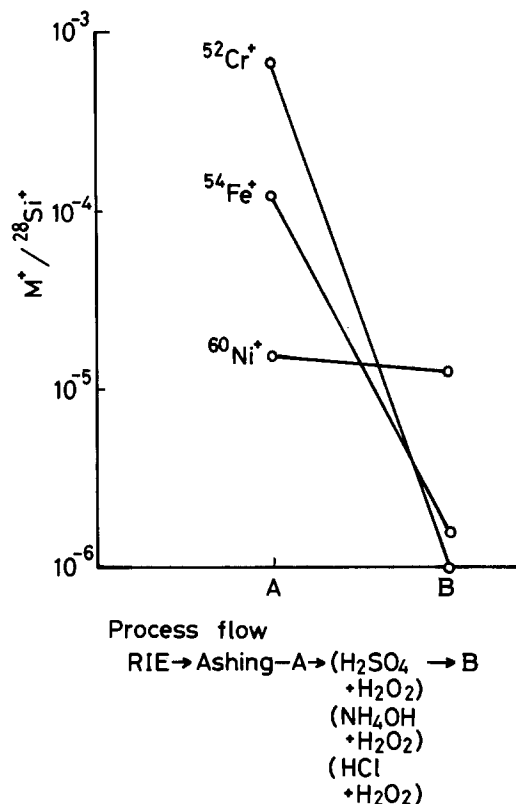


Fig. 2. Relation between remaining Fe, Cr, and Ni amounts and cleaning steps, using stainless steel as the contamination source, expressed by SIMS spectrum intensity ratios, $M^+ / {}^{28}\text{Si}^+$. SIMS measurement was done at A and B steps.

1 μm depth by Wright etching (5) and observed with a microscope.

Results

Removal of heavy metal contamination originating from stainless steel.—SIMS analysis was carried out on stainless steel-contaminated samples and cleaned using the basic cleaning procedure. Fe, Cr, and Ni, which compose stainless steel, were detected on the Si surface, as shown in Fig. 2. Heavy metal mass peak intensities on the Si surface after the basic cleaning procedure were high for Ni, Fe, and Cr in descending order. Cr was removed to the SIMS detection limit level after cleaning. These results indicate that Ni is the most difficult material to remove from Si.

Removal of heavy metal contamination originating from pure metals.—Si wafers contaminated with Fe, Cr, or Ni pure metals were prepared using RIE and SF observation. After applying the basic cleaning procedure, SF's were not observed on the Cr-contaminated Si wafers but were observed on those contaminated with Fe and Ni, as shown in Fig. 3. No SF's were observed on the Fe-contaminated Si wafers when the wafers were etched to a 20 nm depth with an $\text{HNO}_3 + \text{HF} + \text{CH}_3\text{COOH}$ solution before RCA treatment as shown in Fig. 4A. However, on the Ni-contaminated wafers, SF's were observed, as shown in Fig. 4B. In the wet etching process, used in Fig. 4, Si was etched off to an 8 nm depth using the basic cleaning procedure and to 20 nm depth with the mixed solution. Consequently, the Si etched depth was estimated to be about 30 nm.

The relation between remaining Fe, Cr, or Ni amounts and the cleaning steps was investigated by SIMS, using the ratio of mass intensities to ${}^{28}\text{Si}^+$. Remaining amounts of the three elements decreased with each step in the cleaning procedure, as shown in Fig. 5. The amount of Cr was below the SIMS detection limit level after the basic cleaning steps with no Si wet etching. For Fe, the amount was the same as for Cr if the Si wet etch procedure was employed before RCA treatment. However, Ni remained

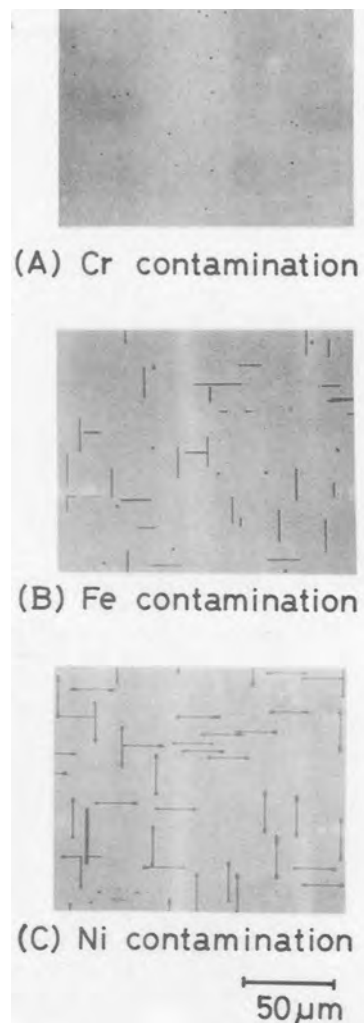


Fig. 3. SF observation results after basic cleaning procedure. SF's were made visible by Wright etching method.

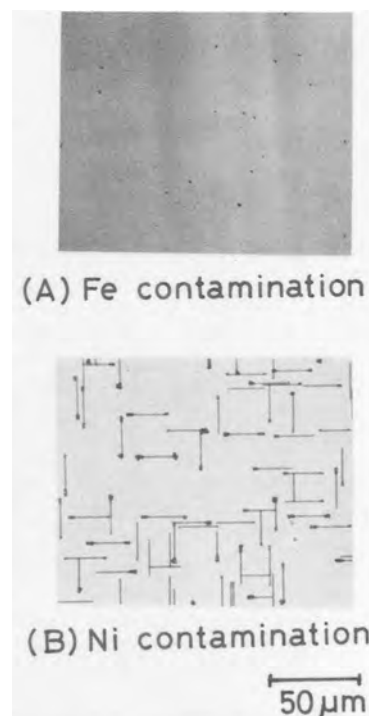


Fig. 4. SF observation results after adding 20 nm Si wet etching to basic cleaning procedure. SF's were made visible by Wright etching method.

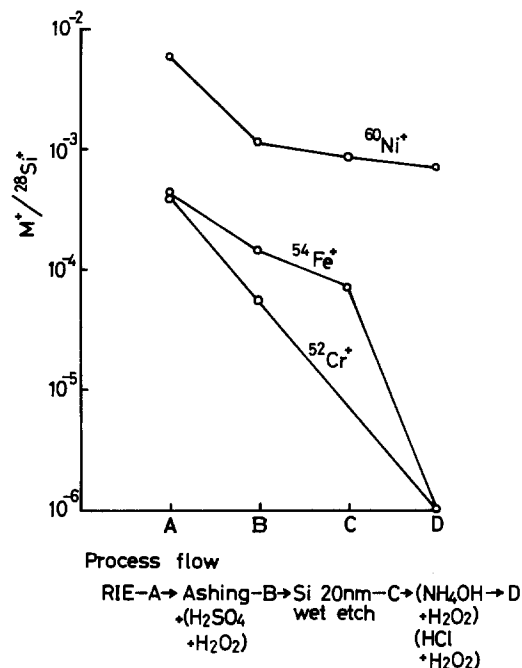


Fig. 5. Relation between remaining Fe, Cr, and Ni amounts and cleaning steps, using pure metals as the contamination source, expressed by SIMS spectrum intensity ratios, $M^{+}/^{28}\text{Si}^{+}$. SIMS measurement was done at A, B, C, and D steps.

high even after all cleaning steps were carried out. These results support the SF observation.

Metal plate wet etching rates were investigated using the solutions employed in the basic cleaning procedure. Ni was etched in considerable quantity, as much as Fe, with the HCl + H₂O₂ solution, as shown in Table I.

Thus, the etching of metals in Si is different from that of metal itself. The chemical state of the Ni atom added to Si wafers during RIE was of concern and was investigated by XPS analysis.

XPS analysis of the Ni-contaminated wafer.—Possible Ni atom chemical states were considered to be either of a metallic state, a compound with Si, or a compound with the etching gas element. The compound with Si, nickel silicide, is known to be formed at 200° ~ 300°C (6) and to be insoluble in acids except for hydrofluoric acid (7). XPS analysis was carried out on the Si surface immediately after Ni contamination. A Ni and a nickel oxide were detected, while nickel silicide was not, as shown in Fig. 6. Nickel oxide formation is considered to be caused by the Ni oxidation during ashing treatment.

On the basis of XPS analysis results mentioned above, nickel removal investigations were carried out using wet cleaning methods.

Ni-contaminated layer removal.—Several kinds of wet etching solutions were applied before the RCA treatment in the basic cleaning procedure. These are summarized in Table II. The treatments were aimed at accomplishing the following: treatments a, b, and c were for Ni removal. Treatment d was to remove nickel oxide with HCl and nickel with HNO₃. Treatment e was for Ni removal and was carried out in diluted HCl using a 5 mA dc current between the Ni-contaminated sample and a Si cathode

Table I. Etching rates for heavy metals by the solutions used in the basic cleaning procedure

Solutions	Etching rates for metals (at./cm ² -min)	
	Ni	Fe
H ₂ SO ₄ + H ₂ O ₂	2 × 10 ¹⁸	1 × 10 ¹⁸
Diluted HF	2 × 10 ¹⁷	2 × 10 ¹⁶
NH ₄ OH + H ₂ O ₂	1 × 10 ¹⁶	1 × 10 ¹⁶
HCl + H ₂ O ₂	5 × 10 ²⁰	5 × 10 ²¹

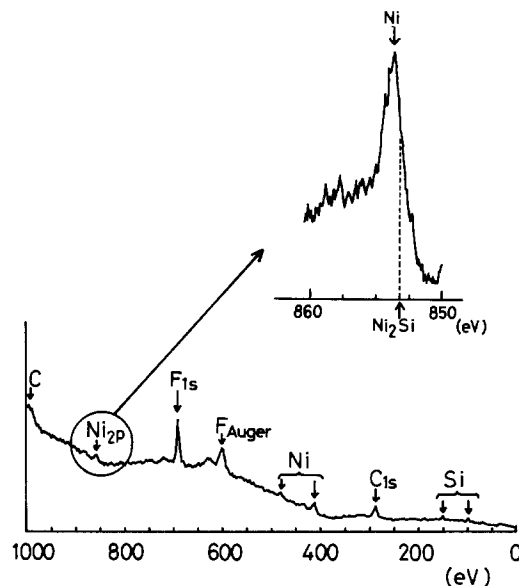


Fig. 6. Si wafer XPS analysis immediately after Ni contamination

electrode. The results obtained indicate SF occurrence in all the samples and that Ni was impossible to remove from the Si surface.

Discussion

The experimental results are summarized as follows: (i) Cr is removed using the basic cleaning procedure; (ii) Fe is removed by adding 20 nm Si wet etching to the cleaning procedure; and (iii) Ni is not removed despite the application of several cleaning procedures. The reason Ni cannot be removed is discussed below.

Consider a simple model in which metal atoms sputtered from metal plates are ionized in glow discharge and impinge on the Si wafer surface with an acceleration energy equivalent to the cathode fall potential. Metal ions such as Fe⁺, Cr⁺, and Ni⁺ are implanted at a finite depth from the Si surface. Here, the metal atom depth profiles become important in interpreting wet cleaning characteristics.

The Ni depth profile in Si wafers was measured using SIMS profile analysis. It is found that Fe and Ni were introduced to 50 and 60 nm depths, respectively, as shown in Fig. 7. The SIMS profile analysis generally presents a deeper profile due to a tailing phenomenon in highly concentrated impurity analysis (8). Thus, the impurity profile depth shown in Fig. 7 must be slightly exaggerated. For example, as already mentioned, Fe was removed by etching the Si to approximately a 30 nm depth, while Fig. 7 shows that Fe exists to 50 nm. The Fe depth in the wafer is shown to be 20 nm larger using SIMS profile analysis than that found in actual wet etching. Considering the Fe case, Ni is inferred to etch at most 40 nm in the Si wafer. This inference also comes from Ni ion's small acceleration energy of 700 eV for the 0.2 W/cm² power condition. It thus follows that Ni could be removed by etching the Si to approximately 40 nm.

Fe and Ni profiles were estimated using the "step etch" method. Namely, metal-contaminated Si wafers were

Table II. Treatments for Ni removal applied before RCA treatment in the basic cleaning procedure

Treatment	
a	Stir in a (NH ₄) ₂ S ₂ O ₈ 200g, HCl 10 cm ³ and H ₂ O 1000 cm ³ solution at 70°C
b	Stir in a K ₂ Cr ₂ O ₇ 13g, H ₂ SO ₄ 50 cm ³ and H ₂ O 100 cm ³ solution at 70°C
c	Stir in an HCl 300 cm ³ and HNO ₃ 100 cm ³ (aqua regia) solution at 70°C
d	Stir in HNO ₃ after stirred in HCl at 70°C
e	Electrolytic etching in 12% HCl

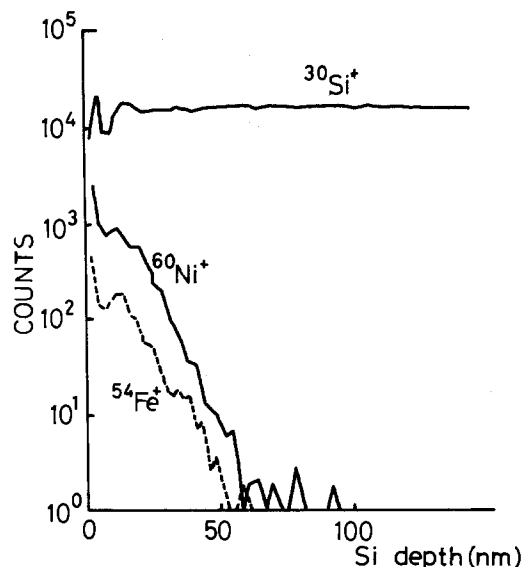


Fig. 7. Ni and Fe depth profiles in Si wafers estimated by SIMS profile analysis, expressed by counts of each metal isotope detected by SIMS.

etched to a certain depth using a $\text{HNO}_3 + \text{HF} + \text{CH}_3\text{COOH}$ solution after ashing followed by diluted HF etching. SIMS analysis was performed after these steps. Results are the same as if Ni is penetrated to a depth of 150 nm, while they show that Fe was below the SIMS detection limit level at 30 nm. This is shown in Fig. 8. Etching of the Ni-contaminated Si wafer using the mixed solution stopped at 150 nm depth. It was necessary to dip the Ni-contaminated wafer into an HF solution to restart etching. Some layer seemed to prevent the etching.

Thus, the fact that Ni in Ni-contaminated Si wafers, contaminated during RIE, cannot be removed is believed to be caused by Ni redeposition onto the Si wafers in the wet cleaning procedure. High Ni metal etching rates, and discrepancy in Ni depth profiles between the SIMS profile analysis and step etching, would be explained by this readhesion concept.

These results indicate that one means of protecting Si wafers against heavy metal contamination during RIE is to select Ni-free materials for the fixtures in the dry etching chamber.

Conclusion

Wet cleaning effects on Si wafers have been investigated for removing heavy metal-contaminated layers introduced during RIE. Si wafers were intentionally contaminated with stainless steel constituent elements, *i.e.*, Fe, Cr, and Ni, during RIE. Wet cleaning procedures were designed to combine washing in $\text{NH}_4\text{OH} + \text{H}_2\text{O}_2$ solution and $\text{HCl} + \text{H}_2\text{O}_2$ solution with etching employing a $\text{HNO}_3 + \text{HF} + \text{CH}_3\text{COOH}$ solution. The amount of heavy metal removed was estimated by SIMS and SF observation in the Si wafers after wet cleaning. The results show that Fe and Cr are removed by etching the Si wafers to approxi-

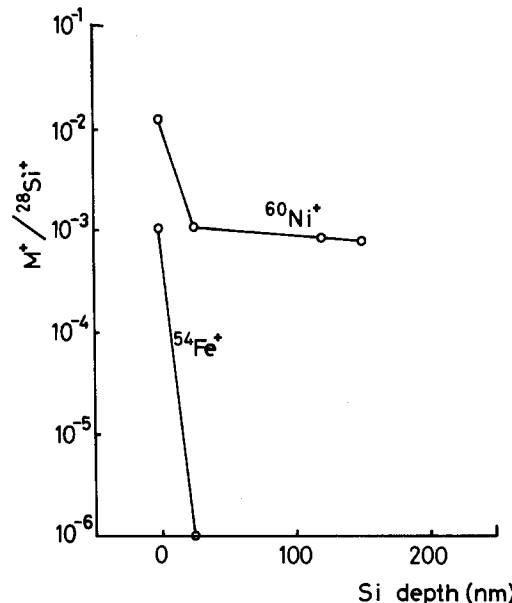


Fig. 8. Heavy metal depth profile in Si wafers estimated by step etch method, expressed by SIMS spectrum intensity ratios, $M^+/^{28}\text{Si}^+$.

mately 30 nm using wet cleaning procedures. However, Ni cannot be removed, even though Ni-contaminated Si wafers were etched to 150 nm. This failure to remove Ni is probably due to Ni redeposition to the Si surface during wet etching. Usage of Ni-free materials for fixtures in the dry etching chamber will be one way to avoid heavy metals contamination in Si wafers.

Acknowledgment

The authors wish to thank Toyoki Kitayama for his valuable suggestions and encouragement and Izumi Kawashima for carrying out the SIMS analysis.

Manuscript submitted June 25, 1984; revised manuscript received April 11, 1985.

Nippon Telegraph and Telephone Public Corporation assisted in meeting the publication costs of this article.

REFERENCES

1. H. R. Deppe, B. Hasler, and J. Hopfner, *Solid State Electron.*, **20**, 51 (1977).
2. Y. Ozaki, K. Hirata, S. Yabumoto, and M. Oshima, "Proceedings of the 2nd Symposium on Dry Processes," p. 55, Institute of Electrical Engineering, Tokyo (1980).
3. L. M. Ephrath and R. S. Bennett, *This Journal*, **129**, 1822 (1982).
4. W. Kern and D. A. Puotinen, *RCA Rev.*, **31**, 187 (1970).
5. M. W. Jenkins, *This Journal*, **124**, 757 (1977).
6. I. Ohdomari and K. Suguro, *J. Vac. Soc. Jpn.*, **22**, 411 (1979).
7. S. P. Murarka, *J. Vac. Sci. Technol.*, **17**, 775 (1980).
8. C. W. Magee, R. E. Honig, and C. A. Evans, Jr., "Depth Profile by SIMS: Depth Resolution, Dynamic Range and Sensitivity," p. 172, Springer Series in Chemical Physics 19, Springer-Verlag, Berlin (1982).

Deep-UV Contact Lithography Using a Trilevel Resist System for Magnetic Bubble Devices with Submicron Minimum Feature

H. Umezaki, N. Koyama, Y. Maruyama, Y. Sugita, and R. Suzuki

Hitachi Limited, Central Research Laboratory, Kokubunji, Tokyo 185, Japan

ABSTRACT

Deep UV lithography using a trilevel resist system has been developed to delineate submicron patterns for magnetic bubble memory devices. The trilevel resist system consists of PIQ[®] as a bottom polymer layer, spin-coated TiO_x as an intermediate layer, and MRS as a top imaging resist. All these layers can be spun and baked sequentially. MRS resist patterns are defined by deep-UV contact printing and transferred to TiO_x layer and PIQ layer sequentially using reactive ion etching with CF₄ gas for TiO_x and O₂ gas for PIQ. Using this trilevel resist process, 0.4 μm lines and spaces were fabricated and contiguous disk patterns of 2 μm bit period for bubble memory devices of 16 Mb/cm² were also fabricated successfully.

Magnetic bubble memory devices with the bit capacity of 1 and 4 Mb are now in volume production(1). These devices are all Permalloy devices in which track patterns for bubbles consist of Permalloy patterns. These patterns have gaps between neighboring bits. The minimum feature of these patterns is 1 μm, and the patterns are fabricated using contact printer or 10× projection printer with conventional UV light. High density ion-implanted bubble memory devices of 4-16 Mb in memory capacity are now under development (2, 3). Bubble propagation tracks of these devices are fabricated by implanting H₂ or Ne ions into bubble garnet through mask patterns. Since the mask patterns, named contiguous disks, have no gaps between neighboring bits, the requirement for lithography can be relaxed compared with Permalloy devices. However, for higher density devices of 4-16 Mb/cm², the delineation of patterns with the minimum feature of 0.5-1.0 μm is required even using this approach to fabricate 4-16 Mb/cm² devices.

Conventional UV lithography, however, is insufficient for this purpose because of its lack of practical resolution. Deep-UV lithography is known to be superior to UV lithography and has the high resolution capability in submicron range (4). Deep-UV contact lithography uses the same technique as the conventional UV lithography, except for light source and resist. A Xe-Hg lamp is well known to be the deep UV-light source. As deep-UV resist, we employ the negative-type MRS¹ resist, which is composed of poly(p-vinylphenol) and 3,3'-diazidodiphenyl sulfone (5, 6, 7). The MRS resist has properties of high sensitivity to 200-300 nm radiation, high resolution, and good resistance to dry etching.

The mask patterns for ion-implanted bubble devices should satisfy the following requirements: (i) the thickness is large enough to stop incident ions; (ii) the material is highly heat resistant not to be deformed during implantation; and (iii) the edge profile is steep and smooth to obtain a clearly defined propagation track. To satisfy these requirements, we employ the polyimide resin PIQ(8)² with the thickness of 1.5 μm as a mask material and transfer MRS patterns to PIQ layer using trilevel resist technique (9).

In this paper, the characteristics of MRS resist such as resolution capability and process latitude in resist profile control and linewidth control are reported. The trilevel resist process using the MRS resist as top imaging resist, the spin-coated TiO_x as an intermediate layer, and the PIQ as a bottom polymer layer is presented. Experimental results demonstrating the performance of the process are also included.

Experimental

The MRS resist films were spin-coated on substrates to thickness of 0.3-0.6 μm and prebaked at 80°C for 20 min.

¹MRS stands for micro resist for shorter wavelength, and is commercially available from Hitachi Chemical Company Limited under the trade name RD2000N.

²PIQ stands for Polyimide Iso-indroquinazolinedione, and is a trade name of Hitachi Chemical Company Limited.

The thickness was changed for the purpose of the experiment and adjusted by diluting the resist solution with cyclohexanone. Exposure was carried out using the contact aligner Cobilt CA800 equipped with a 500W Xe-Hg lamp (Ushio Electric, Incorporated) and an aluminum mirror. Since the spectral photosensitivity of the MRS resist is restricted to 200-300 nm wavelength, a cold mirror is not necessary to expose the MRS resist. The photomask used in the experiment consisted of a quartz substrate and a thin layer of chromium patterns which were delineated by electron-beam writing. The thickness of the quartz substrate was 2.4 mm. After exposure, the MRS resist was developed in MF312 developer (Shipley) diluted with water at 1:4 and rinsed in deionized water.

In order to compare the resolution capability of MRS with conventional UV resist, the resolution of AZ1350J (Shipley) was also investigated. To perform the experiment under the same condition, the same photomask and the same aligner were used, except for a light source, *i.e.*, a Xe-Hg lamp for MRS and a Hg lamp for AZ1350J. The AZ1350J resist was developed in the AZ developer (Shipley), diluted with water at 1:1, and rinsed in deionized water.

The trilevel resist system studied here consists of MRS/TiO_x/PIQ. A schematic diagram of the process is shown in Fig. 1. A substrate was coated successively with the thick polymer layer of PIQ (1.5 μm), the thin layer of spin-coated TiO_x (0.1 μm), and the thin MRS resist layer (0.3 μm). The TiO_x film was obtained by spin-coating and baking an organotitanium solution which will be described in detail later. The top imaging resist MRS was defined by the deep-UV contact printing. Transfer of the resist patterns to TiO_x layer was performed by reactive ion etching (RIE) in CF₄ plasma. The patterns in TiO_x layer were then replicated in thick PIQ layer by RIE in pure O₂ plasma.

Results and Discussion

Characteristics of MRS.—The resolution of MRS was compared with the conventional UV resist AZ1350J. The results are shown in Fig. 2. Both resist patterns were defined by the same contact aligner using the same photomask patterns of lines and spaces. The thicknesses of these two types of resist were both 0.6 μm. It can be seen from the figure that the resolution of AZ1350J is about 0.5 μm and that of MRS is less than 0.4 μm. The resolution of MRS is thus superior to that of AZ1350J. As for AZ-type resist, Smith *et al.* demonstrated the linewidth of 0.4 μm using a contact printer and conformable photomask (10). In our experiment, however, the resolution is about 0.5 μm. This is presumably due to the difference of photomask structures. In our experiment, a hard mask plate was used and this should cause the degradation of resolution.

The MRS resist thus exhibits a high resolution. But this resist is also known to have such a property that the cross-sectional profile varies sensitively according to de-

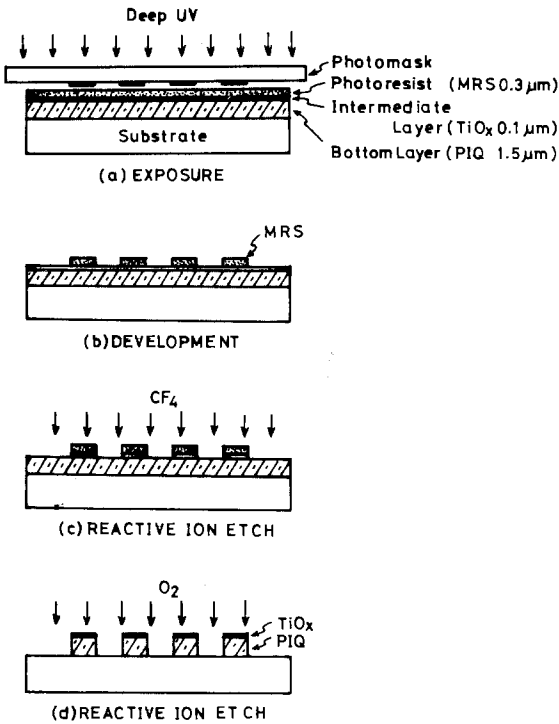


Fig. 1. Schematic diagram of the trilevel resist process

velopment conditions (5). Examples of this phenomenon are shown in Fig. 3. The resist thickness is $0.6 \mu\text{m}$ for the left-hand samples and $0.25 \mu\text{m}$ for the right-hand samples. A development time was changed by 15s from the minimum time required to delineate a pattern. In the case of $0.6 \mu\text{m}$ thick resist, the profile changes with increasing a development time and results in the undercut profile. On the other hand, for the resist with the thickness of $0.25 \mu\text{m}$, the profile does not change and is always steep in all development conditions.

The undercut profile shown here is caused by a strong absorption of deep-UV light by MRS resist (5). In the case of $0.6 \mu\text{m}$ thick resist, the deep-UV light cannot reach at the lower layer, owing to a strong absorption, and the resists at the lower part are removed by prolonged development. In the case of $0.25 \mu\text{m}$ thick resist, however, the thickness is so small that the deep-UV light can penetrate all through the resist. Therefore, the resist profile is always steep at every development condition. This property is desirable, since the steep profile ensures that the good linewidth control and the restriction on development condition can be relaxed compared with the case of thick MRS resist.

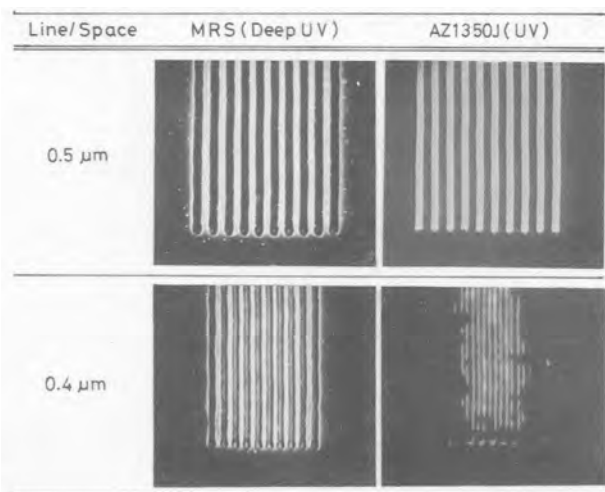


Fig. 2. Comparison of the resolution of MRS resist (deep UV) and AZ1350J resist (UV) delineated by contact printing.

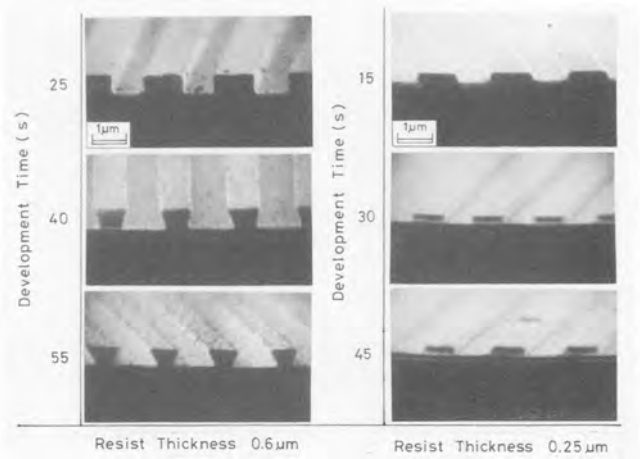


Fig. 3. MRS resist profiles as a function of development time. The thicknesses are $0.6 \mu\text{m}$ for the left-hand samples and $0.25 \mu\text{m}$ for the right-hand samples.

Figure 4 shows the linewidth variation of thin MRS resist patterns as functions of exposure and development time. The results of UV resist AZ1350J are also shown in the figure. The thicknesses of MRS and AZ1350J are $0.27 \mu\text{m}$ and $0.26 \mu\text{m}$, respectively. The test patterns used in the experiment were lines and spaces with the widths of 1.0 , 0.75 , and $0.5 \mu\text{m}$, respectively. The patterns on the photomask were transferred to the resists with each exposure and development condition. The exposure time was changed from the minimum time to delineate a pattern to about eight times the minimum time. The development time was changed from 5 to 160s. Under these exposure and development conditions, linewidth for MRS resist and spacewidth for AZ1350J resist were measured by scanning electron microscope (SEM) observation.³

The contour lines shown in the figure were obtained from the values of measurement points and indicate the same linewidth is obtained. Therefore, as the density of contour lines is small, the latitude of exposure and development condition becomes large. It can be seen that the density of contour lines for MRS resist is smaller than that for AZ1350J resist. That is, the linewidth variation of MRS caused by a fluctuation of exposure or development condition is smaller than that of AZ1350J resist. The rectangular regions in the figure correspond to the latitude of linewidth control $\pm 20\%$, that is, 1 ± 0.2 , 0.75 ± 0.15 , and $0.5 \pm 0.1 \mu\text{m}$, respectively. As shown in the figure, the rectangular region of MRS resist is larger than that of AZ1350J resist for each linewidth. The rectangular region of $0.75 \mu\text{m}$ patterns for MRS resist is almost the same as that of $1.0 \mu\text{m}$ patterns for AZ1350J resist. This indicates that the $0.75 \mu\text{m}$ pattern can be fabricated with the same

³Since the types of these two resists are different, i.e., MRS is the negative-type resist and AZ1350J is the positive-type resist, the line pattern for MRS resist corresponds to the space pattern for AZ resist when the same photomask pattern is used.

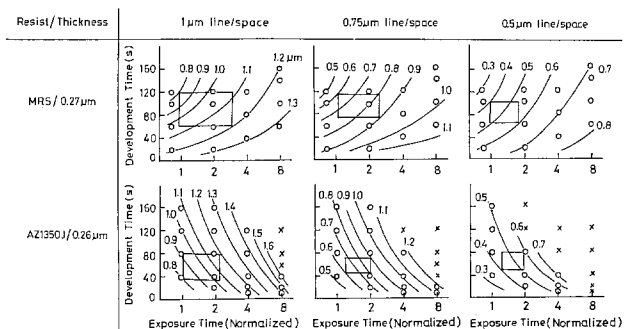


Fig. 4. Linewidth variations of MRS resist and AZ1350J resist patterns as functions of exposure and development times.

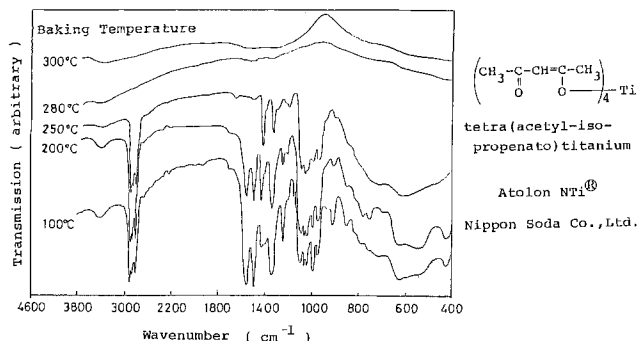


Fig. 5. Fourier transform infrared spectra for Atolon NTi films which were baked at temperatures from 100° to 300°C.

tolerance as that for 1 μm pattern of AZ1350J resist. As for 0.5 μm pattern, the MRS pattern can be obtained at every exposure and development condition. The condition for AZ1350J resist is restricted, as can be seen in the figure.

Here it should be noticed that the thin resist cannot be used in itself as a mask pattern for etching or ion implantation. Therefore, we introduced the trilevel resist process where thin MRS resist was used as the top imaging resist.

Trilevel resist process.—The present trilevel resist system is composed of PIQ, TiO_x , and MRS as already indicated in Fig. 1. An intermediate layer TiO_x was obtained from the organometal solution of tetra(acetyl-isopropenato)titanium (Atolon NTi®; Nippon Soda Company Limited). Figure 5 shows the Fourier transform infrared spectra for Atolon NTi films which were baked at temperatures from 100° to 300°C. The baking treatment was performed in the air atmosphere for 30 min in all cases. The strong absorptions due to organic compounds are observed for the samples baked at less than 250°C, but they disappear when the baking temperature is greater than 280°C. From these results, it can be said that the inorganic TiO_x is obtained by baking Atolon NTi at temperature higher than 280°C.

The TiO_x films thus obtained have some advantages compared with spin-on glass (SOG) (11) or SiO_2 films deposited by plasma enhanced chemical vapor deposition (PECVD) (9). These materials are widely used as an intermediate layer for trilevel resist process. Table I shows the comparison of these materials. A deposition process of TiO_x and SOG is simple because there is no need of evacuation process, which is necessary for PECVD. The adhesion of MRS or AZ resist to the TiO_x film is excellent, and the adhesion promoter such as hexamethyl disilazane (HMDS) is not needed here. On the other hand, the adhesion promoter is necessary for SOG and SiO_2 . The stability of Atolon NTi solution is good compared with the SOG solution. In the case of SOG solution, proper storage is required since the silicate material can easily be hydrolyzed by moisture in the air to form SiO_2 -like crystals. These crystals cause defects in a spin-on film. The TiO_x films obtained from Atolon NTi solution pose no such problem, because the hydrolysis in this case hardly occurs and defects in the films are few. The defects in PECVD SiO_2 film are usually caused by particles which eventually flake off from the surrounding wall of PECVD chamber. Therefore, careful cleaning procedures are required to decrease defects in a film.

Table I. Comparison of intermediate layers for trilevel resist process.

Material	TiO_x (Spin-On)	SOG (Spin-On)	SiO_2 (PlasmaCVD)
Process Simplicity	○	○	X
Adhesion of MRS or AZ	○	X	X
Defect	○	△	△

Linewidth control.—Linewidth control of the patterns delineated by the trilevel resist process depends on three factors, i.e., image transfers of photomask patterns to resist layer, resist patterns to intermediate layer, and intermediate patterns to bottom layer. As described previously, the accuracy of image transfer to MRS resist is superior to that of AZ resist. In the present case, the MRS patterns are transferred to TiO_x and PIQ layer successively. Therefore, these etching processes must be controlled precisely. The TiO_x etching process is especially critical since the thin (0.3 μm thick) MRS resist must be used to etch TiO_x layer using reactive ion etching. To control a linewidth precisely in TiO_x etching, therefore, the sufficient etching selectivity is required. For this purpose, we investigated etching conditions, that is, an etching gas and RF power. The results are shown in Fig. 6. The etching gases studied here were CF_4 , CF_4/O_2 , CHF_3 , and CHF_3/Ar , and the RF power was changed from 100 to 400W. The vacuum pressure was 5 Pa in every case. It can be seen that the etching rate of TiO_x in CF_4 plasma is relatively high and the etching rate ratio of TiO_x to MRS is also high. When O_2 gas is mixed in CF_4 gas, the etching rate of TiO_x increases. However, the etching rate of MRS also increases and the ratio becomes smaller. In the case of CHF_3 plasma, a deposition process occurs when an RF power is small (100-200W). At high RF power (400W), the etching becomes possible and the etching rate ratio is high. CHF_3/Ar plasma etching behavior is almost the same as the case of CHF_3 plasma.

In order to obtain the high etching rate ratio, the CHF_3 or CHF_3/Ar plasma with 400W RF power is most favora-

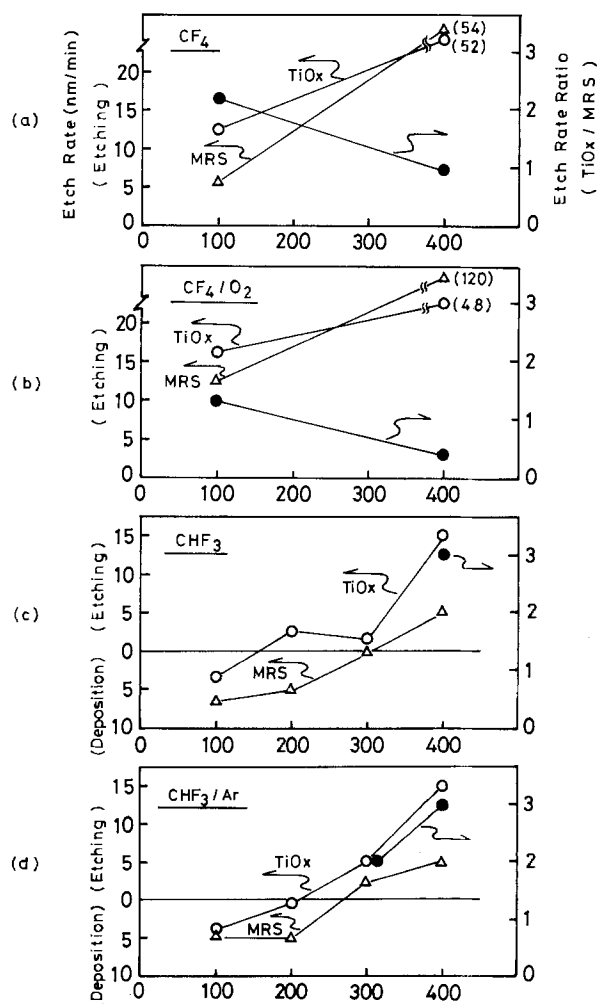


Fig. 6. Etching rate of TiO_x and MRS resist and etching rate ratio of TiO_x/MRS as a function of RF power. a: CF_4 50 sccm. b: CF_4 50 sccm + O_2 5 sccm. c: CHF_3 50 sccm. d: CHF_3 50 sccm + Ar 15 sccm. Vacuum pressure was 5 Pa in every case. The substrate on which wafers were placed was SiO_2 for CF_4 and $\text{CF}_4 + \text{O}_2$ gases and Teflon for CHF_3 and $\text{CHF}_3 + \text{Ar}$ gases.

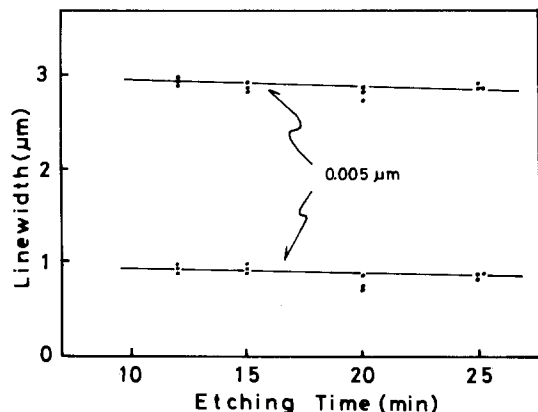


Fig. 7. Linewidth variations of TiO_x patterns as a function of etching time. Etching gas was CF_4 with the flow rate of 50 sccm. Vacuum pressure was 5 Pa, and RF power was 100W.

ble. However, the plasma discharge is unstable at that condition and the reproducibility of etching becomes poor. The stability of plasma discharge was improved when the vacuum pressure was increased (to 10 Pa). But, at the high vacuum pressure, the deposition process again occurred.

From these results, we selected the CF_4 as an etching gas and the RF power to be 100W. Under these conditions, the linewidth variation was measured as a function of etching time. The results are shown in Fig. 7. The linewidth decreases linearly with increasing the etching time, and the decreasing rate is $0.005 \mu\text{m}/\text{min}$. The rate is so small that the linewidth can be controlled precisely. The linewidth variation is only $\pm 0.025 \mu\text{m}$ when the etching time was changed from the standard time (for example at 15 min) by ± 5 min.

Figure 8 shows the etching rates of PIQ, MRS, and Atolon NTi films in O_2 RIE. The Atolon NTi film was baked at 200° or 300°C . The RF power was 100W, and the vacuum pressure was 0.27 Pa. It can be seen that the etching rates of PIQ and MRS are almost the same: 23 nm/min. The Atolon NTi baked at 200°C is etched slightly, and the etching rate is 0.7 nm/min. However, the Atolon NTi baked at 300°C is not etched in this measurement time. As mentioned previously, the Atolon NTi baked at 200°C still contains organic contents and is, therefore, slightly etched by O_2 RIE. On the other hand, the Atolon NTi baked at 300°C changes to the inorganic material TiO_x and remains intact during O_2 RIE. From these results, it can be concluded that the Atolon NTi film baked at 300°C serves as a good mask material for an etching of PIQ by O_2 RIE.

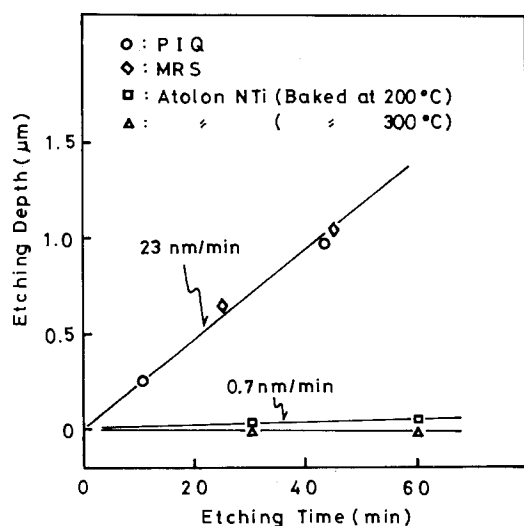


Fig. 8. Etching rates of PIQ, MRS, and Atolon NTi by O_2 reactive ion etching. Atolon NTi films were baked at 200° and 300°C . RF power was 100W, and vacuum pressure was 0.27 Pa.

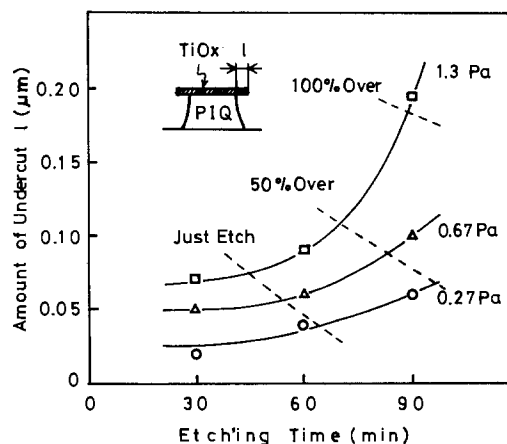


Fig. 9. Amounts of undercut as a function of etching time. Vacuum pressure was changed from 0.27 to 1.3 Pa. RF power was 100W.

The vacuum pressure in O_2 RIE is a key parameter for linewidth control (12). When the vacuum pressure is too high, an undercut profile occurs. On the other hand, the plasma discharge becomes unstable as the vacuum pressure is too low. To obtain the practical condition, we investigated the amount of undercut of the PIQ pattern under the protective TiO_x layer as a function of vacuum pressure. The results are shown in Fig. 9. The vacuum pressure was changed from 0.27 to 1.3 Pa. The amounts of undercut were measured by an SEM observation. When the pressure is 1.3 Pa, the amount of undercut increases rapidly with increasing the etching time and reaches $0.2 \mu\text{m}$ at the etching time of 90 min, which is about twice the time required to eliminate $1.5 \mu\text{m}$ thick PIQ layer. The amount of undercut decreases when the vacuum pressure is low. At the pressure of 0.27 Pa, the undercut becomes very small and the amount is $0.06 \mu\text{m}$ even at the etching time of 90 min, which is about 50% greater than the time required to eliminate PIQ layer. With our RIE apparatus, the lowest pressure above which the plasma discharge is stable is about 0.13 Pa. Therefore, the vacuum pressure of 0.27 Pa was selected.

Applications.—Figure 10 is an SEM photograph of lines and spaces patterns delineated by the trilevel resist process with a deep-UV contact printing. Linewidths are 0.75 and $0.4 \mu\text{m}$, respectively. The patterns consist of 1.5 mm thick PIQ with $0.1 \mu\text{m}$ thick TiO_x on the top surface.

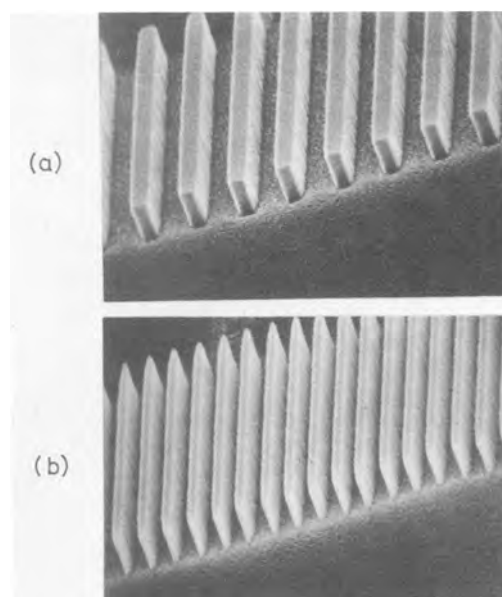


Fig. 10. SEM photographs of lines and spaces patterns delineated by the trilevel resist process with a deep-UV contact printing. Linewidths are 0.75 (a) and $0.4 \mu\text{m}$ (b).

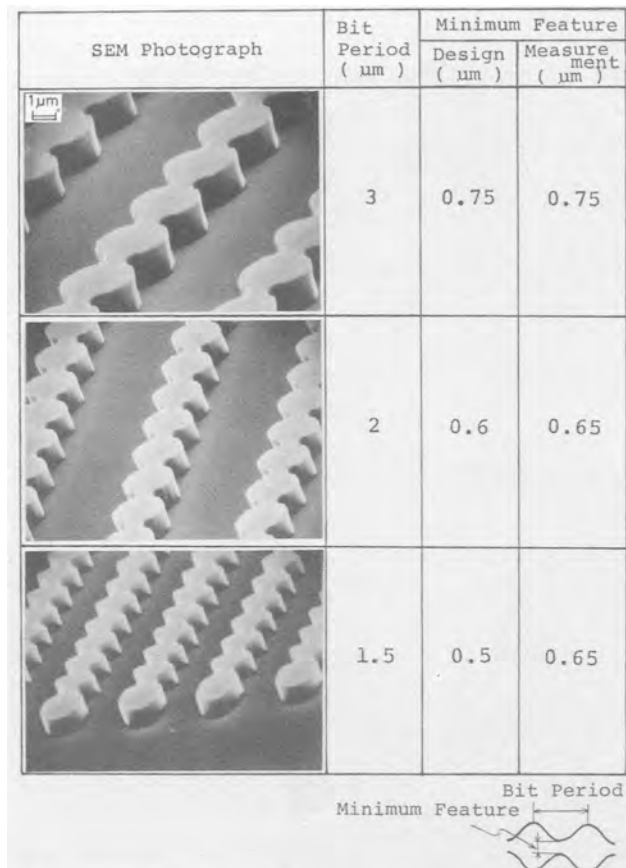


Fig. 11. Contiguous disk patterns for ion-implanted bubble memory devices delineated by the trilevel resist process with deep-UV contact printing.

As can be seen in the figure, the undercut of PIQ layer is very small and submicron patterns of 0.75 and 0.4 μm are delineated successfully.

Figure 11 shows the contiguous disk patterns for ion-implanted bubble memory devices. Bit periods of these patterns are 3, 2, and 1.5 μm and the minimum features are designed to be 0.75, 0.6, and 0.5 μm , respectively. The thicknesses of PIQ are 1.5 μm thick for 3 and 2 μm period patterns and 1.0 μm thick for a 1.5 μm period pattern. These thicknesses are necessary to stop accelerated ions used in each ion implantation. It can be seen that the edge profiles of these patterns are steep and smooth, which are the characteristics necessary for the mask pattern against an ion implantation, as mentioned previously. Patterns of 0.75 μm minimum feature for 3 μm period pattern are defined precisely, and that for 2 μm period pattern is also allowable. However, the discrepancy between a design and measurement value becomes large in the case of 1.5 μm bit period pattern. Therefore, the practical resolution limit of deep-UV contact printing is seen to be about 0.6 μm , and the minimum bit period is about 2 μm . The result is different from that for lines and spaces test patterns. The difference is caused by a diffraction effect. Since a contiguous disk pattern contains a cusp shape at the minimum feature part, the corner of the cusp is rounded by a diffraction effect and the width of the neck, which is the minimum feature, becomes large. That is, a diffraction in practical pattern is not so simple as in lines and spaces pattern and causes a degradation of resolution limit.

From the results obtained here, it can be said that deep-UV contact lithography can be applicable to 2 μm period ion-implanted bubble devices of 16 Mb/cm² in storage density.

Conclusion

Deep-UV contact lithography using trilevel resist system has been developed for magnetic bubble devices with submicron minimum feature. The trilevel resist system consists of MRS resist, TiO_x, and PIQ. The MRS resist patterns were delineated by deep-UV contact printing and the patterns were then transferred into TiO_x and PIQ sequentially using reactive ion etching in CF₄ plasma and in O₂ plasma, respectively. The thickness of MRS is 0.3 μm . The thin MRS resist like this can provide a submicron pattern with a greater process latitude than that of UV printing with AZ resist. The TiO_x film was obtained by spin coating and baking an organotitanium solution. Therefore, the three layers of the present process can all be formed by spin coating method. The adhesion of MRS resist to TiO_x film is good and etching selectivities of TiO_x to MRS (CF₄ RIE) and PIQ to TiO_x (O₂ RIE) are also good. Using the present trilevel resist process, 0.4 μm lines and spaces were delineated and the 2 μm period contiguous disk patterns with the minimum feature of 0.6 μm for bubble memory devices of 16 Mb/cm² were also fabricated successfully.

Acknowledgments

The authors wish to thank S. Nonogaki, T. Iwayanagi, and T. Matsuzawa of Hitachi Central Research Laboratories for their technical advice about MRS resist, and S. Yoshimoto, H. Kanai, H. Nishida, and H. Nozawa of Hitachi Mobarra Works for their helpful discussions during this work. Thanks are also due to N. Koiso, A. Tazawa, K. Asai, and M. Kanou of Hitachi Central Research Laboratories for their technical support.

Manuscript submitted March 22, 1985; revised manuscript received June 17, 1985. This was Paper 529 presented at the New Orleans, Louisiana, Meeting of the Society, Oct. 8-12, 1984.

Hitachi Limited assisted in meeting the publication costs of this article.

REFERENCES

1. S. Matsumoto, M. Hiroshima, and S. Yoshimoto, Paper FA-3 presented at Intermag '83, Philadelphia, April 5-8, 1983.
2. R. Wolf, J. C. North, W. A. Johnson, R. R. Spiwak, L. J. Varnerin, and R. F. Fischer, *AIP Proc. Conf.* **10**, 339 (1972).
3. Y. Sugita, R. Suzuki, T. Ikeda, T. Takeuchi, N. Kodama, M. Takeshita, R. Imura, T. Satoh, H. Umezaki, and N. Koyama, Submitted to *IEEE Trans. Magn.*
4. B. J. Lin, *J. Vac. Sci. Technol.*, **12**, 1317 (1975).
5. T. Iwayanagi, T. Kohashi, S. Nonogaki, T. Matsuzawa, K. Douta, and H. Yanazawa, *IEEE Trans. Electron Devices*, **ed-28**, 1306 (1981).
6. T. Matsuzawa and H. Tomioka, *IEEE Electron Device Lett.*, **ed1-2**, 90 (1981).
7. T. Matsuzawa and H. Tomioka, *IEEE Trans Electron Devices*, **ed-29**, 1284 (1981).
8. K. Sato, S. Harada, A. Saiki, T. Kimura, T. Okubo, and K. Mukai, *IEEE Trans. Parts, Hybrids, Packag.*, **php-9**, 176 (1973).
9. J. M. Moran and D. Maydan, *J. Vac. Sci. Technol.*, **16**, 1620 (1979).
10. H. I. Smith, N. Efremow, and P. L. Kelley, *This Journal*, **121**, 1502 (1974).
11. G. W. Ray, S. Peng, D. Burriesci, M. M. O'Toole, and E.-D. Liu, *ibid.*, **129**, 2152 (1982).
12. C. H. Ting and K. L. Liauw, *J. Vac. Sci. Technol. B*, **1**, 1225 (1983).

Lateral Growth Process of GaAs over Tungsten Gratings by Metalorganic Chemical Vapor Deposition

Hiroimitsu Asai and Seigo Ando

Nippon Telegraph and Telephone Corporation, Musashino Electrical Communication Laboratory, Musashino-shi, Tokyo 180, Japan

ABSTRACT

Lateral epitaxial growth of GaAs over tungsten gratings with 5 μm wide lines and spaces on (001) GaAs substrates is performed using metalorganic chemical vapor deposition. A study is made of the dependence of facet shapes and growth rates of the overgrown layers on grating direction, growth temperature, and arsine (AsH_3) and trimethylgallium (TMG) flow rates. From the perspective of crystallography, all the facets observed in the overgrown layers were found to be classified into four individual groups: $\{110\}$, $\{111\}\text{As}$, $\{112\}\text{As}$, and $\{113\}\text{Ga}$ faces. The GaAs opening direction on the (001) substrate surface is found to be the most essential parameter for determining the crystallographic planes of the facets. Other important controlling parameters for the facet formation are the growth temperature and partial pressure of AsH_3 . The partial pressure of TMG has no influence on the faceting growth. On the other hand, the overall growth rate of the overgrown layer is limited only by the TMG flow rate. These results can be qualitatively explained by the Langmuir-Rideal model.

Lateral epitaxial growth over oxide or metal mask films formed on crystal substrates has recently developed into an attractive technique for fabricating such new devices as permeable base transistors (PBT's) (1-3) and optical wave guides (4). To date, many reports on the lateral growth of GaAs (1-9), Si (10, 11), and InP (12) over metal or oxide mask films have been published.

Halide vapor phase epitaxy (VPE) has been employed as the most general method for overgrowth purposes, because it has several advantages for successfully accomplishing the overgrowth as will be mentioned below. In the VPE growth, there is a thermal equilibrium between the solid and vapor phases. The dependence of surface kinetics on substrate orientation makes an important contribution to the large ratio of lateral to vertical growth rates. In addition, polycrystalline solids, which prevent the lateral overgrowth, do not deposit over large areas of the mask films, because of the desorption or etching processes of source species. In this case, HCl, which is produced or introduced intentionally during the VPE growth, plays an important role in the etching process. In fact, Jastrzebski *et al.* (11) added HCl vapor etching steps intentionally to the Si overgrowth procedure using SiH_2Cl_2 , reporting that the nucleation of poly-Si over SiO_2 was eliminated. However, there are serious problems with the HCl introduction. For example, some kinds of chloride reactants generated during the deposition process react with a quartz reactor or substrates, and, consequently, cause unintentional doping, the so-called "autodoping." Additionally, abrupt interfaces in composition and doping or epitaxial layers containing Al cannot be readily obtained by this method.

For metalorganic chemical vapor deposition (MOCVD), on the other hand, such problems do not exist because of the growth system, which excludes HCl. Moreover, MOCVD is well known to have such advantages as allowing precise control of composition and doping in multicomponent structures. However, lateral overgrowth has been difficult to successfully accomplish using MOCVD, because polycrystalline GaAs can be readily deposited over mask films (13) due to the lack of etching process in this growth mechanism.

Recently, Gale *et al.* (14) and Asai *et al.* (3) demonstrated that the MOCVD lateral GaAs growth can be accomplished without polycrystalline deposits over mask films by optimizing the growth conditions. Lateral overgrowth using MOCVD has developed into an applicable technique for fabricating PBT's. However, the details regarding the GaAs overgrowth process in MOCVD have not yet been made clear.

In this paper, we report on the lateral GaAs growth over a tungsten grating with 5 μm wide lines and spaces on a (001) GaAs substrate using MOCVD. To study the over-

growth process, our attention has been focused on the facet shapes formed at GaAs overgrown film edges and the vertical growth rates of the overgrown films. The dependencies of geometrical shapes of the facets and growth rates on the tungsten grating direction, growth temperature, and source gas flow rates are examined. The tungsten grating direction on the (001) substrate surface is found to be the most essential parameter to determine the geometrical shape of the overgrowth layer. The other controlling parameters are the growth temperature and the partial pressure of arsine (AsH_3). However, the partial pressure of trimethylgallium (TMG) has no influence on the facet formation, though an overall growth rate of the overgrown layer is controlled by mass transport. On the basis of the obtained results, the MOCVD overgrowth mechanism is discussed.

Experimental Procedure

The MOCVD system used for GaAs overgrowth in this work was a conventional horizontal quartz reactor with an RF induction heater. The upper surface of a graphite susceptor was tilted about 7° from the gas flow. The growth temperature was monitored by a thermocouple inserted into the susceptor. An electronic-grade, 10% mixture of AsH_3 in hydrogen was used as an arsenic source. TMG vapor was provided by bubbling hydrogen through this liquid, which was held at 0°C in a stainless steel bubbler. A main impurity in the TMG was Si, whose concentration was nominally 1 ppm. A purified H_2 carrier gas having a 4 liter/min flow rate was introduced with the TMG and AsH_3 into the reactor. The overgrowth was performed under atmospheric pressure.

In order to examine the overgrowth processes, we used the patterned substrates having tungsten gratings, as shown in Fig. 1. After etching Si-doped ($2 \times 10^{18} \text{ cm}^{-3}$), GaAs (001) $\pm 0.5^\circ$ wafers with a $3\text{H}_2\text{SO}_4\text{-1H}_2\text{O}_2\text{-1H}_2\text{O}$ solution, a 400 \AA sputter tungsten grating of 5 μm wide lines and spaces was made as a masking pattern on the wafer with a conventional lift-off technique. A stripe direction of the tungsten grating oriented on the substrate is a very important factor for affecting facet shapes of the overgrown layers, as will be described later.

In this paper, the grating direction is defined as an angle from the $\langle 110 \rangle$ direction on the (001) GaAs surface called the "grating angle." The grating angle was varied from 0° to 90° to examine the dependence of the overgrowth on the grating direction. Taking the crystallographic symmetry of a zinc blende structure into account, this angle region can cover all grating directions on the (001) surface. The determination of the $\langle 110 \rangle$ and $\langle 110 \rangle$ directions on the (001) GaAs wafer was made by means of the etching profile test with a $1\text{H}_2\text{SO}_4\text{-1H}_2\text{O}_2\text{-1H}_2\text{O}$ solution (15).

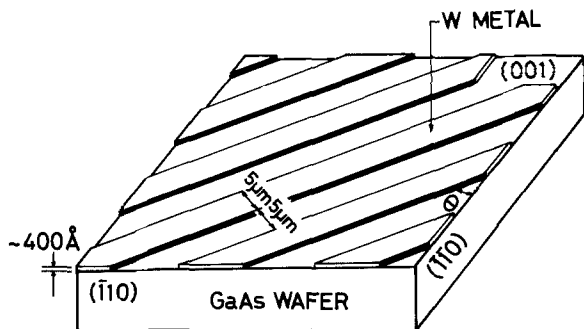


Fig. 1. Schematic picture of a substrate used for overgrowth.

The growth procedure began with substrates having tungsten gratings being loaded into the reactor, after being washed sequentially in trichloroethylene, acetone, and methanol. To compare layer thicknesses, substrates having no grating were also used. The reactor was purged with a purified H_2 gas for about 2h. An AsH_3 gas was introduced when the susceptor temperature reached $400^\circ C$ to protect the substrate from thermal damage. Typical growth time was 2h. Growth conditions were varied widely, as summarized in Table I. When one condition was varied, the others were fixed at standard conditions in order to clarify the effects of the varied condition. This is indicated by the parentheses in Table I.

Our attention in this work focuses specifically on the facet shapes and layer thicknesses formed during overgrowth. In order to determine the crystallographic planes of the facets, $(\bar{1}10)$ and (110) cleavage planes of the overgrown layers were observed for 0° - 45° and 45° - 90° grating directions, respectively, with an optical microscope. All grown layers were stain etched with a $10H_2O$ - $1H_2O_2$ - $1HF$ solution for 15s. Consequently, buried tungsten stripes could be clearly seen as dark lines in the cross-sectional views. The thickness of a selectively grown layer was measured from the step height between the top surface of the layer and the tungsten grating in the cross-sectional view of the sample.

Overgrowth on Various Directional Gratings

In this section, we describe the effects of grating direction on lateral overgrowth from three perspectives. First, for typical grating directions, the relationship between surface morphology and facet formation of overgrown layers is examined. Second, the inclination of the facet with respect to a (001) substrate surface is studied as a function of the grating angle from $\langle \bar{1}10 \rangle$. Third, on the basis of the results, a model for the overgrowth process is discussed.

Cleaved cross sections of the GaAs layers simultaneously grown over tungsten gratings with various directions were observed by an optical microscope. Figures 2a, 2b, and 2c present the cross-sectional photographs of the grown layers over the tungsten gratings oriented at 0° , 30° , and 90° directions from the $\langle \bar{1}10 \rangle$, respectively. These samples were grown under the conditions of $630^\circ C$ and $[TMG]$ and $[AsH_3]$ mole fractions of 3.2×10^{-5} and 1.7×10^{-3} , respectively. Note that Fig. 2a and 2b indicate $(\bar{1}10)$ cleavage planes, while Fig. 2c represents a (110) cleavage plane. It is clear from this figure that the lateral overgrowth strongly depends on the grating direction.

Table I. Growth conditions

Growth temperature ($^\circ C$)	400-800	(630) ^a
[TMG] (mole fraction)	2.3 - 12.8×10^{-5}	(3.2×10^{-5})
$[AsH_3]$ (mole fraction)	0.2 - 7×10^{-3}	(1.7×10^{-3})
$[AsH_3]/[TMG]$	6-220	(53)
Total flow rate (liter/min)	4	
Grating direction from the $\langle \bar{1}10 \rangle$ ($^\circ$)	0-90	

^a Parentheses mean standard growth conditions (see text).

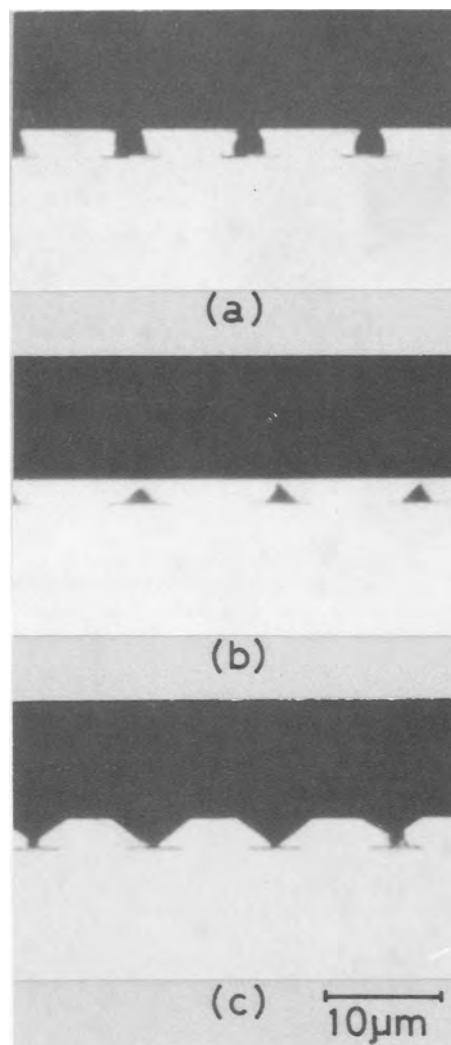


Fig. 2. Photomicrographs of cleaved cross sections of grown layers over tungsten gratings oriented at 0° (a), 30° (b), and 90° (c) from the $\langle \bar{1}10 \rangle$ direction. Note that the a and b show the $(\bar{1}10)$ cleavage planes and that the c represents the (110) plane.

For the 0° grating direction, which corresponds to the $\langle \bar{1}10 \rangle$ direction, the lateral overgrowth facets exhibited planes shaped perpendicularly to the (001) surface (Fig. 2a). For the 30° gratings, the facets had reverse-mesa-shaped planes at the initial overgrowth stage. As the overgrowth continued, the reverse-mesa-shaped GaAs stripes laterally developed and finally joined at the reverse-mesa top to form continuous, flat, specular layers. In the top view of such a sample, one could not observe any disturbance due to the presence of the $5 \mu m$ width-and-space tungsten grating. In the cross-sectional view, however, triangular voids were seen near the centers of the tungsten stripes as a result of reverse-mesa formation during initial overgrowth (see Fig. 2b).

For the 90° grating direction, which corresponds to the $\langle 110 \rangle$ direction, the overgrowth profile indicated ordinary mesa-shaped planes (Fig. 2c). When the overgrowth exhibiting this facet type continued, the top surface of the ordinary mesa became narrower as growth proceeded until the overgrown layer was finally composed of only inclined surfaces. The inclined plane was identified with $\{112\}As$ faces from the facet angle of 37° with respect to the (001) surface. The overgrowth continued further, and if the V-shaped grooves left on the layer surface were filled up one could then expect to obtain an overgrown layer free of voids near the center of the tungsten stripes. In contrast to this expectation, anomalous faceting growth took place actually as shown in Fig. 3. The facets could not be characterized by specific planes.

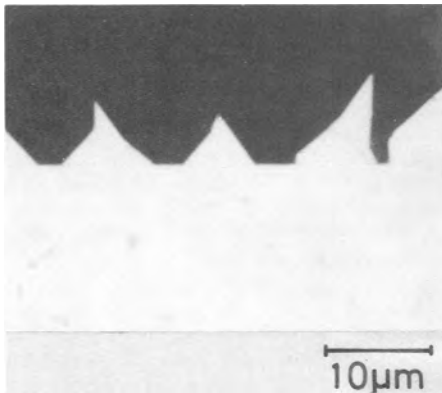


Fig. 3. Photomicrograph of a (110) cleaved plane of an overgrown layer for the 90° tungsten stripe direction which corresponds to $\langle 110 \rangle$.

Surface morphology of MOCVD layers is well known to depend strongly on substrate orientation (16). The layer surface on the $(\bar{1}\bar{1}\bar{1})$ As substrate indicated very defective morphology, including many poly-like hillocks (17). Since $(\bar{1}12)$ As and $(\bar{1}\bar{1}\bar{1})$ As surfaces are composed of a relatively large number of As atoms, the defective growth is considered to take place on the $(\bar{1}12)$ As, similarly to that on the $(\bar{1}\bar{1}\bar{1})$ As. Since the growing surface for the 90° grating direction is only the inclined $(\bar{1}12)$ As face, anomalous faceting growth such as is shown in Fig. 3 is believed to occur.

The overgrown layers are characterized by the facet shapes, as shown in Fig. 2. To determine the crystallographic plane for the facet, the angle of the facet with respect to the (001) surface was measured from cross-sectional photographs of the layers. The facet angle for the tungsten grating direction from 0° to 90° is presented in Fig. 4. All the samples were simultaneously grown under the conditions of 630°C and [TMG] and [AsH₃] of 3.2×10^{-5} and 1.7×10^{-3} mole fraction, respectively. From this figure, the facet angle can be clearly classified into three regions.

In the 0°-10° grating direction region, the facet angle was perpendicular to the substrate surface, which corre-

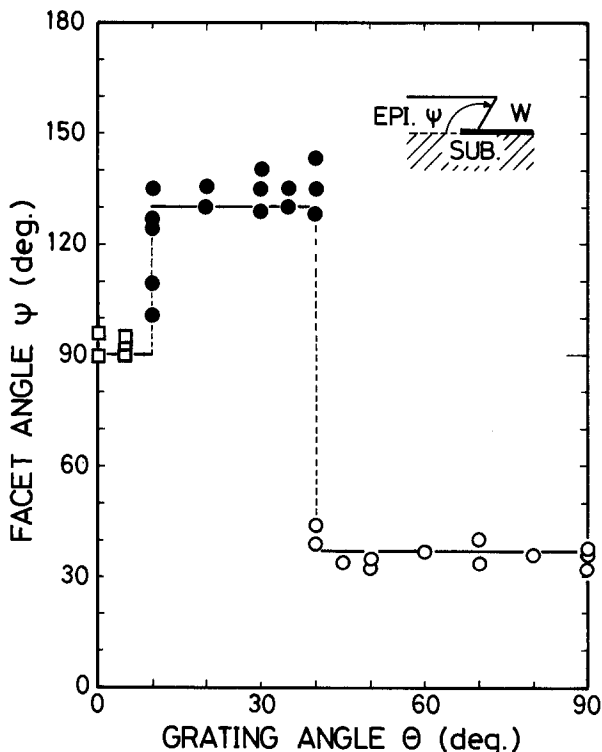


Fig. 4. Facet angle (see inset) with respect to the (001) surface plane as a function of the tungsten grating angle from $\langle 110 \rangle$.

sponds to the {110} crystallographic plane. For the substrates with 10°-45° grating orientations, the sidewalls of the overgrowth layers had an angle of 130° with respect to the (001) surface. This angle coincided with the one of the $\{\bar{1}\bar{1}\bar{1}\}$ As plane with respect to the (001) surface. For the 45°-90° GaAs opening directions from $\langle \bar{1}10 \rangle$, the overgrowth profile observed on a (110) cleavage plane indicated the inclined plane forming an angle of 37°. The angle coincided with the one of the {112}As face with respect to the (001) surface.

In each region of the grating angle, the sidewalls of the overgrown layers were found to retain the same angle with respect to the (001) surface planes as mentioned above. This suggests the following overgrowth process. Lateral overgrowth is seeded from the edges of the masking tungsten stripes by selective epitaxial deposits initially formed only on the exposed regions. However, the lateral growth fronts do not proceed perpendicularly toward the stripe direction.

Microscopically, the lateral growth fronts are composed of two small specific planes formed perpendicularly to the cleavage planes, as shown in Fig. 5. The specific plane can be determined by observation of the cleavage plane. For example, for the 30° grating directions, a small plane observed on the $(\bar{1}10)$ cleavage plane corresponds to the $\{\bar{1}\bar{1}\bar{1}\}$ As crystallographic plane forming an angle of 125.3°, in principle, with respect to (001) surface plane.

This overgrowth process is also supported by the observation of the overgrowth layer surface shown in Fig. 6. In this figure, although almost all growth fronts are parallel to the tungsten stripe, anomalous growth is observed in some areas. The anomalous growth areas are very similar to the zigzag growth process portrayed in Fig. 5. The areas of the films with parallel growth fronts are also believed to be composed of a number of facets, as previously reported by Vohl *et al.* (11). This overgrowth process, therefore, generally occurs in growth over the misoriented masking stripes, whose direction is not parallel to low indexes such as the $\langle \bar{1}10 \rangle$ and $\langle 110 \rangle$ directions.

Dependency of Overgrowth on Growth Parameters

Growth parameters in MOCVD control facet formation as well as layer quality, such as surface morphology and electron mobility. In this section, we describe the dependence of the overgrowth on growth temperature and AsH₃ and TMG mole fractions. Since a smooth surface of an overgrown film was found to be obtainable for the 30° grating direction, as mentioned in the preceding section, the main focus is on the dependency of the lateral growth over the 30° tungsten grating.

Growth temperature.—Growth temperature affects facet formation in overgrowth in conjunction with surface morphology. For typical growth temperatures, we have conducted a study on the relationship between the surface morphology and the facet formation of the overgrown layers. Figures 7a, 7b, 7c, and 7d present the overgrowth layers obtained at 710°, 630°, 600°, and 510°C, respectively, with all other growth conditions being the same, that is, [TMG] = 3.2×10^{-5} mole fraction and [AsH₃] = 1.7×10^{-3} mole fraction. All the specimens shown in

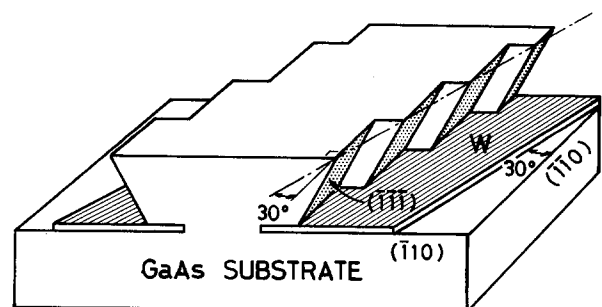


Fig. 5. Schematic picture of overgrowth process onto 30° GaAs stripe openings.

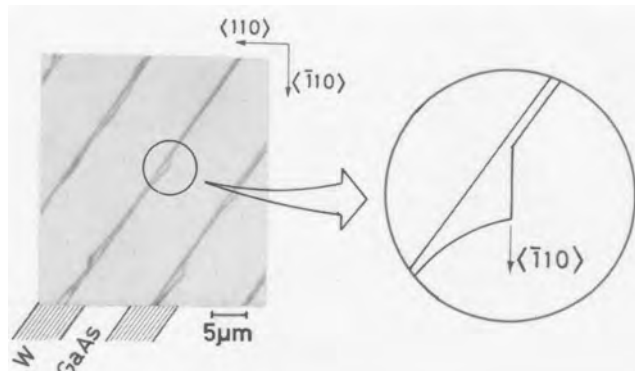


Fig. 6. Photomicrograph of the surface of the overgrown layer just before joining lateral growth fronts seeded from the edges of tungsten stripes.

these figures were grown over 30° gratings from the $\langle \bar{1}10 \rangle$ direction. Note that the cross-sectional views were observed on the $(\bar{1}10)$ cleavage planes.

The sidewall of an overgrown layer at the high temperature of 710°C consists of reverse-mesa- and ordinary mesa-shaped planes as shown in Fig. 7a. At a growth temperature above this value, only the ordinary mesa-shaped planes formed on the exposed GaAs stripes. The cross-sectional views of the samples at 630° and 600°C indicate the same reverse-mesa-shaped planes (see Fig. 7b and 7c). Though the triangular voids are also seen in the layer at 630°C , they were slightly smaller in size than those at 600°C . Therefore, the ratio of lateral to vertical growth rates tends to slightly increase with a decrease in the growth temperature. This tendency demonstrated qualitative agreement with the results using (011) GaAs substrates (12).

The surface of the films obtained at 630°C is flat and smooth (Fig. 7b) On the other hand, the surface of the

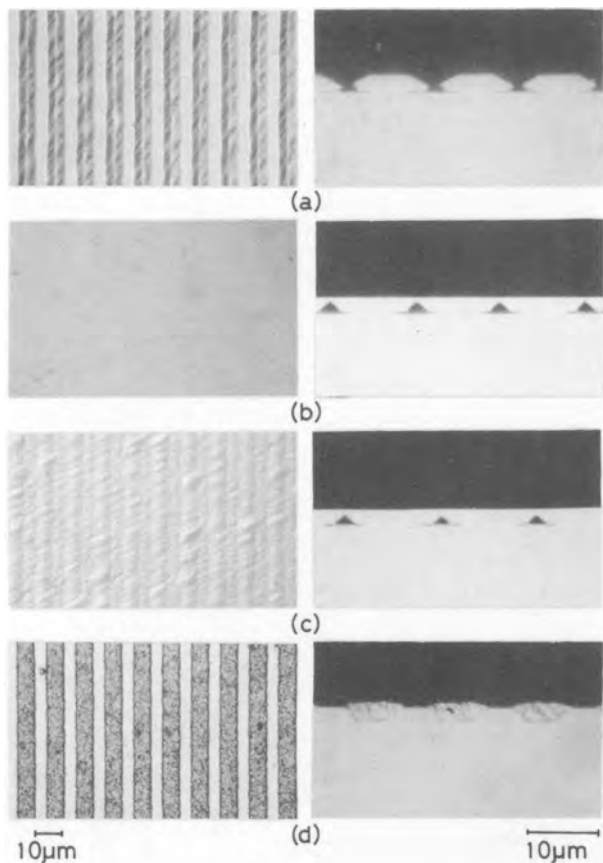


Fig. 7. Photomicrographs of surfaces and $\bar{1}10$ cleavage planes of layers grown over 30° tungsten gratings at 710°C (a), 630°C (b), 600°C (c), and 510°C (d).

film grown at 600°C represents defective morphology, which exhibits a rough-patterned structure reflecting the underlying tungsten grating, as shown in Fig. 7c.

At a growth temperature lower than 530°C , GaAs deposition occurred not only on the exposed GaAs surface but also on the masking tungsten stripes. The deposition of polycrystalline GaAs on the tungsten stripes prevented the lateral epitaxial growth from the edges of the tungsten stripes (see Fig. 7d). Consequently, the well-defined facets cannot be observed for the overgrown layers at the lower growth temperature.

The formation of polycrystalline GaAs over the mask surface, as shown in Fig. 7d, is the major problem encountered during lateral overgrowth. In MOCVD growth in particular, the poly-GaAs deposits readily over the tungsten mask, because the sticking coefficient for Ga is unity. For a growth temperature above 530°C , however, GaAs growth is initiated only on the exposed area. This suggests that Ga adatoms on the tungsten are transferred to the growing GaAs surface. The driving force behind transferring the Ga adatoms is produced by atomic surface diffusion and by the difference between the nucleation probabilities for the GaAs and the tungsten. The atomic surface diffusion length decreases with a decrease in the growth temperature. Nucleation of polycrystalline GaAs, therefore, takes place on the tungsten stripes at low growth temperature.

In addition to the growth temperature, the polycrystalline deposit onto the tungsten surface is very sensitive to the tungsten mask characteristics. For example, the poly-GaAs nuclei form around the defects present on the tungsten surface such as pinholes, topological irregularities, and contaminated regions. These defects considerably increase the nucleation probability on the tungsten surface. Furthermore, the intrinsic properties of a mask surface, such as its surface free energy and number of free surface sites where source species are incorporated (18, 19), also have influence on the nucleation probability for the mask.

The facets of films grown over 30° gratings are affected by the growth temperature, as shown in Fig. 7. To examine the facet shapes in detail, the angle of the facet was measured with respect to the (001) substrate surface. The facet angle for the growth temperature from 550° to 810°C is presented in Fig. 8. Other growth parameters remain the same, that is, $[\text{TMG}] = 3.2 \times 10^{-3}$ mole fraction and $[\text{AsH}_3] = 1.7 \times 10^{-3}$ mole fraction. It is remarkable that the growth temperature of 710°C represents the critical point in change from the reverse mesa to the ordinary mesa geometric shape of the overgrowth layers. The sidewalls of these geometric shapes indicate the facet forming angles of 130° and 27° , respectively. From these angles, the faces constituting the sidewalls of the overgrown layer are identified with the $\{\bar{1}\bar{1}\}\text{As}$ and the $\{11\}\text{Ga}$ crystallographic planes.

On the other hand, with the decrease in the growth temperature, the sidewall inclination of the overgrowth layer changed gradually from 130° to 105° with respect to the (001) substrates. The gradual change is attributed to the reduction in the surface diffusion length of source species with the decrease in the growth temperature. A well-defined facet is not formed due to the reduction of atomic diffusion along the top and side surfaces of the growing layers.

The temperature dependence of the facet formation mentioned above was not observed for all of the grating directions. For example, for the tungsten grating directions of 0° and 90° , which correspond to $\langle \bar{1}10 \rangle$ and $\langle 110 \rangle$, respectively, the facet angle with respect to the (001) surface plane is independent of the growth temperature, as shown in Fig. 9. For the 0° grating direction, the sidewall of the layer observed on the (110) cleavage plane indicates a plane perpendicular to the (001) surface, which corresponds to the $\{110\}$ crystallographic plane. For the 90° grating direction, the overgrowth profile on the (110) cleavage planes exhibits the inclined plane forming an angle of 37° with respect to the (001) surface plane. This

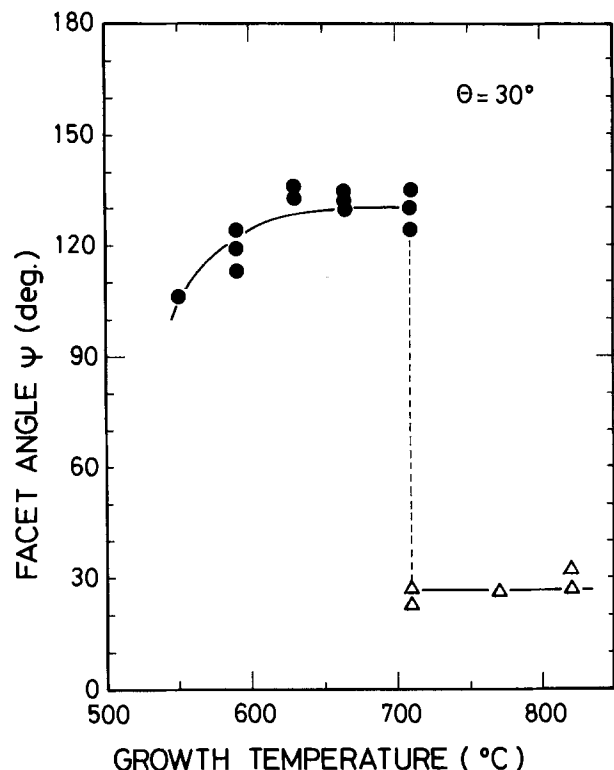


Fig. 8. Facet angle with respect to the (001) surface plane as a function of the growth temperature. Grating direction was 30° from $\langle\bar{1}10\rangle$. Other growth parameters: $[TMG] = 3.2 \times 10^{-5}$ mole fraction, and $[AsH_3] = 1.7 \times 10^{-3}$ mole fraction.

angle coincides with that of the $\{112\}As$ crystallographic plane. With respect to the facet formation, the relationship between the grating angle and the growth temperature is more complex. The details of this will be described below.

AsH₃ and TMG mole fractions.— AsH_3 and TMG mole fractions ($[AsH_3]$ and $[TMG]$) are key parameters in controlling the MOCVD film characteristics, such as p-n conversion. One can expect that the faceting growth onto the GaAs stripe openings is also affected by the $[AsH_3]$ and $[TMG]$ conditions. This represents our final experi-

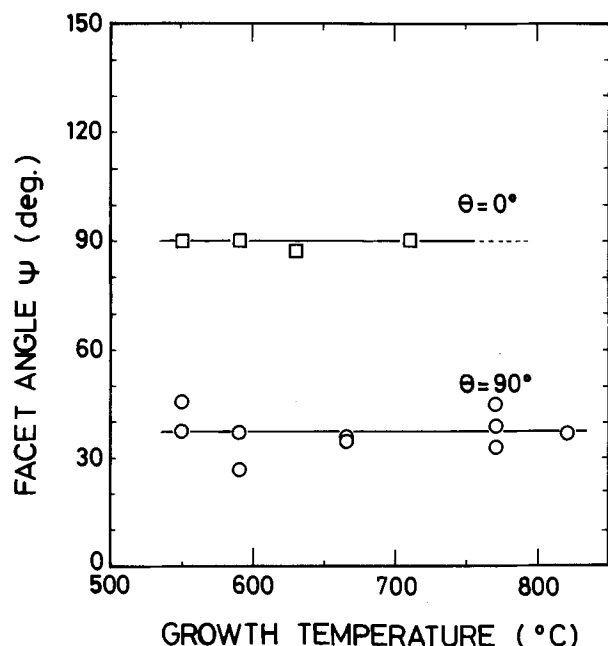


Fig. 9. Facet angle with respect to the (001) surface plane as a function of the growth temperature. Grating directions were 0° and 90° , corresponding to the $\langle\bar{1}10\rangle$ and $\langle 110\rangle$ directions, respectively.

ment on facet dependence. In order to properly separate the $[AsH_3]$ and $[TMG]$ effects, the $[AsH_3]$ condition was varied under a constant $[TMG]$ and vice versa.

Figures 10a, 10b, and 10c are photomicrographs of the (110) cleaved planes of films grown at 6.8×10^{-3} , 1.7×10^{-3} , and 0.4×10^{-3} AsH_3 mole fractions, respectively. For all of the specimens, the tungsten grating directions were 30° from the $\langle\bar{1}10\rangle$, $[TMG]$ was 3.2×10^{-5} mole fraction, and the growth temperature was $630^\circ C$. The geometrical shape of the layer grown at $[AsH_3] = 1.7 \times 10^{-3}$ mole fraction was the reverse mesa, as shown in Fig. 10b. This condition of $[AsH_3]$ was optimal for obtaining the smooth surface of the layer. Even though the AsH_3 mole fraction was increased, the films exhibited the same reverse-mesa-shaped planes. The layer surface, however, became wavy and defective (see Fig. 10a). On the other hand, when the AsH_3 mole fraction was decreased, the ordinary mesa-shaped planes were formed in addition to the reverse-mesa-shaped planes as the sidewalls of the overgrown layer (Fig. 10c). This geometrical shape is very similar to that of the $710^\circ C$ growth temperature (cf. Fig. 7a).

From the cross-sectional photographs shown in Fig. 10, the $[AsH_3]$ dependence of a facet angle with respect to the (001) surface was examined. The facet-angle variation for $[AsH_3]$ of $0.2-7 \times 10^{-3}$ mole fractions is represented in Fig. 11. The observed geometrical shapes of the overgrown layers are shown in the two insets. Up to a mole fraction of $[AsH_3] = 0.8 \times 10^{-3}$, which corresponds to $[AsH_3]/[TMG] = 25$, the sidewalls consisting of ordinary mesa- and reverse-mesa-shaped planes were formed,

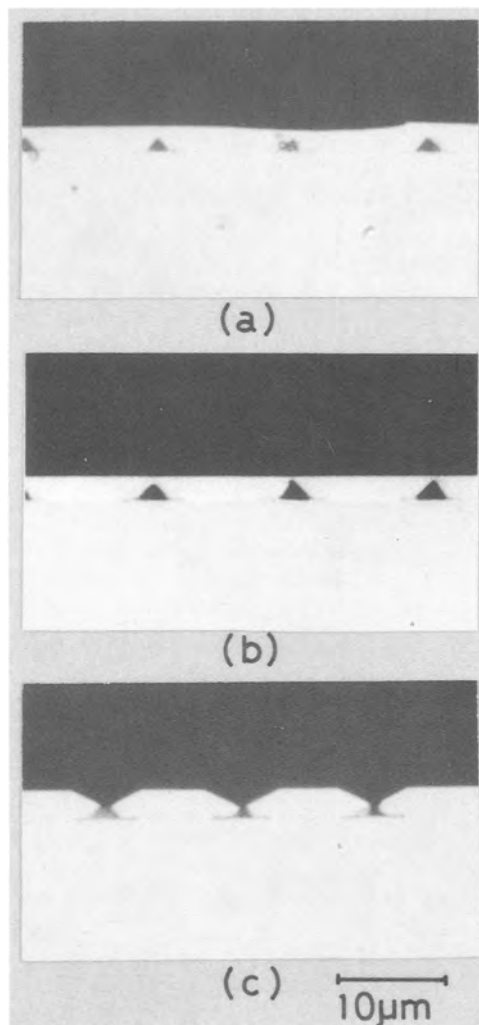


Fig. 10. Photomicrographs of $\langle\bar{1}10\rangle$ cleavage planes of layers grown at $[AsH_3]$ of 6.8×10^{-3} (a), 1.7×10^{-3} (b), and 0.4×10^{-3} (c) mole fractions. All the layers were grown on the tungsten gratings oriented 30° from $\langle\bar{1}10\rangle$.

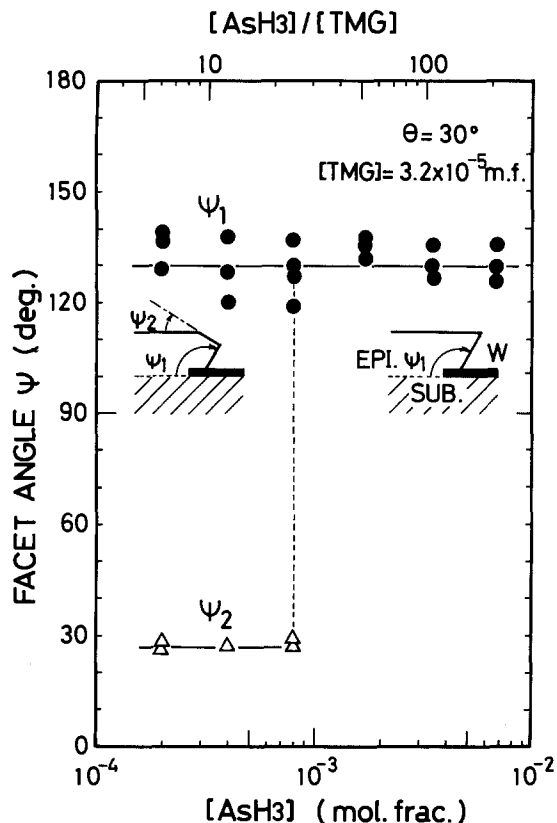


Fig. 11. Facet angle with respect to the (001) surface plane as a function of $[\text{AsH}_3]$. Growth temperature was 630°C .

whose angles with respect to the (001) surface were 130° and 27° , respectively (see the left inset of Fig. 11). From these angles, the facets were found to correspond to the $\{\bar{1}\bar{1}\bar{1}\}\text{As}$ and $\{113\}\text{Ga}$ faces. Above a mole fraction of $[\text{AsH}_3] = 0.8 \times 10^{-3}$, the sidewall indicated only the $\{\bar{1}\bar{1}\bar{1}\}\text{As}$.

From this result only, however, one cannot know whether the growth parameter causing the facet variation is $[\text{AsH}_3]$ or $[\text{AsH}_3]/[\text{TMG}]$. Therefore, we studied the effects of the $[\text{TMG}]$ variation on the overgrowth under $[\text{AsH}_3] = 1.7 \times 10^{-3}$ mole fraction. The facet angle with respect to the (001) surface as a function of $[\text{TMG}]$ is presented in Fig. 12. Under the conditions of $[\text{TMG}] = 2.3\text{--}12.8 \times 10^{-5}$ mole fraction corresponding to

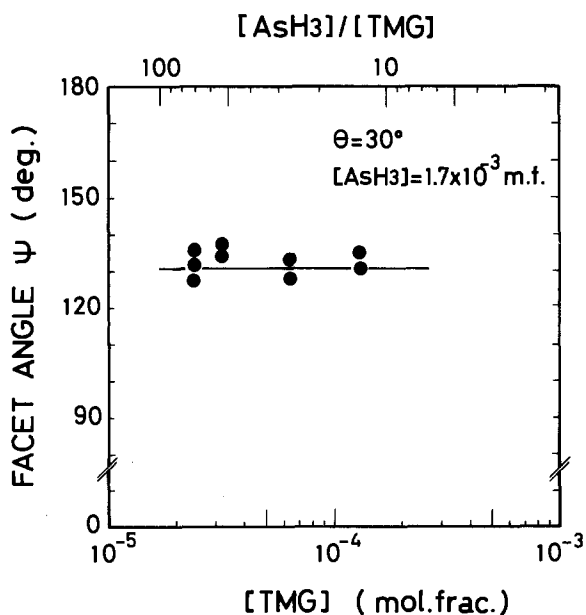


Fig. 12. Facet angle with respect to the (001) surface plane as a function of $[\text{TMG}]$. Growth temperature was 630°C .

$[\text{AsH}_3]/[\text{TMG}] = 13\text{--}74$, the sidewall of the overgrown layer indicates only the facet forming an angle of 130° with respect to the (001) surface. Even below $[\text{AsH}_3]/[\text{TMG}] = 25$, no plane other than the $\{\bar{1}\bar{1}\bar{1}\}\text{As}$ face was formed regarding the sidewalls of the overgrown layers. On the other hand, when $[\text{AsH}_3]/[\text{TMG}]$ was reduced below 25 through a decrease in $[\text{AsH}_3]$ with a constant $[\text{TMG}]$, the $\{113\}\text{Ga}$ face was formed in addition to the $\{\bar{1}\bar{1}\bar{1}\}\text{As}$ face (see Fig. 11). Therefore, the facet formed during the selective growth on the tungsten gratings is concluded to depend on $[\text{AsH}_3]$ rather than $[\text{AsH}_3]/[\text{TMG}]$.

Vertical Growth Rate of Overgrown Layer

Studies of growth rate provide us with basic information on growth mechanisms. For selective growth without poly-GaAs deposition over a tungsten surface, reacting species which arrived from the gas phase to the tungsten surface should be (i) released again into the gas phase, or (ii) transferred to a growing GaAs surface. In case (i), the vertical growth rate on the limited area can be predicted as being essentially the same as the growth rate on the substrate without the tungsten grating. On the other hand, in case (ii), the vertical growth rate in the limited region is apparently enhanced compared to that on the surface without the tungsten grating.

The vertical growth rate was determined from the height of a top side of the overgrown layer on the limited GaAs area. The vertical growth thickness, t , vs. the grating angle is given as the closed circles in Fig. 13, where the growth time was 2h. The layer thickness on the substrate without the tungsten grating is also shown as an open triangle. From this figure, the thickness of the overgrown layer is found to strongly depend on the grating direction. Moreover, the vertical growth rates of the overgrown layers shown in Fig. 13 were larger than the layer thickness on a substrate without the tungsten grating. The vertical growth rate on a limited area is only apparently enhanced. Therefore, the arrival species at the tungsten surface are not released again into the gas phase but are transferred to the growing GaAs surface.

To clarify this situation further, let us consider an average layer thickness, \bar{t} , which is calibrated by filling up the V grooves or the triangular voids as shown in the inset of Fig. 13. The calibrated layer thicknesses are represented as open circles in the figure. The average layer thickness was found to coincide with the layer thickness on the substrate without the tungsten pattern in all the grating directions. Therefore, an amount of the reacting species which lead to the GaAs growth is basically the same. The difference in the heights of the top sides of the layers on the limited areas is only apparent.

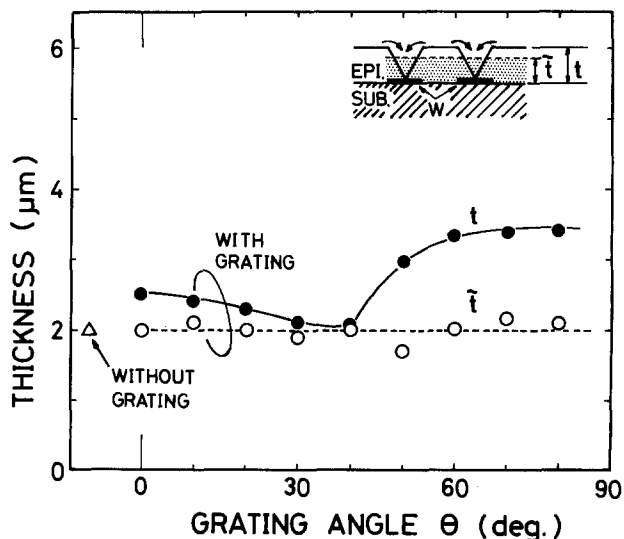


Fig. 13. Layer thicknesses for 2h growth time as a function of grating direction.

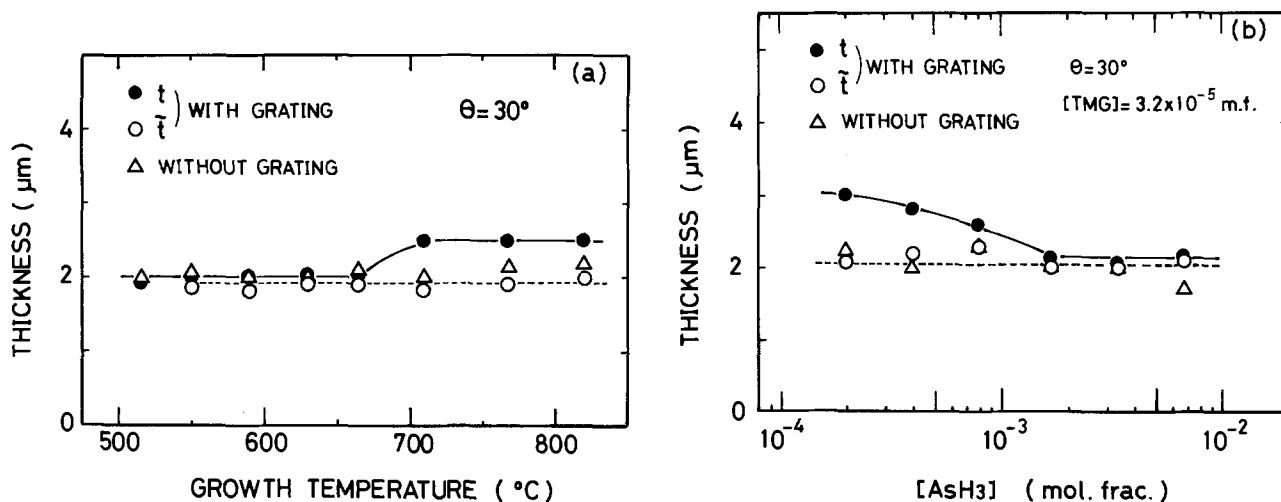


Fig. 14. Layer thicknesses for 2h growth time as functions of growth temperature (a) and $[AsH_3]$ (b). The layers were grown over the 30° tungsten gratings at $630^\circ C$.

Vertical growth rates on the limited area are also studied with respect to growth temperature and $[AsH_3]$. Figures 14a and 14b plot film thickness at a growth time of 2h as functions of the growth temperature and $[AsH_3]$, respectively. All of the films were grown over the 30° tungsten gratings. The apparent and average thicknesses of the selectively grown layers are indicated as the closed and open circles, respectively. The layer thickness on the substrate without the grating is also represented as open triangles. Though the apparent thickness on the GaAs opening varied with the growth temperature and $[AsH_3]$, the average thickness was independent of the growth conditions. This was similar to the layer thickness on the substrate without the grating.

Moreover, the average thickness coincided with the thickness on the substrate without the grating. From the results of the average thickness, it can be concluded that the overall growth rate under this range of growth conditions is essentially limited by mass transport through the stagnant layer in the gas phase. However, surface kinetics cannot be ruled out as an MOCVD growth mechanism, because the various crystallographic faces form with a dependence on the tungsten stripe direction, the growth temperature, and $[AsH_3]$.

Crystallographic Aspect and Overgrowth Mechanism

In this section, we discuss the facets of the overgrown layers on the tungsten gratings demonstrated in Fig. 2, 7, and 10 from a crystallographic aspect. With respect to the crystallographic planes of the formed facets, the relationship between the grating direction and growth condition is studied. On the basis of these discussions, the overgrowth mechanism is examined.

Facet identification.—The facets of the overgrown layers on the tungsten gratings are studied from the crystallographic point of view. From the facet angle of the overgrown layers, the geometric shapes of the layers can be classified into four individual groups, as shown in Fig. 15.

The overgrown facet forming an angle of 90° with respect to the (001) surface plane was observed on $(\bar{1}10)$ cleavage planes for the near $\langle \bar{1}10 \rangle$ grating directions. This result was independent of the growth conditions. From this facet angle, these formed planes correspond to the $\{110\}$ crystallographic planes (see Fig. 15I). In the region of 10° – 45° tungsten opening directions, two types of facet shapes were observed on the $(\bar{1}10)$ cleavage planes. One is represented by the inclined planes forming an angle of 130° with respect to the (001) surface, which corresponds to the $\{\bar{1}\bar{1}\}$ As planes (Fig. 15II). The other is represented by the planes forming an angle of 27° with respect to the (001) surface planes, which corresponds to the $\{113\}$ Ga (Fig. 15III).

The $\{\bar{1}\bar{1}\}$ As and $\{113\}$ Ga planes, in principle, form angles of 125.3° and 25.2° , respectively, with respect to the (001) surface planes. One of these types was changed into the other by the growth temperature or $[AsH_3]$ conditions. For the 45° – 90° tungsten grating directions from $\langle \bar{1}10 \rangle$, only the plane forming an angle of 37° with respect to the (001) surface was observed on the (110) cleavage plane independent of the growth conditions (Fig. 15IV). From the angle of the inclined plane observed on the (110) cleaved plane, the facet corresponds to the $\{\bar{1}12\}$ As, which, in principle, forms an angle of 35.3° with respect to the (001) surface plane.

These facet types shown in Fig. 15 are summarized with respect to the grating direction and growth conditions. The classification of these facet types is plotted out for the growth temperature and grating angle in Fig. 16. Below the growth temperature of $440^\circ C$, no GaAs nuclei are deposited on the exposed GaAs regions nor on the tungsten surface. In the 530° – $440^\circ C$ region, poly-GaAs is deposited on the tungsten surface. Though monocrystalline GaAs was grown onto the exposed GaAs area, the facets could not be observed, owing to the deposition of poly-GaAs on the tungsten surface. Therefore, the temperature range above $530^\circ C$ is a subject of some discussion concerning the facet types.

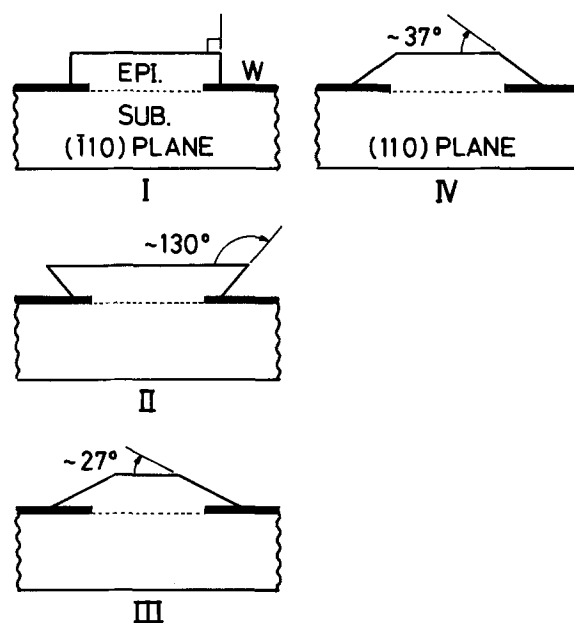


Fig. 15. Schematic diagrams of the overgrowth profiles produced on the (001) GaAs plane under the various growth conditions (see text).

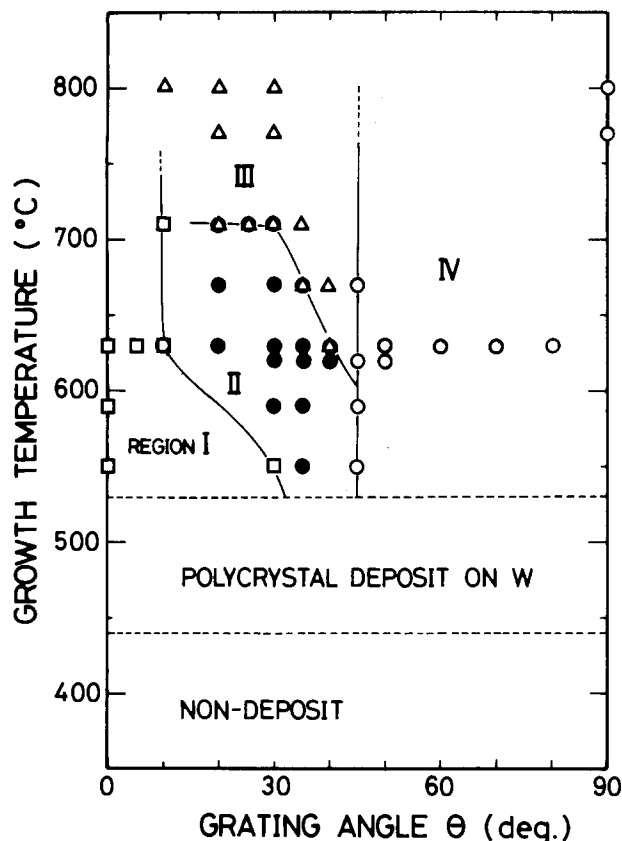


Fig. 16. Classification of facet types for growth temperatures and grating angles.

A similar classification is also mapped for $[\text{AsH}_3]$ and the grating angle in Fig. 17. Regions I, II, III, and IV in Fig. 16 and 17 mean the extent of growth parameters and grating direction, where the overgrowth profiles indicate types I, II, III, and IV as presented in Fig. 15. In these plots, for example, the region II+III means a conditional extent which produces the side wall consisting of the $\{\bar{1}\bar{1}\}\text{As}$ and $\{113\}\text{Ga}$ planes, as shown in Fig. 10c.

It is clear from these figures that the GaAs opening direction on the (001) substrate surface is the most essential parameter for the overgrowth. This is because the facet shape is controlled by the grating direction, except in the

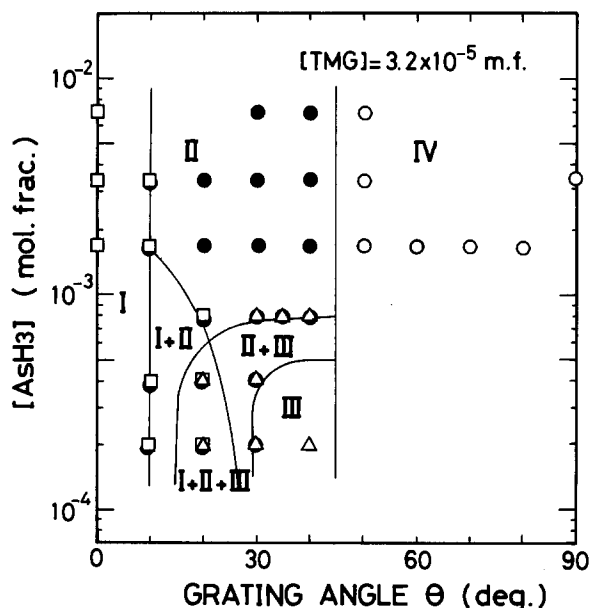


Fig. 17. Classification of face types for $[\text{AsH}_3]$ and grating angle. Growth temperature was 630°C .

$10^\circ\text{--}45^\circ$ region. This reason is not well understood at present, but it is considered to relate to the atomic arrangements, atomic bond directions, and crystallographic polarity on the defined stripe opening of the (001)GaAs substrate surface. The other limitations for the faceting growth are growth temperature and $[\text{AsH}_3]$.

It is noteworthy that the $\{\bar{1}\bar{1}\}\text{As}$ sidewall plane of the selectively grown layer changes to the $\{113\}\text{Ga}$ at the growth temperature of more than 710°C . Additionally important is the fact that the $\{113\}\text{Ga}$ side plane is formed together with the $\{\bar{1}\bar{1}\}\text{As}$ plane at less than a 0.8×10^{-3} mole fraction of $[\text{AsH}_3]$. In short, an increase in the growth temperature and a decrease in $[\text{AsH}_3]$ have a similar influence on facet formation.

Overgrowth mechanism.—We will now discuss our experimental results in terms of the Langmuir-Rideal mechanism, where gas phase gallium species react with surface-adsorbed arsenic (20). Although the reacting species are written as Ga and As for the sake of simplicity, the actual surface species which lead to GaAs growth are considerably more complex in MOCVD (21).

In the Langmuir-Rideal model, the growth rate, R , is given by

$$R = K\Theta_{\text{As}}P_{\text{Ga}} \quad [1]$$

where K is a rate constant, P_{Ga} is the initial partial pressure of the Ga species in the gas phase, and Θ_{As} is the surface coverage of the As species. The Θ_{As} is written as

$$\Theta_{\text{As}} = \frac{\beta_{\text{As}}P_{\text{As}}}{1 + \beta_{\text{As}}P_{\text{As}}} \quad [2]$$

where P_{As} is the partial pressure of the As species in the gas phase and β_{As} is the Langmuir adsorption constant for the As species, that is, the ratio of the rate constant for the adsorption of the As species to the rate constant for desorption.

Assuming that TMG is completely decomposed by the homogenous reaction in the gas phase (22), $P_{\text{Ga}} \approx P_{\text{TMG}}$, where P_{TMG} is the inlet partial pressure of TMG in the gas phase, such that Eq. [1] can be rewritten into

$$R = K\Theta_{\text{As}}P_{\text{TMG}} \quad [3]$$

From this equation, one can expect that the slight difference in growth rate is caused by the Θ_{As} dependence on the surface orientation. However, the dependence of the growth rate on the orientation is not measurable by an experiment using individual substrates with various orientations because $\Theta_{\text{As}} \approx 1$, i.e., $\beta_{\text{As}}P_{\text{As}} \gg 1$, in almost all cases (20). Consequently, Eq. [3] is reduced to

$$R = KP_{\text{TMG}} \quad [4]$$

Therefore, the predicted growth rate demonstrates a linear dependence on the partial pressure of TMG, and is independent of the AsH_3 overpressure.

Let us consider the case where various crystallographic faces are arranged within the surface diffusion length of the reacting species. The growth rate dependence on the orientation predicted from Eq. [3] is enhanced by the diffusion of the reacting species from the face where the growth rate is relatively low to the face with the relatively high growth rate. As a consequence, the growth rate is considered to depend significantly on the surface orientation. The faceting growth is also dominated by this mechanism.

The planes where the growth rate is relatively small are believed to be formed as facets of the overgrowth layer. The Θ_{As} is dependent on the growth temperature and the AsH_3 partial pressure while being independent of the TMG partial pressure. Therefore, the faceting growth is strongly dependent on the temperature and the partial pressure of AsH_3 , while being independent of the partial pressure of TMG. However, the overall average growth rate of the overgrown layer depends only on the partial pressure of TMG.

Conclusion

Lateral epitaxial growth of GaAs over tungsten gratings with 5 μm wide lines and spaces on (001) GaAs substrates was performed using MOCVD. Lateral overgrowth was seeded from the edges of the masking tungsten stripes by selective epitaxial deposits initially formed only on the exposed regions. The facets were formed at the GaAs-overgrown film edges. From crystallographic aspect, all the facets observed in the overgrown layers were found to be classified into four individual groups of {110}, $\{\bar{1}\bar{1}\bar{1}\}$ As, $\{112\}$ As, and $\{113\}$ Ga faces. The GaAs opening direction on the (001) substrate surface was found to be the most essential parameter for determining the geometric shape of the overgrowth layer. The other controlling parameters were the growth temperature and the partial pressure of AsH₃. The partial pressure of TMG had no influence on the facet formation, although the average growth rate of the overgrown layer was controlled by the mass transport of the reacting species including Ga atoms. These results could be qualitatively explained by the Langmuir-Rideal model.

Acknowledgments

The authors wish to thank Dr. Kenji Kumabe for his encouragement throughout this work. They also would like to thank Dr. Nobuhiko Susa, Dr. Hideo Sugiura, and Dr. Kunishige Oe for their useful comments.

Manuscript submitted March 11, 1985; revised manuscript received ca. June 19, 1985.

Nippon Telegraph and Telephone Corporation assisted in meeting the publication costs of the article.

REFERENCES

1. C. O. Bozler and G. D. Alley, *IEEE Trans. Electron Devices*, **ed-17**, 1128 (1980).

2. B. A. Vojak, R. W. McClelland, G. A. Lincoln, A. R. Calawa, D. C. Flanders, and M. W. Geis, *IEEE Electron Device Lett.*, **ed1-5**, 270 (1984).
3. H. Asai, S. Adachi, S. Ando, and K. Oe, *J. Appl. Phys.*, **55**, 3868 (1984).
4. F. J. Leonberger, C. O. Bozler, R. W. McClelland, and I. Melngailis, *Appl. Phys. Lett.*, **38**, 313 (1981).
5. F. W. Tausch, Jr., and A. G. Lapierre III, *This Journal*, **112**, 706 (1965).
6. D. W. Shaw, *ibid.*, **113**, 904 (1966).
7. S. Iida and K. Ito, *J. Cryst. Growth*, **13/14**, 336 (1972).
8. C. O. Bozler, R. W. McClelland, J. P. Salerno, and J. C. C. Fan, *J. Vac. Sci. Technol.*, **20**, 720 (1982).
9. N. Kondo, M. Kawashima, S. Ando, and K. Oe, *Appl. Phys. Lett.*, **45**, 1070 (1984).
10. P. Rai-Choudhury and D. K. Schroder, *This Journal*, **120**, 664 (1973).
11. L. Jastrzebski, J. F. Corboy, J. T. McGinn, and R. Pagliaro, Jr., *ibid.*, **130**, 1571 (1983).
12. P. Vohl, C. O. Bozler, R. W. McClelland, A. Chu, and A. J. Strauss, *J. Cryst. Growth*, **56**, 410 (1982).
13. R. Azoulay, N. Bouadma, J. C. Bouley, and L. Dugrand, *ibid.*, **55**, 229 (1981).
14. R. P. Gale, R. W. McClelland, J. C. C. Fan, and C. O. Bozler, *Appl. Phys. Lett.*, **41**, 545 (1982).
15. S. Adachi and K. Oe, *This Journal*, **130**, 2427 (1983).
16. D. H. Reep and S. K. Ghandhi, *J. Cryst. Growth*, **61**, 449 (1983).
17. H. Heinecke, E. Veuhoff, N. Pütz, M. Heyen, and P. Balk, *J. Electron. Mater.*, **13**, 815 (1984).
18. W. A. P. Claassen and J. Bloem, *This Journal*, **127**, 194 (1980).
19. W. A. P. Claassen and J. Bloem, *ibid.*, **128**, 1353 (1981).
20. W. H. Petzke, V. Gottschalch, and E. Butter, *Krist. Tech.*, **9**, 763 (1974).
21. D. H. Reep and S. K. Ghandhi, *This Journal*, **130**, 675 (1983).
22. M. R. Leys and H. Veenliet, *J. Cryst. Growth*, **55**, 145 (1981).

An Alternative Approach to the Calculation of Four-Probe Resistances on Nonuniform Structures

John Albers

National Bureau of Standards, Semiconductor Devices and Circuits Division, Gaithersburg, Maryland 20899

H. L. Berkowitz*

U.S. Army Electronics Technology and Devices Laboratory, ERADCOM, Fort Monmouth, New Jersey 07703

ABSTRACT

An alternative approach to the calculation of the four-probe resistance of nonuniform resistivity structures is presented. This approach is based upon two simplifications in the form of the four-probe resistance integral. The first arises from the integral's being independent of the probe current density as well as the probe radius. The second simplification involves the rewriting of the integral as one involving only the kernel (without any Bessel functions) and with finite limits which depend only upon the probe spacing. The form of these limits is determined by the analytic calculation of the four-probe resistance for the case of a semi-infinite slab. For the case of a uniform layer over an insulating or conducting boundary, the simplified integral leads to analytic expressions for the four-probe resistance which are compared with the more extensive technique and are also investigated as a function of the probe spacing. For nonuniform resistivity structures, the simplified integral can be easily evaluated by means of the Newton-Cotes numerical procedure. For general multilayer cases, the results obtained from the Newton-Cotes method are compared with those obtained from more extensive numerical techniques and are shown to be in excellent agreement. This allows for a vastly simplified implementation of the previously proposed spreading resistance calibration technique.

Recently, a multilayer expression for the in-line four-probe resistance, $Z(x, S)$, has been derived in the form (1)

$$Z(x, S) = 2\rho(x) \int_0^\infty A(x, \lambda) \{J_0(\lambda S) - J_0(2\lambda S)\} I_\nu(\lambda a) d\lambda \quad [1]$$

where $\rho(x)$ is the resistivity, $J_0(\lambda S)$ is the first-order Bessel function, $A(x, \lambda)$ is the kernel of the integral and is

related to the resistivity structure, $I_\nu(\lambda a)$ is the Hankel transform of the generalized probe-current density normalized to unit current (2), ν is an index which refers to the specific form of the current density, a is the probe radius, and λ is the integration variable. It was shown that the four-probe resistance could always be obtained from the two-probe spreading resistance, $R(x, S)$, from the general expression

*Electrochemical Society Active Member.

$$Z(x, S) = R(x, 2S) - R(x, S) \quad [2]$$

The four-probe resistance was also numerically shown to be (i) independent of the probe radius and the probe-current density, and (ii) simply related to the sheet resistance, $\mathfrak{R}(x)$, when the distance to an insulating boundary is small compared with the probe spacing. The former observation provided the basis for a calibration procedure for determining the value of the probe radius to be used in spreading resistance profile analysis. The use of the four-probe resistance in the calibration procedure requires the evaluation of the integral in Eq. [1]. This evaluation can be greatly simplified, and it is the purpose of the present work to derive a simplified expression for $Z(x, S)$ and hence greatly facilitate the use of the calibration procedure.

Derivation

As the four-probe resistance is independent of the probe current density and the probe radius, Eq. [1] may be rewritten as

$$Z(x, S) = \frac{\rho(x)}{\pi} \int_0^{\infty} A(x, \lambda) \{J_0(\lambda S) - J_0(2\lambda S)\} d\lambda \quad [3]$$

This particular simplification of the integral has been numerically verified for a range of structures. The thrust of the present work is to further simplify the integral by finding a function, $f(1/S)$, such that Eq. [3] can be written as

$$Z(x, S) = \frac{\rho(x)}{\pi} \int_{f(1/2S)}^{f(1/S)} A(x, \lambda) d\lambda \quad [4]$$

In going from Eq. [3] to Eq. [4], the Bessel functions have been removed from the integrand and their effect on the integral has been preserved by the replacement of the limits in Eq. [3] by finite limits which depend only upon S . This particular choice for the limits of the integral is not arbitrary but was motivated by the substitution of the Berkowitz-Lux (3) form of the spreading resistance in both terms in the right-hand side of Eq. [2]. The resulting expression contains the integral of $A(x, \lambda)$ where the lower limit depends upon $1/2S$ and the upper limit depends upon $1/S$. The particular form obtained from this substitution does not adequately represent the results for a wide class of structures. However, this observation provided the insight into the general form which the simplification of the integral would take.

The search for the function, $f(1/S)$, is aided by the calculation of Eq. [3] and [4] for the case of a semi-infinite slab. In this case, $A(x, \lambda) = 1$, and the integral in Eq. [3] can be evaluated analytically (4) to give

$$Z(x, S) = \frac{\rho}{\pi} \int_0^{\infty} \{J_0(\lambda S) - J_0(2\lambda S)\} d\lambda = \frac{\rho}{2\pi S} \quad [5]$$

This indicates that $f(1/S) = 1/S$, as can be verified by direct substitution into Eq. [4]. If this choice is generally correct, then the four-probe resistance will be represented by the equation

$$Z(x, S) = \frac{\rho(x)}{\pi} \int_{1/2S}^{1/S} A(x, \lambda) d\lambda \quad [6]$$

which is far simpler to evaluate and analyze than Eq. [1]. The validity of Eq. [6] was investigated for uniform layers over insulating or conducting boundaries, for a wide class of two-layer structures, and for general nonuniform multilayer structures. The results of these investigations are contained in the next three sections.

Uniform Resistivity Layers over Perfectly Insulating or Conducting Boundaries

The kernel for a uniform resistivity layer over an insulating or a conducting boundary, *i.e.*, $\coth(\lambda x)$, $\tanh(\lambda x)$, may be used to analytically evaluate the integral in Eq. [6] for these cases. Specifically

$$\begin{aligned} Z(x, S) &= \frac{\rho(x)}{\pi} \int_{1/2S}^{1/S} \coth(\lambda x) d\lambda \\ &= \frac{\rho}{\pi x} \ln \left\{ \frac{\sinh(x/S)}{\sinh(x/2S)} \right\} \end{aligned} \quad [7]$$

for an insulating boundary and

$$\begin{aligned} Z(x, S) &= \frac{\rho(x)}{\pi} \int_{1/2S}^{1/S} \tanh(\lambda x) d\lambda \\ &= \frac{\rho}{\pi x} \ln \left\{ \frac{\cosh(x/S)}{\cosh(x/2S)} \right\} \end{aligned} \quad [8]$$

for a conducting boundary. It is important to note in both cases that the probe spacing and the distance to the boundary appear as the ratio x/S . It is this ratio which determines the behavior of the functions.

For the situation where the distance to the boundary is small compared to the probe spacing, *i.e.*, $x/S < 1$, the \sinh function may be replaced by its argument whereas the \cosh function approaches unity. By making use of these limiting values for small x/S , it is straightforward to show that

$$\lim_{x/S < 1} Z(x, S) = \frac{\rho \ln(2)}{\pi x} \quad [9]$$

for an insulating boundary and

$$\lim_{x/S < 1} Z(x, S) = 0 \quad [10]$$

for a conducting boundary. From Eq. [9], it is clear that the idea of a "thin" isolated layer must be phrased in terms of the ratio of the thickness of the layer and the probe spacing. As the probe spacing becomes large compared to the distance to the boundary, the uniform layer may be considered to be "thin." This is important as it places an objective criterion on the use of the idea of thin layers. Equation [10] states for the case of a uniform layer over a conducting boundary that the four-probe resistance approaches zero as the probe separation becomes large compared to the distance to the conducting boundary.

For the situation where $x/S > 1$, the hyperbolic functions contained in Eq. [7] and [8] may be replaced by exponentials of the same argument. Then

$$\lim_{x/S > 1} Z(x, S) = \frac{\rho}{2\pi S} \quad [11]$$

for both the insulating and conducting boundary conditions. Hence, for $x/S > 1$, the results for both the insulating and conducting boundaries approach the semi-infinite slab result given by Eq. [5]. These results are summarized in Fig. 1, where the scaled four-probe function, $(\pi x/\rho)Z(x, S)$, is plotted for a wide range of x/S for each of the three boundary conditions. For $x/S < 1$, the three functions appear as three separate curves. The conducting boundary result decreases rapidly to zero, while the semi-infinite slab result decreases slowly to zero. In this same region, the insulating boundary result has reached its asymptotic value of $\ln(2)$. When x/S is approximately 0.5, the insulating boundary and conducting boundary results begin curving toward the semi-infinite slab results. This curving and merging is finally complete once x/S is approximately 2-3. Beyond this point, all three curves lie on top of each other, as indicated by Eq. [11]. These indicate, once x/S is approximately 2 or greater, that the effects of any boundary (especially an insulating boundary) have been completely removed. This would mean that four-probe resistance measurements made on thick layers, $x/S > 1$, should not be associated with a sheet resistance interpreted in terms of a parallel conduction model, *i.e.*, in terms of a sheet resistance $\mathfrak{R}(x)$, defined by

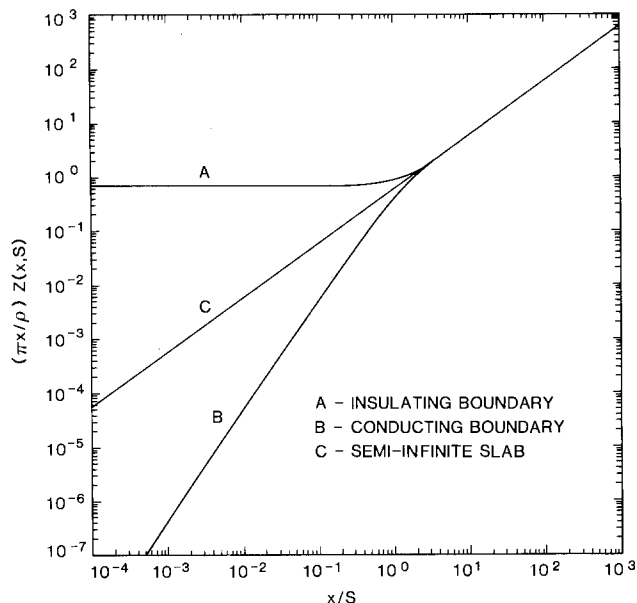


Fig. 1. The four-probe resistance scaled by $(\pi x/\rho)$, i.e., $(\pi x/\rho)Z(x, S)$, is presented for a large range of x/S for several boundary conditions. The curve denoted by A represents the result for an insulating boundary, while the curves denoted by B and C represent the results for a conducting boundary and no boundary (semi-infinite slab), respectively.

$$\Re(x) = \frac{1}{\int_0^x \sigma(x') dx'} \quad [12]$$

Having established the analytical results from the cases of semi-infinite slabs, uniform layers over insulating, or conducting, boundary conditions, what remains to be shown in this section is how well these results agree with the “exact” results obtained from Eq. [1]. Figure 2 contains the results of this comparison for a uniform layer over an insulator. In general, the agreement is very good. In the middle region of x/S values (from about 0.5 up to about 2.0), the maximum difference between the two results is about 10%.

A Two-Layer Structure

A particular example where the equations can be worked out exactly is the two-layer case where the top layer has a larger resistivity than the bottom layer. The resistivities of the bottom and top layers are ρ_1 and ρ_2 , respectively. The form of the kernel of the integral is given by

$$A_2(x, \lambda) = \frac{\rho_1 A_1 + \rho_2 \tanh(\lambda x)}{\rho_2 + \rho_1 A_1 \tanh(\lambda x)} \quad [13]$$

where x is the position of the surface of the top layer and A_1 is the kernel evaluated at the surface of the bottom layer. Introducing the variable q defined as $q = \rho_1/\rho_2$ and expanding the right-hand side of Eq. [13] to terms of order q , leads to the expression

$$\begin{aligned} A_2(x, \lambda) &= (qA_1 + \tanh(\lambda x))(1 - qA_1 \tanh(\lambda x)) \\ A_2(x, \lambda) &= \tanh(\lambda x) + qA_1(1 - \tanh(\lambda x)) + \dots \end{aligned} \quad [14]$$

Substituting this form for the kernel into Eq. [6] and evaluating the integral leads to the following expression of the four-probe resistance for this particular two-layer structure

$$Z(x, S) = \frac{\rho_2}{\pi x} \ln \left\{ \frac{\cosh(x/S)}{\cosh(x/2S)} \right\} + \frac{\rho_1}{\pi x} \ln \{ \tanh(x/S) - \tanh(x/2S) \} \quad [15]$$

Equation [15] represents the four-probe resistance of a

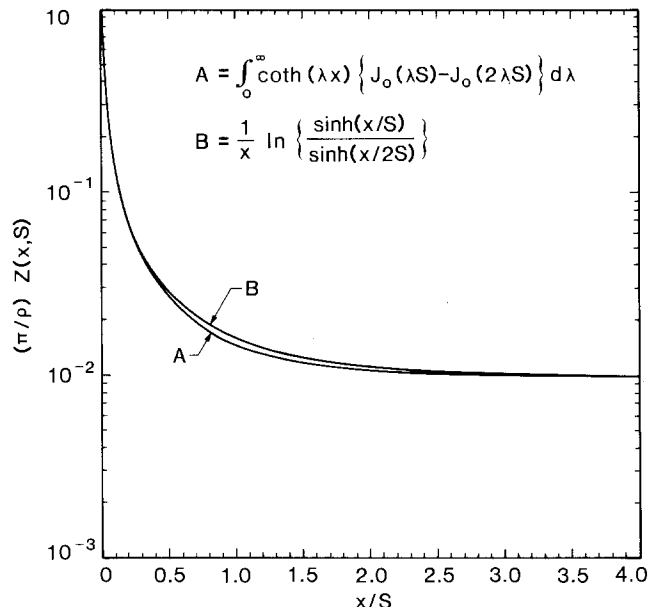


Fig. 2. The four-probe resistance scaled by (π/ρ) , $(\pi/\rho)Z(x, S)$, calculated from Eq. [1] and [7], are presented for the case of a uniform resistivity layer over an insulating boundary condition.

two-layer structure and reduces to Eq. [9] and [11] under the appropriate conditions.

Numerical Evaluation of $Z(x, S)$

A numerical integration scheme is required for the evaluation of the $Z(x, S)$ integral in Eq. [6] for the case of a general nonuniform resistivity structure. Two general techniques were used in the evaluation of the integral in Eq. [6]. The first makes use of the trapezoidal-Romberg technique with a 0.005% convergence criterion on the evaluation of the integral. This integration technique was the one which was used previously (5) to evaluate the spreading resistance correction factor integral. The second technique makes use of the nine-point Newton-Cotes method (6) in the evaluation of the integral. In particular, the logarithmic spacing used in Eq. [12] of Ref. (3) was employed. The purpose of using the first technique was to provide for an “exact” evaluation of the $Z(x, S)$ integral in Eq. [6]. The Newton-Cotes technique was investigated as a faster, more efficient, method. For the Newton-Cotes method of evaluation, the four-probe resistance was calculated using the expression

$$Z(x, S) = \frac{\rho(x)}{\pi} \ln(2) \sum_{i=0}^8 w_{9,i} \lambda_i A(x, \lambda_i) \quad [16]$$

where

$$\lambda_i = \frac{2^{i/8}}{2S} \quad (0 \leq i \leq 8) \quad [17]$$

$w_{9,i} = C_i/8$, and where C_i are the Newton-Cotes weighting factors (6). A comparison of the results of the integration performed with the trapezoidal-Romberg technique and with the nine-point Newton-Cotes method indicates that the latter method gives an excellent representation of the integral of Eq. [6]. Hence, for all subsequent analysis, the Newton-Cotes method will be used. The remaining item to be considered focuses upon the comparison of the four-probe resistances as calculated by Eq. [1] and by Eq. [6] (using the Newton-Cotes method).

The purpose of this section is to present the salient features of the calculation of the function $Z(x, S)$ for both “thin” and “thick” layers. As indicated previously, the concepts of “thin” and “thick” do not refer to the absolute layer thicknesses, but depend rather upon the ratio of the layer thickness (or distance to the insulating boundary) to the probe separation. Obviously, for almost all

practical applications, an isolated layer of up to approximately $10\ \mu\text{m}$ may always be considered to be thin. However, the distinction between thin and thick becomes important for the case of a nonuniformly doped layer over a substrate of the same conductivity type. Here, the total thickness of the wafer must be considered to be the depth to the insulating boundary, *i.e.*, the back of the wafer. Typically, this thickness can be several hundred microns and here the ratio x/S may be on the order of or greater than unity.

A number of implant-type resistivity structures were used with an insulating boundary placed up to several microns below the implanted region. This situation was used to simulate the implant into a junction isolating substrate. In these cases, x/S is always much less than unity and the junction-isolated layer formed by the implant is clearly thin in the sense described above. These structures were used to calculate $Z(x, S)$ using Eq. [1] and [6]. The probe spacings used ranged from 25 up to $1000\ \mu\text{m}$. In all cases, the results of the two techniques were found to be in agreement to within less than 1%. Also, direct evaluation of the sheet resistance showed that the relation between $Z(x, S)$ and the sheet resistance, $\mathfrak{R}(x)$, *i.e.*

$$Z(x, S) = \frac{\ln(2)}{\pi} \mathfrak{R}(x) \quad [18]$$

was satisfied. This would indicate that the Newton-Cotes technique for the evaluation of $Z(x, S)$ as given by Eq. [6] yields the correct result for a thin, *i.e.*, $x/S < 1$, layer.

The same gaussian-type implant structures were used with the insulating boundary placed at $350\ \mu\text{m}$ below the end of the implant structure. This was meant to simulate the situation which would arise from an implant structure into a substrate of the same conductivity type. As discussed above, the back surface of the wafer is now the insulating boundary condition. For the total thicknesses involved, the calculation should probe the results from the region where $x/S > 1$ down to the region where $x/S < 1$. In addition, the substrate resistivity was changed to emulate the approach to junction-type isolation at the end of the implant distribution. When the Newton-Cotes evaluation of $Z(x, S)$ was used and compared with the results of Ref. (1), the maximum deviation was found to be on the order of 10%. However, deviations of this magnitude were not typical of all structures, nor were they typical of any one structure. In general, deviations of about 1-2% were typical. In particular, deviations of this size were found in the surface region of nearly all the structures considered. Typical comparisons of the four-probe resistance integrals are contained in Fig. 3 for illustrative purposes. The overall quality of the Newton-Cotes results indicates that this computationally simpler form of $Z(x, S)$ presented in Eq. [16] and [17] can be used with confidence and at a substantial reduction in computation time. To illustrate the reduction in computation time, the calculations performed in Ref. (1) (using Eq. [1]) usually took several CPU minutes on a minicomputer (equivalent to at least an hour on a microcomputer). The same calculations using the Newton-Cotes method (Eq. [16] and [17]) take several CPU seconds on a minicomputer and on the order of 15-30s on a microcomputer. In addition, the calibration procedure proposed in Ref. (1) is now accessible as a simple add-on to any spreading resistance correction factor algorithm. This calibration procedure is described in detail in Ref. (1) and is implemented exactly as described there. The important difference resulting from the present work is that the calculation of the four-probe resistance for each value of the probe radius (used in the multilayer analysis of the spreading resistance data) can be performed very quickly even on a microcomputer system.

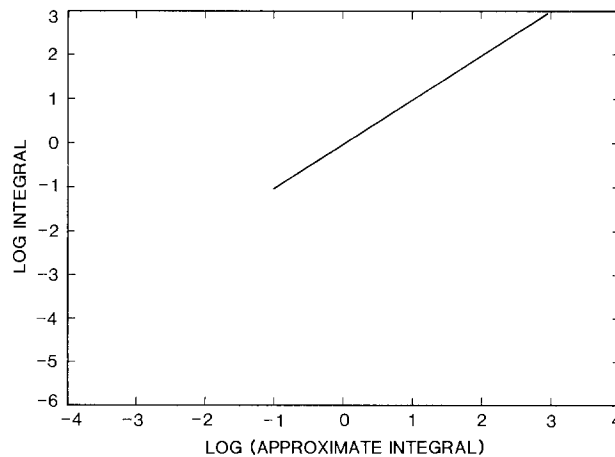


Fig. 3. The four-probe resistance integral as evaluated by the trapezoidal-Romberg method (Eq. [1]) and as evaluated by means of the Newton-Cotes evaluation (Eq. [16]) are plotted against each other in this figure. The data represent a wide range of structures. The data at the lower end represent deviations due to shorting substrates where the four-probe resistance does not provide any useful information.

A listing of the Newton-Cotes evaluation of $Z(x, S)$, written in FORTRAN (but easily translated to other languages), may be obtained from the authors upon request.

Results and Conclusions

A simplified method for evaluating the four-probe resistance has been presented and discussed. The resulting equation for the four-probe resistance involves an integral of $A(x, \lambda)$ over a small interval dictated by the probe spacing. In particular, the larger the value of the probe spacing, the closer the interval is to the origin. In a sense, this signals the importance of the substrate resistivity and the boundary condition as the small λ behavior of the kernel function is dominated by the ratio of the substrate resistivity and the resistivity of the point in question. Analytic expressions have been derived for the cases of a uniform layer over an insulating boundary or a conducting boundary. These expressions have been investigated as a function of x/S . For small values of x/S , the sheet resistance of a uniform layer has been shown to arise for the case of an insulating boundary. For large values of x/S , all three cases have been shown to merge together and provide a caveat in the interpretation of four-probe resistance measurements in terms of a sheet resistance obtained from a laminar conduction model.

A nine-point Newton-Cotes integration scheme has been presented and discussed for the evaluation of the simplified four-probe resistance integral and have been compared with the more complicated methods presented in Ref. (1). Typical differences between the two methods are in the 1-2% range with maximum values on the order of 10%. However, the Newton-Cotes method produces a reduction in computation time down into the region of seconds for both minicomputers and microcomputers. Consequently, the Newton-Cotes technique for evaluating the four-probe resistance can now be readily used in the calibration procedure which was proposed in Ref. (1).

REFERENCES

1. J. Albers and H. L. Berkowitz, *This Journal*, **131**, 392 (1984).
2. H. L. Berkowitz and R. A. Lux, *ibid.*, **126**, 1479 (1979).
3. H. L. Berkowitz and R. A. Lux, *ibid.*, **128**, 1137 (1981).
4. A. D. Wheelon, "Tables of Summable Series and Integrals Involving Bessel Functions," Holden-Day, San Francisco, CA (1968).
5. J. Albers, *Solid-State Electron.*, **23**, 1187 (1980).
6. F. Scheid, "Numerical Analysis," pp. 109-110, McGraw-Hill, New York (1968).

Complete Process Modeling for VLSI Multilayer Structures

Kouichi Sakamoto, Kenji Nishi, Tetsuo Yamaji, Tatsuro Miyoshi, and Shintaro Ushio

Oki Electric Industry Company, Limited, 550-1 Higashiasakawa, Hachioji, Tokyo 193, Japan

ABSTRACT

A new one-dimensional process simulator, ASPREM or advanced SUPREM, has been developed. ASPREM features the capability for multilayer structures and the incorporation of many up-to-date models. In this paper, general features of ASPREM are first described. Then details of many up-to-date models, such as oxidation-enhanced diffusion with or without polysilicon, impurity diffusion in polysilicon and SiO_2 , and stress effects to phosphorus diffusion after high dose ion implantation are reported with experimental results. Finally, applications to base-emitter self-aligned technology (BEST) transistors are described, followed by brief concluding remarks.

More than half a decade has already passed since the first process simulators, SUPREM and its extended version, SUPREM-II, were introduced from Stanford University (1, 2). Several process simulators have since been developed from different organizations (3-6). Most of them are designed for simulating two-dimensional impurity profiles, since the lateral diffusion is becoming more important with shrinking minimum pattern size. However, because of mathematical complexities of moving boundary problems, major efforts have been made to solve efficiently the diffusion equation for simplified structures. No great efforts have been made to develop more accurate physical models for multilayer structures. We currently need process simulators for multilayer structures which always appear in VLSI devices.

The authors introduced the prototype of multilayer process simulator as early as 1981 (7). Many process models have since been developed and incorporated in this simulator which is currently called advanced SUPREM or ASPREM. Some of the newly developed models are oxidation-enhanced diffusion models of impurities under high concentration or with polysilicon on top of the substrate, diffusion models within silicon dioxide and polysilicon, and stress effects to phosphorus diffusion under various ambients.

Recently, SUPREM-III has been developed by Stanford University as a one-dimensional process simulator to handle multilayer structures (8). Though basic features of ASPREM are similar to those of SUPREM-III, ASPREM excels in such models as impurity diffusion within polysilicon and SiO_2 .

In this article, general features of ASPREM are first described. Then, some of the up-to-date process models are reported in detail. Finally, applications to base-emitter self-aligned technology (BEST) transistors (9) are described.

Process Models in ASPREM

General features.—ASPREM can handle multilayer structures including SiO_2 , Si_3N_4 , and polysilicon. Thickness, dopant profiles, and, in the case of the silicon substrate and polysilicon, sheet resistances can be calculated after each process step. In the case of MOS transistors, threshold voltage can also be calculated with varying back bias voltages.

Basic models for impurity diffusion are based on a vacancy mechanism formulation (10), except that impurities can diffuse by interstitialcy mechanism during oxidation. According to this model, increased charged vacancies account for enhanced diffusion under high concentration of impurities. In the case of phosphorus diffusion, the model developed by Fair *et al.* (11) is used with some modification on the evaluation of stress, which is described later. Recent developments on high concentration diffusion of phosphorus have shown that not vacancies, but self-interstitials or both, account for enhanced diffusion (12, 13). At this stage, however, Fair and co-workers' model is still the only quantitative model which can handle high concentration diffusion of phosphorus.

The oxidation process uses the Deal-Grove model (14). For the heavily doped silicon substrate, the model devel-

oped by Ho *et al.* (15, 16) has been implemented in ASPREM to account for the enhanced oxidation rate. Ho and co-workers' model is also used for the oxidation of heavily doped polysilicon, where carrier concentration is replaced by impurity concentration within grains. The ambient-pressure dependence of the oxidation rate is also included. The parabolic growth rate depends linearly on the ambient pressure, whereas the linear growth rate depends on the power of ambient pressure, with the power being less than unity (17). The possible explanation for the nonlinear relationship of the linear growth rate on ambient pressure may exist in atomic-level reaction of oxidants with silicon atoms in the substrate. Details can be found elsewhere (17).

As-implanted impurity profiles are assumed to be a joint-half gaussian distribution for arsenic, phosphorus, and antimony, and a modified Pearson IV distribution for boron in all materials including SiO_2 and Si_3N_4 (10). An exponentially decaying tail is assumed only within the silicon substrate because channeling could occur only within the single crystal. In addition to basic elements, ASPREM can handle implantation of compounds such as BF and BF_2 , which have gained increasing importance in applications to the formation of a shallow junction in CMOS devices. Here, we assumed that a resulting boron profile is the same as the one in which boron ions are implanted with the artificial energy calculated by multiplying the mass ratio of boron in the compound to the original implant energy (18). This is reasonable when we assume that, upon entering the substrate, the implanted compound immediately decomposes into its constituting elements, while conserving kinetic energy and momentum.

In the following, some of the process models including oxidation-enhanced diffusion, and impurity diffusion in polysilicon and SiO_2 , are described in detail.

Oxidation-enhanced diffusion.—The impurities such as boron and phosphorus diffuse faster in the silicon substrate during oxidation. This phenomenon, called oxidation-enhanced diffusion (OED), has been explained by the excess silicon self-interstitials generated at the oxidizing silicon surface, and depends on generation, recombination, and diffusion of interstitials. Taniguchi *et al.* (19) already reported the practical model of OED in which the increment of the diffusivity due to oxidation, ΔD , is proportional to the power of oxidation rate and decreases exponentially with the depth from the silicon surface. Some of the authors also reached the similar equation for ΔD , except that ΔD depends on the impurity concentration at the oxidizing silicon surface (20), as seen in Fig. 1. Thus, ΔD is expressed as follows

$$\Delta D = \frac{D_0}{1 + a \cdot C_s/n_i} V_{ox}^{0.3} \exp\left(-\frac{E_0}{kT}\right) \exp\left(-\frac{x}{L_1}\right) \quad [1]$$

where V_{ox} is the oxidation rate, C_s is the surface impurity concentration, n_i is the intrinsic carrier concentration, E_0 is the activation energy, T is the temperature, k is the Boltzmann constant, x is the depth from the silicon sur-

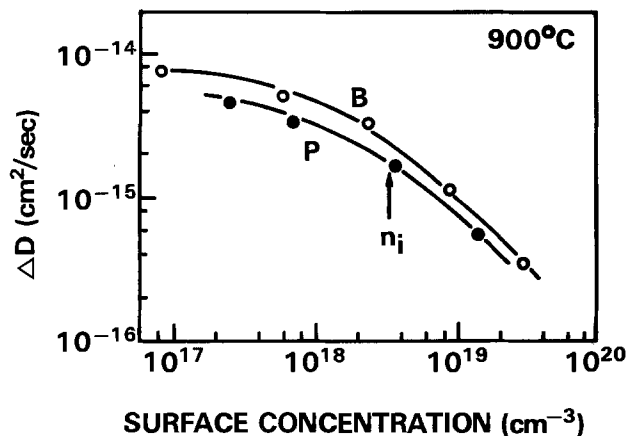


Fig. 1. D vs. surface impurity concentration for boron and phosphorus at 900°C .

face, L_1 is the characteristic length, D_0 is the fitting parameter which depends on impurity species, and a is also a fitting parameter which is fixed to 1.8. When C_s is much lower than n_i , Eq. [1] reduces to the one in Taniguchi's model. On the other hand, when C_s is much higher than n_i , ΔD in Eq. [1] becomes zero, indicating that no oxidation-enhanced diffusion occurs.

Oxidation-enhanced diffusion with polysilicon.—When there is a polysilicon layer on top of the silicon substrate, we must take the effects characteristic of polysilicon into account. Since the oxidation rate of polysilicon is similar to that of the silicon substrate, except for the difference in crystal orientation, we can expect that the amount of silicon self-interstitials generated by oxidation at the polysilicon surface is also similar to the one at the single-crystalline silicon surface. However, when silicon self-interstitials diffuse into the substrate through a polysilicon film, they may be easily trapped at polysilicon grain boundaries.

Some of the authors already reported (20) that ΔD of boron and phosphorus in the silicon substrate during oxidation of a polysilicon film on top of substrate is exponentially dependent on the polysilicon thickness, as shown in Fig. 2. Similar results were also obtained by Swaminathan (21). Hence, the complete expression for the impurity diffusion in the substrate during oxidation of polysilicon on top of it can be written as

$$\Delta D = \frac{D_0}{1 + a \cdot C_s/n_i} V_{\text{ox}}^{0.3} \exp\left(-\frac{E_0}{kT}\right) \exp\left(-\frac{x}{L_1}\right) \exp\left(-\frac{z}{L_2}\right) \quad [2]$$

where z is the polysilicon thickness and L_2 is the characteristic absorption length of interstitials in polysilicon.

Since the parameter, L_2 , depends on the annihilation of silicon self-interstitials at grain boundaries, it depends on the area of grain boundaries and, thus, on the grain size. From Fig. 2, in which the grain size is about $0.1 \mu\text{m}$, the obtained length for L_2 is 1100\AA , independent of impurity species. We note that this value is similar to Swaminathan's results (1000\AA). As for the L_2 dependence on the grain size, g , the following equation is used

$$L_2 = (g'/g \cdot (1/L'^2 - 1/L_1^2) + 1/L_1^2)^{-1/2} \quad [3]$$

where g' is $0.1 \mu\text{m}$ and L' is the absorption length when $g = g'$ and is 1100\AA as already stated. Usually, g is smaller than $10 \mu\text{m}$. In that case, it is easy to check whether or not L_2 is linearly dependent on g . Since g is linearly dependent on the reciprocal of grain boundary area and L_2 is expressed as $\sqrt{D_{\text{int}}\tau}$ where D_{int} is interstitial diffusivity and τ is a lifetime, linear dependence of L_2 on \sqrt{g} implies that τ is linearly dependent on the reciprocal of grain boundary area. When g approaches infinity, *i.e.*, the polysilicon approaches single-crystalline silicon, L_2 reduces to L_1 .

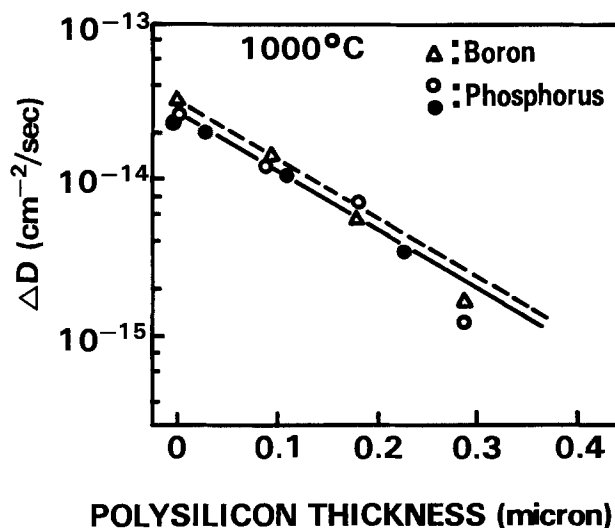


Fig. 2. D vs. polysilicon thickness for boron and phosphorus at 1000°C . The data are taken from Ref. (20).

This model has been implemented in ASPREM and has contributed to accurately simulate impurity profiles for polysilicon-source such as a base and an emitter region with doped polysilicon in conventional bipolar devices and BEST.

Stress effects on phosphorus diffusion.—Phosphorus diffusivity usually increases with increasing phosphorus concentration. However, when the phosphorus concentration exceeds several 10^{20}cm^{-3} , the enhancement factor decreases. Fair attributed this to the decrease of vacancy concentration caused by reduced bandgap, ΔE_g , due to the strain (22). However, he did not try to measure the values of strain experimentally, but rather obtained the relationship between ΔE_g and phosphorus concentration by fitting the calculated results to the experimental junction depths.

Using his relationship for the simulation of implanted phosphorus diffusion, we became aware that his estimates of E_g are too large. Sakamoto, one of the authors, and Sasaki tried x-ray double-crystal diffractometry in order to obtain the actual strain values in the phosphorus-implanted wafers after annealing in nitrogen or oxygen ambient (23). Figure 3 shows the actual maximum strain, s_m , vs. peak concentration of unprecipitated phosphorus. Also shown is the strain calculated from Fair's relationship by using Wortmann and co-workers' equation between ΔE_g and stress (24) and also the well-established relation of stress and strain. The strain calculated from Fair is larger than actual strain, as expected. It should be noted that the maximum strain depends on annealing ambients. As a best fit equation for s_m in the substrate and peak concentration of unprecipitated phosphorus, C_p , after annealing in nitrogen, the following equation is obtained

$$s_m = 1.9 \times 10^{-24} C_p + 4.2 \times 10^{-14} \sqrt{C_p - 1.3 \times 10^{20}} \quad (\text{cm}^{-3}) \quad [4]$$

The first term of the right-hand side alone is the strain after annealing in oxygen. The second term is added when the samples are annealed in nitrogen. More detailed experiments have revealed that the second term decreases inversely proportional to oxygen partial pressure when the samples are annealed in a mixture of nitrogen and oxygen (23). It is beyond the scope of this paper to discuss the difference in the strain after annealing in various ambients. We only note that this could be due to the difference in the type of residual lattice defects in implanted layers after annealing (25).

Equation [4] is used in ASPREM to calculate ΔE_g , which is used to obtain the reduced vacancy concentration and, thus, phosphorus diffusivity. In Fig. 4, we show examples of phosphorus diffusion in nitrogen or oxygen ambients.

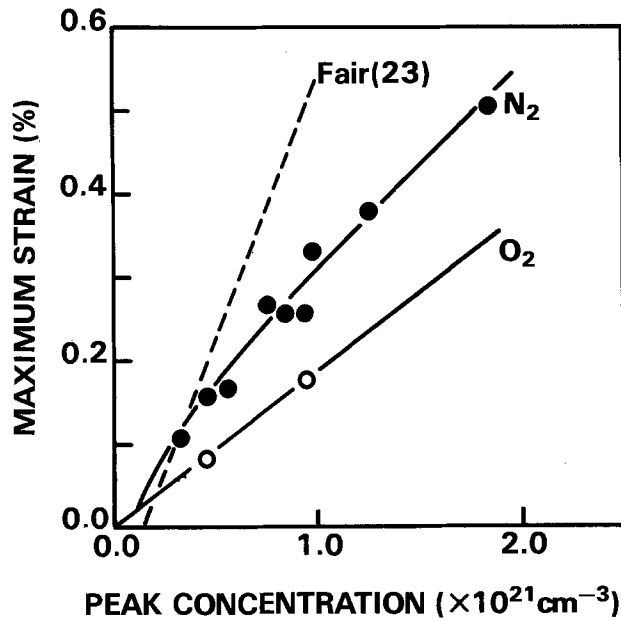


Fig. 3. Maximum strain vs. phosphorus peak concentration after ion implantation and subsequent annealing in nitrogen or oxygen.

Si(100) wafers were implanted with phosphorus at 40 keV with a dose of $1 \times 10^{16} \text{ cm}^{-2}$ and were annealed at 900°C for 20 min in nitrogen. After these wafers were subsequently annealed at 900°C for 100 min in nitrogen or oxygen, phosphorus profiles were obtained by secondary ion mass spectroscopy (SIMS). Phosphorus tails extend deeper when annealed in oxygen, showing enhanced diffusion. Oxidation-enhanced diffusion expressed by Eq. [1] alone cannot account for this large enhancement, since ΔD in Eq. [1] is much smaller than phosphorus diffusivity in nitrogen when surface concentration is as high as that shown in Fig. 4. On the other hand, simulation results using ASPREM, which includes strain effects from phosphorus diffusion, are in good agreement with SIMS profiles. Thus, it is concluded that enhanced diffusivity

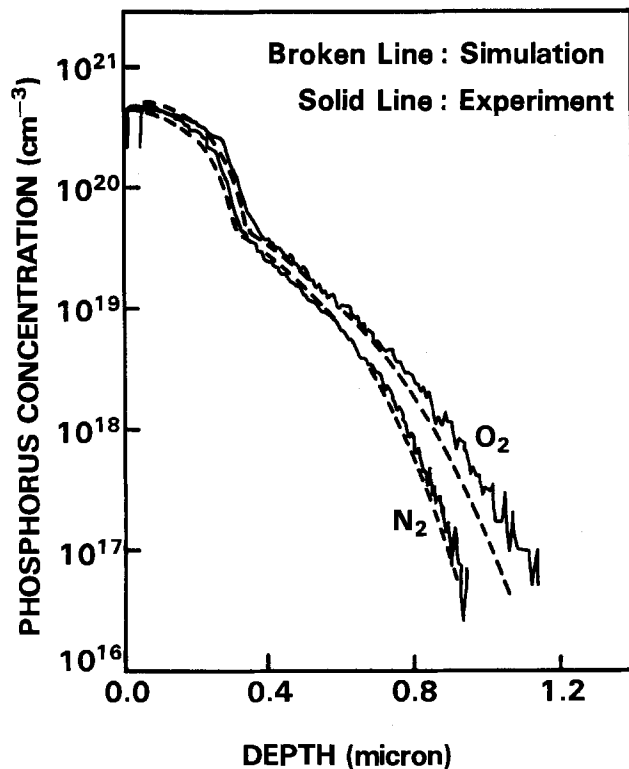


Fig. 4. Experimental and simulated phosphorus profiles after ion implantation and subsequent annealing in nitrogen or oxygen.

of high concentration phosphorus in oxygen is mainly due to the smaller strain compared with that in nitrogen.

Diffusion model in polysilicon.—The polysilicon layer has been found increasingly important in the fabrication of VLSI. The polysilicon layer is used for interconnects, gate electrodes, high valued resistance, and as a diffusion source for shallow junctions. Although several papers have been published for impurity diffusion in polysilicon, there has not been an effective diffusion model (8, 26, 27).

Difficulties in dealing with impurity diffusion in polysilicon arise from the fact that impurities can exist in two regions: within grains and at grain boundaries (21, 26). Another multilayer simulator, SUPREM-III, does not distinguish these two regions for diffusion analysis, although it includes segregation effects for the calculation of carrier concentration. In order to understand the diffusion mechanism in polysilicon, however, it is essential to include the effects of impurity segregation at grain boundaries. We have tried to model impurity diffusion in polysilicon including these effects.

Figure 5 shows a schematic cross section and impurity concentration in polysilicon. In the proposed model, we specify impurity concentration within grains and at grain boundaries independently. The sum of these concentrations gives the total impurity concentration. Impurities in each region can diffuse independently along the X-axis (depth direction). Diffusion along the Y-axis is also taken into account for impurities within grain boundaries by estimating the diffusion length within grains. Impurities in the two regions transport to each other through the interface of grains and their boundaries.

The model is summarized in the equations

$$C = C_i + C_b \quad [5]$$

$$\frac{\partial C_i}{\partial t} = \frac{\partial}{\partial x} \left(D_i \frac{\partial C_i}{\partial x} \right) - h' (mC_{is} - C_b) \quad [6]$$

$$\frac{\partial C_b}{\partial t} = \frac{\partial}{\partial x} \left(D_b \frac{\partial C_b}{\partial x} \right) + h' (mC_{is} - C_b) \quad [7]$$

where t is time, C is total impurity concentration, C_i (C_b) is impurity concentration within grains (at grain boundaries), D_i (D_b) is impurity diffusivity within grains (at grain boundaries), C_{is} is impurity concentration within grains near boundaries, h' is the coefficient for impurity transport through the interface of grains and their boundaries, and m is the segregation coefficient in thermal equilibrium. The value for m is taken from Mei and co-workers model (28) by taking the grain size into account. Equations [6] and [7] show impurity diffusion within grains and at their boundaries, respectively. The impurities at each region can diffuse independently except that they transport each other at the interface of grains and their boundaries. The amount of impurity transport is expressed by the second term of the right-hand side in Eq. [6] and [7]. Since the magnitude of m , which depends on the grain size, affects which of the impurities within

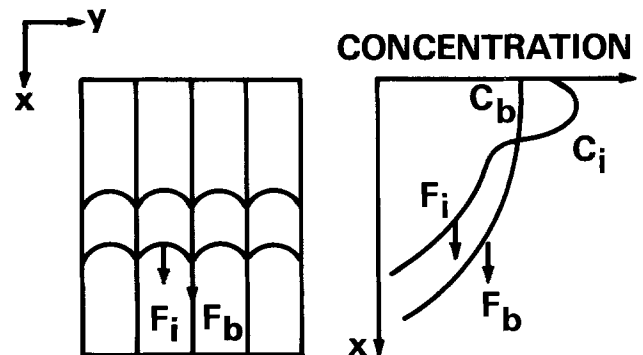


Fig. 5. Schematic model for impurity diffusion in polysilicon. F_i (F_b) and C_i (C_b) are impurity flow and impurity concentration within grains (at grain boundaries), respectively.

Table I. Impurity diffusivities at polysilicon grain boundaries

	Pre-exponential factor (cm ² /s)	Activation energy (eV)
Boron	0.82	2.74
Phosphorus	5.1	2.91
Arsenic	1100	3.53

grains or at grain boundaries is dominant in polysilicon, it is necessary to analyze impurity diffusion independently at each region.

Because of slower diffusion within grains, C_{is} may be different from C_i , which is the average impurity concentration within grains. We use $d \cdot C_i$ for C_{is} where d is $g/\text{minimum}(g, \sqrt{4D_i t})$. d reflects the effects of impurity diffusion within grains along the Y-axis and approaches unity for longer annealing. As the value for h' , we usually use a transport coefficient, h , which depends on temperature and impurity species. However, when C_{is} exceeds solid solubility of impurities within grains, impurity flow from grain boundaries into grain insides can be neglected. This is accomplished by equating $h' = 0$ when C_{is} is greater than solid solubility.

D_i is taken as impurity diffusivity within the silicon substrate, since grain insides are single crystalline. On the other hand, we have obtained D_b by fitting the simulated results to the experimental profiles by SIMS. D_b for boron, phosphorus, and arsenic through the temperature range 800°-900°C is shown in Table I, and is three orders of magnitude higher than D_i .

Figure 6 shows simulated and experimental profiles of boron and phosphorus. The samples are ion implanted with a dose of 10^{16} cm^{-2} to the 0.5 μm thick polysilicon with grain size of 0.1 μm , grown on (100) silicon. They are subsequently annealed at 800°C in nitrogen for 46 and 10 min for boron and phosphorus, respectively. In these profiles, we can distinguish surface and tail regions. In the surface region, impurities retain as-implanted profiles, indicating that no significant diffusion occurred. This slower diffusion is limited by impurity diffusion within grains. In the tail region, the profiles show a gentle slope indicating faster diffusion. This is due to very fast impurity diffusion through grain boundaries. It is

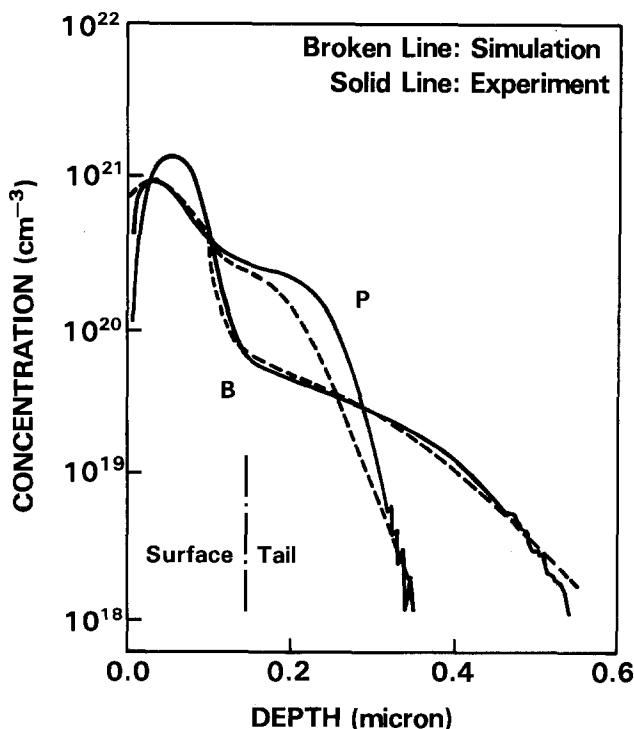


Fig. 6. Boron and phosphorus profiles in polysilicon after ion implantation and subsequent annealing in nitrogen.

noted that impurities at grain boundaries cannot be transported into grain insides, since C_{is} in the tail region exceeds solid solubility. On the other hand, at the diffusion front, the profile shows a relatively steep slope indicating slower diffusion. This is caused by a significant amount of impurities at grain boundaries transported into grain insides. Good agreements between simulated profiles and SIMS profiles show that the proposed model works effectively for impurity diffusion in polysilicon.

It should be pointed out here that simulation of oxidation of heavily doped polysilicon is also significantly improved by employing the proposed model for impurity diffusion in polysilicon. We use Ho and co-workers' oxidation model (15, 16) for polysilicon as well as for the silicon substrate. In their model, the oxidation rate depends on the surface carrier concentration. By assuming that surface carrier concentration is equal to surface impurity concentration within grains, simulated SiO_2 thickness after oxidation of polysilicon agrees well with the experimental result, which also confirms the effectiveness of the proposed model in polysilicon.

Phosphorus diffusion in SiO_2 .—While phosphorus diffusion in SiO_2 is important for MOS gate region, its mechanism has remained one of the least-known fields in VLSI processes. There have been a few reports on phosphorus diffusivity in SiO_2 (29, 30), but their values spread by several orders of magnitude. We have extensively studied phosphorus diffusion in SiO_2 , and obtained the diffusivity in relation to local phosphorus concentration.

Phosphorus with different doses was implanted to a thick oxide film thermally grown on (100) silicon. The wafers were subsequently annealed in dry oxygen at various temperatures. Figure 7 shows examples of phosphorus profiles measured by SIMS. A flat profile where phosphorus concentration is higher than 10^{20} cm^{-3} indicates that very fast diffusion occurred in this region. On the other hand, a steep slope in the lower phosphorus concentration region indicates slower diffusion. An assumption that phosphorus diffusivity, D_{ox} , depends only on the local phosphorus concentration has led to the following expression for the phosphorus diffusivity

$$D_{ox} = D_{i,ox} + bC_{ox}^n \quad [8]$$

where $D_{i,ox}$ is phosphorus diffusivity in low concentra-

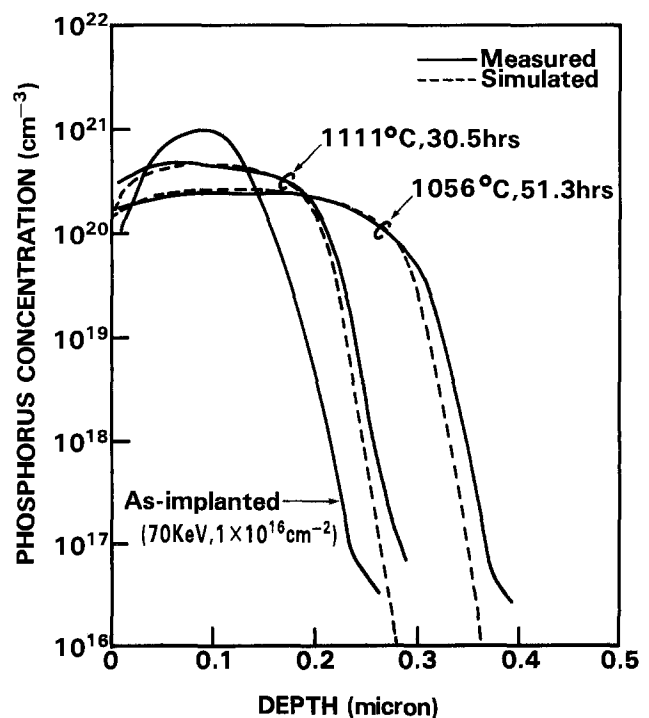


Fig. 7. Experimental and simulated phosphorus profiles in SiO_2 after ion implantation and subsequent annealing in nitrogen.

tion, C_{OX} is phosphorus concentration, and both b and n are fitting parameters. Best fit values for $D_{1,OX}$, b , and n are

$$D_{1,OX} = 3.22 \times 10^{-2} \exp[-4.1 \text{ (eV)/}kT] \text{ cm}^2/\text{s} \quad [9]$$

$$b = 1.13 \times 10^{-20} \exp[-7.1 \text{ (eV)/}kT] \text{ cm}^{6.5}/\text{s} \quad [10]$$

$$n = 1.5 \quad [11]$$

In Fig. 7, simulated results are also shown with experimental profiles. We can see good agreement between simulations and experiments.

The tendency of increasing phosphorus diffusivity with phosphorus concentration in the high concentration region is similar to Ghoshtagore's experiments (30) in which phosphorus was diffused from PSG. The obtained phosphorus diffusivity in thermal SiO_2 in our experiments is also similar to his results. This may indicate that Eq. [8] is generally applicable to phosphorus diffusion in SiO_2 .

Examples

In order to demonstrate the capabilities of ASPREM, we show here an example of simulated impurity profiles from a bipolar process called BEST, which was first introduced from OKI as a high performance bipolar technology with extensive use of polysilicon (9).

The schematic cross section of BEST transistors is shown in Fig. 8. The simulated region is at a cross section through emitter and active base region, which constitutes an essential part of BEST transistors. Two different fabrication processes, named A and B, were simulated. A detailed description of process sequence A is as follows: epitaxy, oxidation in oxygen at 900°C for 20 min, BF_2 ion implantation with dose of $1 \times 10^{14} \text{ cm}^{-2}$ at 40 keV for base formation, annealing in nitrogen at 900°C for 30 min, SiO_2 etching, polysilicon deposition with thickness of 3000\AA , polysilicon oxidation in oxygen at 900°C for 30 min, Si_3N_4 deposition with thickness of 2000\AA , annealing in nitrogen at 900°C for 30 min and at 950°C for 50 min, Si_3N_4 and SiO_2 etching, oxidation in dry O_2 at 900°C for 30 min, arsenic implantation for emitter with dose of $1.2 \times 10^{16} \text{ cm}^{-2}$ at 60 keV, oxidation in steam at 950°C for 40 min at 0.67 atm, and annealing in nitrogen at 1000°C for 35 min.

Process B is intended to form shallower emitter and base regions, and boron was implanted after polysilicon was deposited. The process sequence is as follows: epitaxy, polysilicon deposition with thickness of 3000\AA , oxidation in oxygen at 900°C for 30 min, Si_3N_4 deposition with thickness of 2000\AA , annealing in nitrogen at 900°C for 30 min and at 950°C for 50 min, Si_3N_4 and SiO_2 removal,

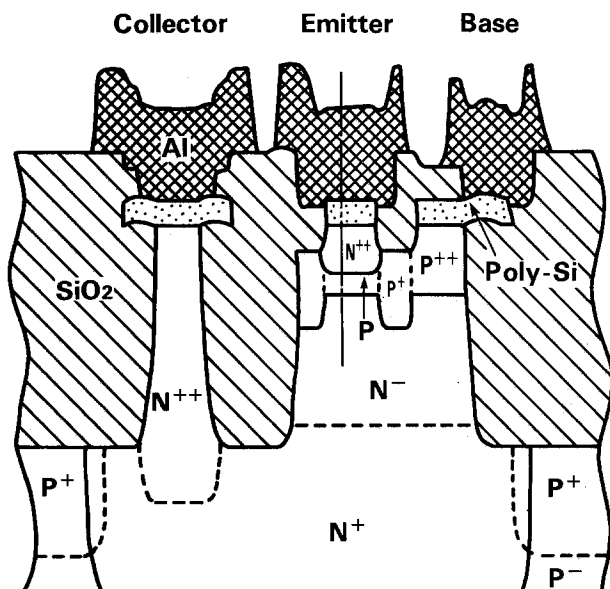


Fig. 8. Schematic cross section of a BEST transistor. Base/emitter region (indicated by a vertical line) is simulated by ASPREM as an example.

polysilicon oxidation in steam at 950°C for 40 min at 0.67 atm, annealing in nitrogen at 1000°C for 15 min, boron implantation with dose of $4.5 \times 10^{14} \text{ cm}^{-2}$ at 70 keV, SiO_2 removal, oxidation in oxygen at 900°C for 30 min, annealing in nitrogen at 950°C for 30 min, arsenic implantation with dose of $1.2 \times 10^{16} \text{ cm}^{-2}$ at 60 keV, followed by annealing in nitrogen at 950°C for 60 min.

Figures 9a and b show simulated and experimental impurity profiles for processes A and B, respectively. First of all, it should be pointed out that overall agreement between simulated and measured impurity profiles are satisfactory for both the processes. A kink in the boron profile around a base/emitter junction can be attributed to the retarded diffusivity by the electric field generated from a steep profile of high concentration arsenic and is also simulated well. The electric field also affects the diffusion of phosphorus, which piles up around the base/emitter junction. This is caused by electric-field-driven phosphorus flow against the gradient of phosphorus concentration. Although it is not clear from Fig. 9, we note that the simulated SiO_2 thickness after oxidation of heavily arsenic-doped polysilicon agrees well with the actual thickness, which is a by-product of distinguishing impurities within grains from those at grain boundaries in the polysilicon diffusion model as discussed.

Measured profiles show a pile-up of arsenic at the polysilicon/Si interface. Although this phenomenon needs more study, the effect on the overall arsenic profile can be negligible. We can see a discontinuity of phosphorus profile at the polysilicon/Si interface. This is due to the use of a relatively large segregation coefficient, which

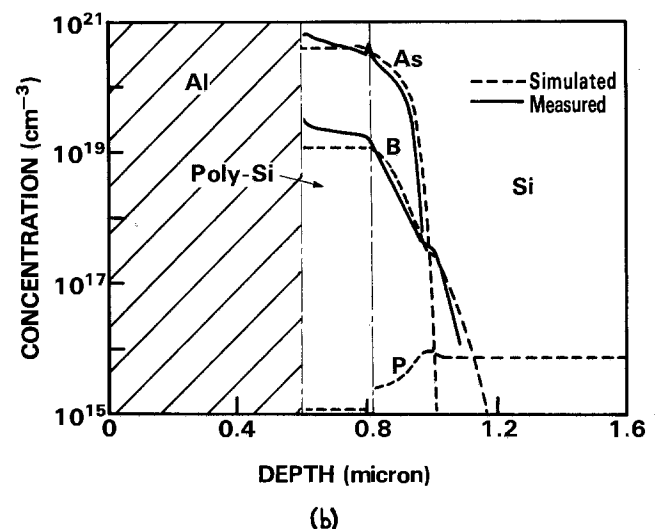
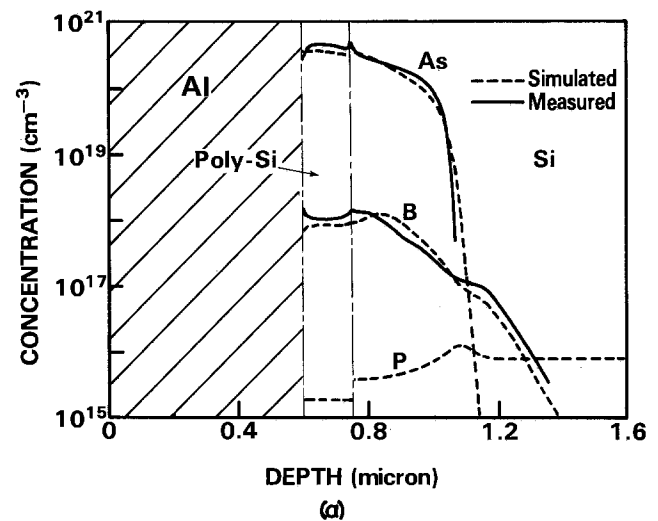


Fig. 9. Experimental and simulated impurity profiles at base/emitter region of a BEST transistor for (a) process A and (b) process B.

has been determined from another experiment on diffusion from a heavily phosphorus-doped polysilicon. Since, in ASPREM, the segregation coefficient is defined as the ratio of impurity concentration in Si to that within grains in polysilicon, interface discontinuity could appear for different process conditions. Further study is necessary for interface phenomena.

Conclusions

A multilayer simulator, ASPREM, has been developed. ASPREM features many up-to-date process models, which include an oxidation-enhanced model with or without polysilicon, strain effects to high concentration phosphorus diffusion, a diffusion model in polysilicon, and a phosphorus diffusion model in SiO₂. The details of these models have been discussed. As a multilayer simulator, ASPREM can be applied to the complete VLSI processes including bipolar and MOS transistors. The effectiveness of ASPREM has been demonstrated by BEST transistors. Especially, accurate simulation of diffusion and oxidation for polysilicon source emitter is worth noting, since similar processes are important for MOS transistors as well.

In addition to being applicable to current processes, ASPREM will serve as an effective tool in developing new multilayer models. This is significant, since multilayer structures are becoming more important, while few established models for multilayers exist.

Acknowledgment

We acknowledge Mr. Kawakatsu for sample preparation of BEST transistors and Mr. Ichikawa for SIMS measurements. We also acknowledge Mr. Higashi and Mr. Mizokami for their encouragement to complete this work.

Manuscript submitted Feb. 19, 1985; revised manuscript received June 4, 1985. This was Paper 411 presented at the Denver, Colorado, Meeting of the Society, Oct. 11-16, 1981.

OKI Electric Industry Company Limited assisted in meeting the publication costs of this article.

REFERENCES

1. D. A. Antoniadis, S. E. Hansen, R. W. Dutton, and A. G. Gonzalez, Stanford Electronics Laboratory Technical Report No. 5019-1, Stanford Electronics Laboratory, Stanford, CA, May 1977.
2. D. A. Antoniadis, S. E. Hansen, and R. W. Dutton, Stanford Electronics Laboratory Technical Report No. 5019-2, Stanford Electronics Laboratory, Stanford, CA, June 1978.
3. K. Taniguchi, M. Kashiwagi, and H. Iwai, *IEEE Trans. Electron Devices*, **ed-28**, 575 (1981).
4. D. J. Chin, M. K. Kump, H. G. Lee, and R. W. Dutton, *ibid.*, **ed-29**, 336 (1982).
5. C. D. Maldonado, F. Z. Custode, S. A. Louis, and R. Pancholy, *ibid.*, **ed-30**, 1462 (1983).
6. K. A. Salsburg and H. H. Hansen, *ibid.*, **ed-30**, 1004 (1983).
7. K. Nishi, K. Sakamoto, and S. Ushio, Abstract 411, p. 998, The Electrochemical Society Extended Abstracts, Vol. 81-2, Denver, CO, Oct. 11-16, 1981.
8. C. P. Ho, J. D. Plummer, S. E. Hansen, and D. W. Dutton, *IEEE Trans. Electron Devices*, **ed-30**, 1438 (1983).
9. S. Shimizu and H. Kitabayashi, *IEDM Tech. Dig.*, 332 (1979).
10. D. A. Antoniadis and D. W. Dutton, *IEEE Trans. Electron Devices*, **ed-26**, 490 (1979).
11. R. B. Fair and J. C. C. Tsai, *This Journal*, **124**, 1107 (1983).
12. S. M. Hu, P. Fahey, and R. W. Dutton, *J. Appl. Phys.*, **54**, 6912 (1983).
13. K. Nishi and D. A. Antoniadis, *ibid.*, **56**, 3428 (1984).
14. B. E. Deal and A. S. Grove, *ibid.*, **36**, 3770 (1965).
15. C. P. Ho and J. D. Plummer, *This Journal*, **126**, 1516 (1979).
16. C. P. Ho and J. D. Plummer, *ibid.*, **126**, 1523 (1979).
17. L. N. Lie, R. R. Razouk, and B. E. Deal, *ibid.*, **129**, 2828 (1982).
18. R. G. Wilson, *J. Appl. Phys.*, **54**, 6879 (1983).
19. K. Taniguchi, K. Kurosawa, and M. Kashiwagi, *This Journal*, **127**, 2243 (1979).
20. K. Sakamoto, K. Nishi, and T. Miyoshi, Paper presented at the 1982 Symposium on VLSI Technology, Japan Applied Physics Society and IEEE Electronic Device Society, Oiso, Japan, August 1982.
21. B. Swaminathan, Ph.D. Thesis, Stanford University, Stanford, CA (1983).
22. R. B. Fair, *J. Appl. Phys.*, **50**, 860 (1979).
23. M. Sasaki and K. Sakamoto, in "Semiconductor Processing," ASTM STP 850, Diensh C. Gupta, Editor, American Society for Testing and Materials, Philadelphia (1984).
24. J. J. Wortmann, J. R. Hauser, and R. M. Burger, *J. Appl. Phys.*, **35**, 2122 (1964).
25. S. Prussin, *ibid.*, **45**, 1635 (1974).
26. G. Zaeschmar, *ibid.*, **54**, 2281 (1983).
27. A. D. Buonaquisti, W. Carter, and P. H. Holloway, *Thin Solid Films*, **100**, 235 (1983).
28. L. Mei, M. Rivier, Y. Kwart, and R. Dutton, in "Semiconductor Silicon 1981," H. R. Huff and R. J. Kriegler, Editors, p. 1007, The Electrochemical Society Softbound Proceedings Series, Pennington, NJ (1981).
29. M. Ghezzi and D. M. Brown, *This Journal*, **120**, 146 (1973).
30. R. N. Goshtagore, *Thin Solid Films*, **25**, 501 (1975).

Degradation Mechanism of Lightly Doped Drain (LDD) n-Channel MOSFET's Studied by Ultraviolet Light Irradiation

M. Saitoh, H. Shibata, H. Momose, and J. Matsunaga

Toshiba Corporation, Semiconductor Device Engineering Laboratory, 1, Komukai Toshiba-cho, Saiwai-ku, Kawasaki 210, Japan

ABSTRACT

The degradation of lightly doped drain (LDD) n-channel MOSFET's has been investigated in detail making use of ultraviolet light irradiation, and the following results have been obtained. The degradation of the parasitic MOSFET consisting of the gate, the LDD region, and the insulator in between, which dominates the deterioration of the total performance, can be divided into two phases. In the initial phase, the degradation is rapid compared to that in the succeeding phase. The initial phase degradation is due not to surface-state generation, but to electron capturing of the oxide covering the LDD region which has a large number of traps. The quality of the insulator above the LDD region should be carefully controlled in order to make highly reliable LDD MOSFET's.

As the device dimensions are reduced in VLSI's, hot carrier-induced MOSFET degradation becomes a problem of more importance, and many efforts have been made to solve it. Along with the studies on the degradation mechanism (1-15), explorations of highly reliable MOSFET's have also been made (16-22). Consequently, lightly doped drain (LDD) MOSFET has been proposed and widely believed to have high reliability.

Hsu *et al.* (21, 22), however, reported recently that when the LDD MOSFET's and the conventional MOSFET are compared under the same substrate current during the stress, the former shows two orders of magnitude faster deterioration in transconductance (G_m) than the latter. This fact seems to suggest that the LDD MOSFET's have their own degradation mechanism which makes them of little advantage to the conventional MOSFET.

Thus, in order to make highly reliable LDD MOSFET's, the degradation mechanism of the LDD structure should be made clear. For this purpose, we tried to make use of ultraviolet (UV) light irradiation, in which the energy distribution of generated hot carriers is almost independent of the impurity concentration of the LDD region. This fact makes experimental results easy to interpret.

Experimental

The MOSFET's examined were fabricated in a conventional poly-Si gate N MOS process with and without LDD (N^-) region (conventional MOSFET's were cofabricated as a reference).

After gate patterning, gate oxide over source/drain area was etched off by wet chemical etchant. Phosphorus ions were implanted to form N^- diffusion, while no ion implantation was made for the wafers of conventional MOSFET's. Then, so-called postoxidation was done.

A new type sidewall, self-defined polysilicon sidewall (SEPOS), was used at the sidewall making step for LDD Tr's. The process flow for the SEPOS is shown in Fig. 1. Onto the postoxide, LPCVD polysilicon was uniformly deposited, and then the surface was slightly oxidized. SiO_2 reactive ion etching (RIE) followed to leave oxide frame only at the vertical sides of the polysilicon steps. After subsequent polysilicon RIE, the oxide-framed polysilicon sidewall was completed. Then, arsenic ions were implanted to make N^+ regions. The polysilicon sidewall was removed by plasma etching, and CVD SiO_2 was deposited on it. Passivation was made by depositing BPSG (boro-phosphosilicate glass) onto the CVD SiO_2 film.

Surface impurity concentration of channel (boron) and N^+ (arsenic) regions were 1.5×10^{16} and 2×10^{20} cm^{-3} , respectively. That of N^- (phosphorus) regions was varied from 3.8×10^{17} to 3.2×10^{18} cm^{-2} (ion dose from 5×10^{12} to 4×10^{13} cm^{-2}). The effective channel length was 0.5-0.7 μm , and gate oxide thickness 25 nm. The N^- region length ranged from 0.24 to 0.36 μm , depending upon phosphorus concentration.

Samples were irradiated with UV light of 4.63 eV, as shown in Fig. 2, using a commercial EPROM eraser

which can erase EPROM data within 10 min. During the irradiation, all the electrodes were connected to the ground potential. All measurements were carried out at room temperature (21°-25°C).

Results

The changes in the linear region of drain current *vs.* gate voltage characteristics after 4h UV light irradiation are shown in Fig. 3 for low (3.8×10^{17} cm^{-3}) and high (1.7×10^{18} cm^{-3}) N^- LDD samples and, for comparison, for a conventional sample. The low N^- one reveals a drastic increase in threshold voltage and a certain amount of decrease in transconductance G_m , while the high N^- one shows only a small decrease in G_m . No change can be observed for the conventional one. Figure 4 compares their subthreshold characteristics. It is found that the low N^- one shows smaller subthreshold slope than the others, and the curve shows parallel shift in the positive direction after irradiation, while no change is observed for the high N^- and the conventional samples.

Figure 5 shows the time dependencies of (i) the increase in V_{th} which is defined as V_G giving rise to I_D of 10^{-7} A for $V_D = 0.1$ V and (ii) the decrease in I_{th} which is defined as I_D for $V_G = V_{th}(\text{initial}) + 3.5$ V, for the low N^- sample. Here, errors coming from temperature fluctuation are corrected. Two curves drawn in the same frame are the data

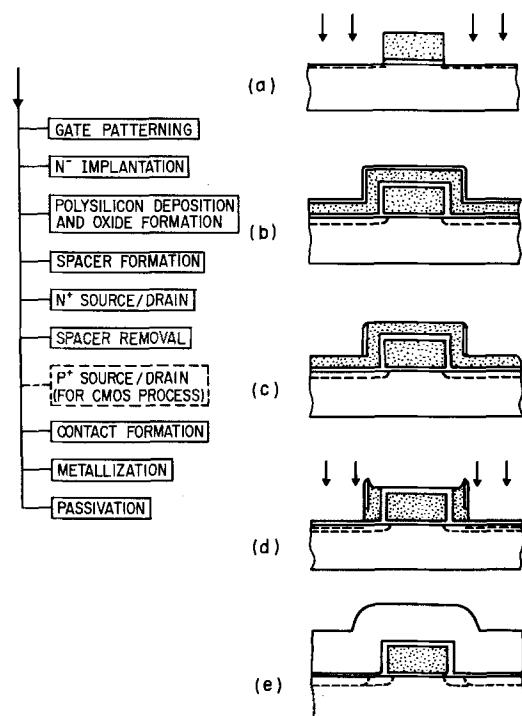


Fig. 1. Process flow for self-defined polysilicon sidewall (SEPOS).

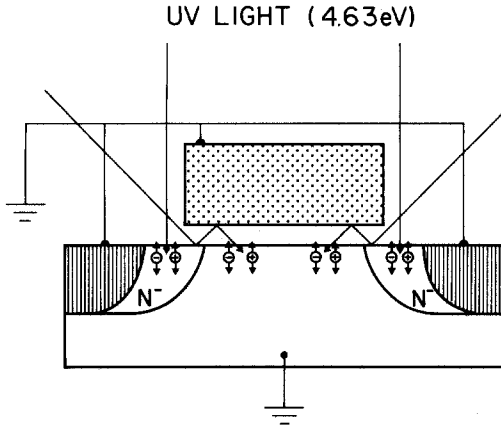


Fig. 2. Ultraviolet (UV) light irradiation using an EPROM eraser

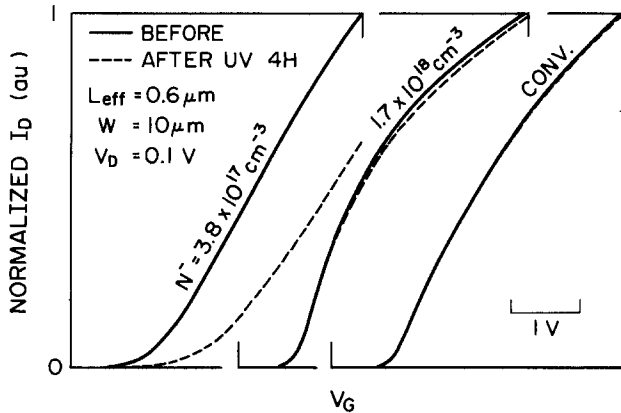


Fig. 3. Changes in the linear region of I_D vs. V_G characteristics caused by 4h UV light irradiation for a 3.8×10^{17} and a $1.7 \times 10^{18} \text{ cm}^{-3}$ N^- concentration LDD MOSFET, and a conventional MOSFET.

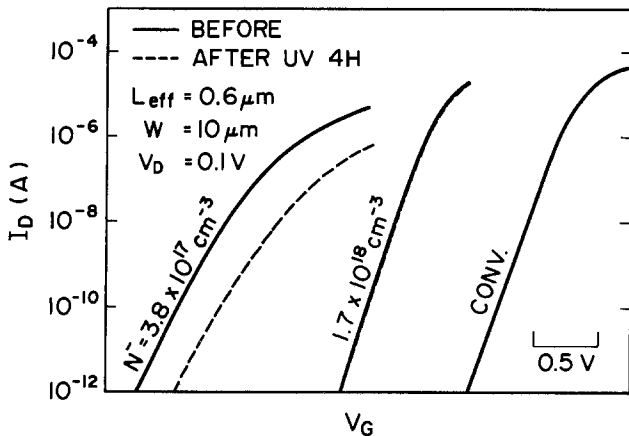


Fig. 4. Replots of the I_D - V_G curves in Fig. 3. Changes in sub-threshold characteristics are compared.

for different samples under the same experimental condition. The threshold voltage V_{th} shows rapid increase within 0.5h and comes to clear saturation thereafter, although the saturation values are largely different from sample to sample. On the other hand, I_{to} does not show such clear saturation. Figure 6 shows the results corresponding to Fig. 5 in the case of high N^- sample. The similar behavior is observed, though the V_{th} shift is very small.

Electrical stress was also studied, where the stress condition was $V_D = V_G = 6V$. Transconductance change ΔG_m and threshold voltage shift ΔV_{th} were measured in this case as a function of stress time. Source and drain were reversed during measurements. Samples of 6.9×10^{17} , 1.7×10^{18} , and $3.2 \times 10^{18} \text{ cm}^{-3}$ N^- concentrations showed a

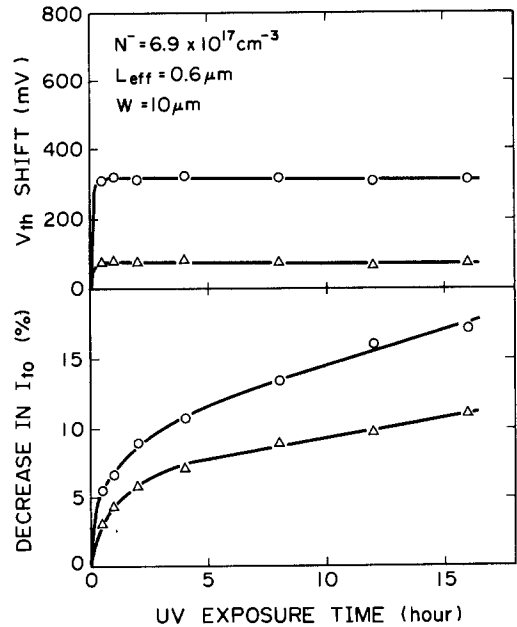


Fig. 5. Increase in V_{th} and decrease in I_{to} as a function of UV exposure time. Here V_{th} is defined as V_G giving rise to 10^{-7} A of I_D for $V_D = 0.1V$, and I_{to} as I_D for $V_G = V_{th}(\text{initial}) + 3.5V$. Concentration of N^- region is $6.9 \times 10^{17} \text{ cm}^{-3}$.

decrease in G_m (which is revealed in Fig. 7) but a negligibly small ($< 10 \text{ mV}$) V_{th} shift. In contrast, in the case of $3.8 \times 10^{17} \text{ cm}^{-3}$ N^- concentration samples, G_m shows a negligibly small decrease ($< 1\%$) and V_{th} a fairly large increase, as shown in Fig. 8.

In Fig. 9, ΔG_m (ΔI_{to} for UV irradiation case) corresponds to the phase 1; initial rapid degradation stages (see Discussion section) are shown as a function of N^- concentration for both UV irradiation and electrical stress cases. In the former case, ΔG_m decreases with N^- concentration, while in the latter case it seems almost independent of the concentration.

Discussion

From the results shown in Fig. 3 and 4, we can derive a model for the LDD MOSFET's and the effect of UV light irradiation (Fig. 10). The features of the model are (i) LDD MOSFET's consist of a main Tr (A in Fig. 10a) and para-

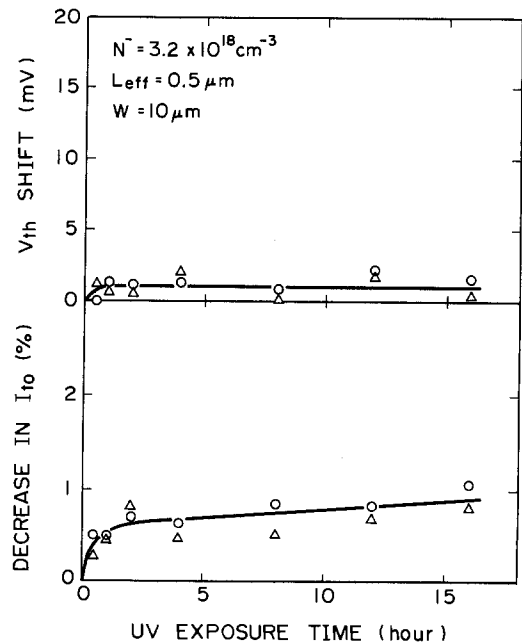


Fig. 6. The same data as in Fig. 5, except for N^- concentration of $3.2 \times 10^{18} \text{ cm}^{-3}$.

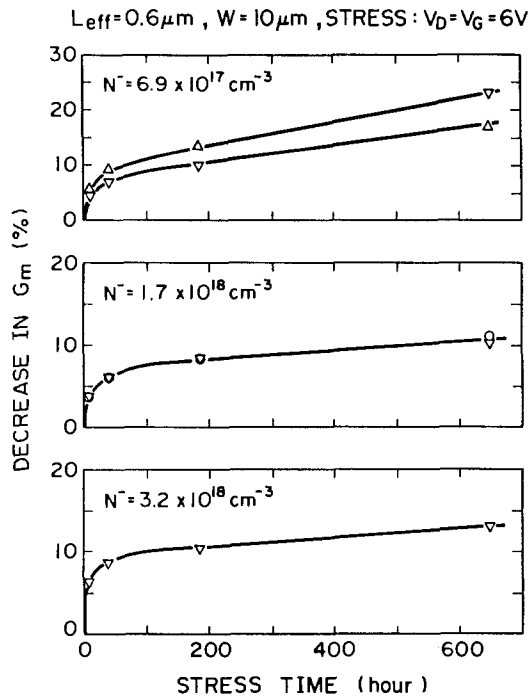


Fig. 7. Decrease in G_m as a function of electrical stress time. Here G_m is defined as $(\partial I_D / \partial V_G)_{max}$. Concentration of N^- region is from 6.9×10^{17} to $3.2 \times 10^{18} \text{ cm}^{-3}$. Threshold voltage shift V_{th} is negligibly small (10 mV) for all cases. Definition of V_{th} is the same as in Fig. 5.

sitic Tr's (B in Fig. 10a) connected in series and (ii) UV irradiation brings change only to the parasitic Tr's. This is known from the fact that the conventional sample does not change. It is considered that in the low N^- concentration region ($3.8 \times 10^{17} \text{ cm}^{-3}$, for example) the threshold voltage of the parasitic Tr's is higher than that of the main Tr and they dominate the total I_D - V_G characteristics. Therefore, a drastic change including subthreshold curve shift occurs for low N^- sample. In the high N^- concentration region ($1.7 \times 10^{18} \text{ cm}^{-3}$, for example), the threshold voltage of the parasitic Tr's is lower than that of the main Tr. So, the expected threshold voltage shift in the parasitic Tr's results only in the transconductance decrease.

The relatively gentle subthreshold slope of the parasitic Tr comes from its depletion-type operation, the process-induced gate oxide thickening there, and/or the relatively large amount of surface states (although the amount does not increase by UV irradiation as shown by the parallel shift of the subthreshold curve). The fact that the para-

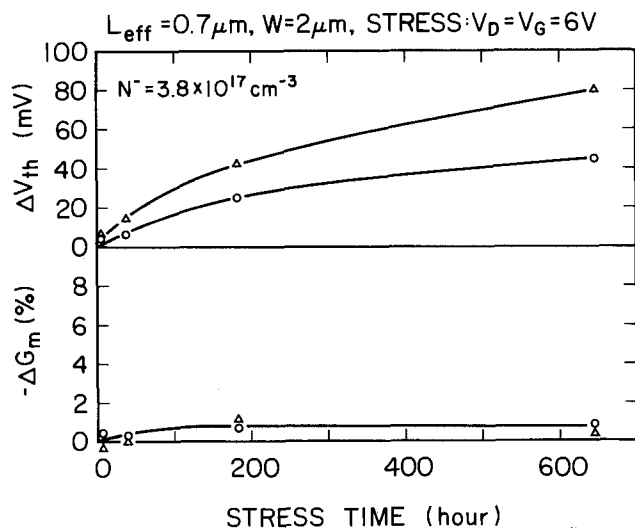


Fig. 8. Threshold voltage shift V_{th} and decrease in G_m as a function of electrical stress time. Concentration of N^- region is $3.8 \times 10^{17} \text{ cm}^{-3}$.

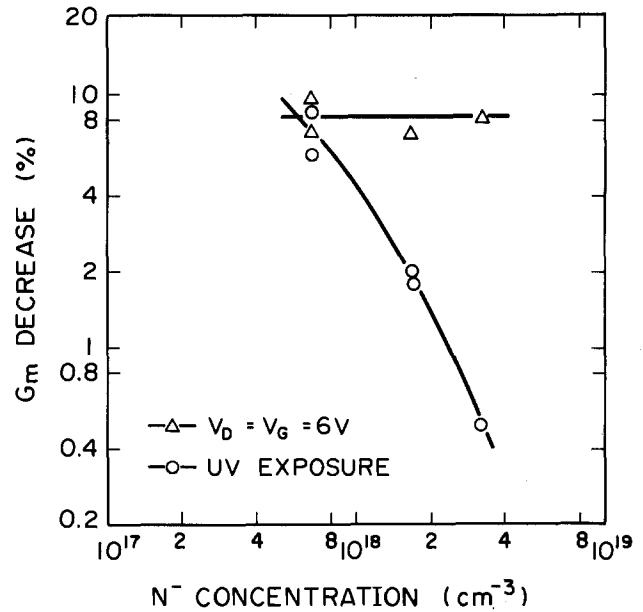
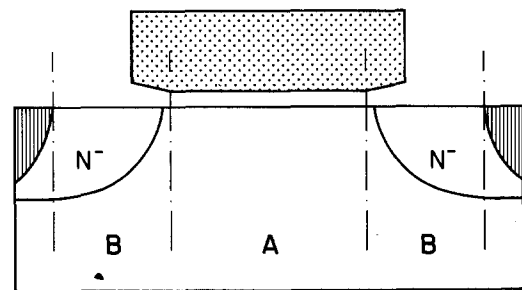


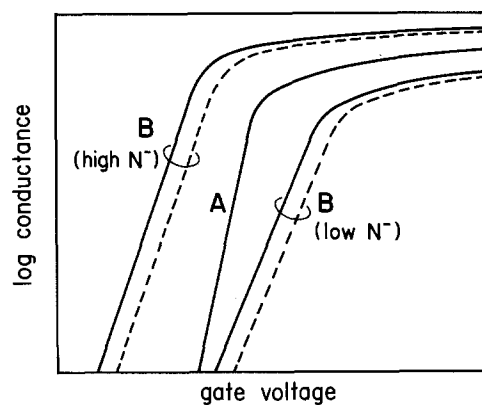
Fig. 9. G_m (for electrical stress) and I_{D0} (for UV irradiation) corresponding to phase 1 charge (see text).

sitic Tr of low N^- concentration before UV irradiation has a threshold voltage higher than that of the main Tr suggests that a certain amount of negative charge (or interface states) exists above the N^- regions when the fabrication process is finished.

As can be seen in Fig. 5, the change in the characteristics of the parasitic Tr can be divided into two phases: phase 1 is the part until the saturation in the V_{th} shift vs. UV exposure time curve, and phase 2 is the one after the saturation. Consequently, the total I_D - V_G characteristics of



(a)



(b)

Fig. 10. A model for the LDD MOSFET's and their own degradation mechanism. LDD MOSFET's consist of a main Tr (A) and parasitic Tr's (B). Degradation characteristics of LDD Tr arise from threshold voltage shift of the parasitic Tr's.

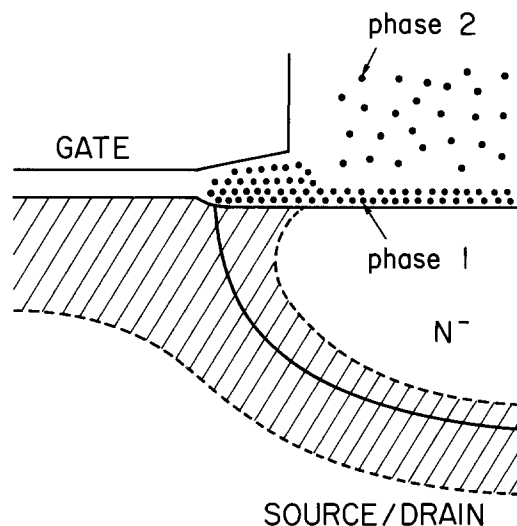


Fig. 11. A model for the location of fixed negative charge which changes the characteristics of parasitic Tr's.

the LDD Tr in triode operation can be expressed by

$$V_D/I_D = \frac{1}{G_{m1}(V_G - V_{th1})} + \frac{1}{G_{m2}(V_G - V_{th2})} + \frac{1}{G_{m3}(V_G - V_{th3})}$$

where V_{th1} , V_{th2} , and V_{th3} are the threshold voltages of the main Tr, of the parasitic Tr which corresponds to the phase 1 change, and of the parasitic Tr which corresponds to the phase 2 change. By UV light irradiation, V_{th1} does not shift, V_{th2} shifts rapidly and then becomes saturated, and V_{th3} shows relatively slow and long lasting shift. The picture derived from the above discussion is illustrated in Fig. 11. The phase 1 charge may be due to built-in traps in both the oxide grown from Si of N^- region and that grown from phosphorus-doped gate polysilicon during the postoxidation step. On the other hand, the phase 2 charge may be due to those in the LPCVD SiO_2 .

Because of the parallel shift of the subthreshold curve (Fig. 4), it is concluded that the V_{th2} shift comes not from surface-states generation, but from increase of trapped negative charges. This is also true for the V_{th3} shift if the barrier height for hot holes is not lowered by the trapped electrons, because the energy of UV light-generated hot holes, 3.51 eV, (4.63 eV photon energy - 1.12 eV bandgap of Si) is smaller than the potential barrier of Si- SiO_2 interface for holes (~3.7 eV) (2).

The dependence of ΔG_m on N^- concentration in the UV irradiation case (Fig. 9) is explained by the higher N^- sample's having lower sensitivity to the fixed charge above the N^- region. Here, the amount of the fixed charge is assumed to be the same for all the N^- concentrations, which is reasonable, as the UV light-induced hot carrier injection phenomenon does occur almost equally for all the N^- concentrations. In the electrical stress case, however, the saturation amount of the phase 1 charge seems to increase with the N^- concentration. In other words, it increases with the energy and population of hot carriers injected; higher N^- must lead to higher energy and population (23). This is why ΔG_m for the phase 1 (Fig. 9) seems to have little dependence on N^- concentration. Anyway, essentially the same mechanism seems to dominate the degradation both in the UV irradiation case and the electrical stress case.

Here it should be noted that the $6.9 \times 10^{17} \text{ cm}^{-3}$ N^- concentration sample reveals the behavior of low N^- sample (i.e., large V_{th} shift) in UV irradiation case (Fig. 5), while it reveals that of high N^- sample (i.e., negligibly small V_{th} shift) in electrical stress case (Fig. 7). It may come from the difference in the spacial and energetic distribution of

hot carriers from UV irradiation to electrical stress. However, we cannot make further comment on this, because the difference from sample to sample is too large, as can be seen in Fig. 5-8.

Finally, we would like to note that the quality of the insulator above the N^- region should be carefully controlled, as well as the impurity profile of the region, in order to make highly reliable LDD MOSFET's.

Conclusions

From a study making use of ultraviolet light irradiation, the following conclusions have been derived.

The LDD n-channel MOSFET has its own degradation mechanism as follows. The oxide covering the LDD (N^-) region, which is grown from the N^- region and the phosphorus-doped gate polysilicon, has a large number of electron traps. Electrons injected into the oxide are captured by these traps and shift the threshold voltage of the parasitic, depletion-type MOSFET in the positive direction. CVD SiO_2 by the side of the gate also has electron traps which play the similar role. The former shift is rapid compared to the latter one and becomes saturated in a certain amount. In contrast, the latter shift is slow and long lasting. This mechanism dominates the degradation of the LDD MOSFET's as far as the energy of hot-carriers is too low to activate another mechanism such as surface-state generation.

Acknowledgments

The authors would like to acknowledge Dr. Y. Nishi and Dr. H. Nozawa for helpful discussion.

Manuscript received April 25, 1985. This was Paper 455 RNP presented at the Cincinnati, OH, Meeting of the Society, May 6-11, 1984.

Toshiba Corporation assisted in meeting the publication costs of this article.

REFERENCES

1. T. H. Ning, P. W. Cook, R. H. Dennard, C. M. Osburn, S. E. Schuster, and H.-N. Yu, *IEEE Trans. Electron Devices*, **ed-26**, 346 (1979).
2. P. E. Cottrell, R. R. Troutman, and T. H. Ning, *ibid.*, **ed-26**, 520 (1979).
3. R. B. Fair and R. C. Sun, *ibid.*, **ed-28**, 83 (1981).
4. H. Matsumoto, K. Sawada, S. Asai, M. Hirayama, and K. Nagasawa, *ibid.*, **ed-28**, 923 (1981).
5. Y. Nakagome *et al.*, in "Proceedings of the 14th Conference on Solid State Devices," p. 99, Tokyo (1982).
6. K. K. Ng, G. W. Taylor, and A. K. Sinha, *IEEE Trans. Electron Devices*, **ed-29**, 1323 (1982).
7. E. Takeda and N. Suzuki, *IEEE Trans. Electron Device Lett.*, **edl-4**, 111 (1983).
8. S. Tam, F.-C. Hsu, C. Hu, R. S. Muller, and P. K. Ko, *ibid.*, **edl-4**, 249 (1983).
9. E. Takeda *et al.*, *ibid.*, **edl-4**, 329 (1983).
10. K. K. Ng and G. W. Taylor, *IEEE Trans. Electron Devices*, **ed-30**, 871 (1983).
11. S. Horiguchi *et al.*, in "Extended Abstracts, 15th Conference on Solid State Devices and Materials," p. 257, Tokyo (1983).
12. C. Hu, *IEDM Tech. Dig.*, 176 (1983).
13. M.-S. Liang *et al.*, *ibid.*, 186 (1983).
14. F.-C. Hsu and S. Tam, *IEEE Trans. Electron Device Lett.*, **edl-5**, 50 (1984).
15. F.-C. Hsu and K.-Y. Chiu, *ibid.*, **edl-5**, 148 (1984).
16. S. Ogura *et al.*, *IEEE Trans. Electron Devices*, **ed-27**, 1359 (1980).
17. P. J. Tsang, S. Ogura, W. W. Walker, J. F. Shepard, and D. L. Critchlow, *ibid.*, **ed-29**, 590 (1982).
18. E. Takeda, H. Kume, T. Toyabe, and S. Asai, *ibid.*, **ed-29**, 611 (1982).
19. E. Takeda, T. Makino, and T. Hagiwara, in "Extended Abstracts, 15th Conference on Solid State Devices and Materials," p. 261, Tokyo (1983).
20. Y. Matsumoto, T. Higuchi, S. Sawada, S. Shinozaki, and O. Ozawa, *IEDM Tech. Dig.*, 392 (1983).
21. F.-C. Hsu and H. R. Grinolds, *ibid.*, 742 (1983).
22. F.-C. Hsu and H. R. Grinolds, *IEEE Trans. Electron Device Lett.*, **edl-5**, 71 (1984).
23. J. M. Pimbley and G. Gildenblat, *ibid.*, **edl-5**, 256 (1984).

Redistribution and Electrical Properties of S Implanted in GaAs

S. S. Chan

Avantek, Incorporated, Santa Clara, California 95051

B. G. Streetman*

Department of Electrical and Computer Engineering, University of Texas at Austin, Austin, Texas 78712

J. E. Baker

Materials Research Laboratory, University of Illinois at Urbana-Champaign, Urbana, Illinois 61801

ABSTRACT

The redistribution and electrical characteristics of ion-implanted S in GaAs have been investigated using secondary ion mass spectrometry (SIMS) and Hall profiling in the dose range of 7×10^{12} to 1×10^{15} cm⁻². A significant dose dependence of the redistribution has been observed, with the light dose implants exhibiting the most severe diffusion during annealing. In the presence of a sufficiently high level of Si doping, the redistribution of implanted S is reduced for annealing temperatures up to 800°C, possibly due to the formation of a S-Si complex. Suitably chosen S + Si dual implants show a similar effect and result in a higher activation efficiency than is achievable by Si-only implants of the same total dose. Implantation damage produced by Ar and S dual implants also causes significant redistribution changes. Low levels of damage enhance the S redistribution during annealing, while a high level of damage strongly inhibits it for temperatures up to 900°C. Where the S redistribution is inhibited by damage, however, electrical activity is reduced or lost.

The redistribution of ion-implanted impurities during annealing is often nonfickian, owing to the presence of defects (1-5), self-interstitials (6), or another chemical species which interacts with the implanted impurity (7, 8). Both enhanced and retarded diffusion have been observed as a result. Data from early work show that implanted S in GaAs undergoes considerable redistribution upon annealing, with only fair to poor electrical activation (9-14). More recent studies using capless annealing in an H₂-As₄ atmosphere indicate less redistribution (15, 16), while other reports using dielectric encapsulation (17, 18) continue to describe severe S migration.

The redistribution characteristics of S-only implants for a variety of doses annealed at 900°C with Si₃N₄ encapsulation have been reported by Yeo *et al.* (17). The dose dependence of such redistribution has also been investigated by Wilson *et al.* (19) for a much larger dose range, using SiO₂ encapsulation and a melt-ambient capless technique (20). Some evidence of a possible S-Si interaction which retards the redistribution of S has been pointed out by Yoder (21) in the data of Oakes and Degenford (22). Wilson and Jamba (23) also showed that S redistribution during annealing is much reduced if the GaAs substrate has been preamorphized by equal doses of Ga and As ions before S implantation.

In this work, we examine the possibility of modifying the redistribution of implanted S in the presence of Si and/or excess implantation damage. To that end, the redistribution of implanted S is examined along with its electrical properties as a function of implantation dose and annealing temperature, and Si doping. We study S implants in the presence of implanted Si and Si introduced during crystal growth. An effort is made to isolate the effects of implantation damage by examining Ar coimplants with S which approximate the damage of the corresponding S + Si dual implants.

This study is performed using Si₃N₄ encapsulation, which is the most common encapsulant capable of preventing both Ga and As loss from the sample surface (24, 25).

Experimental Procedures

Redistribution characteristics of S-only implants were studied by performing 250 keV implants into Cr-doped semi-insulating GaAs substrates. Possible S-Si interactions were studied by dual implants of S and Si into Cr-

doped GaAs and also by implanting S into Si-doped MBE-grown layers. For studies of the effects of implantation damage on S diffusion, S and Ar dual implants were employed.

The energies of dual implants were chosen such that the projected ranges of the different ion species were approximately the same. All implantations were performed at room temperature with the substrates tilted 7° from the surface normal to avoid channeling effects. Annealing was performed in flowing forming gas using an oxygen-free RF plasma-deposited Si₃N₄ cap (24, 25). The resulting impurity distributions were measured with secondary ion mass spectrometry (SIMS), using a Cs⁺ primary beam for S or Si studies, and an O₂⁺ beam to detect Cr. Absolute concentrations for implanted species in unannealed samples were obtained by measuring the depths of the sputtered SIMS craters with a Sloan Dektak mechanical stylus and setting the integrated areas of uncalibrated SIMS profiles equal to the implantation doses. These were then used as standards for calibrating the SIMS profiles in annealed samples by comparing matrix and impurity secondary ion counts. Cr concentrations in the GaAs substrates were obtained by comparing with a GaAs sample having a known Cr implant. The accuracies of the depth scales are estimated to be 5-10%, and are limited by the Dektak accuracy, the uniformity of the sputtering rate, and the flatness of the bottom of the craters created. The uncertainties and reproducibility of the impurity concentrations obtained are estimated to be 10-20%, limited by the stability and reproducibility of the impurity ion yields relative to the matrix ion yield, both during a run and between runs. To enhance SIMS sensitivity, S implants were performed in most cases using the ³⁴S isotope to avoid mass interference from O₂ during SIMS analysis, achieving a detection limit of $\sim 10^{15}$ cm⁻³.

Carrier concentration and mobility profiles were obtained by double ac Hall measurements combined with chemical layer removal (26) using a 1:1:200 mixture of 30% H₂O₂, conc sulfuric acid, and deionized water. The Cr-doped GaAs substrates were first tested for possible type conversion during annealing by implanting with Ar ions and checking for electrical conductivity after a high temperature anneal. No type conversion has been found for these samples after annealing at temperatures up to 800°C. Such conversion does occur at 900°C, however, rendering electrical data for samples annealed at this temperature invalid.

*Electrochemical Society Active Member.

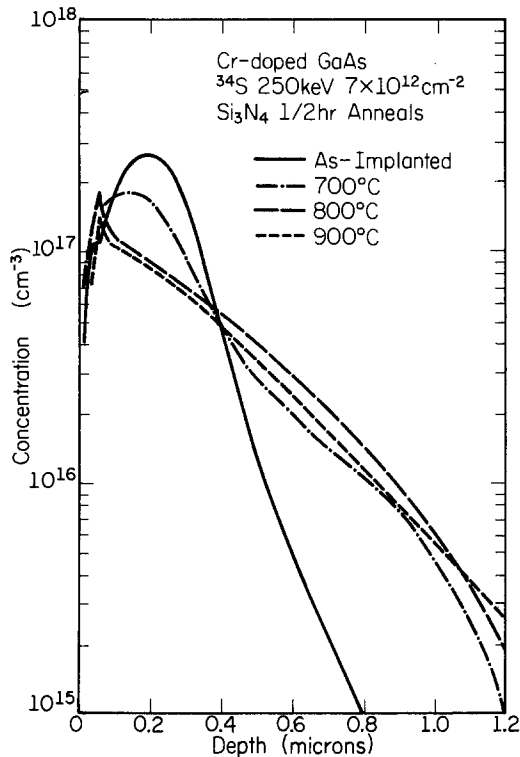


Fig. 1. SIMS profiles of ^{34}S due to a $7 \times 10^{12} \text{ cm}^{-2}$ implant and after several anneals.

Results and Discussion

S-only implants.—The redistribution of S-only implants was investigated first as a function of dose and annealing temperature to form a basis for comparison with later dual implants. Shown in Fig. 1 and 2 are the SIMS profiles of S implanted at 250 keV before and after annealing at 700°, 800°, and 900°C for doses of 7×10^{12} and 10^{15} cm^{-2} . The higher dose is above the amorphization threshold of $1.4 \times 10^{14} \text{ cm}^{-2}$ as estimated using the critical energy dep-

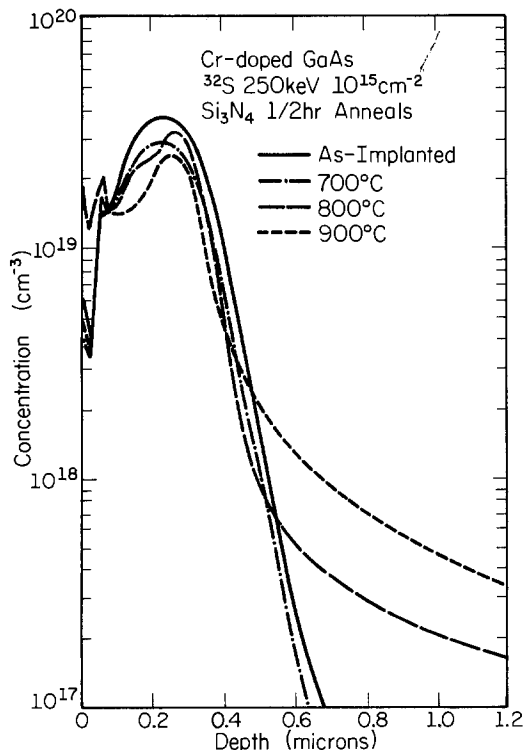


Fig. 2. SIMS profiles of ^{32}S due to a 10^{15} cm^{-2} implant and after annealing.

osition model (27) and Winterbon's energy deposition tables (28). In addition to these doses, data from an intermediate dose ($7 \times 10^{13} \text{ cm}^{-2}$) will be discussed.

Two artifacts of SIMS measurements should be noted here and distinguished from the rest of the data. Thin native oxides on the sample surfaces (inevitably formed as a result of atmospheric exposure) usually cause enhancement of secondary ion yields which are quite unrelated to the actual concentrations of the chemical species being monitored (29). Also, a short time is required before the sputtering rate and the rate of primary ion incorporation into the surface reach their steady state. As a result, the matrix and impurity counts have a period of instability corresponding to the first few hundred angstroms of sputtering, and the impurity profiles are discounted in this region.

The unannealed S profiles are skewed for both doses, with peaks occurring at $0.21 \pm 0.02 \mu\text{m}$. LSS statistics (30, 31) predict a projected range of $0.19 \mu\text{m}$ and a straggle of $0.07 \mu\text{m}$.

In the vicinity of their peaks, the unannealed distributions are approximately gaussian with a straggle $\Delta R_p \approx 0.11 \mu\text{m}$. The tail of the distribution is close to gaussian for the high dose case (Fig. 2), but is considerably deeper than gaussian for implants below the amorphization threshold (Fig. 1). Similar observations have been reported for implanted Se in GaAs and have been attributed to interstitial migration in crystalline GaAs during implantation when the total dose does not exceed the amorphization threshold (23).

Upon annealing, dose-dependent redistribution occurs similar to that reported by Wilson *et al* (19). For the low dose implant (Fig. 1), S diffuses significantly at temperatures as low as 700°C. At 800° and 900°C, the as-implanted peak is entirely lost. The tail regions of the profiles (*i.e.*, $> 0.9 \mu\text{m}$) for all three annealing temperatures are approximately gaussian locally. The diffusion coefficients in these regions are estimated to be 9×10^{-13} , 1×10^{-12} , and $8 \times 10^{-12} \text{ cm}^2/\text{s}$ for 700°, 800°, and 900°C, respectively. These values are consistent with those reported by Sansbury and Gibbons (10) for implanted S, but are almost an order of magnitude higher than the results of Kendall (32) and two to three orders of magnitude higher than those reported by Young and Pearson (33) for S indiffusion experiments into GaAs substrates. Some S outdiffusion into the Si_3N_4 cap also seems to take place, as evidenced by decreasing integrated areas under the S profiles with increasing annealing temperature. The high dose implant behaves differently (Fig. 2). The as-implanted peak is retained with only minor distortions even after a 900°C anneal. However, penetrating tails are still formed after 800° and 900°C annealing.

Implanted S in the presence of implanted Si.—Possible impurity interactions between S and Si (21, 22) were investigated by using dual implants in which various doses of Si were coimplanted at 220 keV with medium ($7 \times 10^{13} \text{ cm}^{-2}$) doses of S at 250 keV. At these ion energies, the range statistics of the two species are approximately the same, and the ratio of S to Si concentrations remains almost constant throughout the as-implanted layer.

Shown in Fig. 3 and 4 are the SIMS profiles of a $7 \times 10^{13} \text{ cm}^{-2}$ S implant in the presence of a $3 \times 10^{14} \text{ cm}^{-2}$ Si coimplant after annealing at 800° and 900°C, respectively. Shown also for comparison are the corresponding S distributions due to S-only implants and the Cr profiles in the dual implants. It is apparent that the Si coimplant substantially reduces the redistribution of S upon annealing at both temperatures and roughly preserves the as-implanted shape of the S profiles. However, at 900°C a secondary peak appears in the S profile when Si is coimplanted. Little outdiffusion into the cap occurs at either temperature, and SIMS analysis shows that the Si distribution is essentially unchanged by annealing.

Increasing the Si dose in the coimplant experiment to $5 \times 10^{14} \text{ cm}^{-2}$ or decreasing it to $1 \times 10^{14} \text{ cm}^{-2}$ gives the same general results shown in Fig. 3 and 4. However, further reducing the Si dose to $3.5 \times 10^{13} \text{ cm}^{-2}$ brings about

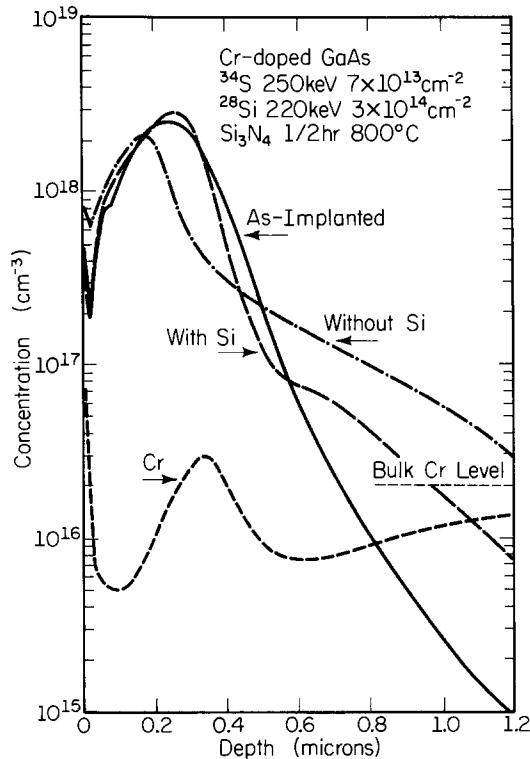


Fig. 3. SIMS profiles of ^{34}S due to a $7 \times 10^{13} \text{cm}^{-2}$, 250 keV ^{34}S implant in the presence of a $3 \times 10^{14} \text{cm}^{-2}$, 220 keV ^{28}Si coimplant and annealed at 800°C ("with Si"). Shown also for comparison are the SIMS profile of ^{34}S if the ^{28}Si coimplant is absent ("without Si") and the Cr distribution in the dual implants.

an entirely different behavior. With 800°C annealing (not shown), there is somewhat more S redistribution with the Si coimplant than in the case of the S-only implant. At 900°C, however, the Si coimplant causes the implanted S to be largely swept out of the implanted region (Fig. 5).

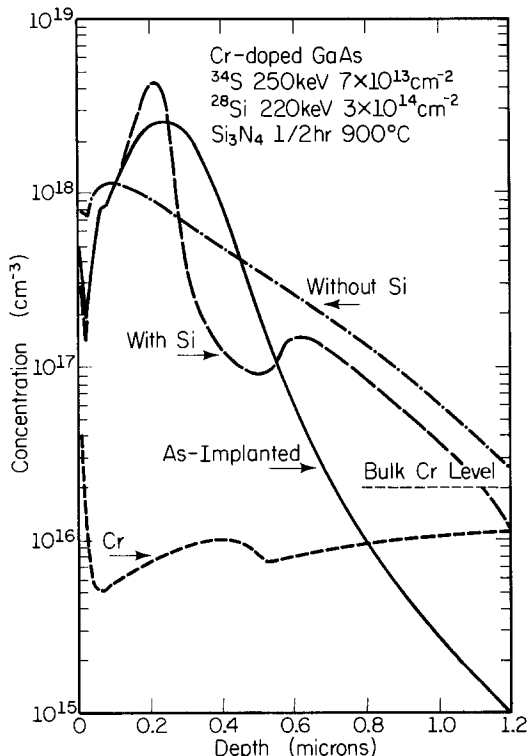


Fig. 4. SIMS profile of ^{34}S due to a $7 \times 10^{13} \text{cm}^{-2}$, 250 keV ^{34}S implant in the presence of a $3 \times 10^{14} \text{cm}^{-2}$, 220 keV ^{28}Si coimplant and annealed at 900°C ("with Si"). Shown also for comparison are the SIMS profiles of ^{34}S if the ^{28}Si coimplant is absent ("without Si") and the Cr distribution in the dual implants.

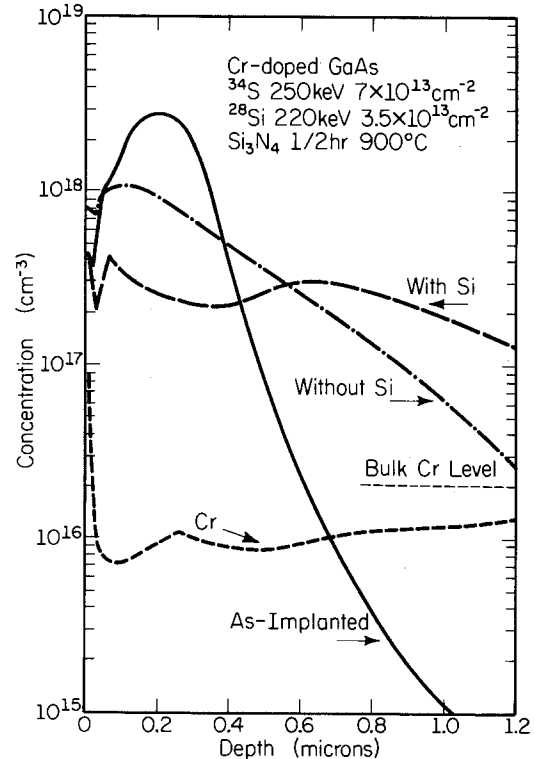


Fig. 5. SIMS profile of ^{34}S due to a $7 \times 10^{13} \text{cm}^{-2}$, 250 keV ^{34}S implant in the presence of a $3.5 \times 10^{13} \text{cm}^{-2}$, 220 keV ^{28}Si coimplant and annealed at 900°C ("with Si"). Shown also for comparison are the SIMS profiles of ^{34}S if the ^{28}Si coimplant is absent ("without Si") and the Cr distribution in the dual implants.

This appears to be a case of very pronounced defect-enhanced redistribution. The Si profile is again found to be little changed by annealing. The as-implanted S profile in Fig. 5 is somewhat narrower and has a peak closer to the surface than the corresponding profile in Fig. 4. The only difference in the implantation conditions is the dose of the Si coimplant, with the lower Si dose (which is not amorphizing) associated with the shallower and narrower as-implanted S profile. We believe that the discrepancy is mostly due to the uncertainties in the depth scale.

The behavior of the Cr originally present in the substrates is found to be quite independent of the dose of the Si coimplant. Annealing at 800°C results in the formation of a local Cr accumulation within a region characterized by extensive Cr depletion (Fig. 3). The local Cr accumulation can be attributed to gettering by residual damage (5), or Cr precipitation at nucleation sites provided by residual damage (4). At 900°C, the local Cr accumulation virtually disappears (Fig. 4 and 5), leaving a broad ($\sim 3 \mu\text{m}$) Cr depletion region.

S implantation into Si-doped MBE layers.—The above experiments suggest a possible S-Si interaction which slows down the redistribution of S when the Si concentration is sufficiently high. However, to discriminate between the effects of the implanted Si and the additional damage associated with the Si implant, S implants at 250 keV and $7 \times 10^{13} \text{cm}^{-2}$ have been performed into GaAs layers doped with Si ($N_A \approx 2.2 \times 10^{18} \text{cm}^{-3}$) during MBE growth. Upon annealing at 800°C (Fig. 6), the S redistribution is clearly less severe than if there is no Si doping, but is still considerable. There is also little outdiffusion of S into the cap (the integrated S concentration is $6 \times 10^{13} \text{cm}^{-2}$). The diffusion tail in this case is almost exponential, which is consistent with the view that fast diffusing S is slowed by trapping (34, 35) in the presence of Si doping. However, when the annealing temperature is raised to 900°C, the S redistribution is not inhibited by the Si doping.

Influence of Si on the S profile is not observed when the Si doping in the MBE layer is reduced to 1×10^{18}

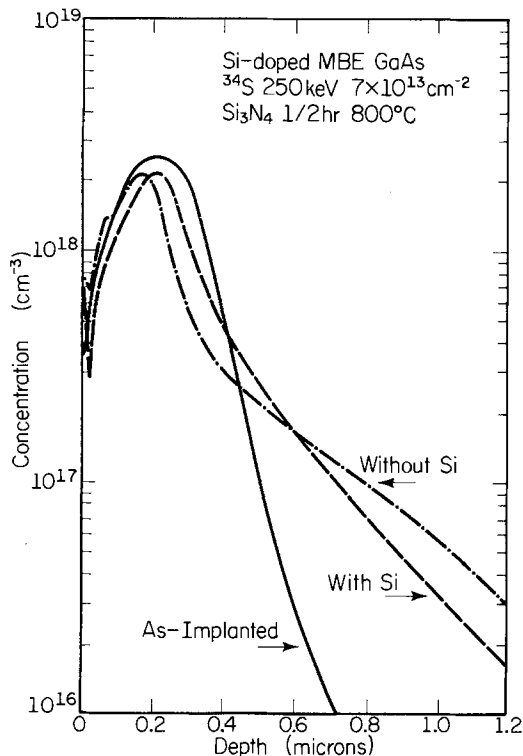


Fig. 6. SIMS profiles of ^{34}S due to a $7 \times 10^{13} \text{ cm}^{-2}$ ^{34}S implant into heavily Si-doped ($N_d \approx 2.2 \times 10^{18} \text{ cm}^{-3}$) MBE GaAs annealed at 800°C ("with Si"). Shown also for comparison is the SIMS profile of ^{34}S if the Si doping is absent ("without Si").

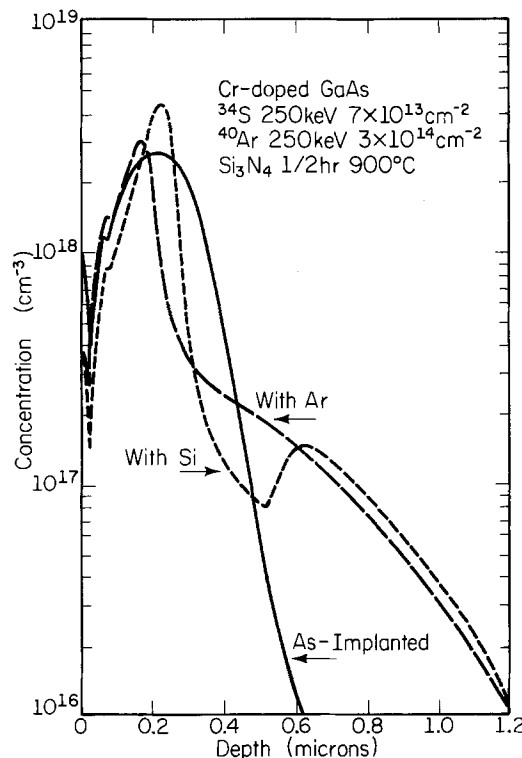


Fig. 7. SIMS profile of ^{34}S due to a $7 \times 10^{13} \text{ cm}^{-2}$, 250 keV ^{34}S implant in the presence of a $3 \times 10^{14} \text{ cm}^{-2}$, 250 keV ^{40}Ar coimplant and annealed at 900°C ("with Ar"). Shown also for comparison is the SIMS profile of ^{34}S due to the same implant in the presence of a $3 \times 10^{14} \text{ cm}^{-2}$, 220 keV ^{28}Si implant annealed at the same temperature ("with Si").

cm^{-3} . This supports the view that the S-Si interaction is a short-ranged one, such as the formation of a nearest neighbor complex as suggested by Yoder (21). Such a S-Si complex may be a slower diffuser than S because of a large physical size or because Si itself has a very low diffusivity in GaAs. At sufficiently high temperatures, such complexes are expected to break up. This is apparently the case for the 900°C anneals observed here, in which S redistribution is not strongly slowed by the presence of Si.

S and Ar dual implants.—The results on S-implanted MBE layers suggest that the reduced redistribution of implanted S at 900°C observed in the case of Si coimplants (Fig. 4) must involve factors other than Si doping. It is therefore useful to investigate the role of implantation damage in such redistribution. To simulate the damage due to the Si implants, Ar was coimplanted with S at 250 keV to the same doses as the Si coimplants discussed above. In the case of a $7 \times 10^{13} \text{ cm}^{-2}$ S implant and a $3 \times 10^{14} \text{ cm}^{-2}$ Ar coimplant, the extent of S redistribution after 800°C annealing is observed to be somewhat less than if a Si coimplant had been used. When the annealing temperature is raised to 900°C , an approximately gaussian tail appears (Fig. 7) which largely coincides with the Si coimplant case, but without the secondary peak observed in Fig. 4.

For the same S dose ($7 \times 10^{13} \text{ cm}^{-2}$), when the dose of the Ar coimplant is raised to $5 \times 10^{14} \text{ cm}^{-2}$, very little S redistribution is observed for 800°C annealing. At 900°C , somewhat more redistribution is observed, but it is much less than in S-only implants and somewhat less than in S + Si dual implants. Again, the secondary peak observed for Si coimplants does not occur. When the dose of the Ar coimplant is lowered to $3.5 \times 10^{13} \text{ cm}^{-2}$, defect-enhanced redistribution is observed, similar to the corresponding low dose Si coimplant (Fig. 5).

Electrical properties.—Unlike Column IV dopants such as Si, S is not amphoteric and may therefore be capable of yielding heavier n-type doping in high dose implantations. Of particular interest are the electrical properties of S-only implants and the combinations of S + Si and S +

Ar dual implants where the redistribution of S is inhibited.

Figure 8 shows carrier concentration and mobility profiles due to a $7 \times 10^{13} \text{ cm}^{-2}$ (medium dose) S implant at 250 keV into Cr-doped GaAs, annealed at 800°C . Shown also for comparison is the atomic S distribution as measured by SIMS. It is apparent that activation efficiencies and carrier mobilities ($\sim 4000 \text{ cm}^2/\text{V-s}$) are high in the tail

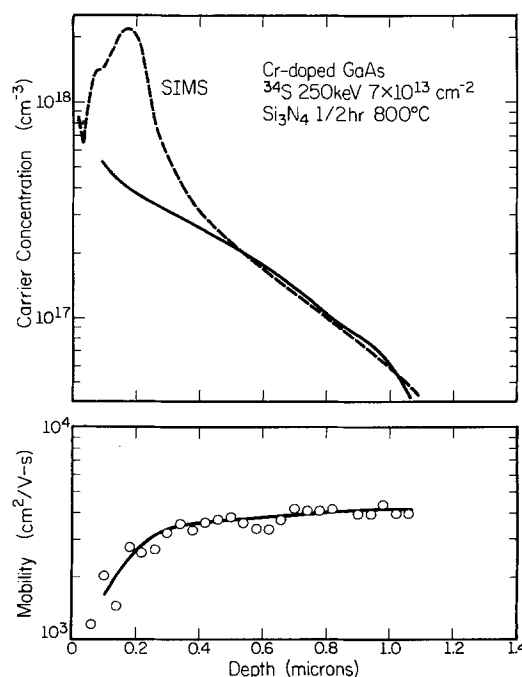


Fig. 8. Carrier concentration and mobility profiles due to a $7 \times 10^{13} \text{ cm}^{-2}$ ^{34}S implant at 250 keV, annealed at 800°C . The SIMS profile is also shown for comparison.

of the atomic distribution. However, in the vicinity of the SIMS peak, a substantial fraction of the implanted S is electrically inactive and the carrier mobilities are also low relative to the active electron concentration. While little published data are available concerning the solid solubility of S in GaAs at 800°C, electron concentrations as high as $3 \times 10^{18} \text{ cm}^{-3}$ have been obtained by H_2S doping during VPE growth at 750°C (36). Group VIA elements (S, Se, Te) are known to form electrically inactive complexes or precipitates at high concentrations, but this does not happen until the active electron concentration exceeds $\sim 1 \times 10^{18} \text{ cm}^{-3}$ (37, 38). Apparently, the low activation in the vicinity of the SIMS peak is due to residual damage remaining after the 800°C anneal. The overall doping efficiency after correcting for outdiffusion into the cap is 36%.

When the S dose is lowered to $7 \times 10^{13} \text{ cm}^{-2}$, the carrier concentration profile after an 800°C anneal assumes a shape similar to the corresponding SIMS profile (shown in Fig. 1), and carrier mobilities are relatively high ($\sim 3700 \text{ cm}^2/\text{V-s}$) throughout. In contrast, raising the S dose to 10^{15} cm^{-2} results in electrical activity only in the tail region of the atomic profile, with a maximum electron concentration of $\sim 4 \times 10^{17} \text{ cm}^{-3}$. The overall activation is only 2.3%. This is consistent with an increasing amount of residual damage in the vicinity of the SIMS peak as the dose is increased. However, other factors may also be involved as discussed below.

Shown in Fig. 9 are the carrier concentration and mobility profiles due to a dual implant of $7 \times 10^{13} \text{ cm}^{-2}$ S at 250 keV and $3 \times 10^{14} \text{ cm}^{-2}$ Si at 220 keV, annealed at 800°C. Shown also for comparison (dashed line) is the carrier concentration profile due to a $3.7 \times 10^{14} \text{ cm}^{-2}$ Si-only implant at 220 keV annealed at the same temperature. SIMS profiles presented in Fig. 3 indicate that the redistribution of S in this case is reduced in the presence of the Si coimplant. Figure 9 shows also that the activation efficiency of the dual implant is higher than that of a Si-only implant of an equivalent dose. The peak electron concentration due to the dual implant is also 45% higher ($1.6 \times 10^{18} \text{ cm}^{-3}$ vs $1.1 \times 10^{18} \text{ cm}^{-3}$). A surface inactive layer of $0.25 \mu\text{m}$ exists in both cases and is presumably due to incomplete lattice recovery from implantation damage. This dual implant can be used to achieve a higher peak electron concentration and lower sheet resistivity than is obtainable by Si implantation alone, without encounter-

ing the problems caused by the high diffusivity of S-only implants. The improved n-type activation may result from S preferentially occupying As sites, thus forcing more of the Si to occupy Ga sites where they act as donors.

While SIMS profiles indicate that S + Ar dual implants in which the Ar dose in amorphizing are very effective in inhibiting S redistribution, no measurable electrical activity is detected for these dual implants after an 800°C anneal. The redistribution of Cr in these cases is very similar to those shown in Fig. 3 and 4, and is therefore quite insufficient to result in complete compensation of the implanted S. While the degree of recovery of the GaAs lattice achievable after high dose Ar implants is also in question, the following experiment showed that additional factors are involved. The experiment consisted of amorphizing a Cr-doped GaAs substrate with a $5 \times 10^{14} \text{ cm}^{-2}$ Ar implant and then annealing it for 15 min (instead of the usual 30 min) with Si_3N_4 encapsulation. The cap was removed and the partially annealed sample implanted with $7 \times 10^{13} \text{ cm}^{-2}$ S at 250 keV. Annealing was again performed with a second nitride cap at 800°C for an additional 15 min. The implantation damage associated with the amorphizing Ar implant was therefore annealed for a total time of 30 min, while the damage associated with the S implant was annealed for only 15 min. Electrical profiling showed that in this case the implanted layer recovered sufficiently to give a significant peak carrier concentration ($\sim 5 \times 10^{16} \text{ cm}^{-3}$) with a relatively high mobility (2000-4000 $\text{cm}^2/\text{V-s}$). It appears, therefore, that the total lack of electrical activity is only associated with annealing implanted S in the presence of a very large density of defects (as found in an amorphized substrate). This may occur through the formation of thermally stable but electrically inactive complexes which are too large to diffuse rapidly. This is also consistent with the observation that, in the case of high dose ($1 \times 10^{15} \text{ cm}^{-2}$) S-only implants, very low concentrations of carriers are found in the vicinity of the peak of the S distribution, where a similar mechanism may occur due to the presence of a high density of implantation damage.

Summary and Conclusions

The redistribution characteristics of ion-implanted S in GaAs have been investigated and found to be strongly affected by implantation damage and Si doping. In general, a high density of implantation damage inhibits the redistribution, while a low level of damage enhances it. As a result, implanted S profiles after annealing are characterized by relatively little change in the vicinity of the implant peak (for sufficiently high doses) and the formation of penetrating tails away from the peak due to defect-enhanced redistribution. The presence of Si doping in a sufficiently high concentration slows the redistribution of S for temperatures up to 800°C, possibly by the formation of a S-Si complex. Above 800°C, the complexing effect of Si is no longer sufficient to inhibit S redistribution.

In S + Si dual implants using a medium dose ($7 \times 10^{13} \text{ cm}^{-2}$) of S and a larger dose of Si, both the Si and the additional implantation damage due to the Si coimplant have a part in inhibiting redistribution of S during annealing. The secondary peak in the S profile after a 900°C anneal in this case (Fig. 4) is possibly due to a complex interaction between Si trapping, inhibited S redistribution in regions of heavy implantation damage, and enhanced redistribution in regions of lower level damage. Christel and Gibbons (39) have presented calculations which show that local stoichiometric disturbances due to unequal recoil of Ga and As can result in regions of excess As, followed by a deeper region of excess Ga, with a transition region in between. It is clear that Ga and As vacancies affect impurity diffusion; there is also experimental evidence that the Ga divacancy plays a significant role in aiding the diffusion of S in crystalline GaAs (33). Hence, the anomalous redistribution evident in Fig. 4 and 7 may involve such local stoichiometric imbalances. It is conceivable that locally enhanced out-diffusion of S from

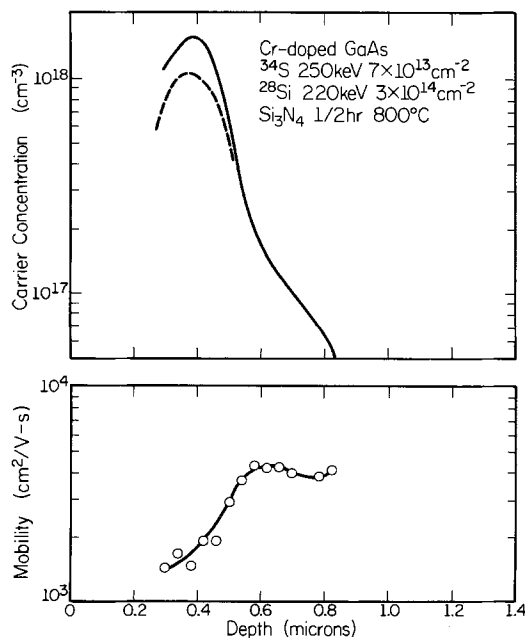


Fig. 9. Carrier concentration and mobility profiles due to a dual implant of $7 \times 10^{13} \text{ cm}^{-2}$ ^{34}S at 250 keV and $3 \times 10^{14} \text{ cm}^{-2}$ ^{28}Si at 220 keV annealed at 800°C. The dashed line is the carrier concentration profile due to a $3.7 \times 10^{14} \text{ cm}^{-2}$ single ^{28}Si implant at 220 keV annealed at the same temperature.

a particular region (due to stoichiometric imbalances or otherwise) may result in a local minimum in the S profile and an apparent S buildup in adjacent regions, as is indicated in these figures.

The electrical activation of single S implants after 800°C annealing is fair for low and medium dose implants and poor for high dose implants. Activation is especially low near the peaks of medium and high dose implants where implantation damage is considerable. The level of damage required to prevent significant S redistribution during annealing will also prevent it from becoming electrically active. Apparently, annealing under these conditions produces thermally stable but electrically inactive S-defect complexes which do not diffuse significantly. In contrast, suitably chosen S + Si dual implants both inhibit the redistribution of S (up to 800°C) and result in a higher activation efficiency than is achievable by high dose Si-only implants of the same total dose. In this case, S implantation can be advantageously applied to achieve high donor concentrations without significant S migration. However, the results presented here indicate that such improvements exist in a rather narrow range of coimplant conditions and that residual defects in the surface layer remain after annealing.

Acknowledgment

The authors wish to thank H. Morkoc and T. J. Drummond of the Coordinated Science Laboratory and Department of Electrical Engineering, University of Illinois at Urbana-Champaign, for growing the MBE layers used in this work. This work was supported by the Joint Services Electronics Program under Contract N00014-79-C-0424, the Office of Naval Research under Contract N00014-76-C-0806, and the National Science Foundation under Grant DMR-80-20250.

Manuscript submitted Feb. 22, 1985; revised manuscript received July 2, 1985.

The University of Texas assisted in meeting the publication costs of this article.

REFERENCES

1. C. W. Farley and B. G. Streetman, *J. Electron. Mater.*, **13**, 401 (1984); also, *This Journal*, **131**, 946 (1984).
2. A. Lidow, J. F. Gibbons, V. R. Deline, and C. A. Evans, Jr., *Appl. Phys. Lett.*, **32**, 149 (1978).
3. B. J. Masters and E. F. Gorey, *J. Appl. Phys.*, **49**, 2717 (1978).
4. V. Eu, M. Feng, W. B. Henderson, H. B. Kim, and J. M. Whelan, *Appl. Phys. Lett.*, **37**, 473 (1980).
5. P. K. Vasudev, R. G. Wilson, and C. A. Evans, Jr., *ibid.*, **36**, 837 (1980).
6. E. B. Stoneham and J. F. Gibbons, in "Ion Implantation in Semiconductors," S. Namba, Editor, p. 57, Plenum Press, New York (1975).
7. A. J. N. Houghton and B. Tuck, *Solid-State Electron.*, **25**, 441 (1982).
8. P. N. Favennec, M. Gauneau, H. L'Haridon, B. Devaud, C. A. Evans, Jr., and R. J. Blattner, *Appl. Phys. Lett.*, **38**, 271 (1981).
9. J. M. Woodcock, J. M. Shannon, and D. J. Clark, *Solid-State Electron.*, **18**, 267 (1975).
10. J. D. Sansbury and J. F. Gibbons, *Rad. Eff.*, **6**, 269 (1970).
11. R. G. Hunsperger and O. J. Marsh, *ibid.*, **6**, 263 (1970).
12. F. H. Eisen and M. B. Welch, in "Ion Implantation in Semiconductors 1976," F. Chernow, J. A. Borders, and D. K. Brice, Editors, p. 97, Plenum Press, New York (1977).
13. M. Fujimoto, H. Yamazaki, and T. Honda, in "Ion Implantation in Semiconductors 1976," F. Chernow, J. A. Borders, and D. K. Brice, Editors, p. 89, Plenum Press, New York (1977).
14. H. Müller, J. Gyulai, J. W. Mayer, F. H. Eisen, and B. Welch, in "Ion Implantation in Semiconductors," S. Namba, Editor, p. 19, Plenum Press, New York (1975).
15. R. M. Malbon, D. H. Lee, and J. M. Whelan, *This Journal*, **123**, 1413 (1976).
16. H. Kanber, M. Feng, V. K. Eu, R. C. Rush, and W. B. Henderson, *J. Electron. Mater.*, **11**, 1083 (1982).
17. Y. K. Yeo, Y. S. Park, and R. Kwor, *J. Appl. Phys.*, **53**, 1815 (1982).
18. R. Kwor, Y. K. Yeo, and Y. S. Park, *ibid.*, **53**, 4786 (1982).
19. R. G. Wilson, D. M. Jamba, V. R. Deline, C. A. Evans, Jr., and Y. S. Park, *ibid.*, **54**, 3849 (1983).
20. C. L. Anderson, K. V. Vaidyanathan, H. L. Dunlap, and G. S. Kamath, *This Journal*, **127**, 925 (1980).
21. M. N. Yoder, in "Semi-Insulating III-V Materials," G. J. Rees, Editor, p. 281, Nottingham, England (1980).
22. J. G. Oakes and J. E. Degenford, GaAs Monolithic Microwave Subsystem Technology Base Report N00014-78-C-0268, Westinghouse Electric, Pittsburgh, PA (1980).
23. R. G. Wilson and D. M. Jamba, *Appl. Phys. Lett.*, **39**, 715 (1981).
24. K. V. Vaidyanathan, M. J. Helix, D. J. Wolford, B. G. Streetman, R. J. Blattner, and C. A. Evans, Jr., *This Journal*, **124**, 1781 (1977).
25. M. J. Helix, K. V. Vaidyanathan, B. G. Streetman, H. B. Dietrich, and P. K. Chatterjee, *Thin Solid Films*, **55**, 143 (1978).
26. W. V. McLevige, P. K. Chatterjee, and B. G. Streetman, *J. Phys. E*, **10**, 335 (1978).
27. M. Lin, *Electron. Lett.*, **14**, 695 (1978).
28. K. B. Winterbon, "Ion Implantation Range and Energy Deposition Distributions," Vol. 2, IFI/Plenum Publishing Corporation, New York (1975).
29. C. A. Andersen, *Int. J. Mass. Spectrom. Ion Phys.*, **2**, 61 (1969).
30. J. Lindhard, M. Scharff, and H. Schiott, *Mat. Fys. Medd. Dan. Vid. Selsk.*, **33**, 1 (1963).
31. J. F. Gibbons, W. S. Johnson, and S. W. Mylroie, "Projected Range Statistics, Semiconductors and Related Materials," 2nd ed. Dowden, Hutchinson and Ross, Stroudsburg, PA (1975).
32. D. L. Kendall, in "Semiconductors and Semimetals," Vol. 4, R. K. Willardson and A. C. Beer, Editors, p. 163, Academic Press, New York (1968).
33. A. B. Y. Young and G. L. Pearson, *J. Phys. Chem. Solids*, **31**, 517 (1970).
34. T. Hirao, K. Inoue, S. Takayanagi, and Y. Yaegashi, in "Ion Implantation in Semiconductors 1976," F. Chernow, J. A. Borders, and D. K. Brice, Editors, p. 1, Plenum Press, New York (1977).
35. J. A. Davies and P. Jespersgard, *Can. J. Phys.*, **44**, 1631 (1966).
36. H. Poth, H. Bruch, M. Heyen, and P. Balk, *J. Appl. Phys.*, **49**, 285 (1978).
37. H. C. Casey, Jr., and M. B. Panish, "Heterostructure Lasers, Part B: Materials and Operating Characteristics," p. 98, Academic Press, New York (1978).
38. L. J. Vieland and I. Kudman, *J. Phys. Chem. Solids*, **24**, 437 (1963).
39. L. A. Christel and J. F. Gibbons, *J. Appl. Phys.*, **52**, 5050 (1981).

Furnace and Rapid Thermal Annealing of P⁺/n Junctions in BF₂⁺-Implanted Silicon

M. E. Lunnon and J. T. Chen

Philips Research Laboratories, Signetics Corporation, Sunnyvale, California 94086

J. E. Baker

Materials Research Laboratory, University of Illinois, Urbana, Illinois 61801

ABSTRACT

Shallow p-n diodes with junction depths between 0.15 and 0.3 μm have been fabricated by rapid thermal and furnace annealing of boron fluoride implants made into single-crystal wafers. The implants were performed at 30 keV with a dose of 1×10^{15} or 3×10^{15} ion-cm⁻². For very shallow junctions, the residual implant damage is found to degrade the reverse bias diode leakage characteristics. The residual damage can be nearly eliminated and shallow junction characteristics can be improved by preamorphizing the wafers with a single 50 keV silicon implant at a dose of 1×10^{15} ion-cm⁻².

This report examines methods of obtaining shallow source-drain regions for p-channel devices used in complementary-metal-oxide-semiconductor (CMOS) structures. Shallow junctions (< 0.3 μm) will be required with the scaling down of device dimensions to increase component density. Ion implantation of boron into crystalline silicon, which is used to introduce the dopant into source-drain regions, is accompanied by a channeling effect which leads to increased penetration of the implanted profile. Because of the relatively high diffusion coefficient of boron in silicon, dopant redistribution occurs during furnace annealing.

In this study, boron is replaced by boron fluoride (BF₂) as the implanted species in order to obtain a shallow implanted profile in monocrystalline silicon (1). Rapid thermal annealing is utilized to minimize boron diffusion during dopant activation (2). The electrical carrier profiles and residual implantation damage are compared for rapid thermal and furnace annealing. In this way, the effect of the proximity of residual damage to the p-n junction is investigated by measurement of the p-n diode characteristics. These measurements are also performed on wafers with a surface layer amorphitized by a silicon implant, followed by a boron fluoride implant and a rapid thermal or furnace anneal. Other workers have used multiple silicon (3) or germanium (4) implants to displace the implantation damage from the device regions. It will be shown that a single, low energy silicon implant can be used to eliminate channeling of boron in a subsequent low energy, boron fluoride implantation and that the residual damage is greatly reduced compared to boron fluoride implanted into monocrystalline silicon.

Experimental

Boron fluoride was implanted at 30 keV with a dose of 1×10^{15} or 3×10^{15} ion-cm⁻² into 10 cm diam, (100) silicon wafers doped with phosphorus to a resistivity of 4-6 $\Omega\text{-cm}$. The 30 keV boron fluoride implant is equivalent to a boron implant at 6.7 keV. In some cases the silicon wafers had been preamorphized with a silicon implant at an energy of 50 keV and with a dose of 1×10^{15} ion-cm⁻². The silicon and boron fluoride implants were made with the ion beam tilted at an angle of 7° to the wafer normal in a random direction to minimize channeling. The substrates were held at approximately room temperature.

The implanted wafers were annealed either in a standard furnace or an AG210T HeatpulseTM system using a nitrogen ambient. The temperature control system in the Heatpulse system has a temperature feedback mechanism which enables the wafer to be held at a constant annealing temperature. The duration of the anneal is defined here as the time spent at the constant annealing temperature.

The boron and fluorine concentration profiles were obtained by secondary ion mass spectrometry (SIMS) using O₂⁺ primaries and positive secondary ions. The sheet resistance was measured by contour mapping with a four-point probe (5). The electrical carrier concentrations and the p-n junction depths were determined from spreading resistance profiles.¹ The junction depth measurements were reproducible to within $\pm 0.02 \mu\text{m}$. The implantation damage, before and after annealing, was examined by transmission electron microscopy (TEM).

Diode structures were fabricated using the implant and anneal conditions described above to evaluate the electrical characteristics of the p-n junctions. Current-voltage measurements were performed on oxide isolated, circular diodes of 1 mm diam.

Results and Discussion

Figure 1 shows the boron concentration profiles after implantation of boron fluoride into crystalline or into

¹ Measurements made by Solelec Laboratories, Incorporated, Sunnyvale, California 94089-2221.

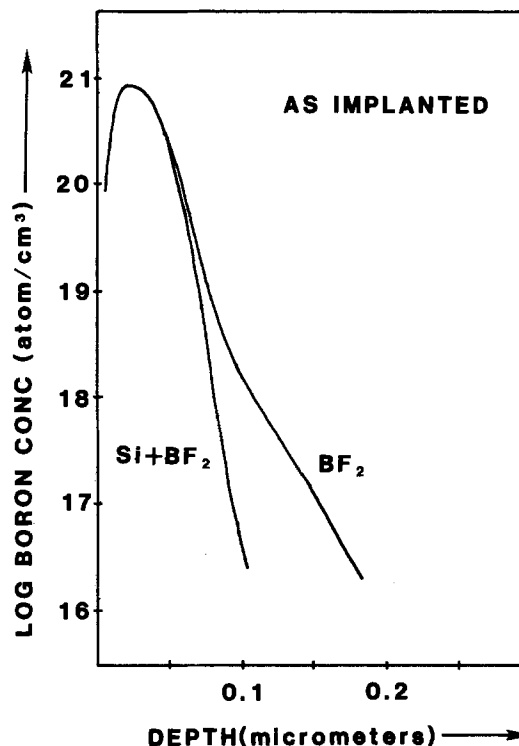


Fig. 1. SIMS measurements of the boron profiles after implanting BF₂ at 30 keV with a dose of 3×10^{15} ion-cm⁻² into monocrystalline and amorphous silicon.

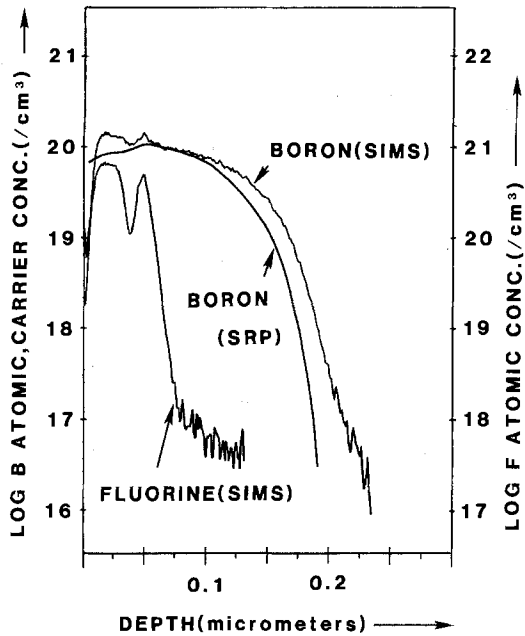


Fig. 2. SIMS and spreading resistance profiles for a BF_2 implant at 30 keV and with a dose of 3×10^{15} after rapid thermal annealing at 1100°C for 5s.

amorphous silicon and illustrates the channeling effect observed with implantation into crystalline silicon. Figure 2 shows the boron and fluorine dopant concentration profiles, together with the boron electrical carrier concentration profile, after rapid thermal annealing of the implant made into crystalline material. The fluorine outdiffuses during the anneal, leaving a broad fluorine peak close to the wafer surface, together with a sharp peak at a depth of 50 nm. It will be shown below that this is the location of the residual implantation damage. However, the retained fluorine does not affect the boron electrical activation because only the tail region of the implanted boron remains inactive. Similar spreading resistance profiles were obtained after each of the implant and anneal conditions described in Table I. The junction depths shown in Table I were measured from the spreading resistance profiles at a carrier concentration of 10^{15} cm^{-3} , which corresponds to the background doping concentration.

The depth of the residual ion implantation damage was measured from TEM cross sections. Figure 3a depicts the initial implantation damage caused by a 30 keV boron fluoride implant with a dose of $3 \times 10^{15} \text{ ion-cm}^{-2}$. An amorphous layer is formed with a heavily damaged crystalline region just below the amorphous-crystalline interface. After rapid thermal annealing, a band of implantation damage remains at this depth (Fig. 3b). The TEM planar section (Fig. 3c) shows this damage to consist of irregularly shaped dislocation loops. The depth from the

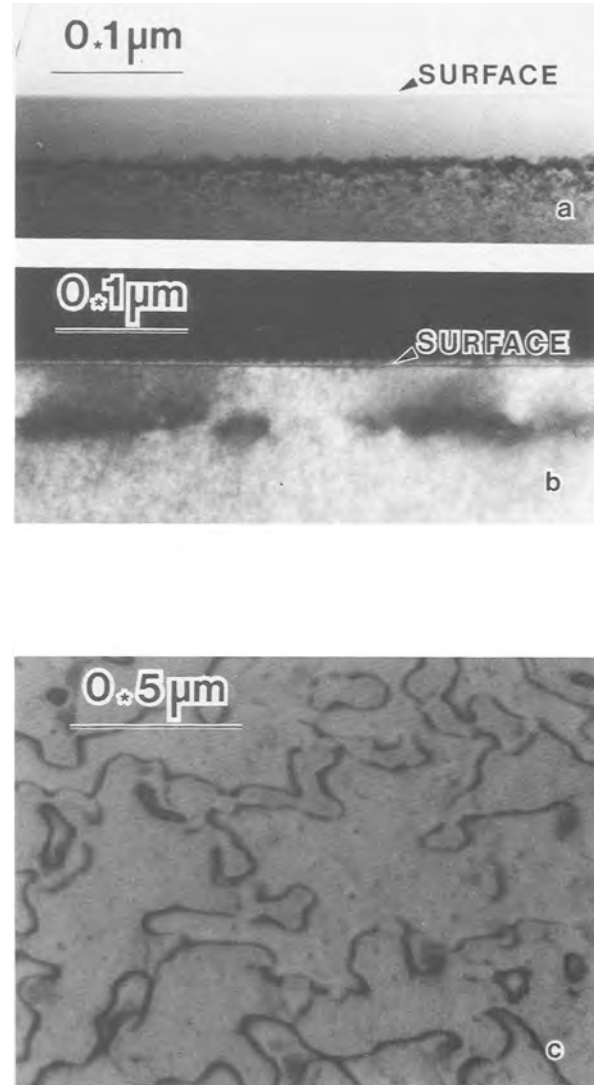


Fig. 3. a: TEM cross section showing the amorphous layer formed after a BF_2 implant at 30 keV with a dose of 3×10^{15} . b: TEM cross section showing the residual implant damage after the structure in a has been rapid annealed at 1100°C for 5s. c: TEM planar section of the residual damage shown in b.

wafer surface to the lower edge of the band of dislocation loops is listed in Table I. A similar defect structure occurs after furnace rather than rapid thermal annealing.

Shown in Fig. 4a is the amorphous layer formed after a silicon implant at 50 keV and a dose of $1 \times 10^{15} \text{ ion-cm}^{-2}$ followed by a boron fluoride implant at 30 keV and a dose of $1 \times 10^{15} \text{ ion-cm}^{-2}$. In this case, the silicon implant energy and dose was chosen to produce an amorphous layer (110 nm deep) which would contain the entire boron distribution from the subsequent boron fluoride implant. After the furnace anneal described in Table I, implantation damage is located at a depth of 80 nm but only small dislocation loops remain with an average loop diameter of 200 nm (Fig. 4b). A similar defect structure is observed if the boron fluoride implant is omitted, indicating that the damage is characteristic of the silicon implant. Almost complete elimination of implant damage has been reported for multiple silicon implants followed by a boron implant and furnace annealing (6). It has been shown here that this can be achieved by furnace annealing of dual silicon and boron fluoride implants.

There are several comparisons which can be made from Table I that illustrate the interdependence of residual implant damage, junction depth, diode leakage characteristics, and sheet resistance. First, the values listed in Table I for rapid thermal anneals are compared with those after furnace annealing for boron fluoride implanted into crys-

Table I. Structural and electrical properties of the p⁺/n junctions. The annealing conditions are: A, furnace anneal at 600°C for 30 min and at 950°C for 10 min; B, rapid thermal anneal for 5s at 1100°C

Implant	Si (50 keV)		BF ₂ (30 keV)		1×10^{15}	1×10^{15}
	1×10^{15}	3×10^{15}	A	B		
Anneal			A	B	A	
Sheet resistance (Ω/\square)			143	130	78	72
Defect depth (μm)			0.065	0.063	0.063	0.060
Junction depth (μm)			0.24	0.15	0.30	0.20
Reverse bias leakage current density (5V) (nA-cm^{-1})			1	23	1	10

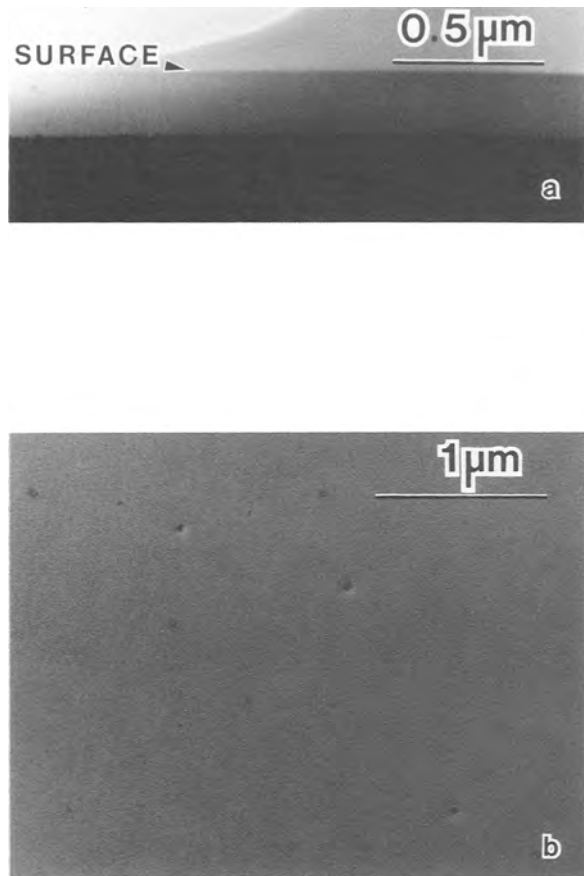


Fig. 4. The TEM cross section (a) shows the amorphous layer formed after a 40 keV silicon implant at a dose of 1×10^{15} followed by a BF₂ implant at 30 keV with a dose of 1×10^{15} . The planar section (b) shows the residual damage after a two-step furnace anneal at 600°C for 30 min and 950°C for 10 min.

talline silicon with a dose of 1×10^{15} or 3×10^{15} ion-cm⁻². It can be seen that a lower sheet resistance combined with a shallower junction depth can be achieved with rapid thermal annealing. This is consistent with the ability of rapid thermal annealing to thermally activate the implanted dopant while minimizing dopant diffusion. The higher annealing temperature of the rapid thermal anneal may account for the relatively low values of the sheet resistances. Although low sheet resistance values

and shallower junction are obtained, rapid thermally annealed diodes have relatively high leakage current densities. There is a correlation between increased leakage and a smaller separation between the residual damage and the p/n junction depth. This finding is now compared with the equivalent results for the dual silicon and boron fluoride implants. After furnace annealing, a low leakage current density (1 nA-cm^{-2} at -5V) combined with a small separation ($0.12 \mu\text{m}$) between the implant damage and the p/n junction is found. This suggests that the reverse bias characteristics are improved by a reduction of the residual defect density through use of the dual implant.

Conclusions

Shallow p-n diodes with good leakage characteristics are obtained by rapid thermal annealing or furnace annealing of boron fluoride-implanted, single-crystal silicon wafers. Generally, rapid thermally annealed diodes have shallower junction depths with lower sheet resistances but higher leakage current densities than furnace-annealed diodes. The high leakage current density is attributed to the close proximity of residual implant damage to the p-n junction.

The residual damage can be greatly reduced by pre-amorphization of the silicon wafers using a single silicon implant at 50 keV with a dose of 1×10^{15} ion-cm⁻². In this way, shallow junctions with good leakage characteristics can be obtained.

Acknowledgments

The authors gratefully acknowledge the technical assistance of K. Belton for TEM specimen preparation. Funding for the SIMS analyses was provided by the National Science Foundation under MRL Grant DMR-8-20250.

Manuscript received Feb. 22, 1985.

Philips Research Laboratories assisted in meeting the publication costs of this article.

REFERENCES

1. R. G. Wilson, *J. Appl. Phys.*, **54**, 6879 (1983).
2. J. E. Seidel, *IEEE Electron Devices Lett.*, **ed1-4**, 353 (1983).
3. C. Carter, W. Maszara, D. K. Sadana, G. A. Rozgonyi, J. Liu, and J. Wortman, *Appl. Phys. Lett.*, **44**, 459 (1984).
4. D. K. Sadana, W. Maszara, J. J. Wortmann, and G. A. Rozgonyi, *This Journal*, **131**, 943 (1984).
5. D. S. Perloff, F. E. Wahl, and J. Conragan, *ibid.*, **124**, 584 (1977).
6. B-Y. Tsaur and C. H. Anderson, Jr., *J. Appl. Phys.*, **54**, 6336 (1983).

Two-Dimensional Ion Implantation Profiles from One-Dimensional Projections

M. D. Giles

AT&T Bell Laboratories, Murray Hill, New Jersey 07974

J. F. Gibbons

Stanford Electronics Laboratories, Stanford University, Stanford, California 94305

ABSTRACT

Two-dimensional ion implantation profiles can be constructed from one-dimensional projections more quickly than by direct calculation. This method can be applied to many common target structures that can be reduced to an equivalent nonplanar single-layer target. This paper shows how the Boltzmann transport equation method can be extended to calculate two-dimensional effects for the implanted ion, damage distributions, and stoichiometry disturbances. The same approach can also be used with Monte Carlo methods.

The Boltzmann transport equation (BTE) approach (1) has been successfully applied to many ion implantation problems, predicting range and damage distributions, recoil distributions (2), and stoichiometry disturbances in compound semiconductors (3). The effects of ion backscattering can also be included if a multiple-pass scheme is used (4). All of this work has been restricted to one dimension. As device dimensions shrink, the lateral spread of implanted ions can no longer be neglected because of their effect on device behavior, providing the motivation to extend the method to two dimensions. Direct two-dimensional calculation is possible (5), but the computation time can be considerable. This paper describes a simpler method based on construction of two-dimensional information from one-dimensional projections.

Calculation of a two-dimensional profile by any method begins with the calculation of the results of implantation at a single point, yielding the point response function. There are then two levels of complexity possible. The simplest approach is to use the same response function at each point along the surface. A more general solution recomputes the response function at each point across the target. The simpler solution requires that the target have the same structure at each point along the surface, apart from the presence or absence of an opaque mask. This is satisfied exactly by a planar target even if it contains many planar layers. It is also approximately satisfied by a nonplanar single-layer target. The general solution can be used for any target shape and composition at the cost of an extra order in computation. These possibilities are illustrated in Fig. 1. Most cases of practical interest, such as silicon-silicon dioxide-polysilicon structures, are nonplanar multilayer (see Fig. 1f) and so require a general calculation scheme. We would like to treat these cases as a nonplanar single layer (see Fig. 1e) to speed up the calculations. This is made possible by a small scaling of the layers to form an equivalent silicon structure, as has been done previously for one-dimensional calculations. We will therefore concentrate on the single-layer case.

There are several approaches to the calculation of a point response in a single-layer target. The most common is to revert to a moments approach (6, 7) which allows the construction of a two-dimensional gaussian profile or a hybrid Pearson-Gaussian profile, and this has been used in several early two-dimensional simulation programs (8-10). At the other end of the spectrum in complexity, a full two-dimensional Monte Carlo (11) or Boltzmann (5) calculation can be performed. As will be seen, this can represent an unnecessarily large amount of work for this problem. As an intermediate approach, one-dimensional projections of the profile can be calculated and used to reconstruct the two-dimensional response function. It is found that two projections, one vertical and one lateral,

are sufficient to do an accurate reconstruction. This method can be applied to both the Monte Carlo and Boltzmann schemes.

Method

Monte Carlo.—The initial result from a program such as TRIM (12) is a three-dimensional histogram of the final ion positions in the target. In a one-dimensional calculation, the histogram is flattened onto one vertical dimension to describe the final profile. The number of ion tracks that is necessary to describe the distribution is governed by the desired statistical error in the distribution; if a histogram box contains N ions, then the error is approximately \sqrt{N} . This dictates the use of at least 10^4 ions to maintain roughly 10% accuracy over the first decade of the profile. For a two-dimensional direct calcula-

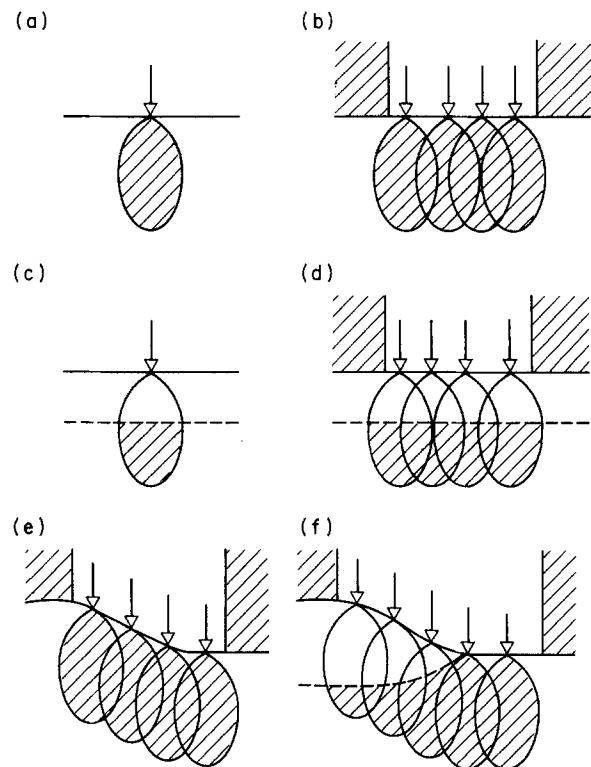


Fig. 1. Examples of point-response functions and corresponding targets. a: Point response for a single-layer target. b: Superposition in a mask window. c: Point response for a multilayer target. d: Superposition for a planar multilayer target. e: Superposition for a nonplanar single-layer target. f: General superposition using different point response functions.

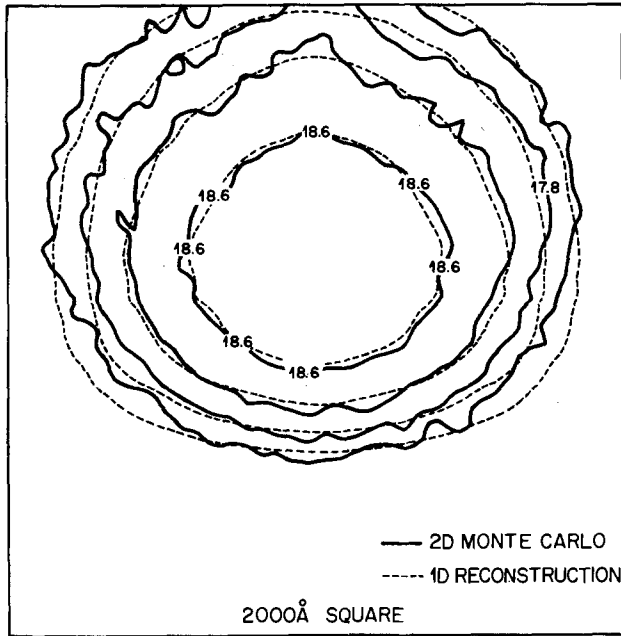


Fig. 2 Comparison of a direct two-dimensional Monte Carlo calculation (10^5 ions) with a reconstruction from projections (10^4 ions) for 20 keV boron implanted into silicon at a dose of 10^{15} cm^{-2} .

tion, the ions are spread over a plane rather than a line, so more ions must be followed to maintain statistical accuracy—between 10^5 and 10^6 ions are necessary, with a corresponding increase in calculation time.

In the alternative method proposed here, lateral information is obtained by flattening the histogram into one dimension laterally. The point response is then taken to be the product of the vertical and lateral projections. Because one-dimensional information is used throughout, 10^4 ion tracks are sufficient to define the result. The statistical error in the lateral projection is actually less than for the vertical profile because the lateral case is symmetric and the half-width is less than the total profile depth, so the histogram is spread over fewer bins. Figure 2 compares direct calculation using 10^5 ions with a reconstruction from 10^4 ions for 20 keV boron implanted into silicon. This comparison shows that the direct calculation is satisfactorily reproduced over the first two decades and justifies reconstruction from only two projections.

Boltzmann.—A one-dimensional Boltzmann vertical calculation does not contain lateral information because projection of the ion motion onto an axis is an integral part of the calculation. However, by changing the initial and boundary conditions, a lateral projected profile may be

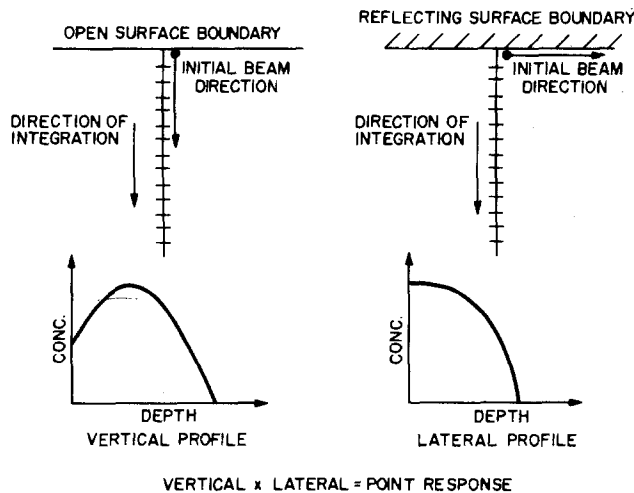


Fig. 3. Comparison of Boltzmann calculation method for vertical and lateral profiles.

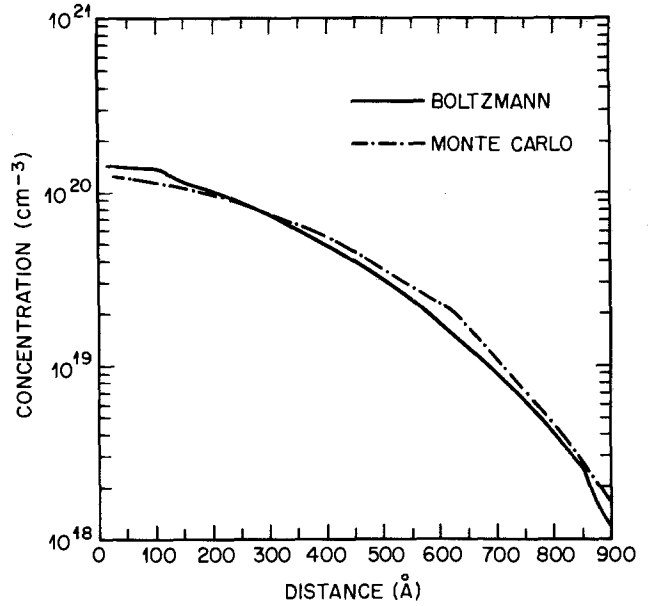


Fig. 4. Comparison of Monte Carlo and Boltzmann methods for lateral profile of 20 keV boron in silicon. Dose: 10^{15} cm^{-2} .

obtained. In a vertical calculation, the direction of integration is parallel to the initial beam direction. At each integration step, the ion motion is projected onto the integration direction so that the final result is a vertical projected profile. The surface is considered as an open boundary so that ions may be ejected out of the target. For a lateral calculation, the direction of integration is perpendicular to the initial beam direction. The same projection operation therefore produces a lateral projected profile. The surface is considered as a reflecting boundary so that only one half of the symmetric lateral distribution need be calculated. The two calculation conditions are compared in Fig. 3. For the lateral calculation, multiple passes (4) are essential because the beam angle causes many ions to be considered as backscattered. The multiple pass approach allows the motion of backscattered ions to be fully considered. Typical calculations require five passes, each of which is much shorter than a vertical calculation, leading to an overall calculation time of roughly twice the vertical time. The time to construct a point response for VLSI applications is in the range of

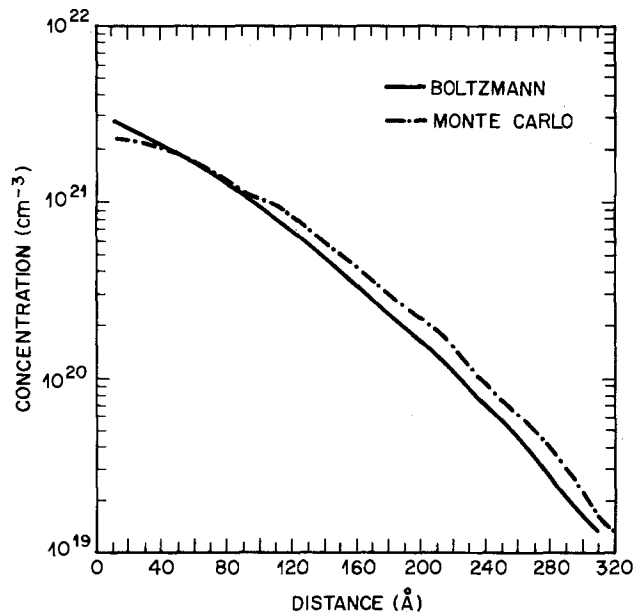


Fig. 5. Comparison of Monte Carlo and Boltzmann methods for lateral profile of 50 keV arsenic in silicon. Dose: 10^{15} cm^{-2} .

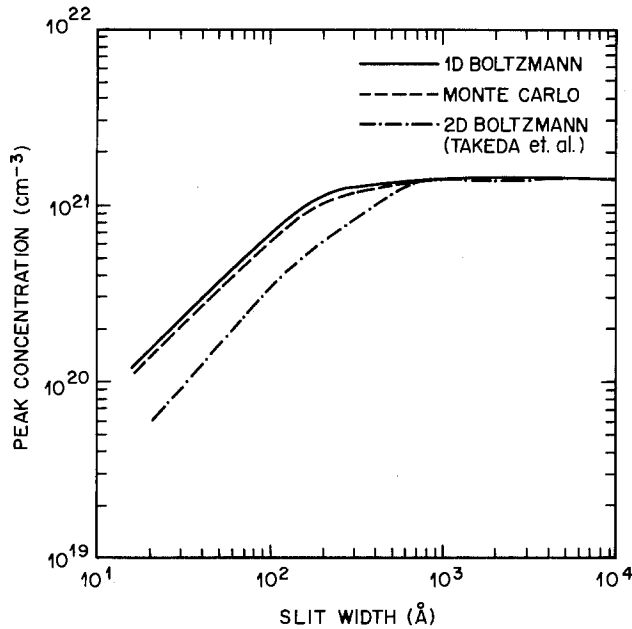


Fig. 6. Comparison of calculations for peak concentration for implantation of 50 keV arsenic through a narrow slit into silicon. Dose: $5 \times 10^{15} \text{ cm}^{-2}$.

5-50s on a Cray-1 computer, compared with 50-500s for the same calculations using a vectorized Monte Carlo code.

Figures 4 and 5 compare lateral profiles calculated by the Monte Carlo and Boltzmann methods, showing very good agreement, and also confirming the accuracy of the calculations because the methods are independent. Comparison is also possible with the two-dimensional Boltzmann work of Takeda *et al.* (5). Figure 6 shows the change in peak concentration with slit width for implantation of 50 keV arsenic through a narrow window on a silicon substrate. All three methods show the same trends, but the data from Takeda *et al.* indicate a wider spread in the point response for their work.

Direct measurement (13) of true lateral profiles has not yet been achieved to sufficient accuracy for a useful com-

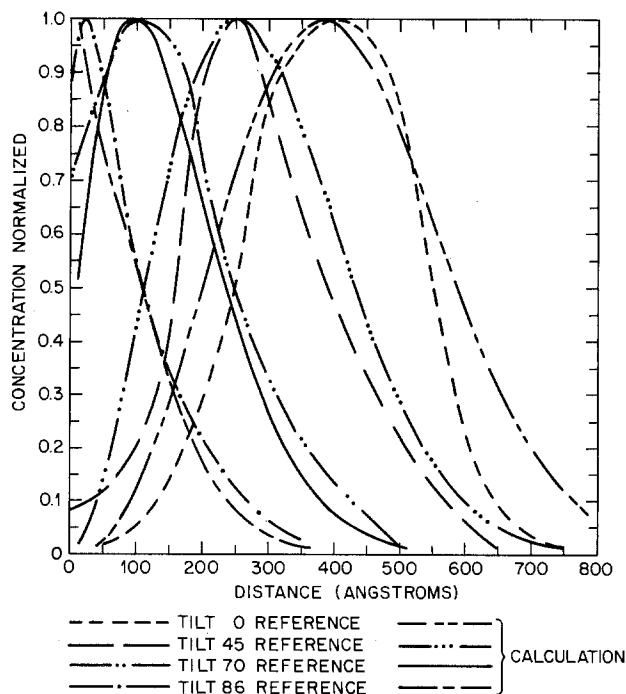


Fig. 7. Comparison of Boltzmann calculation with experiment for 60 keV arsenic implanted into silicon at various beam angles.

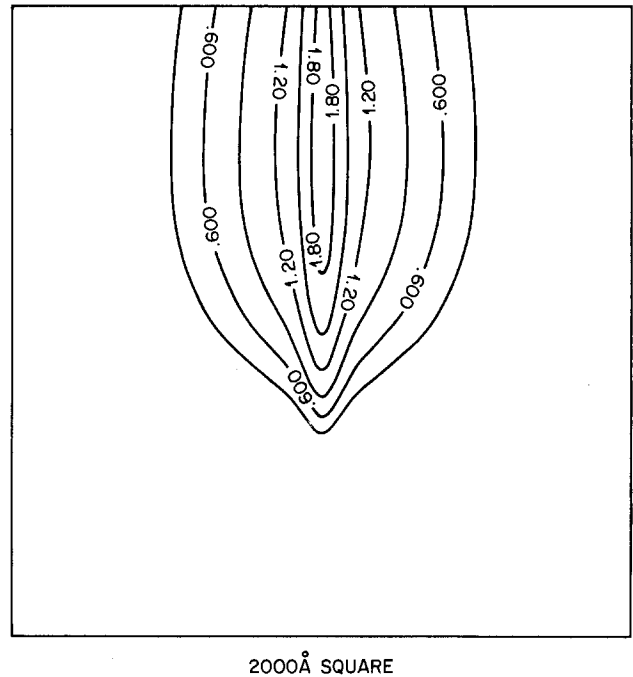


Fig. 8. Damage point response function for 20 keV boron implanted into silicon. Dose: 10^{15} cm^{-2} .

parison to be made. The closest thing possible to an experimental comparison at this time is to compare with profiles from tilted-beam experiments (14-17). In the BTE approach, this corresponds to tilting the initial beam direction and leaving the surface boundary open. Figure 7 compares calculation with experiment (17) for 60 keV arsenic implanted at various angles, showing the same movement of the peak position with tilt angle. The poor fit to the deeper profiles is believed to be in part due to inaccuracy in the measured profiles. For example, the experimental data for normal incidence seem truncated in comparison with the calculated curve and also in comparison with the other experimental curves and published data (18).

In one dimension, the BTE approach has also been used to calculate damage distributions (1), stoichiometry disturbances (3), and recoils in multilayer targets (2). In

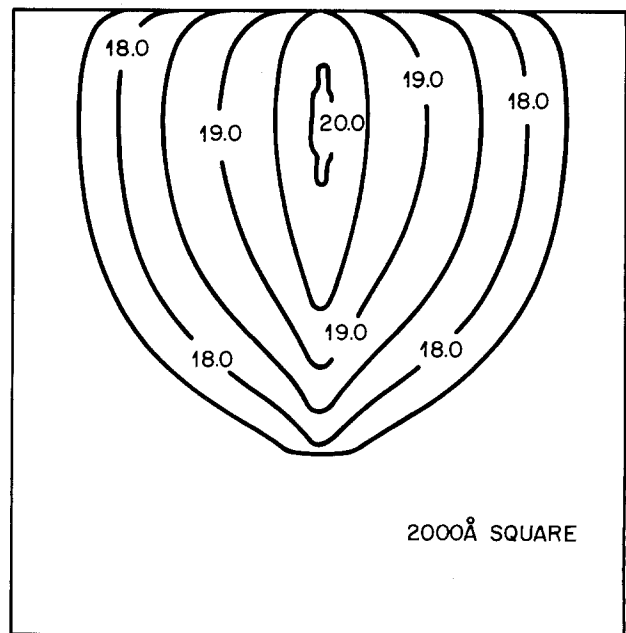


Fig. 9. Recoil atom point response function for 50 keV silicon implanted into gallium arsenide. Dose: 10^{15} cm^{-2} .

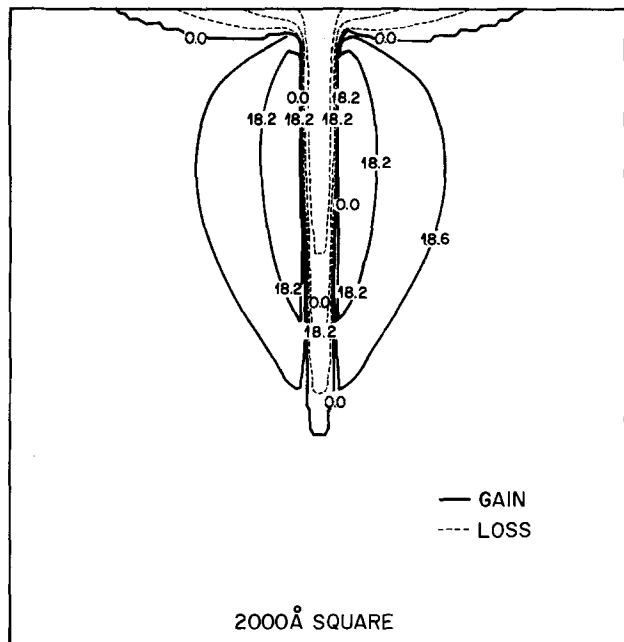


Fig. 10. Net substrate displacement from 50 keV silicon implanted into gallium arsenide. Dose: 10^{15} cm^{-2} .

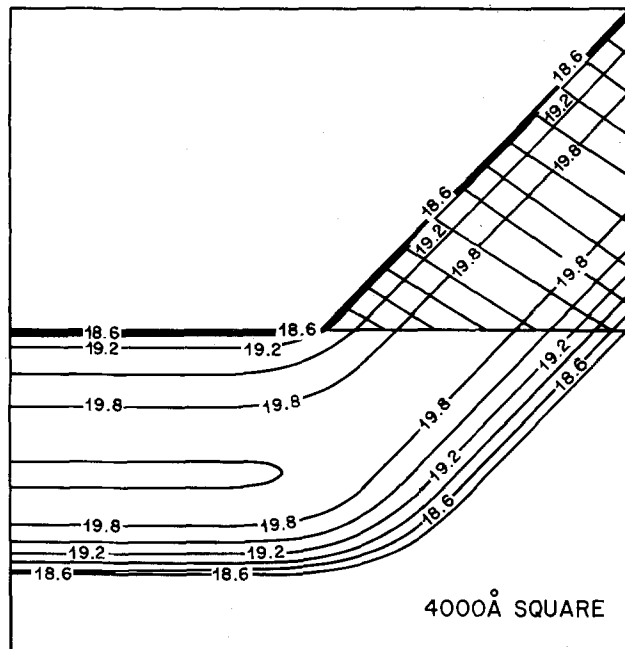


Fig. 12. Concentration profile for 20 keV boron into silicon at a 45° mask edge.

two dimensions, we have restricted ourselves to single-layer targets, but calculation of damage and stoichiometry is still possible by constructing point response functions for the appropriate quantities. Figure 8 shows a calculation for damage from a 20 keV boron implant into silicon. The general shape is similar to that of the concentration profile, although the dynamic range is less. For displacement and stoichiometry calculations, it is necessary to construct responses for displaced atoms and the corresponding vacancies separately. The net disturbance is then the difference in the two response functions. Figure 9 shows the concentration response for recoils from 50 keV silicon implanted into gallium arsenide, considering the substrate atoms together because their masses are so similar. The corresponding profile for vacancies is almost identical. The difference in these two correlated

quantities gives the net imbalance, as shown in Fig. 10. This shows some surface loss of recoiled atoms and net displacement of atoms from the beam axis outward.

Example Profiles

Once the point response function has been calculated, it is easy to obtain two-dimensional profiles at various mask edges by convolution. Figures 11 and 12 illustrate calculations for 20 keV boron at an abrupt and a 45° mask edge, respectively. The construction time for each profile, given the one-dimensional sections, is much less than 1s on a Cray-1. Figure 13 shows a similar calculation for a damage distribution at a 45° mask edge. Finally, Fig. 14 shows net substrate atom displacement for a 50 keV silicon implant through a narrow window with abrupt edges into GaAs, which can be compared with the point response of Fig. 11.

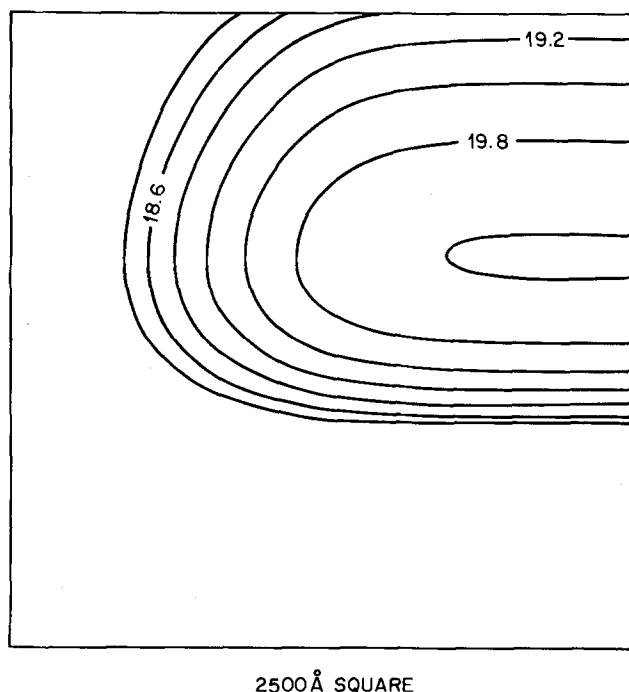


Fig. 11. Concentration profile for 20 keV boron into silicon at an abrupt mask edge.

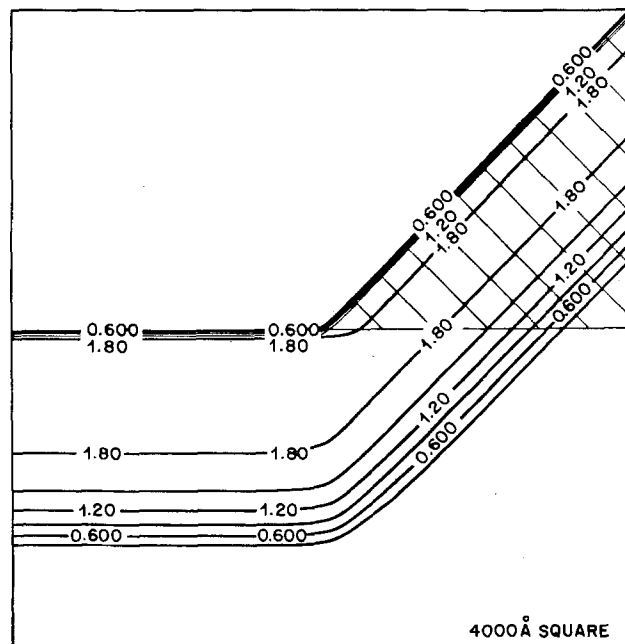


Fig. 13. Damage distribution from 20 keV boron into silicon at a 45° mask edge.

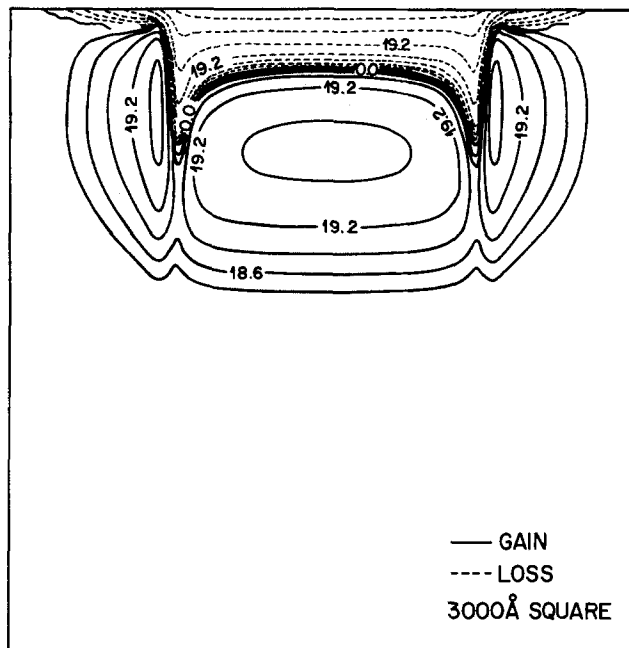


Fig. 14. Net substrate displacement from 50 keV silicon into gallium arsenide at an abrupt mask window.

Conclusions

The method of construction from projections allows two-dimensional implantation profiles to be calculated in the same order of magnitude of time as one-dimensional results, at the loss of some generality. Through scaling, the method can be used for practical useful structures, and it can be applied to both Monte Carlo and Boltzmann schemes. Through appropriate choice of point-response function, damage and stoichiometry effects can also be calculated. There is little advantage in using a more complex method unless a full, general solution is required and the increased computing resources are available.

Acknowledgments

The major portion of this work was funded at Stanford Electronics Laboratories through the support of DARPA

(Contract no. MDA903-79-C-0257). Thanks are due to W. Fichtner of AT&T Bell Laboratories for making available the Monte Carlo code and encouraging the presentation and publication of this work.

Manuscript submitted March 25, 1985; revised manuscript received July 8, 1985. This was Paper 489 presented at the New Orleans, Louisiana, Meeting of the Society, Oct. 7-12, 1984.

AT&T Bell Laboratories assisted in meeting the publication costs of this article.

REFERENCES

1. L. A. Christel, J. F. Gibbons, and S. Mylroie, *J. Appl. Phys.*, **51**, 6176 (1980).
2. L. A. Christel and J. F. Gibbons, *Nucl. Instrum. Methods*, **182/183**, 187 (1981).
3. L. A. Christel and J. F. Gibbons, *J. Appl. Phys.*, **52**, 5050 (1981).
4. M. D. Giles and J. F. Gibbons, *Nucl. Instrum. Methods*, **209/210**, 33 (1983).
5. T. Takeda and A. Yoshii, *IEEE Electron Devices Lett.*, **ed-4**, 430 (1983).
6. J. Lindhard, M. Scharff, and H. E. Schiøtt, *Mat. Fys. Medd. K. Dan. Vidensk. Selsk.*, **27**, No. 15 (1963).
7. H. Runge, *Phys. Status Solidi A*, **39**, 595 (1977).
8. D. Chin, M. Kump, and R. W. Dutton, Stanford University Process Analysis Program, July 1981.
9. C. D. Maldonado, *Appl. Phys. A*, **31**, 119 (1983).
10. B. R. Penumalli, *IEEE Trans. Electron Devices*, **ed-30**, 986 (1983).
11. W. P. Petersen, W. Fichtner, and E. H. Grosse, *ibid.*, **ed-30**, 1011 (1983).
12. J. P. Biersack and L. G. Haggmark, *Nucl. Instrum. Methods*, **174**, 257 (1980).
13. P. Roitman, J. Albers, and D. R. Myers, *J. Appl. Phys.*, **55**, 4436 (1984).
14. S. Furukawa and H. Matsumura, *Appl. Phys. Lett.*, **22**, 97 (1973).
15. H. Okabayashi and D. Shinoda, *J. Appl. Phys.*, **44**, 4220 (1973).
16. W. A. Grant, J. S. Williams, and D. Dodds, *Rad. Eff.*, **29**, 189 (1976).
17. L. De Cata, J. S. Williams, and H. B. Harrison, *Nucl. Instrum. Methods B*, **4**, 368 (1984).
18. J. Nakata and K. Kajiyama, *Jpn. J. Appl. Phys.*, **21**, 1363 (1982).

High Speed Integrated Circuit Using Silicon Molecular Beam Epitaxy (Si-MBE)

E. Kasper

AEG-Telefunken Forschungsinstitut, D 7900 Ulm, Germany

K. Wörner

Telefunken electronic GmbH, D 7100 Heilbronn, Germany

ABSTRACT

Si-MBE is a low temperature deposition method for epitaxial silicon layers with thickness and doping profile control on a submicron level. The MBE equipment described in detail is designed for high throughput of round wafers (ten 3 in. wafers per day). The apparatus consists of six subsystems, the reliable and simple operation of which has been proved during a 2 yr test period. For the first time we report on fabrication of high performance integrated circuits using Si-MBE material. Frequency dividers were fabricated using, apart from MBE, a commercial process line. Clock frequencies of up to 2.8 GHz were realized by these dividers with integrated transistors with transit frequencies up to 7 GHz.

Si-MBE promises several advantages which should make it a powerful instrument for future material and device fabrication. Remarkable properties are low process temperature, precise control of thickness and doping profile on a submicron scale, and high flexibility concerning the choice of material combinations and layer numbers.

Up to now, much effort has been directed toward the technological development of the Si-MBE system and toward the fabrication of materials (1, 2) and of basic devices (3) demonstrating the capability of the method; see also, for instance, recent reviews (4, 5) and the excellent bibliography (6). Several groups now are intensively thinking about industrial application of the method, and they are bearing in mind that facts like cost, throughput, and yield are of the same importance as technical feasibility (7, 8).

Si-MBE may influence the fabrication of integrated circuits in an evolutionary or revolutionary way. For near-future applications, the evolutionary way accepting the well-established IC-process sequence has to be chosen. Our experience with this evolutionary way is described in the following report, which covers (i) layer growth in high throughput Si-MBE equipment with a ten-wafer cassette within a load-lock chamber; (ii) influence of surface treatment, buried layer structures, and postepitaxial processes on crystal perfection and dopant profiles of the MBE-layers; and (iii) fabrication of a GHz frequency divider. Apart from MBE all other process steps were taken from a process sequence routinely used for manufacturing these frequency dividers.

Si-MBE apparatus.—Si-MBE systems provide inside of a clean UHV chamber several individually regulated molecular beams (silicon, dopants, alloy materials, metals) which are directed onto the cleaned surface of a heated substrate. Our homemade apparatus (9) has been designed for high throughput fabrication of electronic-grade material. A wafer cassette positioned in a separate UHV-storage chamber which is connected to the growth chamber by a gate valve enhances the throughput. Crystal quality is improved by an extremely clean environment provided by low residual gas content (process pressure) and by the use of silicon as material for components which are in line of sight with the substrate. For simple operation, effusion cells emitting neutral molecular beams are used as dopant sources. Handling of round wafers without contaminating the back side is ensured by a special transport mechanism and by radiation heating of the substrates positioned in an annular holder made from silicon. This equipment, reliably working for two years, consists of the following six subsystems.

1. An ultrahigh vacuum system which allows a clean environment during the total process time. A proper choice

of pumps, vacuum parts, materials and their pretreatments, and of the procedure is necessary to obtain a process vacuum not substantially worse than the base vacuum. Our system (see Fig. 1) is pumped down by a turbo-molecular pump getting the gas molecules out of the vacuum chamber and by a high speed titanium-sublimation pump gettering the gas molecules inside the vacuum chamber (9). Materials used for components are copper and stainless steel for cold parts and molybdenum, titanium, boron nitride, graphite, and silicon itself as often as possible for hot parts. All components are preheated 50 K above their operation temperature and scrubbed by electrons. All hot components are heat shielded to reduce thermal load. The heat shieldings of the material sources are water cooled to avoid thermal coupling. Intentionally, we do not use liquid nitrogen-cooled "cold walls" in the line of sight of the substrate, because methane (CH_4) adsorbed on the cold wall can easily be desorbed by electrons. Typical process pressure is 10^{-10} mbar. The main residual gas is hydrogen.

2. The substrate heater should be able to uniformly heat large diameter wafers up to temperatures necessary for thermal cleaning and growth. The most promising type is a radiant heater positioned near the back side of the wafer, where care is taken to reduce thermal stresses on the wafer below the stress level activating slip line generation (10). This is successfully done with our substrate heater by using a graphite meander radiation source and a substrate holder made from silicon avoiding temperature differences at the rim of the wafer by providing equal absorption properties of substrate and ring holder. Crystal

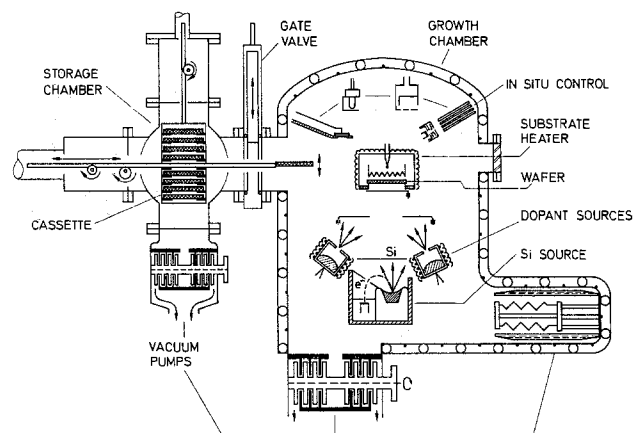


Fig. 1. Sketch of our Si-MBE apparatus. Growth chamber on the right side. Load-lock with cassette on the left side. Both UHV chambers are connected by a gate valve with 150 mm aperture.

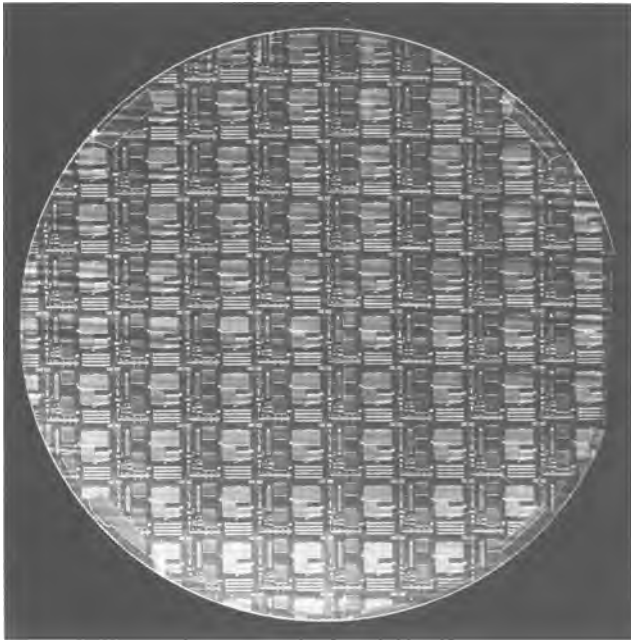


Fig. 2. X-ray topograph of a wafer with a $3 \mu\text{m}$ film grown on patterned oxide ($0.2 \mu\text{m}$ thick). Slip lines and dislocations were avoided by uniformly heating the substrate. Contrast arises from the strain field of the patterned oxide.

perfection and absence of slip lines are routinely checked by x-ray topography (see Fig. 2). Power consumption for heating a $75 \text{ mm } \varnothing$ wafer at a growth temperature of 750°C amounts to 700W .

3. The silicon molecular beam is generated by E-gun evaporation from pure silicon source material in the central portion melted and heated up to approximately 2000 K . Molten silicon is so reactive as to attack all other known crucible materials. The purity of the Si beam is enhanced by protecting the commercial E-gun from bombardment of backscattered electrons and ions by a silicon shielding. On a 30 cm distant substrate, typical growth rates are in the range of several micrometers per hour. Whereas E-gun evaporation is considered to be a reliable, clean, well-controlled process, it should be mentioned that it is also a source of particle beams (backscattered electrons, secondary electrons, silicon ions) and of electromagnetic radiation (light, x-rays, bremsstrahlung) influencing surface physics (adsorption, desorption, dissociation).

4. Dopant beams are generated by evaporation from effusion cells. For dopant materials we use Sb (for n-doping) and Ga (for p-doping). With Sb as a dopant material, concentrations up to the saturation limit of $2 \times 10^{19}/\text{cm}^3$ (at a growth temperature of 750°C) can be obtained (10, 11). But, near the saturation limit, incomplete electrical activation and degradation of the crystal perfection occurs. Well below the saturation limit, resistivity, Hall mobility of the layers, and their temperature dependence are similar to P- or As-doped bulk material (10-14). Thermodynamical calculations (15) predict a molecular beam that mainly consists of Sb_4 molecules. We found, by mass spectrometric analysis of the antimony beam, Sb atoms as well as Sb_2 and Sb_4 molecules. Up to now, a quantitative comparison with the calculations (15) has not been performed, because molecules are partly dissociated within the ionization chamber of the mass spectrometer and the sensitivity of the quadrupole mass spectrometer varies with atomic mass.

With Ga as a dopant material, carrier levels up to $2 \times 10^{18}/\text{cm}^3$ were achieved (16-18). The relatively high ionization energy of the Ga acceptor (70 meV) results in a dependence of resistivity on dopant concentration, quite different from B-doped bulk material. Already at Ga dopant levels above $1 \times 10^{17}/\text{cm}^3$ the acceptors start to be only partially ionized as proved by Hall effect measurements.

The upper Ga-dopant concentration amounts to approximately $1 \times 10^{19}/\text{cm}^3$ (growth temperature: 550°C). The carrier concentration belonging to this saturation limit amounts to $2 \times 10^{18}/\text{cm}^3$ at room temperature ($2.3 \times 10^{16}/\text{cm}^3$ at 77 K). With hole levels above $1 \times 10^{17}/\text{cm}^3$, device designers have to bear in mind the properties of the Ga acceptor.

Dopant atom incorporation can be enhanced and sharpness of interfaces can be improved by a technique we have called doping by secondary implantation during molecular beam epitaxy (DSI-MBE) (19). With this technique, silicon ions which are always produced by E-gun evaporation are accelerated by an electric field (typical potential difference between substrate and E-gun amounts to several hundred volts) toward the substrate. We believe that a main part of the low energy silicon ions implants atoms of the adsorbed dopant layer by impact (secondary implantation) into the growing MBE layer. The effect itself has been confirmed by another group (20), but the mechanism is a subject of controversial opinions.

5. *In situ* measurements of fundamental growth parameters are possible in the UHV environment of the growth chamber. Usually, analysis of the surface, the residual gas composition, the molecular beam intensities, and the temperatures of the substrate and effusion cells is employed. More than usual effort is directed by us toward mass spectrometry of dopant fluxes, absolute calibration of temperatures, and analysis of backscattered electrons.

Mass spectrometry of dopant fluxes is performed by a separate mass spectrometer sensitive to the range of atomic mass numbers 1-500 and by using a multiplier for ion counting. A shielding with properly positioned apertures protects the parts of the crossed-beam ion source of the spectrometer from being contaminated with dopant material or silicon. During operation of the effusion cells the mass numbers of Ga, Sb, Sb_2 , and Sb_4 isotopes can be detected. Using this mass spectrometer, we investigated the relation between effusion cell temperature and dopant flux density, the response of flux intensity on power variations of the cell heater, and the thermal cleaning of freshly loaded dopant materials from oxide layers.

Crystal perfection and dopant incorporation are influenced by the substrate temperature and the temperature of the evaporating surface of the dopant material. These temperatures differ from the reference temperatures measured by thermocouples mounted into the substrate heater and the effusion cells. The temperature differences between surface and reference thermocouple depend on design of substrate heater and effusion cell, on substrate doping (different absorption of radiation), on volume of cell load, and in some cases on thermal coupling from E-gun to substrate (significant only at very low growth temperatures) or from substrate heater to effusion cell (significant for wafer diameters greater than 50 mm and antimony effusion cell).

Intensity and energy spectrum of backscattered electrons, secondary electrons, and ions are measured by a Faraday probe with variable grid voltage. The primary source of electrons is the E-gun itself. Because of the magnetic field of the E-gun, the electron path is curved and only fast backscattered electrons can escape from the E-gun. The slow (several electronvolts) secondary electrons are generated by the impact of backscattered electrons onto the chamber wall. One can understand that the intensity and energy spectrum of the electrons scattered to the substrate sensitively depend on the design of the growth chamber. Near the substrate, the flux density of scattered electrons is in the order of $10^{12} \text{ electron}/\text{cm}^2\text{s}$.

6. The wafers are put into the growth chamber and removed through a load-lock chamber also pumped down to ultrahigh vacuum (see Fig. 1). Thereby the clean UHV environment within the growth chamber is maintained during several weeks until material must be reloaded or parts must be replaced. We have installed within the load-lock chamber a wafer cassette, the use of which further reduces the mean time for insertion of a wafer. On a nor-

mal working day, with this equipment, a 1 μm epitaxial layer can be deposited on ten 75 mm diam wafers.

Growth of device quality material.—The procedure consists of chemical cleaning of the substrate surface, insertion of the cassette into the load-lock chamber, pump down of the load-lock during the night, and epitaxy during the following day. One wafer after another is taken up from the cassette and transported by a transfer system to the growth chamber and put back after epitaxy. In the growth chamber, the wafer is inserted into the substrate heater. After a short heat cleaning step (900°C, 5 min), process parameters are adjusted to their proper values and growth is started by opening the main shutter and the cell shutters. Growth temperatures are between 550° and 800°C. The growth process is monitored by the *in-situ* control instruments and finished at the desired layer thickness by closing the shutters.

For establishing the growth of high quality layers one has to consider the importance of a clean environment, the role of surface diffusion of adatoms, the time dependence of dopant incorporation, and the existence of radiation (light, x-rays) and charged particles (electrons, ions) inside the growth chamber.

Models of ideal growth assume a clean surface on which pure beams of silicon and dopant material are impinging. Under real growth conditions, there will be undesired contaminating atoms, radiation, and charged particles. Actually, essential characteristics of Si-MBE are the attempt to suppress the contamination to a level as low as possible and the toleration of the level of electromagnetic and particle radiation inherently connected with the use of an E-gun. There are two principal sources of contamination, namely, the substrate surface itself mainly chemisorbed with oxygen and carbon, and residual gas. The chemisorbed substrate surface must be cleaned *in situ*, otherwise the deposited layer grows as a polycrystal. We use a short (5 min) thermal cleaning step at 900°C to remove the oxide layer. Strongly chemisorbed carbon cannot be removed by this moderate heating step. It is essential, therefore, to use a chemical pretreatment resulting in low carbon chemisorption (12, 21). It seems to us that careful handling, pure materials, and rapid transfer into the UHV chamber are more important than the choice between the different etching procedures. Carbon contaminants in the rising water not detected by electrical resistivity measurement may cause a nonreproducible carbon coverage. Remaining 5h in usual laboratory atmosphere increases the carbon coverage by a tenth of a monolayer as proved by ESCA measurements.

For perfect growth, the pressure and composition of the residual gas must also fulfill severe requirements during the cleaning and growth process. Heavy hydrocarbons must not be detected by a sensitive quadrupole-mass spectrometer. Partial pressures of oxygen, water, and also nitrogen should be well below the 10^{-11} mbar range. Only hydrogen as main component is allowed to be present at a partial pressure of several 10^{-10} mbar (22).

Fast surface diffusion of silicon adatoms was claimed (23) to play a dominant role for low temperature epitaxial growth under MBE conditions. Smooth surface, temperature-independent growth rate, and negligible desorption were explained by vertical growth via lateral motion of monatomic steps generated by the unintentional misorientation of commercial substrates (typically 1/4°). BCF (Burton, Cabrera, Frank) theory (24), assuming steps to be a capture site for diffusing adatoms, predicts negligible desorption only for an adatom diffusion length much higher than the step distance. A low energy barrier of surface diffusion (<1 eV) is compatible with the experimentally observed desorption and growth rates (23). These experiments should be compared with the strongly temperature-dependent growth rate, the desorption, and the moderate surface diffusion (energy of surface diffusion \approx 1.6 eV) observed with vapor phase epitaxy (25). Possibly, the difference in the energy barrier of surface diffusion is caused by hydrogen adsorption (26) during VPE or by radiation-enhanced motion during MBE.

Surface segregation, low sticking coefficients, and large time constants for incorporation of the dopants Sb and Ga (10, 12, 13, 17) rule out monatomic steps also to be an effective capture site for adsorbed dopant atoms, because during growth a step passes a point on the surface roughly every second. Therefore, BCF theory cannot describe dopant material incorporation during MBE. Other models (27, 28) describe the time dependence of dopant incorporation at least qualitatively.

There are considerable differences about the sticking coefficients of dopant material given in literature. Uncertainty of temperature was believed to be the cause of these differences (27). We have built three MBE equipments with different design but with the same careful calibration of cell and substrate temperatures. The sticking coefficient in every Si-MBE apparatus differs from the other. This experimental fact leads us to consider radiation and charged particle beams influencing the desorption, dissociation, and incorporation of dopant atoms. After every redesign of the apparatus, dopant level adjustment should take place. Electromagnetic and particle radiation also influence adsorption/desorption (29), contamination, and possibly silicon adatom migration as described above.

GHz-frequency divider.—A simple application of Si-MBE is to replace the epitaxial layer on an integrated circuit usually made by conventional vapor phase epitaxy by an MBE layer without changing pre- or postepitaxial processes or circuit layout. Clearly, in doing so the full potential of MBE will not be utilized, but this is an effective way to analyze the compatibility of the MBE process with the other IC manufacturing process steps. Improvements should be based on low growth temperature, reduced autodoping, and precise thickness control.

As a test vehicle, we selected a frequency divider used for television tuners. Initially, this commercial device was developed for an operating frequency up to 900 MHz (ultrahigh-frequency band of European television). Meanwhile, one needs frequency dividers up to X-band frequencies (12 GHz). Of late, Si bipolar IC's entered the lower microwave regime (30). Whereas in 1980 the fastest bipolar LSI circuits were considered to be based on integrated transistors with a transit frequency of $f_T = 4$ GHz (31), now the frequency limit of integrated bipolar transistors is shifted with laboratory examples toward $f_T = 14$ GHz (32) using a sidewall base contact structure (SICOS) technology. The highest reported clock frequency of a GHz-frequency divider is 5.5 GHz (33). These authors used a half-micron bipolar technology with advanced super self-aligned processes (SST-1A). Propagation delays for nonthreshold logic (NTL) of 42 ps/gate, power-delay products of 20 fJ/gate, and transit frequencies of 12.4 GHz were obtained with this technique. The highest operation frequency of the divider has been obtained at a high power dissipation of 884 mW. Encouraging results were also obtained with other special laboratory techniques. Using the direct nitride passivated base surface (DNP-II) process (34) resulted in a f_T value of 10 GHz and a clock frequency for the divider of 3.9 GHz at a power dissipation of 316 mW. Using vertically isolated self-aligned transistors (VIST) (35) resulted in a low power consumption of 84 mW at 2.5 GHz ($f_T = 6$ GHz) for a four-stage frequency divider (1:16).

We used, apart from Si-MBE, a 2 μm linewidth process sequence, which was developed for manufacturing of commercially available frequency dividers (36). Process sequence and circuit design were chosen to allow for the high yield production of a GHz-frequency divider with power dissipation below 100 mW. One layout of the test circuits is shown as a chip photograph (Fig. 3). This test chip contains a preamplifier, a master-slave flip-flop in ECL technique as binary divider, and test devices.

Prior to epitaxy, an As buried layer ($R_S = 8 \Omega/\square$) was diffused and a B-channel stopper was implanted to avoid inversion layers below the isolation oxide. Thermal processes after epitaxy were diffusion of the collector contact, oxidation of the isolation oxide, and annealing of

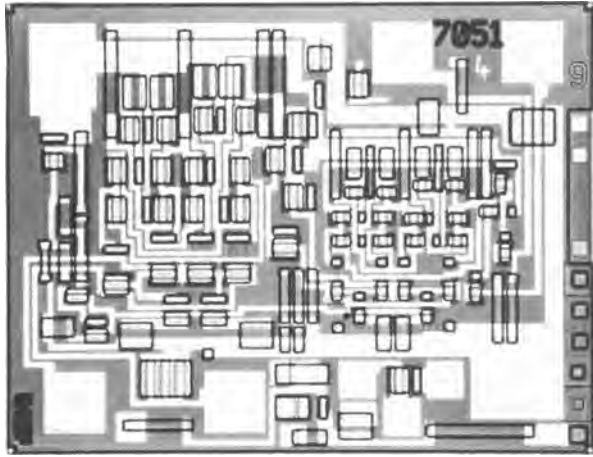


Fig. 3. Chip photo of a frequency divider with test devices. Layout-set number 7051.

base, base contact, and emitter implantation (Table I). The vertical structure of the integrated transistors is shown in Fig. 4. The effective thickness d_{eff} of the collector is lower than the epitaxial thickness d due to out-diffusion of the buried layer and due to the depth penetration of the base contact. Typical emitter depth amounts to $0.25 \mu\text{m}$, typical base width is $0.1 \mu\text{m}$, and base contact penetrates $0.55 \mu\text{m}$. In this experiment, the thickness d was reduced from 2.5 to $0.9 \mu\text{m}$, thereby reducing the effective thickness d_{eff} (see Fig. 4) from 1.6 to $0.2 \mu\text{m}$. The differences between d and d_{eff} are larger for thicker layers because of the prolonged time for oxidation of the isolation oxide. Alternatively, another test circuit was used (layout-set number 852) with diffused isolation and diffused emitter. The frequency limit of transistors with oxide isolation is roughly 2 GHz higher than the frequency limit (5 GHz) of transistors with diffused isolation (7).

With these test circuits we investigated yield as a function of the surface treatment, influence of pre- and post-epitaxial process steps on the quality of the MBE film, and transit frequency of the frequency divider and of integrated transistors as a function of the epitaxial layer thickness.

All fundamental growth experiments were performed on homogeneous substrates with flat, well-defined surfaces. Epitaxy for IC fabrication, however, starts on the surface of a heat-treated substrate, parts of which are oxidized, diffused, and ion implanted. These processes generate surface steps which are large compared with the monatomic misorientation steps present at flat surfaces. Surface contamination, defect propagation from substrate to layer, and growth mode can be influenced by these varied start conditions. Yield measurements can give general information about the significance of such varied start conditions. We obtained detailed information about causes of yield reduction by several methods for analysis of surfaces and defect structure (ESCA, TEM, x-ray topography, interference microscopy, defect etching). Initially, yield was considerably reduced when we replaced VPE layers by MBE layers. This was caused by residual

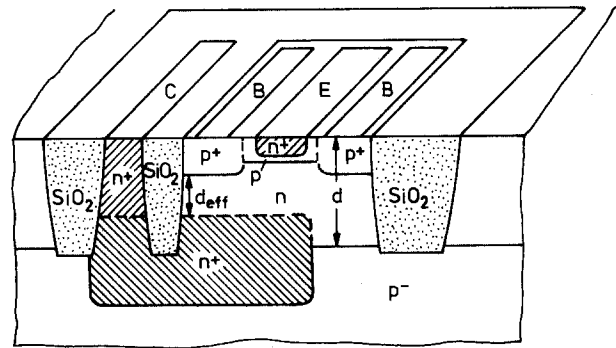


Fig. 4. Frequency divider. Vertical structure of integrated transistors with oxide isolation.

contamination at surface steps when applying the usual chemical cleaning treatment immediately before insertion into the magazine of the load-lock chamber. High device yield (up to 90%) was obtained by applying the following cleaning procedure. A modified cleaning solution based on hydrogen peroxide [known as RCA-etch (37)] yields low stacking fault and dislocation densities ($1 \times 10^3/\text{cm}^2$). This etching sequence is preceded by a centrifugal wafer spray. High purity water wets the spinning wafer; N_2 finally dries it for removal.

The buried layer zones themselves with their high As-dopant concentration do not degrade the high crystalline quality of the overlying film. Transmission electron micrographs clearly show that the epilayer grown onto buried layers exhibits the same lattice perfection as the part grown directly on the p-type substrate.

Autodoping is a well-known problem of epitaxy on substrates with buried layers. In order to investigate autodoping we grew layers on p-substrates, half of which were doped with arsenic in the same way as buried layer zones. Then we profiled doping level and junction abruptness on several spots on both halves of the wafer by C-V and spreading resistance measurements (see Fig. 5). We found that (i) junctions are abrupt within measurement accuracy (38) and carrier diffusion length (approximately a Debye length) and (ii) doping level is not influenced by the underlying substrate doping. That means practically that autodoping should not be considered when layer growth is performed by Si-MBE.

Postepitaxial processes may be influenced by the content of carbon, oxygen, or hydrogen, or by the concentration of interstitials or vacancies. Using the same process sequence as for the fabrication of the commercial devices, we did not find any hint that MBE material behaves other than VPE material with respect to postepitaxial processes.

The frequency limit depends on the thickness of the epilayer. Figure 6 exhibits the frequency limit, f_T , as a function of the emitter current, I_E , for several epitaxial thicknesses. Epitaxial dopant density is $1 \times 10^{19}/\text{cm}^3$. The emitter area is a single stripe $2.5 \mu\text{m}$ wide and $25 \mu\text{m}$ long. Collector-base voltage, U_{CB} , was fixed at 2 V . Frequency limit increases with increasing current up to a saturation value obtained at current densities of 1×10^8 – $2.5 \times 10^8 \text{ A/m}^2$. Frequency limits in excess of 4 GHz are obtained already at current densities above $3 \times 10^7 \text{ A/m}^2$ with epilayers 0.9 – $2.5 \mu\text{m}$ thick. The upper frequency limit of 7 GHz is obtained with epilayers about $1.2 \mu\text{m}$ thick. With thinner epilayers (see no. 192 in Fig. 6) the collector-base capacity increased, due to the reduced effective thickness decreasing the frequency limit (6 GHz for $d = 0.9 \mu\text{m}$). With thicker layers the collector resistance increases with increased effective thickness, reducing the frequency limit (5.8 GHz for $d = 2 \mu\text{m}$). The latter effect is more pronounced with lower epidoping level. With a doping level of $3 \times 10^{15}/\text{cm}^3$ (Sb), we obtained a frequency limit f_T of 6 GHz with $d = 1.2 \mu\text{m}$, $f_T = 4 \text{ GHz}$ with $d = 2 \mu\text{m}$, and $f_T = 2.5 \text{ GHz}$ with $d = 2.5 \mu\text{m}$. For low power consumption,

Table I. Postepitaxial processes. Heat cycles above 500°C

Aim	Process
Contact to buried collector	P diffusion, diffusion temperature dependent on epitaxial thickness (900° – 1000°C)
Oxide isolation	High pressure oxidation (20 bar) at 800°C , duration dependent on epitaxial thickness
Base, base contact, emitter	Room temperature implantation (B and As), furnace annealing at temperatures between 900° and 950°C

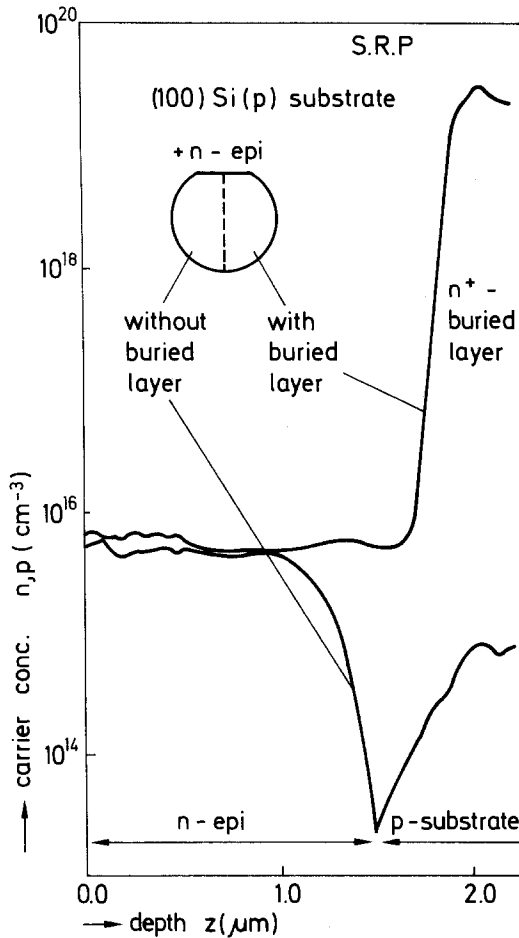


Fig. 5. Spreading resistance measurement of carrier profile of the epilayer on p-substrate with and without buried layer.

high frequency limits should be obtained at low collector-base voltage (U_{CB}) levels. An example is given in Table II. With integrated transistors of these frequency limits, frequency dividers with clock frequencies up to 2.8 GHz could be fabricated.

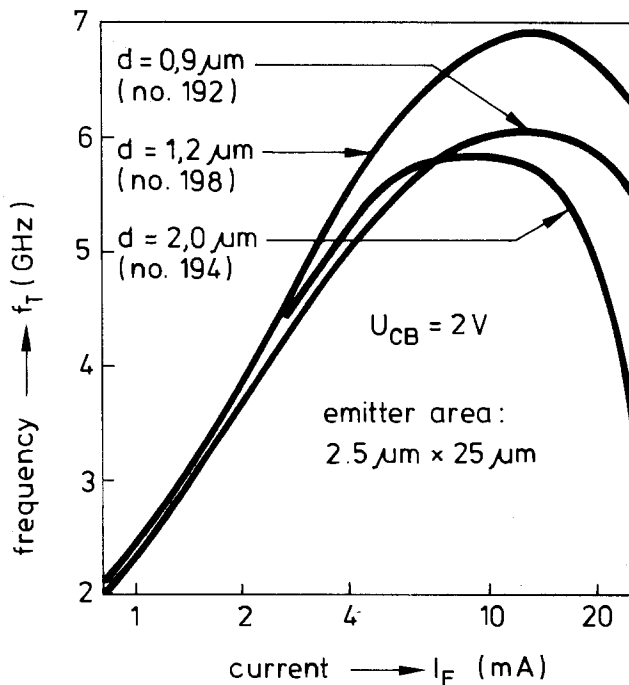


Fig. 6. Transit frequency f_T as a function of emitter current I_E for transistors with different epilayer thickness d .

Table II. Frequency limit f_T as function of the collector-base voltage U_{CB} at an emitter current $I_E = 5 \text{ mA}$ (no. 179, epilayer thickness 1.35 μm)

U_{CB} (V)	0.5	1	2	4	5	6
f_T (GHz)	5.45	5.75	6.1	6.35	6.45	6.6

Conclusions

We have proved for the first time that use of Si-MBE material enables the fabrication of high speed integrated circuits with excellent performance. Apart from Si-MBE, the process sequence of a commercial frequency divider has been used. High crystal perfection on buried layer substrates, absence of autodoping, and compatibility with postepitaxial processing are offered by this conventional use of an epitaxial layer.

Further improvement should be expected by using the full capability of Si-MBE, including, in addition low process temperatures and precise control of submicron layers, the high flexibility of materials, profiles, and structures.

The layers have been grown in an Si-MBE apparatus which was designed for industrial application. Simple handling, high throughput, and reliable operation were demonstrated since the installation of this equipment in 1982. Based on the principles of this equipment (storage chamber with a cassette, excellent vacuum conditions, low process temperatures, large area wafer heater, high precision *in situ* process control), development of the next generation equipment should also fulfill high requirements with respect to low cost and high throughput production of Si-MBE layers.

Acknowledgments

Technical assistance by Mr. H. Kibbel, layer assessment by Mr. H. J. Herzog and Mr. H. Jorke, and discussion with Dr. U. König and Dr. Th. Ricker are acknowledged. Part of the work was sponsored by the Ministry of Technology of Germany.

Manuscript submitted Oct. 10, 1984; revised manuscript received June 25, 1985.

AEG-Telefunken Forschungsinstitut assisted in meeting the publication costs of this article.

REFERENCES

- J. C. Bean, L. C. Feldmann, A. T. Fiory, S. Nakahara, and I. K. Robinson, *J. Vac. Sci. Technol. A*, **2**, 436 (1984).
- E. Kasper, H. J. Herzog, and H. Kibbel, *Appl. Phys.*, **8**, 199 (1975).
- J. Freyer, E. Kasper, and H. Barth, *Electron. Lett.*, **16**, 865 (1980).
- Y. Ota, *Thin Solid Films*, **106**, 1 (1983).
- F. C. Allen, S. S. Iyer, and R. A. Metzger, in "Proceedings of the SPIE Technology Symposium," p. 2, Los Angeles, January 1982.
- J. C. Bean and S. R. McAfee, *J. Phys. (Paris)*, **43**, C5-153 (1982).
- E. Kasper and K. Wörner, Abstract 51, p. 73, The Electrochemical Society Extended Abstracts, Vol. 84-1, Cincinnati, OH, May 6-11, 1984.
- R. G. Swartz, G. M. Chin, A. M. Voshchenkov, P. Ko, B. A. Wooley, S. N. Finegan, and R. H. Bosworth, *IEEE Electron. Devices Lett.*, **edl-5**, 20 (1984).
- U. König, H. J. Herzog, H. Jorke, E. Kasper, and H. Kibbel, in "Collected Papers of MBE-CST-2," p. 193, Tokyo (1982).
- U. König, H. Kibbel, and E. Kasper, *J. Vac. Sci. Technol.*, **16**, 985 (1979).
- U. König, E. Kasper, and H. J. Herzog, *J. Cryst. Growth*, **52**, 151 (1981).
- Y. Ota, *This Journal*, **124**, 1795 (1977); **126**, 1761 (1979).
- J. C. Bean, *Appl. Phys. Lett.*, **33**, 654 (1978).
- Y. Shiraki, in "Collected Paper of MBE-CST-2," p. 179, Japanese Society of Applied Physics, Tokyo (1982).
- R. R. Hultgren, "Selected Values of Thermodynamic Properties of Metals and Alloys," Report of the Minerals Research Laboratory, University of California, Berkeley, CA (1962).

16. U. König, H. Jorke, and H. Kibbel, Paper presented at the 2nd European MBE-workshop, Institute of Physics, Brighton, England (1983).
17. G. E. Becker and J. C. Bean, *J. Appl. Phys.*, **48**, 3395 (1977).
18. S. S. Iyer, R. A. Metzger, and F. G. Allen, *ibid.*, **52**, 5608 (1981).
19. H. Jorke, E. Kasper, and H. Kibbel, Paper presented at the 3rd International MBE-Conference, San Francisco, CA, August 1984.
20. R. A. A. Kubiak, W. Y. Leong, and E. H. C. Parker, Paper presented at the 3rd International MBE-Conference, San Francisco, CA, August 1984.
21. A. Ishizaka, K. Nakagawa and Y. Shiraki, in "Collected Papers of MBE-CST-2," p. 183, Tokyo (1982).
22. E. Kasper and H. Kibbel, *Vak. Tech.*, **33**, 13 (1984).
23. E. Kasper, *Appl. Phys. A*, **28**, 129 (1982); or T. de Jong, Thesis, University of Amsterdam, Amsterdam, The Netherlands (1983).
24. W. K. Burton, N. Cabrera, and F. Frank, *Trans. R. Soc. (London)*, **243A**, 299 (1951).
25. R. C. Henderson and R. F. Helm, *Surf. Sci.*, **30**, 310 (1972); R. F. C. Farrow, *This Journal*, **121**, 899 (1974).
26. A. A. Chernov and M. P. Rusaikin, *J. Cryst. Growth*, **45**, 73 (1978).
27. R. A. Metzger and F. G. Allen, *J. Appl. Phys.*, **55**, 931 (1984).
28. M. Tabe and K. Kajiyama, in "Collected Papers of MBE-CST-2," p. 187, Japanese Society of Applied Physics, Tokyo (1982).
29. B. A. Joyce, *Surf. Sci.*, **35**, 1 (1973).
30. C. P. Snapp, *Microwave J.*, **93**, (August 1983).
31. H. Nakashiba, I. Ishida, K. Aomura, and T. Nakamura, *IEEE Trans. Electron Devices*, **ed-27**, 1390 (1980); K. Wörner, H. Caluss, H. M. Rein, and H. Kostka, *Dig. Techn. Papers*, p. 73, ESCIRC 78, Amsterdam, The Netherlands (1978).
32. T. Nakamura, K. Nakazato, T. Miyazaki, T. Okabe, and M. Naga, 1984 IEEE International Solid-State Circuit Conference, *Dig. Techn. Pap.*, p. 152 (1984).
33. T. Sakai, S. Konaka, Y. Kobayashi, M. Suzuki, and Y. Kawai, *Electron. Lett.*, **19**, 283 (1983).
34. S. Watanabe, S. Shinozaki, N. Kusama, S. Miyazaki, and T. Nakata, IEEE 1984 Monolithic Circuits Symposium, *Dig. Pap.*, p. 24 (1984).
35. T. Fujita, H. Sakai, K. Kawakita, and T. Takamoto, *Jpn. J. Appl. Phys.*, **22-1**, 125 (1983).
36. K. Wörner, *IEEE Trans.*, **ce-30**, 297 (1984); Data sheet U 822 BS /U 824 BS, Telefunken electronic GmbH, Heilbronn, Germany.
37. See, for instance, W. Kern, *Semicond. Int.*, p. 94 (April 1984).
38. L. A. Hing and J. E. Curron, *Electron. Lett.*, **19**, 1091 (1983).

Diffusion of Oxygen in Silicon Thermal Oxides

E. A. Taft*

General Electric Company, Schenectady, New York 12301

ABSTRACT

A method for comparing the oxidation rates of silicon under an initial 1000Å of thermal oxides is described. Ellipsometry is used to measure the thicknesses of a pair of samples before and after a relatively short time of additional oxide growth in dry oxygen. Excluding the known orientation effect, a large variation in growth rate at a given temperature is noted. The rate is directly related to the index of refraction of the initial oxide. As this index is known to depend upon the initial growth temperature, the apparent oxygen diffusion "activation energy" must include this newly documented temperature factor. Parabolic and linear rate constants are presented and are compared with literature values. This study gives further evidence that silicon thermal oxides are metastable structures.

The linear-parabolic model of Deal and Grove (1) is still the generally accepted interpretation of thermal oxide growth on silicon. Though recognized early by, e.g., Hopper *et al.* (2) and Irene and van der Meulen (3, 4) as not an exact model, careful experimental work did not result in much improved interpretation. Additions to the linear-parabolic approach continue to appear (5-9), and new physical possibilities are advanced (10-12), but the basic model remains. (Only a few of many papers are referenced here.)

This paper will present new oxygen diffusion data which should be considered within the linear-parabolic model framework. The experimental approach follows the lead of Taft (13) and of Irene *et al.* (14), who show density differences in silicon thermal oxides. The effect of this oxide structure variation on the diffusion rate of oxygen is examined.

The diffusion of gas through a network is strongly dependent on the relative size of the interstices of the network and diameter of the diffusant molecule (15). If the density of vitreous silicon oxides varies by several percent, the interstitial volume also varies. The diffusion of the oxidant through a silicon thermal oxide might be expected to strongly depend upon changes in this interstitial volume. Hence, as the index of refraction and density does vary with the oxide formation temperature (13), the diffusion constant of the oxidant should not be expected to be the same for all thermal oxides. Rate growth variations have been reported in other multiple oxidation studies (10, 16).

* Electrochemical Society Active Member.

It has been observed that the oxides are metastable in that they can be reheated up to the formation temperature without appreciable change in the index of refraction. Heating to a higher temperature will cause the film structure to relax to the index appropriate to that for a film grown at this higher temperature. Irene *et al.*, (14) have documented this oxide stability. This fact is a necessary part of the diffusion study.

This paper will also present data on the linear and parabolic rate constants of oxide growth in dry oxygen on <111> and <100> silicon wafers. The purpose here is not so much to give new data but to provide an informed starting place for comments on the rate constants and to show that the oxides reported are typical. The effective activation energy of the parabolic rate constant especially is discussed.

Experimental

Oxides were grown in dry oxygen on <100> and <111> single-crystal silicon at various temperatures to about 1000Å thick. The wafers were cleaned in hot H₂SO₄-H₂O₂ and given an HF acid dip to remove native or previously grown oxide. They were then hydrogen fired to 1200°C for 10 min. This high temperature cleaning (2, 17) gave initial ellipsometer readings of about 3Å as found by Claussen and Flower (17). The index of refraction and thickness was carefully checked with a Gaertner L119 ellipsometer. A second measurement was made the following day to test oxide stability. Pairs of wafers of the same orientation from different temperature runs were chosen to be of the same thickness to < 1%. Dilute HF

etching was used on one wafer, when necessary, to obtain a close thickness match. These pairs of wafers were then placed in an oxidation furnace at the lower of the original growth temperatures of the pair. A growth time for adding 5-10% to the original thickness was chosen. This new oxide is now considered as an incremental growth over a small part of the growth curve near 1000Å. The thickness and index of the incremented oxides were carefully remeasured. Again, a second measurement was made the following day to check reproducibility of measurements.

Also, oxide growth-time curves for 700°-1170°C temperature in dry oxygen were developed. <100> and <111> wafers of 1 1/2 in. diam were employed for this work also. The thickness data were taken in the 100-1500Å range with the Gaertner L119 ellipsometer.

Results

The matched thickness wafer pairs did not have matched growth rates. The oxide grown originally at the higher temperature always had a greater incremental growth thickness. The ratio of these new growth thicknesses was at first plotted against the initial growth temperature differences of the pairs. Only a trend was observed. As noted before (13), the index is a better measure of the state of the oxide film than growth temperature. Furnace contamination, generally water vapor, which might occur in our small tube furnace will give an effectively higher temperature to a sample. The incremental thickness ratio was then plotted against the difference in initial index for each pair of samples. This curve is shown in Fig. 1.

A point on this graph is found from the example of the following wafer pair. One wafer had an oxide thickness of 973Å with an index of 1.4686. The oxide was grown at 1000°C. A second wafer oxide grown at about 1170°C was chosen at nearly the same thickness at 975Å. Its index was 1.4623. After 20 min in the oxidation furnace at 1000°C, the first oxide was 57Å thicker at 1030Å with the index unchanged at 1.4685. The second oxide increased slightly in index to 1.4636 and was 107Å thicker at 1082Å. The initial indexes were different by 0.0063 and the ratio of incremental growths was 107/57, or 1.88. This point appears in Fig. 1.

The thickness of the oxide was measured immediately if a dilute HF etch was used. When checked the following day, it was noticed that, invariably, the thickness had increased by several angstroms. Subsequent measurements

were unchanged. Wafers from the oxidation furnace which were not etched appeared to have stable thicknesses. (Wafer pairs included samples with neither oxide etched and samples where either the high or the low temperature oxide was adjusted in thickness. No correlation was observed during subsequent measurements.) The thickness chosen for etched oxides was from the later stabilized value; repeatability was closer than $\pm 1\text{Å}$. The reproducibility of the index measurement was $< \pm 0.0005$. The thickness and index of refraction of the oxide readings taken on subsequent days were generally within these values. Additional readings were sometimes taken to verify the stability of the films, or to check for errors in this manually operated two-zone ellipsometer arrangement. The angle of incidence is the most critical setting. The observed reproducibility is well within the resetability of this angle.

After the short extended growth of the oxide pairs, it was typically found that the index of the lowest temperature film had not changed. This result might be expected, as the new growth was but a continuation at the temperature of the initial growth. The index of the higher temperature film was typically found to be higher than initially. In this case, the oxide added at the lower temperature would be expected to have a high index. The initial high temperature oxide remains unchanged with the lower temperature exposure. The averaged index of the composite film is then greater than the original index. A calculation from ellipsometer readings using a two film case shows that the agreement of thickness and indexes of refraction is good. One further note—Fig. 1 contains points from both <100> and <111> silicon oxidation pairs.

The thickness-time growth curves of <111> and <100> silicon oxide were analyzed by hand fitting to an equation of the form $t = A(X - 20) + B(X^2 - 20^2)$ (3). Minutes of growth is t ; A and B are the reciprocal rate constants; and X is the oxide thickness in angstroms. The rate constants are plotted in Fig. 2 and 3. The points for the lowest temperatures are not reliable, as large corrections were made for initial growth (18). The growth curves of Hopper *et al.* (2) and of Irene and van der Meulen (3), which were carefully analyzed, are not in particularly good agreement with each other. For this reason and the fact that there was some scatter in the 15-30 points making up our growth curves, the hand fitting of the equations seemed adequate.

Discussion

Diffusion.—Figure 1 shows that there are large readily measurable variations in the incremental growth rate of oxide films in the same environment. The variations appear to correlate to the sensitivity of the oxygen diffusion constant to the packing (in amorphous material) of the solid oxides. This conclusion is a restatement of commentary from the introduction. The sequence of the argument goes from our measured index of refraction change to the measured (14) and calculated density change through the Lorenz-Lorentz relation to an inferred interstitial volume change. The 0.43% decrease in index of refraction leads, in our example, to the 88% increase in the diffusion rate of oxygen through a thermal oxide on silicon.

This result indicates that another source for a temperature coefficient for diffusion in silicon thermal oxides has been identified. In the usual linear-parabolic analysis of oxidation, the coefficient for the parabolic rate contains the diffusion term. The temperature variation of this parabolic rate is often compared to the variation of molecular oxygen diffusion found for fused quartz (1). The possible constraint imposed by this comparison has now been removed, and a larger temperature variation may be considered more favorably.

If the incremental thickness differences in the oxide films described were attributed to only the parabolic term in the growth rate, these differences would also apply directly to the diffusion constant change. When the index changes of Fig. 1 are converted to inverse tempera-

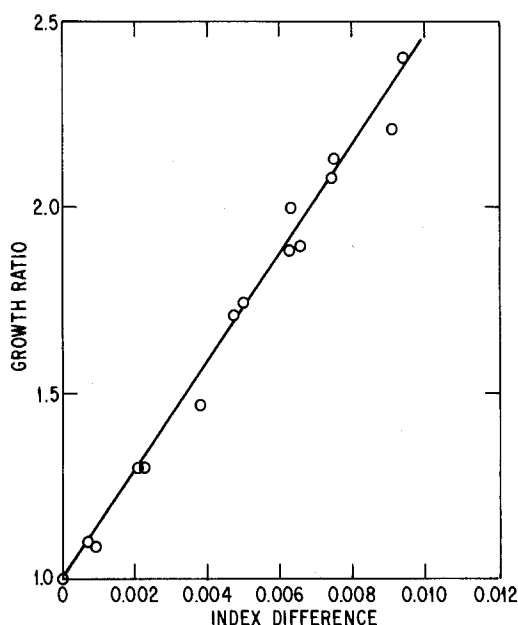


Fig. 1. Incremental growth ratio for pairs of oxidized wafers relative to the initial index of refraction difference in the low and the high temperature oxides.

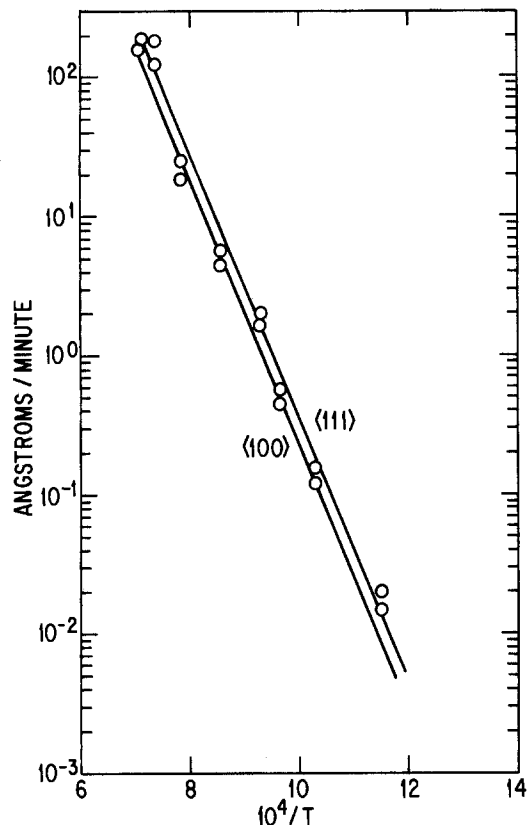


Fig. 2. Linear rate constants for dry oxides on $\langle 111 \rangle$ and $\langle 100 \rangle$ silicon.

ture through Ref. (13) and plotted against the logarithm of incremental thickness, a curve corresponding to an energy of ~ 0.3 eV is found for $\langle 111 \rangle$ silicon.

This structurally dependent diffusion rate of oxygen in silicon oxide is decreasing with decreasing temperature as does the normal temperature dependent diffusion rate for, e.g., fused quartz. In a series of grown oxide films, the net result is a steeper diffusion *vs.* inverse temperature curve or a higher apparent activation energy for diffusion. The activation energy for molecular oxygen in fused quartz according to Norton (19) is 1.17 eV. Adding the temperature effect found here, the net activation energy should be $1.17 + 0.3$ or 1.47 eV. This is for oxide formed on $\langle 111 \rangle$ silicon in dry oxygen. Taft (13) shows that oxides on $\langle 100 \rangle$ silicon have a slightly steeper index-temperature variation than those on $\langle 111 \rangle$ material. As the data of Fig. 1 also apply to $\langle 100 \rangle$ silicon, the apparent activation energy for diffusion in these oxides could be about 1.6 eV. It should be mentioned that these are minimum corrections. Consideration of the linear rate contribution or of the small effect of the two-layer oxide after regrowth will make for somewhat larger corrections.

The numbers are, of course, approximations, as the added factor is determined from data on a series of structurally different oxides. The data also indicate a T rather than $1/T$ relation with diffusion. It might be expected that the observed Arrhenius plot of the parabolic rate constant for oxide films would be nonlinear over an extended temperature range (8, 20, 21).

Rate constants.—As the major point of this paper is to present the oxygen diffusion effect, the rate constants determined in Fig. 2 and 3 are meant to serve in a corroborative role. The oxides grown here will be shown to be similar to those generally accepted in the literature. In the temperature range 900°–1200°C used for the diffusion measurements, the literature is fairly consistent.

Our activation energy for the linear rate constants is about 1.88 eV. This value is similar to that found by Hopper *et al.* (2), Kamigaki (6), and Lie *et al.* (8). Slightly greater values at ~ 2.0 eV are found by Deal and Grove (1) and Deal *et al.* (7). Slightly lower values are found by

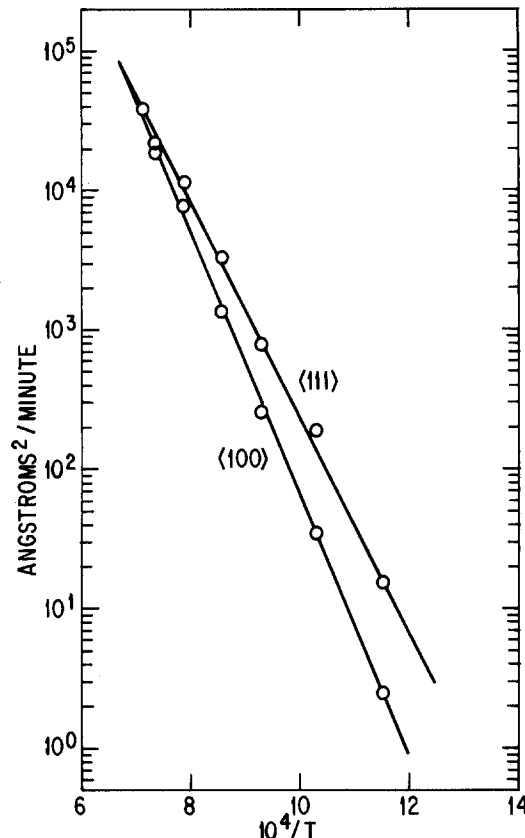


Fig. 3. Parabolic rate constants for dry oxides on $\langle 111 \rangle$ and $\langle 100 \rangle$ silicon.

Irene (22, 23), Irene and van der Meulen (3), and Irene and Dong (20). The latter group finds the activation energy for $\langle 100 \rangle$ to be slightly higher than for $\langle 111 \rangle$ silicon. Also they find that the activation energy is not constant with temperature. Our rate constants for oxide on $\langle 111 \rangle$ silicon are slightly higher than those of Lie *et al.* (8) and Hopper *et al.* (2), and considerably higher than those of Deal and Grove (1) and Irene and van der Meulen (3). At 1000°C, the constant agrees with Revesz and Evans (24). The rate constant for oxide grown on $\langle 111 \rangle$ silicon appears to be about twice that grown on $\langle 100 \rangle$ silicon at the same temperature. This observation has been previously reported by van der Meulen (4), Irene (22), and Kamagaki (6). It appears that the linear rate constants for oxides grown in this experiment compare favorably to those reported in the literature.

Our activation energy for the parabolic rate constants is dependent upon the orientation of the silicon. For $\langle 111 \rangle$ silicon, it is ~ 1.45 eV, and for $\langle 100 \rangle$ silicon it is ~ 1.85 eV. For $\langle 111 \rangle$ silicon, our value is close to that of Lie *et al.* (8) and Hopper *et al.* (2), as was also noted for the linear term. Values nearer to 1.2 eV were found by Deal and Grove (1), Deal *et al.* (7), and by Revesz and Evans (24). Irene (22) and Irene and van der Meulen (3) found higher values. A larger activation energy for the $\langle 100 \rangle$ orientation is noted by Irene (22). Irene and Dong (20), Lie *et al.* (8), and Han and Helms (21) do not find a constant activation energy. The rate constants for $\langle 111 \rangle$ silicon are near those obtained by Lie *et al.* (8) and Hopper *et al.* (2) and smaller than the Deal and Grove (1) values. As with the linear term, our rate constants for the parabolic term are in reasonable agreement with reported values.

The actual oxide growth time for, e.g., a 1000Å oxide on $\langle 111 \rangle$ silicon at 1000°C, is found to be in better agreement among the several references given than are the derived rate constants. While our rate constants do not agree as well with those of Deal and Grove (1) as they do with others, the calculated growth times for this oxide are within a few percent of each other. It appears that the dry oxides grown for this diffusion experiment are much like other oxides reported.

Summary

Incremental growth rates in dry oxygen of oxides on silicon in the same furnace are found to differ by more than two. These rates are directly related to the index of refraction of the initial oxide film and thus to the original growth temperature. Therefore, there seems to be a change in diffusion rate because of a change in the oxide structure with growth temperature. This structure factor when added to the activation energy for the diffusion of oxygen through fused quartz could account for the higher effective activation energy of the parabolic rate constants usually observed. The activation energy for growth of oxide on <100> silicon should be higher than that on <111> silicon.

Acknowledgment

I should like to express my thanks to H. R. Philipp for his encouragement in the course of this work.

Manuscript submitted Jan. 28, 1985; revised manuscript received June 20, 1985.

General Electric Company assisted in meeting the publication costs of this article.

REFERENCES

1. B. E. Deal and A. S. Grove, *J. Appl. Phys.*, **36**, 3770 (1965).
2. M. A. Hopper, R. A. Clarke, and L. Young, *This Jour-*

- nal*, **122**, 1216 (1975).
3. E. A. Irene and Y. J. van der Meulen, *ibid.*, **123**, 1380 (1976).
4. Y. J. van der Meulen, *ibid.*, **119**, 530 (1972).
5. D. W. Hess and B. E. Deal, *ibid.*, **122**, 579 (1975).
6. Y. Kamigaki and Y. Itoh, *J. Appl. Phys.*, **48**, 2891 (1977).
7. B. E. Deal, D. W. Hess, J. D. Plummer, and C. P. Ho, *This Journal*, **125**, 339 (1978).
8. L. N. Lie, R. R. Razouk, and B. E. Deal, *ibid.*, **129**, 2828 (1982).
9. W. A. Tiller, *ibid.*, **127**, 625 (1980).
10. M. Hamasaki, *Solid-State Electron.*, **25**, 479 (1982).
11. W. A. Tiller, *This Journal*, **130**, 501 (1983).
12. S. M. Hu, *J. Appl. Phys.*, **55**, 4095 (1984).
13. E. A. Taft, *This Journal*, **125**, 968 (1978).
14. E. A. Irene, D. W. Dong, and R. J. Zeto, *ibid.*, **127**, 396 (1980).
15. F. J. Norton, *J. Appl. Phys.*, **28**, 34 (1957).
16. Chien-Jih Han and C. R. Helms, *This Journal*, **132**, 402 (1985).
17. B. H. Claussen and M. Flower, *ibid.*, **110**, 983 (1963).
18. E. A. Taft, *ibid.*, **131**, 2460 (1984).
19. F. J. Norton, *Nature*, **171**, 701 (1961).
20. E. A. Irene and D. W. Dong, *This Journal*, **125**, 1146 (1978).
21. C. J. Han and C. R. Helms, *ibid.*, **132**, 516 (1985).
22. E. A. Irene, *ibid.*, **121**, 1613 (1974).
23. E. A. Irene, *Appl. Phys. Lett.*, **40**, 74 (1981).
24. A. G. Revesz and R. J. Evans, *J. Phys. Chem. Solids*, **30**, 551 (1969).

Oxidation Properties of Nickel in the Temperature Range 1073-1500 K

F. A. Elrefaie,¹ A. Manolescu,² and W. W. Smeltzer*

Institute for Materials Research and Department of Metallurgy and Materials Science, McMaster University, Hamilton, Ontario, Canada L8S 4M1

ABSTRACT

Oxidation of nickel after preoxidation at 1473 K was investigated during isothermal stages in oxygen atmospheres, $10^3 \leq P_{O_2} \leq 10^5$ Pa, at temperatures in the range 1073-1500 K. The reaction kinetics were parabolic; the parabolic oxidation rate constant was proportional to $P_{O_2}^{1/n}$ with the value of n varying from 5.5 ± 0.2 at 1073 K to 6.2 ± 0.2 at 1473 K. The activation energy of oxidation was 225 ± 4 kJ/mol NiO. Marker measurements indicated that the polycrystalline columnar NiO scales, which exhibited a preferred (100) texture, grew by predominant outward nickel diffusion. The measured values of the parabolic oxidation rate constants were higher by a factor of ≤ 3 than values calculated using nickel self-diffusion coefficients of single-crystal NiO, due probably to a component of nickel migration along easy diffusion paths developed in the polycrystalline scales.

Oxidation of nickel is expected to follow parabolic kinetics when the kinetics are controlled by lattice diffusion of nickel via cation vacancies in the NiO scale. Application of Wagner's theory for parabolic oxidation (1) to the high temperature scaling of nickel has been examined by several investigators as reviewed in Ref. (2-5). The agreement between experimental and calculated values of the parabolic oxidation rate constant is satisfactory to a first approximation at temperatures higher than 1273 K; at lower temperatures, this agreement breaks down and can attain a discrepancy as high as 5-7 orders of magnitude at 773 K. This discrepancy arises because nickel migration along easy diffusion paths in the polycrystalline NiO layer such as dislocations and subgrain and grain boundaries plays a predominant role in the reaction mechanism. The purpose of this research, accordingly, was to investigate the influence of a preformed thin NiO layer, which was relatively free of easy diffusion paths, on the subsequent morphological development and oxida-

tion mechanism of scales grown during isothermal stages at 1073-1473 K.

Experimental

Nickel plate specimens, $2 \times 1 \times 0.05$ cm, were prepared from 99.995 atom percent (a/o) purity sheet containing impurity contents as listed in Table I. These specimens after abrasion on 600 and 800 SiC grit paper and ultrasonic cleaning in methanol were annealed in flowing ultrahigh purity argon at 1473 K. An annealed specimen, average grain size ~ 0.1 μ m, was polished on napless cloths to 1 μ m diamond paste using kerosene and cleaned as above prior to placement in the oxidation apparatus.

Oxidation kinetics were measured gravimetrically using a recording semimicrobalance assembly as described elsewhere (6). The oxidizing atmospheres maintained at 10^5 Pa were static air, flowing oxygen, or oxygen-argon mixtures of oxygen partial pressures ranging from 1×10^3 to 2×10^4 Pa. A specimen was oxidized initially at 1473 K for 120-300s, then the furnace temperature was altered to a lower value, whereupon the specimen was oxidized isothermally and subsequently at several other temperatures in the same atmosphere.

*Electrochemical Society Active Member.

¹Present address: Department of Metallurgical Engineering, Cairo University, El Giza, Egypt.

²Present address: Ontario Hydro Research Laboratory, Toronto, Ontario, Canada.

Table I. Impurity contents of nickel, 99.995 a/o pure

Element	B	C	N	O	F	Na	Mg	Al	Si	S	Cl
ppma	0.3	7	0.6	4	0.5	0.04	1	1	10	0.8	0.01
Element	K	Ca	Ti	Cr	Mn	Fe	Cu	Ag	Ba	Pb	
ppma	0.02	0.3	0.05	0.03	0.2	20	3	0.02	0.2	0.02	

Marker studies were carried out by placing platinum wire, 25 μm diam, around a nickel specimen which was sandwiched between two $\alpha\text{-Al}_2\text{O}_3$ disks and heated at 1273 K in argon for 10.8 ks to assure the absence of a gap between the wire and specimen surface.

Optical and electron microscopy was used to investigate the morphology of the NiO layers. Preferred orientations of the oxide grains within the polycrystalline scales were determined using an inverse pole figure method (7) whereby the texture coefficient of an (hkl) plane, P_{hkl} , of oxide is given by

$$P_{\text{hkl}} = \frac{I_{\text{hkl}}/I_{\text{r,hkl}}}{\frac{1}{n} \sum I_{\text{hkl}}/I_{\text{r,hkl}}} \quad [1]$$

In this expression, I_{hkl} and $I_{\text{r,hkl}}$ are integrated intensities from the (hkl) peak of oxide within the scale and of randomly oriented powder, and n is the number of peaks examined.

Results

Oxidation kinetics.—Typical oxidation curves are illustrated by the parabolic-type plots in Fig. 1. In this case, a nickel specimen was initially oxidized in air at 1473 K for 300s before altering the furnace temperature to 1098 K. Although this latter temperature was attained after 5.4 ks, the slope of the kinetic curve plotted in parabolic form continued to decrease and eventually reached a constant value after 30 ks from which the parabolic rate constant was determined. When the temperature was then changed over ~ 50 K ranges, parabolic oxidation behavior was established after 600–1800s from temperature stabilization.

Values of the parabolic oxidation rate constant obtained at specified temperatures are plotted vs. oxygen pressure in Fig. 2. This rate constant was proportional to $P_{\text{O}_2}^{1/n}$ where $n = 5.5, 5.8, 5.4, 6.3,$ and 6.2 at 1073, 1173, 1273, 1373, and 1473 K, respectively, within an estimated error of ± 0.2 .

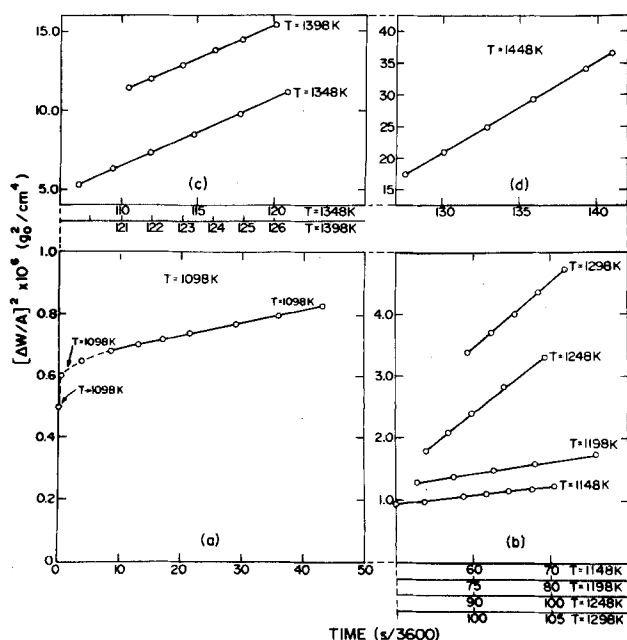


Fig. 1. The parabolic oxidation of nickel in air at temperatures in the range 1098–1448 K. The specimen was preoxidized at 300s at 1498 K before altering temperature to 1098 K, followed by subsequent oxidation at 1098 K (a), 1148, 1198, 1248, and 1298 K (b), 1348 and 1398 K (c), and 1448 K (d).

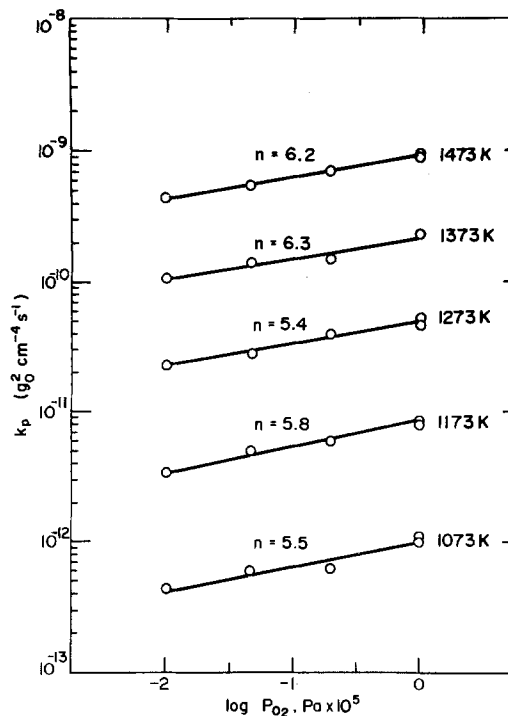


Fig. 2. The dependence of the parabolic oxidation rate constants on oxygen pressure according to the relationship $k_p = k_p^0 (P_{\text{O}_2})^{1/n}$.

Arrhenius plots of the parabolic rate constants for oxidation of nickel in the various atmospheres are shown in Fig. 3. The activation energies calculated from the slopes of the least squares linear fits are given in Table II; an average value of 225 ± 4 kJ/mol NiO is estimated at constant oxygen pressure within $10^3 \leq P_{\text{O}_2} \leq 10^5$ Pa.

Oxide microstructure.—As illustrated in Fig. 4, a uniformly thick NiO layer was formed at 1473 K upon oxidizing nickel for 300s. One or two oxide grains extended

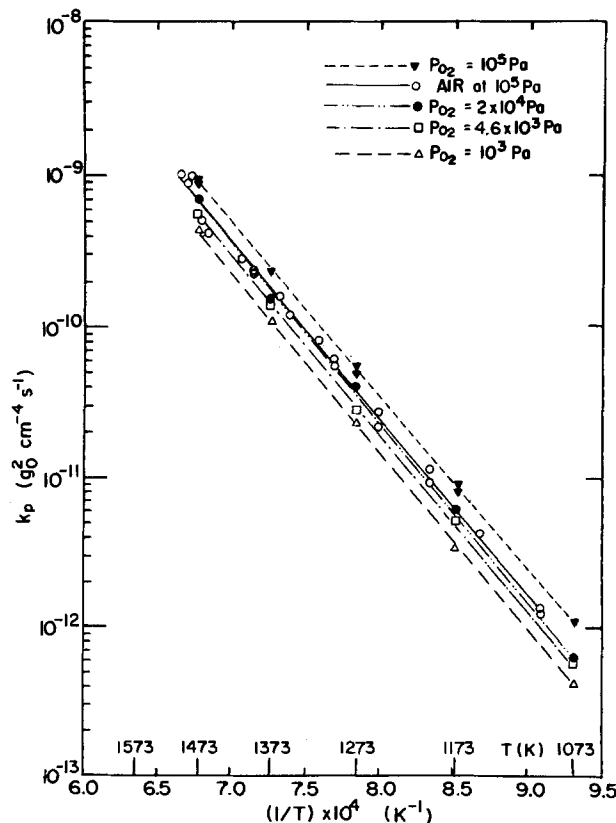


Fig. 3. Arrhenius plots of the parabolic oxidation rate constants in the temperature range 1073–1500 K at different oxygen pressures.

Table II. Activation energies for parabolic oxidation of nickel in various atmospheres

Atmosphere total pressure: 1 atm (1×10^5 Pa)	Temperature range (K)	Activation energy (J/mol NiO)
Oxygen	1073-1473	221,750
Air	1098-1500	223,840
O ₂ -Ar: $P_{O_2} = 2 \times 10^4$ Pa	1073-1473	228,030
O ₂ -Ar: $P_{O_2} = 4.6 \times 10^3$ Pa	1073-1473	223,840
O ₂ -Ar: $P_{O_2} = 10^3$ Pa	1073-1473	228,030

across this layer, and it exhibited a relatively flat outer surface. This scale morphology can be contrasted to that of the NiO layer formed when nickel was directly oxidized at the lower temperature of 1098 K for a long period of 155 ks as shown in Fig. 5. In this latter case, the small grains of $\sim 3 \mu\text{m}$ diam within the NiO layer were encased by oxide ridges, and they exhibited little preferred texture, as indicated by the values of P_{hkl} calculated for (111), (200), (220), and (311) planes, $0.9 < P_{hkl} < 1.1$, using Eq. [1].

A typical morphology of the oxide layers obtained after complete cycles of oxidation over several temperatures is shown in Fig. 6. The photomicrograph shown in Fig. 6a manifests the formation of a compact oxide layer having good adherence to the metal. The fracture cross section, Fig. 6a, illustrates formation of columnar NiO grains extending completely across the scale which are of smaller lateral dimension adjacent to the metal. The external surfaces of these grains, Fig. 6b, are flat even though the intersections of grain boundaries with the external surface were severely faceted. These fully developed scales exhibited a (100) preferred orientation texture as illustrated by the values of P_{hkl} recorded in Table III. The columnar grains in the scales exhibited little lateral growth during the oxidation cycles, as their average lateral diameter was $\sim 3 \mu\text{m}$ as measured along the midpoint line in the scale.

Marker measurements.—The oxidation run on the nickel specimen with markers was carried out in air according to the reaction sequence illustrated in Fig. 1, followed by a prolonged final oxidation state of 252 ks at 1448 K. Figure 7 illustrates the positions of two markers. The marker in Fig. 7a is located directly on the metal/oxide interface, and NiO internal precipitates exist beneath the marker. A thin layer of NiO was formed beneath the marker shown in Fig. 7b, but such markers re-

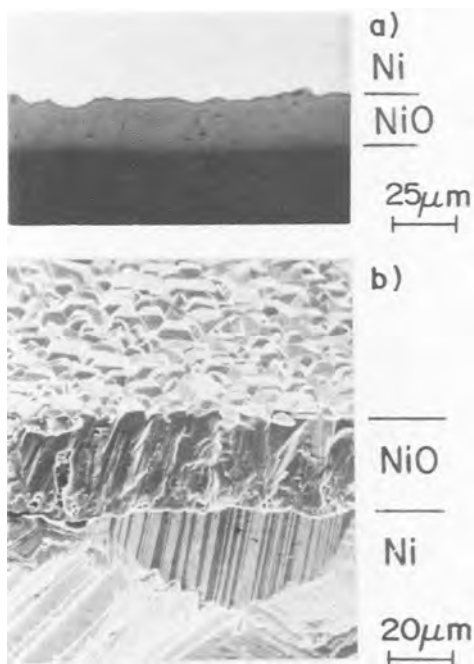


Fig. 4. The NiO layer formed on nickel after oxidation in air at 1473 K. a: Metallographic cross section. b: Fracture cross section.

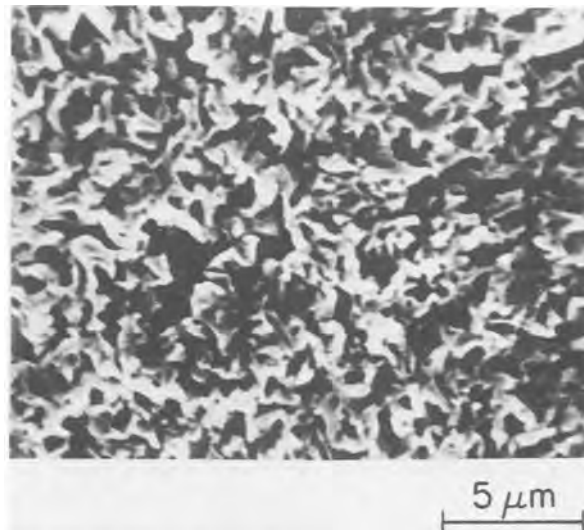


Fig. 5. The topology of NiO layer formed on nickel after direct oxidation in air at 1098 K for 155 ks.

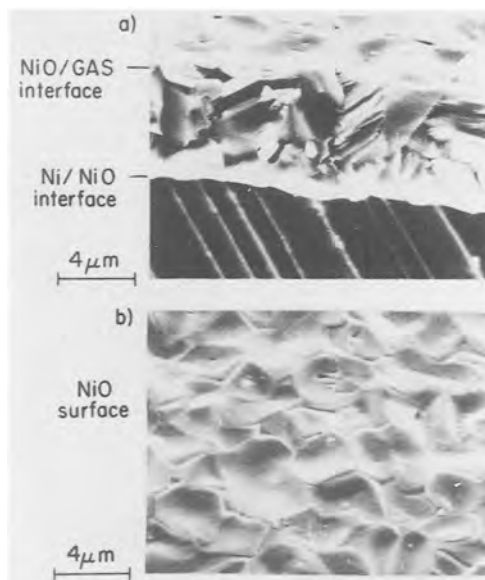


Fig. 6. The NiO layer formed on nickel in air at temperatures in the range 1098-1448 K after the complete oxidation cycle as given in Fig. 1. a: Fracture cross section. b: NiO surface at scale/gas interface.

mained at positions tangent to the main metal/oxide interface. These markers were oxidized with indication of oxide precipitation within the marker matrix. Scale void population was high in the region around a marker and the scale tended to jut out from the marker.

Discussion and Conclusions

Values of the parabolic oxidation rate constant in oxygen atmospheres, $10^3 \leq P_{O_2} \leq 10^5$ Pa, were obtained at temperatures in the range 1073-1500 K by oxidizing nickel specimens isothermally in stages at several temperatures after brief preoxidation at 1473 K. This rate constant was proportional to $P_{O_2}^{1/n}$ where $5.5 \leq n \leq 6.2$, which is in agreement with the hypothesis that nickel migration

Table III. Texture coefficient of (hkl) planes of NiO in scales formed on nickel as calculated by Eq. [1]

Atmosphere $P = 10^5$ Pa	P_{hkl}			
	(111)	(200)	(220)	(311)
O ₂	0.02	2.99	0.06	0.92
Air	0.20	2.00	0.60	1.30
O ₂ -Ar; $P_{O_2} = 10^3$ Pa	0.00	2.68	0.13	1.18

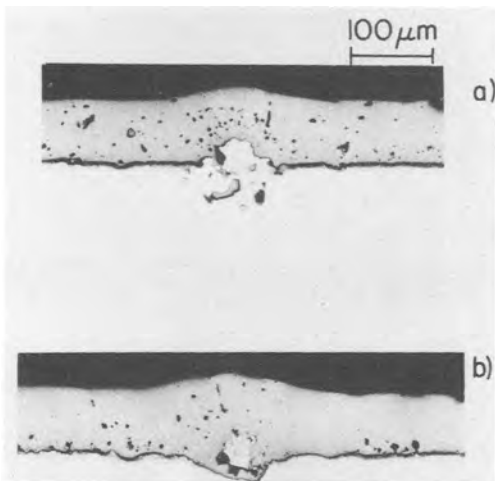


Fig. 7. The positions of platinum markers on a nickel specimen after oxidation according to the reaction cycle given in Fig. 1 followed by prolonged oxidation of 252 ks at 1448 K.

through NiO predominately by doubly charged cation vacancies determined the growth rate of this oxide layer (2-5). An average value of 22 kJ/mol for the activation energy of parabolic oxidation is of approximately the same magnitude, but 225 kJ/mol less than the most recent determination for the activation energy of nickel self-diffusion in single-crystal NiO (8).

The values obtained at different temperatures for the parabolic rate constant at $P_{O_2} = 10^5$ Pa are compared to those from the literature in Fig. 8. Fair agreement exists for all evaluations above 1273 K. The previously reported values at temperatures less than 1273 K are of larger mag-

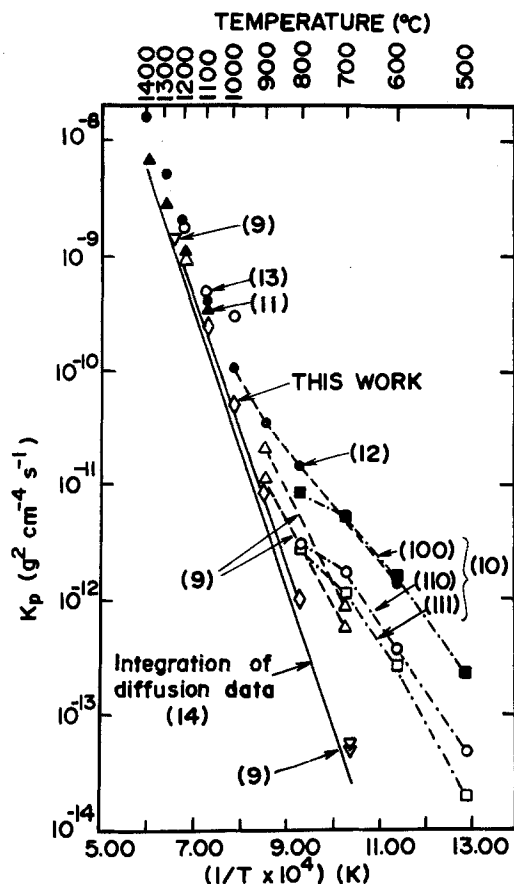


Fig. 8. Arrhenius plots of parabolic oxidation constants at $P_{O_2} = 10^5$ Pa for NiO layer growth on polycrystalline, crystal faces, and pre-oxidized polycrystalline nickel. The numbers on plots are the references. The experimental determinations from Ref. (9) at 973 K are from direct observations of thickening of the NiO grain matrix.

nitude than those reported in this investigation and they yield Arrhenius plots of smaller slopes. In this lower temperature range extending down to 773 K, oxide growth has been interpreted as being controlled by nickel short-circuit diffusion involving easy diffusion paths in the polycrystalline NiO scales formed on nickel polycrystalline sheet or nickel single-crystal faces (2-5). These easy diffusion paths have been assumed to be largely associated with the oxide grain boundaries since these are decorated by a network of outward extending ridges at the external oxide surface when the metal is directly oxidized as illustrated in Fig. 5.

Arrhenius plots of the parabolic rate constants obtained under the condition of preoxidation were linear over the entire temperature range from 1073 to 1500 K, as shown in Fig. 3 and 8. This behavior arose because preoxidation at 1473 K led to formation of a thin oxide layer relatively free of easy diffusion paths. This layer thickened upon subsequent stages of oxidation at lower temperatures into scales containing large columnar oxide grains mainly by nickel lattice diffusion. These conclusions are also consistent with earlier optical measurements on the growth of individual large oxide grains in scales grown at 973 K (9) on polycrystalline nickel as illustrated in Fig. 8.

One can utilize the Wagner theory for parabolic oxidation based upon lattice ambipolar diffusion to quantitatively assess diffusional processes during nickel oxide layer growth. The parabolic rational rate constant (1) is

$$k_p \text{ (eq/cm}^2\text{-s)} = \bar{c} \int_{a'_0}^{a''_0} D \, d \ln a_0 \quad [2]$$

where \bar{c} is the average equivalent nickel concentration in NiO, D is the self-diffusion coefficient of nickel in NiO, and $a_0 = (P_{O_2})^{1/2} = \{P_{O_2} \text{ (Pa)} / 1.013 \times 10^5 \text{ (Pa)}\}^{1/2}$ is the oxygen activity integrated over the limits from the metal/oxide to oxide/oxygen interface. Since D conforms to a $P_{O_2}^{1/n}$ relationship where $4 \leq n \leq 6$ (15), Eq. [2] becomes

$$k_p \text{ (g O}^2\text{/cm}^4\text{-s)} = nD^0(P''_{O_2})^{1/n} \left(\frac{M_0 \rho_{NiO}}{M_{NiO}} \right)^2 [1 - (P'_{O_2}/P''_{O_2})^{1/n}] \quad [3]$$

Here, D^0 is the nickel self-diffusion coefficient at $P_{O_2} = 10^5$ Pa, M_0 and M_{NiO} are the atomic weight and formula weight of oxygen and NiO, respectively, and $\rho = 6.85$ g/cm³ is the density of NiO.

The tracer diffusion coefficient of nickel in NiO, D^* , was determined (14) recently at $P_{O_2} = 10^5$ Pa and at temperatures in the range 795-1673 K

$$D^* \text{ (cm}^2\text{/s)} = 2.2 \times 10^{-2} \exp - 246.9 \text{ kJ/RT} \quad [4]$$

Since the diffusion process is controlled by a vacancy mechanism, D^* is related to D by a correlation factor $D^* = fD$, where $f = 0.78$. At $P''_{O_2} = 1$, Eq. [3] becomes

$$k_p \text{ (g O}^2\text{/cm}^4\text{-s)} = 2.76nD^*[1 - (P'_{O_2})^{1/n}] \quad [5]$$

Based on Eq. [5], k_p values were calculated utilizing values of D^* (Eq. [4]) and $n = 6$ for doubly charged nickel vacancies, since $5.5 \leq n \leq 6.2$ from this investigation, and P'_{O_2} for equilibration of NiO with nickel (17). These calculated values are compared to the experimentally obtained values in Table IV and Fig. 8. These values are in fair

Table IV. A comparison of the measured and calculated values, Eq. [5], of the parabolic oxidation rate constants of preoxidized nickel in oxygen, $P_{O_2} = 10^5$ Pa, and over the temperature range 1073-1473 K

T (K)	Measured k_p (g ² /cm ⁴ -s)	Calculated k_p (g ² /cm ⁴ -s)	$\frac{k_p(\text{meas})}{k_p(\text{calc})}$
1473	$9.2 \pm 0.2 \times 10^{-10}$	5.7×10^{-10}	1.6
1373	2.3×10^{-10}	1.3×10^{-10}	1.8
1273	$5.0 \pm 0.3 \times 10^{-11}$	2.5×10^{-11}	2.0
1173	$8.2 \pm 0.2 \times 10^{-12}$	3.4×10^{-12}	2.4
1073	1.0×10^{-12}	3.2×10^{-13}	3.2

agreement, the measured values being two to three times larger than the theoretical values.

It would appear that the difference between the experimental and calculated values of the parabolic rate constant was not associated with oxide formation by inward diffusion of oxygen because its diffusion is at least two orders of magnitude less than that for nickel diffusion in NiO (18). Marker measurements, moreover, wherein the marker remains at the metal/oxide interface, indicate that the NiO layer grew predominantly by outward diffusion of nickel. Nickel and platinum are completely miscible and the platinum marker did not remain completely inert. Consequently, formation of internal oxide and a concaved oxide beneath the main metal/oxide interface and the markers, Fig. 7, was brought about by dissociation of NiO and inward oxygen migration through the marker. In similar reported marker experiments (11), NiO formed beneath a porous platinum film marker, but fine relatively inert Al_2O_3 powder markers remained at the Ni/NiO interface.

Since the NiO layer during growth was not completely free from easy diffusion paths such as dislocations, subgrain boundaries (sgb), and grain boundaries (gb), the nickel flux should be given in terms of an effective diffusion coefficient

$$D_{\text{eff}} = D + \sum D_i f_i \quad [6]$$

where D_i is a diffusion coefficient for an easy diffusion path and f_i is the fraction of diffusion sites in this path such that $\sum f_i \ll 1$. The comparison between experimental and calculated values of the parabolic oxidation rate constant, Table IV, demonstrates that $D_{\text{eff}}/D \sim 1.5$ -3.

One can readily demonstrate that preferential nickel diffusion via high angle boundaries characteristic of polycrystalline NiO did not play a role in growth of the columnar grained and textured scales. At 1073 K, $D = 2.8 \times 10^{-14}$ cm²/s (14) and $D_{\text{gb}} = 2 \times 10^{-9}$ cm²/s in polycrystalline NiO (16) where the width of the boundaries may be taken as 7×10^{-8} cm (16). The average diameter of the columnar NiO grains was ~ 3 μm . Thus, $D_{\text{gb}} f_{\text{gb}} = 2(2 \times 10^{-9})(7 \times 10^{-8})/(3 \times 10^{-4}) = 9 \times 10^{-13}$ cm²/s, which is 30 times larger, rather than two to three times larger, than D . Metallography, as shown in Fig. 4 and 6, also illustrated that the boundaries of the columnar grains in the preferentially (100)-textured scales did not exhibit evidence of ridges by enhanced oxide growth as did boundaries of grains in untextured oxide scales formed at 1098 K as shown in Fig. 5.

One therefore concludes that the grain boundaries in the textured columnar grained scale did not permit a rapid rate of nickel diffusion as exhibited by high angle boundaries in polycrystalline NiO. It would appear that any enhanced nickel diffusion by boundaries in the columnar scale is of the same magnitude as to be expected by dislocation arrays throughout the scale acting as

subgrain boundaries. Since $D_{\text{sgb}} = 6 \times 10^{-11}$ cm²/s at 1073 K (3, 14), $D_{\text{sgb}} f_{\text{sgb}} = 6 \times 10^{-14}$ cm²/s, yielding $D_{\text{eff}}/D = 2$ if each grain of ~ 3 μm diam is assumed to contain two subgrains. This latter consideration involving a small degree of short-circuit nickel diffusion by dislocation arrays at grain and subgrain boundaries is consistent with the findings that uniformly thick columnar grained (100)-textured scales grew on the preoxidized metal specimens.

Acknowledgments

The author appreciated helpful discussions with A. T. Chadwick and A. Atkinson on the subject of this paper. This research was carried out under the auspices of the Natural Sciences and Engineering Research Council of Canada.

Manuscript submitted March 7, 1985; revised manuscript received June 17, 1985.

McMaster University assisted in meeting the publication costs of this article.

REFERENCES

1. C. Wagner, "Atom Movements," p. 153, ASM, Cleveland, OH (1951).
2. W. W. Smeltzer and D. J. Young, *Prog. Solid State Chem.*, **10**, 17 (1975).
3. A. Atkinson, R. I. Taylor, and A. E. Hughes, in "High Temperature Corrosion," R. A. Rapp, Editor, p. 110, NACE-6, National Association of Corrosion Engineers, Houston, TX (1983).
4. P. Kofstad, in "High Temperature Corrosion," R. A. Rapp, Editor, p. 123, NACE-6, National Association of Corrosion Engineers, Houston, TX (1983).
5. R. A. Rapp, *Met. Trans. A*, **15**, 765 (1984).
6. P. Mayer and W. W. Smeltzer, *This Journal*, **121**, 538 (1974).
7. G. B. Harris, *Philos. Mag.*, **43**, 113 (1952).
8. A. Atkinson and R. I. Taylor, *J. Mater. Sci.*, **13**, 427 (1978).
9. D. Caplan, M. J. Graham, and M. Cohen, *This Journal*, **119**, 1205 (1972).
10. R. Herchl, N. N. Khoi, T. Homma, and W. W. Smeltzer, *Oxid. Met.*, **4**, 35 (1972).
11. K. Fueki and J. B. Wagner, Jr., *This Journal*, **112**, 384 (1965).
12. J. Paidassi and L. Berry, *C. R. Acad. Sci. Paris*, **262**, 1553 (1966).
13. D. L. Douglass, *Corros. Sci.*, **8**, 665 (1968).
14. A. Atkinson and R. I. Taylor, *Philos. Mag. A*, **39**, 581 (1979).
15. M. L. Volpe and J. Reddy, *J. Chem. Phys.*, **53**, 1117 (1970).
16. A. Atkinson and R. I. Taylor, *Philos. Mag. A*, **43**, 979 (1981).
17. B. C. H. Steele, "Electromotive Measurements in High Temperature Systems," C. B. Alcock, Editor, p. 3, American Elsevier Publishing Co., New York (1968).
18. A. E. Hughes, A. Atkinson, and A. T. Chadwick, AERE Harwell Report R-11200 (1984).

Growth Mechanism of Silicon Plasma Anodic Nitridation

M. Hirayama, T. Matsukawa, H. Arima, Y. Ohno, and H. Nakata

Mitsubishi Electric Corporation, LSI Research and Development Laboratory, 4-1 Mizuhara, Itami, Hyogo 664, Japan

ABSTRACT

Nitridation of silicon was performed in a temperature range of 680°-920°C by 13.56 MHz RF oscillation in nitrogen-hydrogen plasma. Growth kinetics and activation energy of nitridation were investigated. The relationship between nitridation time (t) and nitrided film thickness (x_n) was found to be $x_n(2 - 0.00695V_{dc}) = 0.86 \times 10^{-6}t$. External dc voltage (V_{dc}) on plasma nitridation was effective in obtaining a high growth rate of nitrided film on silicon. Activation energy for the plasma anodic nitridation of silicon (0.25 eV) was twice as large as the value of plasma nitridation without an external dc voltage. The role of hydrogen in plasma nitridation was also studied with quadrupole mass spectroscopy.

Progress in MOS VLSI densification requires a large capacitance in a small capacitor area (1). Therefore, the direct nitridation of silicon may be one of the most attractive techniques for the device fabrication process. Compared with the widely used silicon dioxide film, silicon nitride film has a higher dielectric constant. The silicon nitride film is chemically stable and is also much better as a diffusion barrier for impurities and metals. In spite of these advantages, the silicon nitride film deposited on silicon wafers by LPCVD cannot be used for the gate dielectric film of MOSFET because it was interfacial instabilities between the silicon nitride and the silicon substrate. Many attempts at achieving direct nitridation and forming the silicon nitride film have already been made (2, 3). Ito *et al.* reported that uniform amorphous silicon nitride films could be obtained from the reaction of silicon in an ammonia ambient and applied to the LSI device fabrication (4). However, these films were very thin because of the slow diffusion of nitridant species through the nitrided film. To improve the low growth rate, plasma nitridation and plasma anodic nitridation were attempted. A high reaction rate was given by the plasma-excited reactive species compared with the thermal reaction. Plasma anodic nitridation was expected to give an enhanced growth rate, similar to that in the case of the anodic oxidation of silicon (5). Also, the reaction temperature could be decreased below the temperature of the thermodynamical limit because the plasma reaction forms reactive species.

In this paper, the growth mechanism of plasma anodic nitridation will be investigated. To prevent the contamination of oxygen and hydro-oxygen, we used highly purified hydrogen and nitrogen for our experiment.

Experimental

The vacuum system, gas sources, and experimental arrangements for achieving the plasma anodic nitridation of silicon are shown in Fig. 1. They are the same as those used in the earlier study (6). Nitrogen plasma was generated at a pressure range from 0.5 to 2.0 torr by an RF oscillator whose frequency was 13.56 MHz. Anodization voltage applied between the anode and the ground level was supplied by an external dc supply. The nitridation experiments were performed in a temperature range from 680° to 920°C. Boron-doped n-type (100)-oriented CZ silicon wafers, whose resistivity was about 10 Ω -cm, were used for the nitridation. To remove the native oxide on the silicon surface, hydrogen plasma was generated prior to the nitridation process under a pressure below 0.2 torr. The reaction chamber was first pumped down to less than 4×10^{-5} torr with a turbo molecular pump to minimize the residual gases. Then research-grade nitrogen and hydrogen were admitted to the reaction chamber. After the pressure became stable, glow discharge was initiated by applying RF power. The anodizing voltage applied to the sample was typically 150V. The nitridation time was varied between 10 min and 400 min.

In order to study the nitridation mechanism, quadrupole mass analysis of the reacting plasma in the chamber was performed. Transmission electron microscopy (TEM)

was carried out to examine the interface structure of silicon nitride and silicon. Also, characterization of the nitrided film was studied using Auger electron spectroscopy and infrared absorption.

Results and Discussion

Film composition.—The infrared absorption spectrum of Fig. 2 shows the characteristic absorption peak of nitride film at wave number of 865, 895 cm^{-1} . The wafer was nitrided at 920°C for 400 min with an external dc voltage of 150V. A peak at 610 cm^{-1} identified as the phonon absorption of the silicon substrate was observed, but no absorption interpreted as Si-O bonds was found in this spectrum. The 865 and 895 cm^{-1} peaks are due to the stretching vibration of Si-N bonds and seem to be almost the same as the peak described by Frieser (2). However, a peak at 920 cm^{-1} , higher than our measurement, results for Si-N bonds was reported by Ito *et al.* (4).

The chemical composition of films formed by plasma anodic nitridation was examined by Auger electron spectroscopy (AES). The AES analysis revealed the presence of nitrogen and oxygen at the surface of the nitrided samples. Since hydrogen is not detectable with Auger spectroscopy, the hydrogen content of these samples is not known. Carbon peaks were not observed from any AES spectra, so carbon atoms at the sample surface did not exist. Sputter etching was accomplished with a 1.0 keV argon ion to obtain in-depth profiles. A typical Auger spectrum of the plasma anodic nitridation film is shown in Fig. 3. The film was grown for 300 min in a nitrogen-hydrogen mixture with an external dc voltage of 150V. The N_{KLL} and O_{KLL} lines are clearly observed on this spectrum obtained from the surface of the nitrided film. From the results of infrared absorption and the Auger spectrum, it is concluded that the silicon surface was changed to silicon nitride by this plasma anodic nitridation.

Nitridation.—Figure 4 is a cross-sectional view of plasma-anodized silicon and the silicon dioxide boundary using a high resolution transmission electron microscope (TEM). It is observed that the thickness of the nitrided films on the silicon surface is almost the same as it is on the silicon dioxide surface. On the sidewall of the silicon dioxide, the film thickness is small. This nitridation behavior shows anisotropical growth resulting from plasma

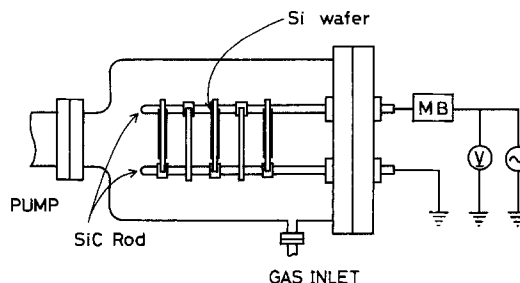


Fig. 1. Schematic diagram of experimental apparatus for plasma anodic nitridation.

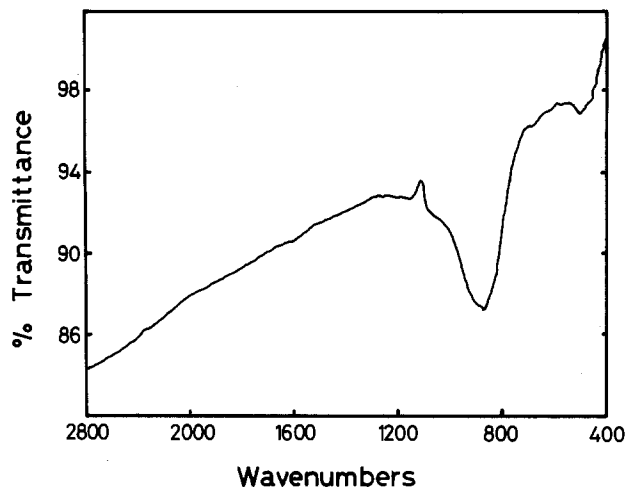


Fig. 2. Infrared transmission curve of nitrided silicon

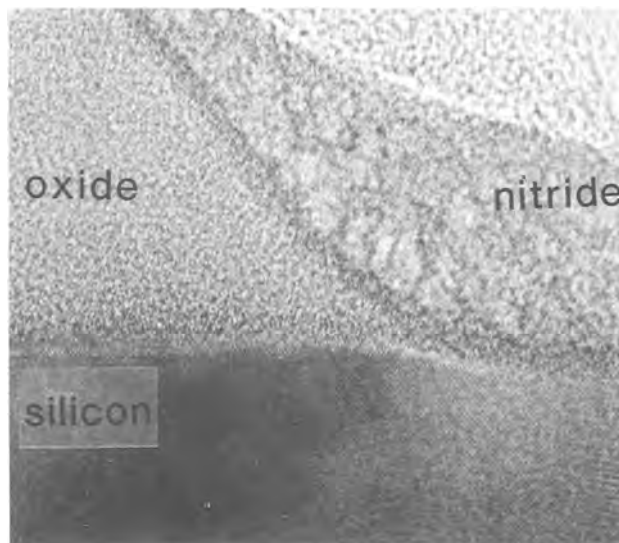


Fig. 4. TEM micrograph of the nitrided film

reaction. The most remarkable point of this TEM photograph is the difference in the interface levels between the silicon-nitrided film and the original silicon-silicon dioxide film. This phenomenon is generally observed on the thermal oxidation of silicon. With the oxidation of silicon, the interface between silicon and silicon dioxide drops down into the bulk silicon, and the thickness ratio of the upper and lower parts of the oxidized film divided by the original silicon surface is generally about half and half. Therefore, in this nitridation experiment, it is supposed that the nitridant species also diffused into silicon and that the silicon surface is actually nitrided like the oxidation of silicon surface.

Growth kinetics.—Figure 5 illustrates the variation of growth rate with the dc power applied to the wafers. The RF power and the temperature were fixed at 500W and 900°C, respectively. The enhancement of the growth rate by the externally applied voltage (V_{dc}) is shown in this figure. It is obvious that the growth rate is remarkably enhanced by the application of the dc bias. The uniformity of the films grown in this system is quite good except in the upper area. For example, with a typical film about 17 nm thick, the standard deviation of the thickness was about 0.8 nm thick within the 4 in. wafer areas.

The dependence of the film thickness on the growth temperature is plotted against the inverse of nitridation temperature in Fig. 6. These lines were obtained from the samples under nitridation conditions listed in the insert.

The nitridation temperature dependences are indicated by the two pairs of parallel curves. From the straight lines shown as solid and dotted, one can obtain apparent activation energies of 0.12 and 0.25 eV, respectively.

Activation energies of the plasma nitridation with or without the external dc voltage indicate only a very weak temperature dependence in the range of 680°-920°C. The gradient difference of the curves is considered to be caused by the application of the external dc voltage on the nitridation. However, these activation energies are somewhat smaller than those reported by Murarka *et al.* for the thermal nitridation of silicon (7).

Next, we will discuss the kinetics of the plasma anodic nitridation of silicon and propose a theory for the anodization mechanisms of silicon. For this purpose, at first, we referred to the model of thermal oxidation of silicon.

In thermal oxidation, there are three basic steps theoretically established by Deal and Grove (8). These three steps are the transportation of oxidant gases, the diffusion of oxidant species in oxide film, and the reaction with the silicon surface. The theory consists of the flux correspondence to each step at each boundary and well explains the experimental results of thermal oxidation. The same analysis based on the solution of the continuity equation has been applied to thermal nitridation (9). It was concluded that the experimental results were adequately explained by the three step model.

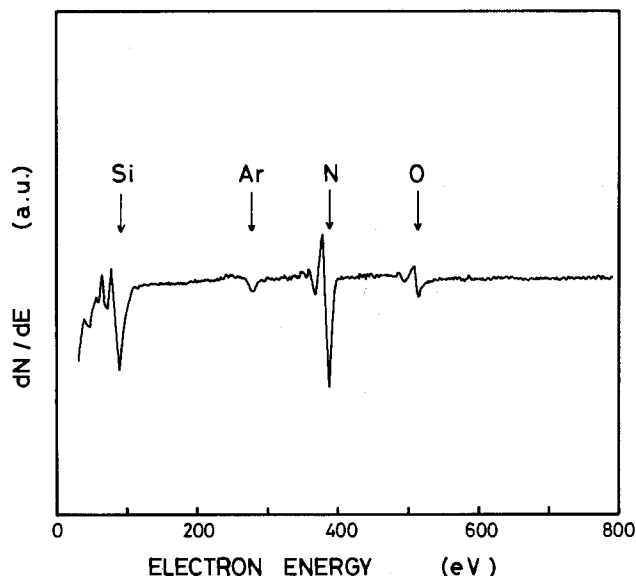


Fig. 3. Typical Auger electron spectrum of plasma anodic nitrided film.

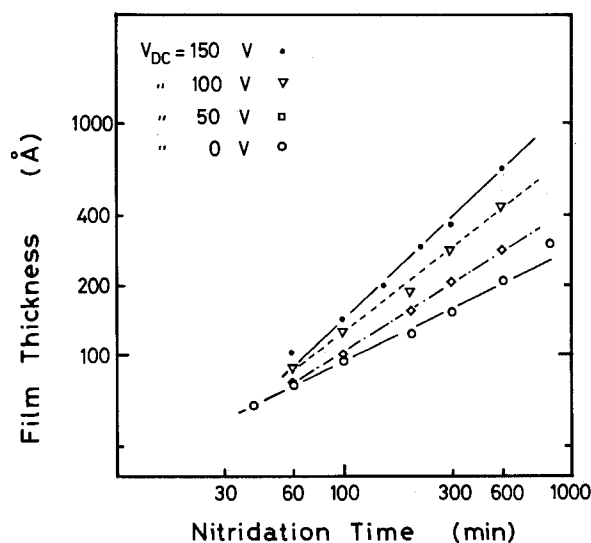


Fig. 5. Dependence of the film thickness on nitridation time

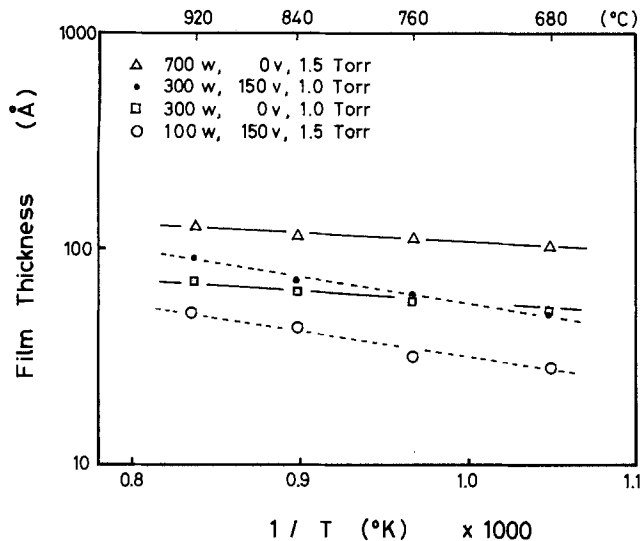


Fig. 6. Dependence of the film thickness on nitridation temperature

In the plasma anodic nitridation of a silicon surface, the growth rate constants and characteristic parameters of nitridation were deduced. When the nitridation time is long, the growth rate has an exact parabolic relationship for the plasma nitridation without the external dc voltage supply. The relationship between the nitridation time and the thickness of the growth film shown with open circles in Fig. 5 can be expressed in functional form as $x_n^2 = Bt$, where x_n and t are the silicon nitride thickness and nitridation time, respectively, and B is the temperature-dependent constant. In this relationship, the constant B is calculated as $0.86 \times 10^{-6} \mu\text{m}^2/\text{s}$.

The significant effect of an external dc voltage on nitridation growth kinetics was suggested by the experimental data. It is clear that the gradient of these curves increases as the external dc voltage increases, as shown in Fig. 5. The growth rate of nitride film on the silicon surface was accelerated with the positive dc voltage supplied on the silicon substrate. Therefore, the relationship between the nitridation time and the nitride film thickness is empirically described as $x_n(2 - mV_{dc}) = Bt$, where the constant m was given as 0.00695 V^{-1} .

The effect of the external dc voltage was investigated from the in-depth Auger profile of the nitrided film. Figure 7 shows a typical profile of the plasma anodic nitrided film. The film was grown for 400 min in a nitrogen-hydrogen mixture at an external dc voltage of +80V. The peak-to-peak heights of the N_{KLL} and O_{KLL} lines were plotted as a function of the sputtering time. The nitrogen and oxygen profiles are described with filled and open

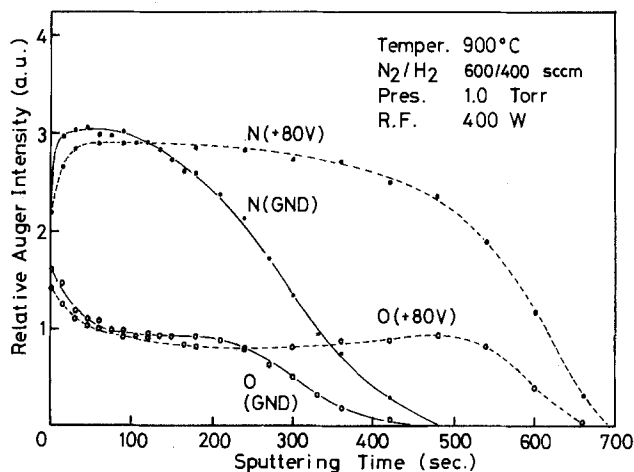


Fig. 7. In-depth Auger profile of the nitrided silicon in nitrogen-hydrogen plasma with positive external voltage.

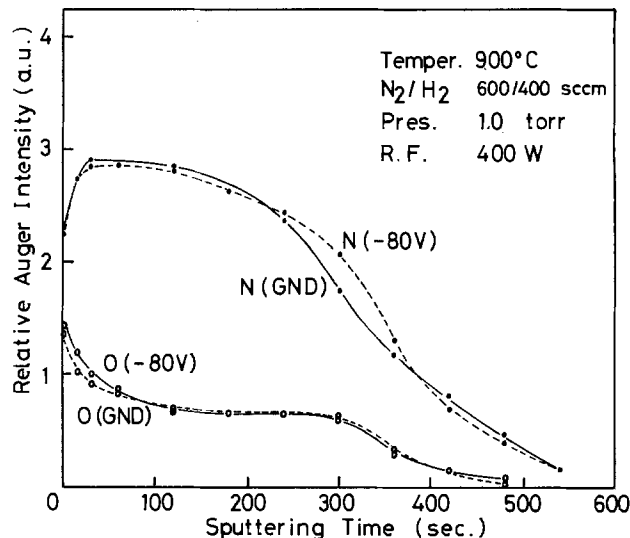


Fig. 8. In-depth Auger profile of the nitrided silicon in nitrogen-hydrogen plasma with negative external voltage.

circles, respectively, for both the samples loaded on the anode and the ground side of silicon carbide rods. The thickness of the films of the anodized sample loaded on the anode was almost twice that of the ground sample. The most interesting feature in Fig. 7 is that the tail of the nitrogen profile reaches deeply into the silicon substrate compared with that of the oxygen profile. Nitrogen apparently diffused into silicon more easily than oxygen, even though the nitridant species seems to diffuse slower through the nitride film in comparison to oxygen through the oxide. The nitrogen fraction is highest near the film surface and decreases toward the interface. It is also shown that the nitridant species has difficulty diffusing through the film and that the surface region is preferentially nitrided.

The effects of the anodization by the application of the external negative dc voltage were studied. The in-depth Auger profiles of nitrided films grown for 400 min in a nitrogen-hydrogen mixture plasma at an external dc voltage of -80V is shown in Fig. 8. Nitrogen profiles for both samples loaded on the cathode (the supplied voltage po-

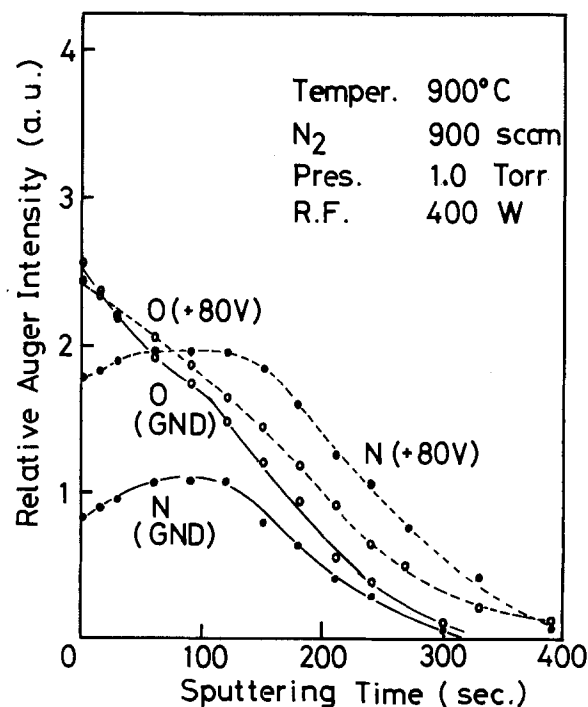


Fig. 9. In-depth Auger profile of the nitrided silicon in nitrogen plasma with positive external voltage.

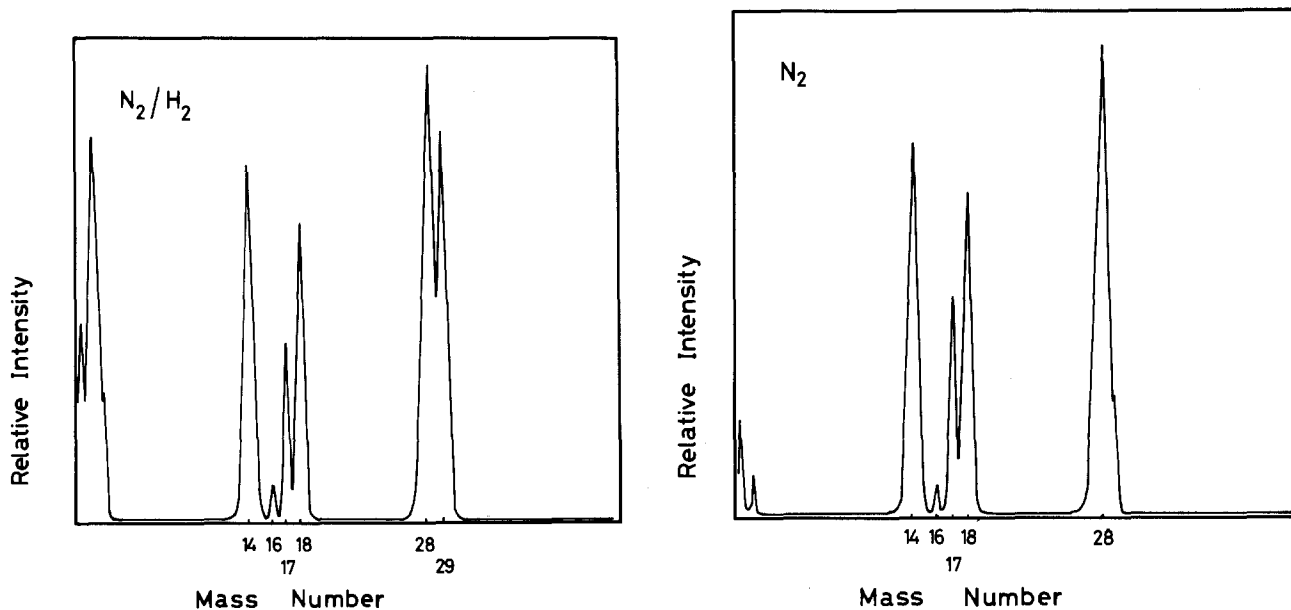


Fig. 10. Quadrupole mass spectra for nitrogen-hydrogen mixture plasma (a, left) and nitrogen plasma (b, right)

larity was changed) and the ground show almost the same curve. Beside the oxygen profiles were drawn almost the same curve one above another for the external dc positive and negative voltages. There exists no difference of film thickness between the samples loaded on the cathode and the ground level.

Role of hydrogen content.—Nitridation using plasma anodization is considerably more complex, and, at present, we can only present a tentative description of the anodization mechanism. It has been previously suggested that the nitridation of silicon is generally subject to parabolic growth behavior. Analysis of growth behavior in plasma anodization indicates that nitridation is essentially a diffusion-limited process and, presumably, the nitridant species migrate to react with silicon at the interface. Figure 9 illustrates in-depth Auger profile of the film grown for 400 min in nitrogen only. The nitrogen profiles were shrunk abruptly for both samples loaded on the anode and the ground. However, the oxygen profiles fully broadened in the direction of the depth of the films. It is quite different from the former profiles of the nitrided film obtained in the hydrogen-nitrogen mixture plasma. The tail of the nitrogen profiles disappeared before the decline and fall of the oxygen profile for both samples loaded on the anode and the ground.

To investigate the difference between the nitrogen-hydrogen mixture plasma and the nitrogen plasma, the quadrupole mass spectrometer was operated during each nitridation process. The base pressure of the spectrometer was kept at 1×10^{-6} torr, and the measurements were started after the nitridation pressure became stable. In Fig. 10a and 10b, mass spectra obtained from the nitrogen-hydrogen mixture plasma and nitrogen plasma are shown. The peaks observed in both spectra at atomic mass unit (amu) 14 and 28 were coincident with N and N₂. The intensities at amu 16, 17, and 18 were the residual oxygen and hydro-oxygen. The amu 2 and 29 peaks appear on the nitrogen-hydrogen mixture spectrum, and the amplitude of the other peak intensities has not changed between the two kinds of plasma. In the nitrogen-hydrogen plasma, H⁺, H₂⁺, nitrogen-hydrogen molecular ions of NH⁺, NH₂⁺, and NH₃⁺ were identified. Those ions might play the role of nitridant species. Also, it is considered that electrically neutral particles such as nitrogen and nitrogen-hydrogen radicals contribute to the nitridation reaction in plasma discharge. One possibility is that the energetic bombardment of these nitridant species in the plasma promotes the reaction of nitridation on the silicon surface to form the thick nitride film.

Conclusions

Growth kinetics of the plasma anodic nitridation of silicon were investigated using the nitrogen-hydrogen mixture plasma. Results of infrared absorption spectrum and the Auger profile indicated the formation of nitrided films on the silicon surface and the TEM micrograph actually showed the nitridation of silicon. The relationship between the nitridation time and the nitride film thickness can be expressed as $x_n(2 - mV_{dc}) = Bt$. In this equation, the temperature dependent constant B is calculated as $0.86 \times 10^{-6} \mu\text{m}^2/\text{s}$ and m is given as 0.00695 V^{-1} . The activation energy of anodization is about twice that of plasma nitridation. Therefore, the external dc voltage is effective in obtaining a higher growth rate of nitrided film on silicon surface. Hydrogen content also greatly contributes to the nitridation of silicon in plasma glow discharge. Some kinds of nitrogen-hydride ions in plasma work as the nitridant species to promote the reaction of nitridation.

Acknowledgments

The authors wish to acknowledge the encouragement of Dr. H. Oka and are also grateful to Professor Dr. W. G. Oldham of California University for valuable discussions.

Manuscript received March 4, 1985. This was Paper 59 presented at the Toronto, Ontario, Canada, Meeting of the Society, May 12-17, 1985.

Mitsubishi Electric Corporation assisted in meeting the publication costs of this article.

REFERENCES

1. R. Dennard, F. Gaensslen, H. Yu, V. Rideout, E. Basous, and A. LeBlac, *IEEE J. Solid-State Circuits*, **sc-9**, 256 (1974).
2. R. G. Frieser, *This Journal*, **115**, 1092 (1968).
3. E. J. M. Kendall, *J. Phys. D, Ser. 2*, **1**, 1409 (1968).
4. T. Ito, S. Hijiya, T. Nozaki, H. Arakawa, M. Shinoda, and F. Fukukawa, *This Journal*, **125**, 448 (1978).
5. V. Q. Ho and T. Sugano, *IEEE Trans. Electron Devices*, **ed-27**, 1436 (1980).
6. M. Hirayama, T. Matsukawa, H. Arima, Y. Ohno, N. Tsubouchi, and H. Nakata, *This Journal*, **131**, 664 (1984).
7. C. P. Murarka, C. C. Chang, and A. C. Adams, *ibid.*, **126**, 994 (1979).
8. B. E. Deal and A. S. Grove, *J. Appl. Phys.*, **16**, 3770 (1965).
9. C. Y. Wu, C. W. King, M. H. Lee, and C. T. Chen, *This Journal*, **129**, 1559 (1982).

Solubilities of α -Fe₂O₃ and Fe₃O₄ in Fused Na₂SO₄ at 1200 K

Y. S. Zhang and Robert A. Rapp*

Department of Metallurgical Engineering, The Ohio State University, Columbus, Ohio 43210

ABSTRACT

The solubility of mixed α -Fe₂O₃ and Fe₃O₄ in fused Na₂SO₄ was measured at 1200 K as a function of the melt basicity at 2.14×10^{-7} atm O₂. At lower P_{O₂}, in separate ranges of basicity where either Fe₃O₄ or else FeS is the stable phase, the solubilities of these compounds in Na₂SO₄ were determined. From these solubility measurements, the activity coefficients of NaFeO₂, FeS, and FeSO₄ in fused Na₂SO₄ were calculated to be 430, 180, and 0.83, respectively. On this basis, the solubilities of the iron oxides α -Fe₂O₃ and Fe₃O₄ and the dominant acidic and basic solutes were calculated for the entire regimes of P_{O₂} and melt basicity in which these phases are stable in Na₂SO₄.

Hot corrosion occurs at high temperatures in oxidizing environments when a molten salt deposit contacts a metal surface. Hot corrosion by molten Na₂SO₄ can cause significant damage in gas turbine and other combustion-product environments. Metal oxides are often the stable phases in contact with fused Na₂SO₄. Therefore, a knowledge of the solubility behavior of metal oxides in molten Na₂SO₄ should assist in understanding hot corrosion processes, especially the initiation of hot corrosion. The solubilities of NiO (1, 2), Co₃O₄ (1, 2), Al₂O₃ (3), and Y₂O₃ (4) in Na₂SO₄ have been reported recently.

The solubility of α -Fe₂O₃ in fused Na₂SO₄ (5) has been previously measured at 1 atm O₂ and 1200 K as a function of the melt basicity, defined as $\log a_{\text{Na}_2\text{O}}$. However, α -Fe₂O₃ is stable only at high P_{O₂} and in a certain basicity regime. As the P_{O₂} in a Na₂SO₄ melt is reduced, Fe₃O₄ becomes stable. From the thermodynamic phase stability diagram for the Na-Fe-S-O system shown as Fig. 1, the solute species and solubilities of the two iron oxides would be expected to depend upon both the melt basicity and the P_{O₂} in the melt. Obviously, solubility measurements at reduced oxygen pressures are needed to provide an overview of the dissolution behavior in the iron-oxygen-sulfur system in Na₂SO₄, and to provide insight for extension to other systems.

In the present work, the solubility of the coexisting oxides, α -Fe₂O₃ and Fe₃O₄, was measured at 1200 K and 2.14×10^{-7} atm O₂. (See Fig. 1.) This measured P_{O₂} corresponds exactly to the thermodynamic value from Ref. (6) for α -Fe₂O₃/Fe₃O₄ equilibrium at 1200 K. However, this result is inconsistent with the JANAF thermodynamic data used previously (5). Furthermore, as shown in the previous work (5) as well as in this work, a plateau in the basic solubility for α -Fe₂O₃ occurs for $\log a_{\text{Na}_2\text{O}} > -8.9$, which is inconsistent with the only available data for $\Delta G^\circ_{\text{NaFeO}_2}$. Therefore, in this work, to retain an internal consistency for the calculation of solute activity coefficients and in the construction of Fig. 1, values of ΔG°_f used for compounds in the system are the same as those listed in the preceding papers (3, 5) except for the use of $\Delta G^\circ_{\text{Fe}_3\text{O}_4} = -730$ kJ/mol and $\Delta G^\circ_{\text{NaFeO}_2} = -479$ kJ/mol. These changes are not great, but are thought to represent an improvement over other reported values (7, 8). The dashed lines of Fig. 1 are calculated lines of isoactivity for the several solute species in the system. Figure 1 shows that at P_{O₂} = 2.14×10^{-7} atm, NaFeO₂ and FeSO₄ should be the dominant basic and acidic solutes, respectively. From the solubility measurements reported here, activity coefficients of NaFeO₂ and FeSO₄ in Na₂SO₄ are estimated later. At even lower P_{O₂}, dissolved FeS should be the predominant acidic solute of Fe₃O₄. In order to obtain the activity coefficient of FeS in fused Na₂SO₄, the solubility of FeS was also measured within the field of FeS stability. Finally, a generalized map for the solubility behavior in the Fe-O-S system has been calculated for the entire ranges of P_{O₂} and melt basicity in which α -Fe₂O₃ and Fe₃O₄ are stable in Na₂SO₄ at 1200 K. The method may serve as a model for the analysis of other metal-oxygen-sulfur systems.

* Electrochemical Society Active Member.

Experimental Apparatus and Procedure

The experimental setup is illustrated in Fig. 2. A closed-end mullite tube served as the reaction chamber which was closed by a gastight, water-cooled stainless steel flange joined by epoxy. Solid-state electrodes were inserted into the Na₂SO₄ melt through stainless steel adaptors with O-rings. Fused Na₂SO₄ and iron oxide powder were contained in an internal alumina crucible supported by an alumina tube which also sheathed a Pt-Pt/10% Rh thermocouple. The temperature was controlled at 1200 ± 3 K using an Electromax (L&N) temperature controller.

The basicity and oxygen pressure in the Na₂SO₄ melt were measured at a Pt wire working electrode by two immersed reference electrodes: a sodium sensor and an oxygen probe. The sodium sensor consisted of a silver wire contacting a Na₂SO₄-10 mole percent (m/o) Ag₂SO₄ melt contained in a closed-end mullite (3Al₂O₃ · 2SiO₂) tube (McDanel MV30), which is a sodium ion conductor (over a grain boundary glass phase) at high temperatures. A platinum wire, spot welded to the silver wire, served as the lead wire. The mullite tube was sealed at the top with an Al₂O₃-base ceramic cement to prevent the loss of SO₃ by the thermal decomposition of the sulfate. The oxygen probe consisted of a painted porous platinum electrode connected to a Pt wire inside a partially stabilized zirconia [3.5 weight percent (w/o) CaO] tube. At 1200 K, the open-circuit voltage (1) between these two reference electrodes is given by

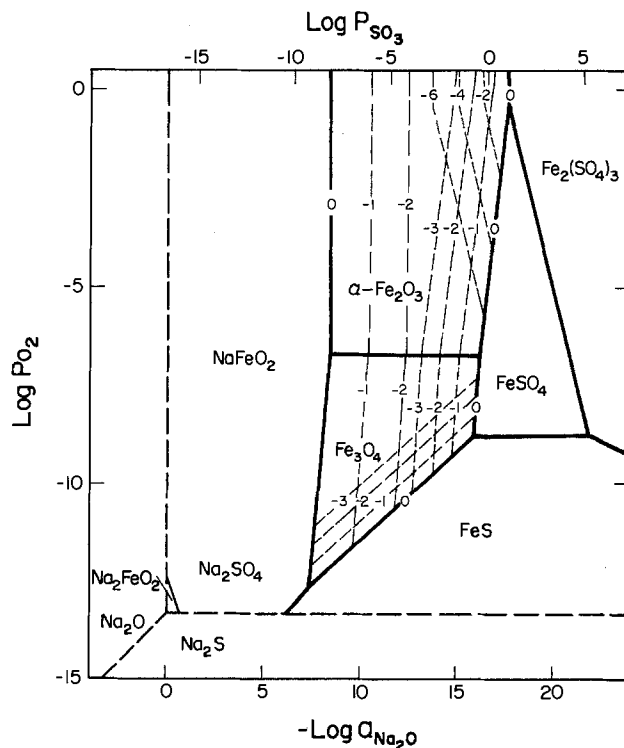


Fig. 1. Thermodynamic phase stability diagram for the Na-Fe-S-O system at 1200 K.

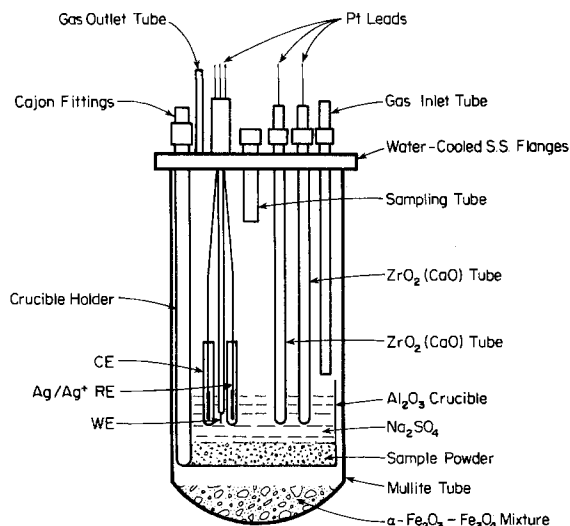


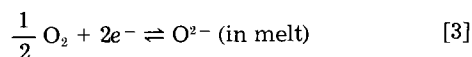
Fig. 2. Experimental setup for solubility measurements

$$E(V) = 1.4943 + 0.119 \log a_{\text{Na}_2\text{O}} (\text{melt}) \quad [1]$$

The open-circuit voltage (1) between the Pt working electrode and the oxygen probe is given by

$$E(V) = 0.0403 + 0.0595 \log P_{\text{O}_2} \quad [2]$$

The basicity of the Na₂SO₄ melt was adjusted by pumping oxide ions into or out of the melt using another partially stabilized ZrO₂ tube. A platinum wire in another mullite tube containing only Na₂SO₄ served as a counterelectrode for the titration. As shown recently (2, 9), upon applying a voltage in this circuit, the oxide ion concentration of the melt may be increased or decreased by driving the reaction



to the left or the right. In this study, different values of voltage were applied to change the electrochemically measured melt basicity, $\log a_{\text{Na}_2\text{O}}$, from -7.5 to -13.6.

About 25g of reagent-grade Na₂SO₄ and 5g of mixed α -Fe₂O₃ (99.9% purity) and Fe₃O₄ (99.99% purity) powder (1:1 molar ratio) were charged into the alumina crucible, and about 150g of an equimolar α -Fe₂O₃ and Fe₃O₄ powder mixture was placed on the floor of the mullite reactor. After drying the salt and the mixed iron oxides at 150°-200°C in a slowly flowing purified argon gas for at least 24h, the system was heated to 1200 K and closed to further gas flow. A suitable voltage was applied to the ZrO₂ pumping electrode with a potentiostat (Wenking ST72). After a few hours, the P_{O_2} in the melt decreased to 2.14×10^{-7} atm, corresponding to the equilibrium oxygen pressure of α -Fe₂O₃ and Fe₃O₄ at 1200 K. Various times were required for the melt basicity to reach a desired value, and thereafter the basicity remained constant. After a day of equilibration, samples of the melt were taken by freezing a small amount of salt onto a cool alumina rod. Each salt sample, about 0.2g, was weighed to an accuracy of 0.1 mg, and dissolved into 100 or 1000 ml of 0.02N HCl solution, depending upon the expected iron concentration in the salt. An atomic absorption spectrophotometer (Perkin-Elmer, Series 360) with a graphite furnace was used to determine the iron content of the aqueous solutions. Only a small amount, 10 μ liter, of the sample solution was added to the graphite furnace in order to avoid any uncertainty introduced by the Na₂SO₄ salt in the solution.

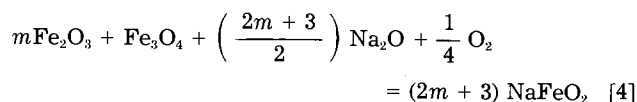
For determining the activity coefficient of FeS in fused Na₂SO₄, the solubility of FeS was measured in the range on Fig. 1 where FeS is the stable phase. The oxygen pressure was kept at 3.5×10^{-12} atm by placing nickel powder in the system, and the melt basicity was adjusted to -12

and -14 by titration. To substantiate the FeS activity coefficient determined in this way, the solubilities of Fe₃O₄ were measured at the same P_{O_2} and at basicities of -8.5, -9.0 and -9.5, respectively.

Results and Discussion

The measured solubility values for mixed α -Fe₂O₃ and Fe₃O₄ in fused Na₂SO₄ at 1200 K and 2.14×10^{-7} atm O₂ are shown in Fig. 3. Each data point in Fig. 3 is the average of several measurements of the concentration of soluble iron in Na₂SO₄ for each salt sample, compared with a certified standard solution for iron.

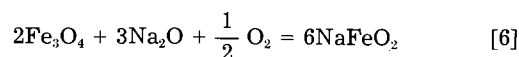
In basic dissolution, the measured dependence of the solubility on the melt basicity indicates that FeO₂⁻ is the solute species for the mixed iron oxides. The dependence is consistent with the following dissolution reaction



For excess Fe₂O₃ and Fe₃O₄ at constant P_{O_2}

$$\frac{\partial(\log a_{\text{NaFeO}_2})}{\partial(-\log a_{\text{Na}_2\text{O}})} = -\frac{1}{2} \quad [5]$$

The individual oxide Fe₂O₃ or Fe₃O₄ obeys this same dependence. Above 2.14×10^{-7} atm oxygen, oxygen is not involved in the basic dissolution of α -Fe₂O₃, so that no oxygen dependence is expected for the soluble NaFeO₂ concentration. At oxygen pressures below 2.14×10^{-7} atm, the basic solubility of Fe₃O₄ is dependent upon P_{O_2} according to the reaction

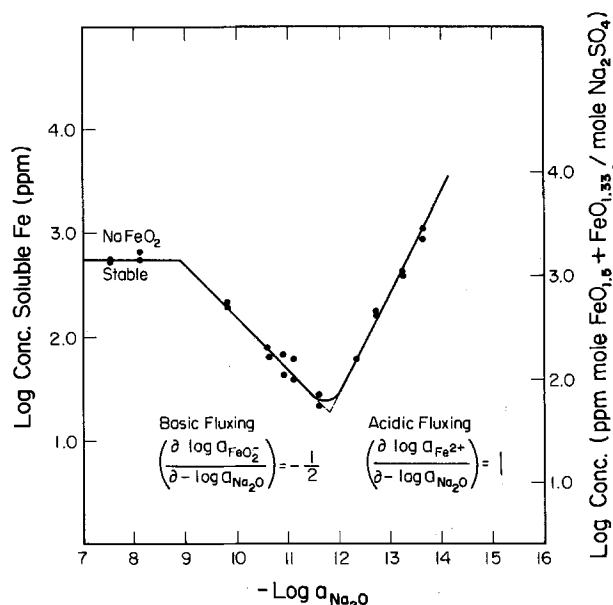


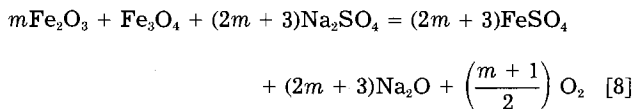
For excess Fe₃O₄ at constant $a_{\text{Na}_2\text{O}}$

$$\frac{\partial(\log a_{\text{NaFeO}_2})}{\partial(\log P_{\text{O}_2})} = \frac{1}{12} \quad [7]$$

The FeO₂⁻ concentration plateau at the left of Fig. 3 results because O²⁻ ions are not involved in the dissolution of NaFeO₂ to form FeO₂⁻ ions.

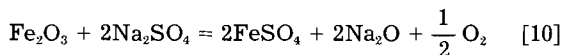
In the acidic dissolution of Fe₃O₄ + α -Fe₂O₃, the Fe²⁺ solute ion is indicated by the $\log a_{\text{Na}_2\text{O}}$ dependence of the solubility. The dependence of the soluble FeSO₄ concentration upon the melt basicity is consistent with the following dissolution reaction

Fig. 3. Solubilities of α -Fe₂O₃ + Fe₃O₄ in fused Na₂SO₄ at 1200 K



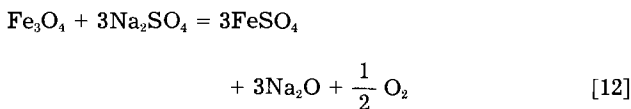
$$\frac{\partial(\log a_{\text{FeSO}_4})}{\partial(-\log a_{\text{Na}_2\text{O}})} = 1 \quad [9]$$

The dependences of the acidic solubilities of $\alpha\text{-Fe}_2\text{O}_3$ and Fe_3O_4 on P_{O_2} can be predicted from the reactions



$$\frac{\partial(\log a_{\text{FeSO}_4})}{\partial(\log P_{\text{O}_2})} = -\frac{1}{4} \quad [11]$$

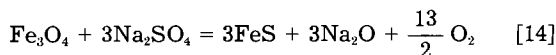
and



$$\frac{\partial(\log a_{\text{FeSO}_4})}{\partial(\log P_{\text{O}_2})} = -\frac{1}{6} \quad [13]$$

The activity coefficient of soluble NaFeO_2 in fused Na_2SO_4 was calculated to be 460, which is close to the value of 400 derived from the previous work (using adjusted $\Delta G^\circ_{\text{NaFeO}_2}$) (5). The activity coefficient of the FeSO_4 solute in Na_2SO_4 was calculated to be 0.83. These activity coefficient values possess significant uncertainties resulting from the uncertainties in ΔG°_f for NaFeO_2 and FeSO_4 . The minimum solubility for the mixed oxides, $\alpha\text{-Fe}_2\text{O}_3$ and Fe_3O_4 , lies at $-\log a_{\text{Na}_2\text{O}} = 11.8$, which generally meets thermodynamic expectation from Fig. 1.

Four measurements of FeS solubility within the range of FeS stability gave an average concentration of 5.68×10^{-3} mole fraction FeS . From these measurements, the activity coefficient of FeS in fused Na_2SO_4 is estimated to be 180. According to Fig. 1, at very low oxygen pressures, Fe_3O_4 can experience acidic dissolution as soluble FeS . The dissolution reaction should be



From Eq. [14], the dependences of Fe_3O_4 solubility as soluble FeS upon the melt basicity and P_{O_2} can be derived as follows

$$\frac{\partial(\log a_{\text{FeS}})}{\partial(-\log a_{\text{Na}_2\text{O}})} = 1 \quad [15]$$

and

$$\frac{\partial(\log a_{\text{FeS}})}{\partial(\log P_{\text{O}_2})} = -\frac{13}{6} \quad [16]$$

This model for Fe_3O_4 dissolution at low P_{O_2} , as well as the FeS activity coefficient, was proved by the three Fe_3O_4 solubility data points in Fig. 4, which were measured at 3.5×10^{-12} atm oxygen ($\log P_{\text{O}_2} = -11.46$) for three different basicities. As seen in Fig. 4, the two acidic solubility measurements agree exactly with those calculated using the measured activity coefficient for FeS and Eq. [15] and [16]. The other point fits the calculated line for basic solubility.

Based on an assumption of constant activity coefficients from these measurements in combination with the previous work (5), the solubilities of the iron oxides, $\alpha\text{-Fe}_2\text{O}_3$ and Fe_3O_4 in fused Na_2SO_4 were calculated for wide ranges of P_{O_2} and melt basicity, as shown in Fig. 4. In the construction of Fig. 4, the activity coefficient of soluble NaFeO_2 was chosen to be 430, the average of the values estimated from the previous study and this work.

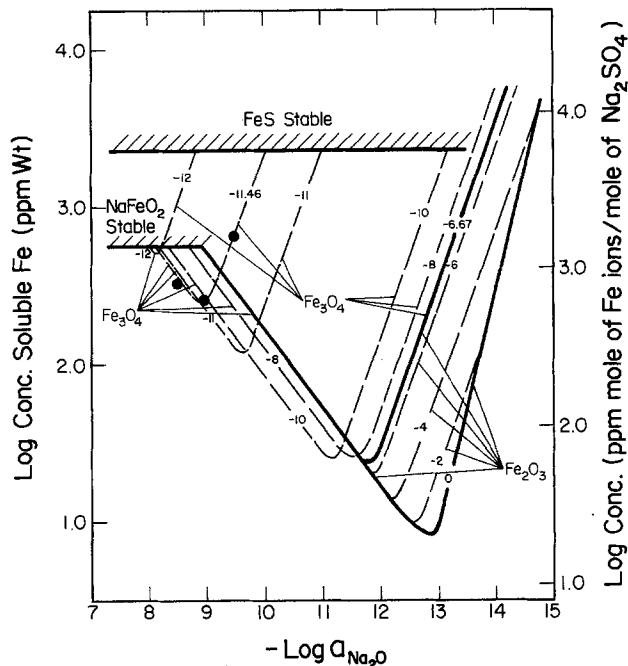
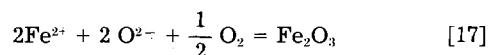


Fig. 4. Measured and calculated solubilities of $\alpha\text{-Fe}_2\text{O}_3$ and Fe_3O_4 in fused Na_2SO_4 at 1200 K.

In Fig. 4, the solid lines represent the measured dependencies of solubilities upon the melt basicity at certain P_{O_2} , while the dashed lines are calculated values. For a specific $\log P_{\text{O}_2}$ value (indicated on the lines), each solubility curve is composed of two segments: the left segment for basic dissolution, and the right for acidic dissolution. In Fig. 4, the basic solubility decreases with decreasing P_{O_2} , except for P_{O_2} equal to or higher than 1.24×10^{-7} atm, whereas the acidic solubility increases with decreasing P_{O_2} . The melt basicity corresponding to the solubility minimum moves to a more basic value with a decrease in P_{O_2} . The only basic solute species of $\alpha\text{-Fe}_2\text{O}_3$ and Fe_3O_4 is FeO_2^- (dissolved NaFeO_2), regardless of the P_{O_2} . The principal acidic solute of $\alpha\text{-Fe}_2\text{O}_3$ is either Fe^{3+} [dissolved $\text{Fe}(\text{SO}_4)_{1.5}$] or Fe^{2+} (dissolved FeSO_4), depending upon both the P_{O_2} and melt basicity. Although the acidic solute for Fe_3O_4 is only Fe^{2+} , it can be described in terms of either dissolved FeSO_4 or else dissolved FeS , depending on the P_{O_2} . In Fig. 4, the acidic solubility lines for Fe_3O_4 at P_{O_2} higher than about 10^{-8} atm represent the concentrations of dissolved FeSO_4 in Na_2SO_4 , while the solubility lines at P_{O_2} lower than about 10^{-10} atm represent the concentrations of dissolved FeS in Na_2SO_4 . Between these two values for P_{O_2} , both solutes are significant.

Figure 4 should be important in understanding the iron oxide fluxing mechanism in the hot corrosion of iron. As an example, consider a piece of iron covered by molten Na_2SO_4 , with a $\log a_{\text{Na}_2\text{O}}$ value in the acidic melt of $\log a_{\text{Na}_2\text{O}} = -13$, with 10^{-1} atm oxygen in the gas phase. At the oxide/melt interface, P_{O_2} should be much lower than 10^{-1} atm resulting from the SO_3 - or O_2 -diffusion limited oxidation of iron, say, 10^{-8} atm. The stable oxide phase at this interface is then Fe_3O_4 , and the solute species is Fe^{2+} . According to Fig. 4, the solubility of Fe_3O_4 at the oxide/melt interface is much higher than that at the melt/gas interface for $\log a_{\text{Na}_2\text{O}} = -13$. Therefore, the migration of Fe^{2+} ions from the oxide/melt interface to the melt/gas interface results in their oxidation to form Fe_2O_3 with a lower solubility



and the Fe_2O_3 may precipitate near the melt/gas interface as porous particles. In this case, the Rapp and Goto criterion (10)

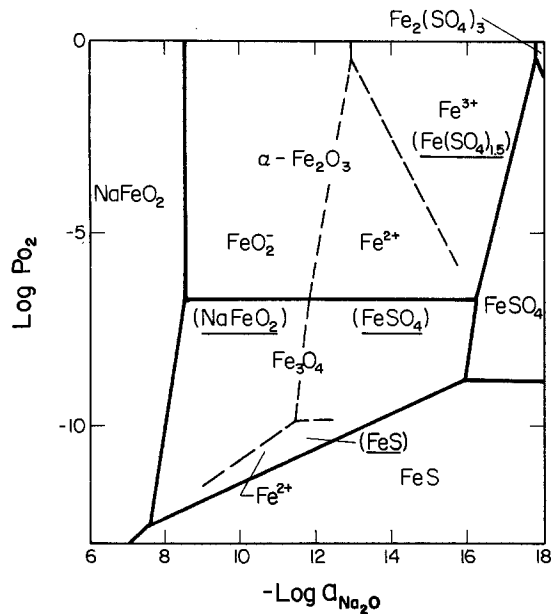


Fig. 5. Dominant solute iron species sections in Na₂SO₄-iron oxide system at 1200 K.

$$\left(\frac{d [\text{Solubility of oxide}]}{dx} \right)_{x=0} < 0 \quad [18]$$

is satisfied. In such a way, hot corrosion continues as the protective Fe₃O₄ scale is dissolved. This model was used by Luthra to interpret the low temperature hot corrosion of cobalt-base alloys (11).

It is useful to identify each of the predominant solute species in the Na₂SO₄-iron oxide system, as shown in Fig. 5. The regimes in P_{O₂} and melt basicity where α-Fe₂O₃ and Fe₃O₄ are stable in Na₂SO₄ are separated by dashed lines into four sectors where different solute species are dominant. The dashed lines denote points of equal solute concentrations (not activities) and therefore possess uncertainties relating back to the solute activity coefficients. The predominance plot may be helpful in the evaluation of the electrochemical reactions in the Na₂SO₄-iron oxide system.

Conclusions

From the solubility measurements and their discussion, the following conclusions can be drawn.

1. The basic solutes of α-Fe₂O₃ and Fe₃O₄ in fused Na₂SO₄ at 1200 K are FeO₂⁻ ions while the acidic solutes are either Fe³⁺ or Fe²⁺, depending upon the P_{O₂} and the melt basicity.

2. The activity coefficient for the basic solute NaFeO₂ in molten Na₂SO₄ at 1200 K was estimated to be 430, and those for Fe(SO₄)_{1.5}, FeS, and FeSO₄ are 3.6 × 10⁻³ (5), 180, and 0.83, respectively.

3. The solubility measurements and calculations may assist in understanding any fluxing mechanism for the hot corrosion of iron, and may aid in the interpretation of electrochemical studies for the Na₂SO₄-iron oxide system.

Acknowledgments

This research was sponsored by the National Science Foundation, Metallurgy Program of the Division of Material Research under Grant DMR 791190. Y. S. Zhang is supported as a Visiting Scientist from People's Republic of China.

Manuscript submitted March 25, 1985; revised manuscript received June 18, 1985.

The National Science Foundation assisted in meeting the publication costs of this article.

REFERENCES

1. D. K. Gupta and R. A. Rapp, *This Journal*, **127**, 2194, 2656 (1980).
2. M. L. Deanhardt and K. H. Stern, *ibid.*, **128**, 2577 (1981).
3. P. D. Jose, D. K. Gupta, and R. A. Rapp, *ibid.*, **132**, 735 (1985).
4. M. L. Deanhardt and K. H. Stern, *ibid.*, **129**, 2228 (1982).
5. Y. S. Zhang and R. A. Rapp, *ibid.*, **132**, 734 (1985).
6. R. A. Rapp and D. A. Shores, in "Techniques of Metals Research," Vol. IV, Part 2, R. A. Rapp, Editor, p. 159, John Wiley and Sons, New York (1970).
7. B. J. Shain, P. C. S. Wu, and P. Chiotti, *J. Nucl. Mater.*, **67**, 13 (1977).
8. JANAF Thermochemical Tables, 2nd ed., National Bureau of Standards 37, U.S. Dept. of Commerce (1971) and supplements.
9. M. L. Deanhardt and K. H. Stern, *J. Phys. Chem.*, **84**, 2831 (1980).
10. R. A. Rapp and K. S. Goto, in "Molten Salts," J. Braunstein and J. R. Selman, Editors, p. 159, The Electrochemical Society Softbound Proceedings Series, Pennington, NJ (1981).
11. K. L. Luthra, in "High Temperature Corrosion," NACE-6, R. A. Rapp, Editor, p. 507, NACE, Houston (1981).

Destabilization of Yttria-Stabilized Zirconia Induced by Molten Sodium Vanadate-Sodium Sulfate Melts

A. S. Nagelberg*

Sandia National Laboratories, Livermore, California 94550

ABSTRACT

The extent of surface destabilization of ZrO_2 -8 weight percent Y_2O_3 ceramic disks was determined after exposure to molten salt mixtures of sodium sulfate containing up to 15 mole percent sodium metavanadate ($NaVO_3$) at 1173 K. The ceramic surface was observed to transform from the cubic/tetragonal to the monoclinic phase, concurrent with chemical changes in the molten salt layer in contact with the ceramic. Significant attack rates were observed in both sodium sulfate and sodium metavanadate-sulfate melts in the presence of sulfur trioxide. The rate of attack was found to be quite sensitive to the mole fraction of vanadate in the molten salt solution and the partial pressure of sulfur trioxide (1×10^{-6} to 1×10^{-3} atm) in equilibrium with the salt melt. The observed approximately parabolic rate of attack was interpreted to be caused by a reaction controlled by diffusion in the salt that penetrated into the porous layer formed by the destabilization. The parabolic rate constant in mixed sodium metavanadate-sodium sulfate melts was found to be proportional to the SO_3 partial pressure and the square of the metavanadate concentration.

Operating temperatures of today's gas turbines are limited by the high temperature mechanical properties of the nickel- and cobalt-based superalloys used for rotating components and by the high temperature corrosion of the metallic coatings on these components. The use of insulating surface layers on critical combustion turbine components is expected to allow higher gas turbine inlet temperatures, thus increasing operating efficiencies.

A thin insulating surface layer is provided by a thermal barrier coating that reduces the underlying metal surface temperature by as much as 150 K and provides a barrier to the ingress of corrosive species from the gas phase. Improved component reliability can be achieved by this reduction in operating temperature. Alternatively, increased gas turbine operating efficiencies are possible since higher inlet gas temperatures can be tolerated.

Several ceramics have been proposed for use as thermal barrier coatings, including Y_2O_3 - and MgO-stabilized zirconia, MgO, and $CaSiO_3$ (1-3). Of these ceramics, zirconia-based ceramics containing 6-12 weight percent (w/o) Y_2O_3 showed superior resistance to cracking and spallation in laboratory tests (1, 3). Clean fuel burner rig tests have shown extended lifetimes. Unfortunately, burner rig tests using sodium or vanadium containing fuels show much shorter ceramic coating lifetimes. Levine (3) reported lifetimes in excess of 10,000 cycles when burning clean fuels. In contrast, when 5 ppm of sodium and 2 ppm vanadium were added to the fuel, lifetimes were less than 100 cycles. The shorter lifetimes have been attributed to chemical attack by fuel impurities and to destabilization of the zirconia-based coating and/or condensation of high thermal expansion phases in the coating pores (1, 3-6).

Zirconia ceramics are partially or totally stabilized by the addition of oxides such as MgO, CaO, and Y_2O_3 . Stabilization refers to the retention of the cubic or tetragonal phases at temperatures at which the monoclinic phase would normally occur in pure ZrO_2 . This stabilization is crucial to coating adherence, since the transformation from tetragonal to monoclinic structure involves a large volume change (~9%) (7). Even though the monoclinic phase is predicted to form at lower temperatures for the stabilized compositions, the slow kinetics of the transformations allow retention of the tetragonal or cubic phases at room temperature. The phase diagram (8) shows that the monoclinic structure is favored at lower temperatures and at lower concentrations of stabilizing oxide.

The zirconia-based ceramics proposed for thermal barrier coatings (6-12 w/o yttria) are found from the phase diagram to be in a two-phase region containing tetragonal and cubic phases at typical turbine operating temperatures (1073-1373 K). As long as coatings remain in either of these two structures, cracking and spallation associated with the tetragonal to monoclinic phase transition

will not occur. However, if the yttria content is reduced slightly, the tetragonal to monoclinic transition will occur upon cooling.

During operation of gas turbines, impurities in the fuel and ingested air are known to lead to the formation of molten surface deposits. The presence of vanadium in the combustion exhaust gases can significantly affect the composition and temperature stability range of the liquid surface deposit. Luthra and Spacil (9) estimated that, for a fuel containing 30 ppm vanadium and 2 ppm sodium, the $NaVO_3 + V_2O_5$ content of the condensate at 1173 K would be nearly 80 mole percent (m/o). For these conditions, a liquid condensate would be stable from 879 to 1279 K. Although these impurity levels are high for presently used clean fuels, numerous gas turbine users have considered using fuels such as residual oils which contain significantly increased impurity levels. For a fuel with only 2-4 ppm vanadium, the calculated $NaVO_3 + V_2O_5$ content of the condensate is 3-15 m/o, respectively. It is thus reasonable to expect that ceramic-coated turbine components may be exposed to salt films containing high vanadium contents (10).

Sodium sulfate in the presence of a sulfur trioxide containing environment has been found to induce destabilization of yttria-stabilized zirconia ceramics (5). The destabilization was attributed to the acidic leaching of yttria from the ceramic substrate. Hamilton and Nagelberg (11, 12) have used Raman spectroscopy to study the phase transformations of stabilized zirconia induced by exposure to molten salt solutions containing sodium metavanadate. They found that the surface attack is very rapid and strongly depended on the metavanadate concentration during exposures in air at 1173 K.

In this study, we have measured the destabilization of the surface of ZrO_2 -8 w/o Y_2O_3 ceramics exposed to molten sodium sulfate and sodium metavanadate-sulfate melts in oxygen-sulfur dioxide-sulfur trioxide atmospheres at 1173 K.

Experimental

High density (greater than 96% of theoretical density) ZrO_2 disks containing 8 w/o Y_2O_3 were obtained from Corning Glass Works, Zircoa Division. Sodium metavanadate ($NaVO_3$) was obtained from Cerac Pure, Incorporated, and sodium sulfate anhydrous from Baker, Incorporated.

Yttria-stabilized zirconia ceramics were exposed to molten salt mixtures containing 0.2, 2.0, 3.9, and 7.7 m/o sodium vanadate in sodium sulfate at 1173 K. Master melts were prepared by melting premixed powders at 1223 K and crushing the solidified salt melt to obtain a uniform composition. Such prepared powders were used to fill 1 ml platinum crucibles in which the 1 cm diam stabilized zirconia disks were immersed during exposure. Initial

*Electrochemical Society Active Member.

melting and ceramic introduction to the salt was done in air. In no case were the immersed ceramics at temperature for more than 5 min during this stage. For experiments using a sulfur dioxide-sulfur trioxide containing atmosphere, the platinum crucibles containing the ceramics were then suspended in a quartz reaction tube in a cold end of the tube under an argon atmosphere. Once the furnace had reached the reaction temperature, the platinum crucibles were inserted into the constant temperature zone of the furnace and the oxygen-sulfur dioxide-sulfur trioxide exposure gas composition introduced. The initial gas mixtures and final equilibrium compositions are given in Table I. The gas mixtures were obtained by mixing either SO_2 or a 1% SO_2 in O_2 mixture with O_2 before passing the gas over a bed of platinum mesh at 1173 K in a precatalyst furnace. A small piece of platinum mesh was also positioned below the salt crucibles in the reaction tube. Exposures were for times up to 500h for sodium metavanadate-sulfate melts and 1600h for pure sodium sulfate melts. For air exposures, the platinum crucibles were placed in a muffle furnace at 1173 K. After exposure, the ceramic disks were removed from the salts by immersion in distilled water. The washed ceramics were subsequently metallographically mounted and polished for examination by optical microscopy, scanning electron microscopy, and electron microprobe analysis.

The solutions containing the dissolved salts were analyzed for elements contained in the salts and original ceramics by atomic absorption and ICP techniques.

Results

Exposure of stabilized zirconia ceramics to a pure sodium sulfate melt at 1173 K in a 1% SO_2 in O_2 environment resulted in a measurable surface destabilization. After 380h, the transformed layer is approximately 40 μm thick. Longer salt exposure showed the monoclinic layer thickness was closely approximated by parabolic growth kinetics, as shown in Fig. 1.

The surface destabilization rate was observed to increase upon the introduction of sodium metavanadate to the salt melt for all the exposures examined. Except for the lowest metavanadate concentration used (0.2 m/o), the increase in the extent of destabilization was dramatic. Figure 2 shows that yttria-stabilized zirconia exposure to a molten salt solution containing 2.0 m/o sodium metavanadate in sodium sulfate at 1173 K in an initially 1.0% SO_2 in O_2 atmosphere resulted in formation of an approximately 50 μm surface layer after 24h. The surface layer formed is identified in the photomicrograph by the increased porosity in the ceramic near the surface. Not very apparent in Fig. 2 is a slight preferential attack of the ceramic along grain boundaries. On several samples examined, a slightly uneven reaction front was observed with the center of grains near the reaction front not appearing as porous as the grain periphery. A more pronounced grain boundary attack was observed by Nagelberg (12) for the molten vanadate attack of magnesia-stabilized zirconia ceramics.

Electron microprobe analysis showed the high porosity region to be depleted in yttrium compared to the bulk ceramic. The surface layer was determined to contain approximately 1 w/o yttrium throughout with no observable concentration gradient except for the center of a few grains near the reaction front. The yttrium concentration in the bulk crystal was 8 w/o, as was expected from the initial composition, and again no observable concentration

Table I. Exposure environment composition

Initial gas composition (%)		Equilibrium composition at 1173 K (%)		
O_2	SO_2	O_2	SO_2	SO_3
90	10	90	7.7	2.4
99	1	99	0.76	0.24
99.9	0.1	99.9	7.6×10^{-2}	2.5×10^{-2}
99.985	0.015	99.99	1.1×10^{-2}	3.7×10^{-3}
1	99	0.25	97	0.15

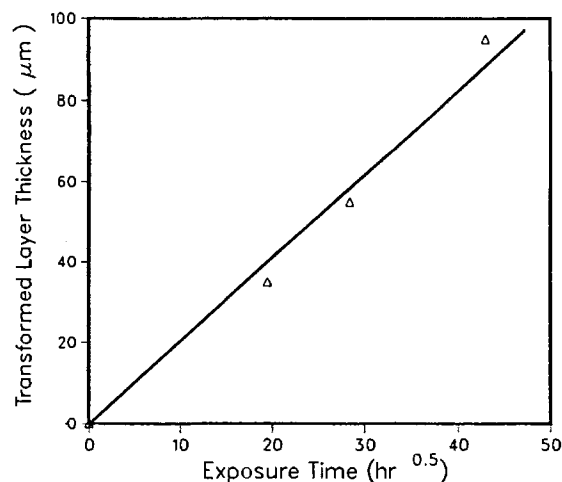


Fig. 1. Transformed layer thickness as a function of the square root of time for ZrO_2 -8% Y_2O_3 exposed to Na_2SO_4 at 1173 K in a 1% SO_2 in O_2 atmosphere.

gradient was observed in the region in proximity to the surface layer.

As expected, chemical analysis of the wash solutions indicated that no zirconium was dissolved in the salt during exposure to the molten salts. The observed dissolved yttrium levels correlated well with the extent of yttrium removal from the ceramic.

The time dependence of the thickness of the yttrium-depleted surface layer for metavanadate concentrations of 0.2, 2.0, and 3.9 m/o are shown in Fig. 3 as a function of the square root of time after exposure to a 1.0% SO_2 in O_2 atmosphere at 1173 K. Similar to destabilization induced by a pure sodium sulfate salt in the presence of sulfur trioxide, an approximately parabolic time dependence appears to be approximately followed for all three vanadate concentrations in the molten salt. The measured parabolic rate constants are given in Table II. Also listed in Table II is a parabolic rate constant for a sodium metavanadate concentration of 1.0 m/o. This value was obtained by assuming parabolic kinetics and a single measured value of the monoclinic layer thickness after a 164h exposure to 1% SO_2 in O_2 atmosphere. The monoclinic layer thickness does indicate a deviation from parabolic behavior toward linear kinetics at longer times.

Variation of the sulfur dioxide (and thus sulfur trioxide) content of the atmosphere above the salt melts was found to cause significant changes in the extent of destabilization of the ceramics. For an atmosphere initially con-

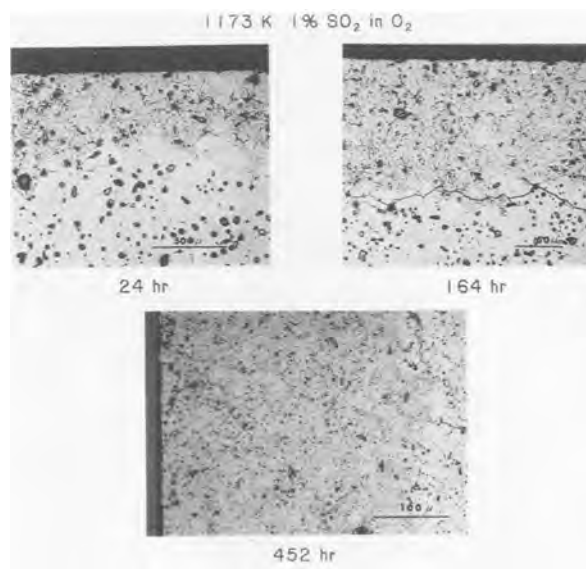


Fig. 2. Photomicrographs of ZrO_2 -8 w/o Y_2O_3 exposed at 1173 K to a 1% SO_2 in O_2 atmosphere for various times.

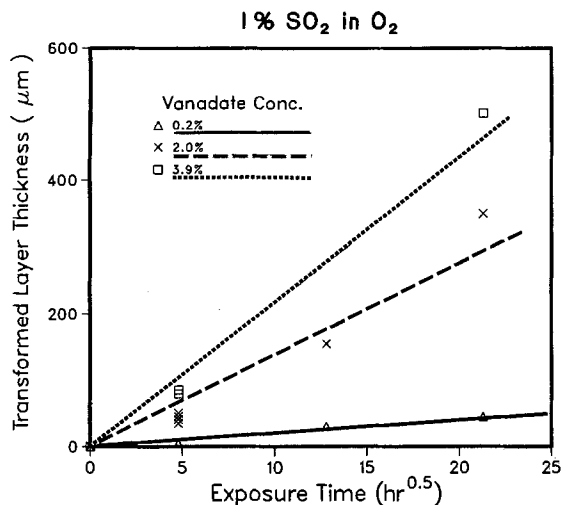


Fig. 3. Transformed layer thickness as a function of the square root of time for $\text{ZrO}_2\text{-8\% Y}_2\text{O}_3$ exposed to $\text{NaVO}_3\text{-Na}_2\text{SO}_4$ melts at 1173 K in a 1% SO_2 in O_2 atmosphere.

taining 0.1% SO_2 in O_2 ($P_{\text{SO}_3} = 2.5 \times 10^{-4}$) and 2.0% metavanadate, the transformed layer was approximately 15 μm thick after 24h. In contrast, an environment initially containing 10% SO_2 in O_2 ($P_{\text{SO}_3} = 2.4 \times 10^{-2}$) results in a 200 μm thick layer in the same time. Results for three vanadate concentrations after a 24h exposure to various partial pressures of SO_3 at 1173 K are given in Fig. 4. The slope of all the lines drawn in Fig. 4 is 1/2.

Using the parabolic rate constants given in Table II, the metavanadate compositional dependence in the presence of an environment containing 0.0025 atm SO_3 is plotted in Fig. 5. The measured parabolic rate constant for exposures to a pure sodium sulfate melt under the same SO_3 partial pressure is also given for comparison as the filled triangle. Except for the parabolic rate constant for the lowest metavanadate concentration (0.2 m/o), the measured rate constants are fitted well by a line with a slope of 2.

Discussion

Hamilton and Nagelberg (13) have reported the rapid attack of yttria-stabilized zirconia by both pure metavanadate melts and mixed sulfate-metavanadate melts at 1173 K in air. From their salt exposures in air, it was established that the formation of a surface monoclinic layer occurred due to the acidic leaching of yttrium from the stabilized zirconia ceramic to form a Y^{3+} salt soluble species. From the phase diagram, it can be seen that the removal of yttrium results in a phase transformation to the monoclinic structure. Associated with the removal of yttrium, an increase in the pyrovanadate content of the salt was also observed. A similar reaction process is believed to be occurring in the presence of an $\text{SO}_2\text{-SO}_3\text{-O}_2$ atmosphere. As would be expected from their results, the monoclinic ceramic surface layers observed in this study were depleted in yttrium uniformly throughout the layer. In addition, the salt was found to contain significant quantities of dissolved yttrium but no zirconium.

The attack rates measured in $\text{SO}_2\text{-SO}_3$ containing atmospheres are a factor of 100-1000 faster than were reported for vanadate-sulfate melts exposed to air. Figure 6 com-

Table II. Parabolic rate constants ($P_{\text{SO}_3} = 2.4 \times 10^{-3}$)

NaVO_3 concentration (m/o)	Parabolic rate constant (cm^2/s)
0.0	1×10^{-11}
0.2	1×10^{-11}
1.0	1.7×10^{-10}
2.0	5.4×10^{-10}
3.9	1.5×10^{-9}

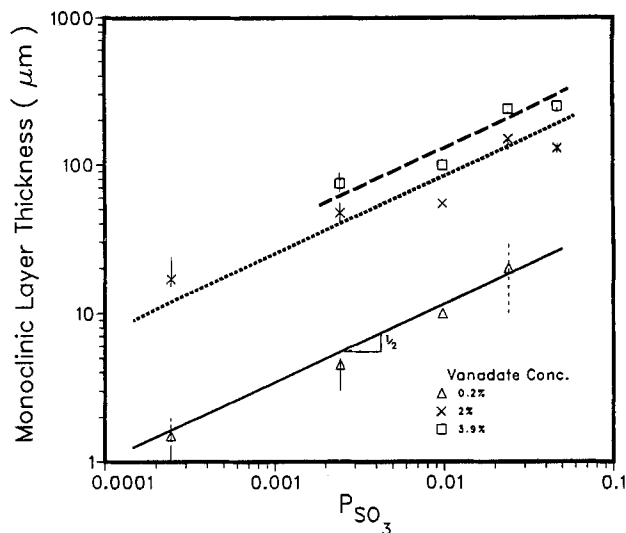
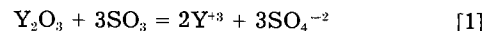


Fig. 4. Transformed layer thickness as a function of partial pressure SO_3 for $\text{ZrO}_2\text{-8\% Y}_2\text{O}_3$ exposed to Na_2SO_4 at 1173 K.

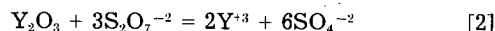
pare the morphology of the scales formed in air with the destabilized surface layer formed in the presence of an equilibrated 99% $\text{SO}_2\text{-1\% O}_2$ atmosphere at 1173 K. The monoclinic surface layers formed in both air and $\text{SO}_2\text{-SO}_3\text{-O}_2$ containing atmospheres were found to be extremely porous, as can be seen in Fig. 6. The only difference between the different salt exposures was the extent of attack.

Similar to the observations of Barkalow and Pettit (5), yttrium leaching from the ceramic was found to occur in the presence of sodium sulfate alone. The addition of sodium metavanadate was found to significantly enhance the rate of formation of a monoclinic surface layer. Since the experimental melts were buffered with respect to the sulfur trioxide partial pressure, it is assumed here that two similar yet different mechanisms are active in the mixed sulfate-vanadate melts.

In pure sodium sulfate melts, a possible dissolution mechanism for Y_2O_3 dissolved in the ZrO_2 [first proposed by Barkalow and Pettit (5)] is the acidic leaching of yttria given by



or considering the existence of the pyrosulfate ion



In either case, the reaction strongly depends on the sulfur trioxide partial pressure. Jones *et al.* (14) have determined

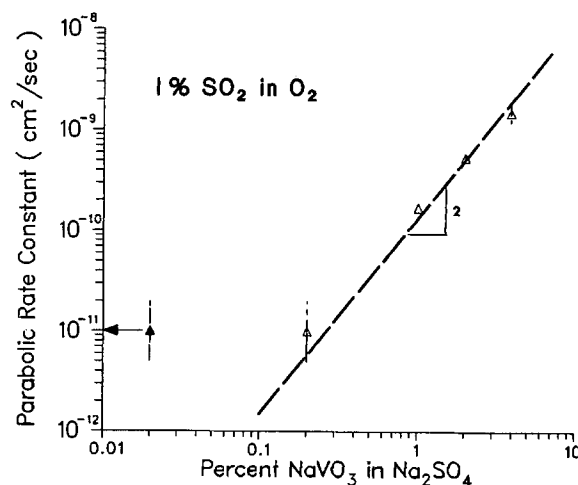


Fig. 5. Parabolic rate constant as a function of the NaVO_3 concentration for $\text{ZrO}_2\text{-8\% Y}_2\text{O}_3$ exposed to Na_2SO_4 at 1173 K in a 1% SO_2 in O_2 atmosphere.

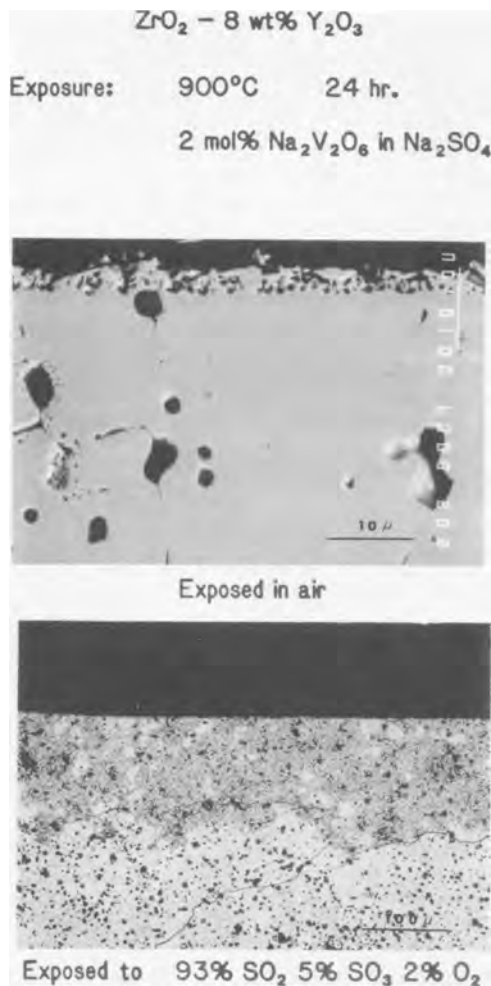
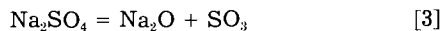


Fig. 6. Photomicrographs of ZrO_2 -8 w/o Y_2O_3 exposed at 1173 K for 24h.

the minimum SO_3 partial pressure to cause sulfation of pure yttria as approximately 2.5×10^{-5} atm at 1173 K. The partial pressures utilized in this study are easily in excess of this value. These authors also noted an increased sulfation rate of the yttria in the presence of Na_2SO_4 .

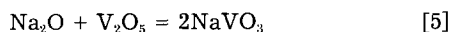
For salt melts containing sodium sulfate, a SO_2 - SO_3 - O_2 atmosphere determines the partial pressure of sulfur trioxide and thus the sodium oxide activity of the melt by Eq. [3]



$$k_1 = a_{Na_2O} P_{SO_3} / a_{Na_2SO_4} \quad [4]$$

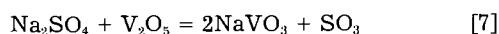
In the absence of a sulfur dioxide-sulfur trioxide-oxygen containing cover gas the Na_2O activity of the salt melt is undefined and is not regulated. Thus, the sodium salt will decompose sufficiently to obtain local thermodynamic equilibrium, making the melt increasingly basic (high activities of Na_2O) during exposure to a flowing gas stream.

When considering mixed sodium metavanadate-sodium sulfate melts, the sodium oxide activity of the molten salt in turn affects the activity of V_2O_5 by Eq. [5]



$$k_3 = a_{NaVO_3}^2 / a_{Na_2O} a_{V_2O_5} \quad [6]$$

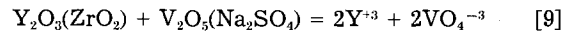
Combining Eq. [3] and [5]



$$k_5 = a_{NaVO_3}^2 P_{SO_3} / a_{Na_2SO_4} a_{V_2O_5} \quad [8]$$

Thus it is found that the V_2O_5 activity is proportional to the partial pressure of sulfur trioxide and the square of

the sodium metavanadate concentration as $NaVO_3$, when it is assumed that the sodium sulfate activity and activity coefficient for the metavanadate are constant. The change in sodium sulfate concentration from 99.8 to 94% represents only a minor variation in comparison to the change in metavanadate concentration. Therefore, it is possible that the dissolution mechanism in metavanadate-sulfate melts is given by



Even though Eq. [7] implies that the sodium sulfate activity and sulfur trioxide partial pressure can be influenced by the presence of metavanadate, we believe the mechanism given by Eq. [9] predominates in vanadate containing melts. Sodium sulfate is expected to behave ideally over the range of metavanadate concentrations utilized and thus varies by approximately 8%. The V_2O_5 activity of the molten salts will be modified to a very limited extent by volatilization of V_2O_5 , since the vapor pressure at 1173 K is close to 10^{-8} atm. Thus the SO_3 partial pressure and the sodium metavanadate concentration will have the prime influence on the V_2O_5 activity of the melt.

The parabolic rate constant for a diffusion-controlled process relates the square of the reaction layer thickness to the exposure time. In addition, for a diffusion-controlled process it is found that the parabolic rate constant is proportional to the diffusion coefficient of the rate-controlling species through an increasingly thickening reaction layer. Both Fig. 1 and 3 showed that the formation of a monoclinic surface layer can be approximately fitted to such a parabolic growth rate.

The measured parabolic rate constants given in Table II are larger than would be expected from a process controlled by cationic diffusion in the ceramic. Extrapolation of the cationic diffusion coefficients in ZrO_2 measured at higher temperatures, 1700-2100 K, give a value of D_{Zr} at 1173 K of approximately 5×10^{-20} cm²/s or more than ten orders of magnitude smaller than the measured rate constants. In addition, the large sulfur trioxide and metavanadate concentration effects are difficult to reconcile with a cationic diffusion-controlled rate.

The monoclinic reaction layer formed is found in all cases to be very porous. For the structural conversion of the tetragonal structure to the monoclinic phase with no change in composition a net volume increase is expected (7). The observed decrease in volume of the monoclinic layer and thus the porosity can be explained by variations in the lattice parameters of the tetragonal and monoclinic phases with composition (15) and the dissolution of yttria in the molten salts. Using the lattice parameters given by Scott (15) for the tetragonal and monoclinic structures and an assumed depletion of yttria from 8 to 1 w/o, a net shrinkage of approximately 4% is expected.

Since the reaction layer forming is a porous outer monoclinic layer and no yttrium concentration gradient was observed, it would be reasonable to expect that the diffusion of $S_2O_7^{-2}$ and V_2O_5 through the porous channels of this layer was the rate-controlling species for sulfate and metavanadate-sulfate melts, respectively. Since approximately parabolic kinetics are followed, it must be assumed that the pore structure is relatively uniform throughout and thus the porous layer exhibits a nearly constant permeability.

Even though the time-dependent formation of a monoclinic reaction layer is closely fitted by a parabolic rate relationship, a small upward deviation from the square root of time dependence was observed at very long times. Haycock (16) has reported that this deviation toward a linear reaction rate can be due to the formation of a surface layer with a diffusivity increased above the rest of the reaction layer. The reaction product of the leaching reaction is soluble in the molten salts and is not expected to lead to clogging of the product layer porosity. As the transformation to the monoclinic structure progresses to completion, it is not unexpected that the size of the pores increases. No increased porosity at the outer regions is apparent in the micrographs. However, the deviation

from parabolic behavior is small and the increased porosity to induce such an effect would be difficult to observe. This deviation implies that, at exposure times significantly longer than those reported here, the rate of destabilization may be influenced by the formation of an outer porous reaction layer and make extrapolation of rates to longer times difficult.

For both sulfate and vanadate-sulfate melts, the above analysis indicates that the parabolic rate constant is strongly dependent on the SO_3 partial pressure. In the presence of sodium vanadate, Eq. [8] predicts a linear dependence of the rate of growth of the monoclinic layer with the SO_3 partial pressure. The parabolic rate constant is proportional to the scale thickness squared at any given time. Thus, the square root dependence of the monoclinic layer thickness after a fixed time exposure of 24h, shown in Fig. 4, indicates that a linear sulfur trioxide dependence of the parabolic rate constant is followed (twice the exponent of the dependence of the layer thickness on the partial pressure of SO_3).

Furthermore, for vanadate containing salts, it is expected from Eq. [7] and [9] that the parabolic rate constant is proportional to the vanadate concentration squared. Figure 5 shows that this metavanadate concentration dependence was also observed.

Comparison of the measured attack rate in a pure sodium sulfate melt and the 0.2% metavanadate melt show the two rates to be approximately identical. It thus must be assumed that the contribution of the metavanadate to the attack rate at these low concentrations is small and that the destabilization rate is essentially due to the reaction given by Eq. [1]. The dependence on metavanadate concentration squared implied by Eq. [8] would predict in association with the parabolic rate constants measured for higher metavanadate contents a parabolic rate constant for the 0.2 m/o metavanadate salt melt of approximately 5×10^{-12} , or half the experimentally measured value. This predicted value from the higher vanadate concentration measurements and the proposed compositional dependence of the vanadate-induced corrosion rate constant is larger than calculated by simply subtracting the parabolic rate constant measured in pure sulfate melt from the observed value. Nevertheless, the discrepancy is within the experimental scatter of the measurement.

The observed molten salt attack rate dependence on vanadate concentration and sulfur trioxide partial pressure strongly favors a reaction mechanism in which diffusion of V_2O_5 in the salt within the pores of the monoclinic layer is rate controlling. Associated with this mechanism would be an absence of a yttrium concentration gradient within the monoclinic product layer. Microprobe results support this conclusion, with the exception of the limited regions in which the center of the ceramic grains near the monoclinic tetragonal interface are untransformed. Even for this case there is no observed gradient in the monoclinic phase. It is felt that this is solely because of a slightly more rapid intrusion of and attack by the molten salt along the grain boundaries and pore surfaces. The observed absence of either sodium or vanadium in the internal pores of the ceramics by the electron microprobe is due to the experimental procedure of dissolving the salt in water to remove the ceramics from the salt melts.

The most extensive surface transformation found in this study or by Hamilton and Nagelberg (13) was for the exposures to the SO_2 - SO_3 containing atmospheres. Comparison of monoclinic layer thickness formed in air with those formed in SO_2 - SO_3 containing atmospheres show a dramatic change in the rate of leaching yttrium from the ceramics. Air exposure to a 2% NaVO_3 salt melt for 24h resulted in the formation of a transformed layer approximately $1.5 \mu\text{m}$ thick, while exposure to the same salt in a 1% SO_2 in O_2 atmosphere results in the formation of an $\sim 50 \mu\text{m}$ thick monoclinic layer. If the square root dependence of layer thickness (and thus linear dependence of parabolic rate constant) on the SO_3 partial pressure holds over extended variations in partial pressure, corrosive attack in an air atmosphere over a 24h period is equivalent

to exposure to an atmosphere containing a SO_3 partial pressure of approximately 2×10^{-6} atm.

The formation of a porous monoclinic reaction layer implies a process that does not simply involve the removal of yttrium from the stabilized zirconia ceramics since the density of the monoclinic product phase (5.56 g/cm^3) (7) is slightly lower than the original tetragonal phase ($\sim 5.7 \text{ g/cm}^3$). Even though a net expansion is expected when the density alone is considered, the significant leaching of yttrium from the ceramic (6-7 w/o) leads to a shrinkage of the ceramic within the reacted layer. Michalske (17) has observed that the transformation of tetragonal zirconia in molten silicates occurs by a dissolution-precipitation reaction. It was found that the tetragonal phase has a higher solubility in the molten salt and first dissolves before the monoclinic phase precipitates. Although no evidence for high solubilities of zirconia in the sulfates was found in this study, a similar process may be occurring in the molten sulfate-vanadate melts and represents a mechanism by which the highly porous reaction layer forms.

Conclusions

The sodium vanadate enhanced surface destabilization of yttria-stabilized zirconia occurs by a leaching of yttrium from the ceramic. Analysis of the molten salts indicated that yttrium alone was being leached from the ceramic. The removal of yttrium from the ceramic surface results in a phase transformation from the tetragonal structure to monoclinic structure. The monoclinic surface layer is observed in micrographs as a highly porous region.

The extent of transformation approximately increased with the square root of time and is believed to be controlled by a diffusion process. At long times, deviation from parabolic kinetics was observed and is believed due to the formation of an increasingly porous outer monoclinic layer. The measured parabolic rate constant was linearly dependent on the SO_3 partial pressure of the atmosphere in equilibrium with the molten salt melt. In addition, the parabolic kinetics for the growth of a monoclinic surface layer as found to be dependent on the sodium vanadate (NaVO_3) concentration of the salts. Since no concentration gradient was observed and a strong reaction rate dependence on the melt thermochemistry was observed, it is believed that the diffusion process controlling the observed reaction rate was diffusion of $\text{S}_2\text{O}_7^{2-}$ (in pure sulfate melts) or both $\text{S}_2\text{O}_7^{2-}$ and V_2O_5 (in mixed metavanadate-sulfate salt melts) through the salt penetrating the porous monoclinic surface layer.

Acknowledgment

This work was supported by the U.S. Department of Energy, Office of Basic Energy Sciences.

Manuscript submitted Jan. 7, 1985; revised manuscript received June 10, 1985.

Sandia National Laboratories assisted in meeting the publication costs of this article.

REFERENCES

1. R. A. Miller, "Analysis of the Response of a Thermal Barrier Coating to Sodium- and Vanadium-Doped Combustion Gases," NASA TM-79205, June 1979.
2. I. Kvernes, in "Proceedings of the Second Conference on Advanced Materials for Alternate-Fuel Capable Heat Engines," EPRI RD-2369-SR, p. 6-1, May 1982, Electric Power Research Institute, Palo Alto, CA (1982).
3. S. R. Levine, R. A. Miller, and M. A. Gedwell, in "Proceedings of the Second Conference on Advanced Materials for Alternate-Fuel Capable Heat Engines," p. 6-185, EPRI RD-2369-SR, May 1982, Electric Power Research Institute, Palo Alto, CA (1982).
4. R. J. Bratton, S. K. Lau, C. A. Andersson, and S. Y. Lee, in "Proceedings of the Second Conference on Advanced Materials for Alternate-Fuel Capable Heat Engines," p. 6-82, EPRI RD-2369-SR, May 1982, Electric Power Research Institute, Palo Alto, CA (1982).
5. R. H. Barkalow and F. S. Pettit, in "Proceedings of the First Conference on Advanced Materials for

- Alternate-Fuel Capable Directly Fired Heat Engines," J. W. Fairbanks and J. Stringer, Editors, p. 704, Castine, ME, Dec. 1979.
6. P. E. Hodge, R. A. Miller, and M. A. Gedwell, "Evaluation of Hot Corrosion Behavior of Thermal Barrier Coatings," NASA TM-81520, April 1980.
 7. "Engineering Property Data on Selected Ceramics: Volume III, Single Oxides," MCIC-HB-07, Vol. III, pp. 12-80, Metals and Ceramics Information Center, Columbus, OH (1981).
 8. V. S. Stubican, R. C. Hink, and S. P. Ray, *J. Am. Ceram. Soc.*, **61**, 17 (1978).
 9. K. L. Luthra and H. S. Spacil, *This Journal*, **129**, 649 (1982).
 10. J. W. Vogan, L. L. Hsu, and A. R. Stetson, in "Proceedings of the Second Conference on Advanced Materials for Alternate-Fuel Capable Heat Engines," p. 6-54, EPRI RD-2369-SR, May 1982, Electric Power Research Institute, Palo Alto, CA (1982).
 11. J. C. Hamilton and A. S. Nagelberg, in "Corrosion in Fossil Fuel Systems," I. G. Wright, Editor, pp. 435-455, The Electrochemical Society Softbound Proceedings Series, Pennington, NJ (1983).
 12. A. S. Nagelberg, Unpublished research.
 13. J. C. Hamilton and A. S. Nagelberg, *J. Am. Ceram. Soc.*, **67**, 686 (1984).
 14. R. L. Jones, D. B. Nordman, and S. T. Gadowski, "Sulfation of Y_2O_3 and HfO_2 in Relation to MCrAlY Coatings," NRL Report 5255, Jan. 1984.
 15. H. G. Scott, *J. Mater. Sci.*, **10**, 1527 (1975).
 16. E. W. Haycock, *This Journal*, **106**, 771 (1959).
 17. T. Michalske, Personal communication.

Cathodoluminescent Properties of Evaporated ZnS:Mn Films in the 2-6 kV Acceleration Voltage Range

D. Theis

Siemens Aktiengesellschaft, Siemens Research Laboratories, D-8000 Munich, Germany

R. Wengert

Siemens Aktiengesellschaft, Siemens Components Division, D-8000 Munich, Germany

ABSTRACT

Evaporated thin films of ZnS:Mn as used for yellow light emitting electroluminescent displays were analyzed with respect to their cathodoluminescent properties in the 2-6 kV acceleration voltage range. In these films, the light output normal to the film plane is 10-20 times lower than in yellow emitting powder phosphors. This result is explained in terms of light piping in the plane-parallel thin film structure as well as in a specific saturation process occurring at high excitation. Suitable measures to suppress the light piping could probably provide a technically useful high resolution CRT thin film faceplate.

Evaporated thin films of manganese-doped ZnS constitute the light emitting layers in ac-addressed electroluminescent displays. Scientific and industrial interest in these matrix displays is growing. [For a comprehensive review, see, e.g., Ref. (1).] Whereas highest luminance has been achieved with displays of the refresh type (2), an inherent memory and accordingly storage capability of the ZnS:Mn films fabricated under special preparational conditions have been discovered (3, 4). It was demonstrated that such panels can be addressed by electron beams and thus constitute the faceplate of a new type of storage CRT's (5, 6).

We were interested in finding out the suitability of evaporated thin ZnS:Mn films for high resolution, lower voltage CRT's without any additional storage features. Only little has been published on the cathodoluminescent properties of these films in the acceleration voltage range between 2 and 6 kV. This voltage range roughly corresponds to a complete penetration of the electrons through the films used. (Film thickness usually was less than 1 μm .) Some exploratory experiments on the cathodoluminescent properties of ZnS:Mn films evaporated on glass will be reported here.

Sample Preparation and Characterization

The samples available for the cathodoluminescent investigations were prepared by electron-beam evaporation. Mn incorporation into the ZnS film was achieved either by evaporating a Mn-doped hot-pressed ZnS pellet or by using a double-source system with separated ZnS and Mn sources. Substrate heating was performed by two 1000W quartz radiators placed in front of the samples.

Figure 1 illustrates the influence of the substrate temperature on the thickness of the film obtained at process times of equal length. One can extrapolate that in the evaporation chamber used no ZnS growth could be ob-

tained at substrate temperatures above $\approx 300^\circ\text{C}$. The temperature was measured by a specially attached and gauged bimetal which could rotate together with the sample during the deposition process. It is interesting to note that the initial growth rate at a given substrate temperature is not constant. The growth rate increases with increasing film thickness and attains a (temperature-dependent) constant value only at a film thickness $t > 200$ nm. In other words, the growth rate in the very fine grained initial layer, which we have visualized by cross-sectional TEM analysis (7), is lower than in film regions,

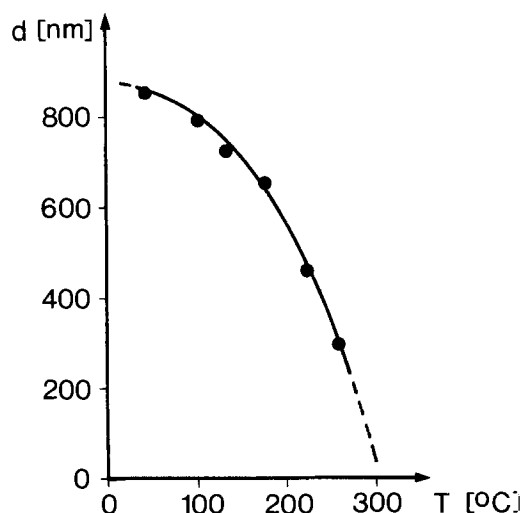


Fig. 1. Dependence of ZnS:Mn film thickness on substrate temperature T (at constant deposition duration, $t = 1000\text{s}$, and at constant evaporation rate).

where we observed the development of nicely shaped conical or columnar grains.

In Ref. (7), the Mn depth distribution in the bulk of our thin film samples was shown to be depending on preparational conditions. Additionally, we examined the photoluminescence intensity distribution emerging from the surface of the sample in normal direction with high spatial resolution. The luminescence observed was excited by the 488 nm line of an Ar laser and corresponds to the well-known ${}^4T_1-{}^6A_1$ transition between the crystal field levels of the Mn^{2+} ions, peaking at 585 nm at room temperature. The observed photoluminescence intensity normal to the surface was homogeneously distributed, indicating a correspondingly homogeneous distribution of Mn within the plane of the film. This result is important for the assessment of the cathodoluminescence intensity distribution.

Cathodoluminescence Apparatus

The specially prepared demountable cathodoluminescence (CL) apparatus is shown in Fig. 2. The rotatable sample holder carries 14 samples ($25 \times 25 \text{ mm}^2$) and a current registration station which allows measurement of the incident electron-beam current with neglectable losses. The inner wall surface area of this current registration box is 460 times larger than the slit aperture area and exhibits a structure which minimizes the escape probability of backscattered electrons of the incident beam to less than 1%. This is very important in the energy range between 2 and 6 kV, where the coefficients for reflection and secondary emission of electrons are strongly dependent on material and voltage. The forward and backward CL light emission of the samples is caught by suitably arranged lightguides and registered by a calibrated photodiode.

For the measurement of fast dynamical effects we used a calibrated photomultiplier whose circuitry had response times below 50 ns. The range of electron penetration d into any material is defined by its specific properties and the kinetic energy of the electrons. An empirical formula for ZnS is given in Ref. (8)

$$d_{ZnS} = 2.83 \times 10^{-2} \times U^2 \quad [1]$$

where d is in micrometers and U is in kilovolts. For the range of interest, this formula yields the following table for penetration depths d_{ZnS} of the electrons

U (kV)	d_{ZnS} (μm)
2	0.11
3	0.26
4	0.45
5	0.71
6	1.02

Luminance vs. Accelerating Voltage, Current Density, and Average Power

Figure 3 shows the cathodoluminescence intensity of ZnS:Mn films vs. the acceleration voltage of the electrons. The arrows indicate the voltage value which is sufficient for a complete penetration of the film according to the above formula (1). The cathodoluminescence intensity tends to saturate at voltages above this value. The saturation is a true bulk saturation and not due to charging effects. This is evidenced by sample 2, which has been prepared under equal conditions but additionally covered with a 30 nm Al film to ensure proper grounding of the film. The achievable saturation luminance increases with increasing substrate temperature during deposition. In Ref. (9) we have established a correlation between substrate temperature, grain size, and normalized cathodo- and photoluminescence intensities.

The current density dependence of the CL emission was measured in a pulsed mode with a 50 Hz repetition rate. We choose two different ways of excitation variation. Either the amount of charge per pulse was increased at constant pulse duration (amplitude modulation) or the pulse duration was varied, keeping $\Delta Q/\Delta t$ constant (pulse length modulation). In Fig. 4, we plot the obtained luminance values. With increasing current density the light emission tends to saturate, leading to a nonlinear dependence of light on current. This behavior has also been observed for the dissipative in-phase current flowing through the ZnS-layer during electroluminescent operation (10). There have been published a lot of speculations in the literature to explain the nature of the observed luminance saturation with increasing current [see Ref. (11) and references therein]. The most probable reason seems to be the one suggested in Ref. (11). The author proposes that saturation arises from an interaction between excited Mn^{2+} which occurs by energy transfer via unexcited Mn^{2+} and results in nonradiative decay. Furthermore, we can confirm the results of Mach and Müller (12), who find a dependence of decay time constant on the exciting beam

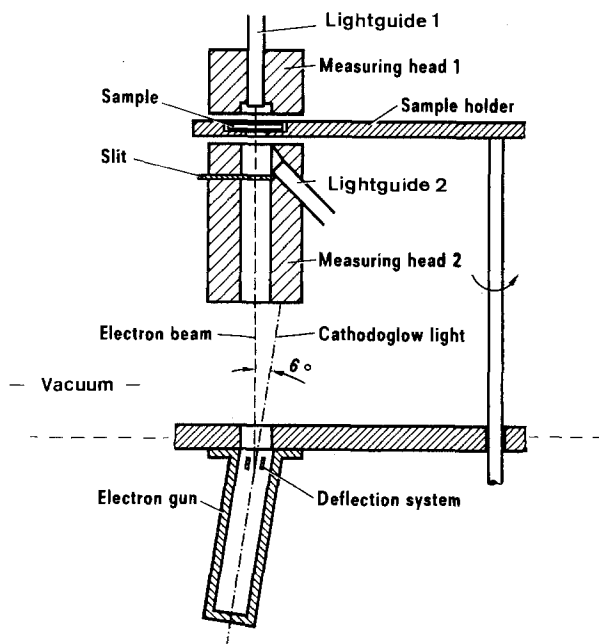


Fig. 2. Measuring system for cathodoluminescent light in forward and backward direction.

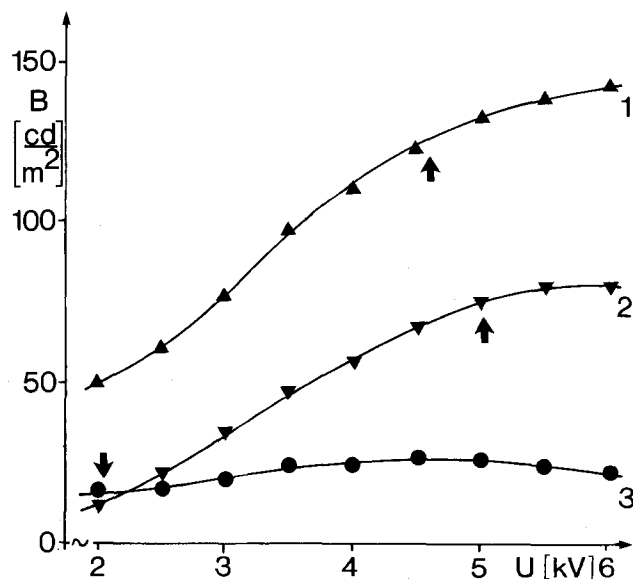


Fig. 3. Backward luminance B vs. accelerating voltage U for three different ZnS:Mn films. Curve 1: 630 nm, 0.4 w/o Mn, substrate temperature $T_s = 180^\circ\text{C}$. Curve 2: 700 nm, 0.4 w/o Mn, $T_s = 180^\circ\text{C}$ (with additional 30 nm Al coverage). Curve 3: 120 nm, 0.7 w/o Mn, $T_s = 180^\circ\text{C}$. The arrows indicate the voltage value where according to Eq. [1] full penetration of the bulk of the film is expected.

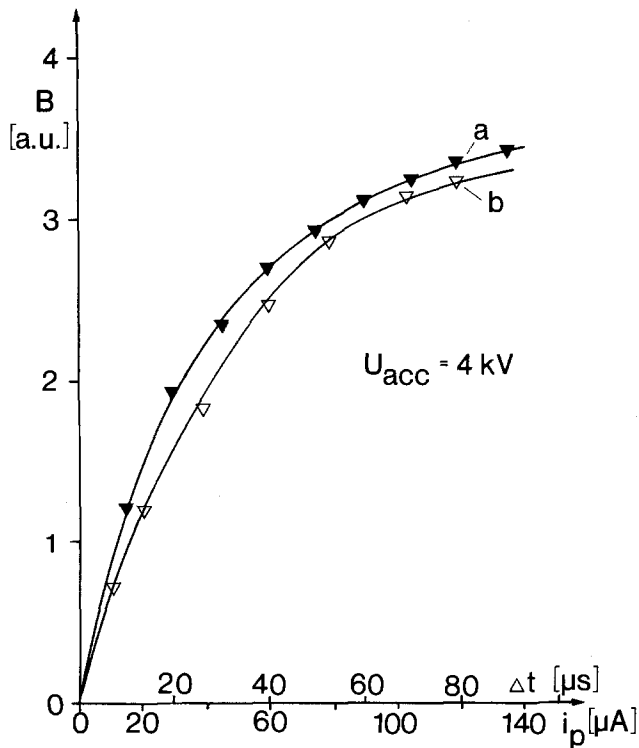


Fig. 4. Luminescence vs. exciting charge. Curve a: Keeping the current amplitude during the pulse at a constant value ($100 \mu\text{A}$) and varying the pulse duration Δt (50 Hz repetition rate). Curve b: Keeping the pulse duration constant ($64 \mu\text{s}$) and varying the current amplitude i_p during the pulse (50 Hz repetition rate). The spot diameter on the sample is 2.6 mm.

current density, i.e., if we increase the charge density per pulse ($60 \mu\text{s}$, 50 Hz repetition rate) from 5 to $25 \mu\text{A}/\text{mm}^2$, the decay time constant τ in samples with 0.4 weight percent Mn shrinks about 30%. This phenomenon is explained in terms of the above-mentioned nonradiative decay channel $\tau_{nr}^*([\text{Mn}^{2+}]^*)$

$$\frac{1}{\tau} = \frac{1}{\tau_r} + \frac{1}{\tau_{nr}[\text{Mn}^{2+}]} + \frac{1}{\tau_{nr}^*([\text{Mn}^{2+}]^*)} \quad [2]$$

where τ_r is the radiative lifetime, τ_{nr} ($[\text{Mn}^{2+}]$) the concentration-dependent nonradiative lifetime, and $\tau_{nr}^*([\text{Mn}^{2+}]^*)$ the nonradiative lifetime depending on the concentration of excited centers.

In Fig. 5 (lower curve), we show how luminance saturation with current density affects the performance of an electron-beam addressed thin film faceplate when dynamical pictures should be displayed. The upper curve in Fig. 5 represents the behavior of an ordinary (Zn, Cd)S:Ag yellow emitting CRT phosphor. Although the efficiency for this phosphor also varies with excitation condition, the effect of this variation is by far not so strong as in the case of ZnS:Mn films. The thin film efficiency decreases by roughly one order of magnitude when the average power per spot (2.6 mm diam) is increased from 0.64 to 60 mW.

If we compare the light emission efficiency of the thin films under equal average power excitation, we find that higher pulse duration always yields a relative decrease in efficiency as one expects from the sublinear behavior of the pulsewidth modulation vs. brightness curve in Fig. 4. The obtainable efficiencies of the thin film are roughly ten times lower than the corresponding values of the phosphor at average power $P_{\text{avg}} < 3.5 \text{ mW}$. This ratio increases to a factor of 20 for $3.5 \text{ mW} < P_{\text{avg}} < 10 \text{ mW}$ and even to a factor of 30 for $P_{\text{avg}} > 10 \text{ mW}$. For steady-state excitation with $P_{\text{avg}} = 60 \text{ mW}$, the efficiency ratio between powders and thin film yields a factor of 20.

In Ref. (12), a very useful factorization of the efficiency η of thin film electroluminescent devices was suggested.

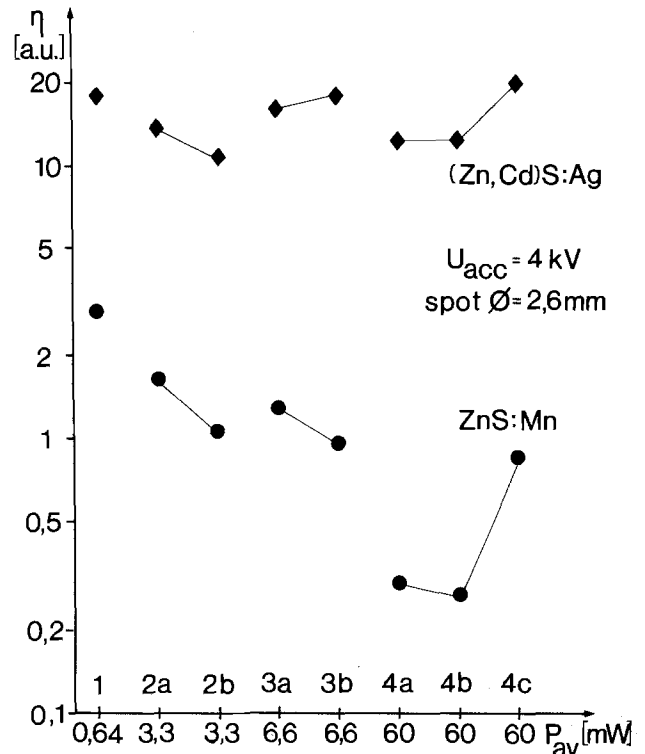


Fig. 5. Relative efficiencies of typical ZnS:Mn thin films and (Zn, Cd)S:Ag powder phosphors vs. different excitation conditions. Point 1: $50 \mu\text{A}$; $64 \mu\text{s}$; 50 Hz; $P_{\text{avg}} = 0.64 \text{ mW}$. Point 2a: $130 \mu\text{A}$; $64 \mu\text{s}$; 100 Hz; $P_{\text{avg}} = 3.328 \text{ mW}$. Point 2b: $130 \mu\text{A}$; $128 \mu\text{s}$; 50 Hz; $P_{\text{avg}} = 3.328 \text{ mW}$. Point 3a: $130 \mu\text{A}$; $125 \mu\text{s}$; 100 Hz; $P_{\text{avg}} = 6.656 \text{ mW}$. Point 3b: $130 \mu\text{A}$; $256 \mu\text{s}$; 50 Hz; $P_{\text{avg}} = 6.656 \text{ mW}$. Point 4a: $120 \mu\text{A}$; 2.5 ms; 50 Hz; $P_{\text{avg}} = 60.0 \text{ mW}$. Point 4b: $120 \mu\text{A}$; 5 ms; 25 Hz; $P_{\text{avg}} = 60.0 \text{ mW}$. Point 4c: 15 μA -cw; $P_{\text{avg}} = 60.0 \text{ mW}$. The spot diameter on the sample is 2.6 mm.

$$\eta = \eta_{\text{exc}} \eta_{\text{lum}} \eta_{\text{opt}} \quad [3]$$

$$\eta_{\text{exc}} = \text{centers excited (cm}^{-3}\text{)}/\text{electrons transferred (cm}^{-2}\text{)} \quad [3a]$$

$$\eta_{\text{lum}} = \text{centers decaying radiatively (cm}^{-3}\text{)}/\text{centers excited (cm}^{-3}\text{)} \quad [3b]$$

$$\eta_{\text{opt}} = \text{photons emitted through the surface (cm}^{-2}\text{)}/\text{photons generated (cm}^{-3}\text{)} \quad [3c]$$

η_{opt} can be further factorized into

$$\eta_{\text{opt}} = \eta_A \eta_{\text{Fr}} \eta_{\text{CAL}} \quad [4]$$

where η_A accounts for absorption losses (and yields the dimension distance⁻¹ required from Eq. [3c], which in terms of dimensions is counterbalanced by η_{exc} , the excitation yield per unit length), η_{Fr} accounts for the Fresnel loss which occurs when light passes from a medium whose index of refraction is n_1 (ZnS) to a medium whose index of refraction is n_2 (air). The well-known formula for the reflection coefficient is

$$R = [(n_2 - n_1)/(n_2 + n_1)]^2 \quad [5]$$

and since the transmission coefficient T is

$$T = 1 - R = 4n_2n_1/(n_2^2 + 2n_2n_1 + n_1^2) \quad [5a]$$

The Fresnel loss efficiency factor is then defined as T/n_1n_2

$$\eta_{\text{Fr}} = 4/(2 + n_2/n_1 + n_1/n_2) \quad [6]$$

$$\eta_{\text{FrZnS}} = 4/(2 + 1/2.4 + 2.4) = 0.83 \quad [6a]$$

The third (and most important) efficiency loss is due to total internal reflection (Snell's law). The critical angle loss factor is determined by

$$\eta_{\text{CAL}} = (n_2/n_1)^2 \quad [7]$$

$$\eta_{\text{CAL,ZnS}} = (1/2.4)^2 = 0.17 \quad [8]$$

Hence, even if we neglect (at low excitation densities) absorption losses, the optical efficiency is

$$\eta_{\text{opt,ZnS}} = 1 \times 0.83 \times 0.17 = 0.14 \quad [9]$$

This figure accounts for a major part of the inferiority in efficiency of the thin film compared to the (Zn, Cd)S:Ag powder (which has practically no light piping losses) at least in the low excitation density region. At higher excitation densities, the above-mentioned reabsorption processes leading to nonradiative decay take place, leading to even worse optical efficiencies. In order to compare the stability of powders and thin films under heavy excitation conditions, we have measured the relative decrease of light output within a few hours. With the same amount of high average excitation energy ($P = 20 \text{ mW-mm}^{-2}$) applied to both types of luminophors, we observed a decrease in efficiency of 60% for the powder and of only 25% for the thin film within 4h. Driven with equally high average energy, the powders degrade by nearly a factor of two faster than the thin films. Since phosphors, however, are much more efficient than the thin films, they need only a fraction of the power necessary to obtain the same level of brightness and accordingly do not degrade substantially in technical applications.

Conclusion

Mainly due to light trapping effects in the ZnS:Mn thin film layer, the cathodoluminescence efficiency of such films is lower than in a yellow light emitting (ZnCd)S:Ag powder phosphor by nearly a factor of ten at low excitation energies. At higher current densities, luminescence-current saturation effects as have been observed in electroluminescence as well further limit the cathodoluminescence efficiency of ZnS:Mn films. The main

disadvantage of high light loss by waveguiding in the transparent ZnS layer can be minimized by proper surface treatment (roughening) and/or additional antireflective layers. With an estimated increase of the optical efficiency by a factor of two or three, the material seems to be quite interesting for high resolution, low degradation CL display applications.

Manuscript submitted March 21, 1985; revised manuscript received June 4, 1985.

Siemens Aktiengesellschaft assisted in meeting the publication costs of this article.

REFERENCES

1. R. Mach and G. O. Müller, *Phys. Status Solidi A*, **69**, 11 (1982).
2. M. Yoshida, Y. Kakihara, T. Yamashita, K. Taniguchi, and T. Inoguchi, *Jpn. J. Appl. Phys., Suppl.*, **17**, 127 (1978).
3. T. Inoguchi and S. Mito, "Topics in Applied Physics," p. 222, Springer, Heidelberg (1977).
4. J. M. Hurd and C. N. King, *Electron. Mater.*, **8**, 879 (1979).
5. M. E. Dunham, D. H. Smith, C. N. King, and G. S. Barta, in "Proceedings of the International Electron Devices Meeting, Washington, 1980," p. 711, New York (1980).
6. O. Sahni, P. M. Alt, D. B. Dove, W. E. Howard, and D. J. McClure, *IEEE Trans. Electron Devices*, **ed-28**, 708 (1981).
7. D. Theis, H. Oppolzer, G. Ebbinghaus, and S. Schild, *J. Cryst. Growth*, **63**, 47 (1983).
8. W. Espe, "Werkstoffkunde der Hochvakuumtechnik," Vol. III, VEB Deutscher Verlag der Wissenschaften, Berlin (1961).
9. D. Theis, *Phys. Status Solidi A*, **81**, 647 (1984).
10. H. Venghaus and D. Theis, Abstract 169, p. 420, The Electrochemical Society Extended Abstracts, Vol. 81-1, Minneapolis, MN, May 10-15, 1981.
11. R. Törnqvist, *J. Appl. Phys.*, **54**, 4110 (1983).
12. R. Mach and G. O. Müller, *Phys. Status Solidi A*, **81**, 609 (1984).

Technical Notes



A Novel Method for Growing Thin Gate Oxide

D. N. Chen¹ and Y. C. Cheng

Department of Electrical Engineering, University of Hong Kong, Hong Kong

In the present trend of miniaturization, thin oxide has become the subject of intense investigation. Recently, we proposed a novel method (1) for routinely growing thin (< 200Å) gate oxide with good stability and integrity. In this "partial-TCE" technique, a low temperature dry oxidation is followed by a high temperature dry oxidation with an appropriate amount of TCE. The former step is to provide a large portion of oxide with high dielectric strength, while the latter step gives a good Si/SiO₂ interface with a passivation ability against sodium contamination.

While it has been reported that addition of water to the oxidizing environment weakens the effect of the chlorine species (2), wet oxides have been shown (3) to possess higher dielectric strength. Taking these effects together, we are interested in examining the effectiveness of a wet partial-TCE process, aiming at obtaining thin oxides with higher dielectric strength. This paper summarizes an in-

¹Permanent address: South China Institute of Technology, Gaungzhou, China.

vestigation of the properties of a wet oxygen partial TCE process consisting of two steps. The substrate is first oxidized in a wet O₂ atmosphere at a lower oxidation temperature to form an initial oxide film, and subsequently the oxidation is continued in a dry oxygen atmosphere containing TCE at a higher temperature. The overall aim is to incorporate the advantage of wet oxidation into the dry O₂ TCE technique. This oxidation process is not complicated, but the advantages of both wet O₂ and dry O₂ TCE can be fully exploited.

Experimental Procedure

All substrates used in the present studies are n-type silicon with a resistivity of 10 Ω-cm, and (111) orientation. These wafers were cleaned by standard cleaning procedure and were then oxidized in a resistance-heated furnace at a temperature range of 850°-1000°C for the initial oxidation period. For each oxidation temperature, wet oxidation was carried out by bubbling oxygen through water maintained at three different temperatures. Initial

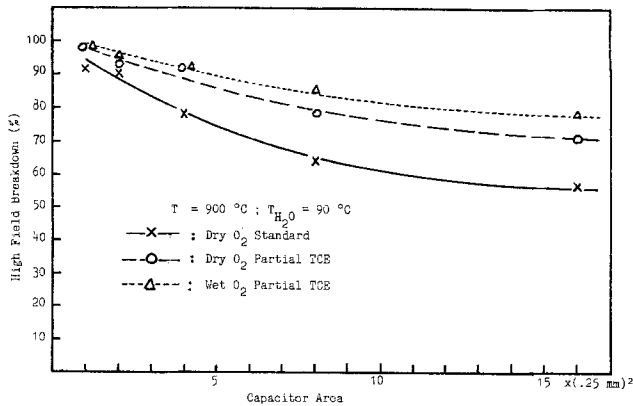


Fig. 1. Dependence of high field breakdown on capacitor area for various processes.

oxide films were grown at 900°C in dry O₂ partial-TCE and in standard dry oxygen in order to compare with the wet O₂ partial-TCE process. Except for those oxidized with a standard dry O₂ process, all other wafers were followed by a TCE oxidation at a higher temperature. Annealing was performed in N₂ or Ar for 1h. Essential processing conditions are summarized in Table I.

Results and Discussions

Measured results on dielectric breakdown show that the distribution is generally in the high field region (e.g., 8-10 MV/cm), with only a small percentage in the low field region (e.g., 0.3-2 MV/cm). Figure 1 shows a plot of the percentage of high field breakdown (i.e., > 5 MV/cm) as a function of capacitor areas. The results in general agree with those of a previous report (1) in that the probability of low field breakdown increases with larger capacitor area. Relatively speaking, samples fabricated by the wet O₂ partial-TCE method have the highest breakdown field compared to other processing techniques. At any oxidation temperature, the higher the water temperature, the stronger is the breakdown field, and the distinction between different water temperature diminishes as the oxidation temperature goes up. These observations confirm the notion that wet oxidation yields oxides with a greater portion of areas having higher dielectric strength, especially when the oxidation temperature is lower. These results are summarized in Fig. 2.

However, the combined influence of the oxidation temperature and water temperature is not so straightforward. At any water temperature, the general trend is that the higher the oxidation temperature, the higher the dielectric breakdown, and this is true for the water temperature

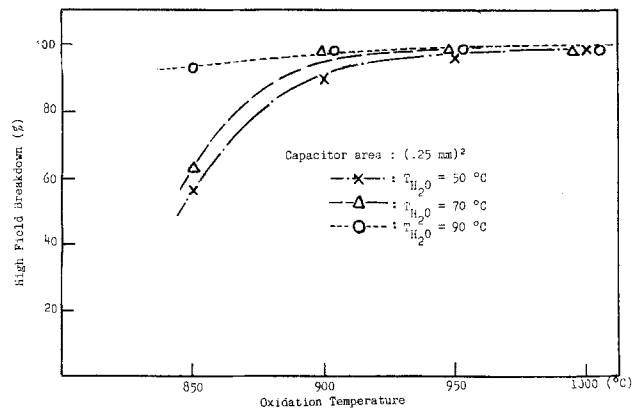


Fig. 2. Influence of water temperature on the relation of high field breakdown vs. oxidation temperature in the initial period.

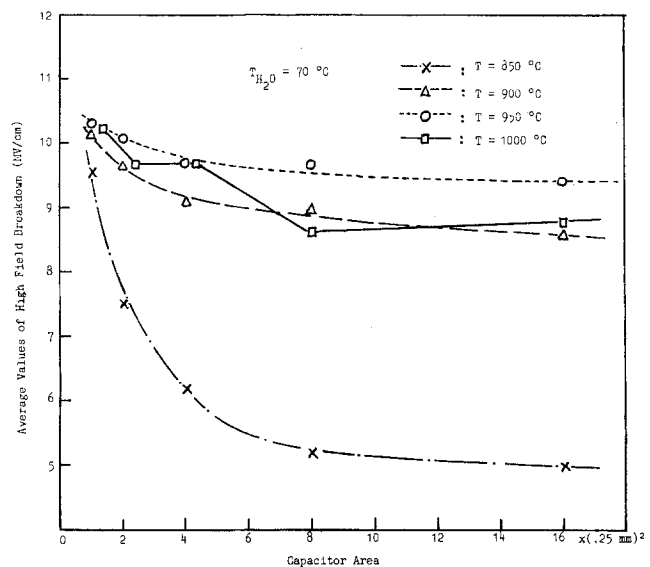


Fig. 3. Dependence of high field breakdown on capacitor area for various oxidation temperatures in the initial period.

at 50°C. Complication, however, arises when the water temperature is 70°C, and the maximum dielectric breakdown field occurs at an oxidation temperature of 950°C rather than 1000°C. These observations suggest that an optimal process condition may exist as far as dielectric breakdown field is concerned (Fig. 3). An analysis of the histograms of breakdown fields indicates that wet oxides

Table I. Processing conditions

Step	Wet TCE	Dry TCE	Standard dry O ₂
1	T = 850°-1000°C T _{H₂O} (°C) = 50; 70; 90 O ₂ = 500 ml/min t = 4 min	T = 900°C O ₂ = 1000 ml/min t = 10 min	T = 900°C O ₂ = 1500 ml/min t = 10 min
2	T = 1060°C O ₂ = 500 ml/min TCE/N ₂ = 80 ml/min t = 11 min	T = 1060°C O ₂ = 500 ml/min TCE/N ₂ = 80 ml/min t = 11 min	T = 1060°C O ₂ = 1500 ml/min t = 13 min
3	Annealing in N ₂ or Ar = 1500 ml/min		

Table II. High field and low field breakdown characteristics (%)

	Ref. (1) Area of capacitor = 0.204 mm ²			Present work Area of capacitor = 0.25 mm ²		
	Standard oxide (352Å)	Partial-TCE oxide (408Å)	Dual TCE oxide (499Å)	Standard oxide (423Å)	Partial-TCE oxide (409Å)	Wet O ₂ TCE oxide (398Å)
> 8 MV-cm ⁻¹	71.6	90.7	90.3	75	88	98
< 4 MV-cm ⁻¹	14.7	1	0	11	3	0

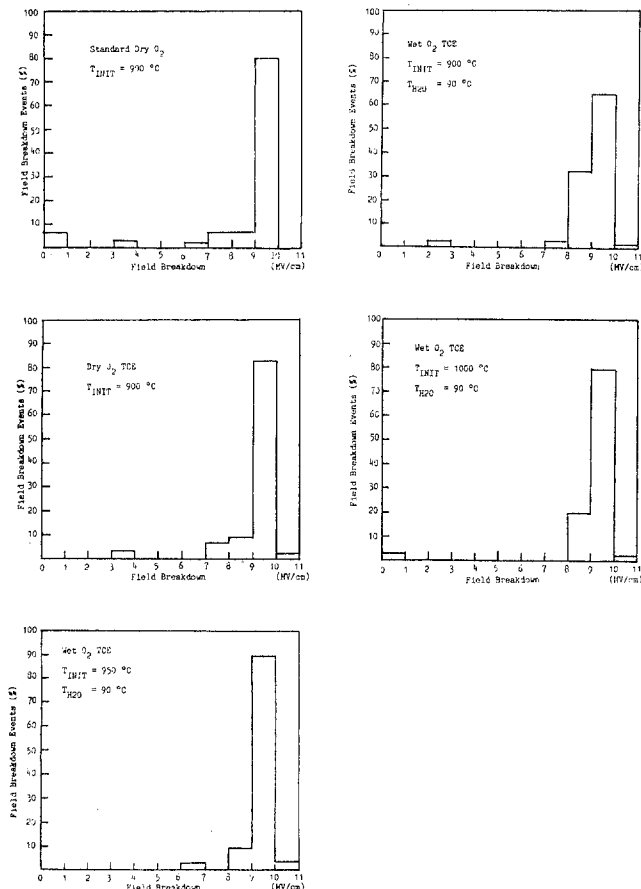


Fig. 4. Comparisons of dielectric field breakdown distribution for different oxidation processes.

grown at a furnace temperature of 950°C with a water temperature of 90°C possess the best field breakdown distribution (Fig. 4).

These results may be explained in terms of a model based on the results of Gibson and Dong (4). They found the existence of micropores in dry oxides by high resolution transmission electron microscope. The oxidant can diffuse to the interface through the micropores, with the explanation that the growth rate is linear for dry oxygen and the oxides give poor breakdown statistics. In the case of wet oxidation, it is postulated that the OH group will reduce the strain in the random network or the OH group will plug the micropores. Thus the potential fluctuation from the water-filled pores will be less than that of empty ones, resulting in a more uniform dielectric breakdown. This may probably explain the fact that there is less dependence of high field breakdown on capacitor area for wet oxides. However, some metallic ions will perhaps be attracted by the micropores, thus forming conducting channels which will cause low field breakdown. Therefore, the probability of low field breakdown will increase with the dryness of the oxidation environment.

In general, our experimental data show that raising the oxidation temperature at a fixed H₂O partial pressure

will improve the relation of high field breakdown vs. capacitor area. This may be due to the fact that water molecules do not dissociate sufficiently at low oxidation temperatures to give enough OH radicals to plug the micropores.

In addition, we also measured the I-V characteristics of oxide films grown in wet O₂ partial TCE atmosphere with water temperature at the range of 70°-90°C. The field breakdown is nondestructive until the current is up to a few tens of microamperes, similar to that of dry O₂ partial-TCE (1). However, an abrupt transition always occurs in oxide films grown in standard dry O₂ process.

To summarize our results of investigation, we compare the high field and low field breakdown values among various oxidation techniques. Table II shows that the present technique yields the highest percentage of high field breakdown (> 8 MV-cm⁻¹) and the lowest percentage of low field breakdown (< 4 MV-cm⁻¹) when compared with other processes in the present work and with other techniques of the previous investigation. We have not examined in detail the effect of the present technique on oxide charges and defect densities. The former had been found to be comparable to that with other techniques, deducing from rough estimates of the flatband voltages. The latter quantity could possibly be lower, as suggested by the observation of a larger equilibrium current of breakdown than samples prepared by other techniques.

Conclusion

The wet O₂ partial-TCE technique has been successfully applied to grow thin oxide films with good integrity. Although the distribution of field breakdown of wet O₂ partial-TCE is very similar to that of dry O₂ partial-TCE for smaller capacitor area, the relation of field breakdown vs. capacitor area and the maximum breakdown current are much better in the wet case than in the dry O₂ case. The weakening effect of water vapor on TCE does not arise in the present oxidation technique, because both the wet oxidation and TCE oxidation are executed separately. Thus, the process conditions can be adjusted separately to an ideal value, if there is any, but they will not influence each other in an adverse manner. We believe that the optimum processing condition can be found if more experiments are performed. Though oxides grown by the present method appear promising, a more complete characterization is needed to perform on other oxide quality besides the dielectric breakdown in order to yield an overall picture of the quality of the thin oxides.

Acknowledgment

This work was supported in part by Industrial Development Board of Hong Kong.

Manuscript submitted Jan. 18, 1985; revised manuscript received June 14, 1985.

REFERENCES

1. Y. C. Cheng and B. Y. Liu, *This Journal*, **131**, 354 (1984); B. Y. Liu and Y. C. Cheng, *ibid.*, **131**, 683 (1984).
2. C. M. Osburn, *ibid.*, **122**, 284 (1975).
3. E. A. Irene, *ibid.*, **125**, 1708 (1978).
4. J. M. Gibson and D. W. Dong, *ibid.*, **127**, 2722 (1980).

Nickel Plating on Porous Silicon

R. Herino,¹ P. Jan, and G. Bomchil*

Centre National d'Etude des Télécommunications, 38243 Meylan Cedex, France

Porous silicon has been obtained by anodic oxidation of monocrystalline silicon in concentrated hydrofluoric acid solutions (1). Thick layers up to several microns can be obtained, with an average density ranging between 30 and 75% of that of the starting material (2), with pore radii between 20 and 100Å according to operating conditions and substrate resistivity (3). Thermal oxidation of PS can lead to thick layers of silicon dioxide, in relatively short times, because of the easy access of gaseous oxygen through the pores (4). It is why PS has been proposed to realize localized dielectric insulation and silicon-on-insulator (SOI) structures in the integrated circuit technology (5). In fact, another application of PS might be possible in the field of metallization, for contacts and interconnections. If a metal could be deposited in the porous volume, a very interesting structure would be obtained for the formation of metal silicides upon heating. Standard vacuum metallization techniques result in a quick pinching off of the pores, leading only to a thin superficial layer of metals. In this work, we report preliminary results which show that electrodeposition is an appropriate method for metallization of the porous silicon volume.

Electroplating on silicon has been studied very early in order to form electrodes. Various metals have been deposited and several solution compositions and solvents have been proposed (6). The main difficulty encountered with plating silicon is a rather poor adhesion of the deposited film when no special surface treatment (such as roughening of the surface by chemical etching) is performed before the electrolysis (7). In this preliminary work, we have been interested in the nickel deposition, which is said to present a rather good adhesion, and which is able to form silicides upon heating at relatively low temperatures. The electrolyte composition that we have used is slightly different from that described by Wurtz and Borneman (7): it was composed of 0.2M NiSO₄, 6H₂O and 0.1M tetraethylammonium perchlorate as supporting electrolyte. The solvent was a mixture of 85% ethylene glycol and 15% deionized water. Substrates were p-Si samples boron doped and (100) oriented with a 0.01 Ω-cm resistivity. The cell was a standard electrolytic cell, with a platinum counterelectrode and a Ag-AgCl reference electrode; illumination of the semiconductor surface was performed with a 100W tungsten-halogen lamp, providing intensities of the order of 10 mW/cm² at the silicon surface. Potentiostatic measurements were performed with a PAR M173 potentiostat, driven by a PAR M175 programmer. All plating experiments were conducted at room temperature. Porous samples were prepared in HF/EtOH electrolyte (25% HF and 50% EtOH), at a constant current density of 200 mA/cm², leading to a porous film of an average density of 45% of that of silicon, with pore radii of about 80Å as determined by gas adsorption experiments (3).

Nickel plating has been performed in the same experimental conditions which lead to bright and adherent films on nonporous silicon surface. Deposition occurs for potentials more negative than -0.55V vs. Ag/Ag⁺; however, for potentials more negative than -0.90V, hydrogen bubbles form at the semiconductor surface. Plating on porous silicon was performed at constant current density, with values between 0.05 and 1 mA/cm², which corresponds to electrolysis potential greater than -0.90V. In this current density range, a faradic efficiency of 70-85% is obtained.

We have studied the Ni concentration profiles in the

*Electrochemical Society Active Member.

¹Université Scientifique et Médicale de Grenoble, Grenoble, France.

porous layers by x-ray microanalysis, with a LINK analyzer mounted on a JEOL electronic microscope. Primary electron energy was set to 22 keV, in order to get a good ionization of L_{αβ} nickel lines. The electronic spot is fixed at a given point of the cleaved porous layer: the x-ray spectrum obtained during this analysis leads by integration (and after an initial calibration) to the atomic ratio of silicon to nickel present at the point where the spot is fixed. Concentration profiles are obtained by analyzing several points at different depths in the porous layer. Figure 1 shows the results obtained with a 10 μm thick porous layer. The cathodic current density used during metallization was 100 μA/cm², and the charges exchanged were 1.3 C/cm² for curve A and 6.7 C/cm² for curve B. It can be seen that nickel has been deposited in the whole thickness of the layers, and that the relative amount of nickel deposited decreases when depth increases. The comparison between curves A and B indicates that longer electrolysis times do not change significantly the nickel concentration at the bottom of the porous layer; on the contrary, it is observed that for longer metallization times the difference between both curves increases towards the surface, suggesting a progressive blockage of the access of nickel atoms to the pores from the bottom to the surface. Similar profiles are obtained at other plating current densities, with a slight increase in the nickel concentration gradient at the highest current density (1 mA/cm²).

When profiles obtained with rather thin porous layers (of the order of 5000Å) are investigated, x-ray microanalysis is no longer a suitable technique because of its relatively low spatial resolution. In this case, secondary ion mass spectroscopy (SIMS) can be used. However, only qualitative results will be presented, as the ratio of the intensity of the nickel signal over the intensity of the silicon signal, because the ionization rate of the element has not been determined. Profiles were not calibrated in depth, because we could not assume that the etching velocity was constant all along the thickness, so that only the depth measured with an alpha-stepper is given. A typical result is shown in Fig. 2, obtained for a 4600Å thick porous layer metallized with a plating current density of 100 μA/cm². It appears that for the small thicknesses the con-

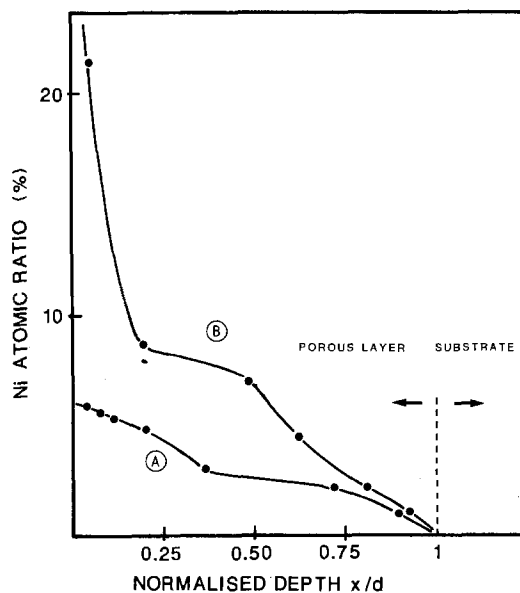


Fig. 1. Nickel concentration profile of metallized thick porous layers (10 μm) determined by x-ray microanalysis. Plating current: 100 μA/cm². Exchanged charge: 1.3 C/cm² (curve A) and 6.7 C/cm² (curve B).

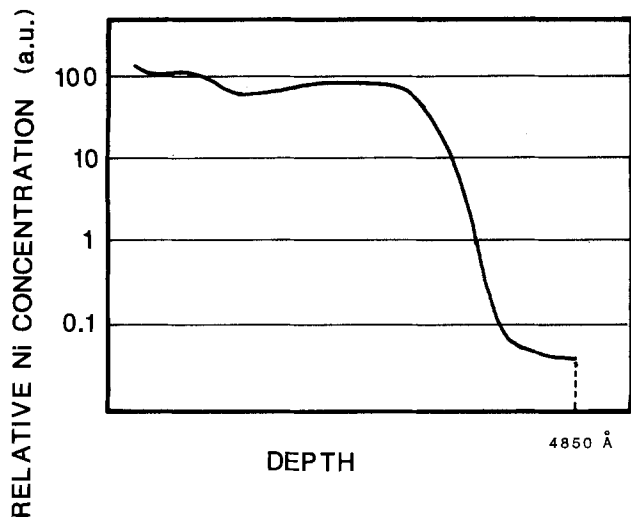


Fig. 2. Nickel concentration profile of a metallized thin porous layer (4800Å) determined by SIMS analysis.

centration profile is quite flat on mainly all the porous layer. The same result is obtained for other current densities up to 1 mA/cm². A rather good metallization of the porous volume is thus obtained in these conditions.

The formation of nickel silicide has been studied by annealing thin layers plated in the above conditions. X-ray diffraction of the as-plated samples (before annealing) shows the presence of a nickel layer, and from the broadening of diffraction peaks, a rather small particle size can be calculated (in the order of 50-70Å); otherwise, porous silicon presents a monocrystalline structure (8). When samples are annealed at different temperatures in the range from 400° to 800°C for 1h in dry nitrogen, nickel silicides are formed. We have observed a mixture of several silicide phases: NiSi₂, NiSi, and Ni₃Si₂. In addition to silicide formation, large stresses have developed, especially at the highest temperature; the diffraction pattern of monocrystalline porous silicon has disappeared, leaving place in the x-ray diagram to Bragg peaks corresponding to polycrystalline silicon.

In conclusion, this preliminary work demonstrates that metallization of the inner structure of porous silicon can be achieved by an electrochemical deposition method.

The metal concentration is found uniform in depth for thin porous layers (5000Å thick), which may present a technological interest, but a large concentration gradient is obtained for thick porous layers (10 μm thick). A detailed study of the concentration profiles as a function of the cathodic current density and of the layer thickness, with porous structures presenting different pore sizes, is now necessary for getting a better understanding of the deposition mechanism in porous silicon. This would allow a comparison between the results on metal deposition on porous silicon and those obtained on microprofiles of different types, which have been studied in detail using theoretical and experimental approaches (9). Such a study, interesting from a fundamental point of view, might be of technological interest, as metallized porous layers seem to be promising structures for obtaining localized metal silicides.

Acknowledgments

The authors are very grateful to Dr. J. P. Gonchond for x-ray microanalysis and to Dr. D. Jourdain for SIMS analysis.

Manuscript submitted April 4, 1985; revised manuscript received June 26, 1985.

CNET assisted in meeting the publication costs of this article.

REFERENCES

1. D. R. Turner, in "The Electrochemistry of Semiconductors," P. J. Holmes, Editor, Chap. 4, p. 180, Academic Press, New York (1962); T. Unagami, *This Journal*, **127**, 476 (1980).
2. Y. Arita and Y. Sunohara, *ibid.*, **124**, 285 (1977).
3. G. Bomchil, R. Herino, K. Barla, and J. C. Pfister, *ibid.*, **130**, 383 (1983).
4. Y. Arita, *J. Cryst. Growth*, **45**, 383 (1978).
5. K. Imai and H. Unno, *IEEE Trans. Electron Devices*, **ed-31**, 297 (1984).
6. J. I. Pankove, in "The Electrochemistry of Semiconductors," P. J. Holmes, Editor, Chap. 7, Academic Press, New York (1962).
7. E. C. Wurtz and E. H. Borneman, *J. Appl. Phys.*, **28**, 235 (1957).
8. K. Barla, G. Bomchil, R. Herino, J. C. Pfister, and J. Baruchel, *J. Cryst. Growth*, **68**, 721 (1984).
9. O. Kardos and D. G. Foulke, in "Advances in Electrochemistry and Electrochemical Engineering," Vol. 2, C. W. Tobias, Editor, p. 145, John Wiley and Sons, New York (1962).

Interface Traps Caused by Ge Pre-Amorphization

D. S. Wen,** J. Liu,** C. M. Osburn,* and J. J. Wortman*

Department of Electrical and Computer Engineering, North Carolina State University, Raleigh, North Carolina 27695 and Microelectronics Center of North Carolina, Research Triangle Park, North Carolina 27709

Modern CMOS VLSI technologies require shallow source-drain junctions for both p-channel and n-channel devices. Junction depths between 0.1 and 0.25 μm will be necessary in order to minimize both source-drain leakage currents and threshold voltage reduction due to short channel effects. This is particularly difficult for p-channel transistors because of the channeling and the high diffusivity of boron in silicon. However, these effects can be minimized by applying both preamorphization techniques and rapid thermal annealing (RTA) (1-3). More recently, silicon preamorphization using germanium implantation was shown to be a suitable choice for Si preamorphization, since it has a high solid solubility in Si and because it does not appear to alter the electrical properties of Si significantly (3). In order to be compatible with self-aligned polysilicon gate technology, the damage caused by high energy implantation must be prevented

from degrading the silicon-silicon dioxide interface. MOSFET characteristics can be degraded if the damage is not removed by annealing. In our recent work, the interface traps caused by the Ge preamorphization were observed even with very low implant energy. A comparison between different isotopes of germanium showed that the effect was due to hydrogen, not germanium. The purpose of this communication is to document the effect and to alert other workers to the adverse impact of GeH implantation.

Experimental

Starting with <100> p-type Si wafers, a 38 nm gate oxide was thermally grown. A 0.25 μm polysilicon layer was then deposited. After POCl₃ doping, a 0.15 μm CVD oxide was deposited to increase the height of the gate barrier up to 0.4 μm. Then, Ge was implanted at several energies with a dose of 2E15 cm⁻². Two isotopes of Ge [Ge(70) and Ge(74)] were used using GeH₄ as the source. The CVD ox-

*Electrochemical Society Active Member.

**Electrochemical Society Student Member.

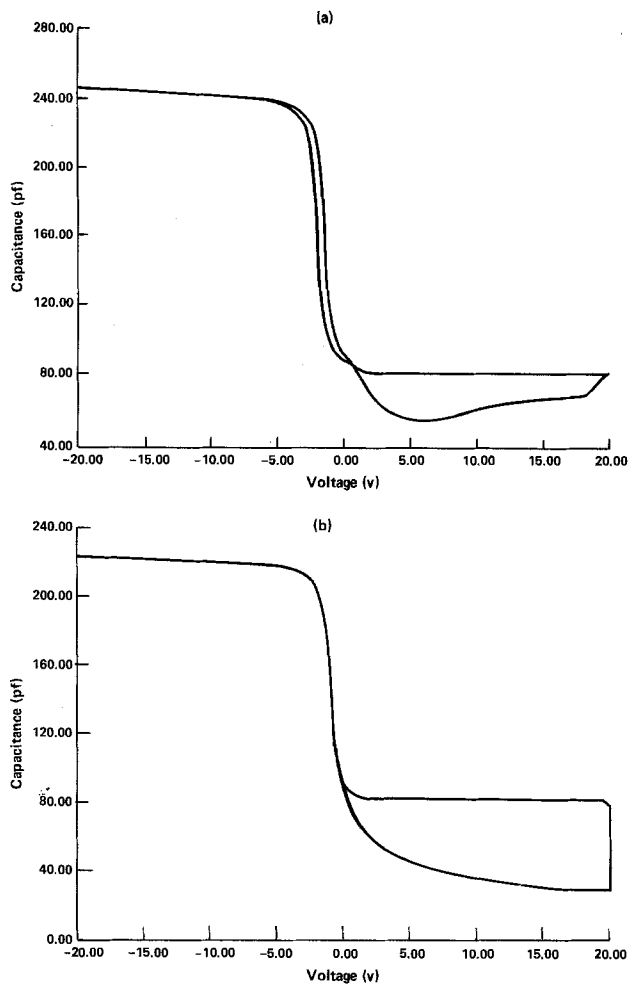


Fig. 1. The C-V characteristics of capacitor with Ge(74) implantation (energy = 75 keV, dose = 2×10^{15}). a: After RTA 1000°C, 10s. b: After RTA 1100°C, 10s.

ide layer on the top of poly was etched off and standard MOS capacitors were generated by plasma etching the polysilicon. Rapid thermal annealing was then performed at 1000° and 1100°C, respectively, for 10s. The C-V characteristics of the capacitors were obtained and the results were compared.

Results and Discussions

Figure 1a shows the C-V characteristics of the MOS capacitors with Ge(74) implantation at 75 keV, after RTA 1000°C for 10s. There is a hysteresis in the C-V characteristics between forward and retrace curves. The minority carrier lifetime of the devices is so low that the device cannot be driven into the deep depletion. Similar results had been obtained on the samples with Ge(74) implanta-

Table I. The LSS projected range of Ge in Si (4)

Energy (keV)	R_p (μm)	ΔR_p (μm)
300	0.17	0.055
150	0.087	0.030
75	0.047	0.017

Table II. The major isotopes of Ge (5)

Isotope	Percentage
Ge(70)	20.55
Ge(72)	27.37
Ge(73)	7.67
Ge(74)	36.74
Ge(76)	7.67

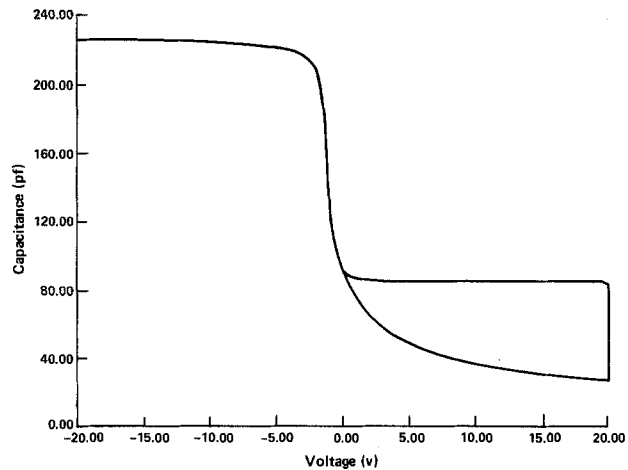


Fig. 2. The C-V characteristics of capacitor with Ge(70) implantation (energy = 150 keV, dose = 2×10^{13}), after RTA 1000°C, 10s.

tion at the energies of 150 and 300 keV. These results indicate that the interface damage exists even with very low implant energy (75 keV). Such damage can be removed only by RTA at 1100°C for 10s (Fig. 1b) and was not observed on the control wafer without implantation. The LSS projected range and standard deviation for Ge in Si are listed in Table I. The estimated depths of amorphous layer are 0.39, 0.21, and 0.11 μm for the energies of 300, 150, and 75 keV, respectively. TEM cross-sectional analysis for Ge implantation at 300 keV showed the amorphous layer to be about 0.4 μm (3). Thus Ge penetration through the thick polygate stack (0.15 μm CVD oxide/0.25 μm

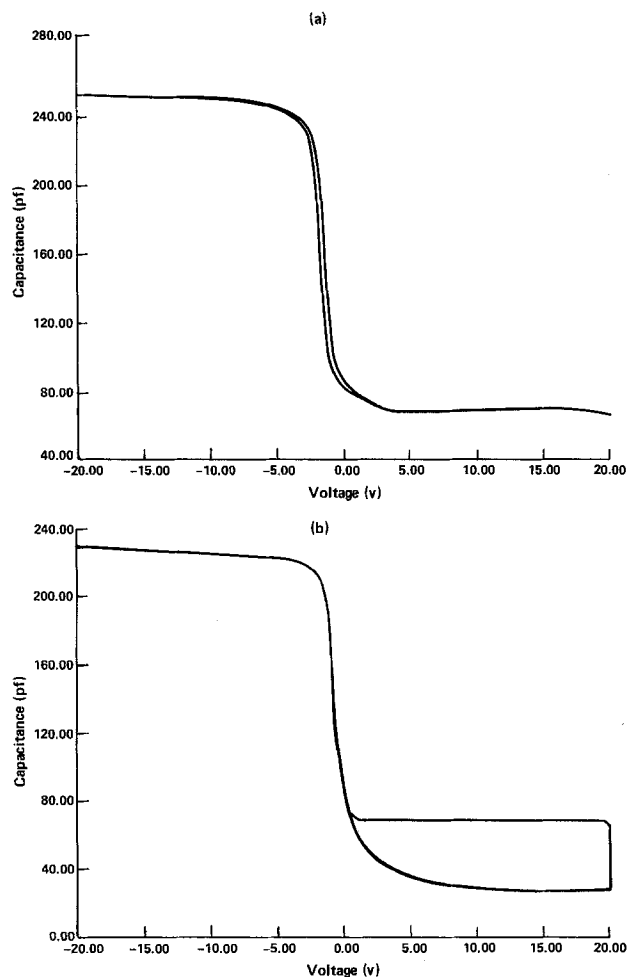


Fig. 3. The C-V characteristics of capacitor with H_2^+ implantation (energy = 100 keV, dose = 1×10^{13}). a: After RTA 1000°C, 10s. b: After RTA 1100°C, 10s.

polysilicon/oxide) was considered unlikely at 75 and 150 keV. Nevertheless, the defects were clearly caused by the implantation process.

Since Ge has several isotopes (Table II), the Ge(74) is usually selected because of the highest percentage. Unfortunately, implantation with 74 amu might include Ge(73)H and Ge(72)H₂ in addition to Ge(74). In an ion implanter with a preanalysis system, the mass analysis takes place at low extraction voltage, and the beam then passes through an acceleration stage to reach its final energy. Postanalysis dissociation of GeH(74) could occur before high energy acceleration, giving the hydrogen atoms enough energy to penetrate the polygate and gate oxide. Indeed, the hysteresis and low lifetime phenomena due to the interface defects are not seen in 150 keV Ge(70)-implanted samples after RTA at 1000°C for 10s (see Fig. 2). As a further verification that defects are due to hydrogen penetration, samples with only H₂ implantation were fabricated in the same manner. C-V hysteresis and low minority carrier lifetime were seen in the C-V curve (see Fig. 3) of 100 keV H₂-implanted wafers; furthermore, the C-V curves exhibited considerable variability from die to die. Based on these experiments, we conclude that anomalously high energy H implantation can occur during Ge(74) implantation. We are unable to determine whether this results from preacceleration dissociation, from charge exchange with residual H₂, or during dissociation of GeH at the wafer.

At 300 keV, the defects were observed in both Ge(70)- and Ge(74)-implanted wafers. It showed that the Ge

penetrated the 0.4 μm gate barrier and caused damage at the oxide-silicon interface, confirming the previous work of XTEM analysis by Sadana *et al.* (3).

Acknowledgments

The authors would like to express their thanks to Dr. D. Sharma and Dr. S. Goodwin-Johansson for their helpful discussion and to Larry Simpson for help with Ge and H implantation. This work was sponsored by the Semiconductor Research Corporation and the Microelectronics Center of North Carolina.

Manuscript submitted April 22, 1985; revised manuscript received June 28, 1985.

The Microelectronics Center of North Carolina assisted in meeting the publication costs of this article.

REFERENCES

1. T. E. Seidel, *IEEE Electron Devices Lett.*, **ed1-4**, 353 (1983).
2. T. E. Seidel, R. Knoell, F. A. Stevie, G. Poli, and B. Schwartz, in "VLSI Science and Technology 1984," K. Beam and G. A. Rozgonyi, Editors, p. 201, The Electrochemical Society Softbound Proceedings Series, Pennington, NJ (1984).
3. D. K. Sadana, W. Maszara, J. J. Wortman, G. A. Rozgonyi, and W. K. Chu, *This Journal*, **131**, 943 (1984).
4. J. F. Gibbons, W. S. Johnson, and S. W. Mylroie, "Projected Range Statistics, Semiconductors and Related Material," Dowden, Hutchinson & Ross, Stroudsburg, PA (1975).
5. W. H. Sullivan, "Trilinear Chart of Nuclides," Oak Ridge National Laboratory, Oak Ridge, TN (1957).



Evidence for a Bipolar Mechanism of Passivity in Mo Bearing Stainless Steels

Y. C. Lu¹ and C. R. Clayton*

Department of Materials Science and Engineering, The State University of New York, Stony Brook, New York 11794

Variable angle XPS studies of the passive films formed on the alloys Fe-19Cr-9Ni and Fe-19Cr-9Ni-2.5Mo in deaerated 0.1M HCl is presented. Passivation in each case was carried out for 1 hour at -180mV (Vs. SCE) following cathodic removal of the air formed film by polarization at -600 mV for 15 minutes. In figure 1 we compare the Cr 2p^{3/2} spectra for each alloy, at 20° (w.r.t. sample surface) to enhance the outer regions of the film and 50° to enhance spectra of the Cr species at the metal-film interface. The complex spectra contains two major peaks with positions corresponding to Cr₂O₃ and CrOOH or Cr(OH)₃. Two minor peaks corresponding to CrO₃ and CrO₄²⁻ are also found. For each alloy the Cr₂O₃ phase appears to be situated at the metal-film interface. Independent studies to be fully presented later, indicate that CrO₃ is incorporated in Cr₂O₃ and that CrO₄²⁻ is incorporated in the Cr(OH)₃ or CrOOH phase. The outer layers of the anodic film in each case contain iron hydroxy-oxides. In particular we note that the Mo bearing alloy produced well defined spectra of Fe²⁺, MoO₂ and MoO₄²⁻. The Mo3d spectra are presented in figure 2. It is possible that FeMoO₄ is formed in the outer layer. The addition of Mo to the alloy also results in the development of the Cr₂O₃ phase and a marked reduction in the Cr(OH)₃ or CrOOH phase.

The nature of the passive film formed in 0.1M HCl appears to follow the behavior expected of a bipolar duplex membrane as described by Sakashita and Sato (1). In figure 3 is a schematic representation of the bipolar behavior of the passive films formed on stainless steel. This model proposes that CrO₄²⁻ and the more abundant MoO₄²⁻ anions may convert the otherwise anion selective hydrated oxides to cation selective phases. While deprotonation is enhanced by the field assisted egress of protons through the cation selective layer, O²⁻ anions resulting from the dissociation of OH⁻ groups, are able to diffuse through the anion selective phase towards the metal-film interface and to react with Cr to

form Cr₂O₃. Due to the fact that Cr₂O₃ and CrO₃ have very similar standard free enthalpies it is not surprising that, as postulated by Revesz and Kruger (2) some CrO₃ is formed in the Cr₂O₃ phase. The deprotonation reaction may take the following course: Cr(OH)₃ → CrOOH + O²⁻ + 2H⁺, as evidenced by RHEED studies reported elsewhere (3). The resulting Cr₂O₃ layer will act as a non-selective ionic barrier for both anion and cation diffusion.

The presence of CrO₄²⁻ and MoO₄²⁻ is not expected since both ions are unstable in low pH media. However, it would appear that they are formed in the solid-state by reaction of lower valent metallic ions with lattice water trapped in the gel-like disordered state at the onset of passivity. The solid-state environment in which the lower valent cations are initially accommodated is, therefore, analogous to a neutral to high pH solution where both CrO₄²⁻ and MoO₄²⁻ are stable. We propose that there is a common link between the effect of solution born inhibitors of the type MeO₄ⁿ⁻ and MeO₄ⁿ⁻ anions incorporated in anodic films at low concentrations. It has been shown from quantum mechanical studies by Rosenfeld that anions of the form MeO₄ⁿ⁻ appear to be electron acceptors with the partial electronic charge residing on the oxygen ligands surrounding the central atom (4). Such systems would therefore provide strong negative fixed charges capable of rectifying ionic current.

A fuller discussion of the proposed mechanism of passivity of stainless steel will shortly be submitted to this journal.

ACKNOWLEDGEMENTS:

It is a pleasure to acknowledge the support of this program by the National Science Foundation under the research grant DMR8106499A01 and equipment grants DMR771831 and DMR811732

*Spectra were calibrated against the following binding energies Au 4f 83.8eV
C 1s 284.6eV

REFERENCES

1. M. Sakashita and N. Sato. Passivity of Metals, Eds., R.P. Frankenthal and J. Kruger, Electrochem. Soc., Princeton, N.J. (1978) p. 479.
2. A.G. Revesz and J. Kruger. *ibid* p. 479.
3. C.R. Clayton, A.R. Brooks, K. Doss and Y.C. Lu in Equilibrium Diagrams and Localized Corrosion, Eds. R.P. Frankenthal and J. Kruger, Electrochem. Soc., Princeton, N.J., (1984), p. 369.
4. I.L. Rosenfeld, Corrosion Inhibitors, McGraw-Hill Inc., New York (1981).

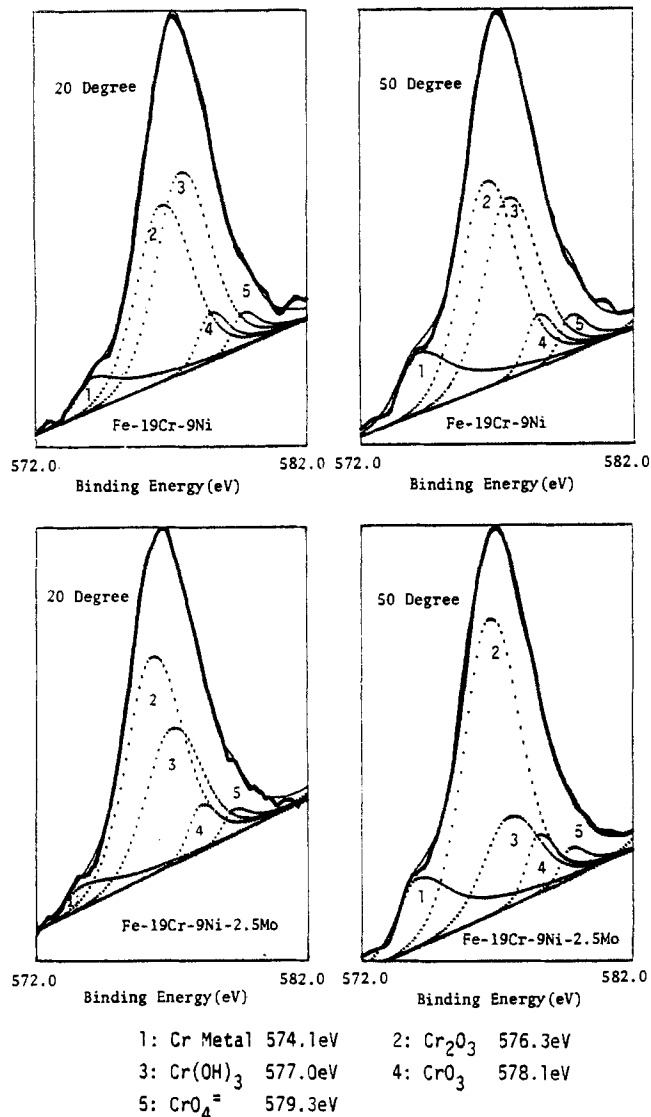


Fig. 1 Cr 2p_{3/2} photoelectron spectra obtained from the anodic films formed on Fe-19Cr-9Ni and Fe-19Cr-9Ni-2.5Mo alloys in 0.1M HCl at -180mV(SCE) for 1 hour.

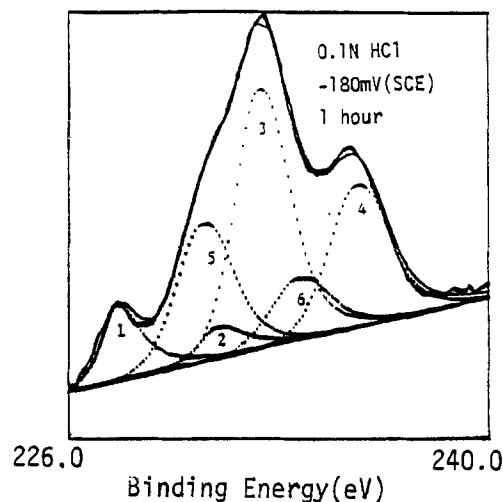


Fig. 2 Mo 3d photoelectron spectrum obtained from the anodic film formed on Fe-19Cr-9Ni-2.5Mo alloy

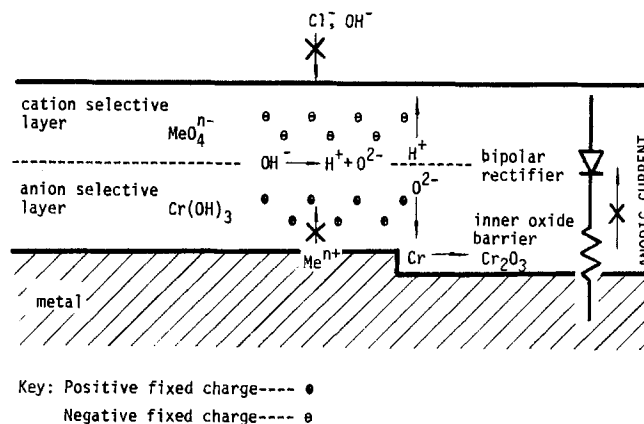


Fig. 3 Schematic representation of the bipolar behavior of the passive film formed on stainless steel

*Electrochemical Society Active Member.

¹Permanent address: Guangzhou Research Institute of Electrical Appliances, Guangzhou, China.

Manuscript received May 3, 1985.

The State University of New York assisted in meeting the publication costs of this article.

Sulfur Dioxide Gas Detection with $\text{Na}_2\text{SO}_4\text{-Y}_2(\text{SO}_4)_3\text{-SiO}_2$ Solid Electrolyte by a Solid Reference Electrode Method

N. Imanaka, Y. Yamaguchi, G. Adachi, and J. Shiokawa

Department of Applied Chemistry, Faculty of Engineering, Osaka University, Yamadaoka 2-1, Suita, Osaka 565, Japan

In recent years, sulfur dioxide exhausted into the surroundings has been seriously deteriorating the environments. The suppression of the exhausted SO_2 gas amount is an urgent necessity.

Lately, alkali-metal sulfates(1-8), have been examined to utilize as solid electrolytes for a sulfur dioxide gas detector. However, alkali-metal sulfates are not suitable materials because of the phase transformation(9-11) and their low electrical conductivities. In electromotive force(EMF) measurements, two main techniques have been investigated. One is an SO_2 gas concentration cell method(1-4,12) using an SO_2 standard gas electrode. The other is to apply the metal sulfate-metal oxide(5,6) or the silver-silver sulfate mixture(7,8) electrode as reference electrode instead of the standard reference gas. The former method is a general technique to examine whether the sample is appropriate for the solid electrolyte or not. However, the size of the SO_2 gas detector of this type becomes larger and complicated. In the case of the sulfate-oxide(5,6) electrode, it is necessary to maintain the solid electrode separated from the electrolyte completely because the electrode may react with the sulfate electrolyte to give a false EMF. The temperature in practical use should be restricted between 783 K and 833 K with a silver-silver sulfate reference electrode method(7,8).

In our previous investigation(12), rare earth sulfates($\text{Ln}=\text{Y}$ and Gd) and silicon dioxide have been mixed so as to enhance the electrical conductivity and to prevent the electrolyte from becoming ductile, respectively. In addition, the suppression of the phase transformation has been attempted by the mixing both $\text{Ln}_2(\text{SO}_4)_3$ ($\text{Ln}=\text{Y}$ and Gd) and SiO_2 . In this study, a metal sulfate-metal oxide($\text{M}=\text{Mg}$, Mn , and Ni) solid electrode has been applied as the reference electrode and directly fixed to the $\text{Na}_2\text{SO}_4\text{-Y}_2(\text{SO}_4)_3\text{-SiO}_2$ solid electrolyte.

The EMF measurement by the sulfate-oxide solid reference electrode method was conducted with the $\text{Na}_2\text{SO}_4\text{-Y}_2(\text{SO}_4)_3\text{-SiO}_2$ solid electrolyte. The apparatus is illustrated in Fig. 1. The platinum net reference electrode was tightly fixed between the electrolyte and the solid reference electrode. The sample was covered

with the bonding agent(SUMICERAM from Sumitomo Chemical Industries Ltd.). A ringed glass packing was adopted so as to separate the test gas from the reference electrode compartment. The test SO_2 and air gas mixture was regulated with the Standard Gas Generator(SCGU-711SD) from Standard Technology Co.. The air gas was introduced into the reference electrode compartment in order to maintain the constant oxygen partial pressure(2.13×10^4 Pa). Platinum was sputtered on both center surfaces(5×10^{-3} m in diameter) of the electrolyte(1.3×10^{-2} m in diameter) by Shimadzu's Ion Coater IC-50. The Pt film thickness was approximately 10 nm. By this sputtering, good contact between the electrolyte and the Pt electrode was obtained. Furthermore, the formation and the decomposition of sodium sulfate might be considered to be made smoother. The preparation of the $\text{Na}_2\text{SO}_4\text{-Y}_2(\text{SO}_4)_3\text{-SiO}_2$ solid electrolyte is discussed in our previous paper(12)(The reaction between Na_2SO_4 , $\text{Y}_2(\text{SO}_4)_3$, and SiO_2 has been completed by this preparation). The EMF measurements were conducted twice with each solid reference electrode and almost the same results were obtained. The EMF results with the $\text{MgSO}_4\text{-MgO}$ solid reference electrode at 973 K are shown in Fig. 2. The values obtained were approximately 280 mV higher than the calculated EMF(6). The $\text{MgSO}_4\text{-MgO}$ reference electrode seemed to react with the $\text{Na}_2\text{SO}_4\text{-Y}_2(\text{SO}_4)_3\text{-SiO}_2$ solid electrolyte during measurement. This chemical reaction might be considerably enhanced the EMF value. The variation of the EMF with the $\text{MnSO}_4\text{-Mn}_2\text{O}_3$ solid reference electrode at 973 K is also presented in Fig. 2. In all measurements, the measured EMF was about 80 mV larger than the calculated value. The $\text{MnSO}_4\text{-Mn}_2\text{O}_3$ electrode, however, did not react with the electrolyte. The difference between the measured and the calculated EMF can be mainly ascribed to the fact that manganese oxides of different oxidation states may have been produced. The results of the EMF measurements with the $\text{NiSO}_4\text{-NiO}$ solid reference electrode at 973 K are shown in Fig. 3 together with the results of Na_2SO_4 as a comparison. The EMF characteristics for Na_2SO_4 decreased significantly in the inlet SO_2 gas concentration less than 0.1 % ($\log(P_{\text{SO}_2})_{\text{in}} = -3.0$)

because of the gas permeation through cracks occurred in the electrolyte. In the case of the $\text{Na}_2\text{SO}_4\text{-Y}_2(\text{SO}_4)_3\text{-SiO}_2$ electrolyte, the measured EMF was in good accordance with the calculated EMF(6), in the inlet SO_2 gas concentration from 30 ppm ($\log(P_{\text{SO}_2})_{\text{in}} = -4.52$) to 1% ($\log(P_{\text{SO}_2})_{\text{in}} = -2.0$). No chemical reaction between the electrolyte and the $\text{NiSO}_4\text{-NiO}$ reference electrode was observed. The EMF characteristics for the $\text{Na}_2\text{SO}_4\text{-Y}_2(\text{SO}_4)_3\text{-SiO}_2$ were appreciably improved both the mixing of $\text{Y}_2(\text{SO}_4)_3$ and SiO_2 simultaneously into sodium sulfate and by the Pt sputtering. In addition, the $\text{Na}_2\text{SO}_4\text{-Y}_2(\text{SO}_4)_3\text{-SiO}_2$ solid electrolyte can be fixed directly to the solid reference electrode.

The $\text{NiSO}_4\text{-NiO}$ solid reference electrode technique has a potential in practical utilization for a sulfur dioxide gas detector.

REFERENCES

1. K. T. Jacob and D. B. Rao, *J. Electrochem. Soc.*, **126**, 1842 (1979).
2. M. Gauthier and A. Chamberland, *J. Electrochem. Soc.*, **124**, 1579 (1977).
3. N. Imanaka, G. Adachi, and J. Shiokawa, *Bull. Chem. Soc. Jpn.*, **57**, 687 (1984).
4. N. Imanaka, G. Adachi, and J. Shiokawa, *Proc. the International Meeting on Chemical Sensors*, Fukuoka, 348 (1983).
5. M. Gauthier, R. Bellemare, and A. Bélanger, *J. Electrochem. Soc.*, **128**, 371 (1981).
6. M. Gauthier and C. W. Bale, *Metall. Trans. B*, **14B**, 117 (1983).
7. W. L. Worrell, *Proc. the International Meeting on Chemical Sensors*, Fukuoka, 332 (1983).
8. W. L. Worrell and Q. G. Liu, *J. Electroanal. Chem.*, **168**, 355 (1984).
9. E. L. Kreidl and Ivan Simon, *Nature*, **181**, 1529 (1958).
10. F. A. I. El-Kabbany, *Phys. Stat. Sol.*, (a) **58**, 373 (1980).
11. A. Kvist and A. Lundén, *Z. Naturforschg.*, **20a**, 235 (1965).
12. N. Imanaka, Y. Yamaguchi, G. Adachi, and J. Shiokawa, *Bull. Chem. Soc. Jpn.*, **58**, 5 (1985).

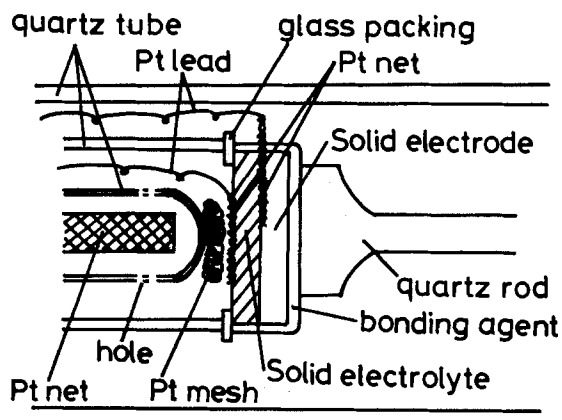


Fig. 1 The apparatus for the EMF measurements (A solid reference electrode method)

Manuscript submitted April 18, 1985; revised manuscript received Aug. 13, 1985.

Osaka University assisted in meeting the publication costs of this article.

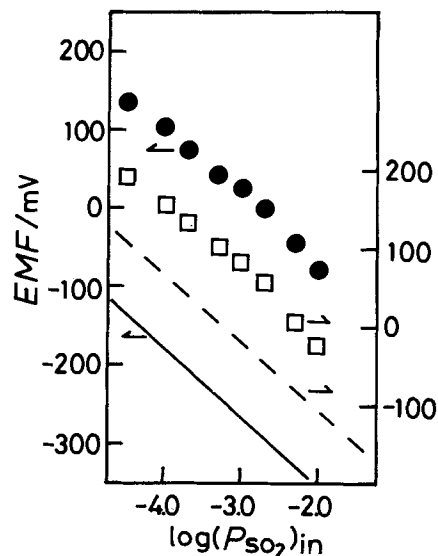


Fig. 2 The variation of the EMF for $\text{Na}_2\text{SO}_4\text{-Y}_2(\text{SO}_4)_3\text{-SiO}_2$ (48.1:11.8:40.1) with $\text{MgSO}_4\text{-MgO}$ (●) and $\text{MnSO}_4\text{-Mn}_2\text{O}_3$ (□) solid reference electrodes at 973 K
— and — — are calculated EMF(6)

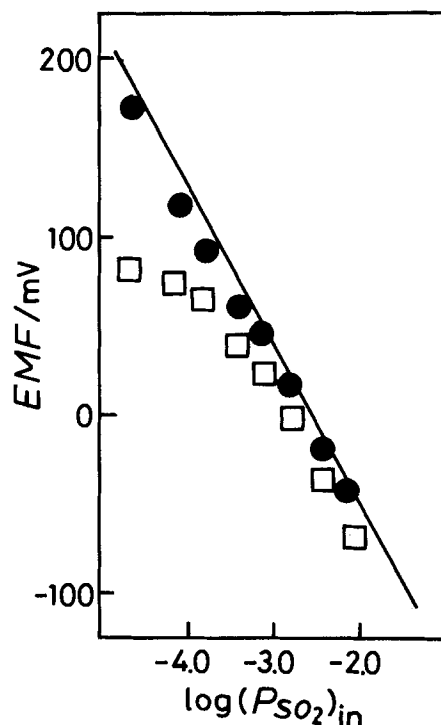


Fig. 3 The variation of the EMF for $\text{Na}_2\text{SO}_4\text{-Y}_2(\text{SO}_4)_3\text{-SiO}_2$ (48.1:11.8:40.1) and Na_2SO_4 solid electrolytes with $\text{NiSO}_4\text{-NiO}$ solid reference electrode at 973 K
● $\text{Na}_2\text{SO}_4\text{-Y}_2(\text{SO}_4)_3\text{-SiO}_2$
□ Na_2SO_4
— calculated EMF(6)



Recharge Kinetics of the Porous Lead Dioxide Electrode

I. The Effect of Structural Changes

Per Ekdunge and Daniel Simonsson

Department of Chemical Technology, The Royal Institute of Technology, S-100 44 Stockholm, Sweden

ABSTRACT

The changes in structure and kinetics during charge of the porous PbO_2 electrode have been studied by means of electrochemical and structure characterizing methods. It was found that the potentiostatic charge current after an initial period of growth, due to nucleation and growth of PbO_2 , is proportional to the decreasing amount of remaining lead sulfate. The polarization curves have a Tafel slope of about 60 mV/decade at overvoltages lower than 0.1V and about 180 mV/decade at higher overvoltages. The form of these curves can be explained by a mechanism with two consecutive single-electron transfer reactions. The results from these specific studies of the positive electrode and charge experiments with complete lead-acid cells show that the fastest way to charge lead-acid batteries is to charge at a constant cell voltage of a value just below that which leads to unacceptable gassing rates.

In spite of its great age, the cheap and reliable lead-acid battery is still the single most used battery in the world. Consequently, it has been and still is the target of intensive research. The research area has been reviewed by Burbank *et al.* in 1971 (1) and by Rüetschi in 1977 (2). Vinal's classic textbook (3) on the subject from a technological point of view has been succeeded by Bode's "Lead-Acid Batteries," published in 1977 (4). In comparison to the discharge process, less scientific interest has been paid to the charge process. This topic has more often been approached with the technological aim of finding the optimal method of charging or procedures for very rapid charging. One of the results of these studies of black-box character is the classical rule of thumb which goes by the name of the ampere-hour law and states that a battery can accept as much current (in amperes) as it needs in capacity (in ampere-hours) until it reaches full charge.

On the other hand, fundamental studies have been made of specific phenomena in the electrodes of the lead-acid battery. Studies have thus been reported on the electrocrystallization of lead dioxide from lead sulfate formed on smooth electrodes of electrodeposited lead dioxide or lead (5-8).

A lot of research has also been devoted to the electrode kinetics of the lead dioxide electrode (*e.g.*, 9-13), but it has been mainly with simplified systems with a plane electrode and where the sulfuric acid has been substituted with an electrolyte which does not give a solid product such as lead sulfate. A real battery electrode deviates significantly from the majority of systems used in these studies. A main difference is its porous structure, which introduces the additional complexities of current distribution and concentration gradients in the pores. The porous structure is in itself of decisive importance for the electrode kinetics. Specific surface area and pore size distribution are important structural parameters. These parameters are not constant in the porous lead dioxide electrode because of the structural transformations that occur between the two solid phases: lead dioxide and lead sulfate. These structural changes have been studied in optical and scanning electron microscopes (14-19) and with structure characterizing methods (19-20).

The overall kinetic behavior of the porous lead dioxide electrode as a result of the mutual dependences of intrin-

sic kinetics, structural changes, current distribution, and concentration changes is still waiting to be explored, especially with regard to the anodic process. The aim of the present work was to determine the relative importance of various structural and kinetic parameters for the rate at which lead-acid batteries can be charged. This is a question of high practical importance, not least in the application as a power source in electric vehicles. The interest was focused on the positive electrode since in most systems this is generally the limiting one, both at discharge and charge.

Experimental

The investigations were performed with commercial battery electrodes from Noack, Sweden, with a thickness of 2.0 mm. The lead grid was alloyed with 2.4-2.6% antimony and lesser amounts of arsenic (0.09-0.11%), tin (0.03-0.04%), and selenium (0.02%). Electrodes for the investigations were cut into the size 60 × 60 mm². The working electrode was placed centrally in a Plexiglas cell. Two lead electrodes were used as counterelectrodes. The electrolyte was 5.0M H_2SO_4 in large excess. The electrode potential was measured relative to a $\text{Hg}/\text{Hg}_2\text{SO}_4$ reference electrode. The potentiostatic experiments were performed with a Wenking 68TS10 potentiostat. In order to obtain a uniform lead sulfate distribution in the electrodes, they were discharged with a low current density ($\sim 20 \text{ A/m}^2$) in the standard case. The discharge was interrupted at a potential of 0.9V. The electrode was at rest for 2h before the charge.

For comparisons, recharge experiments were also performed with complete lead-acid cells with electrodes of the full size. Six cells were assembled; each with three positive and four negative plates. In five of these cells, the distance between the electrodes was 5 mm and was controlled by vertical separator tubes of the type used for tubular electrodes. In one cell, the electrodes were closely packed with ordinary separators between them. The cells were made of Plexiglas. They were closed and gastight; evolved gases were allowed to escape from the cell through an outlet connected to an oxygen sensor (Servomex OA250). The gas evolution rate was measured volumetrically with a graduated tube. The temperature was measured with a thermometer inserted through the lid via a sealing rubber stopper. A thermostat bath was used to

control the temperature in runs at nonambient temperature.

In all experiments, the charges were recorded by electronic coulometers simultaneously with the overvoltage or current.

The structural changes were followed by visual observations with SEM (Jeol JSM2) and by measuring the changes in specific surface area according to the BET method (Micromeritics Accusorb 2100 E) and pore size distribution by means of mercury porosimetry (Aminco 5-7118). Samples taken for these observations were washed according to a special procedure in order to avoid large concentration gradients which can cause redistribution of the lead sulfate in a bipolar process driven by the concentration elements thus created. The samples were placed in a beaker filled with a stirred 5M H₂SO₄ solution. This solution was then progressively diluted with distilled water, which was added continuously with a rate adjusted so that all the sulfuric acid had been washed out overnight. In this way, the concentration gradients within the porous electrode were limited to small values.

The changes in effective conductivity of the pore electrolyte were determined from the ohmic voltage drop required to pass a given current through the unloaded electrode. An x-ray diffraction analysis showed that the active mass of the fully charged positive electrode consisted almost entirely of β -PbO₂.

Results

Galvanostatic and potentiostatic charges.—Charging with a constant current gave the overvoltage-time curves shown in Fig. 1 and 2. In these curves the Ri-free overvoltage has been plotted against a nominal state of charge defined as

$$q = q_d + \int_0^t i dt \quad [1]$$

where q_d is the charge output in the previous discharge. The general form of these curves can be interpreted by formally distinguishing four different regions. When the constant current is applied to the fully discharged electrode, the potential immediately rises to a peak value. The overvoltage then rapidly decreases to a flat minimum at about 10-20% charge. In a third region, the overvoltage increases monotonically until it finally reaches the plateau corresponding to the oxygen evolution reaction on the fully charged electrode.

The potential peak decreases with the decreasing discharge capacity at increasing discharge current. The minimum, on the other hand, first decreases with increasing discharge current density and then increases at very large discharge currents.

Figure 2 shows that the charge curve is flatter at lower current densities. The recharge of a partially discharged electrode requires a lower overvoltage than a fully dis-

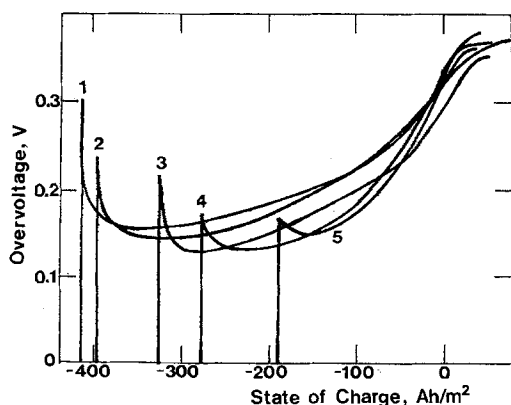


Fig. 1. Overvoltage-time curves at galvanostatic charge with 200 A/m² of an electrode discharged with -30 (curve 1), -100 (curve 2), -200 (curve 3), -500 (curve 4), -1000 A/m² (curve 5).

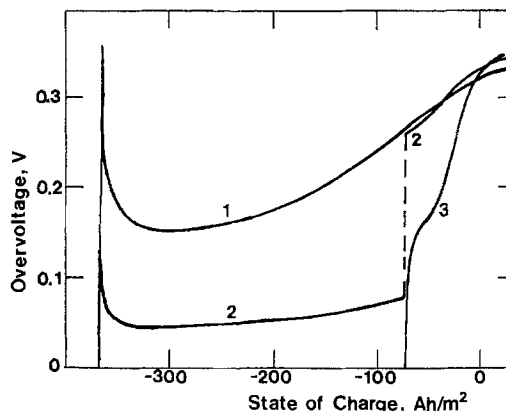


Fig. 2. Overvoltage-time curves at galvanostatic charge of fully discharged (curve 1) and partially discharged (curve 3) PbO₂ electrodes. Current density = 200 A/m². Curve 2: charge with 20 A/m² to 80%, followed by charge with 200 A/m².

charged electrode which has been recharged to the same state of charge. It can also be noted that the inflection point of curve 3 in Fig. 2 is at an overvoltage of approximately the same value as the minimum in the recharge curve (curve 1) of the fully discharged electrode.

The potentiostatic charge curves (Fig. 3) can be interpreted in the corresponding way. The falling potential after the initial peak value at the galvanostatic charge has its correspondence in a rising current at potentiostatic charge. After a maximum (corresponding to the minimum in the galvanostatic charge curve), the current decays almost linearly with the state of charge. Since the current efficiency is somewhat less than 100%, especially at higher overvoltage, the nominal state of charge (q) is somewhat higher than the true state of charge. The curves therefore do not level off at the oxygen evolution current until q assumes positive values. Figure 4 shows that the current density at potentiostatic charge is not a state function with respect to the PbSO₄/PbO₂ composition. The maximum current was roughly the same (within 20%) irrespective of whether the electrode had been discharged to 100, 70, or only 20% (curves 1-3 in Fig. 4). When the electrode had been discharged with a high current density (-1000 A/m²), the potentiostatic charge current was somewhat higher.

The rising transients in Fig. 3 and 4 and the falling overvoltage in Fig. 1 and 2 can be ascribed to nucleation and growth of lead dioxide. This process governs the kinetics only up to 10-20% charge. The amount of charge consumed in this region is independent of the current or the potential. An initial galvanostatic charge with low current

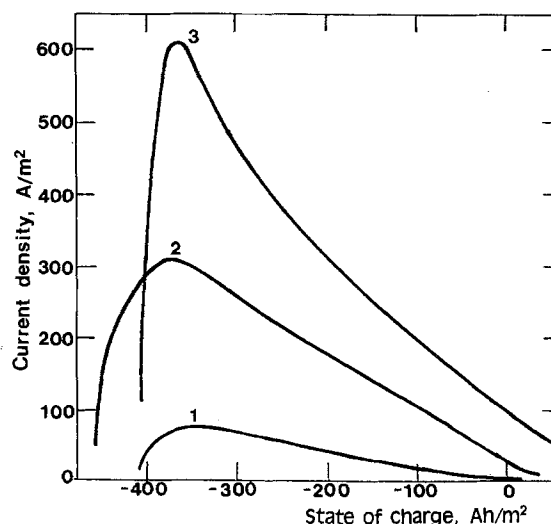


Fig. 3. Potentiostatic charge of a PbO₂ electrode at different overvoltages: 100 (curve 1), 200 (curve 2), 266 mV (curve 3).

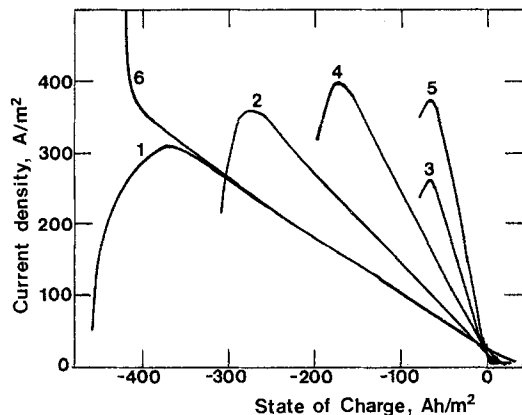


Fig. 4. Potentiostatic charge of an electrode discharged under different conditions. Curves 1-3: discharged with -20 A/m^2 to 100 (curve 1), 70 (curve 2), and 20% (curve 3). Curves 4, 5: discharged with -1000 A/m^2 to 100 (curve 4), and 40% (curve 5). Curve 6: discharged with -20 A/m^2 to 100% and recharged galvanostatically with 20 A/m^2 to 10%.

density (20 A/m^2) to 10% followed by a potentiostatic charge resulted in a monotonically decreasing current coinciding with the decreasing current of the complete potentiostatic charge curve (Fig. 4). The initial deviation between the two curves can probably be explained by the differences in electrolyte concentration profiles. The rising transients were also observed at the potentiostatic charge of only partially discharged electrodes, although its relative importance decreases with decreasing discharge.

The dependence of overvoltage on current density at different states of charge is shown in Fig. 5. These curves were obtained by applying different constant currents of short duration at three different states of charge (20, 50, and 80%), while the electrode was otherwise charged with a low constant current density in order to avoid nonuniform current distribution and the establishment of concentration gradients. The overvoltage was corrected for the contribution from the increasing acid concentration gradient by extrapolation back to time zero. The anticipated linear decrease in current density with the increasing state of charge indicated by the potentiostatic oxidations was tested by a rate equation of the form

$$i = S_m j_o L (q/q_a) \exp\left(\frac{\alpha n F}{RT} \eta\right) \quad [2]$$

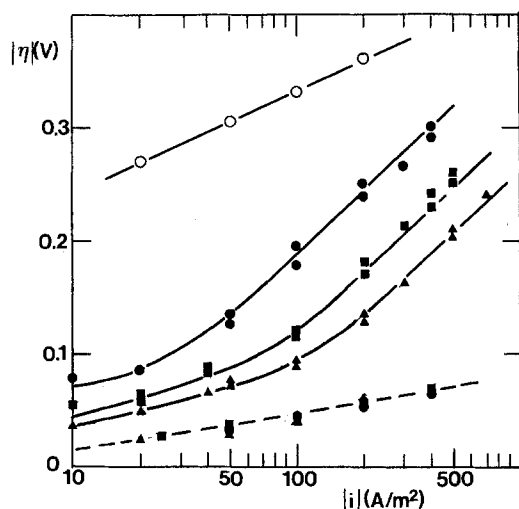


Fig. 5. Polarization curves for two different PbO_2 electrodes fully discharged with -20 A/m^2 and recharged with 20 A/m^2 to 20 (triangles), 50 (squares), 80 (filled circles), and 120% (open circles) (oxygen evolution). Solid lines: anodic current. Dashed line: cathodic current. The anodic polarization curves drawn for the partial charges are fits to the relation $i = S_m j_o L q/q_a$ where j is given by Eq. [12] with $\alpha_r = 0.32$, $S_m 2j_o L = 47 \text{ A/m}^2$, $j_{0,r}/j_{0,o} = 25$, and $\alpha_o = 0.5$.

at higher overvoltage, where the back reaction can be neglected. Piecewise fits of this expression are in good agreement with the experimental points in Fig. 5. At lower overvoltage, $\alpha n \approx 1$ and $S_m j_o L \approx 3 \text{ A/m}^2$. The Tafel slope increases abruptly at an overvoltage of 0.1 V . Above this value, $\alpha n = 0.32$ and $S_m j_o L = 47 \text{ A/m}^2$. Calculations with a rate equation derived from Eq. [2] showed that the current density distribution in the porous electrode was practically uniform at all current densities. When the overvoltage approaches a value of 0.3 V , the side reaction of oxygen evolution becomes significant. The Tafel slope of 95 mV/decade found for this electrode reaction is in agreement with the results of Rüetschi *et al.* (21). Figure 5 also shows the cathodic overvoltage measured in the same way at different states of charge during the recharge process.

Charging of full-size cells.—Preliminary experiments with potentiostatic charge of lead dioxide and lead electrodes, respectively, showed that the positive electrode was the limiting one both at discharge and at charge. The behavior of the lead-acid cell would then be controlled mainly by its positive electrode. Experiments with complete cells with full-size electrodes were therefore undertaken in order to compare the behavior observed for the single lead dioxide electrode with that of the complete cell. Comparisons were made between charging with constant current (I), constant voltage (U), and constant current followed by constant voltage (IU), respectively. The voltage-time curves at charging with constant current are shown in Fig. 6 together with the total volume of evolved gases. The common feature of the different charge curves is a continuously increasing voltage up to a state of charge where the voltage rises abruptly to a much higher level while simultaneously the gassing rate increases rapidly. A cell voltage of, e.g., 2.6 V is reached after 71, 79, and 90% charge at 150, 100, and 50 A/m^2 , respectively. The fraction remaining to be charged into the battery is thus approximately proportional to the current density. This is in accordance with the first-order dependence on lead sulfate as expressed in Eq. [2]. The galvanostatic charge curves in Fig. 6 exhibit a steeper rise in overvoltage than those of a single PbO_2 electrode in Fig. 1.

Charging with constant current until the cell voltage reaches 2.50 V followed by charging at constant voltage gave the results shown in Fig. 7. Compared to charging with constant current, this procedure has the advantage that excessive gassing is automatically avoided by not allowing the voltage to increase above a prescribed value. According to Fig. 7, the charging current decays exponentially during the period of constant voltage. The

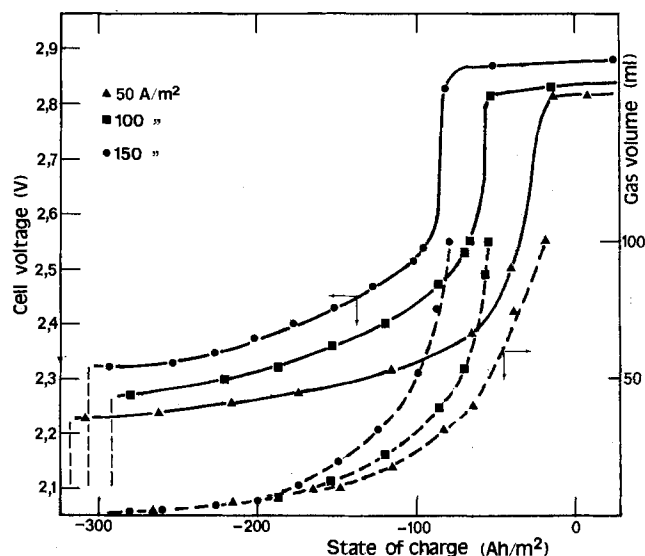


Fig. 6. Changes in cell voltage and accumulated gas volume at galvanostatic charge at different current densities. Discharge current density = -120 A/m^2 .

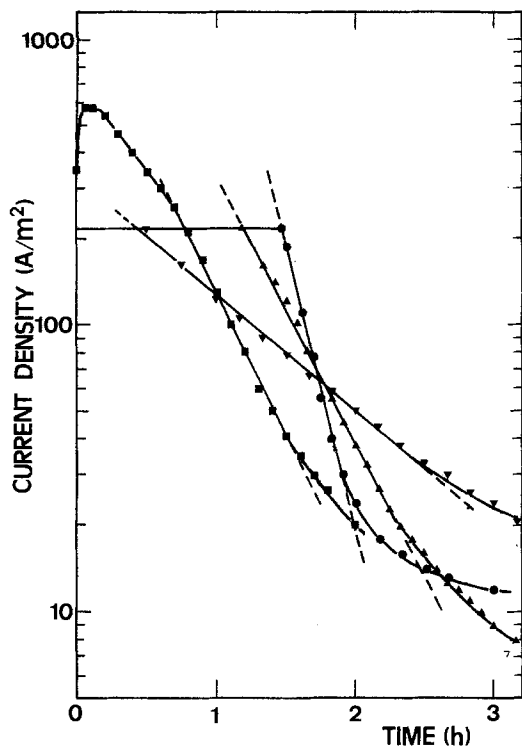


Fig. 7. Current density vs. time at a charge with constant cell voltage = 2.50V (squares), 22°-29°C, and IU charging with current limitation to 22A at different temperatures: 3.5°C (nablas), 25°C (triangles), and 52°C (circles).

experimental curves deviate from the straight $\ln i-t$ lines at lower current densities, since the electrochemical gas evolution becomes a progressively higher fraction of the total, decreasing current. The disadvantage of IU charging is obviously that it does not take full advantage of the high charge acceptance in the beginning. Charging at constant voltage utilizes this possibility of high initial currents. The curve for charging at a constant cell voltage of 2.50V in Fig. 7 is somewhat convex after the maximum. This is due to a temperature rise from 22° to 29°C. In the linear portion of the curve, the temperature varies only between 29° and 28°C.

When Eq. [1] and [2] are combined, we obtain the variation of current density with time

$$i = i_1 \exp[-k(t - t_1)] \quad (\eta \approx \text{const}) \quad [3]$$

where index 1 denotes the time after which Eq. [2] is valid, and

$$k = S_m j_o L \exp\left(\frac{\alpha n F \eta}{RT}\right) / (-q_d) \quad [4]$$

The coefficient k is a rate coefficient which can be determined from the slopes of the linear portions of the curves in Fig. 7. The temperature dependence of k at constant cell voltage follows an Arrhenius relation (see Fig. 8).

Structural changes.—The morphological changes during charge were followed by taking out samples at different states of charge for visual observations by means of a scanning electron microscope. These observations showed that larger lead sulfate crystals were formed at lower rates of discharge (Fig. 9 and 10). The size of the lead sulfate crystals could, furthermore, be related to the volumetric restriction imposed by the porous structure. On the exterior surface, where there are no such restrictions, the lead sulfate can grow to large, closely packed crystals (Fig. 9 and 10). This also holds for larger voids in the porous electrode (Fig. 11), while otherwise the lead sulfate crystals were smaller and randomly dispersed in the porous structure (Fig. 12). In most cases, no firm conclusions could be drawn as for the mechanism of the struc-

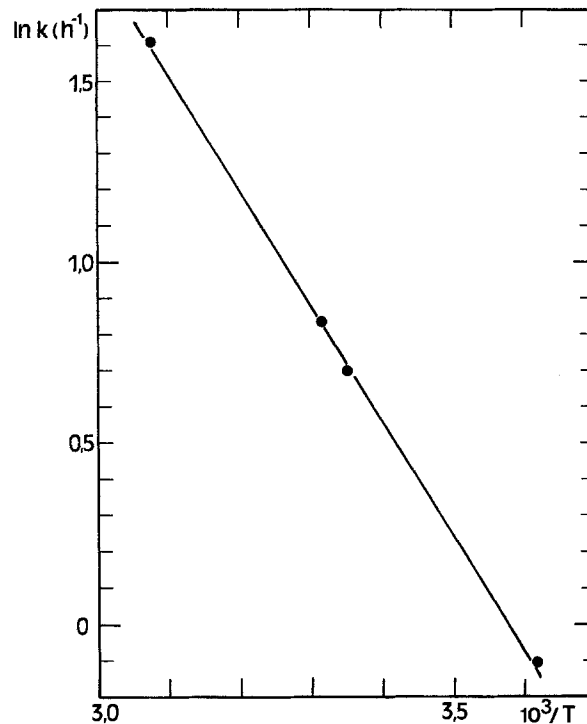


Fig. 8. Arrhenius plot of the charge rate coefficient defined by Eq. [4].

tural transformations: occasionally, we could observe how lead sulfate crystals were transformed into lead dioxide with the macrostructure preserved (Fig. 13). This type of transformation has earlier been observed by Simon *et al.* (14, 16). Interesting observations were made concerning the structural transformations of the larger lead sulfate crystals formed on the exterior surface at low discharge rates. The lead dioxide formed during charge was held within the dimensions of the original lead sulfate crystals. A dense microcrystalline wall of lead dioxide was formed which eventually was ruptured at excess charge and revealed an inside growth of small lead dioxide crystals into the form of a compact kernel (see Fig. 10 and 14-17).

The changes in specific surface area are of great importance when attempting to explain the changes in electrode kinetics. Although the BET method does not distinguish between the surface areas of PbO_2 and PbSO_4 , important conclusions can be drawn when combined

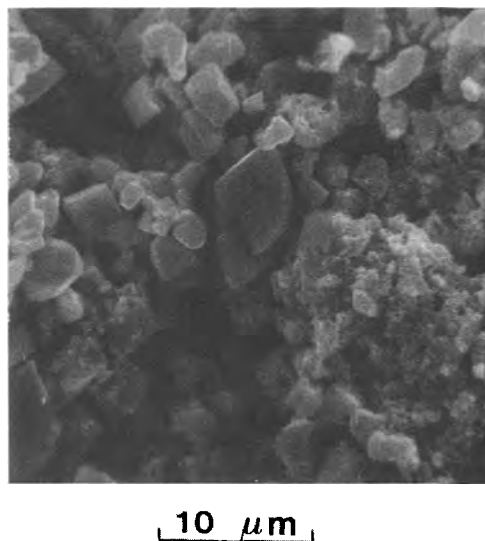


Fig. 9. Lead sulfate crystals formed on the exterior surface of the electrode at a discharge with -200 A/m^2 to -320 Ah/m^2 .

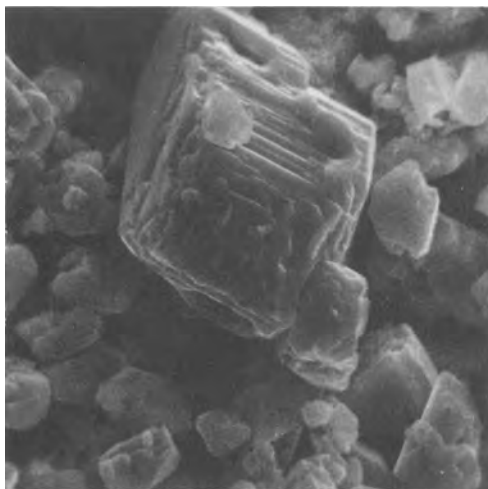
10 μm

Fig. 10. Lead sulfate crystals formed on the exterior surface at a discharge with -30 A/m^2 to -410 Ah/m^2 .

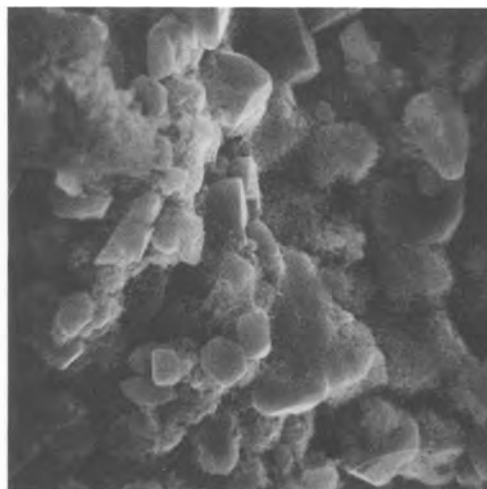
10 μm

Fig. 13. Formation of microporous lead dioxide within the dimensions of the original lead sulfate crystals formed during discharge. Electrode discharged with -30 A/m^2 and recharged with 200 A/m^2 to -48 Ah/m^2 .

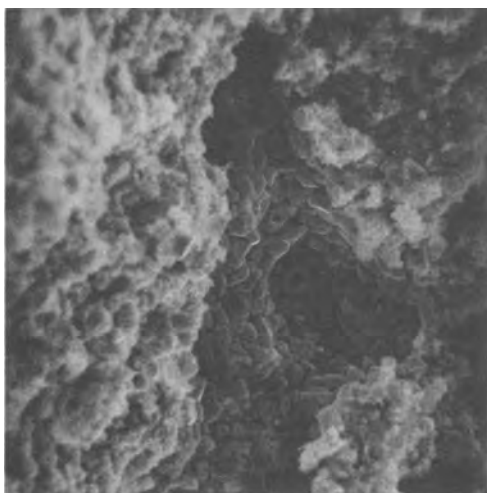
10 μm

Fig. 11. Formation of dense agglomerates of lead sulfate crystals in a larger void. Electrode discharged with -30 A/m^2 .

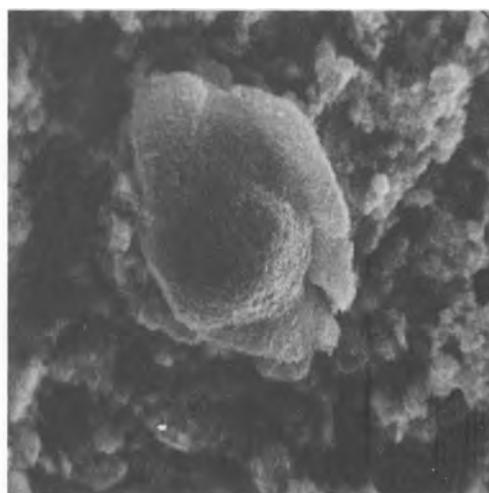
10 μm

Fig. 14. SEM micrograph showing the beginning of the transformation of large lead sulfate crystals into microcrystalline lead dioxide in the form of shell and kernel.

10 μm

Fig. 12. Morphology of the interior of the electrode. Discharge with -30 A/m^2 to -350 Ah/m^2 .

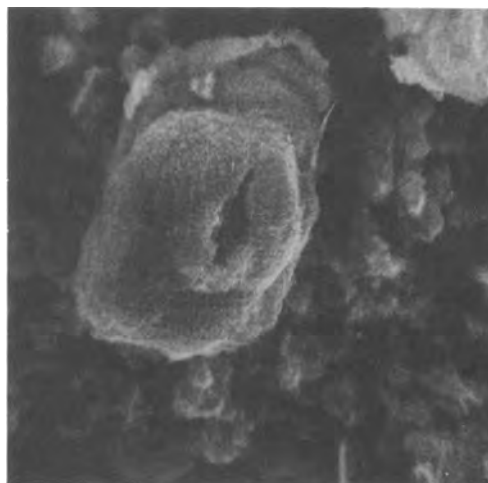
10 μm

Fig. 15. SEM micrograph showing the transformation of large sulfate crystals into microcrystalline lead dioxide in the form of shell and kernel.

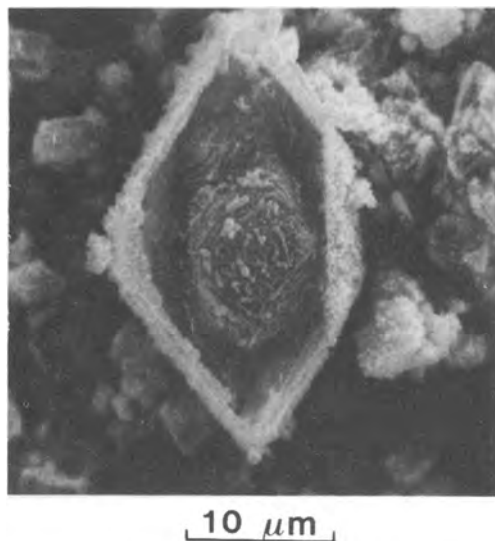


Fig. 16. SEM micrograph of large sulfate crystals transformed into microcrystalline lead dioxide in the form of shell and kernel.

with other pieces of information. The changes in specific surface area during charge are illustrated in Fig. 18. The fully discharged electrode has a specific surface area which is almost three times smaller than that of the fully charged. The latter is $6.4 \text{ m}^2/\text{g}$, which according to the geometric relationship for spherical particles

$$S_p = 6/d_p \quad [5]$$

corresponds to a mean particle diameter of $0.1 \mu\text{m}$. The mean particle diameter of the fully discharged electrode can, in the same way, be calculated to be $0.4 \mu\text{m}$. These values can be compared to those estimated from micrographs, which are about $0.1 \mu\text{m}$ for the lead dioxide and $1\text{-}10 \mu\text{m}$ for the lead sulfate. The specific surface area of the fully discharged electrode must, therefore, to a major extent, be attributed to residual lead dioxide which has not been covered with PbSO_4 but is either electrically insulated or electrochemically nonactive. The dashed line in Fig. 18 represents the change in specific surface area of the lead dioxide only according to a structural model assuming spherical particles shrinking uniformly during discharge. The measured surface area of the fully discharged electrode is lower than that predicted by this model. This is also to be expected since microscopy studies have revealed that much of the PbO_2 remaining at the end of discharge have been encapsulated within PbSO_4 crystals (14, 16). The initially rapid growth of specific sur-



Fig. 17. Detail of Fig. 16

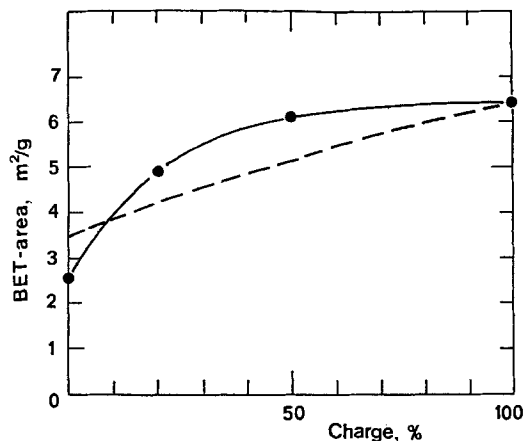


Fig. 18. Changes in specific surface area during charge. The surface area is given in the unit of square meter per equivalent gram of PbO_2 .

face area during charge can thus be attributed to the uncovering of this encapsulated PbO_2 , while at the same time a large inner surface area of PbSO_4 is created inside the PbSO_4 crystals as they dissolve. Although residual PbO_2 may act as nuclei for the lead dioxide formed during charge, new nuclei will probably be formed in parallel at the high initial overvoltage. These new PbO_2 crystals will give an additional contribution to the surface area. After the initially rapid growth of surface area, the continued increase is much slower because the surface area of PbO_2 grows slower than linearly with the amount of charge, while the surface area of PbSO_4 decreases.

The changes in pore size distribution are plotted in Fig. 19. The fully charged electrode had a total porosity of 56%, including closed pores and pores smaller than $0.035 \mu\text{m}$, and a mean pore diameter of but $0.15 \mu\text{m}$. Using a cylindrical pore model, the porosimetry data can also be used to estimate the specific surface area. The values obtained in this way were 40-50% lower than the corresponding values measured by the BET method. Besides the inaccuracy of the cylindrical pore model, part of this discrepancy can be attributed to pores smaller than $0.035 \mu\text{m}$, which contribute little to the pore volume but appreciably to the specific surface area.

The changes in the porosimetry curves in Fig. 19 also reflect the fact that the molar volume of lead sulfate ($48.9 \text{ cm}^3/\text{mol}$) is almost twice that of lead dioxide ($25.5 \text{ cm}^3/\text{mol}$). The plugging effect of the lead sulfate in the pores affects the effective transport coefficients for diffusion and migration. The changes in effective conductivity are plotted in Fig. 20. As expected, the effective conductivity increases during charge, due to the opening up of pores, but then reaches a flat maximum at about 80% charge. The labyrinth factor $\lambda = \kappa_{\text{eff}}/\kappa_{\text{free}}$ of the fully charged electrode is 0.15 including the effect of the grid and about 0.19 after correction for the grid, which occupies about 20% of the total projected electrode area.

Discussion and Conclusions

The results should be interpreted with respect to both the individual factors and their mutual dependence. It can thus be concluded that the initial part of the charge process is governed by the formation of electrochemically active PbO_2 surface. As already discussed, Fig. 18 indicates that this occurs not only by nucleation and growth of new PbO_2 crystals, but also by the uncovering of encapsulated or covered residual lead dioxide. This hypothesis is also supported by the observation that the duration of this process is independent of current density or overvoltage and that it does not affect the later period of the recharge.

The rising potentiostatic transient reaches a maximum after recharge to only 10-20%. While this first, shorter period is controlled mainly by the available surface area of lead dioxide, the major portion of the charge process

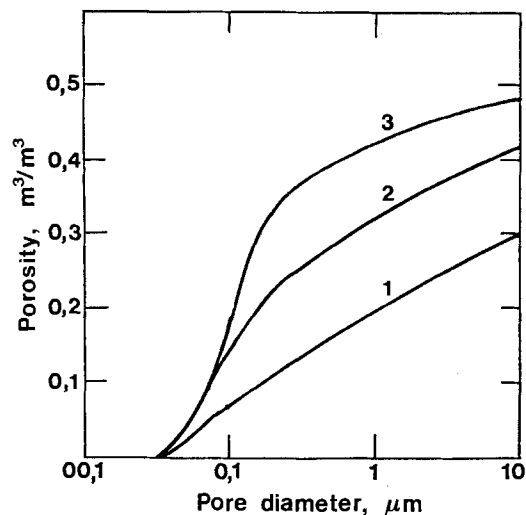


Fig. 19. Pore size distribution of a porous PbO_2 electrode. 1: Fully discharged. 2: 50% charged. 3: Fully charged.

seems to be controlled by the availability of lead sulfate. It is obvious that the anodic and cathodic reactions are different in their dependence on the structural changes and cannot be microreversible at the current densities employed. The cathodic polarization curves in Fig. 5 do not differ significantly from each other, which indicates that the working surface area of the active lead dioxide is relatively constant after a recharge to 20%. This is in agreement with the results from the surface area measurements (Fig. 18) when recalling that the main fraction of this total specific surface area can be attributed to the lead dioxide.

Contrary to this, the anodic reaction is apparently first order with respect to the amount of remaining lead sulfate. The charge reaction, therefore, seems to be confined to a zone very close to the surface of the lead sulfate crystals. An evident explanation would be that the reaction proceeds through a solid-state mechanism. On the other hand, it is more commonly believed that the transformations between lead sulfate and lead dioxide occur via a dissolution precipitation mechanism involving dissolved Pb^{2+} ions. Vetter (22) has shown that such a mechanism is possible in the lead dioxide electrode, and that the volumetric diffusion rate of Pb^{2+} ions over the microscopic distances is sufficiently high to allow an efficient utilization of the whole PbO_2 surface. According to this mechanism, the oxidation reaction can be formally written as

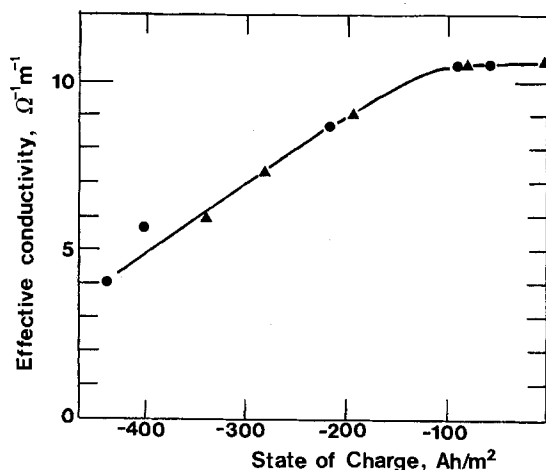
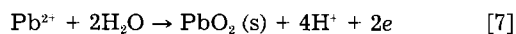
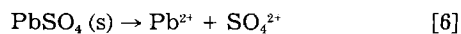


Fig. 20. Changes in effective conductivity during charge. Two different electrodes.

where the latter reaction in turn is composed of several elementary steps. Vetter's analysis can be extended by taking into consideration the interplay of diffusion and intrinsic electrode kinetics in a rate equation. Assuming first-order, purely consecutive reactions, the kinetic equation at high overvoltage for this scheme would be of the form

$$i = \frac{S_2 j_0 \exp\left(\frac{\alpha n F}{RT} \eta\right)}{1 + \frac{S_2 j_0}{2F} \left(\frac{1}{k_0 S_1} + \frac{L}{D_{\text{ce}} S_{1,2}}\right) \exp\left(\frac{\alpha n F}{RT} \eta\right)} \quad [8]$$

Equation [8] takes into account the dissolution rate of PbSO_4 and the diffusion of Pb^{2+} ions over a characteristic distance L and across a mean cross section $S_{1,2}$, which is some weighted average of the surface areas of PbSO_4 (S_1) and PbO_2 (S_2). When the dissolution and diffusion rates are high in comparison to the charge transfer rate, the second term in the denominator vanishes and the current is proportional to the surface area of lead dioxide. It is only at the limiting current density, when the reaction rate is controlled by the dissolution and/or diffusion, that the current is proportional to the surface area of lead sulfate. Equation [8] thus predicts η - i curves for different states of charge which approximately coincide at low current densities, diverge at higher current densities, and finally reach their different limiting values appearing as vertical lines in the η - i diagram. The different curves in Fig. 5 obviously do not follow this pattern. The curves at different states of charge do not coincide until very close to the equilibrium potential, and no distinct limiting currents can be observed at higher overvoltages.

An alternative kinetic model takes into account that diffusion of Pb^{2+} ions and their reaction occur in parallel as well as in consecutive steps. The physical picture is then similar to that in a heterogeneous catalyst particle (23). An order of magnitude calculation shows, however, that even in this case, the diffusion rate of lead ions is sufficient to balance their consumption rate in the charge reaction.

The switch from a low to a high Tafel slope in Fig. 5 can be explained by a mechanism with two consecutive single-electron transfer reactions. This case has been treated by Vetter (24) for the general scheme



Writing down the rate equation for each step and eliminating the concentration of the intermediate S_m between the two equations give the following relation between current density and overvoltage

$$j = 2j_{0,r} \cdot \exp\left(\frac{\alpha_r F}{RT} \eta\right) \frac{1 - \exp\left(-\frac{2F}{RT} \eta\right)}{1 + \frac{j_{0,r}}{j_{0,o}} \cdot \exp\left(-\frac{1 + \alpha_o - \alpha_r}{RT} F \eta\right)} \quad [12]$$

where $j_{0,r}$ and $j_{0,o}$ are the exchange current densities and α_r and α_o are the charge transfer coefficients of reactions [9] and [10], respectively. At high anodic overvoltages, Eq. [12] is simplified to

$$j = 2j_{0,r} \exp\left(\frac{\alpha_r F}{RT} \eta\right) \quad [13]$$

The geometric current density of the porous electrode at uniform current distribution would then be

$$i = S_m L (q/q_0) 2j_{0,r} \exp\left(\frac{\alpha_r F}{RT} \eta\right) \quad [14]$$

which is similar to Eq. [12]. The values of the charge

transfer coefficient α_r and the pre-exponential factor can thus be explicitly determined from the slope and intercept of the Tafel line at overvoltages higher than 0.1V. The obtained value of the charge transfer coefficient, $\alpha_r = 0.32$, is rather low and indicates an unsymmetrical energy barrier. Assuming that $\alpha_o = 0.5$ and using the quotient $j_{o,r}/j_{o,o}$ as a fitting parameter, the complete polarization curve can be constructed from Eq. [12] multiplied by $S_m L(q/q_o)$. The fitted curves are drawn as solid lines in Fig. 5 with a fitted value of $j_{o,r}/j_{o,o} = 25$.

The reality corresponding to the formal Eq. [9] and [10] is not possible to elucidate from current density overvoltage curves only. Several possible mechanisms can be proposed, but the discrimination between these requires further information, for example, about electrochemical reaction orders.

The situation is more complicated when the cathodic Tafel-line in Fig. 5 is taken into consideration. It is remarkably straight in spite of the fact that the current distribution in this case with a low Tafel slope would become successively more nonuniform with an increasing current density, thus leading to an increasing Tafel slope. It has a slope of about 30 mV/decade, which is consistent with results obtained on plane electrodes (25). This slope is consistent with a rate-determining chemical step after both electrons have been transferred. One thinks, on the first hand, of the precipitation of lead sulfate. The observed value of the cathodic transfer coefficient is not consistent with the transfer coefficients obtained for the anodic reaction. The value of the parameter $S_m j_o L$, obtained from the intercept with the $\log i$ axis is about 3 A/m², which is in approximate agreement with the value of $j_{o,o}$ obtained for the anodic reaction. On the other hand, the exchange current density j_o obtained on a flat electrode of electrodeposited β -PbO₂ is of the order of 0.1 A/m² (24). With $S_m = S_2 \approx 10^7 \text{ m}^{-1}$ and $L = 10^{-3} \text{ m}$, this value of j_o gives an estimated value of $S_m j_o L = 10^3 \text{ A/m}^2$. Even after a correction for the roughness factor of the plane electrode, this value is orders of magnitude higher than that obtained for the porous electrode.

The inconsistency between the anodic and cathodic branches at higher overvoltages is difficult to explain in view of the reversibility of the lead dioxide electrode. Probably, a change in mechanism occurs in the region of lower anodic overvoltages: for example, a change from a solid-state to a dissolution-precipitation mechanism. This hypothesis is partly supported by the SEM micrographs, from which the latter mechanism seems to be the more probable at the cathodic reaction, while the first-order dependence on lead sulfate at anodic overvoltages above 30 mV is in favor of a solid-state mechanism.

The SEM micrographs, unfortunately, do not give an unequivocal discrimination between these two mechanisms at recharge. The formation of the core-shell structure in Fig. 16-17 evidently requires transfer of lead species via the solution, while the structure in Fig. 13 is more consistent with a solid-state reaction.

In conclusion, the experimental results can be combined to give an understanding of the effect of the structural changes on the electrode kinetics of the porous lead dioxide electrode. During discharge, the cathodic reaction is distributed (although not uniformly) over the entire PbO₂ surface. As the discharge proceeds, the PbSO₄ crystals grow larger, overlap, and merge into larger but fewer crystals. The total surface area of PbSO₄ will then grow only slowly. This explains why in Fig. 4 approximately the same maximum current is obtained at potentiostatic charge of fully and partially discharged electrodes.

At the same time, the amount of lead dioxide decreases and thus a successively larger amount of charge is needed for the formation of new lead dioxide in the electrocrystallization process. The rising transients in Fig. 4, therefore, have a longer duration after a deeper discharge. The morphology of the lead sulfate crystals formed during discharge, especially the larger crystal size in larger voids and on the exterior surface, indicates that the cath-

odic reaction proceeds via a dissolution-precipitation mechanism. The Tafel slope even indicates that the precipitation of lead sulfate from Pb²⁺ and SO₄²⁻ ions might be the rate-determining step at sufficiently high current densities.

Acknowledgments

This work was financially supported by the National Swedish Board for Technical Development (Project no. 83-3262). The SEM studies were performed by Mats Hallberg.

Manuscript submitted Dec. 5, 1984; revised manuscript received May 21, 1985. This was Paper 22 presented at the New Orleans, Louisiana, Meeting of the Society, Oct. 7-12, 1984.

The Royal Institute of Technology assisted in meeting the publication costs of this article.

LIST OF SYMBOLS

c_{eq}	equilibrium concentration of Pb ²⁺ ions (mol/m ³)
D	diffusion coefficient of Pb ²⁺ ions (m ² /s)
d_p	particle diameter (m)
i	geometric current density (A/m ²)
i_o	apparent geometric exchange current density (A/m ²)
j	true current density (A/m ²)
j_o	true exchange current density (A/m ²)
k	charge rate coefficient (h ⁻¹)
k_o	rate constant for the dissolution of PbSO ₄ (mol/m ² /s)
L	thickness of one symmetric half of the porous electrode (m)
n	number of electrons transferred in the electrode reaction
q	amount of charge remaining to be recharged (Ah/m ²)
q_d	charge output in the previous discharge (Ah/m ²)
S	specific surface area (m ² /kg)
S_m	specific active surface area (m ⁻¹)
S_1	specific surface area of PbSO ₄ (m ⁻¹)
S_2	specific surface area of PbO ₂ (m ⁻¹)
$S_{1,2}$	mean specific cross-section area for the diffusion of Pb ²⁺ ions

Greek Letters

α	charge transfer coefficient
η	charge transfer overvoltage (V)
ρ	density of electrode material (kg/m ³)

Subscripts

r	first electron transfer step
o	second electron transfer step

REFERENCES

- J. Burbank, A. C. Simon, and E. Willihnganz, in "Advances in Electrochemistry and Electrochemical Engineering," Vol. 8, P. Delahay, Editor, p. 157 (1971).
- P. Rüetschi, *J. Power Sources*, **2**, 3 (1977/1978).
- G. W. Vinal, "Storage Batteries," 4th ed., John Wiley and Sons, New York, (1955).
- H. Bode, "Lead-Acid Batteries," Wiley-Interscience, New York (1977).
- M. Fleischmann and H. R. Thirsk, *Trans. Faraday Soc.*, **51**, 71 (1955).
- S. G. Canagaratna, P. Casson, N. A. Hampson, and K. Peters, *J. Electroanal. Chem.*, **79**, 281 (1977).
- P. Casson, N. A. Hampson, and K. Peters, *ibid.*, **83**, 87 (1977).
- N. A. Hampson, S. Kelley, and K. Peters, *J. Appl. Electrochem.*, **10**, 261 (1980).
- D. Spahrber, Dissertation, Technische Hochschule Stuttgart, Stuttgart, Germany (1960).
- N. A. Hampson, P. C. Jones, and R. F. Phillips, *Can. J. Chem.*, **45**, 2045 (1967).
- N. A. Hampson, P. C. Jones, and R. F. Phillips, *ibid.*, **46**, 1325 (1968).
- N. A. Hampson, P. C. Jones, and R. F. Phillips, *ibid.*, **47**, 2171 (1969).
- H. Ogura and T. Sekine, *Denki Kagaku*, **41**, 638 (1973).
- A. C. Simon, C. P. Wales, and S. M. Caulder, *This Journal*, **117**, 987 (1970).
- A. C. Simon, S. M. Caulder, and J. T. Stemmler, *ibid.*, **122**, 461 (1975).
- A. C. Simon and S. M. Caulder, in "Power Sources 5,"

- D. H. Collins, Editor, p. 109, Academic Press, London (1975).
17. S. Hattori, M. Yamaura, M. Kohno, Y. Ohtani, M. Yamane, and H. Nakashima, in "Power Sources 5," D. H. Collins, Editor, p. 139, Academic Press, London (1975).
18. P. Casson, N. A. Hampson, K. Peters, and P. Whyatt, *J. Electroanal. Chem.*, **93**, 1 (1978).
19. P. Reinhardt, M. Vogt, and K. Wiesener, *J. Power Sources*, **1**, 127 (1976/1977).
20. W. Kappus and A. Winsel, *ibid.*, **8**, 159 (1982).
21. P. Rüetschi, J. B. Ockerman, and R. Amlie, *This Journal*, **107**, 325 (1960).
22. K. J. Vetter, *Chem.-Ing.-Tech.*, **45**, 213 (1973).
23. C. N. Satterfield, "Mass Transfer in Heterogeneous Catalysis," Chap. 3, M.I.T. Press, Cambridge, MA (1970).
24. K. J. Vetter, "Elektrochemische Kinetik," Springer Verlag, Berlin (1961).
25. D. Simonsson, *This Journal*, **120**, 151 (1973).

Recharge Kinetics of the Porous Lead Dioxide Electrode

II. The Effect of Sulfuric Acid Concentration

Per Ekdunge and Daniel Simonsson

Department of Chemical Technology, The Royal Institute of Technology, S-100 44 Stockholm, Sweden

ABSTRACT

Anodic polarization curves for partially recharged porous lead dioxide electrodes have been recorded at different sulfuric acid concentrations. These curves can be fitted by the rate equation for two consecutive single-electron transfer reactions. The dependence of the two exchange current densities on the sulfuric acid concentration is strongly negative. The apparent electrochemical reaction order for the first transfer step approaches -3 as the sulfuric acid concentration approaches $7M$. The polarization curves also depend on the acid concentration during the previous discharge. At the same current density, the overvoltage at recharge in $5M$ H_2SO_4 was much higher when the electrode had been discharged in $1M$ H_2SO_4 compared to a discharge in $5M$ H_2SO_4 . This effect can probably be attributed to the larger lead sulfate crystals formed at lower sulfuric acid concentrations.

In the previous paper (1), the recharge kinetics of the porous lead dioxide electrode in $5.6M$ H_2SO_4 was studied with regard to the effects of structural changes. The present paper deals with the effects of changes in sulfuric acid concentration. Although of great importance, this parameter has not been studied often before. Many investigations of the electrode kinetics of the PbO_2 electrode have been made with electrolytes giving soluble $Pb(II)$ species, e.g., $HClO_4$ and $NaClO_4$ (2-5) or HNO_3 (6), since this is the only way to vary the concentrations of Pb^{2+} and H^+ independently and at a constant ionic strength. The results of these studies are not directly applicable to the positive electrode in the lead-acid battery in which the electrolyte is sulfuric acid with a concentration of generally $4.5-5M$. The concentration decreases during discharge and increases during charge. Due to the concentration gradients required for the diffusion process, the sulfuric acid concentration in the interior of the electrode may deviate significantly from that in the free electrolyte. The acid concentration affects not only the electrode kinetics, but also the maximum utilization of the active material of the electrode (7-9).

The complexity of sulfuric acid as the electrolyte in the porous lead dioxide electrode is due to not only its two dissociation steps and the low solubility of lead sulfate, but also to the fact that sulfate ions are specifically adsorbed on the lead dioxide surface (10, 11).

The goal of the experimental studies reported here was to investigate the effect of sulfuric acid concentration on the recharge kinetics and as a specific result obtain a practically useful rate expression, which relates current density to charge transfer overvoltage and includes parameters taking into account the effects of changes in composition of both the solid electrode and the electrolyte. A kinetic expression of this form is of great use in mathematical models for analyzing and predicting the electrochemical behavior of the porous lead dioxide electrode.

Experimental Procedure

The electrochemical measurements were performed in two different cells, one of which has been described earlier (1). The other cell was designed with the porous lead dioxide electrode as a flow-through electrode (Fig.

1). This cell design with its two symmetrical Luggin capillaries was also suitable for the determination of the effective conductivity and for diagnosing the current distribu-

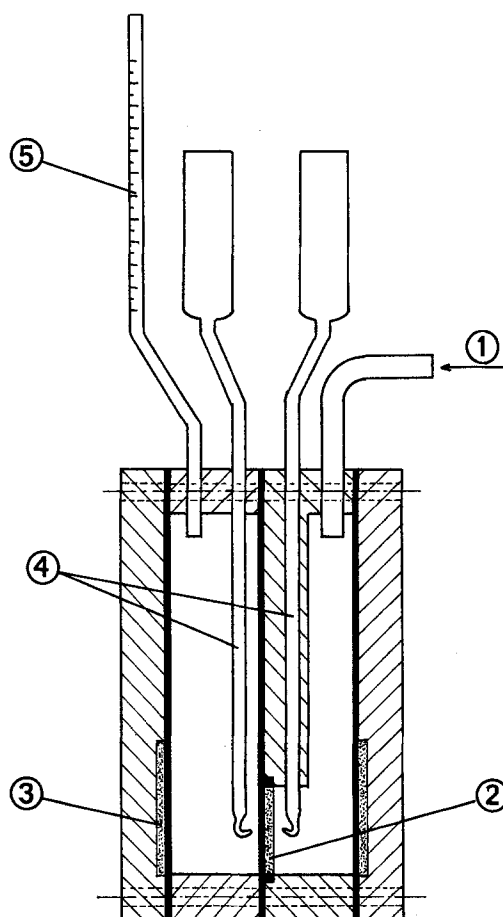


Fig. 1. Experimental cell with the porous PbO_2 electrode as a flow-through electrode. 1: Electrolyte flow from a peristaltic pump. 2: Porous lead dioxide electrode. 3: Lead electrode. 4: Luggin capillaries. 5: Graduated tube.

tion by measuring the electrode potential both at the front and the back of the electrode under current load from one side only (12). All experiments were performed at room temperature (22°C) according to procedures described in the previous paper (1).

Experimental Results

The effect of sulfuric acid concentration on the electrode potential during galvanostatic recharge with 200 A/m² is shown in Fig. 2. The overvoltage (with respect to the equilibrium potential at the actual concentration) evidently increases with an increasing acid concentration. While the change in overvoltage is relatively small when going from 5.0 to 6.0M, the increase is much greater when going from 6.0 to 7.5M. Charging in 10.0M H₂SO₄ made the potential go directly into the oxygen evolution region at the actual current density.

The results illustrated in Fig. 2 were obtained with the electrode always discharged in 5.0M H₂SO₄. Figure 3 shows that the acid concentration during discharge is also of a great importance. At the same recharge conditions, the overvoltage is much higher when the electrode has been discharged in a more diluted acid. In addition, at the low discharge current used (-20 A/m²), the discharge capacity was somewhat higher (about 10%) in 1M than in 5M H₂SO₄.

The influence of the sulfuric acid concentration on the electrode kinetics is demonstrated in the form of polarization curves in Fig. 4 for electrodes previously recharged to 20%. All curves in Fig. 4 have the same general form, with a low slope at overvoltages below 0.1V and a much higher slope at higher overvoltages. The slopes of the lines for the different sulfuric acid solutions are parallel to each other in both regions of overvoltage. At the same charge transfer overvoltage, the current density is approximately twice as high in 1.0M H₂SO₄ as in 5.0M H₂SO₄, although the electrode potential is more than 0.1V lower. This somewhat unexpected result leads to the question which of the ions has the greatest effect. A solution was therefore prepared with the composition of 1.0M H₂SO₄ and 4.0M HClO₄. This solution has approximately the same hydrogen ion activity and ionic strength as 5M H₂SO₄ and approximately the same Pb²⁺ and HSO₄⁻ ion concentration as 1M H₂SO₄. The results with this electrolyte fell between those of 1M H₂SO₄ and 5M H₂SO₄, respectively, but with a higher slope, especially in the high overvoltage region. This indicates that not only the hydrogen ion, but also the anion, is of importance for the kinetics, especially in the low overvoltage region. At higher overvoltage, the curve for 4M HClO₄/1M H₂SO₄ approaches the one for 5M H₂SO₄. Between 5 and 7M H₂SO₄,

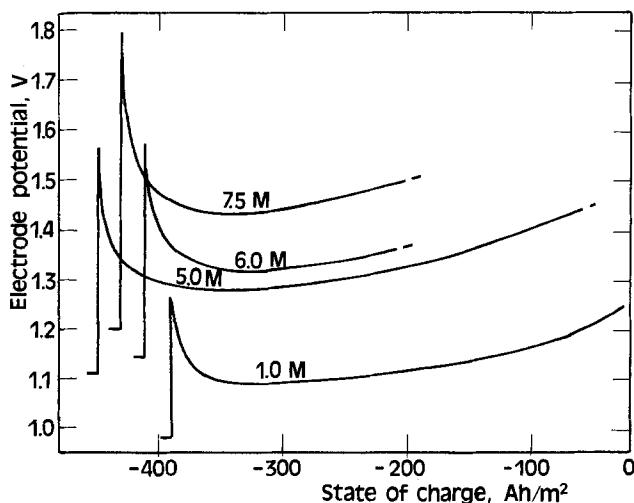


Fig. 2. Galvanostatic recharge curves at different sulfuric acid concentrations. Current density = 200 A/m². The previous discharges were all made in 5.0M H₂SO₄ at -20 A/m². The electrode potential was measured relative to a Hg/Hg₂SO₄ electrode.

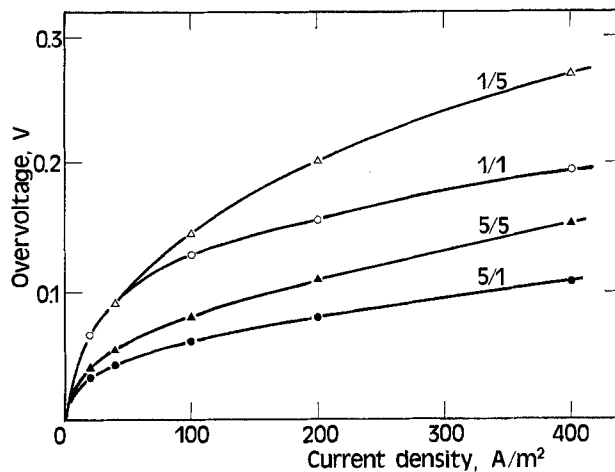


Fig. 3. Overvoltage vs. current density at 1.0 and 5.0M H₂SO₄, respectively. The notation 1/5 means discharge in 1M and recharge in 5M H₂SO₄, etc. Current load from one side only. Electrode fully discharged with -20 A/m² and recharged with 20 A/m² to 20%.

the charge transfer overvoltage is fairly independent of the concentration, especially in the low overvoltage region. For 8M, the polarization curve is very close to those for 5 and 7M in the low overvoltage region. At higher overvoltages, the working electrode potential in this solution enters into the oxygen evolution region, and the measurements at overvoltages approaching 200 mV were therefore made at significant gas evolution. This may explain the increasing deviation from the curves obtained at lower concentration. The current density at these high overvoltages is not simply the sum of the independent predictions of the partial currents for oxygen evolution and PbSO₄ oxidation. In view of the lowered current densities, the effect of oxygen evolution seems rather to be antagonistic.

Exchange current densities for the different electrolytes can be obtained by extrapolation of the linear portions of the polarization curves in the high overvoltage region to

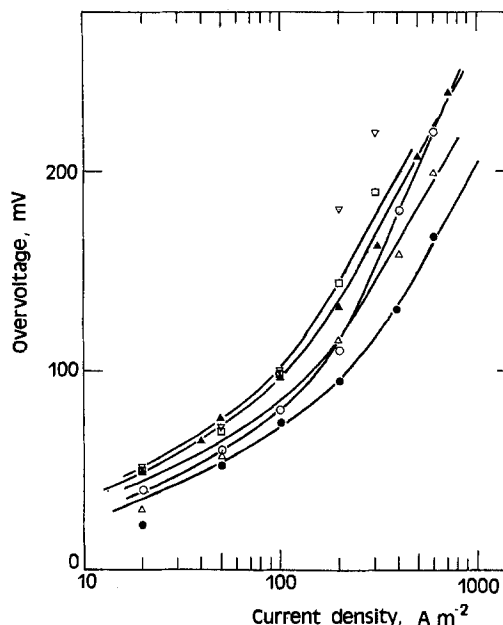


Fig. 4. Polarization curves at different sulfuric acid concentrations: • 1.0M; △ 3.0M; ▲ 5.0M; □ 7.0M; ▽ 8.0M H₂SO₄; and ○ 4.0M HClO₄/1.0M H₂SO₄. Electrode fully discharged with -20 A/m² and recharged with 20 A/m² to 20% in 5.0M H₂SO₄. The lines are predictions for all concentrations but 8M by means of Eq. [1], with exchange current densities for the first electron transfer step taken as the intercepts with the X-axis (see Fig. 5). $\alpha_r = 0.32$ (0.26 for 4M HClO₄/1M H₂SO₄), $\alpha_o = 0.5$, and $j_{0,r}/j_{0,o} = 25$.

their intercepts with the i -axis. These straight lines were drawn with the same slope for the curves for 1-7M H_2SO_4 . The exchange current densities obtained at the different sulfuric acid concentrations are plotted in a bilogarithmic form in Fig. 5.

During charge, the acid concentration in the pores increase continuously due to a limited diffusion rate. It is therefore of great interest to establish the relative importance of this concentration gradient. In Fig. 6, a comparison is made between galvanostatic recharge curves obtained with and without forced electrolyte flow. With regard to the great effect of concentration on the electrode potential, both thermodynamically and kinetically, its resulting effect on the total overvoltage is fairly small.

Evaluation of a Kinetic Equation

At the previous studies with a constant concentration of sulfuric acid, the kinetics could be successfully described by the rate equation for two consecutive electron transfer reactions (1)

$$i = S_m L (q/q_d)^2 j_{0,r} \exp\left(\frac{\alpha_r F}{RT} \eta\right) \frac{1 - \exp\left(-\frac{2F}{RT} \eta\right)}{1 + \frac{j_{0,r}}{j_{0,o}} \exp\left(-\frac{1 + \alpha_o - \alpha_r}{RT} F \eta\right)} \quad [1]$$

The overvoltage, η , in Eq. [1] is defined as the difference between the working electrode potential and the equilibrium potential of the electrode in the actual solution. The effect of structural transformations is explicitly taken into account by the factor (q/q_d) , the extent of discharge. The validity of Eq. [1] is restricted to extents of discharge lower than 0.8-0.9 (1). The effect of sulfuric acid concentration should manifest itself as a functional dependence of the two exchange current densities, $j_{0,r}$ and $j_{0,o}$, on the concentration.

The variation of $j_{0,r}$ with the sulfuric acid concentration can be directly obtained from Fig. 5, since $j_{0,r}$ is the exchange current density obtained by extrapolation of the Tafel lines in the high overvoltage region. The simplest way to express in mathematical terms the variation of $j_{0,r}$ with the sulfuric acid concentration, c , is by a power function

$$j_{0,r} = kc^{-0.43} \quad [2]$$

The maximum error is then about 10%, which is acceptable for most practical applications of Eq. [1]. The value of $j_{0,o}$ determines the potential region where the polarization curve shifts from a lower to a higher slope and can only be determined by curve-fitting of the experimental data

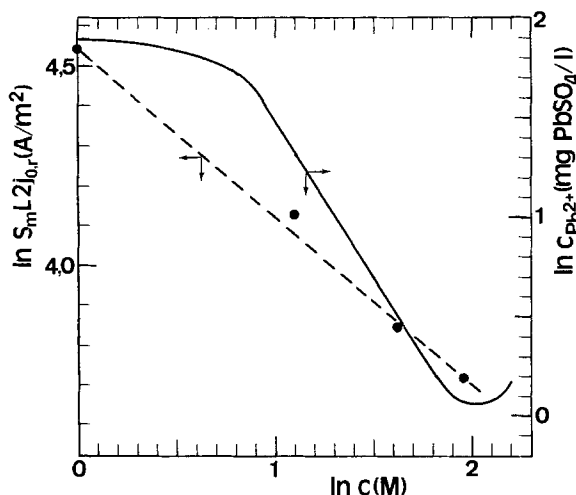


Fig. 5. Bilogarithmic plots of exchange current density vs. sulfuric acid concentration (experimental points) and solubility of lead sulfate vs. sulfuric acid concentration (solid line) according to Ref. (16).

in Fig. 4. Since all polarization curves in Fig. 4 bend at approximately the same charge transfer overvoltage, the quotient $j_{0,r}/j_{0,o}$ was in a first attempt taken to be constant and equal to 25, which is the value estimated earlier (1). The values of the charge transfer coefficients, $\alpha_r = 0.32$ and $\alpha_o = 0.5$, were also taken from this work. The theoretically predicted polarization curves with these input data are drawn as solid lines in Fig. 4. The fit is fairly good, and a possible further improvement by finding optimal values of $j_{0,r}/j_{0,o}$ and α_o for each curve individually would not outweigh the additional complexity of Eq. [1].

At lower overvoltages, below about 50 mV, the predicted curves deviate significantly from the experimental points. This may be explained by the fact that Eq. [1] is valid only for the anodic process at sufficiently high overvoltages. In the previous work, it was thus found that the cathodic polarization curves were not consistent with Eq. [1] either with respect to the structural dependence or with respect to the values of α_o and α_r . It must, therefore, be concluded that the mechanism changes at some lower anodic overvoltage. From a practical point of view, these deviations at lower overvoltages are no real problem since charging at these conditions is far from the optimal strategy. Restricting the validity of Eq. [1] to charge transfer overvoltages higher than 50 mV also means that the exponential term in the numerator can be neglected. Introducing this approximation and the estimated values of the parameters in Eq. [1] then leads to the final useful form

$$i = i_0 c^{-0.43} (q/q_d) \exp(0.32 \eta') / (1 + 25 \exp[1.18 \eta']) \quad [3]$$

$(q/q_d < 0.8; \eta' = \eta F/RT \geq 2)$

where i_0 has the form of an apparent, geometric exchange current density which depends on the value of $j_{0,r}$ and the total active surface area per projected area unit. This quantity, therefore, varies with the thickness and overall activity of the electrode. The other parameters are of a more fundamental electrochemical nature, and can thus be expected to be valid for most lead-acid positive electrodes.

Finally, it should be remarked that Eq. [1] and the interpretations of the measured polarization curves have been based upon the implicit assumption of a uniform current distribution within the porous electrode. This assumption was checked by using Eq. [1] together with Ohm's law for the ionic current density in a numerical calculation of the current distribution (13). The deviation of the current density at the front of the electrode from the average value was then found to be of the order of 10% at the current densities employed. The uniform current distribution can be attributed to the high Tafel slope, especially at higher current densities.

Discussion

The main objective of this study was to evaluate a rate equation, which can be used as a vital part in a mathemat-

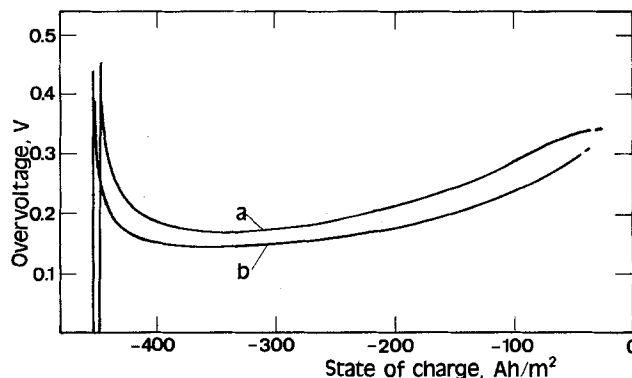


Fig. 6. Galvanostatic recharge curves at 200 A/m². a: Without electrolyte flow. b: With electrolyte flow. The electrode had been fully discharged with -20 A/m².

ical model for the recharge of the lead-acid battery. The experimental conditions were therefore chosen as close as possible to those in real lead-acid batteries. Although the results thus obtained are not suitable for a precise evaluation of fundamental electrochemical parameters, they give valuable hints as regards the mechanism of the electrode process. One very interesting aspect is the strongly negative influence of the sulfuric acid concentration on the recharge kinetics. According to the theory of electrochemical kinetics (14), the exchange current density $j_{0,r}$ in Eq. [1] should be a function of the concentrations according to the expression

$$j_{0,r} = k_r \pi c_i^{z_{r,i}} \exp\left(\frac{\alpha_r F}{RT} \epsilon_0\right) \quad [4]$$

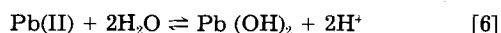
where the exponent $z_{r,j}$ is the electrochemical reaction order with respect to component j . Taking first the logarithm of Eq. [4] and then the derivative with respect to the logarithm of sulfuric acid concentration gives

$$\frac{\partial \ln j_{0,r}}{\partial \ln c} = z + z_{Pb^{2+}} + \frac{\partial \ln c_{Pb^{2+}}}{\partial \ln c} + \frac{\alpha_r F}{RT} \frac{\partial \epsilon_0}{\partial \ln c} \quad [5]$$

The term on the left-hand side can be evaluated from Fig. 5 or Eq. [2]. The second term on the right-hand side takes into account the implicit effect of changes in Pb^{2+} concentration with changes in sulfuric acid concentration. The derivative $\partial(\ln c_{Pb^{2+}})/\partial \ln c$ can be graphically determined from the solubility curve in Fig. 5. Two extreme cases can be distinguished. In the first case, we assume that the mechanism involves soluble Pb^{2+} ions and that the electrochemical reaction order with respect to Pb^{2+} is equal to one. In the second case, we assume a solid-state mechanism where soluble Pb^{2+} ions play no role and $z_{Pb^{2+}} = 0$.

The last term on the right-hand side accounts for the dependence of the equilibrium potential on the sulfuric acid concentration. The derivative of this term can be estimated from, e.g., the correlation given in Ref. (15). When going from 1 to 7M H_2SO_4 , the electrochemical reaction order with respect to sulfuric acid, z , was found to vary from about -0.4 to -3 using the assumption of $z_{Pb^{2+}} = 1$ and from approximately -1 to -3 with $z_{Pb^{2+}} = 0$. The extreme value of -3 was in both cases obtained for 7M H_2SO_4 , at which concentration the solubility of $PbSO_4$ passes a minimum and then starts to increase with a further increase in acid concentration.

Regardless of the role of the Pb^{2+} ions, the reaction order with respect to sulfuric acid concentration is clearly highly negative. An explanation of this effect might be that a protonation equilibrium is established before the first electron is transferred. For example, the mechanism proposed by Hampson *et al.* for acid perchlorate electrolytes (4) involves as the first step



Here $Pb(II)$ stands for either dissolved Pb^{2+} in the case of a dissolution-precipitation mechanism, or solid lead sulfate in the alternative case of a solid-state mechanism. At equilibrium, the activity of $Pb(OH)_2$ is proportional to $[H_2O]^2/[H^+]^2$. If then $Pb(OH)_2$ is the electroactive reactant in the first charge transfer step, the current density should be proportional to this quantity at higher overvoltage where the reverse reaction can be neglected. The activity coefficient of water decreases, and the mean activity coefficient of sulfuric acid increases strongly with increasing acid concentration in the range 1-7M (16). The electrochemical reaction order with respect to the hydrogen ion concentration may thus be as high as -3 . Assuming that the sulfuric acid can be considered as a 1,1 electrolyte which dissociates almost completely in H^+ and HSO_4^- ions (17) means that the concentration of H^+ is equivalent to the sulfuric acid concentration.

The discussion above has so far been restricted to the first anodic charge transfer step, which is rate

determining at overvoltages higher than 100 mV. The lower Tafel slope at lower overvoltages is governed by the denominator in Eq. [1]. The effect of the sulfuric acid concentration is implicit in the quotient $j_{0,r}/j_{0,o}$. According to theory (14)

$$j_{0,r}/j_{0,o} = k_r^{-1}/k_o^+ \exp\left(-\frac{1 + \alpha_o - \alpha_r}{RT} - F\epsilon_0\right) \quad [7]$$

The equilibrium potential ϵ_0 increases with the sulfuric acid concentration. With $\alpha_o = 0.5$ and $\alpha_r = 0.32$, this equation predicts that a change in sulfuric acid concentration from 1 to 5M with $\Delta\epsilon_0 \approx 130$ mV should make $j_{0,r}/j_{0,o}$ decrease by a factor of several hundreds. In view of this, the constancy of this quotient found in our experiments is very puzzling, and Eq. [3] is in this respect hard to give a mechanistic explanation for.

A more direct evaluation of the influences of the Pb^{2+} and H^+ ions would be possible by a comparison of the polarization curves for 5M H_2SO_4 and 1M $H_2SO_4/4M HClO_4$, respectively. The hydrogen activity is nearly the same in these two solutions, whereas the Pb^{2+} ion concentration is approximately four times higher in the latter. The results show, however (Fig. 4), that such a direct comparison is not possible. The Tafel slope for the $HClO_4/H_2SO_4$ solution is higher than for the pure H_2SO_4 solutions, which demonstrates that the kind of anion also affects the electrode kinetics, probably due to adsorption. This fact rules out the possibility of making more exact kinetic-mechanistic studies of the porous lead dioxide battery electrode by varying the concentrations of H^+ , Pb^{2+} , HSO_4^- , and SO_4^{2-} ions at a constant ionic strength by the addition of perchlorate salts. The value of $\alpha_r = 0.26$ for the $HClO_4/H_2SO_4$ solution in the high overvoltage region is comparable to that obtained by Hampson *et al.* (4) for acid perchlorate electrolytes, $\alpha_r = 0.21-0.24$. This value and that for sulfuric acid solutions, $\alpha_r = 0.32$, are both unusually low in comparison to a generally expected value around 0.5. A probable explanation is again the effect of adsorption of the anions.

The effect of the sulfuric acid concentration at discharge on the subsequent recharge (Fig. 3) can be explained by the first-order dependence on the amount of lead sulfate (1). It is well known that the size of the lead sulfate crystals increases with a decreasing sulfuric acid concentration (7-9), which also explains the higher discharge capacity obtained in 1M H_2SO_4 . The lower recharge current at the same amount of lead sulfate indicates that the total surface area of the lead sulfate crystals is the determining factor. While in the case of a single particle size this would imply that the potentiostatic current varies during recharge proportionally to the amount of lead sulfate raised to two thirds, a crystal size distribution gives a higher dependence and may explain the established first-order dependence. Since order of magnitude calculations show that a limiting mass transfer rate of the Pb^{2+} ions is less probable, this result is in favor of a solid-state mechanism.

Acknowledgment

This work was financially supported by the National Swedish Board for Technical Development (Project no. 83-3262).

Manuscript submitted Feb. 7, 1985; revised manuscript received May 21, 1985.

The Royal Institute of Technology assisted in meeting the publication costs of this article.

LIST OF SYMBOLS

- c sulfuric acid concentration (M)
- i geometric current density (A/m²)
- i_0 apparent geometric exchange current density in 1.0M H_2SO_4 (A/m²)
- j_0 true exchange current density (A/m²)
- L thickness of one symmetric half of the porous electrode (m)

q amount of charge remaining to be recharged (Ah/m²)
 q_d charge output in the previous discharge (Ah/m²)
 S_m specific surface area (m⁻¹)
 z electrochemical reaction order

Greek characters

α charge transfer coefficient
 ϵ_0 equilibrium electrode potential (V)
 η charge transfer overvoltage (V)
 η' dimensionless overvoltage [$\eta F/(RT)$]

Subscripts

r first electron transfer step (anodic direction)
 o second electron transfer step (anodic direction)

REFERENCES

1. P. Ekdunge and D. Simonsson, *This Journal*, **132**, 2521 (1985).
2. D. Spahrbiel, Dissertation, Technische Hochschule Stuttgart, Stuttgart, Germany (1960).
3. N. A. Hampson, P. C. Jones, and R. F. Phillips, *Can. J. Chem.*, **45**, 2045 (1967)
4. N. A. Hampson, P. C. Jones, and R. F. Phillips, *ibid.*, **46**,

- 1325 (1968).
5. N. A. Hampson, P. C. Jones, and R. F. Phillips, *ibid.*, **47**, 2171 (1969).
6. H. Ogura and T. Sekine, *Denki Kagaku*, **41**, 638 (1973).
7. S. Hattori, S. Tosaño, and O. Kuzuoka, *ibid.*, **44**, 109 (1976).
8. D. B. Matthews, M. A. Habib, and S. P. S. Badwal, *Aust. J. Chem.*, **34**, 247 (1981).
9. K. Asai, M. Tsubota, K. Yonezu, and K. Ando, *J. Power Sources*, **7**, 73 (1981).
10. I. G. Kiseleva and B. N. Kabanov, *Dokl. Akad. Nauk SSSR*, **122**, 1042 (1958); *ibid.*, **108**, 864 (1956).
11. G. A. Kokarev, V. A. Kolesnikov, and M. Ya. Fioshin, *Elektrokhimiya*, **19**, 196 (1983).
12. L. G. Austin and E. G. Gagnon, *AICHE J.*, **17**, 1057 (1971).
13. J. Newman and C. Tobias, *This Journal*, **109**, 1183 (1962).
14. K. J. Vetter, "Elektrochemische Kinetik," Springer Verlag, Berlin (1961).
15. D. Simonsson, *J. Appl. Electrochem.*, **3**, 261 (1973).
16. H. Bode, "Lead-Acid Batteries," Wiley-Interscience, New York (1977).
17. H. S. Harned and B. B. Owen, "The Physical Chemistry of Electrolytic Solutions," Reinhold Publishing Corporation, New York (1958).

The Influence of Composition and Microstructure on the Corrosion Behavior of Pb-Ca-Sn Alloys in Sulfuric Acid Solutions

D. Kelly and P. Niessen

Department of Mechanical Engineering, University of Waterloo, Waterloo, Ontario, Canada N2L 3G1

E. M. L. Valeriotte*

Cominco Limited, Product Research Centre, Sheridan Park, Mississauga, Ontario, Canada L5K 1B4

ABSTRACT

The corrosion behavior of selected Pb-Ca-Sn alloys after various thermal treatments has been studied. Alloys with high tin content or high tin:calcium ratios had lower rates of intergranular corrosion but were susceptible to intergranular stress corrosion cracking. A low tin:calcium ratio promotes discontinuous precipitation, which produces an interlocking grain structure. This structure is very resistant to stress corrosion. It is experimentally shown that during corrosion of these alloys, stresses are produced across boundaries by the intergranular corrosion products.

In recent years, lead-calcium-tin alloys have become established alternatives to lead-antimony alloys for grids in automotive batteries. Although much research has been done on the Pb-Ca-Sn alloys, some aspects of their behavior, particularly in the corrosive environment of the lead-acid battery, are not fully understood. Valeriotte (1) extensively studied weight loss and integrity of various Pb-Ca-Sn alloys under open-circuit and anodic polarization conditions. His work provided a basis for selecting suitable alloy compositions, but some of his results remain unexplained. For example, he found that, for grids made from expanded continuously cast strip, a Pb-0.09Ca-0.3Sn alloy retained its structural integrity in the corrosive environment better than a Pb-0.06Ca-0.6Sn alloy.

Prengaman (2) has reported that the microstructures as well as the compositions of Pb-Ca-Sn alloys influence their corrosion behavior. He claimed that for alloys which have partially transformed by a slow discontinuous precipitation mechanism, resulting in coarse lamellar or rod-like precipitates, grid life is considerably shortened by "deep penetrating corrosion." Other researchers (3-8) have also claimed that corrosion properties are influenced by alloy composition. However, there is no agreement on what compositions provide the best grid integrity or on how composition influences the corrosion behavior of the Pb-Ca-Sn alloys.

The present study was undertaken to provide a better understanding of the relationships between alloy composition, microstructure, and corrosion behavior.

Alloy Selection

Three alloys were obtained for testing in the form of strip samples, prepared by Cominco Limited (Sheridan Park, Ontario, Canada), using a commercially established continuous casting process (9). These were selected on the basis of work by Borchers and Assmann (8), who found that at the weight ratio of tin:calcium = 8.83:1 (ratio of 3:1 atomic per cent) there is a marked change in both the microstructure of the alloy and in the precipitation strengthening mechanism. Below this ratio, lead-calcium-tin alloys are strengthened by fine Pb₃Ca particles which are formed by a discontinuous precipitation-hardening reaction involving extensive movement of the grain boundaries. [For a more complete discussion of the discontinuous precipitation mechanism, the reader is referred to recent review articles by Williams and Butler (10) and by Gust (11)]. Above the 8.83:1 ratio, the strengthening occurs by the more common continuous precipitation mode in which no boundary movement takes place. Subsequent to the continuous precipitation, a slow, and therefore coarse, discontinuous precipitation reaction can occur. In this reaction, the existing continuously precipitated Pb₃Ca particles are transformed into coarse rod-like particles. This slow reaction is accompanied by a sharp decrease in hardness and strength.

*Electrochemical Society Active Member.

In order to produce a wide range of microstructures, the three alloys used in this study were selected to have Sn:Ca ratios well below, well above, and close to the critical ratio. Alloy compositions and corresponding Sn:Ca ratios are given in Table I.

Experimental Procedures

Specimens of each alloy were cut from 1 mm thick strip to dimensions of 25×150 mm. These were solution treated for 60s in a molten salt bath approximately 3°C below their experimentally determined solidus temperatures. Subsequently, specimens were subjected to each of the following aging treatments: (i) air cool to 180°C , hold for 20 min, air cool to room temperature; (ii) air cool to 100°C , hold for 20 min, air cool to room temperature; and (iii) air cool to 50°C , hold for 11 days, air cool to room temperature.

These treatments were selected to evaluate the effects of a high temperature aging treatment, to simulate the thermal history of a continuously drum-cast strip which is coiled and left to cool (12), and to simulate long-term aging at room temperature. Specimens were stored in liquid nitrogen until the start of corrosion testing.

Corrosion testing was carried out at 50°C , in 1.27 ± 0.02 specific gravity (sp gr) sulfuric acid, at a constant anodic overpotential of 200 mV. In order to monitor corrosion, 81 coupons were examined, nine from each alloy/aging treatment combination. These were removed from the corrosion cell at various corrosion times from 21 to 92 days. Each coupon was examined metallographically to determine the mode and extent of corrosive attack. The depths of both intergranular corrosion and surface corrosion were measured on sections perpendicular to the sample surfaces using a calibrated optical microscope. The maximum depth of intergranular corrosion was measured at ten randomly selected sites on each specimen.

To show that stresses are produced by the corrosion product, two further experiments were designed in which corrosion was greater on one surface of a specimen than the other. It was reasoned that these stresses would cause an initially straight specimen to take on curvature with time.

One experiment was done by thinning a 1 mm thick strip of 903 alloy to 0.5 mm using a chemical polish and then coating one surface of the sheet with Teflon. (This alloy was selected for its large grain boundary area in order to accelerate testing.) The coupon was then placed in a 1.25 sp gr H_2SO_4 solution at room temperature and anodized for five days at a cell voltage of about 3V with a current density of 8 mA/cm^2 .

The second experiment, which more closely approximated normal battery overcharge conditions, was carried out by corrosion of 1 mm thick strip coupon samples of drum-cast Pb-0.18Ca-0.26Sn-0.012Al (1803) at 50°C and 200 mV anodic overpotential ($1.347 \pm 0.002\text{V}$ with respect to a $\text{Hg}/\text{Hg}_2\text{SO}_4/1.275$ sp gr H_2SO_4 reference electrode at room temperature) for 70 and 90 days in a 1.280 sp gr (at 15°C) sulfuric acid solution. These samples were chosen for their unusual duplex microstructure, as will be discussed later. Samples of expanded and of gravity cast grids of other compositions were included in the same corrosion cell (13), but the 1803 samples were tested as coupons because they lacked sufficient ductility for expansion.

Results

Microstructure.—As expected, the alloy/heat-treatment combinations produced a range of different microstructures. Alloy 609, aged at 50°C , had the relatively large

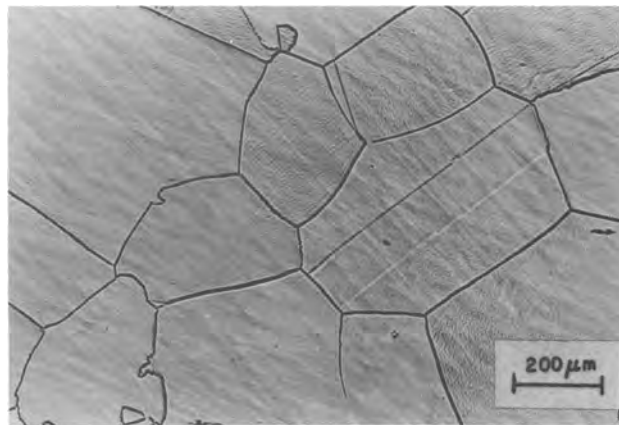


Fig. 1. Equiaxed grain structure of alloy 609

equiaxed grains shown in Fig. 1. During the course of the corrosion experiments, regions of the coarse discontinuous precipitation reaction were observed, increasing in size and number with time. These were also observed, although less frequently, in alloy 606. Figure 2a shows the complex interlocking grain structure of alloy 903 aged at 180°C . To emphasize the interlocking structure, the perimeter of one of the grains has been traced in Fig. 2b. The complexity of the microstructure increased from that of Fig. 1 to that of Fig. 2 with decreasing Sn:Ca ratios and to a lesser extent with increasing temperature.

The complex shape of the grains in Fig. 2 prevents a meaningful determination of grain size. Because of this, the relative grain boundary area of each sample is reported as the number of grain boundaries crossed by a 1 mm linear transverse on the sample surface. The grain boundary data summarized in Table II with respect to alloy and heat-treatment are average values based on a minimum of five measurements.

Corrosion.—Very early in the corrosion tests, it became clear that all alloys were preferentially attacked at grain boundaries, but there was also a general corrosive attack over the surface of the samples. After 75 days of testing, the surface corrosion product on the 609 alloy was $17 \mu\text{m}$ thick, while on the 606 and 903 alloys the layer was $24 \mu\text{m}$.

The influence of the various alloy/heat-treatment combinations on the intergranular corrosion was determined by performing an analysis of covariance with alloy and heat-treatment as independent variables, depth of corrosive penetration as the dependent variable, and time as the covariate. This showed, with a high level of confidence (>99%), that each of the three alloys has a different time *vs.* depth-of-intergranular-corrosion relationship. There was no evidence that the heat-treatments used had a significant effect on the rate of intergranular penetration. Because of this, the curves in Fig. 3 indicate the depth of corrosive penetration for each alloy averaged over the three heat-treatments. It should be noted here that although the heat-treatment does not influence the rate of intergranular corrosion, it does affect the micro-

Table I. Alloy compositions and Sn:Ca ratios

Alloy	Composition (w/o)		Sn:Ca ratio	
	Ca	Sn	Atomic	Weight
903	0.087	0.33	1.3	3.8
606	0.058	0.56	3.3	9.7
609	0.051	0.89	5.9	17.5

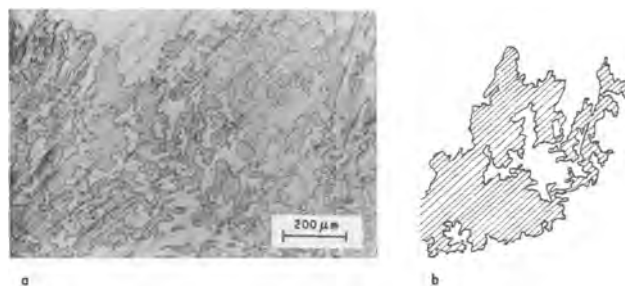


Fig. 2. a: Irregular microstructure typical of alloy 903 aged at 180°C . b: To better illustrate the interlocking of the grains, the perimeter of one of the grains in a has been traced at the same magnification as a.

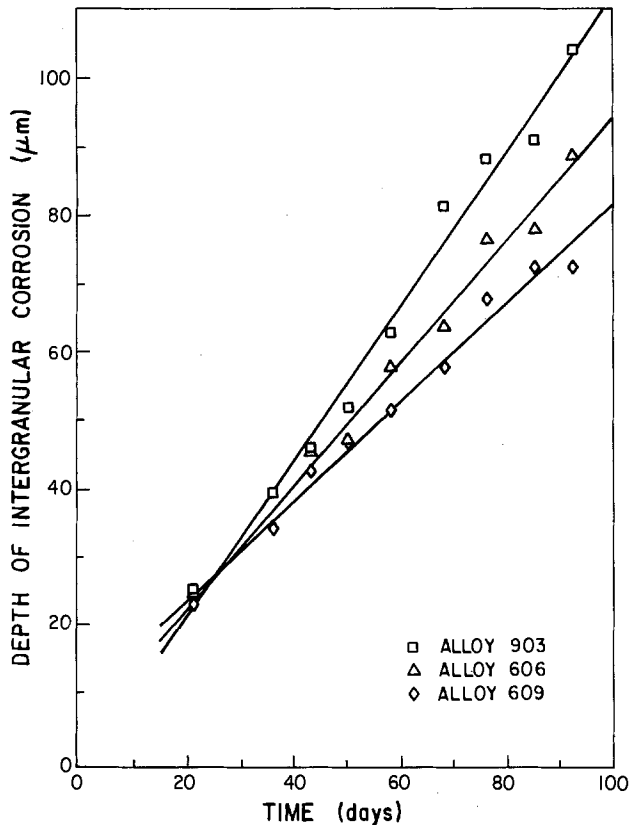


Fig. 3. Depth of intergranular corrosion as a function of time. The rate of intergranular corrosion decreases with increasing tin:calcium ratio and/or increasing tin content.

structure, which, as will be shown later, does play a significant role in the overall corrosion behavior. The results of linear regression analysis for each alloy are summarized in Table III. The rates of corrosive penetration for the 606 and 609 alloys were, respectively, 80 and 64% of that for the 903 alloy.

The linear regression analysis of the data produced lines with nonzero intercepts. However, it must be recognized that the equations represent the line of best fit through the data points. In fact, the 95% confidence limits for the regression line include the origin for alloys 903 and 606. The larger positive intercept for alloy 609 may be indicative of a different corrosion rate at short times.

In several specimens, boundaries which had sustained much more than typical damage were sometimes observed. For example, the average depth of penetration for alloy 609 after 75 days was $64 \mu\text{m}$; however, the boundary shown in Fig. 4 has been penetrated to a depth of $240 \mu\text{m}$. (The measurements for very deeply penetrated boundaries represented samples from a different population and were, therefore, excluded from the averages because of

Table II. Summary of effects of alloy content

Alloy	Heat-treatment temperature ($^{\circ}\text{C}$)	Grain boundaries (mm^{-1}) ^a
903	180	33.0
	100	18.5
	50	20.5
606	180	9.2
	100	5.0
	50	4.0
609	180	2.7
	100	2.3
	50	1.7

^a Average of five measurements.

Table III. Summary of linear regression analysis of depth of intergranular corrosion vs. time for each alloy

Alloy	Intercept	Slope		Correlation coefficient
		Estimate	Percentage of 903	
903	-1.19	1.135	100	0.993
606	4.17	0.905	80	0.993
609	9.05	0.728	64	0.992

Table IV. Depth and frequency of deeply penetrating grain boundaries for alloy 609

Aging temperature ($^{\circ}\text{C}$)	Number of sites of deep penetration observed	Average depth of deep penetration (μm)
180	9	262
100	14	290
50	38	375

their anomalous behavior.) These were observed most frequently in alloy 609, to a lesser extent in alloy 606, and not at all in alloy 903. Also, as shown in Table IV, for alloy 609 the depth and frequency of the deeply penetrated boundaries increased as the heat-treatment temperature decreased. No correlation was found between the time in the corrosion test cell and either the frequency of occurrence or the depth of this "deep penetration."

Metallographic examination of the intergranular corrosion gave no indication that grain boundaries associated with the coarse discontinuous precipitation reaction were penetrated at a faster rate than were other boundaries. The only difference in the corrosion which was associated with the regions of coarse discontinuous precipitation was in regard to the lateral spread of the intergranular corrosion, i.e., the widening of the corrosive wedge. This widening occurred at a faster rate into the regions which contained the coarse rod-like precipitates than into the regions of submicroscopic precipitates.

In the experiment showing the effects of corrosion which was restricted to one surface of the strip, the effect of the intergranular corrosion was clear after 5 days of testing. As expected, the initially straight specimen had become curved with the bare lead alloy on the convex side and the Teflon on the concave side. The radius of curvature was found to be 400 mm after 1 day, 275 mm after 2 days, and 175 mm after 5 days. The increasing curvature of the specimen confirms the existence of substantial forces exerted by the corrosion products on the parent metal.

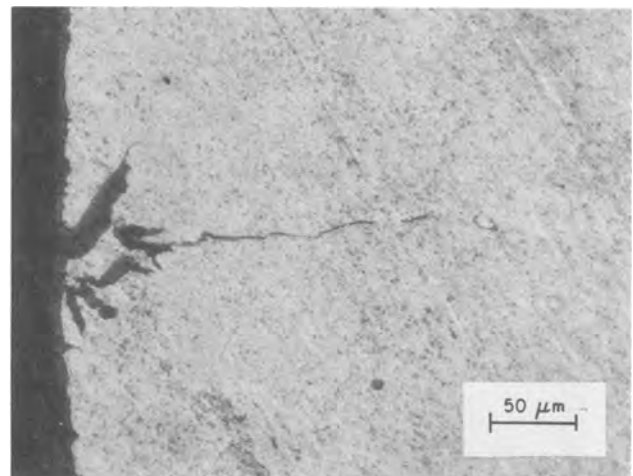


Fig. 4. Deep penetration of grain boundary in alloy 609. Although the average depth of intergranular corrosion is $64 \mu\text{m}$ after 75 days of testing, this boundary has been penetrated to a depth of $240 \mu\text{m}$.

This result was confirmed even more dramatically in the second accelerated corrosion experiment. The samples for this experiment were chosen because of their highly unusual duplex microstructure (Fig. 5), which is not found in cast strip of conventional compositions. Only a small difference in calcium content could be determined between the "drum" side (0.176% Ca) and the "air" side (0.183% Ca), but the microstructures were very different. Although some transformation of the grain boundaries (similar to that seen in Fig. 2) is evident, the microstructure on the drum side (top of Fig. 5) still indicates the effects of nucleation on the cooled drum casting surface and consequent growth of columnar grains during solidification. On the air side, however, the structure is extremely fine and many coarse primary precipitate inclusions, which appear to have nucleated in the melt, have been incorporated into this side of the strip, which solidified last and under very different cooling conditions than the drum side.

As expected (13), weight losses for the 1803 coupons were very high after 70 days (112 mg/cm²) compared to a 903 expanded cast-strip grid in the same cell (42.5 mg/cm²) (13), an 803 (Pb-0.08Ca-0.3Sn) expanded cast-strip grid containing aluminum (39.6 mg/cm²) (14), and 903 gravity cast grids, with and without aluminum [37.6 and 25.6 mg/cm², respectively (13)]. Weight loss for the 1803 grid at 90 days was 178 mg/cm², indicating an accelerating corrosion rate, as previously observed for other Pb-Ca alloys (1). Metallographic examination indicated a much more uniform attack on the fine-grained air side than on the drum side of the coupon, where the attack penetrated more deeply, apparently associated with the straight columnar grain boundaries.

Substantial growth of the coupons accompanied the corrosion. The radius of curvature at the bottom of the coupons (Fig. 6) was about 100 mm after 70 days and 20 mm after 90 days. At the midpoint of the 90 day sample, where it was most warped, the radius of curvature was only 16 mm. The air side became convex and the drum side concave during corrosion, indicating greater horizontal growth on the fine-grained air side. This also suggests that the corrosion rate was greater on the fine-grained air side than on the drum side, assuming that both growth and corrosion are grain-boundary-related phenomena (13).

Discussion

It has been shown that changes in alloy composition and aging treatments produced a wide range of microstructures. The various aging treatments had no effect on the corrosion rate for a particular alloy, but there were significant differences in the rates of corrosion of the alloys studied. This indicates that composition has a significant influence on the corrosion properties of Pb-Ca-Sn alloys, while the temperature of heat-treatment appears to have little effect. Considering the composition effect, if only the level of calcium had affected the

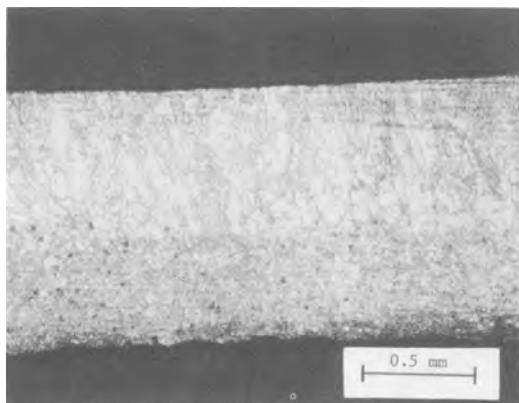


Fig. 5. Novel duplex structure in cross section of etched 1803 alloy cast strip. Top is drum-cast surface; bottom is air side of cast strip.

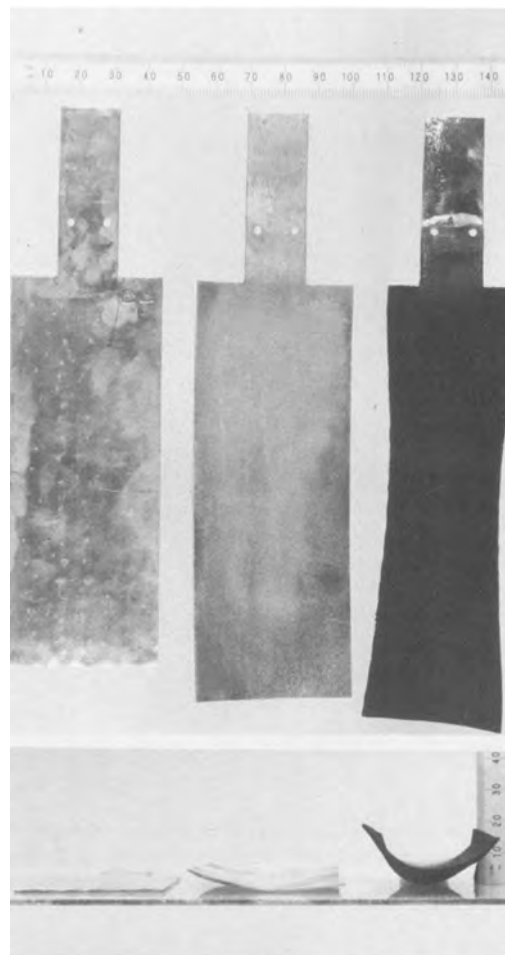


Fig. 6. Corrosion test coupons as prepared (left), after 70 days corrosion and chemical stripping (center), and after 90 days corrosion (right) at 50°C, $\eta_c = 200$ mV. Top photograph is a vertical view illustrating growth; lower photograph is a bottom view illustrating curvature.

corrosion, there would have been little difference in behavior between the 606 and 609 alloys. Since the high tin alloy, 609, had a lower corrosion rate than the 606 alloy, it appears that an increase in either the tin content or in the tin:calcium ratio reduces the rate of intergranular corrosion. Further studies will be required to determine which is more important: the Sn:Ca ratio or only the Sn level.

Increasing the tin:calcium ratio decreased the intergranular corrosion rate, the number of grain boundaries, and the general surface corrosion. Therefore, if weight loss were used as the criterion for selection of grid material, one would expect alloy 609 to be the best material.

This, however, does not consider the influence of the deeply penetrating cracks observed, particularly in alloy 609, on the overall corrosion behavior. To understand the effect of the deep penetrating cracks, it is important to understand their origin. The authors believe they result from stress corrosion (15), and the following mechanism is proposed.

Most commonly, stress corrosion mechanisms involve accelerated rates of cracking in the presence of an applied stress and a corrosive environment. The mechanism in this study is somewhat different since the applied stress results directly from the formation of the corrosion product. A similar mechanism has been observed in stainless steels (16). For Pb-Ca-Sn alloys, it is known that the corrosion product, containing primarily lead oxides, has a larger specific volume (17) than the lead matrix. As a result, the intergranular corrosion product is under compressive stresses due to the physical constraints of the bulk material. This produces tensile stresses which are concentrated across the grain boundary at the tip of the intergranular corrosion. The effect of the stresses pro-

duced by this wedging action of the corrosion product will vary depending on microstructure of the alloy. If alloy 609, with its relatively straight immobile grain boundaries, is considered, it is evident that as the corrosion continues the stresses will increase until, at a critical stress level, an intergranular fracture will be initiated, as shown in Fig. 4. Once a crack exists, more electrolyte will be able to flow to the crack tip, leading to more corrosion and continued crack propagation. This mechanism will likely lead to rapid failure of a grid wire because the increasing volume of corrosion product will cause higher loads, which must be carried by the reduced cross-sectional area of the grid wire. These two factors combine to produce increasing stresses across the boundary and an accelerating rate of crack propagation.

The behavior of alloy 903 (or 1803) under the same stresses will be quite different than that of alloy 609 because crack propagation is impeded by the interlocking of the grains (recall Fig. 2). This forces the intergranular corrosion, or an intergranular crack, to follow a very irregular path. Even though the stresses may be sufficient, very little cracking occurs because there are only short lengths of boundary which are oriented with respect to the applied load such that crack propagation will occur. Thus, the irregular shape of the grain boundaries in alloy 903 prevents the stress corrosion mechanism from occurring.

The results in Table IV are consistent with this mechanism. The higher aging temperatures result in more extensive discontinuous precipitation and hence more irregular grain boundaries. The irregularities can either prevent the initiation of a crack or arrest its propagation. Thus, both the frequency of occurrence and the depth of penetration are reduced as aging temperature is increased.

This proposed mechanism is supported by our previous experimental results (1). Grids made from alloy 606 (and 909) fell apart during grid integrity tests, but those made from alloy 903 retained their integrity.

Subsequent testing (14) on grids made from alloy 609 indicated that they too suffered a loss of grid integrity. Thus, of the three main alloys studied, only alloy 903 with its irregular boundaries resists intergranular separation. The above mechanism is based on the premise that corrosion product produces tensile stresses across the grain boundaries.

The experiments in which one side of the corrosion sample corroded preferentially to the other and thereby produced warping also illustrate the generation of these tensile stresses and show that they are related to grain boundary density.

If, for alloys with relatively straight grain boundaries, these stresses cause grain boundary cracking leading to early failure as was shown by differences in grid integrity (1, 14), this mechanism may also account for Prengaman's "deep penetrating corrosion" (2). Although he associated this phenomenon with the coarse discontinuous precipitation, it was observed in our metallographic studies that the grain boundaries between the areas of coarse precipitation and the matrix are relatively straight. These boundaries are therefore susceptible to the stress corrosion mechanism. Prengaman also states that the deep penetrating corrosion is not observed in alloys in which the entire structure has been transformed by the fine discontinuous precipitation reaction, *i.e.*, those alloys which the present work has shown to exhibit irregular microstructures. The proposed stress corrosion mechanism is accordingly consistent with his observations.

The existence of stresses induced by the corrosion product also suggests an explanation of the grid growth often observed in Pb-Ca-Sn alloy grids. It is probable that the same intergranular stresses which cause cracking in alloys such as 609 will result in creep of coupons or grid wires in alloys such as 903. Because the stresses act along the length of the grid wires, they will increase in length regardless of their orientation in the grid. Furthermore, wires of thin cross section will see higher stresses and

therefore will have higher creep (growth) rates. For the 1803 alloy, the nonuniformity of the growth, due to the nonhomogeneous microstructure, also causes warpage to occur.

Conclusions

1. For the alloys studied, there is an increase in the rate of intergranular corrosion with decreasing tin content or decreasing tin:calcium ratio.
2. Since both the rate of intergranular attack and the grain boundary area increase with decreasing tin:calcium ratio, corrosive weight loss will also increase with decreasing tin:calcium ratio.
3. The measurement of intergranular corrosion rate or weight loss is not sufficient for selecting Pb-Ca-Sn alloys best suited for use in battery grids. It is also necessary to consider the microstructure and its influence on the overall corrosion behavior.
4. The grain boundary cracking observed in Pb-0.06Ca-0.6Sn (606) and Pb-0.05Ca-0.9Sn (609) alloys has been explained by a stress corrosion mechanism. Internal tensile stresses result from the intergranular corrosion product, which has a larger specific volume than the uncorroded metal. These stresses act across the grain boundary and can result in intergranular fracture.
5. Alloys which have irregular grain structures are resistant to the stress corrosion fracture mechanism because the shape of the boundaries impedes crack propagation. However, the stresses caused by the corrosion product do lead to creep of the alloy, particularly along grid wires, giving rise to grid growth in batteries.
6. If the grain size within a battery grid wire or casting is not uniform, the resultant unbalanced tensile stresses arising from intergranular corrosion can lead to warpage of grids or fracture of grid wires.

Acknowledgments

Useful discussions with J. A. Brown and assistance with the corrosion experiments by M. J. Dewar, J. Sklarchuk, and K. Cowan are gratefully acknowledged.

Manuscript submitted Dec. 26, 1984; revised manuscript received July 13, 1985.

Cominco Limited assisted in meeting the publication costs of this article.

REFERENCES

1. E. M. L. Valeriote, *This Journal*, **128**, 1423 (1981).
2. R. D. Prengaman, in "Edited Proceedings, 7th International Lead Conference, Madrid, May 11-14, 1980," pp. 34-47, Lead Development Association, London (1980).
3. J. Perkins and G. R. Edwards, *J. Mater. Sci.*, **10**, 136 (1975).
4. A. M. Howard and E. Willihnganz, *Electrochem. Technol.*, **6**, 370 (1968).
5. G. W. Mao, J. G. Larson, and P. Rao, *This Journal*, **120**, 11 (1973).
6. J. A. Young and J. B. Barclay, in "Proceedings of the 85th Convention of Battery Council International," pp. 37-51, San Francisco, CA, May 1-3, 1973.
7. J. A. Young, in "Proceedings of the 87th Convention of Battery Council International," Hollywood, FL, April 8-10, 1975, pp. 127-134.
8. H. Borchers and H. Assmann, *Z. Metallkd.*, **69**, 43 (1978).
9. Canadian Pat. 978 324 (1975).
10. D. B. Williams and E. P. Butler, *Int. Metals Rev.*, **26**, 153 (1981).
11. W. Gust, in "Phase Transformations," Vol. 1, pp. II 27-68, Institution of Metallurgists, Spring Residential Conference, April, 1979, Chameleon Press, London (1979).
12. P. C. Coghlan, Cominco Ltd., Product Research Centre, Sheridan Park, Ontario, Canada, Private communication.
13. E. M. L. Valeriote, J. Sklarchuk, and M. S. Ho, in "Advances in Lead-Acid Batteries," K. R. Bullock and D. Pavlov, Editors, p. 224, The Electrochemical Society Softbound Proceedings Series, Pennington, NJ (1984).

14. E. M. L. Valerioti, Unpublished data.
 15. D. E. Kelly, M.A.Sc. Thesis, University of Waterloo, Waterloo, Ontario, Canada (1980).
 16. H. W. Pickering, M. G. Fontana, and F. H. Beck, *Corro-*

- sion*, **18**, 230t (1962).
 17. H. Bode, "Lead-Acid Batteries," p. 13, R. J. Brodd and K. V. Kordesch, Translators, John Wiley and Sons, Toronto (1977).

Characteristics of Sulfolane-Based Electrolytes for Rechargeable Lithium Batteries

Yoshiharu Matsuda,* Masayuki Morita, Kazuhiro Yamada, and Kohji Hirai

Department of Industrial Chemistry, Faculty of Engineering, Yamaguchi University, Tokiwa-dai, Ube, Yamaguchi 755, Japan

ABSTRACT

The utility of sulfolane (S)-based electrolytes has been studied for rechargeable lithium batteries. Electrolytic conductivities of LiClO_4 , LiBF_4 , and LiPF_6 were measured in the mixed system of S with 1,3-dioxolane (DOL), tetrahydrofuran (THF), or 1,2-dimethoxyethane (DME). Vapor pressure, viscosity, and relative permittivity of the mixed solvents and/or the electrolytic solutions were also measured, and the results were discussed in connection with the solution conductivity. Conductivity maxima were observed in the mixed solutions containing 60-90 mole percent ethers. The conductivity of S-DME (1:9 by volume)/ LiPF_6 (1M), being the highest of all examined, was $1.5 \times 10^{-2} \text{ S-cm}^{-1}$. The Li cycling characteristics were mainly investigated in the S-ether (1:1) mixed solutions. Efficiencies on the Ni substrate in the S-DME solutions varied less with cycling than those in S-DOL and S-THF. The average efficiency of Li cycling in S-DME increased in the order of $\text{LiClO}_4 < \text{LiBF}_4 < \text{LiPF}_6$. The Li cycling characteristics in the S-ether solutions are discussed from the standpoints of ionic behavior in the solution and chemical reaction at Li-solution interface.

In the course of the development of ambient temperature, rechargeable lithium (Li) batteries, it has been noted that the choice of an electrolyte system is of special importance in the cycling performance of the Li electrode (1, 2). Up to the present, the electrolyte systems in which high Li cycling efficiency has been obtained have been 1,3-dioxolane (DOL)/ LiClO_4 and 2-methyltetrahydrofuran (2-MeTHF)/ LiAsF_6 (3). The Li electrode characteristics in these electrolytes are sufficient to realize a practical rechargeable battery, but some problems such as detonation susceptibility of DOL/ LiClO_4 (4) and relatively low conductance of 2-MeTHF/ LiAsF_6 (5, 6) remain to be solved. Thus, various solvent-salt systems as the electrolytes of the rechargeable Li batteries are still under investigation (3, 7).

Sulfolane (S) is one of the promising solvents for the electrolytes of the rechargeable Li batteries (8, 9). It has high relative permittivity (dielectric constant) and high resistance to electrochemical oxidation or reduction (10). Because of its high melting point (mp) of 28.86°C (10), however, S is not easy to use as the solvent of the ambient temperature cell. To avoid this inconvenience of S, the use of 3-methylsulfolane (3-MeS), whose mp is relatively low ($\sim 0^\circ\text{C}$), has also been attempted (11). On the other hand, the mp of the solvent can be lowered by blending S with low viscosity ethers. This attempt was first made by an EIC group (12), but no quantitative data have been presented yet.

We have examined the S-based electrolytes for the ambient temperature Li batteries. The solvent mixing effects on the electrolytic conductivity and on the electrode characteristics have already been proved in the propylene carbonate (PC)-ether (13, 14) and ether-ether mixed systems (15, 16). In this paper, DOL, tetrahydrofuran (THF), and 1,2-dimethoxyethane (DME) were used as the cosolvent of S. Table I shows the selected physicochemical properties of S, DOL, THF, and DME. The ethers have low viscosity and also relatively high donicity (17). (The donicity of DOL has not been reported, but it should be comparable with those of the other ethers.) The latter implies that some interaction between the ether solvents and cations would be produced in the electrolytic solutions of the S-ether mixed systems. For the present work, the electrolytic conductivity of some Li salts were measured in the

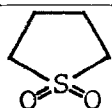
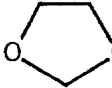
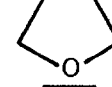

mixed solvents, and the mixing effects of the ethers on the conductivity were investigated. The Li electrode characteristics were studied in the S-ether mixed electrolytes. Differences in the Li cycling behavior between the cosolvent ethers and anion effects of the electrolytes will be discussed in connection with the results of conductivity measurements.

Experimental

The purification of ethers, or DOL (Tokyo Kasei Kogyo), THF (Toyo Soda Manufacturing), and DME (Mitsubishi Yuka Fine Chemicals), was carried out as described previously (14, 16). S (Tokyo Kasei Kogyo) was dehydrated by P_2O_5 and distilled under reduced pressure at $95\text{--}110^\circ\text{C}$ (18). The electrolytic salts, LiClO_4 (Ishizu Pharmaceutical) and LiBF_4 (Morita Chemical Industries), were used after drying under a vacuum at appropriate temperatures (14, 15). LiPF_6 (Morita Chemical Industries) was used as received because it had been sealed under a dry Ar atmosphere and tends to decompose by heating.

The electrolytic conductivity, the relative permittivity, and the viscosity of the solvents and the solutions were

Table I. Viscosity (η), relative permittivity (ϵ_r), donicity (DN), and acceptor number (AN) of the solvents

Solvent	Structure	$\eta/10^{-3} \text{ Pa-s}$ (30°C)	ϵ_r (30°C)	DN ^a	AN ^a
S		9.87	42.5	14.8	19.0
DOL		0.58	6.79	—	—
THF		0.46	7.25	20.0	8.0
DME		0.40	6.92	24	—

*Electrochemical Society Active Member.

^a From Ref. (17).

measured by the same methods as in the previous work (16). The vapor pressure was measured by a static method (19, 20). These measurements were carried out at controlled temperatures (20° or 30°C).

Li cycle efficiency was determined by a galvanostatic charge-discharge test (21), which is an accelerated test for brief evaluation of secondary Li electrode in the electrolyte under consideration. A beaker-type glass cell (volume = 100 cm³) was used for the measurement. The substrate of the test electrode was a Ni sheet (0.95 cm²) mounted on a Teflon holder. The counterelectrode was a Li sheet (2.5 × 3.0 cm) with a Ni mesh current collector. The reference electrode was a Li piece on the tip of a Ni wire (Li/Li⁺). It was connected to the test electrode through a Luggin capillary. The plating and stripping current densities (i_p , i_s) were usually 2 mA/cm², and the plated charge (Q_p) was 0.2 C/cm². The cycle efficiency was defined as $(Q_s/Q_p) \times 100$ [%], where Q_s is stripped charge (15, 22). The plated charge of 0.2 C/cm² is much lower than those to be cycled in a practical full cell (> 10 mAh/cm²) (6). However, even under the present conditions, the results will give an outline of the Li cycling behavior in the electrolyte under consideration, especially in the initial stage of the cycle (21).

Polarization behavior of Li in the S-based electrolytes was also studied on the Ni substrate by using the same apparatus as described above. The polarization curves were potentiostatically measured. At first, the electrode potential was stepwise changed from the rest potential to a cathodic (charging) one, and then the potential changed in the anodic (discharging) direction. The values of current density were recorded after 2 min of the potential setting. These electrochemical measurements were carried out in a dry Ar atmosphere at room temperature (18°-22°C).

Results and Discussion

Conductivity and related properties of S-based electrolytes.—Vapor pressure of an electrolytic solution is of technical interest because it relates to the storage performance of the cell containing that electrolyte. It is also used for interpreting the thermodynamic behavior of the mixed electrolyte solution (20). The vapor pressure of a real mixed solvent is given by Eq. [1]

$$P = P_A^0 x_A \gamma_A + P_B^0 x_B \gamma_B \quad [1]$$

where P , P_A^0 , and P_B^0 are the vapor pressures of the mixed solvent and the pure solvents, A and B, respectively. The x 's and γ 's are the molar fractions and the activity coefficients of the components, respectively. If the mixed solvent is an ideal liquid, Eq. [1] will be identical with Raoult's equation, where γ_A and γ_B are unity.

Figure 1 shows the vapor pressure of the S-ether mixed systems at 20°C as a function of the ether concentration (mole percent [m/o]). The vapor pressure of the mixed solvent increased in the order S-DME < S-DOL < S-THF. Some deviation in the positive direction from the straight line indicates $\gamma > 1$, or the mixed solvents' being nonregular solutions. A certain association of the S molecules in the pure solvent would be weakened by addition of the ether. At that time the S=O bond of S can interact more effectively with noncyclic structure of DME without steric hindrance as compared with those of DOL or THF. The vapor pressure of the S-DME solution containing 1M (mol/dm³) LiBF₄ decreased about 20%, compared with that of the parent S-DME solvent. This was also the case for the solutions of S-DOL/LiBF₄ and S-THF/LiBF₄. The lowering of vapor pressure in the 1M LiBF₄ solutions is largely explained on the basis of the depression of vapor pressure by dissolving the salt. An interaction between the Li⁺ ion and the solvent, binding solvent molecules to Li⁺, would also take part in the lowering of vapor pressure.

Conductance of an electrolytic solution is much affected by the relative permittivity of the solvent and the viscosity of the solution (23). Table II shows the viscosity (η) of the mixed S-ether solutions, and Fig. 2 shows the

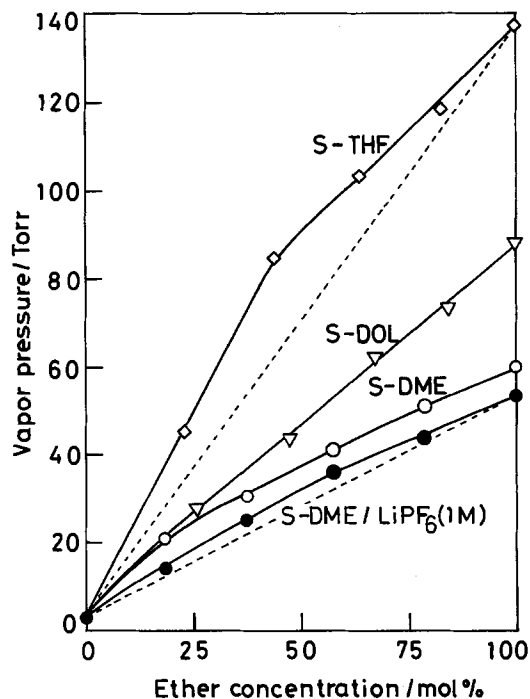


Fig. 1. Vapor pressure of S-ether mixed solvents and S-DME/LiBF₄ (1M) solution.

relative permittivity (ϵ_r) of the mixed solvents. The neat ethers have ϵ_r 's and η 's similar to one another. Therefore, ϵ_r 's and η 's of the mixed S-ether solutions were also comparable to one another. The ϵ_r 's varied almost linearly with a change in the volume percent of each ether, but in the systems of S-THF and S-DOL the variation of ϵ_r against mole percent of the ether revealed a slight positive deviation from an additive property, as shown in Fig. 2. This suggests that there would be some difference in the solvent-solvent interaction between S and the ethers. The variation of η with solvent composition in the S-ether mixed systems was similar to those in the mixed systems with combinations of high and low viscosity solvents such as PC-ether systems (14, 24).

Figure 3 shows the electrolytic conductivity (κ) of the 1M LiBF₄ solution as a function of the solvent composition. The conductivity became maximum at about 70 m/o ether in every S-ether system. This conductivity enhancement would result from a favorable combination of high permittivity of S and low viscosity of the ether (14, 24). The maximum conductivities (κ_{max}) of 1M LiBF₄ were 3.3, 3.7, and 5.0 × 10⁻³ S-cm⁻¹ in S-THF, S-DOL, and S-DME,

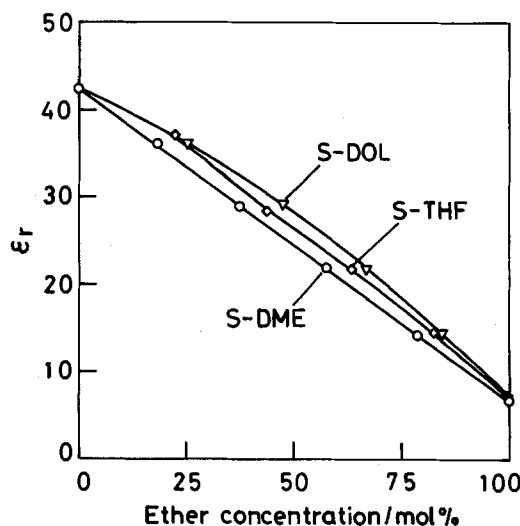


Fig. 2. Variation of relative permittivity with ether concentration for S-ether mixed solvents.

Table II. Viscosity of S-ether mixed solvent (η_0) and S-ether/LiBF₄ (1M) mixed solution (η^*) at 30°C

Solvent composition (v/o of ether)	S-DOL		S-THF		S-DME	
	$\eta_0/10^{-3}\text{Pa-s}$	($\eta^*/10^{-3}\text{Pa-s}$)	$\eta_0/10^{-3}\text{Pa-s}$	($\eta^*/10^{-3}\text{Pa-s}$)	$\eta_0/10^{-3}\text{Pa-s}$	($\eta^*/10^{-3}\text{Pa-s}$)
100	0.58	(1.00)	0.46	(1.29)	0.40	(0.71)
80	0.81	(1.43)	0.72	(1.33)	0.65	(1.21)
60	1.22	(2.17)	1.17	(2.41)	1.07	(2.14)
40	2.08	(4.12)	2.09	(4.68)	1.99	(4.15)
20	3.98	(8.75)	4.17	(10.04)	3.98	(8.92)
0	9.87	(23.29)	9.87	(23.29)	9.87	(23.29)

respectively. The critical distance for ion-pair formation, or Bjerrum's q value (25), at the solvent composition providing κ_{max} (≈ 70 m/o) was estimated to be 1.25-1.53 nm from ϵ_r at that solvent composition. It is reasonable that ionic association takes place in the solution with such a large q (14, 24). Thus, ionic association is responsible for the low conductance of the solution with higher ether concentration than about 70 m/o.

Differences in the conductivity among the different ethers to be mixed with S are at least partly attributable to differences in the solution viscosity. Walden products ($\Lambda\eta$) for 1M LiBF₄ are shown in Fig. 4. In spite of the appreciable differences in the conductivity, the Walden products are almost the same at given ether concentrations. The monotonous decrease in $\Lambda\eta$ with increasing ether concentration, however, means that the Walden rule fails in each S-ether system even at the lower concentration of the ether. This means that ionic association takes place in the solutions of high ether concentration.

Figure 5 shows the conductivity dependence on the DME concentration for 1M solutions of LiBF₄, LiClO₄, and LiPF₆ in S-DME. Solubility of LiPF₆ was rather low in S-DME. It was lower than 1M at DME concentration below 40 m/o or above 95 m/o. Thus, the conductivities of LiPF₆ solutions at such solvent compositions refer to those of saturated (<1M) solutions (closed squares in Fig. 5). The conductivity increased in the order LiBF₄ < LiClO₄ < LiPF₆, and the κ_{max} 's were 5.0, 7.1, and 15.1 ($\times 10^{-3}$ S-cm⁻¹) for LiBF₄, LiClO₄, and LiPF₆, respectively. The DME concentration at which the conductivity reached κ_{max} also depended on the electrolyte salts. These results show that the anions of the salts greatly affect the electrolytic conductance in this system. The Stokes radii of ClO₄⁻, BF₄⁻, and PF₆⁻ are comparable to one another in PC-DME (20), which is an analogous mixed-system to present S-DME. It is, therefore, reasonable that there is no great difference in the size among these three anions in S-DME. The difference in the conductance behavior

among the solutions of LiClO₄, LiBF₄, and LiPF₆ might be attributable to differences in some anion-cation or anion-solvent(s) interaction in S-DME. For example, the formation of ion-pair and triple ions would be responsible for the conductance behavior. The formation in the LiBF₄ solution is probably high, and, therefore, it lowers conductivity. In the LiPF₆ solution, the larger crystallographic size and lower charge density of the PF₆⁻ ion would minimize Li⁺-PF₆⁻ interaction and, hence, higher conductivity would be achieved. Unfortunately, this trend in the conductance behavior, as shown in Fig. 5, could not be proved in S-THF or S-DOL. As LiPF₆ liberates free PF₅, which is a strong Lewis acid, its THF or DOL solution polymerizes under Lewis acid-catalyzed oxidation (26). Because of this polymerization accompanying an increase in the solution viscosity, no accurate conductivity was obtained for the LiPF₆ solutions of S-THF and S-DOL.

Charge-discharge behavior of Li in S-based electrolytes.—Anodic and cathodic current-potential relations were measured by a potentiostatic polarization method. The polarization curves of Li at Ni substrates in S-DME (1:1 mixture = 48 m/o DME) are shown in Fig. 6. The curves were first measured in the cathodic direction from the rest potentials. Li was deposited on the Ni substrate during this cathodic polarization. Then, the measurements were carried out in the anodic direction from -2.0 to +1.5V (vs. Li/Li⁺). The anodic currents (from 0 to +1.5V) are based on the dissolution of Li which has been deposited on the Ni substrate during the preceding cathodic polarization.

A hysteresis observed on each cathodic curve in the solution of LiBF₄ or LiClO₄ seems to originate from a

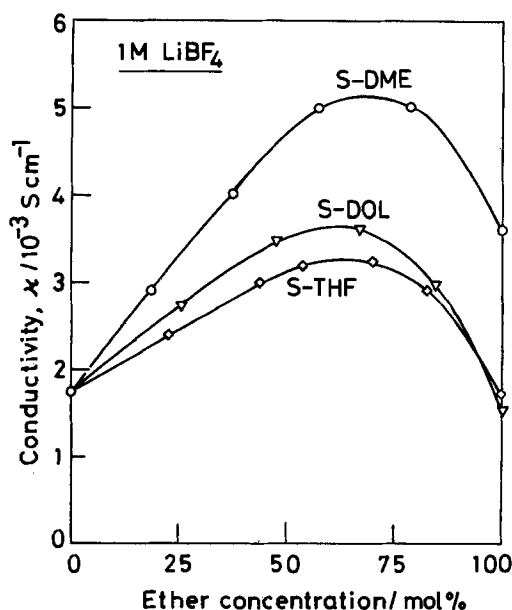


Fig. 3. Variation of conductivity with ether concentration for 1M LiBF₄ in S-ether mixed systems.

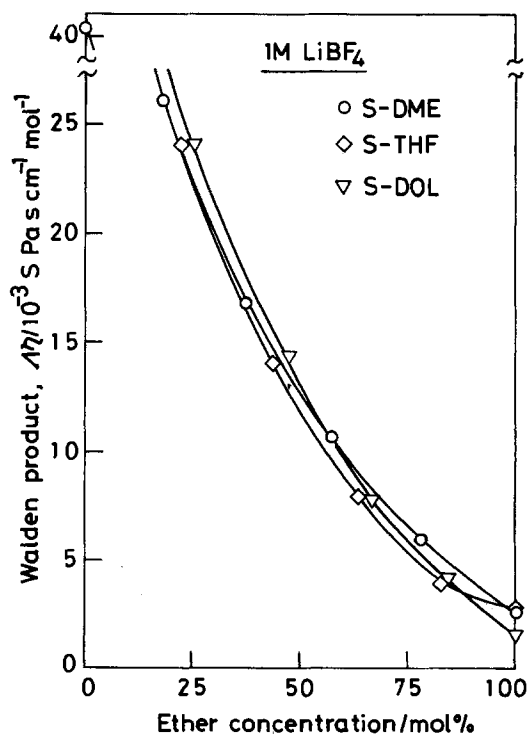


Fig. 4. Variation of Walden product with ether concentration for 1M LiBF₄ in S-ether mixed systems.

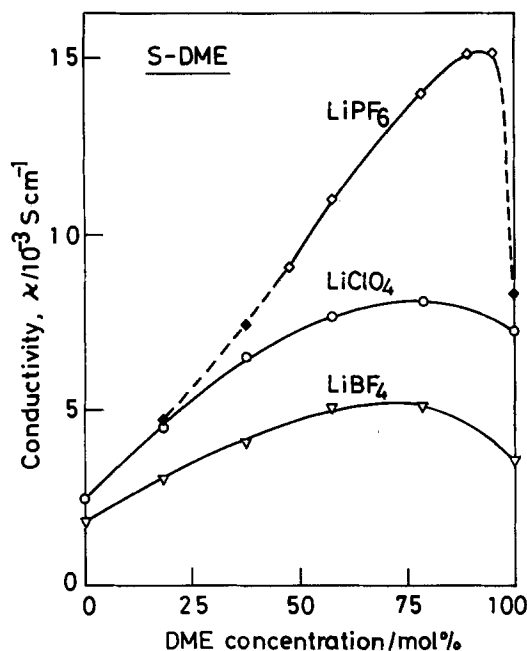


Fig. 5. Variation of conductivity with DME concentration for 1M LiClO_4 , LiBF_4 , and LiPF_6 in S-DME.

change in the real surface area of the electrode by continuous Li deposition during the measurement. The hysteresis was hardly observed in the LiPF_6 solution. In the potential region away from 0 V, the current densities at given potentials increased in the order $\text{LiClO}_4 < \text{LiBF}_4 < \text{LiPF}_6$. That is, the polarization in the LiPF_6 solution was smallest of the three. The anodic current in the LiClO_4 solution dropped at anodic potentials of 0.5V or greater. Active Li remained on the Ni substrate after this anodic polarization in the LiClO_4 solution. Thus, the current drop at about 0.5V is probably due to passivation of Li deposited during cathodic charge.

Variations of Li cycling efficiency in 1M LiBF_4 solutions are shown in Fig. 7. In this case, 1:1 (by volume) mixtures were used as the mixed solvents for convenience. The actual mixing ratios are 58, 54, and 48 m/o ethers for S-DOL, S-THF, and S-DME, respectively. The efficiency in S/ LiBF_4 was about 60% for the initial cycles but decreased with repeated cycles. The reason for this lowering in the efficiency is not clear, but it might be related to passivation of Li or formation of isolated, inactive

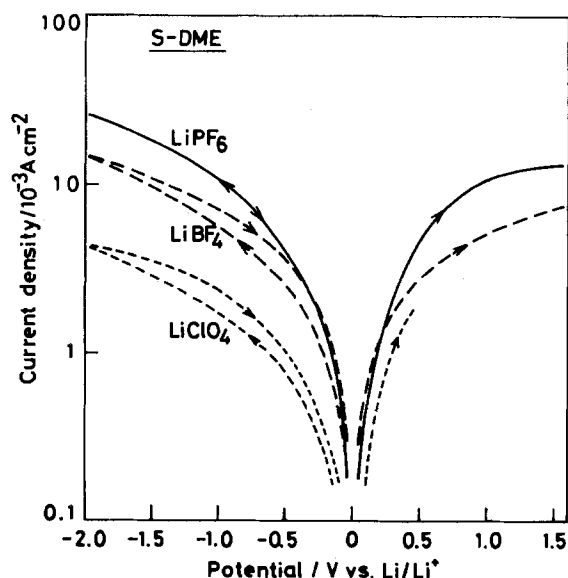


Fig. 6. Current-potential curves of Li on Ni substrate in 1M LiClO_4 , LiBF_4 , and LiPF_6 . Solvent: S-DME (1:1 by volume = 48 m/o DME).

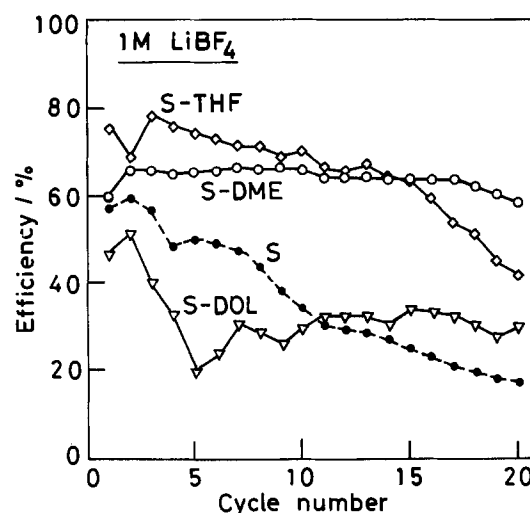


Fig. 7. Variation of efficiency with cycle number in 1M LiBF_4 solutions. $i_p = i_s = 2.0 \text{ mA/cm}^2$. $Q_p = 0.2 \text{ C/cm}^2$.

Li as in the case of PC-based electrolytes (27). The efficiency was little improved by mixing DOL with S.

On the other hand, the use of THF or DME as a cosolvent of S brought relatively high efficiency. This was probably caused by two effects. The one is lowering the polarization of Li during the charge-discharge cycles. The other is coordination of THF and DME to the Li^+ ions. The former mainly results from the improvement of electrolytic conductivity (or ionic mobility) by mixing S with low viscosity THF or DME. The lower polarization should lead to the reduction in the rates of side reactions (e.g., decomposition of the electrolyte solution), which causes the efficiency loss in the cycle. The latter effect, coordination of the ethers, would also contribute to the reduction in the decomposition rate of solvents. In PC-based electrolytes, the interaction between PC and Li^+ accelerates the decomposition of the solvent (28). This would also be the case for S-based electrolytes, although S has a higher resistance to electrochemical reaction than PC has. Isolation of Li^+ from solvent S by coordination of the ether to Li^+ would minimize the reaction rate. Furthermore, it is difficult to rule out the possibility that the added ethers play a part in the superior Li deposition. Such a Li film formed in the ether containing solutions might be different from the film deposited from the solution consisting of neat S.

The cycle efficiency in S-THF was relatively high initially but gradually decreased. In S-DME, however, variation of the efficiency with cycling was rather small. The average cycling efficiency from the first to twentieth cycles on the Ni substrate was 64.2% in S-DME/ LiBF_4 .

In Fig. 8, the cycle efficiencies in the S-DME solutions with different electrolytes were compared with one another. The average efficiency in the LiPF_6 solution was 77.1% and was the highest of all. Relatively low efficiencies were observed in the LiClO_4 solution, which would be related to the results of the current-potential measurements. These differences in the cycle efficiency among the three electrolytes are based on the differences in the electrochemical stability of the solution, which depend on the magnitude of polarization during the charge-discharge process. The morphology of Li deposited on Ni and the electrochemical properties of the film which might be formed on Li would also affect the cycling characteristics. In the LiBF_4 and LiPF_6 solutions, liberation of Lewis acids (BF_3 and PF_5), whose amounts might be different to each other, can also affect the cycling efficiency. Furthermore, the structures of the electrical double layers with different anions might influence the charge-discharge characteristics of the Li electrode. Details of these differences in the cycling behavior between the electrolytic salts are now under consideration.

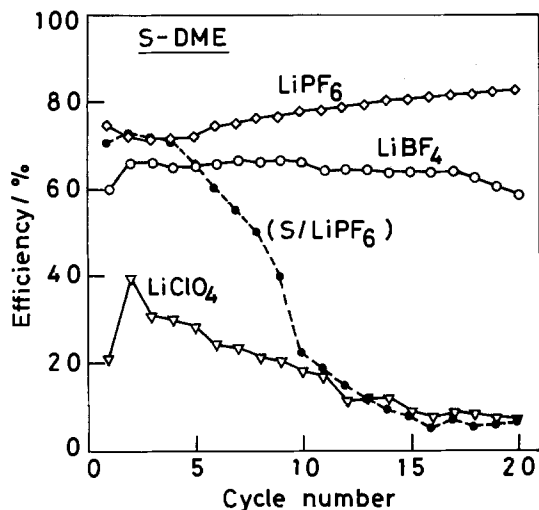


Fig. 8. Variation of efficiency with cycle number in 1M LiClO₄, LiBF₄, and LiPF₆. Solvent: S-DME (1:1 by volume = 48 m/o DME).

The efficiencies in S/LiPF₆, which contains no ether, were as high as those in S-DME/LiPF₆ for few initial cycles, but a marked decreasing of the efficiency was observed, especially after the tenth cycle. Therefore, DME mixed with S apparently functions to keep the efficiency in S/LiPF₆ high.

When the cycles were further extended in S-DME/LiPF₆, about 80% of the efficiency was reproducibly observed up to the fortieth cycle or so. However, the efficiency at additional cycles varied with less reproducibility. Figure 9 shows the potential-time curves during the charge-discharge cycles in S-DME/LiPF₆. Up to the fortieth cycle, the potential variation with time in each cycle was similar to one another. The polarization (potential difference from 0 V) during the charge and discharge increased with continued cycling after the fortieth cycle. The shape of the discharge curve also varied with the cycle. These changes in polarization behavior seem to be associated with the efficiency variation. Repetition of the charge-discharge cycle leads to accumulation of inactive Li which is electrically isolated from the substrate (27). This seems to be the cause of the changes in cycling characteristics at the extended cycles.

Figure 10 shows the effects of current density and mixing ratio of the solvents on the cycling efficiency in S-DME/LiPF₆. Average efficiency during the first ten cycles increased with increasing i_p . As Q_p was kept constant at 0.2 C/cm², increasing i_p implied decreasing the plating (charging) time. Thus, the lower i_p and i_s were, the longer the deposited Li contacted the solution. This would lead to the result that the Li deposited under low i_p is not effectively utilized because of an inert film formed on Li. However, the dependence of the average efficiency on the current density was rather small, compared with that in ether-ether mixed systems (22). Therefore, the film for-

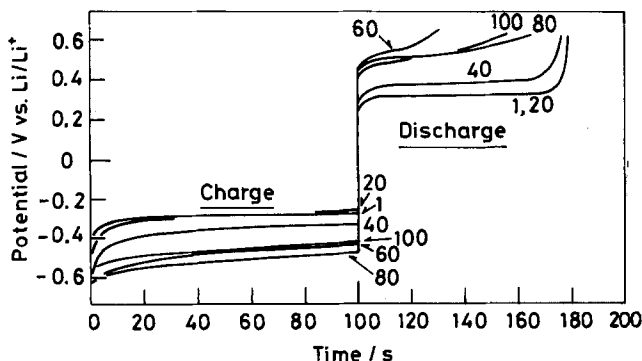


Fig. 9. Potential-time curves of Li on Ni substrate during charge-discharge cycles.

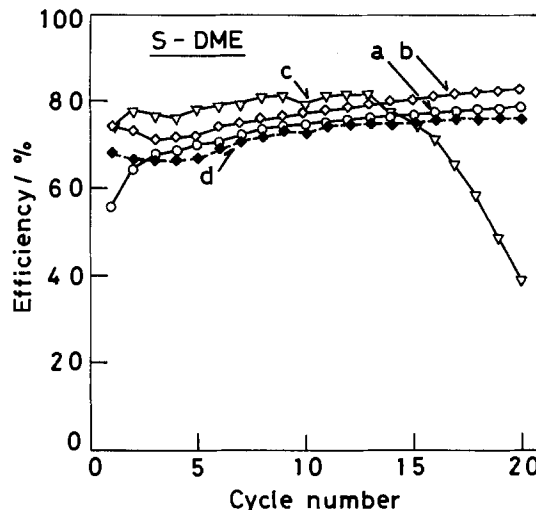


Fig. 10. Variation of efficiency with cycle number in S-DME/LiPF₆. Solvent: 1:1 by volume (a-c), 1:9 by volume = 89 m/o DME (d). i_p ($= i_s$): 1 mA/cm² (a), 2 mA/cm² (b, d), and 5 mA/cm² (c). Q_p : 0.2 C/cm².

mation or production of isolated, inactive Li might proceed with relatively slow rate. On the other hand, cycling at higher i_p and i_s (5 mA/cm²) led to a marked decrease of efficiency after the thirteenth cycle. The polarization of the electrode becomes high when plating is done at high current density. Some side reaction such as cathodic reduction of the solvents might occur during the charge. This results in the efficiency loss with repeating the cycle.

The Li cycle efficiencies were measured in the S-DME/LiPF₆ solutions with various solvent compositions. In Fig. 10, the solvent mixing ratio of 1:9 (by volume) is equivalent to 89 m/o DME in S-DME. The electrolytic conductivity of 1M LiPF₆ in S-DME (1:9) was about 1.5 times of that in S-DME (1:1). The increase in the conductivity brought little improvement to the cycling characteristics. Values of efficiency similar to that in S-DME (1:1) were obtained in the solutions with other mixing ratios (30-90 m/o DME).

Summary

Some properties of the electrolytic solutions consisting of sulfolane (S)-ether mixed solvents were investigated for rechargeable lithium batteries. The results are summarized as follows.

1. Vapor pressure of the mixed solvent increased in the order S-DME < S-DOL < S-THF, and it deviated from the Raoult rule in the positive direction for every system. Relative permittivity of the mixed solvent and viscosity of the electrolytic solution were little dependent on the added ether.

2. Maximum conductivities were obtained in the solutions consisting of the mixed solvent. The conductance behavior varied markedly with the electrolytic salt and cosolvent ether. The highest conductivity of all examined was observed for S-DME (1:9)/LiPF₆ (1M).

3. The polarization of Li on the Ni substrate in S-DME increased in the order LiPF₆ < LiBF₄ < LiClO₄, and the average efficiency of Li cycling increased in its opposite order. The cycling in S-DME/LiPF₆ showed the highest efficiency of all examined.

Acknowledgments

We wish to thank Dr. Y. Takasu for measurements of vapor pressure. We also thank Mr. F. Tachihara for conductivity measurements.

Manuscript submitted April 18, 1985; revised manuscript received July 23, 1985.

Yamaguchi University assisted in meeting the publication costs of this article.

REFERENCES

- J. O. Besenhard and G. Eichinger, *J. Electroanal. Chem.*, **68**, 1 (1976).
- V. R. Koch, *J. Power Sources*, **6**, 357 (1981).
- K. M. Abraham and S. B. Brummer, in "Lithium Batteries," J. P. Gabano, Editor, p. 371, Academic Press, New York (1983).
- G. H. Newman, R. W. Francis, L. H. Gaines, and B. M. L. Rao, *This Journal*, **127**, 2025 (1980).
- J. L. Goldman, R. M. Mank, J. H. Young, and V. R. Koch, *ibid.*, **127**, 1461 (1980).
- K. M. Abraham, J. L. Goldman, and D. L. Natwig, *ibid.*, **129**, 2404 (1982).
- S. B. Brummer, in "Lithium Battery Technology," H. V. Venkatesetty, Editor, Chap. 7, p. 159, John Wiley and Sons, New York (1984).
- B. J. Carter, S. P. S. Yen, D. H. Shen, R. M. Williams, and R. B. Somoano, Abstract 72, p. 179, The Electrochemical Society Extended Abstracts, Vol. 81-2, Denver, CO, Oct. 11-16, 1981.
- J. S. Foos and L. M. Rembetsy, Abstract 73, p. 117, The Electrochemical Society Extended Abstracts, Vol. 83-2, Washington, DC, Oct. 9-14, 1983; J. S. Foos and L. M. Rembetsy, in "Lithium Batteries," A. N. Dey, Editor, pp. 413-421, The Electrochemical Society Softbound Proceedings Series, Pennington, NJ (1984).
- H. V. Venkatesetty, in "Lithium Battery Technology," H. V. Venkatesetty, Editor, Chap. 1, p. 7, John Wiley and Sons, New York (1984).
- S. P. S. Yen, D. H. Shen, R. P. Vasquez, B. J. Carter, and R. B. Somoano, Abstract 74, p. 119, The Electrochemical Society Extended Abstracts, Vol. 83-2, Washington, DC, Oct. 9-14, 1983.
- DOE Project, *J. Power Sources*, **11**, 212 (1984); J. S. Foos, L. M. Rembetsy, and S. B. Brummer, Final Report on Department of Energy Contract no. DE-AC03-76SF00098, Subcontract no. 4514810 (1984).
- H. Ikeda, S. Ueno, T. Saito, S. Nakaido, and H. Tamura, *Denki Kagaku*, **45**, 391 (1977).
- Y. Matsuda, M. Morita, and K. Kosaka, *This Journal*, **130**, 101 (1983).
- Y. Matsuda, M. Morita, and K. Takata, *ibid.*, **131**, 1991 (1984).
- Y. Matsuda, M. Morita, and T. Yamashita, *ibid.*, **131**, 2821 (1984).
- V. Gutmann, *Electrochim. Acta*, **21**, 61 (1976).
- M. D. Monica, L. Jannel, and U. Lamanna, *J. Phys. Chem.*, **72**, 1068 (1968).
- E. Koizumi and S. Ouchi, *Nippon Kagaku Zasshi*, **91**, 510 (1970).
- Y. Matsuda, H. Nakashima, M. Morita, and Y. Takasu, *This Journal*, **128**, 2552 (1981).
- V. R. Koch and S. B. Brummer, *Electrochim. Acta*, **23**, 55 (1978).
- K. Takata, M. Morita, Y. Matsuda, and K. Matsui, *This Journal*, **132**, 126 (1985).
- R. Jasinski, in "Advances in Electrochemistry and Electrochemical Engineering," Vol. 8, P. Delahey and C. W. Tobias, Editors, p. 253, Interscience, New York (1971).
- Y. Matsuda, M. Morita, and K. Kosaka, *Denki Kagaku*, **51**, 119 (1983).
- N. Bjerrum, *K. Danske Vidensk. Selk.*, **7**, No. 9 (1926); R. A. Robinson and R. H. Stokes, "Electrolyte Solutions," p. 16, Elsevier, New York (1966).
- G. H. Newman, in "Lithium Nonaqueous Battery Electrochemistry," E. B. Yeager, B. Schumm, Jr., G. Blomgren, D. R. Blankenship, V. Leger, and J. Akridge, Editors, pp. 143-157, The Electrochemical Society Softbound Proceedings Series, Princeton, NJ (1980).
- E. Peled, in "Lithium Batteries," J. P. Gabano, Editor, p. 43, Academic Press, New York (1983).
- E. B. Yeager, in "Lithium Nonaqueous Battery Electrochemistry," E. B. Yeager, B. Schumm, Jr., G. Blomgren, D. R. Blankenship, V. Leger, and J. Akridge, Editors, pp. 1-12, The Electrochemical Society Softbound Proceedings Series, Princeton, NJ (1980).

Effect of EDTA on the Cathodic Reduction of Oxide Films on Iron in Sodium Hydroxide Solution

Z. Szklarska-Smialowska, T. Zakroczyński,¹ and C.-J. Fan

Department of Metallurgical Engineering, The Ohio State University, Columbus, Ohio 43210

ABSTRACT

Simultaneous electrochemical and ellipsometric investigations of the behavior of iron in 0.05 NaOH solution (pH 12) with and without the addition of EDTA showed that EDTA did not affect the passive film formation but drastically enhanced cathodic reduction of the passive film. Cathodic reduction of the passive film in EDTA-free 0.05M NaOH resulted in the formation of an unreducible porous layer on the iron surface. This layer grew progressively in thickness when periodic passivation-reduction cycles were applied but did not influence the passive film formation. The cathodically formed layer probably consisted of some kind of iron hydroxide and elemental iron. In contrast, when EDTA was added to 0.05M NaOH, the cathodic reduction and removal of the passive film was complete and occurred very rapidly. Cathodic polarization of passive iron carried out potentiostatically in the presence of EDTA was found to provide reliable data on the charge consumed for reduction of the passive film.

In two other studies of ours (1, 2), it was found that the formation of passive films on iron in NaOH and NaOH + NaCl solutions (pH 12.0) resulted in a release of iron cations into the surrounding electrolyte starting in about 2s of the anodic polarization. In addition, it was noticed that after passivation and successive cathodic reduction in both NaOH and NaOH + NaCl solutions, the optical parameters did not return to their initial values before passivation, suggesting that some film still existed on the metal surface. Huang and Ord (3) reported that during cycling of iron in NaOH solution between anodic and cathodic potentials, the thickness of the unreducible film increased during each consecutive cycle. This film had a very low index of refraction and was probably FeOOH. Therefore, it seemed interesting to assess whether the ad-

dition of a complexing agent would interfere with the formation and reduction of oxide films on iron. The ethylenediaminetetra-acetic acid (EDTA) has been chosen to be studied here, because this chelating agent is known to dissolve magnetite in acid and neutral solutions at 50°C and higher temperatures (4). On the other hand, EDTA added to the alkaline electrolyte in iron batteries has been found (5) to increase their capacity.

Experimental

The material used and the experimental procedure were the same as in the two aforementioned studies (1, 2).

Results of Electrochemical and Ellipsometric Measurements

Polarization curves.—Anodic polarization curves measured at a potential sweep rate (PSR) of 0.01 V/s in 0.05M NaOH without and with the addition of either 0.001 or

¹Permanent address: The Institute of Physical Chemistry, Polish Academy of Sciences, Kasprzaka 44/52, 01-224 Warsaw, Poland.

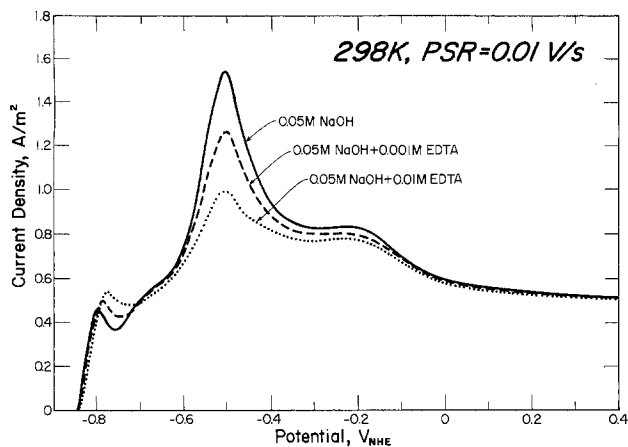


Fig. 1. Anodic polarization curves for iron in 0.05M NaOH containing different amounts of EDTA.

0.01M EDTA are shown in Fig. 1. In the presence of EDTA, a slight decrease of the critical current for passivation occurred, with no effect on the current density in the passive state. It appeared, therefore, that there were no changes in the protective properties and quality of the film grown on iron in either the presence or absence of EDTA in 0.05M NaOH solution.

Current decay curves.—Figure 2 depicts variations of the anodic current density with time at a constant potential of 0.550V, resulting from a rapid (PSR = 80 V/s) change of the electrode potential from -0.950 to 0.550 V. Also in this case, no significant effect of EDTA on the anodic current density was observed, suggesting that EDTA added to 0.05M NaOH did not affect the passive film growth on iron. This conclusion was supported by the results of ellipsometric measurements in 0.05M NaOH + 0.01M EDTA which did not differ from those obtained in 0.05M NaOH (anodic part of the first cycle in Fig. 3).

Passivation-reduction cycling.—Contrary to the anodic polarization, there was a significant effect of EDTA on the course of the cathodic reduction. In 0.05M NaOH, the cathodic polarization of a passivated iron electrode did not permit the optical parameters Δ and ψ to return to their initial values observed for nonpassivated iron. Furthermore, repeated passivation-reduction cycles carried out with the same electrode resulted in an additional irreversibility of optical parameters, so that each consecutive $-\delta\Delta$ vs. t , $\delta\psi$ vs. t , or $\delta\psi$ vs. $-\delta\Delta$ curve was shifted relative to the preceding one (Fig. 3 and 4). In contrast, in the presence of EDTA, the film reduction was fast and complete, and numerous repeated passivation-reduction cycles had the same run.

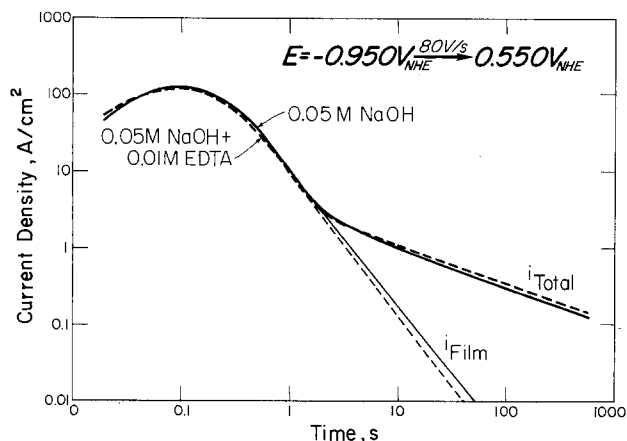


Fig. 2. Changes in current density with time for iron in 0.05M NaOH with and without EDTA and at 0.550V. The extrapolated fine lines correspond to the current consumed for film growth ($t > 2$ s).

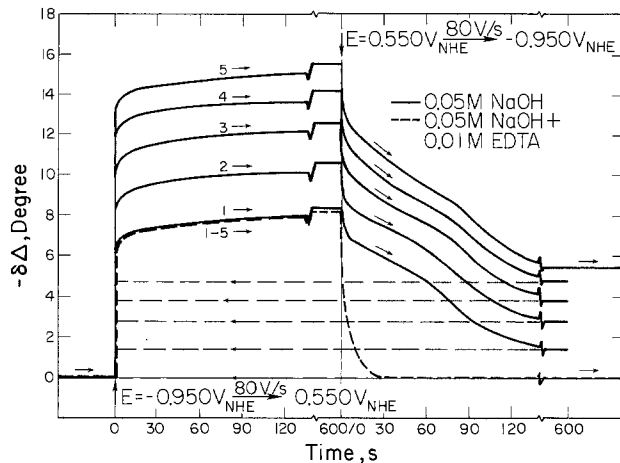


Fig. 3. Changes in $-\delta\Delta$ with time during consecutive five cycles of film growth and film reduction in 0.05M NaOH with and without EDTA.

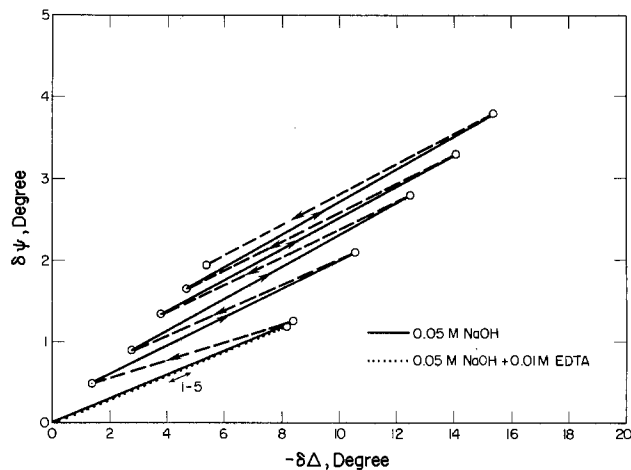


Fig. 4. Relationship between $-\delta\Delta$ and $\delta\psi$ during consecutive cycles of film growth and film reduction in 0.05M NaOH with and without EDTA.

Figure 5 shows changes in $-\delta\Delta$ and $\delta\psi$ in relation to the number of passivation-reduction cycles obtained in two similar experiments. In the first experiment, which was performed in 0.05M NaOH without EDTA, 20 consecutive cycles between -0.950 and 0.550 V were applied, with both potentials maintained each time for 600s. Values of Δ and ψ were taken after a successive reduction at -0.950 V; their changes are marked as $(-\delta\Delta)_{\text{RED}}$ and $(\delta\psi)_{\text{RED}}$, respectively. After 20 cycles, the metal surface was covered with a yellow-brown deposit. In the second experiment, after

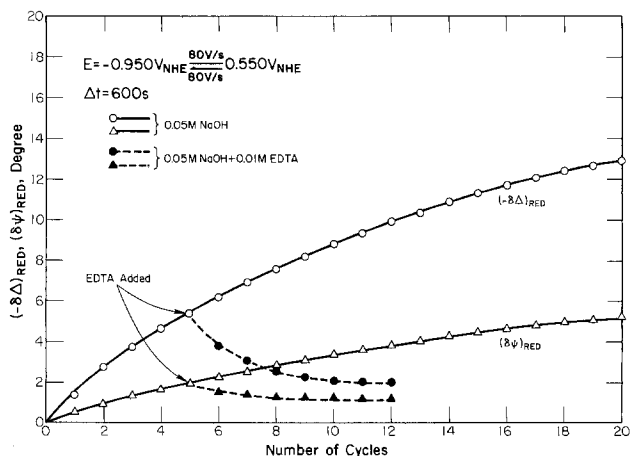


Fig. 5. Changes in optical parameters obtained after successive cathodic polarization of the passivated iron in 0.05M NaOH and the effect of the addition of EDTA.

five passivation-reduction cycles in 0.05M NaOH, EDTA was added at $-0.950V$. At this potential, no significant changes in the optical parameters were observed (even for times longer than 600s). However, during the successively repeated passivation-reduction cycles, a partial restoration of the optical parameters was observed (solid characters in Fig. 5).

In contrast to the optical parameters, both the anodic (at 0.550V) and the cathodic (at $-0.950V$) current densities were not significantly affected by passivation-reduction cycling in either EDTA-free or EDTA containing 0.05M NaOH. The magnitude and the changes of the anodic current density with time shown in Fig. 2 are the same for many cycles.

Since both the pH and kind of anion can play significant roles in the film formation and film reduction processes, additional passivation-reduction cycling experiments were carried out using NaOH, borate, and phosphate solutions of different pH. Figure 6 indicates that in all applied solutions of high pH (> 12), without EDTA the reduction of the passive film in a successive cycle led to a gradual increase of $(-\delta\Delta)_{red}$, whereas in the presence of EDTA the restoration of Δ was complete. In turn, Fig. 7 shows that at pH 9, the passive film was removed in spite of the absence of EDTA.

Reduction and removal of the passive film.—Additional information regarding the influence of EDTA on the reduction of passive films on iron in 0.05M NaOH is provided in Fig. 8, showing changes in $-\delta\Delta$ under various passivation and reduction conditions. When both the

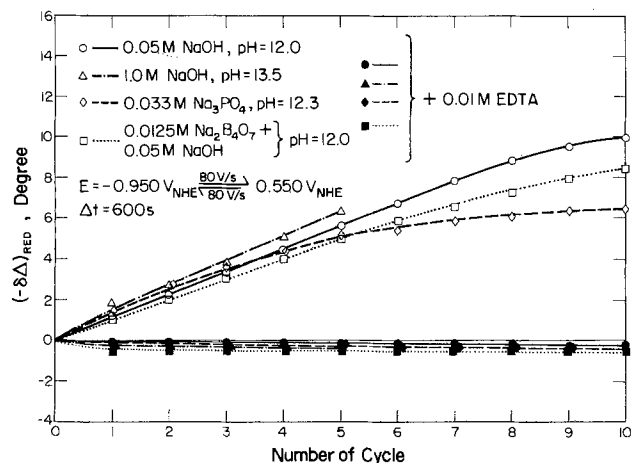


Fig. 6. Changes in $-\delta\Delta$ obtained after successive cycling from anodic to cathodic polarization of iron in solutions containing different anions, with and without EDTA (high pH).

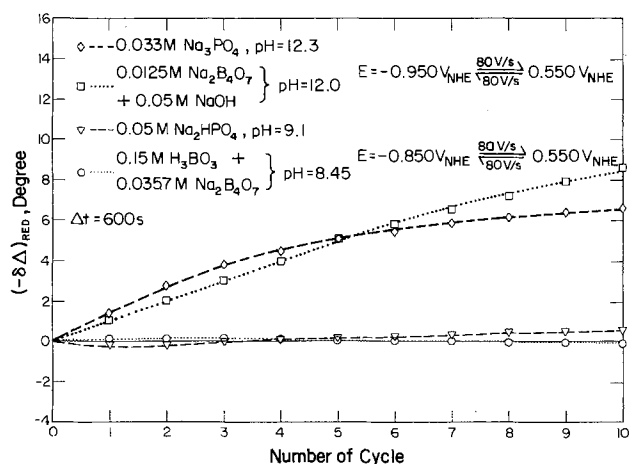


Fig. 7. Changes in $-\delta\Delta$ obtained after successive cycling from anodic to cathodic polarization of iron in borate and phosphate solutions of different pH.

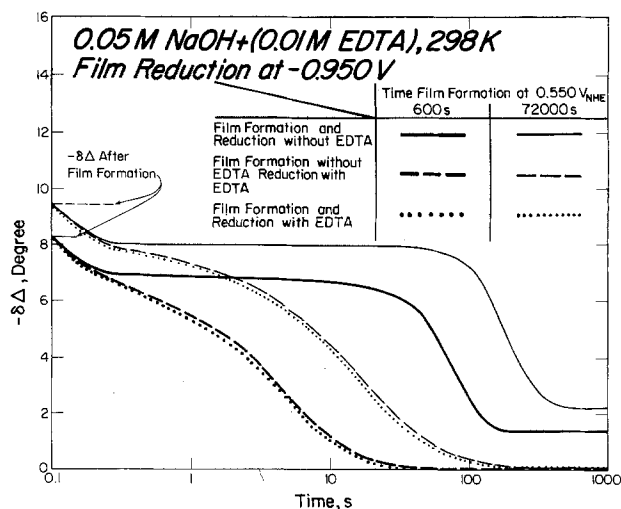


Fig. 8. Changes in $-\delta\Delta$ with time during the cathodic reduction of films grown in 0.05M NaOH with and without EDTA.

passivation and reduction were conducted in the absence of EDTA, restoration of Δ during reduction was slow and not complete; the longer passivation time was employed, the slower restoration was. Moreover, irreversibility was more pronounced when the passivation time was longer. When the passive film grew in 0.05M NaOH and was then reduced in the presence of EDTA, Δ returned to its initial value before passivation. This occurred at a rate which also was passivation-time dependent, but much faster than in the EDTA-free 0.05M NaOH solution. Identical results were obtained when both the passivation and reduction occurred in the presence of EDTA, once again indicating the EDTA did not affect passivation but decisively enhanced the reduction of passive films on iron and caused a full restoration of the optical parameters.

Determination of the film charge density.—Since the cathodic reduction method is often used to determine the charge consumed for the reduction of a passive film and to measure its thickness, additional experiments aimed at assessing the influence of EDTA on the results of film charge measurements have been performed. Relationships between the electrode potential and $-\delta\Delta$ vs. time of galvanostatic reduction are shown in Fig. 9 and 10, respectively. In both those figures, the value of $q_{film} = 67.5 C/m^2$ is marked on the charge density scale. This value was obtained by integration of the curve i_{film} plotted in Fig. 2. It was expected that the same q_{film} value could be obtained on the basis of the reduction experiment. Unfortunately, this proved to be impossible because there was no characteristic point on the potential-time curve (Fig. 9)

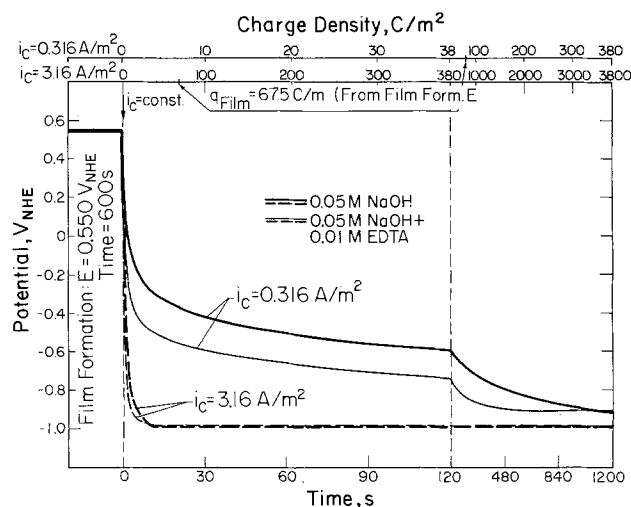


Fig. 9. Variation in potential with time during galvanostatic reductions of the passive film in 0.05M NaOH with and without EDTA.

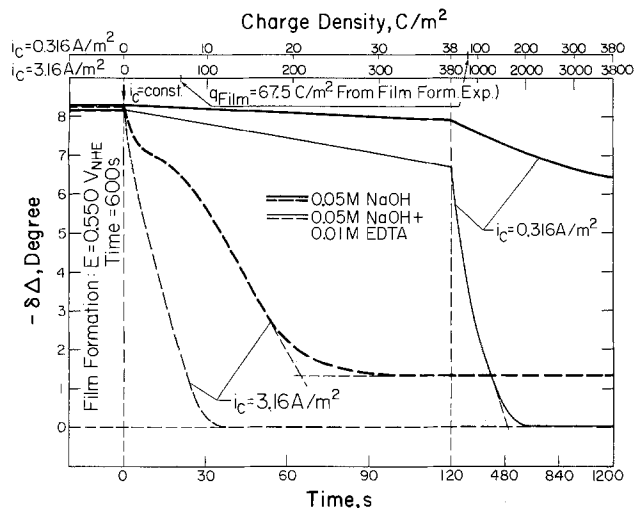


Fig. 10. Changes in $-\delta\Delta$ with time during galvanostatic reductions of the passive film in 0.05M NaOH with and without EDTA.

which could permit differentiation of the film reduction charge from the hydrogen evolution charge. Attempts to evaluate q_{film} taking into account the time after which Δ returned to its initial value ($-\delta\Delta = 0$) in the presence of EDTA or to a constant value in the absence of EDTA (see Fig. 10) were also unsuccessful. However, the q_{film} value obtained in the presence of EDTA at a high current density was about 90 C/m^2 and hence not very far away from the previously determined value of 67.5 C/m^2 .

In the next series of experiments, the cathodic reduction of the passive film was conducted in 0.05M NaOH under controlled potentiostatic conditions at -0.950 V . It was assumed that the reduction of the film ended when $-\delta\Delta$ was constant and that i_c also is constant and associated with the hydrogen evolution reaction (i_H). Another assumption was that during the cathodic reduction the evolution of hydrogen occurred at a constant rate. This was a very rough simplification, because in the initial reduction stage the hydrogen evolution reaction probably was overwhelmed by that of film reduction. Based on these assumptions, the charge consumed for hydrogen evolution, q_H , could be calculated. Finally, q_{film} could be obtained by subtracting q_H from q_{total} . The results of these calculations showed that, again, the q_{film} value was still too high relative to that obtained in the film formation experiments.

The results of measurements taken under the same conditions as above but in the presence of EDTA are much more promising; see Fig. 11 and 12. The obtained value of q_{film} is only 4% lower than the one sought. This difference could be caused by the simplified assumption concerning the constancy of i_H . From those considerations, it follows that potentiostatic measurements conducted in the presence of EDTA in alkaline solutions may lead to reliable data of the charge consumed for the passive film reduction on iron.

Discussion

It was expected that EDTA, which is a potent complexing agent for iron ions, could reduce the propensity to passivation of iron in NaOH. However, neither the course of anodic polarization curves (Fig. 1) nor those of decay curves (Fig. 2) or ellipsometric data (Fig. 3 and 4) support the above expectation. In fact, passive film grown on iron in either EDTA-free or EDTA containing 0.05M NaOH solution exhibit the same protective and optical properties. This fact can be explained by the high ability of iron to be passivated by alkaline solutions.

The most significant finding to be discussed here is the appearance of a layer of iron after its anodic oxidation, followed by cathodic reduction in 0.05M NaOH. This layer does not, however, appear when the cathodic reduction is conducted in 0.5M NaOH containing

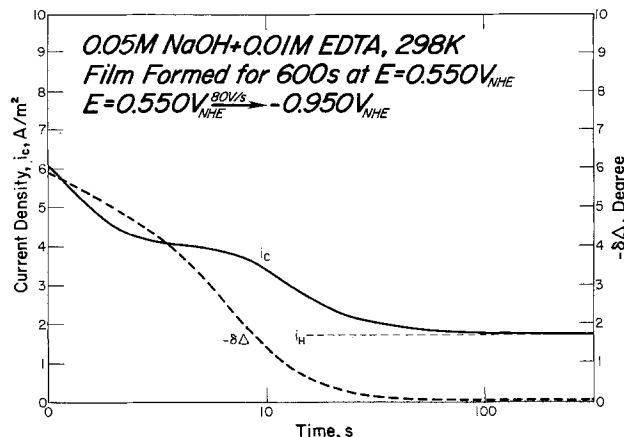


Fig. 11. Changes in current density and $-\delta\Delta$ with time during cathodic reduction of the passive film in 0.05M NaOH + 0.01M EDTA at -0.950 V .

EDTA. The question arises whether this layer consists of a residue of the previous passive film or results from a certain, heretofore unknown, cathodic reaction. The first option seems to be likely, since it is generally accepted that a complete reduction of the passive film on iron is hard to attain in alkaline solutions. However, the presence of some passive film residue on iron would influence its next anodic behavior, which is not observed. In all the repeatedly conducted passivation-reduction cycles, the current density was the same, and both $-\delta\Delta$ and $\delta\psi$ increased a little with increasing cycle number (Fig. 3 and 4).

These observations show that the new passive film formed during each successive passivation does not substantially differ from that formed during the previous passivation. It is obvious, therefore, that the surface layer resulting from the cathodic reduction of passive iron in 0.05M NaOH does not consist of an unreducible residue of the previous passive film.

The above conclusion was supported by the following additional experiment. A fresh iron electrode was pre-treated cathodically at -0.950 V and kept in 0.05M NaOH under open-circuit condition for 20h. Both the corrosion potential and optical parameters varied with time, showing that slight passivation occurred; namely, after 20h, the potential attained about -0.4 V and $-\delta\Delta$ was 5.4° . Then, the electrode was polarized to 0.550 V and kept at this potential for 600s, during which $-\delta\Delta$ increased to 8.3° , i.e., to a value close to that characterizing the passive state of iron after its passivation in one stage from -0.950 to 0.550 V (Fig. 3). The charge consumed for the potential shift from -0.4 to 0.550 V was less than that consumed from -0.950 to 0.550 V , indicating that the presence of a

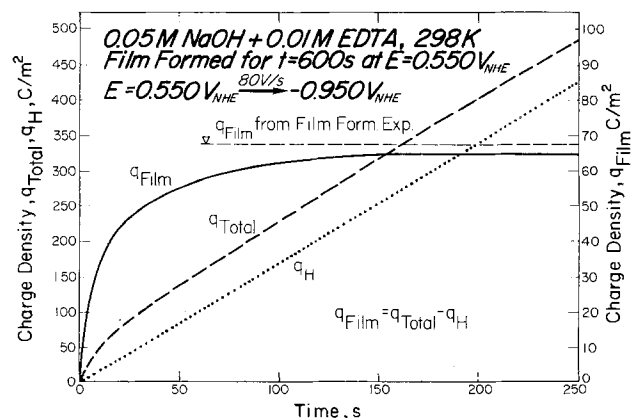


Fig. 12. Effect of time on the total charge density during cathodic reduction of the passive film and on the charge densities consumed for film reduction and hydrogen evolution in 0.05M NaOH + 0.01M EDTA at -0.950 V .

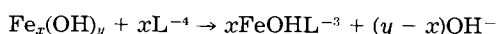
passive film residue does not interfere with the next passivation but assists its attainment.

The layer that forms on iron during the cathodic polarization in 0.05M NaOH has a very low refractive index. The n and k values obtained from the $(\delta\psi)_{\text{red}}$ vs. $(-\delta\Delta)_{\text{red}}$ relationship are about 1.4-1.6 and 0, respectively. None of the known iron oxides exhibit such low n and k values. The thickness of the cathodic layer increases with the number of passivation-reduction cycles applied and may attain several hundred angstroms. It can be supposed, therefore, that this layer is porous and that its refractive index, as measured, is immaterial. Because of its porosity, the layer is nonprotective and does not affect the next passivation.

Another question to be asked regards the origin of the cathodic layer. Two possibilities can be taken into account: first, that this layer is a result of the cathodic reduction of the pre-existing passive film; second, that ferric ions released from the film during passivation undergo reduction and iron is electrodeposited during the next cathodic polarization. To check the latter possibility, the following auxiliary experiment was performed. After 600s of cathodic polarization of an iron electrode at -0.950V in 0.05M NaOH, ferric ions at a concentration of 1×10^{-5} mol/liter were added and ellipsometric parameters were recorded. Although the concentration of ferric ions added was much higher than that which could be produced by dissolution of a pre-existing passive film, the optical parameters did not change during a few hours of cathodic polarization. Consequently, the first alternative appears to be more probable.

The above considerations do not provide a clear solution to the crucial question regarding the nature of the cathodic layer. One possibility is that during cathodic polarization, the passive film, probably FeOOH (1), is reduced to iron in the form of a porous layer. In the presence of this layer, at a constant cathodic potential of -0.950V , the optical parameters do not change in either EDTA-free or EDTA containing 0.05M NaOH solution. This indicates that under these conditions the cathodic layer does not undergo any change. However, optical parameters are decreased by cycling between anodic and cathodic potentials in EDTA containing 0.05M NaOH (Fig. 5), suggesting that by such a procedure the porous layer becomes partly removed. When EDTA is added to the electrolyte after passivation but before application of the first cathodic reduction, *i.e.*, when the iron electrode is covered by the sole passive film, cathodic polarization results in a complete removal of the passive film and there is no porous layer formation. The optical parameters return to their initial values before passivation.

The exact part played by EDTA in the above processes is not quite clear. Since EDTA is a complexing agent of iron cations, it might be supposed that the charge density consumed for the passive film reduction should be less than that for passivation ($\text{Fe}^{\circ} \rightarrow \text{FeOOH}$). In reality, however, the charge used for film removal was close to that corresponding to the reduction of FeOOH into Fe° (Fig. 12). This suggests that in this process, the effect of EDTA was nonexistent or negligible. Therefore, another possibility regarding the nature of the cathodic layer has to be considered. It can be presumed that cathodic polarization of the passive film leads to the formation of porous iron in a highly active state in which it is able to react chemically with water at high pH, producing some compound of unknown composition, say $\text{Fe}_x(\text{OH})_y$. During the next anodic polarization, a new passive film might grow beneath the porous layer, and processes of this kind occur alternately during each successive passivation-reduction cycle. Presumably, in the cathodic layer, $\text{Fe}_x(\text{OH})_y$ predominates in its outer part and Fe° in its inner one, *i.e.*, in the one adjacent to the electrode. EDTA might be supposed to react with $\text{Fe}_x(\text{OH})_y$ according to the following reaction



where L is an EDTA molecule

The results presented in Fig. 7 reveal the essential role of pH in the passive film reduction process. Namely, at high pH (> 12) in the absence of EDTA, cathodic polarization leads to the formation of a porous layer which does not form at lower pH values. The presence of this layer was found on the surface of passivated iron after its cathodic treatment in all the studied solutions of high pH, irrespective of the kind of anion. In solutions of lower pH (8-9), as in those containing EDTA, there is no cathodic film formation at either high or low pH values. There is, however, a different reason for the absence of the cathodic layer in EDTA-free low pH solutions and in solutions of high pH containing EDTA. Namely, $\text{Fe}_x(\text{OH})_y$ does not form at pH 8-9, but at high pH, EDTA removes the cathodic layer by binding $\text{Fe}_x(\text{OH})_y$.

Conclusions

1. EDTA added to 0.05M NaOH has no effect on passive film formation on iron during its anodic polarization.
2. The passive film formed on iron in 0.05M NaOH during anodic polarization as well as at corrosion potential can be completely reduced and removed when cathodic polarization in the presence of EDTA is applied.
3. The cathodic reduction of the passive film in EDTA-free 0.05M NaOH (pH 12) leads to the formation of a porous surface layer which presumably consists of some kind of iron hydroxide, say $\text{Fe}_x(\text{OH})_y$, and elemental iron. This layer has the following properties. It cannot be removed during cathodic polarization in either EDTA-free or EDTA containing 0.05M NaOH. It undergoes partial oxidation when anodic polarization is applied, and then it can be partly dissolved by cathodic polarization in the presence of EDTA. It achieves a significant thickness when periodic passivation-reduction cycles in the absence of EDTA are applied. It is porous, has no protective properties, and therefore does not influence the passive film formation. In solutions of lower pH ($\approx 8-9$), there is no porous layer formation.
4. Summing up, the course of events that probably occurs on the surface of an iron electrode during its anodic and cathodic polarization in the absence or presence of EDTA in 0.05M NaOH might be described as follows.

Electrolyte: 0.05M NaOH.—During the first anodic polarization, passive film formation occurs. During the first cathodic polarization, reduction of the passive film to iron and chemical interaction of the freshly formed porous iron with water molecules occur, producing $\text{Fe}_x(\text{OH})_y$.

Successive cycles of anodic and cathodic polarization.—In anodic polarization, a new passive film grows mainly at the interface between solid metal and porous layer formed in previous cathodic treatment. In cathodic polarization, the newly formed passive film is reduced to active iron which reacts chemically with water molecules, forming $\text{Fe}_x(\text{OH})_y$, mainly in the outer layer of the newly formed and reduced passive film. Periodic cycling between anodic and cathodic potentials results in gradually increasing thickness of the porous layer.

Electrolyte: 0.05M NaOH + EDTA.—In each of the successive cathodic and anodic polarization cycles, passive films form at anodic potentials and are reduced to Fe° at cathodic potentials. Fe° reacts chemically with water molecules, forming $\text{Fe}_x(\text{OH})_y$, but EDTA removes the latter, producing FeOHL^{-3} .

5. Because EDTA assists the reduction of passive films on iron, cathodic polarization conducted potentiostatically in the presence of EDTA can provide reliable data about the charge consumed for passive film reduction.

Acknowledgment

This investigation was supported by The National Science Foundation under Contract no. DMR-8213905.

Manuscript submitted March 16, 1985; revised manuscript received July 5, 1985.

Ohio State University assisted in meeting the publication costs of this article.

REFERENCES

1. T. Zakroczymski, C-J. Fan, and Z. Szklarska-Smialowska, *This Journal*, To be published.
2. T. Zakroczymski, C-J. Fan, and Z. Szklarska-Smialowska, *ibid.*, To be published.
3. Z. Q. Huang and J. L. Ord, *This Journal*, **132**, 24 (1985).
4. EPRI Report, NP-2815 "Cleaning Steam Generators Off-Line (Soaking) with Chelants" Electric Power Research Institute, Palo Alto, CA (1983).
5. T. Yabumoto and K. Ohsawa, *Jpn. Kokai*, **75**, 45, 243.

Activation of the Iron Surface to Hydrogen Absorption Resulting from a Long Cathodic Treatment in NaOH Solution

T. Zakroczymski¹ and Z. Szklarska-Smialowska

Department of Metallurgical Engineering, The Ohio State University, Columbus, Ohio 43210

ABSTRACT

Electrochemical measurements of the permeation rate of hydrogen through pure iron cathodically polarized in 0.1M NaOH, together with ellipsometric and optical observations of the electrode surface, were performed. A long, uninterrupted charging caused disintegration of a subsurface metal layer and, as a result, the metal surface became more prone to both hydrogen absorption and corrosion. The permeation rate through activated iron membranes was controlled by the cathodic current density. An addition of EDTA into 0.1M NaOH increased the activity of the iron surface by removing from it some oxidized products of the chemical reaction of iron with water. Therefore, at the same charging current density, the hydrogen permeation rate through iron membranes was much greater in the presence than in the absence EDTA. On the contrary, a layer of palladium on the input surface impeded the entry of hydrogen.

In a previous paper by one of the authors (1), it was found that a sufficiently long (100-200h) cathodic polarization of ARMCO iron membranes in a dilute NaOH solution resulted in a surprisingly high permeability of the metal to hydrogen. Interruption of the charging current followed by its switching on caused the hydrogen permeation rate to decrease transiently, before the previous permeability was restored. It was supposed that, upon the exposure of the iron to NaOH, a barrier layer formed at the metal/electrolyte interface, hindering the entry of hydrogen into the metal bulk. This barrier could be removed by a sufficiently long, uninterrupted cathodic polarization, leading to a very high permeability level.

In another paper by the authors (2), it was shown that passive films formed on iron in NaOH and then subjected to cathodic reduction in the same electrolyte could not be completely removed. After such a treatment, some unreducible porous layer remained on the iron surface. However, in the presence of EDTA (ethylenediaminetetraacetic acid) in NaOH, the cathodic removal of the passive film on iron was complete.

Therefore, it was deemed interesting to compare the properties of the barrier layer which hindered the entry of hydrogen into iron with those of the porous layer remaining on the surface of iron after passivation followed by reduction in NaOH, and also to check if EDTA would influence the permeation rate of hydrogen through iron.

Experimental

Hydrogen permeation measurements, ellipsometry, and microscopic observations were performed. The classical electrochemical permeation technique (3) was used for permeability measurements, and the nonsteady-state diffusion method (4, 5) was used for diffusivity determination (see Appendix).

The base electrolyte was aqueous 0.1M NaOH. Additional experiments were conducted in the presence of ethylenediaminetetra-acetic acid (EDTA) or in that of both EDTA and As₂O₃. The test membranes, 0.001m thick, were of high purity 99.998% iron (Puratronic iron of Johnson Matthey Chemicals Limited). For all permeability measurements, the input surfaces of membranes were mechanically polished with diamond paste to a 1 μm

finish. The output surface of each membrane was coated with a thin layer of Pd. Palladium electroplating was performed in aqueous solution 0.8g PdCl₂/liter + 60g NaOH/liter and at current densities of 200 A/m² during the first 30s and 100 A/m² during the next 270s. Some permeability measurements were taken in the presence of a Pd layer on the input surface as well. For ellipsometry, a different kind of pure iron, 99.991% Fe (product of Material Research Corporation) was used. These specimens were in the form of slices cut off from a 0.0064m diam rod; they were polished in the same way as the membranes. A manual ellipsometer, Type 436 of Rudolph Research, and a mercury light source of 546.1 nm wavelength were used. The angle of incidence was 71°. Directly measured polarizer and analyzer angles were converted into relative changes of phase (Δ) and amplitude (ψ), respectively. All experiments were carried out at 24° ± 1°C.

Results

Permeability measurements.—Figure 1a shows three examples of hydrogen permeation rate (i_p) vs. time (t) curves obtained for iron membranes in either pure 0.1M NaOH solution or in that containing 0.01M EDTA. The entry side of one of these membranes [marked Fe(Pd)] was covered with Pd. These results were obtained during the first 200s of cathodic polarization at a current density of 90 A/m². As a rule, in this initial charging period, the H permeation rate was relatively small. The addition of EDTA to the electrolyte caused a substantial increase of permeability, whereas the presence of Pd on the input surface of iron had an opposite effect.

Analyses of the first build-up transients as depicted in Fig. 1a are given in Fig. 1b. Because the $\log(i_p \cdot t^{1/2})$ vs. t^{-1} relationships were not linear, only mean values of their slopes and, consequently, mean values of the effective diffusivity of hydrogen (D) could be estimated. As in the case of permeability, EDTA increased and Pd decreased the effective diffusivity. All calculated D values were much lower than those reported in literature for the lattice diffusivity of hydrogen in pure iron at room temperature. This suggests that, during the above initial period of cathodic polarization, the permeability was controlled not by diffusion of H in the metal but by some kinetic impediments acting on the input surface. The present results differ from those found for gas phase diffusion (6, 7) in

¹Permanent address: The Institute of Physical Chemistry, Polish Academy of Sciences, Kasprzaka 44/52, 01-224, Warsaw, Poland.

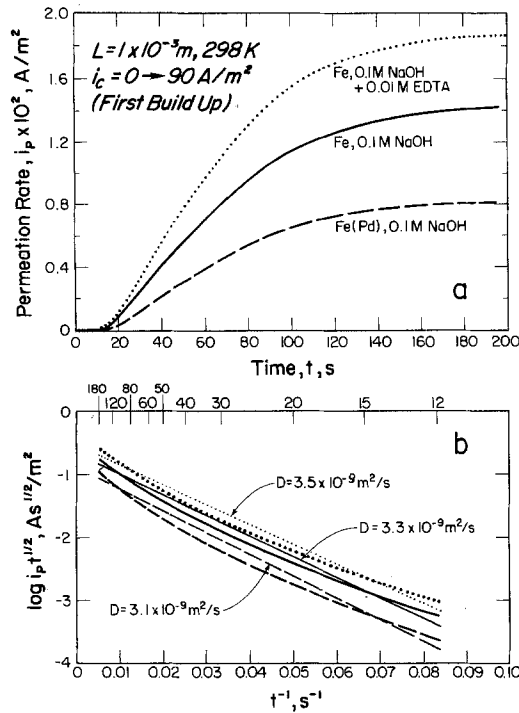


Fig. 1. Build-up transients (a) and their evaluation (b) for nonprecharged membranes. Experimental curves are marked by thick lines, dashes, and dots (compare 1a), while thin marks correspond to averaged straight lines from which the average D values (indicated by arrows) are calculated.

that the presence of palladium did not eliminate permeation control by surface processes.

Figure 2 shows relationships between the hydrogen permeation rate and the square root of cathodic current density for freshly prepared (*i.e.*, not precharged) membranes of the same type as in Fig. 1a, exposed to the same two solutions for 200s. From Fig. 2 it follows that permeability increased with input current density, increasing up to some 20 A/m^2 , but did not at higher currents.

A quite different picture was obtained when the cathodic polarization was continued for 50h or more. As shown in Fig. 3, for both the nonpalladized membranes the permeability increased quite rapidly within, approximately, the 20-50h range, after which a nearly constant permeation rate was obtained; its level was much higher in the presence of than in the absence of EDTA in 0.1M NaOH. Here again, a Pd layer on the input side of the membrane had a significant impeding effect on H permeation. In the presence of EDTA, after about 50h of

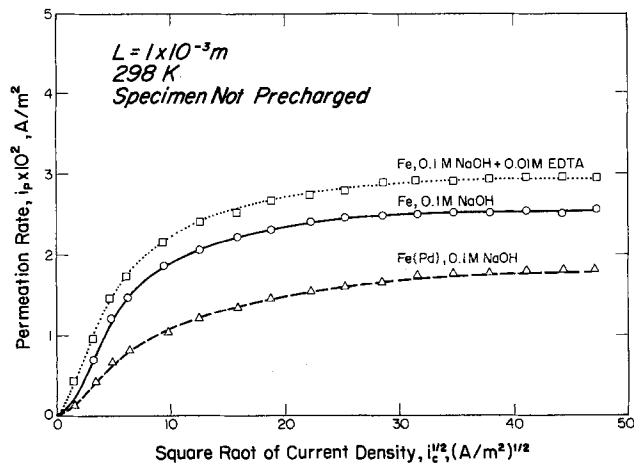


Fig. 2. Relationships between hydrogen permeation rates and the square root of cathodic current density for nonprecharged membranes at $t = 200s$.

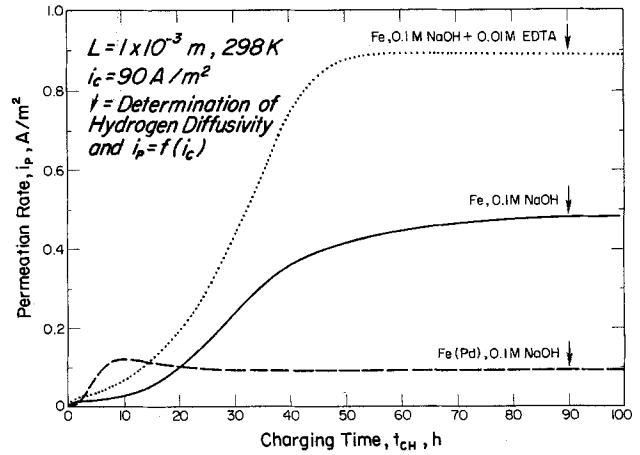


Fig. 3. Changes of hydrogen permeation rate with time

uninterrupted charging, the permeability attained an approximately constant level of 0.9 A/m^2 , *i.e.*, about 50 times that observed after the first 200s. When As_2O_3 was added to the EDTA containing solution after the above steady-state permeability was achieved, the permeation rate still increased up to about 1.8 A/m^2 .

After 90h of interrupted cathodic charging (at times marked in Fig. 3 by arrows), the permeation decay and build-up transients were measured by a rapid variation of the current from 90 to 30 A/m^2 and then back to the previous value of 90 A/m^2 . An example of decay and build-up permeation transients is plotted in Fig. 4a and the result of their analysis in Fig. 4b. By this method, the true diffusivity of hydrogen was determined (4, 5).

There was a very good agreement between the hydrogen diffusivity values calculated from either the permeation decay or the build-up transient recorded in both EDTA-free (Fig. 4) and EDTA containing electrolyte. In the EDTA-free solution, D was a little greater ($8.20 \times 10^{-9} m^2/s$) than in the remaining one ($7.57 \times 10^{-9} m^2/s$). Both were independent of the concentration of hydrogen and close (especially D obtained in EDTA-free solution) to literature data for the lattice diffusivity of hydrogen in pure iron at room temperature (8, 9). In contrast, for membranes coated on the entry side with Pd, nonlinear rela-

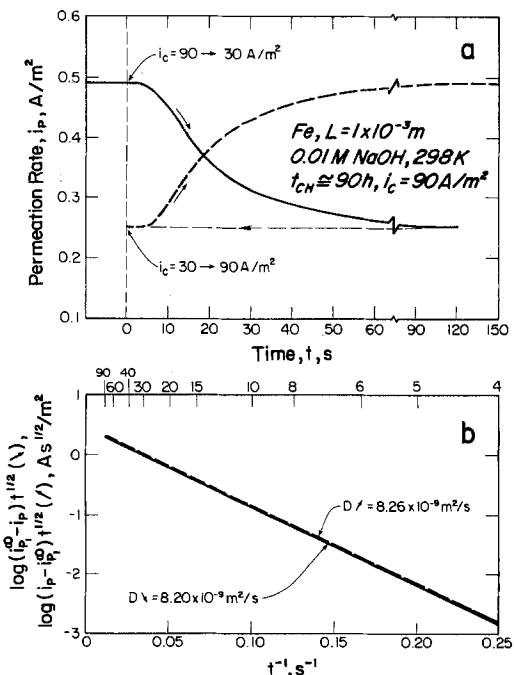


Fig. 4. Permeation decay and build-up transients (a) and their evaluation (b) for precharged iron membrane in 0.1M NaOH.

tionships (similar to those in Fig. 1b) and lower diffusivity values were obtained ($\sim 5 \times 10^{-9}$ m²/s).

Effects of the cathodic current density on the permeation rate of hydrogen through precharged membranes are shown in Fig. 5. In this case, the permeation rate was a linear function of the square root of cathodic current density over its whole applied range, i.e., up to 2250 A/m². The most striking result was again obtained in the EDTA containing solution, where the permeability reached 5 A/m², i.e., a value corresponding to $i_p \times L = 3.12 \times 10^{16}$ H at./m²-s. (Concentration of diffusive hydrogen in the metal beneath the input side was equal to 4.87×10^{-5} at. H/at. Fe.) Fluxes of such a high intensity are hard to obtain in acid, poison-free solutions.

On the entry surface of membranes in which permeabilities higher than about 1 A/m² were obtained, blisters appeared. They were not numerous and covered only a small part of the surface. They did not detectably influence the permeability.

Ellipsometry and observations of the electrode surface.—Changes in $-\delta\Delta$ with time for iron specimens polarized cathodically in 0.1M NaOH at three different current densities are shown in Fig. 6, and the respective relationships between $-\delta\Delta$ and $\delta\psi$ are depicted in Fig. 7. As a rule, cathodic polarization resulted in significant changes of the ellipsometric parameters. The greater the current density applied, the larger the change in Δ and ψ .

Effects of EDTA and Pd on ellipsometric parameters are shown in Fig. 8 and 9. In the presence of EDTA, the increase of $-\Delta$ was less pronounced than that of ψ . The palladized specimen exhibited relatively small changes in both $-\Delta$ and ψ with time.

In more advanced stages of the cathodic treatment, a brownish layer appeared on the surface of all the electrodes. Depending upon the composition of the electrolyte and time, the color of that layer changed from golden or yellow-brown to almost black. Optical and scanning electron microscopic observations revealed that it had a finely dispersed porous structure. Its thickness reached several hundred nanometers.

Evolution of hydrogen bubbles at the cathode surface also changed with time. In the initial charging stage, only a few sites on the metal surface were engaged in this process. Later on, more sites became available for H₂ evolution. Finally, a multitude of very small bubbles was seen to take off rapidly from the whole metal surface. These events developed with time rather slowly and depended equally upon the presence of EDTA in the electrolyte and of Pd on the electrode; hence, they were related to the observed changes in H permeability.

Discussion

In contrast to the behavior of fresh (nonprecharged) iron membranes, where a linear dependence of hydrogen

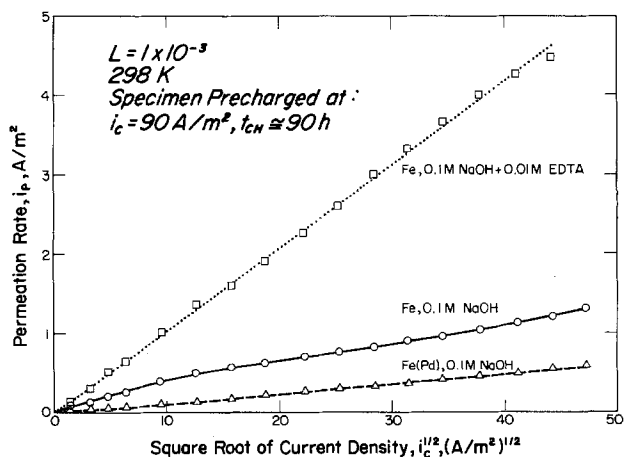


Fig. 5. Relationships between hydrogen permeation rates and the square root of cathodic current density for precharged specimens.

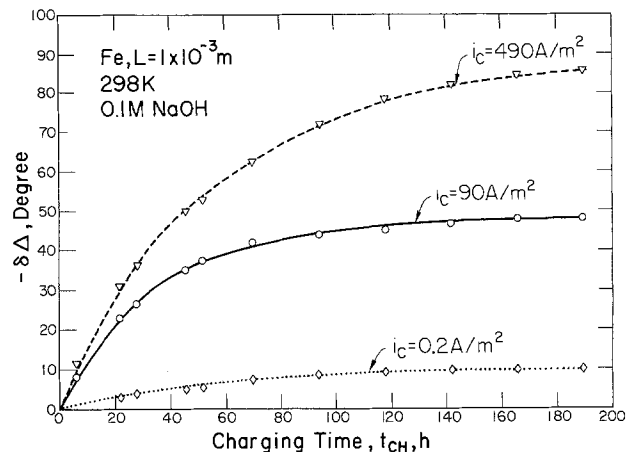


Fig. 6. Changes in $-\delta\Delta$ with time during cathodic polarization of iron in 0.1M NaOH at different current densities.

permeation on the square root of cathodic current density was held over a narrow range of low cathodic current densities (Fig. 2), for all the precharged (activated) membranes the above linear relationship was seen up to very high applied currents (2250 A/m², Fig. 5). This indicated that in the former case some barrier layer existed on the input surface but was absent in the later case. However, despite that same supply of hydrogen to the cathodic surface, in the three experiments referred to in Fig. 5 the hydrogen permeation rate was different, indicating differences in either the state of surface or partial pressure of the atomic hydrogen supplied.

Ellipsometry revealed the formation of some alien layer on the surface of iron treated cathodically in NaOH. After about 24h of cathodic treatment, this layer became visible to the unaided eye. The longer the cathodic polarization was, the thicker the layer was. It was supposed, therefore, that by a long cathodic polarization with simultaneous hydrogen evolution in NaOH, disintegration of a thin subsurface iron layer occurred. The disintegrated iron particles probably were highly active and, because of the high pH at the cathode, could react chemically with water molecules and produce an oxidized iron compound.

It was found previously (2) that passive films formed on iron in NaOH and then subjected to a cathodic treatment in the same electrolyte could not be completely removed because some unreducible porous layer remained on the iron surface. It was assumed that this layer consisted of some kind of iron hydroxide [$\text{Fe}_x(\text{OH})_y$] and elemental iron.

It is believed that the nature of the porous layer formed on iron by cathodic treatment in NaOH is identical with that formed on iron by passivation and then reduction in NaOH. It can be predicted that such an oxidized layer

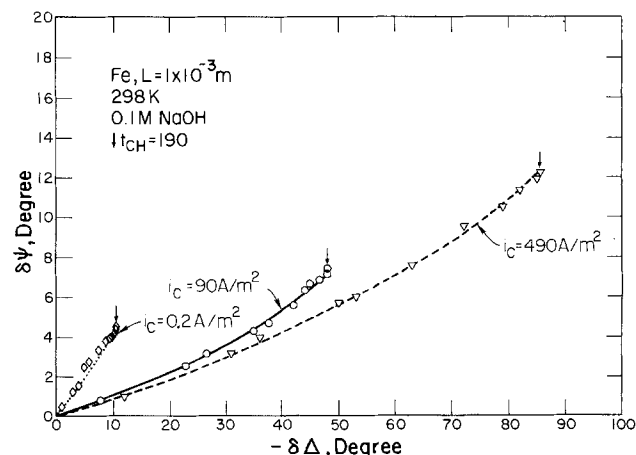


Fig. 7. Relationships between $-\delta\Delta$ and $\delta\psi$ for iron cathodically polarized in 0.1M NaOH at different current densities.

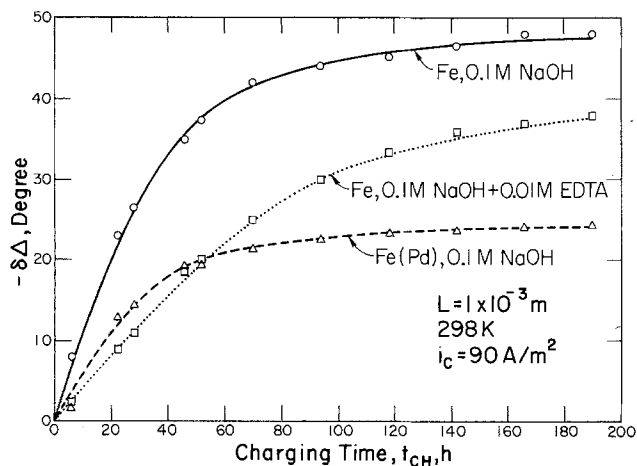


Fig. 8. Changes in $-\delta\Delta$ with time during cathodic polarization of iron in EDTA-free and EDTA containing 0.1M NaOH and of Pd-coated iron in 0.1M NaOH.

would deactivate the iron surface for the absorption of hydrogen, since the access of H atoms to the bare metal surface would be more difficult. At the same time, however, the presence in that layer of disintegrated iron particles of very high areas could make the metal surface more accessible to hydrogen. Consequently, the permeation rate of hydrogen through precharged membranes was greater than through fresh membranes.

In a previous work (2), it was also found that in the presence of EDTA in NaOH cathodic reduction of the passive film was complete, and if no prolonged cathodic treatment was applied, the iron surface was free of any alien layer. Obviously, EDTA removed $\text{Fe}_x(\text{OH})_y$ forming soluble complexes. However, after a long cathodic treatment of iron in EDTA containing NaOH, a porous layer of iron always was present; being evidently free of any oxidized product of the chemical reaction of iron with water, it increased the surface area of the cathode. As a result, in EDTA containing NaOH, the permeation of hydrogen through precharged membranes was much faster than in EDTA-free NaOH (Fig. 3 and 5).

In the presence of Pd on the input side of membranes the hydrogen permeation rate during the first approximate 2-15h of charging was greater than that observed for uncoated Fe, but it diminished then to a much lower, approximately constant value (Fig. 3). The former event could be caused by the fact that, initially, H dissolved in Pd, forming the α phase in which the transport of hydrogen is known to be faster than in the β phase that exists at high H concentrations. Another reason for the later decrease of permeability could be the greater recombination rate of hydrogen on Pd than on Fe, resulting in a decrease of the supply of H atoms to the cathode.

The presence of a layer of Pd on the entry side of the membrane does not prevent disintegration of the subsurface iron layer. This is clearly demonstrated by ellipsometric results shown in Fig. 8, where $-\delta\Delta$ for Fe(Pd) changes with charging time in a way similar to that for unpassivated iron.

Determination of the diffusivity of hydrogen based on decay and build-up transients recorded in NaOH with and without EDTA led to correct values of the diffusion coefficient of hydrogen in iron (Fig. 4). Contrary to expectations, for membranes coated on the input side with Pd, it was impossible to obtain correct diffusivity values using the method of successive permeation transients; the D values obtained were low. Apparently, Pd coatings retarded both the desorption and absorption of hydrogen during decay and build-up transients, respectively. As is known, under cathodic charging conditions, Pd forms a hydrogen-rich beta phase, the formation and decomposition of which is relatively slow. As a result, the relaxation time necessary to establish new boundary conditions was too long to permit application of the nonstationary diffusion equations.

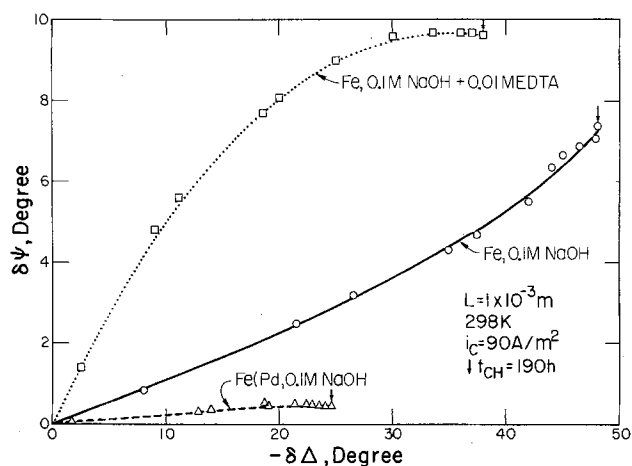


Fig. 9. Relationships between $-\delta\Delta$ and $\delta\psi$ for cathodically polarized iron in EDTA-free and EDTA containing 0.1M NaOH and for Pd-coated iron in 0.1M NaOH.

Conclusions

1. The absorption of hydrogen by iron during the first several hours of its cathodic polarization in 0.1M NaOH occurred relatively slowly and was controlled by the applied current only within a narrow range of low current densities.
2. A long, uninterrupted cathodic polarization of iron in NaOH solutions caused disintegration of a thin subsurface metal layer. As a result, the working surface of the cathode increased and became activated, i.e., more prone to both hydrogen absorption and corrosion.
3. Over the whole range of the applied charging currents (up to 2250 A/m²), the permeation rate of hydrogen through activated iron membranes was controlled by the cathodic current density, i.e., the rate of which the hydrogen atoms were supplied to the metal surface.
4. Disintegration of iron at its interface with NaOH solution led to the formation of a thin porous layer which was probably composed of disintegrated iron and of some oxidized iron compound. Because of its porosity, this layer did not hinder the absorption of hydrogen.
5. EDTA increased the activity of the iron surface by removing from it some oxidized products of its reaction with water at high pH values.
6. A layer of palladium on the input surface impeded the entry of hydrogen into iron.
7. Despite the presence of blisters on the input side of iron specimens and the very large hydrogen fluxes obtained in NaOH with EDTA, the permeation of hydrogen through iron was controlled in these experiments by lattice diffusion.

Acknowledgment

The authors are grateful for the support of this research by the National Science Foundation under contract no. DMR-8213905.

Manuscript submitted March 16, 1985; revised manuscript received July 5, 1985.

Ohio State University assisted in meeting the publication costs of this article.

APPENDIX

Principles of the Nonsteady-State Diffusion Method of Hydrogen Diffusivity Determination

In contrast with the steady-state diffusion, where the rate of hydrogen entry into a flat membrane is balanced by an equal rate of hydrogen exit from the opposite surface of the membrane, in the nonsteady state of diffusion these rates differ from one another. For materials in which the hydrogen diffusion coefficient (D) is independent of the hydrogen concentration, Fick's second law applies, and D can be precisely determined on the basis of build-up or decay permeation transients when the following initial and boundary conditions are fulfilled (4)

$$C = 0; 0 < x < L; t < 0 \quad [\text{A-1}]$$

$$C = C_0; x = 0; t = 0 \quad [\text{A-2}]$$

$$C = 0, x = L; t \geq 0 \quad [\text{A-3}]$$

where C is the concentration of hydrogen at a chosen distance x from the entry side, C_0 is the concentration of hydrogen in the first layer of metal atoms beneath the entry surface, L is the membrane thickness, and t is the time. These conditions mean the following.

1. Before charging, the whole membrane is free of hydrogen.

2. When cathodic charging begins at $t = 0$, a constant H concentration C_0 corresponding to the applied current density settles immediately beneath the entry surface ($x = 0$); this is also true of any other change in the state of the cathodic current density.

3. At the exit side of the membrane (*i.e.*, at $x = L$) the concentration of hydrogen at any t is 0; this is assumed by coating the exit surface with a thin layer of palladium and maintaining it at an appropriate anodic potential at which all the oncoming hydrogen is immediately ionized.

In this work, the following equations were used to calculate the effective diffusivities of hydrogen on the basis of build-up and decay permeation transients

decay

$$\frac{i_p - i_{p_2}^\infty}{i_{p_1}^\infty - i_{p_2}^\infty} = 1 - \frac{2}{\sqrt{\pi\tau}} e^{-1/4\tau} \quad [\text{A-4}]$$

buildup

$$\frac{i_p - i_{p_1}^\infty}{i_{p_2}^\infty - i_{p_1}^\infty} = \frac{2}{\sqrt{\pi\tau}} e^{-1/4\tau} \quad [\text{A-5}]$$

where $i_{p_1}^\infty$ is the initial steady-state permeation rate settled at a chosen cathodic current density $i_{c_1}(t < 0)$, $i_{p_2}^\infty$ is the final permeation rate settled at $i_{c_2}(t = \infty)$, i_p is the actual permeation rate at a chosen time $t > 0$, and τ is a dimensionless parameter equal to Dt/L^2 .

Equations [A-4] and [A-5] can be converted into more convenient forms

decay

$$\log(i_{p_1}^\infty - i_p)\sqrt{t} = \log \frac{2F\sqrt{D}(C_1 - C_2)}{\sqrt{\pi}} - \frac{L^2 \log e}{4D} - \frac{1}{t} \quad [\text{A-6}]$$

buildup

$$\log(i_p - i_{p_1}^\infty)\sqrt{t} = \log \frac{2F\sqrt{D}(C_2 - C_1)}{\sqrt{\pi}} - \frac{L^2 \log e}{4D} - \frac{1}{t} \quad [\text{A-7}]$$

where C_1 and C_2 are hydrogen concentrations in the metal directly beneath the entry surface, corresponding to i_{c_1} and i_{c_2} , respectively, and F is Faraday's constant. The slopes of linear relationships, $\log(i_{p_1}^\infty - i_p)\sqrt{t}$ vs. $1/t$, and $\log(i_p - i_{p_1}^\infty)\sqrt{t}$ vs. $1/t$, permits calculation of $D \downarrow$ and $D \uparrow$ values for decay and buildup, respectively. The linearity of these relationships, symmetry of build-up and decay transients, and equality $D \downarrow = D \uparrow$ all indicate that the permeation of hydrogen is controlled by diffusion and that the boundary conditions for nonsteady-state of diffusion are strictly fulfilled. Nonlinearity, asymmetry, or difference between $D \downarrow$ and $D \uparrow$ indicate that the permeation rate is controlled by some other events, most probably by either trapping or kinetic impediments on the entry surface, or jointly by both these events. However, the trapping of hydrogen in iron is a fast process which usually (especially for a thin membrane) ceases within several minutes after a constant cathodic current is applied, *i.e.*, when all traps present in the volume of the membrane are filled with hydrogen to a content related to the input fugacity of the external hydrogen source. Therefore, when deviations from linearity, symmetry, or equality continue for hours under constant charging conditions, evidence is given that the permeation is affected by some spurious surface effects.

REFERENCES

1. T. Zakroczymski, *Scrip. Metall.*, **19**, 521 (1985).
2. Z. Szklarska-Smialowska, T. Zakroczymski, and C.-J. Fan, *This Journal*, **132**, 2543 (1985).
3. M. A. V. Devanathan and Z. Stachurski, *Proc. R. Soc. London, Ser. A*, **270**, 90 (1962).
4. J. McBreen, L. Nanis, and W. Beck, *This Journal*, **113**, 1218 (1966).
5. T. Zakroczymski, *Corrosion (Houston)*, To be published (1985).
6. A. J. Kumnick and H. H. Johnson, *Met. Trans. A*, **6**, 1087 (1975).
7. G. M. Pressouyre, Ph.D. Thesis, Carnegie-Mellon University, Pittsburgh, PA (1977); also cited in "Advanced Techniques for Characterizing Hydrogen in Metals," p. 89, TMS-AIME, Warrendale, PA (1982).
8. H. G. Nelson and J. E. Stein, NASA Report TND-7265, NASA, Ames Research Center, Moffett Field, CA (1973).
9. N. R. Quick and H. H. Johnson, *Acta Metall.*, **26**, 903 (1978).

Formation and Breakdown of Passive Oxide Films on Nickel in Halide Solutions

B. MacDougall* and M. J. Graham

Division of Chemistry, National Research Council of Canada, Ottawa, Ontario, Canada K1A 0R9

ABSTRACT

The influence of Cl^- , Br^- , and F^- on the passivation of nickel in pH 3.0, 0.15N Na_2SO_4 has been studied. The presence of Cl^- and Br^- only temporarily delays the establishment of passivity; in contrast, F^- has little short-term (< 1s) influence, but a considerable long-term effect with the anodic current falling to only $\sim 1 \text{ mA}\cdot\text{cm}^{-2}$. To study the influence of the different halide ions, passive oxide films were formed on nickel in pH 3.0 Na_2SO_4 , and then subjected to potentiostatic polarization in 0.08M Cl^- , Br^- , or F^- solutions. In Cl^- and Br^- solutions, the anodic current remains very low but increases abruptly with pit initiation. The breakdown results in F^- solution are completely different, with the measured anodic current increasing gradually with time of polarization; the rate of current increase is at first very low, but then increases with time and eventually slows as passivity breakdown approaches completion. While the kinetics of passivity breakdown depend on both the prior passivation treatment and the conditions existing in the F^- solution, the results generally give S-shaped curves, suggesting that the breakdown process is one of nucleation and lateral growth of "holes" in the passive oxide film. This mechanism of film breakdown in F^- is confirmed by replica electron microscopy of the surface at various stages in the breakdown process, with local attack initiating at selected sites and then gradually spreading over the entire surface. The difference in behavior between F^- and Cl^- and Br^- is discussed in terms of the adsorption characteristics of the ions.

Metals and alloys such as nickel, iron, and the stainless steels have the ability to form thin, passive oxide films which are susceptible to either general or local breakdown in the presence of aggressive halide ions. The exact role of these anions, and therefore the fundamental mechanism of passivity breakdown, is still under discussion with various theories proposed to explain the influence of Cl^- and Br^- on pit initiation (1-12). It has been argued that these ions can rupture or break the passive oxide film (12, 13), *e.g.*, by adsorption on the surface, so that underlying metal is exposed to the aggressive environment at potentials high enough to cause pitting. Another suggested mechanism involves direct incorporation of the halide ion into the oxide film with a subsequent increase in pitting susceptibility. The halide ion may, however, initiate passivity breakdown by simply interfering with local film repair, *i.e.*, the oxide may experience continual local breakdown-repair events and the halide ion merely influences the efficiency of local repassivation.

Unlike the highly localized attack observed with Cl^- and Br^- ions, F^- ion has been found to cause an overall breakdown of passivity and general metal dissolution (14-17). At present, however, neither the kinetics and mechanism of F^- -induced passivity breakdown nor the influence of F^- on the formation and development of an oxide film are well known. In this work, the influence of F^- on both the establishment and breakdown of passivity is studied. With regard to the latter, a variety of passive oxide films are formed in non- F^- solutions and then exposed to F^- containing solutions for breakdown of the previously established passivity. In this way, the influence of both prior passivation treatment and conditions in the aggressive F^- solution on the breakdown of passivity is studied. Replica electron microscopy has been used to follow the initiation and propagation of passivity breakdown. The results are analyzed in terms of the nucleation and lateral growth of holes at breakdown sites in the passive oxide film. The behavior of F^- as an aggressive anion is contrasted with that of Cl^- and Br^- .

Experimental

Polycrystalline nickel specimens and Ni(111) single crystals were prepared as described previously (18). Potentials are referred to the saturated calomel electrode, $\text{Hg}/\text{Hg}_2\text{Cl}_2$. Experiments were conducted at 25°C in deaerated pH 3.0 solutions of 0.15N Na_2SO_4 either with or without added NaF, NaCl, and NaBr. To determine the influence of the various anions on the establishment of passivity, electropolished nickel electrodes were cathodi-

cally reduced at $20 \mu\text{A}\cdot\text{cm}^{-2}$ for 5 min (to obtain oxide-free starting surfaces), and the potential was then stepped to a value in the passive region. The resulting current-time transients were obtained on a high speed Brush recorder (risetime < 8 ms) and integration gave the passivation charge. Nickel electrodes were also passivated in F^- -free solutions and then transferred through the air to deaerated 0.08 or 0.01M F^- solution for passivity breakdown. Results from previous work indicate that such air exposure has no influence on the state of the passive oxide film (19). To determine the extent and type of passivity breakdown in the presence of F^- , the surface of a passivated (111) single crystal was examined by replica electron microscopy after treatment in F^- solution.

Results and Discussion

Influence of halide ions on anodic passivation.—Figure 1 shows the influence of the 0.08M concentrations of the various halide ions on the i - t profile upon stepping the potential into the passive region. Cl^- and Br^- ions substantially increase the short-term anodic charge passed in establishing passivity, indicating that they interfere with the passivation process; the extent of interference is greater for Cl^- than for Br^- (Fig. 1 and Table I). In contrast, F^- ion appears to have little influence on the initial stages of passivation, the i - t profile during the first 0.5s being similar to that obtained in its absence. The results are consistent with the expected strong interaction of Cl^- and Br^- ions with the nickel surface, an interaction which should block at least part of the surface for oxide formation. However, the apparently stronger interaction of Cl^- than Br^- is not in agreement with predicted strengths of adsorption of these ions (20-23). The anticipated weak interaction of F^- ion should cause little interference with passivation, as observed.

Although the Cl^- and Br^- ions strongly interfere with the initial surface oxidation (Fig. 1), passivity eventually

Table I. Anodic charge passed during the first 1s after stepping the potential to 0.2V in pH 3.0 Na_2SO_4 solution containing no halide and 0.08M of the various halide ions. Electrode pretreatment was electropolishing and cathodic reduction at $20 \mu\text{A}\cdot\text{cm}^{-2}$ prior to the potential step

Halide ion present	Anodic charge ($\text{mC}\cdot\text{cm}^{-2}$)	Percentage of background charge
—	2.8	100
F^-	3.5	130
Cl^-	18.3	670
Br^-	8.8	320

* Electrochemical Society Active Member.

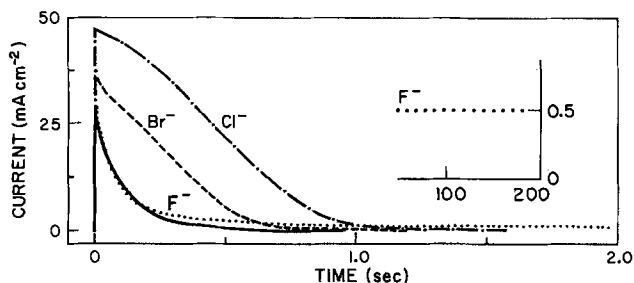


Fig. 1. Current-time transients, obtained on oxide-free nickel in pH 3.0 Na_2SO_4 , upon stepping the potential to 0.2V (solid line). Also shown are transients in solutions with 0.08M Cl^- (dot-dash line), Br^- (dashed line), and F^- (dotted line). The inset indicates the steady current of 0.5 $\text{mA}\cdot\text{cm}^{-2}$ observed after 200s at 0.2V in 0.08M F^- .

occurs and the anodic currents fall to very low values. Indeed, the currents measured 60s after the potential step are only ca. 10-15% higher than in the absence of halide ions. The behavior with F^- is completely different in that the current stops falling a few seconds after the potential step and reaches a steady value of $\sim 0.5 \text{ mA}\cdot\text{cm}^{-2}$ (Fig. 1, inset). Such a high anodic current indicates that passivity has not developed beyond the most elementary stages which is in sharp contrast to the initial ($< 0.5\text{s}$) lack of influence of F^- on passivation. This result could be due to F^- either (i) influencing the nature of the passive film and therefore its stability toward dissolution or (ii) increasing the aggressiveness of the solution. Whatever the reason, it is clear that normal passivity cannot be achieved for nickel in a pH 3.0 Na_2SO_4 solution containing 0.08M F^- .

Galvanostatic charging of nickel in halide ion solutions.—Figure 2 shows a series of galvanostatic charging profiles for electropolished nickel at $4 \mu\text{A}\cdot\text{cm}^{-2}$ in pH 3.0 Na_2SO_4 solutions with different halide ions present. In the absence of halide ion, the potential increases from the immersion value of -0.04V to the oxygen evolution region at 0.96V with no indication of film breakdown or pitting (24). In the presence of 0.08M Br^- or Cl^- , the galvanostatic charging curve is the same as in halide-free solution until the potential is high enough for pitting to occur. This is manifested as a sharp reversal of the potential as the passive oxide film locally breaks down; rapid metal dissolution at the breakdown sites results in the observed anodic depolarization. Thus, neither Cl^- nor Br^- has any apparent influence on the galvanostatic development of the passive oxide film until pitting begins at the higher anodic potentials. This is certainly not the case with F^- , where passivity breakdown begins as soon as the electrode is immersed at $4 \mu\text{A}\cdot\text{cm}^{-2}$ and continues until passivity has completely broken down a short time later. Gal-

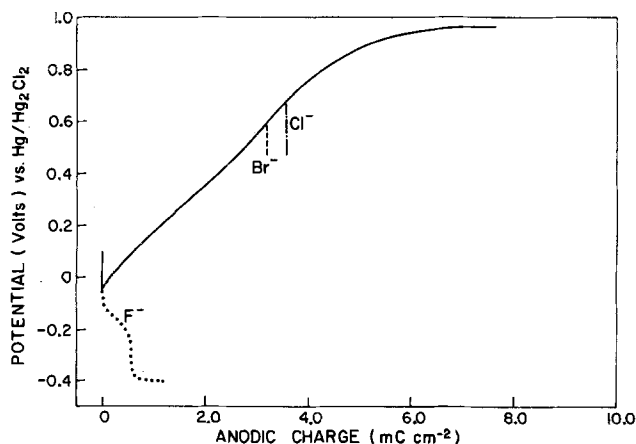


Fig. 2. Anodic galvanostatic charging profiles for electropolished nickel at $4 \mu\text{A}\cdot\text{cm}^{-2}$ in pH 3.0 Na_2SO_4 in the absence of halide ion (solid line), and in solutions containing 0.08M Cl^- (dot-dash line), Br^- (dashed line), and F^- (dotted line).

vanostatic charging in F^- gives rise not to pitting but rather to an overall loss of passivity with corresponding general metal dissolution, which is again in contrast to the localized attack by Cl^- and Br^- .

Potentiostatic breakdown of passivity in F^- solutions.—It is well known that, when prepassivated nickel is exposed to a Cl^- or Br^- solution above the pitting potential, the measured anodic current remains almost constant but then abruptly increases when pit initiation occurs [see, e.g., Ref. (25)]. The time required for the sharp current increase, referred to as the induction time (τ_{ind}) for pit initiation, varies exponentially with the potential of the pitting experiment. In the present work, similar experiments were performed in the presence of F^- both to compare the results with those obtained in Cl^- and Br^- and to understand the nature of passivity breakdown in F^- .

Figure 3 shows the current response for a film preformed in pH 3.0 Na_2SO_4 at 0.6V for 1h and then polarized at 0.2V in 0.08M F^- . The current is initially quite low ($< 0.1 \mu\text{A}\cdot\text{cm}^{-2}$) but after ~ 5 min it begins to increase, at first slowly but then more rapidly. The rate of change of current increases with time during about the first 18 min, but then begins to decrease and a steady state is eventually reached after ~ 23 min. During this time, the current increases by over four orders of magnitude indicating a massive breakdown of passivity. The eventual constant current is actually somewhat higher than that obtained when electropolished and cathodically reduced nickel is polarized at 0.2V in the F^- solution (Fig. 1); this is probably due to the increased surface roughness associated with breakdown in F^- (see below, especially Fig. 7). The results thus suggest that complete breakdown of passivity occurs in F^- after a certain time of exposure. The breakdown results shown in Fig. 3 are reproducible from experiment to experiment to within $\pm 2\%$. This high degree of reproducibility means that the increase of anodic current can be used to carefully study the kinetics of passivity breakdown in F^- as a function of condition of formation of the prior passive film as well as the conditions in the breakdown solution.

If the current, i , at any time, t , in F^- solution is a measure of the extent of passivity breakdown, then the ratio $\alpha = (i_{\text{max}} - i)/i_{\text{max}}$ is the fraction of the surface still covered by the passive film. The term $(1 - \alpha)$ is therefore a measure of the extent of passivity breakdown; $[(1 - \alpha) = i/i_{\text{max}}]$. When the results from Fig. 3 are plotted in the form of $(1 - \alpha)$ vs. t , an S-shaped curve is obtained (Fig. 4). Passivity breakdown is initially slow and then accelerates, eventually slowing again towards the end of breakdown.

Influence of electrode pretreatment on F^- -induced film breakdown.—To investigate the influence of state of pas-

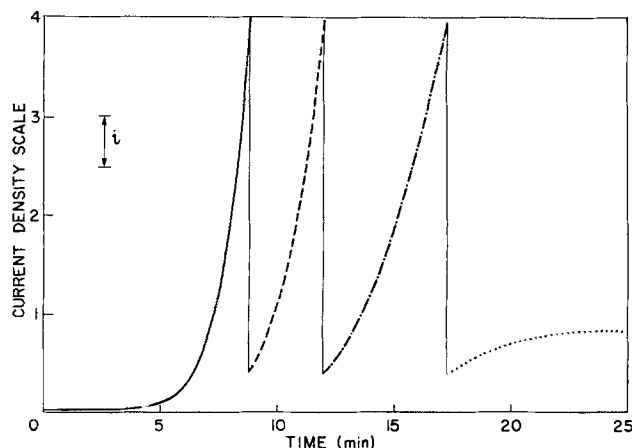


Fig. 3. Change of current with time for a prepassivated nickel electrode in 0.08M F^- (pH 3.0) at 0.2V; prepassivation treatment was 1h at 0.6V in pH 3.0 Na_2SO_4 . The current marker, i , represents $0.5 \mu\text{A}\cdot\text{cm}^{-2}$ (solid line), $5.0 \mu\text{A}\cdot\text{cm}^{-2}$ (dashed line), $50 \mu\text{A}\cdot\text{cm}^{-2}$ (dot-dash line), and $500 \mu\text{A}\cdot\text{cm}^{-2}$ (dotted line).

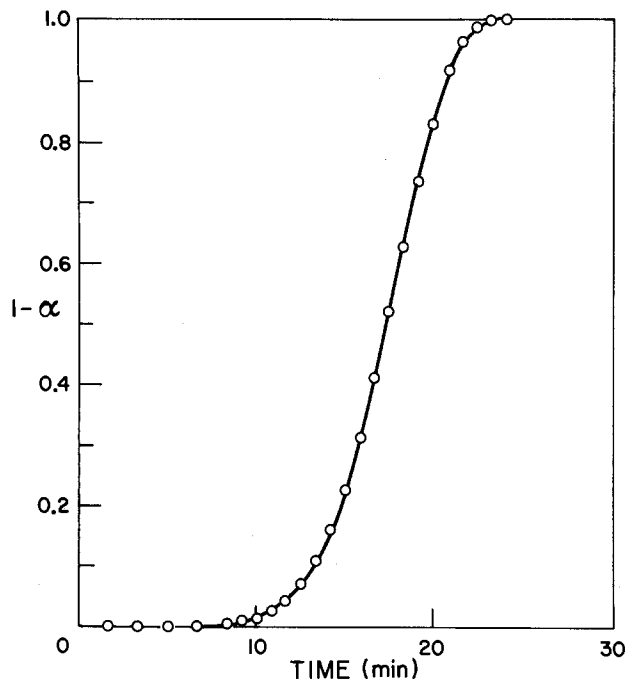


Fig. 4. Results of Fig. 3 plotted in terms of $(1 - \alpha)$ vs. time where $\alpha = (i_{\max} - i)/i_{\max}$.

sivity on the rate of film breakdown in F^- , $(1 - \alpha)$ vs. t profiles were obtained for electropolished nickel (EP Ni) and nickel prepassivated in pH 3.0 Na_2SO_4 at 0.6V for 3 min and 16h and at 0.2V for 1h. The results, shown in Fig. 5, indicate that the rate of passivity breakdown at 0.2V in 0.08M F^- is highly dependent on the prior state of the film. Both the potential and time of anodization have a major influence on the stability of the film toward F^- -induced breakdown. Either a higher passivation potential or a longer passivation time gives an increase in the induction time before measurable breakdown occurs as well as a slower rate of activation after breakdown has begun. The order of resistance of these films toward attack by F^- is the same as that previously observed for open-circuit breakdown in slightly acid sulfate solutions (26), with the film on EP Ni being the least stable. In that previous work, an increase in the open-circuit film stabil-

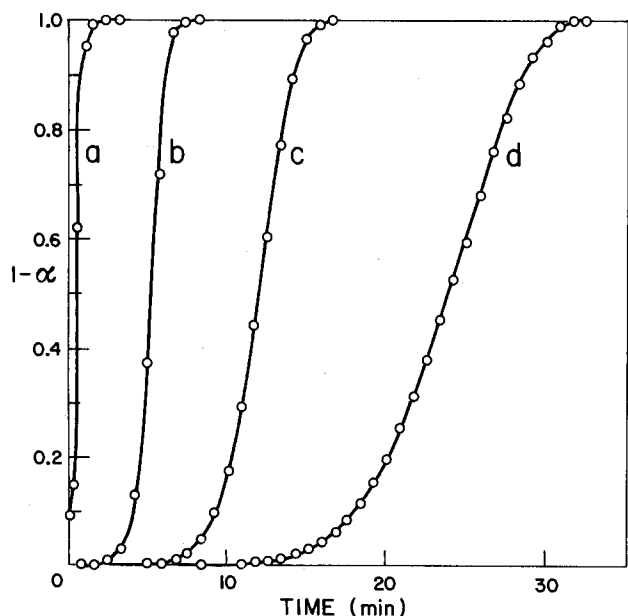


Fig. 5. $(1 - \alpha)$ vs. time profiles for different oxide films formed in pH 3.0 Na_2SO_4 and broken down at 0.2V in 0.08M F^- (pH 3.0). Prepassivation treatments are: electropolishing (a); 1h at 0.2V (b); 3 min at 0.6V (c); and 16h at 0.6V (d).

ity was shown to be associated with a decrease in the density of film defects rather than any change in film thickness.

Influence of breakdown conditions in F^- solutions.— Figure 6 shows the influence of potential of breakdown in F^- solution on the $(1 - \alpha)$ vs. t profile for a standard passive film, i.e., one formed at 0.6V for 1h in pH 3.0 Na_2SO_4 . The film breakdown kinetics are highly dependent on the applied potential in the F^- solution, the rate of passivity breakdown increasing dramatically with increasing anodic potential (cf. profiles a and b). Both the induction time and the rate of subsequent breakdown are strongly influenced by the breakdown potential. The kinetics of passivity breakdown are also dependent on the $[F^-]$ in solution, the breakdown time being much longer in 0.01M F^- solution in comparison to 0.08M F^- , all other conditions being constant (cf. profiles c and a). The lower $[F^-]$ more than compensates for a high potential, so that breakdown is slower than at 0.1V in 0.08M F^- solution (cf. profiles c and b). These results indicate that by a proper selection of the conditions in F^- solution, breakdown of even the most defective oxide films (e.g., the film on EP Ni) can be studied in detail.

Mechanism of passivity breakdown in F^- solutions.— While the above results demonstrate which parameters influence passivity breakdown in F^- , questions remain concerning the breakdown mechanism. The most probable modes of attack by F^- are either general layer-by-layer thinning of the oxide film with time (27) or local attack at specific sites with a gradual spreading of this attack across the surface. To distinguish between these two possibilities, replica electron micrographs of a Ni (111) surface were obtained at various times during breakdown in F^- . The Ni (111) electrode was prepassivated at 0.6V for 1h and then transferred to a 0.08M F^- solution for breakdown at 0.2V. The $(1 - \alpha)$ vs. t profile is very similar to that shown in Fig. 4 for a polycrystalline electrode, i.e., an initial induction period is followed by a rapid increase in $(1 - \alpha)$ with an eventual slowing down as a steady state is approached. The micrographs associated with three extents of breakdown, having $(1 - \alpha)$ values of 0.5, 10, and 99%, are shown in Fig. 7a, 7b, and 7c. It is apparent that the F^- attack begins at a few specific points on the surface (Fig. 7a) and that both the number of attack sites and their radii increase as the attack progresses (Fig. 7b). Eventually, the attack spreads over most of the surface as new sites of attack appear and the existing sites spread laterally (Fig. 7c); by this time, close to complete passivity breakdown has occurred. This form of attack is in sharp contrast to that observed when electropolished and cathodically reduced nickel is polarized at 0.2V in 0.08M F^- solution (Fig. 7d). In this case, there is no evidence of local attack since there was no passive oxide film to break down. A general attack is observed with uniform roughening of the metal surface. Similar surface features are observed after F^- breakdown of the oxide film on EP Ni. Since dissolution of this highly defective oxide is very rapid (Fig. 5a), there is little time for localized attack to develop. The almost immedi-

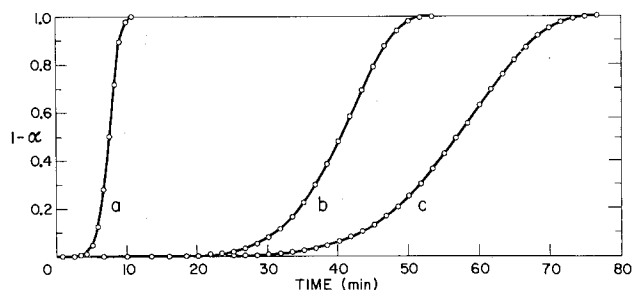


Fig. 6. $(1 - \alpha)$ vs. time profiles for an oxide film formed at 0.6V for 1h in pH 3.0 Na_2SO_4 and broken down under different conditions in pH 3.0 F^- solution. Breakdown conditions are: 0.4V in 0.08M F^- (a); 0.1V in 0.08M F^- (b); and 0.4V in 0.01M F^- (c).

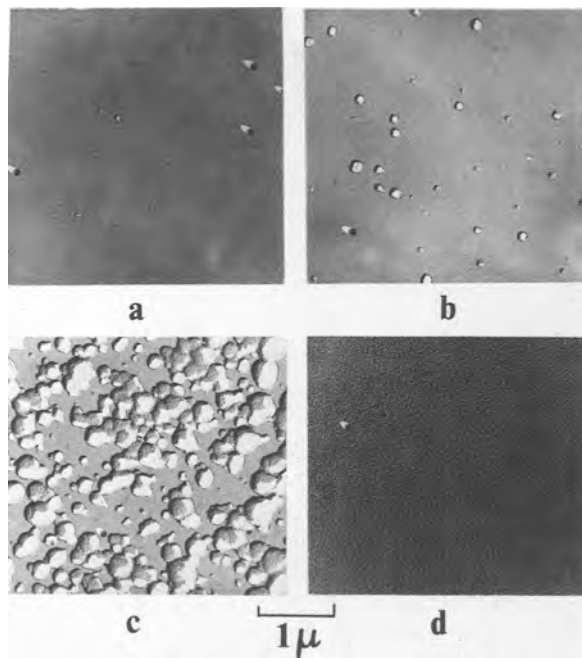


Fig. 7. Replica electron micrographs of a Ni(111) single crystal prepassivated at 0.6V for 1h in pH 3.0 Na_2SO_4 and then exposed to 0.08M F^- (pH 3.0) at 0.2V for times required to give $(1 - \alpha)$ values of 0.5% (a), 10% (b), and 99% (c). d: The micrograph obtained after electropolishing, cathodic reduction, and passivation at 0.2V in 0.08M F^- . Shadowed spheres are 900Å polystyrene balls.

ate disappearance of the oxide film thus gives rise to the same general dissolution features observed in the absence of an oxide film.

The results presented for the breakdown of passivity in F^- suggest that the process is one of nucleation and lateral growth, i.e., local breakdown of the oxide film is nucleated, perhaps at defect sites in the film, and the attack then spreads laterally across the surface. The mechanism is akin to that discussed in detail by Evans (28) for nucleation and growth of new phases (with the generation of S-shaped kinetics) and analogous to the more recent computer modeling work of Kozłowska *et al.* (29) for the cathodic removal of thin oxide films on platinum. In this later work, initial oxide removal was considered to be the result of a nucleation process at specific sites on the surface giving rise to "lakes" or "holes" in the film. Continued cathodic reduction occurred at the periphery of the established holes, and the rate of reduction increased with the extent of reduction until the holes began to overlap. The potential had a strong influence on the reduction rate since it determined the density of sites where holes would be nucleated. In the present work, local breakdown of the passive NiO film in F^- solution results in its replacement by a poorly passivating film characteristic of the particular potential. The resulting local high rates of metal dissolution give rise to the local surface attack which is seen by electron microscopy. The rate of passivity breakdown will be determined by both the density of breakdown sites and their rate of radial growth. The dependence of the breakdown rate on the prior passivation treatment is easy to understand since this prior treatment determines the defect density of the oxide film and therefore the number of sites susceptible to breakdown. The increase in breakdown rate at higher potentials in F^- could be due to an increase in the number of film defects at which breakdown is nucleated as well as to a change in the lateral growth rate of developing holes. Electron microscopy indicates that the nucleation is progressive, as opposed to instantaneous, since the number of breakdown sites increases with time (Fig. 7). This local breakdown of oxide by expanding holes and newly appearing nuclei eventually results in complete removal of the passive film with subsequent general metal

dissolution. At that point, the passive oxide has been replaced by a poorly inhibiting film.

The precise mechanism by which F^- locally breaks down passivity and destroys the film is still open to question. It is known that F^- forms stable complexes with transition metal cations (rather than metal atoms) so it has more effect on the metal oxide film than on the metal itself (30-33). This fact may explain the different behavior of F^- vs. Cl^- and Br^- (Fig. 1 and 2). There is a suggestion in the literature that F^- forms a surface complex with passive oxide films on nickel and iron which enhances the rate of cation transfer from the oxide lattice into solution (14, 15). However, it may be that F^- in solution does not directly influence the initial breakdown of the passive oxide film at all but simply influences local repair after breakdown has occurred. Breakdown occurs even in the absence of F^- , and its extent is determined by the state of perfection of the film and the aggressiveness (pH) of the solution.

Whatever the precise mechanism of F^- -induced breakdown of passivity, the present results clearly show that the attack is initially localized at a few sites on the surface. With long exposure to F^- solution, the eventual general breakdown of passivity is a result of the spreading of this local attack, as well as attack occurring at new sites. There appears to be a direct correlation between the defect state of the oxide film and its resistance to breakdown in F^- , the defects in the film likely being the sites of attack by F^- . While F^- is quite different from Cl^- and Br^- in terms of its ability to eventually cause a general breakdown of passivity, it appears that breakdown is initiated in much the same way as by Cl^- and Br^- , viz., by a highly localized attack at a few specific sites on the surface.

Manuscript submitted Feb. 27, 1985, revised manuscript received ca. July 8, 1985.

The National Research Council of Canada assisted in meeting the publication costs of this article.

REFERENCES

1. Z. Szklarska-Smialowska, *Corrosion (Houston)*, **27**, 223 (1971).
2. T. P. Hoar and W. R. Jacobs, *Nature (London)*, **216**, 1299 (1967).
3. T. P. Hoar, D. C. Mears, and G. P. Rothwell, *Corros. Sci.*, **5**, 279 (1965).
4. C. L. McBee and J. Kruger, in Proceedings of U. R. Evans International Conference on Localized Corrosion, 1971, p. 252, NACE, Houston (1974).
5. J. R. Galvele, *This Journal*, **123**, 464 (1976).
6. H. H. Strehblow and B. Titze, *Corros. Sci.*, **17**, 461 (1977).
7. B. MacDougall, *This Journal*, **126**, 919 (1979).
8. N. Sato, *Electrochim. Acta*, **16**, 1683 (1971).
9. M. Janik-Czachor, *Werkst. Korros.*, **30**, 255 (1979).
10. K. E. Heusler and L. Fischer, *ibid.*, **27**, 551 (1976); *ibid.*, **27**, 697 (1976).
11. M. Janik-Czachor, *This Journal*, **128**, 513C (1981).
12. H. H. Strehblow, *Werkst. Korros.*, **27**, 792 (1976).
13. T. P. Hoar, *Corros. Sci.*, **7**, 341 (1976).
14. H. H. Strehblow, B. Titze, and B. P. Lochel, *ibid.*, **19**, 1047 (1979).
15. H. H. Strehblow and B. P. Lochel, in "Proceedings of the Fifth International Symposium on Passivity," Bombannes, France, M. Froment, Editor, p. 379, Elsevier, Amsterdam (1983).
16. A. Cakir and J. C. Scully, in "Passivity of Metals," R. P. Frankenthal and J. Kruger, Editors, p. 385, The Electrochemical Society Corrosion Monographs Series, Princeton, NJ (1978).
17. B. MacDougall, in "Proceedings of the Ninth International Congress on Metallic Corrosion," Toronto, Ont., Canada, Vol. 2, p. 168, National Research Council of Canada, Ottawa, Ont., Canada (1984).
18. B. MacDougall and M. Cohen, *This Journal*, **121**, 1152 (1974).
19. B. MacDougall and M. Cohen, *ibid.*, **123**, 191 (1976).
20. M. W. Breiter, *Electrochim. Acta*, **8**, 925 (1963).
21. M. Jesionek and Z. Szklarska-Smialowska, *Corros. Sci.*, **23**, 183 (1983).

22. W. Paik, M. A. Genshaw, and J. O'M Bockris, *J. Phys. Chem.*, **74**, 4266 (1970).
23. Y-C. Chiu and M. A. Genshaw, *ibid.*, **73**, 3571 (1969).
24. B. MacDougall and M. J. Graham, *Electrochim. Acta*, **27**, 1093 (1982).
25. B. MacDougall, in "Proceedings of the Fifth International Symposium on Passivity," Bombannes, France, M. Froment, Editor, p. 275, Elsevier, Amsterdam (1983).
26. B. MacDougall and M. Cohen, *This Journal*, **124**, 1185 (1977).
27. J. J. Kelly, *Electrochim. Acta*, **24**, 1273 (1979).
28. U. R. Evans, *Trans. Faraday Soc.*, **41**, 365 (1945).
29. H. Angerstein-Kozłowska, B. E. Conway, and J. Klinger, *J. Electroanal. Chem.*, **87**, 301, 320 (1978).
30. C. C. Seastrom, *Corrosion*, **20**, 179t (1964).
31. K. Azuma and H. Kametari, *Trans. Metall. Soc. AIME*, **230**, 835 (1964).
32. M. J. Pryor and U. R. Evans, *J. Chem. Soc.*, **71**, 3330 (1949).
33. S. Ahrland, J. Chatt, and N. R. Davies, *Quart. Rev.*, **12**, 265 (1958).

Polarization and Corrosion of Electrogalvanized Steel—Evaluation of Zinc Coatings Obtained from Waste-Derived Zinc Electrolytes

M. Dattilo

U.S. Department of the Interior, Bureau of Mines, Rolla Research Center, Rolla, Missouri 65401

ABSTRACT

The corrosion of electrogalvanized 1070 steel wire has been investigated in molar quiescent ammonium chloride and ammonium sulfate under near-neutral conditions. Zinc coatings obtained from waste-derived electrolytes were evaluated *vs.* coatings from relatively pure zinc electrolytes. The waste source of zinc was brass smelter flue dust. Corrosion rates were measured by Tafel line extrapolation and the polarization resistance technique. Values of the Tafel slopes and the corrosion currents were also compared with those for pure zinc (99.999%). Corrosion rates were found to be affected by the medium employed, pH, and bimetal diameter reduction (drawing). Drawn electrogalvanized steel displays higher values of the Tafel slopes than do the as-plated samples. The Tafel slopes are different from those obtained on pure zinc. This is assumed to be due to inhomogeneous surface features obtained from additive adsorption (during plating) and residual lubricants used in the drawing process as well as surface structure. The corrosion rates of electrogalvanized samples plated in the waste-derived zinc electrolytes were similar to the corrosion rates of samples plated in relatively pure zinc electrolytes. Therefore, wastes are a potential source of zinc for electrogalvanizing.

Large quantities of zinc bearing waste materials exist; therefore, the Bureau of Mines is investigating processes that can benefit from using this resource. Previous Bureau work has shown that zinc coatings obtained in waste-derived electrolytes are comparable to coatings from relatively pure electrolytes when evaluated in salt spray tests (1). Most uses for zinc require high purity material; and since wastes normally contain other metals which coextract with zinc, they are less suitable for the production of primary cathode zinc. Zinc electrowinning is accomplished in pure electrolytes. Cathode current densities for this process range from 20 to 100 mA/cm², and the plating times from 18 to 48h. This allows buildup of impurity levels that lower cell efficiency as well as cathode purity. Removal of these impurities involves several process steps (2-3) requiring greater cost to the producer. In electrogalvanizing, however, high current densities (200-600 mA/cm²) and short plating times (minutes) are employed, thus allowing higher impurity levels in the plating electrolyte (4-5).

Electrogalvanizing is accomplished in a continuous process. The steel substrate is cleaned, plated, and subjected to multiple diameter reductions (drawing) in the case of wire products. This working of the metal surface causes a change in its structure and corrosion properties. It also allows better adherence of materials such as rubber or polymer for structural applications.

There is a considerable amount of reported data on zinc corrosion in acid, alkaline, neutral, and near-neutral media (6-13), and corrosion rates are highly influenced by the medium employed. Normally, electrogalvanized steel is evaluated in aerated NaCl; however, it has been shown that the corrosion rates measured electrochemically are in error because of two competing cathodic reactions and corrosion products on the surface. Deaerated ammonium salt solutions appeared to be an excellent choice for a corrosion medium because of reproducible electrochemical measurements and suppression of oxide film formation (11).

This report deals with the corrosion of electrogalvanized steel obtained by plating in a brass dust-derived zinc

electrolyte. Evaluation of these coatings was necessary *vs.* coatings obtained from industrial-type electrolytes to determine if wastes are viable sources of zinc for electrogalvanizing.

Experimental

Electrolytes and plating.—Synthetic zinc electrolytes were prepared by dissolving French process zinc oxide (prepared from zinc metal) in reagent-grade sulfuric acid. Reagent-grade NH₄Cl and H₃BO₃ were added as desired for conductivity and buffering. Waste electrolytes were obtained by extraction of brass smelter flue dust (64.6% zinc) with 180 g/liter sulfuric acid. This yielded an impure electrolyte containing ~120 g/liter zinc and ~1 g/liter copper. Copper was removed by addition of 2 g/liter zinc dust at 75°C for 30 min. A thorough account of this procedure has been given in a previous report (1). Compositions of the electrolytes are shown in Tables I and II along with the additions.

Steel wire 1070 (0.234 cm diam) was prepared for plating by first degreasing with trichloroethylene and then electrocleaning in 600 g/liter H₂SO₄ using a current density of 400 mA/cm² (1). Wires were then rinsed and plated at constant cathode current density of 600 mA/cm² for 30s at 40° and 60°C over a pH range of 2-5. The wire was rotated during plating at 105 rpm. The anode in the plating cell was a 99.999% zinc rod so as to maintain constant zinc concentration. Cathode area was 7 cm², and the anode area was > 10 cm² in all cases.

Drawing.—Bimetal drawing was accomplished on wire plated as above. The samples were ~10 cm long and were

Table I. Synthetic zinc electrolyte compositions (g/liter)

Electrolyte	Zn	NH ₄ Cl	H ₃ BO ₃	Licorice
P-1	120-145	18	12	0.3
P-2	120-145	18	12	0
P-3	120-145	18	12	0.1
P-4	120-145	18	12	0.5

Table II. Waste zinc electrolyte compositions (g/liter)

Electrolyte	Zn	Cd	Cl	Cu	Ni	NH ₄ Cl	H ₃ BO ₃	Licorice
W-1	120-130	0.002	2.1	0.003	0.003	18	12	—
W-2	120-130	0.01	1.11	< 0.001	0.002	18	12	—
W-3	120-130	0.002	2.1	0.003	0.003	18	12	0.1

drawn through a hard die to reduce the diameter ~10% in the first pass. (Samples drawn twice were reduced 20% on the second pass.) Industrial dies and lubricant were used. The dies used were 6° conical type.

Corrosion media.—The electrolytes for this corrosion study were 1M NH₄Cl and 1M (NH₄)₂SO₄. Analytical reagent-grade salts were dissolved in distilled water. The pH was adjusted to 6 ± 0.1, except in specific experiments, by small additions of NH₄OH, H₂SO₄, or HCl. Prior to immersion of samples, the solutions were deaerated with oxygen-free nitrogen. Polarization measurements were performed at 25° ± 2°C.

Solutions were analyzed by atomic absorption for zinc content during weight loss tests.

Sample preparation.—Samples were prepared by degreasing in boiling trichlorethylene followed by rinsing with absolute ethanol and distilled water. The surface was then dried in a filtered air stream. 1 cm² surface area was used in all measurements.

In the solution analysis (weight loss) experiments, 5.6 cm² area was used.

Measurements were made after the simple degreasing preparation so as to retain the characteristic surface of electrogalvanized steel. Zinc rods (99.999% pure) were machined to give a flat face and polished with 600 grit SiC, then etched in 50% HCl and degreased.

Polarization measurements and cell.—The cell used was a commercially available 1-liter glass vessel. The counterelectrode was platinum mesh, and the reference was a saturated calomel electrode. The reference electrode was placed in an electrolyte bridge tube with fritted glass tip designed for low leakage and minimum IR drop. All measurements were made with a scanning potentiostat, and current and potential were constantly monitored by digital electrometers.

The sample was placed in the corrosive medium and allowed to equilibrate which takes ~15 min, and then the corrosion potential (E_{corr}) was measured. Next the polarization resistance (R_p) was determined. The potential was adjusted to 5 mV cathodic of E_{corr} and the scan was begun in the anodic direction at a rate of 0.1 mV/s, and stopped at a value 5 mV anodic of E_{corr} .

Following the measurement of R_p , the electrode was allowed to stabilize again at E_{corr} . The cathodic scan was then obtained from E_{corr} scanning at 0.25 mV/s. After completion of the cathodic scan, the corrosion potential was redetermined and the anodic scan was initiated at the same sweep rate (0.25 mV/s). All measurements were made in quiescent electrolytes.

Results

Polarization data.—Anodic and cathodic polarization curves of 99.999% zinc in 1M NH₄Cl and 1M (NH₄)₂SO₄ are shown in Fig. 1 and 2, respectively. Typical polarization curves of electrogalvanized steel in 1M (NH₄)₂SO₄ and 1M NH₄Cl are shown in Fig. 3 and 4. These figures show both as-plated and drawn samples. The current-potential relationships are similar to pure zinc, but close inspection shows intrinsic differences. In Fig. 3 [(NH₄)₂SO₄], the anodic branch shows an inflection at ~ -1.05V. In NH₄Cl (Fig. 4), a similar current-potential relation is obtained. The inflection in the anodic portion suggests more than one anodic reaction.

These curves were obtained at pH 6 ± 0.1. At lower pH values, there is a considerable shift of the corrosion potential to more anodic values. Figure 5 shows the polarization curve of drawn electrogalvanized steel at pH 6 and 4.

Table III. Corrosion of pure (99.999%) zinc

	i_{corr}^E ($\mu\text{A}/\text{cm}^2$)	b_a	$-b_c$	E_{corr}	i_{corr}^R ($\mu\text{A}/\text{cm}^2$)
1M (NH ₄) ₂ SO ₄	16.8	41	125	-1.154	17.1
1M NH ₄ Cl	10.5	30	174	-1.133	—

The current is increased at lower pH and it is difficult to determine a cathodic Tafel slope; therefore, pH 6 was chosen for all measurements given in this report.

Calculation of corrosion rates.—The values obtained for the corrosion rates of electrogalvanized steel (EG) samples and 99.999% zinc are given in Tables III-V. Arithmetic mean values are listed in the tables at the 95% confidence level. Corrosion currents were measured by Tafel line extrapolation of the anodic portion to give i_{corr}^E (11). Both the anodic and cathodic Tafel slopes were measured directly from the polarization curve.

Corrosion currents were also calculated using the polarization resistance technique. The well-known Stern-Geary equation was used to calculate i_{corr}^R (14-16)

$$i_{\text{corr}}^R = \frac{b_a b_c}{2.303 (b_a + b_c) R_p} \quad [1]$$

Values of the Tafel slopes for the anodic (b_a) and cathodic (b_c) reactions are also listed in the tables.

Polarization resistance measurements yield a straight line about E_{corr} for zinc (10-11). Because of the widespread knowledge of this method, no curves are given.

Corrosion rates measured by atomic absorption analysis of test media during immersion tests are given in Table VI. The data is for as-plated wire in 1M (NH₄)₂SO₄ calculated from Faraday's law (17).

Discussion

The results were determined according to the mixed potential theory of coupled corrosion reactions developed by Wagner and Traud (17) and the assumption of a charge transfer-controlled process using the Stern-Geary equation (15-16). Pure zinc yielded values of the Tafel slopes and corrosion rates in good agreement with those deter-

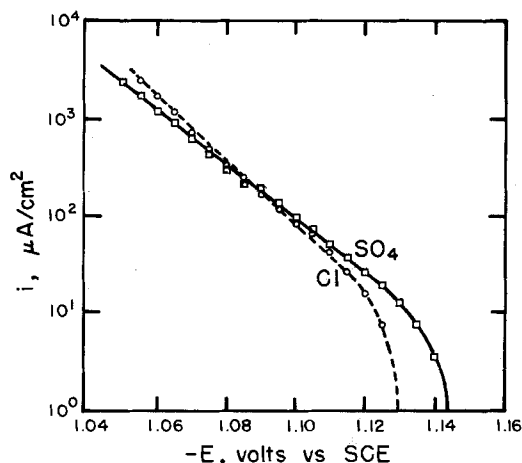


Fig. 1. Anodic polarization of zinc in 1M NH₄Cl and (NH₄)₂SO₄ at pH 6.

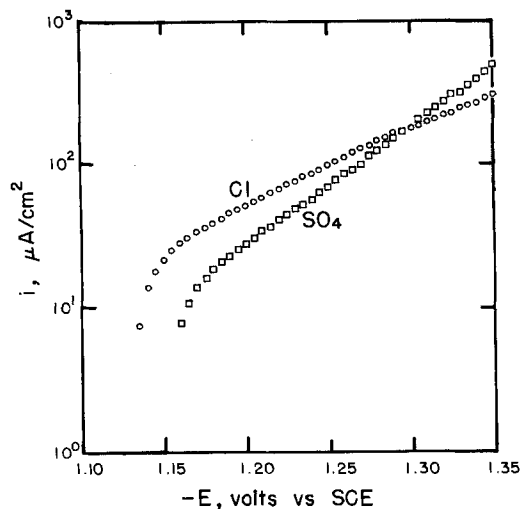


Fig. 2. Cathodic polarization of zinc in 1M NH₄Cl and (NH₄)₂SO₄ at pH 6.

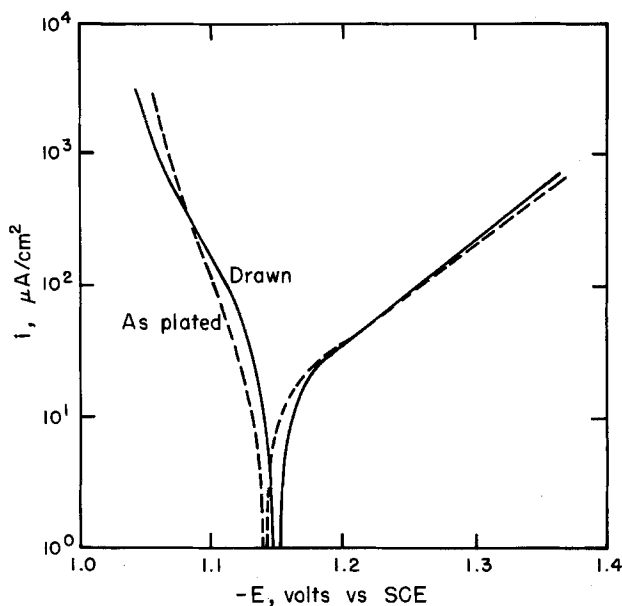


Fig. 4. Polarization of as-plated and drawn EG steel in 1M NH₄Cl at pH 6.

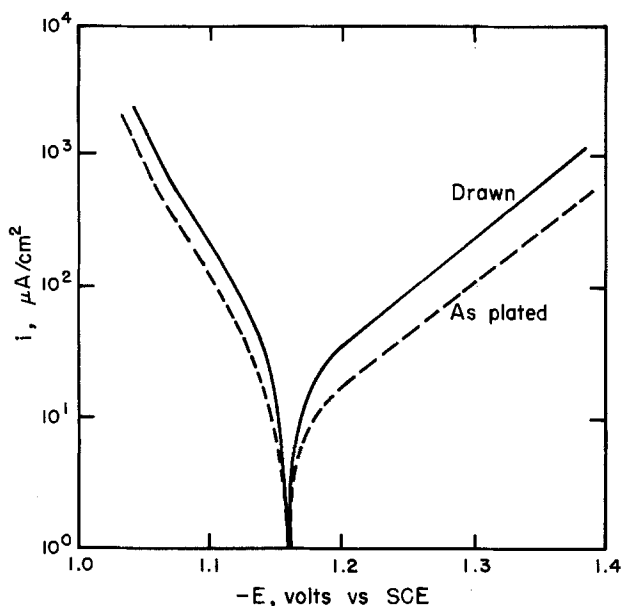


Fig. 3. Polarization of as-plated and drawn electrogalvanized steel in 1M (NH₄)₂SO₄ at pH 6.

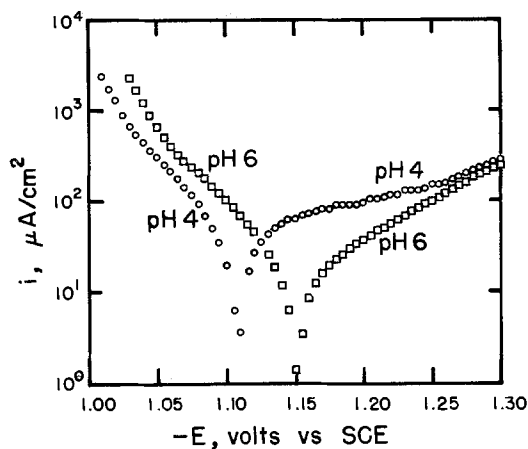


Fig. 5. Comparison of polarization of drawn EG steel in 1M (NH₄)₂SO₄ at pH 4 and 6.

mined by other investigators (11). Electrogalvanized (EG) steel displayed different values of the Tafel parameters, b_a

and b_c , for the anodic and cathodic reactions, respectively. This implies differences in the processes of corrosion according to some authors (11, 14, 18).

On the average, drawn EG steel corrodes more rapidly than does the as-plated material. This is certainly related

Table IV. Corrosion rate data for measurements in 1M (NH₄)₂SO₄

Plating electrolyte	b_a (mV)	E_{corr} (V)	$-b_c$ (mV)	i_{corr}^E ($\mu A/cm^2$)	i_{corr}^R ($\mu A/cm^2$)	N^a	Surface condition
P-1	71 ± 4	-1.157 ± 0.004	124 ± 5	21.9 ± 5.6	24.6 ± 5.1	9	Drawn
W-2	82 ± 5	-1.159 ± 0.003	119 ± 4	21.6 ± 6.6	18.6 ± 4.1	11	Drawn
P-1	55 ± 5	-1.155 ± 0.005	148 ± 10	12.5 ± 4.9	12.9 ± 3.0	7	As-plated
W-2	51 ± 7	-1.158 ± 0.005	149 ± 12	5.4 ± 2.2	9.8 ± 2.5	6	As-plated
P-2	77 ± 24	-1.157 ± 0.003	120 ± 3	11.7 ± 3.3	14.1 ± 5.0	4	Drawn
P-3	78 ± 9	-1.150 ± 0.014	125 ± 22	21.2 ± 14.5	20.9 ± 11.7	4	Drawn
P-4	70 ± 3	-1.151 ± 0.005	118 ± 7	16.2 ± 8.4	17.1 ± 8.9	4	Drawn

^a Number of determinations.

Table V. Corrosion rate data for measurements in 1M NH₄Cl

Plating electrolyte	b_a (mV)	E_{corr} (V)	$-b_c$ (mV)	i_{corr}^E ($\mu A/cm^2$)	i_{corr}^R ($\mu A/cm^2$)	N^a	Surface condition
P-1	56 ± 3	-1.145 ± 0.007	132 ± 7	24.0 ± 12.4	23.9 ± 7.6	4	Drawn
P-1	35 ± 2	-1.138 ± 0.004	135 ± 13	10.5 ± 5.6	11.9 ± 4.0	3	As-plated

^a Number of determinations.

Table VI. Corrosion rates of as-plated electrogalvanized wire in deaerated 1M ammonium sulfate (Factor for calculating i_{corr} in microamperes per square centimeter from solution analysis: $F = 34.2$)

Plating electrolyte	Test	i_{corr} ($\mu\text{A}/\text{cm}^2$)	t (h)
P-1	1	14.5	25.2
		24.6	49.2
		21.8	73
P-1	2	17.2	4.3
		22.1	21
P-1	3	22.4	18.6
		10.4	24
W-2	1	19	48
		24	71
		4.7	24
	2	7.7	48
		13.5	72

to surface structural changes incurred in the deformation of the malleable zinc coating. Figure 6 shows that the as-plated and drawn surfaces are distinctly different. The zinc coating from the synthetic electrolyte P-1 (Fig. 6A) shows larger grains than the waste electrolyte-derived deposit (Fig. 6B). The drawn surface (Fig. 6C) shows a relatively smooth surface with "die" lines. X-ray analysis shows perturbation of the crystallographic orientations upon drawing the as-plated surface as expected.

As-plated wire was also evaluated by weight loss (solution analysis) and the results show that zinc is dissolved at a rate consistent with electrochemical measurements under the assumption given above.

Waste-derived EG steel corrodes at a rate slightly lower than does the EG coating from a relatively pure zinc electrolyte. This result is presumably due to the finer-grained coating from the waste electrolyte. Salt spray corrosion tests yielded the same result: the waste coating outlasted the coatings from electrolytes prepared from French process zinc oxide (1).

Electrogalvanized wire used for evaluation was plated at two different temperatures, 40° and 60°C, representing the range normally used to produce this type of product. Also, a pH range of 2-5 was evaluated since various processes require different acid contents. Figures 7 and 8 depict the affects that plating temperature and electrolyte pH have on electrogalvanized steel corrosion rates. The corrosion currents are averages of the extrapolated and polarization resistance values. It can be seen that, in general, the higher plating temperature (60°C) yields the more corrosion-resistant product, especially after the wire is drawn.

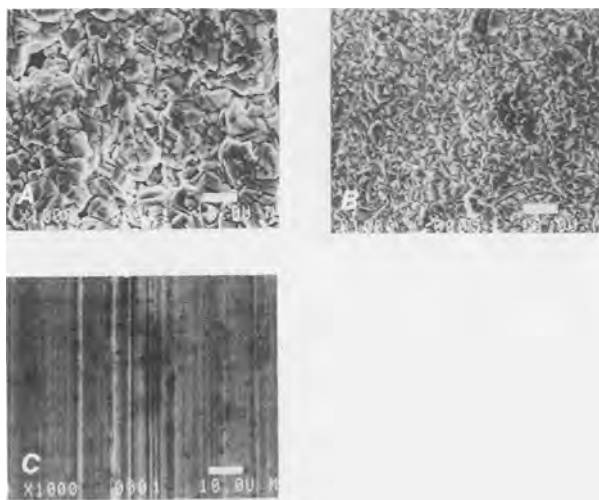


Fig. 6. SEM photographs of as-plated EG steel plated in synthetic (A), waste-derived zinc electrolytes (B), and drawn EG steel (C).

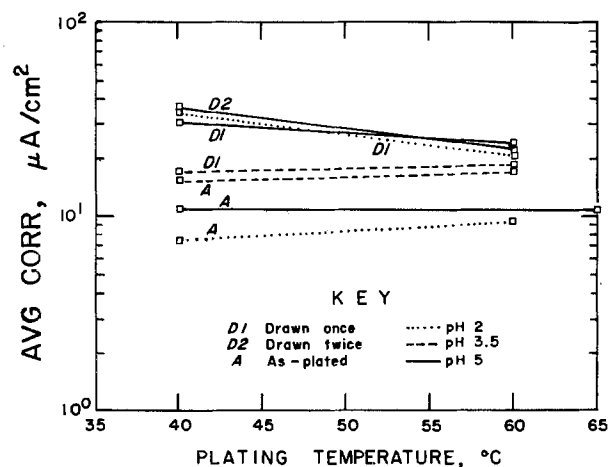


Fig. 7. Average corrosion current densities of as-plated and drawn EG steel plated in pure electrolyte P-1.

Another process variable that was evaluated was the affect of the licorice additive concentration in the pure electrolyte and the drawn wire corrosion properties. Results given in Table IV for drawn wire plated in electrolytes P-1 through P-4 show that no licorice and 0.5-g/liter licorice yield results for the final product that are better than those with intermediate licorice content. Licorice is a common additive for acid zinc plating.

The observation of the inflection in the anodic Tafel curves in Fig. 3-5 during active corrosion of the EG steel deserves comment. Tafel slopes for the dissolution of zinc on EG steel are larger than those obtained when corroding pure zinc. This is assumed to be caused by the affects of additives in the plating electrolyte and embedded drawing lubricants in the case of the drawn surface. Battery alloy zinc shows a similar inflection in the anodic polarization curve (11), so that competing anodic processes due to inhomogeneities appear to be the cause (16).

Electrogalvanized steel appears to corrode by a simple charge transfer process since the correlation between weight loss and the electrochemical techniques is acceptable. Because the medium for corrosion was deaerated, hydrogen evolution is the cathodic process coupled with anodic zinc dissolution. The use of an ammonium salt provides an increase of the rate of the cathodic hydrogen evolution process, and these media were sufficiently aggressive in their attack without the problems of surface films observed in aerated salt solution. Because electrogalvanized steel is covered with paint, rubber, or polymer in actual service and the corrosion processes are determined by real environments subject to numerous variables, the choice of medium is somewhat arbitrary.

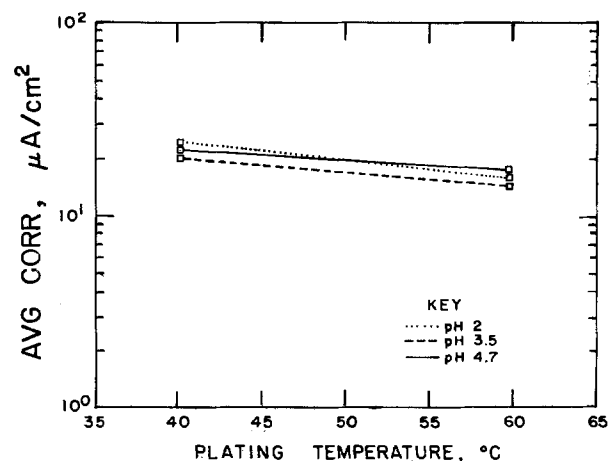


Fig. 8. Average corrosion current densities of drawn EG steel plated in waste-derived electrolyte W-2.

Conclusions

It has been shown that electrogalvanized steel plated in waste-derived zinc electrolytes corrode at rates similar to those of pure electrolyte coatings. Electrogalvanized steel displays different Tafel parameters than does pure zinc because of surface differences. The correlation between the weight loss determined by solution analysis and the electrochemical techniques of Tafel line extrapolation and polarization resistance is excellent for as-plated steel wire in ammonium sulfate solution. This allows a rapid evaluation of corrosion performance.

Because of the increased use of electrogalvanized steel for automotive application, rapid analysis is needed for process monitoring which is not provided by salt spray and performance testing. Other process variables such as plating temperature, pH, and additive concentrations can also be evaluated as to their effect on corrosion.

If wastes are to be used as raw materials in industrial processes, the final product must meet the requirements specified. Electrochemical techniques provide a means of determining corrosion rates in a short time and have been used to show that wastes are a viable source of zinc for electrogalvanizing.

Manuscript submitted Nov. 19, 1984; revised manuscript received July 1, 1985. This was Paper 6 presented at the Cincinnati, Ohio, Meeting of the Society, May 6-11, 1984.

REFERENCES

1. M. Dattilo, E. R. Cole, and T. J. O'Keefe, *Conserv. Recycl.*, **8**, 399 (1985); presented at Federation of Materials Recycling Conference, July 18, 1984, Proceedings to be published.
2. V. R. Miller and D. L. Paulson, *Resourc. Conserv.*, **9**, 95 (1982).
3. J. B. Stephenson, E. R. Cole, and D. L. Paulson, *ibid.*, **6**, 203 (1981).
4. E. H. Lyons, *Trans. Electrochem. Soc.*, **78**, 317 (1940).
5. E. H. Lyons, *ibid.*, **80**, 387 (1941).
6. H. Leidheiser, Jr., Y. Momose, and R. D. Granata, *Corrosion*, **38**, 178 (1982).
7. J. J. Podesta, R. C. V. Piatti, and A. J. Arvia, *ibid.*, **38**, 599 (1982).
8. R. F. Ashton and M. T. Hepworth, *ibid.*, **24**, 50 (1968).
9. R. D. Armstrong and G. M. Bulman, *J. Electroanal. Chem.*, **25**, 121 (1970).
10. L. M. Baugh, *Electrochim. Acta*, **24**, 657 (1979).
11. L. M. Baugh, *ibid.*, **24**, 669 (1979).
12. K. Boto and L. F. G. Williams, *J. Electroanal. Chem.*, **77**, 1 (1977).
13. K. Boto and L. F. G. Williams, *This Journal*, **124**, 656 (1977).
14. J. O'M. Bockris and A. K. N. Reddy, "Modern Electrochemistry," Vol. 2, Plenum Press, New York (1970).
15. M. Stern and A. L. Geary, *This Journal*, **104**, 56 (1957).
16. M. Stern, *ibid.*, **104**, 645 (1957).
17. C. Wagner and W. Traud, *Z. Elektrochem.*, **44**, 391 (1938).
18. J. O'M. Bockris, B. E. Conway, E. Yeager, and R. E. White, "Comprehensive Treatise of Electrochemistry," Vol. 4, p. 2, Plenum Press, New York (1981).

Transpassive Dissolution of Ni in Acidic Sulfate Media: A Kinetic Model

Michel Keddam, Hisasi Takenouti, and Ning Yu

LP0015 CNRS "Physique des Liquides et Electrochimie," associé à l'Université Pierre et Marie Curie, 75230 Paris Cedex 05, France

ABSTRACT

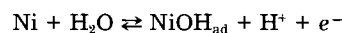
The transpassive dissolution of Ni in acidic sulfate media, including the influence of crystallographic orientation, was investigated. The surface plane had low index values, that is (100), (110), and (111). This study was largely based on the analysis of complex impedance. (100) and (110) specimens showed identical electrochemical behaviors, whereas the (111) specimen showed a current density about 20% lower. A reaction mechanism describing the dissolution of the passive film was proposed. This dissolution step was postulated to be catalytic, in the sense that the passive film transformed into a soluble species by anion was not consumed by the transpassive dissolution itself. Calculated polarization curves as well as electrode impedances at various polarization points were in a good agreement with experimental results.

Beyond the passivity range and preceding the oxygen evolution reaction, Ni electrode in an acidic sulfate medium exhibits a transpassive dissolution followed by a secondary passivity. A very marked intergranular dissolution which is to be directly related to localized corrosion of austenitic stainless steel immersed in an oxidizing medium is observed in this potential range (1).

This paper is aimed at a better understanding of the transpassive dissolution of Ni, including the influence of the crystallographic orientation which is likely to play an important role in the course of localized attack. Of major interest may be the interaction of the crystallographic orientation with the electrochemical behavior of the passive layer. Nickel single crystals with low index surface plane (100), (110), and (111) were investigated along with a polycrystalline specimen. The use of single crystals also avoids, to a large extent, complications due to poorly defined surface area and potential distribution within intergranular grooves and crevasses (2). This study was largely based on complex impedance measurements which yield a far more realistic picture of the reaction mechanism.

A mechanism of transpassive dissolution, based on potential decay experiments (3), was first proposed by Sato

and Okamoto in 1963



where the subscripts "ad" and "sol" indicate, respectively, a species adsorbed on the electrode surface and one that dissolved in the solution bulk. This dissolution mechanism is close to that proposed by Bockris *et al.* for the active dissolution of iron (4). The sole difference is the use of H₂O molecule as reactant instead of OH⁻ for the iron dissolution. The valency of transpassive dissolution was reported by many authors to be equal to two (5-7).

Osterwald observed that when a polarization device was switched from potentiostat to galvanostat, nearly sine wave potential oscillations took place (8, 9). On the basis of the stability theory, he deduced the existence of two time constants (second-order dynamical system) associated with a negative resistance in the frequency response. This prediction was experimentally verified by Epelboin and Keddam (10).

In 1975, on the basis of impedance data, Jouanneau *et al.* proposed a very general model for Ni dissolution cov-

ering the whole range from activity to oxygen evolution including transpassivity (11). They remarked, furthermore, that the transpassive dissolution is highly dependent on anion. Hence, they introduced reaction paths implying anion in addition to hydroxyl ion. The skeletal model includes ten adsorbed intermediate species and 12 reaction paths besides two dissolution processes and two oxygen evolution reactions. Nevertheless, the model does not distinguish explicitly the active and the transpassive dissolution. In other words, it includes no dissolution process of the passive film. Therefore, the transpassive dissolution is preceded by the reduction of bivalent passive film to a monovalent intermediate species at potentials more anodic than the passivity range. This unlikely feature seems to be an important weakness in consistency of this model. Furthermore, the model is much too intricate to be checked by numerical simulations or to fit experimental data with enough reliance. This is why we devised a new reaction mechanism.

Experimental

Electrode.—Single-crystal specimen rods, 9 mm diam, prepared by Bridgman or Czochralski method, were supplied by Cristal-Tec (France). The purity was evaluated to be 99.95%. The specimen rods were mounted in a stainless steel shaft to form a rotating disk electrode. The specimen was then covered by a thin heat curing epoxy-phenolic resin at 200°C under pressure (3.5 bar). This particular preparation of electrode allowed us to avoid any underlying attack between metal and insulating material.

The electrode surface was then polished on emery paper under water flow up to 1200 grade, and then electrochemically polished in 10% perchloric acid in ethylene glycol monobutyl-ether at 5°C. The misorientation with respect to the corresponding index plane was kept to less than 1°.

Electrolyte.—The electrolyte was prepared by mixing dilute sulfuric acid and sodium sulfate solutions to obtain the desired pH value at different total concentrations of sulfate ions. The electrolyte was deaerated by Ar bubbling before and during experiments. The solution temperature was kept at $25 \pm 0.2^\circ\text{C}$.

Cell.—A cylindrical glass cell contained about 0.35 liter solution. The working electrode, rotated at about 1200 rpm, was set at the center. This rotation speed was high enough to avoid control by mass transport. A platinum gauze counterelectrode, ca. 200 cm², was set around the cell wall. The reference electrode, located halfway between these two electrodes, was mercurous sulfate in saturated K₂SO₄ (SSE). The potential given in this paper was corrected for ohmic drop due to the electrolyte resistance determined by the high frequency limit of electrode impedance and dc current.

Measurements.—dc and ac measurements were performed potentiostatically with the Schlumberger-Solartron equipment (1186-1172 TFA). The electrode impedance was measured under sine-wave perturbation of small amplitude ($\Delta E < 5$ mV) at various dc polarization points.

Calculations.—Numerical simulations were performed using FORTRAN-77 language with double precision (*i.e.*, 16 bytes for a complex variable) on a Gould 32/27 computer. A reaction model was first translated into a set of differential equations corresponding to the mass and charge balances. Then this set of equations was solved for steady-state and linearized nonsteady-state conditions yielding mathematical expressions of the dc current and the frequency dependence of the impedance at any given potential. A detailed description of the procedure has been given elsewhere (12). Specific equations relevant to the model of transpassive dissolution of Ni are shown below.

Numerical simulations were performed by varying the values of the kinetic parameters. No fitting program was

used, but the values were adjusted manually for each run to approach sufficiently to the experimental data. Models able to reproduce neither analytically nor numerically the experimental results were discarded. The steady-state polarization curve was first simulated. At this stage, a certain number of kinetic parameters had little or no influence on the calculated curve. Then the impedance diagrams at various polarization points were tried to be reproduced by numerical calculations.

Results and Discussion

In Fig. 1, the steady-state polarization curve of the transpassive dissolution of (111) single-crystal Ni in 1M H₂SO₄ is shown. This curve exhibits a fairly well-defined Tafel relationship spreading over two orders of magnitude, in agreement with Ref. (5). The steady state was reached within a few minutes at a given potential for single-crystal specimens. This contrasts to the case of a polycrystalline specimen on which the steady state was reached only after 10-15 min of polarization, due probably to the formation of grooves and crevasses at grain boundaries. The current maximum can be seen near 1.0V, due to the secondary passivation process. Beyond 1.1V, the oxygen evolution reaction sets in, leading to a further current increase.

The influence of crystal plane on the polarization curve is illustrated in Fig. 2. Except for the full passive range (13), (100) and (110) specimens showed identical polarization curves. On the contrary, the current density of (111) specimen is about 20% lower in the transpassive dissolution range, and roughly half at the current maximum. The results were highly reproducible, and the difference observed was significantly greater than the experimental error. The same difference was also observed in the polarization curves obtained in other solutions. On the contrary, no significant difference can be seen in the oxygen evolution range.

Figure 3 depicts different impedance diagrams obtained at the polarization points labeled A to F in Fig. 1 on the (111) specimen. Over the entire transpassive dissolution range, in addition to the high frequency capacitive loop related to the double-layer capacitance and the

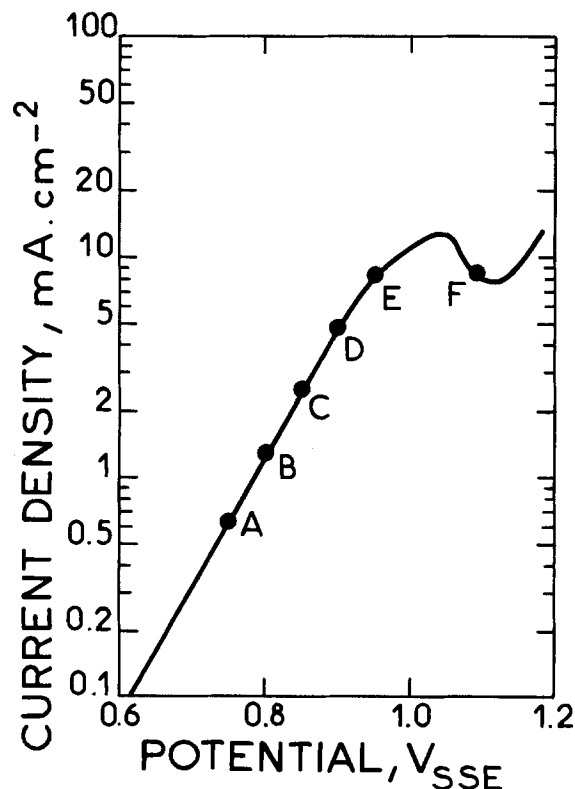


Fig. 1. Steady-state polarization curve of the transpassive dissolution; (111) Ni single crystal in deaerated 1M H₂SO₄ at 25°C. A to F correspond to the diagrams given in Fig. 3.

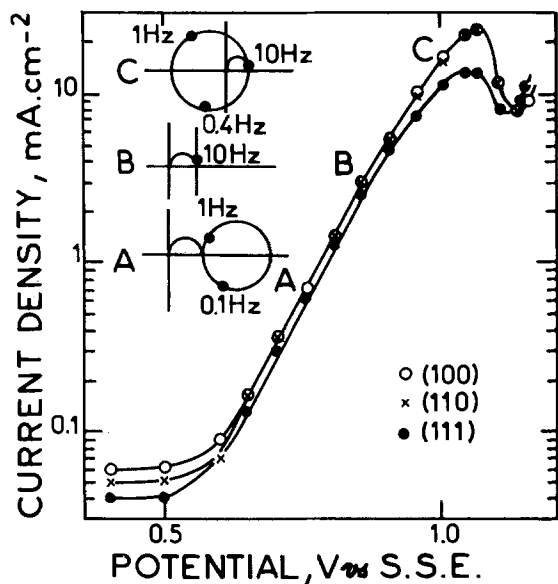


Fig. 2. Polarization curves for different crystal planes. Diagrams A to C illustrate schematically the evolution of electrode impedance with potential.

charge transfer resistance, two loops, one capacitive and another inductive, can be seen. Hence, the impedance diagram intersects the real axis at a frequency ranging from 0.1 to 0.4 Hz, depending upon the electrode potential. At a potential near 0.88V, the impedance becomes infinite at this frequency (wave-trap circuit). At potentials less anodic than this critical value, the real part of impedance remains always positive. On the contrary, at more anodic potentials, the real part of the impedance exhibits a negative contribution. This change of the impedance diagrams is illustrated in Fig. 2. The impedance diagram above the critical potential is in fact stable under potential but unstable under current regulation (14), as correctly predicted by Osterwald (9).

The impedance diagrams of (100) and (110) specimens are quite similar to those shown in Fig. 3. A slight differ-

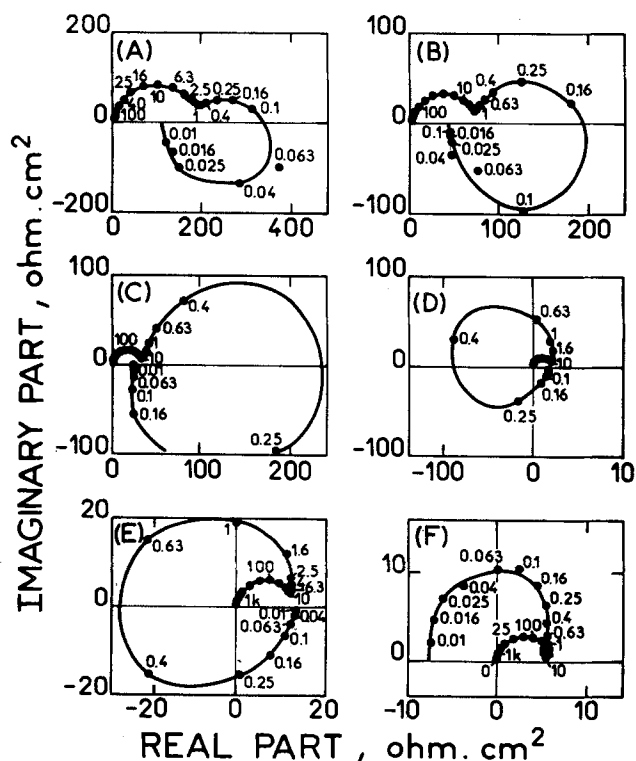


Fig. 3. Impedance diagrams of (111) Ni single crystal. A to F are measured at dc points labeled on Fig. 1.

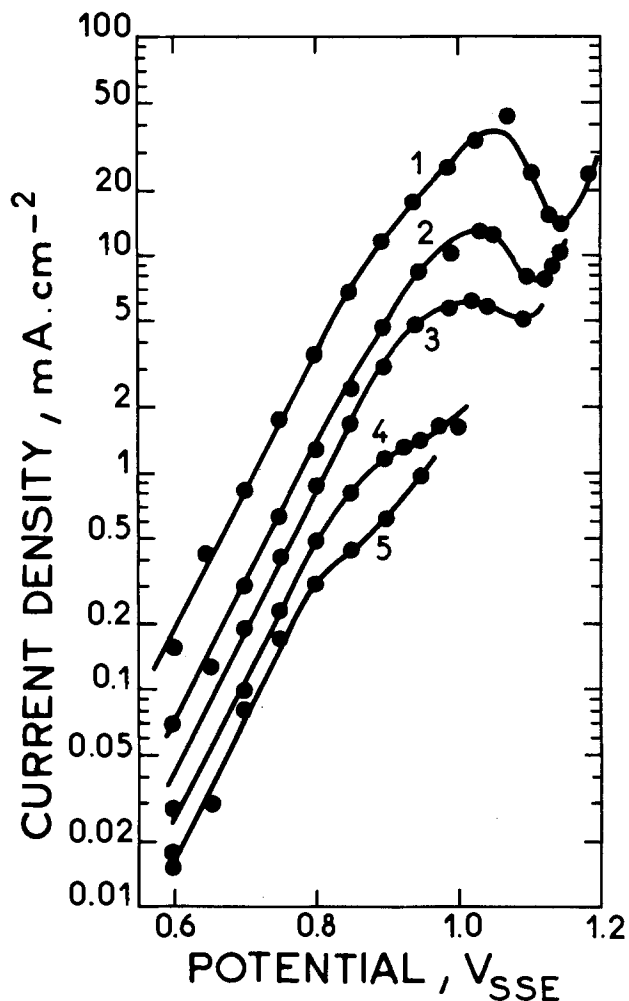


Fig. 4. Influence of solution pH on polarization curves: (111) Ni in 2M H_2SO_4 (curve 1) and in a molar SO_4^{2-} of various pH. Curve 2: pH 0.0. Curve 3: pH 0.6. Curve 4: pH 1.6. Curve 5: pH 3.

ence in the observed impedance modulus can be related to the difference of the dc component. The similarity of the polarization curves, and more significantly of the complex impedances, exhibited by these three specimens indicates that the electrode kinetics is not clearly dependent on the crystallographic plane.

In order to obtain additional data about the reaction mechanism, the solution pH and the total sulfate concentration were independently varied. Figure 4 depicts the influence of solution pH on the polarization curve for (111) single-crystal specimen. When the solution pH increases, the dissolution current decreases. The apparent reaction order of dissolution rate with respect to H^+ concentration is ca. 0.25. That is, the influence of solution pH is small. Furthermore, its increase seems to enhance the passive state instead of the dissolution, as in active Fe dissolution. These two points contrast definitively with the consecutive dissolution mechanism proposed by Bockris *et al.* (4) for active Fe.

Figures 5 and 6 illustrate the influence of total sulfate concentration at a constant pH. At a low pH value (0.35), as can be seen in Fig. 5, no clear relationship between the dissolution current and the sulfate concentration can be established. It may be worth noting that, at this pH, sulfate anions are mainly HSO_4^- . At pH 3.0, on the contrary, the major solution anion is SO_4^{2-} , for which the results are shown in Fig. 6. Somewhat more significant change than at pH 0.35 can be seen. The apparent reaction order with respect to the total sulfate concentration is 0.2. That is, the influence of sulfate concentration is small for a weakly acid and negligible in a strongly acid medium in spite of the fact that the very nature of anion plays a crucial role in transpassive dissolution (11). This strongly

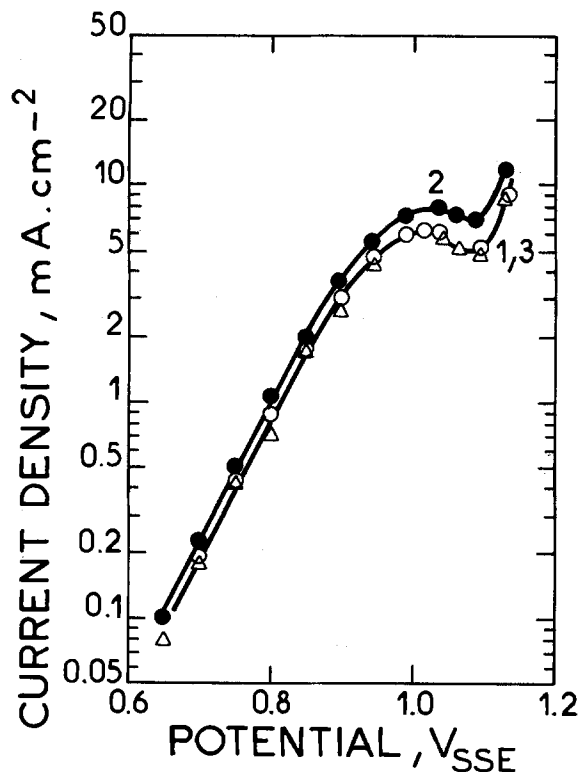


Fig. 5. Influence of sulfate concentration on polarization curves: (111) single-crystal Ni. 1: 0.5M H_2SO_4 . 2: 0.5M H_2SO_4 + 0.5M Na_2SO_4 . 3: 0.5M H_2SO_4 + 1M Na_2SO_4 . Solution pH: 3.5.

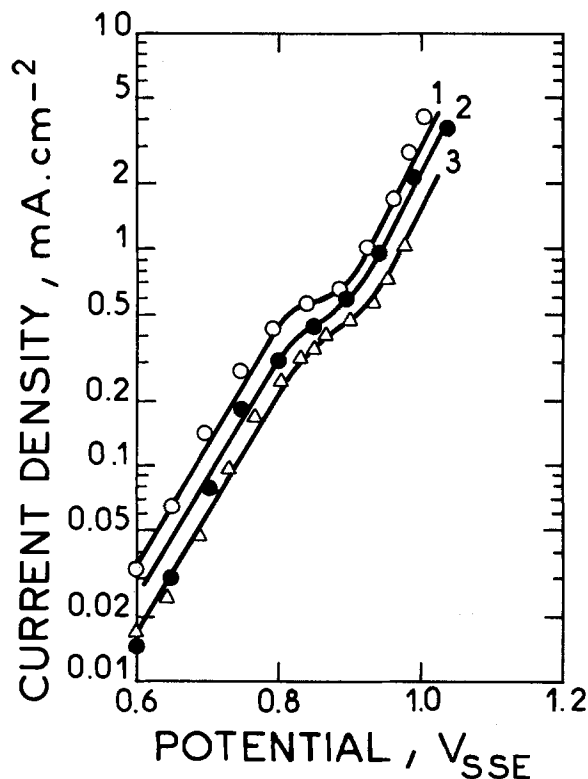


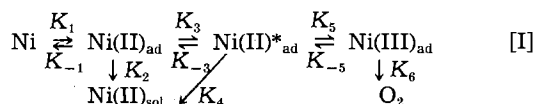
Fig. 6. Similar to Fig. 5 with pH 3 solution of total sulfate concentration 1M (1), 0.1M (2), and 0.01M (3).

suggests a catalytic effect of anion on the dissolution of the passive layer, as established recently in the case of F⁻ by spectroscopic and electrochemical techniques (15).

In this potential range, the metal surface is completely covered by a bivalent passive layer. At high enough anodic potentials, SO_4^{--} and/or HSO_4^- are assumed to attack the passive film and to transform it into a soluble species. The secondary passivity is to be explained by another type of passive film such as $Ni(OH)_3$. This concept contrasts drastically with those proposed in the literature, in which the transpassive dissolution is considered to be similar to the active dissolution (3, 11).

Reaction Model

The impedance data clearly put forward a far more intricate mechanism than the single charge transfer step expected in Ref. (5) from the Tafel law obeyed over a large range of current densities. Neither polarization curves nor electrode impedances allow us to determine the chemical nature of reaction intermediate species, but only allow some guess about their potential and time dependence. Therefore, a skeletal reaction model was preferably used without explicating reaction chemistry but only on the valency state of intermediate species



The reaction step [I] depicts the formation of the passive film. Since the potential range of interest in this work is far anodic to the active dissolution, the latter process is discarded from the reaction scheme. The K_2 step is the chemical dissolution process of the passive film which determines the constant current density in the full passive range. The K_3 step denotes the transformation of the passive film into a somewhat more soluble species, likely containing anion, leading to the transpassive dissolution itself (K_4 step). The K_5 step accounts for the secondary passivity, whereas the K_6 step describes the oxygen evolution reaction. This reaction is assumed to take place on top of the secondary passivity adsorbate since its

contribution is detectable only after the current maximum. This model implies three intermediate species sharing simultaneously the electrode surface. The fractional coverage of Ni(II), Ni(II)*, and Ni(III) are, respectively, denoted by θ_1 , θ_2 , and θ_3 .

In spite of this formalism, the model validity can be extended to a situation where the kinetics is partly controlled by depth profiles of potential and/or concentration within a film. In this range of potential, the electrode surface must be considered as completely covered by the passive film and no bare nickel is allowed to contact electrolyte. Therefore, K_1/K_{-1} step can be considered as the transfer of Ni(II) across the film from the metal to a surface site on the passive layer. A high field migration is consistent with an exponential dependence on the applied potential. Adsorption states are assumed to be located at the film/electrolyte interface.

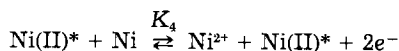
The mass balance of the three intermediate species given above can be expressed by

$$\beta \frac{d\theta_1}{dt} = K_1 \Sigma - (K_{-1} + K_2 + K_3)\theta_1 + K_{-3}\theta_2 \quad [1]$$

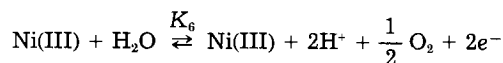
$$\beta \frac{d\theta_2}{dt} = K_3\theta_1 - (K_{-3} + K_5)\theta_2 + K_{-5}\theta_3 \quad [2]$$

$$\beta \frac{d\theta_3}{dt} = K_5\theta_2 - K_{-5}\theta_3 \quad [3]$$

where $\Sigma = 1 - \theta_1 - \theta_2 - \theta_3$ and β stands for the surface concentration (4.0×10^{10} mol \cdot cm $^{-2}$) of adsorbed species at $\theta_1 = 1$. These equations indicate that K_4 and K_6 steps do not intervene in the mass balance. In a preliminary work, it was found that experimental data cannot be accounted for by the K_4 dissolution step obeying usual electrochemical kinetics. Though not demonstrated analytically, a catalytic process seems to be needed to simulate the experimental results on the basis of this reaction scheme. Furthermore, the formation of a catalytic surface species is also in agreement with a small dependence of the reaction rate on anion concentration. Such a reaction can be represented for instance by



This particular mechanism allows us to separate the relaxation time constant from the current flow through the electrode interface. In fact, in this reaction scheme, the dissolution of Ni(II)* is not accompanied with its consumption. The consequence of such a reaction from the viewpoint of electrode impedance was described in detail in the case of Fe dissolution (12). For oxygen evolution reaction, the secondary passive species Ni(III) also plays a catalytic effect, but these kinetics are introduced only to simplify the mass balance equation. In fact, this reaction is beyond the scope of this work and is introduced merely to explain the current increase due to the oxygen evolution. The reaction process may be explicated for instance as



The charge balance dQ/dt , that is, current flow I , can be written as follows

$$I = F[2K_1\Sigma - 2K_{-1}\theta_1 + (2K_4 + K_5)\theta_2 - (K_{-5} - 2K_6)\theta_3] \quad [4]$$

where F is the Faraday.

The Tafel law and the Langmuir-type isotherm are postulated to describe the potential dependence of K_1

$$K_1 = K_{10} \exp(b_1 E) \quad [5]$$

where K_{10} and b_1 are independent of θ , K_1 is expressed in $\text{mol}\cdot\text{s}^{-1}\cdot\text{cm}^{-2}$, and the unit of b_1 is V^{-1} . For an equilibrium reaction, $(b_+ + b_-) = RT/nF$. This condition was found much too drastic to fit experimental results over a wide range of experimental conditions. This implies that K_1/K_{-1} , K_2/K_{-2} , and K_3/K_{-3} cannot be considered as true elementary equilibrium processes but depict merely an overall reaction reversibility. Furthermore, the K_{-1} value in the transpassive dissolution range is so small that this process may be considered as practically irreversible.

The steady state is defined by $d\theta_i/dt = 0$, hence from Eq. [1]-[4] one yields the steady-state polarization current \bar{J}

$$\bar{J} = 2F(K_2\bar{\theta}_1 + K_4\bar{\theta}_2 + K_6\bar{\theta}_3) \quad [6]$$

where

$$\bar{\theta}_1 = K_1 K_{-3} K_{-5} / D; \quad \bar{\theta}_2 = K_1 K_3 K_{-5} / D; \quad \bar{\theta}_3 = K_1 K_3 K_5 / D$$

and

$$D = (K_1 + K_{-1} + K_2)K_{-3}K_{-5} + K_1K_3(K_5 + K_{-5})$$

$\bar{\theta}$ indicates the steady-state value of fractional coverage. The faradaic impedance Z_F is to be derived from the Taylor expansion of Eq. [1]-[4] limited to the first order. The result of this straightforward calculation is given below

$$\frac{1}{Z_F} = \frac{1}{R_t} - F[2(K_1 + K_{-1}) \frac{d\theta_1}{dE} + (2K_1 - 2K_4 - K_5) \frac{d\theta_2}{dE} + (2K_1 + K_{-5} + 2K_6) \frac{d\theta_3}{dE}] \quad [7]$$

where

$$\begin{aligned} \frac{1}{R_t} &= F\{[2(b_1 - b_{-1})K_{-1} + b_1K_2]\bar{\theta}_1 + [2b_4K_4 + (b_5 - b_{-5})K_5]\bar{\theta}_2 + 2b_6K_6\bar{\theta}_3\} \\ \frac{d\theta_1}{dE} &= \frac{X_1Z_2Z_3 - X_1K_5K_{-5} - (K_1 - K_{-3})(X_2Z_3 + K_{-5}X_3) - K_1(X_3Z_2 + X_2K_5)}{Z_D} \\ \frac{d\theta_2}{dE} &= \frac{Z_1X_2Z_3 + X_1K_3Z_3 + Z_1X_3K_{-5} - K_1K_3X_3}{Z_D} \\ \frac{d\theta_3}{dE} &= \frac{Z_1Z_2X_3 + (K_1 - K_{-3})K_3X_3 + Z_1X_2K_5 + X_1K_3K_5}{Z_D} \end{aligned}$$

Table I. Kinetics parameters used in simulation calculation

$K_1 = 1 \times 10^{-8} \exp(5E)$	$K_4 = 5 \times 10^{-11} \exp(10E)$
$K_{-1} = 2.8 \times 10^{-7} \exp(-5.5E)$	$K_5 = 3 \times 10^{-13} \exp(10E)$
$K_2 = 5 \times 10^{-12} \exp(7E)$	$K_{-5} = 3 \times 10^{-8} \exp(-4.5E)$
$K_3 = 2 \times 10^{-13} \exp(5E)$	$K_6 = 2 \times 10^{-14} \exp(12.5E)$
$K_{-3} = 7.6 \times 10^{-9} \exp(-4.5E)$	

with

$$Z_D = Z_1Z_2Z_3 + (K_1 - K_{-3})K_3Z_3 - Z_1K_5K_{-5} + K_1K_3K_5$$

$$X_1 = [(b_1 - b_{-1})K_{-1} + (b_1 - b_2)K_2 - (b_3 - b_{-3})K_3]\bar{\theta}_1$$

$$Z_1 = K_1 + K_{-1} + K_2 + K_3 + j\omega\beta$$

$$X_2 = [(b_3 - b_{-3})K_{-3} - (b_5 - b_{-5})K_5]\bar{\theta}_2$$

$$Z_2 = K_{-3} + K_5 + j\omega\beta$$

$$X_3 = (b_5 - b_{-5})K_{-5}\bar{\theta}_3$$

$$Z_3 = K_{-5} + j\omega\beta$$

ω is the angular frequency ($\text{rad}\cdot\text{s}^{-1}$) and $j = \sqrt{-1}$.

It is assumed that the double-layer capacitance C_d ($= 100 \mu\text{F}\cdot\text{cm}^{-2}$) is linked in parallel with the faradaic impedance, and hence the overall electrode impedance is expressed by

$$\frac{1}{Z} = \frac{1}{Z_F} + j\omega C_d \quad [8]$$

By a trial-and-error method, a set of kinetic parameters shown in Table I was found to simulate suitably the experimental results on (111) single-crystal specimen in 1M H_2SO_4 . The polarization curve obtained by numerical calculation is shown in Fig. 7. The calculated curve is in fairly good agreement with experimental results.

In the same figure, the changes of fractional coverage by Ni(II), Ni(II)*, and Ni(III) are shown. This figure illustrates that the electrode is practically completely covered ($\theta_1 + \theta_2 + \theta_3 \approx 1$), and the passivating species θ_1 decays in the transpassive range and undergoes a transformation into the soluble transpassive species θ_3 . The fractional coverage of this species remains rather small in the whole potential range, and shows a maximum near $E = 0.88\text{V}$, corresponding to the critical potential.

From calculated results, at the foot of the transpassive range, Ni dissolution through K_2 path is still significant, but, beyond $E = 0.7\text{V}$, the K_4 path prevails in the whole range of transpassive nickel dissolution.

Figure 8 shows the impedance diagrams obtained by simulation according to the model at various dc polarization points labeled A' to F' in Fig. 7. The change in the diagram shape with potential is well reproduced by the model. In particular, the critical potential beyond which the negative real part is observed is seen to be well simulated. On the contrary, at potentials close to the current maximum, experimentally, the impedance diagram again takes a shape similar to Fig. B' or C'. This was not successfully reproduced by the kinetic parameters given in Table I. Another discrepancy with the model is the R_t value. Calculated charge transfer resistance is a few times smaller than that measured experimentally for high cur-

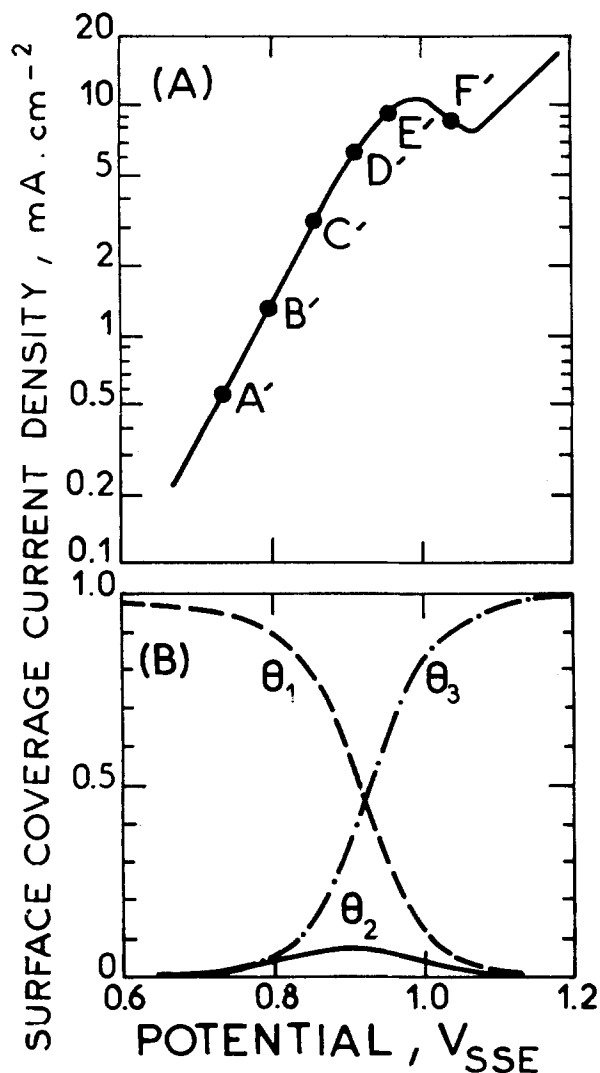


Fig. 7. A: Calculated polarization curve of the transpassive dissolution of Ni (cf. Fig. 1). B: Fractional surface coverage by Ni(II) (θ_1), Ni(II)* (θ_2), and Ni(III) (θ_3).

rent densities. However, it is reasonably hoped that these points can be improved by the choice of a better set of kinetic parameters.

Conclusion

Experiments on the transpassive dissolution of Ni in acidic sulfate media were performed with single-crystal specimens having three different orientations (100), (110), and (111). The polarization curves, as well as the impedance diagrams, of (100) and (110) are identical, whereas (111) showed a slightly lower dissolution current.

The dissolution rate is weakly dependent on the solution pH. The lower the pH value, the faster the dissolution rate. This experimental observation contrasts to the influence of solution pH on the active dissolution of Fe in an acidic medium. The influence of sulfate concentration is also weak or negligible, although the anion plays a crucial role in the very existence of transpassive dissolution. These experimental data led us to consider the transpassive dissolution as a catalytic dissolution of the passive film.

A reaction model for the transpassive dissolution and the secondary passivity, implying three adsorbed species and two dissolution paths, is proposed. A numerical simulation of this model reproduces the experimental results with a satisfactorily good agreement in the case of (111) Ni specimen in 1M H_2SO_4 .

Consideration of the role of OH^- , HSO_4^- , and SO_4^{--} in the framework of the model will constitute the next step of this work.

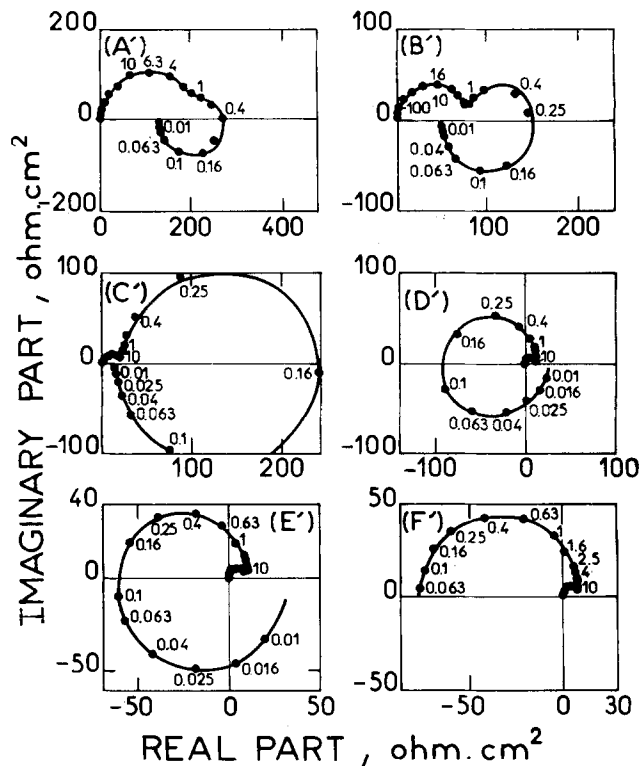


Fig. 8. Calculated impedance diagrams at dc polarization points labeled on Fig. 7A by corresponding letters.

Acknowledgment

One of the authors (N.Y.) gratefully acknowledges the Ministry of Education of the People's Republic of China for providing his fellowship.

Manuscript submitted Oct. 22, 1984; revised manuscript received April 14, 1985. This was Paper 258 presented at the New Orleans, Louisiana, Meeting of the Society, Oct. 7-12, 1984.

CNRS assisted in meeting the publication costs of this article.

REFERENCES

1. L. Beaunier, M. Froment, and C. Vignaud, *J. Electroanal. Chem.*, **119**, 125 (1981).
2. R. de Levie, in "Advances in Electrochemistry and Electrochemical Engineering," Vol. 6, P. Delahay, Editor, p. 239, John Wiley and Sons, New York (1967).
3. N. Sato and G. Okamoto, *This Journal*, **110**, 605 (1963); *ibid.*, **111**, 897 (1964).
4. J. O'M. Bockris, D. Drazic, and A. R. Despic, *Electrochim. Acta*, **4**, 321 (1961).
5. K. Arnold and K. J. Vetter, *Z. Elektrochem.*, **64**, 407 (1960).
6. K. Schwabe, U. Ebersbach, and W. Leimbrock, *Electrochim. Acta*, **17**, 957 (1972).
7. M. Turner, G. E. Thompson, and P. A. Brook, *Corros. Sci.*, **13**, 985 (1973).
8. J. Osterwald and H. G. Feller, *This Journal*, **107**, 473 (1960).
9. J. Osterwald, *Electrochim. Acta*, **7**, 523 (1962).
10. I. Epelboin and M. Keddam, *ibid.*, **17**, 177 (1972).
11. A. Jouanneau, M. Keddam, and M. C. Petit, *ibid.*, **21**, 287 (1976).
12. M. Keddam, O. R. Mattos, and H. Takenouti, *This Journal*, **128**, 257, 266 (1981).
13. C. J. Mauvais, R. M. Latanision, and A. W. Ruff, Jr., *ibid.*, **117**, 902 (1970).
14. I. Epelboin, C. Gabrielli, M. Keddam, and H. Takenouti, in "Comprehensive Treatise of Electrochemistry," Vol. 4, J. O'M. Bockris, B. E. Conway, E. Yeager, and R. E. White, Editors, p. 151, Plenum Press, New York (1981).
15. H. H. Strehblow and B. P. Löhel, in "Passivity of Metals and Semiconductors," Vol. 4, M. Froment, Editor, p. 379, Elsevier, Amsterdam (1983).

An Improved Accelerated Test Chamber for Electrolytic Metal Migration and Corrosion

J. J. Steppan*

Department of Chemical Engineering, Vanderbilt University, Nashville, Tennessee 37235

W. R. Seebaugh

Department of Mechanical and Materials, Vanderbilt University, Nashville, Tennessee 37235

J. A. Roth

Department of Chemical Engineering, Vanderbilt University, Nashville, Tennessee 37235

L. C. Hall

Department of Chemistry, Vanderbilt University, Nashville, Tennessee 37235

ABSTRACT

Many accelerated electrolytic metal migration and corrosion investigations have been performed in accelerated test chambers with unknown gas concentration and flow characteristics. This paper outlines the development of a well-characterized accelerated test chamber. The length (mean flow path) to hydraulic diameter ratio of the closed-circuit rectangular flow channel is 20. Velocity and concentration measurements showed minimal horizontal or vertical gradients in the test section. The range of standard deviations (m/s) for the velocity profiles in the test section was 0.0037-0.16 at mean velocities of 0.11-2.9 m/s, respectively. Similarly, the range of standard deviations [ppm(vol.) SO₂] for the SO₂ concentration profiles was 1.0-1.2 for a standard gas mixture of 102 ± 1.1 ppm SO₂ in the air. The effect of gas velocity upon the rate of metal migration was demonstrated in the described test chamber using a new accelerated test in an SO₂ environment. This test, the PEG-400 drop test, is a moderate accelerated test with metal migration rates that are less than the water-drop test but greater than a temperature humidity bias test with or without pollutants. The gas velocity was found to have a significant effect upon the rate of copper migration. The effects of gas velocity, humidity, and pollutant concentrations upon the metal migration and corrosion rates can be investigated in this accelerated test chamber.

Accelerated life tests are performed on electronic components to predict the actual lifetime and reliability of these components. Electrolytic metal migration and corrosion are common reliability problems encountered in the microelectronics industry. Accelerated metal migration and corrosion investigations are performed in test chambers in which the temperature, humidity, pollutant concentration, air velocity, and applied bias can be varied or cycled. Typically, little attention is paid to velocity or concentration profiles and gradients in these chambers. Most accelerated metal migration and corrosion laboratory tests are performed in test chambers which have unknown or uncontrolled velocity and concentration gradients.

The accelerated test chambers used in metal migration and corrosion studies can be classified as one of three types: flow-through chambers (1-11), commercial humidity cabinets (12-16), and sealed containers (17-20). The flow-through chambers are usually constructed of glass, Plexiglas, or Teflon and are best suited for studies using humidified air with or without pollutant gases. Some investigators using a flow-through chamber (1-6) mix humidified air and pollutants in the test chamber, which does not provide consistent pollutant and water concentrations in the chamber. Other investigators (7-11) mix the humidified air and pollutant gas streams before introductions into the test chamber.

Most flow-through chambers are rectangular. Rectangular chambers exhibit velocity gradients, stagnant regions in the corners, and eddy currents at the entrance and exit (21). Antler and Dunbar (22) observed different corrosion rates on copper coupons in different locations within their accelerated test chamber. This was attributed to nonuniformity of velocity and water vapor and SO₂ concentrations, especially at the entrance and exit of the test chamber.

It has been shown that the rates of corrosion of silver (23-25), of copper (25), and of copper migration (21) are dependent upon the gas velocity past the specimens. Sharma *et al.* (26) include a velocity term in their acceleration corrosion rate expressions. Other investigators do not discuss velocity effects.

The majority of metal migration and corrosion studies reported in the literature apply only to the specific system in which the accelerated tests were performed. It is difficult to establish the significance of comparisons between accelerated test results obtained using uncalibrated test chambers. Accelerated test chambers have not been standardized. Thus, investigators must standardize or characterize their test chambers so that comparisons with other experimenters and field tests can be made. This is essential for the development of acceleration factors used to predict electronic machine life under actual conditions.

The accelerated test of interest was first devised by Carbone and Corl (27). It involves placing a drop of 400 average molecular weight polyethylene glycol (PEG-400) between a pair of biased electrodes. The PEG film absorbs water and gaseous pollutant species from the ambient environment. These species ionize in the PEG or PEG-water film, causing an increase in the electrical conductivity of the film. Copper ions are formed at the anode and migrate to the cathode where they are reduced, producing dendrites. When the dendrites form a continuous filament between the electrodes, the device shorts. The time for the electrode system to short (t_s) is a measure of the relative rate of metal migration. The metal migration rates for this accelerated test (PEG-400 drop test) are moderate. The short times are longer than the water-drop test, but shorter than exposing dry electrodes to a temperature-bias-humidity test with or without pollutants.

The first objective of this paper is to outline the development of a well-characterized test chamber suitable for

*Electrochemical Society Student Member.

accelerated metal migration and corrosion studies. The second objective is to determine the effect of velocity upon the rate of copper migration for the PEG-400 drop test in an SO₂ environment.

Apparatus and Experimental Methods

Two conceptual approaches to the design of the accelerated test chamber were considered. The principal goal was to obtain a steady, reproducible flow at the test section. Generally, this may be accomplished by (i) providing sufficient entrance length upstream of the test section to provide a fully developed velocity profile across the test section or (ii) by minimizing the length of the upstream to provide a nearly uniform flow across the test section.

The velocity profile in a duct becomes fully developed at a certain distance from the entrance to the duct. For laminar flow in circular tubes (28), the approximate entrance length is given by

$$\frac{x_t}{D} = 0.05 \text{ Re} \quad [1]$$

where x_t is the entrance length, D is the tube diameter, and Re is the flow Reynold's number (ratio of the product of linear-flow-velocity, test-medium-density, and tube-diameter to the test-medium-viscosity). Similarly, the entrance length for turbulent flow (28) is given by

$$\frac{x_t}{D} = 4.4 \text{ Re}^{1/6} \quad [2]$$

For a desired velocity variation 0.11-2.9 m/s (Reynold's number range of approximately 1,100-29,000 for a 0.15m diam tube), the entrance length is 8.3-16m for laminar flow (0.11-0.20 m/s) and 2.4-3.7m for turbulent flow. These lengths are not practical for an accelerated test chamber, since the laminar entrance length must be used as the upstream length for investigations covering both the laminar and turbulent regimes.

Alternative designs were considered, since it was desirable to limit the overall size of the test chamber while obtaining reproducible and constant velocity and concentration profiles at the test section. Steady, nearly uniform flow at the test section with a minimum duct length can be achieved by careful design. This may be accomplished by either accelerating flow through a short nozzle or interrupting the flow by a pressure reducing device that occupies the duct a short distance upstream of the test section. The flow is stabilized just ahead of the test section using either of these methods.

The second option, use of a flow restrictor, was selected. A closed-circuit test chamber was constructed of clear acrylic plastic to permit use of flow visualization aids. The rectangularly configured flow channel design is advantageous, since the size of the chamber is small (0.91 × 0.91 × 0.15m) and the pollutant gas is recycled, requiring only a small make-up stream. The ratio of total length of flow channel (mean flow path) to hydraulic diameter is 20 for this chamber. The flow restrictor is a bundle of polyethylene straws held in the duct by a polyvinylchloride screen. Flow visualization studies were conducted using Dry Ice vapor to observe the air flow patterns. Vanes were installed at the two corners of the chamber between the drive fan and the flow restrictor to eliminate stagnant regions. The final configuration of the accelerated test chamber is shown in Fig. 1.

Velocity profile measurements.—Air velocity measurements were made at multiple locations in the test section with a Flow Corporation Model 55 air velocity meter. The (x, y, z) coordinate system (see Fig. 2) was used to define these locations. The x = 0 plane is the exit side of the air distributor. The air velocity was varied from 0.11 to 2.9 m/s by varying the fan speed. The velocity measurements were taken in the z = 0.013, 0.064, and 0.11 planes of the test section.

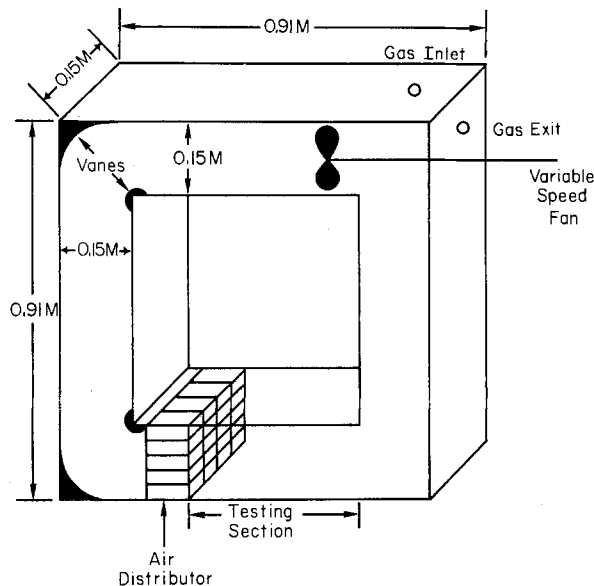


Fig. 1. Accelerated test chamber

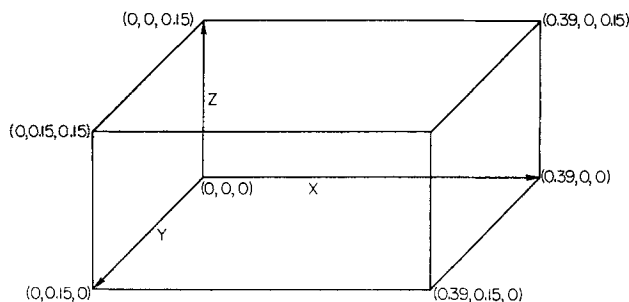


Fig. 2. Coordinate system for velocity measurements

Concentration profile measurements.—A Matheson Certified Standard gas mixture of 102 ppm (vol.) SO₂ in air was introduced into the accelerated test chamber with the fan creating a velocity of approximately 1.0 m/s. Gas samples (5.0 × 10⁻⁷m³) were taken from locations in the test section after steady state was reached (approximately 1800s). The SO₂ concentrations were determined with a Tracor Model 565 gas chromatograph equipped with a Hall 700A electrolytic conductivity detector. Gas samples were taken in the z = 0.11 plane to determine the horizontal concentration gradient, if any. Samples were also taken at x = 0.30, y = 0.076, and z = 0.025, 0.091, and 0.11 to determine vertical concentration gradients. Gas samples taken directly from the cylinder were used as standards for comparison with samples taken from the accelerated test chamber.

Copper migration measurements.—The test specimens for the copper migration investigation consist of copper electrodes (approximately 5.0 × 10⁻⁵m thick) on a substrate of nonfire retardant epoxy reinforced with woven Fiberglas cloth. The "point-to-plane" electrode configuration was manufactured by a vendor using a lithographic technique. Figure 3 shows the point-to-plane electrode design. The electrode pairs used in this investigation had spacing of approximately 2.2-2.5 × 10⁻⁴m between the point and plane. There was some inconsistency in initial electrode spacings and condition due to problems inherent with the manufacturing process.

The test specimens were cleaned to remove residual photoresist and manufacturing fluxes in order to obtain a reproducible electrode surface. The electrode cleaning procedure appears in Table I. This cleaning procedure produced visually clean electrodes at 60 times magnification with long blank short times compared to accelerated short times, i.e., $\frac{t_s(\text{accelerated})}{t_s(\text{blank})} \ll 1$. Care was taken

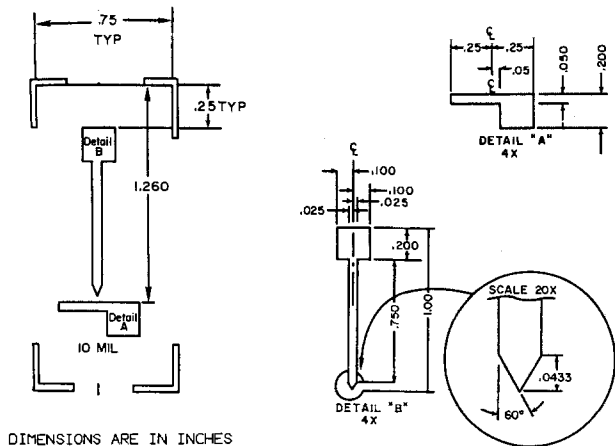


Fig. 3. Point-to-plane electrode design

not to touch the copper metallurgy, and latex gloves were worn when handling the specimens.

After the specimens were cleaned, two electrode pairs were placed in a Plexiglas holder and the electrode spacings were measured using a calibrated eyepiece micrometer at a magnification of 60 times. The sample holder was then placed in the test chamber and electrical connections were made to the electrodes with alligator clips. The plane was biased negatively and was located upstream of the point (+). Unreproducible results were obtained when the bias was reversed in preliminary metal migration investigations involving PEG-water drops doped with ammonium perchlorate. The applied potential was measured to ensure good electrical contacts and was then turned off. The chamber was sealed and the fan was turned on. The velocity across each specimen was measured prior to the introduction of the SO₂. The fan motor was located on the floor and drove the fan blade by means of a flexible shaft in order to eliminate any vibrations. The samples were then covered with a polyethylene cover to prevent the SO₂ environment from coming in contact with the copper electrodes before steady state was reached. The chamber was then resealed and the 104 ppm SO₂-air mixture was introduced. The SO₂ concentration was monitored by gas chromatography using a ten-port gas sampling valve to compare the feed and test chamber concentrations. Once steady state was reached, the polyethylene cover was removed through a septum in the chamber wall and a 6.0 μliter drop of PEG-400 was placed between each electrode pair, and a potential of 9.0V was applied. The leakage current of each electrode pair was monitored as a function of time. The time until short (*t_s*) was determined at several gas velocities in the laminar and transition flow regimes. A short is defined as a surge in leakage current, typically 1.0-10 μA, and visual observation of a dendritic structure bridging the electrodes. Upon completion of the short time runs, the fan speed was increased to 5.7 m/s [minimum velocity for reproducible psychrometric measurements (30)] and the relative humidity was determined by psychrometry.

Results and Discussion

The Dry Ice vapor (CO₂) flow patterns qualitatively showed a reproducible velocity profile with no eddy cur-

Table I. Copper electrode cleaning procedure

1. Dip card in hot (50°-60°C) HNO₃ [25% (by volume)] for 60s or longer if copper lines are not clean after 60s.
2. 15s rinse with deionized water.
3. Ultrasonicate in hot (50°-60°C) HCl [25% (by volume)] for 1800s.
4. 15s rinse with deionized water.
5. 15s rinse with isopropanol.
6. Ultrasonicate in isopropanol for 900s.
7. Store cards in isopropanol until ready for use (do not store for more than 24h).
8. Dry card with nitrogen before using.

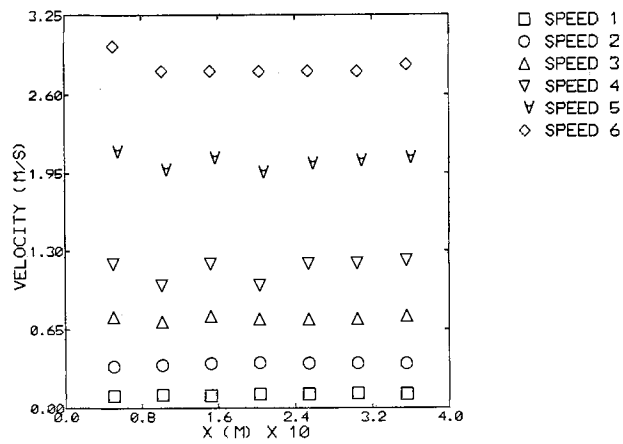


Fig. 4. Longitudinal velocity profiles in test section

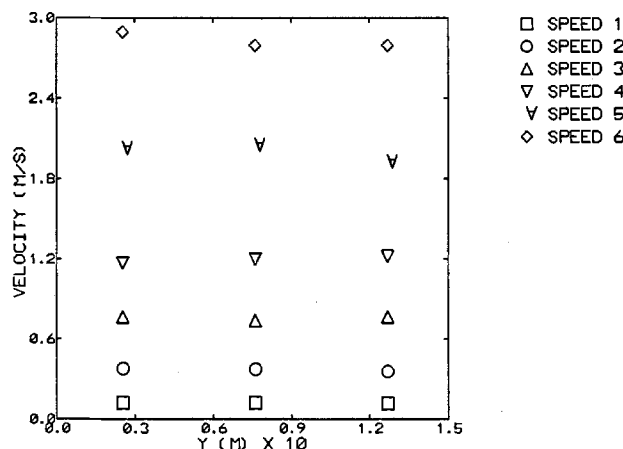


Fig. 5. Transverse velocity profiles in test section

rents or stagnant regions in the velocity range from 0.11 to 2.9 m/s. This velocity range corresponds to a Reynold's number range of approximately 1,100-29,000.

Velocity profile results.—Figure 4 shows the velocity profile along the center of the accelerated test chamber at *z* = 0.064m. Figure 5 shows the velocity profiles across the chamber at the same height. The mean velocity values and their standard deviations appear in Table II.

The velocity profile results show no organized patterns, but some scatter in the transverse and longitudinal directions in the test section of the accelerated test chamber. The range of standard deviations (m/s) in the test section was 0.0037-0.16 at mean velocities of 0.11-2.9 m/s, respectively.

The introduction of test specimens and electrical connections disturbs the velocity profile downwind of the

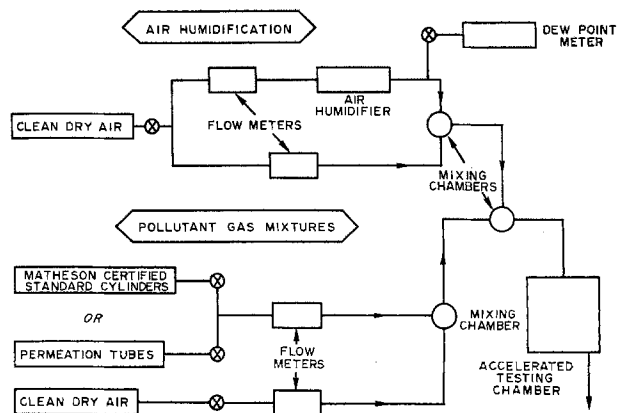


Fig. 6. Gas mixing system

Table II. Velocity results in test section

Mean velocity (m/s)	Standard deviation (m/s)
<i>z = 0.013m plane</i>	
(<i>x = 0.051-0.36m; y = 0.025-0.13m</i>)	
0.13	0.016
0.38	0.0060
0.81	0.035
1.2	0.092
2.1	0.079
2.9	0.16
<i>z = 0.064m plane</i>	
(<i>x = 0.051-0.36m; y = 0.025-0.13m</i>)	
0.11	0.0083
0.36	0.014
0.75	0.030
1.1	0.092
2.0	0.056
2.8	0.081
<i>z = 0.11m plane</i>	
(<i>x = 0.051-0.36m; y = 0.025-0.13m</i>)	
0.11	0.012
0.36	0.018
0.72	0.022
1.0	0.080
1.9	0.056
2.6	0.060
<i>z = 0.30m plane</i>	
(<i>y = 0.0039-0.055m; z = 0.013-0.11m</i>)	
0.11	0.0037
0.36	0.012
0.72	0.036
1.0	0.10
1.9	0.082
2.6	0.093

samples. Thus, it is important to design a sample holder with a small cross-sectional area. The sample holder used in this accelerated test holds two test specimens. Both specimens have identical velocity profiles across them.

Concentration profile results.—Replicate samples of standard 102 ppm (vol.) SO₂-air mixture were analyzed by gas chromatography with a maximum standard deviation of 1.1 ppm. The standard deviation of the vertical point concentration analyses in the test section was 1.2 ppm. Similarly, the standard deviation of the horizontal point concentration analyses was 1.0 ppm. The concentration profile results show that there are minimal horizontal and vertical concentration gradients in the test section.

The gas mixing system shown in Fig. 6 can be used to prepare humidified air-pollutant mixtures for accelerated testing of electronic components. The effects of velocity, humidity, and pollutant concentrations upon the rate of metal migration or corrosion can be investigated singly or in combination.

Copper migration results.—The effect of velocity upon the relative rates of copper migration was investigated by varying the velocity while holding the SO₂ concentration [104 ± 1 ppm (vol.)], relative humidity (20.0-31.6%), electrode spacing (2.2-2.5 × 10⁻⁴m), and applied potential (9.0V) constant. The time until a short occurred (*t_s*) was determined at each velocity. The Q test (31) was used to eliminate outlier points at the 90% confidence level. Figure 7 shows the relationship between the short time (*t_s*) and velocity (*V*) in the laminar and transition flow regimes. The decrease in short time with increased velocity indicates that the diffusion of pollutants and water from the gas phase to the PEG-film significantly contributes to the rate of copper migration. This relation is easily explained by transport phenomena or hydrodynamic theory (26, 32). The higher the velocity past the PEG-400 film, the thinner the diffusion (boundary) layer, and thus, the rate of gas-liquid mass transfer of SO₂ increases. Ishino *et al.* (23) report that the diffusion of pollutants to metal surfaces is the controlling step of corrosion processes in the field. The sudden break in the *t_s*-*V* relationship in the transition region is predicted by hydrodynamic theory for any process which is significantly affected by velocity.

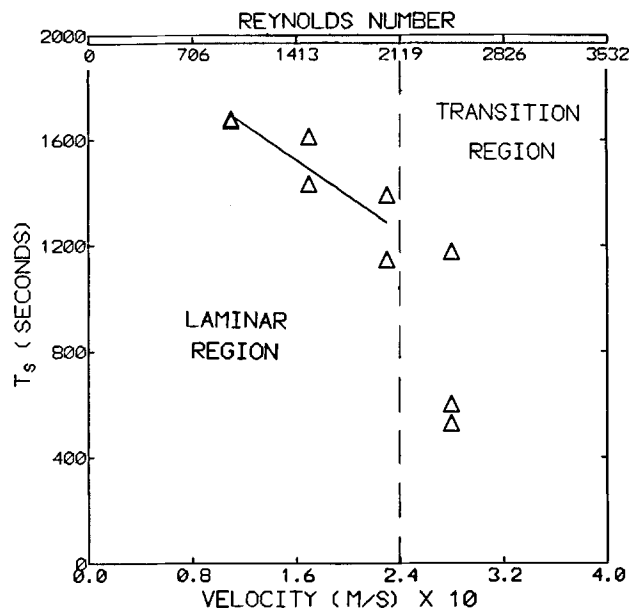


Fig. 7. Effect of velocity upon relative rate of copper migration

Thus, the break in the *t_s*-*V* relationship supports the idea that the gas-liquid mass-transfer step, and therefore the velocity significantly affects the rate of copper migration.

Conclusions

An accelerated test chamber has been developed with reproducible velocity and concentration profiles with minimal velocity and concentration gradients. The length to hydraulic diameter ratio of the chamber is 20. This chamber provides a constant and reproducible atmosphere in which the rates of electrolytic metal migration and corrosion can be determined as a function of pollutant concentration and humidity at constant velocities.

The results of PEG-400 drop tests performed in the described accelerated test chamber show that the velocity significantly affects the rate of copper migration. This velocity effect agrees with hydrodynamic and diffusion theories.

Acknowledgments

The work upon which this paper is based was supported by a contract from IBM (project number MR201). The assistance of Maureen Steg with the velocity profile measurements is acknowledged.

Manuscript submitted Nov. 13, 1984; revised manuscript received July 2, 1985.

REFERENCES

- W. H. Abbott, *IEEE Trans. Parts, Hybrid, Packag.*, **php-10**, 24 (1974).
- L. G. Feinstein and N. L. Sbar, *IEEE Trans. Components, Hybrids, Manuf. Technol.*, **chmt-2**, 159 (1979).
- F. N. Fuss, C. T. Hartwig, and J. M. Morabito, *Thin Solid Films*, **43**, 189 (1977).
- M. Iannuzzi, *IEEE Trans. Components, Hybrids, Manuf. Technol.*, **chmt-6**, 191 (1983).
- M. Iannuzzi and R. P. Kozakiewicz, *ibid.*, **chmt-5**, 345 (1982).
- D. W. Rice, P. Peterson, E. B. Rigby, P. B. P. Phipps, R. J. Cappell, and R. Tremoureux, *This Journal*, **128**, 275 (1981).
- N. L. Sbar, *IEEE Trans. Parts, Hybrids, Packag.*, **php-12**, 176 (1976).
- N. L. Sbar and L. G. Feinstein, *ibid.*, **php-13**, 208 (1977).
- N. Schwartz and D. D. Bacon, *This Journal*, **125**, 1487 (1978).
- E. S. Sproles, Jr., and S. P. Sharma, *IEEE Trans. Components, Hybrids, Manuf. Technol.*, **chmt-6**, 343 (1983).
- O. A. Svedung, L. G. Johansson, and N. G. Vannerberg, *ibid.*, **chmt-6**, 349 (1983).
- G. DiGiacomo, in "20th Annual Proceedings of the Reliability Physics Symposium," pp. 27-33, San

- Diego, CA, March 30-April 1, 1982, IEEE, New York (1982).
13. M. Iannuzzi, *IEEE Trans. Components, Hybrids, Manuf. Technol.*, **chmt-6**, 181 (1983).
 14. H. M. Naguib and B. K. MacLaurin, *ibid.*, **chmt-2**, 196 (1979).
 15. N. L. Sbar and R. P. Kozakiewicz, *IEEE Trans. Electron Devices*, **ed-26**, 56 (1979).
 16. S. P. Sharma, *This Journal*, **125**, 2005 (1978).
 17. P. J. Boddy, R. H. Delaney, J. N. Lahti, E. F. Landry, and R. C. Restrict (Part 1) and R. H. Delaney and J. N. Lahti, (Part 2) in "14th Annual Proceedings of the Reliability Physics Symposium, 108-117, April (1976).
 18. J. N. Lahti, R. H. Delaney, and J. N. Hines, in "17th Annual Proceedings of the Reliability Physics Symposium, 39-43, April, (1979).
 19. D. J. Lando, J. P. Mitchell, and T. L. Welsher, in "17th Annual Proceedings of the Reliability Physics Symposium, 51-63, April (1979).
 20. J. C. Williams and D. B. Herrmann, in "IRE Trans. Reliab. Qual. Control." pp. 11-20, February (1956).
 21. J. J. Steppan, M. S. Thesis, Vanderbilt University, Nashville, TN (1983).
 22. M. Antler and J. J. Dunbar, *IEEE Trans. Components, Hybrids, Manuf. Technol.*, **chmt-1**, 17 (1978).
 23. M. Ishino, M. Kishimoto, K. Matsui, and M. Shoichi, *ibid.*, **chmt-3**, 63 (1980).
 24. J. A. Lorenzen, in "17th Annual Proceedings Inst. Envir. Sciences, pp. 110-116 (1971).
 25. F. N. Fuss, R. F. Leach, and W. H. Yocum, *Proceedings of the 1979 International Microelectronics Symposium*, 325-330 (1979).
 26. S. P. Sharma, J. H. Thomas, III and F. E. Bader, *This Journal*, **125**, 2002 (1978).
 27. S. P. Carbone, and E. A. Corl, in "Atmospheric Corrosion," W. H. Arbor, Editor, pp. 173-175, John Wiley and Sons New York (1982).
 28. F. M. White, "Fluid Mechanics," pp. 312-313, McGraw Hill Book Company, New York (1979).
 29. B. J. W. Tuin, M.S. Thesis, Vanderbilt University, Nashville, TN (1984).
 30. J. H. Arnold, *Physics* (NY), **4**, 334 (1933).
 31. R. B. Dean, and W. J. Dixon, *Anal. Chem.*, **23**, 636 (1951).
 32. R. B. Bird, W. E. Stewart, and E. N. Lightfoot, "Transport Phenomena," John Wiley and Sons, Inc. New York (1960).

Electroreduction of Chromium (VI) in Aqueous Acid Solutions

A. F. Diaz* and D. Schermer

International Business Machines Corporation, General Products Division, San Jose, California 95193

ABSTRACT

The cyclic voltammogram of chromium (VI) in aqueous acid solution shows a reduction peak at 0.3-0.4V when a platinum electrode is used vs. Na SCE. The reaction is electrochemically irreversible, and, with phosphoric acid in the solution, the voltammogram is different than with any other acid because an insoluble chromium (III) phosphate film is formed on the electrode. This film is insulating and forms in a self-healing manner. Although it passivates the electrode towards further Cr(VI) reduction, it remains active to protons and oxygen. The film is very tight, and the diffusion of small molecules such as ferrocene across the film is significantly reduced. In aqueous sulfuric acid, the Cr(VI) reduction reaction is diffusion limited with no indications of adsorption on the electrode surface either before, during, or after the reaction.

Chromium conversion coatings (1-4) are used commercially on aluminum surfaces to provide a protection layer. The coating process is a galvanic process which proceeds spontaneously upon contact of the aluminum substrate with the aqueous acid solution containing chromium (VI). The driving force for the reaction is ca. 2.5 eV (5). Therefore, the reaction is controlled kinetically and has no thermodynamic limitation. The chemistry is complicated and involves electron transfer between aluminum, which is oxidized to aluminum (III) and chromium (VI), which is reduced to chromium (III). The net reaction is shown in Eq. [1]



The chromate solutions contain phosphoric acid, which precipitates Cr(III) as chromium phosphate, the protective layer. Therefore, the resulting protective film is a composite of chromium phosphate and mixed aluminum oxide-fluoride salts. Initially formed films are gelatinous and soft, but they become insoluble, hard, and strongly adherent when dried.

The chromate phosphate process works quite well when relative thick coatings are desired (several microns thick) because the coating covers the aluminum completely. However, the coating is not uniform in thickness on a microscopic level. The thickness of the film is difficult to control because the Cr(VI) species must penetrate the aluminum oxide layer and come in near contact with the aluminum metal in order for electron transfer to occur. Therefore, variations in the protective layer thickness will result from differences in the oxide layer and the corresponding diffusion rates along the aluminum surface. In addition, the chromium phosphate films are subject to disruption due to the diffusion of

ions and hydrogen gas evolution. As a result, the quality of the thin film coatings is noticeably poor. They are very irregular, and areas of the substrate are often left uncoated.

The overall process is quite complicated, and it is not clear how the quality of the thin films is influenced by the quality of the aluminum surface and by the inherent nature of the chromium reaction. Therefore, as an approach, the reduction of chromium (VI) was studied under conditions which would permit us to understand the reaction in the absence of complications due to the chemistry of the aluminum surface. The reaction was probed electrochemically using a platinum surface in both sulfuric and phosphoric acid solutions. The reaction is electrochemically irreversible and limited by diffusion of the electroactive species in solution. In sulfuric acid solution, the reaction produces soluble products, whereas in phosphoric acid an insoluble chromium (III) phosphate film is produced which insulates the electrode surface.

Experimental

The electrochemical equipment used in this study was available from previous studies (6). Most of the measurements were made using a 0.2 cm² platinum working electrode, a gold wire counterelectrode, and a saturated sodium chloride standard calomel reference electrode. A 0.156 cm² gold working electrode was also employed. The solutions were prepared using either Baker "Analyzed" reagent-grade chromium trioxide and mineral acids or using commercially available Alodine 407 which contains 4.4M phosphoric acid and 2M chromic oxide. Reagent-grade ferrocene from Aldrich Chemicals was recrystallized before use. Burdick acetonitrile and tetraethylammonium tetrafluoroborate were used without further purification.

* Electrochemical Society Active Member.

The electron micrographs were measured with a Hitachi S405A scanning electron microscope. The films were coated with a 100Å film of gold prior to the measurement in order to improve the resolution of the micrograph. The ESCA analyses were performed with a Hewlett-Packard 5950B ESCA spectrometer. The energy reference for the instrument is set for Au at 84.0 eV.

Results and Discussion

Chromium (VI) on Pt in aqueous sulfuric acid.—The reduction of 0.01M chromium (VI) in aqueous sulfuric acid (0.18M) was studied by cyclic voltammetry using a platinum electrode. As shown in Fig. 1, the scans were initiated at 0.6V, which is a potential near the open-circuit potential. Better reproducibility was obtained when the voltage was swept to 1.2V before sweeping in the cathodic direction. The cyclic voltammogram shows a peak for the Cr(VI) to Cr(III) reaction at 0.3V. The nature of the electroactive species in aqueous dilute sulfuric acid can be approximated from the magnitude of the various equilibrium constants. Chromium (VI) is primarily in the form of the dissociated ions of chromic acid, H_2CrO_4 , and chromium (III) is in the form of dissociated hydrated ions, $Cr(H_2O)_6^{3+}$ (7). The peak heights scale approximately linearly with the square root of the sweep rate as anticipated for a diffusion-controlled process. This relationship is also plotted in Fig. 1. The plot is not truly linear. Only the first three points extrapolate to the origin, and the points for the faster scan rates deviate down from linearity. Considering the points at the slower scan rates which extrapolate to the origin, a value for $i/Av^{1/2}$ equal to 0.042 A/cm² (V/s)^{1/2} is calculated. This provides a value for $n(\alpha nD)^{1/2}$ equal to 14.1×10^{-3} cm/s^{1/2} using the Randles-Sevcik equation for an irreversible reaction (8). With n equal to 3, αD is calculated to be 0.74×10^{-5} cm²/s.

The reaction is electrochemically irreversible, and the products remain soluble with no evidence of change in the activity of the electrode surface as a result of the formation of an insulating film. In the anodic sweep, there is a small anodic peak at 1.0-1.2V which must be due in part to the oxidation of chromium (III) which is formed while the electrode is resting at 0.6V before the scan is initiated, plus the oxidation of the platinum surface. The oxidation of the platinum surface is a relatively unimportant reaction in these conditions. For example, the voltammogram measured using an aqueous sulfuric acid solution, containing no chromium (VI), does not show a peak at 0.6V (anodic scan); it shows only a gradual increase in the current. Furthermore, the reduction peaks, which appear at 0.25 and 0.47V, are 15-20 times smaller. Finally, in the potential region cathodic of 0.0 V (not shown in Fig. 1), the cathodic current increases rapidly, owing to the re-

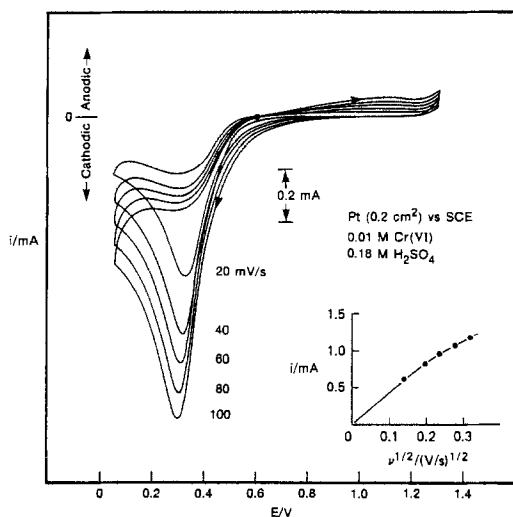


Fig. 1. Cyclic voltammogram for the reduction of Cr(VI) in 0.18M aqueous sulfuric acid using a platinum electrode. The inset shows a plot of the peak current vs. the square root of the sweep rate.

duction of protons and oxygen in the electrolyte solution. The reactions occurring in this voltage range were not investigated further. The results obtained with the platinum electrode/sulfuric acid solution could be reproduced with a gold electrode or a hydrofluoric acid solution.

Chronocoulometry of the platinum electrode/sulfuric acid solution reconfirms that the reaction is diffusion limited. As seen in Fig. 2, the consumption of charge is linear in $t^{1/2}$. For these measurements, the potential was stepped from 0.6 to 0.2, 0.0, and -0.2 V, respectively. The same slope was obtained in every case, and a value for $nD^{1/2}$ equal to 9.63×10^{-3} cm/s^{1/2} is calculated using the integrated form of the Cottrell equation (8). With n equal to 3, the diffusion coefficient for the chromium (VI) reaction is 1.03×10^{-5} cm²/s. To the extent that there may be some reduction of platinum oxide, the linearity in the chronocoulometric plots suggests that it is not very important under these conditions. When the potential was stepped to values cathodic of -0.3 V, the current response was no longer linear with $t^{1/2}$ due to the concurrent reactions of oxygen and protons at the electrode surface.

The electrochemical stoichiometry of the reaction has been assumed equal to 3 F/mol. The same stoichiometry, 3.03 F/mol of chromate, is observed for the electrochemical reduction of Cr(VI) in aqueous ammonium-buffered solution (9) and of $CaCrO_4$ (<0.04 M) in LiCl-KCl eutectic melt (10). In the report by Delnick and McCarthy (10), the cyclic voltammogram of the melt solution is described as having a single irreversible wave at -0.45 V vs. Ag/Ag^+ reference electrode. The reaction is a one-step process yielding $LiCrO_2$ exclusively. The stoichiometry also varies with the reaction conditions and is different in aprotic solvent (11). In acetonitrile, the first reduction reaction of chromate on a dropping mercury electrode is a one-electron reversible reaction. The $\log(i)$ vs. E plot for this reaction has a slope of 16.7 (11) with $n = 1$ and $\alpha = 0.98$. However, under the same conditions but using a solid gold electrode, the reaction is again irreversible and produces mainly Cr(II) and Cr(O) (11).

A comparison of D (1.03×10^{-5} cm²/s) from the chronocoulometry experiment with αD (0.74×10^{-5} cm²/s) from the cyclic voltammetry experiment provides a value for α equal to 0.72. This value can be determined experimentally from the low current levels at the initial part of the reduction peak. The voltammogram is shown in Fig. 3 along with the $\log(i)$ vs. E plot (inset). The measurement was made using a slow sweep rate, 4 mV/s, between 0.7 and 0.4V. $\log(i)$ is linear with E , and the slope of the line (nF/RT) is 13.1. From the slope, αn is estimated to be equal to 0.77, which does not fit for α equal to 0.72 and n equal to three. This gross discrepancy between the two values cannot be reconciled unless the peak shown in Fig. 1 envelopes several peaks and the stoichiometry changes from one in the initial part of the peak to three as the scan progresses through the voltage range of the peak.

Chromium (VI) on Pt in aqueous phosphoric acid.—The results obtained using solutions prepared from commer-

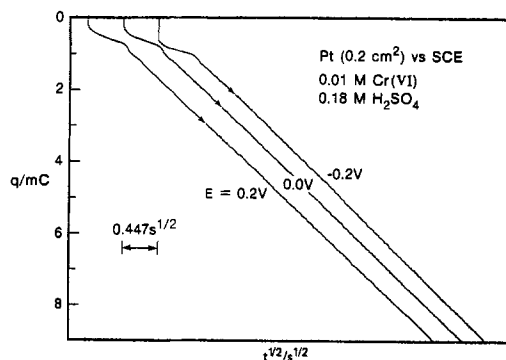


Fig. 2. $Q-t^{1/2}$ plot for the reduction of Cr(VI) in 0.18M sulfuric acid using a platinum electrode. The curves correspond to separate measurements where the potential was stepped from 0.6V to 0.2, 0.0, and -0.2 V, respectively.

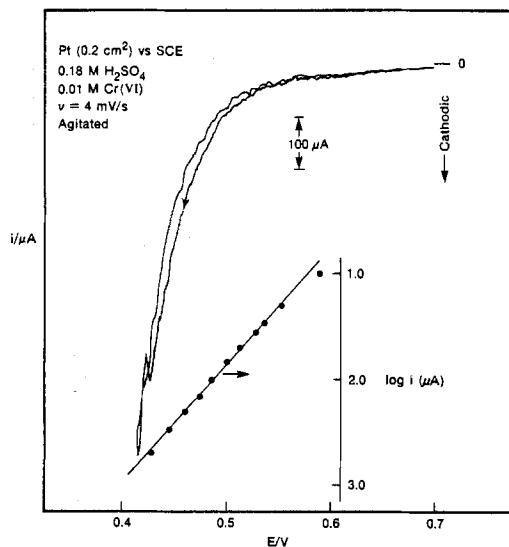


Fig. 3. Current-voltage plot at the foot of the wave for the reduction of Cr(VI) in 0.18M aqueous sulfuric acid using a platinum electrode. The measurement was made using a sweep rate of 4 mV/s and with agitation of the solution. The inset shows a plot of $\log i$ vs. V .

cially available Alodine 407 are quite different. The Alodine solution was diluted 1 to 200 with distilled water and used directly for analyses. This solution consists of 0.01M Cr(VI) and 0.022M phosphoric acid. The chemical nature of Cr(VI) can be estimated in this acid solution by considering the various equilibria for the proton dissociation of phosphoric ($\log K = -2$) and chromic acid ($\log K = 0$) plus the condensation of chromic acid to form the mixed anhydride with phosphoric acid ($\log K = 0.95$) and with dihydrogen phosphate ($\log K = 0.48$) (7). Using these values, it can be calculated that the Cr(VI) species exists primarily in the anhydride form where the equilibrium mixture is 0.0075M $H_2CrPO_7^-$ and 0.0025M $HCrPO_7^-$.

The measurements were more difficult to make with this solution because the reaction product, chromium (III) phosphate ($\log K_{sp} = -17$ to -23) (7), precipitates on the electrode surface. It is essential that the potential applied to the electrode be swept anodically to 1.2V before the excursion in the cathodic direction in order to oxidize away the deposit. Without this treatment, reproducible voltammograms are not obtained, where, in the subsequent sweeps, the peak becomes considerably smaller and displaced. Repeated scanning over this potential range without cleaning the electrode causes the electrode to become completely passivated. Finally, cleaning the electrode by the anodic sweep treatment is successful only with freshly formed films. Electrodes which were removed from the electrochemical cell and whose film had dried had to be cleaned by abrasion.

The scan for the voltammetric analysis of this solution was initiated at 0.6V, scanned anodically to 1.2V, and then cathodically to 0.0 V. Two oxidation waves appear in the initial anodic scan at ca. 0.8 and 1.0V and are due to the oxidation of chromium (III) phosphate which is formed on the electrode during the short time that the cell is at rest before the scan is initiated, plus the oxidation of the platinum electrode. As can be seen in the voltammogram shown in Fig. 4, the change in the electrolyte from sulfuric to phosphoric acid causes the peak to shift to 0.38V and reduces the current response by an order of magnitude even though the Cr(VI) concentration is similar in both solutions. Thus, the effective surface area is only ca. 10% of the geometric area of the electrode. The peaks have a more symmetrical shape, are much broader, and still increase with the sweep rate. The increase in the peak height is more closely linear with the rate (inset a) but is not truly linear with either the rate or the square root of the rate (inset b). These characteristics suggest a shift in the mechanism to a surface-localized reaction occurring in the absence of diffusion. However, the peak

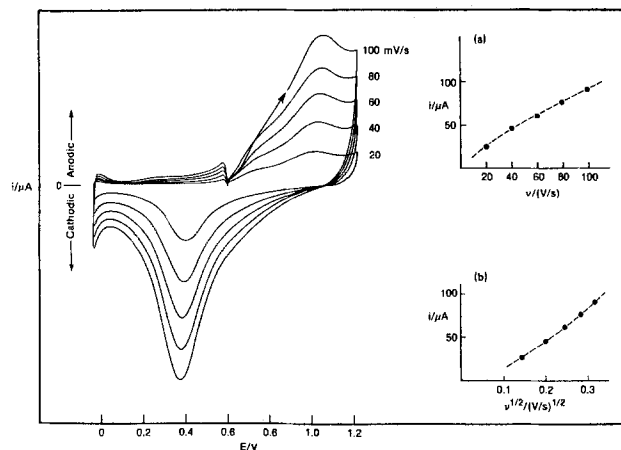


Fig. 4. Cyclic voltammogram for the reduction of Cr(VI) in 0.022M aqueous phosphoric acid solution using a platinum electrode. The insets show a plot of the peak current vs. the sweep rate (a) and square root of the sweep rate (b).

width at half-height is approximately 0.3V and much larger than the expected value of $93/n$ mV. Thus, the electroreduction reaction is much more complicated in the presence of phosphoric acid and is strongly influenced by the chromium phosphate deposit on the electrode surface.

Although definite conclusions cannot be drawn from this data, the characteristics of the voltammogram may result from the gradual decrease in the effective electrode area during the scan caused by the formation of the passivating layer. A continuous decrease in the area will cause the current to drop off faster than is expected for a diffusion-controlled reaction, thus giving the peak a symmetrical appearance. The surface does not fully passivate during the time of a single scan with the sweep rates used, and the film is easily penetrated by protons and oxygen. As a result, the current in the cathodic sweep increases at ca. 0.0V.

The oxidation and reduction of the platinum surface is important with these conditions. For comparison, voltammetric analyses were made of an aqueous 0.03M phosphoric acid, with no chromic acid present, and using the same potential limits and scan rates as above. The voltammogram shows a gradual increase in the anodic current during the initial anodic sweep. In the cathodic scan, the cathodic current increases gradually, starting at ca. 1.0V, and the peak appears at 0.2V. The current response is comparable to the case with chromic acid present. Thus, with the chromic acid/phosphoric acid solution (Fig. 4), the anodic current resulting from the oxidation of the surface in the initial anodic scan must lie under the peaks observed at 0.8-1.0V. And, in the cathodic scan, the presence of the prewave at 0.6V is due to the reduction of the platinum surface (12). The peak at 0.2V does not appear when chromic acid is present.

From the chronocoulometric measurements, it is seen that the surface is readily passivated and maximum current levels are quickly attained. For these measurements, the applied voltage was stepped from 0.6 to 0.2V, and the amount of charge consumed was measured with time. The results are plotted in Fig. 5, where it can be seen that the charge is linear with neither time nor the square root of time, but continually decreases as the electrode becomes passivated. The current levels off after approximately 20s, and the amount of charge consumed is approximately 3 mC/cm², which corresponds to approximately five monolayers of chromium phosphate.

Finally, the voltammogram for chromium (VI) in phosphoric acid solution can be changed to resemble the voltammogram observed in solutions containing only sulfuric acid by the addition of sulfuric acid. With the addition of 0.18M sulfuric acid to the above solution, the voltammogram changes and resembles the one measured in aqueous solution containing only sulfuric acid. The re-

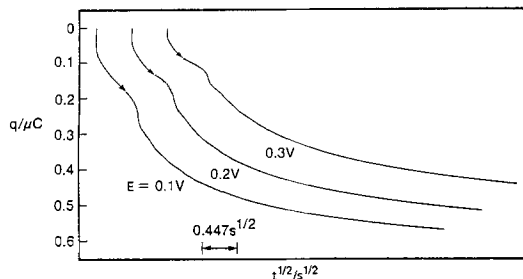


Fig. 5. $Q-t^{1/2}$ plot for the reduction of Cr(VI) in 0.022M aqueous phosphoric acid using a platinum electrode.

duction peak is shifted cathodically from 0.38 to 0.33V at 20 mV/s, and the size of the peak recovers. In addition, there now appears a slight cathodic depression at ca. 0.3V in the anodic sweep.

Concentrated chromium (VI) solution.—The results with the dilute solutions are very different from those reported using a high concentration (2.5M) of chromic acid (13, 14). As can be seen in Fig. 6, the voltammogram is much more complicated and is consistent with the voltammogram published by Hoare (12, 13). Analysis of this concentrated solution is not straightforward since the electrode is easily contaminated. As a result, we observed wide variations in both the size of the signal and the reproducibility of the results between runs. As before, the reproducibility was improved when the voltage was scanned anodic to 1.4V before scanning cathodically. The most striking difference is in the size of the signals. The peaks are ca. ten times smaller than the peak produced by the dilute solution even though the solution is 250 times more concentrated, suggesting again that the electrode surface is heavily contaminated by an insulating film. In addition, the oxidation of the platinum surface strongly interferes with the analysis of these solutions. The film that is formed probably results from the chemical reaction between platinum and chromate, and consists of the oxides of these metals (12, 13). The peak at 0.3V observed with the dilute solutions is now shifted to 0.4V, and two additional reduction peaks appear in this voltage range, one at 0.6V and one at 0.9V. With these solutions, the oxidation peaks in the range 1.0-1.2V, corresponding to the oxidation reactions of Cr(III) and the platinum surface, are considerably larger.

The decrease in current density with increasing concentrations of chromate has been reported by Wallace (14). In the concentration range 0.2-1.0M chromate, the current density for the reduction reaction on a nickel-plated steel surface was found to be lower at the higher concentrations (14).

Passivating chromium phosphate films.—Films of chromium phosphate were prepared at constant potential, 0.2V, and using the dilute solution 0.01M chromic

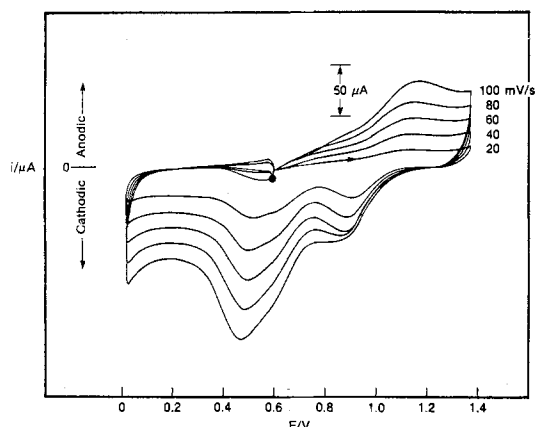


Fig. 6. Cyclic voltammogram for the reduction of Cr(VI) in 2.5M aqueous chromic acid using a platinum electrode.

acid and 0.022M phosphoric acid. Films prepared using ca. 1 mC/cm² were too thin, and no information was obtained about the topology or the presence of cracks or defects from scanning electron microscopy using 40,000 magnification. ESCA analysis was only semiquantitative because of the limited amount of material. The ESCA spectrum shows a small signal for chromium (575 eV) and phosphorus (189 eV) in the ratio of 1 to 2.

Since the SEM analysis was not helpful for determining the integrity of the film, measurements of the diffusion of ferrocene across the film were made. For these determinations, films on the platinum electrode were mounted as a working electrode in a cell containing 0.001M ferrocene in acetonitrile. The voltammogram of this solution shows a signal for the oxidation of ferrocene which is ca. 50 times smaller and has a distinctively different shape than the peak observed on bare platinum (see Fig. 7). This measurement could be repeated with no obvious damage to the film. Films prepared in this way were quite reproducible where the variation in the current response was 10-30% between films. From the size and the shape of the peak in Fig. 7, it is clear that the film covers the platinum electrode completely. There are no open areas, cracks, or defects. If the current was due to the reaction of ferrocene occurring at exposed areas of the electrode provided by cracks or defects, the shape of the voltammogram would resemble that for a clean electrode surface and the size of the signal would depend on the extent of exposure.

The film does permit some level of diffusion, and the current levels observed permit us to estimate the diffusion of ferrocene across the chromium film. The diffusion velocity (D/u) is 2×10^{-4} cm/s, and was estimated using the equation provided by Lacaze for a process where there is limited diffusion across an insulating thin film on the electrode surface (15), $i_{lim}/A = nFC D/u$. This equation was derived from the case where there is no selectivity for ion migration from the solution into the film and there is a linear concentration gradient of the electroactive species across the thin film. The concentration of the electroactive species is zero at the metal film interface and equal to the bulk concentration at the film solution interface. For this calculation, n is 1, F is Faraday's constant, C is the concentration of ferrocene, D is the diffusion coefficient for ferrocene across the film, and u is the thickness of the film. Considering that the film is 20-25Å thick, the diffusion constant for ferrocene in the film is 0.5×10^{-10} cm²/s. The chromium phosphate films

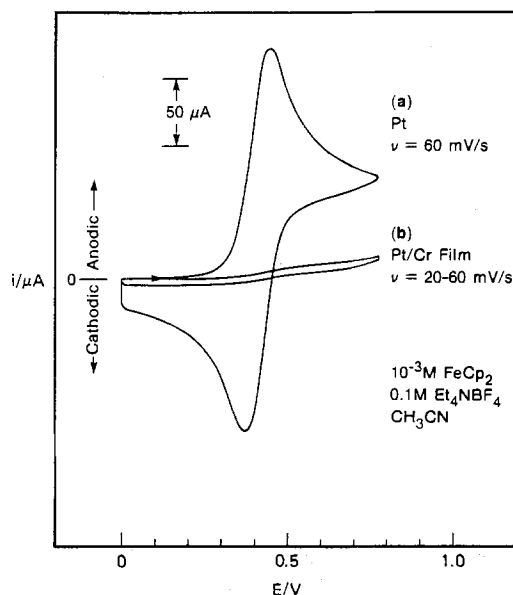


Fig. 7. Cyclic voltammogram for the oxidation of ferrocene in acetonitrile solution containing 0.1M tetraethylammonium tetrafluoroborate. a: Bare platinum electrode. b: Platinum electrode coated with chromium phosphate film.

are quite stable on the electrode in the acetonitrile electrolyte and can be used repeatedly. For example, with the thicker films of chromium phosphate, the electrode was totally insulated from the solution and no current response was observed in the voltammogram, even with repeated scanning between 0 and 1.0V. In contrast with the behavior in aprotic solvent, they are not stable in aqueous solution containing ferrocyanide ion. Electrochemical analysis of this solution with the coated electrodes resulted in the destruction of the film during the anodic scan.

The diffusion of ferrocene across the chromium phosphate film is much slower than has been observed with passivating organic films on electrode surfaces. Diffusion through the organic thin films (600-30,000Å) varies with the structure of the polymer (16). The smallest diffusion coefficients have been observed with polysilanes which have values of 5×10^{-10} cm²/s. The hydrocarbon polymers have values in the range $14-1300 \times 10^{-10}$ cm²/s.

Conclusions

The electrochemical reduction of Cr(VI) is well behaved in dilute acid solutions. The reaction is electrochemically irreversible and diffusion limited. In aqueous sulfuric acid with low concentrations of Cr(VI), soluble Cr(III) products are formed. In concentrated solutions, the electrode is partially passivated by the formation of insoluble Cr(III) salts. In solutions containing phosphoric acid, insoluble chromium phosphate is formed on the electrode even at dilute Cr(VI) concentrations. The film insulates the total surface very efficiently, and the diffusion of molecules, such as ferrocene, across the film is significantly reduced.

Acknowledgments

The authors wish to thank R. Galwey, A. Tuason, V. H. Le, and L. Van Ness for their technical assistance, and M.

Henneberg, R. Balanson, M. Bergkamp, and T. Tilbury for their support of this project.

Manuscript submitted Feb. 4, 1985; revised manuscript received July 15, 1985.

IBM Corporation assisted in meeting the publication costs of this article.

REFERENCES

1. C. W. Ostrander, in "Electroplating Engineering Handbook," 3rd ed., A. K. Graham, Editor, p. 437, Van Nostrand Reinhold Company, New York (1971).
2. S. Wernick and R. Pinner, "The Surface Treatment and Finishing of Aluminum and Its Alloys," 4th ed., Vol. 1, p. 263, Robert Draper Ltd., London (1972).
3. F. A. Lowenheim, "Electroplating," 3rd ed., p. 442, McGraw-Hill Company, New York (1974).
4. B. Laszloni, *Gepgyartastechnologia*, **12**, 495 (1972).
5. W. M. Latimer, "Oxidation Potentials," 2nd ed., Prentice Hall, Inc., New York (1952).
6. A. Diaz, J. I. Castillo, W. Lee, and J. A. Logan, *J. Electroanal. Chem.*, **129**, 115 (1981).
7. "Stability Constants of Metal Ion Complexes," The Chemical Society Special Publication 17, The Chemical Society, London (1964).
8. R. N. Adams, "Electrochemistry at Solid Electrodes," Marcel Dekker, New York (1969).
9. J. Matysik and M. Korolczuk, *J. Electroanal. Chem.*, **88**, 421 (1978).
10. F. M. Delnick and D. K. McCarthy, *This Journal*, **130**, 1875 (1983); see references therein for earlier work on the electrochemical reduction of chromates in molten salt solutions.
11. M. Otto, R. Wagner, and H. Hennig, *Inorg. Chim. Acta*, **64**, L11 (1981).
12. J. P. Hoare, *This Journal*, **130**, 1475 (1983).
13. J. P. Hoare, *Plat. Surf. Finish.*, **71**, 50 (1984).
14. A. J. Wallace, Jr., *ibid.*, **67**, 66 (1980).
15. M. Delmar, M. C. Pham, P.-C. Lacaze, and J.-E. Bubojs, *J. Electroanal. Chem.*, **108**, 1 (1980).
16. A. Diaz and R. D. Miller, *This Journal*, **132**, 834 (1985).

Electrochemical and Metallurgical Aspects of Laser-Enhanced Jet Plating of Gold

M. H. Gelchinski, L. T. Romankiw,* D. R. Vigliotti, and R. J. von Gutfeld*

IBM T. J. Watson Research Center, Yorktown Heights, New York 10598

ABSTRACT

Experimental results for a new plating technique using a laser in combination with a pressurized jet are described. Electrochemical and hydrodynamic parameters affecting the gold deposits are discussed. Scanning electron micrographs of the deposited gold surfaces indicate increased smoothness and decreased nodularity as well as disappearance of voids with increasing laser power density. A marked decrease in voids with increasing laser power is also observed in cross-sectioned samples. At the highest laser power densities used, with a 0.5 mm diam nozzle, plating rates of up to 12 μ m/s have been observed. In general, the rate increases with increasing laser power density. Measurements of the Knoop hardness of the deposits gave values in the range characteristic for soft gold.

The development and potential benefits of the laser-enhanced plating (LEP) technique have been described in several previous publications (1-8). Investigations of the experimental parameters, mechanisms, and applications were carried out for laser-enhanced copper plating (1-4) and more recently for laser-enhanced gold plating (5-7). High quality gold deposits, at plating rates of approximately 1 μ m/s, were obtained. Recently, it was suggested that the plating rate of LEP is limited by the substrate heat conductivity (10). Based on experimental and theoretical considerations, it is claimed in Ref. (10) that the application of a thin layer of a relatively poor heat conducting material may lead to a higher local heat increase and significantly improved plating rate and selectivity of gold deposits.

* Electrochemical Society Active Member.

We have demonstrated (6, 8) that plating rates in LEP are limited by the concentration of ions in solution and the supply of ions into the plating region. Dendritic or powdery depositions were obtained when plating was carried out from a commercially available plating solution containing as much as 32.4 g/liter (4 tr oz Au/gal) at plating rates greater than 1 μ m/s. An attempt to avoid operation at the limiting current density region by using high concentration solutions in conjunction with a higher power laser did not substantially increase the plating rate, though a larger volume per second could be deposited by defocusing the laser to a larger spot size.

To improve the mass transport and consequently the plating rate, we developed a new technique, laser-enhanced jet plating (LEJP) (9), which combines the earlier LEP technique with a free-standing jet of electro-

lyte to achieve localized high speed, resulting in gold-plated spots and lines of high metallurgical quality. The principal advantage of the free-standing jet is its ability to provide a rapid resupply of fresh ions into the region of plating to overcome the mass transport limitation. In addition, the jet stream limits the region of plating without the use of masks. In the present application, the jet stream also acts as an optical waveguide or light pipe for the laser beam. This paper reports the electrochemical and metallurgical aspects of LEJP of gold deposits.

General Concept—Total Internal Reflection

When a light beam emerges from a medium of higher refractive index, such as water, into a lower index medium, such as air, at a finite angle, it is bent away from the normal to the interface as it enters the lower index medium (air). When the incident angle for a water-air interface is greater than 49° , the beam will undergo total internal reflection in the water with the angle of reflection being equal to the angle of incidence. In our experiments, the laser is directed collinearly through an optical window into a free-standing jet of plating liquid. In such a configuration, the jet both resupplies the ions and acts as an optical waveguide to contain the laser beam by reflecting diverging light from the jet periphery-air interface. The waveguide also tends to homogenize the power density in the radial direction.

Experimental Setup and Procedure

The experimental setup is shown in Fig. 1. A CW argon laser beam with maximum output power of 25W was passed through a beam expander prior to entering the cell and focused approximately at the center of the jet orifice with a 50 mm focal length lens. The flow system is comprised of a solution container, a pump which recirculates the electrolyte after impingement on the cathode, and the jet cell. The components of the flow system are connected with polypropylene and tygon tubes. The pump is equipped with 316 stainless steel bearings. The jet cell, shown schematically in Fig. 2, is a hollow Lucite cylinder, consisting of an inlet chamber, maintained under pressure with the jet nozzle. The nozzle is made from a section of capillary tube glassed onto a flat Pyrex plate. The end plates of the cell are quartz windows. A platinum wire serves as an anode and is inserted into the fluid chamber. Air bubbles trapped in the fluid chamber are eliminated by a bleeder valve. A nozzle orifice of 0.5 mm diam is used, giving rise to gold spots of similar diameter. To maintain a constant current, we used a PAR 173 potentiostat set to operate galvanostatically. The cathode is attached to a microprocessor-controlled X-Y-Z table via an extension arm. The Anorad microprocessor also controls the on-off gating of the argon laser and can be made to operate the on-off controls of the potentiostat. Programs we use move the cathode to a desired position, followed by gating on both the laser and potentiostat simultaneously while the jet runs continuously. In several experiments, the potentiostat was controlled manually. Plating takes place only when the current and the laser beam are on.

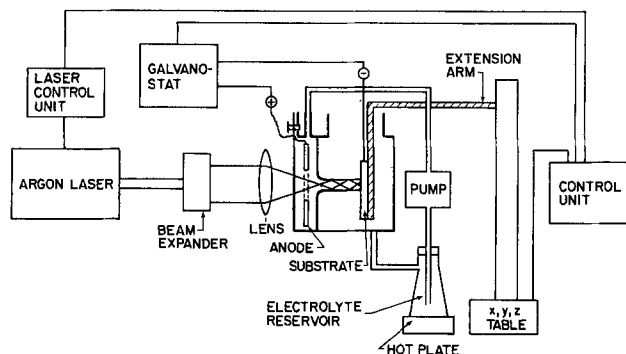


Fig. 1. Experimental setup

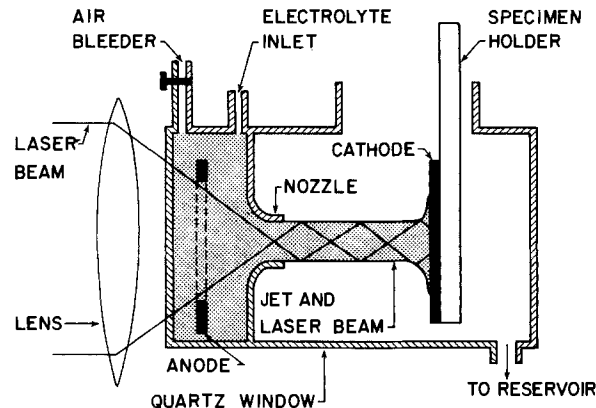


Fig. 2. Schematic representation of the jet cell and the waveguide effect

In either mode of operation, the height of the deposit was measured from the time the sample was moved into position for the particular dwell time programmed with the potentiostat supplying constant current.

For all electroplating runs, we used a high speed cyanide acid solution (Sel-Rex Autronex 55 GV without addition of the cobalt complex) containing 4 tr oz/gal of metallic gold. The electrolyte was preheated to 60°C . The linear flow velocity was 1.0×10^3 cm/s, which corresponds to a Reynolds number of 5.5×10^3 at the nozzle orifice. The nozzle-cathode spacing was typically 0.5 cm.

For metallurgical cross sectioning, the samples were nickel plated prior to mounting in epoxy to preserve the original profile of the deposit during the metallurgical sectioning. After sectioning, the potted samples were polished, etched to reveal the structure, and examined by an optical microscope. Scanning electron microscopy was used to study the morphology of the deposits. Thickness was measured from the photographs of the cross-sectioned samples under the optical microscope. These values agreed with those measured with a Talysurf prior to potting in epoxy.

Results

Jet plating.—Morphology of jet plating deposits at high current densities.—Initial studies were conducted with the jet system without laser irradiation in order to compare the jet-plated gold to LEJP gold under otherwise the same plating conditions. The substrates used were 200 μm (8 mil) thick beryllium-copper, plated with approximately 1 μm nickel from a sulfamate plating bath. To prevent contamination of the gold solution, the substrate was precleaned in acetone and methanol. This cleaning proce-

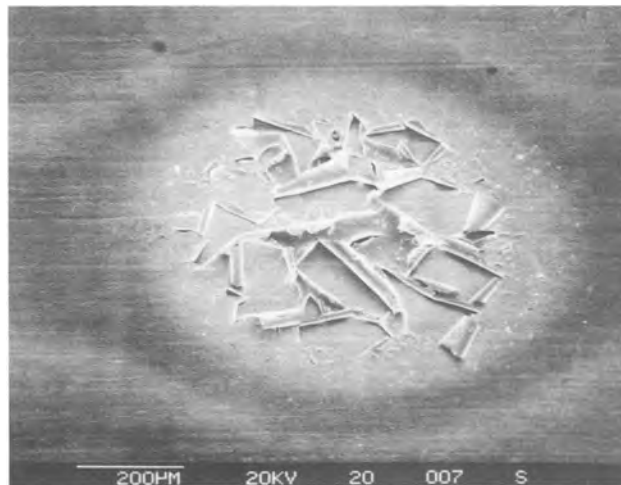


Fig. 3. SEM micrograph of a jet-plated (no laser) gold spot plated at room temperature. Current density ~ 10 A/cm 2 . (Note that deposition is badly cracked and peeled due to stresses and residual nickel oxide on the substrate.)

ture, however, was insufficient to dissolve the thin native nickel oxide layer usually present on plated nickel.

Plating at room temperature with the aforementioned cleaning procedure at current densities above 5 A/cm^2 resulted in a cracked deposit which peeled off very easily (Fig. 3) owing mainly to high internal stresses and poor adhesion. Increasing the electrolyte temperature to 60°C resulted in a nodular deposit, shown in Fig. 4a-4b, composed of small, isolated nodules separated by large voids. Cross sections of these deposits are shown in Fig. 5a-5c. One observes large voids throughout the deposit irrespective of film thickness, indicating that the voids initiate at the nickel-gold interface apparently due to a combination of the presence of nickel oxide on the surface (with a resulting low density of nucleation sites) and very high local current density. This type of columnar deposit with columns physically separated from each other is typical of metal deposition resulting from a low density of nucleation sites in combination with plating near or at the limiting current density.

Laser-enhanced jet plating.—Effect of laser power on morphology.—The effect of laser power on the morphological structure of laser-enhanced jet deposits is demonstrated in the scanning electron microscope (SEM) micrographs of Fig. 6a-6d. The deposits were plated for 0.5s at a current density of 12.5 A/cm^2 . Figure 6a shows that deposits obtained with a relatively low laser power result in a nodular microstructure. This surface is composed of uniform, small, isolated nodules separated by open voids which penetrate deeply into the deposit. This morphology is similar to the structure obtained with jet plating

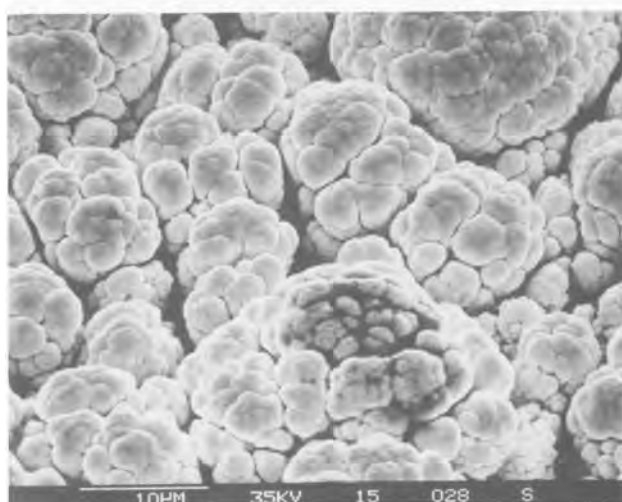
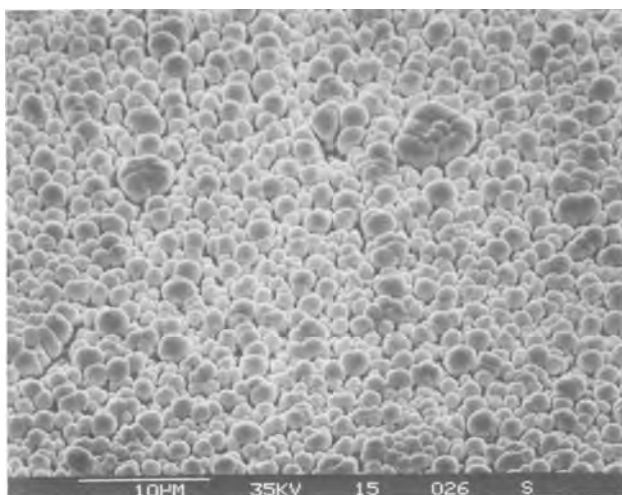


Fig. 4. SEM micrographs of jet-plated (no laser) gold spots plated at 60°C . The current density is 12.5 A/cm^2 . a: Plating time = 1s; thickness $\sim 3 \mu\text{m}$. b: Plating time = 10s; thickness $\sim 25 \mu\text{m}$.

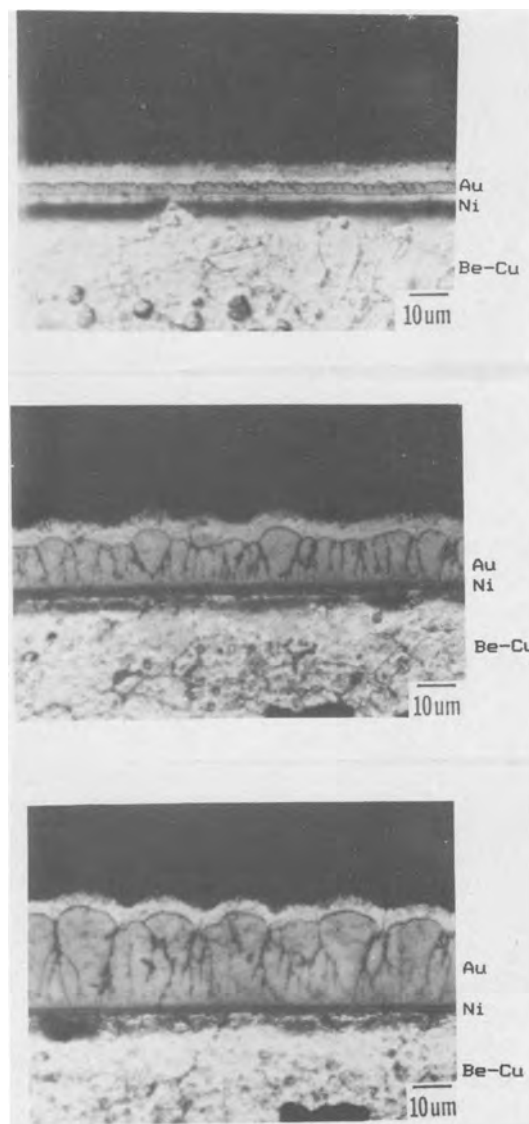


Fig. 5. Cross section of jet-plated gold spots without the use of laser power during deposition. The current density is 11 A/cm^2 . Plating times and resulting thickness are: 1s, $3 \mu\text{m}$ (a), 5s, $12.5 \mu\text{m}$ (b), and 10s, $25 \mu\text{m}$ (c). Note that the voids and pores appear throughout the deposits, irrespective of film thickness.

without laser irradiation, as shown in Fig. 4. This implies that 10W of laser power (an incident power density of $\sim 5 \times 10^3 \text{ W/cm}^2$) is insufficient to alter the microstructure of the deposit for these particular plating conditions.

Increasing the laser power to 15W still resulted in a somewhat nodular deposit (Fig. 6b) although the nodules are larger and more connected. A substantial morphological change occurred when the laser power was raised to 20W ($1 \times 10^4 \text{ W/cm}^2$), Fig. 6c. This power was sufficient to produce a visually bright, smooth deposit with very few surface cracks and nodules. When the laser power was increased to 25W, a more continuous morphology was produced (Fig. 6d).

The morphological changes caused by the laser illumination in LEJP are more pronounced when thick deposits are produced, as illustrated in Fig. 7a-7d. These deposits were plated for 5s at a current density of 12.5 A/cm^2 . Figures 7a-7c show that the nodules become larger (suggesting large crystallites or grains) as the laser power increases from 10 to 20W. With 10W of laser power, a nodular deposit was obtained. This deposit appears to contain two types of morphologies: small nodules with distinct, tight boundaries which form larger nodules separated by deep voids. At 15W, the number of voids decreases (Fig. 7b). One can also see that the surface of the deposit became smooth. Increasing the laser power to 20W leads to

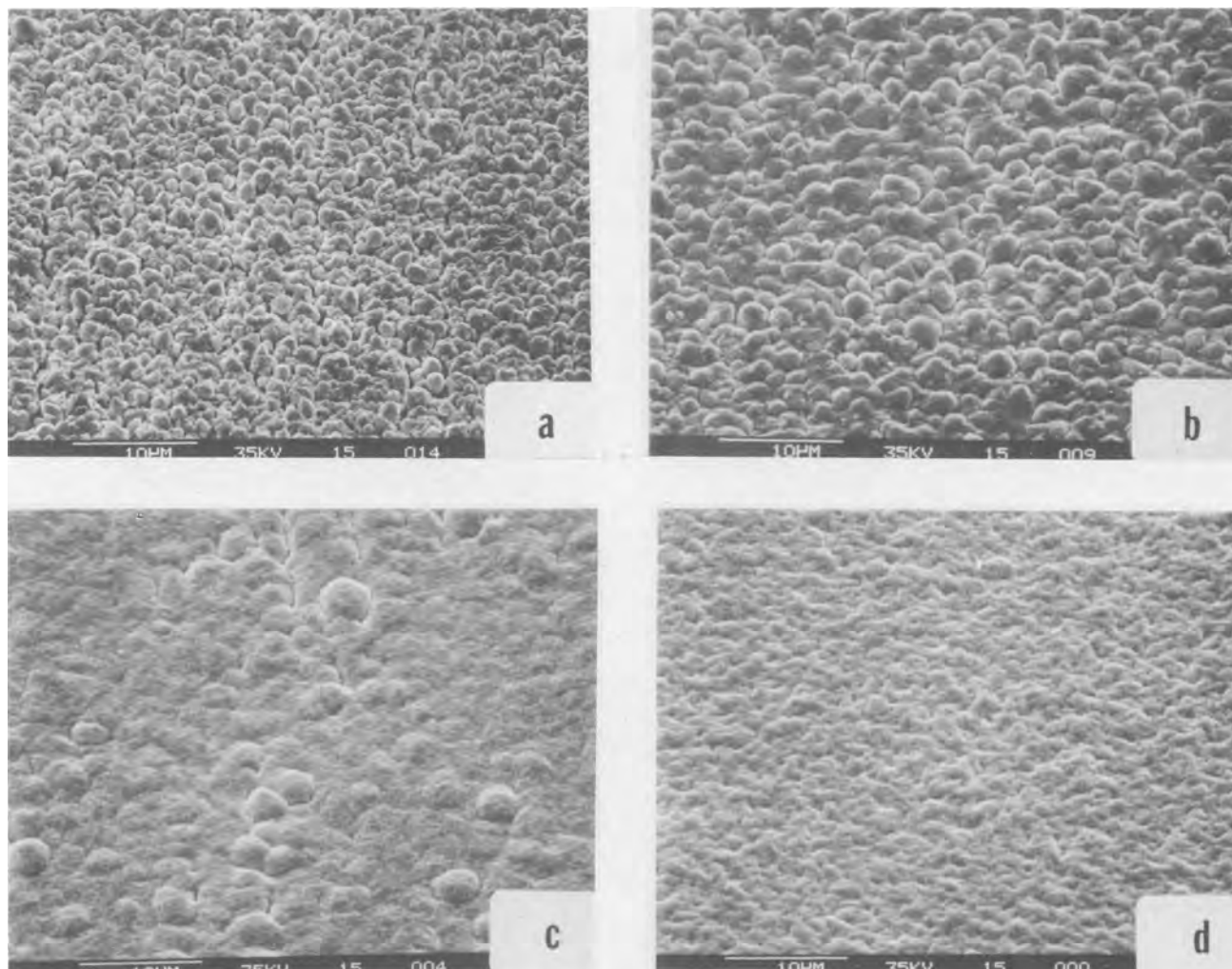


Fig. 6. Effect of laser power on the morphology of LEJP of gold deposits as shown in SEM. The current density is 12.5 A/cm^2 . Plating time = 0.5s. Laser power: 10W (a), 15W (b), 20W (c), 25W (d).

a pronounced morphology modification as shown in Fig. 7c. Here, the structure appears to be that of large crystallites ($\sim 10 \mu\text{m}$) without voids or cracks. Finally, at 25W, a smooth deposit is produced (Fig. 7d).

Cross-sectioned samples of laser-jet plated gold spots are shown in Fig. 8a and 8b. These deposits were plated at a current density of 12.5 A/cm^2 in conjunction with 25W of laser power. Examination of their morphology indicates dense deposits consisting chiefly of small crystallites, free of cracks and voids. Upon electroetching, the samples were found to possess a columnar structure, typical of pure soft gold deposits. We have observed a similar behavior in the morphology of gold laser-jet deposits on both copper and beryllium-copper substrates with increasing laser power.

Effect of laser power on plating rate.—The effect of the laser power on the plating rate was measured for deposits plated at a constant current density of 12.5 A/cm^2 . Figure 9 shows the variation of the plating rate as a function of laser power. The curve of Figure 9 is divided into two regions which have two different slopes. The first region, extending from 0 to 15W, results in only a moderate enhancement in the plating rate. Above 15W the rate enhancement due to the laser illumination is significant and reaches $\sim 10 \mu\text{m/s}$ at 25W, compared to $2.5 \mu\text{m/s}$ without the laser. This increase in plating rate can be explained in terms of an increase in plating efficiency described in more detail in the Discussion section.

Effect of current density on plating rate and microhardness.—The plating rate, in conjunction with 20W of laser power, increases linearly with the current density, as

demonstrated in Fig. 10. This indicates that deposition is carried out at potentials below the limiting current density at a constant plating efficiency.

Microhardness was measured on polished cross sections using a Leitz Miniload microhardness tester with a 25g load. The results of the variation of microhardness with current density are shown in Fig. 11. The Knoop hardness number at a 25g load decreases slightly with increasing current density. Microhardness testing indicates that LEJP from a pure gold solution results in a soft gold deposit, *i.e.*, Knoop values ranging from 70 to 90 kg/mm^2 . The low Knoop values of LEJP deposits are indicative of a high purity deposit and large crystallites, consistent with the morphological findings. It is important to mention that these morphological results are also a function of jet velocity, jet diameter, ambient bath temperature, as well as plating solution parameters.

Discussion

Two factors are probably responsible for the production of the rough, dull, and porous deposits obtained for jet plating, without laser illumination, at high current densities. First, plating was performed near or at the limiting current density. Second, the substrate was covered with a thin native oxide layer. In general, plating at the limiting current density yields a rough nodular or powdery deposit (11, 12) due to the depletion of the ions and due to OH formation at the cathode. For jet-plated deposits, the long voids between the columns are found to occur throughout the film irrespective of thickness, apparently initiating at the nickel-gold interface. This indicates that an oxide layer greatly reduces the number of nuclea-

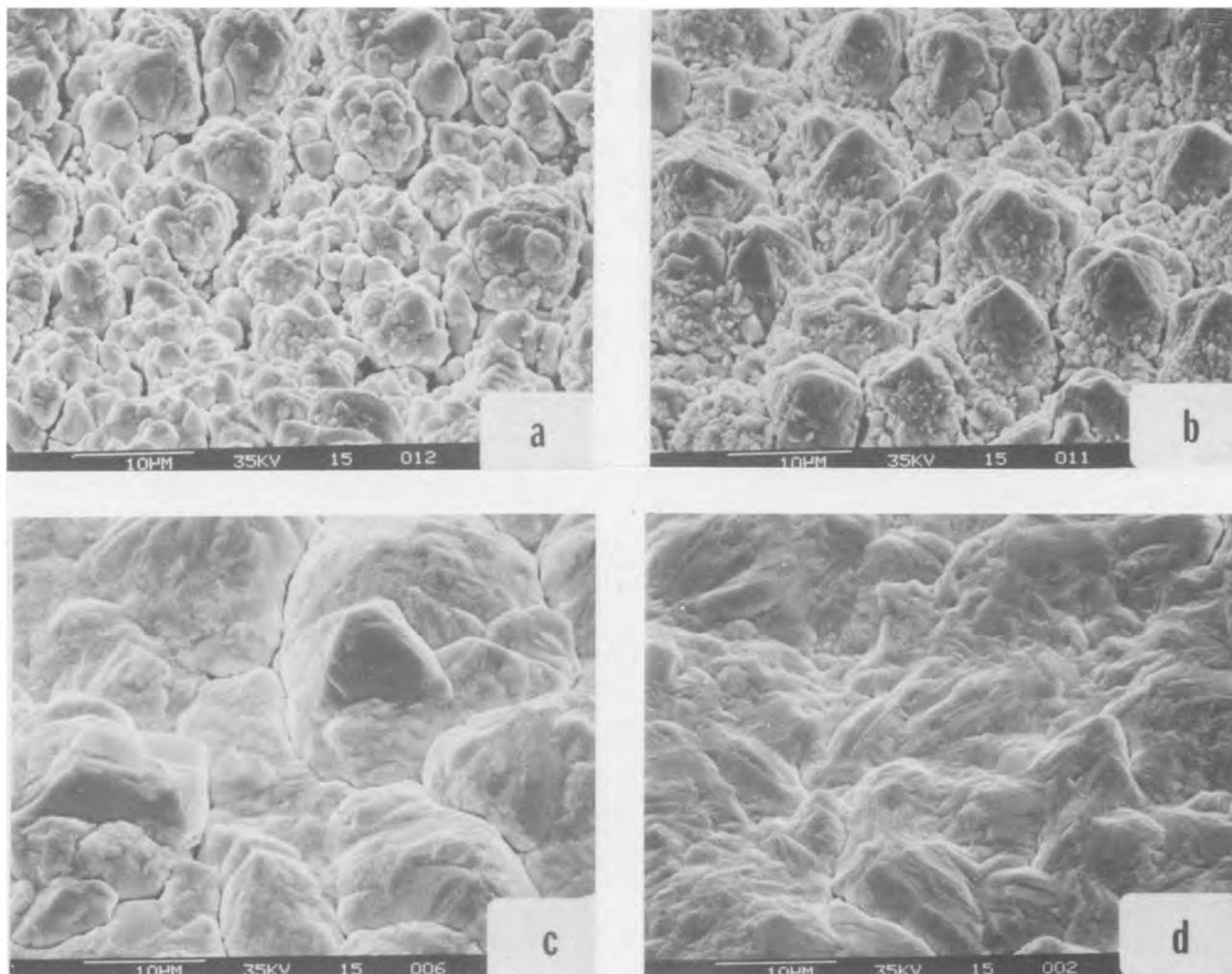


Fig. 7. Effect of laser power on the morphology of LEJP of thick gold deposits as shown by SEM. The current density is 12.5 A/cm^2 . Plating time = 5s. Laser power: 10W (a), 15W (b), 20W (c), 25W (d).

tion sites. Because of the very fast deposition rate, the surface mobility of Au ions is insufficient to quickly backfill the voids. This forces the fast growing grains to grow in columns perpendicular to the substrate without making connections in the lateral direction thereby giving rise to voids. Our beryllium-copper substrates have a very thin nickel film so that acid etching was not possible. Based on our previous work, there is evidence that the laser dissolves thin oxides so that elaborate precleaning is not generally required for laser-enhanced plating.

Introducing the laser into the jet system substantially improves the morphology of the deposit and enhances the plating rate. Three major factors may contribute to the enhanced plating rates observed when laser light is absorbed by an electrode: (i) an increase in the kinetic rate due to locally higher temperature, (ii) increased rates of mass transport due to microstirring arising from locally steep thermal gradients in and around the region of the laser absorption, and (iii) a shift in the equilibrium potential to more positive values due to locally higher temperatures. From this study, it appears that there is an increase

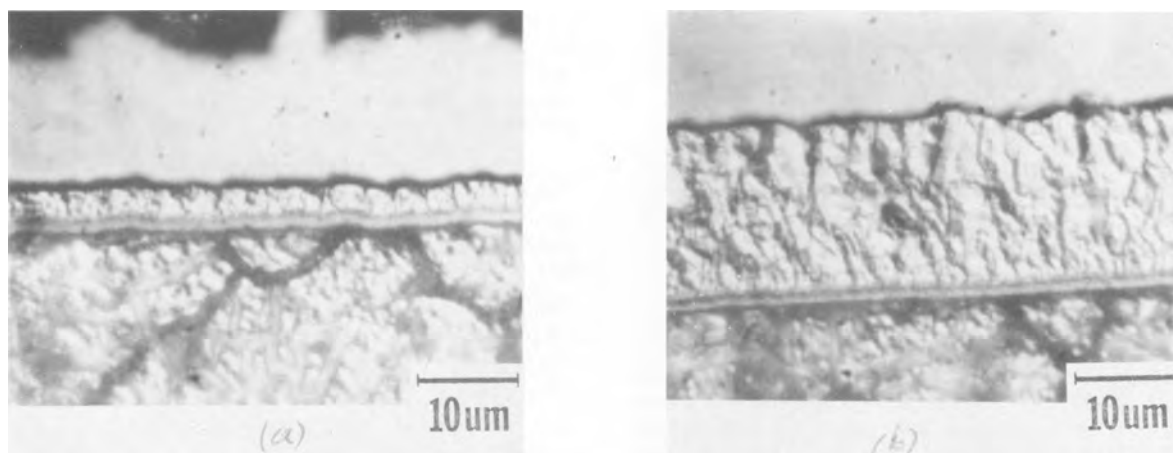


Fig. 8. Cross sections of laser-jet plated gold spots (LEJP) on nickel-plated Be-Cu substrates. The current density is 12.5 A/cm^2 . Laser power = 25W. Laser-jet plating times and resulting thicknesses are: 0.5s, $42 \mu\text{m}$ (a), 2.5s, $18 \mu\text{m}$ (b).

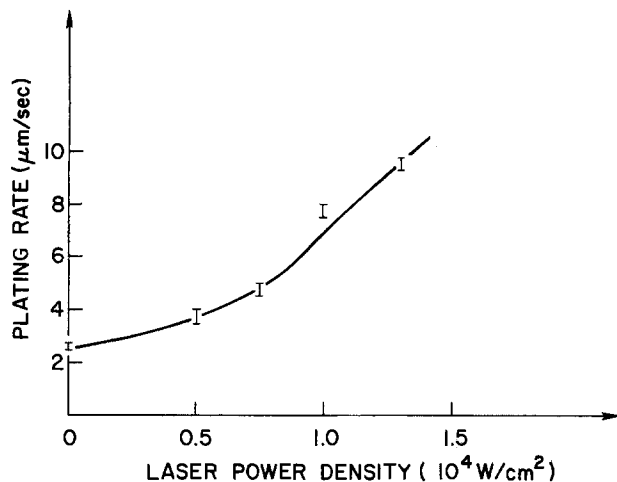


Fig. 9. Influence of laser power density on plating rate of LEJP. The current density is 12.5 A/cm^2 .

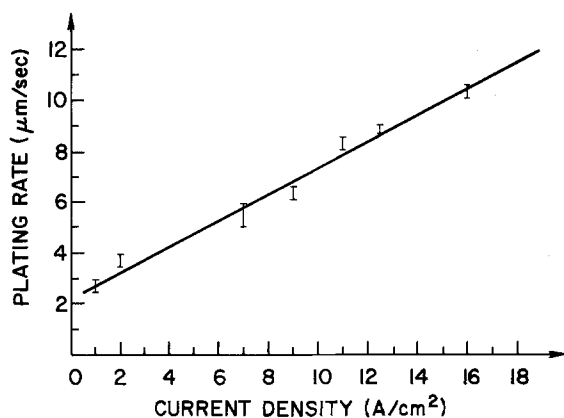


Fig. 10. Effect of current density on LEJP plating rate. The laser power is 20W . (Laser power density = $1.0 \times 10^4 \text{ W/cm}^2$.)

in plating efficiency with an increase of the laser power (see Fig. 9).

Figure 12 shows the shift in rest potential in Sel-Rex Autronex 55GV solution used in our experiments as a function of temperature. This shift is approximately $1 \text{ mV}/^\circ\text{C}$ over the range investigated. This is probably due to a weakening of the gold complex. The laser irradiation shifts the current-voltage curve to more positive potentials. This shift and an increase in surface mobility of Au leads to a dramatic change observed in the morphology of the laser-enhanced deposit.

From the point of view of the morphology of the deposits, without laser irradiation, a typical I-V curve for gold can be divided into two regions: (i) a low current density region (low overpotentials) where normally dense deposits are obtained and the plating rate is reasonably efficient, and (ii) high current density region where simultaneous hydrogen evolution reaction is substantial. This results in nodular, dendritic, and even powdery deposits at the highest current densities because of the very high rate of hydrogen evolution that occurs simultaneously. At these high current densities, we estimate the plating efficiency from our results to be $\sim 15\text{-}20\%$ in the absence of laser radiation and approximately 60% under otherwise the same plating conditions but utilizing 25W of laser power. Due to the shift of the I-V curve to the more positive potentials and an increase in Au surface mobility, it is possible to obtain dense Au deposits in the LEJP plating, while at similar current densities in the absence of laser irradiation, the deposits are nodular and/or powdery. The higher the laser power density, the greater the shift to more positive rest potentials and accompanying decrease of the hydrogen evolution rate. This shift seems adequate to account for the changes observed in the morphology at different laser powers as is seen in

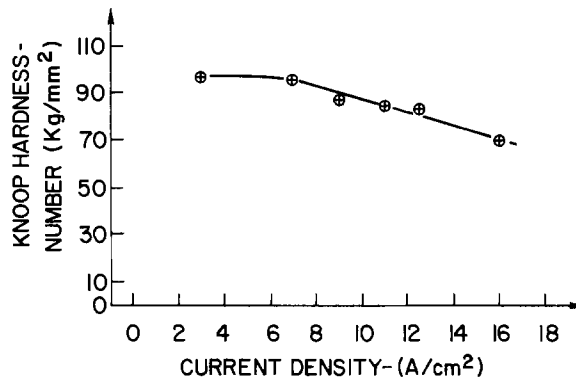


Fig. 11. Effect of current density on LEJP deposit microhardness. Films were deposited at a laser power of 25W . Hardness was measured on the cross-sectioned area with a 25g load.

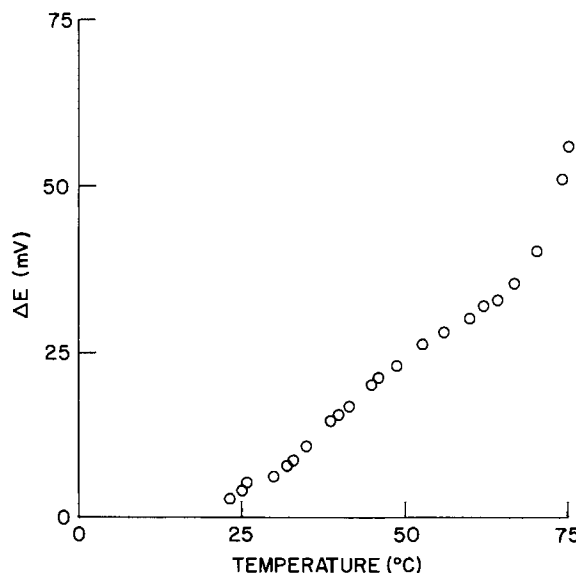


Fig. 12. Shift of the rest potential with temperature for the Sel-Rex Autronex 55 GV solution in absence of cobalt.

Fig. 6a-6d and 7a-7b. We also believe that the laser-heated solution dissolves the nickel oxide on the substrate, creating a clean surface for electrocrystallization. On such a surface, lateral crystallite growth becomes less inhibited. This results in denser deposits. In addition, the dissolution of oxide greatly improves adhesion of the deposit.

The potential shift caused by the laser irradiation can also be used to explain the differences in the plating rates obtained by jet plating and LEJP, at similar current density. Plating at more positive potentials means less hydrogen evolution, i.e., less current consumed for side reactions.

LEJP of gold from a commercial solution (without cobalt complex) possesses a columnar microstructure typical of soft pure gold. The slight decrease in microhardness with the increase of current density cannot be explained at this time.

Acknowledgments

We are grateful for the technical assistance of C. F. Aliotta in obtaining the scanning electron micrographs and for the helpful technical discussions with Dr. D. A. Smith, Dr. R. E. Acosta, and Dr. J. M. Locarnini.

Manuscript submitted Nov. 28, 1984; revised manuscript received ca. March 4, 1985.

IBM Corporation assisted in meeting the publication costs of this article.

REFERENCES

1. R. J. von Gutfeld, E. E. Tynan, R. L. Melcher, and S. E. Blum, *Appl. Phys. Lett.*, **35**, 651 (1979).
2. R. J. von Gutfeld, E. E. Tynan, and L. T. Romankiw, Ab-

- stract 472, p. 1185, The Electrochemical Society Extended Abstracts, Vol. 79-2, Los Angeles, Oct. 14-19, 1979.
- J. Cl. Puipe, R. E. Acosta, and R. J. von Gutfeld, *This Journal*, **128**, 2539 (1981).
 - R. J. von Gutfeld, R. E. Acosta, and L. T. Romankiw, *IBM J. Res. Dev.*, **26**, 136 (1982).
 - R. J. von Gutfeld, M. H. Gelchinski, and L. T. Romankiw, Paper 663 RNP presented at the Denver, CO, Meeting of the Society, Oct. 11-16, 1985.
 - M. H. Gelchinski, L. T. Romankiw, and R. J. von Gutfeld, Abstract 131, p. 206, The Electrochemical Society Extended Abstracts, Vol. 82-2, Detroit, MI, Oct. 17-21, 1982.
 - R. J. von Gutfeld, M. H. Gelchinski, and L. T. Romankiw, in "Proceedings of the SPIE Conference on Laser Processes of Semiconductor Devices," SPIE 385, p. 118 (1983).
 - L. T. Romankiw, M. H. Gelchinski, R. E. Acosta, and R. J. von Gutfeld, in "Electroplating Engineering and Waste Recycle—New Developments and Trends," D. D. Snyder, U. Landau, and R. Sard, Editors, p. 66, The Electrochemical Society Softbound Proceedings Series, Pennington, NJ (1983).
 - R. J. von Gutfeld, M. H. Gelchinski, L. T. Romankiw, and D. R. Vigliotti, *Appl. Phys. Lett.*, **43**, 876 (1983).
 - H. K. Kuiken, F. E. P. Mikkers, and P. E. Wierenga, *This Journal*, **130**, 554 (1983).
 - N. Ibl, in "Advances in Electrochemistry and Electrochemical Engineering," Vol. 2, P. Delahay and C. W. Tobias, Editors, p. 49, Interscience, New York (1962).
 - A. R. Despic and Y. I. Popov, in "Modern Aspects of Electrochemistry," Vol. 7, p. 199, Plenum Press, New York (1972).

Mechanisms of Electroless Metal Plating

II. Formaldehyde Oxidation

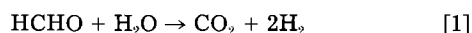
Perminder Bindra* and Judith Roldan

IBM Corporation, Thomas J. Watson Research Center, Yorktown Heights, New York 10598

ABSTRACT

A detailed investigation of the decomposition of formaldehyde was carried out to account for the fact that formaldehyde decomposition on Group VIII metals, *e.g.*, palladium, occurs without simultaneous hydrogen generation, while on Group IB metals, *e.g.*, copper, formaldehyde decomposition is accompanied by hydrogen evolution. It was found that, in principle, metals may be divided into three main classes: (i) metals with positive free energy of hydrogen adsorption, (ii) metals with free energy of hydrogen adsorption close to zero, and (iii) metals with negative free energy of hydrogen adsorption. In the case of class (i) metals, formaldehyde oxidation is accompanied by hydrogen evolution. For class (ii) metals, there is no simultaneous hydrogen evolution. Class (iii) metals show low catalytic activity for formaldehyde oxidation. Hence, formaldehyde cannot be used as a reducing agent for electroless plating of class (iii) metals.

In electrolytic metal deposition, the electrons required for the reduction of the metal ions are supplied by an external current source. In electroless metal deposition, on the other hand, the electrons required for reduction are supplied by the catalytic or electrocatalytic oxidation of a reducing agent. The electrocatalytic oxidation of reducing agents such as methanol has been widely studied (1). Relatively little work has been done on the oxidation of formaldehyde, an important reducing agent for electroless copper deposition (2). It is generally agreed, however, that the oxidation of both of the organic molecules proceeds via dissociative adsorption leading to dehydrogenation as the precursor reaction. The oxidation of formaldehyde in acid media has been shown (3) to proceed as follows



In alkaline media, two types of behavior are observed. On Group VIII metals, such as platinum and palladium formaldehyde oxidation occurs without simultaneous hydrogen generation (4), while on Group IB metals, such as copper, silver, and gold, formaldehyde oxidation is accompanied by hydrogen evolution (1a). One of the objectives of this investigation is to account for this behavior. To this end, a quantitative study of the kinetics and mechanism of formaldehyde oxidation on one metal from each group, namely, platinum and copper, has been carried out and the overall stoichiometries of the oxidation reaction on each metal determined.

The second objective has been to determine the effect of the nature of the metal on the electrocatalytic oxidation of formaldehyde. This is a qualitative study in which the catalytic activities of several metals were compared by cyclic voltammetry. The measurements were performed in both acid and alkaline media and the data are plotted in the form of the so-called volcano plots pro-

posed by Balandin (5) for gas phase heterogeneous catalytic reactions and by Parsons (6) and Gerischer (7) for electrocatalytic (electrochemical) reactions.

Experimental

The electrochemical measurements were performed in a standard three-compartment cell. The auxiliary electrode chamber and the reference electrode chamber were separated from the working electrode chamber by sintered glass frits. The potential of the working electrode was monitored via a Luggin capillary with its tip placed 1 mm from the working electrode. Formaldehyde concentrations were estimated using standard quantitative analysis equipment. It is noted that in aqueous (acid) solution formaldehyde exists mainly as a hydrate, methylene glycol, while in alkaline solution the predominant species is methylene glycolate anion (8).

All the solutions were prepared with water purified by running deionized water through a Milli-Q water purification system, Continental Water Systems. Perchloric acid and sodium hydroxide were ultrapure Baker products and were diluted without further purification. Formaldehyde solutions were prepared by dissolving solid paraformaldehyde in pure water to the required concentration and determining the concentration iodometrically (9). Iodine and thiosulfate solutions were also prepared from Baker chemicals by the methods described by Vogel (10). Solutions were deaerated by continuous bubbling with purified argon.

Pine Instruments rotator and electrodes were used for all rotating disk measurements. The electrodes, which had a geometric area of 0.458 cm², were polished to a near mirror finish on a wheel using successively finer grades of alumina abrasive. The electrodes were then degreased with alcohol and thoroughly rinsed with purified water before each measurement.

The counterelectrode was a large (10 cm²) gold foil, and the reference electrodes were Hg/HgO (1M NaOH) for

*Electrochemical Society Active Member.

measurements in alkaline solution and $\text{Hg}/\text{Hg}_2\text{SO}_4$ for measurements in acid solutions, respectively. The electrode potentials are referred to the reversible hydrogen electrode (RHE) at the solution pH.

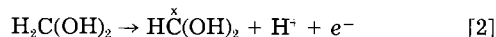
Cyclic voltammetry and current-potential curves were obtained with a PAR 173 potentiostat in conjunction with a PAR 175 universal programmer. The curves were recorded on a Yokogawa Model 3033 X-Y-t recorder. The charge passed during the formaldehyde decomposition efficiency measurements was recorded with the help of a PAR 179 coulometer. pH values were measured on a Beckman-Altrex pH meter, with a pH electrode designed for measurement at high pH.

Results

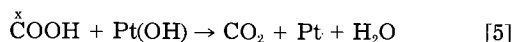
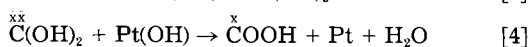
Cyclic Voltammetry

Formaldehyde oxidation on noble metals such as Au, Pt, Pd, Rh, and Ir in 1M HClO_4 was compared by the cyclic voltammetry technique. In 1M NaOH solution, the list of metals was extended to include Ag, Cu, and Ni. Cyclic voltammograms for formaldehyde oxidation on some of these metals are described below, and the voltammograms for the other metals are also included but will be described elsewhere (11).

Platinum.—A typical cyclic voltammetry curve for Pt in 0.1M $\text{HCHO} + 1\text{M HClO}_4$ is shown in Fig. 1, together with the curve obtained in the base electrolyte. The general features of this voltammogram are similar to the voltammogram for Pt in $\text{HCOOH} + 0.5\text{M}$ sulfuric acid (12). In each case, three peaks occur in the anodic scan, though in the case of formaldehyde the first peak occurs at 0.7V vs. RHE instead of at 0.5V vs. RHE as for formic acid. This peak is attributed to a simple charge transfer step

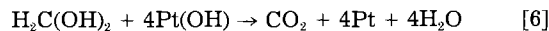


where $\overset{\times}{\text{H}}\text{C}(\text{OH})_2$ represents an adsorbed radical occupying a single site on the substrate. The first anodic peak is followed by a "passive" region (as opposed to an "inhibitive" region in the case of formic acid) before the onset of the second oxidation peak. In the second anodic peak, the strongly adsorbed intermediates of the type $\overset{\times\text{xx}}{\text{C}}\text{OH}$ are removed from the substrate by oxidation reactions such as



With the removal of the strongly adsorbed intermediates, more $\text{Pt}(\text{OH})$ sites are created and solution phase formal-

dehyde is oxidized sequentially to give the following overall stoichiometry



It is not clear whether the decrease in current after the second anodic peak is due to the formation of inactive PtO (13) or due to self-poisoning of the formaldehyde oxidation reaction by some sort of a secondary disproportionation reaction (14). In any case, oxidation of formaldehyde does not totally cease after the second anodic peak as in the case of formic acid. At around 1.1V, the current increases rather abruptly, and this increase in current is attributed to the reaction of a $\text{PtO}(\text{O})_{\text{ad}}$ species with formaldehyde. At 1.25V, the potential scan was reversed.

In the cathodic scan, a broad anodic peak spread over 0.4V is observed. This peak has substructure which indicates two peaks at 0.8 and 0.6V, and the familiar shoulder also observed in the case of formic acid is observed at 0.4V. The peak at 0.8V occurs at approximately the same potential as the first anodic peak and is attributed to the formation of the weakly bound intermediate $\overset{\times}{\text{H}}\text{C}(\text{OH})_2$ via the charge transfer reaction described in Eq. [2]. At more cathodic potentials, the weakly bound $\overset{\times}{\text{H}}\text{C}(\text{OH})_2$ undergoes a disproportionation reaction to give the strongly bound and "poisonous" species $\overset{\text{xxx}}{\text{C}}\text{OH}$ and the current decreases until it reaches zero at $\sim 0.3\text{V}$.

The cyclic voltammetry curves obtained with and without formaldehyde in alkaline solution are shown in Fig. 2. There is a clear difference in the voltammograms obtained in acid and alkaline media, and it is almost certain that this difference is due to the fact that at pH = 14 the active species in the electrolyte is the methylene glycolate anion, $\text{H}_2\text{C}(\text{OH})\text{O}^-$, while at pH = 0 the active species is the formaldehyde hydrate or methylene glycol, $\text{H}_2\text{C}(\text{OH})_2$. The fact that surface oxidation on Pt in acid electrolyte commences at 0.8V and in alkaline electrolyte at 0.6V does not seem to have much effect. Formaldehyde oxidation currents are much higher in 1M NaOH than in 1M HClO_4 , suggesting that the reaction is base catalyzed. There is no evidence of strongly adsorbed intermediates either in the hydrogen region or in the double-layer region. Inhibition of the oxidation reaction first begins at 0.7V. This may be due to the formation of inactive PtO or a self-poisoning reaction described earlier. The peak at 1.0V in the anodic and cathodic scans is probably due to the formation of $\text{PtO}(\text{O})_{\text{ads}}$ which is able to react with formaldehyde. The reaction totally ceases at 1.5V. It is tempting to suggest that this is due to the formation of inactive PtO_2 even though it is inconsistent with the results of Biegler *et al.* (15) which show that a complete PtO_2 layer forms at much more anodic potentials.

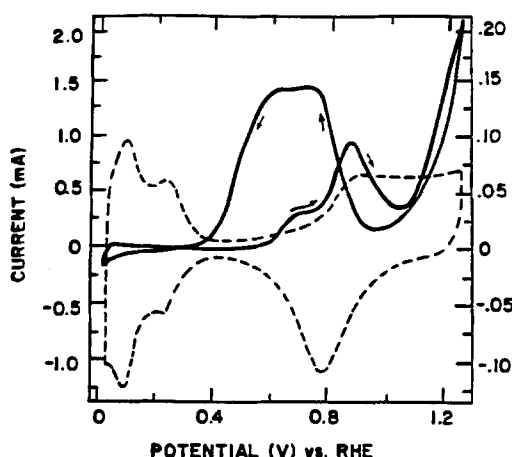


Fig. 1. Cyclic voltammograms for Pt in 1M HClO_4 (dashed curve, scale on right) and 1M $\text{HClO}_4 + 0.1\text{M HCHO}$ (solid curve). Ar saturated; electrode area = 0.458 cm^2 ; scan rate = 0.1 V/s ; temperature = 25°C .

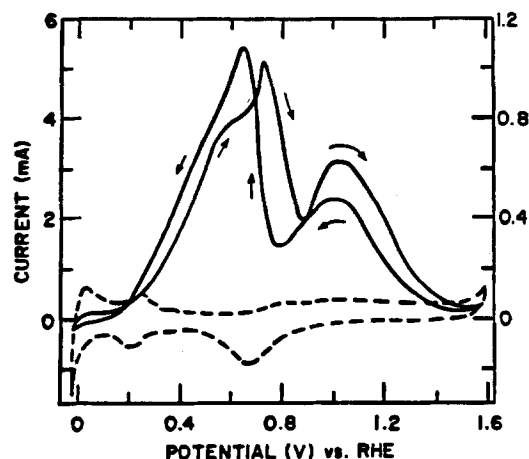


Fig. 2. Cyclic voltammograms for Pt in 1M NaOH (dashed curve, scale on right) and 1M NaOH + 0.1M HCHO (solid curve). Ar saturated; electrode area = 0.458 cm^2 ; scan rate = 0.1 V/s ; temperature = 25°C .

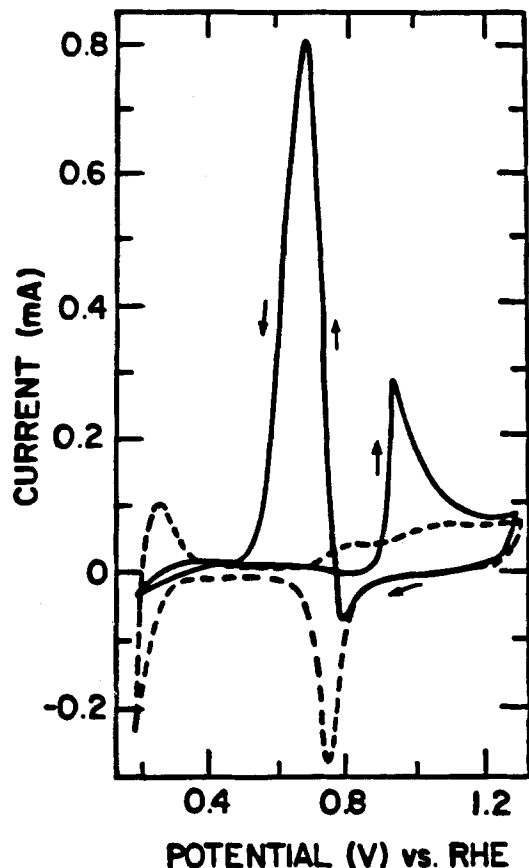


Fig. 3. Cyclic voltammograms for Pd in 1M HClO₄ (dashed curve) and 1M HClO₄ + 0.1M HCHO (solid curve). Ar saturated; electrode area = 0.458 cm²; scan rate 0.1 V/s; temperature = 25°C.

Palladium.—Figures 3 and 4 show the cyclic voltammograms for Pd in the presence and absence of formaldehyde in 1M HClO₄ and 1M NaOH, respectively. In acid solution, there is only one anodic peak in the anodic scan which occurs at 0.95V. Hydrogen adsorption on Pd is suppressed in the presence of formaldehyde in the electrolyte, indicating the presence of strongly adsorbed intermediates on the surface. Between 0.4 and 0.7V, the anodic current in the presence and absence of formaldehyde has the same value. From 0.7V until the anodic peak

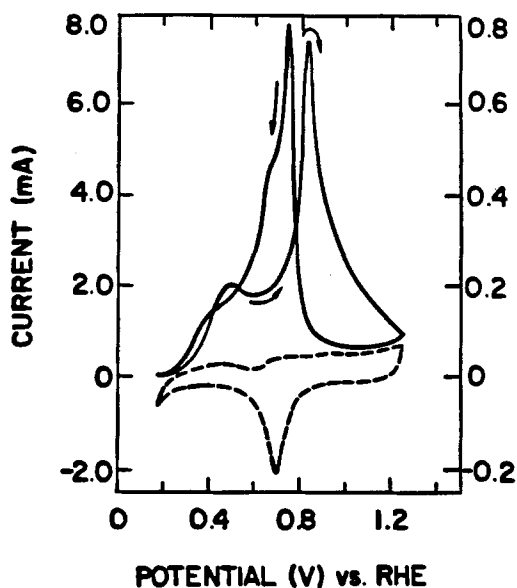


Fig. 4. Cyclic voltammograms for Pd in 1M NaOH (dashed curve, scale on right) and 1M NaOH + 0.1M HCHO (solid curve). Ar saturated; electrode area = 0.458 cm²; scan rate = 0.1 V/s; temperature = 25°C.

at 0.95V, the current in the presence of formaldehyde is much lower than the base electrolyte current. This confirms the presence of strongly adsorbed intermediates which prevent the formation of Pd(OH) or PdO. At 0.95V, there is an abrupt increase in current and an asymmetrical peak is observed. This peak is most likely due to the reaction between PdO(O)_{ads} and the poisonous intermediates as well as bulk phase, H₂C(OH)₂, just as in the case of Pt in acid solution. The current due to formaldehyde oxidation ceases around 1.2V, presumably due to the formation of inactive PdO₂.

In the cathodic scan, one large anodic peak is observed. This peak commences at the threshold of oxide reduction on Pd. The acceleration of oxide reduction by strongly adsorbing organic intermediates has been described by Capon and Parsons (12). The oxidation peak, however, is rather narrow, suggesting langmuirian adsorption of the intermediate.

The voltammogram obtained in alkaline solution (Fig. 4) is quite different from that obtained in acid solution. It is clear from Fig. 4 that the anodic and the cathodic scans show some hysteresis, though the general formaldehyde oxidation characteristics are the same. In the anodic scan, the first anodic peak occurs at 0.5V. This peak is attributed to the first charge transfer reaction of the type described in Eq. [2]. The reduction in current following the peak is due to surface coverage by strongly adsorbed intermediates. The large peak at 0.85V is, as in the case of Pt in alkaline solution, due to the interaction of Pd(OH) with formaldehyde. The reduction in current is due either to the formation of inactive PdO or a self-poisoning secondary reaction. In the cathodic scan, there is one large anodic peak at 0.7V and two shoulders at 0.65 and 0.4V. The anodic peaks in the cathodic and anodic scans are of approximately the same magnitude. The cyclic voltammograms for formaldehyde oxidation in 1M NaOH on Pt and Pd are quite similar. The catalytic activity is slightly greater for Pd.

Nickel.—The cyclic voltammograms obtained with and without formaldehyde in 1M NaOH solution are shown in Fig. 5. In the base electrolyte, only one peak is observed during the anodic scan. This peak occurs at 0.55V and is attributed to the chemisorption of an OH layer to form NiOH or Ni(OH)₂. The rapidly increasing current at potentials exceeding 0.8V is due to the formation of phase oxide. In the cathodic scan, the phase oxide reduction appears reproducible but there is no complementary peak for the desorption of the OH layer. This suggests that a breakdown of the adsorbed layer is required in order to nucleate the growth of the phase oxide.

In the presence of formaldehyde, hydrogen adsorption on Ni is suppressed. The anodic peak at 0.55V due to the adsorption of OH is no longer there as the surface is pre-

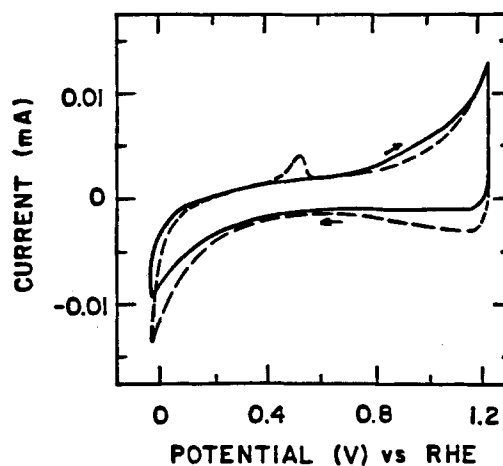


Fig. 5. Cyclic voltammograms for Ni in 1M NaOH (dashed curve) and 1M NaOH + 0.1M HCHO (solid curve). Ar saturated; electrode area = 0.458 cm²; scan rate = 0.1 V/s; temperature = 25°C.

ferentially covered by carbonaceous radicals. Oxidation of such radicals or of methylene glycolate anion occurs at potentials greater than 0.6V. There is suppression of the phase oxide formation until the adsorbed species have been oxidized from the surface. Clearly, Ni is not a very good catalyst for formaldehyde oxidation. Hence, formaldehyde is not used as a reducing agent in electroless Ni plating solutions even though the decomposition potential is favorable for such an application.

Copper.—The cyclic voltammetry curve for copper in 1M NaOH + 0.1M HCHO is given in Fig. 6 together with the background curve. The first anodic peak in the background curve is attributed to the formation of Cu_2O . At slow scan rates ($dv/dt < 10$ mV/s), this peak is preceded by a prepeak at 0.55V due to $\text{Cu}(\text{OH})_2^-$ formation. The current between 0.8 and 1.0V increases as $\text{Cu}(\text{OH})_2$ is formed and decreases when the passivating species CuO forms. There is some evidence of film dissolution in this potential range. At around 1.2V the anodic current increases again, probably due to the reaction $\text{Cu}(\text{II}) \rightarrow \text{Cu}(\text{III})$ (16). The background curve shows a cathodic peak at 0.5V. This peak is due to the reduction of Cu_2O . The cathodic peak which starts at around 0.2V is due to the reduction of a surface layer by consisting of more than one species. The Cu/NaOH system is very complex and requires more work for full interpretation than expended in this study.

In the presence of formaldehyde, the first anodic peak occurs at 0.55V as a result of the reaction of formaldehyde on the freshly reduced Cu surface. This peak has been used for the volcano plots and other analysis. Cu_2O is not catalytically active. The interaction of formaldehyde with $\text{Cu}(\text{OH})_2$ causes a large increase in the anodic current at 0.8V. The current decreases at 0.9V as a result of the formation of inactive CuO . Once the inactive CuO has been removed via dissolution (16) or the conversion of $\text{Cu}(\text{II})$ to $\text{Cu}(\text{III})$, a large anodic current due to the oxidation of formaldehyde on the fresh Cu surface appears again. During the cathodic sweep, the curve in the presence of formaldehyde coincides with the background curve until 0.25V when a large cathodic current due to formaldehyde reduction is seen.

Silver and gold.—The cyclic voltammogram for Ag in 1M HClO_4 (Fig. 7) is essentially featureless. There is hardly any evidence of hydrogen adsorption prior to hy-

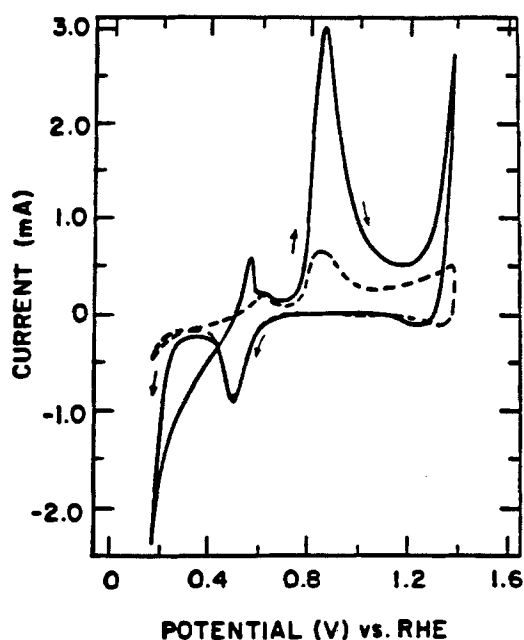


Fig. 6. Cyclic voltammogram curves for Cu in 1M NaOH (dashed curve) and 1M NaOH + 0.1M HCHO (solid curve). Ar saturated; electrode area = 0.458 cm^2 ; scan rate = 0.1 V/s; temperature = 25°C .

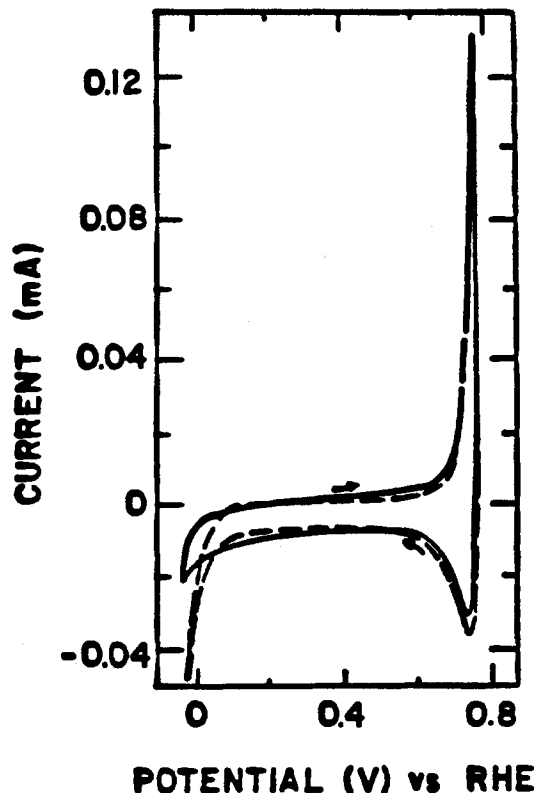


Fig. 7. Cyclic voltammogram curves for Ag in 1M HClO_4 (dashed curve) and 1M HClO_4 + 0.1M HCHO (solid curve). Ar saturated; electrode area = 0.458 cm^2 ; scan rate = 0.1 V/s; temperature = 25°C .

drogen evolution at around 0 V. In the anodic scan, oxide formation is immediately proceeded by Ag dissolution. A peak due to oxide reduction and/or Ag deposition is seen at 0.7V in the cathodic scan. In the presence of formaldehyde in the acid solution, the cyclic voltammogram is hardly affected. There is suppression of the hydrogen adsorption/evolution current and oxide formation is somewhat inhibited, but there is no clear evidence of formaldehyde adsorption or oxidation. In alkaline solution (Fig. 8), the base electrolyte curve on Ag shows evidence for the formation and stripping of "Ag-oxides," but the currents are very small. In the presence of formaldehyde, there is an abrupt increase in the anodic current at around 0.2V. A broad oxidation peak is observed which is asymmetrical and has the maximum at 0.4V. Between 0.4 and 1.1V, the anodic current is due to the oxidation of adsorbed as well as solution phase formaldehyde. As the solution phase formaldehyde is depleted in the vicinity of the electrode, the oxidation current comes down. This also accounts for the decreasing current in the cathodic scan.

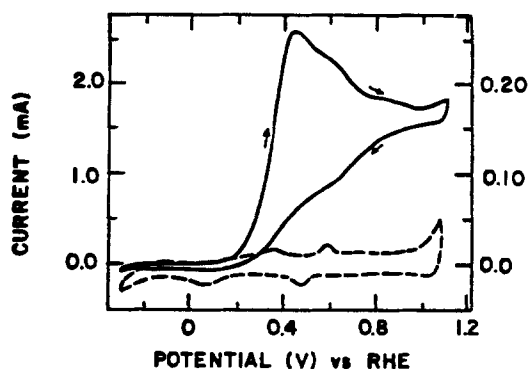


Fig. 8. Cyclic voltammogram curves for Ag in 1M NaOH (dashed curve, scale on right) and 1M NaOH + 0.1M HCHO (solid curve). Ar saturated; electrode area = 0.458 cm^2 ; scan rate = 0.1 V/s; temperature = 25°C .

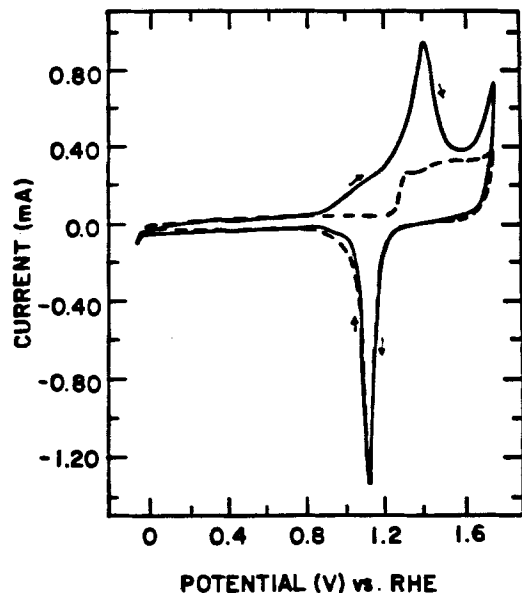


Fig. 9. Cyclic voltammery curves for Au in 1M HClO₄ (dashed curve) and 1M HClO₄ + 0.1M HCHO (solid curve). Ar saturated; electrode area = 0.458 cm²; scan rate = 0.1 V/s; temperature = 25°C.

The cyclic voltammery curve obtained in the presence and absence of formaldehyde in acid and alkaline electrolytes on Au are shown in Fig. 9 and 10, respectively. In acid solution, the double-layer region on gold is extensive and OH adsorption commences at 1.2V. There is hardly any evidence of formaldehyde oxidation at room temperature. At slightly elevated temperature, three peaks due to formaldehyde oxidation are observed in the anodic scan. This suggests that the activation energy for formaldehyde adsorption on Au is rather low. Each of the anodic peaks is associated with the adsorption of -OH species on the Au surface, suggesting once again that -OH catalyzes the formaldehyde oxidation reaction. In alkaline solution, -OH adsorption on Au occurs around 0.7V. However, this does not seem to affect the formaldehyde oxidation reaction which begins at 0.2V in the anodic scan. There is an anodic peak at 0.4V and some structure between 0.4 and 0.8V; otherwise, there is a steady oxidation current until 1.2V. At 1.2V, the formation of AuO or Au₂O₃ passivates the gold surface and formaldehyde oxidation current is gradually reduced. In the cathodic scan,

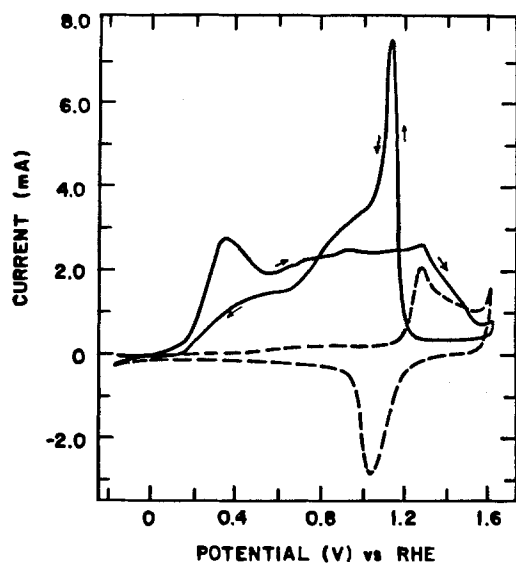


Fig. 10. Cyclic voltammery curves for Au in 1M NaOH (dashed curve) and 1M NaOH + 0.1M HCHO (solid curve). Ar saturated; electrode area = 0.458 cm²; scan rate = 0.1 V/s; temperature = 25°C.

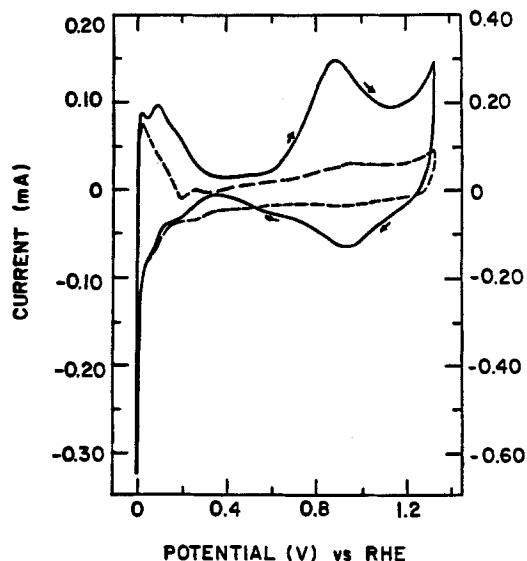


Fig. 11. Cyclic voltammery curves for Ir in 1M HClO₄ (dashed curve) and 1M HClO₄ + 0.1M HCHO (solid curve). Ar saturated; electrode area = 0.458 cm²; scan rate = 0.1 V/s; temperature = 25°C.

there is evidence of the oscillatory phenomena observed for carbonaceous reducing agents on solid electrodes. The anodic peak at 1.1V during the cathodic sweep is attributed to this oscillatory behavior. This peak potential is a function of the sweep rate.

Iridium and Rhodium.—Figures 11 and 13 show the cyclic voltammery curves for Ir and Rh in 0.1M HCHO + 1M HClO₄, respectively. The base electrolyte curves show that the "double-layer" regions for Ir and Rh are much smaller than the "double-layer" region for Pt. The oxide reduction peak on Rh occurs at ~0.4V vs. RHE, while for Ir there is no distinct oxide reduction peak but the cyclic voltammogram is symmetrical about the potential axis in the oxygen adsorption region. In the case of Rh, there is clear evidence that during the anodic scan, OH adsorption on the metal is suppressed in the presence of formaldehyde in the solution. This is followed by a large asymmetrical peak due to formaldehyde oxidation,

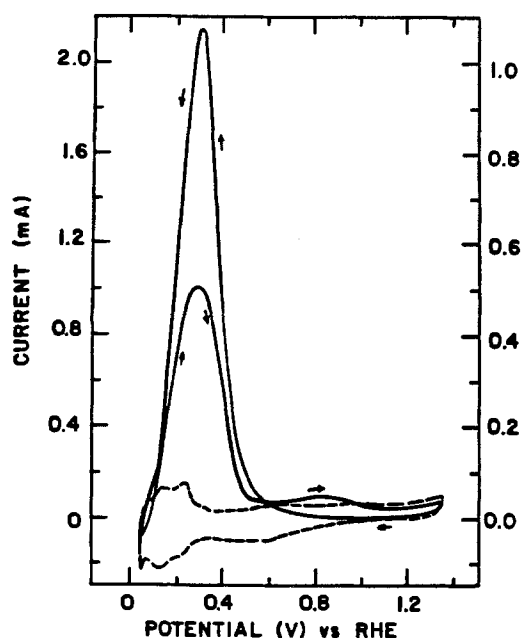


Fig. 12. Cyclic voltammery curves for Ir in 1M NaOH (dashed curve) and 1M NaOH + 0.1M HCHO (solid curve). Ar saturated; electrode area = 0.458 cm²; scan rate = 0.1 V/s; temperature = 25°C.

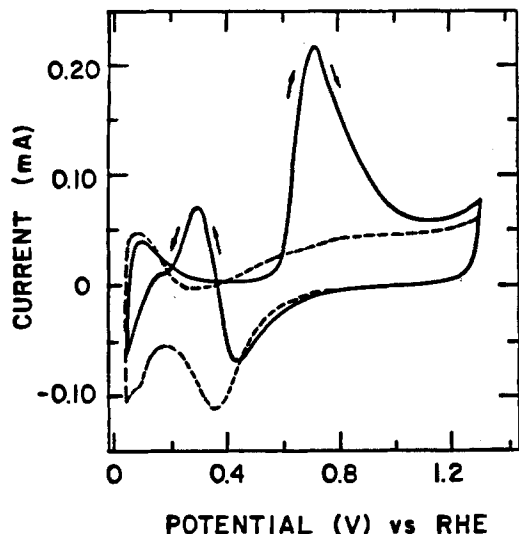


Fig. 13. Cyclic voltammograms for Rh in 1M HClO_4 (dashed curve) and 1M $\text{HClO}_4 + 0.1\text{M HCHO}$ (solid curve). Ar saturated; electrode area = 0.458 cm^2 ; scan rate = 0.1 V/s ; temperature = 25°C .

demonstrating that formaldehyde oxidation is catalyzed by $\text{Rh}(\text{OH})$ species. The decrease in current is due to the formation of inactive RhO or Rh_2O_3 . In the cathodic scan, an anodic peak at 0.3V and a shoulder at 0.2V are observed. The anodic peak is attributed to the first dehydrogenation reaction (Eq. [2]) leading to the formation of weakly bound $\text{HC}(\text{OH})_2$ species and the shoulder is due to the disproportionation of this species. In general, the behavior of formaldehyde in acid electrolyte on Rh resembles its behavior on Pt.

For Ir, in the presence of formaldehyde there are several peaks during the anodic scan. In this case, hydrogen adsorption is not suppressed; in fact, there are two peaks due to formaldehyde oxidation in the hydrogen adsorption/desorption region. The current begins to rise again at 0.6V and a broad peak appears at around 0.9V , indicating that the adsorption of OH on Ir also catalyzes formaldehyde oxidation. During the cathodic scan, there is further evidence of formaldehyde oxidation between 0.4 and 0.2V .

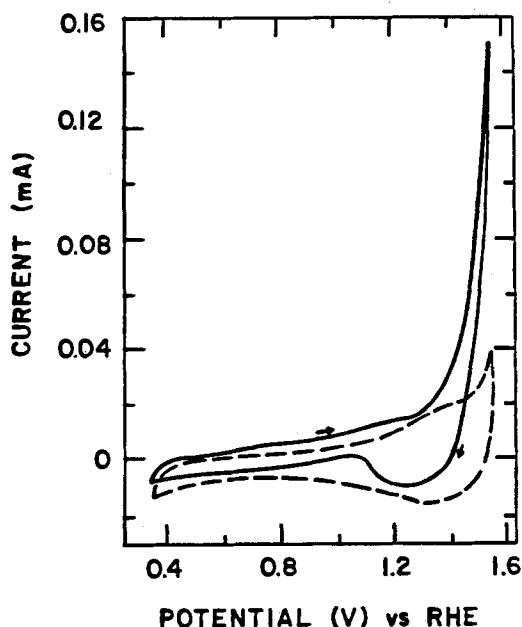


Fig. 14. Cyclic voltammograms for Rh in 1M NaOH (dashed curve) and 1M $\text{NaOH} + 0.1\text{M HCHO}$ (solid curve). Ar saturated; electrode area = 0.458 cm^2 ; scan rate = 0.1 V/s ; temperature = 25°C .

Figures 12 and 14 show the cyclic voltammograms for Ir and Rh in the presence and absence of formaldehyde in 1M NaOH , respectively. Rh shows a fairly featureless curve in the base electrolyte. In the presence of formaldehyde, there is a dramatic increase in current at $\sim 1.3\text{V vs. RHE}$. Ir shows a somewhat broadened hydrogen adsorption region in alkaline solution. In the presence of formaldehyde, there is an abrupt increase in current in the hydrogen region leading to a broad peak at 0.3V . In the cathodic scan, the current due to formaldehyde oxidation begins to set at 1.0V , long before oxide reduction is complete. The anodic peak in the cathodic scan also occurs at 0.3V and is at least twice the magnitude of the anodic peak during the anodic scan. Data not published here have shown that these peaks are a function of temperature and that at high temperatures the two peaks are of the same magnitude. Clearly, formaldehyde oxidation of Ir is quite complex and has been described in detail in a subsequent publication (11).

Kinetic Parameters

Tafel slopes.—A potential step method was used to obtain Tafel plots on platinum substrates free from strongly adsorbed intermediates. The technique involved pretreatment of the electrode at an anodic potential (1.0V vs. RHE) where the strongly adsorbed intermediates are oxidized, prior to stepping the potential into the potential region where oxidation of formaldehyde first begins. Currents are measured on electrodes rotated at 1600 rpm , at a standard time interval of 1s after the application of the potential step. Hardly any hysteresis was observed when the potential was retraced. No corrections for the IR drop were made, as the measurements were performed in the region of low current densities where this correction was found to be insignificant. The Tafel plots on copper electrode were constructed from polarization data obtained by the potentiodynamic method. The potential scan rate was 100 mV/s . Tafel plots for formaldehyde oxidation on platinum and on copper are shown in Fig. 15. These plots yield Tafel slopes of 150 ± 5 and $180 \pm 5 \text{ mV/decade}$ for platinum and copper, respectively.

Reaction orders.—Reaction orders were ascertained with respect to formaldehyde and hydroxide ion only. The reaction order for the reduction of the formate ion, while desirable, is difficult to measure and therefore was not attempted.

Formaldehyde.—Peak currents for the large cathodic peak at varying concentrations of formaldehyde yielded a reaction order of 0.9 ± 0.15 for platinum. Confirmation of first order was obtained from rotating disk data which yielded linear plots of $1/i$ vs. $1/\omega$ (17). The complete rotating disk electrode data will be given elsewhere (11). In the case of copper electrode, the first anodic oxidation peak current was plotted as a function of formaldehyde concentration. Figure 16 shows that the reaction order with respect to formaldehyde on copper is similar to that on platinum and has a value of 0.9 ± 0.1 .

Hydroxide ion.—The pH dependence of formaldehyde oxidation was examined over the range $12.0\text{--}13.7$ by adding varying amounts of concentrated HClO_4 to 0.1M

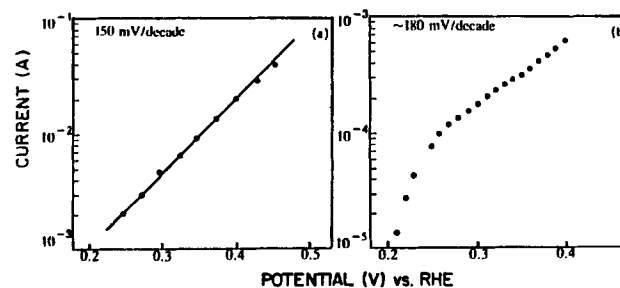


Fig. 15. Tafel plot for HCHO oxidation in 1M NaOH . Ar saturated; electrode area = 0.458 cm^2 . a: Platinum. b: Copper. Temperature = 25°C .

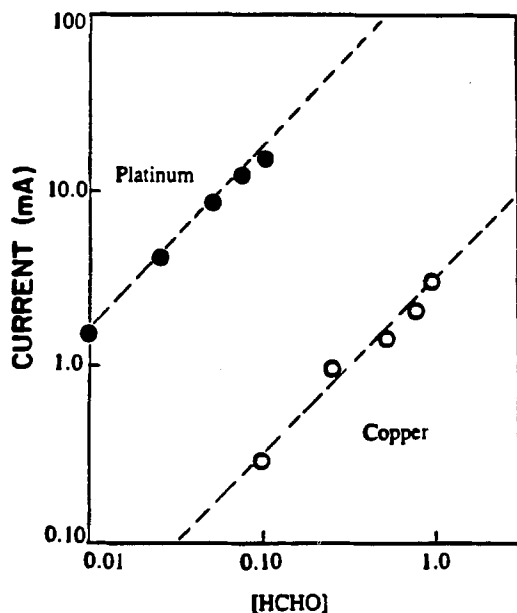


Fig. 16. Reaction order for oxidation of HCHO in Ar-saturated 0.1M HCHO + 1M NaOH. Electrode area = 0.458 cm²; scan rate = 0.1 V/s; temperature = 25°C.

HCHO in 1M NaOH. Plots of peak currents against pH (the large cathodic peak for platinum and the first anodic peak for copper) yielded a reaction order of 0.5 in hydroxide ion for Cu and of 0.0 for Pt. These plots are displayed in Fig. 17. A fractional reaction order implies participation of the hydroxide ion via an adsorbed state, thus confirming that in the case of Cu substrate the anodic peak is due to catalysis by Cu(OH)₂⁻. A reaction order of 0, as in the case of Pt, implies that the reaction is independent of hydroxide ion concentration in the solution.

Stoichiometric number ν .—The stoichiometric number, ν , is generally evaluated either by the activation polarization resistance method (18) or from the anodic and cathodic transfer coefficients (19). These methods could not be applied here because neither the current-potential curves for formaldehyde oxidation at low overpotentials nor the transfer coefficient for formate reduction could be measured. ν was therefore evaluated by applying the Allen and Hickling (20) graphical treatment to the general equation for a multistep reaction (21). This equation has the form

$$i = i_0 \left\{ \exp \left[\left(\frac{n-\gamma}{\nu} - r\beta \right) \frac{F\eta}{RT} \right] - \exp \left[- \left(\frac{\gamma}{\nu} + r\beta \right) \frac{F\eta}{RT} \right] \right\} \quad [7]$$

where η is the overpotential, γ is the number of electrons transferred before the rds in the electronation reaction or the number of electrons transferred after the rds in the de-electronation reaction, n is the number of electrons involved in the overall reaction, β is the symmetry factor of the rds, and r is the number of electrons involved in the rds. The graphical treatment of Allen and Hickling (20) gives a linear plot of $\log \{ i/l - \exp(-nF\eta/\nu RT) \}$ against η for the appropriate value of ν . Plots of $\nu = 1$ and $\nu = 2$ are shown in Fig. 18 for platinum and for copper. It is evident from Fig. 18 that $\nu = 1$ for platinum and $\nu = 2$ for copper. The slope of these plots is $[(n-\gamma)/\nu - r\beta] RT/F$. The numerical values observed in Fig. 18 are 150 mV/decade for platinum and 180 mV/decade for copper, similar to the Tafel slopes observed in Fig. 15.

Discussion

Reaction mechanisms.—The mechanism of formaldehyde oxidation on Pt and on Cu in alkaline media is dis-

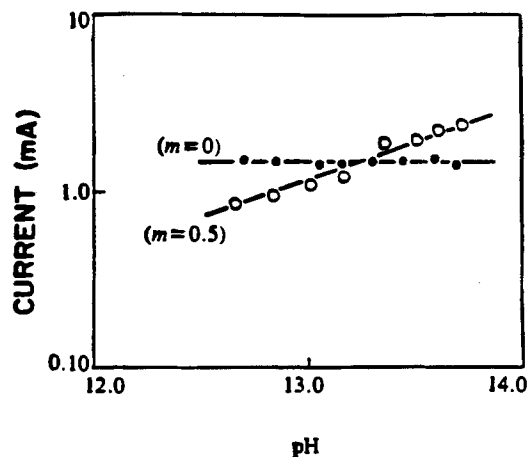


Fig. 17. Dependence of HCHO oxidation on pH for (solid circles) Pt and (open circles) Cu in Ar-saturated 1M NaOH + 0.1M HCHO. Electrode area = 0.458 cm²; scan rate = 0.1 V/s; temperature = 25°C.

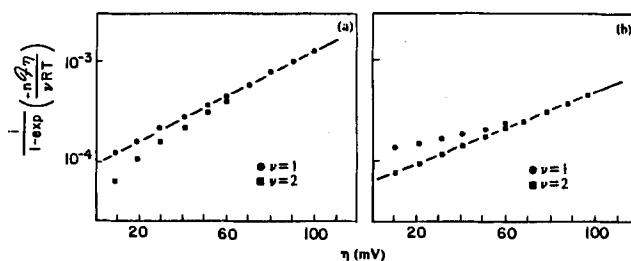


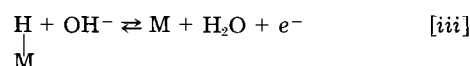
Fig. 18. Allen and Hickling type plots for stoichiometric number determination at Pt (a), and Cu (b).

cussed in this section. Under Langmuir adsorption conditions, the transfer coefficient obtained from the Tafel plot is equal to the transfer coefficient yielded by the Allen-Hickling analysis (Fig. 18), *i.e.*

$$\alpha_a = \frac{n-\gamma}{\nu} - r\beta \quad [8]$$

Equation [8] is solved for γ by inserting the appropriate values for the other parameters. n was evaluated by measuring the coulombic efficiency for formaldehyde oxidation of Pt and Cu (see Fig. 21), while the value of ν on each metal was obtained from the Allen-Hickling plots. The values of r and β were assumed to be 1 and 0.5, respectively, for each substrate. $r = 0$ is rejected because a symmetry factor is needed for an electron transfer step, and $r = 2$ is improbable, as a two-electron transfer would require very high activation energy. The values of the kinetic and mechanistic parameters are collected in Table I.

It is clear from Table I that the Tafel slope for formaldehyde oxidation on both platinum and on copper is $RT/\alpha F$ with α values substantially less than 0.5. This indicates specific adsorption of reacting species or intermediates (22) and suggests an ihp mechanism in which the first electron transfer is rate determining. The data given in Table I are compatible with the following sequence of steps.



or

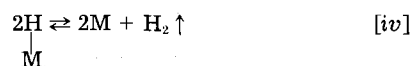


Table I. Kinetic and mechanistic parameters

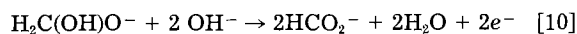
	$\frac{\partial V}{\partial \log i}$	$\frac{\partial \log i}{\partial \log C_F}$	$\frac{\partial \log i}{\partial \log C_{OH^-}}$	α_a	n	ν	r	β	γ
Platinum	150 ± 5	1	0	0.4	2	1	1	0.5	1
Copper	180 ± 5	1	0.5	0.33	1	2	1	0.5	0

M in the above reaction scheme represents the substrate. Steps (i), (iii), and (iv) are in quasi-equilibrium.

The rate equation for the reaction on platinum, based on the data in Table I, is

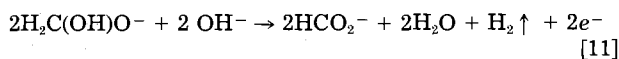
$$i = k FC_F (1 - \theta_F - \theta_H) \exp(i - \beta) \frac{FE}{RT} \exp - (1 - \delta) (r_F \theta_F + r_M \theta_M) \quad [9]$$

where C_F = concentration of formaldehyde, θ_F and θ_M are the coverages of methylene glycol anion (MGA) and hydrogen, respectively, and r_F and r_M are the interaction coefficients for adsorbed MGA and hydrogen, respectively. δ represents the activation coefficient in the case of charge transfer from the adsorbed state and is given by $0 \leq \delta \leq 1$. In the case of platinum, Table I shows that $\gamma = 1$, i.e., one electron is transferred before the rds in the cathodic reaction, or, in this case, the anodic rds is followed by a reversible electron transfer step so that the complete stoichiometry of the reaction on Pt is obtained by adding steps (i), (ii), and (iii), i.e.



The mechanism described in Eq. [10] is similar to that proposed by Buck and Griffith (3) for formaldehyde oxidation on Pt in 1M KOH.

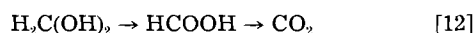
In the case of copper, the oxidation current is obtained by multiplying the right-hand side of Eq. [9] by $C_H^{0.5}$, as in this case $\partial i / \partial C_H = 0.5$ (Table I). The stoichiometry number is 2, so that the overall stoichiometry of formaldehyde oxidation on Cu is obtained by adding steps (i), (ii) and (iv)



This mechanism is in agreement with the proposal of Lukes (4).

Volcano plots.—Volcano plots provide a useful means for comparing the electrocatalytic activities of metals or alloys toward certain reactions. True volcano curves are obtained by plotting the actual catalytic activities as a function of the free energy of adsorption of the reactant or a reaction intermediate (6). Capon and Parsons (12) have shown that, for the electrochemical oxidation of formic acid on various noble metals, a plot of the relative catalytic activity against the formate heat of formation, obtained via gas phase measurements by Sachtler *et al.* (23), gives a volcano-type plot. Such a plot therefore suggests that $HCOO-M$ is a likely intermediate in the $HCOOH$ oxidation pathway.

In this investigation, the relative catalytic activities of various metals toward formaldehyde oxidation were obtained from cyclic voltammograms by the Capon and Parsons (12) method. When these approximate catalytic activities are correlated with the formate heats of formation, volcano-type curves are obtained as shown in Fig. 19 and 20. In acid media (Fig. 19), the convex relation obtained is quite similar to the curve obtained by Capon and Parsons for $HCOOH$ oxidation. It is therefore logical to assume that $HCOO-M$ is also the weakly bound intermediate in the formaldehyde oxidation pathway. Under the circumstances, formaldehyde oxidation in acid media may simply be described as



In alkaline media, there is little doubt that $HCOO^-$ is an intermediate. In fact, on metals such as Pt, a larger over-

potential is necessary to oxidize the $HCOO^-$ further to CO_3^{2-} (1a). It is therefore quite appropriate that Fig. 20 should show a volcano-type correlation. The shapes of the volcano curves are, however, not very helpful in determining the reaction mechanism (6). Consequently, Fig. 20 does not explain why on certain metals such as Ag and Cu formaldehyde oxidation is accompanied by hydrogen evolution while on metals such as Pt and Pd formaldehyde oxidation proceeds without simultaneous hydrogen generation. An explanation for this behavior can be found by examining the detailed mechanism of formaldehyde oxidation on the two types of metal described in the previous section. On Pt, the dehydrogenation reac-

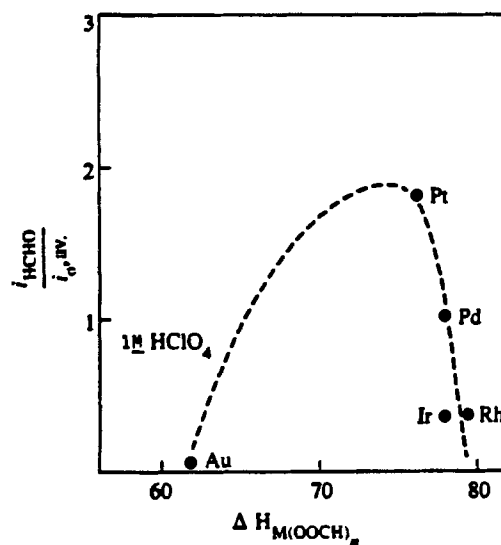


Fig. 19. Plot of the relative catalytic activity for HCHO oxidation in 1M $HClO_4$ as a function of enthalpy of formation of metal formate.

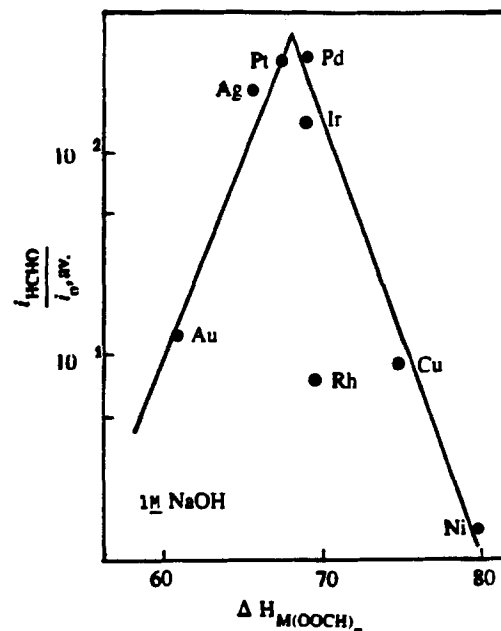


Fig. 20. A plot of HCHO oxidation currents in 1M NaOH vs. enthalpy of formation of metal formate.

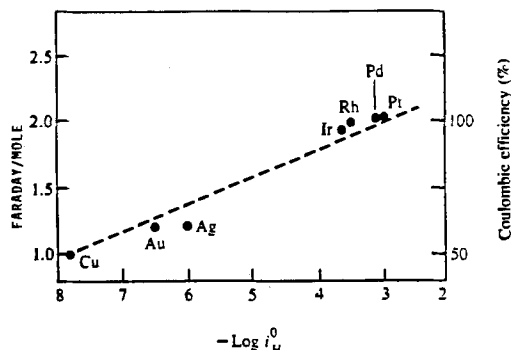


Fig. 21. Plot of coulombic efficiency for HCHO oxidation in 1M NaOH against i_H^0 on various metals.

tion and rds are followed by a hydrogen ionization reaction (reaction scheme [i]-[iv]). At the potentials at which formaldehyde oxidation on Pt occurs, the hydrogen oxidation reaction is entirely possible. On copper, the rds occurs twice, and this is then followed by hydrogen radical recombination reaction. Presumably, at the potential at which formaldehyde oxidation on copper takes place, hydrogen recombination and evolution is kinetically more favorable than hydrogen ionization, though thermodynamically at these potentials hydrogen ionization is the favored reaction. This suggests that whether formaldehyde oxidation on a substrate is accompanied by hydrogen evolution or not depends entirely on the catalytic activity of the substrate toward the hydrogen ionization reaction, i.e., on the free energy of adsorption of hydrogen on the substrate. This is verified in Fig. 21, which shows a linear relationship between the coulombic efficiency of the formaldehyde oxidation reaction on various metals (or the number of electrons realized per formaldehyde molecule decomposed), and $-\log i_H^0 \cdot i_H^0$ is the exchange current density for the hydrogen reaction on these metals and is taken to represent the free energy of adsorption for hydrogen (24). The correlation between simultaneous hydrogen evolution during formaldehyde oxidation and the heat of adsorption for hydrogen on the metals was first suggested by van den Meeraker (25); but the heat of adsorption for hydrogen was erroneously calculated by the Eley-Stevenson (26, 27) method for both transition and sp metals. It has been shown by Trasatti (28) that while this method can give satisfactory results for transition metals, it does not hold at all with sp metals. The correct parameter to be used for the reactivity scale toward hydrogen of the various metals (transition and sp metals) is i_H^0 . This parameter relates to the free energy of adsorption for hydrogen in the presence of the solvent and the field in the double layer.

It is interesting to note in Fig. 21 that the Group IB metals or the sp metals such as Cu, Au, and Ag show low coulombic efficiency even though Ag exhibits approximately the same catalytic activity for formaldehyde oxidation as Pt and Pd (cf Fig. 20). The Group VIII metals or metals with unfilled d bands exhibit high coulombic efficiency giving two electrons per formaldehyde mole-

cules oxidized. Clearly, according to the data in Fig. 21, metals may in principle be divided into three main classes: (i) metals with positive free energy of hydrogen adsorption, (ii) metals with free energy of hydrogen adsorption close to zero, and (iii) metals with negative free energy of hydrogen adsorption. In the case of class i metals, formaldehyde oxidation is accompanied by hydrogen evolution. For class ii metals, there is no simultaneous hydrogen evolution during the formaldehyde oxidation. Class iii metals, such as Ni, showed very low catalytic activity for formaldehyde oxidation to allow accurate measurements of the coulombic efficiency.

Manuscript submitted Feb. 19, 1985; revised manuscript received June 19, 1985.

IBM Corporation assisted in meeting the publication costs of this article.

REFERENCES

- (a) W. Vielstich, "Fuel Cells," Revised English ed., Interscience, New York (1978); (b) M. W. Breiter, "Electrochemical Processes in Fuel Cells," Springer-Verlag, New York (1969); (c) "From Electrocatalysis to Fuel Cells," G. Sandstede, Editor, Washington University Press, St. Louis, MO (1972).
- O. A. Khazova, Yu. B. Vasiliev, and V. S. Bagotskii, *Elektrokhimiya*, **1**, 82 (1965).
- R. P. Buck and L. R. Griffith, *This Journal*, **109**, 1005 (1961).
- R. M. Lukes, *Plating*, **51**, 1066 (1964).
- A. A. Balandin, *Adv. Catal.*, **19**, 1 (1969).
- R. Parsons, *Trans. Faraday Soc.*, **54**, 1053 (1958).
- H. Gerischer, *Bull. Soc. Chim. Belg.*, **67**, 506 (1958).
- R. J. L. Martin, *Aust. J. Chem.*, **7**, 4000 (1954).
- J. F. Walker, "Formaldehyde," 3rd ed., Reinhold, New York (1964).
- A. Vogel, "Textbook of Quantitative Inorganic Analysis," ed. IV, Langman (1978).
- P. Bindra and J. Roldan, To be published.
- A. Capon and R. Parsons, *J. Electroanal. Chem.*, **44**, 239 (1973).
- O. G. Tyunikova, N. B. Miller, A. A. Yakovleva, and V. I. Veselovski, *Elektrokhimiya*, **7**, 690 (1971).
- A. Capon and R. Parsons, *J. Electroanal. Chem.*, **45**, 205 (1973).
- T. Biegler, D. A. J. Rand, and R. Woods, *ibid.*, **29**, 269 (1971).
- J. Ambrose, R. G. Baradas, and D. W. Shoesmith, *ibid.*, **47**, 65 (1973).
- V. G. Levich, "Physicochemical Hydrodynamics," Prentice Hall, Englewood Cliffs, NJ (1962).
- K. J. Vetter, "Electrochemical Kinetics," English ed., Academic Press, New York (1967).
- R. Parsons, *Trans. Faraday Soc.*, **47**, 1332 (1951).
- P. L. Allen and A. Hickling, *ibid.*, **53**, 1626 (1957).
- J. O'M Bockris and A. K. N. Reddy, "Modern Electrochemistry," Vol. 2. Plenum Press, New York (1970).
- D. S. Gnanamuthu and J. V. Petrocelli, *This Journal*, **114**, 1036 (1967).
- J. Fahrenfort, L. L. Van Reyen, and W. M. H. Sachtler, in "The Mechanism of Heterogeneous Catalysis," J. H. DeBoer, Editor, Elsevier, New York (1960).
- S. Trasatti, *J. Electroanal. Chem.*, **39**, 163 (1972).
- J. E. A. M. van Den Meeraker, *J. Appl. Electrochem.*, **11**, 387 (1981).
- D. D. Eley, *Disc. Faraday Soc.*, **8**, 34 (1950).
- E. P. Stevenson, *J. Chem. Phys.*, **23**, 203 (1955).
- S. Trasatti, *J. Chem. Soc. Faraday 1*, **68**, 229 (1972).

Plasma-Sprayed Semiconductor Electrodes: Photoelectrochemical Properties of TiO₂

L. Parent, J. P. Dodelet,* G. G. Ross, and B. Terreault

INRS-Energie, Varennes, Québec, Canada J0L 2P0

S. Dallaire

Institut de Génie des Matériaux, Boucherville, Québec, Canada J4B 6Y4

ABSTRACT

TiO₂ photoanodes have been prepared by the plasma spray technique on titanium, graphite, and alumina substrates. 25-30 μm thick coatings display a good adhesion to the substrate and a highly textured surface. Dark and photoelectrochemical properties of the photoanodes have been measured in oxygen-saturated solutions of NaOH at pH 13. It is shown that the performances of the electrodes are quite insensitive to the plasma power or to the TiO₂ powder granulometry but are very sensitive to the purity of the spraying material, to the substrate, and also to a heat-treatment (H₂ or Ar at 800°C followed by a rapid quenching in air). The maximum quantum yield is obtained at 300 nm for heat-treated TiO₂. It is about 40% on alumina and 70% on the titanium. The heat-treatment affects the conductivity, σ , and the surface density of hydroxyl groups, N_{OH} , of the coatings. For heat-treated TiO₂, typical values are $\sigma = 2.4 (\Omega\text{-cm})^{-1}$ and $N_{OH} = 2.8 \times 10^{15} \text{ cm}^{-2}$. For untreated TiO₂, typical values are $\sigma = 30.6 (\Omega\text{-cm})^{-1}$ and $N_{OH} = 2.1 \times 10^{16} \text{ cm}^{-2}$. The J-V curves of heat-treated TiO₂ sprayed on alumina extend anodically up to 9.5V (*vs.* SCE), where film breakdown occurs. For the same film sprayed on titanium and graphite, the anodic dark behavior is similar to that observed for the bare substrates. It is concluded that polycrystalline TiO₂ coatings, produced by the plasma spray technique, can display photoelectrochemical and dark characteristics similar to the ones obtained with single-crystal material.

Polycrystalline n-TiO₂ has been largely studied as a semiconducting electrode in photoelectrochemical cells. Several techniques for the preparation of the photoanodes are found in the literature, namely, thermal oxidation (1-8), anodic oxidation (8-16), chemical vapor deposition (8, 9, 14, 17-21) and plasma-enhanced chemical vapor deposition (22), sputtering (23, 24), pressed and sintered powders (2, 25, 26), and screen printing (27).

An industrial coating technique, plasma spraying, has also been used to produce polycrystalline electrodes from TiO₂ powders of unspecified purity sprayed on titanium (28) and from raw rutile sprayed on alumina (29). The latter investigation reports an unusual anodic flatband potential ($V_{FB} \approx -0.6V$ SCE) at the pH used (10M NaOH) and a large potential dependence of the photocurrent below 0.4V. At higher anodic potentials, a rapid rise in dark current is attributed by Wang and Henager (29) to the presence of impurities (Si, Fe, Cr, Ni, Mn) in the raw rutile. TiO₂ was again recently sprayed on titanium (30). The obtained results were similar to the ones reported by Wang and Henager except that anodic dark currents, in 0.1M NaOH, rise quickly at potentials higher than $\sim 0.7V$ *vs.* SCE.

In the present work, it will be shown that the current voltage (J-V) characteristics of plasma-sprayed n-TiO₂ photoanodes are largely dependent on the purity of the powder and on the nature of the substrate.

Using this technique, it is possible to produce large surfaces of polycrystalline TiO₂ photoanodes displaying J-V characteristics like the ones observed with monocrystals. On alumina substrates, J-V curves can be obtained up to 9.5V.

Experimental

Powder preparation.—TiO₂ powders were obtained from three different sources. Two of them [Metco 102 ($\leq 44 \mu\text{m}$) and H. C. Starck (5-12 μm)] had the appropriate size distribution for direct feeding of the torch and were used without modifications. X-ray diffraction showed that these powders had the rutile structure. The third one, a high purity anatase powder (99.9%, A. D. MacKay Chemicals), had a particle diameter which was too small ($\leq 5 \mu\text{m}$). It was agglomerated before plasma deposition by atomization in a spray dryer. The atomization was realized from a suspension prepared by mixing demineralized water (30 weight percent [w/o]), polyvinyl alcohol (0.5

w/o; J. T. Baker, 88-89% hydrolized), polyethylene glycol (2 w/o; Carbowax, Fisher Laboratories), and TiO₂. All the organic components were eliminated during the sintering of TiO₂ performed in an alumina crucible at 1200°C in air. This temperature treatment also induces the transformation of the initial anatase form of TiO₂ into the rutile form. Finally, the desired size of powders was sieved with an air jet sieve classifier (Alpine, Augsburg) and the distribution of particles having a diameter smaller than 32 μm was measured with a particle size analyzer (PA-720, Pacific Scientific).

Spraying system.—Plasma spraying was performed with a plasma spray system (Plasmadyne). Three plasmas were used for the production of the coatings: (i) Ar/He (2:1) 30 kW, (ii) Ar/He (2:1) 40 kW, and (iii) Ar/H₂ (20:1) 30 kW. TiO₂ was introduced in the plasma at a constant rate of about 9 g·min⁻¹ and projected in subsonic mode on three different substrates: titanium foils (99.7% from Alfa), alumina disks (99.8% Coors), and graphite slices. Fused silica was also tried out as a substrate but was abandoned because of the poor adhesion of the coating. The distance between the torch and the substrate was always 7.5 cm, and the speed of X-Y sweeping was set to obtain coatings 25-30 μm thick [measured with a Surtronic 3 profilometer (Taylor and Hobson)]. The surface texture of the films was quite sensitive to the particle size distribution. Coatings obtained with powders having a diameter ranging from 32 to 63 μm are rougher than those made with powders of 4-20 μm, but their exposed surface is smaller. With all powders used in this investigation, gray coatings were always obtained.

Hydrogen or argon treatment.—The photoelectrochemical properties of the TiO₂ films were investigated either directly after plasma spraying or after a hydrogen or argon treatment at temperatures up to 800°C. This treatment usually consisted in leaving the electrode for 15 min in a 0.3 liter·min⁻¹ flow of hydrogen or argon. The samples were always introduced in the furnace under argon atmosphere at the temperature of the treatment; upon removal, they were quenched at room temperature.

Photoelectrochemical measurements.—In order to perform electrochemical measurements on the TiO₂-coated electrodes, ohmic contacts were established by directly attaching a lead to the conducting substrates (C, Ti). On alumina, the ohmic contact was obtained with a Ga/In eu-

* Electrochemical Society Active Member.

tectic. All the nonphotoactive parts of the electrode were afterwards covered with silicone rubber to avoid corrosion, leaving an active area of 1.5 cm^2 .

The electrochemical measurements were performed in a three-electrode cell equipped with a quartz window, using a NaOH solution at pH 13 ($\sim 0.1N$) saturated with oxygen at atmospheric pressure. The counterelectrode was a 15 cm^2 Pt foil, and a standard calomel electrode was used as reference.

The working electrode was illuminated with white light from a high pressure 300W Xe lamp equipped with a 10 cm water filter. The maximum UV power (up to 400 nm) incident on the working electrode was $30 \text{ mW}\cdot\text{cm}^{-2}$ (uncorrected for the reflection). Neutral density filters were used to vary the light intensity. Monochromatic light for quantum yield determination was obtained by interference filters having a 10 nm bandwidth. At 300 nm, the incident power on the working electrode is $0.150 \text{ mW}\cdot\text{cm}^{-2}$. The light intensity was measured with a Photodyne 44 XL radiometer. The J-V curves were performed with a Princeton Applied Research Model 173 potentiostat and a Model 175 programmer. The scanning rates were always $10 \text{ mV}\cdot\text{s}^{-1}$. The quantum efficiencies were obtained in a two-electrode configuration using a Keithley 614 electrometer. All the measurements were performed at room temperature.

Conductivity measurements.—The van der Pauw technique (31) was followed to perform the conductivity measurements on TiO_2 sprayed on alumina. For these measurements, a Keithley 225 current source and a Hewlett-Packard 3455 A digital voltmeter were used.

Hydrogen depth profiling.—A novel, quantitative, nondestructive, nuclear microanalysis technique (32) called elastic recoil detection was used to detect the presence of hydrogen in the top layer of plasma-sprayed TiO_2 . This technique uses a 350 keV $^4\text{He}^+$ beam incident under vacuum (10^{-7} torr) on the material to probe the hydrogen concentration to a depth of 600Å. The sensitivity is 1 H atom percent (a/o).

Results and Discussion

Surface aspect of TiO_2 coatings.—Figure 1 is a scanning electron microscope (SEM) picture showing the surface texture of the TiO_2 coating. Irregularities of the surface introduce a much larger actual area as compared to the geometrical one. The surface texture is a function of the size of the sprayed particles and the power of the plasma.

The largest exposed surfaces are obtained with the smallest particles ($4\text{--}20 \mu\text{m}$) and with the highest plasma power (40 kW). In this case, the melted particles leave the torch with a large kinetic energy resulting in a bigger splash upon arrival on the substrate. The electrode surface depicted in Fig. 1 is an intermediate between a flat surface and a colloid.

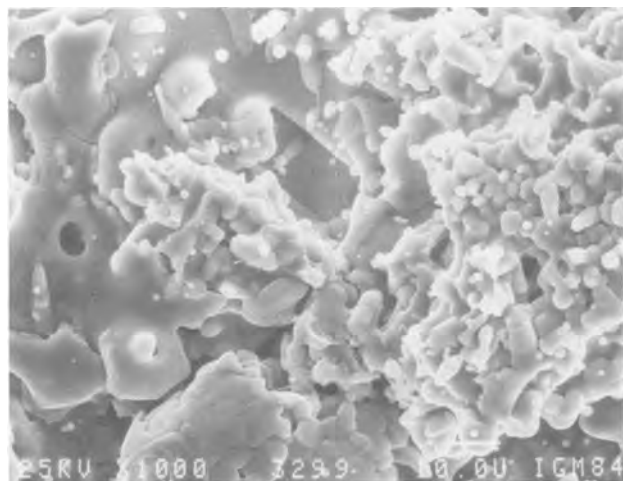


Fig. 1. SEM picture of the surface of a plasma-sprayed TiO_2 electrode

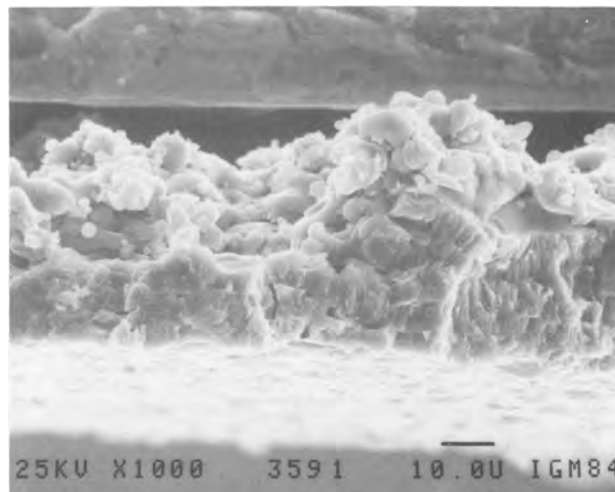


Fig. 2. SEM picture of a fracture of a plasma-sprayed TiO_2 coating removed from its substrate.

No bare spots were detected in the coatings by SEM. However, there are small cracks and pores on the surface through which the electrolyte could eventually penetrate and reach the substrate.

Figure 2 is a SEM picture showing a fracture of a TiO_2 coating removed from its substrate. This picture confirms the film thickness ($25\text{--}30 \mu\text{m}$) measured with the profilometer. The more regular surface seen at the bottom of the picture was the surface in contact with the substrate. This film is typical of plasma-sprayed coatings which always show a vertically oriented crystallization.

Purity of TiO_2 powders and plasma characteristics.—Figure 3 presents the J-V curves obtained for TiO_2 coatings on Ti using three powders having different impurity contents. All these coatings were heated in H_2 at 800°C , and the UV power ($\lambda \leq 358 \text{ nm}$) incident on the electrodes is $9 \text{ mW}\cdot\text{cm}^{-2}$. The smallest photocurrent densities were obtained with TiO_2 from Starck (dash-dotted curve) followed by TiO_2 from Metco (dotted curve). The highest photocurrent densities were obtained with TiO_2 from Mackay (full curve). Chemical analysis of these powders is presented in Table I. The Al content, which is known to improve the quantum yield of TiO_2 (33), is about the same for the three powders. However, the amounts of Cr and Fe, which are known to decrease the UV quantum yield (34), are smaller in the MacKay powder.

The influence of the plasma powder and its type on the photocurrent densities has also been analyzed. No significant differences were observed when the power of the plasma was changed from 30 to 40 kW and when He was replaced by H_2 . Within experimental error, there were no significant differences due to variation in the size of the feeding particles from $4\text{--}20$ to $32\text{--}63 \mu\text{m}$. Cooling the

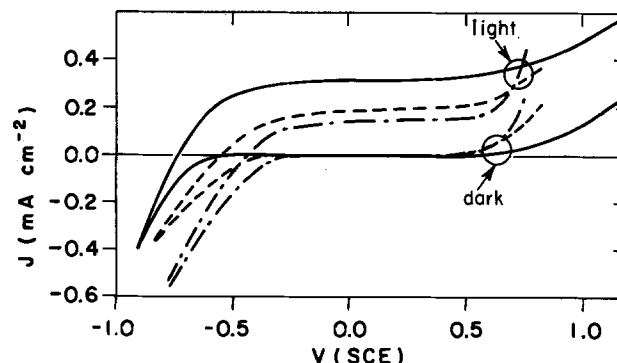


Fig. 3. J-V curves for plasma-sprayed TiO_2 coatings (H_2 treated at 800°C) on titanium using three powders having a different impurity content.

Table I. Chemical analysis of the three TiO₂ powders used in this work (in weight percent)

Elements	Starck	Metco	MacKay ^a
Si	0.015	0.035	0.02
Mn	0.001	0.002	0.001
Cr	0.02	0.002	0.002
Fe	0.05	0.14	0.01
Al	0.02	0.015	0.016
Ni	0.001	0.001	0.001

^a After agglomeration and sintering.

substrate with Dry Ice during coating also has no effect. In light of these results, the experiments that follow were performed exclusively on coatings made with TiO₂ from MacKay by using a 30 kW Ar/He plasma to melt the powders.

Quantum yields and coating conductivities.—Figures 4A and 4B depict the quantum yields, ϕ , for TiO₂ sprayed on titanium and alumina, respectively. When graphite is used as a substrate, the obtained quantum yields are similar to the ones measured for TiO₂ on titanium. The full points represent the values obtained directly after plasma spraying. The open points, on the other hand, are obtained after treating the plasma-sprayed TiO₂ at 800°C in H₂. All these action spectra are corrected for a constant photon flux (3.4×10^{14} photon·s⁻¹·cm⁻²) using the following relation

$$J_{sc} = kI^\gamma \quad [1]$$

where J_{sc} is the short-circuit photocurrent in the two-electrode configuration used for the quantum yield determination, k is a proportionality constant, and γ is the light power exponent. A value of $\gamma = 0.80$ was found for both untreated and H₂-treated TiO₂. The maximum quantum yield is obtained at about 300 nm and reaches values as high as 70% for H₂-treated TiO₂ on titanium. This value compares favorably with the quantum yields reported in the literature (8, 22, 33, 35).

An increase in the quantum yield is always observed for plasma-sprayed TiO₂ electrodes treated in H₂ at temperatures higher than 300°C with a maximum effect at temperatures above 600°C. A similar effect on ϕ is found when

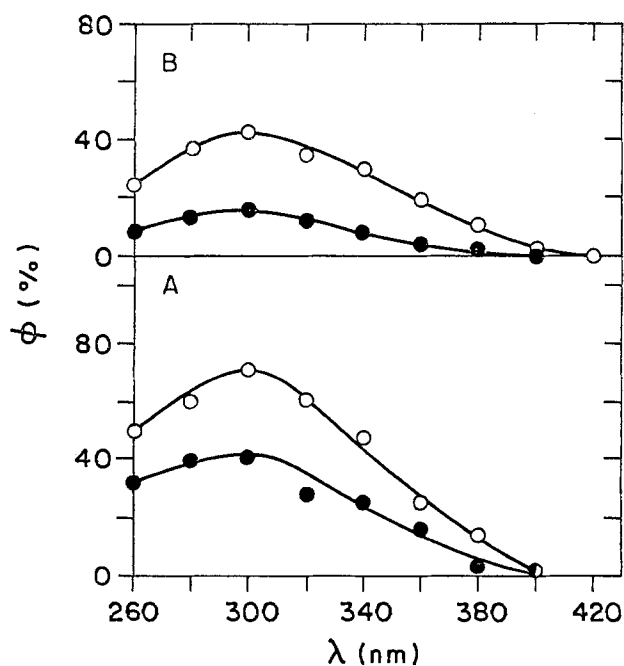


Fig. 4. Quantum yield, ϕ , for H₂- or Ar-treated (open symbols) and untreated (dark symbols) TiO₂ sprayed on titanium (A) and on alumina (B), as a function of the wavelength.

the electrodes are treated in Ar. The H₂ or Ar treatment above 600°C induces a reduction of the coating conductivity, σ . Typically, $\sigma = 30.6$ (Ω -cm)⁻¹ for untreated samples and $\sigma = 2.4$ (Ω -cm)⁻¹ for H₂- or Ar-treated samples at 800°C. As the treatment of the electrode in either H₂ or Ar atmosphere has the same effect on the conductivity of TiO₂, the formation of Ti—H bonds, resulting in a decrease of the charge carrier density N , may not be invoked to explain the decrease of the conductivity of the H₂- or Ar-treated electrodes. It is, however, possible that the quenching of the electrode in air after H₂ or Ar treatment might decrease, by reoxidation, the amount of triply ionized interstitial titanium and doubly ionized oxygen vacancies, which, according to Kofstad (36), are responsible for the semiconducting character of TiO₂. The oxidation effect is quite critical since an electrode left for 15 min in air at 800°C becomes so resistive that no photocurrent can be detected afterwards. A shorter oxidation time generates intermediate quantum yields tending toward the maximum value obtained after the H₂ or Ar treatment. In the remainder of the text, plasma-sprayed TiO₂ heated at 800°C in Ar in H₂ for 15 min and then quenched in air will be referred to as heat-treated electrodes.

Surface hydroxyl group densities.—Figure 5 shows the hydrogen profile, in atom percent, obtained by the nuclear microanalysis technique, for untreated (full line) and heat-treated (broken line) plasma-sprayed TiO₂ before any contact with the electrolyte solution. Even if the probed depth is 600Å, the detected hydrogen probably originates exclusively from the TiO₂ surface. This can be understood in terms of surface irregularities, as depicted in the insert of Fig. 5, where five surface analyzing conditions are illustrated. In case 1, H⁺ ejected from the surface by the impact of 350 keV ⁴He⁺ will be detected as having the maximum energy. It will be identified correctly as belonging to the surface of the sample (0 Å depth). In cases 2 and 3, even if the hydrogen also originates from the actual TiO₂ surface it will be measured by the detector as originating from a certain depth because of the energy loss in traversing the matter. The surface hydrogens represented by cases 4 and 5 will not be detected by the technique because they are shielded from ⁴He⁺ by a too large thickness of material or the ejected H⁺ stops in the layer of TiO₂ before being able to be detected. Another indication that the hydrogen is located mostly on the surface is that the profile of Fig. 5 shows a definite surface peak whose width has the theoretical resolution of the technique.

Taking into account the rutile density (4.25 g·cm⁻³) and a sensitivity limit of 1 a/o of H, one obtains $2.1 \cdot 10^{16}$ H cm⁻² for untreated TiO₂ and $2.8 \cdot 10^{15}$ H cm⁻² for heat-treated TiO₂. The actual area of the coating is not known, but these results indicate that there is a difference of nearly one order of magnitude between both hydrogen surface

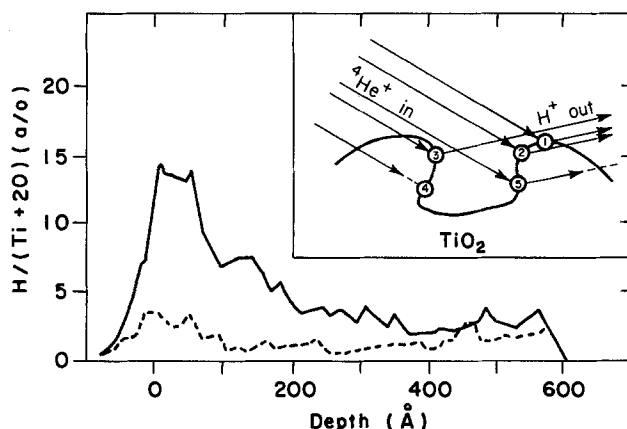


Fig. 5. Depth profiles of hydrogen content (in atom percent) for H₂- or Ar-treated (broken line) and untreated (full line) TiO₂ coatings obtained by nuclear microanalysis. The insert illustrates five analyzing conditions encountered on irregular surfaces.

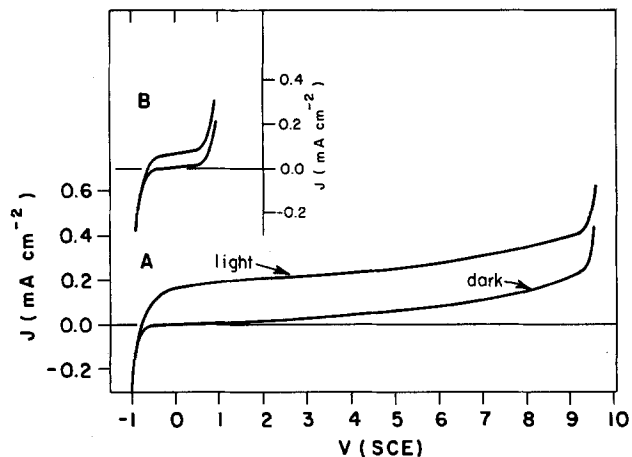


Fig. 6. TiO_2 sprayed on alumina. J-V curves obtained in oxygen-saturated NaOH (pH 13) for H_2 - and or Ar-treated TiO_2 (A) and untreated TiO_2 (B) electrode.

densities. A similar ratio was found for the conductivities of untreated and heat-treated TiO_2 , with the most conducting coating having the largest surface hydrogen density. Surface hydrogen probably belongs to hydroxyl groups chemisorbed on the surface as the result of the interaction of atmospheric water vapor and TiO_2 (37).

TiO_2 substrate and breakdown potential.—Figure 6A displays the J-V curves obtained in NaOH at pH 13 for heat-treated TiO_2 . The breakdown potential of the film happens at 9.5V. When heat-treated TiO_2 of the same purity is sprayed on Ti, a rapid increase of the dark oxidation current is observed for applied voltages $>0.5\text{V}$ (full curve in Fig. 3). It demonstrates that the breakdown observed for TiO_2 sprayed on Ti is not characteristic of the heat-treated sprayed film. It is the oxidized titanium surface of the titanium substrate, in contact with the electrolyte through cracks and pores of the sprayed film, which is responsible for the dark J-V behavior. J-V curves obtained in the dark for bare Ti (always covered by a native oxide layer) in contact with NaOH at pH 13 corroborate this interpretation. These curves are similar to the dark J-V curve displayed in Fig. 6B for untreated TiO_2 sprayed on alumina. The dark anodic behavior of TiO_2 films sprayed on graphite is also dominated by the dark characteristics of the graphite substrate in alkaline solutions.

Conclusion

This work demonstrates that the plasma spray technique is well suited for the production of TiO_2 semiconductor electrodes. The photoanodes are characterized by a highly textured surface and are able to show, after being submitted to a suitable heat-treatment, dark and photoelectrochemical properties comparable to those measured for monocrystalline TiO_2 . This technique would be particularly well suited for large-scale production. The photocatalytic performances of these coatings are now under investigation.

Acknowledgments

This work has been supported by NCR Contract no. RSD.31950-4-0008. We wish to thank D. Spino for his help with the coating production, G. Gobeil for operating the 350 keV accelerator, and Dr. C. H. Langford for his helpful suggestions.

Manuscript submitted Feb. 4, 1985; revised manuscript received July 11, 1985. This was Paper 591 presented at the Toronto, Ontario, Canada, Meeting of the Society, May 12-17, 1985.

INRS-Energie assisted in meeting the publication costs of this article.

REFERENCES

1. A. Fujishima, K. Honda, and K. Kohayakawa, *This Journal*, **122**, 1487 (1975).
2. G. Mavroides, D. I. Tchernev, J. A. Kafalas, and D. F. Kolesar, *Mater. Res. Bull.*, **10**, 1023 (1975).
3. J. F. Houlihan and D. P. Madacsy, *ibid.*, **11**, 1191 (1976).
4. L. A. Harris and R. H. Wilson, *Ann. Res. Mater. Sci.*, **8**, 99 (1978).
5. H. R. Sprünken, R. Schumacker, and R. N. Schindler, *Discuss. Faraday Soc.*, **70**, 55 (1980).
6. K. J. Hartig, J. Lichtscheidl, and N. Getoff, *Z. Naturforsch.*, **36a**, 51 (1981).
7. V. Antonucci, N. Giordano, and J. C. J. Bart, *Int. J. Hydrogen Energy*, **7**, 769 (1982).
8. K. J. Hartig, N. Getoff, and G. Nauer, *ibid.*, **8**, 603 (1983).
9. J. Keeny, D. H. Weinstein, and G. M. Hass, *Nature*, **253**, 719 (1975).
10. H. Gerischer, *J. Electroanal. Chem.*, **82**, 133 (1977).
11. J. F. McAleer and L. M. Peter, *Discuss. Faraday Soc.*, **70**, 67 (1980).
12. J. C. Manchenoir, J. P. Loup, and J. Masson, *Thin Solid Films*, **66**, 357 (1980).
13. K. J. Hartig, N. Getoff, K. D. Kotchev, and St. Kanev, *Solar Energy Mater.*, **9**, 167 (1983).
14. S. E. Lindquist, B. Finnström, and L. Tegner, *This Journal*, **130**, 351 (1983).
15. P. Clechet, C. Martelet, R. Olier, J. P. Thomas, and M. Fallavier, *ibid.*, **130**, 1795 (1983).
16. P. Miller, S. Mamiche-Afara, M. J. Dignam, and M. Muskovits, *Chem. Phys. Lett.*, **100**, 236 (1983).
17. K. L. Hardee and A. J. Bard, *This Journal*, **122**, 739 (1975).
18. K. L. Hardee and A. J. Bard, *ibid.*, **124**, 215 (1977).
19. C. Stalder and J. Augustynski, *ibid.*, **126**, 2007 (1979).
20. R. Schumacker, R. H. Wilson, and L. A. Harris, *ibid.*, **127**, 96 (1980).
21. Y. Takahashi, K. Tsuda, and K. Sugiyama, *J. Chem. Soc., Faraday Trans. 1*, **77**, 1051 (1981).
22. L. M. Williams and D. W. Hess, *Thin Solid Films*, **115**, 13 (1984).
23. A. A. Soliman and H. J. Seguin, *Can. J. Phys.*, **59**, 1674 (1981).
24. M. F. Weber, L. C. Schumacker, and M. J. Dignam, *This Journal*, **129**, 2022 (1982).
25. J. Gautron, P. Lemasson, and J. F. Marucco, *Discuss. Faraday Soc.*, **70**, 81 (1980).
26. P. Salvador, *This Journal*, **128**, 1895 (1981).
27. C. Blaauw, H. M. Naguib, A. Ahmad, and S. M. Ahmed, *Solar Energy Mater.*, **7**, 331 (1982).
28. W. Gissler, P. L. Lensi, and S. Pizzini, *J. Appl. Electrochem.*, **6**, 9 (1976).
29. R. Wang and C. H. Henager, Jr., *This Journal*, **126**, 83 (1979).
30. M. Takeuchi, F. Shimizu, F. Kaneko, and H. Nagasaka, in "Proceedings of the International Ion Engineering Congress," p. 927 (1983).
31. L. J. van der Pauw, *Philips Res. Rep.*, **13**, 1 (1958).
32. G. G. Ross, B. Terreaux, G. Gobeil, G. Abel, C. Boucher, and G. Veilleux, *J. Nucl. Mater.*, **128-129**, 730 (1984).
33. A. K. Ghosh and H. P. Maruska, *This Journal*, **124**, 1516 (1977).
34. H. P. Maruska and A. K. Ghosh, *Solar Energy Mater.*, **7**, 237 (1979).
35. D. Laser and A. J. Bard, *This Journal*, **123**, 1027 (1976).
36. P. Kofstad, *J. Less-Common Metals*, **13**, 635 (1967).
37. W. J. Lo, Y. W. Chung, and G. A. Somorjai, *Surf. Sci.*, **71**, 199 (1978).

On the Thermal Characteristics of Electrolytic Cell

Y. Ogata, S. Kainuma, M. Yasuda,* and F. Hine*

Nagoya Institute of Technology, Nagoya 466, Japan

ABSTRACT

Mathematical analysis of the heat balance of electrolytic cell was investigated. Experimental results with a vertical-type water electrolysis cell under normal conditions agreed with calculation. The water vaporization is a major factor of heat loss from the cell and, hence, it must be reduced. The thermal behavior of a water electrolysis cell was simulated under normal and pressurized conditions with the equations proposed. It was clarified that the heat loss from the cell could be reduced by increasing the operating pressure because the water vaporization was a large factor of heat dissipation at high temperatures. The effects of the thermal insulation and the emissivity of the cell wall were also discussed.

Electrochemical processes consume much more electric energy than the thermodynamic requirement to proceed the reaction under discussion. A part of excess energy is of course utilized to cover the entropy and the heat loss from the system, although it must be minimized as small as possible. The heat transfer through the cell wall is generally a major factor of these losses. In practice, the operating temperature is kept constant by balancing the Joule heat, the heat losses, and the external source such as the heat exchanger if any. Beck and Ruggeri have investigated the heat balance of several electrochemical processes (1). They point out that the diaphragm-type chlor-alkali cell and the chlorate cell dissipate some 15 and 32% of the electricity supplied, respectively, through the cell wall. The heat loss can be reduced by utilizing improved insulation, whereby the operating temperature is affected.

The energy balance of electrochemical processes has been studied by several authors. Fahidy has published the general description emphasizing the heat loss through the cell wall (2-6). These evaluations of the thermal behavior of the electrochemical system under discussion are useful for reducing the energy requirement and hence further improvement of the process economy. Use of the selected electrode materials and separators, minimization of the electrode gap, operation at high temperatures, and other factors must be considered to reduce the cell voltage and generation of unwanted Joule heat. In fact, many electrochemical cells generate excess heat over the minimum requirement. However, it might be possible to equalize the heat generation with the heat loss if the cell is operated at a certain temperature.

As Kawashima (7) and LeRoy (8, 9) state, the cell voltage decreases, but the thermal balance voltage increases when the operating temperature rises. As a result, the cell could be operated with no external heat at a temperature t_{ST} , where the cell voltage is equal to the thermal balance voltage, depending on the cell design and the operating conditions such as the cell current.

This paper deals with a basic formulation for evaluating the thermal characteristics of the electrochemical cell filled with aqueous solution operated under both steady-state and nonsteady-state conditions. A vertical-type water electrolysis cell was used as an example.

Heat Balance of Electrolytic Cell

The heat accumulation Q_A results from a balance of the heat generation by electrolysis Q_E , the heat coming from the external source Q_{EX} , the heat losses due to the solution flow and vaporization of water Q_S and Q_V , respectively, and the heat transfer through the cell wall Q_L .

$$Q_A = Q_E + Q_{EX} - Q_S - Q_V - Q_L \quad [1]$$

$$Q_A = mC_{ps} \frac{dt_s}{d\theta} \quad [2]$$

$$Q_E = 0.86I(V - E_d) - 0.86I \left(\Sigma|\eta| + \Sigma IR - \frac{T_s \Delta S_r}{nF} \right) \quad [3]$$

*Electrochemical Society Active Member.

$$Q_S = GC_{ps} (t_s - t_i) \quad [4]$$

$$Q_V = w\Delta H_v \quad [5]$$

and

$$Q_L = \Sigma UA (t_s - t_a) \quad [6]$$

where E_d is the enthalpic voltage ($\Delta H_r/nF$) (8). It is well known that the specific heat of aqueous solution is large in comparison with that of the cell components. Therefore, it is assumed that the product of the mass and the specific heat of the cell hardware is negligible to mC_{ps} in Eq. [2] in general, or in the case under discussion at least. Of course, the heat capacity of hardware must not be avoided when the cell consists of a narrow channel so that the solution volume is small for example. Both Q_E and Q_{EX} under given conditions must be minimized as small as possible in order to save energy requirements. Of these, reduction of Q_E or the cell voltage V is a main subject for research and development which includes development and utilization of high performance electrodes, separators, and other cell components, and minimization of the ohmic voltage drop between two electrodes. On the other hand, Q_{EX} can be decreased by adequate design of the hardware and utilization of the construction materials, especially thermal insulators. The operating conditions such as the electrolyte flow rate and the temperature are also important factors.

Now let us consider the factors represented by Eq. [1]-[6]. The heat generation Q_E is decreased by increasing the operating temperature because the resistivity of electrolyte, the electrode overvoltages, and the resistance of separators decrease at high temperatures. The solution IR drop is the largest factor of the excess Joule heat, especially at large amperages in most cases. The contribution of $T_s \Delta S_r$ is relatively small at medium temperatures, and its sign, of course, depends on the reaction proposed.

The heat losses, Q_S , Q_V , and Q_L increase with the operating temperature. The flow rate G on the right side of Eq. [4] is given by the cell current and the conversion of feedstock. The heat loss with vaporization of water is relatively small at low temperatures, but it increases significantly at high temperatures close to the boiling point of the electrolytic solution.

The heat loss through the cell wall Q_L depends on the hardware design and the construction materials as well as the operating conditions. The solution temperature is of course a major factor.

The external heat Q_{EX} varies with the operating temperature, as stated above. At t_{ST} , the heat generation is balanced with the dissipated heat, and hence no external heat is required. Its steady-state temperature moves to the high direction when the heat dissipation from the cell is reduced. When Q_{EX} is negative, the excess heat of the cell could be recovered. In fact, it is wasted in most cases because it is inferior to use [see Fig. 7 and 8 in Ref. (9)].

A vertical-type, undivided laboratory cell for water electrolysis with dilute caustic soda solution was operated under normal atmospheric pressure so as to evaluate the heat balance on Eq. [1]. For simplicity, assume that electrolytic solution is not circulated externally. However, the

solution is agitated and circulated extensively in the cell by electrolytic gas lift. Under such conditions, Eq. [7] is obtained

$$\left[m_o - \frac{18 \times 10^{-3}}{2F} \left(1.0 + \frac{1.5 p_{H_2O}}{1.0 - p_{H_2O}} \right) I \theta \right] C_{ps} \frac{dt_s}{d\theta} = 0.86I(V - E_d) - \frac{18 \times 10^{-3}}{2F} \left(\frac{1.5 p_{H_2O}}{1.0 - p_{H_2O}} \right) \gamma_{H_2O} I - \Sigma UA(t_s - t_a) \quad [7]$$

It is assumed that the gas bubbles leaving the cell are saturated with water vapor at the solution temperature t_s . The second term in the brace on the left side of Eq. [7] shows the water consumption due to electrolysis and vaporization.

The left side of Eq. [1], Q_A , is equal to zero under the steady-state conditions. In this case, the temperature t_{sT} was obtained by means of the iteration method. Under nonsteady-state conditions, on the other hand, the temperature varies with time and is evaluated by a Runge-Kutta method.

The cell voltage is represented by Eq. [8]

$$V = E_d^0 + \frac{RT_s}{2F} \ln(1.0 - p_{H_2O})^{1.5} - \eta_a + |\eta_c| + K \frac{l_c I}{A_c \kappa_s} \quad [8]$$

The activity of water was assumed to be unity. A coefficient K consists of the bubble effects, the current distribution on the working electrodes, and other factors (10-12). The overvoltages of the anode and cathode also vary with time because of deactivation and changes of the working surface (13). Since there was concern about discrepancies between calculation and experimental results caused by these factors, the terminal voltage was measured and used in the calculations.

The overall heat-transfer coefficient of a wall U is as follows

$$\frac{1}{U} = \frac{1}{h_s} + \frac{l_p}{k_p} + \frac{1}{h_a} \quad [9]$$

where h_s and h_a are the heat-transfer coefficients of the solution side and of the air side next to the cell wall, respectively, k_p is the thermal conductivity, and l_p is the thickness of the cell wall. Of these factors on the right side of Eq. [9], the first term $1/h_s$ is negligible to other factors, since solution in the cell is circulated vigorously by

gas lift and hydrodynamic boundary layer on the cell wall with the exception of the cell top is sufficiently thin (14). Therefore, we have

$$\frac{1}{U} \approx \frac{l_p}{k_p} + \frac{1}{h_a} \quad [10]$$

Since there is a gas phase at the cell top in most cases, the heat-transfer coefficient of its phase, similar to h_a , must be added in the calculation. Of course, Eq. [10] is valid for the top wall when the cell is filled up with electrolyte.

The heat-transfer coefficient h_a consists of two factors: natural convection and radiation as shown by Eq. [11]

$$h_a = h_c + h_r \quad [11]$$

The coefficient with respect to convection of air along the wall, h_c , is represented by a dimensionless term, the Nusselt number, Nu , which is a function of the Prandtl number, Pr , and the Grashof number, Gr . For the vertical wall, Nu is represented by Eq. [12a] and [12b]. For other cases, the equations can be found in the reference books such as Ref. (15)

$$Nu = 0.13(Pr Gr)^{1/3} \quad \text{for } Pr Gr \geq 10^9 \quad [12a]$$

and

$$Nu = 0.59(Pr Gr)^{1/4} \quad \text{for } Pr Gr \leq 10^9 \quad [12b]$$

where

$$Nu = \frac{h_c H}{k_a} \quad [13]$$

$$Pr = \frac{C_{pa} \mu_a}{k_a} \quad [14]$$

and

$$Gr = \frac{\rho_a^2 \beta_a g H^3 (t_{pa} - t_a)}{\mu_a^2} \quad [15]$$

where β_a is the volume expansion of air and g is the gravity acceleration. The coefficient with respect to radiation, h_r , is shown by the Stefan-Boltzmann equation

$$h_r = \sigma \epsilon \frac{T_{pa}^4 - T_a^4}{T_{pa} - T_a} \quad [16]$$

This equation is applicable to calculating the heat-transfer coefficient for radiation (h_r) from the cell wall in a large room (16). Table I shows the factors employed for

Table I. Physicochemical properties used

Terms	Unit	Equation	Temp. (°C)	Ref.
Enthalpic voltage	E_d (V)	$E_d = 1.4850 - 1.490 \times 10^{-4} t_s - 9.84 \times 10^{-8} t_s^2$		(8)
Vapor pressure of water	p_{H_2O} (atm)	$\log \frac{218.617}{p_{H_2O}} = \frac{\chi}{T_s} \left(\frac{3.2437814 + 5.86826 \times 10^{-3} \chi + 1.1702379 \times 10^{-8} \chi^2}{1 + 2.1878462 \times 10^{-3} \chi} \right)$ where $\chi = 647.27 - T_s$	10-150	(17)
Latent heat of water vapor	γ_{H_2O} (kcal/kg)	$\gamma_{H_2O} = 596.25 - 0.5654 t_s$	35-100	
Specific heat of air	C_{pa} (kcal/kg-K)	$C_{pa} = 0.241$	20-100	
Viscosity of air	μ_a (kg/m-h)	$\mu_a = 6.198 \times 10^{-2} + 1.655 \times 10^{-4} t_f$	0-100	
Thermal conductivity of air	k_a (kcal/m-h-K)	$k_a = 1.840 \times 10^{-3} \frac{T_f^{1.5}}{T_f + 125}$	-191-212	(18)
Density of air	ρ_a (kg/m ³)	$\rho_a = \frac{1.2932}{1 + 3.67 \times 10^{-3} t_f}$		(19)
Thermal conductivity of acrylic resin	k_p (kcal/m-h-K)	$k_p = 0.18$		
Emissivity of acrylic resin	ϵ	$\epsilon = 0.90$		
Specific heat of water	C_{ps} (kcal/kg-K)	$C_{ps} = 1.0007 - 1.226 \times 10^{-4} t_s + 1.903 \times 10^{-6} t_s^2$	20-100	

calculation. Those factors having the reference number in the last column were quoted from the publications, and others were obtained from the handbooks and the like.

The emissivity of the cell wall was estimated, since its availability was limited. The water vapor pressure and the specific heat of the solution employed were nearly the same as of water, since the caustic soda concentration was sufficiently low.

Experimental Procedure

Three vertical cells equipped with Type 304 stainless steel (SS) electrodes were used. Cell A was a rectangular-type SS cell 100 mm wide, 100 mm deep, and 1000 mm high, with one side open where a Lucite resin plate of an adequate thickness was flanged as a heat-transfer wall (see Fig. 1). A Lucite plate 10 mm thick was normally used. The copper-constantan thermocouples were embedded in the resin plate perpendicular to the wall and measured to estimate the heat flux passing through the plate. Besides the resin wall, the cell was thermally insulated with cotton of ca. 100 mm thick. A pair of the SS plate electrodes 40 mm wide and 700 mm high were positioned at the center of the cell, and the electrolysis gap was 10 mm. This cell was capable of 100A while most experiments were carried out at the amperage up to 60A, or 2100 A/m².

Cell B was a plate-and-frame type cell made of Lucite resin and was 90 mm wide, 43 mm deep, and 450 mm high. The experimental setup with this cell was almost the same as with cell A. However, a pair of thermocouples were inserted into the thermally insulated wall to estimate the heat loss from this side as well as the plastic gap on the front.

Cell C was composed of a Lucite resin cylinder of 110 mm id, 120 mm od, and 600 mm height. Two SS rods of 8 mm diam were located at the center of the cell in parallel as the electrodes. The center-to-center distance was 50 mm. The thermocouples were located along the vertical electrode to determine the temperature distribution in the solution.

Dilute caustic soda solution (0.2M NaOH) was electrolyzed. Oxygen and hydrogen were liberated at the anode and the cathode, respectively, and these gases were mixed together in the cell since there was no separator between two electrodes in these cells.

Although most experiments were conducted in the batch-wise manner, cell A was also operated under forced circulation of electrolytic solution, *i.e.*, the solution was pumped from the reservoir to the cell bottom and was recycled from the cell top to the reservoir by gravity. The solution was heated by an electric heater in the reservoir.

Results and Discussion

Verification of the thermal behavior.—Experimental results with cell A under various conditions are shown in Fig. 2. The ordinate is the temperature difference between solution and environment under steady state.

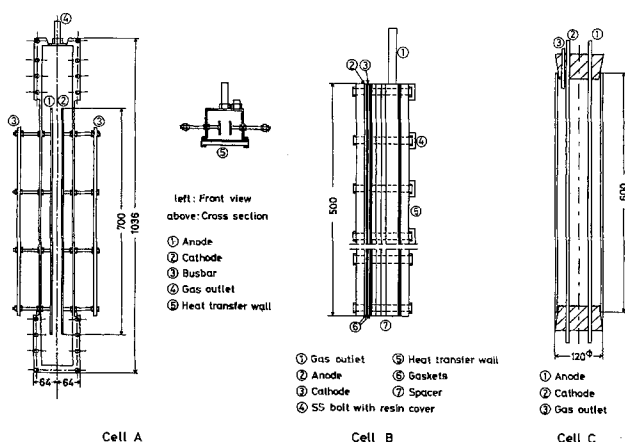


Fig. 1. Electrolytic cells

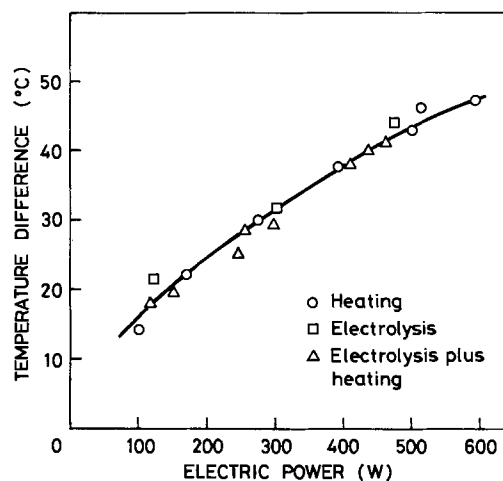


Fig. 2. Temperature difference, $t_s - t_{ar}$, as a function of the electric power supplied to the system.

Since the enthalpic voltage E_d is consumed to proceed electrolysis under a given temperature, the effective voltage as the heat source is $V_{eff} = V - E_d$, and hence the corresponding electric power is $I \times V_{eff}$, where I is the cell current. Also, the electrolyte is heated by an electric heater in the reservoir as stated above. The abscissa of this figure shows $I \times V_{eff} + W_{heater}$, where W_{heater} is the wattage supplied to the heater.

First, the solution was circulated between the reservoir and the cell without electrolysis, so that the heater in the reservoir was only a heat source (circular points). Second, electrolysis was conducted with no outside heater, *i.e.*, the Joule heat by electrolysis is a single source of heating (rectangular points). Finally, electrolysis was conducted with solution heating by using the heater in the reservoir (triangular points). It is clear that three cases agree well, and hence Eq. [3] is considered to be applicable for calculating the heat generation of electrolytic cell. Heat was dissipated from the piping to some extent, but no differ-

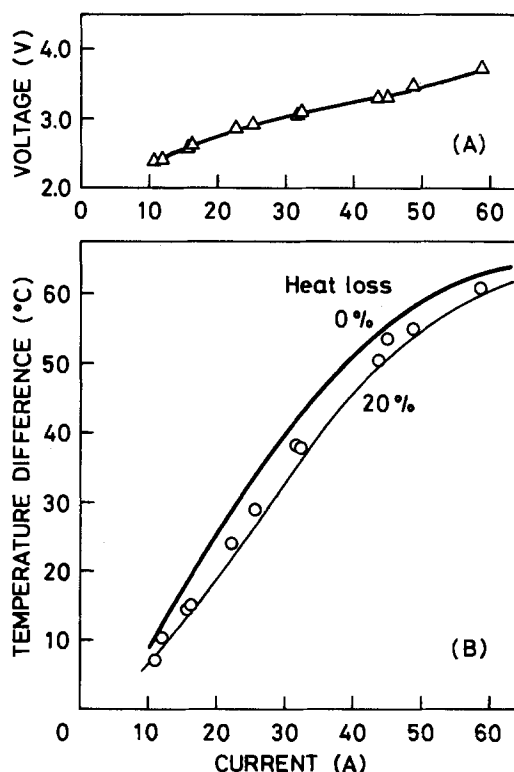


Fig. 3. Cell voltage (A) and temperature difference, $t_s - t_{ar}$ (B) of cell A as functions of the electrolytic current. Wall thickness = 10 mm. Electrode gap = 10 mm.

ence exists among three cases. Therefore, the results shown in Fig. 2 are not affected.

Figure 3 illustrates the experimental results obtained with cell A without solution circulation. The electrolysis gap was 10 mm, and the Lucite resin wall was 10 mm thick. The solution temperature depends on the cell current. According to a preliminary experiment with cell B, the heat loss through the thermally insulated wall was some 20% of the total heat in the range 35°-80°C. The thick and thin lines in draft B illustrate the temperature calculated with assumptions of 0 and 20% of the heat loss, respectively. Almost all the experimental results locate between two curves, so that the heat loss through the insulated wall of cell A is assumed to be 15-20%. While the solution temperature rises with the increase of the cell current up to a temperature difference of 50°C, the slope of the curve decreases because the water vaporization becomes significant at high temperatures.

Although the configuration of cell C was unrealistic as practice, its simple cell design was useful to avoid the heat-transfer problems through the insulated wall as in the cases of cells A and B. The experimental results shown by the circular points in Fig. 4 agreed well with calculation using Eq. [12b] shown by the solid line, since the heat transfer was uniform along the cell wall.

Figure 5 shows the Joule heat with electrolysis, the heat loss through the wall, and the heat loss caused by water vaporization as functions of the electric current passing through cell C. It is clear that the last factor increases greatly with increases of the cell current and, hence, the solution temperature as stated above with cell A.

To investigate the effects of the emissivity of the cell wall on the heat balance, a small cell C was used. That is, the outside surface of the resin cylinder was covered with an adhesive aluminum foil to change the emissivity. Air voidage between the resin and the aluminum foil was negligible and, hence, did not affect the heat transfer. The open points and the closed points in Fig. 6 show the experimental results obtained with and without aluminum foil, respectively. The solid lines illustrate the results of calculation with 0.45 and 0.90 for ϵ . An aluminum foil employed here had a relatively large ϵ shown above against expectation since its surface was coated with synthetic polymer. The emissivity of bright aluminum is said to be less than 0.1. The solution temperature of the cell with aluminum foil is high. In consequence, the emissivity of the cell wall is a large factor of the heat balance of the electrolyzer rather than the thickness of the thermal insulator (see Fig. 12 and its description).

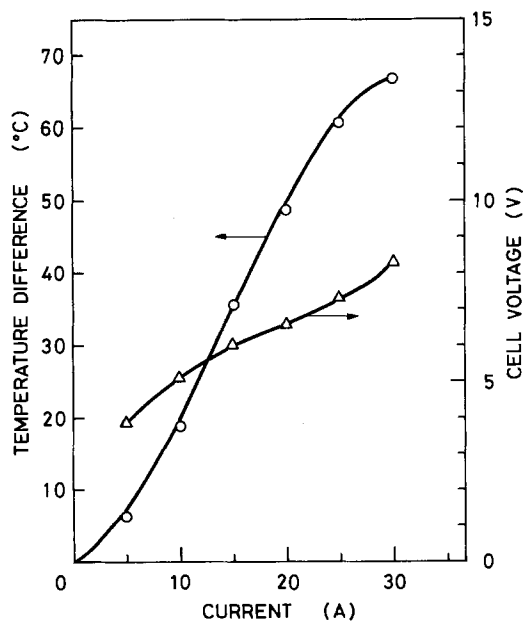


Fig. 4. Temperature difference, $t_s - t_a$, and voltage of cell C under steady-state conditions as functions of the electrolytic current.

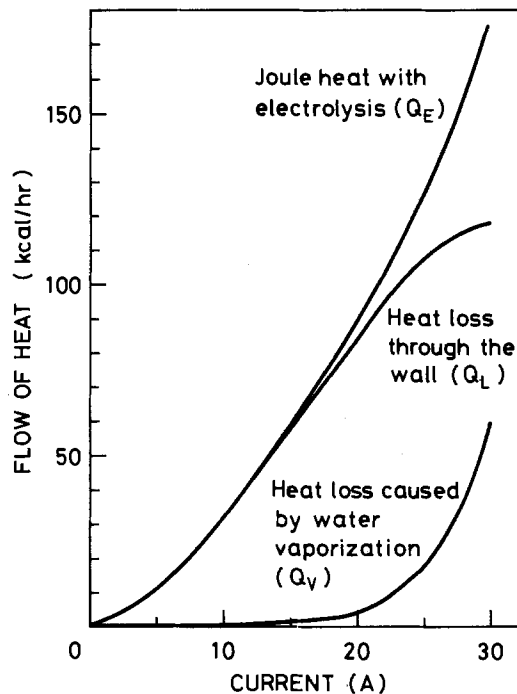


Fig. 5. Flow of heat vs. amperage of cell C

Figure 7 is an example of the solution temperature vs. time curves during electrolysis. The solid lines illustrate the results of calculation with Eq. [7] under respective conditions. The experimental results agree with calculation. Pickett (20) reported, however, disagreement of experiment with theory, probably due to variation of the solution temperature within his cell.

Since calculation described above is feasible to simulate the thermal characteristics of the cell having a simple configuration, the solution temperature in the electrochemical system consisting of the electrolyzers, the solution circulation pumps and reservoir, and other auxiliaries could be calculated exactly if the structure and geometry of hardware, the operating conditions, and the physicochemical properties of materials and electrolyte are given. Also, it is applicable to calculate the thermal

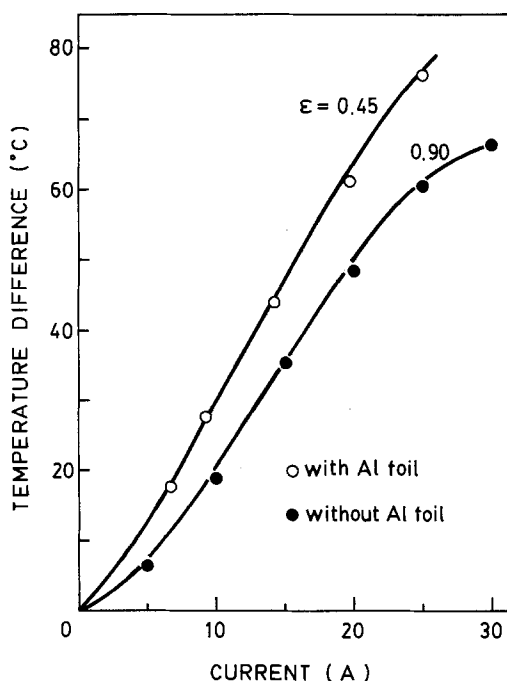


Fig. 6. Effect of the emissivity on the temperature difference, $t_s - t_a$, vs. current curve of cell C. Plots = experimental. Curves = calculated.

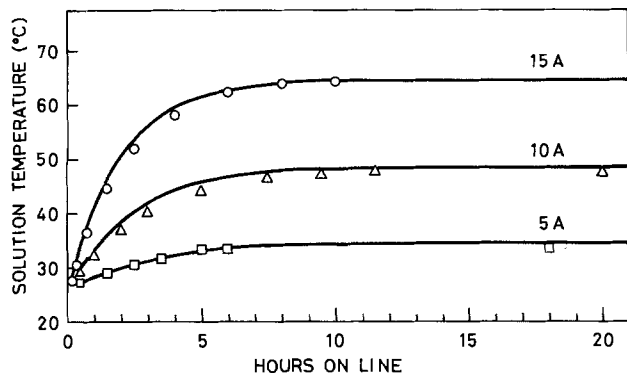


Fig. 7. Transient curves of the solution temperature of cell C. Plots = experimental. Curves = calculated.

behavior of complex systems if the overall heat-transfer coefficient for those systems is available.

Mathematical simulation of the thermal behavior of water electrolysis cell.—Tilak *et al.* have illustrated a useful diagram showing the material and energy balances of a monopolar, tank-type cell for water electrolysis [see Fig. 7 in Ref. (21)]. Calculation of the heat balance of this system operated under normal conditions shown in Table II was conducted to evaluate applicability of the mathematical treatment discussed above.

Assume that the electrolyzer is operated at a given temperature t_s . The cell voltage is V , and the amperage is I . Excess heat is removed by the heat exchanger and the like. Purified water is fed to the cell at the temperature t_f . A part of heat is dissipated from the cell wall by radiation and convection. Hydrogen and oxygen are generated at the cathode and the anode, respectively, and these gases are saturated with water vapor at the cell temperature. They also contain entrainment of electrolytic solution to some extent. The gases are cooled by the respective heat exchangers to the temperature t_c and brought to the gas holder. A small amount of water may go out with hydrogen and oxygen; instead, the condensate is sent back to the cell.

The heat balance of the water electrolysis cell under steady-state conditions is represented by Eq. [17]

$$0.86I(V - E_d) - \frac{18 \times 10^{-3}}{2F} \left(\frac{1.5p_{H_2O}}{p - p_{H_2O}} \right) \gamma_{H_2O} I - \Sigma UA(t_s - t_a) - \frac{18 \times 10^{-3}}{2F} \left(1 + \frac{1.5p_{H_2O}'}{p - p_{H_2O}'} \right) (t_s - t_f) I - \frac{18 \times 10^{-3}}{2F} \left(\frac{1.5p_{H_2O}}{p - p_{H_2O}} - \frac{1.5p_{H_2O}'}{p - p_{H_2O}'} \right) (t_s - t_c) I + Q_{EX} = 0 \quad [17]$$

The fourth and the fifth terms on the left side of this equation are the heats required for water feed and condensate, respectively. The cell voltage V is as follows

$$V = E_d + \eta_a + |\eta_c| + \frac{il_e}{\kappa_s} \quad [18]$$

Table II. Operating conditions of a water electrolysis cell

Electrolyzer:	1.6m wide, 1.2m deep, and 1.2m high, fabricated with carbon steel plate 5 mm thick, equipped with 20 pairs of the electrodes. For carbon steel, $k_p = 45$ kcal/m-h-K and $\epsilon = 0.8$.	
Electrodes:	Anodes = nickel-electroplated carbon steel plate. Cathodes = bare carbon steel plate. Size = 1.0m wide and 1.0m high. Electrode spacing = 20 mm.	
Electrolyte:	28% KOH (6.93m)	
Temperatures: (°C)	Feed water	30
	Condensers	40
	Ambience	30

Table III. Parameters employed for calculating the thermal behavior of the water electrolysis cell

Decomposition voltage (V)	$E_d = E_d^\circ + \frac{RT_s}{2F} \ln \left(\frac{p_{H_2O}^\circ (p - p_{H_2O})^{1.5}}{p_{H_2O}} \right)$
Standard decomposition voltage (V)	$E_d^\circ = 1.5184 - 1.5421 \times 10^{-3} T_s + 9.523 \times 10^{-5} T_s \ln T_s + 9.84 \times 10^{-8} T_s^2$
Anodic overvoltage (V)	$\eta_a = 0.062 \log i + 0.164$
Cathodic overvoltage (V)	$\eta_c = -0.160 \log i + 0.146$
Solution conductivity (1/Ω-m)	$\kappa_s = 26.112 + 1.5451t_s - 1.6271 \times 10^{-3} t_s^2$
Water vapor pressure on solution (atm)	$\ln p_{H_2O} = 0.016214 - 0.13802m + 0.19330m^{0.5} + 1.02391 \ln p_{H_2O}^\circ$ ($m = 6.93$ at 28% KOH)

In this equation, both the diaphragm resistance and the coefficient K in Eq. [8] have been neglected for simplicity. Although the standard decomposition voltage and the overvoltages were found in the published papers (8, 13), the temperature coefficient of the overvoltage was unavailable. The water vapor pressure on the solution and the solution conductivity κ_s were quoted from Ref. (21) and (22), respectively. The relationships of these factors are shown in Table III. Some heats are dissipated from the cell cover and the side wall by radiation and convection, and for simplicity these surfaces are assumed to be flat. Also, conduction from the cell bottom is neglected.

Equation [12a] is employed for calculating convection from the cell cover as well as the vertical surface with a different coefficient 0.14 instead of 0.13 for the vertical surface (15).

Figure 8 shows the results of calculation of the thermal characteristics of a water electrolysis cell operated under normal pressure. Drafts A, B, and C show the solution temperature, the cell voltage, and the three components of heat losses, respectively, as functions of the current density. As is shown in draft A, the solution temperature rises with the increase of current density and becomes asymptotic to the boiling point. The cell voltage is almost a straight line with the current density, except with the range lower than 1000 A/m² where the superficial resist-

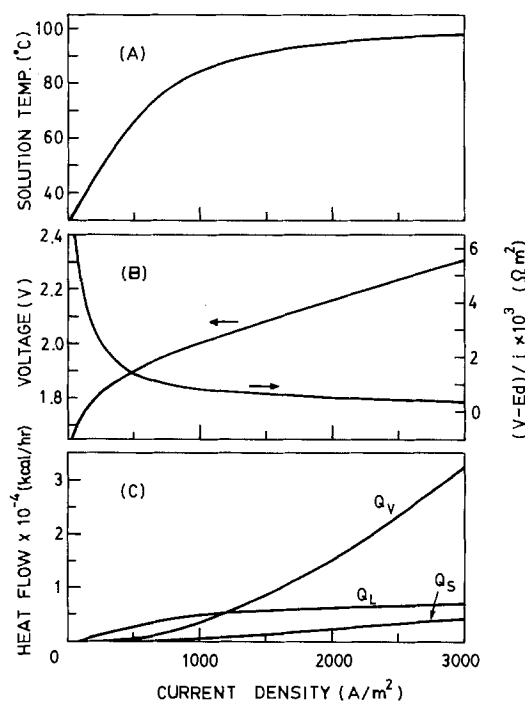


Fig. 8. Solution temperature (A), cell voltage (B), and flow of heat (C) as functions of the current density under normal pressure.

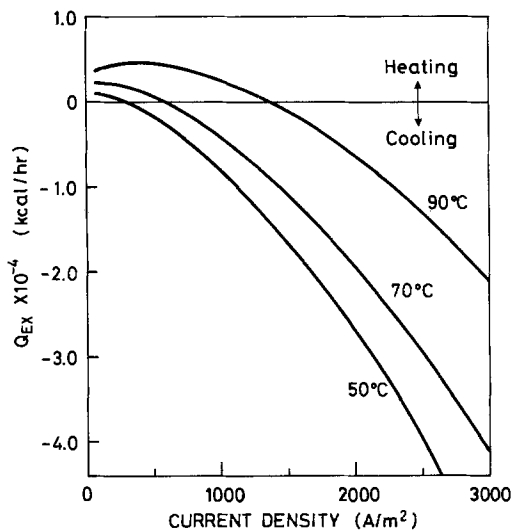


Fig. 9. External heat as a function of the current density of a cell operated under various temperatures and normal pressure.

ance $(V - E_d)/i$ decreases steeply with the increase in amperage as illustrated in draft B.

Although the heat loss through the wall Q_L is the largest factor at low current densities, the electrolytic cell is cooled mainly by water vaporization Q_V when the solution temperature rises at high current densities. The sensible heat of the feedstock Q_S is also a small factor (see draft C).

The ordinate of Fig. 9 represents the heat supply heated from an outside source for electrolyzing under given temperatures. The electrolytic cell requires some heat when operated at low current densities. On the other hand, the excess heat generated by electrolysis at high current densities must be removed. At the current density at $Q_{EX} = 0$, the heat generation is equal to dissipation so that no extra heating or cooling is required. This current density increases when the low overvoltage anode and/or cathode are employed with a minimum gap between them; thereby, the Joule heat generation is minimized. Also, Fig. 8 and 9 indicate that improvement of thermal insula-

tion, and hence decreasing the current density at the break-even thermal conditions, is useless for minimizing the heat loss from the cell wall unless the Joule heat is reduced, since, otherwise, water vaporization is rather stimulated.

The cell operation under high pressures might be favorable for minimizing water vaporization at high temperatures, resulting in high energy efficiency. Reduction of the water content in the cell gas is an additional advantage in practice.

Figure 10 illustrates the heats as functions of the operating pressure at 2000 A/m^2 evaluated by the same manner as of the cell operated under normal pressure discussed above. However, some data necessary for the calculation were estimated by means such as extrapolation, since availability was limited. It is clear that the heat dissipation accompanied water vaporization, Q_V , is decreased greatly by increasing the pressure, while the heat loss from the wall Q_L increases. The sensible heat Q_S and the Joule heat by electrolysis Q_E are almost unchanged.

Figure 11 shows the solution temperature as a function of the current density under constant pressures. The solution temperature is limited to ca. 100°C under atmospheric pressure (1 atm). On the other hand, the cell can be operated at the temperatures higher than 200°C when it is pressurized at 50 atm, and hence a significant reduction of the cell voltage or the energy requirement is anticipated. Miles *et al.* report a voltage saving of some 0.5V at 3000 A/m^2 by changing the operating temperature of the water electrolysis cell filled with 50% KOH from 80° to 208°C (23). According to our calculation, however, the voltage reduction by increasing the operating pressure from 1 to 50 atm, which correspond to 98° and 215°C, respectively, is only 0.1V. This disagreement might be caused by limited data and inadequate extrapolation. Thus, further experiments to obtain the physicochemical properties of electrolyte and the electrode kinetics necessary for the calculation must be conducted.

Figure 12 shows the energy requirement from the outside source as a function of the emissivity of the cell wall (A) and the thickness of the thermal insulator around the cell (B). Although the emissivity of the cell wall is difficult to change in a wide range, minor modification of the hardware surface could be possible. As is shown in Fig. 12A, the external heat supply is decreased considerably by decreasing the emissivity, especially at high cur-

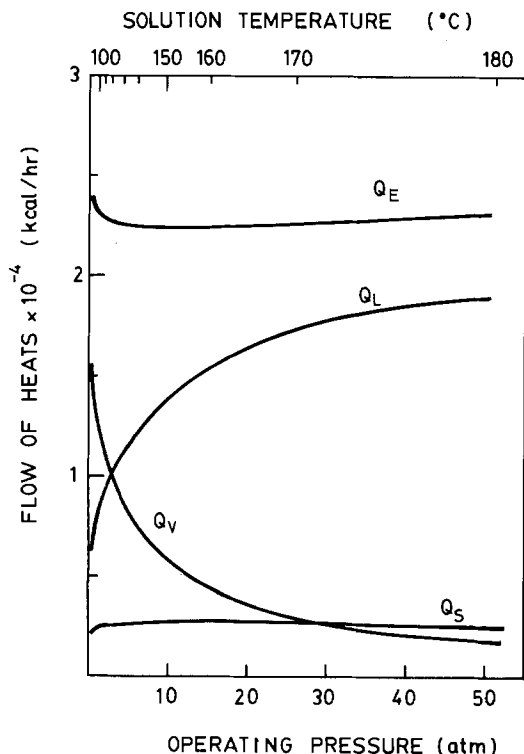


Fig. 10. Breakdown of the flow of heat as a function of the operating pressure of a cell at 2000 A/m^2 .

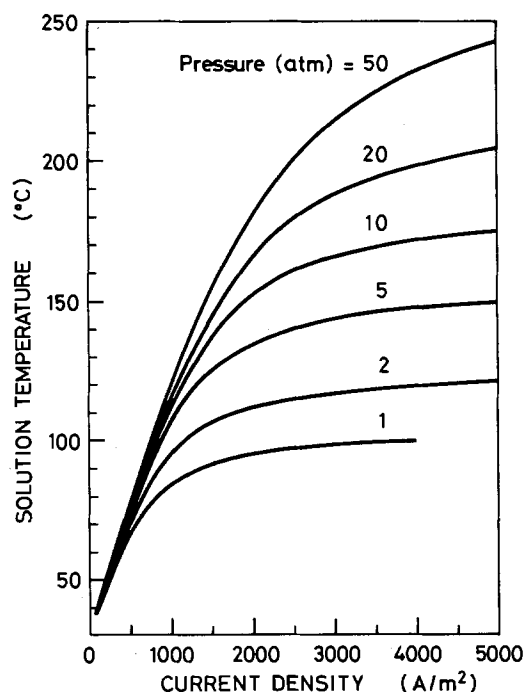


Fig. 11. Solution temperature vs. current density curves under different pressures.

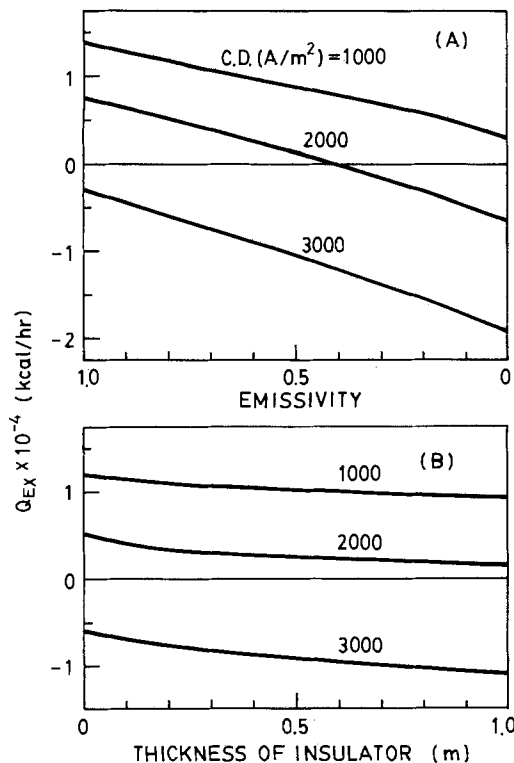


Fig. 12. External heat as a function of the emissivity of the cell wall (A) and the thickness of the thermal insulator (B) of a cell operated at 50 atm and 200°C. For the thermal insulator, $k_p = 0.15$ kcal/m-h-K and $\epsilon = 0.95$.

rents. On the other hand, the reduction of the external heat is not fully accomplished by increasing the thickness of the insulator as shown in Fig. 12B. An insulator thickness 1m thick is impractical for industrial cells.

In conclusion, the heat balance in the electrolytic cell was discussed by using an alkali water electrolytic cell as an example. Experiments were carried out to obtain the results useful for calculation. A vertical-type, rectangular cell ca. 1m high was operated under normal pressure to determine heat transfer through the cell wall. Experimental results were referred to calculation, and they agreed well in both steady-state and nonsteady-state conditions.

It is concluded that a mere increase of the thickness of the thermal insulator around the cell is not beneficial because it causes the rise of the solution temperature, and the water vaporization is stimulated extensively, resulting in the loss of heat. Any component of the Joule heat such as the electrode overvoltage and the solution IR drop must be reduced as well.

It was clarified that the emissivity of the cell wall was a large factor of the heat loss, even at relatively low temperatures. The decrease of the emissivity through any surface modification might help to improve the heat balance of electrolytic cells significantly.

Operation under high pressures and temperatures will minimize unwanted vaporization of water from the electrolytic cell.

Mathematical treatment for water electrolysis under pressurized conditions was carried out with limited physical data, and the energy saving was demonstrated. Further experiments must be conducted to acquire all necessary data needed for calculation.

Acknowledgments

The authors appreciate T. Isobe and T. Sanno for their laboratory work. A part of this study was supported by the Japan Soda Industry Association and the Asahi Glass Foundation for Industrial Technology.

Manuscript submitted March 19, 1985; revised manuscript received ca. July 12, 1985.

Nagoya Institute of Technology assisted in meeting the publication costs of this article.

LIST OF SYMBOLS

A	surface area of the cell wall (m^2)
A_e	area of the working electrode (m^2)
C_{pa}	specific heat of air (kcal/kg)
C_{ps}	specific heat of solution (kcal/kg)
E_d	decomposition voltage (V)
E_d°	standard decomposition voltage (V)
E_d	enthalpic voltage (V)
F	Faraday's constant (kcal/V-eq)
g	gravity acceleration (m/h^2)
G	mass flow rate of solution (kg/h)
Gr	Grashof number
ΔG_r	free energy change for electrode reaction (kcal/mol)
H	height of the cell wall (m)
ΔH_r	enthalpy change for electrode reaction (kcal/mol)
ΔH_v	heat of vaporization (kcal/kg)
h_a	heat-transfer coefficient of the air side (kcal/ m^2 -h-K)
h_c	coefficient for convective heat transfer (kcal/ m^2 -h-K)
h_r	coefficient for radiative heat transfer (kcal/ m^2 -h-K)
h_s	heat-transfer coefficient of the solution side (kcal/ m^2 -h-K)
I	current for electrolysis (A)
i	current density (A/m^2)
K	correction factor
k_a	thermal conductivity of air (kcal/m-h-K)
k_p	thermal conductivity of the cell wall (kcal/m-h-K)
l_e	electrode gap (m)
l_p	thickness of the cell wall (m)
m	mass of solution (kg)
m	molality (mol/kg H_2O)
m_o	initial mass of solution (kg)
Nu	Nusselt number
n	number of charge transfer
Pr	Prandtl number
p	operating pressure (atm)
p_{H_2O}	water vapor pressure on the solution (atm)
$p_{H_2O}^\circ$	vapor pressure of pure water (atm)
$p_{H_2O}^o$	water vapor pressure at t_c (atm)
Q_A	heat accumulation (kcal/h)
Q_E	heat generation by electrolysis (kcal/h)
Q_{EX}	heat from the external source (kcal/h)
Q_{ES}	heat loss accompanied with feedstock (kcal/h)
Q_L	heat loss through the cell wall (kcal/h)
Q_V	heat loss caused by water vaporization (kcal/h)
R	resistance (Ω)
R	gas constant (kcal/mol-K)
ΔS_r	entropy change for electrode reaction (kcal/mol-K)
t_a and T_a	temperature of surroundings ($^\circ C$ and K , respectively)
t_c	temperature of condenser ($^\circ C$)
t_f and T_f	film temperature, $t_f = (t_{pa} + t_a)/2$ ($^\circ C$ and K , respectively)
t_i	temperature of inflow ($^\circ C$)
t_{pa} and T_{pa}	temperature of the cell wall at the air side ($^\circ C$ and K , respectively)
t_s and T_s	solution temperature ($^\circ C$ and K , respectively)
t_{ST}	steady-state temperature (see third paragraph) ($^\circ C$)
U	overall heat-transfer coefficient (kcal/ m^2 -h-K)
V	cell voltage (V)
V_{eff}	part of the cell voltage effective to heat generation (V)
W_{heater}	wattage supplied to the heater (W)
w	rate of vaporization (kg/h)
β_a	volume expansion of air (1/K)
γ_{H_2O}	latent heat for water vaporization (kcal/kg)
ϵ	emissivity
η	overvoltage (V)
θ	time (h)
κ_s	conductivity of electrolytic solution (1/ Ω -m)
μ_a	viscosity of air (kg/m-h)
ρ_a	density of air (kg/ m^3)
σ	Stefan-Boltzmann's coefficient

REFERENCES

1. T. R. Beck and R. T. Ruggeri, in "Advances in Electrochemistry and Electrochemical Engineering," Vol. 12, H. Gerischer and C. W. Tobias, Editors, p. 263, Wiley-Interscience, New York (1981).
2. T. Z. Fahidy, *Appl. Math. Model.*, **4**, 59 (1980).
3. T. Z. Fahidy, *This Journal*, **129**, 953 (1982).
4. T. Z. Fahidy, *ibid.*, **131**, 1054 (1984).
5. T. Z. Fahidy, *J. Appl. Electrochem.*, **14**, 231 (1984).
6. T. Z. Fahidy, *Electrochim. Acta*, **29**, 1321 (1984).

7. N. Kawashima, *Ryuan Gijutsu*, **7**, 9 (1954).
8. N. L. LeRoy and C. T. Bowen, *This Journal*, **127**, 1954 (1980).
9. R. L. LeRoy, *ibid.*, **130**, 2158 (1983).
10. F. Hine, M. Yasuda, R. Nakamura, and T. Noda, *ibid.*, **122**, 1185 (1975).
11. F. Hine and K. Murakami, *ibid.*, **127**, 292 (1980).
12. F. Hine, S. Yoshizawa, and S. Okada, *ibid.*, **103**, 186 (1956).
13. R. L. LeRoy, M. B. I. Janjua, R. Renaud, and U. Leuenberger, *ibid.*, **126**, 1674 (1979).
14. R. B. MacMullin, K. L. Mills, and F. N. Ruehlen, *ibid.*, **118**, 1582 (1971).
15. R. H. Perry and C. H. Chilton, "Chemical Engineers' Handbook," 5th ed., Section 10, McGraw-Hill, New York (1973).
16. J. P. Holman, "Heat Transfer," 5th ed., p. 337, McGraw-Hill, New York (1981).
17. R. B. MacMullin, *This Journal*, **116**, 416 (1969).
18. S. Kamei, "Kagaku Kikai no Riron to Keisan" (Principles and Calculation of Chemical Process Equipments), p. 542, Sangyo Tosho Publishers, Tokyo (1959).
19. "Kagaku Binran" (Handbook of Chemistry), 2nd ed., p. 667, Chemical Society of Japan, Maruzen Publishers, Tokyo (1975).
20. D. J. Pickett, "Electrochemical Reactor Design," p. 355, Elsevier, Amsterdam (1979).
21. B. V. Tilak, P. W. T. Lu, J. E. Colman, and S. Srinivasan, in "Comprehensive Treatise of Electrochemistry," Vol. 2, J. O'M. Bockris, B. E. Conway, E. Yeager, and R. E. White, Editors, Chap. 1, Plenum Press, New York (1981).
22. W. Yang, Unpublished work.
23. M. H. Miles, G. Kissel, P. W. T. Lu, and R. Srinivasan, *This Journal*, **123**, 332 (1976).

Gas Permeation in SPE Method

II. Oxygen and Hydrogen Permeation Through Nafion

Zempachi Ogumi,* Tohru Kuroe, and Zen-ichiro Takehara*

Department of Industrial Chemistry, Faculty of Engineering, Kyoto University, Kyoto 606, Japan

ABSTRACT

The permeation of hydrogen and oxygen through Nafion® of different water contents was investigated by an electrochemical monitoring technique utilizing SPE composite electrodes. For both gases, the solubility, c^0 , was very high compared with the value in aqueous solutions and was on the order of 10^{-2} mol-dm⁻³. The diffusion constant, D , was on the order of 10^{-7} cm²-s⁻¹. While D increased with increasing exchange capacity, c^0 was independent of the capacity. D and c^0 were almost independent of the water content of the Nafion. Hydrophobic cations, R_4N^+ , decreased D . It was concluded that the permeation of gases through Nafion takes place in the intermediate region, which consists of the flexible amorphous part of the polytetrafluoroethylene backbone.

Recently, electrolyzers employing solid polymer electrolyte (SPE) have undergone extensive investigation for applications such as water electrolysis (1), brine electrolysis (2), and electro-organic syntheses (3-5). In gas evolving electrolyzer systems, gas permeation through SPE materials results in decreases in current efficiencies. This has been observed in Kolbe-type reactions using a "both-sides" SPE method as well as in water electrolysis. Similar decreases in efficiencies probably are also observed in SPE fuel cells (6).

Nafion perfluorinated cation exchange membranes are used widely in many electrochemical systems (7-9), including SPE technologies, because of their chemical and thermal stabilities and their high ionic conductivities. The structure of Nafion has attracted the interest of many workers and has been the subject of considerable investigation. An ionic cluster model by Gierke *et al.* (10-12) has been basically accepted widely. This model satisfactorily explains Nafion's mechanical properties (10) and transport behavior (11-15). Yeager and Steck have modified the spherical ionic cluster model and have proposed a model based on irregular ionic clusters, composed of three regions, *viz.*, a hydrophobic backbone, aqueous ionic clusters, and intermediate regions (16).

The present authors have investigated oxygen permeation through Nafion 120 using an electrochemical monitoring technique and have reported previously the diffusion coefficient and the solubility of oxygen (17). The very high solubility of oxygen was briefly discussed, and the influence of the polytetrafluoroethylene backbone was inferred to explain the high solubility.

In the present work, solubilities and diffusion coefficients of hydrogen and oxygen have been examined in detail for different counterions and water contents. Based on the results obtained, the permeation of these gases through Nafion is discussed with reference to the model by Yeager and Steck.

* Electrochemical Society Active Member.

Experimental

Chemicals.—All chemicals, with the exception of hydrazine, were reagent grade. Hydrazine was chemical pure grade. All chemicals were used without further purification. Hydrogen, nitrogen, and argon were of purity higher than 99.9%, oxygen of 99.8%.

Membranes and deposition of platinum.—Nafion 125 (nominal exchange capacity of 0.83 meq/g-dry polymer and thickness of 0.125 mm), Nafion 120 (0.83 meq/g-dry polymer, 0.250 mm), and Nafion 117 (0.91 meq/g-dry polymer, 0.175 mm) were chosen for this study. Nafion is known to change its water content depending on the treatment conditions, such as boiling time and counterions, and the electrolyte concentration of the soaking solutions (18). The membranes were pretreated in the manner of Yeager and Steck (19). Platinum was deposited on one side of the membranes after boiling membranes in the H⁺ form for 3h. The prepared SPE composite electrode, referred to as Pt-Nafion, was soaked in a solution containing a given M⁺ ion for more than 36h at 25°C for equilibration. These composites are referred to as M-type membranes. Solutions containing M⁺ were prepared from M₂SO₄ and distilled water at 0.5 mol-dm⁻³ for alkali metal ion solutions and from R₄NCl at 1 mol-dm⁻³ for tetraalkylammonium ion solutions. Some of the Nafion membranes were treated according to a different procedure in which they were boiled in the Na⁺ form in water for 0.5 or 3h, followed by deposition with platinum. The prepared Pt-Nafion then was soaked in M⁺ ion solutions as described above. Composites prepared thus are referred to as M^a-type (0.5h boiling) and M^b-type (3h boiling) membranes. Platinum deposition was carried out by utilizing a previously described electroless plating method using hydrazine as a reductant (3, 17). The resistivity of the prepared Pt-Nafion was less than 4Ω at 2 cm distance on the surface and it did not increase beyond 6Ω after repeated permeation measurements.

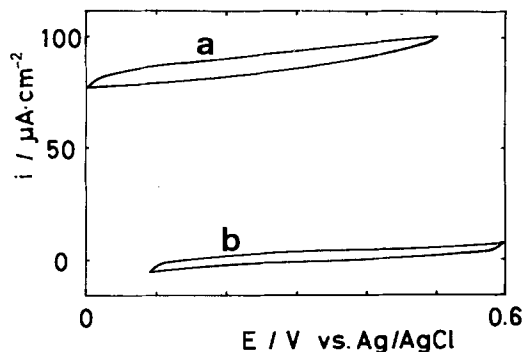


Fig. 1. Polarization curves on Pt-Nafion of K^+ -type membrane. Sweep rate: $0.1 \text{ mV}\cdot\text{s}^{-1}$. Curve a: hydrogen. Curve b: nitrogen in the gas compartment. $0.5M \text{ K}_2\text{SO}_4$ in the solution compartment.

Electrolysis cell and permeation measurement.—The experimental cell was constructed as described elsewhere (17). The solution compartment was filled with solution of the same composition as used previously for soaking and equilibration, in order to prevent the membrane from changing its water content during the measurements. Permeation measurements were carried out in the same manner as in Ref. (17).

Results

E-i relationships.—Figure 1 shows the results from a set of polarization experiments on Pt-Nafion using K^+ -type Nafion 125. Curve a was obtained using 100% hydrogen, and curve b 100% nitrogen. A hysteresis was observed between the forward and reverse sweep in spite of the very slow sweep rate of $0.1 \text{ mV}\cdot\text{s}^{-1}$. This hysteresis can be ascribed to the large capacity of the electrodes, which were deposited on the Nafion in a form similar to platinum black. An almost constant current due to hydrogen oxidation was observed at $0-0.5V \text{ vs. Ag/AgCl}$, which was controlled by hydrogen mass-transfer limitation through the membrane. With nitrogen, the observed current was very small and was regarded as a residual current. During all the hydrogen permeation experiments, the potential of the SPE composite electrodes was set at $0.25V \text{ vs. Ag/AgCl}$ in order to oxidize hydrogen under diffusion limiting conditions. The obtained currents were corrected for the residual current. In all experiments for oxygen reduction, the potential was set at $-0.25V \text{ vs. Ag/AgCl}$ according to our previous results (17).

Permeation results.—All permeation transients for hydrogen oxidation and oxygen reduction showed the small second step following the large first step in both buildup and decay curves as described by curve a in Fig. 2, which was measured for hydrogen oxidation on Na-type Nafion 125. The first large step corresponds to a main fast permeation pass, and the second small one to a slow permeation pass. $J_{1\infty}$ and $J_{2\infty}$ are the steady-state currents for the fast pass and the (fast + slow) pass, respectively. The first step was replotted as curve b in Fig. 2, neglecting the second step. Curve b agrees very well with the theo-

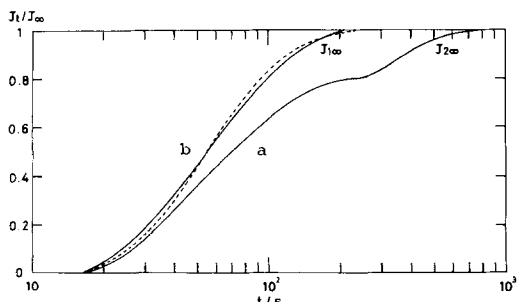


Fig. 2. Hydrogen permeation transient currents through Na-type Nafion 125 at 25°C in $0.5M \text{ K}_2\text{SO}_4$. Solid line a: full transient. Solid line b: transient until $J_{1\infty}$ of curve a. Broken line: theoretical curve.

retical curve for fickian diffusion shown by the broken line in the figure. Although the slow pass was replotted neglecting the fast pass, the resulting curves did not show agreement with the theoretical curve. In this study, only the fast permeation is treated neglecting the slow permeation.

Both the buildup and decay curves for hydrogen permeation through Li-type Nafion 125 did not agree well with the theoretical curve. This poor agreement leads to diffusion coefficients and solubilities of a limited reliability for hydrogen permeation through Li-type Nafion 125.

Evaluation of diffusion coefficients, D , and solubilities, c^0 .—In order to evaluate diffusion coefficients, D , and solubilities, c^0 , using the transient technique, the membrane thickness, l , must be known (17); $D = 0.138 l^2/t_{1/2}$ and $J_\infty = nFDc^0/l$ [see Ref. (17) for details]. Since Nafion without reinforcement is known to change its dimension isotropically by swelling (18), the thickness can be calculated from the volume change at swelling. The thicknesses of Li, Na, K, and Cs types were calculated using the reported water content by Yeager *et al.* (19). The water content in swollen Nafion was also estimated by using the following empirical equation (18, 20) with the above membranes

$$V_w = 2.4AB \exp(3980/EW)$$

The differences between values from the two methods were less than 10%. The thicknesses of membranes of types other than the above four were estimated by using the empirical equation. The results obtained from the permeation experiments are summarized in Table I and Table II for hydrogen and oxygen. Each value is the average of more than three measurements.

Both dry and wet gases were used in the experiments for oxygen permeation using Na-type membranes. Both results were the same within experimental error. This coincidence means that the conditions of the gases are less important than those of the solution contacting the membrane.

Discussion

Solubilities.—Table III summarizes the solubilities of O_2 and H_2 in several media. Both hydrogen and oxygen solubilities are much higher in liquid perfluorocarbon and polytetrafluoroethylene (PTFE), which comprises the backbone chain of Nafion, than in aqueous solutions. Hydrogen and oxygen dissolved 40 and 20-30 times more in PTFE, respectively, than in aqueous solutions. The solubilities in Nafion shown in Tables I and II are as high as in PTFE. In addition to high solubilities, similarity in the solubility ratio of the two gases is observed between Nafion and PTFE. These facts show that the dissolution of both gases in the hydrophobic backbone of Nafion (which has a structure similar to PTFE) is preferred to dissolution in the ionic cluster. In Fig. 3 and Fig. 4, the solubilities of hydrogen and oxygen, respectively, are plotted against the water content of swollen Nafion. The solubilities of both gases are scattered, and it is difficult to find any dependency on the water content. The solubilities of both gases were comparable to each other in the same types of membranes. Table IV lists the solubili-

Table I. Permeation parameters of hydrogen through Nafion 125 of different ionic types at 25°C

	K^a	K^b	Cs	K	Na	Li
Water content mol $\text{H}_2\text{O}/\text{mol SO}_3^-$	9.2* **	9.5	9.9 11.3	12.0 13.3	18.6 18.4	22.2 22.3
$J_{1\infty} \times 10^6 \text{ (A}\cdot\text{cm}^{-2}\text{)}$	83.1	84.0	71.0	82.8	92.0	69.7
$D \times 10^7 \text{ (cm}^2\cdot\text{s}^{-1}\text{)}$	8.02	5.66	4.68	6.03	5.06	4.65
$c^0 \times 10^2 \text{ (M)}$	0.75	1.03	1.09	0.97	1.36	1.18

^a Using empirical equation.

^b By Yeager *et al.*

Table II. Permeation of oxygen through Nafion 125 (A) and Nafion 117 (B) of different ionic types at 25°C

	R' ₄ N ^a	R'' ₄ N ^a	K ^a	R' ₄ N	Cs	K	Na	Li	
A Water content mol H ₂ O/mol SO ₃	8.7	9.0	9.2		9.9	12.0	18.6	22.2	^b
					11.3	13.3	18.4	22.3	^c
	$J_{1\infty} \times 10^6$ (A-cm ⁻²)	50.1	68.2	80.1		59.8	72.1	94.9	108.8
$D \times 10^7$ (cm ² -s ⁻¹)	1.39	1.73	2.16		1.88	2.42	2.61	2.62	
$c^0 \times 10^2$ (M)	1.27	1.38	1.31		1.14	1.09	1.37	1.60	
<hr/>									
B Water content				15.6		15.9	24.6	29.3	^b
$J_{1\infty} \times 10^6$ (A-cm ⁻²)				76.9		89.2	68.4	101.5	
$D \times 10^7$ (cm ² -s ⁻¹)				3.59		4.32	4.29	4.24	
$c^0 \times 10^2$ (M)				1.10		1.07	0.86	1.34	

^a R' = C₂H₅; R'' = CH₃.

^b Using empirical equation.

^c By Yeager *et al.*

ties, c^0 , referred to the volume of the hydrophobic backbone of Nafion, which was calculated by subtracting the volume of the swelling water from the apparent total volume. In this estimation, the partial molar volume of the swelling water was assumed to be equal to that of ordinary free water. The solubility, c^0 , was almost constant within experimental error except for Li- and Na-type Nafion. It is known that gases do not dissolve in the crystalline region but in the amorphous region when they dissolve in polymers (23). The crystalline region of Nafion decreases in the order -SO₂F form (XR resin, the precursor polymer of Nafion) > dry H⁺ form > wet H⁺ form. An increase in the exchange capacity decreases the crystalline region (24).

The above discussion of solubility leads to the expectation that gases are dissolved preferentially in the hydrophobic backbone region of Nafion.

Diffusion coefficients.—Figures 5 and 6 show the diffusion coefficients of hydrogen and oxygen in Nafion, D_H

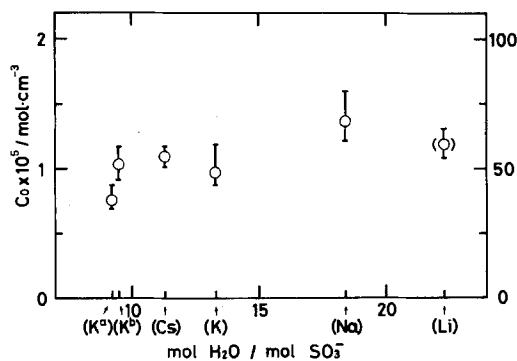


Fig. 3. Hydrogen solubility in Nafion 125 of different ionic types at 25°C.

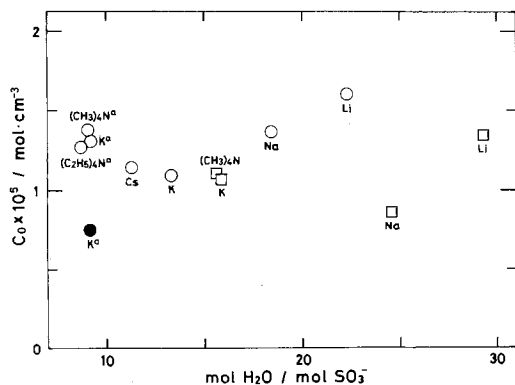


Fig. 4. Oxygen solubility in membranes of different ionic types at 25°C. Open circles: Nafion 125. Closed circles: Nafion 120. Squares: Nafion 117.

Table III. Solubilities of oxygen and hydrogen in several media in $c \times 10^3$ (mol-dm⁻³)

Medium	Temp. (°C)	H ₂	O ₂	Ref.
K-type Nafion 125		9.7	10.9	
K-type Nafion 117			10.7	
Nafion 120	25	24.5		(32)
H ₂ O	25	0.78	1.3	(17)
0.5M H ₂ SO ₄	25	0.72		(17)
0.5M K ₂ SO ₄	25		0.85	(17)
n-C ₄ F ₁₈	25	6.8	26.8	(21)
n-C ₆ F ₁₈	25		23.2	(21)
PTFE	20	31.3	26.8	(22)

and D_O , against $V_p/1 - V_p$, where V_p is the polymer fraction of the swollen membrane. The double circles and

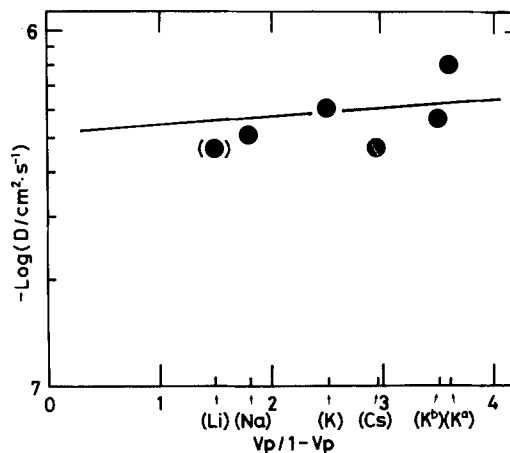


Fig. 5. Dependence of hydrogen diffusion coefficient through Nafion at 25°C.

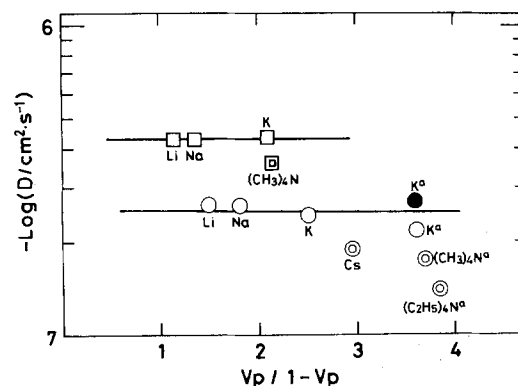


Fig. 6. Dependences of diffusion coefficient of oxygen through Nafion 125 (circles, double circles), Nafion 120 (closed circle), and Nafion 117 (squares, double square) at 25°C.

Table IV. Solubilities, c^0 , of hydrogen and oxygen in polymer part of Nafion. $c^0 \times 10^3$ (mol-dm $^{-3}$)

		(C ₂ H ₅) ₄ N ^a	(CH ₃) ₄ N ^a	K ^a	K ^b	(CH ₃) ₄ N	Cs	K	Na	Li
H ₂	Nafion 125			0.96	1.32		1.46	1.35	2.11	1.97
O ₂	Nafion 125	1.60	1.75	1.67			1.53	1.52	2.13	2.67
	Nafion 117					1.61		1.58	1.49	2.52

double square designate the results obtained by using ions which are known to exist in the intermediate region between the hydrophobic backbone and ionic cluster regions (16). The unit ($V_p/1 - V_p$) of the abscissa was introduced by Yasuda *et al.* in order to describe the transport phenomena of small particles through polymer materials bearing a fixed charge (25). In the case of diffusion through the aqueous part of a swollen polymer, theoretically, $\log D$ decreases against $V_p/1 - V_p$. Yeager *et al.* obtained straight lines of negative slopes for H₂O and Na⁺ transport through swollen Nafion using the above plots. On the other hand, they obtained a constant value of $\log D$ against changing $V_p/1 - V_p$ for Cs⁺ transport through the identical membrane. These results allowed them to propose a structural model of Nafion and to conclude that, while H₂O and Na⁺ permeate through the ionic cluster region, Cs⁺ permeates through the intermediate region which is not affected by the change in water content (16).

IR (26) and NMR (27) measurements have revealed the existence of the interaction of water with perfluorocarbon backbone. Hydrophobic interaction of large hydrophobic cations in Nafion has been recognized in addition to electrostatic interaction with the fixed anion (28-30).

Taking these reported observations into consideration, the results shown in Fig. 5 and 6 that D_H and D_O are independent of $V_p/1 - V_p$ and small in the presence of cations existing in the intermediate region lead to the conclusion that the main diffusion region is not the ionic cluster but the intermediate region. This conclusion is consistent with the discussion in the section on solubility. Yeager *et al.* considered that the intermediate region of Nafion consists of an aqueous part. The region, however, might be too small to satisfy the high solubility and large diffusion coefficient observed in the present work. It is reasonable to assume that the intermediate region available

for dissolution and permeation of gases includes the amorphous part of the perfluorinated backbone. It is known that unhydrolyzed precursor polymer (-SO₂F) comprises ~40% of the crystalline portion of dry polymer (24) and Nafion of exchange capacity 0.83 meq/g-dry polymer and 0.93 meq/g-dry polymer 5 ~ 10%. This means that most parts of the backbone are of a flexible structure and are available for gas permeation in the permeation model through the amorphous part of the hydrophobic perfluorocarbon backbone of Nafion.

The flexible hydrophobic part is expected to show properties similar to PTFE, which dissolves much hydrogen and oxygen as shown in Table III. This was confirmed by the solubility results.

It is expected also that the cation existing in the intermediate region will interfere with the diffusion of gases there. This was proved in the diffusion measurements through membranes with (CH₃)₄N⁺, (C₂H₅)₄N⁺, and Cs⁺ ions, which are considered to have hydrophobic interactions, as shown in Fig. 6 with double circles and the double square. Larger D_O 's were obtained with Nafion 117 than with Nafion 125 and 120. This is because the former should have a larger amorphous part available for the permeation than the latter, because of the higher exchange capacity.

Based on the above discussion, it can be concluded that the permeation of gases through Nafion takes place in the intermediate region of the structural model of Yeager *et al.*, which consists mainly of the flexible amorphous part of perfluorocarbon backbone of Nafion. This is illustrated in Fig. 7.

Of course, this discussion does not exclude permeation through an ionic cluster, although the contribution from such permeation is estimated to be small.

Permeability.—Permeability, P , which is the product of the diffusion coefficient and the solubility, often is used to describe the transport of gases through polymers. Table V contains values of P calculated from D and c^0 . Except for hydrophobic ion-type membranes, P changes with c^0 because D was almost constant. High water content causes an increase of the intermediate region at the cost of the crystalline part of Nafion to produce an increase in P . Hydrophobic R₄N⁺ interferes with the permeation and decreases P .

The ratio P_H/P_O is almost constant, and is similar to the value for PTFE. This similarity supports the concepts of gas permeation through Nafion discussed in the above sections.

Summary

The permeation of hydrogen and oxygen through Nafion of different water content was investigated by an electrochemical monitoring technique using SPE composite electrodes.

Table V. Permeability, P , through Nafion 125 of different ionic types in $P \times 10^{12}$ (cm²-s⁻¹) mol-cm⁻³ Nafion

Ion	R' ₄ N ^a	R'' ₄ N ^a	R' ₄ N	K	K	Cs	K	Na	Li
H ₂				7.70	7.47	6.83	8.14	10.68	9.16
O ₂	2.22	3.03		3.61		2.88	3.68	5.56	7.00
O ₂ ^b			5.78				6.83	6.39	10.68
H ₂									
O ₂				2.13		2.37	2.21	1.92	1.31

^a R' = C₂H₅; R'' = CH₃.

^b Through Nafion 117; cf. H₂: 8.13, O₂: 3.73 through PTFE.

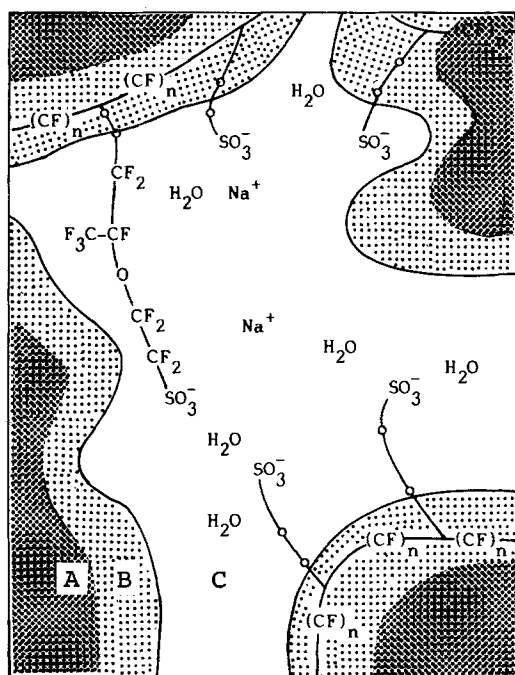


Fig. 7. Schematic model of the permeation region through Nafion. Region A: rigid hydrophobic backbone. Region B: flexible perfluorocarbon where gases permeate. Region C: ionic cluster region containing water similar to bulk water.

The solubility and diffusion coefficient were almost independent of the water content of the membrane. While the high solubility was almost independent of the exchange capacity, the diffusion coefficient of oxygen was higher in Nafion 117 of higher exchange capacity than in Nafion 125 of lower exchange capacity. Hydrophobic cations, R_4N^+ , decreased the diffusion coefficient of oxygen because such ions could intrude and block the diffusion pass. The results lead to the conclusion that gases permeate mainly through the intermediate region, which consists of the flexible amorphous part of the polytetrafluoroethylene backbone of Nafion. The permeability ratio P_H/P_O through Nafion was similar to the ratio in PTFE. This similarity strongly supports the discussion on the permeation pass.

Acknowledgments

Special thanks are due to Professor F. Foulkes of the University of Toronto for his helpful discussions. The authors also wish to thank E. I. du Pont de Nemours and Company for providing membrane samples.

Manuscript submitted April 1, 1985; revised manuscript received June 5, 1985.

Kyoto University assisted in meeting the publication costs of this article.

REFERENCES

1. P. W. T. Lu and S. Srinivasan, *J. Appl. Electrochem.*, **9**, 269 (1979).
2. A. P. Laconti, Japan Tokkyo Kokai, 54-112398 (1979).
3. Z. Ogumi, K. Nishio, and S. Yoshizawa, *Denki Kagaku*, **49**, 212 (1981).
4. Z. Ogumi, K. Nishio, and S. Yoshizawa, *Electrochim. Acta*, **26**, 1779 (1981).
5. Z. Ogumi, H. Yamashita, K. Nishio, Z. Takehara, and S. Yoshizawa, *ibid.*, **28**, 1687 (1983).
6. H. A. Liebhafsky and E. J. Cairns, "Fuel Cells and Fuel Batteries," John Wiley and Sons, New York (1968).
7. R. S. Yeo, J. McBreen, G. Kissel, F. Kulesa, and S. Srinivasan, *J. Appl. Electrochem.*, **10**, 741 (1980).
8. D. Bergner, *ibid.*, **12**, 631 (1982).
9. R. S. Yeo and D.-T. Chin, *This Journal*, **127**, 549 (1980).
10. R. S. Yeo and A. Eisenberg, *J. Appl. Polym. Sci.*, **21**, 875 (1977).
11. T. D. Gierke, Paper 438 presented at The Electrochemical Society Meeting, Atlanta, GA, Oct. 9-14, 1977.
12. R. S. Yeo, *This Journal*, **130**, 533 (1983).
13. H. L. Yeager and B. Kipling, *J. Phys. Chem.*, **83**, 1836 (1979).
14. H. L. Yeager, B. O'Dell, and Z. Twardowski, *This Journal*, **129**, 85 (1982).
15. C. Fabiani, G. Scibona, and B. Scuppa, *J. Membr. Sci.*, **5**, 16 (1983).
16. H. L. Yeager and A. Steck, *This Journal*, **128**, 1880 (1982).
17. Z. Ogumi, Z. Takehara, and S. Yoshizawa, *ibid.*, **131**, 769 (1984).
18. W. G. Grot, G. E. Munn, and D. N. Walmsley, Paper 154 presented at The Electrochemical Society Meeting, Houston, TX, May 7-11, 1972.
19. A. Steck and H. L. Yeager, *Anal. Chem.*, **52**, 1215 (1980).
20. E. I. du Pont de Nemours & Co., Inc., E-05569, 2/76 (catalog).
21. M.H. A. Hamza, G. Serratrice, M.-J. Stebe, and J.-H. Delpuech, *J. Am. Chem. Soc.*, **103**, 3733 (1981).
22. T. K. Gibbs and D. Pletcher, *Electrochim. Acta*, **25**, 1105 (1980).
23. A. S. Michaels and H. J. Bixler, *J. Polym. Sci.*, **50**, 393 (1961).
24. T. D. Gierke, G. E. Munn, and F. C. Wilson, *J. Polym. Sci. Polym. Phys. Ed.*, **19**, 1687 (1981).
25. H. Yasuda, C. E. Lamaze, and L. D. Ikenberry, *Makromol. Chem.*, **118**, 19 (1968).
26. M. Falk, *Can. J. Chem.*, **58**, 1495 (1980).
27. N. Sivashinsky and G. B. Tanny, *J. Appl. Polym. Sci.*, **26**, 2625 (1981).
28. P. C. Lee and D. Meisel, *J. Am. Chem. Soc.*, **102**, 5477 (1980).
29. D. A. Buttry and F. C. Anson, *ibid.*, **105**, 685 (1983).
30. C. R. Martin and H. Freiser, *Anal. Chem.*, **53**, 902 (1981).
31. N. G. Boyle, V. J. McBrierty, and D. C. Douglas, *Macromolecules*, **16**, 75 (1983).
32. R. S. Yeo and J. McBreen, *This Journal*, **126**, 1682 (1979).

Oxidation of Phenol with AC Electrolysis

D.-T. Chin* and C. Y. Cheng

Department of Chemical Engineering, Clarkson University, Potsdam, New York 13676

ABSTRACT

The method of alternating voltage (AV) modulation has been used to determine the effect of alternating current on the polarization behavior of the oxidation of phenol on platinum in aqueous sulfuric acid electrolyte. The study was made with sinusoidal, square, and triangular AV over a range of frequency from 20 to 6000 Hz, and a range of magnitude from 0 to 500 mV rms. A batch electrochemical cell operated on a potentiostatic mode was used to evaluate the conversion of phenol, anode current efficiency, yield of hydroquinone, and energy consumption of the process. The results indicate that AV strongly modified the shape of the polarization curve. It caused a shift in the rest potential toward the negative direction, and increased the dc current density for both the anodic and cathodic reactions. The rate of conversion of phenol increased with increasing magnitude of AV and decreased with increasing AV frequency.

Recently, the rising cost of petrochemical feedstocks and environmental considerations have generated a renewed interest in electro-organic reactions (1). The disadvantages of electro-organic synthesis as compared to the chemical synthetic methods are the slow reaction kinetics, high capital investment of electrolytic cells, and high energy consumption for the electrolysis. The purpose of this work is to improve the reaction rate of electro-organic reactions with an alternating current (ac) electrolysis. Previous investigations in this laboratory on the ac corrosion processes (2-9) have shown that ac enhances the apparent reaction kinetics of electrochemical reactions by improving the exchange current density and transport of reacting ions to the electrode surface. The application of

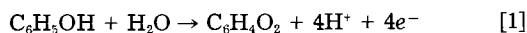
ac to electro-organic reactions has an advantage that there is no need to modify the electrochemical cell, and no catalysts and additives are used, thus avoiding the contamination of reaction products.

Superimposition of an ac component in electrolysis shifts the rest potential and lowers the overpotential of electrode reactions. This property may be used to isolate a desired product, which would be otherwise destroyed at higher overpotentials. Reitlinger (10) has found that ac affected the selectivity of the electro-organic reaction. Ethyl alcohol was oxidized to acetaldehyde without being further oxidized to acetic acid with an alternating current. He also reported that with ac electrolysis p-benzaldehyde sulfonic acid could be obtained from p-toluene-sulfonic acid. Kappana *et al.* (11) applied the ac electrolysis to the oxidation of glucose to calcium gluconate. They showed

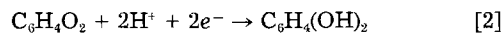
*Electrochemical Society Active Member.

that the current efficiency increased with increasing ac current density and with decreasing ac frequency. Noguchi (12) applied 0.8-2M Hz ac (below 100V) to two Ag-plated electrodes in soy sauce, synthetic vinegar, whiskey, sake, and perfume to decrease the time required for the aging process. He also found that green tea lost its flavor, persimmons lost their bitterness, coffee and cocoa extracts lost their taste, and acrylic ester was polymerized by applying high frequency ac. Polymerization of methylmethacrylate in aqueous solutions of H_3PO_4 and H_2SO_4 was initiated by ac on a platinum electrode (13). The degree of polymerization depended on the type of electrolyte, concentration, and ac current density. Korchinskii (14) found that ac increased the adsorption of acetate ions on a platinum electrode. Nadebaum *et al.* (15) obtained a rate equation for the oxidation of aqueous ethanol to carbon dioxide and ethane when the cell was modulated with a rectangular alternating voltage (AV). Nitskanski (16) exposed eggs to high frequency sinusoidal ac during incubation. The total protein and albumin content increased, and γ -globulin content decreased. Kikuchi and Ueyama (17) found that the electrolysis of a mixture containing N-vinylcarbazole, $LiClO_4$, and ethyl ether or methylcyanide at -22° to $30^\circ C$ gave low molecular weight poly(N-vinylcarbazole) in the anode compartment by superimposing a rectangular ac. The yield of the polymer increased with decreasing temperature, and the molecular weight of the polymer produced with the rectangular-wave ac was greater than that with only dc. Florequin *et al.* (18) found that the use of anodic rectangular current pulses restored the activities of a platinized Pt electrode for the reduction of dimethylacetone and butanone to alkane. Bhadani (19) passed sinusoidal ac through a styrene solution containing sodium tetraphenylboron, and a high molecular weight polystyrene was formed. The yield and molecular weight of polystyrene decreased with increasing ac frequency. Tamura (20) and his co-workers found that superimposed AV at 50 Hz increased the formation of β -type crystals of vinylindene fluoride. Kawahara (21) mixed soybean milk with an acidic medium containing oxalic acid, or lactic acid and $CaHPO_4$, and treated the solution with a sinusoidal ac ($0.25 A/dm^2$) to make Tofu. Alkire and Tsai (22) prepared propylene oxide by electrolysis of propylene in a sodium bromide solution with sinusoidal ac. They obtained a 22% current efficiency at 1 Hz and an ac current density of $175 mA/cm^2$ on a platinum electrode. Adzic *et al.* (23) investigated the oxidation of formic acid to carbon dioxide and water on platinum with a superimposed rectangular alternating voltage. The oxidation rate was higher than that of the constant dc potential electrolysis.

In this study, the method of alternating voltage (AV) modulation (6-9) has been used to determine the effect of sinusoidal, square, and triangular wave ac on the polarization behavior of the oxidation of phenol to benzoquinone



The oxidation of phenol was first reported by Fichter (24), and its industrial importance is reflected by numerous patents (25-31). In an undivided cell, the benzoquinone produced at the anode is subsequently reduced to hydroquinone at the cathode



A bench-scale electrochemical cell operated on a potentiostatic mode was used to evaluate the effect of superimposed ac on the conversion, chemical yield, current efficiency, and energy consumption of the process.

Experimental

An alternating voltage (AV) modulation was used in the present investigation. In this method, a constant AV is superimposed onto a dc potential and the resulting composite potential wave is applied between working and reference electrodes through a potentiostat. The resulting dc and ac current densities are then measured as a function

of dc potential and applied AV. The details of the experimental technique are described in Ref. (6-9), and will not be repeated here.

Electrolyte and cell setup.—The electrolyte used in this work consisted of 0.01-0.1M phenol in 1M sulfuric acid in a temperature range of 23° - $50^\circ C$. A platinum rotating disk electrode mounted on a rotator (Pine Instruments ASR2) and having a surface area $0.458 cm^2$ exposed to the electrolyte was used for the polarization measurement. A stationary platinum foil of $12.5 cm^2$ surface area was used for the potentiostatic batch cell electrolysis of oxidation of phenol. A 1 liter Pyrex glass jar immersed in a constant temperature bath was used as a single-compartment cell. The counterelectrode was a platinum screen, and a saturated calomel electrode (SCE) connected to a Luggin capillary tube was used as the reference electrode.

Polarization measurement.—The platinum rotating disk electrode was used for the polarization measurement. For each run, the electrode was cleaned with methanol and was cathodically activated at $-3.0V$ for 2 min in 1N NaOH solution followed by rinsing in distilled water. The clean electrode was quickly transferred into the cell and installed on the rotator. The potential difference between the working and reference electrodes was controlled by a potentiostat with a built-in sweep generator (Pine Instrument RDE3). The superimposed AV was supplied to the potentiostat from an ac signal generator (Hewlett-Packard 2311A), and the dc potential of the working electrode was swept between 0 and 1500 mV at a sweep rate of 5 mV/s. The dc current was converted to a voltage signal by passing the current through a precision resistor ($10-1000\Omega$) connected in parallel to a capacitor ($16,800 mF$). The voltage drop was fed to a logarithmic converter (Linseis N46), and the output of this converter was fed to a X-Y recorder (Hewlett Packard 7044A) for plotting dc current vs. dc potential. The ac current was determined with a multimeter (Keithley 177) by measuring the ac voltage drop across a second precision resistor; the output from the multimeter was fed to a second X-Y recorder (Linseis 1700) for plotting ac current vs. dc potential. In this way, the dc and ac currents vs. dc potential curves were obtained with the test electrolytes for a range of superimposed sinusoidal, square, and triangular AV varying from 0 to 500 mV rms, and the AV frequency from 20 to 6000 Hz. The experiments were carried out in a temperature range 23° - $50^\circ C$.

Batch electrolysis experiment.—After the polarization measurement, a potentiostatic batch electrolysis was carried out for the oxidation of phenol with the stationary platinum electrode at selected dc potentials superimposed with a constant AV. During the electrolysis, the dc current, ac current, dc cell voltage, and ac cell voltage were recorded as functions of electrolysis time. Electrolyte samples were also withdrawn from the cell at selected time intervals, and the concentration of phenol was analyzed with a bromination and iodometric titration method. At the end of the run, the yield of hydroquinone was determined by an oxidimetric titration with a ceric sulfate solution. The details of the chemical analytical methods used are given in Ref. (32).

Results and Discussion

DC polarization curves without superimposed AV.—To establish the basis for comparing with AV modulation, the dc polarization curves were first obtained for the platinum rotating disk electrode in the test electrolytes without any superimposed AV. It was found that the speed of rotation had no effect on the anodic polarization curves for the oxidation of phenol, and all the data were collected at a rotational speed of 2400 rpm.

The effect of phenol concentration (0-0.1M) on the dc polarization curves at $50^\circ C$ is shown in Fig. 1. The anodic curves are for the oxidation of phenol, and the cathodic curves correspond to the reduction of surface oxides and dissolved oxygen on the platinum surface. The arrows in the figure indicate the location of rest potentials. The

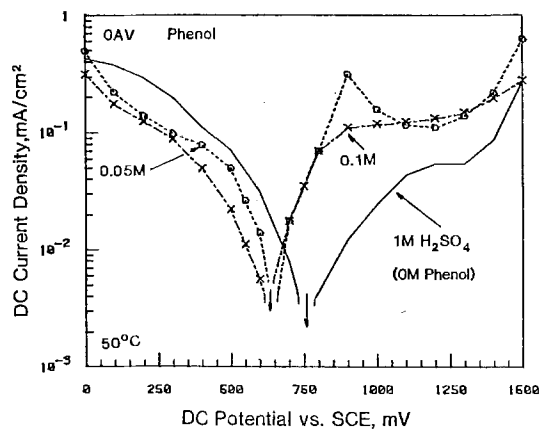


Fig. 1. DC polarization curves without superimposed AV for the oxidation of phenol on a platinum rotating disk electrode in 1M H₂SO₄ at 50°C. The data are given for three phenol concentrations: 0, 0.5, and 0.1M. The arrows indicate the rest potentials. The platinum electrode was rotating at 2400 rpm.

cathodic current density decreased with increasing phenol concentration. This was due to the adsorption of phenol on platinum, which blocked the active sites for the oxygen reduction reaction. For the anodic curves, the blank run with only 1M H₂SO₄ exhibited two potential regions: the curve between 750 and 1250 mV vs. SCE corresponded to the formation of a platinum oxide, and the curve above 1250 mV vs. SCE corresponded to the oxygen evolution reaction on the platinum surface (33). Addition of phenol to the sulfuric acid supporting electrolyte increased the anodic current density and shifted the rest potential to a more negative value of 620 mV vs. SCE. The phenol concentration did not seem to affect the anodic current in the low overpotential regime of 620-900 mV vs. SCE. At the potentials more positive than 900 mV vs. SCE, the adsorption of the oxidation product, benzoquinone (34), on the electrode surface caused the current to decrease with a further increase in potential for the run with 0.05M phenol. This adsorption phenomenon was found to be more pronounced at low phenol concentrations (0.01-0.05M) and at low temperatures (23°C). At the potentials above 1250 mV vs. SCE, the oxygen started to evolve and the current density increased again with increasing potential.

Effect of sinusoidal AV on dc polarization curves.— Figures 2-3 show the typical dc polarization curves for the oxidation of phenol on platinum in 0.1M phenol plus 1M sulfuric acid at 50°C when the electrode was superimposed with sinusoidal AV at the frequencies of 60 and 200

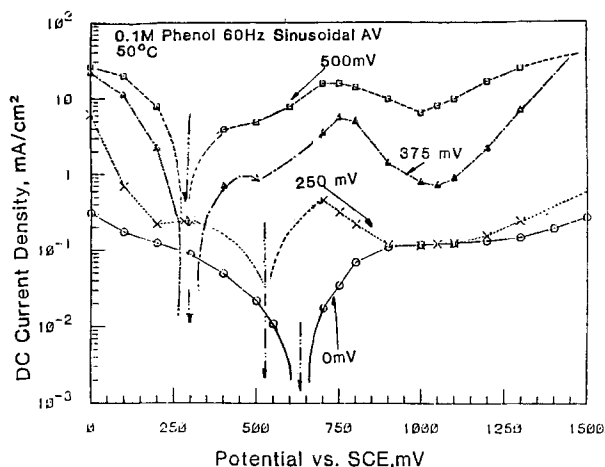


Fig. 2. DC polarization curves with 60 Hz sinusoidal AV for the oxidation of phenol on a platinum rotating disk electrode (2400 rpm) in 0.1M phenol and 1M H₂SO₄ at 50°C. The magnitude of superimposed AV varied from 0 to 500 mV rms as indicated in the figure. The arrows refer to the position of the rest positions.

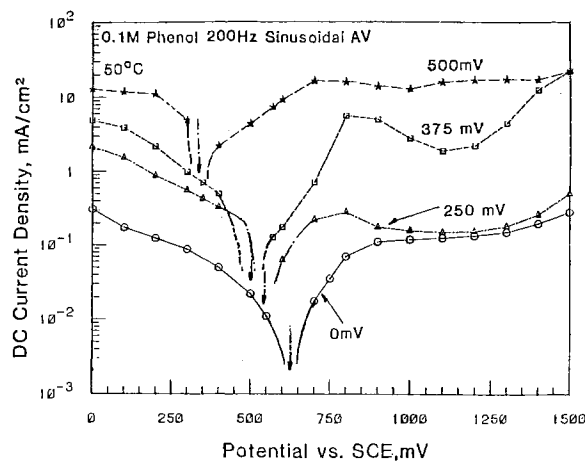


Fig. 3. DC polarization curves with 200 Hz sinusoidal AV for the oxidation of phenol on a platinum rotating disk electrode (2400 rpm) in 0.1M phenol and 1M H₂SO₄ at 50°C. The magnitude of superimposed AV varied from 0 to 500 mV rms as indicated in the figure. The arrows indicate rest potentials.

Hz. The magnitude of AV varied from 0 to 500 mV rms. The dc polarization curves covered both the cathodic and anodic potential regimes, and the arrows in the figures indicate the rest potentials. The results indicate that AV caused an increase in the dc current density for both the anodic and cathodic processes. The rest potential was shifted by the AV toward the negative direction. For the anodic process, the rate of oxidation of phenol was enhanced when the magnitude of AV was greater than 250 mV rms, and the dc current density increased with increasing magnitude of AV. At 60 Hz, for example, the greatest dc enhancement for the anodic process occurred near the dc potential of 750 mV vs. SCE. At this potential, the dc current with 500 mV rms AV was two orders of magnitude greater than the dc current without AV. This rate enhancement can be partly explained by an increase in the apparent electrokinetics under the superimposed AV conditions. Consider an electrode process whose current-potential relation under the activation control is described by the Butler-Volmer equation of the type

$$i = i_0 \left\{ \exp \left(\frac{\phi - \phi_0}{\beta_a} \right) - \exp \left(\frac{\phi_0 - \phi}{\beta_c} \right) \right\} \quad [3]$$

where i_0 and ϕ_0 are the exchange current density and the rest potential without superimposed AV, respectively, and β_a and β_c are the anodic and cathodic Tafel slopes based upon ϕ vs. $\ln i$ plot. When the electrode is polarized with a dc potential, ϕ_{dc} , plus a superimposed sinusoidal AV, then

$$\phi = \phi_{dc} + V \sin \omega t \quad [4]$$

where V is the peak AV potential, ω is the AV frequency in radians per second, and t is the time. Under this condition, the current density flowing across the electrode/solution interface will be composed of a time-averaged dc component, i_{dc} , and a periodic ac component, i_{ac}

$$i = i_{dc} + i_{ac} \quad [5]$$

Substituting Eq. [4] and [5] into Eq. [3] and carrying out the time average on both sides of the resulting equation, one has

$$i_{dc} = i_0 \left\{ \exp \left(\frac{\phi_{dc} - \phi_0}{\beta_a} \right) \overline{\exp \left(\frac{V}{\beta_a} \sin \omega t \right)} - \exp \left(\frac{\phi_0 - \phi_{dc}}{\beta_c} \right) \overline{\exp \left(-\frac{V}{\beta_c} \sin \omega t \right)} \right\} \quad [6]$$

The time-averaged quantities in the above equation are given as

$$\overline{\exp\left(\frac{V}{\beta_a} \sin \omega t\right)} = \frac{1}{2\pi} \int_0^{2\pi} \exp\left(\frac{V}{\beta_a} \sin \omega t\right) d(\omega t) \quad [7]$$

$$\overline{\exp\left(-\frac{V}{\beta_c} \sin \omega t\right)} = \frac{1}{2\pi} \int_0^{2\pi} \exp\left(-\frac{V}{\beta_c} \sin \omega t\right) d(\omega t) \quad [8]$$

These two quantities are always greater than one, and may be considered as the enhancement factors for the anodic and cathodic current under the superimposed AV condition. The numerical calculation for the current enhancement by AV is given in Ref. (6), and it has been shown that it is possible to enhance the dc current density by a factor of 100-1000 with a peak AV of 5-10 β_a .

In addition, the AV had the ability to breakdown the adsorption layer on the platinum surface in a way similar to the breakdown of passive film by AV in the corrosion of iron and stainless steels (5, 7, 9). The phenomenon was similar to the reactivation of the platinum fuel cell electrode by the application of alternate anodic and cathodic potential pulses (35, 36). Thus, the function of AV was to continuously activate the platinum electrode, thus enabling the oxidation of phenol to proceed at a rate higher than that of the steady-state dc electrolysis.

When the frequency of AV was increased, the effect of AV became less obvious. At 6000 Hz, there was no significant increase in the dc current density over a range of AV from 0 to 500 mV rms (32). This was caused by the fact that the double-layer impedance became smaller at high frequencies, and the application of AV was used for the charge and discharge of the electric double layer at the electrode-solution interface.

Figure 4 shows the rest potential of the polarization curves against the magnitude of superimposed AV for a range of AV frequencies from 20 to 6000 Hz. The rest potential was shifted to the negative direction by the applied AV. The reason for this is that the cathodic Tafel slope was larger than anodic Tafel slope, and, according to an analysis by Chin *et al.* (4-5), the rest potential would be shifted toward the negative direction because of an un-

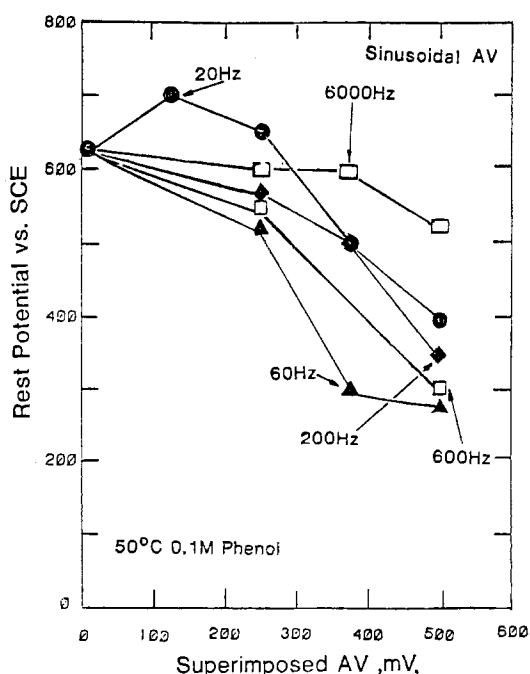


Fig. 4. Apparent rest potential of a platinum rotating disk electrode (2400 rpm) as a function of the root-mean-square of superimposed sinusoidal AV for 0.1M phenol and 1M H_2SO_4 at 50°C. The AV frequency varied from 20 to 6000 Hz as indicated in the figure.

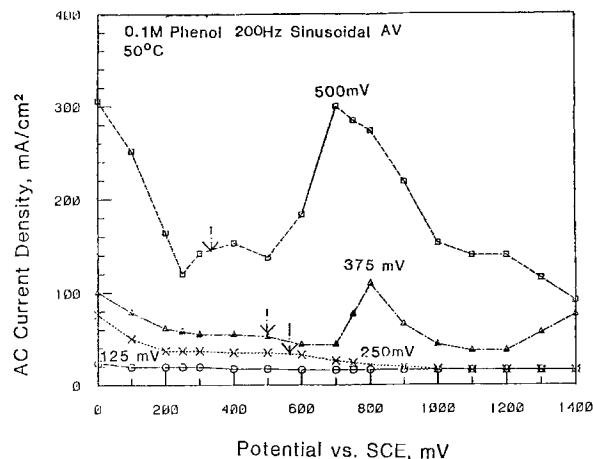


Fig. 5. AC current density vs. dc potential when 200 Hz sinusoidal AV was superimposed on a platinum rotating disk electrode (2400 rpm) in 0.1M phenol and 1M H_2SO_4 at 50°C. The AV magnitude varied from 125 to 500 mV rms as indicated in the figure. The arrows refer to the position of the rest potentials where the dc current density became zero on the electrode.

symmetric behavior between the anodic and cathodic polarization of the present reaction system.

AC current density vs. dc potential.—The typical ac current density vs. dc potential curves at 200 Hz are given in Fig. 5 for a range of sinusoidal AV from 125 to 500 mV rms. The measurements were made with a platinum rotating disk in a solution containing 0.1M phenol and 1M H_2SO_4 at 50°C. The ac current density increased with increasing AV at a given dc potential. For a given root-mean-square of AV, the ac current density increased with AV frequency. The ac current was also a function of dc potential. For the AV less than 250 mV rms, the ac current at the cathodic dc potentials was higher than that in the anodic regime (the arrows in the figure indicate the rest potentials). However, as the magnitude of AV increased beyond 375 mV rms, the ac current density vs. dc potential curves exhibited a maximum within the dc potential range investigated. The maximum ac current occurred approximately at 750 mV vs. SCE, and the height of the maximum increased with increasing AV. The phenomenon is similar to that of ac polarography (34). Accordingly, the dc potential where the maximum ac occurred was in the vicinity of the half-wave potential for the oxidation of phenol.

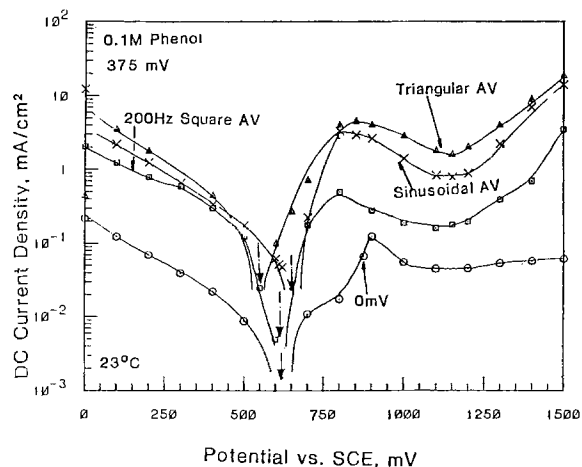


Fig. 6. Effect of AV waveforms on the dc polarization curves of a platinum rotating disk electrode (2400 rpm) in 0.1M phenol and 1M H_2SO_4 at 23°C. The data are given for the 200 Hz sinusoidal, square, and triangular wave AV as indicated in the figure. The AV magnitude was kept at 375 mV rms. For comparison, the polarization curve without any superimposed AV is also given (open circles).

Effect on AV waveforms.—In order to investigate the effect of AV waveforms on the oxidation of phenol, a set of runs was made by superimposing 200 Hz triangular and square-wave AV onto the platinum electrode in 0.1M phenol + 1M H₂SO₄ at 23°C. Figure 6 shows the resulting dc polarization curves for a set of sinusoidal, square, and triangular AV at a constant AV magnitude of 375 mV rms (200 Hz). For comparison, the dc polarization without AV is also shown in the figure. It is seen that the triangular wave resulted in the largest increase in the dc current density for both the anodic and cathodic reactions. This was followed by the sinusoidal and square wave according to the sequence

$$\text{triangular AV} > \text{sinusoidal AV} > \text{square AV} \quad [9]$$

The trend was similar to that of previous mass-transfer studies in ac electrolysis (37-38), where the triangular wave was shown to have the largest limiting ac current density, followed by the sinusoidal and square wave ac. This sequence may be explained by the fact that, for a given root-mean-square value, the triangular wave possesses the highest peak voltage, causing the severest destruction of the adsorbed layer on the platinum surface. Qualitatively, all the three waveforms had the same effect on the oxidation of phenol on the platinum electrode. Distinctions can be made only by the extent of enhancement in the dc current density. All the AV waveforms shifted the rest potentials toward the negative direction, as shown in Fig. 4.

Results of batch electrolysis.—The batch electrolysis experiment was carried out in a single-compartment cell at 50°C with 0.01M phenol in 1M sulfuric acid. In this experiment, phenol was oxidized to benzoquinone on a stationary platinum anode, and the benzoquinone was further reduced to hydroquinone on a platinum screen cathode having a surface area much larger than that of the anode. The cell was operated with a potentiostat by controlling the potential of the anode with respect to a saturated calomel reference electrode. The operating condition was dc potential, 750 mV vs. SCE, and 60 Hz sinusoidal AV varying from 0 to 375 mV rms. This condition was chosen from the polarization curves shown in Fig. 2-3. To manifest the effect of AV frequency on the batch electrolysis, a superimposed AV of 250 mV rms in a range of AV frequency from 20 to 600 Hz was also used. The conversion of phenol (mole converted per mole of phenol charged at the beginning of electrolysis) and the yield of hydroquinone (mole formed per mole of phenol converted) were obtained with a chemical analysis. The dc current I , ac current \tilde{I} , dc cell voltage E , and ac cell voltage \tilde{E} were recorded on a strip chart recorder. The number of dc cou-

lombs passing the cell was obtained by integrating the dc current with respect to the time, and the anodic current efficiency for the oxidation of phenol was calculated according to Faraday's law. The consumption of electric energy during the electrolysis was calculated by

$$W = \int_0^t [E(t)I(t) + \tilde{E}_{\text{rms}}(t)\tilde{I}_{\text{rms}}(t)]dt \quad [10]$$

where W is the electric energy in joules, t is the time in seconds, and the subscript rms refers to the root-mean-square values.

Figure 7 shows the results for the dc current as a function of time when the cell was superimposed with 60 Hz sinusoidal AV varying from 0 to 375 mV rms. The dc current increased with AV. At 375 mV AV, the dc current was 1000 times greater than that without any superimposed AV. The results imply that the applied AV increased the reaction rate. The conversion of phenol is presented in Fig. 8 as a function of time for various applied AV. The figure shows that the conversion increased with increasing AV. However, the slopes of the curves decreased with time because of the loss of current efficiency. Figure 9 shows the effect of AV frequency on the conversion of phenol when 250 mV rms sinusoidal AV was superimposed onto the anode potential. The conver-

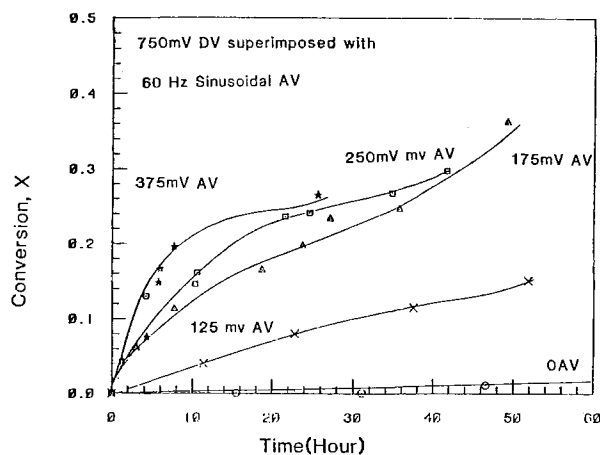


Fig. 8. Conversion of phenol as a function of time for a potentiostatic batch electrolysis with a stationary platinum electrode in 0.01M phenol and 1M H₂SO₄ at 50°C. The potential of the platinum anode was maintained at 750 mV vs. SCE, and was superimposed with 60 Hz AV with a magnitude varying from 0 to 375 mV rms as indicated in the figure.

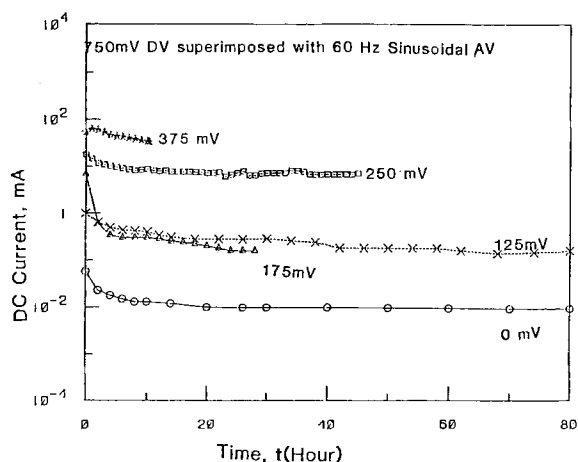


Fig. 7. DC current as a function of time for a potentiostatic batch electrolysis of the oxidation of phenol on a stationary platinum electrode (12.5 cm² surface area) in 0.01M phenol and 1M H₂SO₄ at 50°C. The potential of the platinum anode was maintained at 750 mV vs. SCE and was superimposed with 60 Hz sinusoidal AV with a magnitude varying from 0 to 375 mV rms as indicated in the figure.

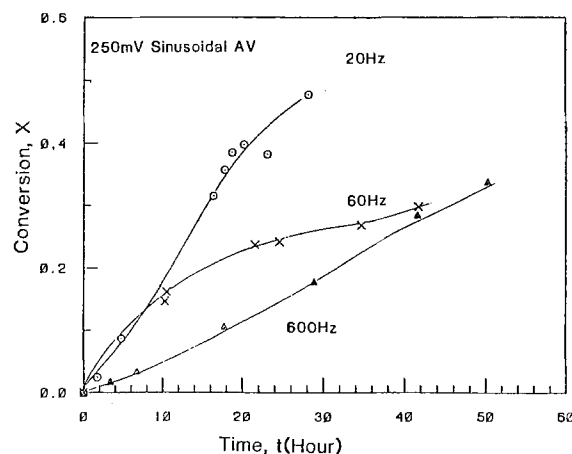


Fig. 9. Effect of AV frequency on the conversion of phenol in a potentiostatic batch electrolysis with a stationary platinum electrode in 0.01M phenol and 1M H₂SO₄ at 50°C. The data are given for three frequencies of sinusoidal AV: 20, 60, and 600 Hz. The magnitude of the superimposed AV was 250 mV rms, and the dc potential of the platinum anode was maintained at 750 mV vs. SCE.

Table I. Results for the oxidation of phenol with a potentiostatic batch electrolysis

	Experimental conditions	Time (h)	DC (C)	Conversion (%)	Current efficiency (%)	Yield (%)	Energy consumption J ($\frac{\quad}{\text{kg-mol phenol}}$)
Present work (12.5 cm ² Pt)	0 AV	172	6.2	—	—	—	—
(0.01M phenol) (50°C)	125 mV rms 60 Hz AV	116	91.5	42	—	29.4	2.9 × 10 ⁸
	250 mV rms 60 Hz AV	45	1278	29.7	65	19.9	1.65 × 10 ⁹
(DC potential 750 mV vs. SCE)	375 mV rms 60 Hz AV	10.3	1699	26.5	44	4.1	2.82 × 10 ⁹
	250 mV rms 20 Hz AV	43.9	2104	55.3	28.6	48.8	3.84 × 10 ⁹
	250 mV rms 600 Hz AV	68	58	25.9	30.2	16.8	3.17 × 10 ¹⁰
Covitz (28) (154 cm ² PbO ₂) (0.32M phenol) (30°C)	80 A/dm ²	0.5	—	40.3	35	61.2	1.49 × 10 ¹⁰

sion of phenol decreased with increasing AV frequency. After 30h electrolysis, the run with 20 Hz AV had 50% conversion, whereas only 25 and 18% conversion were obtained with the 60 and 600 Hz AV, respectively. The dc current with 20 Hz AV was also proportionally greater than those at the higher frequencies.

Table I summarizes the results of the potentiostatic batch electrolysis experiments shown in Fig. 7-9. All the values in the table were obtained at the end of each run. The electric energy consumption was determined by integrating the product of dc current and dc cell voltage, and of ac current and ac cell voltage with respect to the time, and the result is expressed in joules per kilogram-mole of phenol converted at the end of the electrolysis. For the run with only dc potential, the cell current was so small that only 6.2C of electricity were passed after 172h electrolysis, and the conversion of phenol was negligible. With superimposed AV, the dc current increased and the electrolysis time was shortened. The rate of oxidation of phenol increased with increasing magnitude of AV and with decreasing AV frequency. However, as the dc current increased by AV, the anodic current efficiency decreased. The yield of hydroquinone appeared to increase with decreasing AV frequency and to decrease with increasing magnitude of superimposed AV. For comparison, the results of a galvanostatic dc electrolysis using a lead dioxide anode as reported by Covitz (28) are also listed in Table I. The present results for the conversion of phenol, anode current efficiency, and yield of hydroquinone were comparable to those of Covitz's dc electrolysis. On the other hand, the energy consumption of the potentiostatic ac electrolysis (except for the run with 600 Hz AV) was about one order smaller than Covitz's value. This is because AV served as a depolarizer and reduced the electrode overpotential and dc cell voltage by continuously activating the electrodes during the electrolysis. A large portion of the total energy requirement in the present work was caused by the passage of ac current and ac cell voltage.

Conclusions

A study has been made of the effect of AV on the oxidation of phenol on platinum in aqueous sulfuric acid electrolyte. The effects of AV waveforms (sinusoidal, square, and triangular waves), frequency, and magnitude were also examined. The results indicate that, within the frequency range of 20-600 Hz, AV increased the dc current density for the anodic and cathodic processes and shifted the rest potential toward the negative direction. The magnitude of dc enhancement increased with increasing root-mean-square of superimposed AV, and decreased with in-

creasing frequency. The results of a potentiostatic batch electrolysis in an undivided cell revealed that superimposed AV increased the dc current and shortened the electrolysis time. The rate of conversion of phenol increased with increasing AV. The anodic current efficiency, and yield of hydroquinone decreased with increasing AV. The electric energy consumption was smaller than that of a galvanostatic dc electrolysis reported in the literature.

Acknowledgment

Acknowledgment is made to the donors of the Petroleum Research Fund (Grant 14330-AC5-C), administered by the American Chemical Society, for the support of this research.

Manuscript submitted March 7, 1985; revised manuscript received July 16, 1985.

The Petroleum Research Fund assisted in meeting the publication costs of this article.

REFERENCES

1. R. Jansson, *Chem. Eng. News*, **62**, 43 (Nov. 19, 1984).
2. D-T. Chin, in "Proceedings of the 9th International Congress Metallic Corrosion, Toronto, Canada," Vol. 4, pp. 96-103, National Research Council, Ottawa, Ont., Canada (1984).
3. S. R. Pookote and D-T. Chin, *Mater. Perf.*, **17** (3), 9 (1978).
4. D-T. Chin and T. W. Fu, *Corrosion*, **35**, 514 (1979).
5. S. Venkatesh and D-T. Chin, *This Journal*, **128**, 2588 (1981).
6. D-T. Chin and S. Venkatesh, *ibid.*, **126**, 1908 (1979).
7. D-T. Chin and P. Sachdev, *ibid.*, **130**, 1714 (1984).
8. R. Sethi and D-T. Chin, *J. Electroanal. Chem.*, **160**, 79 (1984).
9. J. L. Wendt and D-T. Chin, *Corros. Sci.*, To be published.
10. O. Reitlinger, *Z. Electrochim.*, **20**, 261 (1914).
11. A. N. Kappanna and K. M. Joshi, *J. Ind. Chem. Soc.*, **29**, 69 (1952).
12. I. K. Noguchi, *Res. Rep. Nagoya Ind. Sci. Res. Inst.*, **1**, 19 (1949); *ibid.*, **2**, 32 (1950); *ibid.*, **5**, 26 (1952); *ibid.*, **6**, 20 (1953).
13. N. S. Tsvetkov and E. P. Kovalchuk, *C.A.*, **64**: 5213e (1966).
14. G. A. Korchinski and E. F. Fedorov, *Elektrokhimiya*, **2**, 1395 (1966).
15. P. R. Nadebaum and T. Z. Fahidy, in "Symposium on Electrochemical Engineering," Vol. 1, J. D. Thornton, Editor, p. 145, Institute of Chemical Engineers, London (1973).
16. S. G. Nitskanskii, O. S. Khristeva-Strizhen, and I. I. Nitskanskaya, *C.A.*, **81**: 117281 (1983).
17. Y. Kikuchi and T. Ueyama, *Nippon Kagaku Kaishi*, **5**, 981 (1974).

18. P. Florequin, H. Larmuseau, and X. De Hemptinne, *Ann. Soc. Sci. Bruxelles, Ser. 1*, **88**, 241 (1974).
19. S. N. Bhadani, *Ind. J. Technol.*, **12**, 570 (1974).
20. M. Tamura, K. Ogasawara, N. Ono, and S. Hagiwara, Japan Pat. 7,744,593 (1977).
21. M. Kawahara, Japan Pat. 80,111,767 (1980).
22. R. C. Alkire and J. E. Tsai, *This Journal*, **129**, 1157 (1982).
23. R. R. Adzic, K. I. Popov, and M. A. Pamic, *Electrochim. Acta*, **23**, 1191 (1978).
24. F. Fichter and E. Brunner, *Z. Electrochem.*, **19**, 781 (1913).
25. N. H. Vagenius and R. J. King, U.S. Pat. 2,135,368 (1938).
26. G. C. Jones and R. H. Meen, U.S. Pat. 4,035,253 (1977).
27. G. C. Jones and D. A. Payne, U.S. Pat. 3,994,788 (1976).
28. F. H. Covitz, U.S. Pat. 3,509,031 (1970).
29. F. H. Covitz, U.S. Pat. 3,616,323 (1971).
30. F. H. Covitz and R. V. Carruba, U.S. Pat. 3,616,324 (1971).
31. I. N. Sorokin, U.S.S.R. Pat. 489,525 (1972).
32. C. Y. Cheng, Ph.D. Dissertation, Clarkson University, Potsdam, New York (1983).
33. K-L. Hsueh, E. R. Gonzalez, S. Srinivasan, and D-T. Chin, *This Journal*, **131**, 823 (1984).
34. H. Breyer and H. Bauer, "Alternating Current Polarography and Tensammetry," pp. 203-205, Interscience, New York (1963).
35. S. Schuldiner and T. B. Warner, *This Journal*, **112**, 212 (1965).
36. S. Gilman, in "Electroanalytical Chemistry," Vol. 2, A. J. Bard, Editor, pp. 111-192, Marcel Dekker, New York (1967).
37. C. Y. Cheng and D-T. Chin, *AIChE J.*, To be published.
38. C. Y. Cheng and D-T. Chin, *Chem. Eng. Commun.*, To be published.

Modification of Titanium Electrodes for Detection of Biological Substances

Ichiro Nakabayashi, Tahei Tomida, and Katsuhiko Kawashiro

Faculty of Engineering, The University of Tokushima, Minamijosanjima, Tokushima 770, Japan

ABSTRACT

Several modifications of the surface structure and texture of electrode substrate (titanium) were carried out by the treatments of rolling, heating, and ion bombardment to develop electrodes to detect biological substances. These electrodes were chemically modified with trypsin or aprotinin (trypsin inhibitor). The electric response measured in a specific reaction system of trypsin-aprotinin depended on the characteristics of surface of the electrode substrate as well as the concentration of the biological substances. The ion bombardment in H₂O vapor was found to be more effective in modifying electrodes for biosensors of this type.

Chemically modified electrodes have been developed to detect biological substances such as antigens, antibodies, enzymes, etc. (1-3). Yamamoto *et al.* (1, 2) have proposed a new electrical method using a titanium electrode modified chemically with the counterpart of a biologically active substance described above. This electrical method is expected to have wide applications because of its simplicity, high specificity, and sensitivity.

On the other hand, it is known that the proteins to be modified should be immobilized by the hydroxyl group on the surface of electrodes. It is therefore important to increase the hydroxyl group on the electrode surface.

In this study, several modifications of the surface structure and texture of electrode substrates (titanium) were tried by rolling treatment, heat-treatment, and ion bombardment. With these electrodes, the relation between electric responses and surface properties was also studied for an aprotinin-trypsin system.

Experimental

Preparation of electrode.—Titanium wires (1ϕ × 35 mm) were used as the electrode substrates. Each wire was modified separately by a different treatment as follows: a was heated at 600°C in the air atmosphere for 5 min; b was rolled by length of 50% with a dental roller and then oxidized at 600°C for 5 min; c was treated like b and then annealed at 1300°C in 6.7 × 10⁻³ Pa for 30 min and further oxidized at 600°C in air for 5 min; with d, the substrate of c was exposed to ion bombardment (20 Pa of H₂O vapor) with an energy of 200 eV. The ion bombardment was carried out by the usual radio frequency (RF) diode sputtering method described elsewhere (4).

After these various treatments, these electrode substrates were chemically modified with trypsin or a trypsin inhibitor (aprotinin) by the conventional cyanogen bromide method (5). The chemically modified electrode with bovine serum albumin (BSA) was used as the reference electrode. The chemicals of trypsin (type III), aprotinin (type I-S), and BSA were procured from Wako Pure

Chemicals Company Limited and Sigma and Seikagaku Kogyo Company Limited, respectively. Aqueous solution of barbital sodium (0.1M) served as the buffer solution at pH 8.6. This particular pH was adjusted by 1M hydrochloric acid.

Electrical measurement.—The electric circuit is shown in Fig. 1. A potential difference between the working and reference electrode immersed in a sample solution (18 ml) at 35°C was measured with a vibrating reed electrometer (Takeda Riken Company Limited). The sample solution was stirred with a Teflon stirrer piece at an appropriate speed. The whole system of measurement was set in the dark box shielded electrically with aluminum foil.

Results and Discussion

The electrode potential between the working (aprotinin) and the reference electrode shifted exponentially toward the positive after the addition of trypsin solution (2 ml). On the other hand, the electric response changed in the negative direction by the trypsin electrode-aprotinin solution. The response direction (positive, negative) and the voltage change observed have been well explained by the reasonable assumption of the dipole moment upon the formation of the complex of trypsin-aprotinin (6). This potential shift is attributed to the specific reaction between aprotinin and trypsin at the electrode surface as described by Yamamoto *et al.* (1).

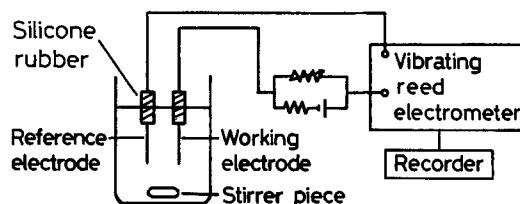


Fig. 1. System for the measurement of potential difference of reference and working electrodes.

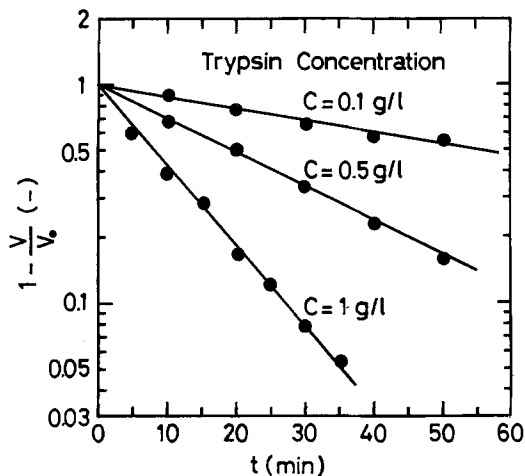


Fig. 2. Semilog plots of potential vs. time for electrode of original titanium wire.

Figure 2 shows the semilog plots of potential vs. time. The slope of each curve in the figure was proportional to the trypsin concentration, and potential shift could be expressed by the equation

$$V = V_0 [1 - \exp(-kCt)]$$

where V_0 is the terminal potential shift, which depends on the amount of couplings, and C is the concentration of an additive. In this case the additive is trypsin.

Figure 3 shows the effect of different surface treatments for substrates on electric responses. The rolled electrode (treatment b) gives a higher potential shift but longer delay time than that of the original titanium wire (treatment a). This may be due to the thick porous oxide layer produced on the electrode surface by the rolling, resulting in the increase of hydroxyl group attached to the surface, and so the long time is needed for the additive to diffuse through the porous layer to the binding sites. Also, the heat-treatment of rolled plate (treatment c) decreases the potential significantly. This is due to the decrease in the hydroxyl group or aprotinin immobilized, owing to the high crystallinity of TiO_2 (rutile) and titanium metal. This was confirmed by x-ray diffraction analysis. The decrease in roughness of the surface and grain boundaries broadened by heat-treatment were also observed in the photograph of scanning electron microscope (SEM).

The response obtained from the H_2O -bombarded electrode (treatment d) was very rapid and sensitive as compared with curves a, b, and c corresponding to the non-

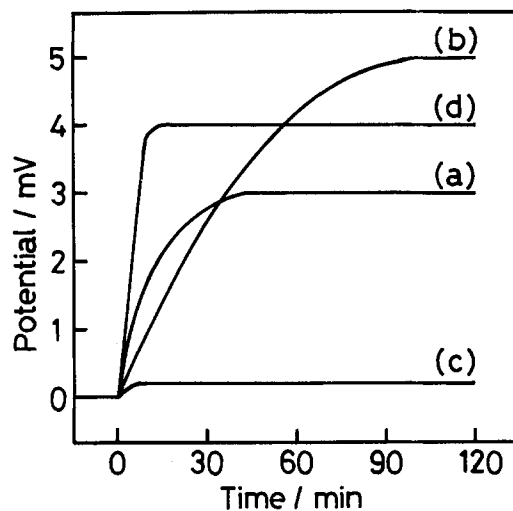


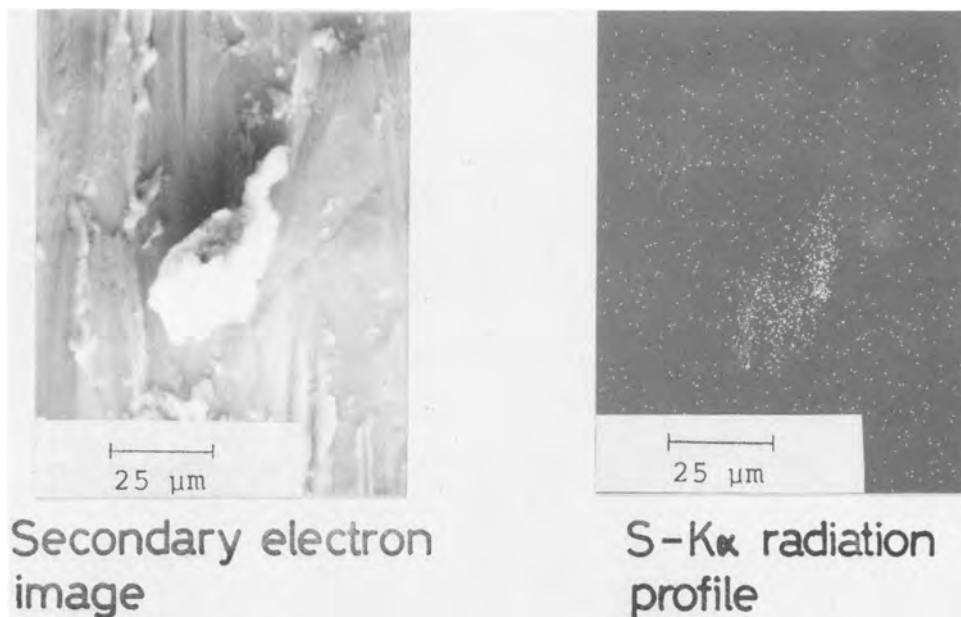
Fig. 3. Effects of surface treatment on electric response. a: Original titanium wire. b: Titanium plate rolled wire. c: Titanium plate annealed at 1300°C in 6.7×10^{-3} Pa. d: Titanium plate annealed at 1300°C and then bombarded in 20 Pa of H_2O vapor.

bombarded electrodes. The potential vs. time behavior of the variously treated electrodes was expressed by the equation described above, except for the data on the high temperature-annealed substrate (c) in Fig. 3, which shows very small potential change. The value of k for the bombarded electrode is about seven times that of the non-bombarded one (a). The effect of the ion bombardment may contribute to increase in the hydroxyl group on the electrode surface. This was confirmed by the detection of the sulfur atoms in the trypsin molecules attached to the hydroxyl group on the surface of electrode.

Figure 4 shows the photographs of the secondary electron image and S- $K\alpha$ radiation profile with an electron probe microanalyzer (EPMA). In the ion-bombarded substrates, a small amount of sulfur was found to be uniformly distributed. On the other hand, only a trace of sulfur was detected in the original or annealed substrate.

X-ray diffraction studies were conducted for the above substrates. It was observed that, for all substrates treated below 600°C , no peaks corresponding to titanium oxide were found in the x-ray patterns. On the other hand, TiO_2 (rutile) crystal was detected in all substrates treated above 600°C . From the x-ray and SEM analyses of rutile crystal which was treated by the ion bombardment in H_2O vapor, no change was observed in its surface texture or crystal structure. However, a thin amorphous layer of titanium

Fig. 4. Texture of trypsin electrode surface and sulfur distribution on it by EPMA.



oxide is assumed to be formed due to the displacement of atoms in the surface layer from their regular sites. In the similar technique employed for Zn_2SiO_4 , this analogy is already established (4). This thin amorphous layer could have a large amount of hydroxyl group in a similar manner as silica gel or porous glass (5).

These results show that the response of potential in the trypsin inhibitor (aprotinin)-trypsin system depends on the characteristics of electrode substrate surface which are modified by the various surface treatments such as rolling, heating, and ion bombardment. Above all, the ion bombardment in H_2O vapor was found to be more effective in modifying electrodes for biosensors of this type.

Acknowledgments

The authors wish to acknowledge their gratitude to Professor O. Tada of the Department of Electronic Engineering, the University of Tokushima, for suitable discussions that led to the development of the modifying elec-

trode. We also would like to thank Mr. Y. Itsuki, K. Itoh, and A. Ugai for their experimental assistance.

Manuscript submitted Feb. 20, 1985; revised manuscript received May 17, 1985.

The University of Tokushima assisted in meeting the publication costs of this article.

REFERENCES

1. N. Yamamoto, S. Shuto, and H. Tsubomura, *Nippon Kagaku Kaishi*, 1562 (1980).
2. N. Yamamoto, Y. Nagasawa, S. Shuto, M. Sawai, T. Sudo, and H. Tsubomura, *Chem. Lett.*, 245 (1978).
3. J. Janata, *J. Am. Chem. Soc.*, **97**, 2914 (1975).
4. O. Tada, K. Tominaga, T. Kondo, and K. Ichinomiya, *This Journal*, **131**, 1365 (1984).
5. H. H. Weetall and C. C. Detar, *Biotechnol. Bioeng.*, **17**, 295 (1975).
6. N. Yamamoto, Y. Nagasawa, M. Sawai, T. Sudo, and H. Tsubomura, *J. Immunol. Meth.*, **22**, 309 (1978).

Laser Interferometry of Pulsed Galvanostatic Deposition of Polycarbazole

R. N. O'Brien*

Department of Chemistry, University of Victoria, Victoria, British Columbia, Canada V8W 2Y2

K. S. V. Santhanam

Tata Institute of Fundamental Research, Bombay 400 005, India

ABSTRACT

The galvanostatic deposition of polycarbazole was conducted by pulsing the current in the frequency range from 0.1 to 500 Hz in solutions of N,N-dimethylformamide containing carbazole and tetra-n-butyl ammonium perchlorate. Compared with its dc deposition, the results obtained here indicated a smooth deposit (pinhole free) and with greater binding to the substrate surface. The SEM studies demonstrate that the range of pulsed frequencies and the potential drop across the electrodes control the deposition process. An advantage of the unsymmetrically pulsed current deposition was the selective reduction of the unpolymerized free radicals at the electrode-solution interface resulting in increasing the surface concentration of the monomer. The development of concentration gradients in the pulsed electrolysis has been followed by laser interferometry, and it shows frequency-controlled growth at the electrode/solution interface.

While the organic synthetic metals have prospective usage as electrodes in fuel cells and in rechargeable batteries (1-3), a key problem in their development has been associated with their stability. One factor which is responsible for this instability, especially with polycarbazole-type electrodes, is caused by the pinholes (nonsmooth deposits) and weakly adhering nature of the deposits produced during their electrodeposition. Problems such as fine-grained and "burned" deposits during electrodeposition of metals, such as Ni, Au, Ag, etc., arise but can be avoided by using a high c.d. pulsed at a low frequency (4) to enhance the metal ion concentration in the diffusion layer (5-7). The effect of pulsed electrolysis has been to increase the allowable rate of deposition. As the mechanism of the electrodeposition of real metals differs from others (synthetic metals), an investigation has been undertaken to study the effect of pulsed current on the deposition of polycarbazole. The results obtained in this study suggest that a smooth deposition can be obtained at moderate frequencies (higher than that employed in the conventional depositions), *i.e.*, < 1 Hz. The need for using higher frequencies than those employed in conventional metal depositions is attributed to two factors: (i) as the synthetic metals are produced by an initial electrochemical oxidation of the electroactive species generating the radical cation for propagating the polymer chain, the reduction of the nonpolymerized radical at the electrode during galvanostatic (current pulsed anodic on/off, anodic/cathodic, or anodic/off/cathodic/off) pulsed electrolysis results in

the enhancement of the surface concentration of the electroactive species (carbazole), and (ii) the negligible destruction of the deposits in the pulsing mode (the polymer is reduced at $E^0 \approx 0.0$ V).

The pulsed electrodeposition of polycarbazole has been followed by laser interferometry, and the diffusion gradients that exist in the pulsed electrolysis are discussed here.

Experimental

The solutions for the electrodeposition of carbazole were prepared in anhydrous N,N-dimethylformamide (DMF, MCB reagent grade). Tetra-n-butyl ammonium perchlorate (South Western Analytical Chemicals) was dried at 100°C for 24h in a drying piston under vacuum before using it as the supporting electrolyte. The dried sample was stored in a dessicator before use in the experiments.

The electrodes employed in this study were of two types. In one type (for multiple beam laser interferometry), glass disks were cut in half and the cut edges were sputtered with Au about 3000-5000Å thick. The sputtering was done for about 10 min.

The glass disks were cleaned in alcoholic KOH solution before carrying out the sputtering. In the second type (for SEM studies and holographic interferometry), rectangular glass plates (0.8 cm wide and 8.5 cm long) were covered with vacuum-deposited Au. The thickness of the film was measured with a profilometer and was estimated at

3000Å. The two electrodes were widely separated in the interferometric cell (separation of 5-10 mm).

The experimental arrangement for laser interferometry has been described previously (8-10). The Au plated glass disk electrodes were mounted into the Teflon cell in a parallel configuration. The optical glass flats were placed on either side of the electrodes and clamped in a brass cell holder. A He-Ne laser (1 mW) was used for producing the interference fringes. The fringe movements were videotaped on a Hitachi video recorder (VTR Model VT-7A) and were displayed on a 20 in. Hitachi color television. An RCA CC 030 microprocessor-controlled camera was used to follow the fringes.

The pulsed electrolysis experiments were carried out using a Keithley constant current source (Model 220) in combination with a Wavetek Model III function generator or Data Royal Corporation F210B waveform generator. The cell voltages were followed using a Tektronix Type 561A oscilloscope with Type 3A6 dual-trace amplifier and Type 3B3 time base. A few experiments were carried out with a Harrison power supply-amplifier 6824A with $\pm 50V$ and $\pm 1A$ suitably modified to generate the pulsed currents.

Results and Discussion

The electrodeposition of polycarbazole was conducted at c.d.'s ranging from 0.06 to $3.5 \text{ mA}\cdot\text{cm}^{-2}$ with galvanostatic pulsed frequencies ranging from 0.5 to 500 Hz. The galvanostatic pulsed current amplitude oscillates symmetrically from the positive to negative direction. Figure 1 shows the potential drop across the electrodes plotted as a function of the applied c.d. during the electrolysis of carbazole. The magnitude of the observed changes in the cell voltage is larger at lower c.d.'s ($< 0.3 \text{ mA}\cdot\text{cm}^{-2}$) owing to the smaller extent of polarization at the electrodes. The interfacial concentration of carbazole or its radical is expected to change periodically (as is the double-layer capacitance, which must charge with the solution resistance) as the potential of the system is changed. At the anode (when the current magnitude is positive), the oxidation of carbazole to a free radical occurs, and at the cathode, reduction of carbazole to its anion with its follow-up reaction will occur (11). The extent to which these reactions proceed is dependent on the imposed c.d. and the actual potentials attained by the electrodes during the electrolysis. Thus, at both the electrodes, the onset of background electrolysis occurs after a long time (several minutes). In the electrolysis conducted at lower frequencies ($< 10 \text{ Hz}$) due to the factors discussed earlier, the oscillating potential range [the maximum (V_{\max}) and minimum (V_{\min}) potential drop across the electrodes] spans a wider range with V_{\min} reaching negative values relative to the V_{\max} and relative to $V = 0$. Figure 2 describes the V_{\max} and V_{\min} distribution as a function of the

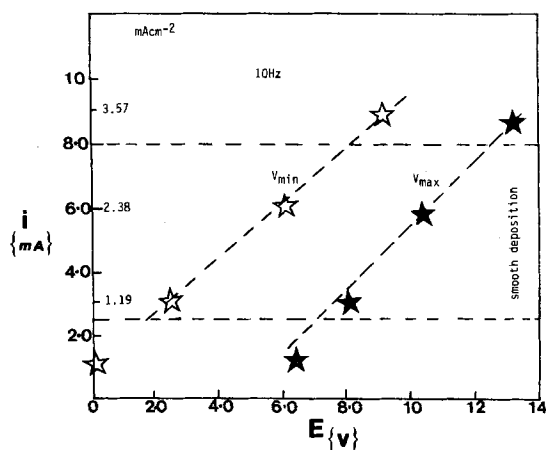


Fig. 1. Current-voltage curves for the electrolysis of 60 mM carbazole and 0.1M $(C_6H_5)_4NClO_4$ in DMF under 10 Hz pulsing. V_{\max} represents the maximum cell voltage, and V_{\min} represents the minimum voltage. Dotted lines indicate the smooth deposition of polycarbazole.

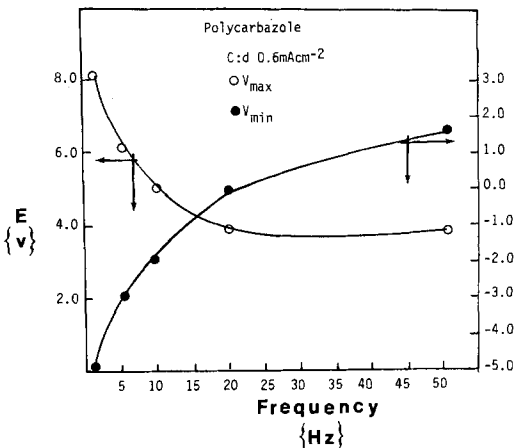


Fig. 2. The effect of frequency upon pulsed electrolysis of 60 mM carbazole. The V_{\max} and V_{\min} attained during the electrolysis is given in the figure.

pulsing frequency during the electrodeposition of polycarbazole in a laser interferometric cell.

The onset of concentration profiles during the pulsed electrolysis of carbazole follows a pattern similar to that of dc electrolysis (12); a smooth down turn of the fringes was observed at the anode, indicating a decrease in refractive index of the medium in that region of the electrolyte. Due to the pulsing current density, the electrode polarity changes with the result that these fringe bendings show a reversal. The fringe shifts at the anode during the progress of the electrolysis show a frequency dependency; at 500 Hz, pulsed electrolysis at a c.d. of $0.30 \text{ mA}\cdot\text{cm}^{-2}$ fringe shifts of 0.85 (240s) and 1.07 (360s) were obtained. At a lower frequency, 50 Hz, a fringe shift of 0.53 (240s), 0.67 (360s), and at an intermediate frequency of 100 Hz a fringe shift of 0.75 (240s) was estimated during the progress of the electrolysis. This decreasing trend was maintained to the lowest frequency, that is, 0.5 Hz. With a view to understanding this fringe shift behavior, we monitored the potentials V_{\max} and V_{\min} during the course of the electrolysis. At the highest frequency examined (500 Hz), the V_{\min} value differed from the V_{\max} by about 0.20V, and at the lowest frequency of 0.5 Hz this difference widens to 12.0V. In the latter situation, the potential drop across the electrodes (V_{\min}) moves to the negative region. In the experiments that were conducted with 500 Hz pulsing, the V_{\max} and V_{\min} were both in the positive region. Based on these results, it is possible to postulate two sets of reactions, one set of reactions when both V_{\max} and V_{\min} are well into the positive region of potentials and another set of reactions when the cell voltage oscillates from positive to negative values (relative variations). We wish to suggest that (at the electrode which is usually the anode) these reactions are the reduction of the free radical cation on the surface of the electrode (produced after the initial oxidation of carbazole) and the redox reaction of the polymerized product. A cyclic voltammetric study of the polycarbazole in background solutions of DMF containing $(C_6H_5)_4NClO_4$ reveals such a reduction of polycarbazole at $E_{pc} = 0.0 \text{ V}$ (13, 14) and a drawn-out oxidation wave of the product at about +0.20V. These reactions are possibly responsible for the differences in the observed fringe shifts.

The effect of pulsed electrolysis on the concentration gradients is much more pronounced at higher c.d.'s ($> 1 \text{ mA}\cdot\text{cm}^{-2}$). This point is illustrated in Fig. 3. Note the developments of concentration gradients in the frames 1 through 4. The fringe bending occurs smoothly up to 60s of electrolysis of carbazole, and thereafter the fringe distortions occur until destroyed at times greater than 900s. An important feature of the high c.d. electrolysis is the stronger distortions of the fringes at the initially cathodically polarized electrode. The sequence of fringe distortions are much more easily seen on the videotapes where hydrodynamic contours are clearly discernible on the television screen. Since in pulsed electrolysis the polarities

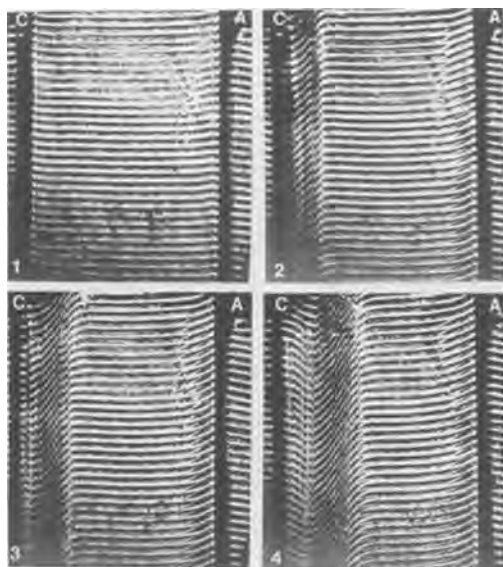


Fig. 3. Laser interferograms obtained during high c.d. electrodeposition of polycarbazole. $i_0 = 16.6 \text{ mA-cm}^{-2}$. $f = 1 \text{ Hz}$. 1: At 60s of electrolysis. 2: 180s. 3: 240s. 4: 360s. The anode is a Au plated glass electrode on the left side, and the cathode is another Au plated glass electrode.

of the electrodes are continuously reversed, one would expect a similar development of fringe distortions at the anode (the other electrode). It is, however, not observed in these experiments. The occurrence of fringe distortions at the cathode is being ascribed to the $(\text{C}_4\text{H}_9)_4\text{N}^+$ reduction (background electrolysis) and the cleavage of the neutral radical produced to the corresponding amine and N_2 . This process occurs more efficiently on the Au cathode than on the polymer-covered Au anode. These results suggest differences in the electrocatalytic behavior of the polymer and Au electrodes.

A more detailed analysis of the concentration gradients and the concentration-distance profiles at the anode can be done by using a holographic interferometric cell,¹ where the distance between the electrodes is larger, 10 mm compared with the 3 mm in multiple beam laser interferometry. The development of these profiles during the electrolysis is shown in Fig. 4 and 5.

The smoothness of the pulsed electrolytic deposition of polycarbazole at a c.d. of 0.30 mA-cm^{-2} with a pulsed fre-

¹ These profiles are obtained from holographic interferometry by using a 5 mW He-Ne laser in combination with a beam splitter. The analyzing beam is attenuated by using a neutral density filter. The details of the experimental arrangement are described in Ref. (14) and (15).

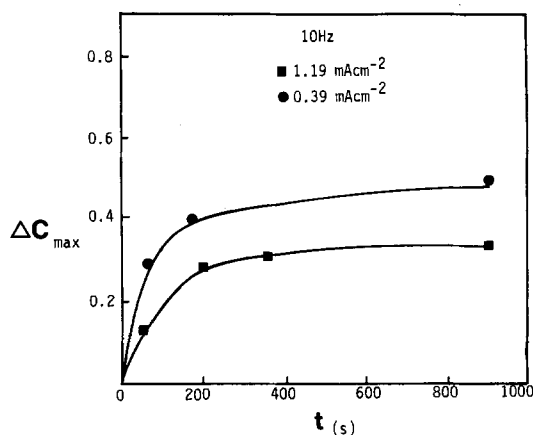


Fig. 4. Holographic interferometry of electrodeposition of polycarbazole under pulsed conditions. $f = 10 \text{ Hz}$. The development of concentration gradients during electrolysis at two different c.d.'s are shown.

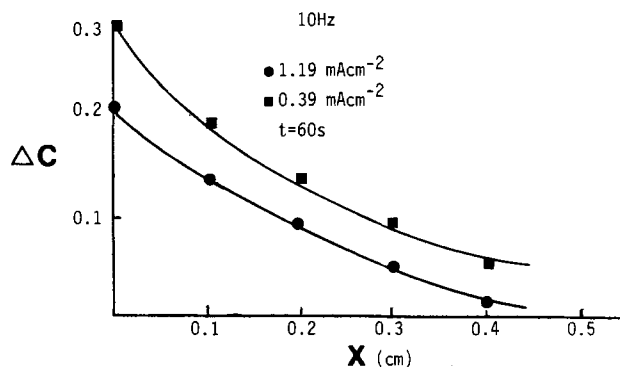


Fig. 5. Holographic interferometry of the electrodeposition of polycarbazole. The development of concentration-distance profiles are indicated at two different c.d.'s. $f = 10 \text{ Hz}$.

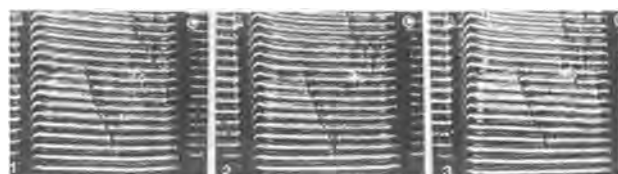


Fig. 6. Laser interferograms of pulsed electrolytic deposition of polycarbazole. 1: 60s. 2: 240s. 3: 360s. $f = 10 \text{ Hz}$. $i_0 = 1.66 \text{ mA-cm}^{-2}$.

quency of 10 Hz is shown in Fig. 6. The fringes are well developed during the progress of the electrolysis, and the frames in Fig. 6 should be compared with those shown in Fig. 3 for the development of distorted contours.

The experiments were also conducted by using unsymmetrical timings in the pulsing circuits but with the same overall frequency. By this method, we would have the oscillating potential spanning different potential regions; however, the frequency of the pulsed electrolysis is maintained at the same value. These experiments would provide a support to the hypothesis (conclusions reached earlier) that the oscillating potential plays a critical role in the development of concentration gradients. For this purpose, a comparison of a symmetrical 10 Hz ($t_r = 50 \text{ ms}$ and $t_f = 40 \text{ ms}$) with an unsymmetrical pulsing ($t_r = 60 \text{ ms}$ and $t_f = 40 \text{ ms}$) gives differences in the potential excursions of $+8.00$ to -2.00V and $+8.00$ to $+4.00\text{V}$, respectively; correspondingly, the gradients are different for the same superimposed frequency. This difference in concentration gradients is shown in Fig. 7.

The conductivity of the polycarbazole films have been measured (10 to $100 \text{ } \Omega^{-1}\text{-cm}^{-1}$) (12). The stability of the film has also been measured. An interesting aspect of the pulsed electrolysis is in the morphological developments that appear on the polycarbazole deposits. For these experiments, two Au sputtered-glass plates were used as

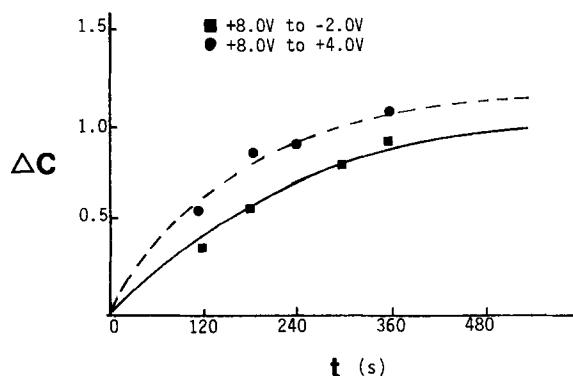


Fig. 7. Differences in the buildup of concentration gradients under symmetrical and unsymmetrical pulsed electrolysis of carbazole. $f = 10 \text{ Hz}$. c.d. = 1.66 mA-cm^{-2} .

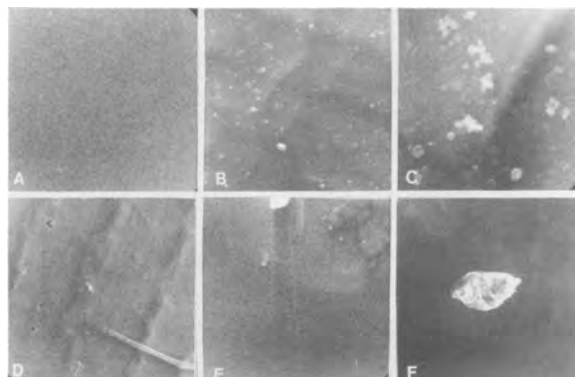


Fig. 8. SEM photographs of the polycarbazole deposits under different conditions. A: 10 Hz, 0.39 mA-cm^{-2} ; B: 10 Hz, 1.19 mA-cm^{-2} , magnification of 550 times. C: 10 Hz, 1.19 mA-cm^{-2} , magnification of 2100 times. D: 1 Hz, 0.39 mA-cm^{-2} , magnification of 550 times. E: 100 Hz, 1.19 mA-cm^{-2} , magnification of 550 times. F: 1.19 mA-cm^{-2} , 100 Hz, magnification of 550 times of edge region.

electrodes in the holographic cell; during these depositions, holographic fringes were monitored. The results of these are given in the earlier section. The pulsed electrolysis was carried out at different c.d.'s in the range of $0.30\text{--}3.57 \text{ mA-cm}^{-2}$ with the pulsing frequencies operating at 1-100 Hz. Films made with current densities of $1\text{--}3.0 \text{ mA-cm}^{-2}$ (10 Hz) are remarkably rugged. They were active over a period of two weeks, as indicated by the SEM and the electrochemical oxidations of organics. The film continued to be active over a period of six months. The anode was washed well with DMF and dried after the experiment. It was then examined under a scanning electron microscope at different magnifications up to 4000 times. A representative set of data on polycarbazole is shown in Fig. 8. The frame A in the figure was obtained at 10 Hz, 0.39 mA-cm^{-2} pulsed electrolysis. The next frame, B, was the deposit obtained at the 10 Hz, 1.19 mA-cm^{-2} electrolysis, and the following frame, C, was the observation of the deposit under a higher magnification (3900 times). In these frames, one can see the crude deposits on the underlying bumpy deposits. The unevenness is much more visible at still higher c.d.'s, 3.57 mA-cm^{-2} , and the deposits tend to peel off from the glass surface. Frame D shows the deposit obtained at the 0.39 mA-cm^{-2} , 1 Hz electrolysis; the development of cracks on the electrode is visible in

the frame. Frame E in Fig. 8 shows the deposit obtained when pulsing at 100 Hz. At these frequencies, the electrode edges develop uneven growth. A magnified view of the edge deposit is shown in frame F. The higher c.d.'s such as 3.57 mA-cm^{-2} do not yield good adherent deposits even though the cell voltage under pulsed (10 Hz) conditions varies from +12.0 to +9.0V. This is believed to be because of the onset of the background electrolysis at these thicker deposits of polycarbazole.

Acknowledgments

The authors wish to acknowledge the support for this work by National Sciences and Engineering Research Council of Canada and the help of Teddy Gathright of Triumph, and D. R. Bapat and Jack Dietrich for their help in gold sputtering and in SEM studies.

Manuscript submitted March 19, 1985; revised manuscript received July 3, 1985.

The University of Victoria assisted in meeting the publication costs of this article.

REFERENCES

1. T. Nagatome, T. Honma, C. Yamamoto, K. Negishi, and D. Omoto, *J. Appl. Phys.*, **22**, L275 (1983).
2. P. Bernier, A. El-Khodary, F. Maurice, C. Fabre, P. Mirebeau, and A. M. Ledunois, *J. Phys. C*, **3**, 583 (1983).
3. M. Armand, *ibid.*, **3**, 559 (1983).
4. H. Y. Cheh, *This Journal*, **118**, 551 (1971).
5. A. Hickling and H. P. Rothbaum, *Trans. Inst. Met. Finish.*, **34**, 53, 199 (1957).
6. N. Ibl, *Metalloberfläche Agnew Elektrochem.*, **33**, 51 (1979).
7. T. Z. Fahidy, *This Journal*, **130**, 296 (1983).
8. K. S. V. Santhanam and R. N. O'Brien, *J. Electroanal. Chem.*, **160**, 377 (1984).
9. R. N. O'Brien and K. S. V. Santhanam, *This Journal*, **129**, 1266 (1982).
10. R. N. O'Brien, *Rev. Sci. Instrum.*, **35**, 803 (1964).
11. K. S. V. Santhanam, R. N. O'Brien, and A.D. Kirk, *Can. J. Chem.*, **47**, 1355 (1969).
12. R. N. O'Brien, N. S. Sundaresan, and K. S. V. Santhanam, *This Journal*, **131**, 2028 (1984).
13. N. S. Sundaresan, V. Swayambunathan, and K. S. V. Santhanam, *Trans., SAEST*, **19**, 85 (1984).
14. R. N. O'Brien and K. S. V. Santhanam, in "Interfinish '84," p. 255 of the World Congress on Metal Finishing, Jerusalem, 1984.
15. V. S. Srinivasan, in "Advances in Electrochemistry and Electrochemical Engineering," Vol. 9, P. Delahay and C. W. Tobias, Editors, John Wiley and Sons, New York (1973).

Ionic Conductivity in Glass and Glass-Ceramics of the $\text{Na}_3\text{YSi}_3\text{O}_9$ and $\text{Na}_5\text{YSi}_4\text{O}_{12}$ Type Materials

Ephraim Banks* and Chy Hyung Kim

Department of Chemistry, Polytechnic Institute of New York, Brooklyn, New York 11201

ABSTRACT

The ionic conductivities in glass and glass-ceramics were studied for $\text{Na}_{3.2}\text{M}_{0.7}\text{Si}_{2.9}\text{P}_{0.1}\text{O}_{8.7}$ ($M = \text{Er, Y, Ho, Dy, Gd, Eu,}$ and Sm) compounds. The results showed comparable conductivity values, in the range of $10^{-4} (\Omega\text{-cm})^{-1}$ at 280°C , with the glasses being somewhat better conductors. Compounds of the type $\text{Na}_5\text{MSi}_4\text{O}_{12}$ ($M = \text{Fe, In, Er, Y, Gd,}$ and Sm), which yielded highly conductive phases in the crystalline ceramic form, were also studied in glassy and glass-ceramic states. In compositions of the latter type, the glasses showed lower conductivity than that in the glass-ceramic or the conventional ceramic phase. However, glass-ceramic samples with $M = \text{Er, Y}$ showed lower activation energies (4.0-4.4 kcal/mol) compared with those in the conventional crystalline phase prepared by Shannon *et al.* (1). The greater conductivity of the glass-ceramic state in the $\text{Na}_5\text{MSi}_4\text{O}_{12}$ phases, compared to the glassy state, is understood in terms of the favorable structure for ionic transport in the crystalline state.

Glasses containing alkali ions are well known as good conductors of electricity. The processing involved in forming glasses and glass-ceramics can eliminate the porosity usually associated with sintered ceramics, and can permit the production of thinner sections, which would decrease the series resistance of a cell. The feasibility of forming ceramics was investigated using known solid electrolyte compositions to yield a highly conductive phase.

Since the compounds of the type $\text{Na}_3\text{YSi}_3\text{O}_9$ were prepared (2), it has been reported that ionic conductivity was improved by the addition of more sodium with a combination of phosphorus substitution and reduction of Y^{3+} content, such as $\text{Na}_{3.2}\text{Y}_{0.7}\text{Si}_{2.9}\text{P}_{0.1}\text{O}_{8.7}$ (3).

The hydrothermal synthesis of $\text{Na}_5\text{YSi}_4\text{O}_{12}$ and its crystal framework was reported by Maksimov *et al.* (4). Since 1977 and 1978 (5, 6), those materials have been known as good superionic conductors owing to the existence of large channels in the structure, which facilitate ionic transport. However, the study of glassy and glass-ceramic forms of these materials has not yet been investigated.

In this work, preparation of $\text{Na}_{3.2}\text{M}_{0.7}\text{Si}_{2.9}\text{P}_{0.1}\text{O}_{8.7}$ ($M = \text{Er, Y, Ho, Dy, Gd, Eu,}$ and Sm) and $\text{Na}_5\text{MSi}_4\text{O}_{12}$ ($M = \text{Fe, In, Er, Y, Gd,}$ and Sm) glasses and glass-ceramics was attempted, and comparisons of their ionic conductivities were made.

Experimental

Appropriate amounts of reagent-grade Na_2CO_3 , M_2O_3 , SiO_2 , and $\text{NH}_4\text{H}_2\text{PO}_4$, according to the composition, were mixed in an agate mortar. The ground mixture was placed into a platinum crucible and heated in a furnace to about 1200°C for $\text{Na}_{3.2}\text{M}_{0.7}\text{Si}_{2.9}\text{P}_{0.1}\text{O}_{8.7}$ samples and 1300°C for $\text{Na}_5\text{MSi}_4\text{O}_{12}$ samples for 2-3h until no air bubbles were found in the fused material. Weight loss measurements showed no appreciable loss by vaporization. Pouring the molten glass into a stainless steel mold before it solidified allowed preparation of disk specimens of 1.25-1.35 cm diam. The disk-shaped glass was then annealed in the furnace from room temperature to 550°C for $\text{Na}_{3.2}\text{M}_{0.7}\text{Si}_{2.9}\text{P}_{0.1}\text{O}_{8.7}$ and 600°C for $\text{Na}_5\text{MSi}_4\text{O}_{12}$ to relieve the strain in the quenched glass and to prevent cracking. It was held at that temperature for 1-2h, and then cooled to room temperature at the natural cooling rate of the furnace. X-ray powder diffraction of the glasses revealed no crystalline structure. The x-ray patterns were obtained on a Philips diffractometer using $\text{Cu K}\alpha$ radiation. The glass disks were cut to thinner sizes using a diamond saw, and were subsequently polished with emery papers (180, 320, 400, and 600). Finally, they were polished with alumina powder ($3 \mu\text{m}$) on a polishing wheel and then washed with acetone.

For the production of glass-ceramic materials, the same general process was applied except that the molten

glasses were poured into a stainless steel plate instead of a mold and pressed to form thin disk specimens. These were placed on a graphite plate to prevent adhesion to the steel plate at high temperature and heated in a furnace from room temperature to 845°C for $\text{Na}_{3.2}\text{M}_{0.7}\text{Si}_{2.9}\text{P}_{0.1}\text{O}_{8.7}$ (845°C for $M = \text{Sm}$; 890°C for $M = \text{Ho, Er, Eu, Gd}$; and 920°C for $M = \text{Y, Dy}$); and 890°C for $\text{Na}_5\text{MSi}_4\text{O}_{12}$ (890°C for $M = \text{Sm}$, 920°C for $M = \text{Er}$ and Gd , and 1000°C for $M = \text{Y}$) materials. No measurements of glass transition temperatures were made. However, the annealing temperatures listed above were determined empirically for each composition, approaching them by tests taken at successively higher temperatures. Microscopic examination showed a polycrystalline structure, with no evidence of a glassy intercrystalline phase.

The glasses were held at that temperature for 2-3h and then cooled to room temperature overnight. These glass-ceramics were polished with emery papers and alumina powder using the technique previously described. The

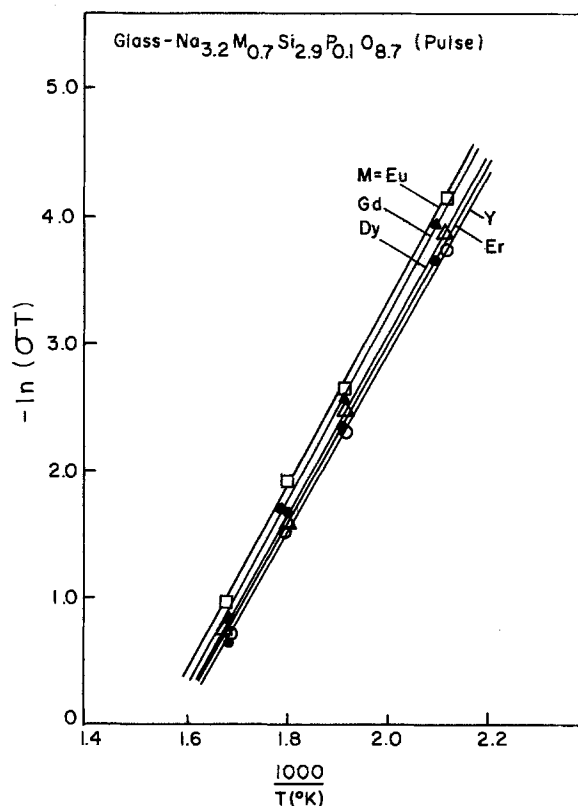


Fig. 1. Arrhenius plots of ionic conductivity for glass $\text{Na}_{3.2}\text{M}_{0.7}\text{Si}_{2.9}\text{P}_{0.1}\text{O}_{8.7}$.

*Electrochemical Society Active Member.

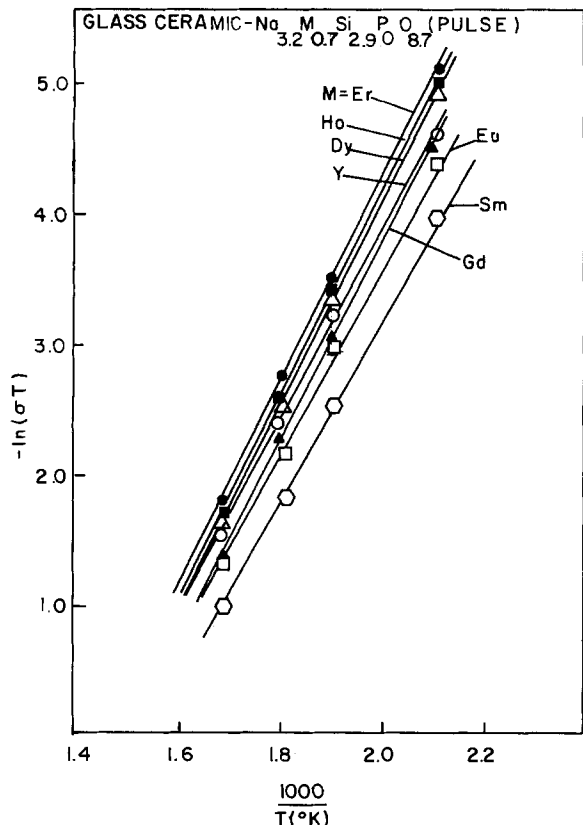


Fig. 2. Arrhenius plots of ionic conductivity for glass-ceramic $\text{Na}_{3.2}\text{M}_{0.7}\text{Si}_{2.9}\text{P}_{0.1}\text{O}_{8.7}$.

x-ray diffraction patterns for the glass-ceramic $\text{Na}_{3.2}\text{M}_{0.7}\text{Si}_{2.9}\text{P}_{0.1}\text{O}_{8.7}$ revealed the same sharp crystalline patterns as the corresponding samples prepared by pressing and sintering. For the glass-ceramic $\text{Na}_3\text{MSi}_4\text{O}_{12}$, the x-ray patterns showed traces of the $\text{Na}_3\text{MSi}_3\text{O}_9$ phase, except for the case of yttrium, which showed only the

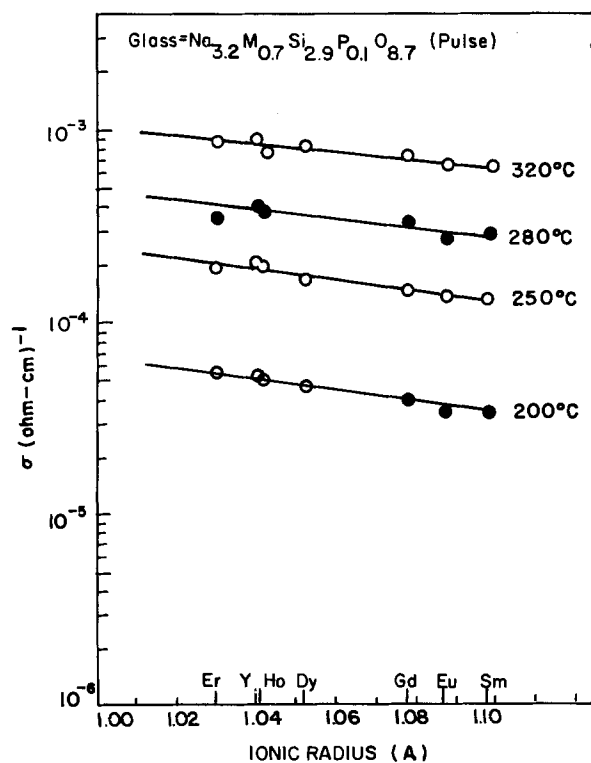


Fig. 3. Variation of ionic conductivity with M^{3+} radius for glass $\text{Na}_{3.2}\text{M}_{0.7}\text{Si}_{2.9}\text{P}_{0.1}\text{O}_{8.7}$.

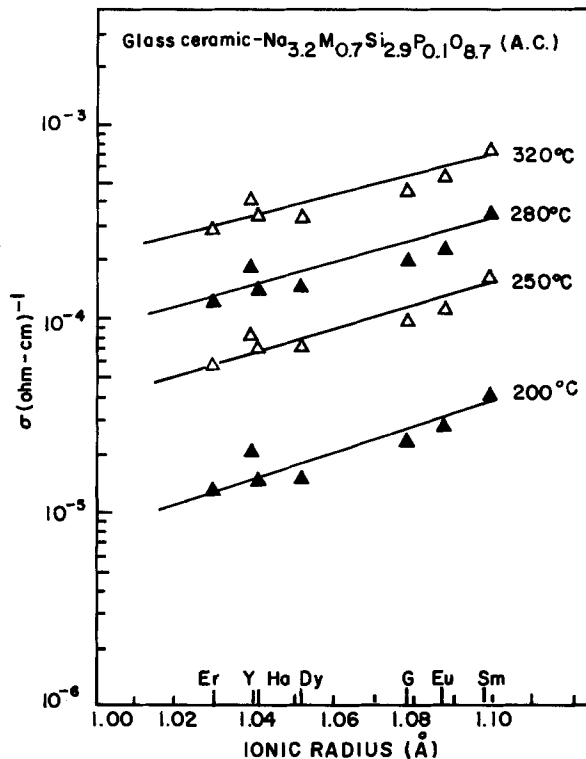


Fig. 4. Variation of ionic conductivity with M^{3+} radius for glass-ceramic $\text{Na}_{3.2}\text{M}_{0.7}\text{Si}_{2.9}\text{P}_{0.1}\text{O}_{8.7}$.

$\text{Na}_5\text{YSi}_4\text{O}_{12}$ phase. No detectable crystalline phases were found by x-ray diffraction of the glassy materials.

The polished disk-shaped samples were coated with chromium ($\sim 400\text{\AA}$) followed by gold to about 2000\AA in thickness by vacuum evaporation, forming irreversible blocking electrodes. Their relative density varied from

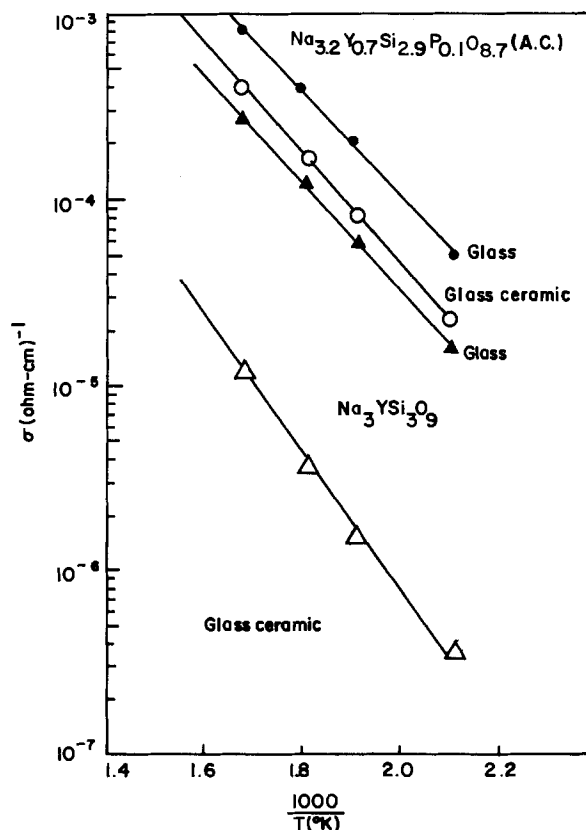


Fig. 5. Ionic conductivity vs. $1/T$ for $\text{Na}_3\text{YSi}_3\text{O}_9$ and $\text{Na}_{3.2}\text{Y}_{0.7}\text{Si}_{2.9}\text{P}_{0.1}\text{O}_{8.7}$.

98-100% in glass-ceramic $\text{Na}_{3.2}\text{M}_{0.7}\text{Si}_{2.9}\text{P}_{0.1}\text{O}_{8.7}$ to 90-99% in the glass-ceramic $\text{Na}_5\text{MSi}_4\text{O}_{12}$. The existence of pores in the glasses was negligible as observed microscopically. Two conductivity measurement techniques, a pulse method and a two-terminal ac method, were used at 200°, 250°, 280°, and 320°C. The pulse method was combined with a dc method which permitted the separation of ionic and electronic contribution to the conductivity. The pulses generated were 80 μs with 200 μs between pulses, but for the glass-ceramic $\text{Na}_5\text{MSi}_4\text{O}_{12}$ a shorter pulse width of 8 μs and a longer pulse repetition time of 1000 μs were chosen to eliminate the polarization effect occurring due to high ionic mobility in those materials. Pulse heights varied from 1 to 8V. For the dc measurement, a constant 0.5V was applied in the circuit, but the electronic contribution was negligible when the known series resistance was 5-10 k Ω . Two-terminal ac measurements were performed at 10^2 - 10^5 Hz and at 1V using a Hewlett-Packard 4274A Multifrequency LCR meter.

Results and Discussion

The glasses produced were transparent. The rigid glasses were devitrified to produce glass-ceramics. A major goal of this study was to compare the ionic conduction of the same composition in glasses and glass-ceramics. Usually, a glass will be a better conductor than a ceramic of the same composition. In this case, the effort was to compare crystalline phases of two materials with their glassy phases, one material being a good superionic conductor and the other being a relatively poor conductor.

$\text{Na}_{3.2}\text{M}_{0.7}\text{Si}_{2.9}\text{P}_{0.1}\text{O}_{8.7}$.—Figures 1 and 2 display the plot of $-\ln(\sigma T)$ vs. $1/T$ for the glass and glass-ceramic samples (curves for M = Ho and Sm are omitted in Fig. 1 due to the close spacing between lines). Tables I and II show the

conductivities and energies of activation in the glass and glass-ceramic phases by the pulse and ac method at four temperatures. The magnitudes of the conductivities were in the order of 10^{-4} ($\Omega\text{-cm}$) $^{-1}$ at 250°C in glass and at 280°C in glass-ceramic phases. Activation energies were in the range of 13.5-15.5 kcal/mol and not very different from those of the corresponding conventional polycrystalline phases (3). The results by the pulse and ac measurement were in good agreement.

Figures 3 and 4 show the dependence of conductivity upon the ionic size of six-coordinate M^{3+} . Most of the radii given here are "crystal radius" radii derived by Shannon (7). As can be seen in Fig. 3, the larger the size of M^{3+} in the glassy state, the lower the conductivity. It might be expected that the sodium ion motion in the amorphous state would be somewhat disturbed by the M^{3+} around the sodium ion and that the degree of disturbance depends on the size of M^{3+} . On the other hand, the conductivity in the glass-ceramic showed a different tendency from the case of glass, as can be seen in Fig. 4. The larger the ionic size of M^{3+} , the greater the conductivity. This result was same as that observed in corresponding conventional ceramic materials (3). When the glass-ceramic has recrystallized, ordering occurs and the position of each type of ion in the structure becomes fixed in the same way. The amount of space for the ionic motion is determined by the size of M^{3+} , which results in different cell volumes. The magnitudes of the conductivities in both glasses and glass-ceramics were comparable. Except when M = Sm, the other rare earth compounds showed higher sodium ion conductivities in glasses than in glass-ceramics.

Comparison of $\text{Na}_3\text{YSi}_3\text{O}_9$ and $\text{Na}_{3.2}\text{Y}_{0.7}\text{Si}_{2.9}\text{P}_{0.1}\text{O}_{8.7}$.—Figure 5 shows the results by ac method. The glassy state

Table I. Ionic conductivity of glass- $\text{Na}_{3.2}\text{M}_{0.7}\text{Si}_{2.9}\text{P}_{0.1}\text{O}_{8.7}$, pulse (ac) methods

M^{III}	Ionic conductivity ($\Omega\text{-cm}$) $^{-1}$				E_a (kcal/mol)
	200°C	250°C	280°C	320°C	
Er	5.40×10^{-5} (5.20×10^{-5})	1.90×10^{-4} (1.88×10^{-4})	3.52×10^{-4} (3.56×10^{-4})	8.61×10^{-4} (7.99×10^{-4})	14.05 ± 0.10 (13.90 ± 0.02)
Y	5.15×10^{-5} (5.06×10^{-5})	2.00×10^{-4} (2.00×10^{-4})	4.00×10^{-4} (3.94×10^{-4})	8.69×10^{-4} (8.23×10^{-4})	14.24 ± 0.02 (14.11 ± 0.02)
Ho	4.94×10^{-5} (5.00×10^{-5})	1.95×10^{-4} (1.88×10^{-4})	3.80×10^{-4} (3.70×10^{-4})	7.50×10^{-4} (7.88×10^{-4})	13.71 ± 0.11 (13.92 ± 0.03)
Dy	4.55×10^{-5} (4.53×10^{-5})	1.70×10^{-4} (1.66×10^{-4})	3.75×10^{-4} (3.31×10^{-4})	8.13×10^{-4} (7.39×10^{-4})	14.36 ± 0.07 (14.06 ± 0.02)
Gd	4.00×10^{-5} (3.90×10^{-5})	1.49×10^{-4} (1.47×10^{-4})	3.30×10^{-4} (3.00×10^{-4})	7.36×10^{-4} (6.50×10^{-4})	14.98 ± 0.06 (14.49 ± 0.04)
Eu	3.35×10^{-5} (3.36×10^{-5})	1.40×10^{-4} (1.30×10^{-4})	2.72×10^{-4} (2.60×10^{-4})	6.41×10^{-4} (5.96×10^{-4})	14.61 ± 0.05 (14.37 ± 0.02)
Sm	3.36×10^{-5} (3.32×10^{-5})	1.36×10^{-4} (1.30×10^{-4})	2.85×10^{-4} (2.65×10^{-4})	6.28×10^{-4} (6.20×10^{-4})	14.80 ± 0.05 (14.76 ± 0.02)

Table II. Ionic conductivity of glass-ceramic $\text{Na}_{3.2}\text{M}_{0.7}\text{Si}_{2.9}\text{P}_{0.1}\text{O}_{8.7}$, pulse (ac) methods

M^{III}	Ionic conductivity ($\Omega\text{-cm}$) $^{-1}$				E_a (kcal/mol)
	200°C	250°C	280°C	320°C	
Er	1.30×10^{-5} (1.32×10^{-5})	5.73×10^{-5} (5.70×10^{-5})	1.20×10^{-4} (1.23×10^{-4})	2.80×10^{-4} (2.80×10^{-4})	15.28 ± 0.03 (15.20 ± 0.05)
Y	2.10×10^{-5} (2.10×10^{-5})	7.80×10^{-5} (8.22×10^{-5})	1.65×10^{-4} (1.81×10^{-4})	3.75×10^{-4} (3.98×10^{-4})	14.54 ± 0.03 (14.96 ± 0.06)
Ho	1.44×10^{-5} (1.58×10^{-5})	6.43×10^{-5} (6.82×10^{-5})	1.39×10^{-4} (1.40×10^{-4})	3.14×10^{-4} (3.25×10^{-4})	15.41 ± 0.07 (15.11 ± 0.04)
Dy	1.54×10^{-5} (1.60×10^{-5})	6.71×10^{-5} (6.93×10^{-5})	1.50×10^{-4} (1.49×10^{-4})	3.32×10^{-4} (3.26×10^{-4})	15.37 ± 0.08 (15.09 ± 0.07)
Gd	2.24×10^{-5} (2.30×10^{-5})	9.19×10^{-5} (9.56×10^{-5})	1.90×10^{-4} (1.91×10^{-4})	4.35×10^{-4} (4.45×10^{-4})	14.94 ± 0.02 (14.83 ± 0.03)
Eu	2.70×10^{-5} (2.80×10^{-5})	1.12×10^{-4} (1.14×10^{-4})	2.20×10^{-4} (2.27×10^{-4})	4.63×10^{-4} (5.10×10^{-4})	14.31 ± 0.08 (14.52 ± 0.02)
Sm	4.11×10^{-5} (4.17×10^{-5})	1.58×10^{-4} (1.66×10^{-4})	3.12×10^{-4} (3.38×10^{-4})	6.50×10^{-4} (7.47×10^{-4})	14.00 ± 0.05 (14.57 ± 0.02)

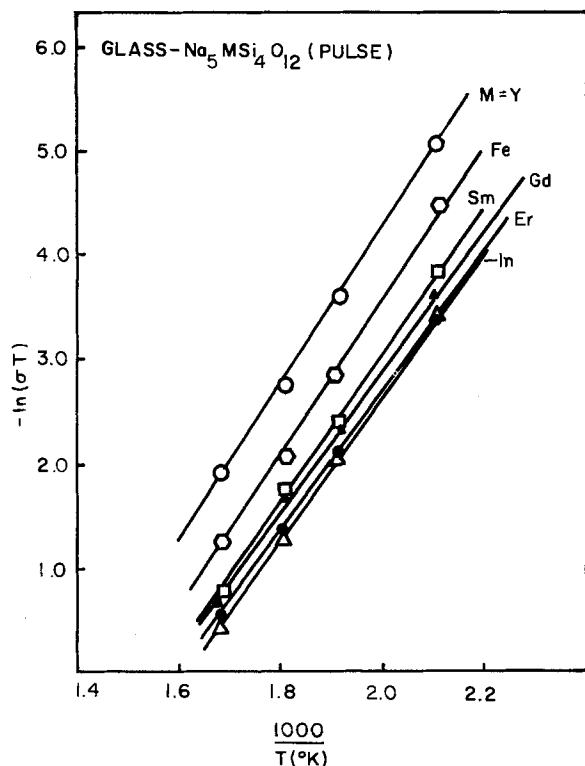


Fig. 6. Arrhenius plots of ionic conductivity for glass $\text{Na}_5\text{MSi}_4\text{O}_{12}$.

has higher conductivities than those of the glass-ceramic state in both materials. Larger conductivity differences between glass and glass-ceramic states were observed in $\text{Na}_3\text{YSi}_3\text{O}_9$. The conductivity of $\text{Na}_{3.2}\text{Y}_{0.7}\text{Si}_{2.9}\text{P}_{0.1}\text{O}_{8.7}$ was always higher than that of $\text{Na}_3\text{YSi}_3\text{O}_9$ in the glassy and glass-ceramic states. The activation energy of glass-ceramic $\text{Na}_3\text{YSi}_3\text{O}_9$ was higher (19.8 kcal/mol) than that of $\text{Na}_{3.2}\text{Y}_{0.7}\text{Si}_{2.9}\text{P}_{0.1}\text{O}_{8.7}$ (14.5 kcal/mol), but in glass the values for both materials were comparable. This is consistent with the view that the conduction mechanism in glass is largely determined by the structure of the glass network and relatively independent of the number of large network modifying ions.

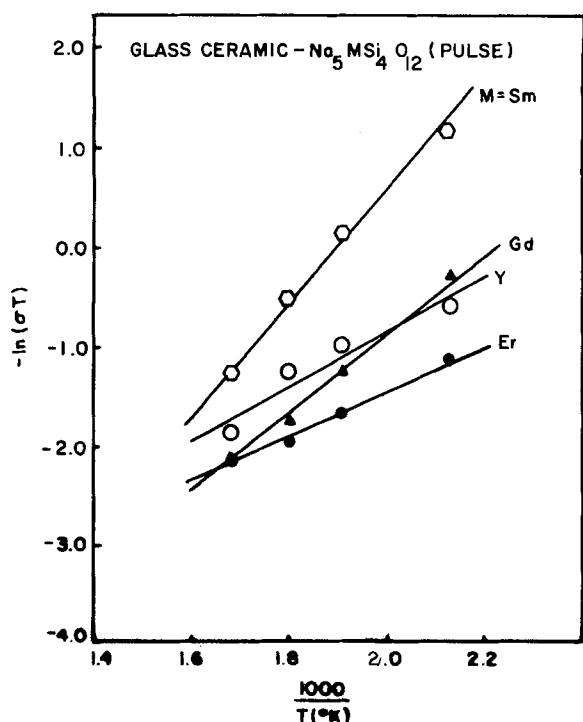


Fig. 7. Arrhenius plots of ionic conductivity for glass-ceramic $\text{Na}_5\text{MSi}_4\text{O}_{12}$.

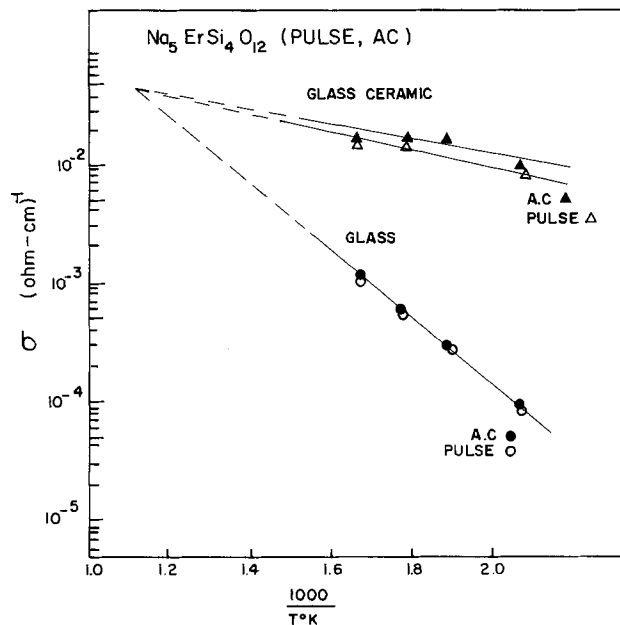


Fig. 8. Ionic conductivity vs. $1/T$ for $\text{Na}_5\text{ErSi}_4\text{O}_{12}$.

$\text{Na}_5\text{MSi}_4\text{O}_{12}$ compounds.—Figures 6 and 7 indicate Arrhenius plots for the glasses and glass-ceramics of composition $\text{Na}_5\text{MSi}_4\text{O}_{12}$. The glasses show similar activation energies. However, in the case of glass-ceramics, the energies of activation were somewhat different depending on the nature of M^{3+} . Activation energies estimated for glass-ceramics with $\text{M} = \text{Er}, \text{Y}$ were lower than those of the corresponding polycrystalline materials prepared by conventional techniques (6) (see Table III). It is thought that this may be an effect of the smaller radii of these ions on the anisotropic nucleation of the $\text{Na}_5\text{MSi}_4\text{O}_{12}$ crystals in the glass. This point should be investigated more systematically.

Figure 8¹ shows the results of measurements on glassy and glass-ceramic $\text{Na}_5\text{ErSi}_4\text{O}_{12}$. The glass-ceramics gave

¹In contrast to earlier Arrhenius plots, Fig. 8 shows the logarithm of the conductivity, rather than its negative, in order to emphasize the higher conductivity and lower activation energy of the glass-ceramic phase.

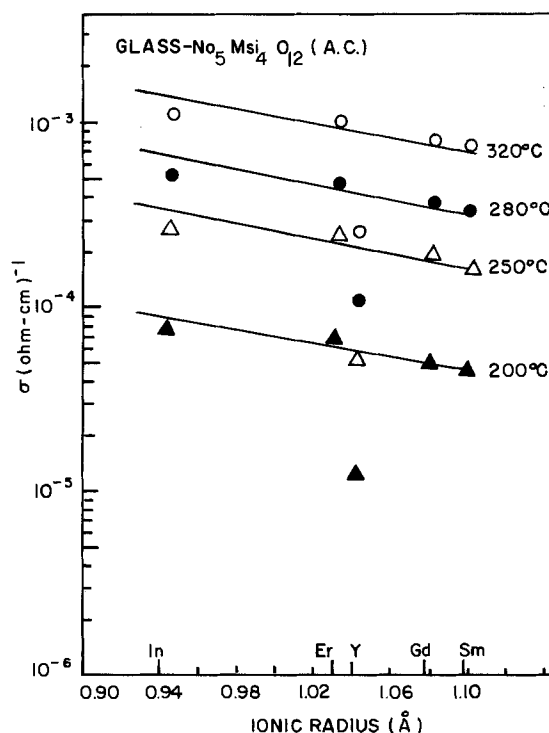


Fig. 9. Ionic conductivity vs. M^{3+} radius for glass $\text{Na}_5\text{MSi}_4\text{O}_{12}$.

Table III. Activation energy (kcal/mol) for $\text{Na}_3\text{MSi}_4\text{O}_{12}$

	M			
	Er	Y	Gd	Sm
Glass-ceramic ^a	4.0	4.4	7.5	11.1
Crystalline	7.5	7.1	6.5	7.3

^a Average of two measurements.

much better conductivities than the glasses, with lower activation energies. This may be explained by the fact that the large open channels (4, 6) in the glass-ceramic structure would not be disturbed as in the case of the amorphous state, and that this may help the motion of mobile sodium ions. It should be noted that all lines cross at a value of $1/T \sim 10^{-3}$, close to zero. The pre-exponential factor is $4 \times 10^{-2} (\Omega\text{-cm})^{-1}$.

The relation between the conductivity and ionic size of M^{3+} in glassy $\text{Na}_3\text{MSi}_4\text{O}_{12}$ is displayed in Fig. 9. The same tendency found in glassy $\text{Na}_{3.2}\text{M}_{0.7}\text{Si}_{2.9}\text{P}_{0.1}\text{O}_{8.7}$ resulted; the larger the ionic size of trivalent metal, the lower the conductivity, with some deviation when $\text{M} = \text{Y}$. The same explanation given for the glasses $\text{Na}_{3.2}\text{M}_{0.7}\text{Si}_{2.9}\text{P}_{0.1}\text{O}_{8.7}$ may be used for this phenomenon in glassy $\text{Na}_3\text{MSi}_4\text{O}_{12}$. The larger ions evidently interfere more with the motion of the mobile sodium ions in the disordered glass.

The result of this comparison of glass and ceramic phase of the same composition appears to confirm the suggestion that compounds with crystal structure having channels for rapid ion migration will have their conductivity decreased in a disordered state, while compounds

whose structure is not conducive to rapid transport and that depend primarily on defect migration for their conductive properties will have higher conductivities in the glassy state, where the defect concentration is increased relative to the crystalline state. This work has also demonstrated the feasibility of forming ceramic solid electrolytes by glass forming techniques without degrading the intrinsic conductivity properties of the crystalline phase, and perhaps even enhancing them.

Acknowledgments

The authors thank Mary Eschwei of the Department of Physics, Polytechnic Institute of New York, for the preparation of electrodes on the samples. This research was supported by the Polytechnic Institute of New York via a teaching assistantship of C. H. Kim. This paper is part of a dissertation submitted to the Polytechnic Institute of New York by C. H. Kim in partial fulfillment of the requirements for the degree of Doctor of Philosophy.

Manuscript submitted Feb. 19, 1985; revised manuscript received July 5, 1985.

REFERENCES

1. R. D. Shannon, B. E. Taylor, T. E. Gier, H.-Y. Chen, and T. Berzins, *Inorg. Chem.*, **17**, 958 (1978).
2. R. D. Shannon, T. E. Gier, C. M. Foris, J. A. Nelen, and D. E. Appleman, *Phys. Chem. Miner.*, **5**, 245 (1980).
3. C. H. Kim, B. Y. Qiu, and E. Banks, *This Journal*, **132**, 1340 (1985).
4. B. A. Maksimov, Y. A. Kharitonov, and N. V. Belov, *Sov. Phys. Dokl.*, **18**, 763 (1974).
5. R. D. Shannon, H.-Y. Chen, and T. Berzins, *Mater. Res. Bull.*, **12**, 969 (1977).
6. R. D. Shannon, *Acta Crystallogr., Sect. A*, **32**, 751 (1976).

Light-Generated Electrode—Rotating Dual Electrodes

B. Miller* and J. M. Rosamilia

AT&T Bell Laboratories, Murray Hill, New Jersey 07974

ABSTRACT

The generation of current for solution redox reactions below the mass-transport limiting current at semiconductor electrodes has been shown to be spatially controllable by light-beam dimension and placement. Thus, a localized electron or hole transfer surface can be created at a semiconductor-redox electrolyte junction by means of a focused laser beam. Such a spot was scanned over a semiconductor disk in a series of experiments within a rotating ring-disk electrode geometry to test the transit and collection properties of the local reaction products. By comparison to related theory for the given geometries, the predicted disk and ring currents as a function of electrode size and location were quantitatively confirmed. These microelectrodes ought to have the enhanced radial transport and reduced resistive losses associated with their micrometallic counterparts, but with flexible manipulation of the geometric parameters. Other results include mapping the generation of selected products over the surface of the semiconductor material and establishing the possibility of detecting kinetic processes by monitoring the collection and transit parameters as a function of radial origin.

It is well appreciated that electrode geometry and mass-transport mode are of primary concern in the various forms of voltammetry (1). Schemes in which a detecting electrode monitors a generating one (e.g., rotating ring-disk electrodes) take further advantage of geometry and mass transport to great effect. Our purpose here is to explore the possibilities inherent in "generator" electrodes whose location and dimensions can be defined by light beams rather than limited to conventional mechanical shaping or masking.

To describe this approach, we refer first to the recent thrust of electrochemical studies to semiconductor photoelectrochemistry. Extensive development has been made of the energy conversion possibilities in the light stimulated formation of electron-hole pairs and their separation to initiate photoanodic (n-type) or photocathodic (p-type) processes. These reactions of minority carriers proceed in the direction forbidden in the dark by the rectifying barrier

associated with the existence of a bandgap in the semiconductor whose edges straddle the levels of the relevant redox potentials. For our present aim, light activation under proper electrode potential control creates an electron-transfer surface defined geometrically by the incident light flux (only restricted diffusive spreading of charge in the solid exists parallel to the interface).

We have applied the above concepts to making spatially controllable electrode surfaces by focusing light spots onto a semiconductor surface through a redox electrolyte. Since laser light can be readily concentrated to form disk profiles of FWHM (full width at half maximum) sizes in the micrometer region, an immediate possibility is the generation of very small electrodes for the ordinarily (dark) current blocking direction. Such electrodes could have the advantages of enhanced radial transport and low relative losses ascribed to such "ultramicro" electrodes (2, 3), could the effective electrode area be restricted to light spot dimensions. Thin rings are another useful pattern readily accessible to light beam definition.

* Electrochemical Society Active Member.

In this initial report, however, we concentrate on the more physically complex arrangement of generator-detector electrode pairs where the generator electrode is that defined by light and semiconductor junction properties. Existing theory allows us in this way to demonstrate our facile control of the features of variable electrode size and location and the useful properties that emerge from this capability. Future work will treat the single electrode possibilities we have alluded to above.

Our experiments employ rotating dual electrodes whose collection characteristics are theoretically related to those of the well-known rotating ring-disk and ring-ring electrodes. With some graphic visualizations and quantitative tests, we demonstrate here that electrodes of defined small dimensions with predictable properties can be produced. The quantitative aspects refer to the collection and transit time features of electrode pairs in the convective diffusion regime.

We first discuss the theoretical and practical considerations necessary for partially illuminated semiconductor electrodes. The collection properties of rotating generator-detector dual electrodes of our geometry are treated by means of dual ring electrode theory (4). The transit time relations for localized generating electrodes to a fixed ring are calculated from the previous treatments for rotating ring-disk electrodes (5, 6).

Semiconductor junctions.—The flux of photons to a given semiconductor area (A) can produce a flow of minority carriers to the interface up to its equivalent current density, i^*/A , should all photons be absorbed and each generate a hole-electron pair. If i^*/A is less than the mass-transfer-limited flux of an appropriate redox species to the interface with current density, i_l/A , then the interfacial potential of the localized redox reaction at cell current $i \equiv i^*$ will be fixed (7, 8).

Consider all the photocurrent generated at only a small area, A (small meaning $A \ll A_D$, where A_D is the area of the entire electrolyte-exposed semiconductor). The photocurrent produced over A is in parallel with the "dark" current of the unilluminated area. In order to detect a process occurring at the illuminated small spot, this dark current must be significantly less than the light-generated value when the electrode is reverse-biased (*i.e.*, held a few tenths of a volt positive of flatband for a n -type material). This situation can be readily achieved for a FWHM spot size $\leq 100 \mu\text{m}$, as we will show, even where A_D/A ratios are of order 2×10^3 , as in our typical electrodes.

The diffusion length of minority carriers in the semiconductor crystals employed in our experiments is $< 10 \mu\text{m}$. Further, the flux of redox species to the illuminated spot to accept the photogenerated carriers is kept from being limiting by the use of sufficient concentrations (0.1M). Diffusive spreading of the carriers outside of spot sizes in the work below can be neglected. Also, the fact that the profile of intensity across the beam is gaussian, rather than rectangular, is not taken into account in the geometric considerations below.

Collection properties of dual electrodes.—The experiments are performed on rotating ring-disk electrodes (semiconductor disks, gold rings). The collection property in the absence of any localization of the reaction within the disk area is expressed by $N = |i_r/i_0|$, where i_r is the ring current (change) produced by disk current, i_0 . The calculation of N from the electrode radii is well known (9). Following Matsuda (10, 11) and Albery and Bruckenstein (9), Filinovskii *et al.* (4) have also derived the collection efficiency, $N_r = |i_{r0}/i_{i0}|$ for a rotating dual ring electrode, where subscripts o and i refer to outer and inner ring, respectively.

Consider all the product generated at current i arises from a spot on the disk for detection at a limiting current level (collection) at a fixed ring. The collection efficiency, $N_s = |i_r/i|$, for this case will approximate that of a dual ring system with radii r_0 , $r_1 = r_0 + \Delta$, r_2 , and r_3 ; r_0 is the distance from the inner edge of the spot to the center

of the disk, Δ is the diameter of the spot, and r_2 and r_3 are the inner and outer radii of the fixed ring, respectively.

For the dual ring system, N_r is given by (4)

$$N_r = \left(\frac{r_3^3 - r_2^3}{r_1^3 - r_0^3} \right)^{2/3} G \left(\frac{r_1^3 - r_0^3}{r_2^3 - r_1^3} \right) + G \left(\frac{r_3^3 - r_2^3}{r_2^3 - r_1^3} \right) - \left(\frac{r_3^3 - r_0^3}{r_1^3 - r_0^3} \right)^{2/3} G \left[\left(\frac{r_1^3 - r_0^3}{r_2^3 - r_1^3} \right) \left(\frac{r_3^3 - r_2^3}{r_3^3 - r_0^3} \right) \right] \quad [1]$$

where

$$G(Z) = \frac{\sqrt{3}}{4\pi} \ln \frac{1+Z}{(1+Z^{1/3})^3} + \frac{3}{2\pi} \arctan \left(\frac{2Z^{1/3}-1}{\sqrt{3}} \right) + \frac{1}{4} \quad [2]$$

The collection efficiencies, N_s , for the current generated at a spot were calculated from Eq. [1] and [2], using the radii defined above.

Transit time.—Another mode of defining location of electrode reaction under these hydrodynamic conditions is through the interval from generation to detection of the reaction at the spot. The transit time, τ , from initiation of a light-activated pulse of current somewhere on the disk to its detection at the inner edge (r_2) of a ring is the quantity of interest. Bruckenstein *et al.* (5, 6) found this transit time in seconds from the generation of a step of current at a disk of radius r_1 to its detection at the ring to be given by

$$w\tau = (43.1) \left(\frac{\nu}{D} \right)^{1/3} (\log r_2/r_1)^{2/3} \quad [3]$$

w is speed in revolutions per minute and ν/D is the Schmidt number, Sc , the ratio of the kinematic viscosity of the solution to the diffusion coefficient of the electroactive species. Prater and Bard (12, 13), with slightly different assumptions about particle trajectories, found a numerical factor of 34.2 rather than 43.1.

This relation should approximate the transit time associated with the transport of photogenerated species from a small spot of diameter Δ . The variation of τ with r_1 in this case can be tested against Eq. [3] by applying light pulses and measuring the transit time oscilloscopically.

Experimental

Acetonitrile (CH_3CN) from Burdick and Jackson was not further purified. Ferrocene $\text{Fe}(\text{Cp})_2$ was obtained from Aldrich, and tetrabutylammonium fluoroborate (TBAFB) from Eastman Kodak Company. Redox electrolyte solutions of 0.1M $\text{Fe}(\text{Cp})_2/1.0\text{M}$ TBAFB/ CH_3CN (14) were stored over activated Linde 3Å molecular sieves. Ambarone 345 polymeric reductive resin (Rohm & Haas) was used to reduce the level of $\text{Fe}(\text{Cp})_2^+$ that might be present in the stock solution.

Rotating ring-disk electrodes (RRDE's) consisted of either n -InP or n -GaAs disks and Au rings. The geometric values of r_1 , r_2 , and r_3 , respectively, were 2.35, 2.47, and 3.11 mm for the n -InP RRDE and 2.37, 2.45, and 3.11 mm for n -GaAs. Collection efficiencies for the n -InP and n -GaAs electrodes are 0.384 and 0.398, respectively. Rotation was provided by a Pine Instruments MSR rotator/controller. The n -InP and n -GaAs electrodes were etched for 3s in concentrated HCl or 1:1 $\text{H}_2\text{SO}_4/\text{H}_2\text{O}_2$, respectively. The etchant procedure for each was repeated until a constant light limited current profile, *i.e.*, current independent of position, was established across the semiconductor disk for a scanned beam. The disk and ring currents were measured using a Pine Instruments Model RDE3 bipotentiostat using graphite rods as reference and counterelectrodes. Potentials are thus reported *vs.* solution redox level.

A block diagram of the instrumentation employed for rastering the RRDE is shown in Fig. 1. A He-Ne laser beam is deflected 90° using a 45° mirror mount and focused to a spot size of about 100 μm on the electrode surface using a 10× microscope objective. A Servo-Tek motor in an assembly equipped with silver-graphite electrode contacts and the RRDE are mounted on an X-Y

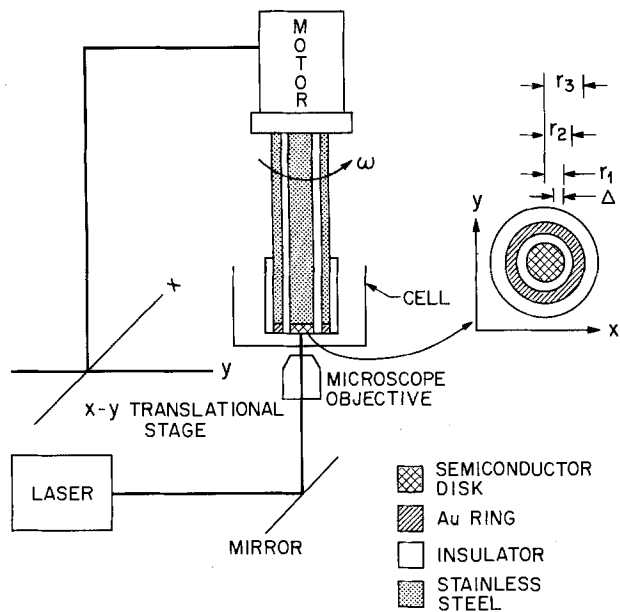


Fig. 1. Schematic of the laser-RRDE scanning system with fixed optics and translated electrode. Insert of electrode face shows fixed disk and ring radii and programmable spot diameter, Δ .

translational stage driven by a Newport Corporation 855C programmable controller system. This arrangement allows the laser beam and an optical flat-bottom cell to be fixed in space while the electrode itself is displaced in X-Y coordinates (the plane of the disk).

Two-dimensional (line) scans were monitored by both a Y1-Y2-t recorder and a microcomputer. The microcomputer provided digital data for analysis of N . The electrode was scanned in the X direction at a fixed Y location at a rate of 0.06 mm/s. Three-dimensional and contour plots were obtained with the same mapping procedures as in Ref. (15), substituting the electrode for the photovoltaic cell.

The only physical modification needed in the above apparatus to measure transit times was adding a controllable shutter in the path of the laser beam to provide a 50 ms pulse of light. A step pulse of disk current is correspondingly generated, followed by a rise in ring current as the product is detected. The i_D and i_R vs. time relations were measured on an oscilloscope, and τ values were determined from these traces (5, 6). The laser beam was moved across the electrode in 0.2 mm steps.

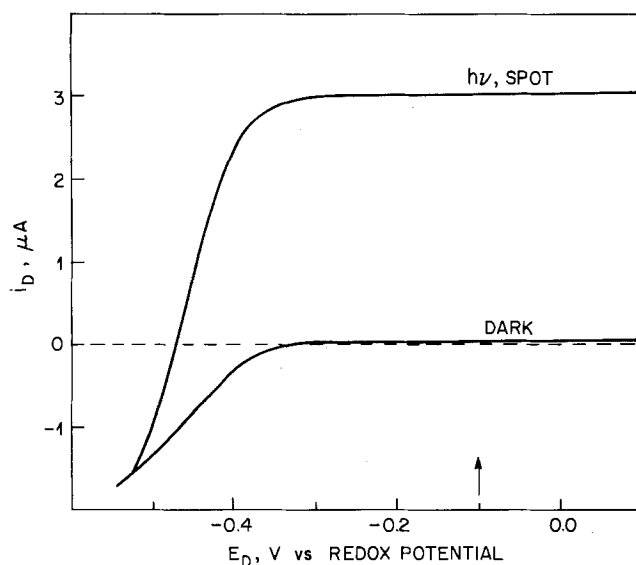


Fig. 2. i_D and E_D curves in dark and with $\sim 100 \mu\text{m}$ laser spot, at a rotating n-InP disk electrode in $0.1M \text{Fe}(\text{Cp})_2/1.0M \text{TBAFB}/\text{CH}_3\text{CN}$. $\omega = 1600 \text{ rpm}$. Scan rate = 7.5 mV/s .

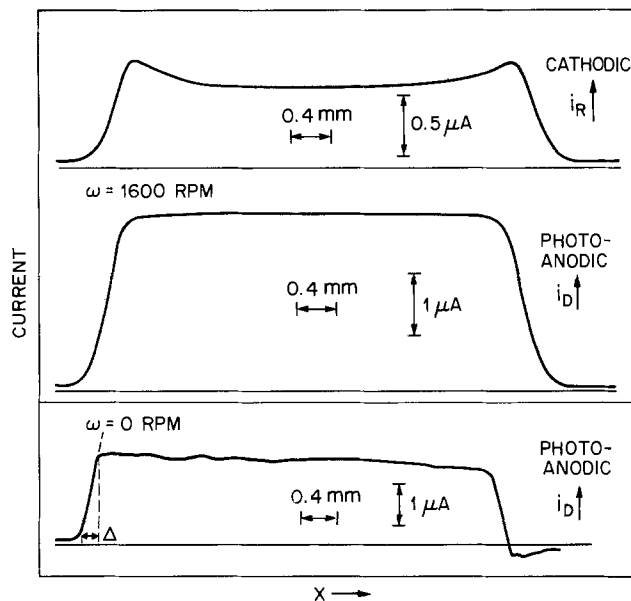


Fig. 3. Two dimension line scans of i_D (photoanodic) and i_R (cathodic) for $\omega = 1600 \text{ rpm}$, and i_D (photoanodic) for $\omega = 0 \text{ rpm}$ as a function of light spot position, x , across a diameter of the n-InP electrode. E_D fixed at $-0.1V$ vs. redox potential. E_R fixed at $-0.2V$ [limiting current region for $\text{Fe}(\text{Cp})_2^+$ reduction].

The laser beam spot size was determined by monitoring a Metrologic Radiometric Si detector in conjunction with a $10 \mu\text{m}$ pinhole attached directly to an X-Y translational stage in front of the detector head. The pinhole is positioned at the focus corresponding to electrode experiments and is scanned across the beam at 0.006 mm/s . The power output as a function of distance traveled is recorded and the corresponding peak width at 50% (FWHM) and 25% of peak height is measured.

Results and Discussion

The i - E curves for the n-InP disk, first in the dark and then with the addition of a laser beam focused on area A (anywhere on its surface area A_D) are shown in Fig. 2. The solution used throughout is $0.1M \text{Fe}(\text{Cp})_2/1.0M \text{TBAFB}/\text{CH}_3\text{CN}$. Although the A_D/A ratio is at least 2×10^3 , the reverse (residual) current at the dark crystal is still very small compared to the photoanodic component generated over the small area. At these ferrocene concentrations, the results are independent of rotation speed. The current density, i/A , in the illuminated spot is about 0.4 mA/cm^2 .

If the disk electrode potential is held in the range indicated by the arrow on the abscissa of Fig. 2 while the electrode face is scanned across the beam, virtually all current is attributable to the light source. Such a scanning experiment is shown in Fig. 3. When the electrode was ro-

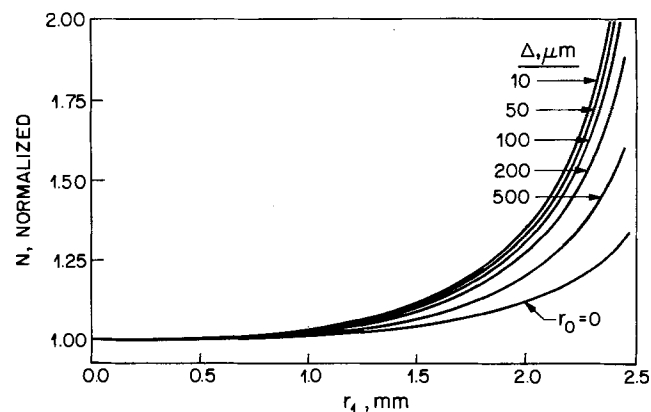


Fig. 4. Theoretical curve of normalized collection efficiency vs. r_1 for several values of Δ and for $r_0 = 0$. Ring diameters r_0 and $r_0 + \Delta = r_1$.

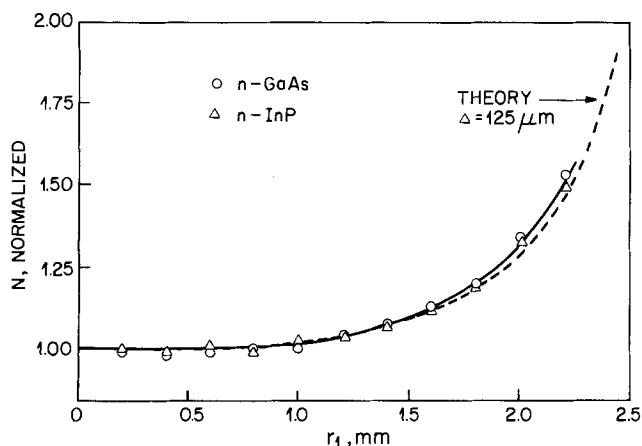


Fig. 5. Experimental curve of normalized collection efficiency vs. r_1 for both n-GaAs (circles) and n-InP (triangles) disk-Au ring electrodes. Values are obtained from i_R vs. X scans as shown in Fig. 2. Theoretical relationship of N vs. r_1 for $\Delta = 125 \mu\text{m}$ (Δ from Fig. 2) is the dashed line.

tated at 1600 rpm, the ring current for the reduction of ferrocenium species was simultaneously monitored. The i_D profile is constant across the disk once the entire spot is on the semiconductor surface. The ring current trace shows the anticipated higher collection for product generated nearer the disk edge where it has less chance of escape before detection. A scan across a stationary disk is also shown under the same beam conditions. The profiles of disk current are essentially flat across the bulk of the disk, independent of rotation rate, under these local light-limited current conditions.

The profiles of rotated and stationary electrode disk currents differ materially only at the edge. The stationary electrode, for any scanned diameter, shows a sharper rise to its constant value since there is no eccentricity attributable to rotation and circular imperfections to broaden this distance. The scan traverse from edge (initial rise) to flat current, as indicated in Fig. 3, is a measure of Δ , the spot diameter. A more direct measure of spot diameter has been made by pinhole profiling under the same focus conditions. The FWHM was $\sim 70 \mu\text{m}$, and the width at 25% peak was $\sim 90 \mu\text{m}$. These values are consistent with the measurements of Δ from the stationary disk current profiles.

A set of theoretical curves calculated from Eq. [1] and [2] for spot collection is shown in Fig. 4. They are plotted normalized to the limiting collection of 0.315 for a small disk at the center of rotation where it becomes independent of spot size. This limiting collection efficiency was obtained using $r_2 = 2.45$ and $r_3 = 3.11$ mm. The plot for $r_0 = 0$ is identical with the set of calculated ring-disk collection efficiencies (9). As the spot becomes smaller, collection for spots near the disk edge becomes relatively larger (r_2 and r_3 fixed). The sensitivity to Δ can be used as a test of the localization of current as defined by $r_1 = r_0 + \Delta$.

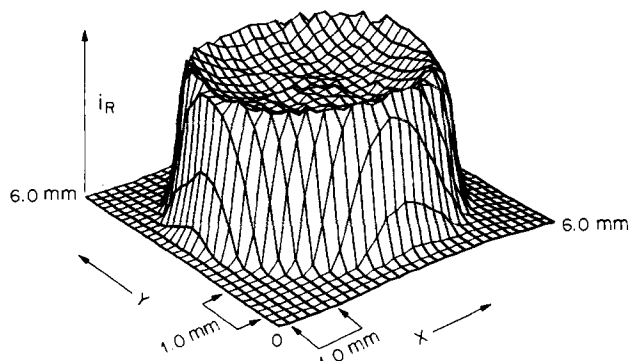


Fig. 6. Three-dimensional surface of i_R as a function of spot location on disk. Experimental conditions as in Fig. 3.

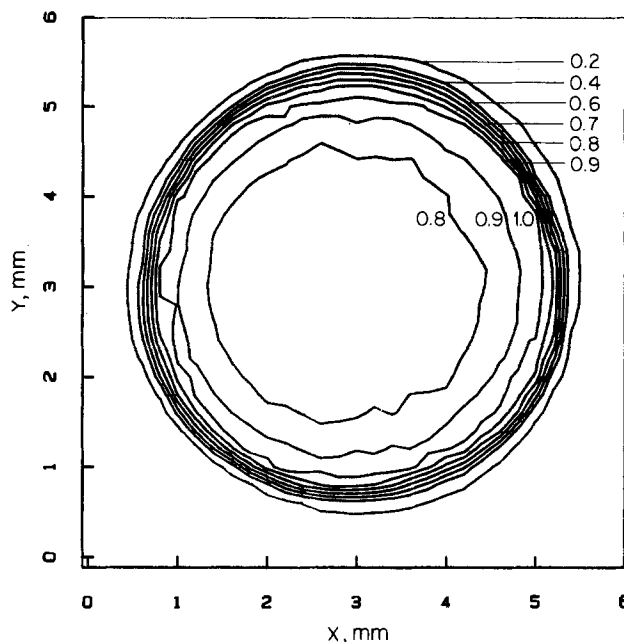


Fig. 7. i_R contour plot projected on disk surface. The maximum ring current is normalized to 1.0. Contour values of 0.2, 0.4, 0.6, 0.7, 0.8, 0.9, and 1.0 are indicated.

In Fig. 5 are plotted the experimental determinations of the function in Fig. 4 from the analysis of data obtained, as in Fig. 3, by a disk scan across a diameter. The theoretical curve for the Δ value obtained from the edge effect for a stationary electrode scan is also plotted in Fig. 5. There is good agreement of predicted and experimental curves. The sensitivity of normalized collection efficiency to the value of Δ is, however, largest at the edge where the difficulty of having perfect geometry and no eccentricity is highest.

The results of the two-dimensional experiments in Fig. 3 and 5 can be expanded to a three-dimensional representation of an X-Y collection (i_R) scan over the full disk area, as shown in Fig. 6. The corresponding i_D map is a flat topped mesa; it is not shown. In principle, the entire disk area is observed through rotation during a single radial scan. Rotationally synchronized data acquisition could give a point-by-point i_R map, rather than the radially averaged one of Fig. 6. The damping imposed by the spiral trajectory and the finite transit time precludes effective use of this fact.

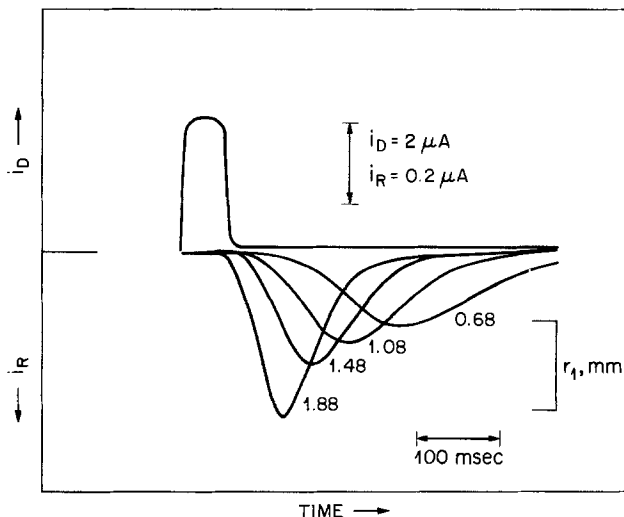


Fig. 8. i_D and i_R vs. time at several values of r_1 for the n-InP disk having $r_2 = 2.47$ mm. $\omega = 1600$ rpm. The laser spot originates from a 50 ms pulse.

Besides the visualization of the collection efficiency as a surface over the moving radial origin of disk current, the X-Y scans allow more facile determination of what is a true radial direction scan. For example, curves shaped as in Fig. 3 can be obtained even though one may be missing the center of the disk in the scan. A radial scan, as opposed to that of any other chord, will, of course, give the largest abscissa in a Fig. 3 experiment. A contour display of the three-dimensional experiment, normalized to unity at the high (near-edge) values, is given in Fig. 7.

This plot offers the information of a two-dimensional scan averaged over the whole disk electrode. The drawing of radii across the disk contours allows one to make Fig. 5 plots with a fuller estimate of the range of reproducibility. In the contours of Fig. 7, the ring residual current has been linearly corrected for any changes in each X-direction scan noted before and after crossing the active disk surface. Step increments are treated as Y-direction.

The transit time experiments were accomplished by producing an i step with a pulse of light controlled by the shutter drive, then monitoring both i_D and i_R on a dual-beam storage oscilloscope. If sufficient time is allowed for the i_R response to return to the residual (dark disk) value, repetitive pulses produce successively coincident i and i_R traces when appropriately triggered by either the shutter pulse or i .

A sequence of i_R traces produced by the same i timing, but for different radial positions at constant rotation speed, is shown in Fig. 8. The i_R traces are extrapolated by a tangent line on the steeply rising part of the peak to a time intercept on the extrapolated residual line. Maximum transit time is obtained at the disk center.

A similar set of traces was obtained for a point near a $r_1/2$ position as a function of rotation speed. These two experiments in which $\omega\tau$ is obtained as a function of r (constant ω) and ω (constant r_1) are plotted in Fig. 9. The quantity $(\log r_2/r_1)^{2/3}$ arising from Eq. [3] is plotted as the radial abscissa (lower), as is ω (upper).

Using the tangent method, the $\omega\tau$ vs. $(\log r_2/r_1)^{2/3}$ line is straight but extrapolates through a finite $\omega\tau$. Since this extrapolation should be zero (point of origin and detection coinciding), the intercept value of $\omega\tau$ was used as a correction in the $\omega\tau$ as $f(\omega)$ plot. When corrected in this manner, $\omega\tau$ is a constant at all ω , as predicted and found for fixed geometry ring-disk electrodes (5, 6). However, the way τ is chosen can be reflected in the value of the $\omega\tau$ product (12).

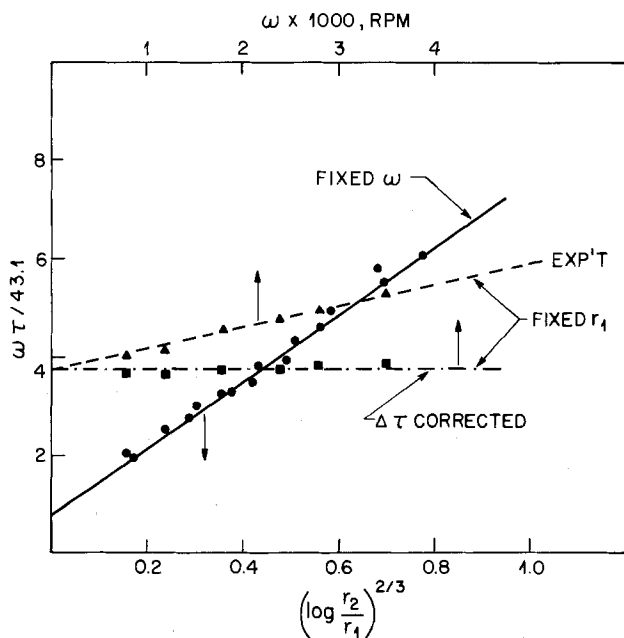


Fig. 9. Plot of $\omega\tau/43.1$ vs. $(\log r_2/r_1)^{2/3}$ at fixed $\omega = 1600$ rpm (solid line) and ω at fixed $(\log r_2/r_1)^{2/3} = 0.569$ (dashed line). Plot of the corrected values $\omega(\tau - \Delta\tau)/43.1$ vs. ω is shown by the dash-dotted line where $\Delta\tau$ is obtained from the Y-intercept of the solid line.

Table I. Summary of $Sc^{1/3}$ values

	$Sc^{1/3}$	$\bar{Sc}^{1/3}$	$Sc^{1/3}$	$\bar{Sc}^{1/3}$
A	$\omega\tau$ vs. $(\log r_2/r_1)^{2/3}$	6.51 ^a	8.20 ^b	
		5.42 ^a	6.5	6.83 ^b
		7.54 ^a		9.50 ^b
B	$\omega\tau$, fixed r_2/r_1	7.03 ^a	8.86 ^b	8.6
		6.60 ^a	8.32 ^b	
C	Δi_L at $p = 0.05/\Delta i_L$ at $p = 0.5$	8.32		
D	i_L vs. $\omega^{1/2}$	8.81		

^a Numerical factor of 43.1 from Ref. (5) was used in Eq. [3].

^b Numerical factor of 34.2 from Ref. (12) was used in Eq. [3].

A summary of $Sc^{1/3}$ values obtained from the slope of three sets of $\omega\tau$ vs. $(\log r_2/r_1)^{2/3}$ experiments and from two sets of constant $\omega\tau$ product at fixed r_2/r_1 is given in Table IA and IB. An Sc value for this solution was further estimated independently in two ways. A Levich plot of limiting current vs. $\omega^{1/2}$ was determined for a known ferrocene concentration, and D was calculated using the kinematic viscosity of 1.0M TBAFB/CH₃CN measured with a Cannon-Fenske viscometer. The frequency response of hydrodynamic modulation of the limiting current was measured for two ratios, p , of modulation frequency/rotational frequency. This two-point method (16, 17) gives a value for Sc independent of concentration. The data are summarized in Fig. 10.

The modulation current ratio for $p = 0.05$ and 0.5 of 0.341 corresponds to a $Sc^{1/3}$ as given in Table IC. $D = 1.2 \times 10^{-5}$ cm²-s⁻¹ calculated from the Levich equation (i_L vs. $\omega^{1/2}$ plots) using $\nu = 8.3 \times 10^{-3}$ cm²-s⁻¹ gives the $Sc^{1/3}$ value in Table ID, which ought to be the most reliable. The consistency of the $Sc^{1/3}$ measurements by all four procedures is adequate within the experimental limits of the $\omega\tau$ repeatability and assumptions for the numerical constant.

Conclusions

The generation of current at locally selected areas of semiconductor (disk) electrodes has been shown to be spatially controllable by light-beam placement and dimension. The quantitative confirmation comes from two properties (transit time and collection) of rotating ring-disk systems for which theoretical relations may be adapted to the local generation problem. By both of the methods the current stimulated by the light beam can be shown to originate in the area fixed by a diameter corresponding to that determined through beam profile and disk edge crossing effects. The properties of the laser

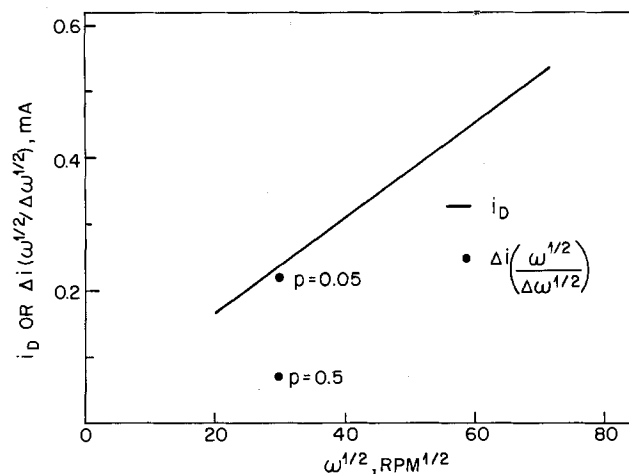


Fig. 10. Plot of i_D vs. $\omega^{1/2}$ for $1.6 \times 10^{-3}M$ Fe(Cp)₂ in 1.0M TBAFB/CH₃CN at a Au disk electrode held at 0.6V vs. SCE. The points represent the Δi response for $p = 0.05$ and 0.5 employing $\omega^{1/2} = 30$ rpm^{1/2} and $\Delta\omega^{1/2} = 2$ rpm^{1/2}.

scanned beam have been extended to a three-dimensional representation of the collection characteristic of the entire surface.

Two general points are intended by these demonstrations. First, directly from the experiments discussed, the flexible localized control of reaction generation in dual electrode systems leads to new schemes of kinetic measurement where a geometric, as well as a hydrodynamic (rotation speed), factor can be a primary variable. An example of this would be in chemical follow-up reactions (EC mechanisms) where the collection as a $f(r)$ would be altered. Another in this category is the use of the r variable to increase sensitivity in the detection of adsorption via the transit-time experiment (6). The illustrated mapping of a surface with respect to collection of ring current from that area is a geometric extension that adds the discrimination of selective product detection to the mapping of photocurrent (18) or differential power efficiency (15) over surfaces of semiconductors. Thus, corrosion current or redox transfer efficiency can be determined over a locally heterogeneous disk, averaged in this case over a radial position.

The second emphasis relates to producing small electrodes of selected shapes in regions of controlled mass transport. Such properties are currently under study. The use here in the context of exposed semiconductor surfaces is limited because of the competitive photocorrosion reactions, through another means to study that competition. The use of buried junctions and "noble" overlayers to augment controlled passivation must overcome, by appropriate design, the lateral spreading of carriers in the overlayer. Such electrodes, if successfully constructed, could allow localized reaction at a choice of surfaces not restricted to semiconductors while retaining the advantageous geometric control properties that cannot now be obtained with metals.

Manuscript submitted March 28, 1985, revised manuscript received May 3, 1985. This was Paper 445 presented at the Las Vegas, Nevada, Meeting of the Society, Oct. 13-18, 1985.

AT&T Bell Laboratories assisted in meeting the publication costs of this article.

REFERENCES

1. A. J. Bard and L. R. Faulkner, "Electrochemical Methods," John Wiley and Sons, New York (1980).
2. A. M. Bond, M. Fleischmann, and J. Robinson, *J. Electroanal. Chem.*, **172**, 11 (1984).
3. R. M. Wightman, *Anal. Chem.*, **53**, 1125A (1981).
4. V. Yu. Filinovskii, I. V. Kadija, B. Z. Nicolich, and M. B. Nakic, *J. Electroanal. Chem.*, **54**, 39 (1974).
5. S. Bruckenstein and G. A. Feldman, *ibid.*, **9**, 395 (1965).
6. S. Bruckenstein and D. T. Napp, *J. Am. Chem. Soc.*, **90**, 6303 (1968).
7. S. Bruckenstein and B. Miller, *This Journal*, **129**, 2029 (1982).
8. S. Bruckenstein, J. M. Rosamilia, and B. Miller, *J. Phys. Chem.*, **89**, 677 (1985).
9. W. J. Albery and S. Bruckenstein, *Trans. Faraday Soc.*, **62**, 1920 (1966).
10. H. Matsuda, *J. Electroanal. Chem.*, **15**, 109 (1967); *ibid.*, **16**, 153 (1968).
11. H. Matsuda, *ibid.*, **35**, 77 (1972).
12. K. B. Prater and A. J. Bard, *This Journal*, **117**, 207 (1970).
13. A. J. Bard and L. R. Faulkner, "Electrochemical Methods," p. 307, John Wiley and Sons, New York (1980).
14. C. M. Gronet and N. S. Lewis, *Appl. Phys. Lett.*, **43**, 115 (1983).
15. J. M. Rosamilia and B. Miller, *Solar Cells*, To be published.
16. K. Tokuda, S. Bruckenstein, and B. Miller, *This Journal*, **122**, 1316 (1975).
17. J. M. Rosamilia and B. Miller, *Anal. Chem.*, **56**, 2410 (1984).
18. T. E. Furtak, D. C. Canfield, and B. A. Parkinson, *J. Appl. Phys.*, **51**, 6018 (1980).

Extension of DC Transient Techniques to the Nonlinear Current Density-Overpotential Range and the Limitations of Linearized Approximations

Z. Nagy* and R. H. Land

Argonne National Laboratory, Chemical Technology Division, Argonne, Illinois 60439

G. K. Leaf and M. Minkoff

Argonne National Laboratory, Mathematics and Computer Science Division, Argonne, Illinois 60439

ABSTRACT

The applicability of the dc relaxation techniques for the measurement of kinetics of fast electrode reactions has been limited generally to the linear current density-overpotential (i - η) range by the mathematical difficulties in obtaining a closed-form solution of the differential equations describing the system, confining the measurements to the vicinity of the equilibrium potential. Evaluation of the experimental data with numerical curve-fitting procedures offers a possibility for the extension of these techniques into the nonlinear i - η range. The feasibility of such extension was demonstrated by a curve-fitting data-evaluation method with a nonlinear multidimensional least squares minimization package coupled to a software package designed to solve systems of nonlinear partial differential equations. The main advantage of this approach is that measurements can be made at high enough overpotentials to avoid signal-to-noise ratio problems without introducing linearization errors in the data evaluation. The error of the linearized i - η relation is not negligible under many experimental conditions. A quantitative evaluation of this error has been made as a function of three dimensionless parameters: $\alpha\nu/n$, $C_0D_0^{1/2}/C_R D_R^{1/2}$, and $\eta nF/RT$. The error in the exchange current density determination, with the assumption of linear i - η relation, will be at least as large as the error of the linearized equation.

The applicability of the dc relaxation techniques for the measurement of kinetics of fast electrode reactions has been limited generally to the linear current density-overpotential range by the mathematical difficulties in

*Electrochemical Society Active Member.

obtaining a closed-form solution of the differential equations describing the electrode system (1). It would be highly desirable to extend the applicability of the relaxation techniques to the nonlinear range because the linearization is valid only within a few millivolts polariza-

tion around the equilibrium potential; this limit is very restrictive for both practical and theoretical purposes. Measurements at low overpotentials are often difficult because of signal-to-noise ratio problems. Furthermore, the assumption that the kinetics and mechanisms of the electrode reaction are independent of potential is often incorrect; therefore, extrapolation from the linear range to higher overpotentials is generally questionable. Evaluation of the experimental data with numerical curve-fitting procedures offers a possibility for using these techniques in the nonlinear current density-overpotential range. It has been shown previously (2-6) that numerical curve-fitting, using nonlinear, multidimensional least squares calculation, is the best data evaluation method for all dc relaxation techniques in the linear range. The curve-fitting program does not require a closed form solution of the diffusional equations: all it requires is a user-supplied subroutine to provide a set of numerical values for the relaxation curve, calculable with parameters supplied by the curve-fitting program, and a set of numerical values for the derivatives of the relaxation curve with respect to all parameters to be determined (the jacobian matrix). These numerical values were calculated with the help of the closed form solutions of the diffusional equations for the linear range (2-6), but the numerical values for the relaxation curve could be equally well calculated, in principle, using a numerical differential equation software package, and the jacobian matrix can be calculated by a forward difference approximation. This approach is reported in the present communication.

The linearized current density-overpotential relation, which, in the past, has been generally used for the calculation of kinetic data from the results of the relaxation techniques, places a restriction on the experiments because the linearized relation is valid only for sufficiently low overpotentials. The meaning of "sufficiently low" is still a matter of some controversy, which is yet another subject of this communication. Generally, 5 mV has been considered a limiting value, although it was shown some time ago (7, 8) that the value of the overpotential alone is not sufficient to set the limit of applicability of the linearization because it will be influenced also by the transfer coefficients of the reaction and the concentrations of the reactants and products. The linearized and full current density-overpotential relations themselves can be directly compared. Kooijman *et al.* (8) used such a comparison and concluded that, under some conditions, overpotentials much less than 5 mV are needed to limit the error of the linearization to less than 1%. On the other hand, the diffusional differential equations must be solved numerically to compare the relaxation curves calculated with the linearized and full relations. Such calculations were carried out for the coulostatic (9) and the galvanostatic single-pulse (10) relaxation techniques, and it was concluded, in contradiction to Kooijman's results, that the error of the linearization was smaller than previously assumed; *e.g.*, an error of less than 2% was found at overpotentials up to 25 mV for the coulostatic technique. However, in the latter calculations, the transfer coefficients were assumed to be 0.5, and this may limit the validity of the conclusion since there is a controversy about the effect of the transfer coefficients (8, 11-13). The effect of the concentrations of the reactants and products is also controversial, especially in the extreme case where the concentration of one species remains constant during the course of the reaction as is the case in metal deposition-dissolution reactions (11-13). Our numerical calculation methods were also useful for determining the error and, consequently, the limitations of the data evaluations based on the linearized current density-overpotential relation and for resolving the above controversies.

Theory of DC Relaxation Techniques

Only a brief outline of the theory of the relaxation techniques will be given here, mainly to define the terms and to enumerate all basic assumptions; detailed reviews are available (1, 14, 15). Experimentally, the techniques in-

volve the application of a perturbing current (or potential) pulse and the resulting potential (or current) relaxation is observed. A redox reaction, $O + ne = R$, or a metal deposition-dissolution reaction, $M^{+n} + ne = M$, is under investigation, with, in the simplest case, only three processes to be considered. These processes are: (i) the reaction at the electrode surface, (ii) the diffusion of the reactant and product to and from the surface, and (iii) the charging of the double-layer capacitance. The reaction can take place in any number of elementary electrochemical and chemical steps; it is assumed that one of these steps is rate determining and that none of the reaction intermediates is lost by diffusion into the bulk solution. The rate-determining step can occur ν times for each occurrence of the overall reaction, where ν is the stoichiometric number of the reaction mechanism. The uniform flux of the reactant to the electrode surface, being equal to the flux of the product away from the electrode, is assumed to be completely supplied by semi-infinite, linear diffusion in the presence of excess supporting electrolyte. This flux is equivalent to the faradaic current density. The double-layer capacitance is assumed to be independent of potential and concentrations within the limits of the experiment. Adsorption and double-layer effects are neglected.

The relaxation process is described by a set of partial differential equations for diffusion, coupled with an ordinary differential equation for the overpotential. The diffusion equations are

$$\frac{\partial C_j^s(x, t)}{\partial t} = D_j \frac{\partial^2 C_j^s(x, t)}{\partial x^2} \quad [1]$$

with the following initial and boundary conditions

$$C_j^s = C_j \text{ for } t = 0, x \geq 0 \quad [2]$$

$$C_j^s \rightarrow C_j \text{ for } t > 0, x \rightarrow \infty \quad [3]$$

$$\left[\frac{\partial C_j^s(x, t)}{\partial x} \right]_{x=0} = \pm \frac{i_f(t)}{nFD_j} \quad [4]$$

where j can stand for O or R, and in Eq. [4] the positive sign corresponds to R and the negative to O. The last condition expresses the equivalence of the faradaic current density and the diffusion flux. The faradaic current density in Eq. [4] is related to the overpotential and the concentrations of the species at the electrode surface¹

$$i_f = i_o \left\{ \left[\frac{(C_R^s)_{x=0}}{C_R} \right]^{1/\nu} \exp \left(\frac{\alpha_a F}{RT} \eta \right) - \left[\frac{(C_O^s)_{x=0}}{C_O} \right]^{1/\nu} \exp \left(- \frac{\alpha_c F}{RT} \eta \right) \right\} \quad [5]$$

where the overpotential is the sum of the charge transfer (activation) and mass-transport (concentration) overpotential terms

$$\eta = \eta_{ct} + \eta_{mt} \quad [6]$$

and

$$\alpha_a + \alpha_c = n/\nu \quad [7]$$

At low overpotentials, Eq. [5] can be approximated by the linearized expression²

$$\eta' = \frac{\nu RT i_f}{nF i_o} + \frac{RT}{nF} \left[\frac{(C_O^s)_{x=0}}{C_O} - \frac{(C_R^s)_{x=0}}{C_R} \right] \quad [8]$$

The ordinary differential equation for the overpotential is

¹Equation [5] can be obtained by adjusting the generalized, multistep Butler-Volmer equation (16, 17) for surface concentration changes by a method equivalent to that used for single-step reactions (18). It is to be emphasized that the transfer coefficients are not equal to, although are functions of, the symmetry factor of a single-step reaction.

²Equation [8] is obtained from Eq. [5] by assuming that $\alpha F/RT \eta \ll 1$; and, consequently, that $(C_j^s)_{x=0}/C_j \approx 1$ (see Eq. [17]).

$$i(t) = i_c(t) + c \frac{d\eta(t)}{dt} \quad [9]$$

with an initial condition of $\eta(0) = 0$, indicating that the total current is the sum of the faradaic and capacitive currents. The overpotential in Eq. [9] is related to the measured potential by Eq. [10], indicating that the measured potential includes the overpotential and the uncompensated potential drop in the solution between the working and reference electrodes

$$E(t) = \eta(t) + i(t)R_s \quad [10]$$

For the galvanostatic and coulostatic (current impulse) techniques, $i(t)$ is controlled and $E(t)$ is measured and vice versa for the voltage and potential step techniques. The kinetic and mechanistic parameters to be calculated from the experimental results are: the exchange current density (i_0), the transfer coefficients (α_c , α_a), and the stoichiometric number (ν). Additionally, there are five more parameters which may have to be determined from the relaxation experiment if their values are not available from independent measurements. These are the double-layer capacitance (c), the diffusion coefficients (D_0 , D_R), the uncompensated solution resistance (R_s), and the total number of electrons exchanged during the overall reaction (n). The following parameters are usually known: the perturbing signal (i or E), the concentrations (C_0 , C_R), and the temperature (T).

A closed-form solution of the differential equations can be obtained using the linearization shown in Eq. [8], and this is the basis for the evaluation of the experimental data taken at potentials near the equilibrium value. Equation [5] is the basis for the data evaluation procedure proposed in this work, making it possible to carry out the experimental measurement at any potential.

Computational Procedures

Curve-fitting data evaluation methods.—Two methods were tested for the data evaluation in the nonlinear range. Both methods are similar in that they involve the numerical solution of Eq. [1] and [9] and the use of numerical optimization techniques to determine the kinetic and mechanistic parameters described above.

Numerical simulation of electrochemical kinetics-diffusion models such as Eq. [1] and [9] have previously been dealt with by finite difference approximation; see, for example, Feldberg (19, 20), Sandifer and Buck (21), and Britz (22). More recently, in an effort to achieve greater accuracy, spline approximation techniques have been combined with collocation methods by Pons (23) and with Galerkin's method by Franceschetti and Macdonald (24). Our approach also uses a spline-based Galerkin procedure as implemented in the software package DISPL2 (25). We, however, combine this numerical simulation with optimization techniques to extend the curve-fitting evaluation of the dc transient techniques to the nonlinear current density-overpotential ranges, for which range closed-form solutions do not exist for the diffusional differential equations.

In the first method, the curve-fitting was accomplished with subroutine LMDIF from the MINPACK-1 package developed at Argonne National Laboratory (26) for nonlinear multidimensional least squares minimization using a modified Levenberg-Marquardt algorithm (27). The same program package was used previously for data evaluation in the linear range (2-6). The subroutine LMDIF requires the user to supply only the function values from which the jacobian matrix is calculated by a forward difference approximation. This means, however, that for an N parameter fitting, the function value has to be calculated $N + 1$ times for each new guess of the parameters. The function values were calculated by solving Fick's diffusion equations numerically using the software package DISPL2 developed at Argonne National Laboratory (25). This package is designed to solve systems of nonlinear partial differential equations in one- and two-dimensional geometries. The numerical approximation is

based on the use of Galerkin's procedure combined with the use of a B-spline basis set in order to reduce the system of partial differential equations to a system of ordinary differential equations. The latter system is solved by means of an ordinary differential equation software package for stiff systems based on the use of multistep time differencing with local error control (28).

The problem was treated as a system of two partial differential equations for C_R^s and C_0^s coupled with an ordinary differential equation for η . The equations were integrated to the full pulse length, t_r , with output at selected intermediate times. The half-axis, $x \geq 0$, was truncated at $x_\infty = 5\sqrt{Dt_r}$, where D was the mean value for D_R and D_0 . The spatial domain was subdivided by a nonuniform spatial mesh, and the B-spline basis used corresponded to piecewise quadratic polynomials with continuous first derivatives to approximate the spatial distribution of $C_j^s(x, t)$. The time integration error was controlled by the local error control in the multistep stiff ordinary differential equation solver, and the spatial discretization was controlled by the number of points and their distribution in the spatial grid.

The second method also used the DISPL2 software package to solve Fick's diffusion equations. However, instead of employing a nonlinear least squares approach, use was made of a general constrained optimization approach implemented in subroutine VMCON1 developed at Argonne National Laboratory (29). To understand the strengths and weaknesses of these two approaches to the data evaluation problem, the differences in the optimization problems, methods, and techniques for generation of jacobian matrices are summarized below.

1. The first method specifically treats the unconstrained nonlinear least squares problem. That is, for m observations y_i and a model $f(X, t_i)$ where X is an N -component vector of parameters, we wish to select X so that

$$\sum_{i=1}^m [f(X, t_i) - y_i]^2 \quad [11]$$

is minimized. The second method solves the problem: minimize $f(X)$, subject to

$$\begin{aligned} c_j(X) &\leq 0; j = 1, \dots, k \\ c_j(X) &= 0; j = k + 1, \dots, l \end{aligned} \quad [12]$$

That is, a general function (not specifically of the form used in Eq. [11]) is minimized subject to constraints which may be inequality or equality constraints. Thus, the second approach allows for constraints on the problem but treats a more general optimization function.

2. The first method uses a modification of the Levenberg-Marquardt algorithm to solve the problem. This algorithm exploits the structure of the nonlinear least squares problem and uses a combination of the steepest descent and the Gauss-Newton methods. The steepest descent method is globally reliable but slow. The Gauss-Newton method is locally reliable and fast. The Levenberg-Marquardt algorithm adaptively combines these two methods to obtain a fast, reliable algorithm. The second method uses an iterative quadratic programming technique developed by Powell (30). This algorithm generates quadratic programming subproblems, *i.e.*, quadratic functions minimized subject to linear equality and inequality constraints. These subproblems can be solved without requiring function evaluations. This second method is essentially a constrained Newton technique and converges quite rapidly. When compared to other constrained optimization methods, the iterative quadratic programming technique requires relatively few function evaluations (31). This is important since the DISPL2 computation is quite time consuming. Nevertheless, this second method does not exploit the structure of the nonlinear least squares function and thus is not likely to be as efficient as the first method. In particular, the first method uses the structure of the sum-of-squares function,

Eq. [11], to obtain approximations of the second derivative of the function in terms of first derivative approximations (the Gauss-Newton method). The second method treats Eq. [11] as a general function and, therefore, cannot provide second derivative estimates as easily.

3. The first method uses a derivative-free version of the Levenberg-Marquardt algorithm. As in most optimization techniques, both methods require the derivatives of the optimization function with respect to the variables. In the first method, this reduces to the jacobian which is obtained by forward-difference approximation. These differences, however, require N additional evaluations of the partial differential equation system. In the second method an attempt was made to obtain the derivatives without resorting to finite differencing. These derivatives can often be obtained in terms of additional ordinary and partial differential equations. As an example, if α_c is a parameter in the curve-fit, the necessary information for the derivatives can be assembled if we can obtain an ordinary differential equation for $d\eta/d\alpha_c$. Such an equation can be derived by differentiating Eq. [9] with respect to α_c and using the initial condition $(d\eta/d\alpha_c)_{t=0} = 0$. In deriving the additional equations needed for the jacobian, some terms were neglected for the sake of practicality. In particular, in deriving the equation for $d\eta/d\alpha_c$ there is an indirect dependence on $\partial C_i^*(x, t)/\partial \alpha_c$. If we seek to calculate these terms in the numerical simulation, two additional partial differential equations are generated. The computational cost of calculating the jacobian via this combined system would be as great as using finite-difference methods for the jacobian (and the computer storage cost would be much greater as well). We, therefore, compromise by neglecting the dependency which leads to the additional partial differential equations. Thus, while we avoid the additional N evaluations of the finite-difference approach, the analytic derivatives obtained have an inherent error.

To summarize, there are two areas of difference between the methods: the numerical method and the jacobian estimate. The first method treats the specific form of Eq. [11] but cannot handle constraints such as [12]. When constraints are necessary (as, for example, to control the range of parameters used for the simulation) other methods should be used. The second method handles constraints but treats a more general minimization function. Therefore, the numerical approach of the second method does not take advantage of the mathematical form of Eq. [11]. Ideally, the first method with the capability of handling constraints should be used. The second area of difference between the methods deals with the jacobian calculation. The first method uses finite-difference estimates to build up the jacobian. The second method adds a differential equation for $d\eta/d\alpha_c$ to estimate the derivatives directly. Either of these jacobian calculation methods could be used with either of the optimization methods. The second approach to estimate the jacobian can lead to considerable savings in computation time when compared with the finite-difference approach. However, it can also lead to larger simulation problems because of the use of approximations to the derivatives.

Evaluation of the curve-fitting methods.—Primarily because of the long computational times required, and also because of the large number of variables involved, it was not practical to carry out a full error analysis and to develop applicability digrams and compare to those calculated for the linear cases (2-6). The main purpose of this work was to show that it is feasible to extend the relaxation techniques to the nonlinear current density-overpotential range. This could be done by a small number of calculations using representative conditions. For similar reasons, the calculations were carried out only for the galvanostatic single-pulse technique.³ Extension to other

³This technique involves a simple current step perturbation of the electrode. To allow for the finite risetime of the pulse generator, the current was taken to rise linearly from zero to the desired value. The correction for this risetime was found to be important for the linear approximation case (3, 32).

techniques is expected to be straightforward. The calculation procedure was similar to that used in the error analysis for the linear range (2-6). It consisted essentially of three steps.

1. Synthetic data were generated, with the use of DISPL2, for a set of parameter values. The relaxation curves were defined by 25 points, equally spaced in time. The pulse length was selected to include the time period containing the most kinetic information (3).⁴ Then, to simulate practical conditions, random measurement errors were introduced by rounding off the calculated potential values, creating data sets with either ± 5 or ± 50 μV errors (3).

2. This set of points was then treated as experimental data, and a curve-fitting calculation was carried out. The number of parameters to be determined was varied from two to seven; the other parameters were assumed to be known from independent measurements. Measurement errors were introduced for the known parameters to simulate practical conditions by using 0.1 or 1.0% different values in the data evaluation than were used in the data generation. The stoichiometric number was treated differently than other parameters because it is an integer parameter, a restriction that the curve-fitting subroutine was not equipped to handle. It was treated as a known parameter but a series of calculations was carried out with different values assigned to it in search of the best fit. The total number of electrons exchanged, another integer parameter, was always considered known. Were this not the case, it could be treated similarly to the stoichiometric number. The transfer coefficients are interrelated through Eq. [7], and only one of them needs to be determined. All parameters were restricted to positive values by a square root transformation, that is, the parameters calculated by the curve-fitting were the square roots of the parameters to be determined. The curve-fitting routines need a starting guess for each parameter to be determined; ten times the actual value of the parameter was usually used, except for the transfer coefficient, which was started from 0.5. Previous work on curve fitting in the linear current density-overpotential range has shown that good results are obtained with guesses not more than one order of magnitude off the true values, except at the very edges of the applicability fields (2-6).

3. Finally, the calculated parameter values were compared to the known values (used in the data generation) and a percent error was calculated. These errors and the standard deviations of the calculated results (33) were used to evaluate the curve-fitting methods.

Determination of linearization errors.—The following procedure was used to evaluate the errors and the limitations of the linearized approximation. Relaxation curves were calculated using both the full current density-overpotential relation, Eq. [5], and the linearized relation, Eq. [8], and the maximum deviation between the two relaxation curves was determined. The differential equations were solved using the DISPL2 software package (25). Closed-form solutions were available for the linearized cases (2-5). Calculations were carried out for all dc relaxation techniques, the galvanostatic (single and double pulse) techniques, the coulometric (current impulse relaxation) technique, and the potential and voltage step techniques. A large variety of conditions (exchange current density, transfer coefficients, concentrations, diffusion coefficients, overpotential, etc.) were used to cover the whole field of applicability of each technique (2-6). Selection of all experimental conditions (*e.g.*, pulse lengths, pulse amplitudes) were also made in accordance with procedures described in the above-mentioned references. Two extreme cases were also considered: the charge transfer-controlled system ($\eta_{ct} \gg \eta_{mt}$) and the mass-

⁴The selection of the proper pulse length for an unknown system by the use of a statistical sensitivity analysis of the parameters determined by the curve-fitting data evaluation was discussed earlier for the linear current density-overpotential range (33). A similar technique can also be used for the nonlinear range.

transport-controlled system ($\eta_{ct} \ll \eta_{mt}$). All calculations were carried out for both anodic and cathodic polarizations and also for the case of a cell containing two identical working electrodes, one being polarized anodically and the other cathodically; in the latter case, η stands for the total overvoltage of the cell.

An additional series of calculations was carried out to determine the deviations between the full and linearized current density-overpotential relations themselves, rather than those of the relaxation curves, for the extreme cases of pure charge transfer- or mass-transport-controlled systems. For $\eta_{ct} \gg \eta_{mt}$, the Butler-Volmer equation can be written in the form of

$$i_t = i_0 \{ \exp(P_1 P_2) - \exp[-(1 - P_1) P_2] \} \quad [13]$$

where $P_1 = \alpha_a \nu / n = (1 - \alpha_c \nu / n)$ and $P_2 = (nF/\nu RT) \eta_{ct}$. Equation [13] can be linearized to

$$i_t = (nF i_0 / \nu RT) \eta'_{ct} \quad [14]$$

if the exponents in Eq. [13] are small. Since every term in the expansion of Eq. [13] is a function only of P_1 and P_2 , the deviation between η_{ct} and η'_{ct} will obviously be a function of two dimensionless parameters: $\alpha \nu / n$ and $nF \eta_{ct} / \nu RT$, where α can stand for either α_a or α_c .

The deviations between Eq. [13] and [14] were calculated as a function of these dimensionless parameters in two ways. At constant current density, the error can be represented as

$$\epsilon_\eta = \frac{100(\eta' - \eta)}{\eta} \quad [15]$$

Alternatively, one can keep the overpotential constant and calculate the current densities needed to produce the same overpotential with the full and linearized equations; an error, ϵ_i , can be defined analogously to Eq. [15]. The two errors are interrelated by

$$\epsilon_i = - \frac{100\epsilon_\eta}{100 + \epsilon_\eta} \quad [16]$$

which can be demonstrated by a geometric consideration of the deviations between the linear and the full equations.

For the case of $\eta_{ct} \ll \eta_{mt}$, the Nernst equation expresses the overpotential as a function of surface concentrations, which, in turn, are dependent on the faradaic current density and time

$$\eta_{mt} = \frac{RT}{nF} \ln \left[\frac{(C_0^s)_{x=0}}{C_0} \cdot \frac{C_R}{(C_R^s)_{x=0}} \right] \quad [17]$$

This can be linearized to

$$\eta'_{mt} = \frac{RT}{nF} \left[\frac{(C_0^s)_{x=0}}{C_0} - \frac{(C_R^s)_{x=0}}{C_R} \right] \quad [18]$$

if $(C_j^s)_{x=0}/C_j \approx 1$. Equations [17] and [18] are not in convenient form because the surface concentrations of the species are generally not known. The mass-transport overpotential can, however, be expressed in terms of measurable parameters by using the relation

$$(C_0^s)_{x=0} D_0^{1/2} + (C_R^s)_{x=0} D_R^{1/2} = C_0 D_0^{1/2} + C_R D_R^{1/2} \quad [19]$$

which can be shown to be true for all relaxation techniques considered here (34). This leads to

$$\frac{(C_1^s)_{x=0}}{C_1} = \frac{1 + \frac{C_2 D_2^{1/2}}{C_1 D_1^{1/2}}}{1 + \frac{(C_2^s)_{x=0} D_2^{1/2}}{(C_1^s)_{x=0} D_1^{1/2}}} \quad [20]$$

where the indexes 1 and 2 can stand for O and R. The fraction in the denominator of the right-hand side of Eq. [20] can be expressed, with the help of Eq. [17], as

$$\frac{(C_0^s)_{x=0} D_0^{1/2}}{(C_R^s)_{x=0} D_R^{1/2}} = \frac{C_0 D_0^{1/2}}{C_R D_R^{1/2}} \exp \left(\frac{nF}{RT} \eta_{mt} \right) \quad [21]$$

Therefore, η_{mt} and η'_{mt} , and the deviation between them, can be expressed in terms of the dimensionless parameters $P_3 = C_0 D_0^{1/2} / C_R D_R^{1/2}$ and $P_4 = nF \eta_{mt} / RT$, both of which are known for a given experiment

$$\eta_{mt} = \frac{RT}{nF} \ln \left[\frac{1 + P_3 \exp(P_4)}{P_3 + \exp(-P_4)} \right] \quad [22]$$

and

$$\eta'_{mt} = \frac{RT}{nF} \left[\frac{1 + P_3}{P_3 + \exp(-P_4)} - \frac{1 + P_3}{1 + P_3 \exp(P_4)} \right] \quad [23]$$

In conclusion, the error of the linearization can be expressed in terms of dimensionless parameters for both the charge transfer- and the mass-transport-controlled cases.

The deviations between Eq. [17] and [18] were calculated in two ways: (i) as a function of $(C_j^s)_{x=0}/C_j$ and (ii) as a function of $C_0 D_0^{1/2} / C_R D_R^{1/2}$ and $nF \eta_{mt} / RT$. The calculations were carried out at constant current (or, more precisely, using the same surface concentrations for both equations), and ϵ_η was obtained. Equation [16] is also valid for the mass-transport-controlled case.

Error of exchange current density measurements due to linearization.—The following procedure was used to calculate the error in the exchange current density determination caused by measurement in the nonlinear i - η range coupled with data evaluation assuming a linear i - η relation. Relaxation curves were generated using both the linear and the nonlinear $i = \eta$ relations and the maximum deviation between the two curves was determined (see above). The curve generated with the nonlinear relation was used as input data for a curve-fitting data evaluation assuming a linear i - η relation (2-5), and the calculated exchange current density was compared to the exchange current density used in the generation of the synthetic data. To ensure that the results reflect only the error caused by the linearization of the i - η relation, no other measurement errors (current density and potential) were introduced into these data sets. The calculations were carried out for a series of overpotential values keeping all other parameters constant.

Results and Discussion

Curve-fitting in the nonlinear i - η range.—Initial calculations have demonstrated that both calculation methods described above give satisfactory results, but we found that the second method requires significantly more computational effort than the Levenberg-Marquardt method (2.5 times more in one case). It is likely that the ability of the Levenberg-Marquardt method to exploit the structure of the nonlinear least squares problem, its use of a hybrid of steepest descent and Gauss-Newton techniques, and the approximating aspects of the analytic jacobian combine to cause the second approach to be relatively slow. We decided to abandon the constrained method for the remainder of this study. (A constrained Levenberg-Marquardt approach would provide the positive features of both methods and may be a subject of further work.) All the results discussed below were obtained with the Levenberg-Marquardt method.

Satisfactory results were obtained for a variety of electrode reaction parameter values and measurement conditions with the number of parameters determined varying from two to seven. Two typical examples are presented in detail in Tables I-III. Table I shows the conditions, and Tables II and III show the results of the calculations. The results indicate that the parameters can be determined with a few percent error (the maximum error was 6.4% in these examples). The synthetic data were calculated with a stoichiometric number of one, while the evaluations were carried out for $\nu = 1, 2$, and 3. To select the correct ν value, one has to select the best fit based (26, 33) on (i)

Table I. System parameters used in the examples

Parameter	Used in	
	Three-parameter fit	Five-parameter fit
Exchange current density ($A\text{-cm}^{-2}$)	6.42×10^{-1}	6.42
Concentration, O and R ($\text{mol}\text{-cm}^{-3}$)	4.21×10^{-5}	4.21×10^{-5}
Diffusion coefficient, O ($\text{cm}^2\text{-s}^{-1}$)	1.00×10^{-5}	1.00×10^{-5}
Diffusion coefficient, R ($\text{cm}^2\text{-s}^{-1}$)	1.00×10^{-5}	2.00×10^{-5}
Double-layer capacitance ($F\text{-cm}^{-2}$)	2.50×10^{-5}	2.50×10^{-5}
Uncompensated solution resistance ($\Omega\text{-cm}^2$)	0.00	0.00
Cathodic transfer coefficient	3.00×10^{-1}	3.00×10^{-1}
Temperature (K)	2.98×10^2	2.98×10^2
Risetime (s)	1.00×10^{-7}	1.00×10^{-7}
Pulse length (s)	1.00×10^{-5}	5.00×10^{-6}
Pulse current density ($A\text{-cm}^{-2}$)	1.44	8.26
Overpotential at the end of the pulse (V)	5.60×10^{-2}	1.73×10^{-1}
Stoichiometric number	1	1
Number of electrons	1	1

Table II. Example of a three-parameter fit

Calculated with a stoichiometric number	Parameter	Percent error of determination	Percent standard deviation	Root mean square residual
1	i_o	1.9	0.15	2.44×10^{-5}
	α_c	2.1	0.24	
	c	0.8	0.08	
2	i_o	136	0.59	1.09×10^{-4}
	α_c	-64	2.67	
	c	-4	0.35	
3	i_o	269	0.73	1.40×10^{-4}
	α_c	-85	8.29	
	c	-5	0.45	

Table III. Example of a five-parameter fit

Calculated with a stoichiometric number	Parameter	Percent error of determination	Percent standard deviation	Root mean square residual
1	i_o	1.4	0.22	2.46×10^{-5}
	α_c	-0.9	0.38	
	c	1.1	0.21	
	D_o	-6.4	0.99	
	D_R	-0.1	0.07	
2	i_o	227	0.33	1.51×10^{-4}
	α_c	95	0.16	
	c	-20	0.90	
	D_o	5,200	12.12	
	D_R	164	0.80	
3	i_o	375	0.37	2.01×10^{-4}
	α_c	55	0.24	
	c	-19	1.21	
	D_o	11,017	12.91	
	D_R	88	0.72	

the standard deviation of the parameters (expressed in the tables as a percentage of the calculated parameter value) and (ii) the root mean square residuals (which expresses the overall quality of the fit). In both cases, $\nu = 1$ gives the best fit. These results demonstrate the feasibility of using a combination of a numerical differential equation solver and a least squares minimization software package for the data evaluation of relaxation techniques in the nonlinear i - η range. Numerous calculations were carried out, but, because of the long computational times involved, a complete error analysis could not be carried out. Therefore, an applicability field cannot be defined for this method. Five runs were made under conditions

near the diffusion-limited edge of the applicability field calculated for the linearized case (3), and it was concluded that the limitations of the nonlinearized and linearized cases are similar. All calculations were carried out for the galvanostatic single-pulse case; no difficulties are expected in the extension of this data-evaluation method to the other dc relaxation techniques.

The present method of data evaluation, which is not limited to the linear i - η range, has several advantages over the previously used curve-fitting data evaluations. (i) Signal-to-noise problems can be minimized by the use of large overpotentials. This is especially important for electrode reaction systems where, in the linear range, one would use very small overpotentials because the error of the linearized equations is large, e.g., when the $\alpha\nu/n$ is far from 0.5 or $C_oD_o^{1/2}/C_R D_R^{1/2}$ is far from unity (see discussion below). (ii) Because of freedom from overpotential limitations, the possible potential dependence of the transfer coefficients can be easily detected by making measurements at a number of current densities. (iii) The values of the exchange current density and the stoichiometric number can both be individually determined, while in the linear range only i_o/ν is determinable. (iv) The transfer coefficients can be directly obtained from the data, while in the linear range they are determinable only from the concentration dependence of the exchange current density. (v) The diffusion coefficients are also directly determinable, while in the linear range only the diffusion parameter ($1/C_oD_o^{1/2} + 1/C_R D_R^{1/2}$) is determinable.

The disadvantage of the method is that it requires considerable computational time, about one to two orders of magnitude more than similar calculations using the linearized approximations. All calculations were carried out with a Digital Equipment Corporation VAX 11/780 machine; with this computer, a curve-fit in the linearized approximation takes a matter of minutes, while it can take several hours for the nonlinear range. (Equivalent execution times on an IBM mainframe computer are about one order of magnitude shorter.)

Linearization errors.—A comparison of the errors caused by the linearization of the current density-overpotential relation for the dc relaxation techniques revealed that, under comparable experimental conditions, all techniques suffered the same error. Therefore, in the following discussion the individual techniques will not be treated separately and all results apply equally to the single- and double-pulse galvanostatic, the coulometric, and the potential and voltage step techniques.⁵ It was also found that the errors calculated by simply comparing the full and linearized current density-overpotential relations were essentially the same as those calculated from the comparison of the relaxation curves. The deviation between the relaxation curves calculated with the full and linearized i - η relations is not constant but changes with time because some conditions (e.g., surface concentrations) change with time. Therefore, what can be stated is that if the linearized i - η relation is in error by $x\%$, as compared to the full i - η relation, for a given system and at y mV overpotential, then for that system the relaxation curve calculated for any relaxation technique using the linearized i - η relation will have a maximum deviation of $x\%$ from an analogous relaxation curve calculated with the full i - η relation (as long as the overpotential never exceeds y mV). It seems prudent, therefore, to use this maximum error to characterize the overall error. These results are presented below in terms of ϵ_r . As expected, the error was found to be a function not only of the overpotential but also of every parameter needed to characterize the electrode reaction system. Because of this, the results of the error analysis can be simply presented only for certain extreme conditions, specifically, for the case of charge transfer control ($\eta_{ct} \gg \eta_{mt}$), and mass-transport control ($\eta_{ct} \ll \eta_{mt}$). For these cases, the results of the er-

⁵However, the use of two working electrodes is not readily applicable for the potential and voltage step techniques because the potential control of the individual electrodes will be lost.

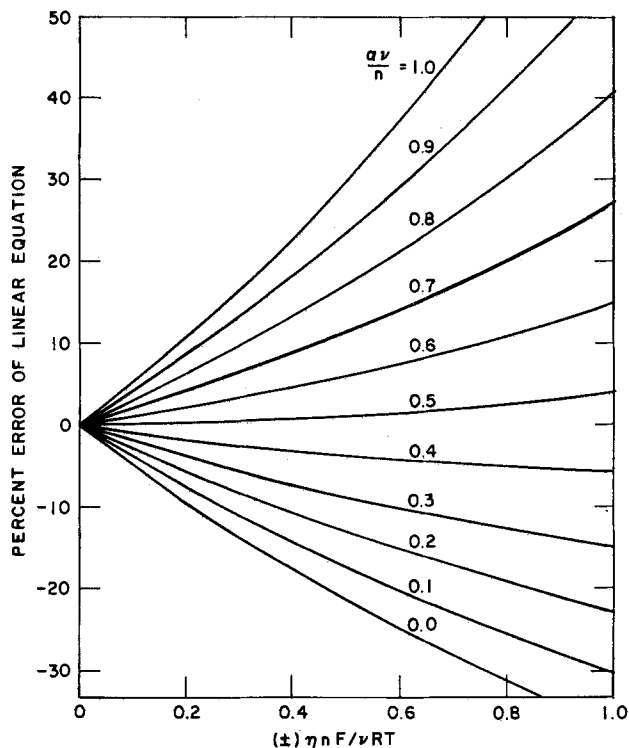


Fig. 1. Error of the linearized i - η relation for the case of charge transfer control ($\alpha = \alpha_a$ for $\eta > 0$; $\alpha = \alpha_c$ for $\eta < 0$).

ror calculations can be presented in terms of the dimensionless parameters discussed earlier.

The results for the charge transfer-control case are shown in Fig. 1. The error increases almost linearly with increasing overpotential parameter ($\eta n F / \nu RT$), and the rate of this increase is a strong function of the transfer-coefficient parameter. The smallest error occurs near, but not exactly at, $\alpha\nu/n = 0.5$ and increases drastically below and above this value.⁶ For example, at $\eta n F / \nu RT = 0.2$, which is approximately 5 mV polarization at room temperature and $n = \nu$, the error is only 1% at $\alpha\nu/n = 0.5$, but increases to 10% under the worst conditions ($\alpha\nu/n = 1$ or 0). One can also express the limitation of the linearized equation as the highest allowed overpotential for the error not to exceed a maximum value. For a 5% error this limit is 30 mV at $\alpha\nu/n = 0.5$ but decreases to 2.5 mV under the worst conditions. Changing the polarity of the current will change the sign of the error; therefore, if two identical working electrodes are used, polarizing one anodically and the other cathodically, much of the error will cancel, as indicated in Fig. 2. This approach to decrease the error of linearization was first suggested by Kooijman *et al.* (8). Considerable error cancellation results at all values of $\alpha\nu/n$ except at 0.5, and the error is close to zero at $\alpha\nu/n \approx 0.65$. The cancellation effect is very significant: the worst-case error at 5 mV polarization decreases from 10% for a single electrode to 2% for the two-electrode case, and the 5% error limit increases from 2.5 to 10 mV at $\alpha\nu/n = 1$ (the worst condition).

The results for the mass-transport-controlled case are shown in Fig. 3. The error increases with increasing overpotential parameter, and the effect is approximately linear. The rate of increase is strongly dependent on $C_0 D_0^{1/2} / C_R D_R^{1/2}$, which, for the sake of simplicity, will be called the mass-transport parameter. Zero error occurs near, but not exactly at, a mass-transport parameter of one. Above and below this value, the error increases steeply but reaches asymptotic limits.⁷ For example, at

⁶It is important to emphasize that α , here and throughout this paper, refers to the transfer coefficient of the multistep Butler-Volmer equation (16, 17). The transfer coefficient is equivalent to the symmetry factor only for the case of a single-step reaction with $n = 1$.

⁷The error calculated at the mass-transport parameter of 1000 and 0.001 is within 0.5% relative error of the asymptotic limit.

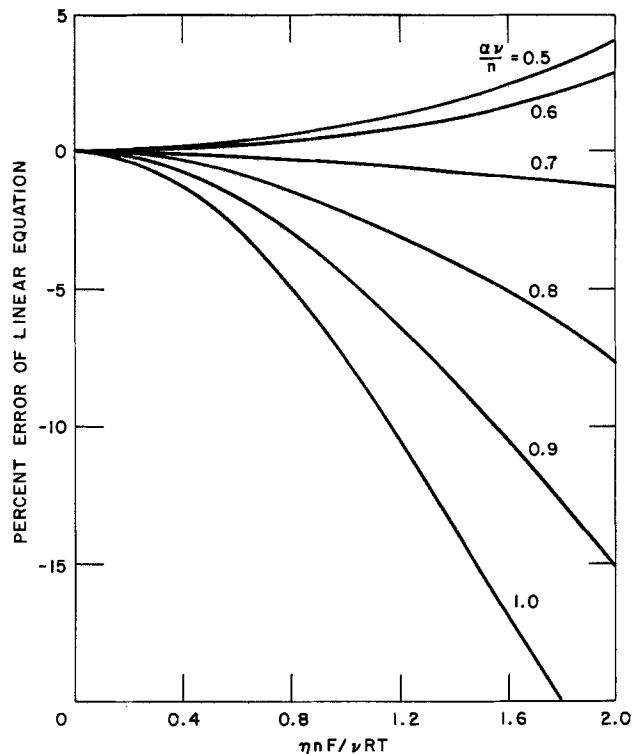


Fig. 2. Error of the linearized i - η relation for the case of charge transfer control and two identical working electrodes. The symbol α stands for the larger of α_a and α_c .

$\eta n F / RT = 0.2$ and mass-transport parameter of one, the error is 1%, but increases to 8% at the asymptotic limit. Alternatively, the maximum allowed overpotential (at room temperature and $n = 1$) for a 5% error is 20 mV at the mass-transport parameter of one but decreases to 2.5 mV at the asymptotic limit. It is to be noted here that for metal deposition-dissolution reactions (the concentration of one species is fixed) the error will always be the asymptotic limit. The sign of the error changes as the sign

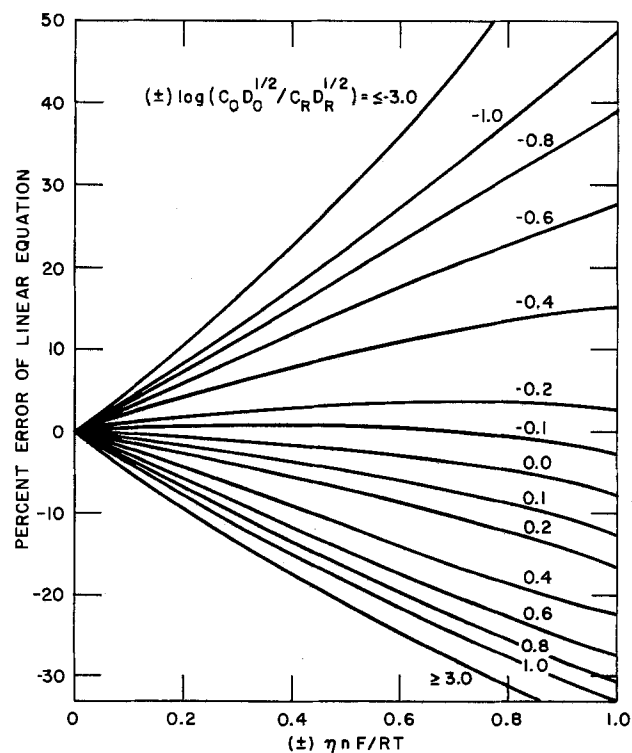


Fig. 3. Error of the linearized i - η relation for the case of mass-transport control.

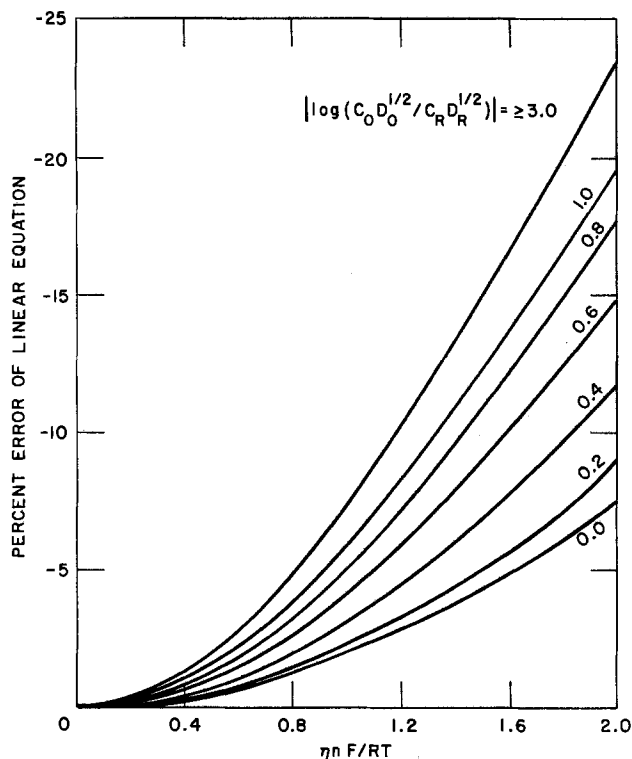


Fig. 4. Error of the linearized i - η relation for the case of mass-transport control and two identical working electrodes.

of the polarization changes; therefore, a cancellation of errors occurs when using two identical working electrodes. This case is shown in Fig. 4. The beneficial effect of this type of measurement is shown by the decrease of the error at the asymptotic limit from 8% for a single electrode to 1.5% for two electrodes; similarly, the maximum allowed overpotential for a 5% error increases from 2.5 to 10 mV.

The error as a function of the $(C_i^s)_{x=0}/C_i$ ratios is shown in Fig. 5. This was calculated by a straightforward

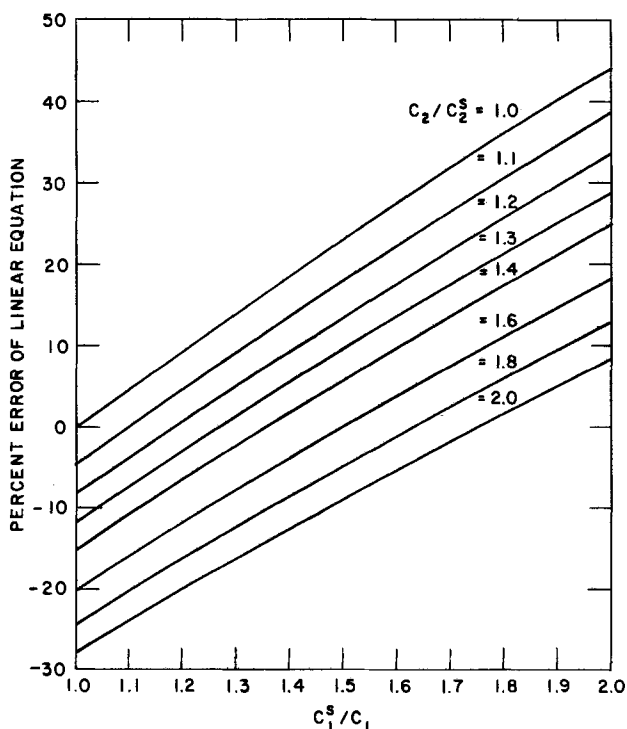


Fig. 5. Error of the linearized i - η relation for the case of mass-transport control as a function of surface concentrations ($1 = \text{O}$ and $2 = \text{R}$ for $\eta > 0$; $1 = \text{R}$ and $2 = \text{O}$ for $\eta < 0$).

comparison of Eq. [17] and [18]. These results are instructive, though the figure cannot be used to predict errors for practical situations. The error depends not only on the individual concentration ratios but also on the ratio of the two ratios. This explains the small error near the mass-transport parameter of one and the large error for metal deposition-dissolution reactions.

The error cannot be represented in a simple way for more general cases because it is a function of too many parameters, some of which may be unknown at the time of an experiment. Specifically, one would need to know how the total overpotential is divided into charge transfer and mass-transport overpotentials. One would also need to know the values of the transfer coefficients and the stoichiometric number. If these are known, or at least estimated, the figures presented in this communication can be used to determine the error of the charge transfer and mass-transport overpotentials and the overall error will be their algebraic sum. If the above-mentioned parameters are not known, one can estimate the maximum error by assuming that the reaction is charge transfer or mass-transport controlled, calculating the worst error for both cases and taking the largest of the two. For example, at room temperature and $\nu = n = 1$, at a 5 mV polarization the worst-case error (at $\alpha = 1.0$ and mass-transport parameter at the asymptotic limit) will be 10%. The actual errors will probably be considerably smaller than the maximum error, in part because the parameters will not have extreme values and in part because the errors of the charge transfer and mass-transport overpotentials can have opposite signs resulting in cancellations. Many numerical calculations were carried out for all relaxation techniques confirming the additivity of errors and the cancellation effects.

There is a small discrepancy for the case of the pure mass-transport control between the errors calculated from the two i - η relations and the errors calculated from the relaxation curves. The first error is calculated by assuming the same surface concentration for all species for both the linear and the full equations, while the latter is calculated for a constant current case. The two errors will be identical only when the double-layer capacitance is zero. For a finite double-layer capacitance, a fraction of the current will be consumed for the double-layer charging and this fraction will not be the same for the linearized and the full i - η cases; consequently, the surface concentrations will be unequal at equal total currents. The results shown in Fig. 3 and 4 are for a double-layer capacitance of zero; the deviation from practical conditions will not be large; for example, for $c = 25 \mu\text{F}\cdot\text{cm}^{-2}$, the results given in Fig. 3 and 4 are correct within a factor of 1.2. The results given in Fig. 1-4 are expressed in terms of ϵ_η (Eq. [15]); for a potentiostatic case, the error of interest is, of course, ϵ_s , which can be obtained from ϵ_η by using the relation given in Eq. [16].

These results are in general agreement with those of Kooijman *et al.* (8) and emphasize again the importance of the value of the transfer coefficients and concentrations in the limitation of the linearized i - η relation. The controversy surrounding this subject (7-13) can be resolved by stating that it is correct that in the limit of $\eta \rightarrow 0$ the linearized relation will be identical to the full relation, independent of the value of other parameters, but the rate of approach to the limit depends on those other parameters. That is, at a given overpotential value, the error of the linearized i - η relation is a function of all system parameters, namely: $\alpha\nu/n$, $C_O D_O^{1/2}/C_R D_R^{1/2}$, and $\eta n F/RT$.

Error of the exchange current density determination due to linearization.—A series of calculations was carried out to determine the error in the exchange current density determination by the dc relaxation techniques caused by measurement in the nonlinear i - η range coupled with data evaluation assuming a linear i - η relation. It was found that, if the electrode system is well within the field of applicability of the techniques (2-5), the percent error of the exchange current density determination is approxi-

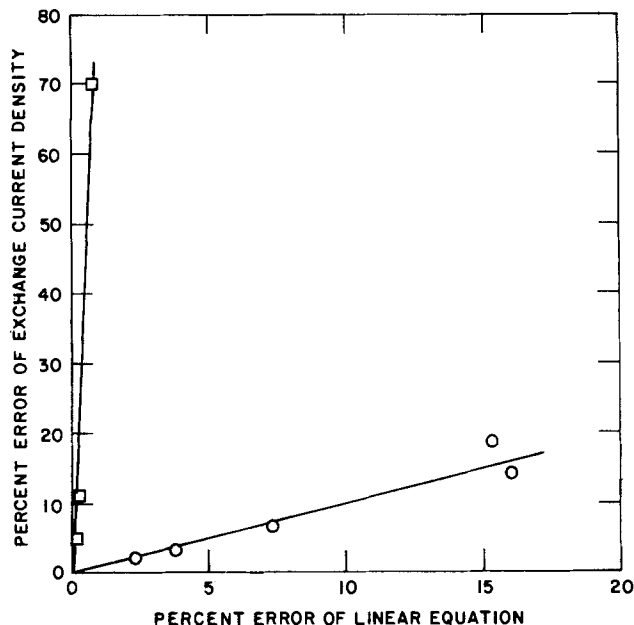


Fig. 6. Error of the exchange current density determination with galvanostatic single-pulse technique assuming linear i - η relation vs. the error of the linearized equation. Circles: electrode reaction well within the field of applicability. Squares: electrode reaction at the edge of applicability.

mately the same as the maximum percent deviation between the relaxation curves calculated with the linear and nonlinear i - η relations. A much larger error in the exchange current density was found at the edge of the applicability fields. This is in agreement with earlier results (2-5) indicating that the limits of applicability of all dc relaxation techniques are sensitive to measurement errors. An example for the galvanostatic single-pulse technique is shown in Fig. 6. The error in the exchange current density determination is plotted against the error of the linearized equation for two electrode reactions: one well within the field of applicability and one at the edge of applicability. [The value of $\log \kappa$ was 3 or 0, while the value of $\log \tau_c$ was -5 for both cases, see Ref. (3); $\alpha v/n$ was 0.3, and the mass-transport parameter was unity.] It can be concluded that the error in the exchange current density determination will be at least as large as the error of the linearized equation.

Summary

The feasibility of the extension of relaxation techniques to the nonlinear current density-overpotential range has been demonstrated. This was accomplished by a curve-fitting data-evaluation method with a nonlinear multidimensional least squares minimization package coupled to a software package designed to solve systems of nonlinear partial differential equations. The main advantage of this approach is that measurements can be made at high enough overpotentials to avoid signal-to-noise ratio problems without introducing linearization errors in the data evaluation. The error of the linearized i - η relation is not negligible under many experimental conditions. A quantitative evaluation of this error has been made as a function of three dimensionless parameters: $\alpha v/n$, $C_0 D_0^{1/2}/C_R D_R^{1/2}$, and $\eta n F/RT$. The error in the exchange current density determination, with the assumption of linear i - η relation, will be at least as large as the error of the linearized equation.

Acknowledgments

This work was supported in part by the Division of Materials Science, Office of Basic Energy Sciences, U.S. Department of Energy, and in part by the Applied Mathematical Sciences subprogram of the Office of Energy Research, U.S. Department of Energy, under Contract W-31-109-ENG-38. We are grateful to Dr. V. A. Maroni for his critical reading of the manuscript.

Manuscript submitted July 30, 1984; revised manuscript received May 6, 1985. Parts of this work were presented as Paper 321 at the Detroit, Michigan, Meeting of the Society, Oct. 17-21, 1982.

Argonne National Laboratory, assisted in meeting the publication costs of this article.

LIST OF SYMBOLS

c	capacity of the double layer ($F \cdot \text{cm}^{-2}$)
C_j	concentration of species j in the bulk solution ($\text{mol} \cdot \text{cm}^{-3}$)
C_j^s	concentration of species j near the electrode surface ($\text{mol} \cdot \text{cm}^{-3}$)
D_j	diffusion coefficient of species j ($\text{cm}^2 \cdot \text{s}^{-1}$)
E	measured potential (V)
F	Faraday constant ($C \cdot \text{mol}^{-1}$)
i	total current density ($A \cdot \text{cm}^{-2}$)
i_f	faradaic current density ($A \cdot \text{cm}^{-2}$)
i_o	apparent exchange current density ($A \cdot \text{cm}^{-2}$)
n	total number of electrons transferred in the overall reaction
N	number of optimization variables
O	(index) oxidant
P_j	dimensionless parameter
R	(index) reductant
R	universal gas constant ($J \cdot K^{-1} \cdot \text{mol}^{-1}$)
R_s	uncompensated solution resistance between the working and reference electrodes per unit electrode area ($\Omega \cdot \text{cm}^2$)
t	time (s)
t_f	pulse length (s)
T	temperature (K)
x	distance from electrode surface (cm)
α_a	anodic transfer coefficient
α_c	cathodic transfer coefficient
ϵ_i	error at constant potential, defined by Eq. [16]
ϵ_η	error at constant current density, defined by Eq. [15]
η	total overpotential (V)
η_{ct}	charge transfer overpotential (V)
η_{mt}	mass-transport overpotential (V)
η'_j	overpotential calculated with the linearized equations (V)
ν	stoichiometric number of the reaction mechanism

REFERENCES

- J. Kuta and E. Yeager, in "Techniques of Electrochemistry," Vol. 1, Chap. 3, E. Yeager and A. J. Salkind, Editors, Wiley-Interscience, New York (1972).
- Z. Nagy, *This Journal*, **128**, 786 (1981).
- Z. Nagy, *Electrochim. Acta*, **26**, 671 (1981).
- Z. Nagy, *This Journal*, **129**, 1943 (1982).
- Z. Nagy and J. T. Arden, *ibid.*, **130**, 815 (1983).
- Z. Nagy, *Electrochim. Acta*, **28**, 557 (1983).
- P. Delahay, "Double Layer and Electrode Kinetics," p. 160, Interscience, New York (1965).
- D. J. Kooijman, M. Sluyters-Rehbach, and J. H. Sluyters, *Electrochim. Acta*, **11**, 1197 (1966).
- J. M. Kudirka and C. G. Enke, *Anal. Chem.*, **44**, 614 (1972).
- F. H. Beyerlein and R. S. Nicholson, *ibid.*, **44**, 1917 (1972).
- R. L. Birke and D. K. Roe, *ibid.*, **37**, 450 (1965).
- D. M. Mohilner, N. Hackerman, and A. J. Bard, *ibid.*, **39**, 1499 (1967).
- D. K. Roe and R. L. Birke, *ibid.*, **39**, 1501 (1967).
- P. Delahay, in "Advances in Electrochemistry and Electrochemical Engineering," Vol. 1, Chap. 5, P. Delahay and C. W. Tobias, Editors, Interscience, New York (1961).
- D. D. Macdonald, "Transient Techniques in Electrochemistry," Plenum Press, New York (1977).
- J. O'M. Bockris and A. K. N. Reddy, "Modern Electrochemistry," Chap. 9, Plenum Press, New York (1970).
- J. O'M. Bockris and Z. Nagy, *J. Chem. Ed.*, **50**, 839 (1973); *ibid.*, **51**, 803 (1974).
- P. Delahay, "Double Layer and Electrode Kinetics," p. 168, Interscience, New York (1965).
- S. W. Feldberg, in "Electroanalytical Chemistry," Vol. 3, p. 199, A. J. Bard, Editor, Marcel Dekker, New York (1969).
- S. W. Feldberg, in "Computers in Chemistry and Instrumentation," Vol. 2, p. 185, J. S. Mattson, H. B. Mark, and H. C. Macdonald, Editors, Marcel

- Dekker, New York (1972).
21. J. R. Sandifer and R. P. Buck, *J. Electroanal. Chem. Interfacial Electrochem.*, **49**, 161 (1974).
 22. D. Britz, "Digital Simulation in Electrochemistry," Lecture Notes in Chemistry 23, Springer-Verlag, New York (1981).
 23. S. Pons, in "Electroanalytical Chemistry," Vol. 13, p. 115, A. J. Bard, Editor, Marcel Dekker, New York (1984).
 24. D. R. Franceschetti and J. R. Macdonald, in "Electrode Processes," S. Bruckenstein, B. Miller, J. D. E. McIntyre, and E. Yeager, Editors, p. 94, The Electrochemical Society Softbound Proceedings Series, Princeton, NJ (1980).
 25. G. K. Leaf and M. Minkoff, in "Advances in Computer Methods for Partial Differential Equations V," p. 429, R. Vichnevetsky and R. Stepleman, Editors, IMACS, New Brunswick, NJ (1984).
 26. J. J. More, B. S. Garbow, and K. E. Hillstrom, Argonne National Laboratory Report ANL-80-74 (1980).
 27. J. J. More, in "Numerical Analysis," G. A. Watson, Editor, p. 105, Lecture Notes in Mathematics 630, Springer-Verlag, New York (1978).
 28. A. C. Hindmarsh, Lawrence Livermore Laboratory Report UCID-30130 (1976).
 29. R. L. Crane, K. E. Hillstrom, and M. Minkoff, Argonne National Laboratory Report ANL-80-64 (1980).
 30. M. J. D. Powell, in "Numerical Analysis," p. 144, G. A. Watson, Editor, Lecture Notes in Mathematics 630, Springer-Verlag, New York (1978).
 31. M. Minkoff, in "Nonlinear Programming 4," p. 519, O. L. Mangasarian, R. R. Meyer, and S. M. Robinson, Editors, Academic Press, New York (1981).
 32. Z. Nagy, *This Journal*, **125**, 1809 (1978).
 33. Z. Nagy, *Electrochim. Acta*, **29**, 917 (1984).
 34. A. J. Bard and L. R. Faulkner, "Electrochemical Methods," p. 161, Wiley, New York (1980).

A Systematic Approach to the Determination of Possible Reaction Mechanisms of Oxygen Reduction on Platinum in Alkaline Medium

J. L. Valdes* and H. Y. Cheh**

Department of Chemical Engineering and Applied Chemistry, Columbia University, New York, New York 10027

ABSTRACT

The reaction mechanisms of oxygen reduction of platinum in alkaline medium are determined once a set of reacting species and elementary reactions is specified. The technique utilized to generate all the possible reaction mechanisms is based upon the principles of combinatorial analysis and linear algebra along with application of the principle of microscopic reversibility. The development of this method by Happel and Sellers has enabled them to study complex mechanisms for some important industrial reactions in heterogeneous catalysis. A preliminary evaluation analysis of the myriad reaction mechanisms for oxygen reduction is accomplished by invoking the concept of a stoichiometric number and a corresponding rate-determining elementary reaction. The number of mechanisms which are consistent with a given experimentally derived stoichiometric number is considerably less. The resulting set of mechanisms forms an important basis for further investigations.

The reduction of molecular oxygen in electrochemical systems has been the subject of many investigations over the past 50 years. It is evident from these studies that a mechanism for this reaction is strongly dependent upon the nature of the electrode material, the surface condition, the composition and purity of the electrolyte, the current density and electrode potential, and the temperature and pressure. Consequently, it is not surprising that the study of mechanisms is rendered difficult, as exemplified by the conflicting accounts which are often found in the literature. The determination of all the possible reaction mechanisms consistent with a given set of elementary steps and chemical species provides a systematic framework for a rigorous theoretical analysis of oxygen reduction. In a continuing effort to develop a clearer understanding of the complex structure of this reaction system, the present study has been undertaken.

In alkaline electrolytes, the reduction of oxygen is primarily considered to proceed through two mechanistic pathways: in one path, a four-electron reduction reaction without the formation of hydrogen peroxide; in the other, an initial electroreduction reaction believed to produce hydrogen peroxide which can be transported to the solution, electroreduced further to water, or catalytically decomposed. The mechanism for oxygen reduction can therefore be envisioned as consisting of a network of various elementary steps interconnecting a set of chemical species. Although this perspective may seem unresolvably complicated at first, the method which is applied here unambiguously determines all the possible mechanisms from a given set of elementary steps and chemical species.

The development of the theory of reaction mechanisms for complex reactions is found in the early work of

* Electrochemical Society Student Member.
 ** Electrochemical Society Active Member.

Horiuti and co-workers (1, 2). The determination of the stoichiometric number by Horiuti in 1948 permitted, to a certain extent, distinctions to be made between the various mechanisms. Horiuti also showed that a chemical reaction mechanism can be described by specifying the number of occurrences required by each of the elementary steps in order for a given overall reaction to take place. The determination of possible reaction mechanisms then amounts to selecting the proper stoichiometric number for each of the elementary steps. Horiuti employed a matrix composed of elementary steps by species to select the stoichiometric numbers and obtain the linearly independent sets or reaction routes. According to Happel and Sellers (3), the concept of linear independence introduced by Horiuti will allow mechanisms to be combined in such a way that certain elementary reaction steps can be cancelled. Although this may be mathematically correct, it is not feasible from a kinetics point of view, since no two mechanisms containing a given elementary step can be equivalent to a third in which that step does not appear. As a result, the procedure developed by Horiuti for determining the possible reaction mechanisms of a simple overall reaction is not exhaustive and therefore does not provide a complete set of mechanisms.

Milner (4), aware of the deficiencies encountered in Horiuti's model, developed a systematic method for generating complete sets of reaction mechanisms from a given number of elementary steps and intermediates. Here the concept of direct paths was introduced to emphasize that while such paths may not be linearly independent of one another, they are undoubtedly kinetically distinct and unique in that each path or mechanism cannot be considered to result from a superposition of any of the other members in that set. Milner found that the number of nonzero stoichiometric numbers specifying a direct

path can be no more than one greater than the number of intermediates. This seemingly simple rule, however, does not hold true when multiple overall reactions are considered. Hence, Milner applied these concepts only to systems of electrochemical interest for the case in which there is a single overall reaction.

An efficient method of generating all the possible reaction mechanisms was developed by Sellers (5). This theory of chemical reaction networks was originally used to analyze a single overall reaction, and it was later extended by Happel and Sellers (3) to include the case of multiple overall reactions. In the present study, we have applied their method to the enumeration of all the possible reaction mechanisms for oxygen reduction at platinum. The following section is a brief summary of the important facets of this theory; however, the reader is referred to the original article for a detailed account of the procedures and mathematical proofs involved.

Theoretical

The reduction of oxygen in alkaline medium takes place through a network of intermediates, and the transitions that take place between one species and the other can be represented by a set of elementary steps. According to Boudart (6), a reaction is an elementary step if it takes place in a single irreducible act at the molecular level just the way it is written in the stoichiometric equation for the reaction. The act of reaction is irreducible when no intermediate between reactants and products can be detected by any available technique. Once a set of elementary steps is specified and reaction intermediates are postulated, all the possible reaction mechanisms can be unambiguously determined. Furthermore, it is not necessary to know *a priori* the overall reaction.

This method assumes that the networks of reaction steps can be decomposed into two sets. The first set consists of those steps which when combined yield the overall production and consumption of chemical species. The second set of steps forms cycle reactions in the sense that there is no net change of terminal species. (The terminal species are those which appear in the overall reaction.) Such cyclic reactions violate the principle of microscopic reversibility (7) and therefore cannot be physically realizable.

Consider a steady-state reacting system where the chemical species are represented in the notation

$$a_1, a_2, a_3, \dots, a_A \quad [1]$$

and the mechanistic elementary steps

$$s_1, s_2, s_3, \dots, s_S \quad [2]$$

Each elementary step in Eq. [2] is composed of certain chemical species and symbolically represents a molecular event whereby these species are transformed into others. Every elementary step has an associated chemical reaction which can be put into the form

$$R(s_i) = \alpha_{i1}a_1 + \dots + \alpha_{iA}a_A \quad [3]$$

where the α 's are the stoichiometric coefficients of the species in each elementary step and the sign depends on the usual convention (positive for a product and negative for a reactant species). Every step s_i has certain scalar values, σ_i , which can take on any value and are used to form all the possible vectors which constitute a one-dimensional mechanistic vector space. The mechanistic vectors can be written as

$$\sigma_1 s_1 + \dots + \sigma_S s_S \quad [4]$$

and the set of all vectors of this form constitutes an S -dimensional vector space and is called the mechanism space. Every mechanistic vector thus has a reaction vector $R(m)$ associated with it where each mechanism m is represented by a mechanistic vector as in Eq. [4]. The set of all possible reaction vectors is called a reaction space, which is of dimension R , corresponding to the maximum number of linearly independent reactions.

The stoichiometric coefficient matrix can be written in the form

$$\begin{matrix} \alpha_{11}, \alpha_{12}, \dots, \alpha_{1A} \\ \alpha_{21}, \alpha_{22}, \dots, \alpha_{2A} \\ \vdots \\ \alpha_{S1}, \alpha_{S2}, \dots, \alpha_{SA} \end{matrix} \quad [5]$$

where the rows correspond to the elementary steps and the columns to the various chemical species. It is then a simple matter to enumerate the possible reaction mechanisms by multiplying the matrix given in Eq. [5] by m . This affords the reaction vectors $R(m)$ in terms of the stoichiometric coefficients and the scalar values, σ_i . Thus, for every mechanistic vector m , a reaction vector $R(m)$ can be found by matrix multiplication. However, the present problem can be considered as the inverse of this, in that the values for σ_i are unknown and we wish to find all the mechanistic vectors which produce a specified reaction vector: namely, the overall reaction vector.

The overall reaction vector consists only of terminal species; hence, the mechanistic vectors which must be determined will have to recycle all the intermediate species. Consequently, a set of mechanistic vectors which regenerates all the species must also be determined. It is evident that such a cycle mechanistic vector affords a reaction which is null and is represented by the equation

$$R(z) = 0 \quad [6]$$

In any chemical system, there is a unique number of mechanisms which are termed direct mechanisms. These are shown by Happel and Sellers (3) to be the fundamental constituents of any mechanism. The first step in the determination of all the possible direct mechanisms is accomplished by a diagonalization of the stoichiometric coefficient matrix given in Eq. [5]. It is sufficient to note in the present context that the process of diagonalization directly provides one with all the mechanistic vectors which produce a particular independent overall reaction. Furthermore, a cycle matrix is formed where the number of rows, C , corresponds to the number of cycle reactions present in the system and the number of columns is given by the total number of species, A . The mechanistic vectors for each of these cycles are also available if a detailed record is kept of all the column and row manipulations during the diagonalization process. It is clear that this type of management is most efficiently realized through the use of a computer algorithm.

The results of any diagonalization process can be shown in the generalized reduced matrix given in Fig. 1. In this matrix, all entries are zero below the diagonal, nonzero in the outlined boxes, and arbitrary above the diagonal. The space of all the nonsteady-state mechanisms, steady-state mechanisms, and cycles is given by: m_1 to m_H , m_{H+1} to m_q , m_{q+1} to m_S , respectively. It is clear that only the terminal species are involved in the steady-state mechanisms, whereas cycles regenerate all the species to form a null reaction according to Eq. [6].

The general expression for any steady-state mechanism can be written as a linear combination of the overall reactions and the cycles

$$m = \mu_{H+1}m_{H+1} + \dots + \mu_S m_S \quad [7]$$

The coefficients of the mechanistic vectors, m_{q+1} through m_S , form the C -by- S cycle matrix. Since the general mechanism is composed of a linear combination of overall reaction vectors and cycles, we must insure that this combination does not lead to any cycles, since this would violate the principle of microscopic reversibility. Thus, in order to find every cycle-free system, we must insure that C columns of the C -by- S cycle matrix add up to zero, which is equivalent to the following matrix equation

$$(\sigma_{H+1} \dots \sigma_q) + (\mu_{q+1} \dots \mu_S)M = 0 \quad [8]$$

where the solution to the above equation is given by

	a_1	a_2	a_I	...	a_{I+R}	a_A
m_1	■							
m_2		■						
...								
m_{H-1}			■					
m_H				■				
m_{H+1}					■			
m_{H+2}						■		
...								
m_{Q-1}							■	
m_Q	ALL ENTRIES ARE ZEROS BELOW THE DIAGONAL, NONZERO IN THE BOXES, AND ANYTHING ABOVE THE DIAGONAL.							■
m_{Q+1}								
...								
m_S								

Fig. 1. Generalized reduced matrix

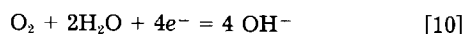
$$(\mu_{Q+1} \dots \mu_S) = -(\sigma_{H+1} \dots \sigma_Q)M^{-1} \quad [9]$$

where M^{-1} is the inverse of the C -by- C cycle matrix. The procedure for enumerating every direct mechanism is simply given by the solution to Eq. [9]. In this case, all the nonsingular C -by- C submatrices of the C -by- S cycle matrix must be considered as viable in generating a direct mechanism. The solution of these sets of linear algebraic equations becomes tedious even for a small cycle matrix, since it is evident that there are at least $S!/[(S-C)!C!]$ possible combinations of C -by- C submatrices which can be generated from a C -by- S cycle matrix. A computer algorithm is thus appropriate for this task.

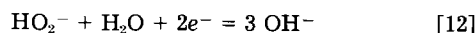
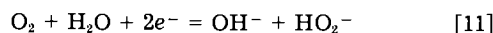
Analysis of Reaction Mechanism

The reduction of oxygen in alkaline solutions is often believed to proceed along two parallel reaction paths. This was the conclusion by Bockris and co-workers (8), using experiments with the rotating ring-disk electrode. In one of these paths, hydrogen peroxide is considered an intermediate which can be partially reduced or electrocatalytically decomposed to water. However, the decomposition reaction of hydrogen peroxide to water is found to take place only in acidic solutions at platinum (9). In the other path, oxygen is reduced to water without hydrogen peroxide as an intermediate. For the purpose of this study, the presence of hydrogen peroxide is included in the reaction scheme. The reason is simply that both pathways will very likely become operable unless "ultra-high" purity solutions are used, which is often difficult to achieve and impractical in most applications.

The overall reaction for the reduction of oxygen in alkaline solutions at platinum is given by the following equation, regardless of whether hydrogen peroxide is formed or not



Furthermore, two other overall reactions account for the possibility of hydrogen peroxide formation. The following equations apply for alkaline solutions



Note that the preceding reactions do not form an independent set, since Eq. [11] and [12] can be combined to yield Eq. [10].

Any critical assessment of the possible reaction mechanisms of oxygen reduction must necessarily include consistency with certain experimental results. There are at least two ways in which this minimum consistency standard can be met.

The first method involves the deduction of mechanistic indicators and was used by Bockris (10) in evaluating the reaction mechanisms for oxygen reduction. Once a

mechanism has been postulated, reaction rate equations are developed. The kinetic expression for a reaction rate depends upon the reaction pathway, upon the behavior of the intermediates, and upon which step is rate determining. The mechanistic indicators obtained reflect how the rest potential changes with logarithm of the current at constant pH, or alternatively, the change of rest potential with pH at constant current. These theoretically derived mechanistic indicators are then compared to experimental results for consistency. Distinction between the various mechanisms is impossible when each is characterized by the same mechanistic indicators, as is often the case. Consequently, this method cannot unequivocally provide conclusive evidence for the existence of one mechanism over the other.

In the present analysis, the stoichiometric number concept is employed as a diagnostic tool for evaluating the reaction mechanisms. The stoichiometric number, originally used by Horiuti in studying mechanisms of single overall reactions, represents the number of times the rate-determining step occurs in order to effect one occurrence of the overall reaction. Partial experimental consistency is obtained by using the cathodic and anodic Tafel slopes, from the polarization curve of the oxygen electrode reaction, in order to calculate the stoichiometric numbers. According to Parsons (11), this can be accomplished from the following expression

$$\nu = \frac{4F}{RT} (1/b_a - 1/b_c)^{-1} \quad [13]$$

where b_a and b_c are the anodic and cathodic Tafel slopes, respectively. Furthermore, the existence of Tafel line regions for the cathodic reduction of oxygen on platinum strongly indicates that the rate-determining step is electron-transfer related. Hence, the stoichiometric number applied to an electron-transfer rate-determining step provides for an important preliminary screening of the possible reaction mechanisms. This limited set of mechanisms can subsequently be analyzed through the method of mechanistic indicators.

The procedure outlined in the theoretical section can be used to generate all the possible reaction mechanisms once a set of elementary steps and chemical species has been postulated. A review of the literature has revealed that the set of elementary steps listed in Table I may be appropriate in describing the molecular interactions that are likely to take place during the reduction of oxygen at platinum in alkaline solutions.

Although the list of elementary steps given in Table I is not exhaustive, it does comprise a comprehensive set of the most important reactions, which forms a basis for the present systematic study. The intermediate species considered are OH , O , O_2H , O_2^- , and O^- , and the terminal species are OH^- , O_2 , H_2O , O_2H^- , and e^- . Although the

Table I. Elementary steps considered in the reduction of oxygen on platinum in alkaline medium

1.		OH^-	=	OH	+	e^-			
2.	OH^-	+	O	=	O_2H	+	e^-		
3.		O_2H^-	=	O_2H	+	e^-			
4.		$2 OH$	=	O	+	H_2O			
5.	OH	+	O	=	O_2H				
6.		$2 O$	=	O_2					
7.	OH^-	+	O	=	O_2H^-				
8.	O	+	e^-	=	O^-				
9.	OH	+	OH^-	=	O^-	+	H_2O		
10.	OH	+	O_2H	=	O_2	+	H_2O		
11.	O	+	O_2H	=	O_2	+	OH		
12.	O_2H^-	+	O	=	O_2	+	OH^-		
13.	O_2H^-	+	OH	=	O_2H	+	OH^-		
14.	OH^-	+	OH	=	O	+	H_2O		
15.	OH^-	+	O_2H	=	O_2	+	H_2O		
16.	OH^-	+	O_2	=	O	+	O_2H		
17.	O_2H^-	+	OH	=	O_2	+	H_2O		
18.	O_2H^-	+	O	=	O_2	+	OH		
19.		$2 OH^-$	=	O	+	H_2O	+	$2e^-$	
20.	O_2H^-	+	OH^-	=	O_2	+	H_2O	+	$2e^-$
21.	O_2	+	e^-	=	O_2^-				
22.	OH	+	O_2H^-	=	O_2^-	+	H_2O		

overpotential, the determination of transfer coefficients and the stoichiometric number, and the dependence of reaction rates upon substitution of isotopic atoms. In principle, if all these criteria were to be taken into account, the number of possible reaction mechanisms would be drastically reduced. However, such a procedure can be quite involved and many of these criteria are particularly sensitive to the specific system investigated. For these reasons, an analysis of the reaction mechanisms will be performed based on simple kinetic criteria in the form of Tafel slopes and stoichiometric number.

We have shown that with the given set of 18 elementary steps, the reduction of oxygen in alkaline solutions involves two overall reactions. One reaction involves the direct reduction of oxygen to water, while in the other oxygen is reduced to hydrogen peroxide. The stoichiometric number concept as developed by Horiuti strictly applies for the case of a single overall reaction. However, if one of the reaction paths in the reduction of oxygen is predominant over the other, and one of the elementary steps in this path is rate determining, then the Tafel slopes will necessarily be characteristic of that rate-determining step. In the reduction of oxygen near the reversible electrode potential, the path which does not have hydrogen peroxide as an intermediate must predominate (17). Consideration of this case permits the use of the stoichiometric number as a diagnostic criterion in mechanism analysis.

Experiments with the oxygen electrode in alkaline solutions at platinum indicate an anodic Tafel slope of RT/F , at low current densities, while at higher current densities the slope is twice as much (12). This is in accordance with the appearance of oxide formation at the higher anodic overpotentials and is suggestive of a change in the mechanism or a change in the rate-determining step. The cathodic Tafel slopes for the reduction of oxygen in alkaline solutions at platinum have been reported as $-RT/F$ at low current densities and $-2RT/F$ for much higher current densities (13-15). Direct substitution of the low current density Tafel slopes into Eq. [13] yields a stoichiometric number of 2.

The results of a diagnostic analysis for case study I using the stoichiometric number concept are shown in Table II. Note that there are 1686 mechanisms which have at least one elementary step with a stoichiometric number of 2. The existence of Tafel lines and the absence of chemical reaction-limited currents indicate that any one of the nine elementary steps which involve electron transfer is likely to be rate determining (18). Consequently, if we consider mechanisms which have a stoichiometric number of 2 associated with an electron-transfer rate-determining step, then the number of possibilities is significantly reduced to 950. The number of mechanisms for this case is also listed separately, according to the particular electron-transfer elementary step. For example, there are 187 possible mechanisms that have a stoichiometric number of 2 in connection with elementary step number 1, which is an electron-transfer reaction. Note that even with these simple criteria we have been able to

Table II. Mechanism diagnostic analysis: case study I

Elementary steps: 18	
Terminal species: O_2, H_2O, OH^-, O_2H^-	
Intermediate species: OH, O, O_2H, O^-	
Total number of mechanisms: 1897	
Stoichiometric number $\nu = 2$	Mechanisms
a) Any rds	1686
b) Charge transfer rds	950
Charge transfer elementary step	$\nu = 2$
1	187
2	187
3	143
8	211
14	129
15	157
16	204
17	139
18	187

Table III. Mechanism diagnostic analysis: case study II

Elementary steps: 13	
Terminal species: O_2, H_2O, OH^-, O_2H^-	
Intermediate species: OH, O, O_2H, O^-	
Total number of mechanisms: 315	
Stoichiometric number $\nu = 2$	Mechanisms
a) Any rds	277
b) Charge transfer rds	82
Charge transfer elementary step	$\nu = 2$
1	32
2	25
3	23
8	66

reduce by one order of magnitude the number of possible mechanisms. However, it is impossible to begin listing all these mechanisms here; thus, a complete list is provided upon request.

Case study II.—In case study II, we examine a set of elementary reactions which excludes those "elementary" steps in which two chemical species and an electron transfer are simultaneously involved. Such reactions tend to have a positive Gibbs free energy of reaction by effecting a concerted mechanism through the presence of three entities at the electrode surface. In this case, elementary steps 14-18, as listed in Table I, will not be considered.

Given the same intermediate and terminal species as in the previous case study, all the possible reaction mechanisms can be determined from the remaining 13 elementary steps. Once again, we find two overall independent reactions. However, unlike case study I, the hydrogen peroxide reaction is given by Eq. [11] instead of by Eq. [12]. Nonetheless, it is important to realize that two independent overall reactions are needed to characterize this chemical reaction system. The results of a diagnostic analysis of these mechanisms based on the stoichiometric number is shown in Table III. The number of possible mechanisms has decreased substantially compared to the previous case. Although simple kinetic criteria like Tafel slopes and the stoichiometric number cannot ultimately determine the reaction mechanism, it is an important step in that direction. Furthermore, when these simple kinetic criteria are supplemented with other system-specific experimental data, as previously mentioned, a greater understanding of the mechanism for oxygen reduction is made possible.

Conclusions

A method for generating all the possible reaction mechanisms consistent with a given set of elementary steps and chemical species has been applied to the reduction of oxygen under alkaline conditions at platinum. In this study, we have employed the magnitudes of the anodic and cathodic Tafel slopes, through a determination of the stoichiometric numbers, as a major basis for mechanistic interpretations. This procedure establishes a limited set of mechanisms, and other diagnostic criteria can be used to even further reduce these possibilities. We have shown how this method can be used in conjunction with diagnostic criteria, as a powerful and systematic tool in the investigation of the mechanism for the reduction of oxygen.

Manuscript submitted Aug. 28, 1984; revised manuscript received May 24, 1985.

REFERENCES

- J. Horiuti and T. Ikusima, *Proc. Imp. Acad. Tokyo*, **15**, 39 (1939).
- J. Horiuti and T. Nakamura, *Z. Phys. Chem. (Frankfurt am Main)*, **11**, 358 (1957).
- J. Happel and P. H. Sellers, *Ind. Eng. Chem. Fundam.*, **21**, 67 (1982).
- P. C. Milner, *This Journal*, **111**, 228 (1964).
- P. H. Sellers, *Arch. Ration. Mech. Anal.*, **44**, 23 (1971).
- M. Boudart, "Kinetics of Chemical Processes," p. 32, Prentice-Hall Inc., Englewood Cliffs, NJ (1968).
- W. J. Moore, "Physical Chemistry," p. 332, Prentice-

- Hall Inc., Englewood Cliffs, NJ (1972).
8. J. O'M. Bockris, M. A. Genshaw, and A. Damjanovic, *This Journal*, **114**, 1107 (1967).
 9. J. O'M. Bockris and L. F. Oldfield, *Trans Faraday Soc.*, **51**, 249 (1955).
 10. J. O'M. Bockris, *J. Chem. Phys.*, **21**, 817 (1957).
 11. R. Parsons, *Trans. Faraday Soc.*, **47**, 1332 (1951).
 12. A. Damjanovic, A. Dey, and J. O'M. Bockris, *Electrochim. Acta*, **11**, 791 (1966).
 13. D. B. Sepa, M. V. Vojnovic, and A. Damjanovic, *ibid.*, **26**, 781 (1981).
 14. D. B. Sepa, M. V. Vojnovic, and A. Damjanovic, *ibid.*, **25**, 1491 (1980).
 15. A. Damjanovic and M. A. Genshaw, *ibid.*, **15**, 1281 (1970).
 16. E. Yeager, *This Journal*, **128**, 160C (1981).
 17. D. S. Gnanamuthu and J. V. Petrocelli, *ibid.*, **114**, 1036 (1967).
 18. F. G. Will, Report no. 76CRD276, p. 34, General Electric Co., Power Systems Laboratory, Schenectady, NY (1976).

Underpotential Deposition of Copper on Gold and the Effects of Thiourea Studied by AC Impedance

Joseph Collin Farmer*

Sandia National Laboratory, Materials Department, Livermore, California 94550

ABSTRACT

This paper reports ac impedance and cyclic voltammetry studies of underpotential deposition (UPD) of Cu on Au in an electrolyte composed of CuSO₄ and H₂SO₄. A theoretical kinetic model was developed which fits the experimental impedance spectra over frequencies ranging from 0.001 to 20,000 Hz. Spectra are characterized by a two-time constant process; two capacitive loops were observed in the Nyquist diagrams corresponding to two distinctive peaks in the Bode phase plot. The high frequency time constant is associated with the double-layer capacitance, while the low frequency process is due to relaxation phenomena associated with the charge transfer involved in Cu²⁺ electrosorption. Thiourea is one of the most important organic additives for commercial CuSO₄ plating baths. Therefore, the coadsorption of thiourea and UPD Cu on Au was also studied by ac impedance. Adsorbed thiourea was found to have a dramatic effect on the high frequency peak in the Bode phase plot. Measurements such as these are proposed as a means of determining organic additive concentrations in Cu plating and electroforming baths.

Underpotential electrodeposition (UPD) of metal monolayers on foreign substrates offers the electrochemist an opportunity to study electrosorption from a fundamental point of view since coverage can be precisely controlled with potential (1-8). It has been shown that in many cases Langmuir, Frumkin, or Temkin adsorption isotherms govern the equilibrium behavior of UPD films (1, 2). Furthermore, the UPD represents the initial stage of nucleation of an electrodeposit on a foreign substrate, and therefore offers insight into early development of bulk deposits (3). The free energy of electrosorption may be indicative of the bonding (adhesion) between the deposit and substrate.

The UPD of Cu on single-crystal Au electrodes of (111) and (100) orientation were studied by Beckmann *et al.*, who used cyclic voltammetry (CV) and reflected high energy electron diffraction (RHEED) (3). They concluded that deposition of about two-thirds of a Cu monolayer on Au (111) resulted in a ($\sqrt{3} \times \sqrt{3}$) R30 superstructure, and that deposition of bulk Cu on Au (111) resulted in an additional (2×2) superstructure, attributed to a surface alloy of Au₃Cu. Their failure to recover all of the deposited Cu by anodic stripping and the dramatic rearrangement of the Au surface after removal of both UPD and bulk deposits support the alloy concept. They state that these observations are indicative of a deposition process more complicated than simple adsorption and that the probable place exchange between Cu and Au atoms in the surface could result in high kinetic barriers to UPD formation.

AC impedance is a powerful tool for addressing questions regarding the kinetics and mechanism of electrosorption. Recently, ac impedance studies of Pb and Tl UPD formation on Ag single crystals were done by Klimmeck and Juttner (4). Their impedance spectra had a frequency range extending from 0.1 to 10,000 Hz and could be explained by the simple Dolin-Ershler model. Earlier, a dynamic impedance technique was used by Nihei *et al.* to study Cu UPD formation on Pt (5). Unfortunately, the data presented in Ref. (5) were obtained at rel-

atively high modulation frequencies (above 1 Hz). As will be shown here, important features in impedance spectra of electrosorption can only be observed at subhertz frequencies extending to 0.001 Hz. Such data cannot be obtained by dynamic impedance measurements and require fast Fourier transform (FFT) techniques (9) or a single-frequency correlator.

This paper reports ac impedance and cyclic voltammetry studies of UPD of Cu on Au in an electrolyte composed of CuSO₄ and H₂SO₄. A theoretical kinetic model was developed which fits experimental impedance spectra over frequencies ranging from 0.001 to 20,000 Hz. Since thiourea significantly affects the morphological properties of Cu electrodeposits and is one of the most important organic additive for commercial CuSO₄ plating baths (10, 11), the coadsorption of thiourea and Cu on Au was also studied by ac impedance. Data were collected at various potentials and concentrations.

Experimental

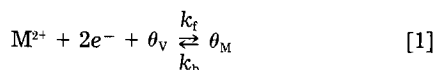
The electrolyte consisted of reagent-grade CuSO₄ (0.01-0.1M) dissolved in dilute H₂SO₄ (0.1M). Distilled, deionized water was used in the preparation. Incremental thiourea additions were then made to this electrolyte (0, 5, 10, 15, and 30 mg/liter). These ranges of concentrations are inclusive of those used in plating baths. Prior to data collection, the electrolyte was stripped with nitrogen and treated by pre-electrolysis at potentials sufficiently cathodic to assure removal of impurities which could interfere with formation of the UPD.

A polycrystalline Au rotating disk working electrode (RDE), a large surface area platinum-sheet counterelectrode, and a double-junction saturated calomel reference electrode (SCE) were used. The cell and RDE rotator were obtained from IBM Instruments (EC/219-1A), and the impedance instrument was obtained from Princeton Applied Research (Model 368). Impedance spectra from 1.3 to 20,000 Hz were obtained using a lock-in amplifier to follow the current response to voltage modulation. At frequencies extending to 0.001 Hz, a fast Fourier transform (FFT) technique was used (9).

*Electrochemical Society Active Member.

Theoretical

In order to interpret impedance spectra for the underpotential deposition of Cu^{2+} on polycrystalline Au, electro sorption mechanisms must be postulated. Then, electrokinetic models and corresponding faradaic impedances are derived based upon these mechanisms. The simplest mechanism is



where M^{2+} is the bulk concentration of Cu^{2+} , θ_v represents the fractional vacancies on the electrode surface, θ_M represents the fractional coverage of the electrode surface by UPD Cu, and k_f and k_b are the forward and reverse rate constants, respectively. Note that θ_v and θ_M totaled together equal unity. The kinetic equation which describes the rate of formation of the UPD via the mechanism shown in Eq. [1] is

$$\frac{d\theta_M}{dt} = k_f \text{M}^{2+} - (k_f \text{M}^{2+} + k_b) \theta_M \quad [2]$$

Based upon Eq. [2], the current involved in the electro sorption process, i , is written as Eq. [3]

$$i = 2F(\theta_M(k_f \text{M}^{2+} + k_b) - k_f \text{M}^{2+}) \quad [3]$$

where F is Faraday's constant. Note that two electrons are involved in the process. In a manner similar to that of Epelboin and Wiart (12), the complex faradaic impedance, Z_f , is then derived from Eq. [3] using Eq. [4]

$$\frac{1}{Z_f} = \left(\frac{\partial i}{\partial E} \right)_{\theta_M} + \left(\frac{\partial i}{\partial \theta_M} \right)_E \cdot \frac{\Delta \theta_M}{\Delta E} \quad [4]$$

where E is the electrode potential. The two partial derivatives of current are defined in terms of physically significant quantities by Eq. [5] and [6]

$$\left(\frac{\partial i}{\partial E} \right)_{\theta_M} = 2F(\theta_M(k'_f \text{M}^{2+} + k'_b) - k'_f \text{M}^{2+}) \quad [5]$$

$$\left(\frac{\partial i}{\partial \theta_M} \right)_E = 2F(k_f \text{M}^{2+} + k_b) \quad [6]$$

Primed rate constants, k'_f and k'_b , represent their respective potential derivatives. The steady-state value of θ_M is required by Eq. [5] and is found by setting the left-hand side of Eq. [2] to zero. The result is

$$\theta_M = \frac{k_f \text{M}^{2+}}{k_f \text{M}^{2+} + k_b} \quad [7]$$

In addition to Eq. [5] and [6], definition of Z_f requires $\Delta \theta_M / \Delta E$

$$\frac{\Delta \theta_M}{\Delta E} = \frac{k'_f \text{M}^{2+} - k_f \text{M}^{2+} (k'_f \text{M}^{2+} + k'_b) / (k_f \text{M}^{2+} + k_b)}{j\omega + k_f \text{M}^{2+} + k_b} \quad [8]$$

The total differential of Eq. [2] and the following relationship

$$j\omega \Delta \theta_M = \frac{d}{dt} \Delta \theta_M \quad [9]$$

are used to obtain Eq. [8]; ω is the angular frequency $2\pi f$ (12). Substituting Eq. [5], [6], and [8] into Eq. [4], one finds that Z_f can be written as

$$\frac{1}{Z_f} = \frac{1}{R_p} - \frac{1}{\rho(1 + j\omega\tau)} \quad [10]$$

an impedance identical to that of the equivalent circuit shown in Fig. 1a, a resistor in parallel with a complex capacitive component. Note that this is a special case of Eq. [7] in Ref. (12), where I_1 is greater than $3I_3$. Here, the circuit components R_p , ρ , and τ are defined in terms of Faraday's constant, the electrokinetic rate constants, and the

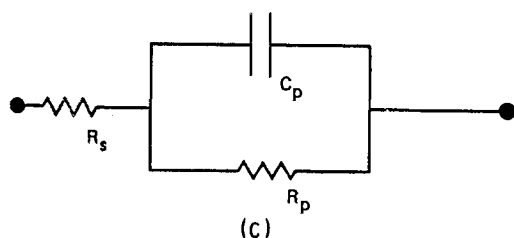
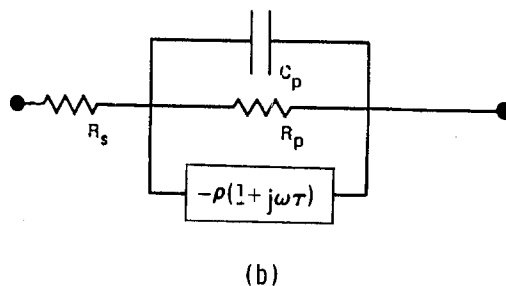
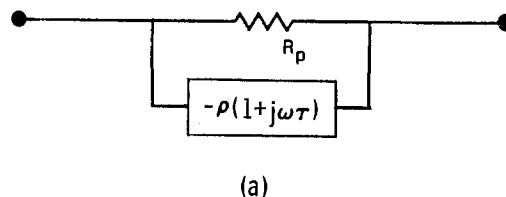


Fig. 1. Equivalent circuit models for the faradaic impedance of electro sorption (a), overall impedance of the electrochemical cell (b), and impedance for the special case of infinite (c).

concentration of Cu^{2+} in the bulk electrolyte which are all found in Eq. [3] above

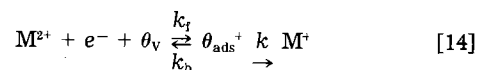
$$R_p = \frac{1}{2F(a + b)k_f \text{M}^{2+}} + \frac{1}{2F(a + b)k_b} \quad [11]$$

$$\rho = R_p \quad [12]$$

$$\tau = \frac{1}{k_f \text{M}^{2+} + k_b} \quad [13]$$

The constants a and b are from the expressions $k_f = A \exp(-aE)$ and $k_b = B \exp(bE)$. It is also important to note that $R_p = \rho$ in this case. As will be discussed, this equality can be used as a basis of distinguishing between various electro sorption mechanisms.

Bruckenstein *et al.* show that Cu^{2+} can be reduced to form soluble Cu^+ and metallic Cu simultaneously at potentials more cathodic than those required for bulk Cu deposition (13). Bowles presents evidence for formation of Cu^+ on Pt in the UPD region near monolayer coverage (14). As will be discussed here, cyclic voltammetry shows a loss of cathodic charge in the UPD region which is believed to be due to formation of a reduced, soluble species like Cu^+ . Therefore, a mechanism is proposed that assumes both the UPD and soluble Cu^+ could form from the same adsorbed intermediate, Cu_{ads}^+ . An additional electron transfer would incorporate this intermediate into the UPD, and its desorption into the electrolyte without charge transfer would yield Cu^+ . This mechanism is represented by Eq. [14] and [15]



where θ_{ads}^+ represents the fractional coverage of the sur-

face by the intermediate, Cu_{ads}^+ , and k is the potential independent desorption rate constant. If the second electron transfer shown in Eq. [15] is assumed to be fast relative to all reaction paths shown in Eq. [14], then θ_{ads}^+ would be in approximate equilibrium with θ_M

$$\theta_M = K\theta_{\text{ads}}^+ \quad [16]$$

where K is the equilibrium constant. The kinetic rate equation for the intermediate is then

$$\frac{d\theta_{\text{ads}}^+}{dt} = k_f M^{2+} - (k_f M^{2+}(1+K) + k_b + k)\theta_{\text{ads}}^+ \quad [17]$$

and the corresponding current involved in this process is

$$i = F(\theta_{\text{ads}}^+(k_f M^{2+}(1+K) + k_b) - k_f M^{2+}) \quad [18]$$

The complex faradaic impedance, Z_f , is then found by substituting Eq. [18] into Eq. [4]. As in the case of simple adsorption (Eq. [1]), one finds that Z_f can again be represented by Eq. [10] and the equivalent circuit shown in Fig. 1a. However, in the case of the soluble intermediate the equivalent circuit components are redefined

$$R_p = \frac{1}{Fk_f M^{2+}} \left(\frac{k_f M^{2+}(1+K) + k_b + k}{k_f M^{2+}(K') + k_b(a+b) + k(a)} \right) \quad [19]$$

$$\tau = \frac{1}{k_f M^{2+} + k_b + k} \quad [20]$$

$$\rho = \frac{k_f M^{2+}(1+K) + k_b + k}{k_f M^{2+}(1+K) + k_b} R_p \quad [21]$$

From Eq. [12] and [21], it is clear that a simple adsorption mechanism (Eq. [1]) can be distinguished from the mechanism involving formation of a soluble intermediate (Eq. [14] and [15]) by the ratio ρ/R_p ; a ratio of unity implies that Eq. [1] is applicable, and a ratio greater than unity implies that Eq. [14] and [15] are applicable, *i.e.*, that k is not zero.

The desorption rate constant, k , has been eliminated in Eq. [22], a ratio derived from Eq. [20] and [21]

$$\frac{R_p}{\tau\rho} = k_f M^{2+}(1+K) + k_b \quad [22]$$

A plot of this ratio as a function of concentration, M^{2+} , should yield a straight line with a slope of $(1+K)k_f$ and an intercept of k_b .

The equivalent circuit shown in Fig. 1a does not account for the double-layer capacitance, C_p , and resistance of the electrolyte, R_s . When these effects are taken into consideration, the electrochemical cell has the same electrical response as the circuit shown in Fig. 1b. The overall complex impedance of the electrochemical cell is written as Eq. [23] (12)

$$Z = R_s + \left(\frac{1 + j\omega R_p C_p}{R_p} - \frac{1}{\rho(1 + j\omega\tau)} \right)^{-1} \quad [23]$$

The complex faradaic impedance, Z_f , and the impedance due to C_p are added as circuit components in parallel; then, the result and R_s are added as circuit components in series. The high frequency time constant of the circuit shown in Fig. 1b is proportional to $R_p C_p$, while the low frequency response is proportional to τ .

The high frequency limit of Eq. [23] is identical to R_s , as shown in Eq. [24]

$$\lim_{\omega \rightarrow \infty} Z = R_s \quad [24]$$

The low frequency limit of Eq. [23] gives a useful relationship between ρ and R_p

$$\lim_{\omega \rightarrow 0} Z = R_s + \frac{\rho R_p}{\rho - R_p} \quad [25]$$

Based upon Eq. [25], two minima (peaks) are observed in plots of phase angle, ϕ , as a function of frequency (Bode phase plot). One peak appears at intermediate high frequencies, and another at intermediate low frequencies (Fig. 2a, curve A). At intermediate high frequencies,

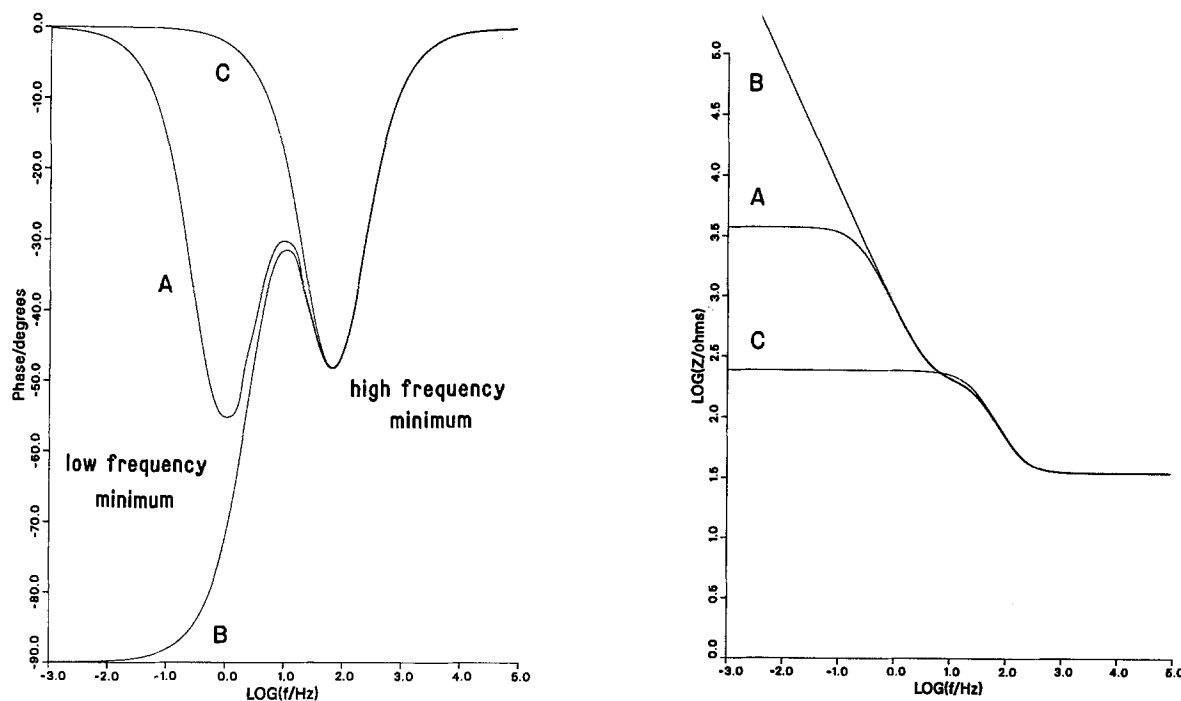


Fig. 2. a (left): Curve A is the Bode phase plot calculated from Eq. [23] and consistent with the electroadsorption mechanism shown in Eq. [14] and [15]. Parameter values are: $R_s = 35\Omega$; $R_p = 205\Omega$; $C_p = 30 \mu\text{F}$; $\rho = 229\Omega$; and $\tau = 0.48\text{s}$. Curve B shows a case where ρ is changed to a value of 205Ω . Since R_p and ρ are equivalent, curve B is consistent with the mechanism shown in Eq. [1]. Curve C shows a case where it is changed to a value of $10,000\Omega$ and is essentially infinite. b (right): Curves A, B, and C are the Bode amplitude plots corresponding to curves A, B, and C in Fig. 2a, respectively.

$(1 + j\omega R_p C_p)/R_p$ is much greater than $1/(1 + j\omega\tau)$, and the overall impedance given in Eq. [23] is approximately

$$Z = R_s + \left(\frac{1 + j\omega R_p C_p}{R_p} \right)^{-1} \quad [26]$$

Equation [26] can be rewritten as

$$Z = R_s + \frac{R_p}{1 + (\omega R_p C_p)^2} - j \frac{R_p(\omega R_p C_p)}{1 + (\omega R_p C_p)^2} \quad [27]$$

The tangent of the phase angle at intermediate high frequencies, calculated from the ratio of the real and imaginary parts of Eq. [27] is

$$\tan \phi = - \frac{R_p(\omega R_p C_p)}{R_s + R_p + R_s(\omega R_p C_p)^2} \quad [28]$$

The phase angle and its tangent both pass through minima at the same frequency. The point where these minima occur can be found by differentiating Eq. [28] with respect to angular frequency, ω , and setting the result to zero. From Eq. [28], the tangent of the minimum phase angle at intermediate high frequencies and the corresponding angular frequency are $\tan \phi_{\min}$ and ω_{\min} , respectively

$$\tan \phi_{\min} = - \frac{R_p}{2(R_s + R_p)} \sqrt{1 + R_p/R_s} \quad [29]$$

$$\omega_{\min} = \frac{1}{R_p C_p} \sqrt{1 + R_p/R_s} \quad [30]$$

These results are consistent with Eq. [15] and [16] given by Mansfeld for a single time constant cell (15).

At intermediate low frequencies, similar approximations are useful. First, it is helpful to rearrange Eq. [23] to the form of Eq. [31]

$$Z = R_s + \frac{\rho R_p(1 + j\omega\tau)}{\rho(1 + j(\omega\tau + \omega R_p C_p) - \omega^2\tau R_p C_p) - R_p} \quad [31]$$

As will be seen, the low frequency time constant, τ , is typically more than three orders of magnitude larger than the high frequency time constant, $R_p C_p$. Thus, at low frequencies ($\omega \leq 1$) all terms in Eq. [31] smaller than $\omega\tau$ are insignificant and Eq. [31] can be written approximately as Eq. [32]

$$Z = R_s + \left(\frac{1}{R_p} - \frac{1}{\rho(1 + j\omega\tau)} \right)^{-1} \quad [32]$$

Then Eq. [33] and [34] are derived for intermediate low frequencies by following the strategy used to develop Eq. [29] and [30]

$$\tan \phi'_{\min} = - \frac{R_p(\omega'_{\min}\tau)}{(\rho - R_p) + \frac{R_s}{\rho R_p} (\rho - R_p)^2 + (\omega'_{\min}\tau)^2 \rho \left(1 + \frac{R_s}{R_p} \right)} \quad [33]$$

Table II. Model parameters estimated by approximate equations

E (mV)	Cu^{2+} (M)	T (mg/liter)	R_s (Ω)	R_p (Ω)	C_p (μF)	(Ω)	(ms)
0	0.01	0	35	205	30	217	35
50	0.01	0	36	85	23	86	19
100	0.01	0	37	109	9	109	14
200	0.01	0	37	161	15	161	5
0	0.1	0	49	144	47	183	19
50	0.1	0	49	54	20	57	12
100	0.1	0	49	65	8	66	12
200	0.1	0	49	234	5	236	24
50	0.1	5	49	199	24	238	52
50	0.1	10	49	352	26	381	42
50	0.1	15	49	449	33	486	45
50	0.1	30	49	601	54	651	111

$$\omega'_{\min} = \frac{1}{\tau} \sqrt{\frac{1 + R_s/R_p + R_s R_p/\rho^2 - 2R_s/\rho - R_p/\rho}{1 + R_s/R_p}} \quad [34]$$

where $\tan \phi'_{\min}$ and ω'_{\min} are the tangent of the minimum phase angle and the angular frequency at the minimum, respectively.

The five quantities defined in Eq. [24], [29], [30], [33], and [34] are easily obtained from inspection of experimental impedance spectra similar to curve A in Fig. 2a and 2b. Values of R_s , R_p , C_p , ρ , and τ can all be calculated by substituting the five quantities into Eq. [24], [29], [30], [33], and [34] (Tables I and II). Alternatively, these parameters can be determined numerically by minimizing the sum of squares. The model variance, parameter variances, and parameter confidence intervals can also be calculated (16, 17).

Equation [23] was used to generate three theoretical impedance spectra. These are compared in Fig. 2a and 2b. Curve A represents Eq. [23] for the case where R_p and ρ are not equivalent and shows two minima in the Bode phase plot, Fig. 2a. Parameter values used in this calculation are given in the figure caption and are based upon values measured for underpotential deposition of Cu on Au at 0 mV and 0.01M Cu^{2+} . Note that the adsorption mechanism shown in Eq. [14] and [15] is consistent with this result. In contrast, curve B represents the case where $R_p = \rho$, which is characteristic of the simple adsorption mechanism shown in Eq. [1]. In this case, the phase asymptotically approaches -90° at very low frequencies, while the minimum in phase at high frequency remains unchanged. Curve C shows only one minimum (peak) and corresponds to the special case where ρ is essentially infinite; the circuit shown in Fig. 1b behaves like that shown in Fig. 1c. Such single time constant impedances can result from electrode reactions which occur without the adsorption of reactants. Every minimum observed in Fig. 2a has a corresponding inflection point in Fig. 2b, the Bode amplitude plot.

Table I. Summary of impedance spectra: quantities used to estimate model parameters

E (mV)	Cu^{2+} (M)	T (mg/liter)	log Z (Ω)		log f (Hz)		Phase minimum ($^\circ$)	
			High frequency	Low frequency	High frequency	Low frequency	High frequency	Low frequency
0	0.01	0	1.54	3.56	1.84	0.00	-48	-51
50	0.01	0	1.56	4.17	2.18	-0.27	-33	-66
100	0.01	0	1.57	5.25	2.53	-0.62	-37	-71
200	0.01	0	1.57	7.07	2.18	-0.93	-43	-71
0	0.1	0	1.69	2.86	1.67	0.55	-37	-28
50	0.1	0	1.69	3.00	2.33	0.35	-21	-43
100	0.1	0	1.69	3.55	2.67	0.14	-24	-55
200	0.1	0	1.69	4.52	2.48	-0.30	-45	-63
50	0.1	5	1.69	3.11	1.88	0.05	-42	-35
50	0.1	10	1.69	3.67	1.69	-0.01	-52	-35
50	0.1	15	1.69	3.77	1.53	-0.03	-55	-35
50	0.1	30	1.69	3.90	1.25	-0.42	-59	-34

Note: The third column contains the thiourea concentration. The fourth and fifth columns contain the log of the amplitude of the complex impedance at the high frequency and low frequency limits. The sixth and seventh columns show the position of the high frequency and low frequency minima in the Bode phase plots, respectively. The last two columns contain the depth of those minima.

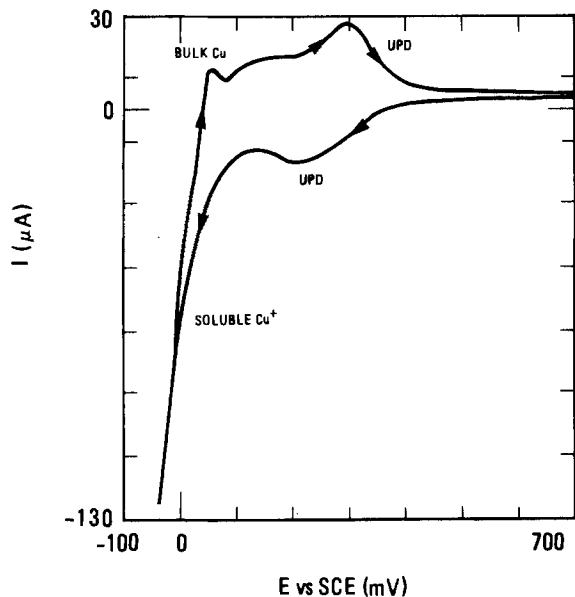


Fig. 3. Cyclic voltammogram of underpotential deposition of Cu on polycrystalline Au rotating disk electrode. The electrolyte consisted of 0.1M H_2SO_4 and 0.1M $CuSO_4$. A sweep rate of 50 mV/s and a rotation speed of 2000 rpm were used.

Results and Discussion

A cyclic voltammogram obtained during underpotential deposition of Cu on Au from an electrolyte consisting of 0.1M $CuSO_4$ in 0.1M H_2SO_4 is shown in Fig. 3. The potential was swept from 700 to -35 mV, SCE at a rate of 50 mV/s, and the RDE rotation speed was at 2000 rpm. Bulk Cu deposition began at approximately -35 mV and resulted in the small stripping peak centered at 0 mV; the amplitude of this stripping peak increased as the reversal potential was increased in the cathodic direction. The broad anodic peak centered at 300 mV is due to stripping UPD Cu from the Au surface. Approximately 4.61×10^{-4} C/cm² of anodic charge was removed from the Au surface during stripping, which corresponds to 1.06 monolayers of Cu. Apparently, surface alloy formation was minimal.

However, three times as much charge was passed during the cathodic portion of the potential cycle. The cathodic charge in excess of that required for the UPD is believed to have resulted in formation of soluble Cu^+ . Cyclic voltammograms at slower sweep rates, such as those shown in Ref. (3), have more well-defined UPD deposition and stripping peaks; a fast sweep rate was used here to avoid excessive diffusion of Cu into the Au surface (3).

Impedance spectra were obtained at electrode potentials of 0, 50, 100, and 200 mV and at each concentration level of Cu^{2+} . In Fig. 4a and 4b, experimental data obtained at a Cu^{2+} concentration of 0.01M and a potential of 0 mV are represented by points and compared to the theoretical model (solid line). This electroadsorption process clearly exhibits the characteristics of the mechanism shown in Eq. [14] and [15], which involves formation of Cu^+ ; the ratio ρ/R_p is greater than unity. Furthermore, the dramatic increase in cathodic current near 0 mV shown in Fig. 1 is attributed to Cu^+ formation; interpretations of impedance spectra and the cyclic voltammogram are consistent. For comparison, data obtained at the same concentration and a more anodic potential, 100 mV, are shown in Fig. 5a and 5b. Changes in potential alter observed impedance spectra of the UPD process dramatically. The ratio of ρ/R_p calculated from Fig. 5a is almost unity.

Figures 6 and 7 show the experimentally determined values of model parameters as a function of electrode potential at Cu^{2+} concentrations of 0.01 and 0.1M, respectively. The cell resistance, R_s , is independent of electrode potential, while all other parameters appear to have a strong dependence on this variable. Variations in R_p and ρ with potential are considered to be significant since these parameters have standard deviations of less than 1% of the absolute parameter values. However, variations in C_p and τ with potential have a much larger error associated with them. Consequently, it is inappropriate to use Eq. [22] to calculate rate constants.

Values of ρ are slightly greater than values of R_p over the entire potential range investigated, which is indicative of the mechanism given in Eq. [14] and [15]. However, in some cases the differences are too small to be reflected in tabulated values (Table II). Such differences give rise to two distinct minima observed in spectra such as those

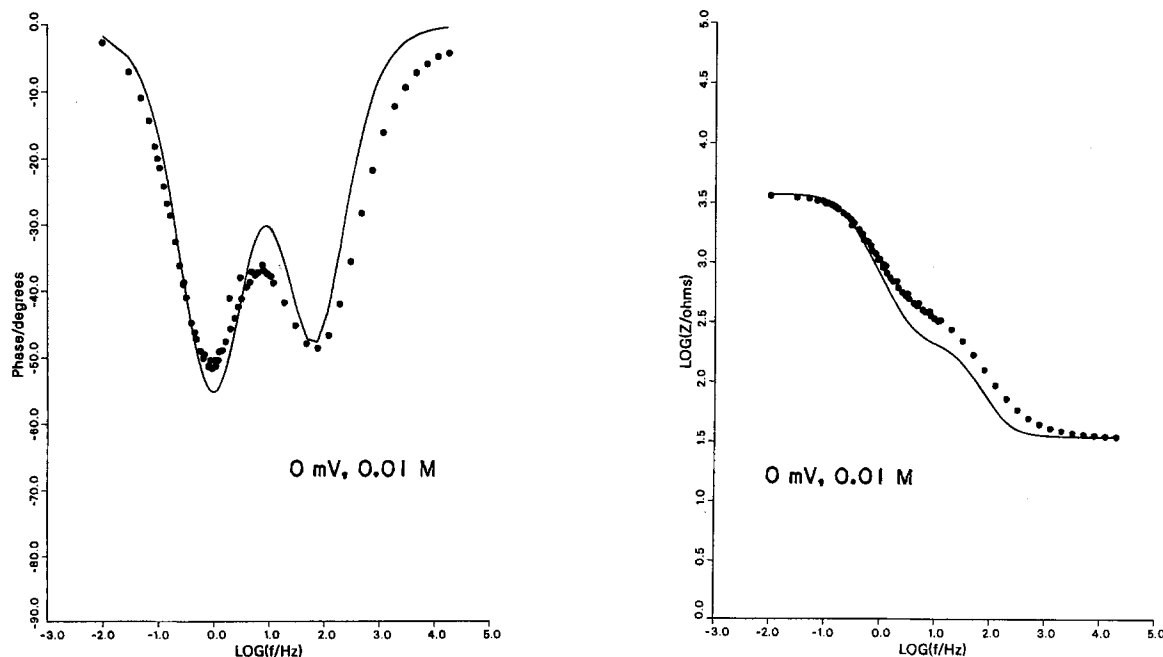


Fig. 4. a (left): A comparison of the theoretical Bode phase plot (solid line) and experimental data (points) for Cu electroadsorption on Au at 0 mV. The electrolyte consisted of 0.1M H_2SO_4 and 0.01M $CuSO_4$. Parameter values were $R_s = 35\Omega$, $R_p = 205\Omega$, $C_p = 30 \mu F$, $\rho = 229\Omega$, and $\tau = 0.048s$. b (right): A comparison of the theoretical Bode amplitude plot (solid line) to experimental data (points) at the same conditions as Fig. 4a.

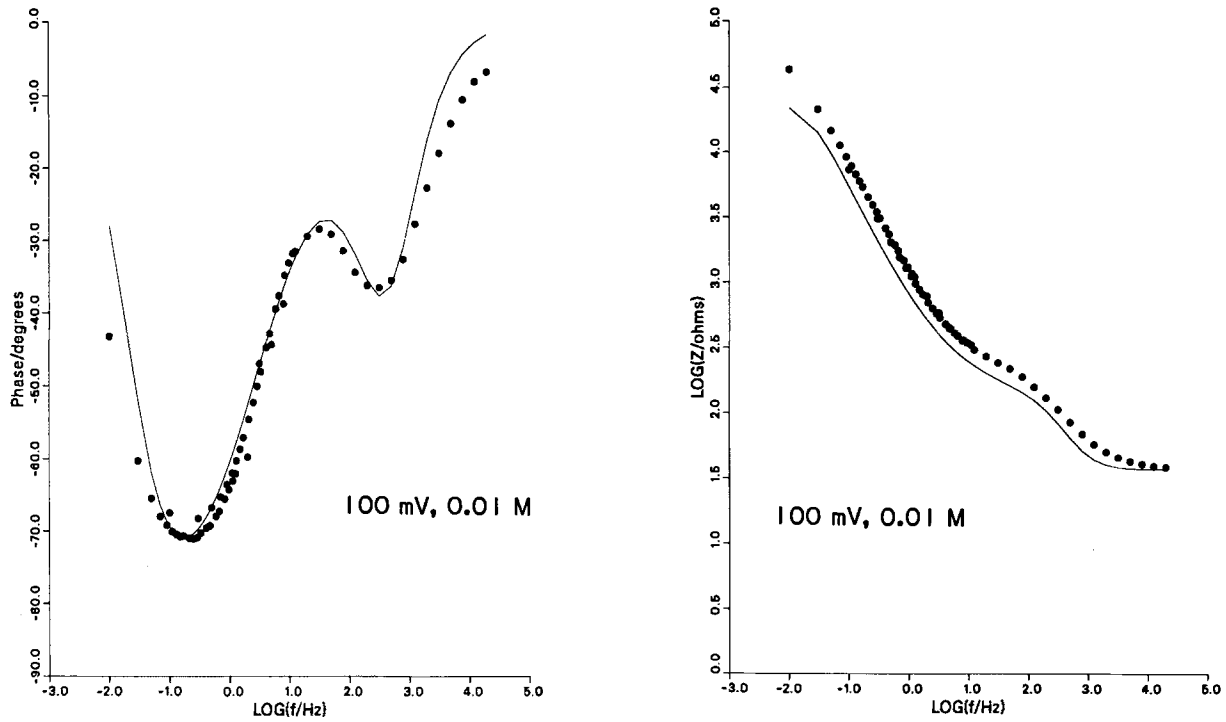


Fig. 5. a (left): A comparison of the theoretical Bode phase plot (solid line) and experimental data (points) for Cu electro sorption on Au at 100 mV. The electrolyte consisted of 0.1M H₂SO₄ and 0.01M CuSO₄. Parameter values were $R_s = 35\Omega$, $R_p = 109\Omega$, $C_p = 9\mu F$, $\rho = 111\Omega$, and $\tau = 0.078s$. b (right): A comparison of the theoretical Bode amplitude plot (solid line) to experimental data (points) of the same conditions as Fig. 5a.

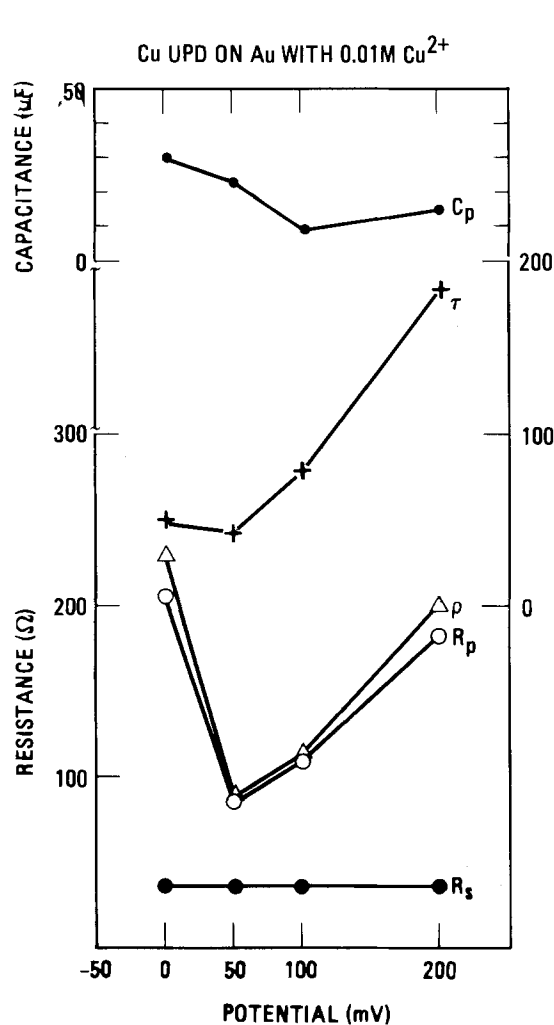


Fig. 6. Potential dependence of impedance model parameters at a CuSO₄ concentration of 0.01M.

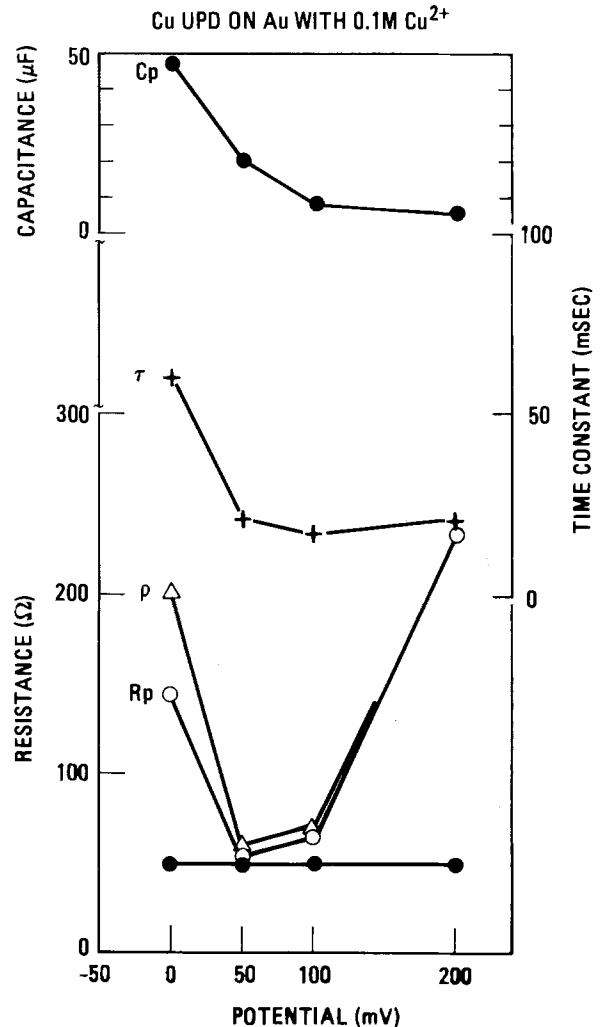


Fig. 7. Potential dependence of impedance model parameters at a CuSO₄ concentration of 0.1M.

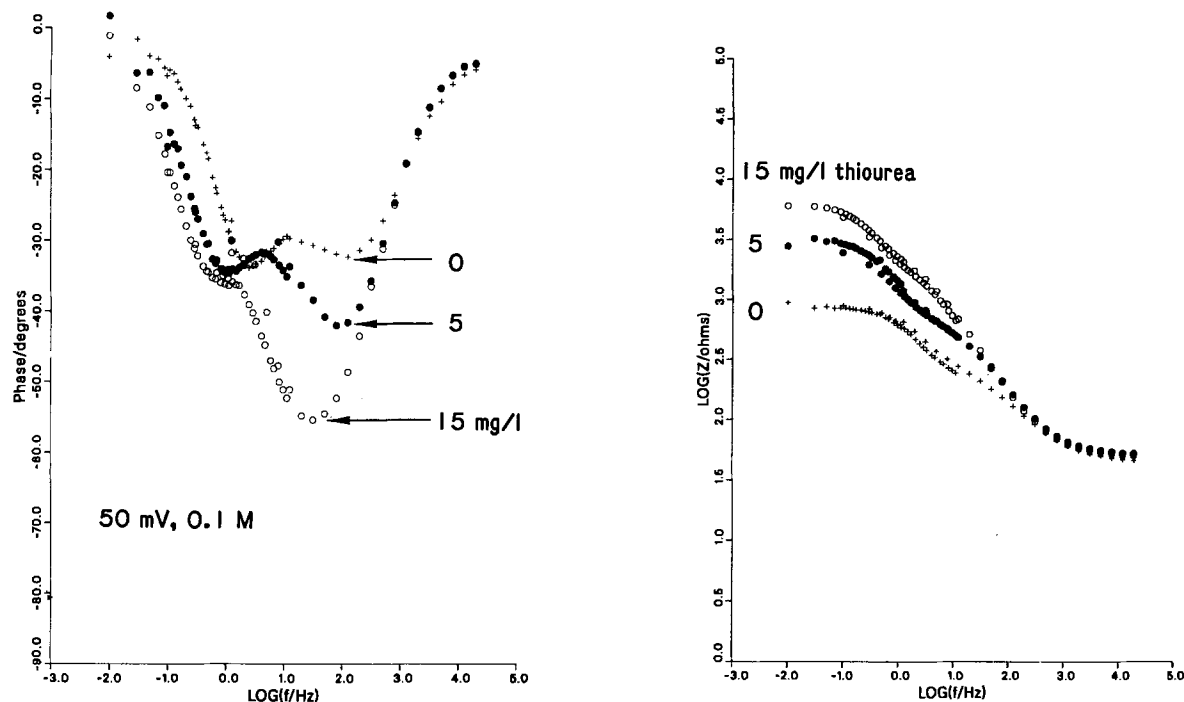


Fig. 8. a (left): Effect of thiourea on impedance spectra (Bode phase plots) at a potential of 50 mV. The electrolyte consisted 0.1M H_2SO_4 , 0.1M $CuSO_4$, and thiourea. Data points represent thiourea concentrations of 0 (crosses), 5 (closed circles), and 15 (open circles) mg/liter. b (right): Effect of thiourea on impedance spectra (Bode amplitude plots) of the same conditions as Fig. 8a. Data points represent thiourea concentrations of 0 (crosses), 5 (closed circles), and 15 (open circles) g/liter.

shown in Fig. 4a and 5a. The simple adsorption process given in Eq. [1] cannot account for such spectra or the difference between ρ and R_p . The rate of dissolution of Cu^+ responsible for the difference in R_p and ρ would be difficult to detect in a ring-disk experiment (13).

Charge transfer resistances for bulk deposition do not exhibit minima and decrease with increasing cathodic potential (12). However, in the cases of Pb and Tl electro-sorption, the observed charge transfer resistances do pass

through minima (4). In these cases of simple electro-sorption, the reason can be found by inspection of Eq. [11]. At the limit of infinite cathodic potential, k_f becomes infinite while k_b becomes zero. Alternatively, at the limit of infinite anodic potential, k_b becomes infinite while k_f becomes zero. At both extremes, the charge transfer resistance, R_p , approaches infinity and the rate of electron transfer drops to zero. At potentials between these limits, R_p passes through a finite, minimum value. Rationalization of the minima in R_p and ρ are observed in Fig. 6 and 7 near 50 mV is more difficult because of the complexity of Eq. [19]. The equilibrium constant K is assumed to be of

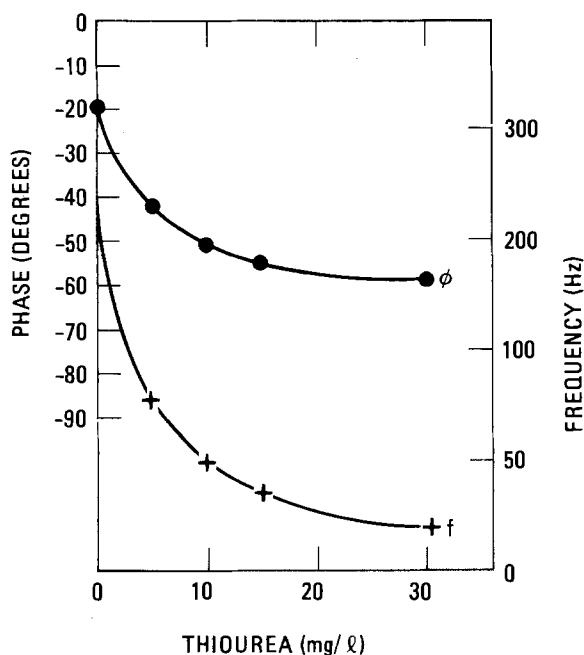


Fig. 9. Empirical effect of thiourea on the high frequency minimum (peak) in the Bode phase plot at the same conditions as Fig. 8a. The depth of the minimum in phase is represented by the curve labeled ϕ and the position of this minimum on the frequency axis is represented by the curve labeled f .

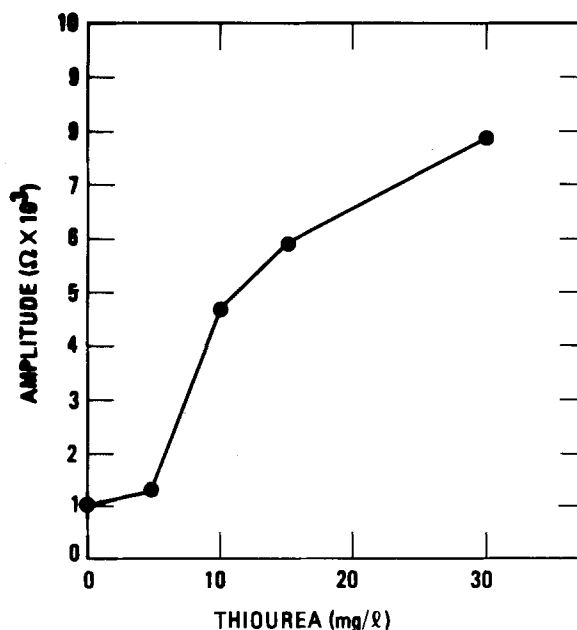


Fig. 10. Empirical effect of thiourea on the impedance amplitude at the low frequency limit. Same conditions as Fig. 8a.

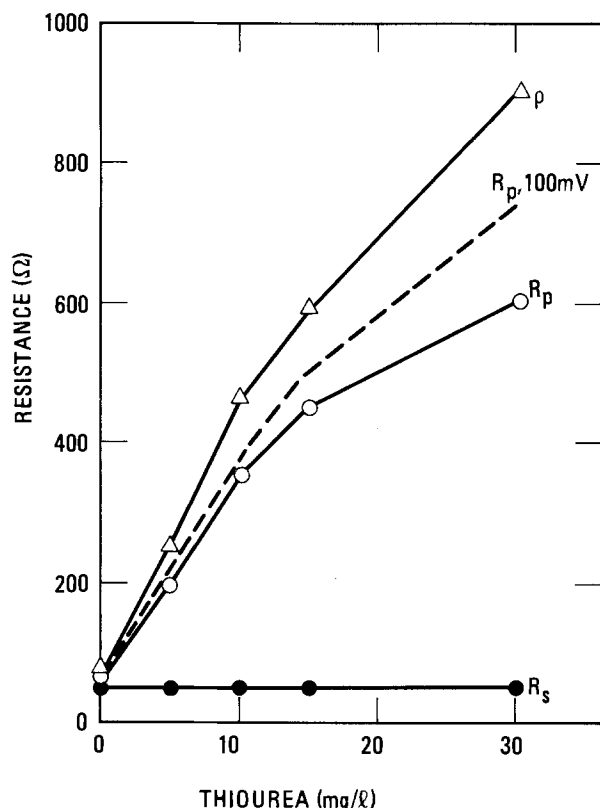


Fig. 11. Effect of thiourea on the impedance model parameters at the same conditions as Fig. 8a. The resistances R_p and ρ increase dramatically with thiourea concentration, while the cell resistance, R_s , remains constant.

the form $K = C \exp(-cE)$, so $K' = -cC \exp(-cE)$. Therefore, the denominator of Eq. [19] is proportional to the difference $(a + b)k_b + k - cKk_tM^{2+}$, which becomes zero as the potential increases in the cathodic direction to some limit; at this limit R_p becomes infinite. At intermediate potentials, R_p passes through a finite, minimum value, while at large anodic potentials it approaches infinity.

Impedance spectra showing the effects of thiourea additions to the electrolyte are shown in Fig. 8a and 8b. These data were obtained at a Cu^{2+} concentration of 0.1M, thiourea concentrations of 0, 5, and 15 mg/liter, and an electrode potential of 50 mV. Note that thiourea increases the depth and changes the position of the high frequency minimum in the Bode phase plot (Fig. 8a and 9). Furthermore, the amplitude of the complex impedance increases dramatically at the low frequency limit (Fig. 8b and 10). These changes translate into increases in the charge transfer resistances R_p and ρ , as expected (Fig. 11). The rate constants k_t and k_b are proportional to the active area available to discharge metal cations. Coadsorption of thiourea during formation of the UPD would decrease the active area by blocking sites, thereby decreasing the magnitude of rate constants and increasing R_p and ρ . Data also indicate that the double layer capacitance, C_p , and the low frequency time constant, τ , increase with thiourea concentration (Fig. 12). This result for C_p is surprising since organic additives have been shown to decrease the double-layer capacitance during Ni deposition (17) and since it implies that thiourea increases the surface charge density on the electrode.

It is important to note that Cl^- is present in most copper plating solutions at concentrations of about 30 ppm and can effect grain refinement of the electrodeposit significantly. This experimental technique might be useful in understanding the role of Cl^- during electrodeposition. Furthermore, there is strong evidence that thiourea is electrochemically decomposed at the cathode (18). This decomposition results in incorporation of sulfur, but no carbon, into the electrodeposit. Note that thiourea decom-

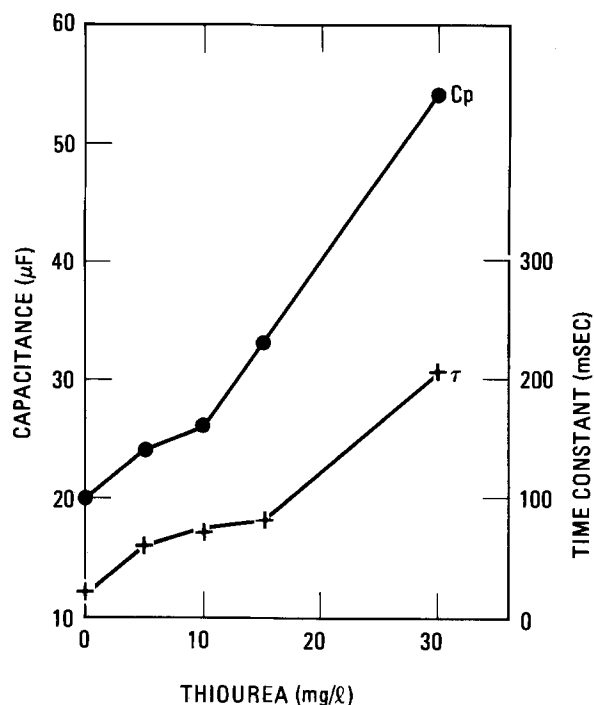


Fig. 12. Effect of thiourea on the impedance model parameters at the same conditions as Fig. 8a.

position was not considered in the electrokinetic model presented. However, sulfide formation at the electrode-electrolyte interface could help explain the unexpected increase in double-layer capacitance with increasing thiourea concentration. Such films would exhibit relatively high dielectric strengths.

These measurements suggest that ac impedance could be used as a means of monitoring total organic additive concentration in copper electroplating baths or as a means of verifying electrolyte purity in additive-free copper electroforming baths. Detection of such low levels of thiourea and other surface active organics by spectroscopic means is not practical at the present time.

Summary

Formation of a Cu UPD on Au has been studied by ac impedance. Spectra are characterized by two capacitive peaks in the Bode phase plot. The high frequency peak is associated with both the double-layer capacitance and the resistance to charge transfer which accompanies electro-sorption. In contrast, the low frequency time constant is due only to relaxation phenomena associated with charge transfer. Data are consistent with an electro-sorption mechanism which involves simultaneous formation of the UPD layer and a soluble intermediate. A method is presented for calculating model parameters from the impedance spectra.

Adsorbed thiourea was found to have a dramatic effect on the high frequency peak in the Bode phase plot. These measurements suggest that ac impedance could be used as a means of monitoring total organic additive concentration in copper electroplating baths or as a means of verifying electrolyte purity in additive-free copper electroforming baths. Detection of such low levels of thiourea and other surface active organics by spectroscopic means is not practical at the present time.

Acknowledgments

This work is supported by the U. S. Department of Energy, DOE, under Contract no. DE-AC04-76DP00789. The support and technical guidance of D. A. Nissen are deeply appreciated.

Manuscript submitted March 12, 1985; revised manuscript received ca. June 5, 1985. This was Paper 237 presented at the Las Vegas, Nevada, Meeting of the Society, Oct. 13-18, 1985.

Sandia National Laboratories assisted in meeting the publication costs of this article.

REFERENCES

1. J. C. Farmer and R. H. Muller, *This Journal*, **132**, 39 (1985).
2. S. Swathirajan, H. Mizota, and S. Bruckenstein, *J. Phys. Chem.*, **86**, 2480 (1982).
3. H. O. Beckmann, H. Gerischer, D. M. Kolb, and G. Lehmpfuhl, *Faraday Sympos.*, **12**, 53 (1977).
4. M. Klimmeck and K. Juttner, *Electrochim. Acta*, **27**, 83 (1982).
5. K. Nihei, T. Ohsaka, and K. Anzai, *Denki Kagaku*, **47**, 415 (1979).
6. K. Engelsmann, W. J. Lorenz, and E. Schmidt, *J. Electroanal. Chem.*, **114**, 1 (1980).
7. W. J. Lorenz, H. D. Hermann, N. Wuthrich, and F. Hilbert, *This Journal*, **121**, 1167 (1974).
8. S. Swathirajan and S. Bruckenstein, *J. Electroanal. Chem.*, **146**, 137 (1983).
9. W. Smyrl, in "Electrochemical Corrosion Testing," F. Mansfeld and U. Bertocci, Editors, pp. 199-214, American Society for Testing and Materials, Philadelphia (1981).
10. D. R. Turner and G. R. Johnson, *This Journal*, **109**, 798 (1962).
11. N. J. Spiliotis, in "Metal Finishing Guidebook and Directory," 46th ed., p. 216, Metals and Plastics Publications, Hackensack, NJ (1978).
12. I. Epelboin and R. Wiart, *This Journal*, **118**, 1577 (1971).
13. S. Bruckenstein and G. W. Tindall, *Anal. Chem.*, **40**, 1051 (1968).
14. B. J. Bowles, *Electrochim. Acta*, **15**, 589 (1970).
15. F. Mansfeld, *Corrosion*, **36**, 301 (1981).
16. G. E. P. Box and G. A. Coutie, *Proc. IEE*, **103**, 100 (1956).
17. J. C. Farmer and H. R. Johnson, in "Proceedings of the 11th World Congress on Metal Finishing," pp. 343-355, Jerusalem, Israel, Oct. 21-26, 1984.
18. J. Llopis, J. M. Gamboa, and L. Arizmendi, in "CITCE Meeting Proceedings," pp. 448-458, Paris (1957).

On the Evolution of Concepts Concerning Events at the Semiconductor/Solution Interface

John O'M. Bockris*

Department of Chemistry, Texas A&M University, College Station, Texas 77843

Shahed U. M. Khan*

Department of Chemistry, Duquesne University, Pittsburgh, Pennsylvania 15282

ABSTRACT

The conventional determination of the Fermi level of electrons in solution is found incorrect. One should not utilize the energy corresponding to the redox potential on the vacuum scale to be equal to the energy of the Fermi level of metal or semiconductor at equilibrium. It is activated vibrational states within ions (rather than fluctuations of energy in the ground vibrational state) which should overlap with the electronic states in the semiconductor. Electronic states in solution relevant to an electrode reaction are not gaussian but are boltzmannian. The Schottky model is sometimes (perhaps often) not applicable to the semiconductor/solution interface. Metallic catalysts in photoelectrochemistry are effective by causing a change of rate-determining step to that at the metal/solution interface.

Increasing investigations of the semiconductor/solution interface suggest that there is need to modify some of the classical concepts. It is desired in this paper to discuss the evolution of these concepts.

The Fermi Level in Solution

The equilibrium between a metal, or semiconductor, and a solution can be expressed in various terms. A quite general relationship states that there must be an equality of the electrochemical potentials $\bar{\mu}_i$ for each given entity between the values in the solid phase (m) and the value in the solution (s). Thus

$$\bar{\mu}_i^{\text{sol}} = \bar{\mu}_i^{\text{solid}} \quad \bar{\mu}_i^{\text{m}} = \bar{\mu}_i^{\text{s}} \quad [1]$$

If one takes the electrons as the species concerned, the advantage is that there is a named concept with which one associates $\bar{\mu}^{\text{m}}$ (m here is taken to mean solid electronic conductor, i.e., it may be a semiconductor as well as a metal). This is the Fermi energy of the electron in the solid.

There is considerable conceptual confusion in relating the meaning of $\bar{\mu}_e^{\text{m}}$ to the concept of the Fermi level energy.

Thus, a simple concept of the Fermi energy, normally given in books in solid-state physics, is to take the approximation that the electron is "free" in the conductivity band. Then, in respect to the bottom of the conduction band, the maximum kinetic energy in the conductivity band is easily shown (7b) to be $n^2\hbar^2/8m_e\lambda^2$, where these quantities have their usual meaning. What is meant by the

chemical potential, μ_e^{m} , is the work done to bring an electron from infinity to this maximum kinetic energy level in the special and unnatural case in which both the surface potential is zero and the charge on the metal is zero. The physical meaning of this μ_e^{m} (the chemical potential of the electron in the bulk of the metal) for electrons in the conductivity band is the interaction which these electrons have with the surrounding metal atom cores.

The relationship between a kinetic Fermi energy $E_{F,m}$ and $\bar{\mu}_e^{\text{m}}$ (or the corresponding μ_e^{m} for an unreal case where the metal is uncharged and there is no surface potential) is that the larger the kinetic Fermi energy, the smaller is $\bar{\mu}_e^{\text{m}}$ (see Fig. 1).

In order to express the equilibrium between metal or semiconductor and solution, it is necessary to know the value of the corresponding μ_e^{s} , the electrochemical potential of the electron in solution. In the normal view, accepted up to now, this μ_e^{s} has been identified with the redox potential (on the vacuum scale) of redox process occurring across the interface.

The origin of this approach relates to a paper by Gerischer (1). In the original derivation, the artificial and unusual case was taken by Gerischer, or perhaps the simplification, that there was a charge-free surface, and also that the solution had a zero value of surface potential, i.e., no dipole potential across the solution-vacuum interface such that μ_e^{s} becomes equal to μ_e^{v} . Later, however, such a concept has been utilized for real situation (2, 3) where $\chi_s \neq 0$ and the Fermi level of solution μ_e^{s} is equated to the negative value of energy corresponding to vacuum-scale redox potential (4, 5), $-nFV_{\text{redox}}$ (vacuum scale).

*Electrochemical Society Active Member.

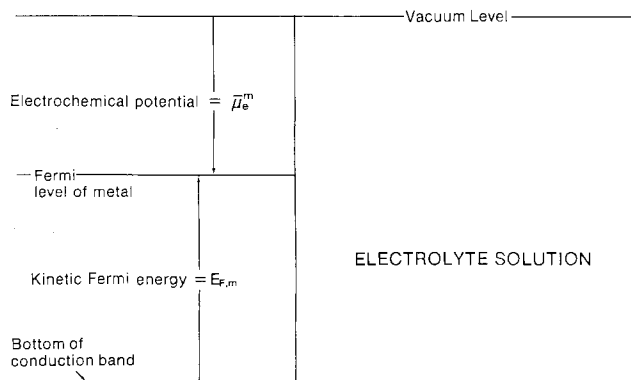


Fig. 1. A schematic diagram to show the kinetic Fermi energy, $E_{F,m}$ and the electrochemical potential of electron, $\bar{\mu}_e^m$, in a metal.

It has been shown (13) that the negative value of energy corresponding to the redox potential in the vacuum scale, $-nFV_{\text{redox}}$ (vacuum scale), is indeed equal to this $\bar{\mu}_e^s$ but not to the μ_e^s . The normal practice, from this beginning, is to find out V_{redox} (vacuum scale) (simply done by taking the value of the hydrogen scale and adding to it the value of the hydrogen electrode on the vacuum scale, approximately $4.5 \pm 0.3V$).

The difficulty comes from the fact that, indeed, solutions neither have zero charge when they are in equilibrium with metals or semiconductors, nor do they have a zero value of the surface potential. Under these circumstances therefore, the identification that $\bar{\mu}_e^s = -nFV_{\text{redox}}$ (vacuum scale) fails. The true identification is that $-nFV_{\text{redox}}$ (vacuum scale) = μ_e^s , not $\bar{\mu}_e^s$.

This matter is one of major importance because of the frequent erroneous use of this $-nFV_{\text{redox}}$ (vacuum scale) in semiconductor photoelectrochemistry to identify as the Fermi level in solution $\bar{\mu}_e^s$ (6-10).

1. Further, the Fermi level in solution must be associated with a "free" movement of electrons within the phase, so that the idea of a "kinetic Fermi energy" can exist.

2. Corresponding to this, it is difficult to conceive of the idea of a Fermi level in a solution in which energy bands for electrons or holes have no real existence.¹

In applying Fermi level concepts to an ionic solution and the electrons which characterize the electronic states of ions in solution, criteria 1 and 2 do not apply, *i.e.*, there is no kinetic energy of free electrons in ions, since the electrons are in the bound state in the ion and cannot contribute to electronic conductivity in solution; and bands in the normal sense do not arise.

Such considerations must not be confused with the idea of spectral bands in water (11a, 18) which correspond to levels associated with atomic or molecular movements and have a radically different meaning from conduction bands for electrons in water. Such concepts would have no remote relevance even in a solution which contained solvated electrons (11b). The carriers (electrons or holes) have no relevance to the electrons in the orbitals within ions in redox systems where the energy considerations are not band-like.

Thus, in summary, it is, at the least, unrealistic, and, at the most, fundamentally incorrect, to discuss a Fermi level or Fermi energy of electrons and holes in ionic solutions.

3. The idea of the energy of a Fermi level characterizing electronic states in solution, and the equating of it for some electron transfer equilibrium to the energy of a Fermi level in the electrode, goes back to concepts appropriate to the metal/metal and metal/semiconductor interfaces. Here, consideration of equalization of Fermi levels in the two phases is correct, because there are free carriers (electrons or holes) in each phase, and each phase is an electronic conductor. The free electrons from one

¹Thus, in theoretical work of Williams *et al.* (11a), a conduction level for electrons in water is referred to, but this is almost at the vacuum level.

metal phase to another metal or semiconductor phase can have a conductive flow at the interface. However, the condition which governs the transfer of electrons and holes at metal or semiconductor/solution interfaces is that the transfer is isoenergetic with respect to the particle in transfer and involves an electron transfer reaction. At the metal/metal, or metal/semiconductor, interfaces, there is no transfer from one phase to a single particle, in which specific quantum levels exist. For the metal/metal and metal/semiconductor interfaces, it is a matter of conductive flow (across a gradient of electrochemical potential) in free electron conduction. At the metal/solution and semiconductor/solution interfaces, it is a matter of a reaction between an individual particle in the solution and electrons in the bands of the electronic conductor. The energy states in solution which are relevant and which must be equal to the energy of the carriers in the semiconductor are the energy of vibronic (vibrational and electronic) states in ions in solution when they are activated² (for which an activation barrier exists). Hence, electron transfer at the electrode/solution interface occurs in the form of an electron transfer reaction (12), but not as a conductive flow, like that in metal/metal or semiconductor/metal interfaces.

4. Finally, in respect to the value of $\bar{\mu}_e^s$ (which exists, conceptually, for any phase independently of whether, in solution, it should be associated with Fermi level concepts), it has been shown elsewhere (13-15) that for a real interface it should be given by

$$\bar{\mu}_e^s = -nFV_{\text{redox}}(\text{vacuum scale}) - nF\phi^s = E_{F,\text{redox}} \quad [2]$$

where the inner potential of solution, ϕ^s , is not experimentally determinable and is at present not known. Equation [2] clearly proves that one cannot use vacuum-scale redox potential as the Fermi level in solution to equate with that in metal or in semiconductor at equilibrium.

Is the Fermi Level in Solution a Necessary Concept?

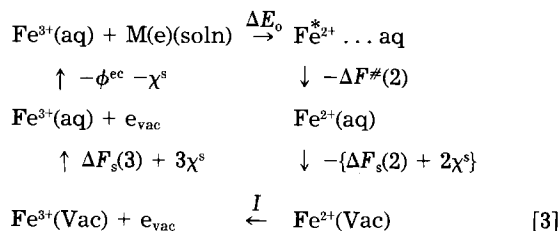
In metal-semiconductor contacts, the equilibrium condition is normally regarded as being given by an equality of the Fermi levels. Such a condition provides a reasonable and convenient way of knowing the energy levels in one phase if one knows the energy levels in the other.

The normal approach in electrochemistry is to imitate the situation for the metal-metal and metal-semiconductor systems. Knowing the electrochemical potential in the solid phase, it has been thought convenient to utilize the Fermi level concept in solution (discussed above) in order to assess, or determine, the equilibrium position with respect to electrons in the solid and liquid phases.

The aspect of the validity of applying Fermi-like concepts to solutions (and, if valid, then the question remains about its numerical value) has been dealt with in the previous section. However, there exists a different kind of question, which may be put forward as follows. Let it be assumed that the Fermi level concept applies to solution, and that the difficulty of the numerical determination of it can be overcome (15b); then the question still remains. Is it a useful concept for kinetic and mechanistic electrochemistry where the principal ideas are quantum-oriented and where the thermodynamic states are utilized only as reference to beginning states, but where the transitions concerned are from quantum levels in the electrode to quantum levels in the solution? The most desirable and useful quantities to know are the electronic donor and acceptor energy levels of the ions in solution. To determine these, one needs to know the difference of energy, ΔE_0 , between the activated and the ground state of acceptor or donor ions in solution and then to express this with respect to the energy of a clearly defined reference state. The best reference state at present seems to be

²One should not consider that the activated state is the excited electronic state of the ion, *e.g.*, in a transition metal-ion due, say, to d-d transition. Such a transition involves very high energy, *e.g.*, of the order of 1.5 eV. Activated states in electrochemical reactions correspond to excited vibrational states of the ion-solvent bond in the ground electronic state of the ion.

the stationary electron at infinity in a vacuum. For example, when $\text{Fe}^{3+}(\text{aq})$ ion is in solution, one can determine this difference in energy, ΔE_0 , by using the following cycle



Hence

$$\Delta E_0 = \phi^{\text{ec}} + \Delta F^{\#}(2) + \Delta F_s(2) - \Delta F_s(3) - I \quad [4]$$

where $\Delta F^{\#}(2)$ is the free energy of activation of $(\text{Fe}^{2+} \dots \text{aq})$, and $\Delta F_s(2)$ and $\Delta F_s(3)$ are the free energies of solvation of Fe^{2+} and Fe^{3+} ions, respectively. I is the ionization energy of Fe^{2+} ions and χ^{s} is the surface potential of solution.

Knowing ΔE_0 and taking the activated electronic level of $\text{Fe}^{2+}(\text{aq})$ to be equal in potential energy to the energy of the Fermi level in the electronic conductor, one can calculate the vibronic energies of the ground state of the acceptor ions in solution with respect to the reference level in vacuum, E_0 , as (see Fig. 2)

$$E_0 = -\Phi^{\text{ec}} + \Delta E_0 \quad [5]$$

Electronic Energy Distribution in Solution

It has been conventional for workers in the field of photoelectrochemistry to follow Russian and German workers in portraying the energy distribution in solution in the form of a gaussian distribution (1, 6-8). Thus, it was thought (16a) that there would be a gap between the vibrational energy levels in solution, as there is a gap between the vibrational energy states of molecules in the gas phase. The energies referred to are those of the electronic states in the ions, as affected by the vibrational-rotational levels of the ion-solvent complex (*i.e.*, vibronic states).

It was argued (16a) that the order of the energy difference (*e.g.*, for H_3O^+) between vibrational levels is around 0.5 eV, and, as the energy of the average oscillator in solution is kT , the probability of energy being transferred to levels above the ground-state level must be negligible. Such a concept was originated in the work of Levich (6), since he erroneously avoided the fact that thermal equilibrium between the ion-solvent bond and the surrounding solvent molecules can give rise to sufficient probability of having the required energy of activation.

On the basis of these concepts, the ground-state vibrational level in the first electronic state was the only one which was considered to be relevant to electron transfer processes at electrodes. In order that the range of energies needed in electrochemical reactions could be obtained, it was thought that fluctuations of the energy around the ground state would be necessary. As fluctuations give rise to gaussian distributions, the energy distribution

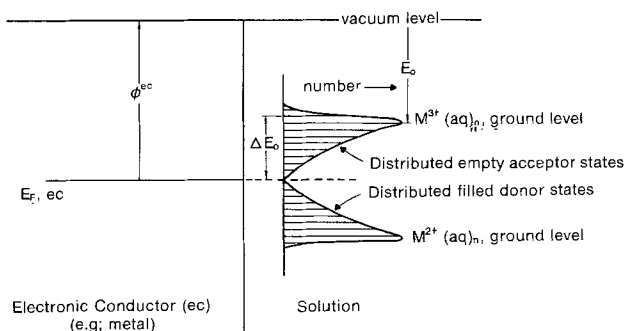


Fig. 2. Maxwellian distribution in solution

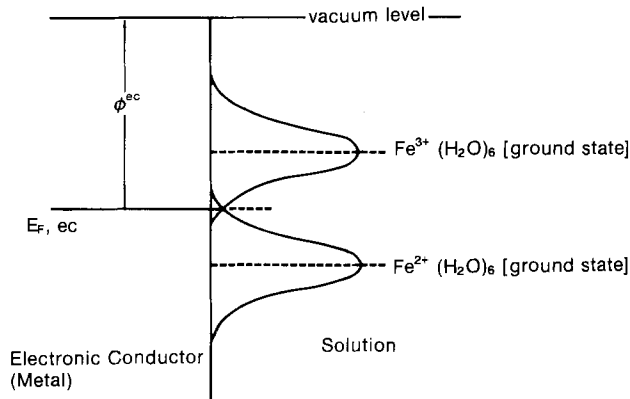


Fig. 3. Gaussian distribution in solution

was drawn in the form of a gaussian bell-shaped curve (1-3, 6-8) (see Fig. 3)³ where the potential energy is considered to vary both around the ground state to an equal degree.

However, the thing which in fact varies when an ion is in solution and then causes the energy of the central ion to vary is not this ground state and its perturbational fluctuation but the normal boltzmannian distribution of the energy in all the vibrational states of the ion-solvent bonds. This energy is not symmetrically distributed around the central point (*i.e.*, the ground state) but is distributed Maxwellianly in the normal way in all presentations of molecular mechanics in solution, except those associated with the Levich-Marcus-Gerischer viewpoint.

Hence, the gaussian concept must now be viewed as nugatory. A very simple and general piece of evidence against an effectively gaussian distribution is that it conforms to the relation (16)

$$\ln i_c = \ln A - \frac{(E_s + e_0 \eta_c)^2}{4E_s kT} \quad [6]$$

where A is a constant, E_s is the solvent reorganization energy of the ion, i_c is the cathodic current density, η_c is the cathodic overpotential, and e_0 is the electronic charge. However, the experimental evidence is clear: the current density/overpotential relation usually observed is boltzmannian, *i.e.*

$$\ln i = B - \frac{E_A + \beta e_0 \eta}{kT} \quad [7]$$

where B is a constant. Equation [7] is not consistent with a gaussian distribution of the relevant energy states of ions in solution but is consistent with the boltzmannian distribution of states in solution (Fig. 2).⁴

³Although conceptually, it seems consistent with the literature development as above, it must be mentioned that the gaussian type of energy distribution arises also in a quite different way. Thus, Eq. [6]—which is usually put forward on the basis of some rather complicated considerations of nonequilibrium thermodynamics and even as quantum mechanical concepts (16a)—arises from very simple considerations of the stretching of bonds in an electrode reaction (16b). In fact, the only necessary condition whereby one obtains Eq. [6] is the energy-distance relation of these bonds to be harmonic (*i.e.*, quadratic) and that no more complex and anharmonic relationships should be taken into account.

This is the origin of why Eq. [6] does not give rise to a Tafel equation. To obtain the latter (universally observed), it is necessary to have a more complex energy-distance relationship to have the activated state necessary for electron transfer and their extension from the equilibrium state, and this relationship then gives rise to a non-gaussian distribution. Alternatively (16c), the energy states which are available to electrons in solution are simply regarded as boltzmannian on the basis that they are the normally distributed quantum states in the ion-solvent bond and do not arise due to fluctuations of the ground state.

⁴The evidence for Eq. [7] is overwhelming in terms of very many systems of different types (17a). The counterevidence consists of a paper by Saveant and Tessier (17b) in which results are given for an undefined organic reaction in which, correspondingly, the rate-determining step is unknown.

Gaussian states are essentially error states and represent the deviation from the equilibrium states which are the subject of the Boltzmannian distributions. Gaussian distributions are associated with every one of these Boltzmannian states.

Treatments in electrode kinetics should not be given in terms of thermodynamic concepts, representing net energy changes.

A Gaussian treatment neglects states above the ground vibrational states. There is, in this treatment, basically one state, corresponding to the ground-state vibrational level of the ion-solvent bond: the ground state. The other states are obtained by fluctuating this ground state.

The energy levels in the ion-solvent complexes are likely to represent an energy continuum for electrons, acceptor or donor, which are to be interchanged between the entities in solution and those in the electrode. This is a result of the quasi-continuum nature in respect to energy levels in solution, as indicated by the broadness of the vibrational spectra observed (18, 19).

Apart from bringing of consistency to the situation in respect to energy distribution and generation of activated states, it is desirable to point out that, were fluctuations of the energy of the ground state to be the origin of electronic states in solution, it would seem unlikely that these could occur at a rate sufficient to meet the needs of even the middle range (mA-cm⁻²) of rates met within chemical reactions. Thus, one could estimate the orders of magnitude for the average rate (*i.e.*, frequency) of activation needed for an ion in solution in the following way.

The number of water molecules which have an energy equal to, say, the activation energy, E_a , of proton discharge on Hg at the reversible potential (0.78 eV) is given by

$$N_{E_a} = N_{E_0} e^{-E_a/kT} = \frac{1}{18} \times 6.0 \times 10^{23} \times e^{-0.78/0.025} = 10^9 \quad [8]$$

molecules per cubic centimeter (where N_{E_0} is the number of molecules per mole in the ground state energy, E_0).

These activated molecules are, therefore, on the average, 10⁻³ cm apart (since 10⁹ activated molecules occupy one cubic centimeter). Hence, in a plane of area 1 cm², there will be 10⁶ activated molecules. If they have a diffusion coefficient, $D = 2.5 \times 10^{-5}$ cm²·s⁻¹, the time of diffusion over a distance $\Delta = 10^{-3}$ cm can be obtained as

$$\tau = \frac{\Delta^2}{2D} = 0.02\text{s} \quad [9]$$

Hence, it is possible to deliver to 1 cm² of an electrode surface some 5×10^7 molecules [$= (N_{E_a})^{2/3}/\tau = 10^6/0.02$] with an energy around 0.78 eV in 1s. The number of reactant H₃O⁺ ions needed to be available at the activated state per unit time in the reaction plane for an i_0 value of 10⁻¹² A-cm⁻² (a rate which corresponds to the activation energy given) is $i_0 N_A/nF = (10^{-12}/10^9) \times 6.6 \times 10^{23} = (6.6 \times 10^6 \text{ ion-cm}^{-2}\cdot\text{s}^{-1})$. A sufficient number of appropriately activated molecules can, therefore, be available.⁵ Though the calculation is rough in nature, it serves, as an order of magnitude level, to show that the rate of supply of activated ions from solution is not unfeasible by thermal activation. Thus, a Maxwell-Boltzmann distribution of donor and acceptor electronic states (20) (see Fig. 1) in solution is possible.

The Schottky Barrier Model

A dominating thought in the electrochemistry of semiconductors has been the so-called Schottky barrier at the semiconductor/solution interface.

It is traditional in the field of semiconductor/solution photoelectrochemistry to take such a barrier as existing

⁵This calculation which has been done here is independent of the value of i_0 , *i.e.*, if there were a reaction at an electrode, with an i_0 of 10 mA, where the current needed would be much more, it would not matter, because then the heat of activation would be very much less, and the probability of finding ions with the right energy will be correspondingly greater.

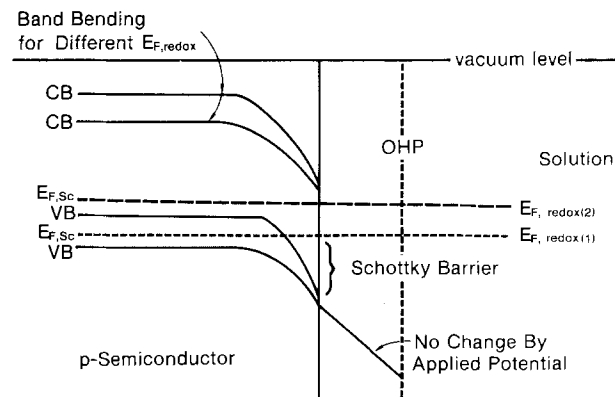


Fig. 4. Schottky barrier model at the interface

inside the semiconductor only, due to difference between the Fermi level in the semiconductor and that in the solution before the equilibrium is established. However, after the equilibrium is established, it is thought that the Fermi level of the semiconductor coincides with the Fermi level in solution and, thus, gives rise to the enhanced (or reduced) band bending (*i.e.*, the Schottky barrier), depending on the relative positions of the two Fermi levels (see Fig. 4) before the equilibrium is established.⁶ Construction of such a barrier at the semiconductor/solution interface is unrealistic, since the existence of a Fermi-like level in solution is doubtful.

Green (21, 22) was the first to question the applicability of Schottky barrier concepts at the semiconductor/solution interface in respect to electrode kinetics. According to the Schottky barrier model, the potential drop inside the semiconductor (*i.e.*, band bending) varies with the externally applied potential, and the other part of the interphasial potential drop is that in the Helmholtz layer in the solution side of the interface which remains (almost) independent of the applied potential (see Fig. 5). The traditional treatments (1-3, 6-8) assume that the above situation nearly always obtains at the semiconductor/solution interface.

Such a treatment leads to a current/potential relationship of the form

$$\frac{\partial V}{\partial \log i} = \frac{RT}{F} \quad [10]$$

⁶When one discusses the potential distribution and the corresponding barrier, one talks about classical and equilibrium situation. The nonequilibrium situation gives rise to the fluctuating barrier which is not relevant for electron transfer kinetic studies. This is because the barrier fluctuates slower than the transfer time of electron across the interface. However, under illumination condition the degree of band bending will be less than dark equilibrium situation.

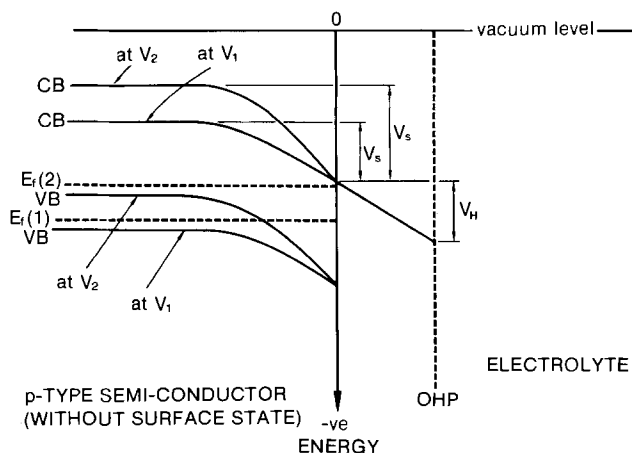


Fig. 5. Schematic diagram of p-type semiconductor/solution interface at two applied potentials, V_2 and V_1 . The diagram shows that the potential drop (p.d.) in the Helmholtz layer exhibits no variation with applied potential and the potential varies inside the semiconductor only.

where V is the electrode potential. Green (21, 22) pointed out that the Schottky barrier considerations were dependent upon the absence of a limiting number of surface states. With the semiconductor in equilibrium, if the surface states exceeded about 3% of the total surface occupancy (e.g., 10^{13} cm $^{-2}$ since there will be 3.5×10^{14} sites available for molecular size of 3\AA in 1 cm^2 of the surface), the changes in potential would be predominantly in the Helmholtz region and not in the space charge region (21, 22), and the pure Schottky barrier model will fail. Correspondingly, the Tafel slope of the dark reaction at semiconductor/solution interfaces would then become

$$\frac{\partial V}{\partial \log i} = \frac{2RT}{F} \quad [11]$$

which indicates a symmetry factor $\beta = 1/2$, as in regular electrode kinetics at metal. Such an observation at semiconductor solution interface indicates the presence of surface states of more than 10^{13} cm $^{-2}$ and, hence, the metallization of the semiconductor. In such situations, variation of the potential will be mainly in the Helmholtz layer. Thus, whether the variation of potential is effective only in the semiconductor side of the interface in the Schottky barrier approximation depends upon the density of occupancy of surface states on the semiconductor.

In situations at the metal/semiconductor interfaces, there is no doubt about the existence of the Schottky barrier to electrons or holes and the variation of band bending (i.e., potential) inside the semiconductor. However, in the case of reactions which are at the semiconductor/solution interface, such a situation may be exceptional. Two events may provoke the existence of surface states in addition to those associated with dangling bonds. One is the specific adsorption of anions and the solvent on the surface of the semiconductor. With hydrogen and oxygen evolution, this is particularly so because the adsorbed intermediate atom on the surface would cause further surface states. The numerical value characterizing the extent of such adsorption is not yet known, but it is reasonable to infer a high degree of adsorption from the published observations of anion adsorption at oxide/solution interfaces (23, 24). The adsorption is higher at nonmetals than in Hg, indicating the formation of charge transfer bonds at the surface. A large extent of specific adsorption at semiconductor/solution interfaces would indicate a high density of surface states and the breakdown of the Schottky barrier approximation. A degree of "metallization" would occur. Correspondingly, the presence of water at the semiconductor/solution interface may give rise to charge transfer bonds between the free antibonding orbitals which exist in oxygen and d-band positions in semiconductor oxides

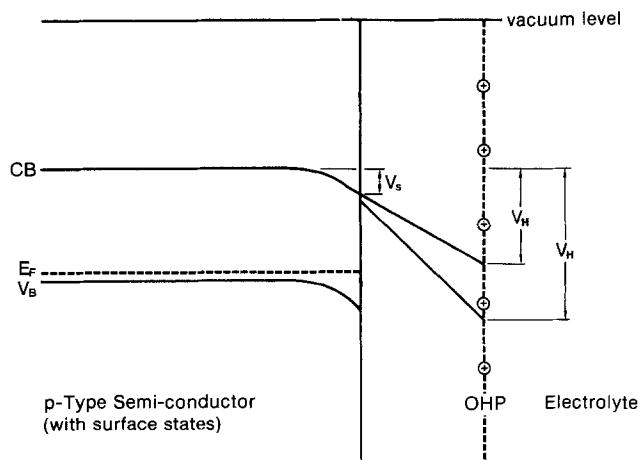


Fig. 6. Schematic diagram of p-type semiconductor/solution interface in presence of high density of surface states. No variation of potential drop (p.d.) inside the semiconductor, V_s , and hence no variation of Fermi level in the semiconductor (pinning); variation of p.d. occurs in the Helmholtz layer, V_H , with applied potential.

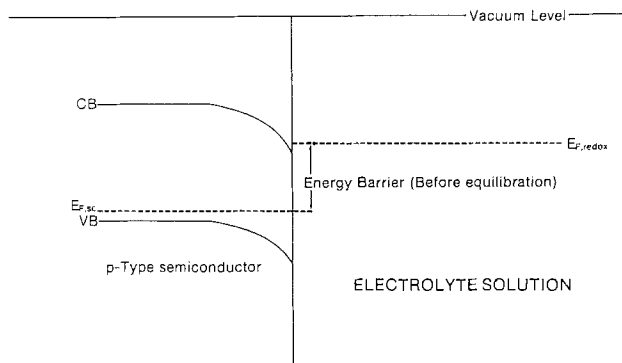


Fig. 7. The barrier for the electron transfer at the interface of semiconductor and redox electrolyte before equilibration of electron of two phases (classical view).

which contain transition metals (24) (e.g., LaNiO_3) and, thus, may increase the density of surface states. Such metallization causes the potential to change over the Helmholtz double layer (see Fig. 6), rather than inside the semiconductor across the space charge region. The metallization also occurs if the doping density is very high, $> 10^{19}$ cm $^{-3}$.

Of course, there must be some p.d. inside all semiconductors; otherwise, they would behave effectively like metals under an applied potential. At present, it seems as though pure Schottky barrier models (25, 26) are applicable to the semiconductor/solution interface as an exception rather than the rule. Recent experiments on the measurement of capacity due to surface states and its dependence on potential even at n-TiO $_2$ electrodes (27) and other p-type electrodes (28) indicate a high concentration of surface states ($\geq 10^{13}$ cm $^{-2}$).

Another matter needing discussion is the identity of the so-called "barrier-to-electron passage" at a semiconductor/solution interface.

Thus, work which is normally carried out at the present time, particularly in photoelectrochemistry, normally regards this barrier in the following way. The thought is that, at the moment of immersion of a semiconductor into a solution, before equilibration of the electrons of the two phases has taken place, there will be a situation shown in Fig. 7, where the Fermi levels are at different positions. In this situation, this hypothetical momentary situation, the energy barrier for penetration of carriers outside the semiconductor is indicated in Fig. 7.

At a short time after the contact has been made, equilibration will arise, and the Schottky barrier will change (in the classical concepts) so that the two Fermi levels, that in the semiconductor and that in the solution, are equal.

Thus, in this classical view (in which the basic concept of a Fermi level in solution is taken as an important entity), the nature of the barrier for the electron exit is taken as the extra bending of the Schottky barrier which arises from the original difference of the Fermi levels in the semiconductor and solution before equilibration (see Fig. 4).

Several difficulties inhabit this view, apart from those which are associated with doubts concerning Fermi level concepts in water, with its lack of clarity of defined band structure. Thus, the barrier outlined in Fig. 4 is a barrier for majority carriers. In photoelectrochemistry, however, a p-type semiconductor is a cathode and an n-type semiconductor is an anode, and the photoexcited minority carrier injection from the electrode to the solution would not experience the Schottky barrier as outlined above but rather would be helped by the bending of the band.

It is not the Schottky barrier which is wrong in the concept, but the fact that photoelectrochemistry involves minority carrier transfer (for n-type semiconductor acts as an anode), and hence a different type of barrier would be involved at the photoexcited semiconductor/solution interface. However, it would not be like photoexcited semiconductor-metal junction, since solution does not in any-

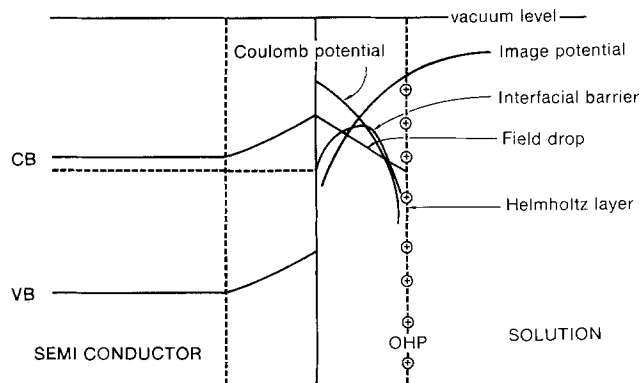


Fig. 8. The schematic diagram of non-Schottky-type barrier at the semiconductor/solution interface (8); the effect of field drop in the Helmholtz layer in solution side and the effect of Coulomb potentials in this layer constitute an extra barrier at the interface.

way behave like metal or semiconductor, which are electronic conductors and have band structure.

However, there is a greater difficulty which pertains to the practices which are present in literature; that is that no account is taken of transfer to quantum states in ions in solution. Thus, the energy barrier which actually exists in an electron transfer reaction is not concerned primarily with the difference of thermodynamic equilibrium states (though this is indeed a basic beginning to the formation of such a barrier), but, as normally conceived in all concepts of kinetic barriers, the height and dimensions of the barriers themselves are concerned with considerations external to the levels of the initial and final states. In particular, in a p-type semiconductor under illumination, electrons exit into solution, and the barrier for the electron is affected by the image forces between the semiconductor and the electron and by the Coulomb interaction between the ion and the electron. The electric field of the interface influences the electron and the height of the barrier in addition to these entities (see Fig. 8). All this has been omitted in the concepts which now exist in the literature. Prior to charge transfer through such an interfacial barrier, the ions in solution need to overcome the activation barrier arising from the potential energy distance relation for the ion-solvent bonds and so forth and attain a suitable distribution of acceptor or donor states such that those states match the electronic states in the electrode to have isoenergetic transfer.

Thus, the conventional treatments which locate the barrier only inside the semiconductor should be revised to take into account the electric potential barrier at the solution side of the interface, along with the activation barrier (Fig. 8) as has been detailed in our recent work (15a).

Fermi Level Pinning

Fermi level pinning has been discussed recently in the photoelectrochemical literature (9, 10) as though it were a new topic.

The idea of Fermi level pinning was introduced into the semiconductor literature in 1953 by Brattain and Bardeen (29). It was Green (21, 22) who introduced the idea in treatments of the semiconductor/solution interface in 1959. The situation was well represented in books discussing semiconductor electrochemistry in the 1960's (30). Fermi level pinning has long been a common and well-known phenomenon in the realm of semiconductor electrochemistry and often has been misused.

Model of Photoelectrocatalysis

Recently, a number of papers have been published (31-37) which show that small metal aggregates on the surface of p-type semiconductors cause a change in the rate of the photoevolution of hydrogen. Two models of photoelectrocatalysis are possible. In one, Model A (36), the function of the catalyst added to the surface (the metal particles in submonolayer amounts) is regarded as speeding up the reaction of electron transfer at the sur-

face to protons in solution in such a way that the surface step becomes nonrate determining and the rate determination (insofar as it varies with the entities on the surface) depends upon factors inside the semiconductor. Thus, interactions at the interface between the metal aggregates and the semiconductor cause a change in reaction rate; since the Fermi level of the semiconductor near the metal aggregates must at equilibrium⁷ be equal to that of the catalytic metal, it follows that, when the work function of the metal is lower than that of a p-type semiconductor, the effect of the metal would be to move the Fermi level inside the semiconductor in a more positive direction (on the potential energy scale), thus increasing band bending (Fig. 9) and, correspondingly, augmenting the photoelectrochemical current density (because when the rate-determining step is inside the semiconductor greater band bending would mean a lessened recombination probability and increased drift velocity of electrons towards the semiconductor-metal interface).

In another model, Model B (32, 37a), the rate-determining step is associated with events taking place at the interface between the metal aggregates and the solution, which could be catalyzed, as in the hydrogen evolution reaction, by metal aggregates on semiconductor surfaces.

Recent work has shown the direction of the shift of the midpoint potential in the exponential section of the $i_{\text{photo}}/\text{potential } E$ curves of metal aggregate-coated p-Si photocathodes, as a function of the presence of a number of individual metals (see Fig. 10). A shift in the positive direction (with respect to the potential of the midpoint for bare Si) implies electrocatalysis of the hydrogen evolution reaction, while a shift in the negative direction implies its inhibition. It has been found that these shifts occur in the order which would be expected if the photoevolution of hydrogen were, in fact, controlled by the kinetics of the dark hydrogen evolution process at the metal/solution interface.

Model A would lead to the expectation that, at a given photoelectrocatalytic rate, the displacement on the potential E axis of the photocurrent/potential curve between the bare and the metal aggregate-covered semiconductor, ΔE , in the positive direction would decrease with increasing work function of the metal.

The trend predicted by Model A is shown by the dashed line in Fig. 11a. The experimental results are represented by the solid line in Fig. 11a. The experimental results show a reverse trend to that predicted by Model A.

To obtain a change in work function so that the direction of change of the photocurrent/potential relations is

⁷Even at nonequilibrium situation under illumination, the band bending varies according to the difference of Fermi energy levels in semiconductor and metal though it may be less than the equilibrium value.

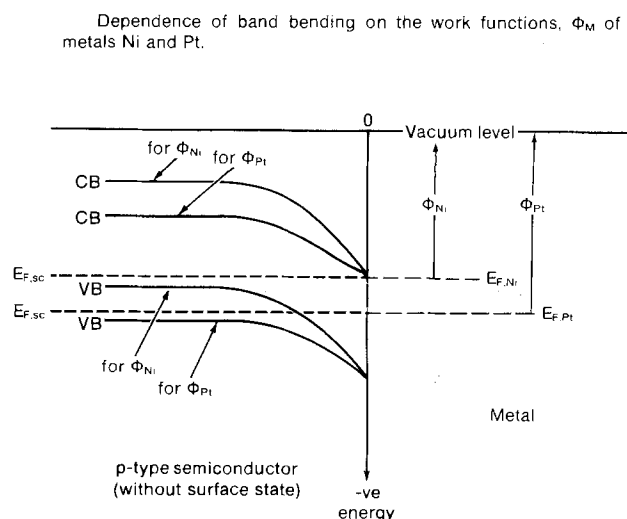


Fig. 9. The dependence of band bending inside the semiconductor on the work function of metal (e.g., Ni and Pt) deposited in the form of islets on the semiconductor surface.

Photocurrent potential dependence for the presence of different metal islets on p-Si electrode.

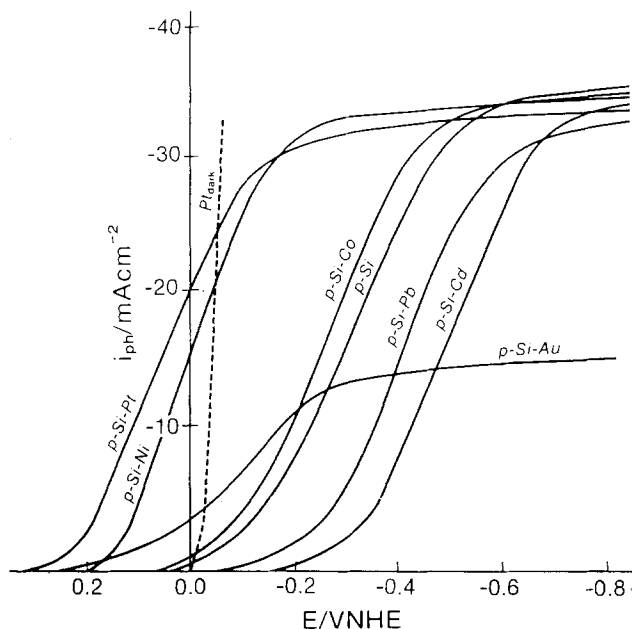


Fig. 10. The photocurrent-potential plot (37a) for various metal islets on p-Si photocathode. p-Si/Pt; p-Si/Ni; p-Si/Au; p-Si/Co; bare p-Si; p-Si/Pb; p-Si/Cd.

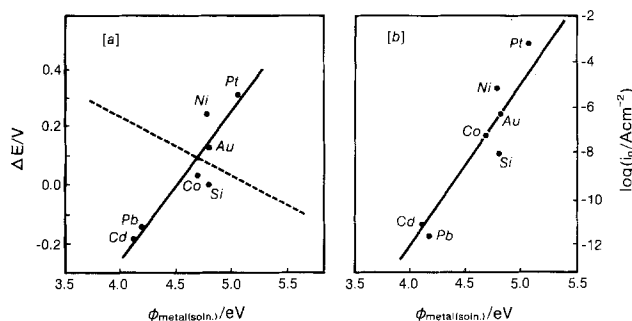


Fig. 11. a: Variation of the potential shift, ΔE , with the work function of the metal pertaining to electrolyte solution, Φ_{metal} (37a). b: The dependence of the log of the exchange current densities, i_0 , for hydrogen evolution reaction at various massive metals on the work function of the metals, Φ_{metal} (37b).

consistent with observation on Model A, it was necessary to assume (36) that H would lower the work function of Pt by about 0.8V (Fig. 11a) and raise that of Cd by about the same amount. The observed values are shown in Table I; it is clear that the necessary shifts are not in the needed direction and do not have the appropriate magnitude.

In Model B, the displacement, ΔE , would be proportional to $\log i_0$ (see Fig. 12), where i_0 is the exchange current density for the hydrogen evolution reaction on massive metal electrodes in the dark (37b). In Fig. 11b, it is

Table I. The values of work functions for different materials in vacuum, ϕ_v , and in solution, ϕ_s , and changes caused by hydrogen, $\Delta\phi_{\text{H}_2}$ (40-44)

Material	ϕ_v (eV)	ϕ_s (eV)	$\Delta\phi_{\text{H}_2}$ (eV)
Rh	4.9	5.0	+0.3
Ru	4.7	4.8	+0.4
Pt	5.5	5.0	+0.1
Ni	5.1	4.7	+0.4
Au	5.2	4.8	+0.2
Co	4.9	4.7	+0.33
Pb	4.0	4.2	—
Cd	3.9	4.1	—

Dependence of potential shift, ΔE on $\log i_0$, exchange current density for hydrogen evolution on massive metals.

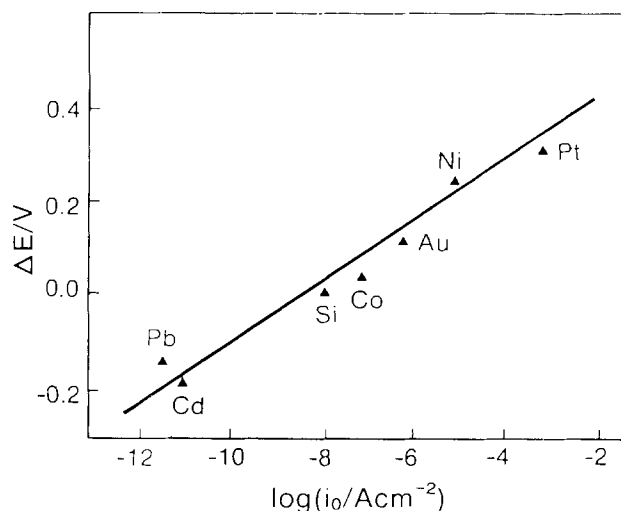


Fig. 12. The dependence of the potential shift, ΔE , with the log of exchange current densities, i_0 , at various metal electrodes (37a).

shown that $\log i_0$ increases linearly with the work function of the metals when they are in solution (38a). Thus, the experimental results show the trend predicted by Model B.

A clear indication that Heller's Schottky barrier model is not operative has been obtained from the experiment carried out on n-Si electrode in dark with and without metal aggregates on it. Figure 12 shows the similar shift in potential, ΔE , as that in photoelectrochemical situation on p-Si. The shift in potential ΔE in dark and in light correlates well and thus agrees well with $\log i_0$ (38b) and with the electrocatalytic model rather than the Schottky model.

These correlations suggest that the rate-determining step in the photoelectrochemical evolution of hydrogen on surfaces decorated with submonolayer quantities of metals of various kinds is one which is rate determined to the metal/solution interface and that interactions at the metal/semiconductor interface do not have a primary influence on the rate of the reaction concerned (except insofar as they make the transition across this interface nonrate determining).

Summary

Traditional and modified views at the semiconductor/solution interface

Concept	Traditional	Modified
Fermi level in solution.	Is equal to redox potential in the vacuum scale.	Must include the inner potential of solution, ϕ^s . No free electron and band structure in solution. Better use of ground state energy of solvated ions.
Electronic energy distribution in solution.	Gaussianly distributed energies of ground state of ions. Fluctuational in nature.	Although such states exist, they seem unlikely to play much part in electrode reactions because they fluctuate too infrequently. Boltzmannian states of ion-solvent bond are origin of relevant states.

Schottky barrier.	Most semiconductor/solution interfaces are like those at the semiconductor/metal interface.	Such (Schottky) barriers are greatly diminished in semiconductor/solution interface. Surface states are always frequent at this interface because of adsorption of species (water, O, H, anions, etc.) from solution.
Relevant interfacial barrier in photoelectrochemical process.	The Schottky barrier.	The principal components controlling the electron exit rate at the semiconductor/solution interface (i.e., the barrier) are activation/stretching or reorientation processes in the ion-solvent complex in the Helmholtz double layer. Interfacial barrier outside the semiconductor surface exists.
Fermi level pinning.	A new (1980) concept in photoelectrochemistry.	Introduced in 1947 (39) and into electrochemistry in 1959 and into photoelectrochemistry in 1978.
Model of photoelectrocatalysis.	Is due to shift of Fermi level in semiconductor due to presence of metal. Hence, band bending (dV/dx) _{sc} changes.	Is due to happenings at metal/solution interface (i.e., electrocatalytic effect).

Acknowledgments

We gratefully acknowledge the financial support of this work by the Robert A. Welch Foundation. The authors acknowledge useful discussion with Professor B. E. Conway, Dr. A. K. Vijh, and Dr. A. Nozik. We gratefully acknowledge the constructive criticism of divisional editor, Dr. R. H. Wilson; it helped to improve the clarity and the strength of the paper considerably.

Manuscript submitted May 17, 1984; revised manuscript received April 29, 1985.

Texas A&M University assisted in meeting the publication costs of this article.

REFERENCES

- H. Gerischer, *Z. Phys. Chem. N.F.*, **26**, 223 (1960).
- H. Gerischer, *Surf. Sci.*, **18**, 97 (1969).
- H. Gerischer, in "Physical Chemistry: An Advanced Treatise," Vol. 9A, H. Eyring, D. Henderson, and W. Jost, Editors, p. 463, Academic Press, New York (1970).
- J. O'M. Bockris and S. D. Argade, *J. Chem. Phys.*, **49**, 5133 (1968).
- S. Trasatti, *J. Electroanal. Chem.*, **66**, 155 (1975).
- H. Gerischer, in "Special Topics in Electrochemistry," P. G. Rock, Editor, p. 235, Amsterdam, The Netherlands (1977).
- (a) R. Memming, in "Electrocatalysis," M. W. Breiter, Editor, p. 178, The Electrochemical Society Softbound Proceedings Series, Princeton, NJ (1974); (b) S. Trasatti, in "Comprehensive Treatise of Electrochemistry," Vol. 1, J. O'M. Bockris, B. E. Conway, and E. Yeager, Editors, p. 45, Plenum Publishing Company, New York (1980).
- R. Memming, in "Electroanalytical Chemistry," A. J. Bard, Editor, Vol. 11, p. 1, Marcel Dekker, New York (1979).
- A. J. Bard, A. B. Bocarsly, F. F. Fan, E. G. Walton, and M. S. Wrighton, *J. Am. Chem. Soc.*, **102**, 3671 (1980).
- F. F. Fan and A. J. Bard, *ibid.*, **102**, 3677 (1980).
- (a) F. W. Williams, S. P. Varma, and S. Hillenius, *J. Chem. Phys.*, **64**, 1549 (1966); (b) J. Jortner, *Mol. Phys.*, **5**, 257 (1962).
- J. O'M. Bockris and D. B. Matthews, *J. Chem. Phys.*, **44**, 298 (1966); *Proc. R. Soc. London, Ser. A*, **292**, 479 (1966).
- J. O'M. Bockris and S. U. M. Khan, *Appl. Phys. Lett.*, **42**, 124 (1983).
- S. U. M. Khan and J. O'M. Bockris, in "Photoelectrochemistry: Fundamental Processes and Measurement Techniques," W. L. Wallace, A. J. Nozik, S. K. Deb, and R. H. Wilson, Editors, p. 39, The Electrochemical Society Softbound Proceedings Series, Princeton, NJ (1982).
- (a) S. U. M. Khan and J. O'M. Bockris, *J. Phys. Chem.*, **87**, 2599 (1983); (b) H. Gerischer and W. Ekaradt, *Appl. Phys. Lett.*, **43**, 393 (1983).
- (a) V. G. Levich, "Physical Chemistry: An Advanced Treatise," Vol. 9B, H. Eyring, D. Henderson, and W. Jost, Editors, Chap. 12, Academic Press, New York (1970); (b) J. Appleby, J. O'M. Bockris, and R. K. Sen, in "MTP International Review of Science," J. O'M. Bockris, Editor, Vol. 6, Butterworths, London (1973); (c) R. W. Gurney, *Proc. R. Soc. London, Ser. A*, **134**, 137 (1931).
- (a) "Comprehensive Treatise of Electrochemistry," Vol. 7, B. E. Conway, J. O'M. Bockris, E. Yeager, S. U. M. Khan, and R. White, Editors, Plenum Press, New York (1983); (b) J. M. Saveant and D. Tessier, *Faraday Discuss. Chem. Soc.*, **74** (1982).
- R. E. Moore, O. Ferral, G. W. Koeppl, and A. J. Kresge, *J. Am. Chem. Soc.*, **93**, 1 (1971).
- K. Nakamoto, "Infrared and Raman Spectra of Inorganic Coordination Compounds," Wiley-Interscience, New York (1978).
- S. U. M. Khan and J. O'M. Bockris, *J. Appl. Phys.*, **52**, 7270 (1981).
- M. Green, *J. Chem. Phys.*, **31**, 200 (1959).
- M. Green, in "Modern Aspects of Electrochemistry," Vol. 2, J. O'M. Bockris and B. E. Conway, Editors, Academic Press, New York (1959).
- W. K. Paik, M. A. Genshaw, and J. O'M. Bockris, *J. Phys. Chem.*, **74**, 4266 (1970).
- J. O'M. Bockris and T. Otagawa, *J. Phys. Chem.*, **87**, 2960 (1983).
- J. F. Dewald, *Bell Syst. Tech. J.*, **39**, 615 (1960).
- P. J. Holmes, "Electrochemistry of Semiconductors," Academic Press, New York (1962).
- W. Siripala and M. Tomkiewicz, *This Journal*, **129**, 1240 (1982).
- P. Janietz, R. Weiche, J. Westfehe, R. Landberg, and R. Dehemlow, *J. Electroanal. Chem.*, **106**, 23 (1980).
- W. H. Brattain and J. Bardeen, *Bell Syst. Tech. J.*, **32**, 1 (1953).
- V. Z. Myamlin and L. V. Pleskov, "Electrochemistry of Semiconductors," Plenum Press, New York (1967).
- J. Nakato, S. Tonomura, and H. Tsubomura, *Ber. Bunsenges. Phys. Chem.*, **80**, 1289 (1976).
- W. Kautek, J. Brobrecht, and H. Gerischer, *ibid.*, **84**, 1034 (1980).
- A. Heller and R. G. Vadimsky, *Phys. Rev. Lett.*, **46**, 1153 (1981).
- A. Heller, R. G. Vadimsky, W. D. Johnston, K. E. Strege, H. J. Leamy, and B. Miller, in "Proceedings of the 15th IEEE Photovoltaic Special Conference," p. 1422, Kissimmee, Florida, May 12-15, 1981, IEEE, New York (1981).
- R. N. Dominey, N. S. Lewis, J. A. Bruce, D. C. Bookbinder, and M. S. Wrighton, *J. Am. Chem. Soc.*, **104**, 467 (1982).
- A. Heller, E. Aharon-Shalom, W. A. Bonner, and B. Miller, *ibid.*, **104**, 6942 (1982).
- (a) M. Szklarczyk and J. O'M. Bockris, *Appl. Phys. Lett.*, **42**, 1035 (1983); (b) J. O'M. Bockris, *Discuss. Faraday Soc.*, **1**, 95 (1947); (c) J. O'M. Bockris, S. U. M. Khan, O. J. Murphy, and M. Szklarczyk, *Int. J. Hydrogen Energy*, **9**, 243 (1984).
- (a) S. Trasatti, *J. Electroanal. Chem.*, **66**, 155 (1975); (b) A. Q. Contractor, M. Szklarczyk, and J. O'M. Bockris, *ibid.*, **157**, 175 (1983).
- J. Bardeen, *Phys. Rev.*, **71**, 717 (1947).
- V. V. Gorodetskii, B. E. Nieuwenhuys, W. M. H. Sachtler, and G. K. Boreskov, *Surf. Sci.*, **108**, 225 (1981).
- G. F. Voronina, L. A. Larin, and T. V. Kalish, *Elektrokhimiya*, **14**, 257 (1978).
- F. C. Tompkins, in "The Solid-Gas Interface," Vol. 2, E. A. Flood, Editor, p. 765, Marcel Dekker, Inc., New York (1967).
- R. V. Culver and F. C. Tompkins, in "Advances in Catalysis and Related Subjects," Vol. XI, D. D. Eley, P. W. Selwood, and P. B. Weisz, Editors, p. 67, Academic Press, Inc., London (1959).
- L. Whatley, B. J. Davis, and R. L. Moss, *Trans. Faraday Soc.*, **66**, 3143 (1970).

The Effects of Surface Energetics on the Cyclic Voltammetry of Metallocenes at Nonilluminated n-InP Electrodes

Carl A. Koval and Robin L. Austermann*

Department of Chemistry, University of Colorado, Boulder, Colorado 80309

ABSTRACT

Electron transfer processes at n-type InP electrodes of moderate to low doping density were investigated by monitoring the cyclic voltammetric dark currents of a series of metallocenes in acetonitrile solutions. The formal reduction potentials of the metallocenes span the bandgap of InP, allowing a comparison of the cyclic voltammetric response as a function of the formal reduction potential and the energetic condition of the electrode surface. The energetic condition of the electrode surface during the cyclic voltammetry experiments was monitored by measurements of the capacitance of the space charge region. A simple chemical etching and electrochemical cycling procedure yielded reproducible surface energetics. The n-InP/acetonitrile interface in the depletion condition responded ideally to changes in electrode potential, as evidenced by linear Mott-Schottky plots, over a range of about 0.9V. It was possible to achieve an accumulation condition at negative potentials, but the interface could not be inverted at positive potentials. The n-InP/acetonitrile interface is less susceptible to surface oxidation than is the p-InP/acetonitrile interface. For each metallocene +1/0 couple, the reversibility of cyclic voltammetric (CV) waves at n-InP was dependent on the doping density of the electrode (N_D) and the proximity of the formal reduction potential ($E^{0'}$) to the conduction bandedge (E_{CB}). Couples with $E^{0'}$ located negative of E_{CB} displayed nearly reversible CV waves. Couples with $E^{0'}$ located in the bandgap were reduced irreversibly at overvoltages of 400-500 mV. A couple with $E^{0'}$ located slightly positive of E_{CB} yielded a partially reversible CV wave at moderate N_D , but the wave became irreversible at low N_D . Oxidation of couples with $E^{0'}$ positive of $-0.5V$ vs. $E^{0'}$ for ferricenium/ferrocene was not observed.

The kinetics of electron transfer processes at semiconductor electrode/solution interfaces have not received as much attention experimentally as redox processes at metal electrode/solution interfaces (1-13). We have previously reported our investigation of electron transfer processes at p-InP electrodes in acetonitrile solutions (1). Herein, we extend our study to electron transfer processes at the n-InP/acetonitrile interface.

The purpose of this study is to investigate the ways that heterogeneous charge transfer kinetics at semiconductor electrodes are affected by various combinations of the formal reduction potentials of solution species and the energetic condition of the electrode surface. Our approach has been to measure cyclic voltammetric dark currents in acetonitrile solutions for ferricenium⁺, cobalticenium⁺, and a number of their derivatives (Fig. 1) at n-InP electrodes of moderate to low doping density. Abbreviated designations and formal reduction potentials, $E^{0'}$, for the metallocenes are listed in Table I. The reasons behind our choices of InP as the electrode material and the series of metallocenes as solution redox probes have been discussed before (1).

The specific knowledge of the energetics of the semiconductor/solution interface that this study requires was derived from measurements of the space charge capacitance taken in the same regions of electrode potential and at scan rates similar to those used in the cyclic voltammetry experiments.

Through these experiments, we have observed a correlation between the dark current flow and the doping density of the electrode, as well as the difference in potential between the conduction bandedge and the formal reduction potential of the solution redox species. The results qualitatively support the Gerischer model of the semiconductor/solution interface (7, 8).

Experimental

Reagents and materials.—Gold-label acetonitrile (Aldrich) was thoroughly dried by refluxing over calcium hydride for 14h in a nitrogen atmosphere.¹ The supporting electrolyte, tetrabutylammonium fluoroborate, TBABF₄, (Southwestern Analytical Chemicals, Incorporated) was dried under vacuum for two days at 25°C. Ferrocene, acetylferrocene, 1,1'-diacetylferrocene (Aldrich), and

*Electrochemical Society Active Member.

¹In some of the initial experiments, the acetonitrile was passed through a column of activated alumina prior to solution preparation. This procedure was discontinued because it was found to have no effect on the electrochemical behavior.

decamethylferrocene (Strem) were purified by sublimation. Cobalticenium hexafluorophosphate (Strem) was used without further purification. 1,2,4,1',2',4'-hexamethylferrocene, bis(diphenylphosphinocyclopentadienyl) cobalt hexafluorophosphate, and bis(diphenylphosphinocyclopentadienyl) cobalt molybdenum tetracarbonyl were used as received (14).

Electrochemical measurements.—All electrochemical measurements were performed in a Vacuum Atmospheres controlled-atmosphere glove box containing helium. An opaque, one-compartment cell was used for all electrochemical measurements. The acetonitrile solutions contained 0.5M TBABF₄ as the supporting electrolyte. The reference electrode was a silver wire immersed in a solution of 0.01M AgNO₃ and 0.5M TBABF₄ in acetonitrile, which was contained in a glass tube that was sealed at one end with a Vycor glass disk (Princeton Applied Research). This reference electrode has a potential of 0.29V vs. SCE (15). Its potential was monitored daily by comparison with the formal reduction potential, $E^{0'}$, of the ferricenium/ferrocene couple, which occurred at approximately 0.1V vs. the Ag/Ag⁺ reference electrode. All potentials herein are reported vs. the $E^{0'}$ for ferrocene^{+/0} (16). The counterelectrode was a platinum foil.

Cyclic voltammetry, CV, was performed with a Princeton Applied Research Model 175 universal programmer and Model 173 potentiostat/galvanostat. The data were recorded on a Houston Instruments Model 2000 X-Y recorder. In experiments involving InP electrodes, the space charge capacitance of the electrochemical cell was

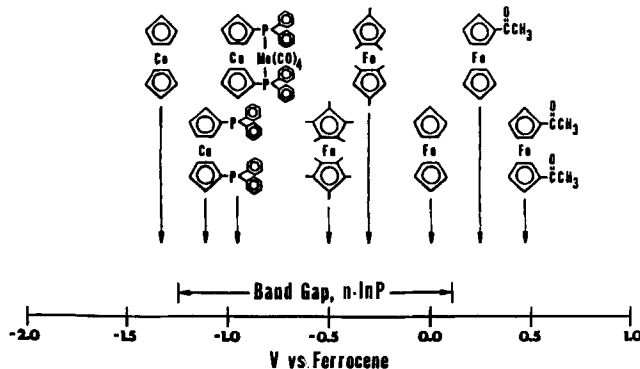


Fig. 1. Formal reduction potentials of the metallocenes in relation to the bandgap of n-InP in acetonitrile solution.

Table I. Designations and reduction potentials for the metallocenes

Designation	Metallocene	$E^{0'}$ (V vs. ferrocene)
FER	Ferrocene	0.00
DFER	Decamethylferrocene	-0.50
HFER	1,2,4,1',2',4'-Hexamethylferrocene	-0.30
AFER	Acetylferrocene	0.24
DAFER	1,1'-Diacetylferrocene	0.47
COB	Cobaltocene	-1.33
PCOB	Bis(diphenylphosphinocyclopentadienyl) cobalt	-1.10
PMCOB	Bis(diphenylphosphinocyclopentadienyl) cobalt molybdenum tetracarbonyl	-0.95

measured by using a Princeton Applied Research Model 5204 lock-in analyzer and a Hewlett-Packard Model 200AB audio oscillator interfaced to a computer acquisition system (17).

The formal reduction potentials of the metallocenes were determined from CV data measured at the platinum electrode as the average of the anodic and cathodic peak potentials. The values of $E^{0'}$ so determined (Table I) were within ± 70 mV of previously reported measurements (14, 18-20). The approximate concentrations of the ferrocene derivatives were estimated by comparing the magnitudes of the CV peak currents obtained at a platinum electrode with peak currents obtained in a solution containing a known concentration of ferrocene. In each CV experiment, the peak current densities obtained at the InP electrode were compared with the peak current densities obtained at a platinum electrode in the same solution. Whenever it was necessary to prepare a solution of the metalocenium⁺ cation, it was generated electrochemically in a two-compartment cell. One compartment contained the platinum foil working electrode and the reference electrode, and the other compartment contained the platinum wire counterelectrode. The compartments were separated by a Vycor frit.

Electrode pretreatment and characterization.—The platinum disk electrode and n-InP (Varian, Cambridge) electrodes were constructed as described previously (1). Prior to each experiment, the n-InP electrodes were etched for 1 min in a 50/50 solution of CH_3OH /concentrated HCl, rinsed with CH_3OH , and dried in a stream of argon. The areas of the InP electrodes were measured by using a photographic procedure.

The doping densities, N_D , and flatband potentials, E_{FB} , of the InP electrodes were determined from capacitance/potential data by using the Mott-Schottky equation (21)

$$1/C_{sc}^2 = (2/e\epsilon\epsilon_0 N_D)(E - E_{FB} - k_B T/e)$$

where C_{sc} is the capacitance of the space charge region, ϵ_0 is the permittivity of free space, ϵ is the static dielectric of the semiconductor (12.5 for InP), E is the electrode potential, and k_B is the Boltzmann constant. The data were modeled to a series RC circuit, and the total measured capacitance was assumed to be equal to C_{sc} (22). Values of C_{sc} were recorded at 100 mV intervals using a cyclic staircase potential program with the step time equal to 10s, which was superimposed upon an ac signal with a frequency of 5 kHz and an amplitude of 20 mV peak to peak. The X-intercepts of the Mott-Schottky plots for all of the electrodes used in this study and the slopes of the Mott-Schottky plots for all but the electrode of lowest doping density were found to be independent of frequency.

The single-crystal n-InP pieces employed in this study were of moderate or low doping density and had a (100)

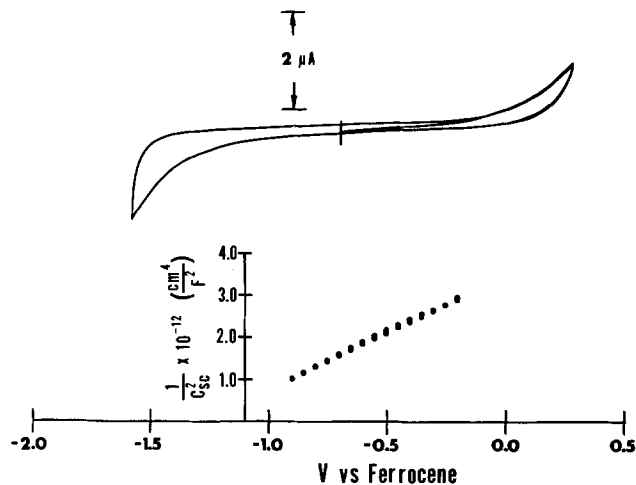


Fig. 2. Cyclic voltammograms for five consecutive cycles and a Mott-Schottky plot for the N18(100) electrode in a solution of 0.5M TBABF₄ in acetonitrile. The Mott-Schottky plot shows a forward (negative) and reverse (positive) scan with an ac frequency of 5 kHz.

crystal orientation with both indium and phosphorous atoms exposed. The reproducibility of the voltammetric responses and surface energetics for different electrodes constructed from the same material was quite good. The characteristics of the three electrodes that were used most extensively in this study are summarized in Table II.

Results

Surface energetics in the absence of electroactive species.—A cyclic voltammogram for five consecutive cycles of an N18(100) electrode in electrolyte solution exhibited very little current in the region from about -1.1 to -0.2 V vs. ferrocene (Fig. 2). When the electrode potential was swept positive of -0.2 V, an anodic wave appeared, and when the electrode potential was swept negative of -1.1 V a cathodic wave appeared that was larger than the anodic wave. Since similar scans in the same solution at a platinum electrode are featureless, these currents can be attributed to oxidation and reduction of the electrode surface rather than to electroactive impurities in the solution. A typical Mott-Schottky plot for this electrode in electrolyte solution is also shown in Fig. 2. The capacitance data were collected in the range of -0.9 to -0.2 V, which is within the bandgap of n-InP, where very little faradaic current appeared in the cyclic voltammogram. The plot is linear, with no hysteresis between the forward and reverse scans.

Capacitance data taken in electrolyte solution in the regions where anodic and cathodic faradaic background current appeared in the CV resulted in Mott-Schottky plots like those shown in Fig. 3. When the electrode potential was swept negative of -1.1 V, the capacitance became constant and independent of potential. This suggests that negative charge resided at the electrode surface at potentials corresponding to the onset of cathodic current in the corresponding cyclic voltammogram (Fig. 2). This potential-independent capacitance appears at a potential closely corresponding to the position of the conduction bandedge. On the reverse scan, there is a small amount of hysteresis in the Mott-Schottky plot. Compared to similar scans at p-InP (1), these data indicate that the negative scan causes little permanent change of the electrode surface. When the electrode potential is swept positive of -0.2 V, the potential corresponding to the on-

Table II. Properties of the n-InP electrodes

Electrode	Area (cm ²)	Orientation	E_{FB} (V)	Doping density (cm ⁻³)
N18 (100)A	0.19	(100)	-1.28 ± 0.04	$(4.1 \pm 0.1) \times 10^{18}$
N18 (100)B	0.13	(100)	-1.23 ± 0.04	$(2.7 \pm 0.1) \times 10^{18}$
N16 (100)	0.25	(100)	-1.08 ± 0.04	$(2.3 \pm 0.1) \times 10^{16}$

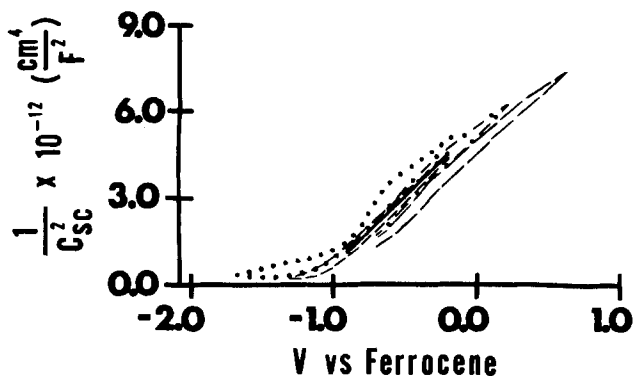


Fig. 3. Mott-Schottky plots for the N18(100) electrode in a solution with 0.5M TBABF₄ in acetonitrile. The switching potentials used are: (---) -0.2 and -1.3V; (····) -0.2 and -1.7V (-·-·-) -0.7 and 0.2V; (—) -0.7 and 0.6V.

set of anodic background current in the cyclic voltammogram, the slope of the Mott-Schottky plot decreases slightly, and there is hysteresis in the reverse (negative) scan. The measured capacitance does not become independent of potential in the positive direction.

To determine if cyclic voltammetric scans into regions where cathodic or anodic background current flows cause a permanent change in the position of the band-edges, a series of measurements of the flatband potential were taken as a function of the number of cyclic voltammograms done in a given potential range (Fig. 4). The triangles show that repetitive scans between -0.9 and -0.2V, where very little background current appeared, resulted in a stable value of E_{FB} after a few initial scans. If the electrode potential was scanned between -0.9 and 0.4V, into the range of anodic background current, E_{FB} shifted in a positive direction (squares), but eventually stabilized after about 30 CV scans. When the electrode was swept between -1.6 and -0.2V, into the range of cathodic background current, E_{FB} did shift in a negative direction (circles), but stabilized after about 20 CV scans.

In order to produce a stable E_{FB} before each CV experiment, each freshly etched electrode was cycled five times in electrolyte solution between -0.9 and -0.2V.

Cyclic voltammetry of metallocenes at n-type InP electrodes.—Representative cyclic voltammetric behavior of the metallocenes at n-InP can be shown by presenting the responses of FER⁺, PCOB⁺, and PMCOB⁺ at the N18(100) and N16(100) n-InP electrodes.

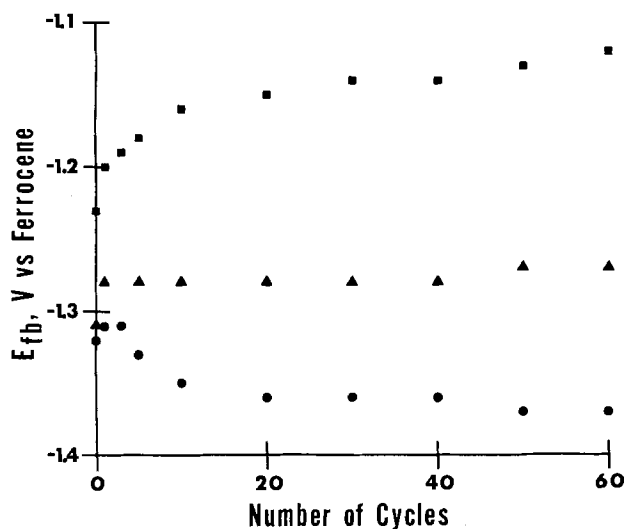


Fig. 4. The flatband potential as a function of the number of cyclic voltammograms done between three different pairs of switching potentials at the N18(100) electrode in a solution of 0.5M TBABF₄ in acetonitrile. Switching potentials: (squares) -0.9 and 0.4V; (triangles) -0.9 and -0.2V; (circles) -0.2 and -1.6V.

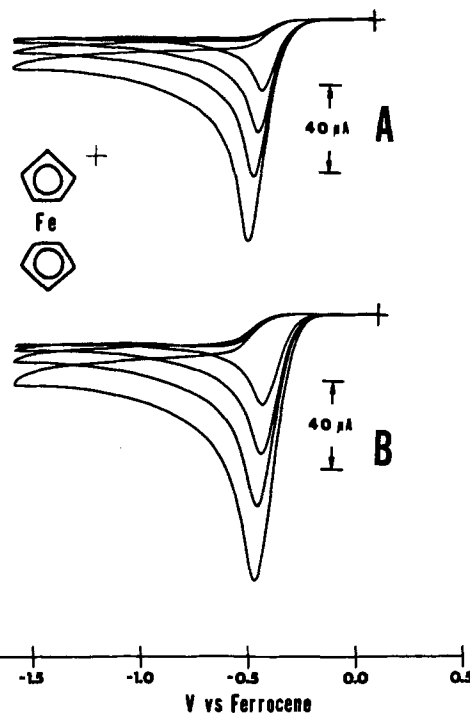


Fig. 5. The cyclic voltammetry of FER⁺ in a solution with 0.5M TBABF₄ in acetonitrile at: (part A) the N18(100) electrode; (part B) the N16(100) electrode at 200, 100, 50, and 20 mV/s with an initial potential of 0.2V.

Ferricenium⁺.—Cyclic voltammograms at the N18(100) electrode (Fig. 5A) and at the N16(100) electrode (Fig. 5B) of FER⁺ at different scan rates show a diffusion-controlled cathodic wave that appears 450 mV negative of the E° of FER⁺ at both electrodes. Neither electrode exhibits an anodic wave on the reverse (positive) scan, even if the electrode potential was swept positive of 1.0V. The cyclic voltammograms of DFER⁺, HFER⁺, and AFER⁺ had a similar appearance to the CV of FER⁺, exhibiting only cathodic waves that occurred 450-600 mV negative of their formal reduction potentials (Table III). Anodic waves were not observed on the reverse scans.

Bis(diphenylphosphinocyclopentadienyl) cobalt molybdenum tetracarbonyl.—A cyclic voltammogram of PMCOB⁺ at the N18(100) electrode (Fig. 6A) and the N16(100) electrode (Fig. 6B) shown at different scan rates also exhibits a diffusion-controlled cathodic wave at both electrodes at less than 100 mV negative of the E° for that compound. The difference in response between the different doping densities lies in the reverse (positive) scan. The N16(100) electrode exhibits no anodic current during the reverse scan, whereas the N18(100) electrode does exhibit a kinetically controlled anodic current during the reverse scan with a magnitude that is less than 60% of the cathodic current.

Table III. Reduction potentials

Compound	Electrode	E_{pc} (V) ^a	E_{onset} (V) ^b	j_0 (A/cm ²)	α
AFER ⁺	N18 (100)B	-0.35	-0.05	1.8×10^{-7}	0.44
	N16 (100)	-0.41	-0.20	6.0×10^{-11}	0.71
FER ⁺	N18 (100)A	-0.48	-0.30	6.7×10^{-7}	0.43
	N16 (100)	-0.45	-0.25	1.6×10^{-11}	1.04
HFER ⁺	N18 (100)A	-0.77	-0.55	2.9×10^{-7}	0.47
	N16 (100)	-0.82	-0.60	4.4×10^{-22}	2.11
DFER ⁺	N18 (100)A	-0.95	-0.60	6.7×10^{-7}	0.46
	N18 (100)B	-0.88	-0.60	3.8×10^{-7}	0.52
	N16 (100)	-0.93	-0.70	3.2×10^{-14}	1.42

^a At 100 mV/s.

^b +/- 0.025V.

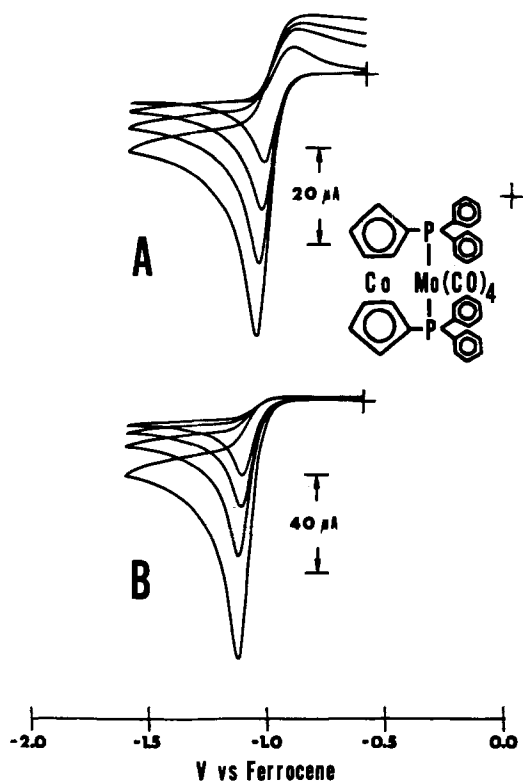


Fig. 6. The cyclic voltammetry of PMCOB⁺ in a solution with 0.5M TBABF₄ in acetonitrile at: (part A) the N18(100) electrode; (part B) the N16(100) electrode at 200, 100, 50, and 20 mV/s with an initial potential of -0.6V.

Bis(diphenylphosphinocyclopentadienyl) cobalt.—The cyclic voltammetry of PCOB⁺ is shown for the N18(100) electrode (Fig. 7A) and the N16(100) electrode (Fig. 7B) at different scan rates. The waves are nearly electrochemically reversible. There is a 62 mV separation between the peak potentials, and the cathodic peak currents are indicative of a diffusion-controlled process. A plot of i_{pc} vs. (scan rate)^{1/2} is linear, but a plot of i_{pa} vs. (scan rate)^{1/2} is not linear for either electrode, indicating that the anodic waves are not diffusion controlled.

The cyclic voltammetric response of COB⁺ was similar to that of PCOB⁺.

1,1'-Diacetylferrocene.—DAFER has a reduction potential that is positive of the valence bandedge of n-InP. No anodic wave appeared on the positive scan for DAFER at the n-InP electrodes. Unfortunately, DAFER⁺ is not sufficiently stable to allow the electrochemical generation of a solution of the cation at a platinum foil electrode, so it was not possible to see if the reduction of the cation would have occurred at n-InP.

Discussion

The n-InP/acetonitrile interface as a function of electrode potential.—The rates and mechanisms of electron transfer across a semiconductor/solution interface are greatly influenced by the position of the electrode Fermi level with respect to the valence band and conduction bandedges at the electrode surface. The three surface energetic conditions of an ideal, nonilluminated n-type semiconductor/solution interface, which can be achieved by changes in the Fermi level, are shown in Fig. 8. These diagrams represent the electrochemical potential of electronic orbitals as a function of distance into the electrode with respect to redox levels in solution (23). Although dark current flow for each of these energetic conditions has been addressed experimentally and theoretically (10, 13), many questions regarding the interpretation of these currents remain unanswered.

In principle, it should be possible to study faradaic redox processes at semiconductor electrodes under accumulation, depletion, or inversion conditions by adjusting

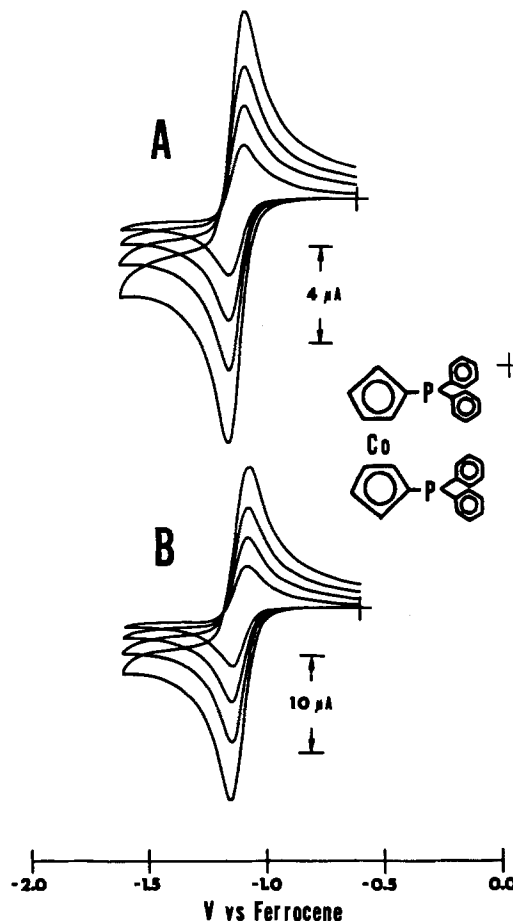


Fig. 7. The cyclic voltammetry of PCOB⁺ in a solution with 0.5M TBABF₄ in acetonitrile at: (part A) the N18(100) electrode; (part B) the N16(100) electrode at 200, 100, 50, and 20 mV/s with an initial potential of -0.6V.

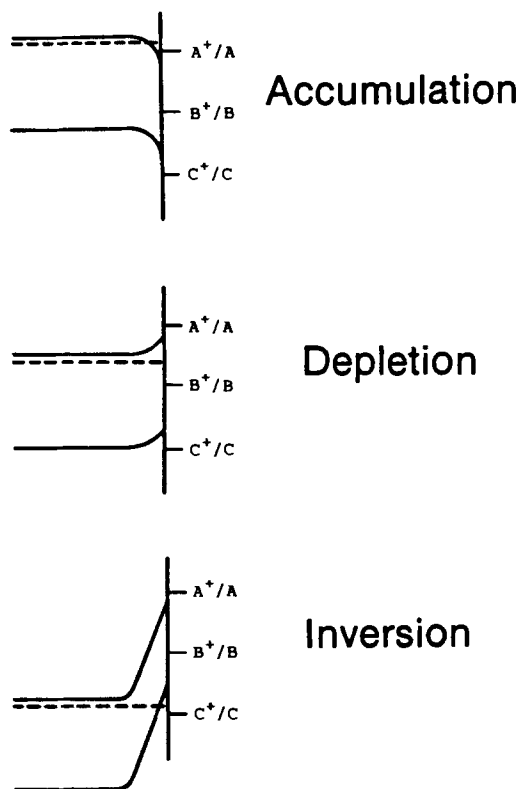


Fig. 8. Accumulation, depletion, and inversion as pictured for the ideal n-type InP/acetonitrile interface in the dark in relation to solution redox levels.

the externally applied potential. Our data indicate that the n-InP/acetonitrile interface responded to changes in the electrode potential in a nearly ideal way if the electrode potential was kept in the range of -1.1 to -0.2 V vs. ferrocene, which corresponded to having the electrode in a depletion condition (Fig. 2). As the electrode potential was swept negative of -1.1 V, the space charge capacitance became independent of potential (Fig. 3). Because the onset of potential-independent capacitance coincides well with the position of the conduction bandedge, we interpret -1.1 V as the onset of accumulation at the n-InP electrodes. On the reverse (positive) scan, as the electrode passes from accumulation to depletion, the Mott-Schottky plot shows the same flatband potential as on the forward scan, indicating that little or no negative shift in the position of the conduction bandedge occurred when the electrode was in accumulation.

When the electrode potential was swept positive of -0.2 V, the measured capacitance did not become independent of potential, indicating that the inversion condition did not occur (Fig. 3). The observed behavior is characteristic of a semiconductor electrode in deep depletion (9, 24). Deep depletion is a nonequilibrium condition in which minority carriers are consumed at the interface in surface reactions, preventing their accumulation in interface states. This accumulation of minority carriers in interface states is required for inversion. One possible surface reaction is the formation of surface oxide. Surface oxide formation at p-InP caused the bandedges to shift in a positive direction and prevented the electrodes from going into accumulation (1). Although there seems to be much less oxide formation at n-InP than there was at p-InP, it is reasonable that this process is preventing the electrodes from going into inversion by consuming minority carriers.

Since the capacitance measurements and the cyclic voltammograms were done at similar effective scan rates and within the same potential regions, it can be assumed that the changes in the surface energetics just described also occurred during the cyclic voltammetry experiments. Our interpretation of the capacitance data suggests that redox processes negative of -1.1 V at n-InP should be indicative of the electrode in accumulation, that is, that metal-like behavior should be observed (10). Redox processes positive of -1.1 V at n-InP should be indicative of the electrode in depletion, that is, kinetically controlled currents should be observed (10). Since the capacitance data indicates that inversion does not occur at n-InP, metal-like behavior would not be expected positive of the conduction bandedge.

Interpretation of cyclic voltammograms.—The reduction potentials of COB^{+0} and PCOB^{+0} are located negative of -1.1 V. It was predicted from the capacitance measurements that the electrode surface would be in accumulation at these potentials. As expected, nearly reversible cyclic voltammograms result for both compounds, regardless of the doping density of the electrode. Kohl and Bard have also observed nearly reversible cyclic voltammograms at n-InP in acetonitrile for redox couples with formal reduction potentials located negative of the conduction bandedge (25).

It is interesting to contrast the cyclic voltammetric behavior of PCOB^{+0} and PMCOB^{+0} (Fig. 6 and 7), which have E^0 values that differ by only 150 mV. The sharp transition from the accumulation condition to the depletion condition, which causes the oxidation waves for PMCOB to become kinetically controlled, is readily apparent from the electrochemistry of these two complexes.

The reduction of AFER^+ , FER^+ , HFER^+ , and DFER^+ , which have formal reduction potentials that span a range of 0.75 V, could be studied at potentials where the n-InP/acetonitrile interface was in the depletion condition. Each of these couples displayed an irreversible cathodic voltammetric wave at potentials where the interface was in depletion. Peak potentials and approximate onset potentials for these waves are listed in Table III. Kohl and

Bard have also observed irreversible cathodic cyclic voltammetric waves at n-InP in acetonitrile for redox couples with formal reduction potentials within the bandgap (26).

There are several fundamental issues related to the electrochemistry of these complexes. First, since the CV waves are irreversible, the operative electron transport mechanism must be unidirectional. Second, it would be useful to discern whether the reduction currents are due to majority carriers (conduction band electrons) or to injection of minority carriers (holes) from the ferricenium cations into the valence band. Third, the role of surface states in the electron transfer process should be addressed. Fourth, the relative contributions of thermionic emission-diffusion over a Schottky barrier and quantum mechanical tunneling should be assessed (27).

The model that is generally used to discuss current flow at the semiconductor/solution interface is shown in Fig. 9. The figure depicts the energetic situation for DFER^{+0} as the redox couple in solution. Since the reorganization energies for the various ferrocene redox couples should be similar (1), the energetics for the other couples can be envisioned by vertically displacing the density of states curves to reflect the different values of E^0 .

One mechanism that is consistent with the irreversible CV waves is thermionic emission-diffusion (TED) of conduction band electrons (26). The height of the barrier to reduction of solution species by TED at an n-type electrode is the amount of band bending, approximately $E_{\text{CB}} - E_{\text{F}}$. This barrier height influences the concentration and flux of conduction band electrons at the semiconductor/solution interface at the energy of the conduction bandedge. It is possible to change the height of this barrier to reduction by moving the Fermi level with an external potential bias. The height of the barrier to oxidation of solution species by TED at an n-type semiconductor is related to the difference in potential between the conduction bandedge and the formal reduction potential of the solution species, $E_{\text{CB}} - E^0$. This barrier height determines the concentration of filled states of the solution species at the semiconductor/solution interface at the energy of the conduction bandedge. For a given solution species, assuming that the potential of the conduction bandedge does not change during a CV scan, this barrier height will not change with the electrode potential. The inability to

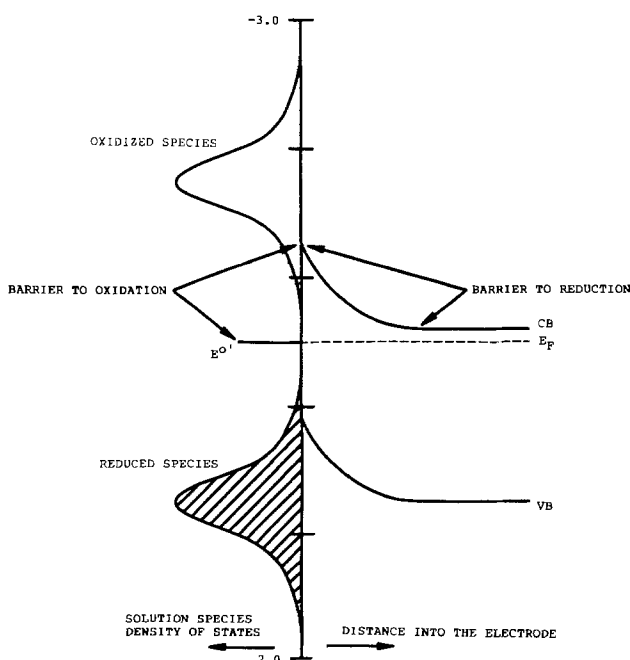


Fig. 9. Illustration of the barriers to oxidation and reduction of solution species at the n-InP/acetonitrile interface. The formal reduction potential shown is for DFER^{+0} . Also shown are the density of states distributions for DFER and DFER^+ in solution.

oxidize the ferrocene derivatives in Table III at n-InP can therefore be attributed to a low concentration of filled states at E_{CB} .

The difficulty with the TED mechanism is that it cannot account for the current densities for reduction of AFER⁺ and FER⁺. Given the high mobility of conduction band electrons in InP (greater than 4000 cm²/V-s) (26), the peak currents for HFER⁺ and DFER⁺, which occur with $|E_F - E_{CB}| < 0.5V$, could be attributed to TED. The band bending at E_{pc} for AFER⁺ and FER⁺, however, is greater than 0.7V, which makes a TED process appear unlikely. Since $E^{o'}$ for AFER⁺ and FER⁺ lies close to E_{VB} , reduction of these compounds may be due to minority carrier injection.

Kohl and Bard proposed a model for reductions at depleted n-ZnO, n-CdS, and n-GaP electrodes that involved filling of a surface state that has a redox energy located within the bandgap by conduction band electrons (25). The experimental evidence for this model was a "leveling" effect, that is, the tendency of different couples to be reduced at a common potential. Such a leveling effect is not observed in the present study at n-InP or in the previous study at p-InP. Instead, the data in Table III indicate that reduction of the ferricenium cations occurs over a wide range of potentials and that E_{pc} is related to $E^{o'}$. It can be argued that surface states with a variety of energies may be involved; however, it appears that this eventuality would lead to oxidation waves for certain couples. For example, if a surface state with an $E^{o'}$ of approximately -0.3V were responsible for the reduction of AFER⁺, this state should allow oxidation of DFER. In Kohl and Bard's model, it is unclear why current flow should be unidirectional unless the surface states are filled by TED from the conduction band.

Reduction of solution species at depleted surfaces can also occur via quantum mechanical tunneling (QMT) of conduction band electrons through the barrier in Fig. 9. Since the barrier width is inversely proportional to N_D , currents due to QMT depend dramatically on doping density. At semiconductor/metal junctions, currents due to QMT are only important at high doping densities (26). The positions and shapes of the CV waves for the complexes in Table III do depend on N_D . Plots of $\ln i_{pc}$ vs. $E_{pc} - E^{o'}$ were used to estimate exchange current densities, i_0 , and transfer coefficients, α , for the redox couples (21). While the use of CV data to obtain these kinetic parameters is questionable (experiments utilizing more reliable methods are in progress), the results tabulated in Table III are intriguing. The exchange current densities and transfer coefficients at the N18(100) electrodes for the different couples are quite similar. A decrease in N_D has the expected effects on these parameters and probably reflects a contribution by QMT to each reduction process. Further evidence for QMT is found in the voltammetry of PMCOB⁺⁰ (Fig. 5). The CV wave for this couple occurs at a depleted surface, but close to $E^{o'}$. When the electrode potential was swept positive of $E^{o'}$ for PMCOB so that oxidation of the neutral species was thermodynamically favorable, no anodic wave appeared at the lower doped electrode. A small, kinetically controlled anodic wave appeared at the moderately doped electrode. The dependence of the current on doping density could indicate that the barrier is thin enough at the moderately doped electrode for electron transfer to occur via quantum me-

chanical tunneling but too thick at the lower doped electrode for tunneling to be possible.

The formal reduction potentials of acetylferrocene and 1,1'-diacetylferrocene are positive of the valence bandedge. The appearance of anodic waves for the oxidation of these compounds would be an indication that the n-InP electrodes entered the inversion condition under this external potential bias. The absence of anodic waves for either of these compounds is another indication that the n-InP electrodes did not enter inversion, maintaining a deep depletion condition instead.

A comparison of this work to studies of the n-Si/acetonitrile interface.—A study of highly doped n-type silicon in acetonitrile solutions using a series of redox couples that includes metallocenes has been done by Chazalviel and Truong (27). The results of their study show many similarities to our results at InP/acetonitrile interfaces. In their system, the redox couples exhibited cyclic voltammetric waves at small overpotentials, even for redox couples within the bandgap. In addition, all of their redox couples produced an apparently diffusion-controlled cathodic wave on the forward (negative) scan, similar to our results at n-InP. Couples that were located positive of the conduction bandedge had no anodic wave on the reverse (positive) scan, and couples that were located negative of the conduction bandedge had an apparently diffusion-controlled anodic wave on the reverse (positive) scan. Redox couples that were located in the vicinity of the conduction bandedge had a kinetically controlled anodic wave on the reverse (positive) scan. These results were obtained at freshly etched electrodes.

They also did a study of the cyclic voltammetric response as a function of time, in which reversible cyclic voltammograms would evolve into irreversible cyclic voltammograms. The results of their study were similar to the results of our previous study on the effect of anodic switching potential on the cyclic voltammetric response at p-InP (1). They attributed the negative shift in the conduction bandedge that they observed to the oxidation of the electrode surface and the formation of SiO₂. Our data indicate that leaving an n-type electrode in accumulation for an extended period of time can cause the reduction of surface oxide and the subsequent negative shift in the position of the conduction bandedge. Shifting the conduction bandedge negative would increase the height of the barrier to oxidation, which can result in the loss of anodic current as a function of time.

Conclusions

When combined with the data for p-InP from our previous paper (1), these results yield a complete description of the surface energetics and dark currents for the InP/acetonitrile interface. Both studies emphasize the use of metallocenes as effective redox probes and, especially, the use of capacitance data in conjunction with voltammetry experiments. The results for n-InP are summarized in Table IV. The behavior of the n-InP/acetonitrile interface is relatively simple compared to the p-InP/acetonitrile interface (1), because the effects due to surface oxide formation at positive potentials are less extensive for n-InP. This observation is consistent with the fact that the majority carriers in n-InP and p-InP are electrons and holes, respectively. If effects caused by surface oxide for-

Table IV. Summary of results at n-InP

Electrode potential (V vs. ferrocene)	Surface energetic condition	Stability of surface energetics	CV dark currents
-1.5 to -1.1	Accumulation	E_{FB} shifts negative. Slight hysteresis in M-S plot.	Nearly reversible waves.
-1.1 to 0.1	Depletion	E_{FB} is stable. Linear M-S plots.	Irreversible waves or reversible waves.
> 0.1	Deep depletion	E_{FB} shifts positive. Hysteresis in M-S plot.	No anodic currents.

mation are considered, the voltammetric responses for metallocenes at n-InP and p-InP can be rationalized qualitatively by using the Gerischer model for electron transfer at semiconductor/solution interfaces (7, 8). In some reports, the predictions of this model are consistent with the theoretical interpretation of current flow across semiconductor/metal junctions (26). One intriguing result of these experiments is that diffusion-controlled CV waves will occur for compounds with formal reduction potentials within the bandgap while the electrode is in depletion, rather than being postponed until the electrode is brought into accumulation or inversion. While deducing the mechanism of charge transport, thermionic emission-diffusion, quantum mechanical tunneling, or a minority carrier process will require additional experiments, the data do not support a mechanism involving surface states.

Acknowledgments

We wish to thank Dan DuBois (Solar Energy Research Institute) for donating samples of the complexes PCOB and PMCOB and Gary Darsey (University of Arizona) for donating a sample of HFER. This project was supported by the Department of Energy (Division of Chemical Sciences) Contract no. DE-FG02-84ER13247.

Manuscript submitted April 18, 1985; revised manuscript received July 23, 1985.

REFERENCES

1. C. A. Koval, R. L. Austerlmann, J. A. Turner, and B. A. Parkinson, *This Journal*, **132**, 613 (1985).
2. W. J. Albery, "Electrode Kinetics," Clarendon Press, Oxford, England (1975).
3. J. O'M. Bockris and A. K. N. Reddy, "Modern Electrochemistry," Plenum Press, New York (1970).
4. K. J. Vetter, "Electrochemical Kinetics," Academic Press, New York (1967).
5. P. Delahay, "Double-Layer and Electrode Kinetics," Interscience Publishers, New York (1965).
6. A. J. Bard and L. R. Faulkner, "Electrochemical Methods," Chap. 3, 12, John Wiley and Sons, New York (1980).
7. H. Gerischer, *Adv. Electrochem. Electrochem. Eng.*, **1**, 139 (1961).
8. H. Gerischer, *Top. Appl. Phys.*, **31**, 115 (1979).
9. S. R. Morrison, "Electrochemistry at Semiconductor and Oxidized Metal Electrodes," Plenum Press, New York (1980).
10. R. H. Wilson, *Crit. Rev. Solid State Mater. Sci.*, **1** (1980).
11. A. J. Nozik, *Ann. Rev. Phys. Chem.*, **29**, 189 (1978).
12. H. Reiss, *This Journal*, **125**, 937 (1978).
13. R. Memming, *Electroanal. Chem.*, **11**, 1 (1979).
14. G. Darsey (University of Arizona, Tempe, AZ) and D. DuBois (Solar Energy Research Institute, Palo Alto, CA), Personal communication.
15. C. K. Mann, *Electroanal. Chem.*, **3**, 57 (1969).
16. R. R. Gagne, C. A. Koval, and G. C. Lisensky, *Inorg. Chem.*, **19**, 2854 (1980).
17. J. A. Turner, J. Manassen, and A. J. Nozik, *Appl. Phys. Lett.*, **37**, 488 (1980).
18. J. L. Robbins, N. Edelstein, B. Spencer, and J. C. Smart, *J. Am. Chem. Soc.*, **104**, 1882 (1982).
19. D. W. Hall and C. D. Russel, *ibid.*, **89**, 2316 (1969).
20. W. F. Little, C. N. Reilly, J. D. Johnson, and A. P. Sanders, *ibid.*, **86**, 1382 (1964).
21. A. J. Bard and L. R. Faulkner, "Electrochemical Methods," John Wiley and Sons, New York (1980).
22. G. Cooper, J. A. Turner, B. A. Parkinson, and A. J. Nozik, *J. Appl. Phys.*, **54**, 6463 (1983).
23. A. J. Bard and L. R. Faulkner, "Electrochemical Methods," p. 634, John Wiley and Sons, New York (1980).
24. S. M. Sze, "Physics of Semiconductor Devices," p. 371, John Wiley and Sons, New York (1969).
25. P. A. Kohl and A. J. Bard, *This Journal*, **126**, 598 (1979); *J. Am. Chem. Soc.*, **99**, 7531 (1977).
26. S. M. Sze, "Physics of Semiconductor Devices," Chap. 9, John Wiley and Sons, New York (1969).
27. J. N. Chazalviel and T. B. Truong, *J. Am. Chem. Soc.*, **103**, 7447 (1981).

Technical Notes



Influence of pH on the Charge Storage Behavior of Thermally Prepared MnO₂ Films

Laurence D. Burke and Michael J. Ahern

Department of Chemistry, University College, Cork, Ireland

It has recently been demonstrated (1) that it is necessary to distinguish between two significantly different forms of oxide. The first is a highly compact, anhydrous form as is found in the rutile phase of thermally prepared IrO₂ (2). The second, involving the same metal oxidation state and usually prepared by wet, nonthermal techniques (e.g., base precipitation and various electrochemical procedures), is a dispersed hydrous oxide (2, 3). The present work is part of a project devoted to a study of the relevance of these ideas, developed mainly from work on noble metal oxide electrochemistry, to the charge storage behavior of the industrially important MnO₂ system. The charge storage behavior of three different types of manganese oxide have been investigated: the first was produced by potential cycling a manganese metal substrate (4); the second by a standard anodic precipitation procedure used commercially to yield battery-grade γ -MnO₂; and the third by thermal decomposition of Mn(NO₃)₂ (5).

Experimental

Hydrous manganese oxide layers were generated by potential cycling (-0.40 to 1.65V, 41 mV·s⁻¹, ten cycles) a slab of manganese metal (ca. 1 mm thick, Alpha/Ventron, 99.9% pure) sealed into glass—with an exposed polished surface of geometrical area ca. 0.1 cm²—in 1.0 mol·dm⁻³ NaOH at 25°C. Thermal MnO₂ deposits on gold wire of geometrical area ca. 0.5 cm², sealed into soda glass, were prepared as follows. The wire was degreased in acetone, submerged in boiling aqua regia for 30s, washed with distilled water, and allowed to dry. It was then briefly immersed in a methanol solution containing 1.74 mol·dm⁻³ Mn(NO₃)₂ · 4H₂O and 0.22 mol·dm⁻³ SnCl₂ · 2H₂O and annealed in air after drying (50°C for 15 min) for 3h at 195°-200°C (5). The presence of SnO₂ in this initial mixed oxide layer enhanced the adhesion of the final deposit to the gold substrate; it did not appear to affect the charge storage behavior of the thermal MnO₂—this was checked

by repeating the coating process, leaving out the $\text{SnCl}_2 \cdot 2\text{H}_2\text{O}$ in the case of the second layer (both deposits gave similar voltammograms with higher currents in the case of the two-coated specimen).

To prepare electrodeposited MnO_2 , graphite rods were first abraded with emery paper, then coated with a metal etch resist (Kodak, KMER) to leave an exposed geometric area of ca. 2 cm^2 ; after immersion for 1 min in a solution containing 10% H_2SO_4 and 5% H_2O_2 (by volume), these were stored overnight, after washing, in distilled water. MnO_2 was deposited onto the resulting surfaces by anodization at $2.0 \text{ mA}\cdot\text{cm}^{-2}$ in an aqueous solution containing $0.30 \text{ mol}\cdot\text{dm}^{-3} \text{ MnSO}_4 \cdot \text{H}_2\text{O}$ and $0.66 \text{ mol}\cdot\text{dm}^{-3} \text{ H}_2\text{SO}_4$ at $80^\circ \pm 1^\circ\text{C}$ (raising the deposition temperature to 95°C made little difference to the subsequent voltammetric results) for 25 min. This is a standard procedure for electrodepositing $\gamma\text{-MnO}_2$ (5, 6). The loading level used was ca. $1.4 \text{ mg MnO}_2\cdot\text{cm}^{-2}$. X-ray analysis confirmed the presence of $\beta\text{-MnO}_2$ and $\gamma\text{-MnO}_2$ as the main bulk constituent in the thermally prepared and electrodeposited material, respectively.

The potentiostatic circuitry has been outlined elsewhere (4). Analar-grade chemicals and triply distilled water were used throughout; the cell temperature was controlled at $25^\circ \pm 0.1^\circ\text{C}$. Experiments involving potential/pH studies were carried out using Michaelis buffer solutions; some problems were encountered due to anion effects, e.g., addition of H_2SO_4 , HCl , and H_3PO_4 to the buffer solutions even at high pH tended to dislodge the oxide deposit, and attempts to maintain constant ionic strength by addition of $1.0 \text{ mol}\cdot\text{dm}^{-3} \text{ Na}_2\text{SO}_4$ also led to a deterioration (including a certain degree of bleaching) of the oxide coating on the working electrode. Generally, it was found that the oxide deposits were stable at pH values down to ca. 9.3.

Results and Discussion

Preliminary description of the voltammetric behavior.—In basic media, two peaks, E_a^I and E_a^{II} , could be distin-

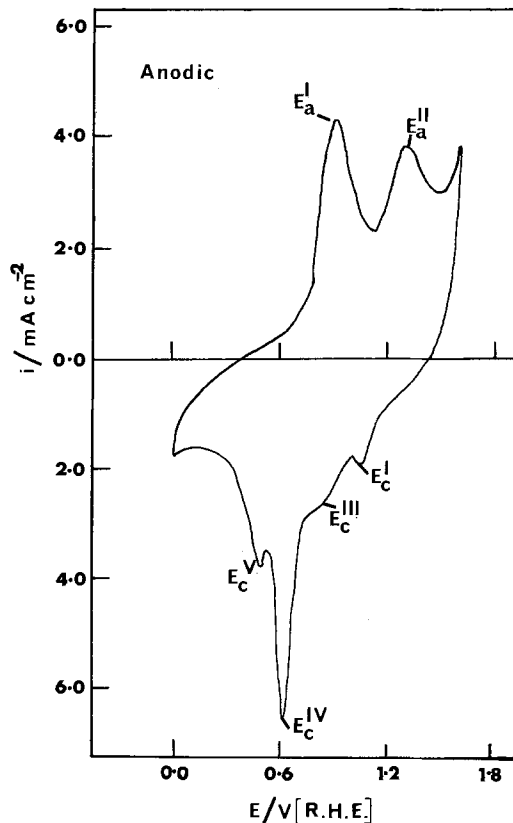


Fig. 2. Cyclic voltammogram for an anodically deposited manganese dioxide layer on graphite; $1.0 \text{ mol}\cdot\text{dm}^{-3} \text{ NaOH}$, 25°C , $0\text{-}1.60\text{V}$, $2 \text{ mV}\cdot\text{s}^{-1}$.

guished on the anodic sweep and about four (or five in the case of the thermal oxide) on the cathodic sweep (Fig. 1-3). Approximate peak maximum potential values are

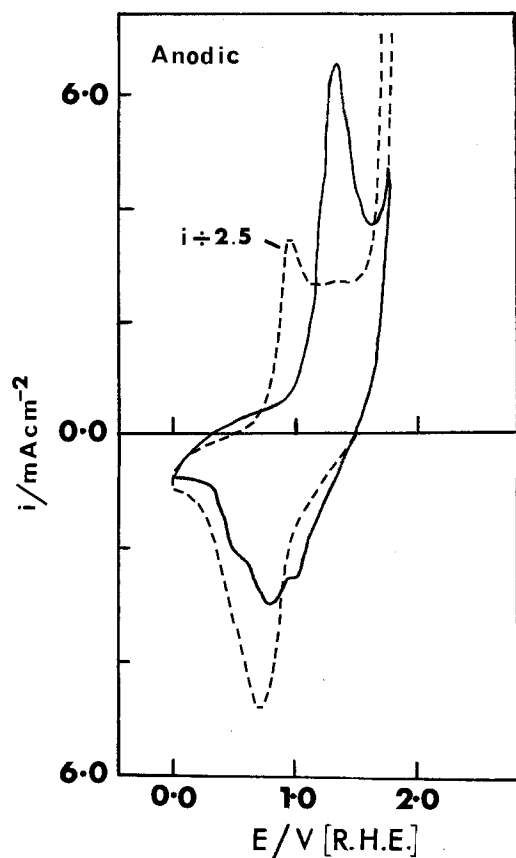


Fig. 1. Cyclic voltammogram for a hydrated oxide coated manganese metal electrode in $1.0 \text{ mol}\cdot\text{dm}^{-3} \text{ NaOH}$ ($\text{pH} = 13.6$, dashed line) (a) borate buffer ($\text{pH} = 9.30$, solid line) at 25°C (b); $0\text{-}1.75\text{V}$, $35 \text{ mV}\cdot\text{s}^{-1}$.

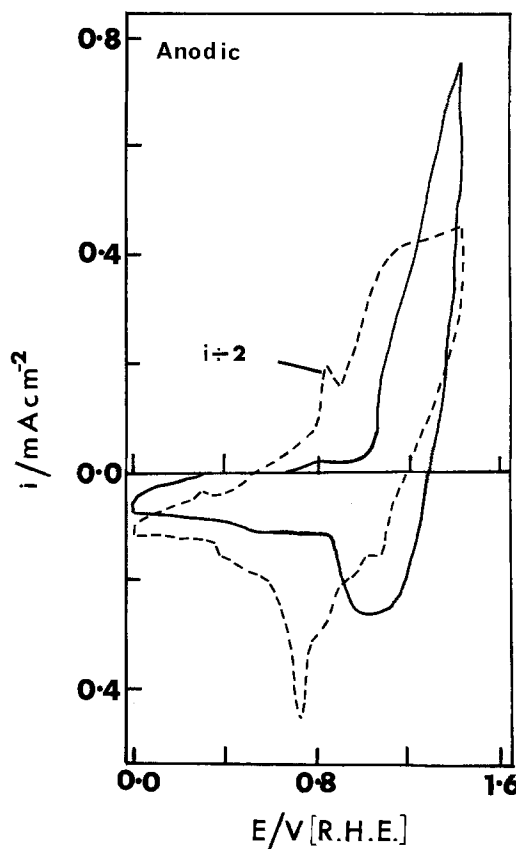


Fig. 3. Cyclic voltammogram for a thermally prepared $\text{MnO}_2/\text{SnO}_2$ deposit on gold: $1.0 \text{ mol}\cdot\text{dm}^{-3} \text{ NaOH}$, $\text{pH} = 13.6$ (dashed line); borate buffer, $\text{pH} = 9.30$ (solid line). $T = 25^\circ\text{C}$. $0\text{-}1.40\text{V}$; $5 \text{ mV}\cdot\text{s}^{-1}$.

Table 1. Approximate peak maximum potentials observed in cyclic voltammograms recorded for the three different types of manganese oxide in 1.0 mol-dm⁻³ NaOH at 25°C (RHE scale)

Type of MnO ₂ deposit (↓)	E _a ^I	E _a ^{II}	E _c ^I	E _c ^{II}	E _c ^{III}	E _c ^{IV}	E _c ^V
(a) Hydrous	0.96	1.37/P	N	N	0.86/P	0.70	0.47/P
(b) Thermal	0.83	1.15/P	1.03/P	0.93/P	0.79/P	0.70	0.39/P
(c) Electro-deposited	0.92	1.32	1.07	N	0.86/P	0.60	0.50

N: not observed.
P: poorly resolved.

listed in Table I; while there seemed to be reasonable agreement between the E_{max} values for the different types of oxide, it is obvious from the original diagrams that most of the peaks are quite broad. In the case of the thermally prepared material, the charge associated with the voltammograms generally increased (Fig. 4) on cycling; evidently, due to some type of rearrangement and hydration process, the depth of charge in this material was increased by this procedure. For most of the present work, the thermal oxide-coated electrodes were pretreated by cycling in 1.0 mol-dm⁻³ NaOH, 15 cycles, 0-1.40V at 28 mV·s⁻¹.

With the hydrous deposit, Fig. 1, only one major anodic and one major cathodic peak was observed. The peak E_{a}^{II} can be seen much more clearly in the case of the electro-deposited layer (Fig. 2). With all three films, the major feature of the cathodic sweep in base was the peak E_{c}^{IV} at ca. 0.70V.

Effect of pH on the redox response under potential cycling conditions.—Voltammograms are also shown in Fig. 1 and 3 for the oxide films in borate buffer solutions of pH = 9.30. Despite the lower peak current density, the anodic peak for the latter in the case of the hydrous film produced by cycling is clearly at a higher potential than in base. Similarly, for the same system, the main cathodic process occurs over a slightly more anodic potential range at pH = 9.30 than at 13.6; however, the anodic shift observed here on altering the pH is more dramatic for the oxidation as compared with the reduction sweep (see also Fig. 6). These shifts for the hydrous film are not kinetic in origin; this is clear from Fig. 5, where it can be seen that at slow sweep rates (< ca. 60 mV·s⁻¹) the peak maximum potentials for the hydrous material are sweep-rate independent. As outlined in Fig. 6, these reversible peak potentials vary in a linear manner with pH, dropping by 137 and 87 mV (anodic and cathodic, respectively) per unit increase in solution pH (pH-independent scale).

It is clear from Fig. 3 that the anodic shift with decreasing pH occurs also in the case of the thermal film. The

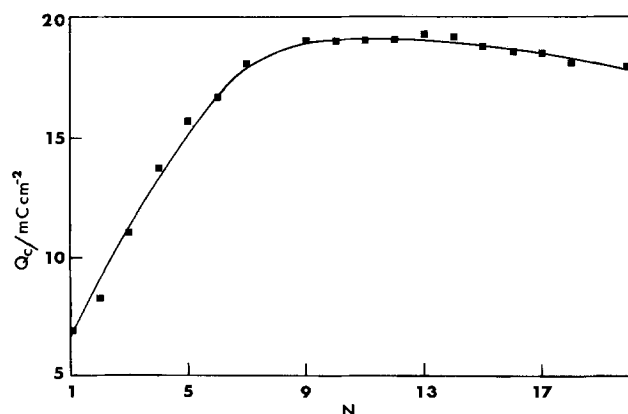


Fig. 4. Effect of the number of pretreatment cycles, N, on the cathodic charge associated with voltammograms (0-1.4V, 28 mV·s⁻¹) recorded for a thermally prepared MnO₂/SnO₂ electrode in 1.0 mol-dm⁻³ NaOH at 25°C.

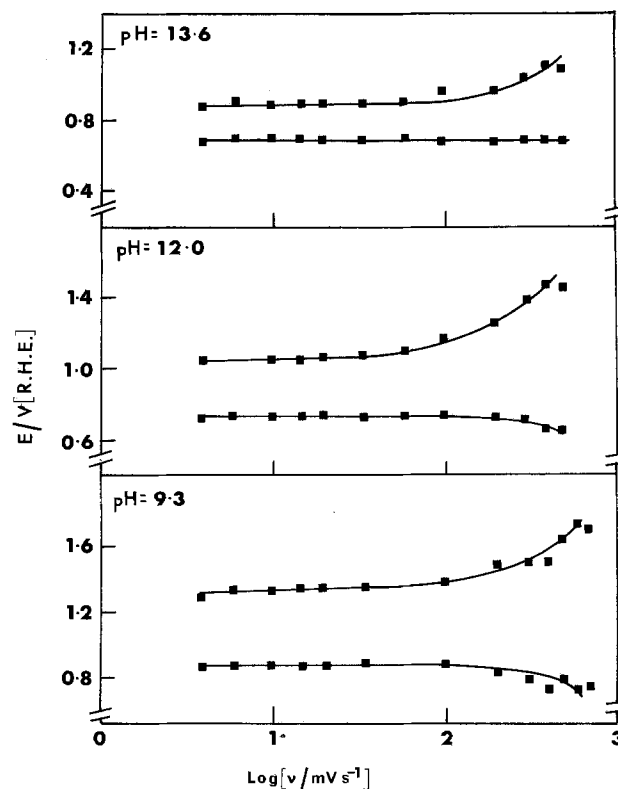
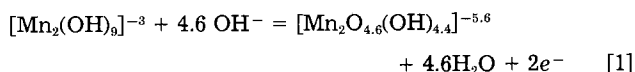


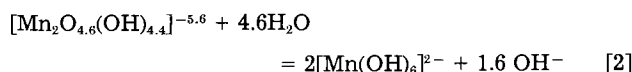
Fig. 5. Effect of sweep rate (ν) on the peak potentials (E_{max}) for the main anodic and cathodic process, at various pH values, for a hydrous film (see Fig. 1).

peaks in this case are not very distinct—especially in the borate buffer solution—but the shift can be illustrated by showing (Fig. 7) the drop in the anodic charge required to attain a given potential under fixed, slow sweep-rate, voltammetric conditions with decreasing solution pH.

The model proposed earlier (1) to explain the redox behavior of hydrous oxide systems—especially their unusual potential/pH dependence—assumes that these materials are loosely cross-linked ion-exchange polymers whose acidity, or ion-exchange capacity, increases with increasing degree of oxidation of the central metal ion. In the case of the material produced by potential cycling (4), the large, apparently sweep-rate independent, potential/pH variation of the anodic peak (ca. 137 mV/pH unit, SHE scale) corresponds to a ratio of hydroxide ions/electrons of 2.3/1. An appropriate equation for the oxidation reaction in this case is



The basic reaction involved here is assumed to be Mn(III)/Mn(IV); however, there is evidently significantly greater proton loss from the more oxidized form of the hydroxy complex. The nonintegral values may be viewed in two ways: (i) a mixture of anionic products, e.g., $[\text{Mn}_2\text{O}_5(\text{OH})_4]^{-6}$ and $[\text{Mn}_2\text{O}_4(\text{OH})_5]^{-5}$, is present in aggregate form, or (ii) the hydroxy species given in this equation are simply mean atomic or group ratio values for material present in an extended array. To explain the difference between the anodic and cathodic response (Fig. 6), it is assumed that the highly anionic oxidation product is unstable, decomposing in a postelectrochemical step as follows



This decomposition is assumed to yield the required starting material for the subsequent cathodic process [which is identical to that proposed earlier for iridium (1),

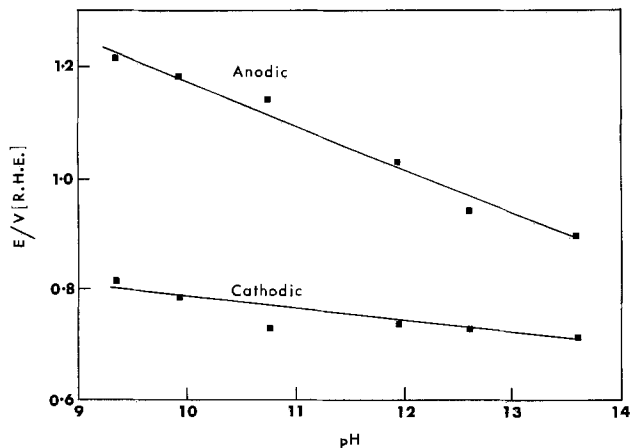


Fig. 6. Effect of pH on E_{\max} for the main anodic and cathodic process recorded for a hydrous film at slow sweep rates. Least squares slope values (RHE scale): anodic, -78 mV/pH unit; cathodic, -28 mV/pH unit. $T = 25^\circ\text{C}$.

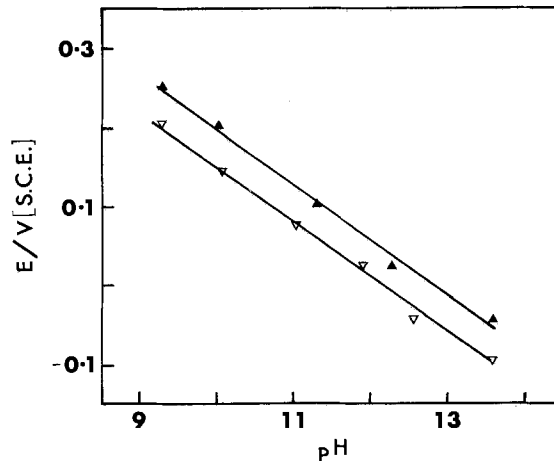
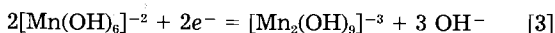


Fig. 8. Effect of pH on the open-circuit potential for a thick (filled triangles) and a thin (open triangles) thermally prepared MnO₂/SnO₂ deposit on gold. Mean least squares slope value (SHE scale): -70.3 mV/pH unit.

where an 87 mV shift was also noted]



In the case of the thermally prepared material, it is assumed that only the outer region of the oxide deposit is electroactive; this is also the region which is most likely to be hydrated. The shift of the charge storage reaction to higher potentials on decreasing the solution pH (Fig. 3 and 7) is also similar to that described earlier in the case of hydrous rhodium oxide deposits [Fig. 8 in Ref. (7)]. The pH effect is clearly the dominant factor here; the other anions, e.g., borate (which must be added to the solutions of lower pH if buffering and ionic strength are to be maintained at reasonable levels), affect the charge storage capacity; although they do not, at least to any marked extent, affect the redox potentials [the same type of decrease in redox potential on raising the solution pH is observed in phosphate and sulfate solutions (8)]. Most

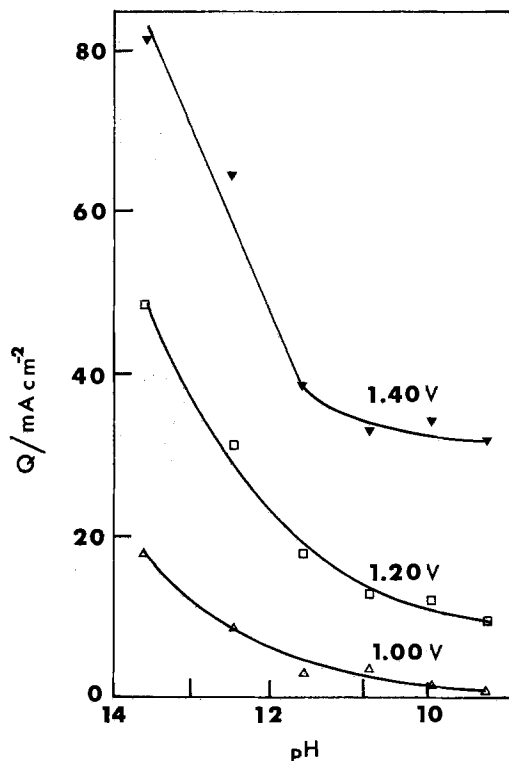


Fig. 7. Effect of pH, in the case of a thermally prepared MnO₂/SnO₂ film, on the anodic charge (above 0.6V) required to reach three specified potentials on the sweep-cyclic voltammetry conditions as outlined in Fig. 3. $T = 25^\circ\text{C}$.

treatments of the manganese dioxide electrode system to date, while briefly mentioning oxide acidity and ion-exchange behavior, have ignored the influence of variation of oxide activity associated with changes in the oxidation state of the central metal ion and, in particular, the influence of such acidity changes on the redox behavior of this type of material. A qualitative treatment of the super-nernstian, i.e., $> 2.303 RT/F$ V/pH unit, shift recorded here may also be given for the case of MnO₂ rather than its hydrated analogs, e.g., $[\text{Mn}(\text{OH})_6]^{-2}$ (Eq. [2]) as follows. According to the most recent view of the MnO₂ system, that of Ruetschi (9), this material is a cation vacancy system in which protons replace Mn⁴⁺ species at certain sites in the oxide, i.e., the latter contains both O⁻ and OH⁻ anions and these are related by the equilibrium



Raising the pH or hydroxide ion activity of the solution increases the hydroxide ion activity in the solid, and therefore lowers the metal ion activity. As outlined in the case of gold (10) and iridium (1), this drop is usually greater for material in the hydroxylated or partially hydroxylated state for the oxidized (Mn⁴⁺) as compared to the reduced (Mn³⁺) cationic species. The former tend to be more acidic, anionic, or prone to hydrolysis: one manifestation of this increased acidity is the super-nernstian potential-pH shift; another, for a battery oxide system not very different from MnO₂, is the strong binding of K⁺ cations in the oxidized Ni(111) system, i.e., $\gamma\text{-NiO} \cdot \text{OH}$ (11).

Open-circuit potential/pH response.—The application of cyclic voltammetry to the study of bulk charge storage reactions in oxides is to date surprisingly limited; the method, however, is extremely useful, as a "spectrum" of the charge/discharge properties of these materials is readily obtained. To eliminate the possibility that the observed super-nernstian shift in the present case is an artifact due to a slow electrochemical or transport step under cyclic voltammetry conditions (though, in view of Fig. 5, this seemed unlikely), the following experiment was carried out with a thermally prepared MnO₂ electrode. The latter, after preliminary cycling in base, was held for a brief period at 0.9V (RHE). It was then transferred to a buffer solution (the order of pH change here with respect to the different buffers was random) and its potential monitored with respect to saturated calomel. Drift was negligible after ca. 30 min. The plotted values (Fig. 8) were taken after a period of 1h. From this type of open-circuit experiment, which in fact was carried out at separate times using different electrodes, a mean potential/pH variation of ca. 70.3 mV/pH unit (SCE or SHE scale) was recorded.

This super-nernstian response on open circuit is in agreement with the report of other authors (12, 13), whose

work involved the use of battery-type (*i.e.*, γ -) MnO_2 . The observed value is lower than that recorded under cyclic voltammetry conditions. A similar effect was again noted in the iridium oxide case (14). The difference is attributed primarily to chemical effects, *i.e.*, the redox processes are rapid, but either the more anionic oxidation product is somewhat unstable (dissociating or rearranging slowly to give a more neutral phase) or the more inert, neutral (*i.e.*, bulk) oxide plays a greater role in the equilibrium value recorded under open-circuit conditions. The potential/pH response observed under cyclic voltammetry conditions may be most relevant to the behavior of MnO_2 under current supply situations in battery systems, *i.e.*, the interaction between oxide acidity and redox behavior seems to be particularly relevant with regard to an interpretation of the charge/discharge characteristics (dynamic as opposed to open-circuit) behavior of MnO_2 .

Acknowledgment

The authors are grateful to Dr. P. McSweeney, Mitsui Denman (Ireland) Limited, Little Island, Cork, Ireland, for x-ray data.

Manuscript submitted Dec. 10 1984; revised manuscript received ca. July 8, 1985. This was Paper 68 presented at the New Orleans, Louisiana, Meeting of the Society, Oct. 7-12, 1984.

REFERENCES

1. L. D. Burke and D. P. Whelan, *J. Electroanal. Chem.*, **162**, 121 (1984).
2. L. D. Burke and R. A. Scannell, *Plat. Metals. Rev.*, **28**, 56 (1984).
3. J. D. E. McIntyre, W. F. Peck, and S. Nakahara, *This Journal*, **127**, 1264 (1980).
4. L. D. Burke and M. J. G. Ahern, *J. Electroanal. Chem.*, **183**, 183 (1985).
5. S. Trasatti and G. Lodi, in "Electrodes of Conductive Metallic Oxides, Part A," S. Trasatti, Editor, Chap. 7, Elsevier, Amsterdam (1980).
6. G. W. Nichols, *Trans. Electrochem. Soc.*, **62**, 393 (1932).
7. L. D. Burke and E. J. M. O'Sullivan, *J. Electroanal. Chem.*, **129**, 133 (1981).
8. L. D. Burke, M. E. Lyons, E. J. M. O'Sullivan, and D. P. Whelan, *ibid.*, **122**, 403 (1981).
9. P. Ruetschi, *This Journal*, **131**, 2737 (1984).
10. L. D. Burke, M. E. Lyons, and D. P. Whelan, *J. Electroanal. Chem.*, **139**, 131 (1982).
11. L. D. Burke and T. A. M. Twomey, in "The Nickel Electrode," R. G. Gunther and S. Gross, Editors, pp. 75-95, The Electrochemical Society Softbound Proceedings Series, Pennington, NJ (1982).
12. R. S. Johnson and W. C. Vosburg, *This Journal*, **99**, 317 (1952).
13. P. Benson, W. B. Price, and F. L. Tye, *Electrochem. Technol.*, **5**, 517 (1967).
14. L. D. Burke, J. K. Mulcahy, and D. P. Whelan, *J. Electroanal. Chem.*, **163**, 117 (1984).

Electrochemical Behavior of Thin Platinum(111) Films Deposited on Mica Surfaces

Hsue-Yang Liu, Fu-Ren F. Fan, and Allen J. Bard*

Department of Chemistry, The University of Texas, Austin, Texas 78712

Atomically smooth Pt electrode surfaces are usually prepared from single crystals and are, of necessity, of limited area. It is possible to prepare "smooth" electrode surfaces by mechanical polishing with a fine polishing agent (*e.g.*, 0.1 μm alumina), but such surfaces are only macroscopically smooth (*e.g.*, with asperities $>1000\text{\AA}$). An alternative approach is to deposit a thin film onto a smooth substrate such as flat glass or quartz. One problem with this approach is the weak adhesion of a thin metal film to the substrates, especially when the electrode is immersed in liquid and subjected to an applied electrode potential. Mica is a naturally occurring material that can be cleaved to produce an atomically smooth surface. It has been used to prepare epitaxially grown single-crystal films (1-9) for UHV experiments, and films of Ag and Au on mica have been applied to electrochemical measurements (8, 9). Thin Ag(111) films have been prepared to study electroreflectance (9a) and to investigate the migration of complexes (8) at electrode/electrolyte interfaces. Au(111) (9b) films were utilized to examine the hydrogen adsorption isotherm in acidic solutions. In this paper, we report the preparation of smooth Pt(111) films grown on freshly cleaved mica surfaces and the electrochemical behavior of such films in aqueous and non-aqueous solutions.

The thin platinum films were prepared by RF sputtering at 2×10^{-2} torr under Ar flow with a Materials Research Corporation Model MRC 8620 triple shutter RAD sputtering module. Films 1000\AA thick were prepared at a deposition rate of 10 $\text{\AA}/\text{s}$. Before deposition, a thin sheet was first peeled off from a thick mica plate (grade 2, ruby c.c.s. mica sheet, United Mineral and Chemical) in air. Mica has been used frequently for surface studies (1-7), and techniques like multiple beam interferometry (10)

can be used to confirm the perfect cleavage and smooth surface.

The crystallography of the resulting platinum film deposited on the mica surface was examined using x-ray diffraction techniques. Figure 1 shows spectra obtained at bare (B) and Pt-deposited (A) mica surfaces. Although the background spectrum (Fig. 1B) due to the bare mica surface is relatively complicated, a peak at $2\theta = 39.5^\circ$ (Fig. 1A) that arises from Pt(111) (ASTM no. 4-0802) can be clearly identified. No peaks associated with other crystal phases were found, so that the crystal phase of the resulting platinum film is clearly (111). Scanning electron microscopy (SEM) was used to check the smoothness of the thin Pt(111) film. There were no distinguishable island features at up to $40,000\times$ magnification. These results indicate that a smooth thin Pt(111) film can be readily prepared on the mica surface (1, 2a).

For electrochemical measurements, the thin platinum film was connected with conductive silver paint (Acme Chemicals and Insulation Company) to a copper wire lead in a glass tube. The electrode surface was masked by 5 min epoxy and silicone rubber cement, except for the area to be examined. The cyclic voltammogram (CV) obtained at the thin platinum film in a solution of 0.5M H_2SO_4 is shown in Fig. 2A. The nature of hydrogen adsorption and oxide film formation on platinum single-crystal electrodes have been the subject of many studies (11-16). As shown in Fig. 2A, at the Pt/mica electrode in the hydrogen adsorption region, only a single peak at -0.2V is observed. These results, when compared with those reported previously under similar experimental conditions (11, 13a), show that the thin platinum film used in the present study behaves as a Pt(111) surface. Therefore, the electrochemical results are consistent with the assignment of the Pt(111) surface as deduced from the

* Electrochemical Society Active Member.

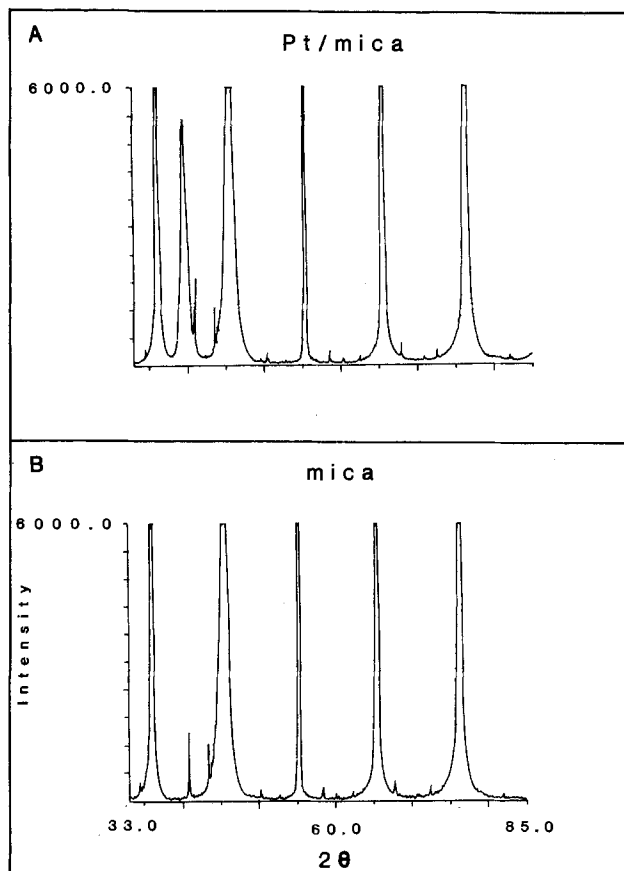


Fig. 1. X-ray diffraction spectra of Pt-deposited mica surface (A) and bare mica surface (B).

x-ray diffraction data. The thin Pt film became flaky if the electrode potential was repeatedly scanned over the hydrogen evolution region. This probably can be attributed to penetration by hydrogen into the platinum lattice.

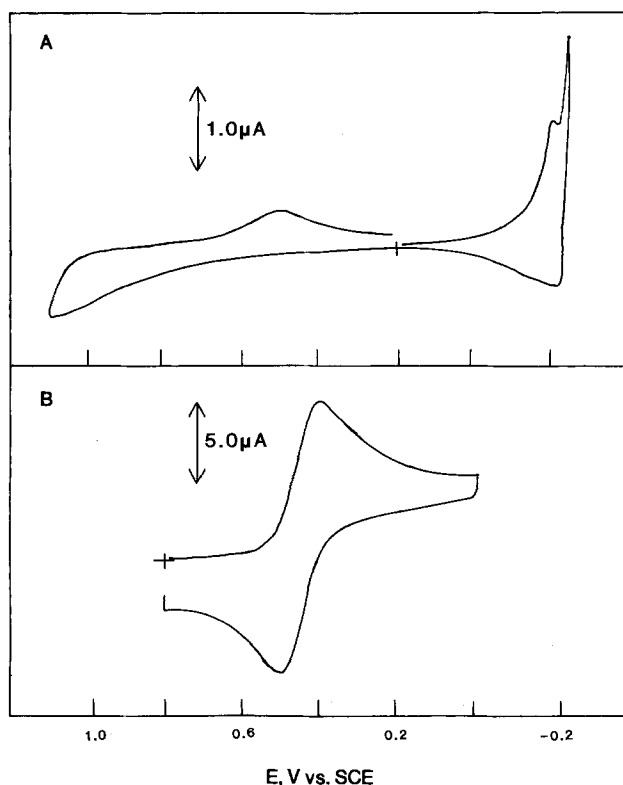


Fig. 2. A: Cyclic voltammetry of thin Pt(111) film in 0.5M H_2SO_4 . Electrode area: 0.08 cm^2 . Scan rate: $10 \text{ mV}\cdot\text{s}^{-1}$. B: Same as A, except the solution containing $1.4 \text{ mM Fe(CN)}_6^{3-}$. Scan rate: $50 \text{ mV}\cdot\text{s}^{-1}$.

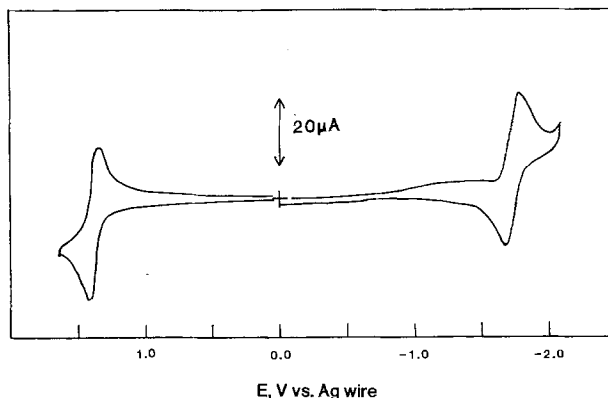


Fig. 3. Cyclic voltammetry of 1 mM DPA in $0.1M \text{ TBAF/MeCN}$ solution at 0.12 cm^2 thin Pt(111) film. Scan rate: $100 \text{ mV}\cdot\text{s}^{-1}$.

However, this thin film was very stable if the electrode potential was not allowed into the hydrogen adsorption or evolution region. The response of $\text{Fe(CN)}_6^{3-/4-}$ at this thin platinum film is given in Fig. 2B. The electrode could be scanned repeatedly over these potentials without loss of Pt from the surface. The observed behavior is similar to that found with bulk Pt electrodes.

To demonstrate the usefulness of this smooth thin Pt(111) film in nonaqueous media, cyclic voltammetry of 9,10-diphenylanthracene (DPA) carried out in $\text{MeCN}\cdot 0.1M$ tetrabutylammonium fluoroborate (TBAF) solution (Fig. 3). Both reversible reduction ($\text{DPA} \rightarrow \text{DPA}^-$) and oxidation ($\text{DPA} \rightarrow \text{DPA}^+$) reactions were observed. The thin platinum film was stable in the solution on repeated scanning of the electrode potential between $+1.65$ and $-2.1V$ vs. Ag wire. Electrogenenerated chemiluminescence (ECL) was also observed with this thin platinum film in the same solution for potential steps (50 ms) between $+1.65$ and $-2.1V$. In past studies, we found that Pt films sputtered on glass would peel from the substrate when subjected to such large potential excursions, presumably because of the significant changes of surface tension at the Pt/solution interface.

The possible application of thin Pt films deposited on mica as optically transparent electrodes (OTE) (17) was also examined. A 500\AA Pt film on mica is transparent in the visible region with relatively constant absorbance (≈ 1.0) with an associated sheet resistance of about $15 \Omega/\square$. These results are comparable to those reported for Pt deposited on quartz (17). However, as demonstrated above, the Pt film on mica appears to show better mechanical stability.

In conclusion, the experiments described here indicate that smooth thin Pt(111) films can be easily prepared on cleaved mica surfaces. Our results also show that these thin films are stable in aqueous and nonaqueous media during electrochemical experiments. Mica surfaces can be used as smooth templates to prepare a wide range of thin film electrodes. We are especially interested in such electrodes for the construction of an ultrathin layer electrochemical cell using mica balance techniques (18). Studies of this application and further characterization of these films are currently under investigation in this laboratory.

Acknowledgment

The support of the National Science Foundation (CHE8402135) and IBM is gratefully acknowledged.

Manuscript submitted June 7, 1985; revised manuscript received Aug. 27, 1985.

The University of Texas assisted in meeting the publication costs of this article.

REFERENCES

- J. W. Matthews, "Epitaxial Growth, Part B," Chap. 9, Academic Press, New York (1975).
- (a) R. L. Palmer and J. N. Smith, Jr., *J. Chem. Phys.*, **60**,

- 1453 (1974); (b) D. G. Welke, M. G. Lagally, and R. L. Palmer, *J. Vac. Sci. Technol.*, **17**, 453 (1980).
3. M. Barkai, E. Grunbaum, and G. Deutscher, *Thin Solid Films*, **90**, 85 (1982).
 4. J. Koshy, *ibid.*, **41**, L13 (1977).
 5. M. H. B. Stiddard, *ibid.*, **94**, 1 (1984).
 6. A. L. Dawar, A. Kumar, R. P. Mail, and P. C. Mathur, *ibid.*, **112**, 107 (1984).
 7. J. Caballero, G. Kremer, and L. A. Moraga, *ibid.*, **117**, 1 (1984).
 8. (a) R. Waser and K. G. Weil, *J. Electroanal. Chem.*, **150**, 89 (1983); (b) R. Waser and K. G. Weil, *Z. Phys. Chem. N. F.*, **139**, 203 (1984).
 9. (a) D. M. Kolb and R. Kotz, *Surf. Sci.*, **64**, 96 (1977); (b) D. A. Scherson and D. M. Kolb, *J. Electroanal. Chem.*, **176**, 353 (1984).
 10. S. Tolansky, "Multiple-Beam Interferometry of Surfaces and Films," Oxford University Press, London (1949).
 11. A. T. Hubbard, *Acc. Chem. Res.*, **13**, 177 (1980).
 12. K. Yamamoto, D. M. Kolb, R. Kotz, and G. Lehmpfuhl, *J. Electroanal. Chem.*, **96**, 233 (1979).
 13. (a) W. E. O'Grady, M. Y. C. Woo, P. L. Hagans, and E. Yeager, *J. Vac. Sci. Technol.*, **14**, 365 (1977); (b) A. S. Homa, E. Yeager, and B. D. Cahan, *J. Electroanal. Chem.*, **150**, 181 (1983).
 14. (a) F. T. Wagner and P. N. Ross, Jr., *ibid.*, **150**, 141 (1983); (b) P. N. Ross, Jr., *ibid.*, **76**, 139 (1977).
 15. B. E. Conway, H. Angerstein-Kozolowska, and F. C. Ho, *J. Vac. Sci. Technol.*, **14**, 351 (1977).
 16. F. Will, *This Journal*, **112**, 451 (1965).
 17. W. R. Heineman, F. M. Hawkridge, and H. N. Blount, in "Electroanalytical Chemistry," Vol. 13, A. J. Bard, Editor, Marcel Dekker, New York (1984).
 18. (a) J. N. Israelachvili and G. E. Adams, *Nature*, **262**, 774 (1976); (b) J. N. Israelachvili, *J. Colloid Interface Sci.*, **44**, 259 (1973); (c) J. N. Israelachvili and G. E. Adams, *J. Chem. Soc. Faraday Trans. 1*, **74**, 975 (1978); (d) H. K. Christenson, *J. Chem. Phys.*, **78**, 6906 (1983); (e) P. F. Luckham and J. Klein, *J. Chem. Soc. Faraday Trans. 1*, **80**, 865 (1984); (f) H. K. Christenson and R. G. Horn, *J. Colloid Interface Sci.*, **103**, 50 (1985).

Hydrogen Insertion at a Vanadium Pentoxide Cathode

S. J. Hibble, A. M. Chippindale, and P. G. Dickens

Inorganic Chemistry Laboratory, University of Oxford, Oxford, England OX1 3QR

The galvanostatic discharge of a vanadium pentoxide cathode using 2M ZnSO₄ as electrolyte at a current density of 50 μA/cm² gives rise to the potential vs. charge curve shown in Fig. 1. The discharge curve is in close agreement with that obtained by Shukler and Kuz'min (1) for V₂O₅/ZnSO₄ at comparable current densities. The final discharge product was dark green and had a powder x-ray pattern little changed from that of the parent V₂O₅ (Table I), there being no evidence of the characteristic x-ray lines of V₂O₄ or V₂O₃, the reaction products proposed by Shukler and Kuz'min.

It has been previously shown that the reduction of platinumized samples of V₂O₅ using "hydrogen spillover" gives rise to a green phase of H_xV₂O₅ at low hydrogen contents (x = 0-0.5) with lattice parameters almost identical to those of V₂O₅ (3). Moreover, the IR spectrum of the discharge product (Fig. 2) closely resembles that of the spillover product in that a peak at 928 cm⁻¹, previously assigned as an —OH bend, is clearly visible.

It is therefore proposed that the discharge product is the hydrogen insertion compound, H_xV₂O₅, the reaction occurring at the V₂O₅ cathode being

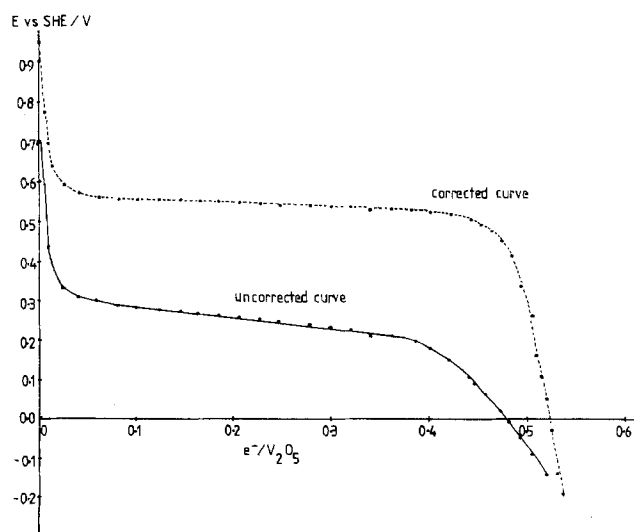
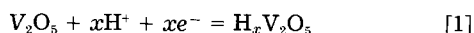


Fig. 1. Discharge curves for V₂O₅ cathode in 2M ZnSO₄ (aq)

The plateau in Fig. 1 indicates the coexistence of two solid phases: namely, V₂O₅ and H_xV₂O₅. Following the end of the plateau, E varies rapidly with the charge passed and corresponds to the formation of a single phase of H_xV₂O₅ with a narrow composition range. The pH of the electrolyte was measured continuously throughout the experiment, and the broken curve shown in Fig. 1 has been corrected to unit hydrogen ion activity using the Nernst equation

$$E_{\text{obs}} = E^{\circ}_{\text{corr}} + \frac{RT}{nF} \log [\text{H}^+] \quad [2]$$

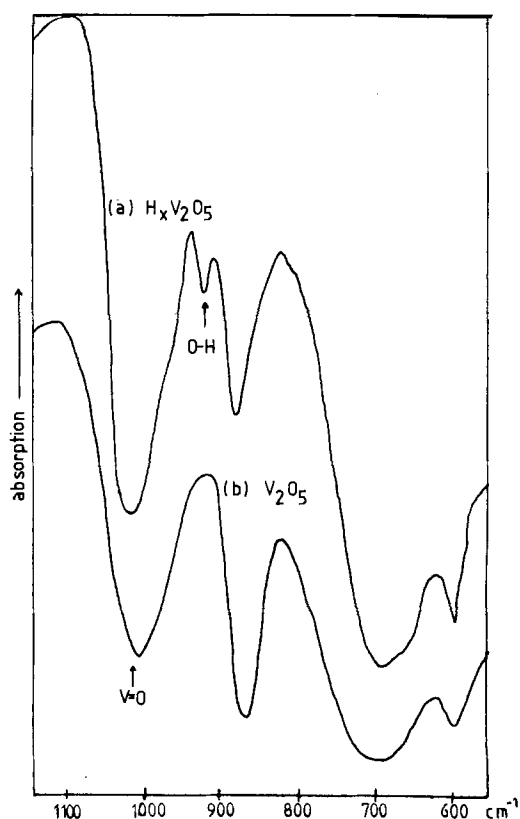


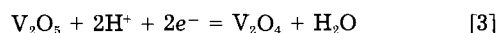
Fig. 2. IR spectra of discharge product (a) and of V₂O₅ (b)

Table I. X-ray powder data for $H_xV_2O_5$

	2θ	d_{obs} (Å)	d_{calc} (Å)	h	k	l
m	15.308	5.787	5.771	2	0	0
s	20.260	4.382	4.368	0	0	1
w	21.729	4.089	4.085	1	0	1
s	26.108	3.412	3.409	1	1	0
m	30.985	2.886	2.886	4	0	0
w	32.429	2.761	2.763	0	1	1
w	33.300	2.690	2.687	1	1	1
wm	34.320	2.613	2.616	3	1	0
w	47.260	1.923	1.924	6	0	0
w	47.981	1.897	1.899	3	0	2
w	48.827	1.865	1.863	0	1	2
w	51.216	1.784	1.784	0	2	0
w	51.888	1.762	1.761	6	0	1

Orthorhombic: Refined lattice parameters: $a = 11.544(7)$, $b = 3.568(3)$, $c = 4.368(4)$ Å. Compare refined lattice parameters for V_2O_5 (2): $a = 11.51$, $b = 3.56$, $c = 4.37$ Å.

The corrected curve shows $0.45e^-$ passed per V_2O_5 up to the end of the plateau region. The cathode reaction proposed by Shukler and Kuz'min is thus unsatisfactory since $2e^-$ per V_2O_5 would be required for the formation of V_2O_4



Our reaction [1] agrees with the expression obtained by Watson and Scott (4) for the pH dependence of the potential of a V_2O_5 cathode in acidic media

$$E = E^\circ - 0.0602pH \quad [4]$$

In conclusion, the cathodic reduction of V_2O_5 in $ZnSO_4$ leads to the formation of the low hydrogen content phase of $H_xV_2O_5$, the lower phase limit being $x = 0.45$.

Acknowledgments

We thank the U.S.A.F. Office of Scientific Research for Grant AFSOR-83-0052. A.M.C. Also thanks the S.E.R.C. for a Research Studentship.

Manuscript received June 25, 1985.

The University of Oxford assisted in meeting the publication costs of this article.

REFERENCES

1. Y. S. Shukler and L. L. Kuz'min, *Shurnal Prikl. Khim.*, **39**, 1327 (1966).
2. ASTM Powder Diffraction File 9-387.
3. P. G. Dickens, A. M. Chippindale, S. J. Hibble, and P. Lancaster, *Mater. Res. Bull.*, **19**, 319 (1984).
4. N. V. Watson and A. B. Scott, *This Journal*, **112**, 883 (1965).

The Electrochemical Deposition of Conducting Poly(3-Methyl-2,5-Thienylene) Films from Aqueous Media

Andrzej Czerwinski,¹ Hans Zimmer, Chiem Van Pham, and Harry B. Mark, Jr.*

Department of Chemistry, University of Cincinnati, Cincinnati, Ohio 45221

Diaz *et al.* have published extensively on the characterization of electrodeposited conducting films of poly(pyrrole) (1) and poly(2,5-thienylene) (2) from nonaqueous media. The electrochemical behavior of solution phase redox couples at electrodes consisting of such conducting polymer films have been described also (1-6). There appears to be a certain disagreement about the effect of small amounts of water in the nonaqueous deposition media on the morphological and electrochemical behavior of poly(pyrrole) films deposited by electrochemical oxidation on platinum (3, 4). Although Taurillon and Garnier have done the stability test of poly(3-methyl-2,5-thienylene)² in 1:1 CH_3CN/H_2O medium and showed that after 10^3 cycles of anodic-cathodic polarization no degradation of the electrochemical properties of the polymer occurs, (5), there have been no reports of the electrodeposition of polythienylene from aqueous media alone. In spite of the fact that the monomeric, 3-methylthiophene is not significantly soluble in an aqueous media (7), it was found, as reported here, that conducting films of poly(3-methyl-2,5-thienylene) could be deposited by electrochemical oxidation of aqueous emulsions of the monomer. The procedure for aqueous deposition and the comparison to nonaqueous electrodeposited film are described.

Experimental

The 3-methylthiophene monomer was a commercial sample and was used as is (Aldrich Chemical Company, Milwaukee, Wisconsin). The polymer film was prepared by an electro-oxidation of the monomer in a standard single-compartment cell-three-electrode potentiostat

* Electrochemical Society Active Member.

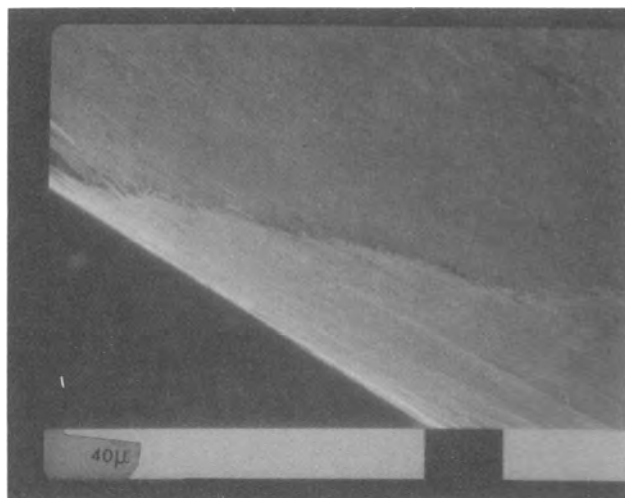
¹ On leave from the University of Warsaw, Warsaw, Poland.

² The divalent radical derived of thiophene in analogy with the phenylene nomenclature is commonly referred to as thienylene. Thus, the compounds dealt with in this and similar publications from this laboratory are named 2,5-poly(thienylenes) and not 2,5-polythiophenes.

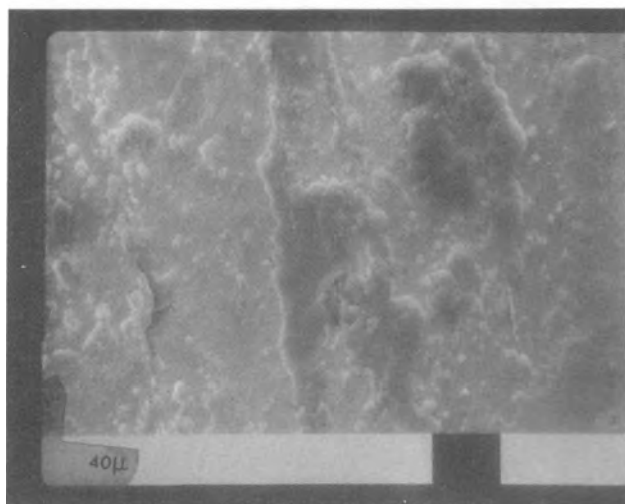
system using both platinum wire working and auxiliary electrodes. A normal calomel electrode (NCE) was used as the reference electrode. As mentioned above, the monomer was essentially water insoluble and the stirred solution was an unstable heterogeneous emulsion. The aqueous phase of the stirred emulsion used for electrodeposition was a 0.1M $NaClO_4$ solution. The electrodeposition potentials were either +1.0 or +1.4V vs. NCE and the solutions were deaerated prior and during the electrolysis by a constant stream of argon. Prior to use, the platinum working electrodes were pretreated by cyclic polarization using -0.25 and +1.15V vs. NCE potential limits in 0.5M aqueous H_2SO_4 solution until previously described (8) reproducible cyclic voltammograms were obtained. The chemical and experimental conditions for the background cyclic voltammograms of the aqueous deposited conducting poly(thienylene) films and the ferro/ferricyanide couple are given in the legends of the figures. The photographs of the electrodes surfaces were taken by SEM (Cambridge Stereo Scan 600) and surfaces were analyzed by an attached energy dispersive analyses of x-rays (EDAX) system. The bare Pt electrode and the film-coated Pt electrodes used in these experiments had identical surface areas.

Results and Discussion

Figure 1 shows the scanning electron micrographs obtained for poly(3-methyl-2,5-thienylene) films electrogenerated on Pt wire electrodes at different applied deposition potentials. Figure 1a depicts the surface morphology of a smooth poly(thienylene) film formed on electrogeneration at +1.0 to +1.1V vs. NCE. The film appears to the eye as a light yellow color and to be transparent. EDAX shows that the film contains a high concentration of sulfur. The SEM indicates that it is apparently nonporous for the magnification indicated. Physically, the film is strongly adherent to the platinum and cannot be removed by electrochemical or chemical means. A film of a few micrometers in thickness can be obtained after about 60h



a



b

Fig. 1. Scanning electron microscope pictures obtained for the 3-methyl-2,5-poly(thienylene) films. a. Electrodeposited at +1.0V vs. NCE. b. Electrodeposited at +1.4V vs. NCE.

deposition time. Figure 1b shows that the poly(3-methyl-2,5-thienylene) deposited at +1.4V vs. NCE is quite rough microscopically as compared to that obtained at +1.0 to 1.1V (Fig. 1a). Furthermore, the film is opaque and appears black to the eye. It also does not adhere strongly to the platinum surface and flakes easily on either electrochemical or mechanical treatment. The SEM suggests that the film is porous. Clearly morphology and chemical nature of the film obtained on electro-oxidative polymerization is highly potential dependent. However, the fact that the film continues to grow with time at both deposition potentials indicates that it is conductive. It should be noted that polymerization under the same conditions for 3-methyl-2,5-dibromothiophene does not occur. It means that when the 2 and 5 positions are blocked by Br atoms the anodic polymerization reaction does not occur. Thus, it is felt that the films obtained on the anodic aqueous oxidation of thiophene results in the 2,5-polymer system.

Figure 2 shows the typical background cyclic voltammogram behavior of an electrodeposited poly(3-methyl-2,5-thienylene) film at +1.0V in a neutral pH 0.1M aqueous NaClO₄ solution. Also shown in Fig. 2 is the typical cyclic voltammogram for the same supporting electrolyte solution at a bare Pt contact electrode. There are marked differences in peak potentials and magnitude of currents,

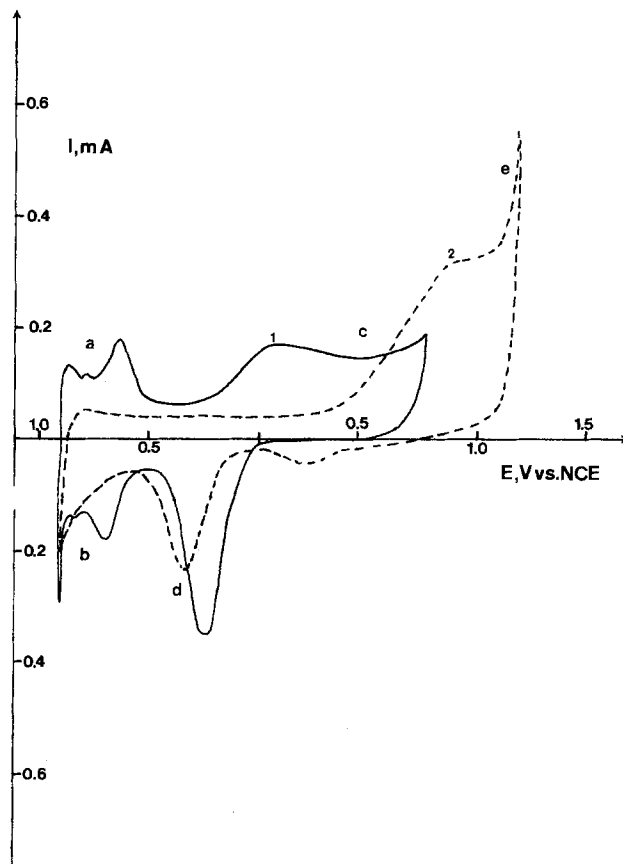


Fig. 2. Voltammogram for Pt electrode film obtained without (curve 1) and with (curve 2) a poly(3-methyl-2,5-thienylene) film obtained in 0.1M NaClO₄. Sweep rate = 50 mV·s⁻¹. The electrodeposition potential was +1.0V vs. NCE.

but the currents for polymer-covered Pt electrodes essentially correspond to the same processes as in the bare Pt contact electrode where peaks at negative potentials (a, b in Fig. 2) correspond to the hydronium ion reduction (b) and adsorbed hydrogen oxidation (a) at a platinum electrode surface, and the peaks at positive potentials (c, d) correspond to the formation of oxygen species (c) and their reduction (d) on platinum. The small peak observed at negative electrode polarization (ca. 250 mV) subsequent to a positive polarization probably corresponds to reduction of some oxidized moiety of thiophene. It should be noted that there is an increase in the magnitude of the current in the positive applied voltage region, which indicates that both the Pt surface and the polymer oxidation processes are contributing to the total anodic current. Also, the potentials of surface oxidation and oxygen evolution on Pt covered with the thiophene polymer are shifted to more positive potentials than on Pt. At the same time, there is a very significant decrease in the current magnitudes in the corresponding hydrogen-platinum surface redox peaks at negative potentials as compared to the bare Pt electrode. These results suggest that the poly(3-methyl-2,5-thienylene) film is microscopically porous and the redox reactions can occur at both the Pt and poly(3-methyl-2,5-thienylene) surfaces. The results of Tourillon and Garnier (5) showed that poly(thienylene) films deposited from nonaqueous media are fibrillar and also have potential dependent swelling properties. In contrast, the films deposited from aqueous media are not fibrillar and do not exhibit any potential dependent swelling. It is also important to note that there are no observable color changes in the positive and negative polarization regions as noted for the nonaqueous deposited film (6). Similar qualitative results were obtained in 0.5M aqueous sulfuric acid electrolyte solutions, as shown in Fig. 3.

As a further test of the electrode response of a +1.0V deposited poly(3-methyl-2,5-thienylene) film from an

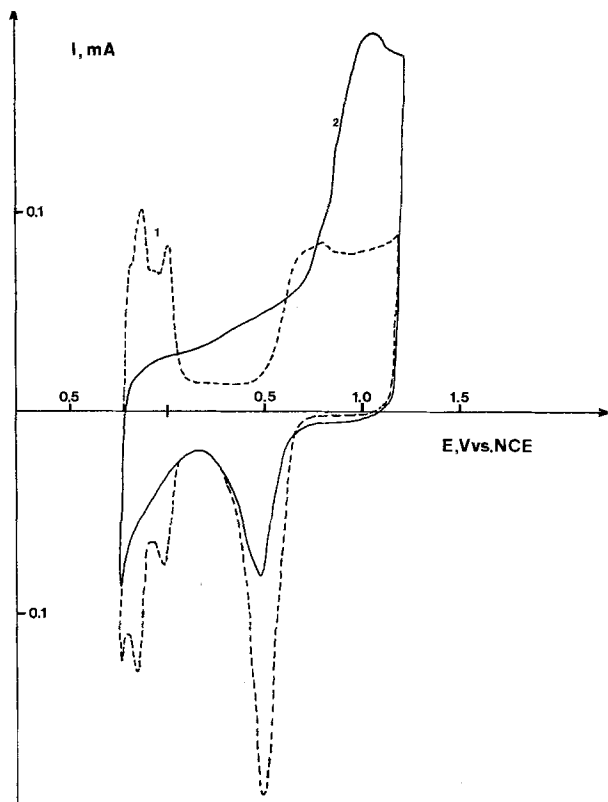


Fig. 3. Voltammograms for Pt electrode without (curve 1) and with (curve 2) a poly(3-methyl-2,5-thienylene) film obtained in 0.5M H_2SO_4 . Sweep rate = $50 \text{ mV}\cdot\text{s}^{-1}$, and electrodeposition potential was +1.4V vs. NCE.

aqueous media, the background cyclic voltammograms obtained in 0.1M acetonitrile solution containing 10^{-3}M nitrobenzene and 10^{-3}M triphenylamine were examined. Typical cyclic voltammograms are shown in Fig. 4. Again, in the positive potential region of the voltammograms, there is a slight increase in the anodic current (e.g., oxidation reaction of triphenylamine) and a slight decrease in

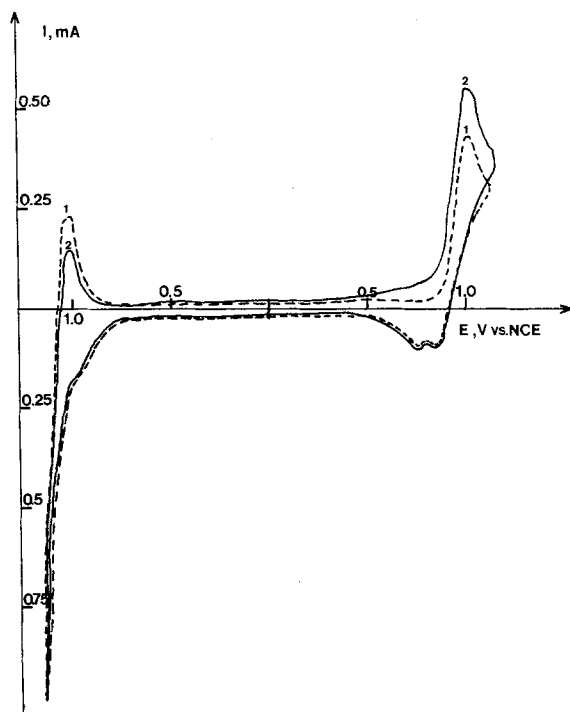


Fig. 4. Cyclic voltammograms of a 0.1 TEAFB/ CH_3CN solution containing 10^{-3}M nitrobenzene and 10^{-3}M triphenylamine at $50 \text{ mV}\cdot\text{s}^{-1}$ vs. NCE. Curve 1 (dotted line): Pt electrode. Curve 2 (solid line): Pt-poly(thienylene) electrode.

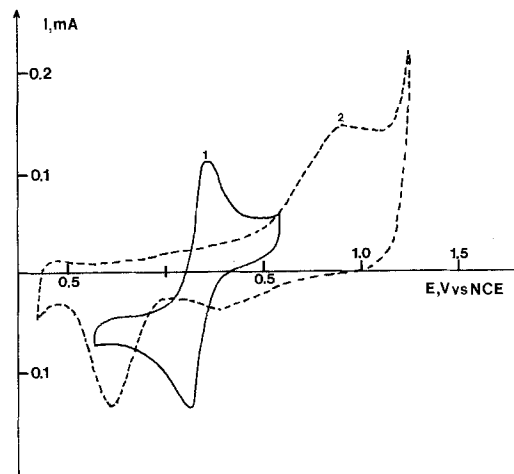


Fig. 5. Cyclic voltammograms for Pt electrode covered by poly(3-methyl-2,5-thienylene) in 0.1 NaClO_4 in the presence of 10^{-2}M $\text{K}_3\text{Fe}(\text{CN})_6$ (curve 1) and without (curve 2).

peak currents in the negative potential region (e.g., nitrobenzene reduction reaction). This is in contrast to the results reported by Diaz *et al.* (6), which showed that the neutral form of poly(thienylene) in acetonitrile solution exhibited no redox waves for negative polarization and, hence, no conductivity. Again, this indicates a significant degree of porosity of the aqueous deposited poly(3-methyl-2,5-thienylene) films as compared to the nonaqueous deposited films investigated by Diaz *et al.* (5). It is also interesting to note that electro-oxidation of the monomer when CuCl_2 is added to the aqueous NaClO_4 solution produces the same polymer film without copper being incorporated. This result is different from that of Tourillon *et al.* (9), who observe that, on oxidation from CH_3CN containing a high concentration of CuCl_2 , metallic clusters of copper are homogeneously distributed in the polymer matrix. The polymer films obtained on deposition at +1.4V show in all cases significantly more Pt electrode-type behavior or a higher degree of porosity, as suggested by the SEM in Fig. 1b.

Furthermore, the cyclic voltammograms for the ferro/ferricyanide redox systems at an electrode formed with a poly(thienylene) film from an aqueous medium at +1.0V vs. NCE are exactly the same in shape as those obtained at a bare Pt electrode, as shown in Fig. 5. However, the magnitude of the peak currents is much lower than that of a bare Pt electrode having the same surface area.

It is clear that the electrodeposition of poly(3-methyl-2,5-thienylene) films from an aqueous emulsion of the monomer produces a conducting film of the polymer which has very different morphology and conducting properties than that produced on electrodeposition from nonaqueous media. It is also clear that the potential of the aqueous electro-oxidation of the monomeric 3-methylthiophene controls the porosity, adherence, etc., of the poly(thienylene) film obtained and a systematic study of the electrochemical and physical nature of the polymer as a function of deposition potential might produce conditions that will yield a nonporous poly(3-methyl-2,5-thienylene) film. Also, a study of films obtained on electro-oxidation from mixed aqueous/nonaqueous solvent systems with variation of the ratio of concentration of the solvents would be interesting. However, no further study of this aqueous electrodeposition is planned in this laboratory.

Acknowledgment

This research was supported in part by the National Science Foundation, Grant no. NSF CHE 8205873, and was also aided significantly by gifts of n-butyl lithium from the Lithium Corporation of America, Bessemer City, North Carolina 28016.

Manuscript submitted Jan. 24, 1985; revised manuscript received May 6, 1985. This was Paper 69 presented at the

Toronto, Ontario, Canada, Meeting of the Society, May 12-17, 1985.

The University of Cincinnati assisted in meeting the publication costs of this article.

REFERENCES

1. A. F. Diaz and J. I. Castillo, *J. Chem. Soc. Chem. Commun.*, 397 (1980); A. F. Diaz, J. I. Castillo, J. A. Legan, and W. Y. Lee, *J. Electroanal. Chem.*, **129**, 115 (1981); E. M. Genies, G. Bidan, and A. F. Diaz, *ibid.*, **149**, 101 (1983); P. Bergmayer and R. W. Murray, *J. Am. Chem. Soc.*, **104**, 6139 (1982); A. F. Diaz, J. M. Vasquez Vallejo, and A. Martinez Duran, *IBM J. Res. Dev.*, **25**, 42 (1981); R. A. Bull, F. F. Fan, and A. J. Bard, *This Journal*, **129**, 1009 (1982); R. Noufi, D. Tench, and L. F. Warren, *ibid.*, **127**, 2310 (1980); R. Noufi, A. J. Frank, and A. J. Nozik, *J. Am. Chem. Soc.*, **103**, 1849 (1981); T. Skotheim, I. Lundstrom, and J. Prejza, *This Journal*, **128**, 1625 (1981); T. Skotheim, L. G. Petersen, O. Inganas, and I. J. Lundstrom, *ibid.*, **129**, 1737 (1982); D. Inganas, T. Skotheim, and I. Lundstrom, *Phys. Scr.*, **28**, 863 (1982); R. A. Simon, A. J. Ricco, and M. S. Wrighton, *J. Am. Chem. Soc.*, **104**, 2031 (1982); G. Cooper, R. Noufi, A. J. Frank, and A. J. Nozik, **295**, 578 (1982); R. Noufi, *This Journal*, **130**, 2126 (1983); A. J. Frank and K. Honda, *J. Phys. Chem.*, **86**, 1933 (1982); K. S. Reddy and A. S. N. Murthy, *Electrochim. Acta*, **28**, 473 (1983); T. Komori and T. Nonaka, *J. Am. Chem. Soc.*, **105**, 5690 (1983); A. F. Diaz, T. J. Castillo, K. K. Kanazawa, M. Salmon, and O. Fajardo, *J. Electroanal. Chem.*, **133**, 233 (1982); M. Salmon, A. F. Diaz, J. A. Logan, M. Krounbi, and J. Bargon, *J. Mol. Cryst. Liq. Cryst.*, **83**, 265 (1982); A. F. Diaz, W. Y. Lee, J. A. Logan, and D. C. Green, *J. Electroanal. Chem.*, **108**, 377 (1982); M. Salmon, A. F. Diaz, and J. Goita, in "Chemically Modified Surfaces in Catalysis and Electrocatalysis," J. S. Miller, Editor, p. 65, ACS Symposium Series 192, American Chemical Society, Washington, DC (1981).
2. G. Tourillon and F. Garner, *J. Electroanal. Chem.*, **135**, 173 (1982); A. F. Diaz, J. Bargon, and R. Waltman, in "Membranes and Ionic and Electronic Conducting Polymer," E. B. Yeager, B. Schumm, Jr., K. Mauritz, K. Abbey, D. Blankenship, and J. Akridge, Editors, p. 332, The Electrochemical Society Softbound Proceedings Series, Pennington, NJ (1982); A. Diaz, *Chem. Scr.*, **17**, 145 (1982); G. Garner, G. Tourillon, M. Gazard, and J. C. Dubois, *J. Electroanal. Chem.*, **148**, 299 (1983); R. J. Waltman, A. F. Diaz, and J. Bargon, *This Journal*, **131**, 1452 (1984); *ibid.*, **130**, 2042 (1983).
3. S. Brimmer, Ph.D. Thesis, University of Cincinnati, Cincinnati, OH (1984).
4. A. F. Diaz, Private communication (1984).
5. G. Tourillon and F. Garnier, *J. Electroanal. Chem.*, **161**, 51 (1984).
6. R. J. Waltman, J. Bargon, and A. F. Diaz, *J. Phys. Chem.*, **87**, 1459 (1983).
7. "Handbook of Chemistry and Physics," 61st ed., R. C. Weast, Editor, CRC Press, Inc., Boca Raton, FL (1980).
8. A. Capon and R. Parsons, *J. Electroanal. Chem.*, **65**, 285 (1975).
9. G. Tourillon, E. Dartyge, H. Dexpert, A. Fentaine, A. Jucha, F. Lagarde, and D. E. Sayers, *ibid.*, **78**, 357 (1984).



1985

Deep Levels in Semi-Insulating LEC GaAs Before and After Silicon Implantation

Salam Dindo,* Ibrahim Abdel-Motaleb, Kerry Lowe,**¹ Wade Tang, and Lawrence Young**

Department of Electrical Engineering, University of British Columbia, Vancouver, British Columbia, Canada V6T 1W5

ABSTRACT

The deep trapping levels present before ion implantation of silicon into the semi-insulating LEC GaAs starting material were investigated using optical transient current spectroscopy (OTCS). MESFET channel current deep level transient spectroscopy (DLTS) was used for the implanted material. With a silicon nitride layer used to encapsulate the GaAs for postimplantation annealing and with implantation directly into the GaAs, it was found that of seven or more deep levels seen in the semi-insulating substrate prior to silicon implantation only the level believed to be EL12 remained. On implanting through a thin Si_3N_4 encapsulating layer and annealing under Si_3N_4 , only EL2 was found. With a silicon dioxide layer as an encapsulant, two traps remained and two apparently unreported levels appeared.

It is widely, but not universally, accepted (1, 2) that a fabrication process based on the implantation of dopant, often silicon, directly into undoped liquid-encapsulated Czochralski (LEC) GaAs wafers is likely to dominate in the manufacture of high speed digital and analog GaAs integrated circuits. This fabrication process is as opposed to such older methods as the use of doped epitaxial layers for the MESFET channels, or that of implanted semi-insulating "buffer" epitaxial layers deposited on chromium-doped Bridgman or Czochralski wafers. With this fabrication process, some of the problems with deep trapping levels which have been extensively reported in the literature are no longer present. For example, in the earlier work, traps in epitaxial layers and at the interface of the buffer layer and the semi-insulating layer (4-6) were a problem. Naturally, problems associated with chromium or the redistribution of chromium (7-9), which with LEC material is no longer needed to obtain semi-insulating material, are no longer present. Nevertheless, the problems with the newer technology still include those due to the presence or redistribution of deep trapping levels. These levels may be due to impurities or native defects and may be present in the starting material or may be induced by process steps. In addition to problems of deep levels, the distribution of the implanted dopant and its percentage activation are crucial to device characteristics and can depend very significantly on the nature of the starting LEC material as well as on the process steps. With silicon as dopant, a high temperature anneal (at about 850°C) is needed not only to repair damage but also to allow the silicon atoms to find gallium sites on which they act as donors. On arsenic sites, they would act as acceptors. To avoid loss of arsenic, the wafers are sometimes sealed or encapsulated with a layer of SiO_2 or Si_3N_4 (10, 11). These are, of course, nominal formulas; the actual films are nonstoichiometric. Onuma *et al.* (12) have demonstrated that the implanted silicon is redistributed by diffusion during the anneal more with SiO_2 than with Si_3N_4 . This was explained as due to the presence of more vacant gallium sites in the GaAs when SiO_2 was used because of increased loss of gallium through the

encapsulant film. It is known that gallium can diffuse through SiO_2 .

The precise ways in which the details of the growth process of the Czochralski GaAs affect (i) the traps initially present, (ii) those generated by the processing, and (iii) the dopant redistribution and activation process need to be better understood and controlled. The growth and polishing techniques used by suppliers of LEC GaAs wafers are regarded as proprietary. Ingot qualification tests are used by device manufacturers.

There is an extensive literature on deep levels in GaAs (13) and on their effects on device characteristics. Only a few references can be given here. Recent papers which are specifically on deep levels in ion-implanted undoped semi-insulating (SI) GaAs include those by Sriram *et al.* (14, 15), by Rhee *et al.* (16, 17), and by Hickmott (18).

In the present work, we applied optical transient current spectroscopy (OTC)—also known as photoinduced transient spectroscopy (PITS)—(19, 21) to the undoped LEC starting material from various manufacturers and after various surface treatments. Metal semiconductor field effect transistors (MESFET's) were then fabricated on material from one manufacturer using three fabrication procedures. The traps present in the MESFET's were investigated using channel current deep level transient spectroscopy (DLTS) (6, 8, 22).

Experimental Procedures

The test devices for OTCS were of the planar type, *i.e.*, a pair of electrodes were deposited side by side on the one surface. As described previously (25), a constant voltage was applied and a GaAsP LED diode (670 nm) provided pulses of light. The transient current following the termination of the light pulses was sampled at times t_1 and t_2 after the end of the illumination using a boxcar integrator. The temperature of the device was scanned. Peaks were observed at certain temperatures due to the individual traps as their time constants $\tau = \tau_0 \exp(W/kT)$ pass through the observation window. Chromium electrodes were used since these give lower dark current than Au + Ge.

The MESFET used for channel current DLTS were long channel devices ("fat FET's") (23) with a channel width of 180 or 200 μm and a gate length of 100 or 120 μm .

* Electrochemical Society Student Member.

** Electrochemical Society Active Member.

Present address: Bell Northern Research, Ottawa, Ontario, Canada K1Y 4B7.

The source and drain were Au + Ge alloyed at 430°C for 5 min. The gates were aluminum.

In the first set of devices, the channel was implanted with $3 \times 10^{12} \text{ cm}^{-2}$ ^{29}Si at 100 keV through windows etched in a 600 nm RF-sputtered SiO_2 layer. The channel was furnace annealed at 850°C for 20 min using a 170 nm RF-sputtered SiO_2 cap. The second and third set of devices were both made using plasma-enhanced chemical vapor deposition (PECVD) Si_3N_4 films laid down in a Plasmatherm Multiversion machine with NH_3 and SiH_4 in He. The second set (labeled II) had their channels implanted through a thin (40 nm) Si_3N_4 film at 125 keV to $3.38 \times 10^{12} \text{ cm}^{-2}$ using ^{28}Si . The Si_3N_4 was thickened to 80 nm before annealing. The implantation of the third set (labeled III) was done directly into the GaAs at 100 keV to $2.25 \times 10^{12} \text{ cm}^{-2}$ of Si. 80 nm of Si_3N_4 was deposited before annealing.

The channel current DLTS experiments were performed with a bias of 50 mV applied between drain and source, small enough to be in the linear region. A reverse bias voltage was placed on the gate such that the channel was nearly pinched off. Pulses of voltage taking the gate to near zero bias were applied. The basic idea is that majority carrier traps are filled by carriers which are allowed to enter the previously depleted channel during the positive going gate voltage pulse. When the gate voltage returns to its more negative value the negative charge due to the trapped electrons partially compensates the positive space charge density in the depleted region. To maintain the fixed voltage drop across the region, it must, therefore, become initially wider than before. The channel is therefore narrowed and the drain current is less. As the occupancy of the traps returns to normal, the drain current increases (with the time constant of the trap depopulation emission process). Hole traps (9) give the reverse sign of effect [it is believed (9) that the hole trap occupancy can be changed because the quasi-Fermi level for holes communicated with the gate Fermi level].

Results

Starting LEC material.—Figure 1a shows an OTCS spectrum of a device made on a Cominco wafer from ingot no. 344. The spectrum is considerably different from those of early (lower-numbered) ingots from this manufacturer reported earlier (25), but is very close to that of a device made on a recent Sumitomo wafer (Fig. 2A). A Litton wafer gave the rather different results shown in Fig. 2b. We have no information on how typical these Litton and Sumitomo wafers were. The negative peak P2 has about the same magnitude for the Cominco and Sumitomo wafers. This peak has been related by Oliver *et al.* (24) to the degree of wetness of the B_2O_3 used in the growth process and we have found that the mechanical abrasion can increase its magnitude (25). We have discussed the mechanism by which negative peaks occur elsewhere (25). The EL2 peak P1 is much less pronounced in this current Cominco and Sumitomo material than in the earlier slices from Cominco used to investigate "thermal stability" (of the semi-insulating property) (25).

Figure 1b shows a spectrum for a specimen on a Cominco wafer of a similarly recent era (no. 453) which had been subjected to an etch by Bell Northern Research using $\text{H}_2\text{O}_2 + \text{H}_2\text{SO}_4$. The same specimen, after measurement, was again etched in an H_2O_2 and H_2SO_4 mixture to give the result shown in Fig. 1c. The effect of this process on the Sumitomo specimen in Fig. 2a is shown in Fig. 2c. These results represent a feature of the OTCS method that the effects of surface treatments can be investigated. These treatments should not be assumed merely to remove surface layers and thus reveal a depth profile of traps since a change in surface traps could also affect the result. Surface traps will presumably be populated by the light pulse and could cause some band bending.

All samples show the same set of peaks but with different amplitudes. Arrhenius plots (Fig. 4) were obtained using a range of rate windows for the OTCS sampling and using a total of ten samples made on Cominco wafers

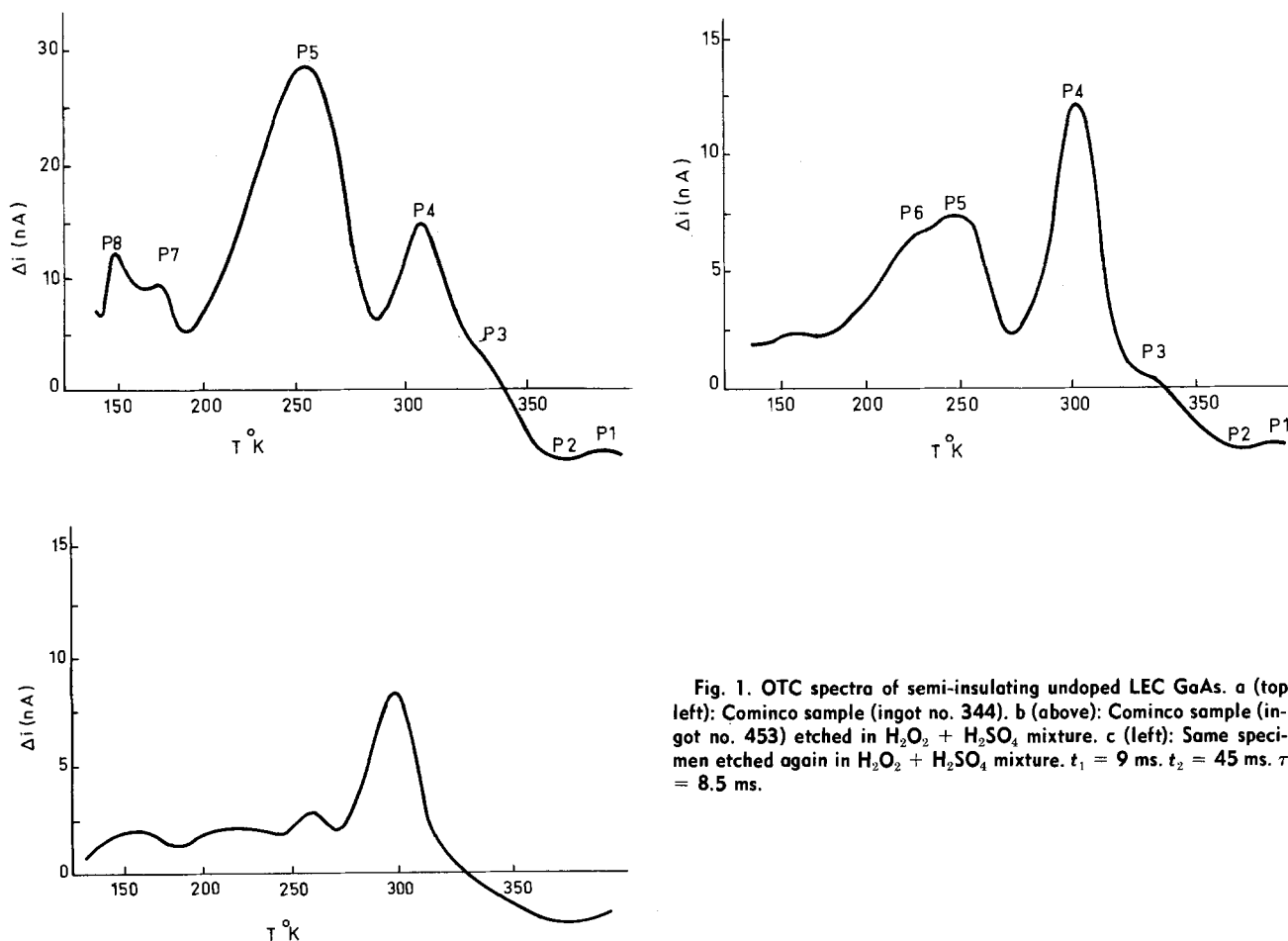


Fig. 1. OTCS spectra of semi-insulating undoped LEC GaAs. a (top left): Cominco sample (ingot no. 344). b (above): Cominco sample (ingot no. 453) etched in $\text{H}_2\text{O}_2 + \text{H}_2\text{SO}_4$ mixture. c (left): Same specimen etched again in $\text{H}_2\text{O}_2 + \text{H}_2\text{SO}_4$ mixture. $t_1 = 9 \text{ ms}$. $t_2 = 45 \text{ ms}$. $\tau = 8.5 \text{ ms}$.

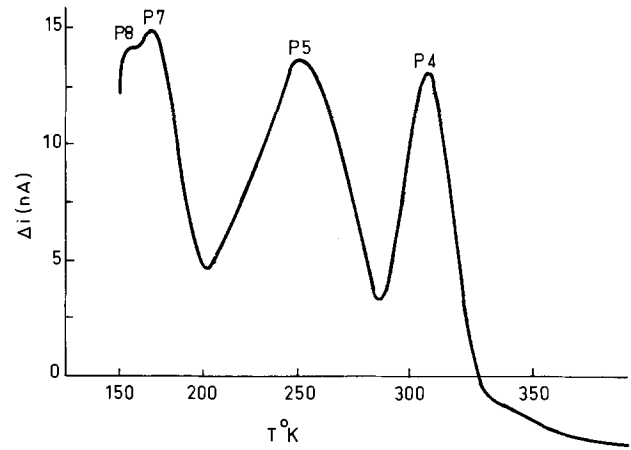
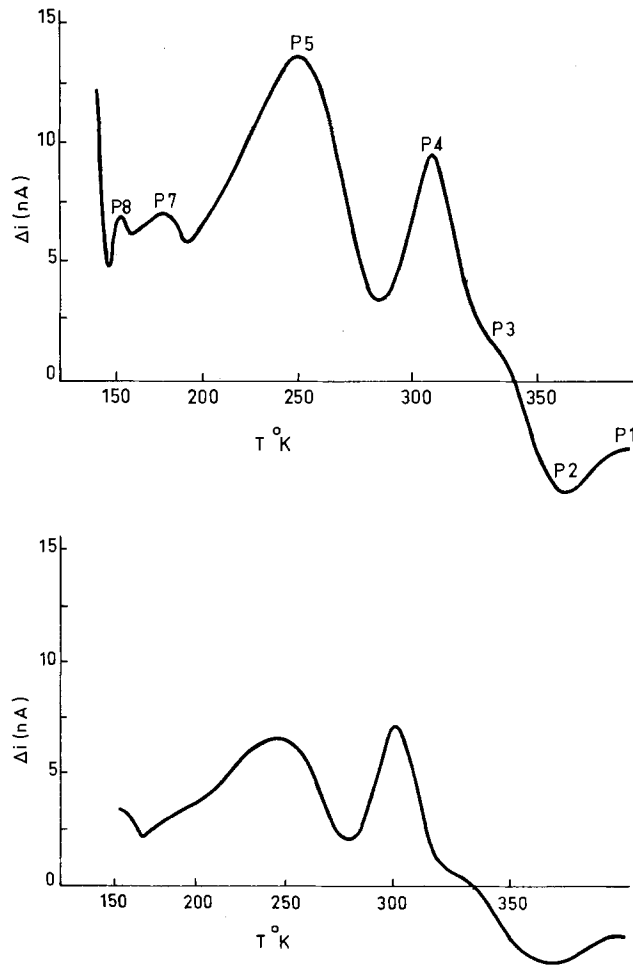


Fig. 2. OTCS spectra of semi-insulating LEC undoped GaAs. a (top left): Sumitomo sample. b (above): Litton sample. c (left): Specimen of a subjected to H_2O_2 and H_2SO_4 mixture etch. Times as in Fig. 1.

(both tail and seed ends). The identifications of the observed peaks with previously reported traps were given in a previous paper (25) and are summarized in Table I for comparison with the channel current DLTS results.

Deep levels in Si-implanted layers.—Channel current DLTS spectra are given in Fig. 3 for MESFET's made from the Cominco material using the three processes above (I: SiO_2 cap. II: Si_3N_4 cap, implantation through Si_3N_4 . III: Si_3N_4 cap, direct implantation into the GaAs). Arrhenius plots for the channel current DLTS peaks are given in Fig. 4a, and, for comparison, Arrhenius plots are also given for the OTCS peaks 4b. Table I summarizes the DLTS and OTCS data.

The devices made with a SiO_2 cap gave four peaks. On the basis chiefly of activation energies, two of these, Q1 and Q2, are the same as two peaks found in the starting material by OTCS, P4 and P5. The closest levels in the compilation of Martin *et al.* (26) seems to be EL12 and EL3. The other two levels Q3 and Q4 were not observed

in the starting material and are therefore process-induced peaks. The data given are for ingot no. 43, but similar results were obtained for ingots no. 51 and 123.

For devices implanted directly into GaAs and annealed under Si_3N_4 , only S1 (0.74 eV) was found. This peak was observed in the starting material by OTCS as P4 and is believed to be EL12. For devices implanted through Si_3N_4 and annealed under Si_3N_4 , only R1 (0.85 eV) was observed. This peak was found by OTCS as P1 and is the EL2 of Martin *et al.* (26). The data are for specimens from ingot no. 344, but similar results were obtained for process II with ingot no. 175. Although crystal manufacturers may change their growth procedures from time to time, the above differences are believed to be determined by the choice of process, not the ingot number.

Table I. Activation energies, capture cross sections, and possible identities of the deep levels found using OTCS (P1-8) in semi-insulating, undoped, LEC GaAs, and of deep levels found by channel current DLTS in MESFET's fabricated by three processes (Q1-4, R1, S1)

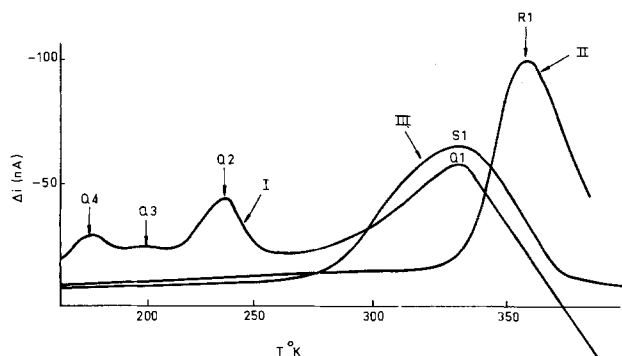


Fig. 3. Channel current spectra for MESFET's using processes I, II, and III. $\tau = 22.4$ ms.

Label	Activation energy (eV)	Capture cross section (cm^2)	Possible identity
P1	0.87	1.05×10^{-12}	EL2
P2	0.65	3.00×10^{-12}	Negative peak
P3	0.79	3.69×10^{-12}	EL12 ?
P4	0.76	2.12×10^{-12}	EL12 ?
P5	0.59	3.46×10^{-12}	EL3 ?
P6	0.52	2.90×10^{-13}	EL4
P7	0.38	3.20×10^{-14}	EL6
P8	0.32	2.50×10^{-13}	HL6
Q1	0.74	2.67×10^{-13}	P4 and EL12
Q2	0.57	4.47×10^{-12}	P5 and EL3
Q3	0.28	1.66×10^{-16}	—
Q4	0.24	1.45×10^{-16}	—
R1	0.85	4.30×10^{-13}	P1 and EL2
S1	0.74	2.10×10^{-13}	

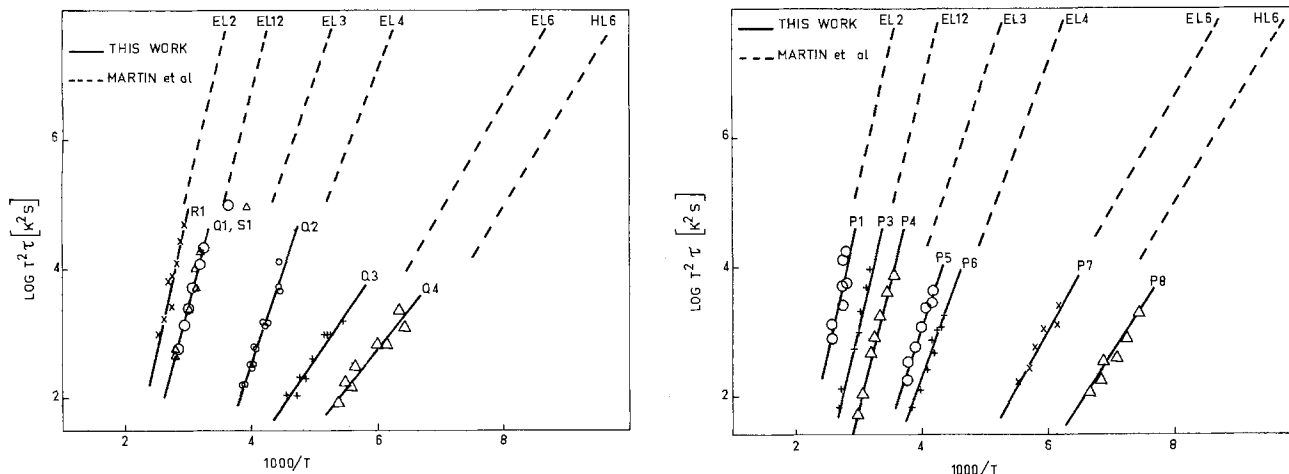


Fig. 4. Signature or Arrhenius plots. a (left): Channel current DLTS data. b (right): OTCS DLTS data.

Relating these results to previous work (Table II), Sriram *et al.* (14, 15) used devices with Si implanted directly into SI LEC GaAs at doses of $2.5\text{--}5.5 \times 10^{12} \text{ cm}^{-2}$ at 100–325 keV and annealed at 860°C under “phosphorus silicon glass.” Using channel current DLTS, they found six levels, of which three were process induced. Their defect A is possibly our level Q4. Rhee and Bhattacharya (16) implanted Si directly into Cr-doped SI LEC GaAs at doses of 10^{12} and 10^{13} cm^{-2} at 100 keV and annealed under SiO_2 (Silox). They found three electron traps, of which one was present in their starting material. In a later paper (17), they found two dominant levels (0.52 eV electron trap and an 0.15 eV hole trap) in directly implanted material, these centers being absent on implantation through Silox. Jervis *et al.* (27) compared the traps produced by implantation (i) direct and (ii) through Si_3N_4 into epitaxial buffer layers and into Cr-doped semi-insulating wafers. They annealed under Si_3N_4 . Using capacitance DLTS with both electrical and optical excitation, they also found an increase in EL2 on implanting through Si_3N_4 .

As regards mechanisms for the extra EL2, one might suggest that when implantation is done through Si_3N_4 knock-on nitrogen atoms (28) compete with displaced As atoms for vacant As sites (since nitrogen is also Group 5). The preempted As atoms could adopt vacant Ga sites to produce As_{Ga} which is, or is associated with, EL2 (29).

With SiO_2 as encapsulant, the loss of Ga is to be expected to have some effect on the types of defect produced. Perhaps occupation of the vacant Ga sites by impurities from the SiO_2 cap could be responsible for the two process-induced traps. The fact that two traps present in the starting material disappeared when annealed under Si_3N_4 but not when annealed under SiO_2 surely has to be related to the Ga vacancy concentration.

Table II. Some deep levels in silicon-implanted GaAs reported in the literature

Label	Activation energy (eV)	Capture cross section (cm^2)	Possible identity (Ref.)
A	0.23	1.90×10^{-17}	Unknown (14)
B	0.22	1.17×10^{-15}	EL14
C	0.53	1.60×10^{-12}	EL4
D	0.85	1.00×10^{-9}	New
E	0.64	5.90×10^{-14}	Cr complex
F	0.75	1.50×10^{-14}	EL2
A	0.52 ± 0.01	$(1.20\text{--}1.60) \times 10^{-18}$	(16)
B	0.17 ± 0.01	$(5.20\text{--}5.50) \times 10^{-23}$	
C	0.21	3.10×10^{-21}	
EB2	0.83	2.20×10^{-13}	EL2 (27)
EB3	0.90	3.00×10^{-11}	
EB4	0.71	8.30×10^{-13}	
EB7	0.30	1.70×10^{-14}	
EB6	0.41	2.60×10^{-13}	

Acknowledgments

This work was supported by the British Columbia Science Council and by the Natural Sciences and Engineering Research Council of Canada.

Manuscript submitted April 19, 1985; revised manuscript received Aug. 2, 1985. This was Paper 707 SOA presented at the Toronto, Ontario, Canada, Meeting of the Society, May 12–17, 1985.

The University of British Columbia assisted in meeting the publication costs of this article.

REFERENCES

- B. M. Welch, Y-D. Shen, R. Zucca, R. C. Eden, and S. I. Long, *IEEE Trans. Electron Devices*, **ed-27**, 116 (1980).
- “GaAs FET Principles and Technology,” J. V. DiLorenzo and D. D. Khandelwal, Editors, Artech House, Inc., Dedham, MA (1982); S. K. Ghandhi, “VLSI Fabrication Principles,” John Wiley and Sons, New York (1983).
- S. Asai, S. Ishioka, H. Kurono, S. Takahashi, and H. Kodra, *J. Jap. Soc. Appl. Phys.*, **42**, Suppl. 71 (1973).
- N. Yokoyama, A. Shibatomi, S. Ohkawa, M. Fukuta, and H. Ishikawa, *Inst. Phys. Conf. Ser.*, **33b**, 20 (1977).
- T. Itoh and H. Yanai, *Jpn. J. Appl. Phys.*, **19-1**, Suppl., 351 (1979).
- T. Itoh and H. Yanai, *IEEE Trans. Electron Devices*, **ed-27**, 1037 (1980).
- Y. M. Houn and G. L. Pearson, *J. Appl. Phys.*, **49**, 3248 (1978).
- A. A. Immorlica, D. R. Chen, D. R. Decker, and R. D. Fairman, *Inst. Phys. Conf. Ser.*, **56**, 423 (1981).
- A. Zylberstein, G. Bert, and G. Nuzillat, *ibid.*, **45**, 315 (1979).
- K. V. Vaidyanathan, M. J. Helix, D. J. Wolford, G. B. Streetman, R. J. Blatner, and C. A. Evans, *This Journal*, **124**, 1781 (1977).
- C. W. Farley and B. G. Streetman, *J. Electron. Mater.*, **13**, 401 (1984).
- T. Onuma, T. Hirao, and T. Sugawa, *J. Appl. Phys.*, **52**, 6128 (1981).
- U. Kaufmann and J. Schneider, *Adv. Electron. Electron Phys.*, **58**, 81 (1982).
- S. Sriram and M. B. Das, *IEEE Trans. Electron Devices*, **ed-30**, 586 (1983).
- S. Sriram, B. Kim, P. K. Ghosh, and M. B. Das, *Inst. Phys. Conf. Ser.*, **63**, 215 (1982).
- J. K. Rhee and P. K. Bhattacharya, *J. Appl. Phys.*, **53**, 3311 (1982).
- P. K. Bhattacharya and J. K. Rhee, *This Journal*, **131**, 1152 (1984).
- T. W. Hickmott, *IEEE Trans. Electron Devices*, **ed-31**, 54 (1984).
- R. D. Fairman, F. J. Morin, and J. R. Oliver, *Inst. Phys. Conf. Ser.*, **45**, 134 (1979).
- C. L. Hurtes, M. Boulou, A. Mitonneau, and D. Bois, *Appl. Phys. Lett.*, **32**, 821 (1978).
- G. M. Martin and D. Bois, in “Semiconductor Characterization Techniques,” P. A. Barnes, Editor, p. 32, The Electrochemical Society Softbound Proceedings Series, Princeton, NJ (1978).

22. M. G. Alderstein, *Electron. Lett.*, **12**, 297 (1976).
 23. A. A. Immorlica, D. R. Becker, and W. A. Hill, *IEEE Trans. Electron Devices*, **ed-27**, 2285 (1980).
 24. J. R. Oliver, R. D. Fairman, and R. T. Chen, *Electron. Lett.*, **17**, 839 (1981).
 25. L. Young, W. Tang, S. Dindo, and K. Lowe, Submitted to *This Journal*.
 26. G. M. Martin, A. Mitonneau, and A. Mircea, *Electron. Lett.*, **13**, 191, 666 (1977).
 27. T. R. Jervis, D. W. Woodward, and L. F. Eastman, *ibid.*, **15**, 619 (1979).
 28. R. T. Blunt, R. Sweda, and I. R. Sanders, *Vacuum*, **34**, 281 (1984).
 29. J. Lagowski, H. C. Gatos, J. M. Parsey, D. Wada, M. Kaminska, and W. Walukiewica, *Appl. Phys. Lett.*, **40**, 342 (1982).

Chemical Vapor Deposition of Ruthenium and Ruthenium Dioxide Films

M. L. Green,* M. E. Gross, L. E. Papa,¹ K. J. Schnoes, and D. Brasen

AT&T Bell Laboratories, Murray Hill, New Jersey 07974

ABSTRACT

The preparation of Ru and RuO₂ thin films by organometallic chemical vapor deposition and an investigation of the films' properties are reported. Ru is of interest for metallization in integrated circuit fabrication because its thermodynamically stable oxide, RuO₂, also exhibits metallic conductivity. As a result, oxidation during processing of Ru is a less critical concern than in current metallization technology. Taking advantage of the benefits of chemical vapor deposition, such as conformal coverage and low temperature, damage-free deposition, we have deposited Ru, RuO₂, and Ru/RuO₂ by pyrolysis of three organoruthenium complexes. Films of a given phase composition were deposited under a wide variety of conditions and exhibited large variations in electrical resistivity and carbon content. The best Ru film, produced from Ru₃(CO)₁₂ at 300°C in vacuum, had a resistivity of 16.9 μΩ-cm and exhibited excellent adhesion to Si and SiO₂ substrates. The best RuO₂ film, produced from Ru(C₅H₅)₂ at 575°C in O₂, had a resistivity of 89.9 μΩ-cm and similarly exhibited excellent adhesion. Rutherford backscattering studies show that Ru and RuO₂ films are effective diffusion barriers between Al and Si up to annealing temperatures of about 550° and 600°C (1/2 h exposure), respectively. Thus, they are significantly better than the currently used W films, which are only effective to about 500°C.

Integrated circuit processing requires the use of conducting films that must maintain their integrity at elevated temperatures. For example, gate electrode metallizations, in addition to being good electrical conductors, must also be resistant to oxidation at temperatures as high as 950°C. Silicides are often chosen for this application. Diffusion barrier films, used to prevent the interdiffusion of Al and Si at source/drain regions (spiking), may be exposed to temperatures as high as 550°C, at which point oxidation, even to a small extent, may degrade the contact resistance between the Al/barrier/Si layers. Tungsten and TiN, currently used as barrier films, are particularly sensitive to oxidation. These examples emphasize the critical concern with the degradation of electrical properties in the film or the film interfaces owing to environmental effects, particularly oxidation.

It is therefore interesting to consider ruthenium as a potential metallization for integrated circuits. Ruthenium dioxide, the most thermodynamically stable oxide of Ru, when formed at temperatures greater than 200°C, is almost as good a conductor as Ru ($\rho_{\text{Ru}} = 6.7 \times 10^{-6} \Omega\text{-cm}$, $\rho_{\text{RuO}_2} = 4.6 \times 10^{-5} \Omega\text{-cm}$, where ρ is the resistivity), and is actually as good a conductor as TaSi₂ ($\rho = 5.0 \times 10^{-5} \Omega\text{-cm}$) and many other silicides currently used as IC metallizations. In electrical contact applications, the advantages of Ru and RuO₂ are well known (1-3). The use of Ru, therefore, alleviates concern regarding oxidation during processing, since RuO₂ is a good electrical conductor. Other conducting oxides exist, but most are either complex oxides (e.g., Bi₂Ru₂O₇, SrVO₃) and, therefore, are more difficult to prepare, or are oxides that are thermally unstable with respect to further oxidation [e.g., 2CrO₂ (conductive) → Cr₂O₃ + 1/2 O₂ (nonconductive)] (4).

This work was undertaken to determine if Ru and RuO₂ films could be prepared by chemical vapor deposition (CVD). Chemical vapor deposition was chosen because of its well-known advantages of conformal step coverage and low deposition temperatures. The properties of CVD

Ru or RuO₂ films have not, to our knowledge, been reported before, and only a few references to such films prepared by this method exist (5-7). However, Ru films have been prepared by electrodeposition (8) and sputtering (9). In addition, RuO₂ films have been prepared by sputtering (10) and by oxidation of Ru or decomposition of RuCl₃ (2).

Experimental

Three organoruthenium compounds, all sublimable solids, were selected as sources for CVD: ruthenium acetylacetonate, ruthenocene, and triruthenium dodecarbonyl. Data on these compounds are tabulated in Table I. Vapor pressure data were available only for ruthenocene. The compounds were purchased from Alfa Chemicals and Strem Chemicals and used without further purification.

Film deposition experiments were carried out using the apparatus depicted in Fig. 1. To prevent condensation of the sublimable source materials, all surfaces of the apparatus outside the reaction zone were maintained at temperatures greater than the source sublimation temperature but lower than its decomposition temperature. Placement of the source boat as close as possible to the substrates minimized the condensation problem.

Typically, the deposition process sequence was as follows. The substrates, (100) Si, (100) Si with 1000Å of thermal oxide (SiO₂), or device wafers, were cleaned in 1%

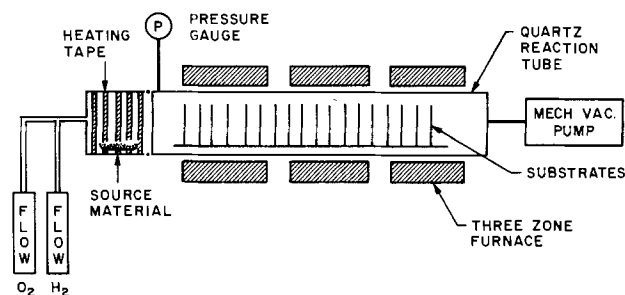


Fig. 1. Chemical vapor deposition apparatus

* Electrochemical Society Active Member.

¹ Present address: IBM Corporation, Charlotte, North Carolina 28201.

Table I. Organoruthenium source materials

Compound	Formula	Ru (w/o)	C (w/o)	H (w/o)	O (w/o)	Form	Vapor pressure	Supplier
Tris-2,4-pentane-dionato ruthenium (III) (ruthenium acetylacetonate)	$\text{Ru}(\text{C}_5\text{H}_7\text{O}_2)_3$	25.4	45.2	5.3	24.1	Solid red crystals	Unknown; decomposes at 220°C	Alfa
Bis(cyclopenta-dienyl) ruthenium (ruthenocene)	$\text{Ru}(\text{C}_5\text{H}_5)_2$	43.8	51.9	4.3	—	Solid yellow crystals	~0.01 torr at 85°C	Strem
Triruthenium dodecacarbonyl	$\text{Ru}_3(\text{CO})_{12}$	47.4	22.5	—	30.1	Solid red powder	Unknown; decomposes at 150°C	Alfa

HF for 1 min, rinsed in distilled H_2O for 10 min, then dried in a stream of N_2 . They were then loaded onto a quartz carrier and positioned vertically in the reaction furnace, which was at 200°C. The furnace was evacuated to about 20 mtorr and then brought up to the deposition temperature while pumping was continued. Once stabilized at this temperature, the gas flow of hydrogen or oxygen, if any, was started. Next, the heating tapes around the source material were turned on and sublimation of the source material was observed to begin. Deposition pressure was monitored with a capacitance manometer. When all the source material had sublimed, gas flow, if any, was stopped, and the furnace was cooled to 200°C. Deposition conditions for various films are listed in Table II.

On removal from the furnace, the samples were subjected to a variety of tests. Sheet resistance was measured with a four-point probe. Film thickness was determined with a mechanical stylus (Dektak II) on steps etched with an aqueous solution containing 5% NaOCl and 3% NaOH. From these two measurements, film resistivity could be determined. Several films, notably those containing RuO_2 , could not be etched by this method. The thickness of these films was determined by transmission electron microscopy (TEM), Auger depth profiling (after having determined the Auger sputtering rate for RuO_2 and Ru), or Rutherford backscattering spectroscopy (RBS). Film structure and composition were determined by x-ray diffraction, Auger spectroscopy, TEM, RBS, and x-ray photoelectron spectroscopy.

Results

Selection of source materials.—Selection of source materials for the deposition of thin metal films by organometallic CVD is based on consideration of several factors. The operational considerations are those of vapor

pressure sufficient to achieve rapid rates of material transport, and temperatures of sublimation and decomposition that are low, but different enough to prevent reaction of the source before reaching the deposition zone. Coupled with these are the more complex issues of decomposition chemistry and reactions with oxidizing or reducing gases.

The formal oxidation state of the metal atom in an organometallic compound is a useful formalism to consider in terms of the ease and purity of metal deposition, but it is not a physical property. The three organometallic ruthenium compounds that we chose to study as CVD sources in this work contain the metal atom in three formal oxidation states: Ru(0) in $\text{Ru}_3(\text{CO})_{12}$, Ru(+2) in $\text{Ru}(\text{C}_5\text{H}_5)_2$, and Ru(+3) in $\text{Ru}(\text{C}_5\text{H}_7\text{O}_2)_3$. The reactivity of the complexes and the ease of reduction to a formally zero-valent metal favors the carbonyl complex, in which the ligands can dissociate cleanly without any further reduction of the ruthenium. The deposition of Ru from the other two sources in the absence of reactive gases, however, requires that the organic moieties act as reducing agents for the metal ion. In the process, the ligands oxidize and decompose to leave nonvolatile carbon residues in the films.

Mass spectra of the organometallic species may also offer some clues about the relative ease of ligand dissociation. The most abundant ion in the mass spectrum of $\text{Ru}_3(\text{CO})_{12}$ is the bare tri-ruthenium cluster, Ru_3^+ (11). In contrast, the parent ion is the most abundant species in the mass spectrum of $\text{Ru}(\text{C}_5\text{H}_5)_2$ and Ru^+ is among the least abundant ions (12); likewise, for $\text{Ru}(\text{C}_5\text{H}_7\text{O}_2)_3$ (13).

Effect of source material on phase structure of film.—Table II summarizes the experimental conditions for the growth of the Ru and RuO_2 films from the various source materials. The phase structure of the films was deter-

Table II. Deposition conditions and phases present for various films

Source	Deposition temperature (°C)	Ambient	Deposition pressure (torr)	Phases present		Comments
				On Si	On SiO_2	
$\text{Ru}(\text{C}_5\text{H}_7\text{O}_2)_3$	500	H_2 O_2	1.0	Ru	Ru	
			0.3-1.0	Ru	Ru	
	600	Vacuum	0.1 max.	Ru	Ru	
			1.0	Ru, RuO_2	Ru, RuO_2	
$\text{Ru}(\text{C}_5\text{H}_5)_2$	500-800	H_2 O_2	0.5-1.0			No films observed Powdery film
			1.0	^a	Ru	
			5.0	Ru^b , RuO_2	RuO_2	
	600	O_2	5.0	Ru	Ru, RuO_2	
			5.0			
			1.0	Ru, RuO_2	Ru, RuO_2	
500-600	Vacuum				No films observed	
$\text{Ru}_3(\text{CO})_{12}$	250	H_2	1.0	^a	Ru	
			1.0	Ru	Ru	
	300	H_2	1.0	Ru	Ru	
			1.0	Ru	Ru	
	300	O_2	1.0	Ru	Ru	
			0.1 max.	^a	Ru	
	300	Vacuum	0.1 max.	Ru	Ru	
			0.1 max.	^a	Ru	
	350	Vacuum	0.1 max.	^a	Ru	
			0.2 max.	^a	Ru	

^a Deposition not performed on this substrate.

^b Minor constituent.

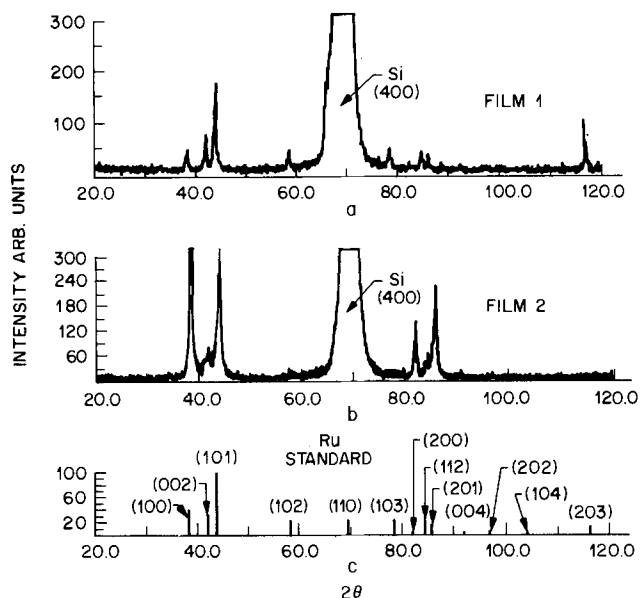


Fig. 2. X-ray diffraction patterns of Ru films: film 1 (acetylacetonate, 500°C, vacuum, on SiO₂) (a) and film 2 (carbonyl, 300°C, vacuum, on Si) (b).

mined by x-ray diffraction. We performed the deposition experiments under a wide range of conditions, with deposition temperatures of 250°-800°C, deposition pressures of 0.1-5.0 torr, and three growth ambients, H₂, O₂, or vacuum. Both Ru and RuO₂ were deposited under a variety of conditions.

Films deposited from the acetylacetonate complex at 500°C contained Ru (hexagonal phase) regardless of the ambient. Note that the thermodynamically favored RuO₂

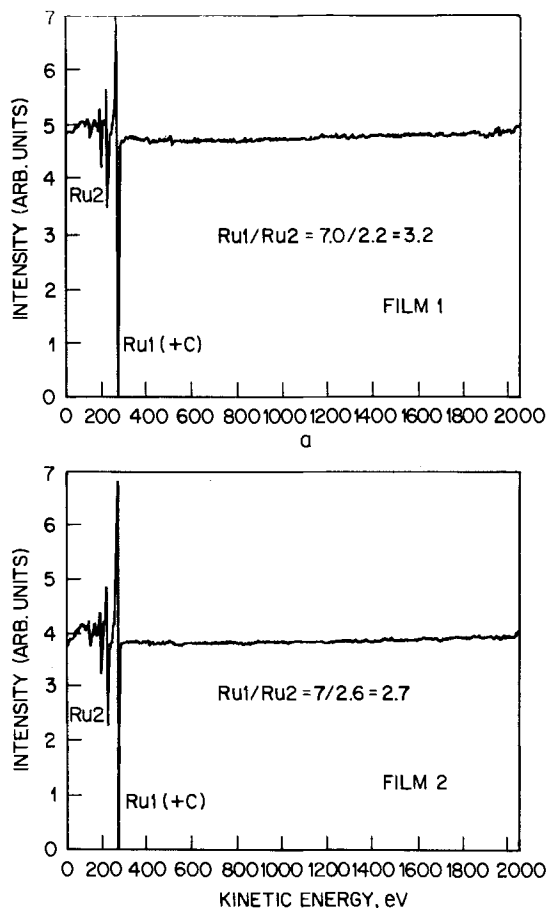


Fig. 3. Auger electron spectroscopy of Ru films: film 1 (acetylacetonate, 500°C, vacuum, on SiO₂) (a) and film 2 (carbonyl, 300°C, vacuum, on Si) (b).

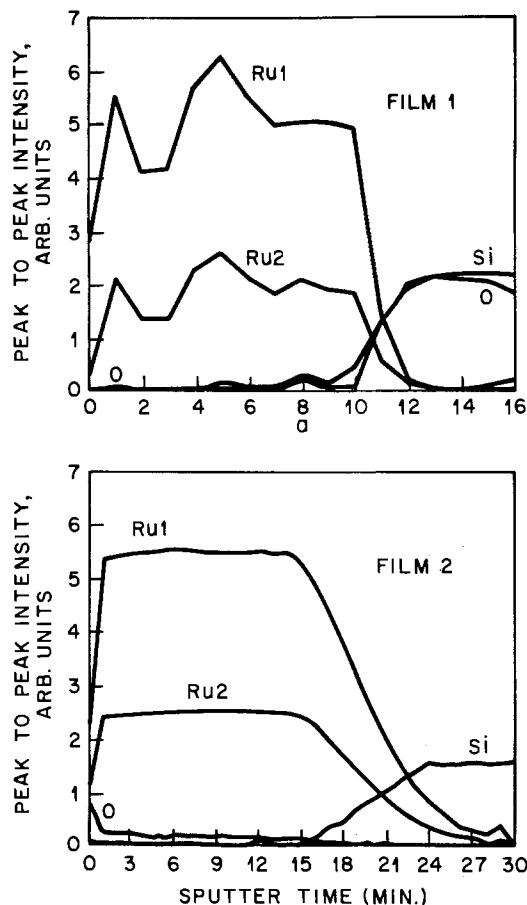
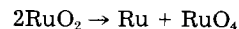


Fig. 4. Auger depth profiles of Ru films: film 1 (acetylacetonate, 500°C, vacuum, on SiO₂) (a) and film 2 (carbonyl, 300°C, vacuum, on Si) (b).

did not form in oxygen at that temperature. Films deposited at 600°C began to exhibit RuO₂ (tetragonal phase). In a hydrogen ambient, the oxygen of the RuO₂ could only have originated from the acetylacetonate ligand. Thus, in spite of the reducing ambient, formation of the oxide becomes kinetically, as well as thermodynamically, favored and the ligand serves to oxidize the Ru. Complete oxidation of the Ru at 600°C, however, is only achieved when excess oxygen is present in the ambient.

Films could only be deposited from ruthenocene in an oxygen ambient. At 500°C in oxygen, a Ru film was deposited, although it was porous. When the deposition temperature was raised to 575°-600°C, the RuO₂ phase began to be stabilized. If the oxygen pressure in the reactor is raised to 5.0 torr, films consisting entirely of RuO₂ will result on SiO₂. A RuO₂ film formed in oxygen at 575°C was found to disproportionate when postdeposition annealed in vacuum at 900°C for 2h. According to the reaction



RuO₂ films could decompose, completely or partially, to Ru and RuO₄, a volatile oxide, as observed.

Films deposited from Ru carbonyl consisted entirely of Ru, regardless of the ambient. However, the results for the other two sources show that oxide formation is not kinetically favored below ~575°C under our experimental conditions, and, owing to depletion of the carbonyl source, we could not achieve deposition above 400°C.

Film microstructures and characteristics.—In this section, the physical properties of selected films will be discussed. Several Ru, RuO₂, and mixed Ru/RuO₂ films were chosen for in-depth analysis because they represent different ambient growth conditions. All these films are continuous, specular, and, with one exception, adherent to their substrates.

Ru films.—Figure 2 illustrates the x-ray diffraction patterns for two Ru films, film 1 (acetylacetonate, 500°C, vacuum, on SiO₂) and film 2 (carbonyl, 300°C, vacuum, on Si). Comparison with the stick-figure diffraction pattern of the Ru standard, Fig. 2c, shows that all the observed peaks are attributable to Ru. In addition, whereas comparison of Fig. 2a and 2c shows film 1 to be a randomly oriented polycrystalline film, film 2 has a pronounced texture, as is shown by the high intensity of the (100) peak.

The Auger spectra of these two films, taken at a depth of 300Å into the film with the ion gun on during analysis, are shown in Fig. 3. In the presence of Ru, carbon is not easy to detect by Auger analysis as the C peak overlaps the Ru 1 peak. However, the Ru 2 peak arises only from Ru, and therefore the ratio Ru 1/Ru 2 should be related to the carbon content; specifically, it should increase with increasing carbon content. Auger analysis of a pure Ru sample (bulk) gave a ratio Ru 1/Ru 2 of 2.64, and the same ratio, as measured from the Ru spectra of the Auger handbook (14), is 2.63. Therefore, the carbonyl film, film 2, is pure with respect to carbon, as Ru 1/Ru 2 = 2.7. X-ray photoelectron spectroscopy (XPS) of this sample, a technique that is more accurate for C in Ru than Auger analysis, can detect no difference between it and the Ru standard. On the other hand, the acetylacetonate film, film 1, with its ratio of 3.2, contains much carbon, as is substantiated by XPS and RBS measurements, which show a carbon level of 60 and 62 atomic percent (a/o), respectively.

Figure 4 shows Auger depth profiles for the two films. Film 1 is much less uniform than film 2, a fact that is consistent with the TEM photomicrographs of Fig. 5. The discontinuous appearance of film 1, Fig. 5a, suggests that the carbon may be interspersed between the Ru grains. The high carbon content of this film, combined with its discontinuous microstructure, is responsible for its high electrical resistivity of $\rho = 1940 \mu\Omega\text{-cm}$. On the other hand,

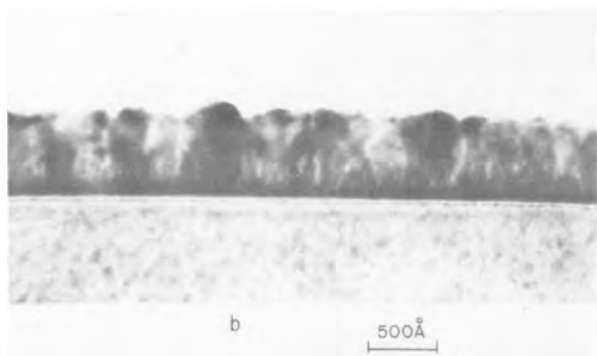
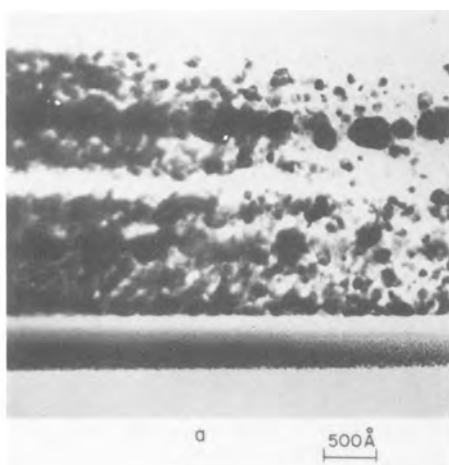


Fig. 5. Transmission electron photomicrographs of Ru films: film 1 (acetylacetonate, 500°C, vacuum, on SiO₂), bright field image (a), and film 2 (carbonyl, 300°C, vacuum, on Si), bright field image (b).

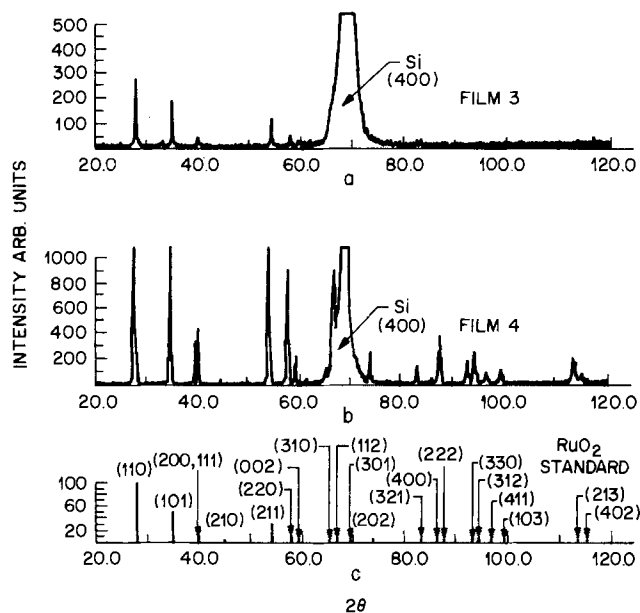


Fig. 6. X-ray diffraction patterns of RuO₂ films: film 3 (acetylacetonate, 600°C, 1.0 torr O₂, on Si) (a) and film 4 (ruthenocene, 575°C, 5 torr O₂, on Si) (b).

film 2, which is uniform and has little, if any, carbon, has $\rho = 16.9 \mu\Omega\text{-cm}$, which is only twice the bulk value of Ru. It is typical for $\sim 1000\text{\AA}$ thick films to have higher resistivities than bulk samples, owing to grain size effects and surface electron scattering. Further observations from Fig. 5 are that the grain size range of Ru in film 1 (Fig. 5a) is about 100-400Å, whereas that of film 2 (Fig. 5b) is about 300Å. Neither film shows an interaction with its substrate, based on the planar interfaces ob-

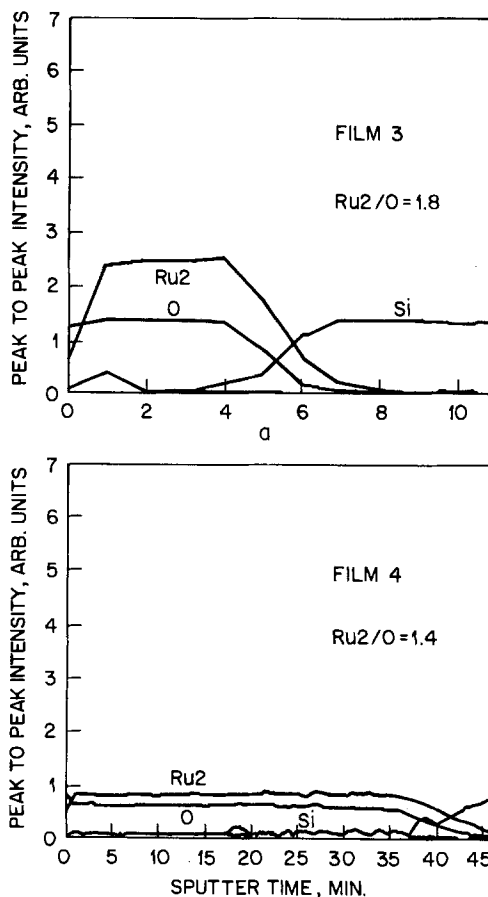


Fig. 7. Auger depth profiles of RuO₂ films: film 3 (acetylacetonate, 600°C, 1.0 torr O₂, on Si) (a) and film 4 (ruthenocene, 575°C, 5 torr O₂, on Si) (b).

Table III. Film properties

Film no.	Source	Deposition temperature (°C)	Deposition pressure (torr)	Ambient	Substrate	Film thickness (Å)	Resistivity (μΩ-cm)	Film color	Film adhesion	Carbon content (a/o)	Microstructure
Ru films											
1	Ru(C ₅ H ₇ O ₂) ₃	500	0.12	Vacuum	SiO ₂	2500	1940	Metallic	Poor	~60	Grain size ~100-400Å randomly oriented
2	Ru ₃ (CO) ₁₂	300	0.09	Vacuum	Si	1029	16.9	Metallic	Excellent	~0	Grain size ~300Å (100) texture
RuO ₂ films											
3	Ru(C ₅ H ₇ O ₂) ₃	600	1.0	O ₂	Si	1449	643	Metallic, purple-blue	Excellent	<20	Grain size ~100-500Å randomly oriented
4	Ru(C ₅ H ₇) ₂	575	5.0	O ₂	Si	6100	89.9	Blue	Excellent	<20	Grain size ~5000Å randomly oriented
Ru/RuO ₂ films											
5	Ru(C ₅ H ₇ O ₂) ₃	600	1.0	H ₂	Si	854	521	Metallic, dark	Excellent	~0	Grain size ~300-1000Å (002) texture (Ru)
6	Ru(C ₅ H ₇) ₂	600	1.0	O ₂	SiO ₂	707	14.8	Metallic, dark	Excellent	<20	Grain size ~500-750Å (200), (111) texture (RuO ₂)

served. This observation is consistent with RBS data that show that little, if any, interdiffusion of the Ru and Si or SiO₂ substrates has occurred.

Table III summarizes the physical properties of the films. Film 2, produced from the carbonyl, is more conductive, contains less carbon impurities, and exhibits better adhesion to its substrate than film 1, produced from the acetylacetonate.

RuO₂ films.—The x-ray diffraction patterns of two typical RuO₂ films are shown in Fig. 6. Film 3 (acetylacetonate, 600°C, 1 torr O₂, on Si) and film 4 (ruthenocene, 575°C, 5 torr O₂, on Si) both show patterns that are completely explainable by referring to the RuO₂ standard (Fig. 6c). Neither film shows any indication of significant texture. The diffraction pattern of film 4 is much more distinct than that of film 3 because, as can be seen in Table III, film 4 is much thicker.

The Auger depth profiles of films 3 and 4 are depicted in Fig. 7. Oxygen is evenly distributed in the films, suggesting that the films are uniform. The apparent oxygen-rich layer on the surface of film 4 is believed to be an artifact of sputtering. The presence of oxygen in these films seems to affect the Auger intensity ratio Ru 1/Ru 2, thereby making it difficult to determine if carbon is present in these films. Whereas for the Ru films, the minimum ratio of Ru 1/Ru 2 is 2.7, the pure Ru value, that ratio for films 3 and 4 is 1.7 and 1.9, respectively. As we had no carbon-free RuO₂ standard to compare these to, the carbon content of these films is not known. However, RBS analysis of film 3 suggests that carbon, if any, is present to the extent of less than 20 a/o, the detectability limit. Based on its similar ratio, the carbon content of film 4 is presumably about the same. The intensity ratio of the Ru 2 and O Auger peaks should, under ideal conditions, be related to the stoichiometry of the RuO₂ phase. However, the ratio Ru 2/O is 1.8 for film 3 and 1.4 for film 4. We believe the variation in this ratio to result from variations in sputtering yields between Ru and oxygen during depth profiling, which is sensitive to grain size and morphology. RBS analysis of film 3 shows that its stoichiometry is RuO₂. The similarity in interplanar spacings observed in the XRD patterns of films 3 and 4 and the RuO₂ standard (Fig. 6c) suggests that film 4 is stoichiometric RuO₂ as well.

The two RuO₂ films are microstructurally different, as is shown in Fig. 8. Film 3 (Fig. 8a) is composed of grains ranging from about 100 to 500Å. Some columnar growth is observable at the Si/RuO₂ interface, but this seems to break down at a thickness of about 700Å, after which the grains appear to be equiaxed. Film 4 (Fig. 8b) is composed of large grains, about 5000Å, that are columnar and well defined. Neither film appears to have interacted to any significant extent with the Si substrate.

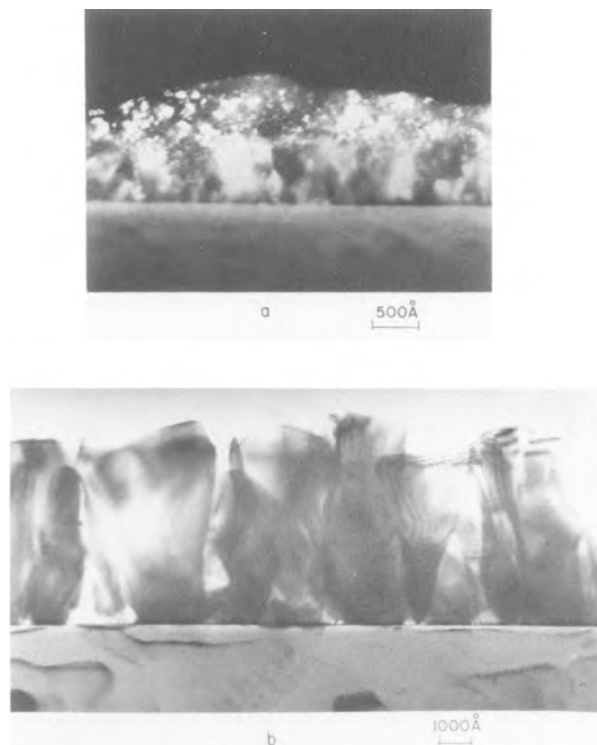


Fig. 8. Transmission electron photomicrographs of RuO₂ films: film 3 (acetylacetonate, 600°C, 1.0 torr O₂, on Si), darkfield image using (110) and (101) reflections (a), and film 4 (ruthenocene, 575°C, 5 torr O₂ on Si), bright field image (b).

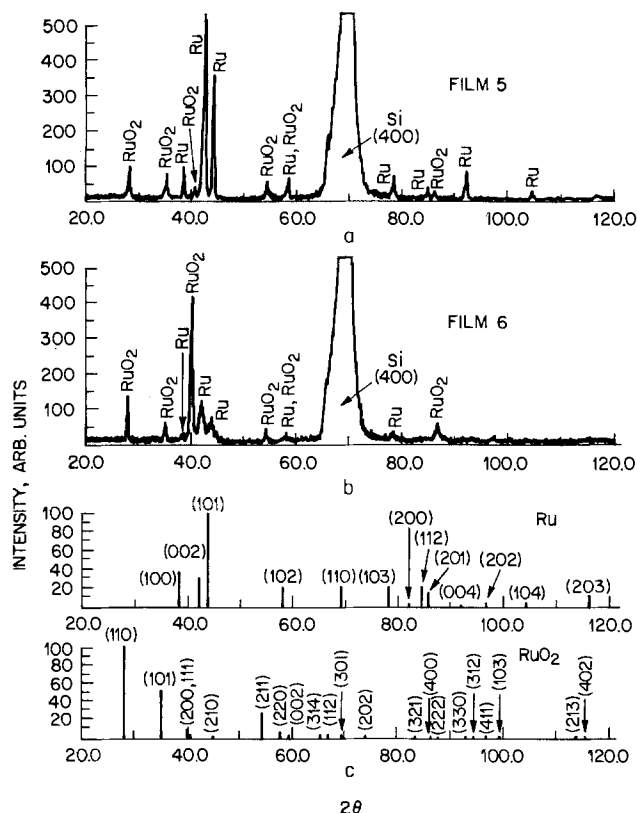


Fig. 9. X-ray diffraction patterns of Ru/RuO₂ films: film 5 (acetylacetonate, 600°C, 1.0 torr H₂, on Si) (a), and film 6 (ruthenocene, 600°C, 1.0 torr O₂, on SiO₂) (b).

The electrical resistivity of film 4 was found to be 89.9 $\mu\Omega\text{-cm}$, which is just about twice that of bulk RuO₂. As film 4 is 6100Å thick and is therefore reasonably close to bulk material, one might expect the bulk resistivity to be observed. The increase in resistivity probably results from less than perfect interconnectivity between the RuO₂ grains, as is suggested by Fig. 8b. The resistivity of film 3 is 643 $\mu\Omega\text{-cm}$, indicating that the fine grain microstructure, coupled with thin film scattering effects, is probably responsible for this high value. The data for these two films are summarized in Table III.

Ru/RuO₂ films.—Under certain deposition conditions, listed in Table II, films composed of both Ru and RuO₂

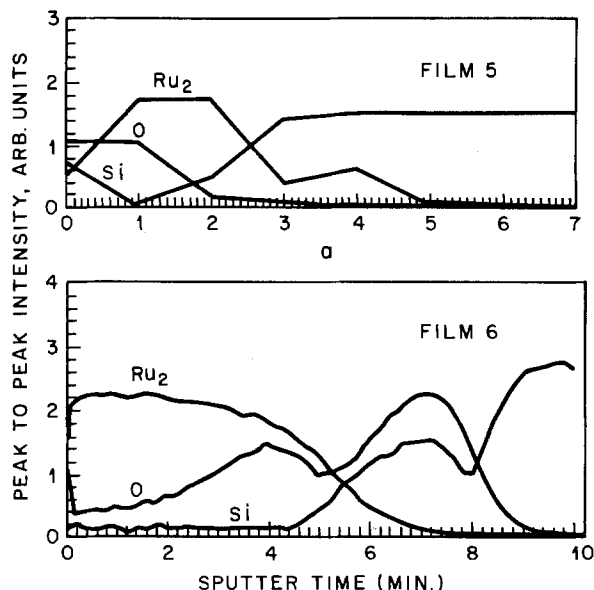


Fig. 10. Auger depth profiles of Ru/RuO₂ films: film 5 (acetylacetonate, 600°C, 1.0 torr H₂, on Si) (a), and film 6 (ruthenocene, 600°C, 1.0 torr O₂, on SiO₂) (b).

phases can be deposited. It is of interest to determine the microstructure of such mixed films. The XRD patterns of two such films are shown in Fig. 9. Film 5 (acetylacetonate, 600°C, 1.0 torr H₂, on Si) is predominantly Ru phase (85% as determined by RBS), whereas film 6 (ruthenocene, 600°C, 1.0 torr O₂, on SiO₂) is predominately RuO₂ phase. Film 5 exhibits a large Ru (002) peak, indicating that the Ru component of the film has some basal plane texture, while the RuO₂ component appears to be of random orientation. The RuO₂ phase of film 6 possesses a texture where the (200) or (111) RuO₂ planes tend to be parallel to the substrate.

Auger depth profile analysis of film 5 (Fig. 10) shows that the sample is Ru rich near the Si interface, and progressively richer in oxygen towards the surface of the film. As this film was deposited in H₂, the only source of oxygen can be from the acetylacetonate radical. Therefore, the Ru-rich layer, first to deposit on Si, seems to catalyze further decomposition into RuO₂. The Auger sample is thinner than the XRD or TEM samples (it is probably from a corner of the wafer). For that reason, Si was able to diffuse to the surface during deposition. Film 5 is also pure with respect to carbon, as the Auger intensity ratio Ru 1/Ru 2 = 2.5. Film 6 has almost the opposite depth profile of film 5. The film is oxygen rich at the SiO₂ interface (Fig. 10b) and Ru rich at the surface. Here, however, the oxygen must be incorporated from the ambient.

Figure 11 illustrates the microstructures of films 5 and 6. Film 5 is composed of equiaxed grains between 300 and 1000Å in diameter. Film 6 is composed of columnar grains between 500 and 750Å in diameter. The resistivity of film 5 is 521 $\mu\Omega\text{-cm}$, whereas that for film 6 is 14.8 $\mu\Omega\text{-cm}$. The high resistivity of film 5 is probably related to the thinness of the film, its small grain size, and the oxygen-rich surface layer. On the other hand, the low resistivity of film 6 may result from the Ru-rich layer at its surface.

Diffusion barrier properties of Ru and RuO₂ films.—Al-Ru-Si and Al-RuO₂-Si thin film diffusion couples were

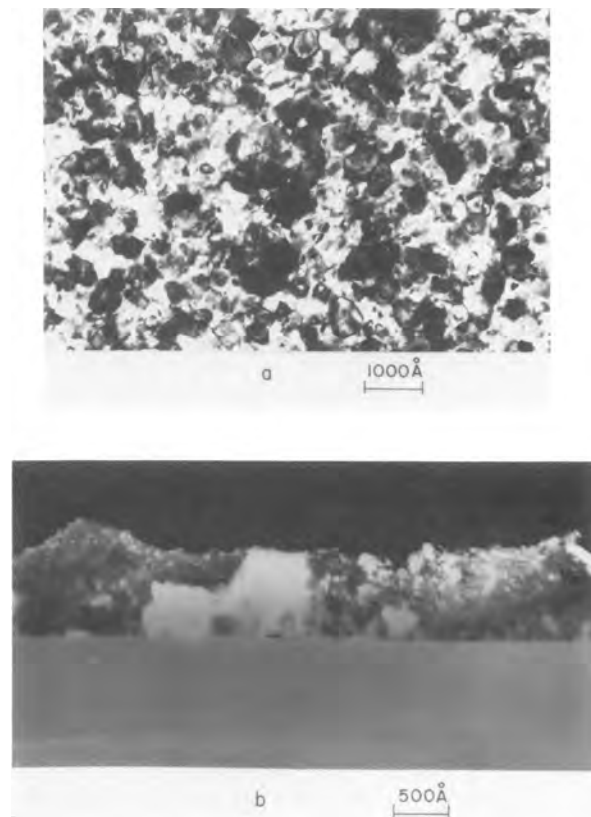


Fig. 11. Transmission electron photomicrographs of Ru/RuO₂ films: film 5 (acetylacetonate, 600°C, 1.0 torr H₂, on Si), bright field image looking through the film (a) and film 6 (ruthenocene, 600°C, 1.0 torr O₂, on SiO₂), darkfield image using (110) and (101) RuO₂ reflections (b).

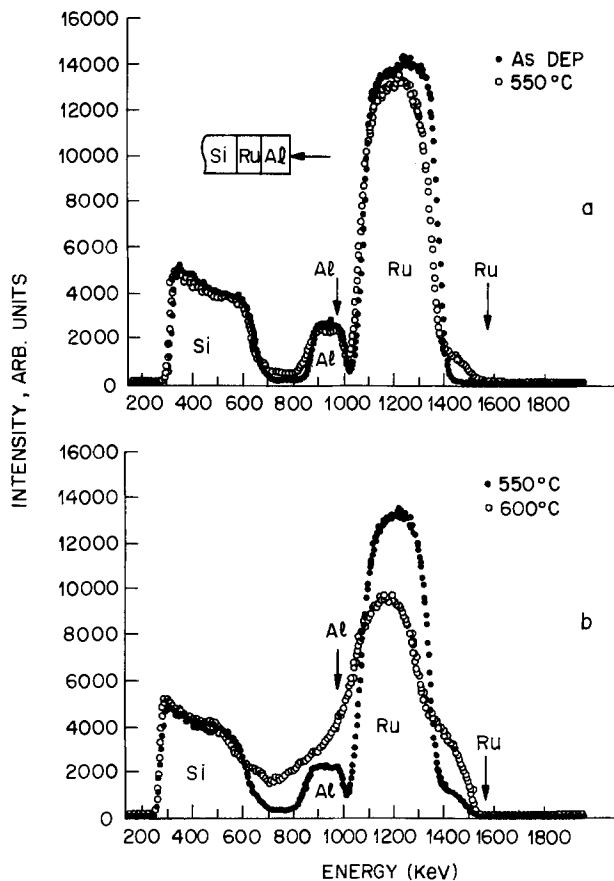


Fig. 12. RBS spectra of an Al-Ru-Si couple (1500Å Al/1029Å Ru/Si substrate), after various heat-treatments. a: Comparison of as-deposited and 550°C(1/2 h, in argon) spectra. b: Comparison of 550°C(1/2 h) and 600°C(1/2 h) spectra. The vertical arrows mark the surface positions of the corresponding elements.

prepared by depositing about 1500Å of evaporated Al on films 2 (Ru) and 3 (RuO₂). The interdiffusion of these couples was studied by RBS as a function of annealing temperature. The ability of Ru or RuO₂ to act as a diffusion barrier between Al and Si would be advantageous for VLSI metallization applications.

Figure 12a compares the RBS spectra of the Al-Ru-Si couple (1500Å Al/1029Å Ru/Si substrate) before (as-deposited) and after a 550°C(1/2 h) anneal in argon. No significant changes in the spectra were noted until 550°C. The interdiffusion of Al and Ru was observed to occur above 550°C, as evidenced by the tail at the leading edge of the Ru peak. This corresponds, however, to only a small amount of Ru in Al. There is some slight evidence for a Ru-Si interaction at this temperature, as the Si leading edge profile has changed to a small extent. Figure 12b illustrates that after a 600°C(1/2 h) anneal the couple has interdiffused significantly. The Al peak is no longer distinguishable, indicating that it has interdiffused with the Ru and possibly the Si. Interdiffusion of Ru and Si has also occurred. XRD of this sample shows the existence of the phases Ru₂Si, Ru₂Si₃, and RuAl₂, as well as remnants of the original elemental Si, Al, and Ru.

Figure 13a illustrates the RBS spectra for the Al-RuO₂-Si couple (1500Å Al/1450Å RuO₂/Si substrate) after 500°C(1/2 h) and 600°C(1/2 h) heat-treatments, both in argon. Up to a temperature of 500°C, no changes in the spectra were observed. After 600°C, a small amount of Al-RuO₂ interdiffusion can be noted, based on the small tail at the Ru leading edge. The general shift of the Ru edges to lower energies after the 600°C anneal probably results from the formation of some Al₂O₃ during the anneal. Also, the difference in Si peak heights (in both Fig. 13a and 13b), is artifactual. Figure 13b shows that interdiffusion is pronounced after a 650°C anneal. The Al peak is smeared out, and the Ru peak is reduced by about 10% (possibly

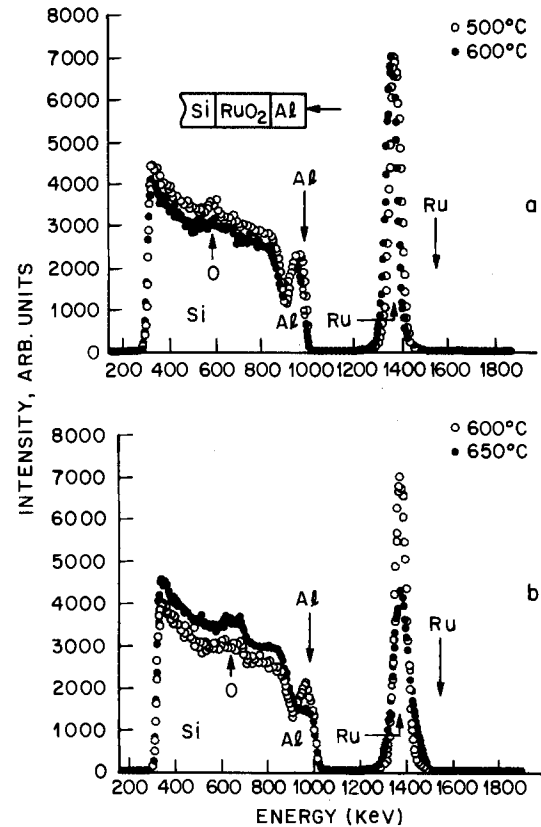


Fig. 13. RBS spectra of an Al-RuO₂-Si couple (1500Å Al/1450Å RuO₂/Si substrate), after various heat-treatments. a: Comparison of 500°C(1/2 h) and 600°C(1/2 h) spectra. b: Comparison of 600°C(1/2 h) and 650°C(1/2 h) spectra. The vertical arrows mark the surface positions of the corresponding elements.

owing to loss by disproportionation of RuO₂ during exposure to air while still hot, see the Effect of source material section). X-ray diffraction of this sample shows the presence of Ru₂Al₃, RuAl₂, and Ru₂Si₃, as well as RuO₂, Ru, Al, and Si. The presence of Ru suggests that Al is reducing some of the RuO₂.

Finally, Fig. 14 illustrates, for comparison, RBS spectra of an Al-W-Si sandwich (1500Å Al/1100Å W/Si substrate). The W was deposited by selective chemical vapor deposition via the H₂ reduction of WF₆. LPCVD W is now being considered as a diffusion barrier for VLSI devices (15-17). It can be seen from Fig. 14 that, for the case of LPCVD W, significant interdiffusion takes place during a 550°C(1/2 h) anneal. XRD shows the presence of WSi₂, W(Si, Al)₂, W₅Si₃, and WAl₁₂. Therefore, Ru and RuO₂ are

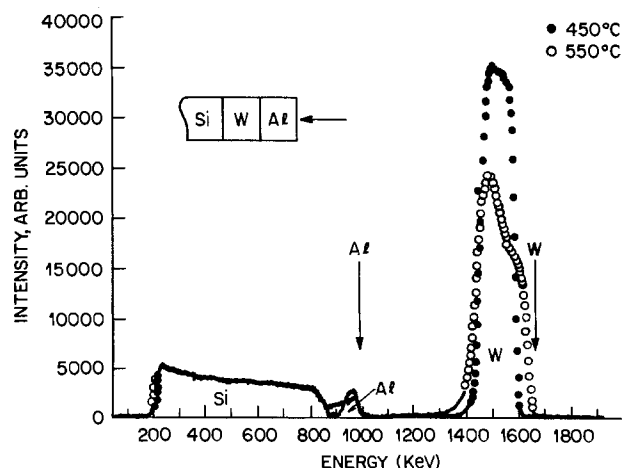


Fig. 14. RBS spectra of an Al-W-Si couple (1500Å Al/1100Å W/Si substrate), after 450°C(1/2 h) and 550°C(1/2 h) heat-treatments. The vertical arrows mark the surface positions of the corresponding elements.

more stable diffusion barriers between Al and Si than LPCVD W by about 50° and 100°C, respectively.

Discussion

Film processing considerations.—Table III shows that Ru, RuO₂, and Ru/RuO₂ films, each with large variations in physical properties, can be produced by varying the experimental conditions. Ruthenium, RuO₂, or Ru/RuO₂ films deposited from the acetylacetonate complex consistently exhibit higher resistivities than the same films deposited from other source materials. The best Ru films are those deposited from the carbonyl at temperatures of about 300°C. An SEM photomicrograph of such a film (Fig. 15) illustrates the excellent conformal coverage typical of LPCVD films. The best RuO₂ films are those deposited from ruthenocene at 575°-600°C.

The deposition of either of these films is consistent with current CVD processing. The fact that both source materials are solids is not in itself a serious drawback, as CVD of Al₂O₃, in which solid AlCl₃ is used as a source material, is already in commercial use (18). However, the temperature difference between sublimation and decomposition of the source material should be as large as possible to avoid severe depletion effects in the reactor. This temperature gap appears to be small for the carbonyl (~75°C), but significantly larger for ruthenocene (~300°C).

Device considerations.—Metallization applications in VLSI devices can be classified as interconnects, diffusion barrier layers, contacts, and gates. In this section, we will consider Ru and RuO₂ as potential films for these applications.

As an interconnect, neither Ru nor RuO₂ can compete with Al, if only because of Al's low resistivity ($\rho = 2.7 \mu\Omega\text{-cm}$) and ease of deposition. However, as a diffusion barrier and contact between Al and Si at source/drain areas, Ru and RuO₂ may have applications. In particular, Ru has a low Schottky barrier height to Si [0.6 eV to n-type Si (19)], similar to that of Cr, Ni, and W, and should therefore exhibit low contact resistance to Si. This is especially true if the Si is highly doped and tunneling conduction mechanisms are operative. Although the barrier height of RuO₂ is not known, it is assumed that, if some oxidation of the Ru occurred, adequate contact resistance would still be maintained.

Furthermore, Al metallization is compatible with Ru or RuO₂ contacts. Although Al₂O₃ is more stable than RuO₂ at the temperatures of interest (~500°C) (20), our results show that Al does not extensively reduce RuO₂. If Al₂O₃ were formed by this reaction, insulating layers would form. Little is known about Ru-Si interactions that result in silicide formation. At least up to deposition temperatures of 600°C, no silicide formation was observed in our work. As contact metallizations will not see these high

temperatures, silicide formation, with its attendant junction erosion and higher contact resistance, is not expected to be a problem. The RBS data of Fig. 12-14 show that Ru and RuO₂ are potentially better diffusion barriers between Al and Si than W.

Gate metallizations should have good conductivity and be stable at high temperatures in oxidizing atmospheres. Ruthenium and RuO₂ conductivities are both stable with respect to oxygen, although RuO₂ might disproportionate at higher temperatures ($T > 750^\circ\text{C}$). Furthermore, Ru gates would not interact with SiO₂ gate oxides, as SiO₂ is more stable than RuO₂ (20). Ruthenium might be the more suitable of the two as a gate metallization as its work function is equal to 4.7 eV (21), just about midway between those of N⁺ and P⁺ silicon. Such midgap metallizations are ideal for CMOS applications where only one gate material, rather than the traditional two, is desired.

In all applications, it should be kept in mind that RuO₂ is thermodynamically unstable in the presence of H₂, even at room temperature (20), and complete reduction to Ru is easily achieved at temperatures greater than about 300°C. Therefore, reducing conditions during heat-treatment are not compatible with the use of RuO₂; vacuum, nitrogen, or inert gas anneals should be used.

A final point should be made about the plasma etchability of Ru and RuO₂. Although no information is available on this subject, it is believed that both materials can be etched in fluoride-based plasmas, as RuF₅ is a low melting and boiling point species ($T_{\text{mp}} = 101^\circ\text{C}$, $T_{\text{bp}} = 250^\circ\text{C}$).

Conclusions

We have deposited Ru, RuO₂, and Ru/RuO₂ films by organometallic LPCVD, and have extensively characterized these films as potential VLSI metallizations. Ruthenium is of interest to us because its thermodynamically stable oxide, RuO₂, exhibits metallic conductivity. As a result, oxidation during processing of Ru would be a less critical concern than in some current metallization technologies. We have found that films of a given phase composition can be deposited under a wide range of conditions, with large variations in electrical resistivity and carbon content. Ruthenium films with electrical resistivity as low as 16.9 $\mu\Omega\text{-cm}$ could be deposited from the carbonyl. Ruthenium films deposited from Ru acetylacetonate were found to be mostly carbon and to exhibit high resistivity. Ruthenium dioxide films with electrical resistivity as low as 89.9 $\mu\Omega\text{-cm}$ could be deposited from ruthenocene. Again, Ru acetylacetonate produced inferior RuO₂ films. Ruthenium/ruthenium dioxide films ranging in resistivity between 14.8 and 521 $\mu\Omega\text{-cm}$ were also deposited. All films, except the Ru film deposited from the acetylacetonate, were adherent to their substrates (either Si or SiO₂). Ruthenium and RuO₂ films were found, by RBS analysis, to be more effective diffusion barriers between Al and Si than LPCVD W, capable of withstanding about 50° and 100°C higher annealing temperatures before significant interdiffusion, respectively. The advantages of Ru and RuO₂ films may also suggest other applications in VLSI metallization, noting that the deposition processes are compatible with current VLSI processing.

Acknowledgments

We would like to acknowledge S. Abys, R. Frankenthal, and D. Siconolfi for Auger analysis, C. C. Chang for XPS analysis, R. Knoell for the TEM work, and W. D. Reents, Jr., for mass spectrometry of the source materials. Helpful discussions were held with L. C. Feldman.

Manuscript submitted May 7, 1985; revised manuscript received July 15, 1985.

AT&T Bell Laboratories assisted in meeting the publication costs of this article.

REFERENCES

1. D. J. Pedder, "Electrical Components Science and Technology," Vol. 2, pp. 259-261, Gordon and Breach, Ltd., New York (1976).

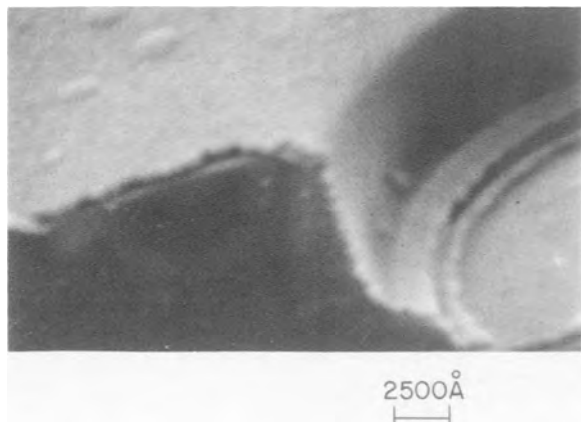


Fig. 15. Scanning electron photomicrograph of a Ru film deposited on a device (film 2, carbonyl, 300°C, in vacuum). The excellent conformal coverage of the film is shown by the film uniformity on the SiO₂ (left) and Si window area (right).

2. R. G. Vadimsky, R. P. Frankenthal, and D. E. Thompson, *This Journal*, **126**, 2017 (1979).
3. R. D. Lanam and A. R. Robertson, *Res. Dev.*, 102 (1984).
4. V. B. Lazarev and I. S. Shapylgin, *Russ. J. Inorg. Chem.*, **23**, 163 (1978).
5. J. N. Crosby and R. S. Hanley, U.S. Pat. 4,250,210 (1981).
6. J. C. Vigié and J. Spitz, *This Journal*, **122**, 585 (1975).
7. D. R. Rolison, K. Kuo, M. Umama, D. Brundage, and R. W. Murray, *ibid.*, **126**, 407 (1979).
8. T. A. Palumbo, *Plating Surf. Finish.*, **66**, 42 (1979).
9. G. A. Augis and L. L. Hines, *IEEE Trans. Comp. Hyb. Manu. Tech.*, **chmt-1**, 46 (1978).
10. M. C. Canart-Martin, Y. Canivez, R. Declercq, L. D. Laude, and M. Wautelet, *Thin Solid Films*, **92**, 323 (1982).
11. C. R. Eady, B. F. G. Johnson, and J. Lewis, *J. Organometal. Chem.*, **37**, C39 (1972).
12. J. Müller and L. D'Or, *ibid.*, **10**, 313 (1967).
13. W. D. Reents, Jr., Unpublished results.
14. L. E. Davis *et al.*, "Handbook of Auger Electron Spectroscopy," Perkin-Elmer, Eden Prairie, MN (1978).
15. N. E. Miller and I. Beinglass, *Solid State Technol.*, **25** (12), 85 (1982).
16. P. A. Gargini, *Ind. Res. Dev.*, **25** (3), 141 (1983).
17. M. L. Green and R. A. Levy, *This Journal*, **132**, 1243 (1985).
18. S. K. Tung and R. E. Caffrey, *ibid.*, **114**, 275C (1967).
19. S. P. Murarka, *J. Vac. Sci. Technol.*, **17**, 775 (1980).
20. E. A. Brandes, "Smithells Metals Reference Book," Chap. 8, Butterworths, London (1983).
21. D. B. Fraser, in "VLSI Technology," S. M. Sze, Editor, Chap. 9, McGraw-Hill, New York (1983).

Thermal Oxidation of Silicon in Dry Oxygen Growth-Rate Enhancement in the Thin Regime

I. Experimental Results

Hisham Z. Massoud*¹ and James D. Plummer*

Integrated Circuits Laboratory, Stanford University, Stanford, California 94305

Eugene A. Irene*²

IBM Thomas J. Watson Research Center, Yorktown Heights, New York 10598

ABSTRACT

In many studies of oxidation kinetics, it has been observed that SiO₂ growth in dry oxygen in the thin regime (<500Å) is faster than the classic description of growth in thicker layers by a linear-parabolic relationship. Growth-rate enhancement in the thin regime was studied in the 800°-1000°C range under a variety of substrate doping densities and O₂ partial pressures using *in situ* ellipsometry. The enhancement in oxidation rate is found to decay exponentially with thickness, and its thickness extent is approximately independent of substrate orientation, doping density, and oxygen partial pressure; its oxygen pressure and substrate doping dependence suggest that it is caused by physical mechanisms associated with the substrate. Such mechanisms are discussed in part II of this paper (11).

Thermally grown layers of silicon dioxide have been an integral part of silicon device technology since their first applications in surface protection and selective masking during diffusion (1) and in stabilizing silicon surfaces (2). Silicon dioxide layers found additional applications in device isolation, impurity gettering, masking against impurities, junction passivation, and insulation between metal layers (3-6). Such applications have made silicon oxidation a vital processing step in both bipolar and MOS technologies. Its most important application, however, is the growth of the gate-dielectric material for MOS transistors where SiO₂ layers become an active component. With continued shrinkage of device dimensions, it has been estimated that submicron channel-length VLSI MOSFET's will use oxide layers thinner than 150Å (7). Thin tunnelable oxides are also used in memory devices such as electrically alterable read only memories (EAROM's). These layers must be grown routinely and reproducibly with high yield and long-term reliability and must not be degraded by subsequent processing.

In early studies of silicon-oxidation kinetics, it was observed that growth rates were higher than predicted by linear-parabolic kinetics for layers thinner than 250Å when silicon was oxidized in dry oxygen (8). Available experimental evidence also indicates that such thin layers are different from thicker layers in other properties such as dielectric breakdown and reliability (9) and interfacial optical properties (10). This study focuses on the growth kinetics of SiO₂ layers in the thin regime (<500Å) in order to achieve a better understanding of the oxidation pro-

cess and to establish a framework within which the difference between thin and thick layers can be better explained.

In this paper, the principles on which the oxidation-rate analysis is based are discussed. The experimental results of the dependence of the growth rate on temperature, substrate orientation, doping density, and oxygen partial pressure in the oxidizing ambient are presented. The rate enhancement is then analyzed quantitatively in the 800°-1000°C range as a function of oxide thickness for lightly doped silicon oxidized in dry oxygen and in oxygen-argon mixtures and for heavily doped substrates oxidized in dry oxygen. The results show that the excess rate decays exponentially with thickness and that it exists under all conditions investigated. The physical mechanisms involved in the early stages of the oxidation of silicon in dry oxygen are discussed in part II of this paper (11).

Experimental Procedures

The thermal growth of silicon dioxide layers on silicon in the thin regime was monitored *in situ* by a high temperature automated ellipsometer. The operation of the automated ellipsometer and the high temperature optical properties of silicon and silicon dioxide are described elsewhere (12, 13). The oxide thickness was measured from the onset of oxidation, where the native oxide is typically 10-15Å, up to ~600Å. The preoxidation cleaning sequence consisted of H₂O₂-based solutions of NH₄OH and HCl with appropriate DI water rinses followed by a dip in dilute HF and a final DI water rinse (14). The wafers were then dried using nitrogen and immediately loaded in the oxidation furnace with argon flowing. Following background intensity measurements, the native oxide thickness was evaluated and was usually found to be in the

*Electrochemical Society Active Member.

¹Present address: Department of Electrical Engineering, Duke University, Durham, North Carolina 27706.

²Present address: Department of Chemistry, University of North Carolina, Chapel Hill, North Carolina 27514.

7-22Å range. The furnace ambient was then switched to the oxidizing ambient of interest. Thickness *vs.* time data in the 800°-1000°C range were obtained for (100), (111), and (110) substrate orientations, with 1.0×10^{15} , 1.8×10^{20} , and 3.2×10^{20} cm⁻³ surface doping concentrations, and in 1.0, 0.1, or 0.01 atm oxygen partial pressure in an oxidizing ambient consisting of mixtures of dry oxygen and argon (15). The lightly doped wafers were either p-type (doped with boron) or n-type (doped with phosphorus). Higher surface doping concentrations were obtained using POCl₃ predeposition and drive-in. A typical example of the data obtained is shown in Fig. 1, where thickness *vs.* time results for the oxidation of lightly doped silicon in dry oxygen in the 800°-1000°C range are plotted. It can be seen that, through the use of *in situ* automated ellipsometry, closely spaced data were obtained. This provides a unique opportunity to investigate the underlying physical mechanisms.

The linear and parabolic rate constants, describing the oxidation process beyond the fast initial regime, were first determined as described elsewhere (16). Knowledge of these rate constants is important in accurately determining the magnitude of growth-rate enhancement in the thin regime and the extent of this enhancement in thickness (or the onset of conventional linear-parabolic growth).

Oxidation-Rate Analysis in the Thin Regime

Kinetic growth laws relating oxide thickness and oxidation time may describe distinctly different rate-limiting processes while having the same mathematical form (17). As an example, in the Deal-Grove linear-parabolic model of oxidation (8), linear growth could result if the rate-limiting step were either the flux at the oxide-gas interface or that at the Si-SiO₂ interface. A parabolic growth law could result if the rate-limiting process were either the diffusion of oxygen to the oxide-silicon interface or the diffusion of silicon to the oxide-gas interface. In both situations, additional information obtained from other experiments was essential in identifying the rate-limiting process. Tracer experiments and oxidation results obtained when changing the flow of oxygen over several orders of magnitude (4-6) provided the additional information that helped identify the diffusion of oxygen and the reaction at the Si-SiO₂ interface as the rate-limiting processes in the parabolic and linear regimes, respectively. Investigations of silicon oxidation in dry oxygen in the thin regime were usually limited in the experimental conditions under which the reaction rate was studied. These limitations were subsequently reflected in the multitude of growth laws obtained such as linear, parabolic, linear-parabolic (with different rate constants), logarithmic, and inverse logarithmic (4-6). A comprehensive study of the reaction rate is therefore necessary because knowledge of a rate law under a limited set of experimental conditions is insufficient to determine the reaction mechanism. This

is why, in this work, a complete characterization of the dependence of the growth rate on all possible processing conditions was undertaken.

To analyze the oxidation process in the early stages of SiO₂ formation, it is important to discuss the assumptions on which the analysis is based. In earlier silicon-oxidation studies, it was shown that the linear-parabolic model is representative of the details of the oxidation process in the thick regime, namely, that oxide growth is the result of the transport of the oxidizing species through an existing layer of oxide and their reaction with silicon atoms at the Si-SiO₂ interface to form SiO₂ (8). Mathematically, this was modeled by three fluxes in series under steady-state conditions— F_1 from the gas to the oxide surface, F_2 through the oxide, and F_3 at the Si-SiO₂ interface.

The resulting growth rate is expressed as (8)

$$\frac{dX_{ox}}{dt} = \frac{B}{(2X_{ox} + A)} \quad [1]$$

where

$$B = \frac{2DC^*}{N_1} \quad [2]$$

and

$$A = 2D\left(\frac{1}{h} + \frac{1}{k_s}\right) \quad [3]$$

and D and C^* are the diffusion coefficient and solubility of the oxidizing species in the oxide, respectively, N_1 is the number of oxidant molecules incorporated into a unit volume of the growing oxide, k_s is the surface reaction-rate constant, and h is the gas phase mass-transfer coefficient.

An oxidation rate higher than predicted by this model could be, in general, the result of additional processes not accounted for in the linear-parabolic model. These processes could be modeled as thickness and/or time dependent, or as a combination of both. Time-dependent processes are in contradiction with the steady-state assumption in the Deal-Grove model (8), and, consequently, silicon oxidation in the initial stages would be treated as a nonsteady-state process. If the oxidation rate increases as the result of additional fluxes, such fluxes would not occur in series with F_1 , F_2 , or F_3 because that would further reduce the overall oxidation rate if they are the rate-limiting process, or the overall growth rate would remain unchanged if they are not. It is therefore concluded that rate enhancement in the thin regime must be described by processes occurring in parallel with any one of these fluxes or with their entire sequence. In a most general case, the additional processes can be represented by excess fluxes ΔF_1 , ΔF_2 , and ΔF_3 in parallel with F_1 , F_2 , and F_3 , respectively, and F_4 in parallel with their total sequence, as illustrated in Fig. 2.

Oxidant-species adsorption at the outer surface of the oxide caused by possible field effects on the oxygen species or by the porous structure of SiO₂ at the onset of oxidation is an example of a process that may be represented by ΔF_1 . Flux ΔF_2 may be the result of field-aided diffusion of ionized oxygen species or the transport of molecular and atomic oxygen in neutral and ionized states across the oxide. The reaction that forms the oxide at the interface could be the result of the reaction of molecular and atomic oxygen (in neutral and ionized states) with silicon-silicon bonds, partially bonded surface-silicon atoms, or silicon vacancies at the Si-SiO₂ interface. These additional surface fluxes can be modeled by ΔF_3 . Flux F_4 possibly represents the transport of oxygen species along microchannels in the oxide to reach the interface and react with the substrate, thereby occurring in its entirety in parallel with the three-flux (F_1 - F_2 - F_3) process. Some of the details of the oxidation reaction can be altered by stress in the oxidizing structure because of its possible effect on the transport and concentration of oxidizing species in the oxide or on the energy required for the surface reaction.

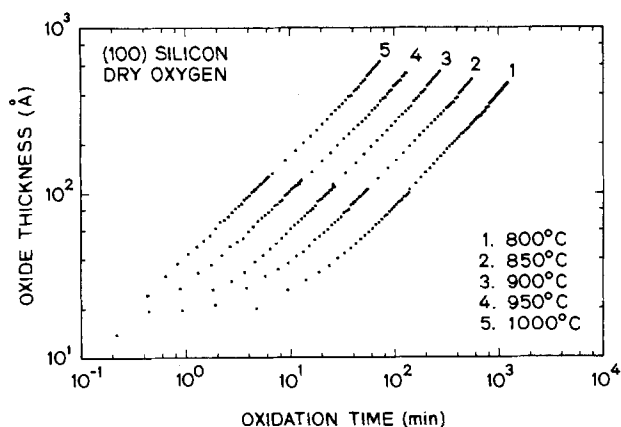


Fig. 1. Oxidation of lightly doped (100) silicon in dry oxygen in the 800°-1000°C range.

The expression for the growth-rate increase caused by the additional fluxes follows the same steps used to derive the linear-parabolic relationship. In steady state

$$F = F_1 + \Delta F_1 = F_2 + \Delta F_2 = F_3 + \Delta F_3 \quad [4]$$

and the total oxidant flux becomes $F + F_4$. If F_1 , F_2 , and F_3 are expressed as in the Deal-Grove model (8), the growth rate for the modified linear-parabolic model illustrated in Fig. 2 can be written as

$$\frac{dX_{ox}}{dt} = \frac{\frac{2DC^*}{N_1} + \left(\frac{2D}{N_1 h}\right)\Delta F_1 + \left(\frac{2X_{ox}}{N_1}\right)\Delta F_2 + \left(\frac{2D}{N_1 k_s}\right)\Delta F_3}{2X_{ox} + 2D\left(\frac{1}{h} + \frac{1}{k_s}\right)} + \frac{F_4}{N_1} \quad [5]$$

Based on the definitions of B and A in Eq. [2] and [3], this relationship becomes

$$\frac{dX_{ox}}{dt} = \frac{B + \left(\frac{2D}{N_1 h}\right)\Delta F_1 + \left(\frac{2X_{ox}}{N_1}\right)\Delta F_2 + \left(\frac{2D}{N_1 k_s}\right)\Delta F_3 + \left(\frac{2X_{ox} + A}{N_1}\right)F_4}{2X_{ox} + A} \quad [6]$$

from which it can be seen that oxidation-rate enhancement in the thin regime can be analyzed as a term added to the parabolic rate constant B in the formulation of the linear-parabolic oxidation rate. It should be noted that the factors multiplying the ΔF_2 and F_4 terms are thickness dependent. Consequently, it can be concluded that, without further assumptions, the above expression does not contribute any additional insight concerning the location of the enhancement process because the dependence of ΔF_1 , ΔF_2 , ΔF_3 , or F_4 on oxide thickness would have to be independently known or assumed. One additional difficulty in delineating the physical processes involved is that, in the initial stages of oxidation, the oxide thickness is so much smaller than A that the linear-parabolic rate becomes approximately thickness independent and equal to the value of B/A . The total growth rate, therefore, can be expressed by two equivalent forms

$$\begin{aligned} \frac{dX_{ox}}{dt} &= \frac{B}{(2X_{ox} + A)} + \Delta R_e(X_{ox}, t_{ox}) \\ &= \frac{B}{A} + \Delta R_e(X_{ox}, t_{ox}) \end{aligned} \quad [7]$$

or

$$\begin{aligned} \frac{dX_{ox}}{dt} &= \frac{B}{(2X_{ox} + A)} [1 + \Delta R_r(X_{ox}, t_{ox})] \\ &= \frac{B}{A} [1 + \Delta R_r(X_{ox}, t_{ox})] \end{aligned} \quad [8]$$

where $\Delta R_e(X_{ox}, t_{ox})$ and $\Delta R_r(X_{ox}, t_{ox})$ are additive "excess" and multiplicative "ratio" rate-enhancement terms, re-

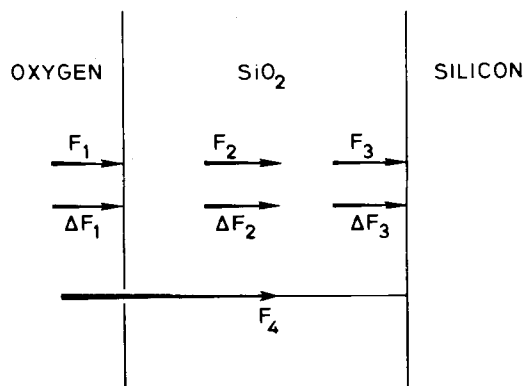


Fig. 2. Modeling oxidation-rate enhancement in the thin regime by adding additional processes in parallel to those described by the linear-parabolic model.

spectively. It is therefore concluded that the oxidation-rate enhancement in the thin regime can be analyzed as either a term added to the linear-parabolic rate or as one that multiplies it. Furthermore, the analysis can be done as a function of oxide thickness or oxidation time. Both analyses were done, and the discussion of the results here will be limited to the analysis as a function of the oxide thickness, which proved to be more physically

significant. As the oxidation approaches the onset of linear-parabolic kinetics, the rate-enhancement terms disappear and the expression for the oxidation rate reduces to that of the linear-parabolic model (Eq. [1]).

In this study, the total oxidation rate was obtained by numerically differentiating experimental X_{ox} - t_{ox} data using a five-point differentiation scheme (18). This approach was made possible only because of the use of *in situ* ellipsometry in obtaining closely spaced data points, as illustrated in Fig. 1. Once the total oxidation rate was calculated, the linear-parabolic contribution was subtracted, resulting in the excess in growth rate ΔR_e characteristic of the thin regime, as given by Eq. [7]. Values of B and B/A appropriate to this study were obtained as described in Ref. (16) and are in general agreement with earlier results.

Experimental Results

The dependence of the growth rate on oxide thickness is discussed for lightly doped silicon oxidized in dry oxygen and oxygen-argon mixtures and for heavily doped silicon oxidized in dry oxygen.

Oxidation of lightly doped silicon in dry oxygen.—The dependence of the silicon-oxidation rate on oxide thickness for (100) silicon in the 800°-1000°C range is plotted in Fig. 3. Similar results were obtained for (111) and (110) orientations (15). In every oxidation run, 33 data points were taken at equal time intervals. A first set of experiments covered the oxide growth up to ~600Å. As a result of the fast initial growth at the onset of oxidation, the number of data points in the first 100Å was limited. This

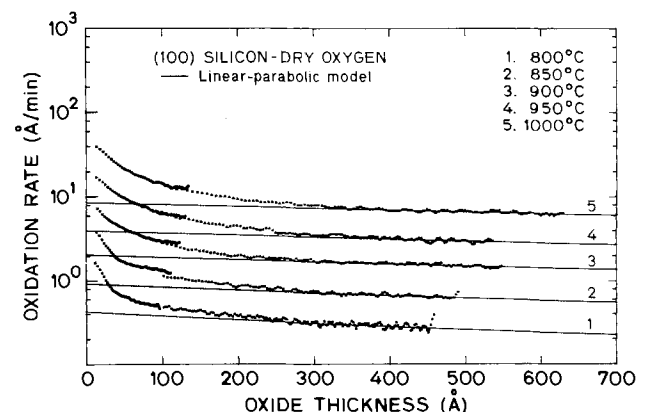


Fig. 3. Oxide-thickness dependence of the growth rate for the oxidation of lightly doped (100) silicon in dry oxygen in the 800°-1000°C range. The solid lines are plots of the linear-parabolic rate.

necessitated that a second set of experiments was carried out in which more closely spaced data points were obtained in the first 100Å.

The oxidation rate expressed by the linear-parabolic model (Eq. [1]) is also plotted as a function of thickness. It is observed that the rate is higher than that predicted by the linear-parabolic model up to 250-350Å and that, beyond this thickness, growth is linear-parabolic. Rate enhancement can be divided into an initial phase extending from the native-oxide thickness up to 40-50Å at 800°C and ~100Å at 1000°C, where the rate rapidly decreases with thickness, and an intermediate phase where it decreases asymptotically to the point of onset of linear-parabolic kinetics. The SiO₂ growth rate on (100) is slower than on (111) and (110) at all temperatures and over the entire thickness range. At all temperatures, the growth rate of SiO₂ on (110) starts higher than in (111) until a certain thickness is reached where this order reverses.

Plots of oxidation-rate enhancement, expressed in the form of an additive term $\Delta R_e(X_{ox})$, for the oxidation of (100) lightly doped silicon oxidized in dry oxygen in the 800°-1000°C range are shown in Fig. 4. These are semilog plots obtained by subtracting the linear-parabolic rate from the total oxidation rate at every oxide thickness. Similar results were obtained for (111) and (100) orientations (15). It can be seen that the excess rate, for all orientations and at all temperatures, has an initial phase extending to ~50Å and an intermediate phase extending from that point to the onset of linear-parabolic kinetics; this suggests that $\Delta R_e(X_{ox})$ can be expressed as the sum of two terms. The parallel straight-line dependence of $\Delta R_e(X_{ox})$ on thickness (on a semilog plot) in the intermediate phase suggests that the fit could be accomplished with a term that exponentially decays with thickness. When $\Delta R_e(X_{ox})$ in the initial phase was calculated and plotted on a semilog plot, it could also be fitted to a second term that decays similarly with thickness. The expression of the total growth rate is then written as

$$\frac{dX_{ox}}{dt} = \frac{B}{(2X_{ox} + A)} + C_1 e^{-(X_{ox}/L_1)} + C_2 e^{-(X_{ox}/L_2)} \quad [9]$$

The following observations apply to the intermediate phase described by C_2 and L_2 .

1. The characteristic length L_2 is approximately independent of temperature in the 800°-1000°C range, and its value is 69, 78, and 60Å for (100), (111), and (110), respectively.

2. The constant C_2 has a single activation energy in the Arrhenius-type plot shown in Fig. 5a, where it can be seen that C_2 fits a simple rate expression in the form of

$$C_2 = C_2^0 e^{-(\Delta E_{C_2}/kT)} \quad [10]$$

The pre-exponential constant C_2^0 and the activation energy ΔE_{C_2} are listed in Table I for the three orientations. For (100) and (111), ΔE_{C_2} is nearly the same, while that of

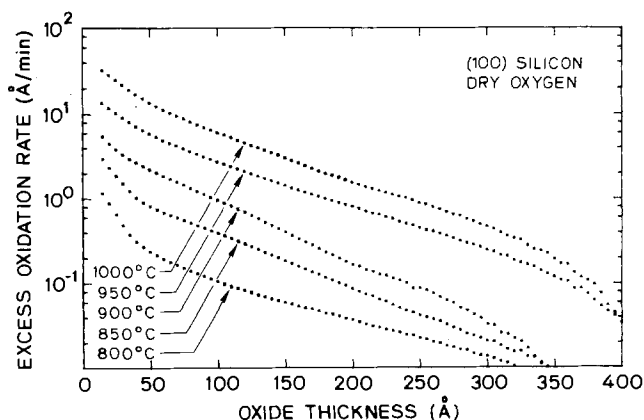


Fig. 4. Oxide-thickness dependence of the excess in growth rate for the oxidation of lightly doped (100) silicon in dry oxygen in the 800°-1000°C range.

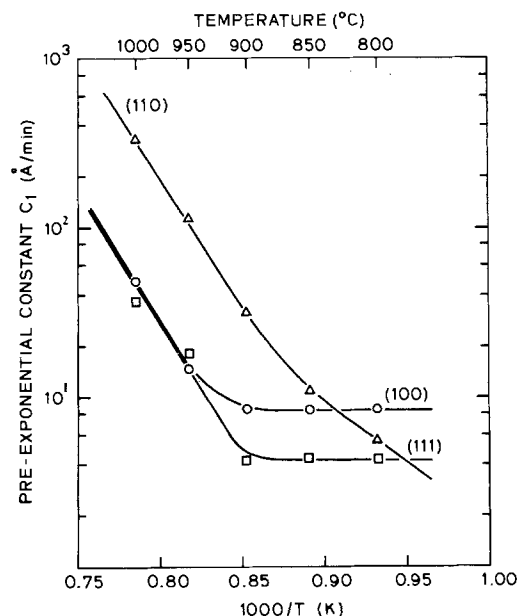
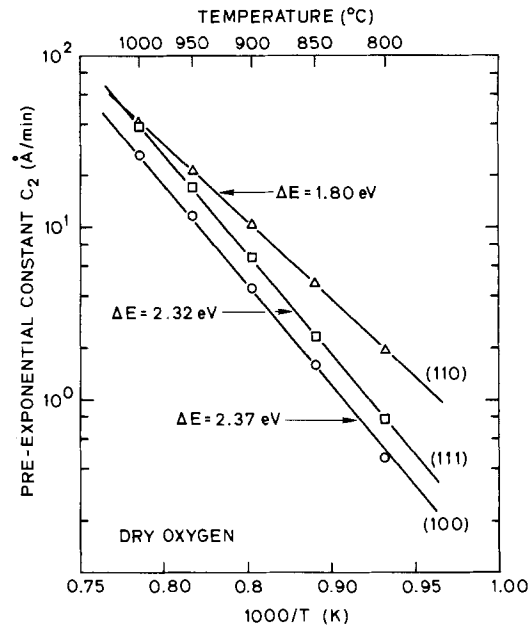


Fig. 5. Temperature dependence of the pre-exponential constants C_2 and C_1 for lightly doped (100), (111), and (110) silicon oxidized in dry oxygen in the 800°-1000°C range.

(110) is lower. The average ratio of C_2 (111): C_2 (100) is 1.52:1.

The following observations apply to the initial phase described by C_1 and L_1 .

1. The characteristic length L_1 increases slowly from 7.7Å at 800°C to 12.4Å at 1000°C for (100) and from 10.9 to 17.1Å for (111). It has a constant value of 14.7Å for (110).

2. The dependence of C_1 on temperature, shown in Fig. 5b, has a break at ~900°C. For (100) and (111), it is temperature independent below 900°C, and the ratio C_1 (100): C_1 (111) is 2.0:1; both orientations have similar values above 900°C. For (110), the activation energy in C_1 changes from that of the other two orientations above 900°C to slightly lower below 900°C. Above 900°C, the initial fitted excess rate can be fitted to an expression analogous to Eq. [10] with the values of C_1^0 and ΔE_{C_1} given in Table I. The lack of a well-behaved trend in the temperature dependence of C_1 may be attributed to the fact that it describes the growth of the first few layers of SiO₂ that has been shown to depend on residual traces of impurities remaining on the surface after cleaning and preoxidation procedures. Although this was not verified experimentally, it is suspected that the first exponential contribu-

Table I. Pre-exponential constants C_2° and C_1° and activation energies ΔE_{C_2} and ΔE_{C_1} for the oxidation-rate enhancement in the thin regime of (100), (111), and (110) lightly doped silicon oxidized in dry oxygen

	(100)	(111)	(110)
C_2° ($\text{\AA}/\text{min}$)	6.57×10^{10}	5.87×10^{10}	5.37×10^8
ΔE_{C_2} (eV)	2.37	2.32	1.80
C_1° ($\text{\AA}/\text{min}$)	3.04×10^{10}	4.87×10^{12}	3.21×10^{14}
ΔE_{C_1} (eV)	2.24	2.80	3.03
T ($^\circ\text{C}$)	C_1° ($\text{\AA}/\text{min}$)	C_1° ($\text{\AA}/\text{min}$)	C_1° ($\text{\AA}/\text{min}$)
$> 900^\circ\text{C}$	8.49	4.33	3.22×10^9
$< 900^\circ\text{C}$	ΔE_{C_1} (eV)	ΔE_{C_1} (eV)	ΔE_{C_1} (eV)
	0.00	0.00	1.87

tion to the excess in oxidation rate is closely related to wafer cleaning and surface preparation procedures.

Using the obtained values of C_1 , C_2 , L_1 , L_2 , B , and B/A in Eq. [9] and integrating numerically to fit the experimental data, it was found that the first decaying exponential $C_1 \exp(-X_{\text{ox}}/L_1)$ affected the fit only slightly at oxide thicknesses up to ~ 50 - 100\AA . Neglecting this term results in errors of less than 5% in fitting the experimental data. A good empirical expression for the oxidation rate, therefore, could include only the second decaying exponential in addition to the linear-parabolic term.

Oxidation of lightly doped silicon in dry oxygen-argon mixtures.—Based on the steady-state assumption in the linear-parabolic model and the validity of Henry's law, the concentration of oxidizing species in the oxide C^* and the parabolic rate constant B (Eq. [2]) are both directly proportional to oxygen partial pressure in the oxidizing ambient. Consequently, the growth rate, expressed as a function of thickness (Eq. [1]), is expected to have a linear dependence on oxygen pressure because A does not depend on C^* (Eq. [3]). From these considerations, it is concluded that, according to the linear-parabolic model, the oxidation rate should be linearly proportional to the partial pressure of oxygen at any thickness. For this reason, oxygen pressure analysis is done in the form of rate *vs.* thickness plots at different pressures.

Figure 6 plots the dependence of the growth rate on oxide thickness for the oxidation of lightly doped (100) silicon in dry O_2 diluted by argon such that the partial pressure of oxygen in the oxidizing ambient is 0.10 atm. Figure 7 plots the results obtained at 0.01 atm. Here again, similar results were obtained for (111) and (110) orientations (15). These experiments did not cover oxide growth up to 500-600 \AA because the oxidation rate is reduced at lower oxygen partial pressures and unusually long oxidations would have been necessary. Oxidation time was limited to 5h. As a result, the linear and parabolic rate constants could not be determined with any degree of confidence; however, lower limits on the values of B and upper limits on those of B/A could be obtained. The quantitative analysis of oxidation-rate enhancement in

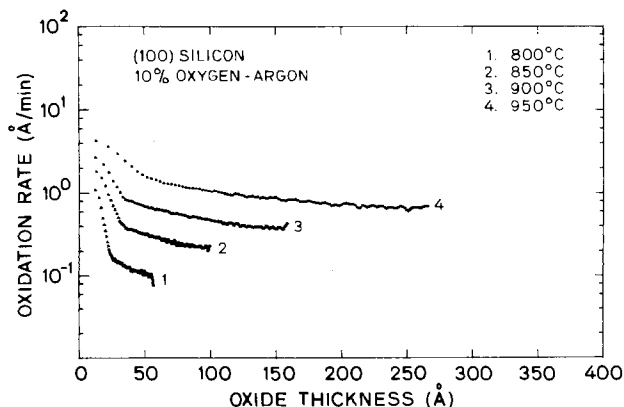


Fig. 6. Oxide-thickness dependence of the growth rate for the oxidation of lightly doped (100) silicon in a dry oxygen-argon mixture corresponding to 0.10 atm of oxygen partial pressure in the 800°-950°C range.

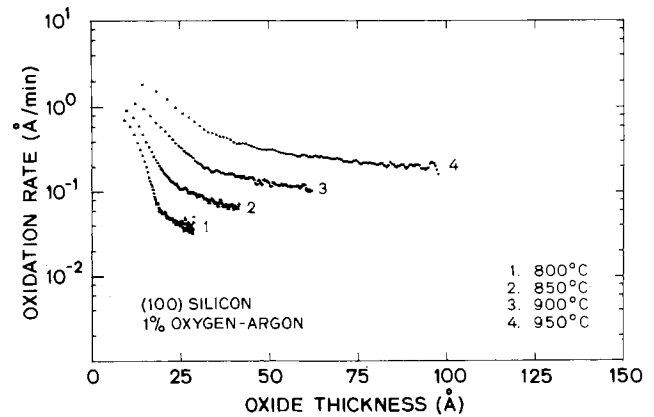


Fig. 7. Oxide-thickness dependence of the growth rate for the oxidation of lightly doped (100) silicon in a dry oxygen-argon mixture corresponding to 0.01 atm of oxygen partial pressure in the 800°-950°C range.

the thin regime at oxygen partial pressures less than 1.0 atm is, therefore, based on the following data analysis and the oxygen-pressure dependence of B and B/A published in the literature.

Oxidation rates at 0.10 and 0.01 atm have a thickness dependence similar to that observed at 1.00 atm where the growth is enhanced in the thin regime and two phases are identified. In all three orientations, the initial phase extends from ~ 30 to 80\AA at 0.10 atm and from ~ 20 to 40\AA at 0.01 atm in the 800°-950°C range. Rate crossover between (111) and (110) occurs at 0.10 atm at all temperatures in the 800°-950°C range where (110) oxidizes faster than (111) below the crossover point. The growth rate of (100) substrates is slowest over the entire thickness range. In contrast, the oxidation of (110) silicon is fastest at 0.01 atm, and crossover is observed between (100) and (111) at 20 and 45\AA at 900° and 950°C, respectively. The rate of SiO_2 growth on (111) is higher than on (100) over the entire thickness range at 850° and 800°C.

A comparison of the oxidation rates at 1.00, 0.10, and 0.01 atm is important in determining the dependence of the concentration of oxidizing species in the oxide on the oxygen partial pressure in the ambient. Figure 8 is a plot of the dependence of the oxidation rate of (111) silicon at 950°C on thickness at the three values of oxygen pressure. Past the initial phase, which extends up to ~ 50 - 60\AA , the growth rates are parallel (or have similar thickness dependence). At any thickness X_{ox} beyond the initial phase, the rate $R_p(X_{\text{ox}})$ at any pressure p can be obtained by dividing the growth rate at 1.00 atm, $R_{1.00}(X_{\text{ox}})$, by a constant K_o such that

$$R_p(X_{\text{ox}}) = \frac{1}{K_o} R_{1.00}(X_{\text{ox}}) \quad [11]$$

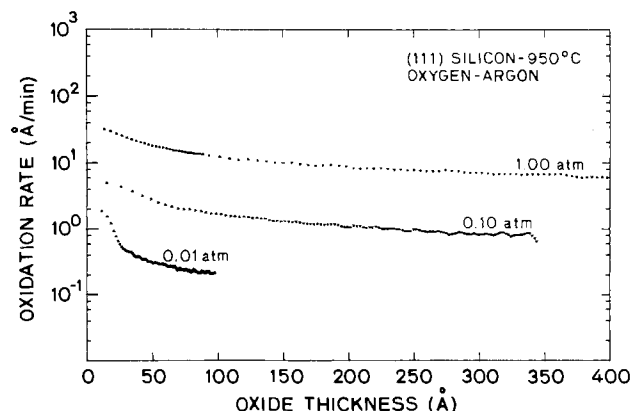


Fig. 8. Oxide-thickness dependence of the growth rate for the oxidation of lightly doped (111) silicon at 950°C in dry oxygen-argon mixtures corresponding to 1.00, 0.10, and 0.01 atm of oxygen partial pressure.

Table II. Temperature dependence of the ratio K_0 of the oxidation rates at 1.00 atm and at 0.10 and 0.01 atm in the 800°-950°C range for (100), (111), and (110) lightly doped silicon oxidized in dry oxygen-argon mixtures

	T_{ox} (°C)	(100)	(111)	(110)
$R_{1.00}/R_{0.10}$	950	6.22	7.45	6.19
	900	6.36	7.16	6.14
	850	6.36	6.05	6.40
	800	6.18	6.17	6.08
$R_{1.00}/R_{0.01}$	950	36.5	57.2	40.6
	900	35.9	48.8	36.2
	850	36.9	35.4	30.2
	800	39.4	33.3	29.6

Values of K_0 for (100), (111), and (110) silicon in the 800°-950°C range are given in Table II.

It can be seen that K_0 is nearly constant at all temperatures and for each value of p . The scatter in the values at 0.01 atm is attributed to the limited thickness range of the experiments. Figure 9 is a plot of the normalized oxidation rate ($R_p/R_{1.00}$ or $1/K_0$) as a function of p . It can be seen that the oxidation rate in the thin regime has a pressure dependence of $\sim p^{0.8}$ which is in agreement with the findings of a high pressure oxidation study in dry oxygen (19) where the linear rate constant B/A was found to have a $p^{0.7}$ - $p^{0.8}$ pressure dependence. The variation in K_0 with temperature at 0.01 atm corresponds to a pressure dependence of $\sim p^{0.74}$ at 800°C to $\sim p^{0.88}$ at 950°C. This is shown in Fig. 9 by the spread of the data points towards lower oxygen partial pressures. It is also in qualitative agreement with a pressure dependence of $\sim p^{0.5}$ observed at low temperatures and $\sim p^{1.0}$ at high temperatures in the 700°-1000°C range, for the normalized linear rate constant obtained by Ghez and van der Meulen (20). Variation in the pressure exponent in the two studies is attributed to different approaches to data analysis; oxidation rates are compared in this study, while linear rate constants were extracted using published values of the parabolic rate constants in the earlier study (20).

The analysis of the effect of oxygen partial pressure on the oxidation rate of lightly doped silicon demonstrated that the growth rate beyond the initial phase has a $p^{0.8}$ pressure dependence. An oxidation study at high pressure in dry oxygen (19) has also shown that the linear rate constant has a $p^{0.7}$ - $p^{0.8}$ pressure dependence and that the parabolic rate constant is linearly proportional to pres-

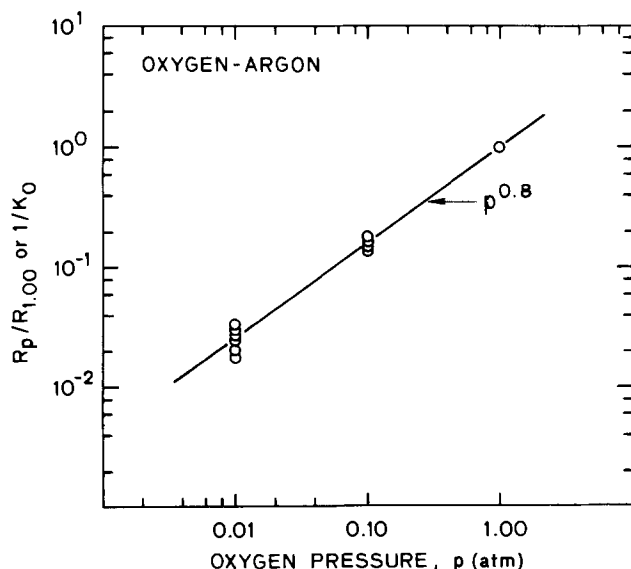


Fig. 9. Dependence of the normalized oxidation rate on the partial pressure of oxygen in the oxidation ambient of (100), (111), and (110) lightly doped silicon in dry oxygen-argon mixtures in the 800°-1000°C range.

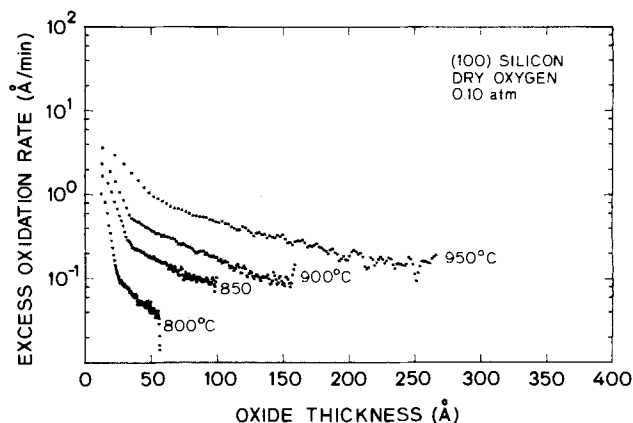


Fig. 10. Oxide-thickness dependence of the excess in growth rate for the oxidation of lightly doped (100) silicon in a dry oxygen-argon mixture corresponding to 0.10 atm of oxygen partial pressure in the 800°-950°C range.

sure. Based on these findings, the quantitative analysis of oxidation-rate enhancement in this study for $p_{O_2} < 1$ atm is based on the assumptions that B is linearly proportional to p and that B/A is proportional to $p^{0.8}$.

The dependence of the excess growth rate $\Delta R_0(X_{ox})$ on oxide thickness for (100) silicon is plotted in Fig. 10 and 11 for $P_{O_2} = 0.10$ and 0.01 atm, respectively. Similar results were obtained for (111) and (110) (15). This excess consists of an initial phase that extends up to ~ 30 - 80 Å at 0.10 atm partial pressure and to thinner oxides at 0.01 atm, and an intermediate phase that merges into linear-parabolic kinetics asymptotically. These results are similar to those observed at 1.0 atm. Here, again, the excess rate could be fitted with two terms exponentially decaying with thickness, as in the form of Eq. [9].

The extent of the intermediate phase, as characterized by the decay length L_2 , was obtained at 0.10 atm and for 900° and 950°C results at 0.01 atm (where the oxide thickness was large enough at the end of the oxidation to identify the intermediate phase). It was found to have values similar to those obtained at 1.0 atm. The pre-exponential constant C_2 is shown in an Arrhenius-type plot for (100), (111), and (110) in Fig. 12, where it can be fitted with a single activation energy of 1.51, 1.58, and 0.85 eV, respectively. The similar values for the activation energies of (100) and (111) and the smaller value for (110) were also observed at 1.0 atm; activation energies at 0.10 atm are, on the average, ~ 0.8 eV smaller than at 1.0 atm.

The exponentially decaying term $C_1 \exp(-X_{ox}/L_1)$ represents the fast growth observed at the onset of oxidation and up to ~ 50 Å. No well-behaved temperature dependence of C_1 was observed, and the characteristic length L_1 decreased from ~ 10 - 20 Å at 950°C to ~ 4 - 7 Å at 800°C. As ob-

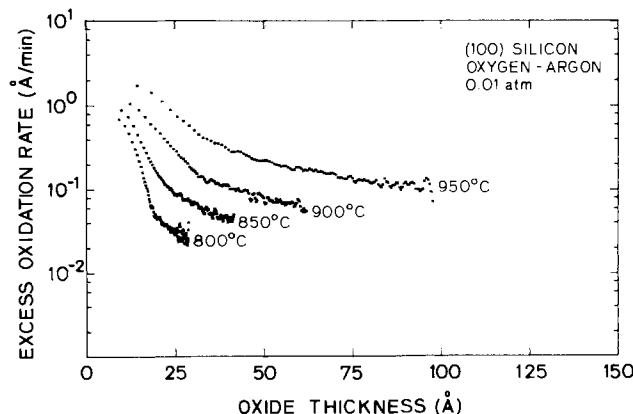


Fig. 11. Oxide-thickness dependence of the excess in growth rate for the oxidation of lightly doped (100) silicon in a dry oxygen-argon mixture corresponding to 0.01 atm of oxygen partial pressure in the 800°-950°C range.

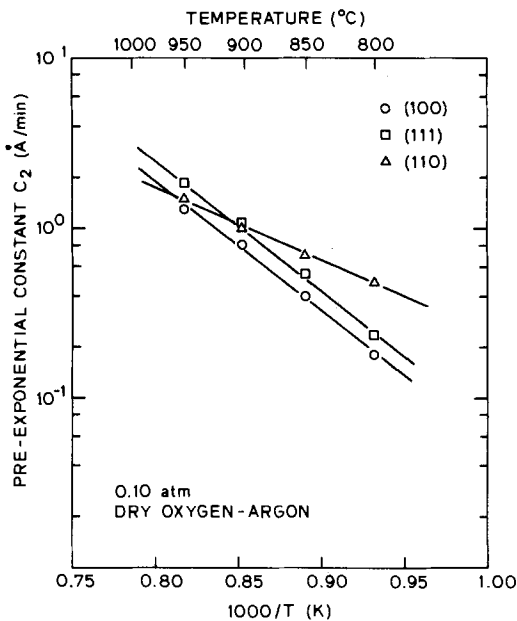


Fig. 12. Temperature dependence of the pre-exponential constant C_2 for the oxidation of lightly doped (100), (111), and (110) silicon in a dry oxygen-argon mixture corresponding to 0.10 atm of oxygen partial pressure in the 800°-950°C range.

served in atmospheric oxidations, this decaying term could also be neglected in the expression of the total oxidation rate with less than 5-7% error in the fit to oxidation data.

The 0.01 atm oxidations were not carried out to oxide thicknesses where the intermediate phase could be quantitatively characterized, except at 900° and 950°C, where the characteristic length of the intermediate phase was found to be similar to 1.0 and 0.10 atm results.

The pressure dependence of the pre-exponential constant C_2 was found to increase monotonically from $p^{0.57}$ at 800°C to $p^{0.88}$ at 950°C for (100), from $p^{0.60}$ at 800°C to $p^{0.93}$ at 950°C for (111), and was nearly constant at $p^{0.83}$ for (110) in the 800°-950°C range. This pressure dependence is similar to that observed for the linear rate constant B/A and discussed earlier.

In summary, oxidation-rate enhancement at lower partial pressures of oxygen has a thickness dependence similar to atmospheric oxidations. The extent of the intermediate phase in oxide thickness is nearly unaffected by oxygen pressure, whereas the activation energy of the pre-exponential constant in the enhancement term is smaller at reduced partial pressures. The pre-exponential constant C_2 was found to have a pressure dependence similar to the linear rate constant B/A .

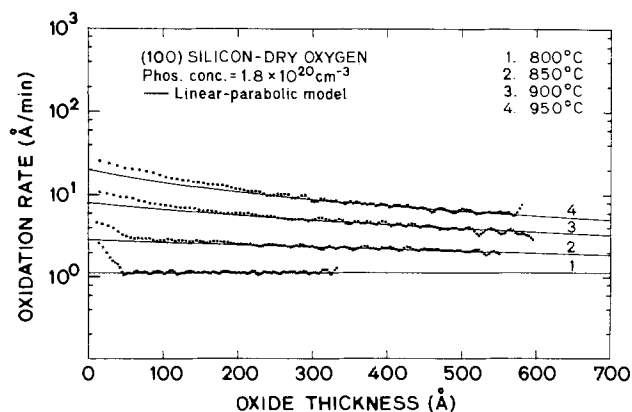


Fig. 13. Oxide-thickness dependence of the growth rate for the oxidation of (100) silicon doped with $1.8 \times 10^{20} \text{ cm}^{-3}$ phosphorus, in dry oxygen in the 800°-950°C range.

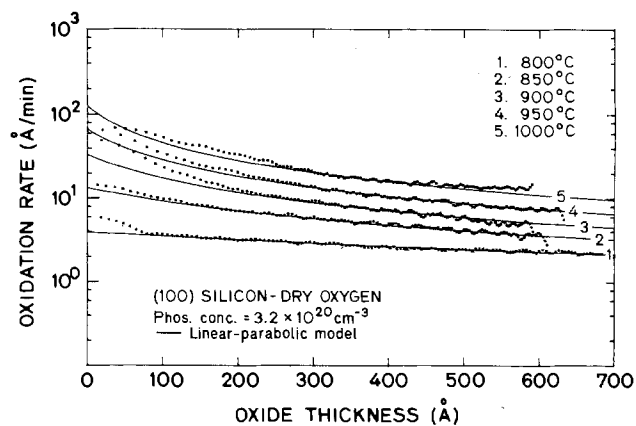


Fig. 14. Oxide-thickness dependence of the growth rate for the oxidation of (100) silicon doped with $3.2 \times 10^{20} \text{ cm}^{-3}$ phosphorus, in dry oxygen in the 800°-950°C range.

Oxidation of heavily doped silicon in dry oxygen.—Figures 13 and 14 plot the thickness dependence of the silicon-dioxide growth rate on (100) silicon wafers doped with phosphorus at $1.8 \times 10^{20} \text{ cm}^{-3}$ (medium doped [MD]) and $3.2 \times 10^{20} \text{ cm}^{-3}$ (heavily doped [HD]) oxidized in dry oxygen in the 800°-950°C and 800°-1000°C ranges, respectively. Based on these plots and the results on lightly doped substrates shown in Fig. 3, the oxidation rate increases with doping at all temperatures and over the entire thickness range. Beyond the initial phase ($< 100\text{\AA}$), lightly doped (LD) substrates exhibit parallel plots of rate vs. thickness in the 800°-1000°C range, whereas, in MD and HD substrates of both orientations, the difference in oxidation rates decreases with increasing thickness. This is expected because, in heavily doped silicon substrates, the linear rate constant B/A is greatly enhanced and the parabolic rate constant B is only modestly enhanced at low temperatures (21, 22); consequently, the transition from linear to parabolic kinetics occurs at a thinner oxide thickness.

The oxidation rate as expressed by the linear-parabolic relationship is also plotted in Fig. 13 and 14 as a function of thickness. The values of B and B/A were determined from the growth data as described elsewhere (16). It can be seen from Fig. 13 and 14 that the growth rate of HD substrates is enhanced during the initial stages of oxidation over a thickness range that decreases from $\sim 300\text{\AA}$ at 1000°C to $\sim 75\text{\AA}$ at 800°C. In MD wafers, the rate enhancement extends over a similar thickness range, approaches a constant value at lower temperatures, and its thickness dependence rate is identical for the two orientations; (111) is 1.5 ± 0.1 larger than (100).

The excess in growth rate $\Delta R_e(X_{ox})$ in the oxidation of heavily doped silicon substrates was calculated by sub-

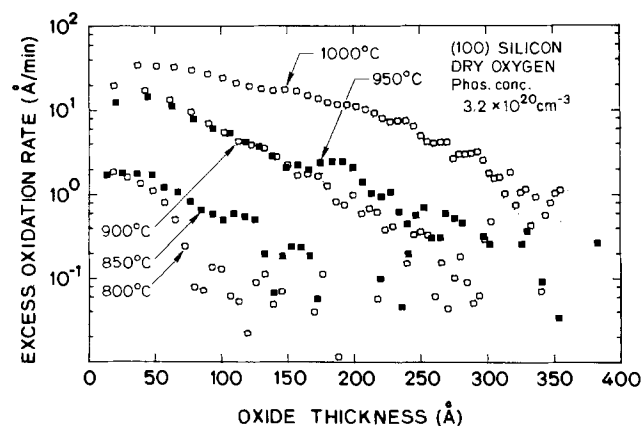


Fig. 15. Oxide-thickness dependence of the excess in the growth rate for the oxidation of (100) silicon doped with $3.2 \times 10^{20} \text{ cm}^{-3}$ phosphorus in dry oxygen in the 800°-1000°C range.

tracting the linear-parabolic contribution as before, but with the appropriate doping dependent values of B/A . It is plotted as a function of oxide thickness in Fig. 15 for (100) HD substrates. Similar results were obtained for (111) HD substrates (15). In comparison with lightly doped substrates, which show two distinct phases in the excess rate, $\Delta R_e(X_{ox})$ for HD substrates has only one apparent phase that decays exponentially with thickness, and it accounts for oxidation-rate enhancement from the onset of oxidation. The absence of the initial growth phase (C_1 , L_1) observed on lightly doped substrates may be due to the large enhancement in the other rates caused by the high doping levels effectively obscuring it. It may also be related to phase separation and/or precipitation of the dopant into the oxide near the interface, as a limited TEM study of the heavily doped samples revealed small heavily doped silicon inclusions in the oxide at the interface. The total growth rate can be therefore expressed as

$$\frac{dX_{ox}}{dt} = \frac{B}{(2X_{ox} + A)} + C_2 e^{-(X_{ox}/L_2)} \quad [12]$$

In the heavily doped wafers, an Arrhenius-type plot of the pre-exponential constant C_2 in Fig. 16 indicates a single activation energy ΔE_{C_2} of 1.87 and 1.77 eV for (100) and (111), respectively. It is interesting to note that C_2 is higher for (100) than for (111) and that its activation energy is smaller than in lightly doped substrates, with (100) and (111) again having similar values. The magnitude and thickness extent of the rate enhancement in both HD and LD substrates are similar. It should also be noted that heavy phosphorus doping in the substrate greatly enhances the linear rate constant B/A but increases the excess oxidation rate associated with the thin regime only moderately. It can be concluded that, to a first order, doping does not affect the oxidation enhancement process in the thin regime.

The excess oxidation rate in MD wafers is plotted in Fig. 17 as a function of thickness in (100) silicon. Similar results were obtained for (111) (15). Only one phase that exponentially decays with thickness is observed. The temperature dependence of C_2 is not a singly activated process, and the characteristic length L_2 is also a strong function of temperature, decreasing from $\sim 85\text{\AA}$ at 950°C

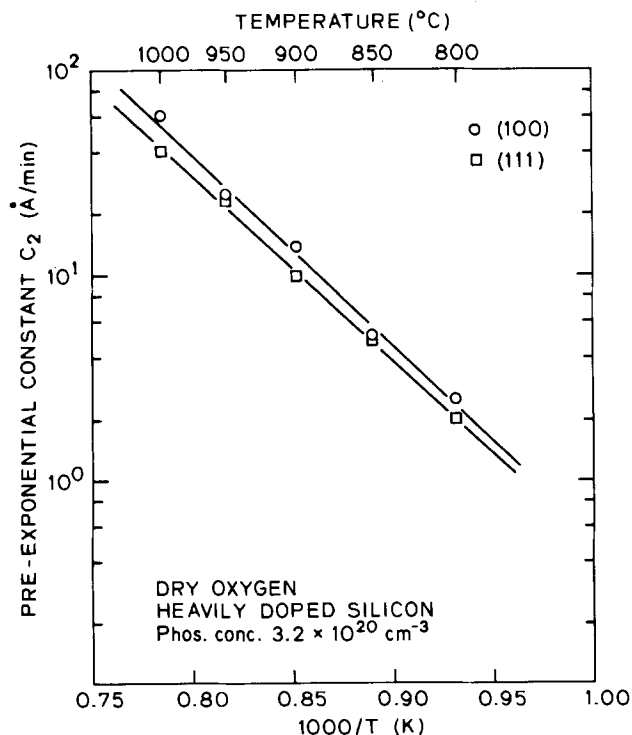


Fig. 16. Temperature dependence of the pre-exponential constant C_2 for the oxidation of (100) and (111) silicon heavily doped with $3.2 \times 10^{20} \text{ cm}^{-3}$ phosphorus in dry oxygen in the 800°C - 1000°C range.

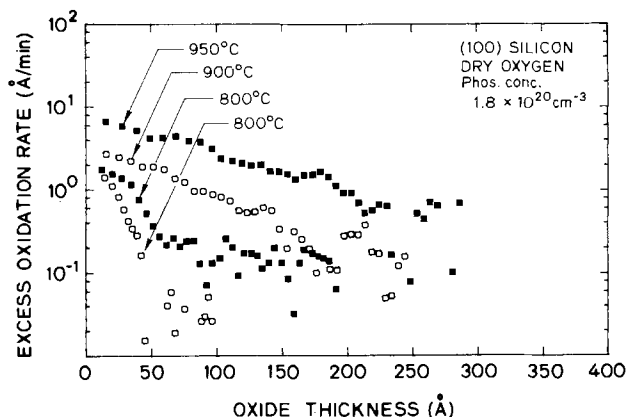


Fig. 17. Oxide-thickness dependence of the excess in the growth rate for the oxidation of (100) silicon doped with $1.8 \times 10^{20} \text{ cm}^{-3}$ phosphorus in dry oxygen in the 800°C - 950°C range.

to $\sim 15\text{\AA}$ at 800°C . The enhancement in the excess term when compared to LD substrates is smaller than that in the linear rate constant at high temperatures but is greater at low temperatures. The results should be analyzed in conjunction with the strong phosphorus redistribution occurring during the early stages of oxidation when phosphorus is depleted near the Si-SiO₂ interface and the concentration of electrically active species is reduced (23, 24).

In the case of heavily doped substrates, the high concentration of phosphorus is sufficient to maintain the solid solubility level in spite of the redistribution occurring simultaneously. This gives rise to an effectively fixed electrically active surface concentration during the oxidation and, therefore, to well-behaved C_2 , L_2 , and B/A . This is not the case, however, with moderately doped substrates where the time dependencies of the redistribution process are clearly involved. The variation of C_2 and L_2 in Fig. 17 is therefore not necessarily an indication of a change in the physical mechanisms involved.

In summary, the magnitude of oxidation-rate enhancement in heavily doped samples in the thin regime is only slightly increased by the doping level in the substrate, and its thickness extent is unaffected. This is in contrast with the large enhancement in the linear rate constant. The excess reaction proceeds with an activation energy lower than in lightly doped substrates. These results indicate that, in a first-order analysis, the surface-reaction mechanism in the thin regime proceeds independently of and in parallel with the mechanism enhancing B/A of heavily doped substrates.

Conclusions

Oxidation-rate enhancement during the early stages of the oxidation of silicon in dry oxygen can be modeled by adding a term that exponentially decays with thickness to the rate expression of the linear-parabolic model. This added term has a prefactor that reflects the excess rate at which the reaction proceeds and a characteristic length that represents its extent in thickness. The activation energy of the excess rate was found to be a function of substrate doping density and oxygen partial pressure in the ambient. The characteristic length was observed to be nearly independent of substrate orientation, doping level, and of the partial pressure of oxygen. The oxidation of medium-doped samples during the early stages reflects the transient redistribution of phosphorus near the interface.

Acknowledgments

The authors would like to acknowledge many helpful discussions with Dr. Bruce E. Deal, Dr. C. P. Ho, and Dr. Reda R. Razouk. This study was sponsored by Darpa Contract no. MDA 903-79-C-0257.

Manuscript received April 15, 1985; revised manuscript received July 11, 1985.

Stanford University assisted in meeting the publication costs of this article.

REFERENCES

1. C. J. Frosch and L. Derick, *This Journal*, **104**, 547 (1957).
2. M. M. Atalla, E. Tannenbaum, and E. J. Scheibner, *Bell Syst. Tech. J.*, **38**, 749 (1959).
3. B. E. Deal and J. D. Plummer, in "Integrated Circuits Process Models," J. D. Meindl and K. C. Saraswat, Editors, Prentice Hall, Englewood Cliffs, NJ, In press.
4. R. B. Fair, in "Applied Solid State Science, Supplement 2, Silicon Integrated Circuits, Part B," D. Khang, Editor, Academic Press, New York (1981).
5. W. A. Pliskin and R. A. Gdula, "Materials, Properties and Preparation," S. P. Keller, Editor, Chap. 11, Vol. 3 in "Handbook on Semiconductors," T. S. Moss, Editor, North Holland Publishing Company, Amsterdam (1981).
6. E. H. Nicollian and J. R. Brews, in "MOS (Metal Oxide Semiconductor) Physics and Technology," Chap. 13, Wiley-Interscience, New York (1982).
7. R. H. Dennard, F. H. Gaensslen, H. N. Yu, V. L. Rideout, E. Bassous, and A. R. LeBlanc, *IEEE J. Solid-State Circuits*, **sc-9**, 256 (1974).
8. B. E. Deal and A. S. Grove, *J. Appl. Phys.*, **36**, 3770 (1965).
9. K. Hamano, *Jpn. J. Appl. Phys.*, **13**, 1085 (1974).
10. E. A. Taft and L. F. Cordes, *This Journal*, **126**, 131 (1979).
11. H. Z. Massoud, J. D. Plummer, and E. A. Irene, *This Journal*, **132**, 2693 (1985).
12. Y. J. van der Meulen and N. C. Hien, *J. Opt. Soc. Am.*, **64**, 804 (1974).
13. P. S. Hauge and F. H. Dill, *IBM J. Res. Dev.*, **17**, 472 (1972).
14. W. Kern and D. A. Puotinen, *RCA Rev.*, **31**, 187 (1970).
15. H. Z. Massoud, Ph.D. Thesis, Stanford University, Stanford, CA (1983).
16. H. Z. Massoud, J. D. Plummer, and E. A. Irene, *This Journal*, **132**, 1745 (1985).
17. I. M. Ritchie and G. L. Hunt, *Surf. Sci.*, **15**, 524 (1969).
18. G. Dahlquist and A. Bjorck, "Numerical Methods," Prentice Hall, Englewood Cliffs, NJ (1974).
19. L. N. Lie, R. R. Razouk, and B. E. Deal, *This Journal*, **129**, 2828 (1982).
20. R. Ghez and Y. J. van der Meulen, *ibid.*, **119**, 1100 (1972).
21. C. P. Ho and J. D. Plummer, *ibid.*, **126**, 1516 (1979).
22. C. P. Ho and J. D. Plummer, *ibid.*, **126**, 1523 (1979).
23. S. A. Schwarz, R. W. Barton, C. P. Ho, and C. R. Helms, **128**, 1101 (1981).
24. R. W. Barton, Technical Report no. J701-1, Stanford Electronics Laboratories, Stanford University, Stanford, CA (1981).

Thermal Oxidation of Silicon in Dry Oxygen: Growth-Rate Enhancement in the Thin Regime

II. Physical Mechanisms

Hisham Z. Massoud*¹ and James D. Plummer*

Integrated Circuits Laboratory, Stanford University, Stanford, California 94305

Eugene A. Irene*²

IBM Thomas J. Watson Research Center, Yorktown Heights, New York 10598

ABSTRACT

In many studies of oxidation kinetics, it has been observed that silicon-dioxide growth in dry oxygen in the thin film regime ($<500\text{\AA}$) is faster than predicted by the linear-parabolic description of the growth of thicker layers. Oxidation-rate enhancement in the thin film regime was studied in the 800° - 1000°C range for a variety of substrate orientations, doping densities, and oxygen partial pressures using *in situ* ellipsometry. The results were reported in part I of this paper. In this part, the physical mechanisms previously proposed to explain the rate enhancement are discussed. No single model was found to apply under all experimental conditions. A new understanding of the growth-rate enhancement in the early stages of silicon oxidation in dry oxygen is introduced.

Silicon oxidation occurs as a result of the transport of oxidizing species through the existing oxide to react with silicon at the Si-SiO₂ interface and form silicon dioxide. Knowledge of the physical processes that affect thermal oxidation is important in optimizing the applications where SiO₂ plays an essential role and in understanding the interaction between oxidation and other related phenomena, such as defect formation/suppression, impurity gettering, stacking fault growth/shrinkage, and impurity-dopant enhanced/retarded diffusion. This knowledge is vital in growing the highest quality oxides to be used as a gate dielectric material in high performance VLSI MOS circuits. The much-discussed growth-rate enhancement in the early stages of silicon oxidation in dry oxygen was investigated using *in situ* ellipsometry, and its dependence on temperature, substrate orientation, doping density, and oxygen partial pressure was reported in part I of this paper (1). The results indicated that the total growth rate in the thin film regime can be expressed as a term

*Electrochemical Society Active Member.

¹Present address: Department of Electrical Engineering, Duke University, Durham, North Carolina 27706

²Present address: Department of Chemistry, University of North Carolina, Chapel Hill, North Carolina 27514

exponentially decaying with thickness added to the linear-parabolic rate. It was also observed that the thickness extent of the initial growth-rate enhancement does not depend, in a first-order analysis, on substrate orientation, dopant density, or oxygen partial pressure and that the pre-exponential constant and its activation energy depend on these experimental parameters.

This paper starts with a summary of the experimental results obtained in this study and reported in part I of this paper (1). The predictions of models already proposed to explain the enhancement in silicon-dioxide growth rate in the early stages of silicon oxidation in dry oxygen are then compared with the experimental results of this study. It will be shown that these models have a limited range of success and could not be applied under all experimental conditions. A possible physical understanding of silicon oxidation in the thin regime which is consistent with all observed experimental results is then introduced.

Summary of Experimental Results

The silicon-dioxide growth rate in the thin regime under a wide variety of experimental conditions (substrate orientation, doping, and oxygen partial pressure) can be expressed as (1)

$$\frac{dX_{\text{ox}}}{dt} = \frac{B}{2X_{\text{ox}} + A} + C_1 e^{-\alpha_{\text{ox}}/L_1} + C_2 e^{-\alpha_{\text{ox}}/L_2} \quad (1)$$

The first term is the linear-parabolic term where B and B/A are the parabolic and linear rate constants, respectively, as defined by Deal and Grove (3). Values for these rate constants used on this study were reported elsewhere (2). The two exponential terms represent the rate enhancement in the thin regime. They are defined in terms of pre-exponential constants C_1 and C_2 and characteristic lengths L_1 and L_2 . The first decaying exponential has a characteristic length on the order of 10\AA , is nonzero for the first $40\text{--}50\text{\AA}$ of oxide growth, and vanishes for oxides thicker than 50\AA . The second decaying exponential has a characteristic length on the order of 70\AA and is present from the onset of oxidation to an oxide thickness of $\sim 250\text{\AA}$, where it decays to zero and where the growth becomes pure linear-parabolic.

In fitting Eq. [1] to oxidation data, it was observed that simplifying the expression of the total oxidation rate to

$$\frac{dX_{\text{ox}}}{dt} = \frac{B}{(2X_{\text{ox}} + A)} + C_2 e^{-\alpha_{\text{ox}}/L_2} \quad (2)$$

would result in only 5-7% error. The following observations summarize the experimental results in part I of this paper (1), as expressed by the dependence of the pre-exponential constant C_2 and the characteristic length L_2 on experimental conditions.

1. For lightly doped silicon substrates oxidized in dry oxygen, it was observed that L_2 is independent of temperature in the $800^\circ\text{--}1000^\circ\text{C}$ range. Its value ($\sim 70 \pm 10\text{\AA}$) is, in a first-order analysis, independent of substrate orientation. The pre-exponential constant C_2 is well behaved in its temperature dependence and fits a single activation-energy rate expression. Similar activation energies of 2.37 and 2.32 eV were obtained for (100) and (111), respectively, and a smaller value of 1.80 eV for (110) (1).

2. For lightly doped silicon substrates oxidized in dry oxygen-argon mixtures, the characteristic length L_2 was similar to oxidations in 100% dry oxygen. The pre-exponential constant C_2 was well behaved in its temperature dependence, again fitting a single activation-energy rate expression. Activation energies for the three orientations were on the average 0.8 eV smaller than oxidations in dry oxygen. The pressure dependence of C_2 was found to be $\sim p^{0.8}$, which is the same as the average pressure dependence of the linear rate constant B/A (1).

3. For heavily doped silicon substrates (doped at solid solubility phosphorus) oxidized in dry oxygen, the characteristic length L_2 was unchanged from lightly doped oxidations. The pre-exponential constant C_2 was also well behaved with temperature with similar activation energies of 1.87 and 1.77 eV for (100) and (111), respectively. By comparison with the magnitude of C_2 for lightly doped oxidations, it was observed that heavy doping only moderately affected the amount of oxidation-rate enhancement in the thin regime.

Oxidation-rate enhancement in the thin regime can, in summary, be expressed by a term exponentially decaying with thickness. Its thickness extent is independent of substrate orientation, doping level, and oxygen partial pressure in the oxidizing ambient. Its magnitude has the same pressure dependence as that of the linear rate constant and is only moderately affected by high phosphorus concentrations in the substrate.

Review of Previous Models

An evaluation of the models already proposed to explain the fast initial regime is given here. These models fall into four groups: (i) space-charge effects where the enhancement is electrochemical in nature, (ii) oxide-structure effects that provide additional oxidant transport, (iii) oxide stress effects influencing the diffusivity of oxidizing species in the oxide and the surface-reaction rate constant at the interface, and (iv) oxygen-solubility considerations in the oxide where growth would be en-

hanced due to oxygen concentrations exceeding its solid-solubility limit.

Space-charge effects.—A number of electrochemical mechanisms have been proposed to enhance the oxidation process in the thin regime (3-9). The transport of oxidant species by thermal diffusion has been proposed to be affected by an electric field existing across the oxide in the early stages of growth. Field-assisted oxidant diffusion was originally proposed by Cabrera and Mott (4) to account for metal-oxidation results. This phenomenon was proposed by Deal and Grove (3) to account for silicon-oxidation results in dry oxygen in the thin regime.

Theoretical analyses of the kinetics of metal oxidation emphasize only two types of rate-determining oxidation mechanisms (4). In the first, the oxide thickness is small in comparison to the extent of possible space-charge regions within the oxide, and the growth kinetics are strongly influenced by the voltage drop across the oxide film caused by contact-potential differences. In the second, the diffusion rate of either the oxidizing species or the metal across the oxide determines the oxidation kinetics; the growth is then purely parabolic. The space-charge effect involves electrons readily available in the metal. These electrons penetrate the oxide either by tunneling or by thermionic emission into its conduction band and then fill the surface states provided by the adsorbed gas molecules at the oxide-gas interface. A steady-state condition is then established in which the net electronic current is close to zero, thereby equalizing the surface-state level and the Fermi level of the metal. This process results in a constant contact-potential difference between the two interfaces and an internal electric field. This field is assumed to be strong enough to alter significantly the activation barrier for the diffusion of ions or other charged defects. As a result, field-dependent transport of ionic defects constitutes the rate-limiting step. The model of Cabrera and Mott (4) yielded an inverse-logarithmic growth law.

The rapid initial oxidation regime in dry oxygen and its absence in wet oxygen or steam have been interpreted by Deal and Grove (3) to be a result of space-charge effects. In their interpretation, the oxidizing species is ionic, and oxidation is enhanced until the oxide thickness becomes larger than the extent of the space-charge region within the oxide. This thickness is on the order of the extrinsic Debye length in the oxide

$$L_{D_{\text{ox}}} = \sqrt{\left(\frac{kT}{q}\right) \frac{k_{\text{ox}} \epsilon_0}{2qC^*}} \quad [3]$$

In dry oxygen, $C^* = 5 \times 10^{16} \text{ cm}^{-3}$, $k_{\text{ox}} = 3.9$ and, therefore, at 1000°C , $L_{D_{\text{ox}}} \approx 150\text{\AA}$, which corresponds well with the oxide thickness beyond which the rapid initial-growth mechanism stops being effective. In contrast, for wet O_2 at 1000°C , using $C^* = 3 \times 10^{19} \text{ cm}^{-3}$, $L_{D_{\text{ox}}} \approx 5\text{\AA}$. Based on the linear pressure dependence of the parabolic rate constant B , Deal and Grove (3) concluded that no dissociation occurs at the oxide-gas interface, which implies that the diffusing species are undissociated molecules of oxygen or water for dry and wet O_2 oxidation, respectively. Coupled with the findings of Jorgensen (5), where an electric field was observed to affect the oxidation of silicon, they suggested that the diffusing species in dry oxygen is a singly ionized oxygen molecule O_2^- . The field created by the space charge of the negatively charged oxygen ions should be directed toward the gas-oxide interface, as illustrated in Fig. 1a.

The transport of the oxidizing species could also be enhanced by a slightly different mechanism (6), illustrated in Fig. 1b. Here, it is assumed that as a molecule of oxygen from the gas is adsorbed at the outer surface, and, after entry into the oxide, it dissociates into a negatively charged oxygen molecule O_2^- and a hole. Holes, diffusing more rapidly than O_2^- , move toward the Si-SiO₂ interface and drag the slower oxygen ions with them by the built-in electric field that results from the coupled motion of two

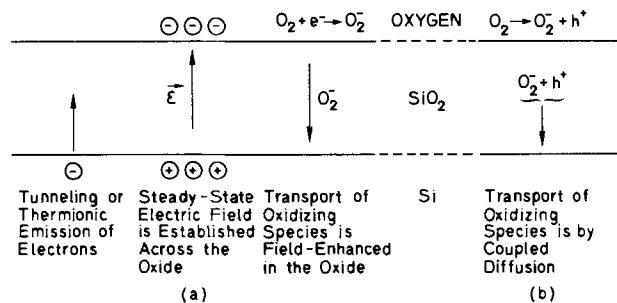


Fig. 1. Enhanced transport of ionized oxidizing species during the initial stages of oxidation in dry oxygen by field enhanced diffusion (a) and by coupled diffusion (b).

charged species with different mobilities. This field aids the motion of the slower species.

Hamasaki (7) proposed that negatively charged oxidant species are prevented from reaching the Si-SiO₂ interface by the oxide field near the interface caused by the positive oxide fixed charge Q_f generated by the oxidation reaction. In this description, electrons reached the outer surface of the oxide by thermionic emission. The initial rapid growth is explained by oxides growing at a fast rate before a sufficient amount of Q_f has been generated by the oxidation reaction. Once formed, the oxide fixed charge establishes an electric field that opposes the transport of negatively charged oxidizing species toward the interface. This description implies that the linear rate constant B/A is a measure of the surface reaction when the oxidizing species are under the influence of the Q_f -induced retarding field. For the same description of the oxidation process, Lu and Cheng (8) further assumed a mathematical form for the distribution of the oxide fixed charge and derived the oxidation rate constants corresponding to the thin (<300Å) and thick regimes

In analyzing the less-than-linear pressure dependence of the linear rate constant B/A , Hu (9, 10) proposed an intermediate oxygen-chemisorption step where chemisorbed molecular oxygen may directly oxidize silicon at a slow rate or dissociate slowly into atomic oxygen which then rapidly oxidizes silicon. The chemisorption isotherm suggested to fit the pressure dependence was the Freundlich isotherm. The extra growth rate in thin regime was proposed to be the result of a possible parallel flux of negatively ionized atomic oxygen (O⁻) becoming more important for small thicknesses. Because of its smaller size, O⁻ ions are expected to diffuse substantially faster than oxygen molecules. The free energy of O⁻ at 1200 K is 1.1 eV (9). The diffusion of ionized atomic oxygen is argued to be possible only if there is substantial electronic conduction by tunneling through the oxide (9). As a result, this mechanism would stop for oxide thicknesses larger than ~150Å.

The above-mentioned models based on space-charge effects predict an inverse-logarithmic relationship between oxide thickness and oxidation time. The qualitative predictions of such a growth law were successful in explaining the absence of enhancement in wet oxygen in comparison to dry O₂ (3). It should be noted, however, that these models are subject to the following considerations.

1. Space-charge effects rely on the presence of ionized oxygen species in the oxide during growth and are based on Jorgensen's observations of the influence of an electric field on the oxidation rate (5). These observations are, however, the subject of much debate. In a recent investigation of the effect of electric fields and oxygen ion beams on silicon oxidation between 25° and 950°C, Modlin (11) reported results opposite of those of Jorgensen (5). When the surface of the oxide was made positive relative to the silicon substrate, the oxidation rate was enhanced, while for negative potentials it was slightly reduced. In reviewing Jorgensen's experimental setup and results, Modlin (11) concluded that the platinum electrodes used in the earlier experiments may have affected the oxida-

tion process dramatically. Modlin's results indicated that, for diffusion-limited thermal silicon oxidation, the diffusing species is neutral molecular oxygen (11).

2. Goodman and Breece (12) noted that, because the solubility C^* of oxygen in the oxide is weakly dependent on temperature, the Debye length $L_{D_{ox}}$ in SiO₂ would be proportional to the square root of the temperature. If this dependence of $L_{D_{ox}}$ holds down to lower temperatures, it is expected to be 125Å at 600°C; however, at that temperature, the growth rate was observed to become approximately linear with time for oxide thicknesses greater than ~25Å (12). Similar behavior was observed for oxidations in water vapor at 600°C (12). The thickness extent of the initial enhanced regime was found to be nearly independent of temperature in this study (1). These experimental observations (1, 12) are in disagreement with the predicted temperature dependence of the extent of the initial regime as expressed by the Debye length in Eq. [3].

3. Further examination of Eq. [3] shows that $L_{D_{ox}}$ is inversely proportional to the square root of C^* . Consequently, for oxidations at lower partial pressures of oxygen (lower values of C^*), the Debye length should increase as would the extent of the fast initial regime. Results obtained in this study at 0.10 and 0.01 atm (1) indicate that the extent of the fast initial regime has a weak dependence on oxygen pressure and tends to decrease slightly at lower partial pressures. van der Meulen's study of the kinetics in the linear regime also showed that, for (111)-oriented silicon oxidized in 10 and 1% oxygen in nitrogen at 850°C, growth is approximately linear beyond 40 and 25Å, respectively (13). As a result, the experimentally observed extent of the fast initial regime has a trend opposite of that predicted from the dependence of $L_{D_{ox}}$ on C^* .

4. In the above descriptions, the oxidation rate is enhanced because of the effect of the electric field (due to electrons or due to Q_f) on the transport of the ionized oxidizing species toward the Si-SiO₂ interface. Because the oxidation process is, in principle, surface-reaction rate limited in the thin film regime, any process that would result in enhancing the transport of oxidant species through the oxide should have no effect on the growth rate. This is dependent on assuming steady-state conditions for the growth process as defined in the linear-parabolic model (3). Additional transport mechanisms that result in increasing the concentration of oxidizing species in the oxide above the solubility limit would enhance the oxidation rate in the thin film regime. Such a mechanism will be discussed when examining oxygen solubility considerations in the oxide.

It should also be noted that although oxygen ions are attracted to the Si-SiO₂ interface in the Deal-Grove (3) and Hu descriptions (9, 10), they are repelled from it in the Hamasaki model (7). Both claim, however, to have the same effect on the oxidation rate. Further examination of the complete expression of the oxide growth in (7) indicates that, for the same flux of incoming oxidizing species, the net growth rate is reduced in the thin regime as compared with the thick regime as a result of the presence of the electric field. This is intuitively clear because such field would repel the ionized oxidizing species away from the Si-SiO₂ interface.

Based on the previous discussion of the temperature and oxygen partial-pressure dependence of the thickness extent of the fast initial regime, it is concluded, at this time, that space-charge effects are not responsible for oxidation-rate enhancement in the initial oxidation regime in dry oxygen.

Oxide structural effects.—A number of proposals have been made to relate the fast oxidation rate in the thin regime to the oxide structure. Revesz and Evans (14) proposed that SiO₂ films are noncrystalline and may contain structural microheterogeneities, especially microchannels, along which diffusing species may transport preferentially. This is illustrated schematically in Fig. 2. It has been demonstrated (15) that the room temperature gaseous permeability of thermally grown SiO₂ layers can

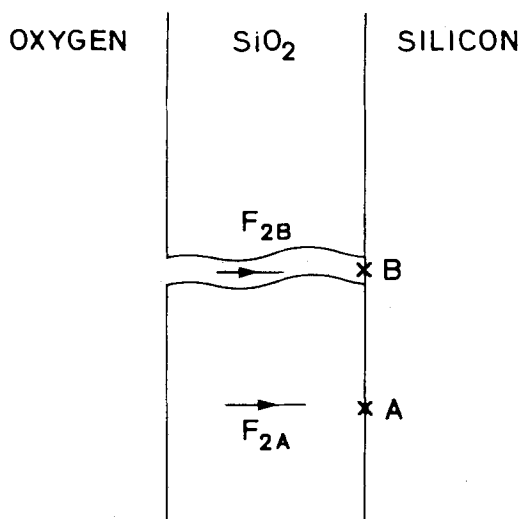


Fig. 2. Micropores in thin oxides affecting the transport oxygen species to the interface.

be considerably higher than in fused silica, and this increase was attributed to microchannels whose diameters are less than 50Å.

The formation of channels has been proposed to be closely related to the mechanism of oxide growth in that both the parabolic rate constant and the extent of the fast initial regime are higher in the (111) than in the (100) orientation of silicon, provided that the H₂O content in the oxidizing ambient is very low (16). This quasi-anisotropic behavior of the SiO₂ film occurs when the channels are aligned perpendicularly to the silicon surface. In dry oxygen, the density of defects, at which interaction between O₂ molecules and SiO₂ occurs, is limited to $\sim 10^{16}$ cm⁻³. In contrast, the density of SiOH groups resulting from the interaction between H₂O and SiO₂ is on the order of 10²⁰ cm⁻³. As a result, in the noninteractive transport of O₂ in SiO₂, channels may be retained, while the interaction between H₂O and SiO₂ acts against such structural ordering.

Direct experimental evidence of the existence of micropores was reported in a study of 90Å thermally grown SiO₂ layers, using high resolution bright-field transmission electron microscopy (17). Contrast phenomena observed in images of films grown in dry oxygen are consistent with the existence of 10Å pores, typically 100Å apart. Similar, films grown in wet oxygen do not display this contrast. The presence of voids or micropores of 5-8Å diam randomly distributed in dry SiO₂ films were also confirmed by Srivastava and Wagner (18). In a study of the initial regime (up to 200Å), Irene (19) attributed the more parabolic-like behavior of the data produced from H₂O containing ambients to a greater protectiveness of wet oxides. Dielectric breakdown measurements revealed that there are fewer defects in the H₂O-grown thin SiO₂ films, and transmission electron microscopy indicated that these films contain inhomogeneities smaller than 50Å. It was concluded, therefore, that the pore structure differs in dry and wet SiO₂ films, provides a short-circuit path to the Si-SiO₂ interface for oxidant species that do not attack the SiO₂ network (such as dry O₂), and is responsible for the variations in the oxidation data and dielectric breakdown.

In another study of the thermal oxidation of silicon up to 200Å in dry O₂ (20), growth followed a linear-parabolic behavior, but with linear and parabolic rate constants different from those characterizing the growth of thicker oxides (>300Å). Here, B/A was larger and B and X₁ were smaller than their corresponding values for thick oxides. Based on these observations and the results of experiments where oxidation was interrupted by a heat-treatment and then reoxidized, Revesz (21) reported that the oxidation of silicon in dry O₂ in the thin regime does not occur under true steady-state conditions because B and B/A change during oxidation. The fast initial regime

does not require any special explanation, therefore, because it is a manifestation of the nonsteady-state oxidation process. The structure of thermally grown SiO₂ films, including the Si-SiO₂ interface, is determined by a combination of ordering and disordering effects. Increased ordering enhances the diffusivity of O₂ molecules along structural channels. The presence of H₂O in the oxidizing ambient has a great disordering effect on the structure of SiO₂ because it interacts with SiO₂ more strongly than does O₂ whose behavior is similar to that of inert gases. Revesz concluded that this is the reason no initial fast regime is observed for oxidations in H₂O.

In the above discussion and as illustrated in Fig. 2, growth-rate enhancement occurs as a result of localized points (such as point B) where microchannels or structural defects meet the Si-SiO₂ interface. This is a result of the concentration of oxygen species in contact with silicon at point B being higher than at other interface areas (such as point A) covered with SiO₂. The oxidation rate at these points is enhanced as a result of a localized higher concentration of oxygen in direct contact with silicon rather than a faster transport of oxygen through the oxide which would not affect the oxidation reaction because oxide growth in the linear regime is rate limited by the surface reaction. The lateral transport of high concentrations of oxidant species at the Si-SiO₂ interface, as a result of micropores in the oxide, may be responsible for localized oxidation-rate enhancement around micropores and microchannels in the thin regime.

Stress in silicon dioxide.—Stress measurements in silicon dioxide have been made at room temperature (22, 23) and at growth temperatures (24). Stress in the oxide measured at room temperature is a result of the mismatch between the thermal expansion coefficients of Si and SiO₂, and it develops as the oxidized wafer cools down from the oxidation temperature to room temperature. The oxide was found in a state of compressive stress. Intrinsic stresses resulting from the mismatch in the molar volume of Si and SiO₂ exist at oxide-growth temperatures. For oxides grown in wet O₂ (23), the intrinsic stress was found to depend on temperature. At 950°C and below, a compressive stress on the order of 7×10^9 dyn/cm² is generated in the oxide. At 975° and 1000°C, the oxide grows in a stress-free state, with possible small tensile stresses above 1000°C. When present, these intrinsic stresses are large enough to cause plastic deformation of the silicon substrate at growth temperatures. The temperature dependence is explained by viscous flow occurring in both steam- and dry oxygen-grown layers at $\sim 960^\circ\text{C}$ (24). Stress in SiO₂ has been linked to phenomena such as dislocation generation at borders of windows etched in oxide layers, bowing and slip processes of wafers, and impurity segregation and precipitation. The temperature dependence of the linear and parabolic rate constants above and below the viscous flow temperature was discussed elsewhere (2). These results suggested that stress in the oxide affects the transport of oxygen through the oxide and its reaction with silicon at the Si-SiO₂ interface. A new formalism that explains the low and high temperature dependence of the linear rate constant on the intrinsic stress was proposed by Irene (26). Intrinsic stress effects on the surface-reaction rate constant are a possible source of oxidation-rate enhancement in the thin film regime. The appearance of high density thermal oxides grown at low temperatures was also explained in terms of a viscous flow model (27, 28).

In a study of silicon oxidation in dry oxygen in the thin film regime, Fargeix and co-workers (29) suggested that the diffusivity of the oxidizing species is not constant across the oxide layer as a result of the influence of stress in the growing film. They proposed that diffusion through the first hundreds of angstroms of the oxide layer is slowed down due to compressive stresses in the SiO₂ film. The increase in the diffusivity far from the oxidizing interface is presumably related to the relaxation of the stresses. These stresses were assumed to be maximum at the Si-SiO₂ interface and to decrease monotonically

ally with a characteristic distance (a relaxation length) from the interface and toward the free surface of the oxide. It was found that this relaxation length (which would replace the characteristic length L_2 in this work) is a strong function of temperature, increasing from $\sim 50\text{\AA}$ at 980°C to larger than 650\AA at 780°C for (100) silicon. This is in contradiction with the experimental results of this study that showed that L_2 is temperature independent. This stress model is also in contradiction with the views of Tiller (30-32) that unless the interface relaxes to become partially incoherent, large amounts of strain energy are stored in the oxide, which results in greatly retarding the oxidation process.

Here again, as in the evaluation of models where the transport of ionized oxidizing species is affected by electric fields, stresses in the oxide, whether they increase or decrease the transport of oxidizing species in the oxide, should have no effect on the oxidation process in a regime where growth is surface-reaction rate limited. It is possible, however, that stress might affect the surface-reaction rate constant, as proposed by Irene (26) for thicker oxides and/or the solubility of the oxidizing species in the oxide.

Oxygen solubility in the oxide.—According to Henry's law, the equilibrium concentration C^* of the oxidant in the oxide is related to the partial pressure p_g of oxidant species in the gas ($C^* = Hp_g$). This relationship holds only in the absence of dissociation or recombination of the oxidant species at the oxide-gas interface and when their chemical potential in the oxide is independent of pressure (dilute case). Increased solubility of O_2 in SiO_2 for very thin layers may be important in describing the fast initial dry oxidation of silicon (33) because it would reflect an increase in the constant of proportionality in Henry's law when the oxide thickness is less than the mean spacing of oxygen solute molecules dissolved in the oxide. For $C^* = 5 \times 10^{16} \text{ cm}^{-3}$ and $3 \times 10^{19} \text{ cm}^{-3}$ in dry and wet O_2 (3), the average spacings are 270 and 32\AA, respectively. For thinner dry or wet oxide films, the description of solubility in terms of an equilibrium bulk quantity becomes questionable because of spatial distribution of the solute molecules is nearly two dimensional.

Details of the equilibrium described by Henry's law involve the balance of the fluxes of solute molecules in and out of the gas-solid interface for a given external gas pressure, as illustrated in Fig. 3. It is generally assumed that the solid is semi-infinite and that no reactions inside the solid affect the details of this equilibrium. These assumptions are not valid for oxidation in dry oxygen for thicknesses smaller than the average spacing between the solute molecules, where the flux of oxygen consumed at the nearby oxidizing interface affects the balance of inward and outward fluxes that establishes the equilibrium conditions at the gas-oxide interface.

To obtain a more realistic description of oxides thinner than the average spacing between oxidant molecules, a two dimensional structure, wherein solute molecules are packed, was suggested by Derbenwick and Anderson (33). It is not clear whether the solubility in such films is equal to the bulk equilibrium solubility in thicker films. The oxidation rate is directly proportional to the concentration of oxidizing species at the Si-SiO₂ interface; a higher solubility in dry SiO₂ films thinner than 270\AA implies a proportionally faster oxidation rate. A simple model to test this solubility concept was proposed (33) based on the assumption that the effective solubility of oxygen into the oxide decreases exponentially in thin oxides. The oxidation-rate expression based on this assumption was similar to that obtained in part I of this paper (1) and resulted into a growth law of the form (33)

$$X_{\text{ox}}(t_{\text{ox}}) - X_{\text{ox}}(0) - L_0 \ln \frac{[C^* + C_0 e^{-X_{\text{ox}}(0)/L_0}]}{[C^* + C_0 e^{-X_{\text{ox}}(t_{\text{ox}})/L_0}]} = \left(\frac{B}{A}\right) t_{\text{ox}} \quad [4]$$

where $X_{\text{ox}}(0)$ is the native-oxide thickness at the start of oxidation ($t_{\text{ox}} = 0$), C^* the equilibrium bulk solubility, $(C^* + C_0)$ the equilibrium concentration at the surface, and

L_0 a characteristic length related to the equilibrium spacing of the solute molecules. The agreement between this expression and experimental data was good at atmospheric pressure but poor at reduced oxygen pressures (33).

The dependence of the excess rate in the thin film regime on oxygen partial pressure is expected to be the same as that of the linear rate constant because of the concentration of the oxidizing species is expected to affect both by the same amount. Furthermore, for the oxidation of heavily doped substrates, the amount of enhancement in the linear rate constant and in the excess rate should be the same because oxygen in the oxide in excess of the solid-solubility concentration would be common to both the linear-parabolic oxidation process present on lightly doped substrates and the reaction present on heavily doped substrates. This expected behavior in the data analysis of heavily doped substrates was not observed experimentally, as the excess rate in the thin regime was found to be approximately independent of the doping level (1). Until an independent measurement of oxygen solubility in thin oxides unquestionably demonstrates that it is enhanced over its values for thick oxides, such a mechanism is unlikely to be responsible for oxidation-rate enhancement in the thin regime.

In conclusion, all models proposed to interpret oxidation-rate enhancement in the thin regime in dry oxygen, whether based on space-charge effects, oxide structure, oxide stress, or enhanced oxygen solubility in thin oxides, have limited success in accounting for growth-rate enhancement observed experimentally in this study, or have no physical, theoretical, or experimental justification. An understanding of silicon oxidation in dry oxygen based on the above results and discussions is now introduced.

Mechanism of Silicon Oxidation in the Thin Regime

In searching for the physical mechanisms responsible for the oxidation-rate enhancement in the thin regime for

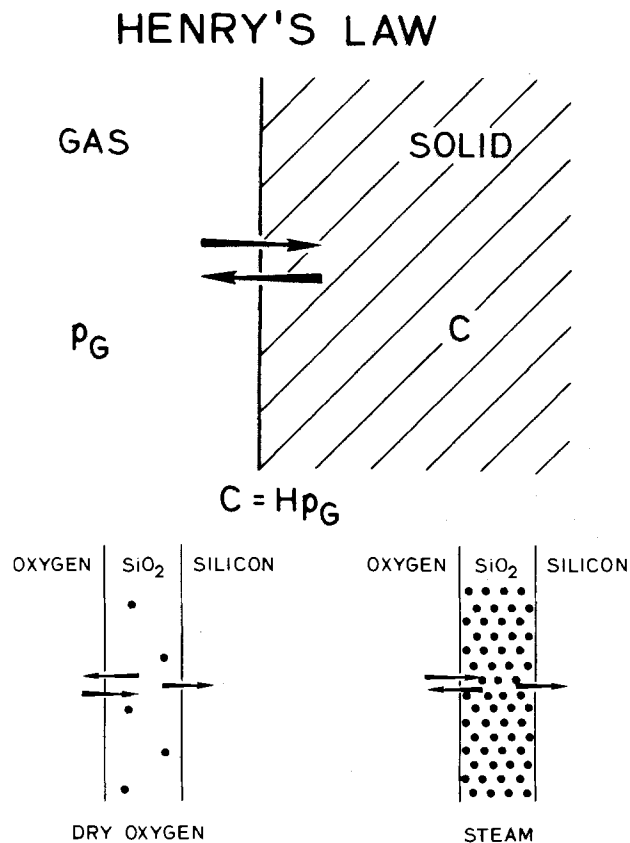


Fig. 3. Henry's law and the equilibrium solid-solubility concentration of oxygen species in the oxide reached through the balance of incoming and outgoing fluxes at the solid-gas interface, as applied to oxides grown in dry oxygen and in steam.

a surface-reaction rate-limited process, one must investigate the possible ways by which the two components of the surface reaction, namely, the concentration of oxygen species and the contribution of the silicon substrate, can be influenced. In other words, one should investigate the mechanisms that would affect the flux of oxidant species F_3 consumed in the surface reaction at the Si-SiO₂ interface. This flux is expressed as $F_3 = k_s C_i$, where k_s is the surface-reaction rate constant (which represents the contribution of the substrate) and C_i is concentration of oxidizing species at that interface. According to the Deal-Grove model (3), the oxidation is surface-reaction rate limited for thin oxides, and the concentration of oxidizing species is uniformly distributed in the oxide and is at the solid-solubility limit.

The thickness extent of the rate enhancement (as given by L_2) does not depend on substrate orientation, doping density, or oxygen partial pressure. These observations suggest that the oxide might be responsible for the rate-enhancement mechanism, assuming that the films do not retain any relationship to the underlying substrate. This is not, however, in agreement with the observed dependence of the parabolic rate constant at low temperatures on substrate orientation (25), which suggests that oxidant diffusivity and/or solubility depend on the substrate orientation. In other words, oxides under stress were observed to carry a signature of the orientation of the underlying substrate. In addition, the orientation dependence of the enhancement term, as reflected in the pre-exponential constant C_2 , indicates that the substrate participates in the reaction during the initial stages. Therefore, it is inconclusive from the results of oxidation of lightly doped substrates as to whether the enhancement mechanism is in the oxide (a process that might affect the concentration of oxygen in SiO₂) or in the substrate (a process by which additional sites at the silicon surface are available for oxidation).

The analysis of the rate enhancement in the thin regime at lower partial pressures of oxygen showed that the pressure dependence of the excess rate is, in a first-order analysis, the same as that of the linear rate constant ($\sim p^{0.8}$). This indicates that, when the oxygen supply to the surface reaction was varied by changing the oxygen partial pressure in the oxidizing ambient, both the linear surface reaction (described in the linear-parabolic model) and the thin film regime surface reaction (responsible for the excess growth rate in thin regime) are affected in the same manner. This result reinforces the fact that oxidation in this thin regime is surface-reaction rate limited, and that the rate enhancement in the thin regime would not be affected by any mechanism that would influence the transport of oxidizing species through the oxide, but by some mechanism that affects the concentration of O₂ at the Si-SiO₂ interface and/or the way in which the silicon substrate contributes to the oxidation reaction. As discussed earlier, oxygen concentrations in the oxide in excess of the solid solubility limit cannot explain the oxidation-rate enhancement of heavily doped wafers and is, therefore, an unlikely mechanism of excess oxidation in the thin film regime. It can be concluded, therefore, that the growth-rate enhancement in the early stages of oxidation is likely a result of an additional surface reaction contributed by the silicon substrate. From these results, however, no conclusion can be made on the nature of this substrate contribution, except that its extent in the substrate is independent of orientation, doping, and oxygen partial pressure.

In heavily phosphorus-doped wafers, it has been observed that the linear rate constant B/A is greatly enhanced by high doping levels in the substrate (34, 35). This observation has been attributed to increased concentrations of silicon vacancies resulting from doping induced shifts in the Fermi level at oxidation temperatures and to the availability of such vacancies at the surface to act as additional sites for thermal oxidation (34, 35). In this study (1), it has been observed that oxidation-rate enhancement in the thin regime is only moderately af-

ected by heavy doping in the substrate. Vacancies may not be responsible for the excess rate because the increase in the linear rate constant with doping is much greater than that in the excess oxidation rate in the thin regime. From this observation, it can be concluded that the thin regime surface reaction is occurring at the Si-SiO₂ interface independently of the surface reaction in heavily doped silicon.

From the above discussion, the understanding of the oxidation process can be summarized as illustrated in Fig. 4. In lightly doped substrates, the reaction at the Si-SiO₂ interface consists of the linear-parabolic reaction [1] and a parallel reaction [2] occurring only in the thin regime. The parallel reaction [2] represents the excess rate term that decays exponentially with thickness. In heavily doped substrates, an additional reaction [3], possibly vacancy related, takes place in parallel with reaction [1] in the thick regime. Reactions [1] and [3] are combined at all thicknesses into a linear-parabolic term where rate constants would reflect their doping dependence. In the thin regime of the oxidation of heavily doped samples, all reactions occur in parallel and the total oxidation rate is the sum of these three fluxes. In this case, the total oxidation rate is the sum of the doping dependent linear-parabolic term and the excess rate term that decays exponentially with thickness. The experimental observations in part I (1) indicate that reactions [2] and [3] are independent.

A number of mechanisms occurring in the substrate could result in increasing the concentration of oxidation sites at the interface. By virtue of its being the surface of an unoxidized silicon substrate, it is expected that some departure from perfect crystallinity would be encountered near the surface. This departure from bulk conditions could be in the form of damage, disorder, bond breaking, bond stretching, surface reconstruction, or vacancies (resulting from band bending caused by surface states pinning down the Fermi level at the surface). This departure from bulk conditions is an inherent property and would exist on any oxide-free surface. Oxidation occurring in a surface zone rather than an oxidizing interface is another possibility. An understanding of the oxidation of silicon based on the availability of additional oxidation sites in a surface layer, the possibility of the oxidation occurring in a surface zone, and the possible interaction of oxygen diffused into the substrate with the surface layer is developed here.

A surface layer in the silicon substrate containing additional sites for oxidation is responsible for the oxidation-rate enhancement in the thin film regime. The concentration of these sites has a profile which decays exponentially with a characteristic length of $\sim 30\text{\AA}$. This decay

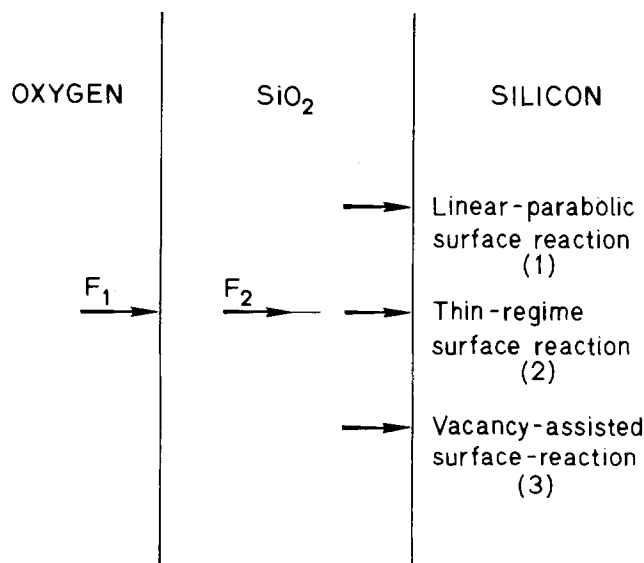


Fig. 4. Components of the interface reaction in the thin regime oxidation of silicon in dry oxygen.

length in silicon corresponds to the average value of $\sim 70\text{\AA}$ observed for the characteristic length L_2 in the data analysis as a function of oxide thickness. The nature of the excess oxidation sites in the surface layer is not yet identified; however, if this layer represents the departure from perfect crystallinity expected at any surface, oxidation could be enhanced because Si-Si bonds have changed angles and/or bond energies or are broken in this layer. The orientation dependence of the rate enhancement reflects the influence of substrate orientation on the manner in which departure from perfect crystallinity occurs. This could also explain why the activation energy of the excess rate is orientation dependent. The dependence of the excess rate on oxygen partial pressure is the result of the limited supply of oxygen species at lower partial pressures. The thickness extent of the rate enhancement is the same at lower oxygen partial pressures because the surface layer is a property of the substrate and does not depend on the ambient. The pressure dependence of the excess rate term at lower oxygen partial pressures indicates that the oxygen supply to the linear surface reaction is affected in the same fashion as that to the excess reaction occurring at the additional sites present in the surface layer. The surface layer is only slightly affected by high concentrations of phosphorus in the silicon, and the resulting abundance of silicon vacancies caused by Fermi-level effects in the substrate adds an independent parallel reaction path to the growth rate in the thin regime. The constancy of the thickness extent of rate enhancement is another indication of the additional oxidation sites being a property of the surface layer. The departure from perfect crystallinity at surfaces is intuitive and is not supported by experimental microscopy studies. It should be remembered, however, that this disorder appears in the first few monolayers on the surface, and the experimental techniques used in such a study should have an appropriately high resolution.

In a thermodynamic analysis of thermal oxidation, Tiller (30-32) developed a two-layer model of the oxide in which the thermodynamic driving force partitions itself differently than in a single-layer film. The hypothesis of an interfacial transitional layer enables the incorporation of a broader range of phenomena known to be associated with thermal oxidation into the kinetic model and could be potentially applied to express oxidation as occurring in a zone rather than on an abrupt surface. For this purpose, one might consider the possible influence of oxygen diffused into the silicon substrate at the onset of oxidation of an oxide-free silicon wafer in dry oxygen. In the brief nonsteady-state period at the start of oxidation when the silicon surface comes in contact with a high concentration of oxygen, it is possible for oxygen to diffuse into the silicon substrate. Because the diffusion of oxygen in silicon is accomplished by a one-jump process of interstitial oxygen from one Si-Si bond to an adjacent one (36), it is possible that oxygen which diffused in the substrate would affect the Si-Si bond breaking energy or angle distribution in the first few monolayers of the silicon surface or would have partially oxidized silicon atoms below the surface. Estimates of the time required for oxygen to diffuse to a profile with a diffusion length of $\sim 30\text{\AA}$ range from 5 ms at 1000°C to 0.35s at 800°C (36). The lack of orientation dependence of the excess rate in the thin regime is, however, not in disagreement with the orientation-independent diffusion of oxygen in silicon. The orientation dependence of the excess rate in the thin regime can be thought of as reflecting the distribution of Si-Si bond breaking, weakening, or bending processes that might be attributed to the presence of oxygen in the silicon surface layer. This may also explain the difference in the activation energy of the excess term with oxygen partial pressure. The dependence of the excess rate on oxygen pressure is a direct result of the reduction of oxygen diffusing into the silicon substrate at lower pressures. Oxygen diffusion is expected to be only slightly affected by the doping density in the substrate, which explains the weak effect of the substrate doping concentration on the

enhancement in the excess rate. This approach can be modeled, in principle, from published data of the diffusion coefficient of oxygen in silicon (36).

Any understanding of growth-rate enhancement in the thin regime has to explain the lack of such a phenomenon when silicon wafers are oxidized in steam or wet oxygen (3). The disordered silicon surface layer is expected to be present on all surfaces irrespective of the oxidizing ambient and, consequently, a growth-rate enhancement should, in principle, be observed in wet oxidations. It is also possible, however, that as water molecules reach the Si-SiO₂ interface to yield H₂ molecules and atomic oxygen, the released hydrogen contributes at high temperatures to a reordering of the Si-Si broken-bond or bond-angle distributions in the surface layer resulting in a reduction or total elimination of the additional oxidation sites. It should also be remembered that atomic oxygen resulting from the decomposition of water at the interface is readily consumed in the surface reaction.

Experimental difficulties are expected when attempting to support any physical process proposed to explain oxidation-rate enhancement in the thin regime because the thickness of interest extends for only a few monolayers of silicon. Progress in advancing the limits of detectability, resolution, and accuracy of high resolution experimental techniques will help identify the underlying physical mechanisms in the fast growth rate of SiO₂ during the early stages of oxidation in dry oxygen.

Conclusions

Physical processes (such as space-charge effects, oxide structure, oxide stress, and oxygen solubility in SiO₂) proposed to account for oxidation-rate enhancement in the thin regime were critically analyzed. An understanding of this phenomenon based on the presence of a surface layer, where a distribution of additional sites of oxidation is found, was proposed and is in agreement with all experimental results. This surface layer represents a property of the surface and can be the result of the departure from bulk properties near the surface. The possible interaction with oxygen diffused into the silicon wafer is also in agreement with this understanding. Further investigations of thermal oxidation will help delineate the features of the silicon surface prior to oxidation and will be valuable in defining the nature of the additional oxidation sites.

Acknowledgments

The authors would like to acknowledge many helpful discussions with Dr. B. E. Deal, Dr. C. P. Ho, Dr. C. R. Helms, Dr. W. A. Tiller, and Dr. D. Modlin. This study was sponsored by Darpa Contract No. MDA 903-79-C-0257.

Manuscript submitted April 15, 1985; revised manuscript received July 11, 1985.

Stanford University assisted in meeting the publication costs of this article.

REFERENCES

1. H. Z. Massoud, J. D. Plummer, and E. A. Irene, *This Journal*, **132**, 2685 (1985).
2. H. Z. Massoud, J. D. Plummer, and E. A. Irene, *ibid.*, **132**, 1745 (1985).
3. B. E. Deal and A. S. Grove, *J. Appl. Phys.*, **36**, 3770 (1965).
4. N. Cabrera and N. F. Mott, *Rep. Prog. Phys.*, **12**, 163 (1948).
5. P. J. Jorgensen, *J. Chem. Phys.*, **37**, 874 (1962).
6. A. S. Grove, "Physics and Technology of Semiconductor Devices," Chap. 2, John Wiley and Sons, New York (1967).
7. M. Hamasaki, *Solid-State Electron.*, **25**, 479 (1982).
8. Y. Z. Lu and Y. C. Cheng, *J. Appl. Phys.*, **56**, 1608 (1984).
9. S. M. Hu, *Appl. Phys. Lett.*, **42**, 872 (1983).
10. S. M. Hu, *J. Appl. Phys.*, **55**, 4095 (1984).
11. D. N. Modlin, Ph.D. Thesis, Stanford University, Stanford, CA (1983).
12. A. M. Goodman and J. M. Breece, *This Journal*, **117**, 982 (1970).

13. Y. J. van der Meulen, *ibid.*, **119**, 530 (1972).
14. A. G. Revesz and R. J. Evans, *J. Phys. Chem. Solids*, **30**, 551 (1969).
15. S. W. Ing, R. E. Morrison, and J. E. Sandor, *This Journal*, **109**, 221 (1962).
16. A. G. Revesz, Abstract 350, p. 897, The Electrochemical Society Extended Abstracts, Vol. 80-2, Hollywood, FL, Oct. 5-10, 1980.
17. J. M. Gibson and D. W. Dong, *This Journal*, **127**, 2722 (1980).
18. J. K. Srivastava and J. B. Wagner, Jr., 463 RNP, *ibid.*, **131**, 196C (1984).
19. E. A. Irene, *ibid.*, **125**, 1708 (1978).
20. M. A. Hopper, R. A. Clarke, and L. Young, *ibid.*, **122**, 1216 (1975).
21. A. G. Revesz, Abstract 281, p. 701, The Electrochemical Society Extended Abstracts, Vol. 81-1, Minneapolis, MN, May 10-15, 1981.
22. R. J. Jaccodine and W. A. Schlegel, *J. Appl. Phys.*, **37**, 2429 (1966).
23. P. G. Borden, *Appl. Phys. Lett.*, **36**, 829 (1980).
24. E. P. EerNisse, *ibid.*, **35**, 8 (1979).
25. E. P. EerNisse, *ibid.*, **30**, 290 (1977).
26. E. A. Irene, *J. Appl. Phys.*, **54**, 5416 (1983).
27. H. Z. Massoud, C. P. Ho, J. D. Plummer, E. A. Irene, and E. Tierney, 1982 IEEE 13th Semiconductor Interface Specialists Conference, Dec. 9-11, 1982, San Diego, CA (Unpublished).
28. E. A. Irene, E. Tierney, and J. Angilello, *This Journal*, **129**, 2594 (1982).
29. A. Fargeix, G. Ghibaudo, and G. Kamarinos, *J. Appl. Phys.*, **54**, 2878 (1983).
30. W. A. Tiller, *This Journal*, **127**, 619 (1980).
31. W. A. Tiller, *ibid.*, **127**, 625 (1983).
32. W. A. Tiller, *ibid.*, **127**, 689 (1981).
33. G. F. Derbenwick and R. E. Anderson, Private communication.
34. C. P. Ho and J. D. Plummer, *This Journal*, **126**, 1516 (1979).
35. C. P. Ho and J. D. Plummer, *ibid.*, **126**, 1523 (1979).
36. G. D. Watkins, J. W. Corbett, and R. S. McDonald, *J. Appl. Phys.*, **53**, 7097 (1982).

Polyimide Adhesion

Mechanical and Surface Analytical Characterization

Rajesh G. Narechania, James A. Bruce,* and Sherrill A. Fridmann

International Business Machines Corporation, Essex Junction, Vermont 05452

ABSTRACT

The effects of surface treatments and cure temperature on polyimide to silicon nitride adhesion strength are discussed. Results show the importance of surface cleanliness and the requirement for an adhesion promoter. X-ray photoelectron spectroscopy (XPS) was used to study the mode of failure at different cure temperatures. As the cure temperature is increased, the mode of failure goes from primarily cohesive to a mixed adhesive/cohesive failure, as inferred from the XPS data.

Polyimide is currently being used as an interlevel insulator in semiconductor device manufacturing (1). Poor adhesion of polyimide at an interface will enhance moisture penetration and as a result will promote a loss in its passivation function. To improve polyimide adhesion, a thorough understanding of the chemistry involved is needed. In addition, it is important to know the mode of failure during adhesion testing.

If the failure is adhesive (polyimide separating from an adhesion promoter or adhesion promoter from nitride), then the adhesion can be enhanced by improving the bonding or thermal stability of the interface (*e.g.*, by means of variations in surface treatments, cure temperatures, or adhesion promoters). However, if the failure is cohesive (separation occurring in the polyimide film itself), then changes in the interface would be ineffective in enhancing the adhesion. Rather, the internal mechanical strength of polyimide would have to be improved by making structural changes, such as molecular weight and degree of cross-linking.

The nature of the underlying surface plays a significant role in the adhesion characteristics of polyimide to that surface. Good adhesion of polyimide to an underlying surface (*e.g.*, an oxygen-rich silicon nitride) requires an adhesion promoter such as 3-aminopropyltriethoxysilane (APS). Work done by Linde shows that APS chemically bonds to both the polyimide and the surface (2). The silane portion of the APS bonds to the surface, while the amino portion reacts with the polyimide precursor, polyamic acid (Fig. 1). It may be noted that, since the APS bonds to the surface through surface hydroxyl groups, enrichment of these groups will favor the adhesion process.

A photoresist adhesion promoter, *e.g.*, hexamethyldisilazane (HMDS), is used to improve the wettability of a nitride surface to photoresist (Fig. 2). In semiconductor processing, photoresist can be applied and stripped sev-

eral times before the application of polyimide. This can leave residual photoresist and/or HMDS on the surface before APS/polyimide is applied. This would prevent the reaction shown in Fig. 1 from occurring as completely as it would on a clean, oxygen-rich nitride surface. Therefore, chemical pretreatments (*e.g.*, plasma cleaning) are needed to assure complete removal of photoresist/HMDS and thereby enhance polyimide adhesion.

Another important factor affecting the bonding (and thus the adhesion) is the cure temperature of the polyimide. The adhesion promoter, APS, has been shown to be thermally unstable at temperatures in excess of 400°C (3). Saiki and Harada have shown a dependence of polyimide adhesion on its cure temperature using a different polyimide with an aminosilane adhesion promoter (4). They found that the temperature dependence of the

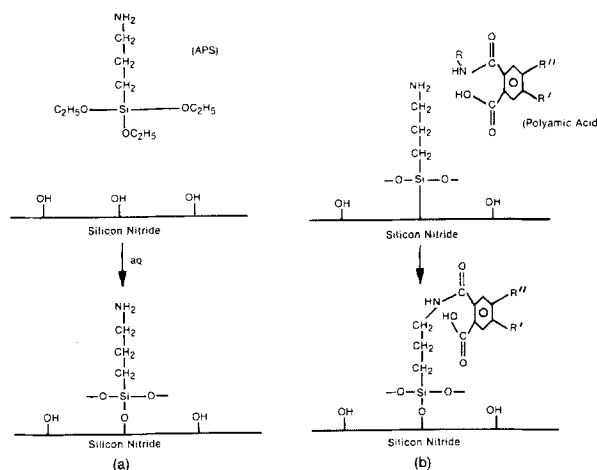


Fig. 1. The reaction of APS with a silicon nitride surface (a) and surface attached APS with polyamic acid (b).

* Electrochemical Society Active Member.

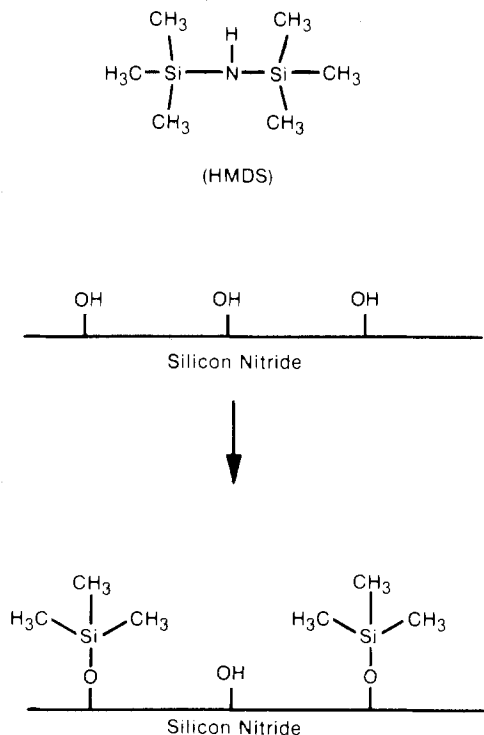


Fig. 2. The reaction of HMDS with a silicon nitride surface

adhesion was due to thermal decomposition of the aminosilane.

It has been shown that a stress of 85°C temperature and 80% humidity can degrade the adhesion of polyimide to a silicon nitride surface (5). Therefore, this test was used as a measure of long-term stability of adhesion to environment.

This paper shows the effects of surface treatment and cure temperatures on polyimide to silicon nitride adhesion strength and investigates the mode of failure during peel testing using x-ray photoelectron spectroscopy.

Methods and Materials

Silicon nitride-deposited wafers were divided into two groups (Fig. 3). In group A, the wafers were oxygen plasma cleaned after applying and removing photoresist and HMDS. This group was divided into two subgroups. In subgroup I, APS was used; in subgroup II, no adhesion promoter was used. The APS was diluted to 0.1% (v/v) with water before puddle-spin application. Polyamic acid was obtained from E. I. du Pont de Nemours and Company, as the amic acid solution of poly(N,N'-(p,p'-oxydiphenylene) pyromellitimide). The commercial equivalent is PI-2540. The polyamic acid was spun onto all the wafers. The wafers in subgroup I were cured in nitrogen at 325°, 350°, 375°, 400°, and 425°C. In group B, no resist was applied on the wafers. This group was divided into two subgroups: plasma clean and no plasma clean. All wafers were then treated with adhesion promoter, spun with polyamic acid, and cured at 400°C.

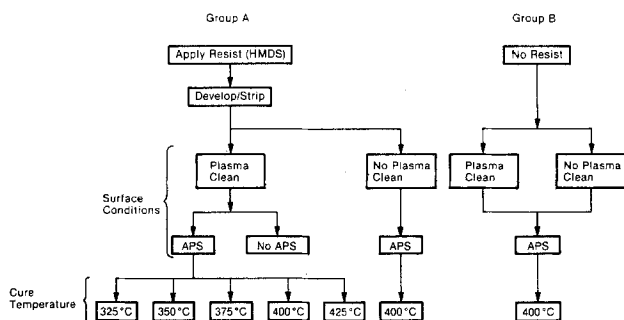


Fig. 3. A flow chart indicating the conditions used to prepare the wafers in group A and group B.

The polyimide-coated silicon nitride substrates were mounted on an X-Y sliding stage. The samples were evaluated by peeling films perpendicularly (Fig. 4) from the nitride surface on the Instron material testing system at a constant rate of 0.2 in./min. A load vs. elongation graph was plotted for each peeled sample, and adhesion peel strength in grams per millimeter was computed. The peel test was repeated on samples that were soaked in the temperature-humidity (T&H) chamber (85°C, 80% humidity) for 168h. Each split consisted of a minimum of ten samples, and the reproducibility was in the range of 5-10%.

X-ray photoelectron spectra were obtained using the Hewlett-Packard Model 5950B spectrophotometer. All data were obtained by scanning in the survey mode over the binding energy range of 0-1250 eV. The resolution in the survey scans was ± 1 eV. These spectra proved to be adequate for quantifying the elements present on the surface and for distinguishing between two different chemical bonding environments for the nitrogen. Spectra were obtained using an Al K α x-ray source and a low energy electron flood gun (2 eV, 0.4 mA) to eliminate possible charging of the sample.

Peel Criteria

A definite criterion for defining and computing peel strength was established (Fig. 5a-5c). A complete peel is defined as one during which the polyimide film across the entire width completely debonds from the adhering surface. A partial peel is one during which the polyimide film does not completely debond across the width from the adhering surface, but only from a portion of the width. During a "no-peel" mode, polyimide does not peel at all from the surface, owing to film fracture. A peel strength measurement at no peel, defined as a "minimum peel strength," represents not the actual peel strength but only its lower limit. The minimum peel strength is not a measure of the film tensile strength because the test is performed in a peel test mode. Also, the largest observed no-peel force in this criterion is an estimate of the minimum peel strength provided no handling damage has occurred.

A polyimide film may not peel either because the film is too brittle to support the cleavage stress at the tip of the peel or because handling damage has occurred. The latter situation will be compounded if the film is brittle.

Historically, a no-peel condition is assumed to manifest excellent adhesion. However, this assumption is inaccurate simply because only the lower limit to the peel strength, and not the peel strength itself, is measured. Prior to a steady peeling from the cleavage site, a film must overcome the plastic deformation of the material (6). Therefore, in a no-peel situation, if the adhesion strength is much higher than the plastic strength of the material, then a high load to break the film is obtained. From this, a minimum peel strength can be computed by dividing

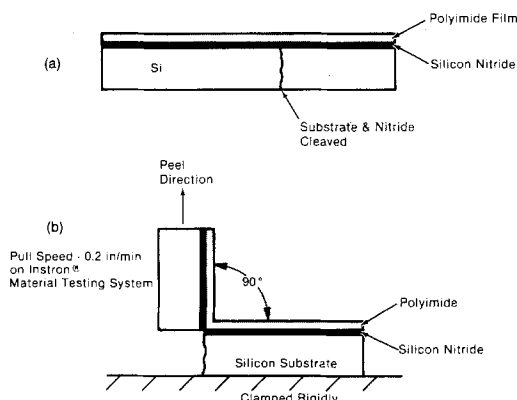


Fig. 4. A cross-sectional representation of a polyimide-coated silicon nitride wafer in which the silicon and the silicon nitride have been cleaved in preparation for the peel test (a) and a sample as it is mounted for the 90° peel test (b).

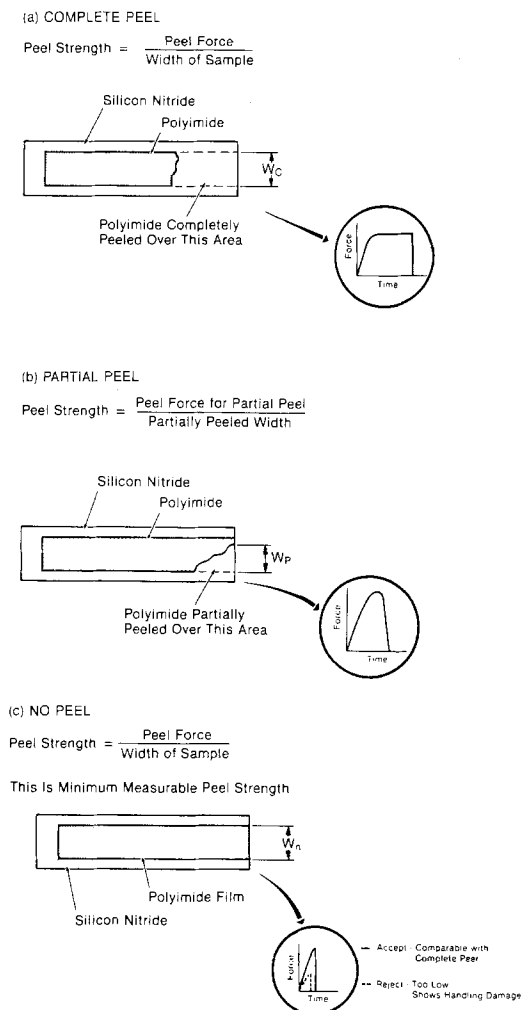


Fig. 5. A representational top view of the polyimide-coated silicon nitride surface after a complete peel (a), a partial peel (b), and no peel (c). A plot of peel force vs. time is shown in the inset for each case.

the load at no peel by the film width. A brittle film will produce a significant load at no peel with high reproducibility if no handling damage is done.

If the minimum peel strength measured in a no-peel situation is within a reasonable limit and comparable to that with complete or partially peeled samples, then the minimum peel strength should be acceptable. However, if the minimum peel strength is significantly lower than when a complete peel is obtained, then the sample tested must be rejected because of the handling damage.

Results

Adhesion strength in all experiments was computed in grams per millimeter according to our peel criteria. All samples were viewed under a microscope to determine the mode of peeling. The results are examined in the three categories below.

Effect of plasma ash conditions on adhesion.—The results in Fig. 6 show that plasma cleaning of HMDS-treated surfaces improved adhesion of polyimide to nitride by 92% for samples not subjected to T&H soak. T&H soaking of plasma-cleaned HMDS-treated samples caused minimal loss of adhesion, whereas those with no plasma clean lost 18% of their adhesive strength.

On the other hand, surfaces not treated with HMDS showed an approximately 40% lower adhesion compared to HMDS-treated samples, whether or not they were plasma cleaned. In addition, these nontreated samples showed adhesion losses of approximately 30% after T&H soak. It is thus evident that adhesion is markedly enhanced by the deposition and subsequent plasma oxidation of HMDS on the surface.

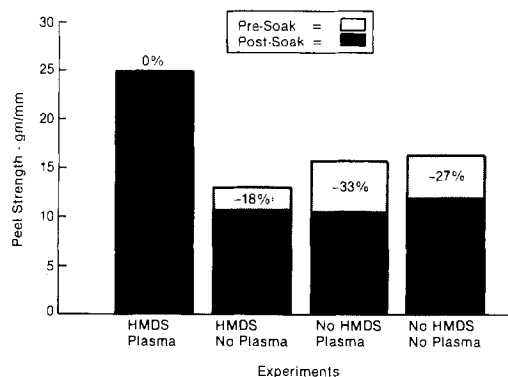


Fig. 6. A comparison of the peel strength before and after the T&H soak for samples prepared with and without plasma clean and HMDS. APS was used in all cases prior to applying polyimide. Polyimide was cured at 400°C.

Effect of APS on the adhesion.—Figure 7 shows that polyimide adhesion strength deteriorated by 40% when adhesion promoter APS was not used. After T&H, the group without APS reduced the adhesion strength to zero. In direct contrast, the group with APS retained adhesion strength after T&H soak.

Effect of cure temperature on polyimide/nitride adhesion.—The peel strengths were computed in this experiment after 168, 336, and 504h of T&H soak (Fig. 8). The results show that after 168h of soak all groups produced a no peel condition, and the minimum peel strength was highest when the polyimide was cured at 425°C. After 336 and 504h of soak, the polyimide cured at 375°, 400°, and 425°C began to peel, whereas those cured at 325° and 350°C produced no peel. Several points may be noted here. (i) There is a general tendency for the measured values to increase with T&H soak time. (ii) For samples which consistently failed to peel (i.e., those cured at 325° and 350°C), these increases can readily be explained as increases in the fracture toughness of the film caused by plasticization due to the T&H soak. (iii) For the samples which consistently peeled at the two longer soak times (i.e., those cured at 375°, 400°, and 425°C), the measurement represents a true adhesive strength.

Surface analytical characterization.—In order to further understand the differences between the various polyimide cure temperatures, XPS was used to examine the silicon nitride surface after peeling. Samples cured at 375°, 400°, and 425°C were peeled after 504h of soak, and then the silicon nitride surface that was exposed by peeling off the polyimide was analyzed by XPS. Samples

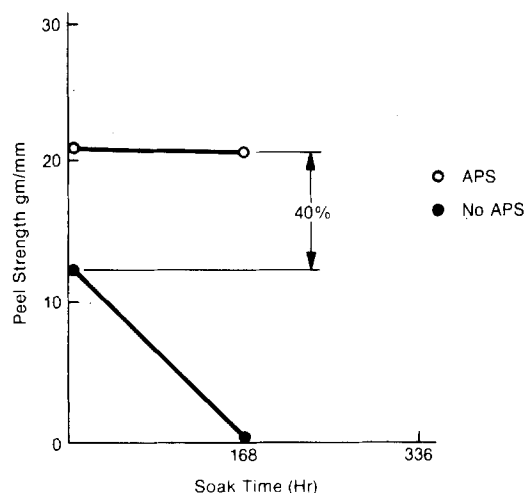


Fig. 7. A plot of peel strength vs. T&H soak time for polyimide-coated silicon nitride wafers prepared with (open circles) and without (closed circles) APS. In both cases, HMDS and plasma clean were used and the films were cured at 400°C.

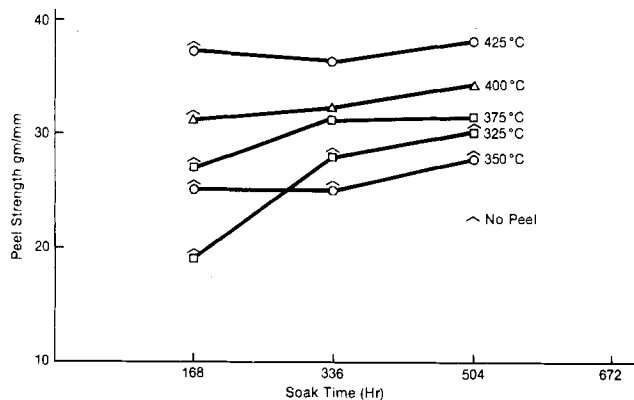


Fig. 8. A plot of the peel strength vs. the T&H soak time for polyimide-coated nitride samples cured at 325°, 350°, 375°, 400°, or 425°C. APS was used in all cases, after HMDS and plasma clean.

cured at 350° and 325°C could not be analyzed because the polyimide did not peel from a large enough area to perform the analysis. Silicon nitride, APS-coated silicon nitride, and polyimide surfaces were analyzed as control samples.

Table I summarizes the results from the XPS analysis. Figure 9 shows survey spectra obtained from some of the samples. Figure 10 shows an expansion of the nitrogen 1s signal from Fig. 9. From Table I and Fig. 9, it can be seen that the silicon signal from the nitride surfaces exposed by peeling increases as the cure temperature increases. There is also a noticeable drop in the carbon content as the cure temperature increases. In all cases, however, the surface exposed by peeling off polyimide does not ap-

Table I. Surface composition as determined by XPS

Surface	PI cure temperature (°C)	Surface composition (a/o)			
		C	N	O	Si
Nitride after peel	375	79	5.5	14	1.1
Nitride after peel	400	78	4.5	15	2.7
Nitride after peel	425	70	7.7	15	7.2
Nitride after peel	425	70	6.2	16	7.4
Polyimide	350	78	5.7	16	—
Silicon nitride	—	6.8	37	14	42
APS on nitride	—	17	30	16	37

proach the composition of the silicon nitride surface alone or the silicon nitride plus APS surface.

From Fig. 10, the nitrogen 1s signal shows signs of two different bonding environments (*i.e.*, two overlapping nitrogen signals of different binding energy) for the sample cured at 425°C, as compared to the sample cured at 375°C. The higher binding energy is associated with the imide nitrogen from the polyimide. The lower binding energy is associated with the nitrogen from either the silicon nitride or the APS. These assignments are confirmed by the spectra of the control sample and are in agreement with reported binding energies for polyimide (7), silicon nitride (8), and APS (9).

Scanning electron microscopy was used to analyze the nitride surface after peeling off the polyimide. No differences were found in the surface morphology for samples cured at 375° or 425°C.

Discussion

Plasma ashing enhances polyimide adhesion to HMDS-treated nitride surfaces due to one or all of the following actions: (i) cleaning of or stripping off photoresist resi-

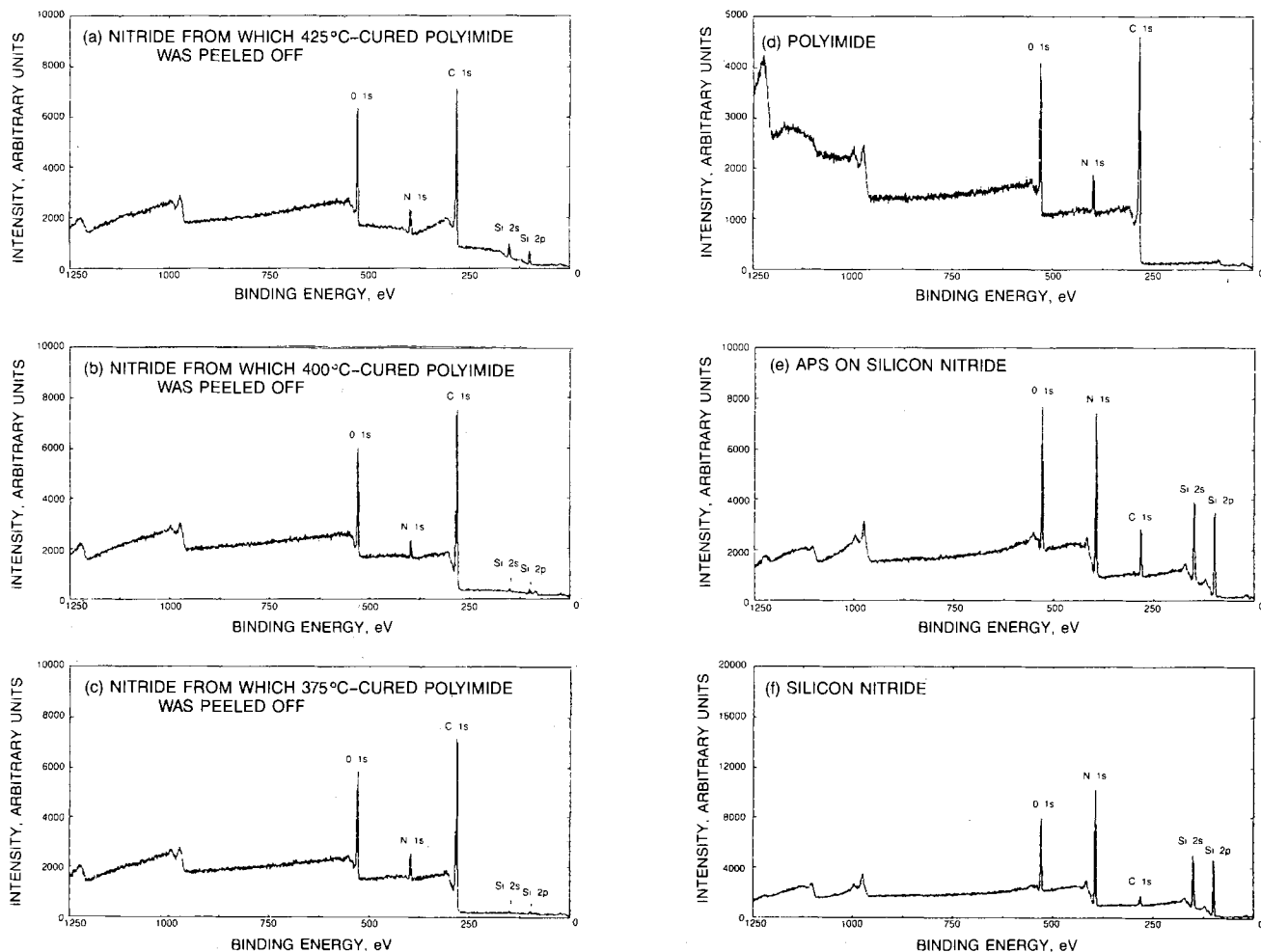


Fig. 9. XPS survey spectra for the nitride surface remaining after peeling off polyimide cured at 425°C (a), 400°C (b), and 375°C (c), as well as the spectra for a polyimide surface (d), a silicon nitride surface coated with APS (e), and an oxygen-rich silicon nitride (f).

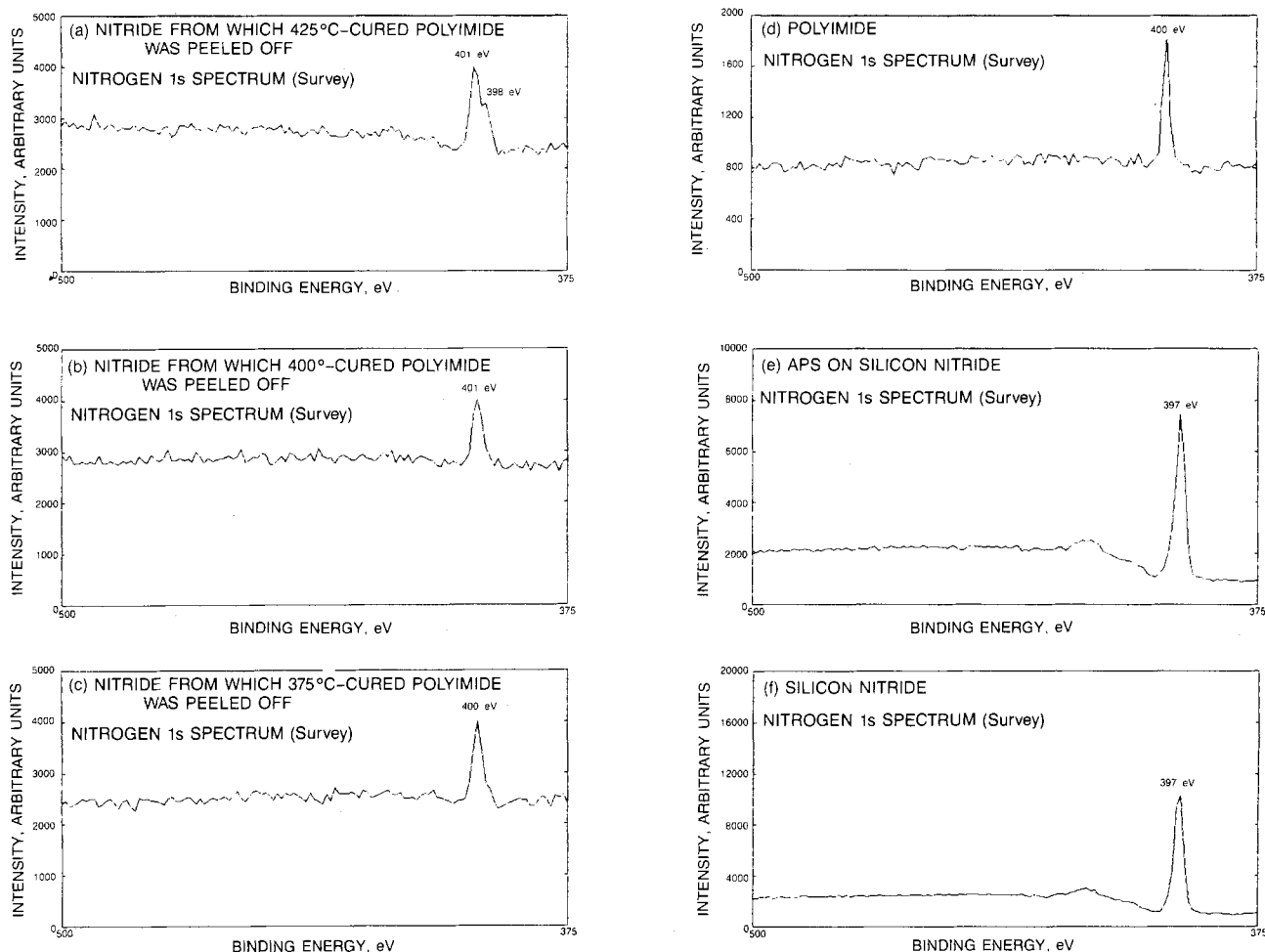


Fig. 10. An expansion of the nitrogen 1s signal from the spectra in Fig. 9

dues and HMDS, (ii) oxidation of HMDS, (iii) oxidation of nitride, and (iv) roughening of the surface. HMDS coating of surfaces enhances adhesion if and only if subsequently plasma cleaned. The omission of HMDS and/or plasma treatment of surfaces results in deterioration in the peel strength post-T&H stress.

APS is a crucial element for polyimide to silicon nitride adhesion. This was previously demonstrated to be true for polyimide to silicon dioxide adhesion (5). Since the silicon nitride surface is oxygen rich, the same chemistry of APS bonding probably occurs on both surfaces.

A higher peel strength at 400° and 425°C than at 350°C is due to the difference in the peel mode: the former values are true adhesive strengths, and the latter are the minimum peel strengths. In order for peel to occur, the tensile strength of the film has to be equal to or greater than the adhesive strength of the bond between film and substrate. This requirement stems from the fact that a certain amount of elastic and plastic deformation of the polyimide must be overcome before peeling can be initiated, given that the adhesion is relatively good (6). However, if adhesion is relatively poor, neither elastic nor plastic deformation is a significant factor. Finally, if the adhesion strength is extremely good, and the plastic deformation of the film is relatively low, then the material can be interpreted as being brittle. This is the case observed in the 325° and 350°C cured polyimide.

The higher cure temperatures produce stronger polyimide than at lower temperatures, but this may not be true for adhesion strength. A higher peel strength at cure temperatures of 375°C and above does not necessarily mean that the adhesion is better than at lower cure temperatures where minimum peel strengths are observed. Higher cure temperatures lead to greater elongation than at lower cure temperatures: hence, high cure temperature superficially shows increased adhesion strength. Our re-

sults show that 350°C is the safest cure temperature where both adhesion and plastic properties are adequate.

The XPS data shows that a thin organic film is left on the nitride surface after peeling polyimide. For the sample cured at 375°C, the three following observations can be made. First, the silicon signal is very small. Second, only one binding energy can be detected for the nitrogen. Third, the carbon, nitrogen, and oxygen signals appear almost identical to the spectrum for polyimide. The film remaining on this sample, therefore, is concluded to be polyimide, implying a largely cohesive failure mechanism. For the sample cured at 425°C, three observations can also be made. First, a significant silicon signal can be detected (although it is still much smaller than the signal from nitride or nitride plus APS). Second, two distinct nitrogen signals can be seen. Third, the carbon signal is reduced somewhat in intensity as compared to the polyimide reference. This indicates that the remaining polyimide film is thinner on the average than for the sample cured at 375°C, and that therefore the underlying nitride or APS films can also be detected.

While there is no ambiguity in the fact that the average thickness of the remaining polyimide film decreases with increasing cure temperature, there is uncertainty as to whether the film remains continuous or becomes discontinuous. If the film remains continuous and no underlying nitride or APS is laid bare, then the failure mode remains cohesive. If, on the other hand, the film becomes discontinuous, *i.e.*, contains microregions where the nitride and/or APS are laid bare, then the failure becomes a mixture of adhesive and cohesive.

Independently of any physical or chemical considerations for the mechanism and mode of adhesion failure, the two extreme situations alluded to above can be quantified from the XPS data. Specifically, for the continuous film case, its thickness may be estimated by

using escape depths. The escape depth of a silicon 2p electron through organic material such as polyimide is about 30Å (10). Using conventional formulas for calculating attenuation of photoelectron signals by overlaying layers (11), and the Si 2p intensities measured in this study, the calculated thickness for the residual polyimide film ranges from 60 to 105Å for cure temperatures ranging from 375° to 425°C, respectively. Alternately, if one assumes that a discontinuous film of polyimide remains on the nitride, the calculated area percent coverage of polyimide ranges from 98% (2% of nitride laid bare) to 89% (11% of nitride laid bare) for cure temperatures of 400° or 425°C, respectively. These calculations assume that nitride is exposed upon peeling. Calculations made assuming that APS is exposed upon peeling would give even lower coverages. Calculations such as these provide some realistic boundaries on the mode of adhesion failure.

As can be seen in Fig. 1b, the polyamic acid chain undergoes scission upon bonding to the APS. This could result in a cohesive failure of the polyimide near the nitride interface, which would be consistent with the cohesive failure mechanism described above. This would not, however, explain an increasingly thinner film remaining after the peel as the cure temperature increases. The chain scission occurs during bonding to APS and is complete at a temperature far below the final cure temperature of the polyimide.

Decomposition of APS could explain this trend. A previous work has shown that the onset of thermal decomposition for the APS/polyimide system occurs in the region of 400°C (3). Any such decomposition occurring at the nitride/polyimide interface would be likely to favor adhesive failure at higher cure temperatures, particularly if these same conditions improve the fracture toughness of the polymer itself.

The fact that no differences were found in the morphology of the nitride surface after peeling for samples cured at 375° or 425°C does not rule out a mixed mode failure mechanism at the higher cure temperatures due to the limited resolution (~100Å) of the SEM.

A mixed mode of failure at higher cure temperatures could be due to inhomogeneities in the nitride/APS/polyimide laminate across the wafer and, therefore, differences in its decomposition behavior in localized areas.

Summary

Our results show the significance of the surface condition of silicon nitride for polyimide adhesion. Surface pretreatments (e.g., plasma cleaning) and adhesion promoters are necessary in order to obtain good polyimide adhesion to silicon nitride. The use of an adhesion promoter plays a crucial role in obtaining and maintaining good adhesion. The cure temperature affects the thermal stability of the interface. At higher cure temperatures, the failure becomes increasingly adhesive in nature due to thermal degradation at the nitride/APS/polyimide interface. All of these results are related to chemical bonding and stability of the nitride/APS/polyimide interface.

Acknowledgments

The authors wish to thank Harold Linde for helpful discussions, Cherie Beach for technical assistance with the peel testing, and Rene Kirby and Tanya Lee for SEM analysis.

Manuscript submitted April 15, 1985; revised manuscript received July 10, 1985.

IBM Corporation assisted in meeting the publication costs of this article.

REFERENCES

1. D. Bergeron, J. Kent, and K. Morrett, in "Proceedings of the 22nd Annual IEEE Reliability Physics Conference," Las Vegas, April 1984, IEEE, New York (1984).
2. H. Linde, *J. Polym. Sci., Polym. Chem. Ed.*, **20**, 1031 (1982).
3. H. Linde, *ibid.*, **22**, 3043 (1984).
4. A. Saiki and S. Harada, *This Journal*, **129**, 2278 (1982).
5. L. Rothman, *ibid.*, **127**, 2216 (1980).
6. A. Crocombe and R. Adams, *J. Adhesion*, **13**, 241 (1982).
7. H. Leary, Jr., and D. Campbell, *Surf. Interface Anal.*, **1**, 75 (1979).
8. H. Leary, Jr., and D. Campbell, *Org. Coat. Appl. Polym. Sci. Proc.*, **46**, 433 (1981).
9. S. Raider, R. Flitsch, J. Aboaf, and W. Pliskin, *This Journal*, **123**, 560 (1976).
10. M. P. Seah and W. A. Dench, *Surf. Interface Anal.*, **1**, 2 (1979).
11. T. A. Carlson, "Photoelectron and Auger Spectroscopy," pp. 261-262, Plenum Press, New York (1975).

Electrical Properties of Silicon Dioxide Films Fabricated at 700°C

III. High Pressure Thermal Oxidation

L. P. Trombetta* and R. J. Zeto*

Electronics Technology and Devices Laboratory (ERADCOM), Fort Monmouth, New Jersey 07703-5302

F. J. Feigl* and M. E. Zvanut

Department of Physics and Sherman Fairchild Laboratory, Lehigh University, Bethlehem, Pennsylvania 18015

ABSTRACT

High quality thermal oxides of silicon have been fabricated on silicon substrates over the oxidation temperature range 635°-1100°C. Dry, high pressure oxidation (DRYPOX) was used to grow oxides at temperatures below 1000°C. The high pressure range investigated was 2-500 atm. Standard capacitance-voltage techniques have been used to characterize these oxides in terms of oxide fixed charge (Q_f) and interface trap densities (D_{it}). Additionally, avalanche injection of both electrons and holes has been used to evaluate the charge trapping properties of these films. The electron trapping properties of 685°C, high pressure oxides were compared with "conventional" 1000°C oxides fabricated at 1 atm and with oxides fabricated using low pressure chemical vapor deposition (LPCVD) at 730°C. The results of these experiments were as follows: (i) basic electrical properties of high pressure oxides, as well as hole and electron trapping behavior in these oxides, were similar to those of 1000°C conventional oxides; (ii) hole trap densities exhibited a broad minimum at an oxidation temperature between 800° and 900°C; and (iii) electron trapping behavior in 685°C DRYPOX oxides was markedly superior to that in 730°C LPCVD oxides. The LPCVD oxide required an anneal at 1000°C to produce electron trapping characteristics comparable to those of DRYPOX samples processed entirely at temperatures below 700°C.

The development of low temperature processing techniques within the silicon planar technology is desirable for the development of very large scale integration (VLSI) (1, 2). In particular, low temperature oxidation using high pressure is receiving increased attention (3). Significantly reduced oxidation temperatures have been achieved using thermal oxidation of silicon at elevated pressures of either steam (2, 4, 5) or dry oxygen (1, 6, 7). Additionally, reductions in arsenic and boron diffusion have been demonstrated using high pressure steam to reduce oxidation temperatures (8, 9). A reduction in silicon stacking faults has also been obtained using high pressure steam (10).

High pressure oxidation using dry oxygen (DRYPOX) was first introduced by Zeto *et al.* (11). These authors investigated the kinetics of oxidation in dry oxygen at pressures up to 130 atm. Dry, high pressure oxidation kinetics have also been investigated by Lie *et al.* (1). A comprehensive review of early experiments in high pressure oxidation may be found in the work by Zeto *et al.* (12).

Basic electrical properties and device characteristics of silicon metal-oxide-semiconductor (MOS) devices fabricated using either dry oxygen (1, 6) or steam (2, 5) pressure oxidation for the gate oxide have been reported. To date, however, studies of the electrical behavior of dry, high pressure oxides have been rather select with regard to both the properties investigated and sample preparation conditions. The present work is intended as a more comprehensive survey of the relation between electrical quality and DRYPOX oxide fabrication techniques.

This paper is the third in a series on low temperature oxidation technologies. Parts I and II of this series discussed the use of low pressure chemical vapor deposition (LPCVD) using tetraethoxysilane (TEOS) (13) and dichlorosilane/nitrous oxide (14) deposition, respectively. For the present study, SiO₂ films were prepared by thermal oxidation of silicon at temperatures ranging from 635° to 1100°C and pressures ranging from 1 to 500 atm. The electrical quality of these films was evaluated in terms of the Deal oxide charge classification scheme (15) using aluminum gate MOS capacitors. Measurements were made of oxide fixed charge (Q_f), interface trap densities (D_{it}), and mobile ionic contaminants. In addition to these basic electrical properties, oxide trapped charge (Q_{ot}) produced by avalanche electron and hole injection was studied. An understanding of such oxide charging is important because of the phenomena of hot carrier injection into the gate oxide of short channel field effect devices (16) and of "window closing" in electrically eras-

* Electrochemical Society Active Member.

able floating gate avalanche injection MOS (E²FAMOS) charge storage devices (17).

The results reported below include a comparison of DRYPOX films with conventional, high temperature (1000° and 1100°C) dry thermal oxide films and with oxide films produced using LPCVD of dichlorosilane and nitrous oxide at 730°C. These comparisons indicate that the electrical characteristics of DRYPOX films are comparable to conventional 1000°C thermal oxides. Additionally, the electron trapping behavior of DRYPOX films produced at 685°C was markedly superior to that of LPCVD films produced at 730°C and equivalent to LPCVD films given a high temperature (1000°C) post-deposition anneal.

Experimental Details

Sample preparation.—High pressure oxidation was performed in the apparatus shown schematically in Fig. 1. This apparatus consisted of an externally heated vessel constructed of a nickel-based alloy (Rene 41) and was pressurized with a Haskel oxygen pump. Gas was supplied to the pump from conventional high pressure cylinders. A Panametrics high pressure hygrometer was used to monitor the moisture content of the oxidation ambient. Under the conditions of the experiment, the moisture content could be maintained at five parts water per million parts oxidation ambient; this value was independent of the ambient pressure. A water content of even a few parts per million may increase oxidation kinetics. However, oxide thicknesses were reproducible to within 10%

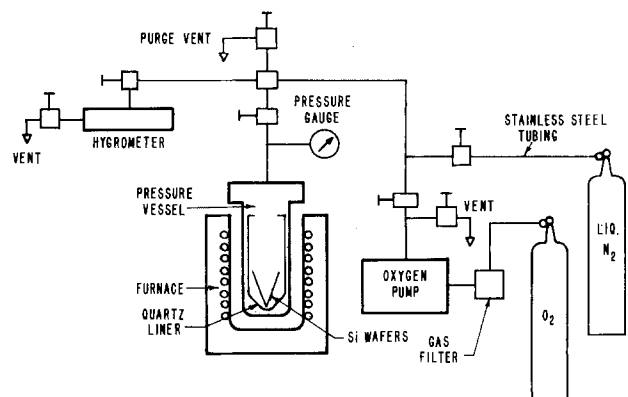


Fig. 1. Schematic diagram of the high pressure apparatus

from run to run, and the moisture content was not considered a problem for the present investigation.

The inside dimensions of the pressure vessel were approximately 1.25 cm diam by 25 cm length. Samples were prepared by dicing polished silicon wafers to dimensions of 0.8 by 2.5 cm and were placed in a quartz test tube prior to insertion into the pressure vessel, as illustrated in Fig. 1. Silicon n-type substrates with phosphorus doping densities of $4\text{--}7 \times 10^{15} \text{ cm}^{-3}$ (3–5 $\Omega\text{-cm}$ resistivity) were supplied by Monsanto Company. Lower resistivity n- and p-type substrates with phosphorus and boron doping densities of $5\text{--}8 \times 10^{16} \text{ cm}^{-3}$ (0.1 $\Omega\text{-cm}$ resistivity) were supplied by Pensilco Company. The lower resistivity substrates were required for avalanche injection. Samples with resistivities significantly higher than 0.1 $\Omega\text{-cm}$ are more susceptible to "edge injection" effects produced by electric field enhancement at geometrical irregularities along the gate electrode perimeter [Ref. (18), p. 505]. With the exception of the wafers used for electron injection studies, all substrates were of n-type silicon with (100) crystallographic orientation. Electron injection studies were performed on p-type (100) wafers. Substrate cleaning consisted of a standard, basic peroxide/acid peroxide clean.

Oxidation in the high pressure system was initiated by first raising the external furnace and then pumping to the desired oxygen pressure. Approximately 35 min was required to reach a set temperature of 800°C. The pressurization time was on the order of seconds. Following oxidation, a dynamic postoxidation anneal was obtained by purging dry nitrogen between the source and the purge vent. The furnace was then lowered and the samples allowed to cool overnight in the vessel.

For comparison purposes, a number of dry thermal oxides were prepared in conventional, 1 atm Thermco furnaces at temperatures of 1000° and 1100°C. Following the oxidation, the furnace was flushed and a postoxidation anneal was performed in dry nitrogen. The samples were pulled from the furnace into a quartz "white elephant" end cap and allowed to cool.

MOS capacitors were formed by depositing circular aluminum electrodes (approximately 0.003 cm² in area) onto the front oxide surface. To provide substrate contact, the back oxide was stripped using HF and covered with aluminum. The aluminum was deposited using an Airco electron-beam metallization system. A postmetallization anneal (PMA) was found to significantly reduce the net charge in as-oxidized samples and was employed routinely. The PMA was performed at 450°C in dry nitrogen for 30 min. Oxidation conditions used for thermal oxide preparation are listed in Table I.

Program of measurements.—Basic measurement techniques.—The basic electrical properties Q_f (oxide fixed charge) and D_{it} (interface trap density as a function of energy in the silicon bandgap), as well as oxide charging characteristics, were obtained using standard capacitance-voltage measurement techniques. Complete details concerning instrumentation and data reduction are available in Ref. (19).

High frequency capacitance-voltage (HF CV) characteristics were obtained using a Boonton 71D capacitance meter operating at 1 MHz. Ramp-IV, or quasi-static capacitance-voltage (QS CV) characteristics, were obtained using an HP 4140B picoammeter/voltage-source measurement system. Q_f was determined via comparison of the measured flatband voltage with that expected for an ideal capacitor. D_{it} was calculated from a comparison of the experimental HF and QS CV curves (20). Substrate doping densities were determined from measured HF CV curves, using oxide thickness values obtained via ellipsometry.

CV and avalanche injection experiments were executed under computer control, using either an HP 9845B computer with an HP IEEE-488 Interface Bus capability (for hole injection and associated CV measurements) or an Apple II with an Interactive Microwave ADALAB Data

Table I. Sample preparation conditions

T_{ox} (°C)	P_{ox} (atm)	t_{ox} (min)	d_{ox} (nm)	g (nm/min)	t_{POA} (h)
A. Varying oxidation temperature					
1100	1	35	77.3	2.1	—
1000	1	105	72.5	0.69	—
900	2	165	85.6	0.52	—
800	150	40	72.5	1.8	—
685	500	165	75.9	0.46	—
635	500	540	66.3	0.12	—
B. Growth rate variation at constant temperature					
800	15	225	86.0	0.4	—
800	73	70	82.0	1.2	—
800	160	40	72.5	1.8	—
800	300	24	79.0	3.3	—
800	500	18	83.0	4.6	—
C. POA time at constant oxidation temperature					
800	150	40	77.0	1.9	0
800	150	40	65.0	1.6	1.5
800	150	40	66.0	1.6	5
800	150	40	73.0	1.8	10
685	500	165	71.0	0.43	0
685	480	165	75.0	0.45	1.5
685	500	165	75.0	0.45	5
685	490	165	75.0	0.45	10
D. p-Substrate samples used in electron-injection experiments					
685 ^a	500	60	39.8	0.66	0
685 ^a	500	60	47.3	0.79	5
685 ^b	500	165	90.0	0.54	0
685 ^b	500	165	90.0	0.54	5
1000	1	105	79.3	0.75	0
1000	1	105	79.3	0.75	0.5

T_{ox} = Oxidation temperature. P_{ox} = Oxidation pressure. t_{ox} = Oxidation time. d_{ox} = Average sample thickness. g = Average growth rate = d_{ox}/t_{ox} . t_{POA} = Time of postoxidation anneal.

^a Wet DRYPOX.

^b Dry DRYPOX. See text for explanation of wet and dry.

Acquisition System (for electron injection and associated CV measurements).

Avalanche injection measurements.—Oxide charge trapping kinetics were investigated using constant current avalanche injection techniques. The circuitry used to produce and measure avalanche currents was based on that developed by Nicollian *et al.* for electron injection (21). In this technique, application of a high voltage sinusoidal signal to the sample results in the injection of a dc current of minority carriers into the gate oxide; some fraction of these carriers is trapped as the carriers traverse the oxide film. The injection current is maintained constant using a feedback mechanism which applies a corrective dc voltage to the gate electrode in response to changes in a preset current level. The circuit described by Nicollian *et al.* was modified for the present work by employing a triangular driving waveform, as suggested by Aitken and Young (22).

Oxide charging during avalanche injection was monitored via automatic measurement of the flatband voltage as a function of the cumulative injection fluence. This was accomplished by periodically interrupting the injection to measure the flatband voltage. The flatband voltage measurements generally required 5–10s.

The cumulative injection fluence, $F(t)$, was defined as

$$F(t) = \frac{1}{q} \int_0^t j dt \quad [1]$$

where j is the dc avalanche current density and q is the elementary charge. Typically, hole injections were performed at a dc hole current of 0.125 nA (40 nA/cm²) and proceeded for 40s between flatband voltage measurements. In all cases presented here, hole currents were set at or below 0.22 nA (70 nA/cm²). The large corrective feedback voltages necessary to maintain current densities larger than this value were observed to cause electron injection from the gate electrode via Fowler-Nordheim emission (19). As a result of experimental limitations, a

drop in hole current of up to 0.05 nA (16.7 nA/cm²) was observed over the course of the measurement. This drop was accounted for by measuring the hole current and directly calculating the fluence for each data point from Eq. [1].

Current densities during electron injection experiments were typically 20 μA/cm². The electron injection current did not vary by more than 1% from the preset level; therefore, a measurement of the current during each injection cycle, as described for hole injection, was not necessary. The procedure for electron injection and analysis has been described previously (14).

The flatband voltage measured relative to its value prior to charge injection (*i.e.*, the flatband voltage shift) is a measure of the centroid-weighted areal density of charge trapped in the oxide layer. The number density of oxide traps is obtained using the relation

$$N_{ot}(F) = |Q_{ot}(F)|/q = -C_{ox}\Delta V_{FB}(F) \quad [2]$$

where $Q_{ot}(F)$ is the areal oxide charge density, C_{ox} is the oxide capacitance per unit area, A is the electrode area, and ΔV_{FB} is the flatband voltage shift.

Hole trapping analysis.—Flatband voltage shift data were analyzed using a first-order kinetic model for oxide charge buildup. Such a model assumes the presence of one or more types of oxide charge trap, each of which is characterized by a saturated number density $N(\infty)$ and a capture cross section σ . The number density of filled traps as a function of time, $N_{ot}(t)$, is given by

$$\frac{dN_{ot}(t)}{dt} = \frac{1}{q} j\sigma[N(\infty) - N_{ot}(t)] \quad [3]$$

where j is the injected current density.

The hole trapping data of the present work were best fit assuming the presence of two types of hole traps. In this case, the solution to Eq. [3] for constant current density j , and with the initial condition $N_{ot}(t = 0) = 0$ is

$$N_{ot,h}(F_h) = N_{1h}(\infty) (1 - \exp(-\sigma_{1h}F_h)) + N_{2h}(\infty) (1 - \exp(-\sigma_{2h}F_h)) \quad [4]$$

Equation [4] gives the number density of trapped holes, $N_{ot,h}$, as a function of the cumulative hole injection fluence, F_h . The filling of oxide charge traps by first-order kinetics has been discussed extensively in the literature (14, 23, 24).

An iterative chi-squared curve-fitting procedure was used to fit Eq. [4] to the data, and the best-fit values of the parameters $N_{1h}(\infty)$, $N_{2h}(\infty)$, σ_{1h} , and σ_{2h} were obtained. Additionally, the total saturated hole trap density, $N_h = N_{ot,h}(\infty) = N_{1h}(\infty) + N_{2h}(\infty)$, and the initial hole trapping efficiency, η , were calculated from these parameters. The initial trapping efficiency is defined as the slope of the charging curve extrapolated to zero fluence, and is given by

$$\eta = \left. \frac{dN_{ot,h}}{dF} \right|_{F=0} = \sigma_{1h}N_{1h} + \sigma_{2h}N_{2h} \quad [5]$$

Electron trapping analysis.—During electron injection, an increase in the flatband voltage due to a buildup of negative charge throughout the oxide bulk was observed. In most cases, a subsequent decrease, or "turnaround," in the flatband voltage shift was observed at a fluence dependent upon processing conditions. The turnaround has been interpreted as being due to the generation of donor-like electron trapping centers in the vicinity of the Si-SiO₂ interface (25). These centers are believed to be responsible for the so-called "anomalous positive charge" which has been widely studied (24, 25-27).

Combining the effects of electron trapping in the bulk and the generation of anomalous positive charge at the Si-SiO₂ interface, the net oxide charging is described by the equation

$$N_{ot,e}(F_e) = -N_{ot,b}(F_e) + N_{ot,i}(F_e) \quad [6]$$

where $N_{ot,b}$ and $N_{ot,i}$ are the number density of filled bulk oxide electron traps and interface anomalous positive charge, respectively. Equation [6] gives the number density of net oxide charge, $N_{ot,e}$, as a function of the cumulative electron injection fluence, F_e . The individual charging components are given by

$$N_{ot,b}(F_e) = N_{ot,b}(\infty) [1 - \exp(-\sigma_c F_e)] \quad [7a]$$

$$N_{ot,i}(F_e) = N_{ot,i}(\infty) [1 - \exp(-\sigma_e F_e)] \quad [7b]$$

where $N_{ot,b}(\infty)$ and $N_{ot,i}(\infty)$ are saturated trap densities and σ_c and σ_e the capture cross sections for bulk electron traps and anomalous positive charge generation, respectively. Equations [6] and [7] were fit to the electron trapping data using a chi-squared fitting routine to obtain the best fit parameters $N_{ot,b}(\infty)$, $N_{ot,i}(\infty)$, σ_c , and σ_e .

Experimental Results

Basic electrical characteristics: Q_f and D_{it} .—In measuring oxide fixed charge densities, between five and ten capacitors from a given wafer were tested. The substrate doping density was 3-5 Ω-cm. Midgap interface trap densities $D_{it,m}$ (*i.e.*, D_{it} taken 0.55 eV above the silicon valence bandedge) were measured on only two or three capacitors per wafer. For both measurements, a standard deviation of 20% was observed on a wafer-to-wafer basis.

Samples were selected periodically throughout the course of these experiments and tested for mobile ion contamination using conventional "bias-temperature-stress" techniques [Ref. (18), p. 428]. The results of these tests indicated a density of less than 8×10^{10} cm⁻² mobile ions in all the oxides tested.

Oxide fixed charge and midgap interface trap densities were examined as a function of oxidation temperature in the range 635°-1100°C. The oxidation conditions for this set of oxides are listed in Table IA. Q_f values were in the range $0.9-3 \times 10^{11}$ cm⁻², and $D_{it,m}$ values were in the range $1-3 \times 10^{11}$ cm⁻²-eV⁻¹. No consistent trend in either parameter was observed over the temperature range 635°-900°C. Oxides grown in conventional furnaces at 1000° and 1100°C had values of Q_f and $D_{it,m}$ which were lower by a factor of approximately 2.

The effect of oxide growth rate at 800°C oxidation temperature was investigated by varying the oxygen pressure. Specific oxidation conditions employed to obtain this growth rate variation are listed in Table IB. Q_f and $D_{it,m}$ as a function of oxide growth rate are listed in Table II. For both properties, a variation of less than a factor of 2 is indicated for an oxide growth rate variation of more than a factor of 10.

Q_f and $D_{it,m}$ were investigated as a function of post-oxidation anneal time between 0 and 10h for wafers oxidized at 800° and at 685°C. The oxidation conditions employed are listed in Table IC. In all cases, the POA was performed at the oxidation temperature. $D_{it,m}$ and Q_f obtained as a function of POA time are listed in Table III. These data indicate a reduction in both Q_f and D_{it} for increasing POA time at both temperatures.

The effect of a 5h POA on oxides fabricated at 685°C on p-type substrates is given in Table IV. This table also contains data obtained on a conventional thermal oxide

Table II. Oxide growth rate investigation

g (nm/min)	Q_f (10^{11} cm ⁻²)	$D_{it,m}$ (10^{11} cm ⁻² -eV ⁻¹)	N_h (10^{12} cm ⁻²)
0.4	1.4	1.8	3.0
1.2	1.7	1.5	3.5
1.8	2.1	1.2	4.1
3.3	2.4	1.7	3.1
4.6	1.3	1.8	3.3

As-grown oxide fixed charge Q_f , midgap interface trap density $D_{it,m}$, and total hole trap density N_h as a function of oxide growth rate g . Oxidation temperature is 800°C. Estimated error in Q_f and $D_{it,m}$ is $\pm 20\%$; in N_h , it is $\pm 10\%$.

Table III. Postoxidation anneal time investigation

T_{ox}/P_{ox} (°C/atm)	t_{POA} (h)	Q_f (10^{11} cm^{-2})	$D_{it,m}$ ($10^{11} \text{ cm}^{-2} \text{ eV}^{-1}$)	N_h (10^{12} cm^{-2})
800/150	0	2.4	0.75	3.2
	1.5	1.7	0.75	3.4
	5	0.8	0.2	3.0
	10	1.2	0.48	3.6
685/500	0	2.5	0.45	4.9
	1.5	0.85	—	4.5
	5	0.6	0.45	4.3
	10	0.27	0.3	—

As-grown oxide fixed charge Q_f , midgap interface trap density $D_{it,m}$, and total hole trap density N_h as a function of POA time. The estimated error in Q_f and $D_{it,m}$ is $\pm 20\%$; in N_h , it is $\pm 10\%$.

Table IV. Basic electrical properties

Sample/anneals	Q_f (10^{11} cm^{-2})	$D_{it,m}$ ($10^{11} \text{ cm}^{-2} \text{ eV}^{-1}$)
685°C dry DRYPOX		
No POA	2.3	0.7
685°C POA (5h)	-1.1	0.2
685°C wet DRYPOX		
No POA	2.9	1
685°C POA (5h)	0.9	0.7
1000°C 1 atm		
No POA	0.4	0.7
1000°C POA (0.5h)	-0.5	0.5
730°C LPCVD		
No PDA	1	4
1000°C PDA (0.5h)	7	1

Comparison of oxide fixed charge Q_f and midgap interface trap density D_{it} using 685° and 1000°C thermal and 730°C LPCVD oxidation technologies. Estimated error for all entries is $\pm 20\%$. See text for definition of anneals.

grown at 1000°C in 1 atm dry oxygen. The POA specified for the thermal oxides refers to a postoxidation anneal at the oxidation temperature. Oxidation conditions are given in Table ID. Table IV also gives Q_f and $D_{it,m}$ values obtained on a 50 nm thick, 730°C LPCVD oxide film (14). The PDA listed for this oxide refers to a 30 min post-deposition anneal. It should be noted that the LPCVD oxides were metallized using a tungsten filament evaporation system rather than the E-beam metallization system used for the DRYPOX and conventional oxides.

Table IV lists data obtained on two sets of 685°C thermal oxides produced under nominally identical conditions. Although Q_f and $D_{it,m}$ values were similar for both the "wet" and "dry" oxides, electron-injection experiments revealed differences in oxide quality. These differences will be discussed below. The similarity in basic electrical quality following POA/PDA treatments is noteworthy.

Avalanche hole injection.—High frequency and quasi-static CV curves obtained before and after a typical hole injection experiment are shown in Fig. 2a for a 685°C

DRYPOX oxide. The shift in the capacitance curves to more negative voltage is a result of the buildup of positive charge near the Si-SiO₂ interface.¹ In addition, the distortion in both the high frequency and quasi-static capacitance curves following hole injection is indicative of the generation of interface traps.

Interface trap densities were observed to increase throughout the silicon bandgap with increasing hole injection fluence, as shown in Fig. 2b. These spectra are typical of those obtained on all of the samples examined. Specifically, a nonuniform increase in D_{it} toward the upper half of the bandgap (0.7-0.9 eV above the valence bandedge), and a uniform increase throughout the mid-gap region (0.2-0.7 eV above the valence bandedge) were observed.

Reproducibility experiments were performed on five wafers processed under nominally identical conditions. The results indicated a variation of 20% in the individual kinetic parameters $N(\infty)$ and σ_h . However, the total hole trap density, $N_h = N_{th}(\infty) + N_{th}(\infty)$, displayed a variation of less than 10% on a wafer-to-wafer basis. Variations on a single wafer were observed to be approximately 10% in the individual kinetic parameters and 5% in the total hole trap density.

The only significant variation observed in hole trapping characteristics was as a function of oxidation temperature. This variation is shown in Fig. 3, where the total hole trap density N_h is plotted for oxidation temperatures ranging from 635° to 1100°C. Figure 3 displays a minimum in the total hole trap density at an oxidation temperature between 800° and 900°C. Average values for individual kinetic parameters obtained from several wafers at each temperature, as well as the total hole trap density and initial trapping efficiency η , are listed in Table V. Specific oxidation conditions for these runs are listed in Table IA. Figure 4 shows hole charging curves representative of each oxidation temperature.

Low resistivity substrates (0.1 Ω -cm) oxidized under the conditions listed in Table IB were examined for variations in hole trapping kinetics with varying oxide growth rate at a constant oxidation temperature of 800°C. Total hole trap densities for this set of oxides are listed in Table II. No consistent trend in hole trapping kinetics was observed over the range in growth rate studied.

Low resistivity samples (0.1 Ω -cm) oxidized under the conditions listed to Table IC were examined for the effect of varying postoxidation anneal time on the hole trapping kinetics. Table III lists total hole trap densities obtained from these samples. Evidently, a POA under the conditions investigated has little effect on the hole trapping kinetics.

Aitken (28) has demonstrated that the use of electron beam metallization may introduce neutral traps into the MOS oxide. To investigate this effect in the present work, hole trapping kinetics were compared between two samples, one metallized using electron-beam evaporation techniques, the other using tungsten filament evaporation.

A relaxation of the flatband voltage shift following hole injection was observed in all of the samples studied. The post-injection C-V curves of Fig. 2a and the D_{it} spectra of Fig. 2b were measured 300h following hole injection, during which time the flatband voltage shift had relaxed by some 30% of its value immediately following the injection.

Table V. Hole trapping kinetics

T_{ox} (°C)	N_{th} (10^{12} cm^{-2})	N_{sh} (10^{12} cm^{-2})	σ_{th} (10^{-16} cm^2)	σ_{sh} (10^{-15} cm^2)	N_h (10^{12} cm^{-2})	η (10^{-3})
635	2.2 ± 1.4	3.8 ± 1.4	9 ± 8	16 ± 0.2	6 ± 0.0	88 ± 5
685	1.4 ± 0.4	3.8 ± 0.5	2.2 ± 0.6	16 ± 7	5.2 ± 0.2	65 ± 3
800	1.2 ± 0.3	2.6 ± 0.5	1.4 ± 0.2	13 ± 2	3.8 ± 0.6	35 ± 8
900	1.2 ± 0.1	2.6 ± 0.4	1.6 ± 0.2	10 ± 2	3.8 ± 0.4	27 ± 10
1000	1.3 ± 0.4	2.8 ± 0.4	2.6 ± 0.6	17 ± 0.4	4.1 ± 0.1	55 ± 12
1100	0.7 ± 0.2	6.8 ± 0.2	2.0 ± 0.4	28 ± 3	7.5 ± 0.4	188 ± 17

Average kinetic parameters for hole trapping as a function of oxidation temperature. Errors indicated for $T_{ox} = 685^\circ, 800^\circ,$ and 1000°C represent one standard deviation about the mean. For the other temperatures, errors indicate the range of values observed.

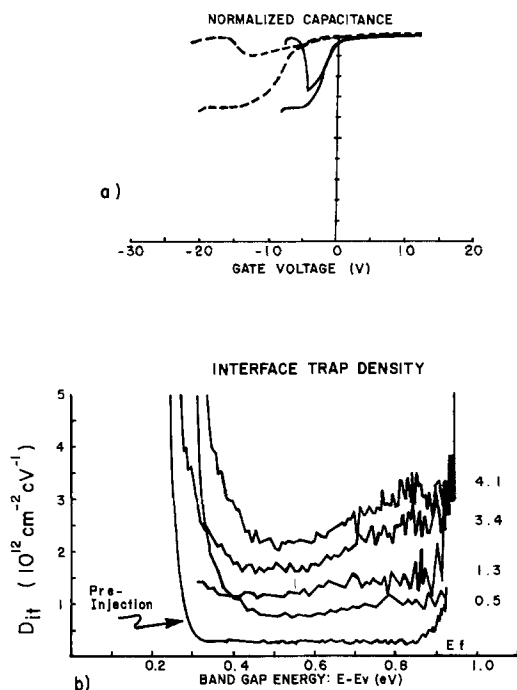


Fig. 2. 685°C DRYPOX oxides. a: High frequency and quasi-static capacitance-voltage characteristics before (solid line) and after (dashed line) avalanche hole injection to a fluence of $3.4 \times 10^{13} \text{ cm}^{-2}$. b: Interface trap densities vs. energy above the silicon valence bandedge (E_v) and following injection to the fluence indicated. Fluences are in units of 10^{13} cm^{-2} .

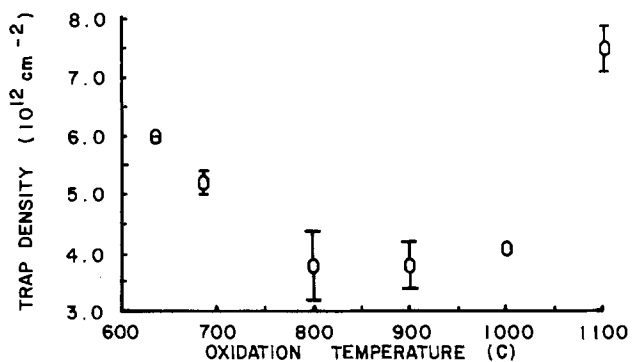


Fig. 3. Total hole trap density as a function of oxidation temperature. No POA was employed. Error bars for $T_{\text{ox}} = 685^\circ, 800^\circ,$ and 1000°C represent one standard deviation about the mean. For the other temperatures, the errors bars represent the range of values observed.

tion. The results indicated that (i) the hole trapping efficiency was larger by approximately a factor of 2 in samples metallized via electron-beam evaporation, (ii) the hole trap density was approximately 20% larger in samples metallized via filament evaporation, and (iii) the oxidation temperature dependence of the hole trapping kinetics was the same using either metallization technique (19).

Avalanche electron injection.—Avalanche electron injection was performed on the samples listed in Table ID, as well as on LPCVD oxides deposited at 730°C. Fixed charge densities Q_f and interface trap densities $D_{it,m}$ for all of these samples are presented in Table IV.

Typical high frequency and quasi-static C-V curves obtained before and after electron injection are shown in Fig. 5a for a 685°C DRYPOX oxide. The shift in the capacitance curves to more positive voltage is due to the buildup of negative charge throughout the bulk of the oxide. In addition, the distortion in both the high frequency and quasi-static capacitance curves is indicative of the buildup of interface traps. Interface trap densities determined before and after electron injection are given in Fig. 5b, where D_{it} is compared to samples oxidized at 685°C in

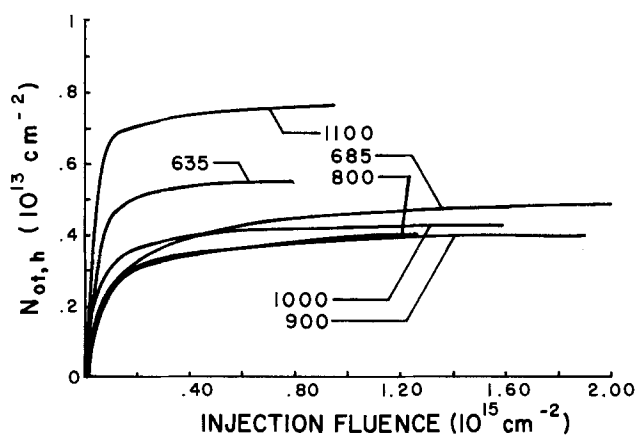


Fig. 4. Hole charging curves with oxidation temperature as a parameter. Oxidation temperatures are shown in degrees centigrade.

500 atm pressure and at 1000°C in 1 atm pressure. Figure 5b demonstrates that D_{it} following electron injection is higher in the 685°C oxide than in the conventional oxide by a factor of approximately 3.

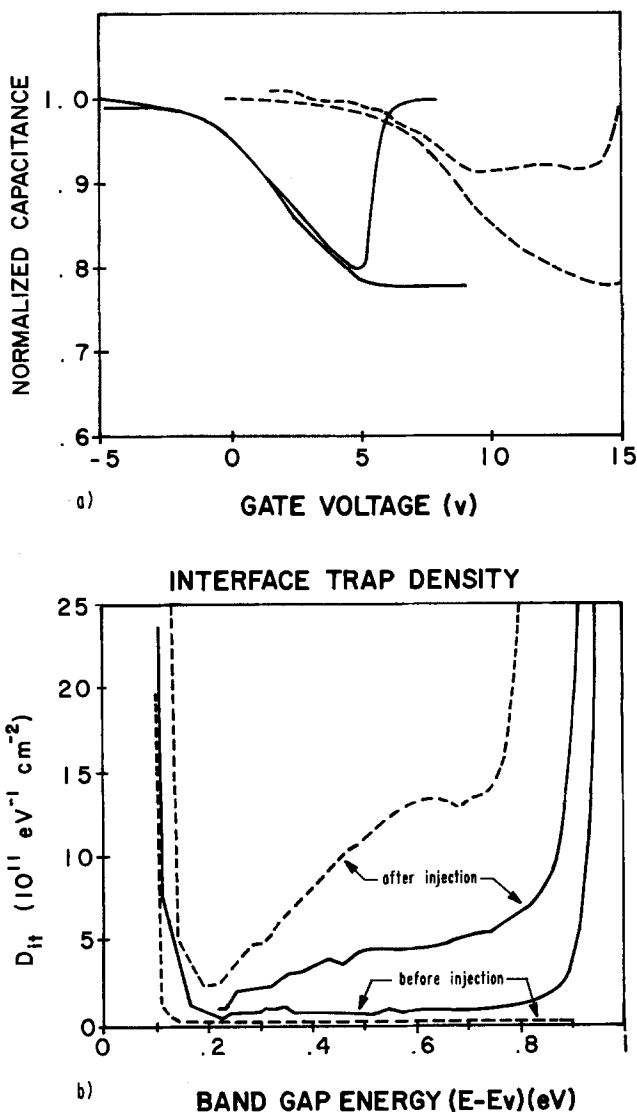


Fig. 5. (a) High frequency and quasi-static capacitance-voltage characteristics and (b) interface trap densities vs. energy above the silicon valence bandedge (E_v) before and after avalanche electron injection to a fluence of $3 \times 10^{18} \text{ cm}^{-2}$. In a, solid lines are before and dashed lines are after injection for a 685°C, 500 atm dry DRYPOX oxide. In b, solid lines are for a 1000°C conventional oxide and dashed lines are for a 685°C DRYPOX oxide.

Individual kinetic parameters for electron trapping in 685°C DRYPOX, 1000°C conventional, and 730°C LPCVD oxide films are given in Table VI. This table shows that the dominant capture cross section for bulk electron trapping, σ_e , is a function of sample preparation. In particular, the 1000°C conventional oxides and the "dry" DRYPOX samples had dominant capture cross sections in the range $(3-5) \times 10^{-18} \text{ cm}^2$. The "wet" DRYPOX samples exhibited a dominant capture cross section of $1 \times 10^{-17} \text{ cm}^2$. The presence of an electron trap with a capture cross section in the range 10^{-17} cm^2 has been associated with water contamination in SiO_2 films (24). Therefore, it is plausible that the DRYPOX films exhibiting the larger electron capture cross section were inadvertently contaminated with water. It was for this reason that the designations "dry" DRYPOX and "wet" DRYPOX were introduced. These assignments are consistent with the larger growth rates observed for the wet oxides (see Table ID).

Differences in electron charging curves between wet and dry DRYPOX samples are evident in Fig. 6. The so-called "flatband voltage turnaround" is evident in the dry oxide at a fluence of $2 \times 10^{18} \text{ cm}^{-2}$, and in the wet oxide at $0.25 \times 10^{18} \text{ cm}^{-2}$. A pronounced turnaround effect has also been associated with water contamination (24, 26). As discussed in the Electron trapping analysis section, the flatband voltage turnaround is due to the buildup of anomalous positive charge at the Si-SiO₂ interface, and was modeled by a second trap density and capture cross section. Values for these kinetic parameters are listed in Table VI as $N_{ot,i}$ and σ_e , respectively.

Prior to a PDA, electron trapping in the LPCVD sample was so extensive that oxide breakdown occurred at fluences too low to allow extraction of the trapping parameters. However, this low fluence data did allow accurate determination of the trapping efficiency, η , which was approximately 2×10^{-3} . This value is two orders of magnitude larger than the efficiency exhibited by the unannealed 685°C dry DRYPOX oxides. Following a PDA, the trapping efficiency of the LPCVD oxides were comparable to those of the DRYPOX samples.

Figure 7 compares electron charging curves in dry DRYPOX and 1000°C conventional oxides. The effect of POA on these charging curves is also explored. Figure 7 demonstrates that the oxide-trapped charge density and, consequently, the initial electron trapping efficiency, were greater in the 685°C oxide by a factor of approximately 2. A POA had little effect on the bulk trapping of these oxides, but reduced the turnaround effect in all cases. These results are also evident in the kinetic parameters of Table VI. Due to the limited amount of data, no kinetic parameters for the turnaround process could be extracted for the 1000°C oxides.

Table VI. Electron trapping kinetics

Sample/anneals	$N_{ot,b}$ (10^{11} cm^{-2})	$N_{ot,i}$ (10^{11} cm^{-2})	σ_c (10^{-18} cm^2)	σ_e (10^{-18} cm^2)
685°C dry DRYPOX				
No POA	30	10	4	0.4
685°C POA	30	9	3	0.2
685°C wet DRYPOX				
NO POA	40	30	10	1
685°C POA	20	20	10	1
1000°C 1 atm				
No POA	8	—	5	—
1000°C POA	11	—	4	—
730°C LPCVD				
No PDA	—	—	—	—
1000°C PDA	10	—	10	—

Comparison of electron trapping kinetic parameters using 685°C and 1000°C thermal and 730°C LPCVD oxidation technologies. LPCVD data taken from Ref. (14). Estimated error for all entries is $\pm 20\%$. See text for definition of anneals.

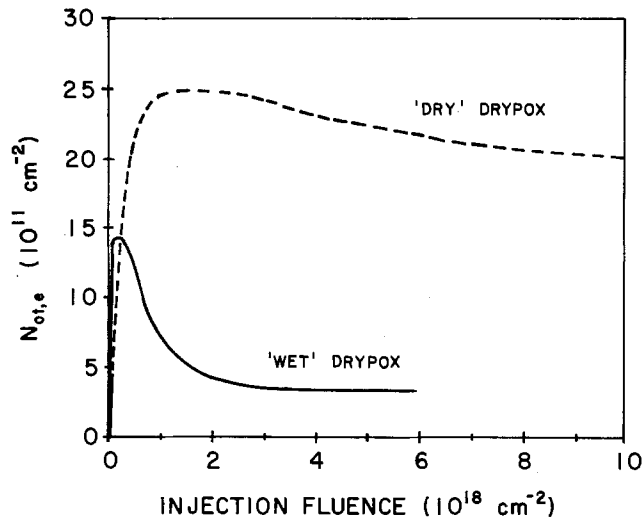


Fig. 6. Electron charging curves for wet and dry DRYPOX oxides

The use of electron-beam metallization may contribute to electron trapping in oxide films (28). No study of electron trapping in DRYPOX oxides metallized by techniques other than electron-beam evaporation was made.

Summary and Discussion

As-grown oxide characteristics.—In general, the levels of oxide fixed charge and interface trap densities found in DRYPOX samples are similar to those reported in the literature (29, 30) for oxides produced using conventional techniques. In particular, oxide fixed charge levels on the order of 10^{11} cm^{-2} were observed, and were found to decrease upon postoxidation annealing. Interface trap densities on the order of $10^{11} \text{ cm}^{-2} \cdot \text{eV}^{-1}$ were observed following a conventional postmetallization anneal. Variations in oxidation temperature over the range 635°–1100°C and in oxide growth rate at 800°C over the range 0.4–4.6 nm/min had no systematic effect on these properties.

Low levels (less than $8 \times 10^{10} \text{ cm}^{-2}$) of mobile sodium contamination were detected in all of the oxides investigated. However, as noted in the Basic electrical characteristics section, values of Q_f and D_{it} were lower in the conventional oxides than in the 1 atm oxides by a factor of approximately 2. Because no dependence of either Q_f or D_{it} on oxidation pressure was observed (recall the oxide growth rate experiments), this difference is believed to be due to systematic differences in cleanliness between the pressure vessel and the conventional oxidation tubes. Specifically, the pressure vessel allowed the oxidation ambient to contact both the silicon wafers and the vessel

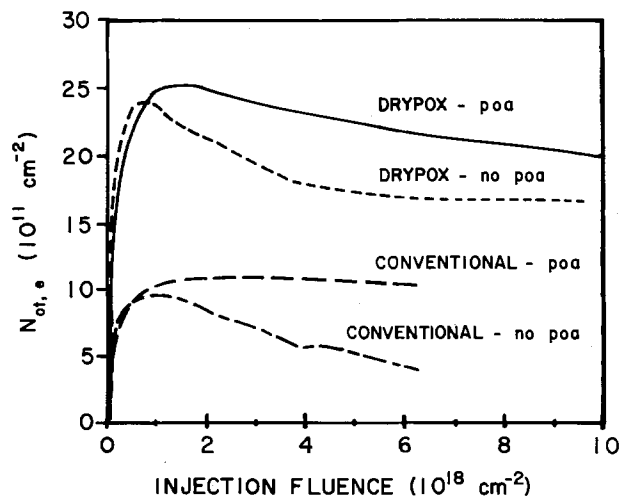


Fig. 7. Comparison of 685°C DRYPOX and 1000°C conventional oxides, with and without a POA at the oxidation temperature.

wall, thereby introducing the possibility of contamination by oxide scale from the vessel wall.

Some differences in the annealing behavior of the low temperature oxides, as compared with conventional oxides, were noted. Specifically, the time required to minimize oxide fixed charge levels was increased with respect to that required at higher temperatures. At anneal temperatures of 1000°C, a minimum in oxide fixed charge has been observed following a POA for approximately 30 min (29). Deal (30) reports a minimum in oxide fixed charge following a POA for 10-20 min at anneal temperatures between 950° and 1100°C. The results of the present work indicate that annealing at 800°C requires an increase of approximately a factor of 10 over these values. After 10h, or an increase of approximately a factor of 20 in POA time, the fixed charge levels observed for a POA at 685°C had not minimized. This behavior is summarized in Table III.

Charge trapping.—Capture cross sections on the order of 10^{-15} and 10^{-14} cm² with corresponding trap densities on the order of 10^{12} cm⁻² were obtained from hole trapping kinetic analyses. Average values for these parameters, obtained as a function of oxidation temperature from 635° to 1100°C, are listed in Table V. Hole trapping kinetic parameters obtained on 1000°C oxides were similar to those reported in the literature (22, 31).

An increase in D_{it} following avalanche hole injection has been observed by Lai (31, 32). Lai reported a uniform increase in fast interface traps throughout the bandgap, with a peak at approximately 0.8 eV above the silicon valence bandedge appearing after the injection and capture of electrons on trapped hole sites. In the present work, a nonuniform buildup of fast interface traps was observed immediately following hole injection, as illustrated in Fig. 2b.

Hole trapping studies have been reported by a number of investigators (22, 33-35). That hole trapping occurs very close to the Si-SiO₂ interface is suggested by etch-back techniques (33) and by photocurrent-voltage measurements (35). A centroid 3-5 nm from the Si-SiO₂ interface is supported by the observation in this work that trapped positive charge decays with time, irrespective of the sign of an applied dc bias, suggesting that quantum mechanical tunneling to the silicon substrate from traps very near the silicon interface is taking place (19, 36). Similar tunneling effects have been observed by other investigators (22).

The most interesting aspect of the hole trapping kinetics obtained in this study is the minimum in total trap density observed between 800° and 900°C. That this effect is due to temperature and not a commensurate change in growth rate was directly demonstrated. A study by Lie *et al.* (1), using dry oxidation at a pressure of 10 atm and over the temperature range 800°-1100°C, suggests a minimum at 900°C in the hole trap density. No analysis of the trapping kinetics was presented by Lie *et al.*

Hole trapping kinetics were unaffected by a post-oxidation anneal for times up to 10h at 800°C and 5h at 700°C. These results are listed in Table III. They differ with the assertion by Lai that a POA below 900°C reduces hole trap densities (31). Hole trapping was also unaffected by a change in growth rate from 0.4 to 4.6 nm/min at an oxidation temperature of 800°C.

The increase in hole trap density observed in this work for oxidation temperatures above 900°C is consistent with a model of hole trapping proposed by EerNisse and Derbenwick (37). These authors suggest that hole traps are produced by viscous flow of the oxide at temperatures greater than 950°C. However, the present work demonstrates that viscous flow is not a necessary condition for the generation of hole traps. Specifically, an increase in the hole trap density is observed for oxidation temperatures below 800°C, where no viscous flow should occur (37, 38).

Another mechanism for the generation of hole traps may be related to the presence of compressive mechanical stress at the Si-SiO₂ interface. A correlation between

Si-SiO₂ interface stress and hole trapping has been suggested by other investigators (31, 39). Irene (38) has suggested that oxide stress develops during oxidation at temperatures below 800°C as a result of the inability of the oxide to undergo viscous flow. The magnitude of stress so generated should increase as the temperature is reduced (38).

It is interesting to note that interface stress generation for oxidation temperatures above 900°C has also been investigated. Specifically, Jaccodine (40) has demonstrated that the difference in the thermal expansion coefficients of Si and SiO₂ results in thermal "warping" of an oxidized wafer, and thereby in Si-SiO₂ interface stress which increases with increasing oxidation temperature. Thus, given that oxide stress increases for oxidation temperatures below 800°C (according to Irene's model) and above 900°C (according to Jaccodine's model), the presence of a minimum at 800°-900°C in the hole-trap density is consistent with models in which stress is responsible for hole trapping.

The argument presented above does not preclude viscous flow as a mechanism for the production of hole traps. In fact, Aitken and Young (22) have observed larger hole trap densities in samples annealed for 90 min at 1000°C than in unannealed samples, suggesting that viscous flow contributes to hole trapping. However, if viscous flow indeed plays a role in hole trapping, the results of the POA experiments in the present work show that it is not operative over a time scale of 10h at 800°C.

Weinberg *et al.* (41) have suggested that hole trapping may be due to an oxygen deficiency at the Si-SiO₂ interface. In terms of their model, the increase in hole trapping below 800°C may be interpreted as a depletion of oxygen from this interface at the lower oxidation temperatures. The data of the present work do not allow a distinction to be made among the relative effects of interface stress, viscous flow, and oxygen deficiency.

Values of bulk and interface trapping kinetics determined from electron-injection experiments are also similar to those reported in the literature for conventional oxides (24). The electron trap density and postelectron injection interface trap densities are slightly higher in the low temperature oxides than in the conventional oxides.

Comparison between a dry DRYPOX oxide and an LPCVD oxide fabricated at 730°C indicates that the electron trapping efficiency of the as-deposited LPCVD oxide was 2 orders of magnitude higher than that of the DRYPOX oxide. The LPCVD oxides required a PDA at 1000°C to produce electron trapping characteristics similar to that of the DRYPOX oxides fabricated entirely at temperatures below 700°C.

Conclusions

High quality oxide films have been produced at temperatures which are low compared with conventional processing by using high pressure oxidation in dry oxygen ambients. Characterization of these oxides has demonstrated their electrical properties, as well as the dependence of these properties on process variables, to be similar to those exhibited by higher temperature thermal oxides prepared using more conventional techniques.

Oxide fixed charge and interface trap levels before electron injection were similar among all of the samples studied. As such, it is interesting to note differences in oxide quality which were manifest only upon electron injection. With regard to electron injection, thermal oxides fabricated at 685°C were found to be superior to LPCVD oxides fabricated at approximately the same temperature.

Acknowledgments

Research at Lehigh University was supported by the U.S. Army Research Office under contract DAAG29-81-K-0007. F. J. Feigl was supported in part by the Electronics and Solid State Science Program of the Office of Naval Research, and M. E. Zvanut by a Sherman Fairchild Fellowship.

Manuscript submitted May 8, 1985; revised manuscript received July 29, 1985. This was Paper 64 presented at the

Toronto, Ontario, Canada, Meeting of the Society, May 12-17, 1985.

ERADCOM assisted in meeting the publication costs of this article.

REFERENCES

- L. N. Lie, R. R. Razouk, and B. E. Deal, *This Journal*, **129**, 2828 (1982).
- L. E. Katz, B. F. Howells, L. P. Adda, T. Thompson, and D. Carlson, *Solid-State Technol.*, **21** (12), 87 (1981).
- D. R. Craven and J. B. Stimmel, *Semicond. Intl.*, 59 (June 1981).
- L. E. Katz and B. F. Howells, *This Journal*, **126**, 1822 (1979).
- R. R. Razouk, L. N. Lie, and B. E. Deal, *ibid.*, **128**, 2214 (1981).
- R. J. Zeto, C. G. Thornton, E. Hryckowian, and C. D. Bosco, *ibid.*, **122**, 1409 (1975).
- R. J. Zeto, C. D. Bosco, E. Hryckowian, and L. L. Wilcox Abstract 82, p. 229, The Electrochemical Society Extended Abstracts, Vol. 77-1, Philadelphia, PA, May 8-13, 1977.
- P. Deroux-Dauphin and L. P. Gonchond, in "VLSI Science and Technology/1984," K. E. Bean and G. A. Rozgonyi, Editors, p. 311, The Electrochemical Society Softbound Proceedings Series, Pennington, NJ (1984).
- D. Fuoss and J. A. Topich, *Appl. Phys. Lett.*, **36**, 275 (1980).
- L. E. Katz and L. C. Kimerling, *This Journal*, **125**, 1680 (1978).
- R. J. Zeto, E. Hryckowian, C. D. Bosco, G. J. IaFrate, R. W. Brower, and C. G. Thornton, Abstract 206, p. 504, The Electrochemical Society Extended Abstracts, Vol. 74-2, New York, NY, Oct. 13-17, 1974.
- R. J. Zeto, N. O. Korolkoff, and S. Marshall, *Solid-State Technol.*, **22**, 62 (1979).
- R. H. Vogel, S. R. Butler, and F. J. Feigl, *J. Electron. Mater.*, **14**, 329 (1985).
- M. E. Zvanut, F. J. Feigl, S. R. Butler, and S. L. Titcomb, *ibid.*, **14**, 343 (1985).
- B. E. Deal, *This Journal*, **127**, 979 (1980).
- T. H. Ning, C. M. Osburn, and H. N. Yu, *J. Electron. Mater.*, **6**, 65 (1977).
- D. J. DiMaria, K. M. DeMeyer, and D. W. Dong, *IEEE Electron. Device Lett.*, **Ed1-1**, 179 (1980).
- E. H. Nicollian and J. R. Brews, "MOS Physics and Technology," John Wiley and Sons, New York (1982).
- L. Trombetta, Ph.D. Thesis, Lehigh University, Bethlehem, PA (1984).
- R. Castagne and A. Vapaille, *Surf. Sci.*, **28**, 557 (1971).
- E. H. Nicollian, C. N. Berglund, P. F. Schmidt, and J. M. Andrews, *J. Appl. Phys.*, **42**, 5654 (1971).
- J. M. Aitken and D. R. Young, *IEEE Trans. Nuclear Sci.*, **ns-24**, 2128 (1977).
- F. J. Feigl, in "VLSI Electronics: Microstructure Science," Vol. 6, N. Einspurch and G. Larrabee, Editors, Chap. 3, pp. 195-204, Academic Press, New York (1983).
- F. J. Feigl, D. R. Young, D. J. DiMaria, S. Lai, and J. Calise, *J. Appl. Phys.*, **52**, 5665 (1981).
- D. R. Young, E. A. Irene, D. J. DiMaria, R. F. DeKeersmaecker, and H. Z. Massoud, *ibid.*, **50**, 6366 (1979).
- R. A. Gdula, *This Journal*, **123**, 42 (1976).
- S. K. Lai and D. R. Young, *J. Appl. Phys.*, **52**, 4231 (1981).
- J. M. Aitken, *J. Non-Cryst. Solids*, **40**, 31 (1980).
- F. Montillo and P. Balk, *This Journal*, **118**, 1463 (1971).
- B. E. Deal, *ibid.*, **121**, 198C (1974).
- S. K. Lai, *J. Appl. Phys.*, **54**, 2540 (1983).
- S. K. Lai, *Appl. Phys. Lett.*, **39**, 58 (1981).
- R. J. Powell and G. F. Derbenwick, *IEEE Trans. Nuclear Sci.*, **ns-18**, 99 (1971).
- M. H. Woods and R. Williams, *J. Appl. Phys.*, **47**, 1082 (1976).
- D. J. DiMaria, Z. A. Weinberg, and J. M. Aitken, *ibid.*, **48**, 898 (1977).
- S. Manzini and A. Modelli, in "Insulation Films on Semiconductors," J. F. Verweij and D. R. Wolters, Editors, p. 112, Elsevier Science Publishers, New York (1983).
- E. P. EerNisse and G. F. Derbenwick, *IEEE Trans. Nuclear Sci.*, **ns-23**, 1534 (1976).
- E. A. Irene, E. Tierney, and J. Angilello, *This Journal*, **129**, 2594 (1982).
- C. W. Gwyn, *J. Appl. Phys.*, **40**, 4886 (1969).
- R. J. Jaccodine and W. A. Schlegel, *ibid.*, **37**, 2429 (1969).
- Z. A. Weinberg, R. D. Young, J. A. Calise, S. A. Cohen, L. C. DeLuca, and V. R. Deline, *Appl. Phys. Lett.*, **45**, 1204 (1984).

Formation of Silicon-on-Insulator Structures by Implanted Nitrogen

L. Nesbit,* S. Stiffler, G. Slusser, and H. Vinton*¹

IBM General Technology Division, Essex Junction, Vermont 05452

ABSTRACT

The formation of a buried Si_3N_4 by high dose nitrogen ion implantation to form a silicon-on-insulator (SOI) structure is studied by transmission electron microscopy (TEM) and by secondary ion mass spectroscopy (SIMS). Silicon wafers are implanted with a dose of $7.5 \times 10^{17} \text{ N}^+$ ion/cm² at an energy of 160 keV at wafer temperatures of 400°, 500°, and 600°C. The wafers are subsequently annealed at 1200°C for 2h to form the buried silicon nitride layer. Both the as-implanted and postannealed microstructures are examined as a function of the implant temperature by TEM cross-sectional analysis. The microstructures of implanted wafers annealed for intermediate times are also examined to elucidate the development of the final microstructure. The as-implanted nitrogen profile and its redistribution during subsequent annealing at 1200°C are studied by SIMS.

The synthesis of silicon-on-insulator (SOI) structures for high density CMOS circuits has received considerable attention in recent years. Various techniques are currently being developed to form SOI structures which will, it is hoped, result in a high quality, thin, single-crystal silicon layer on an insulating layer or substrate (1-3). One of the more promising techniques for forming such a structure is that of ion implantation in which a high dose of a particular atomic or molecular species is implanted into silicon to form a buried insulating compound with silicon upon annealing at an elevated temperature. Most of the interest and research to date has concentrated on the im-

plantation of atomic or molecular oxygen into silicon wafers and then annealing such wafers to form a buried SiO_2 layer. One of the drawbacks to implanting oxygen is that in order to form a sharp Si/SiO₂ interface, an oxygen dose on the order of $2.0\text{-}2.5 \times 10^{18} \text{ O}^+$ ion/cm² must be implanted into the silicon wafers (4-6). This results in a highly defective top silicon layer after a high temperature anneal, typically at 1150°C. This residual top silicon layer is only 100-400 nm thick (4-6), depending on the implant energy and dose. If this top residual silicon layer is too thin, it may be necessary to grow an epitaxial silicon layer to increase the thickness of the top silicon layer (7, 8).

Implanting nitrogen to form SOI structures has several possible advantages over implanting oxygen (9). First of all, hot filament, high current nitrogen implant sources

*Electrochemical Society Active Member.

¹Present address: University of Vermont, Burlington, Vermont 05401.

with relatively long lifetimes are easier to construct and maintain than similar oxygen sources. Second, the highly defective layer at the top Si/insulator interface for implanted oxygen is absent in the case of implanted nitrogen. This point will be clearly demonstrated in this paper. Third, annealing of the as-implanted nitrogen distribution at sufficiently high temperatures results in the formation of a top silicon layer sufficiently thick so as to preclude the need for a subsequent epitaxial silicon growth step. Finally, a continuous buried silicon nitride layer may be formed at about 40-50% of the dose necessary to form a buried SiO₂ layer with an abrupt top Si/SiO₂ interface (4, 5). These latter two advantages imply that SOI by implanted nitrogen is a potentially simpler process with greater wafer throughput than SOI by implanted oxygen.

The behavior of high doses of implanted nitrogen is substantially different than that of implanted oxygen, both in the as-implanted state and after subsequent annealing. Maeyama *et al.* (10) have shown that the as-implanted nitrogen profile has a gaussian distribution for doses as high as 1.5×10^{18} N/cm² at 150 keV as determined by Rutherford backscattering spectroscopy (RBS). This dose is about 50% in excess of the theoretical dose required for the peak nitrogen concentration to equal that of stoichiometric Si₃N₄. On the other hand, oxygen doses for which the peak oxygen concentration is theoretically in excess of stoichiometric SiO₂ result in the peak oxygen concentration saturating at 66.7 atom percent (a/o) oxygen with the excess oxygen diffusing to the front and back implant tails during implantation (11, 12).

Annealing silicon with a nitrogen dose on the order 1×10^{18} N⁺ ion/cm² at a sufficiently high temperature (*e.g.*, 1200°C) results in a continuous buried polycrystalline silicon nitride layer. Assuming a silicon nitride density of 3.18 g/cm³ (13), a dose of 1.05×10^{18} N⁺ ion/cm² is required at 150 keV for the peak nitrogen concentration to equal that of Si₃N₄. If the dose is too low, a continuous silicon nitride layer will not form, although Tsujide *et al.* (14) found that a dose of 3×10^{17} N⁺ ion/cm² results in silicon nitride precipitates, albeit not a continuous silicon nitride film. Annealing at temperatures less than 1200°C generally does not result in the crystallization of the silicon nitride, even if the dose is on the order of 1×10^{18} N⁺ ion/cm².

Implanting nitrogen at temperatures less than 350°C results in an amorphous top silicon layer, which recrystallizes into polycrystalline silicon upon annealing (9, 15). Implanting at temperatures at or in excess of 350°C apparently results in self-annealing of at least part of this top silicon layer during implantation so as to produce a monocrystalline layer after annealing (9, 15).

For relatively low doses of nitrogen (*e.g.*, 1×10^{16} N⁺ ion/cm²), nitrogen readily diffuses in silicon at anneal temperatures as low as 900° and 1000°C. In particular, the nitrogen tends to diffuse toward and pile up at the surface silicon/native oxide interface and at the interface between the heavily damaged and single-crystal silicon layers (16, 17).

The purpose of this paper is to present microstructural and chemical results on the formation of a buried silicon nitride layer in <100> silicon wafers resulting from high dose, high temperature nitrogen ion implantation. The silicon wafers were implanted with a dose 7.5×10^{17} N⁺ ion/cm² at 400°, 500°, or 600°C. The resulting wafers were then annealed at 1200°C, unless otherwise noted. The microstructure is documented by transmission electron microscopy (TEM) analysis, and the distribution and movement of nitrogen is monitored by secondary ion mass spectroscopy (SIMS).

Experimental Procedure

Silicon wafers of <100> orientation and of p-type doping with a resistivity of 10-12 Ω-cm were first oxidized to grow 25 nm of thermal SiO₂ on the wafer surfaces. The purpose of this oxide layer was to inhibit sputtering and minimize contamination of the underlying silicon surface during implantation. Some thinning of this

top oxide layer was observed as a result of the implantation process. The wafers were implanted on an Eaton NOVA NV-10-160 high current ion implanter with a heated end station. The wafers were mechanically scanned and the temperature was monitored and controlled by a calibrated infrared detector. The wafers were preheated in the implanter to within 50°C of the desired implant temperature before initiating the implantation. Once the implantation started, the wafer temperature was maintained at the intended wafer temperature ($\pm 20^\circ\text{C}$) by a combination of ion beam heating, heat from the end station heaters, and compressed air cooling through the heater coils. The ion beam current was about 4.5 mA across an area of 6.5 cm², resulting in a localized beam current density of 0.7 mA/cm² at the wafer. The wafers were implanted at a 7° tilt at temperatures of 400°, 500°, or 600°C, with 7.5×10^{17} N⁺ ion/cm² accelerated at a potential of 160 keV. The total implantation time for ten 100 mm wafers at a dose of 7.5×10^{17} N⁺ ion/cm² was about 12h. Assuming a gaussian as-implanted nitrogen distribution, the peak nitrogen concentration for a dose of 7.5×10^{17} N⁺ ion/cm² is 3.75×10^{22} N at./cm³, which is about 69% of the nitrogen concentration of stoichiometric Si₃N₄, assuming a density of 3.18 g/cm³ for α-Si₃N₄ (13). The wafers were left unannealed or subsequently annealed at 1100° or 1200°C in argon, with most anneals at the latter temperature. Those wafers which were annealed received 125 nm of chemical vapor deposited (CVD) SiO₂ in order to protect the wafer surfaces from possible oxidation during the high temperature anneal. The actual annealing procedure consisted of inserting the wafers into a furnace set at 1000°C, ramping the furnace temperature up to 1100° or 1200°C, annealing for the designated amount of time, ramping the furnace temperature down to 1000°C, and finally pulling the wafers from the furnace. About 50 min was required to ramp the furnace temperature from 1000° to 1200°C or from 1200° to 1000°C. Typical annealing times at 1100° or 1200°C were 2h, although shorter times were also used in order to determine the development of the annealed microstructure. The microstructure of the implanted nitrogen samples was studied by cross-sectional and planer transmission electron microscopy, using a Philips 400T TEM. The defect densities were determined from planer TEM specimens, with an operating g-vector of <400>. SIMS analysis was accomplished on a Cameca IMS-300 with an O₂⁺ beam at a current of 500 nA. A 750 μm square was rastered and Si₂N⁺ was monitored at a mass of 70 in order to determine the nitrogen profile. An O₂ bleed was supplied at the sample surface in order to minimize artifacts caused by changes in oxygen surface concentration. The lower detection limit of nitrogen in silicon by this SIMS technique was determined to be 6×10^{18} N at./cm³.

Results

As-implanted structure.—The as-implanted microstructure, as determined by TEM cross-sectional analysis, may consist of as many as four distinct layers or regions, as shown in Fig. 1. The measured thicknesses of the top three layers as a function of implantation temperature are listed in Table I. The top layer consists of defective single-crystal silicon with a high dislocation density. Im-

Table I. As-implanted^a layer thicknesses

Implantation temperature (°C)	Layer thicknesses (nm)				
	A	B	C	D = B + C	E = A + B
600	165	165	85	250	330
500	150	55	195	250	205
400	170	0	245	245	170

A = Thickness of the top, highly defective single-crystal Si layer.

B = Thickness of the mottled single-crystal Si layer.

C = Thickness of the amorphous layer.

^a Wafers were implanted with 7.5×10^{17} N⁺ ion/cm² at 160 keV at the designated temperature.

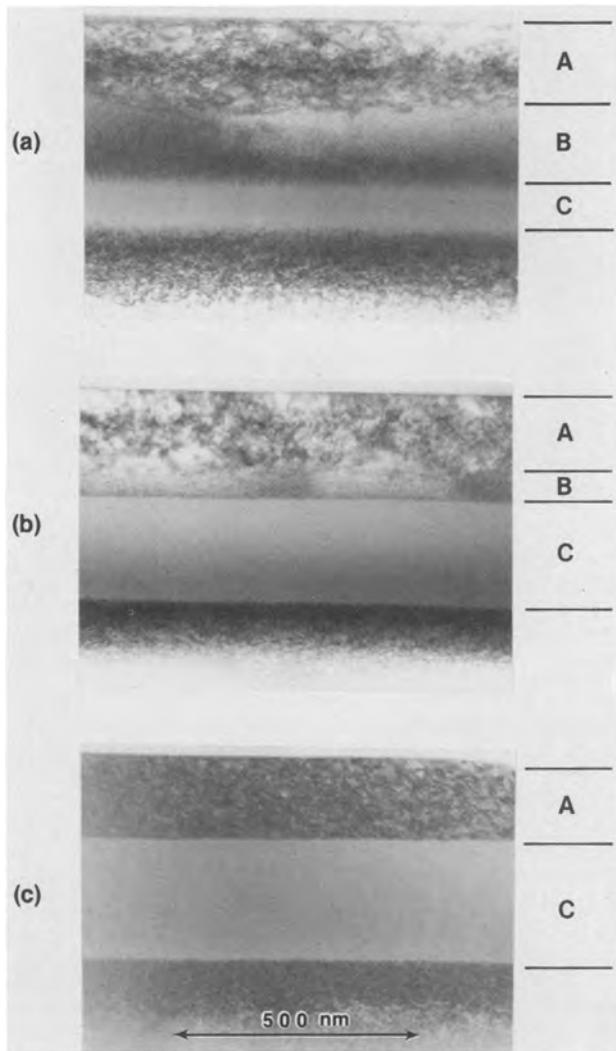


Fig. 1. TEM cross sections of silicon as implanted with 7.5×10^{17} N^+ ion/cm² at 160 keV and 600°C (a), 500°C (b), and 400°C (c). The letters next to the micrographs correspond to the column designations in Table I.

mediately under this top layer is a second layer, which has a mottled or textured appearance, particularly at or near the interface between this layer and the third layer, which is amorphous. Below the amorphous layer is a fourth layer consisting primarily of highly defective single-crystal silicon, although Fig. 1a indicates the presence of some of the mottled microstructure in the fourth layer next to the amorphous layer. This fourth layer is approximately 150 nm thick, regardless of the implant temperature, and corresponds to the lower tail of the implanted nitrogen profile.

The thickness of the top, highly defective single-crystal silicon layer is about 150-175 nm and is designated by the letter A in Table I and Fig. 1. The thickness of this top silicon layer is not a definitive function of the implantation temperature, as indicated in column A of Table I. The density of defects in this layer is on the order of 10^{10} - 10^{11} dislocation/cm² and appears to be independent of the implantation temperature.

The second layer, designated by the letter B, is basically single-crystal silicon as determined by electron diffraction and various other electron microscopy techniques. Despite the mottled appearance of this layer, it contains no classical linear or planar defects, such as dislocations or stacking faults. Lattice imaging of one set of {111} planes in this layer reveals that these planes extend throughout this layer to the completely amorphous layer, except for small, included regions of amorphous material about 1-3 nm diam (see Fig. 2). These small amorphous regions are undoubtedly silicon with a high

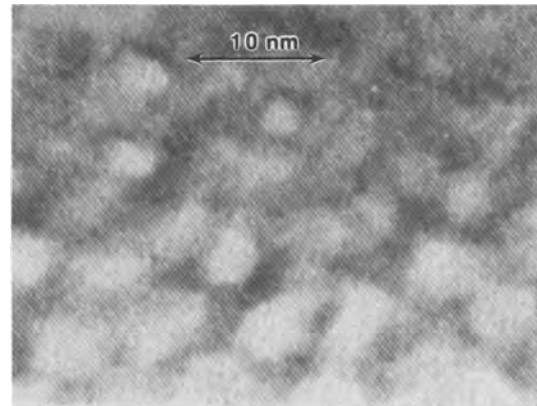


Fig. 2. TEM cross section of silicon as implanted with 7.5×10^{17} N^+ ion/cm² at 160 keV and 600°C. One set of silicon {111} planes is imaged in the second layer near the interface between single-crystal layer and the buried amorphous layer.

concentration of nitrogen, although this hypothesis could not be quantitatively substantiated. The measured periodicity of the mottled microstructure is approximately 5 nm, as determined from micrographs similar to Fig. 1a. The approximate periodicity of the amorphous regions as observed in Fig. 2 is 5-7 nm. Thus, the mottled appearance of this layer in Fig. 1a and 1b is apparently due to the inclusion of small regions of amorphous material in a matrix of single-crystal silicon.

In the electron diffraction pattern corresponding to this layer, the silicon fundamental spots are surrounded by nearly symmetrical halos or rings of diffuse scatter as shown in Fig. 3. The diameters of these rings of diffuse scatter are indicative of a repeated structure with a periodicity of 5-7 nm. These numbers correspond to the periodicity of the mottled microstructure (Fig. 1a) and to the periodicity of the amorphous regions (Fig. 2). Thus, the nearly periodic nature of the mottled microstructure layer gives rise to diffuse scatter about the silicon fundamental spots in electron diffraction.

Below this mottled second layer is a completely amorphous layer, designated by the letter C in Fig. 1 and Table I. As indicated in column C of Table I, the thickness of the totally amorphous layer increases as the implantation temperature decreases. Conversely, the mottled single-crystal silicon layer becomes thinner and ultimately nonexistent at 400°C (Fig. 1c). Examination of column D of Table I indicates that the sum of the mottled and amorphous layer thicknesses is nearly constant as a function of the implantation temperature. Thus, as the implant temperature decreases, the thickness of the amorphous layer increases at the expense of the thickness of the mottled silicon layer. Also, as the implant temperature decreases, the interface between the amorphous layer and the above single-crystal layer becomes more abrupt (cf. Fig. 1a-1c).

SIMS analysis of the as-implanted nitrogen distribution indicates that the nitrogen profile is slightly nongaussian with a higher concentration nitrogen tail toward the surface of the silicon wafer than toward the bulk of the wafer

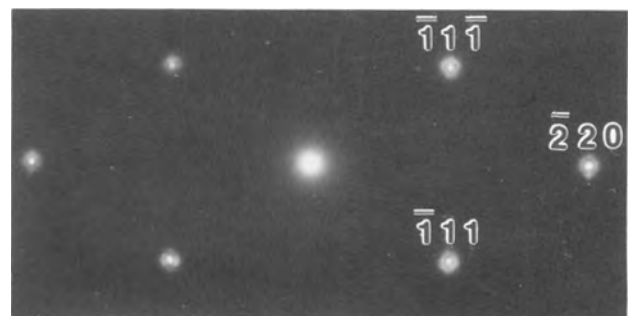


Fig. 3. Silicon $\langle 110 \rangle$ diffraction pattern corresponding to the mottled, second layer in Fig. 1a. Rings of diffuse scatter are observed around the fundamental spots.

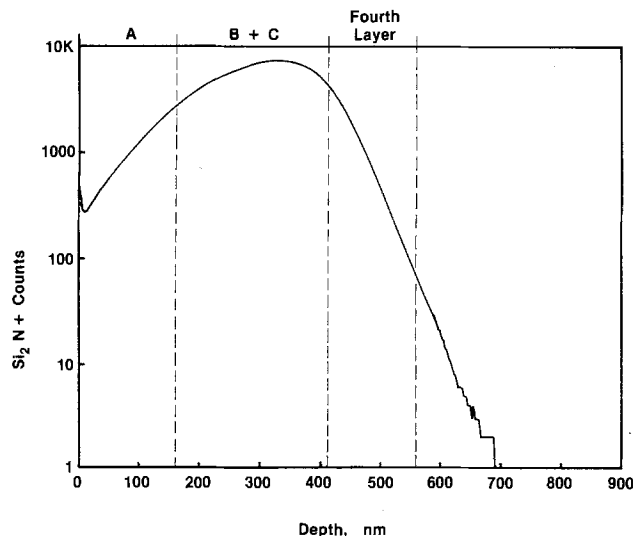


Fig. 4. Nitrogen profile in a $\langle 100 \rangle$ silicon wafer implanted with a dose of $7.5 \times 10^{17} \text{ N}^+$ ion/cm 2 at 160 keV. The approximate thicknesses of the various layers observed in the as-implanted microstructures are indicated by the dotted lines. See Table I for an explanation of letters A, B, and C. The "fourth layer" is the highly defective layer below the amorphous layer.

(see Fig. 4). The general shape of this distribution is typical of a light element implanted at high energies into a heavier element target in which the primary mechanism of ion stopping is electronic interactions between the ions and the atoms. A $\text{Si}_2 \text{N}^+$ count value of 10K in Fig. 4 corresponds to an approximate nitrogen concentration of $3 \times 10^{22} \text{ N at./cm}^3$. As can be seen in Fig. 4, the as-implanted nitrogen peak concentration is less than that predicted by a strictly gaussian distribution. This discrepancy is obviously due to skewness of the nitrogen distribution and to the slight nitrogen pile up at the SiO_2/Si interface. The nitrogen profiles are virtually identical for wafers implanted at 600° and 400°C, implying that the as-implanted nitrogen profile is not a function of the implant temperature. Also, there is no substantial diffusion of nitrogen at 600°C for implantation times as long as 12h. The approximate locations of the various layers tabulated in Table I, as well as the location of the highly defective fourth layer, are indicated in Fig. 4.

Development of the annealed structure.— Upon annealing the as-implanted silicon wafers at 1200°C for 2h a continuous layer of buried, polycrystalline $\alpha\text{-Si}_3\text{N}_4$ forms under a single-crystal silicon layer which has a relatively low defect density. Before proceeding on to a detailed examination of the microstructures of the top silicon and the buried silicon nitride layers, it is helpful to see how the final annealed SOI structure develops from the as-implanted structure. In order to ascertain this development, nitrogen-implanted silicon wafers were annealed at 1200°C for times ranging from 10 min to 2h.

The first event to occur is the nucleation and growth of the polycrystalline $\alpha\text{-Si}_3\text{N}_4$ phase within the amorphous layer of the as-implanted structure. The particular crystalline phase of silicon nitride was determined by electron diffraction. The $\alpha\text{-Si}_3\text{N}_4$ phase nucleates at discrete points and grows in a radial manner out from a given nucleation site within the plane of the buried amorphous layer (see Fig. 5). As a given $\alpha\text{-Si}_3\text{N}_4$ nucleus grows within the amorphous layer, it divides into numerous grains separated by low angle grain boundaries, as determined by electron diffraction and microstructural analysis. The low angle grain boundaries appear to form within a few hundred nanometers of the nucleation site. Eventually, Si_3N_4 grains from adjacent nucleation sites impinge upon each other and form high angle grain boundaries at the points of impingement, as shown in the upper portion of Fig. 5.

For wafers implanted at 600°C, the horizontal growth front of the $\alpha\text{-Si}_3\text{N}_4$ spans the entire thickness of the

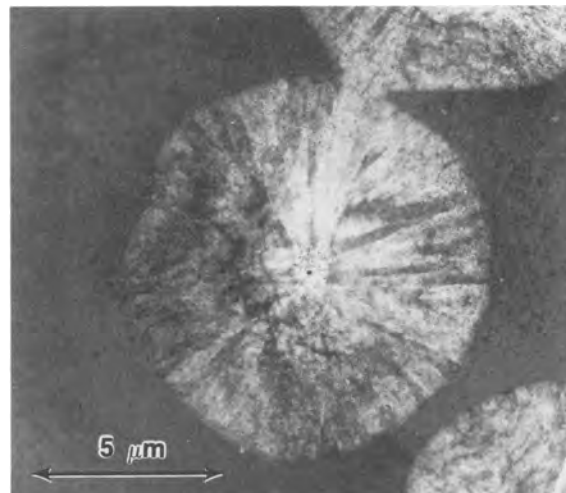


Fig. 5. Planer view of the partially crystallized Si_3N_4 layer in silicon implanted with $7.5 \times 10^{17} \text{ N}^+$ ion/cm 2 at 160 keV and 600°C. The specimen has been annealed at 1200°C for 10 min in argon. Low angle grain boundaries are present between the grains emanating from a common nucleation site. A large angle grain boundary has formed where grains from two adjacent nucleation sites have impinged upon each other.

amorphous layer. Also, for wafers implanted at 600°C, 20-30% of the amorphous layer is crystallized after 10 min at 1200°C, and the layer has completely crystallized after 2h at 1200°C. The horizontal growth rate of the $\alpha\text{-Si}_3\text{N}_4$ phase within the amorphous layer at 1200°C is estimated at 200-400 nm/min. The time necessary to completely crystallize the buried silicon nitride layer depends not only on the growth rate, but also on the nucleation rate of the $\alpha\text{-Si}_3\text{N}_4$ phase within the amorphous layer.

After the $\alpha\text{-Si}_3\text{N}_4$ phase forms within the amorphous layer, a dendritic structure develops perpendicularly to the plane of the buried nitride layer for implant temperatures of 500° and 600°C. This dendritic structure starts to form a few hundred nanometers behind the growth front of the silicon nitride phase at the interface between the amorphous layer and the mottled layer of the as-implanted structure. The dendritic structure is more pronounced (i.e., the dendrites are longer) along the top $\text{Si}/\text{Si}_3\text{N}_4$ interface than along the lower interface for reasons which will be discussed later. Also, the dendritic structure is more pronounced for wafers implanted at 600°C than at 500°C. As the silicon nitride dendrites grow into the mottled silicon layer, the mottled microstructure is transformed to that of defect-free single-crystal silicon, as shown in Fig. 6. The growth front of the silicon nitride in the amorphous layer is to the left of the left edge of the micrograph in Fig. 6. Notice that some of the mottled microstructure is still present in the left portion of the micrograph, but is absent in the right portion of the micro-

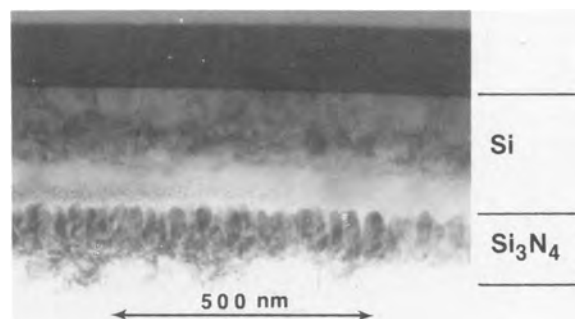


Fig. 6. TEM cross section of silicon implanted with $7.5 \times 10^{17} \text{ N}^+$ ion/cm 2 at 160 keV and 600°C, and subsequently annealed at 1200°C for 10 min in argon. The mottled microstructure just above the $\alpha\text{-Si}_3\text{N}_4$ layer is present in the left portion of the micrograph nearest the amorphous-to-crystalline $\alpha\text{-Si}_3\text{N}_4$ growth front but is absent in the right portion of the micrograph.

graph. This transformation of the mottled microstructure to that typical of defect-free single-crystal silicon occurs only after the nucleation and growth of the underlying α - Si_3N_4 phase. Thus, in the right portion of Fig. 6 an intermediate microstructure has developed consisting of highly defective top silicon layer retained from the as-implanted microstructure, an intermediate, defect-free single-crystal silicon layer, and a bottom, polycrystalline α - Si_3N_4 layer, with a dendritic or cellular structure prominent along the top interface. Continued annealing at 1200°C results in the elimination of the highly defective top silicon layer and the formation of single-crystal silicon with a substantially lower dislocation density (see Fig. 7).

During the 1200°C anneal, the top silicon layer regrows to form a thin layer of $\langle 100 \rangle$ -oriented single-crystal silicon with a dislocation density on the order of 5×10^8 dislocation/cm². This dislocation density is nearly independent of the implantation temperature for wafers annealed at 1200°C, but it is much lower than the 10^{10} - 10^{11} dislocation/cm² in the top silicon layer of the as-implanted specimens. The dislocations in the regrown silicon layer extend from the crystalline nitride layer to the free surface of the silicon layer and are the only observable defects for wafers implanted at 500° or 600°C. Burger's vector analysis indicates that these dislocations are primarily screw in nature.

For the 600°C implant temperature, the α - Si_3N_4 dendrites grow into the mottled silicon layer, but not all of this layer is consumed by the α - Si_3N_4 phase. This is demonstrated by the fact that for the 600°C implant temperature the thickness of the final top silicon layer (column F, Table II) is greater than the thickness of layer A (column A, Table I), but less than the combined thickness of layers A and B (column E, Table I).

For wafers implanted at 400°C and annealed at 1200°C, silicon twins are also observed in the top silicon layer in addition to the dislocations. These twins lie along the silicon {111} planes and begin at about 170 nm below the silicon surface and extend down to the silicon nitride layer. The twins do not extend all the way through the top sili-

con film. The twin nature of these planar defects in Fig. 7c was confirmed by the observation of {111} twin spots in electron diffraction patterns of the top silicon film.

The final microstructure after a 1200°C, 2h anneal consists of a top layer of single-crystal silicon over a buried layer of α - Si_3N_4 for all of the implant conditions investigated. TEM cross sections of silicon implanted at 600°, 500°, or 400°C and subsequently annealed at 1200°C for 2h are shown in Fig. 7a-7c. The thicknesses of the top silicon layer and of the polycrystalline silicon nitride layer are 215-240 and 180-195 nm, respectively (see columns F and G of Table II). These thicknesses do not appear to be dependent on the implantation temperature. However, the overall thickness of the top silicon layer plus the buried silicon nitride layer remains nearly constant with implantation temperature (column H of Table II). Notice that at least for the higher implant temperatures that no highly defective intermediate layer forms just above the buried insulator as in the case of SOI by ion-implanted oxygen (6).

For wafers implanted at 600°C but annealed at 1100°C, the silicon nitride does not crystallize except at gross defects, such as at pits in the top silicon layer. In those scattered instances where the silicon nitride does crystallize, it does so in a manner similar to that at 1200°C. Since the silicon nitride generally does not crystallize at 1100°C, the top silicon layer retains the high density of defects resulting from the nitrogen implantation. These results, along with the above annealing results at 1200°C, indicate that the crystallization of the silicon nitride layer is a prerequisite for the regrowth of the top silicon layer into low defect density silicon.

Nitrogen redistribution.—The redistribution of nitrogen in the silicon as a function of annealing time at 1200°C is shown in Fig. 8. Compare this with Fig. 4. The silicon wafers were implanted with 7.5×10^{17} N⁺ ion/cm² at 160 keV at a temperature of 600°C and subsequently annealed. The ordinate of these graphs is in units of Si_2N^+ counts, which is a measure of the nitrogen concentration in the silicon wafer. Again, a value of 10K Si_2N^+ counts, approximately corresponds to a nitrogen concentration of 3×10^{22} N at./cm³.

After annealing for only 10 min, the nitrogen concentration profile in Fig. 8a displays three distinct peaks. A surface nitrogen peak and a high, broad peak corresponding to the buried silicon nitride layer are readily observed. A slight shoulder is observed on this peak towards the surface of the wafer, and this is believed to correspond to the silicon nitride dendritic structure growing towards the wafer surface. As noted above, the silicon nitride begins to crystallize after only 10 min at 1200°C, and the dendritic structure forms immediately behind the crystallization front. Between the surface nitrogen peak and the peak corresponding to the buried silicon nitride layer is a third nitrogen peak. The concentration of nitrogen at the apex of this peak is lower than the as-implanted nitrogen concentration at this depth (cf., Fig. 4 and 8a). This intermediate nitrogen peak results from the diffusion of nitrogen from this region to either the Si/SiO₂ interface at the silicon surface or to the buried polycrystalline silicon nitride layer. This intermediate nitrogen peak decays with annealing time until it is

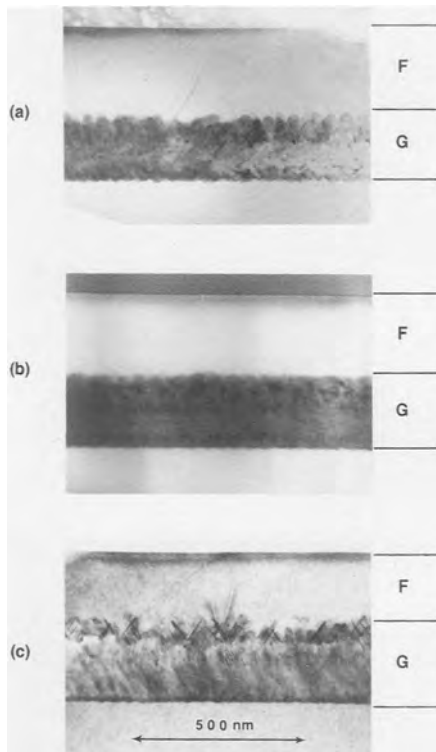


Fig. 7. TEM cross sections of silicon implanted with 7.5×10^{17} N⁺ ion/cm² at 160 keV and 600°C (a), 500°C (b), and 400°C (c), and subsequently annealed at 1200°C for 2h in argon. The letters next to the micrographs correspond to the column designations in Table II.

Table II. Annealed^a Si/Si₃N₄ layer thicknesses

Implantation temperature (°C)	Layer thicknesses (nm)		
	F	G	H = F + G
600	240	180	415
500	215	195	415
400	215	190	405

F = Thickness of the top single-crystal Si layer.

G = Thickness of the polycrystalline Si₃N₄ layer.

^a Wafers implanted with 7.5×10^{17} N⁺ ion/cm² at 160 keV and at the designated temperature were annealed at 1200°C for 2h in argon.

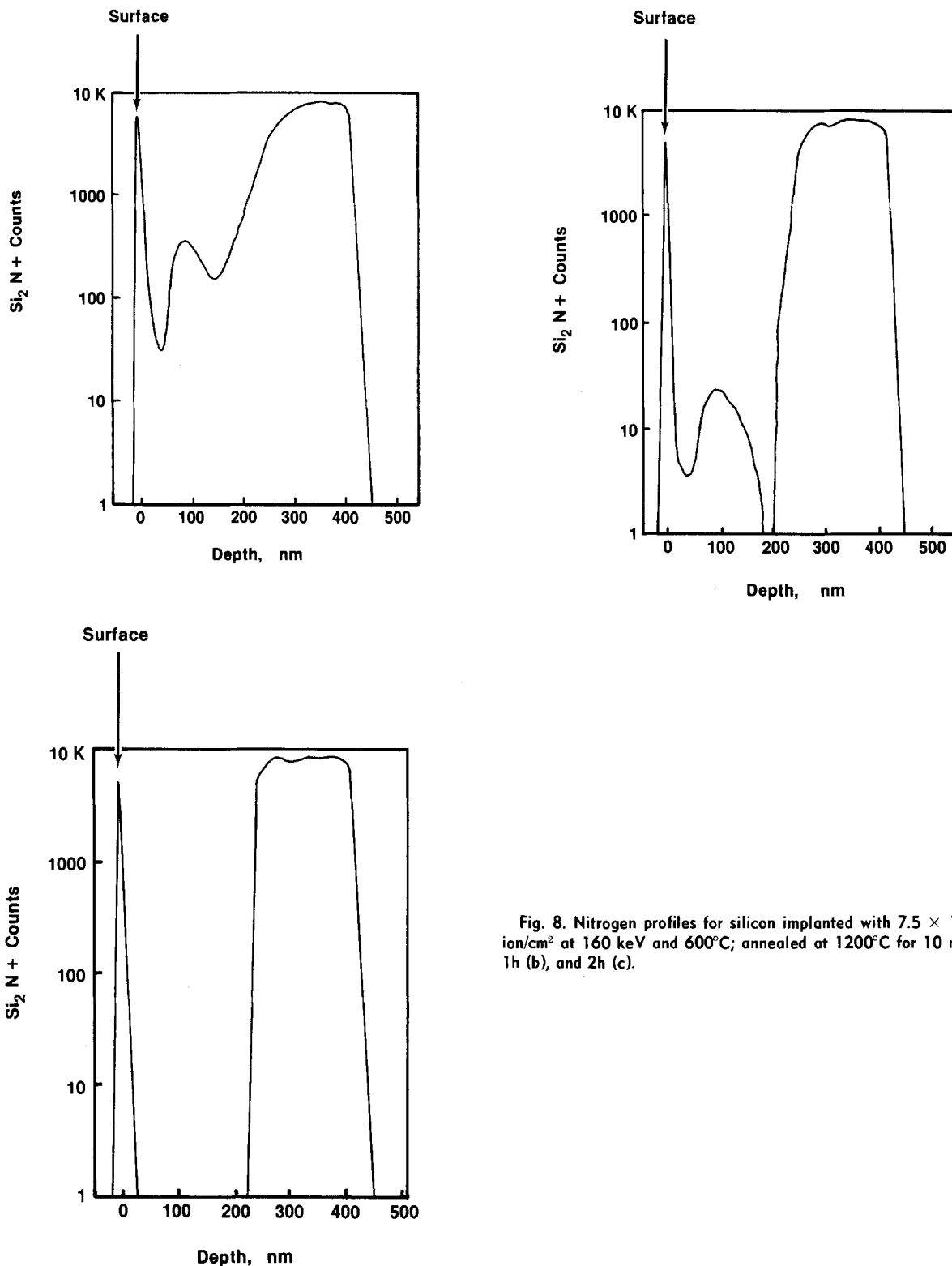


Fig. 8. Nitrogen profiles for silicon implanted with $7.5 \times 10^{17} \text{ N}^+$ ion/cm² at 160 keV and 600°C; annealed at 1200°C for 10 min (a), 1h (b), and 2h (c).

less than $6 \times 10^{18} \text{ N at./cm}^3$ (the detection limit of SIMS) for an anneal time of 2h as indicated in Fig. 8c. After a 1h anneal, the nitrogen concentration just above the buried Si/Si₃N₄ interface is substantially lower than the nitrogen concentration in the silicon next to the nitrogen peak at the Si/SiO₂ interface. Thus, the polycrystalline buried nitride layer acts as a better sink for nitrogen than the top Si/SiO₂ interface.

Close examination of the surface of the silicon wafer after a 2h 1200°C anneal did not reveal the presence of any polycrystalline silicon nitride. However, attempts to strip the pyrolytic oxide from the silicon wafers after the 2h anneal required the use of 49% HF for 1-2 min before the wafers would dewet. A solution of five parts NH₄OH to one part HF (5:1 BHF) did not dewet the wafers at 10 min of

etching time. These results along with similar results reported by Josquin (13, 14) suggest that an amorphous silicon nitride film forms at the Si/SiO₂ interface.

Discussion

The as-implanted microstructures resulting from the experimental conditions of this investigation basically consist of a buried amorphous layer under a layer of single-crystal silicon for all implant temperatures studied. The formation of an amorphous layer by ion implantation is enhanced by high ion doses, high damage density, low implant temperatures, and by the implantation of a heavier element into a lighter target material (18). A model for amorphizing silicon by ion implantation by Morehead and Crowder (19) predicts that, for an implant

temperature of about 350°C or more, an amorphous layer should not form for any dose of nitrogen in silicon. Their model, however, does not quantitatively consider the effect of dose rate (ion beam current density); nor is the effect of substantial changes in the composition of the silicon resulting from high dose implants considered. They do suggest that higher dose rates will favor the formation of an amorphous layer at higher implant temperatures.

As previously noted, Zimmer and Vogt (9) found for nitrogen doses of 1.3×10^{18} N⁺ ion/cm² at 150 keV that an amorphous layer extending to the silicon surface forms at implant temperatures below 350°C. Upon annealing such a structure, a top layer of polycrystalline silicon forms. However, if the implant temperature is in excess of 350°C, sufficient self-annealing presumably occurs to maintain a surface layer of monocrystalline silicon from which the remaining silicon recrystallizes during annealing. Based upon Rutherford backscattering data, Bourguet *et al.* (15) suggest that for a dose of 2×10^{17} N⁺ ion/cm² a buried amorphous layer forms, but that this amorphous layer extends to the surface of the wafer for a dose of 2×10^{18} N⁺ ion/cm² for an implant energy of 180 keV at or near room temperature.

The results of this study indicate that a buried amorphous layer forms at elevated implant temperatures (400°-600°C) and at a dose of 7.5×10^{17} N⁺ ion/cm². Since the wafers at all three implant temperatures were implanted at the same dose rate and the nitrogen profiles are identical for wafers implanted at 400° and at 600°C, the differences in the as-implanted microstructures observed in Fig. 1a-1c are due solely to differences in the implant temperature. Clearly, the formation, thickness, and position of the buried amorphous layer is a function of the implant temperature.

For an implant temperature of 400°C, the center of the amorphous layer corresponds to the projected damage peak for nitrogen implanted into silicon at 160 keV as calculated from the model of Sigmund and Sanders (20). Based upon their model, the projected damage peak is at 81% of the projected nitrogen ion range or at about 295 nm for 160 keV. Thus, the center of the amorphous layer at 400°C corresponds to the region of maximum implant damage.

As the implant temperature increases, the amorphous layer appears to become thinner and a single-crystal layer with a mottled microstructure begins to form. This mottled layer forms primarily between the amorphous layer and the top highly defective single-crystal silicon layer, although some of this mottled microstructure also forms below the amorphous layer (Fig. 1a). Examination of the thickness data in column D in Table I indicates that the sum of the mottled and amorphous layer thicknesses is nearly constant as a function of the implant temperature. Thus as the implant temperature increases, the thickness of the mottled layer increases at the expense of the amorphous layer. Since this mottled layer is defect-free single-crystal silicon, except for 1-3 nm diam regions of amorphous material, the elevated implant temperatures apparently promote the *in situ* recrystallization of a portion of the amorphous layer during the nitrogen implantation. At 600°C, the center of the amorphous layer corresponds to the projected range or the peak nitrogen concentration of as-implanted N⁺ ions into silicon at 160 keV. Given the asymmetry of the as-implanted nitrogen concentration profile (Fig. 4), and the fact that the mottled microstructure forms predominately above the amorphous layer, the extent to which the mottled layer forms at a given implant temperature appears to be a function of the local nitrogen concentration. In particular, as the implant temperature increases, a higher nitrogen concentration is required to insure the retention of a buried amorphous layer. Conversely, as the implant temperature increases, the mottled layer is capable of incorporating a larger concentration of nitrogen.

The development of the final annealed microstructure proceeds first by the crystallization of the amorphous layer into polycrystalline silicon nitride, and then by the

changing of the mottled layer into normal single-crystal silicon with no amorphous pockets (at implant temperatures of 500° and 600°C). Finally, the highly defective top single-crystal silicon layer transforms to single-crystal silicon with a relatively low density of dislocations which span the entire thickness of the top silicon layer. Once the polycrystalline silicon nitride forms, it acts as a sink for the diffusion of nitrogen from the surrounding silicon, particularly for the top silicon layer. As the nitrogen diffuses towards this buried layer, a silicon nitride dendritic structure forms along the Si/Si₃N₄ interface, indicative of morphological instability along this interface. Concurrent with the development of this dendritic structure is the disappearance of the mottled microstructure. This indicates that the 1-3 nm regions of amorphous material may be rich in nitrogen compared to the surrounding silicon matrix. As the nitrogen thus diffuses out of the amorphous pockets in the mottled layer, the silicon lattice relaxes to its perfect state.

For silicon implanted at 600°C and annealed at 1200°C, the dendritic structure is more prominent along the upper Si/Si₃N₄ interface than along the lower interface. This is due more to the lower nitrogen concentration gradient above the amorphous layer than below it, as indicated in Fig. 4. As the silicon nitride crystallizes, the nitrogen in the silicon along the back Si/Si₃N₄ interface of the amorphous layer is rapidly depleted, thus minimizing the development of the dendritic structure. However, along the top Si/Si₃N₄ interface, the dendrites grow into silicon which has a more gradually decreasing nitrogen concentration gradient. Hence, a more prominent dendritic structure develops along this interface. As the implantation temperature increases from 500° to 600°C, the dendritic structure becomes more prominent. This is because the dendritic growth starts at the interface between the amorphous silicon layer and the mottled layer. At higher implant temperatures, this interface is closer to the projected range of the nitrogen and, hence, at a higher nitrogen concentration. Consequently, the dendrites associated with the higher implant temperature start deeper within the silicon and grow farther towards the top surface before the lack of nitrogen inhibits their growth.

In order to understand the development of the various annealed microstructures (Fig. 7a-7c) from their respective as-implanted microstructures (Fig. 1a-1c), it is necessary to examine the pertinent data from Tables I and II as plotted in Fig. 9. In Fig. 9, the total thickness of the top silicon layer for both the as-implanted (Table I, column E) and the annealed (Table II, column F) microstructures is plotted as a function of the implant temperature. For the 600°C implant temperature, the annealed top silicon layer is considerably thinner than the total thickness of the initial single-crystal layers. Consequently, upon annealing,

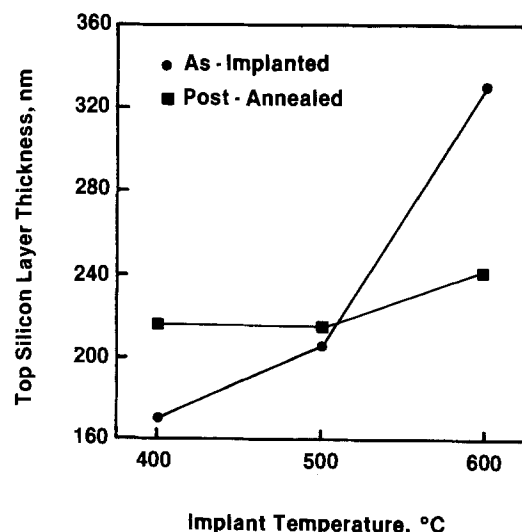


Fig. 9. The total as-implanted and annealed silicon layer thicknesses as a function of the implant temperature.

the α - Si_3N_4 grows dendritically into the mottled layer. For an implant temperature of 500°C, the final silicon layer is of virtually the same thickness as the total top silicon layers in the as-implanted microstructure. As a result, there is virtually no dendritic silicon nitride growth into the mottled silicon layer (see Fig. 7b). For an implant temperature of 400°C, the thickness of the top silicon layer is greater than the thickness of the top silicon layer in the as-implanted microstructure. Consequently, the top silicon layer grows down into the amorphous layer during the anneal. The extent of this silicon growth is about 45 nm, which is approximately the distance of vertical growth of the twins observed in Fig. 7c. Also, the upper extent of the twins in Fig. 7c is located at the position of the interface between the amorphous and single-crystal silicon layers in Fig. 1c. Thus, the regrowth of the top silicon layer for an implant temperature of 400°C and a subsequent anneal at 1200°C is characterized by a twinned microstructure. Based upon this data and the microstructures in Fig. 7, the optimum implant temperature for the studied nitrogen dose and implant energy is about 500°C. At this temperature, the α - Si_3N_4 dendritic growth is minimized and the silicon twins do not form.

The mechanism whereby the final, low dislocation density top silicon film develops is not understood at this time. In particular, the manner in which the high density of defects in the top silicon layer of the as-implanted microstructures (at all implant temperatures) migrate from the silicon is unknown. It is known, however, that the crystallization of the amorphous layer to α - Si_3N_4 is a prerequisite for the formation of the low defect density top silicon layer. Thus the high defect density in the top, as-implanted silicon layer is probably associated with a relatively high concentration of nitrogen in the silicon. As the nitrogen concentration decreases from the top silicon layer, the defect density in this layer correspondingly decreases.

Also unknown at this point is the reason for the formation of the dislocations which form in the top silicon layer and span the entire thickness of this layer. Since the density of these dislocations is independent of the implant temperature, they do not appear to be a function of the as-implanted microstructure for the temperature range of this study. These dislocations could form from the defects in the as-implanted silicon. They could also be due to plastic deformation of the silicon resulting from differences in the thermal expansion coefficients of silicon and alpha silicon nitride. A third possibility is that the dislocations could be due to the difference in the atomic volumes of implanted silicon and the resulting crystalline silicon nitride. Despite their presence, the dislocation density in the top silicon layer of nitrogen-implanted and annealed silicon as described above is relatively low compared to the defect density in the as-implanted microstructure.

The nitrogen profiles as a function of anneal time at 1200°C (Fig. 8) indicate that the implanted nitrogen diffuses to the top Si/SiO₂ interface and to the buried polycrystalline silicon nitride layer. This buried α - Si_3N_4 layer is a better diffusion sink for nitrogen than the nitride layer at the top Si/SiO₂ interface. In particular, the nitrogen profile for implanted silicon annealed at 1200°C for 1h (Fig. 8b) indicates that the equilibrium nitrogen concentration in silicon in contact with crystalline alpha silicon nitride is lower than for the amorphous silicon nitride at the Si/SiO₂ interface. The silicon nitride layer at the Si/SiO₂ interface is amorphous since no polycrystalline material is observed via TEM. Also, it is not known if this nitride is stoichiometric Si_3N_4 . However, Josquin (16, 17) has shown that this nitride layer is capable of inhibiting silicon oxidation.

A comparison of the nitrogen in Fig. 4 and 8a indicates that the peak annealed nitrogen concentration is only slightly greater than the peak as-implanted nitrogen concentration. As previously noted, a value of 10K Si₂N⁺ counts corresponds to a nitrogen concentration of 3×10^{22} N at./cm³. The fact that the peak nitrogen concentrations

are virtually identical implies that the silicon nitride may not be fully dense or that it may have a lower density than anticipated from Ref. (13). This explanation would not be too unreasonable, since the buried nitride has numerous high and low angle grain boundaries. Another explanation for the lower than expected nitrogen concentration in the annealed silicon nitride may be that the nitride has a high solid solubility for silicon, since no silicon precipitates were observed in this layer by electron diffraction.

Conclusions

Both the as-implanted and the postannealed microstructures of silicon implanted with 7.5×10^{17} N⁺ ion/cm² at 160 keV are a function of the implant temperature in the range of 400°-600°C. Within this implant temperature range, the as-implanted microstructure consists of a highly defective monocrystalline top silicon layer and a buried amorphous layer.

At implant temperatures of 500° and 600°C, a mottled microstructure forms between the top, highly defective silicon layer and the buried amorphous layer at the expense of the amorphous layer. This mottled layer is single-crystal silicon except for the inclusion of small (1-3 nm) regions of amorphous silicon. The mottled layer apparently results from the recrystallization of the amorphous layer during implantation. The extent to which this mottled layer forms is a function of the implant temperature and of the local nitrogen concentration.

Annealing at 1200°C results in a continuous buried nitride layer and the formation of a top silicon layer with a relatively low density of dislocations. The buried nitride layer forms by the precipitation of a α - Si_3N_4 phase throughout the amorphous layer. This is followed by the dendritic growth of the α - Si_3N_4 phase partially into the mottled silicon layer for silicon implanted at 500° and 600°C. For silicon implanted at 400°C, the top silicon layer grows towards the buried nitride layer, rather than the silicon nitride growing towards the top surface. For all of the above implant temperatures, the final thickness of the top silicon layer is 215-240 nm.

The formation of the polycrystalline silicon nitride layer is a prerequisite for the regrowth of the top layer into low defect density silicon. The high density of defects in the as-implanted top silicon layer migrate out of the silicon as the nitrogen concentration decreases in this layer.

The final annealed top silicon layer is characterized by dislocations which span the entire thickness of the silicon layer. The density of these dislocations is about 5×10^6 dislocation/cm² and appears to be independent of the implant temperature. The regrown silicon resulting from the 400°C implant is characterized by growth twins at the top Si/Si₃N₄ interface, in addition to the dislocations.

From a microstructural viewpoint, the absence of growth twins and the minimization of the silicon nitride dendritic growth imply that 500°C is an optimum implant temperature for the formation of SOI by implanted nitrogen.

Although the as-implanted microstructure is a function of the implant temperature, the actual as-implanted nitrogen distribution is independent of the implant temperature. During the 1200°C anneal, the nitrogen in the top silicon layer diffuses towards the precipitated α - Si_3N_4 layer and towards the top silicon/SiO₂ interface. The silicon nitride layer along this top interface does not crystallize during the 1200°C anneal.

The results of this study also indicate that a nitrogen dose substantially less than predicted for a stoichiometric silicon nitride layer may result in a continuous buried insulator. This is due to the diffusion of part of the nitrogen from the surrounding silicon to the polycrystalline buried silicon nitride.

Acknowledgments

The authors wish to acknowledge S. Kingsland for his work in implanting the wafers and G. Blanchard for conducting the SIMS analysis. The encouragement of J.

Wursthorn and useful discussions with J. Lasky are also appreciated.

Manuscript submitted March 4, 1985; revised manuscript received May 9, 1985.

IBM Corporation assisted in meeting the publication costs of this article.

REFERENCES

- G. W. Cullen, Editor, *J. Cryst. Growth*, **63**, 429 (1983).
- H. W. Lam, *1983 IEDM Tech. Dig.*, 348 (1983).
- "Comparison of Thin Film Transistor and SOI Technologies," H. W. Lam and M. J. Thompson, Editors, Materials Research Society Symposia Proceedings, Vol. 33, Elsevier Science Publishing Co. Inc., New York (1984).
- C.-E. Chen, T. G. W. Blake, L. R. Hite, S. D. S. Malhi, B.-Y. Mao and H. W. Lam, *1984 IEDM Tech. Dig.*, 702 (1984).
- D. J. Foster, A. L. Butler, and P. H. Bolbot, *ibid.*, 704 (1984).
- C. G. Tuppen, M. R. Taylor, P. L. F. Hemment, and R. P. Arrowsmith, *Appl. Phys. Lett.*, **45**, 57 (1984).
- R. F. Pinizzoto, *J. Cryst. Growth*, **63**, 559 (1983).
- Y. Homma, M. Oshima, and T. Hayashi, *Jpn. J. Appl. Phys.*, **21**, 890 (1982).
- G. Zimmer and H. Vogt, *IEEE Trans. Electron Devices*, **ed 30**, 1515 (1983).
- S. Maeyama and K. Kajiyama, *Jpn. J. Appl. Phys.*, **21**, 744 (1982).
- T. Hayashi, H. Okamoto, and Y. Homma, *ibid.*, **19**, 1005 (1980).
- M. R. Taylor, C. G. Tuppen, R. P. Arrowsmith, R. M. Dobson, A. E. Glaccum, M. C. Wilson, G. R. Booker, and P. Hemment, in "Microscopy of Semiconductor Materials Conference," p. 485, Institute of Physics Conference Series 67, Institute of Physics, London (1983).
- P. Popper and S. N. Ruddlesden, *Trans. Br. Ceram. Soc.*, **60**, 603 (1961).
- T. Tsujide, M. Nojiri, and H. Kitagawa, *J. Appl. Phys.*, **51**, 1605 (1980).
- P. Bourguet, J. M. Dupart, E. Le Tiran, P. Auvray, A. Guivarc'h, M. Salvi, G. Pelous, and P. Henoc, *J. Appl. Phys.*, **51**, 6169 (1980).
- W. J. M. J. Josquin, *Nucl. Instrum. Meth.*, **209/210**, 581 (1983).
- W. J. M. J. Josquin and Y. Timminga, *This Journal*, **129**, 1803 (1982).
- J. F. Gibbons, *Proc. IEEE*, **60**, 1062 (1972).
- F. F. Morehead, Jr., and B. L. Crowder, in "Proceedings of the 1st Conference on Ion Implantation," L. Chadderton and F. Eisen, Editors, pp. 25-30, Gordon and Breach, New York (1971).
- P. Sigmund and J. B. Sanders, in "Proceedings of the International Conference on Applications of Ion Beams to Semiconductor Technology," P. Glotin, Editor, pp. 215-233, Editions Ophrys, Grenoble, France (1967).
- Y. Yatsurugi, N. Akiyama, Y. Endo, and T. Nozaki, *This Journal*, **120**, 975 (1973).

Sidewall-Tapered Oxide by Plasma-Enhanced Chemical Vapor Deposition

Gregory C. Smith* and Andrew J. Purdes*

Texas Instruments, Incorporated, Semiconductor Process and Design Center, Dallas, Texas 75265

ABSTRACT

Plasma-enhanced chemical vapor deposition (PECVD) was used to deposit SiO₂ layers with tapered sidewalls on silicon-doped aluminum steps. The deposition rates ranged from several hundred to 2000 Å/min. The plasma deposition process was performed in a single-wafer reactor, although the process is compatible with batch processing. The sidewall angles of up to 30° to the vertical are formed by the angular dependence of the sputter etch yield due to ion bombardment. A large negative bias voltage with respect to the plasma is maintained at the substrate during the low pressure process.

The topography of deposited dielectrics has become increasingly important as lateral device dimensions approach, and in some cases become smaller than, the heights of topographical features on VLSI devices. The importance of dielectric surface topography stems primarily from the need to coat the dielectric layer conformally with metal and then to etch the metal cleanly. Dielectric films deposited by sputtering or PECVD without strong ion bombardment have surface topography which can be represented by Fig. 1. This profile is the result of shadowing, which causes low deposition rates at the corners near the bottom of steps relative to the rates at the top (1). This results in the reentrant surfaces and cracks seen in Fig. 1. The deposited dielectric can be planarized by applying resist and etching back to replicate the smoothness of the resist surface in the oxide remaining after etch. However, voids can be opened where the reentrant surfaces had closed on themselves during the deposition. If the dielectric topography of Fig. 1 is not planarized before deposition of the metal by evaporation or sputtering of the metal, conductors will be discontinuous on the reentrant dielectric surfaces as a result of shadowing.

Chemical vapor deposition of the subsequent metal can be successful in producing conformal films on even reentrant dielectric surfaces (2). This solves the open-circuit problem but may result in shorting of adjacent

etched conductors because the anisotropic etch of the metallization layers is shadowed by the overhanging dielectric. Hence, regardless of the subsequent metal deposition method, reentrant-deposited dielectric topography is unacceptable.

A well-established method for developing tapered oxide sidewalls during the deposition process is bias sputtering. Bias sputtering of quartz uses sputter etching of the depositing oxide surfaces to tailor the topography of the sputtered film. The sputter etching of the wafers during the deposition is accomplished by providing RF power to the substrate plate from a separate power supply or a power split with the target. Sputter etch rates are maximum for surfaces oriented at about 45° to the incoming ion flux. The steady-state surface topography under sputter etching is either a surface oriented normal to the incoming ion flux or one oriented at a 45° angle to the flux (3, 4). If sputter etching and sputter deposition are done simultaneously, the resulting topography will resemble that of Fig. 2. To completely planarize the oxide, a thick deposition with the topography of Fig. 2 can be made. Then the sputter etch rate is increased so that the net deposition rate on the sloped surfaces is zero, burying the protrusions with a planar film (4). However, planarization can take hours, depending upon the lateral dimensions of the largest circuit feature, and may not be required if the topography of Fig. 2 is acceptable. In these experiments on plasma-deposited films, only tapering of the sidewall was attempted.

* Electrochemical Society Active Member.

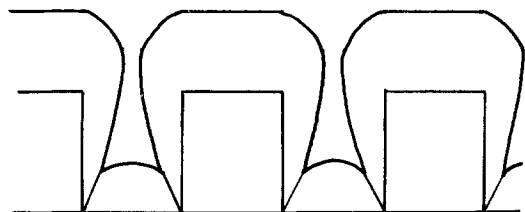


Fig. 1. Breadloafed plasma-deposited oxide over metal steps

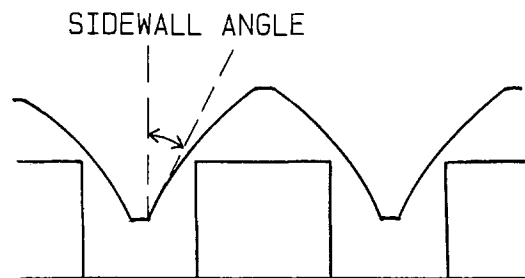


Fig. 2. Sidewall-tapered oxide over metal steps

The topography shown in Fig. 2 has liabilities when compared with conformal film topography or with full planarization. With tapered oxide, the top corner of the underlying metal is isolated from the subsequent metal layer by only a thin insulator, resulting in large capacitance between metal layers and possible reliability problems resulting from film cracking and charge leakage. Also, the bottom of the sidewall is displaced from the underlying metal edge by an amount greater than the average dielectric thickness, consuming valuable chip area. However, unlike planarization, tapering allows contacts cut to the top and bottom of steps to be the same depth. This eliminated the necessity for overetching the contacts to the step tops in order to clear the deep contacts. The problems of poor step coverage and shorts in metal subsequently deposited and etched on conformal oxides will be reduced on sidewall-tapered oxide.

Most of the problems of bias sputtering in producing tapered oxide sidewalls are related to the use of the quartz sputtering target as a source for the deposition. The sodium contaminant levels in quartz targets can be significant, contributing to contamination of the films. Limits on the deposition rate are set by the target. The rate at which the target can dissipate heat limits the allowable target power and thus the deposition rate. For these reasons, experiments were done to determine the feasibility of PECVD tapered oxide as an alternative to bias sputter deposition.

Experimental

The deposition reactor used was a parallel-plate reactive ion etch (RIE) apparatus (Fig. 3). This was chosen because of the highly negative dc bias potentials on the sub-

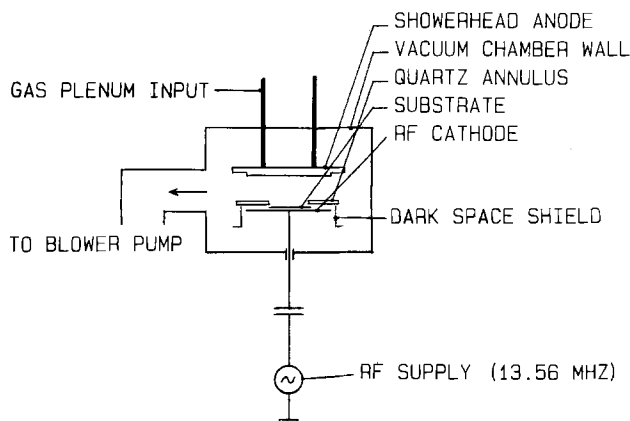


Fig. 3. Deposition reactor for sidewall-tapered plasma oxide

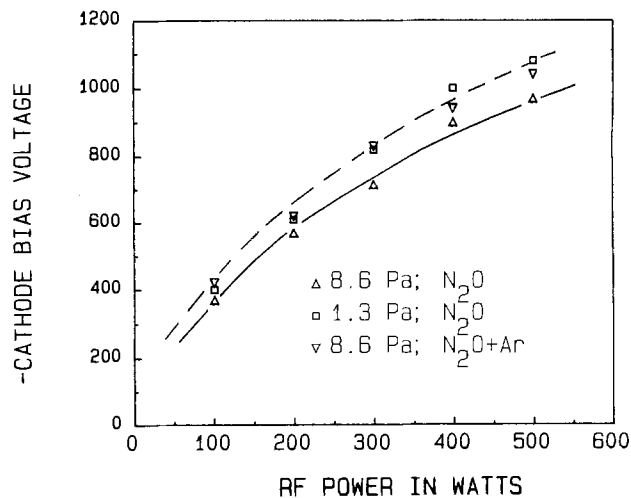


Fig. 4. DC bias voltage of the RF cathode

strate electrode during etch, which enhance the energy of ion bombardment and sputter etch rate. In RIE, the reactor walls and gas inlet plenum are grounded and the plate on which the substrates rest is RF driven, with a blocking capacitor in the matching network. The RF-driven electrode assumes a negative dc potential of large magnitude if the area of the grounded surfaces in contact with the plasma is large compared to the area of the dc floating-RF driven electrode (5). The potential stabilizes when the ion drift current due to the field near the negative substrate electrode equals the diffusion current out of the plasma, which is mostly electron current (6). This ion drift current is used in the present work to sputter etch the surface of the depositing oxide.

The RIE reactor used in these experiments had a 15 cm diam substrate electrode and a 25 cm diam grounded anode and gas inlet plenum in a parallel-plate configuration (see Fig. 4). The plasma was observed to completely fill the vacuum chamber for most deposition conditions tried. The chamber walls and gas inlet chamber are grounded and have large area in contact with the plasma compared with that of the capacitively coupled 13.56 MHz RF-driven substrate electrode. This assures that the substrate electrode assumes a negative dc bias voltage of large magnitude.

Vacuum was established and maintained by a Roots-type blower pump for depositions performed at pressures higher than 8.6 Pa. For pressures lower than 8.6 Pa, vacuum was maintained by a diffusion pump backed by a rotary vane pump. Pressure was monitored by a capacitance manometer. Gas flows were established prior to deposition by evacuating and isolating the chamber and then flowing each gas to be used in the run and adjusting the rate of rise of pressure. The rate of pressure rise required had been previously calculated from the required flow and the vacuum chamber volume. Flows were controlled during deposition using Brooks Rotameter™ flow tubes.

One p-type 75 mm <100> silicon wafer was used in each deposition run. It was centered on the surface of the substrate electrode. A quartz annulus of 26 cm od, 7.5 cm id, and 0.16 cm thickness covered the substrate electrode with the hole over the wafer. This had the effect of increasing local sputter etch and deposition rates on the wafer. The deposition rate and sputter etch rate with and without the annulus are compared in Table I. All deposi-

Table I. Sputter etch and deposition rates with and without the quartz annulus in angstroms per minute

	Oxide sputter etch rate	Oxide deposition rate (with SiH ₄)
With annulus	78	1194
Without annulus	49	1081

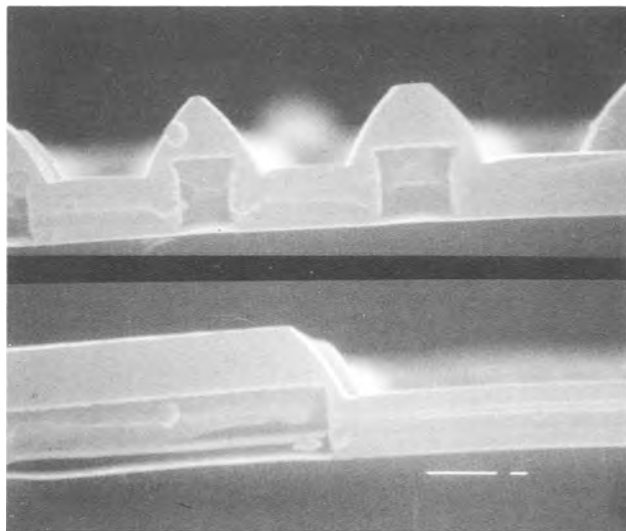


Fig. 5. Topography of plasma-deposited sidewall-tapered oxide. Process: 50 sccm nitrous oxide, 50 sccm argon, 10 sccm silane, 1.3 Pa pressure, 300W RF power, 2.5 cm plate spacing, 30 min.

tion rates, sputter etch rates, and sidewall angle data shown in the Results section were measured on oxides deposited or sputter etched using the annulus. The values quoted in Table I are for 300W, 13 Pa, 100 sccm N_2O sputter etches. The depositions involved the same parameters plus 10 sccm SiH_4 gas flow.

DC bias voltage was measured with a $100\times$ attenuating probe and a 100 MHz oscilloscope. Bias voltage as a function of input power is shown in Fig. 4. The gas ambients used were chosen because they are typical oxidizing ambients in plasma deposition of silicon dioxide. The figure shows that the achieved bias voltages are only weakly dependent on the sputtering ambient or the pressure.

Measurements of oxide thickness were performed with a Nanospec; some measurements were checked with an ellipsometer. SEM samples prepared for measurements shown and plotted in Fig. 5, 11, and 12 were patterned silicon-doped aluminum with $1\ \mu m$ of oxide deposited on them. They were cleaved at liquid nitrogen temperatures to embrittle the aluminum and stained in potassium hydroxide. In order to compare the topography of films deposited by different deposition processes, a standard underlying topography was used with standard thickness of the tapered oxide deposited upon it. The quality of the oxide topography was defined in the present work as the angle shown in Fig. 2, which will be called the sidewall angle. If this angle is negative the surface is reentrant. The standard underlying topography consisted of $1.0\ \mu m$ high steps on $3.0\ \mu m$ pitch. Step and space widths were nominally the same ($1.5\ \mu m$), but as measured the spaces ranged from 1.5 to $2.2\ \mu m$ wide. These were then coated with an oxide thickness of about $1\ \mu m$ for the comparison of sidewall angle.

The sloped oxide shown in Fig. 5 is on the standard topography with space width of $2.2\ \mu m$. Widely separated steps exhibit slightly more favorable sidewall topography than do narrowly spaced steps because of less severe shadowing of the deposition. Hence, comparison of the topography of films produced by different deposition processes needs to be performed with consistent underlying topography and deposited film thicknesses, so similar topographic aspect ratios can be compared. The variation of space width from 1.5 to $2.2\ \mu m$ in the underlying topography in the present work is not believed to be a significant effect on the accuracy of sidewall angle measurements in Fig. 11 and 12.

Results and Discussion

Successful deposition of the sidewall-tapered oxide depends on sputter etching the depositing oxide at a high rate. In order to determine the sputter etch rate of the ox-

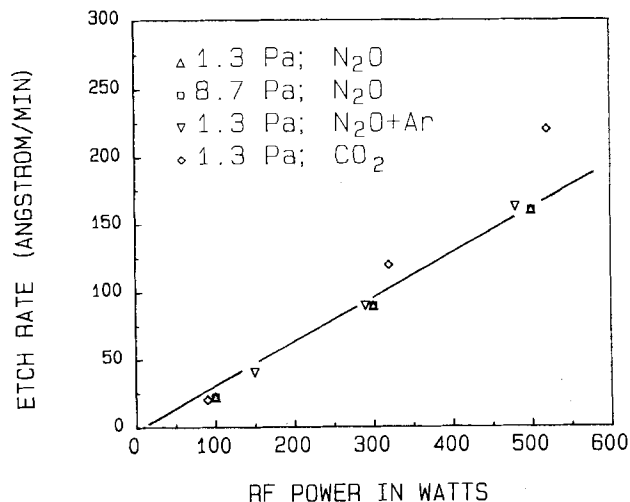


Fig. 6. Sputter etch rates in typical oxidizing gases used for plasma oxide deposition.

ide during deposition, the silane was eliminated from the gas ambient and plasma oxide-coated silicon wafers were used to determine thickness before and after the etch. The sputter etch rates recorded were, of course, for surfaces oriented perpendicular to the ion flux. Maximum sputtering rates of three to five times this value are possible on surfaces oriented at 60° - 80° to the ion flux. Figure 6 shows the rates measured in the indicated oxidizing ambients. The rate is apparently independent of ambient and pressure and is proportional to the RF power.

An experiment was performed to compare sputter etching in N_2O and reactive ion etching in CF_4 as means for tapering sidewalls of previously deposited, patterned, and anisotropically etched oxide steps. One wafer with oxide steps $1\ \mu m$ high was sputter etched for 15 min in N_2O at 200W at 1.3 Pa pressure. Another was etched in CF_4 under similar conditions of pressure and power for 5 min. The CF_4 plasma removed 4900Å of oxide ($980\ \text{Å}/\text{min}$), tapering the oxide sidewalls at a 10° angle. The N_2O sputter etched only 1500Å of oxide ($100\ \text{Å}/\text{min}$) but tapered the sidewalls at a 19° angle to the vertical, as measured from SEM photographs. From this result, it was decided that sputter etching would be the sidewall tapering method used in this work. For a given rate of taper, the oxide removal was substantially less for sputter etching. In a process involving both deposition and etching, sputter etching to produce the tapered sidewall would reduce the net deposition rate less than RIE etching in CF_4 would. Choosing sputter etching as the tapering method also avoided any coupling which might have resulted between the etch and

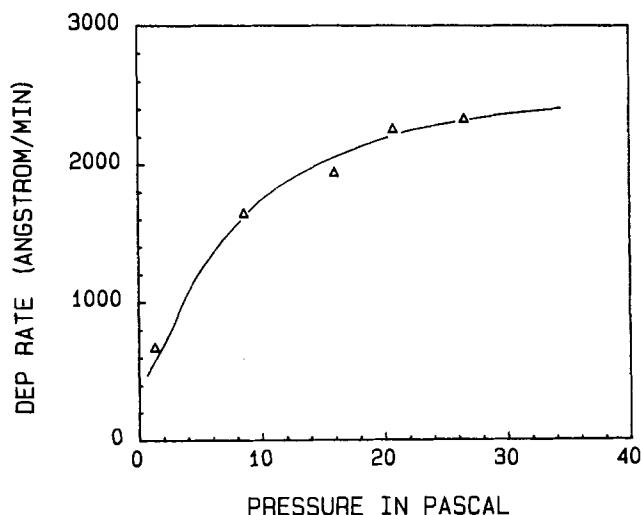


Fig. 7. Dependence of deposition rate on pressure for 10:1 nitrous oxide:silane flow ratio, 500W RF power, 8.7 Pa pressure.

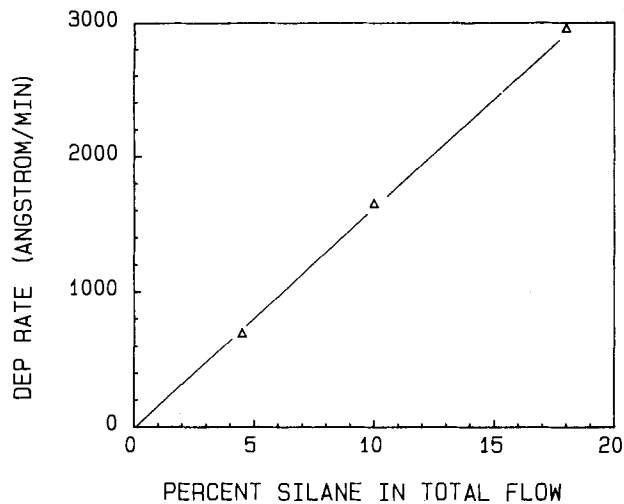


Fig. 8. Dependence of deposition rate on silane fraction at constant 8.7 Pa pressure and 500W power.

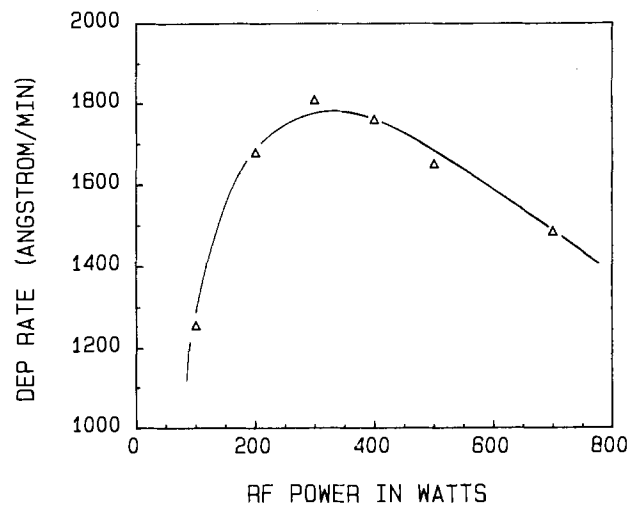


Fig. 9. Dependence of deposition rate on power for 10:1 nitrous oxide:silane flow ratio, 8.7 Pa pressure.

deposition chemistries leading to gas phase nucleation or other undesirable effects. Therefore, the results shown herein are on films tapered by sputter etching.

The net deposition rate of the oxide is plotted as a function of adjustable parameters in Fig. 7-9. Increasing the pressure increases the deposition rate as shown in Fig. 7. Deposition rates of up to 2300 Å/min were achieved at the 10:1 $N_2O:SiH_4$ ratio, and even higher rates can be achieved with lower ratios. It will be shown later, however, that increasing the deposition rate without an accompanying increase in the sputter etch rate causes degradation of the topography of the deposited oxide.

Figure 8 shows that the deposition rate of the oxide is linearly dependent upon the silane/nitrous oxide fraction at constant total flow. As seen in Fig. 10, there did not appear to be much effect of the silane/total flow ratio on the index of refraction except in those films deposited in a 50:50 nitrous oxide:argon mixture to which the silane was added. Here the ratio of silane to nitrous oxide was twice as high as in the other films. As expected, the index was higher (1.52) at largest silane fraction than the average for the other films (1.46). Not expected was the dip in index at 9% silane in all deposition ambients. This effect was strongest in the $N_2O + Ar$ oxides.

The dependence of deposition rate on RF power at constant pressure and flows is shown in Fig. 9. As power is increased from 100 to 300W, the reactant utilization increases, causing the rise in deposition rate. Above 300W, however, the net deposition rate falls because of the saturation of reactant utilization and the increase of the per-

pendicular sputter etch rate. Tapering the sidewalls during oxide deposition required sputter etch rates of one-fifteenth to one-fifth the deposition rate. All sputter etch rates quoted were measured on oxide surfaces normal to the ion bombardment direction.

Plots of sidewall angle as functions of power and pressure are shown in Fig. 11 and 12. The metal coverage at the oxide step bottom in the subsequent deposition increases with the sidewall angle. A 20°-30° sidewall angle indicates favorable topography for subsequent metal deposition. Sidewall angle increases with RF power in all ambients. The high pressure deposition in $N_2O + SiH_4$ required the highest RF power level to achieve sidewall tapering (angles > 20°). This is because the deposition rate increases with pressure and the sputter etch rate is independent of it. In order to increase the sputter etch rate to taper the sidewalls, the power must increase. Of the low pressure depositions, the CO_2 and $N_2O + Ar$ oxidizing ambients required the lowest RF power levels to taper the oxide sidewalls.

Stress in films deposited in pure N_2O and silane at 1.3 and 8.6 Pa pressure was measured by determining the change in radius of curvature of 2.5 cm diam., 125 μm thick silicon wafers before and after a thick oxide deposition (> 0.5 μm). The results are shown in Fig. 13. Stress was compressive, tending toward lower values as the RF power was increased. The stress in films deposited at 1.3 Pa pressure was higher than in films deposited at 8.6 Pa, except at 300W. The only unacceptably high stress value was the 100W, 1.3 Pa point (5 Gdyn/cm²). This set of depo-

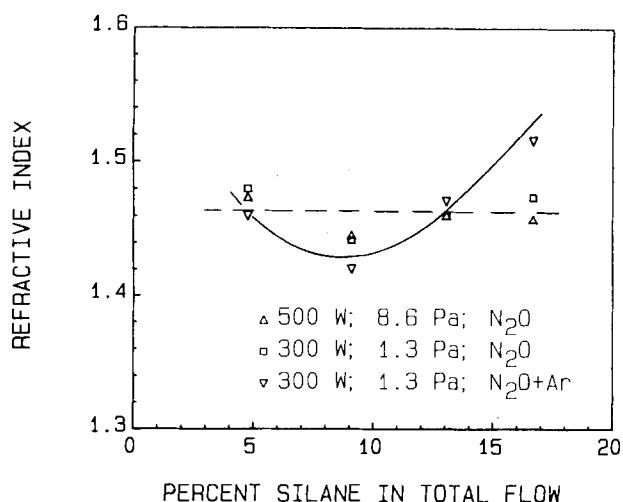


Fig. 10. Variation of the refractive index with nitrous oxide:silane ratio.

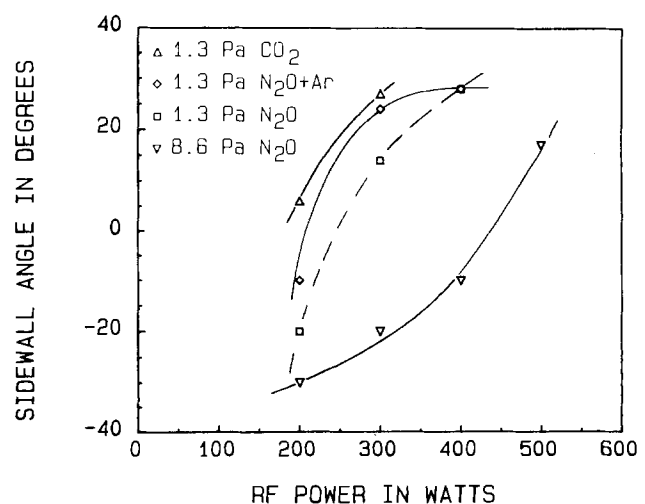


Fig. 11. Variation of the oxide sidewall angle with RF power. Standard topography is 1 μm high aluminum steps on 3 μm pitch.

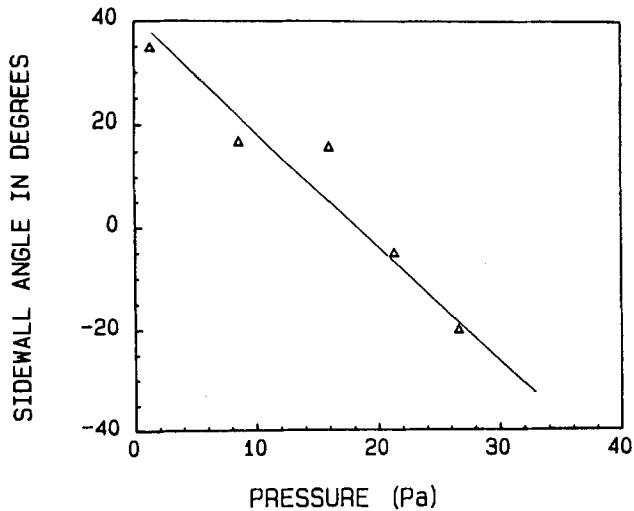


Fig. 12. Dependence of oxide sidewall angle on pressure for 500W RF power, 10:1 nitrous oxide:silane ratio.

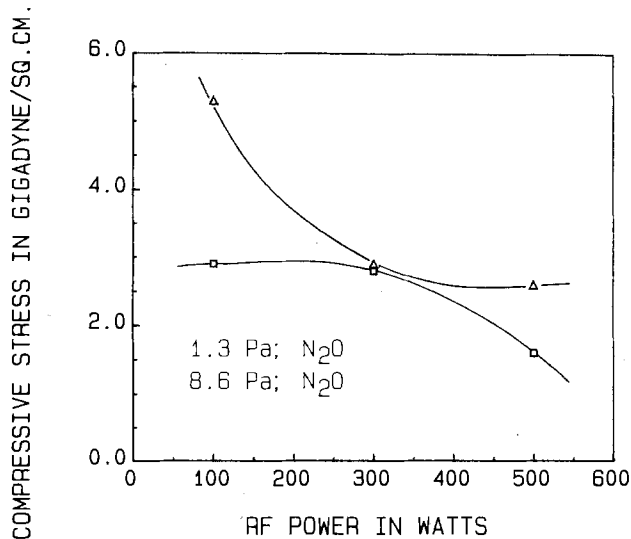


Fig. 13. Dependence of compressive stress on RF power of the deposition

sition conditions does not result in tapered sidewall oxide anyway.

Breakdown strength measurements were made on tapered oxide deposited at 200W and 1.3 Pa in this reactor. Median breakdown fields of 2.6-3.4 MV/cm were obtained on oxides deposited using CO₂ and SiH₄. In an effort to explain these low numbers, x-ray fluorescence was performed on 10,000Å films deposited using the same process. The result was iron contamination levels of 520-852 ppm. The iron is probably from the strongly sputter-etched stainless steel RF cathode and to a lesser degree from the chamber walls. The first approach to eliminating the iron contamination problem will be to use an anodized aluminum RF cathode and, if necessary, an anodized aluminum chamber. The experiments were performed in an environment which lacked particulate control, and this could have made a contribution to the low breakdown fields.

The poor dielectric strength of the tapered oxide films may be tolerable if a standard PECVD film of high breakdown strength can be deposited prior to the tapered oxide deposition, in the same pumpdown. This would provide a low loss capacitor in series with the tapered oxide layer.

Conclusion

A reactive ion etch system has been used to deposit sidewall-tapered oxide by PECVD. The deposition rate is determined by pressure and silane flow for N₂O:SiH₄ ratios of more than 5. The sputter etch rate is independent of pressure and is linear with respect to RF power. These deposition and sputter etch rate parameters are analogous to the target and substrate power in bias-sputtered quartz.

Although sidewall-tapered oxide can be deposited at more than 2000 Å/min, suggesting a single-wafer process, batch processing at lower deposition rates may be a safer approach. This is because of the necessary relationship between the sputter etch rate and the deposition rate in forming the tapered sidewall topography. A high deposition rate requires a high sputter etch rate and, in turn, a large substrate dc bias level. The resulting high energy ion bombardment may be deleterious to the integrity of oxides already on the wafer. Flaking of dielectrics from shielding in a deposition reactor can lead to defects in deposited films. This problem is less serious in batch processing than in single-wafer processing because the thickness of film deposited on the shielding, and therefore the amount of flaking, is less than for a single-wafer process by a factor of the number of wafers in a batch. Lower deposition rates permissible in batch processing are consistent with low sputter etch rates, reduced ion bombardment, and reduced damage to MOS gate oxides already on the wafer.

Although the feasibility experiments for sidewall-tapered plasma oxide were carried out in a parallel-plate RIE-type system, plasma deposition can be performed in a wide variety of ways, offering some flexibility in reactor design. For example, if magnetic fields are used to confine the electrons and increase their ionizing efficiency, increased ion flux to the substrates with smaller biases results. The magnetic field can be used to confine ionizing electrons near the RF-powered substrate as in Ref. (7) or to stabilize a filament-produced high density plasma to which the substrate can be independently biased (8). These approaches may be of use in future attempts to control dc bias and ion bombardment flux independently to reduce damage to the substrates during the tapered oxide deposition.

Acknowledgments

The authors would like to thank Jack Frazier for his help in making most of the measurements.

Manuscript submitted April 15, 1985; revised manuscript received July 8, 1985. This was Paper 413 presented at the New Orleans, Louisiana, Meeting of the Society, Oct. 7-12, 1984.

Texas Instruments, Incorporated, assisted in meeting the publication costs of this article.

REFERENCES

1. R. M. Levin and K. Evans-Lutterodt, *J. Vac. Sci. Technol. B*, **1**, 54 (1983).
2. S. Sachdev, J. A. Fair, C. Fuhs, and W. Coney, Paper presented at the Workshop on Tungsten for VLSI Applications, Albuquerque, NM, Nov. 12-13, 1984.
3. M. J. Nobes, J. S. Colligon, and G. Carter, *J. Mater. Sci.*, **4**, 730 (1969).
4. C. Y. Ting, V. J. Vivalda, and H. G. Schaefer, *J. Vac. Sci. Technol.*, **15**, 1105 (1978).
5. J. W. Coburn and E. Kay, *J. Appl. Phys.*, **43**, 4965 (1972).
6. M. Mitchner and C. H. Kruger, "Partially Ionized Gases," pp. 129-136, John Wiley and Sons, New York (1973).
7. I. Lin, D. E. Hinson, W. H. Class, and R. I. Sandstrom, *Appl. Phys. Lett.*, **44**, 185 (1984).
8. T. D. Mantei and T. E. Wicker, *Solid State Technol.*, **28** (4), 263 (1985).

Precipitation and Diffusivity of Arsenic in Silicon

R. Angelucci, G. Celotti, D. Nobili, and S. Solmi

C.N.R.-Istituto LAMEL, 40126 Bologna, Italy

ABSTRACT

Small angle x-ray scattering measurements were performed on arsenic-implanted laser-annealed silicon slices to investigate the features of precipitation at 900°C for different dopant supersaturations. With decreasing As concentration from 3.2 to $1.1 \times 10^{21} \text{ cm}^{-3}$, the size distribution of the precipitates shifts toward larger values and their shape evolves from that of thin platelets, becoming three-dimensional and approaching at last that of a sphere. The high concentration diffusivity of As at 900°C, deduced from the size of the largest precipitates in specimens doped $1 \times 10^{21} \text{ cm}^{-3}$, turns out to be $2 \times 10^{-14} \text{ cm}^2\text{-s}^{-1}$. Determinations of the shift of the carrier concentration profiles and of the junction depth, after heating at 1000°C, show that the diffusivity of As is not affected by the precipitation and, hence, is controlled by the concentration of the dopant.

The physical nature of the electrically inactive As, which is present in Si at high doping levels, is receiving increasing attention, primarily due to the demands of VLSI. Well-known models hypothesize the formation of complex point defects, or "clusters," in thermal equilibrium (1-6).

Previous work (7) performed on ion-implanted and laser-annealed samples, doped with As in a wide composition range, put into evidence that the electrically active concentration depends only on temperature, a finding leading to the conclusion that a two-phase equilibrium takes place.

The formation of a second phase was also indicated by the isochronal heating behavior, typical of a precipitation process. Precipitates were in fact detected in very heavily doped specimens by small angle x-ray scattering (SAXS), a technique which is suitable because of the noticeably different atomic numbers of Si and As. These determinations provided information on the size distribution and shape of these precipitates, which were found to be in the form of thin platelets. These particles should be coherent with the silicon matrix, as suggested by the absence of extra lines or spots in the diffraction patterns.

As an additional result, the displacement of the carrier concentration profiles due to the heat-treatments showed that the diffusivity of the dopant strongly increased with the implanted dose. This effect, which was particularly evident at high temperature, could be attributed either to the increase of As concentration or to the increased amount of precipitates per unit surface, *i.e.*, to lattice defects in excess generated by the precipitation process.

The present work extends SAXS examinations to less heavily doped compositions (a difficult task owing to the small thickness of the implanted layer) with the aim of controlling the occurrence of precipitation at lower dopant concentrations and of getting further information on this process. In addition, it was intended to verify whether the precipitation process can influence the high temperature diffusivity of As.

Experimental

For these experiments, we used (100)-oriented, CZ-pulled, p-type, boron-doped silicon slices of $1 \Omega\text{-cm}$ resistivity.

The samples were arsenic implanted at an energy of 100 keV at three different doses, *i.e.*, 1×10^{16} , 2×10^{16} , and $5 \times 10^{16} \text{ cm}^{-2}$. All slices were tilted 7° off axis to reduce ion channeling effects during implantation.

To electrically activate the dopant and to recover the radiation damage, the implanted samples were laser annealed by a 20 ns single pulse delivered by a Q-switched ruby oscillator operating in a multimode regime. An optical guide was used to yield a 16 mm diam light spot with an energy density of 1.8 J/cm^2 .

To analyze the influence of dopant concentration on the precipitation and the size distribution of the particles, a set of samples, corresponding to the three implanted doses, was furnace annealed at 900°C for 30 min in nitrogen atmosphere.

A second set of specimens with surface concentration corresponding to the highest dose, but with different amounts of excess dopant per unit surface, was annealed at 1000°C for 10 min, in order to study the effect of precipitation on As diffusivity. The amount of excess dopant was reduced by thinning the laser-annealed wafers using anodic oxidation.

Carrier concentration profiles were determined by a specially designed apparatus which performs automatic anodic stripping followed by incremental sheet resistance and Hall effect measurements (8). The van der Pauw geometry was previously etched on the specimen's surface by a photolithographic process. The thickness of the removed layer was also controlled by Talystep measurements.

The junction depth was evidenced by the standard angle lapping and staining technique using a CuSO_4 solution.

The features of the precipitates (size distribution and shape) were studied by small-angle x-ray scattering, using the techniques which were detailed in a previous paper (7). A new Kratky camera was employed for the present observations: the width of the main slit, defining the incident beam, was $80 \mu\text{m}$. The sample-to-counter distance was 200 mm, and the scattered intensity was recorded every $50 \mu\text{m}$ of counter displacement (corresponding to 0.0143° of 2θ) from 300 to $5000 \mu\text{m}$ (0.086° - 1.43° of 2θ), with a fixed counting time of 1000s.

Results and Discussion

Carrier density profiles of our specimens after laser annealing, which corresponds to complete electrical activation of the dopant, are reported in Fig. 1, together with the profiles after 30 min heating at 900°C. The most heavily doped composition presents the lowest carrier concentration in the plateau region ($\sim 2 \times 10^{20} \text{ cm}^{-3}$), while the more dilute one shows a higher density ($\sim 2.6 \times 10^{20} \text{ cm}^{-3}$). This indicates incomplete precipitation; in fact, the rate of a precipitation process decreases with decreasing supersaturation.

The carrier concentration values in our profiles are slightly higher ($\sim 10\%$) than those we reported in Ref. (7). This results from more accurate determinations of the thickness of the removed layer.

SAXS examinations were performed only on the specimens doped at 2×10^{16} and 1×10^{16} , as the most heavily doped composition was the object of previous investigations which were reported in detail in Ref. (7).

A remarkable increase of the intensity scattered at small angles was observed by comparing the experimental SAXS curves after As implantation and laser annealing with those after heat-treatment of the same specimens at 900°C for 30 min.

As it was concluded in our previous paper (7), the occurrence of this small angle scattering is related to the formation of As precipitates. In agreement with this statement, the present experiments show that the amplitude of this effect decreased with decreasing concentration of the dopant.

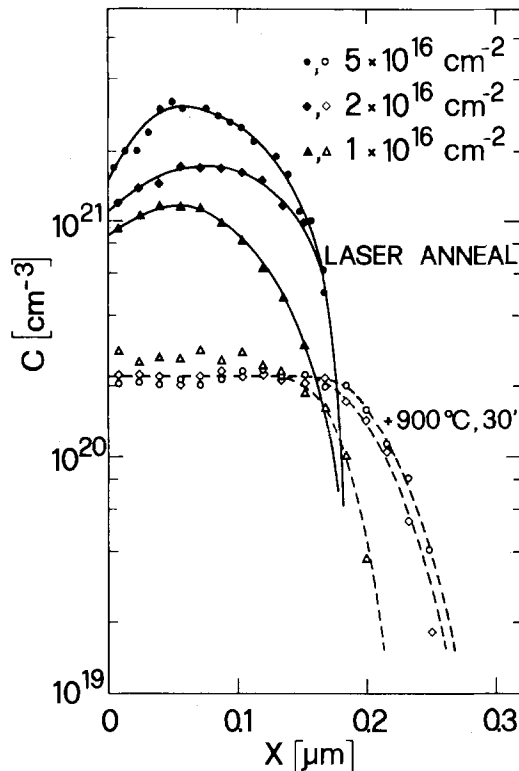


Fig. 1. Carrier concentration profiles of ion-implanted and laser-annealed specimens for three different arsenic doses. Black symbols refer to the initial condition, when all dopant is electrically active, and open symbols to the one after heating 30 min at 900°C.

The Guinier plot ($\log I$ vs. h^2 , where $h = (4\pi \sin \theta/\lambda)$ of the net observed intensity for the specimens implanted with a dose of $2 \times 10^{16} \text{ cm}^{-2}$ is reported in Fig. 2a, while the corresponding plot for the less doped specimen ($1 \times 10^{16} \text{ cm}^{-2}$) is shown in Fig. 2b. In both cases, it can be observed that the scattered intensity decreases with increasing scattering angle, indicating the absence of particle interference effects.

In addition, the deviation of the graph from a straight line in the very small angle region clearly shows that the radius of gyration of the particles is not unique; i.e., the size of the precipitates is, as expected, distributed over a range of values. Indications of the particle size distributions can be obtained by subtraction of the successive less-sloped tangents (9, 10). With this graphical method, the size distribution is approximated by a set of a few discrete fractions of particles of given volume, and the corresponding radii of gyration can be determined. As is known, the radius of gyration for a particle is defined as the root mean square distance of the electrons from the center of charge.

As is shown in Fig. 2, the distributions can in both cases be approximated by three groups of particles. The corresponding radii of gyration turn out to be larger in the less concentrated solution.

The increase of the radii of gyration with decreasing dopant concentration is put in better evidence considering also the results that we obtained by the same method on specimens implanted with the highest As dose [see Fig. 6 in Ref. (7)].

To get further information on the features of the precipitates as a function of dopant supersaturation, the shape of the particles was investigated by analysis of the SAXS intensity data. Figure 3 reports the theoretical slopes for some elementary shapes in the $\log I$ vs. $\log h$ plot, which permits the derivation of this type of information (11) together with the experimental trends for our specimens. The slope of -5.6 observed in the more dilute solution indicates a shape which approximates that of a sphere. The specimens implanted with $2 \times 10^{16} \text{ cm}^{-2}$ show a slope of -4 , which still corresponds to three-dimensional

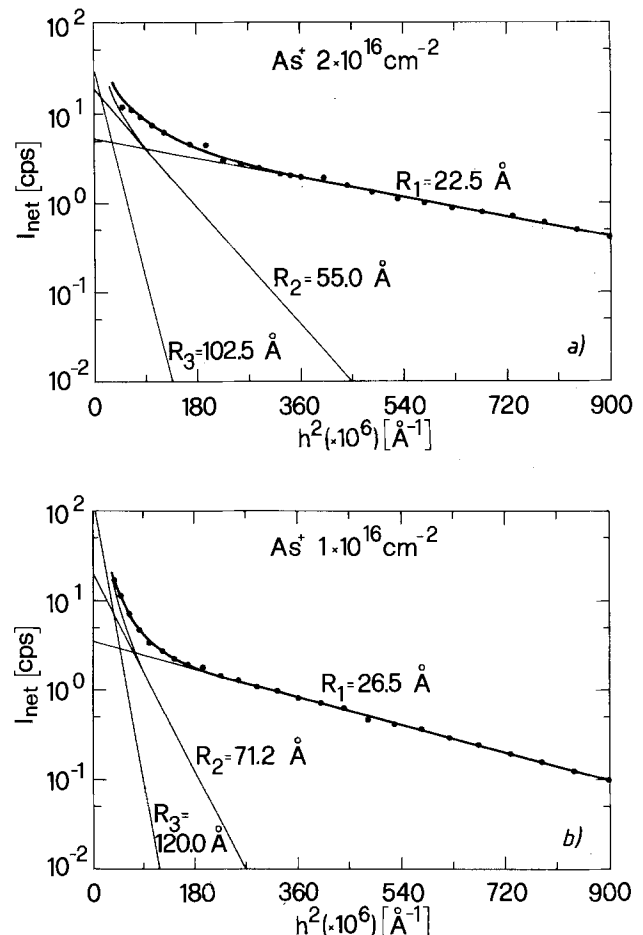


Fig. 2. Guinier plot of the small angle intensity resulting by heating the ion-implanted laser-annealed specimens at 900°C for 30 min. The analysis by the method of the successive less-sloped tangents is also outlined and the proper values of the radii of gyration are indicated. Maximum As concentrations in the profile are (a) $1.7 \times 10^{21} \text{ cm}^{-3}$ and (b) $1.1 \times 10^{21} \text{ cm}^{-3}$.

particles, probably ellipsoids of revolution with semiaxes a , a , and va , with $v \approx 0.5$.

By the same method, we determined on samples implanted with $5 \times 10^{16} \text{ cm}^{-2}$ [see Fig. 8 in Ref. (7)] a slope of -2.5 , which corresponds to platelets having a thickness of the order of an atomic layer.

Consideration of these results puts into evidence that the shape of the precipitates also depends markedly on the concentration of As. The features of As precipitates are summarized in Table I, which includes SAXS results of Ref. (7). For each implanted dose, the maximum dopant concentration C_0 in the profile is indicated, together with the corresponding supersaturation $i = C_0/C_e$, where C_e is the equilibrium solubility of As in silicon at 900°C ($C_e = 2 \times 10^{20} \text{ cm}^{-3}$). Besides the shape of the precipitates, we report for each composition the three radii of gyration in the Guinier distribution, together with the corresponding percentage of precipitate in each group. These fractions were calculated from the corresponding Guinier plot, by taking into account the precipitate's shape (10).

A more rigorous determination of the particle size statistical distribution was also obtained in the form of a continuous curve like the one in Fig. 7 of Ref. (7). This analysis confirmed the trend which is shown in Table I.

These results put into evidence that decreasing the concentration of the dopant from 3.2 to $1.1 \times 10^{21} \text{ cm}^{-3}$ leads to a remarkable decrease of the population of particles of small size and to a corresponding increase of the fraction of particles with the upper radius. At the same time, the shape of the precipitates evolves from that of a thin platelet, becoming three-dimensional and approaching at last that of a sphere.

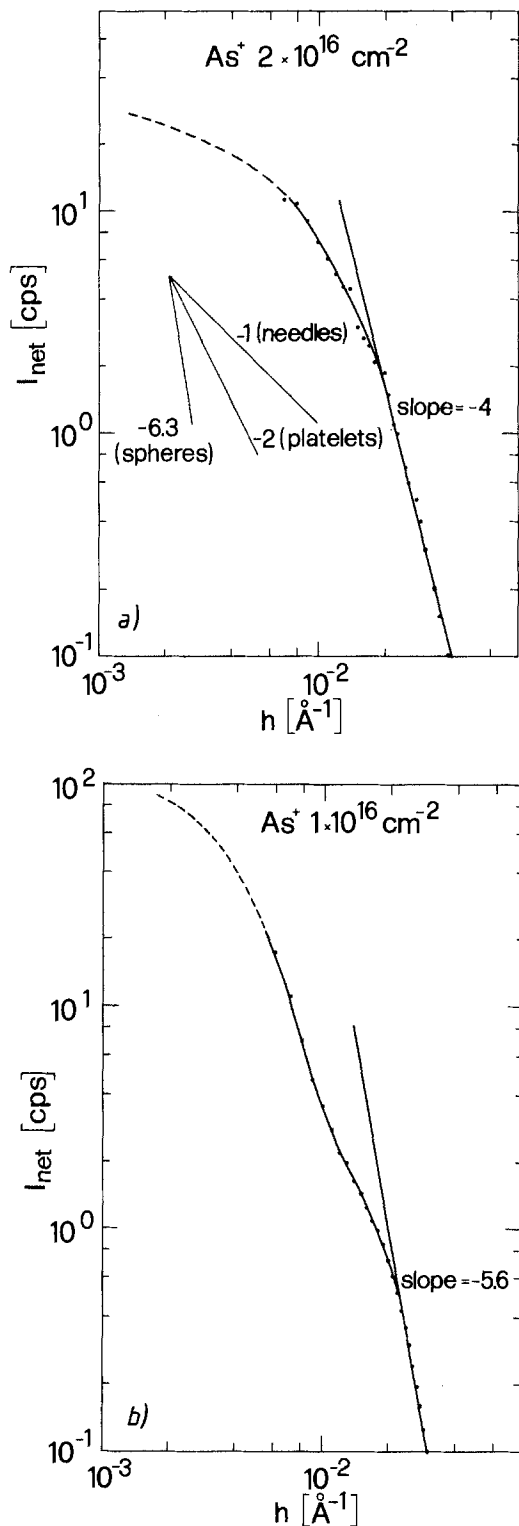


Fig. 3. Experimental slope values providing information on the shape of the precipitates: (a) dose $2 \times 10^{16} \text{ cm}^{-2}$; (b) dose $1 \times 10^{16} \text{ cm}^{-2}$. The theoretical slope values for main limiting cases are reported for comparison.

It seems possible to interpret this behavior on the basis of precipitation kinetics determined by the nucleation

process. A growing particle becomes incoherent because the strain energy term increases with size. The very small difference of the tetrahedral radii of Si and As leads to a very small strain energy and, hence, favors a coherent interface between matrix and precipitate. In the case of a coherent boundary, the strain energy is not very dependent on shape; therefore, with decreasing supersaturation, the nuclei evolve toward a spherical shape because this reduces the surface energy term and hence the reversible work ΔG^* for the formation of the critical nucleus.

On the same line, the increase of the size of the precipitate population is explained as due to the decrease of the precipitate density which results from the decrease of the nucleation frequency with decreasing supersaturation.

Following the classical theory, the nucleation frequency depends on $\exp(-\Delta G^*/kT)$, where, at constant temperature, the term $\Delta G^* = \text{const.}/(\ln i)^2$. From the data in Table I, it is easily seen that decreasing the dopant concentration from 3.2 to $1.15 \times 10^{21} \text{ cm}^{-3}$ leads to an increase in ΔG^* of a factor of 2.5, a figure which can fully explain a marked decrease of the density of the particles and the consequent increase of the population with the largest radius.

We consider now the diffusivity of the dopant. If the radius of the equivalent sphere available to a particle is sufficiently large, the size of the precipitate will be determined by the diffusivity of the solute. This condition is likely to have been satisfied for the largest group of particles in our dilute solution. These specimens, as it is shown in Fig. 1, are still supersaturated after 30 min heat-treatment.

With the hypothesis that the smaller precipitates ($R_1 = 26 \text{ \AA}$ and $R_2 = 71 \text{ \AA}$) depleted the equivalent sphere available for their growth, one obtains for the largest particles ($R_3 = 120 \text{ \AA}$) a radius of the equivalent sphere $r_e \approx 730 \text{ \AA}$, and these regions should be responsible for the residual supersaturation.

With this approximation, the diffusivity of arsenic can be calculated by the diffusion-limited growth model of a spherical particle. By solving the diffusion equation obtained applying the stationary approximation in a finite matrix, one obtains the growth law (12)

$$dr(C_p - C_0) = \frac{2(C_p - C_0)(r_m^3 - r^3)}{2r_e^3 r - 3r_e^2 r^2 + r^4} D dt$$

where C_p is the solute concentration in the precipitate, $r_m = r_e(C_0 - C_e)/(C_p - C_e)$ is the maximum value of the radius attainable by the particle, and D and t have their usual meanings.

With this model, the growth problem is treated by assuming the particle radius r to be nearly constant and solving the time-independent diffusion equation in the matrix (13). Actually, the high concentration inequality existing in our case between the precipitate and the matrix guarantees that r is a slowly varying function of time. The radius r of the particles was deduced from the corresponding radius of gyration R by the relation valid for a sphere: $r = R\sqrt{5/3}$. The value for the largest particles in our dilute samples turned out to be $\approx 155 \text{ \AA}$. In agreement with the results of Ref. (7) which led to the conclusion that the stoichiometry of the precipitates is SiAs, C_p was assumed to be $2.5 \times 10^{22} \text{ cm}^{-3}$. By using these data, the numerical solution of the above equation gave $D = 2.2 \times 10^{-14} \text{ cm}^2 \text{ s}^{-1}$. It is worth noticing that by using the simple growth model in an infinite matrix (14)

$$r^2 = 2Dt(C_0 - C_e)/(C_p - C_e)$$

Table I. Features of arsenic precipitates at 900°C for different dopant concentrations

Implanted dose (cm^{-2})	C_0 (cm^{-3})	i supersaturation	Shape	R_1 (\AA)	f_{R_1}	R_2 (\AA)	f_{R_2}	R_3 (\AA)	f_{R_3}
5×10^{16}	3.2×10^{21}	16	Thin platelets	20	0.80	44	0.17	95	0.03
2×10^{16}	1.7×10^{21}	8.5	Oblate ellipsoids	22	0.77	55	0.18	102	0.05
1×10^{16}	1.15×10^{21}	5.7	Spheres	26	0.60	71	0.17	120	0.23

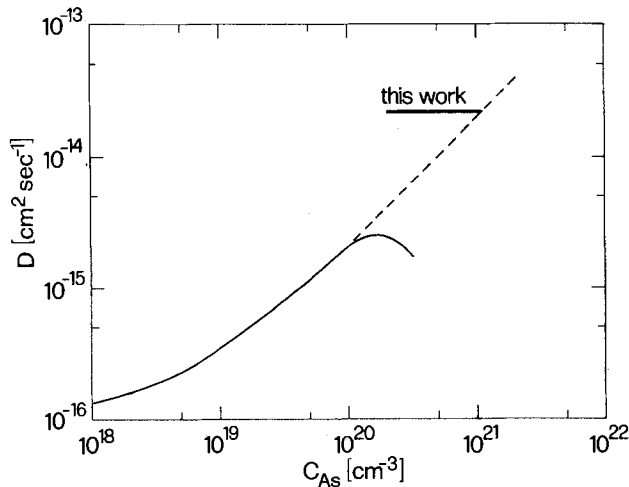


Fig. 4. Diffusion coefficient vs. As concentration at 900°C. The solid line represents the behavior, generally implemented in the simulation programs, which takes into account aggregation phenomena. The dashed line shows the high concentration extrapolation of the model based on the ionized point defects (15). Our experimental value and the corresponding concentration range are also reported.

the diffusivity value turns out to be $1.7 \times 10^{-14} \text{ cm}^2\text{-s}^{-1}$, very close to the previous figure.

This comparison puts in evidence that our diffusivity at 900°C, although underestimated as a consequence of the adopted approximations, should be close to the actual value.

This diffusivity represents an average in the concentration range $(2-10) \times 10^{20} \text{ cm}^{-3}$ and, as is shown in Fig. 4, is in good agreement with the one obtained by extrapolation of the data reported in literature according to the well-known model of diffusion by ionized point defects (15).

We notice that, to the best of our knowledge, our data are the only experimental values concerning such a high concentration of arsenic in silicon. In fact, the diffusivity data reported in literature refer to concentrations up to about 10^{20} cm^{-3} . They were generally deduced applying the Boltzmann-Matano method to the total arsenic profile and show (see Fig. 4) an apparent reduction of the diffusivity for concentrations exceeding the above-mentioned value (2, 4, 6, 15). This trend is due to the fact that the fraction of the dopant which is present in the form of precipitates (or clusters, according to the authors who proposed this model) is not mobile. Therefore, the solid line with hump shown in Fig. 4 refers to the total As diffusivity, while the solid line with dashed continuation shows the substitutional As diffusivity.

We consider now the influence of precipitation on the diffusivity of arsenic.

Previous experiments performed in the temperature range 850°-1000°C put into evidence that the displacement of the concentration profile with the thermal treatment increases with the implanted dose. This effect, which is also shown in Fig. 1, resulted in better evidence at 1000°C [see Fig. 1 of Ref. (7)].

This phenomenon can be attributed either to the increase of dopant concentration or to the increase of the amount of precipitated dopant per unit surface. The increase of arsenic diffusivity with the concentration is commonly attributed to the increase of the concentration of ionized point defects with rising Fermi level (15). On the other hand, one could attribute to the precipitation process the formation of an excess of point defects enhancing the diffusivity of the dopant.

Previous experiments could not discriminate between these two hypotheses, as both the arsenic concentration and the amount of precipitates increase with the implanted dose.

In order to detect the effect of precipitation on the diffusivity of arsenic, we performed the following experiment on a set of specimens implanted with the highest

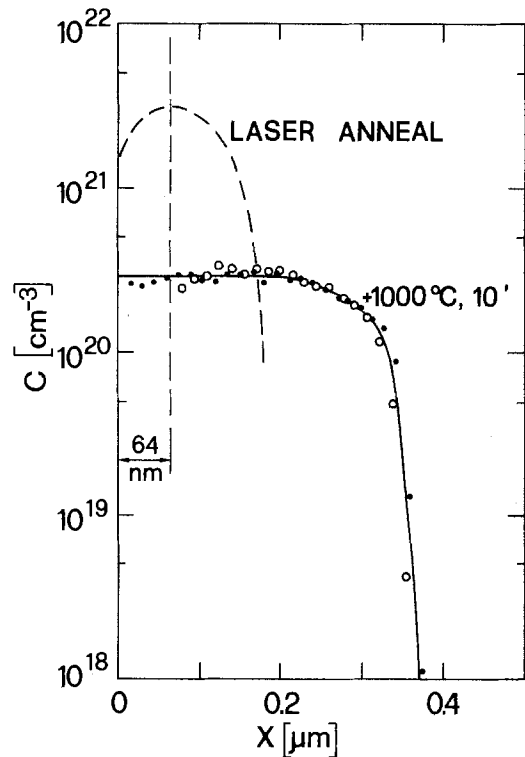


Fig. 5. Carrier concentration profiles of $5 \times 10^{16} \text{ As cm}^{-2}$ implanted samples. Dashed curves show the dopant distribution after laser annealing. Dots refer to the profiles after heating for 10 min at 1000°C; the open symbols concern the specimen thinned 64 nm before this thermal treatment. The two profiles, taking into account the shift of the surface, superimpose.

dose: after laser annealing, part of these samples was thinned by anodic oxidation, removing 64 nm of silicon, thus reducing by a factor of 2 the amount of excess dopant per unit surface, still keeping the same value of the dopant surface concentration ($3.2 \times 10^{21} \text{ cm}^{-3}$). Both types of specimens were subsequently annealed 10 min at 1000°C.

The results of this experiment are reported in Fig. 5, which shows that the profiles coincide, providing thereby conclusive evidence that at high temperatures the diffusivity is controlled by the concentration and does not depend appreciably on the amount of precipitates. The observation of the junction depth supports the same conclusion. In fact, the optical micrograph shown in Fig. 6, showing a specimen selectively thinned as above by anodic oxidation before the heat-treatment, puts into evidence that the junction depth is the same both in the thinned (left side) and the standard (right side) regions.

Conclusions

SAXS experiments performed on ion-implanted, laser-annealed silicon slices doped with arsenic in the concen-

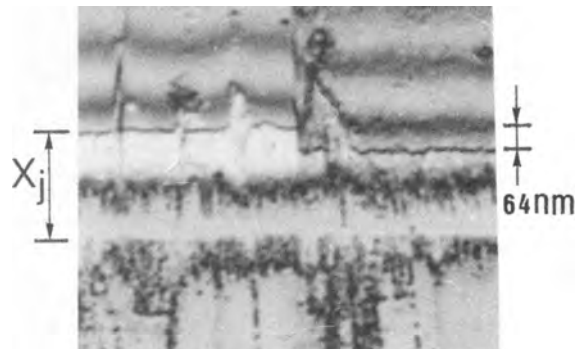


Fig. 6. Optical micrograph taken in a lapped and stained specimen, implanted at $5 \times 10^{16} \text{ cm}^{-2}$, laser annealed and selectively thinned (64 nm) in the left side. After heating for 10 min at 1000°C, the junction depth results are the same in both regions.

tration range $3.2\text{--}1.1 \times 10^{21} \text{ cm}^{-3}$ showed the occurrence of precipitation after heating at 900°C .

The net observed small angle intensity, and hence the amount of the new phase, decreases with decreasing supersaturation of the dopant. Moreover, the size distribution is shifted toward higher values. This implies that, in agreement with the classical theory of nucleation, the density of precipitates decreases with decreasing supersaturation. In addition, the shape of the particles evolves from that of a platelet, becoming three-dimensional and approaching at last that of a sphere.

Consideration of the diffusion-limited growth model for a spherical precipitate, and of the radius ($\sim 150\text{\AA}$) of the largest group of particles in the more dilute solution, led to a diffusivity of arsenic at 900°C of about $2 \times 10^{-14} \text{ cm}^2\text{-s}^{-1}$. This figure, which is an average in the concentration range $2\text{--}10 \times 10^{20} \text{ cm}^{-3}$, is in good agreement with the one expected on the basis of the well-known model of arsenic diffusion by ionized point defects (15).

The experiments performed by reducing the amount of excess dopant per unit surface, still keeping the same value of arsenic surface concentration, showed that, at high temperature (1000°C), the diffusivity is controlled by the concentration. In fact, the shift of the carrier profile and the junction depth do not depend appreciably on the amount of precipitates.

Acknowledgments

The authors wish to thank A. Armigliato and A. Mazzone for the useful discussion and suggestions.

Manuscript submitted May 27, 1985; revised manuscript received Aug. 10, 1985.

C.N.R.-Istituto LAMEL assisted in meeting the publication costs of this article.

REFERENCES

1. S. M. Hu, in "Atomic Diffusion in Semiconductors," D. Shaw, Editor, p. 217, Plenum Press, London (1973).
2. R. B. Fair and G. R. Weber, *J. Appl. Phys.*, **44**, 273 (1973).
3. M. Y. Tsai, F. F. Morehead, J. E. E. Baglin, and A. E. Michel, *ibid.*, **51**, 3230 (1980).
4. J. Morota, E. Arai, K. Kobayashi, and K. Kudo, *ibid.*, **50**, 804 (1979).
5. E. Guerrero, H. Potzl, r. Tielert, M. Grasserbauer, and G. Stingerer, *This Journal*, **129**, 1826 (1982).
6. S. M. Hu, in "VLSI Science and Technology/1985," W. M. Bullis and S. Broydo, Editors, p. 465, The Electrochemical Society Softbound Proceedings Series, Pennington, NJ (1985).
7. D. Nobili, A. Carabelas, G. Celotti, and S. Solmi, *This Journal*, **130**, 922 (1983).
8. R. Galloni and A. Sardo, *Rev. Sci. Instrum.*, **54**, 369 (1983).
9. R. Hosemann and S. N. Bagchi, "Direct Analysis of Diffraction by Matter," North Holland, Amsterdam (1962).
10. M. H. Jellinek, E. Solomon, and J. Fankuchen, *Ind. Eng. Chem. (Anal. Ed.)*, **18**, 172 (1946).
11. J. C. Grosskreutz, in "Handbook of X-Rays," E. F. Kaelble, Editor, McGraw Hill, New York (1967).
12. O. Simmich and H. Löffler, *Phys. Status Solidi A*, **65**, 153 (1981).
13. S. R. Coriell and R. L. Parker, *J. Appl. Phys.*, **36**, 632 (1965).
14. H. B. Aaron, D. Fainstein, and G. R. Kotler, *ibid.*, **41**, 4404 (1980).
15. R. B. Fair, in "Silicon Integrated Circuits (Part B)," D. Kahng, Editor, p. 28, Academic Press, New York (1981).

Ultrafine Aerosol Particles in Semiconductor Cleanrooms

R. P. Donovan and B. R. Locke

Research Triangle Institute, Center for Aerosol Technology, Research Triangle Park, North Carolina 27709

C. M. Osburn* and A. L. Caviness

Microelectronics Center of North Carolina, Research Triangle Park, North Carolina 27709

ABSTRACT

The fabrication of VLSI chips with high yields on small device geometries requires control of particulate contamination during manufacture. One potential source of particulate contamination is the ambient air of the production facility. Monitoring and control of these ambient aerosol particles require increasingly sophisticated instrumentation capable of measuring smaller and smaller particles. This paper identifies three instrument types capable of sizing ultrafine ($\leq 0.1 \mu\text{m}$ diam) aerosol particles in real time: the integral mobility analyzer, the differential mobility analyzer, and the diffusion battery. All three of these sizing instruments use an independent condensation nuclei counter to count particles in size-separated channels. Two of these combinations, the differential mobility analyzer/condensation nuclei counter and the diffusion battery/condensation nuclei counter, have been used to measure the ultrafine aerosol particle size distribution of various quality semiconductor cleanrooms. The data reduction routines of the differential mobility analyzer/condensation nuclei counter combination break down when ultrafine aerosol particle concentration falls below about 1 particle/cm³. The diffusion battery/condensation nuclei counter combination functions to below 0.01 ultrafine aerosol particle/cm³. Data taken by this instrument combination in a state-of-the-art cleanroom at rest show that the peak concentration of ultrafine aerosol particles occurs near $0.1 \mu\text{m}$, the cumulative distribution curve being relatively flat below that size.

Device dimensions continue to shrink in the push toward faster, more powerful silicon chips. Processing technology for submicron chip designs is moving from the laboratory to the production floor.

As the size of the modeled device areas decreases, so does the critical size of certain unmodeled device areas, such as surface defects or bulk imperfections. Surface particles that are too small to affect device behavior when minimum device dimensions are in the $2\text{--}3 \mu\text{m}$ range can

become important when device dimensions are submicron. An arbitrary rule of thumb that defines the size threshold for surface particles of concern is 0.1 times the minimum device dimensions—devices designed with $5 \mu\text{m}$ line widths should be built in manufacturing areas in which $0.5 \mu\text{m}$ particles are monitored and controlled. By this rule, submicron device design and manufacture requires measurement and control of ultrafine particles (size $\leq 0.1 \mu\text{m}$). Outdoor measurements indicate very high concentrations of such ultrafine particles in the urban ambient air (Fig. 1).

*Electrochemical Society Active Member.

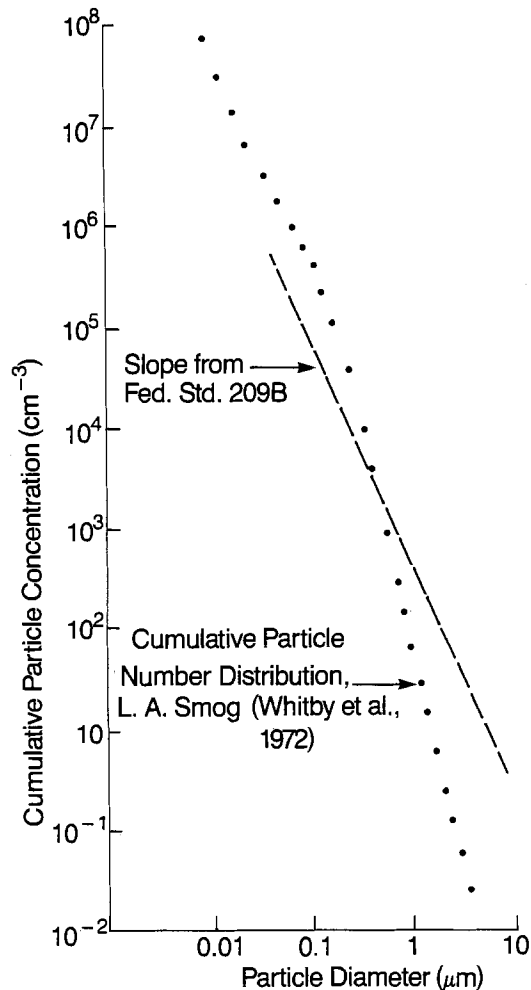


Fig. 1. Cumulative size distribution of ambient urban air (1)

What is of more direct concern to chip manufacturers is the concentration of ultrafine particles in the semiconductor manufacturing area, typically a cleanroom with air quality rated at Class 100 or better,¹ at least under resting conditions (no people in the clean room). Makeup air entering such a facility not only passes through building humidity and temperature conditioning equipment, but is also filtered through an inlet (high efficiency particulate air (HEPA) filter) prior to its introduction to the cleanroom recirculating loop. Typically, makeup air in a cleanroom constitutes only 10-20% of the total air flow so that the bulk of the recirculating cleanroom air passes through the cleanroom HEPA filter bank (inside the cleanroom loop and distinct from the inlet HEPA filter section) many times before discharge. Thus, the recirculating air inside a cleanroom is well filtered and of greatly reduced aerosol particle concentration compared with the ambient air, and is probably of greatly modified aerosol particle size distribution based upon published penetration curves for HEPA filters (3) (Fig. 2). Such curves show very low penetration for both small ($< 0.01 \mu\text{m}$) and large ($> 1 \mu\text{m}$) particles. A maximum in penetration occurs between these limits in the transition region between particle collection mechanisms. This filter property could well be expected to suppress the concentration of ultrafine aerosol particles found in cleanrooms.

Data to support this conclusion are scarce. Serious questions have not been raised about this portion of the cleanroom particle spectrum until recently. Even with the growing interest, however, the instrumentation challenges in measuring ultrafine aerosol particles at the ultralow concentrations characteristic of today's clean-

¹Air quality classifications are defined in Federal Standard No. 209B (2). Figure A-1 is a reproduction of a figure from that standard.

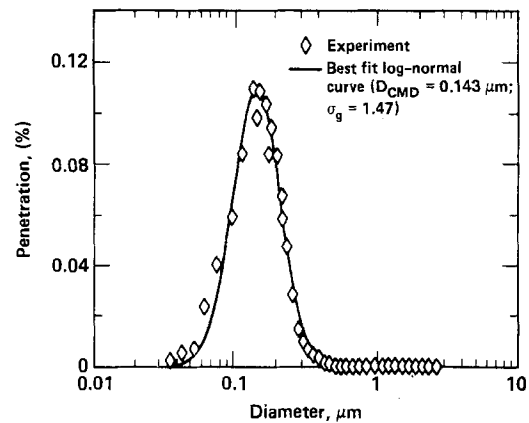


Fig. 2. Particle penetration through a HEPA filter (3)

rooms have not yet been satisfactorily met. This paper reviews candidate aerosol particle measuring instrumentation, selects certain of these instruments for making cleanroom measurements, and presents both differential and cumulative number distributions of aerosol particles measured in semiconductor cleanrooms having various levels of air cleanliness.

Instrumentation Review and Selection

While many aerosol-particle measuring instruments exist, the number capable of detecting ultrafine aerosol particles is not great and, when the added requirements of single-particle detection in real time or near real time are added, the list becomes very short (Table I). Inertial classifiers operate most efficiently in the 1-10 μm range, well above the ultrafine range of interest here. By reducing the operating pressure below atmospheric, the lower limit of size detection by this principle can be pushed into the ultrafine aerosol particle range, but the lack of real-time analytic capability remains a severe shortcoming. Using a quartz crystal (listed under Miscellaneous types in Table I) as the collection stage does provide real-time readout, but single-particle resolution is possible only for larger particles.

Light scattering instruments, such as the optical particle counter (OPC), popular in the 0.3-3 μm size range because of its real-time readout and single-particle counting capability, lose adequate sensitivity on the fringe of the ultrafine particle regime. New designs, using either two lasers for two-sided illumination of the scattering cavity or shorter wavelength lasers, are claimed to detect aerosol particles as small as 0.05-0.06 μm (4). Instrument noise levels, including signals generated by molecular scattering, match the scattering signal from this size particle so that counting small concentrations of ultrafine aerosol particles is limited by background noise over the lower channels in most laser spectrometers. In practice, this statement means that, although laser spectrometers are very successful at determining size distributions at high particle concentrations, they prove less satisfactory at concentrations typical of a cleanroom. This conclusion applies only to the size range below about 0.3 μm , where sampling flow rates must be reduced so that the entire sample flow can be passed through a small volume illuminated by the laser. Although keeping this volume small reduces molecular light scattering and thus allows detection of small particles, the number of particles counted in a sample remains low because of the small cross section through which all of the sample must flow. For ultrafine particle measurements in the cleanroom, the laser spectrometer is of limited use at present.

The traditional basic instrument design used by aerosol technologists to detect ultrafine aerosol particles is the condensation nuclei counter (CNC) (5). This counter solves the small scattering signal problem of ultrafine particles by converting each ultrafine aerosol particle into an optically huge particle. It does this by passing the ultrafine aerosol stream through a supersaturated vapor

Table I. Candidate methods/instruments for measuring aerosol particle size distributions in a semiconductor cleanroom

Type	Measurement principle/ detection method	Size range (μm)	Real-time analysis	Single particle counting/sizing capability
Inertial classifiers				
Cyclones	Centrifugal fractionation/ weighing	3-30	No	No
Centrifuges		0.1-1.0	No	No
Inertial impactors		0.5-5	No	No
Low-pressure inertial impactors		0.05-5	No	No
Aerodynamic particle sizers	Particle acceleration in gas flow/time of flight	0.5-15	Yes	Yes
Light scattering instruments				
Single-particle optical counters	Light scattering	0.2-5	Yes	Yes
Laser spectrometers		0.06-3	Yes	
Electrical mobility analyzers				
Integral samplers	Removal of electrically charged particles in mobility increments	0.01-0.5	Nearly	Sizing but no counting capability
Differential samplers		0.01-1.0	Nearly	
Diffusion batteries	Particle diffusion to a capture surface (i.e., a capillary wall)	0.002-0.3	Nearly	Sizing but no counting capability
Condensation nuclei counters				
With diffusion battery	Particle growth/light scattering after up- stream sizing by	0.002-0.3	Nearly	Yes
With electrostatic classifier (differential mobility analyzer)		Charged particle separation	0.01-1.0	
Miscellaneous types				
Microscopy (optical; electron)	Imaging	> 0.002	No	Yes
Resistivity	Electrical resistivity change by electrolyte displacement	> 0.5	No	Yes
Quartz X-tal cascade impactor	Frequency change by mass loading of a quartz crystal	0.05-35	Yes	No/Yes (Large particles only)
Triboelectric	Contact charge transfer	No unique size dependence	Yes	No

in which each ultrafine particle serves as a site for vapor condensation. By this technique, ultrafine particles grow into 10 μm or larger particles that are easily detected by a built-in optical counter. A CNC can count aerosol particles as small as 0.01 μm (or even smaller, depending on operator technique and sanguinity). However, it provides little size discrimination—a 0.02 μm particle is counted the same as a 0.2 or a 2 μm particle. To obtain a size distribution requires an upstream size separating device such as an electrical mobility analyzer (6) or a diffusion battery (7). Neither of these devices counts particles; they simply remove a certain aerosol fraction from the total aerosol flow (the integral mobility analyzer or the diffusion battery) or else break out a selected size fraction of the total aerosol flow into a separate airstream that can be counted (the differential mobility analyzer).

Size resolution can be quite good using the differential mobility analyzer (6)—the number of size increments between 0.01 and 1 μm can exceed 30 in the commercial version. Size separation in any mobility analyzer depends on the ability of electric fields to remove charged particles from streamlines, and, in the differential mobility analyzer, aerosol charge is controlled by passing the aerosol stream through highly ionized air, which reduces the particle charge distribution to a Boltzmann equilibrium. However, since the particle fraction actually electrically redirected into a separate countable airstream is primarily just the singly charged, unipolar fraction of any given size-band population, most of the particles in a given size range are discarded. (In Boltzmann equilibrium, the charge distribution on particles in any size range is symmetrical and a maximum at zero charge.) In a cleanroom, the small number of total particles present renders this measuring scheme inappropriate; that the total number of particles counted is only a small fraction of what is only a small concentration to begin with means that this counting technique is less satisfactory than other techniques in which all, or nearly all, particles in a given size range are counted. Thus, techniques with poorer size resolution than the differential mobility analyzer may, in

fact, prove better suited for collecting cleanroom size-distribution data in the ultrafine particle size range.

One such alternative is the integral mobility analyzer. This analyzer differs from the differential mobility analyzer in at least two significant features: (i) particles entering the analyzer are charged to saturation by ion diffusion (in the differential mobility analyzer, particle-electrical charge is reduced to a Boltzmann distribution by a Kr-85 neutralizer), and (ii) only one airstream exits the analyzer; particles removed from that airstream are electrostatically precipitated onto an electrically biased center-rod electrode (in the differential mobility analyzer, two streams exit the analyzer, one containing particles having electrical mobilities that fall within a narrow band, and the other the rest of the airstream; some particles are also precipitated). That all particles are unipolarly charged to saturation means that the electrical force acts on all the particles rather than just on a small fraction as is true in the differential mobility analyzer. Thus, one of the major sources of particle loss in the differential mobility analyzer is absent in the integral mobility analyzer.

The second alternative to the high resolution differential mobility analyzer is the diffusion battery. This instrument operates on an entirely different particle capturing principle than the mobility analyzers. Electrical forces play no role in the designed operation of a diffusion battery, the Brownian motion alone of the ultrafine particles being the mechanism whereby the particles collide with the capture surfaces. By passing the aerosol flow through narrow passageways of varying length and noting the incremental particle removal associated with each path-length, the particle-size distribution of the original aerosol can be reconstructed. Thus, though the boundaries between adjacent size channels are not sharp and the resolution of the separation is relatively crude compared to the differential mobility analyzer, the fact that all particles participate in this statistical removal process means that the technique may be better suited for cleanroom measurements than those techniques that count only a fraction of the total particles present.

Other techniques listed in Table I fall short for one reason or another. Microscopy is excellent by all measures except ease and speed of data reduction. One can examine individual particles in great detail, but deducing concentrations and size distributions from microscopic counting is a tedious technique and one prone to error. The resistivity technique requires particle collection and resuspension into an electrolyte. The triboelectric technique depends on control of subtle surface properties and measures a total charge transfer that is not easily converted to a size distribution.

Based on their size range, single-particle particle counting capability, and compatibility with real-time or near-real-time measurement, the instrument combinations of Table I suitable for sampling ultrafine aerosol particles in cleanrooms consist of the following size separating stages (see Appendix B for a discussion of commercial availability: (i) the differential mobility analyzer, (ii) the integral mobility analyzer, and (iii) the diffusion battery.

Experimental

All the above instruments only separate aerosol particles according to size. A downstream CNC is used as the actual particle counter for all three of these particle separating devices. This paper reports the results of using combinations no. 1 (a differential mobility analyzer/CNC) and no. 3 (a diffusion battery/CNC) plus a single-particle optical counter and a laser spectrometer (see light scattering instruments, Table I) in semiconductor cleanrooms of varying air quality. The integral mobility analyzer/CNC (combination no. 2) was not evaluated, so no data from this combination will be presented. Monitoring cleanrooms of the highest air quality has also included periods in which the ultrafine aerosol particle measurement has been by total CNC count alone without any of the size separating stages. While this approach lumps all ultrafine aerosol particles into a single measurement, this single datum can be added to a conventional cumulative size distribution, as generated by an optical particle counter (OPC) or a laser spectrometer. As indicated in Table I, the smallest particle detectable by most OPC's is about 0.2 μm . Laser spectrometers can measure as low as 0.06-0.09 μm but at a much reduced sample flow rate (1 ft^3/min for the OPC; 0.002-0.01 ft^3/min for the laser spectrometer). The low sampling flow rate of the laser spectrometer generally makes it less suitable for cleanroom measurements than the OPC. However, the laser spectrometer is excellent for calibration of ultrafine aerosol instruments at high particle concentration as discussed next.

Prior to extensive site measurements, the two instrument combinations were cross checked with respect to a laser spectrometer. A lengthy series of comparative measurements was carried out using such test aerosols as freshly generated monodisperse salt, freshly dispersed polystyrene-latex (PSL) spheres, polydisperse ambient room air, and prefiltered room air.

With all these aerosol sources, the aerosol particle concentration greatly exceeded that found in a typical cleanroom. This high concentration aids in establishing instrument measurement consistency but does not necessarily adequately rate instrument suitability for cleanroom use. The latter judgment requires tests at actual cleanroom concentrations, a condition created most readily by cleanrooms themselves. Such tests will be described below.

In the calibration test series of this section, the most extensive comparisons were between a differential mobility analyzer/CNC combination, hereafter called simply the DMPS (see Appendix B), and a laser spectrometer, the PMS Model LAS-X, hereafter referred to as the LAS-X. The size ranges detected by each of these two instruments overlap, both measuring aerosol particles in the 0.09-0.5 μm size bracket. Monodisperse PSL spheres are commercially available in several sizes within this range. Figure 3 plots measurements made of 25 PSL aerosol streams using both the DMPS and the LAS-X. Most of

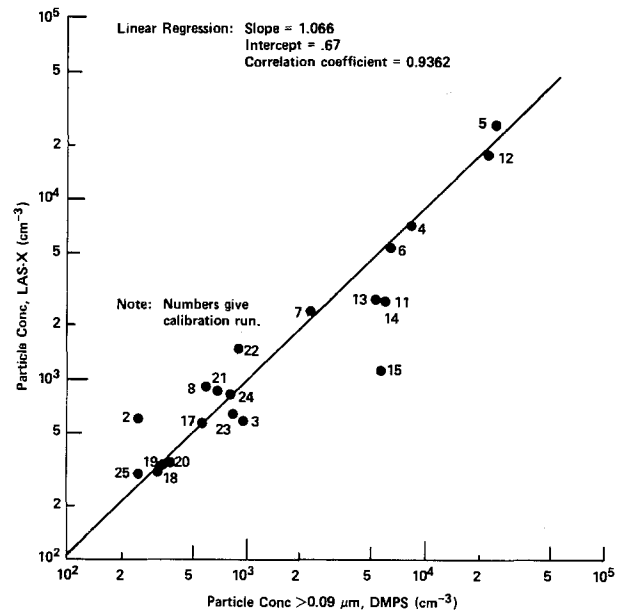


Fig. 3. Concentration measurements of PSL aerosol streams using the DMPS and the LAS-X.

these measurements were made quasi-simultaneously. Since the full range of the DMPS cycle takes 20-30 min and the LAS-X a minute or less at the aerosol particle concentrations generated for the calibrations, the LAS-X count represents the average of many short counting periods spread over the entire DMPS measuring cycle. The regression equation relating the two counts is

$$X = 0.674Y^{1.066}$$

$$r = 0.936 \quad [1]$$

where X is the concentration of particles $> 0.09 \mu\text{m}$ in size as measured by the DMPS (cm^{-3}), Y is the total concentration measured by the LAS-X (cm^{-3}), and r is the correlation coefficient.

Although the DMPS counts fewer particles at low concentration and more at high concentration than the LAS-X, the differences are only about 20% cent over the range of 10^3 - 10^4 particle/ cm^3 . This agreement between the two instruments, each based on completely different sizing principles, is deemed satisfactory for most aerosol particle measurements.

Individual peaks matched reasonably well, as shown in Fig. 4. (The Fig. 4 plot of 0.3 μm PSL spheres is actually the best match among the various PSL comparisons made.) The two LAS-X plots show the value of higher resolution measurements. In one data set, 16 channels span the entire size range of the instrument (0.09-3.0 μm); in the higher resolution setting these same 16 channels span only the range 0.2-0.5 μm . Total concentration varies strongly with size in a monodisperse sample and the high resolution counting mode defines the peak in concentration much better. This high resolution mode of the LAS-X matches the size distribution measured by the DMPS quite well.

In polydisperse aerosol mixtures, aerosol concentration does not vary as much with size as in the monodisperse calibrating aerosols. In this sense, polydisperse aerosol samples represent a less severe test of the aerosol measuring array. However, a polydisperse size distribution more realistically simulates the aerosol found in a cleanroom, especially if it is generated by prefiltering ambient room air. By admitting ambient laboratory air into a closed chamber and then recirculating it continuously through a prefilter, a stable aerosol mixture eventually results that can be used as a source of polydisperse aerosol for instrument array calibration. Figure 5 plots the size distributions measured by the DMPS and the LAS-X

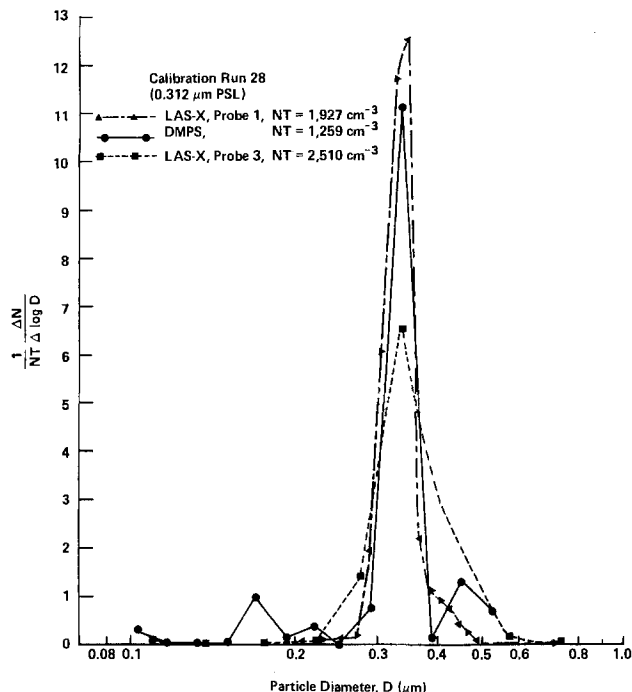


Fig. 4. Differential size distribution of monodisperse $0.3 \mu\text{m}$ PSL spheres as determined by the DMPS and the LAS-X. NT: particle concentration summed over all sizes. Probe settings on the LAS-X refer to particle size spans.

with such a polydisperse source. Again, the agreement is good in the region of size overlap.

Similar calibration runs with a collimated hole diffusion battery (the CHDB/CNC, see Appendix B) show that it sizes $0.08 \mu\text{m}$ PSL particles correctly and agrees well with the LAS-X when measuring polydisperse size distributions at particle concentrations above contemporary cleanroom levels. A representative comparison appears in Fig. 6. This plot shows the size distributions measured by both the CHDB/CNC and the LAS-X for air recirculated continuously through an 80% efficient prefilter in a closed box. Particle concentration (size $> 0.1 \mu\text{m}$) is about 0.1 cm^{-3} , a concentration an order of magnitude lower than the lower concentration limit of the DMPS measuring capability. At this concentration, agreement between the CHDB/CNC and the LAS-X is satisfactory.

Cleanroom Measurements

Four different levels of air quality make up the different cleanrooms sampled as part of this project. In order of decreasing air quality, they were as follows.

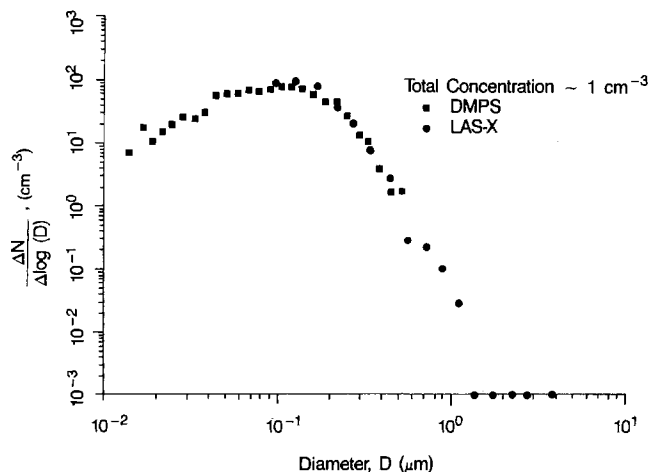


Fig. 5. Differential size distribution of a polydisperse particle mixture as measured by the DMPS and the LAS-X.

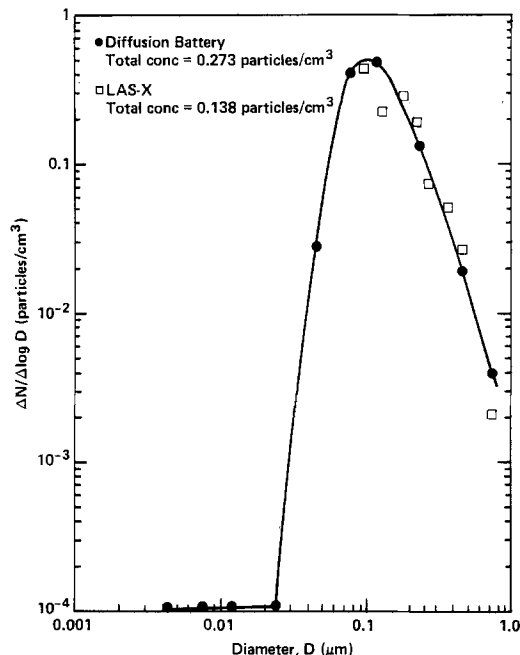


Fig. 6. Differential size distribution of a polydisperse particle mixture (room air recirculated through a prefilter) as measured by the CHDB/CNC and the LAS-X.

1. *The future manufacturing area of the Microelectronics Center of North Carolina (MCNC).*—This facility was not operational at the time of the air sampling, but all filters had been installed and the recirculating fans had been on for at least 3 months during the earliest sampling periods from which data reported here were collected.

2. *A state-of-the-art manufacturing area.*—Measurements were made in this facility both while work was in progress and over a weekend shutdown period. However, the sampling site was remotely located with respect to most production activity so that the air sampled is nearer that of a cleanroom at rest than an operational cleanroom.

3. *The photoresist room of a university fabrication facility.*—This small room is isolated from the main fabrication area and has its own fan and filtration system. Traffic was low during the sampling period.

4. *The main fabrication area of the same university facility.*—This larger room houses all furnaces and other wafer processing equipment. Its room filtration system is smaller than state of the art, and personnel cleanroom procedures are also less rigid. During the sampling period, the mean concentration of aerosols of size equal to or greater than $0.5 \mu\text{m}$ was about 300 ft^{-3} .

The DMPS proved capable of measuring size-distribution spectra in only the Class 300 university facility. (See Fig. A-1 for definitions of air-quality classes.) At the other three sites, the particle concentration was too low for significant counting.

The size-distribution data collected at this site (and at the other sites to be reported on in the following paragraphs) are presented in two forms: as differential size-distribution plots and as cumulative size-distribution plots. The latter plot is the type that appears in Federal Standard no. 209B (2) and forms the basis for the various classes of air quality defined in that Standard. The former type of presentation, showing aerosol concentrations at each aerosol diameter, is perhaps more popular among aerosol technologists. Further reflecting this user association, the concentration units used here will be per cubic centimeter for the differential-distribution plots and per cubic foot for the cumulative-distribution plots. The ordinate of the differential-distribution curve in all plots is $dN/d(\log D)$, and the abscissa $\log D$, where N is the aerosol concentration and D is the aerosol diameter. The use of a log scale in constructing these plots provides

better coverage of typical aerosol ranges; in the differential plots, the ordinate $dN/d(\log D)$ thus is in units of concentration rather than concentration per size increment. Total aerosol concentration as a function of time is the third type of data summary to be presented.

Main fabrication area of a university fabrication facility (DMPS for ultrafine particle data).—Figure 7 presents total aerosol concentration measured by various instruments over the sampling period. The different concentrations measured by each instrument reflect their different size sensitivities. Figures 8 and 9 plot the grand average size distributions as differential and cumulative distributions, respectively. These distributions represent the averages over the entire sampling period depicted in Fig. 7, peaks as well as valleys.

Each datum of the differential number distribution plot (Fig. 8) has error bars corresponding to plus and minus one standard deviation about the mean. In spite of the relatively large error associated with many of the data points, a maximum in the plot clearly occurs in the vicinity of $0.1 \mu\text{m}$. In the cumulative-distribution plot (Fig. 9), this peak represents a flattening of the curve and a departure from the extrapolation of the cumulative-size distribution assumed in Federal Standard no. 209B. (The size distributions published in Federal Standard no. 209B [Fig. A-1] abruptly terminate at $D = 0.5 \mu\text{m}$, so that the distribution below that size is not specified; the curve identified as from Federal Standard 209B in Fig. 9 is thus an extrapolation below $0.5 \mu\text{m}$ that is drawn with the same slope as that of the distribution above $0.5 \mu\text{m}$ which is specified in 209B.) Thus, while the total concentration of aerosols measured by the CNC in this university fabri-

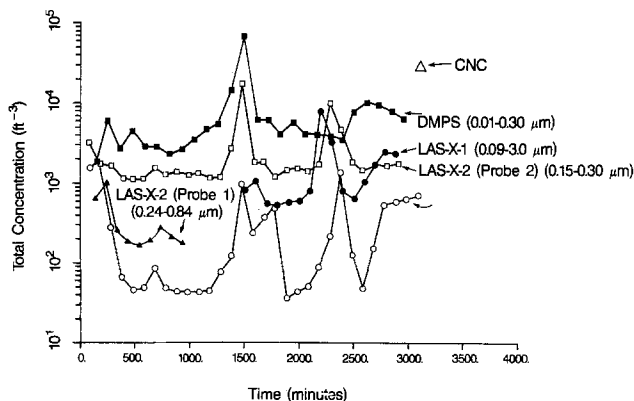


Fig. 7. Total aerosol concentrations, university fabrication laboratory.

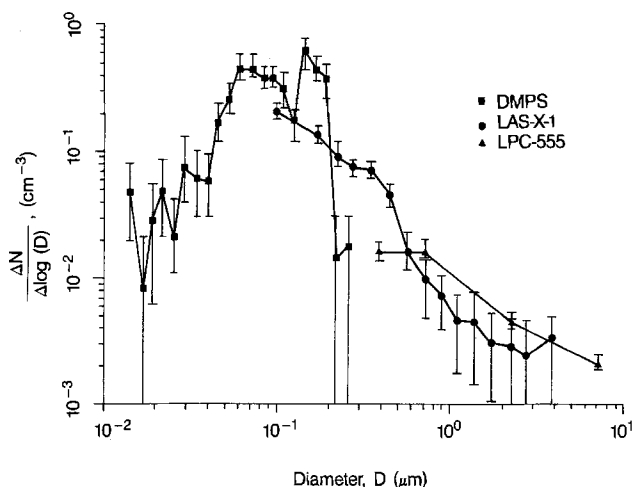


Fig. 8. Grand average differential size distributions, university laboratory.

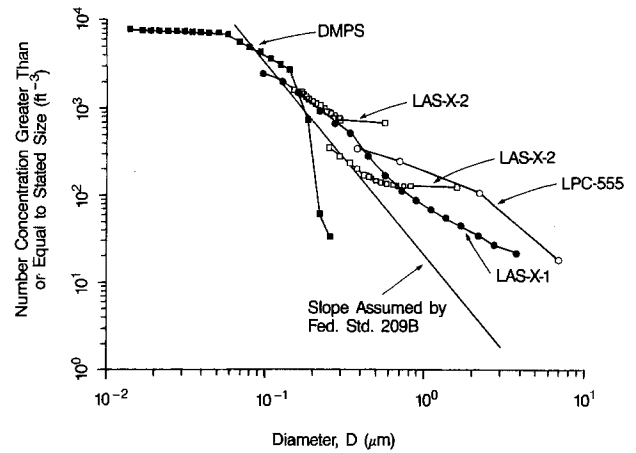


Fig. 9. Grand average cumulative size distribution, university laboratory.

cation laboratory exceeds that measured by the optical counters, it is not as high as would be predicted by a simple extrapolation of the 209B size distribution. This conclusion proves true in all the other cleanrooms monitored as well.

University photoresist room/Class 100 manufacturing area/MCNC (ultrafine particle data by CNC alone).—Detailed size distribution data could not be collected below $0.1 \mu\text{m}$ in any of these facilities because of the inability of the DMPS to detect a statistically significant number of particles. However, by using the CNC alone, a single data point could be collected in the ultrafine-aerosol regime (Table II) and incorporated into a cumulative-distribution plot (Fig. 10).

The cumulative size distribution plot of Fig. 10 combines one CNC count with four conventional optical particle counter cumulative counts. The CNC total count is plotted at $0.01 \mu\text{m}$, which is the size at which the counting efficiency of the CNC falls below about 50% (8). For particles larger than $0.02 \mu\text{m}$, the CNC counting efficiency exceeds 90%; for particles smaller than $0.01 \mu\text{m}$, counting efficiency decreases rapidly to about 10% at $0.005 \mu\text{m}$. Thus, a sub $0.01 \mu\text{m}$ component may be included in the count plotted at $0.01 \mu\text{m}$, but its magnitude should be small. Because of this unknown sub $0.01 \mu\text{m}$ component, the concentration plotted at $0.01 \mu\text{m}$ might be larger than the true concentration, but this error is compensated by the reduced counting efficiency between 0.01 and $0.02 \mu\text{m}$, making $0.01 \mu\text{m}$ a reasonable compromise size for plotting CNC data.

By extrapolating the slope used in defining the air-quality classes of Federal Standard no. 209B from the $0.5 \mu\text{m}$ cutoff of the Standard to the $0.01 \mu\text{m}$ size in the ultrafine regime, it can be seen that the concentration plotted at $0.01 \mu\text{m}$ from the CNC count falls well below the concentration predicted by the extrapolation. This result has been universally true for measurements carried out in cleanrooms of various air qualities and in other areas where air quality depends on filtered air (Fig. 11). Figure 11 plots the ratio of the concentration of particles whose size equals or exceeds $0.01 \mu\text{m}$ (the CNC-determined concentration) to the concentration of particles whose size equals or exceeds $0.3 \mu\text{m}$ (the lower cutoff of the $1 \text{ ft}^3/\text{min}$

Table II. CNC and OPC concentrations measured in various cleanrooms

	CNC conc. (ft ⁻³)	Concurrent OPC conc. (ft ⁻³)
Manufacturing facility	180	3.2
University laboratory		
Fabrication area	27,100	687
Protoresist room	2,860	53

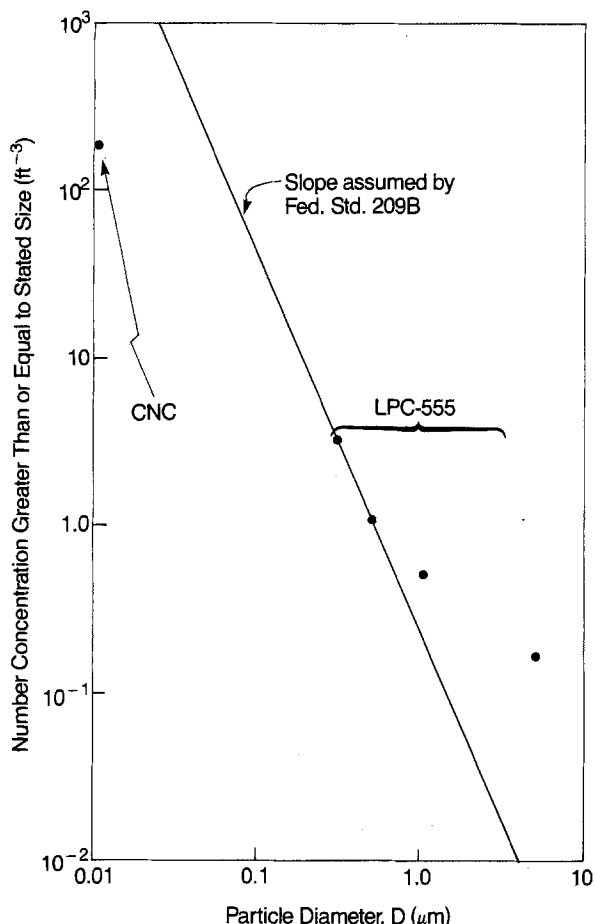


Fig. 10. Cumulative distribution data including that of the CNC alone.

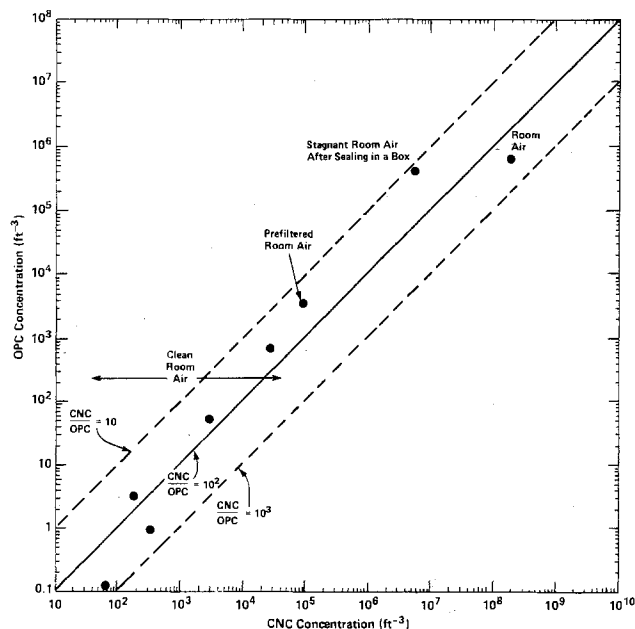


Fig. 11. Comparison of total aerosols counted by the optical particle counter with those counted by the condensation nuclei counter.

OPC [the PMS Model LPC-555] used in these measurements). In Fig. 11, this ratio is written as CNC/OPC. The slope of Federal Standard no. 209B predicts this ratio to be about 1750. The ratios plotted in Fig. 11 all lie between the 10 and 1000 bounds. Interestingly, the highest values of these ratios occur at both the upper and the lower extremes of the concentration range; all the intermediate

values are less than 100. No significance or claim of universality is made for this observation or for any of the data points. Virtually all these measurements were carried out in cleanrooms or sheltered areas at rest; they represent measurements made overnight or over weekends during which time activity was either nonexistent or remote to the sampling points. Human activity would be expected to change both the concentration and the size distribution of the aerosols detected. For example, ambient air measurements made in Los Angeles by Whitby *et al.* (1) show the CNC/OPC ratio as defined above to exceed the 1750 predicted by Federal Standard no. 209B, being on the order of 10^4 (Fig. 1).

The CNC/OPC ratios measured in high quality cleanrooms thus support the conclusion that the flattening of the cumulative size distribution below $0.1 \mu\text{m}$ measured in a low quality cleanroom (Fig. 9) describes the cumulative size distributions of the higher quality cleanrooms as well. Again, this conclusion probably applies only to areas in the cleanroom whose air quality is dominated by the effluent from the HEPA filters rather than emissions from a local source such as equipment or people.

MCNC fabrication area (CHDB/CNC for ultrafine particle data).—The primary purpose of the CHDB/CNC combination was to verify, on a one-time basis, that the flattening of the cumulative size distribution curve below $0.1 \mu\text{m}$ observed in the Class 300 university fabrication laboratory (Fig. 8) and shown to be consistent with CNC/OPC ratios measured in cleanrooms of higher air quality (Fig. 11) also characterizes the air found in a state-of-the-art cleanroom.

The collimated hole diffusion battery consists of long, cylindrical paths through which the aerosol must pass and along which are access ports that allow CNC measurement of concentrations. The pathlength between the entry port and any access port defines a channel length; the longer the channel length, the greater the particle capture by diffusion to the channel wall. A series of concentration measurements at various channel lengths permits the determination of a size distribution because of the dependence of diffusion coefficient upon particle size. The collimated hole diffusion battery consists of 11 channels, typically measured sequentially by connecting the CNC to each port, one after the other. This measurement technique proved unsatisfactory when using one CNC for all diffusion battery channel measurements in series.

A problem occurred because the long measuring interval used (100 min/port) to obtain sufficient counts in each channel stretched the entire measuring cycle over more than half a day, during which time the cleanroom aerosol concentration changed. Thus, early channels sampled one particle population, while later channels sampled a different population. This instability caused the data inversion process to yield nonsensical distributions.

Two corrective actions were taken: (i) a second CNC was added to the instrument combination so that the zero channel concentration (the uncut particle population) was always measured at the same time that a downstream channel was being measured; and (ii) only three downstream channels were actually measured, the intermediate channel values being deduced by curve fitting. The first corrective action means that the channel data could be expressed as a fraction of the 0 channel count and thus variations in total aerosol concentration over the measuring cycle could be compensated for. Changes in size distribution, however, are not compensated.

Using this technique produced results such as those shown in Fig. 12. Figure 12 contains two presentations of the same data. The dots (or solid circles) represent the raw data in which the fractional penetration of the three downstream channels, expressed in terms of the mean channel 0 concentration, have been plotted at the size for which the channel penetration is calculated to be 50% as determined by the calibration of the battery. The calculated distribution shown by the squares is that obtained by using the three measured channel values to derive a best fit curve for the penetration from all channels, and

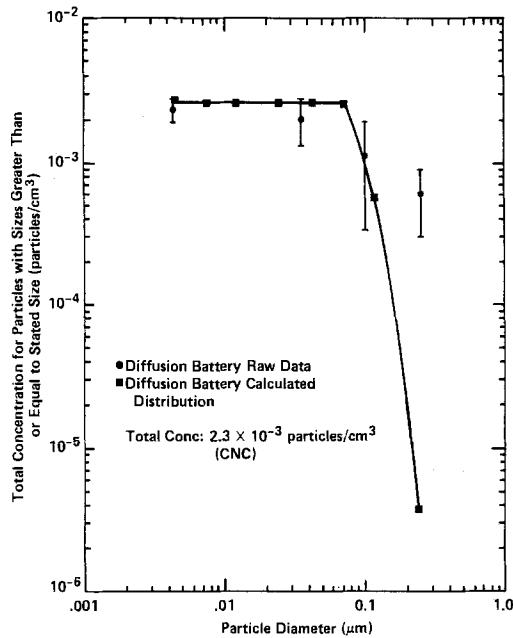


Fig. 12. Cumulative size distribution of ultrafine aerosols in a state-of-the-art cleanroom as deduced from CHDB/CNC measurements.

then substituting this complete set of fitted channel penetration data into published conversion models (9).

This procedure produced a cumulative size distribution having relatively few particles below 0.07 μm for the measuring cycle depicted in Fig. 12. The total mean concentration of condensation nuclei over this measuring period was about 60 ft⁻³, an impressively low number but one that is typical of state-of-the-art cleanrooms at rest. Other measurement runs yielded similar cumulative size distributions.

Conclusions

The cumulative size distributions of ultrafine particles in resting semiconductor cleanrooms flatten out for particles whose diameters are below about 0.1 μm, as might be deduced from the penetration characteristics of a HEPA filter. The large concentrations of ultrafine particles present in ambient air are effectively removed by these filters, and simple extrapolation of the Federal Standard no. 209B curves leads to overestimation of the ultrafine particle populations below about 0.1 μm.

These conclusions apply to cleanrooms at rest. Particle generating activity within an operational cleanroom can easily dominate the ultrafine aerosol concentration in its vicinity and downwind of it. Ultrafine aerosol concentrations in an operational cleanroom, therefore, like larger aerosols, probably depend on the process and people activity and probably are not limited by the air filters. The condensation nuclei counter, in conjunction with a 1 ft³/min optical particle counter, is a practical instrument for measuring ultrafine particle concentrations. This combination does not yield size distribution over the ultrafine particle regime. The only instrument combination so far demonstrated to be capable of ultrafine particle size distribution measurements (0.01-0.1 μm) at semiconductor cleanroom concentrations (less than 1000-5000 ultrafine particle/ft³, for example) is the collimated hole diffusion battery/CNC reported here, and that only with a dual CNC configuration and a modified sampling protocol.

Acknowledgments

Much of the data reported in this paper were collected as part of a research program sponsored by the Semiconductor Research Corporation and the Microelectronics Center of North Carolina.

Manuscript submitted April 8, 1985; revised manuscript received Aug. 8, 1985. This was Paper 474 presented at the

New Orleans, Louisiana, Meeting of the Society, Oct. 7-12, 1984.

Research Triangle Institute assisted in meeting the publication costs of this article.

**APPENDIX A
Air-Quality Classifications**

Figure A-1 is a reproduction of the plot defining classes of air quality in Federal Standard no. 209B (1). The Class 1000 designation, added by a later amendment, has been included in Fig. A-1. Intermediate designations such as 500, 80,000, etc., defined by the 0.5 μm intercept of a curve drawn parallel to those shown, are also defined implicitly. Common usage has been to extend the range of these definitions to include Class 10 and even Class 1 in describing the air quality in contemporary cleanrooms at rest. Note, however, that the Fig. A-1 plot uses a log-log scale so that Class 0 cannot be defined by this procedure. Under a GSA contract, Committee RP50 of the Institute of Environmental Sciences is currently revising and updating Federal Standard no. 209B. Thus, within the next year or two, a new standard, 209C, should be available for critique and suggestions, prior to promulgation for general use.

**APPENDIX B
Commercial Availability of Ultrafine
Aerosol Particle Instrumentation**

The instruments identified as suitable for ultrafine aerosol particle measurement above have limited commercial availability, being marketed by only one company at present (TSI, Incorporated, St. Paul, Minnesota). Each of the three size separators is discussed separately in the following paragraphs. In the case of the differential mobility analyzer, the complete differential mobility analyzer/condensation nuclei counter combination is commercially available and is described as one unit, the differential mobility particle sizer (DMPS).

1. *The differential mobility analyzer.*—The only commercial equipment now readily available is the TSI Model DMPS/C 3932 differential mobility particle sizer, which

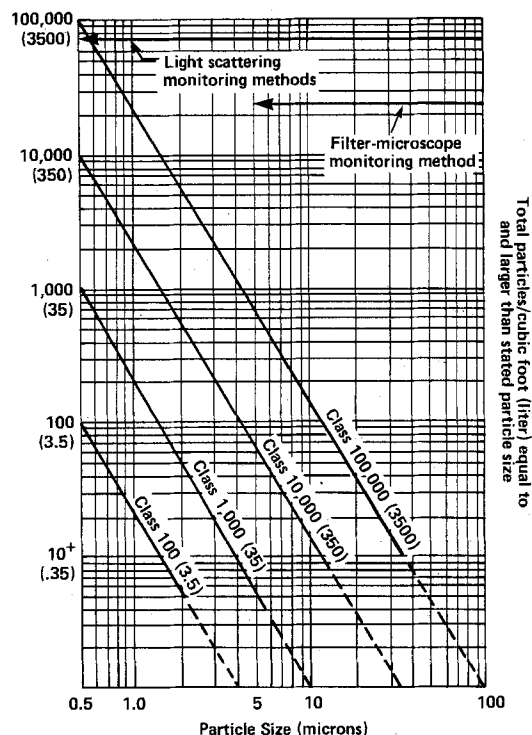


Fig. A-1. Definitions of air quality classes from Federal Standard no. 209B, April 24, 1973, and its Amendment 1, May 30, 1976. Note: Counts below 10 (0.35) particle/ft³ (liter) are unreliable except when a large number of samplings is taken.

includes a CNC (TSI Model 3020) (8) to measure particles separated by a TSI electrostatic classifier Model 3070 (a differential mobility analyzer), the combination being controlled by an Apple IIe personal computer, which also stores and processes the collected data.

2. *The integral mobility analyzer.*—The only commercially available apparatus for this measurement is the TSI Model 3030 electrical aerosol size analyzer. To be capable of single-particle detection, it should be modified by replacing the current measuring electrometer with a CNC.

3. *The diffusion battery.*—The only commercial version is a screen-type diffusion battery (TSI's Model 3040). The diffusion battery used in the measurements presented in this paper, however, used a custom-built collimated hole diffusion battery (CHDB) (7). Any diffusion battery must be followed by a CNC for counting.

4. *The continuous flow condensation nuclei counter.*—While various commercial versions of the condensation nuclei counter have been on the market for years, these older models all relied on an adiabatic expansion to induce condensation. This mode of operation dictated intermittent operation in which sampling flow had to stop while the expansion, condensation, and counting steps took place. When flow resumed into a chamber of lowered pressure, a pulsed flow occurred. The recent introduction of a continuous flow model (TSI Model 3020) (8) avoids these problems by using a thermoelectrically cooled chamber through which the saturated vapor and aerosol continuously flow.

REFERENCES

1. K. T. Whitby, R. B. Husar, and B. Y. H. Liu, in "Aerosols and Atmospheric Chemistry," G. M. Hidy, Editor, pp. 237-264, Academic Press Inc., New York (1972).
2. Federal Standard no. 209B, "Federal Standard Cleanroom and Workstation Requirements, Controlled Environment," April 24, 1973; Amendment 1, May 30, 1976, General Services Administration, Specification Activity, Printed Materials Supply Division, Washington, DC (1976).
3. W. Bergman, A. Bierman, W. Kuhl, B. Lum, A. Bogdanoff, H. Hebard, M. Hall, U. Banks, M. Mazumder, and J. Johnson, "Electric Air Filtration: Theory, Laboratory Studies, Hardware Development, and Field Evaluations," UCID-19952, Sept. 1983, Technical Information Department, Lawrence Livermore Laboratory, Livermore, CA (1983).
4. R. G. Knollenberg, *J. Environ. Sci.*, **28**, 32 (1985).
5. A. W. Hogan, in "Aerosol Measurement," D. A. Lundgren, M. Lippman, F. S. Harris, Jr., W. E. Clark, W. H. Marlow, and M. D. Durham, Editors, pp. 497-514, University of Florida Press, Gainesville, FL (1979).
6. P. Keady, F. Quant, and G. J. Sem, *TSI Quart.*, **9**, 2 (April-June 1983).
7. D. Sinclair, *AIHA J.*, **33**, 729 (1972).
8. J. K. Agarwal and G. J. Sem, *J. Aerosol Sci.*, **11**, 343 (1980).
9. A. Kapadia, Ph.D. thesis, University of Minnesota, Minneapolis, MN (1980); Particle Technology Laboratory Publication no. 413, Dept. of Mechanical Engineering, University of Minnesota, Minneapolis, MN.

Potential-Enhanced Doping of Si Grown by Molecular Beam Epitaxy

R. A. A. Kubiak, W. Y. Leong, and E. H. C. Parker

Solid State MBE Research Group, Sir John Cass Faculty of Physical Sciences and Technology,
City of London Polytechnic, London, England EC3N 2EY

ABSTRACT

Potential-enhanced doping (PED) is a method by which the incorporation efficiencies of certain low sticking coefficient, coevaporated dopants can be enhanced during Si-MBE. PED is implemented by application of a potential to the substrate during deposition. The applied potential is used to control instantaneous dopant incorporation, thereby permitting accurate control over doping levels over a wide dynamic range, as well as offering a powerful method of profile control. PED is especially effective with Sb doping, with enhancements by up to 1000 times being realized, thus permitting doping levels up to the solubility limit to be readily achieved. PED is less efficacious in the case of As doping obtained from III-V compound sources. The electrical, optical, and crystallographic quality of PED:Sb-doped material is comparable to that of bulk Si. Doping transitions of $< 50 \text{ \AA/decade}$ have been obtained for transitions over several decades.

Compared with low energy dopant-ion implantation (1, 2), coevaporation of elemental doping species from thermal sources offers a simple and inexpensive method of doping in Si-MBE. However, not until recently have coevaporative methods, as applied to the preferred MBE dopants Sb, Al, and Ga, proved capable of offering the desired control over doping; these dopants have low, growth temperature-dependent incorporation efficiencies and a propensity to segregate at the growing surface (3-6). Both these factors are severe impediments to obtaining good dopant and profile control. However, two recent developments hold considerable promise in alleviating the limitations of coevaporative doping in Si-MBE. Despite the high temperatures required for evaporation, coevaporated boron behaves as a near-ideal p-type dopant, having a unity incorporation coefficient and being free from any severe surface segregation phenomena (7-9). The second development relates to a method of improved control over dopant incorporation, known as potential-enhanced doping (PED) (8, 10), and is particularly effective in the case of the preferred MBE n-type dopant, Sb (11). This paper reports on PED technique applied to Sb, As, and Ga doping, reports on the material quality obtained, and demonstrates the degree of profile control that can be realized.

Experimental

Epitaxial Si was deposited onto 3 in. diam, (100) Si substrates in a cryopumped three-chamber UHV system de-

scribed earlier (10, 12). Airco Temescal electron-beam evaporators (Type SFIH-270-2) were used to evaporate semiconductor-grade polycrystalline Si with $\rho > 500 \text{ \Omega-cm}$, at growth rates ranging from 0.5 to 20 \mu m-h^{-1} , to thicknesses of 0.2-25 μm . Epilayer growth was performed at temperatures in the range 700°-900°C; although the absolute temperature was known only to within $\pm 30^\circ\text{C}$, reproducibility between experimental runs was better than $\pm 10^\circ\text{C}$.

Consistent with earlier studies (3-6), elemental species were generally used to obtain Sb and Ga doping. However, III-V compounds were also employed as Group V dopant sources to permit (i) comparison of Sb incorporation from Sb₄ (the dominant species generated by elemental Sb) and Sb₂ (the dominant Group V species generated by InSb) and (ii) controllable As doping without the attendant problems of severe memory doping effects caused by the high vapor pressure of elemental arsenic (13). The sources used and the resultant fluxes obtained are summarized in Table I. These materials were evaporated from conventional effusion furnaces of the type used in III-V-MBE, with pyrolytic boron nitride crucibles for all the sources except Ga, which was evaporated from a graphite crucible. The positioning of the thermocouple in the source cells used resulted in an underestimate of the source temperature, precluding calculation of the incident dopant fluxes. The Si and dopant source were situated ~28 cm below the substrate plane, in the configuration presented elsewhere (10).

Table I. The coevaporated sources used to achieve Sb, As, and Ga doping. The dominant and secondary evaporated species are listed

Dopant material	Evaporated species	
	Primary	Secondary
Elemental Sb	Sb ₄	Sb ₂
InSb	Sb ₂	In
GaAs	As ₂	Ga
InAs	As ₂	In
Elemental Ga	Ga	—

The electrical properties of the material were assessed by electrochemical CV profiling (14) and, where appropriate, by Hall measurements. Spreading resistance profiling (SRP), secondary ion mass spectrometry (SIMS), deep level transient spectroscopy, photoluminescence, and Rutherford backscattering (RBS) were further employed on selected samples to evaluate the quality of doped material and the capability for doping control.

Potential-Enhanced Doping

Enhanced incorporation of dopants was induced by application of a voltage (U_s) via a Ta brush in contact with the rotating assembly onto which the substrate is mounted for growth. A schematic representation of the experimental configuration used has been presented elsewhere (10).

The efficacy of PED on dopant incorporation during growth was initially investigated by applying staircase voltage programs of the type shown in Fig. 1a, since the resulting Sb doping profile, as shown in Fig. 1b, is optimized for profile evaluation using the electrochemical-CV method (14). Data obtained for both negative and positive voltages from five epilayers all grown at the same substrate temperature and incident Sb-flux as used in Fig. 1 are presented in Fig. 2. The main features to be noted are (i) negative potentials are significantly more effective at sustaining enhancement than positive potentials, and (ii) only enhancement obtained under negative potentials was reproducible. As a result, only negative voltage PED will be subsequently discussed.

Figure 3 demonstrates PED enhancement obtained over a wide range of growth temperatures ($\sim 730^\circ\text{--}850^\circ\text{C}$) and Sb cell temperatures ($315^\circ\text{--}390^\circ\text{C}$), conditions which

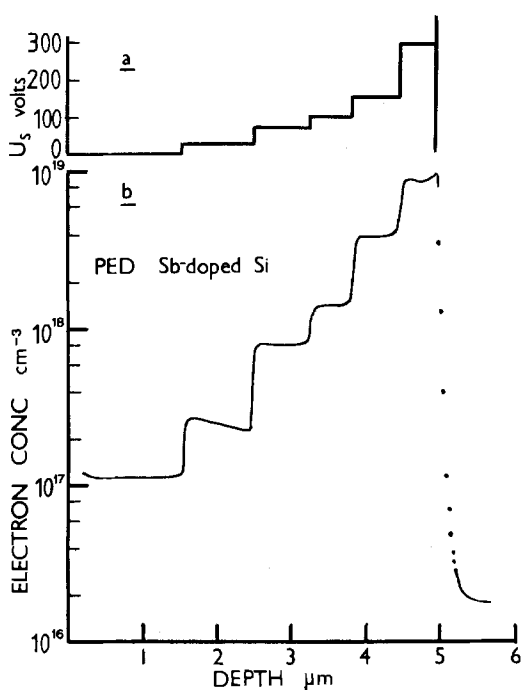


Fig. 1. A typical voltage program (a), and resulting Sb-dopant profile (b), used to establish the efficacy of PED.

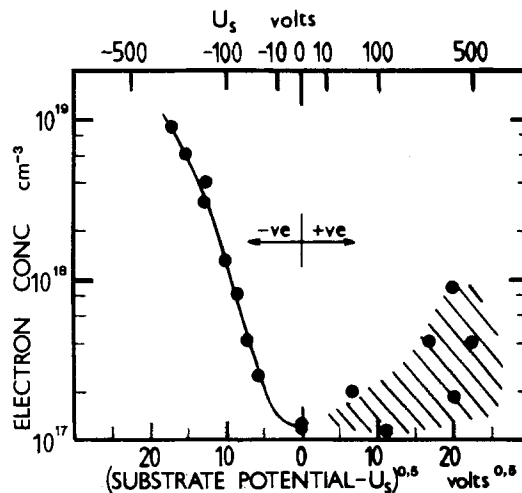


Fig. 2. Variation of Sb doping with applied potential (U_s) obtained from a series of epilayers all grown at the same temperature and Sb flux as used in Fig. 1. For convenience of presentation, the data are presented against the square root of U_s .

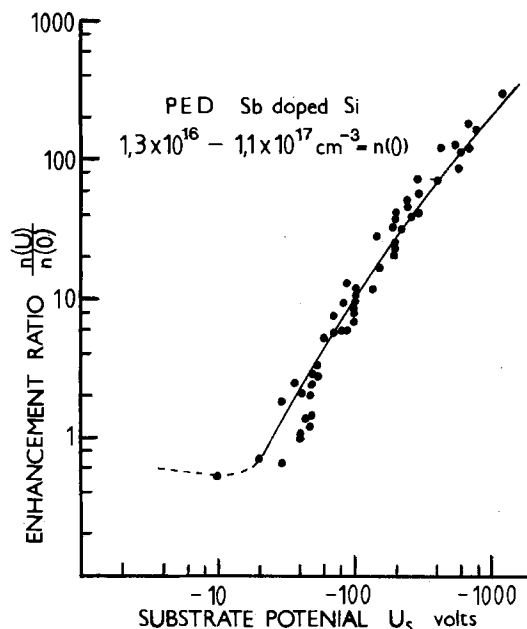


Fig. 3. PED enhancement over a range of growth temperatures and Sb fluxes (generated from elemental Sb and InSb) corresponding to zero potential doping range of 1.3×10^{16} to $1.1 \times 10^{17} \text{ cm}^{-3}$. The ordinate is normalized as an enhancement ratio of doping level at potential U , to that at 0 V: $n(U)/n(0)$.

yielded a zero potential doping range $n(0) = 1.3 \times 10^{16}$ to $1.1 \times 10^{17} \text{ cm}^{-3}$. The ordinate has been normalized as an enhancement ratio of doping level at potential U compared with that at zero volts: $n(U)/n(0)$. It is apparent that PED:Sb doping is highly reproducible. Within the range of growth conditions investigated, a calibration obtained under one set of growth conditions (pertaining to a certain Sb adlayer coverage) can be translated to any other condition. The use of InSb as an Sb₂ source yielded data (10) which coincided with those presented in Fig. 3, indicating that enhanced dopant incorporation was not dependent on the nature of the evaporated Sb species.

Sb forms a two-dimensional surface adlayer with the surface coverage depending on growth temperature and incident Sb flux (5). Based on reported data, the Sb surface coverages obtained under the range of growth conditions employed in this study are considerably less than a monolayer, but still sufficiently high to be detected by Auger electron spectroscopy (AES). Figure 4 shows typi-

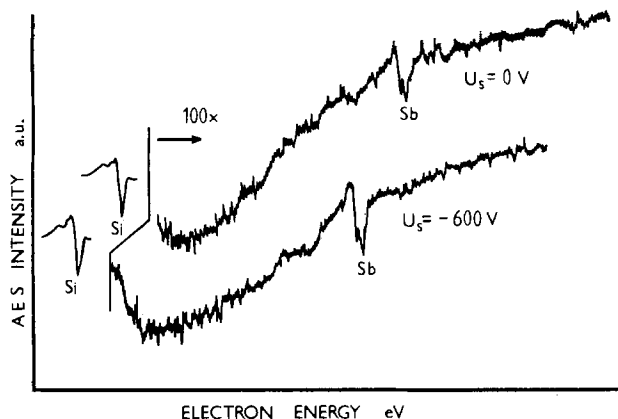


Fig. 4. Auger electron spectra of two epilayers grown under identical growth conditions, except with different applied voltages. The peak heights are identical (within experimental error caused by nonreproducibility of sample positioning), despite a doping level difference of 200.

cal spectra obtained from two epilayers grown at the same temperature and under the same Sb flux, but with differing applied potentials. (The substrate temperature was quenched rapidly immediately on terminating growth to minimize Sb desorption.) Since the measured Sb/Si peak intensity ratio obtained from the two spectra remains practically unchanged, whereas the doping levels differed by a factor of 200, it is surmised that PED enhances incorporation of Sb from the adlayer and does not affect surface coverage (except in a secondary capacity by depletion due to enhanced incorporation). This is consistent with the implication drawn from Fig. 3 that the degree of PED enhancement is independent of adlayer coverage, and hence Sb flux, over the range of growth conditions employed. Although current models for incorporation from dopant adlayers do not distinguish the surface species present, the similarity of enhancement obtained from Sb_2 (InSb source) and Sb_4 (elemental source) suggests a common surface species from which incorporation occurs.

The efficacy of PED:As doping was reported earlier to be less pronounced than in the case of Sb doping (10). Figure 5 shows the enhancement ratio obtained over a range of GaAs source temperatures of 550°–712°C [corresponding to the indicated $n(0)$ doping levels] at a fixed growth temperature of ~810°C. Unlike with PED:Sb doping, Fig. 5 indicates that the enhancement ratio in-

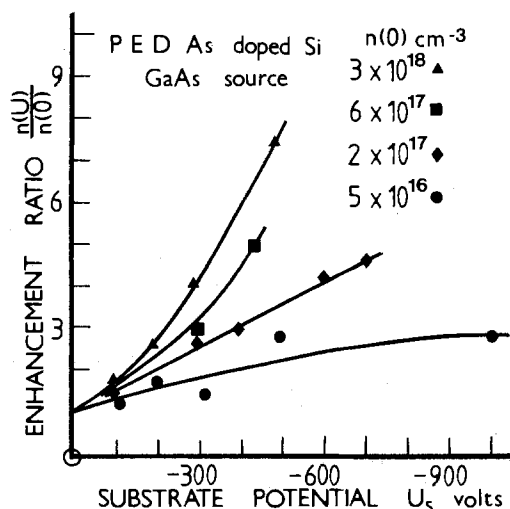


Fig. 5. PED enhancement ratio over a range of As fluxes generated using a GaAs source at constant growth temperature. $n(U)/n(0)$ increases at a given potential with increasing As flux, unlike the case of Sb presented in Fig. 3.

creases with As coverage. This result may indicate either that As adlayer formation is less simple than that of Sb, or, more probably, that the simultaneous presence of a Ga adlayer from the GaAs source affects As incorporation. The latter suggestion is supported by the following observations: (i) SIMS profiles have indicated that Ga is also incorporated during doping from the GaAs source, although the relative levels have not been quantified; (ii) the increasing enhancement ratio with GaAs source temperature is consistent with the reported thermal decomposition behavior of GaAs, i.e., an increasing As_2/Ga flux ratio with increasing temperature (15); and (iii) preliminary investigations using InAs indicate a higher enhancement ratio (factor of ~2) than that obtained from GaAs at a given $n(0)$ coverage, suggesting that In interferes less with As incorporation than does Ga. Although further work is necessary to clarify the effect of the accompanying Group III fluxes obtained from III-V sources, the conflicting responses of the enhancement ratio to arsenide and antimonide sources may imply a shorter surface residence time or a higher spontaneous incorporation efficiency for As compared with that for Sb. Notwithstanding the difficulty in interpreting the effects of the accompanying Group III fluxes from III-V sources, the negligible response of PED:Ga doping (from an elemental source) confirms a species dependence for PED doping (10).

An interesting feature of Sb and Ga doping is that the doping level obtained is independent of growth rate. For example, all the data presented in Fig. 1-3 had no correction applied for growth rate over an experimental range of greater than ten times, and growth of epilayers in which changes in rate were intentionally introduced (with and without PED) confirmed this observation. Although clearly a useful effect, its interpretation in terms of growth step propagation under the adlayer regions (16) requires further study, particularly to account for its occurrence with or without PED. Indeed, this may suggest that spontaneous and enhanced incorporation are dependent on a common mechanism.

Mechanism for PED

The use of electron-beam evaporators for generation of the Si flux also leads to generation of charged particles in the MBE system; secondary (low energy) and backscattered (high energy) electrons are produced, as is a small fraction of low energy Si^+ ions caused by ionizing interactions between the Si flux and the primary electron beam. The application of a potential to the substrate would induce an electrostatic field within the MBE system, which would modify the trajectories of these particles and change the energy with which they impinge on the substrate. The high efficacy of negative potential PED implicates Si^+ ions as the species responsible for the phenomenon, and this is consistent with experiments where dopant incorporation has been enhanced by additional ionization of the Si growth flux by using an electron impact ionizer (17). It is interesting to note that a variety of other effects have been observed (18-21) probably dependent on the same phenomenon.

Enhancement of doping by Si^+ ions would be induced either by attraction of more Si^+ ions to the substrate by the electric field, thus increasing the number of ion-dopant interaction events, or by the increased energy of the ions producing an increased cross section for interaction. To distinguish between these possible mechanisms, an experiment was performed to restrict the flux of Si^+ ions within the MBE chamber to those with direct linear trajectories to the substrate, by using an apertured shroud (22). Since the enhancement ratio of Sb using this procedure was identical to that presented in Fig. 3, we surmise that acceleration of Si^+ ions generated by the evaporators was responsible for the enhancement of incorporation associated with PED.

Jorke *et al.* (17) have proposed that increased Sb incorporation by an applied potential is caused by secondary implantation of the adsorbed Sb atoms by the Si^+ ions. Al-

though such a model is consistent with the PED effect, a better understanding of adlayer chemistry (e.g., the identification of adlayer surface species and the cause for the lack of response of doping level on growth rate), and measurement of experimental parameters such as ion currents, are required to understand the energy dependence indicated in Fig. 3. Alternative mechanisms cannot therefore be discounted at this stage, particularly: (i) Si^+ ion-induced activation of the surface dopant species (e.g., decomposition of the adsorbed species to that required for incorporation, or Si^+ ion-induced enhanced surface diffusion of adlayer species), and (ii) the formation of Si^+ ion-induced preferential incorporation sites.

Assuming that PED-assisted doping involves direct interactions between Si^+ ions and the adlayer, the observed species dependence between Sb: and Ga:PED doping is consistent with their adlayer properties. Whereas Sb forms a two-dimensional coverage (5) permitting ready access of ion-stimulated Sb to incorporation sites, Ga nucleates as three-dimensional islands (4), thereby (i) reducing the cross section for interaction with Si^+ ions by reduced effective surface area and (ii) reducing accessibility of ion-stimulated Ga atoms to incorporation sites.

Material Quality

A range of uniformly Sb-doped epilayers was deposited onto 1-10 $\Omega\text{-cm}$ p-type substrates to facilitate junction isolation of substrate conduction, and resistivity/Hall measurements were performed on cross-shaped samples by using the van der Pauw method (23). The epilayers were sufficiently thick that depletion effects could be ignored (24). Figure 6 shows the measured 300 K mobilities ($\mu = R_H\sigma$) as a function of resistivities of the epilayers; the corresponding carrier concentrations, assuming a Hall factor of unity, are also included. All the epilayers with Sb doping levels greater than $1 \times 10^{17} \text{ cm}^{-3}$ were obtained with the aid of PED. Over the experimental doping range 5×10^{15} to $3 \times 10^{19} \text{ cm}^{-3}$, the mobilities agree well with bulk Hall data (25). Comparison of eCV and SRP data (with its inherent assumption of bulk mobility values) confirms bulk-like mobilities at doping levels down to $< 1 \times 10^{15} \text{ cm}^{-3}$. By contrast, previous reports of Hall data on Sb-doped Si-MBE material obtained without the aid of PED (5, 26) indicated degraded mobilities and heavily defected material at carrier concentrations above 10^{17} cm^{-3} , caused by the associated requirement for heavy Sb

adlayer coverage, which introduces the possibility of cluster incorporation and locally disrupted growth. The upper doping limit obtained in this study ($3 \times 10^{19} \text{ cm}^{-3}$) corresponds to the solubility limit of Sb in Si at typical MBE growth temperatures. The corresponding resistivity of $2 \times 10^{-3} \Omega\text{-cm}$ compares favorably with values used as n^+ contact regions in device structures, where considerably higher doping levels have to be introduced by ion implantation to achieve the same resistivity due to incomplete electrical activation and degraded mobilities. Extensive comparison between electrical (eCV, Hall, and SRP) and chemical (SIMS) measurements indicates that, to within measurement error, all incorporated Sb and As is electrically active.

Since PED doping relies on ion irradiation of the epilayers, it is of concern whether any ion-induced damage is present to degrade material quality. To check on the crystalline quality of the material, RBS dechanneling analysis has been applied to an epilayer doped with PED:Sb at $\sim 1 \times 10^{19} \text{ cm}^{-3}$ ($U_s = -400\text{V}$). The ratio of random-to-channelled signal, χ_{min} , from the epilayer was 0.03, which compares with values obtained from bulk Si: if significant damage had been introduced by PED causing displacement of the host atoms, considerably higher values of χ_{min} would obtain. It is surmised either that annealing of induced damage occurs at the MBE growth temperatures used or that the damage induced by the relatively low Si^+ fluence is small. RBS dechanneling analysis also indicates no significant fraction of Sb on nonsubstitutional sites, which is consistent with complete electrical activation.

The Sb-doped material was grown over a period of several months, interspersed with other studies, during which time improvements in defect densities were realized (22). Defect etching studies revealed that no additional defects could be specifically attributed to PED:Sb doping, since the material remained comparable with undoped Si grown under similar conditions. Again, this contrasts with earlier studies of Sb doping in MBE-Si without PED, where material became heavily defected at doping levels exceeding 10^{17} cm^{-3} due to high adlayer coverages (26). However, our As-doped epilayers had high dislocation densities when doping levels exceeded $\sim 5 \times 10^{18} \text{ cm}^{-3}$, possibly due to incorporation of Ga. PED:Sb doped Si-MBE material characterized using PL indicates the material to behave as bulk Si (27).

Profile Control

Since PED affects the incorporation efficiency of the dopant species from the adlayer, and not adlayer coverage, control over doping profiles should be readily attainable by using suitable voltage programs. Furthermore, sharp doping transitions should be accessible even at low growth temperatures, provided that equilibrium coverage of Sb has been reached (5). The control that can be realized over doping incorporation is demonstrated in Fig. 1. Further studies were undertaken to establish the doping transition widths obtained, and thereby confirm that PED controls Sb incorporation, and not the adsorption/desorption kinetics. Figure 7 shows a Sb doping profile in which the Si and Sb fluxes were maintained constant throughout the growth run, and three n^+ spikes were introduced by stepping the applied potential between 0 and -800V . This SIMS profile indicates the doping transitions to be extremely sharp; the near-surface doping transition (denoted A) had a measured width of $< 50 \text{ \AA}/\text{decade}$, which compares with the resolution limit of SIMS. The asymmetry of the spike features measured in the SIMS profile, and the gradual slight degradation in the shape of the spikes was established to be due to atomic mixing and segregation effects, since improved symmetry is obtained by profiling such structures at 45° to (rather than along) the sample normal (28). SRP and eCV electrical profiles agree within measurement error with the SIMS values at the dopant peaks. However, lower levels are measured (and indeed expected from the calibration shown in Fig. 3) by the electrical profiling

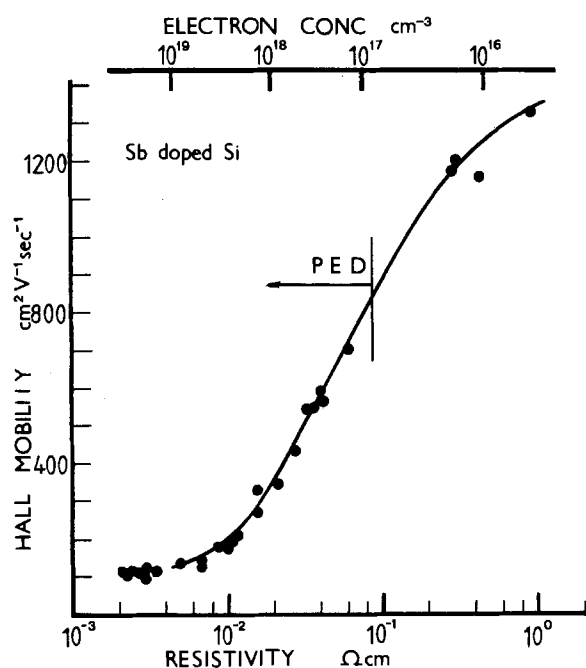


Fig. 6. Room temperature Hall mobility as a function of resistivity (and donor concentration assuming a Hall factor of unity) for uniformly Sb-doped epilayers. Data are superimposed on bulk values (25).

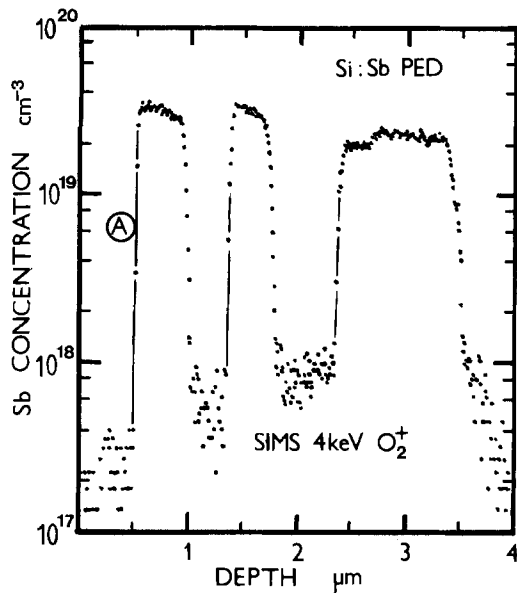


Fig. 7. SIMS profile of an Sb-doped structure grown using PED:Sb. The three n^- spikes were introduced by stepping the applied potential from 0 to $-800V$.

techniques than by SIMS in the n^- valleys due to a mass interference which limits SIMS detection to ^{121}Sb . Comparison of the transition widths obtained by SIMS and SRP indicated similar behavior to that discussed elsewhere for B-doped MBE-Si (9), implying that doping transitions obtained by PED:Sb doping in general exceeded the resolution limit of the three profiling techniques employed.

Conclusions

PED appears to be a powerful method of assisting coevaporation doping in Si-MBE, particularly in the case of n-type Sb. High doping levels are readily and reproducibly obtained using PED:Sb doping without the need for heavy adlayer coverage or low growth temperatures. Bulk-like mobilities up to the solubility limit ($\sim 3 \times 10^{19} \text{ cm}^{-3}$) are obtained. PED likely involves the acceleration of Si^+ ions to the substrate, although the exact mechanism for enhanced doping requires further clarification. Despite the influence of these ions, no degradation in crystallinity can be detected by RBS or defect assessment, and photoluminescence indicates the material to be bulk-like. Used in combination with coevaporative B doping as a p-type source (7-9), these methods offer a powerful alternative to dopant-ion implantation in Si-MBE, particularly where introduction of complex profiles involving sharp or controlled doping transitions over a wide dynamic range is required.

Acknowledgments

We wish to thank Dr. M. Pawlik (GEC Hirst Research Centre), Dr. M. G. Dowsett and Dr. D. F. McPhail (CLP), and Dr. E. Maydell-Ondrusz (University of Surrey) for SRP, SIMS, and RBS analyses, respectively, R. Houghton for associated experimental work, and P. Driscoll for

technical assistance. The work is performed in collaboration with British Telecom Research Labs (Martlesham, UK) GEC Hirst Research Centre (Wembley, UK), and UG Semicon (East Grinstead, UK).

Manuscript received June 17, 1985. This was Paper 129 presented at the Toronto, Ontario, Canada, Meeting of the Society, May 12-17, 1985.

REFERENCES

1. R. A. Swartz, J. H. McFee, A. M. Voshchenkov, and S. N. Finegan, *Appl. Phys. Lett.*, **40**, 238 (1982).
2. Y. Ota, *J. Appl. Phys.*, **51**, 1102 (1980).
3. G. E. Becker and J. C. Bean, *ibid.*, **48**, 3395 (1977).
4. S. S. Iyer, R. A. Metzger, and F. G. Allen, *ibid.*, **52**, 5608 (1981).
5. R. A. Metzger and F. G. Allen, *ibid.*, **55**, 931 (1984).
6. J. C. Bean, *Appl. Phys. Lett.*, **33**, 654 (1978).
7. R. A. A. Kubiak, W. Y. Leong, and E. H. C. Parker, *ibid.*, **44**, 878 (1984).
8. R. A. A. Kubiak, W. Y. Leong, and E. H. C. Parker, Paper presented at the 3rd International Conference on MBE, San Francisco, 1984; *J. Vac. Sci. Technol. B*, **3**, 592 (1985).
9. R. A. A. Kubiak, W. Y. Leong, and E. H. C. Parker, in "Silicon Molecular Beam Epitaxy," J. C. Bean, Editor, p. 169, The Electrochemical Society Softbound Proceedings Series, Pennington, NJ (1985).
10. R. A. A. Kubiak, W. Y. Leong, and E. H. C. Parker, *Appl. Phys. Lett.*, **46**, 565 (1985).
11. R. A. A. Kubiak, W. Y. Leong, and E. H. C. Parker, in "Silicon Molecular Beam Epitaxy," J. C. Bean, Editor, p. 230, The Electrochemical Society Softbound Proceedings Series, Pennington, NJ (1985).
12. R. A. A. Kubiak, W. Y. Leong, R. M. King, and E. H. C. Parker, *J. Vac. Sci. Technol. A*, **1**, 1872 (1983).
13. J. C. Bean, Personal communication.
14. W. Y. Leong, R. A. A. Kubiak, and E. H. C. Parker, in "Silicon Molecular Beam Epitaxy," J. C. Bean, Editor, p. 140, The Electrochemical Society Softbound Proceedings Series, Pennington, NJ (1985).
15. C. T. Foxon, J. A. Harvey, and B. A. Joyce, *J. Phys. Chem. Soc.*, **34**, 1693 (1973).
16. S. S. Iyer, Ph.D. Thesis, University of California, Los Angeles, CA (1982).
17. H. Jorke and H. Kibbel, in "Silicon Molecular Beam Epitaxy," J. C. Bean, Editor, p. 194, The Electrochemical Society Softbound Proceedings Series, Pennington, NJ (1985).
18. T. Itoh, T. Nakamura, M. Muromachi, and T. Sugiyama, *Jpn. J. Appl. Phys.*, **15**, 1145 (1976).
19. T. Narusawa, S. Shimizu, and S. Komiya, *J. Vac. Sci. Technol.*, **16**, 366 (1979).
20. Y. Shiraki, Paper presented at the 3rd International Conference on MBE, San Francisco, 1984; *J. Vac. Sci. Technol. B*, **3**, 725 (1985).
21. F. Arnaud D'Avitaya, Personal communication.
22. R. A. A. Kubiak, W. Y. Leong, R. Houghton, and E. H. C. Parker, in "Silicon Molecular Beam Epitaxy," J. C. Bean, Editor, p. 124, The Electrochemical Society Softbound Proceedings Series, Pennington, NJ (1985).
23. L. J. van der Pauw, *Philips Res. Rep.*, **13**, 1 (1958).
24. S. M. Sze, "Physics of Semiconductor Devices," John Wiley and Sons, New York (1969).
25. F. J. Morin and J. P. Maita, *Phys. Rev.*, **96**, 28 (1954).
26. V. Konig, H. Kibbel, and E. Kasper, *J. Vac. Sci. Technol.*, **16**, 985 (1979).
27. B. Hamilton, Personal communication.
28. M. G. Dowsett, Personal communication.

Rapid Thermal Annealing in GaAs IC Processing

S. J. Pearton, K. D. Cummings, and G. P. Vella-Coleiro

AT&T Bell Laboratories, Murray Hill, New Jersey 07974

ABSTRACT

A variety of annealing steps in GaAs IC processing presently performed in conventional furnaces may be readily transferred to more convenient rapid annealing furnaces. A comparison of the activation characteristics achieved for common implanted species (Si, Se, Be, Mg, and Zn) into semi-insulating GaAs by both annealing regimes is given. The limitations and advantages of the two methods with respect to encapsulation requirements, throughput, and handling are discussed.

The development of GaAs integrated circuits depends upon the routine production of conducting channel and contact regions by ion implantation into semi-insulating substrates. The high temperature annealing step required to activate the implanted ions is crucially important: the activation must be attained with minimal dopant redistribution, and loss of As from the wafer surface must be suppressed. The literature on ion implantation in GaAs has a long and somewhat contradictory history (1, 2), undoubtedly due in large part to the variable quality of substrates available. The need for surface protection, usually achieved by deposition of an encapsulating layer, is also a complicating factor; it is clear that stress induced in the wafer because of differing expansion coefficients (3) and impurities diffusing in from the cap (4), has often been the cause of nonreproducible results reported by many laboratories.

Recent advances in GaAs crystal growing technology, leading to wafers with more uniform properties over a 2 in. diam and better thermal stability, give hope that devices with uniform performance characteristics can be fabricated over large areas (5, 6). Another potential advance in GaAs IC processing comes in the form of rapid thermal annealing (RTA), in which the high temperature cycle is limited to several seconds, rather than 15-20 min as is usual with conventional furnace annealing. The consequent restriction of dopant diffusion (both into the bulk and laterally) is attractive if very small dimension devices are required. Because of the versatility of commercially available rapid annealing furnaces, it also appears feasible to perform other GaAs processing heat-treatments (e.g., contact alloying) in the same furnace. In this paper, we detail experiments to determine the characteristics and suitability of rapid annealing for these heat-treatments.

Experimental

Undoped, semi-insulating (100), LEC-grown wafers were used as substrates for ion implantation. For the production of n or n⁺ regions, various doses (2×10^{12} - 10^{15} cm⁻²) of ²⁹Si or ⁷⁸Se were implanted at energies between 60 and 400 keV. For the fabrication of p or p⁺ regions, ⁹Be, ²⁴Mg, or ⁶⁵Zn was implanted at energies of 40-100 keV and doses of 3×10^{12} - 10^{15} cm⁻².

Rapid annealing was performed in a Heatpulse 210T system¹ under a flow of forming gas. The temperature was monitored by a Cr-Al thermocouple embedded in a 3 in. Si substrate on which the GaAs wafers were annealed. All of the high temperature activation steps were preceded by a 60s, 400°C step to warm the tungsten-halogen lamps. This, combined with an appropriate software routine, ensured that sharp temperature profiles were obtained routinely. An example of a typical temperature profile undergone by an implanted wafer is shown in Fig. 1. For comparison to the rapidly annealed samples, wafers were proximity annealed in a conventional As-H₂ furnace for 20 min at 850°C. In this arrangement, a solid source of As is held in a separate, cooler zone of the furnace (410°C), and the resultant As vapor is carried down the main tube of the furnace by a flow of pure hydrogen. This provides an As vapor pressure above the GaAs wafer

much higher than the equilibrium value which would be obtained from dissociation of the wafer itself.

To avoid possible complications from encapsulating layers, all rapid annealing was also performed using the proximity technique. Figure 2 shows that it is possible to activate Si implants by this method without degrading the wafer surface.² Alternatives, such as placing the wafer on a Si substrate rather than GaAs or leaving the implanted face up during the annealing, lead to surface dissociation at comparatively lower temperatures and shorter times. For routine device production, however, it is clear that encapsulation is required to prevent mechanical damage and baked-on contamination on the implanted face of the wafer.

Electrical activations were determined by C-V profiling using a mercury probe and LCR meter for low dose implants, or a Polaron electrochemical profiler for high dose ($> 10^{13}$ cm⁻²) implants, and by van der Pauw measurements.

Results

Activation of n-type dopants.—The two most suitable species for the production of n-channel regions by ion implantation are Si and Se. This is evident from the comparison of the characteristics of the various implanted donor ions in GaAs given in Table I. Implants of ²⁹Si (60 keV) or ⁷⁸Se (100 keV) at two doses (4×10^{12} or 1×10^{13} cm⁻²) were annealed face down on GaAs substrates for 5s at various temperatures. Figure 3 shows van der Pauw measurements on these wafers; optimum activation is achieved at 950°C for the Si implants at either dose, whereas Se requires a slightly higher temperature (~1000°C), concomitant with the higher degree of damage created by the heavier Se ions. Annealing of either species at still higher temperatures leads to a degradation of electrical properties, owing to site transfer (for the Si) and surface degradation. These optimum activations are essentially identical to those obtained by conventional furnace annealing at 850°C for 20 min.

Electrical profiles of such low dose implants, obtained from C-V measurements, are shown in Fig. 4. The

² Some of these data are taken from Kohzu *et al.* (7).

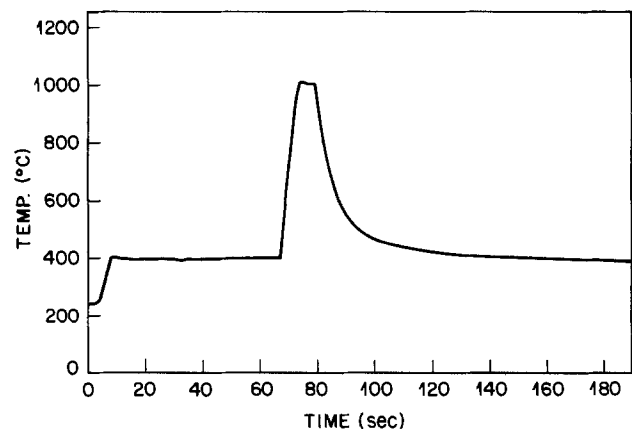


Fig. 1. Typical temperature-time profile for a rapidly annealed wafer

¹ A. G. Associates, Palo Alto, California 94303.

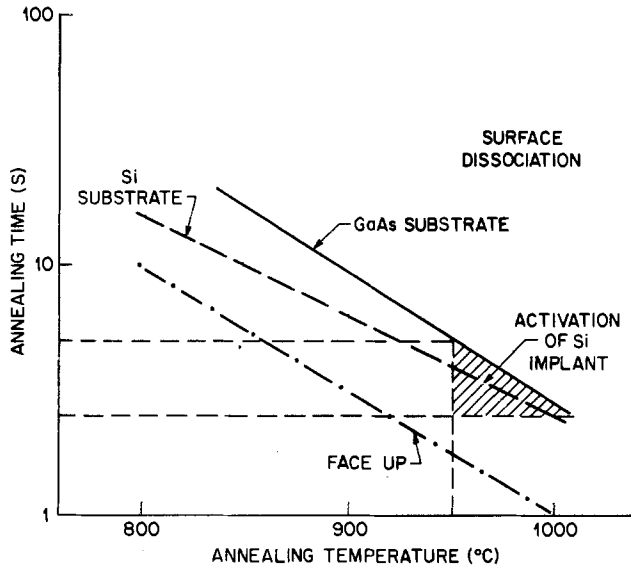


Fig. 2. Surface dissociation of GaAs under RTA. The implanted wafer is placed either face up or face down on a Si or GaAs substrate. Surface dissociation occurs above each line of the plot. Only within the hatched area is good implant activation achieved without surface dissociation of the GaAs wafer. For example, a 1000°C, 5s anneal performed with the implanted wafer face down on another GaAs wafer leads to activation of the Si ions. The same anneal performed with the wafer either face down on a Si substrate or face up leads to surface dissociation of the GaAs wafer.

profiles fit well to those expected from the LSS theory (8). The deviations at the deepest depths are due to two phenomena: first, some channeling of the implanted species during implantation and, second, the increasing series resistance of the sample as pinch off is approached leads to an increasingly inaccurate capacitance determination. There does not appear to be any diffusional broadening during the activation anneal. Although it is not evident from the Se profiles of Fig. 4, it is easier to obtain good activation for deeper (higher energy) implants, presumably because surface effects are less severe than for shallow implants. Once again, the profiles for both Si and Se are similar to those obtained using thermal annealing. The electron mobilities are typically $> 3500 \text{ cm}^2\text{-V}^{-1}\text{-s}^{-1}$ for both rapid and thermally annealed regions, with no systematic differences between the two methods.

The production of n^+ regions for contacts are also required in GaAs device fabrication. It is well established that it is apparently impossible to routinely achieve electrical activities above $2\text{-}3 \times 10^{18} \text{ cm}^{-3}$ by direct ion implantation. These values are below that required for the production of an ohmic contact (9) and alloying of various eutectics is used for their fabrication (10). The total con-

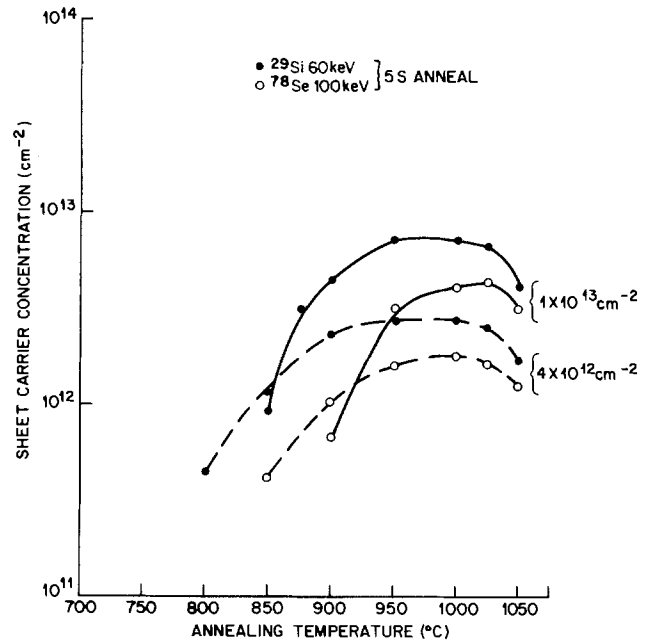


Fig. 3. Donor activation of Si and Se for two doses after 5s anneals at various temperatures.

tact resistance, however, is still dependent on the resistivity of the underlying GaAs and thus it is necessary to produce the highest possible, regularly achievable doping level. Sheet carrier densities for Si and Se implants as a function of dose after rapid annealing for 5s at 950°C are shown in Fig. 5. The eventual saturation in activity is evident from comparison of the experimental results with the full activation line (*i.e.*, slope of activation *vs.* dose curve equals 1). Amorphization of GaAs for room temperature implants occurs at doses of $\sim 10^{14} \text{ cm}^{-2}$ for Si implants and $\sim 5 \times 10^{13} \text{ cm}^{-2}$ for Se implants, and for device applications it seems clear that amorphization should be avoided, if possible. We have found that the carrier mobilities in recrystallized layers are generally poorer than in those where amorphization was prevented, and it is difficult to completely repair the GaAs lattice. There is generally a high density of dislocation loops left after even high temperature ($> 1000^\circ\text{C}$) annealing of initially amorphous layers. We have also previously seen that for very high dose, room temperature implants, thermal annealing, particularly for heavier ion species, is superior to RTA, presumably because full damage removal is difficult on the time scale of RTA unless higher temperatures are used (11). This, in turn, leads to surface dissociation for capless anneals, or else is a very severe test for encapsulating layers that might be used. Getting to

Table I. Characteristics of ion-implanted species in GaAs

Ion	Donors	Comments
Si	Low mass means good activation for RT implant, versatile range.	
Se	Good activation for low dose, RT implant.	
Te	Poor activation for RT implant.	
Ge	Amphoteric species, poor activation, difficult to implant.	
S	Diffuses during annealing.	
Sn	Amphoteric, diffuses during anneal.	
Acceptors		
Be	Very light mass means good activation at low annealing temperature, easy to implant, versatile range, at high concentrations diffuses during anneal.	
Mg	Good activation, versatile range, difficult implant source.	
Zn	Reasonable activation, at high concentrations diffuses during anneal.	
Cd	Reasonable activation, diffuses during implantation at RT, difficult implant source.	

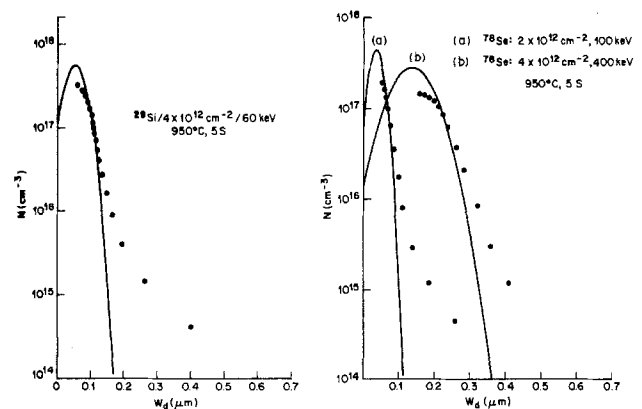


Fig. 4. Electrical profiles for low dose Si and Se implants comparing experimental with theoretically expected profiles. W_d is the depletion depth, and N is the carrier concentration.

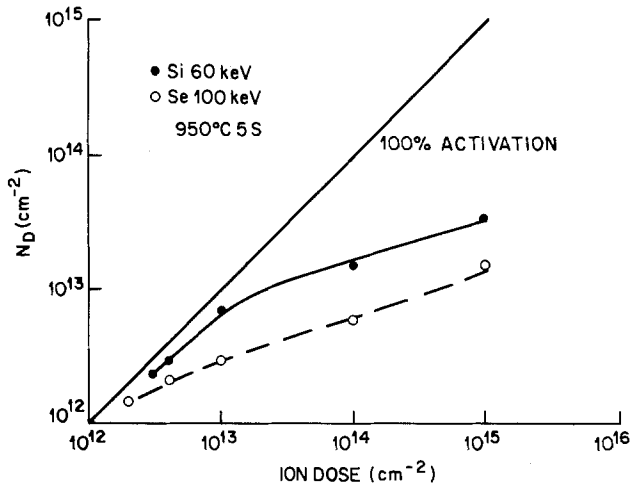


Fig. 5. Activation of Si and Se as a function of implant dose for an anneal of 950°C for 5s.

heavily damaged regions of mobile acceptor impurities such as Mn and Cr also occurs (12), and this will reduce activities and electron mobilities. The point is that if there is little or nothing to be gained electrically by increasing doses above $5\text{--}10 \times 10^{13} \text{ cm}^{-2}$, then doses should be limited to these values. Elevated temperature implantation of heavy species like Se or Te prevents amorphization and leads to higher electrical activities than room temperature implants (13), but for device production it is simpler to use a lighter ion (Si) and room temperature implantation.

Electrical profiles from dual energy Si-implanted wafers are shown in Fig. 6, comparing results from rapidly annealed and thermally annealed samples. Such structures (n^+/n) are used to simultaneously provide an n^+ region for contact to the electron channel (n -region). There is much less diffusion of the Si in the rapidly annealed wafer, bearing in mind that, in the furnace-annealed samples, annealing was performed after each implant [otherwise the two profiles smear together by diffusion (14)]. While single-energy Si implants display essentially no redistribution during furnace annealing, with dual energy implants there is a marked tendency for the Si ions in the n -channel region to diffuse back into the more heavily damaged n^+ region during the activation anneal (14). The fact that good profiles may be achieved by a single dual-implant-rapid anneal schedule means that a tremendous savings in time and handling can be obtained. This is a clear example of a situation where rapid annealing is superior to furnace annealing.

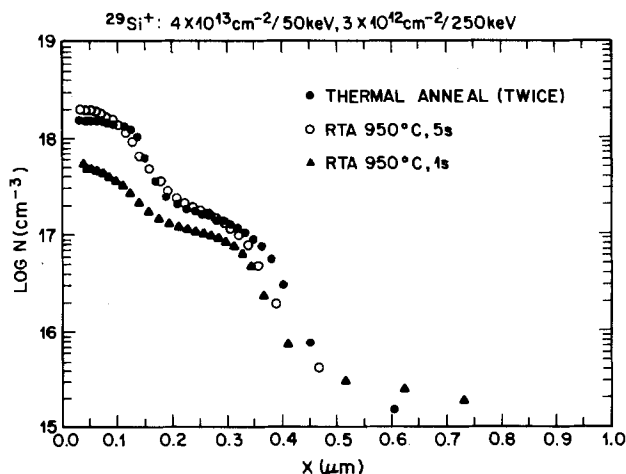


Fig. 6. Electrical profiles from dual Si-implanted wafers, comparing RTA to furnace annealing. The latter was performed after each implant; the former after both implants have been done together.

Activation of p-type implants.—It is widely recognized that p-type implanted regions are activated at lower annealing temperatures than n-type implants (1, 13). In Fig. 7, we show results from rapid annealing of low dose (3×10^{12} and $1 \times 10^{13} \text{ cm}^{-2}$) implants of ^9Be and ^{65}Zn that would be used for p-channel regions. Maximum (and complete) activation of Be is achieved at 800°C for 5s anneals, while the activation of the much heavier Zn ions is less than complete, and the optimum values occur at higher temperatures ($\sim 900^\circ\text{C}$). Results on Mg implants (mass number 24) follow closely those for Be, with slightly lower activation at the lower temperatures (below 750°C). Above 800°C, essentially complete activation is obtained for Mg as well as Be. Again, at the highest temperatures ($\sim 1000^\circ\text{C}$) there is a degradation in activation because of loss of As and diffusion of the implanted species.

Electrical profiles from low dose Be and Mg implants are shown in Fig. 8. The deviations from the expected LSS profiles are due to the rapidly increasing series resistance of the samples affecting the C-V measurements. While there is some channeling during implantation, it is clear from differential Hall measurements that there is little diffusional broadening of the profiles during annealing for the low doses. The mobilities of rapidly annealed p-channel regions are in the range $220\text{--}250 \text{ cm}^2\text{V}^{-1}\text{s}^{-1}$ and are always better after annealing at 800°C and above than 750°C annealing, even though the activation is the same. These mobilities are the same as those achieved by thermal annealing at 800°C for 20 min.

The production of high hole concentrations by implantation and thermal annealing is readily achievable in GaAs, in contrast to the case for donor impurities. This is also true for rapid annealing. Figure 9 shows the activation of Be and Zn implants as a function of dose for capless rapid annealing at 950°C for 3s. Essentially complete activation of Be is achieved up to doses of $\sim 10^{14} \text{ cm}^{-2}$, falling to 40% for a dose of 10^{15} cm^{-2} , where amorphization is obvious. Full activation of Zn implants is not achieved at any dose, with 50% activation at 10^{14} cm^{-2} dose, and 28% activation at 10^{15} cm^{-2} .

Electrical profiles obtained by Polaron profiling and differential Hall measurements on high dose Be and Zn implants are shown in Fig. 10. A peak hole concentration of $3 \times 10^{19} \text{ cm}^{-3}$ was obtained from a 40 keV, 10^{15} cm^{-2} Be implant annealed at 900°C for 1s. Less activation is obtained from Zn implants for equivalent doses. Upon com-

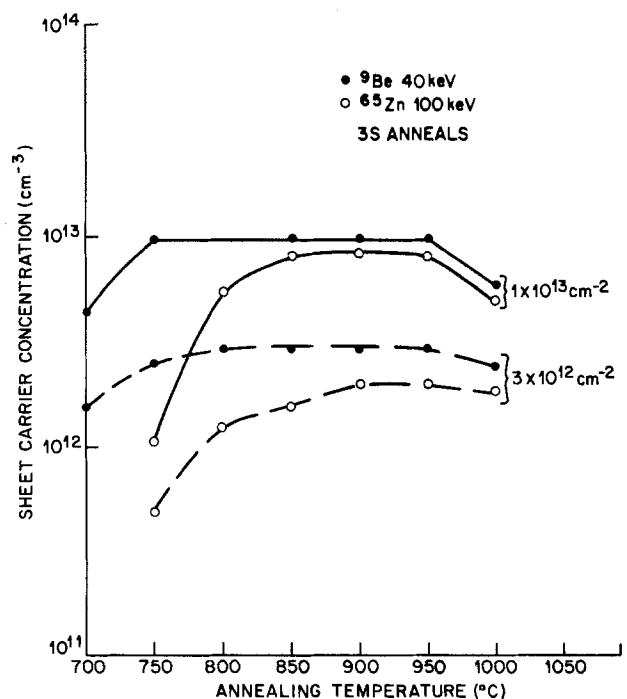


Fig. 7. Acceptor activation of Be and Zn for two doses after 3s anneals at various temperatures.

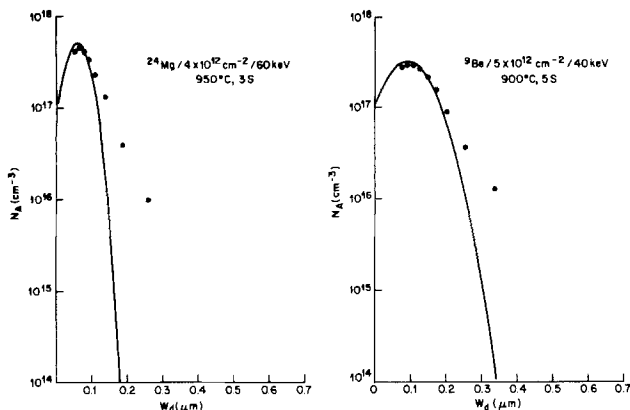


Fig. 8. Electrical profiles for low dose Mg and Be implants after RTA. The deviations from the expected profiles are due to rapidly increasing sample series resistance affecting the C-V data.

parison with the as-implanted profiles (obtained from secondary ion mass spectrometry data), broadening of the profiles during annealing is obvious, particularly for the Be implants. The concentration dependent diffusion of p-type impurities in GaAs is well-documented—thermal annealing usually leads to very broad p^+ profiles (15), while the much shorter time scale of rapid annealing may limit this diffusion. A number of experimenters have attempted to take advantage of this with a “pulsed” diffusion of Zn from a surface source (16). Our own experiments along this line yield results that are comparable to those obtained by implantation and rapid annealing. Again, from a production viewpoint, implantation is preferable to diffusion. The observed characteristics of the available acceptor species in GaAs after implantation and annealing are shown in the lower part of Table I. It appears Be and Mg are the most useful because of their lower mass and hence more versatile implant depths.

Contact alloying.—The process of alloying various eutectics on GaAs is the standard method of forming ohmic contacts, but the details of the method are still not completely understood (9, 10). Conventional furnace annealing of AuGe-based eutectics on GaAs often leads to undesirable morphological features such as balling up and spiking of the eutectic-semiconductor interface. The shorter time scale of rapid annealing would appear to be ideal for ohmic alloying, and several recent studies have indicated the ability of RTA to provide reproducible, morphologically improved alloy contacts with low specific contact resistance to both n- and p-type layers (17, 18).

Our own experiments on split wafer lots have compared the contact resistances obtained by alloying

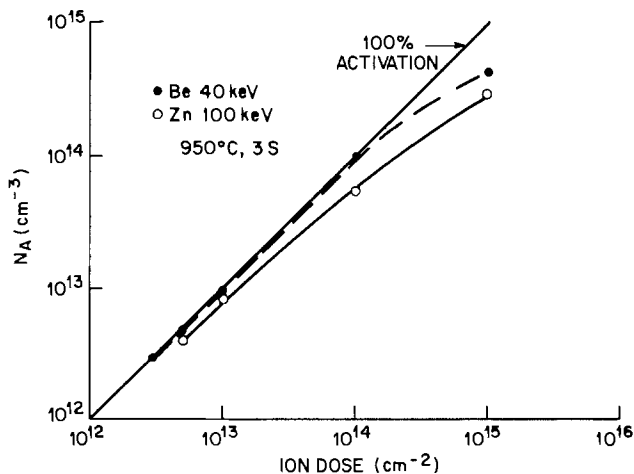


Fig. 9. Activation of Be and Zn as a function of implant dose for an anneal of 950°C for 3s.

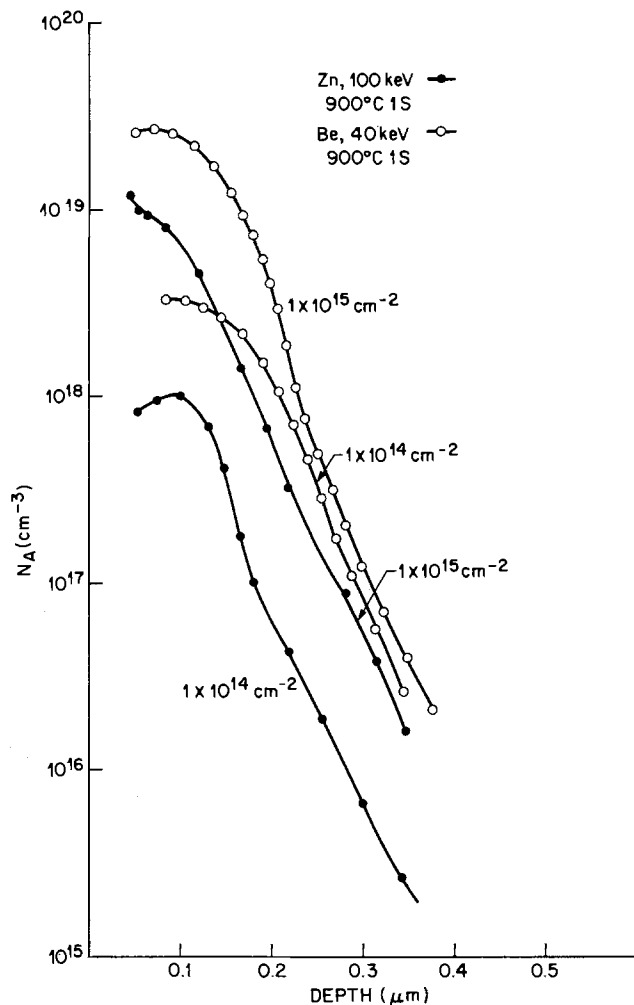


Fig. 10. Electrical profiles of Be and Zn after RTA at 900°C for 1s

AuGeNi to n or n^+ layers created by Si implantation into GaAs, using either a graphite plate heater, or the Heat-pulse RTA system (19). Typical temperature-time profiles from the two annealers are shown in Fig. 11. Contact resistances measured by the transmission line method were obtained at 26 different ohmic test pad positions on the split wafers, and the results from two wafers (n and n^+) are shown in Table II. The rapidly annealed contacts show 30-50% lower specific contact resistances and are more uniform than those obtained using the graphite heater.

Implant isolation.—To produce highly resistive regions between conducting channels in GaAs, moderate doses (10^{12} - 10^{14} cm^{-2}) of protons, helium, boron, or oxygen are implanted to create damage-induced, deep-level compensation of the shallow dopants. The as-implanted resistivity is generally not high enough to achieve effective isolation between neighboring devices, and a low temperature annealing cycle is employed to increase the resistivity to the desired value (20). Obviously, if the temperature is too high, the implant-induced damage is annealed out.

At present, the annealing step is performed in a conventional furnace at 450°-500°C for 10-20 min, but Hall measurements have shown that a much shorter thermal treatment (~20s) in an RTA achieves the same resistivity values for oxygen-implanted wafers. From the production viewpoint, this leads to the attractive scenario of performing all the required heat-treatments for GaAs IC's in a single RTA furnace by cassette-to-cassette loading.

Heterostructure annealing.—A number of experimenters have already demonstrated that normal implant activation annealing in a furnace leads to diffusion of Si ions from the doped AlGaAs layer into the undoped GaAs region of the two-dimensional electron gas (2DEG), with a

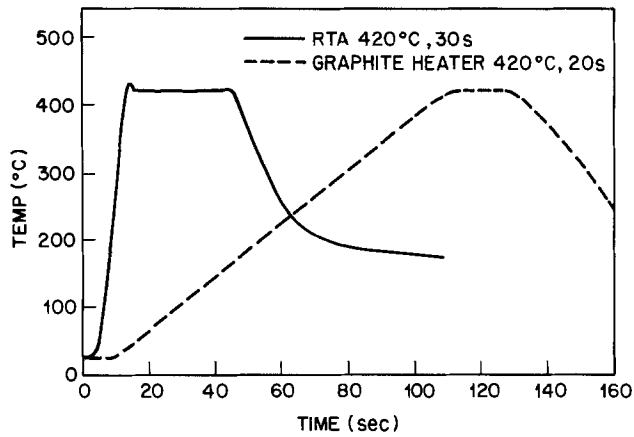


Fig. 11. Temperature-time profiles undergone by wafers during AuGeNi contact alloying in an RTA, compared to a graphite plate heater.

consequent serious degradation of the 77 K electron mobility (21). This falloff, however, is much reduced if a rapid annealing cycle is utilized, and appears to be the only way of annealing heterostructures for device applications without destroying their mobility advantages.

Discussion

The results in this paper demonstrate that the activation and mobility of implanted donor and acceptor species is at least as good using rapid thermal annealing as compared to normal furnace annealing. The uniformity of these properties, which was not discussed in this paper, is also comparable for the two annealing methods, allaying fears that there might be nonuniform heat-transfer to large area (2 in. diam) wafers during RTA (22).

For use as an integral part of device processing, encapsulating layers must be developed capable of withstanding the rapid heating and cooling rates, and the slightly higher annealing temperature of RTA compared to furnace activation. Contrary to the results of some others, we have found that RTA is a more severe test of the encapsulation than is furnace annealing. In particular, the effects of strain or impurities from the cap is most evident on n-channel regions, where an abrupt profile and high electron mobility are essential. The caps which show most promise are AlN (23), Si₃N₄, and PSG (phosphosilicate glass), but a good deal of work remains to be done to get reproducible layers, which can be easily and completely removed after annealing, and which can be deposited in a very uniform manner to allow the use of the through-implantation technique.

The rapid heating and cooling rates during RTA for implant activation are a problem from the viewpoint of slip formation on 2 and 3 in. diam wafers. These morphological features may upset certain subsequent processing steps, notably, photolithography. The slip formation may be reduced or even eliminated by slowing the cooling rate using appropriate software control of the furnace (19). Several Japanese workers have also applied for patents for guard ring structures which prevent slippage of rapidly annealed wafers by eliminating the thermal gradients near the edge of the wafer compared to its center.

Throughput is always a concern from a production viewpoint. This might seem a little strange when talking

about rapid annealing, but in the commercially available systems only one wafer can be annealed at a time, while in a tube furnace 20 or 30 can be annealed together. However, even considering the 1 min preheat for each rapidly annealed wafer, and the cooling time required, the throughput is superior to thermal annealing because of the time taken in the latter case with flushing the furnace, backfilling with H₂, heating up the As source, and the reverse sequence when the heat cycle is complete. (The volume of rapid annealing furnaces is much smaller than for a conventional furnace.) Even with manual loading and unloading, the throughput of wafers in a rapid annealer is ~25 h⁻¹, and this should be increased by cassette-to-cassette handling.

There is wide scope for research into novel alloying and solid phase reactions of metals and GaAs using RTA. For the present, the alloying of AuGeNi in an RTA is more uniform and produces lower specific contact resistances than the more conventional graphite strip heating. Similarly, the isolation implant anneal, another relatively low temperature step in GaAs processing, may be conveniently performed for much shorter times than is currently done.

Perhaps the most obvious need for RTA comes with the fact that to be integrated with other devices, and to reduce their own source-to-drain resistance, selectively doped heterostructure transistors need to be able to withstand high temperature implant activation steps. As mentioned above, normal furnace processing leads to an unacceptable degradation in the transport properties of the 2DEG. Using RTA, we have shown this degradation is considerably less even for devices with 20Å buffer layers, and that acceptable implant activation can be achieved without causing unusually low mobilities in the 2DEG (25). This is a case where RTA is not only a superior alternative to furnace annealing, but also the only feasible method of performing a crucial step in the processing of a very promising technology.

All of the above discussion may be summarized quite simply: it appears eminently feasible to perform all the heat-treatments required in GaAs IC processing in a single RTA furnace. The savings in time, space, and handling appear very attractive, and the actual temperature cycle seen by each wafer can be recorded, eliminating the furnace as a source of error if problems occur in device fabrication.

Conclusions

1. The electrical properties (activation and mobility) of implanted layers following optimum RTA are at least as good as those obtained by furnace annealing.
2. There is less diffusion under optimum RTA conditions than with furnace annealing, with repercussions for the annealing of n⁺/n structures and SDHT's.
3. The alloying of metal-semiconductor contacts is more reproducible with RTA than with furnace annealing.

Acknowledgments

The authors acknowledge the contributions to this work by P. K. Chin, J. S. Williams, T. W. Hou, S. P. Hui, B. Schwartz, S. Singh, A. D. Butherus, N. J. Shah, C. W. Tu, L. J. Kroko, D. J. Talley, L. Yesis, S. Tallia, and S. Skunk.

Manuscript submitted May 3, 1985; revised manuscript received July 22, 1985. This was Paper 703 SOA presented at the Toronto, Ontario, Canada, Meeting of the Society, May 12-17, 1985.

AT&T Bell Laboratories assisted in meeting the publication costs of this article.

REFERENCES

1. J. P. Donnelly, *Nucl. Instrum. Meth.*, **182**, 553 (1981).
2. J. S. Williams, "Laser Processing of Semiconductors," J. M. Poate and J. W. Mayer, Editors, p. 233, Academic Press, New York (1982).
3. H. Nishi, S. Okamura, T. Inada, H. Hashimoto, T.

Table II. Specific contact resistance for Au GeNi alloyed contacts on GaAs

Substrate	Annealer	Average τ_c ($\Omega\text{-cm}^2$)	$\sigma/\text{avg } \tau_c$ (%)
n ⁺	RTA	2.1×10^{-7}	33.7
n ⁺	Graphite	4.8×10^{-7}	40.5
n	RTA	5.5×10^{-7}	33.6
n	Graphite	7.4×10^{-7}	45.5

- Kabota, and T. Nakamura, *Inst. Phys. Conf. Ser.*, **63**, 365 (1982).
4. C. W. Farley and B. G. Sheetman, *J. Electron. Mater.*, **13**, 401 (1984).
 5. D. E. Holmes, H. Kuramoto, C. G. Kirkpatrick, and R. T. Chen, in "Semi-Insulating III-V Materials 1984," p. 204, Shiva, Cheshire, England (1984).
 6. H. M. Hobgood, R. N. Thomas, D. L. Barrett, G. W. Eldridge, M. M. Sopira, and M. C. Driver, in "Semi-Insulating III-V Materials, 1984," p. 149, Shiva, Cheshire, England (1984).
 7. H. Kohzu, M. Kuzuhara, and Y. Takayama, *J. Appl. Phys.*, **54**, 4998 (1983).
 8. J. Linhard, M. Scharff, and H. E. Shiott, *Mat. Fys. Mead. Dun. Vid. Selsk.*, **33**, 1 (1963).
 9. M. I. Nathan and M. Heiblum, *Solid-State Electron.*, **25**, 1063 (1982).
 10. G. S. Marlow, M. B. Das, and L. Tompson, *ibid.*, **25**, 259 (1983).
 11. S. J. Pearton, J. S. Williams, J. M. Poate, D. O. Boerma, and D. C. Jacobson, Unpublished data.
 12. H. Kanber and M. Feng, *SPIE*, **463**, 67 (1984).
 13. F. Eisen, *Rad. Eff.*, **47**, 99 (1980).
 14. J. S. Williams and S. J. Pearton, *Proc. Mater. Res. Soc.*, To be published.
 15. J. Kashara, H. Sakurai, Y. Kato, and N. Watanabe, *Jpn. J. Appl. Phys.*, **21**, L103 (1982).
 16. D. Dobkin and J. F. Gibbons, *This Journal*, **131**, 1699 (1984).
 17. S. K. Tiku, J. B. Delaney, N. S. Gabriel, and H. T. Yan, *Proc. Mater. Res. Soc.*, **35**, 486 (1985).
 18. R. Zuleeg, Private communication.
 19. P. K. Chin and S. J. Pearton, Unpublished data.
 20. Y. Kato, T. Shimada, Y. Shiraki, and K. F. Komabsu-bara, *J. Appl. Phys.*, **45**, 1044 (1974).
 21. S. Takuda, T. Inadu, S. Okamura, and S. Hiyamizi, *Jpn. J. Appl. Phys.*, **23**, L147 (1984).
 22. K. D. Cummings, S. J. Pearton, and G. P. Vella-Coleiro, *Proc. Mater. Res. Soc.*, To be published.
 23. R. Bensalem, N. J. Barrett, and B. J. Sealy, *Electron. Lett.*, **19**, 113 (1983).
 24. N. J. Shah, C. W. Tu, and S. J. Pearton, Unpublished data.

Lateral Epitaxial Growth over Oxide

Lynn O. Wilson and G. K. Celler*

AT&T Bell Laboratories, Murray Hill, New Jersey 07974

ABSTRACT

We model numerically formation of thick dielectrically isolated films by recrystallization from the melt. Si films are deposited over oxidized Si wafers, with a regular array of seeding windows opened in the isolation oxide. A stationary radiative heater melts the entire film and crystallization is controlled by the pattern of openings in the SiO₂. The model provides two-dimensional temperature profiles during melting and solidification as well as the shape of the solid-liquid interface and its motion. It also predicts the amount of superheating and undercooling at the buried oxide as a function of the spacing between the windows in the oxide. The computed results are in agreement with the experimental data and clarify the influence of several processing parameters on melting and crystallization.

Controlled crystallization of silicon from the melt has been explored in recent years as an attractive method of forming single-crystalline Si over an insulating substrate (1). The tools for melting range from scanned cw laser beams and electron beams to scanned graphite filaments to extended stationary heaters. Most efforts have been concentrated on forming thin films over oxidized Si wafers using scanned heat sources.

High voltage and high current integrated circuits are an important class of devices requiring dielectric isolation. They are made commercially in crystalline Si segments, 40-60 μm thick, which are isolated by the SiO₂ film from the polysilicon substrate and from each other (2). Fabrication of dielectrically isolated (DI) wafers is complex and expensive; moreover, the polysilicon substrates tend to bow during thermal processing, reducing device yields. Over the last few years, we have developed a method of forming 10-100 μm thick single-crystalline films by uniform melting with an extended stationary heat source (3, 4). The precursor structure consists of polysilicon deposited over oxidized Si wafers, with a regular array of openings in the oxide. These openings provide seeding needed for epitaxial crystallization and impose lateral temperature gradients necessary for lateral epitaxial regrowth. The latter is possible because the thermal conductivity of the oxide is about ten times lower than that of silicon. The fact that molten Si in contact with the amorphous SiO₂ can be undercooled further facilitates lateral crystallization from the seeding windows. Although extensive crystallization over the oxide has been achieved without detailed knowledge of the thermal profiles and the amount of undercooling, a better understanding of temperature distribution, undercooling, and interface dynamics is necessary to optimize melting and crystallization conditions. This paper describes numerical modeling of this process and compares the computed results with the experimental data.

*Electrochemical Society Active Member.

Description of the Process

Melting and crystallization are carried out in a lamp furnace (5) consisting of two rectangular chambers, each 10 \times 12.5 in. in lateral dimensions, positioned one above the other and separated by a quartz window. Air-cooled tungsten halogen lamps are suspended under a gold-plated reflector in the upper chamber. Wafers are placed on quartz pins \sim 0.5 in. above the water-cooled base of the lower chamber. Samples are heated uniformly from the upper side with a broad-band radiative flux emitted by the lamps. At typical settings required for melting, the spectrum is centered at \sim 1 μm wavelength. At this wavelength, the optical penetration depth is $>$ 100 μm at 20°C, but drops exponentially with temperature to $<$ 1 μm above 1000°C. Cooling is predominantly by blackbody radiation from both the front and back sides of the samples. The presence of the metal base held at a nearly constant temperature $<$ 100°C assures reproducible cooling rates and a gradient across the wafer thickness of the order of 100°C/cm.

Samples for crystallization are prepared by oxidation, photolithography, and deposition of polysilicon and SiO₂ films. (100) starting wafers are cleaned and oxidized in a steam ambient to form the dielectric isolation barrier. The oxide is patterned by photolithography to obtain an array of seeding windows. CVD deposition of polysilicon is carried out at high temperatures in a conventional vertical epitaxial reactor. First, samples are etched briefly with HCl vapor at 1050°C to remove the native oxide from the silicon surface in the seeding windows. Deposition is often done in two steps: (i) nucleation and (ii) rapid growth. Uniform nucleation of Si over SiO₂ is achieved by decomposition of SiH₄ at 1050°C. After a continuous silicon layer has been formed, the temperature is increased to 1150°C and SiH₄ is replaced with SiHCl₃ for a higher, $>$ 1 $\mu\text{m}/\text{min}$, growth rate. The 10-100 μm thick films have columnar grain structure with an average grain diameter $>$ 1 μm and with a surface roughness of 1-3 μm . As a final

step, the surface is capped with a 2 μm layer of LPCVD oxide that is needed to contain molten silicon.

To recrystallize a Si layer on an oxidized Si wafer, the lamps are ramped linearly over 10-30s to a predetermined power setting that exceeds the threshold power for melting, held at that value for 10-100s, and shut off by a linear reduction of electrical power. The sample temperature is monitored with an optical pyrometer that is focused on the back side of the wafer. After a few seconds lag when the power is first applied, the sample temperature increases rapidly until it reaches the melting temperature T_m . This occurs at a power setting of $\sim 80 \text{ W/cm}^2$. The onset of melting is easily determined from the pyrometer output even if the absolute temperatures are not known precisely because of some uncertainty in the value of emissivity. The temperature curve has a knee at the melting temperature and its slope is essentially zero for the melt duration. For this reason, no feedback from the pyrometer to the power supply is used in the crystallization experiments. Almost all the absorbed power exceeding the threshold value is taken by the heat of fusion which for silicon is $\sim 1810 \text{ J/g}$.

Crystallization of the molten Si starts in the seeding windows and proceeds over the oxide. Upon recrystallization, the entire film is usually single crystalline, and it is free of grain boundaries or subboundaries. The remaining dislocations tend to concentrate where two solidification fronts collide. A cross section of the recrystallized film is shown in Fig. 1.

Since all heating is radiative and the reflectivity of molten metallic Si is roughly twice that of the solid, elongated inclusions of superheated solid are present on the surface of the liquid over a range of input powers, from the threshold for surface melting P_1 to a higher threshold for deep melting P_2 (6). The values of P_1 and P_2 depend on surface preparation. Wafers covered with thick polycrystalline layers deposited by CVD have a characteristic roughness caused by the different rates of growth of randomly oriented Si grains. This rough surface is encapsulated with a 2 μm thick transparent film of SiO_2 . Absorptivity of rough surfaces coated with glassy overlayers has been extensively studied for application to solar collectors. Based on calculations of Yablonoivitch (7), we have obtained the value of emissivity $\epsilon_s = 0.84$ near the melting temperature $T_m = 1685 \text{ K}$ for a rough Si surface coated with SiO_2 . The emissivities of a smooth and encapsulated surface would have been 0.72 and for smooth Si without the cap $\epsilon_s = 0.6$.

The emissivity of molten Si is lower than that of the solid. The initial surface roughness and encapsulation still affect the emissivity value. When a Si surface melts, it becomes more reflective and the input of energy into the irradiated surface is reduced. This causes a melting instability: the heated surface breaks up into an array of solid and molten areas that can coexist indefinitely. Two types of breakup have been observed and described (6, 8). Large-faceted molten areas are formed in defect-free single-crystalline surface layers, and networks of thin solid lamellae appear inside them. In heavily defective layers, faceted melting is absent and the entire surface becomes covered with a lamellar network. The solid inclu-

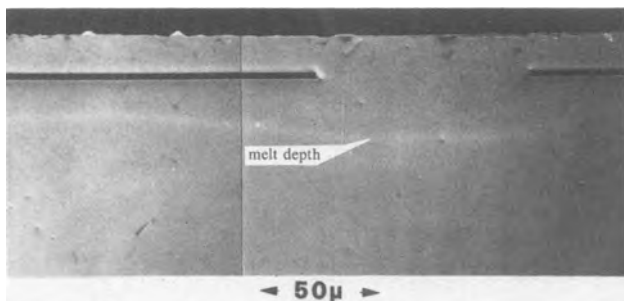


Fig. 1. Optical micrograph of polished cross-section of recrystallized sample after 10s Schimmel etch.

sions reduce the surface-averaged reflectivity to a value permitting a steady-state heat flow, and only superficial melting is present as long as some solid inclusions exist. In our numerical model, it is assumed that the applied input power exceeds P_2 and that the entire surface is uniformly melted.

Formulation

The assumptions used in deriving the governing equations have been discussed in Ref. (9) for a one-dimensional model. In brief, heat-transport within the wafer is predominantly due to conduction, heat input from the lamps is modeled through radiative coupling at the top wafer surface, and radiative cooling at the wafer surfaces is the dominant mechanism for heat loss. Effects due to crystalline anisotropy are ignored. The capping layer is not modeled directly; however, its influence is felt via the values used for the emissivity of solid and liquid silicon at the top surface. Since the development of the two-dimensional equations proceeds analogously, we write the equations below in a dimensionless, nearly final, form.

The basic two-dimensional domain, shown in Fig. 2, represents a cross section of a portion of the wafer. The domain is reflected about its left (or, equivalently, right) edge and repeated to give a periodic array. It consists of a silicon substrate of thickness d_1 , on top of which lies thermal oxide patterned into alternating islands and windows. Shown are half of an island, with half-width w_1 , and half of a window, with half-width w_2 . This layer has thickness d_2 . On top of this is another layer of silicon of thickness d_3 representing the silicon grown by chemical vapor deposition.

We write the governing equations in a nondimensional form, but present all computational results in a dimensional form. For simplicity, we shall use the same notation for the dimensional quantities d_1, d_2, d_3, w_1, w_2 , and for their dimensionless counterparts, when they are divided by a characteristic distance d . Similarly, we use the notation t for time and for dimensionless time, normalized by a characteristic time τ . In practice, this should cause no confusion.

The dimensionless thermal diffusion equation is

$$\text{Pe} \frac{\partial T}{\partial t} = \nabla \cdot (K \nabla T) \quad [1]$$

Here T is the dimensionless temperature and

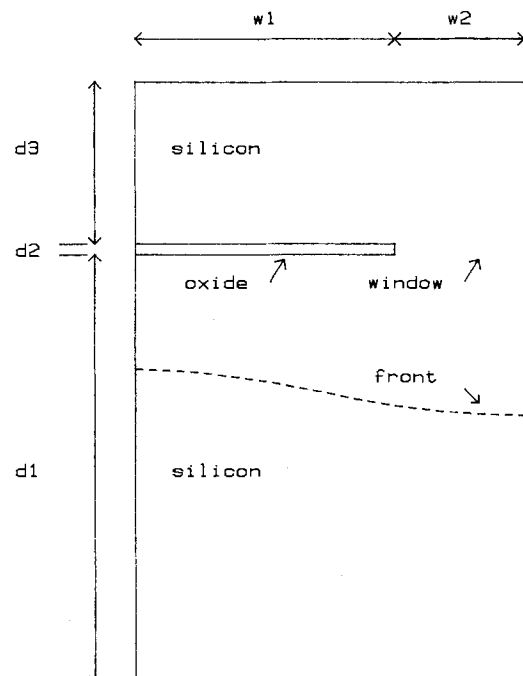


Fig. 2. The computational domain

$$Pe = \frac{\rho Cd^2}{\kappa\tau} \quad [2]$$

is the Péclet number, where ρ , C , and κ represent a characteristic density, heat capacity, and thermal diffusivity, respectively. The dimensionless thermal diffusivity $K(\mathbf{x})$ in Eq. [1] is assumed to take on values $\kappa^{-1}K_s$, $\kappa^{-1}K_L$, and $\kappa^{-1}K_o$ in the solid silicon, liquid silicon, and oxide regions; each of these is constant within its region. The dimensional temperature \bar{T} can be obtained from T by setting

$$\bar{T} = T_m(1 + RT) \quad [3]$$

T_m is the melting temperature of silicon. The radiation number R is given by

$$R = \frac{\sigma d T_m^3}{\kappa} \quad [4]$$

where σ is the Stefan-Boltzmann constant.

Let \mathbf{n} represent the unit outward normal to a surface. By symmetry, no flux crosses the left or right boundary

$$\mathbf{n} \cdot (K\nabla T) = 0 \text{ at } x = 0, x = w_1 + w_2 \quad [5]$$

At the top surface, the flux balance is given by

$$\mathbf{n} \cdot (K\nabla T) = \epsilon P(t) - \epsilon(1 + RT)^4, y = d_1 + d_2 + d_3 \quad [6]$$

where $P(t)$ is the power input from the lamps, while at the bottom surface we have

$$\mathbf{n} \cdot (K\nabla T) = -\epsilon(1 + RT)^4, y = 0 \quad [7]$$

The emissivity ϵ takes on values ϵ_s at the solid top surface, ϵ_l at the liquid top surface, and ϵ_b at the (solid) bottom surface.

Let the position of the melt or solidification front be denoted by $\mathbf{u}(\mathbf{x}, t)$. At the front, the dimensionless temperature is zero

$$T(\mathbf{u}(\mathbf{x}, t), t) = 0 \quad [8]$$

If \mathbf{n}_f represents a unit normal at the front, pointing from the solid to the liquid, the Stefan equation is given by

$$\frac{d(\mathbf{n}_f \cdot \mathbf{u})}{dt} = \frac{R}{PeS} [\mathbf{n}_f \cdot (K_L \nabla T)|_{\mathbf{u}^+} - \mathbf{n}_f \cdot (K_S \nabla T)|_{\mathbf{u}^-}] \quad [9]$$

S is the Stefan number

$$S = \frac{L}{CT_m} \quad [10]$$

where L is the latent heat of silicon.

Initially

$$\mathbf{u}(\mathbf{x}, 0) = \mathbf{u}_0(\mathbf{x}) \quad [11]$$

As we discussed in Ref. (9), for typical values of the relevant parameters, $Pe \approx 2.5 \times 10^{-3}$, so it is reasonable to neglect the left-hand side of Eq. [1] and use the quasi-static approximation

$$\nabla \cdot (K\nabla T) = 0 \quad [12]$$

to decouple partially the system of equations. Furthermore, $R \approx 2.7 \times 10^{-6}$. As we discussed in Ref. (9), for typical wafer thicknesses, the dimensionless temperature T is such that $(1 + RT)^4$ never differs from unity by more than ~2%. Accordingly, we make the approximation

$$(1 + RT)^4 \approx 1 \quad [13]$$

to linearize the boundary conditions [6] and [7].

Finally, we note that $\mathbf{n}_f \cdot \mathbf{u}$ is a function of one, not two, spatial dimensions (e.g., arc length along the front). Mainly for notational simplicity, we make the assumption that $\mathbf{n}_f \cdot \mathbf{u}$ is a single valued function of x and write

$$\mathbf{n}_f \cdot \mathbf{u} = y_f(x, t) \quad [14]$$

in Eq. [9].

These partial differential equations, along with the associated boundary conditions and initial conditions, define a Stefan problem for the position y_f of a moving front and for the temperature T within the domain. The equations are nonlinear because of the coupling between y_f and T . This coupling is reduced, but not eliminated, by means of the quasi-static approximation. The equations are also nonlinear because the material properties differ in the solid silicon, liquid silicon, and oxide. Further nonlinearities due to the radiation boundary conditions have been eliminated via approximation [13].

Note that Eq. [9], with its initial condition [11] and assumption [14], involves time and one spatial dimension. For a given front position, Eq. [12], with boundary conditions [5]-[8] and approximation [13] involves two spatial dimensions.

Parameter Values

In our numerical computations, we used the following parameter values (6, 10, 11)

$$\sigma = 5.672 \times 10^{-12} \frac{\text{J}}{\text{s}\cdot\text{cm}^2\cdot\text{K}^4} \quad [15]$$

$$T_m = 1685 \text{ K} \quad [16]$$

$$\epsilon_s = 0.84, \epsilon_l = 0.58, \epsilon_b = 0.62 \quad [17]$$

$$K_s = 0.216, K_L = 0.64, K_o = 0.02 \text{ W}/(\text{cm}\cdot\text{K}) \quad [18]$$

$$\rho = 2.41 \text{ g}/\text{cm}^3 \quad [19]$$

$$L = 1810 \text{ J}/\text{g} \quad [20]$$

$$C = 1.04 \text{ J}/(\text{g}\cdot\text{K}) \quad [21]$$

Reference (6) details how the values of the emissivity were obtained, taking into account the capping layer on the wafer top and the textures of the surfaces. The density ρ was assumed to be the average of the values for liquid and solid silicon.

For the basic computational subregion (cf. Fig. 2), we generally used

$$d_1 = 160 \mu\text{m}, d_2 = 4 \mu\text{m}, d_3 = 60 \mu\text{m} \quad [22]$$

$$w_1 = 96 \mu\text{m}, w_2 = 48 \mu\text{m} \quad [23]$$

This represents only a portion of the typical repetition

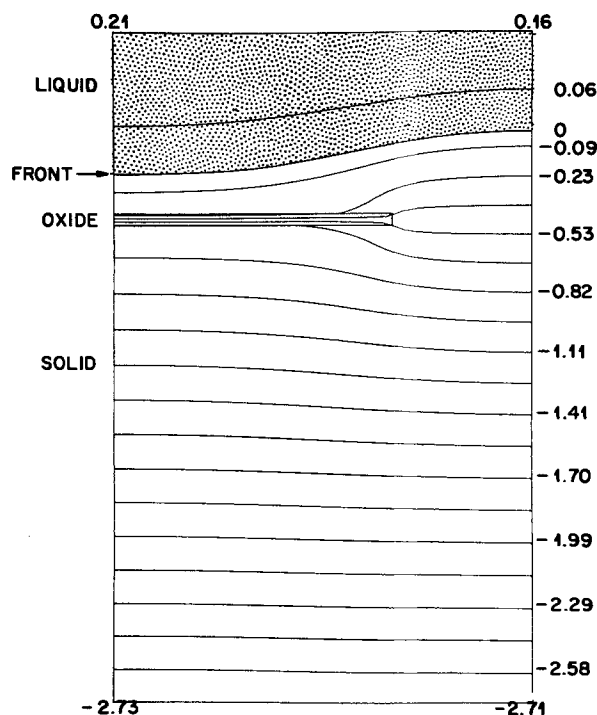


Fig. 3. Typical isotherm distribution when front is above the oxide. Numbers refer to temperature deviation from T_m .

pattern within a wafer. The substrate (d_1) is actually approximately 600 μm thick. The oxide half-width (w_1) varies, but can be as much as several thousand microns. Nevertheless, as will be discussed in more detail later, the dimensions listed above were adequate for most, but not all, considerations. Upon occasion, we used considerably larger values for the oxide half-width or varied the other dimensional parameters.

It is also necessary to specify the power $P(t)$ supplied to the lamps of the furnace. This is a dimensionless function, normalized by σT_m^4 . As we observed in Ref. (6), there are two relevant power thresholds

$$P_1 = 1 + \epsilon_B/\epsilon_S \quad [24]$$

$$P_2 = 1 + \epsilon_B/\epsilon_L \quad [25]$$

In our calculations, we omit consideration of the initial ramping stage, during which we suppose that the power has been ramped past the intermediate region $P_1 < P(t) < P_2$ and has been established at a value $P_{\max} > P_2$. Starting our time measurement from this point [$\Delta_1 = 0$, in the notation of Ref. (6)], we suppose that the power is held constant at $P = P_{\max}$ for Δ_2 seconds, then ramped down linearly to zero over an additional Δ_3 seconds

$$P(t) = P_{\max} \quad 0 \leq t \leq \Delta_2 \quad [26]$$

$$= P_{\max} \left(1 - \frac{t - \Delta_2}{\Delta_3} \right) \quad \Delta_2 \leq t \leq \Delta_2 + \Delta_3 \quad [27]$$

Experimentally, P_{\max} appears to be only a few percentage points greater than P_2 . For most of our calculations, we used

$$P_{\max} = 1.05P_2 \quad [28]$$

We also set

$$\Delta_2 = 17 \quad [29]$$

$$\Delta_3 = 60 \quad [30]$$

To complete the specification of the parameter values for the numerical calculations, we need to define the initial position of the melt front. We assume that it is planar, slightly below (4 μm) the top surface of the wafer

$$y_f(0) = d_1 + d_2 + d_3 - 4 \quad [31]$$

Subsequent computations indicate that the front will quickly readjust itself to a more appropriate shape.

Method of Solution

In this section, we mention some reasons why the Stefan problem we have formulated is particularly challenging numerically. We then sketch the basic method used to solve the problem.

The motion of the front y_f is governed by its initial position (Eq. [11]) and by the difference of the thermal fluxes measured at the two sides of the solid/liquid interface (Eq. [9]). In order to determine the flux difference, it is necessary to know the temperature distribution T within the wafer. This, in turn, is governed by the material properties within the structure (Eq. [12]), the emissivities at the surfaces ([6], [7]), and the position of the front (Eq. [8]). Thus, y_f and T are intricately coupled together.

Notice from parameter [18] that there is more than an order of magnitude range in the size of the thermal conductivities involved. Consequently, we can expect wide variations in the temperature gradients within the structure. These are potentially difficult to compute.

The physical dimensions involved (Eq. [22], [23]) vary considerably. The oxide layer, for example, may be 4 μm thick by several thousand microns long. Since the local computational grid size must be roughly the same as the size of the relevant local dimension, or smaller, a large number of computational grid points is necessarily required.

Note also that the front motion is driven by a thermal flux difference. This presents two computational diffi-

culties. First, the calculation of the temperature gradient (or the flux) is less accurate than the calculation of the temperature itself. Second, we have to take the difference between two fluxes. Since, in the physically relevant operating regime, P_{\max} is only slightly greater than P_2 , we expect the magnitude of the difference to be small compared with the size of either flux. Hence, the calculation of the thermal flux difference is potentially inaccurate.

When solving the Stefan problem numerically, we can, because of the partial decoupling of the nonlinear equation system via the quasi-static approximation, view Eq. [9] as the primary equation. To evaluate its right-hand side at any instant of time, we need to solve Eq. [12] at that instant, with the appropriate front position and other boundary conditions.

For the computational domain (Fig. 2), we consider the entire liquid Si-solid Si-SiO₂ structure to be a region with a crack in it where the melt/solidification front is. Boundary conditions [5]-[7] are applied at the exterior surfaces; boundary condition [8], that the dimensionless temperature is zero, is applied at the interior surfaces, along the front. If the front does not touch the oxide, the crack goes entirely across the computational domain. The problem then can equivalently be solved on two disjoint domains. If the front touches the oxide (which does not melt), the domain is partially cracked.

Suppose that at some instant of time in the course of the computations the temperature T vanishes along a line which is not connected to the current melt/solidification front boundary (the crack). This situation can occur when the front intersects the oxide. We have a choice of saying either (i) that this new line is a new part of the front and melting/solidification proceeds from it as well or (ii) that the line is not part of the front. We now make the significant assumption that the new line is not part of the front. This is justified by experimental observations of a substantial nucleation barrier for melting at the silicon-SiO₂ interface. The presence of a similar barrier during solidification is inferred from the behavior of melts other than Si in contact with the amorphous SiO₂. Pyrometric measurements indicate that the temperature can deviate by at least as much as 10° from T_m before the phase transition takes place at the Si-SiO₂ boundary.

This introduces the possibility that regions of the structure may, at times, be superheated or undercooled. Computational and experimental results corroborating this will be presented in the Superheating and Undercooling section.

The basic computational scheme, oversimplified slightly, is as follows. Assume an initial melt front position at time $t = 0$. Solve the diffusion equation [12] and the associated boundary conditions for the temperature T in the "cracked" domain. Evaluate the flux difference at the front. Substitute this into the Stefan equation [9]. Find the front position at the next "instant" of time. Repeat. This concept is a refinement of ideas used earlier to model an oxidation process [12].

The scheme was implemented by means of two large software packages and an intricate driver program which interwove them.

One of the packages, POST, written by N. L. Schryer, is designed to solve a coupled system of nonlinear partial differential equations involving time and one space variable, and associated ordinary differential equations that are a function of time (13). The numerical technique involves Galerkin's method in space, using B splines and a variable order, variable time-step extrapolated backward difference procedure in time. The POST package is based on the PORT library of portable FORTRAN subroutines for numerical mathematics (14). We used POST to solve Eq. [12].

The other package, PLTMGU, is designed to solve a nonlinear elliptic partial differential equation with two space variables. It was adapted from code written by R. K. Smith to do semiconductor device simulation (15, 16). The solution technique is a multigrid finite element procedure with C^0 piecewise linear finite elements. The

computational domain must have a polygonal boundary. The user supplies a (possibly nonuniform) triangulation of the domain; the code refines this triangulation uniformly. PLTMGU is an outgrowth of yet another software package PLTMG, by R. E. Bank and A. H. Sherman, which used a multigrid scheme with adaptive refinement of the triangulation (17). We used PLTMGU to solve Eq. [9].

One of the more interesting things the driver program does is to provide a triangulation of the computational domain which follows the moving solid-liquid interface. It is desirable to have a nonobtuse triangulation with certain additional properties (18). We devised a triangulation such that the interface lies along edges of triangles, there are no obtuse angles, there is a constant number of triangles, and the triangulation changes reasonably smoothly as the front moves (19).

Computations were performed on a Cray-1. The time required to do a complete calculation of melting and crystallization was approximately 200s.

Most computations were concerned with the restricted spatial domain described in the previous section. Sometimes we wanted to do calculations for a considerably larger domain. It turned out to be impossible to track the front motion under those circumstances, since the computational memory requirements considerably exceeded the capacity of the Cray-1.

However, we were able to obtain a partial solution. If, instead of trying to follow the motion of the front, we assumed the front was in a specific position, we were able to calculate the resulting temperature distribution within the wafer.

This amounted to calculating a static "snapshot" solution. We did this by dispensing with all the computational machinery associated with POST and by calculating on a relatively coarsely triangulated domain without refinement, thereby reducing the space requirements significantly.

Isotherms

The temperature distribution in the structure depends upon the position of the melt/recrystallization front, among other things. A number of characteristics of the thermal profile, however, can be identified and discussed in general. We do so here, but exclude from consideration those cases in which the front intersects the oxide layer: they involve superheating or undercooling and will be discussed below.

Figure 3 shows an isotherm plot when the solid/liquid interface is above the oxide layer; Fig. 4 shows a similar plot when the interface is well below the oxide layer. In each such plot, the isotherm lines represent equally spaced temperatures. In addition, the solid/liquid interface, which corresponds to the zero isotherm, is shown. Both isotherm plots were calculated with a power input $P = P_{\max} = 1.05P_2$, but the observations here are pertinent to both melting and freezing.

Notice that there is a steep temperature gradient across the oxide. The gradient is less steep in the solid silicon and is least steep in the liquid silicon. The isotherms are compressed in the oxide and expand within the window region. At the wafer top, the temperature is slightly greater over the oxide layer than it is over the window region. The wafer bottom has a nearly uniform temperature. This uniformity is even more pronounced if a deeper substrate (d_1) is used in the calculations.

To quantify these ideas further, in Fig. 5 we plot the dimensional temperature $T - T_m$ as a function of the distance from the bottom of the computational domain (cf. Fig. 2) at $x = 0$ (left edge) and $x = w_1 + w_2$ (right edge) when the front is at the position shown in Fig. 3. Similarly, in Fig. 6 we plot the temperature profiles corresponding to Fig. 4.

The left-hand edge corresponds to a vertical slice which goes through the oxide layer well away from the window. In both of the figures, the temperature profile at this edge agrees quite closely with that predicted by the one-dimensional theory (6, 9).

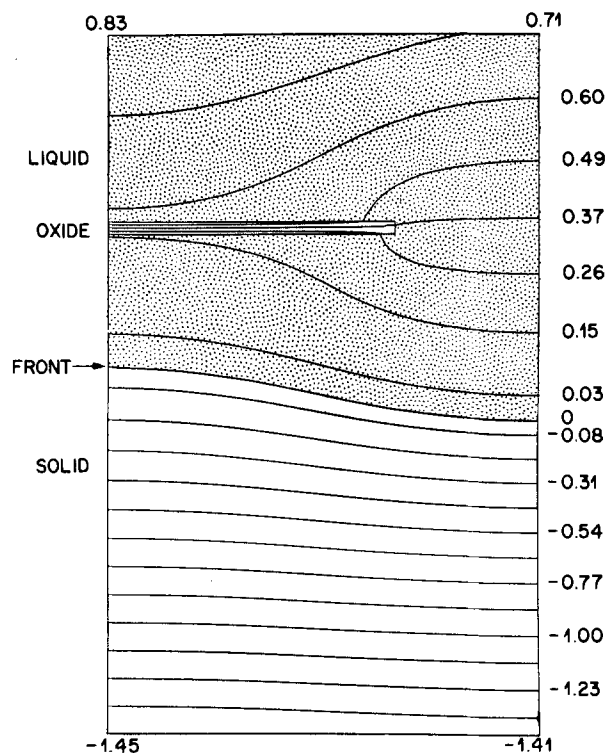


Fig. 4. Typical isotherm distribution when front is below the oxide. Numbers refer to temperature deviation from T_m .

The right-hand edge corresponds to a vertical slice which goes through the center of the seeding window. Here, in the region within a few tens of microns to both sides of the window, the temperature gradient deviates significantly from that predicted by the one-dimensional theory: the effects of the isotherm bunching are still being felt to some extent. It appears that the length characterizing the distance over which the influence of the window can be felt is slightly in excess of $50 \mu\text{m}$.

From Fig. 5 and 6, we observe that the temperature changes by $\sim 1.2^\circ$ over $100 \mu\text{m}$ of solid silicon, $\sim 0.4^\circ$ over $100 \mu\text{m}$ of liquid silicon, and $\sim 0.6^\circ$ across the $4 \mu\text{m}$ of isolation oxide.

The facts that the one-dimensional theory holds at the left-hand side and that the isotherms are very nearly uniformly spaced at the bottom of the computational domain indicate that computations on this domain of restricted size give a reasonably good picture of what is happening when the front does not intersect the oxide. This was confirmed also by static calculations on wider, deeper domains.

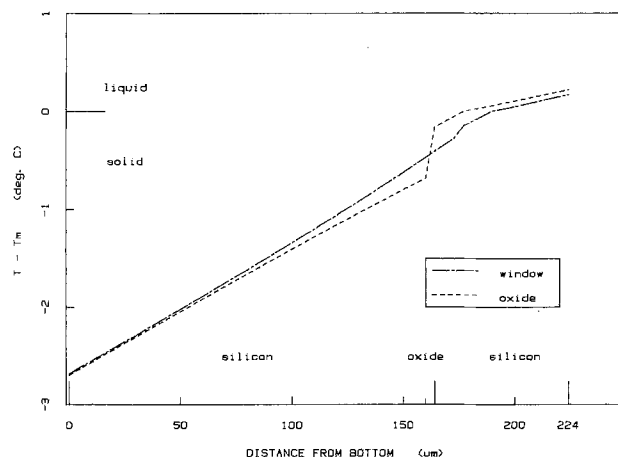


Fig. 5. Deviation of temperature from T_m at the left (dashed line) and right (dot-dashed line) edges of the computational domain as a function of distance from the bottom. Front is above oxide as in Fig. 3.

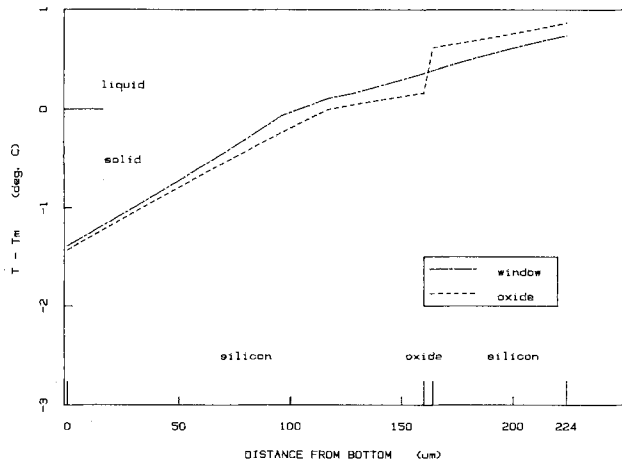


Fig. 6. Deviation of temperature from T_m at the left (dashed line) and right (dot-dashed line) edges of the computational domain as a function of distance from the bottom. Front is below oxide as in Fig. 4.

Motion of the Front

Figures 7 and 8 form composite pictures of the positions of the front at various instants of time during the melting and freezing processes, respectively. The times are not uniformly spaced, since the PDE solver POST automatically adjusts its step size to maintain the desired accuracy. The parameter values used for this calculation are those given in the Parameter section.

Melting.—By assumption, we start with a thin horizontal liquid layer. The melt front quickly readjusts itself so that it is deeper over the oxide. Having done this, it propagates downward toward the oxide with only slight additional steepening. The difference in the heights of the front at the left and right edges of the computational domain is approximately $14 \mu\text{m}$.

The melt front contacts the top of the oxide strip at the left-hand edge first (i.e., in the center of the full strip). The point where the front contacts the oxide quickly propagates to the right, toward the window. As it does so, the remaining portion of the front steepens. Superheating may occur on the other side of the oxide, as we discuss in the next section.

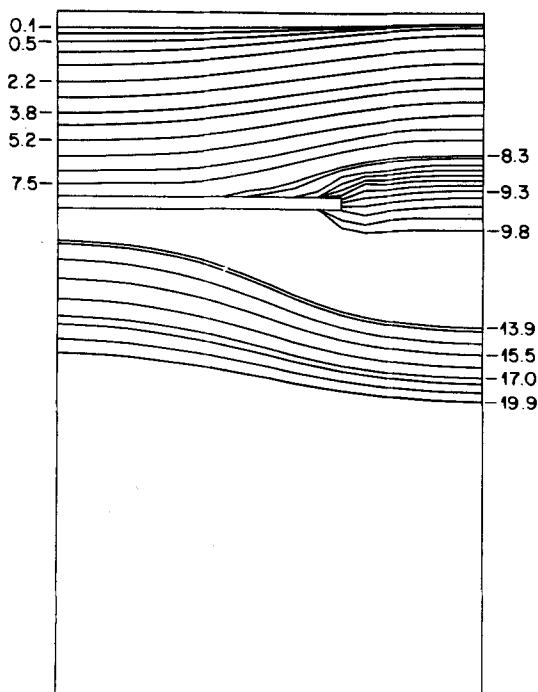


Fig. 7. Calculated melt front positions. Numbers refer to time in seconds.

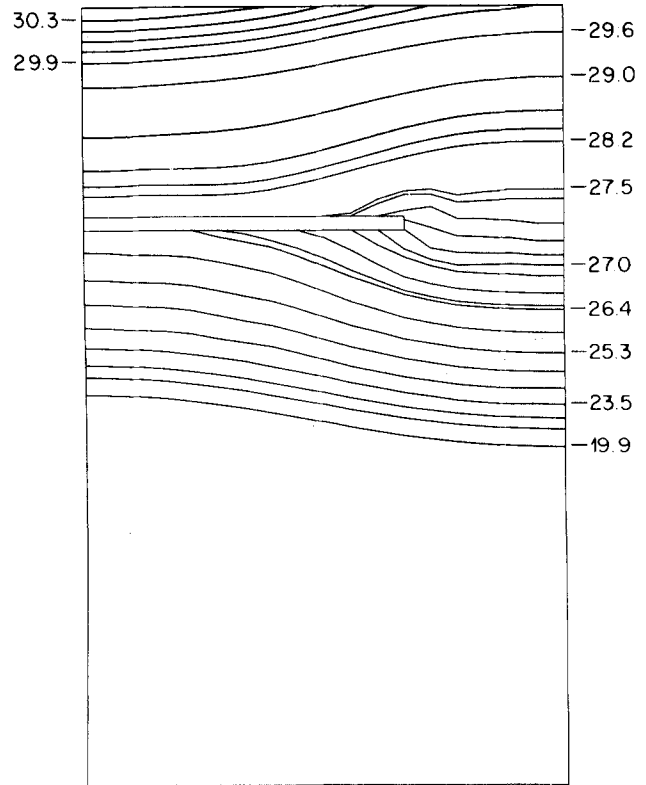


Fig. 8. Calculated solidification front positions. Numbers refer to time in seconds.

Eventually, the front remains only in the window area. Calculations for this regime are extremely difficult to perform accurately. The front flips rapidly, changing its shape from concave downward to concave upward. To some extent, it mimics the general shape of the isotherms which we saw in the preceding section.

Next, the melt front contacts the bottom of the oxide strip at the right-hand edge first, by the window, and moves swiftly to the left. We did not attempt seriously to do calculations for this regime (which involves the reappearance of computational mesh points along the portion of the front which previously disappeared). Nevertheless, we feel that we have an excellent qualitative picture of what is happening.

This type of behavior persists even if the oxide strip is considerably longer than the one used in these calculations. Isotherms, although they may be nearly horizontal over a substantial portion of the region, always have a slight slope which causes the melt contact point to move to the right along the top of the oxide strip and to the left along the bottom of it.

Eventually, the melt front separates completely from the oxide. Since there is a gap in our computations, we had to make an educated guess about the initial front position and starting time for subsequent calculations. Numerical experiments led us to conclude that the height differential of the front is greater when it is just below the oxide layer than when it is above it. In Fig. 7, the differential is approximately $28 \mu\text{m}$. As the melt front continues to travel downward, it tends to flatten out.

As the power $P(t)$ is reduced in preparation for freezing, the front rearranges itself slightly. Relative to the shape for higher values of $P(t)$, the part under the oxide descends slightly and the part under the window rises slightly.

In these computations, the final height differential was approximately $12 \mu\text{m}$.

Freezing.—When freezing begins, the solidification front moves upward toward the oxide, steepening as it does so. The height differential is not quite as large as it was for melting at a comparable position.

The solidification front contacts the bottom of the oxide at the left-hand edge first, and the contact point

moves rapidly to the right, toward the window. Undercooling may occur, as we discuss below. Again, the remaining portion of the front steepens.

When the solidification front remains only in the window area, it again flips rapidly, changing its shape from concave upward to concave downward. As with the melting flip, these calculations are extremely difficult to perform accurately, as is evidenced by some jaggedness in the curves.

Next, the solidification front contacts the top of the oxide strip at the right-hand side, by the seeding window, and moves rapidly to the left. As with the comparable melting case, we did not attempt to compute this portion of the motion.

Eventually, the front detaches itself from the oxide. Numerical experiments lead us to believe that its shape is quite similar to that which it had when it was melting just above the oxide. The front then moves upward with very little change of shape. In the present calculations, the shape changes very little even after the front intersects the top surface of the device.

Surface freezing.—When the top surface starts freezing, the emissivity of the solidified portion jumps to the value ϵ_s , and more power is able to be coupled into the wafer. This tends to shift the isotherm lines downward in the region directly under the solidified surface or under the solidification front near the point where it contacts the surface. This is illustrated in Fig. 9, which was based on calculations with a hypothetical solidification front in the position indicated and a power input $P = 0.95P_2$, where P_2 is the second power threshold, discussed in the Parameter section. The solid lines represent isotherms for which the emissivity of the solid portion of the surface is ϵ_s and the emissivity of the liquid portion is ϵ_L , as expected. The dashed lines represent what the isotherms would have looked like if both the solid and the liquid portions of the surfaces were assumed to have an emissivity ϵ_L .

Consequently, the motion of the solidification front in the vicinity of the contact point is slowed somewhat by comparison with what it would be if the surface emissivity retained the value ϵ_L everywhere. If the power input $P(t)$ is between P_1 and P_2 when the solidification front

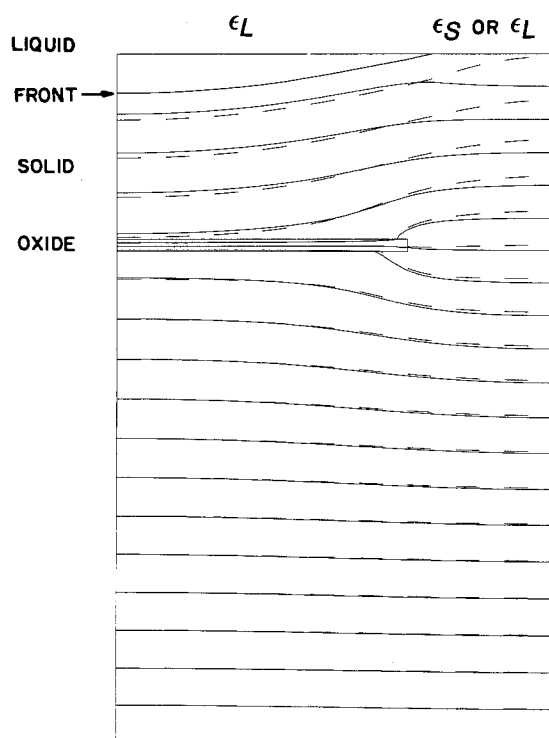


Fig. 9. Effect of emissivity change during surface freezing. Solid lines represent isotherms when solid portion of surface has emissivity ϵ_s , as is true physically. Dashed lines represent isotherms if solid portion were to have emissivity ϵ_L .

reaches the surface, we conjecture that a surface breakup may occur which is similar to the instability present during melting. Small segments of the surface would melt to increase the average reflectivity until there was no net energy gain in the resolidified region. Whether the breakup actually occurs will depend on the size of the resolidified area, its crystalline quality, and the magnitude of $P_2 - P(t)$. Without defects, the surface may tolerate substantial superheating and the excess absorbed power may temporarily halt or even reverse motion of the solidification front if P is held near P_2 .

If the power input $P(t)$ is sufficiently small (certainly if it is less than the threshold P_1), this instability will not be present.

We might also note that if the power input $P(t)$ is less than 1, then, from Eq. [6] and [13], the sign of the thermal gradient at the surface changes whether or not the front intersects the surface. Surface cooling is so rapid that freezing might commence at the surface as well as along the solidification front.

In calculating the interface shape and motion, we assumed all physical properties to be isotropic. In fact, melting and freezing exhibit directional anisotropy, with interface velocity lowest along the $\langle 111 \rangle$ crystalline axes. This often leads to faceting since the growing phase expands more rapidly in directions other than the $\langle 111 \rangle$ until it is bounded by the (111) planes. It is likely that the solidification front instead of assuming the shapes shown in Fig. 8 aligns itself partially or completely with the (111) plane, i.e., makes an angle of $\sim 55^\circ$ with the surface. This could imply more lateral freezing than obtained from our calculations. At the present time, we have no means of testing experimentally the actual shape of the interface.

Rate of movement of front.—We now return to the time-dependent calculations and discuss further the motion of the front, illustrated previously in Fig. 7 and 8. We plot in Fig. 10 the position of the front, measured at the left and right side of the computational domain, as a function of time. Computations were done in segments: melting above the oxide, melting when the front touches the oxide, melting below the oxide, etc., with educated guesses about the time intervals between the computational segments.

Although we do not expect the one-dimensional theory (9) for the front position y_f as a function of time to hold exactly for the two-dimensional problem, it is interesting to compare our results semiquantitatively with it. With a few notational changes, the theory gives, in dimensional form

$$\begin{aligned} y_f(t) &= y_0 - \beta \left(\frac{P_{\max}}{P_2} - 1 \right) t & 0 \leq t \leq \Delta_2 \\ &= y_0 - \beta \left(\frac{P_{\max}}{P_2} - 1 \right) t + \frac{\beta P_{\max} (t - \Delta_2)^2}{2\Delta_3 P_2} & \Delta_2 \leq t \end{aligned} \quad [32]$$

with

$$\beta = \frac{(\epsilon_L + \epsilon_B)\sigma T_m^4}{\rho L} \quad [33]$$

where distance is measured in microns and time in seconds.

Consider first the notion of the front at the right-hand side of the domain, through the seeding window. After an initial adjustment period, the position of the melt front varies nearly linearly with time. The velocity is approximately $6 \mu\text{m/s}$, consistent with the one-dimensional theory. The parameter values are those given in the Parameter section. In the vicinity of the oxide layer, say $20 \mu\text{m}$ above and below it, the velocity of the melt front considerably exceeds that given by the one-dimensional theory. When the melt front gets outside that region, its position again decreases linearly with time at approximately the same rate as it did before being influenced

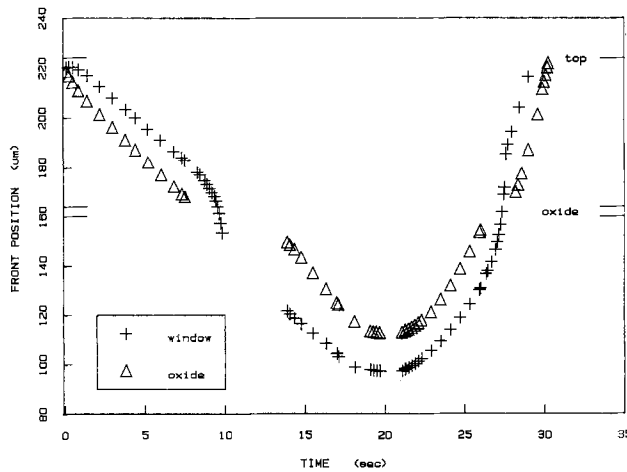


Fig. 10. Front position as a function of time, measured at left and right sides of the computational domain.

significantly by the oxide layer. As the power $P(t)$ is ramped down, the position *vs.* time curve forms a parabola for a while, again reasonably consistent with the one-dimensional theory. In the vicinity of the oxide layer, the velocity of the solidification front increases significantly as the oxide is felt, then decreases again as its influence diminishes.

Next, consider the motion of the front at the left-hand side of the domain, through the middle of the full oxide strip. Above the oxide, the melt front velocity is nearly constant and is nearly the same as that of the front at the right-hand side. The front at this position then disappears for a few seconds, while the remainder of the melt front is doing its flip through the seeding window. When it reappears below the oxide strip, its velocity is nearly constant while the power input is constant, but is slightly larger in magnitude than that of the melt front through the seeding window. When the power is ramped down, the parabolic nature of the position *vs.* time curve is again evident. Again, the front disappears for a while as the solidification front does its flip through the seeding window.

Superheating and Undercooling

When the melt or solidification front is in contact with the oxide strip, the temperature profiles in the structure may change radically. This is particularly true as the front passes through the seeding window. A critical parameter is P/P_2 , which gives a measure of the amount by which the power P exceeds, or is less than, the power threshold P_2 for which the global energy balance is in equilibrium.

Suppose, for example, that $P/P_2 > 1$, so that melting is taking place, and that the melt front is going through the seeding window. Power in excess of P_2 applied to the wafer surface directly above the seeding window, or within a few tens of microns directly above it, affects the advancement of the melt front. However, power applied still further away from the window will have an insignificant effect on the front. If we assume that melting below the oxide layer cannot be initiated at a position unattached to the present melt front, the power in excess of P_2 will go into superheating of a portion of the structure below the oxide layer. The longer the oxide strip is, the greater the amount of superheating will be.

Conversely, if $P/P_2 < 1$, some of the silicon above the oxide layer will become undercooled.

Most of the computations discussed in this section are solutions to static problems. They were done with the "snapshot" version of the code, mentioned in the Method of Solution section, for which the position of the front is assumed, not calculated. We assumed that the front was planar and was located in the seeding window. For the superheating calculations, we positioned the melt front level with the bottom of the oxide layer, at $y = d_1$. For the undercooling calculations, we positioned the solidification front level with the top of the oxide layer, at $y = d_1 +$

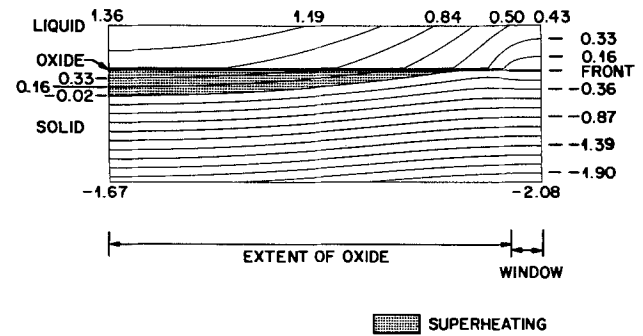


Fig. 11. Isotherms during superheating. The half-width w_1 of the oxide is $600 \mu\text{m}$.

d_2 . Details concerning the precise shape of the front are not expected to affect the thermal profile far from the window, which is what we are primarily interested in here.

We first discuss superheating and undercooling results for a computational domain with $w_1 = 600 \mu\text{m}$, w_2 , d_1 , d_2 , d_3 as before. That is, the domain is similar to that used earlier, except that the oxide strip is made much longer. After that, we discuss the consequences of varying the dimensions of the structure and the power input. Finally, we sketch what happens dynamically as the melt or solidification front moves.

Superheating.—In Fig. 11, we show the isotherms calculated with the configuration described above and a power input $P/P_2 = 1.05$. Note that there is a region directly under the oxide strip which is superheated and that the amount of superheating increases with horizontal distance from the window. This can be better quantified by means of the following two figures. Figure 12 indicates the dimensional temperature profile $T - T_m$ along the bottom of the oxide strip. It dips slightly near the window, then increases rapidly with distance away from it, leveling out at the center of the oxide strip ($x = 0$) as required by symmetry conditions. In Fig. 13, we plot the temperature at the left-hand edge of the computational domain as a function of the distance from the bottom of the domain. This corresponds to a vertical slice which goes through the center of the full oxide strip. As expected (cf. Fig. 3 and 4), the thermal gradients are constant in each of the solid silicon, oxide, and liquid silicon regions.

Undercooling.—Figure 14 depicts the isotherms when the power input $P/P_2 = 0.95$ and the solidification front is planar, at the top of the seeding window. In this instance, there is a region directly over the oxide strip which is undercooled, and the amount of undercooling increases with horizontal distance from the window. In Fig. 15, we

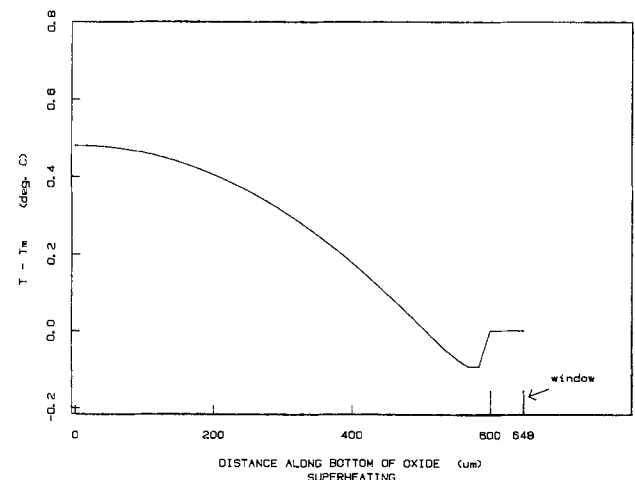


Fig. 12. Deviation of temperature from T_m at the bottom of the oxide strip during superheating.

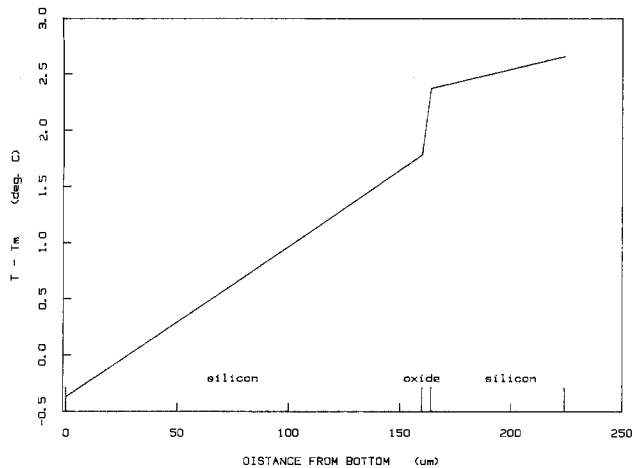


Fig. 13. Deviation of temperature from T_m of the left edge of the computational domain during superheating.

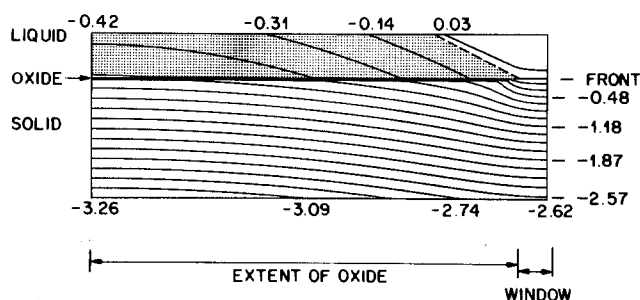


Fig. 14. Isotherms during undercooling. The half-width w_1 of the oxide is 600 μm .

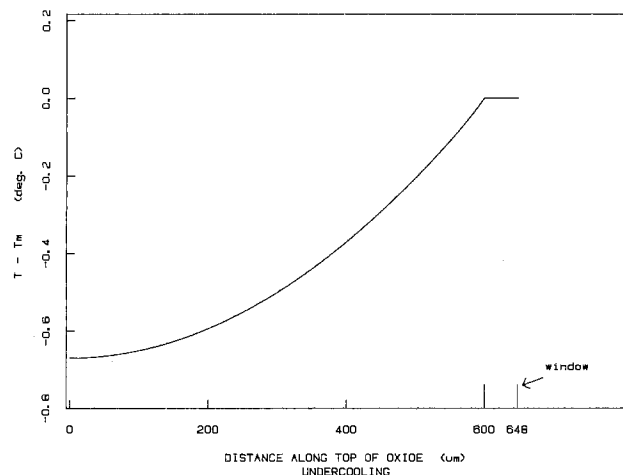


Fig. 15. Deviation of temperature from T_m at the top of the oxide strip during undercooling.

plot the temperature profile $\bar{T} - T_m$ along the top of the oxide strip. It decreases rapidly with distance away from the window, leveling out at the center of the oxide strip.

In many respects, the undercooling results are nearly symmetric to the superheating results. Some differences are worth noting. The curve in Fig. 12 dips before rising (as a function of distance away from the window), while that in Fig. 15 does not rise before dipping. We do not have a good physical interpretation for this effect; however, it is the behavior far away from the window which interests us most here. Also, although the superheating and undercooling at the bottom or top of the oxide at the left-hand side in the two computations are approximately of the same magnitude, the regions affected by superheating or undercooling are quite different. Since the

thermal gradient in liquid silicon is approximately a factor of three smaller than that in solid silicon, the region affected by undercooling is larger. In Fig. 14, a substantial portion of the liquid layer, including most of the surface, is undercooled. A significantly smaller portion of the region in Fig. 11 experiences superheating.

Parameter variations.—We now investigate the sensitivity of the superheating or undercooling to variations in several parameters.

The most critical parameter is w_1 , the half-width of the oxide layer. Using the dimensions of our usual computational domain ($d_1 = 160 \mu\text{m}$, $d_2 = 4 \mu\text{m}$, $d_3 = 60 \mu\text{m}$, $d_4 = 48 \mu\text{m}$), setting $P/P_2 = 1.05$, and varying w_1 , we show in Fig. 16 the magnitude of the superheating at the left edge of the region, under the oxide. The superheating increases substantially, in fact, nearly exponentially, with oxide width. Similarly, with $P/P_2 = 0.95$ and all other parameters as above, we show in Fig. 17 that undercooling, measured at the left edge of the region, over the oxide, also varies nearly exponentially with the oxide width. Notice that, all else being equal, the magnitude of superheating and undercooling are nearly the same for the same amount (5%) of excess or deficit power from equilibrium.

Computations were performed on a limited domain because of storage constraints on the Cray-1. Using a relatively thin substrate d_1 was justifiable earlier (cf. Fig. 3, 4) when the lower portion of the computational domain exhibited a nearly planar behavior. When superheating or undercooling is present (cf. Fig. 11, 14), this is no longer true. In Fig. 17, we include the results of a few calculations using thicker substrates. They indicate that the amount of undercooling in a region with a thicker substrate is somewhat less than was previously calculated,

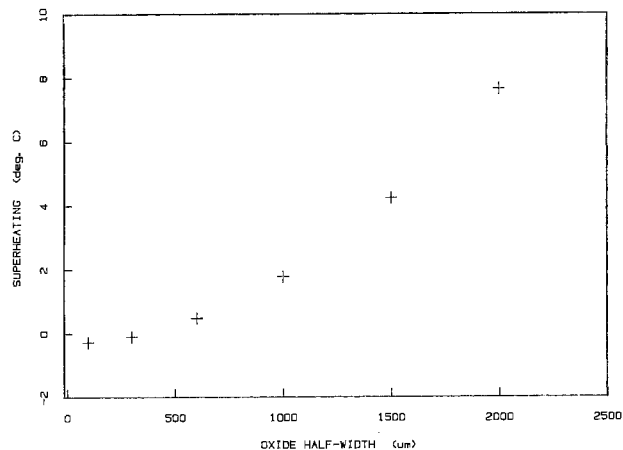


Fig. 16. Magnitude of superheating directly under the center of the full oxide strip as a function of the half-width w_1 .

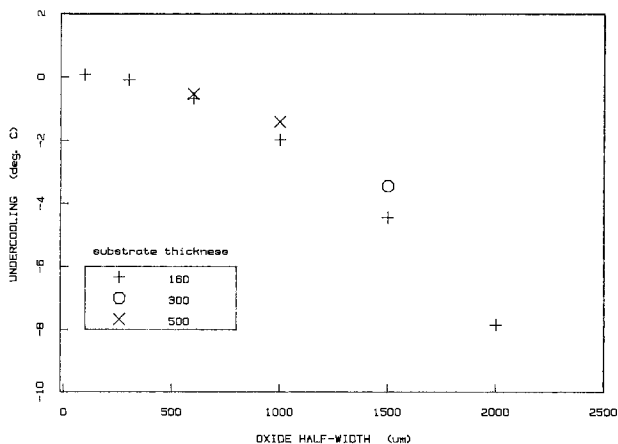


Fig. 17. Amount of undercooling directly over the center of the full oxide strip as a function of the half-width w_1 , for various substrate thicknesses.

and that the discrepancy increases with oxide width w_1 . Symmetric results were obtained for superheating, where our thin substrate calculations overestimate the amount present.

For similar reasons, we expect the thickness d_3 of the polycrystalline layer to play an important role in determining the amount of superheating or undercooling, and it does. In Fig. 18, we illustrate what happens if the thickness of the layer is reduced from 60 to 30 μm , with $P/P_2 = 0.95$ (note the change of scale from Fig. 17). Reducing the thickness of the polycrystalline layer can increase the undercooling significantly, particularly when the oxide strip is long. In a symmetric fashion, reducing the thickness increases the superheating by approximately the same amount when $P/P_2 = 1.05$.

Varying the oxide thickness or the window width within reasonable limits produces comparatively small effects.

Finally, suppose that the domain is fixed (we used $w_1 = 1000 \mu\text{m}$, $w_2 = 48 \mu\text{m}$, $d_1 = 160 \mu\text{m}$, $d_2 = 4 \mu\text{m}$, and $d_3 = 60 \mu\text{m}$) and that the power input is varied. Figure 19 indicates that, for small deviations of P from the threshold P_2 , the amount of superheating or undercooling (measured at the left edge, below or above the oxide, as usual) varies linearly with the power input.

Dynamic picture.—We now sketch briefly what happens dynamically as the melt or solidification front passes in the vicinity of the oxide layer and the seeding window.

If melting is taking place and the melt front is above the oxide layer (cf. Fig. 3), the silicon below the oxide is solid and is below the melting temperature. The isotherms directly underneath the oxide, away from the window, are

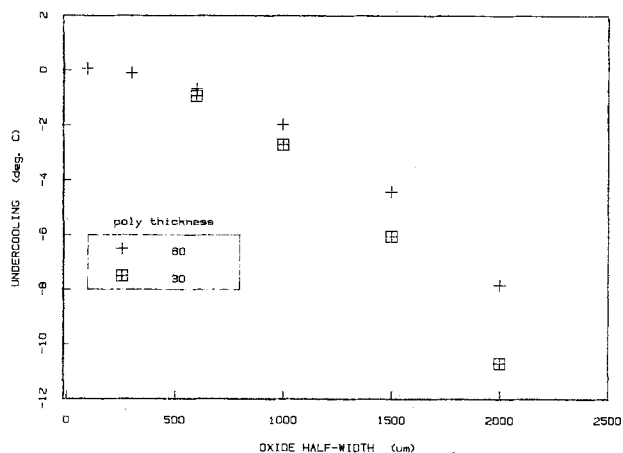


Fig. 18. Amount of undercooling directly over the center of the full oxide strip as a function of the half-width w_1 , for various thicknesses of the polycrystalline layer.

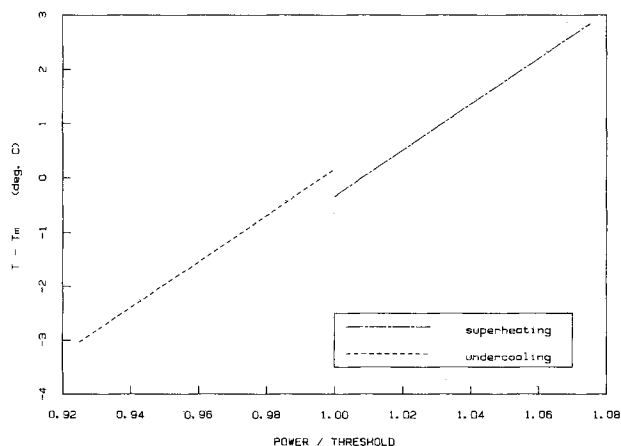


Fig. 19. Amount of superheating or undercooling as a function of power input, normalized by P_2 .

nearly horizontal. As the front starts to intersect the oxide and subsequently move through the seeding window, the temperature under the oxide increases. If the power input is sufficiently greater than the threshold P_2 , the region under the oxide becomes superheated. The superheating starts under the center of the entire oxide strip, far away from the seeding window(s). It then spreads out, extending horizontally under more of the oxide layer and penetrating more deeply into the substrate (cf. Fig. 11). As the melt front proceeds along the bottom of the oxide layer, the superheated region diminishes in size and eventually disappears.

A similar sequence of events, involving undercooling above the oxide layer, happens when the solidification front proceeds through the window.

Experimental Results

Experimentally, we can verify some aspects of the calculations presented above. The temperature is measured with an optical pyrometer at one spot of $\sim 1 \text{ mm}$ diam at the back side of the irradiated wafer. The temperature of the front side is determined by extrapolation, using known values of thermal conductivities and sample thickness. Of course, during most of the process cycle, the front surface temperature is pinned near T_m , with the back side temperature lower by 3-7°C, depending on the depth of melt. A small transient temperature rise and dip are detected when the liquid-solid interface passes through the oxide; they reflect the occurrence of superheating and undercooling, respectively.

The position and shape of the interface cannot be measured directly, but we can detect the maximum melt depth by examining cross sections of recrystallized samples. A series of such cross sections is retraced in Fig. 20. The shape of the interface at various depths is quite similar to those plotted in Fig. 7, and the interface flip in the window is clearly seen.

We already mentioned that superheating and undercooling can be discerned from pyrometer measurements. Superheating at the buried oxide-Si interface also leads to melting of the cooler back side of the sample, away from the heat source. To assure that silicon on this surface melts when T_m is reached, the surface is sandblasted to introduce a high density of crystalline defects. (It should be mentioned here that although a free, clean surface cannot be superheated, the SiO_2 provides excellent passivation of the broken Si bonds and makes superheating possible in defect-free layers.) When samples with a continuous buried oxide are irradiated, molten droplets and voids appear on the back side and vertical molten channels can be detected in cross sections (20).

In samples with windows in the oxide, superheating is a function of the oxide width and position with respect to the windows. When we used wafers with oxide of a half-

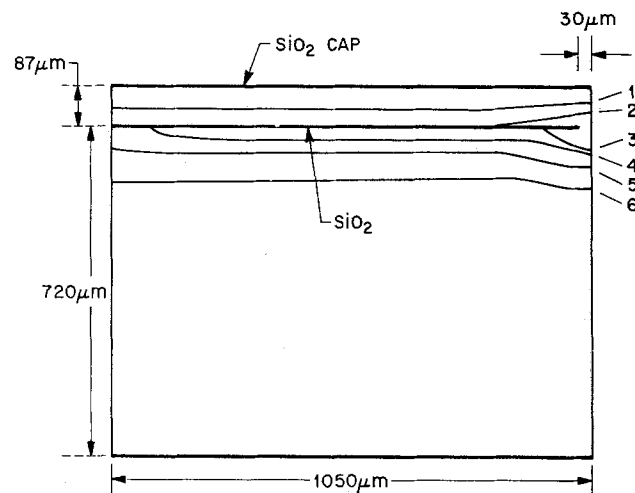


Fig. 20. Composite picture of maximum melt penetrations found experimentally for a series of irradiation energies.

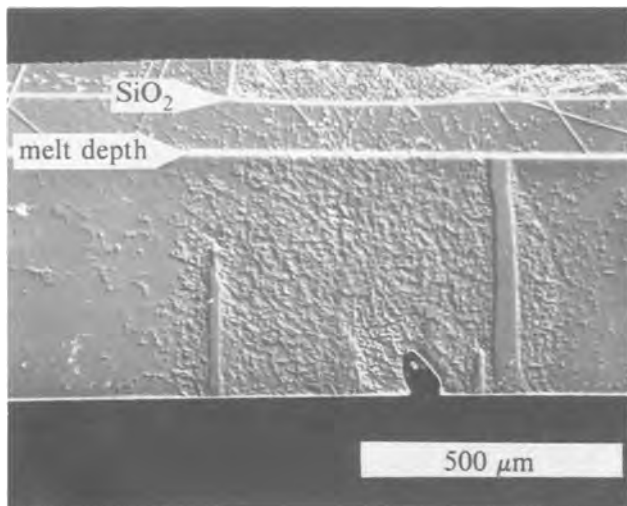


Fig. 21. Etched cross section of a recrystallized sample, showing the depth of the planar melt and the localized melt spikes originating from the superheated back surface.

width $w_1 = 920 \mu\text{m}$ over part of the area and $w_1 = 1840 \mu\text{m}$ over the rest, traces of melting appeared only under the centers of the wide stripes. A cross section of an area with melt spikes emanating from the back side is shown in Fig. 21. For $d_1 = 600 \mu\text{m}$ distance between the buried oxide and the back surface, the temperature drop

$$\Delta T = \frac{d_1}{K} \epsilon_B \sigma T_m^4$$

is about 7°C . This is in excellent agreement with calculated superheating values of $\sim 2^\circ$ and $\sim 7^\circ\text{C}$ for 920 and $1840 \mu\text{m}$ half-widths, as plotted in Fig. 16.

It should be noted that the presence of molten regions at specific locations on the back surface is a positive proof of superheating. If melting were induced by impurities on the back surface, the correlation between the melt sites and the pattern in the buried oxide would be entirely different.

Discussion

We have presented a detailed numerical study of radiative melting and recrystallization of Si structures containing a patterned buried oxide layer. All modeling had to be in a two-dimensional domain because of the presence of slit-shaped seeding windows in the oxide that profoundly modified the shape of isotherms. The numerical results are consistent with the experimental data and provide insight into the details of melting and crystallization processes that cannot be measured directly.

We determined that the velocity of the melt front is $5\text{--}10 \mu\text{m/s}$ for the representative input power of $1.05P_2$. Similarly, the vertical component of the solidification velocity is $\sim 20 \mu\text{m/s}$ when the input power is ramped down in 60s. The top surface directly above the SiO₂ window is always slightly cooler because of the heat sinking effect of the window, but the temperature of the bottom surface is essentially uniform except during brief superheating and undercooling phases.

We found that superheating and undercooling of silicon reach maximum values at the time when the solid-liquid interface passes through the SiO₂ windows. The regions most removed from the windows deviate most from the melting temperature. Superheating is of little practical consequence even though it may cause some undesirable melting at the bottom side of the wafers. Control of undercooling, on the other hand, is essential in achieving successful epitaxial crystallization, since excessive undercooling causes formation of polycrystalline Si. Undercooling increases approximately exponentially with the spacing between the seeding windows and can reach 10°C for

$w_1 = 2000 \mu\text{m}$. Thicker polysilicon over the oxide reduces somewhat the amount of undercooling, and so does a thicker substrate. Undercooling is less when the input power P is close to the threshold P_2 (slow motion of the interface through the window region).

The numerical results indicate that the crystallization velocity has a very large vertical component. The actual physical regrowth is likely to differ somewhat from its numerical counterpart because the directional anisotropy of crystallization was not included in the calculation. It is known that growth of Si crystals is slowest along the $\langle 111 \rangle$ axis, and this leads to faceting in the (111) planes. Therefore it is likely that the solidification front is approximately parallel to the (111) plane and forms $\sim 55^\circ$ angle with the surface.

In any case, the propagation is slower than $100 \mu\text{m/s}$ and has a significant vertical component. This may explain why low angle grain boundaries (subboundaries) that are notorious in thin films (21) are not observed in our experiments. The crystallization front in thin films propagates strictly in the lateral direction, and any impurities present in the melt tend to accumulate ahead of the interface. This builds up their concentration and likely leads to defect formation. In our configuration, the impurities are continuously zone refined toward the top surface, preventing any large buildup at the solid-liquid interface.

Acknowledgments

We gratefully acknowledge contributions of Lee Trimble to the experimental part of the paper and of Kent Smith, Eric Grosse, and Norm Schryer to the numerical part.

Manuscript submitted May 17, 1985; revised manuscript received July 30, 1985.

AT&T Bell Laboratories assisted in meeting the publication costs of this article.

REFERENCES

- G. W. Cullen, (Issue Editor), *J. Cryst. Growth*, **63**, 429 (1983).
- K. E. Bean and W. R. Runyan, *This Journal*, **124**, 5C (1977).
- G. K. Celler, McD. Robinson, and D. J. Lischner, *Appl. Phys. Lett.*, **42**, 99 (1983).
- G. K. Celler, McD. Robinson, L. E. Trimble, and D. J. Lischner, *This Journal*, **132**, 211 (1985).
- D. J. Lischner and G. K. Celler, *Mater. Res. Soc. Symp. Proc.*, **4**, 759 (1982).
- G. K. Celler, L. E. Trimble, and L. O. Wilson, *ibid.*, **35**, 635 (1985).
- E. Yablonovitch, *J. Opt. Soc. Am.*, **72**, 899 (1982).
- G. K. Celler, McD. Robinson, L. E. Trimble, and D. J. Lischner, *Appl. Phys. Lett.*, **43**, 868 (1983).
- L. O. Wilson, G. K. Celler, and L. E. Trimble, In preparation.
- M. E. Glicksman and P. Voorhees, *J. Electron. Mater.*, **12**, 161 (1983).
- A. Bell, *RCA Rev.*, **40**, 295 (1979).
- L. O. Wilson, *This Journal*, **129**, 831 (1982).
- N. L. Schryer, AT&T Bell Laboratories CSTR no. 115 (1984).
- P. A. Fox, A. D. Hall, and N. L. Schryer, Bell Laboratories CSTR no. 47 (1976).
- R. E. Bank, W. M. Coughran, Jr., W. Fichtner, D. J. Rose, and R. K. Smith, In preparation.
- W. Fichtner, L. W. Nagel, B. R. Penumalli, W. P. Petersen, and J. L. d'Arcy, *Proc. IEEE*, **72**, 96 (1984).
- R. E. Bank and A. H. Sherman, "PLTMG User's Guide," CNA152, Center for Numerical Analysis, University of Texas, Austin, TX (1979).
- B. S. Baker, E. Grosse, and C. S. Rafferty, Submitted to *SIAM J. Algebr. Discrete Methods*.
- L. O. Wilson, Submitted to *SIAM J. Algebr. Discrete Methods*.
- G. K. Celler, K. A. Jackson, L. E. Trimble, McD. Robinson, and D. J. Lischner, *Mater. Res. Soc. Symp. Proc.*, **23**, 409 (1984).
- J. C. C. Fan, B.-Y. Tsaur, and M. W. Geis, *J. Cryst. Growth*, **63**, 453 (1983).

The Analysis of Diffusion Data by a Method of Moments

R. Ghez,* J. D. Fehribach,¹ and G. S. Oehrlein*

IBM T. J. Watson Research Center, Yorktown Heights, New York 10598

ABSTRACT

We develop a method for extracting diffusivities from concentration profiles that uses the moments of these profiles. We show that these moments are coefficients of polynomial equations in the fitting parameter Dt ; these equations are easily solved. The method does not rely on the estimation of slopes or of functional values; it is therefore both accurate and simple to use. We apply this method to the case of P redistribution by rapid thermal annealing of ion-implanted Si.

A Basic Diffusion Problem

The analysis of diffusion data requires fitting procedures that are often nonlinear. For example, if the data are representable by a given functional form $C(x, t)$ of the concentration, then the diffusivity D often enters that function parametrically in a nonlinear way. One then needs minimization schemes such as the Davidon-Fletcher-Powell algorithm (1) to determine D . The Boltzmann-Matano analysis (2), sometimes applicable when D is a function of C , provides another example of nonlinear analysis. In this case, the functional form of C is not even required: one operates directly on the diffusion equation. It is well known, however, that this method can handle only very few types of initial and boundary conditions, and that the procedure relies heavily on the accurate estimation of slopes from numerical data. Consequently, we are driven to look for methods for extracting diffusivities from experimental data that are only mildly nonlinear, that do not require curve-fitting, and that do not depend on a given functional form, i.e., one need not even have a solution, analytic or numerical, of the diffusion equation.

A few years ago, one of us (3) proposed a method for the analysis of diffusion data when these are representable by error functions. That method depended on the calculation and numerical estimation of moments of these functions. It was then shown that the unknown parameters could be easily obtained through a simple iterative scheme. Further, that paper offered the pious hope that such methods could be extended to functions outside the class of error functions. Such is the object of this paper.

Our method is best illustrated through the following simple problem; it arose in connection with a study of dopant redistribution in ion-implanted semiconductors (4)

$$\frac{\partial C}{\partial t} = D \frac{\partial^2 C}{\partial x^2} \text{ for } x > 0, t > 0 \quad [1]$$

and

$$C(x, 0) = C_0(x) \quad [2]$$

$$\partial C / \partial x = 0 \text{ at } x = 0 \quad [3]$$

$$C(\infty, t) = 0 \quad [4]$$

The first equation simply states that the mobile species diffuses without any internal loss mechanisms and that the diffusivity D is independent of location x (and of concentration C). The diffusivity, however, can depend² on time t through a temperature schedule $T(t)$. Equation [2] means that the initial condition is an arbitrary profile C_0 . Equations [3] and [4] are boundary conditions: the first

* Electrochemical Society Active Member.

¹On leave from Department of Mathematics, Duke University, Durham, North Carolina 27706

²In that case, the diffusion equation [1] reduced to one having constant coefficients through Kirchhoff's transformation [cf. Ref. (4) or Ref. (5), p. 11]: $t \rightarrow \vartheta = \int D dt$. Equations [5]-[10] remain formally unchanged except for the substitution of ϑ for Dt . The variable ϑ was labeled λ^2 in Ref. (4) because it has dimensions of length squared. One can also interpret this integral as a time average or effective value of D . Thus, $\vartheta = D_{\text{eff}} t$ is proportional to the diffusion time, where it must be understood that D_{eff} is generally a function of time.

assumes that the free surface is insulated (no loss); the second condition states that the concentration, deep inside the material, is negligible.

This problem has an exact solution [Ref. (5), p. 56], namely, a convolution of the initial profile with gaussians centered at "source" points $x = \pm x'$

$$C(x, t) = \frac{1}{2\sqrt{\pi Dt}} \int_0^\infty [e^{-\alpha-x)^2/4Dt} + e^{-\alpha+x)^2/4Dt}] C_0(x') dx' \quad [5]$$

This formula allows the explicit computation of concentration distributions, regardless of the initial profile C_0 . In practice, however, the integral [5] must be evaluated numerically for each value of D . Data fitting can therefore become quite tedious.³ The method that follows is far more direct.

Diffusivity Measurements from Moments of Concentration Profiles

Consider the (nonnormalized and noncentered) moments at time t

$$M_n(t) = \int_0^\infty x^n C(x, t) dx \quad [6]$$

of the concentration distribution, much as one defines moments of probability distributions (6). For any positive integer n , these quantities are easy to evaluate from numerical data if the data are measured over a wide enough range and if the concentration, far from the surface, decays sufficiently rapidly. The following steps are quite simple. Take the derivative of Eq. [6] with respect to time, use Eq. [1] to get

$$\frac{dM_n}{dt} = D \int_0^\infty x^n \frac{\partial^2 C}{\partial x^2} dx \quad [7]$$

and integrate by parts, taking the boundary conditions [3] and [4] into account. One obtains easily integrable differential equations, and thus the relations

$$M_0(t) = M_0(0) \quad [8a]$$

$$M_1(t) = M_1(0) + D \int_0^t C(0, t') dt' \quad [8b]$$

$$M_n(t) = M_n(0) + n(n-1) D \int_0^t M_{n-2}(t') dt', \quad n \geq 2 \quad [8c]$$

The first relation [8a] is nothing but a statement of mass conservation. The second, [8b], expresses the first moment (proportional to the centroid or mean of the distribution) in terms of the time-integral of the surface concentration. The third and most important, [8c], is a recursion between moments. For example, for $n = 2, 4, 6$, we get successively

$$M_2(t) = M_2(0) + 2M_0(0)Dt \quad [9a]$$

³Even in those cases where the integral [5] can be performed exactly [e.g., in Ref. (4)], one must still evaluate transcendental functions in which the diffusivity occurs nonlinearly.

$$M_4(t) = M_4(0) + 12[M_2(0)Dt + M_0(0)(Dt)^2] \quad [9b]$$

$$M_6(t) = M_6(0) + 30[M_4(0)Dt + 6M_2(0)(Dt)^2 + 4M_0(0)(Dt)^3] \quad [9c]$$

We thus see that the moments of even order $2n$ yield polynomial expressions of order n in the variable Dt (or, more generally, in the Kirchhoff variable ϑ , cf. footnote 2), whose coefficients are all measurable. In particular, Eq. [9a] shows that the second-order moment (proportional to the moment of inertia or "dispersion") increases linearly with Dt . Data fitting, i.e., the determination of D then reduces to finding roots of polynomials. This will be illustrated in the next section. On the other hand, no such simple relations exist between the odd-ordered moments because Eq. [8b] expresses M_1 as a time integral over the surface concentration whose values are often difficult to measure. Of course, one can always evaluate the integral in [8b] with the help of Eq. [5]. Thus, we have

$$M_1(t) = M_1(0) + 2\sqrt{Dt} \int_0^\infty C_0(x) i^1 \operatorname{erfc} \left(\frac{x}{2\sqrt{Dt}} \right) dx \quad [10]$$

A moment's reflection, however, shows that all the odd moments are still expressed in terms of transcendental functions of the diffusivity, and that definitely defeats our purpose.

Before applying this method to experimentally determined concentration profiles,⁵ we should make the following remarks. First, the formulas [8]-[10] are independent of the origin of time, i.e., one can evaluate the moments between any two values of time for which the profiles are known. Second, the polynomials [9] have positive coefficients except for the constant term, which is always negative. It easily follows that each of these expressions has only one positive root, namely, the value of Dt that we are seeking. Last, we emphasize that the numerical estimation of moments represents a smoothing operation, as contrasted with point-wise or slope estimates.

A Numerical Example

We use the same data as in Ref. (4); a B-doped (100) Si wafer was P-implanted (energy 50 keV, dose 2×10^{15} cm⁻²) and then short-time annealed (1100°C, 10s). The profiles were acquired by secondary ion mass spectroscopy (SIMS), and they are shown again in Fig. 1. The as-implanted and annealed data are represented by triangles and circles, respectively. The analysis in Ref. (4) was based on the assumption of a gaussian representation of the initial profile (triangles). This is a fair assumption for concentrations greater than 10^{19} cm⁻³. The integral [5] can then be performed exactly, and the resulting expression, shown as a dotted line, fits well the annealed data, at least for the higher concentrations. As we pointed out, however, such expressions are nonlinear in the diffusivity; fitting thus requires minimization schemes. The simplicity of our present method will now be illustrated.

The data are sufficiently dense to provide reasonable estimates of the moments [6]. These were computed from the raw data using the trapezoidal rule, and they are recorded in Table I. These moments form the coefficients of the polynomial equations [9] which are trivially solved for Dt . The corresponding values for the orders 2, 4, and 6 are also recorded in Table I. The values of Dt corresponding to the second and fourth moments are close to one another and to the value 2.98×10^{-11} cm² found earlier (4). On the other hand, the sixth-order moments yield an overestimate of ca. 20%, which can be traced back to a

⁴ We emphasize that any analysis of diffusion profiles yields values of ϑ and not of D , except in ideal cases when the $T(t)$ schedule is either "rectangular" or its rise and decay times are short in comparison with the time at temperature. The extraction of the diffusivity $D(T)$ then requires further information on the $T(t)$ schedule. See also Ref. (7) for an asymptotic analysis of the variable ϑ .

⁵ The present method for extracting effective diffusivities from concentration profiles has been extensively used by Oehrlein *et al.* (8).

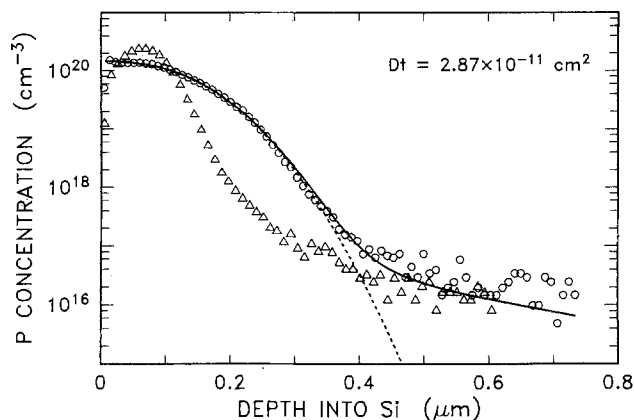


Fig. 1. Time development of an initial P implant in Si. The triangles and circles represent the as-implanted and annealed data, respectively. The solid line represents the best fit by our method of moments, and the dotted line shows the same fit by our former analytic approximation (4).

poor resolution of the higher-order moments. It should always be remembered that the calculations assume integrations [6] over an infinite range. Since the higher-order moments (in this instance, the sixth) tend to weight the tail of the distributions, these tend to amplify experimental uncertainties. Some improvement is possible if one can fit the tail of the distributions to sufficiently rapidly decreasing functions or if one can subtract out the background. The moments can then be estimated more precisely, but our experience with such procedures⁶ indicates but minor shifts in the values of Dt . Finally, we merely insert the measured value of Dt into the integral [5] and evaluate it numerically to obtain the solid line on Fig. 1. Here, we choose the value corresponding to $n = 2$; the curve corresponding to the fourth-order calculation is hardly distinguishable from this case. We note that the solid line represents the data better than the dotted one. This is easily understood since the latter calculation (4) does not take the channeling tail of the initial implant into account.

We should point out that our method may not be entirely applicable to the present experimental data, because P diffusion in Si, at impurity levels greater than 10^{20} cm⁻³, cannot be fully described by the simple diffusion Eq. [1]. [Reference (9) gives a review of this topic.] Therefore, the specific solution provided by our method of moments cannot give a completely accurate description in the case of high level P diffusion. For example, the systematic deviation of the full line from the experimental data in the concentration tail appears physically significant, and it is, most likely, related to the enhanced tail diffusion observed in high dose P experiments (9). Nevertheless, our solution is a very good approximation of a more rigorous treatment, as is clear from Fig. 1, because concentration enhancement effects are only beginning to become significant for our experimental conditions of dose and temperature.

Generalization to Other Diffusion Problems

Our method, as described, appears limited to conservative systems. We now show that it also applies to more general situations, for sources and sinks are a very real

⁶ For example, subtracting a 10^{16} cm⁻³ background level from our data reduces the values of Dt in Table I by 0.3, 1.5, and 4.7% for $n = 2, 4, 6$, respectively. Interestingly, such corrections tend to bring the measured values of Dt into closer agreement.

Table I. Initial and final moments of even orders and corresponding values of Dt computed through Eq. [9]

Order n	$M_n(0)$	$M_n(t)$	$Dt \times 10^{11}$ cm ²
0			—
2	2.14×10^{15} cm ⁻²	2.14×10^{15} cm ⁻²	2.87
4	1.25×10^5 cm ⁰	2.48×10^5 cm ⁰	2.99
6	1.71×10^{-5} cm ²	8.49×10^{-5} cm ²	2.99
6	1.08×10^{-14} cm ⁴	7.32×10^{-14} cm ⁴	3.69

possibility. For example, a dopant that precipitates is described by an internal sink in the diffusion equation. Likewise, a surface sink characterizes a lossy surface.

Consider then a mild generalization of our previous problem. The diffusion equation [1] is replaced by

$$\frac{\partial C}{\partial t^2} = D \frac{\partial^2 C}{\partial x^2} - \sigma_v \quad \text{for } x > 0, t > 0 \quad [11]$$

and the boundary condition at the surface becomes

$$D \frac{\partial C}{\partial x} = \sigma_s \quad \text{at } x = 0 \quad [12]$$

The other conditions [2] and [4] remain unchanged. Here, $\sigma_v(x,t)$ and $\sigma_s(t)$ represent volume and surface sinks, respectively. They are assumed to be known functions. Defining moments of the concentration C as in Eq. [6], and, similarly, moments

$$\mu_n(t) = \int_0^\infty x^n \sigma_v(x,t) dx \quad [13]$$

of the volume sink σ_v , we perform the same steps that led to Eq. [8]

$$M_0(t) = M_0(0) - \int_0^t \sigma(t') dt' \quad [14a]$$

$$M_1(t) = M_1(0) + D \int_0^t C(0,t') dt' - \int_0^t \mu_1(t') dt' \quad [14b]$$

$$M_n(t) = M_n(0) + n(n-1)D \int_0^t M_{n-2}(t') dt' - \int_0^t \mu_n(t') dt', \quad n \geq 2 \quad [14c]$$

For brevity, we have defined the total "surface-equivalent" sink

$$\sigma(t) = \sigma_s(t) + \int_0^\infty \sigma_v(x,t) dx = \sigma_s(t) + \mu_0(t) \quad [15]$$

that occurs in Eq. [14a] and in the subsequent calculations. It represents the degree to which mass conservation, due to diffusion alone, does not hold. Nonetheless, Eq. [14a] is still a statement of global mass balance in the sense that the mass at time t is strictly accounted for by the initial mass and the total losses. Likewise, Eq. [14b] and [14c] generalize the corresponding Eq. [8] when sinks are present. It is now easy to write polynomial expressions analogous to [9]. For example, evaluating [14c] for $n = 2$, we get

$$M_2(t) = M_2(0) + 2M_0(0)Dt - \int_0^t [\mu_2(t') + 2D(t-t')\sigma(t')] dt' \quad [16]$$

which is again a linear equation in D if all other terms are measurable.

Summary

We have developed a method of data analysis that is based on the computation of moments of the concentration distribution. We have shown that these quantities form the coefficients of polynomials in the fitting parameter Dt . Since the moments are easily evaluated numerically from experimental data, it follows that data fitting reduces to finding roots of polynomials. Not only is this procedure much simpler than the usual minimization schemes, but also it must be remembered that the estimation of moments introduces a measure of smoothing. Nowhere is it necessary to estimate slopes or functional values. One can therefore expect increased accuracy in the measurement of diffusivities. It should also be appreciated that the initial profile can be arbitrary, a condition in line with most experimental situations.

We have also demonstrated the method's applicability in the practical case of impurity redistribution in ion-implanted material, but it can be applied equally well to other physical cases that satisfy essentially the same boundary conditions. Although the method requires that the diffusivity be concentration independent and that the boundary conditions be quite simple (given flux, *i.e.*, a Neumann condition), one can anticipate its extension to more complex cases.

Manuscript submitted Feb. 15, 1985; revised manuscript received June 24, 1985.

IBM Corporation assisted in meeting the publication costs of this article.

REFERENCES

1. G. Dahlquist and A. Björk, "Numerical Methods," pp. 438-446, Prentice-Hall, Englewood Cliffs, NJ (1974).
2. B. Tuck, "Introduction to Diffusion in Semiconductors," pp. 199-203, Peter Peregrinus Ltd., Stevenage, England (1974).
3. R. Ghez and M. B. Small, *This Journal*, **128**, 1468 (1981).
4. R. Ghez, G. S. Oehrlein, T. O. Sedgwick, F. F. Morehead, and Y. H. Lee, *Appl. Phys. Lett.*, **45**, 881 (1984).
5. H. S. Carslaw and J. C. Jaeger, "Conduction of Heat in Solids," Clarendon Press, London (1959).
6. W. Feller, "An Introduction to Probability Theory and Its Applications," John Wiley and Sons, New York (1957).
7. J. D. Fehribach, R. Ghez, and G. S. Oehrlein, *Appl. Phys. Lett.*, **46**, 433 (1985).
8. G. S. Oehrlein, R. Ghez, J. D. Fehribach, E. F. Gorey, T. O. Sedgwick, S. A. Cohen, and V. R. Deline, in "Proceedings of the Thirteenth International Conference on Defects in Semiconductors," L. C. Kimmerling and J. M. Parsey, Editors, pp. 539-546, The Metallurgical Society of AIME, Warrendale, PA (1984).
9. S. M. Hu, P. Fahey, and R. W. Dutton, *J. Appl. Phys.*, **54**, 6912 (1983).

Comparisons of GaAs, Tungsten, and Photoresist Etch Rates and GaAs Surfaces Using RIE with CF_4 , $\text{CF}_4 + \text{N}_2$, and $\text{SF}_6 + \text{N}_2$ Mixtures

Nobuhiko Susa

*Nippon Telegraph and Telephone Corporation, Musashino Electrical Communication Laboratory,
Musashino-shi, Tokyo 180, Japan*

ABSTRACT

Etch rates for GaAs, tungsten, and photoresist were compared using CF_4 , $\text{CF}_4 + \text{N}_2$, and $\text{SF}_6 + \text{N}_2$ gases. Etch rate ratio between the W and photoresist can be increased by N_2 gas addition, with a negligibly low GaAs etch rate. GaAs surfaces exposed to $\text{CF}_4 + \text{N}_2$ or $\text{SF}_6 + \text{N}_2$ plasmas were characterized by means of photoluminescence (PL), Schottky contacts, secondary ion mass spectroscopy (SIMS), and Auger electron spectroscopy (AES). The PL intensity measurements and Schottky characteristics revealed that the damage to the GaAs surface was somewhat smaller than that caused by pure CF_4 gas. The AES and SIMS measurements showed that the change in Ga/As composition after reactive ion etching was negligibly small. Results of heat-treatment are also described. Curious annealing characteristics were observed in the $\text{CF}_4 + \text{N}_2$, suggesting the existence of GaN.

As the sizes of high speed electronic devices are scaled down to the submicrometer level, dry processes such as reactive ion etching (RIE) become essential in the development of microdevices. This is because undercutting occurs in fabrication of such devices when conventional wet etching is employed. On the other hand, since RIE is an anisotropic etching method due to the formation of volatile compounds by plasma species and also due to the accelerated ion bombardment in the plasma sheath, high grade photolithography without undercutting is obtained. The energetic ions, electrons, ultraviolet photons, and x-rays in the plasma, however, produce degradation in semiconductor surfaces exposed to it.

Recently, Bozler *et al.* (1) and Asai *et al.* (2) developed a permeable base transistor (PBT), consisting of submicrometer tungsten gratings embedded in a GaAs epitaxial layer. RIE is a suitable technique for patterning the submicrometer W grating on GaAs, because there is no undercutting. In this case, the plasma is required to etch only the W films and not the GaAs layer. Moreover, GaAs surface damage caused by exposure to the plasma must be minimized, because a second GaAs epitaxial layer is grown on the first epitaxial layer after the W photolithography and a damage-free process is needed for the W photolithography to realize a high performance PBT. Although RIE has been extensively studied for application to GaAs etching, few reports on W dry etching, which meets these requirements, have been published (3-5). We have tried several mixtures of several gases to realize W etching without surface damage while maintaining the GaAs etching rate at a negligibly low level. Finally, fluoride gases mixed with nitrogen were found to be suitable for W film etching on GaAs, because the use of these gases resulted in a higher etching rate for the W film than for the photoresist (AZ-1350). Detailed results on the etching rate and conditions with various kinds of gases will be published elsewhere (6). Here, only the etching rates with N_2 gas mixtures will be mentioned briefly in the Etching Rate section.

Surface degradation caused by exposure to $\text{CF}_4 + \text{N}_2$ or $\text{SF}_6 + \text{N}_2$ plasma was characterized by means of carrier concentration, photoluminescence, and Schottky characteristics and was compared with that caused by exposure to pure CF_4 plasma. Changes in surface composition and contamination on the plasma-exposed GaAs surfaces were analyzed by means of Auger electron spectroscopy (AES) and secondary ion mass spectroscopy (SIMS). The results of annealing experiments on the damaged samples are also described in this paper.

Experimental Procedures

The W films used were deposited by conventional RF diode sputtering on (100) GaAs substrates. Since the etching rate for the W film depends on the sputtering pressure, the pressure was fixed at 4×10^{-2} torr, where the

resistivity of the deposited W film was minimal. Details on the deposition conditions and the properties of the W films will be reported elsewhere (7).

The GaAs crystals used were sulfur-doped epitaxial layers 2.6 μm thick grown by conventional vapor phase epitaxy on (100) 2° off GaAs substrates doped with silicon. Their carrier concentrations were 1×10^{17} and above 10^{18} cm^{-3} for the epitaxial layers and the substrates, respectively. The surfaces of the epitaxial layers were exposed to CF_4 , $\text{CF}_4 + \text{N}_2$, and $\text{SF}_6 + \text{N}_2$ plasmas for 15 min and characterized by various methods. Since 300-2000 \AA thick W films (usually used for the PBT) deposited on GaAs were etched within 10 min under the present RIE condition, the plasma exposure time of 15 min was enough to study the GaAs surface damages.

The RIE apparatus used was a commercially available parallel-plate reactor. It consists of a stainless steel chamber and SiO_2 electrodes of 28 cm diam. The chamber can be evacuated to less than 1×10^{-5} Pa with an oil diffusion pump having a liquid N_2 cold trap. All of the RIE experiments in the present paper were done at an RF frequency of 13.56 MHz for 15 min and an input power of 50W (which corresponded in our system to a power density of 0.081 W/cm 2). No substrates were intentionally heated, and their temperatures were apparently near room temperature during the plasma etching. Purities of CF_4 , SF_6 , and N_2 were 99.9999, 99.99, and 99.999%, respectively. The gas flow rates of gases were controlled by mass flow meters.

Etching rates for W films on GaAs were measured for the films etched through $100 \times 200 \mu\text{m}$ windows in the AZ-1350 photoresist mask. After removing the photoresist, the step was measured with a Talystep meter.

The carrier concentration profiles of plasma-exposed GaAs were obtained from the C-V characteristics. The Schottky diodes for the C-V measurements were fabricated by evaporation of Au dots with an area of $1.26 \times 10^{-3} \text{ cm}^2$, and the C-V measurements were done by using a capacitance meter at 1 MHz.

The photoluminescence (PL) intensity was measured at 77 K by illuminating the RIE-processed surfaces with a He-Cd laser (4416 \AA), and was detected with a cooled S-1 type photomultiplier. The penetration depth at the laser wavelength of 4416 \AA is about 300 \AA .

Schottky characteristics, such as barrier height, ideality factor, and leakage current, were evaluated for diodes with Au-Schottky contacts vacuum evaporated on the plasma-exposed surfaces. The diameter of the Schottky contact was 400 μm . Ohmic contacts of alloyed Au-Ge-Ni were made by vacuum evaporation and annealing at 430°C for 150s in H_2 gas flow.

The Ga/As composition ratio and contamination elements, (C, O, F, N) supplied from etching gases and air were analyzed with AES. The in-depth profile was measured by sputtering the GaAs with Ar^+ ion at an etching

rate of about 5 Å/min. The SIMS profiles of C, F, O and N atoms were measured by Cs⁺ ion sputtering with the modified CAMECA IMS-3F.

Etching Rate

When CF₄ gas is employed in RIE, one may expect the etching rate for a W film will be large, while that for GaAs will be negligibly small, because of the volatility of

gallium fluoride (GaF₃, bp > 950°C) is lower than that of gallium chlorides (GaCl₃, bp = 201.3°C) and because the volatility of tungsten hexafluoride (WF₆, bp = 17.5°C) is higher than that of tungsten chlorides (WCl₆, bp = 346.7°C).

However, the GaAs etching rate in our experiments was rather high, as shown in Fig. 1a. Usually, CF₄ gas mixed with O₂ or Ar is used in RIE to change the etching characteristics. We studied these mixtures mainly with respect to the etching selectivity of the W film to the photoresist (AZ-1350). However, these trials resulted in an inadequate etching rate ratio between the W film and the photoresist. Next, CF₄ and SF₆ gases mixed with nitrogen were tried because no reports had been published on these mixtures for either W, GaAs, or photoresist etchings.

The etch rates for the W film, photoresist (AZ-1350), and GaAs as a function of pressure are shown in Fig. 1a, 1b, and 1c for pure CF₄, 90% CF₄ + 10% N₂, and 80% SF₆ + 20% N₂ gases, respectively. Total gas flow rate was fixed at 35 sccm for each case. Input power was 50W, and other etching conditions were identical to those described in the Experimental Procedures section.

Etching rates for GaAs with CF₄ + N₂ and SF₆ + N₂ were found to be negligibly low compared with those for pure CF₄ and SF₆. On the other hand, the etch rate for the W film was rather high when N₂ was added to pure CF₄ and SF₆. In CF₄ + N₂, the etching rates for the photoresist decreased with an increase in the pressure, while in SF₆ + N₂ the etching rates for the photoresist were independent of the pressure. The maximum etching rate ratios of the W film to the photoresist were 4 for CF₄ + N₂ and 10 for SF₆ + N₂. Therefore, the addition of N₂ to CF₄ and SF₆ was concluded to be suitable for etching the W film under the gas mixtures examined, while maintaining a practical, useful high etching rate ratio of the W to the photoresist. Moreover, the GaAs etching rate was negligibly low under these conditions.

More precise studies on the etching conditions and characteristics with various kinds of gases will be published elsewhere (6) as mentioned in the introductory section.

Surface degradation of the GaAs was evaluated in the CF₄ + N₂ and SF₆ + N₂ mixtures. Since the data for the SF₆ + N₂ were similar to those for the CF₄ + N₂, only the results for the CF₄ + N₂ will be described in the following sections.

Carrier Concentration Profiles

Carrier concentration profiles calculated from the C-V characteristics for the GaAs epitaxial layers exposed to pure CF₄ and 90% CF₄ + 10% N₂ plasmas are shown in Fig. 2a and 2b, respectively. The pressure was 25 Pa, and the other RIE conditions were the same as those described in the Experimental Procedures section. The GaAs surfaces were exposed to the plasmas for 15 min. In CF₄, the plasma-induced defects were large enough to diminish carriers near the surfaces. Similar carrier concentration reduction has been reported in RIE when 55% CF₄ + 45% H₂ (8) or pure H₂ (9) was used. On the other hand, no carrier concentration reduction was observed for the CF₄ + N₂, as shown in Fig. 2b. This implies that the surface damage due to CF₄ + N₂ was smaller than that due to pure CF₄.

Since the plasma- or ion-bombardment-induced damage can be repaired by a conventional annealing process (8, 10, 11), annealing experiments were performed in the present study. Carrier concentration profiles for the GaAs epitaxial layers exposed to the pure CF₄ or 90% CF₄ + 10% N₂ plasma are shown in Fig. 2a and 2b, respectively. The carrier concentration profiles for samples annealed in the 10% H₂ + 90% Ar gas flow at 430°C are also shown in the figures. The Au-Schottky contacts were deposited after the annealing, while the Au-Ge-Ni-alloyed ohmic contacts were made before the annealing. Surface deterioration due to exposure to the CF₄ plasma was found to have been repaired by the heat-treatment, as

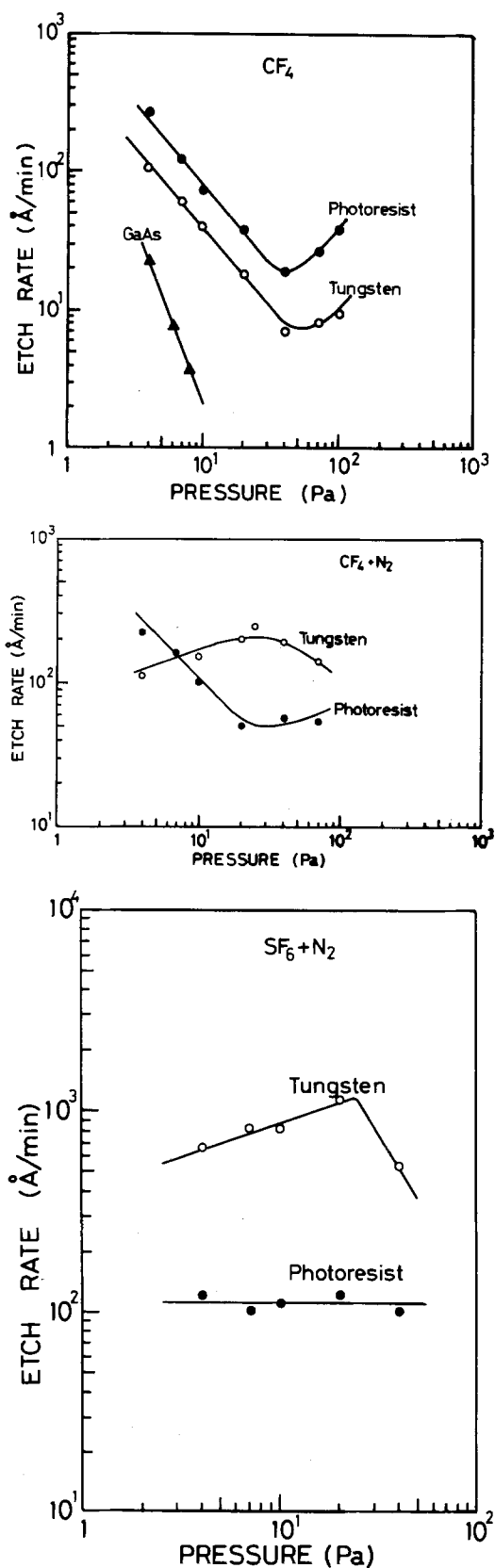


Fig. 1. Etch rate of tungsten, photoresist (AZ-1350), and GaAs as a function of pressure with (a, top) pure CF₄, (b, middle) 90% CF₄ + 10% N₂, and (c, bottom) 80% SF₆ + 20% N₂.

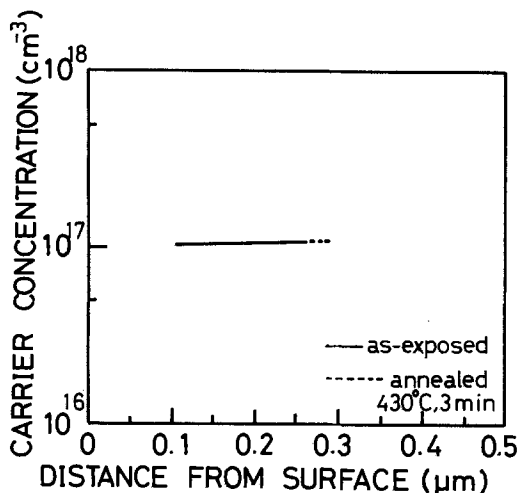
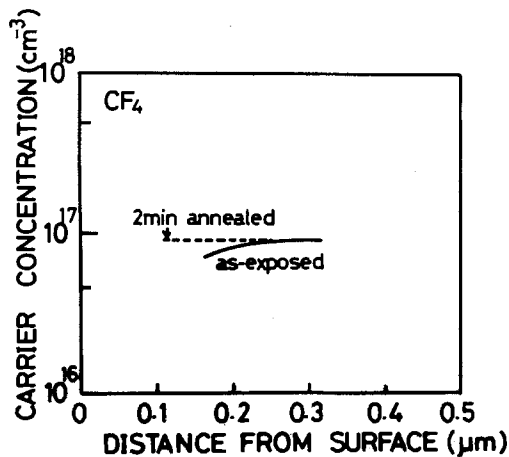


Fig. 2. Carrier concentration profiles for the GaAs epitaxial layers exposed to (a, top) CF_4 and (b, bottom) 90% CF_4 + 10% N_2 plasmas and annealed in H_2 + Ar at 430°C .

shown in Fig. 2a. On the other hand, in the CF_4 + N_2 , the carrier concentration profile was not affected by annealing.

Photoluminescence

Since photoluminescence (PL) spectra and intensity are affected by defects, they are sometimes used to study surface damage induced by ion irradiation. The PL spectra were measured before and after RIE to evaluate the degree of surface deterioration. The PL intensity as a function of wavelength at 77 K for as-grown GaAs and GaAs exposed to the CF_4 + N_2 or CF_4 plasma are shown in Fig. 3. The RIE conditions were identical to those in the carrier concentration measurements. Carrier concentration of the as-grown epitaxial layer was $1 \times 10^{17} \text{ cm}^{-3}$, and its thickness was $2.6 \mu\text{m}$.

When the surfaces were exposed to the plasmas, the PL intensity at an 820 nm peak was reduced by defects produced which acted as nonradiative surface recombination centers. The use of pure CF_4 resulted in a drastic reduction in the PL intensity compared with that of the CF_4 + N_2 mixtures, as shown in Fig. 3. This result agrees with the noticeable reduction (Fig. 2a) in the carrier concentration of the GaAs layer exposed to the CF_4 plasma.

Annealing experiments were carried out at 430°C in 10% H_2 + 90% Ar gas flow for the damaged GaAs surfaces, and a recovery process by the capless heat-treatment was observed by means of PL measurement. The PL intensities as a function of annealing time at the 820 nm peak at 77 K are shown in Fig. 4. The samples measured were the GaAs epitaxial layer exposed to the CF_4 or CF_4 + N_2 plasma, and as-grown GaAs. Data for SiO_2 sputter-deposited GaAs is also shown in Fig. 4 for comparison. In this case, a SiO_2 film with 700\AA thickness was deposited by Ar sputtering for 15 min at 6×10^{-2} torr at an input

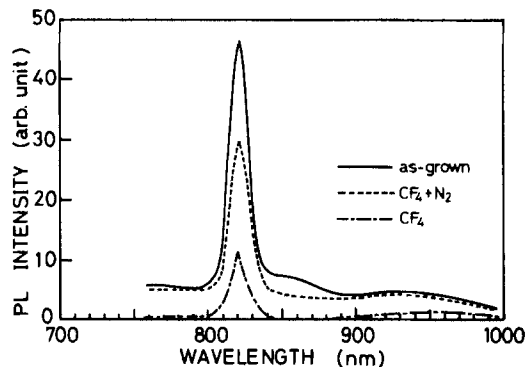


Fig. 3. Photoluminescence (PL) intensity for as-grown epitaxial GaAs and GaAs exposed to CF_4 or CF_4 + N_2 , as a function of wavelength.

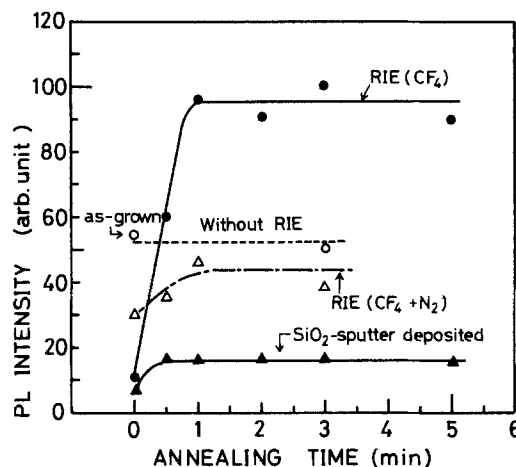


Fig. 4. PL intensity as a function of annealing time at 430°C for as-grown GaAs, GaAs exposed to CF_4 or CF_4 + N_2 , and SiO_2 sputter-deposited GaAs.

power of 50W. This film deposited on the GaAs epilayer was then removed by wet etching with buffered HF solution before the PL measurement.

Interestingly, the values of PL intensity for the samples exposed to the pure CF_4 plasma and then annealed increased until they were nearly double that for the as-grown crystal, even though the PL intensity decreased considerably immediately after exposure to the CF_4 plasma. On the other hand, the PL intensity for the CF_4 + N_2 was somewhat larger than that for the CF_4 before heat-treatment. In the CF_4 , the reason for the abrupt increase in the PL intensity due to the annealing is not clear at present. The As vacancies produced by the ion irradiation due to the CF_4 plasma may be occupied by donor impurities such as sulfur (dopant in the epitaxial layer) which migrated during the heat-treatment. This would cause the carrier concentration near the GaAs surface and the PL intensity to increase. If this is the case, the increase in carrier concentration should occur only near the surface, since it cannot be detected by means of the carrier concentration profile described in the previous section. However, this increase in the carrier concentration can be estimated from a value of capacitance at 0 bias voltage, as will be described in the Capacitance section.

The surface deposited with the sputtered SiO_2 film suffered the most serious damage, as shown in Fig. 4. This is because the GaAs surface was deteriorated seriously by Ar ion bombardment rather than by ion radiation due to the CF_4 plasma. This damage cannot be corrected by the present annealing process.

Schottky Characteristics

In order to characterize the damaged surfaces of GaAs epitaxial layers, Schottky diodes were fabricated by Au vacuum evaporation on the plasma-exposed surfaces. The GaAs surfaces were exposed to pure CF_4 , CF_4 + N_2 , or SF_6

+ N₂ plasma at 25 Pa at 50W for 15 min. Barrier heights were obtained from two different methods which are C-V and forward I-V characteristics (12) and were compared. Ideality factors were also calculated from the forward I-V characteristics (12). Effects of the 430°C heat-treatment on the leakage current, barrier height, and ideality factor were also examined. In these experiments, the Au Schottky contacts of 400 μm diam were evaporated after the annealing, while Au-Ge-Ni alloyed ohmic contacts were formed before the plasma exposure, as in the measurements of the carrier concentration profiles.

Barrier height and ideality factor.—Barrier heights and ideality factors for CF₄ and CF₄ + N₂ are shown in Fig. 5a and 5b, respectively. In the CF₄, a large difference in barrier height between the C-V and I-V characteristics was observed before the heat-treatment, as shown in Fig. 5a. This is because a thin insulator layer or a thin layer with low carrier concentration was formed as a result of the CF₄ plasma exposure, as deduced from the carrier concentration profile shown in Fig. 2a. The barrier heights measured from the I-V characteristics provided more reasonable values than those obtained from C-V measurements. It was found that the short annealing period was sufficient to correct the GaAs surface deterioration caused by the CF₄ plasma.

In CF₄ + N₂, it is interesting to note that the difference in barrier heights obtained from the two methods increased with an increase in the annealing time. This suggests that a higher resistive layer was formed during the heat-treatment. Such a layer, however, cannot be detected in the carrier concentration profile shown in Fig. 2b, probably because the layer was too thin (< 0.1 μm thick). In the present experiment, the barrier heights calculated from the forward I-V characteristics gave a rather exact value.

Ideality factors *n* for the Au-GaAs Schottky contacts before and after the present RIE process were nearly

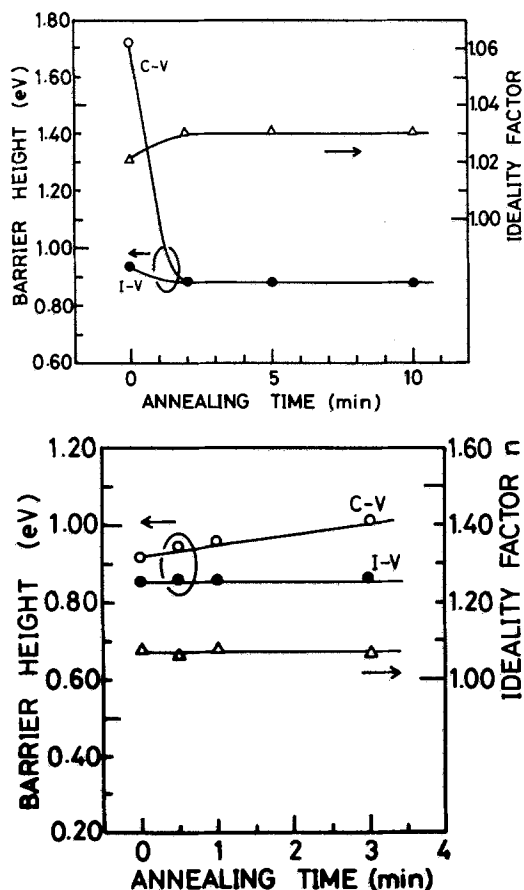


Fig. 5. Barrier heights calculated from the C-V and I-V characteristics, and ideality factor *n* as a function of annealing time at 430°C for samples etched with (a, top) CF₄ and (b, bottom) CF₄ + N₂.

identical, as shown in Fig. 5a and 5b. This was in contrast to the results in previous reports where the *n* factor increased from 1.09 to 1.32 after 700Å GaAs etching for 15 min with 55% CF₄ + 45% H₂ (8), or from 1.1 to 1.2-1.5 after GaAs RIE for 1 min with pure CF₄ (13). This is also due to the lower input power density in the present experiment.

Capacitance.—Capacitances of the Schottky diodes at 0 V bias for the CF₄ and CF₄ + N₂ are shown as a function of annealing time in Fig. 6. Capacitances for the as-grown epitaxial layers are also shown for comparison.

Values of capacitances for CF₄ showed a reduction in carrier concentration due to damage, as shown in Fig. 6. After annealing, the capacitance for the pure CF₄ increased from 89 to 140 pF. The value of 140 pF corresponded to an average carrier density of 1.2×10^{17} cm⁻³ and was higher than that for the as-grown epitaxial layer (129 pF). However, the increase in carrier concentration by annealing occurred only near the surface and could not be detected with the carrier concentration profiles. On the other hand, the capacitance for the CF₄ + N₂ after annealing was 120 pF, which corresponded to a carrier concentration of 8.8×10^{16} cm⁻³ when uniform carrier distribution was assumed.

In the CF₄, the carrier concentration variation induced by the heat-treatment was in qualitative agreement with the variation in PL intensity shown in Fig. 4. However, this was not the case for CF₄ + N₂.

Leakage current.—Leakage currents (backward I-V characteristics of the Au-Schottky diodes) were measured for various kinds of Schottky diodes. Since results for CF₄ + N₂ were similar to those for pure CF₄, only experiments with CF₄ will be mentioned in this section. Leakage currents for as-grown, as-plasma-exposed, and annealed (in 10% H₂ + 90% He gas for 2 min) GaAs epitaxial layers are shown as a function of the reverse bias voltage in Fig. 7. Although reduction of the carrier concentration due to surface damage was observed as shown in Fig. 2a, leakage current did not increase after plasma exposure and was comparable to that for the as-grown epitaxial layer.

Surface Contamination and Composition

Surface contamination and changes in surface composition (Ga/As ratio) caused by RIE were analyzed. Contamination elements such as C, F, N, and O which were supplied from the CF₄, CF₄ + N₂, and air were detected mainly with SIMS. Surface composition (= Ga/As) was measured with AES. The results are described below.

Surface contamination.—Since it has been reported that Si surfaces etched with RIE using CF₄ were contaminated by the composition elements such as C and F contained in the etching gases (14, 15), GaAs surfaces exposed to CF₄ and CF₄ + N₂ plasma were analyzed with respect to C, F, N, and O in the present experiment. In-depth profiles of ¹⁹F⁻ for surfaces exposed to CF₄ plasma at 50W and 25 Pa for 15 min are shown in Fig. 8. Data for

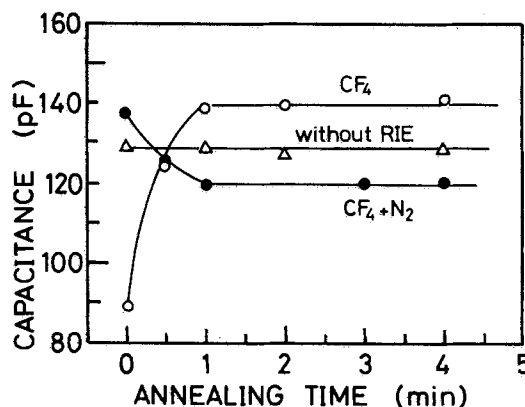


Fig. 6. Capacitances at 0 V bias as a function of annealing time (430°C) for samples etched with CF₄ and CF₄ + N₂. Capacitances of the as-grown GaAs are shown for comparison.

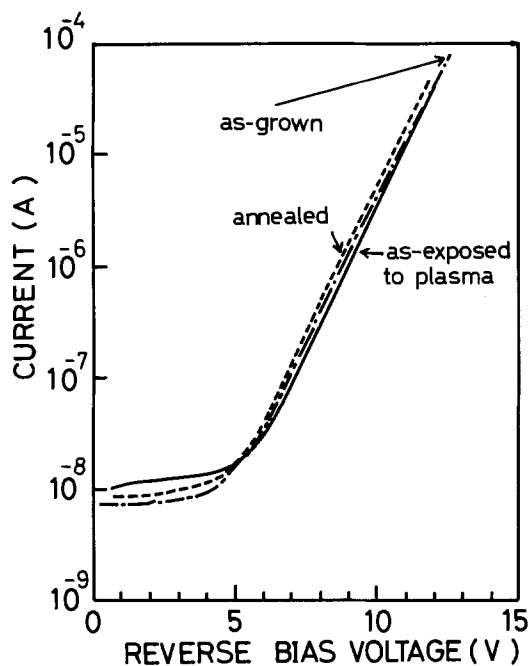


Fig. 7. Leakage currents as a function of reverse bias voltage for as-grown GaAs, and samples as exposed to plasma and then annealed at 430°C.

samples annealed in 10% H_2 + 90% Ar at 430°C for 2 min with and without RIE are also shown for comparison. F contamination was observed after RIE. However, the F on the surface can be easily removed by a simple heat-treatment, as shown in Fig. 8. No C or O contamination was detected on the GaAs surface after RIE in either the CF_4 or CF_4 + N_2 gases.

Changes in composition.—Surface composition change (Ga/As ratio) due to the plasma exposure was analyzed with AES. We measured several kinds of GaAs samples: the epitaxial layer exposed to the CF_4 or CF_4 + N_2 plasma, the layers exposed to these gases and then annealed in 10% H_2 + 90% Ar at 430°C for 3 min, and the as-grown epitaxial layer. In-depth profiles of Ga, As, C, and O for the as-grown and CF_4 plasma-exposed samples are shown in Fig. 9a and 9b as examples. Data for other samples, such as the annealed one, were similar to those shown in Fig. 9a and 9b. Neither AES nor SIMS revealed any C or O contamination due to RIE, although C and O signals due to GaAs surface oxidation and air exposure were always observed, as shown in Fig. 9a and 9b. It has been re-

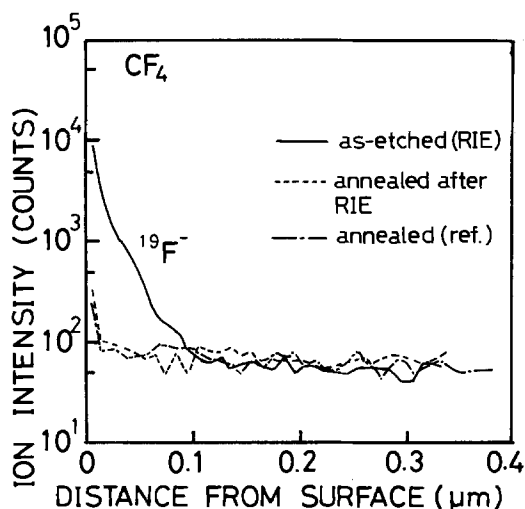


Fig. 8. In-depth profiles of $^{19}F^-$ measured with SIMS for GaAs as exposed to CF_4 plasma, and samples annealed at 430°C with and without CF_4 plasma exposure.

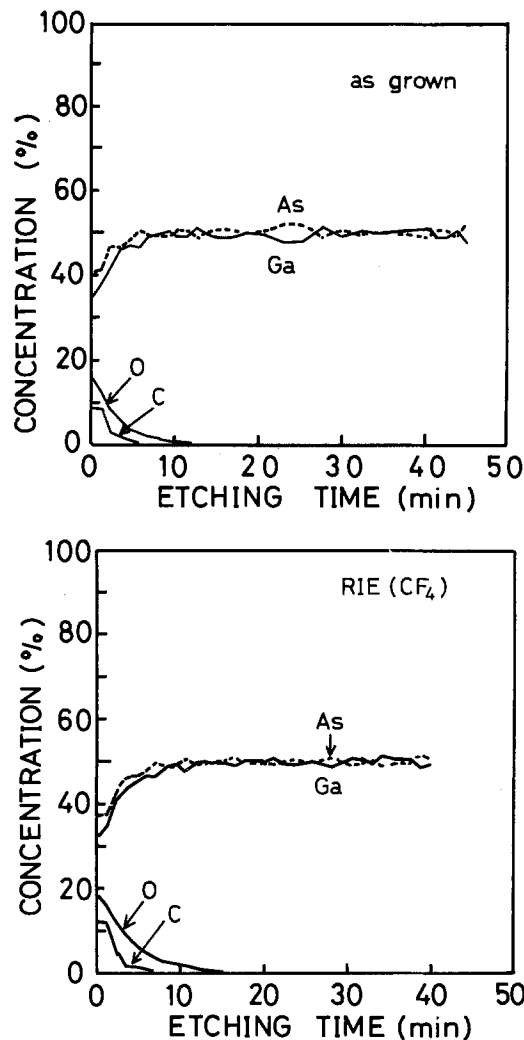


Fig. 9. In-depth profiles of Ga, As, C, and O measured with AES for (a, top) as-grown GaAs and (b, bottom) GaAs exposed to CF_4 plasma.

ported that GaAs surfaces become As or Ga rich as a result of RIE with CF_4 or CCl_4 , respectively (16). However, in the present study, no changes in the Ga/As ratio were observed in any of the samples examined. This is probably due to the input power density of 0.081 W/cm², which is lower than that for GaAs etching by about one order.

Discussion

In order to etch W films while keeping the GaAs etching rate negligibly low and to achieve practical etching selectivity of the W film to the photoresist (AZ-1350), the addition of nitrogen gas to CF_4 or SF_6 was found to be essential in the present experiment. The PL measurements, further, revealed that GaAs surface damage caused by exposure to CF_4 + N_2 or SF_6 + N_2 plasma was somewhat less than that caused by exposure to CF_4 plasma.

Interestingly, these results suggested that GaAs surface treatment with nitrogen plasma should reduce the surface damage. Similar results have been reported by Pankove *et al.* (17) and Matsumoto (18). They concluded that GaN (which has a wider bandgap than GaAs) formation due to the N plasma diminishes the surface recombination velocity for photogenerated carriers and that the PL intensity does not decrease much. Accordingly, the process of immersing the GaAs into nitrogen plasma is a useful method for surface passivation. In their studies, H_2 plasma was used to simultaneously remove As from the GaAs surface as AsH_3 and to produce an As vacancy in parts occupied by a N atom. Nitrogen was detected on the GaAs surface with AES in their experiments. On the other hand, no GaN was detected on the GaAs surface with either SIMS or AES in the present experiment. However, it was observed that the addition of N_2 gas to pure

CF₄ or SF₆ had a noticeable effect on surface damage, as shown in Fig. 2a and 2b and also in Fig. 3. It has been reported that the As was removed preferentially from the surface rather than the Ga when CF₄ was used as the etching gas in RIE (16). Therefore, the GaN formed by replacement of As with N probably prevents the increase in surface recombination velocity, though no Ga-rich layer could be detected in the present experiment (Fig. 9b) owing to the lower input power density and the excessive thinness of the layer.

It is interesting to note that, after annealing, the PL intensity for the GaAs exposed to the CF₄ plasma became about twice as large as that for the as-grown or annealed GaAs which was not exposed to the plasma, as shown in Fig. 4. This is probably because vacancies (probably As vacancies) produced by the ion bombardment were occupied partly by the S donor near the surface through the annealing, causing the PL intensity to increase as a result of the increase in carrier concentration. This increase in carrier concentration for the CF₄ was estimated from the somewhat larger capacitance than that of the as-grown GaAs epitaxial layer with $1 \times 10^{17} \text{ cm}^{-3}$ carrier concentration, as shown in Fig. 6. On the other hand, the capacitance for CF₄ + N₂ was slightly smaller than that of the as-grown crystal after annealing. This is probably because the As vacancies produced by the plasma were partially occupied by N rather than S and a surface layer with lower carrier concentration was formed.

From the results for CF₄ shown in Fig. 2a and 5b, the abnormally large barrier height value obtained from the C-V characteristics is concluded to be due to the formation of an insulator layer or a highly resistive layer between the Au-Schottky contact and the undamaged GaAs. In contrast, for CF₄ + N₂, the difference of the barrier height calculated from the C-V and I-V characteristics increased with an increase in annealing time, as shown in Fig. 5b. This suggests the existence of an insulating or highly resistive layer, or GaN after annealing. The existence of such layers can be estimated from the value of capacitance at 0 bias voltage shown in Fig. 6, although it cannot be detected with the carrier concentration profile, SIMS, or AES.

These results indicated that a W film deposited on the GaAs can be successfully etched in CF₄ + N₂ or SF₆ + N₂ with a negligibly small GaAs etching rate, minimizing the surface damage caused by exposure to the plasma.

Conclusion

A tungsten film was successfully etched on a GaAs substrate in CF₄ + N₂ or SF₆ + N₂ mixtures, with a negligibly low GaAs etching rate. PL intensity measurements revealed that surface damage caused by exposure to the plasma was considerably less than that caused by exposure to pure CF₄ gas. This is probably due to the formation of GaN on the GaAs surface and resultant suppression of surface recombination velocity. Schottky characteristics such as barrier height, ideality factor, and leakage current did not deteriorate much as a result of the low power density employed in the present study.

The GaAs surface was contaminated by F from the CF₄ compound. However, it was found that this F could be easily removed from the surface by annealing at 430°C. The levels of C and O contamination due to RIE were comparable to those for as-grown crystals. Changes in the Ga/As composition ratio after RIE could not be detected with AES or SIMS as a result of the low power density employed and thinness of the damaged layer.

The addition of N₂ to CF₄ or SF₆ gas was revealed to be essential in the W photolithography necessary for the fabrication of microdevices such as PBT's.

Acknowledgments

The authors would like to express their gratitude to Dr. Kenji Kumabe, Dr. Kiyomasa Sugii, Dr. Hideo Sugiura, Dr. Yoshifumi Takanashi, and Dr. Sadao Adachi for their constant encouragement and support. They are also grateful to Yoshikazu Homma for the SIMS measurements and Hamao Okamoto for the AES measurements.

Manuscript submitted March 19, 1985; revised manuscript received June 23, 1985.

Nippon Telegraph and Telephone Corporation assisted in meeting the publication costs of this article.

REFERENCES

1. C. O. Bozler and G. D. Alley, *IEEE Trans. Electron Devices*, **ed-27**, 1128 (1980).
2. H. Asai, S. Adachi, S. Ando, and K. Oe, *J. Appl. Phys.*, **55**, 3868 (1984).
3. C. C. Tang and D. W. Hess, *This Journal*, **131**, 115 (1984).
4. J. N. Randall and J. C. Wolfe, *Appl. Phys. Lett.*, **41**, 247 (1982).
5. K. Tsujimoto, S. Tachi, T. Mizutani, and S. Okudaira, *Proceedings of the Technical Meeting of the Institute of Electrical and Communication Engineers of Japan*, **ssd-84**, 45 (1984).
6. S. Adachi and N. Susa, *This Journal*, To be published.
7. N. Susa, S. Ando, and S. Adachi, *This Journal*, To be published.
8. Y. Yamane, K. Yamasaki, and T. Mizutani, *Jpn. J. Appl. Phys.*, **21**, L537 (1982).
9. Y. Chung, D. W. Langer, R. Becker, and D. Look, *IEEE Trans. Electron Devices*, **ed-32**, 40 (1985).
10. M. Kawabe, N. Kanzaki, K. Masuda, and S. Namba, *Appl. Opt.*, **17**, 2556 (1978).
11. C. Chen and K. D. Wise, *IEEE Trans. Electron Devices*, **ed-10**, 1522 (1982).
12. S. M. Sze, "Physics of Semiconductor Devices," pp. 279-293. Wiley-Interscience, New York (1981).
13. T. Terada, Y. Kitaura, T. Mizoguchi, and K. Hojo, in "Proceedings of the 1983 Spring Meeting of the Japan Society of Applied Physics," 7a-D-4, p. 454 (1983).
14. M. Oshima, *Surf. Sci.*, **86**, 858 (1979).
15. G. S. Oehrlein, R. M. Tromp, Y. H. Lee, and E. J. Petrill, *Appl. Phys. Lett.*, **45**, 420 (1984).
16. N. Yabumoto, M. Oshima, and S. Maeyama, in "Proceedings of the 1982 Dry Process Symposium," Tokyo, III-2, p. 73.
17. J. I. Pankove, J. E. Berkeyheiser, S. J. Kilpatrick, and C. W. Magee, *J. Electron. Mater.*, **12**, 359 (1983).
18. M. Matsumoto, "Proceedings of the Technical Meeting of the Institute of Electrical Engineers of Japan," **emf-84-17**, 59 (1984).

Electrodeposition of Cadmium Telluride Using Phosphine Telluride

Andrzej Darkowski¹ and Michael Cocivera*

Guelph-Waterloo Centre for Graduate Work in Chemistry, University of Guelph, Guelph, Ontario, Canada N1G 2W1

ABSTRACT

Cadmium telluride is electrodeposited on a titanium cathode in a new process that employs tri-*n*-butylphosphine telluride and cadmium ion dissolved in propylene carbonate at about 100°C. Smooth gray films have been obtained with thicknesses up to 5.4 μm. The Te/Cd atomic ratio depends on applied potential and solution composition with values ranging between 0.63 and 1.1. X-ray data indicate that the as-deposited film is amorphous but becomes polycrystalline (cubic) upon annealing at 400°C. The as-deposited film can be deposited as either p or n type, and heat-treatment converts p to n. In photoelectrochemical cells, photocurrents up to 4.2 mA/cm² have been obtained for p-type at -1200 mV vs. Ag/AgCl.

Cadmium telluride is a semiconductor that has been considered as a candidate for solar energy conversion because it has a suitable bandgap. Studies using single-crystal CdTe indicate that solar conversion efficiencies near 10% are possible (1). Preparation of thin film semiconductors by electrodeposition could provide a substantial cost reduction in the manufacture of solar cells if they can replace the single-crystal material. A number of workers have studied the electrodeposition of thin film CdTe using tellurium dioxide as the tellurium source (2). It has been found that the film can be obtained from this process as either n- or p-type, depending on the potential applied (2a). In a more recent paper, tellurocyanide has been explored as a source of tellurium for electrodeposition of the film (3). Possible advantages are that this tellurium source, being in a lower valency, is less likely than tellurium dioxide to oxidize the telluride ion that is produced electrochemically because the free energy difference between oxidized and reduced species is diminished. Also, this source is more soluble than tellurium dioxide (3).

We have been exploring the use of other tellurium compounds as possible tellurium sources for the electrodeposition of thin film CdTe. In particular, we wanted the tellurium in a low valency, and we wanted the compound to be soluble in organic solvents. For these reasons, we have chosen trialkyl- or triarylphosphine tellurides. In this paper, we report the cathodic electrodeposition of thin film CdTe using tri(*n*-butyl)phosphine telluride in propylene carbonate. We have studied the deposition under various conditions of temperature, potential, and solution composition. At a given temperature, the Cd-to-Te ratio in the film depends on the applied potential. Data from x-ray diffraction indicate that the as-deposited film is amorphous. However, it becomes polycrystalline (cubic) when annealed at 400°C in Ar. High temperature annealing also converts p- to n-type.

Experimental

Materials.—Tri(*n*-butyl)phosphine telluride was prepared according to the procedure described earlier (4). Propylene carbonate was distilled from calcium oxide under vacuum. Lithium perchlorate, cadmium perchlorate, and trifluoromethane sulfonic acid were obtained from commercial suppliers. Sodium trifluoromethane sulfonate and cadmium trifluoromethane sulfonate were prepared from the acid and the corresponding base. The salts were vacuum dried at 100°C prior to use.

Substrate.—Titanium substrates were abraded with no. 400 emery paper, sonicated in warm Decon, and rinsed in distilled water. Prior to electrodeposition, the substrate was etched in 5% hydrofluoric acid and sonicated in distilled water.

Electrodeposition.—A cell in which the anode and cathode compartments were separated by a glass frit was employed to avoid contaminants from the anodic process. A Pt anode was used. The solution was kept under a nitro-

gen atmosphere during electrodeposition. Various temperatures ranging from 50° to 120°C were used. Depositions were performed galvanostatically and potentiostatically using a PAR 173 potentiostat/galvanostat. A silver/silver chloride reference electrode was employed for the constant potential deposition. The solutions contained 2-10 mM cadmium perchlorate or trifluoromethane sulfonate, 120 mM lithium perchlorate or sodium trifluoromethane sulfonate, and 7-26 mM phosphine telluride. Current density ranged from 0.1 to 0.5 mA/cm² for constant current deposition, and potential ranged from -650 to -1600 mV(Ag/AgCl) for constant potential deposition.

Chopped light.—In most cases, the majority carrier was determined in a photoelectrochemical cell (PEC) consisting of the photoelectrode, an Ag/AgCl reference electrode, and a Pt counterelectrode immersed in the deposition solution. Dark and light induced current as a function of applied potential was measured using chopped illumination from an ELH lamp. Current and potential were measured using the PAR 173 potentiostat/galvanostat. In some cases, the majority carrier of the film was determined using a PEC that consisted of the thin film photoelectrode and a cuprous sulfide-on-brass counterelectrode (5) immersed in a sulfide/polysulfide solution (3.0M sodium sulfide, 1.3M sulfur, and 0.8M NaOH in water).

X-ray diffraction.—Data were obtained using a Rigaku x-ray diffraction system (a Geigerflex D/Max Model 1A) operating with copper radiation. Data were collected for 2θ from 20° to 80° with a counting rate of 1000 counts.

Composition of films.—Polarographic analysis was used to determine the absolute amounts of cadmium and tellurium in the film. For this purpose, the film was dissolved in concentrated nitric acid at 25°C. We could find no polarographic evidence that the titanium substrate was dissolved using this procedure (6). We investigated two approaches for the polarographic analysis. The first, which we subsequently discarded, involved separation of cadmium and tellurium by base precipitation of cadmium hydroxide followed by separate analysis of the two elements in acid solutions. We found the separation cumbersome, and we found that analysis of Te(IV) in 0.01M nitric acid (7) was not sufficiently accurate because the Te(IV) wave at -1.25V was distorted due to hydrogen evolution.

A more convenient method, which allowed analysis for both Cd(II) and Te(IV) in the same solution, involved the use of an ammonia solution at pH 10 (6). After dissolution in nitric acid, the solution was diluted with 1M sulfuric acid and the excess HNO₃ was evaporated. The concentrated solution was diluted with deionized water and ammonia was used to adjust the pH and prevent the precipitation of cadmium hydroxide. Under these conditions, the Cd(II) and Te(IV) waves are well separated, -0.61 and -0.80V vs. Ag/AgCl, respectively (Fig. 1). At concentrations between 5 × 10⁻⁴ and 5 × 10⁻³M, the Te(IV) wave represents a four-electron reduction, and the tellurium concentration can be determined without using either the

*Electrochemical Society Active Member.

¹On leave from Department of Chemistry, Warsaw Technical University, Warsaw, Poland.

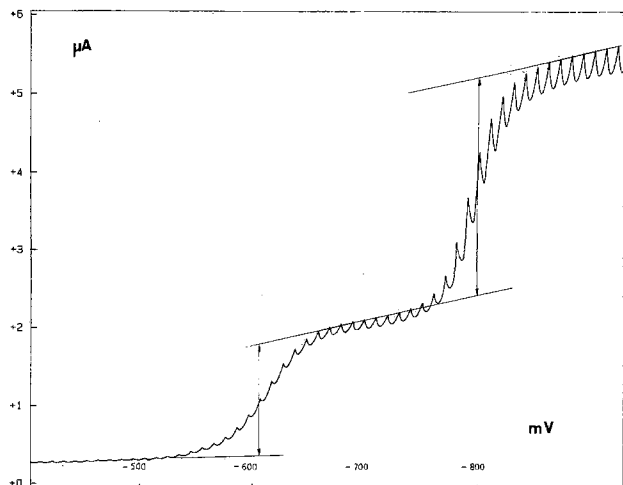


Fig. 1. Polarographic waves due to Cd(II) and Te(IV) with $E_{1/2}$ at -610 and -800 mV vs. Ag/AgCl, respectively. The solution contained 1×10^{-4} M Cd(II), 1×10^{-4} M Te(IV), and 0.1M ammonium sulfate. Obtained for a drop time of 2s.

standard addition technique or standard curves. Accordingly Te(IV) appears to be reduced to elemental tellurium.

Results and Discussion

Cyclic voltammetry for a solution containing Cd(II) alone, phosphine telluride alone, and Cd(II) plus phosphine telluride is presented in Fig. 2 for a titanium working electrode. The Cd(II) wave occurs at a more negative potential than the one for phosphine telluride. In the mixture, the cathodic currents are larger, and the phosphine telluride wave is shifted slightly in the positive direction. It would appear that phosphine telluride interacts weakly with Cd(II).

The composition of the electrodeposited film was determined by polarography. To test the accuracy of the analysis, the procedure was applied to an authentic sample of 99.99% CdTe. This analysis gave a Te/Cd ratio of 1.00 ± 0.01 (Fig. 1) (6).

The cathodic deposition of thin film CdTe on titanium was carried out both potentiostatically and galvanostatically, and the composition and photoresponse were monitored. For potentiostatic deposition at temperatures between 50° and 100°C , films were deposited at potentials between -650 and -1600 mV vs. Ag/AgCl. Table I lists the Te/Cd atomic ratio as a function of applied potential and temperature for solutions containing 0.003M Cd(II) and

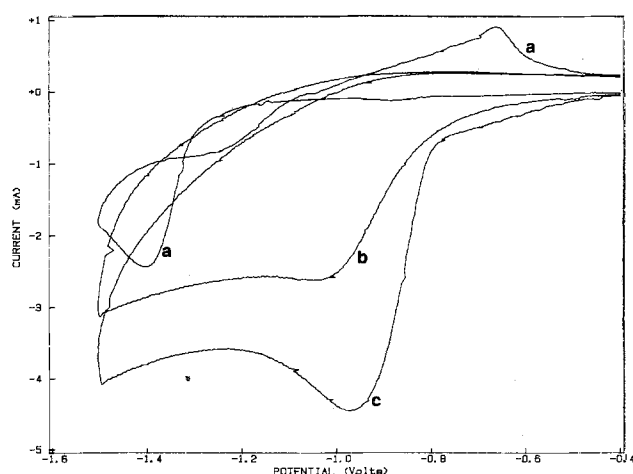


Fig. 2. Cyclic voltammetry in propylene carbonate under N_2 at 100°C and a scan rate of 100 mV/s for 0.003M Cd(II) and 0.10M LiClO_4 (a), 0.018M tri-n-butylphosphine telluride and 0.10M LiClO_4 (b), and 0.003M Cd(II), 0.018M tri-n-butylphosphine telluride, and 0.10M LiClO_4 (c).

Table I. Effect of applied potential on composition and photoresponse of CdTe films

Potential ^a (mV)	Composition ^b (Te/Cd)	Conduc- tivity ^c	Deposition temperature ($^\circ\text{C}$)	Photo- current ^d (mA/cm ²)
-650	0.68	p	95	
-700	0.63	p	95	
-800	0.70 ± 0.05	p	95	0.13
-1000	0.80 ± 0.07	p	100, 95	0.40
-1100	0.8 ± 0.1	p	100, 95	0.63
-1200	0.95 ± 0.05	p	100, 95	—
-1300	1.05 ± 0.05	p	100, 95	—
-1400	1.08 ± 0.08	p	100, 95, 50	0.80 ^e
-1500	1.1	p	100, 95, 50	
-1600	0.9	p	100	
		n	95	

^a vs. Ag/AgCl.

^b By polarography.

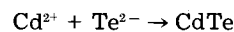
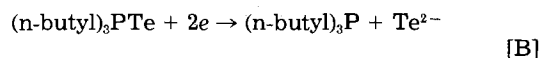
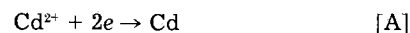
^c Determined by chopped light using the deposition solution in PEC.

^d Determined at -800 mV vs. Ag/AgCl.

^e Determined at 95°C .

^f Constant current deposition at 0.50 mA.

0.012 and 0.018M phosphine telluride. At temperatures between 95° and 100°C , the tellurium content increases as the potential is made more negative, and the Te/Cd ratio appears to level off at about 1.0. At a given potential, this ratio and the deposition current also appear to depend somewhat on the relative Cd(II) and phosphine telluride concentrations. A detailed study is underway. The fact that Te/Cd ratios less than 1.0 can be obtained at more positive potentials indicates that two competing processes may be occurring



The reduction step in process [B] may, in fact, involve a complex series of equilibria because cadmium ion causes a positive shift in the reduction wave assigned to the phosphine telluride (Fig. 2). In addition, excess phosphine also affects this reduction wave.

As the deposition at constant potential progresses, the current density decreases monotonically. For example, at -1100 mV (Ag/AgCl) and 100°C , the current density decreases from an initial value of 1.5 mA/cm² to 0.08 mA/cm² after 20 min for 0.003M Cd(II) and 0.018M phosphine telluride. The rate of current decrease is affected by the concentration of the cadmium ion relative to that of the phosphine. For example, with 0.026M phosphine telluride, the deposition current decreases with time, but the rate of decrease is smaller for 0.006M Cd(II) than 0.003M Cd(II). Thus, for 0.006M Cd(II), the current density decreases from an initial value of 0.75 mA/cm² to 0.50 mA/cm² after 9 min, whereas this decrease takes only about one minute for 0.003M Cd(II) at the same potential. This concentration effect may be an indication that the mechanism for the deposition of CdTe is more complicated than that suggested above. One possibility under investigation is that a cadmium-phosphine telluride complex is involved. Such complexes are known to exist in the case of phosphine selenides (8). The p-type conductivity of the as-deposited film as well as its resistivity may also be partly responsible for the decrease in current with time. At potentials negative of -600 mV, p-type films are deposited as discussed below.

Although the current decreases with time, it is possible to obtain fairly thick films in reasonably short times. Films as thick as 5.4 μm have been obtained in 1h using appropriate Cd(II) concentrations. Film thickness was calculated from the mass of the film (determined by polarography) using the surface area of the film and the reported density for CdTe (9).

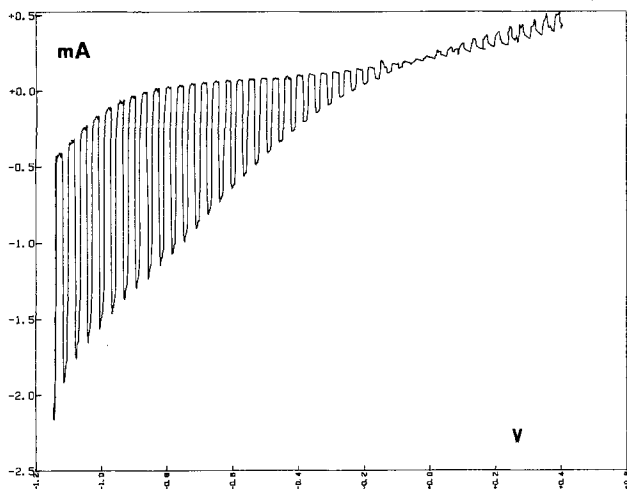


Fig. 3. Photoresponse at 100°C of electrodeposited CdTe film in PEC containing 0.003M Cd(II), 0.018M tri-*n*-butylphosphine telluride, and 0.10M LiClO₄ in propylene carbonate under nitrogen with no stirring.

Figure 3 illustrates the typical chopped light response of CdTe films deposited potentiostatically. This film was prepared by deposition at -1100 mV and 100°C in the dark. In this experiment, the deposition cell was used as the PEC cell. Thus, immediately after completion of the deposition, the film was subjected to chopped light in the same cell and solution, which contained 3.0 mM cadmium perchlorate, 17.5 mM phosphine telluride, and 100 mM lithium perchlorate. Because of the geometry of the cell, it was not possible to determine the light intensity accurately. However, based on the distance of the ELH lamp from the film, the power of the illumination is estimated to be less than 70 mW/cm². Since a cathodic photocurrent is observed, the film is p-type. To assure that the light-induced current is due to photogeneration of minority carriers rather than merely to an increase in photoconductivity, the potential scan was extended to 500 mV positive of the shutoff potential, and the photoanodic current was found to be negligible. Furthermore, in sulfide/poly-sulfide solution, the as-deposited film, which exhibited a photocathodic current, was found to exhibit a photoanodic current at potentials positive of -500 mV vs. Ag/AgCl after it had been annealed at 400°C. Consequently, the chopped light response appears to be a valid indicator of the type of conductivity.

The photocurrent is a factor of eight the value of the dark current since only one side is illuminated. This result is not unusual; enhancements ranging from six to 20 times the dark current have been observed for a large number of films grown under various conditions. The large increase in cathodic current upon illumination indicates that illumination can be used to avoid the large decrease in current that accompanies potentiostatic deposition in the dark (10). In Fig. 3, the potential is scanned from -1113 to +500 mV and the photocurrent is very close to zero at 0 mV (shutoff potential). Correcting for the liquid junction potential using ferrocene [E⁰, +0.34V vs. SCE (11)], the shutoff potential becomes -80 mV vs. SCE. For CdS, the shutoff potential has been found to correlate well with the Mott-Schottky flatband potential in both water and acetonitrile (12). For comparison, values of -30 (13a), +210 mV (13b), and +100 mV (13c) vs. SCE have been reported for p-type CdTe single crystals in water.

Chopped light studies of the film while it is grown have proved to be a great advantage. Thus, by means of these studies, we can monitor the effect of various deposition conditions on the quality of the film without having to remove it from the electrochemical cell. Consequently, time is saved since each film does not have to be incorporated into either a photovoltaic cell or another PEC. Likewise, since the films are not modified in any way for the photoresponse studies, their compositions may be deter-

mined, and the photoresponse may be correlated with the composition and thickness of the film. Finally, it is possible to check the effect of aging and exposure to air on the photoresponse of the film. In this regard, we find that exposure of the dried film to air causes a decrease in the photocurrent. Preliminary results indicate that this decrease is time dependent but stabilizes at about 50% of the original value after 24h. A detailed study is under way.

The observed photocurrents of up to 4.2 mA/cm² for films with surface areas of 1.2 cm² seem promising in view of the poor cell geometry employed. The cell consisted of two compartments separated by a frit, which no doubt caused a large cell resistance. Furthermore, the solution concentrations were quite low, as indicated above. Work is under way to devise a more efficient cell that contains a more suitable redox couple. It should be noted that these photocurrents are obtained at 100°C at applied potentials between -800 and -1300 mV vs. Ag/AgCl.

To date, the conditions providing the p-type film that has the best photocurrent density are 0.003M Cd(II), 0.012M phosphine telluride, 0.10M lithium perchlorate, and a potential of -1200 mV vs. Ag/AgCl. These conditions are being used to make films for photovoltaic cells (14). It is interesting to note that the photocurrent obtained from our as-deposited films is substantially larger than that reported recently for as-deposited thin film p-CdTe obtained by electrolysis of aqueous TeO₂ (2e, 2f). X-ray diffraction data (see below) indicate that both films may be amorphous. Consequently, the difference lies either in the nature of the two films or in the medium and temperature employed (for the TeO₂ grown film, the PEC cell contained aqueous sodium hydroxide at room temperature). These possibilities are under investigation.

A study of the relation between the composition of the film and its conductivity indicates that p-type CdTe is obtained even when the film contains an excess of cadmium. Thus films deposited at potentials in the range from -650 to -1200 mV vs. SCE exhibit p-type conductivity and have Te/Cd ratios of 0.95 or less (Table I). Since a CdTe film containing an excess of cadmium is expected to exhibit n-type behavior (15), we conclude that the excess cadmium is not distributed uniformly throughout the film. Instead, it may be present as small pockets of cadmium metal. Films deposited at -600 mV vs. SCE do not exhibit appreciable photocurrent in the deposition solution.

Preliminary work indicates that the deposition temperature may affect the nature of the conductivity of the film. It is also possible to convert the CdTe film from p- to n-type by annealing it at 400°C in an argon atmosphere for 30 min. In addition, heat-treatment at 400°C converted the film from an apparently amorphous material to a polycrystalline material. X-ray diffraction indicates that the average crystal diameter is about 50 nm in the heat-treated film. The diffraction angles correspond well to those reported for cubic CdTe (Table II). This film had a Cd/Te ratio of 1.0, and no peaks due Cd metal were detected.

In general, the visible appearance of the film depended on the deposition potential employed. Those with the

Table II. Comparison of x-ray diffraction data for thin film CdTe with literature values

2θ	Observed I/I ₀	Reported ^a	
		2θ	Hexagonal I/I ₀
23.7	1.00	23.75	1.00
—	—	—	25.27
39.3	0.46	39.28	0.60
—	—	—	39.25
46.4	0.27	46.42	0.30
—	—	—	45.42
—	—	—	0.75
—	—	—	—

^a ASTM x-ray powder diffraction file numbers 19-193, 4-0554, and 15-770.

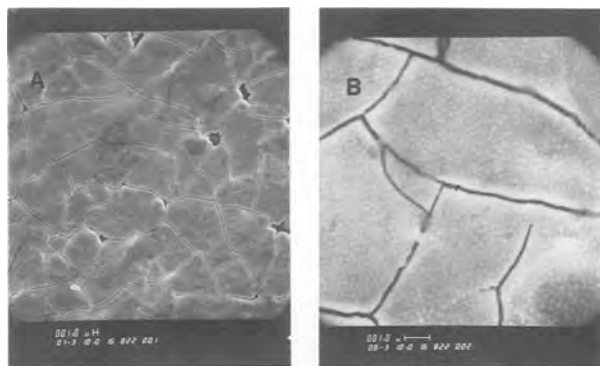


Fig. 4. SEM of thin film CdTe electrodeposited in the dark on titanium at 100°C. The film thickness and Te/Cd ratio are 2.4 μm and 1.0, respectively. Magnification: A:B = 1000:8000.

best appearance were grown at potentials ranging from -1000 to -1300 mV vs. Ag/AgCl. They appear smooth, uniform to the eye, and dark gray in color. At -1600 mV, the film is thin and is not uniformly gray. A SEM of a film grown at constant potential (-1100 mV) is presented in Fig. 4. Cracks are clearly visible. These appear to be a function of the thickness. For thinner films (ca. 0.5 μm), the cracks are fewer and thinner.

Acknowledgment

This work is funded in part by a grant to M. C. from the Natural Sciences and Engineering Research Council of Canada. We are indebted to Professor R. T. Oakley for making us aware of phosphide tellurides.

Manuscript submitted April 8, 1985; revised manuscript received July 10, 1985.

The University of Guelph assisted in meeting the publication costs of this article.

REFERENCES

1. K. Yamaguchi, N. Nakayama, H. Matsumoto, and S. Ikegami, *Jpn. J. Appl. Phys.*, **16**, 1203 (1977).
2. (a) M. P. R. Panicker, M. Knaster, and F. A. Kroger, *This Journal*, **125**, 566 (1978); (b) G. Fulop, M. Doty, P. Meyers, J. Betz, and C. H. Liu, *Appl. Phys. Lett.*, **40**, 327 (1982); (c) J. Llabres, *This Journal*, **131**, 464 (1984); (d) R. N. Bhattacharya, K. Rajeshwar, and R. N. Noufi, *ibid.*, **131**, 939 (1984); (e) K. Uosaki, M. Takahashi, and H. Kita, *Electrochim. Acta*, **29**, 279 (1984); (f) M. Takahashi, K. Uosaki, and H. Kita, *This Journal*, **131**, 2034 (1984).
3. M. Skylas-Kazacos, *J. Electroanal. Chem.*, **148**, 233 (1983).
4. R. A. Zingaro, B. H. Steeves, and K. Irgolic, *J. Organomet. Chem.*, **4**, 320 (1965).
5. G. Hodes, J. Manassen, D. Cahen, and M. David, *This Journal*, **127**, 2252 (1980).
6. A. Darkowski and M. Cocivera, *Talanta*, To be published.
7. D. C. Whitnack, T. Donovan, and M. H. Ritchie, *J. Electroanal. Chem.*, **14**, 205 (1967).
8. (a) P. A. Dean and M. K. Hughes, *Can. J. Chem.*, **58**, 180 (1980); (b) P. A. Dean and L. Polensek, *ibid.*, **58**, 1627 (1980).
9. "CRC Handbook of Chemistry and Physics," 46th ed., R. C. Weast, Editor, p. B161, Chemical Rubber Co., Cleveland, OH (1965).
10. A. Darkowski, J. von Windheim, and M. Cocivera, *This Journal*, To be published.
11. M. E. Langmuir, P. Hoenig, and R. D. Rauh, *This Journal*, **128**, 2357 (1981).
12. J. H. Reeves and M. Cocivera, *ibid.*, **131**, 2042 (1984).
13. (a) J. F. McCann and J. Pezy, *ibid.*, **128**, 1735 (1981); (b) J. O'M. Bockris and K. Uosaki, *ibid.*, **124**, 348 (1977); (c) J. L. Sculfort, R. Triboulet, and P. Lemasson, *ibid.*, **131**, 209 (1984).
14. A. Darkowski and M. Cocivera, *This Journal*, To be published.
15. D. de Nobel, *Philips Res. Rep.*, **14**, 361 (1959).

Thermodynamic Properties of Potassium Polyphosphide KP_{15}

H. S. Marek, C. G. Michel, J. A. Baumann, and M. A. Kuck

Stauffer Chemical Company, Eastern Research Center, Elmsford, New York 10523

ABSTRACT

The equilibrium vapor pressure of phosphorus over crystalline KP_{15} has been measured in the temperature range of 305° – 530°C by means of a Bourdon gauge. The reaction of $6/19 \text{KP}_{15}(\text{s}) = 2/19 \text{K}_3\text{P}_7(\text{s}) + \text{P}_4(\text{g})$ is described by the equation

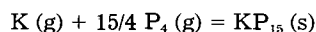
$$\ln p(\text{atm}) = -\frac{14,849 \pm 340}{T} + 19.35 \pm 0.5$$

The calculated standard enthalpy and entropy of this reaction are

$$\Delta H_{298}^{\circ} = 118.8 \pm 2.9 \text{ kJ/mol}$$

$$\Delta S_{298}^{\circ} = 159.0 \pm 4.2 \text{ J/mol-K}$$

The standard enthalpy for the formation of KP_{15} from the elemental gases



was found to be $\Delta H_{v,298}^{\circ} = -651.0 \pm 3.3 \text{ kJ/mol}$. Our data show that the thermal stability of KP_{15} is greater than that of crystalline red phosphorus. In addition, the kinetics of dissociation of KP_{15} were found to be significantly faster than the kinetics of vaporization of crystalline red phosphorus.

The useful semiconductor properties of polyphosphide materials have been recently reported (1). These materials were prepared in our laboratory by several processes. However, until now, very little has been known about their thermodynamic properties.

Metal polyphosphides having the formula MP_{15} (M = alkali metal) constitute a family of P-rich materials with structural units which are derivatives of Hittorf's phosphorus. These polyphosphides, first reported (2, 3) by von Schnering, have a unique atomic framework: a one-dimensional polymer-like structure consisting of parallel

phosphorus tubes of pentagonal cross section linked by M-P bridges.

The crystalline metal polyphosphides (MP_{15}) and Hittorf's phosphorus (4) both contain layers of P tubes. In Hittorf's phosphorus, two consecutive layers of P tubes are aligned crosswise. In the metal polyphosphides, the layers are aligned parallel to each other.

The vapor pressure of various modification of solid red phosphorus has been previously studied as a function of temperature (5). In this paper, we report the equilibrium vapor pressure of phosphorus over crystalline KP_{15} .

Standard enthalpies for the dissociation reaction and for the formation of KP_{15} from the elemental gases were calculated from our pressure-temperature data and compared with the thermodynamics of red phosphorus.

Experimental Technique

The tensimetric apparatus used in this work consists of a quartz Bourdon gauge of the spoon type used as a null-point instrument and controllers to monitor pressure-temperature as shown in Fig. 1. Gauges of various sensitivity were obtained by varying the size and thickness of the spoon. A 25 cm quartz rod pointer was attached to the top of the spoon. Deflection of the rod caused by the vapor pressure in the reaction chamber was detected by observing the displacement of the pointer image from a fixed reference using an optical system. The displacement caused by the vapor pressure on the sample side of the Bourdon gauge was countered by applying argon gas pressure. The argon pressure was measured with a mercury manometer, having an accuracy of 1 torr over a range from 3 to 800 torr. Eleven different Bourdon gauges of various size spoons were used.

Before each experiment, the empty gauge chamber was baked at approximately 550°C with continuous pumping at $\sim 10^{-5}$ torr for several hours. The apparatus was tested using 6N red phosphorus secured from United Mineral and Chemical Corporation. The vapor pressure data of Ref. (5) for material IV were reproduced within 3%.

The sample of KP_{15} (~ 0.1 - 0.5 g) was introduced into the reaction chamber at room temperature under nitrogen. The sample was degassed by pumping for several hours at 150°C and then sealed.

During the experiments, the temperature was varied in steps of $\sim 20^\circ\text{C}$ and maintained constant at sufficiently high temperatures to prevent any condensation of phosphorus.

Sample Preparation

The crystalline KP_{15} materials used in this study were prepared by three different methods. Raman and x-ray powder diffraction spectra shown in Fig. 2 were used as fingerprints to identify these materials. Raman characterization of KP_{15} crystals has been discussed in detail in Ref. (6). Slight differences were observed in the line broadening of the x-ray diffraction peaks, suggesting a variation in the degree of crystallinity of the KP_{15} materials according to the method of preparation. The DTA curve of the crystalline KP_{15} used in the study consists of a single sharp endotherm at 640°C. Repeated heatings of the same sample resulted in virtually identical DTA curves. Samples of commercially available red phosphorus exhibited a sharp endotherm in the 590°-600°C region.

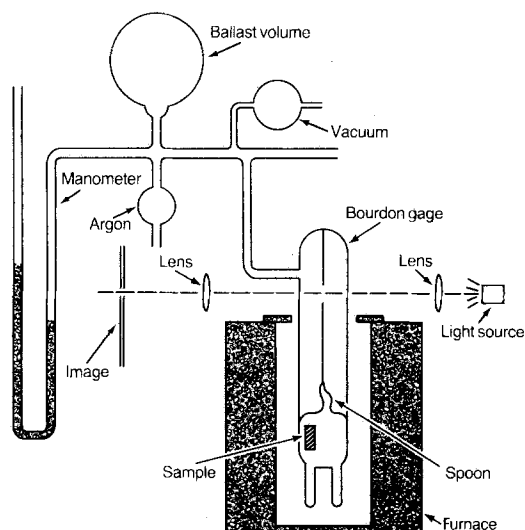


Fig. 1. Schematic of the tensimetric apparatus

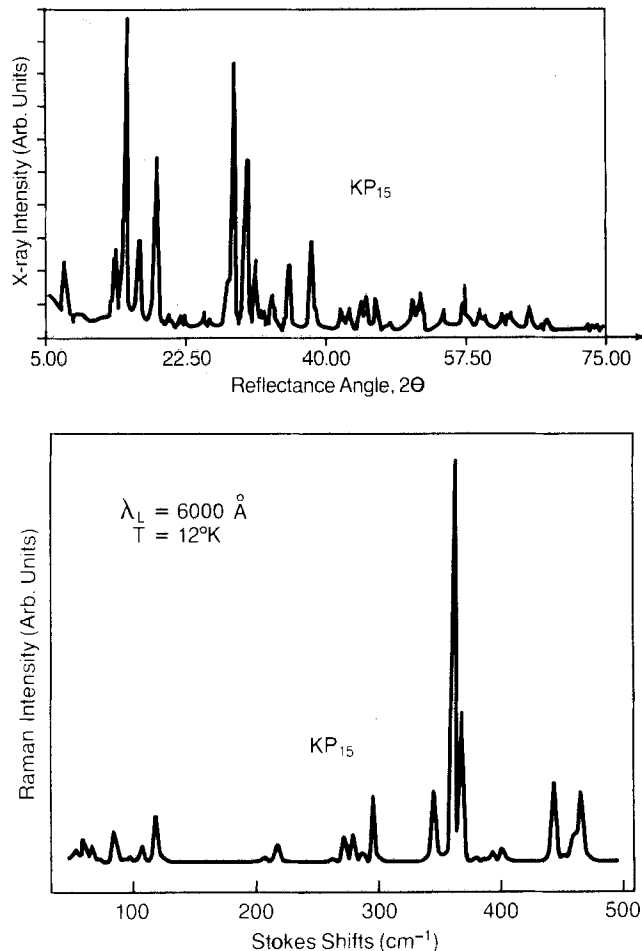


Fig. 2. a: X-ray powder diffraction pattern of KP_{15} whiskers obtained by VT process (Cu- $K\alpha$ radiation). b: First-order Raman spectrum of crystalline KP_{15} .

The different processes used for the synthesis of KP_{15} crystalline materials are described below.

Condensed phase (CP).—Polycrystalline KP_{15} materials were synthesized by the direct solid-state reaction of potassium and red phosphorus. The initial stoichiometric mixture consists of high purity potassium (4N) and electronic grade red phosphorus (6N) ball milled under a nitrogen atmosphere for 48h at 70°-80°C. The resulting mixture was transferred under nitrogen to a Pyrex reaction tube. The tube was heated at 450°C for 100h. Based on the absence of a peak at 590°-600°C in the DTA data, these materials did not contain red P. The DTA results indicated a solid-state conversion from the elements into KP_{15} . However, the broadening of the x-ray powder diffraction peaks was found to be significant for this KP_{15} material. These data suggest that polycrystalline KP_{15} prepared by the CP process have small crystallite size with a low degree of crystallinity.

Vapor transport (VT).—In this process, the KP_{15} samples were synthesized by vapor transport in a sealed quartz ampul by heating the metal and red phosphorus according to the method described by von Schnering *et al.* (2). Modifications were made in our system in order to optimize the yield and to improve the control in the deposition zone of the KP_{15} whiskers.

Large quantities of dark-red, long (> 1 cm) KP_{15} whiskers were obtained by monitoring the heating cycle of the K and P charge and by controlling the temperature ($\sim 450^\circ\text{C}$) in the reaction zone over a large area. The basic structural framework of this material defined by x-ray single-crystal study was found to be the same as that of the KP_{15} structure previously reported (2). However, we obtained the best least squares refinement of x-ray results by lowering the symmetry of the space group in the

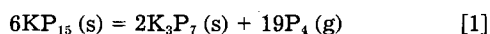
triclinic cell from $P\bar{1}$ to $P1$, corresponding to P tubes slightly shifted from their centrosymmetric positions.

Liquid phase (LP).— KP_{15} crystalline materials were prepared in quasi-equilibrium conditions from the liquid phase (LP) in a sealed tube system. In the LP process, large KP_{15} crystals were grown by slow cooling ($1^\circ\text{C}/\text{min}$) from 660° to 630°C in a specially designed LP apparatus. The volume-to-charge ratio was calculated to maintain the melt composition of $KP_{15,x}$ within the limit $x < 2$ during the growth cycle. The LP growth was terminated at $\sim 630^\circ\text{C}$ by using a tilting furnace.

Unlike CP and VT materials, these LP samples exhibited sharp x-ray diffraction peaks. This feature is characteristic of high quality crystals and suggests that, of the three processes, KP_{15} materials prepared from the liquid phase have the highest degree of crystallinity.

Results

Mass spectral analyses, performed on KP_{15} whiskers in a Knudsen cell, indicated that P_4 was the only significant vapor species present between 280° – 450°C . In this temperature interval, the ion current increased rapidly with a change to a higher isotherm and then slowly tapered off. The observed P_4 evolution suggests that the kinetics of the process is diffusion controlled. In the tensimetric experiment, the composition of the solid phase can be calculated, provided that the composition and the mass of the initial phase and the volume of the reaction chamber are known. The P:K ratio of the final solid product was 2.3:1. Chemical analysis confirmed this ratio. Powder diffraction x-ray analysis also indicated the absence of KP_{15} in the solid product and the presence of a new phase. From the calculated composition of the final solid product in the tensimetric experiment and considering the mass spectral results, the reaction equation can be formulated as follows



This equation is in agreement with the observations from Santandrea *et al.* obtained (7) with their Knudsen effusion technique.

Figure 3 gives the measured vapor pressure as a function of temperature for KP_{15} decomposition obtained from 33 independent data points. In spite of the fairly high temperatures, about 24h were usually required for equilibrium to be established at each temperature step. Approximately 95% of equilibrium was usually established within ~ 2 h. Data were taken only when the measured pressure did not change more than 2 mm in 10h. The time to obtain this equilibrium was faster by about one order of magnitude for KP_{15} than for red phosphorus.

All vapor pressure measurements were taken in the $KP_{15} + K_3P_7$ two-phase region as indicated by the constant pressure at any one isotherm throughout the experiment.

The tensimetric data were obtained during heating. When the system was cooled, the rate of the reverse reaction decreased rapidly and equilibrium was not established even after 100h.

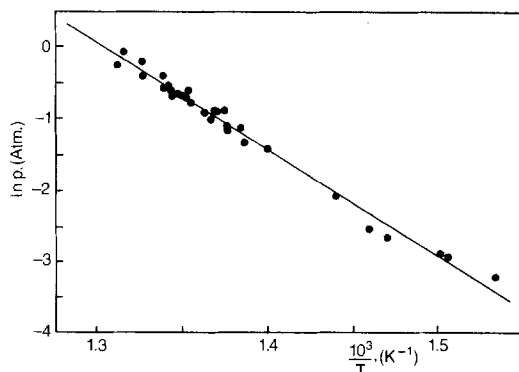
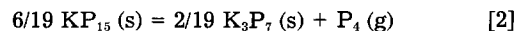


Fig. 3. Measured equilibrium vapor pressure of P_4 over crystalline KP_{15} as a function of temperature.

The pressure data obtained from the KP_{15} crystalline materials prepared from condensed phase, vapor transport, and liquid phase were found to be slightly different. A trend was observed which suggests an inverse correlation between vapor pressure and degree of crystallinity. Therefore, LP materials with the highest degree of crystallinity were used to establish the P - T dependence at low pressure in the plot shown in Fig. 3.

For the reaction



the following equation was obtained from a least squares fit of the experimental data

$$\ln p(\text{atm}) = -\frac{14,849 \pm 340}{T} + 19.35 \pm 0.5$$

Using elemental heat capacities from the literature (8), the standard enthalpy and entropy of the reaction [2] were calculated. They are

$$\Delta H_{298}^\circ = 118.8 \pm 2.9 \text{ kJ/mol}$$

$$\Delta S_{298}^\circ = 159.0 \pm 4.2 \text{ J/mol-K}$$

Since the reaction took place in the two-phase region, $KP_{15} + K_3P_7$, pressures of P_4 at any isotherm were constant. Thus, the enthalpy of formation of KP_{15} can be calculated by a method analogous to that used by Schiffman (9) for binary compounds.

In the present calculation, the activity of P_4 was obtained from the experimental measurements, the activity of K is estimated using the Gibbs-Duhem equation, and it is assumed that the range of homogeneity of KP_{15} is small. For the following reaction



the enthalpy of formation from the elemental gases, calculated by the third law method, is

$$\Delta H_{v,298}^\circ = -651.0 \pm 3.3 \text{ kJ/mol}$$

Discussion

Vaporization of both KP_{15} and crystalline red P yields P_4 vapor. The structural units of these two substances consist of the similar infinite P tubes with pentagonal cross section (2, 3). Thus, it can be expected that the decomposition and vaporization of these substances would have approximately the same enthalpy and entropy changes.

In the temperature range investigated (305° – 530°C), we have found for the reaction [2]

$$\Delta H_T = 123.4 \pm 2.1 \text{ kJ/mol}$$

and

$$\Delta S_T = 160.7 \pm 4.2 \text{ J/mol}$$

The values of thermodynamic functions are comparable with those reported (5) for the crystalline modification of red P in about the same temperature range

$$\Delta H_T = 133.5 \text{ kJ/mol}$$

$$\Delta S_T = 186.2 \text{ J/mol}$$

Recent studies also showed a similarity in the temperature dependence of the heat capacity between KP_{15} (10) and crystalline red P (11). These data demonstrate that the same basic structural units of covalently bonded P tubes dominate the thermodynamic properties of the metal polyphosphides and crystalline red P.

Figure 4 is a comparative plot of the temperature dependence of the vapor pressure for crystalline KP_{15} and the various crystalline modifications of red P (5) referred to as forms I, II, IV, and Hittorf's P. An increase in the degree of crystallinity from form I to form IV is inferred from the methods of preparation of these materials and their corresponding x-ray powder diffraction patterns.

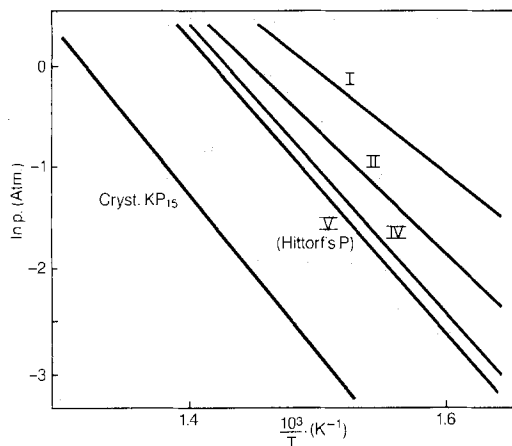


Fig. 4. Plot of the temperature dependence of the vapor pressure for crystalline KP_{15} and the various crystalline modifications of phosphorus I, II, IV, and V.

The Gibbs free energies for the various modifications of red P calculated for the average temperature of our experiment ($T = 683$ K) are¹

$$\Delta G_T(\text{I}) = -2385 \text{ J/mol}$$

$$\Delta G_T(\text{II}) = 397 \text{ J/mol}$$

$$\Delta G_T(\text{IV}) = 2582 \text{ J/mol}$$

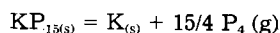
$$\Delta G_T(\text{V})^1 = 3335 \text{ J/mol}$$

$$\Delta G_T(KP_{15}) = 13,690 \text{ J/mol}$$

These data indicate that increases in the degree of crystallinity of the various modifications of red P are directly correlated with lower vapor pressure at any given temperature and, accordingly, an increase in thermal stability as shown in Fig. 4.

The calculated values of the Gibbs free energies indicate that the presence of a K-P bridge within the one-dimensional structure of KP_{15} increases its thermal stability as compared with crystalline P. In addition, analysis of our tensimetric data shows that the kinetics of dissociation of KP_{15} is much faster than the kinetics of vaporization of red P. Hence, at low pressure, KP_{15} appears to be a more suitable source of P_4 than red P (5), especially in processes where the control of P_4 (g) evolution is required.

Enthalpy of formation is calculated from data for the elemental gases instead of from the solid elements. This is because subtracting the elemental gas-solid enthalpy results in the difference between two large numbers which is smaller than the standard deviation of the components and is greatly dependent upon the source used for the elemental enthalpies. However, if the data of Hultgren *et al.* (8) are used for the enthalpy of potassium, the reaction



$$\Delta H_{298}^\circ = 35.10 \text{ kJ/mol}$$

can be compared with the enthalpy of vaporization of red phosphorus (8) of $\Delta H_{298}^\circ = 32.13 \text{ kJ/mol}$.

¹ ΔG_T (V) stands for Hittorf's P.

Enthalpy of formation for KP_{15} from the elemental gases was also calculated by the second law method, with the 33 data points giving

$$\Delta H_{v,298}^\circ = -657.7 \pm 21.3 \text{ kJ/mol}$$

Within the standard deviation, this agrees with the value from our third law calculation of $-651.0 \pm 3.3 \text{ kJ/mol}$. The larger deviation in the second law result is to be expected within the restricted temperature range of this investigation. The third law value is preferred since it is less sensitive to temperature errors.

Summary

We have studied the thermodynamic properties of KP_{15} prepared by different processes. The equilibrium vapor pressure of phosphorus P_4 (g) over KP_{15} solid was measured in the temperature range of $305^\circ\text{--}530^\circ\text{C}$ by using a Bourdon gauge tensimetric apparatus. The standard enthalpy and entropy for the dissociation reaction and for the formation of crystalline KP_{15} were calculated from the P-T data. We have shown that the thermodynamics of KP_{15} dissociation and of crystalline red P vaporization are comparable. The rate of dissociation of KP_{15} crystalline materials was found to be significantly faster than the rate of vaporization of crystalline red P. Our data show that the presence of a K-P bridge within the one-dimensional structure of parallel P pentagonal tubes is correlated with the greater thermal stability of the polyphosphide compounds compared to the crystalline modification of red phosphorus.

Acknowledgments

We would like to thank L. Polgar and P. Racciah for helpful discussions and comments on this paper and D. Olego for taking Raman spectra.

Manuscript submitted April 25, 1985; revised manuscript received July 19, 1985.

Stauffer Chemical Company assisted in meeting the publication costs of this article.

REFERENCES

- R. Schachter, C. G. Michel, M. A. Kuck, J. A. Baumann, D. J. Olego, L. G. Polgar, P. K. Racciah, and W. E. Spicer, *Appl. Phys. Lett.*, **45**, 277 (1984).
- H. G. von Schnering and H. Schmidt, *Angew. Chem.*, **79**, 323 (1967).
- H. G. von Schnering, "Homoatomic Rings, Chains and Macromolecules of Main-Group Elements," p. 317, Elsevier, New York (1977).
- H. Von Thurn and K. Krebs, *Act. Crystallogr. B*, **125**, 125 (1969).
- K. J. Bachmann and E. Buehler, *This Journal*, **121**, 835 (1974).
- D. J. Olego, *Phys. Rev. B*, **31**, 2240 (1985).
- R. P. Santandrea and H. G. von Schnering, in "8 ETPC Abstracts," p. 279, 27/9-1/10 (1982).
- R. Hultgren, P. P. Desai, D. T. Hawkins, M. Gleiser, K. K. Kelley, and A. D. Wagman, "Selected Values of the Thermodynamic Properties of the Elements," American Society for Metals, Metal Park, OH (1973).
- R. A. Schiffman, *J. Phys. Chem.*, **86**, 3855 (1982).
- R. Santandrea, E. Gmelin, C. Santandrea, and H. G. von Schnering, *Thermochim. Acta*, **67**, 296 (1983).
- C. C. Stephenson, R. L. Potter, T. G. Maple, and J. C. Morrow, *J. Chem. Thermodyn.*, **1**, 59 (1969).

Lift-Off Patterning of Sputtered SiO₂ Films (LOPAS) and Its Application to Recessed Field Isolation

T. Yachi and T. Serikawa

Nippon Telegraph and Telephone Public Corporation, Musashino Electrical Communication Laboratory, 3-9-11 Midoricho, Musashino-shi, Tokyo 180, Japan

ABSTRACT

The lift-off patterning of sputtered SiO₂ films (LOPAS) and its application to a new recessed field isolation technique are described. The LOPAS is performed through the following steps: (i) SiO₂ film is sputter-deposited on the photoresist pattern; (ii) slight etching with buffered hydrofluoric acid to remove SiO₂ films on the photoresist sidewalls is done, and (iii) the photoresist is removed. Successful pattern formation using LOPAS strongly depends on the sidewall angle of the under pattern. Recessed field isolation is performed by using LOPAS and silicon substrate oblique ion milling. This recessed field isolation is free of bird's beaks and minimizes the narrow-channel effect.

The field isolation of devices on silicon substrate is of primary importance in fabricating LSI circuits. One well-known technique for defining the field oxide patterns is known as LOCOS (1), in which a nitride film is masked and etched to form the desired pattern, followed by a long high temperature oxidation. The LOCOS process, however, has several disadvantages, such as resulting in bird's beak formation and lateral diffusion of the channel stopper dope into active device areas owing to the oxidation. To overcome these problems, other isolation techniques requiring extra processes, such as two nitride masks (2) and an aluminum mask to etch a silicon groove and lift off plasma-deposited SiO₂ (3), have been reported. Few approaches have been reported to overcome the problems in the LOCOS process through a simple and straightforward process (4).

In a previous paper (5), the authors reported a new simple and straightforward field isolation technique utilizing lift-off patterning of sputtered SiO₂ films (LOPAS) (6). This paper reports the details of this LOPAS process and its application to a new recessed field isolation technique jointly utilizing silicon grooving by oblique ion milling. Combining silicon grooving by oblique ion milling and LOPAS result in isoplanar field oxide formation, which is self-aligned to the channel stop region at a low temperature. With this technique, recessed field isolation, which is suitable for high yield LSI circuits processing, is easily realized through a simple and straightforward fabrication process. Moreover, bird's beaks and lateral channel stopper dope diffusion are not observed.

Experimental

The silicon grooving was performed using a Kaufmann-type ion milling apparatus. Argon ions were accelerated with 600V acceleration voltage and 0.5 mA/cm² ion current density. The substrate holder inclination angle (ion beam incident angle) was changed in the range of 0°-60°. The substrate holder also rotated at 1 rpm during ion milling. Photoresist AZ-1350J 1.3 μm thick was used as an etching mask.

Field oxide film was deposited using an RF planar magnetron sputtering apparatus (7). The target was a SiO₂ sheet, 5 × 15 in. and 1/8 in. thick. The sputtering was carried out at 0.4 Pa in a 95% argon-5% hydrogen mixture. The barrel-type substrate holder of 500 mm diam and 530 mm height had a 10 rpm rotation rate during deposition. The minimum spacing between the substrate and the target was 50 mm. The sputtering power was fixed at 1.5 kW. The substrate temperature was kept below 150°C during sputtering.

The SiO₂ films on the photoresist sidewalls were selectively removed by slight etching in buffered hydrofluoric acid (6). Unwanted SiO₂ film was removed along with the photoresist patterns by dipping the substrates in photoresist strip.

MOS devices were fabricated with a new recessed-isolation technique utilizing silicon grooving by oblique

ion milling and LOPAS. The starting wafers were (100)-oriented p-type silicon with resistivity of 4 Ω-cm. A 50 nm thick gate oxide film was grown in an oxidation ambient with trichloroethylene as an HCl source. Phosphorus-doped polysilicon was chemically vapor deposited, and gate electrodes were defined by plasma etching. Phosphorus was implanted for source/drain formation. Subsequently, the intermediate insulator film was chemically vapor deposited. After annealing at 1000°C for 20 min, windows were formed on the polysilicon and source/drain region. Aluminum metallization was performed for the contact on the polysilicon and source/drain. Finally, annealing was carried out in forming gas at 450°C for 20 min.

In control devices using the LOCOS technique, the field oxide was formed by high temperature oxidation at 1000°C for 6h.

Scanning electron microscopy (SEM) was used to evaluate the various device cross sections. MOSFET threshold voltage was determined using the turn-on voltage in the transconductance-gate voltage curve.

LOPAS

Lift-off process.—SEM photographs at various steps of lift-off patterning of sputtered SiO₂ films (LOPAS) are shown in Fig. 1. As shown in Fig. 1A, the SiO₂ film is fully deposited on the photoresist sidewalls by the planar magnetron sputtering. With slight etching, however, the SiO₂ film on the photoresist sidewall is removed selectively because of the extremely high etching rate, and a narrow groove is formed on the photoresist sidewall (Fig. 1B) (6). The thickness of the SiO₂ on the flat surface, on the other hand, decreased by only about 50 nm. Soaking the sample in a solution to dissolve photoresist material was carried out removing the unwanted SiO₂ film along with the photoresist pattern. Figure 1C shows the final structure.

The successful formation of the SiO₂ pattern depends on the sputtering conditions. SEM photographs of the LOPAS process are given in Fig. 2, following SiO₂ film deposition on an Al-Si pattern. The Al-Si pattern exhibits cylindrical sidewalls, in which the sidewall angle changes from 0° to 90°. During the process, the SiO₂ film is first uniformly deposited on the cylindrical sidewalls of the Al-Si pattern, as shown in Fig. 2A. After slight etching and aluminum removal, the SiO₂ pattern is then formed with a slight projection boarding both sides (Fig. 2B). This formation indicates that the SiO₂ removal by slight etching strongly depends on the sidewall angle of the under pattern. Here, the critical angle for successful SiO₂ pattern formation is determined to be approximately 60°. Additionally, this angle is also strongly dependent on the sputtering conditions, especially the sputtering gas (argon/hydrogen composition) used (7).

In a planar magnetron sputtering deposition system, SiO₂ film properties depend on sputtering conditions, e.g., argon pressure and target-substrate arrangement (8, 9). The SiO₂ thickness and etching rate as a function of the

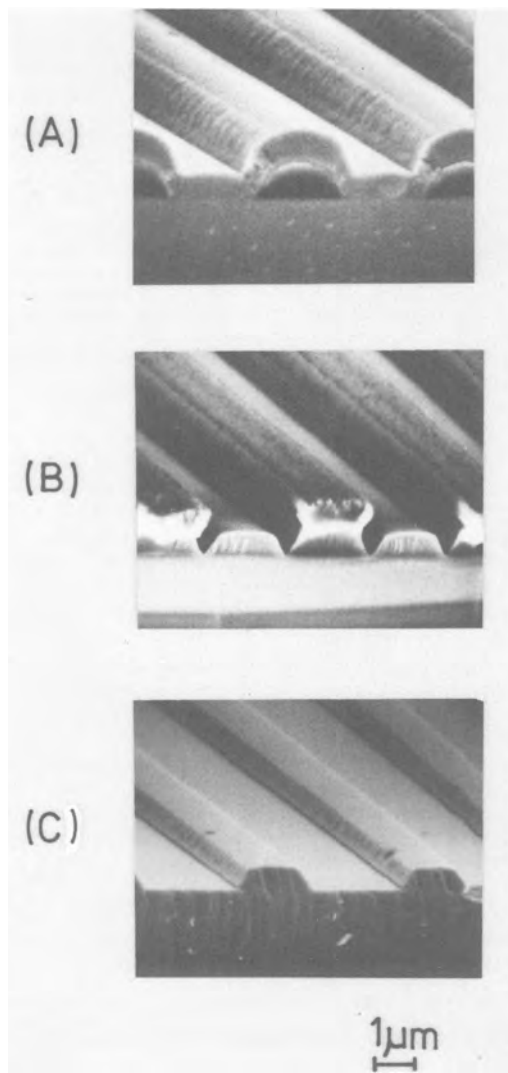


Fig. 1. SEM photographs at various steps of lift-off patterning of sputtered SiO_2 films (LOPAS). A: SiO_2 film deposited on a resist pattern. B: After slight etching. C: Final structure.

position on the substrate holder are shown in Fig. 3 for when the SiO_2 film was deposited at substrate holder stopping. The SiO_2 thickness changes depending on the

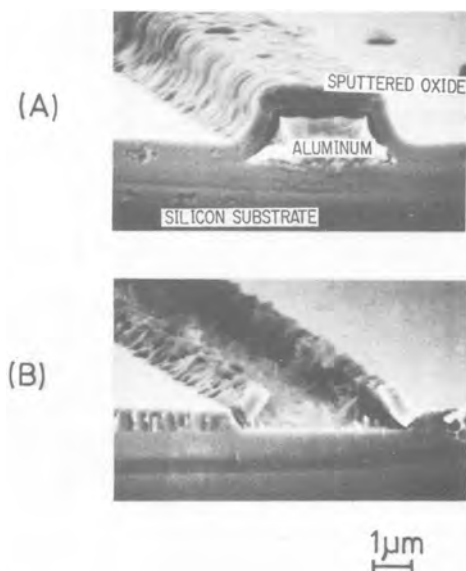


Fig. 2. SEM photographs of LOPAS process using aluminum alloy film. A: SiO_2 film deposited on an aluminum pattern with cylindrical sidewall. B: After lift-off patterning.

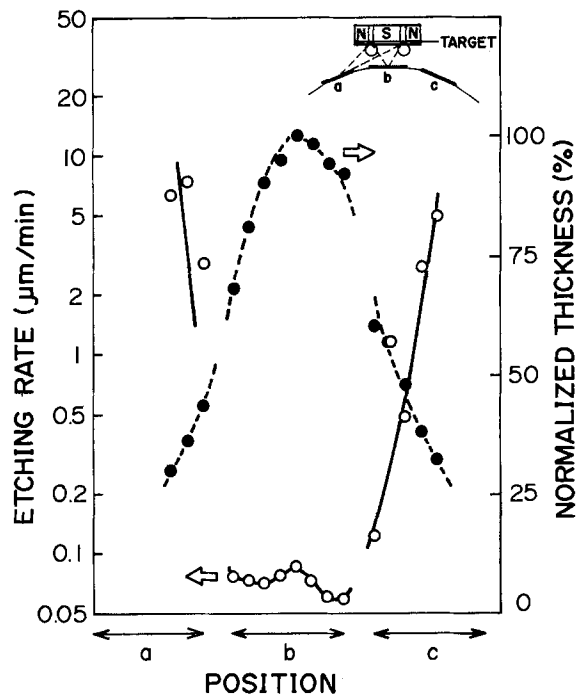


Fig. 3. SiO_2 film deposition rate and etching rate over substrates a, b, and c when the substrate holder was stopped during the deposition.

position. The SiO_2 etching rate also changes extremely depending on the position. For example, on the substrate b parallel to the target, which SiO_2 particles reach with a small incident angle, the SiO_2 etching rate is about $80 \text{ nm}/\text{min}$, comparable to that of the thermal oxide film. On each of the side substrates a and c, which SiO_2 particles reach with a large incident angle, on the other hand, the SiO_2 etching rate increases radically to about ten times higher than that for the film deposited on the substrate paralleled to the target. SiO_2 films deposited with a large incident angle were shown to contain microvoids by observing the surface replica with a transmission electron microscope. This microvoid formation is caused by self-shadowing, which is in turn due to large incident angle (10). Owing to etching along microvoids, the SiO_2 films deposited with a large incident angle have a markedly high etching rate.

Figure 4 demonstrates the incident direction of particles sputtered onto a step profile during substrate rotation in the experimental apparatus having a barrel-type substrate holder. In the calculation, it was assumed that the sputtered particles are emitted from the target, follow the cosine emission distribution, and reach the substrate nearly free of collisions with the argon atoms. This process is thought to be correct at low sputtering gas pressure (11). Although the SiO_2 particles reach the resist sidewall having a steep incident angle in spite of the rotational barrel-type substrate holder, they contain microvoids and are etched at an extremely high rate. This situation is quite similar to that for the side-angled substrates a and c shown in the inset in Fig. 3.

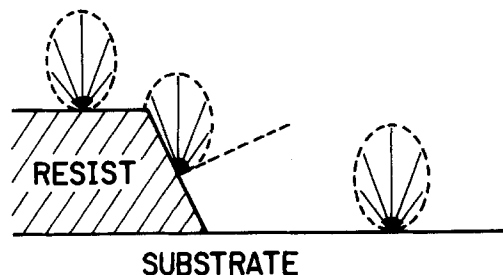


Fig. 4. Incident direction of sputtered particles on a step profile during substrate rotation in the experimental apparatus having a barrel-type substrate holder.

As described above, in planar magnetron sputtering the SiO_2 film on the under pattern sidewall, whose angle is greater than the critical angle, is easily removed by slight etching. This sidewall SiO_2 removing by slight etching successfully performs the lift-off patterning without pattern width reduction. The SiO_2 removing by slight etching is caused by the arrival of the sputtered particles with large incident angle on the under-pattern sidewall.

Recessed LOPAS.—The SiO_2 film on the under-pattern sidewall is removed by slight etching when the under-pattern sidewall angle is greater than the critical angle, as described in the preceding paragraph. Recessed patterning can be performed by SiO_2 sputtering on the silicon groove with two-step sidewall angle, one angle less than the critical angle and the other angle greater than the critical angle. The silicon groove with two-step sidewall angle is easily formed by oblique ion milling (12).

SEM photographs at steps of recessed lift-off patterning of sputtered SiO_2 films (recessed-LOPAS) are shown in Fig. 5. The substrate holder inclination angle is 40° during ion milling. The sidewall angles of the silicon groove are 30° and 80° , respectively (Fig. 5a). The SiO_2 films on the under-pattern with sidewall angle 80° are removed selectively because of the high etching rate. On the other hand, the SiO_2 films on the under-pattern with sidewall angle 30° are not removed, similar to what occurs with a flat surface, as shown in Fig. 5b.

The sidewall angle in the silicon groove depends on the substrate-holder inclination angle during ion milling (12). SEM photographs are shown in Fig. 6 for samples etched with ion beam incident angles of 0° (A), 20° (B), 40° (C), and 60° (D). The samples milled by ion beam incident angles of 40° and 60° have a clear two-step sidewall angle and are formed recessed SiO_2 patterns. With ion beam incident angles of 0° and 20° , the samples do not have a two-step sidewall angle, however, but have, rather, deep ditches in the pattern edge. The horn at pattern edge in a sample milled by incident angle 0° is caused by redeposition during ion milling.

Figure 7 shows the normalized depth of recession (s/d) as a function of the ion beam incident angle. The s/d markedly decreases as the ion beam incident angle increases. The s/d is about 30% for the samples milled by ion beam incident angles 40° and 60° . The two-step sidewall angle formation in silicon groove contributes to the s/d decreasing.

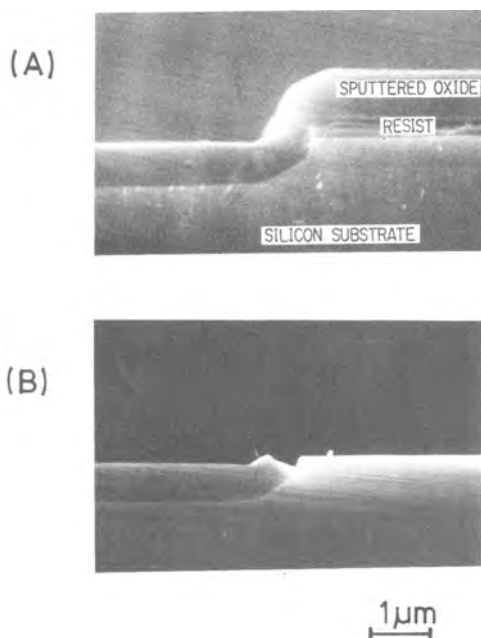


Fig. 5. SEM photographs of LOPAS process on the silicon groove with two-step sidewall angle forming by oblique ion milling. A: SiO_2 deposited on the groove. B: Final structure. The substrate-holder inclination angle is 40° during ion milling.

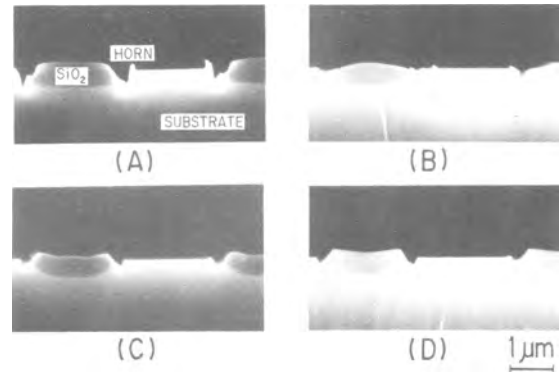


Fig. 6. SEM photographs of the samples that were etched with ion beam incident angles of 0° (A), 20° (B), 40° (C), and 60° (D).

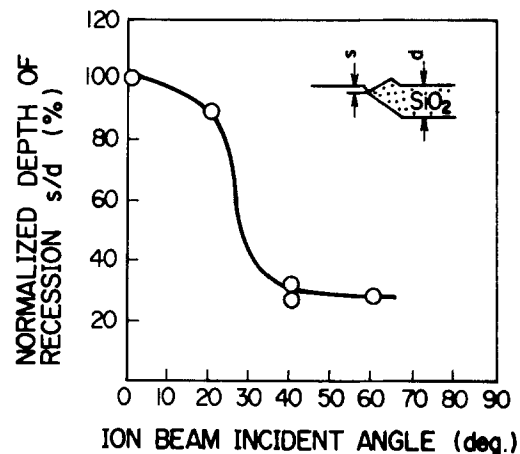


Fig. 7. Recession depth change by ion beam incident angle. Silicon groove depth is $0.6 \mu\text{m}$.

Figure 8 shows the normalized side etching x/d by ion milling as function of ion beam incident angle. The x/d decreases with increasing incident angle. In the case of incident angles 40° and 60° , the x/d is about 20%. This small side etching is caused mainly by etching rate angular dependency (12).

As described above, the recessed SiO_2 patterns are formed by the LOPAS technique and oblique ion milling. At ion incident angle 40° , pattern edge recession and side etching are small.

Application to MOS devices

The recessed-field isolation is performed using recessed LOPAS as described in the preceding paragraph.

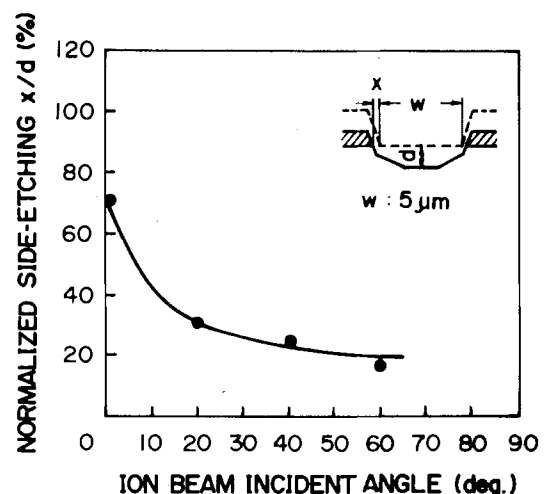


Fig. 8. Side etching change by ion beam incident angle. Silicon groove depth is about $0.6 \mu\text{m}$.

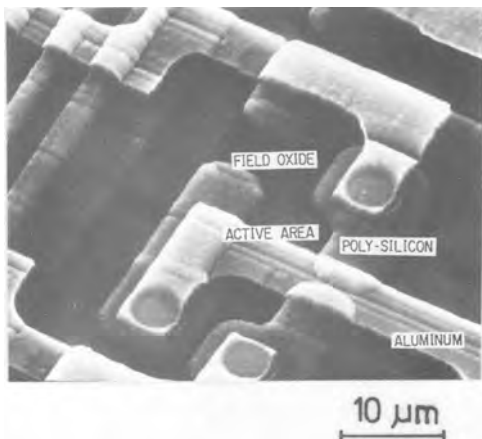


Fig. 9. SEM photograph of the MOS device fabricated using the recessed-field isolation technique.

The process sequence is as follows. (i) Photoresist patterns are formed on the silicon substrate with a thin thermal oxide to protect against contamination. (ii) Silicon grooves are formed by ion milling. (iii) Implantation for channel stopper dope is performed. (iv) SiO₂ films are deposited by planar magnetron sputtering at < 150°C. (v) The samples are dipped in buffered hydrofluoric acid to selectively etch the films on the under-pattern sidewalls at a steep angle. (vi) The photoresist is then removed with resist pattern. In this way, recessed-field isolation free of bird's beaks can form through the low temperature process.

An SEM photograph of MOS device using the recessed field isolation is shown in Fig. 9. The minimum feature size is 2.5 μm. The aluminum line step coverage is better on the recessed-field isolation pattern edge than on the polysilicon gate pattern edge.

Figure 10 shows threshold voltage for MOSFET's using the recessed-field isolation curve (A) and using the LOCOS isolation curve (B) as a function of channel width. In the LOCOS isolation, the threshold voltage shows a markedly narrow channel effect. On the other hand, in the recessed field isolation using LOPAS, the narrow channel effect is minimized by mainly eliminating lateral channel stopper dope diffusion through the low temperature process. The mobilities of the MOSFET's using the recessed-field isolation are similar to those of the control MOSFET's using the LOCOS isolation.

Summary

The lift-off patterning of sputtered SiO₂ films (LOPAS) and its application for a new recessed-field isolation technique have been described. The following results are demonstrated. (i) The successful pattern formation using LOPAS depends on the sidewall angle of the under-pattern. The critical angle is about 60° in sputtering with 95% argon-5% hydrogen mixed gas. (ii) Recessed patterning is easily performed by sputtering on the silicon groove with two-step sidewall angle forming by oblique ion milling. (iii) The recessed-field isolation using

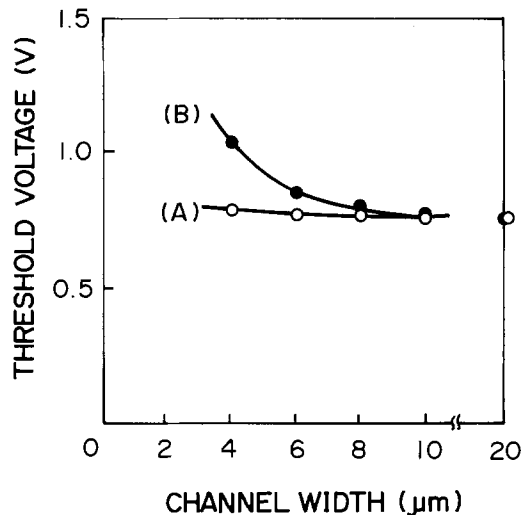


Fig. 10. Changes in threshold voltage with channel width. A: Using recessed field isolation. B: Using LOCOS.

LOPAS is free of bird's beaks and minimizes the narrow-channel effect as a result of the elimination of lateral channel stopper dope diffusion.

Acknowledgment

The authors would like to thank Akiteru Ishimoto, Deputy Director of Division, and Tutomu Wada, Staff Engineer, Electrical Equipment Division, Musashino ECL, NTT, for their helpful suggestions and encouragement. The authors would also like to thank Akio Okamoto, Engineer, Musashino ECL, NTT, and Noriyoshi Yamauchi, Staff Engineer, Ibaraki ECL, NTT, for assistance with MOS device fabrication.

Manuscript submitted March 11, 1985; revised manuscript received July 19, 1985.

Nippon Telegraph and Telephone Public Corporation assisted in meeting the publication costs of this article.

REFERENCES

1. E. Kooi, J. G. van Lierop, and J. A. Appels, *This Journal*, **123**, 1117 (1976).
2. K. Y. Chin, R. Fang, J. Lin, and J. L. Moll, in "Proceedings of the 1982 Symposium on VLSI Technology," (Oiso, Japan), p. 28 (1982).
3. K. Kurosawa, T. Shibata, and H. Iizuka, *IEDM Tech. Dig.*, 384 (1981).
4. J. Y. Chen, R. C. Henderson, J. T. Hall, and J. W. Peters, *This Journal*, **131**, 2146 (1984).
5. T. Yachi, T. Serikawa, and T. Wada, *IEEE Trans. Electron Devices*, **ed-31**, 1748 (1984).
6. T. Serikawa and T. Yachi, *This Journal*, **128**, 918 (1981).
7. T. Serikawa and T. Yachi, *ibid.*, **131**, 2105 (1984).
8. T. Yachi and T. Serikawa, *ibid.*, **131**, 2720 (1984).
9. K. Hara, Y. Suzuki, and Y. Taga, *Jpn. J. Appl. Phys.*, **18**, 2027 (1979).
10. N. G. Nakhodkin and A. I. Shaldervan, *Thin Solid Films*, **10**, 109 (1972).
11. R. E. Jones, Jr., *IBM J. Res. Dev.*, **16**, 27 (1972).
12. N. Yamauchi, T. Yachi, and T. Wada, *J. Vac. Sci. Technol. A*, **2**, 1552 (1984).

Kinetics and Mechanism of Selective Tungsten Deposition by LPCVD

Y. Pauleau* and Ph. Lami

Centre National d'Etudes des Télécommunications, 38243 Meylan, France

ABSTRACT

Tungsten films have been deposited selectively on oxide-patterned silicon wafers by the H_2 reduction of WF_6 in WF_6 - H_2 and WF_6 - H_2 -Ar gas flow systems. The deposition rate of films was investigated as a function of reactant partial pressures. The reaction orders with respect to WF_6 and H_2 are zero and one-half, respectively. Under given experimental conditions, the growth rate of the selectively deposited W films was reduced by 32% when the deposition area increased by a factor of 10-100. This decrease in growth rate can be attributed to the effect of HF on the surface reaction. The selective nature of the process deteriorates with increasing deposition rate, WF_6 partial pressure, H_2 partial pressure, or deposition time. The loss of selectivity seems to be linked to an increase in HF partial pressure in the reactor.

Since the 1960's, the potential advantages of vapor-deposited tungsten as a metallization and interconnection material for silicon devices have become well-known (1). Tungsten is a promising candidate for contact and diffusion barriers, low resistance gates, and interconnect lines in VLSI circuits. W films have been prepared by chemical vapor deposition (CVD) in several gas systems (2). The hexafluoride vapor, WF_6 , is currently used as a starting material. Under appropriate experimental conditions, W can be deposited selectively on oxide-patterned silicon wafers via the H_2 reduction of WF_6 , i.e., the metal can grow on monocrystalline and polycrystalline silicon surfaces while the surrounding oxide regions remain free of any deposit. Several etching and lithography steps are eliminated using the selective process to deposit tungsten on source, drain, and gate regions of MOS circuits. Owing to the advantages of selective deposition and the requirements for VLSI technology, the interest in vapor-deposited tungsten films has been revived (3, 4).

The growth rate of CVD tungsten metallurgical coatings by reduction of WF_6 with hydrogen has been investigated as a function of deposition temperature and reactant partial pressures (5, 6). Lately, the kinetics of W deposition has been examined at lower temperature-pressure combinations compatible with the selective process (7). The deposition rate dependence on the substrate temperature and the partial pressures of WF_6 and H_2 has been found consistent with the results obtained for deposition of tungsten metallurgical coatings. The selective nature of the W deposition process is dependent on various parameters such as deposition temperature, composition of WF_6 - H_2 gas mixtures, and total pressure (8). However, the relationships between selectivity and processing parameters remain essentially qualitative.

The purpose of our experiments was to investigate the kinetics of W deposition via the H_2 reduction of WF_6 and the effect of H_2 and WF_6 partial pressures on selectivity. The metal was deposited on oxide-patterned silicon wafers in two stages. In a first step was grown a self-limiting layer of W via the Si reduction of WF_6 under fixed and constant experimental conditions. Then the growth of metallic films is continued via the H_2 reduction of WF_6 carried out under variable experimental conditions. The deposition rate of metal produced by the H_2 reduction of WF_6 and the selectivity of the deposition process have been determined as a function of the deposition parameters. The growth mechanism of tungsten films will be discussed in the following sections.

Experimental Procedure

The deposition of tungsten films was carried out in a low pressure CVD system with a three-zone resistance-heated horizontal furnace. This experimental setup is quite similar to systems described in previous papers (7-9). The reaction chamber was evacuated with a Roots blower backed by an oil rotary pump. To maintain the to-

tal pressure in the reactor constant, the pumping capacity of the vacuum system could be adjusted by introducing an argon stream at the entrance of the Roots blower. So, total pressure and gas flow could be varied independently of one on another. The temperature setting of the reactor was calibrated with an internal thermocouple, at the same pressure and gas flow as those used during the experiments. The temperature difference across the length of the boat was less than $1^\circ C$. The purities of WF_6 , hydrogen, and argon gases were 99.8, 99.9995, and 99.9995%, respectively. The deposition process was controlled and monitored by a microprocessor.

20-40 Ω -cm p-type (100)-oriented single-crystal silicon wafers of 100 mm diam were used. These wafers were coated with a 40 nm thick thermal oxide layer. Then, a 800 nm thick undoped low temperature oxide (LTO) was deposited on top of the thermal oxide via LPCVD at $430^\circ C$. The test pattern for W selective deposition (Fig. 1) was delineated by standard photolithographic methods; the oxide layers were etched by dipping in a buffered HF solution. After photoresist stripping, a lot of 25 substrates was cleaned in a mixture of (2.5:1) H_2SO_4 : H_2O_2 for 15 min, rinsed in deionized water, and nitrogen spin dried before storage in dust-proof containers. In the reactor, a quartz boat containing 80 wafers is positioned so that the substrate surface is parallel to the gas stream. The wafers are placed in eight rows (A to H) comprising five slots spaced 12 mm apart; two wafers are placed back to back in each slot. Only three or four wafers per deposition run were used as samples; the others were thermally oxidized dummy wafers. Prior to loading in the quartz boat, the test wafers were chemically etched to remove the native oxide layer on the bare silicon regions. This chemical treatment consisted of etching in a (10:1) HF solution for 20s, rinsing in deionized water, and a nitrogen spin dry.

Some W films were prepared via the Si reduction of WF_6 . The substrate temperature was fixed at $285^\circ C$. The partial pressures of WF_6 and argon were 0.005 and 0.245 torr, respectively. The sheet resistance of films was determined as a function of the reaction time which varied between 2 and 12 min. This deposition process comprises several sequences. After loading the quartz boat into the furnace, which is at deposition temperature, the reactor is evacuated, purged with nitrogen at a pressure of 0.25 torr for 10 min, and again evacuated to a base pressure of 5×10^{-3} torr. The argon flow rate corresponding to the deposition conditions is established for 10 min to allow the substrate temperature to stabilize, and then WF_6 is introduced into the reactor for 2-12 min for W deposition on monocrystalline silicon.

The W deposition experiments via the H_2 reduction of WF_6 were carried out in two successive stages. The first stage consisted in the Si reduction of WF_6 performed under the experimental conditions described above. After this step, the reactor is purged with argon for 2 min, and the second stage of deposition via the H_2 reduction of WF_6 proceeds according to the following sequences. The ar-

*Electrochemical Society Active Member.

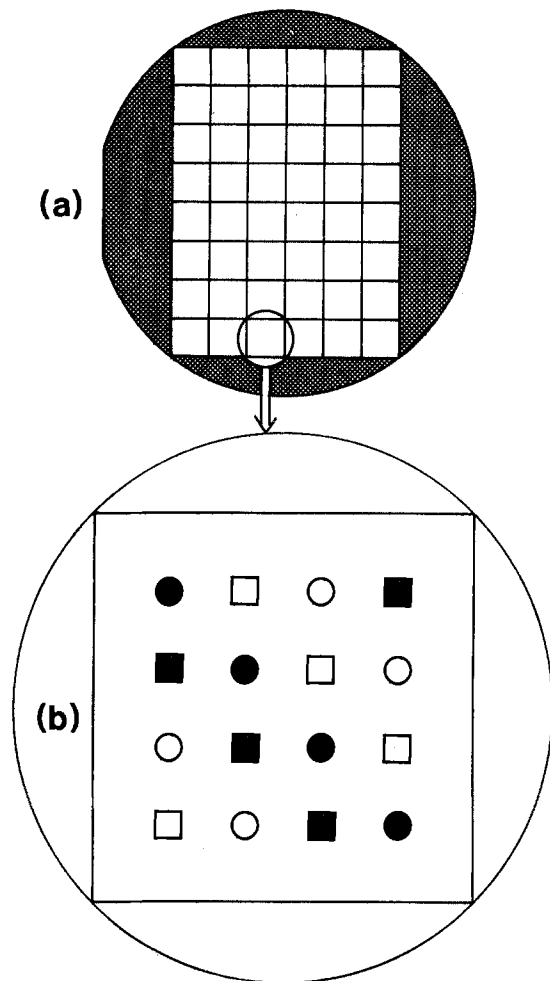


Fig. 1. a: Test pattern for selective deposition of tungsten on silicon wafers. Si (dark areas); SiO₂ (light areas). b: Magnification of 1 cm² of SiO₂ showing square windows of different sizes. Solid squares: 600 μm. Open squares: 400 μm. Solid circles: 200 μm. Open circles: 100 μm.

gon and hydrogen flow rates are established for 10 min, and then the deposition occurs when WF₆ is introduced into the reaction chamber. The deposition duration is fixed at 15 min. The gas flow rates and partial pressures of WF₆, hydrogen, and argon were varied as given in Table I. In all these experiments, the deposition temperature was maintained at 285°C since at this low temperature encroachment problems are suppressed (10) and excellent selectivity can be obtained (8).

The thickness of W films was measured using a stylus profilometer. Tungsten steps were etched in the large deposition zones near the wafer edges (Fig. 1). To delineate the steps, after coating with a protective wax layer, the samples were dipped in a KOH(0.24M)-KH₂PO₄(0.25M)-K₃Fe(CN)₆(0.1M) solution for 1 min (2) after which the wax was stripped in trichlorethylene. The W deposition rate was derived from thickness measurements. To evaluate the selectivity of the process, the test wafers were observed by dark field optical microscopy at a magnification of 500. When a failure of selectivity occurred, minute shiny dots of tungsten could be detected on the oxide regions. Selectivity is less good at the edges of the large sur-

Table I. Processing parameters for selective tungsten deposition at 285°C. (1 torr = 133 Pa)

	H ₂	WF ₆	Ar	Total
Flow rate (liter/min)	1-4	0.015-0.300	1-4	4-7
Pressure (mtorr)	180-1400	3-55	0-1200	250-1400

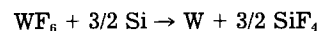
Table II. Symbols used to characterize the selective nature of the tungsten deposition process

△	Selective deposition
◻	Failure of Selectivity
▲	W dots on SiO ₂ up to 1 mm from the edge of the large deposition zones.
◻	W dots on SiO ₂ up to 10 mm from the edge of the large deposition zones.
▲	Non-selective deposition

faces of deposition than in the center of samples. To characterize the quality of selectivity, different symbols are used in Fig. 3-5; the meaning of these symbols is shown in Table II.

Results

Si reduction of WF₆.—The Si reduction of WF₆ proceeds according to the reaction (2, 9)



Tungsten films can form only on silicon regions, and this process is strictly selective. At 285°C and under the partial pressures of WF₆ and argon used, encroachment of W films along the SiO₂-Si interface does not occur. This result is consistent with that obtained by Moriya *et al.* (10). At the initial stage, the reaction of WF₆ with silicon is very fast. The sheet resistance of W films has been found to decrease very rapidly during the first 3 min; for reaction times longer than 3 min, the sheet resistance reaches a constant value (Fig. 2). The minimum resistivity is 30 μΩ-cm, which is in good agreement with values reported in the literature (2). The metallic layers reach a limit in thickness once silicon is completely covered with a continuous, compact W layer. 15 nm thick W films were deposited during this step. The thickness of silicon consumed was about 30 nm. These thickness values deduced from scanning electron microscopic observations of samples are consistent with the data previously published (7, 9, 10).

H₂ reduction of WF₆.—When a WF₆-H₂ gas mixture is introduced into the reactor to deposit W on silicon, Si and H₂ react simultaneously with WF₆ (7, 10) and it is impossi-

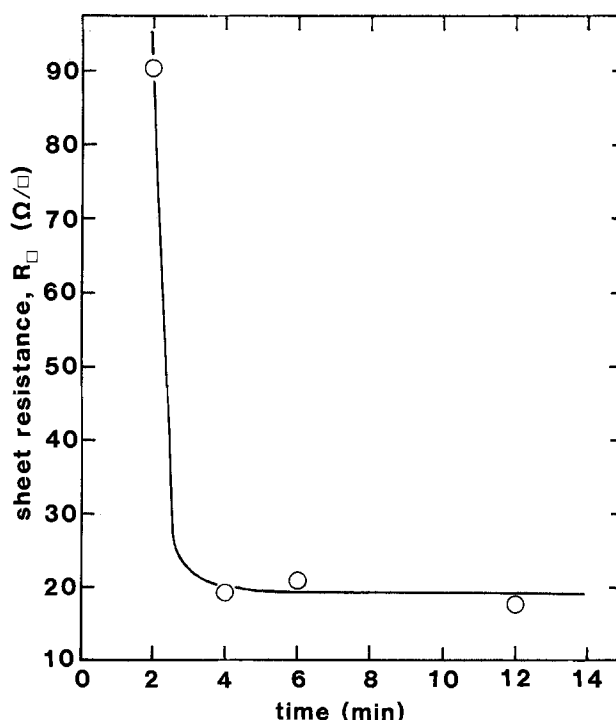
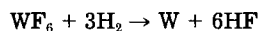


Fig. 2. Sheet resistance of W films vs. reaction time for films produced via the Si reduction of WF₆. Argon pressure = 0.245 torr; WF₆ pressure = 5 mtorr; deposition temperature = 285°C. (1 torr = 133 Pa.)

ble to determine accurately the thickness of W films grown via the H_2 reduction of WF_6 (2, 11)



To eliminate this uncertainty, a first deposition step consisting in the Si reduction of WF_6 was systematically carried out under the experimental conditions already described. W films prepared by the H_2 reduction of WF_6 were deposited on 15 nm thick tungsten layers formed during the first step. To determine the deposition rate, 15 nm of tungsten have been deducted from the total thickness of films obtained by α -step height measurements.

The growth rate of W films on wafers closest to the tube wall (positions 1 and 10 in rows A to H) was zero or very slight compared with the deposition rate on wafers placed within a row. Consequently, the results obtained on the outermost test wafers have been disregarded and only those found for wafers in an internal position (no. 2 to 9 in a row) are reported. The deposited material was determined to be polycrystalline W by x-ray diffraction techniques. In Fig. 3 is plotted the deposition rate of films produced from WF_6 - H_2 -Ar or WF_6 - H_2 gas systems vs. WF_6 partial pressure. The hydrogen partial pressure was varied between 0.18 and 0.81 torr, and the argon partial pressure was adjusted to maintain a constant total pressure of 1.4 torr. The growth rate of W films is essentially independent of the WF_6 partial pressure with or without argon in the gas phase.

The deposition rate of W films prepared from WF_6 - H_2 -Ar gas mixtures under a constant total pressure of 1.4 torr was examined as a function of the H_2 partial pressure. During these experiments, the WF_6 partial pressure could be varied in a wide range (5-50 mtorr) without showing any effect on the deposition rate. The dependence of the growth rate on the H_2 partial pressure is shown in Fig. 4. The deposition rate of W films is proportional to the square root of H_2 partial pressure. The curve (C1) has been plotted using the kinetic data resulting from experiments carried out when the quartz tube, quartz boat, and dummy wafers were clean. Under these experimental conditions, the total surface area of W deposition was about 60 cm², *i.e.*, the deposition area was limited to the silicon area left exposed on the test wafers. The rate constant deduced from the slope of the straight line (C1) is equal to 8.12 nm·min⁻¹·torr^{-1/2}. With the processing parameters used, the quartz ware remains free of any W deposit during 20-25 runs; the cumulated thickness of metal deposited on silicon regions of the test wafers is between 1.5 and 2 μ m. After about 25 runs, a W deposit could be detected on the quartz boat near the test wafer positions and on its downstream part. The quartz tube wall and some dummy wafers were also partially covered with a W deposit. The W layer formed progressively; nevertheless, it spread more and more rapidly during further runs.

Curve (Di) corresponds to kinetic data obtained for experiments performed with dirty quartz ware, *i.e.*, when a slight deposit of metal could be detected on the quartz

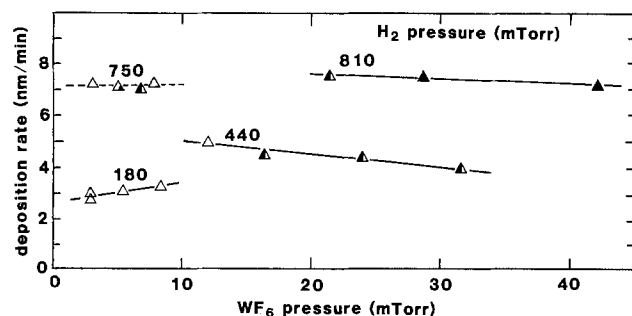


Fig. 3. Deposition rate vs. WF_6 partial pressure for W films deposited at 285°C from WF_6 - H_2 -Ar (solid line) or WF_6 - H_2 (dotted line) gas systems. In WF_6 - H_2 -Ar mixtures, the total pressure was 1.4 torr; the H_2 partial pressures were 180, 440, and 810 mtorr. (1 torr = 133 Pa.) The meanings of symbols used for data points are given in Table II.

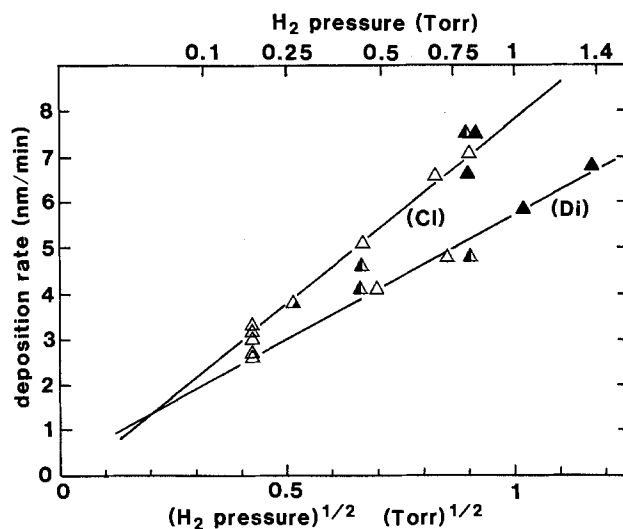


Fig. 4. Deposition rate vs. square root of H_2 partial pressure for W films deposited at 285°C from WF_6 - H_2 -Ar gas mixtures. Total pressure = 1.4 torr. (1 torr = 133 Pa.) Curve C1 results from experiments performed with a clean quartz ware; curve Di is obtained from experiments carried out with a W deposit on the quartz ware. The meanings of symbols used for data points are given in Table II.

boat in proximity to the test wafer positions. Under these conditions, the surface area of W deposition can be estimated at several hundred cm². The rate constant calculated from the slope of the straight line (Di) is 5.47 nm·min⁻¹·torr^{-1/2}. In other words, when a W deposit appears and can be detected on the quartz ware, the growth rate of metal on the test wafers is reduced by 32% whatever the number of selective deposition runs already performed. Nevertheless, the reaction order with respect to hydrogen remains equal to one-half.

The deposition rate of W films prepared from WF_6 - H_2 gas mixture has been determined as a function of H_2 partial pressure (Fig. 5). Curve (C1) shown in Fig. 5 represents the kinetic data obtained for deposition experiments carried out with WF_6 - H_2 -Ar mixtures (Fig. 4). The WF_6 partial pressure was relatively low (3-8 mtorr). Two kinetic regimes can be distinguished. First, under hydrogen partial pressures higher than 0.7 torr, the deposition rate of W films is quite similar to that obtained with argon in the gas phase. Thus, the growth rate displays no

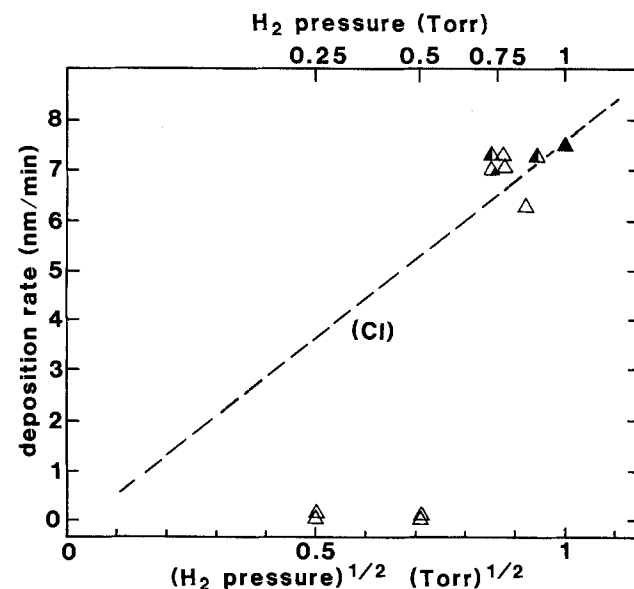


Fig. 5. Deposition rate vs. square root of H_2 partial pressure for films deposited at 285°C from WF_6 - H_2 mixtures. (1 torr = 133 Pa.) WF_6 partial pressure = (3-8) mtorr. Curve C1 (dashed line) reports the data given in Fig. 4. The meanings of symbols used for data points are given in Table II.

dependence on changes in the argon partial pressure. Second, when the hydrogen partial pressure is less than 0.6 torr, the thickness of W films is limited to 15 nm, *i.e.*, the metal can be deposited only via the Si reduction of WF_6 occurring during the first step and the growth rate of W films via the H_2 reduction of WF_6 is about zero.

Selectivity.—The Si reduction of WF_6 yields perfect selectivity since no reaction can take place on SiO_2 .

The symbols in Fig. 3-5 show the selective nature of deposition via the H_2 reduction of WF_6 as a function of WF_6 and H_2 partial pressures. Selectivity dependence on gas partial pressures is valid only for a deposition time of 15 min. For longer deposition times or thicker W films, selectivity would in all likelihood be lost owing to the development of W nuclei on the SiO_2 surface.

Selectivity deteriorates with increasing WF_6 partial pressure (Fig. 3). Under a hydrogen partial pressure of 0.44 torr, deposition remains selective at WF_6 partial pressures of less than 15 mtorr and W films will grow at a rate of only 15 nm/min. Selectivity is preserved at higher deposition rates: under an H_2 partial pressure of 0.75 torr with or without argon in the gas phase, 120 nm thick selective W films have been routinely deposited.

The correlation between selectivity and hydrogen partial pressure is shown in Fig. 4. Failure of selectivity occurs more frequently with increasing hydrogen partial pressure. For a given H_2 partial pressure (0.5 torr, for example), selectivity depends only on WF_6 partial pressure, *i.e.*, a failure of selectivity is observed under a WF_6 partial pressure higher than 15 mtorr. When a W deposit appears on the quartz boat, not only does the deposition rate fall off rapidly, but selectivity is more often lost. Consequently, after ten or 15 deposition runs, the quartz boat and reactor were cleaned in HF- HNO_3 solution to etch an eventual W deposit and oxidized dummy wafers were renewed.

Discussion

Reaction mechanism.—The kinetics of the chemical vapor deposition of W films via the H_2 reduction of WF_6 have been already extensively studied and Bryant (6) has analyzed experimental rate data. The reaction mechanism comprises five main sequences: (i) diffusion of reactants to the surface, (ii) adsorption of reactants on the surface, (iii) reaction in the adsorbed phase on the surface, (iv) desorption of gas products, and (v) diffusion of gas products from the surface.

At high substrate temperatures ($T > 700^\circ C$), relatively low reactant flow rates, and high total pressure, the mass transport process by diffusion in the gas phase is the rate-controlling step (12). Throughout the temperature and pressure ranges investigated for selective tungsten deposition, the kinetic data may be interpreted on the basis of the Langmuir-Hinshelwood model which is currently used in heterogeneous catalysis. In previous studies (5-7), the dissociative adsorption of hydrogen on tungsten was considered as the rate-limiting step. This assumption does not account for the large decrease in deposition rate observed when W deposits on the quartz ware. Nor can this decrease in deposition rate be explained by a depletion of reactant gases due to the large increase in deposition area. Indeed, hydrogen consumption is only 0.4 cm^3/min when 60 cm^2 of metal are deposited at a rate of 10 nm/min. In the reaction scheme proposed in the present work (see Appendix), HF has been considered to affect the surface reaction rate in the adsorbed phase. Details of the procedure used to establish the expression of growth rate of the W films are given in the Appendix.

The actual HF partial pressure, P_c , in the reactor is proportional to the growth rate of tungsten, *i.e.*, to the square root of hydrogen pressure, $(P_B)^{1/2}$, and to the surface area of W deposition; therefore

$$P_c = \beta(a_0 + a_1)(P_B)^{1/2} \quad [1]$$

where a_0 is the surface area for selective deposition and a_1 is the surface area of deposition when a W deposit is detected on the quartz ware, $a_1 \gg a_0$.

Using the value of HF partial pressure given by Eq. [1], the expression [A-15] for the growth rate becomes

$$G_R = [k_R\alpha(1 - \epsilon)N_s\epsilon K_B - k'_R N_s^2 \epsilon^2 K_C \beta(a_0 + a_1)](P_B)^{1/2} \quad [2]$$

Therefore, the reaction orders with respect to WF_6 and H_2 (zero and one-half, respectively) provided by Eq. [2] are in good agreement with the experimental values determined during this study as well as with the findings of other investigators (5-7). By plotting G_R vs. $(P_B)^{1/2}$, two curves can be obtained. When the quartz ware is clean, the surface area, a_1 , is zero and the slope of the straight line (C1) is given by

$$S_{(C1)} = k_R\alpha(1 - \epsilon)N_s\epsilon K_B - k'_R N_s^2 \epsilon^2 K_C \beta a_0 \quad [3]$$

After several runs, when the metal is deposited on the quartz tube, boat, and dummy wafers, the deposition rate decreases and the slope of the straight line (D1) is given by

$$S_{(D1)} = S_{(C1)} - k'_R N_s^2 \epsilon^2 K_C \beta a_1 \quad [4]$$

Thus, the experimental results as given in Fig. 3 and 4 can be described by Eq. [2].

The effect of HF partial pressure on the H_2 reduction of WF_6 has been studied in the past. Berkeley *et al.* (13) have shown that a concentration of HF equal to about 25% of the volume of reactants was sufficient to inhibit the deposition of tungsten from static reacting gases. On the contrary, according to Cheung (5), the addition of up to 40% HF to the WF_6 - H_2 gas flow system did not have more than a dilution effect on the deposition rate. This apparent discrepancy can be explained on the basis of the mechanism proposed (see Appendix) according to which a blocking effect of HF on the deposition process occurs in step [R]. Under relatively high WF_6 partial pressures, such as those used by Cheung, the value for ϵ^2 will be very small. Therefore, Eq. [A-15] can be simplified by neglecting the second term in the right member, which gives

$$G_R = k_R\alpha(1 - \epsilon)N_s\epsilon K_B(P_B)^{1/2} \quad [5]$$

And by neglecting ϵ with respect to unity, the expression becomes

$$G_R = k_R N_s \epsilon K_B \alpha (P_B)^{1/2} \quad [6]$$

Thus, it can be established that the growth rate of W films is independent of HF partial pressure but only under HF pressures higher by a factor of 100-1000 than those used in the present study.

Under hydrogen partial pressures of less than 0.6 torr, the growth rate of W films produced in WF_6 - H_2 gas systems has been found dependent on the orientation of the wafer surface with respect to the gas flow. With the wafer surface parallel to the gas flow, the growth rate is zero (Fig. 5). On the other hand, with the wafer surface perpendicular to the gas flow and under analogous reactant partial pressures, W films were deposited (7, 8). The deposition rate dependence on wafer surface orientation may be linked to the hydrodynamics of the gas system. This point remains the focus of continuing studies.

Selectivity.—The processing conditions leading to the loss of selectivity given in Fig. 3-5 are in good agreement with those put forward by Saraswat *et al.* (8). Losses in selectivity can be linked to an increase in HF partial pressure in the reactor. The selective nature of the W deposition process deteriorates when the growth rate (or HF pressure) is increased and also specially at the edges of the large deposition zones, *i.e.*, in the areas of highest HF pressure. As has already been reported by Cuomo (14), the glass substrate is etched around the W deposition zone by HF liberated from the reduction reaction. In this ablative zone, water vapor is formed on the SiO_2 surface and WF_6 can be hydrolyzed to form tungsten oxyfluoride, WOF_4 . A tungsten compound containing fluorine atoms has been detected by x-ray probe analysis around the ablative zone on the glass substrate (14). At low temperature

(285°C), the etching of SiO₂ due to HF formed by the H₂ reduction of WF₆ is very slight. Nevertheless, water vapor is probably formed on the SiO₂ surface and WF₆ may be locally converted into tungsten oxyfluoride. This compound serves as a nucleating site for W deposition. Hydrolysis is favored under relatively high WF₆ partial pressure and selectivity is reduced with increasing WF₆ pressure (Fig. 3). The nuclei grow slowly during the first minutes of the deposition process; their development thereafter accelerates, and, for longer periods, the selective nature of the deposition process becomes entirely lost.

The advantage of deposition with the wafer surface parallel to the gas flow is a shortening of the HF residence time on the SiO₂ surface. This ought to improve selectivity with respect to wafers placed perpendicular to the gas flow. This point, however, remains to be ascertained by comparative experiments. A parallel configuration implies a higher total pressure than if the wafers are perpendicular to the gas flow. This increase in total pressure has been achieved in the present study by adding argon to the gas system.

Selectivity of W deposition can be further improved by various other means: both deposition area and W growth rate must be as small as possible; a low deposition temperature minimizes the interaction between HF and SiO₂.

Conclusion

The kinetic data for selective tungsten deposition via the H₂ reduction of WF₆ can be interpreted on the basis of the Langmuir-Hinshelwood model. The surface reaction between fluorine and hydrogen atoms in the adsorbed phase is considered as the rate-controlling step. The deposition rate is dependent on the HF partial pressure and, consequently, on the surface area of W deposition. To minimize this surface area and obtain a good reproducibility on the deposition rate, the quartz tube, boat, and oxidized dummy wafers have to be free of any W deposit. The selectivity of the deposition process deteriorates with increasing WF₆ partial pressure and deposition rate. The loss of selectivity seems to be linked to an increase in HF partial pressure in the reactor. The selective nature of the process can certainly be preserved under processing conditions in which HF partial pressure in the reactor and the interaction between HF and SiO₂ are minimized.

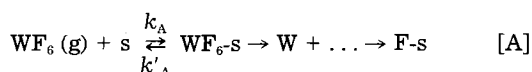
Manuscript submitted April 9, 1985; revised manuscript received July 12, 1985.

Centre National d'Etudes des Télécommunications assisted in meeting the publication costs of this article.

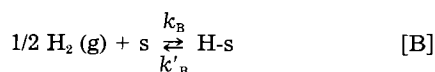
APPENDIX

The different steps of the reaction mechanism for the H₂ reduction of WF₆ can be schematically represented as follows.

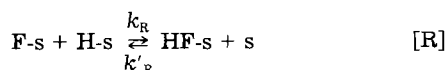
1. Adsorption of WF₆



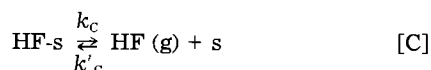
2. Dissociative adsorption of hydrogen



3. Surface reaction in the adsorbed phase



4. Desorption of HF



where k and k' are the rate constants of the direct and reverse reactions, respectively. K is the equilibrium constant with $K = k/k'$.

The Langmuir-Hinshelwood model is based on three main assumptions. First, the adsorption sites, s , on the surface of tungsten are equivalent and the adsorption of different gases (WF₆, H₂, and HF) is a competitive process. Second, the rate-limiting step is the surface reaction in the adsorbed phase; thus, the other surface processes are in equilibrium. Moreover, the surface reaction is assumed to be an opposing reaction, *i.e.*, the adsorbed species, F-s and H-s, can be formed by the adsorption of HF vapor on the tungsten surface. Nevertheless, the overall reduction reaction is not a reverse process. Third, the rate of the surface reaction, $[R]$, is proportional to the concentrations of adsorbed species.

In order to establish an expression describing the growth rate of W films from WF₆-H₂ systems, some additional assumptions have been considered. The adsorption of WF₆ on tungsten produces fluorine atoms, called F-s in reaction [A], which are strongly adsorbed on the surface, *i.e.*, the equilibrium constant, K_A , in process [A] is very high. Some support for this assumption is provided by experimental data on the interactions between tungsten and WF₆ molecules or fluorine atoms (15-17). However, neither the stages from adsorbed fluorine atoms to WF₅ or WF₆ gas molecules nor the steps in the reverse processes have been completely understood. Finally, hydrogen and HF are assumed to be weakly adsorbed on tungsten, *i.e.*, the equilibrium constants, K_B and K_C , are very low.

To simplify the formalism of the rate equations, the subscripts A, B, and C will be used to designate the gases WF₆, H₂, and HF, respectively.

Let N_s be the total number of surface sites per square centimeter and let Θ_s , Θ_A , Θ_B , and Θ_C be the fractions of the surface sites which are free and covered by A, B, and C, respectively. In other words, Θ_s , Θ_A , Θ_B , and Θ_C are the mole fractions of free sites and adsorbed species, WF₆-s, H-s, and HF-s, *i.e.*, $\Theta_s = 1 - \Theta_A - \Theta_B - \Theta_C$. The concentrations of the adsorbed species and free sites on the W surface are given by

$$[\text{WF}_6\text{-s}] = N_s \Theta_A \quad [\text{A-1}]$$

$$[\text{H-s}] = N_s \Theta_B \quad [\text{A-2}]$$

$$[\text{HF-s}] = N_s \Theta_C \quad [\text{A-3}]$$

$$[s] = N_s \Theta_s \quad [\text{A-4}]$$

Since the adsorption step [A] is in equilibrium, the fraction of the surface sites occupied by WF₆ molecules can be expressed as a function of gas pressures (P_A , P_B , and P_C) using the steady-state equation (18)

$$\Theta_A = \frac{K_A P_A}{1 + K_A P_A + K_B (P_B)^{1/2} + K_C P_C} \quad [\text{A-5}]$$

where K_A , K_B , and K_C are the equilibrium constants of the processes [A], [B], and [C], respectively.

Since H₂ and HF are weakly adsorbed and WF₆ strongly adsorbed on the W surface, the equilibrium constants K_B and K_C are very small and can be neglected with respect to K_A . Equation [A-5] can be simplified, and the term Θ_A is almost equal to unity. Setting

$$\epsilon = 1 - \Theta_A \quad [\text{A-6}]$$

the value of ϵ will be very small.

The concentration of adsorbed fluorine atoms is assumed to be proportional to Θ_A and can be expressed by the following equation

$$[\text{F-s}] = \alpha(1 - \epsilon) \quad [\text{A-7}]$$

Consequently, the concentration of fluorine atoms adsorbed on the W surface is independent of gas pressures. The terms Θ_B and Θ_C can be calculated in the same way as Θ_A (18). Since the sum $[K_B(P_B)^{1/2} + K_C P_C]$ is negligible with respect to unity, the simplified expressions of Θ_B , Θ_C , and Θ_s are the following

$$\Theta_B = \epsilon K_B (P_B)^{1/2} \quad [\text{A-8}]$$

$$\Theta_C = \epsilon K_C P_C \quad [\text{A-9}]$$

$$\Theta_s = \epsilon \quad [\text{A-10}]$$

Furthermore, the concentrations of the adsorbed species and free sites on the W surface become

$$[\text{H-s}] = N_s \epsilon K_B (P_B)^{1/2} \quad [\text{A-11}]$$

$$|\text{HF-s}| = N_s \epsilon K_c P_c \quad [\text{A-12}]$$

$$|s| = N_s \epsilon \quad [\text{A-13}]$$

The growth rate of W films, G_R , is equal to the rate of the surface reaction [R] which is considered to be the rate-limiting process. This surface reaction is an opposing reaction, and its rate is given by

$$G_R = k_R |F-s| |H-s| - k'_R |\text{HF-s}| |s| \quad [\text{A-14}]$$

Using Eq. [A-7] and Eq. [A-11]-[A-13], this rate equation takes the form

$$G_R = k_R \alpha (1 - \epsilon) N_s \epsilon K_B (P_B)^{1/2} - k'_R N_s^2 \epsilon^2 K_C P_C \quad [\text{A-15}]$$

REFERENCES

1. J. M. Shaw and J. A. Amick, *RCA Rev.*, **31**, 306 (1970).
2. Y. Pauleau, *Thin Solid Films*, **122**, 243 (1984).
3. N. E. Miller and I. Beinglass, *Solid State Technol.*, **23**, 79 (1980).
4. N. E. Miller and I. Beinglass, *ibid.*, **25**, 85 (1982).
5. H. Cheung, in "Proceedings of the Third International Conference on Chemical Vapor Deposition," F. A. Glaski, Editor, p. 136, The American Nuclear Society, Hinsdale, IL (1972).
6. W. A. Bryant, *This Journal*, **125**, 1534 (1978).

7. E. K. Broadbent and C. L. Ramiller, *ibid.*, **131**, 1427 (1984).
8. K. C. Saraswat, S. Swirhun, and J. P. McVittie, in "VLSI Science and Technology/1984," K. E. Bean and G. A. Rozgonyi, Editors, p. 409, The Electrochemical Society Softbound Proceeding Series, Pennington, NJ (1984).
9. K. Y. Tsao and H. H. Busta, *This Journal*, **131**, 2702 (1984).
10. T. Moriya, K. Yamada, Y. Tsunashima, S. Nakata, and M. Kashiwagi, Extended Abstracts of the 15th Conference on Solid State Devices and Materials, p. 225, Tokyo (1983).
11. Y. Pauleau, *Bull. Soc. Chim. France*, **4**, 583 (1985).
12. W. R. Holman and F. J. Huegel, *J. Vac. Sci. Technol.*, **11**, 701 (1974).
13. J. F. Berkeley, A. Brenner, and W. E. Reid, Jr., *This Journal*, **114**, 561 (1967).
14. J. J. Cuomo, in "Proceedings of The Third International Conference on Chemical Vapor Deposition," F. A. Glaski, Editor, p. 270, The American Nuclear Society, Hinsdale, IL (1972).
15. L. V. McCarty, W. E. Reith, and M. T. Simon, *This Journal*, **121**, 1372 (1974).
16. J. L. Philippart, J. Y. Caradec, B. Weber, and A. Cassuto, *ibid.*, **125**, 162 (1978).
17. M. Metlay and G. E. Kimball, *J. Chem. Phys.*, **16**, 779 (1948).
18. G. W. Castellan, "Physical Chemistry," 2nd ed., p. 795, Addison-Wesley, New York (1971).

A Diffusion Model for Electron-Hole Recombination in $\text{Zn}_2\text{SiO}_4:(\text{Mn},\text{As})$ Phosphors

D. J. Robbins,^{*} N. S. Caswell,^{*} Ph. Avouris,^{*} E. A. Giess,^{*} I. F. Chang,^{*} and D. B. Dove

IBM Thomas J. Watson Research Center, Yorktown Heights, New York 10598

ABSTRACT

Optical techniques have been used to study the extended persistence of luminescence in willemite phosphors coactivated with Mn and As. Absorption and photoluminescence excitation spectroscopy establish that the $\text{Mn}_{\text{Zn}}^{2+}$ impurity ground state lies 3.9 ± 0.1 eV below the conduction bandedge in willemite. Laser pulse excitation at energies > 3.9 eV has been used to generate $\text{Mn}_{\text{Zn}}^{2+}$ luminescence decay curves. At short times ($t < 100$ ms), the shape of these decay curves depends strongly on both temperature and As concentration in the samples (N_{As}). These pulse response curves have been analyzed using a bimolecular kinetic model. The behavior of the model parameters as a function of N_{As} is interpreted in terms of a diffusion-controlled recombination between trapped electrons and ionized Mn centers. When $N_{\text{As}} < 1 \times 10^{19} \text{ cm}^{-3}$, the recombination is dominated by thermal emission of electrons to the conduction band. When $N_{\text{As}} > 2 \times 10^{19} \text{ cm}^{-3}$, diffusion by intertrap tunneling is dominant.

Manganese-activated willemite ($\text{Zn}_2\text{SiO}_4:\text{Mn}$), when coactivated with As, forms the phosphor system designated P39 (1). The active luminescence is the ${}^4\text{T}_1 \rightarrow {}^6\text{A}_1$ intracenter d electron relaxation of the $\text{Mn}_{\text{Zn}}^{2+}$ impurity with lifetime $\tau_e \sim 10$ msec (2). The addition of As introduces a long nonexponential afterglow to the decay. This extended persistence of the P39 phosphor system makes it of considerable current interest as an antiflicker phosphor in displays where the refresh rate must be minimized, such as computer data display.

The $\text{Zn}_2\text{SiO}_4:(\text{Mn},\text{As})$ phosphor was originally reported by Frohlich and Fonda (3). They investigated a number of approaches to increasing the persistence of $\text{Mn}_{\text{Zn}}^{2+}$ luminescence in willemite, including quenching from high temperature, variation of stoichiometry, and incorporation of many coactivator impurities. Of these, the addition of As impurity to $\text{Zn}_2\text{SiO}_4:\text{Mn}$ was found to be most effective in extending persistence. Improved methods of synthesizing the coactivated phosphor have recently been reported (4). In addition, the effects of AlPO_4 substitution in the willemite lattice have been investigated (5), although it is not yet clear that significant improvements in brightness and persistence can be achieved in this way (6).

There has been considerable effort devoted to studying the physics of the phosphorescence process in $\text{Zn}_2\text{SiO}_4:(\text{Mn},\text{As})$. Most of these studies have involved measurement of thermal glow curves (7-14). More recently, photostimulated luminescence and conductivity measurements have been carried out (15-18). However, as yet, there is no general agreement about the recombination mechanism in this phosphor.

It is known empirically that for maximum enhancement of persistence in P39 phosphor the concentrations of Mn and As must be controlled within definite limits. State-of-the-art antiflicker performance is achieved when Mn is $\sim 0.1\%$, substituted for Zn, and the As concentration is somewhat lower. The Mn concentration is about ten times lower than that used in the $\text{Zn}_2\text{SiO}_4:\text{Mn}$ (P1) phosphor system which does not exhibit extended persistence, so that the overall efficiency of the P39 phosphor is reduced. However, there is no quantitative model which can be used to assess whether the presently favored composition of P39 is indeed optimal, or to guide the development of new phosphor systems.

In order to improve our understanding of the mechanism of this phosphor's operation, it is necessary to have more quantitative information about the impurity energy levels in the bandgap of the willemite lattice, about the partitioning of excitation energy between electron traps

^{*}Electrochemical Society Active Member.

[†]On leave from Royal Signals and Radar Establishment, Malvern, England WR14 3PS.

and Mn_{Zn} impurities, and about the rates of recombination between separated electrons and holes in $Zn_2SiO_4:(Mn,As)$ phosphors of different compositions. In this paper, we report the results of various spectroscopic measurements designed to provide this quantitative information. The samples used were either single crystals (19) with varying concentrations of Mn and As impurities or commercial powder phosphors. The techniques employed include absorption and photoluminescence excitation spectroscopy to determine the Mn_{Zn}^{2+} impurity level energy, and time-resolved luminescence to provide information on energy partitioning and recombination rates. Trap population parameters and recombination rate constants were obtained from the time-resolved measurements by computer fitting of the experimental curves with a bimolecular kinetic model. The behavior of these model parameters as a function of As concentration is consistent with recombination occurring by diffusion of trapped electrons, in contrast to conclusions reached in recent work.

The paper is organized as follows. In the second section, the experimental techniques are described, and in the third the results are summarized. The fourth section covers the energy levels for both As and Mn impurities in relation to the bandedges in willemite. The next section develops the simplified diffusion model used to describe electron-hole recombination in the P39 phosphor, and interprets the parameters obtained by numerical fitting of this model to the decay curves. The sixth section is a consideration of the general significance of the power law decay often observed at long times in these phosphors, and the difficulties which prevent firm conclusions about recombination mechanisms being drawn solely from such long-time decay curves. Finally, the last section discusses the optimal composition of the P39 phosphor system in the light of the diffusion-controlled recombination suggested by our results.

Experimental

Spectroscopic measurements have been made on both the $Zn_2SiO_4:Mn$ and $Zn_2SiO_4:(Mn,As)$ systems. The samples used were either commercial powder phosphors or single crystals grown in this laboratory as previously reported (19). The Mn and As impurity concentrations in the single crystals were determined by x-ray microanalysis in a JEOL electron microscope. The Mn concentration in the powder materials was determined using atomic absorption spectroscopy and the As concentration using a colorimetric technique. The impurity concentrations, represented as atoms per formula unit of willemite, are given in Table I. Where a particular crystal was not directly analyzed, the impurity concentration in a crystal grown from a melt of identical composition is indicated; these concentrations are shown in parentheses in the table.

Absorption measurements on single crystals were made using a Cary 17 spectrophotometer with the sample mounted in a variable-temperature He cryostat. For photoluminescence excitation (PLE) spectra, the samples were mounted on a copper block in an evacuable Dewar. The crystals were mounted directly on the copper block using thermal paste, while the powders were first spread as a thin layer on a copper disk. The temperature of the block was controlled by a combination of liquid N_2 cooling and resistance heating. The PLE source was a 150W Hg lamp in conjunction with a broad UV bandpass filter. The excitation wavelength was selected by a Bausch and Lomb monochromator. The luminescence was passed through a low fluorescence edge filter to remove scattered excitation light, and then through a second monochromator acting as a tunable filter at 525 nm near the peak of the Mn^{2+} luminescence spectrum. The signal was detected with an S-20 response phototube and electrometer. The PLE spectra were recorded point by point to allow those phosphor systems with long time constants to reach a steady state. The excitation lamp and monochromator combination was calibrated against a thermopile to allow correction of the PLE spectra.

Table I. Impurity atoms per formula unit of willemite^a

Sample	Mn	As
Crystals		
2173H	(0)	(0.0030)
2348A	0.0015	0.0009
2349A	0.0016	0.0018
2350A	0.0012	0.0041
2279A	(0.0140)	(0.0017)
2159E	(0.0240)	(0)
2228A	0.063	0.0017
Powders		
U-P1	0.0220	(0)
U-P39	0.0012	0.0002 ₃
G-P39	0.0014	0.0011 ₃

^a Nonstoichiometric formula unit $Zn_{1.96}Si_{1.04}O_{4.04}$ [Ref. (19)].

Luminescence rise and decay curves of the phosphors in response to long (2 ms) excitation pulses were measured by introducing a mechanical shutter into the excitation beam. The signal was summed over repeated pulses using a Nicolet 1174 signal averager.

The response to very short (< 10 ns) pulses was measured using two different excitation systems. The first was a Molelectron DL II N_2 -pumped dye laser using either a stilbene dye lasing at 440 nm to generate local excitation of the Mn^{2+} centers without ionization, or the output of a rhodamine 6G dye lasing at 576 nm and frequency doubled to 288 nm by a KDP crystal. The second pulse excitation source was a Lambda Physik excimer laser producing emission at 248 and 193 nm using KrF and ArF, respectively. The repetition rate for both pulse systems was ~0.1 Hz, and repeated pulses were again summed with the Nicolet signal averager.

Results

Room temperature absorption spectra for three crystals are shown in Fig. 1. The absorption strength in the visible region (Fig. 1a-1c) increases with increasing Mn concentration in the crystals; this absorption is due to intracenter d electron transitions of Mn_{Zn}^{2+} impurities on the two inequivalent zinc sites in the willemite lattice (20, 21). Figure 1d compares the absorption spectra of the three crystals in the near-UV region. It is evident that the presence of Mn in the crystal induces absorption. Hence, incorporation of Mn^{2+} in the willemite lattice introduces relatively weak intracenter d electron transitions in the visible region of the spectrum and a strong electronic transition in the near UV. Any optical effects due to As incorporation occur at higher energy and are relatively small by comparison (22).

Figure 2 illustrates the temperature-dependence of the absorption spectrum for crystal 2228A, which has the

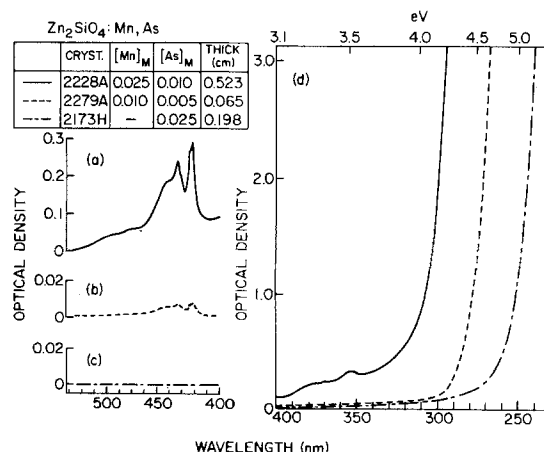


Fig. 1. Room temperature absorption spectra for willemite single crystals. Melt composition and optical path length are given in the key. The incorporated impurity concentrations are given in Table I.

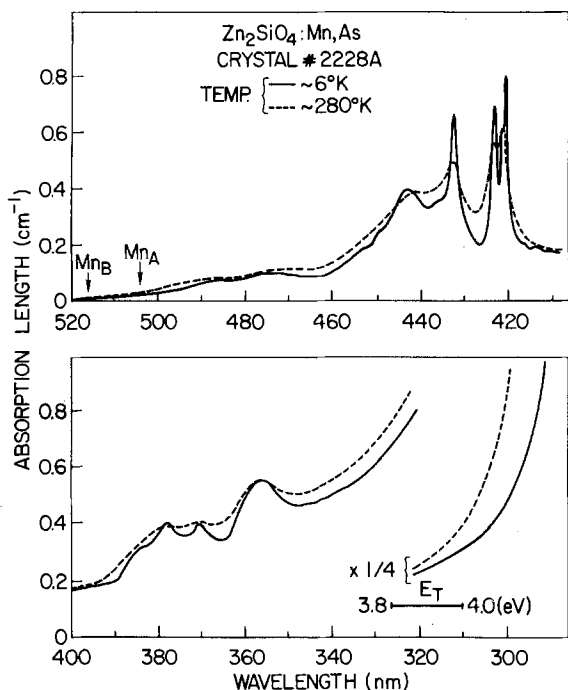


Fig. 2. Absorption spectrum of a willemite crystal at ~ 6 and ~ 280 K. Mn_A and Mn_B are the zero phonon line positions for the ${}^6A_1 \rightarrow {}^4T_1$ transitions of Mn^{2+} ions on the two inequivalent Zn sites of willemite. E_T is the estimated threshold for ionization of Mn_{Zn}^{2+} . Crystal composition is given in Table I.

highest Mn concentration. The d electron transitions in the upper figure show some sharpening at low temperature. The zero phonon line positions for the ${}^6A_1 \rightarrow {}^4T_1$ transitions of the two inequivalent Mn_{Zn}^{2+} centers, Mn_A and Mn_B , are indicated; these lines are too weak to be detected in absorption even at ~ 6 K, although they are easily observable in luminescence (23, 24). The onset of the strong Mn-induced absorption edge is evident near 330 nm (~ 3.8 eV). The intensity of absorption in this edge region clearly increases with increasing temperature.

The threshold for the Mn-induced absorption edge can be more easily determined from the PLE spectrum of the Mn^{2+} luminescence. The spectra in Fig. 3 were taken point by point and corrected as described in the previous section. Figure 3a gives the room temperature PLE spectra for three samples of composition $Zn_2SiO_4:(Mn,As)$ (P39), both crystal and powder; Fig. 3b gives the corresponding PLE spectra for a $Zn_2SiO_4:(Mn)$ (P1) powder sample at 300 and 470 K. It is evident from Fig. 3a and 3b that the form of the room temperature PLE spectrum in the energy range 3.8-5 eV is not very sensitive to the presence of As

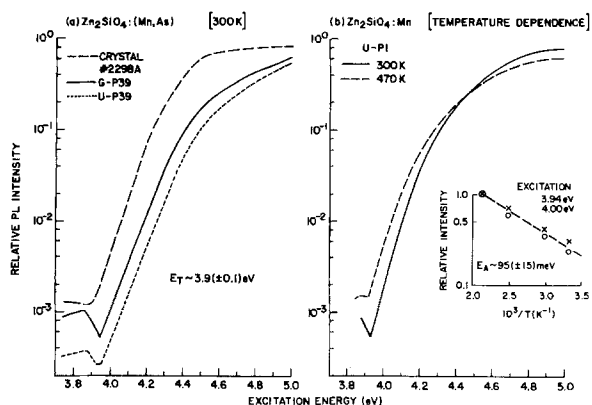


Fig. 3. Photoluminescence excitation spectra for willemite phosphors. The detected signal is the ${}^4T_1 \rightarrow {}^6A_1$ luminescence of Mn_{Zn}^{2+} at 525 nm. The lines are drawn through data taken point by point. a: Room temperature spectra of crystal and powder of composition equivalent to P39. b: Temperature dependence of a powder P1 phosphor. The inset shows the activated form of the spectrum near threshold E_T .

impurity. The sharp increase in the PLE intensity can be used to estimate the threshold for the process leading to Mn^{2+} luminescence, and this is found to be $E_T \sim 3.9 \pm 0.1$ eV. This threshold is marked on the lower part of Fig. 2 and is seen to correspond with the onset of the Mn-induced absorption edge.

The PLE intensity near threshold increases with increasing temperature, as illustrated in Fig. 3b. This behavior parallels the increase in absorption with increasing temperature shown in Fig. 2. The inset to Fig. 3b suggests an activation energy of $\sim 95 \pm 15$ meV for the PLE threshold. This is within the upper range of vibrational energies of the SiO_4^{2-} anion (25) and is consistent with a phonon-assisted absorption process near threshold in willemite.

Although the incorporation of As impurity does not affect the form of the PLE and absorption spectra in the range 2.5-5 eV, the presence of As has a profound influence on the measured decay curve for the Mn^{2+} luminescence. The results of a series of measurements of luminescence decay using an electrical shutter to interrupt the excitation beam are summarized in Fig. 4. As the excitation energy increased, it was found that the measured decay curves showed an initial fast decaying component which possibly arose from relaxation at some defect native to the willemite lattice (9, 17). The detected signal was, therefore, gated with a 2 ms delay to allow the fast component to disappear before measuring the Mn^{2+} decay curves. The time to decay to $1/e$ of the intensity observed at the end of the gate pulse is shown as a function of excitation energy in Fig. 4. Figure 4a gives the results for powder and crystal samples coactivated with Mn and As, and Fig. 4b for powder and crystal samples activated with Mn alone.

In Fig. 4b, the $1/e$ decay time over the whole excitation energy range is close to 10 ms, the value expected for the intrinsic ${}^4T_1 \rightarrow {}^6A_1$ decay of Mn_A and Mn_B centers in willemite at room temperature and with low Mn concentration (23, 24). However, the situation is very different when As is included in the lattice as in Fig. 4a. In this case, the intrinsic decay of ~ 10 ms is observed only for excitation energies < 3.9 eV, i.e., below the absorption threshold E_T determined from the PLE spectra in Fig. 3. At energies above this threshold, the decay time increased to a value > 20 ms and close to 30 ms in the powder sample G-P39. It is important to note that this marked increase in decay time is only observed when two conditions are fulfilled: (i) the excitation occurs above the Mn-induced threshold, ~ 3.9 eV, and (ii) As impurity is present in the crystal. When these conditions are met, the decay shows the extended persistence characteristic of P39 phosphor systems.

The effect of As incorporation on the Mn^{2+} luminescence decay can also be studied using very short excitation pulses from a dye laser or excimer laser at energies above the threshold E_T . Families of decay curves at a series of temperatures in the range 270-390 K were measured for several of the samples listed in Table I. A typi-

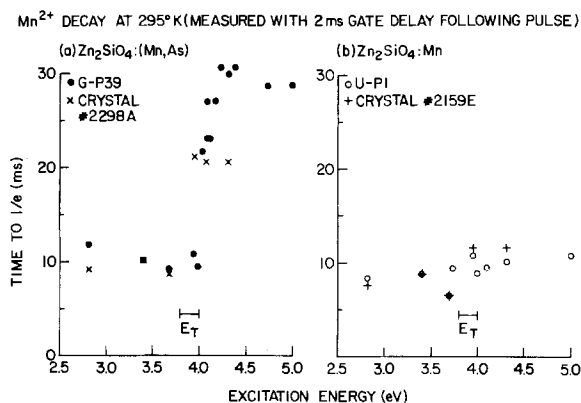


Fig. 4. Mn^{2+} luminescent decay time as a function of excitation energy for $Zn_2SiO_4:Mn$ with As codoping (a) and without As codoping (b).

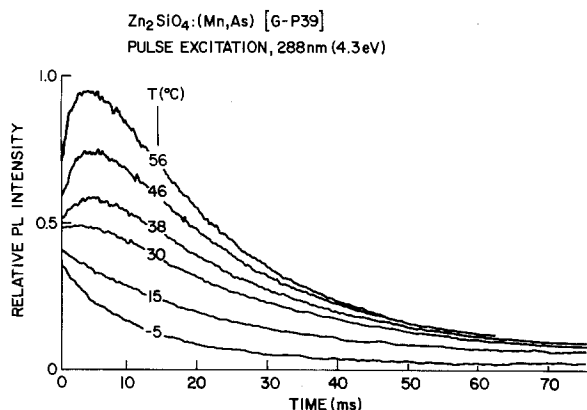


Fig. 5. Pulse response of Mn^{2+} luminescence in a P39 phosphor at different temperatures. The laser pulse was ~ 5 ns. Similar families of curves were obtained with 248 and 193 nm excimer laser pulses.

cal set, for the powder sample G-P39 and taken with a frequency-doubled dye laser at 288 nm (4.3 eV), is shown in Fig. 5. This was the weakest of the pulse excitation sources used; the signal/noise ratio for decay curves measured with the excimer laser at 248 nm (5 eV) and 193 nm (6.4 eV) was always better than that evident in Fig. 5. The dependence of the luminescence intensity on excitation density was checked by attenuating the dye laser beam with neutral density filters; Fig. 6 shows the response to be linear over the measured range.

On the time scale of Fig. 5, the excitation pulses from both the dye laser and the excimer laser correspond to δ -functions at the origin. The appearance of a delayed maximum in the decay curves was only observed for those samples which were simultaneously doped with Mn and As, and then only for pulse excitation above the threshold E_T , i.e., only when conditions (i) and (ii) above were met. Samples without As addition showed a decay curve close to the intrinsic Mn^{2+} decay at all temperatures and no delayed maximum. These pulse decay curves have been fitted numerically to obtain kinetic parameters describing the decay for several of the powder and crystal samples. The details of the fitting, and the correlation between the kinetic parameters and the chemical composition of the samples, are discussed in the fifth section.

Impurity Energy Levels in Zn_2SiO_4

The chemical form in which the As impurity is incorporated in Zn_2SiO_4 is not known. However, the idea that As

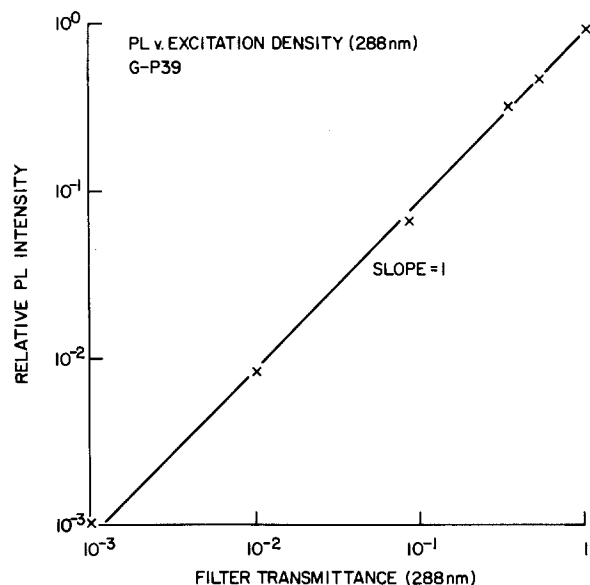
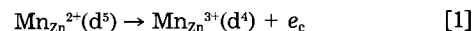


Fig. 6. Photoluminescence intensity of a P39 phosphor excited by 288 nm laser pulses transmitted through attenuating filters. The response is linear with excitation density.

acts as an electron trap in willemite is supported by electrical measurements on As⁺-implanted SiO_2 (26). These show that As⁺ implantation produces a dominant electron trap with capture cross section $(1-2) \times 10^{-15} \text{ cm}^2$ and a gaussian distribution around a median thermal trap energy $E_m = 1.2-1.3$ eV with standard deviation ~ 0.2 eV. The results of thermal glow measurements on $\text{Zn}_2\text{SiO}_4:\text{Mn}$, with and without As addition, have been summarized by Yang *et al.* (27) and Avouris *et al.* (12). The willemite lattice shows glow peaks indicating at least four distinct trap distributions, characterized by trap energies ~ 0.15 , ~ 0.25 , ~ 0.55 , and ~ 0.9 eV. When As is added to the lattice, the glow peak near 273 K (~ 0.55 eV) is greatly enhanced and dominates the thermal glow spectrum, and a new peak is detected near 553 K with activation energy ~ 1.9 eV. This latter peak appears to correlate with the introduction of impurity atoms, the effect of As being particularly large (10); the two dominant peaks may be due to As impurity centers or may represent native defects of the willemite lattice whose concentration is greatly enhanced by the presence of As. These various energy levels are represented as "electron traps" in Fig. 7, the trap energy being measured downward from the conduction band (CB) edge.

In contrast to the situation for As, much is known about the incorporation of Mn^{2+} in willemite. It is incorporated substitutionally at the two inequivalent Zn sites forming the Mn_A^{2+} and Mn_B^{2+} centers (20, 23, 24). The way in which simultaneous doping with As affects the $\text{Mn}_{\text{Zn}}^{2+}$ luminescence decay, evident in Fig. 4 and 5, is most easily explained if it is assumed that the near-UV threshold E_T corresponds to the impurity \rightarrow CB charge transfer transition



The free CB electrons can be efficiently trapped in the presence of a high concentration of As-related centers, leading to slow recombination and enhanced persistence. For excitation below E_T , no ionization is possible and only intracenter excitation occurs to produce the intrinsic Mn^{2+} decay with no enhanced persistence. The threshold E_T , therefore, defines the position of the Mn^{2+} impurity level in the gap as being $\sim 3.9 \pm 0.1$ eV below the CB edge. This is illustrated in Fig. 7 together with the estimated position of the 4T_1 excited level. This positioning of the Mn^{2+} level, deduced from the absorption and PLE spectra in Fig. 2 and 3, is consistent with earlier estimates of ~ 3.96 eV below the CB by Chang and Sai-Halasz (15) based on photostimulated luminescence measurements, and ~ 4 eV by Dove *et al.* (11) based on the threshold for trap filling. In fact, there are two impurity levels corresponding to

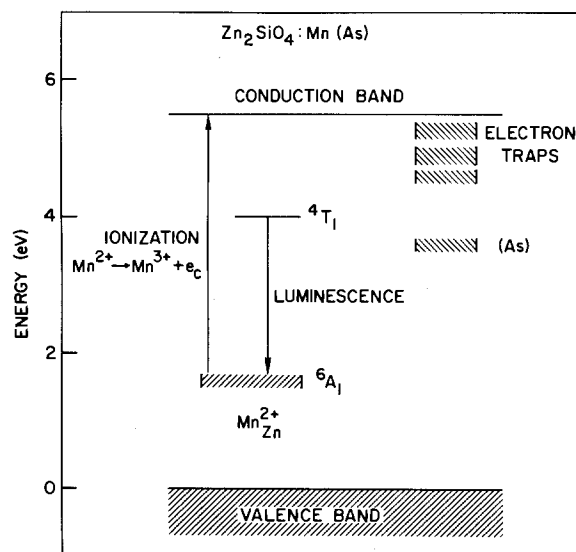


Fig. 7. Impurity energy levels in P39 phosphors. The Mn^{2+} levels are estimated from absorption and PLE spectra. The electron trap levels are taken from thermal glow data.

Mn_A and Mn_B centers; the present experiments detect mainly the lower energy threshold corresponding to the center lying higher in the forbidden gap. This does not affect the arguments presented below.

The assignment of the near-UV absorption edge as an impurity \rightarrow CB charge transfer process implies that the transition occurs from a d-like orbital to an s-like orbital and is, therefore, parity forbidden. This would be quite consistent with the observation that the absorption process is phonon assisted near threshold.

A Recombination Model

Previous work.—The enhanced persistence of the P39 system is due to the slow recombination of spatially separated charges, *viz.*, trapped electrons and ionized Mn_{Zn}^{3+} centers. At long times after the cessation of excitation, it is quite generally found that the decay of inorganic phosphors can be described by an equation of the form (9, 28)

$$I(t) = I_0 \left(\frac{\beta}{\beta + t} \right)^m \quad [2]$$

where the parameters β and m depend on the particular system studied, the excitation density, the time elapsed since cessation of excitation, temperature, and so on.

Kinetic models attempting to describe this decay behavior were developed initially by Randall and Wilkens (7) using first-order kinetic equations, and extended by Garlick and Gibson (8) to include retrapping effects. Medlin (28) subsequently introduced second-order equations to describe the recombination, but found that the behavior of the parameters β and m predicted by the second-order equations was consistent with the experimental data only at temperatures above the glow peak maximum for any trap. At lower temperatures it was necessary to revert to the idea that a first-order trap emptying process was rate limiting. Medlin was then able to obtain a numerical fit to the experimental data by assuming that the trap levels were spread in energy according to a gaussian distribution (28).

More recently, the concept of a quantum-mechanical tunneling recombination between trapped electrons and ionized luminescent centers has been introduced into the kinetic models (12-14, 18). Tunneling from the ground state of an electron trap is a nonthermally activated process. Examples are found in the radiative recombination of donor-acceptor pairs in semiconductors (29) and in the temperature-independent afterglow observed between 4 and 77 K in irradiated KCl:M (M = Ag, Tl) (30). This afterglow is attributed to radiative tunneling recombination between holes trapped as V_k centers and electrons trapped at neutral metal atom sites.

Avouris and co-workers (12, 13) have applied the concept of tunneling recombination to the $Zn_2SiO_4:Mn,As$ system. In this case, however, the proposed tunneling process has an activated form. It is assumed that recombination occurs between a fixed distribution of trapped electrons and the ionized Mn_{Zn}^{3+} centers and that the tunneling process involves thermal activation of a trapped electron to a shallow excited state of large radius. This model is adequate to fit the shape of the glow curves on the low temperature side of the maximum, but above the glow peak it is necessary to assume that thermal emission to the conduction band dominates in the recombination. However, the usefulness of the activated tunneling model is suggested to lie in the explanation which it offers for the form of the phosphorescence decay and the decay of photostimulated luminescence, both of which can show a t^{-1} behavior in $Zn_2SiO_4:Mn,As$ materials. In this context, the model has been further developed by Chang and co-workers (14, 18).

A diffusion model.—There is a need to develop a model for recombination in the P39 phosphor system which can be related to the chemical composition of the material and which can be used as an aid to optimization of the phosphor properties. Attempts to model the long-time decay behavior of the $Zn_2SiO_4:Mn,As$ materials, outlined

above, have not produced agreement on the most appropriate description of the recombination process. In particular, they have not provided quantitative information on decay rates of the kind necessary to develop a useful predictive model of phosphor properties.

We have therefore approached the problem in a different way. First, we have made a systematic comparison of the recombination processes in a series of samples in which the concentration of Mn^{2+} centers is roughly constant, whereas the concentration of As atoms introducing electron traps is increased by more than an order of magnitude. This series includes the powder samples U-P39 and G-P39 and the crystal samples 2348A, 2349A, and 2350A listed in Table I. By this means it is possible to determine whether electrons trapped at As-related centers can become mobile in the lattice by tunneling from trap to trap; the probability of such tunneling increases exponentially with increasing trap concentration. Second, we have studied the recombination mechanism by exciting the phosphors with laser pulses of nanosecond duration and recording the luminescent response over relatively short periods, up to ~ 100 ms. In this way, it proves possible to extract information on the initial partitioning of the excited electrons and on the rates of recombination. Both parameters are essential for a quantitative understanding of the phosphor properties. The remainder of this section outlines the basic theoretical model which is used to analyze the experimental data.

It will be assumed that the traps constitute a disordered system of impurity levels. In the normal way (31), the distribution of trap levels can be described by a density-of-electronic-states function, the width of the distribution arising from differences in charge compensation for the trap centers, random fields, and other sources of inhomogeneity. As mentioned previously, thermally stimulated luminescence data for P39 phosphors suggest the presence of two dominant trapping centers, corresponding to glow peaks near 273 and 553 K. The electron density-of-states (DOS) function will therefore show two major peaks within the willemite bandgap, E_g , as illustrated in Fig. 8.

The effect of a very short laser pulse with energy $\bar{E}_T < hv < E_t$ is to ionize some fraction of the Mn_{Zn}^{2+} centers in the willemite lattice, producing instantaneously equal concentrations of ionized Mn_{Zn}^{3+} centers and free CB electrons. These free electrons rapidly relax to different centers in the lattice. Some recombine immediately with ionized Mn_{Zn}^{3+} centers producing an initial population of excited Mn_{Zn}^{2+} centers in the 4T_1 excited state; the remainder of the CB electrons are captured by traps. If the initial electron population is normalized to unity, and the concentration of electrons in the CB is assumed to be negligible, the following relationships hold

$$M_0^* + n_0 \approx 1 \text{ and } M_0^+ \approx n_0 \quad [3]$$

where M^+ is the population of ionized Mn_{Zn}^{3+} centers, M^* is the concentration of excited Mn_{Zn}^{2+} centers, n is the concentration of trapped electrons, and the subscript 0 denotes the concentration at time $t = 0$ immediately following the laser pulse.

Assuming for simplicity that the electron capture rate is independent of trap depth, and neglecting trap saturation, the initial distribution of the trap population will follow the DOS function

$$n_0(E) = \frac{n_0 N(E)}{N} \quad [4]$$

where $N(E)$ is the DOS function and N is the total trap concentration.

The time dependence of the luminescence obeys the equation

$$\dot{M}^* = -\dot{M}^* - bM^* \quad [5]$$

where b^{-1} is the measured lifetime for the ${}^4T_1 \rightarrow {}^6A_1$ transition of Mn_{Zn}^{2+} . It will be assumed that at low concentrations of Mn impurity the ionized Mn_{Zn}^{3+} centers are immo-

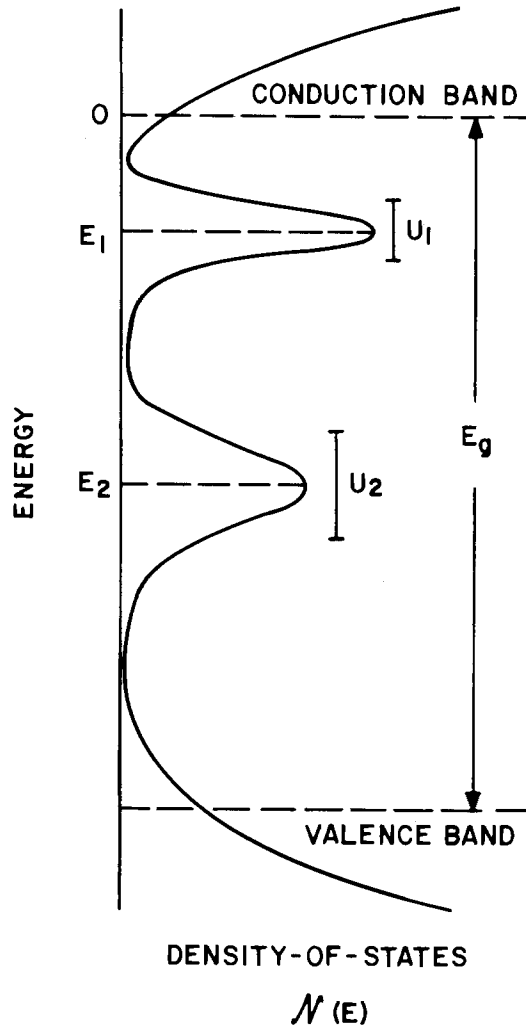


Fig. 8. A schematic representation of the electron trap distribution in P39 phosphors with two dominant trap levels, E_1 and E_2 , corresponding to glow peaks near ~ 273 K and $\sim 583^\circ\text{C}$. The widths of the peaks in the DOS function are U_1 and U_2 , respectively.

ble; recombination is then assumed to occur by diffusion of the trapped electron population. The rate of recombination by diffusion is given by (32)

$$-\dot{M}^+ = 4\pi D'R \left[1 + \frac{R}{(\pi D't)^{1/2}} \right] \cdot M^+ n \quad [6]$$

where D' is a diffusion coefficient and the radius R defines a sphere of influence for the ionized Mn_{2n}^{3+} centers such that an electron impinging on the surface of this sphere undergoes recombination with a probability of unity. To simplify the analysis, we shall neglect the second term in the brackets (which should be important only at very short times) and rewrite Eq. [6] as

$$-\dot{M}^+ \approx (DR)M^+ n \quad [7]$$

where $D = 4\pi D'$.

Following the usual analysis for such disordered systems (31), the diffusive motion of the electrons can take place by two main mechanisms. (i) The first process is a thermally activated emission to the CB followed by diffusion of the free electron. This process is denoted by the diffusion coefficient D_T . (ii) The second is a nonactivated tunneling transfer of an electron from the ground state of one trap to the ground state of another trap. This is denoted by the diffusion coefficient D_N . The observed diffusion coefficient represents the sum of these two processes. If diffusion of trapped holes (i.e., Mn_{2n}^{3+} centers) occurs at high Mn concentration, the effect will simply be to add an extra component to the overall diffusion coefficient (32).

Thermal emission.—For a single trap level of depth E , the thermal emission rate to the CB is given by (33)

$$P_T(E) = \sigma \langle v \rangle > N_c e^{-E/kT} \quad [8]$$

where σ is the capture cross section for the trap, $\langle v \rangle$ is the thermal velocity, and N_c an effective density of states in the CB. The mean distance traveled between emission and recapture, L , is given by $L = : (\sigma N)^{-1}$ and the activated diffusion coefficient by

$$\begin{aligned} D_T(E) &= \frac{1}{6} P_T L^2 \\ &= \frac{\langle v \rangle N_c e^{-E/kT}}{6\sigma N^2} \end{aligned} \quad [9]$$

It should be noted that the thermal diffusion coefficient is inversely proportional to the square of the trap concentration, reflecting the fact that retrapping effects inhibit this thermal diffusion motion.

Tunneling transfer.—The rate of tunneling from trap to trap within a particular DOS peak will have the form (31)

$$P_N = \nu e^{-2\alpha\gamma} e^{-W/kT} \quad [10]$$

where ν is some phonon frequency, γ is the distance between centers, and W is a small activation energy which depends on the width, U , of the DOS peak. The parameter α depends on wavefunction overlap; for deep centers, with localized wave functions, α is large. The term $e^{-2\alpha\gamma}$ therefore ensures short range hops, primarily to nearest-neighbor trap levels. This near-neighbor transfer may require an activation energy approaching the distribution width, $W \sim U$. At the temperatures of interest (≥ 300 K), this thermal energy is available so that the $e^{-2\alpha\gamma}$ term should dominate. If the trap sites are randomly distributed, an effective mean hop length, γ_m , can be defined as a function of concentration and the hopping rate becomes

$$P_N \approx \nu e^{-2\alpha\gamma_m} e^{-U/kT} \quad [11]$$

The length γ_m decreases, and hence P_N increases, as trap concentration increases. The diffusion coefficient for tunneling transfer is then given by (32)

$$D_N \approx \frac{1}{6} P_N \gamma_m^2 \quad [12]$$

In contrast to the thermal motion, the diffusion coefficient for the tunneling transport increases as the trap concentration increases. This simply reflects the fact that wave function overlap, and hence the tunneling rate, increase as the distance between traps decreases. The activation energy U is small compared with the trap depth appearing in the thermal diffusion coefficient, a typical DOS peak having a width ~ 0.1 - 0.2 eV. In principle, the tunneling diffusion coefficient is a function of trap depth, there being a different coefficient for each DOS peak in the trap distribution.

In order to calculate the recombination, it is now necessary to make some assumption about the energy distribution of the trapped electrons as a function of time. For simplicity, we shall assume that both the processes of thermal emission and recapture, and of nearest-neighbor hopping, tend to randomize the electron population so that at all times the electron distribution follows the DOS function

$$n(E, t) = \frac{n(t)N(E)}{N} \quad [13]$$

The rate of recombination can then be written using Eq. [7] and [13] as

$$\begin{aligned} (DR)M^+ n &\approx RM^+ \cdot \int_E [D_T(E) + D_N(E)]n(E) dE \\ &\approx \frac{RM^+ n}{N} \cdot \int_E [D_T(E) + D_N(E)]N(E) dE \end{aligned} \quad [14]$$

The integral in this equation defines the effective diffusion coefficient D which represents the sum of thermally activated and nonthermal tunneling processes

$$D = \frac{1}{N} \cdot \int_E [D_T(E) + D_N(E)]N(E) dE \quad [15]$$

The temperature dependence of the effective diffusion coefficient D will depend upon the overall trap concentration as indicated schematically in Fig. 9 for three trap concentrations, $N_1, D_T > D_N$ at all temperatures so that the observed diffusion coefficient D will show simple activated behavior. However, for the highest concentration, $N_3, D_T < D_N$ at all temperatures and the observed diffusion coefficient will be dominated by the tunneling process showing essentially nonactivated behavior. At the intermediate concentration, N_2 , the diffusion coefficients due to thermal emission and tunneling are comparable so that the observed diffusion coefficient will show a more complicated behavior with some intermediate value for the apparent activation energy.

Fitting to a bimolecular rate equation.—It is a central part of the recombination model developed in the previous section that, throughout the decay, the concentration of ionized $Mn_{Zn^{3+}}$ centers is balanced by an approximately equal concentration of trapped electrons, i.e., we have the conditions

$$M^+ \approx n, \dot{M}^+ \approx \dot{n} \quad [16]$$

Substituting these equalities in Eq. [7] gives

$$-\dot{n} \approx (DR)n^2 = kn^2 \quad [17]$$

where $k = DR$ is a bimolecular rate constant. Thus, the various assumptions and approximations introduced into the model have resulted in a description of electron-hole recombination at ionized $Mn_{Zn^{3+}}$ sites in terms of a bimolecular rate equation. The physical picture underlying this description is that the electrons are isotropically distributed in the lattice and are able to diffuse through it. The kinetics of this system consist of two independent parts, the capture of an electron at a Mn^{3+} site, as discussed above, and its subsequent decay by photon emission. These processes are governed by two rate constants, the bimolecular rate k and the intrinsic $Mn_{Zn^{2+}}$ decay rate b , giving the overall kinetic equation

$$\dot{M}^* = kn^2 - bM^* \quad [18]$$

The solution to Eq. [17] is

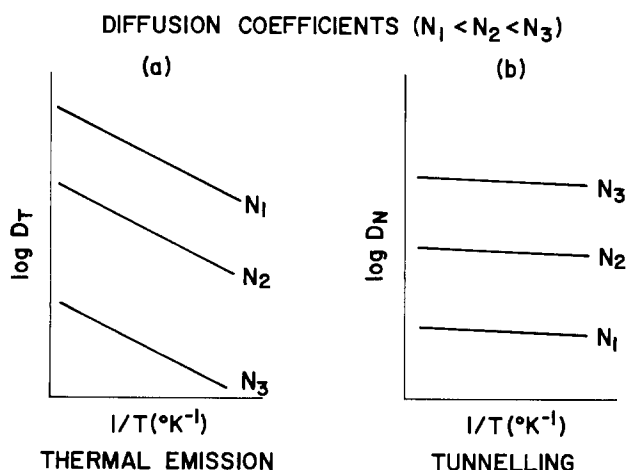


Fig. 9. The schematic temperature dependence of processes contributing to electron diffusion in different P39 phosphors. The relative As concentration in the phosphors is $N_1 < N_2 < N_3$. a: The thermal diffusion coefficient D_T , showing strongly activated behavior favored by low As concentration. b: The tunneling diffusion coefficient D_N , showing weakly activated behavior favored by high As concentration.

$$n = \left(kt + \frac{1}{n_0}\right)^{-1} \quad [19]$$

Substituting Eq. [19] into [18] and solving yields

$$M^*(t) = (M_0^* + n_0)e^{-bt} - \left(kt + \frac{1}{n_0}\right)^{-1} + \frac{b}{k} e^{-(bt + b/kn_0)} \cdot [Ei(bt + b/kn_0) - Ei(b/kn_0)] \quad [20]$$

where $Ei(x)$ is the exponential integral. The luminescence intensity as a function of time is proportional to the excited state population, $M^*(t)$. Equation [20] has been used to generate computer fits to families of luminescence pulse response curves of the kind illustrated in Fig. 5.

The decay rate, b , for each sample was obtained experimentally by measurement of the luminescence decay curve at a series of temperatures using laser pulses at 440 nm to produce only localized, intracenter excitation of the $Mn_{Zn^{2+}}$ ions. These measured decay curves were then approximated by a simple exponential decay. Using the measured values for b , the fitting procedure involved two main parameters, the bimolecular rate constant k and the initial trap population n_0 , together with a normalization factor to scale the fit. Best values of k and n_0 were obtained for each experimental pulse response curve using a nonlinear least squares fitting algorithm developed by Marquardt (35).

The fitted curves reproduced the main features of the experimental data: in particular, the appearance of a delayed maximum in the pulse response curve. However, there was some tendency towards a systematic deviation from the form of the experimental data. A fairly typical result is shown in Fig. 10, which gives the best fit function for one data curve together with the deviation between that fitted curve and the experimental data. This deviation was always significant at short times and may reflect, at least in part, the neglect of the higher-order term in the diffusion (Eq. [6]). This point will be addressed elsewhere (36). In general, however, we feel that the simple bimolecular fitting procedure reported here is quite adequate to establish semiquantitatively the main trends in the recombination rate and trap population as they are influenced by changes in chemical composition in $Zn_2SiO_4:(Mn,As)$ phosphors.

The results of fitting pulse response curves measured over a range of temperatures are summarized in Fig. 11, which shows the best fit values for the bimolecular constant k , and in Fig. 12, which shows the corresponding best fit values for the trap population parameter n_0 . The parameters k and n_0 are normalized to the initial total ex-

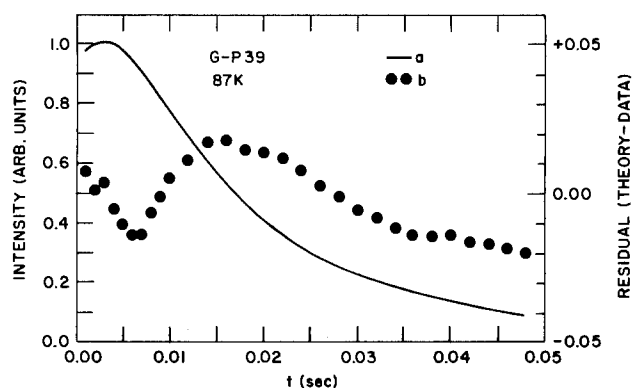


Fig. 10. A typical result from computer fitting of the pulse response curves according to Eq. [21]. a: The solid line (left ordinate) is the calculated function and experimental curve. They are indistinguishable on the scale of this drawing. b: The open circles represent the difference between the calculated function and the experimental curve (right ordinate). The oscillation in the difference curve at short time is a systematic feature of the fitting.

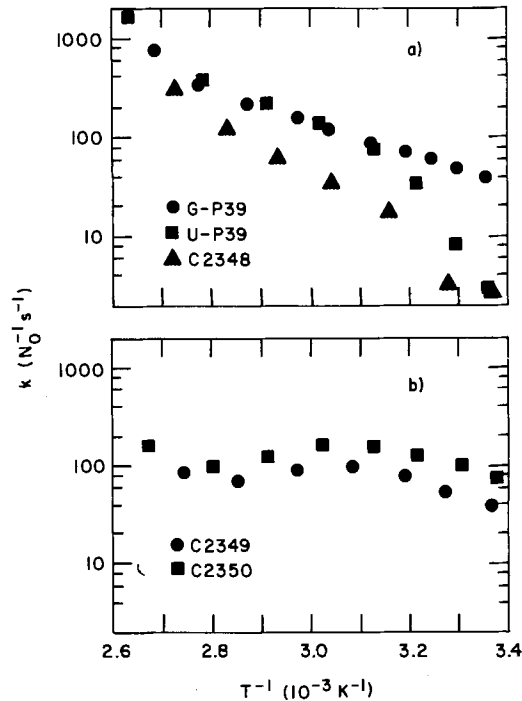


Fig. 11. The bimolecular rate constant k as a function of temperature derived from fitting Eq. [21] to the pulse response curves. Note that the units of k are normalized to the initial concentration of ionized electrons N_0 .

cited state population $N_0 (= M_0^* + n_0)$ which, for numerical convenience, is set to one. As a result, the units of k are $N_0^{-1} \text{s}^{-1}$, while n_0 is a dimensionless fraction. It is assumed that N_0 , which is proportional to the Mn^{2+} absorption cross section, is not a strong function of temperature. The experimental data were obtained from samples U-P39, G-P39, 2348A, 2349A, and 2350A listed in Table I. For all the samples, decay curves were taken using KrF excitation at 248 nm; in addition, the decay of the powder phosphors U-P39 and G-P39 was measured at 193 nm using ArF. No significant differences between these two excitation wavelengths were observed.

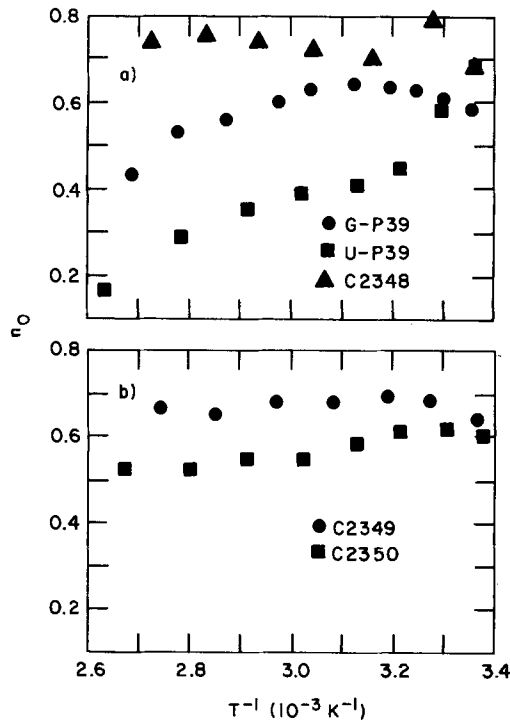


Fig. 12. The initial trap population fraction, n_0 , as function of temperature derived from fitting Eq. [21] to the pulse response curves. The key to the data points is given in the caption to Fig. 11.

Table II. Activation energies and impurity separation

Sample	Activation Energy (eV)	N_{As} (cm^{-3})
U-P39	~ 0.6	2.6×10^{18}
G-P39	~ 0.4	1.3×10^{19}
2348A	~ 0.6	1.0×10^{19}
2349A	Very small	2.1×10^{19}
2350A	Very small	4.7×10^{19}

Table II lists the approximate activation energy for the bimolecular rate constant derived from Fig. 11 for each of the samples, together with the As impurity concentration. The spread in value of n_0 is shown as a function of As concentration in Fig. 13. The behavior of the model parameters divides into two regions as a function of As concentration, the transition occurring when $N_{As} \sim 1.2 \times 10^{19} \text{ cm}^{-3}$.

Region 1 is when $N_{As} \leq 1 \times 10^{19} \text{ cm}^{-3}$. (i) k is activated, $\Delta E \sim 0.6 \text{ eV}$

$$k(300 \text{ K}) \approx 10 N_0^{-1} \text{ s}^{-1}$$

$$k(370 \text{ K}) \sim 10^3 N_0^{-1} \text{ s}^{-1}$$

(ii) n_0 increases as N_{As} increases.

Region 2 is when $N_{As} \geq 2 \times 10^{19} \text{ cm}^{-3}$ (i) k is not activated

$$k(300 \text{ K}) \sim 10^2 N_0^{-1} \text{ s}^{-1}$$

$$k(370 \text{ K}) \sim 10^2 N_0^{-1} \text{ s}^{-1}$$

(ii) n_0 decreases as N_{As} increases.

The sample G-P39 falls in the transition region. It shows an activated recombination, but $\Delta E < 0.6 \text{ eV}$. The bimolecular rate constant at 300 K is $k \sim 50 N_0^{-1} \text{ s}^{-1}$, approaching the nonactivated rate at low temperature. The rate constant at 370 K is $k \sim 10^3 N_0^{-1} \text{ s}^{-1}$, similar to the activated rate at high temperature.

This behavior of the model parameters can be interpreted in terms of the diffusion model developed in the previous section. From Eq. [18], and assuming the radius R to be a constant, the bimolecular rate constant k is proportional to the effective diffusion coefficient D for each sample; in particular, the temperature dependence of k will reflect that of D . In Region 1, the rate constant is activated and the diffusion is dominated by the thermal emission process, D_T , which is favored by low trap concentration, e.g., N_1 , depicted in Fig. 9. The observed activation energy, $\Delta E \sim 0.6 \text{ eV}$, corresponds to a weighted average of thermal trap depths for centers which contribute to trapping and diffusion. This observed value lies within the range of trap energies determined from thermal glow

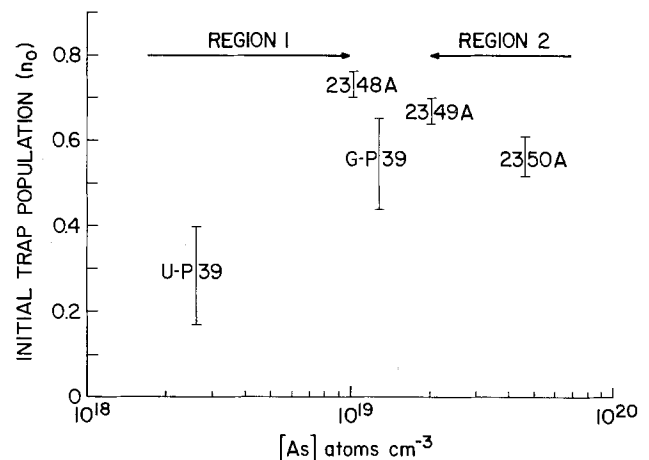


Fig. 13. The initial trap population fraction, n_0 , as a function of As concentration in the samples indicated. The error bars represent the limits of n_0 values obtained by fitting Eq. [21] to the pulse response curves. The significance of Regions 1 and 2 is discussed in the text.

measurements on the dominant glow peak of P39 phosphors center at ~ 273 K.

In Region 2, the rate constant is not activated and the diffusion is dominated by the intertrap tunneling process, D_N , which is favored by high activator concentration. This concentration range would correspond to the high trap concentration, N_3 , depicted in Fig. 9. The sample G-P39 falls in the transition region in which the contributions of thermal emission and tunneling are comparable, analogous to the intermediate trap concentration N_2 depicted in Fig. 9. The diffusion coefficient for this sample is limited by tunneling at low temperature and by thermal emission at high temperature. The effect of comparable contributions from tunneling and thermal emission processes is to reduce the apparent activation energy for the diffusion process.

The behavior of the parameter n_0 can be explained in the following way. The excitation photons excite electrons from the Mn_{Zn}^{2+} centers into the CB with considerable excess energy, e.g., at 248 nm the photon energy, $h\nu = 5$ eV, would ionize the electrons with $(5-3.9) \sim 1.1$ eV excess kinetic energy. This kinetic energy propels the electrons through the lattice and affects the distribution of electrons immediately following the excitation pulse.

In the simplest case, we suppose that each ionized Mn_{Zn}^{3+} center is surrounded by its sphere of influence of radius R and that, if the excited electron comes to rest within this sphere, the recombination with Mn_{Zn}^{3+} center is extremely fast. This would represent a geminate recombination process (37). The parameter n_0 represents the fraction of electrons on As-related traps immediately following the excitation pulse. Thus

$n_0 =$ (probability that an ionized electron escapes the sphere of influence)

\times (probability of a CB electron being captured by a trap)

$$= (\text{probability of escape}) \times \left[\frac{\sigma N}{\sigma N + \sigma^+ M^*} \right] \quad [21]$$

where σ is the capture cross section for traps of concentration N , and σ^+ is the cross section for ionized Mn_{Zn}^{3+} centers. In the absence of As impurity, the probability of escaping the Mn_{Zn}^{3+} sphere of influence will be denoted by p_0 . We shall assume that in the presence of As, electron trapping within the radius R will still produce geminate recombination; hence, the probability of escape in the presence of As, denoted p_{As} , depends upon the probability that an ionized electron is not trapped in traversing the distance R

$$p_{As} = p_0 e^{-\sigma NR} \quad [22]$$

Combining Eq. [21] and [22] gives

$$n_0 = p_0 e^{-\sigma NR} \left[\frac{\sigma N}{\sigma N + \sigma^+ M^*} \right] \quad [23]$$

The exponential term will be close to unity at low trap concentration, so the behavior of n_0 will be determined by the term in brackets. This term increases as trap concentration N increases, and explains the increase in n_0 with increasing N at low concentrations (Region 1) in Fig. 13. At high trap concentrations, however, the term in brackets will approach unity, and the behavior of n_0 will be determined by the exponential term. This term decreases as N increases, which explains the decrease in n_0 with increasing N at higher concentrations (Region 2) in Fig. 13. Estimating crudely from Fig. 13 that the exponential term $e^{-\sigma NR} \sim 0.6$ when $N \sim 5 \times 10^{19} \text{ cm}^{-3}$, gives $(\sigma R) \sim 10^{-20} \text{ cm}^3$. Assuming $R \sim 2$ nm, the distance at which intertrap tunneling becomes significant, allows the trap capture cross section to be estimated

$$\sigma \sim \frac{10^{-20}}{2 \times 10^{-7}} \text{ cm}^2 \sim 5 \times 10^{-14} \text{ cm}^2 \quad [24]$$

This value for the cross section of the As-related traps,

which depends upon the estimate of R , would be typical for coulombic trapping centers, although it is larger than the value $\sigma \sim 1.2 \times 10^{-15} \text{ cm}^2$ reported for As-induced traps in SiO_2 (26).

The Power Law Decay

The expression for the recombination rate contained in Eq. [14] assumes that throughout the decay the trap population $n(E)$ remains proportional to the DOS, $N(E)$. This assumption leads to the definition of the effective diffusion coefficient D in Eq. [15] and thence to Eq. [20], which gives the luminescence intensity as a function of time based on bimolecular recombination kinetics. It is of interest to consider the long-time behavior of Eq. [20] since there have been many attempts to deduce the mechanism of recombination from the form of the decay curves at long times. In the limit $t > > 1/kn_0$, the asymptotic behavior of the exponential integral is

$$Ei(x) \approx \frac{e^x}{x} \left[1 + \frac{1}{x} + \frac{2}{x^2} + \dots \right] \quad [25]$$

Substituting in Eq. [20] and retaining only first-order terms gives

$$M^* \approx -\frac{1}{bt} + \frac{1}{bt} + \frac{1}{bt^2} \propto \frac{1}{t^2} \quad [26]$$

The t^{-2} behavior at long times is characteristic of bimolecular recombination. Measurements of long-time decay on some of the samples studied have shown t^{-2} behavior over extended periods of time (36), consistent with the description in terms of the simplified diffusion model.

On the other hand, it is clear from measurements on many different systems that while the extended decay follows a power law, $I \propto t^{-m}$, the exponent m can vary throughout the decay, taking a wide range of values from $m < 0.5$ to $m > 2$. This exponent varies with temperature and excitation intensity in addition to time elapsed from the cessation of excitation. There are many examples, including P39 and P1 phosphors, in which a t^{-1} behavior is observed over considerable periods in both luminescence decay and the decay of photostimulated luminescence. This t^{-1} behavior has been variously interpreted in terms of trap levels distributed in energy (7, 28) and as evidence of tunneling recombination between Mn_{Zn}^{3+} centers and a fixed spatial distribution of trapped electrons (12-14).

Considering the diffusion model of the previous section, such complexity in the decay behavior might be expected when some of its simplifying assumptions break down. The most important is likely to be the assumption that $n(E) \propto N(E)$ throughout the decay. Since thermal emission is favored for shallower centers over deeper ones, there will be a tendency for the population to accumulate in the deeper levels as the decay proceeds. When this effect is significant, the integral $\int_0^\infty [D_T(E) + D_N(E)]n(E) dE$ will no longer be simply proportional to the total trap population $n(t)$, and simple bimolecular kinetics with t^{-2} decay at long times is no longer to be expected. In addition, as the mean depth of the trapped electrons increases with time, the balance of contributions from thermal diffusion, D_T , and tunneling diffusion, D_N , will change, leading to a time-dependent rate coefficient in the kinetic equations.

Conclusions

Absorption and photoluminescence excitation spectra have confirmed that the Mn_{Zn}^{2+} ground state impurity level in willemite lies 3.9 ± 0.1 eV below the conduction band edge. The ionization cross section for Mn_{Zn}^{2+} shows activated behavior near the threshold, $E_T \sim 3.9$ eV, which can lead to variations in the efficiency of exciting thermally-stimulated glow curves when UV wavelengths near threshold are used to excite the system at different temperatures.

The luminescence pulse response curves for $\text{Zn}_2\text{SiO}_4:(\text{Mn},\text{As})$ phosphors with varying As concentration have been analyzed in terms of a simplified diffusion model. The effective diffusion coefficient D is found to

be activated when the As impurity concentration $N_{As} \approx 1 \times 10^{19} \text{ cm}^{-3}$, suggesting that the electron motion is dominated by thermal emission to the conduction band. However, D is nonactivated when $N_{As} > 2 \times 10^{19} \text{ cm}^{-3}$, suggesting that tunneling between traps is then the dominant mechanism for electron motion; in this limit the recombination rate at 300 K is larger than is the case for activated diffusion. The fraction of excited electrons captured by As-related traps initially increases with increasing N_{As} and then decreases. This effect is explained in terms of competition between geminate recombination at ionized $\text{Mn}_{\text{Zn}}^{3+}$ centers and electron capture at traps. The general validity of the simplified diffusion model, which leads to a bimolecular decay law, is supported by the observation of t^{-2} decay behavior at long times (36). However, this simplified model, while giving reasonable quantitative fits to the experimental data, also shows evidence of systematic deviations which may arise from neglect of higher-order terms in the diffusion equation. The observation of more complex power law decay at long times is probably the result of redistribution of the trapped electron population.

The form of the luminescence pulse response curve, Fig. 5, is insensitive to excitation energy above threshold E_T , and, indeed, we have observed essentially similar behavior for electron beam excitation. From a practical point of view, the optimization of an extended persistence P39 phosphor for CRT displays requires that as large a fraction of excited electrons as possible be captured and stored in traps while the recombination rate should remain as low as possible without introducing "smearing" in refreshed displays. From Fig. 11 and 13, it is evident that for the phosphors studied here with $\text{Mn}_{\text{Zn}}^{2+}$ concentration $\sim 1.6 \times 10^{19} \text{ cm}^{-3}$, the optimum As concentration is $N_{As} \sim 1.2 \times 10^{19} \text{ cm}^{-3}$. At this concentration, the trapped electron fraction is maximum, $n_0 \sim 0.6$, and the recombination rate constant at the phosphor operating temperature, $\sim 300 \text{ K}$, is low, $k \sim 50 \text{ cm}^3\text{-s}^{-1}$. If N_{As} is increased above this level, the fraction n_0 decreases, probably due to an increased rate of geminate recombination, and the recombination rate increases rapidly because of the onset of intertrap tunneling.

Finally, it should be noted that we have studied recombination in P39 phosphor systems over a temperature range approximately $0^\circ\text{-}100^\circ\text{C}$, which corresponds to the high temperature side of the principal glow peak for P39. This temperature range shows the strongest variation in the shape of the luminescence decay curves and is the one of most practical relevance in operation of the phosphor in data displays. We describe the recombination in terms of a diffusive motion of the trapped electrons, this diffusion occurring by thermal emission and intertrap tunneling, the dominant process being determined by the trap concentration. This model correctly predicts the observed change in the kinetics of recombination from activated to nonactivated behavior as N_{As} increases, and is further supported by the observation of t^{-2} decay at long times (36). This recombination model is quite different from the activated tunneling model proposed by Avouris and co-workers (12, 13), who have described the luminescence decay on the low temperature side of the glow peak (i.e., below 0°C) in terms of a tunneling transfer of electrons from excited states of traps in a fixed spatial distribution to the ionized $\text{Mn}_{\text{Zn}}^{3+}$ centers. The Avouris and Morgan model proposes that at temperatures below the glow peak maximum the electrons distributed on trap sites are immobile before recombination by tunneling, whereas at temperatures above the glow peak maximum the trapped electrons are thermally emitted to the conduction band and can recombine with $\text{Mn}_{\text{Zn}}^{3+}$ centers by diffusion. From our results, we expect intertrap tunneling between As centers to be an important factor affecting electron motion at low temperatures, and we have no evidence to suggest a marked change in recombination mechanism at the temperature of a glow peak maximum. The significance of these differences will be discussed in a later paper.

Acknowledgments

The authors are grateful to Y. Thefaine and J. Wilson for assistance in making some of the experimental measurements, to C. F. Guerci for assistance in sample preparation, and to F. Cardone, J. Kuptsis, and R. Savy for the chemical analyses.

Manuscript submitted Jan. 26, 1984; revised manuscript received July 31, 1985.

IBM Corporation assisted in meeting the publication costs of this article.

REFERENCES

1. "Optical Characteristics of CRT Screens," JEDEC Publication 16-C, Electronic Industries Association, Washington, DC (Nov. 1975).
2. D. S. McClure, "Electronic Spectra of Molecules and Ions in Crystals," Academic Press, New York (1959).
3. H. C. Froelich and G. R. Fonda, *J. Phys. Chem.*, **46**, 878 (1942).
4. J. M. Brownlow and I. F. Chang, in "SID/IEEE Display Research Conference Proceedings," p. 66, IEEE, New York (1982).
5. I. F. Chang and M. W. Shafer, *Appl. Phys. Lett.*, **35**, 229 (1979).
6. T. E. Peters and J. R. McColl, Abstract 151, p. 379, The Electrochemical Society Extended Abstracts, Vol. 81-1, Minneapolis, MN, May 10-15, 1981.
7. J. T. Randall and M. H. F. Wilkins, *Proc. R. Soc. London, Ser. A*, **184**, 390 (1945).
8. G. F. J. Garlick and A. F. Gibson, *Proc. Phys. Soc.*, **60**, 574 (1948).
9. H. W. Leverenz, "Luminescence of Solids," John Wiley and Sons, New York (1950).
10. U. Kummel, E. Krantz, and R. Knutter, *Phys. Status Solidi A*, **11**, 181 (1972).
11. D. B. Dove, T. Takamori, I. F. Chang, P. Thioulouse, E. E. Mendez, and E. A. Giess, *J. Lumin.*, **24/25**, 317 (1981).
12. Ph. Avouris, I. F. Chang, D. B. Dove, T. N. Morgan, and Y. Thefaine, *J. Electron. Mater.*, **10**, 887 (1981).
13. Ph. Avouris and T. N. Morgan, *J. Chem. Phys.*, **74**, 4347 (1981).
14. P. Thioulouse, I. F. Chang, and E. A. Giess, *This Journal*, **130**, 2065 (1983).
15. I. F. Chang and G. A. Sai-Halasz, *ibid.*, **127**, 2458 (1980).
16. I. F. Chang, P. Thioulouse, E. E. Mendez, D. B. Dove, and T. Takamori, *J. Lumin.*, **24/25**, 313 (1981).
17. H. Hess and E. Krautz, *ibid.*, **24/25**, 321 (1981).
18. I. F. Chang and P. Thioulouse, *J. Appl. Phys.*, **53**, 5873 (1982).
19. E. A. Giess, C. F. Guerci, J. D. Kuptsis, I. F. Chang, and D. J. Robbins, *J. Cryst. Growth*, **60**, 219 (1982).
20. H. K. Perkins and M. J. Sienko, *J. Chem. Phys.*, **46**, 2398 (1967).
21. D. T. Palumbo and J. J. Brown, *This Journal*, **117**, 1184 (1970).
22. R. Fern and I. F. Chang, Unpublished work.
23. A. L. N. Stevels and A. T. Vink, *J. Lumin.*, **8**, 443 (1974).
24. D. J. Robbins, E. E. Mendez, E. A. Giess, and I. F. Chang, *This Journal*. To be published.
25. K. Nakamoto, "IR Spectra of Inorganic and Coordination Compounds," John Wiley and Sons, New York (1963).
26. R. F. DeKeersmaecker and D. J. DiMara, *J. Appl. Phys.*, **51**, 1085 (1980).
27. E. S. Yang, D. B. Dove, M. W. Shafer, and I. F. Chang, *J. Electron. Mater.*, **10**, 423 (1981).
28. W. L. Medlin, *Phys. Rev.*, **122**, 837 (1961); *ibid.*, **123**, 502 (1961).
29. P. J. Dean, *Prog. Solid State Chem.*, **8**, 1 (1973).
30. C. J. Delbecq, Y. Toyozawa, and P. H. Yuster, *Phys. Rev. B*, **9**, 4497 (1974).
31. N. F. Mott and E. A. Davis, "Electronic Processes in Non-crystalline Materials," Clarendon Press, Oxford, England (1971).
32. S. Chandrasekhar, *Rev. Mod. Phys.*, **15**, 1 (1943).
33. S. M. Sze, "Physics of Semiconductor Devices," John Wiley and Sons, New York (1981).
34. R. M. Fuoss, *Trans. Faraday Soc.*, **30**, 967 (1934).
35. D. W. Marquardt, *J. Soc. Ind. Appl. Matl.*, **2**, 431 (1963).
36. N. S. Caswell, D. J. Robbins, and I. F. Chang, Unpublished work.
37. L. Onsager, *Phys. Rev.*, **54**, 554 (1938).

Backgating in Ion-Implanted GaAs MESFET

Wade C. Tang,* Kerry S. Lowe,*¹ I. Abdel-Motaleb, and Lawrence Young*

Department of Electrical Engineering, University of British Columbia, Vancouver, British Columbia, Canada V6T 1W5

Modification of MESFET drain current characteristics by varying the (negative) voltage applied to a nearby electrode on the semi-insulating substrate is known as backgating (1-5) and is potentially a serious dysfunction for GaAs integrated circuits. Although the name implies an electrostatic field effect which causes a modulation of the channel, the substrate does not normally act simply as a dielectric through which a field is generated by the backgate. Lee *et al.* (3) and Miers *et al.* (4) found that a threshold voltage was required to produce the effect and

* Electrochemical Society Active Member.

¹ Present address: Bell Northern Research Laboratories, Ottawa, Ontario, Canada K1Y 4H7.

that a sharp increase in the current drawn by the backgate occurred at the same threshold. This suggested a trap-filled limit (6) above which injected electrons cause the substrate to become sufficiently conducting to transfer a sufficient part of the applied voltage to the junction of the n-channel with the substrate. In a more recent paper, Blum and Flesner (7) found little or no threshold with devices made using capless proximity annealing of the implanted silicon in contrast to the use of a Si_3N_4 cap in the previous work. They suggested the presence of a p-like layer produced by the outdiffusion of EL2, an idea previously mooted by Chang *et al.* (8) to explain cross talk between devices. Ogawa and Kamiya (10) have now re-

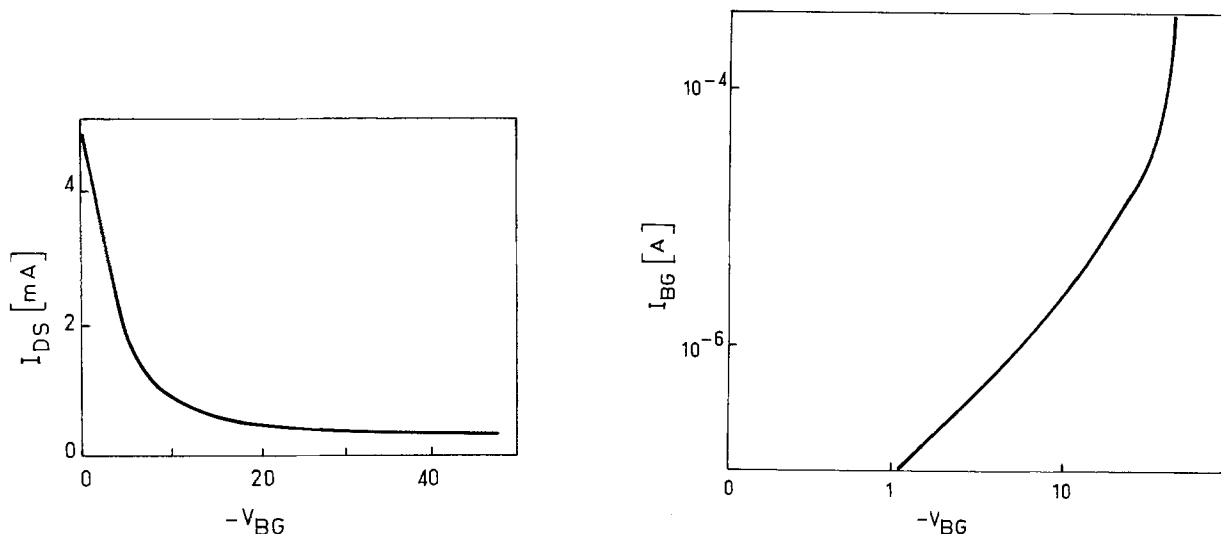


Fig. 1. MESFET annealed under SiO_2 cap. a(left): I_{DS} vs. V_{BG} for $V_{GS} = 0$ showing no threshold. b(right): I_{BG} vs. V_{BG} showing sudden increase in I_{BG} at $V_{BG} \sim -30\text{V}$.

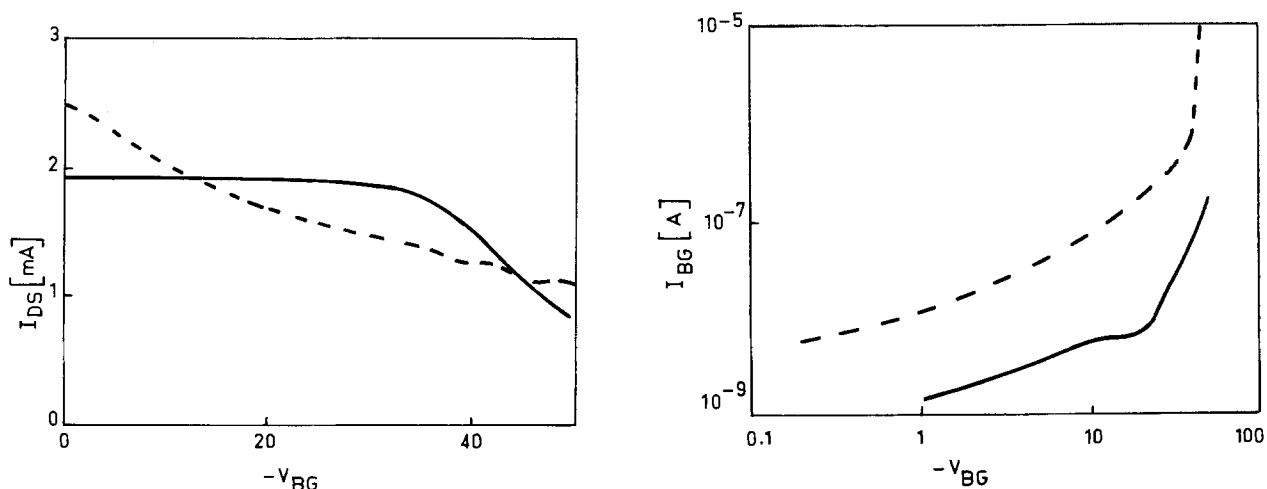


Fig. 2. MESFET annealed under Si_3N_4 cap. a(left): I_{DS} vs. V_{BG} for $V_{GS} = 0$. b(right): I_{BG} vs. V_{BG} . Solid lines: implanted directly. Broken lines: implanted through thin Si_3N_4 .

ported that with Cr-doped wafers the backgating occurred gradually but that there was a threshold for undoped wafers.

In the present communication, we wish to report having obtained a result similar (9) to that of Blum and Flesner with devices made in our laboratory. In one set of MESFET's with 3 and 20 μm long Al gates, $3 \times 10^{12} \text{ cm}^{-2}$ ^{29}Si was directly implanted at 100 keV (at OPTOTEK, Ottawa, Canada) and annealed under a 170 nm RF-sputtered SiO_2 cap at 850°C for 20 min under N_2 . These devices did not require a threshold voltage for backgating (Fig. 1a). Figure 1b shows how I_{BG} rose sharply at (typically) -30V . It was proposed (9) that the model of Chang *et al.* (8) applied to our device. The n^+ layer (due to indiffused Ge under the Au + Ge electrode) with the p-surface conversion layer (due to loss of EL2) and the n-channel form an n + p-n structure. The sharp increase in I_{BG} may perhaps be due to the reverse breakdown of the p-n junction part of this structure.

Results are also given (Fig. 2) for I_{DS} vs. V_{BG} (MESFET gate grounded) for samples on two slices both annealed with a 90 nm PECVD Si_3N_4 cap (deposited with a Plasmatherm Multiversion system). One slice was directly implanted with $2.2 \times 10^{12} \text{ cm}^{-2}$ ^{29}Si , and the other was implanted through 40 nm of Si_3N_4 with $3.4 \times 10^{12} \text{ cm}^{-2}$, both at 100 keV, using the EXTRION 200-20 implanter in our laboratory. This 40 nm was increased to 90 nm before annealing. A "fat FET" mobility profile (5) was done. The devices implanted through Si_3N_4 gave a mobility decreasing with depth. The other gave increasing mobility. As found by Immorlica *et al.* (5), the decreasing mobility profile gave more backgating.

It is clear that the backgating effect can be strongly dependent on the details of the fabrication process and that more than one mechanism can produce the effect.

Precipitation in Fe-Doped Semi-Insulating InP Epitaxial Layer Grown by Metalorganic Chemical Vapor Deposition (MOCVD)

S. N. G. Chu,* S. Nakahara,* J. A. Long, V. G. Riggs, and W. D. Johnston, Jr.*

AT&T Bell Laboratories, Murray Hill, New Jersey 07974

Growth of semi-insulating InP bulk crystals by the liquid-encapsulated-Czochralski (LEC) technique has been achieved routinely by doping with iron (1-8). Resistivity greater than $10^7 \Omega\text{-cm}$ can be attained. However, due to the low segregation coefficient ($k_{\text{eff}} = 2 \times 10^{-4}$) of Fe in InP (8), the pile-up of Fe in the vicinity of the growing solid-liquid interface leads to the formation of a eutectic phase, FeP_2 , which in turn is trapped randomly in the crystal as the growth proceeds (6, 7). Needle- and block-shaped particles 100 μm in size have been observed (7). The estimated dopant concentration at which the particles begin to incorporate into the crystal is around $1 \times 10^{19} \text{ cm}^{-3}$ (6). Recently, Smith *et al.* have also observed a spongelike rod-shaped particle which was identified to be FeP (8).

More recently, Long *et al.* (9) have demonstrated the growth of Fe-doped semi-insulating InP on (001) InP substrates by metalorganic chemical vapor deposition (MOCVD) using $\text{Me}_3\text{In-PMe}_3$ adduct as the In source and $\text{Fe}(\text{C}_5\text{H}_5)_2$ and $\text{Fe}(\text{CO})_5$ as dopant sources. Resistivity as high as $2 \times 10^8 \Omega\text{-cm}$ can be achieved at a dopant level of $\sim 2 \times 10^{18} \text{ cm}^{-3}$. The semi-insulating InP epitaxial layer has been used as the current confinement layer for buried heterostructure lasers (10). Potential applications for the material, such as its use as the base material for microwave devices and as the isolation layer for vertical integration of optoelectronic devices, can also be envis-

Acknowledgments

This work was supported by the B. C. Science Council and by the National Science and Engineering Research Council of Canada. We thank OPTOTEK Limited, Ottawa, for their courtesy in doing implants for us before we had the necessary equipment.

Manuscript submitted April 3, 1985; revised manuscript received June 17, 1985.

The University of British Columbia assisted in meeting the publication costs of this article.

REFERENCES

1. T. Itoh and H. Yanai, *IEEE Trans. Electron Devices*, **ed-27**, 1037 (1980).
2. H. Goronkin, M. S. Birrittella, W. C. Seelbach, and R. L. Vaitkus, *ibid.*, **ed-29**, 845 (1982).
3. C. P. Lee, S. J. Lee, and B. M. Welch, *IEEE Electron Dev. Lett.*, **ed1-3**, 97 (1982).
4. T. H. Miers, W. M. Paulson, and M. S. Birrittella, in "GaAs and Related Compounds," Institute of Physics Conference Series 65, p. 339, Institute of Physics, London (1982).
5. A. A. Immorlica, D. R. Ch'en, D. R. Decker, and R. D. Fairman, in "GaAs and Related Compounds," Institute of Physics Conference Series 65, p. 423, Institute of Physics, London (1980).
6. M. A. Lampert and P. Mark, "Current Injection in Solids," Academic Press, New York (1970).
7. A. S. Blum and L. D. Flesner, *IEEE Electron Dev. Lett.*, **ed1-6**, 97 (1985).
8. M. F. Chang, C. P. Lee, L. D. Hou, R. P. Vahrenkamp, and C. G. Kirkpatrick, *Appl. Phys. Lett.*, **44**, 869 (1984).
9. W. C. Tang, M.A.Sc. Thesis, University of British Columbia, Vancouver, B.C., Canada (1984).
10. M. Ogawa and T. Kamiya, *IEEE Trans. Electron Devices*, **ed-32**, 571 (1985).

aged. Since the perfection of the epitaxial layer is crucial to the ultimate performance of the device, the possibility of precipitation in semi-insulating InP grown by MOCVD needs to be explored. In this study, we report the observation of a precipitate in the Fe-doped epitaxial layer by transmission electron microscopy. The composition and structure of the precipitate will be investigated by x-ray energy dispersive analysis and TEM microdiffraction.

Experimental

Fe-doped semi-insulating InP epitaxial layers used in this study were grown by MOCVD on S-doped (001) InP substrates, using $\text{Me}_3\text{InPMe}_3$ adduct as the In source and $\text{Fe}(\text{C}_5\text{H}_5)_2$ and $(\text{COT})\text{Fe}(\text{CO})_3$ (COT = cyclooctatetraene) as dopant sources. Details of the MOCVD reactor and the growth procedure were described elsewhere (9). The layers were grown at 650°C with a growth rate ranging from ~ 3 to 10 $\mu\text{m/h}$. The defect structure of the as-grown layer was characterized by transmission electron microscopy (TEM) on a (110) cross-section sample. The cross-section TEM (XTEM) sample preparation technique, using a grid masking method, was described previously (11). SIMS depth profiling of the Fe-concentration distribution was done by Charles Evans, Incorporated, using a calibrated standard with known Fe concentration. The composition and structure of the precipitate were investigated by x-ray energy dispersive analysis and electron diffraction. Detailed TEM diffraction study on particles extracted by dissolving the epilayer and particles collected using nitro-

*Electrochemical Society Active Member.

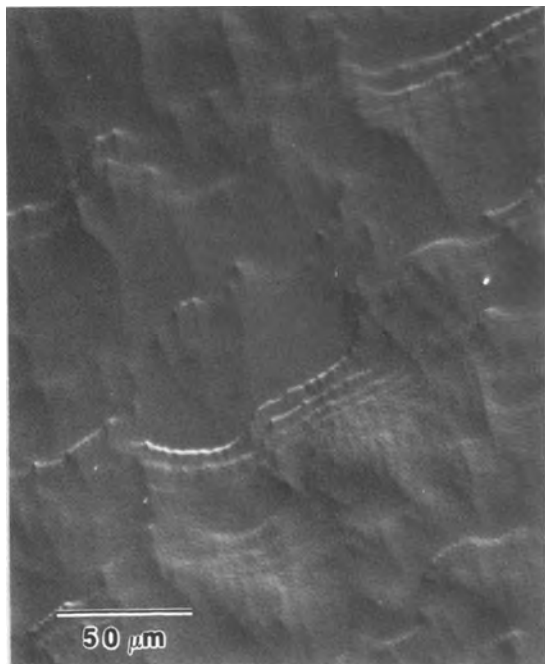


Fig. 1. Nomarski interference photomicrograph of as-grown surface of Fe-doped InP epitaxial layer.

cellulose film (1% amyl acetate) will be discussed elsewhere (14).

Results and Discussion

Although the surface of as-grown Fe-doped InP is highly specular under reflected light, detailed surface morphology is not smooth as revealed by Nomarski interference contrast microscopy (see Fig. 1).

A desert-like surface is typical for a vapor-grown InP layer. The Fe-concentration distribution determined by SIMS depth profiling is shown in Fig. 2. Two peaks near the interface are present. The Fe peak located at the interface ($3.20 \mu\text{m}$) is similar to those observed at substrate/epi layer interfaces regardless of the dopant types. The possible causes have been attributed to surface contamination introduced during wafer handling or out-diffusion of background Fe concentration from the substrate material (12, 13). The appearance of a second peak indicates a transient period in Fe incorporation during the initial stage of epitaxial growth. The average Fe concentration away from the interface is $\sim 1.2 \times 10^{18} \text{ cm}^{-3}$, and the resistivity of the layer is $2 \times 10^8 \Omega\text{-cm}$.

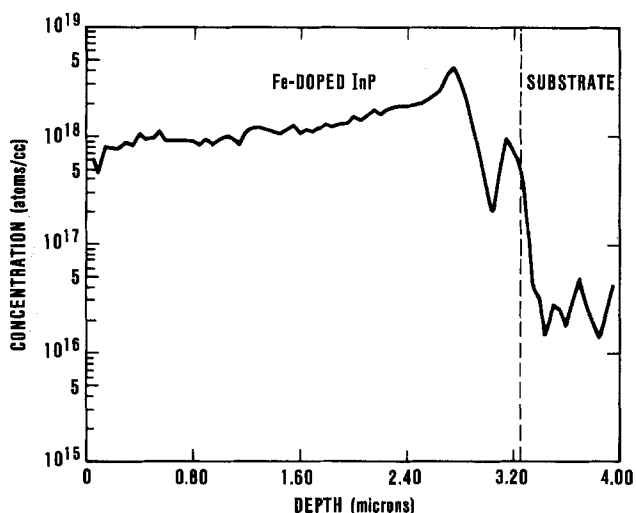


Fig. 2. SIMS depth profile of Fe concentration in InP grown by MOCVD.

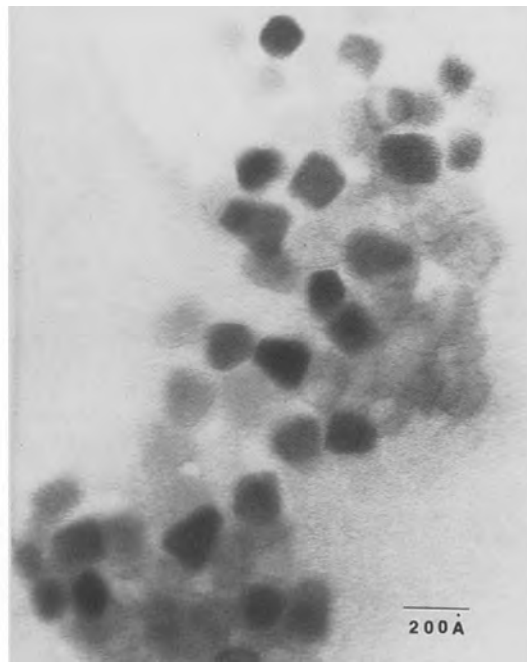


Fig. 3. TEM micrograph of precipitates in Fe-doped InP

Small precipitates of 100-250Å in size are observed by transmission electron microscopy in the (110) cross-section sample. They appear in the form of clusters as shown in Fig. 3. A close examination reveals Moiré fringes associated with most of the particles (see Fig. 4), which indicates that the particles are actually lying on the surface of the sample.

The chemical constituents of the particle were determined by x-ray energy dispersive analysis using a fine electron probe 20Å in size. The spectra taken inside and outside the particle are shown in Fig. 5. Since the detection limit of Fe concentration in InP by this technique is $\sim 5 \times 10^{20} \text{ cm}^{-3}$, a dopant level of 10^{18} cm^{-3} cannot be ob-

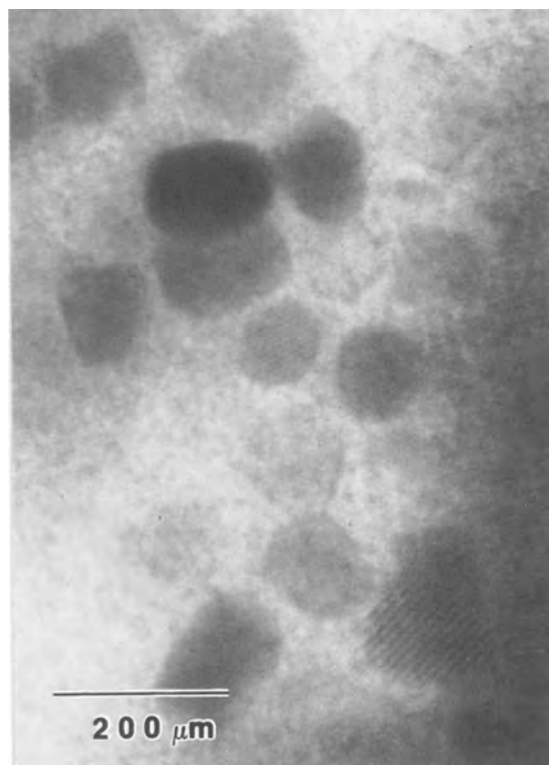


Fig. 4. TEM micrograph showing Moiré fringes associated with the particles.

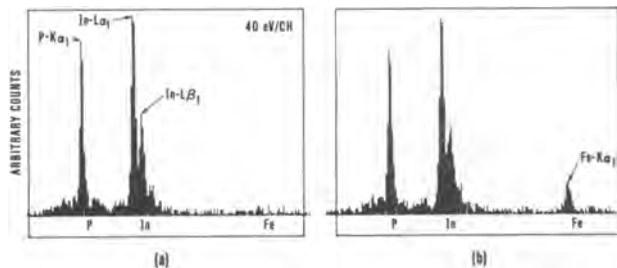


Fig. 5. X-ray energy dispersive spectra taken outside (a) and inside (b) the precipitate.

served. The spectrum taken outside the particles shows only In L lines and P K_α lines (see Fig. 5a). However, an FeK_α peak does appear in the spectrum taken inside the particle (see Fig. 5b). X-ray line scan across the particle further confirms that the iron detected is confined inside the particle. Since the Fe_mP_n compounds have lattice structures different from InP, the type of compound which constitutes the particle can be determined by electron diffraction on extracted particles. The details of the electron-diffraction analysis on the extracted particles will be described elsewhere (14). The major result is shown in Fig. 6, where the electron diffraction pattern is compared with the calculated pattern for FeP₂ and FeP. A careful examination confirms that the particles are FeP.

Since the majority of the precipitates observed in the MOCVD layer are coherent to the InP lattice, the minimization of the strain energy associated with the mismatch thus plays a major role in determining the type of Fe-P compound to be precipitated out. Although the lattice structure of both FeP and FeP₂ are orthorhombic, the difference in lattice constants results in a closer match of FeP ($a = 5.794$, $b = 5.187$, and $2c = 6.190$) to InP ($a = 5.869$) as compared to FeP₂ ($a = 5.460$, $b = 4.985$, and $2c = 5.668$) to InP.

Occasionally, dislocation structures are observed in conjunction with the particles, of which one is shown in Fig. 7. The strong strain contrast associated with the particle is an indication that the high stress concentration developed around the particle is likely to be the cause for dislocation generation. Furthermore, most of the bow-out dislocations contain cusps along the dislocation line, which indicates that the dislocations are pinned by the precipitates during their slipping.

Finally, the density of the precipitates are compared for layers at two different dopant concentrations, *i.e.*, 3×10^{17}

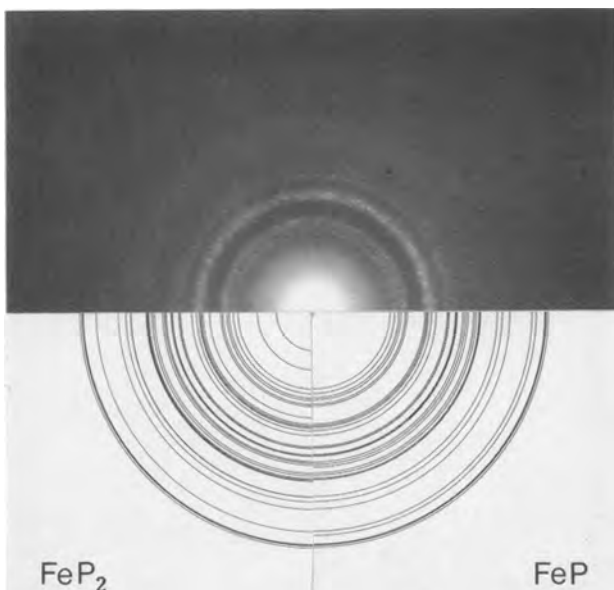


Fig. 6. Comparison of electron diffraction pattern from extracted particles with calculated diffraction patterns from FeP₂ and FeP powders.

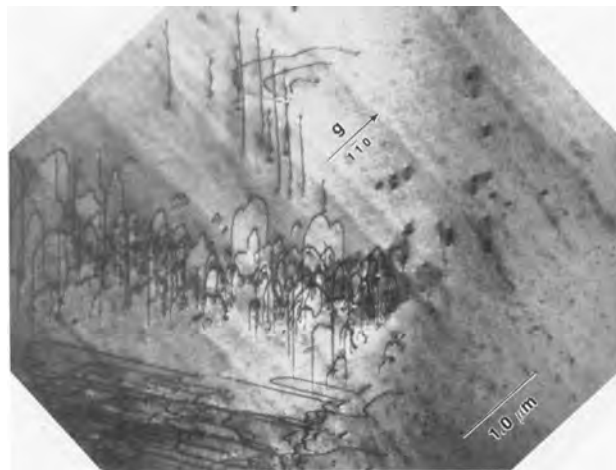


Fig. 7. Dislocation structure in Fe-doped InP epitaxial layer. The dark spots are precipitates.

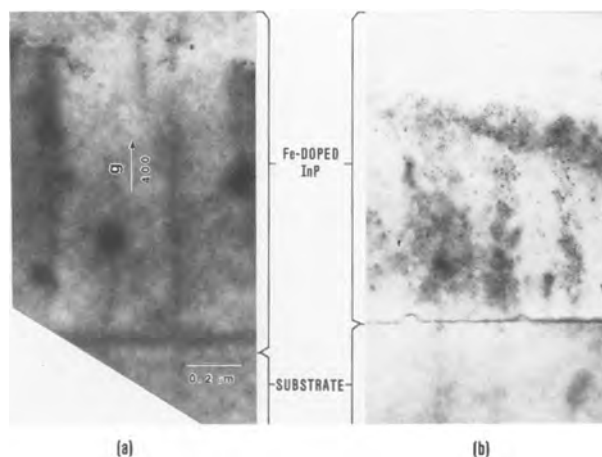


Fig. 8. (110) TEM cross-sectional view of Fe-doped InP epilayers showing particle density at Fe concentrations of $3 \times 10^{17} \text{ cm}^{-3}$ (a) and $2 \times 10^{19} \text{ cm}^{-3}$ (b).

and $2 \times 10^{19} \text{ cm}^{-3}$. The corresponding XTEM micrographs are shown in Fig. 8. In spite of the fact that the majority of the precipitates are lying on the surface of the sample, the drastic increase in the density of the precipitates at a doping level of $2 \times 10^{19} \text{ cm}^{-3}$ is clearly demonstrated. The size of the precipitates, however, is more or less constant, which is expected if it is determined by the misfit strain energy.

Conclusion

We have reported the observation of small coherent precipitates in Fe-doped semi-insulating InP epitaxial layer grown by MOCVD on S-doped (001) InP substrate. Within the iron concentration range of 3×10^{17} to $2 \times 10^{19} \text{ cm}^{-3}$, the density of precipitate increases with increasing iron concentration, while the size of precipitates (100-250Å) remains more or less constant. These are identified as FeP. Due to the differences in lattice structures, precipitation of FeP instead of FeP₂ observed in bulk crystal can be rationalized in terms of the minimization of the misfit strain energy. Occasionally, slip-type dislocation structures were observed associated with the precipitates.

Acknowledgment

The authors would like to thank A. F. Bloemeke and A. T. Macrander for the resistivity measurements. Thanks are also due to Dr. Richard McConville, who kindly took the x-ray line scan shown in Fig. 5. The support and encouragement of J. V. DiLorenzo, L. C. Feldman, and G. Y. Chin for this work are appreciated.

Manuscript received March 29, 1985.

AT&T Bell Laboratories assisted in meeting the publication costs of this article.

REFERENCES

- O. Mizuno and H. Watanabe, *Electron. Lett.*, **11**, 5, 118 (1975).
- D. Rumsby, R. M. Ware, and M. Whitaker, *J. Cryst. Growth*, **54**, 32 (1981).
- C. R. Zeisse, G. A. Antypas, and C. Hopkins, *ibid.*, **64**, 217 (1983).
- E. Kubota, Y. Ohmori, and K. Sugii, *Inst. Phys. Conf. Ser.*, **n63**, 31 (1982).
- M. Morioka, K. Kikuchi, K. Kohe, and S. Akai, *ibid.*, **n63**, 37 (1982).
- S. Miyazawa and H. Koizumi, *This Journal*, **129**, 2335 (1982).
- R. N. Lee, M. K. Norr, R. L. Henry, and E. M. Swiggard, *Mater. Res. Bull.*, **12**, 651 (1977).
- N. A. Smith, I. R. Harris, B. Cockayne, and W. R. MacEwan, *J. Cryst. Growth*, **68**, 517 (1984).
- J. A. Long, V. G. Riggs, and W. D. Johnston, Jr., *J. Cryst. Growth*, **69**, 10 (1984).
- D. P. Wilt, J. A. Long, W. C. Dautremont-Smith, and M. W. Focht, Unpublished work.
- S. N. G. Chu and T. T. Sheng, *This Journal*, **131**, 2663 (1984).
- J. Chevrier, M. Armand, A. M. Huber, and N. T. Link, *J. Electron. Mater.*, **9**, 745 (1980).
- S. N. G. Chu, F. A. Stevie, A. T. Macrander, R. F. Karlicek, C. C. Chang, C. M. Jodlauk, K. E. Strege, D. L. Mitcham, and W. D. Johnston, Jr., *This Journal*, **132**, 1187 (1985).
- S. Nakahara, S. N. G. Chu, J. A. Long, V. G. Riggs, and W. D. Johnston, Jr., *J. Cryst. Growth*, To be published.

Color and Efficiency of Neodymium Iodide Discharges

W. A. McAllister*

North American Philips Lighting Corporation, Bloomfield, New Jersey 07003

Atomic radiation from a number of metals, added as iodides to the high intensity mercury discharge, has provided light sources of exceptional efficiency (100 lm/W) and some improvement in color rendering properties (1). An exception, the tin iodide-mercury discharge has the color rendering characteristics of an incandescent source (2), some Sn-I molecular species being held responsible for the continuum radiation associated with this color improvement (3). Since both continuum and line spectra have been noted in rare earth iodide discharges (4), attractive combinations of efficiency and color rendition might be attainable at the color temperature (2900 K) of an incandescent source. One such material, neodymium iodide, alone or in combination with alkali iodides, has been examined in this work.

Experimental

Arc tubes (400W) were baked at 1050°C under vacuum, electrodes flashed in argon, and raw materials added in a commercial dry train under argon. After evacuation, 20 torr of argon was introduced, and the completed arc tube end coated using a zirconia suspension before mounting in a quartz-jacketed assembly. This evacuated unit was then used for measurement of the spectral power distribution in an integrating enclosure, and the other parameters of interest determined using a computer program formulated for this purpose. When results were attractive, the arc tube was mounted in outer bulb coated with CaS;Eu phosphor in organic lacquer, the resultant change in spectral and other properties were determined as above.

Neodymium was added as wire (99.9% pure, United Mineral) to react *in situ* with mercuric iodide, both the latter and the alkali iodides being introduced as spherical pellets (Anderson Physics Laboratories). A slight excess of neodymium metal over that required for complete reaction with the iodide was found necessary to improve starting. The mercury concentration was 2.5×10^{-4} mol, neodymium iodide 2.5×10^{-5} mol; alkali iodide concentrations are listed in Table I.

Results

The efficiencies and the color characteristics of neodymium iodide discharges are listed in Table I, with the voltage and current values for operation at 400W; included for comparison are figures for bare mercury and sodium-scandium iodide discharges evaluated in the

* Electrochemical Society Member Representative.

same decountable configuration. Neither efficiency nor color temperature is changed from that of the mercury discharge on inclusion of neodymium iodide alone; the improvement in color rendering index (CRI) is associated with continuum radiation throughout the visible (Fig. 1), particularly in the 600-700 nm region. This feature is enhanced considerably upon addition of cesium iodide with the rare earth halide (Fig. 2), with both CRI and efficiency now improving and color temperature remaining at the mercury discharge level (Table I). Use of sodium iodide (4×10^{-5} mol) instead of the cesium salt brought the color temperature down to 4580 K, efficiency and CRI values being lower than those noted with cesium iodide. Addition of 2×10^{-5} mol cesium iodide at this so-

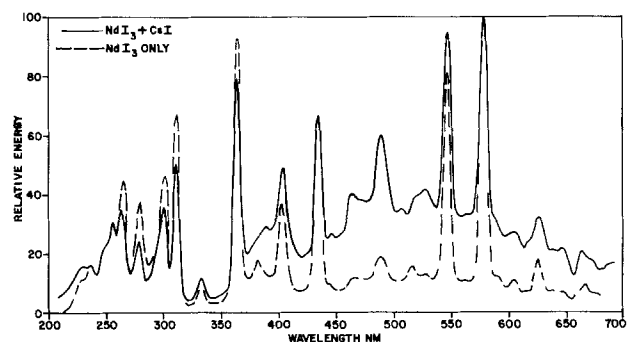


Fig. 1. Spectra of neodymium iodide discharges. Dashed line: NdI_3 only. Solid line: $\text{NdI}_3 + \text{CsI}$.

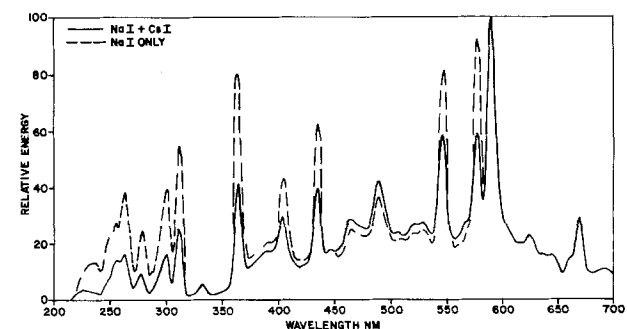


Fig. 2. Spectro of neodymium iodide-cesium iodide discharges. Dashed line: NaI only. Solid line: $\text{NaI} + \text{CsI}$.

Table I. Efficiency and color characteristics of neodymium iodide discharges (lamps)

Additive concentration (mol $\times 10^{-5}$)		Efficiency (lm/W)	Color rendering index	Color temperature (K)	Voltage (V)	Current (A)
CsI	NaI					
—	—	56	57	5490	145	3.05
2.0	—	81 (52.0)	72 (86)	6220 (4280)	138 (140)	3.7 (3.7)
2.0	—	81 (51.8)	73 (89)	6136 (4250)	130 (127)	3.4 (3.7)
—	4.0	73	66	4580	175	3.6
2.0	4.0	84 (69)	69 (59)	5029 (3350)	136 (125)	3.14 (3.3)
2.0	2.7	81 (60)	72 (80)	5080 (3360)	132 (137)	3.2 (3.2)
2.0	1.4	82 (54)	73 (80)	5180 (3480)	150 (150)	2.55 (2.87)
1.0	2.0	87 (63)	76 (88)	5360 (3380)	165 (160)	2.76 (2.8)
Mercury		50	20	5800		
Sodium						
Scandium		100	65	3900		

dium iodide concentration increased the efficiency to 84 lm/W, CRI to 69 and CCT to 5029 K, with the spectral shifts given in Fig. 2. Only slight changes in these values could be effected by altering the CsI/NaI ratios or concentrations (Table I).

Further discharge-related color improvements being unattainable, conversion of ultraviolet to visible red emission was accomplished through use of CaS:Eu,Sn (6) phosphor ($\lambda_{\text{peak}} = 650$ nm) coated on the outer bulb for some arc tubes, the lamps burned for 100h, after which time the data in Table I were assembled. Those with lamps having neodymium and cesium iodides had CRI values near 90, but color temperature was that of cool white source and efficiency that of the mercury discharge. While additions of sodium iodide increased the latter figure and lowered color temperature to values approaching the 2900 K of an incandescent source, color rendition dropped as sodium iodide concentration increased. Then with lower concentrations of the two alkali iodides, efficiency and color rendition improved but color temperature was again near 4000 K; application of a more dense phosphor coating lowered the latter to 3380 K, efficiency now being 63 lm/W and CRI = 80. The spectral changes occurring as phosphor coating weight increased are depicted in Fig. 3, the most dense coating weight providing a trace similar to that of an incandescent source with mercury and sodium lines superimposed.

Discussion

The large increases in efficiency and improvement in color rendition on adding both neodymium and cesium iodides to the mercury discharge are due to greater continuum radiation intensities with insignificant change in the mercury line intensities (Fig. 1). This suggests that the neodymium contribution has been enhanced by formation of a complex with higher vapor pressure than that for the rare earth salt alone (7).

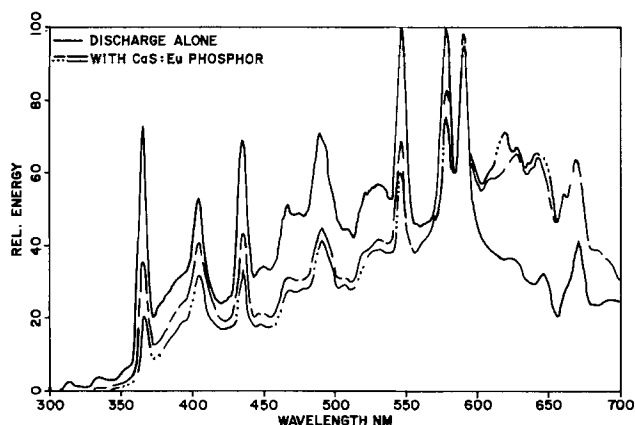


Fig. 3. Spectra of neodymium iodide · cesium iodide · sodium iodide discharge lamps. Solid line: discharge only. Dashed line: discharge + CaS:Eu,Sn phosphor (light density). Dot-dashed line: discharge + phosphor (heavier density).

The continuum radiation (Fig. 2) is not as intense relative to the mercury and sodium lines when sodium iodide is the only added halide and is not altered significantly in absolute terms on addition of cesium iodide. The latter's presence is associated with considerable suppression of mercury line intensities without effect on the sodium line intensity. Thus, the continuum becomes a greater fraction of the overall radiated energy, giving the better color and efficiency characteristics cited above. The mercury line suppression may be due to the formation of $\text{NdI}_3 \cdot \text{CsI} \cdot \text{Hg}$ complex, as postulated by Liu and Zollweg (8). Some support for this speculation is supplied by the facts that (i) the spectra, efficiency, and color properties are unchanged with a three-fold change in sodium iodide concentration, cesium iodide being held constant at 2×10^{-5} mol, and (ii) the mercury lines regain their prominence, and continuum contribution improves, when the cesium iodide concentration is halved at 2×10^{-5} mol sodium iodide.

The bandpass used for these figures made for ease in the analog-to-digital conversion required for the application of correction factors to the raw data and derivation of the efficiency and chromatic parameters. Closer inspection at higher resolution revealed the presence of many lines ascribed to Nd atomic transitions in the band envelopes depicted, yet the continuum persisted even at high resolution (1 nm) slit width. Although some of the continuum below 405 nm has been associated with electron attachment to halogen atoms (9) and the 444 nm band is due to Hg-I (10), most is doubtless due to some molecular neodymium-iodine species, or combinations thereof with the monovalent iodides. Since NdI_3 can dissolve neodymium metal, in excess here, to form $\text{NdI}_{1.95}$ (11) with lower melting point (562°C) than NdI_3 , a contribution from the reduced iodide to the molecular radiation would be expected. However, absorption measurements by others showed no spectral difference in vapor over $\text{NdI}_3 \cdot \text{CsI}$ and $\text{NdI}_2 \cdot \text{CsI}$ mixtures (8). Uncertainty surrounding the geometry of $\text{NdI}_3 \cdot \text{CsI}$ complexes, or for that matter NdI_3 itself (8, 12), makes further speculation on the molecular species involved somewhat presumptuous.

Acknowledgments

The writer gratefully acknowledges the discussions with, and measurements provided by, W. A. Thornton as well as the technical assistance of D. Rachko and E. Chen.

Manuscript submitted Feb. 8, 1985; revised manuscript received ca. July 1, 1985. This was Paper 584 presented at the Hollywood, Florida, Meeting of the Society, Oct. 5-10, 1980.

North American Philips Lighting Company assisted in meeting the publication costs of this article.

REFERENCES

- See, for example, J. F. Waymouth, "Electric Discharge Lamps," MIT Press, Cambridge, MA (1971).
- T. Higashi, L. Mori, and S. Nagano, Paper presented at the CIE Conference, Washington, DC (1967).
- D. M. Speros, R. M. Caldwell, and W. E. Smyser, *High Temp. Sci.*, **4**, 99 (1972).

4. W. Pilz and H. P. Popp, in "Proceedings of the International Conference on Phenomena Ionized Gases (Prague)," p. 409, Czechoslovakian Academy of Science, Prague, Czechoslovakia (1973); D. A. Larson and W. A. Thornton, Final Report, ECOM Contract DAAB07-72-C-0091 (1973).
5. W. A. Thornton, *This Journal*, **116**, 286 (1969).
6. W. Lehmann and F. M. Ryan, *ibid.*, **118**, 477 (1971).
7. C. Hirayama, C. S. Liu, and R. J. Zollweg, in "High Temperature Metal Chemistry," D. L. Hildenbrand and D. D. Cubicciotti, Editors, p. 95, The Electrochemical Society Softbound Proceedings Series, Princeton, NJ (1978).
8. C. S. Liu and R. J. Zollweg, *J. Chem. Phys.*, **60**, 2384 (1974).
9. D. A. Rothe, *Phys. Rev.*, **177**, 93 (1969).
10. R. W. B. Pearse and A. G. Gaydon, "The Identification of Molecular Spectra," 3rd ed., Chapman and Hall, London (1965).
11. L. F. Druding and J. C. Corbett, *J. Am. Chem. Soc.*, **83**, 2462 (1961).
12. J. C. Wells, J. B. Gruber, and M. Lewis, *Chem. Phys.*, **24**, 391 (1977).



COMMENTS

Each issue of the **Journal** will have a section of "Comments." In this section, we provide a means via short pieces, *i.e.*, one column or less, to applaud, dispute, or otherwise discuss the papers published in the **Journal**. Space will be provided for one response by the paper's author(s) to each comment.

Since space available in each issue for the "Comments" section is limited; it is important to be concise.

Comments should be sent to the Editor, Dr. Norman Hackerman, Department of Chemistry, Rice University, P.O. Box 1892, Houston, TX 77251.

Norman Hackerman
Editor

Adsorption of Hydroxide and Sulfide Ions on Single-Crystal n-CdSe Electrodes

K. W. Frese, Jr. and D. G. Canfield
(pp. 2614-2618, Vol. 131, no. 11)

S. Licht:¹ The attempt to determine equilibrium and free energy constants for hydroxide and hydrosulfide/sulfide adsorption onto CdSe in this study is commendable, although certain anomalies render the data uninterpretable.

(i) Surface adsorption of charged particles changes the free energy and potential over that surface.² Hence the equilibria "constant" and free energy for adsorption are potential (*i.e.*, concentration dependent), and it was inappropriate to determine constants for these processes.

(ii) The measured CdSe flatband potentials, V_{FB} , variation of 240 mV/log [OH⁻] and approximately 90 mV/log [HS⁻], even upon assumption of large interaction parameters between adsorbed particles, are inconsistent with their proposed adsorption of monovalent species onto the electrode surface. Regeneration of their data, using their adsorption isotherm, provides a poor fit of their measured

¹ Department of Materials Research, The Weizmann Institute of Science, Rehovot 76100, Israel.

² S. R. Morrison, "Electrochemistry at Semiconductor and Oxidized Metal Electrodes," pp. 60-64, Plenum Press, New York (1980).

data. Hence by rearrangement of their Eq. [8], [OH⁻] in solution may be computed from θ , the relative extent of hydroxide adsorbed on the surface, using their equilibria constant, $K = 50.4$ and their interaction parameter, $f = 1.7$. These computations are presented in Fig. 1 and are compared to their experimental data; their adsorption isotherm fits only at $\theta = 0.5$. An alternate, charge- and potential-consistent model for adsorption onto semiconductors has recently been proposed.³

(iii) Time-dependent chemical substitution reactions occur in the dark between CdSe and alkali polysulfide electrolytes⁴ and will presumably occur to a greater degree in the less stabilizing sulfate and sulfide electrolytes used in the study of Frese and Canfield. Assuming a time- and concentration-dependent modification of the CdSe electrode in sulfate electrolyte to Cd(OH)₂, or in the sulfide solution to CdS, it becomes unclear on which semiconductor their V_{FB} and adsorption properties were characterized.

(iv) Variation in the redox potential of the electrolyte can have a large effect on measured V_{FB} .⁵ The alkaline sulfate and sulfide electrolytes employed in the study were made without added sulfite or sulfur. From the Nernst equation, the sulfate/sulfite and the polysulfide redox couples both have undefined potentials in the respective absence of

³ S. Licht and V. Marcu, Submitted to *J. Electroanal. Chem.*

⁴ D. Cahen, G. Hodes, and J. Manassen, *This Journal*, **125**, 1623 (1978).

⁵ S. U. M. Khan and J. O'M. Bockris, *J. Appl. Phys.*, **52**, 7270 (1981).

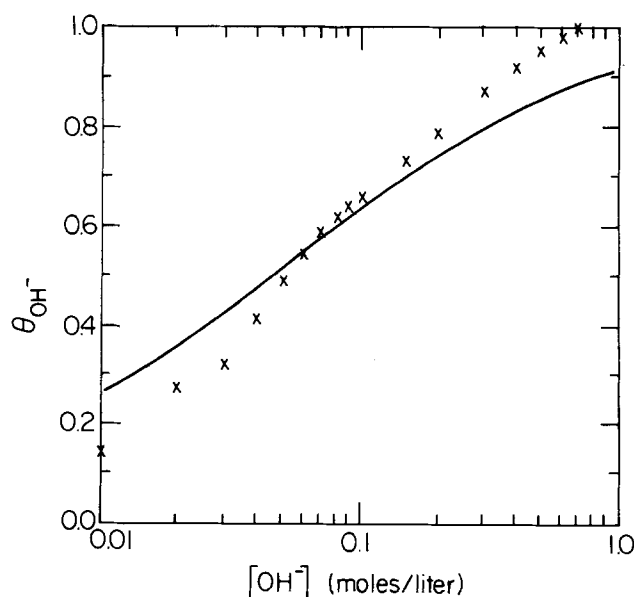


Fig. 1. Extent of hydroxide surface coverage on CdSe, θ , vs. log of hydroxide concentration in solution for n-CdSe (1120) in 0.1M Na₂S₄. Experimental data (points) are from Frese and Canfield. Solid curve: this work. Hydroxide concentrations are calculated upon rearrangement of Eq. [8] in Frese and Canfield, using $K = 50.4$ and $f = 1.7$.

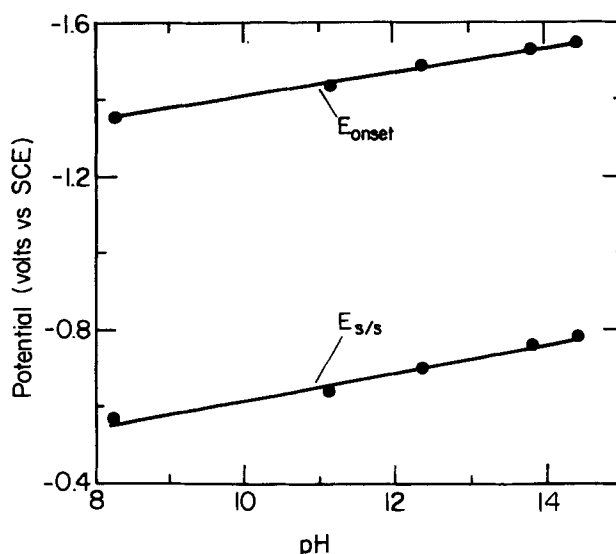


Fig. 2. The measured variation with pH, at room temperature, of polysulfide redox potential (vs. standard calomel electrode) and of the photocurrent onset potential (vs. standard calomel electrode) for a 0.15 cm² CdSe_{0.65}Te_{0.35} single-crystal immersed in an aqueous solution containing 1.8M in CsHS and 3M in sulfur, and various concentrations of CsOH, under tungsten halogen lamp illumination of 75 mW/cm².

significant quantities of sulfite or sulfur. In both cases, impurities and oxidation products of these materials will greatly effect the electrolyte redox potential, which, in turn, may create significant errors in measured V_{FB} .

The differential change of V_{FB} with $[\text{OH}^-]$ might be expected to be similar for the other cadmium chalcogenides. An attempt at measuring cadmium sulfide flatband potential variation with $[\text{OH}^-]$ and $[\text{HS}^-]$ had experimental deficiencies which also rendered the data uninterpretable. That study concluded a 60 mV/pH unit slope for V_{FB} ;⁵ however, their measured pH values were inconsistent by up to 2.2 pH units with pH values readily calculated from their initial concentrations of alkali hydroxide and alkali sulfide added to solution (total hydroxide = alkali hydroxide + hydrolyzed alkali sulfide).⁶ In Fig. 2, my measurements in polysulfide solution of the pH variation of $\text{CdSe}_{0.65}\text{Te}_{0.35}$ V_{FB} , as reflected by trends in photocurrent onset potential, show a slope of 30 mV/pH unit. Note that this slope approximates the observed pH variation of the polysulfide redox potential.

Systematic and consistent application of solution chemistry is vital to the fundamental understanding of CdX/aqueous polysulfide photoelectrochemical solar cells. A recently developed model for the complex distribution of species within aqueous polysulfide solution is useful in understanding these processes.⁷ This correspondent has recently proposed an overall mechanism for the photooxidation of polysulfide in CdX/polysulfide PEC's in which S_4^{2-} , OH^- , and HS^- are shown to be the preferential participants in the reaction process.⁸

K. W. Frese, Jr.⁹ We are aware that the free energy of adsorption and the apparent equilibrium constant are coverage dependent. This was demonstrated by our Eq. [8]-[10] in the paper under discussion. The isotherm we used accounts for this dependence in an approximate way; that is, it assumes that the free energy of adsorption varies linearly with coverage. We disagree that our results are not interpretable, because in the very least the apparent free energy of adsorption can be extrapolated to zero coverage to obtain a meaningful result.

In the case of adsorption of OH^- , we calculated the apparent free energy of adsorption at each coverage up to $\theta = 0.6$. The value of ΔG of -1.7 kcal/mol was found for $\theta < 0.2$; which corresponds to $K = 18$. A slightly more negative value of -2.3 kcal/mol was reported in our paper.

A new feature was revealed by the additional analysis of the OH^- adsorption data. The apparent ΔG becomes negative as coverage increases up to $\theta = 0.6$. This behavior suggests that f in the Frumkin isotherm is actually negative. A possibly similar effect was mentioned in our paper in the discussion of sulfide adsorption. In that case, surface compound formation (CdS) is strongly suspected. Because f appears to be small (about -0.9), we could not distinguish the correct sign in our original analysis. Perhaps compound formation as cadmium hydroxide is suggested by our data.

The use of photocurrent onset potentials to measure the flatband potential as suggested by Licht is not without difficulties. The onset potential depends on light intensity, is influenced by the magnitude of the forward current, and probably depends on the amount of dissolved sulfur. The parallelism between the onset potential and the redox potential in Licht's Fig. 2 probably means that the Helmholtz potential drop is changing due to Fermi level pinning. This means that variations such as the 30 mV/pH of the onset potential reflect the metallic character of the surface (high surface state density) rather than adsorption properties. Our unpublished measurements of the surface state density on n-CdSe in 1M NaOH show that there are only about 1×10^{11} state/cm² in the upper part of the gap. On the contrary, more than 1×10^{14} state/cm² were found in the upper part of the bandgap of CdSe in contact with alkaline sulfide solutions.

⁶ D. S. Ginley and M. A. Butler, *This Journal*, **125**, 1968 (1978).

⁷ S. Licht, J. Manassen, and G. Hodes, Submitted to *Inorg. Chem.*

⁸ S. Licht, Submitted to *J. Phys. Chem.*

⁹ SRI International, Menlo Park, California 94025.

Electrochemical Behavior of Passive Iron in Acid Medium

II. The Passive Film/Solution Interface

M. Keddam and C. Pallotta

(pp. 781-787, Vol. 132, no. 4)

V. Jovancicevic¹⁰ In this paper, the authors raise two interesting questions relating to the passive iron/solution interface. The first one is the relationship between electron and ion charge transfer at the interface, and the second one is about the effect of anions on the kinetics of charge transfer on the film surface. The interpretation of the results involving a loosely structured boundary layer on the top of the inner solid layer needs some remarks.

Keddam and Pallotta argue that the redox reactions, with opposite anion effect on $\text{Fe}(\text{CN})_6^{4-}$ and $\text{Fe}(\text{II})$ oxidation on the passive layer, are allowed by the good electron conductivity of the inner layer and controlled by mass transfer across the transition layer. The effect of anion in the increasing interaction sequence, perchlorate, sulfate, and phosphate, on the passive current is described in terms of the adsorption and subsequent penetration of anions into the loosely structured layer, affecting its passive properties. This model has some similarity to the "chemiconductor" model of the passive film regarding its conductivity.¹¹

The mass-transfer properties and anion interaction with the passive layer are studied by using the angular velocity transient and composition transient of the passive current. Both transients show similar features: first, fast change of the current (minutes), followed by slow attainment of the steady state (hours). Even though the observed effects are similar in these transients, they are interpreted differently. The short-time response is explained as a "mass-transfer-limited process," whereas the long-time response as a decrease of the thickness of the film in the case of the angular velocity transient. In the case of the composition transient, the fast response corresponds to anion adsorption, while the slow response to anion penetration into the film. Recently, similar effects have been obtained with the pH transient where both changes in the thickness and in the surface composition of the layer were suggested.^{12,13}

The adsorption of anions on the surface of the passive layer supported by the results on the colloidal iron oxide is a first step in the formation of $\text{Fe}(\text{III})$ -anion soluble complexes.¹⁴ It is well known that $\text{Fe}(\text{III})$ forms in acid solution stable octahedral aquo complexes where water molecule(s) are substituted by the anion ligands.¹⁵ The stability of the complexes depends on the pH and on the type of anions increasing in the sequence, perchlorate, sulfate, phosphate, as discussed by Keddam and Pallotta. Thus, under steady-state conditions, at constant potential, the different currents correspond to different thicknesses of the film in equilibrium with the solution. When various transients are applied, the passive current increases or decreases, depending on whether more stable or less stable complexes are being formed.

The authors studied kinetics and mass transfer at the passive film/solution interface without clearly giving the reasons for the increase or decrease of the current with the change of the composition of the solution or angular velocity of the electrode. Both effects as well as pH effect can be attributed to the change of the thickness of the passive layer.¹⁶

A relevant aspect of the passive film behavior has been neglected in the study of the current transients which is its potential dependence. Besides the change of the thickness, the potential variation may cause some change in the com-

¹⁰ Department of Chemistry, Texas A&M University, College Station, Texas 77843-3255.

¹¹ B. D. Cahan and C. T. Chen, *This Journal*, **129**, 17, 474, 921 (1982).

¹² O. Reies Iola, A. M. Sukhotin, and L. N. Gerasimenko, *Elektrokhimiya*, **18**, 723 (1982).

¹³ V. Jovancicevic and J. O'M. Bockris, Submitted to *This Journal*.

¹⁴ K. J. Vetter and F. Gorn, *Electrochim. Acta*, **18**, 321 (1973).

¹⁵ F. A. Cotton and G. Wilkinson, "Advanced Inorganic Chemistry," Interscience Publishers, New York (1980).

¹⁶ V. Jovancicevic, In preparation.

position and structure of the passive layer. Thus, using the pH, abrupt change in the solution the relative concentration of Fe(II) in the passive layer could be estimated.¹⁶

S. Kapusta:¹⁷ The dependence of the anodic current measured on passive iron electrode in acid solutions on rotational speed and the correlation of these results with erosion-corrosion phenomena deserve some comments. For the systems under consideration, fluid flow can either promote the transport of matter to and from the surface (convective mass-transfer-controlled dissolution) or it can cause stresses on the surface that may shear the passive film or the metal (corrosion-erosion).

The shear stress on a rotating disk electrode is¹⁸

$$\tau\omega = \rho r \nu^{1/2} \omega^{3/2} G'(0) \quad [1]$$

where ρ is the density of the solution, r the radius of the electrode, ν the kinematic viscosity, ω the angular frequency, and $G'(0)$ a function described elsewhere.¹⁸ One disadvantage of the rotating disk (as compared, *e.g.*, to the rotating cylinder) is that the shear stress depends on position, being maximum at the border of the electrode and (virtually) vanishing at the center. Another often overlooked problem is that the shear stress values obtainable on a practical RDE are small, usually of the order of a few dynes per square centimeter. For instance, for $r = 0.25$ cm and $\omega = 100$ rpm, $\tau\omega = 0.5$ dyn/cm². These stresses may become two to three times larger if the disk is suddenly started, although the stress transients are short.¹⁸

It is doubtful that these small stresses could shear a passive film, since this would imply that the forces bonding the film to the metal surface (or to other, "inner" films) are very weak (less than 1 kcal/mol, *i.e.*, at or below the range of physical adsorption). As an example, we have all experienced the difficulty in removing nitrogen bubbles that tenaciously remain on the center of a RDE even at relatively high speeds. The bubbles are held mainly by buoyancy. One can calculate that even though the bonding forces are very small, rotation alone cannot dislodge these bubbles. To consider such a loosely attached layer part of the passivation film is, at best, arbitrary. However, the authors have based many of their conclusions precisely on this approach.

The stresses involved in actual erosion-corrosion are several orders of magnitude higher, since they may inflict damage to the passive film or the metal itself. These stresses can usually be achieved in multiphase flow, *e.g.*, by particle impact, or, more recently, by focused ultrasonic waves.

Several criteria can be used to distinguish between convective mass transfer and erosion effects. In a first approximation, we may assume that film shearing occurs above a certain threshold shear stress. An increase in ω then should lead to a corresponding decrease in the coverage of the electrode above a certain radius from the center, as can be calculated from Eq. [1] setting $\tau\omega = \text{const}$. If we further assume that the passive current I_p is proportional to the uncovered area, we obtain

$$I_p \propto 1 - \omega^{-3} \quad [2]$$

i.e., a much higher functional dependence of current on ω than reported (*i.e.*, 1/2). Usually, with direct erosion the current varies with the third to sixth power of velocity, while with convective mass transport, the order is ≤ 1.0 .¹⁹

A second difference between convective mass transfer and erosion-controlled reactions is that, with the former, the current follows almost instantaneously any changes in rotational speed and is reversible towards reversal of these changes, while the latter may show an induction period and a certain degree of hysteresis on returning to the starting conditions.

¹⁷ Shell Development Company Westhollow Research Center, Houston, Texas 77001

¹⁸ "Hydrodynamic Resistance and the Heat Loss of Rotating Solids," L. A. Dorfman, Editor, Oliver and Boyd, London (1963).

¹⁹ V. Lotz and E. Heitz, *Werkst. Korros.*, **34**, 454 (1983).

The "staircase" shape of the current transient at constant potential and ω , observed in H₃PO₄ solutions, seems like an experimental artifact, since electrochemical systems do not usually show this type of "digital" behavior.

All this evidence suggests that, indeed, a loosely adherent layer may form, under these experimental conditions, on top of the true passive film. However, dissolution of this layer is to some extent mass-transfer controlled. It is further suggested that this layer is formed by dissolution and reprecipitation, from a saturated solution, of the phosphate and sulfate iron salts. As mentioned earlier, this outer salt layer is not part of the true passive film, but it is rather loosely attached by weak forces and easily overcome (*e.g.*, by rotation). In addition, the anions may also be incorporated into the passive film, as is the case with borate ions, or may otherwise induce localized film breakdown.²⁰ These are, however, well known and documented effects, and I fail to see any new facts in the paper under discussion.

The kinetics of redox reactions on passive electrodes has received considerable attention, and the present results are very interesting. The absence of one of the components of the redox couple, however, introduces some ambiguities in the results, because the system is "unbuffered," *i.e.*, large potential changes occur near the surface as one of the species in the redox couple is generated in the course of the reaction. These potential changes may affect both the conductivity and the composition of the film.

I wish the authors had published some of their polarization curves. In fact, even some old-fashioned exchange current densities and Tafel slope values would have served the purpose. It is frustrating trying to obtain any correlation between reported currents measured at different potentials.

Unexpectedly, the diffusion coefficients of the ferrocyanide ion measured on passive electrodes are consistently lower (approximately 1/2-1/3) than those measured on platinum (although the authors claim that they are similar), even in HClO₄ solutions where passive iron shows a "metallic" (in what sense?) behavior. Was a similar effect observed with Fe²⁺? If not, it could be a specific Fe(CN)₆⁴⁻ effect caused by diffusion through a thin and rotation-dependent layer of [Fe(CN)₆]₂Fe₃ deposited on the surface, as briefly indicated by the authors. If this is the case, however, the ferrocyanide may also interfere with the formation of the overlying salt film, considerably complicating the analysis of ac impedance diagrams.

The EHD diagrams are somehow misleading: Contrary to appearance and expectations, the results for H₃PO₄ solutions, where the more stable "porous" film is formed, fall between those of HClO₄ and H₂SO₄ solutions, instead of being the furthest removed from the ideal diffusion case. This, again, suggests some leveling effect perhaps caused by interference of the Fe(CN)₆⁴⁻ with the normally deposited salt film. Moreover, mechanical removal of this porous film should eliminate the shift towards lower p values, which it does not. Therefore, the evidence overwhelmingly negates any mechanical effect on film stability, while it indicated a mass-transfer-controlled mechanism.

It should be obvious by now that electrochemical techniques alone cannot uniquely define the film composition, and, lacking some independent analytical result, all speculations in this respect will remain just that. Since the films grown in H₃PO₄ solutions may incorporate significant amounts of phosphate ions, it is questionable that the β -FeOOH composition is a valid model. On the other hand, it is to a certain point arbitrary and even confusing to attribute a particular bulk oxide composition to a thin film, (about 40Å in 1M HClO₄),²¹ especially since compositional gradients are unavoidable and interfaces are not well defined.

In particular, the structure and properties of passivation films grown on stainless steels is strongly influenced by the presence of chromium, and any extrapolation from pure iron is not only unwarranted, but is also probably

²⁰ See, *e.g.*, Z. Szklarska-Smialowska, in "Proceedings of the 9th ICMC, Toronto (June 1984)," Vol. 2, p. 112.

²¹ B. P. Lochel and H. H. Strehblow, *Electrochim. Acta*, **28**, 565 (1983).

wrong. Therefore, to attribute the protective effect of molybdenum to intercalation or modification of the iron oxide requires further justification.

M. Keddam:²² We think that this comment brings about some interesting points and deserves the following remarks.

As has been pointed out by Keddam *et al.*,²³ the way in which we have depicted the passive film has some similarity with the semiconductor model in the sense that the high field transport across the inner part of the film is anion dependent. However, our results tend to prove that the anion contents of the inner layer, determining the passive current, is controlled by the highly hydrated outer part of the film. The properties of the latter are determined by the adsorbability of anions on the oxide's surface and by their interaction with the solvent structure.

Regarding the nextcoming papers announced in this comment, we would like to emphasize that, according to data we will show in Fig. 5 of our paper,²³ the film thickness at a given potential, referred to the Flade potential in the same solution, is practically independent of pH and anions. These parameters seem to modify the passive behavior through compositional effects (*e.g.*, ferric to ferrous oxide ratio²⁴) in the inner layer and structural change in the outer layer. Even in the limit, long-term aging changes hardly the thickness but rather proceeds by water out-take and progressive appearance of crystalline iron oxides.²⁴

With respect to pH transients published by Soviet authors and apparently repeated by Dr. Jovancicevic, the short-time response is considerably faster than with anion transient. A likely explanation is to consider that the film/electrolyte potential is determined by pH through an equilibrium between OH and iron oxides. Therefore, pH transients are equivalent to a transient of electrical field strength across the film and induce a fast current step. According to our own experiments, the direction of this step vs. pH step is consistent with this explanation.

²² Physique des liquides et électrochimie, l'Université Pierre et Marie Curie, 75230 Paris Cedex 05, France.

²³ M. Keddam, J. F. Lizée, C. Pallotta, and H. Takenouti, *ibid.*, **131**, 2016 (1984).

²⁴ A. Hugot-Le Goff and C. Pallotta, *ibid.*, To be published.

Regarding the comments of Dr. Kapusta on mechanical disturbances of the passive film, we have never meant that our rotating disk experiments could reproduce the high stresses or solid impacts involved in actual erosion-corrosion. This situation has been dealt with elsewhere.²⁵ Undoubtedly, the shear at the disk is by several orders of magnitude too low for destroying the passive film. However, the argument of a bubble at the very center of the disk submitted to a zero resulting radial force is not convincing.

Owing to the very low passive c.d., mass-transfer control by convective diffusion in its usual sense cannot be accepted as an explanation of the observed response. Therefore, an interpretation must be looked for in a weak hydrodynamical interaction with the passive film. As recognized finally in the comment, the existence of a loosely adherent layer constitutes a satisfactory model. In contrast with Dr. Kapusta's statement, there is no reason at all for thinking of this layer in terms of the salt film which precipitates during fast metal dissolution. In the case of phosphate, *in situ* Raman spectroscopy evidences iron phosphates on top of the passive film.²⁴ Washing out these products removes the corresponding spectrum but does not modify the passive current.

Regarding the RED-OX kinetics, most of the data have been completed and numerically processed since the time of publication of this paper. In fact diffusivities on Pt and on the passive film in HClO₄ are very close. "Metallic" does not refer to the type of conductivity but only to the fast charge transfer ensured by the film.

EHD data fit correctly to a model incorporating diffusion through a "solid" layer²⁶ which persists at high rotation speeds hence explaining the remanent shift towards low *p* values, for phosphate solution, as pointed out in the comment. We agree with the comment that ferrous ferricyanide is able to complicate the interpretation, Fe(II) shows a more complex behavior due to strong interference with the inner film structure. As explained in this paper, it tends to favor the formation of magnetite followed by Raman spectroscopy.

²⁵ J. C. Colson, A. Desestret, M. Keddam, and R. Oltra, *Corros. Sci.*, **23**, 441 (1983).

²⁶ C. Deslouis, M. Keddam, C. Pallotta, and B. Tribollet, "Electrochemical Methods in Corrosion Research," Toulouse, France (July 1985).



In Situ Raman Spectroscopy for the Study of Iron Passivity in Relation to Solution Composition

A. Hugot-Le Goff

LP 15 "Physique des Liquides et Electrochimie," associé à l'Université Pierre et Marie Curie, Tour 22, 75230 Paris Cedex 05, France

C. Pallotta

Facultad de Ciencias Exactas, Ciudad Universitaria, 1428 Nunez, Buenos Aires, Argentina

One of the most complicated topics in metal passivity is the chemical identification of thin films grown on iron electrodes. They are too thin to be analysed by X-rays, and in-situ methods such as Mossbauer spectroscopy or ellipsometry give only indirect results. RHEED (or LEED) which require that the sample be put in vacuum, are not suited to the problem. This explains why several structures, involving some of the numerous possible oxides or oxihydroxides, have been proposed. Raman Spectroscopy has become a useful tool for obtaining chemical and crystallographic identification (1,2).

In this paper, we will try to answer the following two questions :

- Is a defined film composition detectable by Raman Spectroscopy when the passive current, I_p , attains its steady-state value ?

- If a composition is defined, does it depend on the anion composition of the electrolyte ?

Previously we obtained spectra of each compound likely to appear in the passivity state, oxides or oxihydroxides, either as powder, or in single crystal form, together with thermal oxide films of easily controlled thickness (2). We studied the stability of these compounds under exposure to the laser beam. The oxihydroxides undergo a modification leading to the stable forms : hematite α - Fe_2O_3 , and magnetite Fe_3O_4 . However, when the samples were covered by a thin liquid layer during illumination (which reproduces the electrolysis conditions), each of them gave its proper spectrum.

EXPERIMENTAL

Iron electrodes (Johnson Matthey) carefully prepared, as previously described (3), and polished to 1200 grade emery paper, were polarised at different potentials in the full passive range in 1N H_2SO_4 solutions. These samples were placed flat in the cell under the objective of a microscope which served to focus the laser beam (514 nm) on a small area of the sample. This allowed study of local composition changes, and verification that the impact point was not damaged by the laser beam. The front length of objective is about 0.3 mm, permitting good

Manuscript submitted Jan. 28, 1985; revised manuscript received Sept. 10, 1985.

optical yield, and room for a layer of electrolyte sufficient to ensure stability of the electrochemical process. The spectroscope, DILOR OMARS 89, has a diode array detection system which permits addition of spectra and collection of data over long periods. This improves the signal to noise ratio. All potentials are referred to the saturated sulfate electrode (vs SSE).

RESULTS

When the passive potential is more anodic than 0.6 V, even if the current attains its steady-state value ($5 \mu A \cdot cm^{-2}$), a Raman spectrum is observed only after about 12 hours of polarisation. However, it has been shown that a passive film is formed at shorter times (4). The thickness of this "detectable" film was estimated by the amount of O^{16} in the film, as determined by nuclear reaction (5). The thickness was between 10 nm and 17 nm after three days of polarisation, whereas the thickness of the passive film observed after the first hour of polarisation was about 4 nm. Furthermore, for polarisation potentials more cathodic than 0.5 V, no Raman spectrum was observed even for long polarisation times (i.e. 90 hours).

Figure 1 represents two spectra : spectrum a is obtained in-situ after 12 hours of polarisation. Spectrum b corresponds to the same sample taken out of the electrolyte after a longer polarisation time. The electrolyte has an intense spectrum (due to SO_4^{2-} ions) in the 900-1000 cm^{-1} , but in the useful range for iron oxides, the in-situ identification is easy. The species identified under these experimental conditions were a mixture of magnetite (659, 544 cm^{-1}) and hematite (221, 253, 290, 406, 498, 616 cm^{-1}) γ -ferric oxide, as α - or γ - hydrated modifications, which are often assumed to appear, give quite different patterns and one can affirm that they are not present.

However, if the presence of hematite can be conclusively established, the existence of magnetite is not so evident. For the shortest polarisation times, the 544 cm^{-1} peak was not always present ; in this case, one cannot distinguish between the spectrum of magnetite,

CNRS assisted in meeting the publication costs of this article.

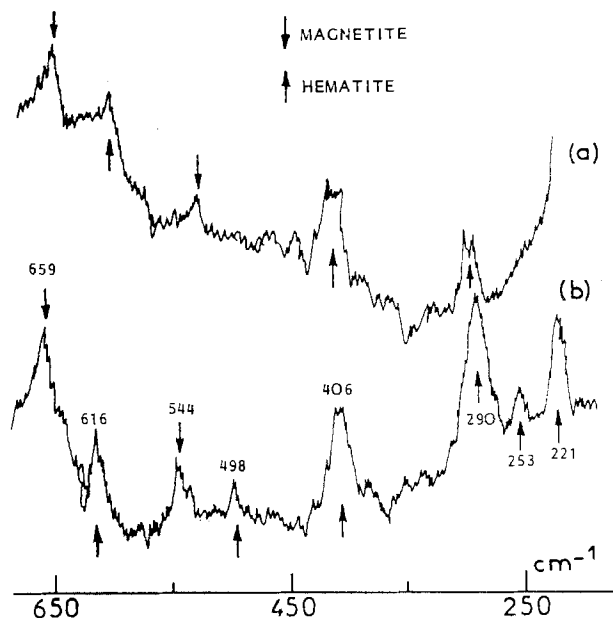


Figure 1 : 1a : in-situ 1b : ex-situ

and that of the short-range oxihydroxide, α -FeOOH, which as the β - and δ -modifications, gives a single faint peak at 670 cm^{-1} . The existence of an amorphous film at the beginning of the passivation is supported by the long ageing necessary under potentiostatic polarisation to obtain Raman spectra. If the lack of a spectrum during the first hours was simply due to the insufficient film thickness, it would be possible to detect some signal by increasing the laser power and the accumulation time. This was not observed. It can be assumed that, during this period, a qualitative change of the initial material, together with a slow thickening takes place. Furthermore, the oxides are detected only if the passivation potential is more anodic than 0.6 V , which is the thermodynamic potential for the formation of iron oxides.

The anions, at constant pH, have a definite effect in determining the I_p value (3). In the case of electrodes passivated for about 15 hours it was shown that the current responds reversibly to a rapid change of the electrolyte composition (6). In order to better understand the role of anions, the solution was rapidly changed (either to $2\text{N H}_3\text{PO}_4$ or to 1N HClO_4). In the first case, when the current attained its new steady-state value ($50\text{ }\mu\text{A}\cdot\text{cm}^{-2}$), the Raman spectrum was recorded, as shown in Fig. 2a. The intensity of the peaks related to hematite is increased, and a new peak at 507 cm^{-1} , corresponding to ferric phosphate, is observed. After several hours of polarisation, only the peaks of hematite remain along with a very intense salt peak.

In the second case, the oxide peaks remain unchanged (Fig. 2b), and two peaks of iron perchlorate are seen at 460 and 625 cm^{-1} . The

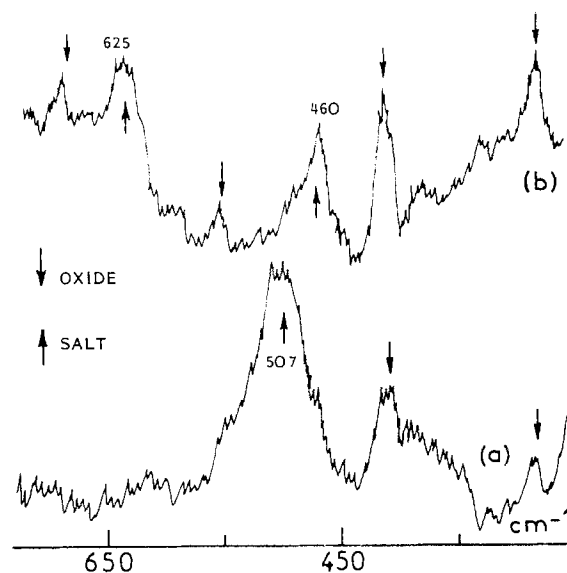


Figure 2 : 2a : $2\text{N H}_3\text{PO}_4$ 2b : 1N HClO_4

salt layer is tightly fixed on the film : and in spite of the solubility of the salt in water, it is necessary to wash the film for a long time to remove it. When the electrode is immersed again, the absence of the salt does not alter the current. From these experiments, it is possible to conclude that :

- The existence of a constant passive current is not related to the presence of species detectable by Raman Spectroscopy.

- The ratio between α -Fe $_2$ O $_3$ and Fe $_3$ O $_4$ depends on anions and, like the value of steady-state current, increases from H $_2$ SO $_4$ to H $_3$ PO $_4$.

This work has to be pursued by further measurements just below the range where the hematite/magnetite mixture is formed. From the present measurements, it is possible to conclude that the presence of crystalline oxide or oxihydroxide in α - or γ -modification in the young passive film is not probable. The structure of this young passive film may be polymeric, like with α -FeOOH structure containing, as proved in(4) a certain amount of Fe(II) ions.

REFERENCES

1. J. Dünwald, A. Otto, Fresenius Z. Anal. 319 (1984) 742.
2. M. Froelicher, A. Hugot-Le Goff, C. Pallotta, R. Dupeyrat, M. Masson "Passivity of metals and Semiconductors", Froment Ed. Elsevier Science Pub. (1983) 101.
3. M. Keddarn, J.F. Lizee, C. Pallotta, H. Takenouti, J. Electrochem. Soc. 131 (1984) 2016.
4. M. Froelicher, A. Hugot-Le Goff, V. Jovancicevic, R. Dupeyrat, M. Masson, J. Phys. C10 (1983) 187.
5. B. Agius, S. Siejka, J. Electrochem. Soc., 122 (1975) 723.
6. M. Keddarn, C. Pallotta, J. Electrochem. Soc. 132 (1985) 781.

The Analysis of Silver in Germanium Selenide Photoresist by Anodic Stripping Voltammetry

P. G. Huggett¹ and J. Greenaway

RCA Laboratories, CH-8048 Zurich, Switzerland

M. L. Hitchmen

Department of Pure and Applied Chemistry, University of Strathclyde, Glasgow, Scotland G1 1XL

ABSTRACT

Germanium Selenide ($\text{Ge}_x\text{Se}_{1-x}$, $x=0.1-0.3$) has shown considerable promise as a very high resolution photoresist when sensitized with silver deposited from an aqueous solution. However, the sensitization step has been found to be irreproducible for films prepared in different batches. It is therefore necessary to assess the silver uptake rate for each production batch. This paper will demonstrate how it is possible to assay absolutely the deposited silver by anodic stripping voltammetry. The technique is shown to be much quicker than the currently accepted analysis by X-ray fluorescence spectroscopy and also to be of reasonable accuracy and precision, provided background currents are subtracted from the voltammogram.

INTRODUCTION

The silver sensitized germanium selenide/polymer, bilayer photoresist system offers considerable advantages over conventional photoresists by extending the capabilities of optical lithography into the submicron regime (1,2). Sensitization of the films is performed by immersion in a solution of AgNO_3 or $\text{KAg}(\text{CN})_2$ which deposits silver. However, this reaction is very dependent upon the nature of the surface of the germanium selenide and this leads to variations from batch to batch in the reaction rates and induction times, even when films are evaporated under very stringent process parameters (3,4). Therefore it is necessary to assess each batch of films produced for the silver uptake rate in order to achieve reproducible photolithographic sensitivity. This has previously been done by X-ray fluorescence spectroscopic analysis (XRF) of sacrificial samples (3), but this technique, whilst highly accurate, requires calibrated sub-standards and is capital intensive and slow.

We have investigated the electrochemistry of the sensitizing reaction, in an attempt to

measure the amount of silver deposited and to elucidate the mechanism of the reaction, by potentiometry and anodic stripping voltammetry. This communication describes the analysis technique and compares results with those from XRF spectroscopy. The method is shown to be a fast, reliable and absolute method of adequate precision for the assay of silver in germanium selenide photoresist films. A full discussion of the mechanism of the reaction will appear in a forthcoming paper (5).

EXPERIMENTAL

Approximately 250nm thick germanium selenide ($\text{Ge}_{15}\text{Se}_{85}$) films were prepared, as described earlier (4), by evaporation onto scrupulously clean substrates. Substrates for XRF analyses consisted of 2 inch silicon wafers. Electrodes for electrochemical analyses consisted of a polymer coated 25x10mm quartz chip with a 100nm layer of sputtered gold and a top coating of germanium selenide. Electrical connection was made by a gold plated clip which punched through the underlying gold film. The edges of the chip and the atmosphere/electrode/electrolyte triple interface were coated with PMMA to avoid edge effects.

Sensitizing and stripping was carried out in 0.1M $\text{KAg}(\text{CN})_2$ buffered at pH10 and thermostatted at 25°C. The counter electrode consisted of a 10x25mm platinum foil held 20mm away and parallel to the germanium selenide electrode. The reference electrode was a saturated calomel electrode (SCE) separated from the working solution by a tube with a frit filled with 0.1M KCN solution to prevent the SCE clogging with AgCl . An air ambient was employed since no differences were found when the experiments were carried out with degassed solvents under nitrogen atmosphere. Electrical measurements were performed with in-house instrumentation. Stripping voltammetry was commenced at the rest potential of the system (ca -0.275V vs SCE) and then the potential was increased by a linear ramp to +1V with respect to the SCE at a rate of 13mV/s.

RESULTS

Two typical traces of current vs voltage with respect to the SCE are shown in Figure 1. Each plot shows 3 peaks which are all assignable to forms of silver; the exact assignment of the peaks will be discussed in a forthcoming paper. The absolute amount of silver stripped off can be determined from the area under the peaks. However, it is clear from the figure that background currents vary from sample to sample. Therefore, in order to subtract the background, it is necessary to apply a different correction for every run. We tried several protocols for background subtraction. The only successful method was to extrapolate the peak flanks to the base line as represented by the shaded areas in Figure 1(a).

The amounts of silver represented by the shaded areas are shown in the Table together with the results of the XRF analyses on the same evaporation batches. The Table shows the results from seven batches, each sample being sensitized for 3 minutes. The XRF data are the mean of 2 samples with an estimated error of better than $\pm 0.5 \mu\text{g}/\text{cm}^2$. The electrochemical data are the mean of 6 samples and at the 95% confidence level, there is an error of $\pm 2.0 \mu\text{g}/\text{cm}^2$ when total areas under the curves are taken, and of $\pm 0.9 \mu\text{g}/\text{cm}^2$ when the background current is subtracted. The larger error for the data using the total area probably represents the variability of the background current. For the corrected values of the silver content the agreement with the XRF values is good.

CONCLUSIONS

We have shown that stripping voltammetry is a useful technique for the absolute assay of silver in germanium selenide photoresist films. Unlike the established XRF and wet chemical analyses, the method offers a fast turn around with sufficient reliability for analyses of silver, which would be essential should germanium selenide photoresist be implemented on a wafer fabrication line.

REFERENCES

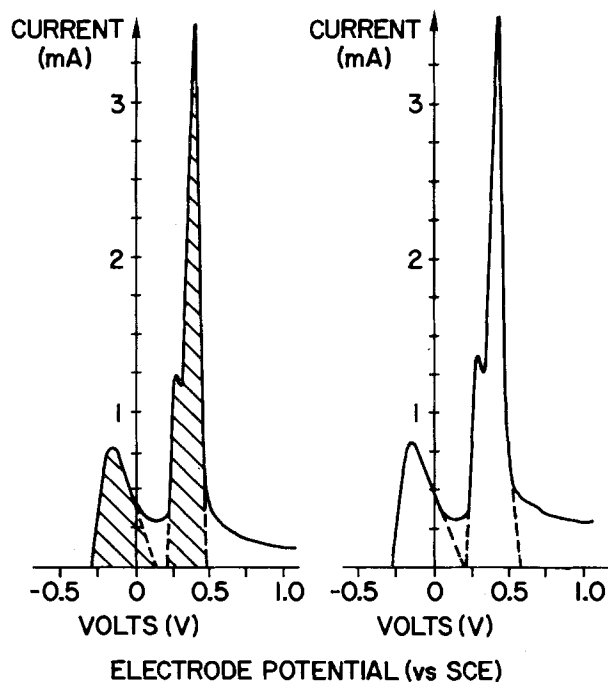
1. A D Doare, A Heller (eds), Proc.Symp. Inorg. Resists, ECS-82-9, (1982).
2. K L Tai, W R Sinclair, R G Vadimsky, J M Moran, J.Vac.Sci.Technol. 16, 1977 (1979).

¹Present address: Plessey Research (Caswell) Limited, Caswell, Towcester, Northants, England NN12 8EQ.

3. S M Vincent, T Y Kometari, Proc.Symp. Inorg. Resists, ECS-82-9, 169, (1982).
4. P G Huggett, K Frick, H W Lehmann, Appl. Phys.Lett., 42, 592, (1983).
5. P G Huggett, J Greenaway and M L Hitchman, results to be published.

Table Comparing Silver Analyses by XRF and Stripping Voltammetry

Evaporation Batch No.	Silver Content ($\mu\text{g}/\text{cm}^2$)		
	XRF	Voltammetry Uncorrected	Voltammetry Background Subtracted
1	12	17	13
2	16	24	18
3	14	24	17
5	13	17	13
6	15	22	16
7	13	16	14



Voltammograms for stripping silver from silver sensitized germanium selenide

Note: differences in the contributions of the background currents

Manuscript received Aug. 19, 1985.

Laboratories RCA Limited assisted in meeting the publication costs of this article.

Alkenylsilane Sulfone Copolymers and Terpolymers as Electron-Beam-Sensitive Positive Resists for Two-Layer Systems

Antoni S. Gozdz, Harold G. Craighead, and Murrae J. Bowden

Bell Communications Research, Incorporated, Murray Hill, New Jersey 07974

The continuing trend towards higher resolution and smaller feature sizes in integrated circuitry has led to the development of multi-layer resist processing schemes to achieve submicron resolution on topographical features [1]. A variety of organosilicon polymers have been investigated in the past decade as potential oxygen reactive ion etching (O_2 RIE) resistant resists for such applications. Although sensitive negative resists for two-layer applications have been developed [2], the sensitivity of similar positive resists is low [3].

Several years ago researchers at RCA reported [4] that poly(vinyltrimethylsilane sulfone) (PVTMSS) is a sensitive positive resist useful as a reactive ion etching (RIE) mask in two-layer resist systems. However, we found that this polymer is difficult to prepare in a soluble form and in a satisfactory yield. In this communication, we report an efficient synthesis, properties and lithographic performance of soluble poly(silane sulfone)s in which the silicon-bearing group is separated from the main chain by one or more methylene groups.

EXPERIMENTAL

Polymers suitable as e-beam resists were obtained by a UV-initiated terpolymerization of allyltrimethylsilane (ATMS) with at least a 6-fold molar excess of 1-butene and sulfur dioxide or in a similar reaction between 3-butenyltrimethylsilane (BTMS) and sulfur dioxide used as a solvent and monomer at -20°C . The polymerization was carried out in sealed Pyrex glass ampoules into which the monomers were transferred using vacuum line techniques. Resist films ca. 3000 Å thick were spun from 3.5% solutions of the polymers in cyclopentanone, and after soft-baking at 120°C they were exposed at 20 keV. Patterns were developed with 1:5 amyl methyl ketone/amyl alcohol solutions and transferred into 1.2 μm -thick hard-baked HPR-204 photoresist by O_2 RIE.

RESULTS AND DISCUSSION

Although poly(olefin sulfone)s are easily degraded upon irradiation, only poly(1-butene sulfone) (PBS) has found wide application as a sensitive, positive e-beam resist [5]. In spite of its many unique properties, its major drawback is its lack of resistance to the various plasma etching techniques used in integrated circuit manufacturing. The introduction of silicon into its structure as reported by the RCA group [4], was

expected to increase its O_2 RIE resistance because of the formation of an SiO_x layer on top of the resist. Unfortunately, we were unable to reproduce the results reported by the RCA group. By following the reported procedure, we could obtain only small amounts of insoluble polymer. However, we prepared and isolated a soluble material under conditions different from those reported in the mentioned patent. After precipitation into methanol, the polymer became insoluble due to hydrolysis of the trimethylsilyl group [6].

Since the solubility of poly(olefin sulfone)s is known to increase with increasing side chain length [7], and an increased reactivity of allylsilanes is well documented [8], we decided to synthesize poly(allyltrimethylsilane sulfone) (PATMSS). This copolymer is insoluble, as is its carbon analog, poly(4,4-dimethyl-1-pentene sulfone) [7]. However, we found that PATMSS may be solubilized by introducing at least 25–30 mol-% of 1-butene into the polymer chain by a UV-initiated terpolymerization of ATMS, 1-butene and SO_2 at below-ambient temperatures, preferably below -10°C . Modeling studies and chemical analyses indicate that ATMS is ca. 9 times more reactive towards SO_2 or SO_2 -capped growing radicals at -20°C than is 1-butene, while vinyltrimethylsilane (VTMS) is ca. 6 times less reactive. Therefore, the successful preparation of a soluble terpoly(ATMS butene sulfone) requires that 1-butene be present in at least a 6-fold molar excess vs. ATMS and that UV radiation be used to initiate the polymerization. If *tert*-butylhydroperoxide is used, an insoluble fraction, enriched in ATMS, was always obtained. Moreover, the polymerization should be carried out to low conversion (10–15%), to avoid an unacceptably heterogeneous terpolymer with inferior lithographic properties.

Very recently, we have found that 3-butenyltrimethylsilane forms a soluble and stable polysulfone which contains 14.6 wt-% Si. In view of the problems associated with PVTMSS and terpoly(ATMS butene sulfone)s, this material is being studied as a very promising poly(silane sulfone) for two-layer applications.

The low reactivity of VTMS may be explained by a steric hindrance caused by a relatively bulky trimethylsilyl group attached to the double bond. The *t*-butyl group in 3,3-dimethyl-1-butene is bulkier and this compound does not copolymerize with SO_2 . Also, the previously reported insolubility of poly(olefin sulfone)s

obtained from lower and branched olefins was explained as a result of their high cohesive energy density [7]. Bowden et al. [5] have found that polymerization of a 1:1 molar mixture of 1-hexene and SO₂ at 0°C gave a product containing a gel fraction which was attributed to cross-linked polymer formed via hydrogen abstraction and chain transfer reaction. Similar arguments may be invoked to explain the insolubility of PATMSS.

The terpoly(ATMS butene sulfone)s containing less than 70 mol-% of ATMS (vs. butene) are high-molecular weight polymers ($M_n > 2-3 \cdot 10^5$, $M_w/M_n = 2-2.5$ by GPC, $[\eta] = 150-250 \text{ cm}^3/\text{g}$ in MEK at 30°C), soluble in a wide range of organic solvents. Their solubility varies with the ATMS/butene ratio. The terpolymers are thermally stable in air up to 170–180°C (TGA) and their T_g was $99 \pm 1^\circ\text{C}$ (DSC). Initial data indicate that poly(3-butenyltrimethylsilane sulfone) (PBTMSS) has similar properties.

Lithographic sensitivity of the terpolymers containing 60–70 mol-% of ATMS (12–13.5 wt-% Si) and of PBTMSS to a 20 keV e-beam was 1.2–2.5 $\mu\text{C}/\text{cm}^2$, dependent on the substrate and development conditions. The terpolymers were used as top imaging layers for O₂ RIE pattern transfer into a thick planarizing layer of a conventional photoresist. Scanning Auger spectroscopic studies showed that they degraded rapidly under O₂ RIE conditions to a 10–100 Å thick SiO_x layer on top of degraded polysulfone. This layer was sufficient to provide protection against O₂ RIE for the underlying planarizing layer. Submicron resolution with vertical walls was readily attained (Fig. 2). However, the O₂ RIE processing latitude of these terpolymers is rather narrow, since their final performance is the result of two competitive processes: oxidative degradation and vaporization, and SiO_x protective layer formation. Thus, under harsher RIE conditions the first group of processes prevail and the resulting patterns contain many defects.

In conclusion, we have synthesized soluble poly(alkenylsilane sulfone)s by a UV-initiated copolymerization of 3-butenyltrimethylsilane with SO₂ or terpolymerization of allyltrimethylsilane with an excess of 1-butene and sulfur dioxide. Their sensitivity to a 20 keV e-beam is ca. 1.5 $\mu\text{C}/\text{cm}^2$ and contrast ca. 1.5–2.5. They are promising for use as sensitive, positive imaging layers for two-layer pattern transfer techniques.

REFERENCES

1. B.J. Lin, in: L.F. Thompson, C.G. Willson and M.J. Bowden, eds., Introduction to Microlithography, ACS Symp. Series No. 219, Washington, D.C. 1983, p.287-350
2. M. Morita, A. Tanaka, S. Imamura, T. Tamamura, and O. Kogure, Japanese J. Appl. Phys., 22, L-659 (1983)
3. E. Reichmanis and G. Smolinsky, in: C.G. Willson, ed., Adv. Resist Technol., Proc. SPIE 469, 1984, p.38
4. K.B. Kilichowski and T.R. Pampalone, U.S. Pat. 4,357,369 (1982); N.V. Desai, E.S. Poliniak, U.S. Pat. 4,396,702 (1983)
5. M.J. Bowden and L.F. Thompson, J. Appl. Polym. Sci., 17, 3211 (1973)
6. A.S. Gozdz and M.J. Bowden, submitted to Polymer Communications
7. K.J. Ivin, H.A. Ende and G. Meyerhoff, Polymer 3, 129 (1962)
8. H. Sakurai, A. Hosomi and M. Kumada, J. Org. Chem., 34, 1764 (1969)

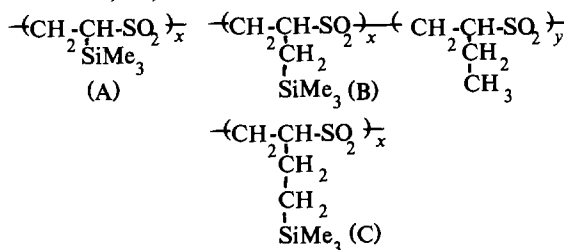


Fig. 1. Structural formulas of PVTMSS (A), terpoly(ATMS butene sulfone) (B) and PBTMSS (C)



Fig. 2. Submicron pattern O₂ RIE'd into 1.2 μm -thick HPR-204 using terpoly(ATMS butene sulfone) as a top imaging layer

Manuscript received July 25, 1985.

Bell Communications Research assisted in meeting the publication costs of this article.

Microphotoelectrochemical Etching of n-GaAs Using a Scanned Focused Laser

R. D. Rauh* and R. A. LeLievre

EIC Laboratories, Incorporated, Norwood, Massachusetts 02062

Localized photoelectrochemical reactions at semiconductor-electrolyte interfaces have been employed for producing photographic images, diffraction gratings, optical lenses, and metal contacts (1). Generally, fabrication of microetched structures have been accomplished at low light intensities ($<100 \text{ mW/cm}^2$) by projecting an image onto the electrode surface and allowing anodic dissolution to occur preferentially in illuminate portions of n-type crystals. An alternative method to forming an etched structure is to guide a focused laser beam in a predefined pattern along the electrode surface. In this way, the etched figures might be "micromachined" with micron scale features without using projection masks. Potential applications include customized marking of semiconductor wafers incorporating integrated circuits, micromachining of sensor elements such as very small scale gas chromatographic columns (2), and direct ruling of grating structures. However, high photoetching rates are necessitated by this approach in order to complete an etched image in a reasonable time.

In this communication, we demonstrate high rate photoassisted etching of $<100>$ n⁺-GaAs ($N_d = 1.5 \times 10^{18} \text{ cm}^{-3}$, Laser Diode, Inc.) using a scanned focused laser. The etching solution is 10% aqueous KOH, in which oxidative dissolution of III-V compounds is mediated by holes (3). The process is accelerated in n-type crystals by holes provided by above bandgap light and the resulting photovoltage that develops between dark and illuminated regions (4).

The experimental arrangement is a variation of that described previously (5). The output of a 1 mw HeNe laser (Uniphase Model 1301) was spatially conditioned, reflected vertically through a cube beam splitter and focused through the etching solution onto the crystal surface using a microscope objective (Melles Griot, 20X, N.A. = 0.5). An eyepiece with reticle placed above the beam splitter permitted visual

*Electrochemical Society Active Member.

Manuscript received Aug. 12, 1985. This was Paper 454 presented at the Las Vegas, Nevada, Meeting of the Society, Oct. 13-18, 1985.

observation of the focused spot and estimation of its diameter, about $2 \mu\text{m}$. The total intensity of the unattenuated beam exiting the objective was determined radiometrically to be $480 \mu\text{W}$. A knife edge measurement of the focused beam profile revealed a nearly Gaussian intensity distribution, with a small amount of anomalous "tailing" out to about $15 \mu\text{m}$ diameter, accounting for $<1\%$ of the total intensity. The crystal's position was controlled by two stepper motors operating at an x-y translation stage in $1 \mu\text{m}$ increments at rates up to 350 Hz. Computer control of the stage motion and of an electronic shutter were employed to "write" figures produced on the monitor directly onto the crystal with user specified x and y scaling.

Holes were etched in the n⁺-GaAs surface with the focused beam at a variety of light intensities (16 W/cm^2 to 16 kW/cm^2) and exposure energies (5 to $1.6 \times 10^5 \text{ J/cm}^2$). The resulting hole diameters and, where possible, hole profiles were determined using optical microscopy and a Sloan Dektak mechanical profilimeter. Figure 1 shows that the etched hole diameters become progressively larger with increasing energy. To first order, this effect is independent of laser intensity, at least within the intensity region investigated. The same result was obtained with dilute $\text{H}_2\text{O}_2/\text{H}_2\text{SO}_4$ and with $\text{Br}_2/\text{methanol}$ etchants as well as with crystals of different orientation and doping level.

The theoretical hole diameters expected for etching with a Gaussian beam of several $(1/e^2)$ diameters, W_0 , are superimposed on Figure 1. Evidently, the experimental hole diameters increase much too sharply with energy to be explained by this mechanism. Furthermore, measurement of the hole profiles revealed conical depressions rather than holes with narrow centers and a shallow "halo". The latter shape might be expected for our slightly nonideal Gaussian beam. Explanations for Figure 1 involving localized heating are not consistent with the independence of the result on light intensity. Indeed, it can be shown by simple theoretical considerations (6) that the local temperature rise will be less than 3°C for the highest

intensity used. An explanation which is consistent both with the observed broadening and hole profile is the diffuse scattering of the focused light within the growing hole. This might be expected under many conditions of "high rate" etching, where revealed surfaces can have a rough microstructure (4,7). The scattered light would be absorbed by the walls, thus causing their erosion by photoetching.

An example of high resolution etching of a character set is shown in Figure 2, demonstrating that this method can be used for the custom marking of wafers. In this case, the characters are formed from an array of pits 0.3-0.5 μm deep, photoetched at 32 J/cm^2 . The smallest alphanumeric characters that we have etched in n^+ -GaAs using this apparatus had an average unit size of $4 \times 4 \mu\text{m}$, equivalent to a character density of $7 \times 10^6/\text{cm}^2$.

The directed laser etching process would find increased utility if higher aspect ratios could be attained without loss of spatial resolution. Significantly, Podlesnik and coworkers (8) recently reported on photoelectrochemical hole drilling in n -GaAs using focused laser light and several different etchants. Using a frequency doubled Ar^+ laser operating at 257 nm, these authors produced holes $>100 \mu\text{m}$ deep and 1-4 μm in diameter, but only at power densities of $\approx 0.1 \text{ W}/\text{cm}^2$. At this power, etch rates were about $0.003 \mu/\text{sec}$, compared to $>10 \mu/\text{sec}$ in the present work. At low etching rates, specular features are produced, and the hole grows by "light guiding". In order to get the same effect at high intensities, conditions of high rate photoelectrochemical polish-etching must be developed. Work is continuing along these lines in our laboratory.

Acknowledgment

This work was supported by the Office of Naval Research.

EIC Laboratories, Incorporated, assisted in meeting the publication costs of this article.

REFERENCES

1. T. Inoue, A. Fujishima and K. Honda, *This Journal*, **127**, 1582 (1980); R.M. Osgood, Jr., A. Sanchez-Rubio, D.J. Ehrlich and V. Daneu, *Appl. Phys. Lett.*, **40**, 391 (1982); F.W. Ostermeyer, Jr., P.A. Kohl and R.H. Benton, *ibid.*, **43**, 642 (1983); R.H. Micheels, A.D. Darrow III and R.D. Rauh, *ibid.*, **39**, 418 (1981).
2. S.C. Terry, J.H. Jerman and J.B. Angell, *IEEE Trans. Electron Devices*, **ED-26**(12), 1880 (1979).
3. H. Gerischer and W. Mindt, *Electrochim. Acta*, **13**, 1329 (1968).
4. F. Kuhn-Kuhnenfeld, *This Journal*, **119**, 1063 (1972).
5. C.A. Kavassalis, D.H. Longendorfer, R.A. LeLievre and R.D. Rauh, *Mat. Res. Soc. Symp. Proc.*, Vol. 29, 151 (1984).
6. M. Lax, *J. Appl. Phys.*, **48**, 3919 (1977).
7. P.A. Kohl, C. Wolowodiuk and F.W. Ostermeyer, Jr., *This Journal*, **130**, 2288 (1983).
8. D.V. Podlesnik, H.H. Gilgen and R.M. Osgood, Jr., *Appl. Phys. Lett.*, **45**, 563 (1984).

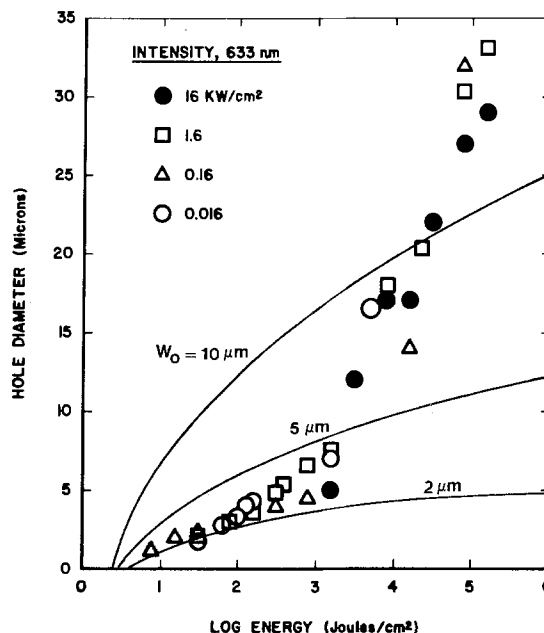


Fig. 1. Etched hole diameters vs. exposure energy for 2 μm diameter laser spot on n^+ -GaAs in 10% KOH; also, theoretical diameters at $>0.1 \mu\text{m}$ depth for a Gaussian beam profile.

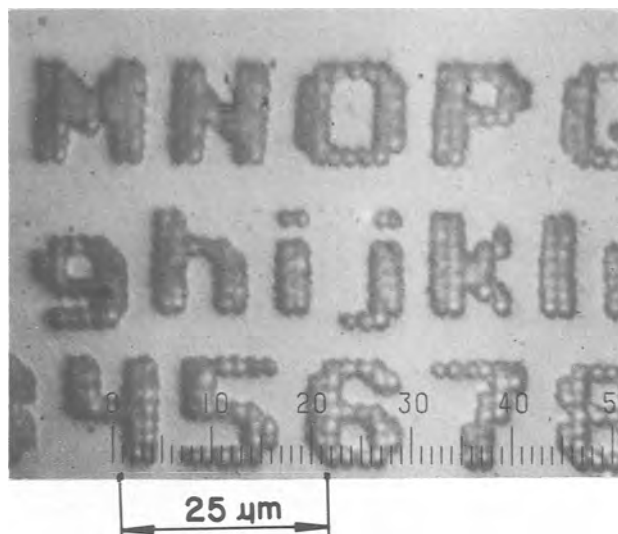


Fig. 2 Photoelectrochemically etched character set in n^+ -GaAs using scanned 2 μm diameter HeNe laser spot ($160 \text{ W}/\text{cm}^2$, 0.2 sec/point). Holes appear raised due to illusion from reflected light.

Elimination of Flux Transients in Molecular Beam Epitaxy

P. A. Maki,* S. C. Palmateer, A. R. Calawa,† and B. R. Lee

General Electric Company, Electronics Laboratory, Syracuse, New York 13221

Film thickness reproducibility in the growth of group III-V compounds by molecular beam epitaxy (MBE) depends on the substrate temperature and on the temperature stability of the group III source. The In, Ga or Al melts are contained in pyrolytic boron nitride (PBN) crucibles of various shapes and sizes. The basic concepts of crucible design for achieving uniform deposition over 2 or 3 inch diameter wafers are well understood.^{1,2} Unfortunately for many of these cell configurations the melt temperature is affected by the radiation shielding provided by the beam shutter³. A flux transient typically lasting 1-3 minutes occurs when the shutter is opened and the cell establishes a new equilibrium temperature. In this letter, we report on a unique PBN crucible which simultaneously exhibits a low flux transient and provides excellent beam uniformity.

Uniformity of molecular beam patterns depends on the source to substrate spacing and the angular flux distribution at the source. The best uniformity is obtained with a large source to substrate spacing and an emitting flux distribution at the cell orifice which is isotropic in the solid angle subtended by the substrate². A conically shaped crucible has these flux characteristics as well as a large cell orifice for high flux density. Flux uniformity at the source is attained by allowing a direct path to the entire substrate from each point on the melt surface. The atoms which escape the crucible without wall collisions are the main component of the flux. The cone angle and hence depth of the crucible is determined by the solid angle subtended by the cell orifice and substrate peripheries. This depth limits the cell volume and reduces practical usage between fillings. Schaff found that partially filled deep crucibles exhibit a

smaller flux transient while retaining a large volume⁴. This is because the melt temperatures deep within the furnace are less sensitive to changes in radiation shielding at the cell orifice. Deep crucibles tend to collimate the beam, however, which limits uniformity.^{2,4}

Our approach to improving the flux transient behavior is to use a two crucible configuration which takes advantage of a deeply recessed melt while maintaining flux uniformity through the use of a beam shaping conical insert. The crucible arrangement is shown in Figure 1. The cell is assembled from a conventional Varian GEN II furnace equipped with a short thermocouple and a 40cc crucible which holds the group III melt⁵. A 16cc conical crucible with its bottom ground off is centered within the 40cc crucible so that intimate contact occurs near their rims.

In our initial studies, we have implemented this cell as a gallium source. Figure 2 shows a plot of the Ga beam equivalent pressure (P_{BE}) versus time for both the new cell and a conventional conical cell. The double crucible cell exhibits only 5% transient over 4 minutes while the conventional cell exhibits a 32% transient over the same time period. A uniformity map of a Si-doped GaAs film grown on a 2 inch diameter substrate is shown in Figure 3. The doping and thickness uniformity is less than $\pm 2\%$. Our initial studies indicate that the GaAs material quality is equivalent to that obtained in our machine from the conventional furnace design⁶. The oval defect density is also comparable ($< 500/\text{cm}^2$).

The small flux transient observed from this cell reflects a more stable melt temperature. This is attained both as a result of the melt location deep in the furnace and through the additional radiation shielding provided by the crucible insert. Beam uniformity is maintained because the recessed aperture of the crucible insert presents a constant melt area to all points on the substrate. A further desirable feature of this cell is its lower operating

* School of Electric Engineering, Cornell University, Ithaca, New York 14853

† Cornell Lecturer. Permanent Address: Lincoln Laboratory, Massachusetts Institute of Technology, Lexington, Massachusetts 02173

temperature. Using the cells as Ga sources, the temperatures required for a GaAs growth rate of $1 \mu\text{m/hr}$ are 1100°C for the new cell, 1000°C for the deep crucible cell and 1200°C for the standard conical cell. The temperatures cannot be directly compared since the thermocouple touches the bottom of each cell and is therefore at a different position for the shallower conical cell. However, we have observed that the power requirements are slightly lower than for the conventional conical cell. We believe this reflects an overall cell temperature which is lower than a conical cell. The lower cell temperature is significant since hot cell parts are thought to be a source of impurities in the MBE environment.

We have demonstrated a practical crucible combination which produces excellent film uniformity with little transient. The usable cell capacity is increased by approximately two times. While demonstrated for gallium, this approach should work equally well for other group III elements.

ACKNOWLEDGEMENTS

We would like to thank J. Berry, JCM Hwang, and R. Finicle for helpful discussions and assistance in this work.

REFERENCES

- (1) For a discussion of cell design, see for example K. Ploog, "Molecular Beam Epitaxy of III-V Compounds," Crystal Growth Properties and Applications, 1980, Vol. 3, Springer-Verlag.
- (2) P.E. Luscher and D.M. Collins, "Design Considerations for Molecular Beam Epitaxy Systems," Progress in Crystal Growth and Characterization, 1979, Vol. 2, pp. 15-32, Pergamon Press Ltd.
- (3) The authors are most familiar with the problem on the Varian GEN II system. Private communications with colleagues indicates that the problem exists to varying degrees on other machines.
- (4) W. Schaff, PhD Thesis, Cornell University, 1984.
- (5) This work was performed on a Varian GEN II. For details on the machine and cell configuration refer to the Varian GEN II operators manual.
- (6) S.C. Palmateer, PhD Thesis, Cornell University, 1985.

Manuscript received June 13, 1985.
General Electric Company assisted in meeting the publication costs of this article.

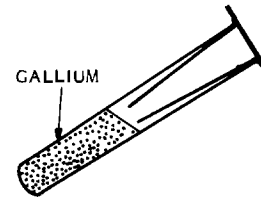


Figure 1. Diagram of Crucible Assembly

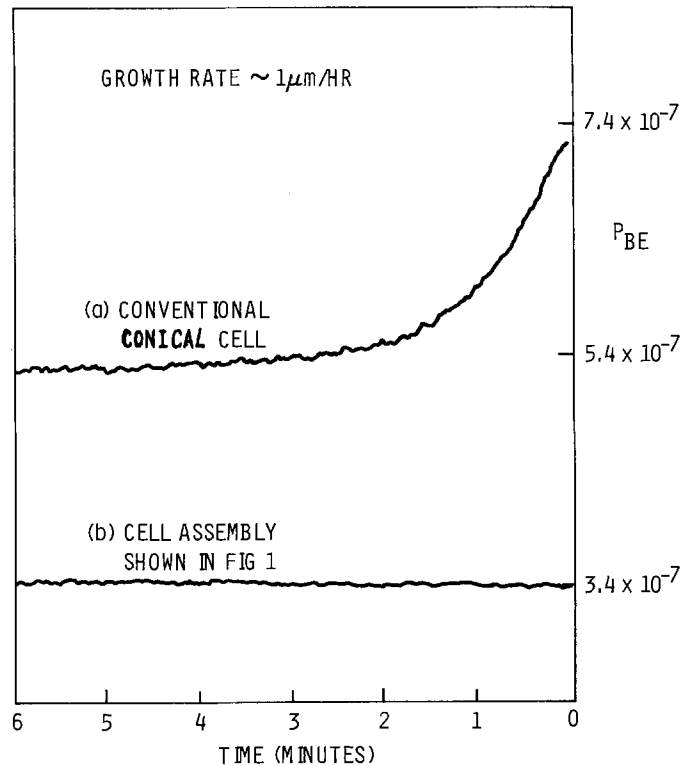


Figure 2. Comparison of Gallium Cell Transient as Measured with Beam Flux Monitor

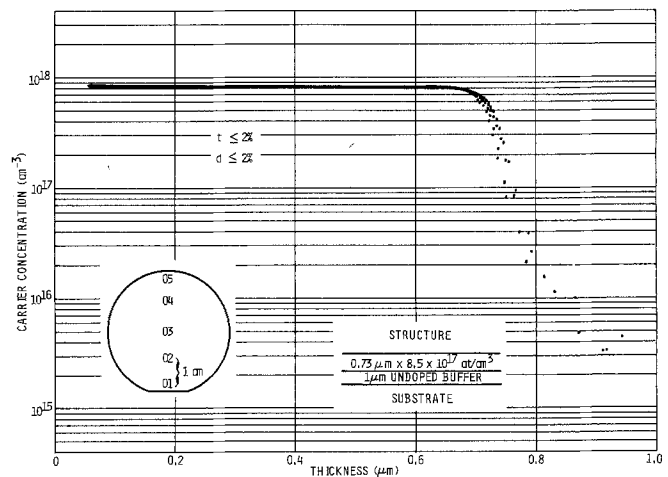


Figure 3. Doping Concentration as a Function of depth from the surface of a Si-doped GaAs Film Grown at 600°C with the Substrate Rotated at 10 RPM

A Measurement of the Effect of Intrinsic Film Stress on the Overall Rate of Thermal Oxidation of Silicon

J. K. Srivastava* and E. A. Irene*

Department of Chemistry, University of North Carolina, Chapel Hill, North Carolina 27514

The effects of intrinsic film stress on Si oxidation kinetics has been receiving considerable attention in recent years(1-5). Oxidation models have appeared that relate the Si-SiO₂ interfacial intrinsic stress to both the interface reaction between oxidant and Si and to a stress altered oxidant transport. The experimental measurement of the film stress itself has been reported, although to date the data is rather sparse(1,6). Recently, in our laboratory more extensive intrinsic stress measurements have been made and these measurements will be reported separately. So while the existence of a compressive intrinsic SiO₂ film stress has been experimentally verified, the experimental verification of the effects of the stress on oxidation kinetics remains a matter of speculation within the various models.

Along with the development of an intrinsic film stress due to the molar volume change during the oxidation of Si, a SiO₂ film density increase occurs and has been measured (6, 10, 11). The density increase of 2-3% is too large to have arisen from the stress optical constant and has therefore been attributed to an accommodation of system to the buildup of stress (6). We consider the intrinsic stress and density increases to have a common origin in the nature of the Si oxidation process on a single crystal Si surface. The present communication provides a rather direct experimental measurement of the effect of the compressive intrinsic film stress and/or oxide density on the Si oxidation kinetics.

We report the result of a simple but careful experiment that shows the parallel between stress and/or density and kinetics in the thicker film regime of Si oxidation where the film thickness, L, is greater than 100nm, and at an oxidation temperature of 800°C. In this thickness range, the transport and interfacial

effects are nearly equivalent. The results show a decrease in the rate of oxidation as had been anticipated for a compressive stress and/or for a higher density film.

EXPERIMENTAL PROCEDURES

All the Si wafers used were lightly P doped n-type (100) oriented commercially available high quality single crystal Si slices. The wafers were cleaned by a slightly modified RCA procedure(7) and followed with an HF dip and thorough deionized H₂O rinse. A batch of ten wafers was oxidized in pure dry O₂ at 800°C to an oxide thickness of between 100-110nm. This thickness was chosen to be near a half of an ellipsometric period (about 140nm for 632.8 nm light) so that both SiO₂ film thickness and refractive index could be accurately measured. The batch was then split in half with one half receiving a one hour 1000°C anneal in pure Ar so as to relieve the stress. This anneal was found to be more than adequate for this purpose(6). At this point all the wafers were measured by ellipsometry. The ellipsometer was of research quality with the capability of polarizer and analyzer resolution to 0.01° and was carefully aligned prior to use. The Δ and Ψ values were converted to SiO₂ thickness and refractive index using a modified version of McCrackin's program(8). We conservatively estimate a thickness and index accuracy of better than 2% and 0.005, respectively. The batch halves were recombined and then the entire batch was oxidized at 800°C in pure O₂. Wafers were selected from each half batch (the annealed and unannealed halves) at various oxidation times so that film thickness and refractive indices could be remeasured.

EXPERIMENTAL RESULTS AND DISCUSSION

Table 1 shows a comparison of the

film thicknesses and refractive indices after the final 800°C oxidation for the oxidation time noted in the left most column. The SiO₂ film thickness is reported as the ² difference between the initial 800°C oxidation to produce the 100-110nm samples and the final oxidation at 800°C to compare the unannealed and annealed samples. In all cases the stress annealed samples grew oxide more rapidly than the stressed samples. The refractive indices indicate that the unannealed samples had the higher density and stress throughout the final oxidation as had been previously reported (6).

Within the Deal and Grove model (9) the transport of oxidant is governed by the parabolic rate constant, k_p and is given as:

$$k_p = 2CD/\rho \quad [1]$$

where C is the dissolved oxidant in SiO₂, D is the oxidant diffusivity and ρ is the SiO₂ density. The transport term can then be reduced by either a decrease in D or an increase in ρ or both. Recently, several studies have shown the likelihood of the intrinsic compressive SiO₂ film stress decreasing D (4,5). Also several studies have shown that the oxide density, ρ , increases with decreasing oxidation temperature (10,11). The experiments reported herein cannot distinguish between these two factors, as both stress and density increase with decreasing oxidation temperature and both anneal out with high temperature treatment (6).

For the interface reaction, a revised formulation now includes the effect of film stress and oxide viscosity (6, 12). In this model (12), the interface reaction constant k_1 is given as:

$$k_1 = kC_oC_{Si}\sigma/\eta \quad [2]$$

where k is a constant, C_o and C_{Si} are the oxygen and silicon concentrations, σ is the intrinsic stress and η is the viscosity of SiO₂. The compressive SiO₂ stress is tensile in Si thereby stretching the Si - Si bonds and increasing the likelihood for oxidation. At low temperatures σ is larger (1, 6) but so is η hence we can neither distinguish σ from η effects nor k_1 from k_p effects. Despite these difficulties, we have demonstrated that the overall rate of

*Electrochemical Society Active Member.

Manuscript received Aug. 9, 1985.

oxidation of Si is reduced in low temperature grown thermal oxide films on Si, and the reduction is linked to the intrinsic film stress. At the present time, more detailed studies aimed at separating film stress and density effects are in progress in our laboratory.

Acknowledgment

This work was supported in part by the Office of Naval Research (ONR).

The University of North Carolina assisted in meeting the publication costs of this article.

REFERENCES

1. E.P. EerNisse, Appl. Phys. Lett., 35, 8(1979).
2. W.A. Tiller, J Electrochem. Soc., 127, 625(1980).
3. E.A. Irene, J. Appl. Phys., 54, 5416(1983).
4. A. Fargeix, G. Ghibaudo and G. Kamarinos, J. Appl. Phys, 54, 2878(1983).
5. R.H. Doremus, Thin Solid Films, 122, 191(1984).
6. E.A. Irene, E. Tierney, and J. Angillelo, J. Electrochem. Soc., 129, 2549(1982).
7. W. Kern and D.A. Puotinen, RCA Review, 31, 187(1970).
8. F.L. McCrackin, NBS Technical Note 499, U.S. Government Printing Office, Washington, D.C.
9. B.E. Deal and A.S. Grove, J. Appl. Phys., 36, 3770(1965).
10. E.A. Taft, J. Electrochem. Soc., 125, 968(1978).
11. E.A. Irene, D. Dong, and R.J. Zeto, J. Electrochem. Soc., 127, 396(1980).
12. E.A. Irene, J. Appl. Phys. 54, 5416 (1983).

Table I

SiO₂ Film Thickness and Refractive Index Comparison for Annealed and Unannealed Samples

Oxidation Time of Second Oxidation (hrs.)	Unannealed		Annealed	
	Thickness (Å)	Ref. Index	Thickness (Å)	Ref. Index
1	9	1.474	23	1.463
2	15	1.475	44	1.465
4	30	1.475	83	1.465
9	78	1.474	163	1.466
19	178	1.473	267	1.466



Electrochemical Studies of Tetrabutylammonium Electrolytes at Carbon Cathodes in Sulfuryl Chloride Cells

Charles W. Walker, Jr., Michael Binder,* William L. Wade, Jr., and Sol Gilman*

U.S. Army Electronics Technology and Devices Laboratory, ERADCOM, Power Sources Division, Fort Monmouth, New Jersey 07703-5302

ABSTRACT

Tetrabutylammonium tetrachloroaluminate [(Bu)₄NAIAlCl₄] has been explored for use as a soluble conducting electrolyte in sulfuryl chloride cells. Cathode capacity and voltage characteristics in this electrolyte are compared to those obtained when using LiAlCl₄ electrolyte. Cathode life in (Bu)₄NAIAlCl₄-SO₂Cl₂ is more than 50 times greater than that found in LiAlCl₄-SO₂Cl₂ due to formation of soluble reaction products. Lowered carbon rest potentials in (Bu)₄NAIAlCl₄ electrolytes are due to the presence of free chloride ions.

The sulfuryl chloride battery has the potential of being used in military and commercial applications based on its high energy and power densities and useful temperature range. The most commonly used electrolyte salts for lithium and calcium sulfuryl chloride primary cells have been LiAlCl₄ or Ca(AlCl₄)₂ (1-6). However, when these electrolyte salts are used, cathode performance is necessarily limited. Chloride ions formed at the cathode during solvent reduction accumulate in carbon cathode pores and react with lithium or calcium cations in the electrolyte to form insoluble, electronically insulating LiCl or CaCl₂. These products clog cathode pores and lead to large diffusion impedances which limit cell life and cathode current density. These limitations are particularly marked in calcium cells because of relatively poor morphology of deposited calcium chloride vs. the lithium chloride product phase (2-4).

In the search for an ideal substitute for LiAlCl₄ and Ca(AlCl₄)₂ electrolyte salts, the requirements would be: (i) the electrolyte salt must be soluble in sulfuryl chloride, have high specific conductivity, and be stable to oxidation by SO₂Cl₂ or reduction by lithium or calcium; (ii) the cation of the electrolyte salt should form a soluble, stable chloride salt in SO₂Cl₂, while the anion should form a soluble, stable lithium or calcium salt in SO₂Cl₂.

In this way, reaction product precipitation will occur not within cathode pores, but rather at some intermediate point between the cathode and anode, where diffusing ions meet (perhaps in the fibers of the anode-cathode separator).

Investigation of a potential candidate electrolyte salt in SO₂Cl₂ representative of the type AlCl₃RCl, where R is a quarternary ammonium compound, is explored in this paper. The salt, tetrabutylammonium tetrachloroaluminate, (Bu)₄NAIAlCl₄, appears attractive because AlCl₄ anions are known to be stable in oxyhalides and tetraalkylammonium cations are difficult to reduce at potentials greater than 2.0V relative to lithium. Furthermore, since only tetrabutylammonium cations are initially present to react with chloride ions formed at the cathode, and since tetrabutylammonium chloride is soluble in sulfuryl chloride, cathode capacity should be increased.

Experimental

Solutions of (Bu)₄NAIAlCl₄-SO₂Cl₂ were prepared *in situ* by successive dissolution. Stoichiometric amounts of

solid (Bu)₄NCl, recrystallized from acetone and ether, were dissolved in a measured volume of distilled SO₂Cl₂ and appropriate amounts of solid, previously sublimed AlCl₃ were slowly added. This allows less chance of AlCl₃ reacting with the SO₂Cl₂ solvent to form complexes. All experiments were performed in a Vacuum Atmospheres Corporation dried argon atmosphere glove box equipped with a circulating air dry train at room temperature with typical moisture level below 10 ppm.

Cyclic voltammetric experiments were carried out in all glass cells using a three-electrode configuration. The data were obtained with a PAR Model 173 Potentiostat/Galvanostat drive by a PAR Model 175 Universal Programmer and read out on a Hewlett-Packard X-Y recorder. A large fine mesh platinum screen surrounding the carbon working electrode served as auxiliary (counter) electrode.

The working electrode was a 3 mm diam glassy carbon rod (Atomergic Chemicals Corporation, Plainview, New York) heat sealed in shrinkable Teflon tubing with the end of the carbon rod ground flush with the Teflon tubing so as to expose only the measured carbon rod cross section. Electrical contact was made to the rear face of the carbon rods using nickel wire attached to the carbon with woods metal. The carbon surface was cleaned between scans by dipping the electrode into an acidic AlCl₃-SO₂Cl₂ solution, rinsing with pure SO₂Cl₂, rubbing over emery paper, and finally rinsing with pure SO₂Cl₂ again.

For initial experiments, our reference electrode consisted of two silver metal strips immersed in 0.01M AgNO₃-acetonitrile (7) which has a rest potential of approximately +0.3V relative to the aqueous saturated calomel electrode (SCE) (8). This well-studied nonaqueous silver reference electrode, however, did not remain stable in the chlorine-like environment of SO₂Cl₂ vapors in our dry box, and the potential of one silver strip relative to the other would drift by approximately 30 mV after only about 30 min. This implied that the silver electrode was affected by the SO₂Cl₂ vapors. We therefore adopted Avigal and Peled's (9) extremely stable reference electrode consisting of a lithium metal strip immersed in LiAlCl₄-SOCl₂ for all subsequent experiments. This lithium reference lies approximately 2.4V below the Ag reference and thus 2.1V below the saturated calomel electrode. The lithium strip in LiAlCl₄-SOCl₂ electrolyte was placed in a small diameter glass tube with an E-pore frit, which

was, in turn, separated from the actual test solution by placing it in another fritted glass tube containing electrolyte test solution. Since thionyl chloride could not contaminate the test solution, stable potential readings were obtained over long periods.

Solutions of 1 methyl, 3 ethyl imidazolium tetrachloroaluminate (IMA Cl_4) were prepared by taking stoichiometric amounts of dry imidazolium chloride powder (kindly provided by Dr. John Wilkes of the Frank Seiler Research Center of the Air Force Academy in Colorado) and slowly adding solid, dry AlCl_3 . Within seconds, the formerly white solid mixture became a clear liquid at room temperature and this liquid was then added to stoichiometric amounts of distilled sulfuryl chloride.

Normally, electrolyte resistance affects scanning voltammograms by decreasing peak currents and shifting oxidation potentials towards more positive potentials. In order to check whether resistances between working and reference electrodes required correcting our voltage sweeps for IR drops, we measured the initial, rapid, IR component between working and reference electrodes during a rapidly applied current pulse in 1.0M $(\text{Bu})_4\text{NAlCl}_4\text{-SO}_2\text{Cl}_2$ solutions. Measured resistances indicated that voltammogram distortion due to IR effects was minimal and no correction for IR losses was made.

Results and Discussion

Figure 1 shows experimental discharge curves at 1.4 mA/cm² constant current for glassy carbon rods in lithium cells containing 1.0M $(\text{Bu})_4\text{NAlCl}_4\text{-SO}_2\text{Cl}_2$ electrolyte compared to discharge curves in base line 1.5M $\text{LiAlCl}_4\text{-SO}_2\text{Cl}_2$ electrolyte. In tetrabutylammonium electrolyte, cathode capacities are greatly increased over those in base line LiAlCl_4 electrolyte. However, both carbon open-circuit and operating voltages are lower for $(\text{Bu})_4\text{NAlCl}_4$ electrolyte salts than for standard LiAlCl_4 -based electrolyte. Our present research goal was to examine the chemistry and electrochemistry of $(\text{Bu})_4\text{NAlCl}_4$, which influence its potential application as a battery electrolyte salt in sulfuryl chloride.

Solubility of tetrabutylammonium tetrachloroaluminate, $(\text{Bu})_4\text{NAlCl}_4$, easily exceeds 1M in both sulfuryl chloride and thionyl chloride at room temperature. Figure 2 compares specific conductivities at room temperature of $(\text{Bu})_4\text{NAlCl}_4$ with two commonly used battery electrolyte salts in SO_2Cl_2 . Tetrabutylammonium electrolyte exhibits conductivities approximately midway between calcium and lithium electrolytes.

We were interested in understanding why carbon rest potentials and carbon cathode load voltages are lower in $(\text{Bu})_4\text{NAlCl}_4\text{-SO}_2\text{Cl}_2$ electrolytes. Rest potentials of carbon electrodes in $(\text{Bu})_4\text{NAlCl}_4\text{-SO}_2\text{Cl}_2$ solutions were approximately 3.3V, while these potentials were approximately 3.9V in either $\text{LiAlCl}_4\text{-SO}_2\text{Cl}_2$ or $\text{Ca}(\text{AlCl}_4)_2\text{-SO}_2\text{Cl}_2$ electrolytes (3). Qualitatively, differences in carbon rest potential

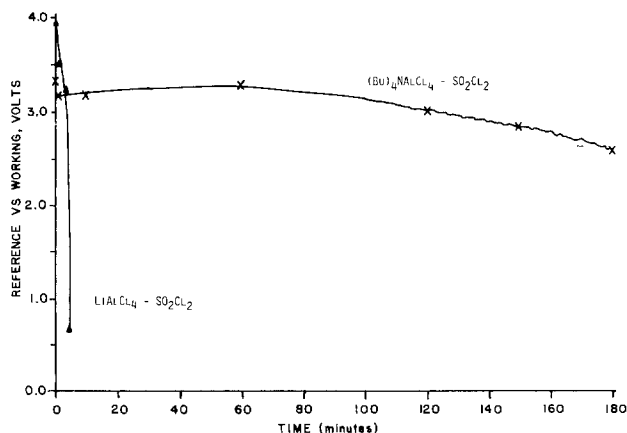


Fig. 1. Potential as a function of discharge time for a 1.4 mA/cm² constant current drain on a smooth carbon electrode in two different electrolyte salts.

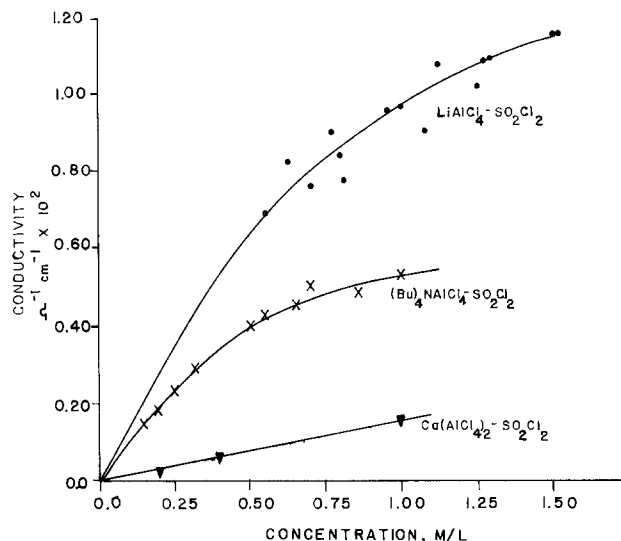
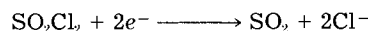


Fig. 2. Room temperature specific conductivities as a function of electrolyte concentrations for three different electrolytes in SO_2Cl_2 .

for the two electrolytes were not entirely unexpected. Standard equilibrium potentials of redox systems are dictated by thermodynamics and depend on specific reaction products. Since no solid preliminary discharge products are formed in $(\text{Bu})_4\text{NAlCl}_4\text{-SO}_2\text{Cl}_2$ electrolytes, free energy change and, hence, open-circuit rest potential would be expected to differ from potentials seen in LiAlCl_4 or $\text{Ca}(\text{AlCl}_4)_2$ electrolytes where solid LiCl or CaCl_2 products are indeed formed.

In the following discussion, we will attempt to show that carbon rest potentials in oxychloride battery electrolytes are largely responsive to the thermodynamics of solvated chloride ion concentration changes in solubility of chloride salts. The smaller the free chloride ion concentration in solution, the higher the carbon electrode rest potential. This is qualitatively predictable from the Nernst equation for sulfuryl chloride reduction. The cathodic reaction is



Neglecting chloride ion activity terms, the Nernst equation for this reaction can be written as

$$E = E^\circ - \frac{0.059}{2} \log [\text{Cl}^-]^2$$

Here E° represents the standard thermodynamic reduction potential for SO_2Cl_2 (which is assumed to be reversible since the theoretically calculated open-circuit cell potential of 3.91V for lithium vs. carbon in $\text{LiAlCl}_4\text{-SO}_2\text{Cl}_2$ electrolytes is exactly what is measured experimentally) and $[\text{Cl}^-]$ represents free chloride ion concentration in the electrolyte.

In $\text{LiAlCl}_4\text{-SO}_2\text{Cl}_2$ electrolyte for example, a carbon electrode has a rest potential of 3.9V relative to lithium. Free chloride ion concentrations in this electrolyte, are low since chloride ions present in solution immediately react with lithium cations to form highly insoluble LiCl . The resulting low free chloride concentration permits high open-circuit potentials. On the other hand, carbon electrode rest potentials in $(\text{Bu})_4\text{NCl}\text{-SO}_2\text{Cl}_2$ electrolyte is only approximately 3.1V relative to lithium since highly soluble $(\text{Bu})_4\text{NCl}$ salt readily ionizes to give high free chloride ion concentrations in solution. There are no counterions present to lower free chloride concentrations.

Figure 3 shows a "potentiometric titration curve" obtained when 1M $(\text{Bu})_4\text{NCl}\text{-SO}_2\text{Cl}_2$ solution was titrated with 1M $\text{AlCl}_3\text{-SO}_2\text{Cl}_2$. The low carbon rest potential under chloride-rich conditions (to the left of the sharp break in the curve) gradually increases as AlCl_3 is added. The combination reaction between added AlCl_3 and Cl^- already in solution effectively reduces net free chloride ion

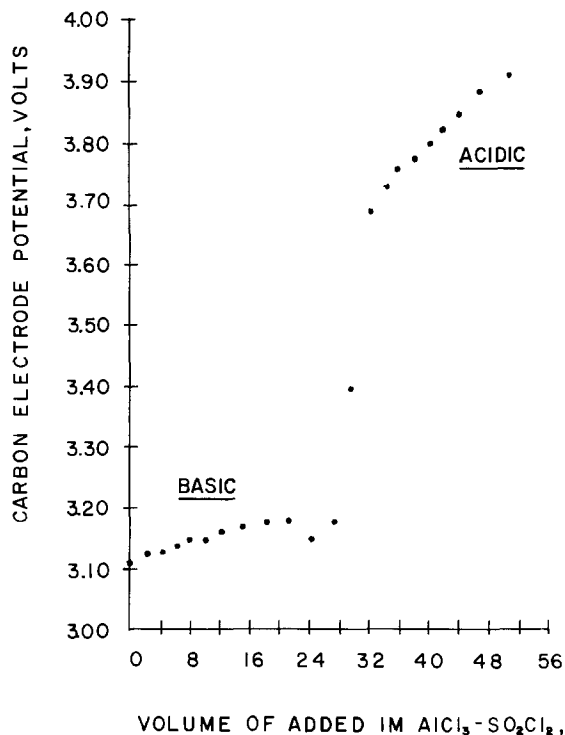


Fig. 3. Carbon rest potentials (relative to a lithium reference electrode) as a function of added $\text{AlCl}_3\text{-SO}_2\text{Cl}_2$ for a 1M/liter $(\text{Bu})_4\text{NCl-SO}_2\text{Cl}_2$ solution.

concentration, and, as chloride ion concentration drops, carbon potential rises. A plot of carbon rest potential in this concentration region plotted against the logarithm of added AlCl_3 concentration (which essentially reflects decreased free chloride ion concentration) yields a straight line with an approximate slope of 60 mV/decade of chloride ion concentration change. This value indicates that, in chloride-rich concentration regions, smooth carbon electrodes behave as quasi-reversible electrodes and a good indicator of free chloride ion activity in SO_2Cl_2 . The steep potential change corresponds to acid-base transition for $(\text{Bu})_4\text{NAlCl}_4$ electrolyte. The drop in potential entailed in going from slightly acid to slightly basic electrolyte solution is the main practical voltage penalty in converting from a lithium- or calcium-based electrolyte to a neutral $(\text{Bu})_4\text{NAlCl}_4$ electrolyte.

As AlCl_3 concentration is increased past the equivalence point, we reach the acidic concentration region (to the right of the sharp break in the curve) where AlCl_3 is present in excess. The carbon rest potential eventually reaches a value equivalent to that seen in $\text{LiAlCl}_4\text{-SO}_2\text{Cl}_2$ solutions where free chloride ion concentrations are normally suppressed by reaction with free Li^+ ions. The slope of carbon working electrode potential for added AlCl_3 in this acidic region is not nernstian and could be due to different thermodynamic reactions such as complexation between AlCl_3 and SO_2Cl_2 occurring with excess AlCl_3 .

If one performs the identical titration experiment using a porous carbon electrode (not shown here), an almost linear relationship between carbon electrode rest potential and AlCl_3 concentration is obtained. The titration curve is completely unlike the sharp potential break indicative of normal potentiometric titrations. This is because a porous carbon electrode is actually an ensemble or network of many smooth carbon electrodes each with a different microenvironment. The sum of these localized regions results in a "smeared out" potential vs. concentration plot.

Since AlCl_3 catalyzes SO_2Cl_2 decomposition to SO_2 and Cl_2 (10), addition of AlCl_3 to SO_2Cl_2 electrolyte may simply be acting as a homogeneous catalyst to produce chlorine (which is soluble in the electrolyte) and thereby raise carbon electrode rest potential to reflect higher potentials of chlorine electrodes. This possibility was, however, ruled out by observation that potentials of porous carbon elec-

trodes in $(\text{Bu})_4\text{NAlCl}_4\text{-SO}_2\text{Cl}_2$ solutions that had been saturated with soluble chlorine gas did not increase by more than approximately 0.1V. Thus, the large increase in carbon rest potential upon AlCl_3 addition is not directly due to chlorine formation.

We have seen lower carbon rest potentials in $(\text{Bu})_4\text{NAlCl}_4\text{-SO}_2\text{Cl}_2$ than those usually observed in SO_2Cl_2 solutions of lithium or calcium salts. Lower potentials correspond to an increase in chloride ion activities. Additional evidence comes from cyclic voltammetry. Sample scans at smooth carbon electrodes are shown in Fig. 4 for neutral, acidic, and basic $(\text{Bu})_4\text{NAlCl}_4\text{-SO}_2\text{Cl}_2$ electrolytes. In contrast to cathodic scans in $\text{LiAlCl}_4\text{-SO}_2\text{Cl}_2$ and $\text{Ca}(\text{AlCl}_4)_2\text{-SO}_2\text{Cl}_2$ electrolytes (4, 5, 11, 12), which show a reduction peak, cathodic sweeps in $(\text{Bu})_4\text{NAlCl}_4\text{-SO}_2\text{Cl}_2$ began at less positive potentials relative to lithium, and cathodic reduction currents simply increased monotonically with no apparent limiting current.

Reduction currents are high because the discharge product (other than the normally formed soluble SO_2) is the extremely soluble $(\text{Bu})_4\text{NCl}$, which, unlike insoluble LiCl or CaCl_2 , does not passivate the carbon cathode. This explains why reduction current profiles do not change significantly after repeated cathodic scans even without cleaning the carbon electrode between scans.

Anodic scans beginning from rest potentials of smooth carbon electrodes in neutral $(\text{Bu})_4\text{NAlCl}_4\text{-SO}_2\text{Cl}_2$ solutions showed two distinct oxidation waves. The first wave, designated as oxidation wave A, occurs in the potential range of approximately +3.5-4.0V relative to the lithium reference, while a much larger oxidation wave, designated as wave B, appears at approximately 5V relative to the lithium reference. Oxidation wave B has been observed in $\text{LiAlCl}_4\text{-SO}_2\text{Cl}_2$ (11, 12) and $\text{LiAlCl}_4\text{-SO}_2\text{Cl}_2$ (4, 5) electrolyte solutions and shown to be due to oxidation of either AlCl_4^- anions or oxidation of the oxyhalide solvent

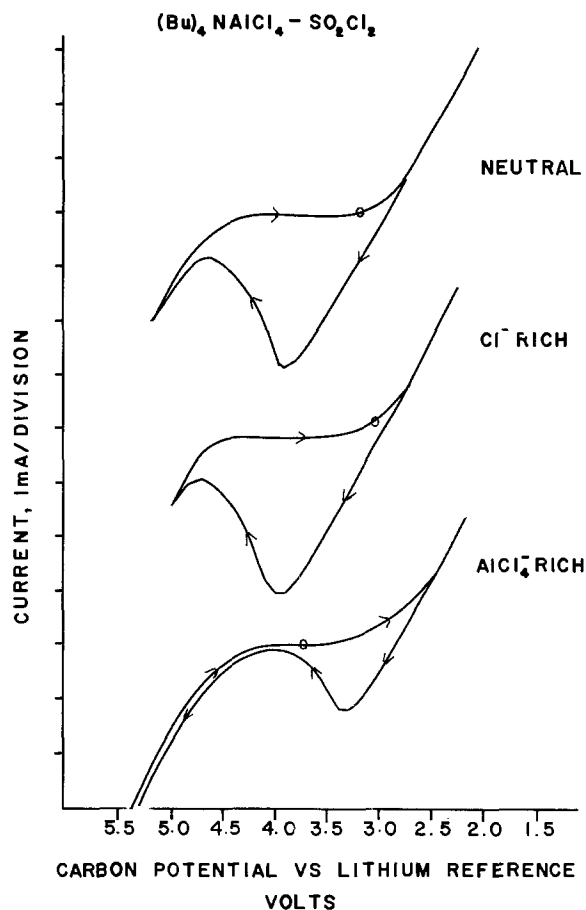
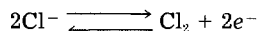


Fig. 4. Cyclic voltammograms at scan speeds of 100 mV/s at a smooth working carbon electrode in neutral, acidic, and basic $(\text{Bu})_4\text{NAlCl}_4\text{-SO}_2\text{Cl}_2$ solutions.

itself to form molecular chlorine. However, neither $\text{LiAlCl}_4\text{-SO}_2\text{Cl}_2$ nor $\text{LiAlCl}_4\text{-SOCl}_2$ solutions show oxidation wave A which is clearly evident in our $(\text{Bu})_4\text{NAlCl}_4\text{-SO}_2\text{Cl}_2$ solutions. A number of observations, although individually not conclusive, collectively support our contention that this oxidation wave represents oxidation of free chloride ions to molecular chlorine. This partial side reaction helps establish lowered carbon rest potentials



Peak current at wave A increases progressively with increasing concentration of soluble Cl^- ion in solution [in the form of added $(\text{Bu})_4\text{NCl}$]. Likewise, as seen in Fig. 4, when AlCl_3 is added to neutral $(\text{Bu})_4\text{NAlCl}_4\text{-SO}_2\text{Cl}_2$, current intensity of wave A decreases and is shifted further cathodic, while wave B increases. When $(\text{Bu})_4\text{NCl}$ is added, available free chloride ion concentration is increased because $(\text{Bu})_4\text{NCl}$ is soluble. When AlCl_3 is added to neutral $(\text{Bu})_4\text{NAlCl}_4\text{-SO}_2\text{Cl}_2$ solutions, free chloride ion concentration decreases because previously available chloride ions are now tied up either as complexed AlCl_4^- anions or as higher-order complexes such as Al_2Cl_7^- or $\text{Al}_3\text{Cl}_{10}^-$. This results in an increase in oxidation wave B intensity (due to an increase in AlCl_4^- oxidation) with a concomitant decrease in oxidation wave A (because of a reduction in overall Cl^- concentration).

Oxidation wave A is not considerably altered in shape or intensity upon repetitive anodic scanning because no insoluble passivating coating is formed on carbon at potentials of oxidation wave A. Variation of peak current for oxidation wave A varies approximately linearly with the square root of scan speeds in the range of 50-200 mV/s, which indicates that oxidation wave A is essentially a diffusion-controlled process. A calculated diffusion coefficient of $10^{-6}\text{-}10^{-7} \text{ cm}^2\text{-s}^{-1}$ for species being oxidized at wave A indicates that chloride could be responsible.

When smooth carbon electrodes were held at various cathodic potentials for different lengths of time and then interrogated by scanning anodic from their rest potential, resulting oxidation current intensity of wave A was a strong function of both the cathodic potentials at which the cathode was held as well as length of time that the electrode had been held cathodic. The longer the electrode was held cathodic, and the more cathodic the holding potential, the larger the subsequent anodic wave at potential A. These facts imply that oxidation wave A is due to oxidation of reduction products (Cl^- or SO_2) normally formed during cathodic scans in SO_2Cl_2 . Furthermore, intensity of oxidation wave A was inversely dependent on the length of time elapsed between the holding potential and subsequent interrogating oxidation sweep. This is understandable since concentration of reduction products available to undergo oxidation depends on diffusion.

Assuming chloride ions are indeed oxidized at oxidation wave A to form molecular chlorine, simultaneous appearance of chlorine gas bubbles is expected. However, no bubbles were visible in $(\text{Bu})_4\text{NAlCl}_4\text{-SO}_2\text{Cl}_2$ solutions even when carbon working electrodes were potentiostated at potential A for up to 10 min. This is because molecular chlorine formed at potential A is highly soluble in SO_2Cl_2 and tends to dissolve in the electrolyte rather than form gas bubbles. For this reason, a chlorine-saturated solution of $(\text{Bu})_4\text{NAlCl}_4\text{-SO}_2\text{Cl}_2$ electrolyte containing a slight excess of $(\text{Bu})_4\text{NCl}$ was prepared. When the smooth carbon working electrode was now held at oxidation wave A, noticeable bubbles were formed. This clearly indicated that chlorine gas was indeed formed at wave A as a result of oxidation of free chloride ions.

The possibility that these gas bubbles were HCl formed from oxidation products of $(\text{Bu})_4\text{N}^+$ was also ruled out. We measured specific conductivity at room temperature of pure SO_2Cl_2 solution saturated with bubbled dry HCl gas. The specific conductivity after HCl gas saturation of $6 \times 10^{-6} \Omega^{-1}\text{cm}^{-1}$ is approximately that of pure SO_2Cl_2 which implies that HCl does not appreciably ionize in SO_2Cl_2

and is therefore relatively insoluble. Had HCl been a product of oxidation wave A, its relative insolubility would have caused bubbles even in nonchlorine-saturated electrolyte solutions. The fact that no bubbles were seen in nonchlorine-saturated solutions implies that, for the most part, oxidation products at wave A are not HCl.

When the carbon working electrode was held at potential A for about 1 min in slightly basic $(\text{Bu})_4\text{NAlCl}_4\text{-SO}_2\text{Cl}_2$ solutions and then rapidly scanned cathodic (at scan rates of 2 V/s to minimize concentration losses due to diffusion) a noticeable reduction wave appeared at approximately 3.5V vs. lithium. This "reversible" reduction wave indicates that the oxidation product of wave A can then become reduced back to chloride ions.

Why is oxidation wave A not observed in lithium-based electrolytes? In lithium or calcium containing electrolyte salts such as LiAlCl_4 or $\text{Ca}(\text{AlCl}_4)_2$ free Cl^- ions are instantly tied up as insoluble LiCl or CaCl_2 and not available for reaction; free chloride ion concentration is vanishingly small. In the presence of $(\text{Bu})_4\text{N}^+$ cation (which is a weaker Lewis acid than Li^+), formed $(\text{Bu})_4\text{NCl}$ is highly soluble in SO_2Cl_2 and Cl^- ion essentially remains free to be oxidized at relatively low potentials of oxidation wave A. This implies that oxidation wave A should be observed in electrolytes such as 1-methyl, 3-ethyl imidazolium tetrachloroaluminate ($\text{Im-AlCl}_4\text{-SO}_2\text{Cl}_2$) where imidazolium cations also allow chlorides to remain soluble in SO_2Cl_2 (since Im-Cl is soluble). As expected, voltammograms (not shown here) of this electrolyte also exhibit distinct oxidation wave at potential A. We therefore conclude that oxidation wave A will be seen in oxyhalide electrolytes where, because of the nature of the cation, large free chloride ion concentrations can exist.

It is not possible to obtain high carbon rest potentials in oxyhalide electrolytes which allow free chloride ions to exist in solution, i.e., electrolytes whose cations form soluble chlorides. The only way to achieve high carbon cathode rest potentials in electrolytes without forming undesirable insoluble chlorides and yet achieve long cathode life is to use standard LiAlCl_4 or $\text{Ca}(\text{AlCl}_4)_2$ electrolyte solutions with excesses of AlCl_3 in order to minimize precipitation of insoluble chlorides. Undesirable anode corrosion due to excess AlCl_3 can perhaps be minimized by protective coatings.

In order to further understand reactions of smooth carbon electrodes in $(\text{Bu})_4\text{NAlCl}_4\text{-SO}_2\text{Cl}_2$ solutions, cyclic voltammetry experiments were carried out in 0.5M $\text{LiAlCl}_4\text{-SO}_2\text{Cl}_2$ electrolyte solutions containing various amounts of added 1.0M $(\text{Bu})_4\text{NAlCl}_4\text{-SO}_2\text{Cl}_2$. The two respective electrolyte concentrations were deliberately chosen. Since specific conductivity of 1.0M $(\text{Bu})_4\text{NAlCl}_4\text{-SO}_2\text{Cl}_2$ at room temperature is approximately equal to that for 0.5M $\text{LiAlCl}_4\text{-SO}_2\text{Cl}_2$ (see Fig. 2) we can, in general, eliminate conductivity as being a major cause of any observed subtle voltammetric changes. Cyclic voltammograms on a smooth carbon electrode are shown in Fig. 5 for various mole fractions of added $(\text{Bu})_4\text{NAlCl}_4\text{-SO}_2\text{Cl}_2$ to a $\text{LiAlCl}_4\text{-SO}_2\text{Cl}_2$ solution. Voltammograms were obtained by scanning the carbon electrodes 2V cathodic from its rest potential, back through the rest potential to 2V anodic from the rest potential, followed by a return to the original carbon rest potential. The arrows indicate cyclic voltammogram scan direction, while initial carbon electrode rest potential is denoted by a line. Scans for pure 0.5M $\text{LiAlCl}_4\text{-SO}_2\text{Cl}_2$ solutions agree well with previous reports by Behl (4, 5) and Abraham and Mank (11, 12).

As a mole fraction of $(\text{Bu})_4\text{NAlCl}_4\text{-SO}_2\text{Cl}_2$ increases, the main reduction peak intensity decreases slightly. At 0.60 mole fraction $(\text{Bu})_4\text{NAlCl}_4\text{-SO}_2\text{Cl}_2$, the return reduction scan, instead of showing near-zero cathodic currents (as normally seen for $\text{LiAlCl}_4\text{-SO}_2\text{Cl}_2$ electrolytes on reverse scans) actually shows substantially larger cathodic currents than for the forward direction scan, i.e., a larger reduction current is seen on the return scan. As the potential is swept further anodic, reduction current decreases and finally crosses the forward reduction current values. This crossover point moves further anodic with

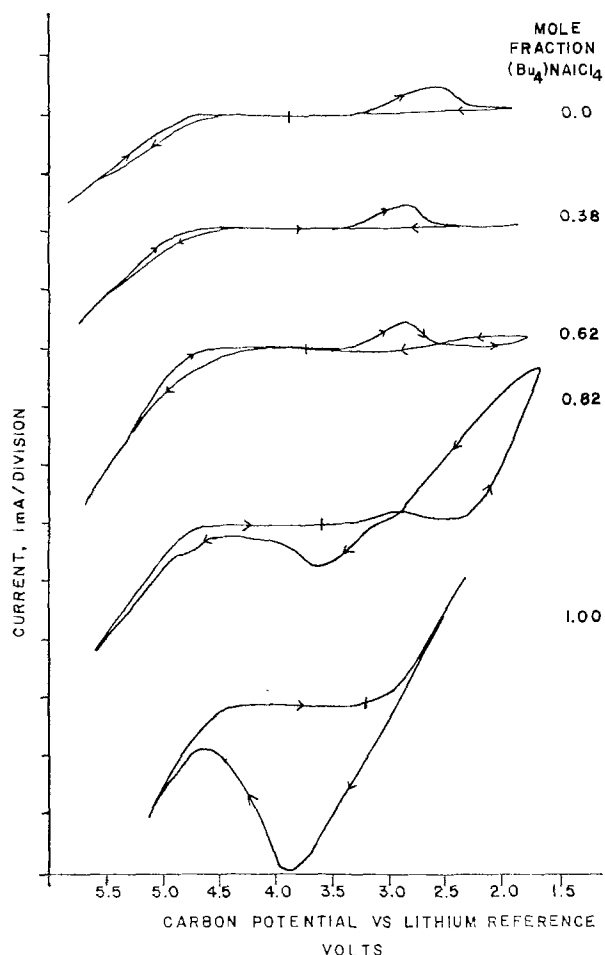


Fig. 5. Cyclic voltammograms at scan speeds of 100 mV/s at a smooth carbon working electrode for various mole fractions of $(\text{Bu})_4\text{NAlCl}_4$ - SO_2Cl_2 in LiAlCl_4 - SO_2Cl_2 .

increasing $(\text{Bu})_4\text{NAlCl}_4$ - SO_2Cl_2 concentrations. For comparison, cathodic scans in neutral $(\text{Bu})_4\text{NAlCl}_4$ - SO_2Cl_2 solutions show cathode reduction current which increases sharply without even reaching limiting current values. This crossover effect seen in mixed Li^+ $(\text{Bu})_4\text{N}^+$ electrolytes appears to be due to increased concentration of reducible species in the vicinity of the carbon electrode.

Although we may rule out the possibility of Li^+ ions being reduced to conductive metallic lithium on the carbon working electrode since carbon potentials were never less

than +1.6V relative to lithium, this crossover is difficult to explain.

The major conclusions from this work are: (i) use of neutral $(\text{Bu})_4\text{NAlCl}_4$ as conducting electrolyte salt in SO_2Cl_2 cells can yield dramatically extended cathode life; and (ii) rest potential of a carbon electrode in sulfuryl chloride-electrolytes is a strong function of dissolved chloride anion concentrations. Highest carbon potentials are obtained when lithium or calcium ions are present or when excess AlCl_3 is present to scavenge free chloride ions. Lowest potentials are obtained when soluble electrolyte salts based on $(\text{Bu})_4\text{N}^+$ are used.

Acknowledgments

We wish to thank Dr. John Wilkes of the Frank Seiler Research Labs for the imidazolium chloride. We wish to thank Dr. Wishvender K. Behl for valuable discussions and experimental suggestions on the cyclic voltammetric experiments and Dr. Mark Salomon for helpful advice on salt purification and electrolyte solubilities. Laura Thorsen greatly assisted in the manuscript preparation. We also wish to thank Dr. Carl Berger, Director of Power Sources for constant encouragement and interest.

Manuscript submitted June 3, 1985; revised manuscript received Aug. 15, 1985.

ERADCOM assisted in meeting the publication costs of this article.

REFERENCES

1. S. Gilman and W. Wade, Jr., *This Journal*, **127**, 1427 (1980).
2. M. Binder, S. Gilman and W. Wade, Jr., *ibid.*, **129**, 897 (1982).
3. M. Binder, W. Wade, Jr., and S. Gilman, in "Proceedings of 30th Power Sources Symposium," Atlantic City, NJ, June 7-10, 1982, The Electrochemical Society, Inc., p. 154 (1983).
4. W. K. Behl, *This Journal*, **130**, 1712 (1983).
5. W. K. Behl, *ibid.*, **127**, 1444 (1980).
6. A. Meitav and E. Peled, *ibid.*, **129**, 451 (1982).
7. G. J. Hills in "Reference Electrodes Theory and Practice," D. J. G. Ives and G. J. Janz, Editors, Academic Press, New York (1961).
8. R. C. Larson, R. T. Iwamoto, and R. N. Adams, *Anal. Chim. Acta*, **25**, 371 (1961).
9. Y. Avigal and E. Peled, *J. Electroanal. Chem.*, **76**, 135 (1977).
10. J. H. Jischke, PhD Thesis, Oregon State University, Corvallis, OR (1976).
11. K. M. Abraham and R. M. Mank, in "Proceedings of the 29th Power Sources Symposium," Atlantic City, NJ, June 9-12, 1980, The Electrochemical Society, Inc., p. 135 (1981).
12. K. M. Abraham and R. M. Mank, *This Journal*, **127**, 2091 (1980).

X-ray Fluorescence and SEM Analysis of Cycled NiOOH Electrodes

S. G. Meibuhr*

General Motors Research Laboratories, General Motors Technical Center, Electrochemistry Department, Warren, Michigan 48090-9058

R. F. Hill

General Motors Research Laboratories, General Motors Technical Center, Analytical Chemistry Department, Warren, Michigan 48090-9058

ABSTRACT

Zinc negative electrodes often contain other metal compounds to minimize shape change during cycling. After cycling in a Zn/NiOOH cell, these materials can be found in the positive nickel hydroxide electrode. Two complementary analytical techniques were used to characterize the distribution and amount of Co, Zn, Ca, and Pb present as components of various compounds in the nickel oxide electrode after cycling. Radioisotope-induced x-ray fluorescence was used to quantify the amounts of the elements at various locations across the electrode face, and scanning electron microscopy was used to determine concentration profiles of Zn within the electrode. Selected area analysis showed that the amount of Zn was lowest in areas of the positive electrode which were opposite sections of the zinc negative electrode that experienced the greatest loss of zinc material: the edges. Large amounts of Pb material were found in the positive electrode when that electrode remained on open-circuit stand after cycling.

The presence of zinc compounds in cycled nickel oxide electrodes and their effect on the electrode performance have been of considerable interest for understanding the behavior of Zn/NiOOH cells. Charkey (1) identified a capacity loss of nickel oxide electrodes by zinc oxide poisoning. He suggested that the deposition of ZnO in the pores of the electrode resulted in a plugging of those pores. Thornell and Pearlman (2) found zinc oxide in sintered nickel oxide plates in varying amounts. They concluded that adsorption of zincate into the electrode caused the capacity to diminish. This capacity loss was reversible when the electrode was subsequently cycled in zincate-free electrolyte. Casey *et al.* (3), in reviewing the reported effect of zinc on nickel hydroxide electrodes, indicated in their Table I essentially no detrimental effect; however, in the text they refer to "the suppression of charge available in the presence of Zn²⁺." Sharpe (4) showed that zincate in the electrolyte lowered the reversibility of the triangular voltage sweep peak on a Ni sheet electrode, presumably by the formation of a resistive film that contained a zinc containing compound.

Pasted zinc electrodes, however, usually contain more than zinc compounds; numerous metal oxides or hydroxides have been utilized to lessen the shape change effect observed on cycling. Such materials as Ti₂O₃ (5, 6), CdO (5, 6), Pb oxides (5-9), Bi₂O₃ (10), Ca(OH)₂ (7, 9, 11, 12), and In(OH)₃ (5-7) have all been tried. Moreover, Kucera *et al.* described the testing of a large Zn/NiOOH battery system (12) that incorporated Ca(OH)₂ into the zinc electrodes. Few researchers have determined whether these zinc electrode additives have any effect on the positive nickel electrode. The work reported here presents analytical methods used to evaluate cycled nickel electrodes.

To determine whether any of the zinc electrode constituents were transferred to the nickel electrode during cycling of a laboratory Zn/NiOOH cell, two analytical techniques—x-ray fluorescence and scanning electron microscopy—were used to examine the nickel electrodes for the presence and distribution of constituents that were originally in the negative electrode. For the purposes of this study, we selected a zinc electrode composition analogous to that used by Jones (9).

Experimental Procedure

Both radioisotope-induced x-ray fluorescence (XRF) measured with an energy-dispersive analyzer and scanning electron microscopy (SEM) coupled with an energy-dispersive x-ray analyzer (EDS) were used to provide information on the amount and distribution of various compounds in cycled NiOOH electrodes. Since

* Electrochemical Society Active Member.

these analytical methods cannot be used to identify compounds, only the constituent elements Ca, Co, Ni, Zn, and Pb were measured.

While the advantages and difficulties of using the SEM/EDS for battery studies is well documented (13), the radioisotopic x-ray fluorescence method is not as well known. The fluorescence method is nondestructive; full-size battery electrodes can be evaluated and they need not be washed free of electrolyte since the analysis is performed in the ambient atmosphere. In contrast, the SEM is best suited for handling small samples and can be used to examine cross sections of battery electrodes.

X-ray fluorescence method.—The radioisotopic x-ray fluorescence system consisted of a radionuclide excitation source, sample, and a Si(Li) detector, as shown schematically in Fig. 1. The detector was coupled to a Nuclear Data 4410 multichannel analyzer through a charge-sensitive preamplifier and an ORTEC 716 shaping amplifier.

Radionuclide excitation source.—Cadmium-109 (0.2 mCi) was used as the excitation source. The source, which was fabricated by New England Nuclear Corporation, was in the form of an annular ring with an inside diameter of 22 mm. The predominant excitation energy is 22.1 keV, the K_α x-ray from silver.

The intensity of the excitation source was selected on the basis of a trade-off between resolution and counting time. The 0.2 mCi source selected for these experiments required a counting time of 2000s to provide counting statistics with standard deviations of <10%. X-ray peak resolution, however, was improved over that obtainable with a more intense source.

Detector.—The Si(Li) detector had an active diameter of 10 mm and a sensitive depth of 5.3 mm. The thickness of the beryllium window was 0.025 mm. The efficiency of the detector was independent of energy for x-ray energies between 6 and 15 keV. Below 6 keV, the efficiency fell off due to adsorption in the beryllium window. At 2 keV, the efficiency was 60% of that at 6 keV.

The resolution of the detector was 180 eV full width at half maximum (FWHM) at 5.9 keV. For a gaussian-shaped peak, the standard deviation (1σ) is equal to FWHM/2.35 (14). X-ray peaks separated by 6σ (~0.5 keV) should be resolved with less than a 1% error.

Mask.—Due to the arrangement of the source, sample, and detector, the maximum effective area of the sample that could be evaluated was 10 cm² (an effective sample diameter of 36 mm). As illustrated in Fig. 1, however, a 3 mm thick acrylic mask was inserted between the sample and detector to reduce the effective sampling area to 1.3

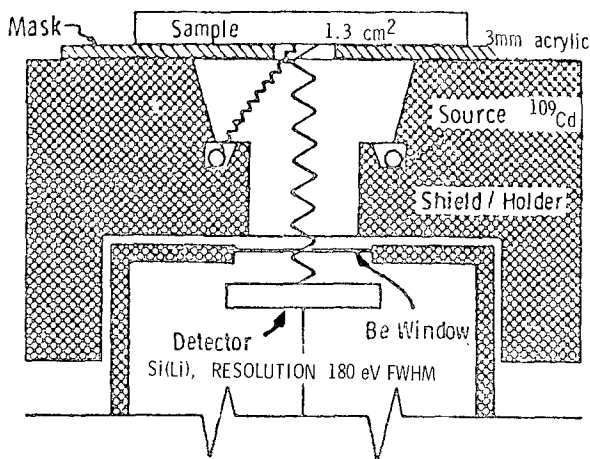


Fig. 1. Source, detector, and sample arrangement for x-ray fluorescence measurements.

cm² so that a more detailed profile of the electrodes could be obtained.

Electrodes.—The zinc electrodes were 16 × 16 cm and similar in composition to those described by Jones (9). These electrodes always contained ZnO, Ca(OH)₂, Pb₃O₄, and a binder in a Ca(OH)₂/ZnO mole ratio of ~0.75 and ZnO to Ni(OH)₂ ratios of from 1.5 to 3. The ratios of these materials varied from cell to cell, but were identical for any given cell. The 16 × 16 cm, nonsintered nickel oxide electrodes were prepared by pasting the nickel hydroxide mix onto a Ni-plated copper perforated-foil current collector. The dry nickel hydroxide mix contained Ni(OH)₂, 60-65 weight percent (w/o) (analyzed typically as containing 61 w/o nickel metal), Co(OH)₂, 3-5 w/o, Dixon KS-2 graphite 20-25 w/o, Thornel VMA carbon fibers (Union Carbide Corporation) 6 w/o, and polytetrafluoroethylene 6 w/o.

The electrodes were assembled into either 20 or 140 Ah capacity cells that used 20 or 25 w/o KOH (7, 9, 12) as electrolyte and the resultant cell was then formed. During cycle testing, the discharges were performed at the C/3 rate to a 1V cutoff and the recharges were made at the C/8 rate to a 2.25V cutoff.

The cycled Zn/NiOOH cells were disassembled in a plastic dry box inflated with dry argon. The individual, flat electrodes were stored in plastic bags inside the inflated dry box until needed for analysis, after which they were washed with distilled water to remove the alkaline electrolyte and then air dried. The electrodes were analyzed by both SEM and XRF methods at one or more

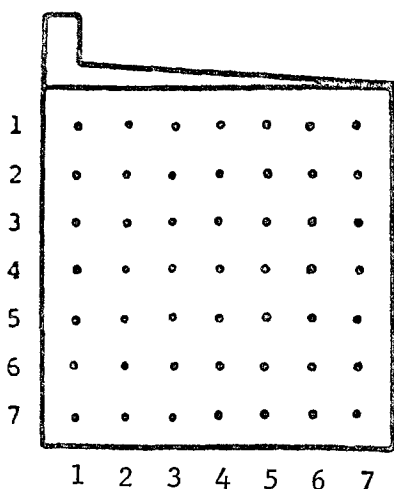


Fig. 2. Electrode shape and analytical grid arrangement

of the sites shown in Fig. 2. Electrodes from 18 cells were examined.

Sample preparation for the SEM surface examination of electrodes was standard. Selected sections cut from some of the electrodes were vacuum impregnated with an epoxy resin for subsequent cross-sectional examination in the SEM. After the epoxy hardened, these samples were polished parallel to the long axis of the electrode section with 600 grit paper to prevent "smearing" of the relatively soft electrode material onto the epoxy surface. X-ray analyses were made on these cross sections in addition to line profile analysis (LPA) for Zn and Ca. The LPA's provide a graphic display of elemental distribution along a line on the sample and therefore can identify the presence of gradients of material within the electrode for both the charged and the discharged condition.

Analytical Approach

The electrode to be evaluated by the radioisotopic x-ray fluorescence method was placed on the source-detector support system, as illustrated in Fig. 1. The 22.1 keV x-rays from the excitation source impinged on the sample and ejected K and L electrons from the various elements in the sample by photoelectric interactions. The excited atoms in turn emitted characteristic K and L x-rays that were counted by the Si(Li) detector.

Characteristic x-rays.—The predominant characteristic x-ray energies for the major constituents in the battery electrodes are listed in Table I. The relative intensities of K_α and K_β for these elements are 150 and 20, respectively, resulting in a K_α/K_β ratio of 7.5 (15). The actual measured ratios range from 5 to 7 due to efficiency changes in the solid-state detector for the various energies and self-absorption in the sample. The average L_α/L_β ratio for Pb was 0.85.

The energy limits that were used to determine the net counts in the various photopeaks are given in Table II. Not all of these photopeaks were present in all analyses, nor were the net counts determined for all photopeaks. For example, the net counts in the Zn K_β photopeak were determined rather than those of the Zn K_α photopeak because of the interference between the Zn K_α and the Ni K_α photopeaks.

Extraneous peaks.—In addition to the characteristic x-ray photopeaks from the elements in the sample, other peaks can be present in the spectrum due to Compton interactions and radiation escaping from the surface of the detector. Since these extraneous peaks can complicate the quantitative determination of some elements, the significance of these peaks must be understood. Equa-

Table I. Predominant characteristic x-ray energies for selected elements

Element	X-ray energy (keV)			
	K _α	K _β	L _α	L _β
K	3.31	3.59	—	—
Ca	3.69	4.01	—	—
Fe	6.40	7.06	—	—
Co	6.93	7.65	—	—
Ni	7.48	8.26	—	—
Cu	8.05	8.90	—	—
Zn	8.64	9.57	—	—
Pb	—	—	10.55	12.61

Table II. Energy limits for various elements

Element, photopeak	Energy limits (keV)
Ca, K _α	3.55- 3.85
Fe, K _α	6.20- 6.60
Co, K _α	6.75- 7.15
Ni, K _α	7.25- 7.75
Zn, K _α	8.40- 8.90
Zn, K _β	9.35- 9.85
Pb, L _α	10.30-10.80
Pb, L _β	12.30-12.90

Table III. Possible extraneous peaks in x-ray fluorescence spectra of Zn/NiOOH battery electrodes

Source	Peak energy (keV)		
	Escape, E _e	Compton, E _c	Backscatter, E _b
Ni K _α	5.78	0.22	7.26
Zn K _α	6.94	0.29	8.35
Pb L _α	8.85	0.43	10.12
Pb L _β	10.91	0.61	12.00
Ag K _α	20.4	1.79	20.31

tions for determining the energy and source of extraneous peaks are presented in the literature (14). Based on those equations, the energy of possible extraneous peaks due to the major constituents in the electrodes and the excitation source were calculated. As noted in Table III, the Compton peaks are at the low energy end of the spectrum and will not interfere with the photopeaks of interest. The backscatter peak, on the other hand, is so close to the characteristic photopeak (Table I) that it cannot be effectively resolved; it will appear as a broadening of the characteristic photopeak for x-ray energies below 10 keV.

The escape peak, on the other hand, can introduce errors. For example, the escape peak from the Zn K_α photopeak (6.94 keV, Table III) is nearly identical to the Co K_α photopeak (6.93 keV, Table I). Preliminary experiments with the Si(Li) detector used in this work indicated that the area under the Zn K_α escape peak was 0.15% of the area under the Zn K_α photopeak. Thus, the cobalt determination must be corrected for the zinc escape peak by subtracting 0.15% of the net counts in the Zn K_α photopeak from the net counts in the Co K_α peak.

Ni ratios.—The raw spectra from the samples were computer smoothed, and then the net counts (total minus background) under the desired peaks were determined. The net counts for the peaks were then divided by the net counts in the Ni K_α peak to provide a nickel ratio. This use of nickel ratios reduced the random errors that can be introduced by statistical processes associated with radiometric measurements, variations in sample density, and variations in counting geometry.

These nickel ratios can be used to estimate the relative amounts of the elements present in the electrode. While no single analytic expression is valid for all elements, a rough approximation for elements within five atomic numbers of nickel is

$$A_z = N(28/Z)^6 \quad [1]$$

where A_z is the relative amount of element with atomic number Z , and N is the nickel ratio calculated from the K_α peaks. This equation was obtained empirically and is based on the relative intensities of the K_α photopeaks from pure metal standards of Ti, Fe, Ni, Cu, Zn, Zr, and Nb when excited with the radiation from a ¹⁰⁹Cd source.

Precision of the method.—To determine the precision of the method, consecutive determinations were made on the same area of a single electrode (no. 20-145). The average counts for Co, Ni, Zn, and Pb photopeaks are listed in Table IV. In one instance, 12 measurements were made; in a second instance, five additional spectra were collected and were computer smoothed to reduce the deviation of counts in the spectra and to compensate partially

Table V. Net counts per unit mass thickness of lead (counting time 2000s)

Nominal absorber thickness (Å)	Actual mass thickness (mg/cm ²)	Net counts/(mg/cm ²)	
		Pb L _α	Pb L _β
5,000	0.69	27,977	32,075
10,000	1.38	25,461	29,777

for poor statistics. The data processing program in the x-ray analyzer incorporated a five-point coefficient smoothing routine that caused the peaks to approximate a gaussian fit. The results in Table IV show (i) that computer smoothing of spectra yielded lower standard deviation values and (ii) that the standard deviation decreased as the amount of the element in the sample increased.

Lead interference.—If the amount of lead present in an electrode is high, it can substantially lower the net counts from the other elements in the electrode due to absorption of the characteristic x-rays by the lead. To evaluate the influence of lead, a series of experiments with lead absorbers was conducted to determine the effect of lead on the net counts from various elements in a nickel oxide electrode.

The lead absorbers were first evaluated separately in repeated experiments. The average net counts per unit mass thickness for the Pb L_α and Pb L_β photopeaks were determined for nominal absorber thicknesses of 5000 and 10,000 Å (Table V). The net counts per milligram per square centimeter dropped off as the thickness of the Pb absorber was increased. This dropoff was due to self-absorption within the Pb absorber. For very thin layers of Pb, self-absorption became minimal.

A second series of experiments was performed to evaluate the influence of the Pb absorbers on the net counts from various elements in a nickel oxide electrode. A NiOOH electrode was evaluated with no absorber, and with 5000 and 10,000 Å thick Pb absorbers between the electrode sample and the detector. Each experiment was repeated four times; the relative net counts for Co, Ni, and Zn were recorded. From the data, it was determined that the 5000 Å thick Pb absorber reduced the net counts in the Co K_α, Ni K_α, and Zn K_β photopeaks by approximately 25% (26%, 24%, and 24%, respectively). The 10,000 Å thick Pb absorber reduced the net counts in the various photopeaks by 43%. The nickel ratios for Pb, (Pb L_α)/(Ni K_α), in these experiments were 0.0137, 0.326, and 0.777, respectively, for the three conditions.

Based on these measurements, Eq. [2] was developed empirically to determine the true net counts (I_0) in the photopeaks for the various elements if Pb had not been present

$$I_0 = I(1 + \text{Pb/Ni}) \quad [2]$$

where Pb/Ni is the nickel ratio based on the actual net counts in the Pb L_α and Ni K_α photopeaks and I is the net counts in the photopeaks selected for any element including nickel. Only Pb was considered in this evaluation because it has the highest x-ray absorption characteristics when compared to other elements in the electrodes.

Table IV. Repeat determinations

	Net counts				Nickel ratio		
	Co K _α	Ni K _α	Zn K _β	Pb L _α	Co/Ni	Zn/Ni	Pb/Ni
Unsmoothed							
Average	2,667	83,398	5,374	1,041	0.0320	0.0644	0.0125
% Std. dev.	6.2	0.45	2.9	18.3	6.2	2.8	18.4
Smoothed							
Average	2,568	83,341	5,469	1,085	0.0308	0.0656	0.0130
% Std. dev.	4.8	0.25	1.6	8.2	4.8	1.5	8.4

Since Eq. [1] was developed for nickel ratios based on the net counts in the K_{α} photopeaks, it cannot be used to estimate the relative concentrations of Pb from the Pb L_{α} photopeak measurements. Equation [3], which was developed from Eq. [2], can be used to estimate the effective mass thickness of Pb on the electrode

$$\text{Pb mass thickness (mg/cm}^2\text{)} = \frac{2.7 (\text{Pb/Ni})}{(1 + \text{Pb/Ni})^{0.8}} \quad [3]$$

where Pb/Ni is the nickel ratio as defined in Eq. [2].

Depth of analysis.—Because the characteristic x-rays from the various elements in the electrodes are of fairly low energy (Table I), self-absorption in the electrode material limits the x-ray fluorescence analysis to relatively shallow depths from the electrode surface. Equations developed for the attenuation of x-rays of various energies through a NiOOH matrix were used to calculate the effective depth (depth from which 90% of the characteristic x-rays detected are emitted) for determining the presence of the various constituents. The effective depth of selected elements is listed in Table VI, which shows that the x-rays detected from Ca, Zn, and Pb originate in a shallow layer close to the surface of the electrode. The depth for Co and Ni determinations, on the other hand, corresponds to about 10% of the total electrode thickness (1-1.5 mm). These depths of analysis, however, are several orders of magnitude greater than those obtained with the electron excitation of the SEM/x-ray method (16).

Results and Discussion

The results of a preliminary analytical experiment in which cycled positive electrodes of different sizes and capacities were reacted in hot concentrated HCl and the resultant filtered solutions were subsequently analyzed by atomic absorption for zinc content are shown in Fig. 3. The amount of zinc, calculated as zinc oxide, was normalized to unit electrochemical activity of the positive electrode. Regardless of how one fits a curve to these data points, it is clear that the content of a zinc compound in the positive electrode increased with cycle duration. The first amounts of zinc were found after the first formation cycle, before the standard cycling process began; thus, the data point below 0 on the X-axis. Although the chemical analysis method detected zinc, it was unsuited for determining the distribution of zinc across the electrode because large sections of electrode would be needed to minimize experimental error. Therefore, we utilized the x-ray fluorescence and SEM methods for more detailed analyses.

In general, after any length of cycle testing in a Zn/NiOOH cell, Zn, Pb, Ca, and any other constituent used to make the negative zinc electrode can be detected in the positive electrode. For example, in cells with zinc electrodes that contained only HgO as additive to reduce the hydrogen overpotential, the HgO has been found in the positive nickel oxide electrode.

Distribution measurements of cycled battery electrodes.—Electrode 20-145 is representative of the majority of the electrodes. Electrode 20-152 experienced an extended open-circuit stand before removal from its cell. Results from this electrode were sufficiently different from the majority that results will be described also.

Electrode 20-145.—This positive electrode, which was used in the repeatability and Pb calibration tests, came from a nominal 20 Ah cell that had been cycled >300

Table VI. Effective depth from which the various elements in NiOOH electrodes are determined

Element	Effective depth (mm)
Ca	0.019
Co	0.096
Ni	0.128
Zn	0.023
Pb	0.038

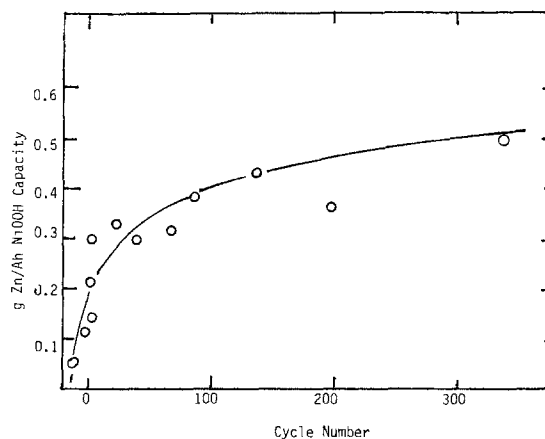


Fig. 3. Amount of zinc material in cycled nickel oxide electrodes determined by chemical analysis.

times at nominally 6 mA/cm² during discharge and 3 mA/cm² during charge. The cell was disassembled in the charged state. The counter zinc electrodes contained Ca and Pb compounds as additives. The positive electrode had a calculated weight of 0.135 g/cm² for the active layer, of which 0.09 g/cm² corresponded to the Ni(OH)₂ material.

Cobalt.—Experimental results showed that the Co remained uniformly distributed across the electrode after the cycling process. From Eq. [1], the average amount of Co remaining in the electrode after prolonged cycling was 3.8% with a range from 3.3 to 4.2%. These values are consistent with the initial concentration of Co in the electrode after taking into account that some Co dissolved in the electrolyte (~30 ppm) during the electrochemical testing, as evidenced by the slight discoloration of the electrolyte.

As pointed out earlier, the zinc escape peak can cause interference with the Co determination. A zinc escape peak of 51 net counts was calculated from the average value of the K_{β} for the zinc and using a K_{α}/K_{β} ratio for zinc of 6.35 as measured. The 51 counts are only about 2% of the net counts recorded in the various Co K_{α} photopeaks. Since this correction is lower than the percent standard deviation determined for the cobalt measurements, the influence of the zinc escape peak on cobalt determinations in positive nickel oxide electrodes can be ignored.

Zinc.—The average relative zinc concentration according to Eq. [1] was 27%; this is consistent with chemical analysis of other cycled positive electrodes, which yielded zinc concentrations varying from 30-35 w/o.

Figure 4 displays the distribution of zinc, milligrams per square centimeter, across the face of the electrode. The top of the electrode and the site positions are identified on the three-dimensional graph. Clearly, there is less zinc material near the top of the electrode than elsewhere, especially near the bottom. The distribution of zinc material from the top of the electrode to the bottom may be due to gravitational effects, but is probably more related to current distribution over the electrode face.

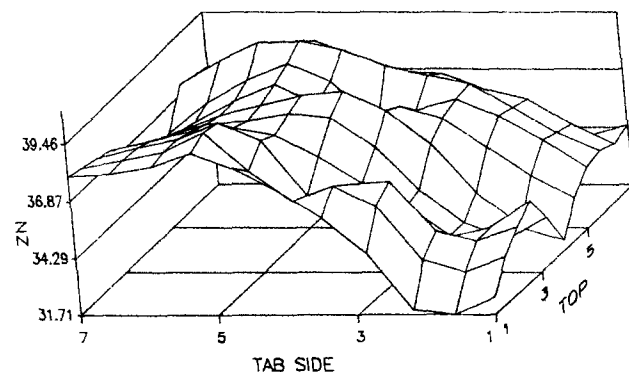


Fig. 4. Three-dimensional representation of zinc distribution across cycled nickel oxide electrode, 20-145, as measured by x-ray fluorescence.

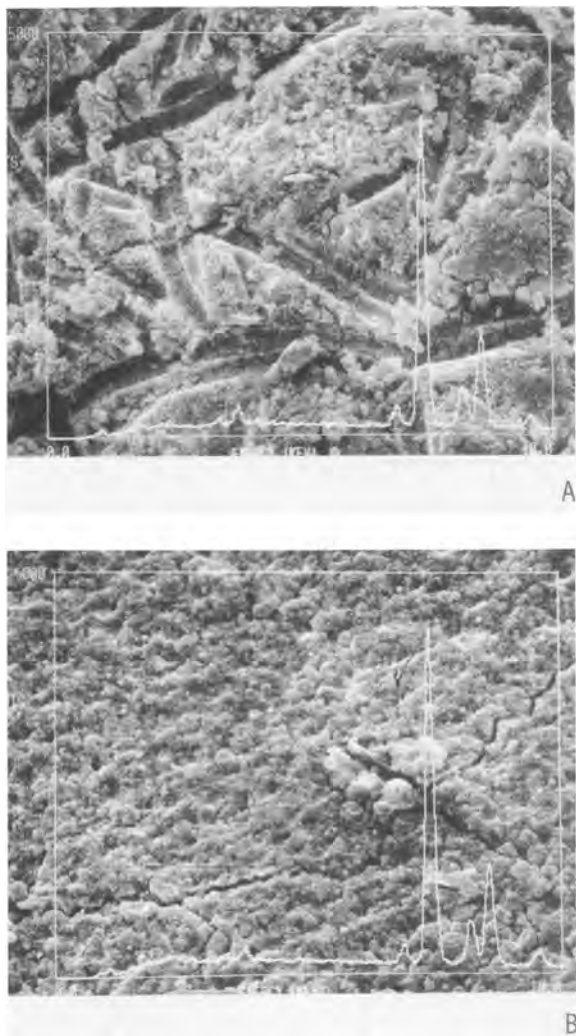


Fig. 5. Scanning electron micrographs of electrode 20-145 together with x-ray spectra. A: Electrolyte side. B: Grid side.

Scanning electron micrographs at 300 times magnification of the electrolyte side and the grid side of the active layer taken from the center of the electrode are shown in Fig. 5 together with their respective x-ray spectra. The electrolyte side of the active layer showed the impression of the separator material. Both surfaces showed high zinc content, corroborating the x-ray fluorescence results. Figure 6 presents a line profile analysis (LPA) for

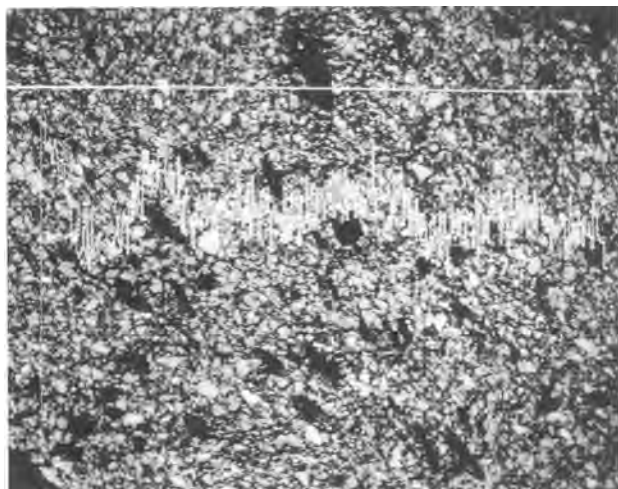


Fig. 6. Line profile analysis for zinc in the cross section from electrode 20-145. Backscatter electron image. Left side is electrolyte.

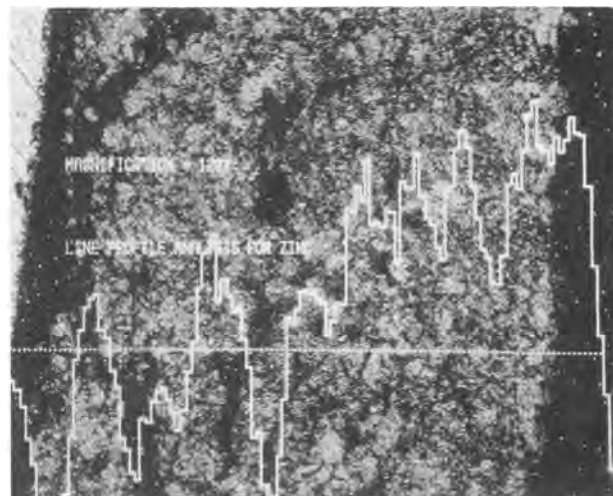


Fig. 7. Line profile analysis for zinc in the cross section of a fully discharged nickel oxide electrode. Backscatter electron image.

zinc in the cross section of the active layer taken from the electrode center; the left side of the micrograph corresponds to the electrolyte side of the active layer. The LPA confirms the uniformity of zinc distribution throughout the inner part of the active layer.

Results of LPA studies made on other discharged and charged positive electrodes are shown in Fig. 7 and 8, respectively. Despite the noise in these LPA's (caused by a too brief of an analysis time), these results demonstrate that in the discharged state, the positive electrode has a higher amount of zinc at the electrolyte side of the active layer than at the grid side. There appears to be a linear increase of zinc from the grid side to the electrolyte side. The fully charged electrode, on the other hand, showed a more uniform distribution of zinc in the active layer.

Lead.—The average Pb concentration corresponds to 0.027% with a range of 0.017-0.043%. The use of Eq. [2] to correct for the presence of Pb in this electrode did not affect the results from Eq. [1] by more than 0.1%; consequently, for concentrations at this level, we can ignore the Pb effect. At this low concentration, Pb could not be detected with the SEM.

Electrode 20-152.—This electrode also came from a nominal 20 Ah cell that had been cycled > 300 times under conditions analogous to that of the previously described electrode. However, the cell remained on open-circuit stand in the discharged state for about 4 months after cycling but before the cell was disassembled. The Pb was in one to two orders of magnitude higher concentration than

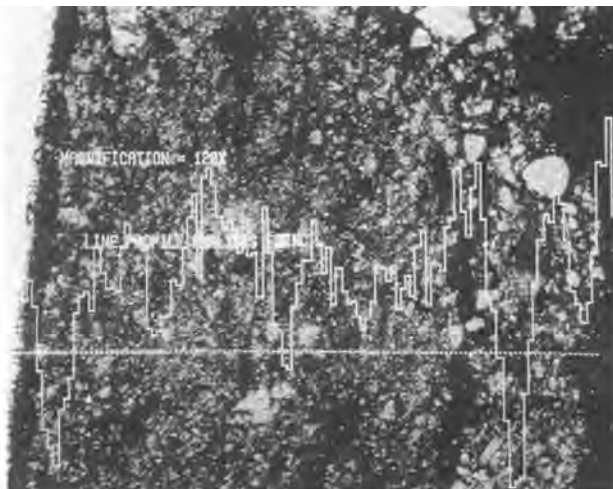


Fig. 8. Line profile analysis for zinc in the cross section of a charged nickel oxide electrode. Backscatter electron image.

in the previous electrode. Other electrodes on prolonged open-circuit stand after cycling have also exhibited similarly higher amounts of Pb regardless of the number of cycles the cell had undergone. The large Pb concentration seriously affected the reported x-ray fluorescence counts for each of the other three elements of interest. It was necessary to use Eq. [2] on the raw data before applying Eq. [1] for the determination of Co and Zn, or Eq. [2] for the determination of Pb.

Cobalt.—The cobalt remained uniformly distributed with an average value of 4.0% and a range of 3.3-5%. The open-circuit stand that this electrode experienced had no detectable effect either on the amount of Co in the positive electrode or on its distribution.

Zinc.—Figure 9 shows a three-dimensional distribution of zinc across the electrode surface; note that the scale, in milligrams per square centimeter, is about twice that used in Fig. 4. Clearly, more zinc material was transferred to the positive electrode during the open-circuit stand. In this situation, however, all four edges showed much less zinc than the upper, central portion of the electrode which showed values two to three times greater than other sections of the electrode.

The average percentage value for zinc was 35% with a range from 20 to 54%. The edge areas showed a lower zinc concentration and corresponded to areas on the negative zinc electrode that also showed a lower amount of zinc material than the central portion of the negative electrode. Also, a densified area on the zinc electrode corresponded to the highest zinc content area on the positive electrode. Further studies are certainly warranted to relate the material distribution in the positive electrode to cell operating conditions.

Lead.—There was more than an order of magnitude variation in Pb content across the electrode face with the highest Pb content in the same area of the electrode as was the highest zinc content. Figure 10 gives the three-dimensional distribution for Pb across the electrode face. In a separate experiment in which a cell was subjected to

only 30 charge/discharge cycles but to an equivalent 4 month open-circuit stand, Pb was detected in the positive electrode at a concentration only slightly less than in the electrode that was cycled > 300 times. Clearly, the open-circuit stand after cycling promotes Pb transfer to the positive electrode. These studies cannot address the question of what mechanism causes this transfer.

Epilog.—Although experimental results are presented for only two electrodes, the other 16 NiOOH electrodes from either other cells or from different locations within one cell all showed, (i) a transfer of Zn, Co, and Pb to the positive electrode during cycling, (ii) a distribution pattern across the positive electrode for Zn that was akin to that of Fig. 4, and (iii) the amount of Zn transferred appeared independent of the zinc electrode composition, at least within the relatively narrow range of component ratios used in this study. We would expect, however, that more zinc would be transferred from a negative electrode that did not contain any calcium compounds. We conclude that any approach that is used to reduce zincate solubility in the alkaline electrolyte, will also lower the amount of zinc transferred to the positive electrode during cycling.

Conclusions

These results show how x-ray fluorescence and cross-sectional scanning electron microscopy coupled with energy dispersive x-ray analysis can be used to quantify the chemical changes that occur in positive nickel oxide electrodes caused by charge/discharge cycling. Analysis at selected areas showed that the distribution of constituents picked up from the negative electrode can be determined.

Manuscript submitted April 15, 1985; revised manuscript received ca. Aug. 5, 1985.

General Motors Research Laboratories assisted in meeting publication costs of this article.

REFERENCES

1. A. Charkey, in "Proceedings of the 11th International Energy Conversion Engineering Conference, Sept. 12, 1976," p. 452, American Institute of Chemical Engineers, New York (1976).
2. S. Thornell and E. Pearlman, in "The Nickel Electrode," R. G. Gunther and S. Gross, Editor, p. 286, The Electrochemical Society Softbound Proceedings Series, Pennington, NJ (1982).
3. E. J. Casey, A. R. Dubois, P. E. Lake, and W. J. Moroz, *This Journal*, **112**, 371 (1965).
4. T. F. Sharpe, Abstract 14, p. 25, The Electrochemical Society Extended Abstracts, Vol. 82-2, Detroit, MI, Oct. 17-22, 1982.
5. A. Himy and O. C. Wagner, in "Proceedings of the 28th Power Sources Conference," Atlantic City, NJ, June 12-15, 1978, The Electrochemical Society, Inc., p. 167 (1979).
6. A. Himy and O. C. Wagner, U.S. Pat. 4,084,047.
7. Y. Maki, M. Fujita, H. Takahashi, and T. Ino, U.S. Pat. 3,816,178.
8. A. Himy and R. Karcher, Abstract 90, p. 246, The Electrochemical Society Extended Abstracts, Vol. 80-2, Hollywood, FL, Oct. 5-10, 1980.
9. R. Jones, U.S. Pat. 4,358,517.
10. J. McBreen and E. Gannon, Abstract 8, p. 13, The Electrochemical Society Extended Abstracts, Vol. 83-2, Washington, DC, Oct. 9-14, 1983.
11. W. J. van der Grinten, Abstract 38, p. 96, The Electrochemical Society Extended Abstracts, Vol. J-6, Chicago, Oct. 15-20, 1967.
12. G. Kucera, H. G. Plust, and C. Schneider, Paper 750147 presented at the Society of Automotive Engineers Meeting, Detroit, MI, Feb. 24-28, 1975.
13. T. J. Hughel and R. H. Hammer, in "7th International Power Sources Conference," D. H. Collins, Editor, p. 35, Oriol Press, Brighton, England (1971).
14. G. F. Knoll, "Radiation Detection and Measurement," p. 91, John Wiley, and Sons, New York (1979).
15. S. I. Salem, S. L. Panossian, and R. A. Krause, *At. Data Nucl. Data Tables*, **14**, 91 (1974).
16. N. C. Barbi, "Electron Probe Microanalysis using Energy Dispersive X-ray Spectroscopy," issued by Princeton Gamma-Tech, Princeton, NJ.

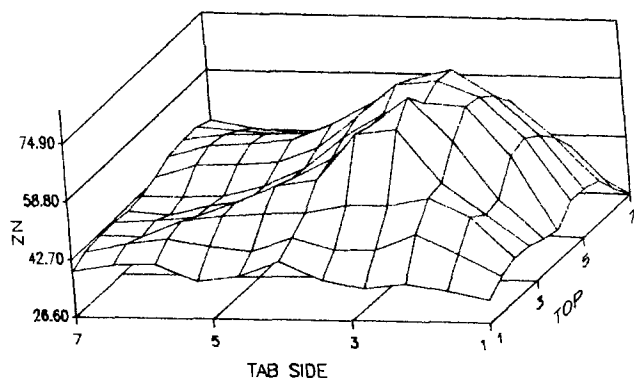


Fig. 9. Three-dimensional representation of the zinc distribution on electrode 20-152 as determined by x-ray fluorescence.

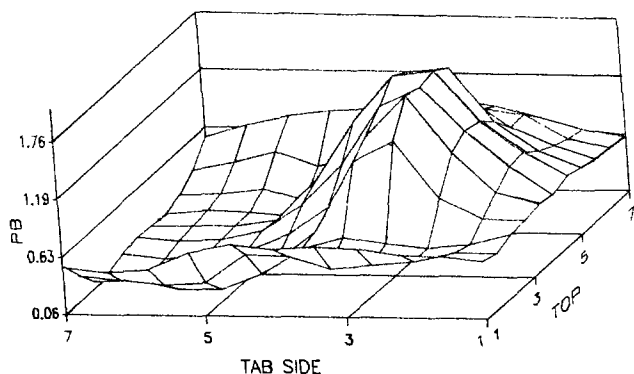


Fig. 10. Three-dimensional representation of the Pb distribution on electrode 20-152 as measured by x-ray fluorescence.

On a Homogeneous Electrochemical Reaction of Prussian Blue/Everitt's Salt System

A Model of MnO₂/MnOOH System

Tsutomu Ohzuku* and Keijiro Sawai

Electrochemistry and Inorganic Chemistry Laboratory, Department of Synthetic Chemistry, Faculty of Engineering, Okayama University, Okayama 700, Japan

Taketsugu Hirai*

Industrial Inorganic Chemistry Laboratory, Department of Applied Chemistry, Faculty of Engineering, Osaka City University, Sugimoto 3-3-138, Sumiyoshi, Osaka 558, Japan

ABSTRACT

Voltammetric, chronopotentiometric, and spectroelectrochemical studies on the homogeneous-phase (single phase) reaction of Prussian blue (PB)/Everitt's salt (ES) system in KCl aqueous solution were carried out as a model for understanding the homogeneous electrochemical reaction of manganese dioxide. Analytical results of voltammetric and chronopotentiometric studies on PB/ES system indicated that the electrode potential was represented by the empirical formula

$$E = E_0 - (RT/nF) \ln ([Fe^{2+}]/[Fe^{3+}]) + (RT/F) \ln [K^+]$$

where the observed n value was 0.5, not 1.0. Results on spectroelectrochemical studies supported the above formulation, and the n value, 0.5, indicated that the effect was thermodynamic, not kinetic. A possible explanation of the problem was given, emphasizing the role of charge carrier in a solid matrix in an electrochemical reaction, and the specific differences between a redox reaction of soluble species in a solution and a redox reaction in a solid matrix were discussed. The electrochemical behavior of MnO₂/MnOOH system was deduced in terms of a homogeneous (single phase) electrochemical reaction from the analogy of PB/ES system.

Mixed valence compounds containing an element in two different oxidation states in a crystal lattice offer a class of electrode system unique in electrochemistry. One of the most useful mixed valence compounds is manganese dioxide (MnO₂), which is used as a cathode for primary batteries. Reaction mechanism of MnO₂ together with the formulation of electrode potential to explain an S-shaped discharge curve has been investigated.

In the discharge process of MnO₂, electrons and protons are introduced into the crystal lattice of MnO₂ without destroying its essential crystal structure, such as ramsdellite/groutite or pyrolusite/manganite. In other words, the original MnO₂ is continuously converted to MnOOH, isostructural with the original MnO₂, by increasing Mn³⁺ and H⁺ (more precisely, OH⁻) concentration in a crystal lattice during the discharge process. Such an electrochemical reaction may be represented as



Johnson and Vosburgh (1) and Newmann and Roda (2) gave the reversible reaction [1], and they formulated the electrode potential directly

$$E = E_0 - \frac{RT}{F} \ln \frac{[MnOOH]}{[MnO_2]} + \frac{RT}{F} \ln [H^+] \quad [2]$$

On the other hand, Kozawa and Powers (3, 4) proposed the equation

$$E = E' - \frac{RT}{F} \ln \frac{[Mn^{3+}]_{solid}}{[Mn^{4+}]_{solid}} \quad [3]$$

instead of Eq. [2] from the analogy of a redox system in an aqueous solution, emphasizing the homogeneous-phase reaction. They explained the characteristic S-shaped discharge curve of MnO₂ fairly well on the basis of homogeneous phase theory (3, 4). Observed S shapes, however, are almost always steeper than those calculated from Eq. [3]. Tye (5) observed -118 mV potential dependence in terms of $\log([Mn^{3+}]/[Mn^{4+}])$ in his electrode potential measurements for composition near to MnO₂. The potential dependence, -118 mV, was also observed in open-circuit voltage curves, low rate discharge curves, and potential-

*Electrochemical Society Active Member.

decay curves at constant current in alkaline solution for both electrolyte MnO₂s and chemically prepared MnO₂s (6).

The value, -118 mV, was two times greater than the expected value -59 mV from Eq. [3], which was not observed for a redox reaction in a solution and consequently which may be an essential character of MnO₂/MnOOH homogeneous-phase reaction if the effect was thermodynamic. Although there have been several arguments on the electrochemical behavior of MnO₂/MnOOH system (7-13), there seems to be general agreement that the electrochemical reduction of MnO₂ proceeds in a homogeneous phase and that the behavior resembles that for a redox couple in a solution phase.

There are, however, some differences between a redox reaction in a solution phase and that in a solid phase, *i.e.*, (i) the redox couple moving freely in a solution *vs.* the redox couple fixed in a solid matrix, (ii) the charge balance due to the movement of ions in a solution *vs.* the movement of foreign ions through a solid matrix, and (iii) the specific oxidation state of single ion in a solution *vs.* the nonstoichiometrically average oxidation state due to the formation of polynuclear species in a solid matrix.

Specific differences between a redox reaction in a solution and that in a solid matrix must, therefore, be recognized as to how such differences reflect on the electrochemical behavior of the redox reaction. In order to understand such specific differences between them, the electrochemical and spectroelectrochemical studies on Prussian blue (PB)/Everitt's salt (ES) electrode, the Fe³⁺/Fe²⁺ redox reaction in a solid matrix, were undertaken.

Physical properties of PB (14-16), such as electronic structure, crystal structure, electronic spectra, molecular magnetism, and the relationship between them are well understood, and reliable methods of preparing thin films of PB chemically (17, 18) and/or electrochemically (19, 20) have been established. Moreover, it is well known that PB having Fe²⁺, Fe³⁺ and bridging CN between them in a cubic lattice is chemically or electrochemically oxidized to Berlin green (BG) isostructural with PB, and also reduced to ES, again isostructural with PB, in an appropriate aqueous solution, indicating that the reaction proceeds in a homogeneous (single) phase. These factors enable us to

study the $\text{Fe}^{3+}/\text{Fe}^{2+}$ redox reaction in a PB matrix as a model for $\text{Mn}^{4+}/\text{Mn}^{3+}$ redox reaction in a MnO_2 matrix in terms of the solid-state redox reaction.

The objectives of the paper are to give specific differences between a redox reaction in a solution and that in a solid matrix and to give some insights into the electrochemistry of $\text{MnO}_2/\text{MnOOH}$ system out of the experimental and analytical results obtained from PB/ES system.

Experimental

Thin films of PB were electrochemically prepared on Pt and In_2O_3 -coated glass electrodes. Electrodes were cathodically polarized at $40 \mu\text{A}\cdot\text{cm}^{-2}$ for 120s in freshly prepared mixed electrolyte [0.02M FeCl_3 , $0.02\text{M K}_3\text{Fe}(\text{CN})_6$] at room temperature as was proposed by Itaya *et al.* (19). Thin films of PB deposited on electrodes were rinsed with distilled water to remove undesirable chemical species from the electrode surface. The prepared electrodes were soaked in the same concentrations of KCl solutions as those to be examined for about 3h before use. The prepared sample was identified as PB having a cubic lattice with $a_0 = 10.2\text{\AA}$ by x-ray examination on thick PB on Pt using an x-ray diffractometer (Shimadzu Corporation, Japan, Type XD-3A).

The electrochemical cell consisted of a working electrode, a Pt counterelectrode, and a saturated calomel electrode (SCE) through a Luggin capillary. The electrolytes were solutions having several KCl concentrations and several pH's. The cell was purged with nitrogen gas to remove oxygen from the system.

Cyclic voltammetry was performed using a potentiostat (Kowa Electronics Works Company Limited, Japan, Model PGS-1525) combined with a function generator (Kowa Electronics Works Company Limited, Model FG-101) and the data were recorded on a Houston Model 100 X-Y recorder.

Chronopotentiometry was performed using a galvanostat (Hokuto Denko Company Limited, Japan, Model HA-211). In the case of chronopotentiometry, the thin film of PB on Pt electrode was kept at $+0.8 \text{ vs. SCE}$ until the residual current reduced to less than $1 \mu\text{A}$, and then the control mode was switched over to galvanostat mode. The electrode potential as a function of time was registered on a recorder (Nippon Denshi Kagaku Company Limited, Model U-228).

Optical absorption spectra as a function of electrode potential were measured using a UV-visible spectrophotometer (Shimadzu Corporation, Model UV-240) equipped with a graphic printer (Shimadzu Corporation, Model PR-1). All experimental work was carried out at room temperature.

Method of Analysis

PB contains Fe^{3+} and Fe^{2+} in different ligand fields in a solid matrix, as is shown in Fig. 1 (21, 22). One is carbon-coordinated iron (low spin), and the other is nitrogen-coordinated iron (high spin). Mössbauer spectra (23, 24) and the magnetic moment (25) of PB suggest the presence of high spin Fe^{3+} , and the infrared spectra (26) of CN stretch frequency in PB agree with the ferric ferrocyanide formulation. Mössbauer spectra, however, cannot be positively identified as either Fe^{2+} or Fe^{3+} due to the anomalous isomer shift of iron cyanide (23), and the magnetic data do not determine the structure because they can be explained equally well by high spin Fe^{2+} and low spin Fe^{3+} (14). Thus, there still remains the question which of the two structures, $\text{Fe}^{3+}\text{-NC-Fe}^{2+}$ or $\text{Fe}^{2+}\text{-NC-Fe}^{3+}$, is right (27).

Whichever structure one takes for PB, Fe^{3+} is reduced to Fe^{2+} with no change in the surrounding ligand field. Therefore, we assume that the electrode potential of PB/ES system is determined by the logarithm of the ratio of two oxidation states existing in the same ligand field. Such an electrochemical reaction may be formulated using a general expression by

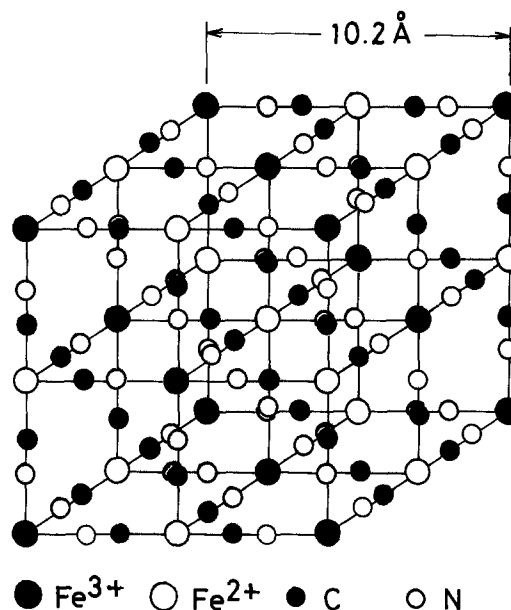
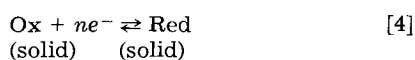


Fig. 1. Idealized skeleton structure of Prussian blue. In Everitt's salt, Fe^{3+} sites are reduced to be Fe^{2+} .

By applying the Nernst equation directly Eq. [4], the electrode potential is represented as

$$E = E'_0 - \frac{RT}{nF} \ln \left(\frac{C_R}{C_O} \right) \quad [5]$$

The condition of an electrochemical reaction in a layered matrix would be formulated as

$$C_O + C_R = C_T \quad [6]$$

where C_O and C_R are the surface concentration of Ox and Red, respectively, in moles per square centimeter, and n is the number of electron participating in the electrochemical reaction [4]. C_T is the total surface concentration of species Ox and Red in moles per square centimeter. In fact, C_O and C_R correspond to the surface concentrations of Fe^{3+} and Fe^{2+} , respectively, existing in the same ligand field in a solid matrix.

Voltammetry.—By solving Eq. [5] with respect to C_R and putting the condition [6] into it, one may have a following expression on the j - E characteristics in voltammetry

$$j = -nF \left(\frac{dC_R}{dt} \right) = Q \frac{\left(\frac{nF}{RT} \right) \exp \left\{ -\frac{nF}{RT} (E - E'_0) \right\}}{1 + \exp \left\{ -\frac{nF}{RT} (E - E'_0) \right\}^2} \left(\frac{dE}{dt} \right) \quad [7]$$

where $Q = nFC_T$, *i.e.*, total charge. Equation [7] was first derived by Hubbard and Anson (28) for a redox reaction in a thin-layered liquid film.

Chronopotentiometry.—Assuming Eq. [4]-[6] and setting the additional conditions for chronopotentiometry

$$C_R = 0, C_O = C_T \text{ at } t = 0$$

$$C_R = C_T, C_O = 0 \text{ at } t = \tau$$

and

$$j_c = nF \left(\frac{dC_O}{dt} \right) = -nF \left(\frac{dC_R}{dt} \right) \quad [8]$$

one may have the following expression by solving Eq. [5] under the conditions [6] and [8]

$$E = E'_0 - \frac{RT}{nF} \ln \left\{ \frac{(t/\tau)}{1 - (t/\tau)} \right\} \quad [9]$$

where τ is the transition time and j_c is the controlled current.

Spectroelectrochemical character.—The broad optical absorption band at ca. 700 nm is characteristic of PB (18, 19). Then, if one assumes that absorbance at ca. 700 nm is directly proportional to the concentration of Fe^{3+} existing in a certain ligand field in a PB matrix, as would be expected by Beer's law, one may define the mole fraction of Fe^{2+} , $X(E)$, as a function of electrode potential (18) as

$$X(E) = \frac{A_{\max} - A(E)}{A_{\max} - A_{\min.}} \quad [10]$$

and the mole fraction of Fe^{3+} , $1 - X(E)$, as

$$1 - X(E) = \frac{A(E) - A_{\min.}}{A_{\max} - A_{\min.}} \quad [11]$$

where A_{\max} is a maximum absorbance and $A_{\min.}$ is a minimum absorbance when absorbance at ca. 700 nm is measured as a function of electrode potential.

Combination of Eq. [5], [10], and [11] gives

$$E = E'_0 - \frac{RT}{nF} \ln\left(\frac{X}{1-X}\right) \quad [12]$$

By using Eq. [7], [9], and/or [12], one can determine E'_0 and n in Eq. [4] from voltammetric, chronopotentiometric, and/or spectroelectrochemical data.

Experimental Results

Voltammetry.—Figure 2 shows the cyclic voltammograms of PB film on Pt electrode at several sweep rates in 1M KCl solution. In recording voltammograms, the initial few cycles were discarded (because the electrode was not well broken in the electrolyte), and then the almost-steady current-potential curves were recorded. The preparation method and pretreatment of electrodes adopted here always gave the same results within an experimental error, and the general observations on voltammograms for PB reduction and ES oxidation agreed well with those of previous workers (17-20).

The voltammetric reduction peaks of PB and oxidation peaks of ES at 200 mV vs. SCE were almost symmetrical

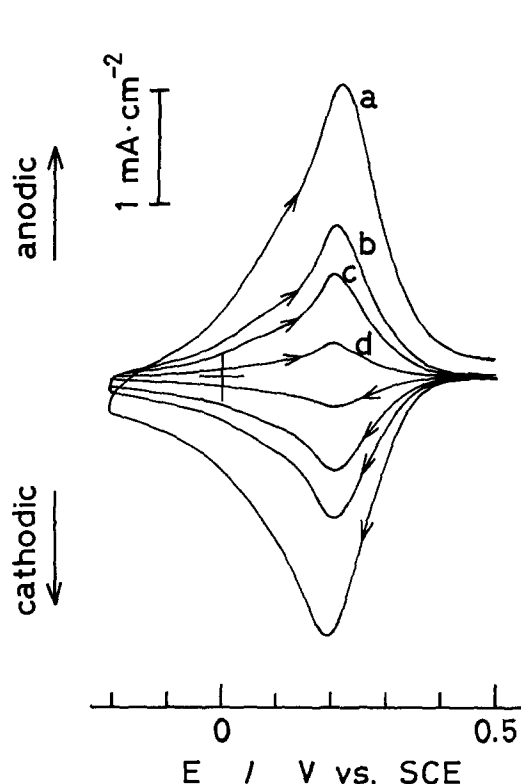


Fig. 2. Voltammograms of a thin film of PB on Pt electrode in 1M KCl solution at room temperature. Sweep rates are 100 (a), 50 (b), 30 (c), and 10 $\text{mV}\cdot\text{s}^{-1}$ (d).

up to the sweep rate of $100 \text{ mV}\cdot\text{s}^{-1}$ and had broad half-width of ca. 180 mV. The coulombs in and out were almost the same for the reduction of PB and the oxidation of ES. Peak currents increased linearly as a function of sweep rate, not the square root of the sweep rate between 5 and $100 \text{ mV}\cdot\text{s}^{-1}$, indicating that there were no diffusion problems.

The peak potentials and the midpoints of them were shifted toward anodic direction with increasing KCl concentrations, as a function of $(RT/F)\ln[a_{\text{K}^+}]$, suggesting a potential response of potassium ion. No shift, however, was observed in varying solution pH of 1M KCl.

Figure 3 shows the comparison between an observed voltammetric curve and the calculated curves from Eq. [7] with $n = 1$ and $Q = 2.5 \text{ mC}\cdot\text{cm}^{-2}$. The observed voltammetric curve was much broader than the calculated curve. Equation [7] requires the half-width of 90 mV for $n = 1$, 45 mV for $n = 2$, 30 mV for $n = 3$ and so forth. On the other hand, observed half-widths were about twice the 90 mV which was expected value from Eq. [7] with $n = 1$, and so the n value in Eq. [7] was calculated to be about 0.5.

Chronopotentiometry.—In measuring chronopotentiograms for PB reduction, PB on Pt electrode was kept at +0.8V vs. SCE until the residual current reduced below a microampere, in order to set the same initial conditions of residual C_R concentrations, and then the control mode was switched over to galvanostatic mode. Transition time τ was determined as the duration time of potential drop from +0.5 to -0.2V vs. SCE. Figure 4 shows the $|j| \cdot \tau$ vs. $|j|$ plots for PB reduction in 1M KCl solution. The $|j| \cdot \tau$ is almost independent of $|j|$, indicating that the electrochemical reaction took place throughout the PB matrix.

Figure 5 shows a comparison between an observed chronopotentiogram for a PB reduction at $50 \mu\text{A}\cdot\text{cm}^{-2}$ ($\tau = 169\text{s}$) and the calculated curves from Eq. [9] with $n = 0.5$ and $E'_0 = +0.175\text{V}$ vs. SCE. Although the calculated value of E'_0 from chronopotentiogram was ca. 25 mV more negative than that from voltammogram, the observed chronopotentiogram, as far as the n value was concerned, agreed well with voltammograms in Fig. 2 and 3.

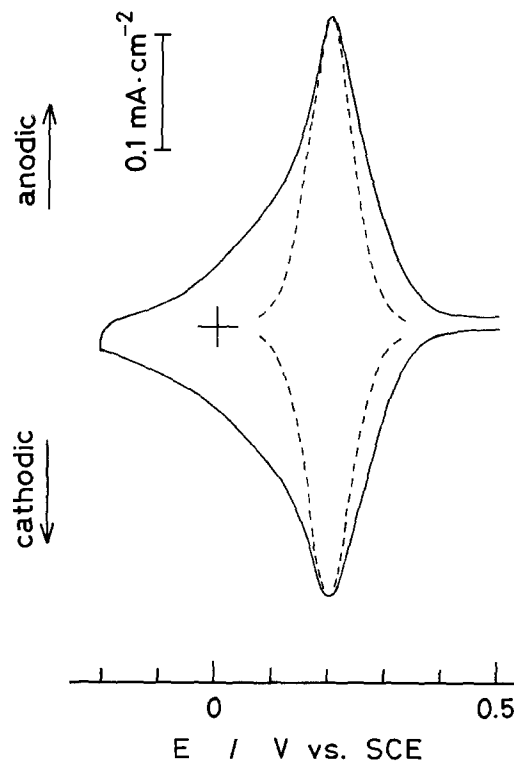


Fig. 3. Comparison between an observed voltammogram for a thin film of PB on Pt in KCl solution at a sweep rate of $10 \text{ mV}\cdot\text{s}^{-1}$ (solid curve) and the calculated voltammogram from Eq. [7] with $n = 1$, $Q = 2.5 \times 10^{-3} \text{ C}\cdot\text{cm}^{-2}$, and $(dE/dt) = 0.01 \text{ V}\cdot\text{s}^{-1}$ (dotted curve).

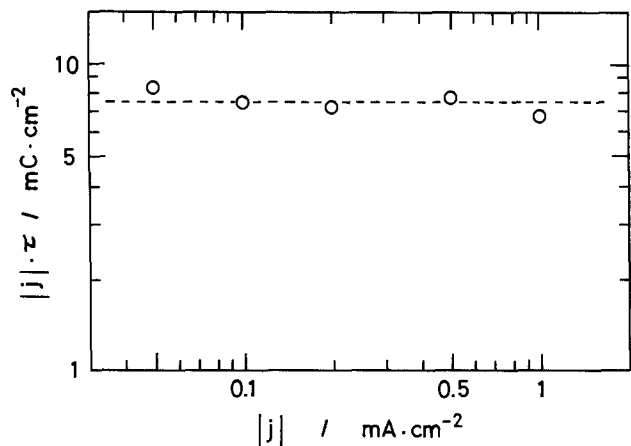


Fig. 4. The $|j| \cdot \tau$ vs. $|j|$ plots for the chronopotentiograms of the reduction of thin film of PB on Pt electrode in 1M KCl solution.

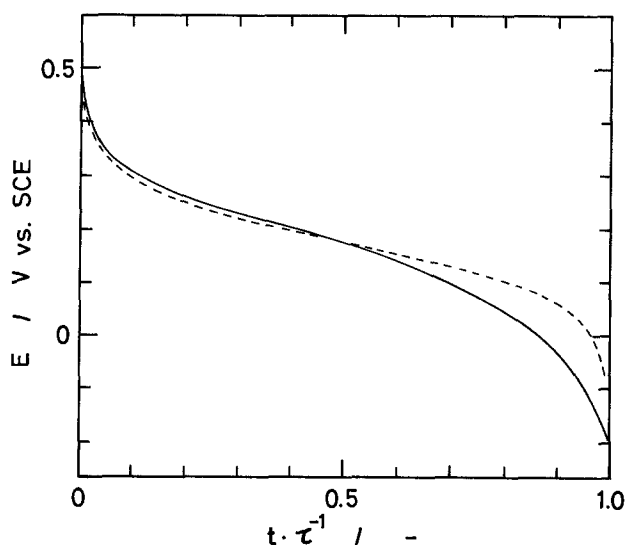


Fig. 5. Comparison between an observed chronopotentiogram (solid curve) for a thin film of PB in 1M KCl solution at $50 \mu\text{A}\cdot\text{cm}^{-2}$ and the calculated chronopotentiogram (dotted curve) from Eq. [9] with $n = 0.5$, $E_0 = +0.175\text{V vs. SCE}$, and $\tau = 169\text{s}$ (experimentally obtained value).

Optical absorption spectra.—Figure 6 shows the optical absorption spectra of PB, ES, and BG on In_2O_3 -coated glass electrode. The spectra of PB, ES, and BG were obtained at +0.5, -0.2, and +1.1V vs. SCE, respectively. The spectra observed agreed well with those of previous workers (18, 19).

In determining $X(E)$ from optical absorbance $A(E)$ from Eq. [10], absorbance at 720 nm was measured potentiostatically point by point in the potential range between +0.5 and -0.2V vs. SCE. A_{max} and A_{min} were determined as the absorbance at +0.5 and -0.2V vs. SCE, respectively. Figure 7 shows the E vs. $X(E)$ plots obtained from optical absorbances using Eq. [10] and [12]. The dotted curve in Fig. 7 shows the calculated curve from Eq. [12] with $E'_0 = +0.175\text{V vs. SCE}$ and $n = 0.5$. The *in situ* optical data indicate that the observed electrode potential is thermodynamic potential.

From these voltammetric, chronopotentiometric, and spectroelectrochemical data, the equilibrium potential of PB/ES system is represented as the empirical formula

$$E = E_0 - \frac{2RT}{F} \ln \frac{[\text{Fe}^{2+}]}{[\text{Fe}^{3+}]} + \frac{RT}{F} \ln(a_{\text{K}^+}) \quad [13]$$

where $[\text{Fe}^{2+}]$ and $[\text{Fe}^{3+}]$ denote the concentrations of Fe^{2+} and Fe^{3+} , respectively, existing in the same ligand field in a solid matrix, and a_{K^+} is the activity of K^+ ion in a solution.

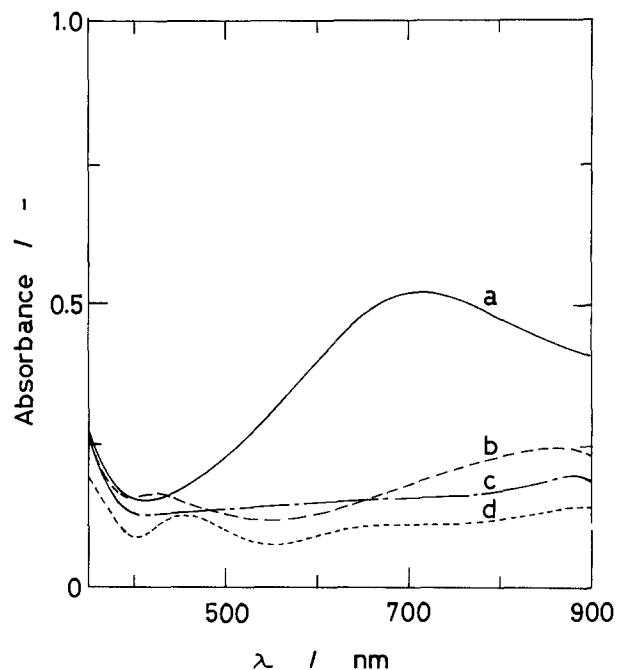


Fig. 6. Absorption spectra in the visible region for PB at +0.5V (a), BG at +1.1V (b), ES at -0.2V vs. SCE (c), and In_2O_3 -coated glass only (d). The spectra were measured in KCl solution.

Discussion

PB/ES homogeneous-phase reaction.—Ellis *et al.* (18) proposed the following equation for the reduction of PB



and they used the Nernst equation directly to Eq. [14] in the form

$$E = E^{\circ} + \frac{RT}{F} \ln \left(\frac{a(\text{PB})a(\text{K}^+)}{a(\text{ES})} \right) \quad [15]$$

where $a(\text{PB})$ and $a(\text{ES})$ were the activities of PB and ES, respectively, $a(\text{K}^+)$ is the activity of potassium ion in a solution, and E° is the standard electrode potential in Eq. [14]. In order to explain their results, they applied the theory of strictly regular solution on estimating $a(\text{PB})$ and $a(\text{ES})$ in Eq. [15], and they discussed the validity of the treatments based on Eq. [14] and [15].

The forms of Eq. [14] and the following Eq. [15] are the same as those applied by Johnson and Vosburgh (1) and Newmann and Roda (2) for the $\text{MnO}_2/\text{MnOOH}$ system,

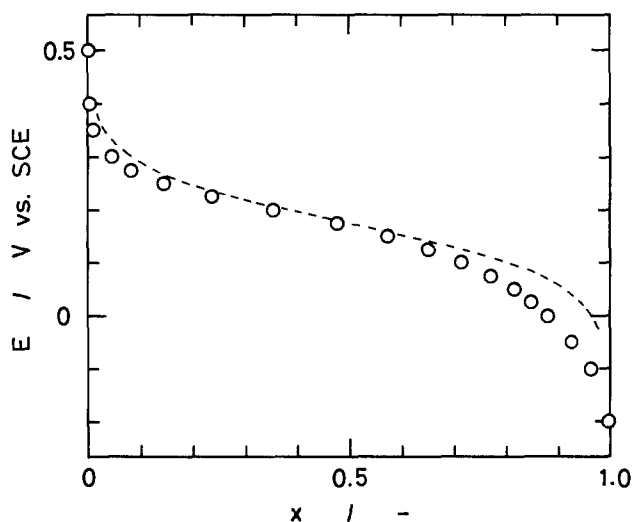


Fig. 7. The E vs. X plots obtained from the absorbance at 720 nm using Eq. [10] and [12]. Absorbance was measured potentiostatically point by point. The dotted curve was calculated from Eq. [12] with $E'_0 = +0.175\text{V vs. SCE}$ and $n = 0.5$.

and, consequently, $\alpha(\text{PB})$ and $\alpha(\text{ES})$ may be calculated by the Newmann and Roda's method (2). The specific definitions of PB (starting material) and ES (reduction product), however, seem to be difficult because the difference between PB and ES is the concentrations of Fe^{2+} and Fe^{3+} existing in the same ligand field and K^+ concentration in a solid matrix. In other words, PB is continuously converted to ES, isostructural with PB, by increasing Fe^{2+} and K^+ concentration in a solid matrix during the reduction process.

Specific differences between the $\text{Fe}^{3+}/\text{Fe}^{2+}$ redox reaction in a solid matrix and in a solution are summarized in Table I. The differences between them are (i) the potential dependence with respect to $\ln([\text{Fe}^{2+}]/[\text{Fe}^{3+}])$ and (ii) the potential response of potassium ion, indicating that the redox reaction in a solid matrix is not explained by the analogy of the homogeneous redox reaction in a solution.

In recent years, Atlung and Jacobsen (9) have proposed a statistical mechanical treatment on dealing with an insertion electrode. We applied their basic concept to the analysis of PB/ES homogeneous-phase reaction. Instead of thinking about an electrode potential based on the Nernst equation using a chemical formula, the phase scheme (7, 8) of PB/ES electrode system in contact with an inert metal and electrolyte was considered, as is illustrated in Fig. 8a, in which R^+ transfer reaction is active.

PB has an electronic conduction which is assumed to proceed by a hopping mechanism, and it has an open structure to accommodate large metal cations and water molecules (15). The equilibrium of electrons at the phase boundary metal/PB, i.e., $e^-(\text{metal}) \rightleftharpoons e^-(\text{PB})$, shall be established. Also, the equilibrium of monovalent ion R^+ at the phase boundary PB/electrolyte, i.e., $\text{R}^+(\text{PB}) \rightleftharpoons \text{R}^+(\text{electrolyte})$, shall be established in such a system.

By applying Guggenheim's assumption to an electrochemical potential (29), one may write the equilibrium conditions in terms of electrochemical potentials for each species between phases

$$\bar{\mu}_e^{\text{metal}} = \bar{\mu}_e^{\text{PB}} \quad [16]$$

$$\bar{\mu}_R^{\text{PB}} = \bar{\mu}_R^{\text{E1}} \quad [17]$$

where

$$\bar{\mu}_e^{\text{PB}} = \mu_e^{\text{PB}} - F\phi^{\text{PB}} \quad [18]$$

$$\bar{\mu}_R^{\text{PB}} = \mu_R^{\text{PB}} + F\phi^{\text{PB}} \quad [19]$$

$$\bar{\mu}_R^{\text{E1}} = \mu_R^{\text{E1}} + F\phi^{\text{E1}} \quad [20]$$

By arranging the equations and converting the potential scale, one may have the following expression for the

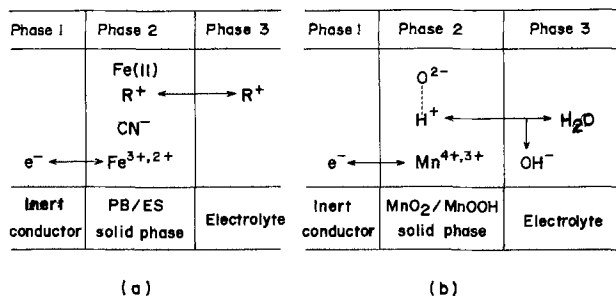


Fig. 8. Phase scheme a: PB/ES homogeneous-phase system in contact with an inert conductor and electrolyte. R^+ (monovalent ion) transfer reaction is active. $\text{Fe}(\text{II})$ is inactive for PB/ES reaction. b: $\text{MnO}_2/\text{MnOOH}$ homogeneous-phase system in contact with an inert conductor and electrolyte. Proton transfer reaction is active.

electrode potential

$$E = \frac{\mu_R^{\text{E1}}}{F} - \frac{(\mu_e^{\text{PB}} + \mu_R^{\text{PB}})}{F} \quad [21]$$

in which μ_R^{E1} denotes the chemical potential of R^+ ion in an electrolyte, and μ_e^{PB} and μ_R^{PB} denote the chemical potentials of electron and R^+ ion, respectively, in a PB solid matrix. The chemical potential of R^+ ion in an electrolyte, μ_R^{E1} , can be represented in terms of the standard chemical potential, $\mu_R^{\circ\text{E1}}$, and the activity of R^+ ion in an electrolyte, a_R , as

$$\mu_R^{\text{E1}} = \mu_R^{\circ\text{E1}} + RT \ln(a_R) \quad [22]$$

On the other hand, μ_e^{PB} and μ_R^{PB} are defined as

$$\frac{\mu_e^{\text{PB}}}{N_0} = \left(\frac{\partial G}{\partial n_e} \right) \frac{\mu_R^{\text{PB}}}{N_0} = \left(\frac{\partial G}{\partial n_R} \right) \quad [23]$$

where N_0 is Avogadro's number.

When PB is reduced electrochemically, Fe^{3+} existing in a certain ligand field in a matrix is reduced to Fe^{2+} in the same ligand field and R^+ ion is inserted into a matrix in order to compensate the additional charge. Electrons and R^+ ions seem to move independently through different sites in the matrix. In such a case, one may formulate μ_e^{PB} and μ_R^{PB} as

$$\frac{\mu_e^{\text{PB}}}{N_0} = \left(\frac{\partial G}{\partial n_e} \right) = \left(\frac{\partial F}{\partial n_e} \right) = -kT \left(\frac{\partial \ln Z_e}{\partial n_e} \right) \quad [24]$$

and

$$\frac{\mu_R^{\text{PB}}}{N_0} = \left(\frac{\partial G}{\partial n_R} \right) = \left(\frac{\partial F}{\partial n_R} \right) = -kT \left(\frac{\partial \ln Z_R}{\partial n_R} \right) \quad [25]$$

Table I. Specific differences between the electrochemical behavior of Prussian blue/Everitt's salt redox reaction and $\text{Fe}(\text{CN})_6^{3-}/\text{Fe}(\text{CN})_6^{4-}$ redox reaction in a solution

Redox reaction	$\text{Fe}(\text{CN})_6^{3-}/\text{Fe}(\text{CN})_6^{4-}$	Prussian blue/Everitt's salt
System	Redox reaction of soluble species	Redox reaction in thin film of solid
Voltammetry		
Shape	Not symmetrical about peak position ^a	Symmetrical about peak position
Midpoint of anodic and cathodic peak ^b	+210 mV vs. SCE	+200 mV vs. SCE
pH response	Yes ^c	No
pK response	No	Yes
Chronopotentiometry ^d		
E_0	+215 mV vs. SCE	+175 mV vs. SCE
n	1.0	0.5

^a If thin liquid film was used, voltammetric peaks symmetrical about the peak position would be obtained.

^b Measured in 1M KCl solution.

^c Due to the protonation of $\text{Fe}(\text{CN})_6^{4-}$.

^d E_0 and n were determined from the equation

$$E = E_0 + \frac{RT}{nF} \ln \frac{1 - (t/\tau)^{1/2}}{(t/\tau)^{1/2}}$$

for the reduction of 0.02M $\text{Fe}(\text{CN})_6^{3-}$ in 1M KCl, and from Eq. [6] for the reduction of PB.

where Z_e and Z_R are the partition functions with respect to electrons and R^+ ions, respectively, and $p \Delta V = 0$ is assumed. Combination of Eq. [21], [22], [24], and [25] gives a general expression on the electrode potential for the reaction, if the partition function Z_e and Z_R are known from electronic structure, crystal structure, interaction between charged species, and so forth.

If the work to put electrons into Fe^{3+} in a matrix is the same for all subsequent steps, which corresponds to a redox reaction between the well-defined oxidation states of ions, the partition function of electrons for such a case would be represented as (30, 31)

$$Z_e(T, V, n_e) = \frac{n_0^e!}{n_e!(n_0^e - n_e)!} \exp\left(-\frac{n_e \epsilon_0}{kT}\right) \quad [26]$$

where n_0^e , n_e , and $(n_0^e - n_e)$ are the number of available sites, the number of occupied sites (Fe^{2+} in this case), and the number of unoccupied sites (Fe^{3+} in this case), respectively, while ϵ_0 is an energy.

Putting Eq. [26] into Eq. [24], one may have the following expression after applying the Stirling's approximation

$$\mu_e^{PB} = \mu_e^{\circ PB} + RT \ln \frac{n_e}{(n_0^e - n_e)} \quad [27]$$

where $\mu_e^{\circ PB}$ is the standard chemical potential of electron in PB/ES system.

The same treatment could be made with respect to R^+ ion in a matrix

$$\mu_R^{PB} = \mu_R^{\circ PB} + RT \ln \frac{n_R}{(n_0^R - n_R)} \quad [28]$$

where n_0^R , n_R , and $(n_0^R - n_R)$ are the number of available sites, the number of occupied sites, and the number of unoccupied sites, respectively, with respect to R^+ ion in a matrix.

For PB/ES system, the number of available sites for electrons and R^+ ions would be the same (21), i.e., $n_0^e = n_0^R = n_0$, and then the combination of Eq. [21], [22], [27], and [28] gives

$$E = E_0 + \frac{RT}{F} \ln(a_R) - \frac{RT}{F} \ln \frac{n_e}{(n_0 - n_e)} - \frac{RT}{F} \ln \frac{n_R}{(n_0 - n_R)} \quad [29]$$

where

$$E_0 = \frac{\mu_R^{\circ E1}}{F} - \frac{(\mu_e^{\circ PB} + \mu_R^{\circ PB})}{F} \quad [30]$$

According to Eq. [29], the 59 mV dependence at 25°C with respect to $\log(a_R)$ and -59 mV potential dependences in terms of $\log(n_e/[n_0 - n_e])$ and $\log(n_R/[n_0 - n_R])$ would be expected, and then the standard electrode potential of PB/ES system, E_0 , would be obtained putting $a_R = 1$, $n_e = n_0/2$, and $n_R = n_0/2$.

The condition of electroneutrality requires $n_e = n_R$, then Eq. [29] becomes

$$E = E_0 - \frac{2RT}{F} \ln \frac{X}{(1-X)} + \frac{RT}{F} \ln(a_R) \quad [31]$$

or

$$E = E_0 - \frac{2RT}{F} \ln \frac{[Fe^{2+}]}{[Fe^{3+}]} + \frac{RT}{F} \ln(a_R)$$

where $X = n_e/n_0$, i.e., the mole fraction of Fe^{2+} .

Equation [31] is the same as the empirical formula [13]. Thus, we have concluded that the observed potential dependence $-2RT/F$ with respect to $\ln([Fe^{2+}]/[Fe^{3+}])$ can be derived from the effect of R^+ ion (K^+ ion, in the present case) in a solid matrix on the electrode potential. In other words, the effect is associated with entropy due to the distribution of R^+ ion in a solid matrix.

MnO₂/MnOOH homogeneous-phase reaction (Mn⁴⁺/Mn³⁺ redox reaction in a solid matrix).—Bode *et al.* (32) first studied the chemical reduction of MnO₂S, and they found the reduction in homogeneous phase is typical of gamma-

MnO₂ down to MnO_{1.5}. Although the term "gamma" is not specific (33), there is a general agreement that both chemical and electrochemical reduction of gamma modification proceed in homogeneous phase (1-4, 10-13, 32, 34-36).

In recent years, Swinkels *et al.* (12) proposed that three or more overlapping discharge processes, each of which is of the simple one-electron type but with different E_0 's, must be considered for an explanation of the larger prelogarithmic factor in the Nernst equation, about twice the -59 mV expected for one-electron transfer. More recently, Ruetschi (38) reported the cation-vacancy model for MnO₂, and formulated the electrode potential of MnO₂ based on his model. We, however, prefer to extend the homogeneous phase theory (3, 4) from the analogy of the PB/ES system.

A schematic phase scheme for the MnO₂/MnOOH homogeneous phase is given in Fig. 8b. For the reduction of MnO₂, Mn⁴⁺ is reduced to Mn³⁺ in a homogeneous solid phase by the arrival of electron together with the formation of new hydroxyl group with proton from a solution, which was confirmed by XRD and IR studies on MnO₂/MnOOH systems (37). In this case, proton transfer at the interface is active.

By comparing the two homogeneous-phase reactions, we may discuss the electrode potential of MnO₂/MnOOH homogeneous phase. In the reduction process of PB, electrons and R^+ ions are introduced into the matrix of PB. The concentrations of Fe^{2+} ions and R^+ ions in the lattice increase gradually, and, finally, PB is converted to ES, isostructural with PB. In such a case, we can formulate the electrode potential of PB/ES homogeneous phase as Eq. [31], in which the potential dependence with respect to $\log([Fe^{2+}]/[Fe^{3+}])$ appeared as $-2.303 \times 2RT/F$ (i.e., -118 mV at 25°C) due to the effect of R^+ ion in a solid matrix as was discussed in the previous section.

It should be recalled here that there are two types of iron sites in PB matrix. One is carbon-coordinated iron (low spin), and the other is nitrogen-coordinated iron (high spin). Because of this, the Fe^{3+}/Fe^{2+} redox reaction in the solid matrix takes at two different electrode potentials, i.e., PB/ES reaction at ca. +0.2V vs. SCE and PB/BG at ca. +0.9V in 1M KCl solution. Thus, the redox potentials appear with a large voltage separation due to the effect of ligand field. For the MnO₂/MnOOH homogeneous system, such a voltage separation may not occur because all manganese ions exist in the same ligand field (oxygen-coordinated manganese). During the reduction of MnO₂, the concentrations of Mn³⁺ ions and OH⁻ ions in a solid matrix increase gradually, and, finally, MnO₂ is converted to MnOOH, isostructural with original MnO₂ (37). In the MnO₂/MnOOH homogeneous phase, electrons move freely along Mn^{4+,3+} sites in the lattice and also proton jump one O²⁻ site to another. Such a situation is very similar to that of PB/ES system. Thus, the previous treatments for the PB/ES system can be made for the MnO₂/MnOOH system.

Kozawa and Powers (3, 4) formulated the electrode potential of MnO₂/MnOOH homogeneous phase as Eq. [3] from the analogy of a redox reaction in a solution. They referred to Fe^{3+}/Fe^{2+} redox reaction in an acid solution as a model for MnO₂/MnOOH homogeneous-phase reaction in order to interpret their homogeneous phase theory. The electrochemical character of Fe^{3+}/Fe^{2+} redox reaction in homogeneous solution phase, however, is different from that in homogeneous solid phase as examined here.

The specific effect of solution pH on the potential response would be due to the proton transfer in the MnO₂/MnOOH homogeneous solid phase, which may be deduced from Vetter's general theories (7, 8). The inserted protons also affect the electrode potential because of the formation of hydroxyl group (enthalpy factor) and their distribution in a solid matrix (entropy factor) in addition to Mn⁴⁺/Mn³⁺ redox reaction. The above description would be the core meaning of proton-electron mechanism (3, 4).

It is therefore reasonable to deduce that the electrode potential of the MnO₂/MnOOH homogeneous-phase sys-

tem is expressed as

$$E = E_0 - \frac{2RT}{F} \ln \frac{[\text{Mn}^{3+}]}{[\text{Mn}^{4+}]} + \frac{RT}{F} \ln (a_{\text{H}^+}) \quad [32]$$

by taking into account for the effect of proton (OH^- ion, in fact) in a solid matrix on the electrode potential. Then, if the electrode potentials of $\text{MnO}_2/\text{MnOOH}$ system were measured as a function of $\log ([\text{Mn}^{3+}]/[\text{Mn}^{4+}])$ at constant pH and if the conditions were well fit to the conditions required by the previous treatments, -118 mV of potential dependence would be observed in this case. Some deviations from Eq. [32], however, may be observed in experimental curves, especially in latter half of the discharge curves, partly because of the secondary modification of discharge product and partly because of the change of ligand field around manganese ion due to the coordination of OH^- ion, which is not the case for the PB/ES system. Tye (10, 13) suggested that the discharge of MnO_2 involved two regions (one between $\text{MnO}_{2.0}$ and $\text{MnO}_{1.75}$ and the other between $\text{MnO}_{1.75}$ and $\text{MnO}_{1.5}$), assuming the intermediate compound $\text{MnO}_{1.75}$, like a PB (50% Fe^{2+} , 50% Fe^{3+} material) between ES (100% Fe^{2+} material) and BG (100% Fe^{3+} material). This may be true, but the specific intermediate compound of $\text{MnO}_{1.75}$ has not been observed yet (37).

A possible refinement of Eq. [32] as to how the partition function in Eq. [26] can be modified in considering the additional factors, especially the change of ligand field around manganese ion due to the coordination of OH^- ion combined with crystal structure and the electronic structure of the $\text{MnO}_2/\text{MnOOH}$ system, will be discussed in future papers together with the experimental and analytical results of MnO_2 .

Acknowledgment

The present work was partially supported by a grant in aid for Scientific Research from the Ministry of Education, Science and Culture.

Manuscript submitted April 6, 1985; revised manuscript received Aug. 15, 1985.

Okayama University assisted in meeting the publication costs of this article.

REFERENCES

1. R. S. Johnson and W. C. Vosburgh, *This Journal*, **100**, 471 (1953).
2. K. Newmann and E. Roda, *Ber. Bunsenges. Phys. Chem.*, **69**, 347 (1965).
3. A. Kozawa and R. A. Powers, *This Journal*, **113**, 870 (1966).
4. A. Kozawa and R. A. Powers, *Electrochem. Technol.*, **5**, 533 (1967).
5. F. L. Tye, *Electrochim. Acta.*, **21**, 415 (1976).
6. T. Ohzuku, C. Ishibashi, and T. Hirai, Extended Abstracts of The 33rd Battery Symposium in Japan, Yokohama, p. 87, Nov. 1982.
7. K. J. Vetter, *This Journal*, **110**, 597 (1963).
8. K. J. Vetter and N. Jaeger, *Electrochim. Acta*, **11**, 401 (1966).
9. S. Atlung and T. Jacobsen, *ibid.*, **26**, 1447 (1981).
10. W. C. Maskell, J. E. A. Shaw, and F. L. Tye, *ibid.*, **28**, 225 (1983).
11. W. C. Maskell, J. E. A. Shaw, and F. L. Tye, *ibid.*, **28**, 231 (1983).
12. D. A. J. Swinkels, K. E. Anthony, P. M. Fredericks, and P. R. Osborn, *J. Electroanal. Chem.*, **168**, 433 (1984).
13. F. L. Tye, *Electrochim. Acta*, **30**, 17 (1985).
14. D. F. Shriver, *Struct. Bonding (Berlin)*, **1**, 32 (1966).
15. M. B. Robin and P. Day, *Adv. Inorg. Chem. Radiochem.*, **10**, 247 (1967).
16. L. Ludi and U. Güdel, *Struct. Bonding (Berlin)*, **14**, 1 (1973).
17. V. D. Neff, *This Journal*, **125**, 886 (1978).
18. D. Ellis, M. Eckhoff, and V. D. Neff, *J. Phys. Chem.*, **85**, 1225 (1981).
19. K. Itaya, H. Akahoshi, and S. Toshima, *This Journal*, **129**, 1498 (1982).
20. K. Itaya, T. Ataka, and S. Toshima, *J. Am. Chem. Soc.*, **104**, 4767 (1982).
21. J. F. Keggin and F. D. Miles, *Nature*, **137**, 577 (1936).
22. F. Herren, P. Fischer, A. Ludi, and W. Halg, *Inorg. Chem.*, **19**, 956 (1980).
23. L. M. Epstein, *J. Chem. Phys.*, **36**, 2731 (1962).
24. J. F. Duncan and P. W. R. Wigley, *J. Chem. Soc.*, 1120 (1963).
25. D. Davidson and L. A. Welo, *J. Phys. Chem.*, **32**, 1191 (1928).
26. G. Emschwiller, *C. R. Acad. Sci.*, **238**, 1414 (1954).
27. H. B. Weiser, W. O. Milligan, and J. B. Bates, *J. Phys. Chem.*, **46**, 99 (1942).
28. A. T. Hubbard and F. C. Anson, *Anal. Chem.*, **38**, 58 (1966).
29. E. A. Guggenheim, *J. Phys. Chem.*, **33**, 842 (1929).
30. R. Kubo, "Netsugaku-Tokeirikigaku (Thermodynamics and Statistical Mechanics)," Shokabo Co. Ltd., Tokyo (1961).
31. R. Kubo, "Tokeirikigaku (Statistical Thermodynamics)," Kyoritsu Shuppan Co. Ltd., Tokyo (1971).
32. H. Bode, A. Schmier, and D. Berndt, *Z. Elektrochem.*, **66**, 586 (1962).
33. T. Ohzuku, H. Higashimura, and T. Hirai, *Electrochim. Acta*, **29**, 779 (1984).
34. J. P. Gavano, B. Morignat, E. Fialdes, B. Emery, and J. F. Laurent, *Z. Phys. Chem.*, **46**, 359 (1965).
35. R. Giovanoli and U. Leuenberger, *Helv. Chim. Acta*, **52**, 2333 (1969).
36. W. C. Maskell, J. E. A. Shaw, and F. L. Tye, *Electrochim. Acta*, **26**, 1403 (1981).
37. T. Ohzuku and T. Hirai, in "Manganese Dioxide Electrode Theory and Practice for Electrochemical Applications," B. Schumm, Jr., R. L. Midaugh, M. P. Grotheer, and J. C. Hunter, Editors p. 141, The Electrochemical Society Softbound Proceedings Series, Pennington, NJ (1984).
38. P. Ruetschi, *This Journal*, **131**, 2737 (1984).

Optimum Additive Distribution for Quick Activation of Sintered Nickel Composite Electrodes

W. Lee*

Naval Surface Weapons Center, White Oak Laboratory, Materials Division, Silver Spring, Maryland 20903-5000

ABSTRACT

The effectiveness of postimpregnation additive addition for quick activation of nickel electrodes of an alkaline cell was clearly demonstrated by nickel composite electrodes which have a sintered body of nickel-coated graphite fibers as the plaque. This treatment during which the $\text{Co}(\text{OH})_2$ additive is added to impregnated composite electrodes achieves full utilization of $\text{Ni}(\text{OH})_2$ active material in the electrodes within five charge-discharge cycles after a brief formation. A model of the additive distribution in the active material is proposed to rationalize the sensitiveness of initial utilization to the manner of additive addition to the composite electrodes.

As an attempt to reduce weight and material cost of nickel positive electrodes of an alkaline cell, nickel composite electrodes have been under development in our laboratory for the last several years (1). The electrodes have a sintered body of nickel-coated graphite fiber as the plaque. Results of charge-discharge cycling tests on these electrodes showed that they can last as long as, or in some cases even longer than, powder-sintered electrodes and have a storage density (over $175 \text{ A} \cdot \text{h}/\text{kg}$ of electrode) over 50% higher than the powder sinter. Despite these successes, the composite electrode suffered one major drawback, *i.e.*, an incomplete or very slow rise in utilization of the $\text{Ni}(\text{OH})_2$ active material with cycling (2). Typically, it took 40-60 cycles to utilize over 90% of the active material containing $\text{Co}(\text{OH})_2$ as an additive. This behavior was not exhibited by powder-sintered electrodes fabricated under the same impregnating conditions as that used for the composite electrodes.

The lower utilization of the composite electrode partly can be explained by the potential drop across the active material occurring in large pores (peak value of pore diameter, $55 \mu\text{m}$, about five times larger than that of powder sinter) (1). However, this utilization loss which was found to be approximately 10% of the maximum utilizable charge is an inherent characteristic of the composite electrode and is not the main issue to be addressed in this report. The main cause of the sluggish utilization was suspected to be an inefficient use of the additive because a homogeneous distribution of the additive throughout the active material is difficult to achieve with the increased pore size. The adverse effect of mal-distributed additives (for instance, in the form of isolated patches) on the utilization of the active material becomes more severe with the increase of the pore size. The importance of the manner of additive addition for the activation of nickel electrodes was reported previously (3-4). Our efforts to unravel the relationship between the activity of the additive and its distribution in the sintered composite electrode are described in this report. A model of additive distribution is proposed based on the cycling test results to rationalize different patterns of the increase in utilization at the initial phase of charge-discharge cycles.

Experimental

Only a brief summary is given here for the procedures which were previously reported in detail (1).

Fabrication of sintered nickel composite plaque.—Graphite fibers ("Thornel" pitch mat) were coated with nickel electrolessly and sintered, under compression, in dry H_2 atmosphere at 800°C . Sintered plaque prepared in two different thicknesses, 0.75 and 2.5 mm, were cut into smaller pieces with dimensions of $2.3 \times 4.5 \text{ cm}$ for impregnation and cycling tests. Porosity of plaques ranged between 80 and 85%.

Impregnation.—Basically, two different types of impregnating methods were employed depending upon

* Electrochemical Society Active Member.

how the $\text{Ni}(\text{OH})_2$ active material is prepared. According to the first type (electrochemical or chemical impregnation), the active material is deposited inside the plaque by precipitation. The second type (suspension impregnation) (5) is a direct loading method, by which externally prepared active material is forced into the porous structure of the plaque.

The electrochemical impregnating method employed was basically that of Pickett (6). In some cases of impregnation, a constant potential was applied between cathode and anode instead of a constant current across the electrodes to avoid heavy surface deposit. Chemical impregnation was performed according to the procedure (polarization method) described in Ref. (7).

The large open-pore structure of the composite plaque makes it possible for the plaque to accept fine $\text{Ni}(\text{OH})_2$ particles suspended in a medium such as ethylene glycol. The loading efficiency of this method depends on the particle size and viscosity of the resulting fluid. Commercial battery-grade $\text{Ni}(\text{OH})_2$ was ground to a particle diameter under $20 \mu\text{m}$ and mixed with an equal weight of ethylene glycol. Gentle rubbing of this fresh made mixture into the plaque and removal of the ethylene glycol by evaporation were repeated several times until a desired loading level was achieved. Typical loading levels ranged from 0.9 to $1.1 \text{ g}/\text{cm}^3$ of electrode volume.

$\text{Co}(\text{OH})_2$ addition.— $\text{Co}(\text{OH})_2$ additive was incorporated into the $\text{Ni}(\text{OH})_2$ active material by coprecipitation, mixing or postimpregnation surface treatment. During electrochemical or chemical impregnation $\text{Co}(\text{OH})_2$ was coprecipitated with the $\text{Ni}(\text{OH})_2$ from the impregnating solution. The active material used for suspension impregnation was prepared by mixing commercial battery-grade $\text{Ni}(\text{OH})_2$ (which already contains 2 weight percent [w/o] of cobalt metal powder) uniformly with 5 w/o of reagent-grade $\text{Co}(\text{OH})_2$. This mixed material was suspended in ethylene glycol and the resulting fluid was forced into the open structure of the composite plaque.

Postimpregnation additive addition was made by cathodically depositing a thin layer of $\text{Co}(\text{OH})_2$ on the surface of the active material in the composite body (either pure cobalt or pure nickel electrode was used as the anode). Either 1.8M $\text{Co}(\text{NO}_3)_2$ or 0.5M cobalt acetate solution in a 1:1 mixture of water and ethanol was used as the impregnating bath with the temperature maintained at 50°C during impregnation. Depending upon the desired thickness of the $\text{Co}(\text{OH})_2$ film, the impregnation time was adjusted from 10s to 2 min with $50 \text{ mA}/\text{cm}^2$ current density.

The $\text{Co}(\text{OH})_2$ film can also be formed chemically by soaking the impregnated electrode in the cobalt compound solution followed by alkaline agent treatment after the solution is drained off.

Cycling test.—Test cells were fabricated using a single nickel composite electrode sandwiched between two commercial cadmium electrodes to produce a positive limiting condition. No additive was added to 31% KOH electrolyte. One complete cycle in the continuous cycling

tests included charging at the C rate for 80 min, 10 min rest, followed by discharge at C/2 rate to 1.0V cutoff. Theoretical total charge capacity of the nickel electrode was determined by the weight gain after impregnation.

Results and Discussion

Definition of percent utilization.—The percent utilization of the charged active material during a discharge cycle is defined as the ratio of the utilizable charge at that cycle to the total charge. Since the valence change of nickel ions during charge-discharge cycles can be greater than one, the possible maximum utilization can exceed 100%. The maximum utilization (or full utilization) of composite electrodes was found to be slightly above 100%.

Utilization of the active material in electrochemically impregnated electrodes.—The first series of the nickel composite electrodes in this study were impregnated by the electrochemical method. Co(OH)_2 additive was incorporated into Ni(OH)_2 active material by coprecipitation. Test cells using these nickel electrodes showed a wide variation in utilization during the first 50 cycles. Since the total charge of Cd electrodes far exceeds that of the nickel electrode, the utilization during the initial cycles should reflect the characteristics of the nickel electrode. According to the shape of the utilization-rise curve (percent utilization vs. charge-discharge cycles), the electrodes can be classified into three different groups as shown in Fig. 1. Type 1 electrodes exhibit an ideal behavior—quick rise to full utilization and no decrease in utilization with additional cycles. Type 2 electrodes show low utilization and never achieve full utilization even after more than 100 cycles. Type 3 electrodes show a slow, almost linear, rise to a near full utilization requiring from 50 to 100 cycles. In this scheme, the electrodes with a heavy surface deposit of the active material are not considered.

The variance in utilization of the charged active material during discharge was surmised to be attributed to the difficulty in achieving a homogeneous additive distribution throughout the active material during electrochemical impregnation. The pore structure of the composite electrodes is characterized by large pore size, a wide distribution of pore diameters, and an irregular pore shape. These factors make it difficult to achieve a uniform current distribution inside the composite body. In addition to probable nonuniform current distribution, the difference in solubility product between Ni(OH)_2 and Co(OH)_2 can result in a precipitation of Co(OH)_2 in isolated patches in the active material. Therefore, different approaches to loading the active material were undertaken to change the condition of additive addition and to ensure more homogeneity in additive distribution.

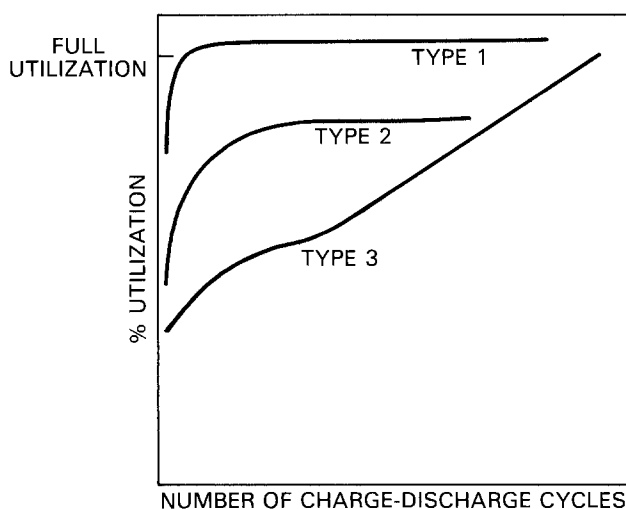


Fig. 1. Classification of the pattern of the rise in utilization exhibited in the nickel composite electrodes.

Utilization of the active material in chemically impregnated electrodes.—The electrodes impregnated by the chemical method inclined to exhibit type 3 behavior (Fig. 1). The chemical method may achieve a different Co(OH)_2 distribution throughout the Ni(OH)_2 active material from that of the electrochemical method because of the ready availability of OH^- ions inside the composite body.

Utilization of the active material in electrodes impregnated by suspension method.—With the suspension method, which allows premixing of Ni(OH)_2 with Co(OH)_2 before insertion into the composite structure, a homogeneous distribution of the additive—at least on the macroscopic scale—is virtually ensured. However, the initial shape of the utilization-rise curve of the electrodes prepared by this method consistently showed type 3 behavior.

Attempts to achieve type 1 behavior by reducing Ni(OH)_2 active material particle size did not prove fruitful (8). There is a small improvement in the initial utilization with the reduction of the particle size. However, when particle size reaches $10 \mu\text{m}$, the utilization decreases again. This is probably due to the difficulty associated with electrolyte penetration into the fine particles of Ni(OH)_2 active material.

These results show clearly that the initial utilization depends on other factors. However, although no drastic improvement was made in the rate of the utilization rise, the behavior of the electrodes impregnated by the suspension method convincingly indicates that a macroscopic homogeneous distribution of additive at least ensures the eventual full utilization.

Surface film of additive on active material.—When a nickel electrode showing a poor utilization was removed from the test cell and treated electrochemically in 7% cobalt solution, the percent utilization increased sharply, as shown in Fig. 2. Since all the nickel electrodes were impregnated either from the bath containing cobalt compound or with Ni(OH)_2 mixed with Co(OH)_2 , this treatment can be seen as a kind of double treatment with cobalt. The difference in the rate of utilization rise between the treated and the nontreated electrode (impregnated by electrochemical method) is clearly seen in Tables I and II and Fig. 3a. It is notable that the 0.75 mm thick composite electrode prepared by electrochemical impregnation followed by the surface treatment reaches 96% utilization in the second cycle. Since the nickel electrodes after the treatment underwent a very brief formation cycle (less than 10 min), the quickness in reaching full utilization is remarkable. The poor performance shown by the electrode without the surface treatment clearly indicates that the Co(OH)_2 precipitant in that electrode must exist at inefficiently utilizable locations inside Ni(OH)_2 active material. The electrodes fabricated by suspension impregnation followed by the surface treatment also demonstrate a large improvement in the utilization as shown in Fig. 3b. However, the improvement is not as pronounced as it was in the case of the

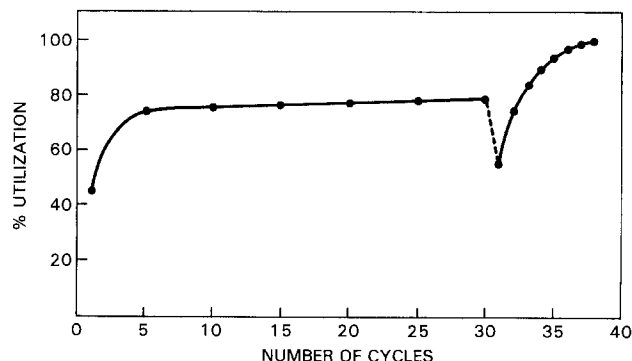


Fig. 2. Sudden increase in utilization of the active material electrochemically impregnated in the composite plaque (0.75 mm thick) after the surface treatment.

Table I. Utilization of the active material electrochemically impregnated in the composite plaque. Electrode is surface treated with cobalt solution after the impregnation

Cycle no.	Utilization (%)	
	0.75V cutoff	1.0V cutoff
1	85	85
2	96	96
3	98	98
4	98	98
5	99	98
6	100	99

Table II. Utilization of the active material electrochemically impregnated in the composite plaque. Electrode is not surface treated after the impregnation

Cycle no.	Utilization (%)	
	0.75V cutoff	1.0V cutoff
1	56	56
2	65	65
3	68	68
4	70	70
5	72	72
6	72	72

electrochemically loaded electrode. This may indicate that the morphology or the crystal phase of the active material—and thus the effect of the surface treatment—is sensitive to the method of impregnation.

The effect of the surface treatment on a thick plate (2.5 mm thick) is shown in Fig. 4. Although there is a marked increase, the increase in utilization is not as steep as for the thinner plate (0.75 mm thick). This may also suggest either that the cobalt solution has not penetrated completely into $\text{Ni}(\text{OH})_2$ active material or that there may be an inherent difficulty with KOH electrolyte infiltration into the thick plate.

Electrodes under discussion up to this point have been impregnated with solutions or mixtures containing a nominal 7% of cobalt compound. To determine whether bulk addition of $\text{Co}(\text{OH})_2$ additive to $\text{Ni}(\text{OH})_2$ active material is necessary for improvement in utilization, some electrodes were impregnated electrochemically in a solution containing only nickel nitrate and subsequently treated (electrochemical deposition) in cobalt nitrate solution after the impregnation. The results of cycling tests for these electrodes are presented in Fig. 5. The results indicate that the utilization behavior of these electrodes, using the Co surface treatment alone, is comparable to those of the previous electrodes impregnated by electrochemical coprecipitation of $\text{Ni}(\text{OH})_2$ and $\text{Co}(\text{OH})_2$ followed by the surface treatment. There was some improvement between 10 and 20s treatment time, however, 120s treat-

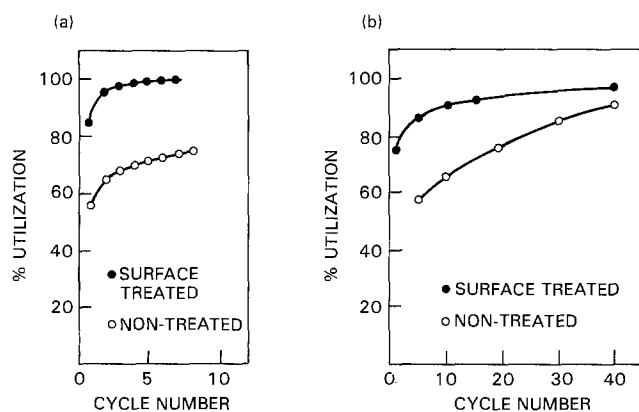


Fig. 3. Effect of the surface treatment on the initial utilization of the composite electrode (0.75 mm thick) impregnated by electrochemical method (a) and suspension method (b).

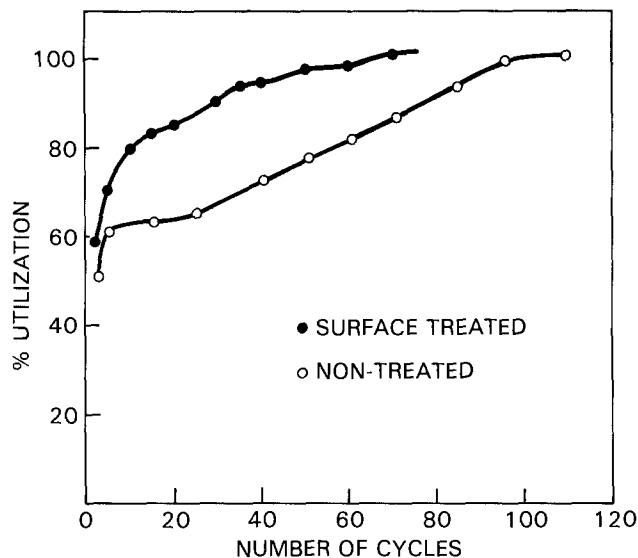


Fig. 4. Effect of the surface treatment on the 2.5 mm thick composite electrode impregnated by electrochemical method.

ment did not provide any further improvement. With less than 20s treatment, $\text{Co}(\text{OH})_2$ normally comprised less than 3% of the $\text{Ni}(\text{OH})_2$ active material on a weight basis. This demonstrates that the amount of the additive can be reduced substantially (from 7 to 3 w/o) by the surface treatment.

Utilization vs. additive distribution in active material.—These results have led to the development of a model to correlate the physical and chemical distribution of active material with the utilization-rise curve. Each type shown in Fig. 1 is represented by a corresponding schematic distribution of both $\text{Ni}(\text{OH})_2$ and $\text{Co}(\text{OH})_2$ particles inside the composite electrode (Fig. 6).

The case of an inhomogeneous additive distribution is pictured as type 2. $\text{Co}(\text{OH})_2$ is deposited more heavily in some local sites or forms an isolated patch. This kind of distribution certainly achieves only partial benefit of the additive. This mal-distribution may arise during electrochemical impregnation from nonuniform current distribution in the porous body and the difference in solubility product between the two hydroxides. $\text{Co}(\text{OH})_2$, because of its low solubility product, tends to precipitate faster than $\text{Ni}(\text{OH})_2$, provided that the local concentration of Co^{2+} ion in the precipitation region does not drop markedly.

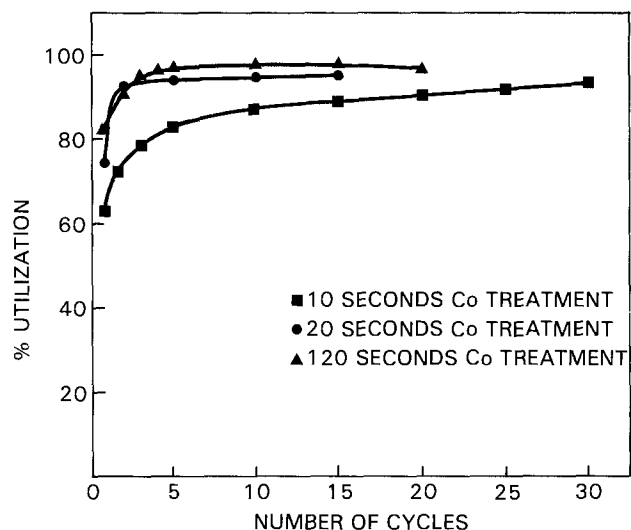


Fig. 5. Effect of the duration of the surface treatment in cobalt nitrate solution on the utilization of the composite electrode (0.75 mm thick). Before the treatment, the active material in the electrode is electrochemically impregnated in a bath that does not contain cobalt nitrate.

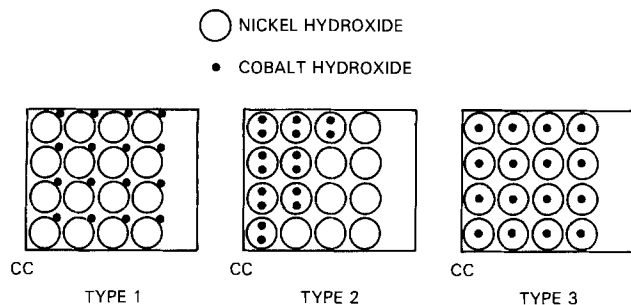


Fig. 6. Model of active material distribution in the composite electrode. Each model represents the corresponding type shown in Fig. 1. CC denotes current collector.

$\text{Co}(\text{OH})_2$ in a form of isolated patch or buried deep inside $\text{Ni}(\text{OH})_2$ active material plays a diminished role to activate the active material. The utilization varies from electrode to electrode, depending on the distribution of $\text{Co}(\text{OH})_2$, but full utilization is seldom attained.

Type 3 shows the case in which a macroscopic homogeneity of additive is achieved, but, on a small scale, the additive still exists as a lump or is buried within the bulk of $\text{Ni}(\text{OH})_2$. These electrodes show a rather slow increase in utilization, but approach full utilization only after 50 or more cycles. Unlike the situation in type 2, $\text{Co}(\text{OH})_2$ in this case can eventually play its role to enhance the activity of $\text{Ni}(\text{OH})_2$ as the active material is rearranged during charge-discharge cycles. The physical rearrangement of the active material in the composite is confirmed by SEM photographs taken before and after the cycling (1). However, the driving force behind the additive rearrangement, if any, is not understood yet. Electrodes prepared by suspension method or chemical impregnation usually show this type of behavior.

The morphology of active material in an electrode of ideal behavior (type 1 of Fig. 1) is depicted by type 1 (Fig. 6). In this electrode, the additive is not only uniformly distributed on a macroscopic scale, but also covers thoroughly the regions of $\text{Ni}(\text{OH})_2$ active material, reachable by electrolyte ions, with its thin film. The additive on the surface of $\text{Ni}(\text{OH})_2$ active material can activate it more effectively than when buried under the material. The fact that the influence of an additive in $\text{Ni}(\text{OH})_2$ is a surface effect was also demonstrated by Weininger (3) in his experiment using film electrodes. Another advantage of the surface treatment by additives in activating nickel electrodes was shown by Winkler (4) in that the additive between $\text{Ni}(\text{OH})_2$ particles can help maintain the primary structure of $\text{Ni}(\text{OH})_2$. However, the quick rise of utilization by this type of treatment strongly suggests an electrocatalytic role of additives at the initial phase of cycling in the charge-discharge reaction on the electrode surface.

In the case of powder-sintered electrodes, the distinction between type 1 and type 2 may be blurred because of their much smaller pore size. The exact location of

$\text{Co}(\text{OH})_2$ is not as critical in determining their utilization as in the case of the composite body. Because of the large open pore structure of the composite plaques, the physical and chemical distribution of the active material in the plaques is far more sensitive to the impregnating conditions. Thus, depending on the conditions, the composite electrodes can exhibit any of the three different types of the behavior classified above.

Each type described thus far represents an extreme case. In many cases, the composite electrode could be better represented by a combination of these. The classification made above offers helpful guidance in understanding one aspect of the complicated behavior of the nickel composite electrode.

Conclusion

The manner of adding $\text{Co}(\text{OH})_2$ additive was found to be critically important for quick rise in utilization of $\text{Ni}(\text{OH})_2$ active material in the sintered nickel composite body. By a proper surface treatment on the active material with the additive, the composite electrode can be activated to full utilization of its charge capacity in just a few charge-discharge cycles.

This phenomenon reflects the unique pore structure of the sintered composite body and is not observed in the powder-sintered body. It is proposed that the manner of adding the additive sensitively determines the pattern of its distribution throughout the active material in the composite body and, accordingly, dictates the utilization behavior of the composite electrodes.

Manuscript submitted April 15, 1985; revised manuscript received Aug. 22, 1985.

The Naval Surface Weapons Center assisted in meeting the publication costs of this article.

REFERENCES

1. W. A. Ferrando, W. Lee, and R. A. Sutula, *J. Power Sources*, **12**, 249 (1984).
2. W. Lee, R. A. Sutula, and W. A. Ferrando, in "Porous Electrodes," H. C. Maru, T. Katan, and M. G. Klein, Editors, p. 32, The Electrochemical Society Softbound Proceedings Series, Pennington, NJ (1984).
3. J. L. Weininger, in "The Nickel Electrode," R. G. Gunther and S. Gross, Editors, p. 1, The Electrochemical Society Softbound Proceedings Series, Pennington, NJ (1982).
4. H. Winkler, Br. Pat. 777,417 (1957).
5. W. A. Ferrando and W. Lee, in "Proceedings of the 31st Power Sources Symposium," Cherry Hill, NJ, June 11-14, 1984, The Electrochemical Society Inc., p. 177 (1985).
6. D. F. Pickett, AFAPL-TR-75-34, Air Force Wright Aeronautical Lab., Wright-Patterson Air Force Base, OH (1975).
7. S. U. Falk and A. J. Salkind, "Alkaline Storage Batteries," pp. 48-52, John Wiley and Sons, New York (1969).
8. W. Lee, W. A. Ferrando, and R. A. Sutula, NSWC Technical Report, TR 84-122, Naval Surface Weapons Center, White Oak, MD (1984).

Some Chemical and Electrochemical Reactions of 2-Methyltetrahydrofuran with Lithium

J. B. Kerr¹

Union Carbide Corporation, Battery Products Division, Westlake, Ohio 44145

ABSTRACT

Gas chromatographic analyses of $\text{LiAsF}_6\text{-2MeTHF}$ electrolytes were carried out to determine the decomposition products resulting from chemical and electrochemical reactions of the solvent with lithium. Storage at elevated temperatures showed that 2-pentanol was the major product, while electrochemical cycling in a lithium half-cell yielded 1-pentanol as the major product. These results indicate that the chemical reaction involves heterolytic, anionic cleavage of the solvent molecule, while the electrochemical reaction involves homolytic, radical-type cleavage. The results support the existence of a solvated lithium ion in electrochemical reactions of lithium.

In recent years, much attention has been given to the development of rechargeable lithium batteries operating at room temperature with nonaqueous electrolytes (1). In this connection, it has been demonstrated that 2-methyltetrahydrofuran (2MeTHF) has excellent properties when used in conjunction with lithium hexafluoroarsenate. Charging efficiencies in the region of 96-98% have been achieved (2, 3). The nature of the reactions which cause the inefficiencies has been investigated by Koch (4), and arguments have been put forward that the kinetically limiting step is the addition of an electron to the solvent molecule from a lithium atom to give a radical ion. This radical ion may decompose to yield the products, for example, butoxy anion from tetrahydrofuran. It has been argued (2) that the source of the better behavior of the substituted 2 MeTHF lies in the inductive effect of the methyl group adjacent to the oxygen atom, which would raise the energy level of the lowest unoccupied molecular orbital (LUMO), thus making the molecule more difficult to reduce. The formation of a "brown film" on the surface of the lithium has also been observed, and it has been proposed that this film may enhance the stability of the lithium-solvent interphase.

An interesting hypothesis has been proposed (5, 6) that the actual electroplating and electrodisolution of lithium may involve a solvated lithium atom. Thus, a solvated lithium ion would approach the electrode and be reduced by electron transfer across the double layer (while still solvated). The solvated lithium atom would desolvate, and the atom would then form a part of the solid electrode phase. This solvated lithium atom may be similar to the radical ion proposed by Koch (4), but in this case the electron may be delocalized through several solvent molecules. It is possible that, should the assembly gain enough energy for the electron to become localized on one solvent molecule, rapid cleavage of the carbon-oxygen bond would then occur, leading to decomposition products and encapsulation of lithium.

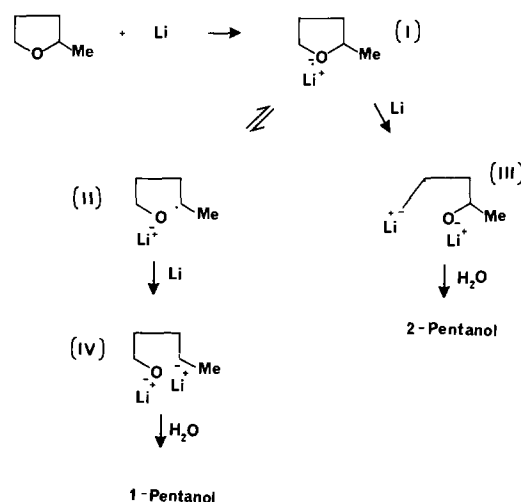
If it were possible to deduce from the products the nature of the species involved in the cleavage reaction, then some information about the solvated lithium atom concept might be obtained. This may be done in the case of 2MeTHF. Scheme I shows the formation of the lithium ion-radical ion pair (I) and its possible decomposition pathways. There may, of course, be more than one solvent molecule involved in I. Homolytic cleavage of the carbon-oxygen bond may occur at this point to form species II. The factors which favor such a cleavage direction are that secondary radicals are more stable than primary radicals and that the charge may prefer to lie on the more electronegative oxygen atom rather than on the carbon. Further reduction of this species by lithium would yield species IV which would ultimately yield 1-pentanol upon addition of water. If, on the other hand, cleavage of species I alone does not occur and that cleavage occurs

simultaneously with the injection of a second electron into the molecule, one would expect that the cleavage direction would be the opposite to the previous case, and species III would form, which eventually would lead to the formation of 2-pentanol. This prediction is once more based on the inductive effect of the methyl group, which would tend to destabilize the secondary anion relative to the primary anion.

The cleavage of species I to give species II may be a reversible process. Such reversible cleavages have been noted before (7). Thus, the irreversible step may be the further reduction of the radical ion by a second lithium atom. This is in accord with the observed stabilities of THF, 2MeTHF, and 2,5-dimethyltetrahydrofuran. The reduction of the favored secondary radicals to give the secondary anions should be harder than the reduction of a disfavored primary radical to give a more favored primary anion. The concept of the solvated lithium atom would then fit in very nicely with this scheme where the event which causes destabilization of the solvated atom is the advent of a second lithium atom to the complex. It should be a simple matter to analyze the products from storage of the electrolyte at elevated temperature as described by Koch (4) and also from electrolyte which had been used to cycle lithium.

Experimental

General.—Electrolyte preparation and the electrochemical experiments were conducted at room temperature (20°-25°C) under an argon atmosphere in a Vacuum Atmospheres Corporation dry box equipped with a Model HE-473 Dri-train to remove moisture and oxygen. Chromatographic analyses were carried out using a Shimadzu GC-9A with fused silica columns (25 m × 0.23 mm id). The inlet system was a cold on-column injection sys-



Scheme I

¹Present address: PPG Industries, Incorporated, Barberton, Ohio 44203

tem to avoid possible thermal reactions from a hot injection chamber. The detector was a flame ionization detector and the column stationary phases were either Carbowax 20M or bonded cyanopropyl phase (Quadrex CPS-2). GC/MS analyses were also carried out using a Finnegan 4000 machine with capillary columns and low column temperatures.

Materials.—2MeTHF (Aldrich) was distilled off CaH_2 under argon. Sodium and benzophenone were added to this collected solvent, and the mixture was refluxed under argon until the solution turned blue indicating the formation of the sodium-benzophenone ketyl. The solvent was then distilled through a vigreux column (1m) and collected in a flask with a stopcock so that the solvent could be transferred to dry box without exposure to the atmosphere. The solvent was then stored over molecular sieves in amber bottles in the dry box. Lithium hexafluoroarsenate (U.S. Steel Agri-Chemicals, electrochemical grade) was used as received.

Electrochemical measurements.—Cells were fabricated from polyethylene cylinders having a 1 cm^2 hole. End plates, also made of polyethylene, were used to hold the electrodes in place. The electrodes were lithium and a nickel plate. A lithium reference electrode was formed by means of a small hole in the cell cylinder through which lithium could be extruded by means of a screw which also provided electrical contact (see Fig. 1). Cell cycling was carried out by means of a ECO Model 553 potentiostat driven by a PAR 175 programmer, and the cell voltages were recorded on a Bascom-Turner Model 4020 electronic recorder.

The cycling regime was the same as that described by Koch and co-workers (3). That is, an initial charge of lithium was plated onto nickel or stainless steel plate ($3.4 \text{ C}\cdot\text{cm}^{-2}$). $1.1 \text{ C}\cdot\text{cm}^{-2}$ was then stripped followed by a $1.1 \text{ C}\cdot\text{cm}^{-2}$ plate. The cycle was continued until failure. All current densities were $5 \text{ mA}\cdot\text{cm}^{-2}$, and no differences were observed when either nickel or stainless steel was used as the substrate. The lithium figure of merit (Li_{FOM}) is then given by the number of completed cycles times $1.1 \text{ C}\cdot\text{cm}^{-2}$ divided by $3.4 \text{ C}\cdot\text{cm}^{-2}$.

Electrolyte preparation and storage.— LiAsF_6 was slowly added to the purified 2MeTHF in the dry box so that the temperature of the solvent remained below 30°C throughout. The prepared electrolytes were then stored over lithium chips or lithium-mercury amalgam in dark-end bottles in the dry box at room temperature ($20^\circ\text{--}25^\circ\text{C}$) until use.

Storage of electrolytes at elevated temperatures (65°C) was accomplished in the manner described by Koch (4). The solvent (2 ml) and freshly cut lithium chips were placed in culture tubes (Corning C9826) equipped with Teflon-lined screw caps. Teflon tape was wrapped around the culture tube threads prior to capping, and the tubes were then stored in an oven for 30 days at 65°C . As found by Koch, some solvent loss occurred during this procedure.

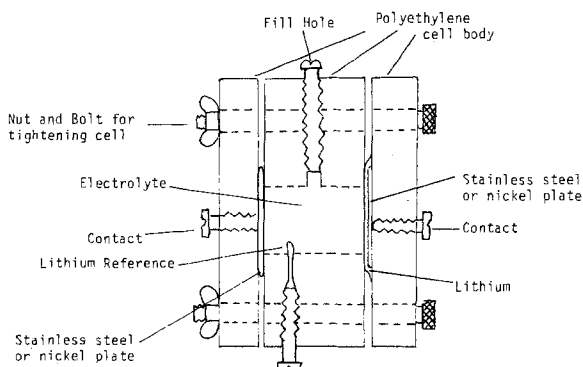


Fig. 1. Cell used for lithium cycling tests

Analysis of electrolytes after electrochemical cycling or elevated temperature storage.—The electrolytes (2.5 ml) were added to distilled water (80 ml) together with the lithium electrodes or chips. Sometimes the lithium electrodes were reacted with water separately from the electrolyte to see if differences existed between the products formed on the solid and in solution. The aqueous solutions were continuously extracted into pentane for 24h, and the pentane was dried (MgSO_4) and carefully evaporated on a rotary evaporator until the volume of the solution was about 2 ml. This pentane solution was then analyzed by GC and GC/MS.

Results and Discussion

Table I shows the results of the GC analyses of the electrolytes which had been stored at 65°C . Our analysis was primarily directed toward the detection of the pentanol isomers. In nearly all cases, other products were detected and our analytical method clearly showed the presence of the impurity, 2-methylfuran (2MeF), which has been remarked upon by others (8, 9) (see Fig. 2b). It was noted that a small amount of 2-pentanol was formed from simple storage of 2MeTHF at elevated temperature. Storage of lithium in 2MeTHF alone showed some corrosion of the lithium and upon analysis of the hydrolyzed contents, pentanols were found. The electrolyte mixture, LiAsF_6 -2MeTHF, turned black in the absence of lithium and the GC analysis showed a multitude of products (see Fig. 2a), indicating that a polymerization reaction had occurred. It is important to note that the liquid showed no signs of solidifying throughout the storage period despite these reactions. A similar experiment has been reported by Foos (11), and the visual observation of the color changes was similar. However, in the previous report, analysis of the darkened electrolyte by NMR spectroscopy showed no change in the spectrum. It is important to note here that the 2MeTHF peak in the gas chromatographic analysis accounts for at least 80% of the sample and that, therefore, the other components in the mixture must be rather dilute. This may account for the lack of change in the spectrum. The presence of lithium in the solution completely

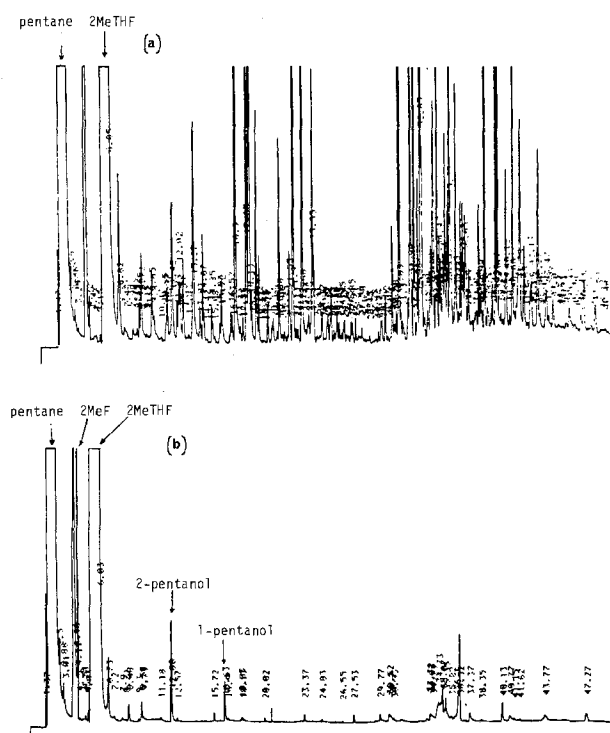


Fig. 2. Gas chromatograms of LiAsF_6 -2MeTHF electrolytes after 30 days at 65°C and extracted into pentane. GC conditions: Quadrex CPS-2 $25\text{m} \times 0.25 \text{ mm}$ fused silica column, cold on-column injection. Oven temperature: 10°C for 2 min, $3^\circ/\text{min}$ to 120°C : a: 1.5M LiAsF_6 -2MeTHF alone. b: 1.5M LiAsF_6 -2MeTHF plus lithium.

Table I. Storage of 2MeTHF, 2MeTHF-LiAsF₆ (1.5M) at 65°C for 30 days in the absence and in the presence of lithium. Visual observations and GC analysis

Tube contents	Visual appearance	GC analysis (area percentage) ^a			
		2MeTHF	1-pentanol	2-pentanol	(Ratio) ^b
2MeTHF	Remains clear	85.8	0	0.001	(—)
2MeTHF+Li	Solution remains clear. Lithium shows some corrosion ^c	41.9	0.001	0.0022	(1:2:2)
LiAsF ₆ -2MeTHF	Solution turns dark after 7 days	80.5	No pentanols formed; many other products formed (see Fig. 2a)		
LiAsF ₆ -2MeTHF+Li	Solution remains clear. Lithium shows brown film corrosion ^c	87.9	0.0015	0.006	(1:4) (See Fig. 2b)

^a Area percentage is defined as the integrated area under the peak normalized over all peaks in the chromatogram. The accuracy for 2MeTHF is poor due to detector overload.

^b Ratio of 1-pentanol to 2-pentanol.

^c In similar tests reported by Goldman *et al.* (2), the lithium surface remained shiny.

Table II. Product analysis from GC analysis of hydrolyzed and extracted electrolyte in lithium half-cell cycling tests: 1.5M LiAsF₆-2MeTHF. Current density: 5 mA-cm⁻²

Electrolyte treatment	Li _{FOM}	GC analysis (area percentage) ^a			
		2MeTHF	1-pentanol	2-pentanol	(Ratio) ^b
Stored over Li chips	27.8	26.8	0.0017	0.0012	(1:0.7)
	30.7	45.0	0.001	0.0006	(1:0.6)
	23.0	63.7	0.008	0.003	(1:0.38)
	15.8	56.8	0.003	0.00015	(1:0.5)
None	14.9	93.6	0.0096	0.008	(1:0.8)
	17.5	88.3	0.0002	0.0003	(1:1.3)
Stored over Li(Hg)	22.3	—		No pentanols detected	
	20.7	38.3	0.000	0.0003	(—)

^a Area percentage is defined as the integrated area under the peak normalized over all peaks in the chromatogram. The accuracy for 2MeTHF is poor due to detector overload.

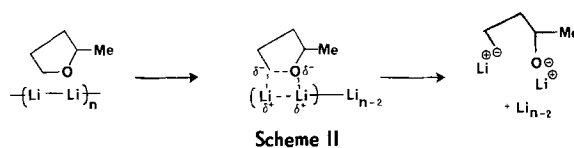
^b Ratio of 1-pentanol to 2-pentanol.

suppresses the polymerization reactions, and the lithium showed signs of the formation of the brown film. GC analysis showed the presence of pentanols, and, in both cases where lithium was present, 2-pentanol was found to be the major isomer. A further point to be noted is that the impurity, 2MeF, was detected in the solutions after the storage period in approximately the same concentrations as before the storage as judged by the integration of the peak areas. This is quite surprising since one might expect such a highly unsaturated molecule to be easily reduced by the lithium.

In Table II, the results of gas chromatographic analyses of the cycled electrolytes are listed. The first column shows the method used to store the electrolyte in the dry box after it is prepared from the distilled solvent and dried salt prior to cycling. The lithium figure of merit (Li_{FOM}) calculated according to the method described in the Experimental section is given in column 2, and the GC analyses from that particular cycling experiment are given in the same row in columns 3-6. The numbers listed for the GC analyses are the raw integration numbers and are for the purposes of comparison only. The accuracy of the 2MeTHF integration in particular is in question due to detector overload. In cases where the area percentages for the 2MeTHF peak are below 50%, the area for the pentane solvent has been included in the normalization. These numbers do, however, give an indication of the concentrations of pentanols found. We have noted, as have others (10), that there is a stability problem with cyclic ether based electrolytes in the absence of lithium, and the effects of this are illustrated by the Li_{FOM} numbers in the table. In nearly all cases, the major pentanol isomer found is the 1-pentanol. This is in striking contrast to the result from the thermal storage experiments in Table I. It was also noted that the impurity, 2MeF, was still detected after the cycling experiments were complete, indicating once more that this highly unsaturated molecule has in-

triguing properties. Indeed, 2MeF has been shown recently to be an excellent additive in the use of tetrahydrofuran in secondary lithium cells (9).

Although there is some variation in the ratios of the pentanol isomers found in both Tables I and II, it is quite clear that there is a difference between the two sets of results. This implies that the mechanism of solvent breakdown is different in the two cases. It should be noted that the mechanism which is operating in the thermal decomposition route of Table I will be competing with the electrochemical route which predominates in Table II and that this may account for some of the variations noted in the isomer ratios. From the purely electronic considerations outlined above, the thermal process involves an anionic cleavage while the electrochemical process involves a cleavage which is radical in nature. The thermal process could be rationalized according to Scheme II, which shows the formation of a surface complex with the lithium followed by cleavage and removal from the lithium metal. The developing negative charges are shown. Such schemes have been proposed before for the reaction of lithium metal with alkyl halides to form organolithium compounds (12). Such a scheme also implies that steric effects may play a role and indeed, it has been reported that steric effects are significant in the reaction of 2,5-dimethyltetrahydrofuran with lithium (13), the *cis* isomer being the more stable. The electrochemical situation, on the other hand, must provide the means for a less concerted cleavage where only one lithium atom is involved. This could be where the lithium atom is surrounded by



several solvent molecules as envisaged by the solvated lithium atom concept and that the attack by the second electron or lithium atom occurs after cleavage. Once again, it has been reported that steric factors affect the cycling behavior of 2,5-dimethyltetrahydrofuran (13) such that the *cis* isomer gives better performance. Such an observation indicates that the surface continues to influence the reaction pathway. A further nuance to the situation is that the cleavage reaction may be reversible in the electrochemical situation and that the advent of another electron disturbs the equilibrium. The steric effect does not support this idea, however, unless the species and hence the stereochemistry is still influenced by the surface to a large extent.

The role played by the 2MeF in this process is most unclear. It has been proposed that the furan may form a protective film on the lithium surface, thereby retarding chemical reactions with the electrolyte (9). We have briefly tried the use of this additive at 4 volume percent (v/o) concentration in the half-cell test and found that the performance degraded markedly in this situation. Abraham *et al.* (9) examined concentrations of 0-1.2 v/o in 2MeTHF electrolyte and found beneficial effects. It is interesting to note that, in thermal storage experiment involving LiAsF₆-2MeTHF in the absence of lithium, the level of 2MeF appeared to be considerably diminished compared with 2MeTHF alone. This may indicate that the furan is consumed by the polymerization reactions. When lithium is present, however, the 2MeF level remains at a fairly high level. It therefore seems possible that some kind of complex is formed between the furan and the polymerization initiator (*e.g.*, AsF₆) and that the presence of lithium may prevent irreversible decomposition of the

complex to give polymerization. This reversible complexation may well explain the continued presence of the furan after electrochemical cycling experiments.

Manuscript submitted Dec. 17, 1984; revised manuscript received July 19, 1985.

Union Carbide Battery Products Division assisted in meeting the publication costs of this article.

REFERENCES

1. K. M. Abraham and S. B. Brummer, in "Lithium Batteries," J. P. Gabano, Editor, p. 372 Academic Press, New York (1983).
2. J. L. Goldman, R. M. Mank, J. H. Young, and V. R. Koch, *This Journal*, **127**, 1461 (1980).
3. V. R. Koch, J. L. Goldman, C. J. Mattos, and M. Mulvaney, *ibid.*, **129**, 1 (1982).
4. V. R. Koch, *ibid.*, **126**, 181 (1979).
5. P. P. Schmidt and B. S. Pons, *Electrochim. Acta*, **27**, 867 (1982).
6. P. P. Schmidt and B. S. Pons, *ibid.*, **27**, 875 (1982).
7. A. J. Bellamy and J. B. Kerr, *Acta Chem. Scand.*, B33, 370 (1979).
8. S. P. S. Yen, D. Shen, R. P. Vasquez, F. J. Grunthaler, and R. B. Somoano, *This Journal*, **128**, 1434 (1981).
9. K. M. Abraham, J. S. Foos, and J. L. Goldman, *ibid.*, **131**, 2197 (1984).
10. V. R. Koch, J. L. Goldman, and R. M. Mank in "Battery Design and Optimization," S. Gross, Editor, p. 377, The Electrochemical Society, Softbound Proceedings Series, Princeton, NJ (1979).
11. J. S. Foos, *This Journal*, **131**, 2308 (1984).
12. B. J. Wakefield, "The Chemistry of Organolithium Compounds," p. 22, Pergamon Press, Oxford, England (1974).
13. V. R. Koch, *This Journal*, **128**, 1293 (1981).

Corona Corrosion of Aluminum in Air

A. Goldman

Laboratoire de Physique des Décharges¹ (CNRS), Ecole Supérieure d'Electricité, 91190 Gif sur Yvette, France

R. S. Sigmond

Electron and Ion Physics Research Group², Norwegian Institute of Technology, N-7034 Trondheim-NTH, Norway

ABSTRACT

Aluminum suffers severe pitting corrosion when used as an anode in negative corona discharges in ambient air. This paper gives a comprehensive account of the electrochemical interaction between a low electric field metal surface, especially aluminum, and the unipolar gaseous electrolyte created by an air corona. Introductory sections on coronas and corona corrosion give the necessary background. Physical and chemical analysis of the gaseous, liquid, and solid corrosion products of aluminum in air coronas demonstrate their close resemblance to the products formed in aqueous nitrate electrolytes.

Electrochemical passivation and corrosion of aluminum have been extensively studied. From the practical point of view, the formation of stable anodic oxides and hydroxides is important for fabrication of electrolytic capacitors and for protection of exposed aluminum, as is, vice versa, the destruction of these oxides by corrosion. Scientifically, the aluminum-water electrochemical system is comparatively simple and can be studied with some hope of physical understanding (1-3). Applied corrosion studies are done under actual conditions of use or by accelerated testing. A typical example is the corrosion testing of aluminum alloy or aluminum-clad steel wires for overhead power transmission lines, either by using a test chamber of adjustable climatic conditions or by exposing the lines to coastal climatic conditions by suspension on racks. One purpose of this communication is to suggest that testing also should include the parameters

of applied high voltage, electrical field stress, and corona currents encountered in normal use.

More academic studies of aluminum passivation and corrosion invariably are performed in liquids, especially electrolytes, usually under potentiostatic or galvanostatic conditions. This paper points out that similar tests and measurements can and should be performed using weakly ionized gases as unipolar electrolytes. Since a corona discharge is one of the more practical ways to produce such a gaseous electrolyte and since this medium was used when we discovered the effects of gaseous electrolytic action on aluminum, we have coined the terms "corona electrochemistry" and "corona corrosion" for the corresponding surface effects observed in weakly ionized gases (4, 5). We show here that unipolar gaseous electrolytes have properties that in important aspects resemble those of liquid electrolytes with similar passivation and corrosion effects on metal electrodes. On the other hand, there are important differences that can be taken advantage of, as the free and sometimes independently adjustable flow of excited neutral species, analogous to radicals

¹Later referred to as LPD.

²Later referred to as ELION.

in liquid electrolytes. Furthermore, quite weak corona currents can have a surprisingly vicious pitting effect on susceptible metals. Corona conditions that cause serious trouble do not occur daily. However, the corona discharge is the industrially most important type of gas discharge, being used for dust precipitation, water purification, treatment of plastic, paper, and textile surfaces, and xerography. Failure to acknowledge the corrosive power of coronas and to take proper countermeasures may lead to costly construction errors. Finally, very weak negative ion corona currents may have the same passivating effect on metal surfaces in air as the corresponding anodic protection current has in aqueous solutions.

A second type of gaseous electrolyte, not to be treated here, must be mentioned. Bipolar gaseous plasmas have been used as chemical reactors (6) since the nitrogen oxide producing arcs of Birkeland and Eyde, and are now applied in plasma etching processes in the integrated circuit industry. These plasmas differ from unipolar corona media by having (i) much higher charged particle densities that only can coexist in a quasi-neutral mixture (by plasma definition), and (ii) much higher temperatures of the neutral particles, often in approximate thermal equilibrium with the charged particles. In our coronas, plasma may exist in thin filaments (streamers) (see the next section). Otherwise, our corona conditions resemble those in the thin boundary layer between a plasma and a solid surface.

An Overview of Low Current Corona Discharge

The corona discharge is the source of charged particles in our experiments with unipolar gaseous electrolytes. We will first give a short summary of their pertinent properties, restricting the treatment to point-to-plane coronas (Fig. 1). A more thorough introduction is found in Ref. (8).

A unipolar corona discharge is, by definition, a gas discharge where the geometry confines the gas ionization processes to the ionization region around the active electrode (here, the point). The corona is called positive or negative according to the polarity of the active electrode. In the space between the ionization region and the passive electrode (the plane), called the drift region, the ions and electrons drift, diffuse, and collide and react with neutral gas molecules. Direct collisions and reactions between the charged particles in coronas are unimportant. They interact, however, strongly via their space-charge field, so that the current density and electric field distributions in atmospheric coronas at currents above some microamperes are completely dominated by space-charge effects (9). This leads to current density distributions at the plane $j(r)$, current-voltage characteristics $I(U)$, and electric field distributions $E(z, r)$ that are simple and independent of the detailed shape and surface condition of the active electrode. The corrosion effects to be discussed take place on the passive electrode, the plane.

In air and most other gases containing electron attaching molecules, two types of dc coronas are found.

Unipolar conduction coronas.—These are variously called positive glow coronas, negative Trichel pulse coronas, and negative glow coronas; they have ionization regions that are concentrated close to the active electrode. At microampere currents and above, they burn either stably or, more often, in short pulses of such high repetition rate that the ion flow in the drift region is practically continuous. The predominant ions are of the corona polarity, that is, positive ions in positive coronas and negative ions in negative coronas. The part of the drift region current in negative air coronas carried by electrons is usually small below 10–20 μA total current, because of electron attachment. At higher currents, the space charges make the electric field distribution more uniform. This and the higher applied voltage sharply increase the drift region field, increasing the electron/negative ion ratio. Note that the rapidly pulsed nature of ionization region processes is important for the corrosion of the negative point electrode. This may affect the drift region and the plane elec-

trode by sputtering (10) or by evaporation of point metal or corrosion products (11, 12).

In this study, unipolar conduction coronas have been used. The exception is the ac coronas treated below, which have bipolar components.

Streamer (bipolar) conduction coronas.—These occur at higher point-to-plane currents, especially at positive point polarity. Under these conditions, the ionization region produces a conducting plasma faster than the plasma can be absorbed by the point electrode. Consequently, a conductive plasma filament of some 30 μm diam (the streamer) grows out of the point toward the plane, carrying the plasma producing ionization region ahead of it with velocity around 10^6 m/s (values for atmospheric density air). When this streamer hits the plane, a cathode spot is produced, the gap field is redistributed along the plasma channel, and this channel either dies out (by electron attachment) or later converts to a thermally ionized spark channel. A positive streamer hitting a plane cathode will subject it to a pulsed glow discharge treatment, bombarding it with positive ions of energies that may exceed 100 eV. This is in sharp contrast to the mainly thermal energy ion influx to the plane in our unipolar current coronas.

Note that both corona forms may coexist: a 50 μA positive corona might consist of 20 μA continuous unipolar current, diffusely distributed over the plane (see below), with 30 μA of streamers, repetitive at 10 kHz, hitting the plane just opposite the point.

The unipolar current density, j , in positive and negative point-to-plane coronas is distributed over the plane according to the Warburg (13–16) law

$$j(\theta) = j_0 \cos^5 \theta \quad [1]$$

$$j_0 \approx I/2d^2 \quad [2]$$

with $\tan \theta = r/d$ and where I is the unipolar corona current and d the gap width. The field and ion flow lines are slightly more separated than in the space-charge-free case, by space-charge repulsion. The observed distributions $j(\theta)$ usually fall quite abruptly to zero around $\theta \approx 65^\circ$, due to the fact that ions drift along the field lines and that field lines ending outside $\theta = 65^\circ$ usually originate on the point surface outside the ionization region. The Warburg distribution is shown in Fig. 1.

In point-to-plane unipolar current coronas, as well as in wire-cylinder or wire-plane ones, space-charge fields tend to make the total field more uniform at increasing currents. It can be shown (9) that the unipolar current I at a given voltage U_0 cannot exceed the saturation limit

$$I_{\text{sat}} = 2\mu\epsilon_0 U_0^2/d \quad [3]$$

where μ is the ion mobility and ϵ_0 ($= 8.85$ pF/m) the per-

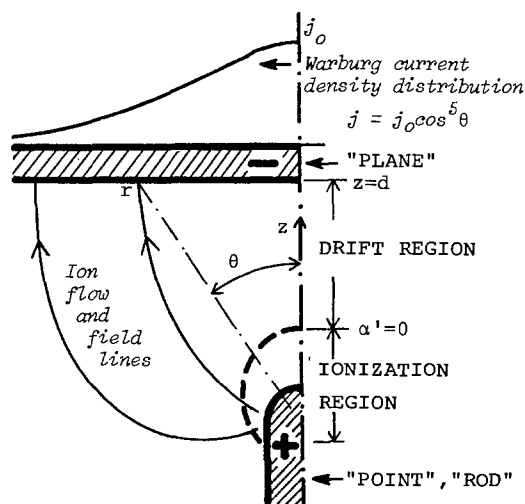


Fig. 1. A typical point-to-plane corona geometry, here shown with positive point, and some commonly used terms (7). The surface $\alpha' = 0$ marks the outer limit of the ionization region, where the production of electrons by ionization just balances the loss by attachment.

mittivity. For ions in air at atmospheric density, this gives

$$I_{\text{sat}} (\mu\text{A}) \approx 4 U_0^2 (\text{kV}^2)/d (\text{mm}) \quad [4]$$

If currents above this are observed, they are either partly bipolar (Eq. [3] and [4] invalid) or electron carried (μ for electrons must be used).

Space-charge dominated currents driven by high potentials (5-10 kV) make corona discharges nearly perfect galvanostatic ion and electron current generators on a macroscopic level.

An important feature of the point-to-plane coronas is the electric wind. As charged particle flow in atmospheric density coronas is completely viscous (collision dominated), virtually all momentum and energy extracted by the ions from the electric field are transferred to the neutral gas molecules. A fairly strong, axial gas jet results (17, 18), often employed to blow out candles in demonstration experiments and to carry ions to gramophone records for removal of excess surface charge. However, this jet also transmits up to half the discharge power to the plane (19) in the form of heat and excited atoms and molecules.

Our electrochemical view of the point-to-plane corona discharge is shown in Fig. 2, illustrating schematically the various reaction regions and channels in the corona gas and on the surrounding conducting and nonconducting surfaces. The importance of synergy between neutral activated species and charged species is demonstrated below.

Introduction to the Corona Corrosion Phenomenon

As the term "passive electrode" implies, gas discharge workers traditionally look upon the low field corona electrode as a passive receiver and neutralizer of impinging ions and as a boundary condition $U = 0$ for the electric potential. The present investigations started with the observation that negative point-to-plane coronas quite rapidly etch pits in plane Al foil anodes in the winter air of Paris but not in that of Trondheim. This difference brought out the importance of humidity (Trondheim's air may be very dry in winter) (4).

A typical point-to-plane corona had the parameters: (i) the gas was 1 atm air 50% relative humidity (RH), flowing at 5-10 liter/h; (ii) the point was a rounded Pt wire of 0.2 mm diam or a conical Rh point $\approx 10 \mu\text{m}$ tip radius (not critical); (iii) the plane was Al foil, 15 μm thick, commercial or high purity (purity not critical); the point-to-plane distance, d , was 10 mm; (iv) current/voltage was Trichel current pulses of 2-3 μs interval, 50 μA average current, and 7-9 kV negative point voltage. The maximum (central) current density is then $\approx 25 \mu\text{A}/\text{cm}^2$.

As seen side-on, using photomultiplier and photon counting or sampling, light comes from the ionization (cathode) region in 30-40 ns pulses simultaneously with the Trichel pulses. Its spectrum corresponds mainly to excited states of the N_2 molecules (second positive system), with some contribution from excited N_2^+ ions (first negative system). No photons are seen side-on from the drift or anode plane regions (see the Apparatus section). This conforms to earlier observations (21, 22).

The Al anode within minutes is covered by a growing layer of glassy, viscous liquid substance, which eventually solidifies and cracks, together with whitish granules. Within hours, holes of some microns diameter pierce the foil, concentrated in a (sometimes annular) region of growing radius around the corona axis. The holes often are nearly cylindrical, with 90° edges in an otherwise flat surface, but this depends to some extent on the foil thickness. The holes grow in number rather than in diameter during the discharge. After many hours, larger holes may be formed, most probably by the merging of many smaller holes. After perforation of the foil, a glassy, initially semiliquid deposit forms on the back side, covering somewhat more than the perforated area. Sometimes at higher RH's the electric wind will even blow hemispherical bubbles out of the holes on the back side. At lower

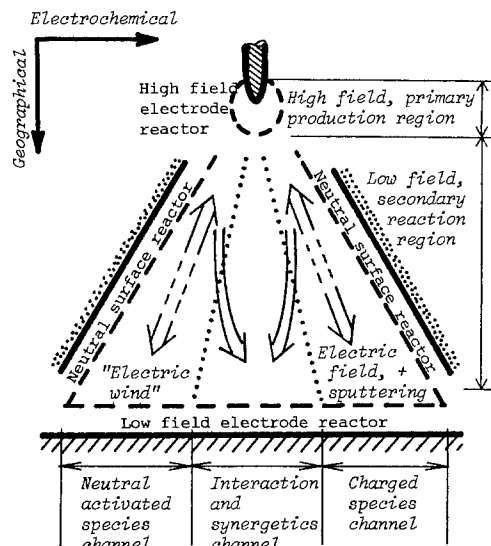


Fig. 2. Schematic diagram illustrating the main reaction regions and reaction channels of a corona electrochemical reactor (20). Two intermixed streams of energetic particles emerge from the ionization region where they are produced: neutral activated species, carried by the electric wind, and charged species, carried by the electric field. The activated neutrals interact with the gas, the neutral (insulating or insulated) surfaces, and the low field electrode. Charged particles interact with the gas and with the low field electrode. The low densities preclude significant interaction between the two streams and their reaction products, except at the low field electrode surface, where important synergetic effects appear.

RH's, especially, "worms" of a loose, white material seem to crawl out of the holes, mostly on the front side, but also on the back. In and around the perforated area on the front side, concentric rings appear both of white-and-gray and of interference color character. The central 1 or 2 mm, where the electric wind jet impinges, are often metallic looking, free of most crust and granules, but very pitted. Figure 3 shows a collection of macroscopic and microscopic photographs of these phenomena, to be discussed later; see also Fig. 14.

As discussed below, the corona pitting corrosion of aluminum seems typical for negative coronas in ambient air. It depends on a negative ion current influx to the plane with synergetic contribution from the electric wind. In the absence of hydrated negative ions, as in dry air negative coronas, or for neutral (insulated) foils, or for cathode foils in positive coronas, pitting is not noticeable after 2-6 day exposures. Finally, pitting seems absent on gold anode foils in air but develops on stainless steel anodes in SF_6 coronas (23).

In the following sections, we discuss several experimental investigations of corona corrosion. The main guideline has been to search for a possible correlation with electrochemical corrosion in aqueous solutions.

Apparatus for Corona Exposure

In Situ Observations of Light and Surface Potentials

A variety of corona electrode systems with associated apparatus for control of electric current, gas flow, and composition and for *in situ* measurements have been used. The most typical set of corona parameters was listed in the preceding section, and some results were presented in Fig. 3.

General corona exposure.—Figure 4 shows our "quad" stainless steel corona chamber with four internal, identical corona units. This allows four samples to be exposed simultaneously to corona in gas of identical composition. As for most closed systems, the gas flow is not sufficient to keep the chamber gas free from corona by-products, but the strong electric winds ensure uniform conditions throughout the chamber. Of the two corona units shown, one is used for direct exposure of a foil sample, while the other works with a grid as the anode and the foil mounted

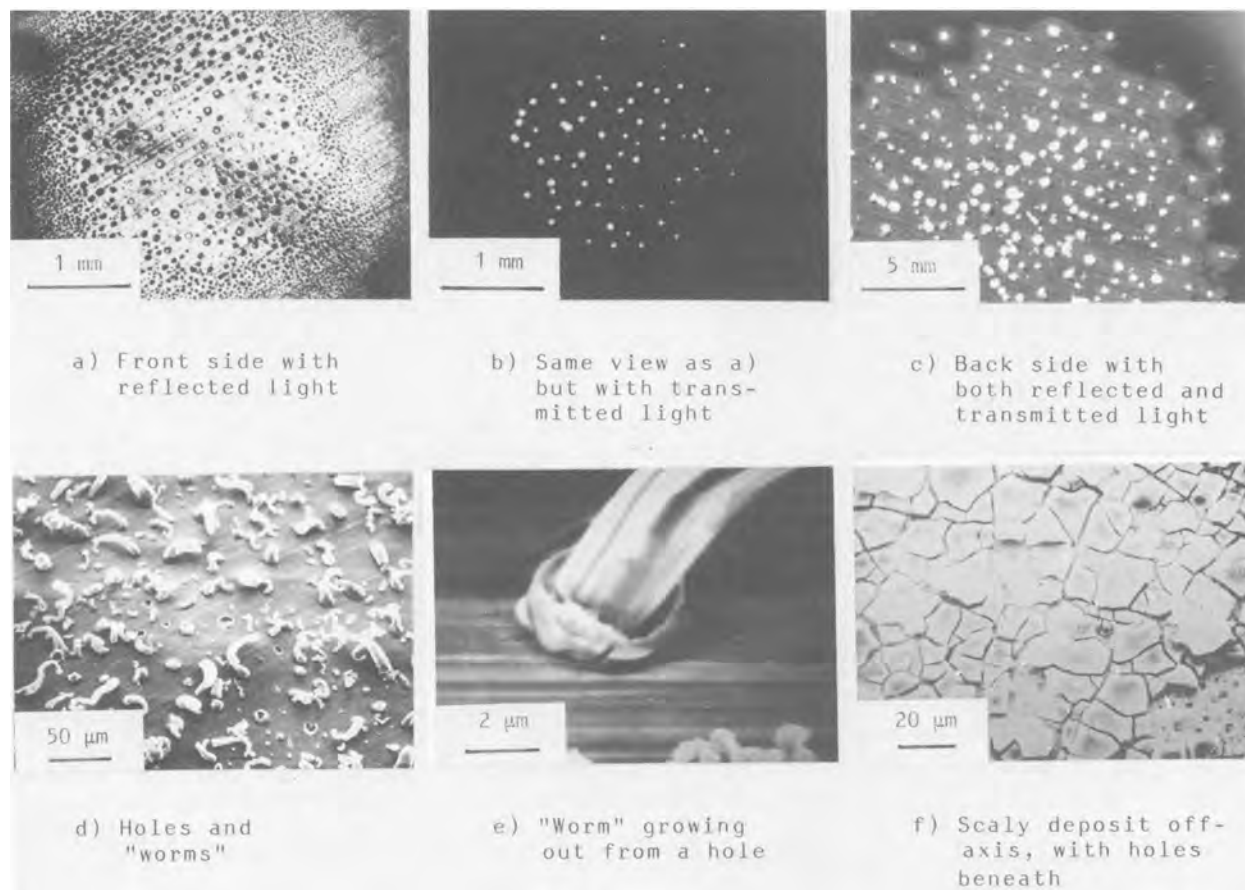


Fig. 3. Macroscopic and microscopic aspects of Al foils ($15\ \mu\text{m}$ thick, except for $c = 40\ \mu\text{m}$) corroded by negative coronas in air of about 50% RH (except for $c = 36\%$ RH). a, b: $d = 8\ \text{mm}, l = 50\ \mu\text{A}$ for 4h. c: $d = 8\ \text{mm}, l = 50\ \mu\text{A}$ for 160h. d, e: $d = 10\ \text{mm}, l = 130\ \mu\text{A}$ for 7h. f: $d = 8\ \text{mm}, l = 50\ \mu\text{A}$ for 4h.

insulated behind it, receiving no net current but exposed to the electric wind. In this case, only the former foil shows noticeable pitting.

Corona exposure with in situ light detection.—Figures 5a and 5b show systems for corona exposure with simultaneous detection of light pulses from the foil (Fig. 5a), or with automatic registration of the increasing light transparency due to foil perforation (Fig. 5b). The latter is a convenient way of obtaining the pitting rate quantitatively (see the Corona Pitting Rate section). The

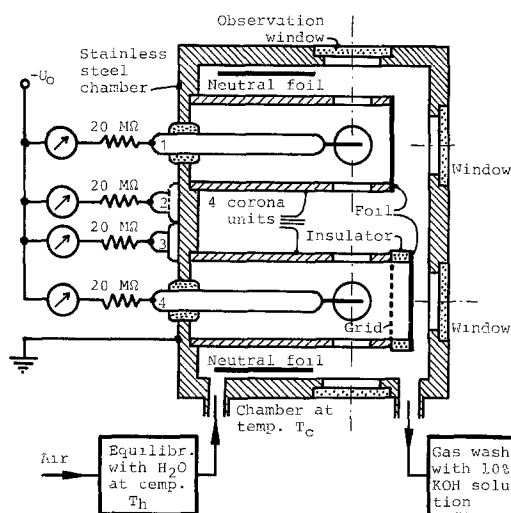


Fig. 4. Quad corona chamber for the parallel exposure of four sample Al foils. Only two of the four corona units in the chamber are shown; no. 1 with grounded foil anode, and no. 4 with grounded grid anode and insulated foil (ELION).

former gives information about the pits themselves through the light pulse shapes (Fig. 6).

In Fig. 6, the light pulses shown were measured using the monochromator, photomultiplier, and sampling oscilloscope of Fig. 5a, looking sideways on or towards the back of a negative Trichel pulse corona in open air. They belong to the second positive system of N_2 . Those marked b-c-d radiate from the back of corona perforated Al foils $16\ \mu\text{m}$ thick. For all curves, the first large pulse, around time zero, is light originating in the ionization region near the negative point during the Trichel pulse generation phase. Its size is nearly independent of the corona current and voltage, and it appears unchanged when seen through needle-made holes in uncorroded foils, curve e. The delayed pulses, in contrast, are absent from needle-made holes. Further, spectrally similar delayed pulses will radiate from grid wires of $20\text{--}100\ \mu\text{m}$ diam placed in front of any anode foil, curve a. All delayed pulses come earlier and increase in amplitude when the corona voltage and current are increased. No light is seen looking obliquely at the front (corona facing) side of exposed foils; all delayed light comes from the back. Storage of a corona perforated foil for months in laboratory air will not destroy this delayed photon pulse emission, but soaking in water does.

The observed light pulses have delays which are consistent with the expected travel time of an electron swarm that originates in the cathode region during the main Trichel current pulse and that escapes subsequent attachment in the space-charge-intensified corona field. The light is emitted only when the electrons enter new regions of sufficiently high electric field, like around the grid wires, curve a. Such regions evidently do not exist in or around holes made with a needle in a foil anode and still less on the back of such a perforated foil, curve e. Thus, the delayed light pulses (curves b-c-d) show conclusively that (i) electrons are conducted into and through corona

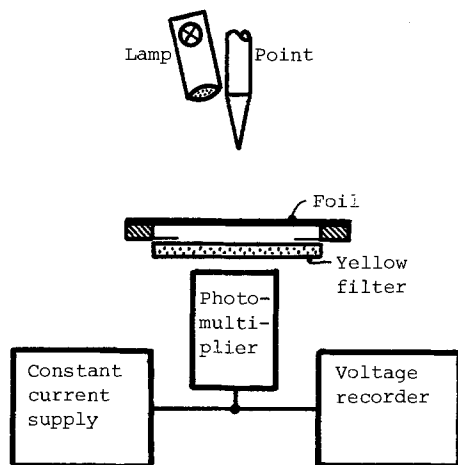
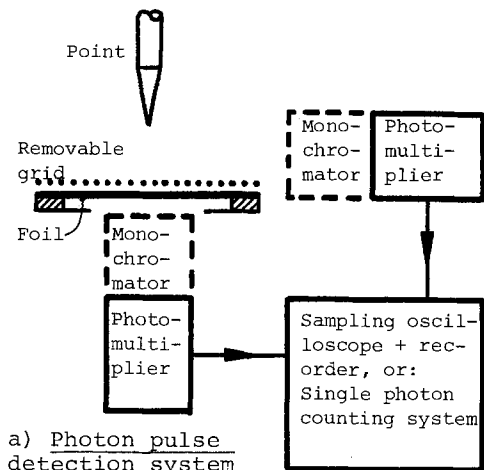


Fig. 5. Systems for corona exposure and *in situ* optical measurements, used in open laboratory air and in enclosed systems.

made holes, and (ii) high field regions exist in or near the back-side mouth of those holes. This means that the front of the foil and the pit walls are covered by an insulating layer, which charges up sufficiently to funnel electrons through the holes to the bare metal on the back side. Heavy negative ions will follow the same trajectories as

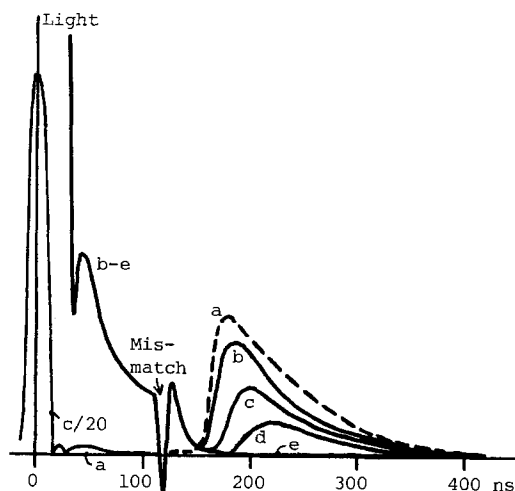


Fig. 6. Light pulses from negative Trichel pulse coronas in open air (4), seen with the system of Fig. 5a and belonging to the second positive system of N_2 . a: Light from grid 8 mm from cathode, $U_0 = 8.5$ kV, $I = 50$ μ A. Light through and from corona made holes in the Al foil, $d = 9$ mm. b: $U_0 = 8.4$ kV; $I = 40$ μ A. c: $U_0 = 7.8$ kV; $I = 30$ μ A. d: $U_0 = 7.1$ kV; $I = 20$ μ A. e: Light through needle-made holes in new Al foil, $I = 50$ μ A.

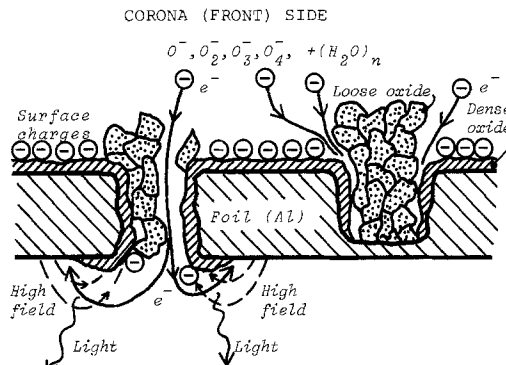


Fig. 7. A tentative picture of pitting and perforation of an Al foil anode in a negative air corona.

electrons, since charged particle trajectories in electrostatic field configurations are independent of particle charge and mass. We are thus led to the tentative picture of a corona corroding foil shown in Fig. 7.

The apparatus shown in Fig. 5a was originally made to look for sparks from the front side of corona-exposed anode foils. Such sparks would have told about erratic spark breakdown of the insulating layer due to accumulating charges, which could be a mechanism for pit formation or initiation. However, no sparks were ever observed.

Corona exposure with in situ surface potential measurements.—The charged insulating layers indicated by the light pulse measurements have been investigated by contactless surface potential measurements.

Figures 8a and 8b show apparatus adapted to nearly *in situ* mapping of surface potential distributions of corona-exposed foils. The rotating disk/field probe system (Fig.

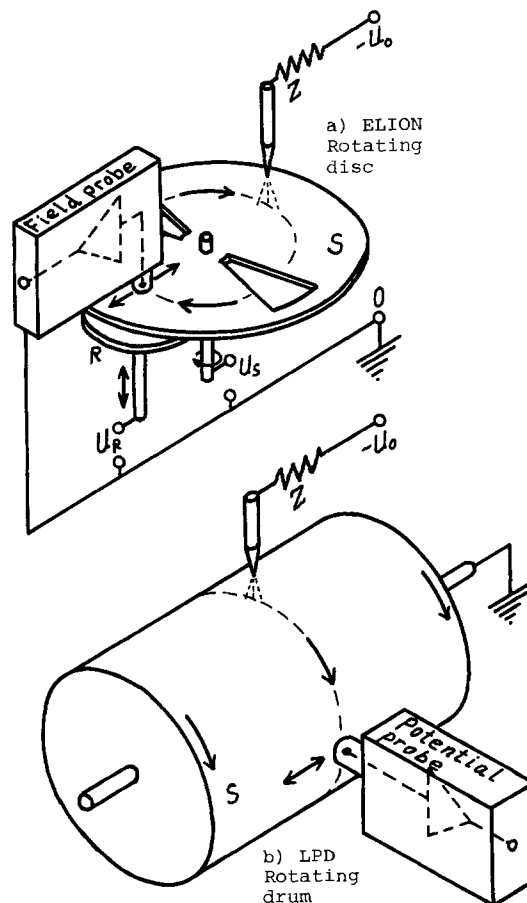


Fig. 8. Apparatus for corona exposure and surface potential measurements. S: Rotating disk or drum, carrying sample. R: Reference electrode (Au).

8a) brings the exposed elements from the corona to the probe within milliseconds, but is somewhat complicated to calibrate and has important centrifugal air flow effects. A slower rotating drum system (Fig. 8b) with a directly calibrated Monroe potential follower probe has also been used.

Typical results are shown in Fig. 9. Figures 9a and 9b were obtained using a continuously rotating disk under 20-30% RH with the corona point electrode perpendicular (Fig. 9a) and inclined toward the disk axis (Fig. 9b). The curves demonstrate that (i) the Al surface potential can reach hundreds of volts under these dry conditions, (ii) the potential distribution has a trough near the corona axis where the potential stays approximately constant, and (iii) this trough is related to the electric wind, which in Fig. 9a is deflected outwards by the centrifugal air flow and in Fig. 9b is forced inwards by the inclination of the point electrode. The curves in Fig. 9c are an example

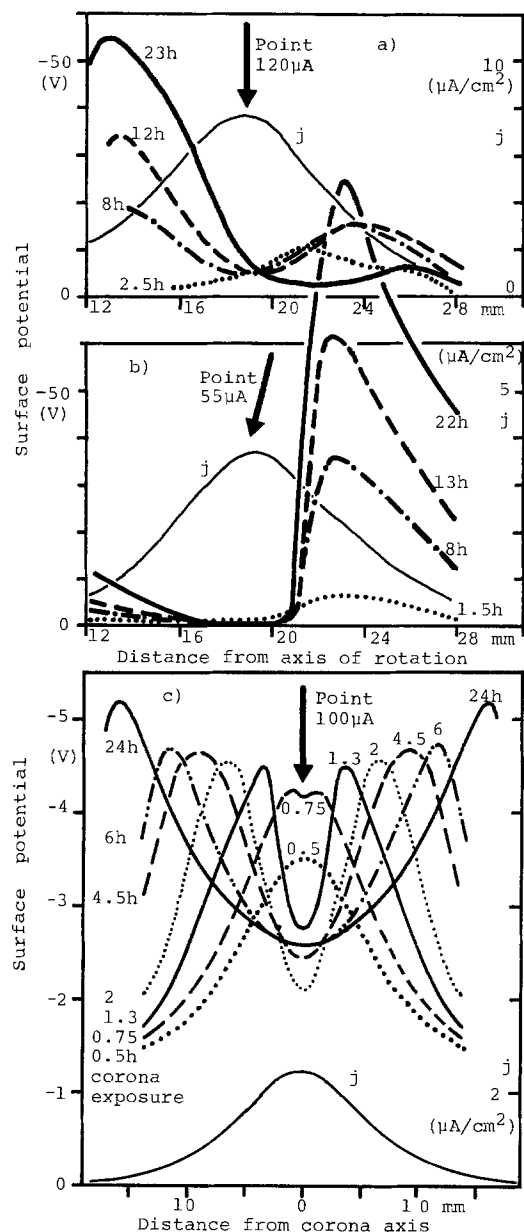


Fig. 9. The development of surface potential distributions observed on rotating Al foils exposed to negative coronas in ambient air. a: Rotating disk, diameter 60 mm, 1470 rpm (Fig. 8a), perpendicular point at $d = 7$ mm, $I = 120 \mu\text{A}$, RH 20-30% (5). b: Rotating disk, diameter 60 mm, 1470 rpm (Fig. 8a), inclined point at $d = 7$ mm, $I = 55 \mu\text{A}$, RH 20-30% (5). c: Rotating drum, diameter 83 mm, 66 rpm (Fig. 8b), perpendicular point at $d = 10$ mm, $I = 100 \mu\text{A}$, RH \sim 40-50%. In the cases a and b, no pitting holes were found. In case c, holes were found along the bottom of the central potential valley. The current density curves (j) are theoretical, calculated using Eq. [1], and averaged over the circumferences of rotation.

of surface potential profiles obtained by the rotating drum method under 40-50% RH. At these humidity levels, surface potentials are appreciably lower than in drier air, generally not exceeding 10V. Figure 9c clearly shows how the central valley forms and develops under symmetrical distributions of electric current and wind.

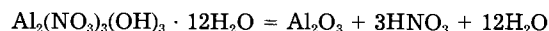
The Corona Corrosion Products

One advantage of corrosion studies using a gaseous electrolyte like a corona discharge, is that solid corrosion products are not dissolved by the electrolyte and are readily available for study by chemical or physical methods. On the other hand, the solid and semiliquid corrosion products on the Al foil are difficult to analyze, as their solubility and composition seem to depend on the conditions of formation, storage and age. Thus, measurements performed at atmospheric pressure (chemical, Debye-Scherrer) gave results quite different from those performed in vacuum (Auger electron microprobe, ESCA).

The conclusions of our investigations of the layers on Al foils corroded in 50% RH air can be summarized as follows.

Morphologically, it is a particularly ill-defined amorphous, porous, or semiliquid substance.

Chemically, the layers seem originally to consist of a mixture of $\text{Al}(\text{NO}_3)_3$, $\text{Al}(\text{OH})_3$, and Al_2O_3 , in different stages of hydration. Typical composition corresponds to the hypothetical compound



By heating or aging, this loses nitrate and water, and some nitrate is converted to ammonia. These conclusions are strengthened by our investigations using physical methods.

A more detailed account is given in the following subsections.

Study by physical methods.—Morphology.—Some typical macroscopic and microscopic aspects were shown in Fig. 3. The electron micrograph in Fig. 10 shows typical agglomerates of 1-3 μm diam with little or no crystalline structure revealed by electron diffraction patterns.

The corona-exposed surface appeared divided into a central, metallic looking region and surrounding annular regions of different texture and color, as mentioned earlier. The region adjacent to the central zone is always the richest in granular, worm-like, or other badly adhering corrosion products, giving this region a darker hue and lower secondary particle yields than the rest. It is also the most difficult to observe by electron-beam methods, because of charging effects. Note that the pitting by prolonged exposure extends further out than this inner annular region.

By corona exposure in very humid air (\approx 50% RH), the deposit was partly a viscous liquid.

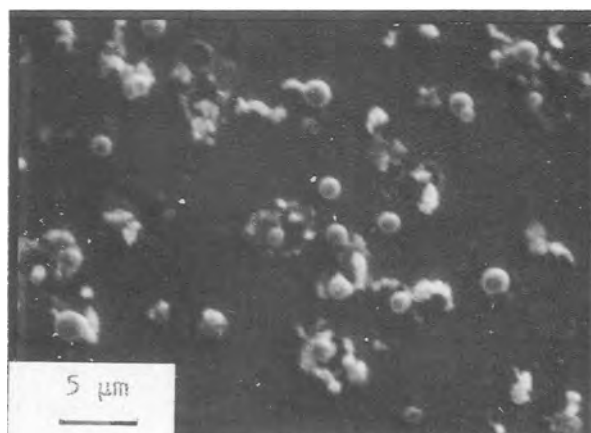


Fig. 10. Electron micrograph showing agglomerates of 1-3 μm diam, formed on Al foil exposed to negative corona in 50% RH air (courtesy of M. Foos, Ecole Des Mines, Nancy, France).

On cathodic and on neutral Al foils, pitting was not noticeable, but corrosion products appeared as loose whitish amorphous powder.

Interference measurements.—In dried air, no pitting takes place, but the Al is covered by a hard, transparent layer of growing thickness. Typical colored interference rings appear, which allow measurement of the optical layer thickness. Assuming the layer to consist of $\gamma\text{-Al}_2\text{O}_3$, the amount formed has been calculated and found to agree well with the Faraday equivalent of the corona exposure.

Melting point determination.—Freshly formed corrosion products from neutral and anodic Al foils (exposed in the quad chamber in 50% RH air) were heated in air under a microscope. The whitish scales and powder melted to a high viscosity liquid around 35°C, but the temperature had to be raised continually to keep it semiliquid. At our temperature limit, about 200°C, it solidified to a white amorphous deposit.

Auger electron spectrometry (ELION).—Anodic, cathodic, and neutral (insulated) corona-exposed Al foils were studied in a Varian automatic Auger electron microprobe. Scaly deposits, whitish "worms" protruding out of corrosion pits, and little corroded surface areas all showed the presence of Al and bound O, but little or no N. X-ray microprobe analyses confirmed these results. Secondary ion mass spectrometry (LPD) showed that the negative corona corrosion layer emits large amounts of O and OH ions. Pt transferred from the corona point was always found.

Used as a scanning electron microscope, the Auger spectrometer again showed that the corrosion products on pitted anodic foils were easily charged and broken off by the electron beam.

Since the pump-down time of this instrument is > 5h, the absence of N may be due to vaporization.

ESCA (LPD).—Figure 11 summarizes the results for foils exposed in negative and positive coronas. For these exposures, a conical point electrode with a large tip radius ($\approx 300 \mu\text{m}$) was used to obtain discharges without streamers in both polarities, for comparison. N_{1s} signifies nitrogen bound in nitrites and in organic-type compounds. Note the complete absence of NO_3 on the cathode foil. The difference between the ESCA and AUGER results must be ascribed to the difference in pump-down times.

Debye-Scherrer x-ray and electron diffraction analyses (ELION).—On newly exposed foils, some weak crystalline patterns were found but could not be identified. No clear patterns of known aluminum oxides were seen. The glassy scale deposit on some neutral Al foils (mounted insulated in quad chamber) analyzed some weeks after exposure gave a weak NH_4NO_3 diffraction pattern. This was produced by an aging process of the original hydrated aluminum nitrate (24), as also shown by chemical analysis (see below).

Chemical and mass spectrometric analyses.—A main purpose of the quad chamber was to provide samples for chemical analysis of the corrosion products. Two parallels were always used, so that each run would deliver one pair of directly exposed foils, one pair that were exposed only to the electric wind through a grid anode, and one pair of neutral foils placed outside the four corona units. Laboratory air was given the desired dew point by bubbling it through pure thermostated water and led through the temperature controlled chamber at about 10 liter/h. The exhaust gas was bubbled through 10% KOH solution, which afterwards was analyzed for NO_x .

Most foils were exposed to 31 μA negative or positive coronas for 50h, and some for 166h, at 8 mm gap width. They were extracted with hot water, usually immediately after exposure, and the water-soluble contents of Al^{+++} , NO_x^- (given as NO_3^-), NH_4^- , and F^- were determined by standard chemical methods. The main source of error was the solubility of the corrosion products, which varies with the age of the specimen. The results are summarized as follows.

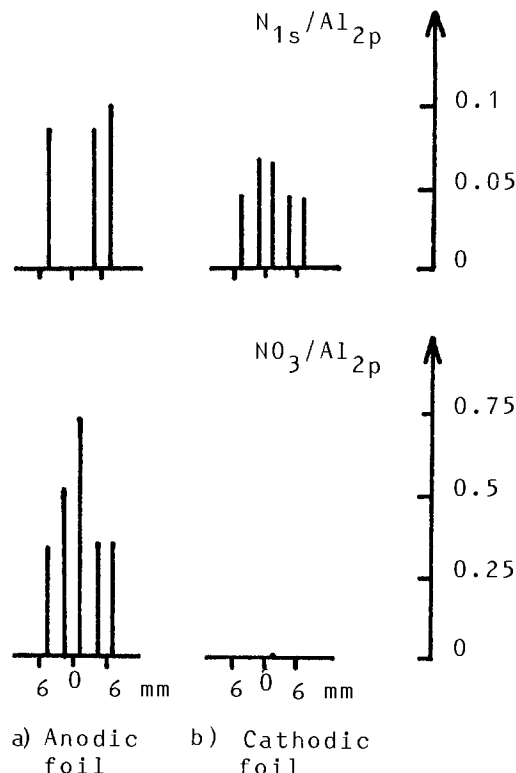


Fig. 11. ESCA analysis of different sections of 15 μm Al foils exposed for 24h to $-20/+20 \mu\text{A}$ negative corona and positive glow corona in 50% RH air. $d = 10 \text{ mm}$. The negative foil had nearly penetrating pits in the central region.

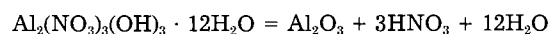
The chamber temperature is the most important parameter both for the weight increase during exposure and for the about equally large weight loss during extraction with water. For foils exposed to 31 μA negative corona for 50h, these quantities fall almost linearly from about 13 mg at 10°C to 3 mg at 70°C.

The relative composition of water-soluble corrosion products shows no clear pattern of variation with corona parameters. The principal ions are Al^{+++} and NO_3^- . NH_4^+ is found in quantity only in samples aged for some months, and is presumably formed from NO_3^- . F^- was always below the 0.003 mg detection limit.

On anode foils in negative coronas and on neutral foils in positive and negative coronas, the Al^{+++} weight percentages in the water soluble layer are scattered in the range 8-14%. On cathode foils in positive coronas, it is about 11% at 70% RH, falling to nearly zero at 30% RH.

The NO_3^- weight percentage in the water soluble layer is usually in the range 35-45% for all foils, positive, negative, or neutral.

It is noted that the hypothetical compound



contains 11% Al and 37% NO_3 . HNO_3 does not attack aluminum under ordinary circumstances, and attempts to corrode foils in air bubbled through HNO_3 were negative. However, the gas exhaust from a corona discharge in air clearly is not an ordinary environment. In particular, the fact that the nature of this environment changes with corona polarity is evident from the data in Table I. The NO_3^- depositing power of the gas from positive coronas is

Table I. Comparative measurements of NO_3^- amounts formed on the Al foils and in the gas by negative and positive coronas

NO_3^- amounts	Negative coronas	Positive coronas
On plane electrodes	$\times 5$	1 (reference)
On neutral foils	$\times 1.3$	1
In exhaust gas	1	$\times 4$

less than that of negative coronas, all other parameters being equal. This agrees with the ESCA results.

Freshly formed corrosion products, mostly a whitish powder, from neutral Al surfaces were readily dissolved in methyl alcohol and introduced into a mass spectrometer with a direct insertion probe facility. The ion source block was kept at 100°C. Mass spectra recorded just after insertion showed large peaks corresponding to NO^+ , N_2O^+ , NO_2^+ , N_2O_2^+ and, particularly, HNO_3^+ . These peaks decreased in height by orders of magnitude within 10 min, thus demonstrating the volatility of the nitrogen containing compounds.

Corona Pitting Rate

Of prime importance is the pitting rate of an anode surface in an air corona and its dependence on parameters like corona current I , local current density $j(r)$, distance from the corona axis r , point-to-plane distance d , air temperature T , and relative humidity RH. From an applied point of view, it would be especially valuable if a critical current density j_c exists below which corrosion is uniform and does not cause pitting. Such a density $j_c \approx 1 \mu\text{A}/\text{cm}^2$ was found previously (5), but the present work lowers this limit to $0.1 \mu\text{A}/\text{cm}^2$.

Methods of measurement.—A point-to-plane corona with a thin foil sample as anode offers several ways to characterize pitting.

First is corona exposure (penetration time t_p , central current density j_0) required for first pit to perforate foil. (Apparatus: Fig. 5b; difficulties: none.)

Second is an increase of foil transparency to light *vs.* time t for given corona parameters. (Apparatus: Fig. 5b; measuring the transparency of the foils to gas flow confirmed that they were not only transparent but also perforated, as also proved by corrosion products observed on the back side; difficulties: corrosion products mask holes to a varying degree.)

Third is radius r_p of foil area containing completely penetrated pits *vs.* exposure time t and current density j at r_p . The macroscopic current density $j(r_p)$ is well known from Warburg's law, Eq. [1]. (Apparatus: Fig. 4, 5b, or others; the foils are removed for microscopic examination; difficulties: sensitivity limit for the detection of small holes.)

Fourth is radius r_c of foil area containing pits, penetrated or not, *vs.* exposure time t and current density $j(r_c)$. (Apparatus: Fig. 4, 5b, or others; the foils are removed for microscopic examination; difficulties: what is a pit?)

It must be stressed that the shape, size, and density of pits are not independent of the Al foil thickness. Pits often stop growing in diameter after penetration, and a thin foil may in this way favor the formation of a high density of small pits. However, no systematic study has been made of this phenomenon.

Dependence on temperature and humidity.—As reported in Ref. (5), all foils exposed in the quad chamber were examined in a microscope to determine the pitted area (the fourth method), the final optical transparency, and the general pit shape. The RH of the air is the determining parameter, regardless of absolute humidity or chamber temperature (Fig. 12). All samples were exposed at gap width 8 mm and with $31 \mu\text{A}$ corona current. The radius r_c could be correlated with current density $j(r_c)$ (Fig. 12). Pitting was found to be most severe around 40% RH, with a minimum current density for pitting of $1.5 \mu\text{A}/\text{cm}^2$. Subsequent exposures of foils in 50% RH air, using maximum (central) current densities $1.5 \mu\text{A}/\text{cm}^2$, seemed to confirm the existence of a critical current density, with only crystallographic attack and no pitting visible, at $1 \mu\text{A}/\text{cm}^2$. However, the following tests show pitting also at lower (off-axis) current densities.

Dependence on corona gap width and current at 50% RH.—First, by *in situ* observations using apparatus Fig. 5b with the photomultiplier replaced by an enlarging objective coupled to a video camera, it was ascertained that

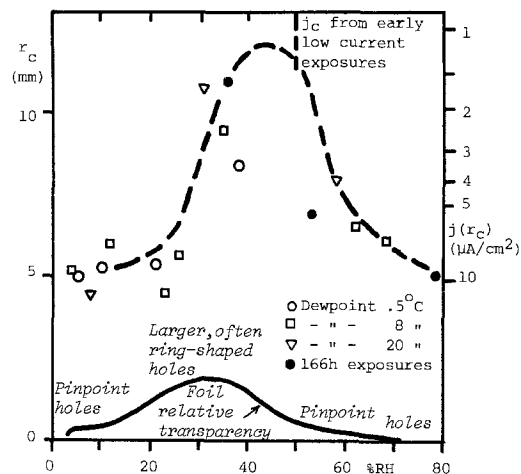


Fig. 12. Pitted area radius r_c , current densities j at r_c calculated using Eq. [1], and foil transparency *vs.* air RH, for $31 \mu\text{A}$, 50h (and 166h) negative corona exposures of $15 \mu\text{m}$ Al foils at $d = 8 \text{ mm}$ (5).

hole formation generally progresses uniformly outwards from the center of the foil. Thus, the first and third methods above were combined, so that the time of appearance of the first central hole was automatically recorded, giving t_p for the central corona-exposure conditions, while the total exposure time gave t_p for holes at radius r_p of the perforated area periphery.

A systematic study of the pitting rate of $15 \mu\text{m}$ thick foils was then carried out at 22°C and 50% RH. The results are presented in Fig. 13a-13c for corona gap widths $d = 5, 7, \text{ and } 10 \text{ mm}$, respectively, as plots of penetration time t_p *vs.* the local current density j . The plots reveal that the exposed surfaces can be divided into two regions: (i) the central inner region of about 2 mm radius, often of metallic appearance, where the pitting efficiency (per unit current density) is very high and dependent on corona gap width and current, and (ii) the outer region, where the pitting rate and efficiency are lower and independent of corona gap width. All points are scattered around the line (Fig. 13d)

$$t_p(\text{h}) = 100j (\mu\text{A}/\text{cm}^2)^{-0.37} \quad [5]$$

If pitting proceeds at a constant rate, Eq. [5] predicts a pit depth growth rate

$$p (\mu\text{m}/\text{h}) = 0.15j (\mu\text{A}/\text{cm}^2)^{0.37} \quad [6]$$

Lines in Fig. 13a-13c are also drawn for the arithmetic averages of the penetration times in the corona center ($r = 0$). These penetration times go through a minimum value in the range $10\text{--}30 \mu\text{A}/\text{cm}^2$, beyond which they increase with current density, in contrast to the penetration times in the outer region.

Till now, we have found no unifying interpretation for these results, but will advance fragmentary, partly conflicting considerations.

1. The difference between the central and the outer regions is connected with the electric wind. As shown experimentally by Fieux and Boutteau (17) and others (15, 25-28) and theoretically by Sigmond (18), this wind forms a narrow jet. When it impinges on the central region, the momentum, energy, and molecules transmitted can (i) dry or blow away any semiliquid electrolyte, explaining the often brilliant looking central patch, and (ii) supply the corrosion process with energy. Note that the shorter penetration times and the brilliant central patches are observed together in the same low current density range. Moreover, the influence of the jet decreases with increasing gap width (19), which could explain why, at $d = 10 \text{ mm}$, the penetration times in the central region do not differ much from those in the outer region.

2. Godard *et al.* (29) state that an increase in the corrosion rate usually entails a more than proportional increase in the pit density, and thus a decrease in the growth rate of the individual pits. In our case, this means longer first

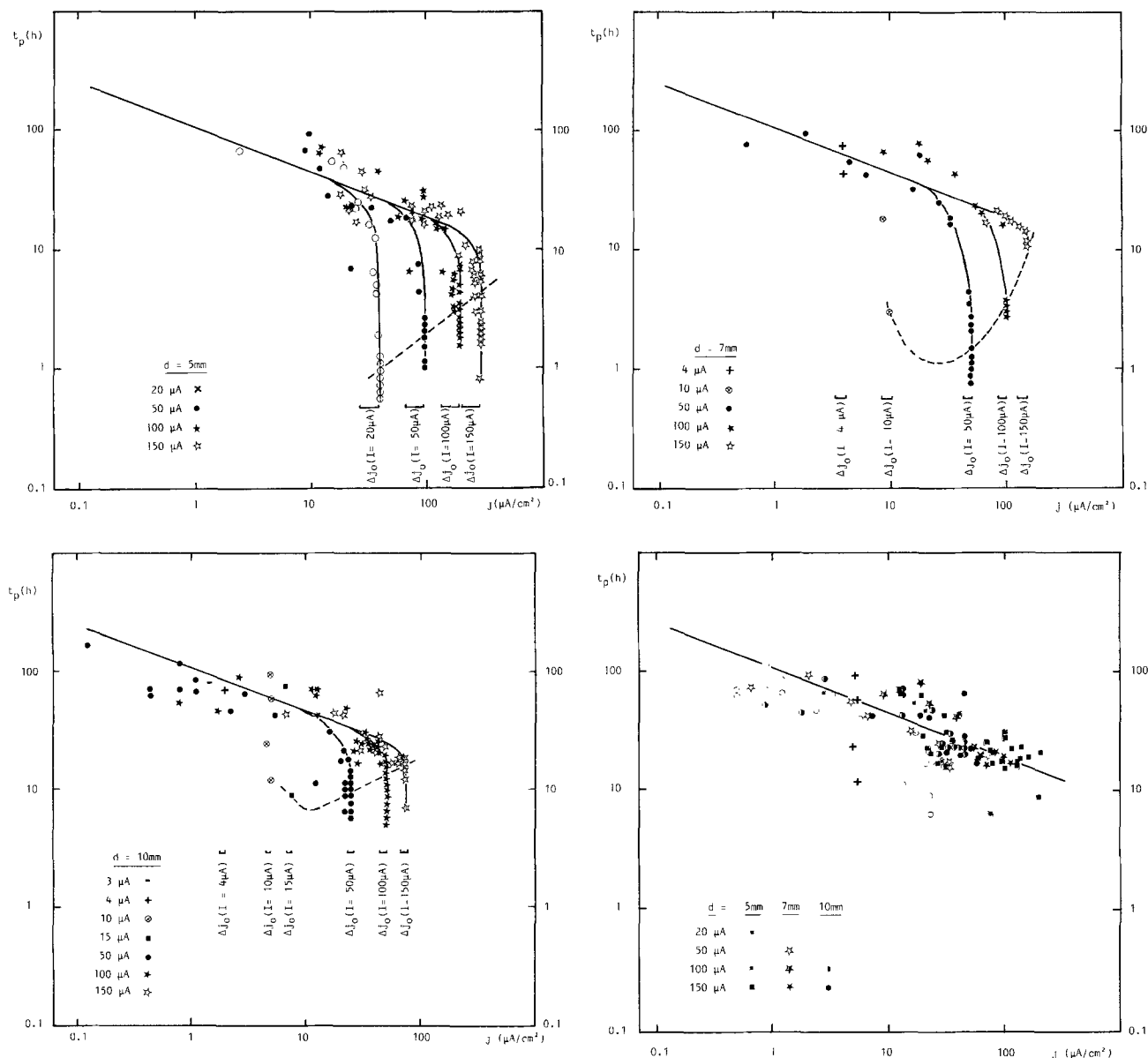


Fig. 13. Plots of penetration times t_p vs. the local current density j for 15 μm Al foils exposed to negative coronas in air of 50% RH at 22°C, with gap widths of 5 mm (a), 7 mm (b), and 10 mm (c), and various corona currents. The Δj_0 bars indicate the points representing holes in a central region of 2 mm radius. The points representing holes outside this region are all plotted together in d, showing that they group along a common line t_p (h) = 100j ($\mu\text{A}/\text{cm}^2$)^{-0.37}. This line is also plotted, for reference, in a, b, and c with lines joining the points of the central region. The dashed lines represent the arithmetic averages of the t_p values on the corona axis.

pit penetration times at higher current densities, as observed in the central region, which is simultaneously subjected to ion flow and to electric wind effects. However, it also entails that holes should first appear far outside the center and then spread inwards. Annular perforated regions have sometimes been observed, but not regularly.

The present measurements give no clear support to our earlier inference (5) of a critical current density for pitting around 1 $\mu\text{A}/\text{cm}^2$. Admittedly, we do not know the real local current density at the spot where a pit is formed, but we have observed off-axis holes formed at macroscopic current densities down to 0.1 $\mu\text{A}/\text{cm}^2$ (Fig. 13c).

Pitting in special geometries.—To get a clearer picture of the influence of the electric wind, two special corona arrangements were tested.

Counterflow.—A suction tube was centered around the stem of the point in an open-air point-to-plane corona, and the suction velocity regulated to reverse the electric wind flow without substantial effects on the electrical corona characteristics or on the much faster ion flow (30). Pit penetration times t_p for the central foil region were increased from their previous low values to values closer to

the curve t_p (h) = 100j ($\mu\text{A}/\text{cm}^2$)^{-0.37} characterizing the outer region.

Inclined point.—Space-charge-controlled ion flow to the plane in a point-to-plane corona is nearly unaffected by the point geometry, while the electric wind jet is directed nearly along the normal to the point surface at the corona cathode spot. Thus, when the point electrode axis was inclined 45° to the foil normal, the current density distribution along the foil was nearly unaffected, with a maximum directly under the point (Fig. 14b). The electric wind jet, on the other hand, was seen by laser light/smoke photographs to flow at ~ 30° to the foil normal (Fig. 14a). In this way, the ion current maximum and the wind jet impact area were separated. The resulting foil corrosion is shown in Fig. 14c. The strongly corroded region, with holes, has now moved nearly to the jet impact area. Between this area and the point electrode direction is seen a spiked extension of the metallic looking area. Farther away, a second perforated area was sometimes found. The point itself was symmetrically etched by the corona, as for a perpendicularly placed point electrode.

The counterflow and inclined-point experiments, together with experiments with an insulated foil behind an

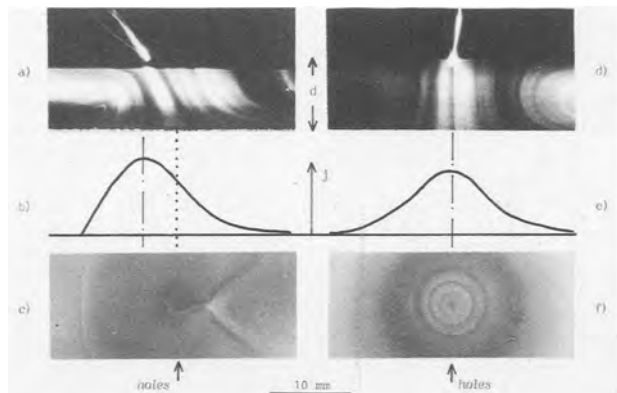


Fig. 14. The inclined point experiment. a: Laser/smoke photograph of the burning negative corona (at $d = 10$ mm, $I = 50$ μ A). b: Measured current density profile. c: Photograph of the Al foil exposed for 24h to the 50 μ A negative corona. d, e, and f: As a, b, c, respectively, but with a perpendicular point.

anode grid, show conclusively that the jet alone causes no noticeable pitting, but that it strongly accelerates the pitting action of the negative charged current to the foil. Experiments with 12 μ m thick Al foils covered by a temperature indicating liquid crystal layer on the back side confirmed that the temperature rise due to the jet plus corona current is only a few degrees (19, 30), which indicates that the jet action cannot be purely thermal.

Pitting in ac coronas.—AC (50-60 Hz) coronas are of importance in high voltage lines and equipment. Preliminary tests in the quad chamber showed that foils exposed to ac corona were pitted to a degree corresponding to the negative corona exposure time, as is expected. This result is of relevance to structures exposed to the corona from highly stressed conductors.

AC (or dc) high voltage lines, however, are not well represented by our point-to-plane corona experiments. Even when such lines receive negative charges emitted by a neighboring line, or emitted by themselves in the preceding half-cycle, the conditions are different from those of our anode foils. The electric field near the line is high, leading to collisional destruction (detachment) of negative ion complexes (31) and even to renewed ionization, and the electric wind is modified or even reversed.

To test for possible corona corrosion effects, one 1 mm diam Al wire and one 1 mm diam Al alloy wire were driven for one week at 50 kV ac with 7.5 μ A/cm² ac corona current in air 20°C 50% RH. Microscopic examination showed that the wire surfaces turned grayish, but no pitting was found. Fatigue tests showed no significant change in strength, thus scientifically confirming the fairly well-established empirical fact that high voltage lines can be driven with some kilowatt per kilometer corona power losses and still last for many years. However, corona corrosion effects on metal parts (line supports, etc.) near corona spots may be serious, although they may easily and wrongly be diagnosed as corrosion caused only by climatic conditions.

Discussion

We first sort out the factors that dominate various aspects of the corrosive media on and just in front of the plane surface electrode. We then discuss the corona corrosion phenomena in an attempt to coordinate our findings with recent electrochemical studies of aluminum in aqueous media.

Charged and neutral particle flows to the plane electrode.—Each ion or electron impinging on the low-field electrode in a point-to-plane corona will impart energy (32)

$$W = W_{\text{heat}} + W_{\text{ionization}} + W_{\text{work function}} \leq 10\text{-}15 \text{ eV} \quad [7]$$

which is always less than 1% of the total energy delivered to each charged particle by the applied field. Thus, for

each charged particle we expect a substantial number of activated neutrals, which are driven in a gas jet toward the plane by the momentum imparted to the gas by the moving charges. Calorimetric measurements (19, 30) show that about 50% of the total power input to a 50 μ A negative point-to-plane air corona of 3 mm gap width is transferred to the plane by the electric wind, and that the relative power transferred falls with increasing current and distance as $I^{-1/2}$ and d^{-1} , respectively. The corresponding surface temperature increases are usually small ($< 10^\circ\text{C}$).

Let us now compare the diffusive flux of neutral particles to the plane with that of ionized species for the case of water. For H_2O molecule flux by thermal movement

$$J_{\text{Ht}} = n_{\text{H}_2\text{O}} \bar{v} / 4 = 4.4 \times 10^{25} \text{ molecule/m}^2\text{-s} \quad [8]$$

taking $n_{\text{H}_2\text{O}} \approx 3 \times 10^{23} \text{ m}^{-3}$ (50% RH at 20°C) and $\bar{v} = 590$ m/s. For H_2O , flux carried as water of hydration by the current, if each ion is singly hydrated

$$J_{\text{Hc}} = j/e \approx 3 \cdot 10^{18} \text{ molecule/m}^2\text{-s}, \approx 10^{-7} J_{\text{Ht}} \quad [9]$$

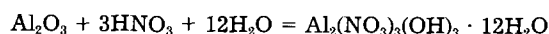
for a 100 μ A, 1 cm point-to-plane corona. Thus, even trace quantities of neutral species in the electric wind are expected to influence the plane electrode surface more than the same species carried selectively by the ions. Note, however, that hydrated ions may carry the water and energy to where they are needed for a specific reaction.

The interaction of the impinging charges with the surface layer depends on the sign of the charges and the nature of the layer. If the charge transfer process is electronic, positive ions will be neutralized and negative ions will lose their electrons, leaving activated neutral particles which probably differ little from those impinging in far greater numbers via the electric wind. If, however, surface layers like $\gamma\text{-Al}_2\text{O}_3$ form, through which charge transport is almost exclusively ionic, then the current density will determine the surface layer potential drop, and the ions (plus neutrals) will be the major constituents in the electrochemical processes.

A recent study (33) of neutral gaseous reaction products from atmospheric pressure air coronas very similar to ours shows these to be O_3 and NO_x . In our corona current range, O_3 production always dominates, in negative and positive coronas. The NO_x production is lower for negative than for positive coronas, in agreement with our exhaust gas measurements (see above). The large amounts of dissociated and excited nitrogen and oxygen in coronas were not directly measured, but are inferred from calorimetric studies (19, 30). Furthermore, it follows from different gas discharge studies (34-36) that the material of the electrodes can have a significant influence on the gas chemistry.

A mass spectrographic study (37) of the ions arriving at the plane electrode in 22 mm, 20 μ A point-to-plane coronas in 50% RH ambient air at 40 kPa shows, in positive coronas the series $\text{H}^+(\text{H}_2\text{O})_n$, $\text{NO}^+\text{NO}(\text{H}_2\text{O})_n$, and $\text{NO}_2^+(\text{H}_2\text{O})_n$ with maxima at $n > 10$, and in negative coronas $\text{CO}_3^-(\text{H}_2\text{O})_n$, $\text{O}_2^-(\text{H}_2\text{O})_n$, $\text{O}_3^-(\text{H}_2\text{O})_n$, and $\text{NO}_2^-(\text{H}_2\text{O})_n$ with maxima near $n = 2$. The conditions in our shorter, higher current coronas at atmospheric pressure should not be significantly different.

To sum up, the front surfaces of our Al foil specimens are subjected to an air flow containing H_2O (according to the RH), O_3 , and NO_x as the main neutral additions, comparable amounts of excited/dissociated N_2 and O_2 , and hydrated H^+ , NO^+ , and NO_2^+ (positive coronas) or hydrated CO_3^- , O_2^- , O_3^- , and NO_2^- (negative coronas). The observed wet surface layers are probably formed because of the hygroscopic properties of the Al- and N-oxides. As noted above, the NO_x^- and Al^{+++} percentages in the water soluble part of our anodic corrosion layers correspond to the hypothetical compound of



Comparison between electrochemical corrosion phenomena in coronas and aqueous solutions.—Our earlier experiments (5) indicated that only crystallographic attack occurs in coronas below about $1 \mu\text{A}/\text{cm}^2$, while our later observations have lowered this possible limit to $0.1 \mu\text{A}/\text{cm}^2$. The concept of a critical anodic current density for pitting may sound strange in a field where the notion of a critical pitting potential is firmly entrenched (38, 39). However, in the case of aluminum, Nguyen and Foley (40) have misgivings in reconciling a critical potential with the essentially chemical process of pitting by soluble complex formation. We shall see that the two concepts of critical current density and critical potential are not mutually exclusive theoretically or experimentally, even for aqueous electrolytes.

Experimentally, the onset of pitting in aqueous electrolytes is accompanied by marked current or voltage fluctuations, depending on the power supply impedance. Inspection of published curves (2, 39) reveals that on little-corroded surfaces these fluctuations start at current densities around $1 \mu\text{A}/\text{cm}^2$. Furthermore if Al is anodized for a given time in a nonpitting electrolyte above the critical potential (-0.55V SHE for Cl^-) and a pitting agent added, a certain induction time elapses before the onset of the current fluctuations that signify pitting. The induction time increases with the previous anodizing time and is presumably the time needed for (spotwise?) thinning of the barrier layer to a certain thickness where pitting can start. But such a given thickness of barrier oxide has a reasonably unique resistivity, which means that a reasonably unique ratio exists between critical potential and critical current density. Videm (2) suggests, in agreement with Hoar and Yahalom (41), that only O^{--} anions may migrate through $\gamma\text{-Al}_2\text{O}_3$ below $550 \text{ V}/\mu\text{m}$, while at higher fields outward migration of Al^{+++} also will take place. Also, below $550 \text{ V}/\mu\text{m}$, the transformation rate of $\gamma\text{-Al}_2\text{O}_3$ to porous oxides was found to be faster than the $\gamma\text{-Al}_2\text{O}_3$ production at the metal-oxide interface.

The above considerations about the initiation of pitting should apply equally well to corona exposure of anodic foils in medium and high humidity air, where a semiliquid layer accumulates on the surface, outside of the region most affected by the electric wind. The local current density here certainly is a more appropriate parameter than the surface potential, because of the galvanostatic character of the corona, *i.e.*, the current at the surface is controlled by the resistance of the gas phase.

When a sufficiently deep pit has formed in a corona or in an aqueous environment, the conditions inside and outside a pit are no longer the same. If the dissolved complexes are positive ions, they will attract more anions and thus lower the critical pitting potential inside the layer (42, 43). In water-starved coronas, the production of hydrated complexes may exhaust the water supplied by diffusion into the pit, so that anions and cations must move by jumping from one hydrated layer to the next, with free water available only at the boundary between the semi-solid layers and the outside electrolyte (42). The electric field inside developed pits may then be high, in agreement with our observation of light emission from the back side of corona perforated foils (see above). Our observations of insulating pit walls in coronas are paralleled by those of Edeleanu (44) in the case of liquid electrolytes.

As for the structure and composition of the corona corrosion products, the results described in the previous section indicate that layers uniformly corroded (anodized) in dry air are simply hard aluminum oxide without any well-defined structure. The products of corona pitting probably start out as a mixture of $\text{Al}(\text{NO}_3)_3$, $\text{Al}(\text{OH})_3$, and intermediate compounds, all in various stages of hydration and often in a glassy liquid form. With time, on heating, or by exposure to vacuum, this converts to oxide containing less and less nitrate and water. These consequences of a drier environment are the main differences between Al corrosion products of negative coronas in air and of anodic pitting in nitrate solutions.

Thus, the major difference between anodic Al corrosion in a humid air corona and in an aqueous electrolyte lies in the existence and effects of the electric wind. For aqueous electrolytes, a suitable counterpart would be a liquid jet containing free radicals. The experiments described in the previous section leave no doubt about the important synergetic effects of the electric wind when combined with the charged particle influx. However, at present, virtually nothing is known about the precise mechanisms involved.

Conclusion

We have reported the present state of knowledge about corrosion of anodic surfaces in unipolar corona discharges in air, a phenomenon that first appeared in the literature in 1979 (4). The workers in this field are few, the corona-exposure times long, and the diagnostics costly and difficult, which is our excuse for the incomplete and even fragmentary nature of some of the data. We are, however, confident that we have proved the following.

1. The low field (drift) region of a humid air corona acts as an efficient pitting electrolyte on anodic metal surfaces. Cathodic low field surfaces (in positive coronas) are pitted at least ten times less.
2. The basic corona pitting mechanism in humid air is, in principle, not different from anodic pitting in aqueous nitrate electrolytes.
3. The corona pitting efficiency is much amplified by the impinging "electric wind" from the active (point) corona electrode. This wind contains much of the corona energy in form of heat and excited neutral particles, but does not cause pitting without the simultaneous influx of charged particles (synergism).
4. AC (50-60 Hz) point-to-plane coronas cause pitting corresponding to their negative half-cycles. Corona from/to high voltage ac lines will not cause significant pitting on the lines themselves, but corona from high voltage dc lines will certainly pit nearby metal.
5. Corona discharge (as from a point or wire at 5-15 kV) changes the surrounding air into a unipolar gaseous electrolyte, which will have roughly the same detrimental or beneficial effects on nearby objects as an aqueous nitrate electrolyte. Thus, for instance, certain corrosion resistance tests will be possible on structures *in situ* without the need for liquid test cells.

Acknowledgments

We gratefully acknowledge discussions and assistance from M. Goldman, and technical assistance from R. Baumgartner (both LPD, Ecole Supérieure d'Electricité, Gif, France) and from R. Dahl and D. Brenna (ELION, Norwegian Institute of Technology, Trondheim, Norway). The kind advice from the Divisional Editor Dr. R. P. Frankenthal is much appreciated. This work has received support from CNRS (France), NTNF (Norway), and via the Cultural Interchange programs of the two countries. It was partly done within the program of the Franco-British Research Group on Gas Discharges.

Manuscript submitted June 8, 1984; revised manuscript received Aug. 20, 1985.

CNRS and NTNF assisted in meeting the publication costs of this article.

REFERENCES

1. V. V. Skorchelletti, "Theory of Metal Corrosion," Israel Program for Scientific Translations, Jerusalem (1976).
2. K. Videm, "The Electrochemistry of Uniform Corrosion and Pitting of Aluminium," Kjeller Report KR-149, Institute for Atomic Energy, Kjeller, Norway (1974).
3. G. E. Thompson and G. C. Wood, in "Treatise on Materials Science and Technology," Vol. 23, S. C. Scully, Editor, Chap. 5, Academic Press, London (1983).
4. A. Goldman and R. S. Sigmond, *J. Phys. C*, **40**, 443 (1979).
5. R. S. Sigmond, A. Goldman, and D. Brenna, in "Pro-

- ceedings of the 6th International Conference on Gas Discharges and their Applications," Part 1, p. 82, IEE Conference Publication 189, IEE, London (1980).
6. A. Goldman and J. Amouroux, in "Electrical Breakdown and Discharges in Gases," NATO ASI Series, Vol. B.89b, E. E. Kunhardt and L. H. Luessen, Editors, p. 293, Plenum Press, New York (1983).
 7. M. Goldman and R. S. Sigmond, *IEEE Trans. Electr. Insul.*, **ei-17**, 90 (1982).
 8. R. S. Sigmond and M. Goldman, in "Electrical Breakdown and Discharges in Gases," NATO ASI Series, Vol. B.89b, E. E. Kunhardt and L. H. Luessen, Editors, p. 1, Plenum Press, New York (1983).
 9. R. S. Sigmond, *J. Appl. Phys.*, **53**, 891 (1982).
 10. G. Buchet and A. Goldman, in "Proceedings of the 1st Int. Conf. on Gas Discharges," p. 459, IEE Conference Publication 70, IEE, London (1970).
 11. R. Le Ny, These Docteur 3e Cycle, Université Nantes, Nantes, France (1981).
 12. R. Le Ny, in "Electrostatics 1983: Proceedings of the 6th Conference on Electrostatic Phenomena," p. 173, Institute of Physics Conference Series 66, Institute of Physics, Bristol, England (1983).
 13. E. Warburg, *Wied. Ann.*, **67**, 69 (1899).
 14. E. Warburg, in "Handbuch der Physik," Vol. 14, p. 154, Springer-Verlag, Berlin (1927).
 15. A. Goldman, E. O. Selim, and R. T. Waters, in "Proceedings of the 5th Int. Conf. on Gas Discharges," p. 88, IEE Conference Publication 165, IEE, London (1978).
 16. Y. Kondo and Y. Miyoshi, *Jpn. J. Appl. Phys.*, **17**, 643 (1978).
 17. R. Fieux and M. Boutteau, *Bull. Dir. Etudes Recherch. EDFB*, **2**, 55 (1970).
 18. R. S. Sigmond, in "Proceedings of the 7th International Conference on Gas Discharges and their Applications," p. 140, Peregrinus, London (1982).
 19. A. Goldman, in "Proceedings 3rd International Conference on Gas Discharges," p. 275, IEE Conference Publication 118, IEE, London (1974).
 20. R. S. Sigmond and M. Goldman, in "Electrostatics 1983: Proceedings of the 6th Conf. on Electrostatic Phenomena," p. 81, Institute of Physics Conference Series 66, Institute of Physics, Bristol, England (1983).
 21. M. Goldman and A. Goldman, in "Gaseous Electronics," Vol. 1, M. N. Hirsh and H. J. Oskam, Editors, Chap. 4, Academic Press, New York (1978).
 22. R. S. Sigmond, in "Electrical Breakdown of Gases," J. M. Meek and J. D. Craggs, Editors, Chap. 4, John Wiley and Sons, New York (1978).
 23. A. Goldman, I. D. Chalmers, and J. L. Dorémieux, in "Proceedings of the 4th International Symposium on High Voltage Engineering," Paper 32.07, National Technical University, Athens (1983).
 24. T. H. Nguyen and R. T. Foley, *This Journal*, **127**, 2563 (1980).
 25. A. Boulloud and J. Charrier, in "Proceedings of the 6th International Conference on Gas Discharges and their Applications," Part 1, p. 110, IEE Conference Publication 189, IEE, London (1980).
 26. J. Dubois, *J. Phys. D*, **13**, 405 (1980).
 27. A. Kurimoto and O. Farish, *Proc. IEE*, **127A**, 89 (1980).
 28. N. G. Douglas, I. S. Falconer, and J. J. Lowke, *J. Phys. D*, **15**, 665 (1982).
 29. H. P. Godard, W. B. Jepson, M. R. Bothwell, and R. L. Kane, "The Corrosion of Light Metals," John Wiley and Sons, New York (1967).
 30. A. Goldman, in "Proceedings of the 3rd International Symposium on High Voltage Engineering," Paper 53.12, IEEE North Italy Section, Milan, Italy (1979).
 31. R. S. Sigmond, in "Proceedings of the 16th International Conference on Phenomena in Ionized Gases," Invited Papers Vol., Düsseldorf University, Düsseldorf (1983).
 32. M. Goldman, A. Goldman, and R. S. Sigmond, *Pure Appl. Chem.*, **57**, 1353 (1985).
 33. R. Peyroux and R. M. Millot, in "Proceedings of the 7th International Conference on Gas Discharges and their Applications," p. 173, Peregrinus, London (1982).
 34. M. Goldman, M. Lécuyer, and M. Palierne, in "Gaseous Dielectrics III: Proceedings of the 3rd International Symposium on Gaseous Dielectrics," L. G. Christophorou, Editor, p. 327, Pergamon Press, New York (1982).
 35. J. Amouroux, M. F. Revoil, and M. Goldman, in "Proceedings of the 5th International Symposium on Plasma Chemistry," p. 388, Heriot-Watt University, Edinburgh, Scotland (1981).
 36. M. P. Bergougnan, A. Gicquel, and J. Amouroux, *Rev. Phys. Appl.*, **18**, 335 (1983).
 37. R. Peyroux, P. Coxon, and J. Moruzzi, in "Proceedings of the 7th International Conference on Gas Discharges and their Applications," p. 169, Peregrinus, London (1982).
 38. K. Nisancioglu and H. Holtan, *Corros. Sci.*, **18**, 835 (1978).
 39. K. Nisancioglu and H. Holtan, *ibid.*, **18**, 1011 (1978).
 40. T. H. Nguyen and R. T. Foley, *This Journal*, **126**, 1855 (1979).
 41. T. P. Hoar and J. Yahalom, *ibid.*, **110**, 614 (1963).
 42. Yu. A. Popov, Yu. V. Alekseev, and Ya. M. Kolotytkin, *Sov. Electrochem.*, **14**, 1260 (1978); *ibid.*, **14**, 1390 (1978); *ibid.*, **15**, 342 (1979); *ibid.*, **15**, 449 (1979); *ibid.*, **15**, 564 (1979); *ibid.*, **15**, 568 (1979); *ibid.*, **15**, 770 (1979); *ibid.*, **15**, 774 (1979); *ibid.*, **15**, 926 (1979).
 43. N. Sato, *This Journal*, **129**, 255 (1982); *ibid.*, **129**, 260 (1982).
 44. C. Edeleanu, *J. Inst. Metals*, **89**, 90 (1960-1961).

Surface Composition of Stainless Steels during Anodic Dissolution and Passivation Studied by ESCA

I. Olefjord, B. Brox, and U. Jelvestam

Department of Engineering Metals, Chalmers University of Technology, S-412 96 Göteborg, Sweden

ABSTRACT

A molybdenum containing austenitic steel was exposed in hydrochloric acid at various potentials in the active and passive ranges of the alloys. The surface compositions were analyzed by the ESCA technique. The influence of pretreatment by ion bombardment and mechanical polishing on the passivation behavior was investigated. The passive film formed on the surface consists mainly of a mixed Fe-Cr-Mo oxide. The average content of Cr^{3+} in the oxide is about 70%. The inner layers of the oxide product consist mainly of Cr oxide. The Ni content in the oxide is low. The concentration and the chemical state of Mo is potential dependent. At low potentials in the passive range, the four-valency state is predominant, while at high potentials Mo exists mainly in its six-valency state. On the surface of the oxide, a layer of hydroxide is present. Chloride ions are incorporated into the passive film. The thickness of the passive film increases with the potential in the passive range from 10 to 15 Å. The composition of the metal phase changes during active dissolution. Thus, the alloying elements are enriched on the surface and thereby control the dissolution rate, control overpotentials, and provoke passivation of the alloy.

Stainless steels belong to a class of metals and alloys which protect themselves by forming reaction products on their surfaces. The so-called passive film consists mainly of oxides, and its thickness is in many cases only a few atomic layers. The corrosion behavior of the steel is dependent on the properties of the passive film. The composition of the film is determined by the composition of the alloy and by the environmental conditions to which the steel is exposed. Exposure of the steel in chloride or other halogen ion environments may cause breakdown of the passive film followed by localized attack of the metal. Binary Fe-Cr alloys are especially susceptible to localized attack. By alloying these steels with Ni and Mo, the resistance against localized attack is markedly improved, but even high alloyed steels may be attacked in higher chloride containing acid solutions at least at elevated temperature. Thus, localized corrosion attack on stainless steels is one of the most serious problems in the use of these alloys. Therefore, it is important to clarify the factors controlling the chemical composition and the stability of the passive film.

By using surface-sensitive techniques (ESCA and Auger) (1-12) it has been possible in the past to get information about the composition of very thin reaction products formed on the surfaces. The ESCA method is unique in the sense that it gives information about the chemical state of the elements. The method allows us to estimate the thickness of the passive film due to the fact that the mean free path of the photoelectrons is of the same order of magnitude as the thickness of the film.

It has now been clarified that the passive film formed on austenitic steels consist mainly of Cr oxide, that the Ni content in the film is very low, and that Mo is present in the oxide. In earlier work (7, 10-12), it has been demonstrated that Fe is selectively dissolved during passivation. The alloying elements are thereby enriched on the surface in their metallic states.

The aim of this paper is to describe the surface condition of an austenitic stainless steel during its dissolution and passivation in a hydrochloride aqueous solution. Attention is directed to interpretation of the chemical states of the elements of the passive film and the distribution of chloride ions in the film.

Experiments

The polarization experiments were performed in an electrochemical cell connected to the preparation system of the ESCA instrument. Figure 1 shows a schematic view of the instrumentation. It consists of separate ESCA (HP 5950 A) and Auger (PHI 545) analyzers. The sample-preparation system allows simultaneous and independent analyses of both instruments. The electrochemical cell consists of a Teflon vessel with an opening to which the

specimen is tightly screwed. A soft Teflon gasket prevents leakage. The cell is equipped with a Pt counterelectrode and an external reference electrode (SCE). The potential was controlled by a potentiostat (Wenking POS73). The solution was mechanically stirred in the cell and deaerated by argon bubbling. Before the electrolyte was used, it was deaerated by argon bubbling for 2h. The closed glass vessel in which the cell is located is streamed through by argon gas during the experiment and during transfer of the sample to the vacuum system. The arrangement is designed to minimize contact between the surface and oxidizing gases.

The steel used is a commercial austenitic stainless steel. Its composition, in weight percent, is: 0.040C, 0.62Si, 1.64Mn, 0.020P, 0.003S, 16.7Cr, 15Ni, 4.28Mo, 0.1Cu, 0.27Co, 0.27N, balance Fe. The electrolyte was 0.1M HCl + 0.4M NaCl. The samples were pretreated by polishing on emery paper to 600 grit finish and then electropolished in perchloric acid. Before exposure in the acid, the samples were either ion etched or mechanically polished on Al_2O_3 powder, grain size $\sim 0.3 \mu\text{m}$. The two different pretreatments were used to clarify their influence on the composition of the passive film.

Immediately after ion etching or grinding, the sample was fixed at the cell and the electrolyte was poured into the cell. The potential of the sample was applied in the following sequence: cathodic range, -450 mV for 10 min; corrosion potential for 5 min; cathodic potential -450 mV for 10 min; the chosen passive potential or corrosion potential. The dissolution at the corrosion potential was performed to dissolve the outer atomic layers of the metal and thereby obtain a surface state representing a self-corroding condition.

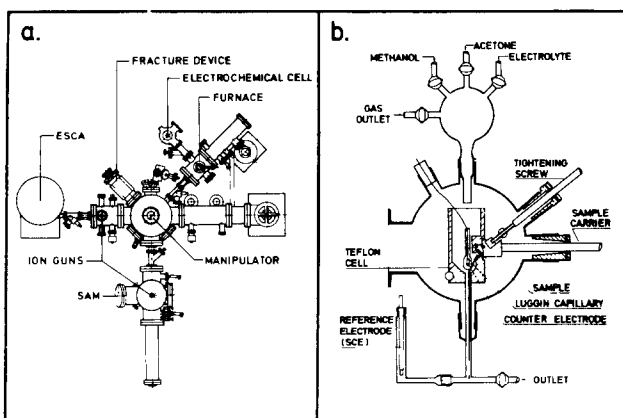


Fig. 1. a: The ESCA/Auger instrument. b: The electrochemical cell

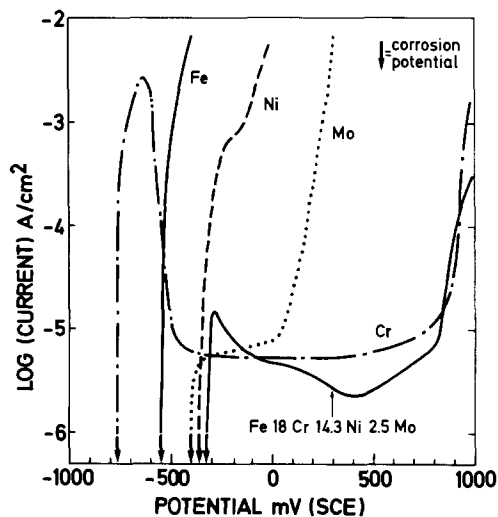


Fig. 2. Polarization diagrams

Anodic polarization curves were recorded in the test solution for the alloy and the pure metals Fe, Cr, Ni, and Mo. The samples were activated in the way described above and then swept in the anodic direction (20 mV/min). The anodic polarization curves are shown in Fig. 2. It appears that Cr is the only element which is passivated over a wide range in this solution. The passivation range of the alloy is almost as wide as for pure Cr. One difference between Cr and the alloy is that the maximum current density in the active range is about two orders of magnitude higher for Cr than for the alloy. Figure 2 also shows that Cr is the least noble of the elements. It also appears that the corrosion potential of the alloy is slightly higher than the corrosion potential of Ni and Mo.

Calibration

The chemistry of the passive film is very complex. The interpretation of the ESCA spectra, in particular Cr and Mo signals, is not straightforward. Therefore, the spectra of these elements recorded from pure metals, alloys, and compounds will be described in detail.

The metallic state of Cr $2p_{3/2}$ is shown in Fig. 3a. The two peaks, the solid and the point-dashed, are recorded from ion-etched pure metal and the alloy, respectively. The peak representing the pure metal is significantly narrower than the peak representing the Cr peak in the alloy. The full width at half maximum of the two peaks are 1.6 and 2.4 eV, respectively. The broadening is characteristic for the elements Cr and Mo in the alloy. The peaks in the spectra representing Fe and Ni in the same alloy are not broadened compared to the peaks obtained from the pure metals. This observation indicates that in an alloy containing Cr and Mo these alloying elements interact with each other in the surface region.

The spectra shown in this paper are the as-recorded signals. The signals are split into their components by using a gaussian/lorentzian distribution. For example, the solid and the dashed peaks in Fig. 3b represent the metallic and the oxide states of Cr, respectively. The solid inverse S-curve is the background, and the dotted curve is the sum of the background and the peaks representing the metallic and oxide states. The dotted curves are shown to demonstrate how well the deconvoluted states represent the recorded peak.

The rows b and c in Fig. 3 show the Cr and the oxygen spectra recorded after oxidation of pure Cr at 500°C in oxygen, 10^{-4} torr, for 0.5 and 5 min, respectively. The oxidation was performed in the preparation chamber. The short oxidation time gives an oxide that only partly covers the surface. The contribution from the metallic state of Cr, binding energy BE = 573.8 ± 0.2 eV, is easily readable. [The spectrometer is calibrated by setting the binding energies of carbon (graphite) and Ni to 284.3 and 852.8 eV, respectively.] The binding energy of the oxide state

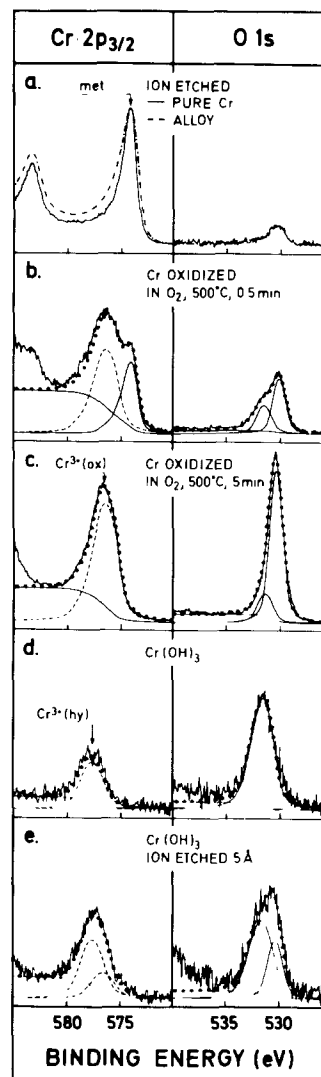


Fig. 3. ESCA spectra recorded from Cr and oxygen. a: Ion-etched pure Cr and Fe18Cr14.3Ni2.5Mo (a/o). b and c: Cr oxidized in O₂. d: Cr(OH)₃. e: Cr(OH)₃ ion-etched 5 Å.

(dashed curve) is 2.5 eV higher than BE of the metallic state (the chemical shift). After oxidation for prolonged time (Fig. 3c), the surface is completely covered by the oxide. The position of the oxide state of Cr, BE = 576.3 eV, is the same as after oxidation for short time. The recorded oxygen signal consists of two peaks. The main peak at 530.0 eV corresponds to oxygen in Cr₂O₃, while the small peak at 531.4 eV represents oxygen in hydroxide.

Figure 3d shows the spectra recorded from Cr(OH)₃. This compound was produced from an aqueous solution, pH = 3, containing 0.01M CrCl₃ to which one droplet of concentrated NH₄OH was added. The solid product from the reaction, CrCl₃(aq) + 3NH₄OH(aq) → Cr(OH)₃(s) + 3NH₄Cl(aq), was allowed to settle on a gold support on the bottom of the reaction cup. After dilution and drying, the sample was moved to the ESCA instrument. The spectra show that the positions of Cr and oxygen signals are shifted to higher binding energies. The shifts compared to Cr₂O₃ are 0.8 and 1.4 eV, respectively. The ratio between the intensities of oxygen and Cr³⁺ is 1.5. This is about twice as much as obtained from the Cr oxide. The difference in chemical shifts for Cr³⁺ and oxygen in oxide and hydroxide gives information on the structure of the passive film. However, as shown in Fig. 3e, a slight ion etching of Cr(OH)₃ noticeably changes the spectra: extra peaks appear on the low binding energy sides of the main peaks; the positions of these peaks correspond to the positions of Cr³⁺ and O²⁻ in Cr₂O₃. Thus, ion etching of Cr(OH)₃ decomposes it to Cr₂O₃. [SiO₂ is used as cali-

brating compound for the ion etching rate.] Prolonged ion etching increases the relative amount of transformed compounds and gradually a stationary state is reached. After ion etching to 100Å below the original surface, the intensity of the signal corresponding to the oxide state is three times higher than the intensity of the hydroxide state. This experiment has been reported earlier (3). In that case, it was also shown that heating of $\text{Cr}(\text{OH})_3$ in vacuum causes the same effect as ion etching. In this study, it was also found that $\text{Cr}(\text{OH})_3$ is transformed to Cr_2O_3 when bombarded with low energy electrons (10 eV) from a flood gun (normally used for neutralizing the surface of an insulator during ESCA analysis).

Figure 4 shows Mo 3d and signals recorded from pure Mo and oxide products. The binding energy of Mo $3d_{5/2}$ in its metallic state is 227.4 eV. The full width at half maximum is 1.0 eV. From the alloy, the corresponding width is 1.2 eV. The spectra in the rows b and c were obtained after oxidation in dry oxygen and H_2O vapor, respectively. Oxidation in pure oxygen, 1 torr, at 400°C for 10 min gives MoO_3 . The binding energy of the six-valency state of Mo $3d_{5/2}$ is 232.2 eV (chemical shift is 4.8 eV). Oxidation in H_2O vapor gives a completely different spectrum. Figure 4c shows the signals recorded after oxidation in H_2O vapor, 1 torr, at 720°C. The position of the peak at BE = 229 eV, marked Mo^{4+} , is found to be the same as in MoO_2 . The signal marked "hy" is an extra peak located between the six- and the four-valency states of Mo. The binding energy of this state is 230.6 eV. (Chemical shift is 3.2 eV.) It is broader than the Mo^{4+} and the Mo^{6+} signals. The position of the peak representing the four-valency state is strongly dependent on the coordination of the Mo^{4+} ions. Thus, it is expected that Mo^{4+} peaks recorded from pure MoO_2 and from a mixed oxide containing Mo^{4+} are not situated in the same positions. It was suggested in Ref. (12) that the Mo^{hy} peak represents the four-valency state in an oxyhydroxide. Indications underlying this statement are the broadening of the peak and the shift of its position. The latter is characteristic for hydroxide, for example, $\text{Cr}(\text{OH})_3$ discussed above and $\text{Ni}(\text{OH})_2$ (13). An extensive study of the oxides of Mo will be published later (14).

The composition and the thickness of the passive film were obtained from the expressions (11)

$$I_M^{\text{ox}} = D_M^{\text{ox}} S_M^{\text{ox}} (1 - \exp[-\alpha^{\text{ox}}/(\lambda_M^{\text{ox}} \sin 38.5)]) \exp(-\alpha^c/(\lambda_M^{\text{ox}} \sin 38.5)) \quad [1]$$

$$I_M^{\text{met}} = D_M^{\text{met}} S_M^{\text{met}} \exp[-(\alpha^{\text{ox}} + \alpha^c)/(\lambda_M^{\text{ox}} \sin 38.5)] \quad [2]$$

$$C_M^{\text{ox}} = D_M^{\text{ox}}/\Sigma D_N^{\text{ox}} \text{ alt. } C_M^{\text{met}} = D_M^{\text{met}}/\Sigma D_N^{\text{met}} \quad [3]$$

where I^{ox} and I^{met} are the measured intensities from the element M in the oxide and metal phases. D is the density of the element; S the relative photoelectron yield factor, experimentally determined, taking into account geometrical and attenuation factors; λ the attenuation length of the photoelectrons (11); α^{ox} and α^c the thicknesses of the passive film and the contamination layer, respectively.

The attenuation of the photoelectrons due to the contamination is taken into account individually for each sample by measuring the intensities of the metal elements before and after a slight ion etching of the surface, which just removes the contaminants. Then, the thickness of the contamination layer, α^c , is calculated from Eq. [2]. The thickness of the passive film, α^{ox} , is estimated from Eq. [1] and [2].

Results

Figure 5 illustrates ESCA spectra recorded from the sample after polarization in 0.1M HCl + 0.4M NaCl. The spectra in the three rows were recorded after 5 min at the corrosion potential (Fig. 5a) and 1h at the passive potentials -100 mV and +500 mV (SCE) (Fig. 5b and 5c, respectively). The alloying elements—Ni, Fe, Cr and Mo—are present in their metallic states. Except for Ni, they are also oxidized. Even when the sample was treated at the

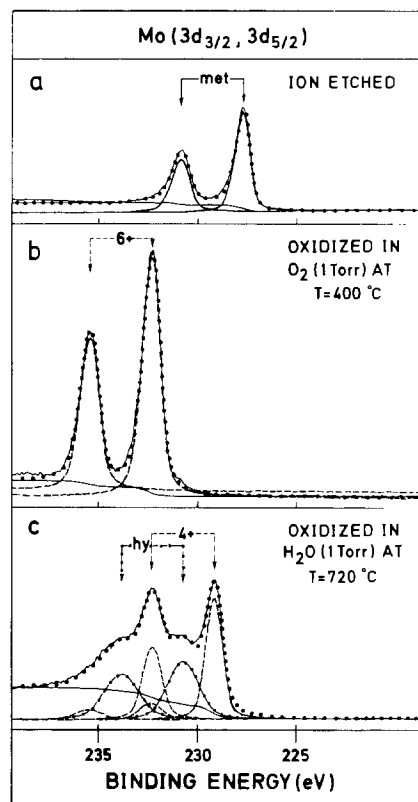


Fig. 4. ESCA spectra recorded from Mo. a: Ion-etched. b: Oxidized in O_2 c: Oxidized in H_2O vapor.

dissolution potential (-320 mV) for 5 min, oxide products are present on the surface. It is suggested that these are formed during rinsing and transferring of the sample to the analyzer. The oxide film is extremely thin; its thickness, estimated by the formula above, is 4Å. The cations in the film correspond to oxidation of less than one atomic plane of the metal.

The ESCA spectra recorded are deconvoluted by using the positions and peak widths obtained from the calibration study, except in the case of the metallic state of Cr, Ni, and Mo, because these signals are broadened when they are recorded from alloys containing these elements.

After passivation, the Cr^{3+} peak is the strongest of the peaks representing the oxidized states. From the figure, it appears that two oxide peaks representing Cr-hydroxide and Cr-oxide are present. The hydroxide state (chemical shift of 3.3 eV) is dominating at -320 and at -100 mV. Iron is present as Fe^{2+} and Fe^{3+} . The intensity of the latter is the strongest. The obtained intensity ratios, $\text{Fe}^{2+}/(\text{Fe}^{2+} + \text{Fe}^{3+})$, are 0.30 ± 0.09 , 0.44 ± 0.03 , and 0.40 ± 0.07 at the three potentials (-320, -100, and +500 mV vs. SCE). Thus, due to the uncertainty it is not possible to conclude about the changes of the valency-state ratio of Fe in the passive state.

The deconvolution of the Mo spectra is shown in Fig. 6. It appears that, in spite of the fact that the spectra are broad with no distinct peaks, the set of Mo states described above satisfy the recorded peaks very well. The oxide state of Mo is dependent on the passivation potential. At low potential, the dominating state is the four-valency state, while at high potential the contribution from the six-valency state is more pronounced. It also appears from Fig. 6 that the peak representing the metallic state is broader than the pure metal state. This is suggested to be due to strong interaction between Mo and the alloying elements Ni and Cr.

In Fig. 5 the metalloids oxygen, carbon, and chlorine are also shown. The main origin of carbon is acetone and methanol, in which the surface was rinsed. The three peaks correspond to the bondings C—H, C—OH, and C=O. The oxygen signal also consists of three peaks. That at low binding energy corresponds to O^{2-} in the ox-

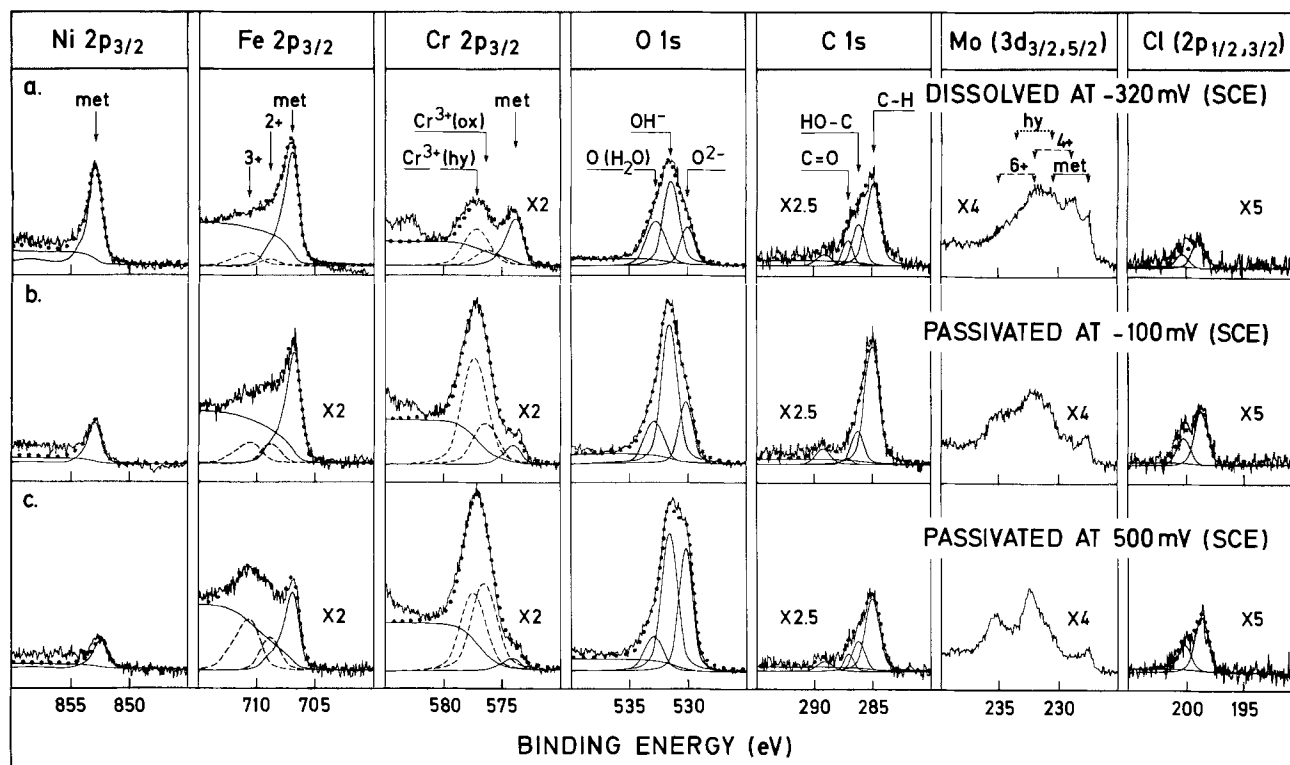


Fig. 5. ESCA spectra of the Fe18Cr14.3Ni2.5Mo alloy recorded after polarization. a: Active range, -320 mV (SCE). b: Passive range, -100 mV (SCE). c: Passive range, $+500$ mV (SCE).

ides Cr_2O_3 , MoO_3 , and Fe_2O_3 . The peak denoted OH^- has the same position as oxygen in $\text{Cr}(\text{OH})_3$ and Mo-hydroxide. This peak overlaps with the signal from the OH group of methanol. The third peak represents water as well as oxygen in acetone. The samples polarized at the dissolution potential were treated in acetone only. The passivated samples were rinsed in acetone and methanol. The difference in rinsing treatment can be read from the figure. It appears that the oxygen peaks recorded after passivation are narrower than after dissolution. This shows that methanol completely removes acetone from the surface, but, on the other hand, this also implies that water bonded in the passive film could be removed. In interpretation of the oxygen signals, the intensity of the peaks representing OH^- and H_2O are reduced by the contribution from methanol and acetone. The contribution is estimated to be $2.5 \times I(\text{C})$, where $I(\text{C})$ is the intensity of the corresponding carbon peak ($\text{C}-\text{OH}$ or $\text{C}=\text{O}$). It appears from the figure that Cl^- ions (BE = 198.5) are present in the oxide product. No Na^+ ions were detected; thus, Cl^- ions are not bound as salt crystals on the surface. Later, it will be shown that the Cl^- ions are incorporated in the film.

Figures 7-11 show the results obtained from quantitative evaluation of the ESCA spectra. The data obtained are given for each individual experiment at the dissolution potential -320 mV and the passive potentials -100 and $+500$ mV. The notations MP and IE refer to the pretreatments, mechanical polishing and ion-etching, respectively. The cation contents in Fig. 7 are calculated from the intensities obtained in the as-polarized condition, i.e., before ion etching. Thus they do not take into account any in depth variations of the composition. Furthermore, all oxide states are summed.

The passive films formed at -100 and $+500$ mV (SCE), polarized for 1h (Fig. 7), consist mainly of Cr^{3+} compounds (oxide and hydroxide). The Cr^{3+} content is about 70%. It seems to be constant and does not vary with the potential. The measured Fe^{ox} (Fe^{2+} and Fe^{3+}) content is in the range 20 to 25 atom percent (a/o) at -100 mV (SCE) and slightly higher at $+500$ mV (SCE). The higher Fe^{ox} concentration at $+500$ mV compensates for the lower Mo^{ox} content at this potential. The measured Mo^{ox} is 7-9 a/o at -100 mV

(SCE) and about 5 a/o at the higher potential. It appears from the figure that the cation content is independent of the pretreatment of the surface. It could be expected that the Mo content of the samples pretreated by ion etching should be higher because ion etching causes enrichment of Mo on the surface due to the lower sputtering rate of Mo.

The oxide products formed on the surface during rinsing and transferring of the polarized sample to the dissolution potential, -320 mV (SCE), depend on the pretreatment procedure. Figure 7 shows that the mechanically polished (MP) samples polarized for 5 min at the dissolution potential consist mainly of Fe^{ox} . The Cr^{3+} is only 35 a/o, which is half of the value obtained after passivation. The Mo^{ox} content is about 15 a/o, which is twice as much as obtained after passivation at -100 mV. The samples prepared by ion etching and polarized for 5 min show much higher Cr^{3+} contents (52 and 55 a/o). The Fe^{ox} and Mo^{ox} concentrations are about 35 and 10 a/o, respectively. Polarization for 1h gives about the same result. It is suggested that the high Cr^{3+} content in the film is indirectly an effect of the ion etching. The etching causes enrichment of Mo on the surface and makes it impossible to keep the surface in its active state; instead, it is passivated.

The thicknesses of the surface oxide products are shown in Fig. 8. It appears that the thickness of the passive film increases with the potential. The values at -100 and $+500$ mV (SCE) are 10 and 15 Å, respectively. After treatment at the dissolution potential, the thickness of the oxide formed on the mechanically polished surface is 5 ± 1 Å. The average value of the ion-etched samples is about 40% higher.

Figure 9 shows the measured Cl^- ion content vs. the thickness of the oxide layer. The values are given before and after a slight ion etching. The ion etching was performed to establish whether the Cl^- ions were adsorbed on the surface or bonded in the oxide. The results show that Cl^- ions are found in the oxide. The figure indicates that at the corrosion potential the highest Cl^- content occurs on the surface covered with the thinnest oxide. The content of Cl^- ions increases with the potential in the passive range. The distribution of Cl^- ions through the

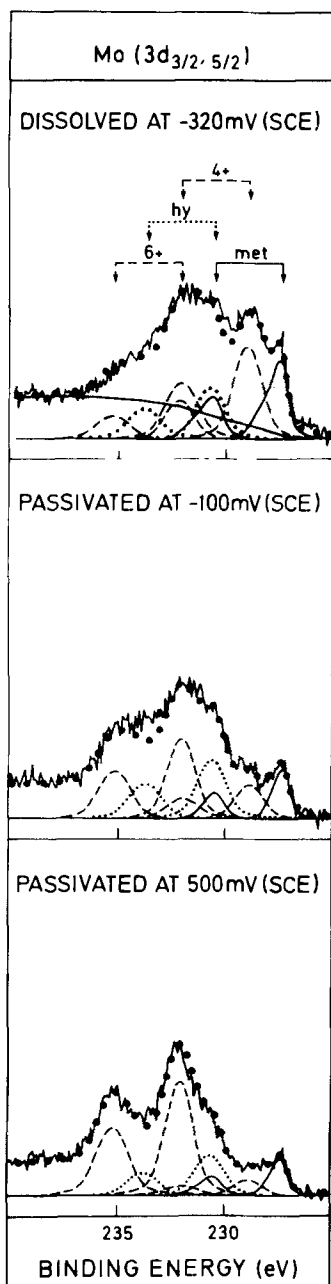


Fig. 6. Deconvoluted ESCA spectra of Mo from Fig. 5

passive film, obtained from ion etching, is shown in Fig. 10. Neglecting selective sputtering effects, it appears that the highest Cl^- concentration exists in the outer layer of the film.

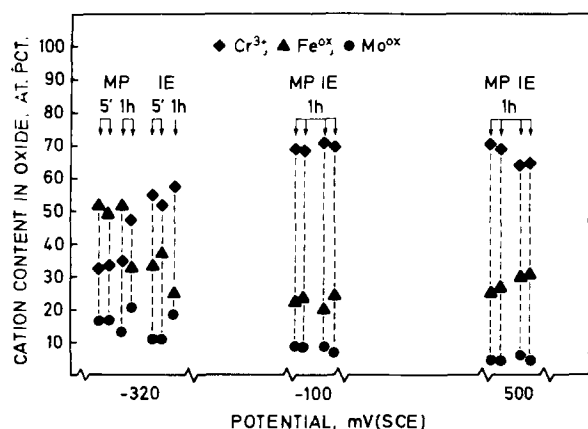


Fig. 7. The cation contents of the reaction products formed at -320 mV (SCE) and of the passive films formed at -100 mV (SCE) and at $+500$ mV (SCE).

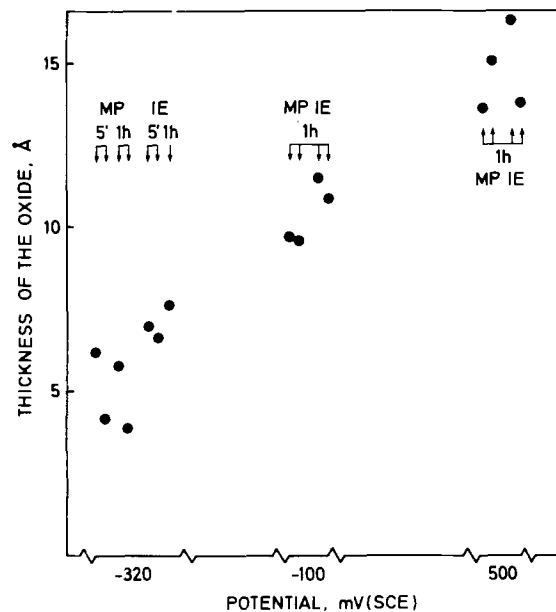


Fig. 8. Thickness of the oxide product vs. the potential

Figure 11 shows distribution of the ions through the passive film obtained by polarization to $+500$ mV (SCE). All Mo concentrations are multiplied by a factor of 10. The data points are average values from four measurements. Before ion etching, the difference between the total charges of cations and anions is less than 2%. The most characteristic feature of the figure is the high OH^- concentration in the outer layer. After ion etching, the OH^- content decreases and the O^{2-} increases. However, it has been demonstrated above that this is at least partly an artifact due to ion etching. It also appears that the outer layer contains hydration water. The profile shows that Cr^{3+} is the dominating species in the inner layer of the passive film. That this result should be an artifact can be excluded because prolonged sputtering into the bulk of the alloy with oxygen present in the sputtering gas (low pressure) gives a ratio between Fe^{ox} and Cr^{3+} which is almost identical to the alloy composition. The profile shows that Fe^{2+} is mainly present in the outer "hydroxide" phase. The content of Fe^{2+} in the inner layer may be an effect of the ion etching because Fe^{3+} is partly reduced to Fe^{2+} . It is suggested that the low Fe^{2+} content in the inner layer is not due to the fact that Fe^{2+} is reduced to the

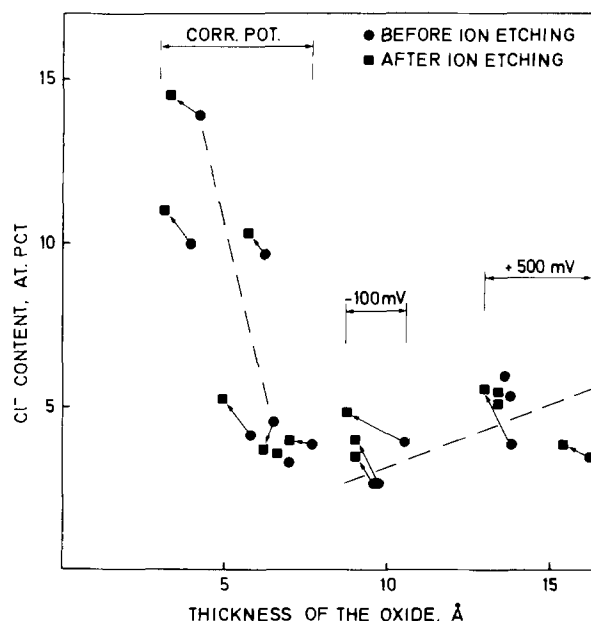


Fig. 9. Cl^- ion content vs. the thickness of the oxide product

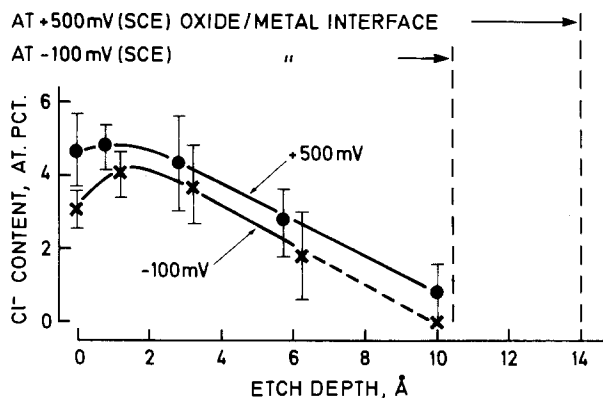


Fig. 10. Cl^- distribution at -100 mV (SCE) and at $+500$ mV (SCE)

metallic state of Fe because, in our experimental setup, we have never observed reduction of Fe^{3+} via Fe^{2+} to Fe^{met} . The Mo content in the passive film is less than 2%. At this potential, Mo is mainly present in the outer layer as Mo^{6+} , while at low potential Mo^{4+} is dominating. Both Fe and Mo are detected in the inner layer of the oxide.

Due to the fact that the oxide products on the alloy are very thin, it is possible to get information about the composition of the metallic state underneath the oxide. The dots in Fig. 12a mark the calculated (by using the formulas [2] and [3]) composition of the metal phase after polarization to the corrosion potential of the sample. The composition obtained is apparent because the formulas [2] and [3] do not take into account the real distribution of the alloying elements in the surface region. The solid bars show the bulk composition of the alloy. It appears from the figure that the apparent Fe concentration is about 10 a/o units lower than the Fe content of the alloy. It also shows that Ni is markedly enriched in the surface region because the apparent Ni content is about twice as high as the figure given from the chemical analysis of the alloy. Furthermore, Mo is slightly enriched, while Cr is depleted in the surface region.

Above, it has been emphasized that the oxide products present on the surface after polarization to the corrosion potential are mainly formed during rinsing and transferring of the sample. It is suggested that the depletion of Cr in the metal phase is caused by selective oxidation during handling of the sample because the Cr

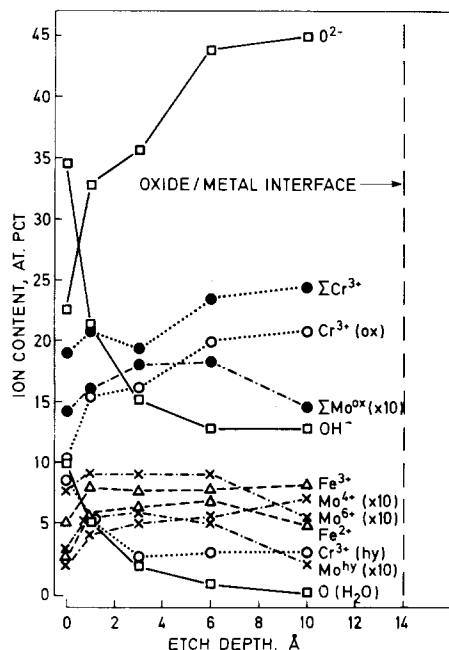


Fig. 11. Ion content vs. etch depth at $+500$ mV (SCE)

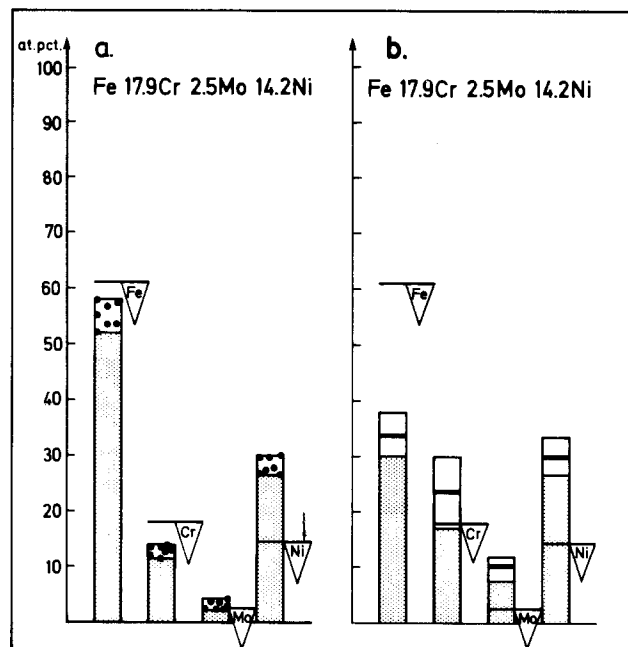


Fig. 12. The composition of the metal phase during dissolution at active potential. a: The apparent metal content. b: The estimated metal content in the outermost atomic layer (15).

content in the oxide is higher than in the alloy. Iron, on the other hand, shows lower concentration in both the oxide and the metal phases compared to the bulk concentration. This observation shows that Fe is dissolved selectively during dissolution at the corrosion potential. Thereby the alloying elements are enriched on the surface.

The observation that Fe is selectively dissolved during dissolution of stainless steel in the active range of the alloy has been reported earlier (10-12). An extensive analysis of the distribution of the alloying elements in the neighborhood of the surface is given in Ref. (15). In that paper, the cations present in the oxide were converted to their metallic state. Also, it was assumed that the alloying elements differ from the bulk concentration in the three outer atomic planes.

The composition of the outermost atomic plane is shown in Fig. 12b [using the procedure in Ref. (15)]. The solid lines in each bar show the average value, while the white area is the standard deviation. The figure shows that during anodic dissolution the alloying elements Cr, Ni, and Mo are significantly enriched in the surface region.

In Fig. 13, the precision of the quantitative method is demonstrated. The alloy was polished on emery paper in methanol and transferred to the analyzer. It is suggested that no selective dissolution of the alloy occurs during polishing in methanol. The apparent composition is shown in Fig. 13a. The cations in the oxide (8\AA) formed during transfer were converted to their metallic state, and the composition of the outermost layer was calculated (Fig. 13b). The calculated concentration of the alloying elements in the outermost atomic plane in this case is very close to the bulk composition of the alloy. Thus, the enrichment of the alloying elements during active dissolution of the alloy is a real effect.

Discussion

This study confirms the duplex structure of the passive film with an outer layer of hydrated hydroxide and an inner layer of oxide. The thickness of these layers cannot be determined exactly, but the sputtering profiles of oxygen in OH^- and H_2O states show that the hydroxide layer is at least one third of the whole film. Both layers consist of mainly Cr^{3+} compounds. Of the total cation content, the content of Cr^{3+} is at least 70 a/o. Nickel in its oxide state cannot be detected in the passive film. Iron is

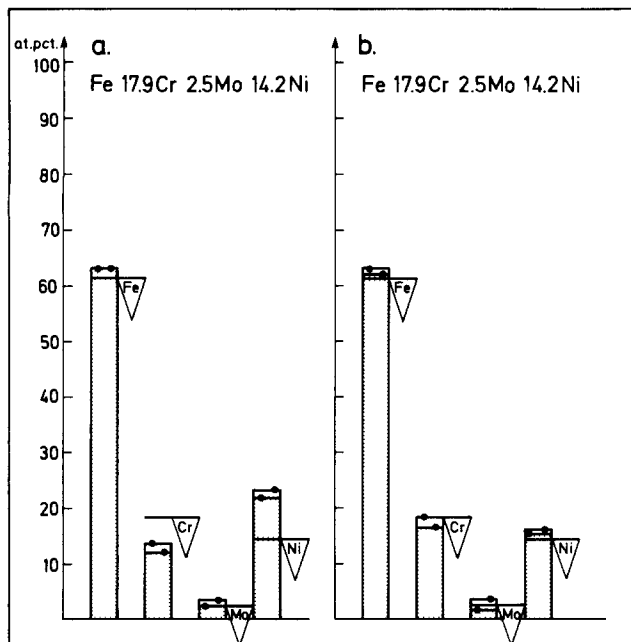


Fig. 13. The austenitic steel polished on emery paper in methanol. a: The apparent content b: The estimated composition of the outermost layer (15).

present in its di- and tri-valent states. The molybdenum content in the passive film is low, a few atomic percent. At -100 mV (SCE), the Mo four-valency state is dominant, while at $+500$ mV (SCE) Mo is present mainly as Mo^{6+} . The oxidation states of both Mo and Fe are reduced during ion etching. Considering the above, it can be concluded that the inner oxide layer consists mainly of Cr and Fe in their three-valency states.

The analysis shows that Cl^- ions are present in the surface products. The amount increases with the potential in the passive range. A suggested explanation for this behavior is that the field strength is higher at the high potential, even in spite of the fact that the layer is thicker. The incorporation of Cl^- in the film is completely different from the situation when stainless steel is exposed in sulfuric acid (12). In that case, SO_4^{2-} ions are merely adsorbed on the surface and completely removed by a slight ion etching. The difference in behavior is suggested to arise from the fact that the Cl^- ion is the same size as the OH^- ion and, therefore, can easily be substituted in the outer hydroxide layer.

The role of Mo has been discussed in the literature. Sugimoto *et al.* (6, 16) and Hashimoto *et al.* (8, 9) suggest that the stability of the oxide film in acid chloride solutions is the result of hexavalent molybdenum oxide forming on the surface. Hashimoto explains the fact that Mo alloyed steels show a much lower current in the passive region by a model in which the passive film is not homogeneous; instead, it contains a high density of microcracks through which current can leak. The microcracks are filled with water, and this is responsible for the high current. In the case of Mo-alloyed steels, Mo^{6+} ions are formed in the cracks and thereby decrease the size of the active sites. It was also mentioned that this Mo^{6+} compound is formed on the surface during active dissolution preceding passive film formation. This idea is to some extent contradictory to the results reported in this study. It has been shown that the six-valency state of Mo is obtained at high potential. At low potential, Mo^{4+} dominates. Also, comparing the result from passivation of pure Mo (17) no six-valency Mo compound is found at potentials lower than $+250$ mV (SCE). However, from a thermodynamic point of view (18), Mo^{6+} is expected even at lower potentials; Mo is oxidized to MoO_3 above -182 mV and to MoO_4^{2-} above -242 mV (SCE) (standard conditions). Interpretation of these compounds by ESCA is not an easy task due to the fact that the positions of the signals repre-

senting Mo in the compounds are very close to each other.

Our result indicates that Mo is uniformly distributed through the layer. Support for this statement is that the high energy peak of the complex Mo^{4+} signal is dominating after passivation and that both Mo^{4+} and Mo^{6+} exist through the layer. We suggest that the role of Mo in the passive film is that it stabilizes the oxide products. At least the outer hydroxide layer is influenced. It is known that some Mo complexes [*i.e.*, $\text{Mo}_3\text{Cl}_4(\text{H}_2\text{O})_2(\text{OH})_2 \cdot 6\text{H}_2\text{O}$] are insoluble in acid while corresponding Fe-Cr-compounds are soluble. It has been suggested by Wanklyn (19) that hydrated MoO_2 occurs in the passive film. We conclude that the outer part of the passive film consists of a mixed hydroxide containing Mo, Fe, and Cr. The latter is directly observed in the spectra.

We have reported (12) that in the case of ferritic steels exposed in 0.5M H_2SO_4 the passive film consists almost entirely of Cr_2O_3 in the inner layer. It was suggested that it is this inner oxide layer that is rate determining for the dissolution. The observation that the oxide consists of mainly three-valency cations implies that the defect density of the passive film is low. However, both lower (Fe^{2+}) and higher (Mo^{4+} and Mo^{6+}) valency cations are present in the film. It is suggested that the defects created by Fe^{2+} are canceled by the defects created by Mo^{4+} and Mo^{6+} . Thus, an almost defect-free oxide is formed in which ionic conductivity is extremely low.

It is found that the thicknesses of the passive films formed on this austenitic steel in hydrochloric acid (0.1M HCl) and on a Mo containing ferritic steel (12) in sulfuric acid (0.5M H_2SO_4) follow the same potential dependence. Even the absolute thickness is almost the same. In the case of non-Mo containing steel (12), the film was noticeably thicker at low potential. Thus, the thickness of the passive film seems mainly to be dependent on the Mo content in the alloy.

At the dissolution potential of the alloy, the alloying elements Ni, Cr, and Mo are enriched on the surface in their metallic states. The enrichment is caused by selective dissolution of Fe. The high Ni content is directly observed from the measurements. The contents of Cr and Mo were obtained by converting the cations in the oxide to their metallic states. It was not possible to avoid a slight oxidation of the surface during handling in spite of all precautions taken. It could be argued that Cr in its oxide state is present on the surface even during active dissolution because pure Cr is passive at the dissolution potential of the alloy (Fig. 2). However, even Fe and Mo are present as oxide on the surface after the dissolution treatment. Iron is the dominating cation in the oxide product, but pure Fe is definitely not passive at the corrosion potential of the alloy. A further indication for the statement that most of the oxide is formed after polarization is that the oxide product formed on the surface of an etched sample in the protecting atmosphere of the cell is thicker than the products discovered after polarization to the corrosion potential.

The selective dissolution of Fe is controlled by the interatomic forces over the interface (metal/solution) and between the alloying elements. Earlier (11), it has been suggested that the elements form a surface phase with lower Fe content than the bulk composition of the alloy. The alloy system forms at high temperature intermetallic compounds (σ -, X-, and Laves phases). During active dissolution, corresponding phases are suggested to be formed due to interaction between the atoms. The initiation of the enrichment is described by the model: at the corrosion potential of the alloy, the dissolution rates of Fe and Cr are higher than the dissolution rate of Mo and Ni because Fe and Cr are less noble than Mo and Ni; interatomic forces between Cr and Mo slow down the dissolution rate of Cr, and thereby it is enriched on the surface. After the initiation, a steady state is reached where the overall dissolution rate is lowered.

The analysis shows that the thickness of the passive film increases with the potential in the passive region.

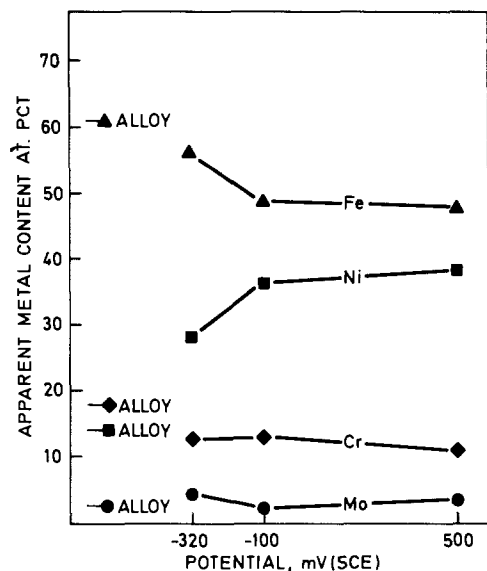


Fig. 14. The apparent metal content of the alloy vs. the potential (SCE).

Because Ni is not present in the oxide (or to only a low extent) and dissolves with a lower dissolution rate than Fe, it is enriched under the passive film. Figure 14 shows the apparent composition of the metal phase. It appears that the apparent Ni content is about twice as high as the bulk composition and that it increases with the potential. Because the excess of Ni atoms is located in a few atomic planes close to the oxide/metal interface, the Ni content of the outermost of these is higher than the value given in the figure.

Because all electrochemical reactions between the metal and the environment take place in the outermost atomic plane, the surface composition and the surface state contribute to the overall reactions and control factors as dissolution rate, overpotential, corrosion potential, and passivability. From the polarization diagram, Fig. 2, it appears the corrosion potential of the alloy is close to the corrosion potential of pure Mo and Ni. It has been emphasized that one beneficial effect of Mo and Ni is the enrichment of these elements on the surface during the anodic dissolution (10, 11, 15) that always precedes passivation. Thereby, the dissolution rate is lowered and the passivation of the alloy is provoked.

Conclusions

The passive film formed on a Mo containing austenitic steel consists of Cr oxide containing Mo and Fe. Chro-

mium is present in hydroxide and oxide compounds. The Ni content of the film is very low. The valency states of Mo are Mo^{4+} at low potentials and Mo^{6+} at high potentials. Chloride ions are incorporated into the oxide passive film. The alloying elements Cr, Ni, and Mo are enriched on the surface during active dissolution. The enrichment is caused by selective dissolution of Fe. The enrichment of the alloying elements provoke passivation of the alloy.

Acknowledgment

The authors gratefully acknowledge the Swedish Board of Technical Development for financial support.

Manuscript submitted April 15, 1985; revised manuscript received Aug. 22, 1985. This was Paper 234 presented at the New Orleans, Louisiana, Meeting of the Society, Oct. 7-12, 1984.

Chalmers University of Technology assisted in meeting the publication costs of this article.

REFERENCES

1. I. Olefjord, in "Proceedings of the 6th Scandinavian Corrosion Congress," p. 11, Swedish Corrosion Institute, Stockholm (1971).
2. H. Fischmeister and I. Olefjord, *Monatsh. Chem.*, **102**, 1486 (1971).
3. I. Olefjord and H. Fischmeister, *Corros. Sci.*, **15**, 697 (1975).
4. J. E. Castle and C. R. Clayton, *ibid.*, **17**, 7 (1977).
5. B-O. Elfström, *Mater. Sci. Eng.*, **42**, 173 (1980).
6. K. Sugimoto and Y. Sawada, *Corros. Sci.*, **17**, 425 (1977).
7. I. Olefjord and B-O. Elfström, in "Proceedings of the 8th International Symposium on Reactivity of Solids," J. Wood, O. Lindquist, C. Helgesson, and M.-G. Vannerberg, Editors, p. 791, Plenum Press, New York (1977).
8. K. Hashimoto, K. Asami, and K. Teramoto, *Corros. Sci.*, **19**, 3 (1973).
9. K. Hashimoto, and K. Asami, *ibid.*, **19**, 251 (1979).
10. I. Olefjord, *Mater. Sci. Eng.*, **42**, 161 (1980).
11. I. Olefjord and B-O. Elfström, *Corrosion (Houston)*, **38**, 46 (1982).
12. I. Olefjord and B. Brox, in "Passivity of Metals and Semiconductors," M. Froment, Editor, p. 561, Elsevier Science Publishers, Amsterdam (1983).
13. P. Marcus, J. Oudar, and I. Olefjord, *J. Microsc. Electron.*, **4**, 63 (1979).
14. B. Brox and I. Olefjord, *Corros. Sci.*, To be published.
15. B. Brox and I. Olefjord, in "Stainless Steel 84," p. 134, The Institute of Metals, London (1985).
16. K. Sugimoto and Y. Sawada, *Corrosion*, **32**, 347 (1976).
17. B. Brox and I. Olefjord, *Corrosion (Houston)*, To be published.
18. A. A. Pozdeeva, E. I. Antonovskaya, and A. M. Sukhotin, *Prot. Met.*, **1**, 15 (1963).
19. J. N. Wanklyn, *Corros. Sci.*, **21**, 211 (1981).

Kinetics and Mechanism of Passive Film Formation on Iron in 0.05M NaOH

T. Zakroczyński,¹ Chwei-Jer Fan, and Z. Szklarska-Smialowska*

Department of Metallurgical Engineering, The Ohio State University, Columbus, Ohio 43210

ABSTRACT

Simultaneous electrochemical and ellipsometric studies of the anodic film growth on iron in 0.05M NaOH have revealed that passivation occurs in two stages. During the first stage, which lasts for about 2s, the anodic current is consumed only for film growth, whereas in the second stage ($t > 2s$) release of iron cations into the electrolyte also occurs. The chemical composition of the passive film formed for times longer than 2s corresponds to FeOOH with a constant density and a complex index of refraction of $\tilde{n} = 1.84(1 - 0.075i)$. During the first stage of film formation ($t < 2s$), the film density and the complex index of refraction change from values characteristic of the electrolyte to those of FeOOH, which is probably related to the fact that the amount of water occluded in the passive film decreases with time. The film thickness increases with increasing anodic potential. A major increase in film thickness occurs during the first 0.2-0.5s.

Although numerous papers have been published in the field of iron passivity, there is little comprehension of some fundamental aspects of this phenomenon. This is particularly true of the passive film formation on iron in alkaline solutions, since the major part of research work has been performed in neutral or near-neutral borate electrolytes. Therefore, literature data concerning alkaline solutions are scanty. Foley *et al.* (1) found the passive film on iron in 0.1M NaOH to be γ -Fe₂O₃, but their conclusion was based on electron diffraction studies conducted on dried films. Froelicher *et al.* (2) used Raman spectroscopy to study *in situ* the passivation of iron in various solutions. In a 1M KOH solution, in which oxidation/reduction cycles had been applied to an electrode, only Fe₃O₄ was found. Donnwald *et al.* (3) also studied the passive film on iron in 1M KOH by Raman spectroscopy. In their study, the iron samples were cycled from cathodic to transpassive potentials at a rate of 1 mV/s. From the spectra obtained, the film appeared to be composed of Fe₃O₄. The trivalent compound which came nearest to matching the spectra was amorphous δ -FeOOH. When the cycle rate was increased to 50 mV/s, a weakly attached reddish-brown layer was formed. This layer was thought to be α -FeOOH, which covered the Fe₃O₄ layer. Huang and Ord (4) took ellipsometric measurements on an iron electrode which was cycled galvanostatically in 0.05M NaOH. They concluded that a low density outer layer built up progressively over an inner layer of a compact oxide which was identified as Fe₃O₄. The inner layer reached a maximum thickness of approximately 3.8 nm at oxygen evolution and was removed completely by cathodic reduction, whereas the outer layer thickness grew by more than 10 nm/cycle. According to the authors, the outer layer is not merely a by-product layer but is alternately oxidized and reduced on each cycle, and has different refractive indexes in its oxidized and reduced states. More recently, Sarver and Szklarska-Smialowska (5) have found that, in NaOH solution of pH 12, as in borate solutions (6), the growth of the passive film occurs in four stages. In the first two stages, which last for only approximately 1s, the thickness of the film achieves 60% or more of its final thickness. They conclude that the composition of the film is probably closer to FeOOH than to Fe₃O₄ or Fe₂O₃.

The present paper is the first of a series of works of which the objective is to use electrochemical and ellipsometric techniques to characterize the passivity of iron in alkaline solutions. In particular, efforts are made to elucidate some fundamental aspects, such as (i) the mechanism and kinetics of film growth, (ii) composition, structure, and physical properties of the passive film, and (iii) effects of environmental factors—electrolyte composition (Cl⁻, chelating agents) and potential.

*Electrochemical Society Active Member.

¹ On leave from the Institute of Physical Chemistry, Polish Academy of Sciences, Kasprzaka 44/52, 01-224 Warsaw, Poland.

The subject of this study is passivation of iron in 0.05M NaOH solution (pH = 12.0).

Experimental

The material used was pure iron. Its chemical composition is given in Table I. The specimen was machined from a rod of 6.35 mm diam, and was mounted in a Teflon holder. The exposed metal surface, which was perpendicular to the rod axis, had an area of 31.7 mm². The specimen was first ground to a 600 grit finish and then mechanically polished with diamond paste to 1 μ m finish. After polishing, the specimen was ultrasonically cleaned in methanol and placed in the ellipsometric cell. An automatic ellipsometer, Rudolph Model Type 2000, was employed. The wavelength was 546.1 nm. The angle of incidence was 71.0° in most experiments.

Simultaneous ellipsometric and electrochemical measurements were performed. Before each measurement, the specimen was cathodically reduced at $-0.950 V_{NHE}$ for 10-15 min. Next, the electrode potential was rapidly changed (sweep rate 80 V/s) to the desired potential in the passive region and changes in electrochemical and ellipsometric parameters were recorded. A high speed electronic recorder (Bascom-Turner Model 3120 T) was used to collect data during the first 2s, and electromechanical recorders (Bio-Rad Model 1322) were applied to collect data at a slower speed during the entire experiment. All measurements were carried out at $24^\circ \pm 1^\circ C$. A Hg/HgO/0.1M NaOH reference electrode ($\cong 0.160 V_{NHE}$) was used for electrode potential measurements. All potential values given below are in the normal hydrogen electrode scale. The optical constants of iron, the films on its surface, and the film thicknesses were calculated using the McCrackin computer program (7) with some modifications.

Results

Electrochemical data.—Figure 1 shows the potentiodynamic anodic polarization curves measured at four different potential sweep rates. With increasing potential sweep rate, both the maximum current density at the potential corresponding to the active/passive transition and the current density in the passive region increased.

Figure 2 depicts changes in the anodic current density *vs.* time observed when the electrode potential was rapidly changed from $E = -0.950 V$ to the following four potentials in the passive region (E^*): -0.350 , -0.050 , 0.250 , and $0.550 V$. At first, the current density (i_{Total}) increased with time, and after about 0.1s achieved a maximum value. Maximum current density increased when a more positive potential was applied. Afterward, the current decreased quite rapidly, and then much more slowly for times longer than 2s. In this final stage, the log current density was a linear function of log time with a slope of about -0.5 .

Table I. Chemical composition of the iron used in this study (ppm)

C	N	O	Na	Mg	P	S	Cl	K	Co	Ti	Cr	Cu	Zn	Fe
12.0	10.0	60.0	1.6	0.9	0.7	2.6	0.8	1.8	0.8	1.4	1.6	0.6	1.9	Balance

Figure 3 shows changes in the anodic charge density corresponding to changes in the current density taken from Fig. 2. The meaning of i_{film} in Fig. 2 and the method used to determine q_{film} in Fig. 3 are described in the Discussion section.

Ellipsometric data.—The optical parameters of the bare metal after polishing and cleaning measured in air were $n = 2.43$ and $k = 1.36$. After exposure to 0.05M NaOH and cathodic treatment at $E = -0.950V$, the optical parameters changed their values, as shown in Fig. 4. After about 900s, the complex index was $\tilde{n} = 2.72 (1 - 1.27i)$, lower than that reported in the literature for a bare iron surface, for instance, in borate (8, 9) or orthophosphate (10) solutions. During continuous cathodic polarization, the optical parameters n and k continued to change; n decreased, and k increased with time (Fig. 4).

Ellipsometric parameters α and ϵ , which were recorded during anodic polarization, were converted to $\delta\Delta$ and $\delta\psi$, where Δ and ψ are relative phase and amplitude parameters. Relationships between $-\delta\Delta$ and $\delta\psi$ for the four applied potentials are shown in Fig. 5, while changes in $-\delta\Delta$ with time are plotted in Fig. 6.

Discussion

Metal dissolution and passivation.—In the first place, the characteristic relationship between the anodic current density and time shown in Fig. 2 deserves special notice. Generally, a sudden change in the electrode potential from a slightly cathodic to an anodic value may result in changes of the anodic current with time which depend upon the processes occurring at the metal/electrolyte interface. The following three cases of the current vs. time relationship, schematically presented in Fig. 7, can be considered.

Active dissolution: curve A-B-C.—The anodic current increases to a constant level B-C depending upon the applied potential and other experimental conditions. Assuming that all products of the anodic processes

occurring on the metal surface are rapidly transferred into the bulk of solution, no surface impediments take place. The slope of the A-B curve depends upon the potential sweep rate.

Full passivity: curve A-M-O.—Products of the anodic processes accumulate on the metal surface and form a passivating film. The anodic current increases more slowly than in the previous case. The surface film thickens, becomes more dense (or compact), and hinders more and more the anodic processes. At point M, the anodic current reaches a maximum value and begins to decrease when the impeding effect overcomes the ability of the metal to be ionized. If all the anodic reaction products are used for surface film formation with no release of cations to the surrounding electrolyte, the current would finally fall to zero at point O.

Incomplete passivity: curve A-M-N-P.—After reaching some limiting thickness and density at point N, the film does not grow any more and its hindering effect on the anodic current assumes a constant and time-independent level.

Incomplete Passivity: curve A-M-N-Q.—If the film density ρ attains a constant value at point N but the film thickness d still increases or, on the contrary, d assumes a constant value but ρ can still increase, changes in the

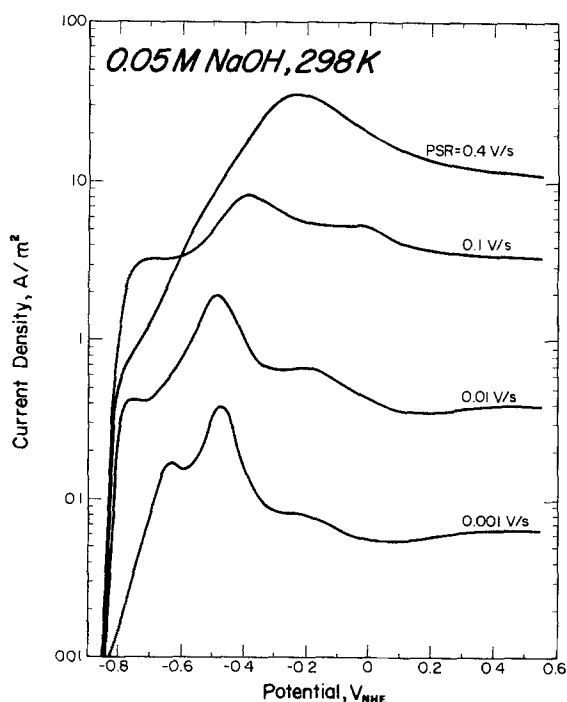


Fig. 1. Anodic polarization curves for iron in 0.05M NaOH measured at four different potential sweep rates.

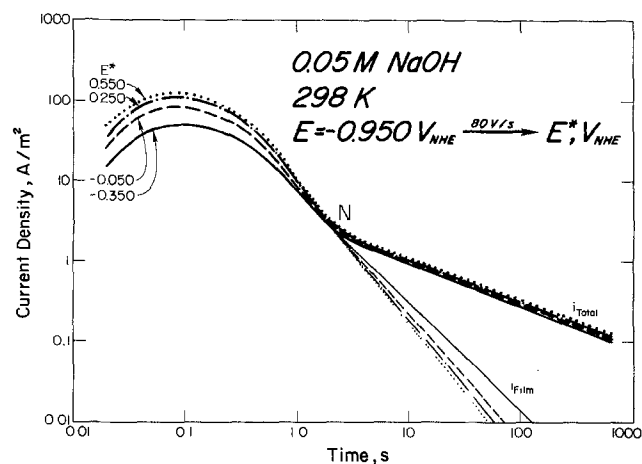


Fig. 2. Changes in current density with time at different potentials. The extrapolated fine lines correspond to the current consumed for film growth ($t > 2s$).

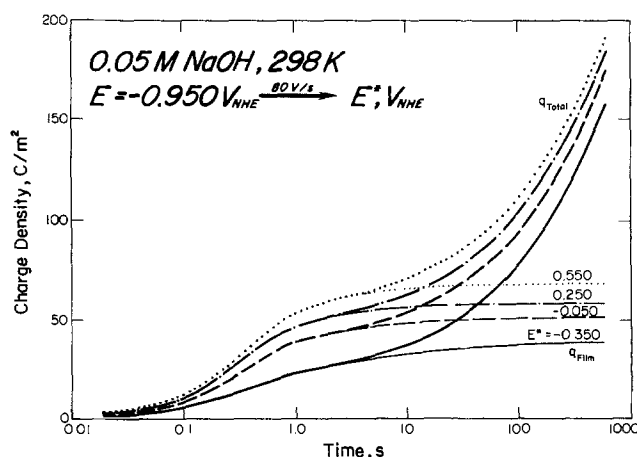


Fig. 3. Changes in charge density with time corresponding to changes in current density in Fig. 2.

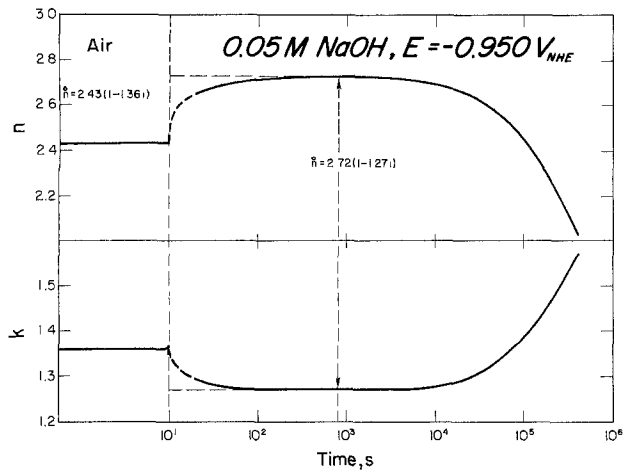


Fig. 4. Changes in optical parameters with time during cathodic treatment of iron in 0.05M NaOH.

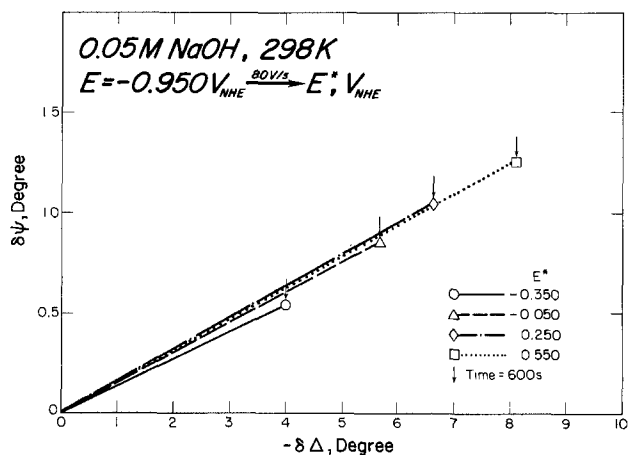


Fig. 5. Experimental relationships between $\delta\psi$ and $-\delta\Delta$ for passive films grown on iron in 0.05M NaOH at different potentials.

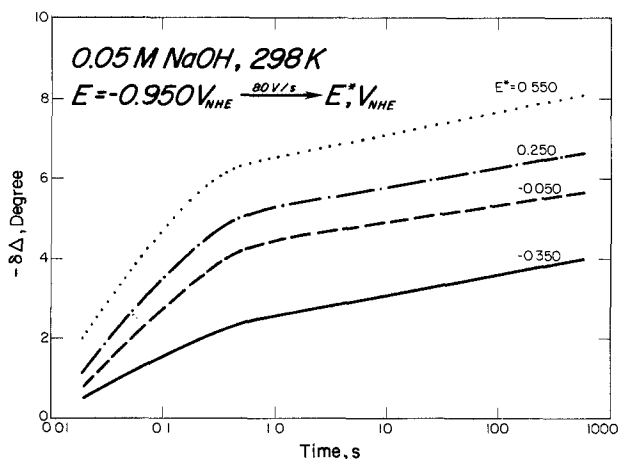


Fig. 6. Changes in $-\delta\Delta$ with time at different potentials

anodic current would be represented by line N-Q. Of course, simultaneous changes of d and ρ with time cannot be excluded.

It is obvious that the above model is simplified. However, it seems likely that when the characteristic deflection point N (Fig. 7) is observed after a relatively short period of time, one can presume that up to this moment there is practically no dissolution of the metal in the sense of forwarding metal cations into the bulk of solution.

Comparison of the experimental curves shown in Fig. 2 (coarse lines) with those schematically plotted in Fig. 7 leads to the conclusion that the real course of events ob-

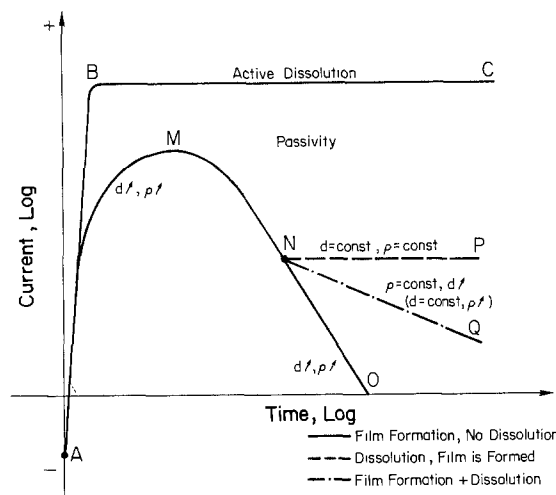


Fig. 7. Schematic representation of possible changes in current density with time as a result of film formation during the anodic polarization of iron.

served in these measurements corresponds to the above case 3b (curve A-M-N-Q in Fig. 7). It is apparent that up to $t = 2$ s there is practically no release of metal cations to the bulk of solution. In this first stage, all reaction products are consumed by the film, which grows thicker and becomes denser. Later on, however, film growth occurs simultaneously with release of metal cations to the surrounding electrolyte.

The next question to be asked is: what share of the total current is consumed by film growth for $t > 2$ s? This share, i_{film} , was estimated by extrapolating the linear parts of M-N curves shown in Fig. 2 (fine lines), which are characterized by a slope of about -1 . The magnitude of this slope suggests that the changes in current density are associated with the film growth, as has been observed for tantalum, aluminum (11, 12), and stainless steel (13). In this manner, the charge consumed for film growth, q_{film} , could be evaluated. The results are represented by fine lines in Fig. 3.

Complex index of refraction, film composition, and thickness.—The complex index of refraction could be calculated from Δ and ψ values. The computer simulation generated the relationship between film thickness, $\delta\Delta$ and $\delta\psi$ for different combinations of n and k . First, certain combinations of n , k , and film thickness (d_{EL}) were selected by matching the experimentally obtained $\delta\Delta$ and $\delta\psi$ values with the computer-generated ones. Second, the film charge density, q_{film} , was used to calculate the thickness, d_{CH} , of the film of an assumed composition, using the following equation

$$d_{\text{CH}} = \frac{q_{\text{film}}M}{zF\rho} \quad [1]$$

where M is the molecular weight of the species formed, z is the number of electrons per elementary reaction, F is the Faraday constant, and ρ is the density of the species formed. The d_{CH} values were calculated for different possible compounds, namely, FeOOH , Fe_3O_4 , $\text{Fe}(\text{OH})_2$, $\text{Fe}(\text{OH})_3$, and Fe_2O_3 , and for $t = 600$ s, during which the film density was believed to attain a constant level. The calculated d_{CH} values and the observed values of $\delta\Delta$ and $\delta\psi$ for the applied anodic potentials and $t = 600$ s are given in Table II and in Fig. 8. The experimental values of $\delta\psi$ vs. $-\delta\Delta$ are plotted in Fig. 8 by open characters, whereas the values of d_{CH} vs. $-\delta\Delta$ are marked by solid ones. The computer-generated relationships $\delta\psi = f(-\delta\Delta)$ and $d_{\text{EL}} = f(-\delta\Delta)$ which fit best to the experimental results are presented by continuous lines. The best fit has been found for the following complex index of refraction: $\tilde{n} = 1.84 (1 - 0.075i)$, which seems to correspond most closely to FeOOH .

Table II. Film charge density (q_{film}), film thickness calculated from charge (d_{CH}) for possible compounds in the film and ellipsometric parameters ($-\delta\Delta$ and $\delta\psi$)
time = 600s

	Potential, E^* (V_{NHE})			
	-0.350	-0.050	0.250	0.550
q_{film} (C/m^2)	38.8	51.4	58.4	68.1
d_{CH} (nm)				
FeOOH, $M = 88.85$ $\rho = 4.28 \text{ g/cm}^3$ $z = 3$	2.78	3.69	4.18	4.89
Fe ₃ O ₄ , $M = 231.54$ $\rho = 5.18 \text{ g/cm}^3$ $z = 2.67$	6.73	8.92	10.12	11.82
Fe(OH) ₂ , $M = 89.96$ $\rho = 3.40 \text{ g/cm}^3$ $z = 2$	5.31	7.04	7.99	9.33
Fe(OH) ₃ , $M = 106.87$ $\rho = 3.60 \text{ g/cm}^3$ $z = 3$	3.98	5.27	5.98	6.99
Fe ₂ O ₃ , $M = 159.7$ $\rho = 5.24 \text{ g/cm}^3$ $z = 3$	4.08	5.41	6.14	7.17
$-\delta\Delta$, degree	4.00	5.68	6.65	8.10
$\delta\psi$, degree	0.54	0.85	1.05	1.26

To ascertain that the ellipsometric data measured were true, additional measurements using different angles of incidence have been carried out. In Fig. 9, the computer-generated relationships $\delta\psi = f(-\delta\Delta)$ for $\tilde{n} = 1.84 (1 - 0.075i)$ and those experimentally observed at two angles of incidence, namely, 71° and 60°, and at $E^* = 0.550V$, are compared. The accordance is very good. Moreover, it can be concluded that the angle of incidence mainly used in this work (71°) has been chosen correctly because it provides significant changes in both the ellipsometric parameters Δ and ψ .

Film growth kinetics.—The kinetics of film growth was estimated on the basis of electrochemical and ellipsometric results as follows. Using Eq. [1], the film charge density vs. time (Fig. 3) was converted into the relationship $d_{CH} = f(t)$, shown in Fig. 10. On the other hand, considering the $-\delta\Delta$ vs. t relationship (Fig. 6), and also that of d_{EL} vs. $-\delta\Delta$ (Fig. 8), d_{EL} could be determined as a function of t , assuming that the film had a constant refractive index of $\tilde{n} = 1.84 (1 - 0.075i)$. The results are shown in Fig. 11.

The above two different calculation methods of film thickness did not lead, however, to satisfactorily consistent results. The film thickness calculated from the charge consumed during the first passivation period was less than that determined ellipsometrically (Fig. 12). Taking into consideration the fact that the film thickness d_{CH} was obtained from the film charge density under the as-

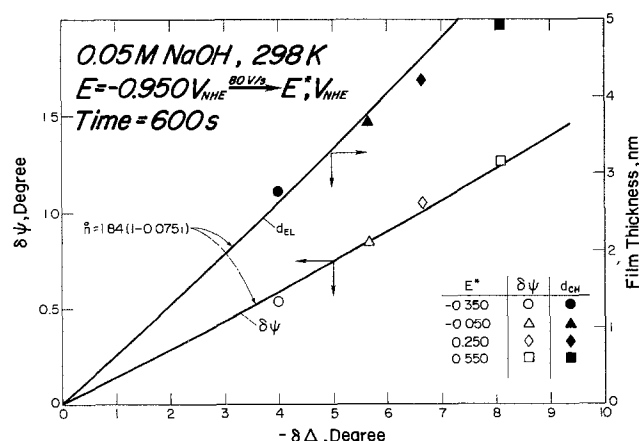


Fig. 8. Relationships between $-\delta\Delta$ and $\delta\psi$ parameters and between $-\delta\Delta$ and film thickness.

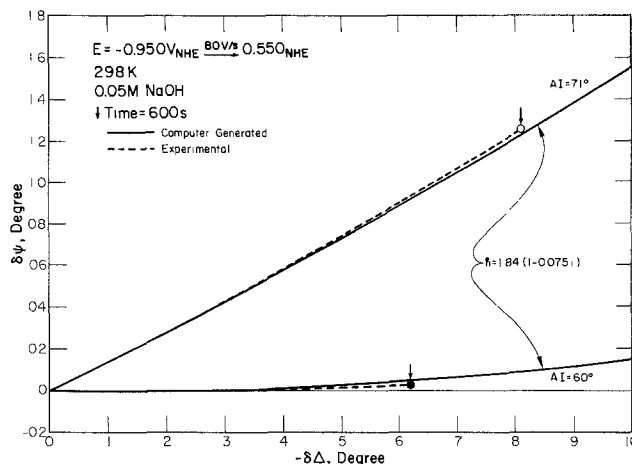


Fig. 9. Computer-simulated and experimentally obtained relationships between $-\delta\Delta$ and $\delta\psi$ parameters for two angles of incidence.

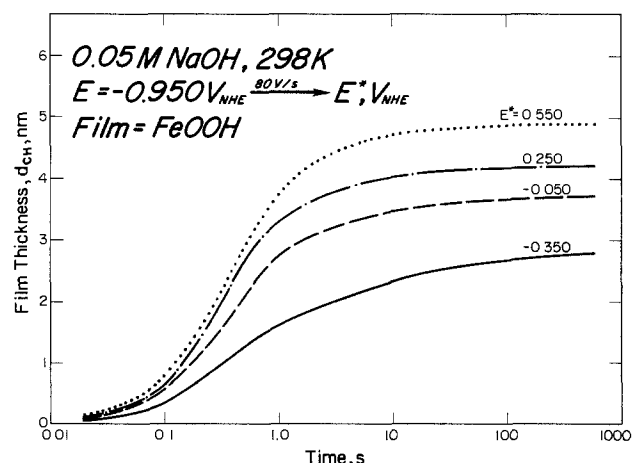


Fig. 10. Film thickness calculated from the electric charge vs. time at different potentials.

sumption of M , ρ , and z constancy, the film thickness determined ellipsometrically seems to be more credible.

As is seen in Fig. 11, the film grows in two stages, both being characterized by a linear relationship between the film thickness and the logarithm of time. During the first fast stage, lasting for about 0.5s, the slope of the d_{EL} vs. $\log t$ curve is controlled by the applied potential, E^* , while later on, in the second slow stage, the slope becomes practically independent of E^* . During the first 0.5s, the film attains about 60% ($E^* = -0.350V$) to about 80% ($E^* = 0.550V$) of its final thickness.

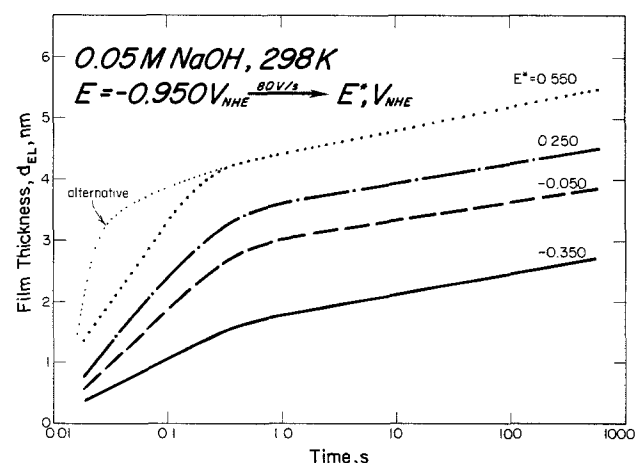


Fig. 11. Film thickness evaluated from ellipsometric data vs. time at different potentials.

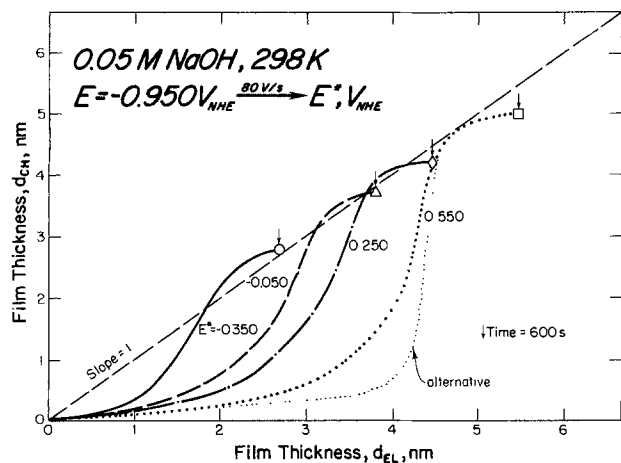


Fig. 12. Relationship between film thickness determined electrochemically and ellipsometrically.

The fast film growth has proved to be governed by the following empirical equation

$$\frac{d d_{el}}{d \log t} = Z (E - E_{cor}) \quad [2]$$

where d_{el} is the film thickness in angstroms, Z is a constant equal to $1/\epsilon$, where ϵ is the electric field strength, E is the applied anodic potential in volts, E_{cor} is the corrosion potential of iron in the given electrolyte, and t is the passivation time in seconds.

Because the above relation appears to be quite significant, analyses of results obtained in previous studies (6, 14) were carried out and graphically compared in Fig. 13, showing that in all the tested solutions $d d_{el}/d \log t$ is a linear function of the applied anodic potential. The straight lines start from E_{cor} , and their slopes Z range from 18-25 Å/V, depending upon the electrolyte. These results suggest that in all the three solutions indicated in Fig. 13 the film formation begins at the corrosion potential of iron in the given solution and that cations transferred from the metal in its active state participate in film growth.

During the slow stage, the film grows at a rate of about 3 Å per decade of time.

Film density.—The fact that the film thickness determined from charge consumed during the first 2 s is much less than that determined ellipsometrically (Fig. 12) was unexpected. It could be inferred that the film density was time dependent and differed from that used for the calculation of d_{CH} , namely $\rho = 4.28 \text{ g/cm}^3$. Presumably, during anodic polarization both the film thickness and density increase with time. Generally, the film density can be considered to change from a low value characteristic of the liquid phase electrolyte (ρ_{liquid}) to a final value characterizing the solid phase film having an established density (ρ_{solid}). Intermediate stages can be treated as containing a mixture of solid and liquid phases in which the

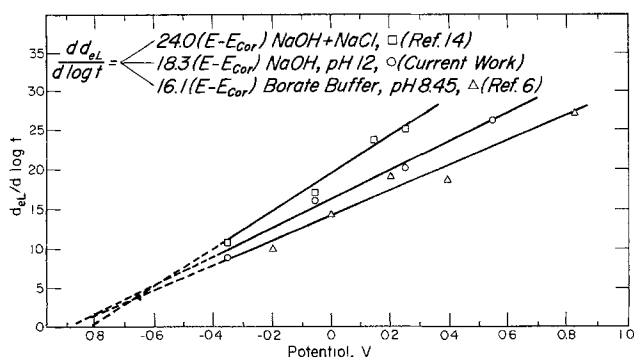


Fig. 13. Kinetics of film growth on iron in different solutions as a function of the anodic potential.

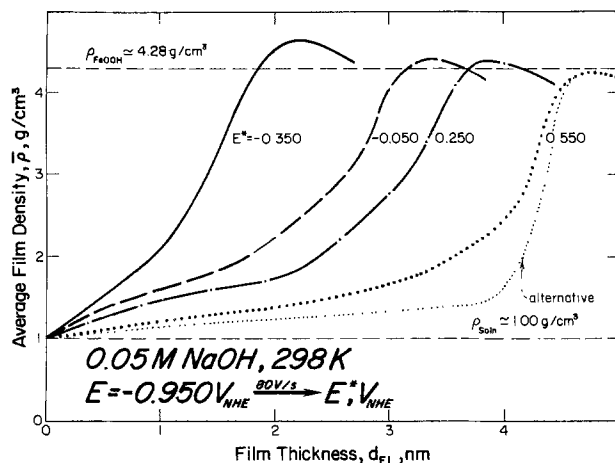


Fig. 14. The average film density as a function of film thickness

water content decreases with passivation time; consequently, the density increases with time. A similar point of view was expressed by Kruger and Calvert (15).

The actual (average) film density can be calculated from the following equation

$$\rho_{aver} = \frac{d_{CH}}{d_{EL}} (\rho_{solid} - \rho_{liquid}) + \rho_{liquid} \quad [3]$$

The results of these calculations are shown in Fig. 14 and 15. The average film density reaches its final value in about 2 s (Fig. 15), *i.e.*, when the current density *vs.* time curve changes its slope at point *N* (Fig. 2). In turn, inflection points of the average film density *vs.* log time curves are observed after about 0.5 s (Fig. 15), *i.e.*, when the film thickness (d_{EL}) *vs.* log time curves change their slope (Fig. 11).

Further considerations.—As previously concluded, for times longer than 2 s, $\bar{n} = 1.84 (1 - 0.075i)$ fits to the obtained ellipsometric data. However, the exact course of events that occur within the first 2 s of film growth cannot be strictly defined because lower values of \bar{n} , for example, those indicated in Fig. 16, may also fit to the experimental $\delta\psi$ *vs.* $-\delta\Delta$ curve. Assuming that during the first 2 s of anodic polarization the optical parameters of the passive film (n and k) change from values characteristic of the aqueous electrolyte ($n = 1.34$, $k = 0$) to those characterizing FeOOH ($n = 1.84$, $k = 0.075$) and that these changes occur according to Fig. 17, variation of the film thickness *vs.* $-\delta\Delta$ would follow the dotted line in Fig. 18, showing that the film thickness calculated taking into consideration the lower optical parameters is greater than that calculated for $\bar{n} = 1.84 (1 - 0.075i)$. Consequently, for example, at $E^* = 0.550 \text{ V}$, the actual relationships of d_{EL} *vs.* $\log t$ and d_{CH} *vs.* d_{EL} may be represented by "alternative" curves plotted in Fig. 11 and 12, respectively. This means

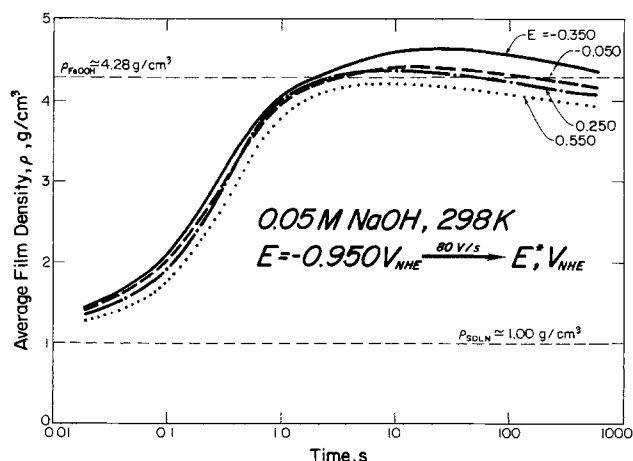


Fig. 15. The average film density as a function of time

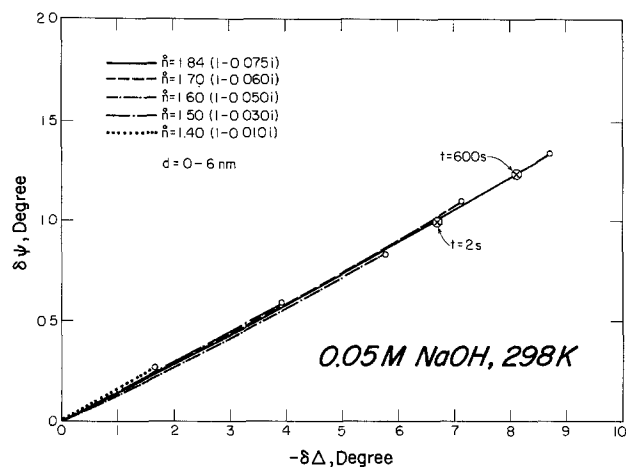


Fig. 16. Relationship between $-\delta\Delta$ and $\delta\psi$ for different complex indexes of refraction.

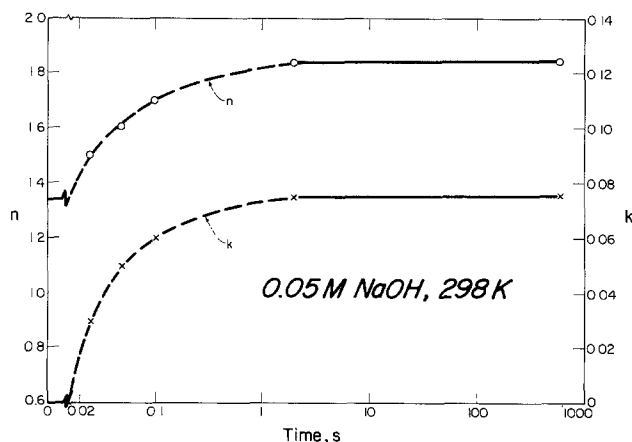


Fig. 17. Changes in n and k with time

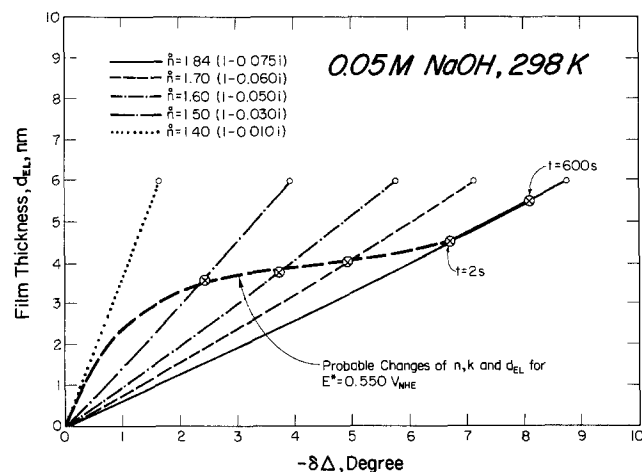


Fig. 18. Film thickness vs. $-\delta\Delta$ for different complex indexes of refraction.

that within the first 2s of film growth the actual film density may be less than that calculated above, and at $E^* = 0.550V$ the ρ vs. d_{EL} relationship may follow the "alternative" curve plotted in Fig. 14.

Conclusions

1. Passivation of iron in 0.05M NaOH at a constant anodic potential occurs in two main stages. During the

first stage, which lasts for about 2s, the anodic current is practically consumed only by the film formation. For times longer than 2s, both the film formation and iron dissolution occur simultaneously.

2. The complex index of refraction of the passive film formed on iron polarized anodically in 0.05M NaOH for times longer than 2s is $\tilde{n} = 1.84 (1 - 0.075i)$. The chemical composition of this film corresponds most closely to FeOOH.

3. During the first 2s, the complex index of refraction and the film density change from the corresponding values of the electrolyte to those of FeOOH, suggesting that the amount of water molecules incorporated in the passive film decreases continuously with time. However, some changes in microstructure further occur in spite of the fact that a constant complex index of refraction and a constant film density are achieved.

4. The film thickness increases rapidly during the first 0.2-0.5s, and then much more slowly. The film is thicker when a higher anodic potential is applied.

5. The fast film growth kinetics (first stage of film growth, $t < 2s$) is governed by the following formula

$$\frac{dd_{el}}{d \log t} = Z(E - E_{cor})$$

During the slow stage, the film grows at a rate of about 3\AA per decade of time.

Acknowledgment

This study was supported by the National Science Foundation under Contract no. DMR-8213905.

Manuscript submitted March 16, 1985; revised manuscript received Aug. 8, 1985.

The Ohio State University assisted in meeting the publication costs of this article.

REFERENCES

1. C. L. Foley, J. Kruger, and C. J. Bechtoldt, *This Journal*, **114**, 994 (1967).
2. M. Froelicher, A. Hugot-Le Goff, C. Pallotta, R. Dupeyrat, and M. Masson, in "Passivity of Metals and Semiconductors," M. Froment, Editor, p. 101, Elsevier Science Publishers, Amsterdam (1983).
3. J. Donnwald, R. Lossy, and A. Otto, in "Passivity of Metals and Semiconductors," M. M. Masson, Editor, p. 107, Elsevier Science Publishers, Amsterdam (1983).
4. Z. Q. Huang and J. L. Ord, *This Journal*, **132**, 24 (1985).
5. J. M. Sarver and Z. Szklarska-Smialowska, in "Equilibrium Diagrams; Localized Corrosion," R. P. Frankenthal and J. Kruger, Editors, p. 357, The Electrochemical Society Softbound Proceedings Series, Pennington, NJ (1984).
6. Z. Szklarska-Smialowska and W. Kozlowski, *This Journal*, **131**, 234 (1984).
7. L. McCrackin, "A FORTRAN Program for Analysis of Ellipsometric Measurements," U.S. Govt. Printing Office, Washington, DC (1969).
8. J. Kruger and J. P. Calvert, *This Journal*, **110**, 670 (1963).
9. C. Lucas, J. B. Lumsden, Z. Szklarska-Smialowska, and R. W. Staehle, *ibid.*, **122**, 1571 (1975).
10. Z. Szklarska-Smialowska and R. W. Staehle, *ibid.*, **121**, 1393 (1974).
11. H. A. Johanson, G. B. Adams, and P. Van Rysselberghe, *ibid.*, **104**, 339 (1975).
12. D. A. Vermilyea, *Acta Met.*, **1**, 282 (1953).
13. M. Stern, *This Journal*, **106**, 376 (1959).
14. T. Zakroczymski, Chwei-Jer Fan, and Z. Szklarska-Smialowska, *ibid.*, **132**, 2868 (1985).
15. J. Kruger and J. P. Calvert, *ibid.*, **114**, 43 (1967).

Passive Film Formation on Iron and Film Breakdown in a Sodium Hydroxide Solution Containing Chloride Ions

T. Zakroczyński,¹ Chwei-Jer Fan, and Z. Szklarska-Smialowska*

Department of Metallurgical Engineering, The Ohio State University, Columbus, Ohio 43210

ABSTRACT

The results of measurements of the optical parameters and thicknesses of passive films grown on iron in an alkaline (pH 12) chloride containing solution suggest that these films were composed of FeOOH and that they resisted pitting when water content was sufficiently reduced. The passive film was formed in two distinct stages. During the initial stage, lasting about 2s, the thickness of the film reached about 60-80% of its final value. The film thickness did not appear to affect its pitting resistance significantly. A model for passive film growth and Cl⁻ induced local passivity breakdown is proposed.

Only several papers dealing with pitting of iron in alkaline solutions could be found. Heusler and Fischer (1) reported that iron did not suffer pitting in a borate solution of pH >10.4 when chloride ions were injected after passivation of the specimen. Oranowska and Szklarska-Smialowska (2) studied the behavior of iron in a saturated Ca(OH)₂ solution of pH 12.5 without and with 0.05 or 0.1M CaCl₂ added. They found that, in the presence of Cl⁻, breakdown of passivity occurred by a spontaneous onset of uneven general corrosion. Breakdown took place as the potential of iron attained a critical value. Film thickness in the presence of Cl⁻ was greater relative to that in Ca(OH)₂ solution. Alvarez and Galvele (3) reported pitting of iron in NaOH + NaCl solution above a certain critical potential which was more positive than that found in neutral NaCl solution. In these experiments, the iron sample was in contact with Cl⁻ from the beginning of the tests. Tousek (4) also observed pitting of iron in 0.1M KOH + 0.4M KCl when the metal was kept passive in this solution and the potential was shifted to values situated above the critical pitting potential.

It therefore can be presumed that these changes in the behavior of iron during passivation in alkaline solutions in the absence or presence of Cl⁻ are associated with some variations of the composition and structure of the passive film. It can also be expected that, depending upon the experimental conditions, the thickness and microstructure of passive films will differ even at the same pH of the electrolyte.

The effect of film thickness on the susceptibility of iron to pitting as studied by McBee and Kruger (5). They found that for the thicker passive film the longer time was needed for its breakdown in NaCl solution. Sarver and Szklarska-Smialowska (6) observed pitting of iron in a Na₂SO₄ solution of pH 12 when the protective "barrier layer" of the film was not yet completely formed.

The purpose of this work was to study the effect of chloride ions on passive film growth on iron in NaOH, and to determine the influence of film growth conditions on the vulnerability to pitting.

Experimental

The passivity of iron in 0.05M NaOH solution containing chloride ions was studied using the same pure iron and procedures identical to those described in the previous paper (7).

Results

Electrochemical data.—Anodic polarization curves were measured in 0.05M NaOH without and with an addition of either 0.005 and 0.05M NaCl using different potential sweep rates (PSR). The initial potential was -0.950V, and the final one was 0.550V. The results plotted in Fig. 1 indicate that the presence of chloride ions does not affect

*Electrochemical Society Active Member.

¹On leave from the Institute of Physical Chemistry, Polish Academy of Sciences, Kasprzaka 44/52, 01-224 Warsaw, Poland.

the shape of the polarization curves. Examination of the specimen surfaces after measurements did not reveal any indication of general or localized corrosion in either NaOH or NaOH + NaCl solution.

After the final value of potential (0.550V) was achieved, changes in the anodic current density vs. time at this potential were recorded (Fig. 2). It is seen that, irrespective of the PSR employed, in both the 0.05M NaOH and 0.05M NaOH + 0.005M NaCl solutions the current decay curves recorded after the same initial treatment (*i.e.*, the same PSR) are practically identical. However, in the third solution, containing 0.05M NaCl, only one of the four curves shown in Fig. 2 follows the same course as the other two, namely, the curve obtained after application of the slowest PSR of 0.001 V/s. The remaining three curves deviated from the usual course; the higher the PSR previously employed was, the greater the deviation was. After some lapse of time, during which the current density decreased, film breakdown occurred, and the current density began to increase rapidly in an irregular manner, this phenomenon accompanied pitting (or general corrosion in the case of PSR = 0.4 V/s).

Pitting also occurred when the specimen was first passivated at a constant potential of 0.550V for 60, 120,

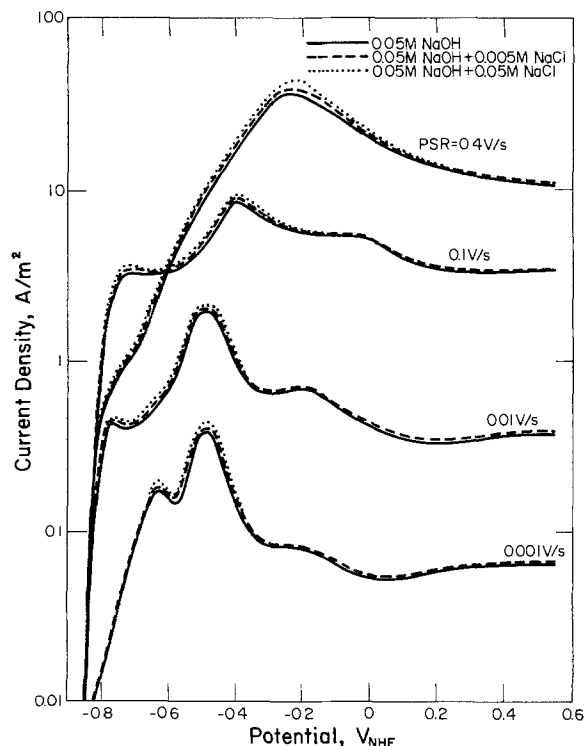


Fig. 1. Anodic polarization curves for iron in 0.05M NaOH with and without the addition of NaCl at four different potential sweep rates.

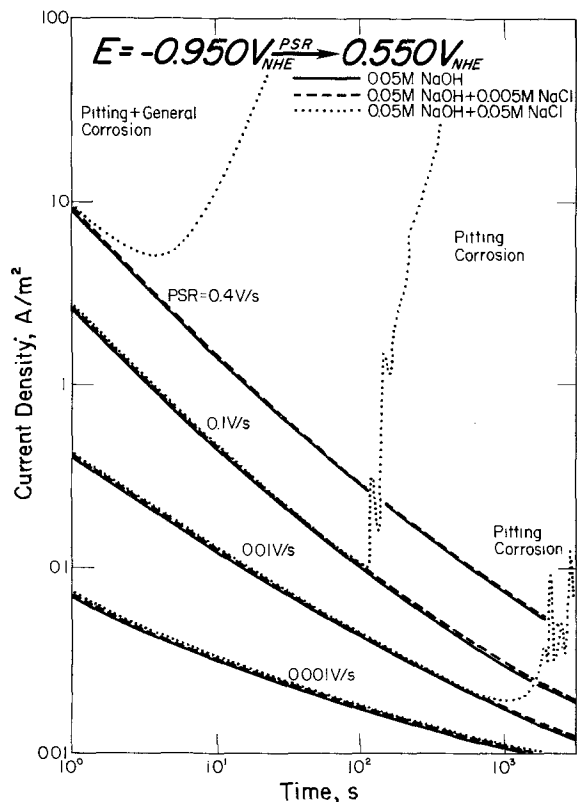


Fig. 2. Changes in current density with time for iron in 0.05M NaOH with and without the addition of NaCl at 0.550V. This potential was attained by shifting it at different PSR starting from -0.950V.

180, or 300s in 0.05M NaOH, after which the electrolyte was adjusted to contain 0.05M NaCl. In contrast, pitting did not occur when chloride ions were added after 600s. Specimens treated this way maintained their resistance to localized corrosion during immersion for 160h in 0.05M NaOH + 0.05M NaCl at room temperature. Figure 3 shows changes in the current density with time before and after the addition of chloride ions to 0.05M NaOH. However, the reproducibility of these measurements was not good. For instance, in the case of four consecutive experiments of passivation in 0.05M NaOH lasting 180s, the following induction times for pitting were observed: 10, 12, 240, and 300s.

Figure 4 shows changes in the anodic current density vs. time recorded when the electrode potential was rapidly changed from -0.950V to the following four potentials in the passive region (E^*): -0.350, -0.050, 0.150, and 0.250V. Similarly, as in the case of 0.05M NaOH (7), the current density (i_{total}) increased to a maximum, and then decreased. The maximum current density was higher

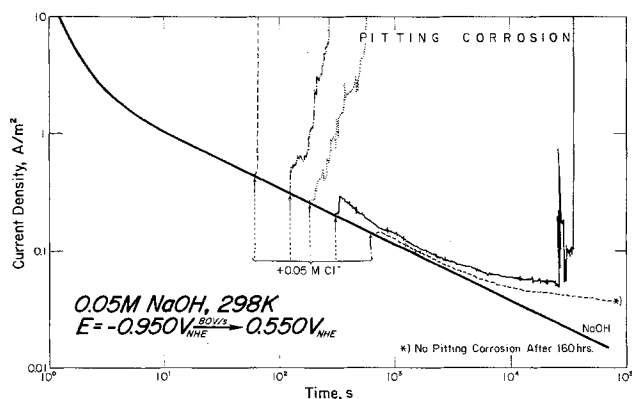


Fig. 3. Changes in current density with time caused by the addition of NaCl after different times of film growth in 0.05M NaOH at 0.550V.

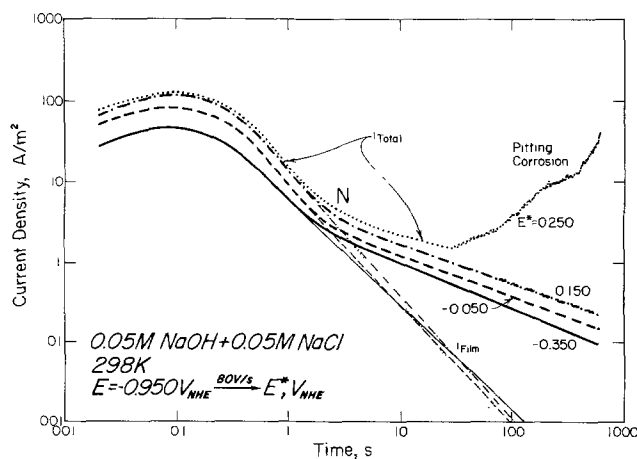


Fig. 4. Changes in current density with time for iron anodically polarized at different constant potentials in 0.05M NaOH + 0.05M NaCl. Fine lines show the current consumed for film growth ($t > 2s$).

when a more positive potential was applied. After about 2s (at point N), the slope of the current density vs. time curve decreased and the log current density became a linear function of log time with a slope of about 0.5. However, in contrast with the behavior of iron in 0.05M NaOH (7), in the presence of NaCl the current density in the final stage proved to be potential dependent, i.e. greater at higher anodic potentials. As is seen in these experiments, namely, 0.250V, film breakdown occurred after some 30s, which was followed by pitting.

Changes in charge density with time, corresponding to the current densities given in Fig. 4, are plotted in Fig. 5. In these two figures, extrapolated values of current density (i_{film}) and charge density consumed for film growth (q_{film}) are marked by fine lines [see Ref. (7)].

Ellipsometric data.—The relationships between $-\delta\Delta$ and $\delta\psi$ at four applied potentials for $t = 600s$ are depicted in Fig. 6. The complex index of refraction calculated on the basis of these results is $\hat{n} = 1.76(1 - 0.05i)$. Measurements of $-\delta\Delta$ vs. time have shown that in NaOH + NaCl, as in pure NaOH, $-\delta\Delta$ first increases rapidly with time, but rises much more slowly after some 0.2s.

Evaluation of experimental data.—Based on the results obtained and using the procedure described in detail earlier (7), the most probable film composition and the film thickness were evaluated. The experimental relationships between $-\delta\Delta$ and $\delta\psi$, and d_{CH} (calculated assuming that the film compound is FeOOH) and $-\delta\Delta$ for $t = 600s$ are presented in Fig. 6 by open and closed characters respectively. Correspondingly, the computer-generated relationships of $\delta\psi$ vs. $-\delta\Delta$ and d_{EL} vs. $-\delta\Delta$, which fit best

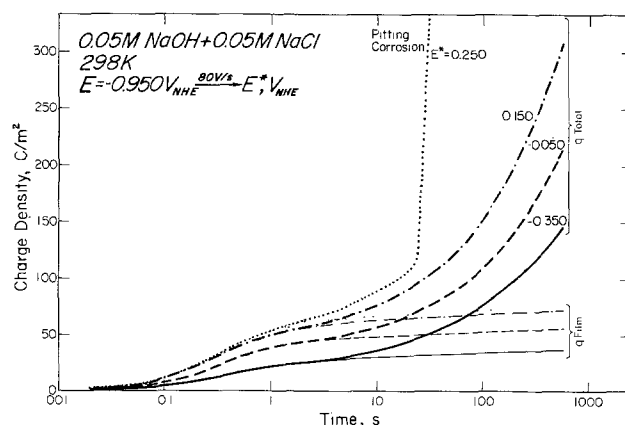


Fig. 5. Changes in charge density with time corresponding to changes in current density in Fig. 4.

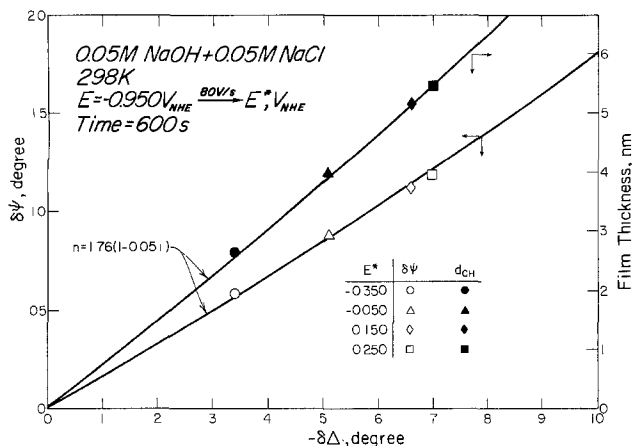


Fig. 6. Changes in $-\delta\Delta$ with time at different potentials

to the experimental results, are also plotted in Fig. 6 as solid lines.

The film thickness evaluated from ellipsometric data, d_{EL} , as a function of time is shown in Fig. 7. The relationship between d_{CH} and time is plotted in Fig. 8. The film thickness, d_{CH} , was calculated from the charge density consumed for film growth.

Discussion

Film composition, thickness, and density.—The complex index of refraction found for the film formed in 0.05M NaOH + 0.05M NaCl is slightly different from that found in 0.05M NaOH. However, there is no reason for assuming a significantly different composition and structure of both those films. The film grown in 0.05M NaOH + 0.05M NaCl, as is that grown in 0.05M NaOH (7), is considered to be FeOOH.

Comparison of the data shown in Fig. 8 with those in Fig. 7 indicates that the film thicknesses measured, either electrochemically or ellipsometrically, after 2s of film growth at the same potential, are identical. However, for shorter growth time periods, the ellipsometric method gives larger values of film thickness than does the electrochemical method, as shown in Fig. 9. Similar results were obtained in 0.05M NaOH (7). Assuming that film thicknesses determined ellipsometrically are close to reality, it can be concluded that in the initial stage of film growth the compound being formed has a significantly lower density than that used for the calculation of d_{CH} , namely $\rho = 4.28 \text{ g/cm}^3$, which corresponds to FeOOH. Figure 10 shows the calculated average density of films formed at different potentials as a function of film thickness determined ellipsometrically. However, a lower complex index of refraction relative to that found in 0.05M

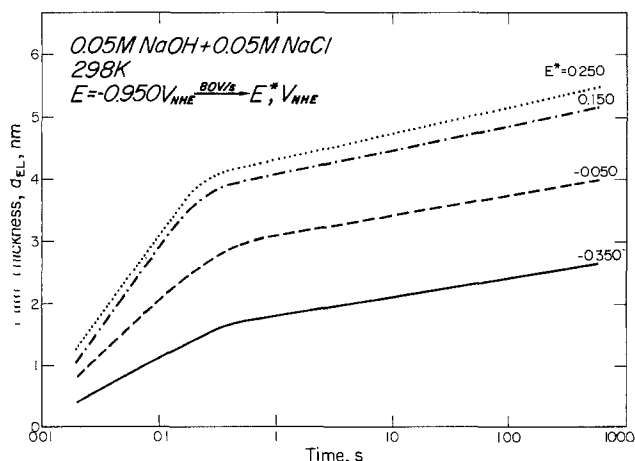


Fig. 7. Film thickness evaluated from ellipsometric data vs. time at different potentials.

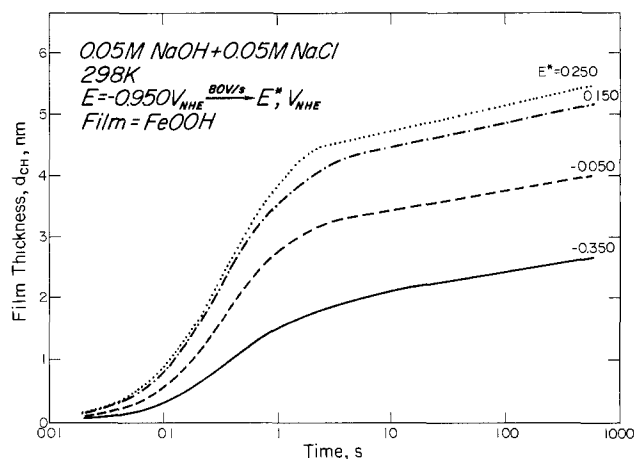


Fig. 8. Film thickness calculated from the electric charge vs. time at different potentials.

NaOH (7) suggest a lower film density. Therefore, additional calculations were carried out by using a tentative value of $\rho = 4.00 \text{ g/cm}^3$. The results obtained are also presented in Fig. 10 (fine lines).

The initial low density of the film is thought to be caused by a large content of incorporated water, which decreases continuously as passivation progresses. Hence, in the initial passivation stage, the metal surface appears to be covered by a layer resembling more a supersaturated iron hydroxide solution than a solid substance. Revie *et al.* (8) found that the passivation of iron in chloride containing solutions results in binding a greater amount of water in the film relative to Cl⁻-free borate solutions.

For times longer than 2s the film density is constant and there is only a small increase of film thickness. Therefore, taking into consideration a continuous decrease of the current density during prolonged passivation of iron in NaOH, it can be concluded that some microstructural changes occur in the film, resulting in an improvement of its protective properties towards pitting.

It is also necessary to mention that despite the very good fit of experimental data to the whole $\delta\psi$ vs. $-\delta\Delta$ relationship for $\tilde{n} = 1.76(1 - 0.05i)$, during the first 2s of film growth, when the film density increases very rapidly with time, other, much lower \tilde{n} values may also fit to the experimental data. Accordingly, during the first 2s of film growth its thickness (d_{EL}) may be greater than that presented in Fig. 7 and 9. Consequently, the film densities would be lower than those shown in Fig. 10 (7).

Passive film breakdown.—Films grown in 0.05M NaOH at 0.550V and next subjected to the action of Cl⁻ at the same potential exhibited greater resistance to pitting the

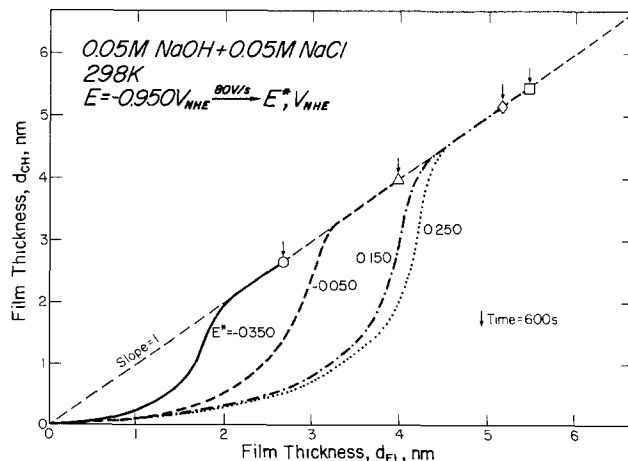


Fig. 9. Relationship between film thickness determined ellipsometrically and electrochemically.

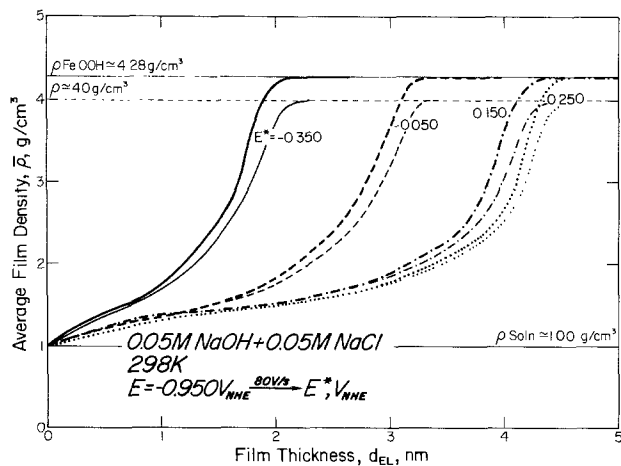


Fig. 10. The average film density as a function of film thickness

longer anodic polarization in absence of chloride ions had previously been applied. On specimens polarized for 1 or 2 min, pitting occurred almost instantaneously when NaCl was added; however, after passivation lasting for 5 min, the induction time for pitting was about 400 min, and after 10 min of passivation pitting did not occur even on exposure to the NaCl containing solution for about 160h (Fig. 3). It was so in spite of the fact that in later passivation stages thickening of the film was insignificant: after 60s of anodic polarization at 0.550V the film was by about only 1 nm thicker than that obtained in 2s, and within the further 20 min its thickness increased by only 0.3 nm. All this indicates that prolonged anodic polarization results in significant changes in the protective properties of the passive film, with little effect on film thickness.

Films grown in 0.05M NaOH + 0.05M NaCl behave differently compared with those grown in 0.05M NaOH, and their behavior depends upon the rate at which the potential is shifted from the cathodic (-0.950V) to the highly anodic value (0.550V) at which the iron electrode is then maintained. Namely, when PSR is high (0.4 V/s), both pitting and general corrosion start within 2-3s after the final constant potential of 0.550V is reached. After application of a lower PSR, for instance 0.01 V/s, pitting starts within about 1000s. A still lower PSR (0.001 V/s) results in a total resistance to any corrosive attack. These results indicate that in the presence of chloride ions in NaOH, consolidation of the passive film on iron to a state of high resistance towards pitting is more difficult relative to that in NaOH.

Reproducibility of the above experiments, especially of measurements of the induction time for pitting, was poor. This suggests a fortuitous character of those events, which was probably related to inhomogeneity of the film. The measured optical and electrochemical properties were averaged for the whole working area of the electrode, while the pitting susceptibility could differ from one point to another. Although in these experiments iron of a relative high purity was used, some "weak" sites in the passive film could probably occur, at which a relatively large amount of Cl^- and water could be agglomerated.

The role of water in the breakdown of passive films on stainless steels was strongly emphasized by Okamoto and Shibata (9, 10). They presumed that from among the three types of oxygen bonding, that of the M-OH type might be the most effective in capturing cations and accelerating repassivation, while the M-OH₂ type could be easily replaced by chloride ions. Consequently, the higher resistance to pitting of steels containing chromium was explained by the high capability of repassivation related to the presence of M-OH bonds in the film (10). Chloride ions, which are adsorbed on the film surface, are thought to migrate into its bulk with assistance of the electric

field and replace the water molecules. In this case, no repair of the film can occur.

Pou *et al.* (11) suggest that water in the passive film on iron facilitates chloride ion penetration. They have found that the thickness of the passive film remains unchanged for various times of exposure to chloride ions before and after breakdown.

On the basis of the results obtained, it is apparent that a compact film composed of FeOOH is much more resistant to pitting than films composed of $\gamma\text{-Fe}_2\text{O}_3$: for example, those formed in borate buffer solutions. However, even a FeOOH film can be destroyed by aggressive anions if it contains incorporated water. Through water "paths" in the film, iron cations can easily migrate to the film/electrolyte interface, while chloride ions move in the opposite direction, reacting with iron cations. As a result of hydrolysis, pH decreases and the metal dissolves locally.

However, the existence of water in the film is not a sufficient condition for pitting. At potentials lower than the pitting potential (E_{np}), water also becomes incorporated into the film, but pitting does not occur. So, under the experimental conditions employed in this study, pitting did not occur at potentials lower than about 0.250V (Fig. 4). Presumably, at potentials lower than E_{np} a sufficiently low pH is not produced within the water paths of the film, because the concentration of chloride ions adsorbed on the film surface is not high enough and/or their migration to water paths is too slow.

Conclusions

The results of this study indicate that pitting of iron can occur in the presence of Cl^- in NaOH solution of pH 12, but only when the passive film is not yet sufficiently consolidated, *i.e.*, when it probably contains a substantial amount of incorporated water. As suggested by ellipsometric data, the film formed either in the absence or presence of Cl^- in NaOH is composed of FeOOH. When fully consolidated, this film is highly resistant to pitting. The thickness of the film does not seem to play an important role in film breakdown.

Acknowledgment

This study was supported by the National Science Foundation under Contract No. DMR-8213905.

Manuscript submitted March 10, 1985; revised manuscript received Aug. 8, 1985.

The Ohio State University assisted in meeting the publication costs of this article.

REFERENCES

1. K. E. Heusler and L. Fisher, *Werkst. Korros.*, **27**, 551 (1976).
2. H. Oranowska and Z. Szklarska-Smialowska, *Corros. Sci.*, **21**, 735 (1981).
3. M. G. Alvarez and J. R. Galvele, *ibid.*, **24**, 27 (1984).
4. J. Tousek, *Corros. Sci.*, **15**, 147 (1975).
5. C. L. McBee and J. Kruger, in "Localized Corrosion," NACE-3, p. 252, NACE, Houston, TX (1974).
6. J. M. Sarver and Z. Szklarska-Smialowska, in "Equilibrium Diagrams; Localized Corrosion," R. P. Frankenthal and J. Kruger, Editors, p. 357, The Electrochemical Society Softbound Proceedings Series, Pennington, NJ (1984).
7. T. Zakroczyński, Chwei-Jer Fan, and Z. Szklarska-Smialowska, *This Journal*, **132**, 2862 (1985).
8. R. W. Revie, J. O'M. Bockris, and B. G. Baker, *Surf. Sci.*, **52**, 644 (1975).
9. G. Okamoto and T. Shibata, in "Passivity of Metals," R. P. Frankenthal and J. Kruger, Editors, p. 646, The Electrochemical Society Corrosion Monographs Series, Princeton, NJ (1978).
10. G. Okamoto and T. Shibata, in "Proceedings of 3rd International Congress on Metallic Corrosion, Moscow," Vol. 1, p. 396 (1969).
11. T. E. Pou, O. J. Murphy, V. Young, J. O'M. Bockris, and L. L. Tongson, *This Journal*, **131**, 1243 (1984).

The Anodic Dissolution of Copper into Phosphoric Acid

I. Voltammetric and Oscillatory Behavior

S. H. Glarum* and J. H. Marshall

AT&T Bell Laboratories, Incorporated, Murray Hill, New Jersey, 07974

ABSTRACT

Anodic electrochemical dissolution of metals is often used in commercial electropolishing, and the copper/phosphoric acid system is a classic example. Surface films are believed essential for polishing, but their composition and role remain elusive. Current oscillations, which may be excited, have been attributed to film formation and breakdown. This study examines the information obtained from voltammetric measurements using rotating disk electrodes. Steady-state currents are limited by a diffusion process whose rate is dependent only upon the solution viscosity and is otherwise independent of its composition. Our results indicate a key role for water and suggest that the film may be a highly viscous, dehydrated surface layer. The oscillations are due to negative impedance surface characteristics.

The anodic dissolution of copper into phosphoric acid solutions represents both a process of technological significance and one with interesting scientific implications. The oscillations which can occur at the onset of the anodic limiting current regime are one of the more intriguing features of this system. These oscillations have been reviewed by Pointu *et al.* (1) and others have studied related aspects of the phenomenon (2-5). A model often invoked to explain this behavior posits the formation and dissolution of a partially soluble, inhibiting surface layer (6, 7). While such a layer may be a necessary condition, it is not sufficient in itself to explain oscillatory behavior. We felt this system might therefore lend itself to a useful impedance study, but first found it advisable to re-examine its voltammetric or steady-state characteristics.

Although the electropolishing region for the $\text{Cu}/\text{H}_3\text{PO}_4$ system has stimulated interest over the years, differences in interpretation remain unresolved. Unanimous agreement exists regarding the diffusional behavior of the limiting current in the electropolishing region, whether based upon transient currents in stagnant solutions or steady-state currents at rotating electrodes (8-14). Contention arises, however, as to the identity of the rate-controlling species. Elmore has proposed Cu^{++} ions (8). With the surface concentration of Cu^{++} fixed by film solubility, dissolution would then be limited by Cu^{++} diffusion into the bulk electrolyte. Several subsequent studies have also favored this interpretation (2, 13, 14).

The principal challenge to this view was first raised by Edwards (10), who examined the influence of bulk Cu^{++} concentration on the dissolution process. Should Elmore's interpretation be correct, the current would be proportional to the difference between a fixed concentration at the electrode surface and a variable concentration in the bulk electrolyte. Edwards found that while addition of Cu^{++} ions to the electrolyte did reduce the dissolution rate, when correction was made for a substantial viscosity increase, the rate was independent of the bulk concentration! Edwards's experiments have been repeated, and his conclusion favored by those making such studies (11-12).

Edwards proposed that phosphate anions, presumably H_2PO_4^- in these acid solutions, were the rate-limiting species. Epelboin and Wagner have called attention to the role of water itself in these concentrated solutions (15, 16). Epelboin has suggested the presence of an anhydrous layer at the electrode, while Wagner has noted the need for water in the hydration of Cu^{++} ions. Scant attention has been paid the role of water in discussions of the copper dissolution process, although it seems evident that significant amounts are required for solvation.

Early interpretations of the copper/phosphoric acid system were based largely on current transient behavior at stagnant electrodes. The intervening development of rotating disk electrode techniques makes more quantitative studies now possible. The importance of diffusion,

*Electrochemical Society Active Member.

concentration, and viscosity has been demonstrated by previous work, and it therefore seemed worthwhile to undertake a more comprehensive examination of this system with the concurrent measurement of these parameters.

To this end, we have employed cyclic voltammetry and rotating disk electrodes. Diffusion coefficients for dilute solutions of cupric ions were determined for a range of phosphoric acid concentrations from cathodic rotating disk limiting currents. Cyclic voltammetric measurements were made for dissolution into these solutions, solutions containing high copper concentrations, and solutions with phosphoric acid replaced by polyphosphoric acid. Viscosities and densities were measured in all cases. Using the rotating disk electrode, we have extended the rate of the dissolution process by an order of magnitude. We also report here on those features of the oscillations revealed by voltammetry - waveforms, frequencies, potential, and current dependence.

Our findings show that the dissolution process is much more complex than dissolving film models would imply. Viscosity gradients and electromigration fields introduce major complications within the diffusion layer. A striking result is that the current, for the solutions explored, depends only upon the viscosity of the electrolyte, and is otherwise indifferent to its composition. This may reflect the importance of water in a fuller understanding of the dissolution process.

Experimental

Voltammetric measurements were made using PAR 173/175/179 components in a potentiostatic configuration. Electrolyte resistance seriously distorts current-voltage plots, and feedback compensation is undesirable for systems prone to oscillation. Uncompensated current and potential signals were first stored in a signal averager and then transferred to diskettes for subsequent analysis. High frequency impedance measurements evaluated the electrolyte resistance. Voltammetric data were then processed to include corrections for electrolyte resistance and plotted in either linear or semilog fashion.

Both 1/16 and 1/4 in. diam copper rotating disk electrodes were used. These were polished to a 15 μm level prior to each series of measurements. Potentials were measured with respect to a calomel electrode isolated from the bath by a capillary bridge. The bath was thermostated at 25°C. Viscosities were measured with suitable Ostwald viscometers, and densities were determined from the weight of 10 cm^3 volumes.

Phosphoric acid (Fisher 85%) and polyphosphoric acid (Aldrich) were used as supplied. Copper phosphate was prepared from CuCO_3 and 30% phosphoric acid. The carbonate was added slowly until effervescence abated. The solution was then filtered and heated to boiling, with a precipitate appearing near 70°. The boiling solution was filtered, giving a fine, bright blue powder which dried rapidly. Although early references are to $\text{Cu}_3(\text{PO}_4)_2 \cdot 3\text{H}_2\text{O}$

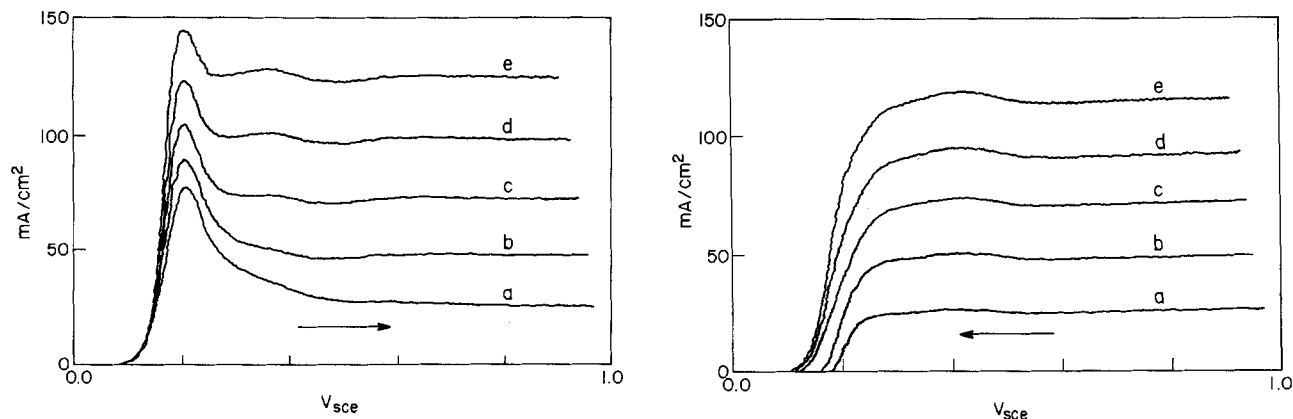


Fig. 1. a (left): Anodic sweep voltammograms at 24 mV/s for a 1/16 in. diam. copper electrode in 85% phosphoric acid. For plots a-e, the disk rotation speeds are 25, 100, 225, 400, and 625 rad/s. b (right): Cathodic sweep voltammograms complementing the plots in Fig. 1a.

(MW = 435) (17), a study by Bassett and Bedwell indicates the correct composition to be $\text{CuHPO}_4 \cdot \text{H}_2\text{O}$ (MW = 179) (18). The apparent molecular weight per Cu atom was found electrochemically by comparison of limiting currents with CuSO_4 solutions in 1M H_2SO_4 . Actual copper concentrations ranged from 10 to 30 mM. Measurements for several preparations gave 150 ± 5 , in agreement with the older formula, and this value was adopted for determining Cu^{2+} concentrations in solutions with added copper phosphate.

Results

Figures 1a and 1b show current-voltage plots derived from cyclic voltammetric measurements for the dissolution of a 1/16 in. diam copper electrode into 85% phosphoric acid. As the applied potential is swept anodically (Fig. 1a), the current rises exponentially until a maximum is reached at $0.2 V_{sce}$. Tafel plots for this portion of the curve have 38 mV/decade slopes over two decades and are independent of disk rotational speed (Fig. 2). Above $0.2 V_{sce}$, the current drops to a nearly constant level, and this plateau extends to ca. $1.5 V_{sce}$. In this constant current regime, we found the current level to vary as the square root of disk rotational speed. The current remains nearly constant during the cathodic retrace, with only a minor maximum at $0.42 V_{sce}$. Below $0.3 V_{sce}$, the current drops rapidly, passing through a zero value because of the buildup of a finite Cu^{2+} concentration in the diffusion layer.

The surface was visually examined *in situ* throughout this potential range with a stroboscopic microscope at magnification ca. 100 \times . In the exponential region of Fig. 1a, the surface first darkened to a ruddy color, and a sharp grain-boundary pattern gradually developed due to surface etching. When the potential was advanced into the limiting current region, the surface returned to a paler complexion and granular features slowly disappeared. After several minutes, the "bright" surface resembled an undulating landscape, with only a few "dark" line segments betraying former grain boundary positions. As the potential was slowly returned to $0 V_{sce}$, the electrode again darkened and etch patterns reappeared. The ruddiness of the surface at etching potentials may be attributed to cuprous oxide (19). However, this coloration disappeared in the polishing region, and we saw no changes which suggested the presence of black cupric oxide (2, 5, 19).

Cyclic voltammetric plots are shown in Fig. 3a and 3b for a 1/4 in. diam copper electrode in 85% phosphoric acid. Although this concentration is identical to that for the Fig. 1 plots, electrical current oscillations now appeared. IR corrections were made after measurements, as for the plots in Fig. 1. The applied sweep range was again $0-1 V_{sce}$, and the difference between the maximum plotted anodic potential and 1V is a measure of this correction.

During the anodic sweep towards more positive potentials, oscillations began ca. $0.42 V_{sce}$. This position was independent of disk rotational speed (current level), although there is a threshold level, and the width of the oscillatory range increases with this level. Oscillations occur at potentials where the I-V plot exhibits a shallow minimum, and not in the nearby region of larger negative slope. Oscillations were also seen during cathodic return traces (Fig. 3b). The current/rotational speed threshold is higher, and the potential range is shifted to $0.38 V_{sce}$, the location of a slight maximum in nonoscillatory plots.

Figure 4 shows several of the diverse waveforms we have observed in these experiments. For these measurements, we used a 1/4 in. electrode in 70% acid solutions. At a rotational speed of 300 rad/s and 0.36V, low amplitude sinusoidal oscillations first appear with a 24 Hz frequency (Fig. 4a). Upon increasing the potential 20-40 mV, a complex 8 Hz waveform develops (Fig. 4b and 4c), and this turns to a sawtooth shape at a slightly higher potential (Fig. 4d). At 0.54V, near the upper limit of the oscillating potential region, a 6 Hz, pulseline waveform is seen (Fig. 4e). With a further potential increase, the period lengthens before oscillations cease altogether (Fig. 4f). When the rotational speed was then raised to 400 rad/s,

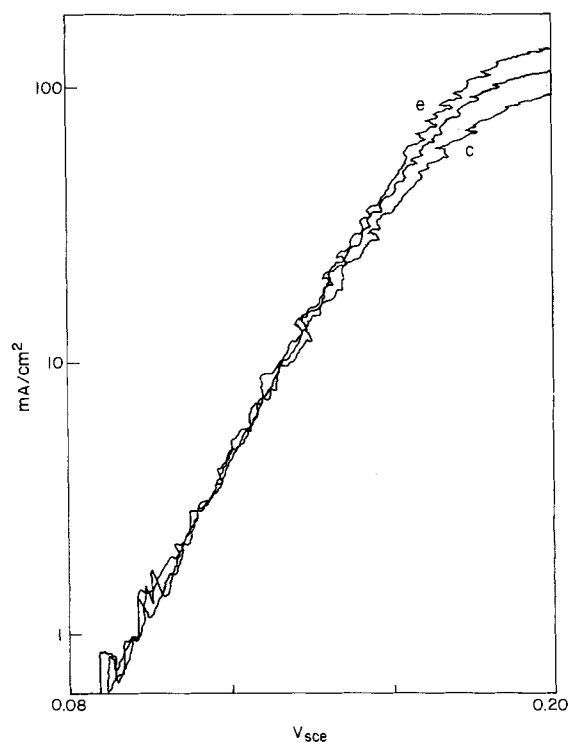


Fig. 2. Tafel plots for the exponential region in Fig. 1a for curves c-e.

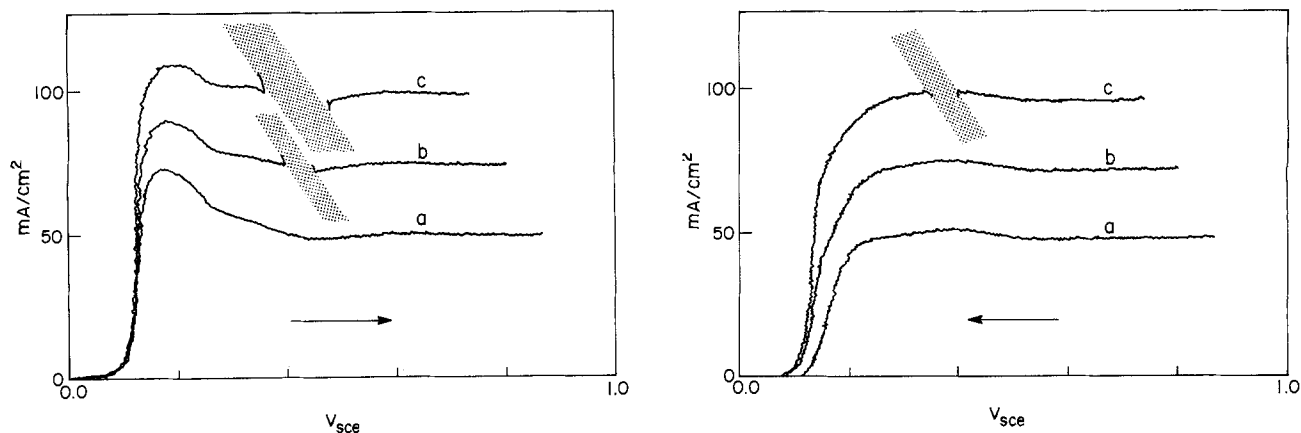


Fig. 3. a (left): Anodic sweep voltammograms at 24 mV/s for a 1/4 in. diam. copper electrode in 85% phosphoric acid. For plots a-c, the disk rotation speeds are 100, 225, and 400 rad/s. The shaded regions indicate areas swept by oscillations. b (right): Cathodic sweep voltammograms complementing the plots in Fig. 3a.

the waveform shifted to a large amplitude, 11 Hz, distorted sinusoidal oscillation (Fig. 4g). Because of the increase in current level, the potential had dropped to 0.49V. These waveforms were obtained by storing the current signal in a signal averager (one pass). The waveforms are extremely sensitive to small variations in potential and disk rotational speed, but, once established, they were stable and could be maintained unchanged for minutes.

For the oscillations in Fig. 4, the oscillating current amplitude represents a large fraction of the mean current level, with a maximum:minimum ratio of about 2:1. The concomitant surface potential variations because of electrolyte resistivity amount to several hundred millivolts. Integration to find the time-dependent charge/cycle for these waveforms gave values of $2-3 \times 10^{-3}$ C/cm² or, in terms of Cu/Cu²⁺ transitions, $6-9 \times 10^{15}$ at./cm².

As measurements were made under potentiostatic conditions, one may question the potentiostat's contribution to the oscillation waveforms. Anticipating the results of our impedance measurements, oscillations are related to negative impedance characteristics of the electrode interface, and the phase of the potentiostat feedback signal can be reversed. Although a formal analysis suggests a region of conditional stability, an empirical evaluation was

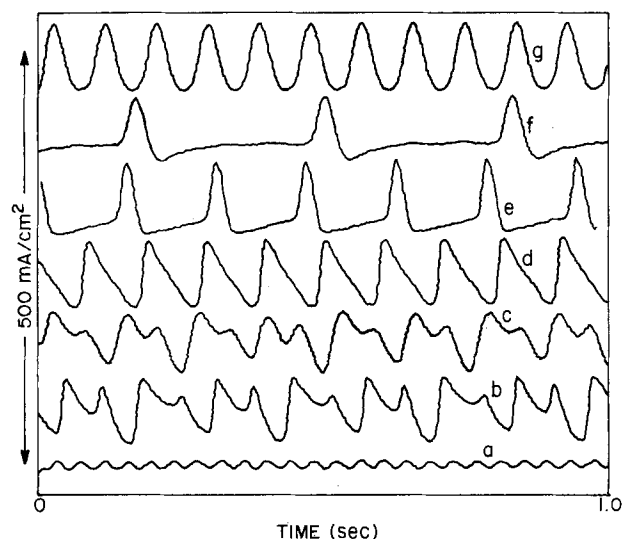


Fig. 4. Oscillation waveforms seen for a 1/4 in. diam copper electrode in 70% phosphoric acid. For curves a-f, the disk rotation speed is 300 rad/s and mean IR-corrected potentials are 0.36, 0.38, 0.40, 0.42, 0.54, and 0.56 V_{sce}. Waveform g was found when the rotation speed was raised to 400 rad/s for the potentiometer setting giving waveform f. The corrected mean potential is 0.49 V_{sce}. The current origin is arbitrary for each plot, but the differential vertical scale is indicated.

made by the insertion of a variable resistance in series with either the working or counterelectrode. In the latter case, no changes in the waveforms were seen for resistance variations 0-500Ω, indicating that the oscillations are independent of potentiostat parameters.

When resistance was inserted in series with the working electrode, however, the waveforms were drastically altered. Under conditions where oscillations were never otherwise seen, they could be induced with a sufficiently large resistance. Formally, one can envision this resistance as equivalent to an increase in electrolyte resistance, apart from nonuniform current distribution effects, and we expect electrolyte resistance to play a major role in shaping the oscillations. While unusual surface behavior is needed for the oscillations to occur, their actual form will depend upon electrolyte conductivity and the electrode configuration. If a is the disk radius, the surface impedance varies as a^{-2} , whereas the electrolyte resistance varies as a^{-1} (20). Consequently, the larger the electrode, the greater the relative importance of electrolyte resistance. A comparison of 1/16 and 1/4, in. diam electrodes shows that oscillatory conditions are more readily established for the latter. The fundamental oscillation frequencies we have encountered fall in the 3-25 Hz range. This range is substantially above that reported in previous studies (≤ 1 Hz) (1, 2, 4). Because of the role of electrolyte conductivity, the size and shape of electrodes are factors in determining oscillatory behavior, and the waveforms are not intrinsic characteristics of the metal-electrolyte interface.

The diffusion-like behavior of the limiting current region has been demonstrated by both rotating disk and transient measurements, but the nature of the current limiting species remains an open question, cupric ions and phosphate anions being most often proposed. The diffusion coefficient of Cu²⁺ in phosphoric acid solutions was obtained from cathodic limiting current measurements for 10-20 mM solutions of copper sulfate for a range of H₃PO₄/H₂O concentrations at a platinum disk electrode. Results for the diffusion coefficient as a function of viscosity are plotted in Fig. 5. Measurements by Krichmar *et al.* based on limiting reduction currents at a microelectrode are also shown (21). Although the viscosity dependence is similar, their absolute values are 50% greater. A least squares fit gives

$$D(\text{cm}^2/\text{s}) = (5.7 \pm 0.1) \times 10^{-6} \nu (\text{cS})^{-1.06 \pm 0.01}$$

For $\nu = 1$ cS, our results extrapolate to the value reported by Tindall and Bruckenstein for Cu²⁺ in 0.2M sulfuric acid (22). The inverse variation with viscosity closely follows Stokes-Einstein behavior, and indicates no change in the size of the diffusing ion over the range studied. The diffusion coefficient is quite small in 85% phosphoric acid, 1.9×10^{-7} cm²/s, because of the high solvent viscosity.

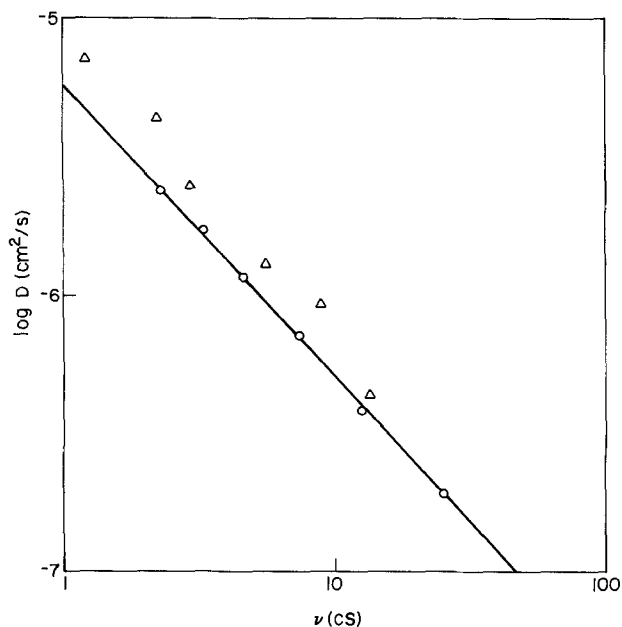


Fig. 5. Variation of the Cu^{++} diffusion coefficient with kinematic viscosity for phosphoric acid solutions. Circles: our results. Triangles: Ref. (21).

Anodic limiting currents were measured at $1.0 V_{\text{sc}}$ and several rotational speeds. Results at 100 rad/s are plotted vs. viscosity in Fig. 6. Data at 25 rad/s had an identical slope. The initial solution was 85% acid, and this was diluted in the course of the experiment.

In a second series of experiments, an 85% acid solution was made 1M in Cu^{++} by addition of copper phosphate. The limiting current decreased 50%, but the viscosity increased from 26 to 50 cS. This solution was then diluted to provide a range of viscosities and Cu^{++} concentrations (0.8-1.0M). These results are also shown in Fig. 6 and lie on the same line as those for Cu^{++} -free solutions, in agreement with Edwards's observation that the limiting current is independent of bulk Cu^{++} concentration when viscosity changes are considered (10).

Edwards has proposed that anion diffusion is the limiting process for anodic dissolution. This hypothesis was tested by substituting polyphosphoric acid/water solutions for the electrolyte. This acid consists of a mixture of species containing predominantly two to five phosphorus atoms per moiety and should have a distribution of anionic entities and diffusion coefficients distinct from those of orthophosphoric acid (23). The electrochemical properties of these solutions were quite similar to those of the simple acid, including oscillatory behavior. When limiting currents were plotted vs. viscosity (Fig. 6), we again found results fitting our previous relationship except that the linear plot was extended to a higher viscosity range. As a further test, the 85% acid was made 1M in Na_3PO_4 . Limiting currents again fell on the common current-viscosity function which characterizes all our results.

Discussion

A satisfactory explanation for the anodic dissolution process should account for those factors determining the limiting current, the potential distribution between metal and electrolyte, and the roles of the diverse chemical species. In addition to the major components, copper, phosphoric acid, and water, ionic forms of Cu^{++} , H_3O^+ , and H_2PO_4^- are certainly present, although their explicit manner of hydration or complexation remains unknown. Copper (I) species also merit serious consideration. Anodic copper dissolution into sulfuric acid, at least near the equilibrium potential, proceeds through a rapid oxidation forming solute Cu^+ ions (24). Some of these escape into the bulk electrolyte, but the majority are converted to Cu^{++} by further electrochemical oxidation. The Cu^+ con-

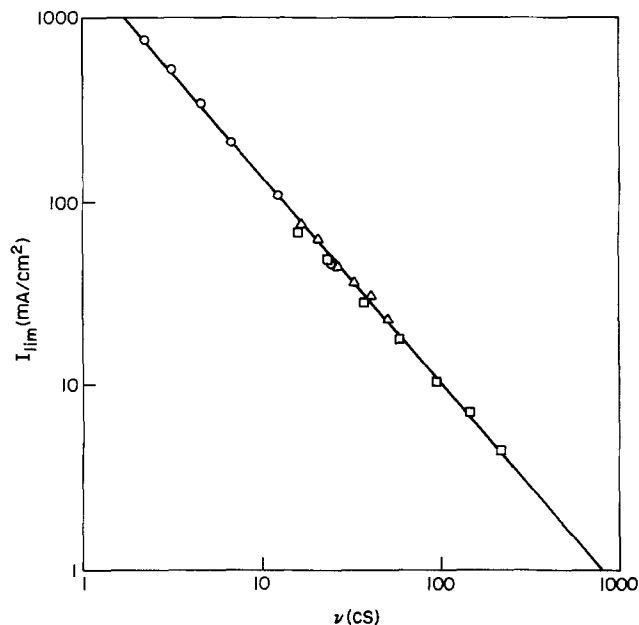


Fig. 6. Variation of the anodic limiting current density with kinematic viscosity for a disk rotation speed of 100 rad/s. The solutions are phosphoric acid solutions (circles), phosphoric acid solutions containing 0.8-1.0M Cu^{++} (triangles), and polyphosphoric acid solutions (squares).

centration rises exponentially with potential until limited by solubility or disproportionation. The 40 mV/decade Tafel slope, characteristic of dissolution into sulfuric acid, is also seen in Fig. 2 and suggests a similar reaction path.

Proposals for surface films have included cuprous and cupric oxides (1, 2, 4, 5) in addition to "copper phosphate" (7, 13). Lorking reports the appearance of a red-brown film (Cu_2O) at etching potentials (19). For more positive potentials, the "oxide film becomes transparent," and a detaching black film was noted. Our observations of a rotating disk electrode confirm the former feature, but we never witnessed a darkening indicative of black CuO . Its formation may vary with experimental conditions, but its presence does not appear essential to reproduce the characteristic features of the polishing region. Analysis of ellipsometric measurements has indicated film thicknesses > 40 and $< 120\text{\AA}$ (25). The thickness was independent of potential. An electron-diffraction study detected an amorphous layer sufficiently thick, $> 30\text{\AA}$, to obscure diffraction by the metallic substrate (7). This film was soluble in phosphoric acid and crystallized on heating to give a copper phosphate diffraction pattern.

We consider the most important results from voltammetric measurements to be (i) the square root dependence of the anodic limiting current on disk rotational speed, (ii) the appearance of limiting current behavior following establishment of the steady-state diffusion layer, (iii) the apparent dependence of the limiting current only upon solvent viscosity, and its independence otherwise on $[\text{Cu}^{++}]$ or the nature of the phosphate species, and (iv), the occurrence of oscillations when uncompensated electrolyte resistance exceeds a threshold value.

The first pair of results show that steady-state behavior is determined by a gradient or gradients with the hydrodynamic diffusion layer. The valence of dissolution has been established to be 2.0, and the total current can therefore be equated to the flux of Cu^{++} ions (13). Irrespective of the reason for limiting current behavior, the Levich equation

$$I_{\text{lim}} = 0.62 zFD^{2/3} \nu^{-1/6} \Omega^{1/2} c$$

may be used to determine the Cu^{++} surface concentration, c , as the disk rotational speed, Ω , is known, and the viscosity and diffusion constant for Cu^{++} , ν and D , are independently measured. For 85% copper-free acid solutions, we find a value of 0.92M. With 1M Cu^{++} added to the bulk

electrolyte, measurements indicate a concentration difference of 0.82M.

From a least squares analysis of the data plotted in Fig. 6

$$I_{lim} \sim \nu^{-1.13 \pm 0.01}$$

When the viscosity dependence of the diffusion coefficient is substituted in the Levich equation

$$c \sim \nu^{-0.25}$$

The nonzero exponent may reflect either limitations of the Levich equation or a solubility variation with acid concentration.

The Levich equation may overestimate the true concentration because of its neglect of ionic migration effects. At 1M, the Cu^{++} concentration probably exceeds the concentration of hydrogen ions, the dominant ionic current carriers, because of the limited dissociation of phosphoric acid. A potential gradient will then develop in the diffusion layer to assist Cu^{++} migration. By way of illustration, let us consider Cu^{++} , H^+ , and H_2PO_4^- , with concentrations c , h , and a , as the dominant solute species. The Nernst ionic mobility equation for the Cu^{++} ion flux is

$$-J_c = D_c \left(\frac{dc}{dx} + \frac{2e}{kT} c \frac{d\phi}{dx} \right)$$

where ϕ is the electric potential in the diffusion layer. Ultrasonic relaxation measurements show fast dissociation kinetics for H_3PO_4 , $\sim 10^{-8}\text{s}$ (26). We shall therefore assume quasi electroneutrality, rapid dissociation equilibrium for phosphoric acid, and very rapid hydrogen ion diffusion. The latter assumption lets us describe the potential in terms of h

$$e\phi/kT = -h'/h$$

while the former give

$$2c + h = a$$

$$ah = K = h_0^2$$

h_0 being the hydrogen-ion concentration in the bulk, copper-free electrolyte. Combining these equations

$$-J_c = D_c c' [1 + 2c/(c^2 + h_0^2)^{1/2}]$$

and integration across a layer of thickness δ , with c varying from c_0 to 0, results in

$$J_c = (D_c/\delta) [c_0 + 2(c_0^2 + h_0^2)^{1/2} - 2h_0]$$

For $c_0 \gg h_0$, the observed limiting current will be thrice the diffusion value. Suitable estimates for h_0 are difficult to come by. If we adopt a dissociation constant based on the dilute solution value scaled for 14M H_3PO_4 and 14M H_2O , $h_{0\approx} 0.16\text{M}$, and the calculated surface concentration for Cu^{++} is reduced from 0.9 to 0.4M. While this is but an estimate because of assumptions made, it is reasonable to conclude that migration effects should be important and that concentrations will be overestimated when they are neglected. Even if we had assumed a 1M H^+ concentration, c_0 would still be reduced to a 0.6M value.

The Levich equation has a further shortcoming in its assumptions of constant viscosity and diffusion constant throughout the diffusion layer. Empirically, we find that addition of 1M $[\text{Cu}^{++}]$ to 85% acid doubles its viscosity. Across the diffusion layer, therefore, we expect 2:1 variations in both ν and D , with the region of highest viscosity nearest the electrode.

If we forego the possibility of novel migration effects, the dependence of I_{lim} on disk rotation rate and potential says that the surface concentration of Cu^{++} is independent of both potential and the current level. Let us consider the view that this "pinned" value corresponds to the solubility limit for a copper phosphate film. Experimental values range about 1M. We have maintained a stable 1.3M solution in 85% acid for several months. Thus, the magnitude of the limiting current appears consistent with the postulate of a copper phosphate film, although the agree-

ment is less satisfactory when migration is considered. Chemical analysis of the anolyte layer has shown 1.5-2.5M concentrations, with higher values evidently corresponding to supersaturated solutions as precipitates appeared on standing (9). Supersaturation of the surface layer would seem inconsistent with the solubility limit model, for it is difficult to visualize a mechanism whereby the degree of supersaturation would remain independent of ionic fluxes.

If the current is to attain a stationary level, the film must grow with a rate dependent on its thickness until its rate of growth matches its rate of solution. Novak *et al.* found the thickness to be potential independent and postulated mobile cationic vacancies without explaining the limits to film growth (25). The presence of fields within a film should contribute significantly to internal ionic transport rates and hence the steady-state thickness. If transport is purely diffusive, the flux will vary inversely with thickness. The ellipsometric measurements were made at one flux level, 15 mA/cm² (65% acid). At the rotating disk electrode, we find normal limiting current behavior at 300 mA/cm² (60% acid). For a film transport rate varying inversely with thickness, the 40-120Å ellipsometric thickness reduces 20-fold to a rather meaningless value.

A less subtle difficulty with the film solubility model is that, for a given viscosity, the limiting current is independent of the bulk Cu^{++} concentration. The points plotted in Fig. 6 for a 1M solution are coincident with data for copper-free solutions within the 10% scatter. A diffusion model requires an unreasonably high surface concentration, $> 10\text{M}$, to explain this concurrence.

We have shown that migration effects are expected because of the high Cu^{++} concentrations involved. A potential difference of 13 mV across the diffusion layer suffices to generate a current equal to the diffusion-limited value, and this current does not explicitly require a concentration gradient. One may conjure a surface film as a hypothetical injection source, but explaining the dependence of current on hydrodynamic conditions is awkward. For the model analyzed, fixed relationships between the concentrations a , c , and h , lead to a potential gradient proportional to c' . Whether a more intricate chemistry, taking into account, for instance, water variations, would lead to migration currents in saturated solutions remains to be shown. The expressions appear too complex for functional solution, and a surfeit of unknown parameters makes numerical attempts seem unprofitable.

Difficulty in explaining the absence of an influence of $[\text{Cu}^{++}]$ on the limiting current, apart from a viscosity change, has led to proposals that other species must be involved. If we assume diffusion coefficients in the range 10^{-6} - 10^{-7} cm²/s, the Levich equation leads to concentrations 0.6-3M for $z = 1$ in 85% acid, and rules out all but the principal species present. High proton mobility makes hydrogen ions a special case. The product of their diffusion coefficient and concentration can be derived from the electrolyte conductivity. When combined with the Levich equation, one finds the limiting current to be equivalent to a 0.5 mM concentration. The existing concentration is certainly much larger, eliminating H^+ from contention.

The remaining possibilities are H_2PO_4^- , H_3PO_4 , and water. Edwards has suggested a depletion of phosphate anions (10). Anions are required to maintain charge neutrality as cupric ions are added to the solution, but the rapid dissociation of H_3PO_4 provides an ample supply (26). Anion concentration should be greatest at the electrode surface, and, once a stationary profile is established within the diffusion layer, there is no necessity for anion diffusion or the further dissociation of H_3PO_4 in this region.

The consequences of a water depletion region have not had serious consideration, apart from Epelboin's mention of an "anhydrous layer" (15). If the viscosity were determined by a single species, water would be the prime candidate. Water is consumed at the electrode by the hydra-

tion demands of Cu^{++} ions, and the correlation of the limiting current with viscosity suggests that it plays a key role in the dissolution process. When 1 mol of Cu^{++} is added to 1 liter of 85% acid (14M H_2O), the viscosity increases to that for a 9M solution. Formulas for copper phosphate favor one water of hydration per Cu^{++} , and the viscosity increase can simplistically be attributed to the formation of hexa-aquo ions.

The major difficulty with a direct water diffusion model is the need for a diffusion coefficient $< 10^{-7}$ cm^2/s , even assuming $z = 1/3$ ($3\text{H}_2\text{O}/e^-$). Of course, the total water content might not be "free" in the sense of being available for hydration. The water activity in 85% acid, based on vapor pressure measurements, is 0.09 of the value for pure water, whereas the mole fraction is 0.5 (27). The reduced activity shows that Cu^{++} must compete with phosphoric acid for the water present.

As the Cu^{++} concentration builds within the diffusion layer, one may imagine the formation of a region of higher viscosity which hinders subsequent material transport. Additional Cu^{++} ions would tie up most of the remaining water until restricted by the buildup of charge or the amount of water present. In the limit, a dehydrated, amorphous surface film comprised of ions and acid would result. This picture is not dissimilar to a film of limited solubility, and it does bring viscosity more directly into the dissolution process. The steady-state rate, however, would now depend on the rate at which bulk water slakes the viscous layer.

Although oscillation waveforms are difficult to analyze, their existence places constraints on possible interpretations of the polishing region. That the oscillations arise because of negative impedance characteristics of the interfacial region is qualitatively shown by their dependence on external cell loading. Admittance measurements will furnish a quantitative proof. DeLevie has discussed the general aspects of electrochemical negative resistance oscillators (28). Negative resistive behavior can often be associated with a negative slope in current-voltage plots. Figures 1a and 1b, however, show no unusual features in the potential region where oscillations occur. The explanation will appear in admittance measurements which do exhibit negative real values for frequencies below 30 Hz. The admittance goes to zero with frequency, in accord with the slope of the current-voltage curves. For the copper-phosphoric acid system, negative impedance behavior is strictly a dynamic effect. The region of negative slope in Fig. 1a is not a negative resistance region, but a monotonic decay which proceeds independently of potential.

Whether a circuit containing a negative impedance element is stable or oscillatory depends on its loading by other elements. In the electrochemical case, loading is due both to electrolyte resistance and external circuitry. It is the voltage drop across these elements which correlates the behavior of otherwise independent portions of the electrode surface. The formation and breakdown of a surface film is often proposed as a qualitative explanation for oscillatory behavior (4, 5). Negative impedance behavior demands both processes be correlated with potential changes. While one can rationalize an increase in film thickness with potential, it is less evident that a decrease in potential should facilitate breakdown, and a more explicit explanation must be proposed for film thinning.

Under the experimental conditions prevailing in Fig. 4, the copper surface is dissolving at a 2500 $\text{\AA}/\text{s}$ rate. During each cycle, 100-200 \AA are lost, while the charge represented by the oscillating portion of the current amounts to a few copper monolayers. The diffusion distance for Cu^{++} ions in one oscillation period is ~ 1 μm , a fraction of the total diffusion layer thickness. Current oscillations extend both above and below a mean level set by nonoscillatory conditions for the same potential and current.

These parameters may be useful for visualizing the scale of spatial and temporal changes at the electrode, but their meaning is ambiguous. Does the charge per cycle

reflect film thickness? Our result might be so interpreted, but Poncet *et al.* find 500-1000 layers dissolving per cycle (1). The difference reflects our higher oscillation frequencies. The diffusional transit time for Cu^{++} ions through the diffusion layer is about 2s. The oscillations, therefore, do not propagate through this layer, and cannot be explicitly dependent on its thickness. Bidirectional current swings seem to imply a greater inhibition than exists in the nonoscillating steady state.

Mathematical models which have been developed to simulate chemical oscillations involve alternative pathways with mutual catalytic interactions (29). Possible species relevant to the system of interest are Cu^{++} , water, and the "film." In addition to its thickness, the film may involve varying concentrations of Cu(I) and Cu(II) . Apart from the conventional rate constants, it may also be necessary to consider the effects of migration fields and viscosity gradients on the diffusion kinetics.

The anodic dissolution of copper in phosphoric acid solutions is not a simple process. In particular, the view of a surface concentration of cupric ions set by film solubility, with the reaction rate then determined by the diffusion of these ions, provides an inadequate accounting for too many features of the process to be acceptable. Sufficient evidence exists to support the view of a surface film. However, whether the film is a true solid phase with distinct boundaries or a highly viscous layer maintained by water depletion has not been proved. The chemical composition of this region remains uncertain, as does the spatial distribution of the large overpotential present. Voltammetric measurements, by themselves, contain information sufficient to characterize and test only relatively simple electrode reactions. While they may reveal the inadequacies of proposed mechanisms, they primarily set limits for more detailed descriptions to meet. A realistic interpretation of the dissolution reaction awaits more elaborate experimental techniques which can better probe the nature of the interfacial region.

Manuscript submitted Nov. 21, 1984, revised manuscript received June 24, 1985. This was Paper 256 presented at the New Orleans, Louisiana, Meeting of the Society, Oct. 7-12, 1984.

AT&T Bell Laboratories assisted in meeting the publication costs of this article.

REFERENCES

1. P. Poncet, M. Braizaz, B. Pointu, J. Rousseau, and N. Muhlstein, *J. Chim. Phys.*, **75**, 287 (1978).
2. L. Meunier, in "Conference Record of the 2nd CITCE, Milan," p. 242 (1951).
3. F. H. Giles and J. H. Bartlett, *This Journal*, **108**, 266 (1961).
4. V. A. Dmitriev and E. V. Rzhetskaya, *Russ. J. Phys. Chem.*, **35**, 425 (1961).
5. B. Pointu, *Electrochim. Acta*, **14**, 1207, 1213 (1969).
6. T. P. Hoar and T. W. Farthing, *Science*, **169**, 324 (1952).
7. E. C. Williams and M. A. Barrett, *This Journal*, **103**, 363 (1956).
8. W. C. Elmore, *J. Appl. Phys.*, **10**, 724 (1939); *ibid.*, **11**, 797 (1940).
9. H. F. Walton, *This Journal*, **97**, 219 (1950).
10. J. Edwards, *ibid.*, **100**, 189C (1953).
11. Z. Zembura and W. Michalik, *Bull. Acad. Polon. Sci.*, **5**, 1073 (1957).
12. M.-C. Petit, *Electrochim. Acta*, **18**, 217 (1963).
13. K. Kojima and C. W. Tobias, *This Journal*, **120**, 1026 (1973).
14. G. H. Sedahmed, M. Z. El-Abd, I. A. S. Mansour, A. H. Ahmed, and A. A. Wragg, *J. Appl. Electrochem.*, **9**, 1 (1979).
15. I. Epelboin, *J. Chim. Phys.*, **49**, 37C (1952).
16. C. Wagner, *This Journal*, **101**, 225 (1954).
17. "Gmelins Handbuch der Anorganische Chemie," 8th ed. Vol. 60, p. 420 (1961).
18. H. Bassett and W. L. Bedwell, *J. Chem. Soc.*, 854 (1933).
19. K. F. Lorking, *Electrochim. Acta*, **7**, 101 (1962).
20. J. Newman, *This Journal*, **113**, 501 (1966).
21. S. I. Krichmar, A. Ya. Pronskaia, and K. F. Afendik, *Elektrokhimiya*, **2**, 967 (1966).

22. G. W. Tindall and S. Bruckenstein, *Anal. Chem.*, **40**, 1402 (1968).
23. F. Uhlig and H. R. Snyder, "Advances in Organic Chemistry," Vol. I, p. 35, Interscience, New York (1960).
24. E. Mattson and J. O'M. Bockris, *Trans. Faraday Soc.*, **55**, 1586 (1959).
25. M. Novak, A. K. N. Reddy, and H. Wroblowa, *This Journal*, **117**, 733 (1970).
26. L. W. Green, P. Kruus, and M. J. McGuire, *Can. J. Chem.*, **545**, 3152 (1976).
27. K. L. Elmore, C. H. Mason, and J. H. Christensen, *J. Am. Chem. Soc.*, **68**, 2528 (1946).
28. R. DeLevie, *Electroanal. Chem.*, **25**, 257 (1970).
29. J. Wojtowicz, in "Modern Aspects of Electrochemistry," Vol. 8, B. E. Conway and J. O'M. Bockris, Editors, p. 47, Plenum Press, New York, (1973).

The Anodic Dissolution of Copper into Phosphoric Acid

II. Impedance Behavior

S. H. Glarum* and J. H. Marshall

AT&T Bell Laboratories, Murray Hill, New Jersey 07974

ABSTRACT

Impedance measurements have been used to study the electrochemical dissolution of copper rotating disk electrodes in phosphoric acid as a function of potential and current density. A space-charge layer is formed at large overpotentials. The thickness of this layer is potential dependent, $\sim 100\text{\AA}$ at $+1.0\text{V}$, but independent of current density. Diverse relaxation behaviors are seen at lower potentials. Reactive equivalent-circuit elements are largely independent of current density, while conductive elements are directly proportional to current density, indicating that the structure of the interface is controlled by the electric potential rather than by kinetics. Current oscillations during dissolution reflect a negative impedance relaxation at low frequencies. This impedance is explained by the dependence of the dissolution process on high mobility hydrogen ions and the coupling of $[\text{H}^+]$ with electric fields external to the metal surface.

Current oscillations accompanying electrode reactions have been observed in diverse systems, but their origins remain largely conjectural (1, 2). Few studies have been directed towards the investigation of the phenomenon itself. Impedance measurements would appear to offer a promising avenue for approaching this curious behavior, and their relation to electrochemical oscillations has been discussed by DeLevie (3). Apart from some limited admittance measurements by DeLevie and co-workers on the reduction of In(III) in the presence of SCN^- (4), we are unaware of prior applications of the technique to the study of electrochemical oscillators. Our attention has been attracted to the anodic dissolution of copper metal into phosphoric acid. Oscillations in this system were reported by Jacquet in 1936 (5). Poncet *et al.* have studied this system with voltammetric techniques and proposed that surface oxides are connected with the instabilities (6). The large amplitude oscillations encountered in such experiments are difficult to analyze as they are governed by nonlinear effects. Impedance measurements offer more quantitative information and can be carried out under nonoscillatory conditions.

The copper-phosphoric acid system is well suited for an impedance investigation. Oscillations occur at frequencies $> 1\text{ Hz}$, a range amenable to measurement. Moreover, as the dissolution current is independent of potential over a wide potential range but can still be varied hydrodynamically, rotating disk electrodes make feasible independent evaluations of the influences of potential and current density. We found it desirable to undertake a parallel voltammetric study prior to an extensive impedance investigation, and these findings appear in Ref. 1. In the present paper, we report and discuss impedance behavior in 85% acid solutions at dissolution potentials extending to the oxygen evolution region. The system exhibits an unusually rich range of response functions and data obtained above and below the actual potential range where instabilities appear provide useful insights into the structure of the interfacial region.

The impedance of an electrolytic cell is often best summarized by an equivalent circuit. This is merely a collection of resistive, capacitive, and Warburg elements chosen to mimic the experimental dependence of impedance *vs.* frequency. Inevitably, one requires circuit elements for electrolyte conductivity and double-layer capacitance,

and their interpretation is relatively direct. Faradaic current flow, however, can lead to a complex impedance function in parallel with the double-layer capacitance. Interpretation of this portion of the circuit requires some modeling of possible electrode reactions to relate equivalent circuit elements to functions of chemical interest. Given sufficient equations to define an electrode process, their transformation into a set of perturbation or modulation equations is straightforward although somewhat arcane to the unversed. Because we shall encounter a diversity of response functions in this study, we have relegated to an appendix a generalized procedure for the derivation of impedance function. In discussion, we shall consider equations describing various mechanisms and present their equivalent impedance without digression into the intermediate algebra.

Experimental

General experimental procedures are given in the first part of this paper (1). For impedance measurements, only 1/16 in. diam copper rotating disk electrodes and 85% phosphoric acid solutions were employed. Reported potentials were measured with respect to a saturated calomel electrode and have not been corrected for electrolyte IR drop. The frequency range explored in this work was 1 Hz-200 kHz. This lower limit was deemed adequate because of the rapid rate of electrode dissolution and the fact that complex-plane plots when extrapolated to zero frequency were compatible with the slopes of steady-state current-voltage curves.

A Rockland 5100 Frequency Synthesizer furnished a sinusoidal source for ac measurements (7). This signal passed through a series of variable, active, lead-lag networks into a PAR 173/179 potentiostat system. AC measurements were made with a PAR 129A two-phase lock-in amplifier of the potential difference between the working and reference electrodes and the drop across an external reference resistor in series with the working electrode. The lead-lag networks were adjusted so that the former difference was approximately constant over the frequency range scanned (2 mV , 0°), and the reference resistor was selected so that the latter drop was $\leq 2\text{ mV}$. For optimum bandwidth and minimum noise, the PAR 179 plug-in was kept on the 1A range and its digital circuitry disabled. Both 0° and 90° square-wave reference signals were extracted from the 5100 and used to drive directly

*Electrochemical Society Active Member.

the phase-detector switches, bypassing the lock-in circuitry of the 129A and extending its frequency response. Typically, 500 measurements logarithmically spaced between 200 kHz and 100 Hz were made in 5-10s. At lower frequencies, four sample-and-hold circuits captured the unfiltered output of the phase detectors, permitting two independent measurements per cycle. Accuracy was established with precision RC components chosen to emulate characteristic cell impedances. For a series RC circuit with a 3 kHz relaxation frequency (75Ω , $0.7\ \mu\text{F}$), the series resistance obtained by a deconvolution of the measured admittance was constant to $\pm 0.2\%$ between 200 and 1.5 kHz, while series capacitance values showed a 1% scatter between 30 kHz and 300 Hz. The latter test is especially critical as only a resistive reference was used. Evaluation of a capacitance from voltage measurements is then frequency-dependent and would reflect errors associated with the high sweep rates used.

Results

Figure 1 is a current-voltage plot for the $\text{Cu}/\text{H}_3\text{PO}_4$ interface under conditions typically employed in this study. Distinctive behaviors make it convenient to partition this curve into four regions. In region I, extending to 0.15V, the current rises exponentially. A limiting current level is then established across region II, 0.15-0.35V. The current peak is sweep-rate dependent, being greater for faster rates. In region III, 0.35-0.55V, current oscillations may appear. Here, the current-voltage curve reveals merely a slight minimum/maximum during anodic/cathodic sweeps. Above 0.55V, in region IV, a stable current plateau is maintained until the oxygen evolution region is reached beyond 1.5V.

The electrode was observed *in situ* under $140\times$ magnification during experimentation. As the potential was raised from its open-circuit value, $\sim 0.05\text{V}$, a well-defined etching pattern developed. The polished copper surface first darkened to red-brown, and then sharply demarcated grain boundaries appeared. Individual grains then acquired variegated russet complexions. Crossing regions II and III, the range of tones diminished, with lighter hues favored. A two-tone surface eventually formed and was superseded by a monochrome surface. Grain boundaries remained sharply defined, but the color at this stage was reminiscent of the original bright copper surface. In region IV, these boundaries gradually faded, leaving a featureless surface. When the potential was then lowered, grain boundaries reappeared at $\sim 0.50\text{V}$, and the pattern of coloration was retraced as the potential was further reduced. The etch pattern characterizing region I was stable under open-circuit conditions. At no time was black or dark color observed which might indicate the presence of CuO .

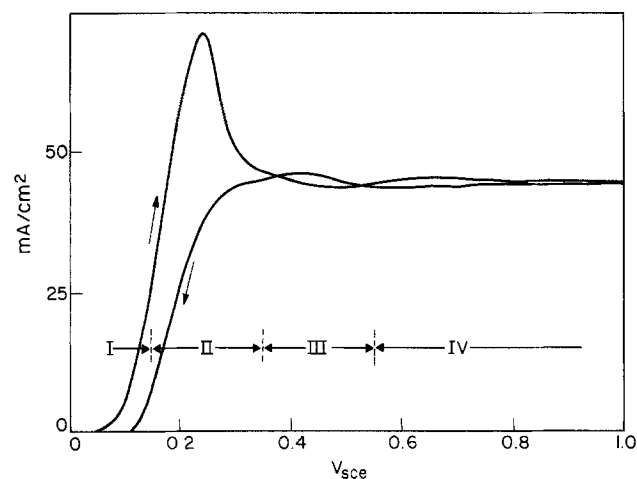


Fig. 1. Voltammetric behavior of the $\text{Cu}/\text{H}_3\text{PO}_4$ interface measured at 20 mV/s sweep rate and 100 rad/s disk rotation. Regions I-IV discussed in the text are shown.

Admittance measurements involved diverse variations of frequency, potential, and current density. Both frequency-sweep measurements at constant potential, $Y_\omega(\omega)$, and potential-sweep measurements at constant frequency, $Y_\omega(\eta)$ proved valuable. The former functions, when plotted in the complex plane, best reveal overall features of relaxation processes. The shapes of these plots are guides to equivalent circuit descriptions. Combinations of $Y_\omega(\eta)$ measurements were used to extract the potential dependence of individual circuit elements after suitable frequencies had been determined from the complex-plane plots.

Complex admittance plots for potentials spanning regions I and II are shown in Fig. 2. Equivalent circuit A in Fig. 3 approximates the response measured in region I. At high frequencies, the admittance is governed by R_0 and C_0 , and the shapes are semicircular. At lower frequencies, plots approach the real axis at 45° . This behavior is better revealed when R_0 and C_0 are deconvoluted from the measured data (Fig. 4). Both G_1 and W increase rapidly with potential in region I. We see, however, clear deviations from the asymptotic slope below 1 kHz. Within region II, these deviations develop into an "inductive" loop which dips below the real axis for frequencies < 300 Hz. Then, rather abruptly, at about 0.25V, this loop is replaced by a capacitive dispersion which approaches the origin at low frequencies. A small but reproducible increase in R_0 is evident in the high frequency intercepts of Fig. 2. The potential dependence of R_0 and C_0 was extracted from $Y_\omega(\eta)$ data at 10 and 100 kHz (Fig. 5). The former function shows a small increase in region II. The latter rises across region I from an initial value of 28 to $35\ \mu\text{F}/\text{cm}^2$ and then plummets abruptly above 0.26V.

Within region III, the low frequency dispersion no longer approaches the origin from the first quadrant but first circles it through quadrants II and III (Fig. 6). The magnitude of this three-quadrant loop is greatest near 0.45V. Plots near this potential but for different electrode rotational speeds show the magnitude of the loop to be proportional to the static current density (Fig. 7). As $\omega \rightarrow 0$, the origin is still approached, but from the third quadrant at an angle $\leq 3\pi/2$. Equivalent circuit B in Fig. 3 can approximate these shapes provided that elements G_2 and C_2 have negative values and $C_1 + C_2 < 0$. The high frequency dispersion, not shown in these figures, remains

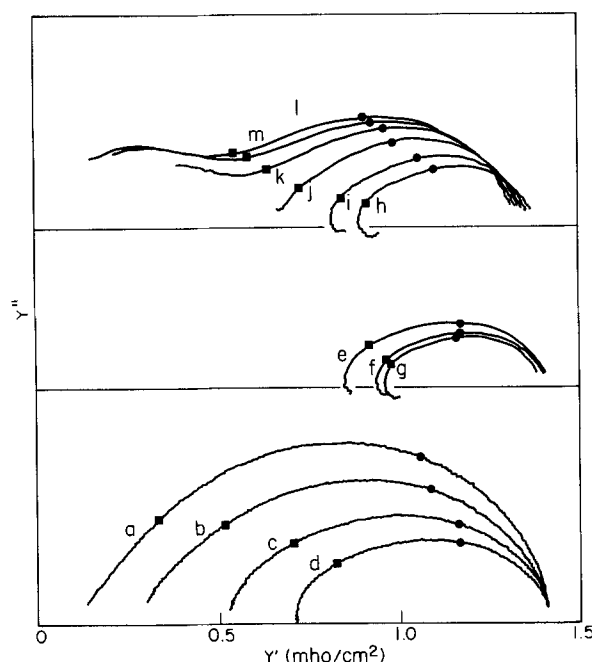


Fig. 2. Admittance plots for potentials in regions I-II. For curves a-m, potentials are 0.06-0.30V in 0.02V increments. The frequency range plotted is 50 Hz-200 kHz with 1 kHz (squares) and 10 kHz (circles) points indicated. Disk rotation: 100 rad/s.

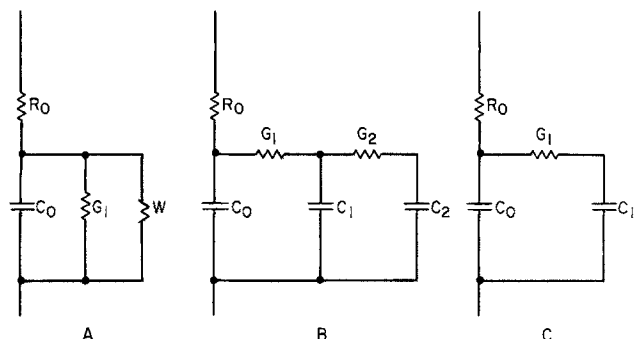


Fig. 3. Equivalent circuits A, B, and C discussed in the text

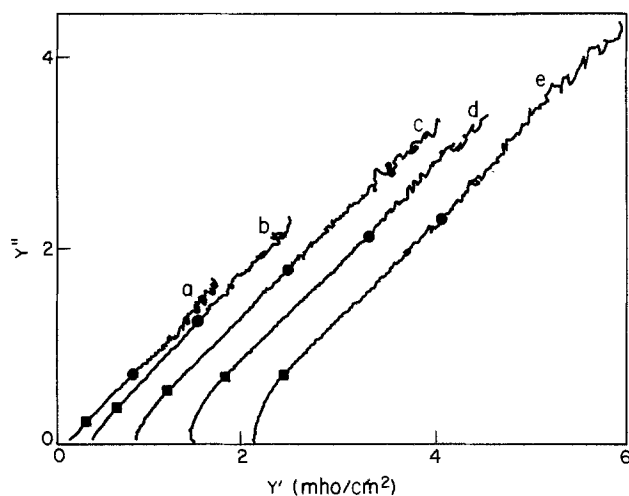


Fig. 4. Admittance plots for data in curves a-e of Fig. 1 after subtraction of the contributions from R_0 and C_0 .

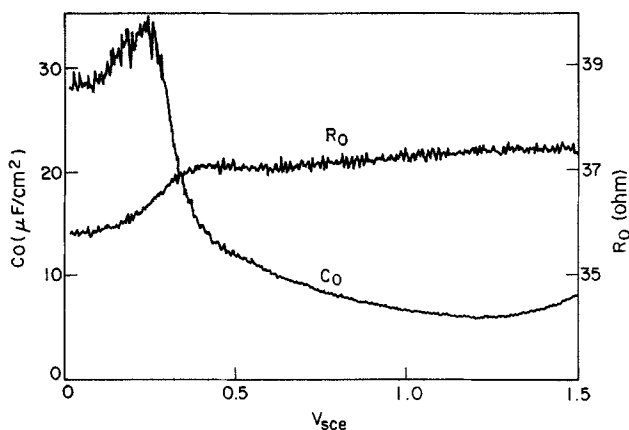


Fig. 5. Dependence of the high frequency cell resistance and capacitance on potential derived from 10 to 100 kHz measurements. Resistance values are plotted as measured for the value is not inversely proportional to electrode area.

determined by R_0 and C_0 , while the low frequency dispersion is given by G_1 , G_2 , C_1 , and C_2 .

Complex admittance plots at plateau potentials, region IV, show two nearly semicircular dispersions, Figure 8 plots the full dispersion (1 Hz-200 kHz) for a sequence of current densities at 1.00V. The amplitude of the low frequency dispersion is directly proportional to the current density. Figure 9 plots the low frequency dispersion for potentials 0.60-1.50V. The amplitude shows only a slight decrease with potential over this range. The cusp separating the dispersions lies between 100 and 1000 Hz, and is unusually sharp. Above +1.0V, it overlaps itself, forming a closed loop in the first quadrant.

Apart from this loop, the response corresponds to equivalent circuit C in Fig. 3. G_1 and C_1 may be found by analysis of the low frequency dispersion. $Y_w(\omega)$ measure-

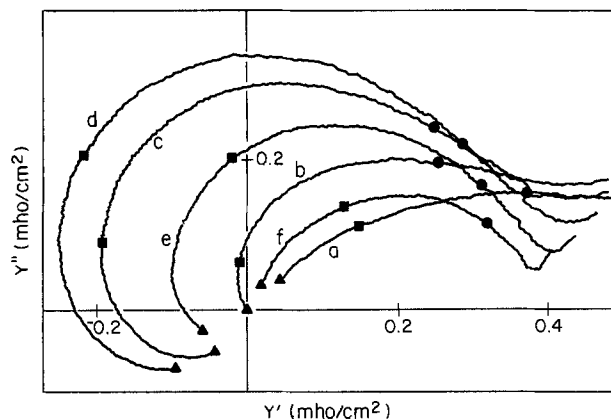
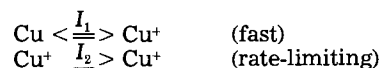


Fig. 6. Admittance plots for the low frequency dispersion in region III. Curves a-f correspond to potentials 0.30-0.55V in 0.05V increments. The plotted frequency range is 1-1000 Hz with 1 Hz (triangles), 10 Hz (squares), and 100 Hz (circles) points shown. Disk rotation: 100 rad/s.

ments at 20 and 100 Hz were analyzed assuming that either a semicircle or a depressed circular arc described the low frequency dispersion. Both approximations gave essentially the same results, and those for the former are plotted in Fig. 10. G_1 values are largely independent of potential, even when the analysis is extended into region III, C_1 values decrease with potential from a maximum 3600 $\mu\text{F}/\text{cm}^2$ at 0.65V to 1300 $\mu\text{F}/\text{cm}^2$ at 1.50V. Below 0.65V, C_1 appears to decrease, but the analysis neglects the negative contribution of C_2 which becomes important within region III.

Discussion

Behavior in region I follows the Mattson-Bockris model developed to describe dissolution into surface acid (8)



The dc current rises at 38 mV/decade rate (1). Admittance measurements are empirically represented by equivalent circuit A in Fig. 3. The high frequency resistance, R_0 , equals the value obtained under zero-current conditions and is due to electrolyte resistivity. The high frequency capacitance, C_0 , ranges from 28 to 32 $\mu\text{F}/\text{cm}^2$. This "conventional" double-layer value reveals no unusual surface polarization characteristics. The minor increase may reflect surface roughening.

To model this reaction mechanism, let $c = [\text{Cu}^+]$ and assume that at the interface ($x = 0$)

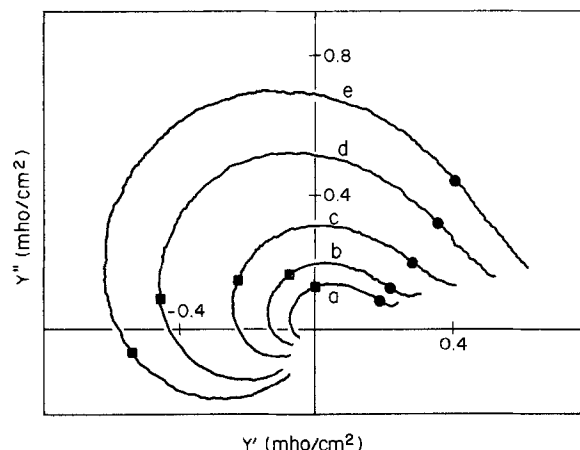


Fig. 7. Admittance plots for the low frequency dispersion in region III at 0.44V. The plotted frequency range is 1-500 Hz with 10 Hz (squares) and 100 Hz (circles) points shown. For curves a-e, disk rotation speeds are 25, 50, 100, 200, and 400 rad/s.

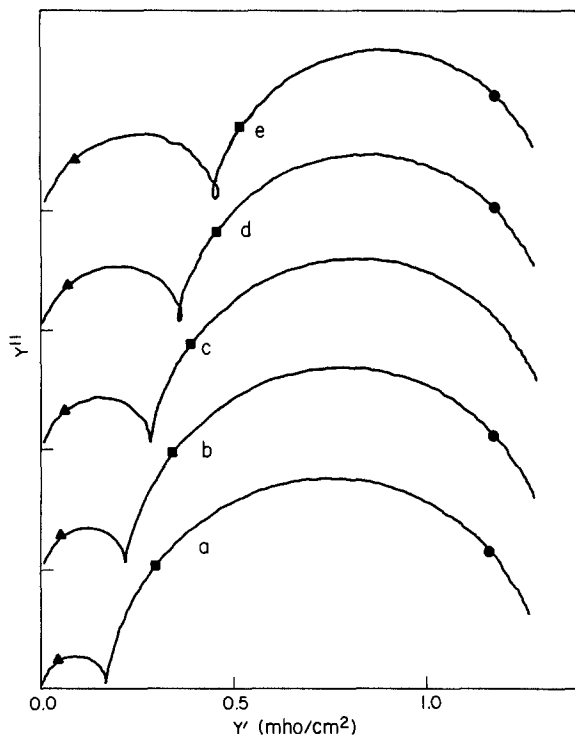


Fig. 8. Admittance plots in region IV at 1.00V. The plotted frequency range is 1 Hz-200 kHz with 10 Hz (triangles), 10 kHz (squares), and 100 kHz (circles) points shown. 100 Hz and 1 kHz points straddle the minimum. For curves a-e, disk rotational speeds are 25, 50, 100, 200, and 400 rad/s.

$$c = c(\eta) = c_0 \exp(e\eta/kT)$$

$$I_2 = I_{20} [(c/c_0) \exp(\beta e\eta/kT)]$$

$$I_1 - I_2 = -DF (\partial c/\partial x)_{x=0}$$

The last expression accounts for the diffusive escape of Cu^+ from the interface before final oxidation. The reaction admittance is therefore (cf. Appendix)

$$Y = G_1 + (i\omega)^{1/2}W$$

$$G_1 = 2(dI_2/d\eta)$$

$$W = D^{1/2}F(\partial c/\partial \eta)_i = D^{1/2}eFc/kT$$

in accord with circuit A of Fig. 3. Cupric ion diffusion, which in principle would add a Warburg term in series with G_1 , may be ignored in an ac analysis because of the high concentration present.

Numerical values for G_1 and W can be derived from the data in Fig. 4. G_1 is given by the extrapolated low frequency intercept and log plots show a linear increase with potential until a maximum is reached at 0.18V. Presuming D , the Cu^+ diffusion coefficient, scales inversely with viscosity as does the Cu^{++} coefficient (1), we estimate $D = 5.5 \times 10^{-7} \text{ cm}^2/\text{s}$ and obtain Cu^+ concentrations of 1.5, 2.6, and 3.7 mM at 0.04, 0.06, and 0.08V (Fig. 4a-4c) (9). $W(\eta)$ peaks near 0.14V. Calculated $[\text{Cu}^+]$ values appear reasonable, but the peak indicates a leveling off near the 5 mM level. Although Cu^+ diffusion is important in determining the electrode impedance, its contribution to the dc current is $< 1\%$. Surface discolorations are seen well below potentials where deviations from this model appear. Color changes point to formation of Cu_2O , but, evidently, this conductive oxide layer does not affect dissolution in region (1).

The onset of region II is marked by maxima in G_1 and W (circuit A in Fig. 3) and the attainment of the limiting current in static measurements. Admittance plots show the development of a low frequency "inductive" loop dipping below the real axis (Fig. 4g-4i). This loop disappears

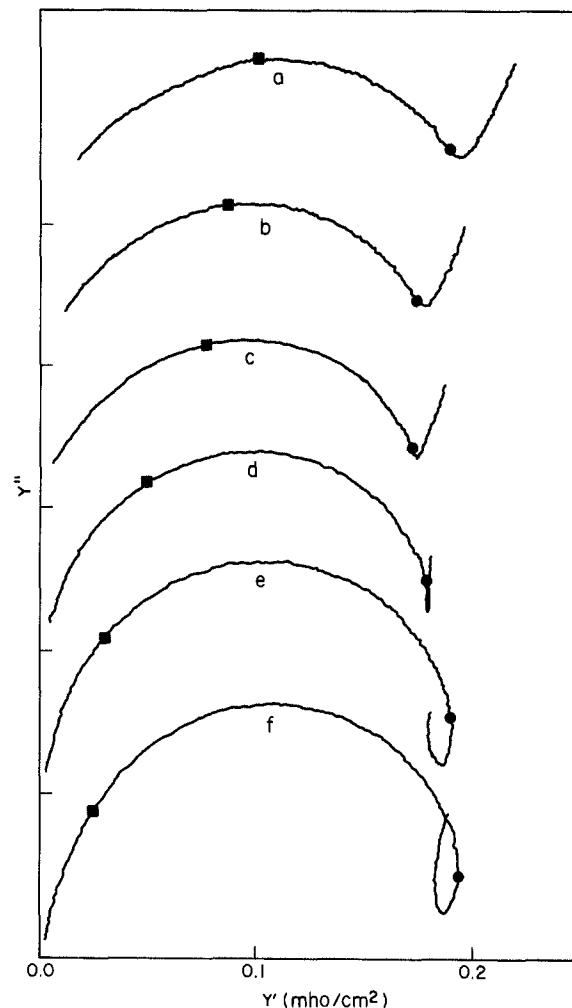
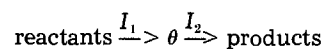


Fig. 9. Admittance plots in region IV. For curves a-f, potentials are 0.60, 0.70, 0.80, 1.00, 1.200, and 1.50V. A disk rotation speed of 25 rad/s was used to reveal more clearly the high frequency loop. The plotted frequency range is 1 Hz-1 kHz with 10 Hz (squares) and 100 Hz (circles) points shown.

at 0.24V and is replaced by a capacitive low frequency dispersion at higher potentials (Fig. 4k-4m). Similar behavior has been observed in the anodic dissolution of Fe in H_2SO_4 , and explained by an adsorbed intermediate Fe(I) species (10)



To model this mechanism, assume both partial currents are functions of potential, η , and the degree of surface coverage by a cuprous intermediate, θ

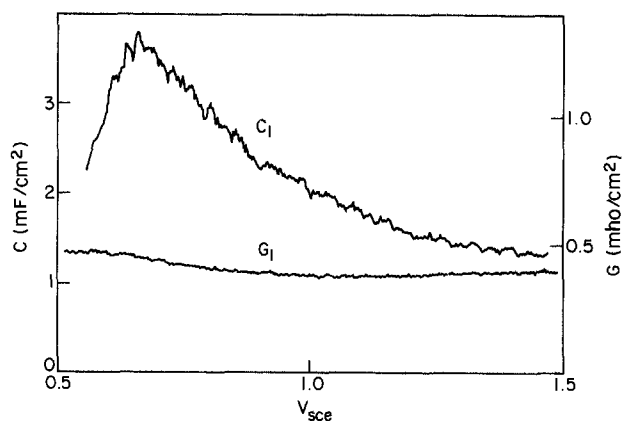


Fig. 10. Variation in region IV of parameters C_1 and G_1 (circuit C of Fig. 3) obtained from 20 and 100 Hz measurements at 37 mV/s sweep rate and 100 rad/s disk rotation.

$$I_1 = I_1(\eta, \theta)$$

$$I_2 = I_2(\eta, \theta)$$

$$Q_{\max} d\theta/dt = I_1 - I_2$$

The last expression accounts for the growth and dissolution of the intermediate layer, with Q_{\max} the charge associated with complete monolayer formation ($\theta = 1$). These expressions lead to the admittance

$$Y = G_1 + (G_2 - G_1)/(1 + i\omega\tau)$$

where

$$G_1 = [\partial(I_1 + I_2)/\partial\eta]_{\theta}$$

$$G_2 - G_1 = [\partial(I_1 - I_2)/\partial\eta]_{\theta} [\partial(I_1 + I_2)/\partial\theta]_{\eta} [\partial(I_2 - I_1)/\partial\eta]_{\theta}^{-1}$$

$$= [\partial(I_1 + I_2)/\partial\theta]_{\eta} (d\theta/d\eta)$$

$$\tau = Q_{\max} [\partial(I_2 - I_1)/\partial\theta]_{\eta}^{-1}$$

G_1 and G_2 are the high and low frequency real axis intercepts. If $G_2 > G_1$, the dispersion appears in quadrant IV. For coverage which increases monotonically with potential, an inductive dispersion corresponds to an increase in coverage with current at constant potential.

Introducing as more explicit functions

$$I_1 = I_{10} (1 - \theta) \exp(e\beta_1\eta/kT)$$

$$I_2 = I_{20} \theta \exp(e\beta_2\eta/kT)$$

we find

$$G_1 = (e\bar{I}/kT) (\beta_1 + \beta_2)/2$$

$$G_2 = (e\bar{I}/kT) [(1 - \theta)\beta_1 + \theta\beta_2]$$

$$\tau = 2\theta (1 - \theta) Q_{\max} \bar{I}$$

where \bar{I} is the dc current level. No dispersion is predicted if either $\beta_1 = \beta_2$ or $\theta = 0.5$. At 0.20V, the low frequency dispersion maximum occurs at 105 Hz ($1/\tau = 2\pi f$), and combining this value for τ with the measured dc current we obtain $\theta(1 - \theta)Q_{\max} = 1.9 \times 10^{14} e^-/\text{cm}^2$. The disappearance of the dispersion at 0.24V implies $\theta \sim 0.5$, and the value for Q_{\max} is consistent with the formation of a monolayer in region II by an electrochemical intermediate.

The expressions for G_2 and G_1 suggest examination of the dimensionless parameter (kTG/eI) as a measure of an anodic transfer coefficient. Taking G_1 from deconvolutions of the high frequency dispersions, we find values decreasing from 2.0 at 0.15V to 0.50 at 0.30V. Over this range, \bar{I} is relatively constant, and the change corresponds to the decrease in size of the low frequency dispersions in Fig. 2. Although values are of order unity, as required for a transfer coefficient interpretation, their dependence on potential implies a more complex mechanism. Limiting current behavior ($G_2 \rightarrow 0$) is only predicted in the limit $\theta \rightarrow 1$ if $\beta_2 \rightarrow 0$, hinting at complications in the second stage of the reaction.

Above 1 kHz, the relaxation is similar to that for region I. The presence of a Warburg contribution is evident in the nonsemicircular appearance of the high frequency dispersions in Fig. 2. W values decrease 50% from their maximum as the potential increases in this region. The high frequency capacitance drops gradually from 32 to 18 $\mu\text{F}/\text{cm}^2$ across region II. The latter decrease is consistent with the formation of a thin insulating layer. A small increase in R_o , $\sim 0.04 \Omega\text{-cm}^2$, may be discerned in the shift of high frequency, real axis intercepts within region II (Fig. 2). When the limiting current level is reached, a large $[\text{Cu}^{++}]$ gradient exists across the diffusion layer. Electro-neutrality forces a corresponding increase in anion concentration which, through the limited dissociation of H_3PO_4 , reduces $[\text{H}^+]$ and consequently electrolyte conductivity in the diffusion layer. In the absence of this effect, we calculate the resistive contribution of the diffusion layer to be $0.013 \Omega\text{-cm}^2$ and the observed change is of a

similar magnitude. Outside region II, R_o values were independent of potential.

We associate region II with the formation of a monolayer of an intermediate Cu(I) species. A transition from low to high coverage is demonstrated by the inductive to capacitive change in the low frequency dispersion and the double-layer capacitance decrease. The latter indicates the monolayer to be a poor electronic conductor. The Cu(I) intermediate cannot be identified with Cu_2O , a good conductor, which is visibly more evident in region I than II.

Although region III is physically the most intriguing, we shall postpone its discussion and pass to region IV. Complex-plane plots show two well-resolved dispersions, each nearly semicircular in appearance (Fig. 7). Apart from the anomalous overlap cusp, the dispersion may be approximated by equivalent circuit C in Fig. 3. At the highest frequencies, response is dominated by R_o and C_o . The former is constant, being fixed by electrolyte resistivity, but the latter exhibits a marked decrease from 18 to 6 $\mu\text{F}/\text{cm}^2$ across regions III and IV. Moreover, C_o is independent of the dc current level. Five measurements at +1.0V for disk rotational speeds ranging between 25 and 400 rad/s yielded values constant to within 3%.

A significant drop in the high frequency capacitance of an electrode can indicate formation of a blocking layer. One interpretation for the origin of limiting current behavior in this system has been the solubility limit of a surface film (11, 12). The rate of dissolution for such a film is proportional to the current density, and film thickness should decrease at higher current levels. The independence of C_o upon current density contradicts this description.

The continuous decrease in C_o with increasing potential suggests trying a Mott-Schottky plot of $1/C^2$ vs. potential (Fig. 11). (Mott-Schottky behavior characterizes a constrained solution of the Poisson-Boltzmann equations and need not imply electronic polarization of a semiconductor interface.) This plot is linear within region IV to 1.2V, at which point C_o begins to increase. The extrapolated intercept of the linear segment lies at +0.35V, the beginning of region III. The simplest model which describes this behavior is a surface layer of thickness l and uniform negative charge density ρ , leading to the Mott-Schottky relations

$$n_d = \rho l^2/2\epsilon$$

$$1/C^2 = (2/\epsilon\rho)\eta_d$$

$$C = \epsilon/l$$

η_d is the potential drop across the layer. From the slope of the plot in Fig. 11, $\epsilon\rho = 5.0 \times 10^{21} e^-/\text{cm}^2$ and $l/\epsilon = 1.3\text{A}$ at +1.2V, the dielectric constant, ϵ , being normalized to its free space value. Physically meaningful parameters imply a high dielectric constant. For 85% H_3PO_4 , $\epsilon = 80$ (13) and for this value $\rho = 6 \times 10^{19} e^-/\text{cm}^3$ and $l = 100\text{\AA}$. The need for a high dielectric constant suggests the charged layer is quasi-aqueous in composition. The layer thickness agrees satisfactorily with previous limits, 13-124 \AA , based on electron diffraction (14), ellipsometry (15), and a reinterpretation of impedance data (16).

The next parameter for consideration is G_1 (circuit C in Fig. 3), a resistive element which determines the initial faradaic current response to a change in potential. G_1 was found to be directly proportional to the limiting current, implying an exponential current-potential relationship. Consider

$$I = I_o(x\dots) \exp(e\beta\eta/kT)$$

where $x\dots$ represents parameters other than the potential. Formally

$$G = (\partial I/\partial\eta)_{x\dots} = (e\beta/kT)\bar{I}$$

with \bar{I} the steady-state current. For data taken at +1.0V, this expression yields $\beta = 0.23 \pm 0.01$ for current densities of 20-80 mA/cm 2 . If β is independent of potential, then, in the limiting current region, so should be G_1 (Fig. 10).

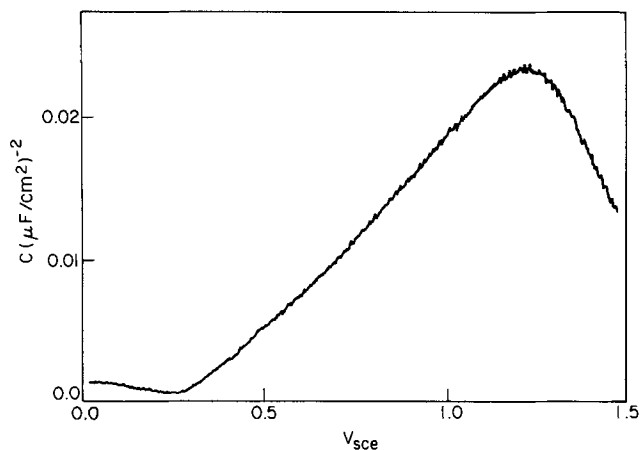


Fig. 11. Mott-Schottky plot for the high frequency capacitance $(1/C_0)^2$ vs. η . C_0

An exponential I - η relation indicates kinetics limited by a barrier whose height is potential dependent. Assume this barrier lies at the metal interface on the inner boundary of the space-charge layer and that the potential drop across this barrier is the difference between the potential of the metal electrode, η , and the potential drop across the space-charge layer, η_d . Thus

$$I = I_0 \exp [e\beta(\eta - \eta_d)kT]$$

where β is the barrier transfer coefficient. The hydrodynamic dependence of the limiting current shows that the steady-state current is determined by concentration gradients external to the surface layer. Consequently, following a potential perturbation, there must be a relaxation of η_d until the injection and dissolution currents are again equal. This relaxation is reflected in the low frequency dispersion seen in Fig. 7 and 8. The semicircular shapes indicate that this relaxation may be approximated by an RC circuit, with the dispersion involving the capacitance, C_1 (Fig. 3C).

For a given potential, C_1 is only slightly dependent on the current density. At +1.0V and rotational speeds of 25, 50, 100, 200, and 400 rad/s, we obtain values of 1600, 1800, 2000, 2100, and 2500 $\mu\text{F}/\text{cm}^2$. In contrast, G_1 ranged 0.5 to 1.9 mho/cm^2 . Against potential, however, C_1 values decrease from 3000 $\mu\text{F}/\text{cm}^2$ at +0.55V to 1300 $\mu\text{F}/\text{cm}^2$ at +1.5V (100 rad/s, Fig. 10). The magnitude of C_1 indicates the associated charge must be faradaic. Between 0.55 and 1.5V, $\int C_1 d\eta$ gives an injected charge of $2 \times 10^{-3} \text{ C}/\text{cm}^2$. This amount is too large to correspond to uncompensated space charge, and we propose that it represents Cu^{++} ions required for growth of the surface layer.

Let us examine growth relaxation for a layer requiring Q coulombs per unit thickness

$$dQ/dt = (dQ/dl) (dl/dt) = I(\eta - \eta_d) - I_d$$

with the rate of change of film thickness proportional to the difference between the electrode current and an unmodulated dissolution current, I_d . The response is that of a conductance, G_1 , and a capacitance, C_1 in series

$$Z = 1/G_1 + 1/(i\omega C_1)$$

$$G_1 = (\partial I/\partial \eta)$$

$$C_1 = (dQ/dl) (\epsilon/\rho l)$$

The capacitance is directly proportional to the high frequency capacitance, assuming a constant density.

Crystallographic data for the compounds CuO , $\text{Cu}_3(\text{PO}_4)_2$, and $\text{CuHPO}_4 \cdot \text{H}_2\text{O}$ give respective molar volumes of 12.4, 85, and 56 cm^3 (17, 18). The $2 \times 10^{-3} \text{ C}/\text{cm}^2$ of integrated charge corresponds to respective layer thicknesses of 13, 29, and 56 \AA . All values are less than the 100 \AA thickness deduced from C_0 . Both C_0 and C_1 decrease similarly with increasing potential. At +0.55V, their ratio is 240, while at +1.0V it is 285. If we suppose that both re-

flect a common surface layer, then from the space-charge density of $6.0 \times 10^{19} e^-/\text{cm}^3$, we deduce molar volumes (Cu^{++}) of 70-80 cm^3 . The molar volume of H_3PO_4 in the electrolyte is also 70 cm^3 . This density is less than that of crystalline $\text{CuHPO}_4 \cdot \text{H}_2\text{O}$. The lower density, together with the high dielectric constant inferred from C_0 values, suggests an amorphous structure containing a high density of dipoles able to reorient in the internal electric fields present.

The most interesting electrical behavior lies in the negative impedance region, III. Here complex admittance plots show a low frequency dispersion circling the origin through three quadrants (Fig. 6, 7). As $\omega \rightarrow 0$, the origin is approached from the third quadrant at an angle $\sim 3\pi/2$, corresponding to a negative capacitance. Current-voltage curves in region III show a small dip/rise in anodic/cathodic sweeps. The magnitude of these changes is sweep-rate dependent, and offers independent confirmation for a negative capacitance. Phenomenologically, any circuit exhibiting the observed response can be made to oscillate by insertion of a series resistance sufficient to shift the negative real axis intercept to the origin. Equivalent circuit B in Fig. 3 can simulate the observed dispersion provided elements R_2 and C_2 are negative and $|C_2| > C_1$. Let us examine its stability with respect to a current fluctuation, $\delta I(t)$, under potentiostatic control ($\delta V(t) = 0$). For simplicity, we drop the high frequency capacitance, C_0 , and combine R_0 and R_1 into a single resistance, R . In addition to depending upon the electrolytic cell, this parameter includes any external resistance we might choose to insert in series with the working electrode. The impedance function $Z(i\omega, R, R_2, C_1, C_2)$ is readily found algebraically. Under constant applied potential the time-dependent current fluctuation is obtained by replacing $i\omega$ with d/dt

$$\delta V(t) = 0 = Z(d/dt, R, R_2, C_1, C_2) \delta I(t)$$

or

$$\{RR_2C_1C_2 \frac{d}{dt^2} + [R(C_1+C_2) + R_2C_2] \frac{d}{dt} + 1\} \delta I(t) = 0$$

Circuit stability depends on the sign of the second term. If positive, fluctuations decay exponentially. If negative, they grow until limited by nonlinearities in the circuit elements. We have assumed R_2 and C_2 to be negative. For R sufficiently small, the circuit is stable, but by increasing R we may always achieve an unstable condition. As the critical point is approached, small amplitude oscillations will occur at a frequency, $\omega = RR_2C_1C_2^{-1/2}$ [cf. Fig. 4a, Ref. (1)]. This is the frequency at which the admittance plot crosses the negative real axis. As experimentally verified (1), larger electrodes are more prone to oscillation because of the greater contribution of electrolyte resistance to the cell impedance. For $C_2 < 0$ but $C_1 + C_2 > 0$, the circuit is unconditionally stable, and complex-plane plots approach the origin at an angle $\pi/2$.

A negative differential capacitance implies a net decrease in the charge stored in the interfacial region following a potential increase. Integration of this capacitance across the negative impedance region gives a drop of $2 \times 10^{-3} \text{ C}/\text{cm}^2$. The magnitude indicates a faradaic charge too large to be accommodated by the thin surface layer present at these potentials. Rather, the charge must be associated with a modulation of the flow of ions into the diffusion layer. We have previously shown that electric fields significantly enhance Cu^{++} fluxes in this quasi-neutral region (1), and we believe these fields are closely related to the instabilities. There is an empirical resemblance between electrochemical behavior and the semiconductor Gunn effect (19). Both involve instabilities in systems with large static fluxes. In semiconductors, the effect is explained by a decrease in carrier drift velocity with an increase in the local electric field. Soliton charge density waves can form within a bulk phase. Instabilities at injecting contacts have also been analyzed, and calculated current-voltage curves bear a marked resem-

blance in shape and position of the negative impedance region to the electrolytic curves (20, 21).

The Gunn effect depends upon a change in band structure with field. Electrolytes lack this option, but offer possibilities arising from a multiplicity of charge bearing species. If we neglect anion migration, our system contains mobile hydrogen and copper ions. We have measured diffusion coefficients in phosphoric acid for the latter and, based upon conductivities, we infer a mobility ratio as high as 10^3 (1). A mechanism by which the balance between high mobility H^+ and low mobility Cu^{++} is shifted towards the latter in high field regions could lead to a direct Gunn analog. We have not been able to rationalize such an ionic field effect, but can construct a potential parallel. Assume behavior in the diffusion layer is expressed by the equations

$$\partial c/\partial x = +(ze/kT) cE - J_c/D_c$$

$$\partial h/\partial x = (e/kT) hE - J_h/D_h$$

$$\partial E/\partial x = (F/\epsilon) (zc + h - a)$$

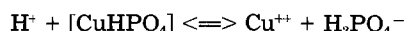
where c , h , and a are concentrations, E the electric field, and J and D fluxes and diffusion coefficients. For rapid proton diffusion [H^+] follows a local Boltzmann relation

$$h(x) = h_0 \exp[-e\eta(x)/kT]$$

The rapid dissociative equilibrium of phosphoric acid ($ha = h_0^2$) implies (22)

$$a(x) = h_0 \exp[+e\eta(x)/kT]$$

even though anions have been assumed immobile. Copper phosphates are very insoluble in neutral and alkaline solutions and an equilibrium maintained by a reaction such as



may be imagined. Hypothesize a bulk phase in which [—] represents trapped Cu^{++} ions. A local increase in [Cu^{++}] leads to an increase in [H^+] and hence a drop in the local potential. The consequent change in electric field tends to drive neighboring Cu^{++} ions towards the center of the fluctuation. Should this force be sufficient to overcome diffusional spreading, the fluctuation will grow.

While the feasibility of a bulk instability may be conjectural, a dissolution interfacial analog offers one explanation for negative impedance behavior. If [—] represents the surface layer, the dissolution current can be written as

$$I_d = k^+ [H^+] - k^- [Cu^{++}] [H_2PO_4^-]$$

or

$$I_d = h_0 \{k^+ \exp(-e\eta_2/kT) - k^- \exp(+e\eta_2/kT) [Cu^{++}]\}$$

with η_2 the potential at the boundary of the surface and diffusion layers. Although the dissolution reaction does not involve charge transfer *per se*, its potential dependence is similar to a charge transfer reaction, save for the sign reversal in the exponents. Negative impedance behavior follows from the fact that the current decreases with an increase in local potential. Although hydrogen ions are a minor constituent of the system, they are strongly coupled to the dissolution reaction and the electric potential. An increase in potential drives these ions away from the interface, thereby decreasing the rate of dissolution.

To find the impedance of the diffusion layer, we must first consider electric field effects on Cu^{++} migration. Given

$$dc/dt = \partial \frac{\partial}{\partial x} (\partial c/\partial x + (zec/kT)\partial \eta/\partial x)$$

and assuming quasi neutrality with $zc = a \gg h$, this equation simplifies to

$$dc/dt = (z + 1)D_c \partial^2 c/\partial x^2$$

In regions where H^+ is a minority carrier, migration leads to an apparent threefold enhancement of the diffusion coefficient. The "diffusion" current is then given by

$$I_d = -z(z + 1)FD_c (\partial c/\partial x)_{x=0}$$

and the diffusion layer impedance becomes

$$Z_d = \eta_2^*/I_d^* = 1/G_d + [i\omega]^{1/2}W_d]^{-1}$$

with

$$G_d = (\partial I_d/\partial \eta_2)$$

$$W_d = zF(i\omega(z + 1)D_c)^{1/2} (\partial c/\partial \eta_2)_1$$

Both G_d and W_d have negative values, and the equivalent circuit consists of a negative resistance and a negative Warburg element in series.

The extent to which this negative impedance is reflected in measured impedances depends upon an additional relationship connecting changes in η_2 with those of η or η_1 . For thin surface layers, we expect the coupling to be large, whereas for thicker layers it should become negligible. The measured negative impedance is about an order of magnitude larger than Z_d calculated assuming $c \sim 1M$. An analysis of ellipsometric data has suggested the presence of a 2000-3500Å viscous region adjacent to the electrode (15). Although such a region would conveniently account for a greater negative impedance, its existence is not revealed by other parameters dependent upon the diffusion layer.

Negative impedance behavior also appears in region IV in the loop separating the two principal dispersions. An interpretation using the model proposed for region III can be forced by an ad hoc relationship between η_2 and η or η_1 , but an alternative explanation can be positive charge injection into a negatively charged space-charge region. Discussion of region IV has been based on the control of injected current by a barrier at the metal interface with a height dependent on the potential difference between the metal and the adjacent surface layer, $\eta - \eta_1$. The potential in the layer, η_1 , is not zero by virtue of negative space-charge within the film, *i.e.*

$$\eta_1 = -\rho l^2/2\epsilon$$

with $\rho < 0$. The low frequency dispersion arises from an increase in layer thickness with potential. Following an increase in η , the current rises, the film thickens, and η_1 also rises until $\eta - \eta_1$ is restored to its original value. If, however, prior to growth, the injected charge reduces the negative charge density, a small negative capacitance develops. For

$$I = I(\eta - \eta_1)$$

$$\eta_1 = -ql/2\epsilon$$

$$dq/dt = I$$

with q the charge in the layer, we find

$$Z = 1/G + 1/i\omega C)$$

$$G = \partial I/\partial \eta$$

$$C = -2\epsilon/l$$

The magnitude of the negative capacitance is comparable with the high frequency interfacial capacitance. Over longer periods of time film growth leads to a much larger positive capacitance, but, for frequencies well above those characterizing the growth process, this mechanism may account for the high frequency loops.

Questions unresolved concern the role of Cu^+ ions in regions III and IV, and those factors determining the space-charge density. It was concluded in Ref. (1) that a water depletion layer was important in determining the steady-state current. Water has not entered into this discussion, except perhaps implicitly in the rate constants in expressions for I_d . Cu^+ defects in the surface layer might account for the space-charge polarization. The ratio of [Cu^{++}] to the

space-charge density, $C_i/C_0 \approx 250$, is close to the $[\text{Cu}^{2+}]/[\text{Cu}^+]$ ratio expected for the solution phase. Independent experiments, e.g., ring disk studies, sensitive to the Cu^+ dissolution current may resolve some of these uncertainties.

Conclusions

Four stages describe the dissolution of copper into phosphoric acid. Initially, a two-step oxidation process involving soluble Cu^+ occurs. A surface monolayer forms when $[\text{Cu}^+]$ reaches a 5 mM level. At higher potentials, a negatively charged surface layer develops, reaching a thickness $\sim 100\text{\AA}$ at +1.0V. Current injected into this layer is limited by a barrier at the metal interface. The layer grows until the injection rate matches the hydrodynamically determined dissolution rate. Thickness is determined by potential, not current density, indicating it is the space-charge rather than a kinetic IR drop which controls the barrier height. During the initial phase of layer growth, a negative impedance develops which is responsible for current oscillations. As a mechanism, it is proposed that electric fields external to the barrier lower $[\text{H}^+]$ with increasing potential and therewith reduce the dissolution rate.

Manuscript submitted Nov. 21, 1984; revised manuscript received June 24, 1985. This was Paper 256 presented at the New Orleans, Louisiana, Meeting of the Society, Oct. 7-12, 1984.

At&T Bell Laboratories assisted in meeting the publication costs of this article.

APPENDIX

Assume as given a set of equations sufficient to describe a time-dependent electrode process. Time-dependent variables will include the current, I , the total applied potential, η , and a sequence of other variables, x_i , specific to the model. The steady-state value of each variable is subject to an arbitrarily small sinusoidal modulation so that

$$I(t) = \bar{I} + I^* \exp(i\omega t)$$

$$dI/dt = i\omega I^* \exp(i\omega t)$$

and similar expressions follow for η^* and x_i^* . For each of the equations describing the model, there is an equivalent modulation expression obtained from a first-order perturbation expansion about the steady state. If, for example

$$I = I(\eta, x_i)$$

then

$$I^* = (\partial I / \partial \eta)_{x_i} \eta^* + (\partial I / \partial x_i)_{\eta} x_i^*$$

The impedance is obtained by solving this set of linear equations for the ratio η^*/I^* . The admittance is the reciprocal of this ratio. Diffusional equations are frequently encountered, and the modulation counterpart of

$$dc(x,t)/dt = Dd^2c(x,t)/dx^2$$

is

$$i\omega c^*(x) = Dd^2c^*(x)/dx^2$$

with the Warburg solution

$$c^*(x) = c^*(0) \exp[-(i\omega/D)^{1/2}x]$$

The alternative solution with positive exponent becomes important for finite width diffusion regions at low frequencies ($\omega < D/l^2$).

REFERENCES

1. S. H. Glarum and J. H. Marshall, *This Journal*, **132**, 2872 (1985).
2. P. Poncet, M. Braizaz, B. Pointu, and J. Rousseau, *J. Chim. Phys.*, **74**, 452 (1977).
3. R. de Levie, *Electroanal. Chem.*, **25**, 257 (1970).
4. R. de Levie and A. A. Husovsky, *J. Electroanal. Chem.*, **22**, 29 (1969); R. de Levie and L. Pospisil, *ibid.*, **22**, 277 (1969); L. Pospisil and R. de Levie, *ibid.*, **25**, 245 (1970).
5. P. Jacquet, *Bull. Soc. Chim. Fr.*, **3**, 705 (1936).
6. P. Poncet, M. Braizaz, B. Pointu, and J. Rousseau, *J. Chim. Phys.*, **75**, 287 (1978).
7. S. H. Glarum and J. H. Marshall, *This Journal*, **131**, 691 (1984).
8. E. Mattson and J. O'M Bockris, *Trans. Faraday Soc.*, **55**, 1586 (1959).
9. G. W. Tindall and S. Bruckenstein, *Anal. Chem.*, **40**, 1402 (1968).
10. I. Epelboin, M. Keddam, and J. C. Lestrade, *Discuss. Faraday Soc.*, **56**, 264 (1973).
11. W. C. Elmore, *J. Appl. Phys.*, **10**, 724 (1939); *ibid.*, **11**, 797 (1940).
12. K. Kojima and C. W. Tobias, *This Journal*, **120**, 1026 (1973).
13. "Gmelins Handbuch," 8th ed., Phosphor C, p. 186 (1965).
14. E. C. Williams and M. A. Barrett, *This Journal*, **103**, 363 (1956).
15. M. Novak, A. K. N. Reddy, and H. Wroblowa, *ibid.*, **117**, 733 (1970).
16. K. Kojima and C. W. Tobias, *ibid.*, **120**, 1202 (1973).
17. G. L. Shoemaker, J. B. Anderson, and E. Kostiner, *Acta Cryst. B*, **33**, 2969 (1977).
18. A. Boudjada, *Mater. Res. Bull.*, **15**, 1083 (1980).
19. M. P. Shaw, H. L. Grubin, and P. R. Solomon, "The Gunn-Hilsum Effect," Academic Press, New York (1979).
20. H. L. Grubin and R. Kaul, *IEEE Trans. Electron Devices*, **ed-22**, 240 (1975).
21. K. W. Boer and G. Dohler, *Phys. Rev.*, **186**, 793 (1969).
22. L. W. Green, P. Kruus, and M. J. McGuire, *Can. J. Chem.*, **54**, 3152 (1976).

The Study of the Anodic and Cathodic Corrosion Process of Coated Iron with the Electrochemical Impedance Technique

J. Hubrecht and J. Vereecken*

Department of Metallurgy and Electrochemistry, Faculty of Applied Sciences, Vrije Universiteit Brussel, 1050 Brussels, Belgium

ABSTRACT

In order to study the anodic and cathodic corrosion process of painted iron separately, two similar specimens are mounted as a differential aeration couple. Application of the electrochemical impedance measurement technique, scanning electron microscopy, and x-ray analysis demonstrate a different paint-degradation rate according to the anodic or cathodic polarization. The blistering phenomenon is shown to be a consequence of the anodic process. The electrochemical impedance points out diffusion control in the cathodic cell and charge transfer control in the anodic cell.

The study of the quality of organic corrosion inhibiting coatings assumes an investigation of the interaction between the corrosive environment, the coating itself, and the metal substrate. More particularly, the course of the subcoating corrosion process and the mechanism of the coating deterioration are important topics. Interaction means that one should investigate the metal/coating/environment system preferably as an integral one. Furthermore, the system is time dependent, so one should be able to monitor it *in situ*. Since the underlying corrosion phenomenon has an electrochemical nature, first of all electrochemical techniques provide a proper method.

The electrochemical impedance technique is especially useful in examining interface processes, and coating performance (1-10). Two important advantages of this technique are that: (i) it often displays the constituting characteristics of the system separately (surface layers, charge transfer, mass transfer, etc.) and (ii) there is no pronounced perturbation of the system, since one usually works with small amplitude signals.

Still, the interpretation and modeling of electrochemical impedance data is not an easy matter.

In order to evaluate what role oxygen plays in corrosion of the integral metal/coating/environment system, an attempt is made to subdivide the system artificially into the oxidation and reduction process. Impedance data, together with scanning electron microscopy and x-ray analysis, are used to investigate the paint degradation and to determine the corrosion mechanism under the coating.

Experimental

After polishing with 600 grit paper, cleaning ultrasonically, and degreasing with ethanol each ARMCO iron plate is coated with a water-base emulsion paint, consisting of ERCUSOL AS250 (a styrene-acrylic polymer) with red iron oxide and strontium chromate pigments.

As described elsewhere (5), the coated specimen is mounted as the bottom plate of a glass cylinder, which is filled with an aqueous 0.5M NaCl solution. The circular surface of the exposed part has an apparent area of 19.6 cm². The experiment runs at room temperature.

For the application of the electrochemical impedance technique, a platinum grid is used as a counterelectrode and an SCE as a reference electrode. The metal substrates of two identical cells are connected electrically, and the cell solutions are connected electrolytically. Pure oxygen is supplied continuously in cell 1, pure nitrogen in cell 2. In this way, a differential aeration couple is created, and the net current between both cells can directly be measured, as can the mixed potential of the metal substrate *vs.* a SCE.

Cell 1 has an average coating layer thickness of 220 μm , and cell 2 190 μm . To have some idea about the reproducibility, the experiment has been repeated with a similar pair of cells (cells 3 and 4) over a shorter time period. Table I presents the cell specifications.

* Electrochemical Society Active Member.

The electrochemical impedance of the separate cells is measured after first disconnecting both cells and holding them potentiostatically at the latest measured mixed potential.

The electrochemical impedance measurement mounting consists of a 1250 frequency response analyzer (FRA) and a 1186 electrochemical interface (potentiostat) both from Solartron/Schlumberger. The FRA is controlled by a Tektronix 4051 desktop computer to perform automatic measurements, data transmission, and data output. The frequency range of the applied voltage sine wave ranges from 65.5 kHz to 10 mHz, and the amplitude is 20 mV.

After a 92 day test period, cells 1 and 2 are dismantled. The coated plates are rinsed with distilled water and ethanol, dried, and embedded in a cold mounting epoxy resin. A cross section is made with a diamond saw. The samples are then polished with 600 grit paper, rinsed with ethanol, coated with carbon, and subsequently analyzed with scanning electron microscopy (SEM) and x-ray analysis (JEOL JSM-50A and ORTEC 6200).

Results

Figure 1 represents the net corrosion current directly measured between cells 1 and 2, and cells 3 and 4. The current between cells 1 and 2 shows an almost linear increase during the first 15 days of the immersion and finally reaches a kind of plateau of about 200 nA. Cells 3 and 4, however, show a much steeper current increase, and the plateau is situated at 500 nA.

The mixed potential of the connected cells 1 and 2, or corrosion potential (Fig. 2), drops by 200 mV in about 4 days; thereafter, the decrease is much slower. The latter trend is very similar to, if somewhat faster than, the corrosion potential behavior of a single cell (called no. 5 in Table I) with 190 μm of the same paint in 0.5M NaCl under air atmosphere (5) (Fig. 2).

Similarly to the current variation of the couple cell 3/cell 4, their potential variation is also faster than for the couple cell 1/cell 2 (Fig. 2).

After an immersion time of 11 days, the cell 1/cell 2 couple is cut for about 10 min. The potential of cell 2, nitrogen supplied, is found to fall by 57 mV; the potential of cell 1, oxygen supplied, rises by 32 mV.

Typical impedance data of cell 1 and cell 2 after 26 days are depicted in a Cole-Cole plot in Fig. 3. The impedance is expressed in $\Omega\text{-cm}^2$ of the apparent area. It is explained elsewhere (5) that the impedance response of a sub-

Table I. Cell specifications

Cell no.	Average coating layer thickness (μm)	Atmosphere
1	220	O ₂
2	190	N ₂
3	224	O ₂
4	211	N ₂
5	190	Air

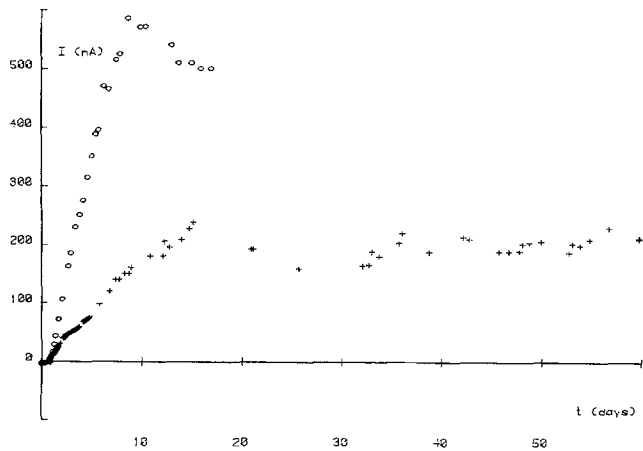


Fig. 1. Net corrosion current I as a function of immersion time t . Crosses: between cell 1 and cell 2. Circles: between cell 3 and cell 4.

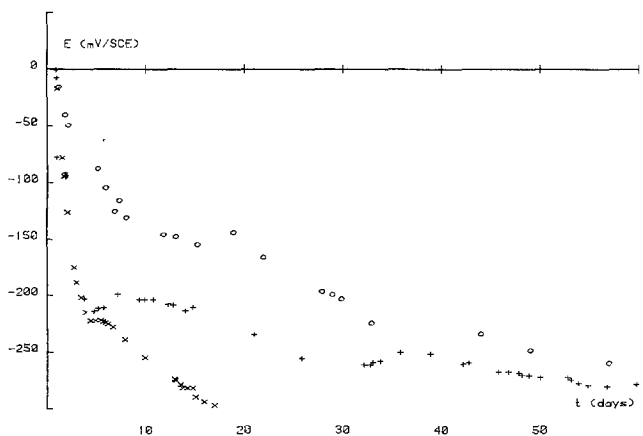


Fig. 2. Mixed (corrosion) potential E as a function of immersion time t . +: Couple 1/2. x: Couple 3/4. o: Single corrosion cell.

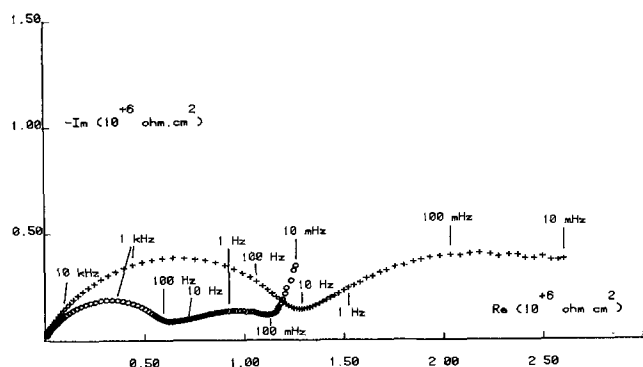


Fig. 3. Complex impedance plot after 26 days. o: Cell 1. +: Cell 2. Parameter: frequency.

mersed coated iron sheet, as specified above, contains three distinct sections according to the frequency domain. The flattened semicircle which is found at high frequencies (HF) is known to reflect the physical behavior of the coating. At intermediate frequencies (IF), the impedance follows the impedance of the electrochemical double layer and charge transfer at the metal substrate, and at low frequencies (LF) the impedance of the mass transfer.

It is noticed from Fig. 3 that the impedance curve of cell 2, and more particularly its HF part, extends over a much wider area than the one of cell 1. If R is taken as the diameter of the HF flattened semicircle, or otherwise as the abscissa of the HF minimum in the curve, then R is $1.29 \times 10^6 \Omega\text{-cm}^2$ for cell 2 and $6.43 \times 10^5 \Omega\text{-cm}^2$ for cell 1 after 26 days.

Further, cell 1 shows a charge transfer response and a mass-transfer response, whereas the data of cell 2 comprise a charge transfer response and no mass-transfer response.

Viewing the impedance data of cell 2 after 11, 26, and 46 days (Fig. 4), one can see that the same behavior is maintained, although the size of the curve is markedly decreasing. The same holds for cell 1 (Fig. 5); still, one can object that the mass transfer becomes increasingly determining with immersion time.

Figure 6 (oxygen-supplied cells no. 1 and 3) and Fig. 7 (nitrogen-supplied cells no. 2 and 4) demonstrate that the experiment is reproducible as for the shape of the impedance curve, but not for its magnitude (Table II). Moreover, going from cell 1 to cell 3 (Fig. 6), the real part of the lowest frequency impedance does not decrease in the same proportion as R . The same is observed in going from cell 2 to cell 4 (Fig. 7).

In the case of the cell 2 sample, the coating shows a blistered surface and can easily be removed after the immersion experiment. The blisters have a maximum diameter of about 1 mm, and an approximate density of 80

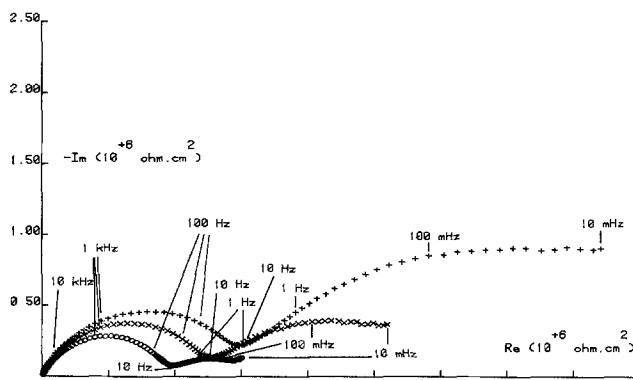


Fig. 4. Complex impedance plot of cell 2. +: 11 Days. x: 26 Days. o: 46 Days. Parameter: frequency.

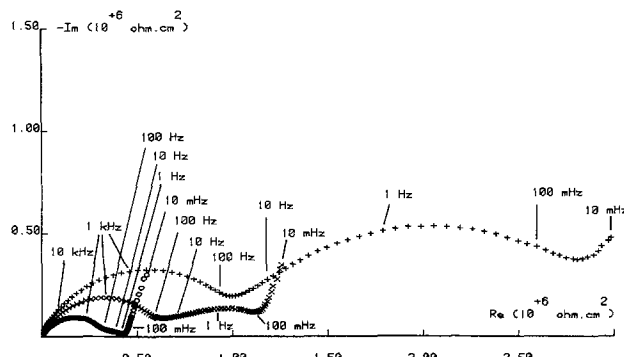


Fig. 5. Complex impedance plot of cell 1. +: 11 Days. x: 26 Days. o: 46 Days. Parameter: frequency.

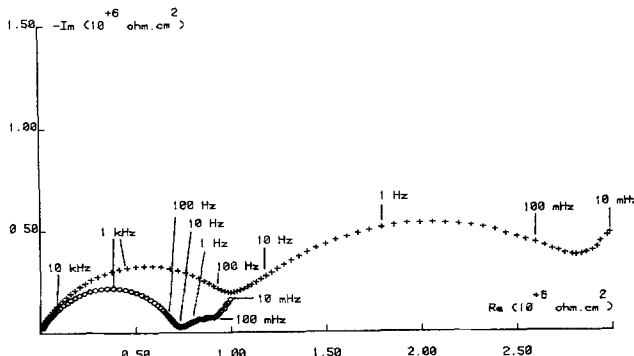


Fig. 6. Complex impedance plot. +: Cell 1 after 11 days. o: Cell 3 after 10 days. Parameter: frequency.

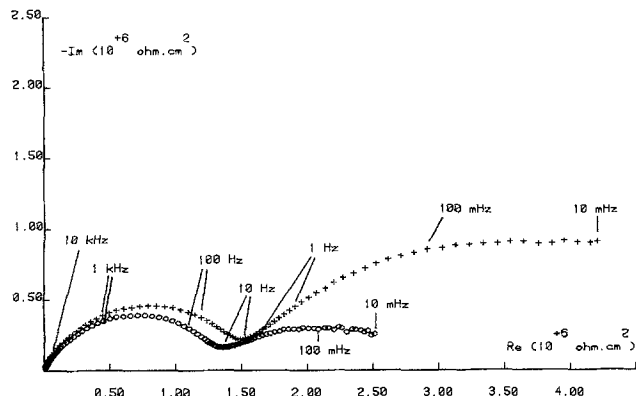


Fig. 7. Complex impedance plot. +: Cell 2 after 11 days. o: Cell 4 after 10 days. Parameter: frequency.

cm⁻². The blisters are not cracked. During optical inspection of the coating/metal interface, voluminous light brown products are observed at the blister sites alternated with a thin uniform dark brown layer. During the immersion test, no products are visible on top of the coated sample and the bulk solution pH fluctuates around 6. In the case of the cell 1 sample, the coating shows an intact surface and no blisters at all, and is still uniformly attached to the substrate; at any place where the coating is pushed off, the metal surface is blank. The bulk solution pH is about 8 during the immersion test.

Figure 8 shows a cross section of the cell 2 sample with an accumulation of oxidation products at a blister. Those products contain Fe, O, and Cl; in the surrounding organic coating, Cr is detected, but it is not in the anodic products. SEM and x-ray microanalysis do not reveal any reaction products at the coating/metal interface of the cell 1 sample.

Discussion

The similarity between the corrosion potential behavior of the single cell and the mixed potential behavior of the differential aeration couple demonstrates that the latter experiment is a good simulation of the real corrosion process. Moreover, the oxygen-supplied cells no. 1 and 3 must behave as cathodes, and the nitrogen-supplied cells no. 2 and 4 as anodes. There are more arguments in favor of those statements: the measured net current, the spontaneous shift of the potential of cell 1 to more positive values and of cell 2 to more negative values when they are disconnected, and the intact condition at the metal/coating interface of cell 1 and the oxidation products at the metal/coating interface of cell 2. The simulation also points out that differential aeration may be one factor determining the anodic and cathodic sites of a corroding coated metal.

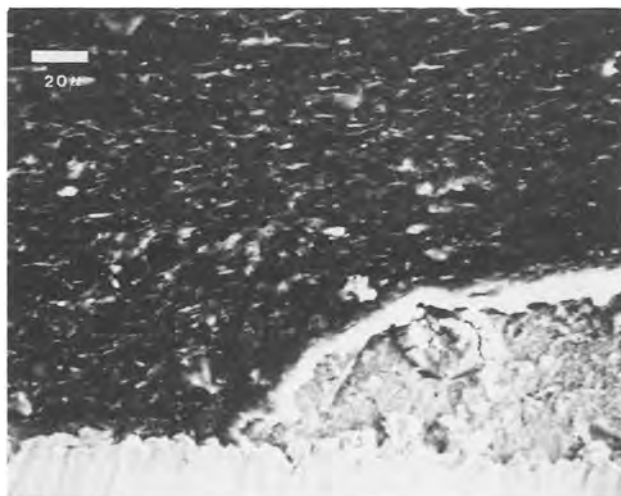


Fig. 8. SEM picture of a cross section of the cell 2 sample. Above: Coating layer. Under: Iron plate. Right: Oxidation products.

Relying on the model proposed earlier for the metal/coating/electrolyte system (10), the quantity R may be a measure for the resistance of the immersed coating layer, or pore resistance, as conduction is ensured via pores in the coating. The R values for both the cell 1 and cell 2 specimen have been drawn as a function of the immersion time (Fig. 9). The reduction of the coating resistance as a consequence of penetration by the conducting solution and coating degradation is a known phenomenon. Nevertheless, the resistance of the cell 1 coating is lower than that of cell 2, although the slight difference in average thickness (Table I) points in the reverse sense, and although the immersion conditions are the same. This fact is repeatable (Fig. 10). The active section A of the coating available for permeation of electrolyte, reacting and reaction products is only a small fraction of the apparent surface area A_a of the coating. A measure for A can be calculated from the measured resistance R and the thickness l of the coating and the specific resistance ρ of the solution which is 23 Ω -cm for cell 1 and cell 2, according to

$$\frac{R}{A_a} = \rho \frac{l}{A}$$

Figure 11 is a plot of the active section A vs. the immersion time for both cell 1 and cell 2. One finds that the active coating section of the cell 1 sample increases linearly with immersion time, whereas the slope for the cell 2 sample is markedly smaller.

At this point, it may be convenient to discuss the appearance of the samples after the immersion test. It is shown by visual and SEM inspection and x-ray analysis that the anodic process in cell 2 is responsible for the formation of products which contain Fe, O, and Cl. As a result of iron oxidation under the coating, hydrolysis (and thus decrease of the solution pH), Cl⁻ penetration

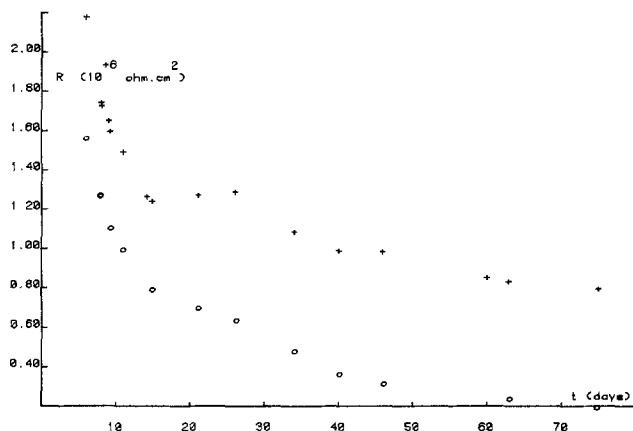


Fig. 9. Immersed coating resistance R vs. immersion time t . o: Cell 1. +: Cell 2.

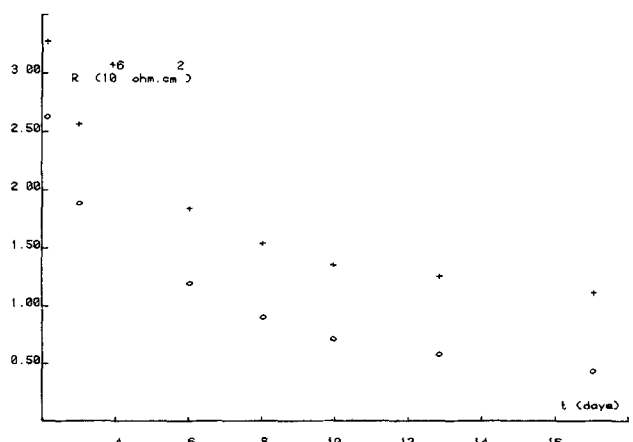


Fig. 10. Immersed coating resistance R vs. immersion time t . o: Cell 3. +: Cell 4.

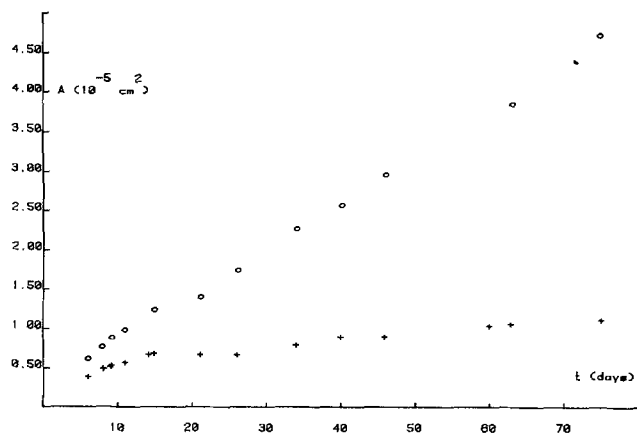


Fig. 11. Active section A of the immersed coating vs. immersion time t . o: Cell 1. +: Cell 2.

through the coating, and Cl^- contribution to the oxidation process, oxidation products are formed and precipitated. They are much more voluminous than the iron itself, and push up the coating. Blister formation is the consequence, which also makes the coating easily detachable.

On the other hand, during the cathodic process in cell 1 oxygen penetrates the coating and is reduced to OH^- , which is proved by the rising of the pH in the bulk solution. One would expect cathodic delamination to occur (11-17), but under the present circumstances no such delamination is detected after 92 days of continuous immersion. An explanation may be found in the rather good performance of the styrene containing copolymer in alkali environment (11) due to the evacuation of OH^- from the metal/coating interface through the water-base emulsion coating, of which the permeability is even increased by the chromate pigment (5).

The better performance of the cell 1 coating is only seemingly contradictory with the R behavior as determined by impedance measurements. Indeed, it is supposed that the coatings of cell 1 and cell 2 behave in the same way as long as only movement of dissolved substances through the coating is occurring. Voluminous deposits, however, as formed by the anodic process in cell 2 cannot move through the coating and actually block the pores. The consequence is that the R drop is slowed down in the anodic cell. This enforces the insight that blister formation in the anodic case is caused by mechanical action of the oxidation products at the coating/metal interface.

Also, the steepest active section increase for cell 2 seems to occur during the first 15 days. It is striking that, as soon as the rate of increase in A in cell 2 slows down, the current reaches its maximum value.

Another system characteristic is that, at a frequency of 10 mHz, the impedance shows the reduction process to be controlled by the diffusion of electroactive species (Fig. 3), and that the longer the immersion the stronger becomes the latter effect (Fig. 5). On the other hand, the oxidation process is still controlled by the charge transfer.

From the low frequency data of the repeated experiment (Table II), it is clear that the rate of the faradaic process in the case of the cell 3/cell 4 couple is much higher than in the case of the cell 1/cell 2 couple, although the difference in coating behavior as reflected by the R value read from the impedance curve is not so drastic as that.

Table II. Maximum real impedance part at 10 mHz in $10^6 \Omega\text{-cm}^2$ (see Fig. 6 and 7)

Cell 1 (11 days)	Cell 3 (10 days)	Cell 2 (11 days)	Cell 4 (10 days)
3.0	1.0	4.2	2.5

The difference in net measured currents for both couples, presented in Fig. 1, confirms the above corrosion rate observations. Still, a nice mathematical relation between the impedance values and the net current is not obvious. It is supposed that perhaps impedance data at frequencies lower than 10 mHz may supply additional information. The problem is, however, that measurements at lower frequencies are disturbed by the spontaneous change of the system.

Conclusion

The simulation of the corrosion process of coated iron with the aid of a differential aeration couple led to some interesting findings concerning the separate action of the anodic and cathodic reaction. Electrochemical impedance measurements show that the pore resistance decreases more rapidly in the coating of the cathodic sample than in the one of the anodic sample. But visual inspection, scanning electron microscopy, and x-ray analysis show that at the anodic metal/coating interface oxidation products are formed which deposit, accumulate, block the coating pores, and cause blistering. Also as revealed by the impedance, the cathodic kinetics seem to be controlled by diffusion phenomena and the anodic kinetics by the charge transfer.

The Stern-Geary theory seems to be respected, as the real part of the 10 mHz impedance of the separate cells is inversely related to the net measured current.

Acknowledgment

The authors would like to thank Dr. M. Piens of the Coatings Research Institute, 1342 Limelette, Belgium, for his kind assistance in practical and theoretical problems.

Manuscript submitted Dec. 18, 1984; revised manuscript received ca. June 24, 1985.

Vrije Universiteit Brussel assisted in meeting the publication costs of this article.

REFERENCES

1. M. Piens, J. Hubrecht, and J. Vereecken, in "Proceedings of the 8th ICMC," p. 1021, Mainz, Germany (Sept. 1981).
2. J. Hubrecht, M. Piens, and J. Vereecken, Abstract 146, p. 369, The Electrochemical Society Extended Abstracts, Vol. 81-2, Denver, CO, Oct. 11-16, 1981.
3. J. Hubrecht and J. Vereecken, p. 51, NACE Corrosion Research Symposium Extended Abstracts, New Orleans, April 2-4, 1984.
4. J. Hubrecht and J. Vereecken, in "Proceedings of the 9th ICMC," Vol. 3, p. 85, Toronto, Canada, June 3-7, 1984.
5. J. Hubrecht, J. Vereecken, and M. Piens, *This Journal*, **131**, 2010 (1984).
6. F. Mansfeld and M. Kendig, in "Proceedings of the 9th ICMC," Vol. 3, p. 74, Toronto, Canada, June 3-7, 1984.
7. G. A. M. Sussex and J. D. Scantlebury, in "Proceedings of the 8th ICMC," p. 1074, Mainz, Germany (Sept. 1981).
8. Y. Sato *Prog. Org. Coatings*, **9**, 85 (1981).
9. G. W. Walter, *J. Electroanal. Chem.*, **118**, 259 (1981).
10. M. Piens and R. Verbist, in "Proceedings of the NACE Meeting on Corrosion Control by Organic Coatings," p. 163, Lehigh University, Bethlehem, PA (1980).
11. U. R. Evans, "The Corrosion and Oxidation of Metals," 1st suppl. vol., E. Arnold, London (1968).
12. M. Kendig, F. Mansfeld, and S. Tsai, Abstract 54, p. 91, The Electrochemical Society Extended Abstracts, Vol. 82-2, Detroit, MI, Oct. 17-21, 1982.
13. H. Leidheiser, Jr., Abstract 67, p. 109, The Electrochemical Society Extended Abstracts, Vol. 82-2, Detroit, MI, Oct. 17-21, 1982.
14. J. J. Ritter, Abstract 78, p. 126, The Electrochemical Society Extended Abstracts, Vol. 82-2, Detroit, MI, Oct. 17-21, 1982.
15. M. Kendig, S. Tsai, and F. Mansfeld, *Mater. Perf.*, **23**, (6), 37 (1984).
16. J. M. Sykes, and K. McLeod, p. 46, NACE Corrosion Research Symposium Extended Abstracts, New Orleans, LA, April 2-4, 1984.
17. W. Wang and H. Leidheiser, Jr., Abstract 244, p. 343, The Electrochemical Society Extended Abstracts, Vol. 84-2, New Orleans, LA, Oct. 7-12, 1984.

Simplified Calculation of pH and Ion Concentrations in High Temperature Phosphate Solutions and Phosphate-Hydroxide Mixtures

Sidney Barnartt*

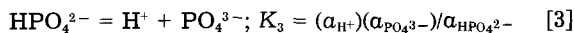
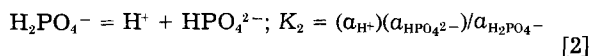
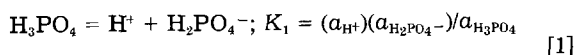
Consulting Chemist, Monroeville, Pennsylvania 15146

ABSTRACT

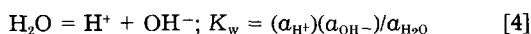
A simplified method is developed for calculating pH and ion concentrations in dilute alkali phosphate-alkali hydroxide mixtures. It is an approximate method which assumes that all of the phosphate is present as H_2PO_4^- and HPO_4^{2-} ions. Comparisons with more general calculations, based on four phosphate species and activity coefficients derived from the Debye-Hückel theory, show good agreement over the temperature range 25°-250°C and Na/P ratios of 1.5-9.

Sodium phosphates have been used extensively as alkali additives to water to mitigate corrosion in high pressure boilers and steam generators. Knowledge of solution pH at operating temperature and of the effect of strong alkali additions is important for corrosion control (1-3). A simplified method of calculating pH and concentrations of phosphate ions in dilute solutions made from sodium phosphates and sodium hydroxide is presented in this paper. The method is shown to yield good precision over a wide range of Na/P ratios at elevated temperatures.

Solutions made from sodium salts of orthophosphoric acid can contain three phosphorus-based ions plus undissociated H_3PO_4 . The following equilibria exist between the dissolved species



where a denotes activity and K the equilibrium constant. There is an additional equilibrium constant for water ionization



Here $a_{\text{H}_2\text{O}}$ is assumed to be unity in dilute solutions.

The pH of a phosphate solution depends upon what combination of alkali hydroxide and phosphoric acid or phosphate salts is used to make the solution. At a fixed temperature, total phosphate molality m_p , and overall atomic ratio Na/P fix the pH of the solution and the concentrations of the dissolved phosphorus containing species.

Equilibrium constants for reactions [1]-[4] are known as a function of temperature within the range 25°-300°C (4-6). These can be used, with the Debye-Hückel theory for evaluating activity coefficients, to calculate pH as a function of temperature.

*Electrochemical Society Emeritus Member.

tion of temperature. A computer program for this calculation is available (7); data in that reference show very good agreement between calculated pH values and published experimental measurements.

A simplified approximation yielding pH and ion concentrations is described below. The concentration ranges and temperatures over which the simplified method provides adequate precision are determined by comparison with the general Debye-Hückel method.

The data base used to generate the temperature dependence of the four equilibrium constants needed for these calculations is given in Table I. Standard Gibbs free energy of reaction values are listed here as a function of temperature. As described in the Appendix, the seven reactions listed provide an internally consistent set of values of ΔG° , the standard free energy of formation from elements at a given temperature, for the seven dissolved species of interest. Convenient polynomials were developed to yield the ΔG° values over the temperature range 25°-300°C. The polynomials are presented in Table II. Equilibrium constants for reactions [1]-[4] are readily obtained from the free energy data in Table II.

Computational Procedures

General method.—The four equilibrium constants, Eq. [1]-[4], are used with the following relations expressing mass balance and electrical neutrality

$$m_p = m_{\text{H}_3\text{PO}_4} + m_{\text{H}_2\text{PO}_4^-} + m_{\text{HPO}_4^{2-}} + m_{\text{PO}_4^{3-}} \quad [5]$$

$$m_{\text{H}^+} + r(m_p) = m_{\text{H}_2\text{PO}_4^-} + 2(m_{\text{HPO}_4^{2-}}) + 3(m_{\text{PO}_4^{3-}}) + m_{\text{OH}^-} \quad [6]$$

Here m_p is the total phosphate molality and r is the atomic ratio Na/P, both known quantities. The sodium ion molality is $r(m_p)$ assuming Na^+ forms no significant amount of ionic complex or neutral molecule in the solutions considered.

An initial set of molalities is obtained by setting the activity coefficient of each dissolved species equal to unity, then solving Eq. [1]-[6] to get the concentrations of the six

Table I. Standard free energy of reaction at elevated temperatures

Reaction	Ref.	ΔG° (kcal-mol ⁻¹)						
		°K: 298.2 °C: 25	333.2 60	373.2 100	423.2 150	473.2 200	523.2 250	573.2 300
[1-A] $\text{H}_3\text{PO}_4(\text{aq}) + \text{OH}^- = \text{H}_2\text{PO}_4^- + \text{H}_2\text{O}$	(5)	-16.16	-16.27	-16.47	-16.81	-17.22	-17.66	-18.10
[2-A] $\text{H}_2\text{PO}_4^- + \text{OH}^- = \text{HPO}_4^{2-} + \text{H}_2\text{O}$	(5)	-9.27	-8.88	-8.42	-7.88	-7.34	-6.79	-6.18
[3-A] ^a $\text{HPO}_4^{2-} + \text{OH}^- = \text{PO}_4^{3-} + \text{H}_2\text{O}$	(6)	-2.28	-1.42	-0.44	0.78	2.00	3.22	4.44
[4-A] $\text{H}_2\text{O} = \text{H}^+ + \text{OH}^-$	(4)	19.10	19.85	20.94	22.54	24.47	26.80	29.64
[5-A] $\text{H}_2 + \frac{1}{2}\text{O}_2 = \text{H}_2\text{O}(l)$	(8, 10)	-56.68	-55.34	-53.83	-51.99	-50.19	-48.43	-46.70
[6-A] $\frac{1}{2}\text{H}_2 = \text{H}^+ + e^-$	(8-10)	0	0.502	0.939	1.268	1.340	1.139	0.647
[7-A] $\text{P} + \frac{1}{2}\text{H}_2 + 2\text{O}_2 + 2e^- = \text{HPO}_4^{2-}$	(8-10)	(defined) -260.31	-255.46	-249.15	-240.17	-229.97	-218.69	-206.03

^a Values at 473.2-573.2 K were obtained by linear extrapolation of the experimental $\log K/T^{-1}$ graph.

Table II. Standard free energy of formation^a of dissolved substances in aqueous phosphate solutions, 298.2-573.2 K

Substance	ΔG_f° at 298.2 K (cal/mol)	a	b	c
H ₂ O	-56,680	38.707	-8.826E-3 ^b	0
H ⁺	0(defined)	16.621	-5.17E-2	0
OH ⁻	-37,580	40.52	0.11455	0
HPO ₄ ²⁻	-260,310	131.21	0.2407	0
H ₂ PO ₄ ⁻	-270,140	114.53	0.1607	-1.126E-4
PO ₄ ³⁻	-243,490	161.18	0.3221	1.076E-4
H ₃ PO ₄ (aq)	-273,080	111.50	0.1055	-2.542E-4

^a $(\Delta G_f^\circ)_T = (\Delta G_f^\circ)_{298.2} + a(\Delta T) + b(\Delta T)^2 + c(\Delta T)^3$; $\Delta T = T - 298.2$

^b E-3 denotes $\times 10^{-3}$.

dissolved species. A second (improved) approximation is obtainable by inserting values for activity coefficients in Eq. [1]-[4].

The Debye-Hückel theory of ionic interaction (11-13) is used to calculate the activity coefficients of ions, while the activity coefficient of undissociated H₃PO₄ is assumed to be unity. For an ion of charge z_i (positive or negative) in a solution of ionic strength I , the Debye-Hückel theory gives the ionic activity coefficient γ_i for dilute solutions as

$$\ln \gamma_i = - \frac{(z_i e)^2 \kappa}{2DkT(1 + \kappa a_i)} \quad [7]$$

with

$$\kappa = (8\pi e^2 N_A I / 1000 D k T)^{1/2} = BI^{1/2}$$

where ionic strength is defined in terms of molarity c as $I = 1/2 \sum c_i z_i^2$. Here a_i is the ion-size parameter and is taken to be 4Å. D is the dielectric constant of the solution and is taken to be that of water at temperature. Also, N_A is Avogadro's number, k is the Boltzmann constant, e is the charge of an electron, and κ^{-1} is the thickness of the ionic atmosphere of excess charge around ion i . Equation [7] is usually rewritten as

$$-\log \gamma_i = Az_i^2 I^{1/2} / (1 + Ba_i I^{1/2}) \quad [7']$$

where A and B are temperature-dependent constants which have been tabulated (12, 14). This equation with $z_i = 1$ yields the value of $\gamma_{H^+} = \gamma_{OH^-} = \gamma_{H_2PO_4^-}$ and $z_i = 2$ yields $\gamma_{HPO_4^{2-}}$, while $z_i = 3$ gives $\gamma_{PO_4^{3-}}$.

Insertion of these values of γ into Eq. [1]-[4] leads to a new set of molality values from Eq. [1]-[6], which in turn yields a second set of γ values, and the cycle is repeated until unchanging m and γ values result.

With the use of the Debye-Hückel theory in unextended form (Eq. [7]), the calculation should give a good approximation up to the maximum concentrations employed in this report, namely, 0.001*m* total phosphate. Therefore, this method is used in the present study as the standard against which the simplified method, described next, is quantitatively evaluated.

Simplified method.—The basis of the simplified calculation to be described is the deduction that alkaline phosphate solutions over a wide range of pH and temperature contain two phosphate species primarily (> 99%). This is clearly revealed by a plot of activity ratio as a function of pH, shown in Fig. 1 for 25°C and 300°C. These lines are described by Eq. [1]-[3], which can be expressed in the general form

$$\log(\text{activity ratio}) = \log K + pH \quad [8]$$

Thus the line labeled H₂PO₄⁻/HPO₄²⁻ gives the activity ratio of these two ions at a given pH. Line location depends only on the numerical value of the equilibrium constant K .

The pH range $P'P''$ shown in Fig. 1 includes all solutions in which the sum of the H₂PO₄⁻ and HPO₄²⁻ activities exceed 99% of the total phosphate activity. At 25°C, a third species, H₃PO₄, exceeds 1% of phosphate activity be-

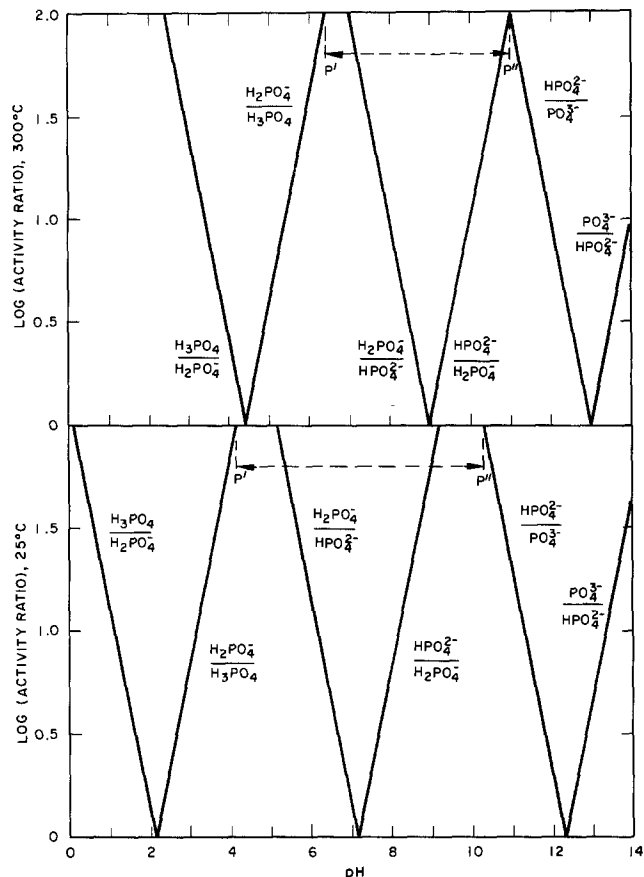


Fig. 1. Activity ratios of phosphate solutions as a function of pH at 25° and 300°C.

low pH 4.1, whereas PO₄³⁻ becomes the third species at significant concentration above pH 10.3. Figure 1 shows that the range $P'P''$ shifts in the direction of higher pH when the temperature is raised to 300°C.

From plots similar to Fig. 1 at intermediate temperatures, the pH ranges for two-species solutions, defined by the 99% limits imposed above, yield the limit curves of Fig. 2. The bottom curve gives the low pH limit and the

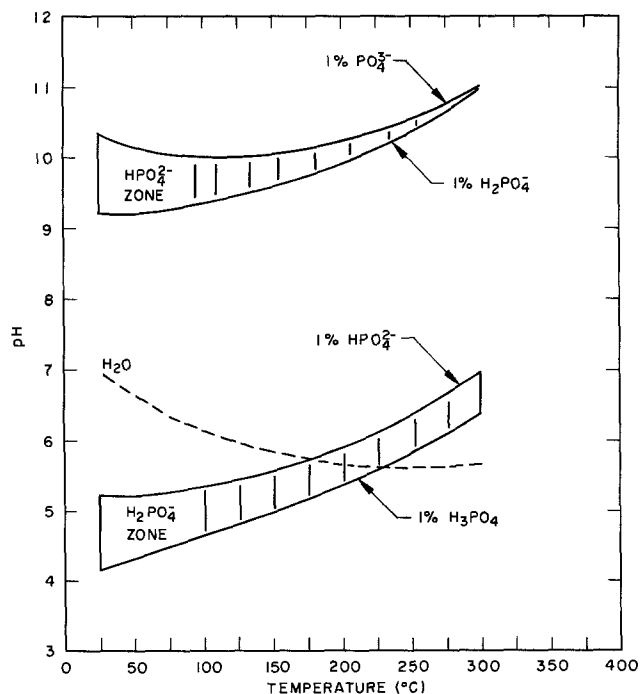


Fig. 2. pH of solutions dominated by the two phosphate ions H₂PO₄⁻ and HPO₄²⁻.

top curve gives the high pH limit for two-species solutions. The upper shaded zone gives the pH range over which 99-100% of the phosphate activity is due to the single ion HPO_4^{2-} . Similarly, H_2PO_4^- makes up 99-100% of the phosphate activity within the lower shaded zone.

Included for comparison as the broken curve in Fig. 2 is the pH of pure water as a function of temperature (4). At room temperature, the two-species solution range includes neutral solutions and extends into the acid region down to pH 4.1 before undissociated H_3PO_4 builds up to a concentration of 1% of the phosphate activity. Neutral solutions remain within the two-species range up to a temperature of about 225°C. As the temperature is raised from 225° to 300°C the neutral solution contains an increasing fraction of undissociated H_3PO_4 .

The broad pH range for two-species solutions over the whole temperature interval 25°-300°C suggested a simplified procedure for calculating pH and ion concentrations which involves two assumptions: (i) ionic activities are established by only two equilibria, namely, water ionization (Eq. [4]) and H_2PO_4^- dissociation (Eq. [2]); (ii) ionic activity coefficients can be approximated by unity. Under these conditions, Eq. [2], [4]-[6] become

$$K_2 = (m_{\text{H}^+})(m_{\text{HPO}_4^{2-}}) / m_{\text{H}_2\text{PO}_4^-} \quad [2']$$

$$K_w = (m_{\text{H}^+})(m_{\text{OH}^-}) \quad [4']$$

$$m_p = m_{\text{H}_2\text{PO}_4^-} + m_{\text{HPO}_4^{2-}} \quad [5']$$

$$m_{\text{H}^+} + r(m_p) = m_{\text{H}_2\text{PO}_4^-} + 2(m_{\text{HPO}_4^{2-}}) + m_{\text{OH}^-} \quad [6']$$

A given solution fixes total phosphate molality m_p and Na/P ratio r , and the temperature specifies numerical values of K_2 and K_w . Thus, these four equations can be solved to obtain the molalities of the four ionic species. To that end, a convenient equation for m_{H^+} , obtained by substitution into Eq. [6'], is

$$m_{\text{H}^+} - K_w/m_{\text{H}^+} + m_p[r - 2 + (1 + K_2/m_{\text{H}^+})^{-1}] = 0 \quad [9]$$

Equation [9] may be solved by trial by application of the Newton-Raphson method for stepwise improvement of the trial value of m_{H^+} . This method uses

$$x_2 = x_1 - f(x_1)/(df/dx) \quad [10]$$

where x_1 is the initial approximation to m_{H^+} , x_2 the improved approximation, and f is the function of m_{H^+} (left-hand side of Eq. [9]). Successive improvements are continued until m_{H^+} is evaluated with the desired precision. Then m_{H^+} is substituted into Eq. [2'], [4'], and [5'] to evaluate the other three molalities.

Results

Single salt solutions of disodium phosphate and of trisodium phosphate were used in an initial comparison of the simplified and general calculation methods. Figure 3 presents pH variations with temperature for Na_2HPO_4 and Na_3PO_4 solutions at concentrations of 10^{-5} , 10^{-4} , and $10^{-3}m$. For 10^{-5} and $10^{-4}m$ solutions, the two calculation methods are in very good agreement over the entire range 25°-300°C. At $10^{-3}m$, the two methods agree within 0.1 pH unit at temperatures up to 250°C, but at 300°C the deviation begins to exceed 0.1 pH.

The set of solutions compared in Fig. 3 conforms to the pH limits of Fig. 2 for two-component solutions, except for the uppermost portion of the top Na_3PO_4 curve (broken section) which is outside those limits. The good agreement revealed in Fig. 3 between the two methods of calculation demonstrates that the simplified method yields pH with sufficiently high precision.

Figure 3 shows that heating from 25° to 300°C raises the H^+ concentration in these solutions, just as it does for pure water. What is not revealed is the fact, which emerges from the computed values of m_{OH^-} , that heating also raises the OH^- concentration. This is true for all of these phosphate solutions. The ratio of m_{OH^-} to total phosphate (m_p) can be used to illustrate the effect. For $10^{-3}m$ Na_2HPO_4 , the ratio m_{OH^-}/m_p increases from 0.0116

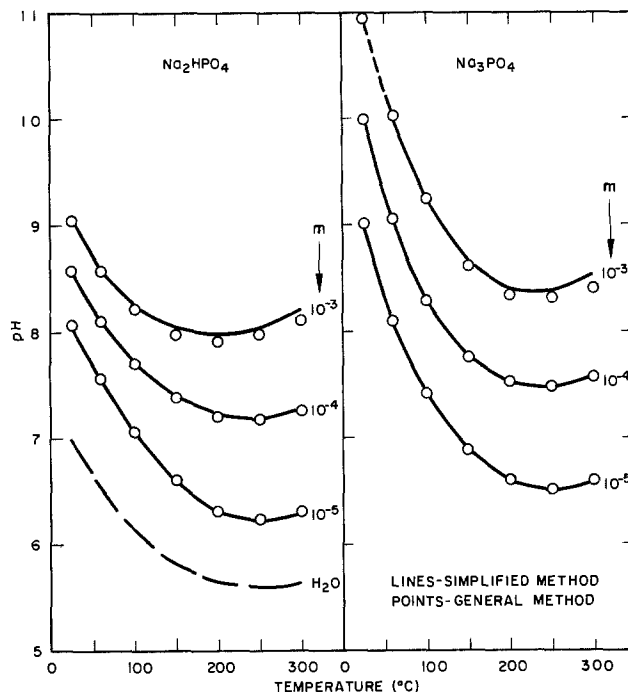


Fig. 3. pH of dilute Na_2HPO_4 and Na_3PO_4 solutions

at 25°C to 0.793 at 300°C, and for $10^{-3}m$ Na_3PO_4 it increases from 0.949 to 1.616 for the same temperature change. In the latter case, the molalities of the three dominant ions at 300°C are ($\times 10^3$) $m_{\text{OH}^-} = 1.616$, $m_{\text{H}_2\text{PO}_4^-} = 0.623$, and $m_{\text{HPO}_4^{2-}} = 0.377$. Here, the most abundant ion is OH^- . This can be significant for accelerated alloy corrosion in boilers or steam generators, if the corrosion mechanism involves a passivating phosphate film which suffers localized breakdown when OH^- exceeds a critical concentration.

Phosphate ion concentrations in the solutions of Fig. 3 are plotted in Fig. 4. The ordinate is the concentration of the divalent ion HPO_4^{2-} as a percentage of total phosphate. At low temperatures, the divalent ion is the dominant species in either Na_2HPO_4 or Na_3PO_4 solutions. As the temperature is raised, the divalent ion converts gradually to the monovalent ion by reaction [2], and at 300°C the monovalent ion is the dominant one in these dilute solutions. The simplified method yields concentrations in good agreement with those generated by the general method over the whole temperature range at 10^{-5} and $10^{-4}m$. For $10^{-3}m$ solutions, the two methods of calculation begin to deviate noticeably at 200°C and the deviation increases with increasing temperature.

Similar calculations of pH and ion concentrations were performed for a wide variety of Na/P ratios ranging from monosodium phosphate, Na/P = 1, to solutions made with Na_3PO_4 and added NaOH up to a molar ratio $\text{NaOH}/\text{Na}_3\text{PO}_4 = 6$ (or Na/P = 9). Ion concentration results are collected in Table III for $10^{-3}m$ total phosphate, which is the highest concentration examined. This concentration yields maximum deviations between the simplified and general computational methods. The blocked case at the upper right corner of Table III represents the only solution in which H_3PO_4 exceeds 1% of total phosphate (general calculation). The enclosed block at the lower left includes all of the solutions examined which contained $\text{PO}_4^{3-} \geq 1\%$ of total phosphate. Within the latter block, deviations of the simplified method from the general method increase with increasing Na/P ratio but decrease with increasing temperature. Solutions outside of the two blocked areas are those in which the two ions, H_2PO_4^- and HPO_4^{2-} , account for more than 99% of the total phosphate molality. Within this group, the deviation of the simplified calculation (Method 1) increases with increasing Na/P ratio and with increasing temperature.

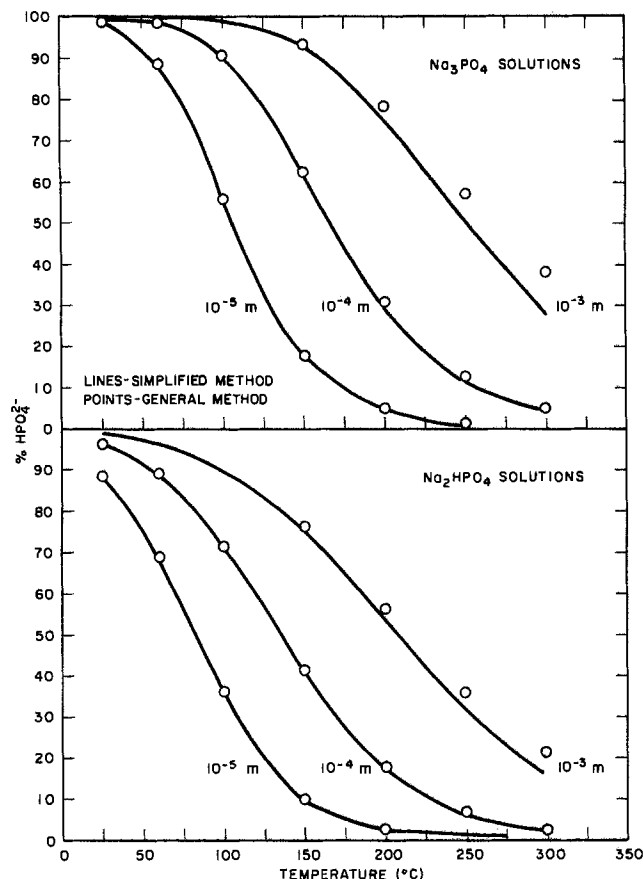


Fig. 4. Conversion of divalent to monovalent phosphate ion with increasing temperature in dilute Na_2HPO_4 and Na_3PO_4 solutions.

Although a few of the concentration deviations listed in Table III are relatively large their effect on pH is minimal, as revealed by the parallel pH listing in Table IV. Throughout the lower left block, agreement between the simplified and general methods remains very good. Even at the lowest temperature and highest Na/P ratio, where the pH of 11.8 is well outside the limits given by Fig. 2,

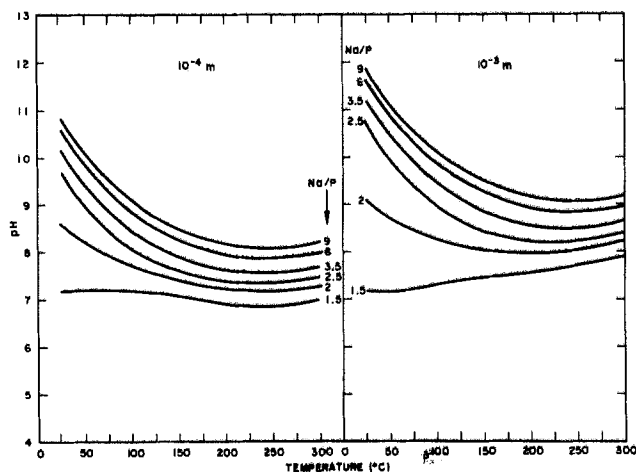


Fig. 5. Effect of Na/P ratio on pH variation with temperature in 10^{-4} and 10^{-3} m phosphate solutions.

the deviation does not exceed 0.07 pH unit. The good agreement in that blocked section results mainly from two compensating errors in the simplified calculation, namely (i) activity coefficients too high (set at unity) and (ii) PO_4^{3-} concentration too low (set at zero). The calculated H^+ concentration tends to be too small from the first error and too large from the second. For all of these solutions, the net result is that the H^+ concentration from the simplified calculation remains close to but always slightly smaller than the value given by the general method.

The largest pH deviation in Table IV is seen to occur for monosodium phosphate solution at 300°C (upper right block), where undissociated H_3PO_4 appears although only at 1.2% of total phosphate. In the whole of Table IV, the pH deviation exceeds 0.1 unit only in the temperature range 150°C - 300°C for monosodium phosphate and only at 300°C for the other solutions.

The temperature variation of pH given in Table IV for 10^{-3} m phosphate solutions is shown graphically in Fig. 5, together with similar curves for 10^{-4} m solutions. These data were generated by the simplified method. The curves illustrate that the pH rise from an NaOH addition,

Table III. Temperature dependence of H_2PO_4^- and HPO_4^{2-} concentrations in 10^{-3} m PO_4 solutions

Component salts	Na/P	Method ^a	25°C		60°C		100°C		150°C		200°C		250°C		300°C	
			% H_2PO_4^-	% HPO_4^{2-}	% H_2PO_4^-	% HPO_4^{2-}	% H_2PO_4^-	% HPO_4^{2-}	% H_2PO_4^-	% HPO_4^{2-}	% H_2PO_4^-	% HPO_4^{2-}	% H_2PO_4^-	% HPO_4^{2-}	% H_2PO_4^-	% HPO_4^{2-}
NaH_2PO_4	1.0	1	99.2, 0.8	99.2, 0.8	99.3, 0.7	99.5, 0.5	99.7, 0.3	99.9, 0.1	99.9, 0.05							
		2	99.0, 0.9	98.9, 0.9	98.9, 0.9	98.9, 0.7	98.9, 0.6	98.8, 0.4	98.8, 0.4	98.5, 0.3						
NaH_2PO_4 = 1	1.5	1	50.0, 50.0	50.1, 49.9	51.1, 48.9	56.6, 43.4	68.6, 31.4	81.8, 18.2	91.5, 8.5							
		2	50.0, 50.0	50.1, 49.9	51.0, 49.0	56.0, 44.0	67.2, 32.8	79.7, 20.3	88.8, 11.2							
Na_2HPO_4	2.0	1	1.3, 98.7	3.8, 96.2	10.2, 89.8	25.3, 74.7	46.6, 53.4	67.9, 32.1	84.1, 15.9							
		2	1.2, 98.7	3.6, 96.4	9.6, 90.4	23.9, 76.1	43.8, 56.2	63.9, 36.1	78.8, 21.2							
Na_2HPO_4 = 1	2.5	1	0.03, 99.97	0.3, 99.7	2.2, 97.8	12.1, 87.9	32.9, 67.1	57.2, 42.8	77.7, 22.3							
		2	0.03, 97.2	0.26, 99.2	1.9, 98.0	10.8, 89.2	29.6, 70.4	52.0, 48.0	69.9, 30.1							
Na_3PO_4	3.0	1	0.02, 99.98	0.15, 99.8	1.1, 98.9	7.4, 92.6	24.6, 75.4	49.0, 51.0	72.1, 27.9							
		2	0.01, 94.5	0.13, 98.7	1.0, 98.8	6.4, 93.5	21.4, 78.6	43.0, 57.0	62.3, 37.7							
NaOH = 0.5	3.5	1	0.01, 99.99	0.1, 99.9	0.77, 99.2	5.2, 94.8	19.4, 80.6	42.6, 57.4	67.2, 32.8							
		2	0.01, 91.8	0.1, 98.2	0.65, 99.0	4.5, 95.5	16.4, 83.6	36.2, 63.8	55.6, 44.3							
NaOH = 1	4.0	1	0.01, 99.99	0.07, 99.93	0.59, 99.4	4.0, 96.0	15.9, 84.1	37.6, 62.4	62.9, 37.1							
		2	0.00, 89.2	0.06, 97.6	0.48, 99.0	3.4, 96.5	13.1, 86.9	31.0, 69.0	50.0, 50.0							
NaOH = 3	6.0	1	0.00, 100	0.04, 99.96	0.29, 99.7	2.1, 97.9	9.1, 90.9	25.2, 74.8	49.8, 50.2							
		2	0.00, 79.7	0.02, 95.1	0.23, 98.7	1.7, 98.1	7.0, 92.9	18.9, 81.1	34.0, 66.0							
NaOH = 6	9.0	1	0.00, 100	0.02, 99.98	0.17, 99.8	1.2, 98.8	5.5, 94.5	16.7, 83.3	37.7, 62.3							
		2	0.00, 67.7	0.01, 91.3	0.13, 97.9	0.93, 98.6	4.0, 95.9	11.4, 88.5	21.5, 78.4							

^a Method 1 is simplified calculation; Method 2 is general.

Table IV. Temperature dependence of pH in $10^{-3}m$ phosphate solutions

Component salts	Na/P	Method ^a	pH at temperature (°C)						
			25	60	100	150	200	250	300
NaH ₂ PO ₄	1.0	1	5.10	5.11	5.16	5.27	5.38	5.49	5.60
		2	5.11	5.14	5.21	5.37	5.60	5.89	6.23
NaH ₂ PO ₄ = 1	1.5	1	7.20	7.22	7.31	7.46	7.57	7.72	7.91
		2	7.13	7.15	7.23	7.37	7.50	7.65	7.80
Na ₂ HPO ₄	2.0	1	9.09	8.63	8.27	8.04	7.97	8.05	8.22
		2	9.03	8.57	8.21	7.97	7.90	7.97	8.10
Na ₂ HPO ₄ = 1	2.5	1	10.69	9.76	8.98	8.43	8.22	8.25	8.40
		2	10.64	9.72	8.94	8.37	8.16	8.17	8.27
Na ₃ PO ₄	3.0	1	10.99	10.06	9.27	8.67	8.40	8.39	8.53
		2	10.94	10.02	9.23	8.61	8.34	8.31	8.39
NaOH = 0.5	3.5	1	11.17	10.23	9.44	8.83	8.53	8.50	8.63
		2	11.11	10.19	9.40	8.77	8.47	8.42	8.49
NaOH = 1	4.0	1	11.29	10.36	9.57	8.95	8.64	8.59	8.71
		2	11.24	10.32	9.52	8.89	8.58	8.51	8.56
NaOH = 3	6.0	1	11.60	10.66	9.87	9.25	8.91	8.84	8.95
		2	11.53	10.61	9.82	9.17	8.85	8.76	8.78
NaOH = 6	9.0	1	11.84	10.90	10.11	9.49	9.15	9.07	9.16
		2	11.77	10.85	10.05	9.41	9.07	8.97	8.97

^a Method 1 is simplified calculation; Method 2 is general.

e.g., to a solution made from Na₂HPO₄, is relatively small at 200°-300°C compared to the pH rise at room temperature from the same addition.

Variations of pH with total phosphate concentration are shown by the plots in Fig. 6, which compare pH at 300°C with that at room temperature. Each plot shows an almost linear increase of pH with log (concentration) over the range covered, 10^{-5} - $10^{-3}m$. At 25°C, the pH shift on increasing the Na/P ratio from 1.5 to 9 becomes larger as concentration increases, but at 300°C the curves tend to be parallel.

Although sodium was used as the alkali cation in the solutions discussed, other alkali cations such as Li⁺ or K⁺ should yield the same ion concentrations if salts of these cations can be assumed to remain completely dissociated in dilute solutions.

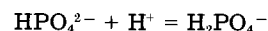
Conclusions

1. Dilute solutions of monosodium, disodium, or trisodium phosphate or their mixtures contain mainly two dissolved phosphate species: H₂PO₄⁻ and HPO₄²⁻ ions.

2. A simplified calculation of pH and ion concentrations is developed, considering only equilibrium between

these two of the four dissolved phosphate species. It yields pH within 0.1 pH unit over the temperature range 25°-250°C.

3. In solutions of disodium phosphate only and of trisodium phosphate only, almost all the phosphate is present as the divalent ion HPO₄²⁻ at room temperature. On heating, this gradually converts to the monovalent ion by the reaction



accompanied by an increase in H⁺ concentration, and at 300°C the monovalent ion predominates.

4. In solutions of monosodium phosphate only, almost all the phosphate is present as H₂PO₄⁻ throughout the temperature interval 25°-300°C.

5. The two ions H₂PO₄⁻ and HPO₄²⁻ predominate also in solutions of Na₃PO₄ with added NaOH. As NaOH is gradually added, the PO₄³⁻ ion does appear in increasing although low concentrations. Nevertheless, the simplified pH calculation remains valid within 0.1 pH unit for a wide range of compositions: Na/P ratios from 1.5 to 9.0 over the temperature range 25°-250°C.

Manuscript submitted April 8, 1985; revised manuscript received Aug. 9, 1985.

APPENDIX

Free Energies of Formation at Elevated Temperatures

The following seven constituent substances are involved in phosphate solution equilibria: H₂O, H⁺, OH⁻, H₂PO₄⁻, HPO₄²⁻, PO₄³⁻, and undissociated H₃PO₄. Maximum use was made of experimental high temperature thermodynamic data from the literature in calculating standard Gibbs free energies of formation from the elements for the seven substances. Literature data for phosphate equilibria and water ionization are given in Table I, reactions [1-A]-[4-A], as standard free energies of reaction.

Similar data were needed for three additional reactions, and the formation reactions for substances H₂O, H⁺, and HPO₄²⁻ were chosen: reactions [5-A]-[7-A] in Table I. These free energies were calculated from molar heat capacities of reaction, Δc_p , by use of the well-known thermodynamic relation

$$\Delta G_T^0 = \Delta G_{298}^0 - \Delta S_{298}^0 (T - 298) + \int_{298}^T \Delta c_p dT - T \int_{298}^T \frac{\Delta c_p}{T} dT \quad [\text{A-1}]$$

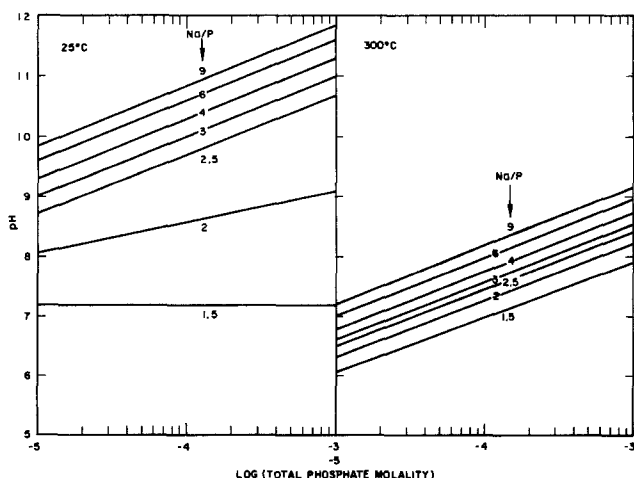


Fig. 6. Effect of Na/P ratio on pH at 25° and 300°C as a function of concentration.

where ΔS° is the standard entropy change for the reaction. The method of Kubaschewski and Alcock (10) was followed, in which Eq. [A-1] is utilized in the following equivalent form for easy evaluation of the integrals

$$\Delta G_r^\circ = \left[\Delta H_{298}^\circ - \int_0^{298} \Delta c_p dT \right] - T \left[\Delta S_{298}^\circ - \int_0^{298} \Delta c_p d \ln T \right] + \int_0^T \Delta c_p dT - T \int_0^T \Delta c_p d \ln T \quad [\text{A-2}]$$

Since Δc_p is available in the general form

$$\Delta c_p = e + fT + gT^2 + hT^{-2}$$

where e , f , g , and h are tabulated constants (10, 15), the integrals become

$$\int_0^T \Delta c_p dT = eT + 1/2 fT^2 + 1/3 gT^3 - hT^{-1} \quad [\text{A-3}]$$

$$\int_0^T \Delta c_p d \ln T = e \ln T + fT + 1/2 gT^2 - 1/2 hT^{-2} \quad [\text{A-4}]$$

It should be noted that the term $e \ln$ (zero), which formally should be included in Eq. [A-4], can be omitted since it cancels out in Eq. [A-2]. Molar heat capacities for ions H^+ and HPO_4^{2-} were obtained by the method of Criss and Cobble (9) based on their entropy correspondence principle.

Free energies of reaction listed in Table I yield free energies of formation for all of the ions and compounds involved. Then for each substance the free energy as a function of temperature was fitted, by multiple linear regression analysis on a computer, to the cubic polynomial

$$(\Delta G_r^\circ)_T = (\Delta G_r^\circ)_{298} + a(\Delta T) + b(\Delta T)^2 + c(\Delta T)^3 \quad [\text{A-5}]$$

with $\Delta T = T - 298$. Table II gives values of the polynomial coefficients for each of the species. This tabulation is a useful and internally consistent set of numerical data for calculating equilibrium constants of high temperature phosphate solutions.

REFERENCES

1. V. M. Marcy and S. L. Halstad, *Combustion*, **35**, 45 (1964).
2. W. D. Fletcher and D. D. Malinowski, *Nucl. Technol.*, **28**, 356 (1976).
3. N. Pessal, A. B. Dunlap, and D. W. Feldman, *Corrosion*, **33**, 130 (1977).
4. F. H. Sweeton, R. E. Mesmer, and C. F. Baes, Jr., *J. Solution Chem.*, **3**, 191 (1974).
5. R. E. Mesmer and C. F. Baes, Jr., *ibid.*, **3**, 307 (1974).
6. N. C. Treloar, CERL Laboratory Note RD/L/N270/73, Nov. 1973.
7. J. M. Wright and G. E. Von Nieda, WAPD-TM-1302 (1979), Bettis Laboratory, Westinghouse Electric Corp.; copies of the computer program are available from National Energy Software Center, Argonne National Laboratory, Argonne, IL.
8. D. D. Wagman *et al.*, "The NBS Table of Chemical Thermodynamic Properties," U.S. National Bureau of Standards, Washington, DC (1982).
9. C. M. Criss and J. W. Cobble, *J. Am. Chem. Soc.*, **86**, 5385, 5390 (1964).
10. O. Kubaschewski and C. B. Alcock, "Metallurgical Thermochemistry," 5th ed., Pergamon Press, New York (1979).
11. P. Debye and E. Hückel, *Z. Phys.*, **24**, 185 (1923).
12. R. A. Robinson and R. H. Stokes, "Electrolytic Solutions," 2nd ed. revised, p. 468, Butterworths, London (1970).
13. H. S. Harned and B. B. Owen, "The Physical Chemistry of Electrolytic Solutions," 3rd ed., Reinhold, New York (1958).
14. R. G. Bates, "Determination of pH," 2nd ed., John Wiley and Sons, New York (1973).
15. K. K. Kelley, *U.S. Bur. Mines Bull.*, 584 (1960).

Changes in Oxide Films on Nickel during Long-Term Passivation

B. MacDougall,* D. F. Mitchell, and M. J. Graham

National Research Council of Canada, Division of Chemistry, Ottawa, Ontario, Canada K1A 0R9

ABSTRACT

The nature of the long-term anodic currents observed when nickel is potentiostatically polarized in the passive potential region has been investigated. Passive oxide films are formed in O^{18} (or O^{16}) solutions and then exposed to O^{16} (or O^{18}) solutions for continued anodic polarization. The change in the O^{18} (or O^{16}) content of the film is determined by SIMS using the polyatomic species $^{58}\text{Ni}^{16}\text{O}_2^-$ and $^{58}\text{Ni}^{16}\text{O}^{18}\text{O}^-$. The extent of oxygen replacement in the passive film increases with increasing time of exposure to the new solution and eventually complete replacement occurs. The kinetics of replacement are highly dependent on the conditions of pretreatment in the O^{18} (or O^{16}) solution, *i.e.*, on the defect state of the oxide and on the aggressiveness of the exposure solution. The results can best be interpreted in terms of a model where the passive oxide film is locally breaking down and being replaced by new oxide formed in the fresh solution. The current efficiency for local repassivation is only $\sim 20\%$, the rest of the charge going towards metal dissolution. Transformation of a passive oxide film, via local breakdown-repair events, occurs at essentially the same rate in Cl^- as in SO_4^{2-} solutions, suggesting that the important role of Cl^- in pit initiation is to interfere with local repassivation rather than to directly break or thin the film.

A fundamental question in the field of passivity concerns the nature of the electrochemical processes giving rise to the long-term anodic currents, i_a 's, observed upon potentiostatic polarization in the passive potential region. For nickel in sulfate and borate solutions, i_a decreases with time (at constant potential) according to a linear $\ln i_a$ - $\ln t$ relationship, and may eventually reach a steady value (1, 2). Results of this kind are often interpreted in terms of high field growth of an oxide film with the rate of growth eventually decreasing to the point where it is comparable to the rate of chemical dissolution of the oxide (3, 4); this situation would result in the constant i_a frequently observed after long times of anodic polarization. However, for nickel in sulfate and borate solutions the majority of the anodic current is not associated with ox-

ide film growth, even in the region of linearity between $\ln i_a$ and $\ln t$, since the current efficiency (c.e.) for metal dissolution is $> 80\%$ (1). In addition, the limiting NiO film thickness of 12\AA is the same over the pH range 2.0-8.4, which also suggests that the simple high field oxide growth model is inappropriate for explaining the measured i_a 's. Anodic processes which might be contributing to the measured i_a include (i) nickel dissolution through the passive oxide film driven by a high electric field (5, 6) (ii) general chemical dissolution of the oxide (7-9) with the outer layer dissolving and reforming, and (iii) localized chemical dissolution of the passive film with patches of oxide breaking down completely and being replaced by new patches formed as a consequence of local film repair (1, 2, 10-13). A better understanding of which process gives rise to the long-term i_a 's observed in non-

* Electrochemical Society Active Member.

aggressive solutions may also throw light on the highly localized pitting corrosion observed in Cl^- and Br^- solutions.

In the present work, experiments have been designed to determine whether passive oxide films on nickel undergo changes during long-term passivation, *i.e.*, to correlate i_a with changes in the oxide film. To this end, passive oxide films are formed in H_2O^{18} (or H_2O^{16}) solutions and then exposed to H_2O^{16} (or H_2O^{18}) solutions for continued passivation. SIMS is used to determine the change in the O^{18} (or O^{16}) content of the film and the distribution of O^{18} and O^{16} throughout the thickness of the film (14). The results are discussed in terms of the mechanism of breakdown of passive oxide films in sulfate solutions. Data are also presented which allow a comparison to be made between the influence of Cl^- and SO_4^{2-} on oxide film breakdown.

Experimental

Polycrystalline nickel specimens were prepared as described previously (15). Potentials are referred to the saturated calomel electrode, $\text{Hg}/\text{Hg}_2\text{Cl}_2$. Experiments were conducted at 25°C in deaerated solutions of pH 7.65 borate buffer and 0.15N Na_2SO_4 solutions with pH's 1.0, 1.5, and 3.0. The borate solution was 23% oxygen-18 isotope enriched, and samples which were passivated in this solution were subsequently polarized in nonenriched pH 1.0 and 1.5 Na_2SO_4 solutions. Samples were also passivated in 10% oxygen-18 isotope-enriched pH 3.0 Na_2SO_4 solutions and then transferred to nonenriched pH 1.0, 1.5, and 3.0 Na_2SO_4 solutions. The extent of oxygen replacement was followed as a function of prior electrode treatment, aggressiveness of the exchange solution and time in this solution. The extent of O^{18} incorporation into passive oxide films formed on electropolished nickel was also studied.

The O^{18} content in the oxide films was determined by secondary ion mass spectrometry (SIMS) using a PHI 590 Auger system with a PHI SIMS II attachment and a PHI differentially pumped ion gun (14, 16). Sputtering was performed with a 1 keV xenon ion beam at 33° off normal at a rate of $\sim 4 \text{ \AA}/\text{min}$. The ion species analyzed were the polyatomic species $^{58}\text{Ni}^{16}\text{O}_2^-$ (mass = 90) and $^{58}\text{Ni}^{16}\text{O}^{18}\text{O}^-$ (mass 92); the $^{60}\text{Ni}^{16}\text{O}_2^-$ species also contributes to mass 92, but this is always subtracted prior to calculating the ^{18}O content in the film. The sputter profiles give the depth distribution of ^{18}O throughout the passive oxide film.

Results and Discussion

Determination of O^{18} in oxide films.—An electropolished nickel electrode was cathodically reduced and then anodized in pH 7.65 borate buffer solution with 23% oxygen-18 at 0.4V for 5 min. SIMS analysis of the sample is given in Fig. 1; the mass 16 and 18 signals are given along with the mass 90 and 92 signals. The O^{18} content in the film ($x\%$) can be determined from the signal ratio $92/90 + 92$, taking into account that the probability for mass 90 is $(1 - x)^2$ and that that for 92 is $2x(1 - x)$. Analysis of the data indicates, as would be anticipated, a constant O^{18} composition of 23% throughout the passive film. The mass 18 and 16 signals also indicate a 23% enrichment factor, after sputtering away the outer layer of oxide. The atomic signals have an enhanced sensitivity for surface hydroxyl species, probably picked up during air transfer to the UHV chamber, which is not reflected in the polyatomic mass 90 and 92 signals. The subsequent advantages of using the polyatomic species for quantitative SIMS analysis have been discussed in detail previously (14).

Transfer of samples from O^{18} to O^{16} solutions.—SIMS was used to determine the O^{18} content of films formed in 23% O^{18} borate buffer (pH 7.65) and then transferred to pH 1.0 Na_2SO_4 (no O^{18}) for continued potentiostatic polarization. With increasing time of exposure to the latter solution, the O^{18} content is found to decrease from the initial 23% to only 1.5% after 1h (Table I and Fig. 2). The SIMS sputter profiles indicate a constant O^{18} level through the oxide film, independent of the total amount of O^{18} in the

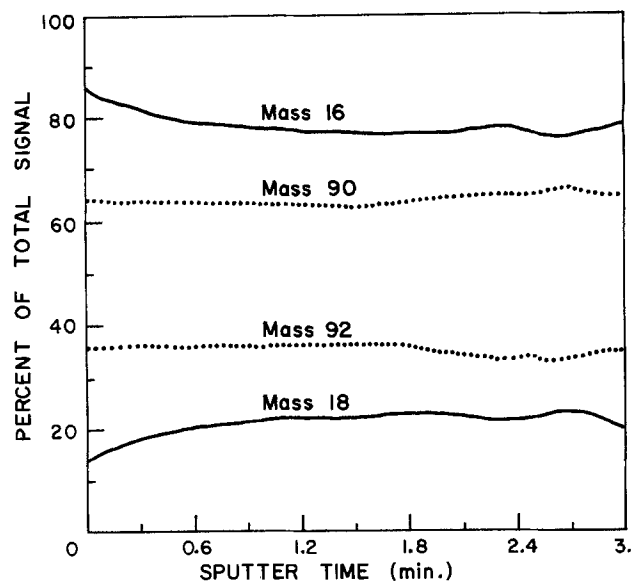


Fig. 1. Percentage of SIMS signals [$\text{mass } 18 \times 100/\text{mass } (18 + 16)$], [$\text{mass } 16 \times 100/\text{mass } (18 + 16)$], [$\text{mass } 92 \times 100/\text{mass } (90 + 92)$], and [$\text{mass } 90 \times 100/\text{mass } (90 + 92)$] for nickel anodized in a 23% oxygen-18 electrolyte. Mass 90 is $^{58}\text{Ni}^{16}\text{O}_2^-$, mass 92 is $^{58}\text{Ni}^{16}\text{O}^{18}\text{O}^-$ (the $^{60}\text{Ni}^{16}\text{O}_2^-$ signal contribution to mass 92 was subtracted prior to calculation), mass 18 is $^{18}\text{O}^-$, and mass 16 is $^{16}\text{O}^-$. Sputtering was by 1 keV xenon at a rate of $\sim 4 \text{ \AA}/\text{min}$.

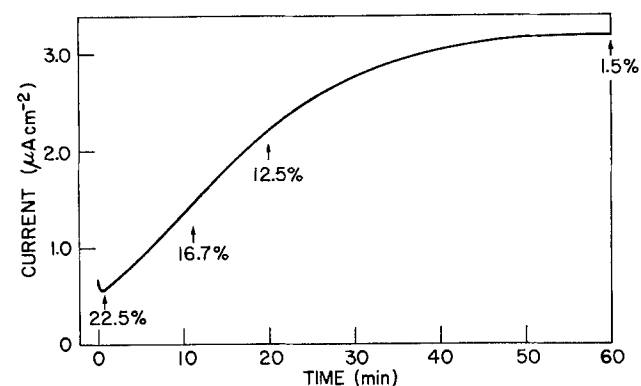


Fig. 2. Increase of anodic current, i_a , with time for nickel prepassivated in pH 7.65 borate buffer solution (23% O^{18}) at 0.4V for 5 min and then transferred to a pH 1.0 Na_2SO_4 (100% O^{16}) solution for continued polarization at 0.4V. Also shown is the percentage of O^{18} detected in the oxide film by SIMS at various times of exposure to the pH 1.0 Na_2SO_4 solution.

film. This suggests that the O^{18} is being replaced by O^{16} throughout the entire thickness of the film, not just in the outer layer. The results show that the passive oxide film, formed in O^{18} is slowly breaking down and subsequently reforming in the O^{16} solution so that eventually

Table I. Influence of nickel pretreatment in pH 7.65 borate buffer solution, containing 23% O^{18} , and subsequent extent of exposure to pH 1.0 Na_2SO_4 (100% O^{16}) on the O^{18} content in the oxide film. O^{18} contents determined by SIMS. All pretreatments involved electropolishing (EP) and cathodic reduction (CR), with the exception of the last one, where no CR was employed

Electrode pretreatment	Exposure conditions in pH 1.0 Na_2SO_4	Percentage of O^{18} in oxide film
5 min at 0.4V	—	23.0
5 min at 0.4V	1 min at 0.4V	22.5
5 min at 0.4V	10 min at 0.4V	17.0
5 min at 0.4V	20 min at 0.4V	12.5
5 min at 0.4V	1h at 0.4V	1.5
1h at 0.65V	20 min at 0.4V	22.0
EP + 5 min at 0.4V	—	7.5

the entire previously formed film will have broken down and been reformed in the new solution. This breakdown is most probably local in nature, *e.g.*, associated with oxide chemical dissolution at film defects (2). The rate of replacement of O^{18} with O^{16} is much slower for a film previously formed at 0.65V for 1h in the 23% O^{18} borate solution (Table I). This result is consistent with the less defective nature of that film and therefore with the smaller number of breakdown sites.

Influence of solution aggressiveness on rate of oxygen replacement.—To determine the influence of aggressiveness of the breakdown solution on the rate of oxygen replacement, samples pretreated in 23% O^{18} borate solution at 0.4V for 5 min were exposed to pH 1.5 Na_2SO_4 at 0.4V for 60 and 150 min. During these times, the O^{18} content of the film decreased from 23 to 13 and 7.5%, respectively. However, if the standard passive film with 23% O^{18} was exposed to a pH 3.0 Na_2SO_4 solution at 0.4V for 90 min, the O^{18} level falls to only 20.5%. The rate of replacement is thus significantly lower the higher the pH of the exposure solution (*cf.* Table I), supporting the view that local chemical dissolution of the oxide is responsible for film breakdown. The local nature of the breakdown and repair of the film ensures that the O^{18} content in the oxide remains constant throughout the film.

Samples were also passivated in nonenriched pH 3.0 Na_2SO_4 solutions at 0.4V for various times, after which the passivation was continued at the same potential in a similar solution which was 10% enriched in O^{18} . SIMS was then used to determine the rate of uptake of O^{18} into the oxide film. The results, given in Table II, indicate that the film formed exclusively in the enriched solution contains 10% O^{18} . The films formed for 5 min in the O^{16} solution pick up an increasing amount of O^{18} with time of exposure to the O^{18} solution. Eventually, the oxide would contain 10% O^{18} , *i.e.*, the amount obtained when the film is formed from the beginning in the enriched solution, since all elements of the prior passive film will break down if the time is sufficiently long (5). The rate of O^{18} uptake is much less after a longer prepassivation treatment, *i.e.*, 75 min at 0.4V, since the oxide film is substantially more stable and therefore more resistant to breakdown.

Also given in Table II are the results for O^{18} uptake, with time, after immersion of electropolished (EP) nickel into the 10% O^{18} solution at 0.4V. The initial (60s) value of 4.1% is probably at least partly due to an increase in thickness of the oxide film from 7 to 10Å (15); any additional amount would be due to dissolution and reformation of the oxide in the 10% O^{18} solution. [Note that the increase for a similar experiment in 23% O^{18} borate solution is 7.5% (Table I), consistent with 30% of the film being formed in the O^{18} solution.] The SIMS results again indicate that in all cases the O^{18} is distributed uniformly throughout the oxide film, suggesting that the additional 3Å of NiO does not form on top of the original 7Å thick EP film. Instead, it appears that the oxygens of the EP film are incorpora-

Table II. O^{18} content of films initially formed on nickel in pH 3.0 Na_2SO_4 solution (100% O^{16}) and then transferred to 10% O^{18} -enriched pH 3.0 Na_2SO_4 solution for continued polarization at the same potential of 0.4V. Also given are the O^{18} contents of films formed by immersing electropolished (EP) Ni into 10% O^{18} solution at 0.4V, both with and without cathodic reduction (CR) of the prior oxide. O^{18} contents determined by SIMS

Electrode treatment	Percentage of O^{18} in oxide film
EP + CR, $V_A \rightarrow 0.4V$ in H_2O^{18}	10.0
EP, $V_A \rightarrow 0.4V$ in H_2O^{18} (60s)	4.1
EP, $V_A \rightarrow 0.4V$ in H_2O^{18} (25 min)	7.4
5 min at 0.4V in H_2O^{16} ; 60s in H_2O^{18}	0.2
5 min at 0.4V in H_2O^{16} ; 15 min in H_2O^{18}	0.8
5 min at 0.4V in H_2O^{16} ; 95 min in H_2O^{18}	4.1
75 min at 0.4V in H_2O^{16} ; 15 min in H_2O^{18}	0.3

ted into the new passive film, *i.e.*, that there is a reorganization of the EP film upon anodic polarization.

Nature of anodic currents, i_a 's.—When the rate of replacement of O^{18} with O^{16} is correlated with the anodic charge passed (Fig. 2), quantitative information can be obtained about the nature of the long-term i_a 's flowing in the passive potential region. The results in Fig. 2 suggest that only 20-25% of the measured i_a is associated with actual dissolution and reformation of the oxide film, *i.e.*, $NiO + 2H^+ \rightarrow Ni^{2+} + H_2O$ and $Ni + H_2O \rightarrow NiO + 2H^+ + 2e$. The measured charges are four to five times greater than those required to bring about a particular degree of replacement, assuming 100% efficiency for oxide repair. The other 75-80% of the anodic charge must be associated with inefficient film repair (after local breakdown) via parallel nickel dissolution, *i.e.*, $Ni \rightarrow Ni^{2+} + 2e$. The results thus indicate that the i_a 's after a long-term anodization are not a direct measure of the rate of oxide chemical dissolution [*cf.* Ref. (2)]. From this work, the model which explains the anodic passive currents is one where the oxide film is dissolving locally and immediately reforming with a *c.e.* < 100% because of parallel nickel dissolution. This process occurs at random points on the surface, the number of sites involved at any instant in time depending on the state of the oxide (which determines the defect density) and the aggressiveness (pH) of the solution.

Influence of Cl^- on i_a .—The change of i_a with time in pH 1.0 Na_2SO_4 at 0.4V, for a sample prepassivated in pH 3.0 Na_2SO_4 at 0.6V for 15 min, is shown in Fig. 3. There is a steady increase of current with time in the lower pH solution until a steady state is reached after about 40 min. The final current is identical to that obtained if the anodizing had been in the pH 1.0 solution from the start, *i.e.*, the new state of the oxide film is that associated with long-term passivation at 0.4V in pH 1.0 Na_2SO_4 . The oxide film formed in the pH 3.0 Na_2SO_4 solution is obviously undergoing a conversion to a more defective form in the pH 1.0 solution. This conversion at the lower pH is probably related to the fact that the limiting stability of the oxide film is highly pH dependent and it is not possible to reach the same stable state at pH 1.0 as could be achieved at pH 3.0 (1). The conversion again involves localized, random breakdown of the film produced at pH 3.0 and its subsequent local replacement in pH 1.0 solution. The time needed to reach a steady state in pH 1.0 solution is highly dependent on the prior passivation treatment, this time being ~ 5h for a sample pretreated for 18h at 0.6V in pH 3.0 Na_2SO_4 . This result is consistent with a rate of film breakdown which is directly dependent on the state of perfection (*i.e.*, the defect state) of the prior oxide film as well as the aggressiveness of the breakdown solution. The rate of increase of i_a with t is thus a measure of the rate of film breakdown and can be used to check the

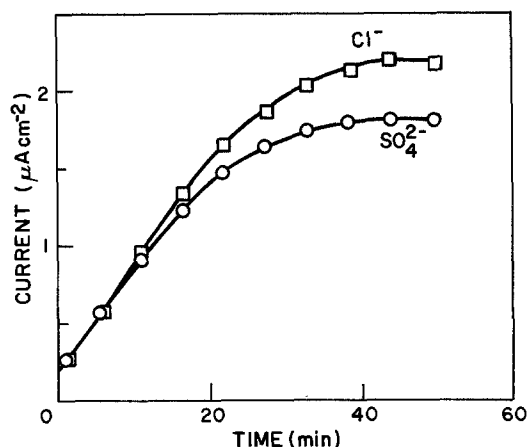


Fig. 3. Increase of anodic current i_a with time for nickel prepassivated in pH 3.0 Na_2SO_4 at 0.6V for 15 min and then exposed to a pH 1.0 Na_2SO_4 solution at 0.4V (circles). Also shown is the influence of 0.003M Cl^- in the pH 1.0 Na_2SO_4 on the change of i_a with time (squares).

influence of added Cl^- on the breakdown (*i.e.*, conversion) rate of the oxide. The *i/t* profile for a film formed in pH 3.0 Na_2SO_4 at 0.6V for 15 min and then transferred to a pH 1.0 Na_2SO_4 solution with 0.003M Cl^- solution at 0.4V is also shown in Fig. 3. The eventual current is somewhat higher than that observed for breakdown in pH 1.0 Na_2SO_4 , but this is simply due to Cl^- incorporation into the oxide film making the film more defective, *i.e.*, producing more sites at which breakdown will occur at any instant in time (17-19). When this is taken into account, the kinetics of conversion of the prior film are similar in the presence or absence of Cl^- ion, *i.e.*, the Cl^- does not appear to accelerate the process of film breakdown. This is consistent with the model, which suggests that Cl^- has no direct influence on breakdown of the passive oxide film but simply interferes with local repassivation events which are continuously occurring at numerous sites on the oxide surface (12, 18). It is also in agreement with the observation that addition of Cl^- to a solution in which a passivated sample is held potentiostatically does not result in any measurable increase in i_a until $t > t_{\text{ind}}$, the induction time at which pitting begins (20).

When the $[\text{Cl}^-]$ used in the experiment indicated in Fig. 3 is 0.015M instead of 0.003M, pitting begins ~ 16 min after immersion in pH 1.0 Na_2SO_4 solution, as indicated by a sharp increase in i_a . Before this time, however, the *i/t* profile is almost identical to that observed with 0.003M Cl^- , indicating that even when sufficient Cl^- is present to cause pitting (and V_a is therefore above the pitting potential), the film is dissolving at more or less the same rate as that observed in SO_4^{2-} solution. These results again suggest that the aggressive Cl^- ion has no direct influence on localized passivity breakdown but instead modifies the local repair kinetics so as to greatly decrease the c.e. for film repair, *i.e.*, that Cl^- interferes with repassivation.

In conclusion, the results obtained from the $\text{O}^{16}/\text{O}^{18}$ experiments in this work support the model of the passive oxide film wherein local breakdown/repassivation events are constantly occurring at selected sites on the metal surface.

Acknowledgment

The authors thank Mr. G. I. Sproule for the SIMS analysis.

Manuscript submitted Feb. 25, 1985; revised manuscript received Aug. 4, 1985.

The National Research Council of Canada assisted in meeting the publication costs of this article.

REFERENCES

1. B. MacDougall, *This Journal*, **103**, 114 (1983).
2. B. MacDougall, D. F. Mitchell, and M. J. Graham, *Isr. J. Chem.*, **18**, 125 (1979).
3. G. Okamoto and N. Sato, *J. Electrochem. Soc. Jpn.*, **27**, E125 (1959).
4. K. J. Vetter, "Electrochemical Kinetics," pp. 748-786, Academic Press, New York (1967).
5. V. M. Novakouski and Y. A. Lickhachev, *Electrochim. Acta*, **12**, 267 (1967).
6. V. M. Novakouski, *ibid.*, **10**, 353 (1965).
7. N. Valverde and C. Wagner, *Ber. Bunsenges. Phys. Chem.*, **80**, 330 (1976).
8. N. Valverde, *ibid.*, **80**, 333 (1976).
9. D. A. Vermilyea, *This Journal*, **113**, 1076 (1966).
10. B. MacDougall and M. Cohen, *ibid.*, **124**, 1185 (1977).
11. B. MacDougall, *ibid.*, **125**, 1183 (1978).
12. B. MacDougall, *ibid.*, **126**, 919 (1979).
13. B. MacDougall, D. F. Mitchell, and M. J. Graham, *Corrosion*, **38**, 85 (1982).
14. D. F. Mitchell, G. I. Sproule, and M. J. Graham, *Appl. Surf. Sci.*, **21**, 199 (1985).
15. B. MacDougall and M. Cohen, *This Journal*, **121**, 1152 (1974).
16. D. F. Mitchell, R. J. Hussey, and M. J. Graham, *J. Vac. Sci. Technol. A*, **2**, 789 (1984).
17. B. MacDougall, D. F. Mitchell, G. I. Sproule, and M. J. Graham, *This Journal*, **103**, 543 (1983).
18. B. MacDougall and M. J. Graham, *ibid.*, **131**, 727 (1984).
19. B. MacDougall, in "Proceedings of the 9th International Congress on Metallic Corrosion," Vol. 2, p. 168, Toronto (1984).
20. B. MacDougall, in "Passivity of Metals and Semiconductors," M. Froment, Editor, p. 275, Elsevier, Amsterdam (1983).

Screening Design Test for Cyclic Voltammetric Evaluation of Zinc Sulfate Electrolyte

R. K. Singh and T. J. O'Keefe*

Materials Research Center, University of Missouri-Rolla, Rolla, Missouri 65401

ABSTRACT

A statistical screening design program was conducted to determine the effects of certain operating parameters in the cyclic voltammetric evaluation of zinc sulfate electrolyte. The variables studied included solution temperature, sulfuric acid and zinc concentrations, and scan rate. Solution temperature was found to be the most significant factor affecting the initial potential, followed by scan rate and zinc concentration. Based on screening design data, mathematical equations were developed to predict polarization behavior of addition-free zinc sulfate electrolytes. A few preliminary tests on the effect of impurities and organic additives, such as Sb(III) and glue, on potential, deposit morphology, and crystal orientation were also made.

Cyclic voltammetry techniques have been used successfully to monitor the electrolyzability of zinc electro-winning solutions (1, 2). By measuring the zinc deposition polarization effects, a definite correlation has been shown to exist between the cathode polarization, deposit morphology, and current efficiency of zinc electrodeposition for a number of systems (3-6). Most of these studies have concentrated on the role of impurities and organic additives in the solutions. However, the activation overpotential and deposit morphology are also affected by other operating variables such as temperature, zinc

concentration, sulfuric acid concentration, and parameters for conducting the test. Therefore, before using this technique for determining an optimum overpotential, it is necessary to delineate the effect of these processing variables if the impurity and organic additive concentrations are to be properly evaluated.

Systems with many independent variables lend themselves to more efficient study by varying several factors at once in a statistical experimental design. The relative importance of independent or factor variables can be ascertained from a Plackett-Burman screening design. A Plackett-Burman design is based on a simplified first-

* Electrochemical Society Active Member.

Table I. Variables and their levels used in the screening design

Variable	Factor level		
	Low	Center	High
x_1 Zinc concentration (g/liter)	50	60	70
x_2 H ₂ SO ₄ concentration (g/liter)	150	175	200
x_3 Solution temperature (°C)	25	35	45
x_4 Test scan rate (mV/s)	0.5	1.25	2
x_5 Dummy			
x_6 Dummy			
x_7 Dummy			

order empirical model, but will also yield information indicating overall curvature, or deviations from the linear model, and give an indication of the presence of interaction effect among variables.

The object of the present study was to determine by means of a screening design, the individual effects and interactions, if any, of temperature, zinc and sulfuric acid concentrations, and scan rate on the nucleation potential of zinc electrodeposition. The conditions chosen were similar to those employed in commercial zinc electro-winning operations. In addition, other tests were made to determine the effects of Sb(III) and glue addition on polarization behavior and deposit morphologies.

Experimental

Screening design.—An eight-run Plackett-Burman screening design was chosen to investigate the importance of parameters listed in Table I. Other types and sizes of statistical design are available (7, 8), and each has its merits and drawbacks, depending on the type of information that is desired.

The design procedure employed follows closely that described by Murphy (7), which lists in tabular form the high and low (+ and -) test level arrangement to be used. As explained in the article, the choices for the screening design result from using only a specific fraction of the 2^p factorial design.

Variables considered in the present study included zinc concentration, sulfuric acid concentration, electrolyte temperature, and voltammetric scan rate. The high, low, and intermediate values of the factor levels are listed in Table I. The choice of factor level was based on pre-screening tests and conditions appropriate to industrial zinc electro-winning practice.

Table II shows the matrix of the design, with each variable at two levels, a plus symbol denotes the high level, and a minus symbol low level. Although seven variables can be studied in this design, only four variables were studied, leaving three variables as dummies to estimate the presence of interaction among variables. To estimate curvature effects and experimental error, three center-point runs were added to the design runs. To guard against systematic trends in uncontrolled (or unknown) variables during execution of the design, the order in which the runs were made was randomized. The center points were evenly spaced over experimental run orders, i.e., as the first, middle, and last run of the design.

Solution preparation.—Tests were conducted using both synthetic zinc sulfate solution and an industrial zinc electrolyte for each design point. Synthetic zinc sulfate solution was prepared by dissolving high purity French Process zinc oxide in reagent-grade sulfuric acid. Industrial zinc electrolyte was obtained from Cominco Limited (Trail, Canada). For a given design run, solution compositions were adjusted by adding reagent-grade sulfuric acid and deionized water to give a desired zinc and sulfuric acid concentration. When studying the effect of impurity and/or glue additions, the required amounts were added from the respective stock solutions. Sb(III) stock solution was prepared by dissolving potassium-antimony tartarate [K(SbO)C₄H₄O₆ · ½ H₂O] in deionized water. Glue stock solution was prepared by dissolving Pearl Glue (obtained from Cominco Limited, Trail, Canada) in deionized water and stored in a refrigerator to avoid its degradation.

Cyclic voltammetry.—The cyclic voltammetry experiments were conducted in a Pyrex "H" cell employing an

Table II. Statistical design and results

Design point run no.	Response (volt ^a at 10 mA/cm ²)		Factor variable ^b						
	Industrial solution	Synthetic solution	x_1	x_2	x_3	x_4	x_5	x_6	x_7
1	-0.866	-0.878	-	-	-	-	+	+	+
2	-0.876	-0.892	+	-	-	+	+	-	-
3	-0.885	-0.900	-	+	-	+	-	+	-
4	-0.845	-0.867	+	+	-	-	-	-	+
5	-0.843	-0.855	-	-	+	+	-	-	+
6	-0.813	-0.818	+	-	+	-	-	+	-
7	-0.825	-0.829	-	+	+	-	+	-	-
8	-0.832	-0.836	+	+	+	+	+	+	+
Industrial solution		Σ+	-3.366	-3.387	-3.313	-3.436	-3.399	-3.396	-3.386
		Σ-	-3.419	-3.398	-3.472	-3.349	-3.386	-3.389	-3.399
		Difference	+0.053	+0.011	+0.159	-0.087	-0.013	-0.007	+0.013
		Factor effect	+0.013	+0.003	+0.040	-0.022	-0.003	-0.002	+0.003
Synthetic solution		Σ+	-3.413	-3.432	-3.338	-3.483	-3.435	-3.432	-3.436
		Σ-	-3.462	-3.443	-3.537	-3.392	-3.440	-3.443	-3.439
		Difference	+0.049	+0.011	+0.199	-0.091	+0.005	+0.011	+0.003
		Factor effect	+0.012	+0.003	+0.050	-0.023	+0.001	+0.003	+0.001

^a vs. SHE.

^b + indicates high values of factor variable levels; - indicates low values of factor variable levels.

Center-point responses from industrial solution design: -0.847, -0.851, -0.852

Average: -0.850

s: 0.003

Center-point responses from synthetic solution design: -0.864, -0.859, -0.865

Average: -0.863

s: 0.003

$$\text{Factor effect of } x_i = \frac{\Sigma(\text{responses at high } x_i) - \Sigma(\text{responses at low } x_i)}{(\text{number of factorial runs})/2}$$

Example: For x_3 or temperature in industrial solution design

$$\text{Factor effect} = \frac{(-0.843 - 0.813 - 0.825 - 0.832) - (-0.866 - 0.876 - 0.885 - 0.845)}{(8/2)}$$

$$= +0.040$$

aluminum working electrode (area 1 cm²), a titanium/manganese dioxide counterelectrode, and a mercurous sulfate reference electrode (+0.667V vs. SHE). A constant-temperature bath was used to maintain the desired temperature and a Petrolite Potentiodyne Analyzer (Model M-4100) was used to record the cyclic voltammogram. The polarization behavior was recorded as a log current vs. potential plot.

The working electrode was prepared by wet polishing on 600 grit paper. The electrode was washed in an ultrasonic cleaner after polishing and then rinsed with deionized water and dried with hot air. The electrode was then placed in the H cell and allowed to come to the test temperature.

After reaching the test temperature, a voltammogram was obtained by varying the potential from -0.633V vs. SHE to a more cathodic potential where the total current was 50 mA. At this point, the scan was reversed and driven to the original starting potential. The test was terminated after reaching the starting potential.

Deposit examination.—For a given set of experimental conditions, the zinc deposits were obtained by scanning up to a current of 50 mA and holding the potential constant at this point for 2 min. The electrode was taken out of solution and washed thoroughly with deionized water and dried in hot air. The deposits were examined by x-ray diffraction to determine their orientations and scanning electron microscopy was used for surface morphology evaluations.

Results and Discussion

Addition-free electrolyte.—A cyclic voltammogram typical of those obtained for the solutions investigated is shown in Fig. 1. The reactions occurring at various points on the polarization curve have been discussed previously (9). In brief, the reactions occurring are: in region AB, hydrogen gas evolution; in region BC, hydrogen gas evolution and zinc deposition on the aluminum substrate; in region CD, hydrogen gas evolution and zinc deposition on zinc; in region DEF, zinc dissolution and hydrogen gas evolution; and in region FG, hydrogen gas evolution on aluminum substrate.

The response variable chosen was the front scan potential of the working electrode at a current density of 10 mA-cm⁻² (i.e., point Y in Fig. 1). Table II shows the values

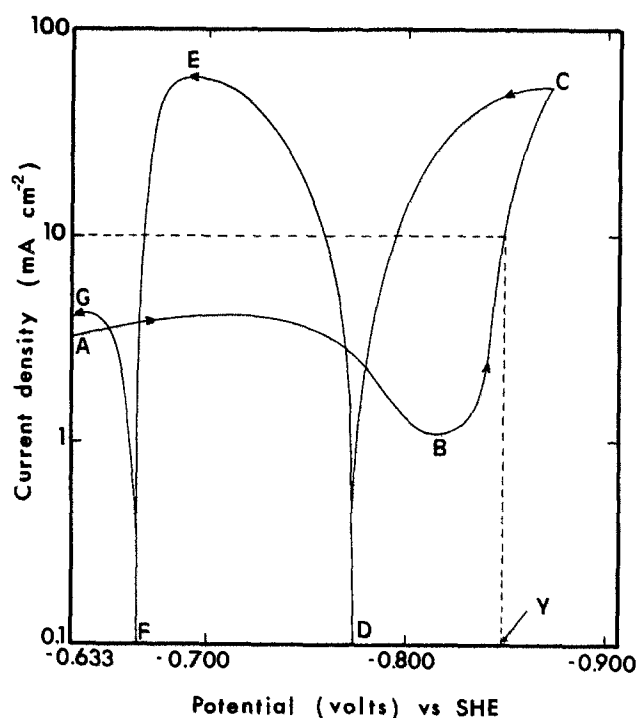


Fig. 1. Cyclic voltammogram for industrial electrolyte (60 g-liter⁻¹ Zn, 175 g-liter⁻¹ H₂SO₄); 35°C, 1.25 mV-s⁻¹.

of the response (Y) observed for each of the 11 runs (eight design runs + three center-point runs) for the synthetic and industrial solutions.

In any screening design, the calculated factor effect establishes the best estimate of the relative importance of a factor. The precision of the estimate is generally stated in the form of a confidence interval, which is an interval said to include the "true" effect at a stated confidence level. Factor effects whose confidence interval passes through zero are considered to be statistically insignificant at the chosen confidence level. Calculation of factor effects and confidence interval, based on a 95% confidence level, for the present study is listed in Tables II and III. The three center points of each design were used to estimate the response error for the given design.

Because the way response variable is defined in this case, factor effects with positive values indicate depolarization while negative values indicate increased polarization (or potential changing in a more negative or cathodic direction) when the independent variable is changed from low to high level. As can be seen from Table III, within the range of factor levels considered in the design, solution temperature is the most significant factor followed by test scan rate and zinc concentration. Sulfuric acid concentration is not a significant factor in either of the designs. Increased temperature and zinc concentration cause depolarization (2 mV-°C⁻¹ and 0.65 mV-g⁻¹-liter for industrial electrolyte, and 2.5 mV-°C⁻¹ and 0.60 mV-g⁻¹-liter for synthetic electrolyte), whereas increased scan rate results in polarization (14.7 mV-mV⁻¹-s for industrial electrolyte, and 15.3 mV-mV⁻¹-s for synthetic electrolyte) of the measurements. The fact that the sulfuric acid concentration was not significant is interesting, because a few prescreening tests at 50 g-liter⁻¹ and 100 g-liter⁻¹ acid concentrations had indicated a considerable depolarization as compared to the 150 g-liter⁻¹ acid level. The reason for the nonsignificance of sulfuric acid concentration may be due to its optimum level being already available at the low factor level of 150 g-liter⁻¹. For the given level of variables, there is a measurable difference in the response of the two types of solutions. This can be attributed to the differences in the basic makeup (i.e., presence of residual impurities) of the two solutions. Impurities like Sb, Ge, Pb, Cd, etc., are known to effect the polarization behavior of the system even at very low concentrations (1). This also indicates the importance of preliminary screening of a given electrolyte.

The effect of dummy factors is also shown in Table III. These factors are a measure of any interaction among independent variables in the system. Since all three dummy factor estimates are found to be statistically insignificant, it can be concluded that there are no interactions among variables within the boundaries of this study.

If the system is linear, the centroid of all the design points and the average response from the center points

Table III. Summary of factor effect intervals at 95% confidence limit

Variable	Industrial solution	Synthetic solution
x ₁ Zn concentration	+0.013 ± 0.009 ^a	+0.012 ± 0.009 ^a
x ₂ H ₂ SO ₄ concentration	+0.003 ± 0.009	+0.003 ± 0.009
x ₃ Temperature	+0.040 ± 0.009 ^a	+0.050 ± 0.009 ^a
x ₄ Scan rate	-0.022 ± 0.009 ^a	-0.023 ± 0.009 ^a
x ₅ Dummy	-0.003 ± 0.009	+0.001 ± 0.009
x ₆ Dummy	-0.002 ± 0.009	+0.003 ± 0.009
x ₇ Dummy	+0.003 ± 0.009	+0.001 ± 0.009

^a Denotes factor effects which are statistically significant at 95% confidence level.

$$\text{Confidence interval} = \text{factor effect} \pm \frac{ts}{\sqrt{N/4}}$$

at 95% confidence limit and $\nu = 2$, $t = 4.303$, where t is the student's t variable, N is the number of design point runs (eight), s is the standard deviation from center points (0.003 for both types of solutions), and ν is the degrees of freedom.

Table IV. Estimation of curvature effects

	Industrial solution	Synthetic solution
Center point average	-0.850	-0.863
Design point average	-0.848	-0.859
Curvature effect ^a	-0.002	-0.004
Confidence interval (at 95% confidence level) ^b	-0.002 ± 0.009	-0.004 ± 0.009

^a Curvature effect = center point average - design point average.

^b Confidence interval = curvature effect ± $ts\sqrt{1/N + 1/C}$ where t is the student's t variable, s is the standard deviation, N is the number of design point runs, and C is the number of center-point runs.

should be equal. If, however, the system deviates from the linear model, overall curvature can be estimated as the difference between the average response of the center points and the average response of the design points. Table IV shows the calculation of the curvature effect for both designs. At 95% confidence level, the confidence intervals on curvature are -0.002 ± 0.009 for industrial solution and -0.004 ± 0.009 for synthetic solution, values which are not statistically significant.

When responses and factors are continuous in scale, it is useful to consider the factor-response relationship in terms of a mathematical model. Since the overall curvature and interaction among variables are insignificant in both designs, a first-order linear model, as given below, was considered to predict the responses at a given level of the variables

$$\hat{Y} = \bar{Y} + m_1x_1 + m_2x_2 + \dots + m_ix_i$$

where \hat{Y} is the predicted response (potential of working electrode at 10 mA-cm⁻² of current density in front scan region), Y the average measured response from the design points, $m_i = (1/2)$ (factor effect of x_i), and

$$x_i = \frac{\text{factor level} - (\text{high level} + \text{low level})/2}{(\text{high level} - \text{low level})/2}$$

where the factor level is the value of interest between the high and low levels.

Neglecting statistically insignificant factor effects, the predicted equations (see the Appendix for calculations) are as follows

Industrial solution: $\hat{Y} = -0.939 + 0.0007 [\text{Zn}] + 0.0020 (T) - 0.015 (S)$

Synthetic solution: $\hat{Y} = -0.964 + 0.0006 [\text{Zn}] + 0.0025 (T) - 0.0153 (S)$

where [Zn] is the zinc concentration in grams per liter, (T) the temperature in degrees Centigrade, and (S) the test scan rate in millivolts per second.

Using the above equations, calculated potential values were obtained for the values of the factors used in this study. Figures 2 and 3 compare the calculated potential values and those obtained experimentally for industrial and synthetic solutions, respectively. The fit of the model is quite good, and an "F" test showed that the variability between the predicted and experimental potential values is within the experimental error of the system for both types of solutions.

Effect of impurities and organic additives.—Impurities like Sb, Ge, Sn, Cu, Pb, etc., and organic additives like glue gelatin, and gum are known to influence the zinc deposition overpotential, deposit morphology, and orientation (3-6, 10, 11). The results of a few preliminary tests carried out with Sb(III) and glue additions are given in Table V. It is clear that when experimental variables are fixed for a given electrolyte, the addition of Sb(III) causes strong depolarization (column C and column D in Table V), and addition of glue results in a strong polarization (column A and column B in Table V) of the zinc electrodeposition process.

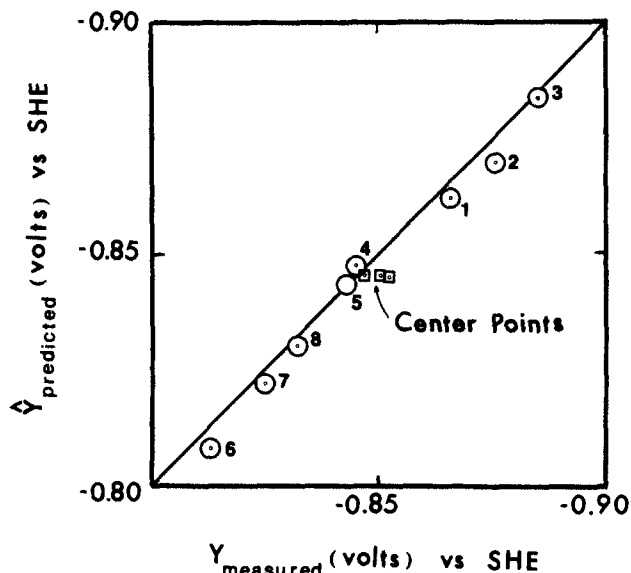


Fig. 2. Predicted vs. measured potential values at 10 mA-cm⁻² of current density for industrial electrolyte. The number beside the points refers to the design point run number in Table II.

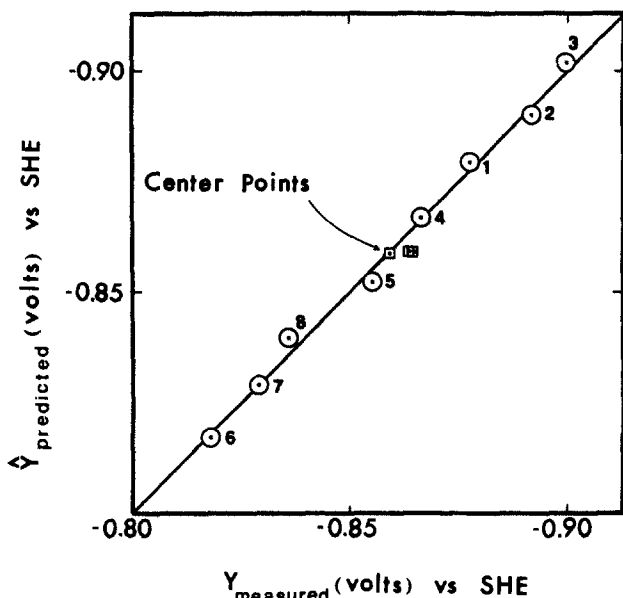


Fig. 3. Predicted vs. measured potential values at 10 mA-cm⁻² of current density for synthetic electrolyte. The number beside the points refers to the design point run number in Table II.

Figures 4-7 illustrate representative structures obtained using various experimental conditions and Sb(III) or glue additions. The morphology of deposits obtained from the addition-free electrolyte (Fig. 4 and 5) consists of parallel, hexagonal zinc platelets packed together and randomly

Table V. Zinc deposition polarization measurements on industrial electrolyte by cyclic voltammetry. A and C: Addition-free electrolyte. B: 10 mg-liter⁻¹ glue. D: 0.04 mg-liter⁻¹ Sb³⁺

Parameters	Experimental conditions			
	A	B	C	D
Zn (g/liter)	70	70	50	50
H ₂ SO ₄ (g/liter)	150	150	150	150
Sb ³⁺ (mg/liter)	—	—	—	0.04
Glue (mg/liter)	—	10	—	—
Temperature (°C)	44	44	25	25
Scan rate (mV/s)	0.5	0.5	2	2
V at 10 mA/cm ²	-0.815	-0.840	-0.880	-0.847

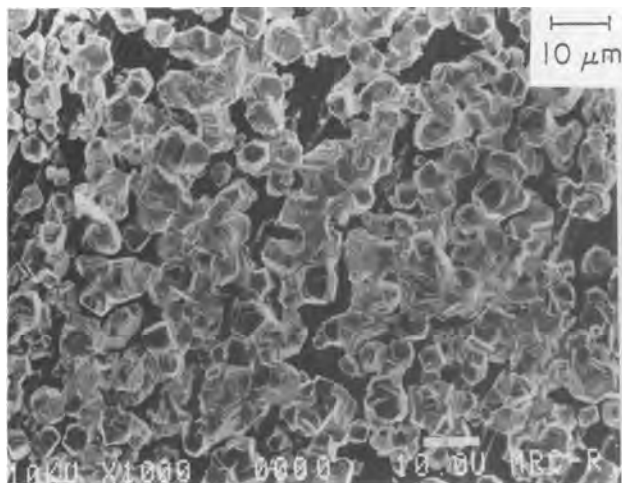


Fig. 4. SEM photomicrograph for the deposit obtained from industrial electrolyte ($Zn = 70 \text{ g-liter}^{-1}$, $H_2SO_4 = 150 \text{ g-liter}^{-1}$, 44°C , $0.5 \text{ mV}\cdot\text{s}^{-1}$). Potential at $10 \text{ mA}\cdot\text{cm}^{-2} = -0.815\text{V}$.

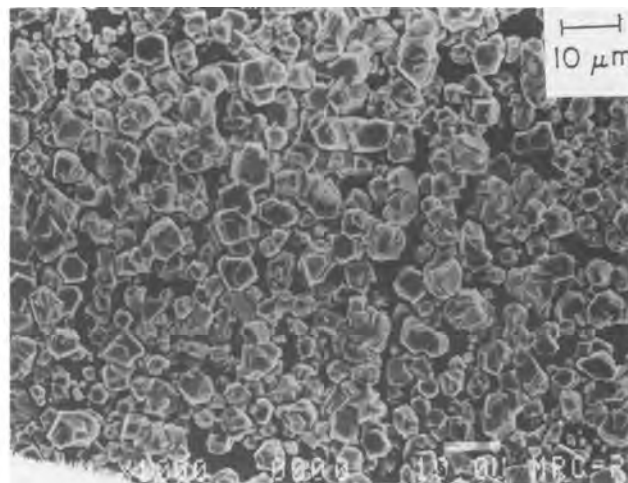


Fig. 6. SEM photomicrograph for the deposit obtained from industrial electrolyte with Sb(III) addition ($Zn = 50 \text{ g-liter}^{-1}$, $H_2SO_4 = 150 \text{ g-liter}^{-1}$, $Sb(III) = 0.040 \text{ mg-liter}^{-1}$, 25°C , $2 \text{ mV}\cdot\text{s}^{-1}$). Potential at $10 \text{ mA}\cdot\text{cm}^{-2} = -0.847\text{V}$.

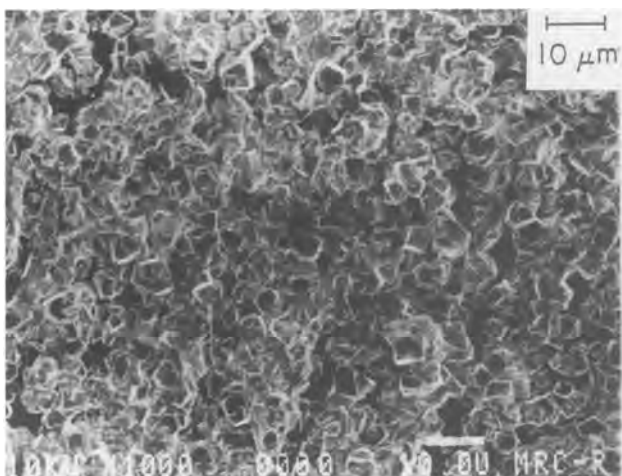


Fig. 5. SEM photomicrograph for the deposit obtained from industrial electrolyte ($Zn = 50 \text{ g-liter}^{-1}$, $H_2SO_4 = 150 \text{ g-liter}^{-1}$, 25°C , $2 \text{ mV}\cdot\text{s}^{-1}$). Potential at $10 \text{ mA}\cdot\text{cm}^{-2} = -0.880\text{V}$.

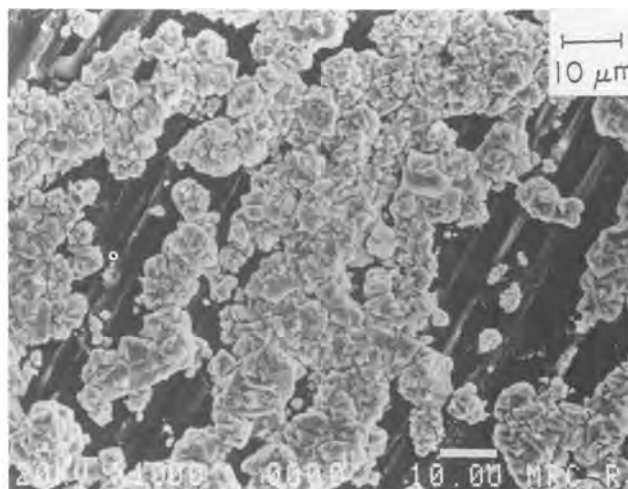


Fig. 7. SEM photomicrograph for the deposit obtained from industrial electrolyte with glue addition ($Zn = 70 \text{ g-liter}^{-1}$, $H_2SO_4 = 150 \text{ g-liter}^{-1}$, $\text{glue} = 10 \text{ mg-liter}^{-1}$, 44°C , $0.5 \text{ mV}\cdot\text{s}^{-1}$). Potential at $10 \text{ mA}\cdot\text{cm}^{-2} = -0.840\text{V}$.

disposed. The morphology obtained with the Sb(III) addition (Fig. 6) is most marked by larger crystal facets as compared to those for addition-free solution. The effect of $10 \text{ mg}\cdot\text{liter}^{-1}$ glue additions on the deposit morphology is shown in Fig. 7. The deposit appears more compact and of finer grain size than the deposit from addition-free electrolyte. The dominant feature is the appearance of zinc platelet edges with the basal plane lying more perpendicular to the substrate.

The x-ray diffraction studies on deposits for the determination of preferred crystal orientations were not conclusive. Very weak effects of antimony or glue additions to the electrolyte were observed. It is felt that, because of short duration of electrodeposition period in these tests, crystal orientations of the deposits were affected by the aluminum substrate. This substrate influence on the crystal orientation diminishes gradually as the thickness of the electrodeposit increases.

Previous studies on zinc electrocrystallization (3, 4) have shown a correlation between the deposit morphology/orientation and zinc deposition overpotential. The trends observed in the present study are in agreement with these investigations. However, a point of clarification is also indicated from the present data. A comparison of Fig. 6 and 7 shows that, although the overpotential values for the two deposits are similar, the morphologies and crystal orientations are not. Similarly, from the data in Table V, it is seen that two solutions

(Table V, B and D) with entirely different impurities and/or organic additives may also indicate a false similarity on their respective voltammograms because of differences in the operating parameters and test conditions used to generate the curves. A practical implication borne out of this is that it might be incorrect to relate a given overpotential value to a characteristic morphology/orientation unless other parameters and test conditions are also fixed in the system.

Conclusions

The screening design tests showed that the temperature is the most significant variable in cyclic voltammetric evaluation of zinc electrolytes. The test scan rate and zinc concentration are also important variables, whereas sulfuric acid concentration (in the range of $150\text{--}200 \text{ g-liter}^{-1}$) is not.

In addition to illustrating the importance of various factors, the statistical design permits the development of a model which can be used to predict the potential, and hence the polarization or depolarization behavior, of a given electrode/electrolyte system. The predicted equations have given a good fit to the experimental data within the range of variables in this study. However, its sensitivity can further be improved by using a full response surface design such as the Box-Behnken or the more elaborate Box-Wilson design.

One other very important fact that is evident from the data is that the deposit morphology is a function not only of the magnitude of the overpotential measured, but also of the conditions used in generating the polarization curve and the type of species in the electrolyte that is dominant in the growth. As indicated in previous research, for any fixed operating parameters and electrolyte system, increases in antimony or glue amounts give depolarizing and polarizing effects, respectively, in proportion to their concentrations. In turn, the morphologies that result can be correlated with the overpotential changes. However, it has been shown that, for example, a polarizing effect can be caused by lowering the temperature and zinc content. Even though the magnitude of increase in overpotential noted is nearly identical to that produced by adding glue, the morphologies will be different. No particular problem results from this feature, but it should be pointed out that it would be risky to try to characterize an unknown electrolyte by polarization techniques alone. A base reference must first be established prior to making evaluations of impurity and/or organic contents based on the overpotential measurement.

Acknowledgments

The authors wish to acknowledge the National Science Foundation, for their continued financial support of this research under Contract CPE 8004272. Thanks are also due to Cominco Limited for supplying the electrolyte and glue sample.

Manuscript submitted Dec. 17, 1984; revised manuscript received July 15, 1985.

The University of Missouri assisted in meeting the publication costs of this article.

APPENDIX

Calculation of Predicted Response for Industrial Solution

$$\hat{Y} = \bar{Y} + m_1x_1 + m_2x_2 + \dots + m_jx_j$$

where \hat{Y} is the predicted potential at 10 mA/cm², \bar{Y} the average measured potential at 10 mA/cm² = -0.848, $m_j = 1/2$ (factor effect for variable x_j), and

$$x_j = \frac{\text{factor level} - (\text{high level} + \text{low level})/2}{(\text{high level} - \text{low level})/2}$$

where the factor level is the value of interest between the high and low levels.

Significant main factor effects are

$$\begin{array}{ll} x_1: \text{Zn concentration} & FE_1 = +0.013 \\ x_3: \text{temperature} & FE_3 = +0.040 \\ x_4: \text{scan rate} & FE_4 = -0.022 \end{array}$$

	High	Low		Notations
x_1 : Zn concentration	70	50	(g/liter)	[Zn]
x_3 : temperature	45	25	(°C)	(T)
x_4 : scan rate	2	0.5	(mV/s)	(S)

Now, these values can be substituted into the equation for \hat{Y}

$$\hat{Y} = -0.848 + \left[\left(\frac{0.013}{2} \right) \frac{[\text{Zn}] - (70 + 50)/2}{(70 - 50)/2} \right] + \left[\left(\frac{0.040}{2} \right) \frac{(T) - (45 + 25)/2}{(45 - 25)/2} \right] + \left[\left(\frac{0.22}{2} \right) \frac{S + (2 + 0.5)/2}{(2 - 0.5)/2} \right]$$

Simplifying yields

$$\hat{Y} = -0.848 + [0.00065([\text{Zn}] - 60)] + [0.002(T - 35)] - [0.01466(S - 1.25)]$$

$$\begin{aligned} \hat{Y} &= -0.848 + 0.00065 [\text{Zn}] - 0.039 + 0.002(T) \\ &\quad - 0.07 - 0.01466(S) + 0.0183 \\ &= -0.939 + 0.0007[\text{Zn}] + 0.002(T) - 0.015(S) \end{aligned}$$

REFERENCES

1. R. Kerby and C. Krauss, in "Lead-Zinc-Tin '80, TMS-AIME World Symposium on Metallurgy & Environmental Control," Las Vegas, NV, Feb. 1980, p. 187, AIME, Warrendale, PA (1980).
2. R. C. Kerby, "International Conference on the Application of Polarization Measurements in the Control of Metal Deposition," Victoria, British Columbia, May 1982, p. 84, Elsevier (1984).
3. B. Lamping and T. J. O'Keefe, *Metall. Trans. B*, **7**, 551 (1976).
4. D. J. Mackinnon and J. M. Brannen, *J. Appl. Electrochem.*, **7**, 451 (1977).
5. D. J. Mackinnon, J. M. Brannen, and R. C. Kerby, *ibid.*, **9**, 55 (1979).
6. D. J. Robinson and T. J. O'Keefe, *ibid.*, **6**, 1 (1976).
7. T. D. Murphy, Jr., *Chem. Eng.*, p. 168, June 6, 1977.
8. C. Lipson and N. J. Sheth, "Statistical Design and Analysis of Engineering Experiments," McGraw-Hill Book Company, New York (1973).
9. Y. Wang, T. J. O'Keefe, and W. J. James, *This Journal*, **127**, 2589 (1980).
10. M. Maja, N. Penazzi, R. Fratesi, and G. Roventi, *ibid.*, **129**, 2695 (1982).
11. D. R. Fosnacht and T. J. O'Keefe, *Metall. Trans. B*, **14**, 64 (1983).

Ionic Electrodeposition of II-VI and III-V Compounds

I. Development of a Simple, Butler-Volmer Equation-Based Kinetic Model for $M_1X_1(\text{CdTe})$ Electrodeposition

R. D. Engelken*

Electronic/Photovoltaic Materials Research Group, Department of Engineering, Arkansas State University, State University (Jonesboro), Arkansas 72467

T. P. Van Doren

Department of Electrical Engineering, University of Missouri-Rolla, Rolla, Missouri 65401

ABSTRACT

A simple kinetic model has been developed for the electrodeposition of CdTe and other 12-16 (II-VI) or 13-15 (III-V) compounds from solutions containing reducible ions of both constituents and is based upon a generalized Butler-Volmer equation that considers ion transport limitations near the cathode. Although the deposition itself is a non-equilibrium process, the reaction between the plated cadmium and tellurium is assumed sufficiently rapid that any infinitesimally small volume in the deposit remains in quasi-chemical equilibrium, as defined by the equilibrium constant-mass action expression involving the activities of the solid constituents and conservation of mass, as invoked by a unity mole fraction sum. Exponential activity coefficients are postulated consistent with "regular" solution models. Although neglecting second-order effects such as hydrogen generation, IR and space-charge voltage drops within the deposit, and possible phase segregation, the model yields a convenient algorithm to numerically simulate voltammetric (j - E) curves and calculate the mole fractions and activities of cadmium, tellurium, and cadmium telluride existing at the deposit surface for any deposition potential.

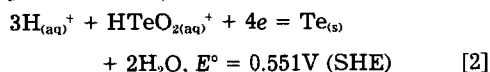
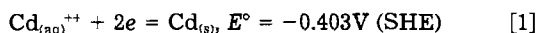
The electrodeposition of binary chalcogenides (1-12) such as CdTe (13-31, 47) and CdSe (32-37) from solutions containing both the metal and chalcogen in reducible ionic form has been a topic of recent experimental research. The major problems associated with compound semiconductor electrodeposition are, first, producing stoichiometric, nondegenerate material, and, second, achieving large-grained, nonamorphous deposits.

Unfortunately, there has not been extensive published theoretical work on the ionic "alloy" (22) electrodeposition of compound semiconductors (31, 48). Noteworthy is Kroger's (38) work describing the equilibrium state of a compound electrodeposit. Although similar in some respects to metallic alloy electroplating, as described in the works of Brenner (39), the very negative Gibbs free energies of formation for 12-16 (II-VI) and 13-15 (III-V) compounds, the possible semiconducting nature of the deposits, the large differences in the standard reduction potentials (E°) of selenium, tellurium, arsenic, and antimony and most metal ions, the changing nature of the deposit during deposition, and the presence of metastable states present complexities to any theoretical description.

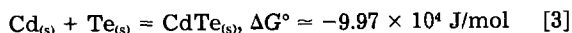
This paper presents a simple model for the kinetics corresponding to ionic electrodeposition of M_1X_1 compounds, as originally developed in detail in Ref. (15) and disseminated in abbreviated form in Ref. (16, 17). The model will be developed in terms of CdTe electrodeposition from acidic solutions of Cd^{2+} and HTeO_2^+ but could be applied to any M_1X_1 compound. Although several simplifying assumptions have been made, the model allows for the simulation of the electrodeposition process and leads to potentially useful predictions about the electrodeposition and associated voltammetric sweeps of such compounds.

Experimental Environment and Assumptions Corresponding to the Model

The primary cathode reactions are



and



and occur at a bare inert (C, Pt, etc.) potentiostat-con-

*Electrochemical Society Active Member.

trolled cathode immersed in an aqueous ($\text{pH} \approx 2.5$) solution containing CdCl_2 , CdSO_4 , etc., and TeO_2 . The reaction at an inert, cadmium, or tellurium anode could be O_2 evolution, Cd^{2+} dissolution, or HTeO_2^+ dissolution, respectively, but has no direct effect upon the cathode kinetics. The volume of the solution is large so that the electrochemical reactions produce negligible changes in pH and cadmium and tellurium ion activities (concentrations). Any hydrogen current is assumed to have no direct effect on the cadmium and tellurium current densities and the resultant deposit surface stoichiometry. Hydrogen is not bound or occluded in the "pure" Cd_xTe deposit. However, the hydrogen ion concentration will affect the tellurium current density through its effect on the tellurium Nernst potential and exchange current density. The total current densities discussed will be the sum of only the cadmium and tellurium current densities and will not include the approximately exponential H_2 current-voltage component.

Telluride or polytelluride anion formation from the six- or ten-electron reduction of Te(IV) ions is assumed negligible with the deposition voltages used. The deposit is formed by the solid-state reaction of plated cadmium and tellurium atoms rather than precipitation of Te_2^{2-} , Te^- , HTe^- , or H_2Te and Cd^{2+} .

The solution is stationary with no stirring and negligible thermal convection currents to avoid dependence of the cathodic diffusion-limited current density upon the agitation-dependent diffusion layer thickness. Any anodic diffusion-limited current, corresponding to cadmium and tellurium dissolution and ion hydration, is very large and not encountered at voltages considered in this paper.

The cathode-reference voltage is assumed to be completely dropped across the double (primarily Helmholtz) layer at the deposit-electrolyte interface. This implies that the electrolyte is very conductive, that voltage drops in the deposit bulk or surface space-charge regions are compensated or insignificant, that the electrochemical reactions and/or ion mass transport are the rate-determining steps, and that the current densities are described by Butler-Volmer kinetics. Because of large concentrations of surface states at a semiconductor surface due to irregularities, defects, and adsorbed electrolyte species, semiconducting electrodes do often behave quasi-metallically with a Tafel-like current-voltage characteristic (46). Furthermore, the deposit will be a nondegenerate semiconductor over a very small x range in Cd_xTe due to native dopants such as atomic vacancies and interstitials.

The deposit is assumed to be homogeneous over its surface area but may change in composition with depth into the deposit. Any nonhomogeneities caused by different grain orientations, grain boundaries, etc., are negligible, and the deposit is best considered an amorphous "gel" that grows complete layer by layer with a layer thickness approaching that of a monolayer. Kinetic parameters for cadmium and tellurium, such as rate constant and transfer coefficients, are assumed constant and independent of the deposit surface composition or structure.

Any small volume in the deposit is assumed to always be in quasi-chemical equilibrium described by

$$\frac{a_{\text{CdTe}}}{a_{\text{Cd}}a_{\text{Te}}} = \exp\left[\frac{-\Delta G^\circ_{\text{CdTe}}}{RT}\right] = K \quad [4]$$

and

$$\sum_1 x_i = 1 \quad [5]$$

Atomic migration within the deposit is assumed negligible, and, therefore, phase segregation and solubility limitations are ignored, consistent with the low temperature deposition system. The deposit exists as a homogeneous, metastable Cd_xTe material with $0 \leq x \leq \infty$ and x dependent upon the cadmium and tellurium current densities.

This model corresponds only to the deposition of material onto a bare inert substrate, as occurs with a negatively sweeping deposition potential, and not to the dissolution of material. Thus, it would not describe the anodic "backsweep" of a voltammetric measurement.

The Generalized Butler-Volmer Equation

The cathodic current densities are described by a generalized Butler-Volmer equation (40)

$$j_i = \frac{z_i F k_i^\circ \left[\left[\prod_m a_{\text{rm}}^{\nu_m} \right]^{\bar{\alpha}_i + \bar{\alpha}_i} \exp\left[\frac{-z_i F \bar{\alpha}_i}{RT} (E - E_i^\circ)\right] - \left[\prod_m a_{\text{pm}}^{\nu_m} \right]^{\bar{\alpha}_i + \bar{\alpha}_i} \exp\left[\frac{z_i F \bar{\alpha}_i}{RT} (E - E_i^\circ)\right] \right]}{1 + \frac{z_i F k_i^\circ}{j_{c,l_i}} \left[\left[\prod_m a_{\text{rm}}^{\nu_m} \right]^{\bar{\alpha}_i + \bar{\alpha}_i} \exp\left[\frac{-z_i F \bar{\alpha}_i}{RT} (E - E_i^\circ)\right] \right]} \quad [6]$$

where z_i is the number of electrons required to reduce the cadmium ($z_i = 2$) or tellurium ($z_i = 4$) ions, k_i° is a rate constant ($\text{mol}/\text{cm}^2\text{-s}$), a_{rm} is the cathode surface activity of reactant m (Cd^{2+} , HTeO_2^+ , H^+) in the formation of solid constituent, i , a_{pm} is the deposit surface activity of product m (Cd , Te , H_2O) in the reaction, ν_m is the stoichiometric coefficient, j_{c,l_i} is the cathodic diffusion-limited current density for ion i (Cd^{2+} or HTeO_2^+), and the other symbols have their standard meanings and/or are defined in the List of Symbols.

The k_i° value is temperature activated

$$k_i^\circ = k_{0i} T \exp\left[-\frac{E_{A_i}}{RT}\right] \quad [7]$$

where E_{A_i} is an activation energy and k_{0i} is a constant that includes any zeta potential drop (assumed small and constant) in the diffuse Gouy-Chapman layer. The units for k° are ($\text{mol}/\text{cm}^2\text{-s}$), rather than the usual (cm/s), because dimensionless activities rather than concentrations (mol/cm^3) have been used in the Butler-Volmer equations. Both $\bar{\alpha}_i$ and $\bar{\alpha}_i$, the transfer coefficients, can take on any value but normally $\bar{\alpha}_i + \bar{\alpha}_i = 1$. Note that z_i is not necessarily the charge (z') on ion i ; for example, $z_{\text{Te}} = 4$ but the tellurium ion is HTeO_2^+ .

The diffusion-limited current density, neglecting convection, can be described by (41)

$$j_{c,l_i} = z_i F D_i \left[\frac{c_{0i}}{(1 - t_{+i})\delta} \right] \quad [8]$$

if the mass transport of the ion i is rate determining, D_i , the diffusion coefficient, ($\sim 10^{-5} \text{ cm}^2/\text{s}$) is directly proportional to temperature, and δ , the diffusion layer thickness,

is normally 10^{-5} - 10^{-2} cm . If γ_i is an insensitive function of concentration over concentrations from 10^{-6} to $0.1M$, then ($a_{0i}^{z_i}/1000\gamma_i$) can be substituted for c_{0i} in Eq. [8]. Even though the above equation relates c_{0i} , $a_{0i}^{z_i}$, and j_{c,l_i} , j_{c,l_i} is taken as an independent, adjustable parameter because of uncertainty in D_i , t_{+i} , γ_i , and δ .

Butler-Volmer Eq. [6] (one for each constituent) reduces to Nernst-like, open-circuit (reversible) potential equations

$$E_{\text{Nernst}_i} = E_i^\circ - \frac{RT}{z_i F} \ln \left[\frac{\prod_m a_{\text{pm}}^{\nu_m}}{\prod_m a_{\text{rm}}^{\nu_m}} \right] = E_i, (E_{\text{Cd}}, E_{\text{Te}}) \quad [9]$$

for $j_i = 0$. If the electrochemical reactions [1]-[3] are reversible, this equation corresponds to the Nernst equation. Indeed, j_i can be zero for all components only at equilibrium, and this zero current condition for all constituents can be used to define the deposit activities at equilibrium (15, 38).

Equation [6] also predicts that $j_i(E \rightarrow -\infty) = j_{c,l_i}$ and can be easily manipulated into a form involving exchange currents, j_0 , and overpotentials, η

$$j_0 = z F k_i^\circ \prod_m (a_{\text{rm}}^{\nu_m})^{\bar{\alpha}_i} \prod_m (a_{\text{pm}}^{\nu_m})^{\bar{\alpha}_i} \quad [10]$$

and

$$\eta = E - E_i \quad [11]$$

It also corresponds to (42)

$$\begin{aligned} a_i^{z_i} &\approx a_{0i}^{z_i} \left[1 - \frac{j_i}{j_{c,l_i}} \right] \\ \text{cathode} & \\ \text{surface} & \end{aligned} \quad [12]$$

when γ_i is nearly constant over the range of concentrations normally used. When $j_i \rightarrow j_{c,l_i}$, ion i becomes depleted at the cathode surface and negative (anodic) j_i causes a buildup of ion i .

The electrochemical reactions [1] and [2] are assumed to occur in a single step. Although neglecting the possible multiple-step nature of both reactions, this assumption simplifies the model and sidesteps a lack of conclusive information about the individual steps and equilibrium constants of all but the rate-determining step. The transfer coefficients, $\bar{\alpha}_i$, could, however, take into account the multiple-step nature of the reactions in a semiempirical, phenomenological manner.

Mass Conservation and Thermodynamic Considerations

It can be shown that

$$\frac{n_{\text{Cd}}}{n_{\text{Cd}} + n_{\text{Te}}} = \frac{\frac{j_{\text{Cd}}}{z_{\text{Cd}}}}{\frac{j_{\text{Cd}}}{z_{\text{Cd}}} + \frac{j_{\text{Te}}}{z_{\text{Te}}}} = x_{\text{icd}} = x_i \quad [13]$$

where x_{icd} is the total (gross) mole fraction (total number of cadmium atoms in an infinitesimal deposit volume divided by the sum of the total number of cadmium and tellurium atoms in the same volume) and n_i is the number of moles of constituent i in the volume. Similarly

$$x_2 = x_{\text{Te}} = \frac{\frac{j_{\text{Te}}}{z_{\text{Te}}}}{\frac{j_{\text{Cd}}}{z_{\text{Cd}}} + \frac{j_{\text{Te}}}{z_{\text{Te}}}} \quad [14]$$

and

$$x_{\text{Cd}} + x_{\text{Te}} \equiv 1 \quad [15]$$

Since these quantities involve all cadmium and tellurium atoms, both those "free" and those bound in CdTe molecules, they correspond to initial values that exist before the rapid reaction of the atoms that results in Eq. [4] being satisfied. Values of x , n , a , etc., that exist after the reaction which produces this equilibrium are designated by the subscript f to denote final values.

The activity coefficients of M_iX_i compounds such as CdTe are modeled by

$$\gamma_{\text{Cd}} = \exp \left[\frac{\beta}{RT} x_2^2 \right] \quad [16]$$

$$\gamma_{\text{Te}} = \exp \left[\frac{\beta}{RT} x_1^2 \right] \quad [17]$$

and

$$\gamma_{\text{CdTe}} = \exp \left[\frac{\beta}{2RT} (1 - 4x_1x_2) \right] \quad [18]$$

where β is a compound-dependent constant. $\gamma_{\text{CdTe}} \rightarrow 1$ as $x_{1,2} \rightarrow 0.5$ at perfect CdTe stoichiometry and $\gamma_{\text{Cd,Te}} \rightarrow 1$ as $x_{2,1} \rightarrow 0$. Equations [16]-[18] can be shown to satisfy the Gibbs-Duhem relation and are suggested by the Guggenheim model (43) for the "regular" solid solution and the regular associated solution (RAS) model of Jordan (44, 45). β , although theoretically dependent upon bonding or interchange energies between the metal and nonmetal atoms, is best considered an adjustable, potentially measurable, and semiempirical parameter. Based upon Jordan's measurements (45), β_{CdTe} is probably between -10^4 and -10^5 J/mol. $\beta = 0$ corresponds to an ideal solid solution and unity activity coefficients.

One can define an effective mole fraction equilibrium constant, K'

$$K' \equiv \frac{x_{\text{CdTe}}}{x_{\text{Cd}}x_{\text{Te}}} \quad [19]$$

Using the above activity coefficient expressions and the fact that $x_1 + x_2 \equiv 1$, one finds that

$$K' = K \exp \left(\frac{\beta}{2RT} \right) = \exp \left[\frac{1}{RT} \left(\frac{\beta}{2} - \Delta G^\circ \right) \right] \equiv \exp \left(\frac{\beta'}{RT} \right) \quad [20]$$

where

$$\beta' \equiv \frac{\beta}{2} - \Delta G^\circ \quad [21]$$

Since 1 mol of CdTe requires 1 mol of cadmium and 1 mol of tellurium for its formation

$$n_{\text{CdTe}} = n_{\text{Cd}} - n_{\text{Cd}} = n_{\text{Te}} - n_{\text{Te}} \quad [22]$$

Now

$$K' = \frac{x_{\text{CdTe}}}{x_{\text{Cd}}x_{\text{Te}}} = \frac{n_{\text{CdTe}}}{n_{\text{Cd}}n_{\text{Te}}} [n_{\text{Cd}} + n_{\text{Te}} + n_{\text{CdTe}}] \quad [23]$$

Therefore, by use of Eq. [22] and [23]

$$n_{\text{Cd}} = n_{\text{Cd}} + \frac{K' n_{\text{Cd}} n_{\text{Te}}}{n_{\text{Cd}} + n_{\text{Te}} + n_{\text{CdTe}}} \quad [24]$$

Substitution of

$$n_{\text{Te}} = n_{\text{Te}} + n_{\text{Cd}} - n_{\text{Cd}} \quad [22]$$

and

$$n_{\text{CdTe}} = n_{\text{Te}} - n_{\text{Te}} \quad [23]$$

into Eq. [24] and manipulation yield

$$n_{\text{Cd}} = n_{\text{Cd}} + \frac{K' n_{\text{Cd}} (n_{\text{Te}} + n_{\text{Cd}} - n_{\text{Cd}})}{n_{\text{Cd}} + n_{\text{Te}}} \quad [25]$$

Solving for the positive, physically permissible value of n_{Cd} yields

$$n_{\text{Cd}} = \frac{n_{\text{Cd}} - n_{\text{Te}}}{2} + \left[\left(\frac{n_{\text{Cd}} - n_{\text{Te}}}{2} \right)^2 + \frac{n_{\text{Cd}} n_{\text{Te}}}{1 + K'} \right]^{0.5} \quad [26]$$

Since

$$x_{\text{Cd}} = \frac{n_{\text{Cd}}}{n_{\text{Cd}} + n_{\text{Te}} + n_{\text{CdTe}}} \quad [27]$$

and

$$n_{\text{CdTe}} = n_{\text{Te}} - n_{\text{Te}} \quad [22]$$

$$x_{\text{Cd}} = \frac{n_{\text{Cd}}}{n_{\text{Cd}} + n_{\text{Te}}} = \frac{1}{1 + \frac{1}{\left(\frac{n_{\text{Cd}}}{n_{\text{Te}}} \right)}} \quad [28]$$

By defining

$$\frac{n_{\text{Cd}}}{n_{\text{Te}}} \equiv h = \frac{b_{\text{Cd}} j_{\text{Cd}}}{b_{\text{Te}} j_{\text{Te}}}, \quad \left(b_i = \frac{1}{z_i} \right) \quad [29]$$

one obtains

$$\frac{n_{\text{Cd}}}{n_{\text{Te}}} = \frac{h - 1}{2} + \left[\left(\frac{h - 1}{2} \right)^2 + \frac{h}{1 + K'} \right]^{0.5} \quad [30]$$

and

$$\begin{aligned} x_{\text{Cd}} &= \frac{1}{1 + \frac{1}{\frac{h - 1}{2} + \left[\left(\frac{h - 1}{2} \right)^2 + \frac{h}{1 + K'} \right]^{0.5}}} \\ &= \frac{h - 1 + \left[\left(\frac{h - 1}{2} \right)^2 + \frac{h}{1 + K'} \right]^{0.5}}{h + 1 + \left[\left(\frac{h - 1}{2} \right)^2 + \frac{h}{1 + K'} \right]^{0.5}} \\ &= \frac{\frac{b_{\text{Cd}} j_{\text{Cd}}}{b_{\text{Te}} j_{\text{Te}}} - 1 + \left[\left(\frac{\frac{b_{\text{Cd}} j_{\text{Cd}}}{b_{\text{Te}} j_{\text{Te}}} - 1}{2} \right)^2 + \frac{\frac{b_{\text{Cd}} j_{\text{Cd}}}{b_{\text{Te}} j_{\text{Te}}}}{1 + K'} \right]^{0.5}}{\frac{b_{\text{Cd}} j_{\text{Cd}}}{b_{\text{Te}} j_{\text{Te}}} + 1 + \left[\left(\frac{\frac{b_{\text{Cd}} j_{\text{Cd}}}{b_{\text{Te}} j_{\text{Te}}} - 1}{2} \right)^2 + \frac{\frac{b_{\text{Cd}} j_{\text{Cd}}}{b_{\text{Te}} j_{\text{Te}}}}{1 + K'} \right]^{0.5}} \end{aligned} \quad [31]$$

Since Eq. [19] is symmetrical with respect to x_{Cd} and x_{Te} , one can derive a similar expression for x_{Te} by an interchange of Cd and Te subscripts

$$\begin{aligned} x_{\text{Te}} &= \frac{\frac{b_{\text{Te}} j_{\text{Te}}}{b_{\text{Cd}} j_{\text{Cd}}} - 1 + \left[\left(\frac{\frac{b_{\text{Te}} j_{\text{Te}}}{b_{\text{Cd}} j_{\text{Cd}}} - 1}{2} \right)^2 + \frac{\frac{b_{\text{Te}} j_{\text{Te}}}{b_{\text{Cd}} j_{\text{Cd}}}}{1 + K'} \right]^{0.5}}{\frac{b_{\text{Te}} j_{\text{Te}}}{b_{\text{Cd}} j_{\text{Cd}}} + 1 + \left[\left(\frac{\frac{b_{\text{Te}} j_{\text{Te}}}{b_{\text{Cd}} j_{\text{Cd}}} - 1}{2} \right)^2 + \frac{\frac{b_{\text{Te}} j_{\text{Te}}}{b_{\text{Cd}} j_{\text{Cd}}}}{1 + K'} \right]^{0.5}} \end{aligned} \quad [32]$$

By defining

$$M \equiv \frac{b_{\text{Cd}} j_{\text{Cd}} - 1}{b_{\text{Te}} j_{\text{Te}}} = \frac{2j_{\text{Cd}} - 1}{j_{\text{Te}}} \quad [33]$$

one obtains

$$\frac{b_{\text{Cd}} j_{\text{Cd}}}{b_{\text{Te}} j_{\text{Te}}} = \frac{2j_{\text{Cd}}}{j_{\text{Te}}} = 2M + 1 \quad [34]$$

$$\frac{b_{Te}j_{Te}}{b_{Cd}j_{Cd}} = \frac{j_{Te}}{2j_{Cd}} = \frac{1}{2M+1} \quad [35]$$

$$x_1 = \frac{2M+1}{2M+2} \quad [40]$$

$$\frac{\frac{2j_{Cd}}{j_{Te}} + 1}{2} = M+1 \quad [36]$$

$$\gamma_{Cd} = \exp \left[\frac{\beta}{RT} \left(\frac{1}{2M+2} \right)^2 \right] \quad [41]$$

$$\frac{\frac{j_{Te}}{2j_{Cd}} + 1}{2} = \frac{M+1}{2M+1} \quad [37]$$

$$\gamma_{Te} = \exp \frac{\beta}{RT} \left[\left(\frac{2M+1}{2M+2} \right)^2 \right] \quad [42]$$

and

$$\frac{\frac{j_{Te}}{2j_{Cd}} - 1}{2} = \frac{-M}{2M+1} \quad [38]$$

and x_{iCd} and x_{Te} expressed as functions of M .

The Nernst equations for the electrochemical Eq. [1] and [2] are

$$E_{Cd} = -0.403 - \frac{RT}{2F} \ln \left(\frac{a_{Cd}}{a_{Cd^{++}}} \right) \quad [43]$$

and

$$E_{Te} = 0.551 - \frac{RT}{4F} \ln \left(\frac{a_{Te}}{a_{HTeO_2^+}} \right) - \frac{3RT}{4F \log_{10}(e)} [pH] \quad [44]$$

Equations [33]-[38], in conjunction with Eq. [13], [14], [16], and [17], yield

$$x_2 = \frac{1}{2M+2} \quad [39]$$

Substitution of all of the above-derived terms into the individual Butler-Volmer Eq. [6] yields

$$j_{Cd} = \frac{2Fk_{Cd}^{\circ} \left[a_{Cd^{++}}^{\bar{\alpha}_{Cd} + \bar{\alpha}_{Cd}} \exp \left[\frac{-2F\bar{\alpha}_{Cd}(E+0.403)}{RT} \right] - \exp \left[\frac{2F\bar{\alpha}_{Cd}(E+0.403)}{RT} \right] \right] \exp \left[\frac{\beta}{RT} \left(\frac{1}{2M+2} \right)^2 \right]}{\left[1 + \frac{2Fk_{Cd}^{\circ}}{j_{Cd}} a_{Cd^{++}}^{\bar{\alpha}_{Cd} + \bar{\alpha}_{Cd}} \exp \left[\frac{-2F\bar{\alpha}_{Cd}(E+0.403)}{RT} \right] \right]} \left[\frac{M + \left[\frac{M^2 + \frac{2M+1}{1 + \exp \left(\frac{\beta'}{RT} \right)} \right]^{0.5}}{M+1 + \left[\frac{M^2 + \frac{2M+1}{1 + \exp \left(\frac{\beta'}{RT} \right)} \right]^{0.5}} \right] \right]^{\bar{\alpha}_{Cd} + \bar{\alpha}_{Cd}} \quad [45]$$

$= f_{Cd}(E, M)$

$$j_{Te} = \frac{4Fk_{Te}^{\circ} \left[(a_{HTeO_2^+} \cdot a_{H^+}^3)^{\bar{\alpha}_{Te} + \bar{\alpha}_{Te}} \exp \left[\frac{-4F\bar{\alpha}_{Te}(E-0.551)}{RT} \right] - \exp \left[\frac{4F\bar{\alpha}_{Te}(E-0.551)}{RT} \right] \right] \times \dots}{\left[1 + \frac{4Fk_{Te}^{\circ}}{j_{Te}} (a_{HTeO_2^+} \cdot a_{H^+}^3)^{\bar{\alpha}_{Te} + \bar{\alpha}_{Te}} \exp \left[\frac{-4F\bar{\alpha}_{Te}(E-0.551)}{RT} \right] \right] \times \dots} \times \dots$$

$$\dots \times \left[\exp \left[\frac{\beta}{RT} \left(\frac{2M+1}{2M+2} \right)^2 \right] \left[\frac{\frac{-M}{2M+1} + \left[\frac{\left(\frac{-M}{2M+1} \right)^2 + \frac{1}{(2M+1) \left[1 + \exp \left(\frac{\beta'}{RT} \right) \right]} \right]^{0.5}}{M+1 + \left[\frac{\left(\frac{-M}{2M+1} \right)^2 + \frac{1}{(2M+1) \left[1 + \exp \left(\frac{\beta'}{RT} \right) \right]} \right]^{0.5}} \right] \right]^{\bar{\alpha}_{Te} + \bar{\alpha}_{Te}} \right] \quad [46]$$

$\dots \times$

1

Further manipulation reduces j_{Te} to Eq. [47]

$$j_{Te} = \frac{4Fk_{Te}^{\circ} \left[(a_{HTeO_2^+} \cdot a_{H^+}^3)^{\bar{\alpha}_{Te} + \bar{\alpha}_{Te}} \exp \left[\frac{-4F\bar{\alpha}_{Te}(E-0.551)}{RT} \right] - \exp \left[\frac{4F\bar{\alpha}_{Te}(E-0.551)}{RT} \right] \right] \times \dots}{\left[1 + \frac{4Fk_{Te}^{\circ}}{j_{Te}} (a_{HTeO_2^+} \cdot a_{H^+}^3)^{\bar{\alpha}_{Te} + \bar{\alpha}_{Te}} \exp \left[\frac{-4F\bar{\alpha}_{Te}(E-0.551)}{RT} \right] \right] \times \dots} \times \dots$$

$$\dots \times \left[\exp \left[\frac{\beta}{RT} \left(\frac{2M+1}{2M+2} \right)^2 \right] \left[\frac{-M + \left[\frac{M^2 + \frac{2M+1}{1 + \exp \left(\frac{\beta'}{RT} \right)} \right]^{0.5}}{M+1 + \left[\frac{M^2 + \frac{2M+1}{1 + \exp \left(\frac{\beta'}{RT} \right)} \right]^{0.5}} \right] \right]^{\bar{\alpha}_{Te} + \bar{\alpha}_{Te}} \right] \quad [47]$$

$\dots \times$

1

$= f_{Te}(E, M)$

[47]

Computational Algorithm

There now exist two equations with two unknowns (j_{Cd} , j_{Te}) for a specified E value. To solve the equations for the unknowns, division of Eq. [45] by Eq. [47] is required to yield

$$f(E, M) = \frac{j_{Cd}(E, M)}{j_{Te}(E, M)} = \frac{j_{Cd}}{j_{Te}} = \frac{2M + 1}{2} \quad [48]$$

which can be interpreted as a single equation in M for a specified E value or a single equation in E for a specified M value.

One can iterate through E and solve for the M value required to satisfy Eq. [48] or iterate through M and solve for the required E value. M can range from $-1/2$ to ∞ if $j_{Cd,l} \rightarrow \infty$, and will saturate at a value

$$\frac{2j_{Cd,l} - 1}{j_{Cd,l} - 1}$$

otherwise. $M = 0$ corresponds to "perfect stoichiometry" with $j_{Cd} = j_{Cd,l}/2$ since

$$x_{iCd} = \frac{1}{1 + \left[1 + \exp\left(\frac{\beta'}{RT}\right) \right]^{0.5}} = x_{iTe} \quad [49]$$

and

$$\gamma_{Cd} = \exp\left(\frac{\beta}{4RT}\right) = \gamma_{Te} \quad [50]$$

Hence

$$a_{iCd} = x_{iCd}\gamma_{Cd} = a_{iTe} = x_{iTe}\gamma_{Te} \quad [51]$$

Once the (E , M) points are calculated, substitution into the individual j_{Cd} and j_{Te} equations (Eq. [45] and [47], respectively) yields j_{Cd} , j_{Te} , and their sum, j_{total} (neglecting hydrogen generation). Thus, it is possible to calculate curves of j_{total} vs. E as approximations to voltammograms conducted with the solutions.

Subsequently, x_{iCd} , x_{iTe} , γ_{Cd} , γ_{Te} , a_{iCd} , and a_{iTe} , existing at the deposit surface for a given deposition potential, can be calculated by substituting M into Eq. [31], [32], (by replacing the current density ratios by the appropriate M containing term), [41], and [42], and then multiplying x_i by γ . Then x_{iCdTe} is obtained from

$$x_{iCdTe} = 1 - x_{iCd} - x_{iTe} \quad [5]$$

Use of Eq. [18] for γ_{CdTe} with x_1 and x_2 defined by Eq. [39] and [40] yields

$$a_{iCdTe} = \gamma_{CdTe} x_{iCdTe} \quad [52]$$

At this point, all partial current densities, mole fractions, and solid-state activities are known as functions of deposition potential. Furthermore, f_{Cd} and f_{Te} can be considered functions of $a_{Cd^{2+}}$, $a_{HTeO_2^+}$, T , $j_{Cd,l}$, $j_{Te,l}$, k_{Cd}^0 , k_{Te}^0 , α_{Cd} , and α_{Te} , and the effects of these parameters upon the current densities and stoichiometries can be also explored. Calculated j - E and x - E curves and subsequent interpretation and discussion will be presented in the second part of this sequence (49) for a representative set of equation parameters.

Conclusions

An analytical model/computational algorithm has been developed for the calculation of constituent current densities, mole fractions, and activities as functions of deposition potential for the electrodeposition of CdTe or other M_iX_i compounds onto bare, inert cathodic substrates from solutions containing metal and nonmetal ions. The model utilizes a generalized Butler-Volmer equation that includes the cathodic diffusion-limited current density. The deposit is assumed to remain in quasi-chemical equilibrium as described by the conventional equilibrium

constant expression and a unity mole fraction sum. An exponential form for the solid-state activity coefficients is assumed, as suggested by various "regular" solution models, but this development could utilize other activity coefficient-mole fraction relationships. The model does not take into account second-order effects such as hydrogen generation or impurity reduction, the possible semi-conducting nature of the deposit over a narrow stoichiometry range, and incomplete or slow metal-nonmetal reactions, but does allow computer simulation of the electrodeposition process for metal selenides, tellurides, arsenides, and antimonides and leads to several interesting predictions, as will be discussed in the next paper (49).

Acknowledgments

The authors thank Dr. Albert Mink and Dr. Hal McCloud at Arkansas State University and Dr. J. Derald Morgan, Dr. Jack Boone, Dr. Bruce Poling, Dr. Burns Hegler, Dr. Yildirim Omurtag, and Mr. Alok Berry at the University of Missouri-Rolla for their help, comments, and discussion, and Sherry Engelken, Maxine Smith, and Betty Minton at Arkansas State University for the manuscript preparation.

Manuscript submitted March 8, 1985; revised manuscript received Aug. 20, 1985. This was Paper 430 presented at the New Orleans, Louisiana, Meeting of the Society, Oct. 7-12, 1985.

LIST OF SYMBOLS

a_i	activity of constituent or ion i
a_o	bulk ion activity
b_i	reciprocal of number of electrons required to reduce ion i , defined in conjunction with Eq. [29]
c_o	bulk ion concentration (mol/cm ³)
c_i	ion i concentration (mol/cm ³)
D	diffusion coefficient
e	electron or exponential base
E	deposition potential
E_A	activation energy, defined in Eq. [7]
E_i	reversible, open-circuit, or Nernst potential of constituent i (Cd, Te)
E^0	standard reduction potential
f	general functional expression or final value
F	Faraday's constant
ΔG^0	Gibbs' free energy
h	dimensionless molar ratio, defined by Eq. [29]
i	general subscript variable, species, initial value indicator, or current (obvious from context)
j_i	current density of constituent i
$j_{Cd,l}$	diffusion-limited current density
j_o	exchange current density
k^0	fundamental rate constant, defined in Eq. [7]
k_o	pre-exponential rate constant multiplier
K	activity equilibrium constant, defined in Eq. [4]
K'	mole fraction equilibrium, defined in Eq. [19]
m	summation or product subscript, or general metal
M	general metal, or dimensionless current ratio variable, defined in Eq. [33]
$n_{i,i}$	number of moles of constituent i before solid-state reaction
$n_{f,i}$	number of moles of constituent i after equilibrium
p	chemical product indicator
q	electronic charge indicator
r	chemical reactant indicator
R	universal gas constant
t_+	transference number
T	temperature (K)
x	general stoichiometry indicator (e.g., Cd, Te)
x_i	mole fraction of constituent i
$x_{1,2}$	total (gross) mole fraction of constituent 1 or 2 (Cd or Te)
X	general Group V or VI element
z_i	number of electrons required to reduce ion i to the element
z'_i	charge on ion i
α	cathodic transfer coefficient
α	anodic transfer coefficient
β	solid-state activity coefficient parameter, defined in Eq. [16]-[18]
γ	activity coefficient
δ	diffusion layer width
ν	stoichiometric coefficient

Σ general summation indicator
 Π general product indicator

REFERENCES

- R. D. Engelken and H. E. McCloud, *This Journal*, **132**, 567 (1985).
- R. D. Engelken, T. P. Van Doren, J. L. Boone, A. K. Berry, and A. Shahnazary, To be published.
- R. D. Engelken and H. E. McCloud, Abstract 429, p. 617, The Electrochemical Society Extended Abstracts, Vol. 84-2, New Orleans, Louisiana, Oct. 7-12, 1984.
- E. Fatas, R. Duo, P. Herrasti, F. Arjona, and E. Garcia-Camarero, *This Journal*, **131**, 2243 (1984).
- A. S. Baranski and W. R. Fawcett, *ibid.*, **127**, 766 (1980).
- R. N. Bhattacharya, *ibid.*, **130**, 2040 (1983).
- A. S. Baranski, W. R. Fawcett, A. C. McDonald, R. M. DeNobriga, and J. R. McDonald, *ibid.*, **128**, 963 (1981).
- D. K. Roe, L. Wehzhao, and H. Gerischer, *J. Electroanal. Chem.*, **136**, 323 (1982).
- A. S. Baranski, W. R. Fawcett, and C. M. Gilbert, *This Journal*, **130**, 2423 (1983).
- A. S. Baranski, M. S. Bennett, and W. R. Fawcett, *J. Appl. Phys.*, **54**, 6390 (1983).
- A. S. Baranski and W. R. Fawcett, *This Journal*, **131**, 2508 (1984).
- Y. W. Chen, J. A. Turner, and R. Noufi, Abstract 316, p. 445, The Electrochemical Society Extended Abstracts, Vol. 84-2, New Orleans, Louisiana, Oct. 7-12, 1984.
- K. Rajeshwar and R. N. Bhattacharya, Abstract 427, p. 615, The Electrochemical Society Extended Abstracts, Vol. 84-2, New Orleans, Louisiana, Oct. 7-12, 1984.
- K. Rajeshwar and R. N. Bhattacharya, Abstract 428, p. 616, The Electrochemical Society Extended Abstracts, Vol. 84-2, New Orleans, Louisiana, Oct. 7-12, 1984.
- R. D. Engelken, Ph.D. Thesis, University of Missouri, Rolla, MO (1983).
- R. D. Engelken, Abstract 429, p. 619, The Electrochemical Society Extended Abstracts, Vol. 84-2, New Orleans, Louisiana, Oct. 7-12, 1984.
- R. D. Engelken, Abstract 510, p. 723, The Electrochemical Society Extended Abstracts, Vol. 85-1, Toronto, Ont., Canada, May 12-17, 1985.
- J. L. Boone and T. P. Van Doren, Final Report, Solar Energy Research Institute Grant DE-FG02-79ER-10532, University of Missouri, Rolla, MO, 1982.
- T. P. Van Doren, J. L. Boone, R. D. Engelken, and Z. Maczenski, in "Proceedings of the Eighth Annual University of Missouri-Rolla — Missouri Department of Natural Resources Conference on Energy," p. 35, University of Missouri-Rolla, Rolla, MO (1981).
- M. P. R. Panicker, M. Knaster, and F. A. Kroger, *This Journal*, **125**, 566 (1978).
- H. J. Gerritsen, *ibid.*, **131**, 136 (1984).
- C. Ogden and D. Tench, Final Report, DOE Contract AC02-77CH-00178, Rockwell International, Thousand Oaks, CA (1981).
- G. Fulop, M. Doty, P. Meyers, J. Betz, and C. H. Liu, *Appl. Phys. Lett.*, **40**, 327 (1982).
- J. Llabres, R. Noufi, R. J. Axton, and S. K. Deb, in "Photovoltaics Advanced Research and Development 5th Annual Meeting," p. 93, Solar Energy Research Institute, Golden, CO (1983).
- B. M. Basol, E. S. Tseng, R. L. Rod, S. Ou, and O. M. Stafudd, in "Proceedings of the Sixteenth IEEE Photovoltaic Specialists Conference," IEEE, New York (1982).
- M. R. Panicker, Ph.D. Thesis, University of California, Los Angeles, CA (1980).
- R. N. Bhattacharya, K. Rajeshwar, and R. N. Noufi, *This Journal*, **131**, 939 (1984).
- J. Llabres, *ibid.*, **131**, 464 (1984).
- B. M. Basol and E. S. Tseng, in "Materials and New Processing Technologies for Photovoltaics," J. A. Amick, V. K. Kapur, and J. Dietl, Editors, p. 463, The Electrochemical Society Softbound Proceedings Series, Pennington, NJ (1983).
- R. Rod, R. Bunshah, O. Stafudd, B. Basal, and P. Nath, Final Report, DOE Contract DE-AC04-79ET23008, Monosolar, Inc., Santa Monica, CA (1980).
- M. Takahashi, K. Uosaki, and H. Kita, *This Journal*, **131**, 2305 (1984).
- S. Chandra and R. K. Pandey, *Phys. Status Solidi A*, **59**, 787 (1980).
- B. L. Funt, M. Leban, and A. Sherwood, American Chemical Society Symposium Series 90, p. 242, American Chemical Society, Washington, DC (1979).
- G. J. Houston, J. F. McCann, and D. Haneman, *J. Electroanal. Chem.*, **134**, 37 (1982).
- M. S. Kazacos and B. Miller, *This Journal*, **127**, 869 (1980).
- M. S. Kazacos and B. Miller, *ibid.*, **127**, 2378 (1980).
- K. Colbow, D. J. Harrison, and B. L. Funt, *ibid.*, **128**, 547 (1981).
- F. A. Kroger, *ibid.*, **125**, 2028 (1978).
- A. Brenner, "Electrodeposition of Alloys-Principles and Practice," Academic Press, New York (1963).
- L. I. Antropov, "Theoretical Electrochemistry," p. 378, MIR, New York (1972).
- L. I. Antropov, "Theoretical Electrochemistry," p. 325, MIR, New York (1972).
- L. I. Antropov, "Theoretical Electrochemistry," p. 326, MIR, New York (1972).
- J. W. Christian, "The Theory of Transformations in Metals and Alloys: Part I. Equilibrium and General Kinetic Theory," p. 170, Pergamon Press, Oxford, England (1975).
- A. S. Jordan, in "Calculation of Phase Diagrams and Thermochemistry of Alloy Phases," p. 100, AIME, Warrendale, PA (1979).
- A. S. Jordan, *Metall. Trans.*, **1**, 239 (1970).
- S. R. Morrison, "Electrochemistry at Semiconductor and Oxidized Metal Electrodes," pp. 113-117, Plenum Press, New York (1980).
- R. N. Bhattacharya and K. Rajeshwar, *This Journal*, **132**, 732 (1985).
- M. W. Verbrugge and C. W. Tobias, *ibid.*, **132**, 1298 (1985).
- R. D. Engelken and T. P. Van Doren, *ibid.*, **132**, 2910 (1985).

Ionic Electrodeposition of II-VI and III-V Compounds

II. Calculated Current Density and Stoichiometry vs. Deposition Potential Curves for Parameter Values Representative of CdTe and with One Partial Current Density Diffusion Limited

R. D. Engelken*

Electronic/Photovoltaic Materials Research Group, Department of Engineering, Arkansas State University, State University (Jonesboro), Arkansas 72467

T. P. Van Doren

Department of Electrical Engineering, University of Missouri-Rolla, Rolla, Missouri 65401

ABSTRACT

This article presents the results of a computer simulation of the kinetic model, developed in the first part of this paper for the electrodeposition of 13-15 (III-V) and 12-16 (II-VI) (notably CdTe) compounds from solutions containing reducible ions of both deposit constituents. The simulation utilized parameter values approximating those of CdTe. The calculated graphs of current density and constituent mole fractions vs. deposition potential indicated that the potential of perfect stoichiometry (PPS), the potential at which $x_{\text{Cd}} = x_{\text{Te}}$ and $x_{\text{CdTe}} \approx 1$, can lie positive of the pure cadmium Nernst potential (E_{Cd}) at the sharp positive shoulder of a nearly constant current plateau. This plateau corresponds to cadmium underpotential depositing on a nearly 1:1 basis with tellurium only because of the reduction in cadmium activity associated with compound formation. This is named conventional underpotential deposition (CUD). n-CdTe can be deposited within this plateau region, but native p-CdTe can be deposited only within a very small potential range positive of the PPS. When the cadmium and tellurium ion concentrations are of the same order of magnitude, the PPS can be shifted negative of E_{Cd} and onto the steep portion of the cadmium current curve. If the diffusion-limited current densities are matched so that equal molar fluxes occur at the cathode, the PPS shifts onto the diffusion-limited, nearly-constant current region negative of E_{Cd} so stoichiometric CdTe (MX) can be plated over a broad potential range. This is named matched diffusion-limited current (MDLC) deposition. The activity coefficient parameter, β , has negligible effect on the PPS during CUD, but varies the width of the plateau region. Less negative $\Delta G_{\text{MX}}^{\circ}$ values shift the PPS negative and decrease the plateau width. A discussion of various experimental measurements and differences with and similarities to the calculated results is also presented.

Because of recent interest in the electrodeposition of electronic-grade compound semiconductor films from solutions of the constituent ions, and the shortage of published theoretical work on the subject (2-5, 14, 16, 17), the first part of this paper (1) presented a simple model/computational algorithm to simulate the ionic electrodeposition of 13-15 (III-VI) and 12-16 (II-VI) compounds, notably CdTe, through the calculation of the cadmium and tellurium current densities, mole fractions, and activities corresponding to a given deposition potential. The present paper presents the results of such a computer simulation for parameters representative of CdTe.

These calculated results lead to several interesting predictions. Among these are the following.

First is the existence of an underpotential cadmium current density (j_{Cd}) plateau structure several hundred millivolts wide over which n-type CdTe can be plated.

Second is the existence of a corner, at the positive shoulder of this plateau, which corresponds to the potential (point) of perfect stoichiometry (PPS) at which intrinsic CdTe (MX) can be plated.

Third is the electrodeposition of native nondegenerate p-CdTe only over an extremely narrow range in potential positive of the PPS.

Fourth is the shifting of the PPS negative of the cadmium Nernst potential (E_{Cd}) and the disappearance of the plateau structure for nearly equal and usually small cadmium and tellurium ion concentrations (c_{Cd} , c_{Te}) and diffusion-limited current densities, (j_{Cd} , j_{Te}), and the deposition of stoichiometric CdTe by the matched diffusion-limited current (MDLC) deposition mode.

Fifth is the lack of sensitivity of the PPS upon β , the activity coefficient parameter, when the PPS lies on the positive shoulder of the plateau during conventional underpotential deposition (CUD).

Representative Parameter Values and Computational Technique

Table I presents the parameter values used in the calculations discussed in the first part of this paper (1). In several cases, these values were derived or extrapolated from

*Electrochemical Society Active Member.

incomplete, questionable, or widely varying data and the kinetic parameters k° , E_{A} , α , and $j_{\text{C},l}$ are best considered as only order of magnitude estimates. Reference (6) was useful in the determination of these representative values.

Even though $k_{\text{CdTe}} > k_{\text{Cd}}$, it includes the factor $(a_{\text{H}^+})^{-3\alpha_{\text{Te}}}$ and is based upon a much smaller exchange current density than for cadmium. In both cases, $\alpha + \bar{\alpha} = 1$; this simplifies the calculations but $\bar{\alpha}_{\text{Te}}$ may be considerably smaller than 0.45 for small cathodic currents.

The activity coefficient parameter, β , corresponding to a regular solid solution model, was typically $-67,800$ J/mol, an ad hoc value not too different from $-12,970$ J/mol found by Jordan (13) for liquid CdTe near its freezing point, but only an estimate for β_{CdTe} which probably lies between -10^4 and -10^5 J/mol. In conjunction with $\Delta G_{\text{CdTe}}^{\circ} \approx -9.97 \times 10^4$ J/mol, the mole fraction equilibrium constant parameter, β' , was calculated to be $\beta' = \beta/2 - \Delta G^{\circ} \approx 6.58 \times 10^4$ J/mol.

The $j_{\text{C},l}$ values were estimated from

$$j_{\text{C},l} \approx \frac{z_i \text{FD}c_{\text{oi}}}{\delta} \quad [1]$$

However, due to uncertainty in δ , $j_{\text{C},l}$ was taken as an adjustable parameter but generally "tracks" $c_{\text{Cd}^{++}}$ or $c_{\text{HTeO}_2^+}$.

In addition to the rate constant equation

$$k_i^{\circ} = k_{\text{oi}} T \exp[-E_{\text{A},i}/RT] \quad [2]$$

temperature corrections were also applied to E_{oi} and D_i through

$$E_{\text{Cd}}^{\circ}(T) \approx -0.403 - 9.3 \times 10^{-5}(T - 298.16 \text{ K}) \quad [3]$$

$$E_{\text{Te}}^{\circ}(T) \approx 0.551 - 3.7 \times 10^{-4}(T - 298.16 \text{ K}) \quad [4]$$

and

$$D_i = D_i(298.16 \text{ K}) \times (T/298.16 \text{ K}) \quad [5]$$

The D_i correction implies that

$$j_{\text{C},l}(T) \approx j_{\text{C},l}(298.16) \times (T/298.16 \text{ K}) \quad [6]$$

Table I. Parameter values used in the computer simulation and approximately representative of cadmium, tellurium, and cadmium telluride

PARAMETER	VALUE	UNITS
k°_{Cd}	$4.7 \cdot 10^{-7}$ (25°C)	$\frac{\text{moles}}{\text{cm}^2 \cdot \text{s}}$
k°_{Cd}	$3.9 \cdot 10^{-7}$	$\frac{\text{moles}}{\text{cm}^2 \cdot \text{s} \cdot \text{K}}$
k°_{Te}	$8.9 \cdot 10^{-6}$ (25°C)	$\frac{\text{moles}}{\text{cm}^2 \cdot \text{s}}$
k°_{Te}	$6.7 \cdot 10^{-6}$	$\frac{\text{moles}}{\text{cm}^2 \cdot \text{s} \cdot \text{K}}$
$E_{A_{Cd,Te}}$	13410	$\frac{\text{J}}{\text{mole}}$
$\alpha_{Cd,Te}$	0.45	
$\alpha_{Cd,Te}$	0.55	
Z_{Cd}	2	
Z_{Te}	4	
Z'_{Cd}	2	
Z'_{Te}	1	
E°_{Cd}	-0.403	V (SHE, 25°C)
E°_{Te}	0.551	V (SHE, 25°C)
$\frac{dE^{\circ}_{Cd}}{dT}$	$-9.3 \cdot 10^{-5}$	$\frac{V}{K}$
$\frac{dE^{\circ}_{Te}}{dT}$	$-3.7 \cdot 10^{-4}$	$\frac{V}{K}$
β_{CdTe}	$-6.78 \cdot 10^4$	$\frac{\text{J}}{\text{mole}}$
ΔG°_{CdTe}	$-9.97 \cdot 10^4$	$\frac{\text{J}}{\text{mole}}$
pH	2.5	
$D_{Cd,Te}$	$\approx 10^{-5}$	$\frac{\text{cm}^2}{\text{s}}$ (25°C)
δ	$10^{-5} - 10^{-2}$	cm

neglecting any possible change in $c_{o,i}$ with temperature (avoiding saturated solutions).

The "standard" operating values were $T = 25^\circ\text{C}$, $a_{Cd^{++}} = 0.019$ ($c_{Cd^{++}} = 0.1\text{M}$), $a_{\text{H}_2\text{TeO}_3} = 2.51 \times 10^{-5}$ ($c_{\text{H}_2\text{TeO}_3} \approx 2.51 \times 10^{-5}\text{M}$), $\text{pH} = 2.5$, $j_{c,l_{Te}} = 100 \mu\text{A}/\text{cm}^2$, $j_{c,l_{Cd}} = 200 \text{mA}/\text{cm}^2$, and $\beta = -6.78 \times 10^4 \text{J}/\text{mol}$.

The computer program was written in Harris REAL*12 (Quadruple Precision) FORTRAN 77 and was executed on a Harris H-800 computer system at Arkansas State University. In the root finding routines, the absolute value of a function at a "root" had to be $\leq 10^{-18}$.

As discussed in the first part of the paper, the program involved finding the

$$M = \frac{\left(\frac{2j_{Cd}}{j_{Te}}\right) - 1}{2} \quad [7]$$

value that satisfied Eq. [48] of that article (1)

$$\frac{j_{Cd}}{j_{Te}} = \frac{2M + 1}{2} = \frac{f_{Cd}(E, M)}{f_{Te}(E, M)} = f(E, M) \quad [8]$$

for a specified E value. This was done by starting at $M = -1/2$ and iterating positively through M until the root was crossed, and then using the conventional bisection method to "chop" in on the correct M .

This M value was reinserted into separate equations for j_{Cd} , j_{Te} , $j_{Cd} + j_{Te}$, x_1 , x_2 , x_{Cd} , x_{Te} , γ_{Cd} , γ_{Te} , and γ_{CdTe} to calculate these values. After this, $a_{Cd} = x_{Cd}\gamma_{Cd}$, $a_{Te} = x_{Te}\gamma_{Te}$, $x_{CdTe} = 1 - x_{Cd} - x_{Te}$, and $a_{CdTe} = \gamma_{CdTe}x_{CdTe}$ were obtained. At this point, the deposition current densities and associated deposit surface stoichiometries were specified as functions of deposition potential.

Calculated Data and Associated Discussion

Figure 1 exhibits calculated voltammetric curves for various temperatures. The "experimental" parameter values used are indicated on the graph. The cathodic cur-

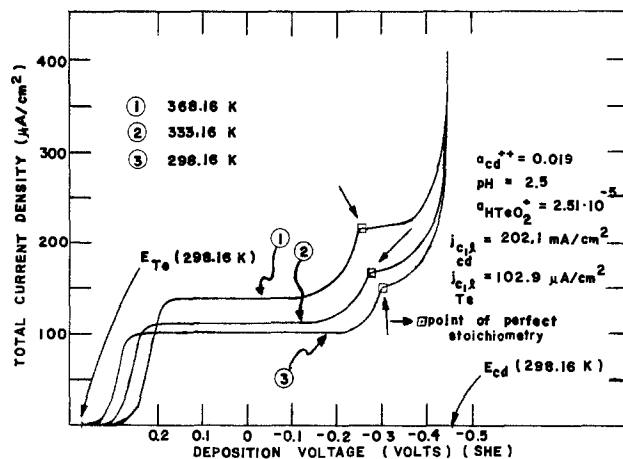


Fig. 1. Plots of total current density vs. deposition potential with temperature as a parameter. Note the underpotential cadmium current density plateau structure and sharp corner at its positive edge. This corner potential is the potential of perfect stoichiometry (PPS).

rent density (j) increases above zero at the tellurium Nernst potential, E_{Te} , ($\approx 0.37\text{V}$ [SHE] at 25°C) and increases nearly exponentially for $E < E_{Te}$. After a 0.1V potential decrease, $j = j_{Te}$ begins to saturate and asymptotically approaches $j_{c,l_{Te}}$. Since the "sweep rate" is infinitesimally slow, the capacitive current is zero and there is no peak at the j_{Te} shoulder due to a transient decrease in $c_{\text{H}_2\text{TeO}_3}$ at the cathode surface.

After a further 0.3-0.5V decrease in potential along the nearly constant $j = j_{Te} \rightarrow j_{c,l_{Te}}$ curve, another distinct increase in j occurs between -0.1 and -0.3V . This new current component exhibits an abrupt but continuous shoulder. Negative of this shoulder exists a current plateau with a relatively small slope.

This second structure is due to the underpotential electrodeposition of cadmium caused by $a_{Cd} < 1$ due to bonding of the plated cadmium with tellurium in the Cd_xTe deposit as described by

$$\frac{a_{CdTe}}{a_{Cd}a_{Te}} = \exp\left[\frac{-\Delta G^{\circ}_{CdTe}}{RT}\right] = K \quad [9]$$

and

$$\frac{a_{Cd}}{\gamma_{Cd}} + \frac{a_{Te}}{\gamma_{Te}} + \frac{a_{CdTe}}{\gamma_{CdTe}} = 1 \quad [10]$$

where $a_{Cd}/\gamma_{Cd} = x_{Cd}$ and $a_{Te}/\gamma_{Te} = x_{Te}$ are functions of j_{Cd}/j_{Te} as described by Eq. [31] and [32] of Ref. (1).

The sharp shoulder at the positive end of the underpotential j_{Cd} plateau occurs exactly at the potential of perfect stoichiometry (PPS), the potential at which $x_{Cd} = x_{Te}$, $a_{Cd} = a_{Te}$, $x_{CdTe} = a_{CdTe} = 1$, and $2j_{Cd} = j_{Te}$. The PPS for the room temperature curve is -0.300V (SHE) and is indicated by a box and an arrow. At the PPS, nearly intrinsic CdTe should be plated and $a_{Cd} = a_{Te} = [1/K]^{0.5}$, since $a_{CdTe} = x_{CdTe} = 1$.

Within the current density plateau, j_{Cd} is controlled by j_{Te} ; that is, because $E > E_{Cd}$, cadmium can plate only when it can react with tellurium. Any cadmium-rich regions will quickly redissolve due to $a_{Cd} \rightarrow 1$, causing a large anodic term in Eq. [45] of Ref. (1), the cadmium Butler-Volmer equation.

Within the plateau, the material is slightly cadmium rich and corresponds to n-CdTe doped by cadmium interstitial atoms. After an approximately 0.1V decrease in potential within the plateau region, the potential is near enough E_{Cd} (-0.454V at 25°C) that the cathodic exponential term in Eq. [45] in Ref. (1) becomes large and j_{Cd} begins its conventional exponential rise. At extremely negative voltages, it would approach its diffusion-limited value of $202.1 \text{mA}/\text{cm}^2$.

The PPS shifts positively with increasing temperature (T). This, in conjunction with a negative shift in E_{Cd} with T , widens the plateau. Thus, higher values for T widen

the voltage range over which CdTe can be plated as well as increasing the grain size.

Figure 2 plots PPS vs. $(1000/T)$ with the same conditions as for Fig. 1 except for just slightly larger $j_c, l_{Te} = 124.0 \mu A/cm^2$ and $j_c, l_{Cd} = 247.1 mA/cm^2$. The graph is nearly linear, indicative of the $1/RT$ containing terms appearing as arguments of the deposition voltage and rate constant terms

$$\exp\left(\frac{\pm 2F\alpha_{Cd}(E - E^0_{Cd})}{RT}\right)$$

and

$$k^0 = k_0 T \exp\left[\frac{-E_A}{RT}\right] \quad [2]$$

The slight bow is due to the minor temperature dependences of j_c, l_{Te} and E^0_{Cd} . Precise temperature control is indicated during electrodeposition to avoid shifting of the PPS and the resultant increase in native doping due to cadmium vacancies or interstitial atoms.

Figure 3 logarithmically plots x_{Cd} , x_{Te} , and x_{CdTe} vs. deposition potential for the room temperature curve in Fig. 1. With a PPS of $-0.300V$, the "free" cadmium and tellurium mole fractions are very small ($x_{Cd} \approx x_{Te} \approx 1.6 \times 10^{-6}$), equal, and changing very rapidly. x_{CdTe} approaches unity ($\approx 1 - 3.2 \times 10^{-6}$). For $E > PPS$, x_{CdTe} decreases and x_{Cd} continues its rapid decrease, while x_{Te} increases rapidly as the deposit becomes nearly pure tellurium at $-0.2V$. At $-0.27V$, x_{Te} becomes larger than x_{CdTe} and indicates a $0.03V$ range in which native p-CdTe is the predominant constituent. These rapid changes are a consequence of a sharply decreasing j_{Cd} for $E > PPS$ in Fig. 1.

For $E < PPS$, x_{CdTe} falls off relatively slowly and remains approximately unity for $0.04V$. CdTe is the dominant deposit constituent until $-0.41V$ where $x_{Cd} > x_{CdTe}$. Near $-0.46V$, $x_{Cd} \rightarrow 1$, $x_{CdTe} < 10^{-2}$, and $x_{Te} \approx 10^{-12}$. The -0.30 to $-0.34V$ range represents a $40 mV$ plateau width in which $x_{CdTe} > 0.97$. This corresponds to the j_{Cd} plateau in Fig. 1 in which j_{Cd}/j_{Te} is changing relatively slowly. Thus, CdTe is predominant over $0.14V$.

Figure 4 plots the logarithm of $3.11 \times 10^{22} (\text{MAX}[x_1, x_2] - 0.5)$ vs. deposition potential corresponding to Fig. 3. The ordinate is a measure of

$$\frac{A_{Cd}(E) - A_{Cd}(E = PPS)}{\text{volume}} \quad [11]$$

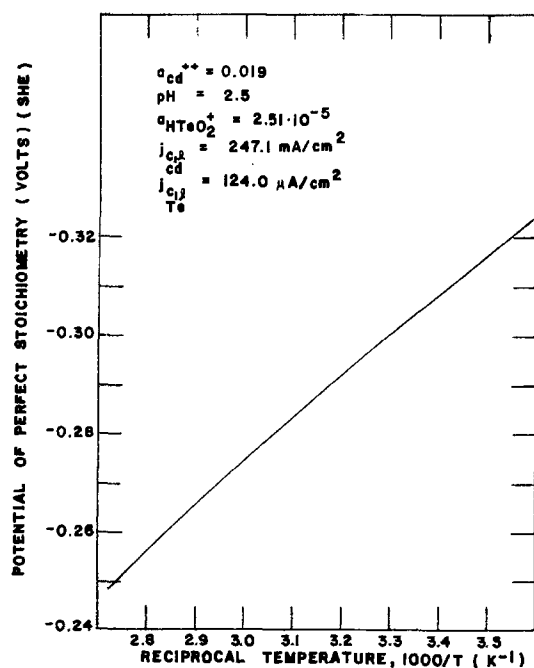


Fig. 2. Plot of the deposition potential required for perfect stoichiometry (PPS) vs. reciprocal temperature for conditions similar to those in Fig. 1. The PPS shifts positively with increasing temperature.

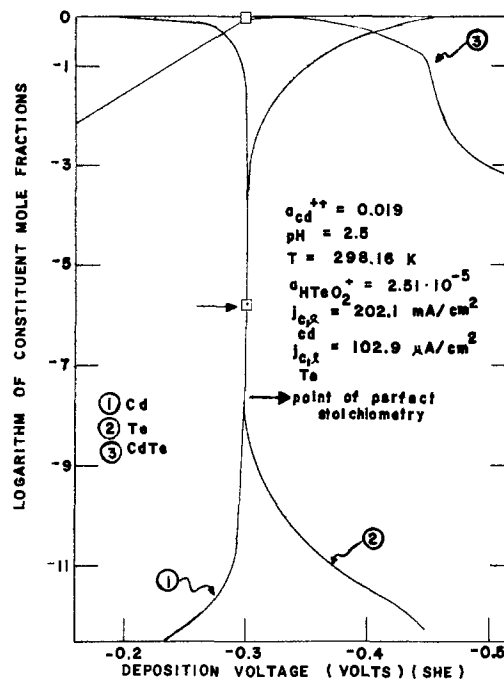


Fig. 3. Logarithmic plots of constituent mole fractions vs. deposition potential for curve 3 in Fig. 1. Note the rapid transitions at the PPS and relatively slow decline in x_{CdTe} negative of the PPS.

for $E < PPS$ and the same expression with Cd replaced by Te for $E > PPS$. A_i is the number of atoms of i . These quantities represent a measure of the native doping density as defined as the per volume number of atoms of constituent i minus the number existing at perfect stoichiometry. Since cadmium vacancies and tellurium interstitial atoms are thermodynamically equivalent, the tellurium excess will be a measure of the acceptor density due to singly ionized cadmium vacancies, and the cadmium excess is a measure of the cadmium interstitial donor density.

Although neglecting multiple ionized vacancies and interstitials and self-compensation effects, Fig. 4 indicates

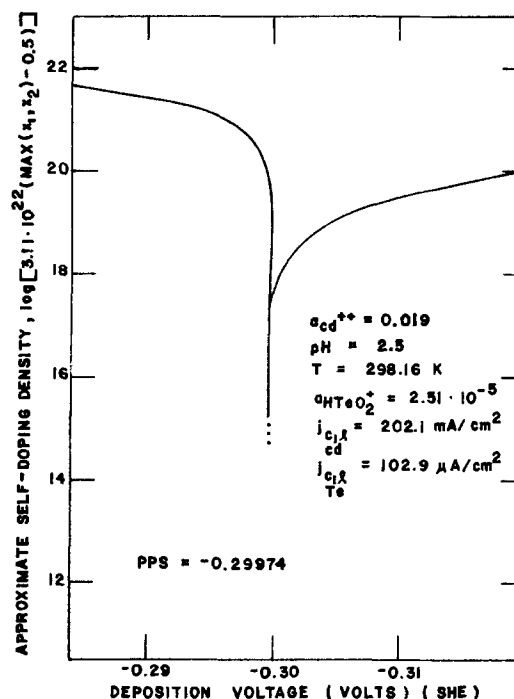


Fig. 4. Plot of approximate native doping density vs. deposition potential corresponding to the curves in Fig. 3. The native doping density, as defined as the number of cadmium or tellurium atoms per cm^3 in excess of that number at perfect stoichiometry, undergoes a dramatic and sudden decline at the PPS.

that the voltages range over which nondegenerate, electronic-quality CdTe can be electrodeposited is probably very narrow. The intrinsic carrier density for CdTe is approximately $10^6/\text{cm}^3$ at 300 K while Fig. 4 indicates that the native doping density is less than $10^{19}/\text{cm}^3$ only between -0.2997 and -0.3046V . Furthermore, the excess cadmium density remains less than $10^{20}/\text{cm}^3$ over a reasonably broad 0.02V range (-0.30 to -0.32V), corresponding to the plateau, while the tellurium excess (cadmium deficiency) is less than $10^{20}/\text{cm}^3$ over less than a millivolt positive of -0.29974V , the PPS. Thus, the electrodeposition of nondegenerate native p-CdTe would be difficult and require extremely stringent potential control, while nondegenerate n-CdTe might be plated over a critical but controllable $5\text{-}10\text{ mV}$ range.

Figure 5 shows the calculated voltammograms as a function of $a_{\text{Cd}^{2+}}$. The plateau width decreases with decreasing $a_{\text{Cd}^{2+}}$ and the plateau and associated abrupt shoulder at the PPS disappear when $a_{\text{Cd}^{2+}}$ decreases to 10^{-4} . As $a_{\text{Cd}^{2+}}$ decreases, E_{Cd} and the PPS become more negative. In fact, the PPS becomes negative of E_{Cd} for $a_{\text{Cd}^{2+}} = 2.56 \times 10^{-4}$ because small $a_{\text{Cd}^{2+}}$ do not produce enough underpotential deposition to match j_{Te} . For $a_{\text{Cd}^{2+}} \leq 10^{-4}$, j_{Cd} comes on scale.

Figures 6 and 7 exhibit the effect of $a_{\text{HTEO}_2^+}$ upon the voltammograms. For large enough ($a_{\text{HTEO}_2^+}/a_{\text{Cd}^{2+}}$), no distinct j_{Cd} plateau structure appears and the PPS is shifted onto the steep, nearly exponential portion of the j_{Cd} plot. When $a_{\text{HTEO}_2^+} \ll a_{\text{Cd}^{2+}}$, the j_{Cd} value is sufficiently small that the underpotential j_{Cd} can match it and shift the PPS positive of E_{Cd} .

For example, in Fig. 6, with $a_{\text{HTEO}_2^+}$ values of 15.2×10^{-3} and 4.64×10^{-3} , the PPS's are both negative of E_{Cd} (-0.454V) and are on the steep portion of the j_{Cd} curve. In Fig. 7, with $a_{\text{HTEO}_2^+}$ values of 1.00×10^{-4} and 2.51×10^{-5} , the PPS's have increased positive of E_{Cd} and the sharp inflection becomes apparent at the onset of the plateau structure.

Thus, too large a ($a_{\text{HTEO}_2^+}/a_{\text{Cd}^{2+}}$) value erases the plateau structure, shifts the PPS onto the exponential portion of the j_{Cd} curve, and makes the electrodeposition of electronic-quality CdTe very difficult. Smaller ($a_{\text{HTEO}_2^+}/a_{\text{Cd}^{2+}}$) values result in $2j_{\text{Cd}} \equiv j_{\text{Te}}$ being satisfied at $E > E_{\text{Cd}}$, and the occurrence of the underpotential j_{Cd} plateau within which a CdTe-rich deposit can be plated. This mode of binary compound electrodeposition involving a constant, diffusion-limited current density for the more noble component, a larger concentration of the ion of the less noble constituent, an underpotential current plateau, and a sharp shoulder (PPS) at the positive side of the plateau is named conventional underpotential deposition (CUD) and corresponds to the Class I compounds discussed by Kroger (3). CUD is inherently a voltage-controlled process

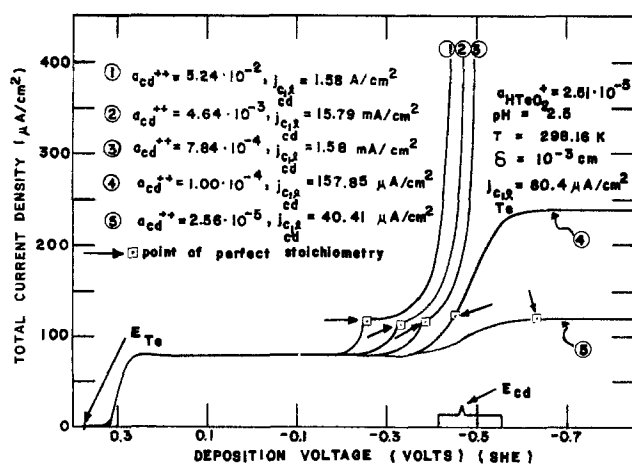


Fig. 5. Plots of total current density vs. deposition potential with cadmium ion activity as a parameter. Note the disappearance of the plateau structure and shifting of the PPS negative of the cadmium Nernst potential for the smallest $a_{\text{Cd}^{2+}}$.

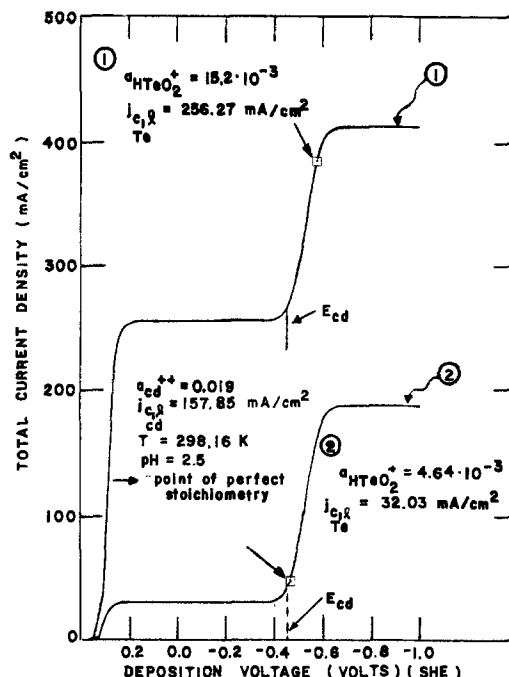


Fig. 6. Plot of total current density vs. deposition potential with tellurium ion activity as a parameter. Note the disappearance of the plateau structure and shifting of the PPS negative of the cadmium Nernst potential for the largest $a_{\text{HTEO}_2^+}$.

with nondegenerate CdTe being plated only within a narrow and precisely controlled voltage range about a PPS dependent upon j_{Cd} , l_{Te} and temperature. For random potential variations about the PPS due to noise, shifts in the PPS due to temperature fluctuations and depletion of the tellurium ions, or the selection of a slightly incorrect deposition potential, the chances of depositing n-CdTe are much greater than depositing p-CdTe, as evidenced by Fig. 4. Films deposited with $E > \text{PPS}$ would likely exhibit p-type behavior as a result of the p-nature of excess tellurium, rather than due to true nondegenerate p-CdTe (15). The most useful voltage should lie slightly positive of the center of the plateau where n-CdTe could be plated with noise immunity because of the small $|dj/dE|$ value.

Matched Diffusion-Limited Current (MDLC) Deposition Mode

In Fig. 6, the PPS lies on the steep exponential portion of the j_{Cd} curve for the largest ($a_{\text{HTEO}_2^+}/a_{\text{Cd}^{2+}}$) values. Because of the large $|dj/dE|$ and dx/dE values at these PPS's, the electrodeposition of electronic-grade CdTe would be difficult and require exact knowledge and stability of the PPS.

However, it is also possible to electrodeposit perfectly stoichiometric CdTe with a vanishing dx/dE value by increasing ($a_{\text{HTEO}_2^+}/a_{\text{Cd}^{2+}}$) until $[j_{\text{Cd}}, l_{\text{Te}}/z_{\text{Te}}] = [j_{\text{Cd}}, l_{\text{Cd}}/z_{\text{Cd}}]$ ($C_{\text{HTEO}_2^+} \approx C_{\text{Cd}^{2+}}$) and then choosing a potential where $j_{\text{Cd}} \approx j_{\text{Cd}}$ and $j_{\text{Te}} \approx j_{\text{Cd}}$. This will ensure nearly equal molar ion fluxes at the cathode for all potentials negative of the shoulder occurring when $j_{\text{Cd}} \rightarrow j_{\text{Cd}}$. The advantage of this deposition mode is that the deposit stoichiometry (as determined by $j_{\text{Cd}}/j_{\text{Te}}$) is nearly independent of potential.

Figure 8 is j - E plot with ($a_{\text{HTEO}_2^+}/a_{\text{Cd}^{2+}}$) deliberately chosen slightly less than unity. The PPS ($\approx -0.53\text{V}$), just positive of the j_{Cd} shoulder, still corresponds to a large $|dj/dE|$ value. Figure 9 logarithmically plots x_{Cd} , x_{Te} , and x_{CdTe} vs. deposition potential for the voltammogram of Fig. 8. The x_{CdTe} and x_{Cd} values fall off rapidly for $E > \text{PPS}$, while x_{Te} rapidly approaches unity. For $E < \text{PPS}$, x_{CdTe} approaches the constant, voltage-independent value of 0.858 while x_{Cd} and x_{Te} approach the constant values of 0.142 and 1.79×10^{-11} , respectively. At the PPS, $x_{\text{Cd}} = x_{\text{Te}} = 1.72 \times 10^{-6}$ while $x_{\text{CdTe}} = 1$ ($\equiv 1 - x_{\text{Cd}} - x_{\text{Te}}$).

Increasing $C_{\text{HTEO}_2^+} \approx a_{\text{HTEO}_2^+}$ to equal $C_{\text{Cd}^{2+}} \approx a_{\text{Cd}^{2+}} = 1.2 \times 10^{-5}$ would increase $j_{\text{Cd}}, l_{\text{Te}}$ to $30.98 \mu\text{A}/\text{cm}^2 \approx 2j_{\text{Cd}}, l_{\text{Cd}}$ assum-

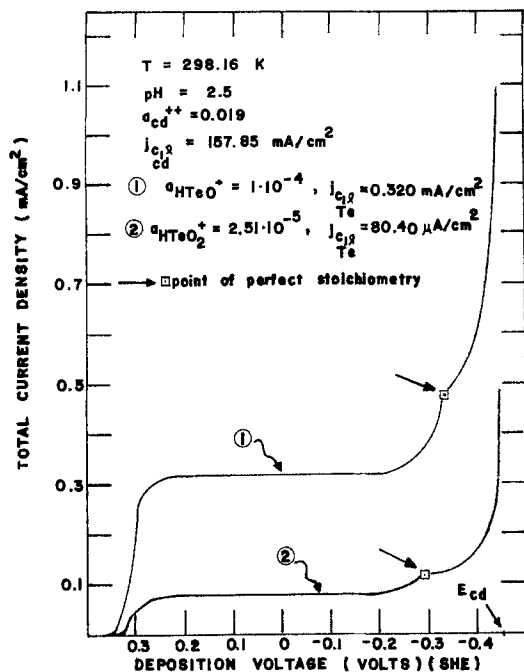


Fig. 7. As in Fig. 6 for different $a_{\text{HTeO}_2^+}$ values

ing nearly equal D_i . This would shift the PPS of Fig. 8 negative of the voltammogram shoulder onto the horizontal section of the curve. A unique PPS would still exist but due to the nearly zero $|dj/dE|$ value, one could define a broad potential range over which x_{CdTe} is greater than some number near unity. In Fig. 9, x_{CdTe} would remain just slightly less than unity (0.999966 at the PPS) for all $E < \text{PPS}$.

To maintain a small but experimentally adjustable $|dj/dE|$ value at the PPS, $j_{c,\text{Cd}}/j_{c,\text{Te}}$ could be chosen just slightly greater than one so that the PPS was just negative of the voltammogram shoulder. This would allow one to deposit both n- and p-CdTe over broad potential ranges negative and positive, respectively, of the PPS. If $j_{c,\text{Cd}} \equiv j_{c,\text{Te}}$, only p-CdTe could be plated; perfectly stoichiomet-

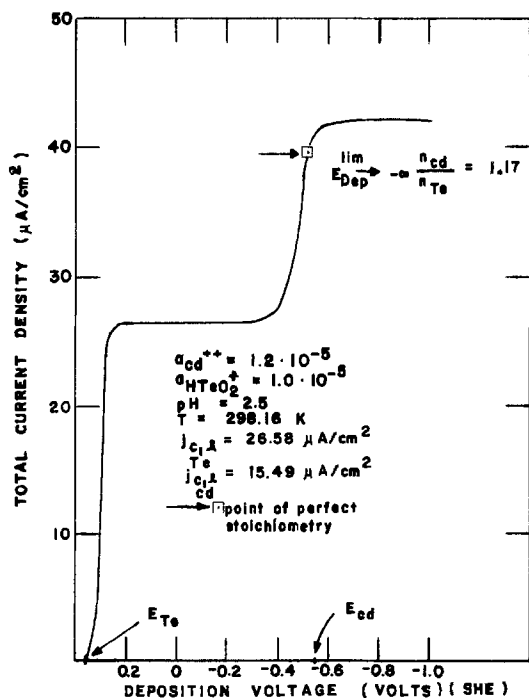


Fig. 8. Plot of total current density vs. deposition potential for nearly equal cadmium and tellurium ion activities and nearly matched diffusion-limited current densities. Note that the PPS is almost on the horizontal diffusion-limited cadmium current density region.

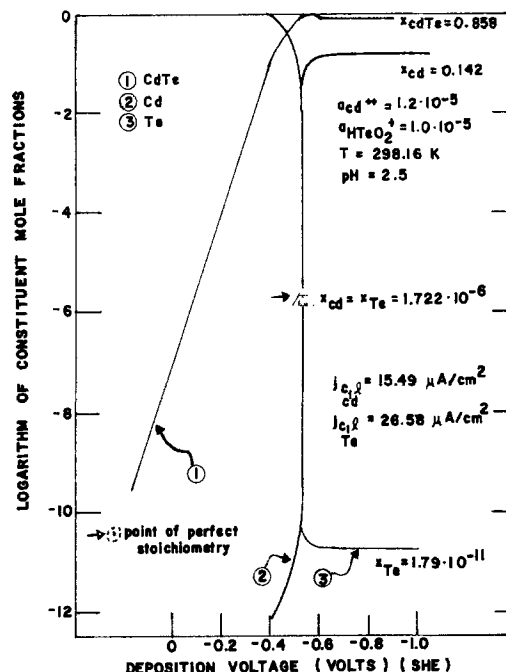


Fig. 9. Logarithmic plot of constituent mole fractions for the curve in Fig. 8. The cadmium telluride mole fraction does not appreciably decrease for potentials negative of the PPS.

ric CdTe would occur only at $E \rightarrow -\infty$. This voltage range expansion for both n- and p-CdTe is the advantage of having matched diffusion-limited currents, given the narrow deposition potential range corresponding to p-CdTe in the CUD mode (Fig. 4).

This deposition involving small $c_{o,i}$'s, nearly equal and matched $j_{c,l}$'s, PPS's negative of the metal $j_{c,l}$ shoulder, and small $|dj/dE|$ values is named the matched diffusion-limited current (MDLC) deposition mode. In principle, MDLC deposition could be used with large $c_{o,i}$ and $j_{c,l}$ values, but would be complicated by the limited solubility of TeO_2 in aqueous solutions and the possible formation of $\text{Te}^=$, $\text{Te}_2^=$, HTe^- , or H_2Te for $E < -1\text{V}$, as required to make $j_{\text{Cd}} \rightarrow j_{c,\text{Cd}}$. MDLC can, however, be implemented with small $c_{\text{Cd}^{++}}$ and $c_{\text{HTeO}_2^+}$ values.

As opposed to CUD, MDLC deposition is inherently a current-controlled process since $|dj/dE|$ is very small. The ratio ($j_{c,\text{Cd}}/j_{c,\text{Te}}$) must not drop below unity or n-CdTe will never be produced. If ($j_{c,\text{Cd}}/j_{c,\text{Te}}$) is too much greater than unity, the PPS will be shifted positive of the $j_{c,\text{Cd}}$ shoulder to a region of large $|dj/dE|$ and dx_i/dE in which deposition of perfectly stoichiometric material would require precise voltage control.

Unfortunately, $j_{c,\text{Cd}}$ and $j_{c,\text{Te}}$ vary with temperature due to changes in D_i and, more importantly, changes in complex dissociation (e.g., CdCl_2^{2-x}) and TeO_2 solubility with changing temperature and pH. Increasing stirring or cathode rotation rates (or increasing thermal convection currents with increasing temperature) decrease δ at the cathode surface and increase both $j_{c,\text{Cd}}$ and $j_{c,\text{Te}}$. Depletion of small unsaturated $c_{o,i}$ with prolonged deposition also decreases both $j_{c,l}$ values. These factors tend to complicate effective MDLC deposition. A large volume, stationary electrolyte at room temperature containing no excess undissolved TeO_2 or cadmium salt would be desirable. Potentials just negative of the $j_{c,\text{Cd}}$ shoulder and $j_{c,\text{Cd}}$ values just slightly greater than $j_{c,\text{Te}}$ would result in a still small but nonzero $|dj/dE|$ value that would allow one to compensate for small drifts in the $j_{c,l}$ values by changes in the deposition potential.

Effect of the Activity Coefficient Parameter, β , Gibbs Free Energy, ΔG° , and Metal Standard Reduction Potential, E° , upon the Calculated Voltammograms

As described by Eq. [16]-[18] in Ref. (1), the activity coefficients used in this model were

$$\gamma_{Cd} = \exp \left[\frac{\beta}{RT} x_2^2 \right] \quad [12]$$

$$\gamma_{Te} = \exp \left[\frac{\beta}{RT} x_1^2 \right] \quad [13]$$

and

$$\gamma_{CdTe} = \exp \left[\frac{\beta}{2RT} (1 - 4x_1x_2) \right] \quad [14]$$

Figure 10 demonstrates that the PPS does not depend sensitively upon the activity coefficient parameter, β . In fact, the PPS visually appears as the same point, and the total currents for $E >$ PPS visually coincide for all curves.

However, β does have a strong effect upon the j_{cd} plateau for $E <$ PPS. The apparent plateau width ranges from slightly greater than 0.1V for $\beta = -1$ J/mol to little more than an inflection for $\beta \cong -10^5$ J/mol. Thus, the more "ideal" ($\beta \cong 0$, $\gamma_i \cong 1$) the solid metastable Cd_xTe solution, the larger will be the potential range over which reasonably pure n-CdTe can be electroplated. It might be possible to use carefully performed voltammetric studies (in the absence of hydrogen or Te(-II) generation) to determine β for solid CdTe from experimental plateau widths. Fortunately, if accurate k_i and $\bar{\alpha}_i$ are known, the PPS can be calculated even with large uncertainties in β and the lack of PPS dependence upon β implies the PPS's insensitivity to the functional forms used for γ_i . Thus, the PPS is a distinct and important quantity characterizing the electrodeposition of M_1X_1 when $j_x = j_c, l_x$.

Figure 11 shows the effect of the Gibb's free energy of formation, ΔG_{MX}^0 , for the imaginary compound M_1X_1 having the same parameter values as CdTe except for β , which was set to zero to accent the plateau structure. The voltammetric curves for $\Delta G^0 = -10^5$ and -10^6 J/mol coincide within the resolution of the graph and possess pronounced j_{cd} plateau structures with a PPS near -0.31 V (SHE). There is substantial underpotential cadmium deposition beginning near -0.2 V because of the strong bonding between M and X . However, as ΔG^0 is positively increased to -10^4 J/mol, the plateau structure disappears, the PPS shifts from -0.31 to -0.43 V (still positive of E_m , -0.454 V), and the metal M does not begin to plate to any

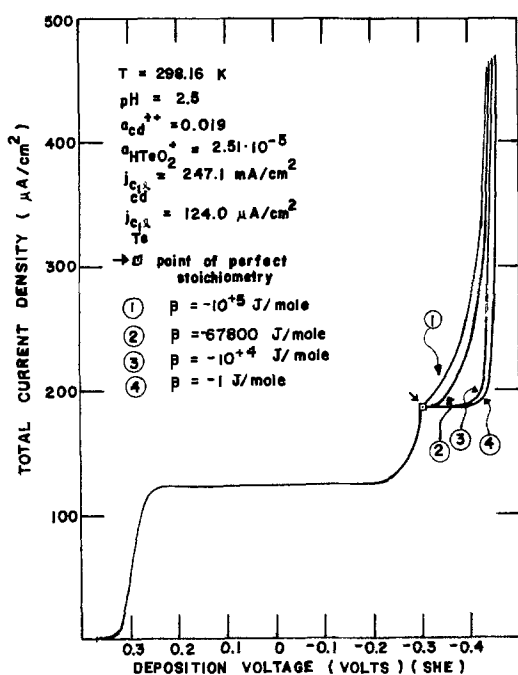


Fig. 10. Plots of total current density vs. deposition potential with the activity coefficient parameter, β , as a parameter. Note that the PPS is insensitive to β , but the plateau width increases with less negative β values.

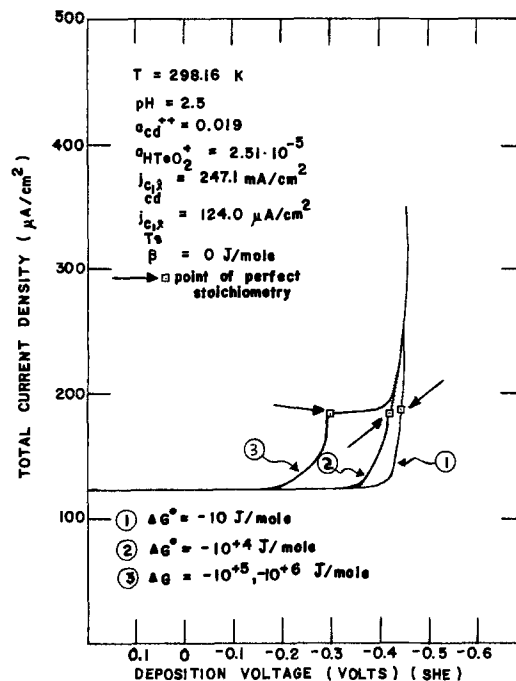


Fig. 11. Plots of total current density vs. deposition potential with ΔG_{MX}^0 , the free energy of formation of compound MX , as a parameter. With small $|\Delta G^0|$, the plateau structure disappears as the two partial current densities become nearly independent.

extent until -0.35 V. The PPS lies on the steep quasi-exponential portion of the metal current curve.

As ΔG^0 increases to -10 J/mol, the PPS shifts to -0.441 V, very close to E_m . There is no significant underpotential deposition until $E = -0.4$ V. The small $|\Delta G^0|$ value indicates weak interconstituent bonding and electrodeposits more like mechanical mixtures than compounds.

The rapid increase in equilibrium a_M (equals x_M for $\beta = 0$) in the deposit as ΔG^0 changes from -10^5 to -10^4 J/mol causes the distinct differences in the curves. The mole fraction equilibrium constant [Eq. [20] in Ref. (1)] is

$$\frac{x_{MX}}{x_M x_X} = K' = \exp \left[\frac{1}{RT} \left(\frac{\beta}{2} - \Delta G^0 \right) \right] \equiv \exp \left(\frac{\beta'}{RT} \right) \quad [15]$$

For $\beta = 0$ and $T = 25^\circ\text{C}$, K' is 3.30×10^{17} with $\Delta G_{MX}^0 = -10^5$ J/mol, but is only 56.5 with $\Delta G_{MX}^0 = -10^4$ J/mol. The much larger x_M and a_M with the smaller $|\Delta G^0|$ value result in a larger anodic pre-exponential multiplier in the cadmium Butler-Volmer equation [Eq. [45] of Ref. (1)], thus, greatly diminishing the underpotential deposition.

Although this model assumes that the solid-state reaction between plated cadmium and tellurium is sufficiently rapid (a rate constant approaching infinity) that the deposit is always described by Eq. [9], [10], and

$$a_i = \gamma_i x_i \quad [16]$$

with γ_i given by Eq. [12]-[14], a finite rate of reaction might be phenomenologically accounted for by a less negative $\Delta G_{eff}^0(t)$, the time varying effective free energy. As plated cadmium and tellurium react toward equilibrium, x_{Cd} , x_{Te} , a_{Cd} , and a_{Te} will decrease and x_{CdTe} and a_{CdTe} will increase until equilibrium is reached. At all previous times

$$\left[\frac{a_{CdTe}}{a_{Cd} a_{Te}} \right] (t) \equiv K_{eff}(t) \equiv \exp \left[\frac{-\Delta G_{eff}^0(t)}{RT} \right] \quad [17]$$

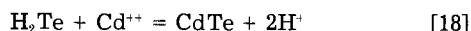
where $\Delta G_{eff}^0(t)$ drifts negatively with time and approaches ΔG^0 .

Thus, the calculated voltammograms for $\Delta G_{MX}^0 > -9.97 \times 10^4$ J/mol might approximate the behavior of experimental current-voltage curves if cadmium and tellurium react more slowly than assumed. As $\Delta G_{eff}^0(t) \rightarrow +\infty$, no

solid-state reaction occurs and the j_i are totally independent. The effects of incomplete reaction between the cadmium and tellurium atoms near the deposit surface include a negative shift in the PPS and a reduction or disappearance of the plateau region.

Figure 12 exhibits the effect of the metal standard reduction potential E_m^0 , upon the voltammograms for imaginary compounds with the same free energy as CdTe. If $j_x \rightarrow j_c, l_x$ at the potential where significant underpotential metal deposition begins to occur, the voltammograms are identical except for the horizontal offset due to different E_m^0 values. This similarity is a consequence of $\Delta G_{MX}^0 = -9.97 \times 10^4 \text{ J/mol}$ being used for all three curves. Since only the term $(E - E_m^0)$, and never E alone, occurs in the metal Butler-Volmer equation and the pre-exponential multipliers depend only upon ΔG^0 , β , $\alpha_{x(\text{IV})}$, $\alpha_{M^{++}}$, j_c, l_x and j_c, l_M , and not E , the j_i 's are always functions of the relative potential $(E - E_m^0)$ rather than the absolute potential E , as long as $j_x \approx j_c, l_x$. When $j_x < j_c, l_x$ at voltages where significant underpotential metal deposition can occur, as when $E_m^0 \approx E_x^0$, the voltammetric structure differs from that exhibited in this paper and perfectly stoichiometric M_xX_1 can be plated at voltages positive of both E_m and E_x . This mode of deposition is named pure underpotential deposition and corresponds to Class II compounds in Kroger's work (3).

Figure 12 indicates that it is not necessary to have $E_m^0 \approx E_x^0$ to electrodeposit the stoichiometric alloy or compound, as is sometimes assumed. The underpotential j_M plateau with its small $|dj/dE|$ values should occur for most base metal chalcogenides. CdTe should be as easy to plate as PbTe or SnTe. At very negative voltages where H_2Te or HTe^- can be generated, the film growth mechanism could change to a precipitation-like reaction such as



and change the observed voltammetric structure for ZnTe or MnTe electrodeposition.

Comparison of Theoretical Results with Experiment

Other workers investigating CdTe electrodeposition have observed plateau-like structures in voltammograms. These often exhibited characteristics different from those of the calculated curves, probably because of the pres-

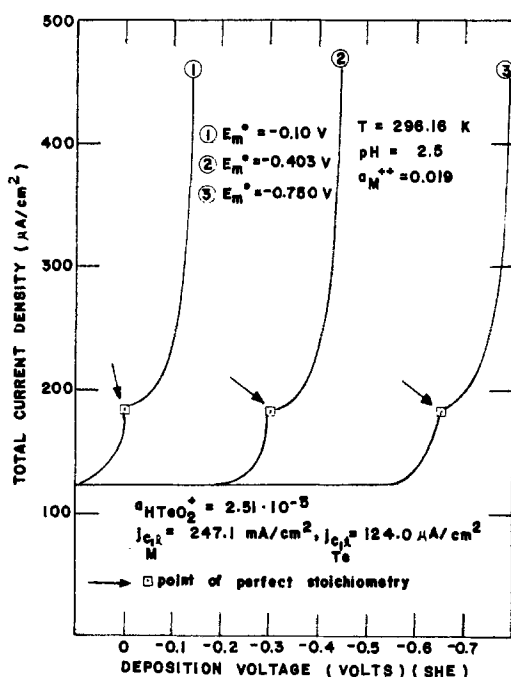


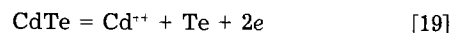
Fig. 12. Plots of total current density vs. deposition potential with E_m^0 , the standard reduction potential of the metal in compound MX , as a parameter. The shapes of the curves are independent of E_m^0 as long as the tellurium current density is diffusion limited.

ence of second-order effects such as hydrogen generation and nonideal voltammetric characteristics of tellurium (multiple steps, very low transfer coefficients, and large overpotentials). These last factors could shift the j_c, l_{Te} peak negative of the calculated shoulder voltage. It is possible that, in some instances, substantial cadmium begins to plate before j_{Te} becomes diffusion limited. In this case, to be discussed later in this sequence of articles, the voltammograms would not be as simple to interpret as those curves calculated in this paper.

Figure 13 exhibits a voltammogram obtained by the authors with a graphite cathode in an aqueous solution ($pH = 2.6$, $T = 90^\circ C$, sweep rate $\approx 50 \text{ mV/s}$) saturated in TeO_2 , $0.24 M$ in Cd^{++} , and containing a graphite anode and Ag/AgCl reference electrode. At $25^\circ C$, the potentials of the standard calomel (SCE) and Ag/AgCl reference electrodes are 0.242 and $0.222 V$, respectively, vs. the standard hydrogen electrode (SHE).

Near $0.1 V$ (Ag/AgCl), a shoulder appears in the current, possibly due to $j_{Te} \rightarrow j_c, l_{Te}$. The current (i) is nearly constant with a slight decrease for about $0.3 V$, and a strong rise and a peak occur near -0.2 and $-0.35 V$, respectively. The current only slowly increases within the apparent plateau until i_{Cd} rapidly increases near $-0.7 V$.

Three strong anodic peaks occur in Fig. 13. There appears to be a correlation between these peaks and the three cathodic structures. The negative-most anodic peak is due to dissolution of cadmium metal plated at the end of the cathodic sweep, which, when stripped, leaves a Cd_xTe deposit. When the potential becomes sufficiently positive, cadmium will strip from the surface $CdTe$ layers according to



thus producing the middle anodic peak and leaving a tellurium surface that is stable until the voltage reaches a more positive critical potential where tellurium and any remaining CdTe is quickly stripped.

The above interpretation is supported by the cathodic photocurrent behavior of the sweeps. On the initial negative going sweeps, photocurrents commence at the apparent underpotential i_{Cd} shoulder (the middle cathodic wave) and remain until pure cadmium deposition begins. On the anodic backsweep, the cadmium dissolution peak appears and photocurrent reappears at the peak's positive foot. Photocurrent remains strong until voltages just negative of the center anodic peak, corresponding to CdTe dissolving into Cd^{++} and tellurium. Between the middle anodic peak and the large tellurium dissolution peak, there is negligible photocurrent.

The photocurrent's sudden disappearance at the middle anodic peak is probably due to the transformation of remaining surface layers from semiconducting CdTe to

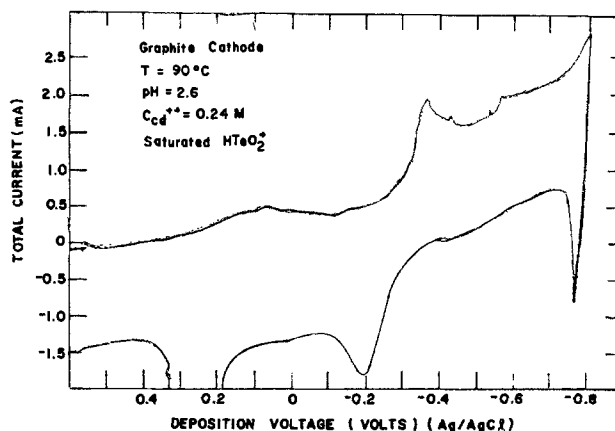


Fig. 13. Experimental voltammetric data for acidic aqueous solutions of cadmium and tellurium ions and a graphite cathode. Three cathodic waves and three anodic peaks appear and may correspond to the plating and dissolution, respectively, of tellurium, cadmium telluride, and cadmium.

quasi-metallic tellurium. The photocurrent onset on the shoulder of the center cathodic wave is probably due to the sudden onset of nondegenerate CdTe deposition (near the PPS).

The apparent PPS's, as determined from the shoulder of the second cathodic wave, the middle anodic peak, and the photocurrent onset, were in the -0.2 to $-0.4V$ (SHE) range, consistent with those values calculated. Much of the middle cathodic wave is probably due to hydrogen and possibly enhanced tellurium reduction, and this is probably why there is such a large difference in the apparent magnitudes of i_{Te} and i_{Cd} . Furthermore, the initial tellurium reduction appears sluggish, probably indicating transfer coefficients and rate constants smaller than assumed in the calculations. It is possible that the first cathodic wave is due to reduction of Te (VI) to Te (IV), as speculated by Bhattacharya and Rajeshwar (7) (discussed below), and that significant tellurium plating does not occur until within the second wave. However, the shoulder or inflection point of the middle cathodic wave is almost certainly the potential at which CdTe deposition commences and should be near the PPS.

Other workers have made observations qualitatively substantiating the authors' analytical model. AMFTEK (8) found that a deposition voltage of -578 mV (Ag/AgCl) led to electronic-grade CdTe in a solution with a temperature of $80^\circ C$, a pH of 2, a Cd^{++} concentration of $1.2M$, and a tellurium ion concentration of $1.6 \times 10^{-4}M$. The resistivity of the films varied from 10^3 to $10^6 \Omega\text{-cm}$ as the deposition potential varied over less than a 20 mV range about -578 mV. This range is consistent with Fig. 4 showing the approximate native doping density, while -578 mV (Ag/AgCl) is consistent with the calculated PPS's.

The Rockwell group (9) determined that a potential of -725 mV (SHE) produced near-stoichiometric CdTe in a $1M$ HCl, $0.1-1M$ Cd^{++} , and $10^{-3}M$ TeO_2 -based solution at temperatures from room temperature to boiling. This potential was critical with a 2-6% change in the cadmium/tellurium ratio per millivolt change in potential noted. The calculated PPS with $a_{HTeO_2^+}$ of order 10^{-3} is between -0.4 and $-0.5V$ (SHE), qualitatively agreeing with Rockwell's value. Rockwell alluded to the existence of an underpotential cadmium current plateau.

The Monosolar group (10) found that the cadmium/tellurium ratio could be varied from 0.75 to 0.82 by varying the deposition potential from -300 to -700 mV (SCE). Evidently, this ratio did not exceed unity until voltages negative of E_{Cd} . The high temperatures ($\approx 95^\circ C$) probably resulted in a large TeO_2 solubility that led to large values of j from 200 to $500 \mu A/cm^2$. Thus, it is reasonable that the PPS was negative of E_{Cd} , consistent with Fig. 6. The largest CdTe grain sizes ($5.7 \mu m$) occurred with a potential of -400 mV (SCE). They could not grow p-type material, even with arsenic, antimony, and gold acceptors, consistent with the narrow potential range calculated for nondegenerate p-CdTe.

Panicker *et al.* (11) found that electrodeposited CdTe films changed from n- to p-type for potentials between -0.45 and $-0.5V$ (SCE) with a solution ($T = 85^\circ C$, pH = 3.4, stir rate = 160 rpm) $1.2M$ in Cd^{++} and saturated in TeO_2 . A plateau-like region beginning between -0.4 and $-0.5V$ (SCE) was observed at $25^\circ C$ and various acidic pH's, was approximately 200 mV wide, and ended with the deposition of pure cadmium. The onset of the plateau at $25^\circ C$ correlates with the n-p transition at $85^\circ C$.

Llabres (12) found an apparent PPS of -660 mV (SCE) for CdTe electrodeposition on stainless steel and ITO from a solution ($T = 82^\circ C$, pH = 2.0-3.5) $1M$ in $CdSO_4$ and saturated with TeO_2 . Plots of bulk resistivity *vs.* deposition potential indicated that the value at $-0.66V$ (SCE) ($\approx 2 \times 10^3 \Omega\text{-cm}$) was several hundreds times that at $-0.58V$ (SCE) ($\approx 5 \times 10^2 \Omega\text{-cm}$). The potential range for single-phase (lacking segregated tellurium) p-CdTe electrodeposition ranged from -0.62 to $-0.66V$, a narrow 40 mV range but considerably larger than that implied in Fig. 4. The tellurium and cadmium atomic percentages decreased and increased, respectively, as the cathodic po-

tential was made more negative. Although not explicitly mentioned, it is likely that n-CdTe was plated over a narrow range of voltages negative of $-0.66V$, a value close to E_{Cd} .

Takahashi *et al.* (5) deposited CdTe from aqueous solutions $1M$ in $CdSO_4$, $10^{-3}M$ in TeO_2 , and $0.05M$ in H_2SO_4 . They observed diffusion-limited currents with voltages between -0.3 and $-0.65V$ (Ag/AgCl) and a strong current increase at $-0.65V$. A linear relationship between this limiting current and $c_{HTeO_2^+}$ was noted, but c_{CdSO_4} had little effect. An increase in the strength of the separate tellurium x-ray diffraction peaks occurred for more positive potentials, and no free cadmium peaks were observed for potentials between -0.2 and $-0.6V$. The films transformed from p- to n-type at $-0.45V$, possibly the PPS.

Plots of photocurrent of already deposited films *vs.* applied voltage indicated that maximum photocurrent occurred for films deposited at $-0.40V$ (Ag/AgCl). No photocurrents were observed for initial potentials positive of $-0.20V$ or negative of $-0.55V$. Thus, the PPS is probably between -0.40 and -0.45 , and the range of potential corresponding to nondegenerate CdTe electrodeposition is approximately $0.35V$. They argue that during deposition of pure CdTe

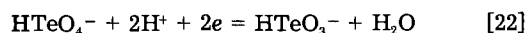
$$i_{total} = \frac{6D_{Te}Fc_{HTeO_2^+}}{\delta} \quad [20]$$

while

$$i_{Te} = \frac{4D_{Te}Fc_{HTeO_2^+}}{\delta} \quad [21]$$

where D_{Te} is the diffusion coefficient of $HTeO_2^+$. Thus, at perfect stoichiometry, i_{total} equals $1.5i_{Te}$, as corroborated by the authors' current model and calculations.

Bhattacharya and Rajeshwar (7) conducted voltammograms with platinum microelectrodes in acidic aqueous solutions $\approx 5.0 \times 10^{-4}M$ in TeO_2 . They observed a tellurium ion reduction wave near $0.4V$ (SCE) and verified the diffusion-limited nature of i_{Te} from the linear wave peak *vs.* (sweep rate)^{0.5} characteristics. They attributed this wave to the reaction



Another reduction wave began near $-0.1V$ (SCE) and peaked near $-0.25V$, as shown in Fig. 3 of their article. The current dipped slightly near $-0.3V$ and increased near $-0.4V$, the negative end point of that particular sweep. Near $-0.4V$, a black deposit, speculated to be tellurium, was formed and was stripped near $0.55V$ during the anodic back sweep.

CdTe films were deposited at potentials from -0.65 to $-0.85V$ (SCE) (potentials probably negative of E_{Cd}), with current densities ranging from 0.3 to 0.5 mA/cm², a pH of 2.5-3.0, and a temperature of 40° - $50^\circ C$ from aqueous solutions $1M$ in $CdSO_4$ and 10^{-5} - $10^{-3}M$ in TeO_2 . The Cd:Te ratio for films grown on titanium averaged 45:55, consistent with tellurium-induced p-type conductivity in the as-deposited films. Annealing at $\approx 600^\circ C$ increased the Cd:Te ratio and changed the films to n-type, as corroborated by photoelectrochemical measurements. Addition of copper to the solutions and films resulted in extrinsic p-type conductivity (15).

Although there are significant variations in the apparent tellurium deposition onset potential, PPS, plateau structure, etc., among the various workers previously discussed, several general trends emerge.

1. For large tellurium ion concentrations (10^{-4} - $10^{-3}M$) and subsequent large j_c, i_{Te} , as occur at low pH's and high temperatures, the apparent PPS lies very near or even slightly negative of E_{Cd} ($E^0 = 0.403V$ [SHE]).

2. Underpotential cadmium deposition does occur, as evidenced by apparent PPS's up to 200 mV positive of E_{Cd} .

3. The range of deposition potential over which electronic-grade CdTe can be plated is relatively narrow (20-400 mV).

4. The apparent tellurium deposition onset potential ($\cong E_{Te}$) lies negative of that predicted from the kinetic parameters assumed in the authors' calculations, and j_{Te} may not always become diffusion limited before significant underpotential j_{Cd} occurs. There may exist a large overpotential for tellurium deposition, and the α_{Te} value may be much smaller than 0.5. The large cathodic reduction wave that commonly occurs a few hundred millivolts positive of E_{Cd} is partially due to underpotential cadmium deposition, as analytically predicted and substantiated by various microanalysis, x-ray diffraction, and photocurrent measurements, but is probably partially due to enhanced tellurium deposition and hydrogen generation.

5. Tellurium may exist as Te (VI) and Te (-II) in addition to the Te (IV) and Te (0) assumed in the authors' model.

6. Tellurium segregation does occur for sufficiently large Te:Cd ratios, as evidenced by x-ray diffraction data.

7. CdTe exhibiting native p-type conductivity can be deposited over a reasonably broad range of potential. However, due to the probable existence of separate p-tellurium phases, it is unclear if this is due to p-CdTe or tellurium.

Except for trend 6, and possibly 7, these trends are consistent with the results of the authors' model and calculations, but would require parameter value changes and model expansions to precisely incorporate. Indeed, the simulated voltammograms were originally intended to be only approximately analogous to CdTe. It would be interesting to conduct voltammograms in organic solutions of N-N dimethylformamide or dimethylsulfoxide, $TeCl_4$, and $CdCl_2$. $TeCl_4$ is extremely soluble ($> 10^{-3}M$), does not undergo hydrolysis, and exists as yellow $TeCl_3^+$ and $TeCl_5^-$ ions in these solvents. The key advantage of the organic baths is the absence of hydrogen generation and ion hydrolysis. Thus, their use in voltammetric measurements should more conclusively prove the validity of the authors' model and calculations.

Conclusions

This paper has presented the results of a computer simulation of the model, developed in the first part of the paper (1), corresponding approximately to CdTe (or M_2X_3) electrodeposition from solutions containing both cadmium and tellurium ions in a reducible form.

The calculated graphs lead to the following conclusions.

1. For diffusion-limited tellurium current densities, there exists an underpotential cadmium current density plateau over an approximately 100 mV range in potential which occurs because cadmium can plate at potentials negative of its pure element Nernst potential (E_{Cd}) only on a nearly 1:1 basis with tellurium. This is because a solid-state reaction between the cadmium and tellurium is required to reduce the cadmium activity enough that the anodic term in the cadmium Butler-Volmer equation is small. This activity reduction and underpotential cadmium current is enhanced by more negative β and ΔG_{MX}^0 values.

2. At the sharp positive shoulder of this plateau lies the potential of perfect stoichiometry (PPS), where $x_{Cd} \cong x_{Te}$, $a_{Cd} \cong a_{Te}$, $x_{CdTe} \cong a_{CdTe} \cong 1$, and the material is nearly intrinsic, neglecting self-compensation effects in the native doping. The PPS shifts positively with increasing temperature and $\alpha_{Cd^{++}}$ (assuming $\alpha_{HTeO_2^+}$ remains constant). If $\alpha_{HTeO_2^+}$ increases with temperature due to enhanced TeO_2 solubility, the PPS may shift negatively with temperature due to larger tellurium diffusion-limited currents.

This mode of deposition, involving PPS's positive of the Nernst potential of the more electronegative deposit constituent, occurring at the positive edge of this constituent's current plateau, and occurring when the more noble constituent's current is diffusion limited, is named conventional underpotential deposition (CUD).

3. With CUD, cadmium-rich, n-type, and probably nondegenerate CdTe is deposited within a several hundred millivolt wide potential range between the PPS and

E_{Cd} . High resistivity p-CdTe ($x_{CdTe} > x_{Te}$) can be deposited only within a very narrow potential range positive of the PPS.

4. For cadmium and the tellurium ion concentrations (activities) sufficiently close together, the PPS may shift negative of E_{Cd} and the plateau structure may disappear. Under these conditions, the PPS can lie on the steep, quasi-exponential portion of the cadmium current density curve and cause a strong dependence of deposit mole fractions on deposition potential.

5. In the CUD mode, the PPS is nearly independent of β , the activity coefficient parameter. This makes the PPS a key quantity for characterizing ionic MX electrodeposition. However, less negative β values broaden the plateau region, with a maximum plateau width occurring with $\beta = 0$ (ideal solid solution) because less negative β values increase γ_{Cd} and a_{Cd} and delay the onset of quasi-exponential cadmium currents. The plateau width decreases and the PPS shifts negatively with less negative ΔG_{MX}^0 values because a smaller MX equilibrium constant and larger free M mole fraction (activity) increase the anodic current density in the M Butler-Volmer equation.

6. If the ion concentrations are very nearly equal, the two diffusion-limited current densities are close together, and the molar fluxes are equal, the PPS may shift onto the nearly constant current region corresponding to both ions being diffusion limited. In this case, the dj_{total}/dE and, hence, dx_i/dE values are very small, so electronic-grade CdTe can be deposited over a broad potential range. This method of deposition is named the matched diffusion-limited current (MDLC) mode.

7. Experimental voltammetric and stoichiometry vs. potential measurements by various workers have differed but have shown that underpotential cadmium deposition does occur with apparent PPS's (based upon microanalysis measurements, maximum photocurrent, or n-p transitions) in qualitative agreement with the calculated results. Plateaulike structures appear, but these may be experimentally complicated by hydrogen and enhanced tellurium deposition. Careful voltammetric, composition, photocurrent, and conductivity-type measurements should be performed as a function of deposition potential with organic solvents such as N-N dimethylformamide or dimethylsulfoxide containing a tellurium halide ($TeCl_4$) and cadmium salt. These baths should avoid hydrogen generation and allow large tellurium ion concentrations and temperatures above 100°C to be used, thus, leading to more general and easy-to-interpret data and better corroboration of the analytical model and calculated results.

Acknowledgments

The authors thank Dr. Albert Mink, Dr. Hal McCloud, and the Computer Center at Arkansas State University and Dr. Jack Boone, Dr. Burns Hegler, Dr. Bruce Poling, Dr. Yildirim Omurtag, Dr. J. Derald Morgan, and Mr. Alok Berry at the University of Missouri-Rolla for their support and assistance. Also thanked are Sherry Engelen, Betty Minton, and Maxine Smith for manuscript preparation and James Dodd and John Hayenga for figure preparation.

Manuscript submitted March 8, 1985; revised manuscript received Aug. 20, 1985. This was Paper 430 presented at the New Orleans, Louisiana, Meeting of the Society, Oct. 7-12, 1984.

REFERENCES

1. R. D. Engelken and T. P. Van Doren, *This Journal*, **132**, 2904 (1985).
2. R. D. Engelken, Ph.D. Dissertation, University of Missouri, Rolla, MO (1983).
3. F. A. Kroger, *This Journal*, **124**, 2028 (1978).
4. A. Brenner, "Electrodeposition of Alloys—Principles and Practice," Academic Press, New York (1963).
5. M. Takahashi, K. Uosaki, and H. Kita, *This Journal*, **131**, 2305 (1984).
6. R. J. Latham, N. A. Hampson, and S. I. Zhdanov, "Encyclopedia of Electrochemistry of the Elements," A. J. Bard and H. Lund, Editors, Chap. I-4, IV-8, Marcel Dekker, Inc., New York (1973).
7. R. N. Bhattacharya and K. Rajeshwar, *This Journal*,

- 131, 2032 (1984).
8. G. Fulop, M. Doty, P. Meyers, J. Betz, and C. H. Liu, *Appl. Phys. Lett.*, **40**, 327 (1982).
 9. C. Ogden and D. Tench, Final Report, DOE Contract AC02-77CH00178, Rockwell International, Thousand Oaks, CA (1981).
 10. R. Rod, R. Bunshah, O. Stafsudd, B. Basal, and P. Nath, Final Report, DOE Contract DE-AC04-79ET23008, Monosolar, Inc., Santa Monica, CA (1980).
 11. M. P. R. Panicker, M. Knaster, and F. A. Kroger, *This Journal*, **125**, 566 (1978).
 12. J. Llabres, *This Journal*, **131**, 464 (1984).
 13. A. S. Jordan, *Metall. Trans.*, **1**, 239 (1970).
 14. M. W. Verbrugge and C. W. Tobias, *This Journal*, **132**, 1298 (1985).
 15. R. N. Bhattacharya and K. Rajeshwar, *ibid.*, **132**, 732, (1985).
 16. R. D. Engelken, Abstract 430, p. 619, The Electrochemical Society Extended Abstracts, Vol. 84-2, New Orleans, LA, Oct. 7-12, 1984.
 17. R. D. Engelken, Abstract 510, p. 723, The Electrochemical Society Extended Abstracts, Vol. 85-1, Toronto, Ont., Canada, May 12-17, 1985.

Coupled Electrocatalysis and Gas Phase Diffusion in a Stabilized-Zirconia Tubular Flow Oxygen Pump

L. M. Rincon-Rubio, B. C. Nguyen,* and D. M. Mason**

Department of Chemical Engineering, Stanford University, Stanford, California 94305

ABSTRACT

A tubular electrochemical reactor constructed from a 10 mole percent Y_2O_3 -stabilized ZrO_2 electrolyte tube with porous Au electrodes on its inner and outer surfaces was operated as an oxygen pump in the temperature range 650°-850°C. Gas mixtures with different O_2 content were circulated through the inside cathodic wall of the tube, where O_2 was electrochemically reduced and pumped out through the outer anodic wall of the tube to an annular chamber. The current-overpotential behavior of the cell was found to be dominated by catalytic rate processes at the cathode. The electrochemical kinetics can be described by a modified Butler-Volmer expression. The behavior of the tubular flow reactor in the integral mode of operation was studied by numerically solving the convective-diffusion equation of change for O_2 molecules in the gas phase, incorporating both radial and axial diffusion and electrochemical reaction on the tube wall. The finite-difference method of successive over-relaxation was used to solve the governing mass-transfer equation. When the axial change in O_2 concentration at the tube wall is accounted for, the computed integrated currents agree very well with the experimentally measured values, allowing the prediction of total ionic current and fractional reactant conversion for a given set of flow and physical variables. Under certain conditions, axial diffusion is found to be quite pronounced, with concentration disturbances penetrating the region well upstream of the inlet to the reaction zone ($\xi = 0$), and significantly decreasing the O_2 concentrations at $\xi = 0$ from values in the entering feed stream.

There has been considerable interest in recent years in employing solid-oxide electrolytes in practical devices such as oxygen sensors, oxygen pumps, electrolysis cells, and fuel cells. Among the oxygen anion conductors, those compounds based on ZrO_2 with the fluorite structure, so-called stabilized ZrO_2 , have been the most widely investigated (1, 2). The ionic conduction is due to the migration of oxygen ions via a vacancy mechanism. The vacancies involved are oxygen vacancies, V_{O}^{oo} , with an effective charge of +2, which are created in order to preserve the electrical neutrality of the solids when ZrO_2 is doped with metal oxides containing cations with valence lower than +4, such as CaO, MgO, Y_2O_3 , or Sc_2O_3 (3, 4). In all these devices, a region of solid stabilized ZrO_2 of a particular desired geometry is used to separate a pair of compartments containing gases with different O_2 activities. In most cases, metals such as Ag, Au, Pd, or Pt are employed as electrodes. At equilibrium, there is no current flowing through the cell and the theoretical open-circuit potential of the cell is given by the Nernst equation, which for a predominantly ionic conductor can be written as

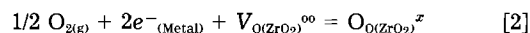
$$E_o = \frac{RT}{4F} \ln \frac{P_{O_2}^{II}}{P_{O_2}^I} \quad [1]$$

where 4 is the total number of electrons transferred in this particular electrode reaction involving O_2 .

When a stabilized ZrO_2 electrochemical cell is operating as an oxygen pump, O_2 can be removed from gas mixtures at any predetermined rates by applying an appropriate external voltage to the cell. As a result of a finite current I circulating through the closed circuit, the cell potential E needed to drive the system is increased above the theoretical value, E_o , because of potential losses asso-

ciated with ohmic resistance of the electrolyte and electrodes and also with nonohmic rate processes such as charge transfer, adsorption, slow gas phase and/or surface diffusion of reactants or products. In order to increase cell efficiencies, it is necessary to identify the major sources of these so-called polarization overpotentials and to determine the functional relationship between overpotential and current density. Electrode polarization phenomena in these solid oxide electrolyte cells are strongly influenced by factors such as gas composition, temperature and total current, electrode morphology, adsorption of reactants and/or products on the solid electrolyte and/or on the electrode. In recent years, even though significant progress has been made in the field of electrode kinetics, it is still very difficult in the case of ZrO_2 -stabilized cells to derive unambiguous general current-overpotential relationships for a particular reacting system.

The reduction of O_2 which takes place at the cathode of a stabilized ZrO_2 electrochemical cell involves species from three different phases and the overall reaction can be written



A variety of physical-chemical processes have been proposed as rate-determining steps for the above reaction, including diffusion of O_2 through the electrode (5), dissociation of O_2 or electron transfer (6), surface diffusion of adsorbed O on ZrO_2 (7), mass transport in the gas phase (8, 9), electronation of O_2 (10), surface diffusion of adsorbed O on the metal electrode (11, 12), and gaseous diffusion in electrode pores (13). Much of the disagreement among the investigators is found actually to arise due to differences in electrode morphology, operating conditions, and cell geometries. Recently, the effects of electrode morphology (11, 14), electrode particle size, and

*Electrochemical Society Student Member.

**Electrochemical Society Active Member.

type of electrolyte on the nature of the electrode polarization have been emphasized (15, 16).

Cell geometries employed in most of the previous studies have not been amenable to analysis employing fluid mechanics theory, and in cases where gas phase diffusion has arisen as the rate-determining step a simple linear driving force relationship of the type below has been used

$$\frac{i}{nF} = \frac{D_j}{\delta} (C_{jb} - C_{js}) \quad [3]$$

where i is the current density, n is the total number of electrons transferred in the reaction, F the Faraday constant, D_j is the effective diffusion coefficient of species j in the gas phase, δ is the thickness of the diffusion layer next to a solid surface, and C_{jb} and C_{js} represent the concentration of species j in the bulk and at the electrode surface, respectively (17, 18). This so-called lumped mass-transfer model is useful in correlating data in complicated geometries not amenable to analytical attack. With the simple tubular geometry under consideration, the gas phase diffusion process near the electrode/electrolyte surface can be more exactly described by the distributed mass-transfer model (19)

$$\frac{i}{nF} = D_j \left. \frac{\partial C_j}{\partial y} \right|_{y=0} \quad [4]$$

where $(\partial C_j/\partial y)|_{y=0}$ represents the concentration gradient of species j at the electrode/electrolyte surface. The value of this gradient is obtained either by solving the convective mass-transfer equation for component j for the entire cell or by using empirical mass-transfer correlations if available for the given cell geometry. Most previous studies have been devoted to unraveling the complicated kinetics occurring in solid-oxide electrolyte reactors. No study has been made of the effects of combined fluid mechanics and electrochemical kinetics on the optimal design and operating conditions of cells in practical devices.

A tubular cell was constructed and operated as an oxygen pump, both in a differential mode to study electrochemical kinetics, and then in an integral mode to obtain the high conversion data encountered in practice. The analysis of the experimental results obtained for the cathodic reduction of O_2 on porous Au electrodes have been presented elsewhere (20). For high inlet O_2 concentration ($P_{O_2} > 9.9 \times 10^{-3}$ atm), the current-overpotential data were correlated with a modified Butler-Volmer expression

$$I = I_{\text{app}} \left[e^{\frac{3}{2} \frac{F\eta_c}{RT}} - e^{-\frac{1}{2} \frac{F\eta_c}{RT}} \right] \quad [5]$$

where I_{app} is an apparent exchange current density which is only a function of temperature and inlet P_{O_2} and η_c is the cathodic overpotential assumed to be constant over the whole electrode surface. When $P_{O_2} < 1.0 \times 10^{-3}$ atm, the experimental results no longer obey Eq. [5]. In the region of low P_{O_2} , the cell was found to operate as an integral reactor with high overall conversion (20). The decrease in the O_2 wall concentration along the length of the cell reduced the gas phase mass-transfer rates as well as the reaction rates. Correspondingly, there was a large decrease in I_{app} with downstream position which is not accounted for by Eq. [5]. The purpose of this paper is to investigate whether Eq. [5] can be employed as a boundary condition in a more general convective-diffusion model to correlate the experimental data in the region of low P_{O_2} . The mathematical equations derived from this model were solved numerically using the method of successive over-relaxation (SOR). It is hoped that the results obtained here with the relatively simple O_2/Ar system will permit a better understanding of the dynamic behavior of other chemical systems such as hydrocarbon gas mixtures reacting in a tubular solid-electrolyte fuel cell reactor.

Theory

Convective-diffusion equation and boundary conditions.—The combined effects of gas phase mass-transfer

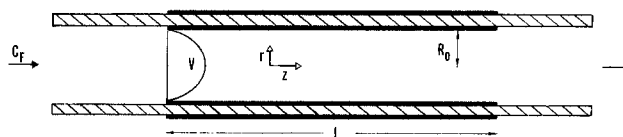


Fig. 1. Tubular flow geometry

and electrochemical kinetics on the O_2 concentration profiles and overall conversions were investigated for different operating variables. The tubular stabilized-zirconia cell employed in the present study is schematically shown in Fig. 1. It is assumed that gas mixtures of initial oxygen composition C_F flow through the inner tubular chamber of the reactor with a fully developed laminar velocity profile $V(z)$. Furthermore, it is assumed that the flow is incompressible and isothermal. Oxygen molecules diffuse from the bulk gas phase to the tube wall, where they undergo an electrochemical reaction at a rate given by a modified form of Eq. [5]

$$i(\xi) = K(T) \theta^{1/2}(\xi, \rho) \Big|_{\rho=1} \left[e^{\frac{3}{2} \frac{F\eta_c}{RT}} - e^{-\frac{1}{2} \frac{F\eta_c}{RT}} \right] \quad [6]$$

where $\rho = r/R_0$, $\xi = z/R_0 N_{pe}$, $\theta = C/C_F$, F is Faraday constant, and N_{pe} is the Peclet number, defined as $N_{pe} = R_0 \langle V \rangle / D$ with R_0 the tube radius, $\langle V \rangle$ the average flow velocity, and D the diffusion coefficient of O_2 . In Eq. [6], the local current density $i(\xi)$ is a function of ξ and the dimensionless O_2 concentration $\theta(\xi, \rho)$ is allowed to vary with both ξ and ρ inside the reactor, with $\theta|_{\rho=1}$ being its value at the tube wall at a given axial position ξ . Moreover, $K(T)$ is the experimentally determined rate constant defined as $K(T) = A(T) P_F$, where P_F is the partial pressure of O_2 in the feed stream; the values of $A(T)$ are given in Table II. At steady state, the convective-diffusion equation for gaseous O_2 can be written in dimensionless form as

$$(1 - \rho^2) \frac{\partial \theta}{\partial \xi} = \frac{\partial^2 \theta}{\partial \rho^2} + \frac{1}{\rho} \frac{\partial \theta}{\partial \rho} + \frac{1}{N_{pe}^2} \frac{\partial^2 \theta}{\partial \xi^2} \quad [7]$$

The boundary conditions for Eq. [7] and the matching conditions at $\xi = 0$ are

$$\xi \rightarrow -\infty \quad \text{for all } \rho \quad \theta = 1 \quad [8a]$$

$$\infty < \xi < 0 \quad \text{for } \rho = 0 \quad \frac{\partial \theta}{\partial \rho} = 0 \quad [8b]$$

Table I. Experimental values of the constant $A(T)$ used in the expression for current density (Eq. [6])

Temperature (K)	A ($A/\text{atm}^{1/2}$)
1123	4.17×10^{-2}
1023	1.39×10^{-2}
923	4.92×10^{-3}

Table II. Comparison of dimensionless concentration θ obtained for three different grid configurations using the SOR scheme with the semianalytical results from Ref. (30). The following parameters were used: $N_{pe} = 10$; dimensionless heterogeneous reaction rate constant = 10; dimensionless homogeneous reaction rate constant = 1

Grid configuration (This work)	N	M	$\theta_{\xi=0}$	$\theta_{\xi=1.125}$	Relative CPU time
(2:1)	21	21	0.7844	0.1559	0.70
(4:1)	21	21	0.7714	0.1484	1.00
(4:1)	21	21	0.7714	0.1484	1.00
(4:2)	21	21	0.7714	0.1484	1.11
(4:1)	21	21	0.7714	0.1484	1.00
(4:1)	31	21	0.7715	0.1483	2.26
(4:1)	21	21	0.7714	0.1484	1.00
(4:1)	21	31	0.7716	0.1483	2.20
Dang(30)	—	—	0.7719	0.1488	—

$$\text{for } \rho = 1 \quad \frac{\partial \theta}{\partial \rho} = 0 \quad [8c]$$

$$0 < \xi < \frac{L}{R_0 N_{pe}} \quad \text{for } \rho = 0 \quad \frac{\partial \theta}{\partial \rho} = 0 \quad [8d]$$

$$\text{for } \rho = 1 \quad \frac{\partial \theta}{\partial \rho} = \frac{-R_0}{C_r D} \frac{i(\xi)}{4F} \quad [8e]$$

$$\xi = \frac{L}{R_0 N_{pe}} \quad \text{for all } \rho \quad \frac{\partial \theta}{\partial \xi} \rightarrow 0 \quad [8f]$$

$$\xi = 0 \quad \theta \rightarrow \text{continuous} \quad [8g]$$

$$\frac{\partial \theta}{\partial \xi} \rightarrow \text{continuous} \quad [8h]$$

Boundary condition [8a] states that far upstream from the reactor entrance, the O₂ concentration is uniform ($C = C_r$), whereas boundary condition [8f] is a simplifying approximation which has been shown to be valid for any finite value of the mass diffusivity particularly when the concentration gradients in the radial direction are not extremely large anticipating the results, as seen in Fig. 3b, 4b, and 5b (21). That $\partial\theta/\partial\xi$ approaches zero at $\xi = L/R_0 N_{pe}$ (or $z = L$) is borne out by the behavior depicted in Fig. 3a, 4a, and 5a.

In order to evaluate the point-to-point change in the O₂ concentration at the tube wall, Eq. [7] must be solved together with boundary conditions Eq. [8a]-[8h]. The values of the wall O₂ concentration thus obtained can then be introduced into Eq. [6] to evaluate $i(\xi)$ as a function of ξ along the reactor. The total ionic current can be calculated according to

$$I = \frac{2\pi R_0 L}{R_0 N_{pe}} \int_{\xi=0}^{\xi=L/R_0 N_{pe}} i(\xi) d\xi \quad [9]$$

where L is the active cell length of the Au electrodes. If Eq. [6] is valid, then the computed values of I should agree with the measured values of the current circulating through the cell at steady state. The radially averaged bulk or mixing cup O₂ concentration at any given axial position is calculated in accordance with

$$C_{Av}(z) = \frac{\int_0^{R_0} 2\pi r v C(z, r) dr}{\int_0^{R_0} 2\pi r v dr} \quad [10]$$

which reduces for the case of fully developed laminar flow to

$$\theta_{Av}(\xi) = \int_0^1 \rho (1 - \rho^2) \theta(\xi, \rho) d\rho \quad [11]$$

Numerical methods.—The behavior of tubular reactors with catalytic walls in which chemical reaction as well as diffusion processes play important roles has been the subject of many investigations. Previous investigators have made simplifying assumptions such as neglecting the effect of axial diffusion (22-25) to facilitate the mathematical analysis of the problem, and the solutions have generally been given in terms of orthogonal eigenfunction expansions (24, 26-27). However, in the present case as well as other important situations in electrochemistry, the mass diffusivity is large and the axial velocity is low. Under solid-electrolyte working temperatures (600°-1000°C), mass diffusivities are high and ignoring axial diffusion leads to incorrect solutions to the problem, especially near the entrance of the reactor. On the other hand, the inclusion of an axial-diffusion term changes the nature of the governing equations from parabolic to elliptic type. Walker (28) studied the tubular-reactor problem with axial diffusion and first-order homogeneous and heterogeneous reactions and obtained asymptotic results for the far downstream region. Dang (29-30) presented an exact analysis of a similar problem for the entire domain $-\infty < z$

$< \infty$. In this analysis, the eigenvalues and eigenfunctions in the upstream region ($z < 0$) and positive downstream ($z > 0$) region are first obtained separately and then both solutions are matched at the reactor entrance $z = 0$. It has been shown that, for the case of a first-order heterogeneous reaction, the error arising in the inlet dimensionless concentrations if axial diffusion is not included can be as large as 50% for small N_{pe} , and with the error increasing when either N_{pe} decreases or the heterogeneous reaction rate constant increases (29). When the heterogeneous rate expressions are not first order, boundary condition [8e] becomes nonlinear, and one usually has to resort to numerical methods in order to obtain complete solutions to the problem. Because of the simple geometry of a tubular reactor, finite-difference schemes have been used in the past to analyze heat- or mass-transfer problems in such systems. Cleland and Wilhelm (25) used a finite-difference approach to study diffusion and reaction in a viscous-flow reactor but did not consider axial diffusion. Poirier (31) used a similar technique to extend the results of Cleland to second-order reactions. In the field of heat transfer, investigators have frequently used numerical techniques to approximate solutions to the classical Graetz problem with constant wall temperature and uniform heat-flux density boundary conditions (32-33).

In the present work, first and second derivatives are approximated by central difference operators resulting in a leading error of the order of $(\Delta\xi)^2$ and $(\Delta\rho)^2$ for derivatives in the axial and radial direction, respectively (34). The finite difference equation corresponding to Eq. [7] is

$$[1 - (j - 1)^2(\Delta\rho)^2] \frac{\theta_{i+1,j} - \theta_{i-1,j}}{2\Delta\xi} = \frac{\theta_{i,j+1} - 2\theta_{i,j} + \theta_{i,j-1}}{(\Delta\rho)^2} + \frac{1}{(j - 1)\Delta\rho} \frac{\theta_{i,j+1} - \theta_{i,j-1}}{2\Delta\rho} + \frac{1}{N_{pe}^2} \frac{\theta_{i+1,j} - 2\theta_{i,j} + \theta_{i-1,j}}{(\Delta\xi)^2} \quad [12]$$

where $\theta_{i,j}$ is the dimensionless O₂ concentration at the (i, j) mesh point with $i = 1, 2, \dots, M$ and $j = 1, 2, \dots, N$. Due to the elliptic nature of Eq. [7], boundary conditions are assigned around the complete domain of integration. As a result, it is not possible to use a simple marching procedure to obtain the solution. Therefore, the large system of equations that arises after applying Eq. [12] at every mesh point has to be solved simultaneously. Fortunately, the number of zero elements in the coefficient matrix associated with this system of equations is much greater than the number of nonzero elements. For this type of matrix, iterative methods of solution are in general found to be more efficient than direct methods, since no computation is required with zero coefficients and considerably fewer numbers need to be stored in the computer (34-36). It is convenient when working with iterative methods to express the finite-difference equation [12] in the form of a five-point difference equation (34)

$$\theta_{i,j} = \frac{1}{A_j} [B_j \theta_{i,j+1} + C_j \theta_{i-1,j} + D_j \theta_{i,j-1} + E_j \theta_{i+1,j}] \quad [13]$$

with

$$A_j = A = \frac{2}{(\Delta\rho)^2} + \frac{2}{N_{pe}^2 (\Delta\xi)^2}$$

$$B_j = \frac{1}{(\Delta\rho)^2} + \frac{1}{2(j - 1)(\Delta\rho)^2}$$

$$C_j = \frac{1}{N_{pe}^2 (\Delta\xi)^2} + \frac{1 - (j - 1)^2(\Delta\rho)^2}{2\Delta\xi}$$

$$D_j = \frac{1}{(\Delta\rho)^2} - \frac{1}{2(j - 1)(\Delta\rho)^2}$$

$$E_j = \frac{1}{N_{pe}^2 (\Delta\xi)^2} - \frac{1 - (j - 1)^2(\Delta\rho)^2}{2\Delta\xi}$$

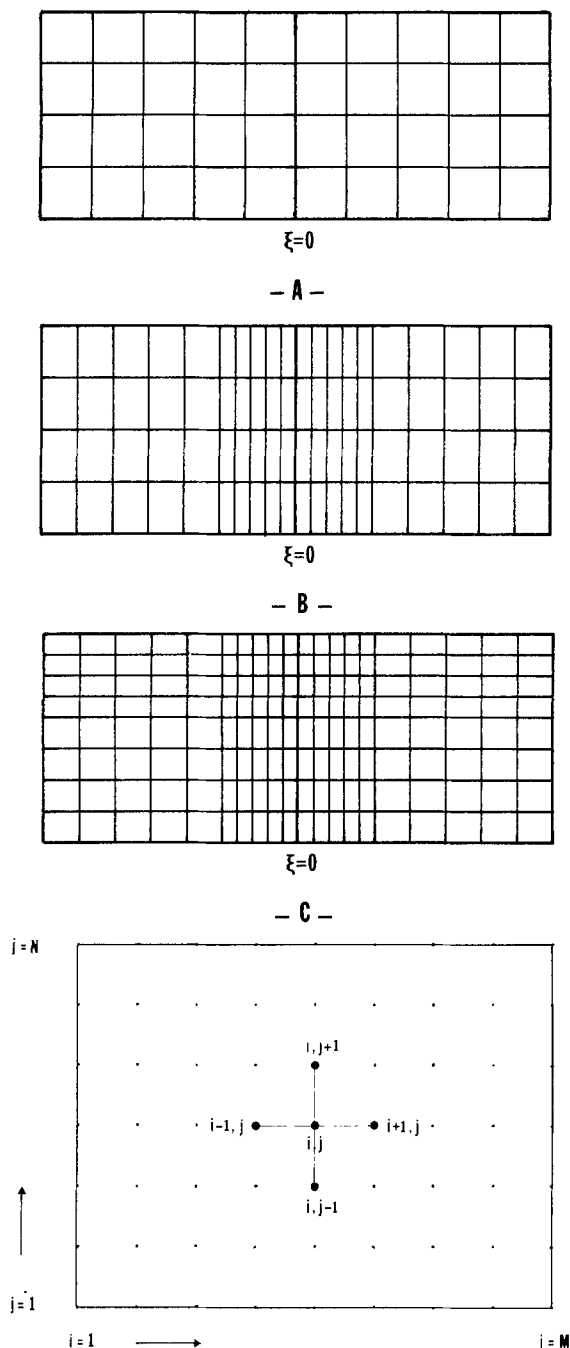


Fig. 2. A: Grid configuration (2:1): two axial zones and one radial zone. B: Grid configuration (4:1): four axial zones and one radial zone. C: Grid configuration (4:2): four axial zones and two radial zones. D: Details of the rectangular grids used in the numerical computations.

The three grid configurations which were used in this study are schematically shown in Fig. 2a-2c. Each of the axial regions contains $M \times N$ mesh points, where N is the number of points along the radial direction and M is the number of points in the axial direction as shown in Fig. 2d. For all internal points, Eq. [13] is applicable. The equations describing the points at the boundaries of each region are obtained by combining Eq. [13] with the appropriate boundary conditions Eq. [8a]-[8f] as shown in the Appendix. A FORTRAN computer program based on the SOR method together with a ten-step Newton linearization loop (34, 35) was written to solve the resulting system of nonlinear algebraic equations. The algorithm for the SOR scheme can be written for internal mesh points as

$$\theta_{i,j}^{(n+1)} = \frac{1}{A} [B_j \theta_{i,j+1}^{(n)} + C_j \theta_{i,j-1}^{(n+1)} + D_j \theta_{i,j-1}^{(n+1)} + E_j \theta_{i+1,j}^{(n)}] W - (W-1) \theta_{i,j}^{(n)} \quad [14]$$

when n represents the previous n^{th} iterative step and the expression in square brackets is seen to contain some terms calculated earlier in the present $(n+1)^{\text{th}}$ iteration and W is the acceleration parameter characteristic of the SOR method, usually in the range $1 < W < 2$. The numerical procedure involved assuming initial values of the concentration at all mesh points, usually 0.90 for θ in the region $\xi < 0$ and 0.10 for θ in the region $\xi > 0$. These initial guess values were then iteratively improved with Eq. [13] and Eq. [A-1]-[A-11] until the difference in the dimensionless concentrations between successive approximations reached a termination condition. The criterion used for terminating the computation was

$$\sum_{i=1}^M \sum_{j=1}^N [|\theta_{i,j}^{(n+1)} - \theta_{i,j}^{(n)}| + |\theta_{i,j}^{(n+1)} - \theta_{i,j}^{(n)}|] < 10^{-5} \quad [15]$$

Experimental Procedures

The reactor was constructed with a 10 mole percent Y_2O_3 -stabilized ZrO_2 tube (15 cm long and 2.5 cm od). Working and reference Au electrodes were made from unfluxed Engelhard gold paste no. A-3156. The working electrodes (10 cm long) have a superficial area of 80 cm^2 and an average thickness of $5-8 \mu\text{m}$. All experimental runs were carried out at atmospheric pressure and in the temperature range $650^\circ-850^\circ\text{C}$. Certified standard O_2/Ar mixtures and research-grade O_2 from Matheson were used. The cell was operated as an oxygen pump in which O_2 mixtures circulated in the inner chamber and air circulated in the outer chamber. In order to avoid reducing the zirconia electrolyte, the external voltage applied to the cell never exceeded 1.5V. Additional details regarding the apparatus and procedures are given elsewhere (20).

Numerical Results and Discussion

In order to check the accuracy of the numerical scheme, the FORTRAN computer program was employed to investigate a similar mass-transfer problem which involves a simple first-order heterogeneous reaction at the tube wall as well as a first-order homogeneous reaction. The numerical results obtained for the dimensionless oxygen concentration θ at the reactor entrance ($\xi = 0$) and at the reactor outlet ($\xi = 1.125$) are then compared with semianalytical results available in the literature (30). Three different grid configurations were tested as depicted in Fig. 2a-2c, and the results are given in Table II. As expected, subdividing the basic configuration into four axial regions (4:1) increased the computing time as compared with two axial regions (2:1), but the accuracy was significantly improved as a result of a finer mesh size around $\xi = 0$ where a step change occurs in the wall boundary condition. Further subdivision into two radial regions with finer step size near the wall (4:2) increased the computing time but did not considerably improve the accuracy of the solution. The grid configuration (4:1) with four axial zones and one radial zone was thus chosen on this basis for all standard runs. Different radial step sizes were tested with this grid configuration. As shown in Table II, increasing the number of radial or axial steps from 2 to 3 more than doubled the computing time but did not improve the solution significantly. Based on these results, values of $M = 21$ and $N = 21$ were used throughout this work.

Complete concentration profiles were obtained for experimental conditions with Peclet numbers ranging from 1 to 20, temperatures from 650° to 850°C , O_2 feed concentrations from 0.009 to 21 volume percent (v/o), and cathodic overpotentials from 50 to 1000 mV. Over-relaxation parameters in the range 1.7-1.9 were found to be the most appropriate, with the larger values corresponding to runs with Peclet numbers $N_{pe} < 2$. For higher N_{pe} , smaller relaxation parameters had to be used in order to avoid divergence or oscillations in the rate of convergence Q

$$Q = \frac{\sum_i \sum_j [|\theta_{i,j}^{(n+1)} - \theta_{i,j}^{(n)}| + |\theta_{i,j}^{(n+1)} - \theta_{i,j}^{(n)}|]}{\sum_i \sum_j [|\theta_{i,j}^{(n)} - \theta_{i,j}^{(n-1)}| + |\theta_{i,j}^{(n)} - \theta_{i,j}^{(n-1)}|]} \quad [16]$$

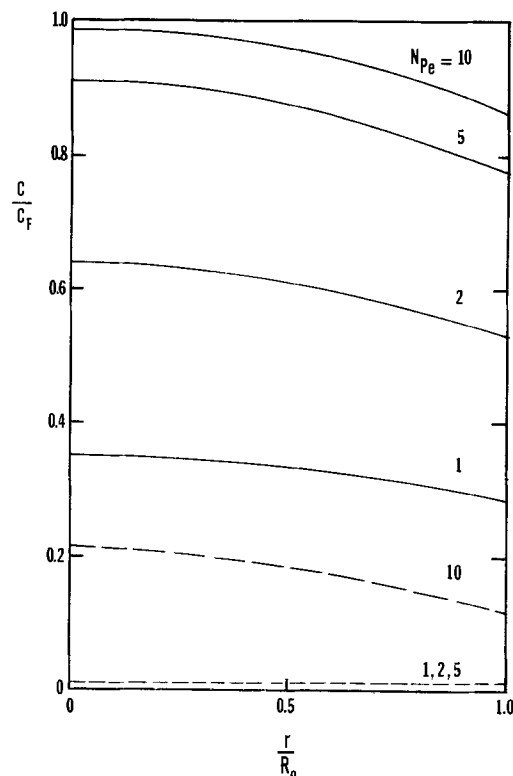
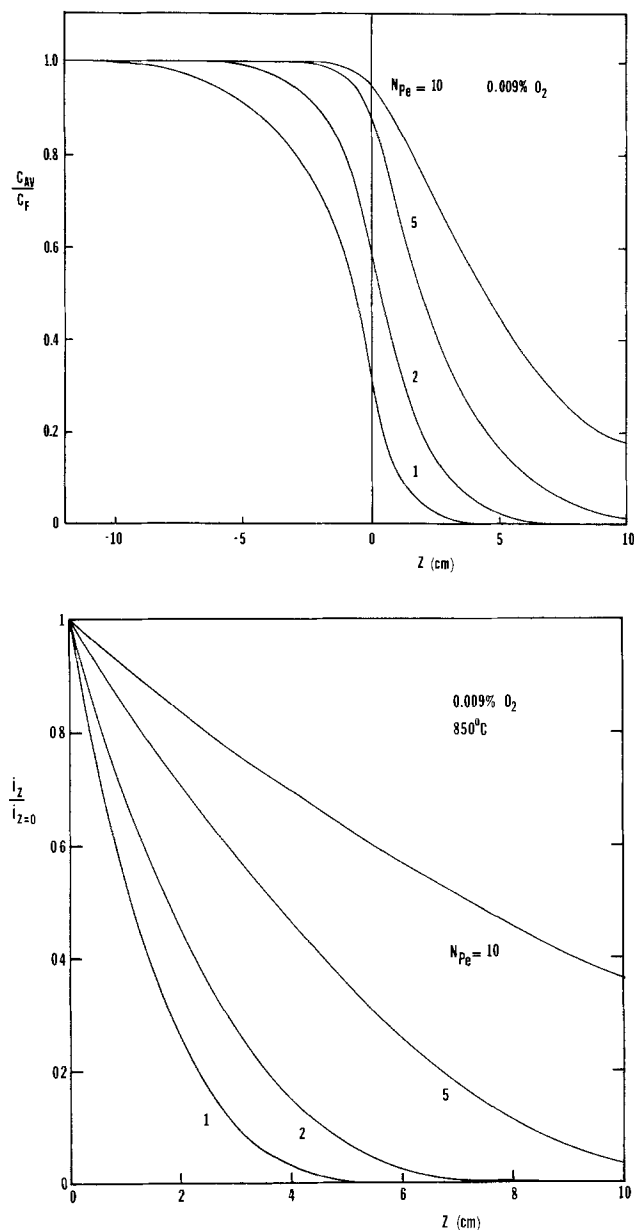


Fig. 3. a(top left): Dimensionless average oxygen concentration vs. axial position with Peclet number as a variable. ($T = 850^\circ C$, $\eta_c = 700$ mV, $C_F = 0.009$ v/o). b(above): Dimensionless oxygen concentration vs. dimensionless radial position at $Z = 0$ (solid curves) and $Z = L$ (dashed curves) with Peclet number as a variable. ($T = 850^\circ C$, $\eta_c = 700$ mV, $C_F = 0.009$ v/o). c(left): Dimensionless local ionic current vs. axial position with Peclet number as a variable. ($T = 850^\circ C$, $\eta_c = 700$ mV, $C_F = 0.009$ v/o).

By choosing the appropriate value of W , the rate of convergence Q was significantly improved and the total number of iterations necessary to reach the termination condition Eq. [15] was reduced to about one-quarter of those necessary when $W = 1$, which corresponds to the Gauss-Seidel iterative scheme. The rate of convergence increased with increasing N_{Pe} and η_c . In the first case, the faster convergence was related to a smaller dimensionless axial step size, while increasing η_c resulted in a larger concentration gradient at the wall. In general, the number of iterations required for termination ranged from about 150 for $N_{Pe} = 20$, high η_c and $C_F = 0.009$ v/o to about 500 for $N_{Pe} = 1$, low η_c , and $C_F = 21$ v/o. The local ionic currents are calculated according to Eq. [6]; Simpson's rule for integration was used to evaluate the averaged bulk concentrations according to Eq. [11].

As expected, the shape of the concentration profiles was highly influenced by the magnitude of N_{Pe} as shown in Fig. 3a. As the convective velocity, and thus N_{Pe} , decreases, backmixing increases owing to the effect of axial diffusion penetrating further into the region upstream from the reactor entrance causing the dimensionless average concentration at $\xi = 0$ to depart significantly from unity. As seen in Fig. 3b, when N_{Pe} decreases, the radial concentration profiles become somewhat flatter due to the increasing importance of the mixing effect of radial diffusion. The expected decrease in the local ionic-

current ratio flowing through the electrolyte as a function of axial position is evident in Fig. 3c for different N_{Pe} .

The concentration and current profiles obtained for different inlet O_2 concentrations C_F is shown in Fig. 4a-4c. For a given η_c , the average amount of O_2 that reacts at the wall relative to the concentration in the feed C_F increases with decreasing C_F , tending to increase the effect of axial diffusion as seen in Fig. 4a. From Fig. 4b, it can be seen that the radial concentration profiles become steeper at lower values of C_F as well as flatter downstream from the entrance because of the effect of convective mass transport. The expected decrease in $i(\xi)$ with axial position is shown in Fig. 4c for different C_F , and the growing importance of the electrochemical reaction at the wall is evident at lower concentrations.

The influence of the overpotential η_c upon the concentration profiles is shown in Fig. 5a-5b. An increase in η_c causes a significant increase in the electrical driving force term of the rate expression Eq. [6] in such a way that the reaction rates at the wall become much higher. As seen in Fig. 5a, this increase in the reaction rates causes backmixing to become more pronounced, with the O_2 concentrations at $\xi = 0$ deviating further from unity as η_c is increased. The overall conversions also increase with increasing η_c in such a way that, in two cases, conversions on the order of 99.99% are attained at moderate values of η_c , as seen in Fig. 5a. In these cases, further increases in

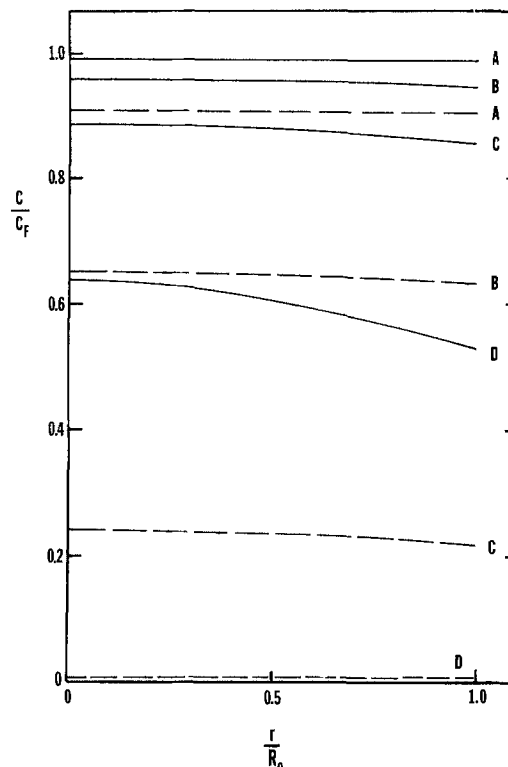
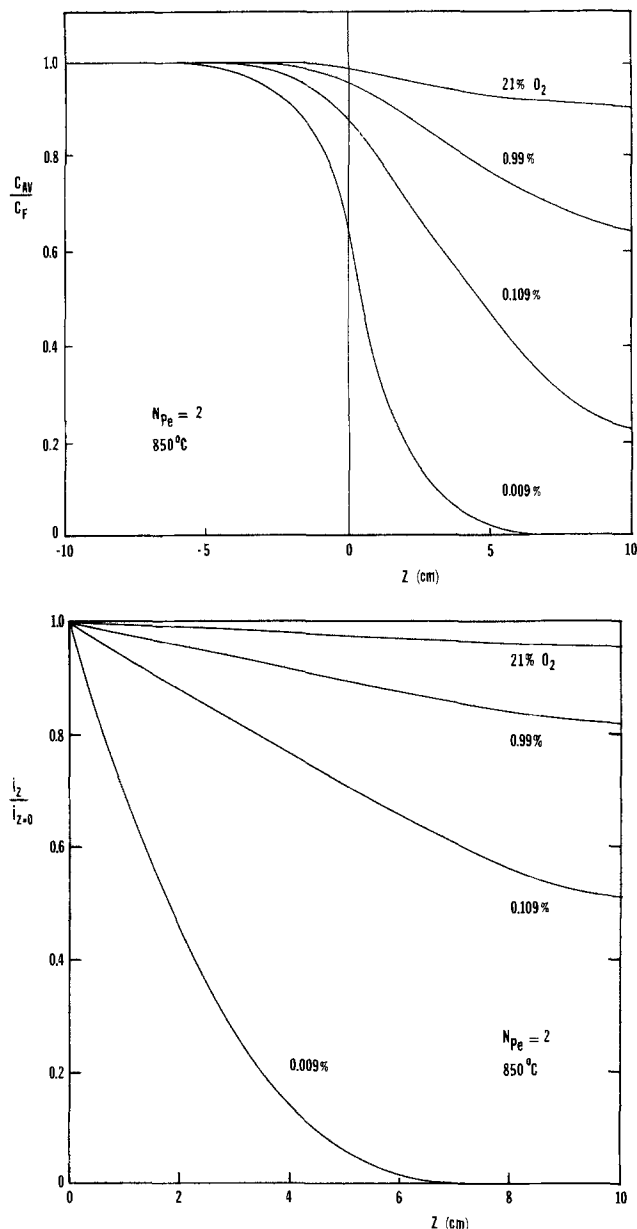


Fig. 4 a(top left): Dimensionless average oxygen concentration vs. axial position with oxygen concentration in the feed as a variable. ($T = 850^\circ C$, $N_{Pe} = 2$, $\eta_c = 700$ mV.) b(above): Dimensionless oxygen concentration vs. dimensionless radial position at $Z = 0$ (solid curves) and $Z = L$ (dashed curves) with oxygen concentration in the feed as a variable. ($T = 850^\circ C$, $N_{Pe} = 2$, $\eta_c = 700$ mV; A = 21 v/o O_2 , B = 0.99%, C = 0.109%, and D = 0.009%.) c(left): Dimensionless local ionic current vs. axial position with oxygen concentration in the feed as a variable. ($T = 850^\circ C$, $N_{Pe} = 2$, $\eta_c = 700$ mV.)

η_c do not lead to an appreciable increase in the overall conversion and the calculated total currents approach limiting values. These limiting values of current correspond to the current plateaus experimentally observed at low P_{O_2} (20). Figure 5b shows that as η_c is increased the radial concentration profiles become steeper, owing to the presence of a high slope of concentration at the wall and the high reaction rate (see Eq. [4]).

The variation of the current density (based on electrode superficial area) with respect to axial position is shown in Fig. 6a-6d for four different inlet O_2 concentrations. At a given η_c , the area under the $i(z)$ vs. z curves determines the value of the total ionic currents. It is seen in Fig. 6a that when air is circulated through the inner chamber, a nearly uniform current distribution results along the reactor for all applied potentials investigated and the reactor is operating in a differential regime. However, when gas mixtures of lower O_2 content are circulated through the oxygen pump, the reactor departs significantly from the differential regime. At moderate to high values of η_c , there is a substantial drop in $i(z)$ with axial position along the reactor. As shown in Fig. 6b and 6c, corresponding respectively to $C_F = 0.99$ and 0.109 v/o, this situation becomes evident when η_c is in the proximity of 1000 mV. For lower inlet O_2 concentrations, the marked decrease in $i(z)$ at high η_c as seen in Fig. 6d indicates that the applied potential E has reached a point beyond which any further increase in E does not give rise to an increase in current.

In these cases, the local current density $i(z)$ drops to negligibly small values at a distance before the end of the active cell region. The length of reactor effectively used is then significantly less than the actual total cell length as evidenced in Fig. 6d. In this particular case, when η_c reaches 1000 mV, most of the ionic current originates in an effective reaction zone corresponding to approximately one-third of the total cell length. The length of the cell being effectively used can be increased by increasing the flow rates and keeping the overall conversion at around 99.99%. During this process, the total ionic current will also increase. Eventually, the gas flow rate reaches a value at which the effective cell length is equal to the total cell length. Beyond this point, further increases in the flow rate will lead to a decrease in the overall conversion.

The effect of temperature on the axial concentration profiles is summarized in Fig. 7. The general trend can be interpreted in terms of an increase in the rate of the electrochemical reaction with increasing temperature as would be expected from the Arrhenius rate expression.

In order to test the validity of the above convective-diffusion model and the accuracy of the numerical solutions, the total ionic currents obtained numerically from Eq. [9] for different values of temperature, inlet O_2 , η_c , and flow rate were compared with the experimentally measured values. For intermediate and high O_2 concentrations ($C_F \geq 0.99$ v/o), the reactor was operating effectively in the differential mode with low overall conversion

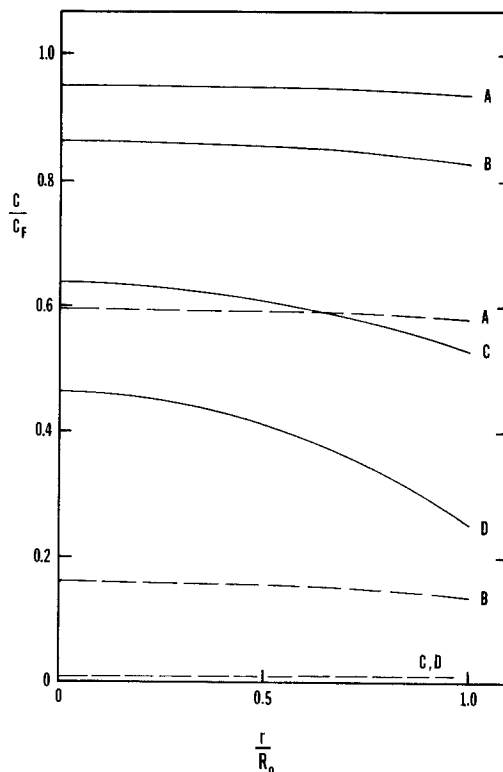
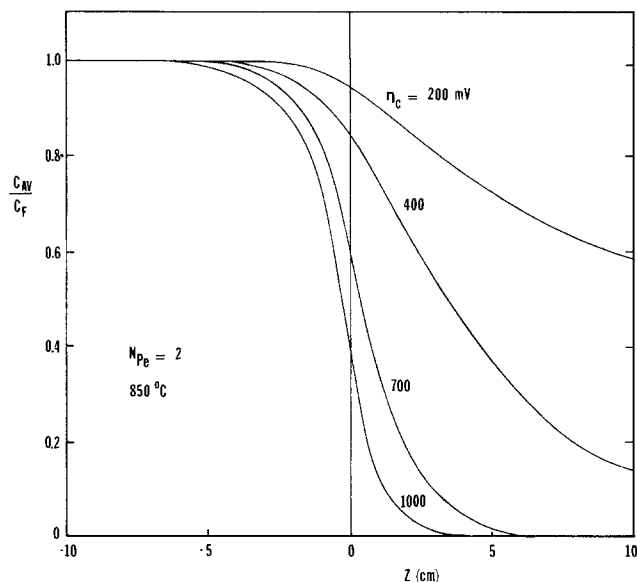


Fig. 5. a(left) Dimensionless average oxygen concentration vs. axial position with cathodic overpotential as a variable. ($T = 850^{\circ}\text{C}$, $N_{\text{Pe}} = 2$, $C_{\text{F}} = 0.009$ v/o). b: Dimensionless oxygen concentrations vs. dimensionless radial position at $Z = 0$ (solid curves) and $Z = L$ (dashed curves) with cathodic overpotential as a variable. ($T = 850^{\circ}\text{C}$, $N_{\text{Pe}} = 2$, $C_{\text{F}} = 0.009$ v/o; A = 200 mV, B = 400 mV, C = 700 mV, and D = 1000 mV.)

throughout the complete overpotential range. As a result, Eq. [6] can be directly used to correlate the current-overpotential data because the change in the O_2 concentration at the tube wall along the reactor is negligible as shown from the above results. However, for lower O_2 concentrations ($C_{\text{F}} < 0.109$ v/o), the reactor enters the integral mode of operation as η_{c} is increased. In this case, it is seen in Fig. 8 and 9 that when changes in O_2 concentration at the tube wall with respect to axial position along the reactor are computed, the resulting total currents obtained from numerical integration of Eq. [9] agree very well with the measured curves of the steady-state current circulating through the cell, indicating that Eq. [6] still provides a valid description of the electrode kinetics associated with the cathodic reduction of O_2 . That the reactor is operating in the integral mode is confirmed by mixing cup fractional conversions ranging from 0.7 to 0.99 in these figures.

The analysis developed here for a tubular solid-electrolyte flow reactor is flexible enough to be applicable with appropriate modifications to any complex form of heterogeneous rate expression. Thus, the investigation of the electrochemical kinetics and/or overall reactor performance for a wide variety of reacting systems, including the decomposition of oxygen bearing species (37), oxidative dehydrogenation of hydrocarbons (38), and the anodic oxidation of gaseous hydrocarbons (39), is amenable to analyses by the numerical scheme presented herein. This model is currently being applied to the electro-oxidation of hydrocarbon gas mixtures such as produced from coal to produce electrical energy as well as valuable chemicals in the so-called "chemical cogeneration" mode of operation. For such fuel cell systems operating with large overall conversions, the assumption of isothermal flow might not be adequate due to thermal effects of the reaction on the wall, and it might be necessary to include an energy balance. The energy balance would then need to be solved numerically together with the convective-diffusion equation. Finally, in cases where large concentration gradients arise in the radial direction, boundary condition Eq. [8f] is less valid, and it might become necessary to recast the mass-transfer problem in the region $L/R_0 N_{\text{Pe}} < \xi$

$< +\infty$ by employing the exact boundary condition $\partial\theta/\partial\xi \rightarrow 0$ as $\xi \rightarrow \infty$. These two additional complexities are currently being incorporated into the numerical scheme.

Conclusions

It has been shown that by solving a general convective-diffusion equation which incorporates axial as well as radial diffusion and a complex electrochemical reaction at the wall, the performance of a tubular stabilized-ZrO₂ oxygen pump operating in the integral mode can be satisfactorily described. The electrochemical kinetics associated with the cathodic reduction of O_2 at the wall was correlated with a modified Butler-Volmer equation. The resulting system of nonlinear equations was numerically solved by the method of successive overrelaxation (SOR). The numerical results indicate that axial diffusion exerts the greatest influence on the concentration profiles at low N_{Pe} , low inlet P_{O_2} , and high values of η_{c} . The total ionic currents computed from these concentration profiles are consistent with those observed experimentally.

Acknowledgments

Acknowledgment is made to the Donors of The Petroleum Research Fund, administered by the American Chemical Society, for partial funding of this research. Financial support from the Government of Venezuela through the Fundacion Gran Mariscal de Ayacucho is also gratefully acknowledged. The authors are grateful to John Hessler of the Civil Engineering Machine Shop for his suggestions and cooperation during the construction of the tubular reactor.

Manuscript submitted March 15, 1985; revised manuscript received July 30, 1985.

APPENDIX

To obtain the equations describing the points on the grid boundaries, Eq. [13] must be combined with the appropriate boundary condition as follows.

(i) For points at $\xi = -\infty$, Eq. [8a] is used

$$\theta_{i,j} = 1 \quad [\text{A-1}]$$

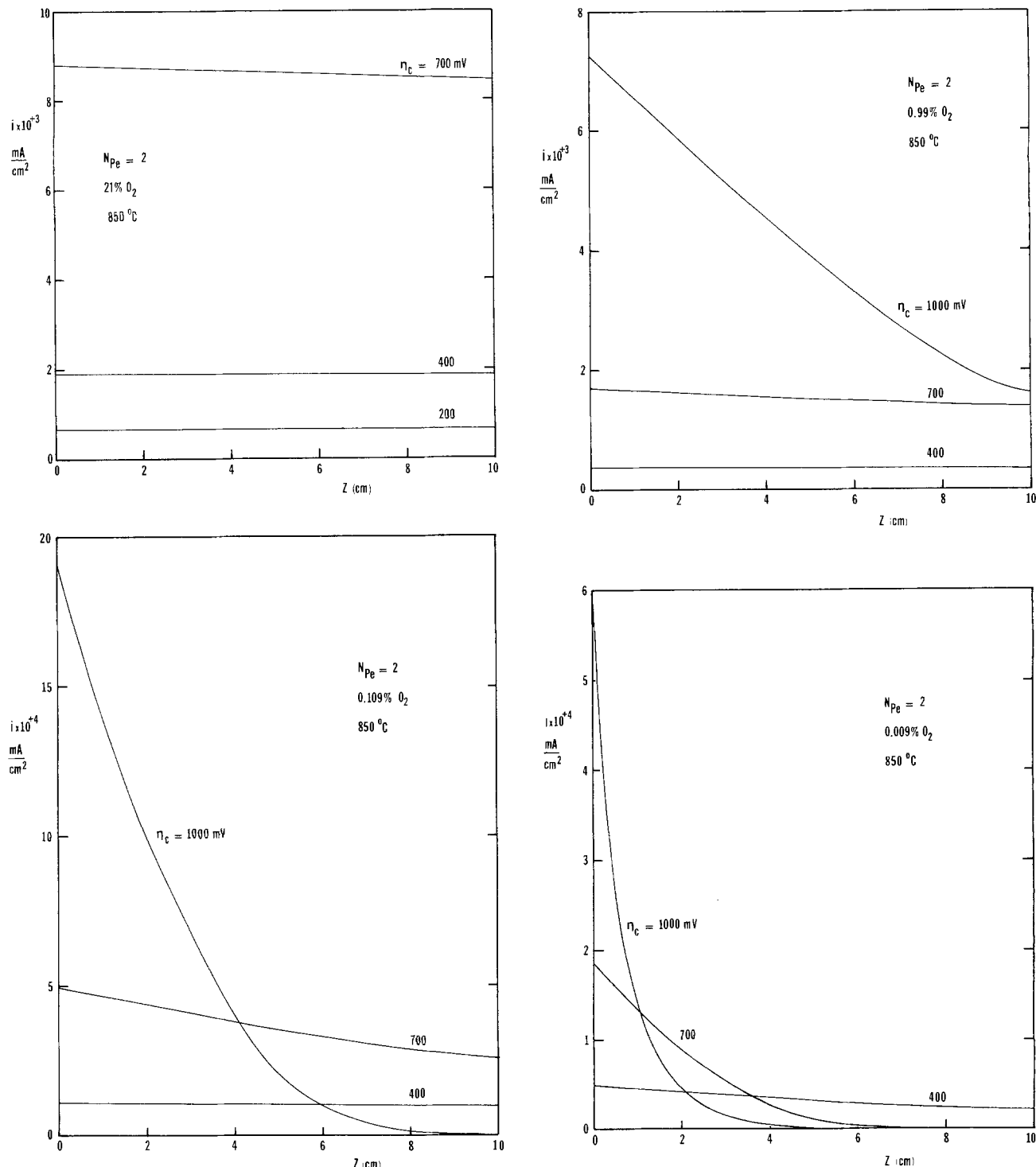


Fig. 6. a(top left): Local ionic current vs. axial position with cathodic overpotential as a variable. ($T = 850^\circ\text{C}$, $N_{Pe} = 2$, $C_F = 21$ v/o.) b(top right): Local ionic current vs. axial position with cathodic overpotential as a variable. ($T = 850^\circ\text{C}$, $N_{Pe} = 2$, $C_F = 0.99$ v/o.) c(bottom): Local ionic current vs. axial position with cathodic overpotential as a variable. ($T = 850^\circ\text{C}$, $N_{Pe} = 2$, $C_F = 0.109$ v/o.) d: Local ionic current vs. axial position with cathodic overpotential as a variable. ($T = 850^\circ\text{C}$, $N_{Pe} = 2$, $C_F = 0.009$ v/o.)

with lengths corresponding to $\xi = -\infty$ at which boundary condition Eq. [A-1] is satisfied being found by trial and error.

(ii) In order to use a central difference operator for points at the wall, it is usual to introduce a "fictitious" concentration θ_{i,N^*+1} at the external mesh point ($i, N^* + 1$) (26). From Eq. [8c], it is then obtained that

$$\theta_{i,N^*+1} = \theta_{i,N-1} \quad [\text{A-2}]$$

If Eq. [13] is written for all points at the wall, i.e., for $i = N$ and then all the terms involving θ_{i,N^*+1} replaced with Eq. [A-2], the following equation is obtained for points at the wall in the region $\xi < 0$

$$\theta_{i,N} = \frac{1}{A} [C_N \theta_{i-1,N} + D_N \theta_{i,N-1} + E_N \theta_{i+1,N}] \quad [\text{A-3}]$$

with

$$C_N = \frac{1}{N_{Pe}^2 (\Delta\xi)^2} \quad D_N = \frac{2}{(\Delta\rho)^2} \quad E_N = \frac{1}{N_{Pe}^2 (\Delta\xi)^2}$$

(iii) Similarly, for points at the wall in the reaction zone ($0 < \xi < L/R_0 N_{Pe}$), the finite difference form of Eq. [8e] becomes

$$\theta_{i,N^*+1} = \theta_{i,N-1} - 2(\Delta\rho) \frac{R_0}{C_F D} \frac{K(T)}{4F} \theta_{i,N^{*+1/2}} [e^{\frac{3}{2} \frac{F\eta_c}{RT}} - e^{-\frac{1}{2} \frac{F\eta_c}{RT}}] \quad [\text{A-4}]$$

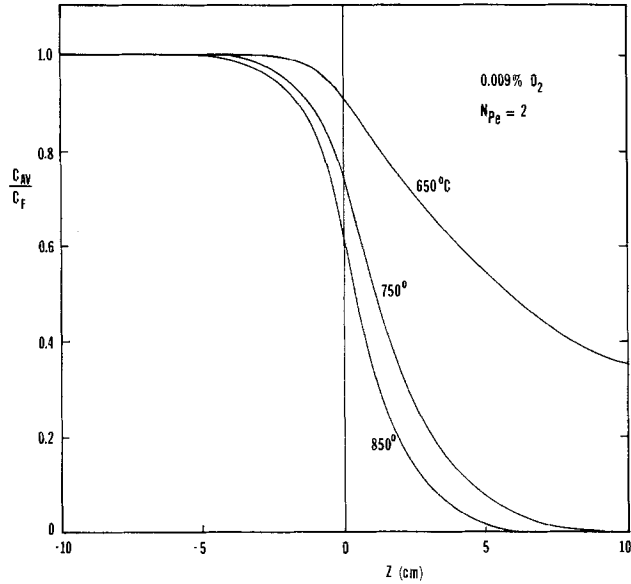


Fig. 7. Dimensionless average oxygen concentration vs. axial position with temperature as a variable. ($N_{Pe} = 2$, $C_F = 0.009$ v/o, $\eta_c = 700$ mV.)

and combining Eq. [A-4] with Eq. [13] to eliminate the unknown $\theta_{i,N+1}$ yields

$$\theta_{i,N} = \frac{1}{A} [C_N \theta_{i-1,N} + D_N \theta_{i,N-1} + E_N \theta_{i+1,N}] - 2B_N(\Delta\rho)$$

$$\frac{R_o}{C_F D} \frac{K(T)}{4F} \theta_{i,N}^{1/2} \left[e^{\frac{3}{2} \frac{F\eta_c}{RT}} - e^{-\frac{1}{2} \frac{F\eta_c}{RT}} \right] \quad [A-5]$$

with

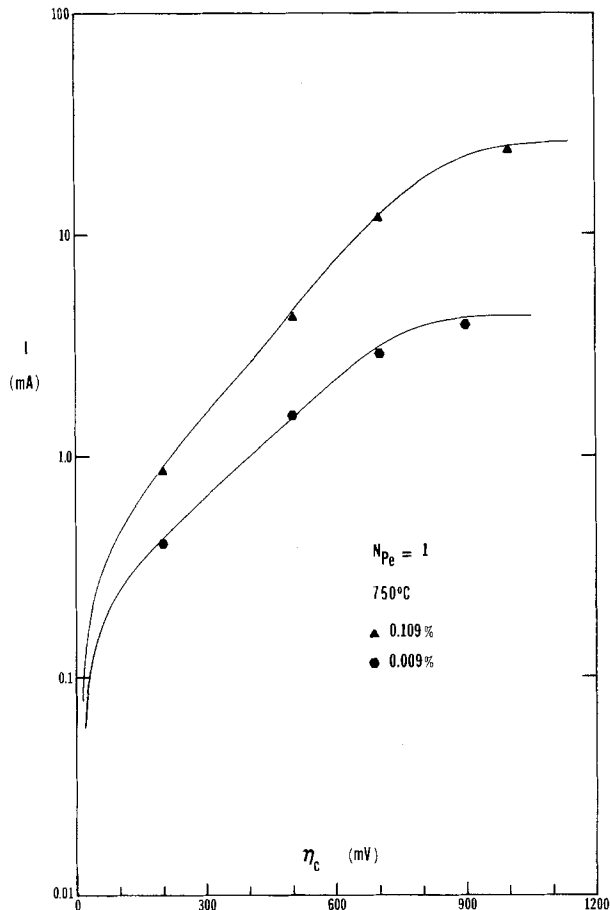


Fig. 8. Plot of $\log I$ vs. η_c for low P_{O_2} at 750°C showing comparison with numerical results (points).

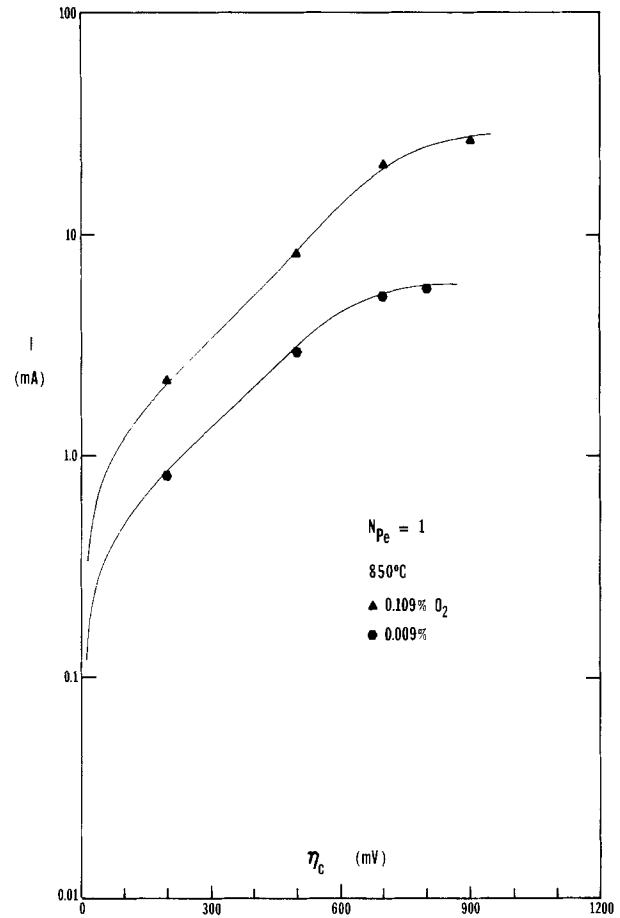


Fig. 9. Plot of $\log I$ vs. η_c for low P_{O_2} at 850°C showing comparison with numerical results (points).

$$B_N = \frac{1}{(\Delta\rho)^2} + 0.5 \quad C_N = \frac{1}{N_{Pe}^2(\Delta\rho)^2}$$

$$D_N = \frac{2}{(\Delta\rho)^2} \quad E_N = \frac{1}{N_{Pe}^2(\Delta\xi)^2}$$

(iv) By combining Eq. [8b] or [8d] with Eq. [13], the following equation is obtained for the points at the centerline ($i = 1, 2, \dots, M$ and $j = 1$)

$$\theta_{i,1} = \frac{1}{A} [B_1 \theta_{i,2} + C_1 \theta_{i-1,1} + E_1 \theta_{i+1,1}] \quad [A-6]$$

with

$$B_1 = \frac{2}{(\Delta\rho)^2} \quad C_1 = \frac{1}{N_{Pe}^2(\Delta\xi)^2} \quad E_1 = \frac{1}{N_{Pe}^2(\Delta\xi)^2} - \frac{1}{2\Delta\xi}$$

(v) Proceeding in a similar fashion with Eq. [8f] and Eq. [13] yields the equation for the internal mesh points at the far right boundary ($i = M$ and $j = 2, 3, \dots, N - 1$)

$$\theta_{M,j} = \frac{1}{A} [B_j \theta_{M,j+1} + C_j \theta_{M-1,j} + D_j \theta_{M,j-1}] \quad [A-7]$$

with

$$B_j = \frac{1}{(\Delta\rho)^2} + \frac{1}{2(j-1)(\Delta\rho)^2} \quad C_j = \frac{2}{N_{Pe}^2(\Delta\xi)^2}$$

$$D_j = \frac{1}{(\Delta\rho)^2} - \frac{1}{2(j-1)(\Delta\rho)^2}$$

(vi) To obtain the equation for the single point located at the wall of the far right boundary ($i = M$ and $j = N$), Eq. [8e], [8f], and [13] are used together

$$\theta_{M,N} = \frac{1}{A} [C_N \theta_{M-1,N} + D_N \theta_{M,N-1}] - 2B_N(\Delta\rho)$$

$$\frac{R_o}{C_F D} \frac{K(T)}{4F} \theta_{M,N}^{1/2} \left[e^{\frac{3}{2} \frac{F\eta_c}{RT}} - e^{-\frac{1}{2} \frac{F\eta_c}{RT}} \right] \quad [A-8]$$

with

$$B_N = \frac{1}{(\Delta\rho)^2} + 0.5 \quad C_N = \frac{1}{N_{pe}^2(\Delta\xi)^2} \quad D_N = \frac{1}{(\Delta\rho)^2}$$

(vii) Finally, Eq. [8d], [8f], and [13] are used to obtain the equation for the point located at the centerline of the far right boundary ($i = M$ and $j = 1$)

$$\theta_{M,1} = \frac{1}{A} [B_M \theta_{M,2} + C_M \theta_{M-1,1}] \quad [A-9]$$

with

$$B_M = \frac{2}{(\Delta\rho)^2} \quad C_M = \frac{2}{N_{pe}^2(\Delta\xi)^2}$$

The basic grid configuration used in this study contains four axial regions and one radial region (Fig. 2b). Whenever this layout was used, Eq. [13] was applied at all internal mesh points and Eq. [A-1]-[A-9] to boundary points as indicated. Matching conditions Eq. [8g] and [8h] were used to solve for the values of the concentration at $\xi = 0$

$$\theta_{M,j^I} = \frac{(\Delta\xi)^j}{(\Delta\xi)^{II}} \theta_{2,j^{II}} + \theta_{M-1,j^I} / 1 + \frac{(\Delta\xi)^j}{(\Delta\xi)^{II}} \quad [A-10]$$

$$\theta_{1,j^{II}} = \theta_{M,j^I} \quad [A-11]$$

where superscripts I, II denote the values of θ in the region $\xi < 0$ and $\xi > 0$, respectively.

REFERENCES

- P. Hagenmuller and W. van Gool, "Solid Electrolytes: General Principles, Characterization, Materials, Applications," Academic Press, New York (1978).
- E. C. Subbarao, "Solid Electrolytes and Their Applications," Plenum Press, New York (1980).
- T. H. Etsell and S. N. Flengas, *Chem. Rev.*, **70**, 339 (1970).
- E. C. Subbarao and H. S. Maiti, *Solid State Ionics*, **11**, 317 (1984).
- R. J. Brook, W. L. Pelzmann, and F. A. Kroger, *This Journal*, **117**, 593 (1970).
- J. E. Bauerle, *J. Phys. Chem. Solids*, **30**, 2657 (1969).
- M. Kleitz, Doctoral Thesis, University of Grenoble, Grenoble, France (1968).
- S. V. Karpachev and Yu. M. Ovchinikov, *Sov. Electrochem.*, **5**, 181 (1969).
- C. S. Tedmon, H. S. Spacil, and S. P. Mitoff, *This Journal*, **116**, 1170 (1969).
- R. E. W. Casselton, *J. Appl. Electrochem.*, **4**, 25 (1974).
- S. Pizzini, M. Bianchi, P. Colombo, and S. Torchio, *ibid.*, **3**, 153 (1973).
- S. Pizzini, in "Fast Ion Transport in Solids," P. Vashista, J. N. Mundy and G. K. Shenoy, Editors, p. 461, North-Holland, New York (1979).
- T. H. Etsell and S. N. Flengas, *This Journal*, **118**, 1890 (1971).
- H. Yanagida, R. J. Brook, and F. A. Kroger, *ibid.*, **117**, 593 (1970).
- D. Y. Wang and A. S. Nowick, *ibid.*, **128**, 55 (1981).
- M. J. Verkerk, M. W. J. Hammink, and A. J. Burggraaf, *ibid.*, **130**, 70 (1983).
- F. A. Kroger, *ibid.*, **120**, 75 (1973).
- T. M. Gur, Ph.D. Thesis, Stanford University, Stanford, CA (1976).
- D. J. Pickett, "Electrochemical Reactor Design," Elsevier Scientific Publishing, New York (1979).
- B. C. Nguyen, L. M. Rincon-Rubio, and D. M. Mason, Submitted to *This Journal*.
- J. F. Wehner and R. H. Wilhelm, *Chem. Eng. Sci.*, **6**, 89 (1956).
- D. E. Rosner, *AIAA J.*, **2**, 489 (1956).
- J. P. Vignes and P. J. Trambouze, *Chem. Eng. Sci.*, **17**, 73 (1962).
- R. L. Solomon and J. L. Hudson, *AIChE J.*, **13**, 545 (1967).
- F. A. Cleland and R. H. Wilhelm, *ibid.*, **2**, 489 (1956).
- A. J. Lupa and J. S. Dranoff, *Chem. Eng. Sci.*, **21**, 861 (1966).
- P. J. Ogren, *J. Phys. Chem.*, **79**, 1749 (1975).
- R. E. Walker, *Phys. Fluids*, **4**, 1211 (1961).
- V. D. Dang, *Chem. Eng. Sci.*, **33**, 1179 (1978).
- V. D. Dang, Paper 105b presented at the National Meeting of the American Institute of Chemical Engineers, Los Angeles, CA, Nov. 14-19, 1982.
- R. V. Poirier and R. W. Carr, *J. Phys. Chem.*, **75**, 1593 (1971).
- D. K. Hennecke, *Warm. Stoffubert.*, **1**, 177 (1968).
- F. H. Verhoff and D. P. Fisher, *J. Heat Trans.*, **95**, 132 (1972).
- G. D. Smith, "Numerical Solution of Partial Differential Equations—Finite Difference Methods," Clarendon Press, Oxford (1978).
- W. C. Rheinboldt, Paper no. 14 presented at the SIAM Regional Conference Series in Applied Mathematics, Philadelphia, PA (1974).
- R. Vichnevetsky, "Computer Methods for Partial Differential Equations," Prentice-Hall, Englewood Cliffs, NJ (1981).
- S. Pancharatnam, R. A. Huggins, and D. M. Mason, *This Journal*, **122**, 869 (1975).
- J. N. Michaels and C. G. Vayenas, *J. Catal.*, **85**, 477 (1984).
- B. C. Nguyen and D. M. Mason, Submitted to *This Journal*.

Toward an Understanding of the Adhesion of PVA-Deposited MP1 Phosphor DVST Screens

Gordon Sletmoe

Tektronix, Incorporated, Beaverton, Oregon 97077

ABSTRACT

MP1 is an MgO surface-modified version of in-house prepared P1 phosphor ($Zn_2SiO_4:Mn$). Reports of "loose phosphor" at CRT Test for a particular lot of this material prompted the present study. Before determining why adhesion varied from lot to lot, it first was necessary to discover the factors governing MP1 adhesion. Contrary to expectations, the surface magnesium was found to exist in two forms: (i) free MgO, which is bad for adhesion, and (ii) $MgSiO_3$, which is beneficial. Process modifications could, however, turn MgO to an advantage by first causing the dissolution of much of this material and then later the redepositing of a small but important portion of it at the phosphor/phosphor and phosphor/substrate interfaces.

In-house P1 phosphor has long been used in our direct-view storage tubes (DVST's) because of its high luminescent efficiency for low voltage bombardment (i.e., 130-300V). More recently, phosphor life was improved roughly four times, with minimal loss of efficiency, by coating the P1 with fine particle MgO, followed by subsequent firing in air at 800°C. This temperature was thought to be high enough to cause chemical combina-

tion of the coating with the underlying silicate material of the P1, while not degrading the basic crystalline properties of the P1 structure. The morphology of the underlying P1 structure as well as that of the magnesium-rich surface nodules are apparent in Fig. 1.

Because of the low voltage operation, DVST screens are not aluminized but rely on an indium-tin oxide (ITO) coating on the glass (together with conductive collectors)

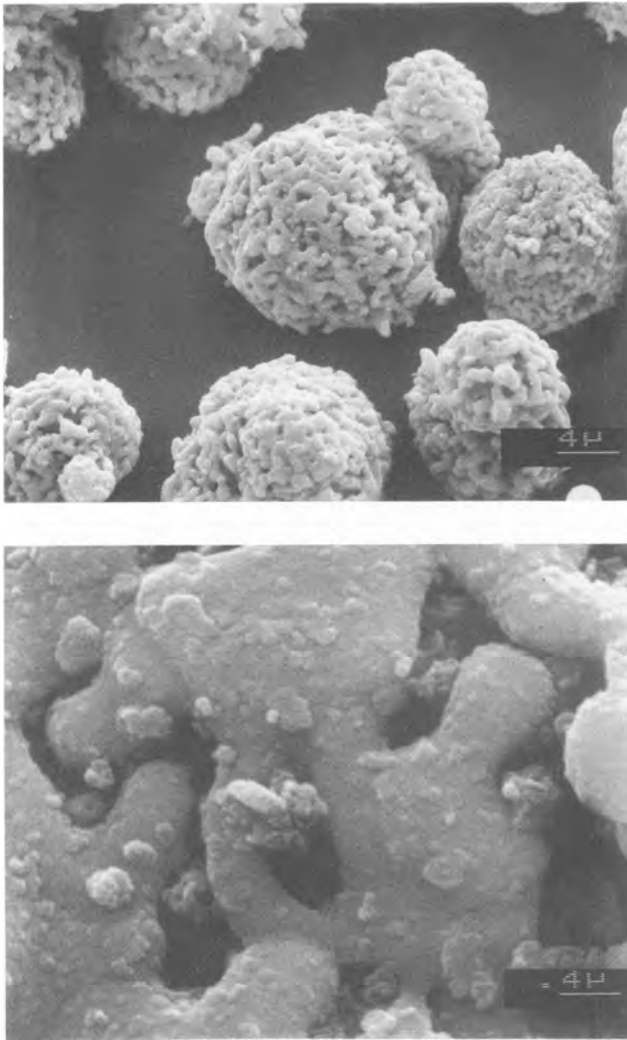


Fig. 1. SEM photographs of MP1 phosphor particles. Figure 1b (bottom) is a ten times enlargement of the center of Fig. 1a (top).

to maintain the phosphor potential and to collect secondary electrons. Without an aluminum overcoat, individual phosphor grains experience significant coulombic attraction under certain operating conditions, as when the nearby wall bands are at a potential of +150V and the screen is suddenly switched to +300V.

To prevent phosphor from covering the collector dots, the polyvinyl alcohol/ammonium dichromate (PVA/AD) photodeposition process is used for depositing phosphor. Exposure is through the glass, with the collectors serving as their own photomask. A slurry version of this process is used to prepare the devices under study. The slurry, consisting of phosphor suspended in a solution of PVA and AD in a mixture of water and an organic solvent, is settled for 20 min before exposure. This permits most of the phosphor to settle to the bottom of the fluid. After exposure through the glass, a controlled fraction of the phosphor is immobilized by the gelled PVA, while the remainder may be decanted off. Remaining unreacted material is then removed by extensive water rinsing in the spray rinser. Finally, the screen is dried and then sent on for bakeout.

In the case of spherically curved screens (as with the 19 and 25 in. devices), slurry depth—and hence ultimate phosphor loading—is kept uniform by the centrifugal effect of slow rotation of the screens during the settling and exposure steps.

Experimental

During the initial phase of this project, Production Engineering had developed a "blow-off" type of adhesion tester, the results of which correlated well with loose

phosphor at test. This would allow the evaluation of adhesion on coated face plates rather than on completed CRT's, thereby greatly increasing the number of tests which could be evaluated. It was a simple arrangement of a glass tube positioned at a fixed distance from the substrate under test. Dry nitrogen flow rate was controlled by a variable pressure regulator. Pressure was advanced in a regulated manner until a massive blow off was experienced. With an arbitrary adhesion value of 10 units, the standard deviation was of the order of 1 unit. If ten samples of the same type were measured, the uncertainty of the mean value at the 95% confidence level would be $\pm 2/3$ of a unit.

Now the most interesting findings of this study pertained to the complex interaction between the deposition process and the surface composition of the phosphors. Before discussing this, however, let us first consider some information concerning the influence of substrate type as well as phosphor particle size upon adhesion.

Figure 2 depicts several adhesion effects related to the substrate. The production problem was experienced on ITO-coated, curved 19 in. screens (with a relatively rough, stippled surface). For comparison the adhesion of the same material (Lot no. 18A) on other substrates is shown. Also shown is how these data compare to the adhesion of another lot of material (Lot no. B17). To obtain the 19 in. data, two panels were specially modified to have four different kinds of surfaces on the same panel (i.e., naturally stippled and specially smoothed, both coated by ITO as well as uncoated). By repeated deposition of phosphor, measurement of adhesion, removal of phosphor, and redeposition, etc., a fairly strong and internally consistent data base was built up. For convenience in this and most subsequent adhesion experiments, the normal collector dots were omitted.

The greatest adhesion difference here was that between curved 19 in. screens and flat 5 in. screens, regardless of surface coating or roughness. A second significant, although less striking, observation was that adhesion was better to specially polished 19 in. screens as compared to those with the regular texture. Whereas ITO vs. uncoated had little effect on 19 in. targets or with Lot no. B17 on 5 in. targets, there was a substantial ITO effect for Lot no. 18A on 5 in. screens.

The most plausible explanation for this data is thought to be (i) that smooth substrates are more favorable than rough, (ii) Lot no. 18A is generally better adhering than Lot no. B17, and finally, (iii) although the process was held as constant as possible between flat and curved substrates, there were unavoidable differences which led to the improved adhesion of the flat screens. Some of the experimentation to be discussed was aimed at discovering which process variables were responsible for this. More important to the remainder of the program is that the adhesion of various lots of MP1 on flat screens generally paralleled their adhesion on curved screens. This

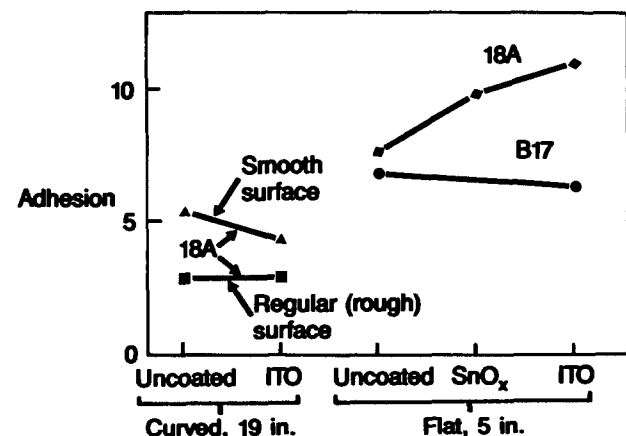


Fig. 2. Adhesion vs. CRT type, surface coating, and phosphor lot

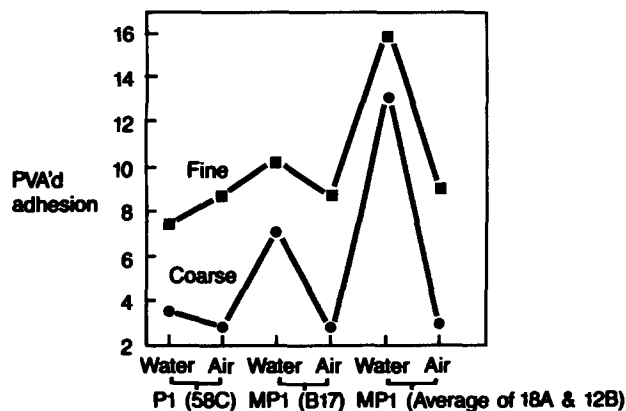


Fig. 3. Adhesion vs. particle size for various lots and treatments

made it possible to use the more convenient flat screens for the remaining experimentation.

Figure 3 shows some results due primarily to the nature of the phosphor. Lot no. B17 was the poorly adhering lot of MP1 noted in Fig. 2. P1 (Lot no. 58C) was the lot of P1 phosphor used in the preparation of this MP1. Because the MP1 Lots no. 18A and 12B exhibited nearly identical adhesion behavior, their results were combined in this figure.

The three groups of materials were each fractionated by two techniques: (i) sedimentation in water, and (ii) air classification in a commercial air fractionator. In every case, the fines had better adhesion than the coarse material. Although of interest, this is of little practical value, as fines do not generally have the efficiency or other performance characteristics required. Especially with the MP1's, note also the regular difference between the water-settled and the corresponding air-fractionated samples. Now as determined from particle size analyses of the various fractions, air fractionation was found to be much more efficient than water settling. Thus, the better adhesion of water-settled particles was not because they were finer than the air-classified material. The most likely reason for the better adhesion of water fractionated MP1's is that their surfaces were favorably modified by this exposure to water. This will be examined in detail below.

Although the PVA process is of primary interest to this work, it was possible to gain valuable insight from the following nonstandard screen deposition technique. Large beakers or battery jars were affixed with side arms and stopcocks near the base, to draw off fluid when required. Clean, flat face plates were then placed horizontally near the bottoms of the containers (but above the location of the drain line). After the covering of the substrates to be coated to a depth of several inches with the fluid of interest (the selection of fluids is discussed below), a phosphor slurry in the same fluid was uniformly sprinkled into the container. Phosphor was then allowed to settle onto the face plate. After suitable settling time, fluid was carefully drained off, leaving only a thin meniscus of fluid on the horizontal plate. This was then evaporated to dryness before removing the coated target.

In one test, we utilized an organic solvent, methyl ethyl ketone (MEK), as the settling fluid, to avoid hydrolysis of the magnesium surface coating. In further experiments, DI water was used as the settling medium, allowing for the possibility of simple hydrolysis, without the influence of acidity or residual chromium (as the AD) or organic residues (from the PVA). To eliminate extraneous variables, targets processed as above were given the same PVA bakeout treatment and subsequent warm/dry handling after bake until adhesion measurement was carried out, as were the standard PVA targets.

Figure 4 compares the adhesion of two lots of MP1, settled in the two fluids just described as well as deposited by the standard PVA process. Several conclusions may be drawn. Water settling results in substantially more adhesion than does MEK settling. The most probable cause

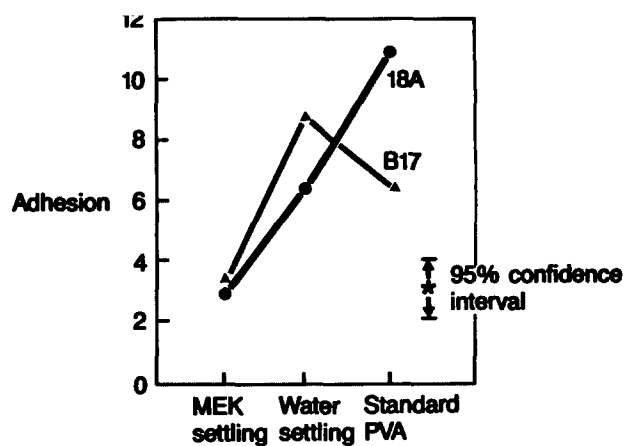


Fig. 4. Adhesion vs. settling technique for two phosphor lots

of this is related to hydrolysis of the magnesium surface coating by the water. Also, note the substantial improvement for Lot no. 18A but not for Lot no. B17 in going from water settling to the PVA reaction. Additional experimentation was called for to understand this.

With the settling technique just described, we could incorporate the PVA chemicals—one at a time—into the aqueous system, to see if we could trace adhesion differences to any one factor. Results from such work are shown in Fig. 5. Here, we see minor differences resulting from the addition of AD or straight PVA. For reference, the standard PVA data are also given. The most important result here was the great improvement resulting from the addition of acetic acid (HAc). HAc was utilized in this case as a prototype of a weak acid such as AD but without any residual chromium.

The great improvement with HAc led us to try to capitalize on this by incorporating HAc in the PVA slurry. Results were disappointing; there was only slight improvement in adhesion of the PVA samples upon addition of HAc. To understand this, we must first consider the acid/base reaction occurring between the HAc and the phosphor surface, as illustrated in the following pH study.

The pH of a solution of 1 ml glacial acetic acid in 100 ml water was about 2.7. When 10g of an MP1 were added to this solution (with continuous stirring), the pH jumped almost instantly to 6.93. Over the first 20 min, it further rose to a value of 7.19, which was close to the value of 7.22 at which it leveled off. Thus, not only was virtually all of the HAc neutralized by the MP1 phosphor, but the time required for this was within the time frame available during normal PVA processing.

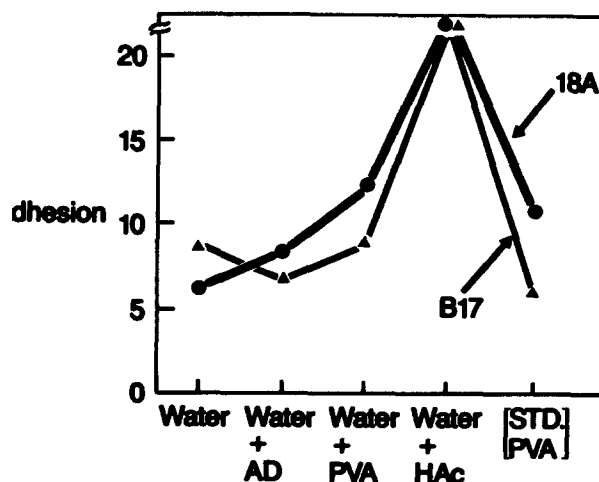
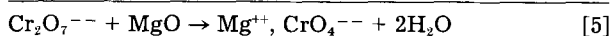
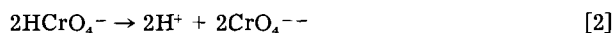


Fig. 5. Adhesion as a function of additive type, in modified water settling.

Assuming this reaction resulted in the formation of soluble ions such as Mg^{++} (an assumption amply validated by the results to follow), then the fate of these soluble ions is thought to explain the observed differences between the two systems.

In the PVA system, most of the soluble ions generated in the above acid/base reaction are thought to be rinsed away during the extensive spray rinse step. In the water settling process, however, there is no analogous rinse step. Instead, whatever ions remain in the meniscus of fluid on the plate after draining are allowed to evaporate to dryness on the settled phosphor coating. Upon subsequent bakeout, Mg^{++} and Ac^- or OH^- ions would react to leave a residue of MgO . Because of capillary effects during evaporation, this material would tend to be located at the interstices between, phosphor/phosphor and phosphor/substrate—right where it would be most effective in promoting adhesion of the subsequent dry film.

At this point, it seemed possible that the various lots of MP1 owed their differing adhesion tendencies to variable concentrations and/or reactivity of magnesium compounds on their surfaces. This led us to attempt to render all of the MP1 lots the same by etching with HAc. This effort was unsuccessful, most likely because HAc is too reactive, attacking the P1 underlayer as well as the magnesium-rich surface coating. This led to the use of the more gentle AD to etch these materials. Before looking at the results of this, let us first consider why AD should react with MgO at all



As shown in Eq. [1], chromate ion from the AD hydrolyzes to bichromate ion. The equilibrium constant is of the order of unity. Bichromate ion then can dissociate to protons plus chromate ion, as in Eq. [2]. At the same time, as shown in Eq. [3] and [4], MgO hydrolyzes to magnesium hydroxide, which, in turn, sparingly dissociates to magnesium and hydroxide ions. The net effect is as shown in Eq. [5]. Because the dissociation constant of water is many orders of magnitude less than the dissociation constant of chromate ion or the solubility constant of magnesium hydroxide, Eq. [5] is shifted far to the right.

In practice, with finely divided MgO in a typical PVA/AD slurry, this reaction will go nearly to completion in the 20 min settling time employed. This has been observed in pH vs. time experiments similar to the one described above. By way of comparison, reagent $MgSiO_3$ powder is scarcely attacked by AD under these conditions (i.e., the slightly acidic pH caused by the AD remains unchanged, and there is a very low level of solubilized Mg^{++} in the reaction fluid).

Figure 6 illustrates the effect of processing upon residual magnesium levels. (All magnesium is reported here as MgO .) Starting with a typical level of 5.5 weight percent (w/o) on the incoming phosphor, roughly one-third of this is lost in preparing samples for MEK settling. Clearly, this fraction is loosely adhering and is of little value to subsequent adhesion. Additional MgO fails to survive water settling. Presumably, the removal of this loosely adhering or readily hydrolyzable material accounts for the improved adhesion of water-settled vs. MEK-settled targets. Additional MgO is lost in going to the PVA'd targets. Some or all of this increment is from solubilization by AD (as discussed above). Finally, etching of the MP1 with excess AD results in removal of still more MgO . The remainder is probably $MgSiO_3$.

Figure 7 shows the resulting adhesion by removing all of this loose as well as dissolvable MgO from a variety of lots of varying intrinsic performance. Points above and

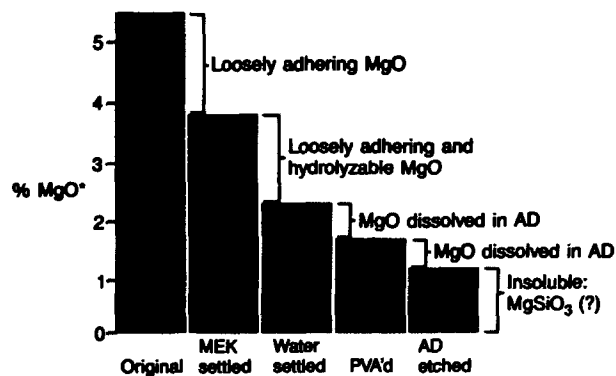


Fig. 6. Residual percentage of MgO as a function of MP1 treatment

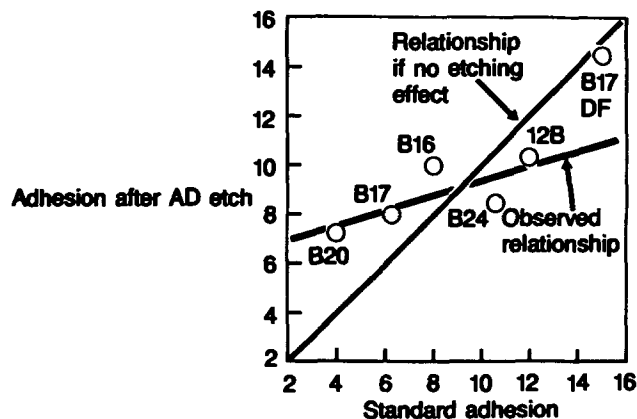


Fig. 7. The effect of AD etching upon adhesion of various MP1 lots

to the left of the diagonal benefited by this treatment, whereas points below and to the right were degraded. What was observed (except for the special case of Lot no. B17DF) was a leveling. Poorly adhering materials were helped while good adhering materials were degraded. This suggests that the principal difference in lots has to do with the amount and kind of loose and/or soluble MgO on the surface, whereas the underlying $MgSiO_3$ has the same adhesion in all cases. Lot no. B17DF was a refined version of the poorly adhering Lot no. B17. Here, presumably, a substantially higher fraction of the total magnesium had become chemically bound to the silicate structure. (Unfortunately, double firing degraded other performance characteristics, so this was not a practical solution. Nevertheless, it pointed in the right direction.)

To see if adhesion could be improved through PVA process optimization, the study represented by Fig. 8 was performed. The shaded area represents the somewhat reciprocal combination of exposure times and AD

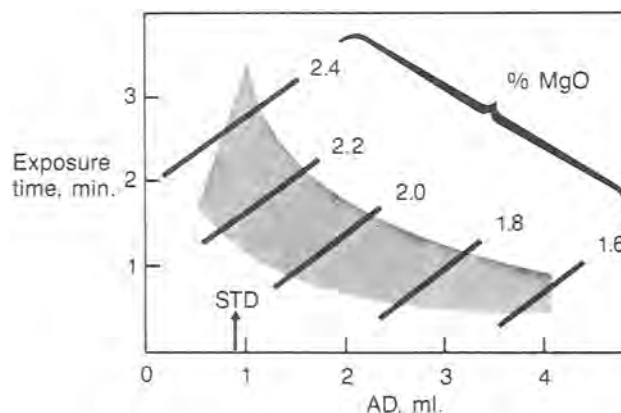


Fig. 8. Residual percentage of MgO and acceptable target weight envelope as a function of PVA variables.

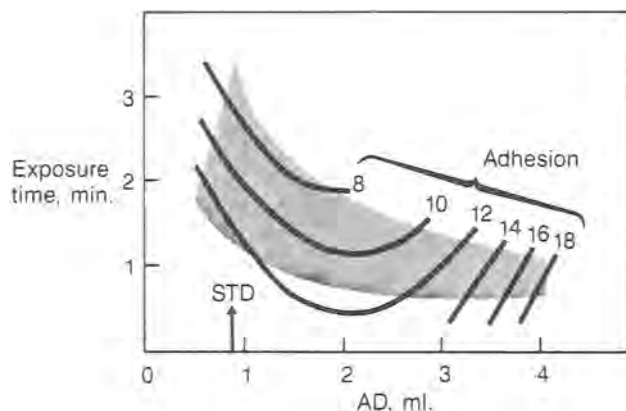


Fig. 9. Adhesion as a function of PVA variables

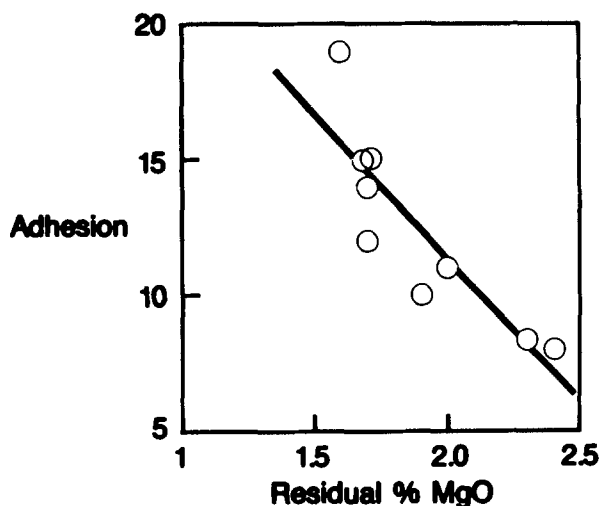


Fig. 10. Adhesion as a function of residual percentage of MgO

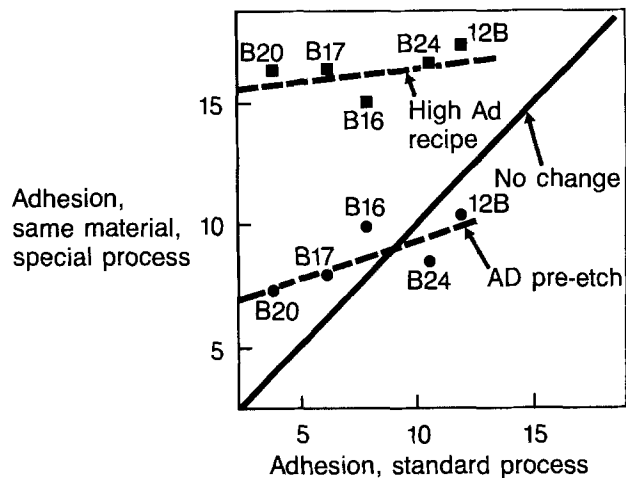
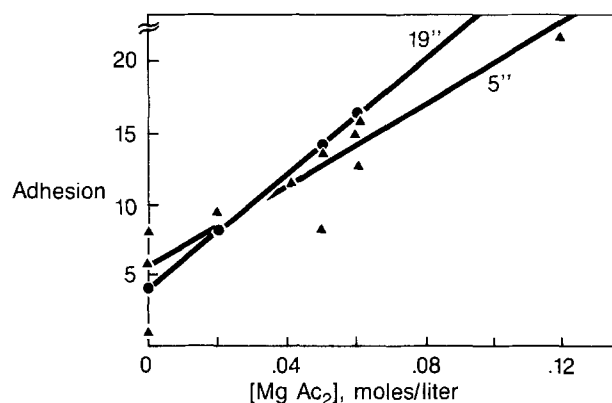
concentrations which yielded acceptable target weights per unit area. Screens within this "process window" would be expected to give us acceptable performance. Note the decreasing residual percentage of MgO with increased AD level. Figure 9 shows the results of this reduced percentage of MgO, where adhesion was dramatically improved. The individual data points of this array showed an excellent correlation of increasing adhesion *vs.* decreasing percentage of MgO, as shown in Fig. 10. An adverse consequence of the high AD recipe is increased residual chromium on the final target, which results in some loss of efficiency. This trade-off would have to be considered carefully in going to this new recipe.

Figure 11 is a composite, comparing the advantages of a high AD recipe to the removal in advance of MgO by AD etching. In both cases, we see a leveling effect for bad and good lots. In both cases, much of the loose and/or soluble MgO has been removed. Why, then, was the high AD recipe so much more beneficial to adhesion than the pre-etch? The best answer seems to be as follows.

1. Pre-etch removes most of the soluble magnesium, making all the samples roughly similar. Differences in amounts of unetchable MgSiO_3 account for the resulting adhesion differences.

2. The high AD recipe also has the effect of removing a substantial portion of the soluble magnesium, although not as completely as with the pre-etch treatment.

3. Unlike with the pre-etch, however, the solubilized ions are formed right in the PVA slurry. Whereas many of these ions are removed during the subsequent spray rinse step (hence the low residual percentage of MgO with this treatment), a small but important amount of

Fig. 11. The effect upon adhesion of the "high AD" recipe *vs.* AD etching of various MPI lots.Fig. 12. Adhesion improvement via postdeposition MgAc_2 soak

magnesium ions is left on the phosphor to dry in the interstices and subsequently to be converted on bakeout back to MgO. To this small but effectively located amount of MgO is attributed the improved adhesion of this group relative to the pre-etched samples.

4. But why does extra AD improve adhesion, whereas added HAc in the PVA system (as discussed earlier) resulted in only slight adhesion improvement? The answer seems to be related to the fact that, in the high AD recipe, extra chromium is bound by the gelled PVA (as evidenced by high residual chromium levels in the baked targets). This bound chromium electrostatically holds an equivalent amount of Mg^{++} ions, preventing them from being rinsed away. Although small on a percentage weight basis, this strategically placed amount of material has a profound effect upon adhesion.

In support of this hypothesis. Fig. 12 indicates a group of targets, both 5 and 19 in., which were prepared in the normal manner. However, before bakeout they were soaked briefly in magnesium acetate solutions of the indicated concentration. After drying and bakeout, the magnesium acetate would have been converted to MgO. SEM studies at the highest MgAc_2 concentrations clearly showed residual MgO "glue" at the interfaces. Intermediate levels of this treatment caused minimal negative impact on luminescent efficiency, while substantially improving adhesion.

Conclusions

1. The magnesium in MPI is present in two forms: (i) MgO—soluble in AD; much of it loosely adhering, and (ii) MgSiO_3 (or related silicate)—insoluble in AD; tenaciously adhering to the phosphor.

2. Adhesion is favored by: (i) removal of MgO, (ii) the presence of MgSiO_3 , (iii) the formation of Mg deposits at

the phosphor/phosphor and phosphor/substrate interfaces, (iv), small particle size, and (v) smooth substrate.

3. Processes to improve adhesion include (i) high AD recipe in the PVA process, and (ii) postdeposition soaking in MgAc_2 solution. (In both cases, there is some fall off in efficiency with improved adhesion.)

4. Better phosphor lots presumably have less loosely adhering and/or soluble MgO deposits. This is achieved by more rigorous MgO firing conditions. (Again, care must be taken so as not to degrade efficiency.)

Acknowledgment

Many thanks go to Paula Larson for her invaluable contribution to the success of this project.

Manuscript submitted May 29, 1985; revised manuscript received Aug. 10, 1985. This was Paper 447 presented at the Toronto, Ontario, Canada, Meeting of the Society, May 12-17, 1985.

Tektronix, Incorporated, assisted in meeting the publication costs of this article.

Photoelectrochemical Properties of Ferrites with the Spinel Structure

L. G. J. de Haart and G. Blasse

Department of Solid State Chemistry, Physics Laboratory, Utrecht University, 3508 TA Utrecht, The Netherlands

ABSTRACT

The diffuse reflection spectra and the photoelectrochemical properties of the ferrites ZnFe_2O_4 , MgFe_2O_4 , and $\text{Li}_{0.5}\text{Fe}_{2.5}\text{O}_4$ with spinel structure are presented. A marked difference between the reflection spectra and the photocurrent action spectra is discussed. The onset wavelength of the photocurrent lies at about 550 nm. Steady-state photocurrents are severely limited by a relatively low absorptivity in the visible region and by surface recombination at low potentials. From an admittance spectra analysis, a value for the flatband potential of ZnFe_2O_4 was obtained, *viz.*, -0.5V vs. SCE in 1M NaOH.

The use of n-type semiconducting materials in photoelectrochemical (PEC) cells for solar energy conversion has been studied extensively in the last decade (1). In this period, much attention has been paid to iron(III)-oxide, $\alpha\text{-Fe}_2\text{O}_3$. With its bandgap of 2.2 eV, $\alpha\text{-Fe}_2\text{O}_3$ is quite suitable for solar energy conversion (2-12).

Stoichiometric $\alpha\text{-Fe}_2\text{O}_3$ is an insulator. It can be made n-type semiconducting by doping with higher valent ions. Shinar and Kennedy (10) studied extensively the way in which the performance of doped $\alpha\text{-Fe}_2\text{O}_3$ anodes depends on the nature and the concentration of the dopant. Doping with lower valent ions can lead to p-type semiconducting $\alpha\text{-Fe}_2\text{O}_3$, which acts as a photocathode in a PEC cell (13, 14).

$\alpha\text{-Fe}_2\text{O}_3$ can also be made n-type semiconducting by reduction. However, reduction treatments result mainly in the formation of a conducting Fe_3O_4 layer on the surface of the electrode. It has been proposed that recombination occurs in this layer (10, 15). This inhomogeneity after the reduction treatment is assumed to be due to the inability of the corundum structure ($\alpha\text{-Fe}_2\text{O}_3$) to tolerate large concentrations of spinel (Fe_3O_4) inclusions [Ref. (15)].

In view of this, we studied the photoelectrochemical properties of ferrites with the spinel structure. Many of these ferrites show n-type semiconducting behavior. Since these ferrites and Fe_3O_4 have the same crystal structure, they can form solid solutions. This prevents segregation on the surface.

The spinels $\text{CO}_{0.90}\text{Fe}_{2.10}\text{O}_4$ and $\text{CoFe}_{1.86}\text{Ti}_{0.14}\text{O}_4$ were investigated for use as photoanodes by Archer *et al.* (16). These materials show an almost uniform spectral response in the wavelength region from 400 to 760 nm. The quantum yield is, however, very low. A large bias had to be applied to obtain significant steady-state photoresponse.

For our investigations, we selected the spinels ZnFe_2O_4 , MgFe_2O_4 , and $\text{Li}_{0.5}\text{Fe}_{2.5}\text{O}_4$. The Zn^{2+} ion has $3d^{10}$ configuration, and the Mg^{2+} ion and the Li^+ ion both have noble gas configuration. These ions do not give rise, therefore, to optical absorption in the near-UV and visible regions. Absorption and photoeffects observed in these spectral regions must then be accounted for by transitions in which the iron ions are involved. In this way, a comparison can be made with $\alpha\text{-Fe}_2\text{O}_3$.

ZnFe_2O_4 has the normal spinel structure (17), $\text{Li}_{0.5}\text{Fe}_{2.5}\text{O}_4$ is an inverse spinel (18), and in MgFe_2O_4 the degree of inversion is around 0.9 (19), depending on the quenching temperature. The occupation of the tetrahedral and octahedral positions in the spinel structure for these compounds is thus: $\text{Zn}[\text{Fe}_2]\text{O}_4$, $\text{Fe}[\text{Li}_{0.5}\text{Fe}_{1.5}]\text{O}_4$, and $\text{Mg}_{0.1}\text{Fe}_{0.9}[\text{Mg}_{0.9}\text{Fe}_{1.1}]\text{O}_4$. In this sequence, there is a decrease in the number of iron ions on the octahedral positions. This enables us to investigate the effect of this occupancy on the photoelectrochemical properties.

Experimental

Samples were prepared by usual ceramic techniques using high purity oxides and carbonates as starting materials. Firing was performed between 1050° and 1200°C in air.

Samples were checked by x-ray powder diffraction. Diffuse reflection spectra were recorded at room temperature on a Perkin-Elmer Lambda 7 UV/VIS spectrophotometer.

For the preparation of the electrodes, stoichiometric amounts of the thoroughly mixed oxides and/or carbonates were pre-fired at 600°-700°C in air. After regrinding, the mixture was pelletized at 120-150 kg/cm². The pellets were sintered at 1150° ($\text{Li}_{0.5}\text{Fe}_{2.5}\text{O}_4$), at 1200° (ZnFe_2O_4), and at 1270°C (MgFe_2O_4) for 3-4h in air and cooled slowly to room temperature. The density ratio of the pellets was about 90% for the MgFe_2O_4 samples and more than 95% for the ZnFe_2O_4 and $\text{Li}_{0.5}\text{Fe}_{2.5}\text{O}_4$ samples. The surfaces of the pellets were polished using emery paper (grain size: 40 μm).

By heating the pellets in a stream of nitrogen at around 700°C for 2-2.5h, they became n-type conducting. The resistivities of the pellets (~ 1 mm thick) dropped to 1-2 k Ω for the $\text{Li}_{0.5}\text{Fe}_{2.5}\text{O}_4$ pellets, to 3-5 k Ω for the ZnFe_2O_4 pellets, and 8-10 k Ω for the MgFe_2O_4 pellets. A silver paste (Degussa, leitsilber) was applied to the back of each pellet to provide electrical contact.

The surfaces of the electrodes were examined for their structure and composition with a Cambridge Stereo Scan 150 electron microscope, equipped with an energy dispersive elementary analysis system (Link Systems, Cambridge, England).

The PEC cell arrangement and photoelectrochemical measurement procedures for steady-state conditions have been described previously (20). All photocurrent densities have been corrected for variations in the light intensity by normalizing them to the number of photons at $\lambda = 470$ nm. Current-voltage scans with hand-chopped illumination were recorded on a Bryans X-Y recorder 29000 A3. Electrode potentials are referred to the saturated calomel electrode (SCE). All photoelectrochemical measurements were performed in 1M NaOH.

The admittance spectra of a PEC cell with a ZnFe_2O_4 anode were studied in the frequency range from 25 mHz to 10 kHz using a Solartron 1172 frequency response analyzer. The ac signal amplitude was kept at 20 mV (rms). Representative admittance spectra were analyzed using a computer program for nonlinear least squares fitting to complex data (21). This procedure has been applied before to analyze admittance spectra of PEC cells with TiO_2 and SrTiO_3 anodes (22, 23).

Results and Discussion

Diffuse reflection spectra.—In Fig. 1, the diffuse reflection spectra of the composition $\text{ZnFe}_{0.02}\text{Al}_{1.98}\text{O}_4$ and of the compound ZnFe_2O_4 are shown. The spectrum of $\text{ZnFe}_{0.02}\text{Al}_{1.98}\text{O}_4$ shows an intense absorption band around 275 nm. Around 500 nm, a shoulder can be observed. Going from the composition $\text{ZnFe}_{0.02}\text{Al}_{1.98}\text{O}_4$ to ZnFe_2O_4 , a marked increase of the absorption strength in the short-wavelength part of the visible region is observed. At about 800 nm, a separate band is observed.

The Fe^{3+} ion has $3d^5$ configuration, which in an octahedral as well as a tetrahedral crystal field gives rise to a 6A_1 ground state. Since this is the only sextet state, all crystal-field (CF) transitions are both spin and, octahedral symmetry, parity forbidden. In tetrahedral symmetry, the latter selection rule is slightly relaxed. Nevertheless, these transitions are extremely weak.

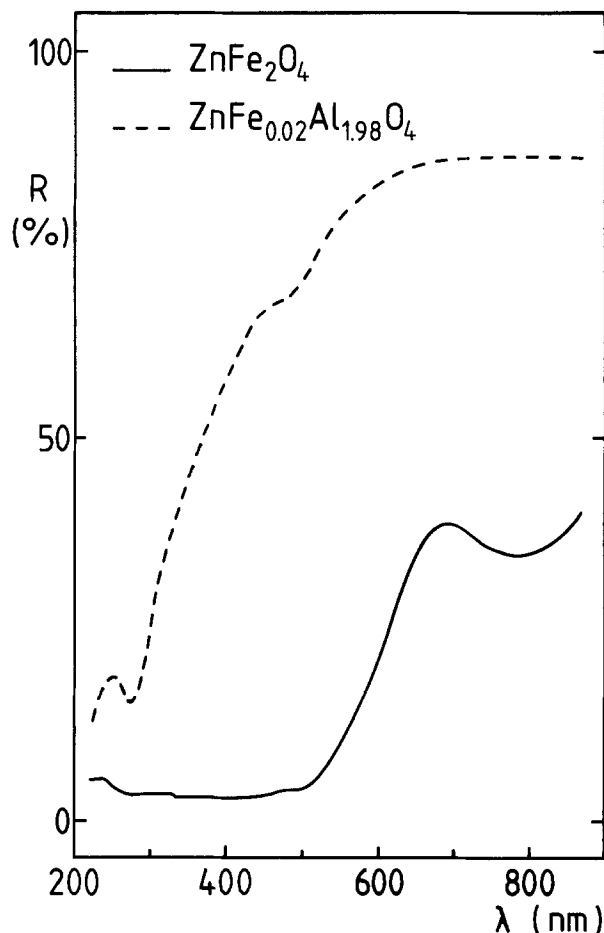


Fig. 1. Diffuse reflection spectra of $\text{ZnFe}_{0.02}\text{Al}_{1.98}\text{O}_4$ and of ZnFe_2O_4 .

The shoulder around 500 nm in the spectrum of $\text{ZnFe}_{0.02}\text{Al}_{1.98}\text{O}_4$ can be assigned to the CF transition ${}^6A_1 \rightarrow {}^4A_1$, ${}^4E(G)$ on octahedral Fe^{3+} (24-26). The band around 800 nm in the spectrum of ZnFe_2O_4 can be assigned to the CF transition ${}^6A_1 \rightarrow {}^4T_1(4G)$ on octahedral Fe^{3+} (24). This CF transition is not observed in the spectrum of $\text{ZnFe}_{0.02}\text{Al}_{1.98}\text{O}_4$. The position of this transition depends strongly on the crystal-field strength. With increasing crystal field, the transition shifts to lower energy. In the case of $\text{ZnFe}_{0.02}\text{Al}_{1.98}\text{O}_4$, the Fe^{3+} ion occupies a relatively small lattice site, resulting in a stronger crystal field than in ZnFe_2O_4 . For $\text{ZnFe}_{0.02}\text{Al}_{1.98}\text{O}_4$, the CF transition ${}^6A_1 \rightarrow {}^4T_1$ is expected at a lower energy, which is beyond the limit of the instrument used.

In the wavelength region between 300 and 450 nm, additional CF transitions on octahedral Fe^{3+} are expected. In the spectrum of $\text{ZnFe}_{0.02}\text{Al}_{1.98}\text{O}_4$, these are, however, masked by the tail of the strong absorption band around 275 nm. This band must be assigned to the $\text{O}^{2-} \rightarrow \text{Fe}^{3+}$ charge transfer (CT) transition. In $\text{Al}_2\text{O}_3:\text{Fe}^{3+}$, this CT transition is situated around 260 nm (27).

The spectrum of ZnFe_2O_4 shows a very strong absorption in the wavelength region from 200 to 500 nm compared to the absorptivity of the CF transitions. Around 300 nm, this is not unexpected, because the $\text{O}^{2-} \rightarrow \text{Fe}^{3+}$ CT transition is situated in this region. However, neither this CT transition nor the CF transitions can account for the intensity of the absorption in the wavelength region from 350 to about 500 nm. It should be noted that the absorption strength decreases in the region from 200 to 500 nm (28), a fact which the present type of spectra does not reveal.

The diffuse reflection spectrum in the visible region of ZnFe_2O_4 is again shown in Fig. 2, now together with the diffuse reflection spectra of MgFe_2O_4 and $\text{Li}_{0.5}\text{Fe}_{2.5}\text{O}_4$. Both latter compounds show the same relatively strong absorption as ZnFe_2O_4 in the region from 350 to about 500 nm. Around 620 nm, shoulders can be observed in the spectra of MgFe_2O_4 and $\text{Li}_{0.5}\text{Fe}_{2.5}\text{O}_4$. For these two com-

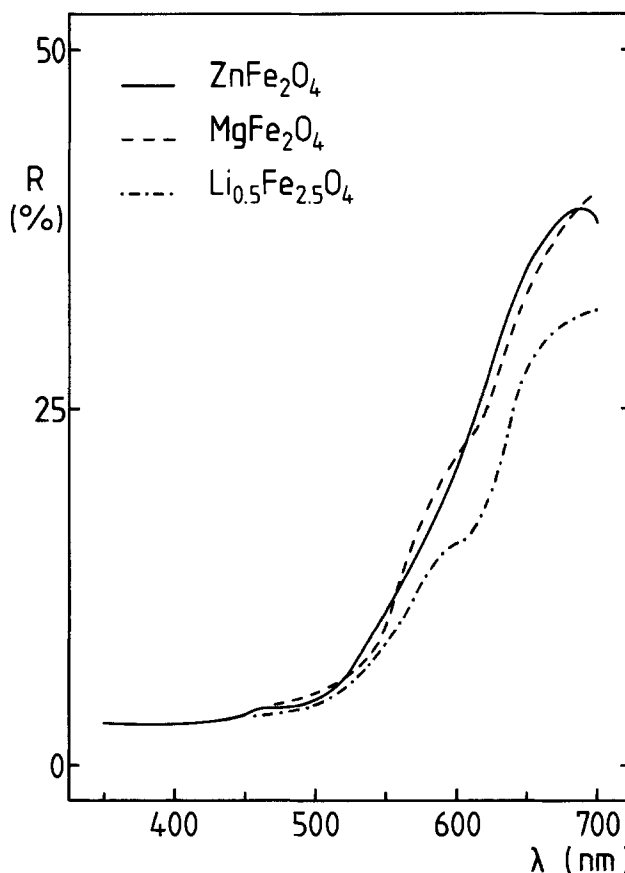


Fig. 2. Diffuse reflection spectra in the visible region of ZnFe_2O_4 , of MgFe_2O_4 , and of $\text{Li}_{0.5}\text{Fe}_{2.5}\text{O}_4$.

pounds, containing Fe^{3+} on tetrahedral sites, these shoulders can be assigned to the CF transition ${}^6A_1 \rightarrow {}^4T_1(4G)$ on tetrahedral Fe^{3+} (25).

We will return to the strong absorption observed in the region from 350 to 500 nm below in relation with the photocurrent action spectra observed for these ferrites.

Photocurrent measurements.—The steady-state photocurrent action spectra of the ferrites are shown in Fig. 3. The photocurrents start around 550 nm, but remain rather low in the visible region. Only with UV irradiation, a reasonable efficiency is obtained. For ZnFe_2O_4 with $\lambda = 300$ nm and at $V = +0.5\text{V}$, the quantum efficiency amounts approximately 25%. The spectra resemble closely the photocurrent action spectra reported for $\alpha\text{-Fe}_2\text{O}_3$ (2, 3, 6, 10). Note that for the three ferrites the photocurrent action spectra are similar (see Fig. 3). From this we conclude that the photoeffects occur on the Fe^{3+} ions on octahedral sites. This makes it tempting to relate the decrease in efficiency, observed in Fig. 3 going from ZnFe_2O_4 to MgFe_2O_4 , to the number of Fe^{3+} ions on octahedral sites in these spinels. We will show below, that care has to be taken with such an interpretation.

A comparison between the photocurrent action spectra and the diffuse reflection spectra shows, that there is a great difference between these spectra in the wavelength region from 350 to 500 nm. This will be discussed below.

In Fig. 4 a current-voltage scan is shown for a $\text{Li}_{0.5}\text{Fe}_{2.5}\text{O}_4$ anode. The insert shows the low potential part scanned with a 10-fold enlargement of the current axis. At these low potentials the photocurrents are highly transient. The transients near -0.3V are still anodic. This indicates that the flatband potential is situated at a more cathodic potential.

Significant steady-state photocurrent response starts only at $+0.3\text{V}$. Above this potential, the transients decrease and above $+0.6\text{V}$ they vanish. The dark current starts to increase steeply at $+0.6\text{V}$ due to oxygen evolution. After long-term polarization at these high anodic potentials in the dark, gas bubbles could be observed on the electrode surface. The same has been observed for $\alpha\text{-Fe}_2\text{O}_3$ electrodes (2, 4, 7).

Figure 5 shows the steady-state photocurrent-voltage curves for the three ferrites, measured with monochromatic irradiation at 300 nm. The curves measured at 380

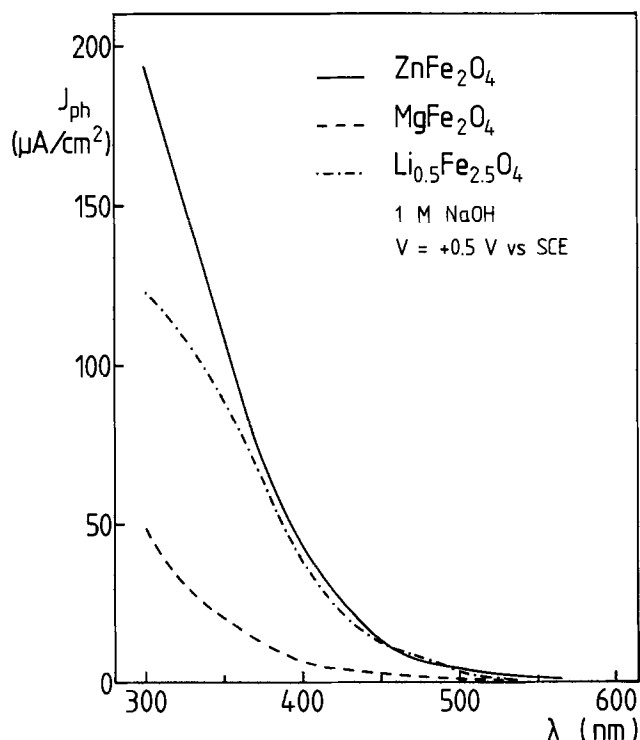


Fig. 3. Variation of the steady-state photocurrent density with irradiation wavelength for ZnFe_2O_4 , MgFe_2O_4 , and $\text{Li}_{0.5}\text{Fe}_{2.5}\text{O}_4$.

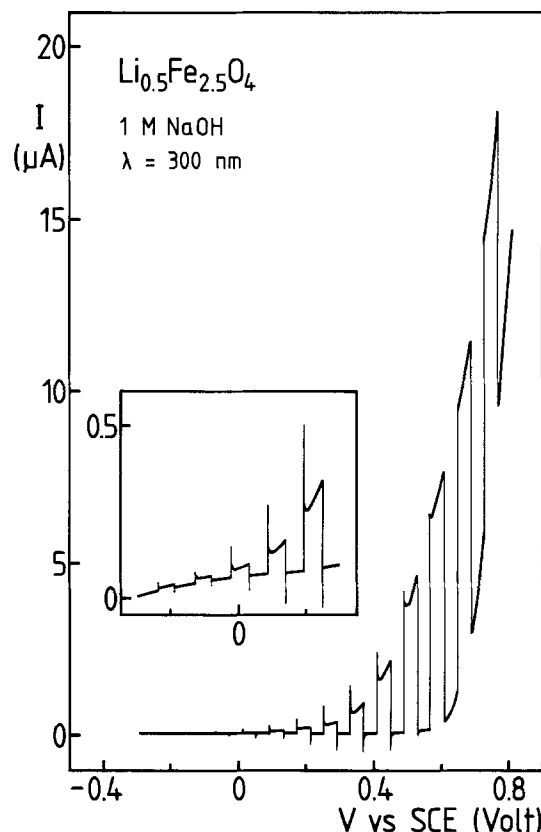


Fig. 4. Photocurrent-voltage scan obtained for a $\text{Li}_{0.5}\text{Fe}_{2.5}\text{O}_4$ anode by scanning from left to right at 0.66 mV/s with hand-chopped irradiation ($\lambda = 300\text{ nm}$) at 1 min intervals. The insert shows the low potential region scanned with a tenfold increase in the current axis.

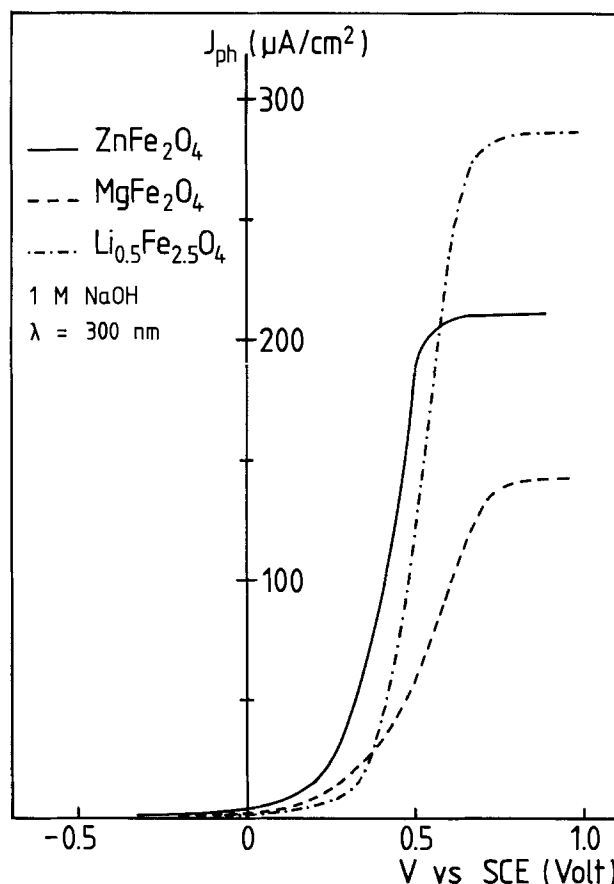


Fig. 5. Variation of the steady-state photocurrent density with applied potential (vs. SCE) for ZnFe_2O_4 , MgFe_2O_4 , and $\text{Li}_{0.5}\text{Fe}_{2.5}\text{O}_4$.

and 460 nm show the same voltage dependence. In the potential region from -0.3V to about $+0.3\text{V}$ a low photocurrent is observed, which increases very slowly. Above $+0.3\text{V}$, the photocurrent increases steeply with increasing potential and tends to reach saturation above $+0.7\text{V}$. For some electrodes, however, the photocurrent showed a maximum value around $+0.7\text{V}$ followed by a fast decrease with increasing potential. This feature was also observed for $\alpha\text{-Fe}_2\text{O}_3$, by Ono *et al.* (29).

Photocurrent-voltage curves reported for $\alpha\text{-Fe}_2\text{O}_3$ (2, 5, 7, 9, 12) show a similar behavior as reported here for the ferrites. In several cases, however, the onset potential of the photocurrent (*i.e.*, the potential at which the photocurrent starts to rise steeply) was situated at more cathodic potentials, although the measurements were performed in the same electrolyte (2, 5, 12). Transients were also observed for $\alpha\text{-Fe}_2\text{O}_3$ electrodes (4, 9, 12, 30). These features, as well as the low steady-state photocurrent in the potential region from -0.3 to $+0.3\text{V}$, can be explained in terms of surface recombination or back reaction of the photogenerated species (30). Oxygen (or a hydroxyl radical) produced by the photogenerated holes produces a back reaction and a cathodic current component by reacting with an electron at the surface. This is equivalent to a surface electron-hole recombination (31). This cathodic current component decreases as the potential is made more positive (30).

The steady-state photocurrent in the saturation region is higher for the $\text{Li}_{0.5}\text{Fe}_{2.5}\text{O}_4$ anode than for the ZnFe_2O_4 anode. This shows that care has to be taken in relating the observed efficiency to the number of Fe^{3+} ions on octahedral sites in these spinels, as the photocurrent action spectra attempt to do.

Capacitance measurements.—The admittance spectra of the PEC cell with the ZnFe_2O_4 anode were measured in the potential region from -0.4 to $+1.0\text{V}$ at regular intervals. At high anodic potentials ($V \geq +0.6\text{V}$, high dark currents were observed and gas evolution on the electrode surface could be observed, similar to the behavior of the $\text{Li}_{0.5}\text{Fe}_{2.5}\text{O}_4$ anode at these potentials (see Fig. 4). The results of the analysis of the ac response data obtained at these potentials were not reliable. We limited the analysis, therefore, to the data obtained between -0.4 and $+0.4\text{V}$. In this potential region, the dark current was less than $1 \mu\text{A}/\text{cm}^2$. The admittance spectra measured between -0.4 and $+0.4\text{V}$ could all be accurately fitted to the equivalent circuit given in Fig. 6. This circuit can be represented by $Q_{\text{SC}}R_{\text{F}}PC_{\text{A}}R_{\text{A}}SPQ_{\text{B}}R_{\text{B}}PSR_{\text{S}}S$, following the notation presented in Ref. (21-23) (P stands for parallel and S for series). The Q element represents a constant-phase-angle (CPA) admittance of the form (21).

$$Y_Q = k_j (i\omega)^\alpha \quad [1]$$

For $\alpha = 1$, this Q element represents the admittance of a capacitor, while for $\alpha = 0$ this element reduced to a resistor. The Q element is usually attributed to current inhomogeneities (32).

The equivalent circuit of Fig. 6 is adopted from the one Tomkiewicz (33) used to model the n-TiO₂/electrolyte in-

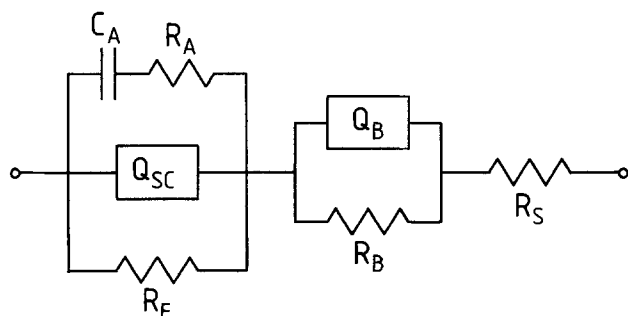


Fig. 6. The equivalent circuit to which the ac response data obtained for the PEC cell with a ZnFe_2O_4 anode were fitted. The symbols are explained in the text.

terface. We inserted the branch $Q_{\text{B}}R_{\text{B}}P$ and replaced C_{SC} by a Q_{SC} element. Dare-Edwards *et al.* (12) used the circuit after Tomkiewicz to fit the ac response data of a PEC cell with a Fe_2O_3 electrode. A circuit similar to the one we used, with capacitances and Q elements exchanged, was used by 't Lam *et al.* (22) to model the ac response data of a PEC cell with a TiO_2 anode.

In the branch $Q_{\text{B}}R_{\text{B}}P$, the Q element approaches the behavior of a pure capacitance ($0.91 \leq \alpha_{\text{B}} \leq 0.98$). The values of the elements in the part $Q_{\text{B}}R_{\text{B}}P R_{\text{S}}S$ of the equivalent circuit are independent of the applied potential. This part can be related to processes in the bulk of the semiconductor and in the electrolyte (22, 23).

The other part of the circuit, $Q_{\text{SC}}R_{\text{F}}PC_{\text{A}}R_{\text{A}}SP$, must then be representative for processes at the semiconductor/electrolyte interface. The resistance R_{F} can be related to the faradaic dark current. The values of R_{F} are quite large ($> 1 \text{M}\Omega$). This agrees very well with the low dark currents observed ($< 1 \mu\text{A}/\text{cm}^2$). The values of C_{A} show a marked voltage dependence. At -0.4V , C_{A} is around $10 \mu\text{F}$, but this value decreases rapidly with increasing potential and approaches a constant value above $+0.2\text{V}$. Dare-Edwards *et al.* (12) found the same voltage dependence for the capacitance C_{SS} in their analysis. The branch $C_{\text{SS}}R_{\text{SS}}S$ in their equivalent circuit, which is analogous to the branch $C_{\text{A}}R_{\text{A}}S$, models surface states of a particular energy.

The element Q_{SC} is related to the space-charge capacitance C_{SC} . The values of α_{SC} are between 0.91 and 0.94, showing that Q_{SC} approaches closely a pure capacitance. Therefore, we may relate the values of k_{SC} to the actual C_{SC} values (23).

In the depletion region the relation between the space-charge capacitance C_{SC} and the potential V is given by the Mott-Schottky equation (34)

$$C_{\text{SC}}^{-2} = \frac{2}{\epsilon\epsilon_0 e N_{\text{D}} A^2} \left(V - V_{\text{FB}} - \frac{kT}{e} \right) \quad [2]$$

where ϵ is the relative dielectric constant, ϵ_0 the permittivity of free space, e the electronic charge, N_{D} the donor density, A the interfacial surface area, and V_{FB} the flatband potential. We have used the values of k_{SC} to construct a Mott-Schottky plot (k_{SC}^{-2} vs. V). This is shown in Fig. 7. From the V axis intercept, a value for the flatband potential V_{FB} was obtained, *viz.*, $V_{\text{FB}} = -0.5\text{V}$ vs. SCE. From the slope, a value for N_{D} can be derived. With $\epsilon = 20$ for ZnFe_2O_4 (35), and $A = 50 \text{nm}^2$, this yields $N_{\text{D}} = 5.6 \times 10^{21} \text{cm}^{-3}$. This value is rather high compared with the number of Fe^{3+} ions on octahedral sites in ZnFe_2O_4 ($2.7 \times 10^{22} \text{cm}^{-3}$).

According to Schoonman *et al.* (36), surface roughness can account for this high value of the donor density. Rough electrodes have acutal interfacial areas ($A = A_0 + \Delta A$), which are greater than the geometrically determined surface areas (A_0). The edge of the depletion layer inside the electrode follows the surface roughness for small values of the electrode potential. Only for large values the edge of the depletion layer will approach A_0 (37).

In Fig. 8, an electron micrograph of the surface of the ZnFe_2O_4 electrode is shown. This picture reveals that we are indeed dealing with a rough surface.

Goodman (37) modified the MS equation to account for surface roughness. However, for small band bending the MS plot will still be linear and may be used to determine V_{FB} . A reliable value for N_{D} will be hard to obtain. The value found by applying Eq. (2) is usually too high (36).

Values of the flatband potential for $\alpha\text{-Fe}_2\text{O}_3$, which are mentioned here for comparison, have been reported by several authors. The ac response data analysis of Dare-Edwards *et al.* (12) resulted in a nonlinear MS plot. This could, however, be extrapolated to $V_{\text{FB}} = -0.5\text{V}$ vs. SSE (1M KOH) ($\text{SSE} = -0.02\text{V}$ vs. SCE). These authors limited the analysis to a five-component equivalent circuit and used only pure capacitances, although their electrode surface was unpolished. This might explain the nonlinear MS plot.

Quinn *et al.* (3) reported a value of -0.67V vs. SCE (2M NaOH) for a single crystal. Kennedy and Frese (6) re-

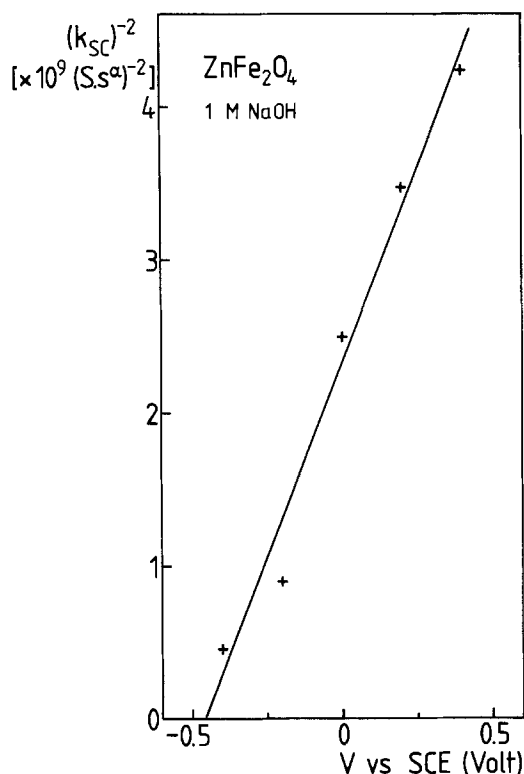


Fig. 7. Mott-Schottky plot of the k_{sc} data obtained for the PEC cell with α - $ZnFe_2O_4$ anode.

ported $-0.73V$ vs. SCE ($2M$ NaOH) for a reduced polycrystalline electrode and $-1.00V$ vs. SCE ($1M$ NaOH) for a Ti-doped polycrystalline electrode. Curran and Gissler (7) reported $-0.95V$ vs. SCE ($1M$ NaOH) for both a sintered Fe_2O_3 electrode and the thin Fe_2O_3 layer of flame-oxidized iron. All these authors used monofrequency impedance measurements to obtain these values. Unfortunately, they are little coherent, which makes a comparison with our value for $ZnFe_2O_4$ difficult.

General Discussion

In relation to the photoeffects observed for α - Fe_2O_3 and for the ferrites reported here, the question arises of which optical transitions generate the charge carriers. Particularly for the visible region, where a marked difference between the diffuse reflection spectra and the photocurrent action spectra is observed, this is of interest. The CF transitions of Fe^{3+} , which cannot account for the intensity of

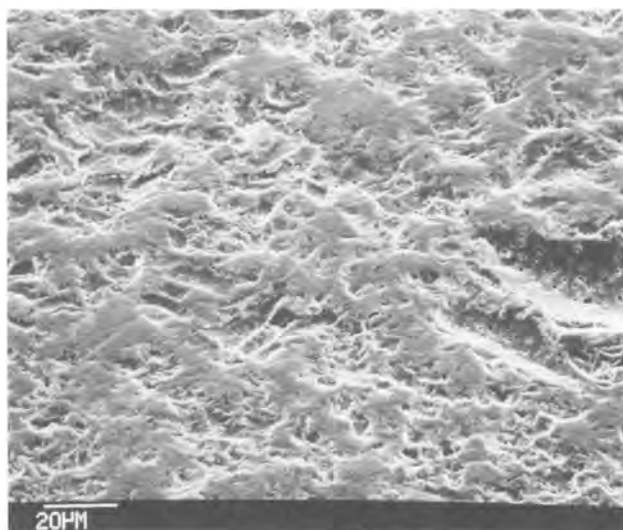


Fig. 8. Scanning electron micrograph of the surface of the $ZnFe_2O_4$ electrode.

the absorption in this region, are excluded beforehand. The localized nature of these transitions make carrier generation improbable, *i.e.*, they will not give rise to photocurrents of any importance. The relatively large absorption coefficient in the visible region might indicate another type of charge transfer transition, *i.e.*, metal to metal, which can be schematically envisaged as $2Fe^{3+} \rightarrow Fe^{2+} + Fe^{4+}$ (A). Kennedy and Frese (5) came to the same conclusions. Also Pollert *et al.* (38) discussing the photoelectrochemical properties of the magnetoplumbite $PbFe_{12}O_{19}$ arrived at this assignment. This metal-to-metal CT transition starts around 2.2 eV, *i.e.*, the onset wavelength of the photocurrent. In the UV part of the photocurrent action spectra, the already mentioned ligand-to-metal CT, *i.e.* $O^{2-} + Fe^{3+} \rightarrow O^- + Fe^{2+}$ (B) accounts for the electron-hole pair generation.

The total photocurrent consists of two contributions: one from carriers generated in the depletion layer, and another from carriers generated in the bulk which diffuse into the depletion layer before recombining (1). The diffusion current depends on the minority carrier diffusion length, which is usually quite short for metal oxide semiconductors. For a small absorption coefficient, the light will penetrate deep into the semiconductor bulk, where most of the photogenerated charge carriers will recombine before reaching the depletion layer. With increasing absorption coefficient, the charge carrier generation in the depletion layer increases, as does the photocurrent efficiency. A higher absorption coefficient for UV radiation than for visible radiation (*cf.* the diffuse reflection spectra section) accounts, therefore, for the higher efficiency observed in the UV region.

We have summarized the results of this consideration in schematic band-structure diagram shown in Fig. 9. This is adopted from a semi-empirical energy-level diagram for α - Fe_2O_3 (39). Since we excluded the CF transitions on Fe^{3+} , the excited-state levels originating from the $Fe^{3+}:3d^5$ configuration have been omitted in this diagram. The two CT transitions responsible for the electron-hole pair generation are indicated (A and B, respectively, see Fig. 9).

From Fig. 9 it can be seen that we are left with two types of holes, each at a different energy level. Upon irradiation with visible light, the holes are in the Fe_e^{3+} band. Under UV irradiation, the holes are created in the oxygen

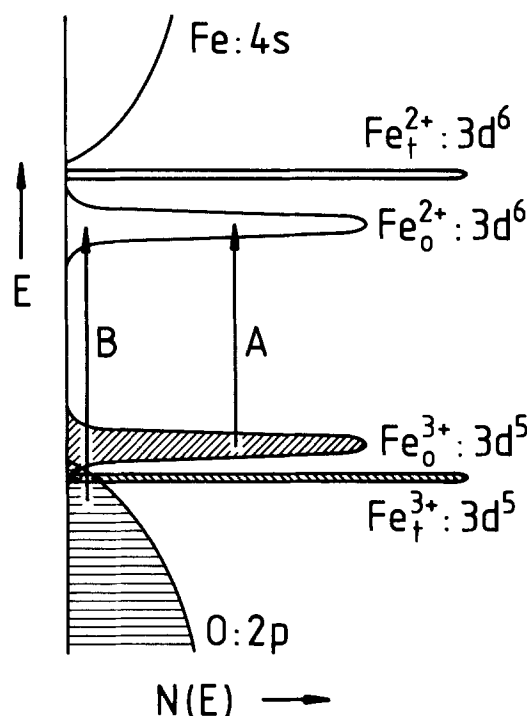


Fig. 9. Schematic band structure of ferrites with spinel structure. A and B indicate the CT transitions discussed in the text.

valence band. The photocurrents measured for 300, for 380, and for 460 nm irradiation show the same voltage dependence. This indicates, that the conduction path for the holes is the same, whether irradiation is performed with visible light or with UV light. The low hole mobility reported for p-type $\alpha\text{-Fe}_2\text{O}_3$ (40) indicates that the hole migrates in the $\text{Fe}_{0^{3+}}$ band rather than in the oxygen valence band. Dare-Edwards *et al.* (12) arrived at a similar conclusion for $\alpha\text{-Fe}_2\text{O}_3$.

The value for V_{FB} (-0.5V vs. SCE) obtained from the admittance spectra analysis agrees with the value expected from the photocurrent-voltage curves observed. The values obtained for the capacitance C_A , which can be associated with surface states, clearly show the decreasing importance of these surface states with increasing band bending. This strongly supports the explanation given before for the transients and the low steady-state photocurrent observed in the low potential region.

In conclusion, we have shown that ferrites with the spinel structure can be used as photoanodes in a PEC cell. Photocurrents are observed up to around 550 nm, but the efficiency in the visible region is limited by a relatively low absorptivity. The flatband potential lies close to, but anodic of, the hydrogen evolving level. However, in the region of low band bending, steady-state photocurrents are severely limited because of surface recombination of the photogenerated electron-hole pairs.

Acknowledgments

The authors wish to thank Professor J. Schoonman for helpful discussions. They are indebted to Mr. J. Pieters for performing the electron microscope analysis. The investigations were supported by the Netherlands Foundation for Chemical Research (SON) with financial aid from the Netherlands Foundation for Technical Research (STW).

Manuscript submitted April 17, 1985; revised manuscript received Aug. 20, 1985.

Utrecht University assisted in meeting the publication costs of this article.

REFERENCES

- H. P. Maruska and A. K. Ghosh, *Solar Energy*, **20**, 443 (1978); K. Rajeshwar, P. Singh, and M. DuBow, *Electrochim. Acta.*, **23**, 1117 (1978); M. A. Butler and D. S. Ginley, *J. Mater. Sci.*, **15**, 1 (1980).
- K. L. Hardee and A. J. Bard, *This Journal*, **123**, 1024 (1976).
- R. K. Quinn, R. D. Nasby, and R. J. Baughman, *Mater. Res. Bull.*, **11**, 1011 (1976).
- L.-S. R. Yeh and N. Hackerman, *This Journal*, **124**, 833 (1977).
- J. H. Kennedy and K. W. Frese, Jr., *ibid.*, **125**, 709 (1978).
- J. H. Kennedy and K. W. Frese, Jr., *ibid.*, **125**, 723 (1978).
- J. S. Curran and W. Gissler, *ibid.*, **126**, 56 (1979).
- S. M. Wilhelm, K. S. Yun, L. W. Ballenger, and N. Hackerman, *ibid.*, **126**, 419 (1979).
- P. Iwanski, J. S. Curran, W. Gissler, and R. Memming, *ibid.*, **128**, 2128 (1981).
- R. Shinar and J. H. Kennedy, *Solar Energy Mater.*, **6**, 323 (1982).
- J. H. Kennedy and M. Anderman, *This Journal*, **130**, 848 (1983).
- M. P. Dare-Edwards, J. B. Goodenough, A. Hamnett, and P. R. Trevellick, *J. Chem. Soc., Faraday Trans. 1*, **79**, 2027 (1983).
- A. H. A. Tinnemans, T. P. M. Koster, J. Schoonman, D. H. W. Thewissen, and A. Mackor, To be published.
- C. Leygraf, M. Hendewerk, and G. A. Somorjai, *J. Catal.*, **78**, 341 (1982); *J. Solid State Chem.*, **48**, 357 (1983).
- P. Merchant, R. Collins, R. Kershaw, K. Dwight, and A. Wold, *ibid.*, **27**, 307 (1979).
- M. D. Archer, G. C. Morris, and G. K. Yim, in "Progress in Electrochemistry, Studies in Physical and Theoretical Chemistry," Vol. 15, D. A. J. Rand, G. P. Power, and I. M. Ritchie, Editors, p. 89, Elsevier, Amsterdam (1981).
- J. M. Hastings and L. M. Corliss, *Rev. Mod. Phys.*, **25**, 114 (1953).
- M. Schieber, *J. Inorg. Nucl. Chem.*, **26**, 1363 (1964); A. Tomas, P. Laruelle, J. L. Dormann, and M. Nogues, *Acta Crystallogr.*, **C39**, 1615 (1983).
- L. M. Corliss, J. M. Hastings, and F. G. Brockman, *Phys. Rev.*, **90**, 1013 (1953); C. J. Kriessman and S. E. Harrison, *ibid.*, **103**, 857 (1956).
- R. U. E. 't Lam, L. G. J. de Haart, A. W. Wiersma, G. Blasse, A. H. A. Tinnemans, and A. Mackor, *Mater. Res. Bull.*, **16**, 1593 (1981).
- A. Roos, D. R. Franceschetti, and J. Schoonman, *J. Phys. Chem. Solids*, To be published.
- R. U. E. 't Lam, J. Schoonman, and G. Blasse, *Ber. Bunsenges. Phys. Chem.*, **85**, 592 (1981).
- R. U. E. 't Lam, L. H. J. M. Jansen, and J. Schoonman, *ibid.*, **88**, 163 (1984).
- T. Birchall, N. N. Greenwood, and A. F. Reid, *J. Chem. Soc. A*, **2382** (1969).
- K. W. Blazey, *J. Appl. Phys.*, **45**, 2273 (1974).
- S. P. Tandon and J. P. Gupta, *Spectrosc. Lett.*, **3**, 297 (1970).
- H. H. Tippins, *Phys. Rev. B*, **1**, 126 (1970).
- I. Balberg and H. L. Pinch, *J. Magn. Magn. Mater.*, **7**, 12 (1978).
- H. Ono, H. Morisaki, and K. Yazawa, *Jpn. J. Appl. Phys.*, **21**, 1075 (1982).
- K. L. Hardee and A. J. Bard, *This Journal*, **124**, 215 (1977).
- D. L. Laser and A. J. Bard, *ibid.*, **123**, 1837 (1976).
- P. H. Bottelberghs, in "Solid Electrolytes," P. Hagenmuller and W. van Gool, Editors, p. 145, Academic Press, New York (1978).
- M. Tomkiewicz, *This Journal*, **126**, 1505 (1979); *ibid.*, **126**, 2220 (1979).
- R. Memming, in "Electroanalytical Chemistry," Vol. 11, A. J. Bard, Editor, p. 1, Marcel Dekker, New York (1979).
- P. A. Miles, W. B. Westphal, and A. von Hippel, *Rev. Mod. Phys.*, **29**, 279 (1957).
- J. Schoonman, K. Vos, and G. Blasse, *This Journal*, **128**, 1154 (1981).
- A. M. Goodman, *J. Appl. Phys.*, **34**, 329 (1963).
- E. Pollert, J. Hejtmanek, J. P. Doumerc, J. Claverie, and P. Hagenmuller, *J. Phys. Chem. Solids*, **44**, 273 (1983).
- J. B. Goodenough, in "Progress in Solid State Chemistry," Vol. 5, H. Reiss, Editor, p. 145, Pergamon Press, Oxford, England (1971).
- R. F. G. Gardner, F. Sweett, and D. W. Tanner, *J. Phys. Chem. Solids*, **24**, 1175 (1963); *ibid.*, **24**, 1183 (1963).

Polarization Relaxation in Electrodeposited Polyphenylene-Oxide Films

S. H. Glarum* and J. H. Marshall

AT&T Bell Laboratories, Murray Hill, New Jersey 07974

ABSTRACT

Impedance measurements of electrodeposited polyphenylene-oxide films, $\sim 250\text{\AA}$ thick, show a polarization relaxation for the metal/polymer/electrolyte interface. The initial polarization following a potential perturbation is distributed across the film. Relaxation follows to a much larger polarization characteristic of a bare metal/electrolyte interface. Kinetics are controlled by ion transport within the film and relaxation times range between 1 and 10^{-4} s. Results are reported for films in strong acids and bases. In the former case, ionic permeability can be reversibly altered by factors $> 10^3$.

Electrochemical syntheses of thin polymer films and their electric properties are topics of increasing importance given the growing interest in microelectrochemical applications. Polymerizations which proceed through oxidative coupling mechanisms are especially attractive for electrochemical studies because the reaction is localized at the electrode surface by fixed electron-transfer requirements for monomer addition (1). Polymer films can be formed in this manner from phenols (2), pyrroles (3), and anilines (4). The latter polymers are electronic conductors under polymerization conditions, and thick films can be produced electrochemically. In contrast, polyphenylene-oxides are insulators and the reaction is quickly quenched when thicknesses of 10^2 - 10^3\AA are reached. This dimension, shared with both Langmuir-Blodgett films and biologic membranes, introduces possibilities for a variety of studies of both fundamental and practical interest. Transport processes too slow to be macroscopically significant occur quite expeditiously on this scale. From a practical viewpoint, such processes may set lower limits for the scaling of macrodesigns.

In a series of papers, Dubois and co-workers have characterized many of the chemical and physical properties of polyphenylene oxide films (5). They propose that the initial polymerization step is the oxidation of a phenolate ion to a radical species. This radical has large spin densities at its *ortho* and *para* ring positions, and, if these sites are not blocked by substituents, the radical adds to an oxygen atom at the end of a growing polymer chain with the removal of H^+ and a second electron.

In this paper, we report on studies of the electric properties of electrodes coated with polyphenylene oxide films in aqueous electrolytes. When a potential difference is applied across the metal/polymer/electrolyte interface, the polymer layer is initially polarized. This polarization decays because of charge transport through the film, and we have used ac techniques to measure this relaxation. Polymers of 2,6-dimethylphenol (DMP) and 4-*t*-butylphenol (TBP) have been examined in detail. The *ortho* positions are blocked in DMP and coupling should take place at the *para* position, leading to a "linear" polymer. The *ortho* and *para* roles are reversed for TBP. Bruno *et al.* report that polymerization does not take place when the *para* and one of the *ortho* positions are blocked (5). We have observed that 2,4-dimethylphenol does form passivating layers when oxidized in aqueous base and, the TBP polymers may contain branching points.

Experiment

Platinum rotating disk electrode, 1/16 in. diam, were used for this work. Prior to polymer deposition, they were polished with $0.05\ \mu\text{m}$ alumina. Unless otherwise indicated, films were grown potentiostatically for 20 min at $\pm 0.25\ V_{\text{sc}}$ (DMP) or $+0.35\ V_{\text{sc}}$ (TBP). These potentials lie just above the monomer oxidation threshold and well below the oxygen evolution region. On one occasion, it was

noted that, if the platinum surface was fully oxidized prior to introduction of the phenol, dark red material covered much of the surface. Electrode rotation rates of 100 rad/s were used during film growth, although no dependence on this rate was found. Sufficient monomer is present in a $20\ \mu\text{m}$ electrolyte layer to meet the demands of the polymerization reaction.

The phenols (Aldrich) were used as received. Solutions were vigorously degassed with argon and the electrolytic cell was thermostated at 25°C . A B&L stereo-zoom microscope ($280\times$) with coaxial illumination was routinely employed for surface examinations. The apparatus for impedance measurements has been described previously (6).

Results

Aqueous solutions, $0.15N$ in NaOH and $0.02M$ in the phenol monomer, were used for the preparation of polymer films. Dubois *et al.* have used more concentrated phenol solutions in methanol (5). In the absence of phenol, substantial currents, presumably due to the oxidation of methanol to formaldehyde, are found at electropolymerization potentials with platinum electrodes. Stoichiometry between current and electrodeposited material is absent with alcoholic solutions because of oligomer solubility, and deposition efficiency is but a few percent. Films grown from aqueous solutions are soluble in methanol and are apparently of lower molecular weight material. On the basis of *in situ* impedance measurements, however, films grown from methanol solutions do not appear to be perceptibly thicker than their aqueous counterparts. While the former were not removed with methanol, their electrical response was altered, with a nearly exponential relaxation being replaced by a broader, nondescriptive dispersion. We interpret the latter as due to an inhomogeneous modification of the polymer layer.

When a freshly polished platinum electrode is immersed in the growth solution, the open-circuit potential is near $-0.1\ V_{\text{sc}}$. Based on cyclic voltammetric measurements for phenol-free solutions, this potential corresponds to the beginning of the oxidation plateau characteristic of platinum surfaces. The electrode was then scanned anodically from this potential (Fig. 1). Between 0.1 and $0.4\ V_{\text{sc}}$, depending on the phenol, the current begins to rise exponentially. Formation of an insulating layer passivates the surface and the current rapidly drops to a constant level characteristic of the oxidation of a bare platinum surface.

The shape of the oxidation wave does not change significantly with electrode rotation (100 - 0 rad/s) but, as seen in Fig. 1, the area beneath the wave is proportional to the scan rate. A constant faradaic charge is involved in formation of a surface film and integrations give 4.2×10^{-3} and $2.5 \times 10^{-3}\ \text{C/cm}^2$ for DMP and TBP films. Assuming $2e^-$ per monomer oxidized, 2.6 and $1.9\ \mu\text{g/cm}^2$ are deposited, respectively. The density of a bulk DMP polymer is 1.05 , leading to a nominal 250\AA thickness.

Growth kinetics can be examined through the current transients which follow jumps from open circuit to poten-

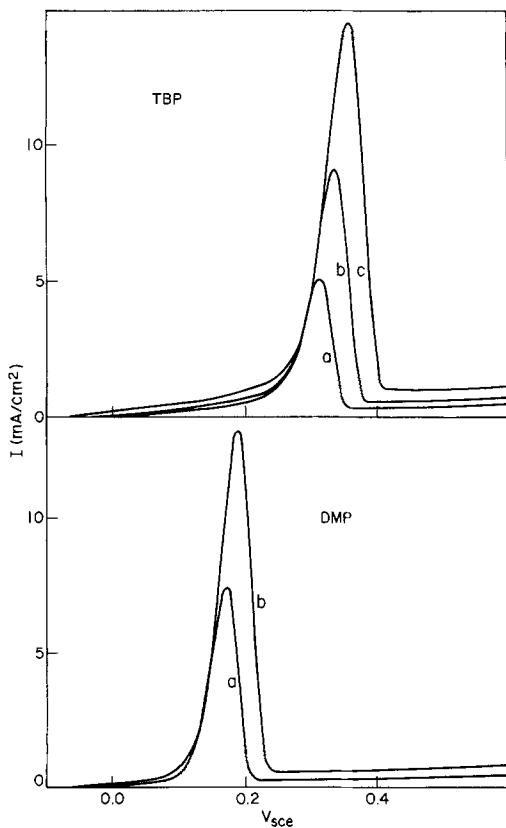


Fig. 1. Anodic current-voltage sweeps for 20 mM solutions in 0.15N NaOH of 4-t-butylphenol (TBP) and 2,6-dimethylphenol (DMP). a:10 mV/s. b:20 mV/s. c:40 mV/s. Electrode rotation:100 rad/s.

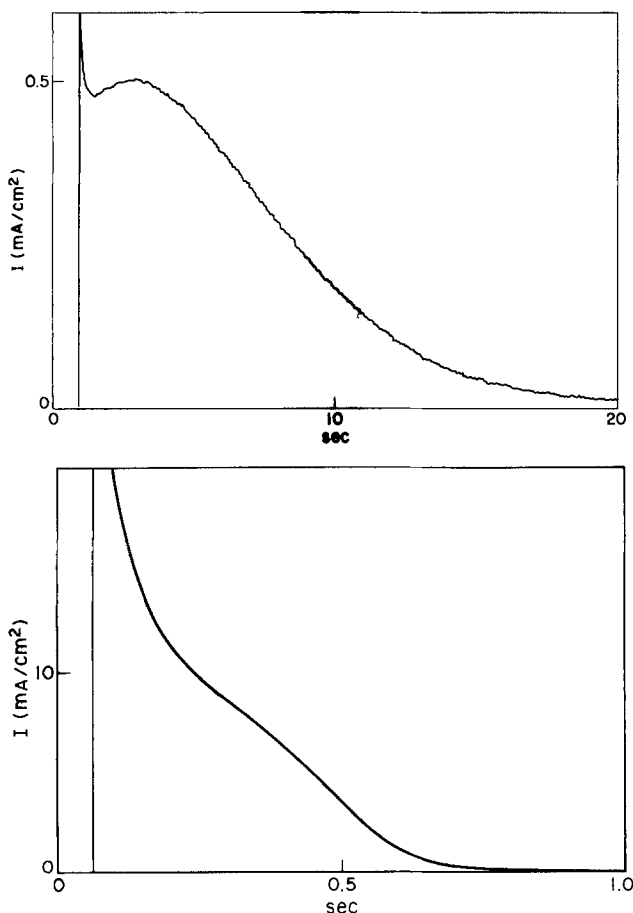


Fig. 2. a (top): Initial current transient for DMP film growth following a potential jump from -0.1 to $+0.15$ V_{sce} . b (bottom): Initial current transient for DMP film growth following a potential jump from -0.1 to $+0.35$ V_{sce} .

tials above the polymerization threshold (Fig. 2a and 2b). The initial current is less at the lower potential and passivation takes 10-20s. At a higher potential and higher initial current, passivation is largely completed with 0.5s. Integration of these transients yields the same coulombic values found from potential-sweep plots and supports the conclusion of a stoichiometry between current and deposited material. The transients can be followed to longer times until constant limiting currents less than $1 \mu A/cm^2$ are reached after 20 min (Fig. 3 and 4). For TBP films the decay varies approximately as $1/t$. For DMP films, there appears to be an exponential drop to an intermediate plateau, followed by a second drop to the limiting current.

Surfaces were examined microscopically before and after film growth. With normal (coaxial) illumination, no changes in surface features were evident, although there appeared to be a more yellow cast to the surface. With oblique illumination, only scattered light enters the microscope and features too small for direct resolution can be detected. No additional scattering was seen with TBP films, and micropolishing marks were equally apparent before and after film formation. The DMP films, however, were uniformly speckled blue. We attribute this

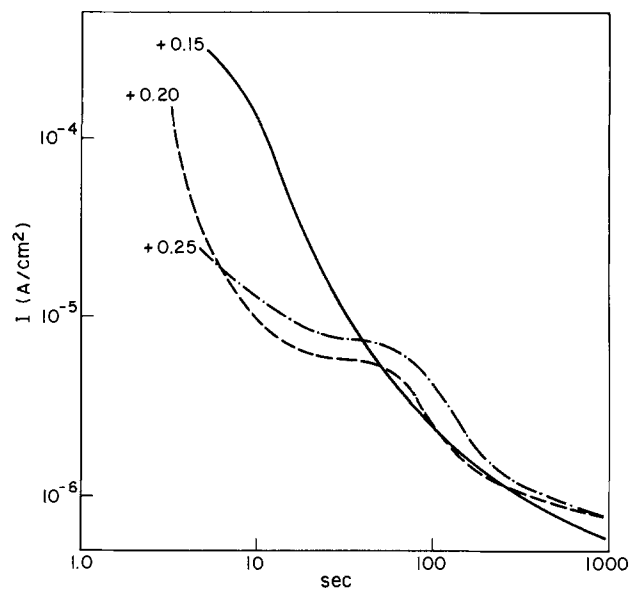


Fig. 3. Long-term current decay for DMP film growth at several potentials.

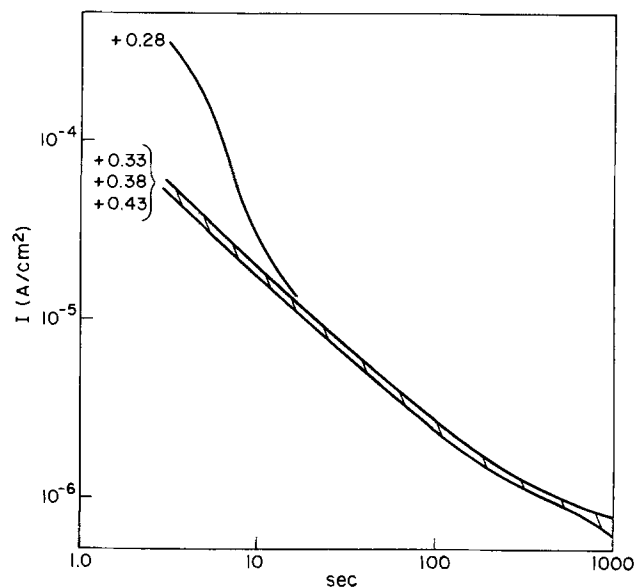


Fig. 4. Long-term current decay for TBP film growth at several potentials.

scattering to refractive index variations between crystalline and amorphous regions.

Most ac measurements were made with 100 Hz-200 kHz frequency scans, although occasionally lower frequency scans, 1-500 Hz, proved helpful. Even at 200 kHz, the film impedance was too high for a reliable evaluation of the electrolyte resistance. To determine this parameter, the film was removed, either by dissolution or repolishing, and the impedance of the bare electrode measured. With the electrolyte resistance in hand, corrections were made for the nonuniform current distribution at disk electrodes, the electrolyte resistance was subtracted from the corrected impedance, and results were plotted in the complex capacitance plane, *i.e.*, $i\omega C^* = (Z^* - R_{el})^{-1}$.

Figure 5 shows such a plot. It is representative of most measurements. The shape is approximately semicircular and well described over most of the frequency range by a circular arc centered 10° below the real axis. Straightforward extrapolations give 0.26 and $48 \mu\text{F}/\text{cm}^2$ for the high and low frequency intercepts. The relaxation time given by the frequency at the top of the arc is $180 \mu\text{s}$ ($1/2 \pi f$). The depressed center can formally be attributed to a relatively narrow distribution of relaxation times. There are no distortions to suggest the presence of more than one dispersion, except possibly at the lowest frequencies. A small dc conductance results in large deviations in C^* plots in this region.

Discussion

Interpretation of the complex capacitance function for the metal/polymer/electrolyte interface is best approached in terms of the behavior of an idealized blocking electrode (see Appendix). We suppose the polymer film contains positive and negative ions of arbitrary mobilities. Within the film, ionic fluxes are governed both by concentration gradients and an electric field. The gradient of this field is determined by the space charge resulting from unequal concentration profiles for anions and cations. The boundary conditions required to complete the description are rapid ion exchange at the polymer/electrolyte interface, pinning concentrations within the film at this boundary, and blocking conditions or null ionic fluxes at the metal/polymer boundary.

Macdonald has offered a formal solution for this problem couched in terms of a symmetric two-electrode cell (7). The half-cell response is, however, equivalent to the problem posed for concentration changes vanish through symmetry at the midplane. Macdonald's solution is rather complicated, in part because of the *ab initio* separation of ionic and dielectric displacement currents. Our Appendix offers an alternative expression somewhat more amenable to evaluation. The problem involves finding the time-dependent response of an equilibrium configuration to a perturbation. An analytic solution has so far been achieved only for the perturbation of a spatially uniform

configuration corresponding to the potential of zero charge (pzc). Gouy-Chapman theory describes equilibrium configurations at other potentials. Our result for the complex capacitance function can be written as

$$C^* = [(\epsilon + \sigma/i\omega)l][1 + \mathfrak{F}(i\omega)]$$

with

$$\sigma = (eF_c/kT)(D_p + D_n)$$

The numerator contains the leading high frequency terms and depends on bulk parameters, ϵ , the dielectric constant, and σ , the conductivity. Relaxation of the charge distribution to create a space-charge polarization is described by the function $\mathfrak{F}(i\omega)$. Five physical parameters are needed to describe the response: the thickness and dielectric constant of the film, the ionic concentration within the film, and the diffusion coefficients for both ions.

The nature of the solutions is best revealed by complex-plane plots for C^* (Fig. 6). Parameters were chosen for these computer-generated curves so that the low frequency capacitance intercept was much larger than the high frequency intercept. The shape of these plots then depends only upon the ratio of the diffusion coefficients. When these are equal, the calculated plot is a semicircle. Despite the complexity of $\mathfrak{F}(i\omega)$, the response is experimentally indistinguishable from a simple exponential relaxation. When the diffusion coefficients differ by orders of magnitude, the dispersion separates into a high frequency semicircle and a low frequency circular arc. The latter is characteristic of a diffusional relaxation process. The ratio of the dispersion amplitudes, $\sqrt{2}$, is set by the assumptions of a 1:1 electrolyte.

The potential perturbation initially creates a uniform perturbing field within the film. Under the guidance of this field, the more mobile ions drift towards or away from the metal/polymer interface, creating a space-charge region which quenches the field in the bulk of the film. This portion of the relaxation appears exponential in time. The slow ions can enhance the space-charge polarization by a factor $\sqrt{2}$, but, in the absence of a field within the film, their redistribution kinetics are diffusive.

If we accept this model, interpretations for parameters derived from experimental C^* plots are straightforward. For $D_p = D_n$ and $C_o \gg C_g$

$$C_g = \epsilon/l$$

$$C_o = \epsilon/\lambda$$

$$\omega_{\max} C_o = \sigma/l$$

$$1/\lambda^2 = 2eF_c/\epsilon kT$$

with C_g and C_o being the asymptotic high and low frequency intercepts, ω_{\max} the frequency at the C^* maximum, and λ a Debye length defined by the last equation which

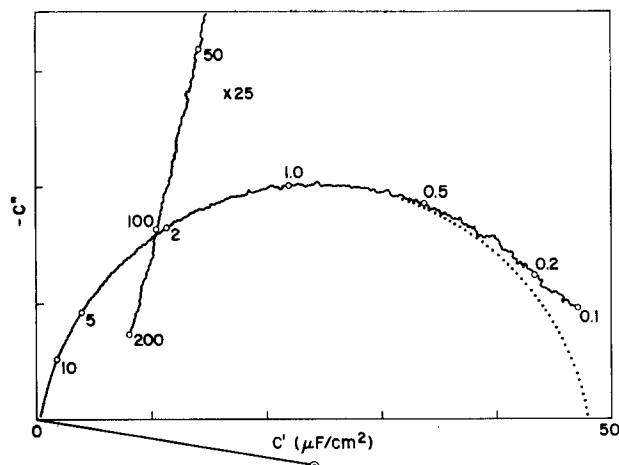


Fig. 5. Complex-capacitance plot for a TBP film in 0.05N NaOH at $-0.1 V_{sce}$ (open-circuit potential).

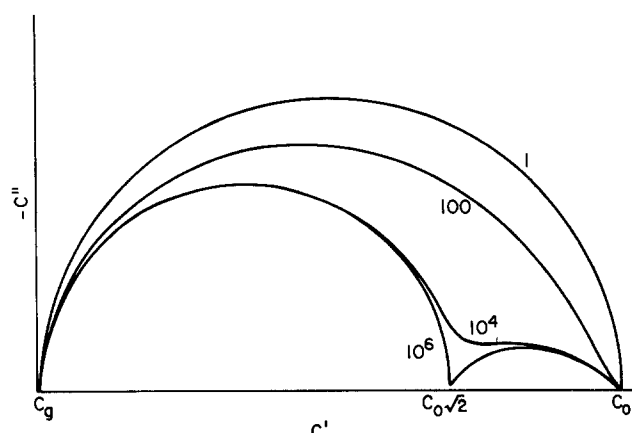


Fig. 6. Theoretical complex-capacitance plots for the space-charge relaxation model. Values indicate the diffusion coefficient ratio D_p/D_n .

describes the width of the space-charge region. C_g is the geometric capacitance of the polymer film. Applying these results to the data plotted in Fig. 5 with $l = 250\text{\AA}$, we find $\epsilon = 7$, $\sigma = 7 \times 10^{-7}$ mho/cm, $c = 0.9M$, and $D = 10^{-10}$ cm²/s. However, $\lambda = 1.0\text{\AA}$, and the validity of macroscopic electrostatics used in the model appears questionable. The dielectric constant for analogous bulk polymers is 2.5. Were this the correct value for the film, the true thickness would be 85 \AA and inconsistent with growth coulometry.

Our suspicions regarding the small Debye length are confirmed by measurements at different potentials which show no changes in C_o . According to Gouy-Chapman theory, C_o should vary as $\cosh(e\eta/2kT)$. In fact, C_o is suspiciously similar in magnitude and potential dependence to the capacitance of a bare platinum electrode in the electrolyte. This capacitance has limiting high frequency values in the range 40-50 $\mu\text{F}/\text{cm}^2$. However, it also exhibits a very broad dispersion of unknown origin extending to very low frequencies. Examination of the width of classic cyclic voltammetric plots in the "double-layer" region gives values of several hundred microfarads per square centimeter. The correlation appears to be best between the low frequency film capacitance and the high frequency film-free capacitance.

When the electrolyte concentration was reduced to 10 mM, neither bare nor coated electrodes showed a capacitance dip indicative of the pzc. The absence of this dip points to specific ionic adsorptions. The magnitude of the capacitance requires a dielectric constant ca. 20 at the interface, which is rationalized in terms of a layer of water molecules (8). While the relation between interfacial structure and capacitance is ambiguous, it seems safe to conclude for polymer-coated surfaces that the equilibrium polarization is localized at the metal interface, the low frequency capacitance reflects the properties of this interface, and a water layer separates the metal and polymer. The low frequency capacitance cannot be relied on, however, for the evaluation of ionic concentration, and a diffusion coefficient cannot be extracted from the film conductivity.

The model analyzed assumes that ionic transport within the film limits polarization relaxation. Although experiments show but one dispersion, it is not immediately evident that the relaxation is not limited by interfacial rather than bulk kinetics. If the rate-limiting process were spatially localized at the outer and/or inner film boundaries, minimum capacitance values would be set by the geometric widths of these regions. Rapid transport within the bulk would eliminate a bulk electric field and hence the dielectric displacement polarization of the bulk. The magnitude of the high frequency capacitance rules out localized interpretations for the observed relaxation.

With some insight into the physical significance of the complex capacitance, the behavior of this function was examined during the period of film formation. Rapid initial changes precluded detailed measurements in the first few minutes. High-frequency measurements, however, showed the capacitance dropped from an initial value, $\sim 60 \mu\text{F}/\text{cm}^2$, to a limiting value within seconds. Thus the film thickness, given by C_g , is quickly established. Relaxation measurements at longer times were possible, and Fig. 7 plots the values for C_g , C_o , and the film conductivity, $G = \sigma/l$. No significant variations are seen for the capacitive parameters showing that the film thickness and the nature of the metal/polymer interface are not changing. The C_o values further indicate the absence of a steady-state electric field within the bulk of the film to assist phenolate anion transport.

The film conductivity shows a steady drop over this period. As the film thickness is invariant, the decrease must be attributed either to reduced ionic mobilities or solubilities. The steady-state current, representing phenolate oxidation, is independent of potential (Fig. 3, 4), and we may assume that it represents a diffusion limited current so that

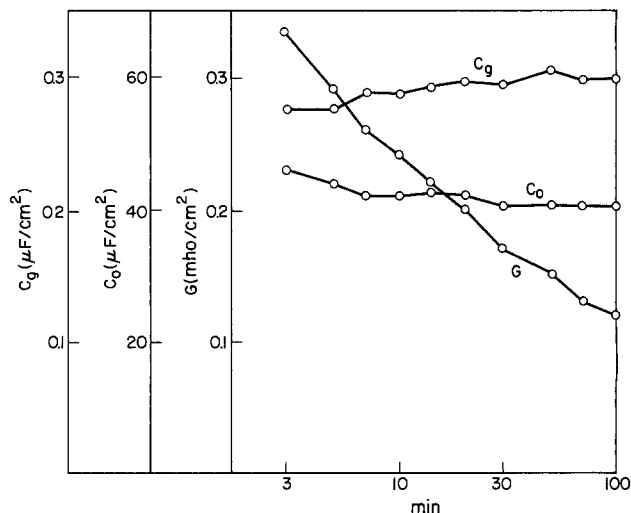


Fig. 7. Variation of the relaxation parameters during TBP film growth at $+0.35 V_{sce}$.

$$I_m = 2FD_m K_m c_{m0}/l$$

with D_m the monomer diffusion coefficient, K_m the monomer partition coefficient, and c_{m0} the monomer concentration in the electrolyte. Film conductivity is primarily due to electrolyte ions and

$$G = 2eFD_e K_e c_e/kTl$$

The product of the diffusion and partition coefficients gives a permeability coefficient. Comparison of the steady-state current with the film conductivity indicates that the electrolyte permeability is $\sim 10^3$ times that of the monomer.

While the structure and ion transport mechanisms in these films are not known, the polymers are polyethers and have some features in common with polyethylene- and polypropylene-oxides. The latter form a variety of complexes with alkali metal salts and possess dielectric constants and room temperature conductivities similar to those measured here for polyphenylene oxide films (9). Armand has proposed that the stability of these complexes arises from cation solvation by a helical arrangement of the ether oxygens, and that the complexes are cationic conductors along these channels (10). Later measurements have indicated that cation and anion diffusion coefficients are nearly equal (11).

Figure 8 plots film conductivities obtained from relaxation measurements for TBP films in contact with various concentrations of three strong bases, NaOH, LiOH, and NPr_4OH . Measurements were made at open-circuit potentials, ca. $-0.1 V_{sce}$, just above the cathodic reduction peak for the platinum oxide region. For the latter two bases, this conductivity appears proportional to the electrolyte concentration. Conductivity is highest for NaOH solutions but appears to be less sensitive to concentration. Data were acquired using a single film and making successive 2:1 dilutions. The anomalous behavior of NaOH solutions is an artifact of an aging process which causes a conductivity increase with time.

Figure 9 shows aging results for separate TBP films in 0.5 and 0.05N NaOH and LiOH solutions. The electrodes had been stored in water prior to measurement. The conductivity of films in NaOH is seen to be proportional to concentration when aging is considered. There were some indications of systematic increases in C_g and C_o totaling no more than 10%, but this variation is commensurate with extrapolation uncertainties.

The large conductivity differences show that film permeability is strongly cation dependent, but we cannot separate solubility and diffusion effects. Electroneutrality requires the exchange of both cation and anions between polymer and electrolyte. The conductivity cannot be due to fixed ionic concentrations within the film, which

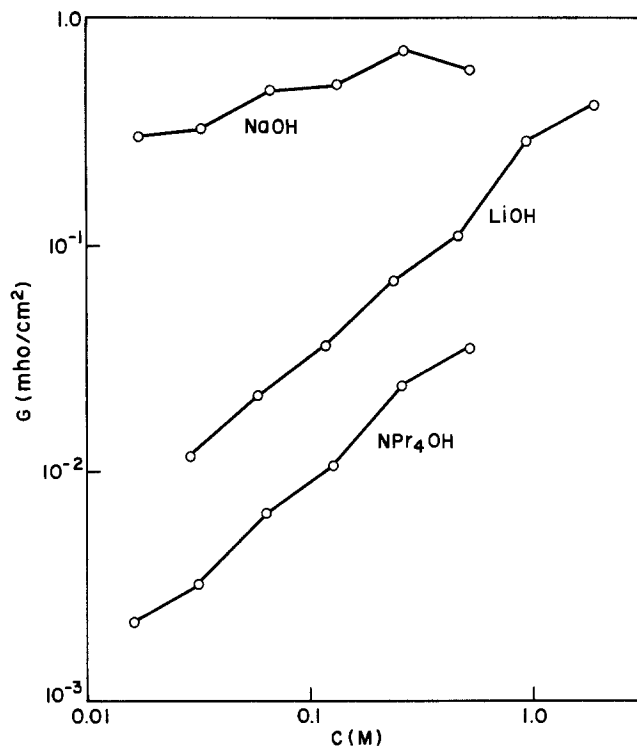


Fig. 8. Variation of film conductivity with electrolyte concentration or basic solutions.

would be the case if phenolate residues determined this value.

The time scale of the aging process is too long to be explained by diffusion of water or electrolyte into the film. Aging cannot be exclusively due to the incorporation of water or hydroxyl ions, for the effect is most marked with NaOH solutions. A configurational or structural relaxation of polymer molecules which opens up ionic transport paths seems most plausible. If polymer hydrolysis is involved, the effects are reversible. In a series of experiments, aging changes were measured during a 3h immersion period in 0.1N NaOH. The electrode was then rinsed in water for 15 min and dried under vacuum for 1h. The original parameters, including C_g , were found on remeasurement.

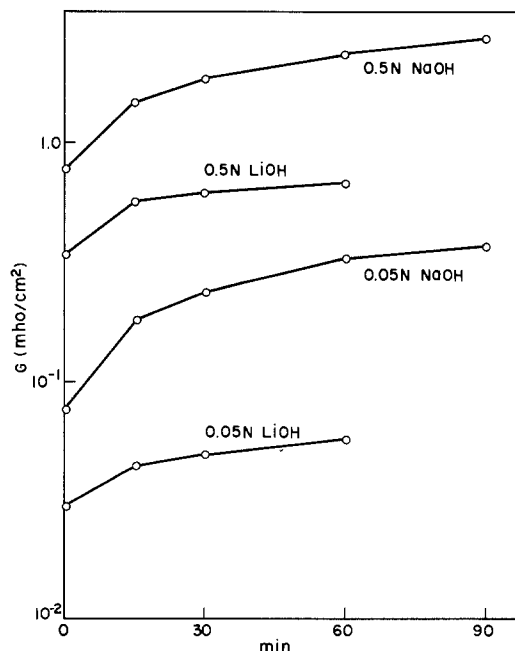


Fig. 9. Aging changes of TBP film conductivity in several basic electrolytes.

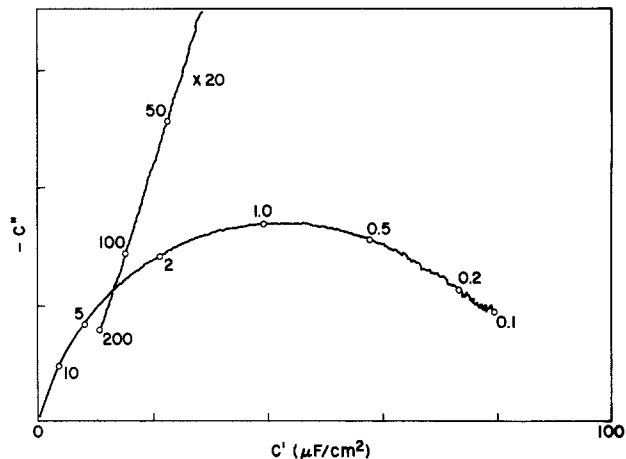


Fig. 10. Complex-capacitance plot for a "fast" TBP film in 0.2M H_2SO_4 at +0.6 V_{sc} . Frequencies are in kilohertz.

Polyphenylene oxide films are also stable in strong acids. For such solutions, however, two markedly different behaviors were observed. Figure 10 shows a fast relaxation in 0.2M H_2SO_4 , with $C_g = 0.28 \mu F/cm^2$, $C_o = 80 \mu F/cm^2$, and a relaxation time of 180 μs . These parameters are essentially identical to those obtained from Fig. 5 for a NaOH solution. The higher C_o value parallels the higher capacitance for a platinum oxide surface in sulfuric acid. In Fig. 11, we see a much slower relaxation for supposedly similar film. Even when the frequency scan was lowered to 1 Hz, the C^* maximum was not reached, and we can estimate a relaxation time $\geq 1s$. Moreover, the plot does not resemble the high frequency extension of a nearly semicircular arc. For three decades, the plot has a slope near unity, corresponding to $(i\omega)^{-1/2}$ dependence and suggesting a diffusion-controlled relaxation process.

As a rule, fast responses are found for films freshly formed and slow responses appear with films allowed to dry out, either under ambient or vacuum conditions. A given film can be reversibly cycled between fast and slow states. A vacuum treatment leads to a slow relaxation, while immersion in NaOH solutions restores fast behavior. The presence of water in the polymer seems implicated in the fast response films. The polymers are hydrophobic, and the facile removal of water is plausible (5). Immersion of a "slow" film for 2h in either water or acid gives no more than a threefold relaxation time decrease, whereas a similar treatment in base yields a 300-fold decrease.

A simple ion transport mechanism would not lead to diffusional relaxation. This behavior occurs while the capacitance is still close to its geometric value, and consequently an electric field must exist within the film as a driving force for ion migration (cf. Fig. 6). Diffusion of an electroneutral species appears to govern the relaxation.

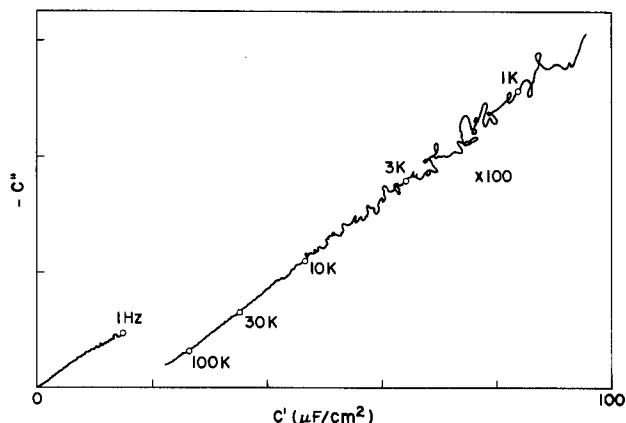


Fig. 11. Complex-capacitance plot for a "slow" TBP film in 0.1M H_2SO_4 at +0.6 V_{sc} . Frequencies are in hertz.

Given the film thickness, a 1s relaxation time corresponds to a diffusion coefficient of order 10^{-11} cm²/s. This value seems too large to associate with water in a polymer matrix. Possibly polar or ionic groups at the ends of polymer chains are involved.

We have also observed that film conductivity in acid solutions can be altered by factors of 2-5 following potential changes. Suppose we measure the response of a "fast" film at +0.2 V_{sce} in the double-layer region of a platinum electrode. After the potential has been lowered to -0.2 V_{sce} and then returned to +0.2V_{sce}, thereby adsorbing and desorbing a monolayer of H atoms, the relaxation time is increased and the high frequency slope of C* plots is reduced. When the potential is then raised to +1.1 V_{sce}, oxidizing the metal surface, film conductivity is increased, and its higher value is maintained on return to +0.2 V_{sce}. Accompanying these potential changes are large pH transients as H⁺ and OH⁻ ions are taken up and released at the metal interface. We cannot draw an obvious connection between pH changes and the much larger effects of film dehydration. Alternative experiments more directly revealing the role of water in modifying the structure of the polymer films and their ionic permeability are necessary.

Our discussion so far has been restricted to results for TBP films. Corresponding measurements for DMP films gave similar results both qualitatively and quantitatively. Relaxation parameters, the influence of electrolytes, and aging effects were not distinctively different. Because of their thinness, film conductivities are readily measured. The slow response films in sulfuric acid have equivalent bulk conductivities of 10^{-10} mho/cm, making them respectable insulators. While lower values are normally cited for conventional insulating materials, they are not based on measurements with concentrated electrolytes as contacts. If the conductivity were ascribed to pinholes filled with electrolyte, the fraction of the surface covered by such holes would be 10^{-9} . Perhaps our most interesting observation is that the permeability of thin polymer layers can be reversibly altered by several orders of magnitude. These materials are not simply passive matrices. Effective utilization of this property will depend upon a clearer understanding of the structures and dynamics within thin films.

Our results also point out some difficulties inherent in thin film applications. The usefulness of ion-selective membranes depends on the relative ionic contributions to conductivity of the membrane through diffusion and partition coefficients (12). If one boundary of the membrane is a blocking contact, relaxation will lead to an equilibrium polarization at this contact which depends only on the properties of this interface and not the selective properties of the overlying matrix. In the case of a platinum contact, this interface turns into a pH sensor within a second for the films used in this work (13). Similar behavior can be anticipated with SiO₂ contacts.

Considerable interest exists in combining electrochemical polarizations with field-sensitive semiconductor surfaces (14). It is perhaps worth noting that the capacitance is closely related to the field at the surface, $C = \epsilon \Delta E(0)/\Delta V$. Capacitance relaxation measurements should permit an assessment of material performance for such applications without the additional complexities of microcircuit fabrication.

Manuscript submitted April 17, 1985; revised manuscript received Aug. 9, 1985.

APPENDIX

The purpose of this Appendix is to outline the derivation of an analytic expression for the complex capacitance of a blocking electrode more tractable than Eq. [44] of Ref. (7). The fundamental equations to be solved are

$$\begin{aligned} dp/dt &= -dJ_p/dx; J_p = -D_p [dp/dx - (ez/kT) p(x, t)E(x, t)] \\ dn/dt &= -dJ_n/dx; J_n = -D_n [dn/dx + (ez/kT) n(x, t)E(x, t)] \\ dE/dx &= (ez/\epsilon) [p(x, t) - n(x, t)] \end{aligned}$$

$$V(t) = - \int_0^l E(x, t) dx$$

with $p(x, t)$ and $n(x, t)$ cation and anion concentrations with diffusion coefficients D_p and D_n . $E(x, t)$ is an electric field, and $V(t)$ is the potential drop across the film with thickness l . Time-dependent parameters are considered to be harmonic perturbations of a uniform equilibrium distribution, i.e.

$$p(x, t) = c_0 + p^*(x) \exp(i\omega t)$$

$$n(x, t) = c_0 + n^*(x) \exp(i\omega t)$$

$$E(x, t) = E^*(x) \exp(i\omega t)$$

Substitution leads to a characteristic equation with roots

$$\begin{aligned} \gamma_{\pm}^2 &= 1 + (i\omega\lambda^2/2)(1/D_p + 1/D_n) \\ &\quad \pm \{1 + [(i\omega\lambda^2/2)(1/D_p - 1/D_n)]^2\}^{-1/2} \\ 1/\lambda^2 &= e^2 z^2 c_0 / \epsilon k T \end{aligned}$$

and

$$E^*(x) = E^*_0 + \sum_1^4 E^*_i \exp(\gamma_i x / \lambda)$$

with the coefficients E^*_i determined by boundary conditions. Similar expressions follow for $p^*(x)$ and $n^*(x)$.

At a blocking electrode, the perturbation current, $I^* = i\omega\epsilon E^*(0)$ and consequently the complex capacitance can be expressed in terms of the coefficients E^*_i

$$C^* = I^*/i\omega V^* = (\epsilon/l) \frac{E^*_0 + \sum E^*_i}{E^*_0 + \sum E^*_i [\exp(\gamma_i l/\lambda) - 1]/(\gamma_i l/\lambda)}$$

From the boundary conditions

$$p^*(l) = n^*(l) = J_p(0) = J_n(0) = 0$$

one readily finds

$$\sum E^*_i = E^*_0 (D_p + D_n) i\omega\lambda^2 = E^*_0 (\sigma/i\omega\epsilon) = E^*_0 / i\omega\tau$$

With considerably more effort, the denominator can be evaluated giving

$$C^* = \frac{(\epsilon + \sigma/i\omega)l}{1 + f_+ + f_-}$$

with

$$f_{\pm} = (\gamma_{\pm}^2 - \gamma_{\mp}^2)^{-1} [(\gamma_{\pm}^2 - 2)/i\omega\tau - 2] [\tanh(\gamma_{\pm} l/\lambda)/(\gamma_{\pm} l/\lambda)]$$

REFERENCES

1. G. Mengoli, in "Advances in Polymer Science," Vol. 33, H.-J. Cantow *et al.*, Editors, p. 1, Springer-Verlag, New York (1979).
2. D. S. McKinney and J. P. Fugassi, U.S. Pat. 2,961,384 (1960).
3. A. F. Diaz, J. I. Castillo, J. A. Logan, and W.-Y. Lee, *J. Electroanal. Chem.*, **129**, 115 (1981).
4. A. F. Diaz and J. A. Logan, *ibid.*, **111**, 111 (1980).
5. F. Bruno, M. C. Pham, and J. E. Dubois, *Electrochim. Acta*, **22**, 451 (1977); M. Delamar, M. Chemini, and J. E. Dubois, *J. Electroanal. Chem.*, **169**, 145 (1984), and references therein cited.
6. S. H. Glarum and J. H. Marshall, *This Journal*, **131**, 691 (1984).
7. J. R. Macdonald, *Phys. Rev.*, **92**, 4 (1953).
8. C. A. Barlow, in "Physical Chemistry," Vol. IXA, "Electrochemistry," H. Eyring, Editor, p. 167, Academic Press, New York (1970).
9. M. C. Wintergill, J. J. Fontanella, J. P. Calame, and D. R. Figueroa, *Solid-State Ionics*, **11**, 151 (1983).
10. M. B. Armand, J. M. Chabagno, and M. J. Duclot, "Fast Ion Transport in Solids," p. 131, North-Holland, Amsterdam (1979).
11. P. R. Sorensen and T. Jacobsen, *Electrochim. Acta*, **27**, 1671 (1982).
12. R. P. Buck, *Crit. Rev. Anal. Chem.*, **5**, 323 (1975).
13. Y. Ohnuki, H. Matsuda, T. Ohsaka, and N. Oyama, *J. Electroanal. Chem.*, **158**, 55 (1983).
14. R. P. Buck and D. E. Hackleman, *Anal. Chem.*, **49**, 2315 (1977).

Photoelectrochemical Properties of Sputtered and Plasma-Oxidized Iron Oxide Films

Lynn C. Schumacher, Suzanne Mamiche-Afara, Michael F. Weber,^{*,1} and Michael J. Dignam*

Lash Miller Chemical Laboratories, University of Toronto, Toronto, Ontario, Canada M5S 1A1

ABSTRACT

The results for iron oxide, thin film ($\sim 500\text{\AA}$) electrodes, formed both by reactive sputtering from an iron target and by plasma oxidation of a sputter-deposited iron film, are reported. The reactively sputtered electrodes were formed by deposition onto sputter-deposited films of both iron and conducting indium tin oxide (ITO), while the plasma oxidized electrodes were formed with ITO only. The performance of the electrodes as photoanodes for O_2 evolution was found to be strongly dependent on a number of fabrication parameters, the best results being achieved for films formed on ITO and then vacuum annealed, both at 350°C . In this case, the performance matched or exceeded that reported in the literature for other methods of fabrication of polycrystalline iron oxide. Annealing these films in oxygen resulted in a decrease in photocurrent by a factor of three to four, as well as a 0.7V suppression of the photocurrent onset potential. The effect was reversed on reannealing *in vacuo*. Postfabrication treatment of electrodes in various aqueous solutions was found to effect their performance significantly. More specifically, a substantial enhancement of the photocurrent in the onset region was achieved by treatment in a boiling KSCN solution. Mott-Schottky plots and conductivity measurements are presented to illuminate these phenomena.

Iron oxide has two valuable properties as an oxygen photoanode in relation to the photoelectrochemical conversion and storage of solar energy: (i) it is stable against photodissolution; and (ii) its bandgap and flatband potential are close to the values required for achieving the maximum conversion efficiency in an unbiased, tandem, photoelectrochemical cell configuration. On the other hand, it suffers from poor transport properties, limiting quantum yields to $<27\%$ even for single crystals (1).

The stability of Fe_2O_3 against photodissociation is attributed to the fact that the optical transition, leading to the generation of electron-hole pairs, is a d-to-d transition (2) and hence not bond breaking. In contrast, most of the lower bandgap materials do undergo photodissociation.

Recently (3, 4), we determined the efficiency limits of a number of different unbiased configurations for the photoelectrochemical splitting of water using solar radiation. The calculations took account not only of the thermodynamics of the photophysical processes, but also of the transport properties of the semiconductor(s) and junctions. We concluded that a single bandgap device, under zero bias, is unlikely to achieve a conversion efficiency higher than $\sim 4.5\%$, this requiring a semiconductor of bandgap $\sim 2.6\text{ eV}$. However, for a tandem photoelectrochemical cell (tandem PEC), consisting, *e.g.*, of a photovoltaic of bandgap $\sim 1.4\text{ eV}$ in optical and electrical series with a photoanode of bandgap $\sim 2.0\text{ eV}$, a conversion efficiency $\sim 17\%$ in unbiased operation becomes a practical goal. Thus while Fe_2O_3 is unable to split water in a single-bandgap, unbiased PEC (its flatband potential is too anodic) it does possess close to the optimum bandgap and flatband potential for use in an unbiased tandem PEC, the former being $2.0 \pm 0.2\text{ eV}$ (5), the latter 0.3V with respect to the reversible hydrogen electrode (1).

The photoelectrochemical properties of both bulk Fe_2O_3 (1, 6-11) and thin film Fe_2O_3 (12-17) have been extensively studied. As already noted, the photostability of Fe_2O_3 has been attributed to the fact that the carrier generating transition is d-to-d. Unfortunately this same feature leads to low hole mobility and hence poor transport properties, since the d bands in which the holes are generated are narrow. It is, in fact, the small overlap of the d orbitals that leads to the narrowness of their band, so that this solution to photostability works directly against achieving good transport properties.

Sputtering is a convenient, inexpensive, readily automated method for producing thin film systems. Film properties can be varied by controlling the substrate temperature, sputtering gas composition and pressure, RF power, substrate bias, and magnetic field strength (in

magnetron sputtering). An important additional advantage of thin films over bulk specimens arises when dealing with relatively high impedance materials, since the film thickness can be tailored to achieve an optimum balance between photon absorption and impedance and recombination losses.

We report here the photoanodic and impedance properties of iron oxide films formed by (i) reactive sputtering of iron in an oxygen plasma onto a presputtered iron film, and (ii) sputtering iron onto a presputtered indium tin oxide (ITO) film, followed by oxidizing it in an oxygen plasma. We have also investigated oxide films formed onto ITO by reactive sputtering; Auger analysis indicates, however, considerable doping of the iron oxide film by the underlying ITO, thus complicating interpretation of the data. Properties of these doped films, while mentioned briefly here, will be treated in detail in a later publication.

Experimental

Sputtering.—Two different sputtering systems were used in the course of this investigation. For the films formed by reactive sputtering onto iron, a Varian, single-target, RF diode system was used. It was modified to include a 15 cm diam heated substrate table capable of achieving temperatures up to 400°C . The films on ITO were formed using a three-target Perkin Elmer Model 2400 RF system, also modified to include a heated, rotatable substrate table with an upper temperature limit of 420°C .

All films were deposited onto microscope slides which had been ultrasonically cleaned in 2-propanol, degreased via hot 2-propanol vapor, then held at $\sim 300^\circ\text{C}$ under vacuum (1×10^{-7} torr) for several hours in the sputtering chamber.

Sputter-deposited iron oxide on iron.—Following presputtering of the iron target in 8×10^{-3} torr argon, $\sim 5000\text{\AA}$ of iron metal was sputtered onto the glass slides at 1000V target bias and an argon pressure of 8×10^{-3} torr, the deposition rate being $\sim 100\text{ \AA}/\text{min}$. Immediately following the iron deposition, oxygen was bled into the plasma, and in most cases the argon flow stopped, leading to reactive sputtering in pure oxygen. The oxygen pressure and substrate temperature were varied from run to run. Following deposition of the desired thickness of iron oxide, the RF field was turned off, the substrate table cooled to room temperature, and the samples removed from the sputtering chamber.

Sputter-deposited iron oxide on ITO.—Deposition of the conducting ITO film proceeded by presputtering the target (Materials Research Corporation 99.97% pure In_2O_3 -9 mol percent SnO_2) in an argon, oxygen mixture, the total

* Electrochemical Society Active Member.

¹ Present address: 3M Center, St. Paul, Minnesota 55133.

pressure being 8×10^{-3} torr and the partial pressure of oxygen about 5×10^{-6} torr. Presputtering was continued until the oxygen partial pressure remained constant at 5×10^{-6} torr under fixed feed conditions. Precise control of the oxygen partial pressure was found to be essential for forming transparent ITO films of good conductivity. The best results were obtained at 1200V target bias, substrate temperature of 320°C, and oxygen partial pressure of 5×10^{-6} torr, the deposition rate being 130 Å/min. Films formed in this way to a thickness of 4000Å were a very pale green in color and had a specific conductivity $\sim 10^4$ mho-cm⁻¹.

Following ITO deposition, the iron target (Materials Research Corporation 99.995% purity) was presputtered at 1000V target bias in 8×10^{-3} torr argon for 30 min, at which time oxygen was introduced into the chamber and the argon flow stopped. The target was then presputtered at 900V target bias in 8×10^{-3} torr oxygen for 1h before deposition of the Fe₂O₃ at a rate of 17.5 Å/min. The long presputtering procedure was found to be necessary to eliminate CO₂ from the system. Mass spectrometric analysis of the chamber gases revealed that the CO₂ peak (mass 44) decreased by two to three orders of magnitude during the presputtering process. Failure to carry out this presputtering procedure led to irreproducible results.

Following deposition of the iron oxide, if no annealing was planned, the heater was allowed to cool to room temperature and the samples removed. If annealing was planned, the substrate table was adjusted to the desired temperature and the films annealed for 10-12h either *in vacuo* or in 2×10^{-2} torr oxygen.

Plasma-grown iron oxide on ITO.—Following deposition of 4000Å of ITO according to the procedure outlined above, the iron target was presputtered at 1000V bias in 8×10^{-3} torr argon for 30 min before depositing the iron film on top of the ITO, the deposition rate being 60 Å/min. When up to ~ 240 Å of iron are exposed to the same plasma conditions as were used to reactively sputter iron oxide (900V target bias, 8×10^{-3} torr oxygen), it is fully oxidized in less than 1.5 min. This thickness of metal (240Å), when fully oxidized, will yield ~ 510 Å of Fe₂O₃ assuming bulk densities. The final films were either annealed, or not, using the same procedure followed for the reactively sputtered films.

Thickness determination.—Deposition rates were determined by three different methods: using an Inficon XTM quartz crystal thickness monitor; by weighing the film deposited in a given time on a semimicrochemical balance; and using a Sloan, Dektac step profiler. The three methods agreed to about $\pm 20\%$ on assuming bulk density for the films.

Electrode preparation.—For photoelectrochemical and electrode impedance measurements, electrodes were fabricated by attaching tinned copper wire to one end of the coated glass slide using GC silver print. A 6 mm diam Pyrex tube was then fastened over the wire to the glass slide using 5 min epoxy glue. The entire assembly was coated with 734 RTV silicone sealant, except for the active oxide surface of area, typically, 0.06-0.10 cm².

Conductivity measurements.—The room temperature conductivity of the oxide films were determined by forming the oxide directly onto glass substrates. An indium-gallium paste was applied to the oxide at fixed intervals and the current-voltage behavior recorded using a PAR Model 170 electrochemistry system.

Photoelectrochemical and impedance measurements.—Photoelectrochemical response curves were made using a PAR Model 170 electrochemical system in conjunction with a focused xenon lamp source, giving a total incident power density at the electrode surface of ~ 0.7 W/cm². Impedance measurements were made using a PAR dual-phase, phase-sensitive amplifier, Model 129A. The 1 kHz ac signal (3 mV peak to peak) was provided by a Wavetek Model 182A function generator. The phase of the lock-in

amplifier was referenced against the ac voltage across the cell and the in- and out-of-phase components of the cell current were measured via a standard $10\Omega \pm 0.005\%$ resistor in series with the cell. Further experimental details can be found elsewhere (18). All measurements were performed at room temperature, $24^\circ \pm 2^\circ\text{C}$, and in N₂-purged 0.10M NaOH, using triply distilled water and analytical reagent-grade sodium hydroxide.

Spectral measurements.—The absorbance of thin oxide films formed directly on vitreous quartz slides were obtained in the range 190-820 nm using a Hewlett-Packard diode array spectrometer, Model 8451A, with the bare quartz slide as reference.

Action spectra were obtained using a Spex Minimate monochromator and a 150W xenon light source. Quantum efficiencies, ϕ , were calculated using the expression $\phi = 1.2408J/I_0\lambda$, where J is the photocurrent density in microamperes per square centimeter, 1.2408 is a conversion factor relating photon flux density to power flux density, and I_0 is the incident power flux density in milliwatts per square centimeters at wavelength λ (expressed in nanometers). While no corrections were made either for transmission losses or for reflection losses at the oxide-electrolyte interface, the procedure followed took account of losses at the electrochemical cell window, since they are matched by losses at the window of the actinometer cell [aqueous iron oxalate (19)] used to calibrate the radiometer (Moletron Model PR 200). The calibration was performed at six different wavelengths with the radiometer used henceforth over the entire wavelength range of interest, 250-750 nm. The electrochemical cell was positioned so that the monochromator slits were imaged at the photoelectrode surface. Thus, I_0 was set equal to the total power flux divided by the area of the slit image, 0.80 cm². Using a diode detector, it was determined that the slit image was uniform in power flux density to within a few percent.

Results and Discussion

Sputter-deposited iron oxide on iron.—Films formed in this way on substrates held at 100°C or less lead to very small photoanodic currents, in agreement with the result reported by Benko *et al.* (17). Performance improved substantially with increasing substrate temperature, however. Figure 1 and 2 show the dc photoanodic response and action spectrum, respectively, for a film about 500Å thick deposited in a pure oxygen plasma onto the iron substrate held at 350°C then cooled immediately to room temperature. Increasing the substrate temperature to 400°C led to no further improvement. While changing the oxygen pressure had no effect on the measured photocurrents, the inclusion of argon in the sputtering gas resulted in substantially lower photocurrents, as was found previously for sputtered TiO₂ films (18).

The data from the action spectrum are plotted in Fig. 3 in a form appropriate for an indirect bandgap semiconductor [$(\phi h\nu)^{1/2}$ vs. $h\nu$, Ref. (20)]. The data for $h\nu < 2.70$ eV

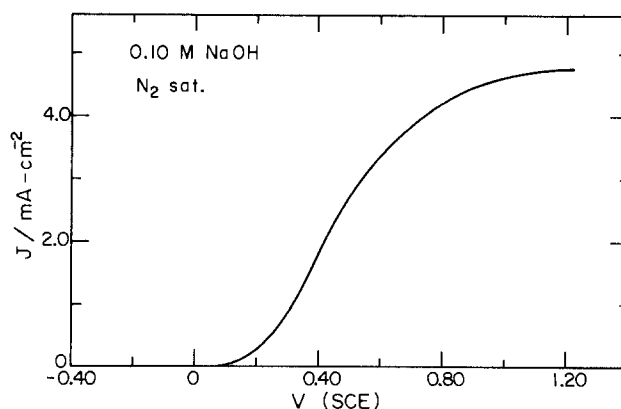


Fig. 1. Photoanodic response curve for 1000Å Fe₂O₃/Fe sputter deposited at 350°C and cooled immediately.

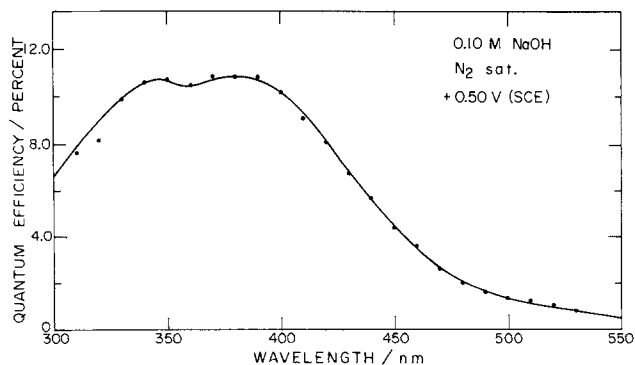


Fig. 2. Action spectrum for electrode of Fig. 1 taken at 0.50V (SCE)

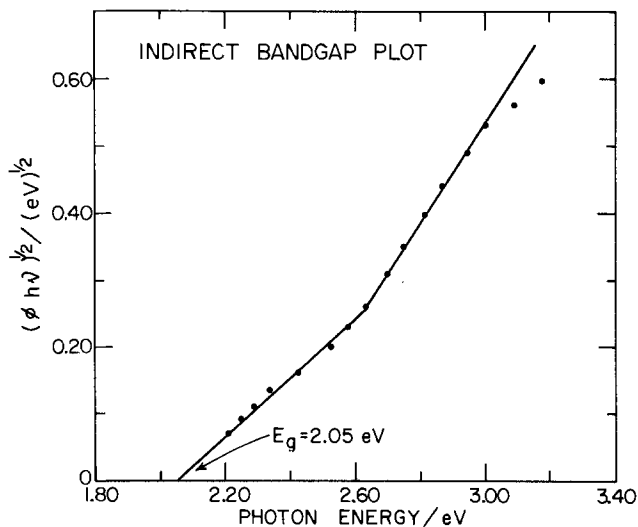


Fig. 3. Indirect bandgap plot for the electrode of Fig. 1, showing a low energy linear region extrapolating to $E_g = 2.05$ eV.

are linear and extrapolate to a bandgap of 2.05 eV, in agreement with the result reported for α - Fe_2O_3 by Morin (5), namely, 2.2 ± 0.2 eV. A Mott-Schottky plot of the impedance data is presented in Fig. 4. The data are similar to results reported for bulk polycrystalline (7) and thermally grown (16) thin α - Fe_2O_3 films. The break occurring at ~ -0.4 V (SCE) has been attributed to deep donor (5, 7, 21) levels which act as electron-hole recombination centers, thereby suppressing the photocurrent onset potential, V_{pc0} to a value ~ 0.3 V anodic of the flatband potential, V_{FB} . Note, however, that V_{pc0} for the film of Fig. 1 is ~ 0.9 V anodic of V_{FB} , representing a further 0.6V anodic suppression of the photocurrent onset compared to that reported for polycrystalline (6) and single-crystal (1) Fe_2O_3 . This could be due to high recombination losses in the bulk and/or at the interface(s), to a kinetic block at the

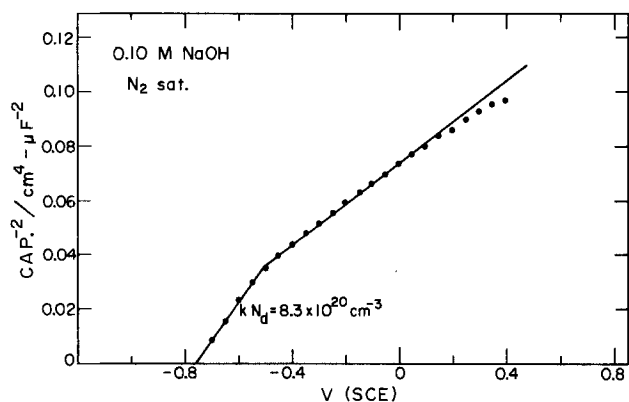


Fig. 4. Mott-Schottky plot (1 kHz) for the electrode of Fig. 1. Since the dielectric constant, K , was not determined, the slopes are reported in terms of the product of K and N_d , the donor density.

oxide-electrolyte interface, or to nonohmic contact of the oxide to the underlying iron metal. This same very large suppression of V_{pc0} is reported by Benko *et al.* for sputtered films of Fe_2O_3 (17). Transient photocurrent studies obtained by chopping the white light at 40 Hz showed photo-onset around -0.70 V (SCE), which is close to the extrapolated flatband from Fig. 4. This indicates that the large suppression of V_{pc0} is not arising due to an anodic flatband shift.

In an attempt to check the ohmic conduction behavior of the oxide-metal contact, an indium-gallium paste was applied to the front surface of the oxide film and the conduction properties of the iron/ Fe_2O_3 /indium-gallium system measured. Highly nonlinear current-voltage curves were obtained in contrast to the behavior of annealed films of Fe_2O_3 on ITO, where ohmic behavior, was obtained. When indium-gallium contacts were made to films of iron oxide reactively sputtered directly onto glass at 350°C and cooled immediately to room temperature, nonlinear i - V behavior was again obtained. However, films which were vacuum annealed (350°C , 10h) showed linear i - V behavior and conductivities of the order of 2.0×10^{-4} mho-cm $^{-1}$. From these results, we cannot conclude that the $\text{Fe}_2\text{O}_3/\text{Fe}$ back contact is ohmic, but the fact that the Mott-Schottky plot extrapolates to the accepted flatband potential and the transient onset potential also occurs near flatband suggests that it is ohmic.

Annealing of the iron/ Fe_2O_3 thin film elements at 350°C *in vacuo* (10^{-7} torr) for 10h led to highly reduced films and no photocurrent.

Sputter-deposited iron oxide on ITO.—As for the iron-supported films, films deposited on ITO at or below 100°C showed only a very small photocurrent. Films deposited onto ITO at 350°C in a pure oxygen plasma and cooled immediately gave results very similar to those deposited onto an iron substrate. Vacuum annealing for 10h at 350°C , however, led to a dramatic improvement in their photoanodic response, as illustrated in Fig. 5, for a film 500Å thick.

While these results showed clearly the pronounced benefit of vacuum annealing, further studies were restricted to plasma-grown films, since Auger depth profile analysis of a 250Å film formed by reactive sputtering onto ITO showed indium doping to the extent of 10-15% at the outer surface, decreasing to 7-8% in the bulk of the film, before increasing again near the $\text{Fe}_2\text{O}_3/\text{ITO}$ back contact.

Plasma-grown iron oxide on ITO.—Auger depth profile analysis of iron oxide films grown in this way showed no detectable indium (<2%) at either the front surface or in the bulk of the film.

Figures 6-8 show the action spectrum, indirect bandgap plot, and Mott-Schottky plot for a 500Å film formed by plasma oxidation at 350°C followed by vacuum annealing for 10h at 350°C . The results are close to those

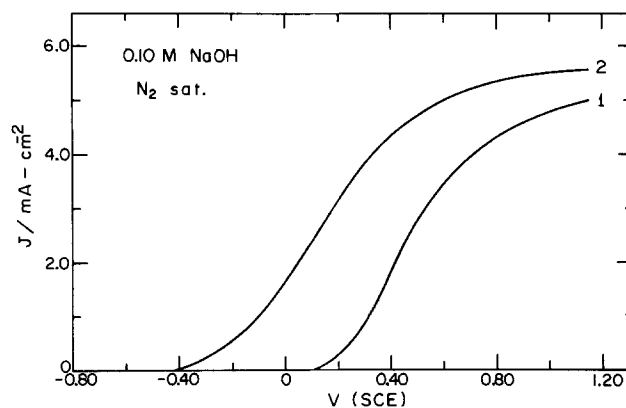


Fig. 5. Photoanodic response curve for 500Å $\text{Fe}_2\text{O}_3/\text{ITO}$ sputter deposited at 350°C then cooled over 3h *in vacuo* (curve 1) or vacuum annealed for 10h at 350°C (curve 2).

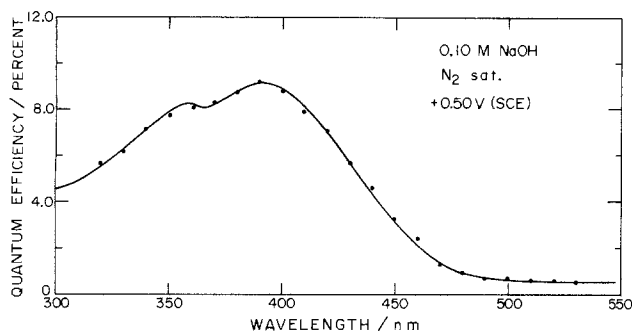


Fig. 6. Action spectrum for 500Å $\text{Fe}_2\text{O}_3/\text{ITO}$ formed by plasma oxidation followed by vacuum annealing, both at 350°C.

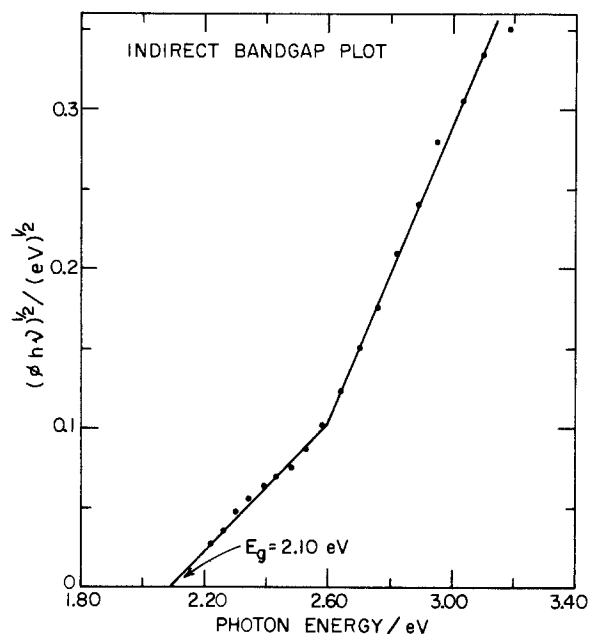


Fig. 7. Indirect bandgap plot for electrode of Fig. 6

for the reactively sputtered and vacuum-annealed films. However, comparison of the Mott-Schottky plots indicates both a higher doping density and a cathodic shift of 0.1V in V_{FB} for the plasma-grown oxide relative to the reactively sputtered oxide.

To ascertain the role of vacuum annealing, some films were annealed for 10h in 2×10^{-2} torr oxygen following film formation. The photoanodic response curve and Mott-Schottky plot for one of these samples are shown in Fig. 9 and 10, respectively, along with those for a sample from the same batch that was returned to the

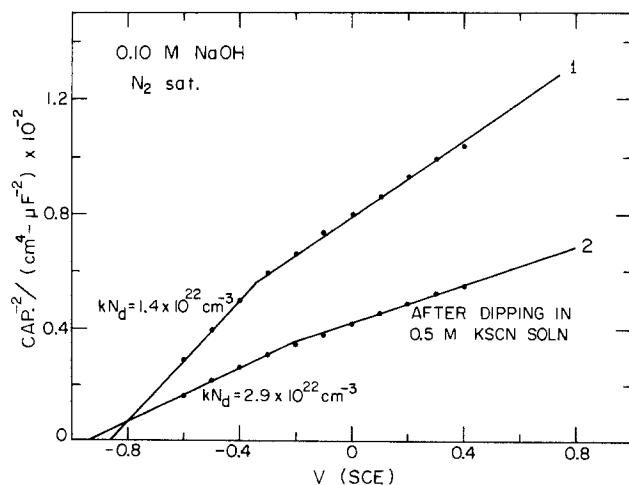


Fig. 8. Mott-Schottky plot (1 kHz) for electrode of Fig. 6, before (curve 1) and after (curve 2) treatment with boiling 0.5M KSCN.

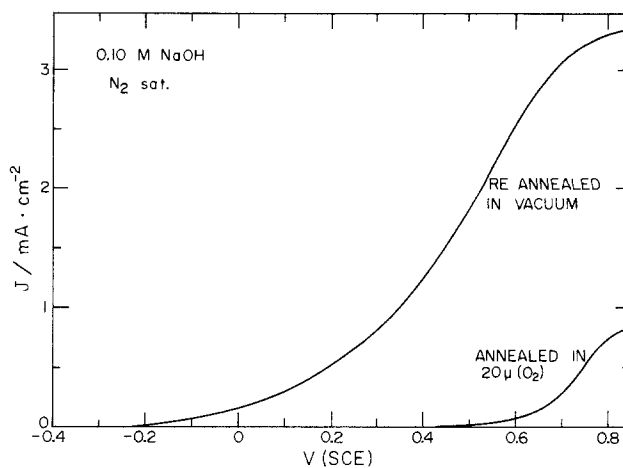


Fig. 9. Photoanodic response curves for 500Å $\text{Fe}_2\text{O}_3/\text{ITO}$ formed by plasma oxidation at 350°C. Both film systems were initially annealed 10h in oxygen at 350°C, but the effect of reannealing at 350°C in vacuum for 10h can be seen.

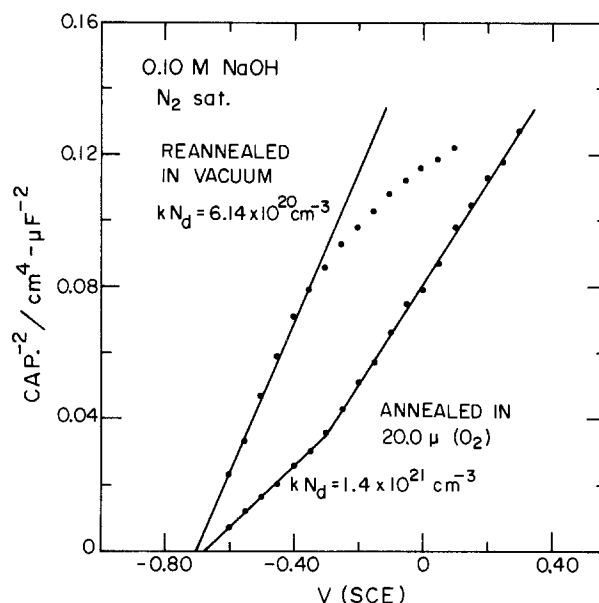


Fig. 10. Mott-Schottky plots (1 kHz) for electrodes of Fig. 9

vacuum chamber and vacuum annealed for 10h at 350°C. The pronounced improvement in both V_{poc} and the photocurrent produced by annealing *in vacuo* rather than in an oxygen atmosphere is clearly illustrated in the results. The reversibility of the changes brought about by annealing alternately *in vacuo* and in oxygen suggests a compositional, rather than structural, basis for the changes. Samples annealed in vacuum initially then reannealed in oxygen also showed the same degraded photocurrent behavior as the films annealed in O_2 initially.

The absorption spectra for 500Å, plasma-formed iron oxide films on vitreous quartz (no ITO present) are presented in Fig. 11. There is a significant difference in the spectra, depending on whether the film is annealed at 350°C for 10h in oxygen or *in vacuo*. Both spectra, however, are similar to that reported by Gardner *et al.* (21) for a 440Å thick iron oxide film formed on alumina by an unspecified procedure. The absorption shoulder at 560 nm (2.2 eV) is consistent with the indirect bandgap determined here (2.05 eV). Also apparent is an absorption peak beginning at about 460 nm (2.7 eV) and reaching a maximum of 385 nm (3.22 eV). This absorption peak has been attributed by Gardner *et al.* (19) to direct charge transfer from oxygen to iron. A direct bandgap plot of the quantum efficiency data (Fig. 12) does indeed produce a linear region from 2.85 to 3.2 eV, which extrapolates to a bandgap of 2.8 eV. This direct

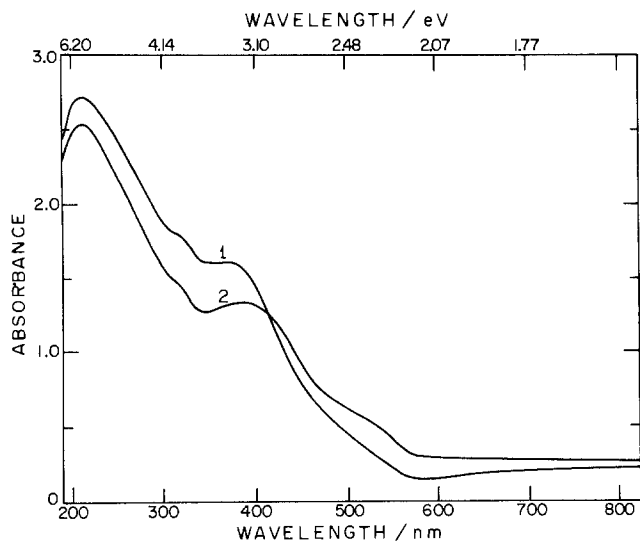


Fig. 11. Absorbance plots for 500Å plasma-formed Fe_2O_3 films on vitreous quartz. Curve 1: annealed 10h in oxygen. Curve 2: annealed 10h *in vacuo*. Note suppression of onset at 2.2 eV of oxygen-onnealed film is reflected in poor photoanodic behavior, Fig. 9.

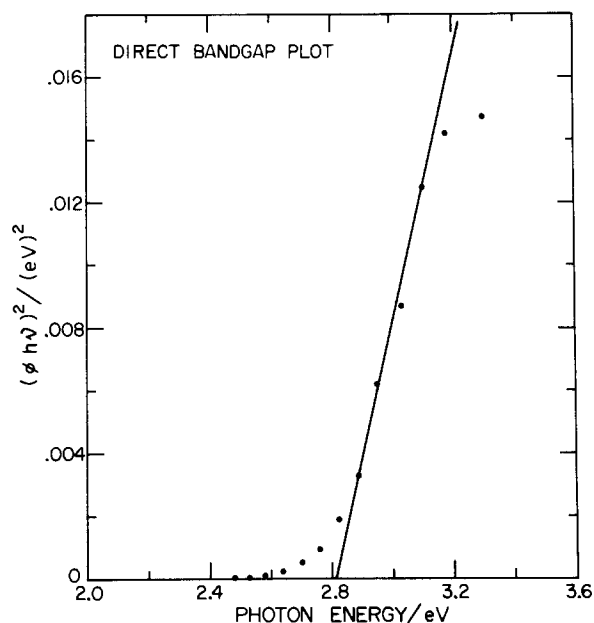


Fig. 12. Direct bandgap plot for electrode of Fig. 6

transition, which is superimposed on the indirect transition, is clearly responsible for the break in the indirect bandgap plots of Fig. 3 and 7.

Conductivity measurements made on films deposited directly onto glass slides, using indium-gallium contacts, yielded values in the range 5×10^{-6} – 10^{-5} mho-cm $^{-1}$ for unannealed samples, and in the range 2×10^{-4} – 2×10^{-3} mho-cm $^{-1}$ for vacuum-annealed samples. This change in conductivity is by a factor substantially larger than one would infer from the slopes of the Mott-Schottky plots (Fig. 10). This result, as well as the spectra of Fig. 11, suggests that vacuum annealing brings about more than simply an increase in the electron donor concentration. We are currently in the process of studying systematically the solid-state properties of plasma-formed iron oxide and the role of vacuum annealing, with this paper concentrating on their photoelectrochemical properties.

Postformation modification of vacuum-annealed, plasma-formed films.—In order to improve the photocurrent onset behavior of the vacuum-annealed films formed by plasma oxidation, postformation treatment with a number of aqueous solutions was tried, with

those producing a significant change, for better or for worse, being reported here.

Figure 13 shows the effect of including different concentrations of sodium vanadate in the 0.10M NaOH electrolyte on the photoanodic response curve. The effect is entirely reversible in that upon rinsing the electrode and returning it to fresh 0.10M NaOH (no vanadate) the original response curve is recovered.

Kyriacou (22) has shown that vanadate ions adsorb and polymerize on the surface of hematite at and above pH 10. The mechanism is assumed to involve the displacement of surface OH^- , which would explain the suppression of the photocurrent observed here in the presence of vanadate ions, as the surface OH^- are presumably the sites for water oxidation.

A number of electron donor complexing agents were tested for their efficacy in increasing the photocurrent, the most active of which was the thiocyanate ion, SCN^- . While treatment of an electrode in 0.50M KSCN for 5 min at room temperature produced no significant change in photocurrent, the same treatment in a boiling solution brought about a marked improvement in the photoanodic response. As can be seen from Fig. 14, the improvement is in the rate of current rise from V_{pco} to saturation (*i.e.*, in the fill factor) rather than in V_{pco} or the saturation current. The improvement, however, is substantial, representing a factor of two to three increase in photocurrent over much of the rising portion of the photoanodic response curve. Mott-Schottky plots for a plasma-oxidized film, both before and immediately after treatment with KSCN, are illustrated in Fig. 8. While the results appear to indicate that the treatment leads to a significant increase in carrier concentration, an additional, specific surface effect is not precluded. An improvement in photoanodic behavior has been reported by Kennedy *et al.* (8) resulting from immersing polycrystalline Fe_2O_3 in 1M KI for 3 weeks. They also observed the onset of a small photocurrent at the flatband potential associated with photo-oxidation of I^- (9). While they attribute these results to surface modification, the possibility of a concurrent change in the bulk properties through incorporation of I^- cannot be ruled out.

Results for treatment with cyanate (OCN^-) and pyrazine are shown in Fig. 14. As for thiocyanate, no effect was observed for treatment at room temperature. All of the nitrogen containing ligands tested led to some improvement in the fill factor for the photoanode when the treatment was carried out in boiling solution. Simply treating an electrode in boiling 0.10M NaOH, however, had no effect on the photocurrent, but such treatment,

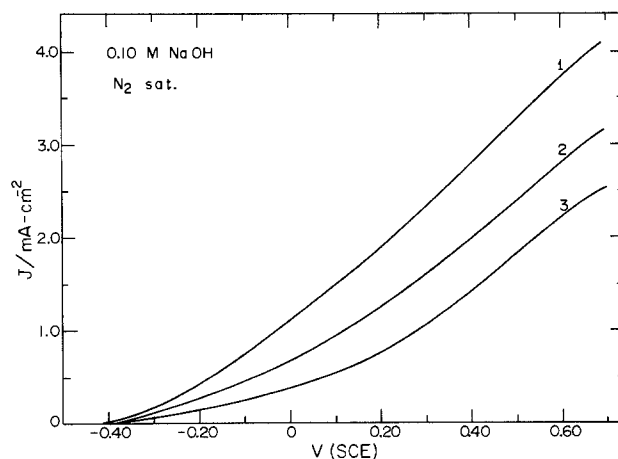


Fig. 13. Photoanodic response curves for 500Å $\text{Fe}_2\text{O}_3/\text{ITO}$ plasma formed and annealed 10h *in vacuo*, both at 350°C, showing the influence of vanadate ion in the electrolyte. Curves 1-3 are for, respectively, 0, 0.0010, and 0.010M NaVO_3 in 0.10M NaOH. The response returns to that of curve 1 when the electrode is rinsed and returned to fresh 0.10M NaOH.

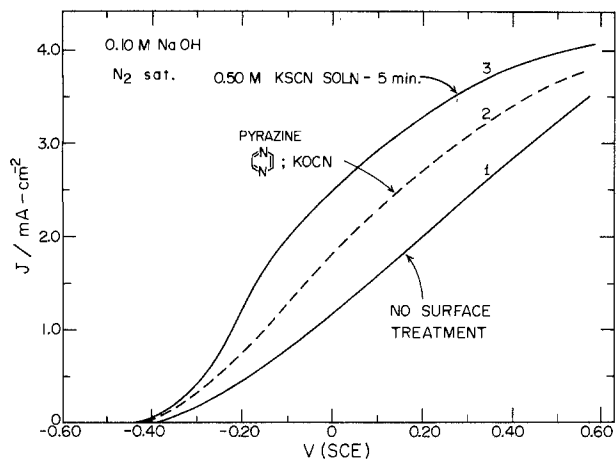


Fig. 14. Photoanodic response curves for electrodes formed as per Fig. 13, then treated in boiling aqueous solutions of different complexing Lewis bases for 5-10 min, the concentration being in the range 0.10-0.50M.

following *e.g.*, the KSCN treatment, restored the photocurrent response to that of an untreated electrode. The change brought about by the complexing agent is evidently fairly easily reversed. Thus, while the photocurrent enhancement was stable for up to 3h, sitting in 0.10M NaOH for 24h at room temperature restored pretreatment behavior.

The results of Lin *et al.* (23) indicate that the active sites for H₂O oxidation are associated with Fe₂⁺ ions on the surface of α -Fe₂O₃. Perhaps the complexing agents stabilize this oxidation state, thereby enhancing the charge transfer step at the oxide-electrolyte interface. Such a proposition is consistent with the fact that the strongest Lewis base, SCN⁻, produced that greatest improvement in the fill factor. Whatever the explanation, however, the improvement achieved is considerable, and suggests the possibility of achieving further improvement in this way. Note, however, that these complexing agents have little or no effect on V_{pc0} , which is $\sim 0.3V$ anodic of V_{FB} . If the source of this anodic shift in V_{pc0} is indeed the presence of deep donor levels, 0.3V below the Fermi level (5, 7, 19), then one could not expect to alter V_{pc0} through surface treatment alone. Likewise, surface treatment is not expected to alter the saturation photocurrent. Thus, while we have shown that treatment with certain complexing agents can result in a substantial improvement in the fill factor, the problems of late photocurrent onset and low quantum yield remain.

Summary and Conclusions

Thin film (500Å) Fe₂O₃ photoanodes, with characteristics closely matching those for polycrystalline iron oxide formed by other methods (8, 15) have been fabricated using atomic sputtering techniques. Achievement of such behavior requires annealing the films at $\sim 350^\circ C$ *in vacuo*. In turn, this treatment dictates a back contact material that does not lead to reduction of the Fe₂O₃ film during the annealing process, eliminating iron for this purpose. Procedures for depositing high conductivity, high transparency ITO films were developed and such films found to form excellent, ohmic back contacts for the Fe₂O₃ films produced either by reactive sputtering or plasma oxidation of iron films. While reactive sputtering produced Fe₂O₃ films containing 7-15% In, no In could be detected in the films formed by plasma oxidation.

The very large improvement in the photoanodic response characteristics brought about by vacuum annealing at 350°C are reversed on annealing in oxygen at 350°C.

Mott-Schottky, spectral, and conductivity measurements were performed on both the vacuum- and oxygen-annealed samples to illuminate the mechanism involved in this process; the problem, however, awaits a thorough investigation.

Treatment of the electrodes in boiling aqueous solution containing electron donor complexing agents resulted in larger fill factors, the most substantial increase resulting from treatment in KSCN. Boiling in 0.10M NaOH apparently removed the complexing agent as the fill factor returned to its original value. The magnitude of the effect appears to be related to the Lewis base strength of the complexing agent, and we have suggested that the complexing agent may facilitate electron transfer at the oxide-electrolyte interface by stabilizing surface Fe²⁺ ions, believed to be connected with the sites for water oxidation (23). Other possibilities exist, however. Inclusion of vanadate ion in the electrolyte suppresses the photocurrent, the mechanism being perhaps the chemisorption of vanadate ion through substitution for the surface OH⁻ ions (22), such OH⁻ presumably being the site for water oxidation.

Acknowledgments

The authors wish to express their appreciation to the Natural Science and Engineering Research Council of Canada for supporting this research, and to Tammy Chan of the University of Western Ontario Surface Science Group for performing the Auger analysis.

Manuscript submitted April 22, 1985; revised manuscript received Aug. 12, 1985.

The University of Toronto assisted in meeting the publication costs of this article.

REFERENCES

- R. K. Quinn, R. D. Nasby, and R. J. Baughman, *Mater. Res. Bull.*, **11**, 1011 (1976).
- S. P. Tandon and J. P. Gupta, *Spectrosc. Lett.*, **3**, 297 (1970).
- M. F. Weber and M. J. Dignam, *This Journal*, **131**, 1258 (1984).
- M. F. Weber and M. J. Dignam, in "Hydrogen Energy Progress V," Vol. 3, T. N. Veziroglu and J. B. Taylor, Editors, pp. 957-968, Pergamon Press, London (1984).
- F. J. Morin, *Phys. Rev.*, **83**, 1005 (1951).
- J. H. Kennedy and K. W. Frese, Jr., *This Journal*, **125**, 709 (1978).
- J. H. Kennedy and K. W. Frese, Jr., *ibid.*, **125**, 723 (1978).
- J. H. Kennedy, M. Anderman, and R. Shinar, *ibid.*, **128**, 2371 (1981).
- M. Anderman and J. H. Kennedy, *ibid.*, **131**, 21 (1984).
- C. Leygraf, M. Hendewerk, and G. A. Somorjai, *J. Catal.*, **78**, 341 (1982).
- J. E. Turner, M. Hendewerk, J. Parmeter, D. Neiman, and G. A. Somorjai, *This Journal*, **131**, 1777 (1984).
- K. L. Hardee and A. J. Bard, *ibid.*, **123**, 1024 (1976).
- L. R. Yeh and N. Hackerman, *ibid.*, **124**, 833 (1977).
- J. S. Curran and W. Gissler, *ibid.*, **126**, 56 (1979).
- K. Itoh and J. O'M. Bockris, *ibid.*, **131**, 1266 (1984).
- S. M. Wilhelm, K. S. Yun, L. W. Ballenger, and N. Hackerman, *ibid.*, **126**, 419 (1979).
- F. A. Benko and F. P. Koffyberg, *ibid.*, **132**, 609 (1985).
- M. F. Weber, L. C. Schumacher, and M. J. Dignam, *ibid.*, **129**, 2022 (1982).
- C. G. Hatchard and C. A. Parker, *Proc. R. Soc. London, Ser. A*, **235**, 518 (1956).
- M. A. Butler and D. S. Ginley in "Semiconductor Liquid Junction Solar Cells," A. Heller, Editor, p. 290, The Electrochemical Society Softbound Proceedings Series, Princeton, NJ (1977).
- R. F. G. Gardner, F. Sweett, and D. W. Tanner, *J. Phys. Chem. Solids*, **24**, 1183 (1963).
- D. Kyriacou, *Surf. Sci.*, **8**, 370 (1967).
- Z. Lin, Y. Cheng, S. Wu, X. Wu, S. Qu, and K. Xie, *Wuli Xuebao*, **32**, 1595 (1983).

Electrochemical Oxidation of Methane in Nonaqueous Electrolytes at Room Temperature

Application to Gas Sensors

Takaaki Otagawa,*¹ Solomon Zaromb,* and Joseph R. Stetter

Argonne National Laboratory, Energy and Environmental Systems Division, Argonne, Illinois 60439

ABSTRACT

The electrochemical oxidation of methane at room temperature was studied using several nonaqueous solvents and electrocatalysts. The best sensitivity and reaction stability were obtained with an electrode composed of platinum black mixed with a 35 weight percent Teflon® dispersion and deposited on a porous Teflon membrane in contact with an electrolyte of 2M NaClO₄ in γ -butyrolactone. A working electrode potential of 800 mV *vs.* Ag/AgCl gave the least current variation with changing relative humidity. However, a potential of 600 mV *vs.* Ag/AgCl gave the highest signal-to-background current ratio. The sensitivity (net current) measured for the electro-oxidation of methane in γ -butyrolactone increased significantly with increasing temperature. The reaction has an activation energy of approximately 12 kcal/mol. An electrochemical methane monitor was constructed exhibiting a sensitivity of 1 μ A/% CH₄ and negligible sensitivity to parts-per-million levels of CO or NO₂. However, it gave responses to > 0.3% H₂, 49 ppm NO, and 50% C₂H₆ that could be mistaken for methane signals.

The potential advantages of amperometric methane sensors have been recognized for detecting natural gas (1) and for meeting the requirements of the U.S. Bureau of Mines' Intrinsic Safe Mine Monitoring System (2, 3).

Although electro-oxidation of methane on a platinum electrocatalyst occurs at an appreciable rate in aqueous phosphoric, sulfuric, and perchloric acids in the 60°-150°C range (4-8), methane's poor electrochemical reactivity at lower temperatures has frustrated attempts to develop room temperature reactors and sensors (1, 9). A high overpotential is required to oxidize methane at room temperature (4, 9), although the electro-oxidation of methane is thermodynamically favored at modest potentials, *i.e.*, the reaction CH₄ (g) + H₂O (l) → CH₃OH (aq) + 2H⁺ + 2e⁻ has $E^\circ = 0.586$ V *vs.* the reversible hydrogen electrode (RHE) (10). At high overpotentials (≥ 0.8 V), the water oxidation reaction proceeds at a high rate and results in intolerable high background currents in sensors containing aqueous electrolytes.

Problems of this type have been encountered and solved in practical sensors by varying the sensing electrode catalyst, the method of catalyst preparation, the electrolyte composition, or the cell geometry (11). The use of nonaqueous electrolytes (*e.g.*, propylene carbonate, glycols, and solid polymers) has been reported as a particularly promising approach for methane oxidation (12).

Several novel amperometric sensors that respond to methane at room temperature, each using a Teflon®-bonded platinum black working electrode and a nonaqueous electrolyte in a three-electrode cell, have been developed recently at Argonne National Laboratory (13-15). The electrochemical studies that led to development of these sensors are described in this paper.

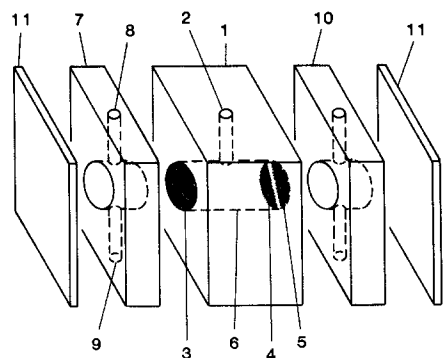
Experimental

Cell construction.—The Teflon-bonded platinum black electrodes were prepared by mixing the desired proportions of commercial platinum black (Engelhard Industries, East Newark, New Jersey), with Teflon 30 dispersion (E.I. du Pont de Nemours and Company, Incorporated, Wilmington, Delaware), and bonding the mixture to a porous Teflon membrane (Zitex™, Chemplast, Incorporated, Wayne, New Jersey), in a way similar to previously reported procedures (16). The platinum black catalyst loading was 14 mg/cm², and the Teflon content of the dehydrated mix was varied between 20 and 45% of weight. Other noble metal black (Engelhard Industries) or oxide electrodes [prepared by coprecipitation of nitrates (17) obtained as reagent-grade chemicals

from Aldrich Chemical Company, Incorporated, Milwaukee, Wisconsin], were made in a similar way.

Each electrode was heat pressed at 100°C and 0.81 kg/cm² for 5 min, with the catalyst pressed against a 40 mesh platinum screen that served both as a support and as an efficient current collector. The electrodes were then sealed onto a polypropylene sensor body, in which the vertically positioned working and counter-reference electrodes were located at opposite ends of the electrolyte chamber (see Fig. 1). The geometric areas of the working, reference, and counterelectrodes were 1.27, 0.42, and 0.84, respectively.

Electrochemical measurements.—The impedance between each pair of electrodes was determined using a conductivity bridge (Model 31, Yellow Springs Instrument Company, Incorporated, Yellow Springs, Ohio), at 1 kHz, after allowing the electrodes to stay in contact with an electrolyte solution overnight. The potential of the platinum/air reference electrode was measured using a microflexible Ag/AgCl reference electrode (Model MI-402, Microelectrodes, Incorporated, Londonderry, New Hampshire). The potential of the working electrode was maintained constant *vs.* the platinum/air reference electrode, which was built into each sensor, using a potentiostat designed and constructed in house. The signal output from the current/voltage converter of the potentiostat was recorded on a three-channel strip-chart



- | | |
|------------------------|--|
| 1. Main compartment | 7. Gas chamber for working electrode |
| 2. Solution inlet | 8. Gas inlet |
| 3. Working electrode | 9. Gas outlet |
| 4. Reference electrode | 10. Gas chamber for counter-reference electrodes |
| 5. Counter electrode | 11. Cover |
| 6. Solution reservoir | |
| working electrode | |

Fig. 1. Basic sensor design

* Electrochemical Society Active Member.

¹ Present address: Life Systems, Incorporated, Beachwood, Ohio 44122.

recorder (Model 1243, Soltec Corporation, Sun Valley, California).

Current/potential curves for methane oxidation at each potential were determined only after allowing the working electrode to equilibrate at the desired potential for at least 12h. The current was initially recorded in a background of "zero" air (*i.e.*, air containing no methane or other known impurities) of a constant relative humidity for at least one hour, until it reached a steady-state value. Subsequently, the steady-state currents were measured for methane samples of the same relative humidity.

Various nonaqueous solvents (99.99% purity, Aldrich Chemical Company, Incorporated), containing 1-3M NaClO₄ or LiClO₄ (99.99% purity, Aldrich Chemical Company, Incorporated), as the electrolytes were prepared and placed in the solution reservoir of the sensor (see Fig. 1). All chemicals were used without further purification.

Gas sample preparation.—High purity methane (99.99%, Scott Environmental Technology, Incorporated, Troy, Michigan) was used for all experiments. The purity of the methane samples was further verified using a sensor array in a portable device for detecting and identifying hazardous vapors developed at Argonne (18, 19). No traces (≥ 1 ppm) of CO, NO, NO₂, or H₂ were detected. Various concentrations of methane in air were prepared by dynamically mixing 99.99% methane and hydrocarbon-free air (Scott Environmental Technology, Incorporated) at proper ratios using two flow meters. All other gas mixtures used in this work (200 ppm CO in air, 49 ppm NO in N₂, 48 ppm NO₂ in air, 200 ppm and 0.5% H₂ in air, and 99.9% C₂H₆) were obtained from Scott Environmental Technology, Incorporated, in premixed cylinders. About 2 liters of each pure gas or gas mixture was first collected into a Teflon gas sampling bag (30 × 30 cm, Pollution Measurement Corporation, Chicago, Illinois) before use.

Humidified methane samples were prepared by passing dry gas samples through a 2.5-5 cm Gore-Tex® (porous Teflon) tube (Gore-Tex TA001, W. L. Gore & Associates, Incorporated, Elkton, Maryland) immersed in water. The relative humidity of the gas mixture was determined by placing a humidity sensor (Model 455, General Eastern Instruments Corporation, Watertown, Massachusetts) in the gas flow path.

In all experiments, the methane samples were pumped with a portable air pump (Model AS-100-1, Spectrex Corporation, Redwood City, California) through a "zero" filter (10 cm length by 2 cm diam) that contained sequential beds of activated carbon, Purafil (KMnO₄/Al₂O₃) and 1% platinum coated on alumina. This purification system was designed to remove CO, H₂, and other trace impurities from the methane gas before it entered the sensor's gas exposure chamber. Unless otherwise stated, all measurements were performed at 23°C. The flow rate for the gas samples through the sensor was typically 100 cm³/min.

An environmental chamber (Model 816, GCA/Precision Scientific, Chicago, Illinois) was used to control the temperature of the experiments. The entire experimental setup, including gas sampling bags for methane and pure air, was placed inside the environmental chamber. The system was allowed to thermally equilibrate at the temperature of interest for at least 3h before any data were taken.

Results and Discussion

Selection of solvent.—The response to dry methane of sensors using a platinum black working electrode (20 weight percent [w/o] Teflon) on a porous Teflon membrane (Zitex H606-122) was recorded for sensors containing 11 solvent and solvent-gel combinations. Table I summarizes the results obtained. Two nonaqueous solvents not listed in the table, benzonitrile and dimethylformamide, did not dissolve enough electrolyte (NaClO₄) to yield a conductivity sufficiently high for use in an amperometric sensor (low conductivities result in small signals and slow responses). Also, solvents with low

boiling points (*e.g.*, acetonitrile) gave small or insignificant signals for methane. These solvents may have been too volatile for the electrodes to be properly wetted. Solvents can also influence the methane signal by inhibiting the reaction at the electrode surface or by inhibiting efficient transport of the methane to the electrode.

Propylene carbonate and γ -butyrolactone gave the best responses to methane under the test conditions. Although the propylene carbonate electrolyte yielded a response of about 10 μ A to 100% methane, it exhibited a continuously changing background current. This current may have been associated with the electrochemical decomposition of propylene carbonate into propylene and carbonate at the potential used in these experiments (20). The low sensitivity and rather slow response of this sensor could be due to partial or complete flooding of the pores in the Teflon-bonded electrode by the electrolyte. To eliminate or reduce pore flooding, the propylene carbonate electrolyte was gelled by adding approximately 10 w/o polymethylmethacrylate. A rapid response but a weak signal was observed for 100% methane. Because polymethylmethacrylate cannot withstand the highly anodic electrode potentials required for methane oxidation, sensors containing this gel were characterized by high background currents and unstable sensor response over short time periods.

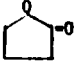

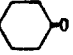

The smallest background current drift was obtained with γ -butyrolactone or sulfolane. Because sulfolane does not dissolve salt readily, the electrolytes obtained had low conductivity, which results in weak sensor signals. On the other hand, the sensitivity achieved with γ -butyrolactone was as high as that achieved with propylene carbonate. The γ -butyrolactone system also exhibited lower cell resistance ($\sim 60\Omega$) than the propylene carbonate system ($\sim 150\Omega$). This result suggested the possibility of achieving more efficient methane oxidation with γ -butyrolactone and a working electrode designed to control pore flooding. Therefore, small quantities (~ 4 w/o) of polymethylmethacrylate were added to γ -butyrolactone, which rendered the electrolyte more viscous. Such additions resulted in methane signals as large as 70 μ A, a result that can be attributed to reduced pore flooding. However, such methane signals are not easily reproduced because of the electrochemical instability of polymethylmethacrylate and the formation of an insulating white polymer film in the electrode pores when the electrode is exposed to moisture.

In summary, the most reproducible methane oxidation currents were achieved with pure γ -butyrolactone electrolyte, which was used as the solvent in the remainder of the experiments.

Optimization of porous electrodes.—A catalyst bed of platinum black with a 20 w/o Teflon content was deposited on different Zitex (porous Teflon) membranes to study the effect of pore size and pore thickness on the electrochemical signal resulting from methane oxidation. Zitex membranes having pores of from 2.5 to 20-30 μ m were used. Only those with pores between 5 and 20 μ m gave large, stable, and repeatable currents. It was apparent from these measurements that mass transport of the reactant to the electrode was important. Satisfactory results were obtained with either Zitex H662-123 (10-20 μ m pores) or Zitex E606-122 (5-10 μ m pores). The Zitex H662-123 membrane performed better because of its open structure, which permitted it to supply gas quickly to the electrode-electrolyte interface. This membrane was used in the following experiments.

As in fuel cell operation, electrochemical gas sensing requires establishing a stable triple-phase (gas-electrode-electrolyte) interface at the working electrode. The Teflon content of the electrode significantly affects the nature of this interface, which has a profound effect on sensor performance, especially sensitivity and response time. Of the three Teflon concentrations tested, the sensitivity to methane was highest at a concentration of 35 w/o Teflon (see Fig. 2). This behavior is similar to that ob-

Table I. Physicochemical properties and sensor response for some nonaqueous electrolyte systems

Compound	Viscosity (Pa-s)	Melting point (°C)	Boiling point (°C)	Dielectric constant	Anodic limit (V)	Cell impedance (W-C, Ω)	Background current (μA)	Signal for 100% CH ₄ at 500 mV bias ^a (μA)
Acetonitrile: CH ₃ CN	0.00036	-42	82	38.8	2.4 (Ag/Ag ⁺)	20 (2M NaClO ₄)	3	None
Nitromethane: CH ₃ NO ₂	0.000619	-29	101	39.4	2.7(SCE) ^b	150 (~2M LiClO ₄)	12	None
Acetic acid: CH ₃ COOH	0.00122	16.7	118	6.2	2.0(SCE)	130 (1M CH ₃ COONa)	40	None
γ-Butyrolactone: 	0.00167	-4	206	39	?	60 (1-3M NaClO ₄)	10	10
Dimethylsulfoxide: (CH ₃) ₂ SO	0.00193	6	189	48	0.7(SCE)	90 (2M NaClO ₄)	30	None
Propylene carbonate: 	0.0022	-49	242	64.4	1.7(SCE)	150 (2M NaClO ₄)	10-25	10
Cyclohexanone: ^c 	0.0028	-16	156	18	?	200 (2M LiClO ₄)	350	None
Sulfolane: 	0.00987	28	285	44	2.3(SCE)	430 (1.5M LiClO ₄)	1.75	0.15
γ-butyrolactone-polymethylmethacrylate ^d	>0.010					60	20	40-70
Acetonitrile-gel ^e	>0.010					20	1.8	None
Propylene carbonate gel ^e	>0.010					130	6.4	1.5

^a Corresponds approximately to 0.8V vs. Ag/AgCl in the same solution.

^b Saturated calomel electrode.

^c Black liquid formed.

^d Not reproducible.

^e 4-10 w/o polymethylmethacrylate.

Source: Anodic limits are from Ref. (22).

served for porous gas diffusion electrodes used in fuel cell technology (16, 21). At low Teflon concentrations, the active electrocatalyst layer was filled with electrolyte, resulting in internal diffusion control; hence, observed oxidation currents were small. Indeed, in the case of 20 w/o Teflon, an increase in the potential of the working elec-

trode did not enhance oxidation currents for methane, which clearly indicated a diffusion-controlled condition rather than one limited by electrocatalyst activity. As the Teflon concentration was increased to 35 w/o, the degree of pore flooding in the electrode decreased, and the control of the reaction rate changed from diffusion to electrochemical activation. An increase in the Teflon concentration beyond 35 w/o resulted in lowered electrochemical activity caused by a decrease in the catalyst's effective conductivity and surface area.

In the case of 35 w/o Teflon, the addition of polymethylmethacrylate gave oxidation currents of the same magnitude as those obtained with pure γ-butyrolactone. This observation supports our conclusion that the maximum degree of utilization of the catalyst may have been achieved with a Teflon concentration of 35 w/o.

Electrode performance characteristics.—Effect of the electrolyte.—The electrolyte used with the γ-butyrolactone solvent was NaClO₄. No substantial differences were observed in methane oxidation currents when LiClO₄ was substituted for NaClO₄. The solubility of NaPF₆, which is reported to be electrochemically more stable than perchlorates (22), is too low in γ-butyrolactone to produce a usable electrolyte.

There have been reports of explosion incidents involving LiClO₄ in dioxolane (23) or nitromethane (24, 25). In both cases, the electrolyte was in direct contact with metallic Li. Our literature search has not uncovered any reports of explosion incidents involving NaClO₄ in γ-butyrolactone, and we believe that our operating conditions (10°-42°C ambient temperature, low operating current densities) are sufficiently different from those in the reported incidents to render the probability of an explosion hazard with this system extremely remote.

The variation in the magnitude of the methane oxidation current with the concentration of NaClO₄ in γ-butyrolactone is shown in Fig. 3. The highest current is

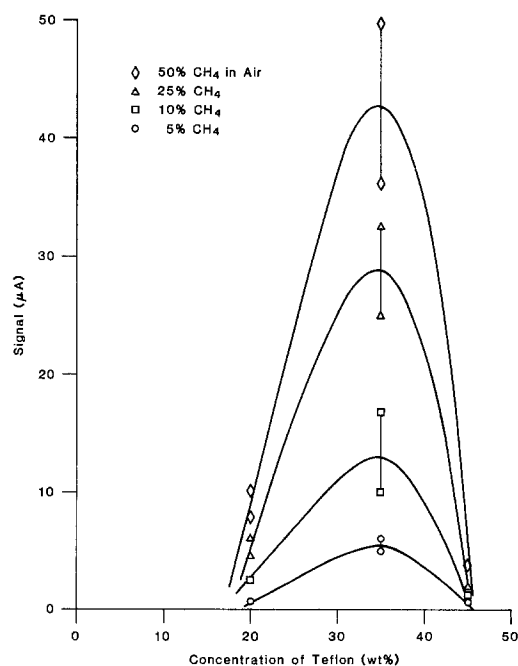


Fig. 2. Net response to various concentrations of methane in air as a function of Teflon concentration. Pt block: 14 mg/cm². Zitetex: H662-123. Electrolyte: 2M NaClO₄ in γ-butyrolactone. Electrode potential: 0.85V vs. Ag/AgCl. Flow rate: 100 cm³/min with a zero filter.

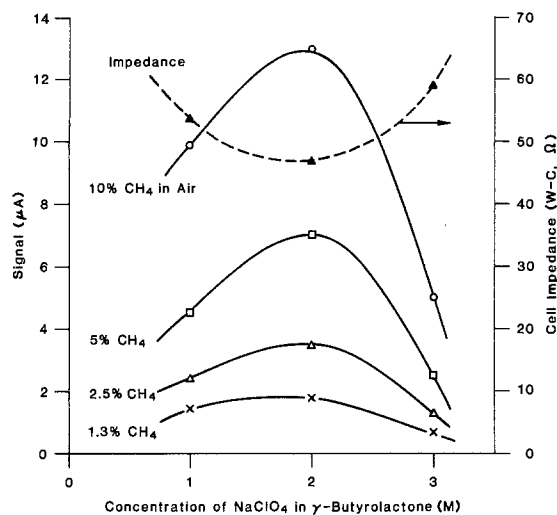


Fig. 3. Net response to various concentrations of dry methane in air and cell impedance as functions of the concentration of NaClO_4 in γ -butyrolactone. Pt black: 14 mg/cm^2 . Teflon: 35 w/o. Zitex: H662-123. Electrode potential: $0.75 \text{ V vs. Ag/AgCl}$. Flow rate: $100 \text{ cm}^3/\text{min}$ with a zero filter. Data were taken on cells freshly filled and equilibrated with each electrolyte for at least 12h.

observed for 2 M NaClO_4 , and the smallest impedance between the working and counterelectrodes is also observed at this concentration. The remaining experiments were therefore carried out with 2 M NaClO_4 in γ -butyrolactone.

Effect of the working-electrode potential.—The effect of the electrode potential on methane oxidation was studied at two relative humidities (75% and 30% RH). The typical response (net current due to electro-oxidation of methane) vs. potential at 75% RH is plotted in Fig. 4. The background current increases sharply with increasing potential, presumably due to oxidation of water, and the observed net oxidation currents for methane go through maxima at a potential of $800 \text{ mV vs. Ag/AgCl}$. A decrease in sensitivity at a potential of 900 mV is attributed to the large background current ($\sim 90 \mu\text{A}$) at this potential. At 75% RH, the current is substantially proportional to methane concentration over a wide range of concentration (0-90%) and potential (500-900 mV vs. Ag/AgCl).

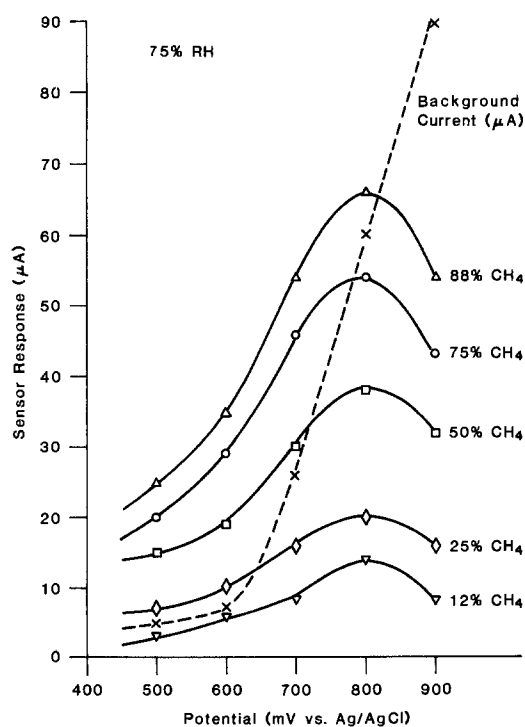
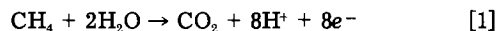


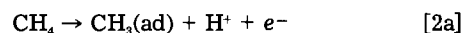
Fig. 4. Net response to various concentrations of methane in pure air vs. working electrode potential at 75% relative humidity.

At 30% RH, the methane currents gradually increase as the potential becomes more anodic. These currents display a diffusion-limited region at potentials above $800 \text{ mV vs. Ag/AgCl}$ for concentrations of methane below 50%. The background current remained below $20 \mu\text{A}$ at the potentials used. However, at 30% RH, the response becomes nonlinear for methane concentrations greater than 50% at potentials greater than $700 \text{ mV vs. Ag/AgCl}$.

The variation of sensitivity with potential for the two relative humidities studied is illustrated in Fig. 5. The sensitivity values were calculated by applying the least squares method to plots of the steady-state current vs. concentration. At potentials lower than $800 \text{ mV vs. Ag/AgCl}$, increased availability of water vapor increases the methane current, which suggests that water is important in the mechanism of the anodic oxidation of methane. At these potentials, a probable reaction is (26)



However, at $800 \text{ mV vs. Ag/AgCl}$, the effect of humidity becomes negligible, indicating a change in the dominant mechanism for the electro-oxidation of methane. The predominant reaction at this potential could be (8)



Thus, a working electrode potential of $800 \text{ mV vs. Ag/AgCl}$ gives the highest response to methane and the least variation in response at various relative humidities. However, the use of this potential in a practical sensor might be limited by the excessive background current ($60 \mu\text{A}$, cf. Fig. 4), even though this current could be compensated by using a nearly identical sensor or working electrode that is not exposed to methane (15).

The ratio of sensitivity to background current at 75% RH is plotted against the potential in Fig. 5. In this case, the optimum potential for observing the oxidation current due to methane is $600 \text{ mV vs. Ag/AgCl}$. The effect of relative humidity at this potential could be minimized by preconditioning the gas samples to an approximately constant humidity before introducing them to the working electrode. This approach could lead to a practical instrument configuration for certain field applications.

Effect of temperature on methane oxidation.—The effect of temperature on methane oxidation is summarized in Table II. The currents due to methane oxidation are substantially proportional to methane concentration from 0 to 100% methane at each temperature. However, the

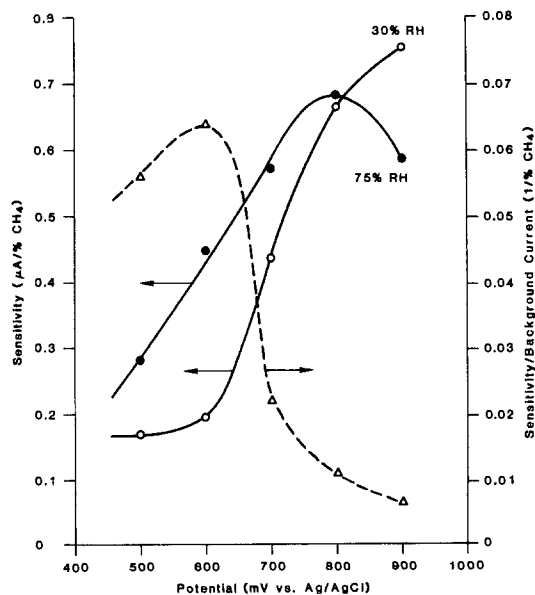


Fig. 5. Sensitivity at 30% and 75% RH and ratio of sensitivity to background current at 75% RH vs. working electrode potential.

Table II. Summary of temperature effect on sensor response

Temperature (°C)	Pt/air reference electrode potential (V vs. Ag/AgCl at 25°C) ^b	Background current (μA)	Response to percentage of methane in pure air (μA, net signal) ^a					Sensitivity (μA/% CH ₄)
			100	75	50	25	12	
10	0.346	19	19	14	7	2.5	1.4	0.209
25	0.329	51	50	38	23	10	5	0.524
35	0.317	60	82	60	40	17	8	0.847
42	0.308	150	165	120	80	40	20	1.64

^a The working electrode potential was adjusted to 800 mV vs. Ag/AgCl at 25°C and maintained at the indicated temperature and at the same flow rate (100 cm³/min). The relative humidity at 25°C was 76%.

^b The Ag/AgCl reference electrode was maintained at 25°C and inserted into the sensor (kept at the indicated temperature) during the brief duration (~10s) of relative potential measurement. No attempts were made to correct for possible changes in the temperature of the Ag/AgCl electrode during this brief measurement period or for any temperature gradients at the liquid junction that could have affected the liquid junction potential.

sensitivity and the background current are dependent on temperature. The sensitivity increases by a factor of eight as the ambient temperature is raised from 10° to 42°C, although the potential of the platinum/air reference electrode decreases slightly (< 0.04V), as measured by the Ag/AgCl electrode.

The Arrhenius plots of the temperature/current data are shown in Fig. 6. In these measurements, the working electrode potential at each temperature was adjusted to 800 mV vs. Ag/AgCl at 25°C in accordance with the readings of the Pt/air reference-electrode potential of Table II. No substantial differences in the magnitude of the signals were observed with or without the adjustment of the potential.

The apparent activation energies for the observed methane oxidation at constant potential, ΔE^\ddagger , calculated using the equation $\Delta E^\ddagger = -2.3R [\partial \log(i) / \partial (1/T)]_v$, average 12 kcal/mol. The values of the activation energy are lower than those measured in inorganic acids. For instance, in 1N H₂SO₄, a value of approximately 30 kcal/mol has been reported (8). The electro-oxidation of methane in γ -butyrolactone containing 2M NaClO₂ may proceed by a different mechanistic path than in sulfuric acid. An activation energy of 8.9 kcal/mol has been reported for the electro-oxidation of methane in trifluoromethanesulfonic acid monohydrate (27). These studies demonstrate the profound influence of the electrolyte on the ability to oxidize hydrocarbons electrocatalytically and ultimately on the design of electrochemical sensors.

Reactivity of other gases.—To design a practical methane monitor, the electrochemical sensors must be specific to methane and give a minimum signal in response to other pollutants that may be present. Figure 7 illustrates the response vs. time behavior of the experimental sensor upon exposure to several gas mixtures in air or N₂ at 78% RH. The interference gases were either passed directly into the sensor or first through a zero filter. No oxidation currents were observed for 200 ppm CO, 200 ppm H₂, or 48 ppm NO₂. Without a zero filter,

strong responses were observed for 25% CH₄, 0.5% H₂, and 49 ppm NO. Upon insertion of the zero filter, the signal for 0.5% H₂ decreased by about one-third, whereas the signals from 25% CH₄ and 49 ppm NO remained substantially unchanged. The response to 50% C₂H₆ was comparable to that of 50% methane.

Therefore, H₂, NO, and C₂H₆ yielded responses that might be mistaken for methane signals, even after some chemical filtration. Although the zero filter is designed to remove CO, some H₂, and other trace impurities, the effectiveness of this kind of filter is variable. An improved filter with an appropriate selection of heterogeneous catalysts might enhance the selectivity of the electrochemical approach to methane detection. Alternatively, the methane sensor could be used in conjunction with either a gas chromatograph or with sensors responding to H₂, NO, and C₂H₆, but not to methane (so that the methane concentration could be computed from the responses of all four sensors).

Methane electro-oxidation catalysts.—Preliminary investigations were conducted on various electrocatalysts, including platinum mesh, platinum black, platinum black/carbon, iridium black, palladium black, carbon, Co₃O₄, and Co₃O₄/carbon. Of the noble metals tested, only platinum black yielded a significant activity for methane oxidation, but it exhibited a relatively slow response time of approximately 4 min. The platinumized platinum mesh alone produced no signal, but when used as a current collector in conjunction with platinum black, it reduced the response time (to 90% of final signal) from about 4 to about 1 min. The Co₃O₄ catalyst produced weak signals and a slow response, presumably due to the excessive resistivity of this catalyst, which yielded an electrode resistance of about 1 k Ω , even with a current collector. To reduce the high resistance of the Co₃O₄ catalyst, the oxide was mixed with fine carbon black powders (Cabot Corporation, Boston, Massachusetts, or Gulf Oil Products Company, Baytown, Texas). However, the carbon black did not significantly improve the conductivity of the oxide.

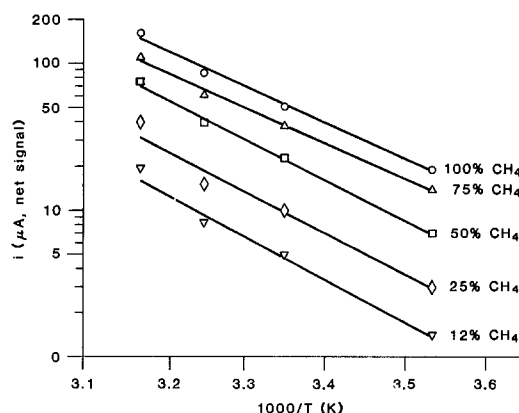


Fig. 6. Plots of current (log scale) vs. $1/T$ at various concentrations of methane in pure air. Electrode potential: 0.8V vs. Ag/AgCl.

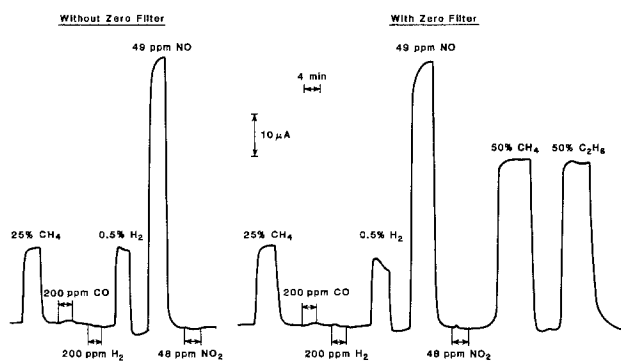


Fig. 7. Response to selected interfering gases in air passed through a zero filter or no filter. Unless specified, signals are taken in pure air. Electrode potential: 0.7V vs. Ag/AgCl.

Efficiency of the electro-oxidation of methane.—It is possible to estimate a dynamic steady-state efficiency for the electro-oxidation of methane at a porous platinum black electrode in the γ -butyrolactone/ NaClO_4 system. An elementary argument shows that the number of moles per second being supplied to the sensing electrode gas chamber for a 50% methane sample at $100 \text{ cm}^3/\text{min}$ is $3.41 \times 10^{-5} \text{ mol/s}$. If the overall reaction [1] is assumed to occur, then the maximum obtainable current at 100% efficiency would be $i = 8F \text{ dn}/\text{dt} = 26.3 \text{ A}$. A typical signal of $50 \mu\text{A}$ was obtained for 50% methane at $800 \text{ mV vs. Ag/AgCl}$, which yields an estimated efficiency of 1.9×10^{-6} . Although the dynamic steady-state efficiency for methane oxidation is quite low under these conditions, this current suffices to detect relatively low methane levels.

In contrast, the estimated efficiency for the oxidation of NO on the same platinum black electrode in the γ -butyrolactone/ NaClO_4 system is 6.6×10^{-2} . This efficiency yields a response ratio about 35,000 times greater per molecule of NO relative to that of methane. Since the size and weight of methane molecules are comparable to or smaller than those of NO molecules, the low efficiency for methane oxidation cannot be due to a diffusion-limited process. Therefore, the far smaller efficiency of methane oxidation must be due to the kinetics of the reaction on the platinum black electrode. The catalytic activity of platinum for methane oxidation at room temperature in the γ -butyrolactone/ NaClO_4 system is very poor when compared with that of other gaseous species. Further, the rate of CO oxidation is approximately 100 times faster on platinum electrodes than on gold electrodes (28). Thus, widely varying sensor responses can be produced by variations in the electrode catalyst. A search for new electrocatalysts to increase the efficiency of methane oxidation could result in significant improvements in the ultimate detection limit of an amperometric sensor.

Application to Gas Sensors

Significant electrochemical oxidation of methane at room temperature was observed using a Teflon-bonded platinum black ($14 \text{ mg}/\text{cm}^2$) electrode. The electrode, which contained a 35 w/o Teflon dispersion, was deposited on a porous Teflon (Zitex) membrane with $10\text{--}20 \mu\text{m}$ diam pores. The electrolyte was $2M \text{ NaClO}_4$ dissolved in γ -butyrolactone solvent. This system can be used to construct a room temperature electrochemical methane monitor (14, 15). As an example, Fig. 8 illustrates the typical response characteristics of a sensor for seven different concentrations of methane ranging from 1.3 to 50%. The response is substantially linear with the methane concentration, and the response and recovery times are about 1 min. Concentrations as low as 0.3% methane in air can be distinguished from the background current and noise, and the response and recovery times are substantially independent of methane concentration.

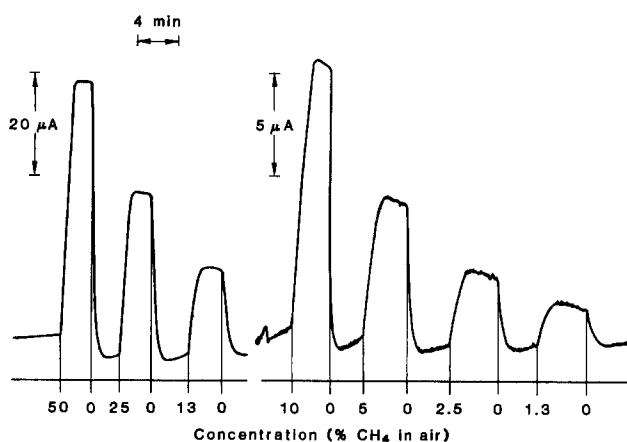


Fig. 8. Typical chart recordings of amperometric sensor responses to various concentrations of methane in dry air. Electrode potential: $0.75V$ vs. Ag/AgCl . Source: Ref. (14).

To develop a monitor for lower methane concentrations (i.e., 0.5%) that has a detection alarm level of say 0.1% (1000 ppm) methane in air, further enhancement of the sensor signal-to-noise ratio is needed, as are increases in the efficiency of the electro-oxidation reaction. Also required are improvements in the selectivity of the sensor, as well as compensation for, or a reduction in, the temperature dependence of the methane oxidation currents and background currents.

Acknowledgments

This work was supported by the U.S. Bureau of Mines under Contract HO233005. The authors acknowledge Dr. A. F. Cohen of the U.S. Bureau of Mines, Pittsburgh Research Center, for her technical suggestions and discussions, and Mr. S. R. Narug for carrying out some of the experiments.

Manuscript submitted March 2, 1985; revised manuscript received Aug. 8, 1985. This was Paper 545 presented at the New Orleans, Louisiana, Meeting of the Society, Oct. 7-12, 1984.

Argonne National Laboratory assisted in meeting the publication costs of this article.

REFERENCES

- U. Bonne and L. L. Altpeter, in "Workshop Proceedings—Gas Distribution and Safety Instrumentation," p. 168, Discussion Gas Research Institute, Chicago (1983).
- J. R. Stetter, W. R. Penrose, S. Zaromb, and A. F. Cohen, "Feasibility of Developing Low-Power, Low-Current Methane Sensors for the Intrinsically Safe Mine Monitoring System," Argonne National Laboratory Report ANL/ES-138 (1983).
- J. R. Stetter, S. Zaromb, W. Penrose, T. Otagawa, and A. F. Cohen, in "Proceedings of the International Meeting on Chemical Sensors, Fukuoka, Japan, Sept. 1983," T. Seiyama *et al.*, Editors, p. 214, Elsevier, New York (1983).
- W. T. Grubb and C. J. Michalske, *Nature*, **201**, 287 (1964).
- L. W. Niedrach, *This Journal*, **111**, 1309 (1964).
- R. V. Marvet and O. A. Petrii, *Elektrokhimiya*, **3**, 153 (1967).
- A. H. Taylor and S. B. Brummer, *J. Phys. Chem.*, **72**, 2856 (1968).
- S. Y. Hsieh and K. M. Chen, *This Journal*, **124**, 1171 (1977).
- A. B. LaConti and H. J. R. Magee, *ibid.*, **118**, 506 (1971).
- A. McDougall, "Fuel Cells," p. 24, The Macmillan Press, Ltd., London (1976).
- J. R. Stetter, "Scientific and Technical Aerospace Reports (STAR)," National Aeronautics and Space Administration Report NASA-CR-153048 (1977).
- S. B. Brummer *et al.*, "New Electrolytes for Direct Methane Fuel Cells," U.S. Department of Energy Report DOE/ET/11321-T1 (1979).
- T. Otagawa, S. Zaromb, and J. R. Stetter, Abstract 545, p. 796, The Electrochemical Society Extended Abstracts, Vol. 84-2, New Orleans, LA, Oct. 7-11, 1984.
- T. Otagawa, S. Zaromb, and J. R. Stetter, "Development of a Methane Monitor Meeting the Bureau of Mines' Intrinsically Safe Mine Monitoring System (ISMMS) Requirements," Argonne National Laboratory Report ANL/ES-144 (Sept. 1984), also published by U.S. Bureau of Mines.
- T. Otagawa, S. Zaromb, and J. R. Stetter, *Int. J. Sensors Actuators*, In press.
- J. Giner, J. M. Parry, S. Smith, and M. Turchan, *This Journal*, **116**, 1692 (1969).
- T. Otagawa and J. O'M. Bockris, *ibid.*, **129**, 2391 (1982).
- J. R. Stetter, S. Zaromb, W. R. Penrose, M. W. Findlay, T. Otagawa, and A. J. Sincali, in "Proceedings of the Hazardous Material Spills Conference," Nashville, TN, J. Ludwigson, Editor, p. 183, Government Institutes, Inc., Rockville, MD (1984).
- J. R. Stetter, S. Zaromb, W. R. Penrose, T. Otagawa, A. J. Sincali, and J. O. Stull, in "Proceedings of the 1984 JANNAF Safety and Environmental Protection Subcommittee, Chemical Propulsion Information Agency, Laurel, MD, In press.

20. A. N. Dey and B. P. Sullivan, *This Journal*, **117**, 222 (1970).
21. B. V. Tilak, R. S. Yeo, and S. Srinivasan, in "Comprehensive Treatise of Electrochemistry," Vol. 3, J. O'M. Bockris *et al.*, Editors, p. 81, Plenum, New York (1981).
22. "Organic Electrochemistry," M. M. Baizer, Editor, p. 228, Marcel Dekker, New York (1973).
23. G. H. Newman, R. W. Francis, L. H. Gaines, and B. M. L. Rao, *This Journal*, **127**, 2025 (1980).
24. J. A. Titus, *Chem. Eng. News*, **49** (23), 6 (1971).
25. R. S. Egly, *ibid.*, **51** (6), 30 (1973).
26. M. G. Sustersic, R. Córdova, O., W. E. Triaca, and A. J. Arvia, *This Journal*, **127**, 1242 (1980).
27. A. A. Adams and R. T. Foley, *ibid.*, **126**, 775 (1979).
28. J. M. Sedlak and K. F. Blurton, *ibid.*, **123**, 1476 (1976).

Oxygen Evolution on Nickel Oxide Electrodes

J. C. Botejue Nadesan and A. C. C. Tseung*

Chemical Energy Research Centre, Department of Chemistry, The City University, London, England EC1V 0HB

ABSTRACT

The anodic oxygen evolution reaction on Teflon-bonded NiO and Li-doped NiO in KOH solution was studied by potentiostatic and galvanostatic techniques as a function of hydroxyl ion concentration, and the kinetic equations were derived. It was shown that the rate-determining step (rds) for NiO at current densities of 100-1000 mA-cm⁻² is S + OH⁻ → SOH + e, and the Tafel slope is approximately 118 mV/decade at 25°C. The rds for Li-doped NiO at current densities of 10-1000 mA-cm⁻² is SOH + OH⁻ → SO⁻ + H₂O, and the Tafel slope is approximately 60 mV/decade. The likely reason for this difference in rds is related to the concentration of Ni²⁺ and Ni³⁺ ions in NiO and Li-doped NiO electrodes.

Nickel metal has long been known as the most suitable material for anodes in alkaline water electrolyzers (1-3). However, a major drawback in the use of this metal is that the potential drifts unavoidably toward more positive values with time.

Work at the City University has indicated that there is a correlation between the minimum voltage for oxygen evolution on semiconducting oxides and the potential of the lower oxide/higher oxide couple (4-7). In the case of nickel cobalt oxide and Li-doped cobalt oxide, the minimum voltage for oxygen evolution is approximately 1.45V *vs.* RHE, comparable to the published values of the lower oxide/higher oxide couple for nickel and cobalt oxide. The purpose of the present work is to study the mechanism of oxygen evolution on NiO as well as Li-doped NiO.

Experimental

Stoichiometric quantities of Ni(NO₃)₂ · 6H₂O and LiNO₃ · 6H₂O required to prepare 10g of 10, 5, and 0 atom percent (a/o) Li-doped NiO was dissolved in 100 cm³ of distilled water and freeze dried (8). The decomposed powder was sintered at 600°C for 5h. The catalyst structures were confirmed by x-ray diffraction analysis.

The catalyst powders were then fabricated into fluorinated ethylene propylene (FEP)-bonded electrodes (9), supported on 60 mesh nickel screens of geometric area 1 cm². Catalyst loadings were approximately 23 mg-cm⁻², and the FEP solid content approximately 25%.

The oxygen evolution performance of the preanodized electrodes were tested at 25°C in a thermostated three-compartment Pyrex cell. The electrodes were mounted in the submerged mode in 5 mol-dm⁻³ KOH electrolyte, prepared by dissolving KOH pellets in doubly distilled deionized water. A piece of platinum was used as the secondary electrode, and the potentials were measured against the reversible hydrogen electrode (RHE). A chemical electronics potentiostat (H. B. Thompson, Model 251) was used in the galvanostatic and potentiostatic modes. The interrupter technique (10) was used to measure the ohmic drop between the Luggin capillary and working electrode.

Experimental reaction order parameters were obtained by simple analysis of the polarization data in KOH concentrations of 0.6, 0.8, 1.0, and 1.2 mol-dm⁻³ KOH at 25°C. Anodic charging of the electrodes was studied by applying a current of 10⁻⁴ A-cm⁻² to the electrodes, held at 1V *vs.* RHE and recording the potential time response on a Y-T recorder.

*Electrochemical Society Active Member.

Results and Discussion

Table I lists the specific surface area (ssa) and resistivities of the NiO and Li-doped NiO. It is interesting to note that there is a significant difference in the resistivity of the Li-doped NiO and the pure NiO, confirming that Li⁺ ions have indeed diffused into the NiO lattice, thereby creating trivalent nickel ions. The existence of divalent and trivalent nickel cations are responsible for the greatly enhanced conductivity of the doped oxides, and this should also have a significant effect on their electrochemical activity.

Figure 1 gives a comparison of catalytic activity for oxygen evolution on NiO and Li-doped NiO electrodes. It is evident from the figure that the oxygen evolution potential of NiO decreases with increase in lithium content. Two reasons could be put forward to explain this trend: (i) an increase in electrical conductivity with increase in lithium doping (*cf.* Table I), (ii) an increase in the Ni³⁺ ion concentration with lithium doping.

A consideration based solely on increased electrical conductivity will not explain the trend observed, especially the difference in performance of the 5 and 10 a/o Li-doped NiO, both having an electrical resistivity of approximately 1 Ω-cm. However, if the Li⁺ ions enter the NiO lattice, this would oxidize corresponding amounts of Ni²⁺ ions to Ni³⁺ ions; thus, 10 a/o Li-doped NiO will have a higher percent of Ni³⁺ ions than 5 a/o Li-doped NiO; Ni³⁺ ions could be the active sites for the oxygen evolution reaction, and hence, greater the Ni³⁺ ion concentration better the performance. This trend is more in accordance with the oxygen evolution trend.

An interesting point to note is that the Tafel plots for the two compounds are different. NiO has three slopes. At high current densities (100-1000 mA-cm⁻²), the slope was ~ 132 mV/decade. At current densities between 5 and 100 mA-cm⁻², the slope was ~ 85 mV/decade, and at current densities lower than 5 mA-cm⁻² the Tafel slope was ~ 43 mV/decade. On Li-doped NiO, two slopes were observed, *i.e.*, at high current densities (~ 10-1000 mA-cm⁻²) the

Table I. Characterization of NiO and Li-doped NiO catalysts

Nominal Li content (a/o)	10	5	0
Temperature of sintering (°C)	600	600	600
Duration of sintering (h)	5	5	5
Total Li (a/o)	10.0	5.2	0
Li in lattice (a/o)	9.23	4.8	0
Free Li (a/o)	0.6	0.15	0
BET ssa (m ² /g)	2	3.6	3.8
Resistivity (Ω-cm ²)	2	1.3	1896

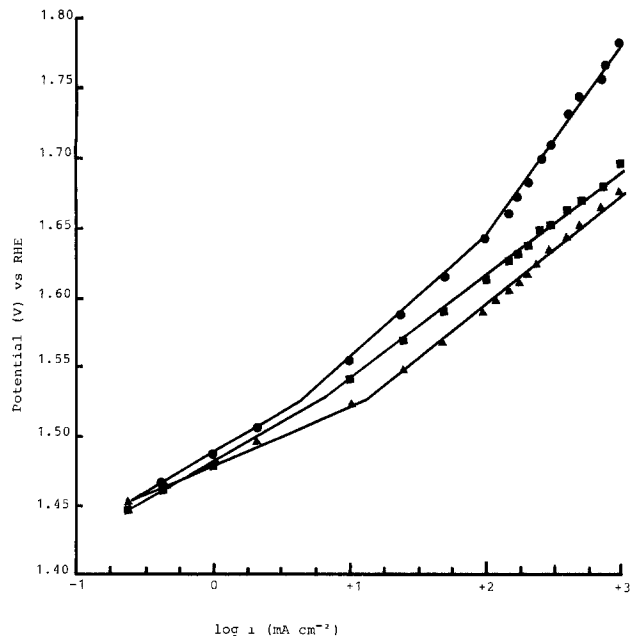


Fig. 1. Tafel characteristics for the evolution of oxygen on NiO (circles), 5 a/o Li-doped NiO (squares), and 10 a/o Li-doped NiO (triangles) in 5 mol-dm⁻³ KOH at 25°C.

slope was ~ 73 mV/decade, and at current densities than 5 mA-cm⁻² the slope had a value of ~ 44 mV/decade.

The experimental reaction order parameters for oxygen evolution on NiO and 5 a/o Li-doped NiO are as shown in Fig. 2.

Figure 3 shows the potential response of a NiO electrode (catalyst loading 20.45 mg-cm⁻²) held at 1V vs. RHE on applying an anodic current of 10⁻⁴ A-cm⁻². The response curve for NiO has two potential arrest regions before oxygen evolution. The first potential arrest occurs at approximately 1.31V, and the second at a potential of approximately 1.45V vs. RHE. The potential response of a 5 a/o Li-doped NiO electrode (catalyst loading 21.4 mg-cm⁻²) under similar experimental conditions is given in Fig. 4. The trace, unlike that of NiO, shows only one potential arrest region before oxygen evolution, i.e., at ~ 1.42 V vs. RHE. The thermodynamic potential of Ni³⁺ \rightarrow Ni²⁺ is 1.304V vs. RHE, and that of Ni³⁺ \rightarrow Ni⁴⁺ is 1.434V vs. RHE (11). Therefore, the potential arrest observed at 1.31V on the NiO charging curve is due to the formation of Ni³⁺ ions, and the potential arrest at 1.45V on both com-

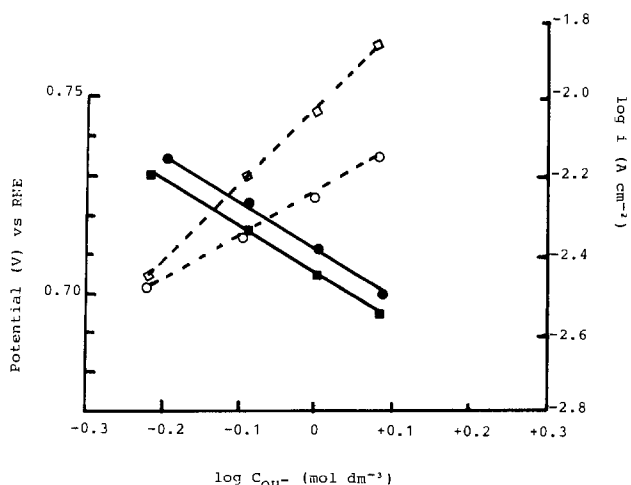


Fig. 2. KOH concentration dependence of oxygen evolution on NiO (solid circles) and on 5 a/o Li-doped NiO (solid squares) at a constant current density of 5×10^{-3} A-cm⁻² at 25°C. The figure also shows the KOH concentration dependence of oxygen evolution on NiO (open circles) and on 5 a/o Li-doped NiO (open squares) at a constant potential of 0.72V vs. SHE at 25°C.

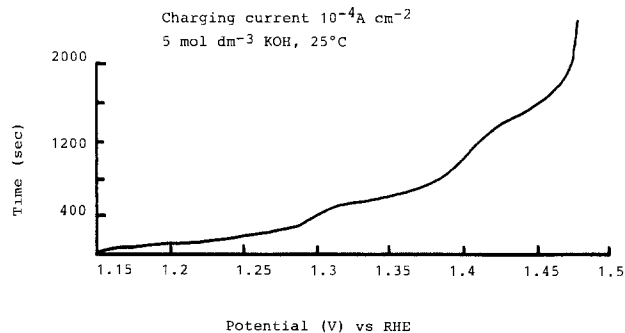


Fig. 3. Anodic charging curve on a FEP-bonded NiO electrode of catalyst loading 21.2 mg-cm⁻².

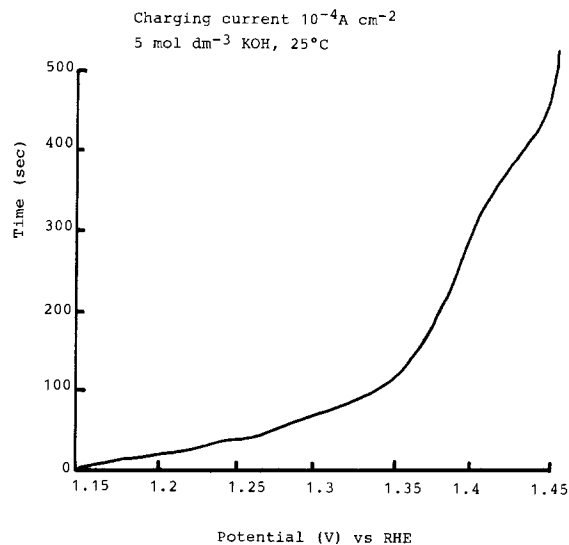


Fig. 4. Anodic charging curve on a FEP-bonded 5 a/o Li-doped NiO electrode of catalyst loading 20.67 mg-cm⁻².

pounds corresponds to the formation of Ni⁴⁺ ions. Another difference between the two curves was the time taken to reach oxygen evolution potential. The time is longer on NiO than on 5 a/o Li-doped NiO. This is most probably due to the lower conductivity of the NiO, and therefore a slower rate of oxidation.

From the charging curves, it is inferred that the majority of ions on 5 a/o Li-doped NiO are Ni³⁺; this is as expected due to lithium doping. Before oxygen evolution these ions form Ni⁴⁺ ions. Therefore, the Ni³⁺ ions can be considered to be the active sites for oxygen evolution on Li-doped NiO. NiO is a nonstoichiometric oxide; hence, it will have a certain percentage of Ni³⁺ ions, but the majority of ions will have a valency of 2+. The experimental results where the oxygen evolution performance increases with increase in the Li doping of the oxides (Fig. 1) also supports this hypothesis. It should be noted that the postulations of the charge transfers were based on the potential values and no analysis of the Ni²⁺ and Ni³⁺ ions or the structure of the species containing these ions was carried out.

A survey of likely reaction paths (12) for the oxygen evolution on NiO and Li-doped NiO shows a consistency with the path previously proposed by Rasiyah and Tseung (6). It is shown that the rate-determining step (rds) for NiO at current densities of 100-1000 mA-cm⁻² is S + OH⁻ \rightarrow SOH + e, and the Tafel slope is approximately 118 mV/decade at 25°C. The rds for Li-doped NiO at current densities of 10-1000 mA-cm⁻² is SOH + OH⁻ \rightarrow SO + H₂O, and the Tafel slope is approximately 60 mV/decade. The likely reason for this difference in rds is related to the concentration of Ni²⁺ and Ni³⁺ ions in NiO and Li-doped NiO electrodes.

The rate equations derived for the two catalysts are as follows.

Table II. Comparison of kinetic data for the oxygen evolution reaction on NiO and 5 a/o Li-doped NiO

Kinetic parameter	Theoretical	Experimental
<u>NiO</u>		
$(E/\log i)_{\text{OH}^-, \tau}$	$2.303 \times 2 \times RT/F$ = 118 mV/decade	128 mV/decade
$(E/\log C_{\text{OH}^-})_{\text{l}, \tau}$	$-2 \times 2.303RT/F$ = -118 mV/decade	-116 mV/decade
$(\log i/\log C_{\text{OH}^-})_{\text{e}, \tau}$	1	1.14 ~ 1
<u>5 a/o Li-doped NiO</u>		
$(E/\log C_{\text{OH}^-})_{\text{OH}^-, \tau}$	$2.303RT/F$ = 59 mV/decade	73 mV/decade
$(E/\log C_{\text{OH}^-})_{\text{l}, \tau}$	$-2 \times 2.303RT/F$ = -118 mV/decade	-123 mV/decade
$(\log i/\log C_{\text{OH}^-})_{\text{e}, \tau}$	2	1.86 ~ 2

At high current densities and at limitingly low coverage of SOH, the rate equation for NiO is

$$i = FK_1C_{\text{OH}^-} \exp(EF/2RT) \quad [1]$$

The Tafel slope on NiO changes to ~ 85 mV/decade at lower current densities. As mentioned earlier, the change may be as a result of the change in the rate-determining step, i.e., due to oxygen being evolved on Ni^{3+} ions. The concentration of Ni^{3+} ions on NiO are limited, and hence, with increase in current density the Ni^{2+} ions become the active sites. Unfortunately, it was not possible to carry out reaction order studies at the intermediate current density region as the demarcation when the active sites for oxygen evolution changes from Ni^{3+} to Ni^{2+} is not very clear, specially at low KOH concentrations.

The rate equation for oxygen evolution on Li-doped NiO is

$$i = (FK_1K_2/K_{-2}) C_{\text{OH}^-}^2 \exp(EF/RT) \quad [2]$$

Table II compares the experimentally obtained and the theoretically predicted values of the kinetic parameters for oxygen evolution on NiO and 5 a/o Li-doped NiO. The experimentally obtained values agree well with the theoretically predicted values.

On all the Tafel plots (i.e., NiO and Li-doped NiO), a slope of ~ 40 mV/decade was observed at current densities less than 1 mA-cm⁻². The potentials at these currents correspond to higher oxide formation, and, therefore, the

Tafel slope of ~ 40 mV was not considered to be related to oxygen evolution but to oxide formation reactions.

Conclusions

The difference in the rate-determining step for the evolution of oxygen on NiO and Li-doped NiO at high current densities is related to the difference in the $\text{Ni}^{3+}/\text{Ni}^{2+}$ ion concentration. In the case of NiO, the evolution of oxygen at high current densities is postulated to be on Ni^{2+} sites and at low current densities from the Ni^{3+} sites, which are the minority ions. By doping the NiO lattice with Li^+ ions, the concentration of Ni^{3+} ions is increased proportionately, and, hence, sufficient Ni^{3+} ions are available for the evolution of oxygen even at high current densities.

Acknowledgment

This work was supported by the European Economic Commission.

Manuscript submitted Oct. 22, 1984; revised manuscript received June 11, 1985.

REFERENCES

1. D. H. Smith and A. T. Kuhn, "Industrial Electrochemical Processes," p. 217, Elsevier, Amsterdam (1971).
2. P. W. T. Lu and S. Srinivasan in "Proceedings of the International Conference of Alternative Energy Sources," Vol. 8, N. Veziroglu, Editor, p. 3577, Hemisphere Publishers (1978).
3. M. H. Miles, G. Kissel, P. W. Lu, and S. Srinivasan, *This Journal*, **123**, 332 (1976).
4. A. C. C. Tseung and S. Jasem, *Electrochim. Acta.*, **22**, 31 (1977).
5. N. P. Rasiyah and A. C. C. Tseung, *This Journal*, **131**, 803 (1984).
6. N. P. Rasiyah and A. C. C. Tseung, *ibid.*, **130**, 365 (1983).
7. N. P. Rasiyah and A. C. C. Tseung, *ibid.*, **130**, 2384 (1983).
8. A. C. C. Tseung and H. L. Bevan, *J. Mater. Sci.*, **5**, 604 (1970).
9. A. D. S. Tantrum and A. C. C. Tseung, *Nature*, **222**, 556 (1969).
10. K. R. Williams, "An Introduction to Fuel Cells," p. 58 Elsevier, Amsterdam (1966).
11. M. Pourbaix, "Atlas d'Equilibres Electrochimiques at 25°C," Gauthiers Villara, Paris (1963).
12. "Electrodes of Conductive Metallic Oxides, Part B," S. Trasatti and S. Lodi, Editors, Chap. 10, Elsevier, New York (1981).

Calculation of Current Distribution and Electrode Shape Change by the Boundary Element Method

J. Deconinck and G. Maggetto

Department of Electrical Engineering, Vrije Universiteit Brussel, 1050 Brussels, Belgium

J. Vereecken*

Department of Metallurgy, Electrochemistry and Materials Science, Vrije Universiteit Brussel, 1050 Brussels, Belgium

ABSTRACT

The boundary element method coupled with a Newton-Raphson iteration technique is used to determine current distributions in electrochemical systems, particularly for applications involving electrode shape change such as electroplating and electrochemical machining (ECM). The derivation of the system of equations with the appropriate boundary conditions is presented. Primary and secondary current distributions are calculated for applications including simultaneous deposition and dissolution on opposing electrodes. In the case of copper electrorefining, a comparison between theory and experiment is made. An example of surface leveling in ECM is also given.

The quantitative determination of current distribution and the simulation of changing electrode shape in applications such as electroplating and electrochemical machining are of industrial interest.

It is well known that only the current distribution of rather simple geometries with linear boundary conditions can be solved with analytical techniques. In all other cases, numerical methods must be used. Prentice (1) gives a good survey of literature.

In this paper, it is shown that the boundary element method, in combination with a Newton-Raphson iteration method (to treat the nonlinearity introduced by the boundary conditions), is very well suited to calculations of current distribution and electrode shape change.

Equations

When the solution is sufficiently stirred, the general problem of electrochemical transport can be divided into two regions: a homogeneous bulk solution where potential theory applies, and a boundary layer at the electrodes where all mass-transport effects must be considered. In many practical cases, this diffusion boundary layer is very thin, so that the effects of these phenomena can be encompassed in the boundary condition. This introduces the concept of concentration overpotential, which must be added to the activation overpotential characterizing electrode kinetics.

The distribution of potential in an electrochemical system can then be described by the following equation and boundary conditions (Fig. 1)

$$\nabla \cdot (-\sigma \nabla U) = 0 \quad [1]$$

in the electrolyte Ω bounded by $\Gamma = \Gamma_1 \cup \Gamma_2 \cup \Gamma_3$

$$U = V - \eta_1(U') \quad [2]$$

on the anode Γ_1

$$U = -\eta_2(U') \quad [3]$$

on the cathode Γ_2

$$U' = \frac{\partial U}{\partial n} = 0 \quad [4]$$

on the boundary Γ_3 (insulator, axis of symmetry), with U being the potential field, U' the electric field normal to the boundary, V the potential difference between anode and cathode minus the Nernst-potential difference, η , the total overpotential (activation and concentration) on the anode ($\eta_1 \geq 0$), η_2 the total overpotential on the cathode ($\eta_2 \leq 0$), and σ the electric conductivity of the solution. Often, σ is assumed to be constant.

*Electrochemical Society Active Member.

In order to describe the electrode shape change, Faraday's law in differential form must be solved

$$\frac{d\bar{h}(\bar{x}_i, t)}{dt} = -\theta \frac{m}{zF\rho_m} \sigma U'(\bar{x}_i, t) \bar{I}_n + \bar{u}(\bar{x}_i, t) \quad [5]$$

with $\bar{h}(\bar{x}_i, t = 0) = 0$. \bar{h} is a vector describing the displacement of each point \bar{x}_i of the boundary with respect to the boundary Γ at $t = 0$. At each moment, the electric field U' satisfies Eq. [1]-[4] with the electrolyte Ω and its boundaries Γ changing in time. \bar{u} is the vector describing the rate and the direction of the displacement of each point \bar{x}_i of the boundary. Usually, \bar{u} is taken as time independent.

Note that, from the mathematical point of view, Eq. [5] is also applicable to boundaries where U' is zero.

For the purpose of determining potential and current distribution along electrodes, membranes, and boundaries, it is advantageous to transform Eq. [1] into an equivalent relation involving only the boundaries.

The Boundary Element Method

Several approximation methods are available to reduce the continuum problem to a discrete system of algebraic equations. Using the method of weighted residuals, one can classify (2) all such methods including the finite difference method (FDM) and the finite element method (FEM).

Although it is more general to derive the boundary element method (BEM) using the weighted residual method (3) or a variational principle (4), it is much more straightforward, in the case of the Laplace equation, to use Green's identity

$$\int_{\Omega} (-w \nabla^2 U + U \nabla^2 w) d\Omega = \int_{\Gamma} w \frac{\partial U}{\partial n} d\Gamma - \int_{\Gamma} U \frac{\partial w}{\partial n} d\Gamma \quad [6]$$

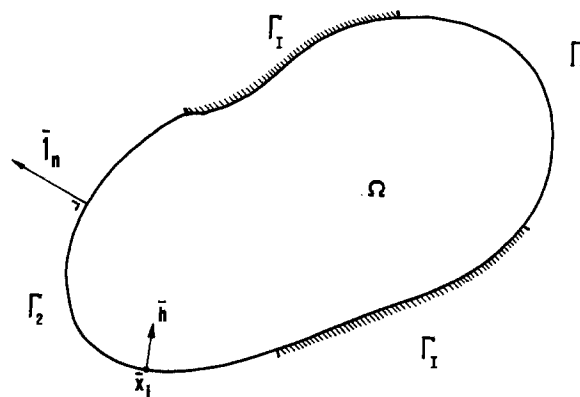


Fig. 1. General representation of an electrochemical system

where w and U are arbitrary, sufficiently continuous functions. We can choose U equal to the unknown potential field and define w in such a way that the following equation is satisfied

$$\nabla^2 w = \delta_i \tag{7}$$

where δ_i is the Dirac delta function at point i . The function w is called the fundamental solution and represents the solution for the Laplace equation in an infinite isotropic space with a unit potential source at a given point i .

In a two-dimensional system, the fundamental solution is

$$w = \frac{1}{2\pi} \ln\left(\frac{1}{r}\right)$$

and, in three dimensions, one has

$$w = \frac{1}{4\pi r}$$

Using Eq. [1] and the appropriate choice of w , Eq. [6] can be reduced to

$$c_i u_i + \int_{\Gamma} U \frac{\partial w}{\partial n} d\Gamma = \int_{\Gamma} w \frac{\partial U}{\partial n} d\Gamma \tag{8}$$

where c_i is equal to 1 at a point i inside the domain Ω , equal to 1/2 at a point on the boundary Γ , and equal to zero at any point outside Ω (Fig. 1). Equation [8] enables us to calculate the value of the potential at any point on the domain if U and U' are known on the boundary Γ . Furthermore, when the point i lies on Γ , Eq. [8] is a functional relation between U and U' ensuring their compatibility as boundary functions for the Laplace equation.

In order to evaluate the integrals in Eq. [8], the boundary is subdivided into a number (M) of segments or "boundary elements" Γ_j (Fig. 2). On each element, it will be supposed that the functions U and U' can be approximated by a combination of linearly independent trial functions ϕ_k . An example is

$$U = \sum_{k=1}^l \phi_k U_k \text{ and } U' = \sum_{k=1}^l \phi_k U'_k \tag{9}$$

where U_k and U'_k are the values of the potential and its normal derivative at l well-defined points of the element Γ_j , namely, the nodal points.

Substitution of Eq. [9] into Eq. [8] and the evaluation of the integrals over each element Γ_j yields the following equation for a nodal point i on the boundary

$$\sum_{j=1}^N H^*_{ij} U_j = \sum_{j=1}^N G^*_{ij} U'_j \tag{10}$$

Such an equation can be written for each node i , producing an $N \times N$ system of equations having the following matrix form

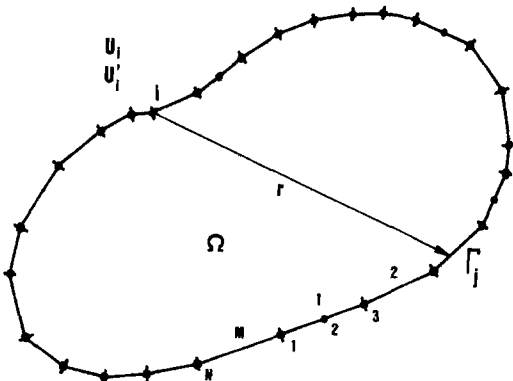


Fig. 2. Discretization of the boundary in M elements and a total of N nodal points.

$$[H]^* \{U\} = [G]^* \{U'\} \tag{11}$$

Introducing the boundary conditions and passing all unknowns into the right-hand term yields

$$[G] \begin{Bmatrix} U'_1 \\ U'_2 \\ U_1 \end{Bmatrix} = [H] \begin{Bmatrix} V - \eta_1(U'_1) \\ -\eta_2(U'_2) \\ 0 \end{Bmatrix} \tag{12}$$

This is a system of nonlinear equations with the unknowns U'_1 and U'_2 being the normal electric field at the nodal points on the anode and cathode, respectively, with U_1 being the potential at the nodal points on the insulating boundaries.

Effectively, by the particular choice of w , the field Eq. [1] is automatically satisfied, and a point collocation is used to match the boundary conditions.

It should be noted that the normal electric field at each node is found directly. It is not necessary to differentiate the potential with respect to the surface normal (as it is in FDM or FEM).

Another important advantage is that only the boundaries need to be discretized. This results in a smaller system of equations to be solved and a considerable reduction of effort in terms of defining the nodal structure. Moreover, with straight-line elements used to discretize the boundary with polynomial trial functions, the integrals can be calculated analytically, giving very accurate results.

Solution of the Nonlinear System of Equations

When the overpotential functions η_1 and η_2 are linearized, as is frequently done, the system of Eq. [12] can be solved directly. Otherwise, one needs an iterative process to obtain the solution. Often, a successive approximation method or a Newton-Raphson iteration technique is used.

Since the matrices $[G]$ and $[H]$ depend only on geometry, the Newton-Raphson process is easily implemented (5, 6).

Defining a function

$$\psi \begin{Bmatrix} U'_1 \\ U'_2 \\ U_1 \end{Bmatrix} = [G] \begin{Bmatrix} U'_1 \\ U'_2 \\ U_1 \end{Bmatrix} - [H] \begin{Bmatrix} V - \eta_1(U'_1) \\ -\eta_2(U'_2) \\ 0 \end{Bmatrix} \tag{13}$$

it is found, after some calculation, that the values of the unknowns at iteration step $(n + 1)$ are related to those at step n as follows

$$\begin{Bmatrix} U'^{n+1}_1 \\ U'^{n+1}_2 \\ U_1^{n+1} \end{Bmatrix} = \begin{Bmatrix} U'^n_1 \\ U'^n_2 \\ U_1^n \end{Bmatrix} - [K_T^n]^{-1} \cdot \psi \begin{Bmatrix} U'^n_1 \\ U'^n_2 \\ U_1^n \end{Bmatrix} \tag{14}$$

where the tangential matrix $[K_T^n]$ is

$$\begin{aligned} K_{Tij}^n &= G_{ij} - \eta'_1(U_1^n) \cdot H_{ij} \text{ for } \forall j \in \Gamma_1 \\ &= G_{ij} - \eta'_2(U_2^n) \cdot H_{ij} \text{ for } \forall j \in \Gamma_2 \\ &= G_{ij} \text{ for } \forall j \in \Gamma_1 \end{aligned}$$

η'_1 and η'_2 are the derivatives of the functions η_1 and η_2 with respect to U' .

Both solution techniques were tested for several example problems. Using a Newton-Raphson technique, convergence was obtained after three to six iterations, whereas the successive approximation method always required more than 100 iterations. Using finite elements in combination with a Newton-Raphson iteration process, Alkire *et al.* (7) also obtained convergence after three to four iterations. The authors' previous experience with finite elements (8) as well as the results of Prentice (9) confirm that, in the case of successive approximations, many iterations are necessary for convergence.

Therefore, it is clear that whichever numerical method is used to discretize the field Eq. [1], a Newton-Raphson

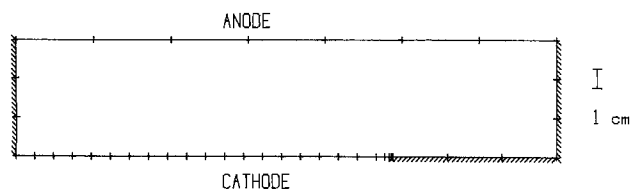


Fig. 3. Copper electrorefining in a rectangular cell with edge effect: element distribution (45 nodal points).

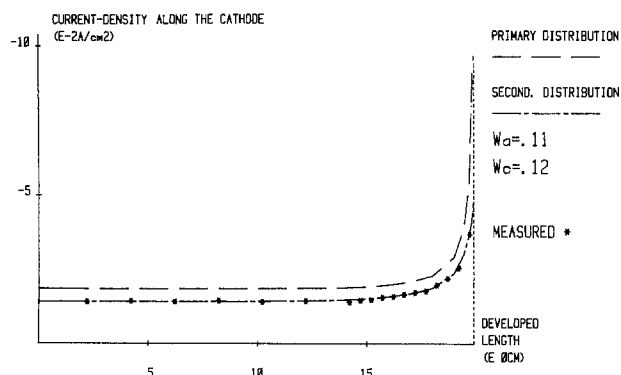


Fig. 4. Copper electrorefining in a rectangular cell with edge effect. Current distribution along the cathode. Primary distribution and comparison between calculated and measured secondary distribution.

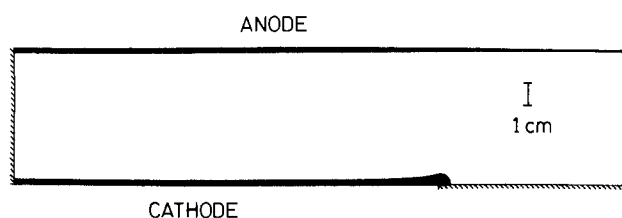


Fig. 5. Copper electrorefining in a rectangular cell with edge effect. Simulation of simultaneous dissolution and deposition after 110h electrolysis (53 nodal points).

iteration process is highly advantageous for treating the nonlinear boundary conditions.

Determination of Electrode Shape Change

After resolution of Eq. [1]-[4], Eq. [5] can be solved with a forward-difference approximation (Euler).

As already mentioned, all calculations are restricted to the boundaries of the system ($U, U', \bar{I}_n, \Delta \bar{h}_n$). This implies that the method is well adapted to simulate electrode shape change or ECM since no internal nodes are to be re-ordered after each time step.

This method was implemented on a H-P 1000 21 MX/E (196K) minicomputer. With this configuration, a two-dimensional or axisymmetric current-distribution problem with 75 unknowns takes no longer than a few minutes.

Examples

Copper electrorefining.—Copper electrorefining from a 0.8M CuSO_4 , 0.8M H_2SO_4 solution ($\rho = 4.67 \Omega\text{-cm}$) was studied in a cell with a singularity (Fig. 3).

To model the overpotentials on anode and cathode in the program, an interpolation by cubic natural splines between measured points, obtained with a standard three-electrode configuration, was used. The advantages are that no Tafel relation is to be fitted, and that the derivatives of the functions $\eta'_1(U')$ and $\eta'_2(U')$ (used in the Newton-Raphson process) are easily obtained.

In order to evaluate the computed current distribution, a cell with removable segmented cathode was built. This cathode was an electronic printboard etched to obtain fine parallel strips of 4.2 mm, 0.8 mm from each other. To avoid disturbing the system with the measurements (no supplementary voltage drop should be created), we used

a dc current probe to measure the current through each strip.

In Fig. 4, comparison between calculation and experiment is summarized (applied voltage: 0.5V). The agreement is within 5%.

Since reactions on anode and cathode take place, we introduced two Wagner numbers

$$W_a = \frac{\partial \eta_1}{\partial J} \Big|_{J_{av}} \frac{J_{av}}{\rho L}$$

on anode and

$$W_c = \frac{\partial \eta_2}{\partial J} \Big|_{J_{av}} \frac{J_{av}}{\rho L}$$

on cathode. As a general, the characteristic length L is taken equal to the shortest distance between anode and cathode.

Using the cell geometry of Fig. 3 in the same circumstances, the simultaneous dissolution and deposition of copper was simulated. Figure 5 gives the obtained calculated profile after 110h electrolysis.

Two remarkable features are the overgrowth over the insulating boundary and the orthogonal incidence between the electrode and the boundary. The latter can be rationalized as follows. If we replace the insulating boundary in line with the cathode by an equivalent symmetry plane, we see that there is no reason to expect the deposit profile to not be perpendicular to this plane. The overgrowth phenomenon is due to the fact that once metal is deposited on the cathode, deposition continues in all directions perpendicular to the new cathode surface.

In order to verify these results an experiment was performed. After electrolysis, the cathodes were embedded in a resin, cut over the length, and polished before measurement. The mean of six profiles was taken.

Figure 6 gives a comparison between the numerical result after 68h and an experiment that ran for the same length of time under the aforementioned conditions. In practice, one common strategy for reducing the edge effect is to interpose a screen or "shield" masking the edge. The influence of such a screen is represented in Fig. 7

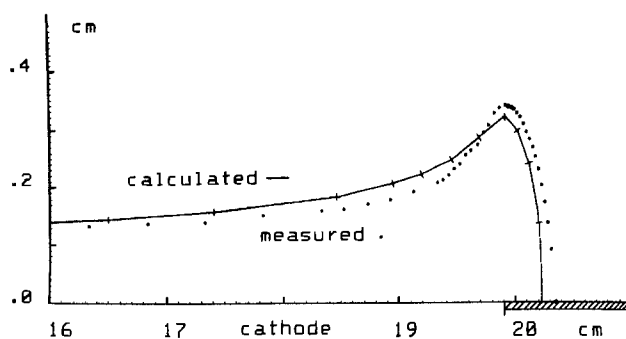


Fig. 6. Copper electrorefining in a rectangular cell with edge effect. Comparison between numerical result and experiment (68h electrolysis).

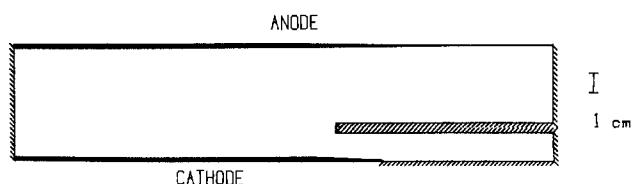


Fig. 7. Copper electrorefining in a rectangular cell with partial masking of the edge effect. Simulation of dissolution and deposition.

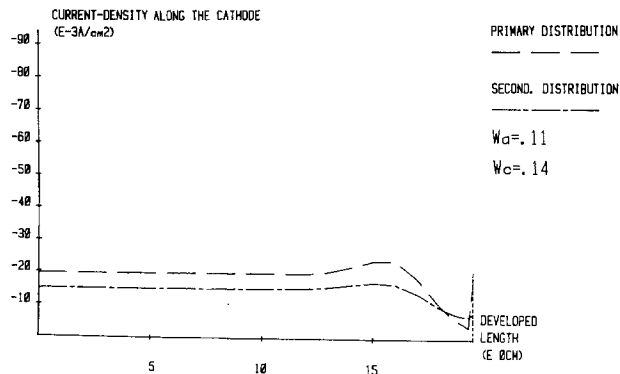


Fig. 8. Copper electrorefining in a rectangular cell with partial masking of the edge effect. Primary and secondary current density distribution along the cathode at $t = 0_+$ (63 nodal points).

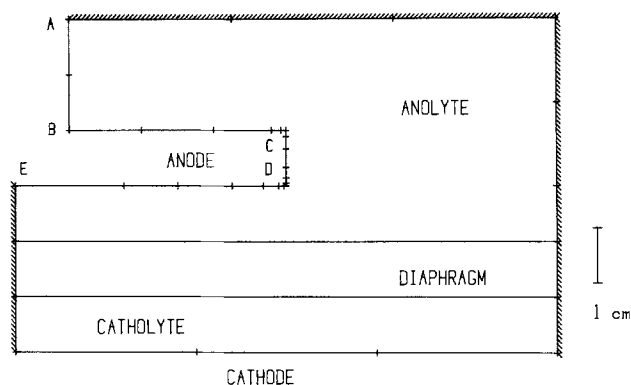


Fig. 9. Diaphragm cell for the production of chlorine. Element distribution (74 nodal points). Resistivities: anolyte = $1.0 \Omega\text{-cm}$; catholyte = $3.0 \Omega\text{-cm}$; diaphragm = $10.0 \Omega\text{-cm}$.

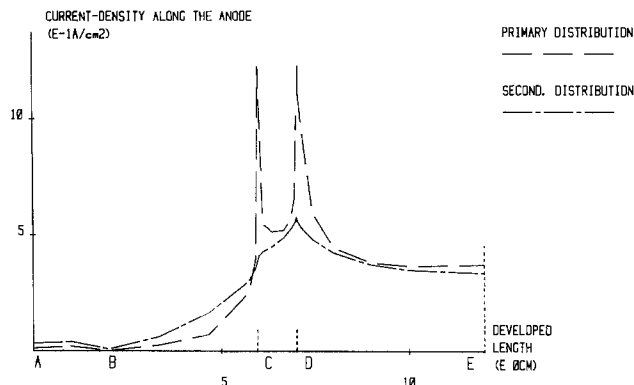


Fig. 10. Diaphragm cell for the production of chlorine. Primary and secondary distribution along the anode: $W_a = 0.09$, $W_c = 0.18$. Applied voltage: 5.0V.

and 8 (the optimal position of the screen was not investigated).

Production of chlorine in a diaphragm cell.—This example shows that it is possible to deal with systems having uniform subregions of differing conductivity. Let us consider the repetitive part of a diaphragm cell for the production of chlorine shown in Fig. 9.

The overpotential functions on anode and cathode were natural cubic spline interpolations of measured values from the literature (10).

The resulting primary and secondary distributions along the anode are given in Fig. 10.

Influence of the Wagner number on the shape change.—The influence of overpotentials on simultaneous deposition and dissolution of a sinusoidal profile is illustrated. Figures 11, 12, and 13 represent the electrode shape changes for three Wagner numbers; the applied voltage is 0.5V and total charges (C) are almost the same.

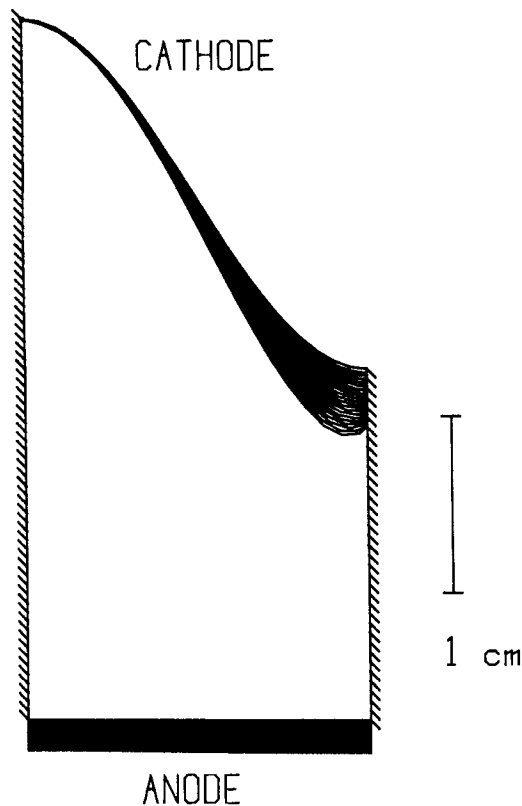


Fig. 11. Sinusoidal profile. Simulation of deposition and dissolution. Resistivity: $4.67 \Omega\text{-cm}$. $W_c = 0.001$ with overpotential relation $\eta_2 = 0.001J$. $W_a = 0$. $Q = 9787C$.

The boundary was divided into only 41 elements with a total of 45 nodal points. Twenty time steps were used. On the cathode, the shapes obtained by Prentice (9) are confirmed, and it is seen that, even for a small Wagner number, the dissolution rate of the anode is uniform for the interelectrode distance in question.

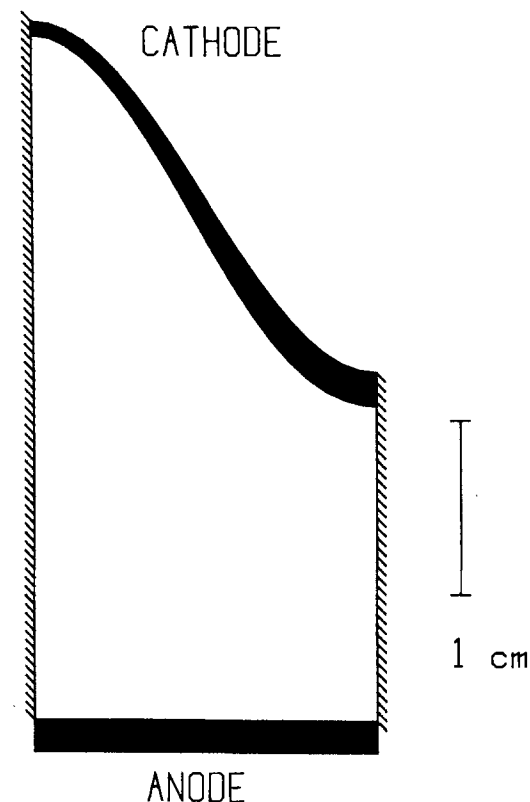


Fig. 12. Sinusoidal profile. Simulation of deposition and dissolution. Resistivity: $4.67 \Omega\text{-cm}$. $W_c = 1.07$ with overpotential relation $\eta_2 = 10J$. $W_a = 0$. $Q = 9963C$.

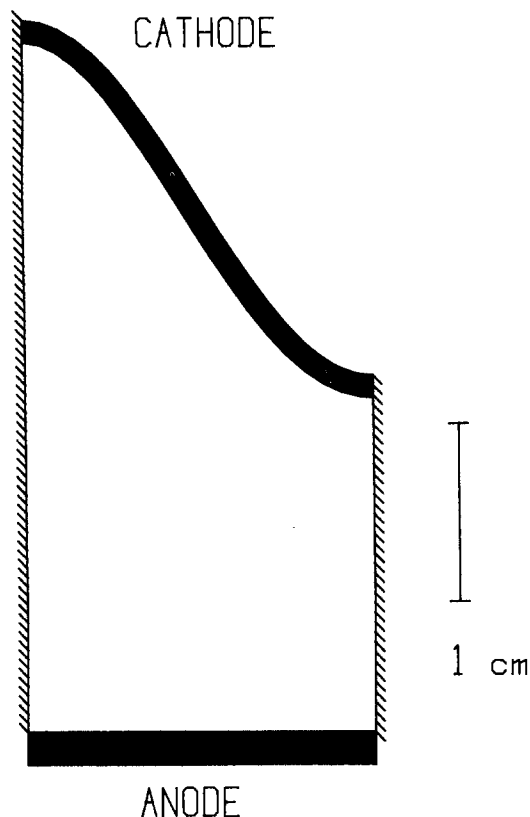


Fig. 13. Sinusoidal profile. Simulation of deposition and dissolution. Resistivity: $4.67 \Omega\text{-cm}$. $W_c = 107$ with overpotential relation $\eta_2 = 1000J$. $W_a = 0$. $Q = 9719C$.

Electrochemical machining.—An iron anode of irregular shape stands in front of a flat cathode (Fig. 15). The electrolyte has a resistivity of $5 \Omega\text{-cm}$, the applied voltage is $10V$, and the cathode moves at the rate of 1.2 mm/min . No overvoltages were considered.

Figure 14 gives the primary current distribution along the anode, and Fig. 15 gives the obtained profile after each time step (0.15 min). The results confirm the notion that small irregularities take longer to vanish.

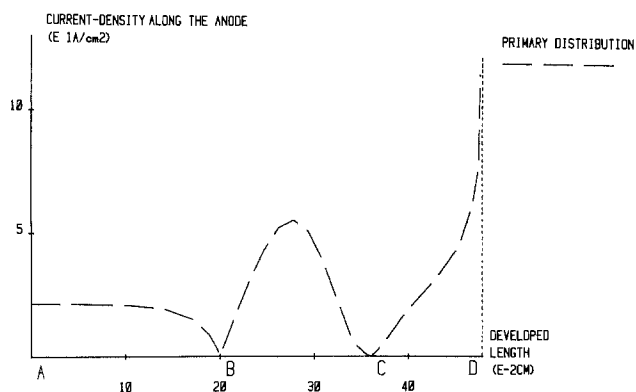


Fig. 14. Surface leveling in ECM. Primary current distribution ($W_a = W_c = 0$) along the anode at $t = 0_+$ (geometry of Fig. 15).

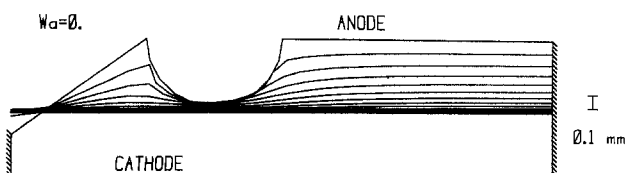


Fig. 15. Surface leveling in ECM. Evolution of the anode profile. The steady-state gap is about 0.46 mm .

Conclusions

A new method, the BEM in combination with a Newton-Raphson iteration, is presented to determine current distribution and electrode shape change.

The main advantages are that: discretization and calculations are restricted to the boundary; data input is easy; accuracy is great; a reduced number of unknowns is needed; the normal derivative is obtained directly and accurately; convergence on the nonlinear boundary conditions is fast (Newton-Raphson); singularities are well described because the element distribution can be refined in their vicinity; and problems with infinite domain can be solved.

The method has also its disadvantages. They are as follows:

(i) The method is less general. For example, to transform the Laplace equation into an integral equation we need an isotropic medium; otherwise, the function w is hard to find. The "domain methods" (FDM and FEM) are local discretizations and permit a variation of conductivity. In the BEM, the conductivity must be piecewise uniform (cf. Fig. 9).

(ii) The underlying mathematics are somewhat more difficult. In particular, the integrals necessary to compose the matrices G and H can be troublesome since they are singular when the distance r in the function w becomes zero.

(iii) The matrices G and H are fully populated, whereas the FDM and FEM generate sparse matrices.

(iv) To simulate electrode shape change, at each time step the matrices G and H are to be recalculated since each nodal point of the boundary is related to all others.

Manuscript submitted Sept. 24, 1984; revised manuscript received ca. Aug. 2, 1985.

Vrije Universiteit Brussel assisted in meeting the publication costs of this article.

LIST OF SYMBOLS

F	Faraday constant
G, G^*	influence matrices depending only on geometry
G_{ij}, G^*_{ij}	influence coefficients defining the interaction between the nodal points i and j
H, H^*	influence matrices depending only on geometry
H_{ij}, H^*_{ij}	influence coefficients defining the interaction between the nodal points i and j
\bar{h}	displacement of the boundary
J, J_{av}	(average) current density normal to an electrode
K_T	tangential matrix
K_{Tij}^n	coefficient of the tangential matrix at time step n
L	characteristic length
m	molecular weight
M	total number of elements
N	total number of nodal points
Q	total charge
r	distance between a field point and an observation point
t	time parameter
U	potential field
U_i	value of the potential at a point i
U_1	values of U at nodal points on the insulating boundary Γ_1
U'	electric field normal to the boundary
U'_i	value of the electric field normal to the boundary at a point i
U'_1, U'_2	values of the electric field at nodal points on anode and cathode, respectively
\bar{u}	displacement rate of a point on the boundary
V	potential difference between anode and cathode minus the Nernst-potential difference
w	fundamental solution
W_a, W_c	Wagner number on anode and cathode, respectively
\bar{x}_i	point on the boundary
z	charge number
\bar{z}	direction normal to the boundary (outward pointing)
$\Delta\bar{h}_n$	increment of \bar{h} at time step n
Γ	boundary
Γ_j	boundary element

Γ_1, Γ_2	anode and cathode, respectively, part of the boundary
Γ_1	insulating part of the boundary
δ_i	dirac delta function
η_1, η_2	overpotential on anode and cathode
η'_1, η'_2	derivative of η_1 and η_2 with respect to U'
θ	current efficiency
ρ	electrolyte resistivity
ρ_m	metal density
σ	electrolyte conductivity
ϕ_k	shape function
ψ	function defined to be zero after convergence
Ω	computational domain

REFERENCES

- G. A. Prentice and C. W. Tobias, *This Journal*, **129**, 72 (1982).
- C. A. Brebbia, *Appl. Math. Modelling*, **2**, 160 (1978).
- C. A. Brebbia and S. Walker, "Boundary Element Techniques in Engineering," Newnes-Butterworths, London (1980).
- D. W. Kelly, G. G. W. Mustoe, and O. C. Zienkiewicz, "Recent Advances in Boundary Element Methods," p. 359, Pentech Press, London; Plymouth (1978).
- J. Deconinck, G. Maggetto, P. Versyck, and J. Vereecken, Extended abstracts of the 34th ISE Meeting, Erlangen, Germany (1983).
- O. C. Zienkiewicz, "The Finite Element Method," MacGraw-Hill, New York (1977).
- R. Alkire and T. Bergh, *This Journal*, **125**, 1981 (1978).
- J. Deconinck, Internal Report, Vrije Universiteit Brussel, Brussels, Belgium (1977).
- G. A. Prentice, Ph.D. Thesis, University of California, Berkeley, CA (1980).
- J. O'M. Bockris, B. E. Conway, E. Yeager, and R. E. White, in "Comprehensive Treatise on Electrochemistry," Vol. 2, p. 121, Table 4, p. 129, Table 5 ($T = 70^\circ\text{C}$), Plenum Press, New York (1981).
- J. A. Mc. Geough, "Principles of Electrochemical Machining," Chapman and Hall, London (1974).
- J. Deconinck, G. Maggetto, and J. Vereecken, Extended Abstracts of the 35th ISE Meeting, Berkeley, CA (1984).
- C. Clerc and D. Landolt, *Electrochim. Acta*, **29**, 787 (1984).
- J. Deconinck, Ph.D. Thesis, Vrije Universiteit Brussel, Brussels, Belgium (1985).

Technical Notes



Electrochemical Determination of Hydrogen Transport Through Copper

David W. DeWulf and Allen J. Bard*

Department of Chemistry, The University of Texas, Austin, Texas 78712

The diffusion of hydrogen into metals and other materials has been widely studied because of its importance in embrittlement, permeation through vessels and pipelines, and hydrogen storage in metal alloys (1). The diffusion of hydrogen in many metals is rapid, and there are many cases, *e.g.*, in a hydrogen pipeline, where a practical impermeable material is desired. We became interested in this problem in connection with submarine fiber optic cable systems, where a transmission loss increase caused by hydrogen permeation occurs at wavelengths important in communications (2-5). The question of finding a suitable material to block this permeation led to consideration of copper. We report here studies of hydrogen permeation in copper by the electrochemical method of Devanathan and Stachurski (6, 7). This method has been applied to hydrogen and oxygen diffusion studies in a number of materials (8-15).

Experimental

The basic experiment followed previous studies (6-8). A thin (15 and 25 μm) copper foil was clamped as a separator (bielelectrode) between two half-cells; the clamping arrangement consisted of O-ring seal joints and utilized Teflon spacers. The area of Cu exposed to each half-cell was 0.78 cm^2 . The counterelectrodes in each half-cell compartment were Pt foil. A saturated calomel electrode (SCE) served as a reference electrode in the detection half-cell. The Cu foil bielelectrode acted as an anode. This compartment was filled with 0.2M KOH, and this side of the Cu foil was coated with Pt to improve the kinetics of hydrogen oxidation. The potential of the Cu bielelectrode anode was held at a potential of -0.30V vs. SCE with a Princeton Applied Research Model 173 potentiostat. A constant current (19.5 mA) was applied between the cath-

ode side of the Cu foil and the Pt counterelectrode; the catholyte was 0.2M H_2SO_4 containing 10 $\text{mg}\cdot\text{liter}^{-1}$ As_2O_3 . Copper foils (99.999%, 25.0 μm and 99.8%, 15.0 μm) were purchased from Aesar, Incorporated, Seabrook, New Hampshire. A Pt film, 0.1 μm thick, was formed on one side by Ar ion sputtering from a Pt target (Material Research Corporation Model 8620 sputtering system). Other thicknesses of Cu were obtained by electrodeposition of Cu from a copper pyrophosphate bath (16). The additional thickness of Cu plated was calculated from the number of coulombs passed, the exposed area of the foil, and the bulk density of Cu. In experiments involving deposition of Pd on the Cu, a thin film (0.050 μm) was formed by

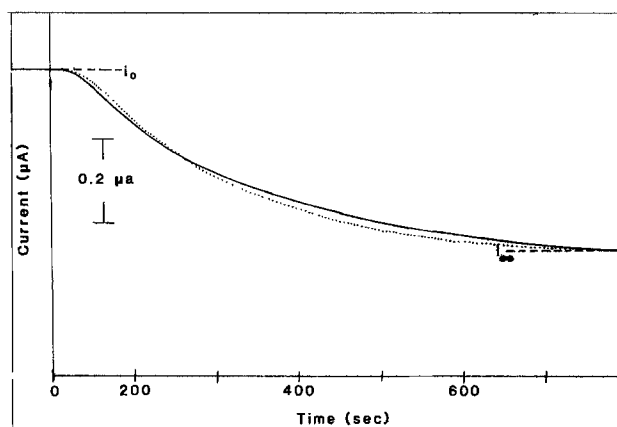


Fig. 1. Anodic current vs. time for a 15.0 μm foil of 99.8% Cu. Solid line: experimental data. Dotted line: best theoretical fit calculated from Eq. [1].

*Electrochemical Society Active Member.

Table I. Results from electrochemical measurements of hydrogen permeation through copper foil at 23°C^a

Foil type	L(μm)	Number of trials	D _{23°C} (cm ² /s)
Puratonic (99.999%)	25.0	3	2.6 × 10 ⁻⁹
	27.5	3	2.3 × 10 ⁻⁹
	30.0	3	2.1 × 10 ⁻⁹
Total 99.8%	15.5	9	2.3 (± 0.3) × 10 ⁻⁹
		5	5.2 (± 0.5) × 10 ⁻⁹

^a *i*_{appl} (cathode side) = 19.5 mA; *E* (anode side) = -0.3V vs. SCE; anolyte, 0.2M KOH; catholyte, 0.2M H₂SO₄ + 10 mg-liter⁻¹ As₂O₃.

vacuum evaporation. All solutions were prepared with reagent-grade chemicals and milli-Q (Millipore Corporation) water.

Results and Discussion

The nature of the anodic current (*i*) (for the oxidation of hydrogen) with time (*t*) for the platinum side of the Cu held at -0.30V vs. SCE and with a constant current of 19.5 mA applied to the cathode side was used to determine the diffusion coefficient, *D*. The basic experiment and treatment followed previous practice (12). The anode side was pre-electrolyzed at -0.30V for 4-8h before the constant current was applied to oxidize any residual hydrogen or impurities. Background currents less than 1 μA were obtained. A typical *i*-*t* curve is shown in Fig. 1. This transient can be fit to the equation (12)

$$\frac{i_t}{i_\infty} = 1 - \frac{4}{\pi} \sum_{n=0}^{\infty} \frac{(-1)^n}{2n+1} \exp \frac{-(2n+1)^2 \pi^2 \tau}{4} \quad [1]$$

where *i*_{*t*} is the permeation current at time *t*, *i*_∞ is the steady-state permeation current, and $\tau = Dt/L^2$ (where *L* is the foil thickness). The τ values were obtained by a computer fit of Eq. [1] to the experimental results. An initial guess for τ could be obtained by noting that at *i*_{*t*}/*i*_∞ = 0.5, $\tau \approx 0.630$. Values of *D* determined in this way at 23°C for two different Cu samples and several thicknesses are given in Table I. The agreement of *D* values for the 99.999% sample for the three thicknesses demonstrates that hydrogen permeation occurs by diffusion. An alternative way of showing this is a plot of *t* vs. *L*² for several values of τ (Fig. 2). As predicted by the equation defining τ , straight lines that intersect the original with a slope of *D*/ τ result.

The diffusion coefficient was significantly higher for the 99.8% sample than for the 99.999% one, suggesting that impurities have an important effect on the rate of hydrogen permeation in Cu. A comparison of the *D* value reported here at 23°C to earlier studies is given in Table II; most involved determinations at much higher temperatures and thus long extrapolations based on the reported heats of activation. The value we report is considerably higher than that previously measured at ambient temperatures (13, 14).

The diffusion coefficient measurement on Cu required that As₂O₃ as a "poison" be added to the catholyte. If As

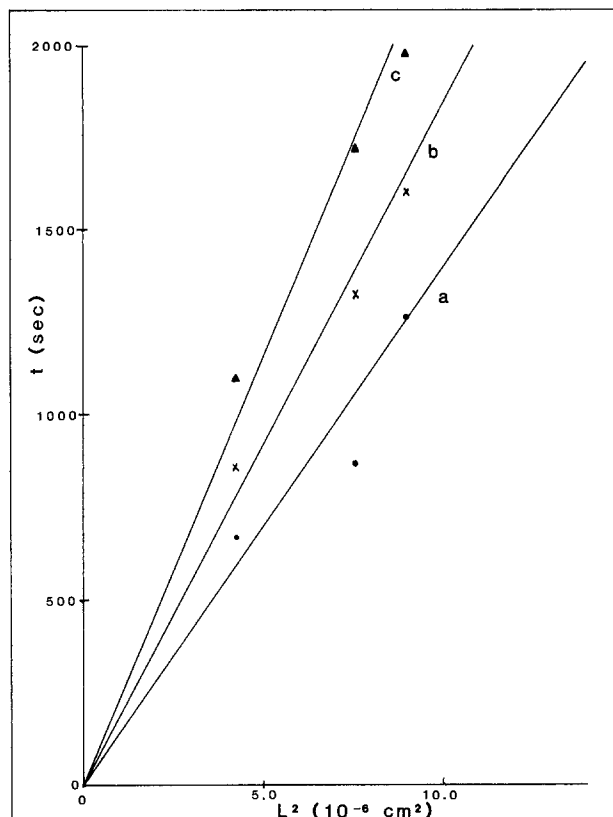


Fig. 2. *t* vs. *L*² at given values of τ (constant *i*_{*t*}/*i*_∞) slopes of all lines = τ/D : (a) $\tau = 0.24$, slope = 1.29×10^8 , intercept = -28; (b) $\tau = 0.38$, slope = 1.73×10^8 (s-cm⁻²), intercept = -28; (c) $\tau = 0.54$, slope = 2.20×10^8 , intercept = -28. *D* calculated from these values is $2.2 (\pm 0.3) \times 10^{-9}$ cm²/s.

(III) was not added to the catholyte, no detectable hydrogen permeation current through the Cu foil was found, even after 6h of electrolysis. This effect is similar to that observed for hydrogen diffusion through Pt (8, 20), where hydrogen permeation is found only when the cathodic side of the metal membrane is poisoned. For other materials, e.g., Pd (20) and pyrite (12), such poisoning is unnecessary. This effect of As (III) has been ascribed to blockage of sites on the electrode surface for recombination of atomic hydrogen to molecular hydrogen, thus increasing the concentration of atomic hydrogen at the surface. Presumably, it is atomic hydrogen that diffuses through the Cu lattice (1, 14, 18, 21). Evidence for the lack of penetration of H₂ through the copper film was obtained by the following experiment. When the catholyte was replaced by moist hydrogen gas, with exactly the same anode and anolyte configuration as before, no detectable permeation current was observed after 30h. Even when a 0.05 μm Pd covering was deposited on the cathodic side and gaseous hydrogen introduced, no permeation current was observed. Since Pd is known to dissociate H₂ and allow permeation measurements in the absence of a poison (20),

Table II. Comparison of diffusion coefficients found in this study at 23°C with previous values

Ref.	Cu Purity	Temperature range (K)	D ₀ (cm ² /s) ^a	Δ <i>H</i> _D (kJ/mol) ^a	D _{23°C} (cm ² /s)
(17)	99.999%	500-900	1.1 × 10 ⁻²	39.64	1.11 × 10 ⁻⁹
(18)	99.999%	700-1200	1.13 × 10 ⁻²	38.85	1.57 × 10 ⁻⁹
(19)		800-1000	2.29 × 10 ⁻²	47.28	1.04 × 10 ⁻¹⁰
(13)	99.9%	289-336	4.96 × 10 ⁻³	40.54	3.46 × 10 ⁻¹⁰
This work	99.999%	296			(3.11 × 10 ⁻⁹) ^b
This work	99.8%	296			2.33 × 10 ⁻⁹
					5.2 × 10 ⁻⁹

^a *D*_T (K) = *D*₀ exp [-Δ*H*_D/*kT*].

^b The value reported by the authors at 292 K is based on application of a constant current to generate hydrogen, but the application of a constant potential boundary condition for the theoretical treatment. This value is a recalculation based on a constant current treatment.

the lack of permeation for the Pd-coated Cu configuration suggests rapid H atom recombination at the Pd/Cu interface. A number of studies have been concerned with the mechanism of "poisoning" by arsenic species (22-26). It is interesting that As acts in a similar way for such different metals as Pt and Cu. From the point of view of blockage of H₂ permeation, the slow step in penetration of hydrogen through a Cu film would be the dissociation of H₂ to hydrogen atoms (or in a membrane sense, the rate of equilibration of hydrogen at the H₂/Cu interface) rather than the rate of diffusion through the film.

Conclusions

The diffusion coefficient (*D*) of hydrogen through a 99.999% Cu foil at 23°C is $2.3 (\pm 0.3) \times 10^{-9}$ cm²-s⁻¹. *D* is affected by the purity of the Cu. With regard to Cu as a barrier to H₂ permeation, the surface properties of the Cu are important, and the rate of H₂ crossing the Cu/gas interface is the rate-determining step.

Acknowledgment

The support of this research by the National Science Foundation (CHE8402135) is gratefully acknowledged. We are indebted to Dr. R. L. Williamson and other members of the Submarine Systems Division, Standard Telephones and Cables, for helpful information concerning submarine fiber optic cables.

Manuscript received July 28, 1985.

The University of Texas assisted in meeting the publication costs of this article.

REFERENCES

1. J. Volkl and G. Alefeld, in "Diffusion in Solids: Recent Developments," A. S. Novick and J. J. Burton, Editors, p. 231, Academic Press, New York (1975).
2. K. Mochizuki, Y. Namihira, and H. Yamamoto, *Electron. Lett.*, **19**, 743 (1983).
3. N. Uesugi, Y. Murakami, C. Tanaka, Y. Ishida, Y. Mitsunaga, Y. Negishi, and N. Uchida, *ibid.*, **19**, 762 (1983).
4. M. Fox and S. J. Stannard-Powell, *ibid.*, **19**, 916 (1983).
5. K. J. Beales, D. M. Cooper, and J. D. Rush, *ibid.*, **19**, 917 (1983).
6. M. A. V. Devanathan and Z. Stachurski, *Proc. R. Soc. London, Ser. A*, **270**, 90 (1962).
7. M. A. V. Devanathan and Z. Stachurski, *This Journal*, **111**, 619 (1964).
8. E. Gileadi, M. A. Fullenwider, and J. O'M. Bockris, *ibid.*, **113**, 926 (1966).
9. H. G. Schoneich and H. Zuchner, *Ber. Bunsenges. Phys. Chem.*, **87**, 566 (1983).
10. R. Kirchheim and R. B. McLellan, *This Journal*, **127**, 2420 (1980).
11. L. Nanis and T. K. G. Namboodhiri, *ibid.*, **119**, 691 (1972).
12. S. M. Wilhelm, J. Vera, and N. Hackerman, *ibid.*, **130**, 2129 (1983); (b) N. Boes and H. Zuchner, *J. Less-Common Met.*, **49**, 223 (1976).
13. Y. Sakamoto and K. Takao, *J. Jpn. Inst. Metals*, **46**, 285 (1982).
14. Y. Sakamoto and K. Hirayama, in "Proceedings of the 3rd International Congress on Hydrogen and Materials," p. 377, Paris, France (1978).
15. Z. Ogumi, Z. Takehara, and S. Yoshizawa, *This Journal*, **131**, 769 (1984).
16. C. Ogden and D. Tench, *ibid.*, **128**, 539 (1981).
17. W. Eichnauer, W. Loser, and H. Witte, *Z. Metallkd.*, **56**, 287 (1965).
18. L. Katz, G. Guinan, and R. J. Borg, *Phys. Rev. B*, **4**, 330 (1971).
19. Yu. I. Belyakov and Yu. I. Zvezdin, *Uch. Zap. Leninograd Gos. Univ., Ser. Fiz. Nauk.*, **345**, 44 (1968).
20. J. P. Hoare and S. Schuldiner, *This Journal*, **103**, 237 (1956).
21. J. K. Gorman and W. R. Nardella, *Vacuum*, **12**, 19 (1962).
22. T. Zakroczymski, Z. Szklarska-Smialkowska, and M. Smialowski, *Werkst. Korros.*, **26**, 617 (1975).
23. E. Lunarska, Z. Szklarska-Smialkowska, and M. Smialowski, *ibid.*, **26**, 624 (1975).
24. T. Zakroczymski, Z. Szklarska-Smialkowska and M. Smialowski, *ibid.*, **26**, 625 (1976).
25. P. Kezierkowski, Z. Szklarska-Smialkowska, and M. Smialowski, *This Journal*, **127**, 2550 (1980).
26. R. D. McCright and R. S. Staehle, *ibid.*, **121**, 609 (1974).

Electrochemical Observations as Related to Marine Atmospheric Corrosion of Chrome-Flashed Stainless Steels

Gardner Haynes and Robert Baboian*

Texas Instruments, Incorporated, Attleboro, Massachusetts 02703

Generally, stainless steels are susceptible to localized corrosion (such as pitting) in chloride containing environments. This occurs in environments where the alloys are totally immersed as well as in those where intermittent wetting occurs, such as marine atmospheres and splash and spray zones. Often the concentration of alloying elements such as molybdenum is increased to provide improved resistance to localized corrosion.

Stainless steels have been plated with a thin layer of chromium (chrome flashed) for decorative purposes for automotive applications (1-3). The chromium electrodeposit is usually about 0.01 mil thick and does not completely cover the stainless steel. It provides a better color match with other trim components, improves appearance, and adds abrasion resistance. It has been established that chrome-flashed stainless steels have better resistance to localized corrosion than their base counterparts in marine atmospheres and chloride environments such as the salt-belt region for automobiles (1-3). Little is known, however, about the performance of chrome-flashed stainless steels under total immersion conditions. The purpose of this work was to elucidate the mechanisms of corrosion resistance of chrome-flashed stainless steels in chloride containing atmospheres and compare its performance in

these atmospheres to its performance when totally immersed.

Experimental

The comparative performance of bare and chrome-flashed stainless steels was evaluated in laboratory accelerated tests and environmental exposure tests. A cyclic immersion testing procedure was used in the laboratory to simulate marine atmospheric exposure. This test for pitting resistance of stainless steels for automotive service consisted of a 10s immersion period in a 5% sodium chloride solution followed by a 90s drying period at 105°F. A multiple crevice washer (ASTM G78-83) was tightened to a torque of 75 in.-lb in the center of 4 × 6 in. sections of 434 stainless steel-clad aluminum and chrome-flashed 434 stainless steel-clad aluminum. These specimens were then run for 100 cycles in the cyclic immersion test.

Bare and chrome-flashed 301 stainless steel-clad aluminum bumpers were exposed in the splash and spray zone at the LCCT test facility in Wrightsville Beach, North Carolina, to determine their performance in an alternate immersion environment. These same materials were totally immersed in seawater at the Texas Instruments test facility in Buzzards Bay, Massachusetts. The aluminum was masked in the total immersion tests so that it could not provide galvanic protection to the stainless steel.

*Electrochemical Society Active Member.

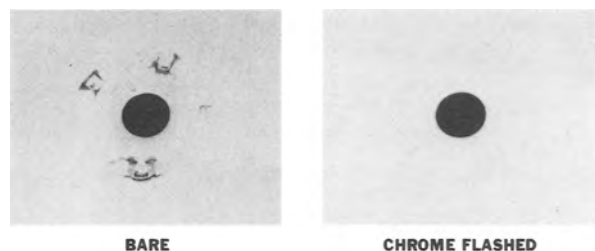


Fig. 1. Appearance of bare and chrome flashed type 304 stainless steel after 100 cycles in the cyclic immersion test.

Electrochemical techniques were used to investigate the mechanisms of corrosion. Cyclic potentiodynamic polarization measurements were made for 301 stainless steel and 434 stainless steel in 5% sodium chloride solution and fresh seawater according to ASTM Designation G61-78. Potential measurements for bare and chrome-flashed stainless steels were made in 5% sodium chloride solution and fresh seawater under conditions of total and alternate immersion.

Results and Discussion

The appearance of the bare 434 stainless steel surface and the chrome-flashed 434 stainless steel surface after 100 cycles in the cyclic immersion test is shown in Fig. 1. Crevice corrosion of the 434 stainless steel occurred at four sites, while no crevice corrosion of the chrome-flashed 434 stainless steel occurred. Similar results were found for 301 stainless steel in the splash and spray zone after 1 yr of exposure. In this case, the bare 301 stainless steel surface had numerous pits, while the chrome-flashed stainless steel did not pit. These results confirm the beneficial behavior of chrome flashing that has been observed in automotive applications.

These results for intermittent wetting can be contrasted with the results of total immersion tests. After six months exposure in seawater, both bare 301 stainless steel and chrome-flashed 301 stainless steel had crevice corroded. The chrome flashing did not provide the improved resistance to pitting or crevice corrosion of the stainless steel that was observed in the marine atmospheres.

Results from cyclic potentiodynamic polarization and the "mixed potential" theory have been used previously to describe the behavior of stainless steels in galvanic

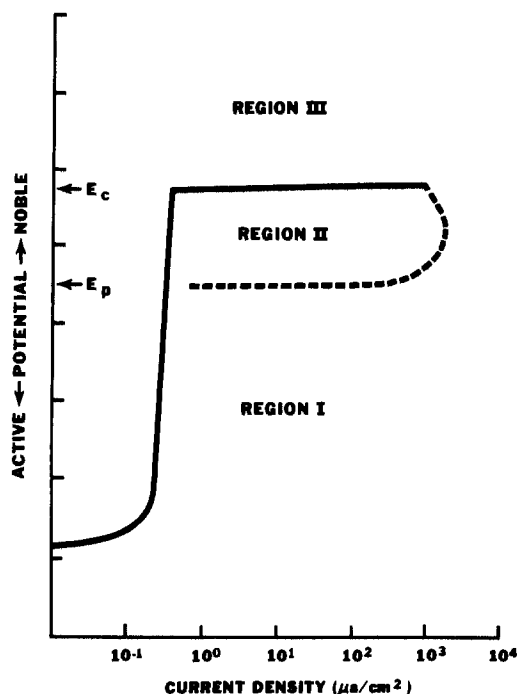


Fig. 2. Schematic potentiodynamic polarization curve for stainless steel in chloride solution showing three corrosion potential regions.

couples (4-8). This same treatment can be used to provide insight into the mechanisms of corrosion in these tests. Referring to the schematic polarization curve in Fig. 2, the corrosion behavior of a stainless steel can be separated into three potential regions: Region I, below E_p , where protection from pitting and crevice corrosion are observed; Region II, between E_p and E_c , where propagation of existing pits and crevices occurs; and Region III, above E_c , where initiation of pitting and crevice corrosion occurs. Galvanic coupling of the stainless steel with another alloy regulates the potential of the stainless steel into one of these regions where the appropriate corrosion behavior for the stainless steel in that region occurs. This behavior has been described for galvanic couples between 321 stainless steel and copper and between 304 stainless steel and carbon steel.

The potentiodynamic polarization curves for 434 stainless steel and 301 stainless steel in 5% sodium chloride solution are shown in Fig. 3. The breakdown potential, E_c , for 301 stainless steel was more noble than the breakdown potential for 434 SS, while the protection potential, E_p , for both alloys was similar. The open-circuit potentials as a function of immersion time in 5% sodium chloride solution are shown in Fig. 4 for 301 stainless steel and chromium. Also shown is the mixed potential for 301 stainless steel galvanically coupled to chromium (1:1 surface area ratio). During this test, the potential of the 301 stainless steel remained in Region II of its polarization curve (Fig. 3), indicating that propagation of existing pits and crevices could occur. The potential of the chromium was much more active than 301 stainless steel, and the mixed potential, as expected, was intermediate. The mixed potential data showed that the galvanic couple between the 301 stainless steel and the chromium regulated the potential of the 301 stainless steel below its protection potential (Region I in Fig. 2), thereby preventing propagation of existing pits and crevices on the 301 stainless steel.

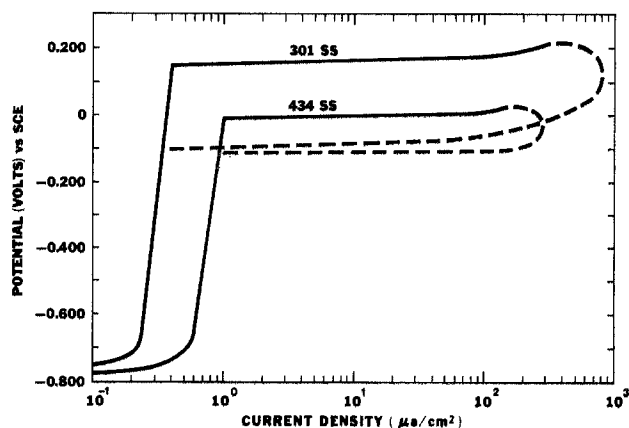


Fig. 3. Potentiodynamic polarization curves for Type 301 SS and Type 434 SS in 5% sodium chloride solution at 30°C (0.6 V/h scan rate).

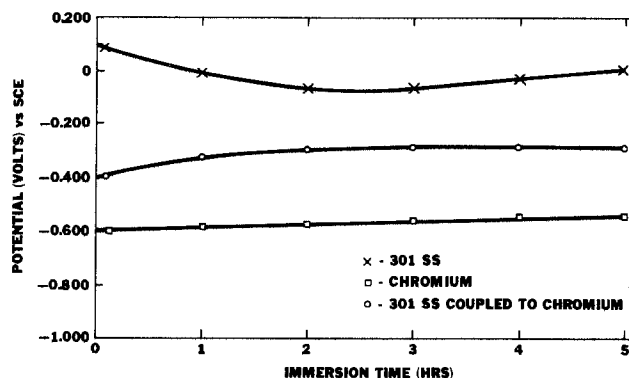


Fig. 4. Corrosion potentials for Type 301 stainless steel and chromium in 5% sodium chloride solution at 30°C.

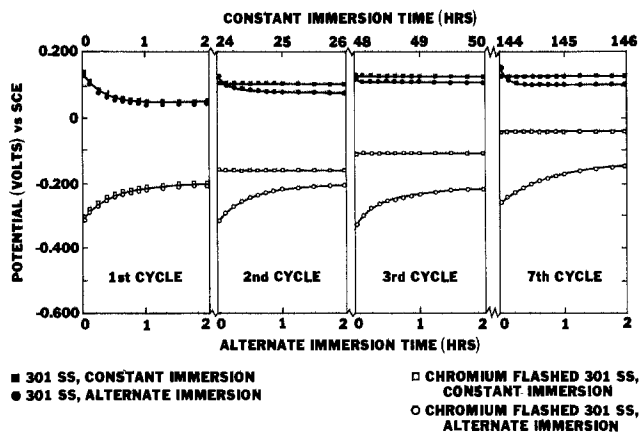


Fig. 5. Corrosion potentials of constantly and alternately immersed chrome flashed 301 stainless steel in 5% sodium chloride solution at 30°C.

Thus, for the 5h immersion period, 301 stainless steel was protected from localized corrosion when coupled to chromium but was susceptible to localized corrosion when isolated.

Since the data in Fig. 4 indicated that the potential of chromium drifted toward more noble values with increased immersion time, additional tests were conducted to determine potentials for longer immersion periods as well as potentials for repeated short immersion periods. These data are shown in Fig. 5 for 301 stainless steel and chrome-flashed 301 stainless steel. Two significant trends are shown. The potential for chrome-flashed 301 stainless steel continuously drifted toward more noble values with longer exposure time. After an extended pe-

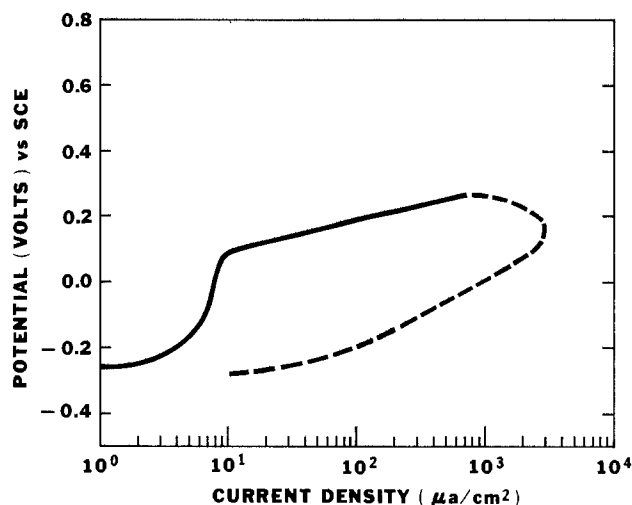


Fig. 6. Potentiodynamic polarization curve for Type 434 stainless steel in seawater at 30°C (0.6 V/h scan rate).

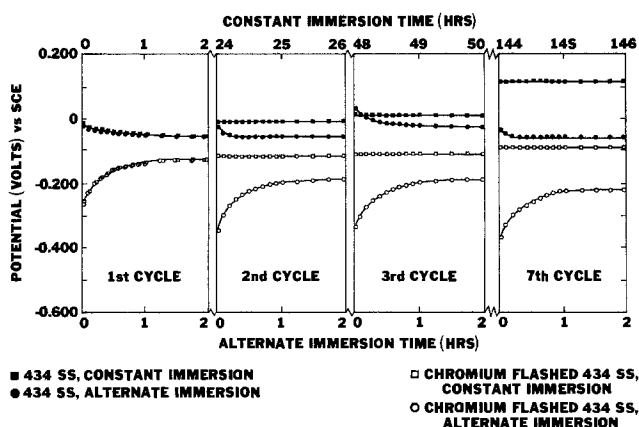


Fig. 7. Corrosion potentials of constantly and alternately immersed chrome flashed Type 434 stainless steel in seawater at 30°C.

riod of time the potential eventually drifted into Region II of the polarization curve for 301 stainless steel (Fig. 3) and, thus, localized corrosion of the 301 stainless steel became possible. Each time the chrome-flashed 301 stainless steel was removed from the solution and reimmersed after 22h, its potential shifted back to the active value initially measured which lies in Region I of the polarization curve for 301 stainless steel (Fig. 3). This behavior continued irrespective of the number of cycles, as shown in Fig. 5. Thus, provided that the chrome-flashed 301 stainless steel is removed from the solution at periodic intervals, the chrome flashing regulates the potential of the 301 stainless steel in Region I (Fig. 3) of its polarization curve and localized corrosion does not occur. This behavior can be attributed to a change in the morphology of the oxide film on chromium with continued exposure or absorption-desorption kinetics for the chloride ion.

Similar results were found for the behavior of 434 stainless steel and chrome-flashed 434 stainless steel in seawater. The cyclic potentiodynamic polarization curve for 434 stainless steel in seawater is shown in Fig. 6, while the results of potential measurements for bare 434 stainless steel and chrome-flashed 434 stainless steel under conditions of constant immersion and intermittent immersion in seawater are shown in Fig. 7. The potential of the chrome-flashed 434 stainless steel gradually became more noble with increased immersion time until the mixed potential resided in Region II of the polarization curve for 434 stainless steel (Fig. 6), thus making localized corrosion of the 434 stainless steel possible. When alternately immersed, the mixed potential of the chrome-flashed 434 stainless steel remained more active (Fig. 7). Thus, under conditions of intermittent wetting, the chrome flashing regulates the potential of the 434 stainless steel in Region I of its polarization curve and prevents localized corrosion of the 434 stainless steel.

Conclusions

Chrome-flashed 301 stainless steel and chrome-flashed 434 stainless steel undergo localized corrosion when constantly immersed in chloride containing environments for extended periods of time. Chrome flashing, however, provides improved resistance to localized corrosion for both alloys in marine atmospheric (and automotive) environments where intermittent wetting occurs.

Cyclic potentiodynamic polarization data and the mixed potential theory can be used to determine the mechanisms of corrosion and explain this behavior. Initially, the more active potential of the chromium polarizes the stainless steel into a region where localized corrosion does not occur. With continued exposure, changes in the nature of the oxide on chromium and/or chloride absorption cause the mixed potential to rise to a value where localized corrosion of the stainless steel occurs. Periodic removal of the chrome-flashed stainless steel from the electrolyte reverses or inhibits these changes so that the mixed potential remains in a region where localized corrosion does not occur.

Manuscript submitted Feb. 14, 1985; revised manuscript received June 3, 1985.

Texas Instruments, Incorporated, assisted in meeting the publication costs of this article.

REFERENCES

- H. L. Black and L. W. Lherbier, ASTM STP 435, p. 3 (1968).
- G. F. Bush, Paper 650A presented at the SAE Meeting, Detroit, MI, January 1963.
- G. F. Bush, *Met. Prog.*, **90**, 56 (1966).
- M. Pourbaix, L. Klimzack-Mathieu, C. Mertens, J. Meunier, C. Vanleughenaghe, L. DeNuncky, J. Laverly, L. Neelemens, and M. Warzee, *Corros. Sci.*, **3**, 239 (1963).
- J. M. Defranoux, *ibid.*, **3**, 75 (1963).
- M. Pourbaix, *Corrosion (Houston)*, **26**, 431 (1970).
- "Electrochemical Techniques For Corrosion," R. Baboian, Editor, NACE, Houston, TX (1977).
- "Galvanic and Pitting Corrosion," R. Baboian et al., Editors, ASTM STP 576, ASTM (1976).

The Production of High Purity Oxygen

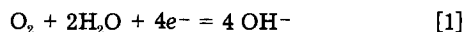
Kurt Buehler¹ and Jack Winnick*

Georgia Institute of Technology, Atlanta, Georgia 30332

High purity oxygen (HPO) (99.99%) is used as a feed for the Space Shuttle fuel cells. NASA stores the HPO on base. The boiloff from the storage tank must be reliquefied instead of vented to maintain the hydrocarbon contamination below 20 ppm. A traditional turnkey distillation process will not allow methane-free HPO to be obtained economically, and electrolysis with an energy-intensive operation becomes uneconomical. We examined use of an oxygen concentration cell as a means of economic, on-site production.

Electrochemical production of oxygen has been reported by Langer (1), Tomter (2), Wynveen (3), and Tseung (4). Langer achieved > 97% oxygen with acidic and basic electrolytes with catalyst-polytetrafluoroethylene gas-permeable electrodes. The over-all four-electron mechanism was found to be operative in both acid and base. Tomter used two porous oxygen electrodes separated by an asbestos matrix saturated with potassium hydroxide. At 0.7V and 71.4°C, Tomter achieved 215.3 mA/cm². He recirculated the electrolyte past the anode to reduce the concentration overvoltage due to oxygen evolution. He did not report product purity. Wynveen used a KOH electrolyte with Pt black electrodes. No oxygen purity was stated, but a four-electron mechanism was found. He achieved current densities of 129 mA/cm² at 40°C. Tseung did not state the oxygen purity achieved; however, a two-electron mechanism reduced the power consumption with H₂O₂ chemically decomposed and collected in the anode compartment.

The concentrator cell operates by reducing oxygen in the feed gas flowing past the cathode



The hydroxyl ions migrate through the asbestos matrix, soaked with saturated potassium hydroxide electrolyte, toward the anode where the reverse reaction occurs releasing pure oxygen off the anode. A dc power supply is necessary to bias the cell. To prevent anodic degradation, the designated cell operating voltage did not exceed 1.2V (5). The feed gas was scrubbed with alkaline solution before entering the cell to prevent loss of electrolyte (3) and carbonate poisoning of the electrodes. The oxygen concentration cell has a hydrophobic cathode and a hydrophilic anode. The hydrophobic electrode permits three-phase reaction sites while the hydrophilic allows two-phase reaction sites. The theoretical voltage needed to bias the cell at open circuit voltage (OCV) can be calculated from the Nernst equation (6)

$$E = (RT/nF) \ln (\text{PO}_2 \text{ anode}/\text{PO}_2 \text{ cathode}) \quad [2]$$

For the four-electron reaction mechanism presented in Eq. [1], the calculated theoretical OCV is 0.01V with air as the feed gas and approximately zero with a propellant-grade oxygen (99.6%) feed gas.

Experimental

The anodes and cathodes were donated by United Technologies (Power Systems Division). The anode, 26 cm² apparent area, consisted of nickel cobalt oxide (NiCo₂O₄) 20 mg/cm², TFE-bonded, on gold-plated 100 mesh nickel screen. The intrinsic surface area of the anode was estimated between (15-20) m²/g (NiCo₂O₄) (5). The cathode, 26 cm² apparent area, consisted of platinum black 10 mg/cm², TFE bonded, on gold-plated 100 mesh, nickel screen. The intrinsic surface area of the cathode was estimated between (20-25) m²/g (platinum black) (5).

*Electrochemical Society Active Member.

¹Present address: NASA/KSC, Kennedy Space Center, Florida 32899.

The actual area of the anode and cathode was approximated at 104,000 and 65,000 cm², respectively. A saturated calomel electrode (SCE) with a porous-plug-type 5 in. body and 1/2 in. diam was used as reference. An asbestos matrix 20 mil thick separated the electrodes and supported twice-distilled water saturated with certified ACS potassium hydroxide.

The current collectors, donated by Exmet, Incorporated, were a perforated expanded-metal material (EXMET), with a sheet thickness of 10 mil, and a strand width of 58 mil. The anodic current collectors were gold plated, which prevented oxidation for the relatively short experiments performed. Ten-gauge silver wires attached to the EXMET provided the electrical leads out of the acrylic cell housing. The cell housing consists of two pieces of acrylic each 5 × 5 × 1 in. Ports were drilled in the acrylic for feed gas inlet and outlet, electrical leads, product gas outlet, and the SCE. The cell housing was sealed with a two-part epoxy resin made by Emerson and Cumings, Incorporated (stycast 2741 and catalyst 15). A Perkin-Elmer Model Sigma 3 gas chromatograph equipped with a thermal conductivity detector analyzed the purity of the oxygen evolving off the anode. A molecular sieve packing removed the water and KOH from the product stream before the gas entered the gas chromatograph.

The current-interruption technique was used to determine ohmic loss, using a Tektronix 5111 single-beam stor-

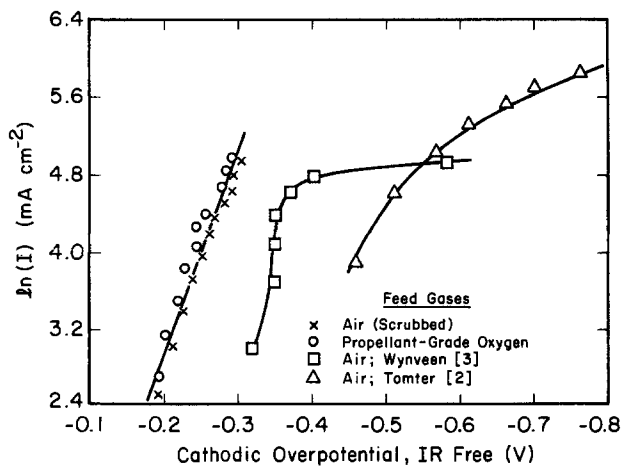


Fig. 1. Experimental cathodic data compared with others

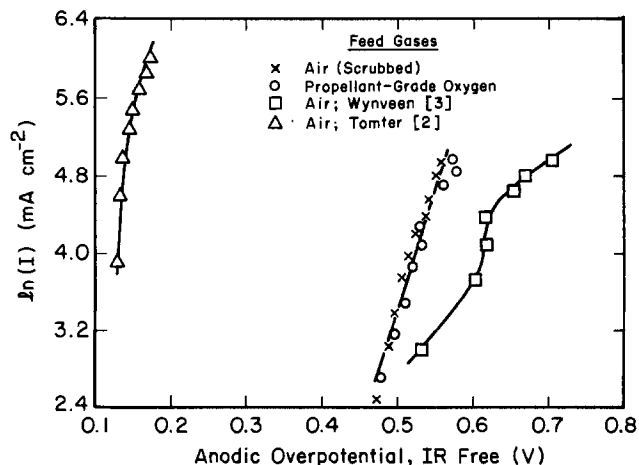


Fig. 2. Experimental anodic data compared with others

Table I. Comparison of anodic Tafel parameters

	Tafel slope (mV/decade)	Exchange current density (apparent) (mA/cm ²)	Exchange current density (actual) (mA/cm ²)
Present study 30% KOH NiCo ₂ O ₄ 25°C	90	1.36 × 10 ⁻⁴	3.4 × 10 ⁻⁸
Ref. (8) 30% KOH NiCo ₂ O ₄ 25°C	60/120	2.0 × 10 ⁻⁶	—
Ref. (9) 1N NaOH Platinum 25°C	60/120	—	1.0 × 10 ⁻⁸
Ref. (10) Saturated NaOH Nickel 25°C	60/120	—	—
Ref. (11) 1N KOH Nickel 23°C	40/170	—	2.2 × 10 ¹¹

age oscilloscope with no. 5BION time base and 5A19N differential amplifier along with a Princeton Applied Research Potentiostat/Galvanostat (Model 371) in the galvanostatic mode.

Electrodes, current collectors, and leads were cleaned before assembling the concentrator cell. The cell was filled with electrolyte through the HPO collector port; experiments were conducted immediately after filling to prevent the conversion of the electrolyte to carbonate by reaction with CO₂. Polarization measurements were taken starting at the lowest current reading and incrementally increasing the bias of the cell up to 1.2V. Cathodic measurements were taken immediately after anodic, and as soon as a reasonable steady state was reached. In this way, a possible change in the electrode surface during cathodic polarization is minimized. Polarization measurements were repeatable and taken in 5h runs. The purity measurements were taken four times in 12h runs.

Results and Discussion

The purity of the oxygen evolving off the anode was found to be 99.996% after the water and KOH were removed with either air or propellant-grade oxygen as cathode feed. The impurities were N₂, Ar, and Kr. The four-electron path was verified through volumetric measurement of the oxygen evolving off the anode; the current

Table II. Comparison of cathodic Tafel parameters

	Tafel slope (mV/decade)	Exchange current density (apparent) (mA/cm ²)	Exchange current density (actual) (mA/cm ²)	Limiting current density (apparent) (mA/cm ²)
Present study Propellant- grade oxygen	100	0.205	8.2 × 10 ⁻⁵	—
Present study Scrubbed breathing air	100	0.205	8.2 × 10 ⁻⁵	400
Ref. (9) 1N NaOH Platinum 25°C Oxygen	60	—	1.0 × 10 ¹¹	—
Ref. (12) 10N NaOH Platinum Oxygen	45	—	—	—

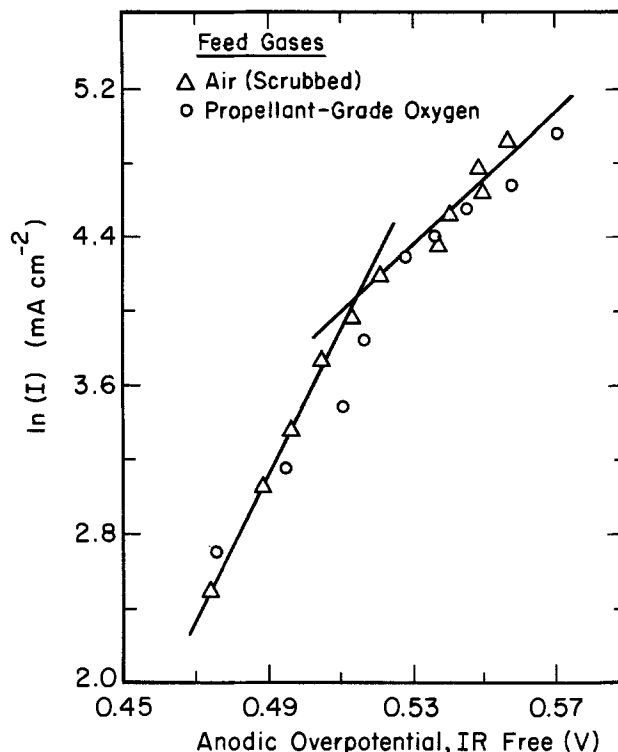


Fig. 3. Experimental anodic data expanded view

efficiency was 100% ± 5%.² The polarization data are plotted in Fig. 1 and 2. The actual cell bias needed is two orders of magnitude larger than the calculated theoretical OCV because of activation, diffusion, and ohmic losses. The ohmic cell losses ranged from 0.0908 to 0.0978Ω; the diffusion losses for the air cathode were negligible compared to the ohmic cell losses.

The Butler-Volmer equation (6), reduced to the Tafel form, was employed to describe the anodic data and the propellant-grade oxygen cathodic data in which diffusion effects can be neglected. Diffusion effects cannot be neglected with the air cathodic data. The mass-transfer limitation is incorporated into the Tafel form of the Butler-Volmer equation in the following manner. The Nernst effect (Eq. [2]) of 0.01V was subtracted from the polarization measurements

$$\ln [I/(1 - I/I_0)] = \ln(I_0) - \frac{F\alpha\eta}{RT} \quad [3]$$

The exchange current densities and Tafel slopes will not be equal at the anode and cathode because of different electrode material and different reaction mechanisms. However, identical values for the cathodic Tafel slope and exchange current are found for the two different feed gases when the data are fit in this manner (Tables I and II).

Our polarizations are somewhat lower than Wynveen's (3) anodic and cathodic data and Tomter's (2) cathodic data (Fig. 1 and 2). However, they are higher than Tomter's anodic data because he recirculated the electrolyte past the anode, eliminating much of the concentration polarization. The break point in the anodic data could not be verified conclusively due to experimental uncertainties [e.g., Ref. (7)]. However, the data obtained compared well with those of Srinivasan (8), who does show a break. Figure 3 presents an expanded-scale view of our anodic data with two lines with Tafel slopes of 60 and 120 mV at low and high overpotentials, respectively. The anodic Tafel parameters found in the present study are compared to the Tafel parameters found in other studies (8-11) in Table I. All these authors show a break point with two Tafel slopes. The Tafel parameters were unaf-

²Water content of the evolved oxygen was not considered, contributing to the uncertainty.

ected by a change in electrolyte, anode, or electrolyte concentration.

The cathodic Tafel parameters found in the present study are compared to the parameters found in other studies (9, 12), in Table II. Platinum was the common electrode, but the electrolyte and electrolyte concentration differ from the present study. No limiting current density was found by the other studies nor was a break point proposed. Our data were corrected for diffusion polarization using the limiting current obtained.

With an expected cell resistance of $0.34 \Omega\text{-cm}^2$ (5), the Tafel parameters incorporated into the Butler-Volmer equation predict current densities of 500 mA/cm^2 with a total cell bias of 1.1V. To produce 5606 kg/week of HPO, a total apparent electrode area of 27.9 m^2 would be required. The power consumption of $4.05 \times 10^{-3} \text{ kWh/liter}$ of O_2 at 500 mA/cm^2 is slightly lower than conventional electrochemical oxygen extractors but higher than Tseung's (4) two-electron mechanism $2.69 \times 10^{-3} \text{ kWh/liter}$ of O_2 .³ The feasibility of implementing Tseung's process to produce 5606 kg of HPO per week seems remote because of the difficulty in scaling up the apparatus,⁴ although the two-electron mechanism is attractive when considering operating costs.

Complete information is now available to design a full-scale system. The economics appear attractive; the operating costs are quite low, but total equivalent cost depends strongly on the purchased cost for the full-scale concentrator cells.

³Apparently incorrectly calculated by Tseung (4).

Acknowledgment

We gratefully acknowledge United Technologies Power Systems Division for providing electrodes and matrix material for the experimental work.

Manuscript submitted April 18, 1985; revised manuscript received Aug. 14, 1985.

REFERENCES

1. S. Langer and K. Haldeman, *J. Phys. Chem.*, **68**, 962 (1964).
2. S. Tomter, *Chem. Eng. Prog.*, **62**, 66 (1965).
3. R. A. Wynveen and K. M. Montgomery, *This Journal*, **114**, 589 (1967).
4. A. C. C. Tseung and S. M. Jasem, *J. Appl. Electrochem.*, **11**, 209 (1981).
5. D. Landsman, United Technologies Power Systems Division, South Windsor, CT, Personal communication.
6. J. O'M. Bockris and A. K. Reddy, "Modern Electrochemistry," Vol. 2, Plenum Press, New York (1971).
7. M. Stern and A. L. Geary, *This Journal*, **104**, 56 (1957).
8. S. Srinivasan, G. Kissel, and C. R. Davidson, *J. Electroanal. Chem.*, **132**, 129 (1982).
9. A. Dey and J. O'M. Bockris, *Electrochim. Acta.*, **11**, 791 (1966).
10. J. P. Hoare, "The Electrochemistry of Oxygen," pp. 117-293, Interscience Publishers, New York (1968).
11. P. W. T. Lu and S. Srinivasan, *This Journal*, **125**, 1416 (1978).
12. T. P. Hoar, *Proc. R. Soc. Edinburg Sec. A*, **142**, 628 (1933).



Anisotropic Wet Etching of Aluminum Electrodes by an Evacuated Etching System

Tohru Hara,* Takeshi Hirayama, and Hirofumi Ando

Department of Electrical Engineering, Hosei University, Kajinocho, Koganei 184, Japan

Masakazu Furukawa

Pioneer Electronics Company, Semiconductor Engineering Laboratory, Kofu, Yamanashi 440, Japan

ABSTRACT

Wet etching of Al/Si (2%) films for fine pattern engraving has been studied using an evacuated wet etching system. The results indicate that isotropic etching by conventional atmospheric wet etching changes to quasi-anisotropic etching with decreasing pressure. The amount of lateral etching beneath the photoresist pattern, which is around $0.8 \mu\text{m}$ in conventional atmospheric wet etching, decreases with decreasing pressure and reaches $0.42 \mu\text{m}$ at a pressure of 9 torr. Uniformity of lateral etching is much better than that by conventional wet and dry etching. This technique is useful in the manufacture of fine-pattern aluminum electrodes, for instance, with $1.0\text{--}1.2 \mu\text{m}$ linewidths.

Wet etching is a well-established technique and has been extensively used for IC production. However, this is typical isotropic etching, and the amount of lateral etching beneath photoresist pattern is much greater than can be achieved by anisotropic etching, such as reactive ion etching (RIE). Therefore, fine-pattern engraving of aluminum electrodes less than $2.5\text{--}3.0 \mu\text{m}$ in linewidth is difficult because linewidth narrowing is evident and etching uniformity is insufficient.

In RIE, however, surface damage induced during the etching is a serious problem (1). The etching selectivity of aluminum to SiO_2 is not so high, for instance, 15/1. Etching uniformity, however, was not acceptable. For instance, uniformity normal to the wafer surface within wafer was about 10% (2).

Thus, the wet etching technique is still useful in the fabrication of conventional bipolar and MOS IC's, owing to its damage-free surface and infinite etching selectivity. If anisotropic etching can be realized by wet etching, it becomes useful for VLSI fabrication. Etching uniformity within a wafer is important in fine-pattern engraving to avoid overetching. Lateral etching uniformity is also important in the fabrication of fine pattern aluminum electrodes. The removal of hydrogen bubbles formed on the aluminum surface should be controlled to attain uniform and reproducible etching.

This paper describes a newly developed aluminum electrode etching technique called evacuated wet etching. The reduction of lateral etching and improvement of etching uniformity within a wafer are also mentioned.

Experimental Procedure

Thin aluminum films, Al/Si (2%), were deposited on 6000\AA thick CVD SiO_2 layer. Negative photoresist patterns with linewidths and spacings of $2/2 \mu\text{m}$ and $3/3 \mu\text{m}$ were defined on the aluminum film.

The etching of the film was performed in hot phosphoric acid without dilution maintained at 55°C , where the etching bath was evacuated to pressures ranging from 9 to 80 torr using a newly developed etching apparatus.¹

*Electrochemical Society Active Member.

¹Type AES 2000, Sigma Corporation, Kawasaki, Japan.

The etching end point was monitored from the time variation of current flowing by the electrochemical potential generated between the aluminum electrode under etching and a platinum electrode dipped in the phosphoric acid. A schematic model of the end point detection procedure is shown in Fig. 1. Variation of current flowing from these electrodes with etching time is shown together with the cross-sectional view of the electrode. At A, etching is proceeding, as seen in the cross-sectional view, A. Current remained constant at i_2 . The etching of the aluminum film normal to the SiO_2 surface was finished at time t_2 , as seen in the cross section B. The current decreased rapidly from i_2 to i_1 at point B. If etching was continued, moreover, lateral etching proceeded as shown in cross section C, where the current remained nearly constant at i_1 , as shown by point C. From observation of the cross-sectional view of aluminum electrode by SEM at different etching times, we have obtained the relation between current and cross-sectional view of the etching (2). From this, the exact end point of the etching can be established.

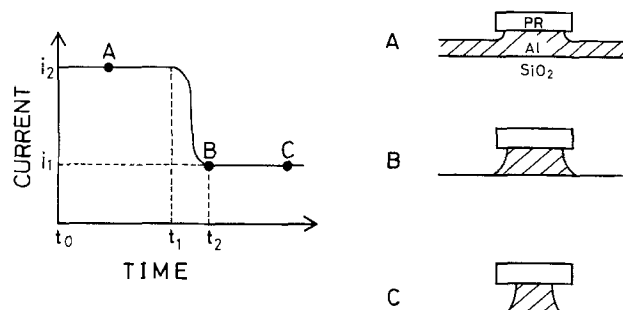


Fig. 1. Schematic model of end point detection using electrochemical potential generated between aluminum electrode and platinum electrode dipped in phosphoric acid. Variation of current flowing from these electrodes and of cross sectional view of the electrode observed by an SEM are shown. Points A, B, and C show etch point of the etching procedure. A: During the etching. B: End point for the etching normal to wafer surface. C: Overetching, lateral etching is proceeding.

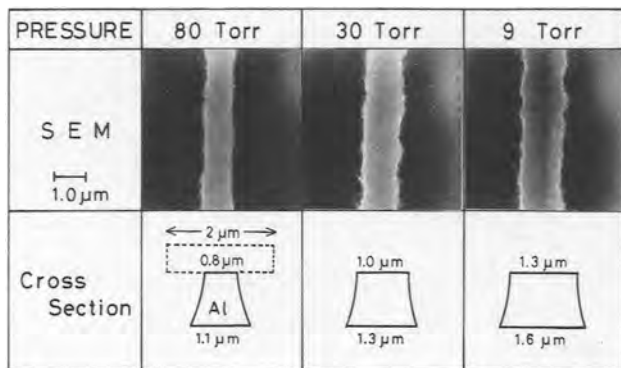


Fig. 2. Top view of SEM micrographs for Al/Si (2%) electrodes etched by evacuated wet system at different pressures. Rectangular test patterns with line/space = $2/2 \mu\text{m}$ were etched in hot phosphoric acid at 55°C at various pressures in the range 9-80 torr. Photoresist patterns were stripped before measurement. Cross-sectional view of each electrode is shown schematically, where the width of electrode at top and bottom is given in micrometers.

Results and Discussion

Etching of the film was performed in phosphoric acid at 55°C with evacuated pressure of 80, 30, and 9 torr. Etching times, determined by end point detection at point B shown in Fig. 1, were around 6 min. Etch rates of the aluminum film normal to the silicon surface were 0.18, 0.17, 0.18, and $0.18 \mu\text{m}/\text{min}$ at pressures of 760, 80, 30 and 9 torr, respectively. This shows that etching rate in this direction is unchanged with evacuated pressure, although bubble sizes removed from aluminum surface decreased rapidly with decreasing pressure. The etching rate uniformity over a 3 in. wafer was better than 5%, which is much better than 10% of conventional wet and dry etching technology (2).

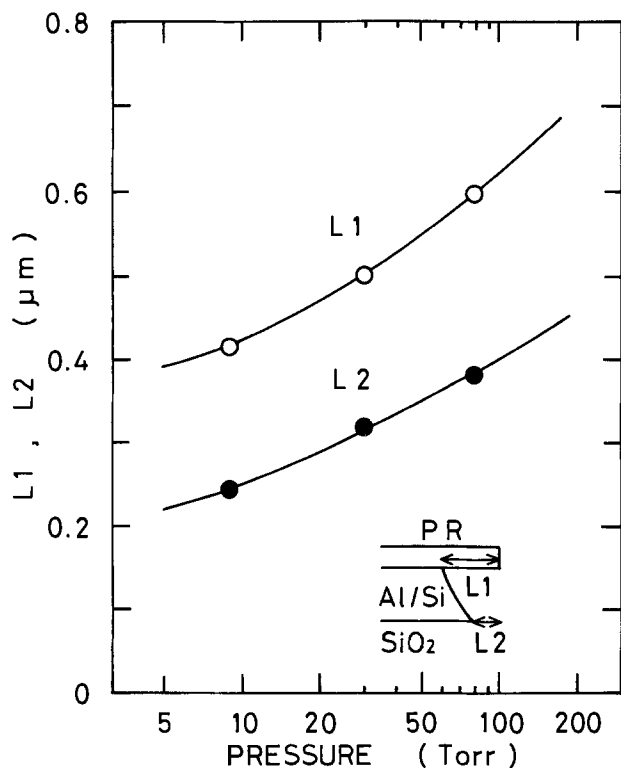


Fig. 3. The amount of lateral etching, L_1 and L_2 , of Al/Si (2%) electrode as a function of pressure in evacuated wet etching system, where L_1 and L_2 are defined in this figure. Rectangular test patterns with line/space of $3/3 \mu\text{m}$ were examined. Mean value of L_1 and L_2 , observed from cross-sectional view of SEM micrographs at 50 points over whole region of wafer, is shown. The electrode was etched in hot phosphoric acid at 55°C .

In the study of lateral etching, etching was stopped at etching point B defined by t_2 in Fig. 1. After photoresist patterns were removed, and the top view of each electrode was observed using a scanning electron microscope (SEM). Figure 2 shows the SEM micrographs for $2/2 \mu\text{m}$ in line/space pattern electrode at etching pressures of 80, 30, and 9 torr, respectively. A cross-sectional view of each electrode is also shown schematically, where aluminum linewidth at top and bottom of each electrode at different pressures are shown numerically in micrometers. Photoresist pattern with $2 \mu\text{m}$ linewidth used in the etching is shown by broken line. As seen in these micrographs, the top linewidth of the aluminum line, which was $0.1\text{-}0.2 \mu\text{m}$ in atmospheric pressure wet etching, increased drastically with decreasing pressure. That is, a linewidth of $0.8 \mu\text{m}$ at 80 torr increased to $1.3 \mu\text{m}$ at 9 torr by the reduction of lateral etching. Bottom width also increased to $1.6 \mu\text{m}$. Typical isotropic etching in atmospheric wet etching changes to quasi-anisotropic etching. This leads to increased linewidth.

The amount of lateral etching for each electrode beneath the photoresist pattern, L_1 and L_2 defined in Fig. 3, was measured from cross-sectional view of SEM micrographs. Mean values of L_1 and L_2 , obtained at 50 points over whole region of the wafer, are shown in Fig. 3 as function of pressure. The value of L_1 was $0.8 \mu\text{m}$ at atmospheric pressure. The values of L_1 and L_2 decrease with decreasing pressure and approach 0.42 and $0.24 \mu\text{m}$, respectively, at a pressure of 9 torr. This shows that isotropic wet etching at atmospheric pressure becomes increasingly anisotropic with decreasing pressure. Therefore, fine pattern electrodes can be manufactured using the reduced pressure wet etching only if uniformity of lateral etching is within acceptable limits.

Uniformity of lateral etching within a wafer was also studied from these data. The standard deviation of L_1 is

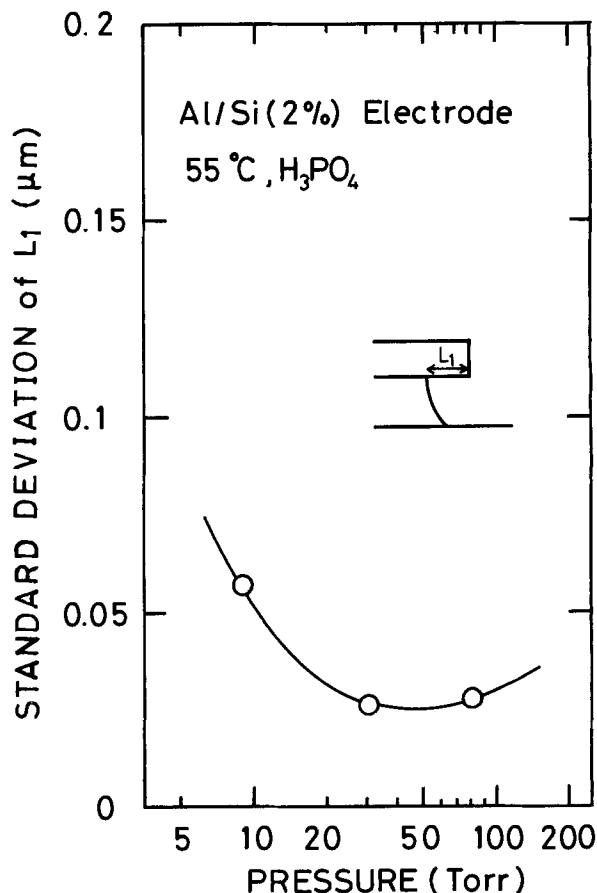


Fig. 4. Uniformity of lateral etching L_1 of Al/Si (2%) electrode shown as a function of pressure in evacuated wet etching system. Test patterns with line/space of $3/3 \mu\text{m}$ were examined. The standard deviation of L_1 , observed at 50 points over whole region of a wafer, is shown. The electrode was etched in hot phosphoric acid at 55°C .

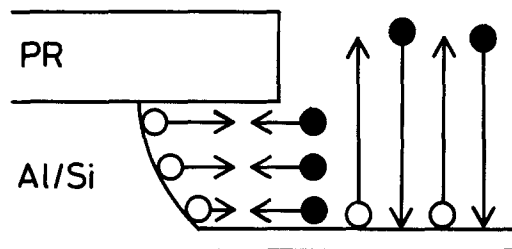


Fig. 5. Model of anisotropic etching in evacuated wet system. Effective diffusion barrier was formed by small hydrogen bubbles on aluminum side wall surface. Here, open and filled circles indicated hydrogen and phosphoric acid, respectively, and arrows show the flux of each molecule.

shown in Fig. 4 as a function of pressure. This shows that lateral etching uniformity was improved remarkably with decreasing pressure. That is, the deviation of $0.2 \mu\text{m}$ at atmospheric pressure decreased to $0.03 \mu\text{m}$ (5%) at 30-100 torr and increased again at still lower pressures. This indicates clearly that evacuated wet etching system offers excellent lateral etching uniformity. Thus, one is able to achieve fine pattern electrode etching with $1.0\text{-}1.2 \mu\text{m}$ linewidth, by the evacuated etching, if the end point detection technique employing electrochemical potential is used.

In wet aluminum etching, hydrogen bubbles are generated on the aluminum film by the chemical reaction with phosphoric acid. Therefore, control of hydrogen bubble removal is important to the improvement of etching uniformity and reproducibility. The fact that the etch rate of aluminum films normal to the wafer surface was constant with time while the lateral (undercutting) etching rate decreased with decreasing pressure suggests the model shown in Fig. 5, which shows the flux of hydrogen bubbles (open circles) and ions of phosphoric acid (filled

circles) during the etching. It is clear from pressure and time variations of the etch rate that the removal rate of hydrogen bubbles through the very narrow channel region ($1 \mu\text{m}$ thick) beneath the photoresist can apparently be restrained with decreasing pressure. Detailed features of this model are reported elsewhere (3).

Conclusions

The consideration of the evacuated wet etching of Al/Si (2%) electrodes resulted in the following conclusions.

1. The etch rate of aluminum films normal to the wafer surface was nearly constant at a value of approximately $0.18 \mu\text{m}/\text{min}$ over the pressure range studied.
2. The amount of lateral etching in the grooves decreased with decreasing pressure, resulting in increased linewidth. Typical undercutting of the conventional (isotropic) wet etching was $0.8 \mu\text{m}$. This was reduced to $0.42 \mu\text{m}$ at 9 torr. Thus, the etching has changed from isotropic to quasi-anisotropic.
3. Uniformity of lateral etching within a wafer was also improved with decreasing pressure. The standard deviation for side etching within a wafer reaches a minimum value of $0.03 \mu\text{m}$ (5%) at 30-100 torr. This is greater uniformity than conventional wet and dry etchings.
4. Overetching for fine pattern aluminum electrodes can be reduced markedly by precisely monitoring the end point. This leads to $1.0\text{-}1.2 \mu\text{m}$ linewidth etching including the deviation.

Manuscript submitted Feb. 20, 1985; revised manuscript received June 20, 1985.

REFERENCES

1. S. W. Pang, *Solid State Technol.*, **27** (4), 249 (1984).
2. T. Hara, Unpublished.
3. T. Hara, T. Hirayama, H. Ando, and M. Furukawa, *Jpn. J. Appl. Phys.*, To be published.

Characterization of Oxide Growth at High Temperatures and Low Pressures from Silane/Nitrous Oxide Reaction

Arthur J. Learn* and R. B. Jackson

Anicon, Incorporated, San Jose, California 95131

ABSTRACT

The reaction of silane and nitrous oxide at high temperatures and low pressures was investigated for a large range of mole ratio of the reactants. For a nitrous oxide/silane mole ratio of approximately 100, silicon dioxide having the stoichiometric refractive index of 1.45 is obtained for growth at $800^{\circ}\text{-}850^{\circ}\text{C}$. For a mole ratio of 2.2 and growth at $700^{\circ}\text{-}750^{\circ}\text{C}$, silicon-rich oxide results with the refractive index increasing linearly from 1.75 to 1.94 with increasing temperature. The growth rate exhibits an Arrhenius-type temperature dependency in the above ranges with activation energies of 1.43 and 0.89 eV for stoichiometric and silicon-rich oxide, respectively. The increase in growth rate for both oxides with increased wafer spacing is quantitatively interpreted, for small wafer spacings, in terms of a modified model developed for semi-insulating polysilicon growth from the same reactants. The refractive index of silicon-rich oxide also increases with increased spacing, which correlates with greater silicon incorporation at higher growth rates. The functional form of the within-wafer thickness profile for both oxides is also consistent with the model referred to, as is the linear dependence of stoichiometric-oxide growth rate on silane partial pressure.

The use of silane and nitrous oxide reactants in the low pressure chemical vapor deposition (LPCVD) of semi-insulating polysilicon (SIPOS) is well documented (1). Nitrous oxide/silane mole ratios, γ , of less than one are employed for this application. Silicon-rich oxides with an excess silicon content on the order of 10% are attractive for use as electron injectors in electrically alterable-memory devices (2) or as an aid to yield improvement on MOS structures with very thin oxides (3). The value of γ used for formation of such films is greater than one and

typically 2-3. Silicon-rich oxides have been prepared by atmospheric-pressure CVD (4) and plasma-enhanced CVD (5). Stoichiometric oxide grown by CVD at high temperatures promises significantly improved conformality (6) and reduced etch rate arising from denser deposits. In particular, a similar wet-chemical etch rate for deposits on horizontal and vertical surfaces could be expected. Such material has been grown by LPCVD (7) with a γ of 50, but little characterization was performed. A preferred silicon bearing reactant is dichlorosilane (8), in some measure due to the more-ready achievement of acceptable thickness uniformity in this case (7).

* Electrochemical Society Active Member.

In the present paper, the growth of silicon-rich and stoichiometric oxide from silane and nitrous oxide by LPCVD in a vertical-flow reactor is characterized. The growth parameters considered are temperature, γ , silane partial pressure and flow rate, and wafer spacing. The effect of these parameters on growth rate, refractive index, and uniformity is considered in most detail.

Experimental

Experiments were performed in a vertical system (9) configured to provide gas flow parallel to the wafer surface. The wafers are held upright in the wafer carrier (boat). A cage is placed around the wafers in order to enhance uniformity of the deposit (9). A caged boat is placed on either side of elongated injectors positioned at the center of the system. An exhaust slot lies opposite the injectors for each boat. Provision is made in the boat for varying wafer spacing in increments of 4.76 mm. The reactant gases, silane and nitrous oxide, are metered through mass flow controllers. Heaters are arranged in such a way as to provide an isothermal chamber for the reaction.

Bare silicon wafers of 100 mm diam were used as substrates. For the high temperature oxide, the ranges investigated for growth parameters were: temperature, 800°-850°C; γ , 36-125; silane partial pressure, 4.0-13.8 mtorr; and silane flow rate, 8-40 $\text{cm}^3\text{-min}^{-1}$. For the silicon-rich oxide, the primary variable considered was temperature, which ranged from 650° to 750°C. Typically, the growth times were in the 30-60 min range. The refractive index and thickness of the resultant films were measured by ellipsometry. As was pointed out (4), for optically absorbing materials such as the silicon-rich oxide, multiple ellipsometric measurements should be made in order to precisely determine thickness. In the present study, the direct ellipsometric readings were considered to be sufficient to reveal significant trends in the data. The growth rate in all cases was calculated on the basis of the thickness at wafer centers. For extensive within-wafer-thickness-uniformity measurements, an interferometric technique was used after determination of the refractive index as above. A significant measure (9) of such uniformity is the ratio of thickness at the wafer center to the average thickness near the wafer edge. Edge measurements were taken at the top, major flat, left and right positions, excluding the outer 6 mm of the wafer.

Some characterization of the films was done by Auger electron spectroscopy. In particular, the silicon content was determined for selected samples. In order to quantify such measurements, a stoichiometric silicon dioxide sample grown thermally was used for calibration. The AES technique was also utilized to test for impurities in the interior of the films.

Results and Discussion

Results were obtained for both high temperature oxide (HTO) and silicon-rich oxide (SIROX). The dependencies for HTO will be discussed first and for SIROX subsequently.

Nitrous oxide/silane mole ratio, γ .—The growth rate and the refractive index of HTO as a function of γ are shown in Fig. 1. Other conditions were held constant at a temperature of 825°C, and silane flow rate and partial pressure of 20 $\text{cm}^3\text{-min}^{-1}$ and 10.8 mtorr, respectively. In general, the data points in Fig. 1 are the result of a single experiment. For a γ of 100, however, several runs were made under ostensibly identical conditions. The ranges of growth rate and refractive index observed are shown in Fig. 1. The leveling off of the refractive index indicates the attainment of stoichiometric HTO for γ near 100. Analysis of such films by AES verified their stoichiometry within the accuracy of this technique (± 2 a/o). The growth rate reaches a maximum at about the same value of γ . This also suggests that the reaction is deficient in oxygen for smaller values of γ . For values of $\gamma > 112$, excess nitrous oxide adsorbed on the substrate surface may inhibit the reaction resulting in reduced growth rate. Somewhat similar behavior, as regards growth rate, is observed (9) for

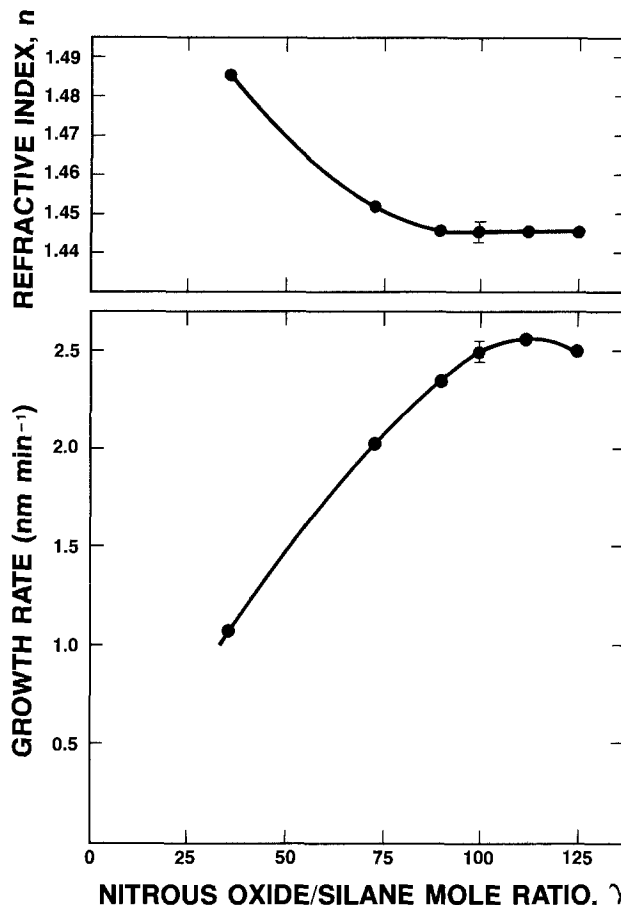


Fig. 1. Oxide growth rate and refractive index as a function of nitrous oxide/silane mole ratio for growth at 825°C with a silane partial pressure of 10.8 mtorr and a silane flow rate of 20 $\text{cm}^3\text{-min}^{-1}$.

the low temperature LPCVD silane/ O_2 reaction. In that case, the growth rate also passes through a maximum, though for $\gamma \approx 1$. The much lower reactivity of nitrous oxide than O_2 , therefore, is apparent.

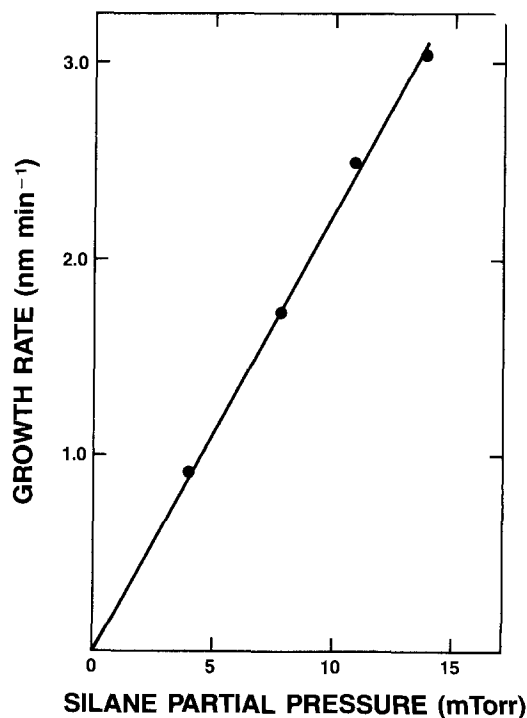


Fig. 2. Oxide growth rate as a function of silane partial pressure for growth at 825°C with a silane flow rate of 20 $\text{cm}^3\text{-min}^{-1}$ and a nitrous oxide/silane mole ratio of 100.

Silane partial pressure.—The growth rate of HTO as a function of silane partial pressure is shown in Fig. 2. In this case, the growth temperature is 825°C, the silane flow is 20 cm³·min⁻¹, and γ is 100. Clearly, a linear dependence of growth rate on silane partial pressure is exhibited. The refractive index for the films of Fig. 2 is not distinguishably different from that for the stoichiometric HTO in Fig. 1.

Silane flow rate.—The growth rate of HTO as a function of silane flow rate is presented in Fig. 3. The temperature and γ are as above, i.e., 825°C and 100, respectively, while the silane partial pressure is 10.8 mtorr. As for the silane/ammonia reaction (10), an increase in growth rate from zero with increased flow is anticipated. This dependency is apparently present for the lower flow rates. The decreased growth rate for the larger flow rates may be a consequence of the reduced residence time for reactants becoming dominant at high flow rates. The refractive index does not exhibit any dependency on flow rate.

Growth temperature.—The logarithm of growth rate as a function of the reciprocal of absolute growth temperature is shown in Fig. 4. The silane flow rate is 20 cm³·min⁻¹, the silane partial pressure is 10.8 mtorr, and γ is 73 for these data. There is a tendency for growth-rate saturation at the highest temperature for this set of growth con-

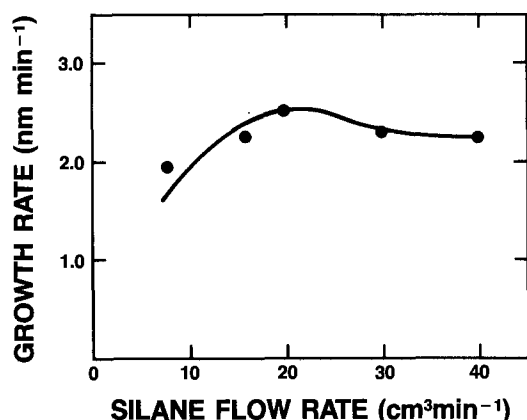


Fig. 3. Oxide growth rate as a function of silane flow rate for growth at 825°C with a silane partial pressure of 10.8 mtorr and a nitrous oxide/silane mole ratio of 100.

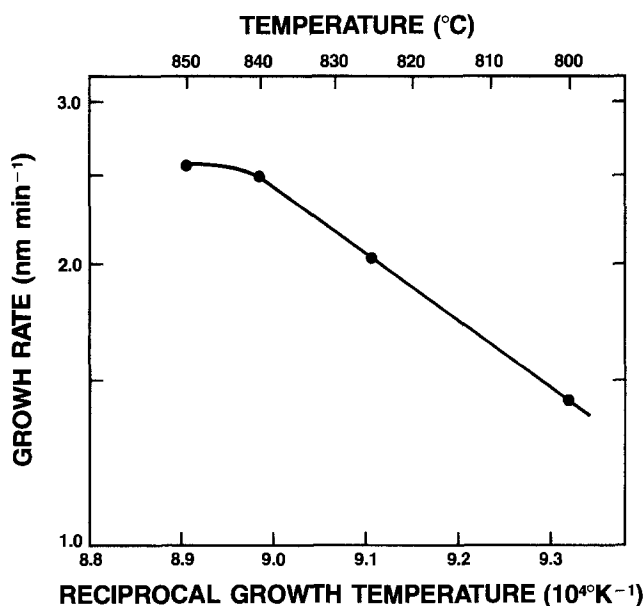


Fig. 4. The logarithm of oxide growth rate as a function of reciprocal absolute temperature for a silane partial pressure of 10.8 mtorr, a silane flow rate of 20 cm³·min⁻¹, and a nitrous oxide/silane mole ratio of 73.

ditions. The lower temperature data points yield an activation energy of 1.43 eV. This activation energy is much larger than the value of 0.52 eV observed (11) for the O₂/silane reaction at temperatures near 400°C. It is, however, lower than the activation energy for the dichloro-silane/nitrous oxide reaction of about 2 eV (8). The refractive index for the highest temperature (850°C) film is approximately 0.02 higher than for the other films.

Wafer spacing.—All of the data listed above were gathered for a wafer spacing of 9.5 mm. The growth rate of HTO at the wafer center as a function of wafer spacing is shown in Fig. 5. The associated growth conditions are a temperature of 825°C, a silane partial pressure of 10.8 mtorr, a silane flow rate of 22 cm³·min⁻¹, and a γ of 90. The growth rate has a sublinear dependency on wafer spacing. A similar dependency is noted for low temperature LPCVD oxide (9). In that case, a proportionality for growth rate, GR , is derived as follows

$$GR \propto d \frac{r_c^2 - r^2}{r_c d + r_w^2 - r^2} \quad [1]$$

where d is wafer spacing, r_c is the inner radius of the cage surrounding wafers, r_w is the wafer radius, and r is the radial position on a wafer. This relationship for GR essentially involves (9) the volume to area ratio of a reaction cell comprised of two adjacent wafers and the portion of the cage between the two wafers. For boats utilized in the vertical-flow reactor, openings in the cage are required in order to allow introduction of reactants to the wafers. The openings are configured as rings of circular holes spaced along the length of the boat. Taking into account these holes, the expression for GR becomes

$$GR \propto d \frac{r_c^2 - r^2 + \frac{d_h^2}{2d}(s+w)n}{r_c d + r_w^2 - r^2 + d_h w n} \quad [2]$$

where d_h is the hole diameter, s is the effective spacing between the cage and the reaction-chamber wall, w is the thickness of the cage wall, and n is the number of holes per reaction cell. The additional volume term is that for cylinders extending from the inner surface of the cage to the chamber wall. The additional area term is that for the peripheries of the holes. For optimum within-wafer thickness uniformity, there is no radial variation of GR , i.e., $d(GR)/dr = 0$. This condition leads to the following equality

$$r_c^2 - r_c d - r_w^2 = n d_h \left\{ w - \frac{d_h}{2d}(s+w) \right\} \quad [3]$$

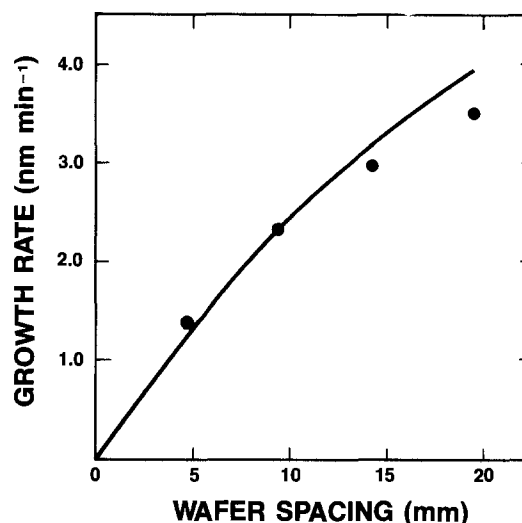


Fig. 5. Oxide growth rate as a function of wafer spacing for growth at 825°C with a partial pressure of 10.8 mtorr, a silane flow rate of 22 cm³·min⁻¹, and a nitrous oxide/silane mole ratio of 90. The curve is a fit of Eq. [2] to the experimental results.

The boat dimensions resulting in this optimum condition for a d of 9.5 mm and a r_w of 50 mm are r_c , n , d_h , and w equal to 52.5, 12, 2.36, and 2.5 mm, respectively. Calculation of s from Eq. [3] yields a value of 87 mm. A boat essentially resides in a reaction chamber of square cross section with a side dimension of 204 mm. Accordingly, the range of s expected is 47-89 mm. The calculated value of s falls within this range, albeit at the high end.

The growth rate at the wafer center as a function of d is given by setting r equal to zero in expression [2]. Using the values for other parameters listed above, the curve in Fig. 5 is obtained. The constant of proportionality was obtained by fitting Eq. [2] to the data point at a d of 9.5 mm. It may be noted that the experimental results fall significantly below this curve for large d .

The uniformity parameter mentioned in the Experimental section, *i.e.*, the ratio of thickness at the wafer center to the average near the edge, is shown in Fig. 6 as a function of d . Relationship [2] can be used to predict this ratio. Comparison is made for r equal to zero and r equal to the wafer radius minus 6 mm. The resultant curve is presented in Fig. 6. Again, as for the GR of Fig. 5, the experimental points fall below this curve for large d . Shifting the GR at wafer center for the two large d up to the level of the curve in Fig. 5 results in the shift in uniformity indicated by the arrows in Fig. 6. A good fit to the theoretical uniformity curve is thereby obtained. The implication is, therefore, that the GR near the edge of wafers varies with d as predicted by Eq. [2]. The different behavior for the edge and center GR may be explained by a diffusion effect. For example, for a d of 19 mm two rings of holes lie between adjacent wafers. Less reactant may diffuse to the wafer center from the more remotely located holes. Such an effect would be less pronounced at the wafer edges, since they are nearer the holes, or for smaller d , for the same reason.

The remainder of the results presented are for SIROX.

Growth temperature.—The logarithm of SIROX growth rate as a function of the reciprocal of absolute growth temperature is shown in Fig. 7. The results were obtained with a nitrous oxide/silane mole ratio of 2.2, a total flow rate of 800 $\text{cm}^3\text{-min}^{-1}$, and a silane partial pressure of approximately 60 mtorr. The straight-line portion of the curve at higher temperatures yields an activation energy of 0.89 eV. This activation energy is comparable to the 0.78 eV value observed (1) for SIPOS for a γ of 0.4. The reaction rate appears to decrease disproportionately at the lowest temperature (650°C). As discussed below, however, the thickness was determined in this case by assuming a value of refractive index and may therefore be somewhat in error.

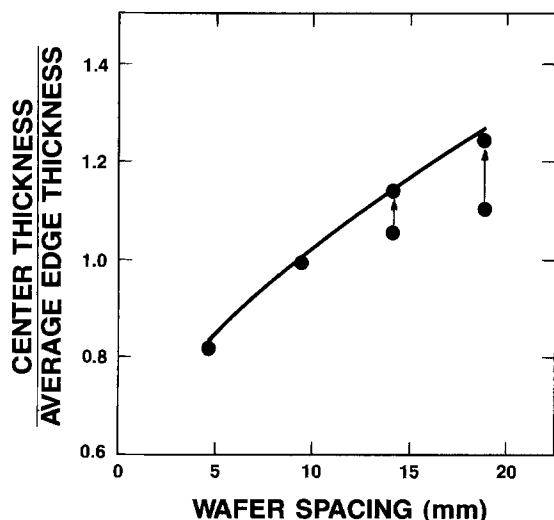


Fig. 6. Oxide-thickness uniformity parameter as a function of wafer spacing. The growth conditions are as listed for Fig. 5. The curve is uniformity as predicted from Eq. [2]. As discussed in the text, the arrows represent corrections for wafer-center growth rates.

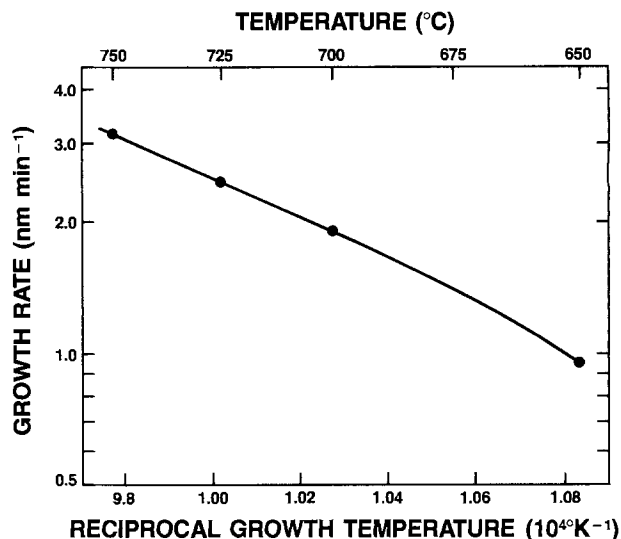


Fig. 7. The logarithm of oxide growth rate as a function of reciprocal absolute temperature for a silane partial pressure of 60 mtorr, a silane flow rate of 250 $\text{cm}^3\text{-min}^{-1}$, and a nitrous oxide/silane mole ratio of 2.2.

The refractive index, n , as a function of growth temperature is presented in Fig. 8. A linear variation of n with growth temperature is indicated. The bars encompass the range of n observed at the different temperatures. There is less variation in n as the growth temperature is reduced. At 650°C, the films were sufficiently thin such that n and thickness could not both be determined. An extrapolated value of 1.56 for n was utilized in measuring thickness. Although perhaps not entirely meaningful, extrapolation of the curve to 1.45 for n indicates growth of stoichiometric oxide at approximately 625°C for γ equal to 2.2.

Wafer spacing.—Growth rate and n are shown as a function of wafer spacing in Fig. 9. Growth was at 725°C, with a nitrous oxide/silane mole ratio of 2.2, a total flow rate of 400 $\text{cm}^3\text{-min}^{-1}$, and a silane partial pressure of 47 mtorr. The curve presented for GR was obtained from Eq. [2] by fitting to the data point for a d of 9.5 mm. The variation of GR with d is virtually identical to that for HTO in Fig. 5. In particular, the experimental GR values fall below the theoretical curve for large d . The data of Fig. 7 were obtained for a d of 9.5 mm, where a growth rate of 2.4 $\text{nm}\text{-min}^{-1}$ is noted at 725°C. For the same d , from Fig. 9, the growth rate is 0.8 $\text{nm}\text{-min}^{-1}$. This change in growth rate corresponds roughly to the combined effects of a twofold reduction in silane flow rate and a 20-25% reduction in silane partial pressure, if a linear dependence of growth rate on these parameters applies.

The refractive index exhibits a monotonic increase with increasing d . Films grown at the extreme wafer spacings

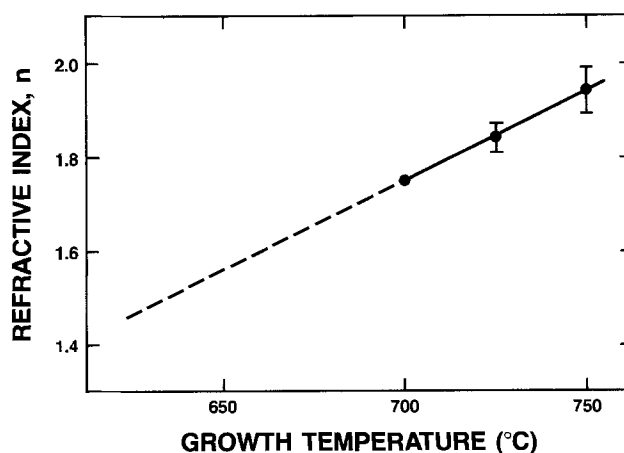


Fig. 8. Refractive index for silicon-rich oxide as a function of growth temperature. The growth conditions are as listed for Fig. 7.

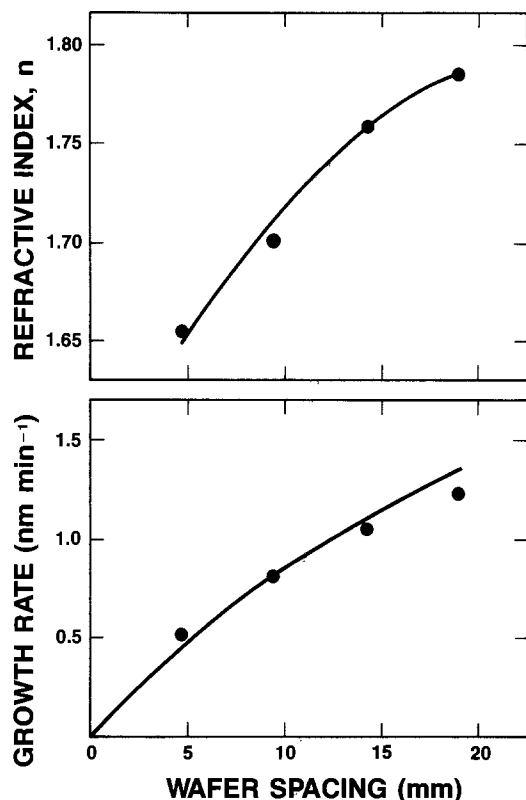


Fig. 9. Silicon-rich oxide growth rate and refractive index as a function of wafer spacing for growth at 725°C with a silane partial pressure of 47 mtorr, a silane flow rate of 125 cm³-min⁻¹, and a nitrous oxide/silane mole ratio of 2.2. The curve is a fit of Eq. [2] to the experimental results.

of 4.76 and 19 mm were tested by AES and found to contain 41 ± 2 and 47 ± 2 a/o silicon, respectively. The higher values of n clearly correspond, therefore, to more silicon-rich composition. In fact, combining the above silicon contents, and their associated values of n from Fig. 9, with the silicon content (33 a/o) and n (1.45) for stoichiometric oxide reveals that a change in n of 0.024 per atom percent of excess silicon applies. In any case, increased silicon incorporation is promoted at the higher growth rates. Such an effect may also account, in part, for the lower n of Fig. 9 than that of Fig. 8 at 725°C. Similarly, the increased n at higher temperatures (Fig. 8) may be partially attributable to the increased growth rates (Fig. 7).

The silicon contents listed above are comparable to those (4) for atmospheric growth at 700°C with the same γ . Also, as is found for the atmospheric films, the AES analysis suggests that the excess silicon exists as a separate phase in the silicon dioxide matrix. For a γ of 2.2 with the atmospheric process, carbon at the several atom percent level and nitrogen in a lesser amount are observed (4) in deposits. Neither of these elements was detected in films of the present study by AES, which has sensitivity down to about 1 a/o.

Center-to-edge uniformities for thickness and n as a function of d are shown in Fig. 10. The thickness-uniformity variation is similar to that for HTO in Fig. 6. As was noted above, the same is true of the GR variation with d . Consequently, the discussion in connection with the HTO data is equally applicable to SIROX. The variation with d of refractive-index uniformity illustrated in Fig. 10 is generally consistent with the dependency of n on growth rate. An exception is the result for the lowest value of d in Fig. 10. Since the center growth rate is less than the edge growth rate in this case, a lower n at the wafer center would be anticipated.

Conclusions

The silane/nitrous oxide reaction was utilized at high temperatures for the low pressure CVD formation of high temperature oxide (HTO) and silicon-rich oxide (SIROX). The nitrous oxide/silane mole ratio was varied from 35 to

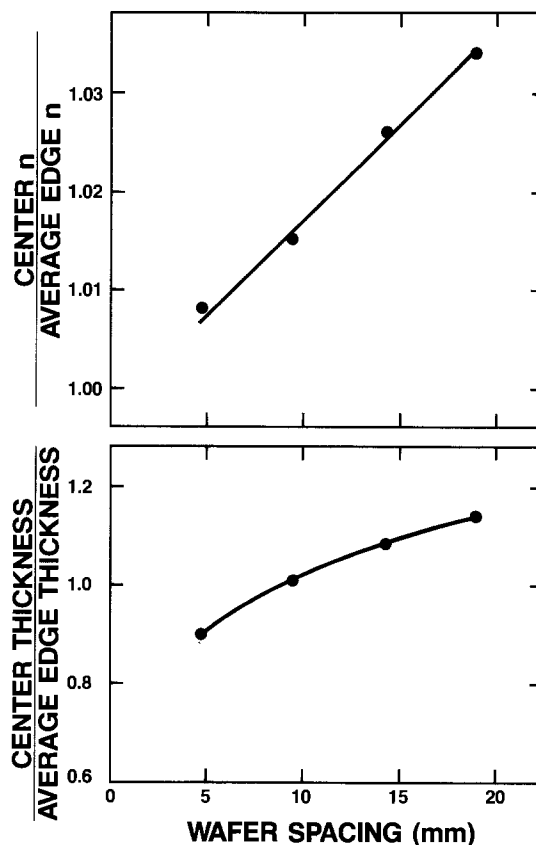


Fig. 10. Thickness and refractive index uniformity parameters for silicon-rich oxide as a function of wafer spacing. The growth conditions are as listed for Fig. 9.

125 for HTO and fixed at 2.2 for SIROX. For low values of this ratio, the HTO growth rate increases, and refractive index decreases as the ratio is increased. The growth rate and refractive index level off for a mole ratio of approximately 100, indicating the attainment of stoichiometric HTO. The growth-rate activation energies for stoichiometric HTO in the 800°-840°C temperature range and for SIROX in the 700°-750°C range are 1.43 and 0.89 eV, respectively. The SIROX refractive index is a strong, linear function of temperature and increases by 0.19 over the 50°C range above. The growth rate of HTO depends linearly on silane partial pressure and passes through a maximum with respect to silane flow rate at high total flow rates. The refractive index and silicon content for SIROX increase with increased wafer spacing. This is a consequence of the monotonic increase in growth rate with increased wafer spacing. Quantitatively, at small wafer spacings, the variation of growth rate at wafer centers for both HTO and SIROX as a function of wafer spacing is in accordance with a modified version of the model developed by Hitchman *et al.* (1) for SIPOS. The within-wafer uniformity variation with wafer spacing in the same range is also consistent with this model. In particular, a reversal in the slope of the center-to-edge thickness profile at a certain wafer spacing is predicted. For large wafer spacings, a diffusion-length effect may cause deviation of the wafer-center growth rate and uniformity from the modeled values. The commonality for all processes to which the model applies appears to be the use of silane as a silicon bearing reactant. This list now includes, SIPOS (1), HTO, SIROX, low temperature LPCVD oxide (9), and silicon nitride (12).

Manuscript submitted Jan. 28, 1985; revised manuscript received Aug. 28, 1985.

Anicon, Incorporated, assisted in meeting the publication costs of this article.

REFERENCES

1. M. L. Hitchman and J. Kane, *J. Cryst. Growth*, **55**, 485 (1981).

2. D. J. DiMaria, K. M. DeMeyer, C. M. Serrano, and D. W. Dong, *J. Appl. Phys.*, **52**, 4825 (1981).
3. S. K. C. Lai, D. J. DiMaria, and F. F. Fang, *IEEE Trans. Electron Devices*, **ed-30**, 894 (1983).
4. D. Dong, E. A. Irene, and D. R. Young, *This Journal*, **125**, 819 (1978).
5. S. Yokoyama, D. W. Dong, D. J. DiMaria, and S. K. Lai, *J. Appl. Phys.*, **54**, 7058 (1983).
6. R. M. Levin and K. Evans-Lutterodt, *Mater. Lett.*, **1**, 29 (1982).
7. R. S. Rosler, *Solid State Technol.*, **20** (4), 63 (1977).
8. A. Philipossian and R. F. Sarkozy, Abstract 448, p. 642, The Electrochemical Society Extended Abstracts, Vol. 84-2, New Orleans, LA, Oct. 7-12, 1984.
9. A. J. Learn, *This Journal*, **132**, 390 (1985).
10. B. A. Capron, Submitted to *This Journal*.
11. A. J. Learn, *ibid.*, **132**, 405 (1985).
12. B. A. Capron and R. B. Herring, Abstract 505, p. 738, The Electrochemical Society Extended Abstracts, Vol. 84-2, New Orleans, LA, Oct. 7-12, 1984.

Reactive Ion Etching of Tungsten Films Sputter Deposited on GaAs

Sadao Adachi

Nippon Telegraph and Telephone Corporation, Atsugi Electrical Communication Laboratories, Atsugi-shi, Kanagawa 243-01, Japan

Nobuhiko Susa

Nippon Telegraph and Telephone Corporation, Musashino Electrical Communication Laboratories, Musashino-shi, Tokyo 180, Japan

ABSTRACT

A correlation between reactive ion etching (RIE) characteristics of W films and their microstructural features has been investigated, and it was found that the α -phase W can be controllably etched compared with the $\alpha + \beta$ mixed modification. The etch rate for the stable, α -phase W films with CF_4 and SF_6 plasmas has been shown to depend strongly on the discharge parameters—RF power and reactor pressure. Effects of the Ar, O_2 , and N_2 additions and the etching selectivity between the W film and photoresist (Shipley AZ-1350) have also been studied in detail. These observations have led to the conclusion that the CF_4/N_2 (SF_6/N_2) mixed system is mostly attractive for a variety of device processing applications. The chemical nature of the RIE-processed W surface has been examined by secondary ion mass spectrometry, and an apparent presence of C, O, F, and S species on the surface has been confirmed. By I-V and C-V measurements of Schottky contacts fabricated on RIE-processed GaAs surface, no indication of damage layers has been detected.

Reactive ion etching (RIE) is of current interest because of its importance for use in the fabrication of VLSI (VLSI) circuits. The processing of refractory metals is also become of great importance for the fabrication of low resistive interconnects and contacts for such semiconductor devices. W film deposition has, therefore, been investigated extensively, and sputtering, electron-beam evaporation, and chemical vapor deposition as well as laser photolysis have been developed as deposition techniques (1). W plasma etching has also been performed widely in both barrel and parallel-plate reactors.

Maeda and Fujino (2) have demonstrated that the refractory metals, such as W and Mo, can be attacked and etched considerably by activated F atoms produced in a barrel-type reactor with a CF_4 discharge. The effects of O_2 additions to SF_6 on W etch rate in a reactor have been studied by Randall and Wolfe (3). They have found that the maximum etch rate occurs with a pure SF_6 discharge and decreases gradually with increasing O_2 additions. Tang and Hess (4) have also carried out a systematic investigation on plasma etching characteristics of W films in CF_4 and SF_6 discharges. They have measured relative F atom concentrations by means of optical emission spectroscopy, and concluded that the W etching is primarily controlled by F atoms in the CF_4 plasmas, but the mechanism is not so simple in the case of the SF_6 plasmas. Recently, Tsujimoto *et al.* (5) have reported fundamental properties of W dry etching, such as etching selectivity between the W and dielectric films and etching profiles of the W films, from the viewpoint of the VLSI applications.

It is the purpose of this paper to clarify a correlation between the RIE characteristics of the W films and their microstructural features and, moreover, to present accurate experimental data on the etch rate of W films (hereafter referred to as R_w) as a function of the discharge parameters, such as RF power and reactor pressure, in a parallel-plate reactor with CF_4 and SF_6 plasmas. Effects of

the Ar, O_2 , and N_2 additions to CF_4 and SF_6 on R_w are also studied in detail. The etching reactions in such plasmas are discussed. Considering the growing importance of submicrometer-design device rule fabrication, it is somewhat surprising that relatively little or, to our knowledge, no attention has been given in the literature to the etching selectivity between the W films and photoresists. Because of this, we simultaneously carried out RIE studies on photoresists. Shipley AZ-1350 was chosen as the photoresist for this study. This resist is positive type and is frequently used in the VLSI processes. The chemical nature of the RIE-processed W surface is examined by secondary ion mass spectrometry (SIMS). The feasibility of the RIE process in the VLSI technology strongly depends on its capability of producing damage free surface. A group of researchers (6, 7) have proposed a new type of the transistor, namely, permeable base transistor (PBT). The unique feature of this transistor is the use of W-metal grating embedded in the single-crystal semiconductor. Because of this importance, Schottky contacts were formed on RIE-processed GaAs surface, and the surface quality was characterized by I-V and C-V measurements.

Experimental

Tungsten deposition.—W films were deposited by conventional RF diode sputtering system on (001) GaAs substrates. The W target used was a commercially available one (99.9% pure). After the system had been pumped down to $\sim 5 \times 10^{-7}$ torr, the target was cleaned by pre-sputtering for about 30 min while the GaAs substrates were isolated from the plasma by a stainless steel shutter. The working gas was argon, 99.999% pure. Sputtering pressures tried were in the range of 1×10^{-2} to 3×10^{-1} torr. Unless otherwise noted, the W films used were deposited at working pressure of 4×10^{-2} torr. The deposition runs were carried out at an RF power of 100W. The substrate temperature was not measured during deposition. A separate series of sputtering experiments, how-

ever, indicated an increase of the substrate temperature to a saturation value ($\sim 200^\circ\text{C}$) as the film deposition was taking place for about 20 min.

RIE apparatus.—The RIE apparatus used in this work was a commercial parallel-plate reactor. It consists of a stainless steel chamber and 28 cm diam SiO_2 electrodes. The etch gases used in this study were CF_4 (99.9999% pure) and SF_6 (99.99% pure) purchased from Asahi Glass Company. High purity argon, oxygen, and nitrogen gases were also added and mixed prior to entering the reactor chamber. The flow rates of individual gases were controlled by thermal mass flow meters. They were corrected with the following gas calibration factors: CF_4 (0.44), SF_6 (0.28), Ar(1.43), O_2 (0.99), and N_2 (1.00). The etching samples, about $5 \text{ mm} \times 5 \text{ mm} \times 320 \mu\text{m}$ size, were loaded at the center of the electrode. In conducting our experiments, we evaluated separately the effects of various plasma parameters on the etch rate with a set of standard etch conditions. They are; 50W (RF power), 10 Pa (reactor pressure), and 35 sccm (gas flow rate).

Etch rates.—Etching studies were performed for the etching selected regions of W films sputter-deposited on (001) GaAs substrates through windows in AZ-1350 photoresist mask. The open windows, $100 \mu\text{m}$ wide and $200 \mu\text{m}$ long, were defined by standard photolithography technique. After etching, removing the AZ-1350 mask, and rinsing in deionized water, the etched depths of the W films were measured from a step height between the etched and unetched surfaces using a Talystep meter. The etch rate of photoresists AZ-1350 was also examined similarly. Hereafter, we refer to this value as $R_{\text{AZ-1350}}$. The etching profile was also examined by cleaving the samples in a direction along the GaAs (110) cleavage plane.

Etched-surface quality.—After RIE processing, the W films were removed from the RIE chamber and characterized by means of the SIMS analysis. Au-evaporated Schottky diodes were fabricated on a RIE-processed GaAs surface, and the surface quality was tested by I-V and C-V measurements.

Microstructure-Related Data on Sputtered-W Films

The purpose of this section is to present a study of the dependence of the properties of Ar-ion-sputtered W films upon deposition condition (working pressure). A series of refractory-metal elements, like W, Mo, and Ta, form stable or, sometimes, metastable crystal structure. In the case of W, its stable structure is the so-called α -W modification with lattice constant $a = 3.156\text{\AA}$ and density $\rho = 19.6 \text{ g/cm}^3$, and its metastable one is the β -W modification of the A-15 cubic crystal structure with $a = 5.038\text{\AA}$ and $\rho = 19.0 \text{ g/cm}^3$.

In the W metallization process used for the fabrication of electron devices, a number of requirements, such as low stress, low interface-state density, and low electrical resistivity, have to be satisfied. Especially, the film resistivity is one of the most important factors for applications to W-gate FET's and circuit interconnects. The room temperature electrical resistivities of the W films sputtered at various pressures were measured by the standard four-point probe method. The results of this experiment are shown in Fig. 1 by the crosses (curve 1). The corresponding sputter deposition rates are also shown in the figure by the open circles (curve 2). It can be seen that the electrical resistivity decreases slightly with increasing working pressure, showing a minimum at about 4×10^{-2} torr, and then increasing sharply. This result is identical to that reported by Hoffman and Thornton (8). The deposition rate also increases gradually with increasing working pressure. It is interesting and important to make clear some correlations between the electrical resistivities and microstructural features of the W films. From this point of view, the crystal structure of the films was examined by an x-ray diffractometer analysis. When the films were deposited at low pressures ($p \leq 4.5 \times 10^{-2}$ torr), they were in a single α -phase because only two peaks of (110) and

(211) of the α -W were detected. When the films were deposited at pressures greater than 4.5×10^{-2} torr, they became α -W/ β -W mixture containing a new phase modification, WO_3 , and the fraction of the β -W modification increased with increasing working pressure. As is shown in Fig. 1, the pure α -W films have a low resistivity. An increase in the film resistivity at higher sputtering pressures corresponds to the appearance of the β -W and WO_3 modifications. It can, therefore, be recognized that relatively large resistivity of the W films deposited at higher pressures is controlled by the amounts of β -W and WO_3 present in the film. Similarly, Petroff *et al.* (9) have found from studies on RF-sputtered films that α -W films consist of large grains (1500 - 2000\AA) free of defects, while β -W films consist of small grains (50 - 100\AA) with a high density of stacking faults and twins. They reported that the high resistivity of the β -W films was attributed to diffuse scattering of electrons by grain boundaries.

The plots of the etch rate against working pressure for the sputter-deposited W film are shown in Fig. 1 by the filled circles. The data were taken in CF_4 plasma with the flow rate of 35 sccm at 10 Pa pressure and 50W RF power. In the figure, the solid line corresponds to that of the as-deposited and without intentional room ambient exposure W films (curve 3a), and the dashed line corresponds to films exposed to room ambient for about two months (curve 3b). It should be noted that the etched depth of the W films in the α -W/ β -W mixture region ($p > 4.5 \times 10^{-2}$ torr) does not increase linearly with etching time (see Fig. 2). When the linear relationship is extrapolated, the line does not pass through the origin, indicating that a lag time exists at the start of the W-film etching in this region. A considerable change in the etch rates of samples with and without room ambient exposure in the α -W/ β -W mixture region, moreover, suggests instability of the ($\alpha + \beta$) W films with room ambient exposure. It is apparent from the figure that the etch rate increases dramatically as the Ar working pressure falls in the ($\alpha + \beta$) W mixture region. This feature is quite similar to that found in the resistivity variation. An identical trend was also seen for the W etching in SF_6 plasma.

Etch Rates

Pure CF_4 and SF_6 plasmas.—The etched depths as a function of etching time for W film and photoresist

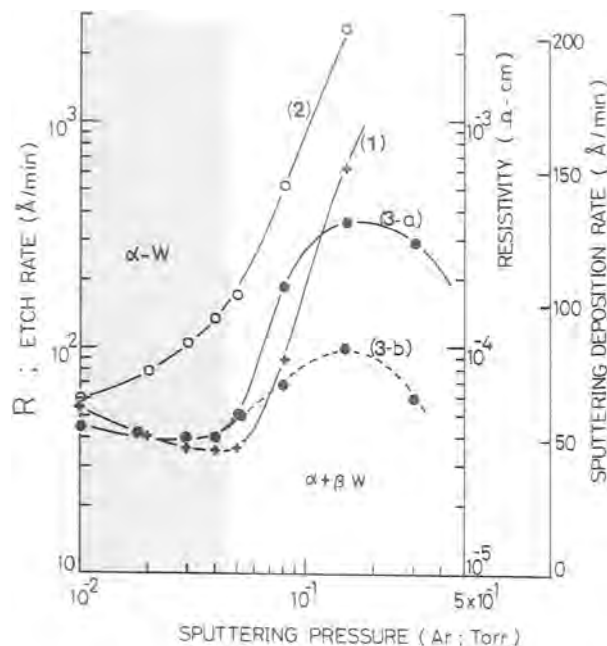


Fig. 1. Plots of electrical resistivity (curve 1), deposition rate (curve 2), and etch rate (curve 3) against working pressure for W films sputter-deposited in Ar using an RF diode sputtering system. Curve 3a corresponds to that of the as-deposited, without intentional room ambient exposure W films, and curve 3b corresponds to that of about two months room ambient exposed ones.

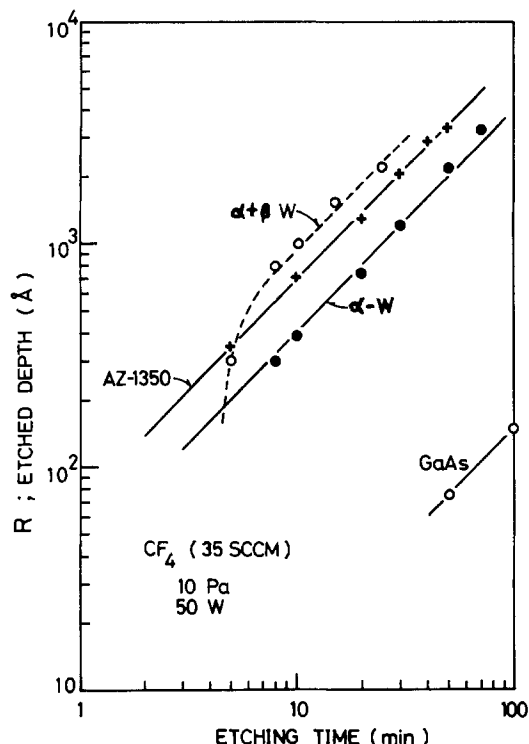


Fig. 2. Relation between etched depth and etching time for α -W (deposited at 4×10^{-2} torr), $(\alpha + \beta)$ W (deposited at 1.5×10^{-2} torr), and AZ-1350 in pure CF_4 plasma.

(AZ-1350) in pure CF_4 plasma are shown in Fig. 2. Similar results were also obtained for SF_6 plasma, except that the α -W film was etched faster than the AZ-1350 photoresist. The etched depth vs. etching time for GaAs in pure CF_4 plasma is also shown in the figure. As clearly seen in the figure, the depth of the α -W film (sputtered at 4×10^{-2} torr) and AZ-1350 photoresist increases linearly with etching time. When this relationship is extrapolated, the line

passes through the origin, indicating that no lag time exists at the start of the α -W and AZ-1350 etching. This etching property of W film is consistent with that reported by Tang and Hess (4). However, the result of $(\alpha + \beta)$ W film is in sharp contrast to that of the α -W films. It is worth noting that the $(\alpha + \beta)$ W film (sputtered at 1.5×10^{-1} torr) shows a clear lag-time effect. This feature of the $(\alpha + \beta)$ W film etching is similar to that observed during Al etching (10). Thin native oxide film always presents an Al surface, and it causes a lag-time effect on the Al etching. An absence of the β -phase in the W films deposited at $p \approx 4.5 \times 10^{-2}$ torr is attributed to their lower oxygen content, resulting in lower resistivity of the films (9). The $(\alpha + \beta)$ W films cannot be etched with good reproducibility and stable etch rates, especially when they are room ambient exposed for a long time, whereas the α -W films can be. Beyond the lag time, the $(\alpha + \beta)$ W films can be etched with relatively high speed compared with the α -W films (see also Fig. 1). Such etching characteristics of the $(\alpha + \beta)$ W films would be caused by surface oxidation (and/or WO_3 transformation) but not by $\alpha \rightarrow \beta$ phase transformation (11). Unless otherwise noted, the stable α -W films (sputtered at 4×10^{-2} torr) were used for RIE studies in the following. It has also been found that both the CF_4 and SF_6 plasmas etch GaAs very slowly. In order for a plasma etching system to be successful, a volatile derivative of the substance to be etched must be produced. Relatively low etch rate of GaAs found here is most likely due to the lower volatility of gallium products (GaF_3 , b.p. $> 950^\circ\text{C}$) (12).

It is known (4) that by increasing RF power the electron density and average electron energy increase and, as a result, the rate of ionization, excitation, and decomposition of gas phase molecules increase. Figure 3 shows the etch rate as a function of RF power for the W films (R_W) and AZ-1350 ($R_{\text{AZ-1350}}$) in pure CF_4 and SF_6 plasmas. The etch rate of GaAs in the CF_4 plasma is also shown in the figure. R_W , $R_{\text{AZ-1350}}$, and also the etch rate of GaAs in the CF_4 plasmas increase with RF power superlinearly within our experimental range; a relation between the etch rates R and RF power P for these substances can be expressed exactly by $R \propto P^{2.0}$. The etch rates in the SF_6 plasma, on the other hand, increase linearly up to $P = 50\text{W}$, and then

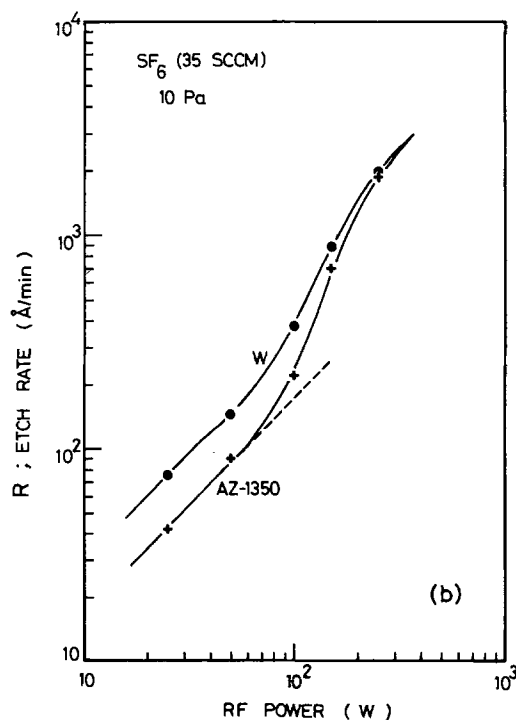
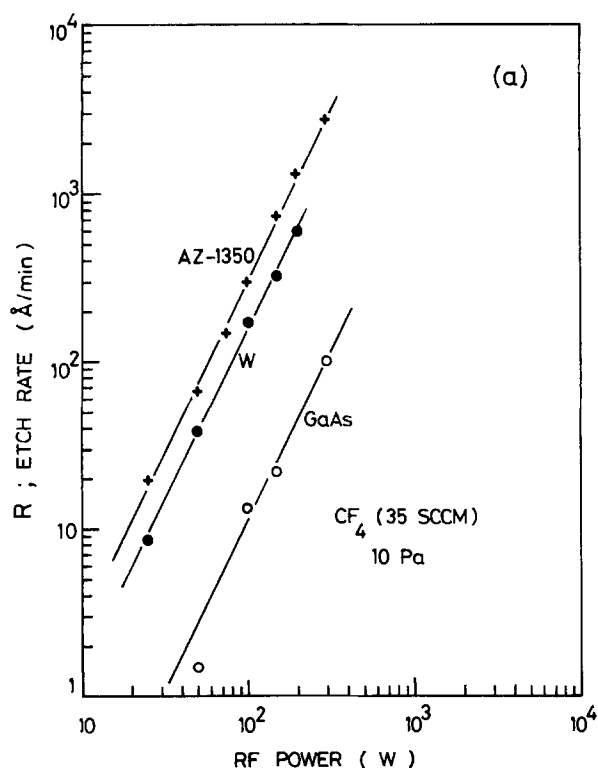


Fig. 3. Etch rate as a function of RF power for α -W, AZ-1350, and GaAs in pure CF_4 plasma (a) and that for α -W and AZ-1350 in pure SF_6 plasma (b).

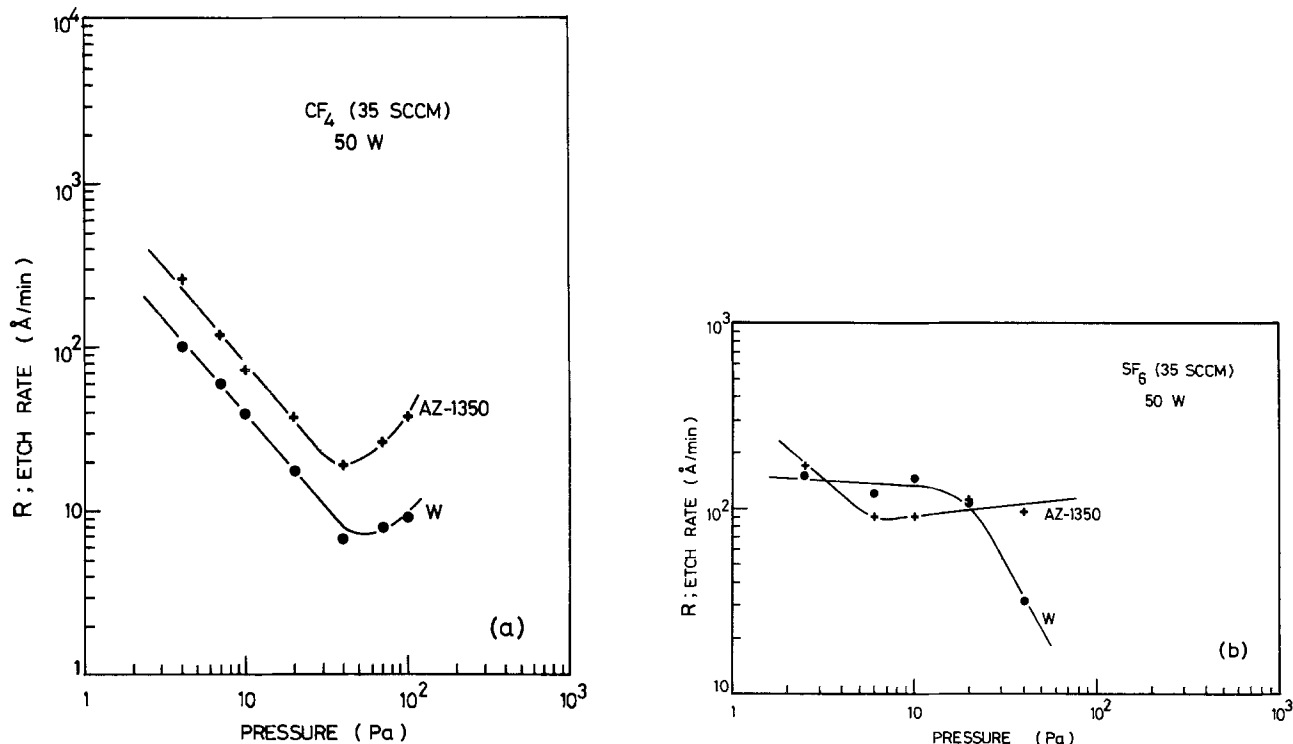


Fig. 4. Etch rate as a function of reactor pressure for α -W and AZ-1350 in pure CF_4 (a) and SF_6 plasma (b)

increase superlinearly for both the W film and AZ-1350 photoresist.

The dependence of R_W and $R_{\text{AZ-1350}}$ on the reactor pressure is shown in Fig. 4. Both R_W and $R_{\text{AZ-1350}}$ in the CF_4 plasmas decrease linearly as the reactor pressure increases, showing a minimum at about 40 Pa, and then increase with further increase of the pressure. The functional pressure dependence of R_W and $R_{\text{AZ-1350}}$ in the SF_6 plasmas is quite different. R_W is nearly constant up to 10 Pa, and decreases drastically with increasing pressure. $R_{\text{AZ-1350}}$, on the other hand, does not depend strongly on pressure within our experimental range.

Effects of Ar, O₂, and N₂ additions.—Inert gas additions can stabilize and homogenize plasmas through the effects of their addition on the thermal properties of the discharge gas or on the electron density and average electron energy resulting from altered electron balance processes. It is also known that radical or unsaturated scavenger effect is expected with the addition of some gases to reactive gas plasmas, e.g., O₂ gas to CF_4 plasmas, where the removal of CF_x radicals prevents their recombination with F atoms and contributes to the ensuing increase in atom density. In the following, the etch-rate data of the W films and AZ-1350 photoresists will be presented as a function of the Ar, O₂, and N₂ additions in the CF_4 and SF_6 plasmas.

The effects of varying Ar partial pressure on R_W and $R_{\text{AZ-1350}}$ in mixed CF_4/Ar and SF_6/Ar systems are shown in Fig. 5. In both mixtures, R_W increases gradually with increasing percent Ar from 0 to 85 (CF_4/Ar) and to 95 (SF_6/Ar). Further increases of percent Ar result in a drastic decrease in R_W . No measurable etched depth on the W film was observed with pure Ar plasma. $R_{\text{AZ-1350}}$ also increases gradually with increasing percent Ar, exhibiting a maximum near 95% Ar in both the CF_4/Ar and SF_6/Ar mixtures. Pure Ar plasma results in considerable etching of the AZ-1350 photoresist ($R_{\text{AZ-1350}} \approx 200 \text{ \AA}/\text{min}$).

Figure 6 shows the effects of varying O₂ partial pressure on R_W and $R_{\text{AZ-1350}}$ in mixed CF_4/O_2 systems. It is known (13, 14) that in the case of Si etching, O₂ additions to CF_4 enhance the products of F atoms and reduce carbon-related residues, thereby increasing the etch rate of Si. R_W in the CF_4/O_2 system goes through a maximum at about 40% O₂. When the percentage of O₂ exceeds 90, R_W de-

creases rapidly and approaches zero as a pure O₂ plasma is approached. Such a trend is very similar to that found for Si etching in CF_4/O_2 plasmas (13, 14). A qualitative feature of W etching in the SF_6/O_2 plasmas is quite different from that in the CF_4/O_2 plasmas. As clearly seen in Fig. 6, R_W in the SF_6/O_2 plasma decreases monotonically with increasing O₂ percentage. $R_{\text{AZ-1350}}$, contrarily, increases gradually and exhibits a maximum at 90% O₂ addition. This trend of $R_{\text{AZ-1350}}$ is nearly identical to that observed in the CF_4/O_2 plasmas.

To our knowledge, there has been no report on the plasma etching of any kind of metals in CF_4/N_2 or SF_6/N_2 mixtures. The effect of varying N₂ partial pressure on R_W and $R_{\text{AZ-1350}}$ in mixed CF_4/N_2 and SF_6/N_2 systems is shown in Fig. 7. In these mixtures, R_W increases dramatically as the addition of N₂ to CF_4 or SF_6 from zero to few percent. Further increases of the N₂ additions result in a slight increase in R_W . The etch rate then decreases as the percent N₂ approaches 100 (pure N₂). The W films were not etched with pure N₂ plasma. $R_{\text{AZ-1350}}$, on the other hand, does not depend so strongly on the N₂ additions, except at the region near pure SF_6 . It is noted that from an aspect of the etching selectivity $S (= R_W/R_{\text{AZ-1350}})$ the CF_4/N_2 (SF_6/N_2) mixture is more suitable than the CF_4/Ar (SF_6/Ar) and CF_4/O_2 (SF_6/O_2) mixtures. In the following, we present the data on R_W and $R_{\text{AZ-1350}}$ as a function of the plasma parameters in the CF_4/N_2 and SF_6/N_2 mixtures.

Figure 8 shows the variation of R_W and $R_{\text{AZ-1350}}$ as a function of the applied RF power in 90% $\text{CF}_4 + 10\% \text{ N}_2$ and 80% $\text{SF}_6 + 20\% \text{ N}_2$ mixtures. The dependence of R_W and $R_{\text{AZ-1350}}$ on RF power in the CF_4/N_2 plasmas can be given by $R_W \propto P^{1.5}$ and $R_{\text{AZ-1350}} \propto P^{2.0}$. The power dependence of the etch rate in the SF_6/N_2 plasmas, on the other hand, can be classified into two regions; $R_W \propto P^{0.5}$ and $R_{\text{AZ-1350}} \propto P^{1.0}$ at RF powers up to 100W, and $R_W \propto P^{1.0}$ and $R_{\text{AZ-1350}} \propto P^{3.0}$ at above 100W.

The etch rates of the W films and AZ-1350 photoresists as a function of the reactor pressure in the CF_4/N_2 and SF_6/N_2 plasmas are shown in Fig. 9. R_W in the CF_4/N_2 mixture increases with increasing pressure, peaking at 20 Pa, and then decreases with increasing pressure. R_W in the SF_6/N_2 mixture also increases with increasing pressure, peaking at 20 Pa, and then decreases abruptly with increasing pressure. $R_{\text{AZ-1350}}$ in the CF_4/N_2 mixture de-

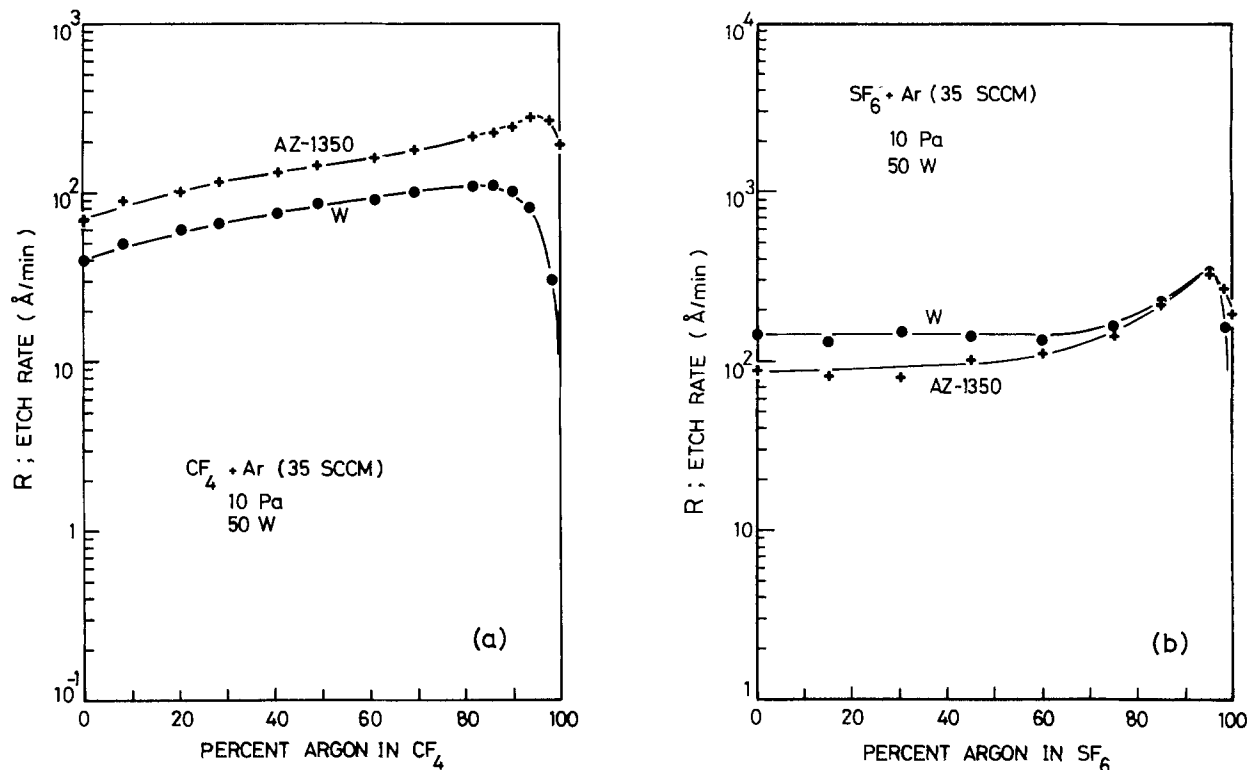


Fig. 5. Effect of varying Ar partial pressure on etch rate of α -W and AZ-1350 in mixed CF_4/Ar and SF_6/Ar plasmas

creases as the pressure increases, showing a minimum at 20 Pa, and then increases very slowly with increasing pressure. $R_{\text{AZ-1350}}$ in the SF_6/N_2 mixture, on the other hand, does not depend on pressure within our experimental range. Such pressure dependence of R_{W} and $R_{\text{AZ-1350}}$ is similar to that found in pure CF_4 and SF_6 plasmas (Fig. 4).

Etching Reaction in Plasma

The chemistry which takes place in a plasma is usually quite complex and involves a large number of elementary reactions (15). There exists a large number of radicals in

fluorinated gases and gas mixtures. The chemical reactions may occur between such radicals and solid materials. If the products which result from the chemical reactions have relatively high volatility, just as in the case of tungsten hexafluoride (WF_6 , b.p. = 17.5°C), they are removed from the solid surface. This is a basic concept of the W plasma etching in the fluorinated gases. We can expect the reaction for W etching in the CF_4 plasma to be

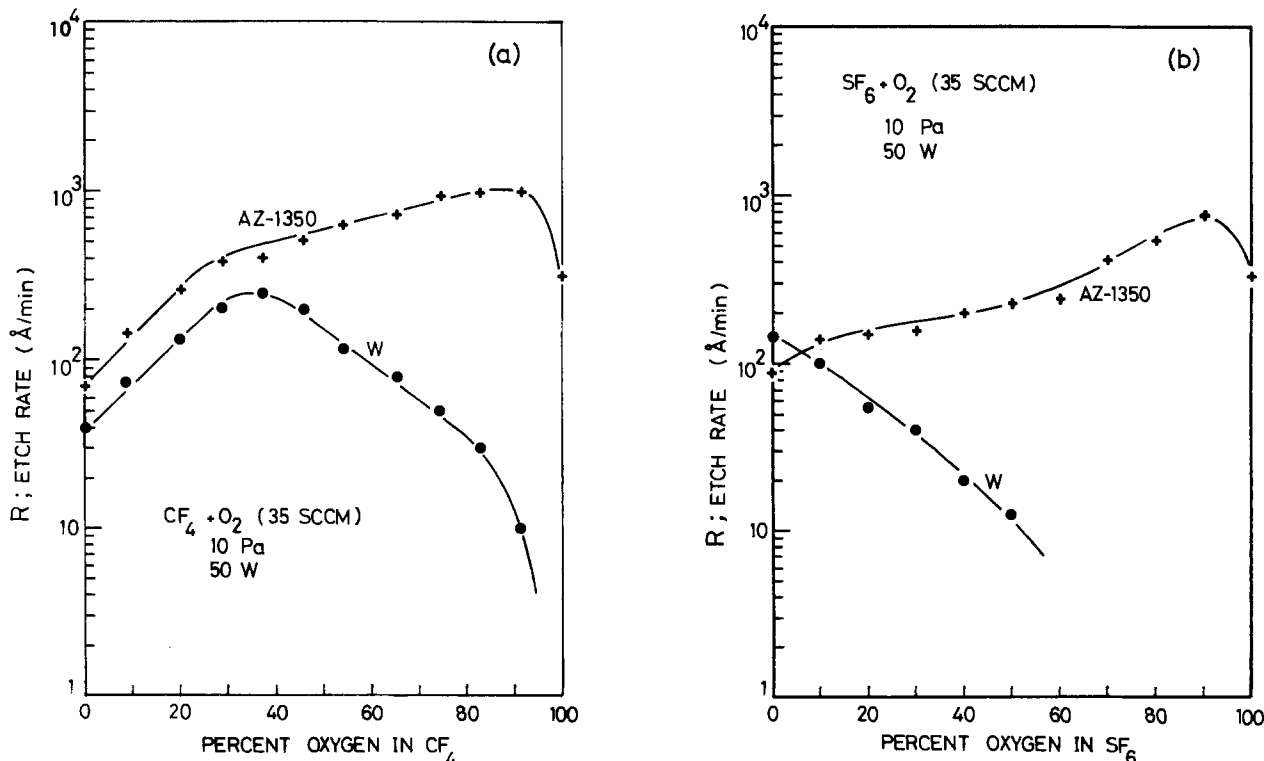
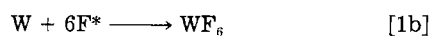
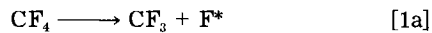


Fig. 6. Effect of varying O_2 partial pressure on etch rate of α -W and AZ-1350 in mixed CF_4/O_2 and SF_6/O_2 plasma

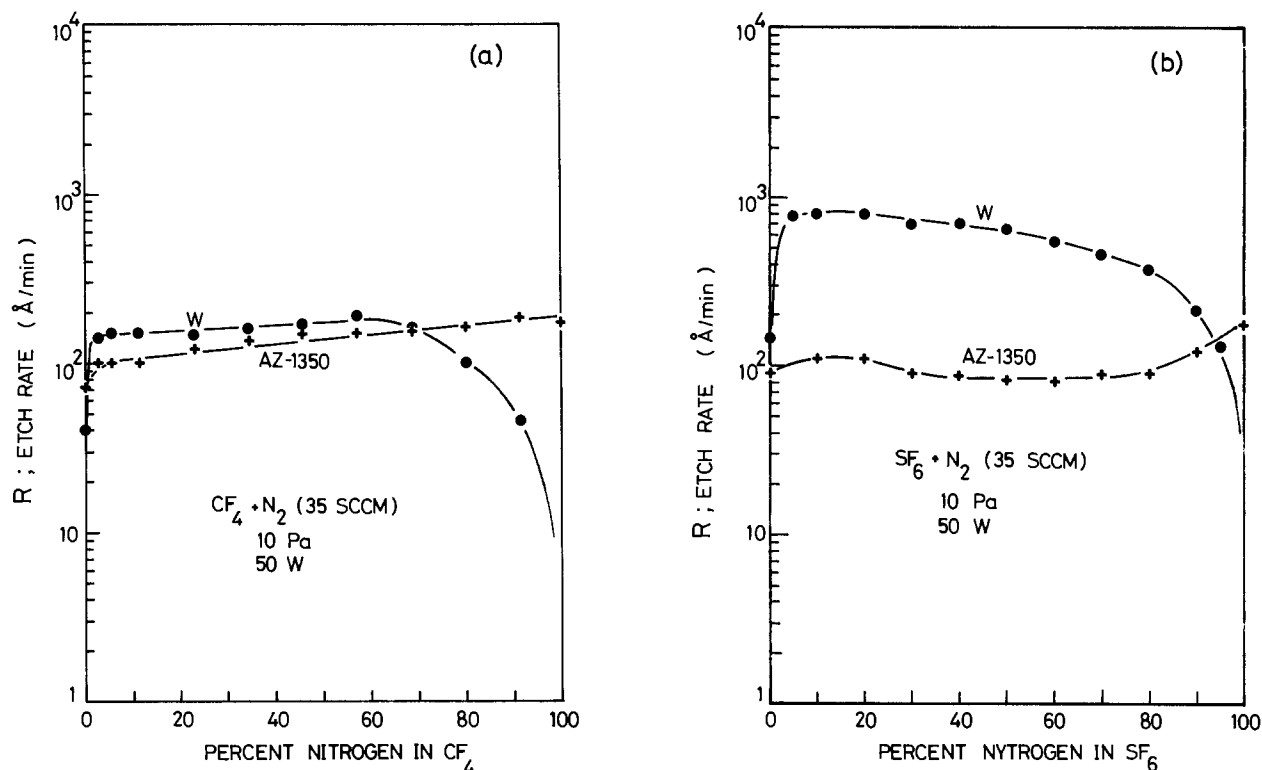


Fig. 7. Effect of varying N₂ partial pressure on etch rate of α -W and AZ-1350 in mixed CF₄/N₂ and SF₆/N₂ plasma

D'Agostino (16) has reported that discharges in pure SF₆ yield no stable reaction products in an alumina reactor without Si or SiO₂ substrates. Various investigators (17), on the other hand, reported SF₄, atomic F, F₂, S₂F₂, and SF₂, among the products of SF₆ discharges. Many of these studies were carried out in quartz discharge tubes where the tube wall participated in the reactions. Because of the SiO₂ electrodes used in the present study, one can expect the same products as reported for the SF₆ plasmas.¹ The

¹See Ref. (16).

etching reaction of W films in SF₆ plasma can also be presumed by Eq. [1b].

The etching of W in pure CF₄ plasma is limited by the supply of reactive species (2, 4). Emission spectra study on pure CF₄ plasma has suggested that the F atom emission intensity decreases with increasing reactor pressure (2). Because of the reactant-supply limited mechanism, R_w in pure CF₄ plasma may be expected to decrease with increasing pressure. That is the fact (see Fig. 4). If the pressures are further reduced, R_w will reach a maximum

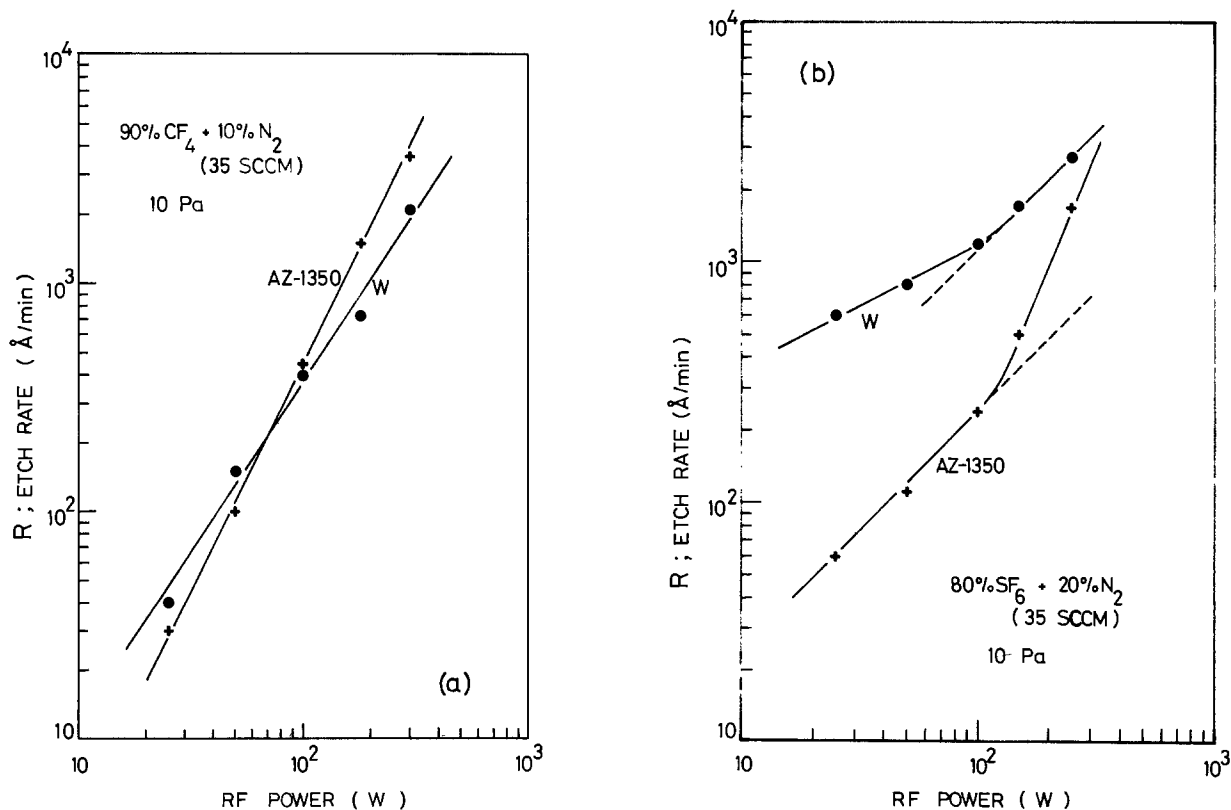


Fig. 8. Etch rate as a function of RF power for α -W and AZ-1350 in 90% CF₄ + 10% N₂ (a) and 80% SF₆ + 20% N₂ plasma (b)

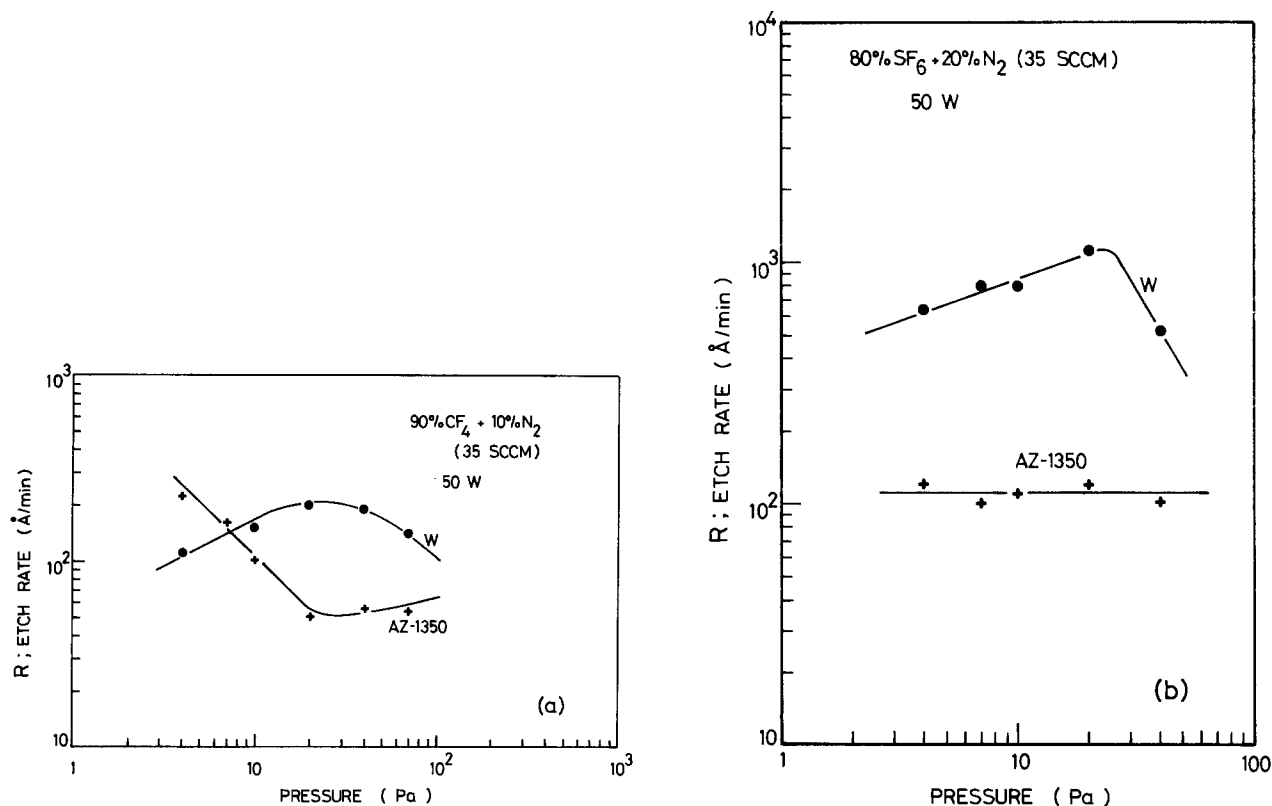


Fig. 9. Etch rate as a function of reactor pressure for α -W and AZ-1350 in 90% CF_4 + 10% N_2 (a) and 80% SF_6 + 20% N_2 plasma (b)

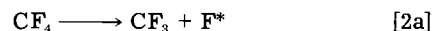
and will then decrease to zero at 0 Pa. We found similar pressure dependence of R_w in the CF_4/Ar and CF_4/O_2 mixtures; in 70% CF_4 + 30% O_2 mixture, for example, R_w increased with increasing pressure, peaking at 10 Pa ($R_w \approx 200$ Å/min), and then decreases with increasing pressure. A decrease in R_w with increasing pressure can also be found in pure SF_6 and 80% SF_6 + 20% N_2 plasmas above 20 Pa (see Fig. 4 and 9).

Noble gas addition, in general, stabilizes and homogenizes reactive gas plasmas that otherwise may be able to provide precise etching control. It can be seen from Fig. 5 that the addition of Ar to CF_4 increases R_w . As one can also see in Fig. 4, R_w in the pure CF_4 plasma increases with decreasing reactor pressure. R_w in the pure SF_6 plasma was constant at pressures up to 10 Pa (see Fig. 4). R_w in the SF_6/Ar system also was constant at Ar percentages from 0 to 60 (see Fig. 5). We have also carried out measurements of R_w and $R_{\text{AZ-1350}}$ as a function of the discharge parameters (RF power, reactor pressure, and gas flow rate) in CF_4/Ar and SF_6/Ar mixtures (30% Ar). The results obtained are very similar to those in pure CF_4 and SF_6 plasmas. It may, therefore, be concluded that the addition of Ar to CF_4 or SF_6 leads no drastic change in the physical and chemical kinetics of the reactions in these etching systems.

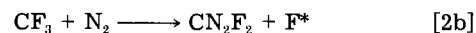
Emission or mass spectra from atomic F as a function of feed composition were measured along with the product distribution in CF_4/O_2 and SF_6/O_2 discharges (4, 5, 13, 14, 16, 17). The corresponding etch rate of W films was also reported (4, 5). In the CF_4/O_2 mixture (4, 13, 14), the F atom density increased with increasing O_2 addition, going through a maximum at certain O_2 composition. The etch rate R_w also indicated a maximum at certain O_2 composition (4). However, the maximum of R_w did not coincide exactly with that of the F atom density, where the increase of the F atom with the O_2 addition is accounted for by a sequence of reactions initiating with the production of CF_3 radicals by electron impact and followed by a reaction of CF_3 with oxygen (and further increase of the O_2 addition decreases the F atom density because, probably, of a decrease in electron energy in the plasma). A noncoincidence of these maxima may be explained by the competition between fluorine and oxygen

for active surface sites, as in the case of Si etching with the CF_4/O_2 (13, 14) and SF_6/O_2 mixtures (16). However, the W etch rate decreased monotonically with increasing O_2 addition in the SF_6/O_2 system (3, 4). This trend is in good agreement with the present result (see Fig. 6). In contrast, Tsujimoto *et al.* (5) have recently reported the etching characteristics of W films in SF_6/O_2 mixtures with a parallel-plate SiO_2 reactor, and obtained a maximum of R_w at about 10% O_2 addition, which was lower than the F atom maximum composition (30% O_2 addition). Unfortunately, however, we cannot suggest the reasons for the striking difference in the etching behaviors between Tsujimoto's result and ours [and also those in Ref. (3, 4)].

Clark (18) has found that for Si etching a 50:50 mixture of CF_4 and N_2 is preferable for smooth, uniform, and controllable etching. CF_4/O_2 mixtures and even pure CF_4 tended to pit the surface of crystalline Si, leading it hazed rather than shiny. The CF_4/N_2 mixtures, on the other hand, gave a smoothly etched Si surface. It is shown in Fig. 7 that a small amount of N_2 addition to CF_4 or SF_6 dramatically increases R_w . Moreover, changes in the N_2 addition within a wide range of compositions can be found to have little effect on R_w . The effects of admitting N_2 into the plasma are found to be similar to those of admitting Ar, but are in contrast to those of admitting O_2 . An addition of few tens percent O_2 tends to increase R_w . That is also the case in the CF_4/N_2 and SF_6/N_2 mixtures. We may expect the basic reaction in the CF_4/N_2 plasma to be



and



By the addition of N_2 to CF_4 or SF_6 , the etching of W will occur via a reaction with F radicals, but nitrogen no longer competes with F for active surface sites. Therefore, such mixtures would provide stable, efficient, and controllable etching of the W films. It is quite likely that an analogous mechanism operates during Si etching in 50% CF_4 + 50% N_2 mixture (18).

The etching processes under consideration are far too complex and the available information rather limited to

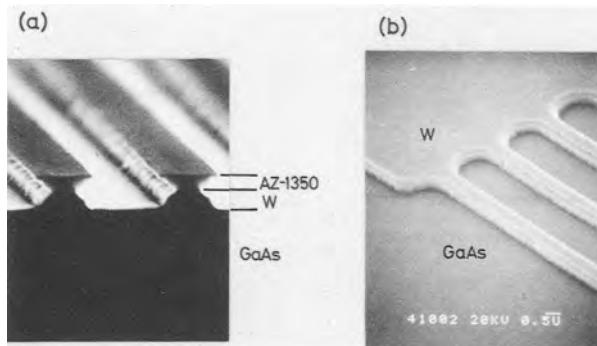


Fig. 10. Cross-sectional SEM image of a resist-patterned α -W film deposited on GaAs (a), and near top-view SEM photograph of the sample with which resist was stripped (b).

allow a qualitative discussion of the decomposition mechanism. Moreover, it is difficult to obtain a complete explanation of the difference in the etching rates with various plasma and physical parameters (RF power, frequency, pressure, flow rate, temperature, reactor geometry, etc.). Detailed etching mechanisms and plasma chemistry will, thus, be the subjects of a separate study.

Etching Profile

Important factors determining the choice of an etching gas are, generally, the etch rates for the materials, the degree of surface quality and undercutting, the gas chemical aggressiveness toward etching masks, and the desired etching profiles for the relevant purpose. Figure 10a shows the cross-sectional SEM image of a resist-patterned W film. This structure was fabricated as follows. After being degreased, wet-etched, and rinsed in deionized water, a GaAs substrate of (001) surface orientation was coated with 0.45 μm thick, RF sputtered W film (α -phase modification). Next, the 2.5 μm period grating pattern was defined by standard photolithography techniques using 0.5 μm thick AZ-1350 photoresist. This was used as an etching mask for plasma etching. The plasma etching was then done with 90% CF_4 + 10% N_2 mixture at 20 Pa reactor pressure, 35 sccm total gas flow rate, and 50W RF power. As can be clearly seen in the figure, a mesa-shaped structure was formed by stripes etched on the W film while this system gave a reverse-mesa-shaped profile on the photoresist mask. The identical situation is also noted for SF_6/N_2 plasmas. Apparently, the profiles give rise to considerable undercutting near the interface between the W film and photoresist. It is believed that a number of radicals and etching products may be ad-

sorbed on an etching substance. These adsorbed species can recombine with incident etchants, thereby influencing etching reaction at the sidewalls. The species may depend on etching materials in question, in this case, W and AZ-1350, and may interact with each other as the etching proceeds. Such effects will lead to an unusual etching profile, as observed in the present study. Similarly, Tsujimoto *et al.* (5) have found that the degree of undercutting of W films depends surprisingly, on the masking materials, such as AZ-1350, PSG (phosphorus-doped glass), and AZ-1350/PSG.

A near top-view SEM photograph of the sample on which the resist was stripped is also shown in Fig. 10b. Fluorine containing reagents and their mixtures with certain additives did not etch GaAs (12). The photograph in Fig. 10b reveals a high quality GaAs surface without any undesirable roughness or etch pits, and also shows that the etching process did not take part on the surface. The smooth surface appearance of GaAs may indicate the desirability of RIE for use in device applications.

Analysis of RIE-Processed Surface

Surface composition.—Figure 11 shows the SIMS in-depth profiles of the α -W films deposited on GaAs. The samples were unetched (Fig. 11a), etched with pure CF_4 (Fig. 11b), and etched with pure SF_6 (Fig. 11c). A relatively large amount of carbon and oxygen is detected near the W surface throughout the samples. The adsorption of C and O probably occurs primarily after the samples are removed from the chamber, although small concentrations of carbon (CO_2) and oxygen (or H_2O) are present during W sputtering or etching. As the interface between W and GaAs is approached, considerable amounts of C and O are also detected. This is due to the air exposure of GaAs surfaces before W sputtering. Clearly, fluorine exists in the samples etched with both pure CF_4 and SF_6 . The fluorine is a decomposition element of the plasma gas. Furthermore, a large amount of sulfur can be detected in the sample etched with pure SF_6 . In-depth profile studies on the samples etched with the CF_4/N_2 and SF_6/N_2 mixtures also gave the same trends as those described here. The fluorine inclusion is in agreement with Auger electron spectroscopy (AES) by Tang and Hess (4). However, they have detected no Auger signal of sulfur on the W surface during etching in SF_6/O_2 plasmas. This is probably a result of the limited detection limit of an AES rather than the SIMS analysis used in this study.

GaAs surface damage induced by RIE.—Since photoluminescence (PL) is sensitive to defects, this method is sometimes used to study damaged layers (19). Figure 12

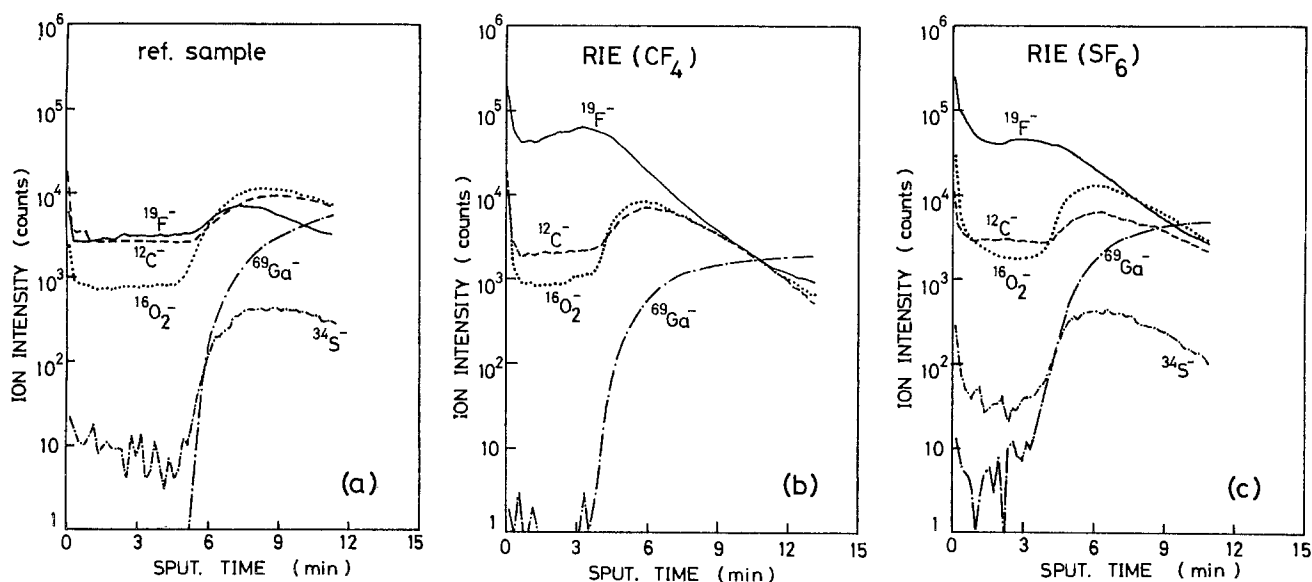


Fig. 11. SIMS in-depth profiles of α -W films deposited on GaAs; (a) unetched, (b) etched with pure CF_4 , and (c) etched with pure SF_6 .

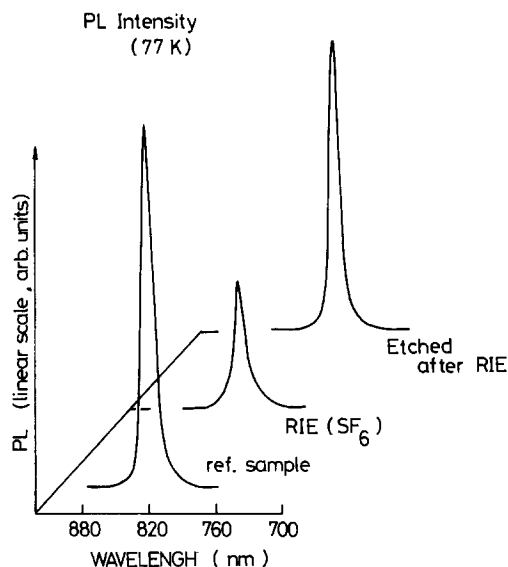


Fig. 12. Photoluminescence peak intensity (~ 1.51 eV) measured at 77 K from GaAs through different processing steps (see text).

shows the PL peak intensity (~ 1.51 eV) measured at 77 K from GaAs through different processing steps; no RIE-processed sample (reference sample), the RIE processed sample, and the wet-etched ($\sim 3000\text{\AA}$) sample after RIE processing. The RIE was done here under the following conditions: SF_6 etching gas, 10 Pa reactor pressure, 35 sccm flow rate, 50W RF power, and 60 min etching time. The samples used were Se-doped GaAs epitaxial layers of $n = 1 \times 10^{17} \text{ cm}^{-3}$.

The surfaces of the samples were excited by a He-Cd laser (4416\AA), and the PL was measured by the conventional method. The RIE was also done with pure CF_4 plasma. The results obtained were similar, as seen in Fig. 12. It is recognized from the figure that the plasma impinging damage which acts as a nonradiative-recombination and/or surface-recombination-velocity reduction centers are produced at the surface of GaAs by the RIE processing. It is also found that the RIE does not lead to a change in the PL spectrum (*i.e.*, only the ~ 1.51 eV peak was observed before and after the RIE processing). In contrast, Kawabe *et al.* (19) have observed relatively large changes in not only the PL intensity, but also the PL spectrum after an Ar ion bombardment of the GaAs surface. After $\sim 3000\text{\AA}$ is removed, almost the same emission intensity as the reference sample begins to appear. The plasma- or ion-bombardment-induced damages can be usually recovered by conventional annealing processes (19, 20).

Furthermore, in order to test the surface quality, Schottky contacts were made on RIE-processed GaAs surfaces and characterized by I-V and C-V measurements (see Fig. 13). The RIE conditions used were the same as those for the PL measurements described above. An evaporated Au metal was used as the Schottky contact. No clear difference was found between the I-V and C-V characteristics between samples with and without RIE-processed GaAs surfaces. For comparison, we also examined Schottky contacts which were fabricated on SiO_2 -sputtered GaAs. An SiO_2 film was deposited with a conventional magnetron-type sputtering equipment at 200W RF power for about 3 min ($\sim 750\text{\AA}$ thick). After removing the sputtered SiO_2 film, the diodes were fabricated in the same manner as described above. The I-V characteristics showed considerably large leakage current. The C-V data taken from the diodes also indicated carrier decrease at a sample surface, in contrast to an almost flat carrier concentration profile obtained from the RIE-processed Schottky diodes. PL measurements also clearly suggested the presence of a damaged layer on the SiO_2 -sputtered GaAs surface. It can, thus, be concluded that distinct damage layer is introduced on GaAs surface

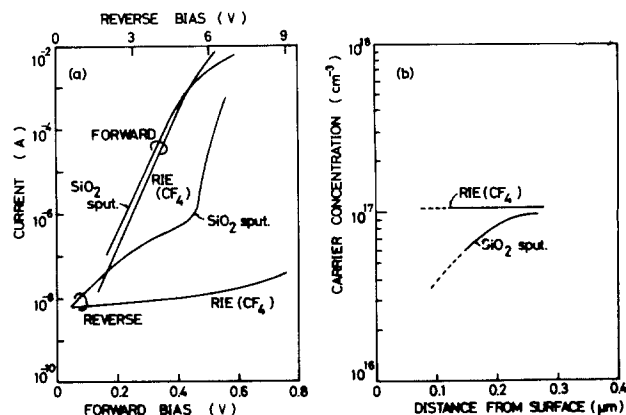


Fig. 13. I-V characteristics (a) and carrier concentration profiles (b) for Au-GaAs Schottky diodes fabricated on the RIE-processed (CF_4) and SiO_2 -sputtered-damaged surfaces.

by the SiO_2 sputtering but is not so clearly introduced by the RIE processing.

Summary

We have studied plasma etching characteristics of sputter-deposited W films on GaAs in a parallel-plate reactor with CF_4 and SF_6 plasmas. Properties of the W films strongly depend upon sputter-deposition condition. The W films sputtered at low Ar pressure ($p \approx 4.5 \times 10^{-2}$ torr) show stable structure, the so-called α -phase modification. When the films are sputtered at higher Ar pressures ($p > 4.5 \times 10^{-2}$ torr), it is possible to identify the presence of the β -phase modification. The reactive ion etching (RIE) characteristics of the sputter-deposited W films strongly reflect such microstructural features. The etch rate of the W films (R_w) is nearly constant in the α -phase region, and it increases abruptly with increasing fraction of the β -phase modification. Etched depth of the α -W films increases linearly with etching time. The α -W/ β -W mixtures, on the other hand, show a clear lag-time effect.

R_w of the α -phase W films strongly depends on the discharge parameters, such as RF power, reactor pressure, and gas flow rate. The etch rate R_w is not strongly dependent upon Ar addition. The addition of O_2 to CF_4 increases R_w considerably, and exhibits a maximum at about 30% O_2 addition. Further increase of the O_2 addition results in a gradual decrease in R_w . On the other hand, the maximum R_w occurs with pure SF_6 discharge and gradually decreases with increasing O_2 additions. A slight addition of N_2 to both CF_4 and SF_6 increases R_w abruptly, and further increase of N_2 shows no stronger effect on R_w (*i.e.*, R_w keeps nearly constant value) within a wide range of N_2 additions. It can be considered that the W etching is controlled by F atoms in the CF_4 plasma and its mixtures, but is not so simple in the cases of the SF_6 plasma and its mixtures.

RIE studies were also simultaneously carried out from an aspect of the etching selectivity between the W films and AZ-1350 photoresists. Relatively large selectivity can be achieved in the CF_4/N_2 and SF_6/N_2 mixtures. The effects of various discharge parameters in the CF_4/N_2 and SF_6/N_2 mixtures on RIE characteristics were also studied in detail with a set of standard etching conditions. Tungsten (R_w) to photoresist ($R_{\text{AZ-1350}}$) etching selectivity extracted from this work, however, should be used with caution. Since SiO_2 and photoresist were simultaneously etched in CF_4 or SF_6 plasmas with an SiO_2 electrode. Oxygen liberated from the SiO_2 electrode would probably enhance the etch rate of photoresist.

The chemical nature of the RIE-processed W surface was examined by SIMS analysis, and presences of C, O, F, and S species on the surface were confirmed. Schottky contacts were fabricated on RIE-processed GaAs surface, and the surface quality was examined by I-V and C-V measurements. No appearance of damage layers was confirmed from these measurements.

Acknowledgments

The authors are grateful to K. Kumabe and K. Sugii for their continual encouragement and critical reading of the manuscript. They thank H. Asai for the x-ray diffractometer analysis. Many thanks are due to S. Ando, H. Sugiura, and Y. Takanashi for helpful discussions and comments. They also wish to thank Y. Homma for the SIMS analysis and helpful discussions.

Manuscript submitted April 8, 1985; revised manuscript received Aug. 6, 1985.

Nippon Telegraph and Telephone Corporation assisted in meeting the publication costs of this article.

REFERENCES

1. T. F. Deutsch and D. D. Rathman, *Appl. Phys. Lett.*, **45**, 623 (1984), and references therein.
2. K. Maeda and K. Fujino, *Denki Kagaku*, **43**, 22 (1975).
3. J. N. Randall and J. C. Wolfe, *Appl. Phys. Lett.*, **39**, 742 (1981).
4. C. C. Tang and D. W. Hess, *This Journal*, **131**, 115 (1984).
5. K. Tsujimoto, S. Tachi, T. Mizutani, and S. Okudaira, Paper SSD84-45 presented to Technical Group of Semiconductors and Semiconductor Devices of IEC Japan.
6. C. O. Bozler and G. D. Alley, *IEEE Trans. Electron Devices*, **ed-27**, 1128 (1980); C. O. Bozler, and G. D. Alley, *Proc. IEEE*, **70**, 46 (1982); B. A. Vojak and G. D. Alley, *IEEE Trans. Electron Devices*, **ed-30**, 877 (1983); D. D. Rathman, B. A. Vojak, D. K. Astolfi, and L. A. Stern, *IEEE Electron Device Lett.*, **ed1-5**, 191 (1984).
7. S. Adachi, S. Ando, H. Asai, and N. Susa, *ibid.*, **ed1-6**, 264 (1985).
8. D. W. Hoffman and J. A. Thornton, *Thin Solid Films*, **45**, 387 (1977).
9. P. Petroff, T. T. Sheng, A. K. Sinha, G. A. Rozgonyi, and F. B. Alexander, *J. Appl. Phys.*, **44**, 2545 (1973).
10. D. W. Hess, *Solid State Technol.*, **24**, (4), 189 (1981).
11. P. M. Petroff and W. A. Reed, *Thin Solid Films*, **21**, 73 (1974).
12. G. Smolinsky, R. P. Chang, and T. M. Mayer, *J. Vac. Sci. Technol.*, **18**, 12 (1981).
13. C. J. Mogab, A. C. Adams, and D. L. Flamm, *J. Appl. Phys.*, **49**, 3796 (1978).
14. R. d'Agostino, F. Cramarossa, S. De Benedictis, and G. Ferraro, *ibid.*, **52**, 1259 (1981).
15. A. T. Bell, *Solid-State Technol.*, **21**, (4), 89 (1978).
16. R. d'Agostino, *J. Appl. Phys.*, **52**, 162 (1981).
17. J. W. Coburn and M. Chen, *ibid.*, **51**, 3134 (1980).
18. H. A. Clark, *Solid-State Technol.*, **19**, (6), 51 (1976).
19. M. Kawabe, N. Kanzaki, K. Masuda, and S. Namba, *Appl. Opt.*, **17**, 2556 (1978).
20. Y. Yamane, K. Yamazaki, and T. Mizutani, *Jpn. J. Appl. Phys.*, **21**, L537 (1982).

Compositional Changes during Alloying of Ohmic Contacts to $\text{In}_{0.53}\text{Ga}_{0.47}\text{As}$

Alan D. Huelsman*

Department of Materials Science and Engineering, Massachusetts Institute of Technology, Cambridge, Massachusetts 02139

Clifton G. Fonstad**

Department of Electrical Engineering and Computer Science and Center for Materials Science and Engineering, Massachusetts Institute of Technology, Cambridge, Massachusetts 02139

ABSTRACT

Auger analysis of alloyed ohmic contacts on n- and p- $\text{In}_{0.53}\text{Ga}_{0.47}\text{As}$ shows that substantial changes occur throughout a relatively thick interfacial layer during normal alloying cycles. Differences in diffusion of the different semiconductor elements are demonstrated and correlated with their reactivity. It is shown that placing a Cr layer at the semiconductor-contact interface effectively eliminates interdiffusion of the semiconductor and metals at elevated temperatures. Au/Cr metallization coupled with shallow, high dose ion implants gives contact resistances comparable to conventional alloyed contacts without the need for alloying.

A reliable means of producing low resistance ohmic contacts to III-V semiconductors has been the subject of much study (1-4). Commonly used contact metallizations involve the evaporation of a multilayer metal-dopant structure or a metal alloy containing a dopant. This structure is then heated to alloy the metals with the semiconductor surface and diffuse the dopant into the semiconductor producing a region of high carrier concentration at the semiconductor surface. The metallization in contact with this highly doped region results in an ohmic contact. The problems with this technique result from the alloying process. The alloying process causes quantities of the metallization to diffuse deeply into the semiconductor, and several compounds or phases are formed at the metal semiconductor interface. These compounds are not stable even at room temperature (5) and especially at high current densities. For shallow junction devices, the metallization can diffuse into the junction region and destroy the device. Contact degradation is an important means of failure in these devices, also.

*Electrochemical Society Student Member.

**Electrochemical Society Active Member.

In order to develop a manufacturable III-V contact technology, a new method of ohmic contact formation must be developed. One approach has been to deposit a layered structure consisting of a dopant layer, e.g., Si or Ge, followed by a refractory metal layer, e.g., Mo, W, or Ta (6, 7) or an amorphous metal layer (8). This structure is then heated as in the case of alloyed contacts. The high melting point of the refractory metals prevent them from forming unwanted compounds at the metal semiconductor interface. These metal layers are typically deposited by sputtering and may be difficult to etch. In addition, they allow only n- or p-type contacts to be formed in a single deposition.

The approach taken here is to create the highly doped region near the semiconductor surface by low energy high dose ion implantation and rapid thermal annealing (RTA). The use of RTA techniques allows high dopant activation to be achieved (9, 10) and at the same time minimizes dopant diffusion. The contact metal consists of a layer of Cr followed by a layer of Au deposited over the implanted regions. This metallization in contact with the highly doped semiconductor surface forms the ohmic

contact. No contact heating is required in this process. Both n- and p-type contacts can be formed in the same Cr/Au deposition. In a previous work, we have demonstrated that the electrical properties of these contacts are comparable to alloyed contacts (11). On n-type material, specific contact resistances of $1.5 \times 10^{-6} \Omega\text{-cm}^2$ for Cr/Au nonalloyed contacts and $2.3 \times 10^{-6} \Omega\text{-cm}^2$ for AuGe/Ni/Au alloyed contacts were achieved. On p-type material, specific contact resistances of $1.4 \times 10^{-4} \Omega\text{-cm}^2$ were achieved for both Cr/Au nonalloyed contacts and Au/Zn alloyed contacts. We now show that the metallurgical properties of these contacts are far superior to those of alloyed contacts.

Auger depth profiling and optical microscopy were used in addition to the electrical measurements described previously (11) to study the effects of heating on alloyed and nonalloyed ohmic contacts to $\text{In}_{0.53}\text{Ga}_{0.47}\text{As}$. The changes in the composition of the contact layer which result from reactions and diffusion during the alloying process have been investigated with respect to alloying temperatures and time. Differences in the reactive and diffusional behavior of the semiconductor constituents, indium, gallium, and arsenic and the dopants, zinc, and germanium were observed. The differences observed can be explained based on differences in reactivity of the different elements with gold. The extensive reaction which takes place in the Au- $\text{In}_{0.53}\text{Ga}_{0.47}\text{As}$ alloying process (4) makes the development of a nonalloyed contact technology of particular importance for this semiconductor.

Experimental Procedures

Contact samples were prepared for Auger spectroscopy by using lift-off to pattern $50 \mu\text{m}$ squares of both the alloyed and nonalloyed types of contact metallization. The metallizations were prepared by thermal evaporation onto $1 \mu\text{m}$ epi layers of n-type ($1 \times 10^{16} \text{cm}^{-3}$) $\text{In}_{0.53}\text{Ga}_{0.47}\text{As}$ grown by liquid phase epitaxy on semi-insulating iron-doped InP. For p-type contact work, p-type regions were produced in these epi layers by selective Be ion implantation at energies of 50, 100, and 225 keV and doses of 5.4×10^{13} , 9.2×10^{13} , and $5.0 \times 10^{13} \text{cm}^{-2}$. The shallow, high dose Si (n-type) or Zn (p-type) implants prior to Cr/Au deposition were done at energies and doses of 50 keV and $3.0 \times 10^{14} \text{cm}^{-2}$ (Si implant) and 120 keV and $1.0 \times 10^{15} \text{cm}^{-2}$ (Zn implant). The implants were annealed using an AG Associates Heatpulse lamp annealing system. The samples were placed face down on a Si wafer, the chamber was

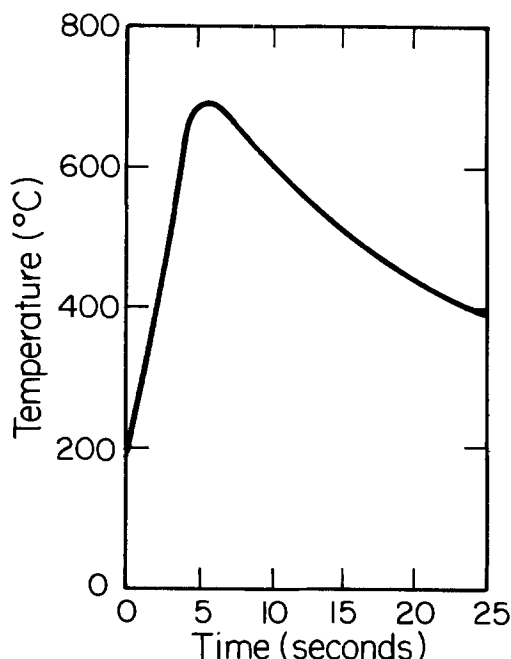


Fig. 1. The time temperature profile used in the rapid thermal annealing of the ion implants.

purged with forming gas, and the anneal cycle completed. The peak temperature was 720°C as measured by a thermocouple mounted alongside the sample. A typical time-temperature profile is shown in Fig. 1. For the p-type measurements, both the Be and Zn implants were annealed at the same time.

Au/Zn contacts were formed by evaporating 1200\AA of an Au 95%/Zn 5% alloy. AuGe/Ni/Au contacts were formed by evaporating first 800\AA of Au 88%/Ge 12% alloy, followed by 200\AA of Ni and 500\AA of Au. Cr/Au contacts were formed by evaporating 200\AA of Cr, followed by 1000\AA of Au. Just prior to loading the samples into the evaporator, a cleaning etch was performed to remove surface oxides. The etch was 10s in buffered HF for the p-type contacts, and for the n-type contacts the treatment was a two-solution etch consisting of a stop solution, 10 ml NH_4OH in 150 ml DI H_2O , and an etch solution, 2 drops NH_4OH , and 2 drops H_2O_2 in 200 ml DI H_2O . The etching sequence for the n-type contacts was 5s in stop, 5s in etch, 5s in stop. For the n-type contacts, the choice of etchant was not critical; either the buffered HF or the NH_4OH based etch were used with equal success.

The contacts to be alloyed were heated in a furnace under a forming gas atmosphere. The alloying procedure was as follows: the samples were loaded onto a quartz boat in the end of the alloying furnace, the furnace was sealed and purged with forming gas, and the samples were slid into the hot zone of the furnace. When the desired temperature was reached, the samples were removed and cooled in forming gas in the end of the furnace tube.

Depth profiles were obtained using an Auger spectrometer¹ equipped with a sputtering gun. The samples were sputtered with a $100 \mu\text{A}$ Ar ion beam accelerated at 4 kV and rastered over a $1 \times 1 \text{mm}$ area. The sputtering rate of Au was measured by sputtering evaporated Au films whose thickness had been determined using a Sloan Dektak II. The sputtering rate of $\text{In}_{0.53}\text{Ga}_{0.47}\text{As}$ was determined by masking a $5 \mu\text{m}$ line, sputtering for 2 min, and measuring the depth with the Dektak. The resolution of the depth profile can be estimated from the interface abruptness observed on a profile of a contact prior to alloying.

Results

Alloyed contacts.—Profiles of Au/Zn contacts as deposited and after three different alloying cycles are shown in Fig. 2. The lowest alloying temperature investigated was 350°C . Ohmic contacts were obtained by alloying for 6 min at this temperature. The interface is abrupt, with the exception of some outdiffusion of indium into the gold. The gold has similarly diffused into the $\text{In}_{0.53}\text{Ga}_{0.47}\text{As}$ with a profile which is complementary to the In profile indicating that at this temperature there is

¹Perkin-Elmer Physical Electronics Model 590, digitally upgraded.

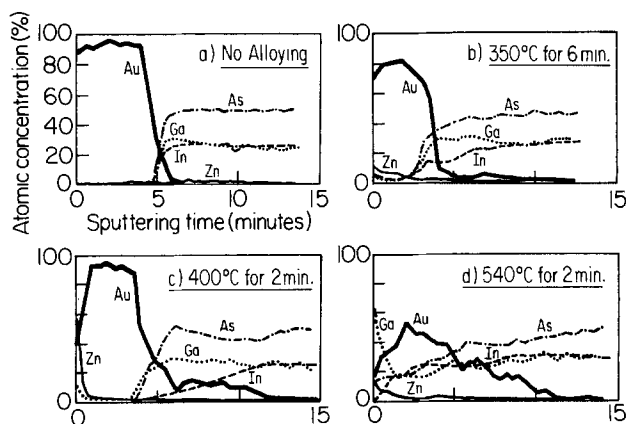


Fig. 2. a: An Auger profile of a Au/Zn alloyed contact as deposited. b: After alloying at 350°C for 6 min. c: After alloying at 400°C for 2 min. d: After alloying at 540°C for 2 min.

some In-Au reaction taking place while the other elements are relatively undisturbed. When the temperature is raised to 400°C, more In-Au intermixing is found to have taken place. In addition, a large amount of Zn has accumulated at the contact surface. This temperature produced ohmic contacts with the lowest specific contact resistance. When the alloying temperature is raised to 540°C, a large degree of metal-semiconductor mixing is found to have taken place. Gold was found to migrate 0.5 μm into the semiconductor, and both In and As are found in the contact layer. In addition, a large amount of Ga has migrated to the contact surface.

Similar effects are observed in the case of AuGe/Ni/Au alloyed contacts on $\text{In}_{0.53}\text{Ga}_{0.47}\text{As}$. Figure 3 shows a depth profile of a AuGe/Ni/Au contact sintered at 420°C for 2 min. Ga has diffused out through the metallization and accumulated on the contact surface. The morphology of the alloyed contacts is always rough. Figure 4b shows a typical photomicrograph of a contact sintered at 400°C. We also found that wire bonding to these alloyed contacts was difficult and unreliable because of the metals (*e.g.*, Ga, Zn) which had accumulated on the contact surface.

Nonalloyed contacts.—A dark field photomicrograph of the Cr/Au contact is shown in Fig. 4a. The contact is perfectly smooth, and the contact morphology did not change with heating.

Composition profiles of nonalloyed Cr/Au contacts before and after heat-treatment are shown in Fig. 5. Even after heating the contact to 500°C for 10 min, very little metal-semiconductor mixing has taken place. In particular, diffusion of semiconductor constituents to the contact surface has been nearly eliminated and gold has not diffused into the semiconductor.

Discussion

During contact alloying, Ga and Zn appear to be diffusing to the contact surface. At the surface, diffusion is against a concentration gradient, a situation which requires a change in phase or chemical environment to drive the process. The accumulation of zinc on the surface of the p-type contacts, for example, could be explained by hypothesizing that Zn reacts on the contact surface. The chemical potential of free zinc on the surface would be less than that in the metallization providing a driving force for Zn diffusion to the contact surface. The diffusion of Ga to the contact surface might be explained using the same mechanism, but with an additional driving force which results from the change in phase of Ga in going from solid form in $\text{In}_{0.53}\text{Ga}_{0.47}\text{As}$ to Ga liquid (12). A similar situation exists in GaAs, where As reacts with the Au or evaporates from the sample surface while Ga remains as a liquid which accumulates on the contact surface (3).

The alloying process which takes place in $\text{In}_{0.53}\text{Ga}_{0.47}\text{As}$ has been shown to be more complex than that which exists in the In or Ga binary compounds and even the InGaAsP quaternary compounds (4, 13). This is due to a difference in the reactivity of In and Ga with respect to the gold contact layer. Whereas Ga does not interact with

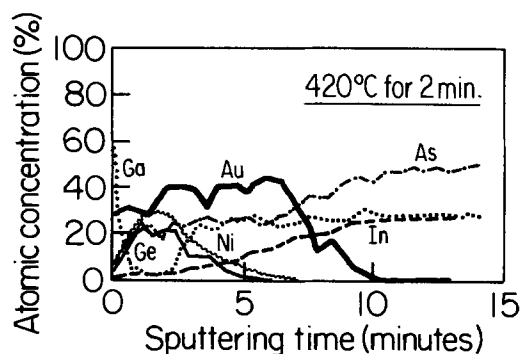


Fig. 3. An Auger profile of a AuGe/Ni/Au contact after alloying at 420°C for 2 min.

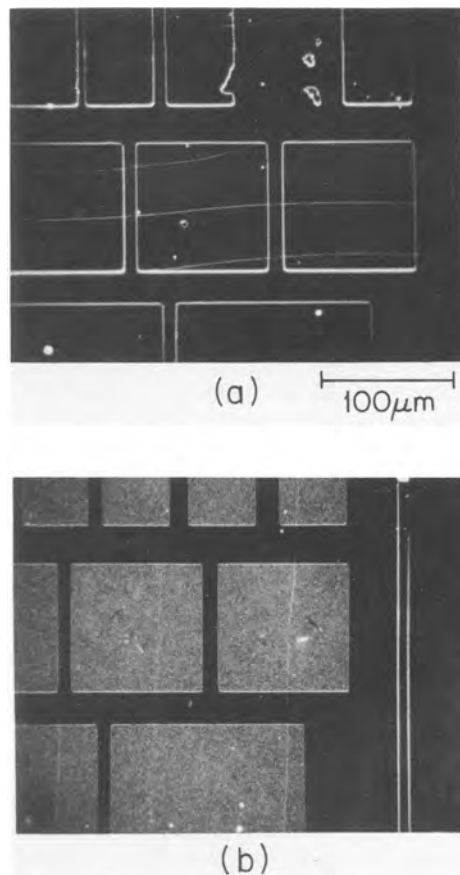


Fig. 4. a: A darkfield photomicrograph of a Cr/Au nonalloyed ohmic contact. b: A darkfield photomicrograph of a typical alloyed ohmic contact.

the Au, the complimentary In and Au concentration profiles indicate that In is forming some phase with the Au. Other work has demonstrated the existence of several phases (5, 14) of In-Au compounds in Au based contacts to $\text{In}_{0.53}\text{Ga}_{0.47}\text{As}$. These compounds have been shown to form at temperatures as low as 160°C (5).

The use of a sandwich contact in this work allows a metal (*e.g.*, Cr) to be used as a diffusion barrier which prevents the In from out-diffusing into and reacting with the

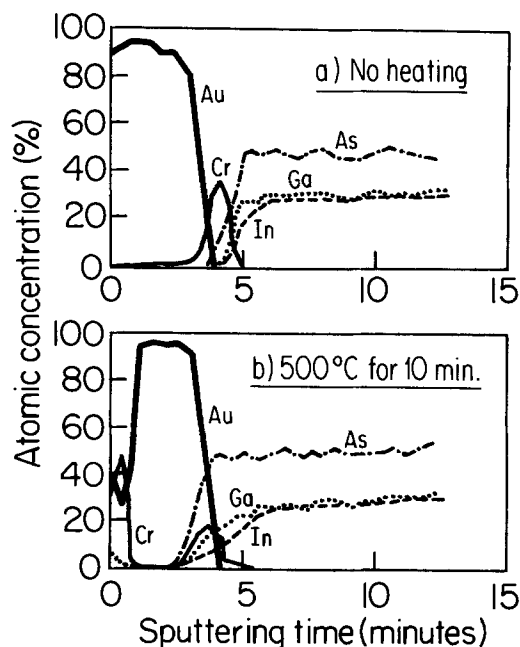


Fig. 5. a: An Auger profile of a Cr/Au nonalloyed contact as deposited. b: After heating at 500°C for 10 min.

Au overlayer, and simultaneously prevents the Au from penetrating into the semiconductor. The appearance of Cr at the contact surface after heating of the nonalloyed contacts indicates that this system is not completely ideal. Other metals, such as Ti and Pt, are known to form diffusion barriers and may also prevent metal-semiconductor intermixing at the $\text{In}_{0.53}\text{Ga}_{0.47}\text{As}$ -Au interface.

Conclusion

The effects of heating on both alloyed and nonalloyed ohmic contacts to $\text{In}_{0.53}\text{Ga}_{0.47}\text{As}$ have been investigated. It was shown that the alloying process causes large amounts of dopant and semiconductor constituents to accumulate on the contact surface. The accumulation of these metals on the contact surface make wire bonding more difficult and make shallow junction devices unreliable. It was further shown that these effects can be eliminated by the use of a Cr/Au nonalloyed ohmic contact which can be used on both n- and p-type material. This contact is thermally stable and has a smooth morphology which provides a good surface for reliable bonding.

Acknowledgments

This work was supported by the Defense Advanced Research Projects Agency, Contract no. N00014-C-80-062 and monitored by the Office of Naval Research. The Center for Materials Science and Engineering is a National Science Foundation Materials Research Laboratory supported in part through Grant no. DMR 81-19295. Extensive use was made of the ion implantation, Auger analysis, and Microelectronics Technologies Central Facilities of the Center during the course of this work.

Manuscript submitted July 1, 1985; revised manuscript received Aug. 19, 1985. This was Paper 712 SOA pre-

sented at the Toronto, Ontario, Canada, Meeting of the Society, May 12-17, 1985.

Massachusetts Institute of Technology assisted in meeting the publication costs of this article.

REFERENCES

1. R. H. Cox and H. Strack, *Solid State Electron.*, **10**, 1213 (1967).
2. K. K. Shih and J. M. Blum, *ibid.*, **15**, 1177 (1972).
3. M. Heiblum, M. I. Nathan, and C. A. Chang, *ibid.*, **25**, 185 (1982).
4. W. Tseng, A. Christou, H. Day, J. Davey, and B. Wilkins, *J. Vac. Sci. Technol.*, **19**, 623 (1981).
5. S. Nakahara and R. J. McCoy, *This Journal*, **128**, 1781 (1981).
6. W. T. Anderson, A. Christou, J. F. Giuliani, and H. B. Dietrich, *IEEE Trans. Ind. Electron.*, **ie-29**, 149 (1982).
7. W. T. Anderson, A. Christou, and J. E. Davey, *IEEE J. Solid State Circuits*, **sc-13**, 430 (1978).
8. K. J. Guo, J. D. Wiley, J. H. Perepezko, J. E. Nordman, D. B. Aaron, E. A. Dobisz, D. E. Madisen, and R. E. Thomas, in "Proceedings of the 2nd Conference on High Temperature Electronics and Instrumentation," Sandra R. Hudson and James R. Kelsey, Editors, Sandia National Laboratory, Albuquerque, NM (1981).
9. K. Tabatabaie-Alavi, A. N. M. M. Choudhury, N. J. Slater, and C. G. Fonstad, *Appl. Phys. Lett.*, **43**, 505 (1983).
10. D. H. Rosenblatt, W. R. Hitchens, S. Shatas, A. Gat, and D. A. Betts, *MRS Symp. Proc.*, **23**, 669 (1983).
11. A. Huelsman and C. Fonstad, *IEEE Trans. Electron Devices*, To be published.
12. L. C. Kimerling, Private communication.
13. I. Camlibel, A. K. Chin, F. Ermanis, M. A. DiGiuseppe, J. A. Lourenco, and W. A. Bonner, *This Journal*, **129**, 2585 (1982).
14. J. M. Vandenberg, H. Temkin, R. A. Hamm, and M. A. DiGiuseppe, *J. Appl. Phys.*, **53**, 7385 (1982).

Evaluation of Silicon Optical Absorption Data for Use in Minority-Carrier-Diffusion-Length Measurements by the SPV Method

Edward S. Nartowitz¹ and Alvin M. Goodman

RCA Laboratories, Princeton, New Jersey 08540

ABSTRACT

We have examined and evaluated the published data for the optical absorption coefficient α of crystalline silicon as a function of the wavelength λ for use in the measurement of minority-carrier-diffusion length L by the SPV method. We have compared the ASTM-recommended expression for $\alpha(\lambda)$ with (i) Runyan's data on which it is based, (ii) the data of Swimm and Dumas, and (iii) the data of Weakliem and Redfield, and find systematic disagreement that can result in significant differences in the values of L determined by the SPV method. We have proposed (i) a set of compromise data based on an average between the extremes of the published data and (ii) an expression for $\alpha(\lambda)$ that agrees with the compromise data to within about 1%. The use of this expression, $\alpha(\lambda) = [(84.732/\lambda) - 76.417]^2$, where $\alpha(\lambda)$ is per centimeter and λ is in micrometers, reduces the uncertainty in resulting values of L by a factor of approximately two. For $L < 60 \mu\text{m}$, a further reduction in uncertainty can be achieved by lowering the maximum value of λ used for the measurements. Finally, we believe that the compromise data that we propose should be considered as an interim choice pending further experimental results that more clearly remove the present uncertainty in the value of $\alpha(\lambda)$.

The constant-magnitude steady-state surface photovoltage (SPV) method for measuring the minority-carrier-diffusion length, L , utilizes a beam of photons incident on the surface of the semiconductor at an energy just above the bandgap (1, 2). For silicon, the bandgap at 300 K is 1.12 eV, necessitating photon wavelengths less than 1.11 μm (3). The absorbed photons generate electron-hole pairs, some of which diffuse toward the illuminated surface and are separated by the electric field of the surface space-charge region, thereby creating a surface photovoltage, ΔV . As the absorption depth is varied by changing the wavelength of the incident light, ΔV is kept constant by adjusting the intensity of the light. For a homogeneous silicon slab with the geometry illustrated in Fig. 1a, it can

then be shown that

$$I_0 = C[1 + (\alpha L)^{-1}] \quad [1]$$

subject to the conditions

$$\alpha W \gg 1 \quad [1a]$$

$$\alpha w \ll 1 \quad [1b]$$

$$W \gg L \quad [1c]$$

$$w \ll L \quad [1d]$$

$$\Delta p \ll n_0 \quad [1e]$$

Here, I_0 is the intensity of the incident light, α is the op-

¹ Permanent address: Science Department, Lawrence High School, Lawrenceville, New Jersey 08648.

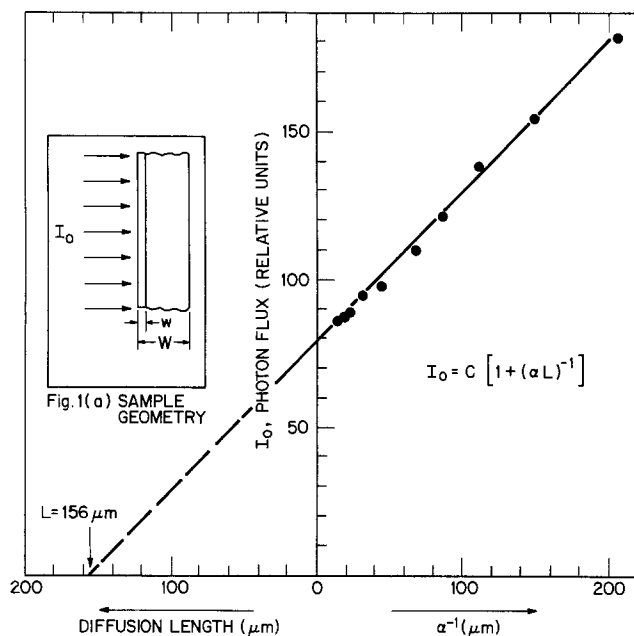


Fig. 1. a: Sample geometry. b: Plot of relative photon flux vs. reciprocal optical absorption coefficient.

tical absorption coefficient, W is the thickness of the silicon wafer, w is the thickness of the surface space-charge region, Δp is the excess minority carrier density at the edge of the surface space-charge region, n_0 is the majority carrier density, and C is a constant. If I_0 is plotted against α^{-1} for each constant-magnitude ΔV point, the result is a linear graph whose extrapolated intercept on the negative α^{-1} axis is L . This is illustrated in Fig. 1b. Thus, the method is critically dependent on a knowledge of $\alpha(\lambda)$.

This method has been applied to the measurement of diffusion lengths in semiconducting materials other than silicon, such as gallium arsenide (1, 4) and indium phosphide (5), where the values of $\alpha(\lambda)$ were separately measured due to the lack of a standard or recommended set of values. For silicon, however, there is an ASTM standard (2) for $\alpha(\lambda)$ which, for the case of stress-relieved silicon, is an empirical fit to data gathered by Runyan (6) in 1967. We refer to this expression for $\alpha(\lambda)$ as the ASTM fit. More recently, absorption data have been gathered on stress-relieved silicon by Swimm and Dumas (7) as well as by Weakliem and Redfield (8). Moreover, Swimm and Dumas point out that their absorption coefficient values are 2-8% lower than those reported by Runyan and up to 16% lower than the ASTM values; they further state that diffusion lengths calculated from their data are approximately 16% greater than those calculated using the ASTM fit.

In the present work, we compare the published absorption data for stress-relieved silicon between 0.70 and 1.05 μm [the ASTM fit (2), the data of Runyan (6), the data of Swimm and Dumas (7), and the data of Weakliem and Redfield (8)]. All of the data considered are based on room temperature measurements. We also compare the values of L calculated using data other than the ASTM fit with the values of L obtained using the ASTM fit, and find significant differences that are strongly dependent on the values of L and the wavelength range covered. In the absence of sufficient objective criteria for selecting one set of absorption data over the other, we generate a set of compromise data which tends to minimize the uncertainty in $\alpha(\lambda)$ and the resultant uncertainty in L . We then compare the resultant L values obtained using the extremes of the $\alpha(\lambda)$ data with the values obtained using our compromise data over various wavelength ranges. We show that the uncertainty in the value of L can be further reduced, especially for low values of L , by an appropriate choice of wavelength range. Finally, we present examples of I_0 vs α^{-1} plots using representative data from measurements of real samples.

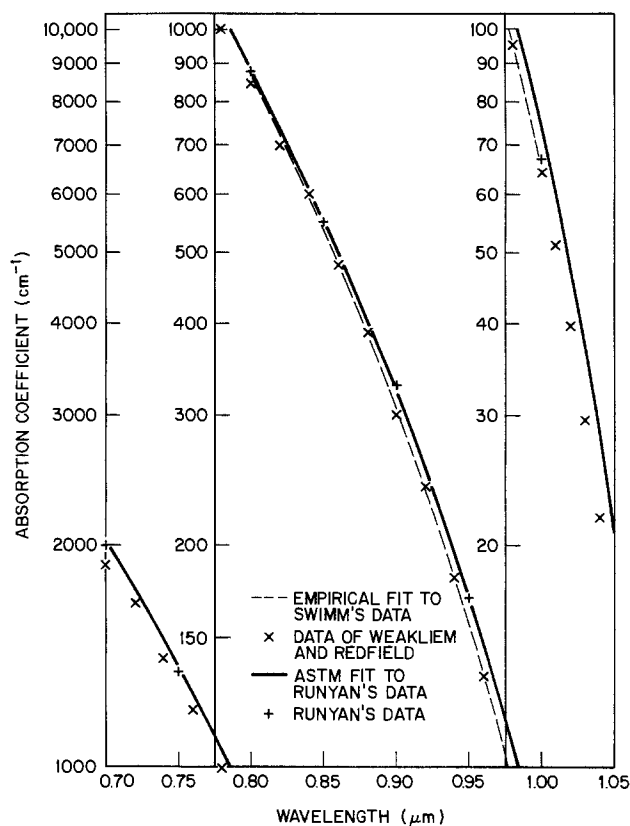


Fig. 2. Published values of the optical absorption coefficient for stress-relieved silicon in the wavelength range $0.70 < \lambda < 1.05 \mu\text{m}$.

In addition to the approach described above, we have also considered an alternative procedure. This procedure, which employs averaging fits to the three data sets, is described in the Appendix. The resulting expression for $\alpha(\lambda)$ differs only slightly from Eq. [2].

Comparison of Published Absorption Data and Resultant L Values

The published values of $\alpha(\lambda)$ for stress-relieved silicon between 0.70 and 1.05 μm are shown in Fig. 2. The data of Weakliem and Redfield agree to within 3% with those of Swimm and Dumas, with closer agreement at higher wavelengths. Like the data of Swimm and Dumas, they are consistently lower than either Runyan's data or the ASTM fit, being approximately 3-10% lower than the former and approximately 2-32% lower than the latter. The larger discrepancies with the ASTM fit occur at high wavelengths where the ASTM fit has very little support from Runyan's data.

The maximum percent uncertainty in $\alpha(\lambda)$ was calculated at each wavelength by dividing the difference between the extremes of the data by the minimum value and multiplying by 100. The results are shown in Fig. 3. The maximum percent uncertainty is seen to be a minimum for the region $0.72 < \lambda < 0.88 \mu\text{m}$ and to rise rapidly for $\lambda > 0.88 \mu\text{m}$.

A comparison of diffusion-length values obtained using different sets of absorption data is shown in Fig. 4. Simulated intensities based on Eq. [1], the ASTM fit, and assumed values of L were used in calculating the diffusion lengths from the data of Swimm and Dumas and from the data of Weakliem and Redfield. The symbols L_A , L_S , and L_W denote the values obtained using, respectively, the ASTM fit, the data of Swimm and Dumas, and the data of Weakliem and Redfield. The figure shows that the differences in L resulting from the use of different sets of absorption data depend (i) on the magnitude of the diffusion length and (ii) on the wavelength range over which the data was taken. For data taken over the range $0.826 < \lambda < 1.005 \mu\text{m}$, curve A and B show that diffusion-length values calculated using the absorption data of Swimm and Dumas and of Weakliem and Redfield are approxi-

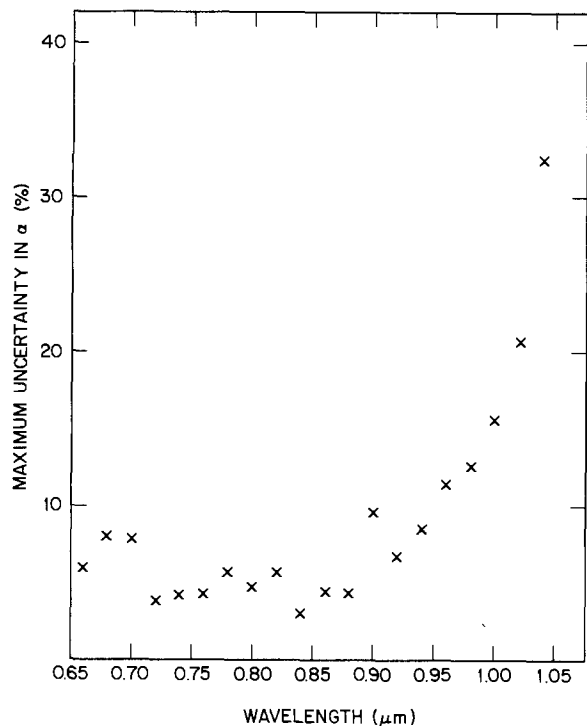


Fig. 3. Maximum percent uncertainty in α vs. λ . At each wavelength, the maximum percent uncertainty was computed by dividing the difference between the extremes of the published values of α by the minimum value of α and multiplying by 100.

mately 20-25% greater than those calculated using the ASTM fit if $L > 60 \mu\text{m}$. For smaller values of L , the discrepancies are much higher, exceeding 55% for $L < 10 \mu\text{m}$ and exceeding 95% for $L < 5 \mu\text{m}$. Curve C and D show a marked improvement in the agreement for diffusion-length values as a result of gathering data over the wavelength range $0.826 < \lambda < 0.960 \mu\text{m}$. This is not surprising since the percent uncertainty in the absorption data is smaller over that range (Fig. 3). For that range, diffusion lengths calculated from the data of Swimm and Dumas and from the data of Weakliem and Redfield agree with those calculated from the ASTM fit to within 15% for $L > 60 \mu\text{m}$ and to within 28% for $L > 10 \mu\text{m}$. For $L < 10 \mu\text{m}$, the discrepancies again rise rapidly.

Proposed Compromise Values and Their Effect on Diffusion-Length Values

The use of wavelength ranges comprising still shorter wavelengths can further reduce the uncertainties for very small values of L . However, the use of such ranges is restricted by Eq. [1b] which, for example, requires that $\alpha^{-1} \approx 3 \mu\text{m}$ for a sample with a doping concentration of approximately $10^{15}/\text{cm}^3$ and $w \approx 1 \mu\text{m}$. Moreover, for other than small values of L , the I_0 vs. α^{-1} plots must include points with large absorption depths, corresponding to longer wavelengths, in order to define more clearly the line that is to be extrapolated to obtain L . Thus, to measure L , it may be necessary to use absorption data over a wavelength range for which there is significant uncertainty in α .

We feel that, at the present time, there is insufficient justification for choosing one set of absorption data over the others. Therefore, in order to minimize the uncertainty in diffusion-length values obtained using the SPV method, we have generated a set of compromise absorption data by averaging the extremes of the published data at each of the various wavelengths. These data are displayed in Fig. 5 in the form of a plot of $\alpha^{1/2}$ vs. λ^{-1} . A straight line fit, after smoothing the data, yields

$$\alpha(\lambda) = \left[\frac{84.732}{\lambda} - 76.417 \right]^2 \quad [2]$$

where $\alpha(\lambda)$ is per centimeter and λ is in micrometers. The

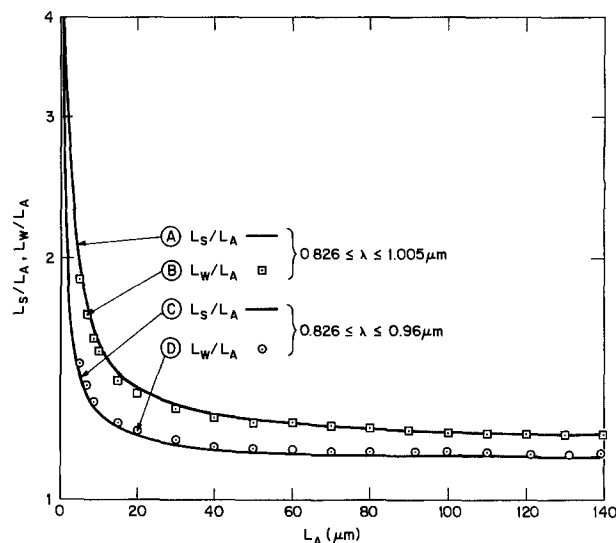


Fig. 4. A comparison of diffusion length (L) values obtained using three different sets of absorption data, two wavelength ranges, and the same $I_0(\alpha)$ values. L_A , L_S , and L_W are the values obtained using, respectively, the ASTM fit, the data of Swimm and Dumas, and the data of Weakliem and Redfield.

λ^{-1} intercept is $0.902 \mu\text{m}^{-1}$, corresponding to an energy of 1.118 eV which is within 0.1 kT of the bandgap of silicon at 300 K. The rms deviation of this fit from our compromise data is 0.7% for $0.70 < \lambda < 1.04 \mu\text{m}$.

In Fig. 6-8, diffusion lengths calculated using previously published data are compared with those calculated using our compromise data. For $0.826 < \lambda < 1.005 \mu\text{m}$ and $L > 60 \mu\text{m}$, L values calculated using compromise data (L_C) are 10-14% lower than those obtained using the data of Swimm and Dumas (L_S) and 8-10% higher than those obtained using the ASTM fit (L_A), (Fig. 6). Thus, the maximum uncertainty in L is 14% as compared to 25% if the ASTM fit absorption values are used (curves A and B, Fig. 8). Figures 6 and 8 clearly show that for low values of L the uncertainty rises sharply, but through the use of compromise data it is reduced from $> 55\%$ to $> 33\%$ for $L < 10 \mu\text{m}$ and from $> 100\%$ to $> 50\%$ for $L < 5 \mu\text{m}$. For $0.826 \mu\text{m} < \lambda < 0.960 \mu\text{m}$, the use of compromise data re-

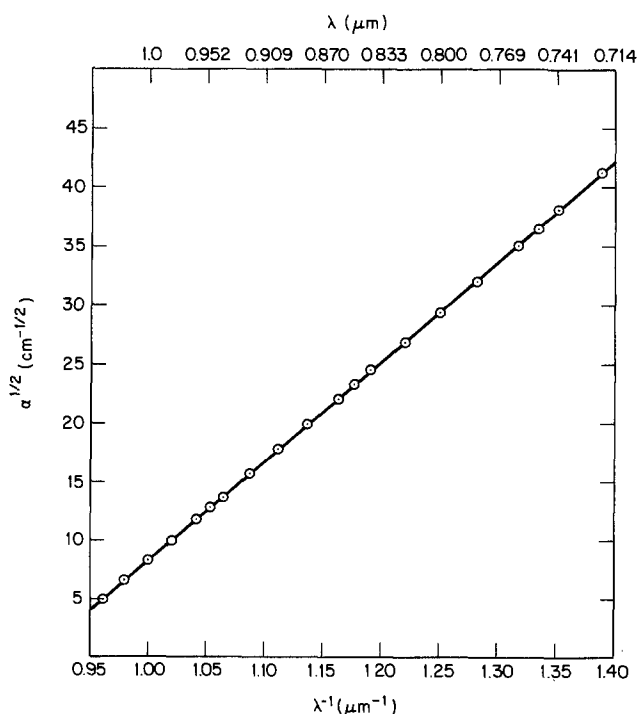


Fig. 5. Square root of the compromise absorption coefficients of stress-relieved silicon at 300 K, plotted vs. reciprocal wavelength.

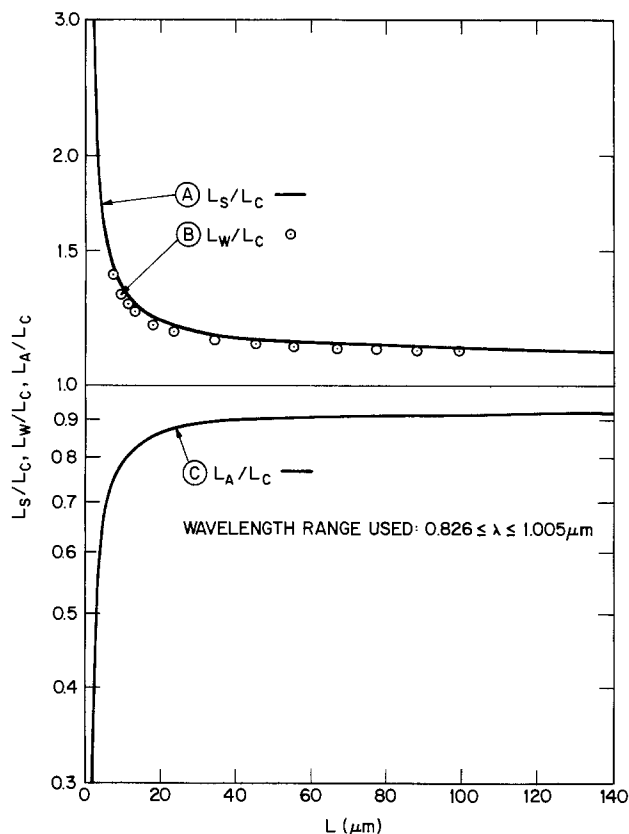


Fig. 6. A comparison between diffusion length (L) values obtained using published absorption data and L values obtained using the compromise absorption coefficients proposed in this paper. L_A , L_S , L_W , and L_C are the values obtained using, respectively, the ASTM fit, the data of Swimm and Dumas, the data of Weakliem and Redfield, and the compromise data. The same $I_0(\alpha)$ values were used for each L determination, and the wavelength range was $0.826 < \lambda < 1.005 \mu\text{m}$.

duces the uncertainty in L to less than 25% for $L > 6 \mu\text{m}$ and less than 12% for $L > 20 \mu\text{m}$ (Fig. 7, 8).

I_0 vs. α^{-1} Plots of Sample Data

Plots of I_0 vs. α^{-1} for sample data are given in Fig. 9-11. Plots using the compromise data for α^{-1} are seen to have r^2 values ranging from 0.992 to 1.000, where r is the correlation coefficient. These values compare favorably with those obtained using either the absorption data of Swimm and Dumas ($0.989 < r^2 < 0.999$) or the ASTM fit to Runyan's absorption data ($0.993 < r^2 < 1.000$).

Some curvature can be present in these plots due to (i) departure from the assumptions made in the derivation of Eq. [1], (ii) surface damage to the sample wafer (9), or (iii) a nonrandom error in the absorption data over a certain wavelength range. If, for example, all the α values were too low for $\lambda > 1 \mu\text{m}$, the plots would decrease in slope for higher values of absorption depth. This appears to occur to a very small extent in the data of Fig. 10 and 11, especially in the plots using the absorption data of Swimm and Dumas. These graphs show a slight concave-downward curvature that cannot be due to surface damage which produces a concave-upward curvature (9). The use of the compromise absorption data results in little concave-downward curvature. However, the curvature present in any of these plots is too slight to offer a criterion for the selection of one set of absorption data over the others. Similarly, the lack of dependence of r^2 values on the choice of absorption data eliminates their use in establishing any such criteria.

Discussion and Conclusions

We recommend the use of compromise absorption coefficients that significantly reduce the uncertainty in the values of L over all wavelength ranges. Further, for the measurement of diffusion lengths larger than approximately $60 \mu\text{m}$, we recommend gathering data over a wave-

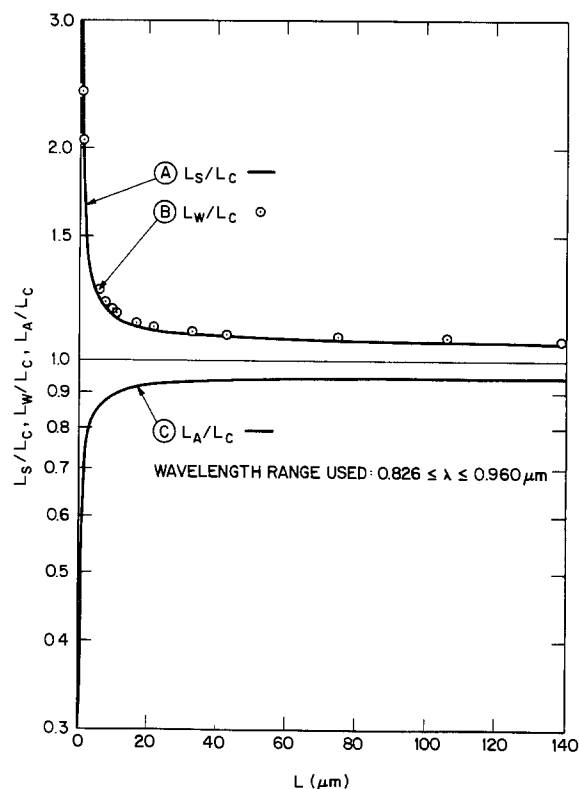


Fig. 7. A comparison between diffusion length (L) values obtained using published absorption data and L values obtained using the compromise absorption coefficients proposed in this paper. L_A , L_S , L_W , and L_C are the values obtained using, respectively, the ASTM fit, the data of Swimm and Dumas, the data of Weakliem and Redfield, and the compromise data. The same $I_0(\alpha)$ values were used for each L determination and the wavelength range was $0.826 < \lambda < 0.960 \mu\text{m}$.

length range extending up to but not exceeding approximately $1 \mu\text{m}$ due to the scarcity of absorption data for silicon beyond $1 \mu\text{m}$.

For $L < 60 \mu\text{m}$, a further reduction in the uncertainty of L can be achieved by lowering λ_{max} the maximum value of λ used for the measurements, i.e., by limiting the measurements to a range of λ where there is better agreement among the various sets of $\alpha(\lambda)$ data. For example, if $L \approx 15 \mu\text{m}$, the uncertainty in an experimentally determined value of L due to disagreement between the various absorption data is reduced from about 26% for $\lambda_{\text{max}} = 1.005 \mu\text{m}$ to about 12% for $\lambda_{\text{max}} = 0.960 \mu\text{m}$ to about 6% for λ_{max}

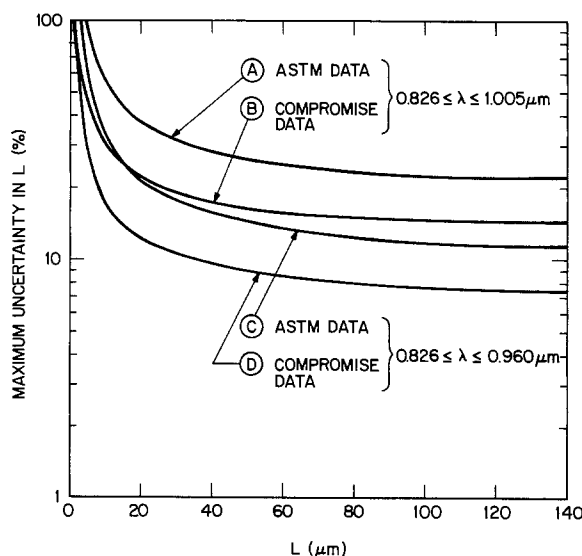


Fig. 8. Maximum uncertainty in the determination of L due to differences in the optical absorption data used. See text for details.

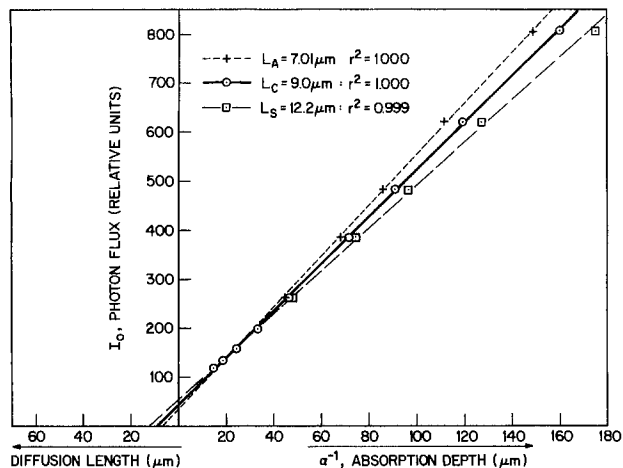


Fig. 9. Plots of I_0 vs. α^{-1} for a "short" diffusion length sample using three sets of optical absorption data. The values of L_A , L_S , and L_C correspond, respectively, to the use of the ASTM fit, the data of Swimm and Dumas, and the compromise data.

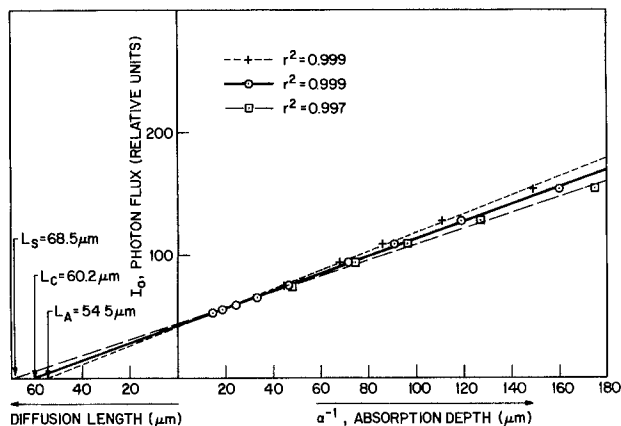


Fig. 10. Plots of I_0 vs. α^{-1} for a "medium" diffusion length sample using three sets of optical absorption data. The values of L_A , L_S , and L_C correspond, respectively, to the use of the ASTM fit, the data of Swimm and Dumas, and the compromise data.

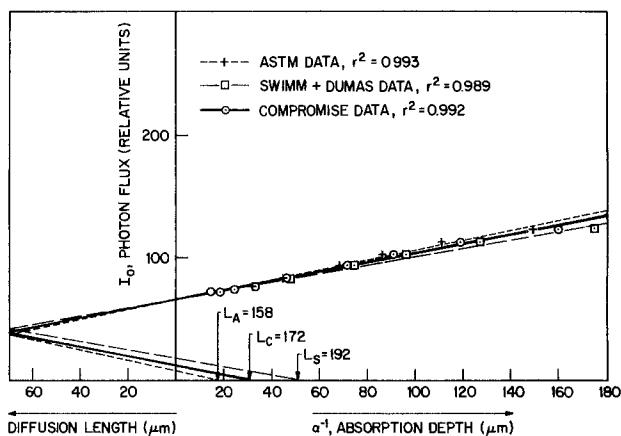


Fig. 11. Plots of I_0 vs. α^{-1} for a "long" diffusion length sample using three sets of optical absorption data. The values of L_A , L_S , and L_C correspond, respectively, to the use of the ASTM fit, the data of Swimm and Dumas, and the compromise data.

= 0.880 μm . However, it should be noted that as the range of values used for the measurements is decreased, any uncertainty (experimental error) in the values of the corresponding I_0 values will have an increased effect on the resulting uncertainty in L . A quantitative treatment of minimization of the total error in L due to uncertainties in both α and I_0 would require an overall error analysis that is beyond the intended scope of this paper. Nevertheless, we recognize in a qualitative way the effects of uncer-

tainties in both α and I_0 , and how the selection of the range of λ used for measurements can affect the resultant error (uncertainty) in L .

Finally, the compromise data that we recommend should be considered an interim choice pending further experimental results that clearly remove the present uncertainty in the variation of the optical absorption coefficient of silicon in the wavelength range $0.7 \leq \lambda \leq 1.04 \mu\text{m}$.

Acknowledgment

We wish to thank H. Weakliem for providing detailed information from Ref. (8) in tabular form, H. Gossenberger for technical assistance, and P. Zanzucchi and R. Martinelli for their helpful reviews of the original manuscript.

Manuscript submitted Dec. 26, 1984; revised manuscript received June 14, 1985.

RCA Laboratories assisted in meeting the publication costs of this article.

APPENDIX

A reviewer of the original manuscript of this paper has suggested an alternative approach to generating compromise $\alpha(\lambda)$ data. In this approach, the data of Runyan (6), Swimm and Dumas (7), and Weakliem and Redfield (8) would be averaged, but the ASTM fit would not be considered. We had originally considered a similar approach, but had discarded it for two reasons: (i) in generating the new $\alpha(\lambda)$ data, it ignores the reality of the ASTM fit which is today's *de facto* standard, and (ii) the various $\alpha(\lambda)$ studies (6-8) do not cover the same wavelength range and do not use the same grid of wavelength values. Nevertheless, we have now calculated an alternative set of $\alpha(\lambda)$ values based on an averaging procedure, and find that these values can be described by an expression having the same functional form as that used for the compromise data with numerical constants that are remarkably close to those of Eq. [2]. The procedure used and the results obtained are described below.

In order to carry out an averaging procedure, it was necessary to have each of the experimental data sets spanning the entire range of interest, 0.7-1.04 μm . The data of Weakliem and Redfield (8) are quite complete in this region, and no special data treatment was necessary; these data are designated $\alpha_w(\lambda)$. The data of Swimm and Dumas (7) cover the range 0.8-1.0 μm , and they give an expression for optical absorption in this region

$$\alpha_s(\lambda) = \left[\frac{85.9}{\lambda} - 77.9 \right]^2 \text{ cm}^{-1} \quad [\text{A-1}]$$

where λ is expressed in micrometers. A least squares fit of Runyan's data (6) to the same functional form gives

$$\alpha_r(\lambda) = \left[\frac{84.765}{\lambda} - 76.271 \right]^2 \text{ cm}^{-1} \quad [\text{A-2}]$$

We then averaged $\alpha_w(\lambda)$, $\alpha_s(\lambda)$, and $\alpha_r(\lambda)$ at 21 points in the interval 0.7-1.04 μm . A least squares fit of those average values gave the expression

$$\bar{\alpha}(\lambda) = \left[\frac{84.801}{\lambda} - 76.594 \right]^2 \text{ cm}^{-1} \quad [\text{A-3}]$$

It is important to note that we have extrapolated $\alpha_s(\lambda)$ and $\alpha_r(\lambda)$ well beyond the wavelength range of the experimental data on which they are based.

A comparison of Eq. [A-3] with Eq. [2] shows very little difference between them. It is also of interest to see how the use of Eq. [A-3] would affect the numerical value of L determined from the experimental data used in Fig. 9-11. Using Eq. [A-3] would have given $L = 9.95 \mu\text{m}$ instead of $L_C = 9.0 \mu\text{m}$ in Fig. 9; $L = 62.7 \mu\text{m}$ instead of $L_C = 60.2 \mu\text{m}$ in Fig. 10; and $L = \sim 179 \mu\text{m}$ instead of $L_C = 172 \mu\text{m}$ in Fig. 11.

REFERENCES

1. A. M. Goodman, *J. Appl. Phys.*, **32**, 2550 (1961); A. M. Goodman, Digest of Technical Papers, International Electron Device Meeting, pp. 231-234, December 1980.
2. ANSI/ASTM F 391-78, 1979 Annual Book of ASTM

- Standards, part 43 (Electronics), p. 770, American Society for Testing and Materials, Philadelphia (1979).
3. S. M. Sze, "Physics of Semiconductor Devices," 2nd ed., p. 15, John Wiley and Sons, New York (1981).
 4. J. Vilms and W. E. Spicer, *J. Appl. Phys.* **36**, 2815 (1965).
 5. S. S. Li, *Appl. Phys. Lett.*, **29**, 126 (1976).
 6. W. R. Runyan, Southern Methodist University Report SMU 83-13 (1967).
 7. R. T. Swimm and K. A. Dumas, *J. Appl. Phys.*, **53**, 7502 (1982).
 8. H. A. Weakliem and D. Redfield, *ibid.*, **50**, 1491 (1979).
 9. A. M. Goodman, *ibid.*, **53**, 7561 (1982).

Observations of the Temperature Gradient Zone Melting Process for Isolating Small Devices

D. J. Lischner, H. Basseches,* and F. A. D'Altroy

AT&T Bell Laboratories, Allentown, Pennsylvania 18103

ABSTRACT

The temperature gradient zone melting process (TGZM) for doping semiconductors is being investigated for the purpose of using it to create the isolation region in a relatively small geometry thyristor. The small size of the chip puts tougher morphological requirements on this liquid zone process than in past TGZM investigations. We discuss here a number of problems encountered which include enhanced diffusion of the aluminum dopant in the silicon, lateral motion of the molten zone at the edge of the wafer, breakup and smearing of the molten zone, and outdiffusion of the aluminum into the passivating oxide layer.

The thyristor semiconductor device usually contains very deep boron diffusions that are mils in depth and in the case of the triac extends through the thickness of the wafer. It requires days to make in furnaces at high temperatures ($> 1250^{\circ}\text{C}$). It runs around the periphery of the chip and is about twice as wide as its depth; thus, on small chips it takes up a large fraction of the chip area. We report here on our investigations to replace the standard solid-state diffusion method for forming these regions with a liquid-zone method known as temperature-gradient zone melting (TGZM). TGZM is a process by which a liquid zone in or on a solid can be caused to move through or across it by impressing a temperature gradient across the zone (1-6, 9). Here, the solid is single-crystal silicon and the liquid is a silicon/aluminum solution. In practice, the process starts at room temperature with evaporated and photolithographically defined aluminum on one side of the silicon wafer. The wafer is radiatively heated from the other side to temperatures considerably higher ($1000^{\circ}\text{--}1200^{\circ}\text{C}$) than the eutectic temperature to form the molten zone. As a result of the one-sided heating, there is a heat flow through the wafer which imposes the thermal gradient across the molten zone. The faces of the zone are thus at a slightly different temperature ($\Delta T < 0.1^{\circ}\text{C}$) and consequently have slightly different aluminum to silicon ratios with the hotter face having more silicon than the colder face. The resulting silicon concentration gradient causes a diffusion of silicon from the hot face to the cold face, leaving the hotter face undersaturated and the colder face supersaturated. As a result, dissolution of additional silicon occurs at the hotter face while precipitation and epitaxial growth of silicon occur at the colder face with the silicon there incorporating aluminum at the solid solubility limit for that temperature ($\approx 2 \times 10^{19}$ at./ cm^3). Thus the molten zone moves through the wafer, up the temperature gradient, leaving in its wake single-crystal silicon doped with aluminum. Due to the speed with which the zone moves through the silicon, on the order of $10 \mu\text{m}/\text{min}$, wafers can be doped through their thickness in minutes. There is also the further benefit of less side diffusion during the doping step. With TGZM, the concomitant side diffusion is a few microns compared to mils for solid-state diffusion.

TGZM itself is not new. It was first discovered by Pfann in 1955 (2), but was not fully developed due to the introduction of planar technology and oxide masking. Its unique properties, though, have kept it of interest; in par-

ticular, there are the two properties that are being made use of here, speed and the ability to form doped areas that are deeper than they are wide.

In the years 1973-1981, Anthony and Cline (3-9) did much to enhance the understanding of this process through the exploration of various solvent/solute systems, in great detail, and they too used the process for isolating thyristors (8) though their device work dealt mainly with large ($\approx 1/4$ in. diam) high voltage, high power SCR's made with the etched groove and glassivation technology. In contrast, we are discussing here the adaptation of the TGZM process to a small chip made with planar technology.

Wafer Processing Prior to TGZM Step

In this section, we describe the characteristics of and preparation of the wafer leading up to the TGZM step. The wafer is 50 mm in diameter, 10-20 $\Omega\text{-cm}$, n-type material. It is 0.30-0.33 mm thick, but is lapped and polished down to 0.2 mm after TGZM. It has a (1,1,1) orientation. The (1,0,0) orientation was not examined since it is known (6) that only lines of aluminum parallel to the $\langle 110 \rangle$ direction can be TGZM'd without forming discontinuities known as "line breaks." There is not a similar constraint for the (1,1,1) wafer. The surface finish is the usual, one side polished and one side etched where the aluminum is deposited on the polished side. Other surface finishes were tried since it was felt that a less perfect surface would aid the initial wetting and alloying of the aluminum and silicon and thus be more successful with respect to being able to TGZM an aluminum grid through the wafer with minimum line breaks. Wafers with as-cut surfaces on both sides had a far greater number of line breaks than wafers with the usual surface finish, while there was little difference between wafers with the usual surface finish and wafers that had both sides etched. Since a polished surface is likely to be the best from the point of view of being able to make a reproducible aluminum to silicon interface, all other experiments were done with wafers with the usual finish and with the aluminum on the polished side.

The formation of the patterned aluminum film starts with film deposition. The TGZM process requires an unusually thick film, far greater than what is required to dope the silicon. A 0.3 mm thick wafer requires the amount of aluminum in a 0.1 μm thick layer to dope it to its solubility limit. However, it has been found that to be able to TGZM a grid structure with a linewidth of 2-5 mil requires a film thickness greater than $\approx 5 \mu\text{m}$. Less than

*Electrochemical Society Active Member.

that results in erratic success with respect to being able to pass the grid through the wafer with no more than a few line breaks. A Varian E-gun deposition system (Model 3140) was used to form the aluminum layer. It can deposit $\approx 14 \mu\text{m}$ of aluminum from two successive pots without breaking vacuum on 75 two inch wafers in 1.5-2h. Patterning the aluminum into a grid with a 35 or 40 mil step and repeat was done with conventional photolithographic techniques except for the aluminum etch step. The etchant used was the PAN solution, phosphorus acid (1690 ml):acetic acid (340 ml):nitric acid (70 ml) at $55^\circ\text{-}65^\circ\text{C}$. Care had to be taken that excessive undercutting did not occur, and cleared wafers were promptly removed from the etchant and rinsed. Etch time is about 20 min, and while in solution the wafers were rotated 90° every 3 min to ensure even etching. Grid lines running parallel to the solution surface etched $\approx 30\%$ faster than those running perpendicular. During the course of etching, the solution was gently stirred by a magnetic stirrer. As a result of the above procedure, the etched aluminum grid line width is 2.3-2.5 mil as compared to the photoresist line width of 3 mil.

The TGZM Step

The aluminum grid is driven through the wafer at $\approx 1200^\circ\text{C}$ with a temperature gradient across the wafer of $\approx 50^\circ\text{C}/\text{cm}$. This is accomplished in a special in-house-built oven based on a design developed at the General Electric Company and has been described elsewhere (10). At the outset of this investigation, a severe line break and smearing problem was encountered. Figure 1 shows the side of the wafer where the aluminum exits. Two things can be seen, numerous line breaks and smearing of the pattern at the intersections. It should be noted that at that time the common practice was to carry out TGZM in an air ambient. Numerous cross sections taken through the line breaks revealed that they always started on the entrance surface (Fig. 2) implying a mechanism other than that which appears in the literature (6), where it is reported that line breaks occur when the moving line-shaped molten zone lowers its surface energy by splitting and bounding itself by (111) planes. With this mechanism, the line breaks would always occur randomly as the zone moves through the wafer. It was hypothesized that both the line breaks and smearing were due to a cocoonlike oxide that forms over the aluminum at the very start of the TGZM process. As the wafer continues to heat the aluminum, which has the largest coefficient of expansion of any of the phases, appears to rupture out of the cocoon at the intersection (Fig. 3) causing the smearing. The line breaks, however, are thought to be caused by the flow of the molten phase down the grid line and out of the rupture. This transverse motion then in some fashion inter-

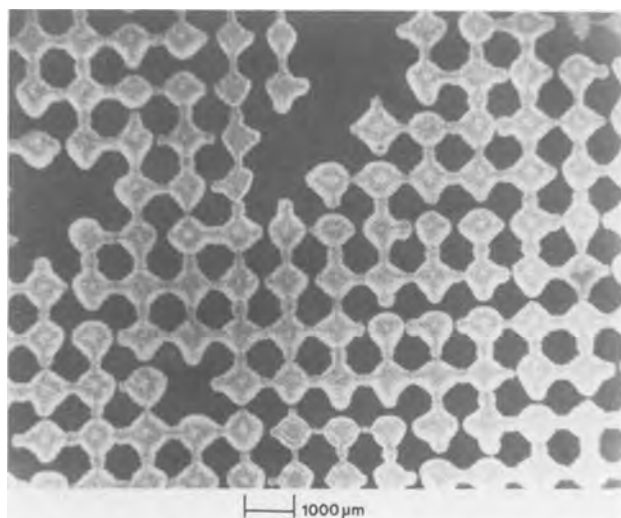


Fig. 1. Photograph of exit side of wafer immediately after TGZM process step. Note discontinuous grid lines and smeared intersections.

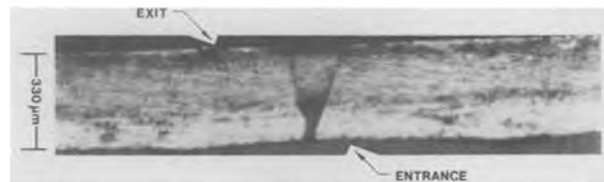


Fig. 2. Photograph of stained cross section of wafer where cross section was made along the length of a grid line. Molten zone passed through wafer everywhere except in dark area which is a line break. Note that line break initiated on entrance surface.

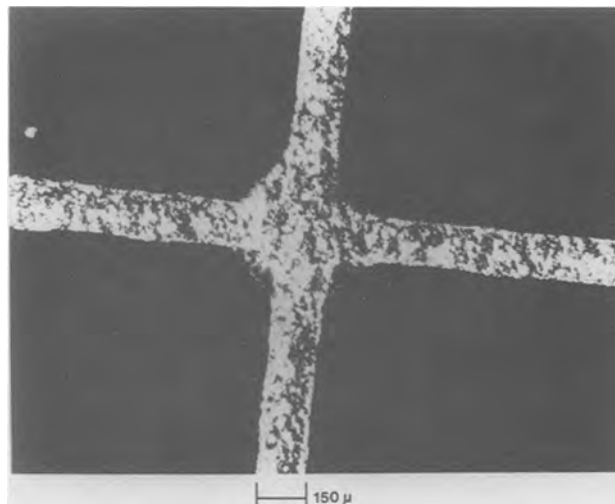


Fig. 3. Photograph of entrance side of wafer at a grid intersection. Note the smearing due to escape of molten zone from under the Al_2O_3 cap.

rupts the initiation of TGZM. When an $\approx 1\%$ O_2 in argon ambient was substituted for air, both problems were almost completely eliminated (Fig. 4). Instead of the continuous, impermeable oxide, a flaky oxide forms over the aluminum.

A pure argon ambient cannot be used because a quartz plate immediately above the wafer develops a coating of SiO_2 formed from the evaporation of Si from the wafer and the wafers thermally etch, by which it is meant that the wafers grew Si whiskers and pitted.

For the molten zone to move everywhere perpendicular to the wafer surface, it is required that the temperature gradient be everywhere perpendicular to the wafer sur-

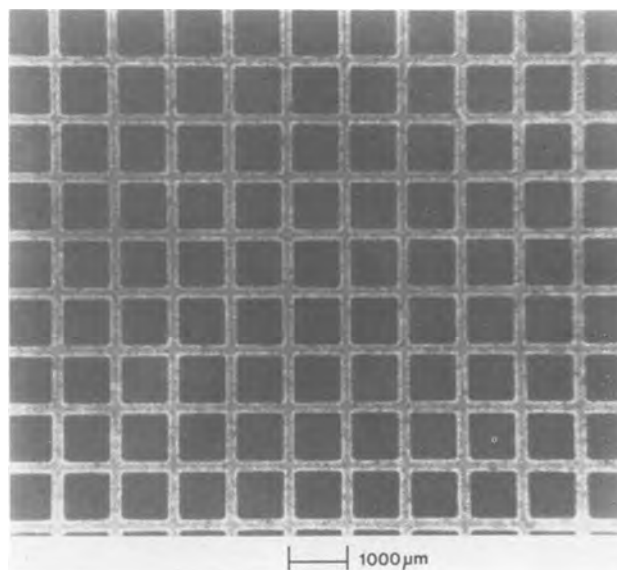


Fig. 4. Photograph of exit side of wafer when ambient during TGZM step was $\approx 1\%$ O_2 in argon.

face. This is in part accomplished by heating the wafer with a radiative flux of sufficient uniformity, and Ref. (10) discusses how sufficient uniformity is achieved in the present oven. However, uncompensated wafers, heated by uniform fluxes of radiation, whether it be one- or two-sided heating as in rapid thermal annealing (10) suffer from lateral temperature gradients that cause the wafer to be cooler at the edge than at the center and this in turn causes the molten zone to move inwards towards the center of the wafer (Fig. 5). This effect is understood (7) and is caused by net radiative losses at the wafer edge. There have been a number of schemes proposed and/or tried to reduce the losses by compensation. For example, it has been suggested that the wafer, during the TGZM step, sit in a hole cut into a large sheet of silicon that is the same thickness as the wafer. It is expected that the inside edge of the hole radiates inwards towards the edge of the wafer sufficient energy to effect compensation of the net loss. Lord has shown through computer modeling (11) that the gap between the wafer and the sheet and the coplanarity of the surfaces of the wafer and sheet must be kept to a fraction of the wafer thickness. This small mechanical tolerance renders this approach impractical. Lien (12) used a thin aluminum ring located on the entrance surface near the edge that was defined along with the aluminum grid during the aluminum etching steps. Here, the heat loss was apparently compensated by the lessened heat loss at the location of the ring, perhaps due to the aluminum's lower emissivity. Though this approach was demonstrated to work, the drawback is the large number of inclusions left in the silicon at the wafer's edge due to the ring's width being tens of mils. Another approach, the authors have developed, uses a thick ring of silicon (3/8 in.) with the wafer hole 1/4 in. larger than the wafer diameter. This eliminates the mechanical tolerance problem associated with the thin silicon sheet approach, but replaces it with the problem of arranging for the ring to have a temperature during TGZM that provides proper heat-loss compensation. When a simple square ring was placed around the wafer (Fig. 6), there was insufficient compensation because the ring had its own very significant edge-loss problem due to its thickness. (The amount of compensation was determined by cross sectioning test wafers and measuring the angle of the molten zone's path.) When a number of such rings are placed side by side and surrounded by silicon blocks, there was additional compensation, but it was still not sufficient. (The wafer, the silicon ring array, and the alumina sheet mentioned below are all supported above the oven floor on pointed quartz pins.) To boost the ring's temperature, 25 mil thick alumina sheets with the same lateral dimensions as the blocks (Fig. 7 and 8) were placed under them to provide thermal isolation from the cold oven floor. (The wafer and ring array are about 1/2 in.

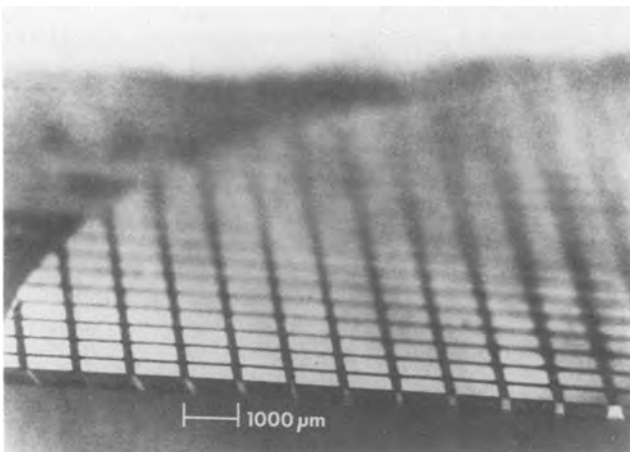


Fig. 5. Photograph of stained wafer cross section made at wafer edge. Note slanted regions due to nonperpendicular temperature gradients caused by edge cooling.

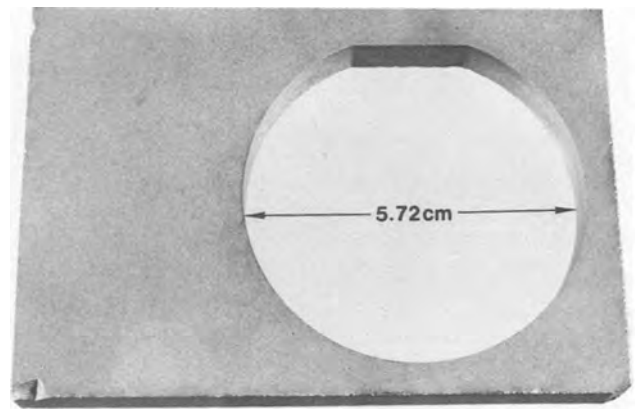


Fig. 6. A thermal trim ring. It measures $4 \times 2\frac{3}{4} \times \frac{3}{8}$ in. and has a $2\frac{1}{4}$ in. diam through hole.

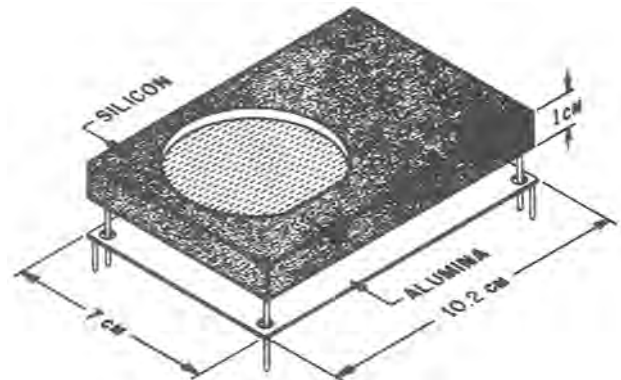


Fig. 7. Drawing of silicon and alumina thermal trim ring pair.

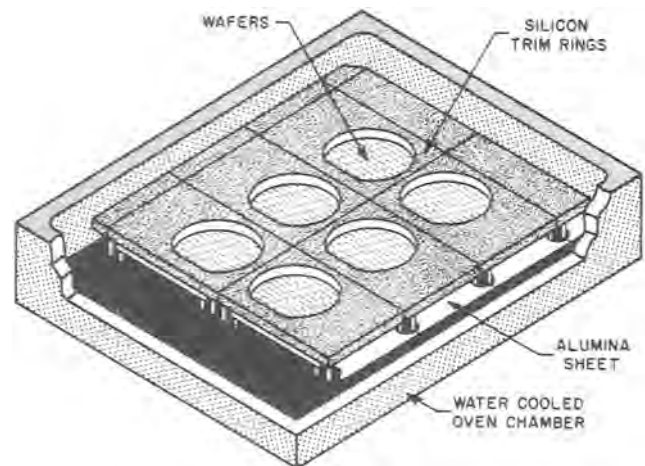


Fig. 8. Drawing of assembled trim rings for six wafers.

above the oven floor, while the alumina sheet is 3/8 in. above the floor.) This arrangement works as can be seen in Fig. 9. There, the angle of the TGZM path at the wafer's edge is plotted against the height of the wafer above the bottom surface of the silicon ring. It is estimated that the thyristors for which this process was developed can tolerate $\pm 10^\circ$ out of perpendicular TGZM isolation. With that criterion, the wafers then have an allowance of $\pm 1/16$ in. in vertical positioning.

Post-TGZM Wafer Preparation

It is a requirement of our device fabrication process that the wafer's surface be flat and polished. This is accomplished in a few steps. First excess aluminum is removed with the PAN etch. This is followed by a grinding or lapping operation to thin the wafer to within approximately a mil or two of its final thickness. A polishing step then reduces the wafer thickness to $8 \pm 1/2$ mil.

Prior to introducing the wafers into the device fabrication line, they are stained to reveal the location of the grid lines with a short Secco etch. Without this step, mask alignment would not be possible. They then enter the line at the initial oxidation step, and between there and base photolithography step device processing is as usual. At base photolithography, a new mask was introduced which was designed to help overcome the fact that the TGZM grid is not as rectilinear or as evenly spaced as the boron-diffused isolation grid, making mask alignment more difficult. The base-level mask has special alignment features to aid this problem. The base level also has widened grid lines to overcome the aluminum out-diffusion problem which is described next.

After the high temperature, long-time base drive-in step (1215°C, 11h), it is observed that this thick initial oxide lying over the grid lines has grossly changed. Based on appearances alone (Fig. 10 and 11), the SiO_2 has devitrified. This is confirmed by TEM cross-sectional analysis which found areas of the SiO_2 capable of diffracting the electron beam. SIMS analysis has detected aluminum in the oxide above the grid line. This evidence suggests that aluminum has outdiffused from the silicon into the SiO_2 and has catalyzed the conversion of the SiO_2 from the amorphous to the crystalline state. It may also be that the SiO_2 in this region forms aluminum silicate. This last possibility is supported by the observation that it is extremely etch resistant. As mentioned above, at base photolithography, the SiO_2 over the TGZM isolation region is etched away prior to the high temperature long drive-in time of the base drive-in. This procedure eliminates the problem of devitrification.

From this point on in the manufacturing process, device fabrication is normal.

The Enhanced Diffusivity Problem

The initial TGZM-isolated thyristor was designed to accommodate spreading of the isolation region due to diffusion of the aluminum to the extent determined by the temperature and times of processing and the published value of the temperature dependent diffusivity. It was found that the TGZM grid linewidth at the end of the wafer processing was wider than expected. Given that final grid linewidth, it is calculated that the diffusivity of the aluminum at 1260°C was $9.5 \times 10^{-11} \text{ cm}^2/\text{s}$, or about three times the published value. This enhanced diffusivity is likely due to the aluminum concentration being at its solubility limit. It was hoped that with TGZM one could capitalize on the minimal concomitant side diffusion to effect a smaller chip design; however, the found enhanced aluminum diffusivity reduces the advantage.

Device Characteristics

Thyristors made with TGZM isolation regions were in almost all respects normal. The reverse blocking current

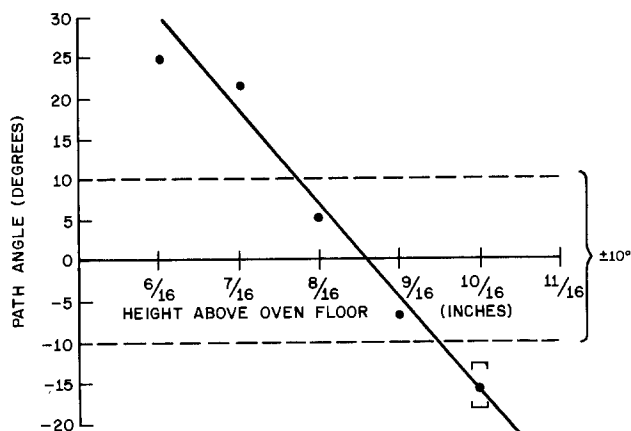


Fig. 9. Graph of angle of slant of TGZM zones at wafer edge vs. height of wafer above bottom of silicon ring. Note that magnitude and sign of the angle can be varied and controlled and that an optimum height with little slant can be identified.

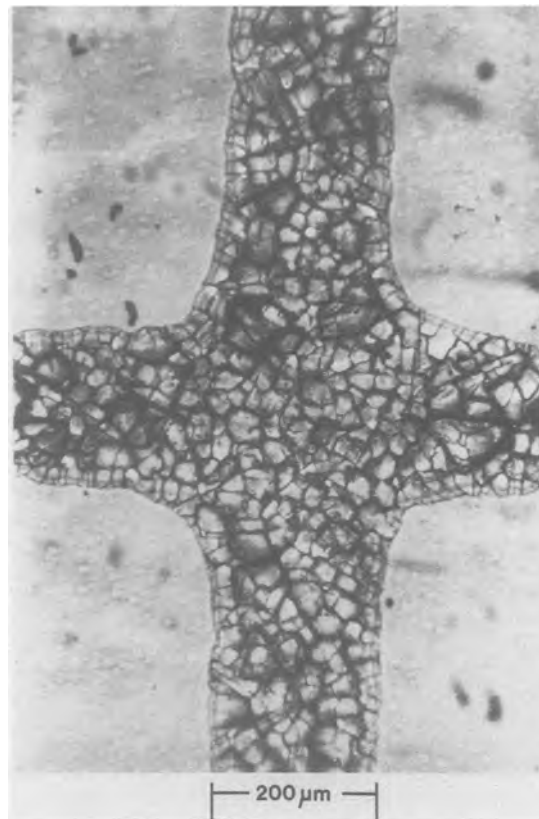


Fig. 10. Photomicrograph of oxide over TGZM region after base drive-in. Note fractured appearance.

was a factor of 2-3 times above the usual. Making some simplifying assumptions on the geometry of the junction, the reverse blocking current density of the TGZM isolated part of the junction was $1.9 \times 10^{-3} \text{ mA/cm}^2$, which is 4.4 times greater than the conventional device current density. This figure is still more than an order of magnitude smaller than the specification limit for this device. The increase in current density may in small part be due to the increased size of the space-charge region associated with the TGZM junction being more graded, but the origin of the remainder is unknown. (It is not due to aluminum contamination of the oxide, since SIM analysis has shown that its outdiffusion is confined to immediately over the grid.)

Groups of thyristors with TGZM isolation regions were subjected to all of the same reliability tests that the conventionally designed units experienced. These included bias-humidity, temperature-bias, and temperature cycling tests. They passed all these tests.

Summary and Conclusions

Adapting TGZM to our 40 mil thyristor has required both the improving of the TGZM process itself and the development and alteration of water preparation procedures. With regard to the process itself, gas ambient control is found to be crucial to being able to pass an aluminum grid with a linewidth of a few mils through the wafer with very few line breaks and little to no smearing

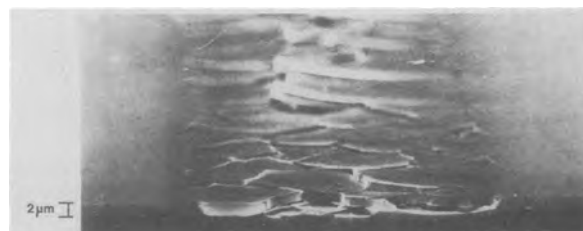


Fig. 11. SEM photomicrograph of devitrified oxide over TGZM region taken with wafer inclined to direction of view.

of the pattern. Also, thermal trim rings were developed which correct the nonperpendicular motion of the molten zone at the edge of the wafer. With regards to wafer preparation procedures, an aluminum etching technique was developed for uniformly defining the grid from the relatively thick aluminum starting film, and it was found that a polished silicon surface is one of the two best surfaces to use under the aluminum in minimizing line breaks and smearing. It is observed that the aluminum in the silicon will outdiffuse into a capping oxide during high temperature treatments causing the oxide to devitrify, and that this problem is avoided by removal of the oxide prior to high temperature processing. We also report the unexpected finding of an enhanced diffusivity that is 2-3 times larger than what is reported in the literature. Finally, with TGZM and with the modification and adaptation of various wafer preparation procedures reported on here 40×40 mil thyristors have been made with normal reliability and normal electrical characteristics.

Manuscript submitted Dec. 5, 1984; revised manuscript received April 19, 1985. This was Paper 92 presented at

the San Francisco, California, Meeting of the Society, May 8-13, 1983.

AT&T Bell Laboratories assisted in meeting the publication costs of this article.

REFERENCES

1. W. G. Pfann, "Zone Melting," 2nd ed., John Wiley and Sons, Inc., New York (1963).
2. W. G. Pfann, *Trans. AIME*, **203**, 961 (1955).
3. T. R. Anthony and H. E. Cline, *J. Appl. Phys.*, **43**, 2473 (1972).
4. T. R. Anthony and H. E. Cline, *ibid.*, **47**, 2316 (1976).
5. H. E. Cline and T. R. Anthony, *ibid.*, **47**, 2325 (1976).
6. H. E. Cline and T. R. Anthony, *ibid.*, **47**, 2332 (1976).
7. T. R. Anthony and H. E. Cline, *ibid.*, **47**, 2550 (1976).
8. T. R. Anthony, J. Boak, L. Chang, and H. E. Cline, *IEEE Trans. Electron Devices*, **ed.-23**, 818 (1976).
9. H. E. Cline and T. R. Anthony, *J. Appl. Phys.*, **49**, 2777 (1978).
10. D. J. Lischner, AT&T Bell Laboratories, Internal publication.
11. H. Lord, AT&T Technology Systems, Engineering Research Center, Internal publication.
12. S. Y. Lien, AT&T Technology Systems, Engineering Research Center, Internal publication.

The Composition and Physical Properties of LPCVD Silicon Nitride Deposited with Different $\text{NH}_3/\text{SiH}_2\text{Cl}_2$ Gas Ratios

Paihung Pan* and Wayne Berry*

IBM General Technology Division, Essex Junction, Vermont 05452

ABSTRACT

The composition and physical properties of low pressure chemical vapor deposition (LPCVD) silicon nitride films were studied. The samples were deposited at 770°C with different $\text{NH}_3/\text{SiH}_2\text{Cl}_2$ reactant gas ratios (R) ranging from 2 to 20. Auger electron spectroscopy (AES) showed that the Si/N ratio was about 0.75, and the compositional uniformity as a function of depth was good for all samples. No excess Si clusters were detected by TEM for the samples annealed at 1000°C in N_2 for 5h. Only N—H bonds were observed by infrared (IR) analysis. The amount of N—H bonds in the as-deposited samples was estimated to be about $5 \times 10^{16} \text{ cm}^{-2}$. The normalized N—H absorption peak area was found to increase by increasing R values, while the amount of N—H bonds was found to decrease after annealing at 1000°C in N_2 for 30 min. The plasma etch rates were found to increase by increasing R values and showed a good correspondence to the trend of increasing the N—H bonds. The film stress for all samples was tensile and had a level of $1 \times 10^{10} \text{ dyn/cm}^2$. No difference was observed in the film's ability to act as an oxidation barrier for samples deposited with different R values.

Silicon nitride films are widely used in the semiconductor industry for the applications of passivation (1), gate dielectric in metal-nitride-oxide silicon (MNOS) (2) and storage capacitor in field effect transistors (3), or bipolar memory (4). It is well known that the low pressure chemical vapor deposition (LPCVD) process is superior to the atmospheric chemical vapor deposition (ATCVD) process from the standpoint of film uniformity and mass production. It is also known that the physical and electrical properties of the deposited films rely on the deposition conditions (5, 6). Film stress levels and pinhole density, which are affected by the process parameters, are particularly important when such films are used for passivation. The film composition and its associated structure are fundamental to understanding the etching behavior and the film's ability to act as an oxidation barrier or as a passivation barrier to mobile ions. Stein (7) has previously reported the direct relationship between the Si—H bonding and the MNOS characteristics for the ATCVD film. Additionally, it has been observed (8) that silicon-rich nitride films have higher electrical leakage current and the presence of Si clusters will enhance the charge injection, which makes the films more suitable for the EEROM application (9).

The composition and structure (10-12) as well as electrical properties (13, 14) of LPCVD Si_3N_4 films have been

reported. The purpose of our study is to understand the properties of the LPCVD silicon nitride as a function of the deposition parameters and then relate these properties to the film composition. In this paper, we report on the LPCVD Si_3N_4 film composition (including Si, N, O, and hydrogen), film stress, etch rate, and the film's ability to act as the oxidation barrier. The samples were deposited with different $\text{NH}_3/\text{SiH}_2\text{Cl}_2$ gas ratios (R).

Experiments

Silicon nitride films were deposited in an LPCVD system. The silicon wafer was chemically cleaned immediately before the deposition. All samples were deposited at 770°C with the $\text{NH}_3/\text{SiH}_2\text{Cl}_2$ reactant gas ratio ranging from 2 to 20. The SiH_2Cl_2 gas flow was kept at a constant of 15 sccm.

Film composition (Si, N, and O) of thin samples (~ 50 nm) was measured by using an Auger system with a beam voltage of 5 kV and a current of $1 \mu\text{A}$. An ATCVD Si_3N_4 sample ($n = 2.01$) of 50 nm, which was deposited with $\text{NH}_3/\text{SiH}_4 = 1200$ at 800°C , served as the standard to determine the Si and N concentration. The amount of oxygen in the film was estimated by referencing to the oxygen concentration (66.7 atom percent [a/o]) of a thermal SiO_2 of 50 nm. The Auger depth profile was used to determine the compositional uniformity as a function of depth.

A Fourier transform infrared (FTIR) system was used to analyze the thick samples (~ 500 nm on both sides of wa-

* Electrochemical Society Active Member.

fer). Transmission spectra were obtained with the incident beam normal to the wafer. The raw spectra were then subtracted from the spectra of the silicon substrate. The total absorption peak area measured by the computer was in the range of 200 cm^{-1} . Samples implanted with H^+ ions at an energy of 25 keV and with a dose of $2 \times 10^{17} \text{ ion/cm}^2$ served as the standard to determine the amount of N—H bonds.

A parallel-plate reactor was used to etch the deposited films $\sim 200 \text{ nm}$ thick. In this etching process, power of 400W, temperature of 40°C , and an RF frequency of 13.56 MHz were applied. The flow of CF_4 and O_2 were 135 and 13 sccm, respectively, and the pressure of the reactor was 250 mtorr. The film thickness, before and after etching, was measured by an ellipsometer, and the etch rates were then determined.

Thick films ($\sim 500 \text{ nm}$ on front side of wafer) were used for stress measurement. The film stress was determined at room temperature by using the x-ray topography technique (15). The refractive index for films 50-100 nm thick was measured by an automatic ellipsometer with an incident beam of $\lambda = 632.8 \text{ nm}$. A transmission electron microscope (TEM) was used to identify the presence of the excess Si phase in thin films (20-40 nm).

Results and Discussion

As shown in Fig. 1, the deposition rate and the pressure was found to increase by increasing the R value. Because pumping speed was kept constant in this experiment, the pressure in the reactor increased by increasing the R value. Based on our other study of deposition rate as a function of pressure, we believe the increase in the deposition rates by increasing the R value was due to the pressure increase. The uniformity of film thickness and refractive index, either across a wafer or across a load of 50 wafers, was found to be within 5% and was independent of the R value. The refractive index for all as-deposited samples was 1.99 ± 0.02 . Within experimental errors, no difference in refractive index was found after annealing at 1000°C in N_2 for 30 min.

After the 10 nm thick surface was sputtered away by Ar ions, the Auger spectra for all samples were obtained. Si, Ar, and N peaks were observed but not a trace of oxygen and carbon was detected, which implies that the oxygen concentration in these films was less than the detection limit (0.5 a/o) of this measurement. Since Ar gas was not used during the film deposition, the Ar peak must be caused by the sputtering Ar ions. Assuming that the electron-beam and the ion-beam effects on both the standard ATCVD Si_3N_4 and the deposited LPCVD samples were the same, the average Si/N ratio for all LPCVD samples was found to be 0.75 ± 0.02 . No dependency on the Si/N ratio as a function of R values was found. The Si/N ratios for these samples are listed in Table I.

As shown in Fig. 2, the Auger depth profile indicated that the uniformity of the Si and N concentration as a function of depth was good. A thin layer of SiO_2 films was observed at the $\text{Si}_3\text{N}_4/\text{Si}$ interface which may affect the electrical properties of the metal-insulator-oxide structure. A detailed Auger study of MNOS structure was reported by Johannessen *et al.* (16). Following the report

Table I. The deposition rate, Si/N ratio, amount of N—H bonds, etch rate, and film stress of Si_3N_4 films deposited with different $\text{NH}_3/\text{SiH}_2\text{Cl}_2$ gas ratios (R)

R	Deposition Rate (nm/min)	Si/N	N-H ($\times 10^{16}/\text{cm}^2$)		Etch Rate (nm/min)		Stress ($\times 10^{10} \text{ dyne/cm}^2$)
			as-deposited	annealed	as-deposited	annealed	
2	1.58	0.74	4.54	2.09	2.34	2.19	1.15
7	1.75	0.73	5.38	3.39	2.41	2.20	1.16
10	1.85	0.76	6.05	4.11	2.50	2.23	1.05
20	2.05	0.74	6.82	4.72	2.56	2.36	1.00

by Pan *et al.* (17), the thickness of this layer was estimated to be about 2-3 nm.

TEM was used to analyze an as-deposited sample and an annealed sample (1000°C in N_2 for 5h). Both samples were deposited with $R = 2$. The TEM diffraction analysis showed diffuse rings for both samples, and no silicon pattern was observed for the annealed sample (Fig. 3a and 3b). The TEM bright field images showed a texture of the film before and after annealing which was 5 and 10 nm, respectively. Both results indicated that the deposited film was amorphous, before and after annealing, and no Si clusters were detected even after annealing for a long time at high temperature. These results and the Auger data of the $\text{Si/N} = 0.75 \pm 0.02$ also indicated that the stoichiometry of these LPCVD samples was Si_3N_4 or very close.

The IR absorption spectrum for a sample, with a thick Si_3N_4 film of about 500 nm on both sides of the wafer, is shown in Fig. 4. The Si—N absorption peak was found to be at 845 cm^{-1} and has the full width at half maximum (FWHM) of 210 cm^{-1} for all samples. No change in either the peak wavenumber or the FWHM value was found after the samples were annealed at 1000°C in N_2 for 30 min. This suggests that the Si—N bonding is nearly the same for both the as-deposited and annealed samples. Since the mass of the hydrogen atom is light and the amount of hydrogen in these samples was small, it was expected that the measured Si—N vibration was not affected by the escape of hydrogen, which was previously bonded to the Si or N atoms.

The N—H bonds at 3350 cm^{-1} were clearly observed for all samples. No trace of Si—H bonds was detected even when the spectrum was expanded 15 times (Fig. 4). This is different from results reported in Ref. (11). As reported in the literature (18, 19), the absorptivity of the S—H bonds is about 1.4 times that of the N—H bonds. This indicated that the amount of the N—H bonds in these films is at least 20 times ($15 \times 1.4 = 21$) that of the Si—H bonds.

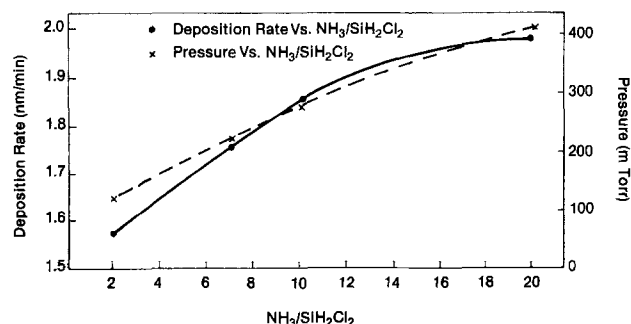


Fig. 1. The deposition rate as a function of $\text{NH}_3/\text{SiH}_2\text{Cl}_2$ ratio (R) or as function of pressure.

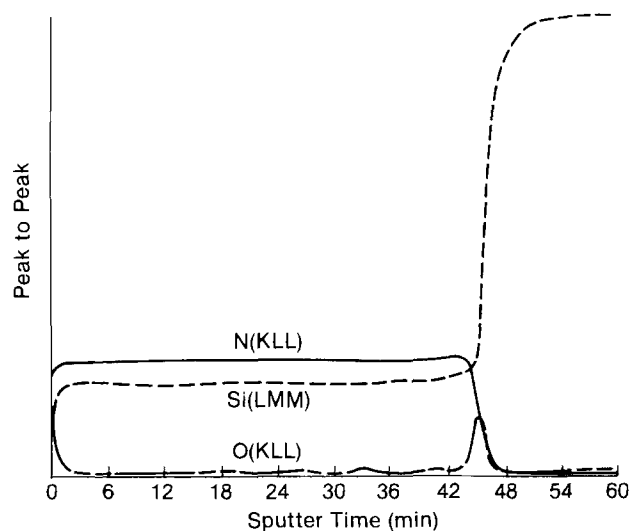


Fig. 2. Auger depth profile of Si_3N_4 film indicating the uniformity of Si, N, as a function of depth.

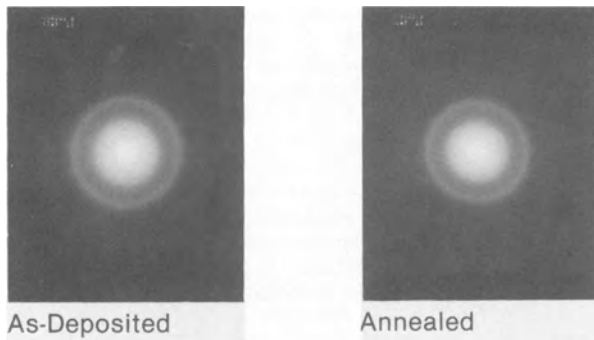


Fig. 3. The TEM diffraction pattern for the Si_3N_4 film deposited with $R = 2$. a: As-deposited sample. b: Annealed sample (1000°C , N_2 , 5h).

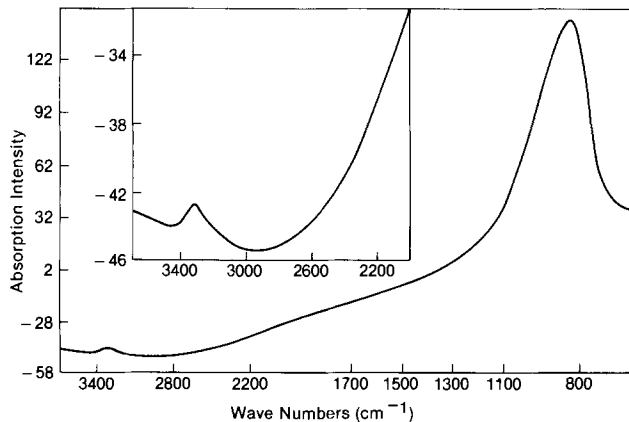


Fig. 4. The infrared spectrum for a Si_3N_4 film ($R = 2$). The spectrum from $2100\text{--}3500\text{ cm}^{-1}$ was expanded 15 times and is shown in the insert.

When the N—H absorption peak area was normalized by the Si—N absorption peak area, we found that the normalized N—H peak area increased by increasing the R values (Fig. 5). The increase of NH_3 gas flow, which enhanced more H and/or N—H during the deposition, will result in this observation. After annealing at 1000°C in N_2 for 30 min, the N—H bonds were decreased for all samples, but the trend of increasing the normalized N—H peak area by increasing the R values was still observed (Fig. 5). The presence of N—H and the lack of Si—H suggested the presence of Si— dangling bonds. The density of the electron spin resonance (ESR) for the Si— dangling bonds in this Si_3N_4 was of the order of $1 \times 10^{16}\text{ cm}^{-3}$ (20) which is close to the value reported by Makino (10). Similar to the ATCVD Si_3N_4 (7, 21), the presence of Si—dangling bonds will affect the device characteristics.

IR spectra for the samples implanted with hydrogen (H^+) were also obtained. Similar to the report by Stein (7)

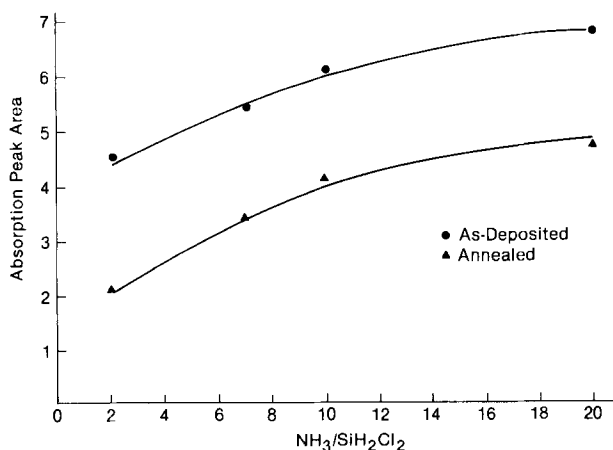


Fig. 5. The normalized N—H bonds as a function of R value

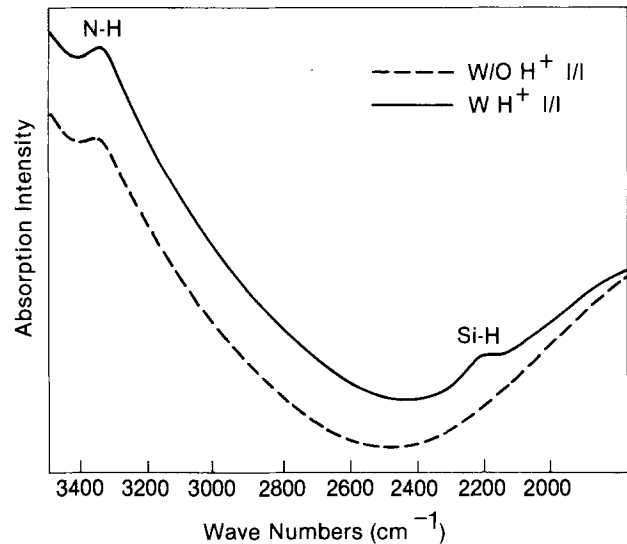


Fig. 6. The infrared spectrum for an as-deposited Si_3N_4 film before and after H^+ ion implantation.

for CVD Si_3N_4 , the Si—H bonds at 2200 cm^{-1} were detected (Fig. 6). The normalized Si—H bonds for the as-deposited sample were found to be higher than that of the annealed sample. After implantation, the increase in the N—H bonds for the as-deposited sample is less than that for the annealed sample (Table II). The presence of more N^+ dangling bonds for the annealed samples, due to the escape of hydrogen during annealing, may provide more chance to form N—H bonds and/or provide less chance for the conversion of N—H to Si—H bonds (7, 22) during the hydrogen implantation. The result that the difference in the total weight is nearly the same for both the as-deposited and the annealed samples suggested that a constant amount of hydrogen ion was bonded to Si or N after implantation.

When one defines that $U(\text{N—H})$ and $U(\text{Si—H})$ are the normalized N—H peak area and the Si—H peak area, respectively, one can write equations as

$$U(\text{N—H}) = A(\text{N—H})/A(\text{Si—N}) \quad [1]$$

$$U(\text{Si—H}) = A(\text{Si—H})/A(\text{Si—N}) \quad [2]$$

for samples before implantation. One can also write equations for samples after implantation as

$$U'(\text{N—H}) =$$

$$\frac{A'(\text{N—H}) - (1/2) \times [A(\text{N—H})/A(\text{Si—N})] \times A'(\text{Si—N})}{(1/2) \times A'(\text{Si—N})} \quad [3]$$

$$= [2A'(\text{N—H})/A'(\text{Si—N})] - [A(\text{N—H})/A(\text{Si—N})] \quad [4]$$

$$U'(\text{Si—H}) = A'(\text{Si—H})/[2A'(\text{Si—N})] \quad [5]$$

$$= [2A'(\text{Si—H})/A'(\text{Si—N})] \quad [6]$$

where $A(\text{Si—N})$, $A(\text{N—H})$, and $A(\text{Si—H})$ are the measured absorption peak area for Si—N, N—H, and Si—H bonds, respectively. $A(\text{Si—N})$ and $A'(\text{Si—N})$ are expected to be equal when the measuring condition is the same. The prime (') indicates after implantation. The factor (1/2) in Eq. [3] and [4] came from the fact that the hydrogen only

Table II. The normalized N—H peak area [$U(\text{N—H})$] and Si—H peak area [$U(\text{Si—H})$], before and after H^+ implantation, for the as-deposited and annealed Si_3N_4 films ($R = 10$). $U(\text{N—H})$ and $U(\text{Si—H})$ are defined in Eq. [1], [2], [4], and [6], and $W = 1.4 \times U(\text{N—H}) + U(\text{Si—H})$

	Before I/I			After I/I			$\Delta W =$ $W(\text{Before I/I})$ $- W(\text{After I/I})$
	$U(\text{N—H})$	$U(\text{Si—H})$	W	$U(\text{N—H})$	$U(\text{Si—H})$	W	
As-Deposited	6.03	0	8.44	7.88	3.58	14.61	6.17
Annealed	4.10	0	5.74	6.71	2.72	12.11	6.37

implanted on one layer of Si_3N_4 contributed only one-half of the measured $A(\text{Si}-\text{N})$.

The increase in the N—H and Si—H peak areas can be obtained by subtracting Eq. [4] from [1] and Eq. [6] from [2]. When one assumes that the implanted hydrogen ions are all chemically formed as Si—H or N—H bonds, and defines that U is the amount of N—H bonds represented by the unit normalized N—H peak area, then one can write

$$U = \frac{H}{[U'(\text{N}-\text{H}) - U(\text{N}-\text{H})] + (1/1.4) \times [U'(\text{Si}-\text{H}) - U(\text{Si}-\text{H})]} \quad [7]$$

where H is the total amount of implanted hydrogen which can be obtained by the integration of hydrogen profile in the implanted sample. The factor (1/1.4) came from the ratio of the absorptivity of the Si—H bonds to that of the N—H bonds (12, 13). The amount of N—H bonds [$Q(\text{N}-\text{H})$] and the amount of Si—H bonds [$Q(\text{Si}-\text{H})$] in the sample can then be estimated by using $Q(\text{N}-\text{H}) = U \times U(\text{N}-\text{H})$ and $Q(\text{Si}-\text{H}) = (1/1.4) \times U \times U(\text{Si}-\text{H})$. In order to use this analysis technique, one sample must be implanted with hydrogen.

From the LSS statistical table (23), the projected range was 230 nm and the standard deviation was 50 nm for the implanted H^+ ions with 25 keV. When the gaussian approximation was assumed, one can estimate that the amount of the N—H bonds in these films is in the order of 5×10^{16} bond/cm². The amount of N—H bonds for all samples is listed in Table I. Because the incident beam was normalized to the wafer and the absorption peak area decreased with decreasing the film thickness, the N—H or Si—H bonds are expected to be present inside the film instead of at the $\text{Si}_3\text{N}_4/\text{Si}$ interface, or on the Si_3N_4 surface.

As shown in Fig. 7, the plasma etch rates were found to increase as the R value increased. After the samples were annealed at 1000°C in N_2 for 30 min, the etch rates for all samples were decreased about 2 nm/min. The trend of the etch rates as a function of R values is the same as that of the normalized N—H peak area. As described earlier, the Si/N ratios were nearly the same and the oxygen contamination was very small (< 0.5 a/o) for all samples. These results indicated that the amount of the N—H bonds or total hydrogen in the sample, which will affect the film density and/or the chemical bonding, should play an important role in the process of plasma etching. The lower etch rate of the annealed film was believed to be due to the densifying effect, which reduced the number of the weaker N—H or Si—H bonds (24) of the as-deposited samples and increase the film density. No loading effects were observed for these Si_3N_4 films under the present etching process.

AES and x-ray photoelectron spectroscopy (XPS) were used to analyze the Si_3N_4 surface after plasma etching. The amount of oxygen (about 8 a/o) on the etched surface was found to be slightly less than that on the unetched surface and the depth of the oxygen distribution for both

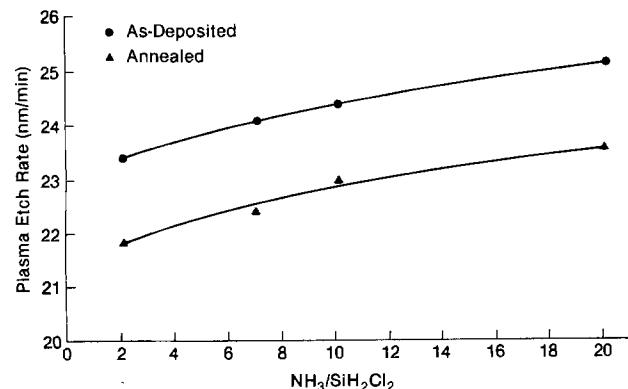


Fig. 7. The plasma etch rates as a function of R value

the etched and unetched samples was nearly the same. These results indicate that the oxygen plasma mainly promoted the dissociation of the CF_4 (25), rather than oxidizing the Si_3N_4 surface during the process of plasma etching.

Film stress for all samples was tensile and at a level of about 1×10^{10} dyn/cm², which is slightly less than the level for the ATCVD Si_3N_4 (26, 27). A slight decrease in stress was observed by increasing the gas ratio, which is shown in Fig. 8. As described previously, the Si/N ratio and the oxygen in all samples were nearly the same. This suggests that the sample with higher hydrogen, either in the form of N—H or Si—H bonds, increases the relaxation of the intrinsic rigidity. The higher surface relaxation for samples deposited with higher deposition rate (26) may be another reason for this observation.

The ability to act as an oxidation barrier was tested by oxidizing the as-deposited and annealed (1000°C, N_2 , 30 min) samples, in wet O_2 ambient at 1000°C for 2h. Auger depth profiles were then used to determine the oxygen distribution. As shown in Fig. 9, one found that the thickness of the oxidized Si_3N_4 was nearly the same (about 10 nm) for both the as-deposited and the annealed samples, which indicated that the pinhole density was small in the as-deposited samples. The observation of no difference in this ability for the samples deposited with different $\text{NH}_3/\text{SiH}_2\text{Cl}_2$ gas ratios indicates that the stoichiometry for all samples is nearly the same. The shape of the Si LVV Auger spectrum at the oxidized layer/ Si_3N_4 interface was identical to that in the LPCVD oxynitride film. This observation suggested that the initial oxygen atoms replaced some nitrogen sites to form an oxynitride layer. When the nitrogen-rich oxynitride was converted into the oxygen-rich oxynitride or SiO_2 , the oxygen atoms in the ambient then diffused through this layer to react with the

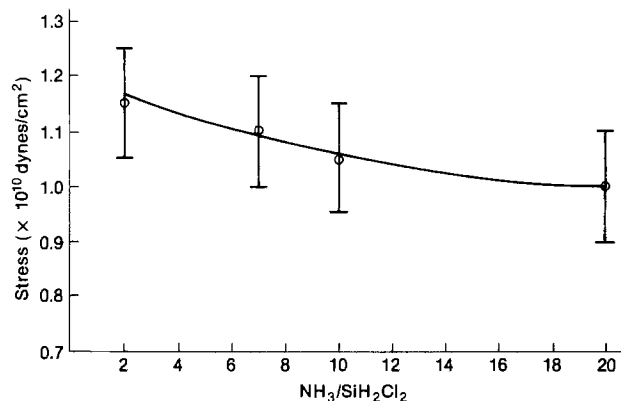


Fig. 8. The film stress of Si_3N_4 deposited with different R values

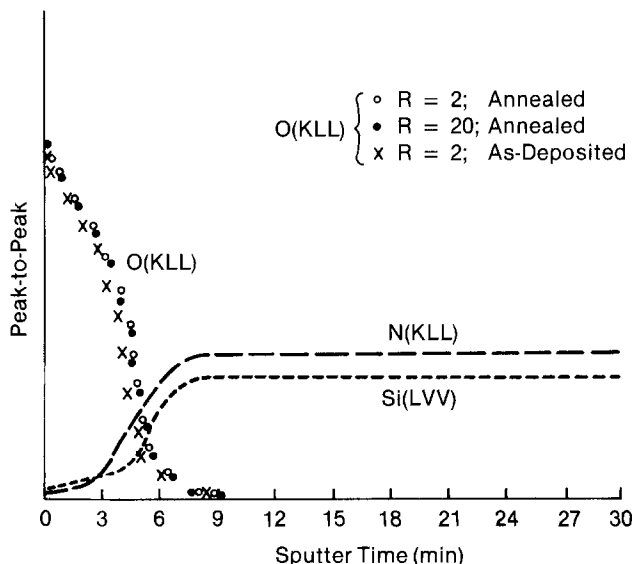


Fig. 9. The Auger depth profile of the oxidized Si_3N_4 films

Si_3N_4 . The slow chemical reaction of Si_3N_4 with oxidant is believed to be the cause of the slow oxidation rate in Si_3N_4 (28). Both replacement of N with O and diffusion of O were observed during the oxidation of oxygen-rich LPCVD oxynitride. The mechanism of the oxygen diffusion in the oxygen-rich oxynitride may be similar to that in SiO_2 film (29).

Summary

LPCVD silicon nitride films were deposited at 770°C with different $\text{NH}_3/\text{SiH}_2\text{Cl}_2$ gas ratios ranging from 2 to 20. Auger analysis was used to determine the Si, N, and O concentration. Comparing with the standard ATCVD Si_3N_4 sample, the Si/N ratio for the LPCVD samples was found to be 0.75 ± 0.02 and was independent of the R values. No excess Si phases were detected by TEM. The amount of oxygen was found to be less than 0.5 a/o. Only N—H bonds were detected by IR analysis, and the presence of Si dangling bonds was detected by ESR. The normalized N—H absorption peak area was increased by increasing the R values. The amount of the N—H bonds in the as-deposited samples was estimated to be about $5 \times 10^{16} \text{ cm}^{-2}$. The plasma etch rates increased by increasing the R values, and the increase in the amount of hydrogen was believed to be responsible. For all samples, the film stress was tensile and the level was in the order of $1 \times 10^{10} \text{ dyn/cm}^2$. The film's ability to act as the oxidation barrier was nearly the same for both the annealed and as-deposited samples, and no dependence on the R values was found for all as-deposited samples.

Acknowledgments

We would like to thank H. Geipel for the critical reading of this paper. Thanks are given to V. S. Nguyen for the information on ESR, S. Burton for doing plasma etch, and E. Cadwell for doing IR analysis. We also want to thank E. Gardner for the encouragement during the course of this work.

Manuscript submitted April 23, 1984; revised manuscript received Jan. 23, 1985. This was Paper 105 presented at the San Francisco, California, Meeting of the Society, May 11-13, 1983.

IBM Corporation assisted in meeting the publication costs of this article.

REFERENCES

1. See, e.g., S. Hiraki, S. Yasuda, T. Ajima, and T. Yonezawa, Abstract 175, p. 461, The Electrochemical Society Extended Abstracts, Vol. 80-1, St. Louis, MO, May 11-16, 1980.

2. See, e.g., J. F. Chang, *Proc. IEEE*, **64**, 1039 (1976).
3. R. R. DeSimone, N. M. Donofrio, B. L. Flur, R. H. Kruggel, and H. H. Leung, *ISSCC*, 154 (1979).
4. A. Bhattacharyya and J. E. Selleck, Abstract 51, p. 144, The Electrochemical Society Extended Abstracts, Vol. 80-1, St. Louis, MO, May 11-16, 1980.
5. H. Nakayama and T. Enomoto, *Jpn. J. Appl. Phys.*, **18**, 1773 (1982).
6. R. S. Bailey and V. J. Kapoor, *J. Vac. Sci. Technol.*, **20**, 484 (1982).
7. H. J. Stein, *This Journal*, **129**, 1786 (1982).
8. D. W. Dong, E. A. Irene, and D. R. Young, *ibid.*, **125**, 819 (1978).
9. D. J. DiMaria and D. W. Dong, *J. Appl. Phys.*, **51**, 2722 (1982).
10. T. Makino, *This Journal*, **130**, 45 (1983).
11. A. E. T. Kuiper, M. P. H. F. Hambraken, A. VanOostrom, and Y. Tamminga, *J. Philips Res.*, **38**, 1 (1983).
12. A. Dixit, C. S. Chen, and C. E. Volk, *This Journal*, **127**, 2239 (1980).
13. V. J. Kapoor and S. B. Bibyk, *Thin Solid Films*, **78**, 193 (1981).
14. F. L. Hamton and J. R. Cricchi, *Appl. Phys. Lett.*, **35**, 802 (1979).
15. W. Berry, *Adv. X-Ray Anal.*, 26 (1983).
16. J. S. Johannessen, C. R. Helms, W. E. Spicer, and Y. E. Strausser, *IEEE Trans. Electron Devices*, **ed-24**, 547 (1977).
17. P. Pan, P. C. Velasquez, and R. W. Douse, *Surf. Interf. Anal.*, **3**, 106 (1981).
18. P. S. Peercy, H. J. Stein, B. L. Doyle, and S. T. Picraux, *J. Electron. Mater.*, **8**, 11 (1979).
19. W. A. Lanford and M. J. Rand, *J. Appl. Phys.*, **49**, 2473 (1978).
20. Work attributed to V. S. Nguyen.
21. S. Fujita, H. Sato, and A. Sasaki, in "Silicon Nitride Thin Insulating Films," V. J. Kapoor and H. Stein, Editors, p. 266, The Electrochemical Society Soft-bound Proceedings Series, Pennington, NJ (1983).
22. H. J. Stein, *Appl. Phys. Lett.*, **15**, 379 (1978).
23. J. F. Gibbons, W. S. Johnson, and S. W. Mylroie, "Projected Range Statistics—Semiconductor and Related Materials," 2nd ed., John Wiley and Sons, New York.
24. "CRC Handbook of Chemistry and Physics," R. C. Weast, Editor, 62nd Edition, CRC Press, Inc., Boca Raton, Florida.
25. See, e.g., A. Jacob, *Solid State Technol.* (4), 95 (1978).
26. E. A. Irene, *J. Electron. Mater.*, **5**, 287 (1976).
27. E. P. EerNisse, *J. Appl. Phys.*, **48**, 3337 (1977).
28. T. Enomoto, R. Ando, H. Morita, and H. Nakayama, *Jpn. J. Appl. Phys.*, **6**, 1049 (1978).
29. B. E. Deal and A. S. Grove, *J. Appl. Phys.*, **36**, 3770 (1965).

CVD Epitaxial Autodoping in Bipolar VLSI Technology

G. R. Srinivasan*

IBM General Technology Division, East Fishkill Facility, Hopewell Junction, New York 12533

ABSTRACT

This paper reviews several aspects of epitaxial autodoping including process effects, flow effects, and the effect of profile tolerance on bipolar device characteristics. Emphasis is placed on the examination of the stagnant boundary layer hypothesis in light of recent evidence. A new derivation of the half-power law that relates the increase in autodoping to an increase in the buried layer area is presented. This law is the limiting law for discrete point sources when they merge to form a continuum.

In high performance bipolar VLSI technology, the trend is toward higher device densities and shallower junctions, both of which are affected by epitaxial autodoping. Autodoping, for example, determines the sharpness of the buried-layer vertical profile, the minimum epitaxial thickness usable for shallow junction devices, and the lateral spacing of the devices. I reviewed the autodoping phenomenon that occurs in CVD epitaxial silicon in 1979 (1), and since then considerable progress has

been made in modeling the hydrodynamic aspects of the dopant redistribution in the epitaxial flow system (2-10). One of the important results of this development as it pertains to the VLSI technology is the theoretical prediction (2), and the subsequent experimental verification (4), of the half-power law which relates an increase in net autodoping due to an increased fraction of the buried layer area in the substrate. Recently, this law has been reconfirmed for substrates containing buried layers of large dimensions (11). The original theory was developed for an array of point sources. In this paper, we will derive

*Electrochemical Society Active Member.

this power law for extended sources, and show that the half power is the consequence of the inverse-distance solution to the flow equation for point sources and its application to a continuum of such sources.

Yet another important outcome of the flow dynamic studies is the finding that for horizontal epitaxial reactor flow systems there is no indication of a stagnant boundary layer (3). This finding has received experimental support recently from direct laser holographic interference observations of the flow in horizontal epitaxial reactors (12, 13) and from theoretical considerations of flow (8).

Further, there have been several recent studies which have examined the interrelationships between autodoping, dopant profiles, and transistor characteristics for bipolar integrated circuits (14-17). In this paper, we will review these flow and device aspects of autodoping in silicon epitaxy.

Process Effects

Autodoping mainly occurs in the pregrowth (prebake) stages of the epitaxial process, and its dependence on prebake parameters (time t_p , temperature T_p) can be described (18) for buried layers by the equation

$$C_A = \alpha \exp(\beta^2 t_p) \cdot \operatorname{erfc}(\beta t_p^{1/2}) \quad [1]$$

where C_A is the maximum concentration in the lateral autodoping peak. If one assumes an Arrhenius behavior for β , which is the ratio of the dopant evaporation velocity to the square root of its diffusivity in silicon such that $\beta = \beta_0 \exp(-\Delta E/kT_p)$, a good agreement between theory and experiment is obtained. Since β contains the evaporation velocity, both the dopant vapor pressure and the reactor pressure are contained in it. The factor α contains both the flow parameters and the growth parameters.

The above equation was derived on the basis that the dopant evaporation kinetics is the controlling mechanism for vapor phase autodoping. The data for arsenic autodoping are consistent with the above model for epitaxial depositions made in a horizontal reactor (18), barrel reactor (15), and vertical pancake reactor (19). More recently, autodoping measurements for epitaxial deposition in a pancake reactor have been reported (20) which show that, while arsenic autodoping is consistent with Eq. [1], phosphorous autodoping shows a different behavior. However, in view of several peculiarities of these data in terms of the differences between the variations of on and off buried layer autodoping with respect to prebake parameters, unexpected growth rate effects, etc., further confirmation is necessary before attempting to model these effects.

The effect of growth rate on autodoping has been modeled using the concept of dopant trapping (1, 18). This trapping model explains the observed increase in autodoping with increased growth rate in terms of the decreased ability of the trapped dopant atoms to diffuse to, and escape from, the rapidly advancing surface.

One of the autodoping effects that is important for integrated circuits is the effect of the initial buried-layer profile, prior to epitaxy. In deriving Eq. [1], an assumption of a rectangular profile was made (18) in order to obtain a closed-form solution to the evaporation equation. Actually, the initial buried layer profile is more complicated, especially if an oxidation-drive-in cycle has been used to form the buried layer. During this cycle, segregation of the dopants into or away from the growing oxide occurs, depending on whether it is a P- or an N-type dopant. For N-type buried layers used in the formation of subcollectors in N-P-N bipolar structures, oxidation cycle produces a dopant pile-up at the SiO₂/Si interface. High performance integrated circuits use high conductivity subcollectors in which the doping is made to the solid solubility limit. Any further pile-up in these buried layers produces mostly electrically inactive dopant and also causes enhanced autodoping.

A method to reduce this pile-up and the consequent autodoping for arsenic subcollectors has been described previously (21). It depends on arriving at a judicious

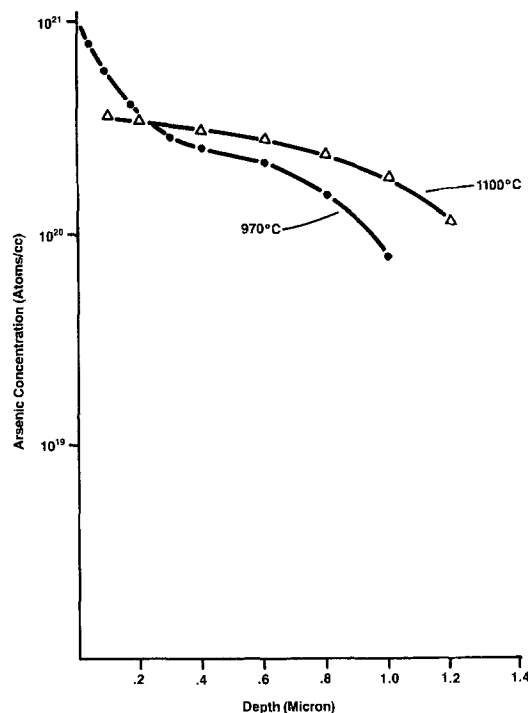


Fig. 1. Rutherford backscattering profiles of pre-epitaxy arsenic buried layers with identical capsule diffusion, but with two different oxidation-drive-in temperatures. Note arsenic pile-up at the silicon surface for the 970°C case.

choice of the oxidation-drive-in temperature which allows the rate of dopant diffusion to be large relative to the rate of oxidation. Figure 1 shows the Rutherford backscattering (RBS) profiles of arsenic buried layers prior to epitaxy from two oxidation temperatures: 970 and 1100°C. Figure 2 shows the spreading resistance profiles for these two cases, after epitaxy, taken on and off the buried layers. The epitaxial conditions were identical for the two cases: SiCl₄, 1150°C deposition temperature, 0.13 $\mu\text{m}/\text{min}$, AMC 7000 radiantly heated barrel reactor. From the RBS profiles in Fig. 1, we see that raising the oxidation temperature from 970° to 1100°C has virtually eliminated the arsenic pile-up at the substrate surface. The off-buried layer spreading resistance profiles in Fig. 2 show that this increase in oxidation temperature has also reduced the autodoping peak concentration by more than 50%. Further, increased electrical activation of the 1100°C oxidation has decreased the postepitaxial buried layer sheet resistance for the same initial predrive-in profile. VLSI circuitry built on wafers using these two subcollector oxidation temperatures showed that 1100°C temperature produced less parasitic subcollector-isolation capacitance from 970°C (21), which is consistent with the autodoping data.

Flow Effects

Since vapor phase autodoping involves a redistribution of dopant vapor emitted by the buried layer sources in the substrate, it is essential to understand the flow effects in the epitaxial reactor before a quantitative formulation of autodoping can be made. Flow effects have been studied in the past, and these include the TiO₂ smoke visual experiments (22), Raman scattering experiments (23), and mass spectrometry (24). Since the TiO₂ visual experiments, it has become customary to analyze the mass transport in the epitaxial reactor flow in terms of a stagnant boundary layer. Recently, however, there have been two independent studies (3, 13) which show that in horizontal epitaxial reactors which are operated at atmospheric pressure with H₂ as the carrier gas there is no stagnant layer formed. In the first study (3), observations of flow-induced anisotropy in the epitaxial autodoping were made using localized autodoping sources in the wafer. The second study (13) involved direct experimental

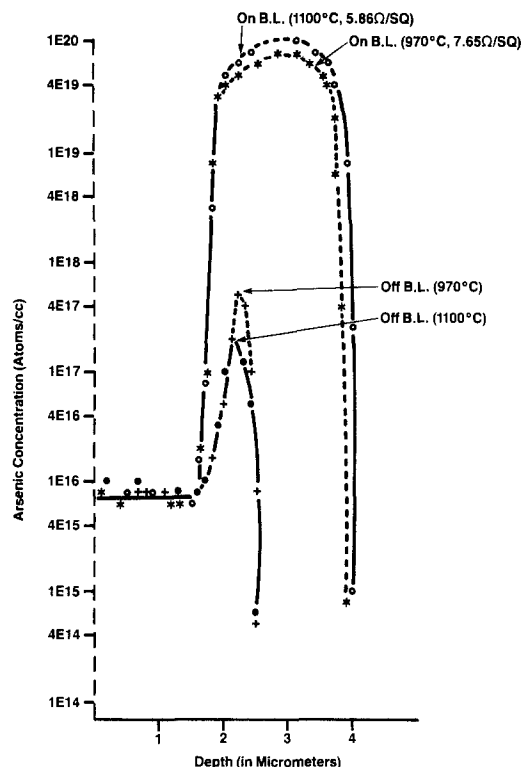


Fig. 2. Spreading resistance profiles after epitaxy from wafers used in Fig. 1. Open circles are on-buried-layer profile from 1100°C oxidation-drive-in wafer, and closed circles correspond to off-buried-layer profile from the same wafer. Stars and plus markers indicate corresponding profiles from 970°C oxidation-drive-in wafer, from a separate run.

observation of the flow using laser interference holography.

We shall first consider the autodoping studies. The ability to emit a calculable quantity of dopant vapor into the flow stream from a geometrically defined area on the substrate and to measure its redistribution in the epitaxial layers provides a powerful technique for the characterization of the reactor flow. Also, since the autodoping source is on the wafer surface, one can investigate the stagnant layer, if present, which would be in contact with the wafer. By using different sizes and shapes of the source and placing them in different directions with respect to the flow, the distribution pattern can be related to the flow dynamics through a mathematical model. Such a study was made (3) for an RF-heated, rectangular, horizontal epitaxial reactor which was air cooled. H_2 was used as a carrier gas. The autodoping sources used were arsenic-diffused buried layers of different shapes. The susceptor was inclined at an angle of 3° to the horizontal plane, and a ramp was used at the flow entrance.

The steady-state transport equation for the redistribution of the dopant vapor which is released at a constant rate into a laminar flow of carrier gas of uniform velocity V , along a direction x is given by

$$D_g \nabla^2 C_g - \frac{V \partial C_g}{\partial x} = 0 \quad [2]$$

where C_g is the dopant concentration at any point (x, y, z) in the flow. The above equation can be solved analytically in closed form for either a point source or a line source placed in a direction normal to the gas flow in the wafer plane. If the redistribution were to occur in a stagnant layer ($V = 0$), solutions to Eq. [2] are spherically symmetric for point sources and cylindrically symmetric for line sources.

For a buried layer of finite area, the solution to Eq. [2] has to be integrated over that area. The integration can be evaluated analytically for simple geometries such as a thin rectangular stripe placed in a direction normal to the

flow for which the transport equation reduces to the modified Bessel equation. The details of this procedure are given elsewhere (3). Explicit expressions were obtained for autodoping variation in the downstream and upstream directions. Figure 3 shows that variation. The dots show experimental measurements, and the solid lines are from the theory. It is evident from the data that pronounced flow-induced anisotropy exists in autodoping.

In order to rigorously test the model, anisotropy ratio R , defined as the downstream to upstream autodoping ratio, was calculated. By this procedure, all unknown quantities in the analytical expression for the stripe autodoping drop out, except for the gas diffusivity, D_g , which is calculable from the kinetic theory of gases. When the calculated values of R were tested against the experimental values for different values of x and V , reasonably good agreement was obtained for $D_g = 2.5 \text{ cm}^2/\text{s}$, which was also consistent with the value obtained by the kinetic theory estimation. Figure 4 shows this comparison. Such an agreement found between the theory and experiment provides a strong support to the model assumptions. We note from this figure that the anisotropy ratio varies from about 2 at low flow velocities to about 100 at high flow velocities. Taken together with the observation (2) that the decay length of the dopant redistribution in the reactor flow system at typical flow velocities is of the order of a few millimeters, this pronounced autodoping anisotropy rules out the existence of a stagnant layer of several millimeter thickness as commonly assumed.

We will now consider the study of epitaxial flow which used an entirely different technique, namely holography. The principle of the holography interference technique (12) is to provide two coherent laser beams to traverse the flow under two different flow conditions and to superimpose them for interference. A reference beam (see Fig. 5) provides for the phase synchronization of the two beams. By recording the beam in one condition of the flow on a hologram and using this holographic plate during a different condition of the flow, interference patterns can be generated which can be interpreted in terms of path differences in the laser beam between the two flow conditions. Since the optical path length depends on the integrated refractive index along that path, which in turn depends on the gas density and the temperature,

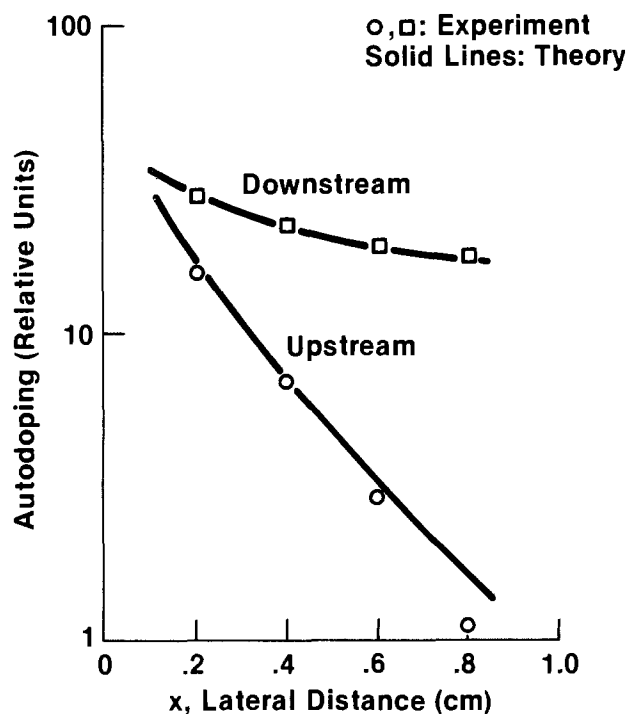


Fig. 3. Variation of autodoping peak maximum with lateral distance. (SiCl_4 , deposition temperature 1150°C, growth rate 0.13 $\mu\text{m}/\text{min}$, H_2 flow rate 15 liter/min).

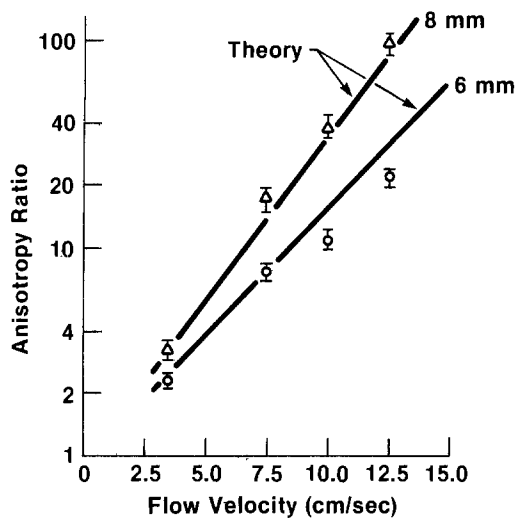


Fig. 4. Variation of the autodoping anisotropy ratio with flow velocity as measured at two distances from the stripe buried layer.

one can, in principle, obtain information on the density and/or temperature distribution in the flow along the beam path. By using an optical shutter, real-time observation of the flow development may be studied. This elegant procedure has been used to study the effect of gas velocity and carrier gas species on the flow pattern in a horizontal epitaxial reactor (13). Important observations for horizontal laminar-flow epitaxial reactors which use H_2 as the carrier gas were that when the reactor walls are kept water cooled, the flow patterns are stable and are insensitive to changes in the flow velocity. It was also found that for H_2 at typical epitaxial flow velocities there was little or no turbulence and no convection in the flow. Based on these observations, it was concluded that there is no stagnant boundary layer formed for H_2 carrier gas in a horizontal epitaxial reactor. However, the interference observations suggest a well-developed parabolic velocity profile in this case.

It is of interest to compare the results of the autodoping study with those of the holographic observations. Both studies indicate the absence of stagnant boundary-layer effect in the horizontal epitaxial reactor. Autodoping measurements show a pronounced flow-dependent anisotropy. However, the autodoping analysis assumes a constant and uniform velocity distribution in the flow, while the holography observations imply a parabolic velocity distribution. One way to reconcile this difference is to assume that the vapor transport involves some average flow velocity which can be related to the flow velocity of the input carrier gas. This velocity averaging procedure will be valid only for laminar flows.

Autodoping in VLSI Substrates and the Half-Power Law

We shall now consider the effect due to a large number of autodoping sources that one encounters in a typical

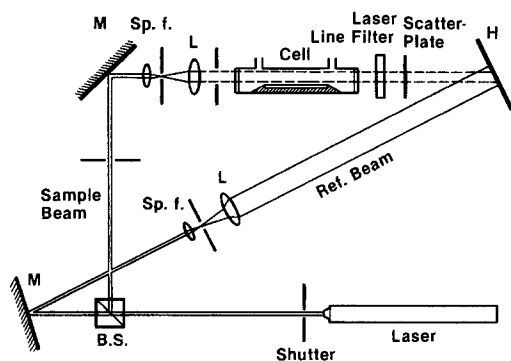


Fig. 5. Schematic diagram of a holographic system. b.s.: Beam splitter. m: Mirror. sp.f.: Spatial filter. l: Lens. h: Hologram. After Ref. (13).

VLSI substrate. For the case of buried layer sources which are so small as to be considered as point sources, the vapor transport equation (Eq. [2]) can be solved and applied to autodoping with the result (2)

$$C_A = (A/r) \exp [(-V/2D_g)(r - x)] \quad [3]$$

where C_A is the autodoping concentration due to a point source at a distance r from it in the wafer plane, A is the proportionality constant, and x is the projection of r along the flow direction. The exponential term in Eq. [3] is the anisotropy factor that modifies the radially symmetric term A/r . Figure 6 shows the autodoping distribution in the wafer plane due to Eq. [3] for $V/2D_g = 1$. For typical deposition conditions, the autodoping extends to several millimeters in the downstream direction and ~ 1 mm in the upstream direction (2).

For a VLSI substrate which contains many thousands of small buried-layer sources, the net autodoping can be calculated by summing the contribution from each of these point sources. By this procedure, it was shown (2) that the net autodoping increases approximately as the square root of the total number n of the point sources on the substrate. The study also showed that the near-half-power law was valid only for the high density arrays of discrete sources separated by distances of less than $10 \mu\text{m}$. For larger separations, the calculation showed a saturation effect, which indicates that the field overlap from these sources is incomplete. The theory also predicted that when $n > 500$ the autodoping variation in the wafer would fall below 5%, thus assuring a uniform autodoping for typical VLSI substrates.

Experimental verification of the half-power law became available subsequently for VLSI wafers which were used for epitaxial deposition in a barrel epitaxial reactor (4). More recently (11), more autodoping data have been published for the deposition in a barrel reactor. These data also confirm the half-power law (see Fig. 7). However, in this latest study, buried layers of large area were used instead of the small ones that are typical of a VLSI pattern. One can intuitively expect the half-power law to be applicable for this case also, although no specific derivation was available. It was speculated that such a power law might be the consequence of the boundary layer in the flow (11). In the treatment that follows, we will present a quantitative formulation of this problem and derive the half-power law for extended sources. We will also show that the half-power law is the limiting law for discrete point sources which are so close to each other as to form a continuum.

Let us consider an extended buried-layer source in the shape of a circle, chosen for symmetry reasons (see Fig. 8). The shape will not really matter, except to simplify the mathematics. The extended source can be considered as a continuous distribution of the point sources, so that the discrete summation of the contribution from each point can be replaced by an integral. For a point source, the so-

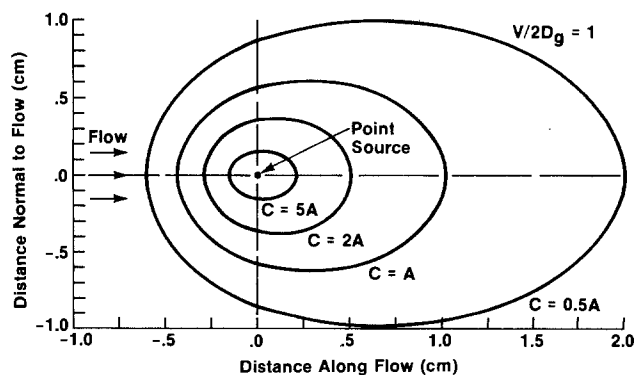


Fig. 6. Impurity distribution due to a point autodoping source in a moving stream of gas of uniform velocity V . Dopant vapor diffusivity in the stream is denoted by D_g , and A is a measure of concentration level.

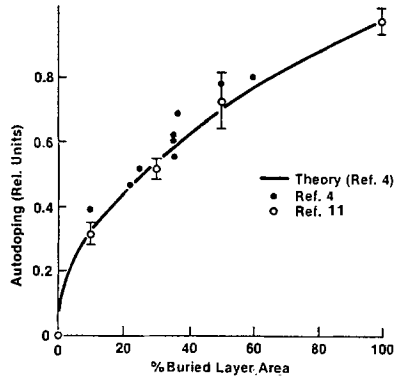


Fig. 7. Autodoping variation with buried layer area [after Ref. (11)].

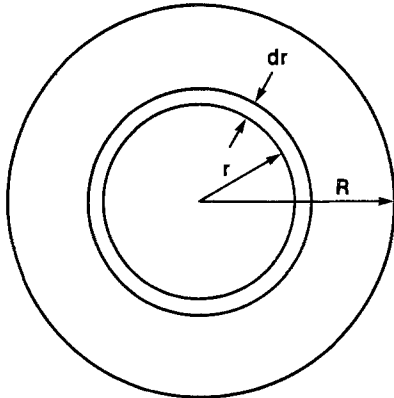


Fig. 8. A circular autodoping source in which an elemental ring of radius r and width dr is shown.

lution is given by Eq. [3], which includes the asymmetry factor contained in the exponential term. When the point sources merge as to form a continuous distribution, the asymmetry for each point disappears due to extensive field overlap from neighboring points, and the solution reduces to

$$C_A = \frac{A}{r} \tag{4}$$

where C_A is evaluated inside the extended source. For evaluations outside the extended source for which asymmetry remains, procedures as described in an earlier work (3) have to be used to sum the contributions from each point within the extended source.

The continuum effect also reduces the transport equation (Eq. [2]) to a Laplace's equation. It is clear that solution given in Eq. [4] satisfies the boundary conditions

$$C_A = 0 \text{ as } r \rightarrow \infty$$

and

$$-\left[4\pi r^2 D_g \frac{dC_A}{dr}\right]_{r=0} = Q (= 4\pi A D_g)$$

where Q is the steady-state evaporation rate used in deriving Eq. [3].

In order to calculate the total contribution of the continuous distribution of point sources in a circle of radius R , we define an elemental ring of width dr at a distance r from the center (see Fig. 8). The contribution from the sources in this elemental ring as evaluated at the center of the circle is given by

$$dC_A = \frac{A}{r} (2\pi r dr)$$

where $2\pi r dr$ is the area of the ring. The total contribution due to all sources contained in the circular area is then

$$C_T = \int_0^R dC_A = 2\pi AR$$

Relating R to the total area a of the extended source, one obtains

$$C_T = ka^{1/2} \tag{5}$$

where $k = 2\sqrt{\pi} A$. Thus, the total autodoping over the buried layer is proportional to the square root of the area of the buried layer.

Since the above equation was derived from integrating the point source solution, it represents a limiting case of the summation of the discrete point sources when the number density approaches infinity for the continuous distribution.

Before concluding this discussion, it is useful to point out that the original theory of discrete point sources showed a significant departure from the half-power law for interpoint source distances of $10 \mu\text{m}$ or larger. Clearly, for this case, the field overlap from point sources is only partial, and one would expect a saturation effect. This was indeed the prediction from the theory. Such a saturation effect manifests itself when one considers the net effect of several wafers in a single epitaxial run. This loading effect has also been observed for depositions in the barrel reactor (25).

Transistor Profiles

In high performance bipolar transistors, it is desirable to have sharp dopant profiles to reduce the diffusion and parasitic capacitances and the charge storage. The epitaxial process controls only the subcollector (and/or subisolation) buried layer profiles. Figure 9 shows a typical high performance bipolar transistor profile. The subcollector profile can be described by the parameters X_{OD} and X_{AT} . X_{OD} refers to the extent of the dopant outdiffusion in the solid silicon during growth, and it depends on the growth temperature and time and surface concentration in the buried layer prior to growth. X_{AT} is the thickness of the so-called autodoping tail which results from vapor phase autodoping. The shape of this tail depends on the flow and process parameters. Considerable attention is paid to control this autodoping tail, since it determines the minimum epitaxial thickness necessary to form a transistor of given junction depths. It should be pointed out that both the lateral autodoping and the vertical autodoping tail are the consequence of the same vapor phase autodoping phenomenon. In fact, it has been shown (1) that the off-buried-layer autodoping peak and the autodoping tail over the buried layer almost exactly superimpose in the upper layers of the epitaxy. Thus, the same factors that control lateral autodoping control also the autodoping tail in the vertical profile. This point is often not appreciated in literature. Thus, the same measures one takes to reduce lateral autodoping also reduce the vertical autodoping, leading to a reduction of the autodoping tail and a sharpening of the buried-layer profile.

Recently (26), it has been possible to model both the lateral and vertical autodoping profiles using a dopant trapping concept. The salient features of this and other epitaxial profile models are reviewed elsewhere (27).

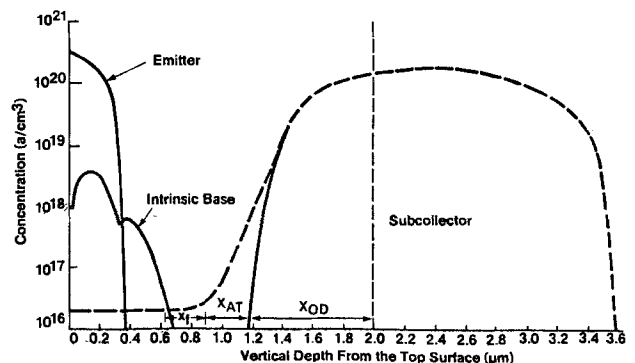


Fig. 9. Vertical profiles from a high performance bipolar device

Progress has also been made (28) to link the "on" and "off" buried layer profiles through a common adsorption layer.

From a device point of view, the factor that is equally important to the reduction of the autodoping tail is the control of its variation. The following discussion makes this clear. The collector/base (C/B) junction determines the breakdown voltage and the junction capacitance. Since most of the depletion occurs in the autodoping tail region, the extent of this tail determines the depletion layer capacitance. Experimental data from high performance NPN bipolar devices (15) show that this capacitance varies as the square root of the C/B junction concentration in accordance with the abrupt junction theory. Thus, depending on where the C/B junction intersects the autodoping tail the performance of the device varies. To avoid this, the C/B junction is always designed to occur in the flatly doped portion of the epitaxial layer, above the autodoping tail, in order to assure a constant and process-independent C/B junction concentration. This concentration is then determined by the intentional doping level and not by autodoping. However, in order to accommodate the variations in the buried-layer profile which is caused by process variations, a certain minimum thickness X_r (see Fig. 9) of the flatly doped epitaxy is maintained between the subcollector profile and the C/B junction. At high current densities of the order of the maximum drift current density J_c ($J_c = qC_0V_s$, where C_0 is the epitaxial flat doping level and V_s is the saturation velocity of the carriers), base stretching is expected to occur (17). Base stretching essentially widens the intrinsic base, which, in turn, increases the base transit time, and hence increases the device delay. Since the stretching stops at the rapidly rising subcollector profile, it is limited by the thickness X_r . It is therefore desirable to minimize X_r while, at the same time, allowing for the profile variations.

One of the ways to reduce the subcollector variations, and hence X_r , is to reduce the epitaxial growth temperature. At lower growth temperature, the variation in the subcollector outdiffusion profile is expected to be less than that at higher growth temperatures, for a given temperature nonuniformity that exists across the wafer, from wafer to wafer and from run to run. The effect of this variation was calculated (15) for two growth temperatures, 1150° and 1050°C, and for a total temperature nonuniformity of $\pm 10^\circ\text{C}$. The calculations showed that the total tolerance in the epi flat region can be reduced by a factor of 3 by reducing the epitaxial growth temperature from 1150° to 1050°C. Considerable improvement in the transistor speed due to such a reduction in X_r is to be expected on the basis of the limitation to base stretching (17).

The lateral autodoping effects also contribute to the collector isolation capacitance. A detailed analysis of this effect has been carried out for both N- and P-type autodoping in high performance NPN bipolar structures that use combined oxide and diffused isolation (14, 16). The P autodoping modifies the isolation-epitaxy junction, whereas the N-type autodoping shifts the isolation-epitaxy junction toward the P⁺ isolation. These calculations show that the junction capacitance can increase by over 60% due to both types of autodoping in a typical VLSI bipolar application.

The above examples show clearly that autodoping effect should be included as a design constraint in high performance bipolar devices. Also, since autodoping increases in proportion to the square root of the device density, it becomes even more important to take autodoping into account for very large scale integration. One of the effective ways to reduce autodoping is by reduced pressure epitaxy. This works well for N dopants such as arsenic. However, for boron, the reduced pressure is found to increase autodoping (29). Thus, for producing high resistivity P epitaxial films over P⁺ substrates for MOS transistor applications, alternate ways of reducing autodoping need to be used. These include extended prebake (temperature and/or time as indicated by Eq. [1]),

lower growth rates (1), and cap-and-flush techniques. In addition, in order to reduce the buried-layer vertical profile variations, it is desirable to reduce the epitaxial deposition temperature. However, at lower deposition temperatures, the vapor phase autodoping increases (18). The autodoping increase can be minimized by including a high temperature prebake at 1150°C in H₂ prior to the deposition at a lower temperature (15, 19, 27, 30, 31). This high-low epitaxial process has the additional advantage of reducing the epitaxial growth defects by over an order of magnitude compared to that without the 1150°C prebake (14, 15, 27, 30). The defect reduction due to the 1150°C prebake in H₂ was first discovered using the SiCl₄ deposition (30) and it has recently been reconfirmed in a separate study (32). For transistor structures with predominantly N⁺ buried layers, a combination of high-low epitaxial process and reduced pressure epitaxial process offers the advantages of both (33).

Manuscript submitted June 8, 1984; revised manuscript received Feb. 15, 1985. This was Paper 207 presented at the Cincinnati, Ohio, Meeting of the Society, May 6-11, 1984.

IBM Corporation assisted in meeting the publication costs of this article.

REFERENCES

1. G. R. Srinivasan, in "Chemical Vapor Deposition," T. O. Sedgwick and H. Lydtin, Editors, p. 77, The Electrochemical Society Softbound Proceedings Series, Princeton, NJ (1977); *This Journal*, **127**, 1334 (1980).
2. G. R. Srinivasan, *IEEE Trans. Electron Devices*, **ed-27**, 1493 (1980); *IEEE J. Solid State Circuits*, **sc-15**, 558 (1980).
3. G. R. Srinivasan, *J. Appl. Phys.*, **51**, 4824 (1980).
4. G. R. Srinivasan, *This Journal*, **127**, 2305 (1980).
5. K. F. Jensen, in "Chemical Vapor Deposition," McD. Robinson, C. H. J. van den Brekel, G. W. Cullen, J. M. Blocher, Jr., and P. Rai-Choudhury, Editors, p. 3, The Electrochemical Society Softbound Proceedings Series, Pennington, NJ (1984).
6. J. C. Gillis, M. L. Hammond, and C. L. Ramiller, in "Chemical Vapor Deposition," McD. Robinson, C. H. J. van den Brekel, G. W. Cullen, J. M. Blocher, Jr., and P. Rai-Choudhury, Editors, p. 21, The Electrochemical Society Softbound Proceedings Series, Pennington, NJ (1984).
7. M. E. Coltrin, R. J. Kee, and J. A. Miller, in "Chemical Vapor Deposition," McD. Robinson, C. H. J. van den Brekel, G. W. Cullen, J. M. Blocher, Jr., and P. Rai-Choudhury, Editors, p. 31, The Electrochemical Society Softbound Proceedings Series, Pennington, NJ (1984).
8. F. Rosenberger, 6th Intl. Conf. Vapor Growth and Epitaxy (1984).
9. K. Chen, *ibid.* (1984).
10. L. J. Giling, *ibid.* (1984).
11. G. K. Acherman and E. Ebert, *This Journal*, **130**, 1911 (1983).
12. L. J. Giling, in "Chemical Vapor Deposition," J. M. Blocher, Jr., G. E. Vuillara, and G. Wahl, Editors, p. 199, The Electrochemical Society Softbound Proceedings Series, Princeton, NJ (1981).
13. L. J. Giling, *This Journal*, **129**, 634 (1982).
14. G. R. Srinivasan, *Solid State Technol.*, **24**, 101 (1981).
15. G. R. Srinivasan, in "Silicon Processing," D. C. Gupta, Editor, p. 151, ASTM STP 804, ASTM, Philadelphia, PA (1983).
16. F. Y. Chang, in "VLSI Science and Technology," C. J. Dell'Oca and W. M. Bullis, Editors, p. 267, The Electrochemical Society Softbound Proceedings Series, Pennington, NJ (1982).
17. D. D. Tang, K. P. Macwilliams, and P. M. Solomon, *IEEE Trans. Electron Devices*, To be published.
18. G. R. Srinivasan, *This Journal*, **125**, 146 (1978); in "Semiconductor Silicon," H. R. Huff and E. Sirtl, Editors, p. 218, The Electrochemical Society Softbound Proceedings Series, Princeton, NJ (1977).
19. V. J. Silvestri, G. R. Srinivasan, and B. Ginsberg, *This Journal*, **131**, 877 (1984); in "Defects in Silicon," W. M. Bullis and L. C. Kimerling, Editors, p. 539, The Electrochemical Society Softbound Proceedings Series, Pennington, NJ (1983).
20. H. R. Chang, Abstract 342, p. 548, The Electrochemical Society Extended Abstracts, Vol. 83-2, Wash-

- ington, DC, Oct. 9-14, 1983.
21. G. R. Srinivasan, *IBM Tech. Disclos. Bull.*, **23**, 999 (1980).
 22. F. C. Eversteyn, P. J. W. Severin, C. H. J. van den Brekel, and H. L. Peck, *This Journal*, **117**, 925 (1970).
 23. T. O. Sedgwick, J. E. Smith, Jr., R. Ghez, and M. E. Cowher, *J. Cryst. Growth*, **31**, 264 (1975).
 24. V. S. Ban, *This Journal*, **125**, 317 (1978).
 25. G. R. Srinivasan and J. E. Basso, *ibid.*, To be published.
 26. M. Wong, R. Reif, and G. R. Srinivasan, in "Proceedings of the International Conference of Simulation of Semiconductor Devices and Processes," K. Board and D. R. J. Owen, Editors, p. 505, Pineridge Press, Swansea, Wales (1984).
 27. G. R. Srinivasan, *J. Cryst. Growth* (1984).
 28. P. C. Murley and G. R. Srinivasan, To be published.
 29. S. B. Kulkarni and A. A. Koziel, Abstract 540, p. 1351, The Electrochemical Society Extended Abstracts, Vol. 80-2, Hollywood, FL, Oct. 5-10, 1980.
 30. G. R. Srinivasan, U.S. Pat. 4,153,486 (1979).
 31. S. F. Chu, G. R. Srinivasan, H. Bhatia, B. M. Kemlage, F. Barson, J. Mauer, and J. Riseman, in "VLSI Science and Technology," C. J. Dell'Oca and W. M. Bullis, Editors, p. 306, The Electrochemical Society Softbound Proceedings Series, Pennington, NJ (1982).
 32. H. R. Chang, in "Defects in Silicon," W. M. Bullis and L. C. Kimerling, Editors, p. 549, The Electrochemical Society Softbound Proceedings Series, Pennington, NJ (1983).
 33. G. R. Srinivasan, *IBM Tech. Disclos. Bull.*, **26**, (7A), 3168 (1983).

Fabrication and Characterization of Epitaxial Heavily Phosphorus-Doped Silicon

Jesús A. del Alamo* and Richard M. Swanson**

Stanford Electronics Laboratories, Stanford University, Stanford, California 94305

ABSTRACT

Phosphorus-doped silicon layers have been grown by epitaxy in a PH_3/SiH_4 system. Doping levels from 2.5×10^{17} to $1.6 \times 10^{20} \text{ cm}^{-3}$ have been obtained. A combination of measurements of electrical resistivity, Hall mobility, and phosphorus concentration by secondary ion mass spectroscopy has yielded accurate values for the electron mobility and the Hall scattering factor. At the lowest doping levels, the phosphorus concentration is proportional to the partial pressure of phosphine in the reactor, while in the high doping regime the dependence is $\sim (p_{\text{PH}_3})^{1/4}$. The growth rate drops by about 20% at the highest doping levels. The defect densities increase quadratically with phosphorus concentration and reach a value of 3000 cm^{-2} at $N_D = 10^{20} \text{ cm}^{-3}$.

The reduction of lateral and vertical dimensions in very large scale integration (VLSI) semiconductor devices requires the doping levels inside the devices to rise so as to provide thin low resistivity layers confined between tightly controlled depletion regions. This trend places increased importance on the accurate characterization of heavily doped silicon.

Material problems have hindered a systematic characterization of heavily doped silicon. Heavy doping studies using diffused or implanted layers suffer from uncertainties caused by their nonuniform doping profiles, while heavily doped as-grown wafers are scarce and inconvenient from a test device point of view. Epitaxially grown heavily doped silicon is a good candidate for carrying out this fundamental study. Epitaxy is a well-known process that produces flat and abrupt impurity profiles, without limitations on layer thickness, and is technologically simple. The doping level, the variable of most interest here, is easy to control.

Epitaxial heavily doped silicon may also be of interest for the fabrication of the base region of VLSI bipolar transistors, if grown under low pressure, low temperature conditions. Its use has already been reported in the fabrication of hyperabrupt IMPATT Si diodes (1).

This paper reports our experience in the growth and characterization of heavily phosphorus doped epitaxial layers. We have reached doping levels of $1.6 \times 10^{20} \text{ cm}^{-3}$, which, to our knowledge, is the highest ever obtained by this technique. In the characterization process, we have measured Hall mobilities and carried out SIMS measurements of the total phosphorus concentration. The outcome of this characterization procedure indicates that the epitaxial material is essentially identical to P-diffused or -implanted Si. We have also measured the Hall scattering factor (2) throughout three orders of magnitude of doping. This parameter establishes the relationship between the conductivity mobility and the Hall mobility.

This paper extends an earlier account of our work (3) and includes new research on the growth and characterization of epitaxial phosphorus-doped silicon.

Experimental Work

All the depositions were carried out in a horizontal, RF-heated epitaxial reactor (Hugle Model HIER II) operating at atmospheric pressure. The quartz reactor tube has an effective cross section of 27 cm^2 above the susceptor. The silicon carbide-coated graphite susceptor is 22.8 cm long and it is tilted at an angle of 2° . This reactor is the same used previously on a fundamental study of silicon epitaxy (4).

Hydrogen was used as carrier gas at a flux of 79 liter/min . Silane was the source of silicon at a partial pressure of 10^{-3} atm except where indicated otherwise. Phosphine was used as dopant source and delivered through a double-dilution system. With PH_3 tanks of 66 ppm, 1%, and 5% in hydrogen, partial pressures from 10^{-8} to $4 \times 10^{-3} \text{ atm}$ were reached in the reaction chamber. With a few exceptions, all depositions were done at a temperature of 1050°C during 10 min. Prior to growth, all wafers were vapor etched in $5 \times 10^{-3} \text{ atm HCl}$ and the carrier gas H_2 during 4 min at 1200°C . The temperature of the substrates was measured with an optical pyrometer calibrated accounting for the emissivity of silicon. The temperature is known within 5°C and was stable during deposition to within $\pm 2^\circ\text{C}$.

The starting material was $\langle 100 \rangle$ boron-doped 0.1-0.2 $\Omega\text{-cm}$ substrates. The 3 in. diam wafers were broken in quarters. One quarter was processed at a time. The cleaning procedure before epitaxy consisted of a standard "reversed RCA" process (5) with a final 50:1 HF dip. After epitaxy the sample was sawed in $7 \times 7 \text{ mm}^2$ die where the characterization was done.

Electrical Characterization

A typical electron profile determined by spreading resistance is shown in Fig. 1. As shown, the carrier distribu-

* Electrochemical Society Student Member.

** Electrochemical Society Active Member.

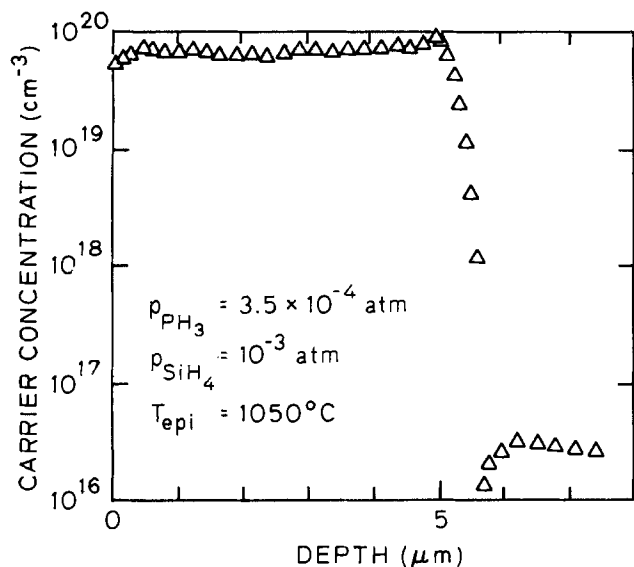


Fig. 1. Spreading resistance profile of a heavily doped epitaxial layer grown at $P_{PH_3} = 3.5 \times 10^{-4}$ atm.

tion throughout the layer is very flat, and an abrupt transition occurs at the interface with the substrate.

In all samples, the thickness of the layer was measured by the groove and stain method, using a copper sulfate solution (6), and an interferometric microscope. The relative error in the measurement is less than 3%. The difference between the electrical and metallurgical junctions, as determined by spreading resistance or staining, has been calculated by Hu (7). For our box profile, he finds a discrepancy of around 6%.

Great care was taken in the measurement of doping level. First, the sheet resistance was measured at a temperature of 23° by the van der Pauw technique (8) by contacting the four corners of the samples. The measurement was corrected to account for the roll off of the doping level near the junction as seen in Fig. 1 (9). The relative error in the sheet resistance was less than 1%. Multiplying the value of sheet resistance by the layer thickness, measured as described before, the resistivity, ρ , is obtained.

Second, the Hall coefficient, R , is measured using the same van der Pauw configuration in a magnetic field of 1.12 kG. The relative error is smaller than 4%. The Hall mobility is obtained as $\mu_H = -R/\rho$ (8). Since $R = -A/qn$, where q is the electron charge, n is the electron concentration, and A is the Hall scattering factor (10), then $-1/qR = nA$. $-1/qR$ therefore represents the electron concentration in the layer if the Hall scattering factor is equal to unity, as commonly assumed in the literature (A is determined below).

In Fig. 2, we compare our measurements of μ_H vs. $-1/qR$ in some of our epitaxial layers with others re-

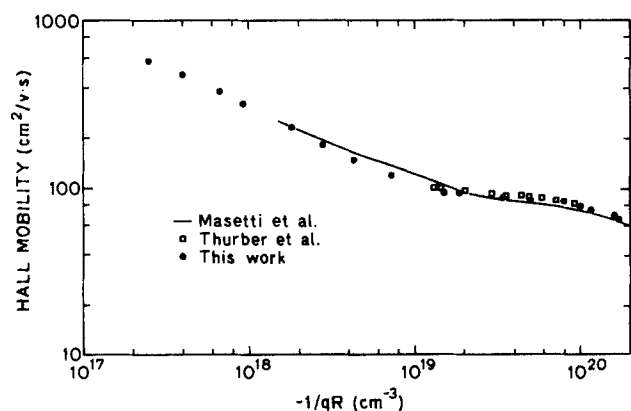


Fig. 2. Hall mobility vs. $-1/qR$ measured in this work and by other authors. There are no error bars in our data because they are smaller than the dots themselves.

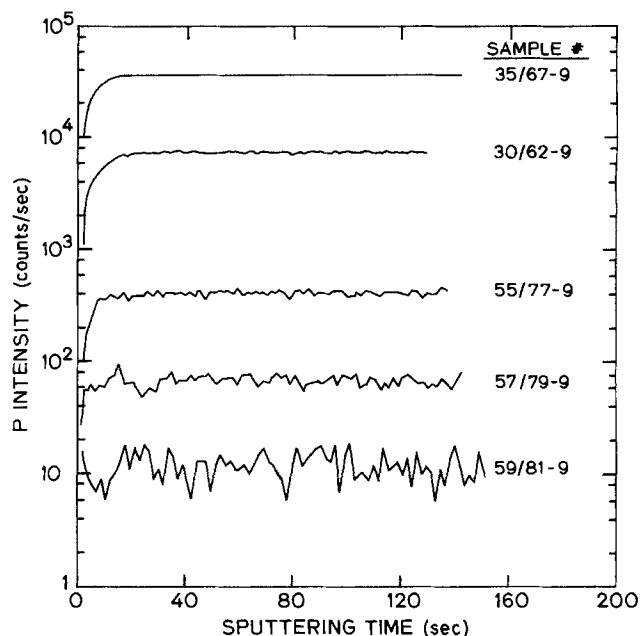


Fig. 3. Phosphorus intensity vs. sputtering time measured by SIMS in a number of samples.

ported on as-grown (11, 12), diffused (13), and ion-implanted (14) P-doped Si. [The data of Ref. (13) and (14) have been represented by a curve fit reported in Ref. (14) so as to not unnecessarily complicate the figure with their large number of data points.] The agreement among these four sets of data is of the order of our experimental error, i.e., around 4% for the mobility. This finding clearly shows that this epitaxial material displays electrical properties identical to phosphorus-doped silicon fabricated by other methods. This fact remains true even at P concentrations higher than 10^{20} cm^{-3} .

The previously described measurements were carried out in two dies of each sample. The differences in value of $-1/qR$ between dies was less than 5%, showing a very good impurity homogeneity. Some of the samples that had a difference smaller than 2% were selected for secondary ion mass spectroscopy (SIMS) measurement of the total phosphorus concentration. These are the samples shown in Fig. 2.

SIMS analysis was carried out in a CAMECA IMS-3f ion microanalyzer with a 10 keV Cs^+ ion beam at a current of 3 μA . The mass 31 ions (corresponding to phosphorus)

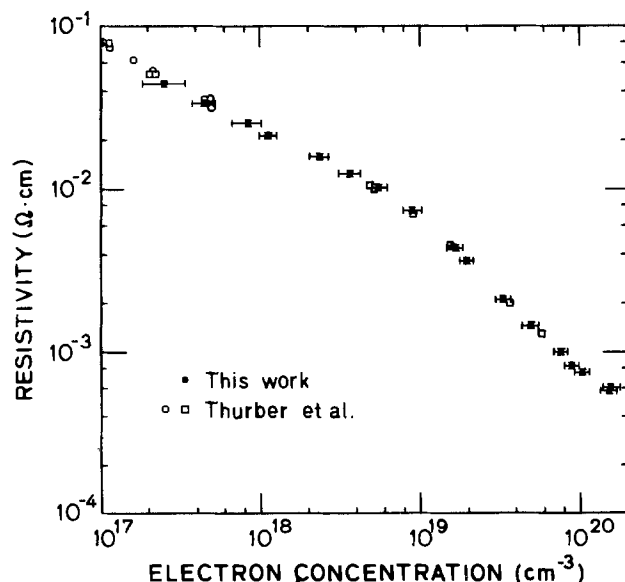


Fig. 4. Electrical resistivity vs. phosphorus concentration measured in this work and by other authors.

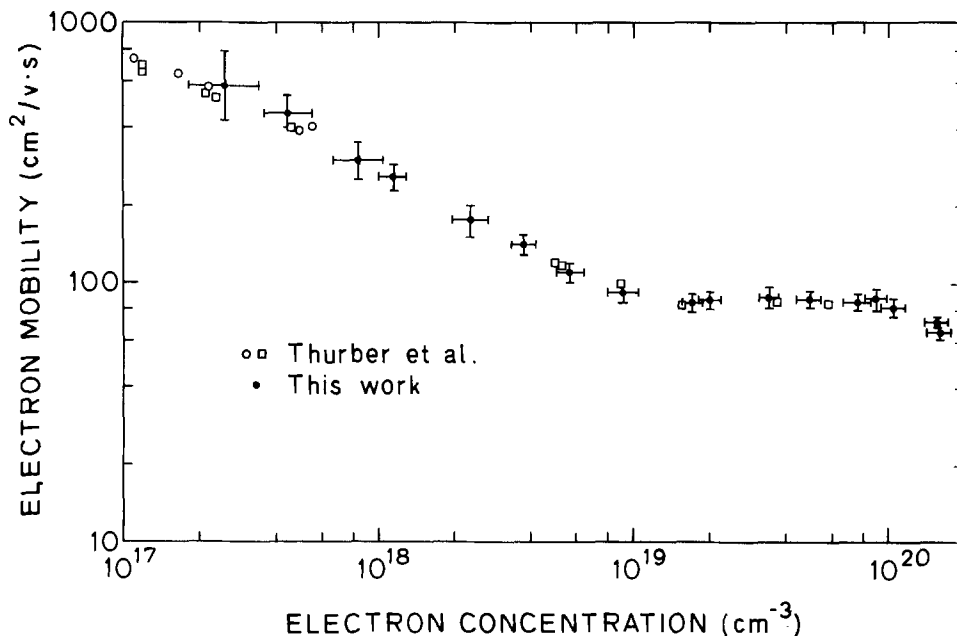


Fig. 5. Conductivity mobility vs. phosphorus concentration measured in this work and by Thurber *et al.* The open circles are data in which n has been measured by the C-V technique. For the squares, the doping level has been determined by neutron activation analysis.

were analyzed from a 30 μm diam area at the center of a crater 400 μm on the side. Some of the phosphorus intensity profiles obtained are shown in Fig. 3. The sputtering etch rate varies from sample to sample around a value of 0.25-0.3 $\mu\text{m}/\text{min}$. We are therefore looking in Fig. 3 at profiles approximately 0.5-0.8 μm deep. Figure 3, like the spreading resistance profile shown in Fig. 1, indicates that the impurity concentration is very flat next to the surface. Deeper profiling was not possible because of a calibration drift in the equipment with time. Because of this same problem, the P intensity in the same sample changed from measurement to measurement and batch to batch. However, the ratio of the P intensity to the Si intensity, the last one measured by means of a Faraday cup, was found to be constant for the same sample throughout all measurements. We assumed this ratio to be proportional to the phosphorus concentration in the layer through a constant denoted as k .

To be able to estimate the P concentration, we extract the value of k by relying on measurements of N_D made by neutron activation analysis (11, 12, 15, 16) by other authors on P-doped Si of similar resistivity values to ours. This process is described in detail in Ref. (2) and will not be repeated here. The constant k is estimated to be within 8%. Figure 4 collects the values of electrical resistivity vs. phosphorus concentration obtained by this procedure, together with those of other authors. The large error bars at low doping levels arise from the gaussian error in P counting (see Fig. 3).

From the data collected in Fig. 4, we can now obtain the conductivity mobility. It is shown in Fig. 5 vs. donor concentrations, together with other measurements from Thurber *et al.* (11, 12). The agreement is again excellent.

The ratio of Hall mobility to conductivity mobility is the Hall scattering factor. Combining Fig. 2 and 5, we can obtain this transport parameter (2), which is represented

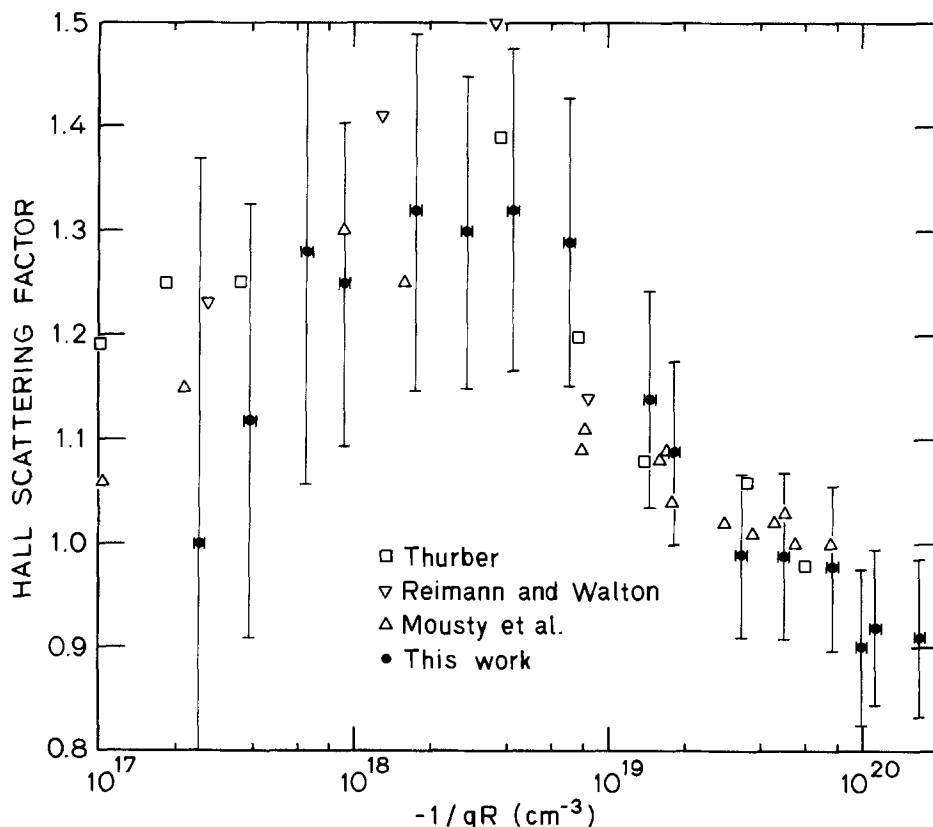


Fig. 6. Hall scattering factor vs. $-1/qR$.

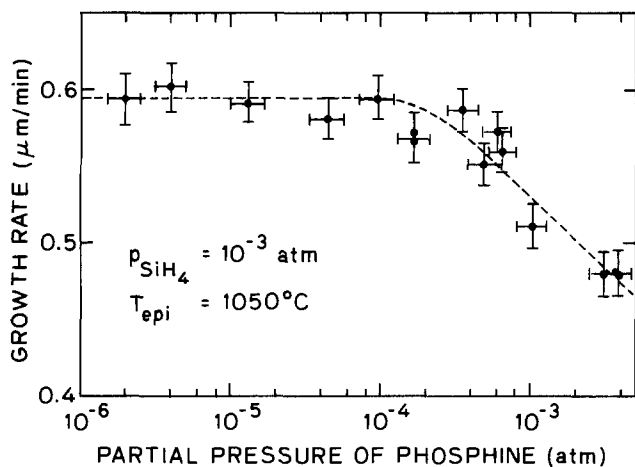


Fig. 7. Epitaxial layer growth rate vs. PH_3 partial pressure

in Fig. 6 vs. $-1/qR$, together with some previous determinations of it made in the literature (15-17). It is striking that A , usually assumed to be one, is clearly different than unity in most of the measurement range. In fact, it reaches a value of around 1.3 in the mid- 10^{18} cm^{-3} doping level and decreases to about 0.9 with $N_D > 10^{20}$ cm^{-3} . The theoretical calculations of A predict a value of 1.03 at low doping levels and 0.87 in the degenerate regime (18). These two limits are seen in our measurements that show, for the first time, that A indeed becomes smaller than unity at high doping. The determination of A carried out in this work requires the assumption of $n = N_D$, or, in other words, that all the impurities are located in substitutional position in the Si lattice, and all are ionized. These assumptions have been studied in detail in Ref. (2) and (9) and been found to be fulfilled within our experimental error. The agreement obtained at the high doping end between our measurements of A and the theoretical prediction confirms these assumptions.

Results

Figure 7 plots the growth rate vs. phosphine partial pressure. The growth rate is fairly constant up to a level of around 4×10^{-4} atm, above which it decreases abruptly. Similar results have been found by Gupta (19) in the $\text{AsH}_3/\text{SiH}_4$ and $\text{B}_2\text{H}_6/\text{SiH}_4$ systems. This phenomenon is probably related to the decay in the growth rate of the SiH_4 epitaxy at high temperatures for high SiH_4 partial pressures observed by Duchemin (20). He postulated that homogeneous nucleation occurs in the gas phase that consumes large amounts of SiH_4 , therefore reducing the SiH_4 available for growth. In our experiments, we

observed that, at the highest phosphine levels, a large amount of nucleation occurred, resulting in the deposition of a Si layer on the walls of the reactor.

Figure 8 collects the resulting phosphorus concentration in the epitaxial layer vs. the partial pressure of PH_3 in the reaction tube. A maximum doping level of 1.6×10^{20} cm^{-3} has been reached, which, to the knowledge of the authors, is the highest ever obtained by epitaxy.

For low phosphine partial pressures, the proportionality between the doping level of the growing layer and the phosphine partial pressure is linear. At a p_{PH_3} of about 10^{-6} atm, corresponding to $N_D \approx 3 \times 10^{19}$ cm^{-3} , the doping level goes as the partial pressure to the 1/4 power. A similar phenomenon has been reported by Bloem *et al.* (21, 22). He observes a transition from a linear regime into a square root regime that occurs at a doping level decreasing with increasing temperature (23). The critical point from this 1/2 regime into the 1/4 regime increases with temperature. At our 1050°C growth temperature, these critical concentrations seem to have merged into a gradual transition that almost erases the 1/2 regime.

To study these phenomena in further detail, we plot in Fig. 9 the critical concentrations vs. growth temperatures obtained by Bloem and us. We denote N_{D1} the doping level at which the 1 to 1/2 transition occurs, and N_{D2} corresponding to the 1/2 to 1/4 transition. At $T = 1500$ K, we can only assess a lower limit of N_{D2} from the experiments of Bloem.

As previously mentioned, N_{D1} decreases with the deposition temperature. This behavior is related not so much to the transition as to the linear regime itself, since at any given phosphine partial pressure the incorporation of dopant decreases as the temperature increases. In fact, this has also been observed by Reif *et al.* (24) in the $\text{AsH}_3/\text{SiH}_4$ system in this dilute regime. They observed a slope of 30 kcal/mol, while we observe from Fig. 9 a value of 38 kcal/mol for our PH_3/SiH_4 system. They explained this behavior as arising from the dominance of surface mechanisms as the doping process in their $\text{AsH}_3/\text{SiH}_4$ system (25).

What is striking about this transition from the linear to the square root regime is that, within the measurement error, it occurs at the same phosphine partial pressure throughout the almost 300°C that separates the highest deposition temperature of Bloem and ours. This value is $\sim 10^{-6}$ atm. As postulated by Swanson and Tucker (23) and Bloem *et al.* (21), this square root proportionality arises from the gas phase decomposition of the PH_3 molecule into the phosphorus monomer, P, and phosphorus dimer, P_2 . In computer calculations of the equilibrium partial pressures of all the components of the PH_3/SiH_4 mixture carried out by Bloem *et al.* (21, 22), it is found that the phosphorus dimer becomes the prevalent species

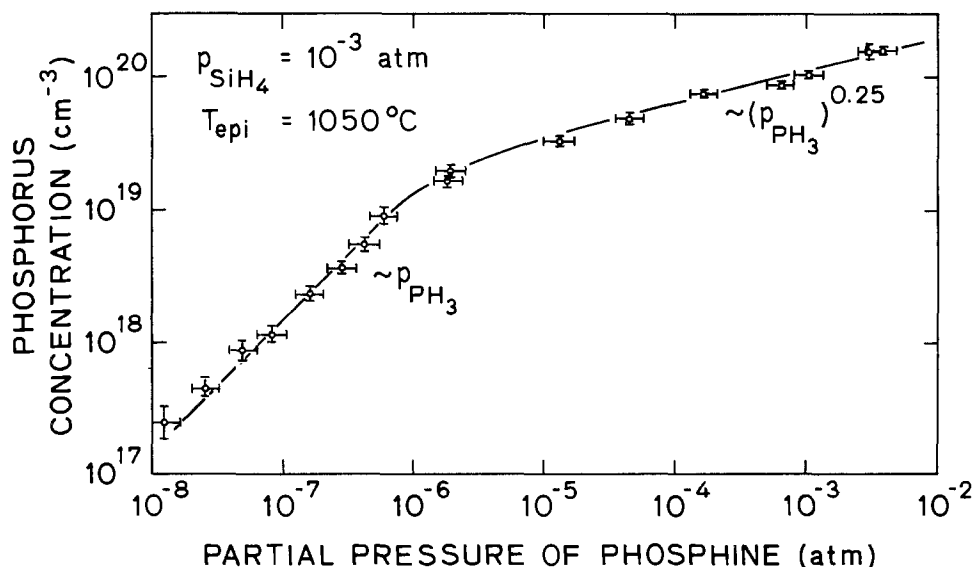


Fig. 8. Phosphorus doping level in epitaxial layer vs. phosphine partial pressure.

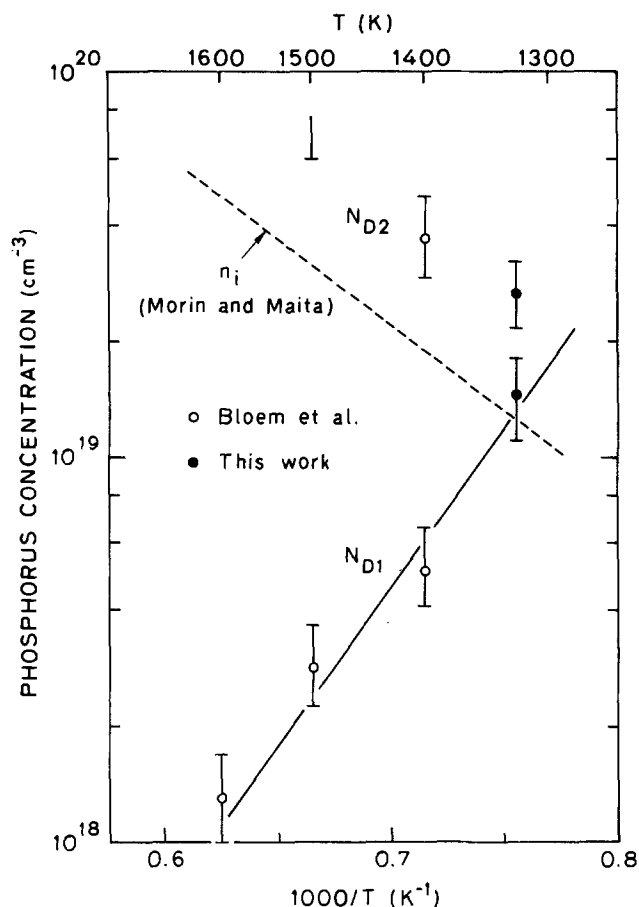


Fig. 9. Temperature dependence of the critical concentrations that separate the different regimes of the N_D vs. P_{PH_3} curve. The extrapolated values of n_i , the intrinsic carrier concentration, of Morin and Maita are also shown.

at partial pressures of phosphine of around 10^{-6} atm, this value being rather independent of temperature. The phosphorus dimer is in equilibrium with all the other species, in particular with the phosphorus monomer P which is further postulated to be the only source of dopant that becomes incorporated to the growing layer. Therefore, as the calculations of Bloem show, at around 10^{-6} atm the concentration of phosphorus monomer becomes square-root dependent on the initial phosphine partial pressure, and this behavior determines the P concentration in the epitaxial layer.

The second transition from 1/2 to 1/4 dependence of the P doping level in the growing layer vs. the phosphine partial pressure (N_{D2} in Fig. 9) has been related to the semiconductor becoming extrinsic due to the high concentration of donors (21). We have also noted in Fig. 9 the values of n_i , the intrinsic carrier concentration in silicon, given by Morin and Maita (26). The absolute values of n_i disagree systematically from N_{D2} by about a factor of two; however, the temperature dependence appears very similar. The highest temperature at which Morin and Maita carried out measurements was about 1000 K, the line plotted in Fig. 9 being an extrapolation of their fitting. It is not surprising, therefore, that the absolute values differ, while the slope is similar. An additional source of the difference can be the bandgap narrowing that arises from the high concentration of donors. This phenomenon tends to increase the value of n_i from its low doping value.

We have further studied the dopant incorporation in the epitaxial layer at high doping levels by analyzing the growth rate dependence. Figure 10 shows the resulting value of $-1/qR$ (the actual doping level is around 0.9 times this value) and growth rate vs. silane partial pressure, for a fixed phosphine partial pressure of 3.8×10^{-3} atm. The growth rate is found to be linear with the silane

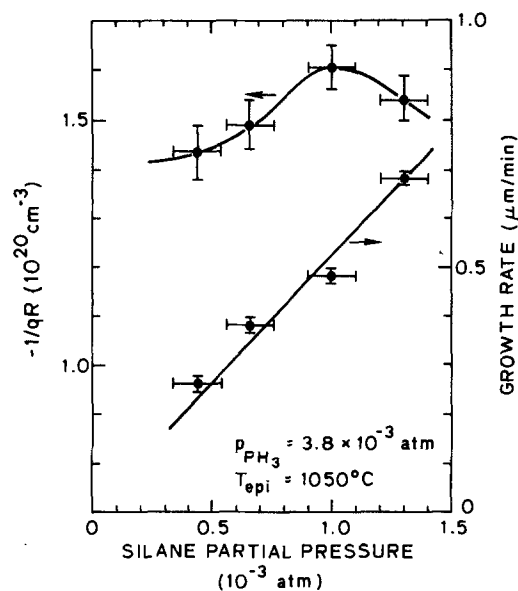


Fig. 10. Values of growth rate and $-1/qR$ (related to doping level through the Hall scattering factor) vs. silane partial pressure at a fixed phosphine level.

concentration. However, the doping level increases with silane partial pressure until it reaches a maximum beyond which it decreases again. This behavior has been observed and explained by Bloem (22, 27) at lower doping levels. For low silane partial pressures and low deposition temperatures, a trapping of phosphorus atoms at the growing interface occurs if the phosphorus diffusion coefficient is sufficiently small so as to prevent the buried atom from diffusing to the growing surface and escape from it. The phosphorus atom in the solid is not in thermodynamic equilibrium with the gas phase. As the growth rate increases and all donors reaching the surface are trapped, the concentration in the layer decreases since they become buried in a fast growing epitaxial layer. This effect is less pronounced at this very high doping regime than in the low 10^{19} cm^{-3} level at higher temperatures, as observed by Bloem, probably due to the larger phosphorus diffusion coefficient that occurs at high doping levels (28).

Finally, Fig. 11 collects the density of etch pits defined by a 5 min Secco etch and its dependence on doping.

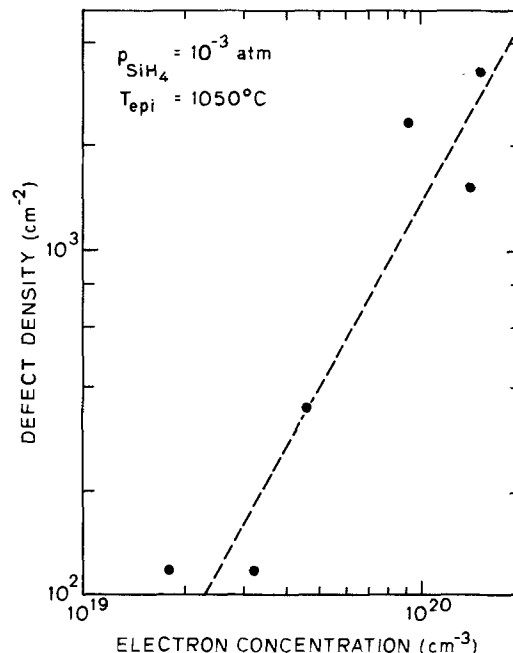


Fig. 11. Density of etch pits defined by Secco etch vs. phosphorus concentration.

There is a strong correlation between doping level and defect density, with the latter increasing roughly on the square of the doping density. The defect seems to be perfect dislocations probably due to strain-induced misfit.

The values here reported, between 100 and 3000 cm⁻² are compatible with the fabrication of the devices for the characterization of minority carrier transport in the heavily doped epitaxial layers. At the time of this writing, vertical and lateral bipolar transistors have been fabricated on these layers, and measurements of hole diffusion length, diffusion coefficient, lifetime, and bandgap narrowing are in progress.

Conclusions

Phosphorus-doped silicon layers have been grown by epitaxy in a PH₃/SiH₄ system. Doping levels as high as 1.6 × 10²⁰ cm⁻³ have been obtained. Electrical characterization of the layers has resulted in detailed measurements of electron mobilities and Hall scattering factor throughout nearly three decades of doping level. A regime in which the phosphorus concentration is proportional to the phosphine partial pressure through a power law with exponent 0.25 has been clearly observed.

Acknowledgments

The authors thank the staff of the Integrated Circuits Laboratory, where all layers were grown. We have benefited from discussions and help from Dr. John Shott, Mr. Richard Crane, Dr. Young Kwark, and Professor Krishna Saraswat. The van der Pauw measurements were carried out in Professor James Gibbons' laboratory. The work was partially funded by the Joint Services Electronics Program. One of the authors (JdA) appreciates the support of The Electrochemical Society during the Summer of 1983, through The Electrochemical Society Energy Research Summer Fellowship funded by the Department of Energy.

Manuscript received April 17, 1985. This was Paper 171 presented at the Cincinnati, Ohio, Meeting of the Society, May 6-11, 1984.

Stanford Electronics Laboratory assisted in meeting the publication costs of this article.

REFERENCES

1. M. Heitzmann and M. Boudot, *IEEE Trans. Electron Devices*, **ed-30**, 759 (1983).

2. J. del Alamo and R. M. Swanson, *J. Appl. Phys.*, **57**, 2314 (1985).
3. J. del Alamo and R. M. Swanson, in "Chemical Vapor Deposition," McD. Robinson, C. H. J. Van der Brekel, G. W. Cullen, J. M. Blocker Jr., and P. Rai-Choudhury, Editors, p. 295, The Electrochemical Society Softbound Proceedings Series, Pennington, NJ (1984).
4. R. Reif, Ph.D. thesis, Stanford University Technical Report no. 4971-1, October 1978.
5. W. Kern and D. A. Puotinen, *RCA Rev.*, **31**, 187 (1970).
6. C. P. Wu, E. C. Douglas, C. W. Mueller, and R. Williams, *This Journal*, **126**, 1982 (1979).
7. S. M. Hu, *J. Appl. Phys.*, **53**, 1499 (1982).
8. L. J. van der Pauw, *Philips Tech. Rev.*, **20**, 220 (1958/1959).
9. J. del Alamo and R. M. Swanson, *J. Appl. Phys.*, **56**, 2250 (1984). See correction in *J. Appl. Phys.*, **57**, 2346 (1985).
10. R. A. Smith, "Semiconductors," 2nd ed., Sect. 5.3.3 and 5.3.4, Cambridge University Press, Cambridge (1978).
11. W. R. Thurber, R. L. Mattis, Y. M. Liu, and J. J. Filliben, National Bureau of Standards, Special Publication 400-64, May 1981.
12. W. R. Thurber, R. L. Mattis, Y. M. Liu, and J. J. Filliben, *This Journal*, **127**, 1807 (1980).
13. G. Masetti and S. Solmi, *Solid-State Electron Devices*, **3**, 65 (1979).
14. G. Masetti, M. Severi, and S. Solmi, *IEEE Trans. Electron Devices*, **ed-30**, 764 (1983).
15. W. R. Thurber, *J. Electron. Mater.*, **9**, 551 (1980).
16. F. Mousty, P. Ostoja, and L. Passari, *J. Appl. Phys.*, **45**, 4576 (1974).
17. P. L. Reimann and A. K. Walton, *Phys. Status Solidi B*, **48**, 161 (1971).
18. J. D. Quirt and J. R. Marko, *Phys. Rev. B*, **7**, 3842 (1973).
19. D. C. Gupta, *J. Electron. Mater.*, **1**, 371 (1972).
20. J. P. Duchemin, *Rev. Tech. Thomson-CSF*, **9**, 33 (1977).
21. J. Bloem, L. J. Giling, and M. W. M. Graef, *This Journal*, **121**, 1354 (1974).
22. J. Bloem, *J. Cryst. Growth*, **31**, 256 (1975).
23. T. B. Swanson and R. N. Tucker, *This Journal*, **116**, 1271 (1969).
24. R. Reif, T. I. Kamins, and K. C. Saraswat, *ibid.*, **125**, 1860 (1978).
25. R. Reif, T. I. Kamins, and K. C. Saraswat, *ibid.*, **126**, 653 (1979).
26. F. J. Morin and J. P. Maita, *Phys. Rev.*, **96**, 28 (1954).
27. J. Bloem, *J. Cryst. Growth*, **13/14**, 302 (1972).
28. S. M. Hu, P. Fahey, and R. W. Dutton, *J. Appl. Phys.*, **54**, 6912 (1983).

The Etching Characteristics of (100) GaAs by K₂S₂O₈-H₂O System

Jiahn-Ann Chen and Si-Chen Lee

Department of Electrical Engineering, National Taiwan University, Taipei, Taiwan, China

Tong-Ing Ho

Department of Chemistry, National Taiwan University, Taipei, Taiwan, China

ABSTRACT

A new etching solution, aqueous potassium peroxodisulfate, was developed for etching GaAs. The peroxodisulfate ion is a powerful oxidizing reagent which can extract two electrons and oxidize the GaAs surface. Because this solution is acidic with pH value of 2, it can dissolve the oxidized product. The most significant feature of the solution is that its etching rate is extremely slow, i.e., 150 Å/min, and can be further reduced by adding NaOH to the solution. It is found that adding HCl does not enhance the etching rate but does significantly improve the morphology of the etched surface.

Chemical etching of semiconductors plays an essential role in electron device technology and is, therefore, widely employed in the fabrication of many useful devices, e.g., n-type GaAs Schottky-barrier field-effect transistors (MESFET's) (1). Most power and low noise analog FET's use a recessed gate geometry in which the gate

stripe is placed in an etched slot to locate it slightly below the semiconductor surface (2). The depth, typically 800-2500 Å, to which the gate is recessed is a critical parameter in FET performance. In the past, this etching was almost always done by wet etching using a chemical solution that is composed of an oxidant (H₂O₂) and an acid or

base solvent (3). The strength of the etchant should be adjusted by dilution to provide an adequate etching rate that is sufficiently slow to allow good control over the recess process. Usually, the dilution is so great that reproducibility is a problem. In this paper, we propose a new solution, $K_2S_2O_8 + H_2O$ for etching GaAs that solves the problem.

Experimental

The samples we studied include (i) Si-doped (100) GaAs with carrier concentration in the range of 10^{18} cm^{-3} and (ii) Cr-doped semi-insulating GaAs crystals. In order to measure the etching profile and etching depth, the GaAs surface was first covered with photoresist, and then a $10 \mu\text{m}$ (or $25 \mu\text{m}$) wide stripe window was opened by standard photolithography techniques. The stripes were visually aligned with respect to the (011) or (0 $\bar{1}$ 1) cleavage planes of the sample. The $\langle 01\bar{1} \rangle$ and $\langle 011 \rangle$ directions in the (100) plane were determined by etching a striped test sample along the natural cleavage plane to see whether the channel is V or U shaped (4).

The etching solution was prepared by dissolving 2.7 or 1.4g $K_2S_2O_8$ powder in 50 cm^3 deionized water. Since the solubility of $K_2S_2O_8$ in 50 cm^3 water is 0.875 g at 0°C and 2.65 g at 20°C (5), the prepared etching solution is already saturated for 2.7g case or undersaturated for 1.4g case. Sometimes, acid (HCl) or base (NaOH) was added to the prepared potassium peroxodisulfate aqueous solution to study its effect on etching rate. The temperature of the etching solution was varied between 9° and 70°C to study the activation energy of the etching process. After etching, the photoresist mask was removed and the sample was rinsed in deionized water. Then, the etching depth and etching profiles were measured along the (011) and (0 $\bar{1}$ 1) planes using either an optical microscope or scanning electron microscope (SEM).

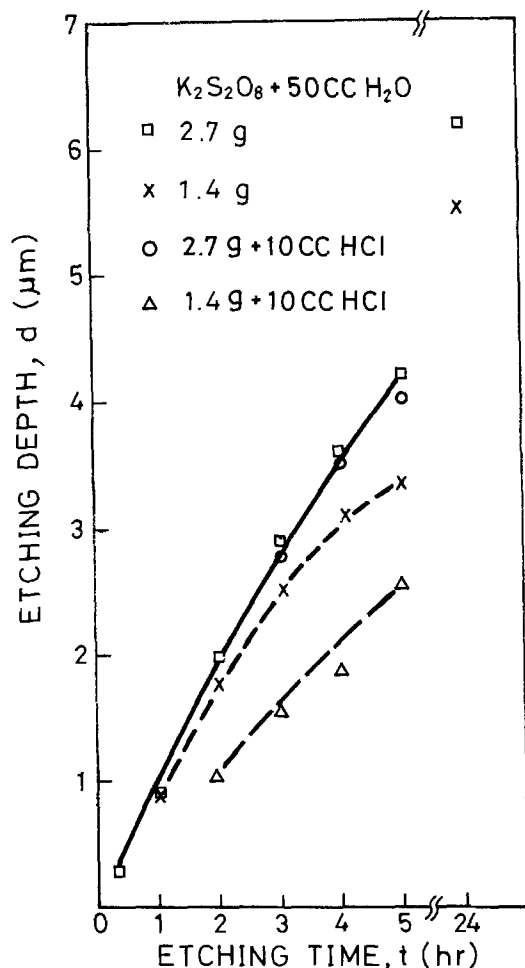


Fig. 1. Etching depth as a function of the etching time. Temperature is 20°C .

Results

Figure 1 shows the etching depth as a function of the etching time using four different solutions, i.e., 2.7 and 1.4g of $K_2S_2O_8$ in 50 cm^3 water and 50 cm^3 water + 10 cm^3 HCl, respectively. It is seen that initially the etching rate at room temperature is constant and extremely slow, i.e., $150 \text{ \AA}/\text{min}$, and then gradually the etching rate slows down even further. It is also clear that the etching rate of the 2.7g $K_2S_2O_8 + 50 \text{ cm}^3 H_2O$ (2.7g KH) is almost the same as that of 2.7g $K_2S_2O_8 + 50 \text{ cm}^3 H_2O + 10 \text{ cm}^3 HCl$ (2.7g KHH) solution, but is faster than those of the 1.4g $K_2S_2O_8 + 50 \text{ cm}^3 H_2O$ (1.4g KH) and 1.4g $K_2S_2O_8 + 50 \text{ cm}^3 H_2O + 10 \text{ cm}^3 HCl$ (1.4g KHH) solutions. To etch 800-2500 \AA depth of GaAs using this saturated solution, it takes as long as 5-16 min and, therefore, is very easy to control. The etching depth of the 1.4g KH solution is initially the same as that of the saturated one, but gradually it falls behind. The reason for this is that the 2.7g KH solution is oversaturated and has $K_2S_2O_8$ solid remaining in the solution. The $S_2O_8^{2-}$ ion grabs two electrons and decomposes into two SO_4^{2-} ions; the solid $K_2S_2O_8$ which remains in the solution will then dissolve to supply the $S_2O_8^{2-}$ ions. Therefore, the concentration of peroxodisulfate ion is always constant during the etching process. However, the concentration of peroxodisulfate ion in 1.4g KH solution (undersaturated) decreases gradually during the etching process which results in a slower etching rate after a long etching time.

Figure 2 shows the etching depth as a function of temperature for a period of 60 min. The activation energies were determined to be 10 kcal/mol for 2.7g KH and 2.7g KHH, 8.7 kcal/mol for the 1.4g KH, and 5.5 kcal/mol for the 1.4g KHH solutions.

It is well known that the dissolution process of a solid surface is either reaction-rate limited or diffusion limited. If the former process is the rate-limiting one, the etched depth d will depend linearly on etching time t , i.e., $d \propto t$, however, if the latter process is the dominant one, d is related to t through $d \propto t^{0.5}$ (6). Usually, the diffusion-limited process has lower activation energy than that of the reaction-rate-limited process, for example, Iida and Ito (7) have studied the etching characteristics of (001) GaAs in

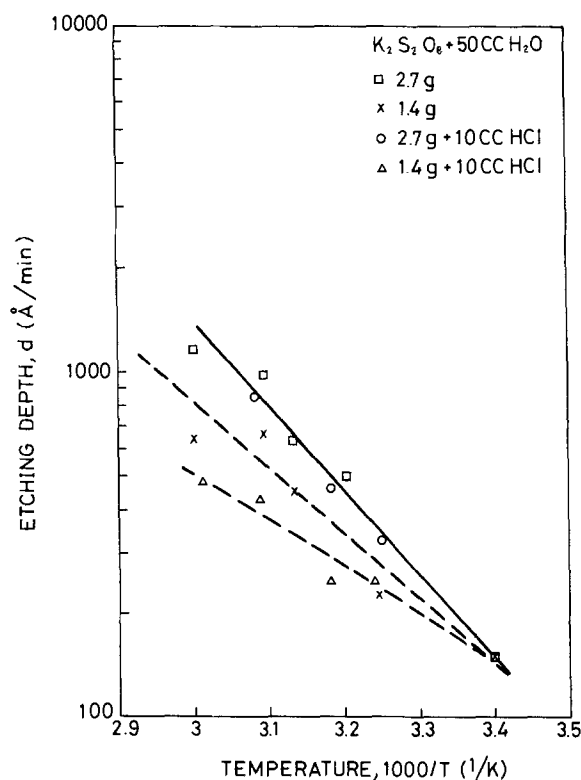


Fig. 2. Etching depth as a function of temperature for a period of 60 min.

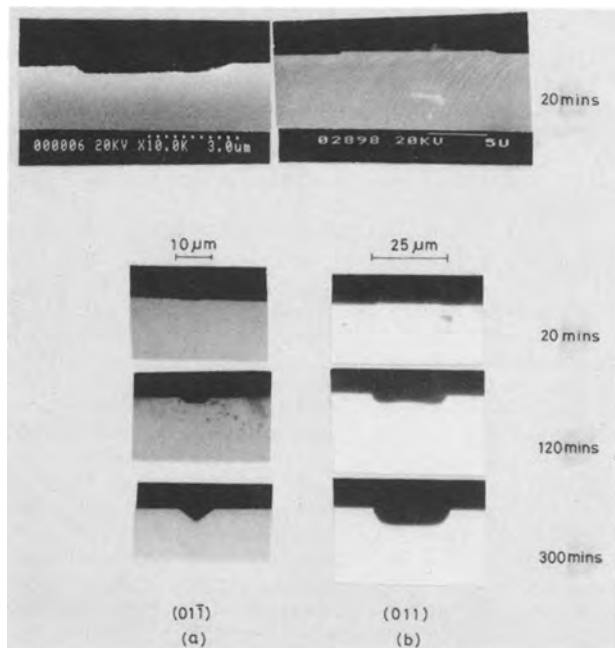


Fig. 3. The etching shape and etching depth for different etching solutions at room temperature. a: 2.7g $K_2S_2O_8 + 50 \text{ cm}^3 \text{ H}_2\text{O}$. b: 2.7g $K_2S_2O_8 + 50 \text{ cm}^3 \text{ H}_2\text{O} + 10 \text{ cm}^3 \text{ HCl}$.

the $\text{H}_2\text{SO}_4\text{:H}_2\text{O}_2\text{:H}_2\text{O}$ system and obtained activation energies of 6-8 kcal/mol for the diffusion-limited process and 8-11 kcal/mol for the reaction-rate-limited process. Since the etching depth depends linearly on time initially, as shown in Fig. 1, the etching process in these etching solutions is probably controlled by a reaction-rate-limited process at least in the initial few hours. Another way to distinguish which process dominates is to measure the etching rate while stirring. The diffusion-limited process shows a notable stirring effect on the etching rate, while the reaction-rate-limited process does not unless the solution is supersaturated. In 1.4g KHH and 1.4g KH solutions, the etching depths for a period of 60 min are 1.0 μm both with and without stirring, which indicates that the reaction-rate-limited process indeed dominates. In 2.7g KHH and 2.7g KH solutions, however, the etching depth for a period of 60 min is 1.4 μm with stirring and 1.1 μm without stirring, which we believe is not because the diffusion-rate-limited process dominates, but because the solution dissolves more $K_2S_2O_8$ under stirring conditions which enhances the reaction rate.

Figure 3 shows the etching time effect on GaAs along $\langle 011 \rangle$ and $\langle 0\bar{1}\bar{1} \rangle$ directions using 2.7g KH and 2.7g KHH etching solutions, respectively. The etching depth for a period of 20 min is the same, *i.e.*, 3000Å, for either etching solution. The etching profiles using 2.7g KH solution with different etching times are shown in Fig. 3a. A V-shaped etching profile was gradually observed on the $(01\bar{1})$ planes. The etching profiles using 2.7g KHH solution on the (011) planes are shown in Fig. 3b. The top and second figures show an etched step with photoresist protecting a narrow stripe. The third and bottom figures show the U-shaped etching profile which results from etching through a 25 μm wide photoresist window. These etching characteristics are similar to other etching solutions (8).

Figures 4a, 4b, and 4c show the etching effect of KH solution alone, with adding acid (HCl) and base (NaOH), respectively. It is clear that the etching rate is the same for both 2.7g KH and 2.7g KHH solutions, as shown in Fig. 4a and 4b, but the morphology of 2.7g KHH is much better than that of 2.7g KH solution. The etching rate, however, is much reduced to below 10 Å/min by adding NaOH into the solution, as shown in Fig. 4c.

Figure 5 shows the morphology of the etched step of GaAs using 2.7g KHH solution for periods of 20 and 60 min, respectively. In general, the etched surface is very

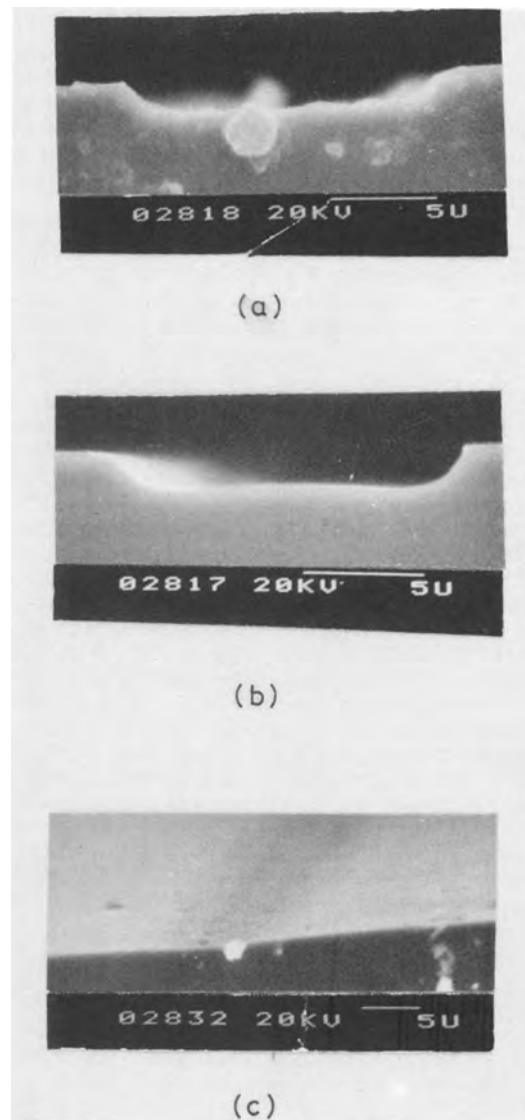
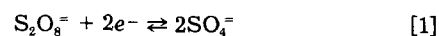


Fig. 4. Etching characteristics of 2.7g $K_2S_2O_8 + 50 \text{ cm}^3 \text{ H}_2\text{O}$ (a), 2.7g $K_2S_2O_8 + 50 \text{ cm}^3 \text{ H}_2\text{O} + 10 \text{ cm}^3 \text{ HCl}$ (b), 2.7g $K_2S_2O_8 + 50 \text{ cm}^3 \text{ H}_2\text{O} + 10 \text{ cm}^3 (1\text{M NaOH})$ (c) solutions. The etching times are all 90 min.

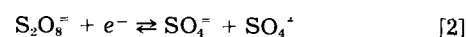
flat. This indicates that adding HCl removes the oxidized products on the GaAs surface more effectively. We also studied the etching rate of Cr-doped (100) GaAs wafers. It is found that by using 2.7g KHH solution the etching depths for a period of 20 min are the same for both Si- and Cr-doped GaAs, *i.e.*, 3000Å. Therefore, the etching rate is not affected by the conductivities of the wafers.

Discussions

Most etchants are generally composed of an oxidant and an acid (base) solvent. The purpose of the oxidant is to oxidize the substrate. The oxidized products are then dissolved in the acid or base solvent. The peroxodisulfate ion is a powerful oxidizing reagent (9). The reduction potential ΔE for the half-reaction



has been estimated to be 2.01 eV (9). The oxidizing mechanism may be varied with reaction conditions; there is good evidence for the formation of the radical anion $\text{SO}_4^{\cdot -}$ by one-electron reduction (10)



In the absence of inorganic or organic reactants, the $\text{SO}_4^{\cdot -}$ radical anions react very rapidly among themselves to reform $\text{S}_2\text{O}_8^{2-}$ with a second-order rate constant of $3.7 \times 10^6 \text{ M}^{-1}\text{-S}^{-1}$ (11). The radical anion $\text{SO}_4^{\cdot -}$ is stable in acidic

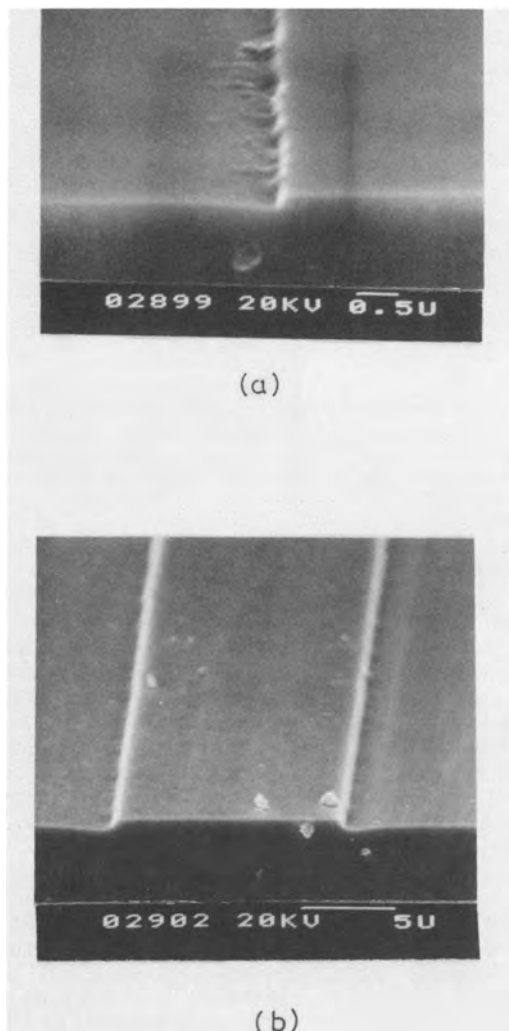


Fig. 5. The etching characteristics of 2.7g $K_2S_2O_8$ + 50 cm³ H_2O + 10 cm³ HCl solution. a: Etching time is 20 min; the etched depth is 3000Å. b: Etching time is 60 min; the etched depth is 9200Å.

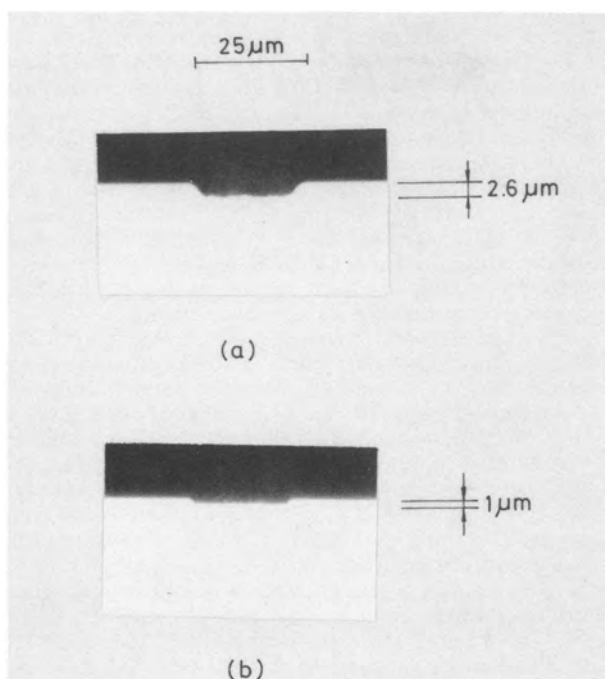
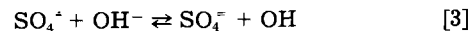


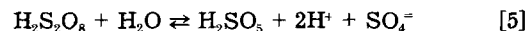
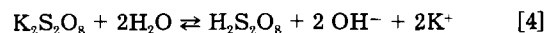
Fig. 6. The etching rate does increase by adding H_2SO_4 into $K_2S_2O_8$ + H_2O solution. a: 2.7g $K_2S_2O_8$ + 50 cm³ H_2O + 10 cm³ H_2SO_4 . b: 1.4g $K_2S_2O_8$ + 50 cm³ H_2O + 10 cm³ H_2SO_4 . Temperature is 20°C. The etching time is 20 min.

and neutral solutions, but very unstable in alkaline solution because of fast reaction with hydroxide ions with a large rate constant $7.3 \times 10^7 M^{-1}S^{-1}$ (12)

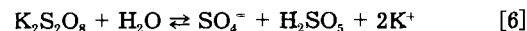


Since the OH radical is less active than $SO_4^{\cdot-}$, the oxidation process is slowed down. This explains the extremely slow etching rate by adding NaOH into KH solution.

In acidic solution, the peroxodisulfate ion is converted to $H_2S_2O_8$ followed by the hydrolysis to obtain the peroxomonosulfuric acid and sulfuric acid (9)



The final reaction is



The pH value of 2.7g KH is 2, and, therefore, it is an acid solution. It is also found that the etching rate was much enhanced by adding H_2SO_4 into KH solution, as shown in Fig. 6. The etching rates were 1300 and 500 Å/min using one H_2SO_4 + five (2.7g KH) and one H_2SO_4 + five (1.4g KH) solutions, respectively. The etched surface morphology was poor. Since the etching rate was not enhanced by adding HCl into KH solution but the etched surface morphology was much improved, as shown in Fig. 3 and 5, it is concluded that the oxidation process is the etching rate-limited process. From Eq. [1], we can find that increasing the concentration of SO_4^{2-} ion will also increase the concentration of $S_2O_8^{2-}$ ion. Therefore, adding H_2SO_4 will enhance both the oxidation and dissolving rate and thus enhances the etching rate which ends up with a poor surface. The HCl enhances only the dissolution rate but not the oxidation, which improves the morphology of the etched surface.

Conclusions

New etching solutions composed of $K_2S_2O_8$, H_2O , and HCl have been developed for the etching of GaAs. The etching mechanism is believed to entail sequential one-electron transfer oxidations of the GaAs followed by dissolution. The final products should be Ga^{3+} , As^{3+} , SO_4^{2-} . This system has an extremely slow etching rate and results in a high quality surface. To etch 800-2500Å depth of GaAs using 2.7g KHH solution takes as long as 5 to 16 min, and, therefore, it is very easy to control. The etching rate does not degrade much after a long period of etching time, i.e., 3 days. It is thus a reliable and reproducible etching solution.

Manuscript submitted June 14, 1985; revised manuscript received Aug. 14, 1985.

REFERENCES

1. W. Baechtold, *IEEE J. Solid State Circuit*, **sc-8**, 54 (1973).
2. R. E. Williams, "Gallium Arsenide Processing Techniques," p. 71, Artech House, Inc., Dedham, MA (1984).
3. D. W. Shaw, *This Journal*, **128**, 874 (1981).
4. G. H. Olsen, M. S. Abrahams, and T. J. Zamerowski, *ibid.*, **121**, 1650 (1974).
5. "Handbook of Chemistry and Physics," 59th ed., R. C. Weast, Editor, CRC Press, Inc., Boca Raton, FL (1979).
6. M. Otsubo, T. Oda, H. Kumable, and H. Miki, *This Journal*, **123**, 676 (1976).
7. S. Iida and K. Ito, *This Journal*, **118**, 768 (1971).
8. S. Adachi and K. Oe, *ibid.*, **130**, 2427 (1983).
9. F. A. Cotton and G. Wilkinson, "Advanced Inorganic Chemistry," 4th ed., p. 534, John Wiley and Sons, Inc., New York (1980).
10. F. Bolletta, A. Juris, M. Maestriand, and D. Sandrini, *Inorg. Chim. Acta*, **44**, 1175 (1980).
11. O. P. Chawla and R. W. Fessenden, *J. Phys. Chem.*, **79**, 2693 (1975).
12. Y. Ogata, K. Tomizawa, and K. Furuta, in "The Chemistry of Functional Groups, Peroxides," S. Patai, Editor, Chap. 21, John Wiley and Sons, New York (1983).

The Mechanism of GaAs Etching in CrO₃-HF Solutions

I. Experimental Results

J. van de Ven

Department of Solid State III, Research Institute of Materials, Catholic University, Toernooiveld, 6525 ED Nijmegen, The Netherlands

J. E. A. M. van den Meerakker and J. J. Kelly

Philips Research Laboratories, 5600 JA Eindhoven, The Netherlands

ABSTRACT

The etching kinetics and electrochemistry of GaAs in aqueous CrO₃-HF solutions were studied. For solutions with a low [HF]/[CrO₃] ratio, etch rates in the dark depend only on the HF concentration and are similar for n-type and p-type GaAs. Illumination strongly increases the etch rate of n-type material but has no effect on p-type dissolution. From current and impedance measurements, it was concluded that Cr^{VI} reduction gives rise to a passivating film on GaAs, which inhibits further hole injection from the oxidizing agent. The limiting quantum efficiencies for Cr^{VI} reduction at illuminated p-type electrodes and for GaAs dissolution at n-type electrodes are significantly greater than unity. At higher [HF]/[CrO₃] ratios the etch rate of both n- and p-type GaAs is determined by Cr^{VI} diffusion in solution. Conclusions concerning the etching mechanism are drawn on the basis of these results.

During the past decade, GaAs and related compounds have become increasingly important for applications in electronic and optoelectronic devices. The crystallographic perfection of these III-V materials directly influences electrical and optical properties and determines device performance and lifetime. One of the most straightforward and powerful methods of defect characterization is, without doubt, wet chemical etching. For GaAs a large number of etchants has been reported (1-4). Most of these etching systems have only been investigated phenomenologically; dissolution rates and surface morphology were studied, but very little attention was paid to the essential chemistry involved.

In this series of papers, a study of the mechanism of the recently developed "DSL-system" for GaAs is presented. DSL refers to "diluted Sirtl-like etchants with the use of light." This system, which is based on CrO₃, HF, and H₂O, has already been described phenomenologically in earlier papers (5-7). With an appropriate choice of solution composition, all crystallographic defects can be revealed in n-type, p-type, and semi-insulating GaAs with high sensitivity. A special feature of this system is that defects are revealed as hillocks on the surface during etching, not only under illumination, but also in the dark. This means that the etch rate of crystallographic imperfections is lower than that of the surrounding material.

Dissolution of GaAs in strongly oxidizing solutions, such as the present CrO₃/HF system, generally takes place via a valence-band process (8, 9). The energy levels of the oxidized states of the redox couple in solution overlap with the valence band of the semiconductor, and holes are supplied to the solid with reduction of the oxidizing agent (8, 9). Localization of holes at the surface of the semiconductor causes rupture of GaAs bonds and results in dissolution. In such "electroless" systems, the rate of reduction of the oxidizing agent, and, consequently, the hole supply to the solid, is equal to the rate of oxidative dissolution of the semiconductor. Since reduction of Cr^{VI} and oxidation of GaAs are potential-dependent reactions, the electrochemistry of the system was studied, together with the etching kinetics, to obtain insight into the mechanism of the etching process. The results of this study are presented in this article. In the second part of this paper, a model is proposed which can explain both the etching and electrochemical results. The morphological aspects of etching in CrO₃-HF solutions will be discussed in a separate paper (10).

Experimental

GaAs crystals, used in this study, were grown by the horizontal Bridgman technique. The wafers were (100)

oriented and supplied by different manufacturers. The n-type samples were silicon doped with a carrier concentration in the range $1.0-2.8 \times 10^{18} \text{ cm}^{-3}$; the p-type samples were zinc doped and had a carrier concentration of $0.8-1.3 \times 10^{18} \text{ cm}^{-3}$. The wafers were first mechanochemically polished. To remove impurities and work damage, various surface pretreatment methods were used. These included anodic polishing in an EDTA electrolyte (11) and etching in H₂SO₄/H₂O₂/H₂O solutions followed, in all cases, by dipping in a diluted HCl solution.

The open-circuit etching kinetics were studied with the same experimental setup as described previously (5). To vary the intensity of the 24 mW, 632.8 nm He-Ne laser at the sample surface, the beam diameter was varied and neutral density filters were used. Homogeneity of the laser spot was maintained within 5% limits. A light power of 150 mW/cm² was used with a spot diameter of 4.5 mm, except for the measurements in which the light intensity was varied. During etching, the solution was not stirred and depletion of solution constituents was not significant. The GaAs samples were partly masked with Apiezon W or photoresist, and the etched depth was measured with a step profiler.

For the electrochemical measurements, both stationary and rotating disk (RDE) electrodes were used. These were mounted in a Teflon cell. Current-potential characteristics were recorded with a Wenking POS73 potentiostat. Impedance measurements were performed with a Solartron 1172 frequency response analyzer using a 10 mV rms signal at 10 kHz. Flatband potentials (V_{FB}) were determined from Mott-Schottky plots (12). A saturated calomel electrode (SCE) was used as a reference, and all potentials are expressed with respect to SCE. A platinum foil served as counterelectrode. A He-Ne laser was also used as light source for the electrochemical measurements.

HF (p.a. grade) was obtained from Merck. In previous work (5), one particular batch of CrO₃ (analar grade), supplied by BDH Chemicals Limited (Poole, England) was used exclusively. In etchants with a low HF concentration ($\leq 2.5M$) containing this CrO₃, the etch rate of n-type GaAs was found to be zero. Subsequent experiments with other batches from BDH (analar grade) and from other suppliers (Merck, p.a. grade and Baker, reagent grade) showed this behavior to be anomalous. The reason for this anomaly is not understood. All etch rates, with the exception of those obtained using the particular batch mentioned above, were reproducible to within 5-10%. The anomalous results with n-type GaAs at low HF concentration are omitted from this work. The electrochemical experiments were performed with CrO₃ (p.a. grade) supplied by Merck. Concentrations are expressed in moles per liter (M).

All measurements were performed at room temperature.

Results

From an extensive study of GaAs etching in CrO_3 -HF solutions reported elsewhere (10), it was clear that the ratio of the HF and CrO_3 concentrations is very important for the etching kinetics. Consequently, the etching and electrochemical results, described in this section, are classified on the basis of this ratio. In the present work, only HF concentrations lower than 10M have been used.

High [HF]/[CrO₃] ratios.—For solutions with [HF]/[CrO₃] ratios > 20, the steady-state open-circuit etch rate of GaAs is independent of semiconductor type and depends linearly on the CrO_3 concentration (Fig. 1). In this range, the HF concentration is not important. The etch rate is sensitive to stirring in the solution. If it is assumed that six holes are required to dissolve one GaAs molecule (13), then the measured etch rate agrees well with that calculated from the diffusion-controlled reduction current of Cr^{VI} , as described below. The etching reaction is obviously determined by diffusion of the oxidizing agent in solution. Consequently, it was not surprising that illumination was found to have no effect on the etching kinetics.

The current-potential curves for n-type GaAs in this range seem to conform to the pattern expected for hole injection from a simple redox system (8). A well-defined cathodic current plateau is observed at potentials positive with respect to the flatband value (Fig. 2). This limiting current depends linearly on the CrO_3 concentration and is directly proportional to the square root of the electrode rotation rate, i.e., cathodic reduction of Cr^{VI} is diffusion controlled. Because of the obvious similarity between curve a of Fig. 2 and the corresponding curve for Ce^{IV} reduction (8), it is tempting to interpret these results in terms of a simple hole-injection mechanism: in the range in which a constant cathodic current is observed, the electron concentration in the space-charge layer is still appreciable, and holes, provided by Cr^{VI} species in solution, recombine with electrons supplied from the bulk (8, 14). At more positive potentials, corresponding to a large band bending, the surface electron concentration is greatly reduced and recombination is no longer possible. The injected holes are held at the surface and cause the solid to dissolve. Since the holes injected from Cr^{VI} are consumed in this reaction, the measured (total) current

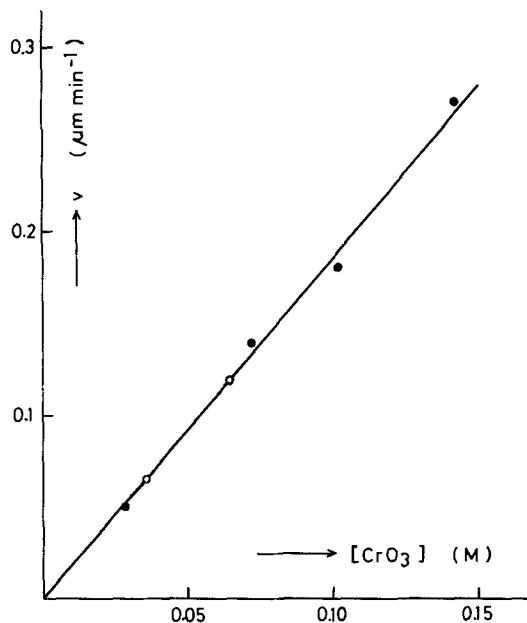


Fig. 1. Steady-state etch rate (v), measured at open circuit, as a function of the CrO_3 concentration for solutions with relatively high [HF]/[CrO₃] ratio. Solid circles: n-Type GaAs. Open circles: p-Type GaAs.

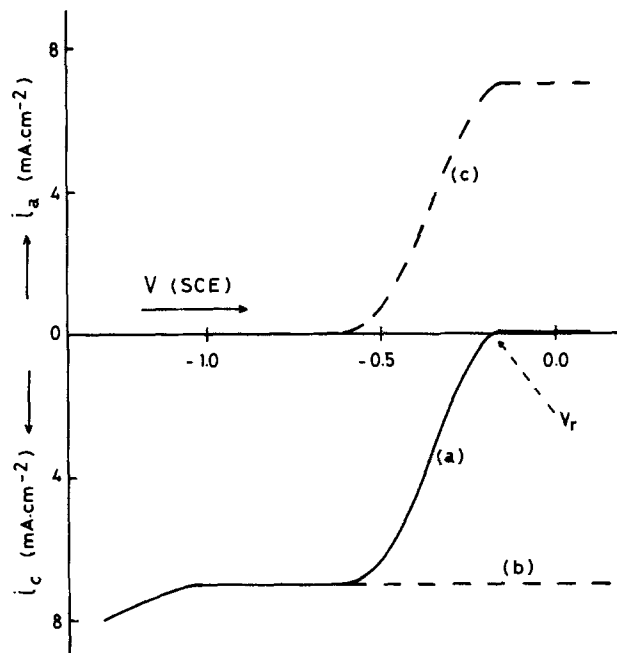


Fig. 2. Curve a is the measured current-potential curve for an n-type GaAs electrode in 0.12M CrO_3 , 9.17M HF solution. Dashed lines b and c show the cathodic and anodic partial curves, respectively. V_r is the rest potential. Scan rate: 10 mV/s.

decreases to a very low value. The diffusion-controlled hole injection current (curve b) is compensated by the anodic dissolution current (curve c).

However, the results obtained with p-type GaAs show that this description cannot be completely valid. The expected characteristics for a p-type electrode (9) are only observed at extremely high [HF]/[CrO₃] ratios. A current-potential curve for an electrolyte with a concentration ratio of 10⁴ is shown in Fig. 3. At more positive potentials, GaAs is anodically dissolved. At negative potentials, a constant cathodic current is observed. From the dependence of this limiting current on CrO_3 concentration and electrode rotation rate, it can be concluded that the reduction reaction is again limited by mass transport of Cr^{VI} species in solution. In this case, it is clear that the open-circuit etch rate must be determined by the diffusion-

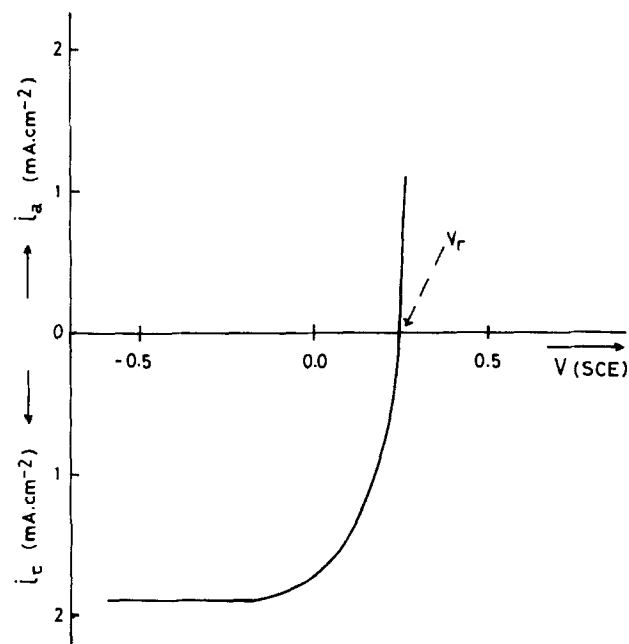


Fig. 3. Current-potential curve for a p-type GaAs RDE in 10⁻³M CrO_3 , 9.0M HF solution at 500 rpm. V_r is the rest potential. Scan rate: 10 mV/s.

controlled reduction of Cr^{VI} . For lower $[\text{HF}]/[\text{CrO}_3]$ ratios (but ones still > 20), the etching kinetics remain unchanged (Fig. 1), but the corresponding current-potential curves deviate considerably from that shown in Fig. 3. The current, which was less well defined, depended strongly on the scan rate, scan direction, and prepolarization potential. Under certain conditions, a current plateau could be observed. However, in most cases a cathodic peak was found at potentials just negative of the rest potential (see results in the following section) and the cathodic current was lower than that expected for a diffusion-controlled process. There seem to be discrepancies, therefore, between the electrochemical results for n- and p-type GaAs and between the electrochemical and etching results of p-type GaAs.

For these CrO_3 -HF solutions, electrode passivation behavior is observed at higher HF concentration. During continued potentiodynamic scanning in the dark, the current gradually decreases. In a 9M HF solution without CrO_3 , the photocurrent at n-type GaAs also decreases in time and a dark layer is formed on the electrode. Removal of this layer and reactivation of the electrode occurs when a small amount of CrO_3 is added to the HF solution. Most probably, the passivating layer consists of an insoluble gallium fluoride $[\text{GaF}_3 \cdot n\text{H}_2\text{O}]$ (15), whose solubility is influenced by the chromium species in solution. Measurements described above were only made at shorter times, for which passivation was not important.

Low $[\text{HF}]/[\text{CrO}_3]$ ratios.—Dark.—For solutions with a $[\text{HF}]/[\text{CrO}_3]$ ratio lower than 10, the open-circuit etch rate of GaAs is practically independent of the CrO_3 concentration but depends strongly on the HF concentration (Fig. 4). A comparison of Fig. 4a and 4b (solid circles) shows that the etching kinetics for p and n-type GaAs in the dark are similar.

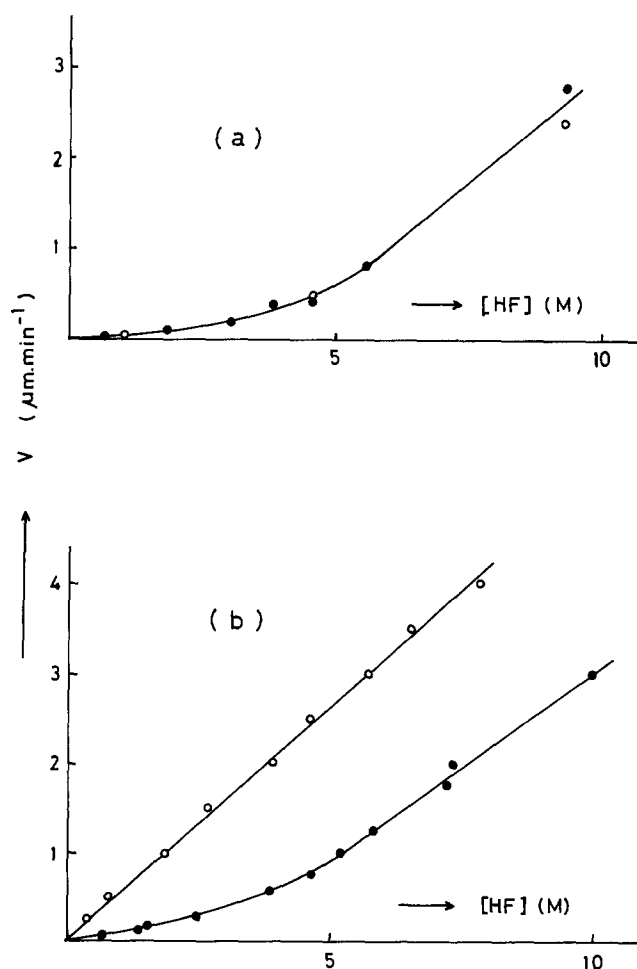


Fig. 4. Open-circuit etch rate as a function of HF concentration for solutions with low $[\text{HF}]/[\text{CrO}_3]$ ratio. Figure 4a refers to p-type, and 4b to n-type GaAs. Solid circles: Dark. Open circles: illuminated.

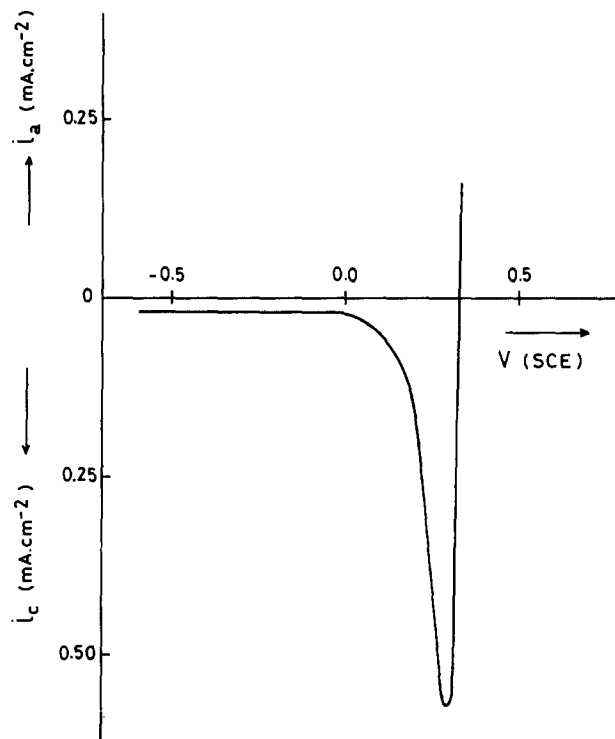


Fig. 5. Current-potential plot for a p-type GaAs electrode in 1.20M CrO_3 , 1.54M HF solution. Scan rate: 2 mV/s.

The current-potential curve of p-type GaAs (Fig. 5) is markedly different from that observed for very high concentration ratios and more pronounced than that found for lower ratios in the concentration range $[\text{HF}]/[\text{CrO}_3] > 20$. At potentials close to or positive with respect to the flatband potential (see Table I), anodic dissolution of GaAs is evident in the sharply rising current. At potentials negative with respect to the rest potential, the cathodic reduction of Cr^{VI} does not give a diffusion-controlled plateau. Instead, a peak is observed (Fig. 5). At more negative potentials, the current decreases to a very low constant value. This latter value depends on the square of the HF concentration (Fig. 6). The peak is reproducible and is independent of the potential scan direction at lower scan rates. As the cathodic current does not depend on the rotation rate of the electrode, it can be concluded that the reduction reaction is kinetically determined.

Analogous behavior was observed for n-type electrodes in these solutions. Instead of a diffusion-controlled cathodic current, a sharp peak is again observed (curve a in Fig. 7). In contrast to p-type GaAs, the peak shows considerable hysteresis even at very low scan rates: the current observed during the cathodic scan was markedly higher than that observed in the return scan. The peak height was, however, reproducible and independent of the scan rate when the potential was scanned in the cathodic direction. The peak currents for n- (cathodic scan)

Table I. Impedance results for an n- and a p-type GaAs electrode in various electrolytes

Electrode	Electrolyte	V_{FB} (SCE)	N_D, N_A (cm ⁻³) ^a
n-GaAs (dark)	0.5M H_2SO_4	-0.98	1.1×10^{18}
	1.20M CrO_3 , 1.54M HF	-0.98	1.3×10^{18}
	0.57M CrO_3 , 1.80M HF	-0.94	1.3×10^{18}
	2.15M CrO_3 , 6.96M HF	-0.95	1.4×10^{18}
n-GaAs (illuminated)	1.20M CrO_3 , 1.54M HF	-0.94	1.4×10^{18}
p-GaAs (dark)	0.5M H_2SO_4	+0.31	1.1×10^{18}
	1.20M CrO_3 , 1.54M HF	+0.31	1.0×10^{18}

^a N_D and N_A are the donor and acceptor concentrations calculated for the n- and p-type electrodes, respectively, from the slope of the Mott-Schottky plots.

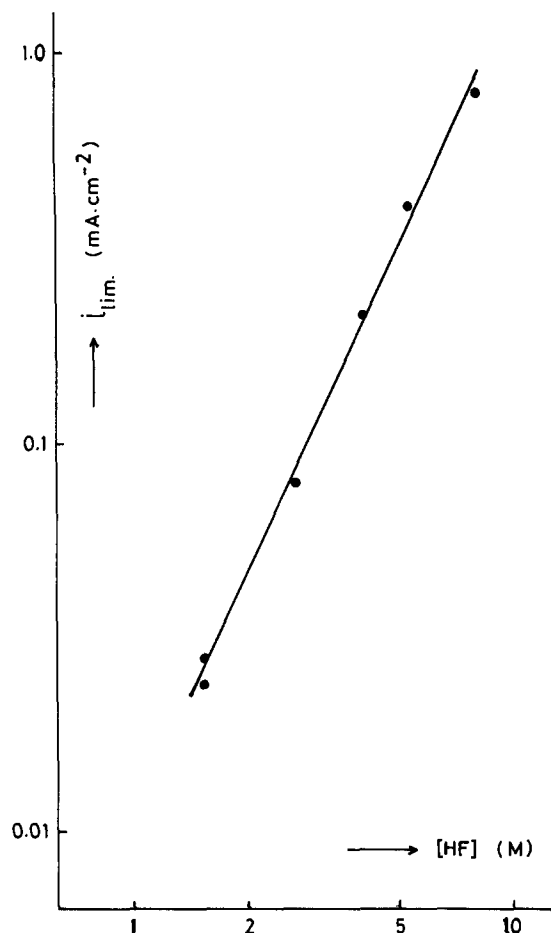


Fig. 6. The limiting cathodic current i_{lim} of p-type GaAs (measured at $-0.50V$) as a function of HF concentration for solutions with relatively low $[HF]/[CrO_3]$ ratio. The CrO_3 concentration was constant ($1.20M$).

and p-type electrodes were identical and depended on the square of the HF concentration (Fig. 8). The peak current was considerably lower than the current calculated from the open-circuit etch rate at the same HF concentration. The etch rate was, however, substantially lower than that expected for a dissolution process limited by diffusion of Cr^{VI} in solution.

It is obvious, both from the etching and electrochemical results presented above, that the reduction of Cr^{VI} is seriously inhibited at GaAs electrodes. From the flatband potential measurements given in Table I for an indifferent electrolyte ($0.5M H_2SO_4$) and various CrO_3 -HF solu-

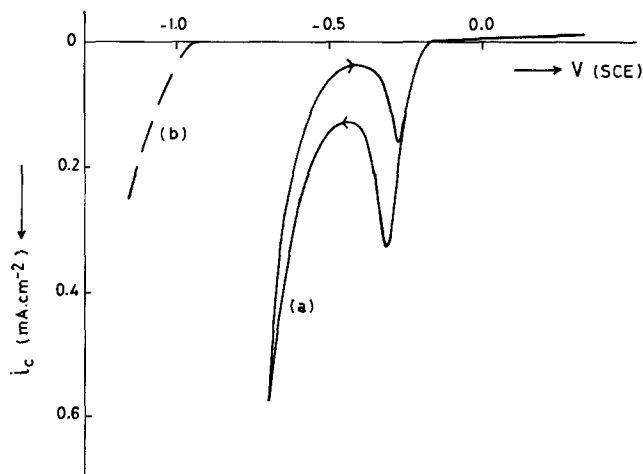


Fig. 7. Curve a is the current-potential curve for an n-type GaAs electrode in $1.20M CrO_3$, $1.54M HF$ solution. Curve b was measured in $0.5M H_2SO_4$ solution. Scan rate: $10 mV/s$.

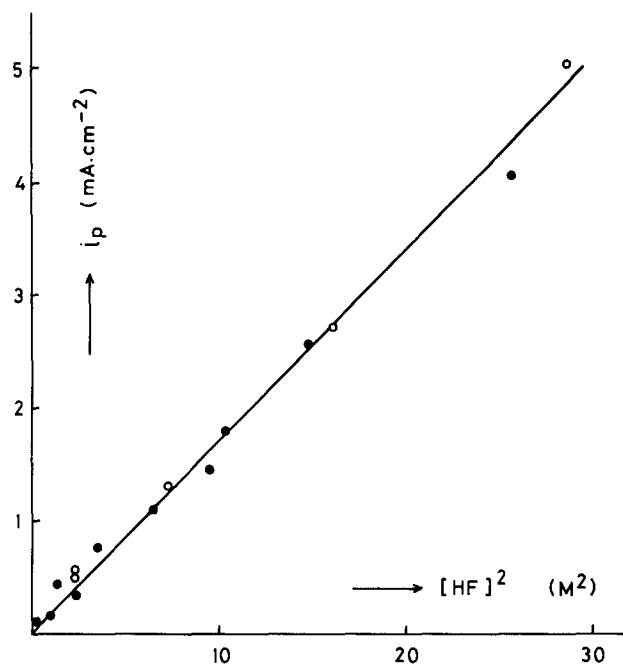


Fig. 8. Cathodic peak current in electrolytes with $[HF]/[CrO_3] < 10$ as a function of $[HF]^2$ for p- (open circles) and n-type (solid circles) electrodes.

tions, it follows that the position of the bandedges of the semiconductor is not significantly affected by the presence of HF or chromium containing species in the electrolyte. Since the standard redox potential of the Cr^{VI}/Cr^{III} couple is very positive (16), efficient hole injection from Cr^{VI} is then expected at GaAs electrodes (8, 9, 12). This is obviously not the case. A similar inhibition of the Cr^{VI} reduction has been observed at metal electrodes and has been attributed to the formation of a blocking film on the electrode surface (17-19). From the results presented above, it must be concluded that a film is also formed on GaAs. For an n-type electrode, the cathodic current at potentials negative with respect to the peak begins to increase again (Fig. 7, curve a) before H_2 evolution is normally observed under these conditions (Fig. 7, curve b). This suggests that electrons, which are available in n-type material in the dark at potentials approaching V_{FB} are capable of reducing the blocking layer.

Further evidence supporting the formation of such a layer in these electrolytes was obtained from measurements with a Pt electrode. At potentials negative with respect to the Cr^{VI}/Cr^{III} redox potential, the electrode was clearly passivated, as only a very small constant cathodic current was observed. In contrast to GaAs electrodes, a current peak was not found at low scan rates. The cathodic current at the Pt electrode began to increase markedly at approximately $0V$ (SCE). Since this potential is more than $200 mV$ too positive for hydrogen evolution, the cathodic current must be attributed to reduction of a chromium species. This again indicates a breakdown of the passive layer, analogous to that found with n-GaAs electrodes.

Illuminated.—While illumination has no effect on the open-circuit etch rate of p-type GaAs (open circles in Fig. 4a), dissolution of n-type material is strongly accelerated by light (open circles in Fig. 4b). The etch rate was found to be linearly dependent on the photon flux at low light intensities but tended to a limiting value at high intensities (10). The photoetch rates, shown in Fig. 4b, were measured at high intensity.

Illumination of a p-type electrode has no effect on the current-potential curve in the vicinity of the rest potential but considerably enhances the cathodic current at more negative potentials (Fig. 9, curve a). For comparison, the photocurrent in a $0.5M H_2SO_4$ solution is also given at the same light intensity (curve b). In the latter case, photo-generated electrons give rise to hydrogen evolution at the

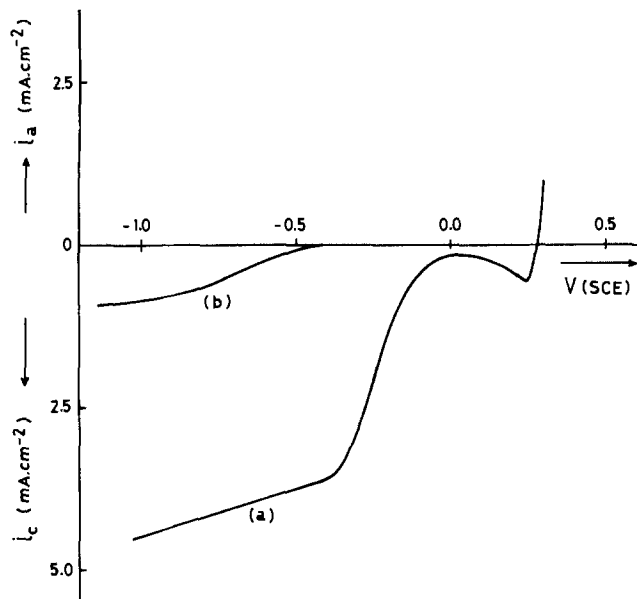


Fig. 9. Current-potential plot for a p-type GaAs electrode in 1.20M CrO_3 , 1.54M HF solution under illumination (curve a). Curve b gives the photocurrent in a 0.5M H_2SO_4 solution at the same light intensity. Scan rate: 10 mV/s.

electrode surface. This electron transfer must compete with an effective electron-hole recombination in the surface region (20). A considerable overpotential must be applied to reduce the surface concentration of the majority carriers and thereby the recombination rate, in order for a photocurrent to be observed. In the limiting photocurrent potential range, a quantum efficiency close to unity was found for H_2 evolution in the H_2SO_4 solution, i.e., one electron is transferred per absorbed photon.

The photocurrent curve for the CrO_3 -HF solution differs in two essential respects from that measured in 0.5M H_2SO_4 . First, current onset in CrO_3 -HF solutions is observed at more positive potentials, which suggests that the redox reaction can compete more effectively with the recombination process. However, recombination still dominates the current-potential characteristics at the rest potential. Consequently, etching of p-type GaAs is unaffected by illumination. Second, the limiting photocurrent for a CrO_3 -HF solution is much higher than the corresponding hydrogen current at the same light intensity. This effect is further demonstrated in Fig. 10, which shows the current, measured at -1.0V in H_2SO_4 and CrO_3 -HF solutions, as a function of light intensity. From these results it follows that six to ten charge carriers are transferred for every photon absorbed. This shows that the creation of minority carriers by light has a significant effect on the blocking film at the electrode surface. As already suggested for n-type GaAs, reduction of the film by electrons very likely frees the surface and allows further hole injection into the valence band by the Cr^{VI} species in solution.

The "depassivation" of a p-type electrode by light could be used to get an indication of the thickness of the blocking layer. Under strong illumination, the passivated surface is freed. When the light is switched off, the electrode, of course, repassivates. We measured the current involved in the repassivation as a function of time. The corresponding charge was equivalent to the formation of a thin film at monolayer or submonolayer coverage.

Illumination of an n-type GaAs electrode gave a limiting dissolution photocurrent (Fig. 11), which was the same as that found in a 0.5M H_2SO_4 solution. Both the rest potential and the cathodic peak are shifted to lower potentials with respect to the dark case. The peak current increases slightly with illumination intensity. The hysteresis observed in the cathodic peak is less pronounced under illumination than in the dark and disappears completely at relatively high light intensity (insert in Fig. 11).

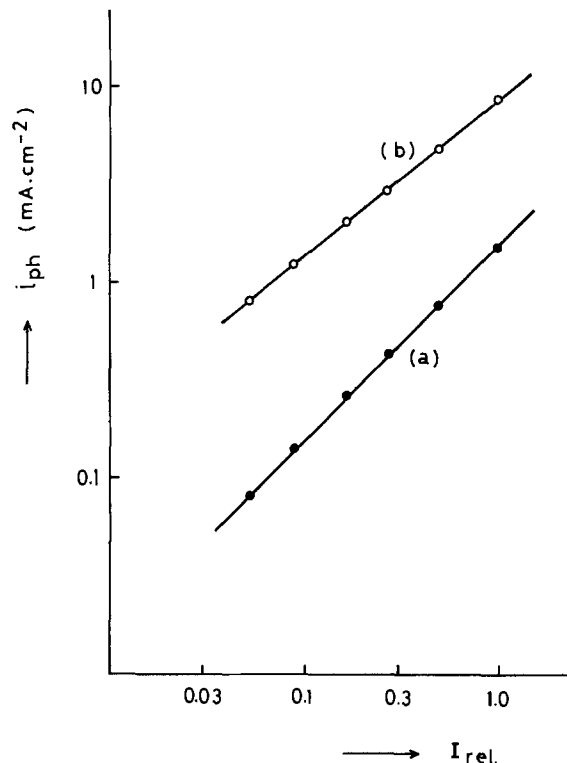


Fig. 10. The limiting cathodic photocurrent at -1.0V as a function of light intensity as obtained with a p-type GaAs electrode in 0.5M H_2SO_4 (a) and in 1.20M CrO_3 , 1.54M HF (b) solutions. The light intensity is given in relative units.

It should be noted that in pure CrO_3 solutions no current was observed. Addition of a small amount of HF activated the electrode and the expected limiting photocurrent was measured.

In order to correlate the photocurrent and photoetching experiments with n-type material, the etch rate was measured at various potentials under potentiostatic conditions. Results in Table II are expressed in terms of a quantum efficiency ϕ defined as

$$\phi = \frac{10^{-4} n F \rho (v_1 - v_d)}{60 M i_{\text{ph}}} \quad [1]$$

where v_1 and v_d refer to the etch rates (in microns per minute) under illumination and in the dark at the same potential, ρ and M are the density and molecular weight of GaAs, F is the Faraday constant, and n ($= 6$) is the number of holes required to dissolve one GaAs molecule. Since the quantum efficiency for photoanodic dissolution of n-type GaAs in indifferent electrolyte is close to unity, the limiting photocurrent i_{ph} determined in H_2SO_4 solution was used as a measure for the photon flux in Eq. [1]. The results in Table II show that, in CrO_3 -HF solutions, quantum efficiencies for etching considerably greater than 1 are obtained both at the rest potential and at more positive potentials.

Discussion

At very high $[\text{HF}]/[\text{CrO}_3]$ ratios, the VB reduction of Cr^{VI} is limited by diffusion of the oxidizing agent in solution and the open-circuit etch rate of GaAs is consequently diffusion controlled (Fig. 1). At lower $[\text{HF}]/[\text{CrO}_3]$ ratios but still larger than 20, an apparent anomaly is observed. Although the etch rate of both p- and n-type material is diffusion controlled, the cathodic reduction of Cr^{VI} at p-type electrodes is not limited by mass transport in solution; at n-type electrodes, a clearly defined diffusion plateau current is observed. At $[\text{HF}]/[\text{CrO}_3]$ ratios lower than 10, both the open-circuit etch rate and the Cr^{VI} reduction rate are kinetically controlled.

For this latter range of concentrations, the reduction reaction is clearly inhibited, despite the favorable corre-

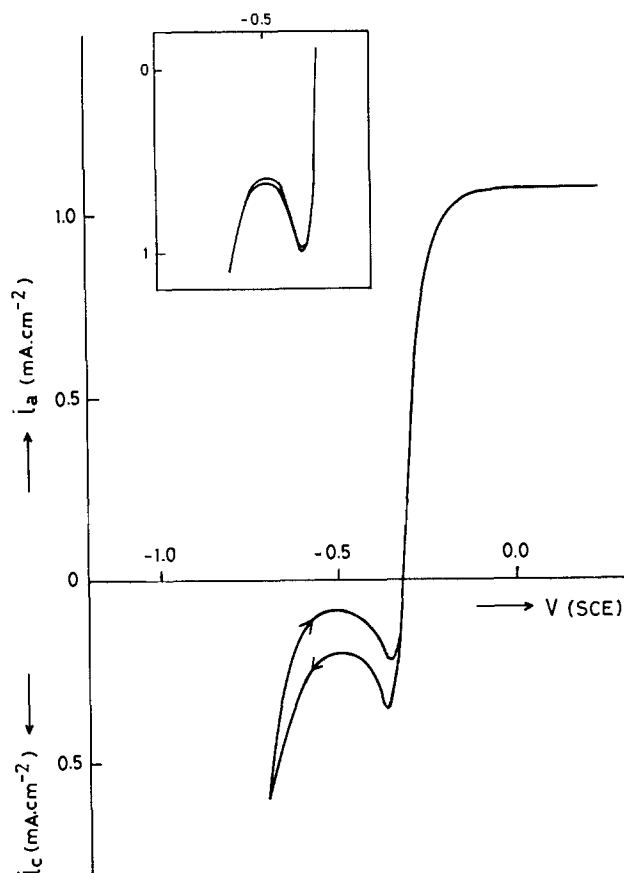
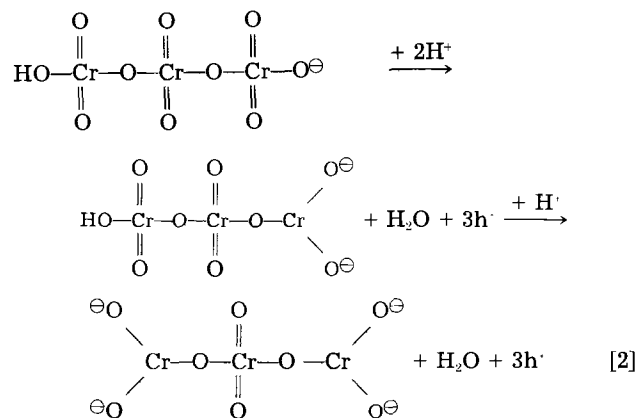


Fig. 11. Current-potential curve for an n-type GaAs electrode in 1.20M CrO_3 , 1.54M HF solution under illumination. In the insert, the cathodic peak is given in both scan directions for a light intensity corresponding to a limiting anodic photocurrent of 3 mA/cm^2 . The scan rate for both curves was 1 mV/s .

spondence of redox potential and semiconductor valence band. It was suggested above that this inhibition is due to the formation of a blocking layer on the electrode. Passivation has also been observed by other workers on Pt and other metal electrodes during Cr^{VI} reduction (17-19). This was ascribed to the formation of mixed valence complexes due to partial reduction of hexavalent chromium in dichromate or trichromate ions (18, 19). Hoare suggests, for example, that the reduction of a trichromate ion can lead to complexes containing trivalent and hexavalent chromium entities (19). Such reactions at GaAs can be represented schematically as follows



Using the analogy with metal electrodes, we conclude that such mixed-valence complexes can adsorb and form a blocking layer on GaAs and thus prevent further reduction of Cr^{VI} .

The Mott-Schottky plots for GaAs in these CrO_3 -HF electrolytes were very similar to those measured in 0.5M H_2SO_4 solution (Table I). No significant difference was observed either in the flatband potential or in the slope

Table II. Measured quantum efficiency for dissolution of n-type GaAs in 0.72M CrO_3 , 0.93M HF solution

Potential ^a	ϕ
Of current minimum	0.0
Of current peak	1.3
Rest potential (V_r)	1.7
$V_r + 0.3\text{V}$	3.0

^a These potentials refer to the illuminated electrode. The light intensity corresponded to a limiting anodic photocurrent density of 3 mA/cm^2 .

(expressed here as a calculated donor or acceptor concentration). It therefore seems likely that the chromium ion products of reaction [2] replace the electrolyte anions in the Helmholtz layer. The Helmholtz potential at low pH is determined by adsorption of H^+ ions and does not depend on the nature of the anion in solution. Consequently, the surface complex does not disturb the existing Helmholtz layer. Of course, this is only possible when the surface layer is thin. The transient current measurements with illuminated p-type electrodes, already described, indicate this to be the case.

The surface coverage due to the film is clearly very sensitive to the HF concentration in solution. This is obvious from the strong HF dependence of the etch rate (Fig. 4) and of the cathodic peak current (Fig. 8) for both types of electrode. The constant cathodic current of p-type electrodes at negative potentials also depends markedly on the HF concentration (Fig. 6).

The electrochemistry of the adsorbed film on GaAs displays some unusual characteristics. From the various measurements, it can be concluded that the surface complex is reduced by electrons from the conduction band. The dark cathodic current at n-GaAs begins much sooner than hydrogen evolution (curves a and b, Fig. 7). Illumination of p-GaAs gives a greatly enhanced cathodic current (Fig. 9 and 10). The species responsible for the surface film must, therefore, have energy levels which correspond to the conduction band or the bandgap (20). Since the quantum efficiency for photocurrent at p-GaAs is much greater than 1, reduction of the adsorbed complex must free a surface site at which several holes can be subsequently injected.

A small constant cathodic current is observed on p-type electrodes at potentials negative with respect to the peak value. Since this current is potential-independent but strongly dependent on HF concentration, we assume that the blocking film can be removed by a chemical reaction with HF. This reaction is second order in HF concentration (Fig. 6).

The most intriguing aspect of this system is an apparent coupling of the GaAs oxidative dissolution and Cr^{VI} reduction reactions. For both p- and n-type electrodes, strong passivation sets in only at potentials at which holes are not kept effectively at the surface and GaAs no longer dissolves anodically (Fig. 5 and 7). Most probably, the adsorbed surface complex can react with an intermediate of the GaAs oxidation reaction, thus freeing a surface site and enabling subsequent hole injection by Cr^{VI} . The behavior of the current peak at lower scan rates supports this conclusion. Under these conditions, current hysteresis was observed for n-type GaAs in the dark. The current was much lower for the anodic scan direction (Fig. 7). At potentials slightly negative with respect to the peak, both n- and p-type electrodes are strongly passivated. Upon increasing the potential, band bending conditions become favorable for keeping holes at the surface. For p-type electrodes and n-type electrodes illuminated at high intensity, holes are readily available. Consequently, the GaAs dissolution reaction can be easily initiated. Intermediates from this process can subsequently react with the blocking film, thus depassivating the surface. In these cases, therefore, the establishment of a steady state is expected to be rapid. For an n-type elec-

trode in the dark, holes are not available from the bulk and must be injected by Cr^{VI} in solution. As this process is strongly inhibited by the presence of the passivating film, retardation effects can be significant. In this case, therefore, current hysteresis can be expected even at low scan rates. In the next article, it will be shown that such a coupling of dissolution and reduction reactions can also account for the enhancement of the etch rate of n-GaAs under illumination and for the surprisingly high quantum efficiency (Table II).

At $[\text{HF}]/[\text{CrO}_3]$ ratios higher than ~ 20 , a discrepancy was noted in the electrochemical behavior of n- and p-type GaAs. While the open-circuit etch rate of both materials depends on diffusion of Cr^{VI} species from the bulk solution to the electrode surface, a diffusion-limited current was only found for n-type electrodes. For p-type GaAs, the reduction rate of Cr^{VI} was diffusion limited only at extreme $[\text{HF}]/[\text{CrO}_3]$ ratios. From the discussion above of the results obtained in solutions with a concentration ratio less than 10, it is clear that the reduction of Cr^{VI} at the open-circuit potential of p-type GaAs must be much higher than the cathodic current at more negative potentials. This is obviously also the case for electrolytes with $[\text{HF}]/[\text{CrO}_3] > 20$ in which the concentration ratio is not extremely high. The fact that a reduced cathodic current is not observed for n-type GaAs under similar conditions (Fig. 2) must be attributed to the presence of electrons at the electrode surface. As discussed above, conduction band electrons can reduce the adsorbed complex. This keeps the surface free for subsequent hole injection. Treating the diffusion-limited cathodic current of n-type GaAs in these solutions as a simple example of hole injection into the valence band is, therefore, not justified.

Acknowledgments

The authors wish to thank Dr. R. Memming, P. H. L. Notten, Dr. L. J. Giling, and Dr. J. L. Weyher for stimulating discussions. J. van de Ven was supported by the Stichting voor Fundamenteel Onderzoek der Materie with

financial support from the Nederlandse Organisatie voor Zuiver Wetenschappelijk Onderzoek.

Manuscript submitted April 9, 1985; revised manuscript received Sept. 5, 1985.

Philips Research Laboratories assisted in meeting the publication costs of this article.

REFERENCES

1. D. J. Stirland and B. W. Straughan, *Thin Solid Films*, **31**, 139 (1976).
2. D. W. Shaw, *J. Cryst. Growth*, **47**, 509 (1979).
3. B. Tuck, *J. Mater. Sci.*, **10**, 321 (1975).
4. A. Munoz-Yague and M. Bafleur, *J. Cryst. Growth*, **53**, 239 (1981).
5. J. L. Weyher and J. van de Ven, *ibid.*, **63**, 285 (1983).
6. J. L. Weyher and W. J. P. van Enckevort, *ibid.*, **63**, 292 (1983).
7. J. L. Weyher and J. van de Ven, In preparation for submission to *J. Cryst. Growth*.
8. F. Decker, B. Pettinger, and H. Gerischer, *This Journal*, **130**, 1335 (1983).
9. J. J. Kelly and P. H. L. Notten, *Electrochim. Acta*, **29**, 589 (1984).
10. J. van de Ven, J. L. Weyher, J. E. A. M. van den Meerakker, and J. J. Kelly, Submitted to *This Journal*.
11. C. R. Elliot and J. R. Regnault, *This Journal*, **127**, 1557 (1980).
12. R. Memming, in "Electroanalytical Chemistry. A Series of Advances," Vol. 11, A. J. Bard, Editor, pp. 1-84, Marcel Dekker, New York (1979).
13. H. Gerischer, *Ber. Bunsenges. Phys. Chem.*, **69**, 578 (1965).
14. J. E. A. M. van den Meerakker, J. J. Kelly, and P. H. L. Notten, *This Journal*, **132**, 638 (1985).
15. "Gmelins Handbuch der Anorganische Chemie," 8er Aufl., Vol. 36, p. 72, Verlag Chemie, Berlin (1936).
16. M. Pourbaix, "Atlas d'Equilibres Electrochimiques," Gauthier-Villars Paris (1963).
17. "Gmelins Handbuch der Anorganische Chemie," 8er Aufl., Teil 52b, Verlag Chemie, Weinheim (1962).
18. J. Lin-Cai and D. Pletcher, *J. Appl. Electrochem.*, **13**, 235, 245 (1983).
19. J. P. Hoare, *This Journal*, **126**, 190 (1979).
20. J. J. Kelly and R. Memming, *ibid.*, **129**, 730 (1982).

The Mechanism of GaAs Etching in CrO_3 -HF Solutions

II. Model and Discussion

J. J. Kelly

Philips Research Laboratories, 5600 JA Eindhoven, The Netherlands

J. van de Ven

Department of Solid State III, Research Institute of Materials, Catholic University, Toernooiveld, 6525 ED Nijmegen, The Netherlands

J. E. A. M. van den Meerakker

Philips Research Laboratories, 5600 JA Eindhoven, The Netherlands

ABSTRACT

A model is presented to describe the dissolution of GaAs in CrO_3 -HF solutions, both in the dark and under illumination. The etching kinetics are shown to be mainly determined by the mechanism of Cr^{VI} reduction at GaAs. An essential feature of the model is the formation of an adsorbed mixed-valence chromium complex which passivates the semiconductor surface. A novel reaction between the adsorbed complex and a surface-state intermediate of the GaAs oxidation reaction is proposed to account for the many surprising aspects of the etching and electrochemical kinetics.

In the first part of this series we described the dissolution of GaAs in CrO_3 -HF solutions (1). It was shown that the HF/CrO_3 concentration ratio determines the etching kinetics; at high values of this ratio, the etch rate depends on diffusion of Cr^{VI} in solution, while at low values etching is kinetically controlled and depends only on the HF concentration. Illumination considerably enhances the

dissolution rate of n-type GaAs but has no effect on p-type material.

In order to gain insight into the etching mechanism, the electrochemistry of the system was investigated. This revealed some unexpected features. The current-potential curves for p- and n-type electrodes have a very characteristic shape at low values of the HF/CrO_3 concentration ra-

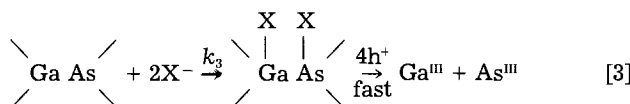
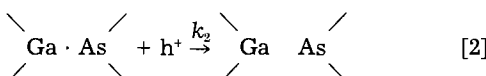
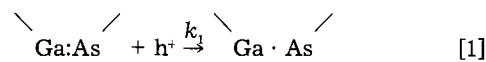
tio. The quantum efficiencies for Cr^{VI} reduction at p-type electrodes and for GaAs dissolution at n-type electrodes were significantly higher than 1. On the basis of these results two main conclusions were drawn: reduction of Cr^{VI} gives rise to a blocking film which plays a decisive role in the surface reactions; and this film can be reduced by a surface-state intermediate of the GaAs oxidation reaction, with the result that the surface is "depassivated."

In this paper, the conclusions from the first article are combined with existing ideas on the mechanism of oxidation of III-V materials to give a model which can account quantitatively for many of the electrochemical and etching results. The discussion will be mainly restricted to those cases in which etching is under kinetic or mixed-kinetic control, i.e., to relatively low HF/CrO₃ concentration ratios (1).

Model

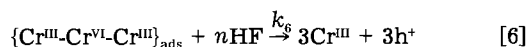
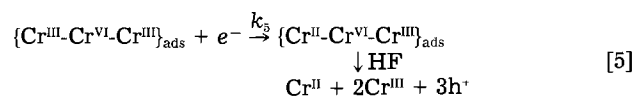
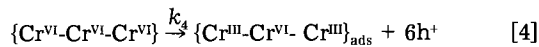
Etching of GaAs in CrO₃-HF solutions involves two electrochemical reactions, oxidative dissolution of the solid, and reduction of the oxidizing agent, Cr^{VI}. In the development of a model for the etching system, it is necessary to consider both partial reactions.

Recent work on the dissolution of GaAs suggests a mechanism involving a series of discrete steps (Eq. [1]-[3]) (2-5)



Localization of valence band (VB) holes at the surface results in the rupture of Ga-As surface bonds. The intermediates formed in reactions [1] and [2] correspond to surface states and have energy levels in the forbidden gap (2, 3). The charge transfer steps are accompanied by chemical attack on the weakened bond by a nucleophilic reagent 2X⁻ from solution. Kinetic studies involving competition between oxidation of the III-V material and of a reducing agent in solution have shown that nucleophilic attack very likely occurs after transfer of the second hole (6). On the basis of current and impedance measurements at different HF concentrations (1), it can be concluded that fluoride species do not participate in the anodic dissolution. Rupture of the first Ga-As bond is generally considered to be the rate-determining step (2, 4). Transfer of a further four holes occurs rapidly, and trivalent gallium and arsenic species are formed in solution (7).

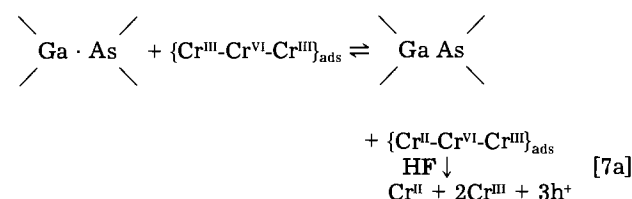
On the basis of the electrochemical results presented in the first article, the reduction of hexavalent chromium at GaAs can be represented as follows



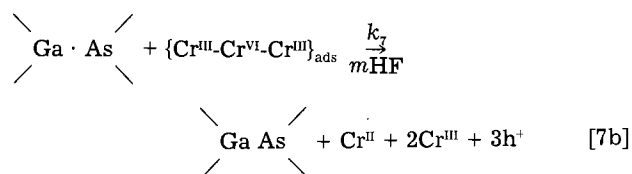
Following the example of Hoare (8), who has extensively studied the mechanism of Cr^{VI} reduction at metal electrodes, we consider the trichromate ion, here denoted by {Cr^{VI}-Cr^{VI}-Cr^{VI}}, to be the electroactive species in solution. An exact knowledge of the solution chemistry is not essential since the model can be readily modified to take into account other hexavalent species. Injection of six holes into the valence band of GaAs in step [4] yields an

adsorbed mixed-valence complex which blocks the surface. This surface complex can be reduced by electrons (step [5]), as is clear from the results with p-type electrodes under illumination and n-type electrodes in the dark (1). This implies that the adsorbed species has an energy level distribution corresponding to the bandgap or the conduction band. Since the redox potential of the Cr^{III}/Cr^{II} couple is in this energy range (9), we assume that one of the terminal Cr^{III} atoms is reduced to Cr^{II}; the central Cr^{VI} species, being sterically protected, is not reduced (8). HF is required to remove the reduced complex and free the surface. The unreduced complex can also be removed in a chemical reaction with HF (step [6]), and the liberated Cr^{VI} species subsequently injects three holes into the VB. This explains the small potential-independent cathodic current observed in the dark on p-type electrodes at negative potentials (1).

A clear relationship has been demonstrated between the reduction of Cr^{VI} and the availability of holes at the electrode surface. The reduction reaction is hindered significantly as soon as (photo) anodic dissolution of GaAs stops (1). These results suggest an interaction between the dissolving GaAs and the surface complex. Considering the likely positions of the relevant energy levels, we conclude that a surface-state intermediate of the dissolution reaction is capable of reducing the adsorbed complex, in a manner similar to that suggested above for electrons (step [5])



The reaction of a mixed valence complex with a surface radical yields a reduced complex which is then removed by HF. We consider electron exchange between the adsorbed complex and the surface state to be reversible. An analysis of the etching results leads us to conclude that the rate of reoxidation of the reduced complex is much faster than its rate of decomposition by HF. Equation [7a] can therefore be replaced by [7b]



in which k_7 is an "effective rate constant" describing both steps of reaction [7a].

In the subsequent sections of this paper, the results of p and n-type GaAs will be examined using the complete set of Eq. [1]-[7].

Application of the Model to p-GaAs

Equations for steady state in the dark.—For a p-type electrode in the dark, reaction [5] can be disregarded. Using Eq. [1]-[4] and [6]-[7], the following expressions for p-type GaAs under steady-state conditions are obtained

$$\frac{d\theta}{dt} = k_4 C_{\text{Ox}}(1 - \theta) - k_6 C_{\text{HF}}^n \theta - k_7 C_{\text{HF}}^m N_1 \theta = 0 \quad [8]$$

$$\frac{dN_1}{dt} = k_1 p_s - k_2 p_s N_1 - k_7 C_{\text{HF}}^m N_1 \theta = 0 \quad [9]$$

$$\frac{dN_2}{dt} = k_2 p_s N_1 - k_3 N_2(1 - \theta) + k_7 C_{\text{HF}}^m N_1 \theta = 0 \quad [10]$$

Here, we denote the surface coverage due to the adsorbed complex by θ ($0 \leq \theta \leq 1$), and the surface density of the dissolution intermediates given in Eq. [1] and [2] by N_1 and N_2 (cm⁻²), respectively. C_{Ox} and C_{HF} refer to the

concentration (mol/cm^3) of trichromate and HF species in solution, and p_s is the surface hole concentration (cm^{-3}). It is assumed that the presence of an adsorbed layer on the surface prevents both the Cr^{VI} reduction (reaction [4] and the later stages of GaAs dissolution which require reaction with X^- from solution (reaction [3]). This inhibition is clear from the $(1 - \theta)$ term denoting the free surface in Eq. [8] and [10]. We also assume that the surface hole concentration is given by the Boltzmann equation

$$p_s = p_0 \exp(eV_{sc}/kT) \quad [11]$$

where p_0 is the bulk hole concentration and the band bending V_{sc}

$$V_{sc} = V - V_{FB} \quad [12]$$

is the difference between the applied and flatband potentials.

Kinetic analysis at the rest potential.—The partial currents for reduction of Cr^{VI} (i^c) and oxidation of GaAs (i^a) can be defined according to the reaction scheme [1]–[7]

$$i^c/F = 6k_4C_{\text{Ox}}(1 - \theta) + 3k_6C_{\text{HF}}^n\theta + 3k_7C_{\text{HF}}^mN_1\theta \quad [13a]$$

$$i^a/F = k_1p_s + k_2p_sN_1 + 4k_3N_2(1 - \theta) \quad [13b]$$

At the rest potential V_r , the total current must be zero. Equating i^c and i^a and rearranging with the aid of Eq. [8]–[10], we obtain

$$9k_4C_{\text{Ox}}(1 - \theta) = 6k_1p_s - k_7C_{\text{HF}}^mN_1\theta \quad [14a]$$

From the measured current-potential curves, it is clear that the limiting cathodic current due to reaction [6] is much smaller than the cathodic peak current. Since the current corresponding to the etch rate at the rest potential is larger than the peak current, reaction [6] can be omitted from a consideration of etching at open circuit. Combining Eq. [8] (with $k_6 = 0$) and [14a], we obtain

$$9k_4C_{\text{Ox}}(1 - \theta) = 6k_1p_s - k_4C_{\text{Ox}}(1 - \theta) \quad [14b]$$

The partial currents at V_r can now be derived from Eq. [8], [9], and [14b]

$$i^a = i^c = \frac{18Fk_1k_4C_{\text{Ox}}C_{\text{HF}}^m}{2k_1C_{\text{HF}}^m + 5k_4(k_2/k_7)C_{\text{Ox}}} \quad [15]$$

From Eq. [15], it is immediately clear that, depending on the ratio of C_{Ox} and C_{HF} , the etch rate may be determined either by the oxidizing agent or by HF, provided the values of the rate constants are not too extreme. This is, indeed, found experimentally (1).

At relatively low HF concentration, the second term in the denominator of Eq. [15] is expected to be dominant. The equation then reduces to

$$i^a = i^c = 18/5 Fk_1(k_7/k_2)C_{\text{HF}}^m \quad [16]$$

Figure 1 shows a log-log plot of the measured etch rates at low HF concentration, taken from the first article (1) and recalculated as current density, vs. the HF concentration. Since it was previously shown that the etching kinetics of p-GaAs and n-GaAs in the dark are the same (1), the etch rates for the latter have also been included in the figure. The experimental results agree with Eq. [16] for etch rates differing by an order of magnitude. The slope of the straight line in Fig. 1 is 1.9 ± 0.1 ; this means that reaction [7] must be second order in HF concentration.

Using $m = 2$, Eq. [15] can be rearranged

$$\frac{C_{\text{Ox}}}{i^a} = \frac{1}{9Fk_4} + \frac{5k_2C_{\text{Ox}}}{18Fk_1k_7C_{\text{HF}}^2} \quad [17]$$

From Eq. [17], it follows that a plot of C_{Ox}/i^a as a function of $C_{\text{Ox}}/C_{\text{HF}}^2$ should give a straight line for all etch rates which are not diffusion controlled. The partial current i^a at V_r was again determined from the open-circuit etch rates. The results for p- and n-type materials are plotted in Fig. 2. Considering that the results in this figure represent a wide range of Cr^{VI} and HF concentrations and etch

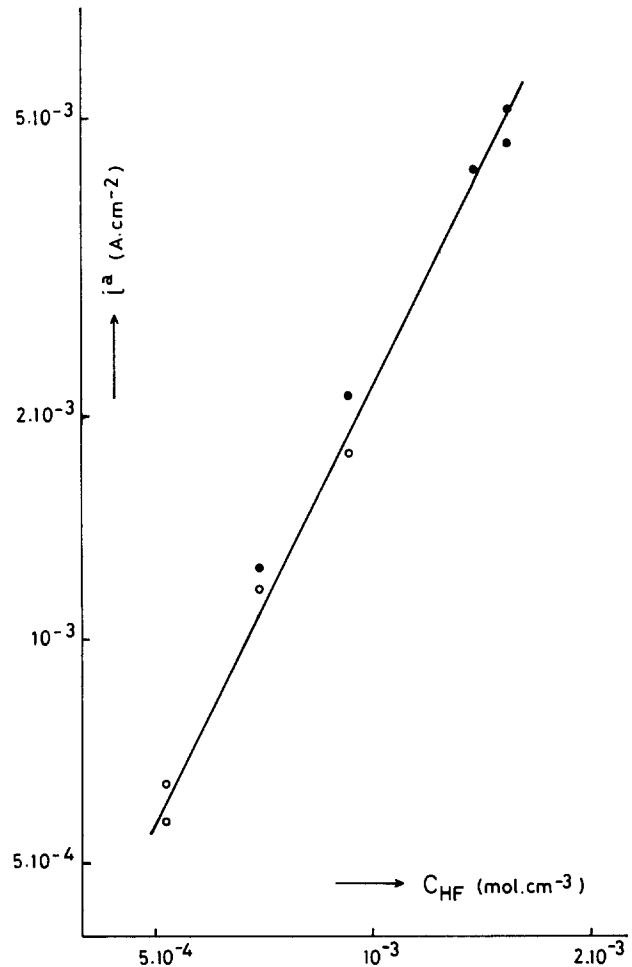


Fig. 1. The etch rate at open circuit for low HF concentrations, expressed as a current density i^a , is plotted as a function of C_{HF} (see Eq. [16]).

rates extending over two orders of magnitude (1), the fit of Eq. [17] should be considered satisfactory. It can therefore be concluded that the model accounts very well for the etching kinetics at open circuit.

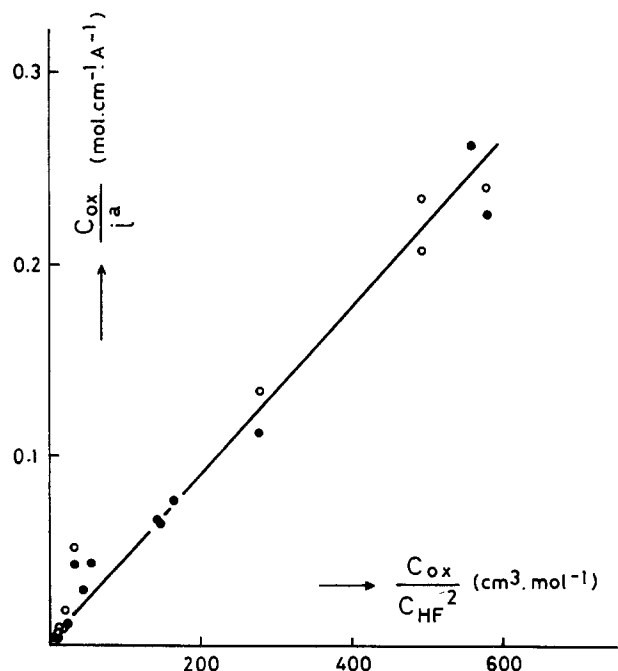


Fig. 2. The etch rate at open circuit, expressed as a current density i^a , is plotted according to Eq. [17].

Determination of rate constants.—In order to calculate the current as a function of potential, it is necessary to know the various rate constants. The constant k_1 is related to anodic dissolution of GaAs. In the absence of the oxidizing agent ($C_{Ox} = 0$), it follows from reaction steps [1]-[3] that

$$i^a = 6Fk_1p_s \\ = 6Fk_1p_0 \text{ at } V = V_{FB} \quad [18]$$

A value of k_1 can thus be obtained from the anodic current-potential curve measured in an indifferent electrolyte. In the present case, Eq. [18] was obeyed and i^a was 1.5 mA/cm^2 at V_{FB} . The resulting k_1 value is given in Table I together with the other constants from the present work.

The term k_2/k_7 can be obtained either from Eq. [16] and Fig. 1 or from Eq. [17] and the slope of Fig. 2. Since k_1 is known, the ratio k_2/k_7 can now be determined. The ratio given in Table I is an average value from the two methods. From Eq. [17] and the intercept of Fig. 2, a value for k_4 can be obtained. This value was found to be not very critical for the further analysis.

At potentials sufficiently negative with respect to V_{FB} , the surface hole concentration is very small. In this range, only reactions [4] and [6] are important. The last term in Eq. [8] can therefore be disregarded and the limiting value of θ can be calculated. The corresponding limiting current $i_{lim} = 9Fk_4C_{Ox}(1 - \theta_{lim})$ is given by

$$i_{lim} = \frac{9Fk_4C_{Ox}k_6C_{HF}^n}{k_4C_{Ox} + k_6C_{HF}^n} \quad [19]$$

At low values of the C_{HF}/C_{Ox} ratio, the limiting current depends only on the HF concentration (1), i.e., $k_4C_{Ox} \gg k_6C_{HF}^n$ and

$$i_{lim} \approx 9Fk_4C_{HF}^n \quad [20]$$

From the experimental dependence of i_{lim} on C_{HF} given in the first article, both n and k_0 can be calculated. Reaction [6] is also found to be second order in HF concentration.

Current-potential curves.—In order to calculate the current in the complete potential range, reaction [6] must be included. The total current is the sum of the partial currents ($i = i^a + i^c$), which are given by Eq. [13]. From the relationship between p_s and θ , which can be obtained from the steady-state Eq. [8]-[10]

$$p_s = \frac{k_4C_{Ox}(1 - \theta) - k_6C_{HF}^2\theta}{k_1 + k_6 \frac{k_2}{k_7} - k_4 \frac{k_2}{k_7} \frac{C_{Ox}}{C_{HF}^2} \frac{(1 - \theta)}{\theta}} \quad [21]$$

the surface coverage can be calculated as a function of p_s . In this way, θ and p_s can be related to the potential via Eq. [11] and [12]. The partial currents, which can also be expressed in terms of p_s and θ (see Eq. [13] and [14]) can therefore be calculated as a function of potential.

Figure 3 shows a calculated curve for a p-type GaAs electrode in a $1.20M$ CrO_3 , $1.54M$ HF solution. For comparison, the measured curve for the same solution is also given (dashed line). Agreement between the two is good: the general form, the cathodic peak height, and the rest potential are predicted by the model. The experimental peak is somewhat broader than expected. This is very likely due to the fact that the Helmholtz potential is not completely constant (10), as is implicitly assumed in Eq. [12]. Figure 4 shows that the calculated dependence of the

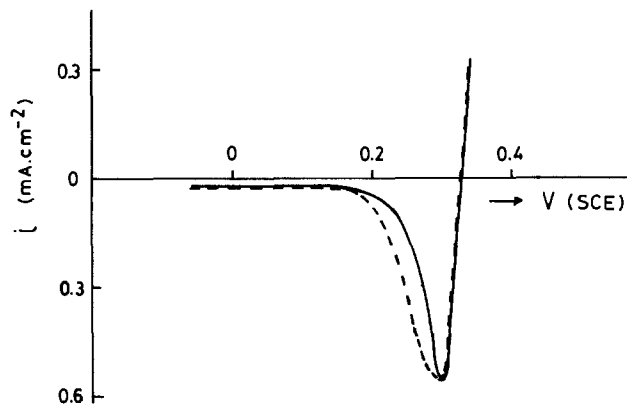


Fig. 3. The solid line gives the calculated current-potential curve for a p-type GaAs electrode in $1.20M$ CrO_3 , $1.54M$ HF solution. The rate constants used were the first four in Table I. The dashed line is the measured curve.

peak current on HF concentration is in excellent agreement with that measured experimentally.

A consideration of the partial currents (Fig. 5) shows how the mechanism operates. As long as the surface hole concentration is sufficient to ensure dissolution of GaAs ($V \geq V_{FB}$), reduction of Cr^{VI} is maintained. Reaction of a surface radical with an adsorbed complex according to reaction [7] leads to decomposition of the complex. Three holes are injected from the liberated Cr^{VI} species, and a surface site is freed at which six holes may be subsequently injected (reaction [4]). Since this process involves the injection of nine charge carriers while only four are required to complete the oxidation of the GaAs pair (reaction [3]), the cathodic partial current can exceed the corresponding anodic current; a current peak, indicated by the dashed line in Fig. 5, is observed. At potentials negative

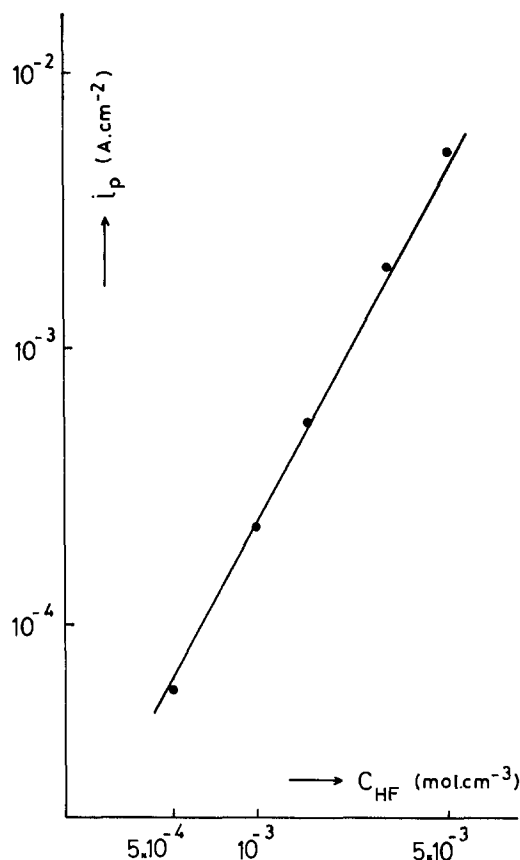


Fig. 4. The cathodic peak current for a p-type GaAs electrode as a function of the HF concentration. The solid line summarizes the measured results from Ref. (1). The points were calculated using the model.

Table I. Estimated values of the various rate constants and rate constant ratios used in this work

k_1	$= 2.5 \times 10^{-27} \text{ mol}\cdot\text{cm}\cdot\text{s}^{-1}$
k_2/k_7	$= 5.5 \times 10^{-25} \text{ mol}^2 \text{ cm}^{-3}$
k_4	$= 5.5 \times 10^{-4} \text{ cm}\cdot\text{s}^{-1}$
k_6	$= 1.3 \times 10^{-5} \text{ cm}^4\cdot\text{mol}^{-1}\cdot\text{s}^{-1}$
k_7	$= 1.5 \times 10^{-33} \text{ mol}\cdot\text{cm}^4\cdot\text{s}^{-1}$
k_7/k_8	$= 1.7 \times 10^{12} \text{ cm}^3 \text{ mol}^{-2}$

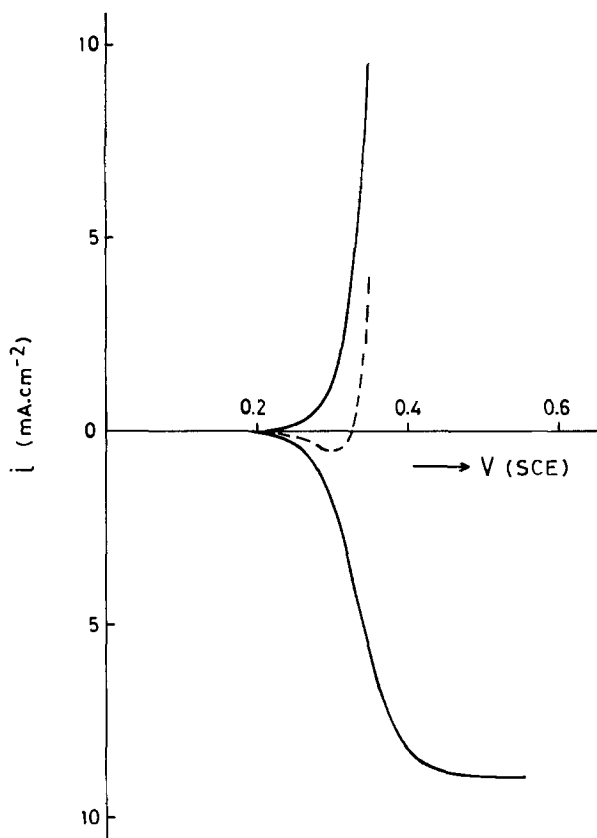


Fig. 5. The solid lines are the anodic and cathodic partial current-potential curves for the case shown in Fig. 3. The dashed line is the total curve.

with respect to the peak, the reduction rate of Cr^{VI} decreases rapidly because of the drop in the GaAs oxidation rate resulting from the drastic decrease in p_s . At potentials more positive than the peak value, the cathodic curve tends to a limiting value while the anodic curve continues to rise exponentially. This leveling off of i_c results from an increase in the contribution of reaction [2], whose rate is directly proportional to p_s . This limits the concentration of reactive radicals at the surface and consequently the rate of reaction [7]. It should be emphasized that the limiting cathodic partial current, shown at positive potentials in Fig. 5, is not a diffusion current. The electrode surface is still blocked and the calculated minimum surface coverage is 0.95 in this case.

A comparison of Eq. [15] and [19] reveals the reason for the apparent discrepancy between the etching and electrochemical results reported for p-GaAs in the first article. A diffusion-controlled reduction of Cr^{VI} was only observed at extreme values of the ratio of the HF and CrO_3 concentrations, while the etch rate depended on mass transport in the solution in a much wider concentration range. The limiting cathodic current of Eq. [19] only becomes independent of C_{HF} when $k_6/k_4 \gg C_{\text{Ox}}/C_{\text{HF}}^2$. Since k_6 is relatively small, this is only possible for high $C_{\text{HF}}^2/C_{\text{Ox}}$ ratios. Open-circuit etching becomes solely dependent on the CrO_3 concentration when $2k_1k_7/5k_2k_4 \gg C_{\text{Ox}}/C_{\text{HF}}^2$; this can be expected at much more modest values of $C_{\text{HF}}^2/C_{\text{Ox}}$ since $2k_1k_7/5k_2k_4$ is two orders of magnitude larger than k_6/k_4 (see Table I). This effect is, of course, due to the participation of GaAs surface intermediates in reaction [7] which results in a depassivation of the surface at open-circuit potential.

Etching morphology.—As described in the first article of this series (1) and in previous publications (11, 12), the CrO_3 -HF etchant is, under kinetically determined conditions, very sensitive to defects in both p- and n-type GaAs. Defects generally correspond to crystallographically disturbed areas of the solid. Since such areas are expected to be less noble than the surrounding material (13),

selective corrosive attack should occur when etching is performed in the dark. Enhanced dissolution of defects should therefore lead to etch pits. Surprisingly, this is not observed with CrO_3 -HF etchants: defects are revealed as hillocks. Although etching morphology will be dealt with in considerable detail in a separate paper (14), we shall here consider briefly the reason for this unexpected effect.

As a simple approximation, we equate the high reactivity of defects with enhanced rate constants (k_1 , k_2) for the dissolution reaction of GaAs. We further assume that the defect has a stronger influence on the second hole trapping step (k_2), which involves the final rupture of the bond, than on the first step (k_1). The effect on the etch rate of such changes in the dissolution rate constants can be judged from Eq. [15]. An increase in the ratio k_2/k_1 gives a lowering of the partial anodic current at the rest potential. The corresponding decrease in etch rate results from a heightened preference of the system for reaction [2] compared to reaction [7]. Since this latter reaction involves a depassivation of the surface, the defects are more effectively protected by the adsorbed layer.

Effect of illumination.—When p-type GaAs is exposed to light of the correct wavelength, electrons are generated in the conduction band (CB) and a cathodic photocurrent is observed at negative potentials (1). Measurements in CrO_3 -HF solutions under these conditions show clearly that illumination also affects the rate at which holes are injected into the VB from Cr^{VI} in solution. We attribute the very high apparent quantum efficiencies found in the limiting photocurrent range to reaction [5]. The surface complex is reduced by an electron, and a surface site is freed. A combination of reactions [4] and [5] involving, in the limiting case, the transfer of ten charge carriers per generated electron (i.e., per absorbed photon) accounts very well for the experimental results (1).

Reduction of the surface complex by electrons, either directly via the CB or indirectly via surface states, is obviously more efficient than H_2 evolution. The onset potential for photocurrent flow in CrO_3 -HF solution is considerably more positive than in an indifferent electrolyte (H_2SO_4). Nevertheless, recombination of electrons with holes must also be important at potentials close to V_{FB} . In previous work (9), it was shown that very effective surface recombination at p-GaAs electrodes can effectively compete with charge transfer to the solution. Therefore, illumination has no effect on the current or on the etch rate near the rest potential.

Application of the Model to n-GaAs in the Dark

Steady-state equations.—For oxidative dissolution of n-type GaAs in the dark, holes must be supplied by injection from solution. In addition, the competing reaction involving recombination of injected holes with electrons from the CB must be considered. This reaction becomes important even at potentials considerably positive with respect to V_{FB} , for which the electron concentration at the surface is relatively low. A representation of the hole balance for an n-type electrode in the dark can be given on the basis of the reaction scheme [1]-[7], where j_p is the hole flux at the surface

$$j_p = 6k_4C_{\text{Ox}}(1 - \theta) + 3k_6C_{\text{HF}}^2\theta + 3k_7C_{\text{HF}}^2N_1\theta - k_1p_s - k_2p_sN_1 - 4k_3N_2(1 - \theta) - j_{\text{rec}} = 0 \quad [22]$$

The j_{rec} term describes the recombination process. Despite the fact that injection occurs mainly at the free surface, we assume a uniform surface concentration for the holes. This is justified if the free surface consists of many very small areas. These areas will, of course, change randomly in time. We also assume that the rate constants determined for p-GaAs can be used for n-type electrodes. The validity of this assumption is supported by results of Gomes and Cardon (15), who studied the competition between redox oxidation reactions and anodic dissolution at III-V electrodes. Since identical kinetics are found for

p-type electrodes in the dark and n-type electrodes under illumination, they conclude that the rate constants are, indeed, independent of semiconductor type.

As a first approximation, we use a very simple recombination mechanism. We consider only direct electron-hole recombination at the surface

$$j_{\text{rec}} = k_r n_s p_s \quad [23]$$

As in the case of p-type electrodes, the majority carrier concentration at the surface n_s is described by the Boltzmann equation

$$n_s = n_0 \exp(-eV_{\text{sc}}/kT) \quad [24]$$

where n_0 is the bulk electron concentration. The magnitude of k_r determines the potential at which a transition occurs between recombination and anodic dissolution (16). An estimate of its value can thus be obtained from the photocurrent-potential curve measured in an indifferent electrolyte. When the photocurrent is equal to half its limiting value, dissolution and recombination rates must be equal ($6k_r p_s = k_r n_s p_s$). The measured potential at which this occurs can be used to calculate n_s (via Eq. [12] and [24]) and consequently k_r . The corresponding value is given in Table I.

Current-potential curves.—Using Eq. [1]-[4], [7]-[10], [12], and [21]-[24] and a procedure similar to that followed above for p-GaAs, both the partial and total currents can be calculated as a function of potential. For convenience, reaction [6] was omitted from all calculations on n-type material. As already shown, the current due to this step is negligible compared to the peak current. Reaction [5] involving reduction of the adsorbed complex by CB electrons was also disregarded, since this only contributes to the current at potentials more than 200 mV negative with respect to the peak value (1).

Calculated results are shown in Fig. 6 for an n-type electrode in the same solution as described above for p-GaAs (Fig. 3). The predicted current-potential curve (Fig. 6a) resembles closely the experimental curve measured with n-GaAs in the vicinity of the rest potential (1). Both the magnitude of the calculated current peak and its dependence on HF concentration are identical to those predicted for p-GaAs and thus in complete agreement with the experimental results.

Again, the mechanism can be more readily understood in terms of the partial reactions (Fig. 6b). At extreme band bending, n_s is very low (Eq. [24]) and recombination can be disregarded. Holes injected from solution are used exclusively to dissolve the electrode. The partial currents are, therefore, equal in this range and the total (measured) current is very low. Since j_{rec} is very small, Eq. [22] becomes the same as Eq. [14], which describes p-GaAs at open circuit. The partial currents for n-GaAs in this potential range are the same as for p-type material at $V = V_r$ (compare Fig. 5 and 6b). At more negative potentials, n_s increases and recombination becomes important. The dissolution rate consequently decreases. A corresponding decrease is observed in the partial reduction current (Fig. 6b). As for p-GaAs, only one hole is required to form a surface radical. On reacting with an adsorbed complex, this can free a blocked site. Subsequent multiple hole injection again gives rise to a current peak (Fig. 6a). It should be noted that, in the case of an n-type electrode, the total (external) current results from recombination of injected holes with electrons (16). This current drops to a very low value on the cathodic side of the calculated peak because the hole injection rate decreases drastically. This results from an increasing surface coverage by the adsorbed complex. It should be noted that the cathodic current, shown in Fig. 6a, begins to flow at potentials at which the photocurrent in an indifferent electrolyte reaches its limiting value.

We have, for simplicity, assumed a surface recombination process to analyze the n-type GaAs case in the dark. However, recombination within the space-charge layer seems more likely considering the very strong band

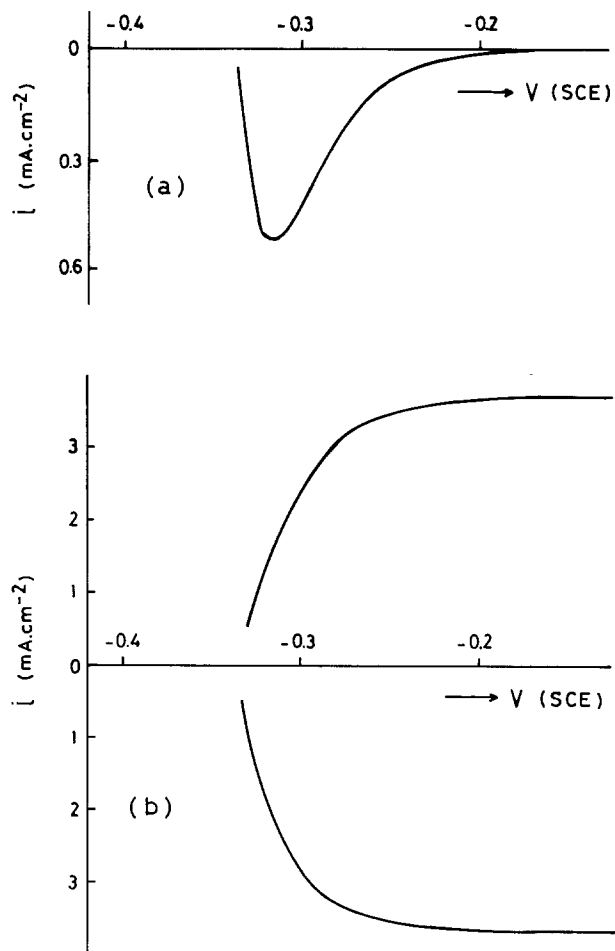


Fig. 6. a: The total current-potential curve calculated for an n-type GaAs electrode in 1.20M CrO_3 , 1.54M HF solution. Direct electron-hole recombination at the surface with a rate constant k_r (Table I) is assumed. b: The corresponding partial curves.

bending involved in the potential range under consideration (16). While the nature of the recombination process may influence the shape of the cathodic peak, its position is always linked to the potential range between photocurrent onset and photocurrent saturation, as observed in an indifferent electrolyte. This has been indicated in the previous section. It can also be shown that the peak current is not dependent on the recombination mechanism, provided that surface intermediates (reactions [1] and [2]) are not involved (see final section).

Etching kinetics.—Using the simple approach as represented by Eq. [22] and [23], it is not possible to calculate the rest potential of the electrode when minority carriers are injected. This potential is determined by a complex combination of factors (17).

An exact knowledge of V_r is, however, not essential for determining the etch rate at open circuit. Under open-circuit conditions, the rates of GaAs oxidation and Cr^{VI} reduction must be equal as the recombination rate must be zero; a nonzero rate would imply electron depletion in the CB. The partial currents at V_r must, therefore, be equal to the potential-independent partial currents shown in Fig. 6b. In order to check that this is the case, we measured the etch rate of GaAs in a 0.72M CrO_3 , 0.93M HF solution as a function of potential. The results in Table II show that the etch rate, determined potentiostatically, has the same potential dependence as that expected from our model (see anodic partial current in Fig. 6b): at potentials positive with respect to V_r , the etch rate is constant and equal to the open-circuit value (this is not a diffusion-controlled rate); at more negative potentials, the etch rate decreases and becomes zero just negative of the cathodic peak value.

Table II. The etch rate of an n-type GaAs electrode, measured in 0.72M CrO₃, 0.93M HF solution, as a function of the applied potential

Potential	Etch rate (nm/min)
Of current minimum	0.0
Of current peak	30 ± 3
Rest potential (V _r)	55 ± 5
V _r + 0.3V	55 ± 5

From the discussion in the previous section, it is clear that the model predicts the same open-circuit etch rates for n- and p-type materials, as is found experimentally. The model, consequently, accounts for the HF concentration dependence of the etch rate.

Application of the Model to n-GaAs under Illumination

Photocurrent-potential curves.—For an illuminated n-type electrode, it is necessary to include a generation term g in Eq. [22] for the hole balance

$$g + 6k_4C_{Ox}(1 - \theta) + 3k_6C_{HF}^2\theta + 3k_7C_{HF}^2N_1\theta = k_1p_s + k_2p_sN_1 + 4k_3N_2(1 - \theta) + j_{rec} \quad [25]$$

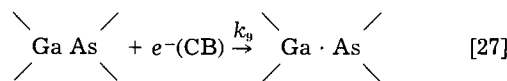
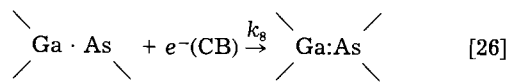
It is found experimentally that the current peak occurs at a potential at least 0.5V more positive than V_{FB} (1). Since this implies a strong electric field at the surface and since the penetration depth of the light is small, we assume that all holes created by light reach the surface (9); g then equals the photon flux. Using Eq. [23]-[25], the partial and total curves can again be calculated. The predicted photocurrent-potential curve is similar to that found experimentally (see Fig. 11 of the first article). At positive potentials, a constant anodic current, whose magnitude depends directly on light intensity, results from photoanodic dissolution of n-GaAs. At more negative potentials, the model predicts a cathodic peak, shifted slightly in the negative direction with respect to the peak in the dark. The calculations also show that this shift is more pronounced at higher light intensity. The predicted peak height under illumination is, however, the same as in the dark and is independent of light intensity. The measured peak showed a weak dependence on photon density (1).

The mechanism of photoetching.—Although the model based on direct electron-hole recombination at the surface accounts reasonably well for the observed current-potential curves, it cannot explain the increase in etch rate at the rest potential during illumination. At V_r , the electrons generated by light at a rate g must be consumed at the same rate, to maintain electrical neutrality in the CB. As generation and recombination rates must be equal ($g = j_{rec}$), Eq. [25] becomes intensity independent at the rest potential and no effect of light on the etch rate can be expected. This also holds for more elaborate models involving recombination centers either at the surface or in the space-charge layer.

In general, two common mechanisms could account for photoetching of n-GaAs at open circuit. In the first, holes generated by light are used for dissolution of the electrode, while the majority carriers, electrons, reduce an oxidizing agent from solution. We do not have such a reduction reaction in the present case. The contribution from reaction [5], the reduction of the surface film by electrons, is too small at the rest potential to account for the increase in etch rate due to light. The second mechanism involves a displacement of the semiconductor bandedges by illumination (10). In this way, hole injection from an oxidizing agent into the VB or surface states, which cannot occur in the dark, may become possible under illumination. A significant shift in the bandedges due to injection from solution or illumination was, however, not observed in this work (Table I of the first article).

To account for photoetching of n-GaAs in CrO₃/HF solutions, a different recombination mechanism was consid-

ered (5), in which the intermediates of the GaAs dissolution reaction act as electron traps



Since these reactions influence the concentration of the radical intermediate responsible for freeing the surface (reaction [7]) they should affect the etch rate. Such a recombination mechanism may not be excluded for the dark case. The rest potential under illumination, however, was found to be more than 100 mV more negative than in the dark (1). The band bending is therefore less extreme and a surface recombination mechanism of the type indicated in Eq. [26] and [27] is even more probable. Normally, one would not expect the second step to be very likely. However, it must be remembered that the intermediate is formed under the blocking layer and nucleophilic attack by X⁻ (reaction [3]) is severely hindered. Analogous recombination steps have been suggested previously by Gomes and co-workers for photoanodic dissolution of n-type III-V electrodes (18, 19).

Equations [9] and [10] now become

$$\frac{dN_1}{dt} = k_1p_s - k_2p_sN_1 - k_7C_{HF}^2N_1\theta - k_8N_1n_s + k_9N_2n_s \quad [28]$$

$$\frac{dN_2}{dt} = k_2p_sN_1 - k_3N_2(1 - \theta) + k_7C_{HF}^2N_1\theta - k_9N_2n_s \quad [29]$$

For convenience in the calculations, we limit ourselves to the case in which all recombination occurs via such a mechanism; the independent j_{rec} term in Eq. [25] is therefore omitted. With the aid of Eq. [8], [24], and [25]-[29] and some straightforward though tedious mathematics, expressions for θ , p_s , k_8N_1 , and k_9N_2 can be obtained as a function of n_s and thus of V_{sc} . Apart from the known parameters, these expressions contain two new terms k_7/k_8 and k_9/k_3 . The former ratio determines the potential at which n-GaAs begins to dissolve when holes are injected from Cr^{VI} in the dark. Its value can be allocated accordingly. The ratio k_9/k_3 must be chosen arbitrarily.

Typical results of such a calculation are given in Fig. 7a. The solid curve shows the total current under illumination as a function of potential. The general form is very similar to that of the measured curves (1). The cathodic peak is shifted with respect to its position in the dark (dashed curve) and illumination enhances slightly the peak current, in agreement with the experimental results. In Fig. 7b the calculated quantum efficiency for dissolution of GaAs, ϕ , defined as

$$\phi = (i_{diss}^* - i_{diss})/gF \quad [30]$$

is plotted as a function of potential; i_{diss}^* and i_{diss} refer to the calculated current densities for GaAs dissolution under illumination and in the dark at the same potential. From this figure, it is clear that a quantum efficiency in excess of one can be expected not only at positive potentials but also at the rest potential, as indicated. A similar result was found experimentally in the potentiostatic etching experiments reported in Table II of Ref. (1). The experimental values were, however, higher than those shown in Fig. 7.

This recombination mechanism is clearly too limited to account quantitatively for all the results observed with illumination. However, the qualitative and semiquantitative agreement between predicted and measured results supports the assumption that dissolution intermediates must play an important role in the electrochemistry of n-type GaAs electrodes illuminated in CrO₃-HF solutions.

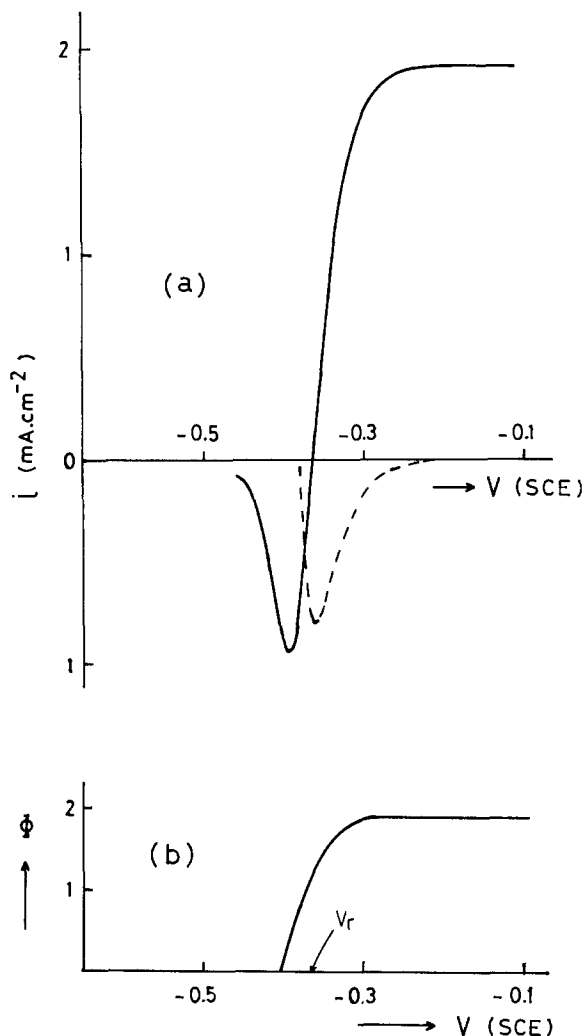


Fig. 7. a: The solid line gives the calculated current-potential curve under illumination for an n-type GaAs electrode in 1.20M CrO_3 , 1.54M HF solution. The dashed line represents the dark case. Recombination is assumed to occur via surface intermediates of the GaAs oxidation reaction. The ratio k_7/k_8 is given in Table I. The ratio k_9/k_3 is assumed to be $2.5 \times 10^{-9} \text{ cm}^3$. b: The calculated quantum efficiency for dissolution of GaAs as a function of potential for the case described in Fig. 7a. The light intensity used corresponds to a flux of $2.1 \times 10^{-8} \text{ mol/cm}^2\text{-s}$.

Summary

The model proposed in this paper for the dissolution of GaAs in CrO_3 -HF solutions involves two important features.

The first is the partial reduction of a hexavalent chromium species in solution results in the formation of an adsorbed mixed-valence complex on the semiconductor surface. This acts as a blocking layer which inhibits both the further injection of holes from Cr^{VI} and the dissolution of GaAs.

The second is that the adsorbed complex can be reduced by a radical intermediate of the GaAs oxidation reaction. The reduced form is then removed from the surface by HF from solution.

An analysis of the kinetics of the partial reactions leads to equations for the etch rate and the current as a function of applied potential.

With regard to etching, the model can explain the following observations: the etch rates of p- and n-type GaAs in the dark are the same; etching changes from kinetic to diffusion control when the ratio of the HF and CrO_3 concentrations is increased; the etch rate of p-type GaAs is not influenced by illumination; and crystallographic defects are revealed as hillocks.

The model accounts very well for the electrochemical results with p-type GaAs: the form of the current-potential curves, including the characteristic cathodic

peak, is explained; the positions of both the rest potential and the peak maximum are predicted; the magnitude of the current peak and its dependence on HF concentration are accounted for quantitatively; and the very high apparent quantum efficiency for the cathodic photocurrent can be understood.

For n-type electrodes, recombination of holes injected by Cr^{VI} with CB electrons must also be taken into account. The essential results for n-type GaAs in the dark can be explained with the aid of a simple model involving direct electron-hole recombination at the surface. The general form and the position of the current-potential curves is accounted for. The peak current is shown to be identical to that of p-type GaAs and to have the same HF concentration dependence.

This simple recombination model failed, however, to explain the results obtained with n-GaAs under illumination. Since, in this case, the rest potential is shifted to values more negative than that observed in the dark, it was concluded that recombination of electrons and holes occurs via surface intermediates of the GaAs oxidation reaction. Although this mechanism predicted a higher cathodic peak current in the dark than was experimentally observed, it could account for the results under illumination. The form of the calculated photocurrent-potential curves agrees with that measured experimentally; the shift of the potential of the cathodic peak from its dark value to more negative potentials at increasing light intensity is predicted; the increase in the magnitude of the peak current with increasing light intensity is explained; and a quantum efficiency greater than one for dissolution of n-GaAs both at open-circuit and more positive potentials can be understood in terms of the model.

Acknowledgments

The authors are grateful to Dr. R. Memming, P. H. L. Notten and Dr. L. J. Giling for helpful discussions. J. van de Ven wishes to thank the Stichting voor Fundamenteel Onderzoek der Materie and the Nederlandse Organisatie voor Zuiver Wetenschappelijk Onderzoek for financial support.

Manuscript submitted April 29, 1985; revised manuscript received Sept. 5, 1985.

Philips Research Laboratories assisted in meeting the publication costs of this article.

REFERENCES

1. J. van de Ven, J. E. A. M. van den Meerakker, and J. J. Kelly, *This Journal*, **132**, 3020 (1985).
2. H. Gerischer and W. Mindt, *Electrochim. Acta*, **13**, 1329 (1968).
3. R. Memming, *ibid.*, **25**, 77 (1980).
4. K. W. Frese, M. J. Madou, and S. R. Morrison, *This Journal*, **128**, 1527 (1981).
5. J. J. Kelly and P. H. L. Notten, *ibid.*, **130**, 2452 (1983).
6. R. Memming, in "Photoelectrochemistry, Photocatalysis and Photoreactors," M. Schiavello, Editor, pp. 107-153, D. Reidel, Dordrecht, Holland (1985).
7. H. Gerischer, *Ber. Bunsenges. Phys. Chem.*, **69**, 578 (1965).
8. J. P. Hoare, *This Journal*, **126**, 190 (1979).
9. J. J. Kelly and R. Memming, *ibid.*, **129**, 730 (1982).
10. J. J. Kelly and P. H. L. Notten, *Electrochim. Acta*, **29**, 589 (1984).
11. J. L. Weyher and J. van de Ven, *J. Phys. C*, **43**, 313 (1982).
12. J. Weyher and J. van de Ven, *J. Cryst. Growth*, **63**, 285 (1983).
13. K. W. Frese, M. J. Madou, and S. R. Morrison, *J. Phys. Chem.*, **84**, 3172 (1980).
14. J. van de Ven, J. L. Weyher, J. E. A. M. van den Meerakker, and J. J. Kelly, Submitted to *This Journal*.
15. W. P. Gomes and F. Cardon, Extended Abstract A18, 32nd Meeting of the ISE, Dubrovnik, Sept. 1981.
16. J. E. A. M. van den Meerakker, J. J. Kelly, and P. H. L. Notten, *This Journal*, **132**, 638 (1985).
17. H. Gerischer and I. Wallem-Mattes, *Z. Phys. Chem. N.F.*, **64**, 187 (1969).
18. D. Vanmaekelbergh, W. P. Gomes, and F. Cardon, *J. Chem. Soc., Faraday Trans.*, **1**, **79**, 1391 (1983).
19. D. Vanmaekelbergh, W. Rigole, W. P. Gomes, and F. Cardon, *ibid.*, **1**, **79**, 2813 (1983).

Quantitative Spectroscopy of Interstitial Oxygen in Silicon

B. Pajot

Groupe de Physique des Solides de l'E.N.S., Tour 23, Université Paris 7, F-75251 Paris Cedex 05, France

H. J. Stein*

Sandia National Laboratories, Albuquerque, New Mexico 87185

B. Cales

CNRS, Centre de Recherche sur la Physique des Hautes Températures, F-45045 Orléans Cedex, France

C. Naud

Optique de la Matière Condensée, Tour 13, Université Paris 6, F-75230 Paris Cedex 05, France

ABSTRACT

Quantitative data are presented on the infrared (IR) absorption of interstitial oxygen in oxygen-rich silicon using Fourier transform spectroscopy. Besides the well-known 515 and 1106 cm^{-1} room temperature IR bands, due to the symmetric and antisymmetric vibrations of the Si_2O entity, respectively, three other bands at 1227, 1720, and 1013 cm^{-1} are reported, whose intensities are scaled with those of the 515 and 1106 cm^{-1} bands. The band at 1227 cm^{-1} has often been confused with an oxygen precipitate band observed at 1225 cm^{-1} in annealed silicon. Evidence is given that the 1227 cm^{-1} band is related to interstitial oxygen. It is also shown that another band at 1720 cm^{-1} is a combination of the antisymmetric mode of Si_2O with a phonon combination of the silicon lattice. A weak band at 1013 cm^{-1} is reported for the first time, and it is attributed to an overtone of the 515 cm^{-1} mode.

Oxygen dissolves in silicon near the melting point (1420°C) up to concentrations of about 2×10^{18} at./ cm^3 by forming two strong Si—O bonds with nearest-neighbor Si atoms (1). In this position, the oxygen atom is termed to be interstitial and noted O_i . This implies a distortion of the lattice as the mean distance between the two Si atoms increases from 0.234 nm in the unperturbed lattice to 0.320 nm when bound through the oxygen atom. Near the melting point, this distortion is somewhat reduced by the generation of Frenkel pairs, but their production rate decreases with temperature and the lattice strain of oxygen-rich Czochralski-grown (CZ) silicon (2) increases with the cooling down of the crystal. A possible channel for global lattice relaxation of the crystal is the precipitation of some form of silica. (It must be pointed out that precipitation of silica produces local strains because of the volume misfit between silicon and silica. These local strains can, in turn, be relaxed by other mechanisms whose discussion is beyond the scope of this paper.) The precipitation kinetics of O_i is such, however, that the O_i concentration at room temperature in most as-grown CZ Si crystals is of the same order of magnitude as that near the melting point, despite the fact that its solubility is of several orders of magnitude less than that at the melting point. It is commonly admitted that, during the cooling down of the CZ Si crystals, precipitation of oxygen can occur (3), especially for crystals with large diameters. This point will be clarified here.

Infrared (IR) vibrational spectroscopy can reveal the presence of dispersed oxygen as well as that of silica precipitates (O_p) produced under deliberate high temperature annealing (4). This technique can allow one to determine the respective amount of each phase if what is due to O_i and what to O_p has been identified unambiguously. This task is complicated by the fact that the most intense IR bands associated with O_i and O_p occur in the same spectral range (950–1250 cm^{-1}), and one of the purposes of this paper is to clearly present what is due to interstitial oxygen since recently, the wrong attribution of a weak absorption band in as-grown CZ Si has led to the statement that silica absorption could be detected in this material. The other purpose is to try to summarize all the features of the room temperature absorption of O_i in silicon, including a discussion on the origin of an O_i -related band

observed at 1720 cm^{-1} and the attribution of another weak band at 1013 cm^{-1} .

Experimental

Different samples about 4 mm thick were cut from a (100)-oriented B-doped CZ slice with $N_a - N_d = 1 \times 10^{15}$ cm^{-3} and $[C_s] = 2 \times 10^{16}$ at./ cm^3 . This slice had been annealed for 2h at 650°C. The spectra shown here have been obtained with a BOMEM DA3.01 Fourier transform spectrometer, using a float-zoned sample with the same free carrier concentration as a reference. The measurements have been performed at $(293 \pm 1)\text{K}$ or at lower temperature using a continuous flow liquid helium cryostat, and they were reasonably independent of the samples. In the determination of the extrinsic absorption coefficient, the effect of multiple reflections is taken into account (5). Neglecting this effect leads to an overestimate of the absorption coefficient, an error which increases for the small values of this coefficient. This must be reminded since we compare values of the absorption coefficient which can differ by two orders of magnitude. No correction has been made for the phonon and free-carrier absorption. The O_i concentration using the ASTM F121-80 norm is 9.9×10^{17} at./ cm^3 . A series of recent independent analyses has shown that the RT calibration factor recommended by the ASTM and the DIN (2.45×10^{17} at./ cm^2), based on the analyses of Graff *et al.* (6), was underestimated and that a value of 3.0×10^{17} at./ cm^2 was more realistic (7).

Results and Discussion

The first extensive studies of the IR absorption of oxygen in silicon after those of Kaiser and Keck (8) were made by Hrostowski (9). They demonstrated that the absorption in as-grown material was characteristic of an Si_2O quasi molecule, today denoted O_i . We consider the so-called 515 and 1106 cm^{-1} O_i -related bands, and we present quantitative data on these bands as well as on weaker bands also related to O_i .

The 515 cm^{-1} band is actually observed at 514.0 cm^{-1} at RT, and it shifts at 517.8 cm^{-1} at liquid helium temperature (LHT). It is due to a symmetric vibrational mode of Si_2O . Although guessed by the first investigators, some doubts had been cast on this attribution (3), but a comprehensive study of the stress-induced dichroism of this band compared with that of the 1106 cm^{-1} band by

* Electrochemical Society Active Member.

Stavola (10) has confirmed the early attribution. The resonance of the 515 cm^{-1} band with the phonon spectrum of Si is responsible for its asymmetric shape, characteristic of a resonance between a discrete transition and a continuum (Fig. 1a). This is also the probable reason for the absence of an isotopic shift due to oxygen (9). This band can be a useful probe of the O_i concentration in annealed silicon containing silica precipitates because of its relative sharpness ($\text{FWHM} \approx 7.6\text{ cm}^{-1}$) and of the weak intensity of the silica precipitates band in this spectral region (10). When measuring the maximum absorption coefficient of this band using the high frequency background as a base line, its ratio to the maximum absorption coefficient of the 1106 cm^{-1} band (this will be hereafter referred to as the relative intensity) is 0.26 ± 0.03 . This figure is an average of measurements made on different Si samples with negligible oxygen precipitation, and the maximum absorption coefficient of the 515 cm^{-1} band can be used to measure $[O_i]$ using calibration factors of $9.4 \times 10^{17}\text{ at./cm}^2$ (ASTM F-121 1980) or $1.25 \times 10^{18}\text{ at./cm}^2$ to comply with Ref. (7).

Figure 1b shows the strong RT absorption of O_i peaking at 1107.7 cm^{-1} , known as the 1106 cm^{-1} band. It can be ascribed to transitions involving the antisymmetric stretching mode (ν_3) of the Si_2^{16}O group starting from thermally excited states of a low frequency anharmonic vibrational mode or a quasi-free rotational mode of the oxygen atom

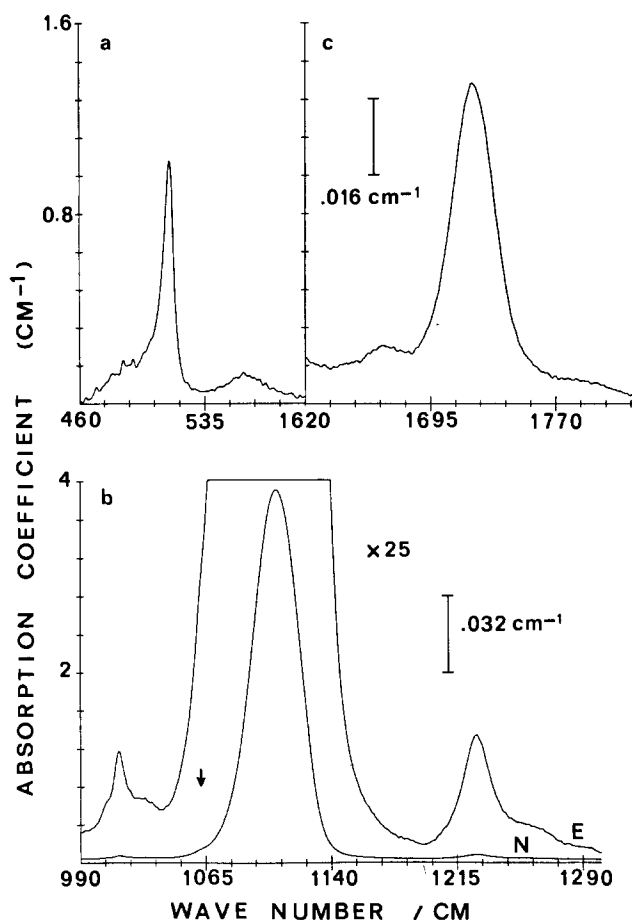


Fig. 1. Absorption coefficient of O_i in a B-doped silicon sample at $(293 \pm 1)\text{ K}$. $[O_i] = 1 \times 10^{18}\text{ at./cm}^3$. The spectral bandwidth (2 cm^{-1}) and the abscissa scale ($15\text{ cm}^{-1}/\text{division}$) are the same for the three spectra. a: The band at 514 cm^{-1} . Note the asymmetric shape and the weak background feature near 560 cm^{-1} . The integrated intensity (l.i.) between 474.5 and 534 cm^{-1} is $(11.8 \pm 0.6)\text{ cm}^{-2}$. b: The bands at 1013 , 1108 , and 1227 cm^{-1} . The ordinate scale for b corresponds to spectrum N. Spectrum E has been expanded by a factor of 25 with respect to spectrum N. The ^{18}O absorption, detected as a shoulder on the low energy side of the 1108 cm^{-1} band, is marked by an arrow. The l.i. is $(136 \pm 1)\text{ cm}^{-2}$ between 1035 and 1185 cm^{-1} . c: The band at 1720 cm^{-1} . The scale expansion with respect to spectrum N of b is 50.

among equivalent minima. The full width at half maximum of the envelope is 33 cm^{-1} , but the individual components are expected to be sharper. The maximum of the envelope is resolution-independent for a spectral band width (s.b.w.) less than 4 cm^{-1} . For a s.b.w. of 8 cm^{-1} , a small decrease of the peak absorption is observed, however. This fact is not in contradiction with individual components having natural widths $\approx 5\text{ cm}^{-1}$ separated by the same quantity. A study of the shape of the envelope as a function of the s.b.w. and of the temperature between 250 and 350 K could help to elucidate this point. In the absence of silica precipitate, the ratio of the peak absorption to the integrated intensity of the 1106 cm^{-1} band is $(2.86 \pm 0.06) \times 10^{-2}\text{ cm}$, and this is a supplementary indication that this band is an envelope.

An asymmetry observed on the low energy side of the 1106 cm^{-1} band is attributed to the ν_3 mode with ^{18}O . (The natural abundance of ^{18}O is 0.002 times that of ^{16}O .) Drastic base-line correction provides a peak value of $(1059 \pm 1)\text{ cm}^{-1}$ for the ^{18}O band, in agreement with the value of 1058 cm^{-1} obtained with an ^{18}O -enriched sample (9). A band at 1013 cm^{-1} and a weaker shoulder at 1006 cm^{-1} are also observed in all the OR samples with a relative intensity of $(6 \pm 2) \times 10^{-3}$. They are seen in the left side of Fig. 1b. A weak band is also observed at the same position (1012.5 cm^{-1}) at LHT; this band was also reported without comment by Oerhlein *et al.* (11). There is a correlation between these bands and the O_i concentration but not with the carbon or boron concentration. Under annealing at 450°C for a relatively long time, these bands broaden and their structure is not so well defined. Bean *et al.* (12) quote a weak band at 1004.1 cm^{-1} in electron-irradiated OR Si after annealing at 450°C . We have indeed observed local mode absorption at 1005.2 and 1011.1 cm^{-1} at room temperature in electron-irradiated OR Si after short-time annealing in the 450°C range. These bands shift to 1006.7 and 1012.2 cm^{-1} at low temperature. The band and the shoulder reported above are certainly different from these oxygen defect-complex bands since the former are still observed after a high temperature (1350°C) redissolution treatment. Bands near 1006 cm^{-1} at ambient have also been associated by Chrenko *et al.* (13) to interstitial lithium trapped electrostatically by the O_i atom in Li-diffused Si, but these bands shift by $\approx 8\text{ cm}^{-1}$ toward high frequencies at low temperature and they do not seem to be related to the bands observed here.

The sharpness of the 1013 cm^{-1} band at room temperature makes its assignment to a combination of the 515 cm^{-1} mode with a phonon mode unlikely, but it could be an overtone of this mode. The absence of a frequency shift between room temperature and LHT could be explained by a change of the anharmonicity of the mode with temperature.

The band at 1227 cm^{-1} best seen on the right side of spectrum E in Fig. 1b is common to all the OR Si samples with a relative intensity of $(11 \pm 2) \times 10^{-3}$. This band should not be confused with the band at 1225 cm^{-1} observed in OR Si after high temperature annealing, which is associated with some kind of silica precipitate (4). Figure 2 shows the 1225 cm^{-1} precipitate band at room temperature in a sample identical to that used to obtain the spectra of Fig. 1 after a two-step annealing: in the first step, 95% of O_i present in the sample was precipitated; in the second step, 50% of the oxygen was redissolved and the 1225 cm^{-1} precipitate band appears clearly. From a comparison of the intensities of the 515 and 1106 cm^{-1} bands in the spectrum of Fig. 2, a contribution of the silica absorption at 1106 cm^{-1} of 17% (0.38 cm^{-1}) to the maximum absorption coefficient at this wave number is calculated. This precipitate band which can generally be observed after preannealing at 600°C followed by annealing at 900°C has long been ascribed to the presence of cristobalite, but this attribution has recently been questioned (14). An important point is that, contrary to the 1227 cm^{-1} band, the shape and the intensity of this precipitate band remain practically unchanged between room temperature and LHT.

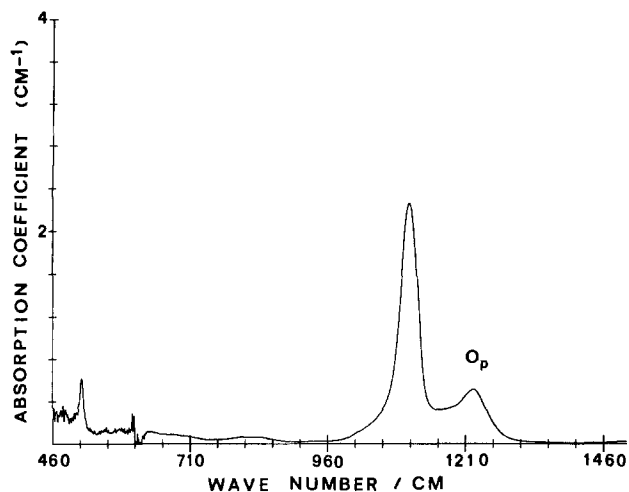


Fig. 2. Absorption coefficient of O_i and O_p in an annealed sample identical to that of Fig. 1. The spectral bandwidth is 2 cm^{-1} . Note the precipitate band near 1225 cm^{-1} . $[O_p] \approx 5 \times 10^{17} \text{ at./cm}^3$ is inferred from this spectrum.

The 1227 cm^{-1} band, on the other hand, is a combination band involving the ν_3 mode of the Si_2O group. This band shifts at 1205.8 cm^{-1} at LHT. The 1205.8 cm^{-1} band has been ascribed by Bosomworth *et al.* (15) to a combination band of the ν_3 mode with a two-quantum excitation of a low frequency anharmonic motion of the oxygen atom tunneling through a potential barrier built by the two silicon atoms of the Si_2O group. This motion is a two-dimensional analog of the low frequency inversion motion of nitrogen tunneling through the potential built by the three hydrogen atoms in the ammonia molecule. In the harmonic oscillator description, it can be visualized as a $|0,0,0\rangle \rightarrow |1,2,0\rangle$ transition where the first number from the left refers to the excitation number of the ν_3 mode, the second one to the excitation number of the low frequency oscillator, and the one at the right to the l value of this oscillator. Aside from the 1205.8 cm^{-1} , a second component at 1216.8 cm^{-1} appears above 15 K and it can be similarly ascribed to a $|0,1,1\rangle \rightarrow |1,3,1\rangle$ transition. (With this labeling, the strong 1136.4 cm^{-1} observed at LHT is a $|0,0,0\rangle \rightarrow |1,0,0\rangle$ transition.) At room temperature, it is expected that the quasi-free rotational motion of the oxygen atom about the Si-Si axis can compete with the low temperature vibrational motion.

The observation of the 1227 cm^{-1} band has been sometimes related to the presence of some kind of silica precipitates in as-grown material. We have tried indeed to measure the concentration of precipitated oxygen in the slice from which the IR sample has been cut. A redissolution experiment (5h at 1350°C in argon ambient followed by room temperature quenching at $\approx 100^\circ\text{C/s}$) on an adjacent sample showed, after removing of $200 \mu\text{m}$ of material on each side of the sample, an increase of the intensity of the 1106 cm^{-1} band by 2%, *i.e.*, by $2 \times 10^{16} O_i \text{ at./cm}^3$. Besides this point, no differences were found in the room temperature spectra of both samples, indicating that in the as-received sample about 98% of the oxygen was already present in the interstitial form.

Figure 1c shows a vibrational band associated with O_i and located at 1720.1 cm^{-1} at room temperature with a relative intensity of 0.016. This band has previously been reported by Lappo and Tkachev (16). The energy difference between this band and the 1106 cm^{-1} band is 612.4 cm^{-1} . (See Table I for the exact position of the bands at 293 K.) At LHT, this band shifts to 1748.6 cm^{-1} ; above 20 K, two new bands appear with decreasing intensities at 1741.2 and 1735.5 cm^{-1} . These bands have also been reported by Krishnan and Hill (17). Their separations from the "hot" bands at 1128.3 and 1121.7 cm^{-1} which are associated (18) with the 1136.4 cm^{-1} band are 612.9 and 613.8 cm^{-1} , respectively. We have checked that the 1720 cm^{-1} band was not correlated with carbon. This band was ascribed by

Table I. Characteristics of the infrared bands associated with interstitial oxygen in silicon at 293 K for a spectral bandwidth of 2 cm^{-1} . The relative intensities are measured taking into account the reflection losses

Origin	Position (cm^{-1})	Relative absorption	FWHM (cm^{-1})
$\nu_{\text{sym}}(O_i)$	514.0 ± 0.6	0.26 ± 0.04	7.6 ± 0.7
$2\nu_{\text{sym}}(O_i)$	1013.2 ± 0.3	$(6 \pm 2) \times 10^{-3}$	8 ± 1
$\nu_{\text{as}}(^{18}\text{O}_i)$	1059 ± 1	NM	NM
$\nu_{\text{as}}(^{16}\text{O}_i)$	1107.7 ± 0.5	1	33 ± 1
$[\nu_{\text{as}} + \nu_{\text{vib}}](^{16}\text{O}_i)$	1226.7 ± 0.7	$(11 \pm 2) \times 10^{-3}$	22 ± 2
$\nu_{\text{as}}(^{16}\text{O}_i) + \nu_{\text{ph}}(\text{Si})$	1720.1 ± 0.6	$(16 \pm 2) \times 10^{-3}$	31 ± 1

Lappo and Tkachev to the combination of two vibrational modes of the Si_2O group, namely, the symmetric one producing the 515 cm^{-1} band and a mode they ascribe to what we label the 1227 cm^{-1} band. The agreement on the frequencies is fair at room temperature, but the LHT results destroy the argument. We propose that this line is due to a combination of the ν_3 antisymmetric mode of the Si_2O group with the two-phonon combination TA + TO at the X point of the Brillouin zone (19). This two-phonon combination is IR active, and it gives rise to the strongest absorption (apparent intensity $\approx 10 \text{ cm}^{-1}$) in the multiphonon spectrum of silicon. The frequencies of this combination are (610 ± 1) and $(613 \pm 1) \text{ cm}^{-1}$ at room temperature and LHT, respectively, but we are unable to detect this difference in our measurements. From the FWHM of the 1720 cm^{-1} band, we infer that the phonon mode distribution is sharp and this is confirmed by the LHT results where the FWHM of the 1748.6 cm^{-1} band is 3.6 cm^{-1} against 0.6 cm^{-1} for the ν_3 band at 1136.4 cm^{-1} .

Conclusion

Two O_i -related IR vibrational bands have been known for a long time in OR silicon. It has been shown here that three other weak vibrational bands are also related to O_i , and that one of them reveals a coupling between the ν_3 mode and the phonon spectrum of silicon. Waldner *et al.* (20) had made similar observations in the study of the local mode absorption of Li B pairs in silicon. One of the bands analyzed here has been previously ascribed to a silica precipitate. The present work rules out this possibility and its consequences. A point which has not been discussed is the origin of a weak and broad band observed at 560 cm^{-1} . This band can be seen in Fig. 1a, where the reference sample contains the same boron concentration as the CZ sample: so, its attribution to a local mode of boron seems unlikely. The presence of this band after redissolution of oxygen seems to preclude its attribution to a silica mode, and its possible relation with oxygen deserves further investigation.

Acknowledgments

We are grateful to Professor J. W. Corbett for having brought Ref. (7) to our attention. The preparation of the samples for the high temperature annealing was performed by S. Squelard.

Manuscript submitted May 27, 1985; revised manuscript received Aug. 14, 1985.

CNRS assisted in meeting the publication costs of this article.

REFERENCES

- Y. Yatsurugi, N. A. Kiyama, Y. Endo, and T. Nozaki, *This Journal*, **120**, 975 (1973).
- Y. Takano and M. Maki, in "Semiconductor Silicon 1973," H. R. Huff and R. R. Burgess, Editors, p. 469, The Electrochemical Society Softbound Proceedings Series, Princeton, NJ (1973).
- F. Shimura, Y. Ohnishi, and H. Tsuya, *Appl. Phys. Lett.*, **38**, 867 (1981).
- W. J. Patrick, in "Silicon Device Processing," C. P. Marsden, Editor, p. 442, N.B.S. Special Publication 337, National Bureau of Standards, Washington, DC (1970).

5. B. Pajot, *Analysis*, **5**, 293 (1977).
6. K. Graff, E. Grallath, S. Ades, G. Goldbach, and G. Tölg, *Solid State Electron.*, **16**, 887 (1973).
7. H. J. Rath, P. Stallhofer, D. Huber, and B. F. Schmitt, *This Journal*, **131**, 1920 (1984).
8. W. Kaiser and P. H. Keck, *J. Appl. Phys.*, **28**, 882 (1957).
9. H. J. Hrostowski and B. J. Adler, *J. Chem. Phys.*, **33**, 980 (1960).
10. M. Stavola, *Appl. Phys. Lett.*, **44**, 514 (1984).
11. G. S. Oehrlein, J. L. Lindstrom, and J. W. Corbett, *ibid.*, **40**, 241 (1982).
12. A. R. Bean, R. C. Newman, and R. S. Smith, *J. Phys. Chem. Solids*, **31**, 739 (1970).
13. R. M. Chrenko, R. S. McDonald, and E. M. Pell, *Phys. Rev.*, **138**, A1775 (1965).
14. P. Gaworzewski, E. Hild, F. G. Kirscht, and L. Vecsernyes, *Phys. Status Solidi; A*, **85**, 133 (1984).
15. D. R. Bosomworth, W. Hayes, A. R. L. Spray, and G. D. Watkins, *Proc. Phys. Soc. London, Sect. A*, **317**, 133 (1970).
16. M. T. Lappo and V. D. Tkachev, *Sov. Phys. Semicond.*, **4**, 418 (1970).
17. K. Krishnan and S. L. Hill, in "Fourier Transform Infrared Spectroscopy (1981)," p. 27, H. Sakai, Editor, S.P.I.E. 289, S.P.I.E., Bellingham, WA (1981).
18. R. C. Newman, *Adv. Phys.*, **18**, 545 (1969).
19. J. L. Birman, in "Encyclopedia of Physics," Vol. XXV/2b, "Light and Matter Ib," L. Genzel, Editor, Springer-Verlag, Berlin (1974).
20. H. Waldner, M. A. Hiller, and W. G. Spitzer, *Phys. Rev.*, **140**, A172 (1965).

A Modeling Study of Superficial Topography for Improved Lithography

L. K. White*

RCA Laboratories, David Sarnoff Research Center, Princeton, New Jersey 08540

ABSTRACT

The contour coating properties of spun-on resist films on topography can influence the lithographic definition of features. In some cases, it is desirable to take these effects into consideration in the layout of a device. Superficial topography, ST, around the perimeter of critical features and large arrays where space permits can improve the uniformity of the spun-on coating contour. A computer simulation procedure is used to design the ST and examples presented for a real device structure coated with representative spun-on positive resist coating. The same ST can also reduce the effects of radial flow-induced coating anomalies that can, in some cases, produce different contours at every location on the substrate. Even planarization sublayers in multilayer resist processes cannot always effectively planarize large arrays relative to a flat expanse. ST can play a beneficial role in many lithographic processes using spun-on films that coat topographical features.

Spun-on resist coatings are the dominant imaging material for IC lithographic processing. Spun-on polymer coatings are also being used more frequently in etchback planarization processes (1) and as passivation coatings. As critical dimensions approach the step heights of the topography, the topography (contour) coating properties of these spun-on coatings become an increasingly important aspect of all these processes. The spun-on coating thickness on topographical features is strongly influenced by the feature size. Different spun-on solutions and spin processes can produce different contour coating properties. Film shrinkage and, in some cases, thermal flow during subsequent cures of the film also influence the coating properties. The spun-on coating thickness on topography is further complicated by adjacent topography which can produce significant changes in the coated contour (2). In large, complex repetitive arrays, the interaction of the edge features of the array with the flat expanse produces significant coating thickness variations. Furthermore, radial flow-induced coating anomalies can actually produce different coating contours, depending on the radial position and orientation of the topography (3, 4).

For lithographic definition of the spun-on resist films, coating thickness variations can greatly influence the final patterned dimensions (5, 6). On highly reflective substrate materials with conventional positive resists and optical g-line exposure (436 nm), standing wave interference phenomena typically produce linewidth deviations as large as 0.5 μm with a 0.0650 μm change in resist thickness. In reality, the exact linewidth deviations may be different depending on the exact thickness change, the substrate reflectivity, resist contrast and processing, and the resolving power of the projection printer relative to the mask dimension. In the past, lithographic considerations in a device layout have concentrated on maximum step height of the topography, minimum line, space, pitch, and contact hole dimensions, and placement accuracies of

interlevel overlays. In this work, we propose that, in some cases, the actual configuration of the topography should be considered to accommodate the contour coating properties of spun-on films during device fabrication. To maintain process latitude and improve yields, spun-on coating thicknesses on topographical features need to be adequately controlled. These considerations become most significant for fine-lined lithography, (*i.e.*, design rules less than 2 μm). Sometimes, it is actually desirable to add topography that serves no electrical function to a design. This topography we shall call superficial topography, ST. The ST can be a permanent structure or a temporary one depending on subsequent processing and space considerations. ST appears to have its most immediate and obvious application at the edge of large complex arrays. The use of ST can improve the coating thickness uniformity on topographical features at the edge of and within the array. A computer simulation technique can be used to design the ST. The same ST can reduce the effects of radial flow-induced coating anomalies.

Designing Superficial Topography

The spun-on film contour coating simulation procedure has been described in detail elsewhere (2-4) and is based on the application of a low pass frequency filter to the uncoated contour (topography). This procedure involves expressing the uncoated contour in the frequency domain, that is, in terms of its Fourier coefficients, a_{nm} and b_{nm} . The spun-coated contour, $T_c(x,y)$, can be approximated as shown below

$$T_c(x,y) \approx \sum_{n=0}^j \sum_{m=0}^k w_n w_m a_{nm} \cos\left(\frac{2\pi nx}{N} + \frac{2\pi my}{M}\right) + w_n w_m b_{nm} \sin\left(\frac{2\pi nx}{N} + \frac{2\pi my}{M}\right) \quad [1]$$

where N and M are the total number of points that span the x and y coordinates. w_n and w_m are the frequency

* Electrochemical Society Active Member.

weighting factors for the x and y coordinates (*i.e.*, the frequency filter). j and k equal $N/2$ and $M/2$, respectively.

The same frequency filter is used for both x and y coordinates. It is determined empirically by measuring the step heights of coated isolated line features. The nonunity weighting factors (w_n and $w_m < 1.0$) that make up the low pass frequency filter are proportional to the logarithm of the period. Two parameters are used to define the filter, P_{\min} and α . P_{\min} represents the minimum period that has weighting factor equal to one and suggests the range of the feature-feature interaction. α is the slope of weighting factor-logarithm period curve and reflects the conformality of the coating. An α parameter of zero would represent a perfectly conformal coating.

For three-dimensional simulations, it is sometimes desirable to include the effects of film shrinkage. Assuming film shrinkage is proportional to thickness, changes in the measured step heights for coated topographical features can be computed according to the relationship shown below

$$H_b = (1 - 1/c) H_i + H_a (1/c) \quad [2]$$

where, H_b is step height before shrink, H_a is the step height after shrink, H_i is the initial uncoated step height, and c is the shrink factor. By measuring thicknesses before, T_b , and after, T_a , curing of the film, the shrink factor is determined as the fraction of the original thickness, T_a/T_b . Figure 1 shows a schematic of the before and after shrink contours and denotes the relevant parameters.

The shrinkage correction can easily be applied to the computed frequency weighting parameters

$$w'_n = (1 - 1/c) + w_n (1/c) \quad [3]$$

w'_n is the shrink-corrected weighting parameter and w_n the normal after-shrink parameter. The normal, after-shrink, frequency weighting parameters are determined from the isolated-line test pattern. Shrink-corrected, w'_n and w'_m , weighting parameters are computed, and a coating contour is calculated from these parameters. The film thickness used is the T_b thickness. The shrink factor is applied to these thicknesses, and the resulting thicknesses are added to the initial uncoated topography to give the shrink-corrected contour. Simulations done without a shrink-correction procedure produce reduced film thicknesses on top of topographical features (*i.e.*, lower step heights and a less conformal coating).

Figure 2a shows the corner portion of a silicon-on-sapphire (SOS) epi-island layout. The step height of the islands is $0.56 \mu\text{m}$. Gates are defined across the islands through the notches on the edge of the islands. The size of the islands is $12 \times 18 \mu\text{m}$. The gaps between the islands are $7 \mu\text{m}$ in the horizontal direction and $2 \mu\text{m}$ in the vertical direction. For this layout, only the gate definition on top of the islands is critical and the space between gates is much larger than the gate length (*i.e.*, width of defined line). Solid, dotted, and dashed lines show where the coating contour cross sections are displayed for the first, second, and fifth rows of gates, respectively. In Fig. 2b and 2c, the ST configurations that we have considered at the edge of the array are denoted by the slash-filled lines.

Table I summarizes the simulation parameter, solution properties, and coating conditions for a few spun-on positive resist films. Figure 3 shows computed shrink-corrected coating contour for the various rows of gates in the epi island layouts, a, b, and c, shown in Fig. 2. The epi island arrays are typically defined by a 512×512 array of

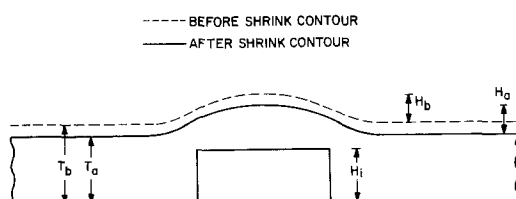


Fig. 1. Schematic of before shrink and after shrink contours

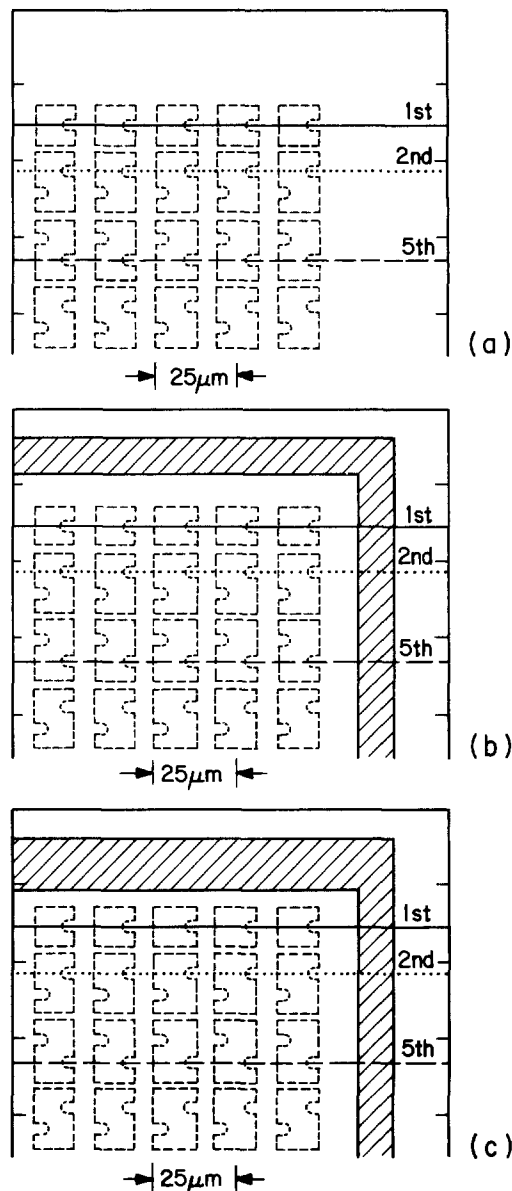


Fig. 2. Epi island layout with and without superficial topography

points spaced at $1 \mu\text{m}$ intervals. The frequency weighting parameters that correspond to a softbaked OFPR 800 coating ($\alpha = 0.60$, $P_{\min} = 200 \mu\text{m}$) were used for all the topographical configurations assuming a 0.90 shrink factor. The computation typically requires 3 min of CPU time on an IBM mainframe computer and a 4 Mbyte machine. These simulated contour traces show thickness variations at the edge of, between, and on top of the islands. The contour height (Y-axis) represents the height of the simulated profilometer trace relative to the uncoated flat expanse. For these designs, only the coating thickness on top of the islands is critical for gate definition. Large thickness variations at the edge of a feature are always present with conventional novalac resin-based positive

Table I. Solution and coating parameters for spun-on films

	OFPR 800	HPR 204	HPR 206
Initial step height (μm)	0.50	0.55	1.01
Spin speed ($\text{rpm} \times 10^3$)	6	6	6
Coating thickness (μm)	0.93	1.05	1.80
Percentage solid ^a	26.9	27.8	33.0
Viscosity ^a (cps)	30	18.5	43
P_{\min} (μm)	165	160	400
α	0.60	0.70	0.53

^a From manufacturer's data sheets.

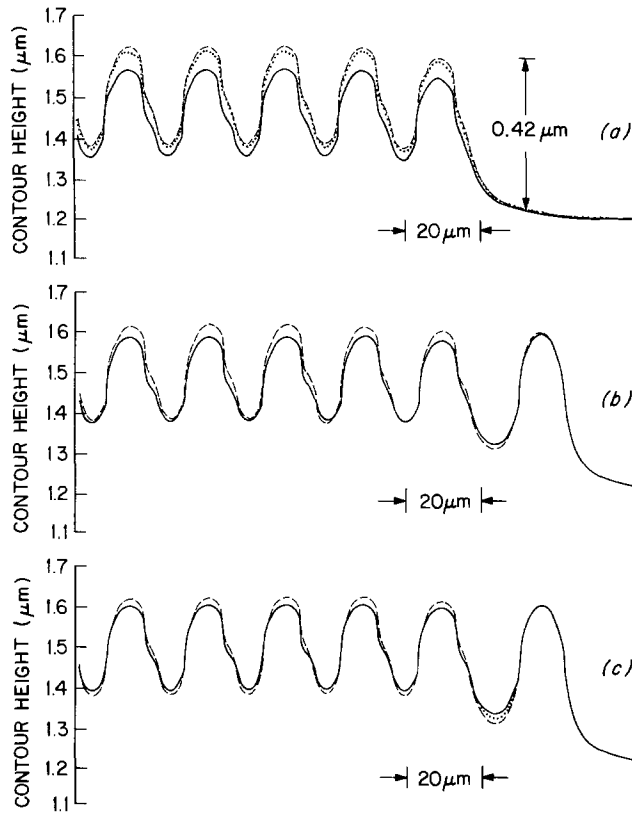


Fig. 3. Simulated contour traces for epi island layout for $P_{\min} = 200$, $\alpha = 0.60$.

resist systems. The ST presented here is only designed to control the resist thickness on top of the epi islands. If pattern definition were important between the islands, thickness variations between the top and bottom of the steps would also be important.

Table II summarizes thickness variations between and within the rows of gates on top of the epi islands for the layouts. For the spin-coated layout without ST (Fig. 3a), the maximum thickness variation between the top of islands is 950Å. The second layout with ST consisting of a 10 μm line spaced 10 μm from the edge of array reduces the maximum thickness variations to 450Å. The third layout with ST further reduces the maximum thickness variations to 250Å. The top section of ST has been widened to 15 μm and is spaced only 5 μm from the edge of the array.

The design of ST depends not only on the layout, but also on the resist material and spin process used. Figure 4 shows additional coating contour simulations for the layout shown in Fig. 2a and 2c. The frequency weighting parameters used are $P_{\min} = 400 \mu\text{m}$ and $\alpha = 0.53$, which may be representative of an HPR 206 coating. No shrinkage correction is used in the simulation. For softbaked positive resist films, a 0.85-0.90 shrink factor does not appreciably change the simulated relative thickness variations on top of the islands; however, small detectable thickness variations between the top and bottom of the simulated

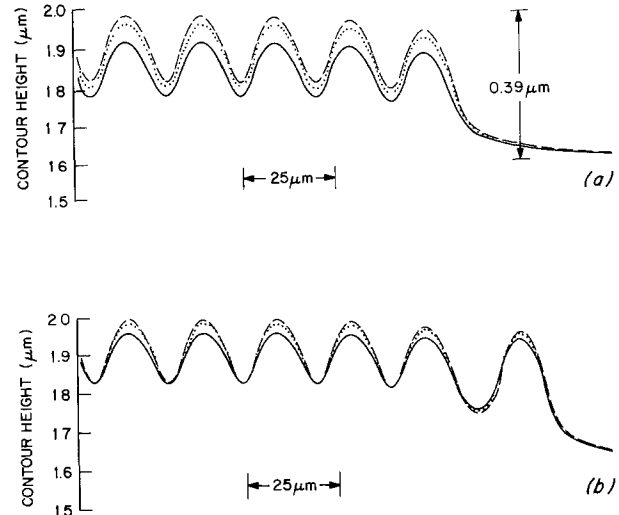


Fig. 4. Simulated contour traces for epi island layout for $P_{\min} = 400$, $\alpha = 0.53$.

contours are present. A shrink-corrected contour (Fig. 3) appears to produce a less smoothed simulated contour. Corners and edges of topography appear more prominent in the shrink-corrected contours. Without ST, the maximum thickness variation on top of the islands is 1100Å. Even with the ST shown in Fig. 2c, the maximum thickness variation is only reduced to 650Å. A more substantial ST is necessary for this particular spun-on coating to reduce thickness variation on top of the islands even further. The configuration of the superficial topography that appears to be most effective in reducing thickness variations tends to match the periodicity within the complex array itself. The simulation also suggests that, at least for this layout, spun-on positive resist coating materials and processes that exhibit longer effective ranges (larger P_{\min} values) tend to produce greater thickness variations within the array.

In practice, it is desirable to keep the thickness variations on top of the islands around a third of the distance between the maximum and minimum standing wave exposure intensity nodes. Thus, for a g-line (436 nm) exposure system, the thickness variation should be around 210Å. For the worst possible case, the standing wave-induced dimensional deviation is approximately halved. Further reduction in these dimensional deviations can be obtained by still tighter thickness control or in some cases by reducing substrate reflectivity. This type of ST is only used to control the maximum resist thickness on top of the islands. The thickness variations at the edge of the island are still present. These edge thickness variations are typically 1200Å, and the presence of a standing wave maximum intensity node is unavoidable. Necking at steps on reflective topography needs to be addressed by other resist processing techniques, such as multilayer resist processes (7, 8). Although these multilayer processes address resist thickness changes within an individual island, they do not necessarily address thickness variations between islands. Even with a thick planarization sublayer, a group of small features tends to behave as a single large feature and little planarization is possible between the flat expanse and the array. Note that, if the spun-on coatings shown in Fig. 3 and 4 had been used as planarization sublayers, the initial uncoated step height of 0.56 μm would have only been reduced to 0.42 and 0.39 μm relative to the flat expanse, respectively. Thus, superficial topography can be important even in multilayer resist processing schemes.

Effect of Radial Flow-Induced Coating Anomalies

The simulations in the previous section only apply for situations where radial flow-induced coating anomalies do not play a prominent role. These anomalies influence the contour coating and thickness variations at various

Table II. Thickness variations of photoresist coatings on top of epi islands

OFPR 800 $P_{\min} = 200$ $\alpha = 0.60$	Within row of gates (Å)	Between first and fifth row of gates (Å)	Total thickness variation (Å)
Layout A	350	600	950
Layout B	100	350	450
Layout C	100	150	250
<hr/>			
$P_{\min} = 400$ $\alpha = 0.53$			
Layout A	400	700	1100
Layout C	250	400	650

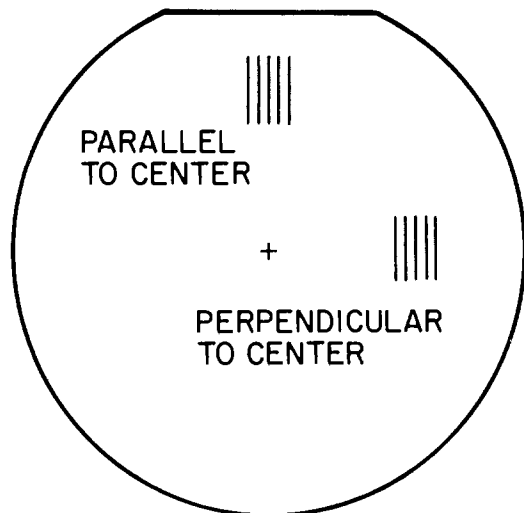


Fig. 5. Schematic of \parallel and \perp orientations with respect to flow from wafer center.

orientations and positions with respect to the centrifugal center of the wafer. Figure 5 shows a schematic of lines oriented parallel (\parallel) and perpendicular (\perp) to the flow of material from the centrifugal center of the wafer. Figure 6 shows profilometer traces that illustrate how coating contours are influenced by the orientation of the feature with respect to the wafer center. Isolated-line features, 40 and 5 μm wide, coated with HPR 206 at a 6 krpm spin speed are shown. The circled "x" denotes the \parallel orientation, and the arrow the direction of flow from the wafer center at the \perp orientation. The numbers above the traces indicate the maximum measured step height in microns, and the numbers below the traces the feature size. The original step height for the feature was 1.01 μm . The profilometer traces for the \perp orientation were taken 25 mm from the center of a 3 in. diam wafer.

Step heights are increased for the \perp orientation, and a buildup of material on the sidewall of the step produces an asymmetrical shape for the coated line feature. The buildup always occurs on the sidewall oriented toward the wafer center. The maximum step height for the orientation does not occur in the center of the cross section of the line but is displaced toward the wafer center side of the line. The edges and corners of features are thus coated differently, depending on whether the edge is adjacent to or opposite the wafer center. When coating failures occur (*i.e.*, thin or no film coverage of a feature), they tend to be located at edges opposite the wafer center, downstream from the radial flow.

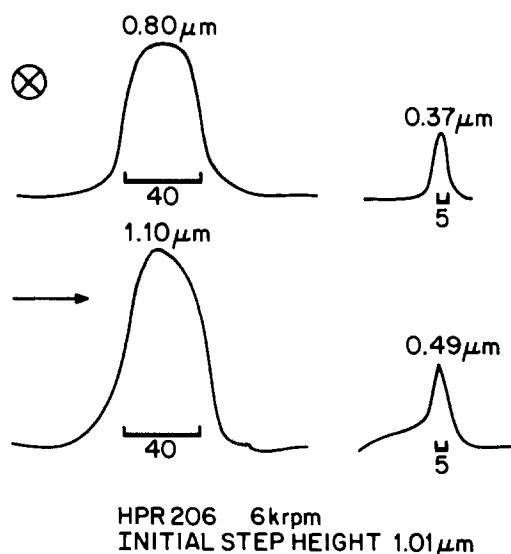


Fig. 6. Profilometer traces of coated isolated-line features at \parallel and \perp orientations.

Radial flow anomalies are more complex than depicted by these two orientations. Intermediate orientations between \parallel and \perp have a complex coating behavior. The \perp orientations themselves have a radial dependence, which essentially introduces a positional dependence for every feature with respect to the centrifugal center (*i.e.*, all features on the wafer can be coated differently). These radial flow anomalies become greater the further away features are from the centrifugal center of the substrate. Larger diameter substrates will show even greater anomalies at their edges. In the center of the substrate, the radial flow anomalies are small and, in terms of the coating contours of line features, the \perp orientations begin to resemble the \parallel orientations.

The flow-induced coating anomalies within large complex three-dimensional arrays can also be significant. Since a group of small features seems to behave as a large feature, the upstream side of the array tends to show thickness buildup and the downstream sides thickness thinning. An example of this effect is shown in Fig. 7 for $10 \times 10 \mu\text{m}$ line-space gratings at \perp orientation and at the center of the substrate. The resist coating is OFPR 800 spun on at 6 krpm, and the uncoated step height is 0.44 μm . The A value represents a coated step height measurement in microns for the first line feature, and the B value the coated step height of a line feature within the array. Although there is some noise present in the B step heights, the difference between A and B step heights is reproducible from wafer to wafer at the same contour trace positions.

The arrows on the figure show the direction of flow from the radial center of the substrate. The middle trace was taken near the centrifugal center of the substrate, and the radial flow induced coating anomalies are expected to be small. Both sides of this grating exhibit the same A and B step heights. In terms of minimizing thickness variations across the whole array, the center positions are always superior. These positions produce coating contours that have small radial flow anomalies, and they are predicted with reasonable accuracy by our simulation procedure. All \parallel orientations of the grating would produce a similar coating contour. The upstream side of the array at a \perp orientation away from the center position (top of Fig. 7) shows the smallest difference between the A and B

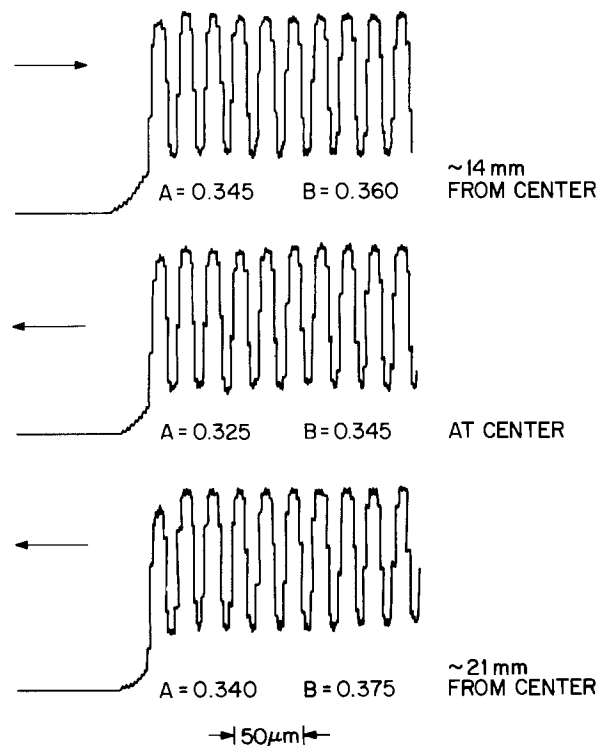


Fig. 7. Profilometer traces of coated $10 \times 10 \mu\text{m}$ grating features at \perp orientations.

step heights. The first line feature exhibits a thickness buildup effect relative to the center trace. The downstream side of the same array away from center position (bottom of Fig. 7) shows the largest difference between the A and B step heights. The first line feature shows a thickness thinning relative to the step height within the array. For this coating, the first line feature on the back side of the array exhibits the most substantial thickness change. This observation suggests that thickness variations produced by radial flow anomalies in some cases may actually exceed those predicted by our contour simulation routine. The exact magnitude of these thickness variations depends on the radial position of the \perp orientation, but the largest radial flow-induced coating anomaly usually occurs at the first feature in the complex array. Superficial topography around the perimeter of the array would help minimize this coating anomaly.

It should also be pointed out that radial flow anomalies can also change the coating contour within the array. The B step heights in presence of radial flow are different from those in the center of substrate and at a parallel orientation. Superficial topography cannot correct this type of coating anomaly. It is important to minimize radial flow-induced coating anomalies during the spin coating process so that topographical features do get coated uniformly and coating failures are minimized. Devices with high step heights and large or long feature sizes are more susceptible to these coating anomalies. Low spin speeds and careful selection of coating materials can be used to minimize, but not eliminate, these effects (3, 4).

This effect, however, is expected to be much smaller for three-dimensional arrays that have both a finite width and length. Smaller feature sizes and more broken arrays produce less substantial radial flow-induced anomalies. In any case, ST around the perimeter of complex arrays can only improve the situation. Since radial flow-induced coating anomalies increase with distance from the center, larger diameter substrates could conceivably benefit more from the use of ST.

Summary

The use of superficial topography to improve coating contour and thickness uniformity at the edge of complex arrays has been proposed. Since a group of small features

tends to act like a single large feature, edge features of an array effectively coat differently during the spin coating process than the same feature within an array. In the absence of large radial flow-induced coating anomalies, the configuration of the superficial topography can be constructed by computer simulation techniques. Different spun-on coatings and topography configurations require different ST to obtain the most uniform coating contours. Films and coating processes that produce long ranges for feature-feature interaction tend to require more substantial ST configurations. Radial flow-induced coating anomalies can produce greater coating nonuniformities within an array. The larger anomalies also tend to occur at the edge of the arrays and on the downstream side of the array. ST also helps reduce these coating difficulties. ST can also be beneficial in multilayer resist processes that employ planarization sublayers, since the sublayers cannot effectively planarize a large array relative to a flat expanse. The contour coating properties of the spun-on resist films used to define critical lithographic levels and spun-on sacrificial films used in planarization etchback procedures are an increasingly important aspect of device processing. Careful consideration of these properties can improve yields, process latitude, and, in some cases, even device performance.

Manuscript submitted May 24, 1985; revised manuscript received Aug. 22, 1985.

RCA assisted in meeting the publication costs of this article.

REFERENCES

1. A. C. Adams and C. D. Capio, *This Journal*, **128**, 423 (1981).
2. L. K. White, *ibid.*, **132**, 168 (1985).
3. L. K. White and N. Miskowski, *J. Vac. Sci. Technol. B*, **3**, 862 (1985).
4. L. K. White, *Proc. SPIE*, **539**, 29 (1985).
5. D. W. Widmann and H. Binder, *IEEE Trans. Electron Devices*, **ed-22**, 467 (1975).
6. M. M. O'Toole, E. D. Lin, and M. S. Chang, *ibid.*, **ed-28**, 1405 (1981).
7. B. J. Lin and T. H. P. Chang, *J. Vac. Sci. Technol.*, **16**, 1669 (1979).
8. J. Moran and D. Mayden, *ibid.*, **16**, 1620 (1979).

Studies of the Vaporization/Decomposition of Alkali Sulfates

K. H. Lau, R. D. Brittain,* R. H. Lamoreaux,* and D. L. Hildenbrand

SRI International, Menlo Park, California 94025

ABSTRACT

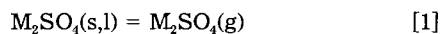
To complement a previous study of the vaporization behavior of K_2SO_4 , the vaporization of Li, Na, Rb, and Cs sulfates has been studied by mass spectrometry and the torsion-effusion method to determine the total pressures, molecular weights, and compositions of the effusing vapors. Both molecular vaporization of M_2SO_4 and dissociation contribute to the vaporization flux. For Na, Rb, and Cs sulfates, the decomposition reaction is $M_2SO_4(s) = 2M(g) + SO_2(g) + O_2(g)$. From the difference between the measured total pressures and calculated decomposition pressures, the contributions attributable to molecular vaporization of Na_2SO_4 , Rb_2SO_4 , and Cs_2SO_4 are about 37, 75, and 95% of the total pressures over the respective sulfates in the temperature ranges of our measurements. Vapor molecular weights determined from simultaneous torsion-effusion and mass-loss measurements are in close agreement with the compositions inferred from the pressure data. Decomposition of $Li_2SO_4(s)$ occurs by the reaction $Li_2SO_4(s) = Li_2O(s) + SO_2(g) + 1/2 O_2(g)$; the Li_2O reacts with the remaining Li_2SO_4 to form a liquid solution phase of unknown Li_2O activity. Li_2SO_4 sublimation accounts for about 0.3% of the pressure over Li_2SO_4 . The derived heats of sublimation in kilojoules per mole at 298 K were determined to be 388.4 ± 4.1 for Li_2SO_4 , 364.0 ± 1.3 for Na_2SO_4 , 340.2 ± 2.8 for Rb_2SO_4 , and 320.1 ± 2.0 for Cs_2SO_4 . Values of the entropies of the gaseous sulfate molecules were derived from slope heats and absolute pressures and are compared with values calculated from molecular constants.

Metal sulfate chemistry is important in technologies such as sulfur removal from combustion gases and high temperature energy generation and conversion. In most of these applications, the high temperature vaporization behavior of sulfates is of particular concern, but the basic

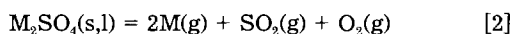
*Electrochemical Society Active Member.

thermodynamics and kinetics needed to treat the technical problems are not adequately known. In the case of alkali sulfates, serious discrepancies exist among sources in the literature not only as to total pressures but in regard to the relative importance of the various vaporization processes.

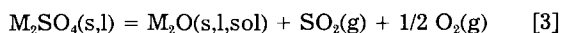
The vaporization of alkali sulfates is complex in that a variety of condensed and vapor phase products may be observed under appropriate conditions. The vaporization behavior may be described as combinations of conceptually simpler individual processes such as molecular vaporization



congruent decomposition



and incongruent decomposition, which results in changes in the condensed phase composition. One incongruent vaporization reaction that may be postulated is



but various condensed phases, both pure compounds and solutions, are possible products.

Previous studies reported that reaction [2] is the principal decomposition mode of Na_2SO_4 (1-3), K_2SO_4 (1, 4), Rb_2SO_4 (1, 5), and Cs_2SO_4 (1, 5); no evidence of incongruent vaporization was found. The percentage of the total vapor pressure attributable to molecular vaporization was not established precisely in most studies, but was reported to increase with the atomic weight of the cation from about 14% for Na_2SO_4 (2) to nearly 100% for Rb_2SO_4 and Cs_2SO_4 (5).

Although several studies of Li_2SO_4 vaporization have been reported, the results are in poor agreement. A mass spectrometric study (1) indicated vaporization according to the decomposition reaction [2], with no molecular sulfate detected, but a later mass-effusion and transpiration study (6) gave indirect evidence for a lithium containing vapor species, presumably $Li_2SO_4(g)$, as the major component of the vapor. This latter study also found evidence of incongruent vaporization, presumably by reaction [3], but concluded that it could not be the major vaporization process.

With the exception of condensed phase solutions, reliable thermodynamic data are available for the various decomposition processes, so that equilibrium decomposition products under neutral vaporization conditions may be predicted from these data. Sulfates of Na, K, Rb, and Cs are calculated to decompose by reaction [2], in agreement with the experimental results. Bonnell and Hastie (7) showed that the $Na(g)$ pressures observed over Na_2SO_4 under neutral vaporization conditions implied that the activity of condensed Na_2O was less than about 10^{-5} . This conclusion agrees with thermodynamic calculations that predict a $Na_2O(g)$ partial pressure of 2×10^{-14} bar for the dissociation of Na_2SO_4 under neutral conditions at 1200 K, whereas the $Na_2O(g)$ pressure over pure $Na_2O(s)$ under similar conditions is predicted to be 2×10^{-8} bar. Similar conclusions can be derived for the decomposition of K_2SO_4 , Rb_2SO_4 , and Cs_2SO_4 . However, under neutral conditions Li_2SO_4 is calculated to decompose primarily by reaction [3]; whether the condensed phase product is a pure substance or a solution is a matter for experimental determination.

A previous study in this laboratory (4) used Knudsen cell mass spectrometry and torsion-effusion vapor pressure measurement to investigate the vaporization behavior of K_2SO_4 . Molecular sublimation accounted for about 63% of the total vapor pressure under the experimental conditions; congruent decomposition by reaction [2] accounted for the remaining pressure. The enthalpy of sublimation at 298 K was 361.9 ± 6.3 kJ-mol⁻¹. The entropy derived from mass spectrometric second-law measurements and torsion-effusion total pressures was 13.8 J-mol⁻¹-K⁻¹ larger than tabulated values calculated from partially estimated molecular constants.

The present studies were undertaken to resolve discrepancies in the earlier data, to obtain quantitative information on the relative importance of molecular vaporization and dissociation, and to derive accurate thermodynamic data for the gaseous sulfates. To this end, the basic approach was the same as in our study of K_2SO_4 vaporiza-

tion. Total pressures were determined by the torsion-effusion method, a purely mechanical technique that requires no knowledge of vapor composition to evaluate total pressures. Partial pressures attributable to decomposition species were calculated using literature thermodynamic data, and the partial pressures due to M_2SO_4 molecules equated to the difference between total and decomposition pressures. Vapor molecular weights, \bar{M}_w , determined from simultaneous torsion-effusion and mass-loss measurements provided a check on our interpretation of the vapor composition. The mass spectra of the effusing vapors were studied in detail, and thermodynamic data were derived for the molecular vaporization and decomposition processes.

Experimental

Mass spectrometric studies were done in the 12 in. radius, 60° sector magnetic instrument equipped with a Knudsen cell source (8). Details of the platinum effusion cell, cell holder, and Pt, Pt-13% Rh thermocouple, and of the experimental technique have been given previously (8). Measurements of the temperature dependence of pressure and ion intensity were made by varying the temperature randomly; however, the data are tabulated in order of ascending temperature so that trends may be more readily identified.

The torsion-effusion apparatus and the associated microbalance, which have been described previously (9-11), were the same as in our K_2SO_4 vaporization study (4). Pt-30% Rh alloy effusion cells with orifice diameters of 0.06 and 0.11 cm and capped with tapered, Pt-coated alumina plugs were used. The system performance was checked against the vapor pressure and molecular weight of KCl, both cells giving results within 5% of the accepted values (12).

The measurements were made using high purity, anhydrous Mallinkrodt AR-grade Na_2SO_4 , Alfa ultrapure $Li_2SO_4 \cdot H_2O$ and Rb_2SO_4 , and Cerac/Pure Cs_2SO_4 . The $Li_2SO_4 \cdot H_2O$ was dried by heating for 2h at 463 K in N_2 . No obvious impurities were found in the mass spectrum, and essentially no outgassing was observed on heating the specimens to measurement temperatures in the torsion-effusion apparatus. In view of the pronounced tendency of molten Na_2SO_4 to wet the walls and to creep out of the effusion cell container, as observed by Kohl *et al.* (13) and in our own preliminary experiments, we charged the cell with a mixture of the solid sulfate and high surface area platinum powder. The inert Pt powder provided a large internal wicking area that confined the molten sulfate by surface tension; two different loadings showed the vapor pressure of the liquid to be independent of the Na_2SO_4/Pt ratio in the region investigated. This technique proved highly effective in eliminating the creep problem in the Na_2SO_4 measurements. Studies on the other sulfates were made at temperatures below the melting points.

Results

Vapor mass spectra.—The mass spectra were examined to obtain quantitative information on the molecular species in the vapor. Table I presents the threshold appearance potentials, neutral precursors, and relative ion intensities at 30 eV ionizing energy. Appearance potentials were evaluated by the vanishing current method. The close agreement of threshold ionization potentials of Na^+ , Rb^+ , Cs^+ , O_2^+ , and SO_2^+ with the spectroscopic ionization potentials (IP) of the corresponding neutrals Na (IP = 5.14 eV), Rb (IP = 4.18 eV), Cs (IP = 3.89 eV), O_2 (IP = 12.08 eV), and SO_2 (IP = 12.34 eV) indicate that the ions are formed by simple ionization processes near threshold. Because of the low appearance potentials of the ions $Li_2SO_4^+$, $Na_2SO_4^+$, $Rb_2SO_4^+$, and $Cs_2SO_4^+$, the corresponding neutrals are also regarded as parent species. At higher ionizing energies, a substantial fraction of the M^+ signal must result from dissociative ionization of M_2SO_4 . Our threshold appearance potentials for $Rb_2SO_4^+$ and $Cs_2SO_4^+$ are about 1 eV lower than those reported by Ficalora *et al.* (1), but agree closely with that of Kohl *et al.* (13) on

Table I. Appearance potentials and relative intensities of ions in mass spectra of Li_2SO_4 , Na_2SO_4 , Rb_2SO_4 , and Cs_2SO_4 vapors

Condensed phase	Ion	T (K)	AP (eV)	Neutral	I ⁺ (30 eV)
Li_2SO_4	Li^+	1114	9.5 ± 0.5	Li_2SO_4	28
	Li_2SO_4^+		9.7 ± 0.3	Li_2SO_4	190
	SO_2^+		12.5 ± 0.5	SO_2	5100
	O_2^+		^a	O_2	1200
Na_2SO_4	Na^+	1239	5.0 ± 0.3	Na	314
	Na_2O^+		11.5 ± 0.5	Na_2SO_4	4.6
	Na_2SO_4^+		8.0 ± 0.3	Na_2SO_4	14
	SO_2^+		12.5 ± 0.5	SO_2	75
	O_2^+		12.0 ± 0.5	O_2	62
Rb_2SO_4	Rb^+	1225	4.0 ± 0.3	Rb	178
	Rb_2O^+		10.6 ± 0.5	Rb_2SO_4	5.9
	Rb_2SO_4^+		7.5 ± 0.3	Rb_2SO_4	40.8
	SO_2^+		12.3 ± 0.5	SO_2	37.5
	O_2^+		12.1 ± 0.5	O_2	9
Cs_2SO_4	Cs_2^+	1170	3.8 ± 0.3	Cs	318
	Cs_2O^+		10.1 ± 0.5	Cs_2SO_4	50
	Cs_2SO_4^+		7.6 ± 0.3	Cs_2SO_4	118
	SO_2^+		12.3 ± 0.5	SO_2	12
	O_2^+		^a	O_2	1.1

^a Not measured.

Na_2SO_4^+ ; Ficalora *et al.* (1) did not detect Li_2SO_4^+ or Na_2SO_4^+ . The species Na_2O^+ , Rb_2O^+ , and Cs_2O^+ , whose measured appearance potentials are far greater than those measured by Hildenbrand and Murad (14) for Na_2O^+ over $\text{Na}_2\text{O}(\text{s})$ (5.5 eV), by Norman and Winchell (15) for Rb_2O^+ (4.9 eV) and Cs_2O^+ (4.6 eV), and by Gorokhov (16) for Cs_2O^+ (4.45 eV), are clearly fragment ions. We found no evidence for molecular SO_3 , reported to be present in other studies.

On the basis of the observed ion signals and the AP data, we conclude that the major species in the vapor effusing from $\text{Na}_2\text{SO}_4(\text{s,l})$, $\text{Rb}_2\text{SO}_4(\text{s})$, and $\text{Cs}_2\text{SO}_4(\text{s})$ are the M_2SO_4 molecular sulfates, the M gaseous alkali metal atoms, SO_2 , and O_2 ; the major species effusing from $\text{Li}_2\text{SO}_4(\text{s})$ are SO_2 and O_2 plus a small amount of molecular Li_2SO_4 . No $\text{Li}(\text{g})$ is detected in the latter. Thus, decomposition by reaction [2] and molecular vaporization by reaction [1] contribute to the vaporization of Na, Rb, and Cs sulfates, whereas Li_2SO_4 vaporizes primarily by decomposition according to reaction [3] with a small contribution from direct sublimation.

To obtain second-law information for the molecular vaporization process, the temperature dependences of the intensities of M_2SO_4^+ species were measured. Second-law heats were derived from least squares analysis of $\log(I^+T)$ as a function of reciprocal temperature, with the results shown in Table II. As a check on this procedure, the decomposition processes were also studied by monitoring M^+ and/or SO_2^+ , for comparison with the established reaction thermodynamics.

Total vapor pressures and vapor molecular weights.—The torsion-effusion total vapor pressures obtained with cells PR-1 and PR-2 and the vapor molecular weights, \overline{M}_w , evaluated from simultaneous torsion and gravimetric effusion experiments are summarized in Tables III, IV, and V. Individual vapor pressures are plotted in Fig. 1-3 as $\log P$ vs. $1/T$. Constants for the effusion cells are included in Table V.

For Na_2SO_4 , a few torsion-effusion measurements were also made on the solid phase, and these are shown in Fig. 1. Several of these were made on a fresh sample of crystalline Na_2SO_4 , and several on the Na_2SO_4 -Pt mixture after completion of the measurements on the liquid. The two sets are in reasonable agreement and join well with the liquid phase pressures at the melting point, indicating that the Pt "wicking" technique gives satisfactory results.

No total pressure measurements are reported for Li_2SO_4 since the mass spectrum indicated only a minor contribution (< 1%) from molecular sublimation. Also, as noted below, it is likely that the oxide product formed in this

Table II. Second-law slope heats derived from ion temperature dependences

Ion	Electron energy (eV)	Data points	T range (K)	T _{avg} (K)	ΔH_T (kJ/mol)
$\text{Li}_2\text{SO}_4(\text{s})$					
Li_2SO_4^+	30	8	1060-1115	1086	326.4 ± 4.0
SO_2^+	17	7	1053-1114	1089	328.4 ± 4.0
$\text{Na}_2\text{SO}_4(\text{s,l})$					
Na_2SO_4^+	50	10	1069-1148	1110 ^a	330.2 ± 1.2
	50	7	1069-1155	1114 ^a	326.2 ± 1.3
	50	7	1168-1237	1199 ^b	291.5 ± 2.9
	50	9	1167-1257	1210 ^b	292.9 ± 1.3
Na^+	8	5	1184-1257	1216 ^b	302.3 ± 2.5
	8	16	1164-1266	1212 ^b	302.9 ± 3.1
SO_2^+	17	7	1176-1262	1217 ^b	297.2 ± 4.9
		$\text{Rb}_2\text{SO}_4(\text{s})$			
Rb_2SO_4^+	50	15	1062-1255	1157	291.1 ± 3.4
	50	14	1055-1258	1165	299.5 ± 1.9
Rb^+	7	6	1144-1274	1212	306.0 ± 2.8
	7	6	1119-1274	1197	305.0 ± 1.1
$\text{Cs}_2\text{SO}_4(\text{s})$					
Cs_2SO_4^+	30	9	992-1112	1045	279.2 ± 2.0
	30	5	983-1139	1056	281.8 ± 2.0
Cs^+	7	6	1080-1174	1127	304.3 ± 1.5

^a Vaporization of $\text{Na}_2\text{SO}_4(\text{s})$.^b Vaporization of $\text{Na}_2\text{SO}_4(\text{l})$.

case is present at reduced activity, thereby complicating the interpretation. For comparison purposes, a few preliminary torsion measurements on Li_2SO_4 indicated a total pressure of 7×10^{-8} bar at 1115 K.

Na_2SO_4 pressures measured with the 0.06 cm diam orifice were about 60% higher than those determined with the larger orifice. A similar orifice-size dependence

Table III. Total vapor pressure of Na_2SO_4 (torsion-effusion method)

Cell PR-1 ($P_E/P_T = 2.116$) ^a			Cell PR-2 ($P_E/P_T = 1.331$) ^a		
T (K)	$P \times 10^6$ (bar)	\overline{M}_w	T (K)	$P \times 10^6$ (bar)	\overline{M}_w
Solid					
1113.7	0.030				
1117.6	0.033				
1121.7	0.040				
1131.7	0.054				
1137.5	0.072				
1145.9	0.094				
Liquid					
1166.4	0.164		1188.2	0.464	
1172.9	0.215		1204.1	0.699	
1174.6	0.202		1220.6	1.034	
1181.9	0.245		1230.2	1.329	
1185.0	0.287		1236.1	1.522	
1188.7	0.289		1255.9	2.272	
1190.3	0.306		1264.7	3.027	
1195.2	0.360		1270.0	3.282	
1199.0	0.380		1284.3	4.490	70.4
1204.3	0.429	67.2	1294.4	5.527	70.3
1209.3	0.508		1302.4	6.635	
1217.3	0.601		1303.6	6.756	62.2
1218.6	0.627				
1219.4	0.633				
1227.9	0.781	69.4			
1236.1	0.959				
1236.9	0.986				
1240.9	1.075				
1251.1	1.377				
1259.4	1.668				
1263.2	1.828				
Mean $\overline{M}_w = 67 \pm 5$ $\overline{M}_w(\text{Na}_2\text{SO}_4) = 142.0$ $\overline{M}_w(\text{decomposition}) = 37.3$ $\log P$ (bar) = $(6.708 \pm 0.262) - (15,729 \pm 135)/T$ (PR-1) $\log P$ (bar) = $(6.798 \pm 0.081) - (15,559 \pm 101)/T$ (PR-2)					

^a P_E/P_T = ratio of equilibrium to steady-state pressures.

Table IV. Total vapor pressure of $\text{Rb}_2\text{SO}_4(\text{s})$ (torsion-effusion method)

Cell PR-1 ($P_E/P_T = 1.259$) ^a			Cell PR-2 ($P_E/P_T = 1.079$) ^a		
T (K)	$P \times 10^6$ (bar)	\overline{Mw}	T (K)	$P \times 10^6$ (bar)	\overline{Mw}
1107.1	0.105		1154.1	0.516	
1117.6	0.149		1170.0	0.810	
1125.9	0.200		1172.6	0.838	
1128.9	0.209		1185.3	1.206	
1146.6	0.344		1201.1	1.819	
1150.4	0.388		1217.6	2.774	
1175.0	0.788	211.5	1220.9	2.997	216.0
1185.7	1.039		1226.1	3.500	
1192.8	1.248		1237.9	4.598	212.7
1203.9	1.675	207.4	1226.4	5.568	203.5
1212.5	2.108	206.7	1248.7	5.963	216.2
1222.2	2.683	199.7	1260.4	7.886	207.8

$$\text{Mean } \overline{Mw} = 209 \pm 4$$

$$\overline{Mw}(\text{Rb}_2\text{SO}_4) = 267.0$$

$$\overline{Mw}(\text{decomposition}) = 69.0$$

$$\text{Log } P(\text{bar}) = (7.839 \pm 0.262) - (16,388 \pm 301)/T(\text{PR-1})$$

$$\text{Log } P(\text{bar}) = (7.777 \pm 0.200) - (16,235 \pm 230)/T(\text{PR-2})$$

^a P_E/P_T = ratio of equilibrium to steady-state pressures.

was found for K_2SO_4 (4). The difference was about 25% for Rb_2SO_4 but was negligible for Cs_2SO_4 . The orifice effect is attributable to undersaturation of the vapor resulting from a kinetic barrier in the vaporization process. The Whitman-Motzfeldt model (11, 17-19) was used to extrapolate the data for Na_2SO_4 and Rb_2SO_4 to zero orifice area to give the equilibrium pressures shown in Fig. 1 and 2; no extrapolation was necessary for the Cs_2SO_4 data. This extrapolation yielded the proportionality constants between steady state and equilibrium pressures for the several cells and samples shown in Tables III, IV, and V. Also shown in Fig. 1-3 are the calculated decomposition pressures for reaction [2]; because of the restriction of congruent vaporization, the calculated partial pressures of M, SO_2 , and O_2 within the effusion cell are not in the integral ratios of 2:1:1 but are adjusted on the basis of their molecular weights so that mass effusion yields stoichiometric M_2SO_4 . In each instance, the total equilibrium pressure is

Table V. Total vapor pressure of $\text{Cs}_2\text{SO}_4(\text{s})$ (torsion-effusion method)

Cell PR-1			Cell PR-2		
T (K)	$P \times 10^6$ (bar)	\overline{Mw}	T (K)	$P \times 10^6$ (bar)	\overline{Mw}
1059.8	0.176		1074.9	0.303	
1072.5	0.272		1086.8	0.415	
1086.1	0.397		1098.0	0.580	
1096.3	0.539		1099.6	0.620	
1107.3	0.738		1111.2	0.856	
1117.2	0.973		1123.1	1.168	313.9
1125.9	1.241		1123.8	1.176	
1134.7	1.553		1135.6	1.680	
1144.4	2.042		1147.4	2.257	336.0
			1148.1	2.339	339.1
			1161.0	3.237	
			1173.5	4.542	341.8

$$\text{Mean } \overline{Mw} = 333 \pm 14$$

$$\overline{Mw}(\text{Cs}_2\text{SO}_4) = 361.9$$

$$\overline{Mw}(\text{decomposition}) = 97.1$$

$$\text{Log } P(\text{bar}) = (7.515 \pm 0.066) - (15,112 \pm 72)/T(\text{PR-1})$$

$$\text{Log } P(\text{bar}) = (7.528 \pm 0.068) - (15,110 \pm 74)/T(\text{PR-2})$$

Torsion-effusion cells

Cell	d (cm) ^a	ΣCa (cm ²) ^a
PR-1	0.11	1.68×10^{-2}
PR-2	0.06	5.08×10^{-3}

^a d = orifice diameter.

ΣCa = effective orifice area.

higher than the decomposition pressure, showing clearly the substantial contribution of molecular vaporization.

Included in Tables III, IV, and V along with the observed molecular weight data are values of \overline{Mw} for the molecular sulfates M_2SO_4 and the corresponding values calculated for the respective decomposition reactions. The experimentally determined values of \overline{Mw} are in each case intermediate between the two extremes, indicating a substantial mole fraction of M_2SO_4 in the vapor, increas-

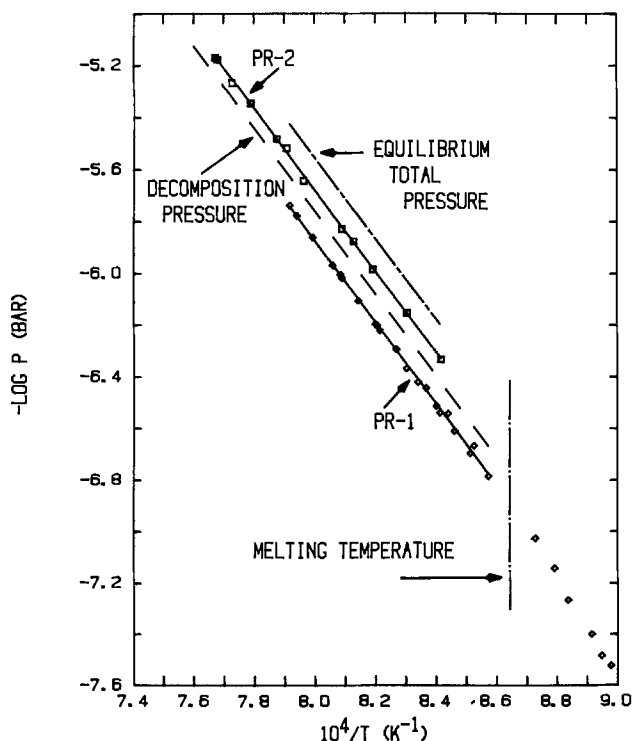


Fig. 1. Total pressure over $\text{Na}_2\text{SO}_4(\text{l})$ measured with two platinum-rhodium effusion cells, showing relation to extrapolated equilibrium pressure and calculated pressure for the decomposition process $\text{Na}_2\text{SO}_4(\text{l}) = 2\text{Na}(\text{g}) + \text{SO}_2(\text{g}) + \text{O}_2(\text{g})$.

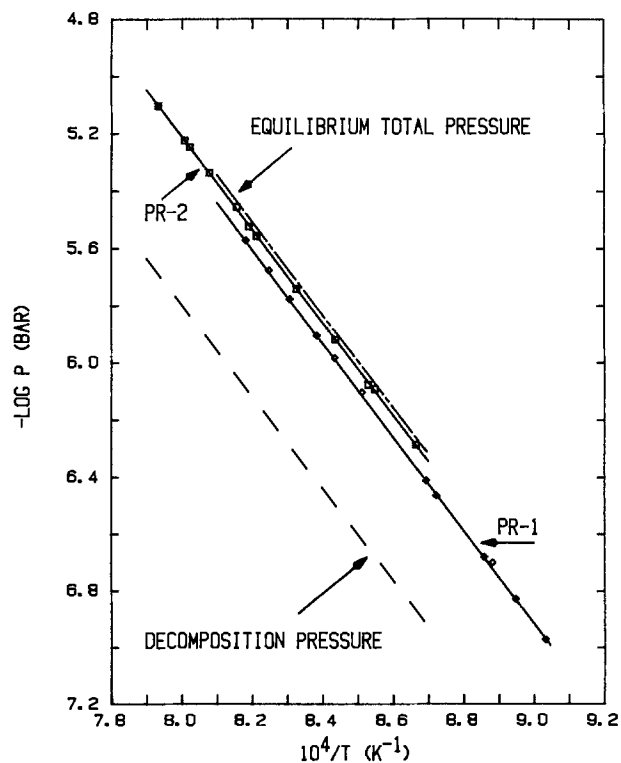


Fig. 2. Total pressure over $\text{Rb}_2\text{SO}_4(\text{s})$ measured with two platinum-rhodium effusion cells, showing relation to extrapolated equilibrium pressure and calculated pressure for the decomposition process $\text{Rb}_2\text{SO}_4(\text{s}) = 2\text{Rb}(\text{g}) + \text{SO}_2(\text{g}) + \text{O}_2(\text{g})$.

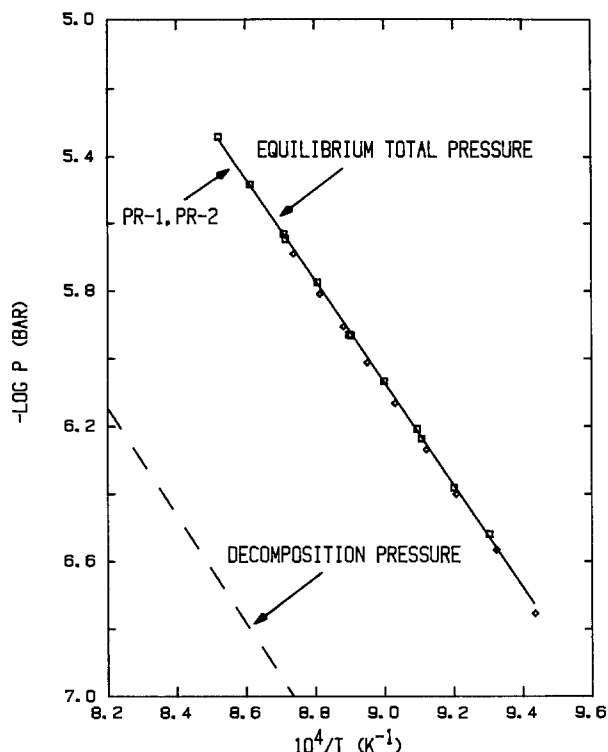


Fig. 3. Total pressure over $\text{Cs}_2\text{SO}_4(\text{s})$ measured with two platinum-rhodium effusion cells, showing relation to extrapolated equilibrium pressure and calculated pressure for the decomposition process $\text{Cs}_2\text{SO}_4(\text{l}) = 2\text{Cs}(\text{g}) + \text{SO}_2(\text{g}) + \text{O}_2(\text{g})$.

ing with the atomic weight of the metal. The quantitative implications of the molecular weight data toward vapor composition will be discussed in a subsequent section.

Residual solid phases.—After the effusion runs, cell residues were examined by x-ray diffraction analysis. Except for the case of Li_2SO_4 , sulfates identical to the starting materials were detected, but no oxides or hydroxides were found; aqueous solutions of the residues had the same pH values as comparable solutions of the starting sulfates. These results indicate that these sulfates vaporize congruently, in accord with the observations of Cubicciotti and Keneshea (3) for Na_2SO_4 and of Cubicciotti (5) for Rb_2SO_4 and Cs_2SO_4 ; identical behavior was observed for K_2SO_4 (4).

Examination of the effusion cell after the exploratory measurements on Li_2SO_4 revealed partial melting of the contents, although the cell temperature had been kept below the Li_2SO_4 melting point, 1132 K. The pH of an aqueous solution of the cell residue was 9.5. There are, apparently, no phase diagram data in the literature for the Li_2SO_4 - Li_2O system. The analogous Li_2CO_3 - Li_2O system (20) has a eutectic at 13 mole percent Li_2O and 978 K, 28 K below the Li_2CO_3 melting point. The evidence for partial fusion during incongruent vaporization below the melting point of either Li_2SO_4 or Li_2O suggests that Li_2SO_4 has a similar phase diagram and that vaporization above the eutectic temperature produces a solution with unknown equilibrium values of Li_2O composition and activity. As only a small fraction of specimen was vaporized in our

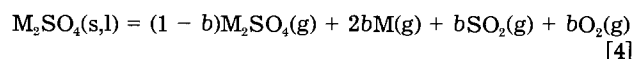
Table VI. Derived vaporization data for $\text{Na}_2\text{SO}_4(\text{l})$, $\text{Rb}_2\text{SO}_4(\text{s})$, and $\text{Cs}_2\text{SO}_4(\text{s})$

T (K)	$P_T \times 10^7$ (bar)	$P_D \times 10^7$ (bar)	$P(\text{M}_2\text{SO}_4) \times 10^7$ (bar)
Na_2SO_4			
1180	5.11	3.14	1.98
1200	8.45	5.26	3.19
1220	13.75	8.66	5.10
1240	22.03	14.04	7.99
1260	34.76	22.42	12.35
1280	54.09	35.27	18.82
Rb_2SO_4			
1180	10.44	2.84	7.60
1200	17.69	4.80	12.89
1220	29.49	7.99	21.50
1240	48.34	13.08	35.26
1260	78.00	21.04	56.96
1280	124.00	33.33	90.67
Cs_2SO_4			
1180	52.80	2.66	50.14
1200	86.31	4.51	81.80
1220	138.84	7.49	131.35
1240	219.92	12.21	207.71
1260	343.30	19.59	322.70
1280	528.51	30.91	497.60

measurements, Li_2SO_4 was present in excess, and its activity in the effusion cell remained essentially unity; the activity of Li_2O in liquid solution was less than unity. In accordance with the law of mass action as applied to reaction [3], the pressure observed in the exploratory run, due primarily to SO_2 and O_2 , is higher by a factor of five than that calculated from literature thermodynamic data (21) for the case of unit activity for $\text{Li}_2\text{O}(\text{s})$.

Determination of vapor composition.—It is difficult to derive accurately the vapor composition from mass spectra alone, because of uncertainty in the relative ionization cross sections of the various neutrals and because of possible effects of fragmentation on species such as Na^+ , Rb^+ , and Cs^+ . However, with both total pressures and molecular weight data available, vapor composition can be determined quantitatively by two independent routes. From the pressure data alone, the difference between the total pressure, P_T , and decomposition pressure, P_D , is the molecular pressure $P(\text{M}_2\text{SO}_4)$. The quantity $P(\text{M}_2\text{SO}_4)/P_T$ is then the fractional contribution of molecular vaporization to the total pressure. Values of P_T taken from the derived equilibrium pressures, of P_D calculated from thermodynamic data, and of $P(\text{M}_2\text{SO}_4)$ obtained by difference are listed at even temperatures in Table VI.

Alternatively, the vapor molecular weight data can be used to define vapor composition. The overall sulfate vaporization process can be described by the expression



where the stoichiometric coefficient b can be used to quantify the contributions of the two processes. For effusion of a complex vapor, the vapor molecular weight \bar{M}_w determined from simultaneous torsion and gravimetric Knudsen measurements is a weight average value related to the values for the individual species by the expression

$$\bar{M}_w = [\sum m_i(\bar{M}_w)^{-1/2}]^{-2} \quad [5]$$

Table VII. Comparison of derived molecular vaporization pressures and vapor molecular weights

M_2SO_4	From total pressures ^a			From molecular weights		
	b	$P(\text{M}_2\text{SO}_4)/P_T$	\bar{M}_w (calc)	b	$P(\text{M}_2\text{SO}_4)/P_T$	\bar{M}_w (meas)
Na_2SO_4	0.47	0.37	68	0.48	0.36	67
K_2SO_4	0.23	0.61	116	0.26	0.59	110
Rb_2SO_4	0.15	0.75	205	0.13	0.76	209
Cs_2SO_4	0.026	0.95	345	0.046	0.91	333

^a $P(\text{M}_2\text{SO}_4) = P_T - P_D$. P_D , the dissociation pressure for reaction [2], was calculated for effusion conditions using the data discussed in the Appendix.

Table VIII. Standard enthalpies of sublimation and formation of gaseous alkali sulfates

M_2SO_4	ΔH° (sub, 298 K) (kJ·mol ⁻¹)		$\Delta_f H^\circ$ (298 K) (kJ·mol ⁻¹)
	This work ^a	Other	
Li ₂ SO ₄	388.4	394.6 ^b	-1048.0
Na ₂ SO ₄	364.0	354.4 ^b	-1023.8
K ₂ SO ₄	361.9	343.5 ^b	-1075.8
Rb ₂ SO ₄	340.2	339.3 ^c	-1095.7
Cs ₂ SO ₄	320.1	320.1 ^b	-1122.5

^a Uncertainty ± 6 kJ·mol⁻¹.

^b Ref. (22).

^c Ref. (23).

where m_i and $(Mw)_i$ are the mass fraction and molecular weights of the i gaseous species. For the overall sulfate vaporization/decomposition process expressed as reaction [4], the observed molecular weight can be related to the coefficient b in the following way

$$\overline{Mw} = \left[\frac{Mw(M_2SO_4)}{(1-b)Mw(M_2SO_4)^{1/2} + 2bMw(M)^{1/2} + bMw(SO_2)^{1/2} + bMw(O_2)^{1/2}} \right]^2 \quad [6]$$

The ratio $P(M_2SO_4)/P_T$ evaluated from the pressure data is also related to \overline{Mw} and b by the expression

$$P(M_2SO_4)/P_T = \left[\frac{(1-b)Mw(M_2SO_4)^{1/2}}{(1-b)Mw(M_2SO_4)^{1/2} + 2bMw(M)^{1/2} + bMw(SO_2)^{1/2} + bMw(O_2)^{1/2}} \right] \quad [7]$$

Therefore, the pressure data alone can be used to derive values of b and then \overline{Mw} for comparison with the directly measured values of \overline{Mw} or, conversely, the latter can be used to evaluate the ratio $P(M_2SO_4)/P_T$ and checked for consistency with the value derived directly from the total pressure measurements.

In Table VII, the pressure ratios $P(M_2SO_4)/P_T$, the average vapor molecular weights \overline{Mw} , and values of the coefficient b obtained by the two different methods are seen to be in remarkably good agreement, giving a high degree of confidence in the vapor composition information. Also included for completeness are results obtained earlier on K₂SO₄ (4). There is a smooth progression from 37% molecular vaporization for Na₂SO₄ to 95% for Cs₂SO₄.

For Li₂SO₄, where the fraction of molecular sublimation was too low to yield meaningful results by the approach described above, an approximate value of $P(Li_2SO_4)/P_T$ was derived from the vapor mass spectrum and a pressure calibration constant based on the vapor pressure of gold. The Li₂SO₄⁺ and SO₂⁺ signals at 1115 K yielded the values $P(Li_2SO_4) = 2 \times 10^{-10}$ bar, $P(SO_2) = 7 \times 10^{-8}$ bar, and $P(Li_2SO_4)/P_T = 0.003$. The estimated SO₂ pressure is in accord with the preliminary torsion value and about a factor of five higher than that calculated for unit activity of Li₂O(s), as expected from the partial melting of the sample and dissolution of Li₂O in Li₂SO₄ at temperatures below the melting point of the sulfate.

Thermodynamics of $M_2SO_4(g)$ species.—The enthalpy change of a reaction is usually calculated from the temperature derivative of the equilibrium constant by the "second-law method" or from individual values of the

Table IX. Entropies of molecular vaporization and absolute entropies of gaseous alkali sulfates

M_2SO_4	T (K)	ΔS_T (vap) ^a	S_T°	
		(J·mol ⁻¹ ·K ⁻¹)	This work ^{a, b}	Other ^c
Li ₂ SO ₄	1115	105.3	474.7	495.7 \pm 42
Na ₂ SO ₄	1200	119.4	549.0	533.3 \pm 17
K ₂ SO ₄	1200	143.6	568.2	554.3 \pm 17
Rb ₂ SO ₄	1100	135.5	567.0	567.1 \pm 17
Cs ₂ SO ₄	1100	132.9	580.4	582.0 \pm 17

^a Uncertainty ± 5 J·mol⁻¹·K⁻¹. For Na₂SO₄(l) = Na₂SO₄(g); for M₂SO₄(s) = M₂SO₄(g) for other alkali sulfates.

^b Calculated using auxiliary data cited in Appendix.

^c Calculated values taken from literature sources discussed in the Appendix.

equilibrium constant by the "third-law method," which is based on knowledge of the absolute entropies of reactants and products. For alkali sulfate vaporization, we defin-

itely prefer the second-law method. The spectroscopic and molecular constant data for the gaseous alkali sulfates are still quite incomplete, although the available data have been reviewed and extended with estimates so as to calculate tables of thermodynamic functions (22, 23). The major uncertainties involve the low frequency deformation vibrations and modes involving the metal atoms, leading to uncertainties on the order of ± 17 J·mol⁻¹·K⁻¹ in the calculated entropies at 298 K (22).

In Table VIII are listed the standard enthalpies of sublimation at 298 K of the molecular sulfates derived from the second-law analysis of the M₂SO₄⁺ ion signals. Values for K₂SO₄ from our earlier work (4) are included for completeness, as are previous values from the literature. Heat capacities and enthalpy increments above room temperature are less sensitive to errors in molecular constants than are the entropies and Gibbs energy functions; therefore, the uncertainties associated with the second-law method are smaller than for the third-law procedure for these molecules. For Na₂SO₄, our selected value is based on the liquid phase measurements because of uncertainty over which of the several polymorphic solid phases is involved and the slow rate of transformation between these phases. The standard enthalpies of formation of M₂SO₄(g) shown in Table VIII were based on the enthalpy of sublimation results of this work and values for the solids (22, 23).

The absolute entropies of the gaseous alkali sulfates were derived from the second-law heats of sublimation and derived values of the M₂SO₄ partial pressures at the

Table X. Pressures of molecular vaporization and decomposition and molar enthalpies and entropies of sublimation at 1100 K

M_2SO_4	$P(M_2SO_4) \times 10^9$ ^a (bar)	$P_D \times 10^9$ ^b (bar)	ΔH° (sub, 1100 K) (kJ·mol ⁻¹)	ΔS (sub, 1100 K) (J·mol ⁻¹ ·K ⁻¹)
Li ₂ SO ₄	0.12	8.9	325.5	106.2
Na ₂ SO ₄	19.2	30.1	321.5	144.6
K ₂ SO ₄	28.7	18.5	322.2	148.5
Rb ₂ SO ₄	83.0	28.0	298.3	135.5
Cs ₂ SO ₄	563	26.5	277.8	132.9

^a For M₂SO₄(s) = M₂SO₄(g).

^b For Li, calculated for reaction [3] assuming unit activity for Li₂O(s). For others, calculated for reaction [2].

experimental temperatures. The results are shown in Table IX along with corresponding values from the literature (22, 23).

Discussion

Our vapor composition data are consistent and are felt to accurately define the relative contributions of molecular vaporization and decomposition to the total vapor pressures of the alkali sulfates. There are, however, some significant differences between these results and those reported earlier. For Na_2SO_4 , results reported before 1979 are reviewed in the JANAF Tables (22), which give a selected value of $P(\text{Na}_2\text{SO}_4) = 1.3 \times 10^{-7}$ bar at 1200 K, compared to our derived value of 3.19×10^{-7} bar; the JANAF value is equivalent to 20% molecular vaporization, compared to 37% found in this study. The subsequent Knudsen effusion results of Halle and Stern (2) which yielded $P(\text{Na}_2\text{SO}_4) = 4.2 \times 10^{-6}$ bar at 1200 K and 14% molecular vaporization are clearly too low. For Rb_2SO_4 and Cs_2SO_4 , Cubicciotti (5) reported less than 1% decomposition in this same temperature region, based on failure to find any evidence for elemental Rb or Cs in the collected effusate. However, these results could have been biased by low sticking probabilities for the alkali atoms on the cool glass collector surface; such behavior has been observed for Mg atoms (24), and we have observed similar behavior for Zn atoms on numerous occasions over the years. It is interesting to note in retrospect that Cubicciotti's comparison (5) of observed effusion data and calculated decomposition pressures indicated about 5% dissociation for Cs_2SO_4 and 20-30% for Rb_2SO_4 , in close agreement with our findings, but this information was discounted as less reliable than the effusate collection results.

The Knudsen effusion data of Cubicciotti (5) on Rb_2SO_4 , when corrected slightly for dissociation, give $P(\text{Rb}_2\text{SO}_4) = 1.5 \times 10^{-6}$ bar at 1200 K, in good agreement with our value of 1.29×10^{-6} bar; similarly, correction of the effusion results of Jagannathan and Wyatt (6) yields $P(\text{Rb}_2\text{SO}_4) = 2.2 \times 10^{-6}$ bar at 1200 K, also in accord with our results. Selected values for Cs_2SO_4 in the JANAF Tables (22), based largely on the effusion data of Cubicciotti (5), lead to $P(\text{Cs}_2\text{SO}_4) = 8.5 \times 10^{-6}$ bar at 1200 K, close to our derived value of 8.18×10^{-6} bar.

Jagannathan and Wyatt (6) concluded correctly that Li_2SO_4 vaporizes incongruently by decomposition to $\text{Li}_2\text{O}(s)$, but their further conclusion that decomposition cannot be the major vaporization process is way off the mark, for unknown reasons. As suggested by Kohl *et al.* (13), interaction of the sulfate samples with alumina-lined tantalum cells may well be responsible for the absence of Li_2SO_4^+ and Na_2SO_4^+ in the mass spectra reported by Ficalora *et al.* (1).

A useful measure of the reliability of the second-law slope heats is given in the comparison of measured decomposition enthalpies derived from parent M^+ and SO_2^+ signals with those calculated from established thermodynamic data. Such a comparison cannot be made for Li_2SO_4 because of the dissolution effects and unknown Li_2O activity mentioned earlier, but in each other instance the M^+ and SO_2^+ second-law values are well within 6 kJ-mol⁻¹ of the calculated values per mole of gas. Comparison of our derived sublimation enthalpies with previous selected values in Table VIII shows the largest deviations for Na_2SO_4 and K_2SO_4 , where those values (22, 23) were obtained primarily from third-law analyses.

As seen in Table IX, the agreement between experimental and calculated entropies is within the estimated error limits in all cases. While the agreement is quite good for Rb_2SO_4 and Cs_2SO_4 , the results indicate that some revision of the estimated frequencies for Li_2SO_4 , Na_2SO_4 , and K_2SO_4 is in order.

Our effusion measurements on Na_2SO_4 , K_2SO_4 , and Rb_2SO_4 showed a pronounced and reproducible dependence on orifice size, while no such effect was observed for Cs_2SO_4 . This orifice-size dependence is generally associated with a kinetic barrier arising from structural or

orientational changes during the transfer from condensed to vapor phase. The decomposition process would clearly require major structural changes during this transition and could be the major contributor to such a kinetic barrier. The absence of an observable orifice-size effect in Cs_2SO_4 , which shows the smallest degree of decomposition, is in line with this reasoning.

Assembled in Table X at a common temperature for ease of comparison are the molecular sublimation and decomposition pressures, and the molar enthalpies and entropies of sublimation. The decomposition pressures show remarkably little variation through the series, while the enthalpies of sublimation show the expected decrease for the heavier salts, leading to higher molecular sublimation pressures.

Acknowledgment

This research was supported by the Division of Chemical Sciences, Office of Basic Energy Sciences, U.S. Department of Energy.

Manuscript submitted May 13, 1985; revised manuscript received Aug. 12, 1985.

SRI International assisted in meeting the publication costs of this article.

APPENDIX

Sources of Thermodynamic and Melting Point Data

Alkali metal atoms, alkali oxides, and oxygen.—Data for the species $\text{M}(g)$, $\text{M}_2\text{O}(s,l)$, and g , and $\text{O}_2(g)$ were taken from the compilation of Lamoreaux and Hildenbrand (21).

$\text{K}_2\text{SO}_4(s,l,g)$, $\text{Na}_2\text{SO}_4(s,l,g)$.—Data were taken from JANAF (1982 supplement) (22).

$\text{Li}_2\text{SO}_4(s,l,g)$.—Data were taken from JANAF (Supplement no. 54) (22).

$\text{Cs}_2\text{SO}_4(s,l,g)$.—Data were taken from JANAF (Supplement no. 56) (22).

$\text{Rb}_2\text{SO}_4(s,l,g)$.—Data were taken from Glushko *et al.* (23).

$\text{SO}_2(g)$, $\text{SO}_3(g)$.—Data were taken from JANAF (1971) (22).

REFERENCES

- P. J. Ficalora, O. M. Uy, D. W. Muenow, and J. L. Margrave, *J. Am. Ceram. Soc.*, **51**, 574 (1968).
- J. C. Halle and K. H. Stern, *J. Phys. Chem.*, **84**, 1699 (1980).
- D. Cubicciotti and F. J. Keneshea, *High Temp. Sci.*, **4**, 32 (1972).
- K. H. Lau, D. Cubicciotti, and D. L. Hildenbrand, *This Journal*, **126**, 490 (1979).
- D. Cubicciotti, *High Temp. Sci.*, **3**, 349 (1971).
- G. V. Jagannathan and P. A. H. Wyatt, *J. Chem. Res. (S)*, 208 (1978).
- D. W. Bonnell and J. W. Hastie, in "Proceedings of the 10th Materials Research Symposium on Characterization of High Temperature Vapors and Gases," Gaithersburg, Maryland (1978), p. 357, NBS Special Publication no. 561, U.S. Govt. Printing Office, Washington, DC (1979).
- D. L. Hildenbrand, *J. Chem. Phys.*, **48**, 3657 (1968); *ibid.*, **52**, 5751 (1970).
- D. L. Hildenbrand and W. F. Hall, *J. Phys. Chem.*, **67**, 888 (1963); *ibid.*, **68**, 989 (1964).
- D. L. Hildenbrand and D. T. Knight, *J. Chem. Phys.*, **51**, 1260 (1969).
- K. H. Lau, D. Cubicciotti, and D. L. Hildenbrand, *ibid.*, **66**, 4532 (1977).
- A. C. P. Pugh and R. F. Barrow, *Trans. Faraday Soc.*, **54**, 671 (1957).
- F. J. Kohl, C. A. Stearns, and G. C. Fryburg, in "Metal-Slag-Gas Reactions and Processes," Z. A. Foroulis and W. W. Smelzer, Editors, p. 649, The Electrochemical Society Softbound Proceedings Series, Princeton, NJ (1975).
- D. L. Hildenbrand and E. Murad, *J. Chem. Phys.*, **53**, 3403 (1970).
- J. H. Norman and P. Winchell, General Atomic Division of General Dynamics Report no. GA-7597 (1967).
- L. N. Gorokhov, in "Proceedings of the Third International Symposium on High Temperature Technology, Asilomar, California, 1967," p. 647, Butterworths, London (1969).

17. C. I. Whitman, *J. Chem. Phys.*, **20**, 161 (1952).
18. K. Motzfeldt, *J. Phys. Chem.*, **59**, 139 (1955).
19. J. H. Stern and N. W. Gregory, *ibid.*, **61**, 1226 (1957).
20. V. Smirnov, I. Ya. Lyubimtseva, L. A. Tsioukina, and Yu. N. Krasnov, *Russ. J. Inorg. Chem.*, **16**, 139 (1971).
21. R. H. Lamoreaux and D. L. Hildenbrand, *J. Phys. Chem. Ref. Data*, **13**, 151 (1984).
22. JANAF Thermochemical Tables, NSRDS-NBS 37, 2nd ed., Suppl. 54 (1978), Suppl. 56 (1979), U. S. Govt. Printing Office, Washington, D. C. (1971); *J. Phys. Chem. Ref. Data*, **11**, 695 (1982).
23. V. P. Glushko, L. V. Gurvich, G. A. Bergman, I. V. Veitz, V. A. Medredev, G. A. Khachkuruzov, and V. S. Yungman, "Thermodynamic Properties of Individual Substances," Vol. IV, Academy of Sciences, Moscow, U.S.S.R. (1982).
24. R. D. Brittain, L. B. Knight, Jr., M. Duncan, and C. H. Joiner, *J. Phys. Chem.*, **79**, 1183 (1975).

Annealing of High Dose Sb-Implanted Single-Crystal Silicon

E. Guerrero and H. Pötzl

Department of Physical Electronics, Institute for General Electrical Engineering and Electronics, Technical University Vienna, and Ludwig Boltzmann-Institute for Solid State Physics, Vienna, Austria

G. Stinger, M. Grasserbauer, and K. Piplitz

Institute for Analytical Chemistry, Technical University Vienna, Vienna, Austria

W. K. Chu

Department of Physics and Astronomy, University of North Carolina at Chapel Hill, Chapel Hill, North Carolina 27514

ABSTRACT

High doses of Sb implanted in silicon and then annealed at a temperature range between 800° and 1200°C cause Sb precipitation and extrinsic diffusion. Sb precipitation has not been completed at temperatures between 800° and 1000°C for 60-400 min duration; a supersaturation of substitutional Sb is detected under the same conditions. The oxidation of such samples causes Sb segregation and anomalous oxide growth. Residual crystal damage after annealing can be observed.

Antimony is a suitable element to study simultaneously diffusion and precipitation in silicon for Sb has a low solubility limit in silicon. A Sb-doped silicon dioxide source is frequently used for the study of antimony diffusion in silicon (1-3). In most of these cases, the Sb concentration in silicon is then just above its solubility limit. These Sb profiles differ from ion-implanted profiles. Sb ion implantation at high doses turns the implanted silicon layer amorphous. The solid phase epitaxy (SPE) growth of this amorphous layer induces a high metastable substitutional antimony concentration at suitable temperatures (4-6). This metastable concentration is far above its solubility limit. After SPE and at temperatures greater than 800°C, antimony precipitation occurs (5, 7).

Experimental results of antimony-implanted silicon annealed at a temperature range between 800° and 1200°C in N₂ or dry O₂ are presented in this work. The behavior of antimony precipitation and diffusion is discussed.

Experimental

FZ <100> silicon crystals of p-type (20 Ω-cm) were implanted with ¹²¹Sb⁺ at room temperature. The implantation energy ranged from 30 to 120 keV, and the dose from 10¹³ to 3 × 10¹⁵ cm⁻². The samples were annealed in N₂ or dry O₂ at 900°-1200°C for 15-120 min. The chemical antimony concentration was measured by SIMS and RBS. The RBS method was also used to determine the substitutional Sb concentration. The SIMS measurements were carried out using a CAMECA IMS-3F ion probe. The electrically active Sb was determined by the four-point probe method combined with anodic oxidation. The measurement error in the concentration was less than 20% for SIMS and less than 30% for electrical measurements. In the depth, the measurement error was less than 10% for both kinds of measurement.

Results and Discussion

Figure 1 shows the RBS measurements of an antimony-implanted and -annealed sample (120 keV, 3 × 10¹⁵ cm⁻², 1000°C, 60 min, in N₂). The figure shows the random and the aligned spectrum of this specimen. For comparison, a

<100>-aligned reference signal of an unimplanted silicon crystal is given (broken line). The higher aligned RBS signal (circles) of Si suggests that after annealing the silicon sample still contains residual damage. The random (squares) and aligned (circles) RBS spectrum for Sb shows that a part of Sb is not substitutional. This not substitutional part can be correlated with the SIMS measurement in Fig. 2. The measured sample in Fig. 2 (curve 2) is the same as in Fig. 1. In this figure, the measured implantation profile (curve 1) prior to annealing is also shown. Below a concentration of ≈ 6 × 10¹⁹ cm⁻³, the annealed profile broadens because antimony diffusion occurs. Above this concentration, the antimony atoms are immobile. Therefore, in this concentration range diffusion does not take place. Curve 2 indicates that the immobile Sb makes up ≈ 70-80% of the implantation dose (area of profile above 6 × 10¹⁹ cm⁻³).

Furthermore, the earlier RBS measurement (Fig. 1) shows that these atoms are not found on substitutional sites. Therefore, it can be concluded that these immobile antimony atoms are precipitates. The concentration of 6 × 10¹⁹ cm⁻³ at which Sb diffusion takes place is higher than the Sb solubility limit of ≈ 4 × 10¹⁹ cm⁻³ (8). Therefore, Sb diffusion occurs before the precipitation process reaches its thermodynamical equilibrium. Moreover, the substitutional antimony concentration may be far above its solubility limit as shown in Fig. 3. The upper profile (curve 1) in Fig. 3 shows the total Sb concentration (solid circles) and the substitutional electrically active concentration (open circles) of a further antimony sample (50 keV, 3 × 10¹⁵ cm⁻², 900°C, 60 min in N₂). At 900°C, the solubility limit of Sb is ≈ 3 × 10¹⁹ cm⁻³ (8). The maximal electrically active concentration shown in Fig. 3 is ≈ 7 × 10¹⁹ cm⁻³. In this case, the substitutional antimony concentration is more than a factor two above the corresponding solubility limit and outside the limits of our experimental measurement error. Therefore, it may be concluded that a supersaturation of substitutional antimony atoms exists and that the precipitation has not reached its thermal equilibrium. This conclusion will be clearly supported later in this paper by the comparison of antimony pro-

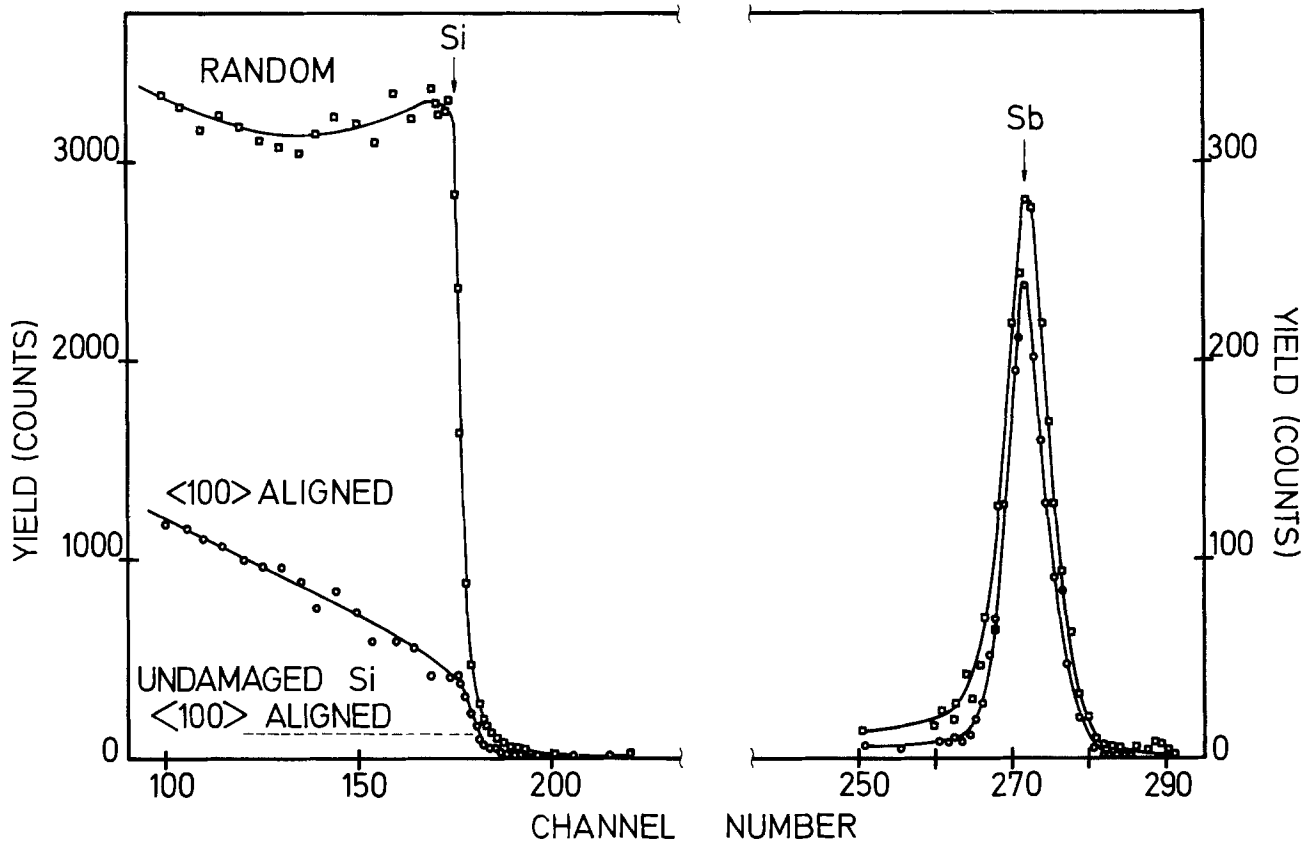


Fig. 1. Random (squares) and $\langle 100 \rangle$ -aligned (circles) RBS spectrum (1, 7 MeV, He^+) of a Sb implanted (120 keV , $3 \times 10^{15} \text{ cm}^{-2}$) and annealed (1000°C , 60 min, N_2) sample. For comparison, the $\langle 100 \rangle$ -aligned signal (dotted line) of an unimplanted specimen is given.

files annealed at different temperatures as in Fig. 6, which shows that the shoulder concentration increases as

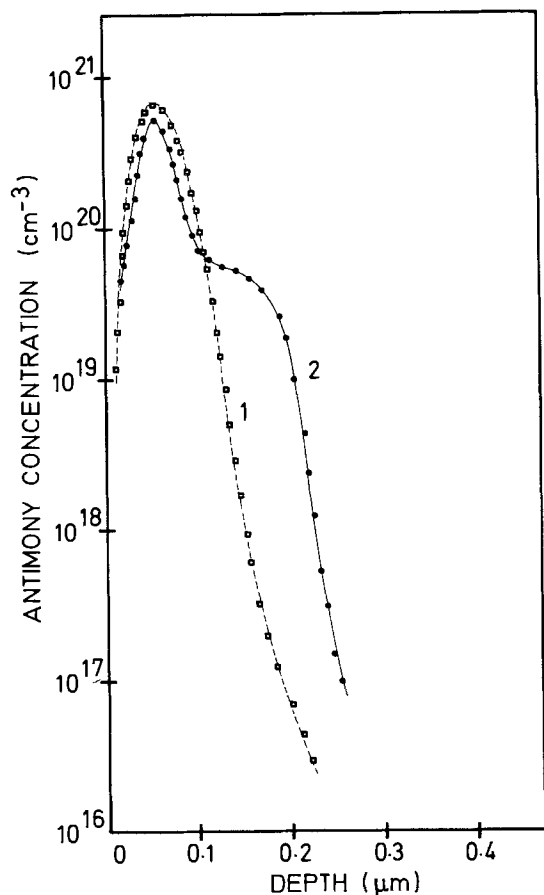


Fig. 2. SIMS measurement of an implanted (squares) (120 keV , $3 \times 10^{15} \text{ cm}^{-2}$) and then annealed (solid circles) (1000°C , 60 min, N_2) Sb-doped sample. The annealed sample is the same as in Fig. 1.

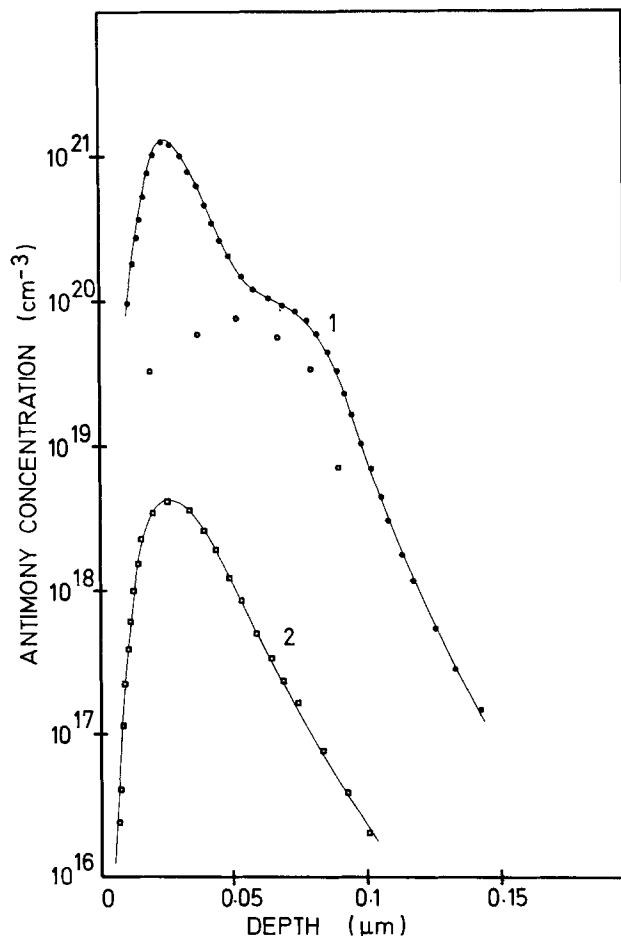


Fig. 3. Sb implantation at 50 keV for $3 \times 10^{15} \text{ cm}^{-2}$ (curve 1) and for 10^{13} cm^{-2} (curve 2). Annealing at $T = 900^\circ\text{C}$ for 60 min (curve 1) and for 120 min (curve 2) in N_2 . In this figure, the SIMS measurement (solid circles, squares) of both curves and the electrical measurement (circles) of curve 1 are shown.

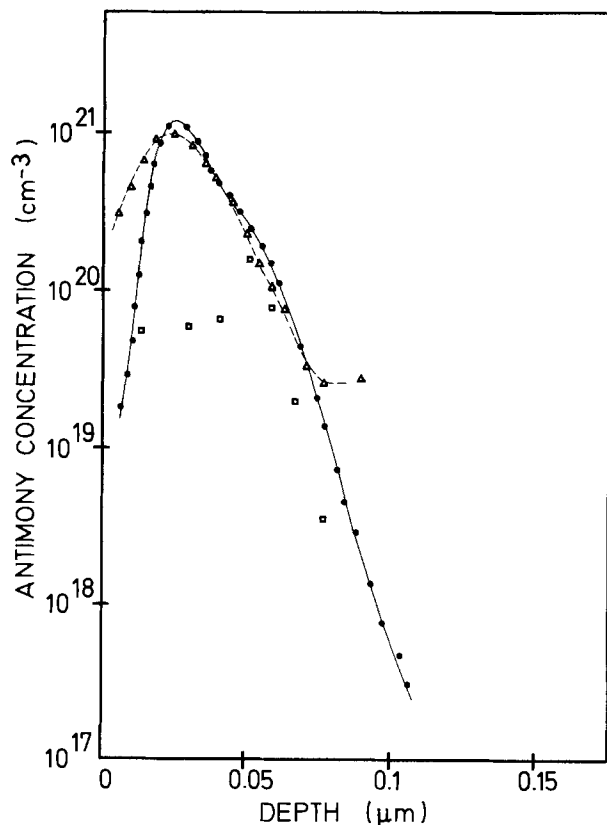


Fig. 4. Sb implantation carried out at 50 keV for a dose of $3 \times 10^{15} \text{ cm}^{-2}$. The annealing was carried out in N_2 , at $T = 800^\circ\text{C}$, for 120 min. In this figure, the SIMS (solid circles), RBS (triangles), and electrical measurements (squares) are given.

the temperature decreases. This experimental result supports the idea that by annealing of high implantation doses the solid phase epitaxy (SPE) causes a high supersaturation of substitutional antimony in silicon. After further annealing Sb precipitation takes place (5, 6).

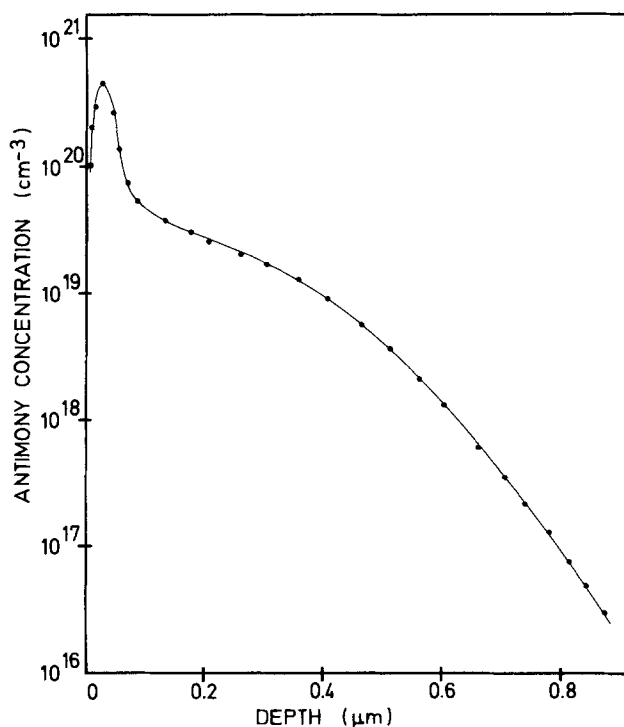


Fig. 5. Sb implantation with the same parameters as in Fig. 3 (50 keV, $3 \times 10^{15} \text{ cm}^{-2}$, curve 1). The annealing was carried out in N_2 at 1200°C for 15 min.

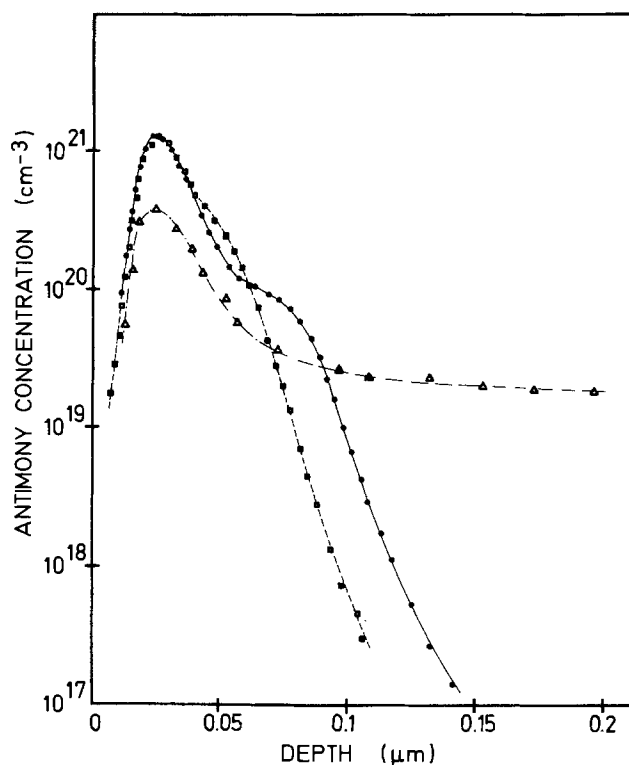


Fig. 6. The SIMS profiles of Fig. 3 (curve 1) (solid circles), Fig. 4 (squares) and Fig. 5 (triangles) are shown.

The decrease of the carrier concentration (n) toward the surface in Fig. 3 cannot be explained with accuracy yet. The possibility of a measurement effect as reported in Ref. (9, 10) by the electrical measurement of As profiles implanted through a oxide cannot be excluded. This, however, does not affect the above conclusions because the main objective of the electrical measurements in this work is to show that the concentration at the shoulder profile is also electrically active being a further support of the presence of substitutional antimony at this level

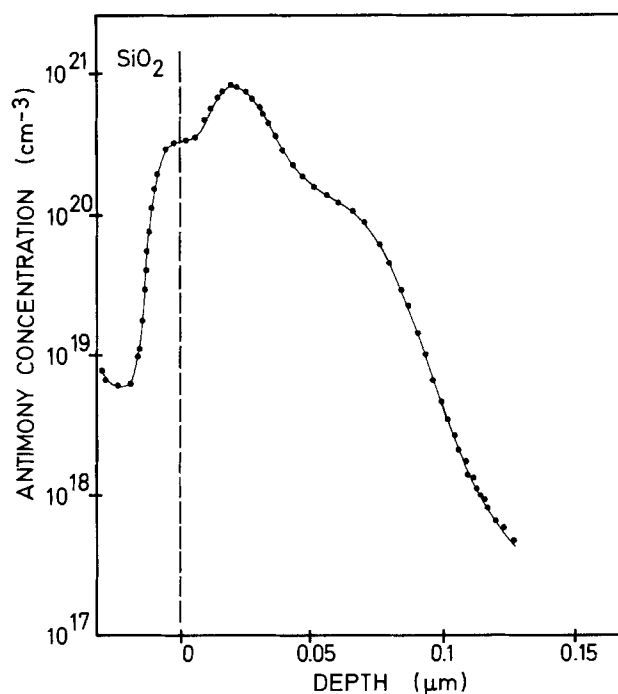


Fig. 7. Thermal annealing of an Sb-implanted sample (80 keV, $3 \times 10^{15} \text{ cm}^{-2}$). A thermal oxidation was carried out at 800°C in dry O_2 for 400 min followed by annealing in N_2 for 15 min. The dashed vertical line represents the SiO_2/Si interface.

(which can diffuse before the precipitation reaches its thermodynamical equilibrium).

Curve 2 in Fig. 3 shows the profile of another antimony sample implanted at 50 keV with a dose of 10^{13} cm $^{-2}$ and annealed at 900°C for 120 min in N $_2$. The maximal antimony concentration of this sample is lower than its solubility limit at this temperature.

A high substitutional antimony supersaturation can be reached by annealing high Sb implantation doses at low temperatures, as shown in Fig. 4. A specimen was annealed at 800°C for 120 min with the same implantation parameters as the sample in Fig. 3 (curve 1). The SIMS (solid circles), the RBS (triangles), and the electrical (squares) measurements are shown. The electrical profile shows a sharp change in the carrier concentration at a depth of ≈ 50 nm. It cannot be discerned if this jump in profile arises from the damage in the crystal. Nevertheless, a broadening of the total antimony concentration profile at $\approx 4 \times 10^{20}$ cm $^{-3}$ is recognizable. This broadening can be clearly seen by comparing the profile in Fig. 3 (curve 1) and the profile in Fig. 4 as done in Fig. 6. Consequently, Sb diffusion at 800°C for 120 min takes place. The substitutional electrical Sb concentration is at least by a factor ≈ 3 above its solubility limit at 800°C. This indicates that the precipitation process at this temperature is slow and has not been concluded. Moreover, this high substitutional antimony supersaturation supports the model in Ref. (5, 6) mentioned earlier.

Annealing at higher temperatures of high Sb-implanted doses was also carried out. A specimen with the same implantation parameters as in Fig. 3 (curve 1) was annealed at 1200°C for 15 min in N $_2$. The measured antimony profile is shown in Fig. 5. The peak in the profile at which the precipitation is located is considerably smaller than in Fig. 2-4. The concentration of $\approx 6 \times 10^{19}$ cm $^{-3}$ at which the tail of the profile begins corresponds with the solubility concentration of Sb at 1200°C (8). Here, the precipitation appears to reach its equilibrium value. The occurrence of supersaturated substitutional antimony is clearly seen by comparing the samples of Fig. 3 (curve 1), 4 and 5 as shown in Fig. 6. From this figure, it may be concluded

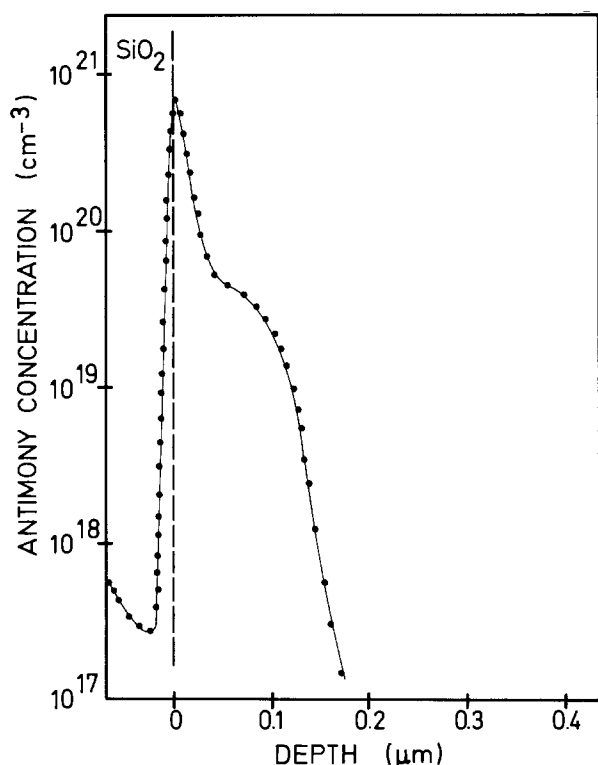


Fig. 8. Sb implantation at 80 keV for 3×10^{15} cm $^{-2}$. Thermal oxidation was carried out at 1000°C in dry O $_2$ for 40 min followed by annealing in N $_2$ for 15 min. The interface SiO $_2$ /Si is given by the vertical dashed line.

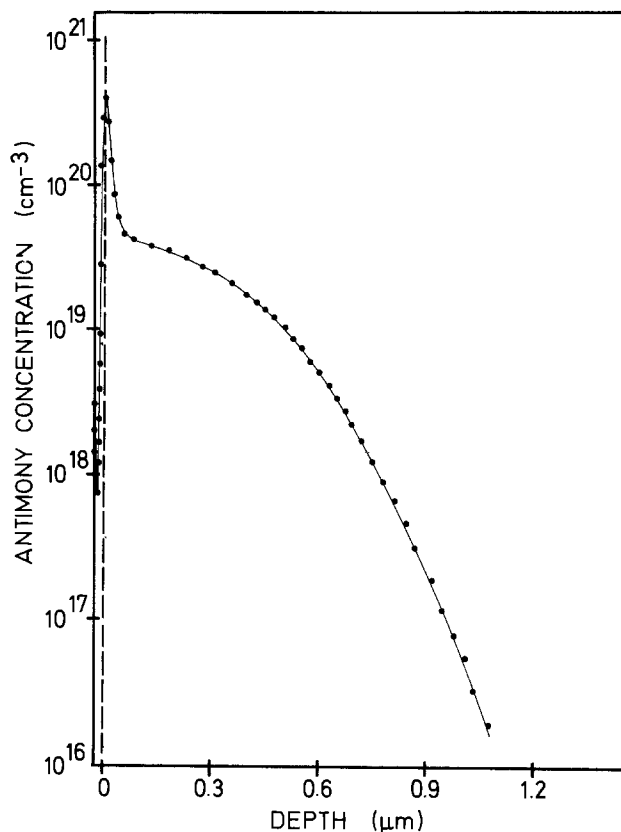


Fig. 9. The implantation parameters are the same as in Fig. 7 and 8. Thermal oxidation was realized in dry O $_2$ at 1200°C for 5 min. Then the sample was annealed in N $_2$ for 15 min. The interface SiO $_2$ /Si is given by the vertical dashed line.

that the supersaturation of Sb increases at lower temperature. Also, the antimony concentration level at which the diffusion takes place is increased by lowering the temperature.

In the following, we describe Sb high dose-implanted silicon specimens which were annealed in oxidizing atmosphere. The samples were implanted at 80 keV with doses of 3×10^{15} cm $^{-2}$. The annealing was performed in dry O $_2$ at 800°C for 400 min (sample 1), at 1000°C for 40 min (sample 2), and at 1200°C for 5 min (sample 3). Then, the samples were annealed at the respective temperature in N $_2$ for 15 min. This last annealing step causes only a

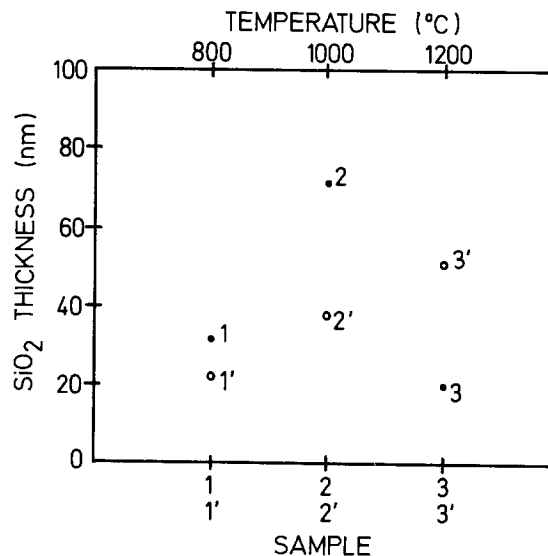


Fig. 10. The thermal oxide thickness of the doped samples 1, 2, and 3 are compared with the respective thermal oxide thickness of the undoped samples 1', 2', and 3'.

further diffusion and precipitation of Sb. At the same time, undoped samples (1', 2', 3') were treated using the respective annealing parameters. The measurements were performed by SIMS avoiding the matrix effect at the SiO₂/Si interface (12, 13). Figure 7 (sample 1), Fig. 8 (sample 2), and Fig. 9 (sample 3) show the antimony concentration profiles in oxide and in silicon. The antimony precipitation and diffusion in these figures show a similar behavior as discussed earlier. Although not much is known about the segregation of Sb at Si/SiO₂, it is assumed that Sb piles up during thermal oxidation in silicon (14, 16). Therefore, the Sb segregation coefficient ($m = C_{(Si)}/C_{(SiO_2)}$) is greater than 1 at the SiO₂/Si interface. However, in Fig. 7-9, $m = 1$ for all three cases, probably because the antimony precipitates influence the Sb segregation. The thickness of the thermally grown oxide is not the same on the Sb doped and undoped specimens. This is shown in Fig. 10. The reason for this deviation cannot be given.

Summary and Conclusions

At higher Sb implantation doses at annealing temperatures between 800° and 1000°C, the antimony substitutional concentration exceeds its solubility limit at these annealing temperatures for times up to 400 min. The amount of Sb substitutional supersaturation is the larger the lower the temperature. At 1200°C after 15 min, Sb precipitation has reached its equilibrium value. At the same time that antimony precipitates, extrinsic Sb diffusion takes place. RBS measurements show residual crystal damage caused by Sb ion implantation and/or antimony precipitation. The Sb segregation coefficient for the SiO₂/Si system does not follow the expected behavior. Moreover, an anomalous thermal oxide growth can be observed.

Acknowledgment

This work has been supported by the Fonds zur Förderung der wissenschaftlichen Forschung (project no.

S 43/10). The authors wish to thank Dr. H. Ryssel (Institut für Festkörpertechnologie, Fraunhofer-Gesellschaft, Munich, Germany) for performing SIMS measurements for control. The authors also wish to acknowledge Siemens AG (Research Laboratories, Munich, Germany) for the preparation of the samples.

Manuscript submitted May 8, 1985; revised manuscript received Aug. 12, 1985.

The Technical University of Berlin assisted in meeting the publication costs of this article.

REFERENCES

1. S. H. Song, T. Niimi, K. Kobayashi, and K. Kudo, *This Journal*, **129**, 841 (1982).
2. S. H. Song and T. Niimi, *ibid.*, **128**, 145 (1981).
3. F. Pintchovski, P. J. Tobin, M. Kottke, and J. B. Price, *ibid.*, **131**, 1875 (1984).
4. J. Narayan and O. W. Holland, *Phys. Status Solidi A*, **73**, 225 (1982).
5. J. Narayan and O. W. Holland, *Appl. Phys. Lett.*, **41**, 239 (1982).
6. J. S. Williams and R. G. Elliman, *ibid.*, **40**, 266 (1982).
7. S. J. Pennycook, J. Narayan, and O. W. Holland, *J. Appl. Phys.*, **54**, 6875 (1983).
8. F. A. Trumbore, *Bell Syst. Tech. J.*, **39**, 205 (1960).
9. T. Hirao, G. Fuse, K. Inoue, S. Takayanagi, Y. Yaegashi, S. Ichikawa, and T. Izumi, *J. Appl. Phys.*, **51**, 262 (1980).
10. T. Hirao, G. Fuse, K. Inoue, S. Takayanagi, Y. Yaegashi, and S. Ichikawa, *ibid.*, **50**, 5251 (1979).
11. J. C. Irvin, *Bell Syst. Tech. J.*, **41**, 387 (1962).
12. G. Stingeder, M. Grasserbauer, E. Guerrero, H. Pötzl, and R. Tielert, *Fres. Z. Anal. Chem.*, **314**, 304 (1983).
13. E. Zinner, *This Journal*, **130**, 199C (1983).
14. D. A. Antoniadis, S. Hansen, and R. W. Dutton, "SUPREM II — A Program for IC Process Modeling and Simulation," Stanford University Technical Report no. 5019-2, Stanford, CA (1978).
15. A. S. Grove, "Physics and Technology of Semiconductor Devices," John Wiley and Sons, New York (1976).
16. H. Müller, J. Gyulai, W. K. Chu, J. W. Mayer, and T. W. Sigmon, *This Journal*, **122**, 1234 (1975).

Technical Notes



Effect of Oxidation Ambient on the Electrical Properties of Thin Silicon Oxide

Richard G. Cosway*

Motorola, Incorporated, Process Technology Laboratory, SRDL, Phoenix, Arizona 85008

Beneficial effects of growing oxide, particularly gate oxide, with some chlorine present have been known for some time. Monkowski's paper (1) provides an excellent review of these effects which include better passivation, minority carrier lifetime enhancement, improved dielectric breakdown characteristics, increased growth rate, and stacking fault suppression over oxides grown in dry O₂.

The purpose of the present investigation was to see if some of the same benefits realized for thicker oxides grown in an HCl containing ambient still apply to thinner (150Å) oxides.

Experimental

The starting material was Czochralski-grown, 75 mm, silicon wafers of <100> crystal orientation phosphorus

*Electrochemical Society Active Member.

doped to 7.5-12.5 Ω-cm. Immediately prior to each run, the diffusion tube, boat, and push rod were cleaned in 10 volume percent (v/o) HCl, 90 v/o N₂ for 1h at 1000°C. All oxidations were carried out at 900°C in a 150 mm quartz tube. Dry O₂ runs had an O₂ flow rate of 10 liter/min, while torch runs had O₂ and H₂ flow rates of 6 and 10 liter/min, respectively. HCl runs used no HCl during the first half of the oxidation cycle and 0.3 liter/min during the last half. Immediately following oxidation, wafers were annealed in N₂ at 900°C for 1h.

Oxide thicknesses were measured on an IBM 7840 film thickness analyzer. Electrical measurements were made on capacitors formed by depositing aluminum (dc magnetron) through a shadow mask to give a nominal size of 7.5 × 10⁻³ cm². The back oxide was stripped and aluminum was deposited so as to give good ohmic contact. The front

and back aluminum was then annealed for 30 min in 5 v/o H_2 , 95 v/o N_2 at 450°C.

C-V plots contained three traces: (i) unbiased, (ii) biased for 1 min at 200°C at 4.5V, and (iii) biased for 1 min at 200°C at -4.5V. Total flatband voltage shifts were obtained by taking the difference between the leftmost and rightmost traces at flatband.

Breakdown voltages were measured using a Tektronix Model 576 curve tracer. The dc voltage was ramped manually until the capacitor ruptured.

Leakage currents were obtained using an HP 4140B picoammeter. Interface-trapped charge values (reported as the density of states at mid bandgap) were obtained from quasi-static C-V measurements using the HP 4140B picoammeter.

Results

Table I shows that oxidation in O_2/HCl gives higher C-V shifts than oxidation in dry O_2 . Wafers oxidized in H_2O/HCl did not give enough good C-V traces to enable a statistically significant evaluation. Most of the capacitors produced in H_2O/HCl were broken down by the bias-temperature-stress of 4.5V at 200°C for 1 min. From the results in Table I, which give the average values and standard deviation from three runs (2 for O_2/HCl) 2 wafer/run and 2 capacitor/wafer, H_2O appears to give a greater total C-V shift than O_2 .

The higher C-V shifts for the O_2/HCl and H_2O oxidations were mostly due to a negative shift after positive BTS (i.e., trace 2 is shifted to the left of trace 1). This may be due to the enhanced equilibrium alkali concentration within the tube in the presence of H_2O and/or HCl (2). Creation of interface traps in the presence of H_2O (3, 4) may also be related to the higher C-V shift. Note that some H_2O is present during the HCl/O_2 oxidation due to the decomposition of HCl .

Table I also shows that yield is determined mainly by oxidant and that the presence of HCl has minimal effect. The yields ($> 10 \text{ MV}\cdot\text{cm}^{-1}$) exclusive of tertiary defects from three runs (two for O_2/HCl) 2 wafer/run and at least 15 capacitor/wafer are shown for each ambient. Comparisons were made among the various ambients using statistical analysis which showed (i) O_2 can be considered equivalent to O_2/HCl and H_2O can be considered equivalent to H_2O/HCl , (ii) H_2O appears to give greater yield than O_2 , and (iii) with 90% confidence, H_2O/HCl gives greater yield than O_2/HCl . The higher yield obtained from H_2O oxidation may be caused by the micropores being filled by OH groups to give more uniform electric fields (3) than would be the case for oxides grown in dry O_2 .

The cumulative failures as a function of applied field is shown in Fig. 1, where it can be seen that the O_2/HCl ambient yields oxides with the most cumulative failures below 11 $\text{MV}\cdot\text{cm}^{-1}$, while oxides grown in H_2O/HCl have the lowest cumulative failure up to 15 $\text{MV}\cdot\text{cm}^{-1}$.

Leakage currents measured at 5 $\text{MV}\cdot\text{cm}^{-1}$ (7.5V for 150Å oxides) gave less than 0.5 $\text{nA}\cdot\text{cm}^{-2}$ for all ambients, and for those capacitors breaking down at $> 10 \text{ MV}\cdot\text{cm}^{-1}$ the average breakdown field was approximately 12.5 $\text{MV}\cdot\text{cm}^{-1}$.

The interface-trapped charge, Q_{it} , for the various ambients is also shown in Table I. All values are the same order of magnitude, with the O_2/HCl oxides yielding the

Table I. Summary of electrical properties for 150Å oxides

Additive	Oxidant	Total flatband shift (mV)	Yield $> 10 \text{ MV}/\text{cm}$ (%)	Interface-trapped charge ^a ($\text{cm}^{-2}\cdot\text{eV}^{-1}$)
No HCl	O_2	13 ± 3	88.4 ± 7.2	3×10^{11}
HCl	O_2	24 ± 7	86.3 ± 12.1	6×10^{11}
No HCl	H_2O	40 ± 26	93.0 ± 9.2	4×10^{11}
HCl	H_2O	—	96.9 ± 6.3	3×10^{11}

^a Determined from the density of states at midbandgap.

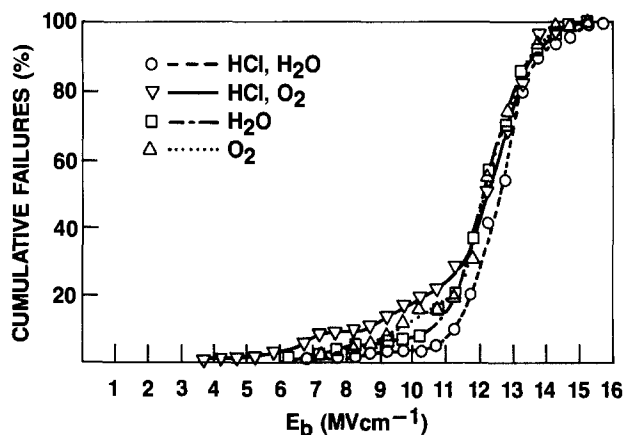


Fig. 1. Cumulative failures as a function of applied field for 150Å oxides grown in various ambients.

highest value of $6 \times 10^{11} \text{ cm}^{-2}\cdot\text{eV}^{-1}$. This may be explained by the findings of Kriegler (5), wherein the use of dry HCl was shown to lead to damage of the silicon surface.

The data for H_2O and H_2O/HCl oxidation were presented only for completeness, since the growth rate in these ambients are too rapid to enable good process control for 150Å oxides.

Discussion

The increased oxide growth rate reported to occur when HCl is present (6) was not observed in the present study. This is probably because the growth takes place in the linear regime of oxidation for these thin films where the HCl was shown to have no effect. The effect of HCl on stacking faults and minority carrier lifetimes was not examined in the current study.

While the passivating properties of the oxides were not measured by intentional contamination, the as-grown films produced in O_2 seemed to contain less alkali impurities (from flatband shifts) than those produced in O_2/HCl (Table I). The as-grown impurity level may be more important than the passivating properties of the oxide for future VLSI applications where downstream processing will be cleaner than today's.

It is possible that cleaning the tube at a considerably higher temperature may reduce the alkali levels observed for the films grown in O_2/HCl ; however, this was not investigated.

The breakdown characteristics of the dry O_2 oxides appear equivalent to those for O_2/HCl oxides (Table I). This, coupled with the arguments presented above, shows that oxides grown in dry O_2 may well be the gate oxides of the future.

By growing oxides in dry O_2 only, retaining HCl solely as a tube cleaning agent, the problems of HCl corrosion can be minimized. Since precise control of HCl flow rate is not necessary for tube cleaning, it can be plumbed to the furnace separately from the other process gases and, as such, can be kept away from the expensive furnace parts that it may corrode.

Another approach is to use an alternate chlorine source to HCl such as TCA (1,1,1-trichloroethane). While this limits the corrosive problems within the gas cabinet, the potential formation of toxic gases (7), explosion potential (8), as well as poorer oxides grown under these conditions (9) make this alternative less than optimal.

Conclusions

The current investigation has shown that the presence of HCl during growth of thin (150Å) oxides materially affects neither the yield ($> 10 \text{ MV}\cdot\text{cm}^{-1}$), average breakdown field above 10 $\text{MV}\cdot\text{cm}^{-1}$, nor the leakage current. For dry oxidation, the presence of HCl actually increases the total flatband shift and slightly increases the interface-trapped charge. H_2O has been shown to give higher yield but worse C-V shifts than O_2 .

Thus, it is feasible to grow thin oxides in dry O₂ only, still utilizing HCl for tube cleaning, however.

Acknowledgments

I would like to thank C.-E. Wu for his valuable contributions to this work including data analysis. I would also like to thank John Seeger for providing the metal deposition, Ginger Stapleton for providing the leakage current and quasi-static C-V measurements, and Fran Sanchez for providing the breakdown and high frequency C-V measurements.

Manuscript submitted April 18, 1985; revised manuscript received Sept. 3, 1985. This was Paper 343 presented at the New Orleans, Louisiana, Meeting of the Society, Oct. 7-12, 1984.

Motorola, Incorporated, assisted in meeting the publication costs of this article.

REFERENCES

1. J. Monkowski, *Solid-State Technol.*, **22**, 58 (1979).
2. S. Mayo and W. H. Evans, *This Journal*, **125**, 106 (1978).
3. E. A. Irene, *ibid.*, **125**, 1708 (1978).
4. D. R. Young, E. A. Irene, D. J. DiMaria, and R. F. Keersmaeher, *J. Appl. Phys.*, **50**, 6366 (1979).
5. R. J. Kriegler, in "Semiconductor Silicon 1973," H. R. Huff and R. R. Burgess, Editors, p. 363, The Electrochemical Society Softbound Proceedings Series, Princeton, NJ (1973).
6. R. J. Kriegler, Y. C. Cheng, and D. R. Colton, *This Journal*, **119**, 388 (1972).
7. Apache Chemical sales information.
8. J. C. Schumacher Co. Product Application Note no. 2.
9. R. G. Cosway and S. Y. Wu, *This Journal*, **132**, 151 (1985).

Effects of Surface Oxide on Leakage Current of Magnetron-Sputtered Ta₂O₅ on Si

Shunji Seki, Takashi Unagami, and Osamu Kogure

Nippon Telegraph and Telephone Corporation, Ibaraki Electrical Communication Laboratories, Tokai, Ibaraki 319-11, Japan

In recent years, tantalum pentoxide (Ta₂O₅) films have attracted much interest for use as storage capacitors in large-scale integrated memory cells and as gate insulators in MOS devices. The higher dielectric constant for Ta₂O₅ films, compared with that for SiO₂ films, makes them attractive for these devices. For these applications, Ta₂O₅ films were prepared by chemical vapor deposition (CVD) and thermal oxidation of a deposited Ta film (1, 2). In these investigations, it has been shown that these films show very high leakage current, and that low temperature heat-treatment around 400°C results in a significant deterioration in the resistivity of Ta₂O₅ films, especially with aluminum electrodes in place. In order to reduce the leakage current, dual-dielectric structures such as Ta₂O₅/SiO₂ have been fabricated. It has been demonstrated that thermal oxide grown by interfacial oxidation between Ta₂O₅ and the silicon substrate reduces the leakage current in the Ta₂O₅ (30 nm)/SiO₂(12 nm)/Si structure (3). However, in this dual-dielectric structure, the effective dielectric constant of the dual-dielectric film is less than 10 due to the existence of the low dielectric constant SiO₂ between Ta₂O₅ and Si. Therefore, Ta₂O₅ films with high dielectric constant and low leakage current are necessary if these films are to be used in electronic devices.

The authors have demonstrated that a low dielectric constant transition layer formed at the silicon interface plays a key role in determining the electrical properties of RF magnetron-sputtered Ta₂O₅ on Si (4). This transition layer can be formed as a result of the interaction between the sputtered particles and the silicon substrate in the initial stage of Ta₂O₅ formation. The present work explores the role of surface oxide on the silicon substrate prior to sputtering deposition in the formation of the transition layer at the interface and the electrical characteristics of the deposited film. This note indicates that the surface oxide exerts an important effect on the leakage current and dielectric properties of Ta₂O₅ films deposited on Si.

Experimental

Leakage current characteristics were measured by using an Al/Ta₂O₅/Si capacitor. Single-crystalline silicon wafers (p-type, <111>-oriented and 2 Ω-cm) were used as substrates. These substrates were cleaned by a mixture of H₂SO₄ and H₂O₂ (volume ratio of H₂SO₄/H₂O₂ = 4/1), and then rinsed in deionized water. Immediately before being installed into the sputtering chamber, the substrates were

dipped into dilute HF to remove the oxide formed during the previous processing steps. Surface oxide thickness at the silicon surface prior to sputtering was adjusted to 1.8 nm (sample A) and 2.5 nm (sample B) by oxidation in the plasma. Surface oxide thickness was measured by ellipsometry and the contact angle of water drops on the surface (5). On these substrates, Ta₂O₅ films were fabricated using an RF magnetron sputtering system. The Ta₂O₅ target was of 10 cm diam and 5 mm thickness. The sputtering was performed in a mixture of argon and oxygen (partial pressure ratio of Ar/O₂ = 90/10). The deposited film thickness was determined by ellipsometry at the wavelength of 632.8 nm. Electron-beam-evaporated aluminum was used for electrodes. Prior to measurements, these MOS capacitors were annealed at 450°C in a hydrogen ambient. After annealing, leakage current characteristics were measured in a dark, shielded box. A negative external voltage was applied to the aluminum electrode in these measurements. In addition to these measurements, dielectric properties of the Ta₂O₅ films were also measured. These measurements were performed for more than 50 capacitors fabricated on the same silicon substrate.

Results and Discussion

Figure 1 shows typical leakage current characteristics for sample A and B. A drastic change can be seen in the leakage current characteristics. The film thickness of sample A is 70.5 nm, and that of sample B is 60 nm. The leakage current in sample A is more than eight orders of magnitude lower than that in sample B when an external electric field of 1 MV/cm is applied. The leakage current in sample A is 1.5×10^{-9} A/cm² at 1 MV/cm. The dielectric breakdown strength is more than 6×10^6 V/cm. It should be noted that this capacitor was annealed in a hydrogen ambient at 450°C with aluminum electrodes on the Ta₂O₅ film. This result clearly indicates that the surface oxide on the silicon substrate prior to sputtering plays a key role in determining the leakage current characteristics, since Ta₂O₅ films in both samples were deposited under the same sputtering conditions.

Figure 2 indicates frequency dispersions in the capacitance of sample A and B. Capacitance was measured at an external bias voltage of -5V applied to the Al electrode. Capacitances at each frequency were normalized by the capacitance measured at 1 MHz. No frequency dispersion

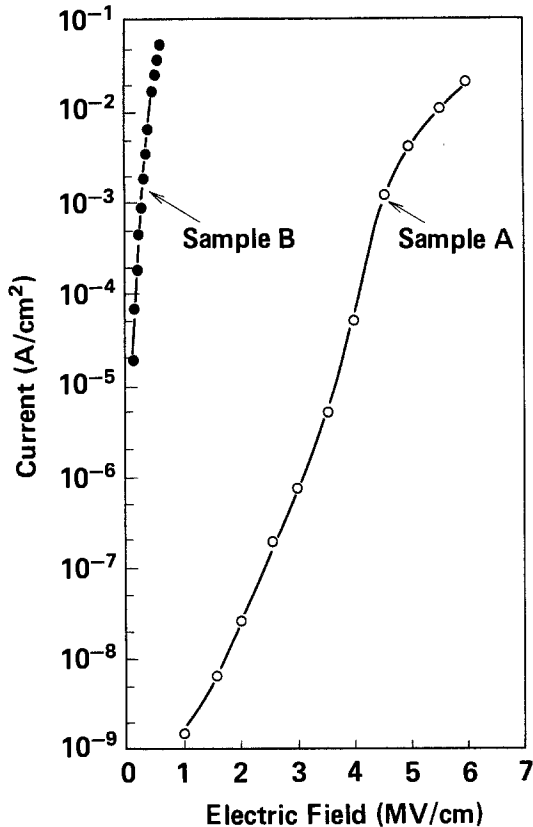


Fig. 1. Current-voltage characteristics of sample A and B. Surface oxide thickness of sample A is 1.8 nm, and that of sample B is 2.5 nm.

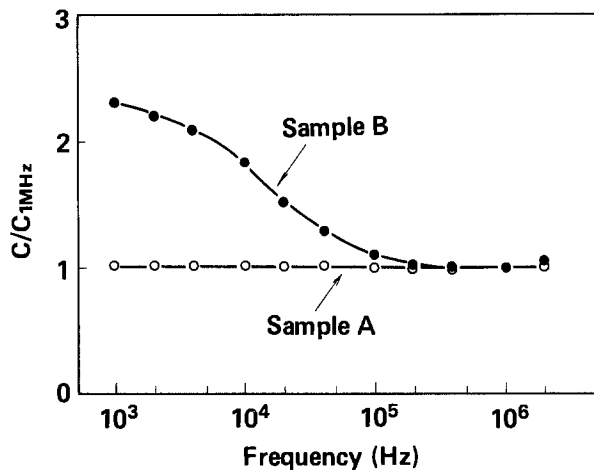


Fig. 2. Frequency dispersion in the capacitance of sample A and B.

has been observed for sample A in the range of 1 kHz-1 MHz. On the other hand, a large frequency dispersion has been observed for sample B. The dielectric constant of sample A is calculated to be 16.5 at 1 MHz. This higher dielectric constant, compared with that of dual-dielectric

structures, makes RF magnetron-sputtered Ta₂O₅ films more attractive for application to electronic devices. Dielectric loss of the film at 1 kHz was less than 0.1% in sample A, but was more than 10% in sample B. These results indicate that high quality Ta₂O₅ films can be obtained on Si by controlling the thickness of the surface oxide.

In addition to the above-mentioned leakage current and dielectric characteristics, a remarkable change was observed in film thickness and index of refraction depending on the surface oxide thickness. When Ta₂O₅ film was deposited on Si substrates with different surface oxide thicknesses for the same sputtering period under the same sputtering conditions, the thickness of the film deposited on the Si substrate with 1.8 nm thick surface oxide was 72 nm, while that of the film deposited on Si with 2.5 nm thick surface oxide was 61.5 nm. The effective indexes of refraction for the films deposited on the former and the latter substrates were 2.04 and 2.12, respectively. This remarkable change in the film thickness and index of refraction might be due to the effect of surface oxide thickness on the transition layer formation mechanism in the initial stage of Ta₂O₅ formation on silicon.

Conclusion

It has initially been indicated that surface oxide prior to sputtering plays a key role in determining the leakage current and dielectric characteristics of magnetron-sputtered Ta₂O₅ on Si. By reducing the surface oxide thickness to as low as 1.8 nm, the leakage current after annealing becomes about 1×10^{-9} A/cm² at 1 MV/cm. The dielectric breakdown strength is more than 6×10^6 V/cm. Furthermore, dielectric constant reaches 16.5, which is much higher than that of the dual-dielectric structure. No frequency dispersion was observed in the film capacitance from 1 kHz through 1 MHz, and dielectric loss of the film was lower than 0.1% at 1 kHz. These results clearly demonstrate that high quality Ta₂O₅ films with high dielectric constant and low leakage current can be obtained on Si with magnetron sputtering by controlling the surface oxide thickness prior to deposition.

Acknowledgments

The authors would like to thank Dr. B. Tsujiyama for his encouragement during the course of this work.

Manuscript submitted May 13, 1985; revised manuscript received July 10, 1985.

Nippon Telegraph and Telephone Public Corporation assisted in meeting the publication costs of this article.

REFERENCES

1. E. Kaplan, M. Balog, and D. Frohman-Bentchkowsky, *This Journal*, **123**, 1570 (1976).
2. D. J. Smith and L. Young, *IEEE Trans. Electron Devices*, **ed-28**, 22 (1981).
3. T. Kato, T. Ito, M. Taguchi, T. Nakamura, and H. Ishikawa, in "1983 Symposium on VLSI Technologies, Technical Digest," p. 86 (1983).
4. S. Seki, T. Unagami, and B. Tsujiyama, *This Journal*, **131**, 2621 (1984).
5. R. Williams and A. M. Goodman, *Appl. Phys. Lett.*, **25**, 531 (1974).

Preparation of Thin ($0.6 \mu\text{m}$) Continuous Monocrystalline Silicon over SiO_2

L. Jastrzebski,* J. F. Corboy, R. Pagliaro, Jr., and R. Soydan

RCA Laboratories, Princeton, New Jersey 08540

Silicon-on-insulator (SOI) technology is a technique under development to obtain monocrystalline silicon over SiO_2 islands, which can be used as an alternative to SOS (1). If this technology can be successfully accomplished in an economical fashion to provide VLSI-quality layers (2), device problems such as latchup (3) and bird's beak (4) can be eliminated wherever this growth technique is applicable.

Several SOI approaches are currently under investigation [for the assets and liabilities of the various approaches see, *e.g.*, Ref., (5)]. With some of the SOI techniques, it is difficult to provide a thin ($\sim 0.5 \mu\text{m}$) silicon layer over oxide islands. For SOI films obtained by epitaxial lateral overgrowth (ELO), a monocrystalline silicon layer is grown by selective CVD from the openings in the oxide mask (deposition conditions are chosen to prevent silicon nucleation over the oxide during homoepitaxial growth) (5-8). The epi layer grows vertically until it is level with the SiO_2 mask and then laterally over the SiO_2 mask as it continues its vertical growth. Growth is continued until the growth fronts, seeded from opposing windows, meet to form a continuous film of silicon. The minimum thickness at which an acceptably smooth, continuous, epitaxial film is obtained depends on the lateral to vertical growth rate ratio (overgrowth ratio) and the width of the SiO_2 islands. Although overgrowth ratios of 10:1 (6) and 40:1 (7) have been reported, low defect densities in ELO films have been reported only for films prepared at a 1:1 ratio (8). If the final SOI film thickness is greater than required for successful circuit applications, *e.g.*, for use as an alternative to $0.6 \mu\text{m}$ thick SOS films, the SOI film could be thinned to the desired thickness by oxidation. Although in the present work we discuss the application of oxide thinning to SOI films obtained by the ELO process, this approach could be used for any SOI film which is too thick for a given device fabrication process. We believe that oxidation thinning is a reliable, economical technique to obtain, in a reproducible way, uniform films of desirable thicknesses ($\sim 0.5 \mu\text{m}$) with smooth surfaces.

The substrates were (100)-oriented silicon patterned with stripes of $0.65 \mu\text{m}$ thick, $6.0 \mu\text{m}$ wide SiO_2 with $6.0 \mu\text{m}$ wide exposed silicon regions between the SiO_2 stripes. The epitaxial films were prepared in a chemical vapor deposition reactor (AMC 7900) at 1050°C at 760 torr using a mixture of SiH_2Cl_2 , HCl , and H_2 . The deposition process was a two-step growth cycle (9). The samples described in this paper were grown at approximately $0.3 \mu\text{m}/\text{cycle}$ for 21 cycles, to give $6 \mu\text{m}$ thick ELO films.

After epitaxial growth, the wafers are removed from the CVD reactor and thinned by oxidation at 1100°C in HCl steam. A maximum of $2.1 \mu\text{m}$ of oxide was grown during each oxidation step, after which the wafers were removed from the oxidation furnace and the SiO_2 film was stripped in buffered HF . When additional silicon thinning was required, the wafers were cleaned and oxidized again. The amount of silicon removed by oxidation was calculated using the formula (10) $t_{\text{Si}} = 0.45t_{\text{ox}}$ (where t is thickness).

Cross-sectional SEM micrographs of the as-grown SOI structure and the structures obtained after each thinning are shown in Fig. 1. The flat continuous nature of the silicon film over and between the SiO_2 strips is evident in Fig. 1E and 1E'. It is clear that the SOI layers thinned to 3.2 , 1.6 , 1.1 , and $0.6 \mu\text{m}$ have the same flatness as the as-grown film

According to our experience, it is not currently possible to obtain continuous $0.6 \mu\text{m}$ thick epitaxial silicon films over $0.6 \mu\text{m}$ thick (or thicker), $6.0 \mu\text{m}$ wide (or wider) SiO_2 using only an epitaxial CVD technique. By combining a CVD growth technique that provides epitaxial silicon with a post epi thinning technique, "oxidation," we are able to obtain this structure.

The process of the oxidation of silicon is well documented (11, 12). The oxidation conditions used to obtain the data presented in this paper were used to demonstrate only the feasibility of oxidation as a thinning technique, and not the practicality of the technique. A practical method of removing 5 - $10 \mu\text{m}$ of silicon would be to use a high pressure (13-15) oxidation procedure.

The time required to grow 0.5 , 1 , 2 , 3 , 4 , 5 , and $6 \mu\text{m}$ of SiO_2 , which corresponds to the removal of 0.22 - $2.7 \mu\text{m}$ of silicon, is given in Table I for oxidation performed at various temperatures in steam at atmospheric pressure and at 20 atm. The columns labeled I and II represent the total time required to remove the amount of silicon shown in the right-hand column, using one oxidation step or two separate but equal length steps (the first oxidation step is followed by oxide removal).

The most practical way of performing thinning by oxidation is to use high pressure (~ 20 atm). From an economical standpoint, the thinning should be performed at high temperatures (1200°C), since the oxidation time is short. If diffusion of impurities need be taken into consideration, as in the case of vertically integrated (three-dimensional) structures, the thinning by oxidation should be carried out at low temperature, high pressure, and with repetitious oxidation steps. For example, during the thinning of $2.25 \mu\text{m}$ of silicon by oxidation at 800°C , at 20 atm, using two successive oxidation steps the impurity

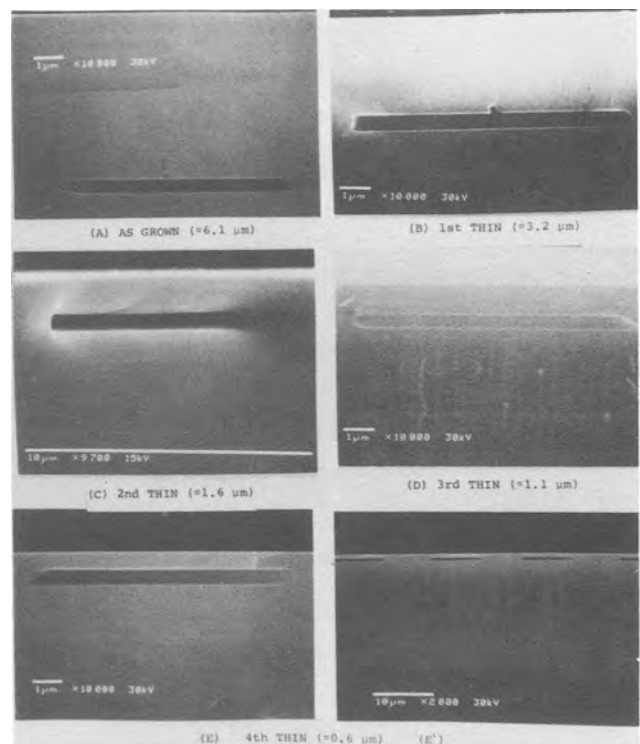


Fig. 1. Cross-sectional scanning electron micrographs of the silicon overgrowth after deposition and after each oxidation experiment.

*Electrochemical Society Active Member.

Table I. SiO₂ thickness (μm) vs. oxidation time (h) as a function of temperature and pressure in pyrogenic steam on (100) silicon

SiO ₂ thickness (μm)	≈ 1 atm								20 atm								Amount of silicon removed (μm)
	1200°C		1000°C		900°C		800°C		1200°C		1000°C		900°C		800°C		
	I ^a	II ^b	I	II	I	II	I	II	I	II	I	II	I	II	I	II	
0.5	0.38	0.18	1.6	1.23	5.4	4.3	21.7	18.7	0.019	0.009	0.084	0.063	0.27	0.22	1.08	0.93	0.22
1.0	1.6	0.76	4.7	3.2	13.4	10.8	50.0	21.7	0.079	0.038	0.25	0.17	0.67	0.54	2.5	2.2	0.45
2.0	7.1	3.2	17.5	9.4	34.2	26.8	133.3	10.0	0.36	0.16	0.90	0.50	1.7	1.3	6.7	5.0	0.90
3.0	16.6	7.6	36.7	19.3	63.3	46.7	233.3	180.0	0.83	0.40	1.9	1.0	3.2	2.3	11.7	9.2	1.35
4.0	33.3	14.2	61.7	35.0	10.0	68.4	366.7	266.7	1.7	0.7	3.2	1.8	7.5	3.4	18.3	13.3	1.80
5.0	60.0	22.7	93.3	53.3	141.7	93.3	508.3	416.7	3.0	1.1	4.7	2.7	7.1	4.7	25.4	20.8	2.25
6.0	86.7	33.2	138.3	73.4	208.3	126.6	633.3	466.7	4.3	1.9	6.7	3.8	10.4	6.3	31.7	23.4	2.7

^a Total time at temperature to grow SiO₂ thickness in one oxidation step.

^b Total time at temperature to grow SiO₂ thickness in two equal-length oxidation steps.

movement (\sqrt{Dt}) is kept to a minimum (D is the diffusion constant of an impurity, and t equals time). The impurity redistribution will be 0.015 μm for boron and 0.005 μm for arsenic using $D_B = 3 \times 10^{-3}$ and $D_{As} = 1 \times 10^{-3}$ $\mu\text{m}^2/\text{h}$. This amount of diffusion will not significantly affect already made devices previously fabricated in the first level of the circuit.

Another issue is the reproducibility and uniformity of SOI films thinned by oxidation. Oxidation is a standard step used by IC processing and the reproducibility of the oxide thickness is controlled to within about $\pm 1\%$ during oxide formation. Also, the uniformity of the oxide across a wafer is $\leq \pm 1\%$. Therefore, the major variations in the thickness of the thinned SOI film during oxidation are associated with the as-grown epitaxial film uniformity and reproducibility. To date, there are not sufficient data on the reproducibility of the ELO process, but the results collected so far indicate that uniformity across the wafer (for identical patterns) is similar to the homoepitaxial layers which is about $\pm 5.0\%$ [for a detailed discussion, see Ref. (16)]. Since this thickness variation will be reflected during thinning, a 6 μm thick SOI film thinned to 0.5 μm will have a ± 0.30 μm thickness variation. For CMOS applications (17), approximately 3 μm thick ELO films overgrowing 3 μm wide SiO₂ islands will be used, and in this case the thinned film thickness variation will be about ± 0.15 μm , which is acceptable for any VLSI application.

We propose that thin (0.6 μm), acceptably smooth, continuous silicon over and between SiO₂ layers can be obtained in an economically viable fashion if CVD growth is combined with thinning by oxidation. This process uses a reliable, economically viable approach to obtain, in a reproducible way, uniform films of desired thicknesses. When combined with high pressure oxidation it can also be used for vertically integrated (three-dimensional) circuits.

Acknowledgment

The authors would like to thank Dr. G. W. Cullen for a critical review of this manuscript.

Manuscript received July 15, 1985.

RCA Laboratories assisted in meeting the publication costs of this article.

REFERENCES

- "Heteroepitaxial Semiconductor for Electronic Devices," G. W. Cullen and C. C. Wang, Editors, Springer-Verlag, New York (1978).
- L. Jastrzebski, *IEEE Trans. Electron Devices*, **ed-29**, 475 (1982).
- R. R. Troutman, *IEDM Tech. Dig.* 296, (1984); J. Hall, K. Fung, J. Seitchik, L. Arledge, and P. Yeng, *ibid.*, 292, (1984).
- W. G. Oldham, *ibid.*, 216 (1982); L. Jastrzebski, A. Ipri, J. F. Corboy, and R. Metz, in "Technical Digest of the 1983 VLSI Technology Symposium, Hawaii," September 1983, p. 50.
- L. Jastrzebski, *RCA Rev.*, **44**, 250 (1983); L. Jastrzebski, *J. Cryst. Growth*, **70**, 253 (1984), special issue, Proceedings of the ACCG-6/ICVGE-6 Conference, July 1984, Atlantic City, NJ.
- T. S. Jayadev, E. N. Okazaki, and H. L. Peterson, Abstract 232, p. 335, The Electrochemical Society Extended Abstracts, Vol. 85-1, Toronto, Ont., Canada, May 12-17, 1985.
- D. D. Rothman, D. J. Silversmith, and J. A. Burns, *This Journal*, **129**, 2303 (1982).
- L. Jastrzebski, *J. Cryst. Growth*, **63**, 493 (1983).
- L. Jastrzebski, J. F. Corboy, J. T. McGinn, and R. Pagliaro, Jr., *ibid.*, **130**, 1571 (1983).
- "Semiconductor Technology Handbook," 5th edition, D. D. Trapp, R. A. Blanchard, L. J. Lopp, and T. I. Kamins, Editors, p. 42, Technology Associates, Portola Valley, California (1985).
- B. E. Deal and A. S. Grove, *J. Appl. Phys.*, **36**, 3770 (1965).
- A. S. Grove, "Physics and Technology of Semiconductor Devices," John Wiley and Sons, New York (1967).
- J. R. Ligenza, *This Journal*, **109**, 73 (1962).
- R. J. Zeto, N. O. Korolkoff, and S. Marshall, *Solid State Technol.*, **62** (7), (1979).
- R. R. Razouk, L. N. Lie, and B. E. Deal, *This Journal*, **128**, 2214 (1981).
- J. F. Corboy and R. Pagliaro, Jr., *RCA Rev.*, **44**, 231 (1983).
- L. Jastrzebski, Paper presented at the European Materials Research Conference, May 1985, Strasbourg, France.

The Fabrication of CMOS Structures with Increased Immunity to Latchup Using the Two-Step Epitaxial Process

L. Jastrzebski,* J. F. Corboy, R. Soydan, R. Pagliaro, Jr., and C. Magee

RCA Laboratories, Princeton, New Jersey 08540

Latchup between p and n transistors in CMOS circuits is one of the primary problems that has to be overcome before the spacing between n and p transistors can be

*Electrochemical Society Active Member.

substantially reduced (1,2). Trenching and the use of heavily doped substrates are currently used to reduce latchup between n and p regions (3). Trenching puts a physical barrier between the n and p regions, whereas

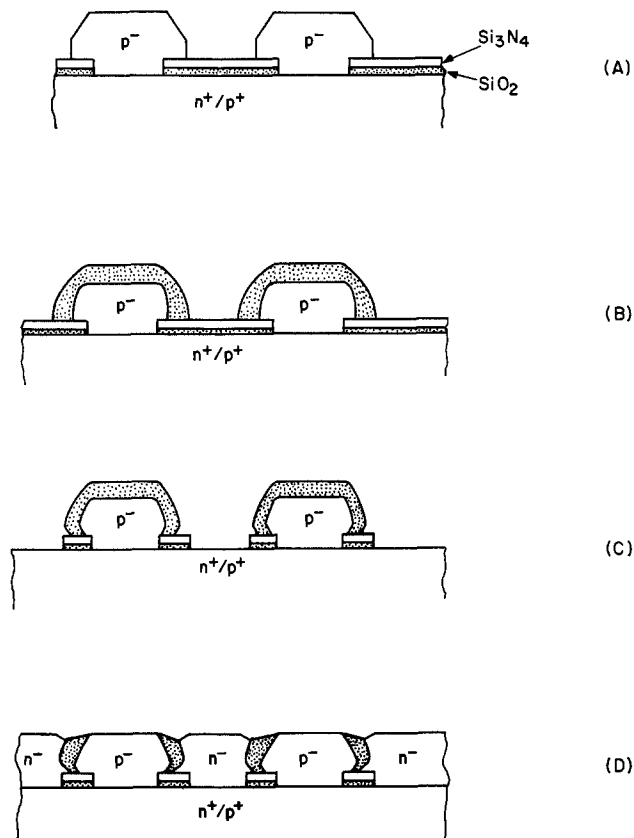


Fig. 1. Processing sequence for a latchup-resistant structure using an epitaxial lateral overgrowth technique.

heavily doped substrates provide a high conductivity, low minority carrier region thereby reducing the minority carrier flow between n and p transistors (4). Currently, 15 μm thick epi layers are being used. This thick epi layer is required to prevent the impurities that out-diffuse from the heavily doped substrate, during well drive, from reaching the bottom of the well region. Due to crystallographic defect generation and practical considerations with present trench technology, only 1-2 μm deep trenches (5) are possible. This leaves a region approximately 13-14 μm thick above the substrate-epi layer interface through which latchup can occur.

Other approaches are being sought to improve CMOS circuits resistant to latchup. One approach is based on

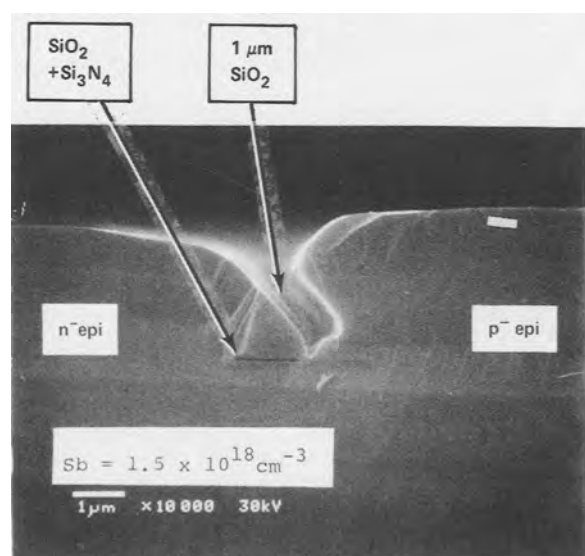


Fig. 2. SEM cross-sectional photomicrograph of n^- and p^- epi layers separated by oxide. The oxide has been removed to enhance clarity in this micrograph.

megaelectronvolt implanting a heavily doped region underneath the well (6), which allows one to have close spacing between the heavily doped regions and the well. Another approach is SOI/SOS technology (7, 8), which yields a totally isolated silicon island. In this paper a new approach to obtain latchup resistant structures is reported. This approach is based on a two-step epitaxial lateral overgrowth (ELO) (9, 10) process. The processing steps are shown in Fig. 1. First, a thin 400 \AA thick oxide (800 $^\circ\text{C}$ in HCl steam) and an 800 \AA thick nitride are grown. A photolithographic pattern corresponding to n or p regions is defined in the photoresist and etched into the $\text{Si}_3\text{N}_4 + \text{SiO}_2$ mask. Subsequently, the first ELO growth step is performed (Fig. 1A). Growth is carried out at 1050 $^\circ\text{C}$ at 100 torr using SiH_2Cl_2 , dopant, and HCl in H_2 in a radiantly heated barrel reactor. The deposition process is a series of two-step cycles. One cycle consists of a deposition step and an etch step. In the deposition step, SiH_2Cl_2 , dopant, and HCl are added to the H_2 carrier for 1 min. At the end of the deposition step, the SiH_2Cl_2 and dopant are removed from the gas stream and the etch step (second step) begins and continues for 1.5 min. The epi layers are grown at a rate of approximately 0.43 $\mu\text{m}/\text{cycle}$ for eight cycles. Dopant is excluded from the first cycle, and the system is purged for 10 min between the first and second cycles to reduce autodoping. Dopant is added to cycles two through eight, and no purge is used between these cycles.

The CVD deposition conditions are such that no silicon nucleates on the Si_3N_4 , but selectively grows in the area of exposed silicon (10), giving the structure shown in Fig. 1A. Subsequently, the epi layer is oxidized at 1050 $^\circ\text{C}$ for 1h in HCl steam to form 1.0 μm of oxide (Fig. 1B). This oxidation step is followed by a wet nitride etch and a "short" wet oxide etch to remove the 800 \AA Si_3N_4 and the 400 \AA SiO_2 layers (Fig. 1C), exposing substrate regions which are not covered by the first epi layer. Subsequently, a second selective epitaxial growth step is performed (Fig. 1D) identical to the first epi growth with the exception of using the opposite conductivity dopant type. After the second growth, the oxide is removed and the wafers are put through the remaining portion of a standard CMOS process.

The n^- and p^- epi layers are isolated from each other by an oxide layer which extends from the epitaxial surface to the $\text{Si}_3\text{N}_4/\text{SiO}_2$ pattern layer on the heavily doped

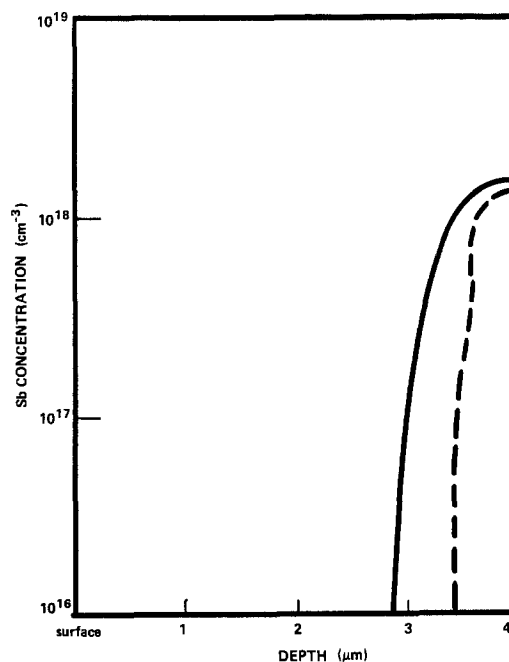


Fig. 3. SIMS profiles of the antimony concentration in the second epitaxial layer (broken line) and in the first epitaxial layer (solid line) after deposition.

substrate surface. A SEM cross-sectional micrograph of the resulting structure is shown in Fig. 2. This structure is not planar. A dip of about $0.8 \mu\text{m}$ exists on the surface in the regions where the two epi layers meet. This nonplanarity should not be an important obstacle in the application of this technology since during SOS processing island edges $\sim 0.6 \mu\text{m}$ high can be tolerated.¹ SIMS profiles of the antimony concentration in the epitaxial layer, which was incorporated via autodoping and out-diffusion from the substrate during the CVD growth process, are shown in Fig. 3. The antimony impurity gradient that extends from the heavily doped substrate into the p^- and n^- epitaxial regions shows a drop in concentration from 10^{18} to 10^{16} cm^{-3} over a distance of $0.3 \mu\text{m}$ in the second epi layer and $0.7 \mu\text{m}$ in the first epi layer. (The first epi layer is exposed to both epi layer temperature cycles.) Since a "well drive" is not required and only low temperature steps are needed to complete the CMOS process, one can expect that these gradients will not be significantly changed during subsequent steps required to complete the CMOS process.

The proposed structure should avoid all of the most significant device problems encountered during ELO, such as high leakage along the interface formed by the ELO film overgrowing an oxide. This interface is different from the interface formed by oxidation of silicon. The leakage along the ELO/oxide interface especially affects performance of NMOS transistors giving leakage in order of $10^{-9} \text{ A}/\mu\text{m}$. It is less apparent in PMOS devices, in which it is usually three orders of magnitude lower (10-12). In the two-step ELO process described, this problem is eliminated by depositing the p^- epi layer first and then thermally oxidizing it. The n channel transistors fab-

¹Also notice that surface nonplanarity is a gradual one; this type of nonplanarity does not affect continuity and definition of poly and metal lines.

ricated in this silicon will be in contact with a "post-epi" thermally grown oxide, not in silicon grown over a SiO_2 layer. The less susceptible p transistors will be made in the second epi layer (n^-) that overgrows the thermally grown oxide. In this way neither the n - or p -channel transistors will be affected by sidewall leakage.

Acknowledgment

The authors would like to thank Dr. G. W. Cullen for a critical review of this manuscript.

Manuscript received July 15, 1985.

RCA Laboratories assisted in meeting the publication costs of this article.

REFERENCES

1. R. R. Troutman, *IEDM Tech. Dig.*, 296 (1984).
2. J. Hall, K. Fung, J. Seitchik, L. Arledge, and P. Yang, *ibid.*, 292 (1984).
3. R. Rung, *ibid.*, 574 (1984).
4. Y. Taur, W. Chang, and R. Dennard, *ibid.*, 398 (1984).
5. C. Teng and C. Slawinski, *ibid.*, 586 (1984).
6. K. Terrill, P. Byrne, H. Zeppe, N. Cheung, and C. Hu, *ibid.*, 406 (1984).
7. L. Jastrzebski, *RCA Rev.*, **44**, 250 (1983).
8. L. Jastrzebski, *J. Cryst. Growth*, **70**, 253 (1985).
9. L. Jastrzebski, J. F. Corboy, and R. Pagliaro, Jr., *This Journal*, **129**, 2645 (1982); L. Jastrzebski, J. F. Corboy, J. McGinn, and R. Pagliaro, Jr., *ibid.*, **130**, 1571 (1983).
10. L. Jastrzebski, *J. Cryst. Growth*, **63**, 493 (1983).
11. L. Jastrzebski, A. C. Ipri, J. F. Corboy, and R. Metz, in "Technical Digest of the 1983 Symposium, VLSI Technology," Sept. 1983, Hawaii, p. 50 (1983).
12. A. Ipri, L. Jastrzebski, J. F. Corboy, and R. Metz, *IEEE Trans. Electron Devices*, **ed-31**, 1741 (1984).
13. K. Tamo, N. Endo, H. Kitajawa, Y. Kernogi, and H. Tsuya, *Jpn. J. Appl. Phys.*, **21**, L564 (1982).
14. L. Jastrzebski and A. Ipri, Unpublished.



A Rechargeable All-Solid-State Sodium Cell with Polymer Electrolyte

K. West, B. Zachau-Christiansen, T. Jacobsen,* and S. Atlung*

Fysisk-Kemisk Institut, The Technical University of Denmark, DK 2800 Lyngby, Denmark

INTRODUCTION

Secondary lithium cells with intercalation or insertion materials as positive electrodes are now an extensively studied subject. However, only few papers covering the corresponding sodium systems have yet appeared. Ostensibly this is due to the lack of reversible sodium/electrolyte half-cells functioning below 200°C. At higher temperatures most electrode materials will react via displacement reactions, which generally have lower electrode potentials and do not possess the inherent reversibility of intercalation reactions.

Liquid organic electrolytes consisting of NaI dissolved in propylene carbonate have been used for electrochemical preparation of sodium intercalated TiS_2 (1,2). The Exxon group has cycled both Na/ TiS_2 and Na/ MoS_3 using sodium triethyl (N-pyrrol) borate dissolved in 1,3-dioxolane as electrolyte (3,4). Most other groups have chosen to use two-electrolyte systems with an ionic conducting ceramic membrane. This membrane separates molten sodium from the liquid electrolyte forming contact to the active material in the positive electrode (5).

In this communication cycling of a cell with solid sodium in contact with a polymer electrolyte and with amorphous MoS_3 as positive electrode is reported.

EXPERIMENTAL

Amorphous MoS_3 was prepared by thermal decomposition of $(\text{NH}_4)_2\text{MoS}_4$ as described by Jacobson *et al* (3).

Sodium electrodes were made by pressing a layer of sodium onto a Ni foil, using polyethylene sheets to aid the spreading. In this way smooth layers of

sodium with thicknesses between 50 μm and 100 μm were obtained.

Polymer electrolyte sheets ($\approx 30 \mu\text{m}$) were prepared by evaporation of acetonitrile solutions of poly-(ethylene oxide) (PEO) and the proper amount of NaI, recrystallized from acetonitrile and vacuumdried at 180°C. The PEO (WSR 301 Polyox, MW = $4 \cdot 10^6$, BDH) was used as received. The films were prepared and handled in an argon filled dry box. The NaI concentration in the films used corresponded to a Na/O ratio of 1:10. With this electrolyte, the operating temperature of the cell is confined to the interval between 98°C (melting of sodium) and 65°C, as the electrolyte conductivity decreases rapidly below this temperature.

Composite MoS_3 electrode films ($\approx 50 \mu\text{m}$) with the overall composition: 72 w/o MoS_3 , 20 w/o PEO, and 8 w/o NaI were prepared by evaporating acetonitrile suspensions/solutions of the ingredients onto nickel foils. In some cases graphite was added as conductive diluent, but no improvement of cell performance at these very low current densities was achieved.

The cell was mounted with spring load in a Ni-plated brass container sealed with a viton O-ring. This container was heated in air to 90°C in a Buchi TO-50 oven.

RESULTS

The first two cycles of the cell

Na / PEO-NaI (10:1) / MoS_3

are shown in fig. 1. The current density used for discharge and charge was 15 $\mu\text{A}/\text{cm}^2$ in these cycles, corresponding to a stoichiometric discharge time of 45 h. The cell was discharged to 1.5 V.

*Electrochemical Society Active Member.

ABE

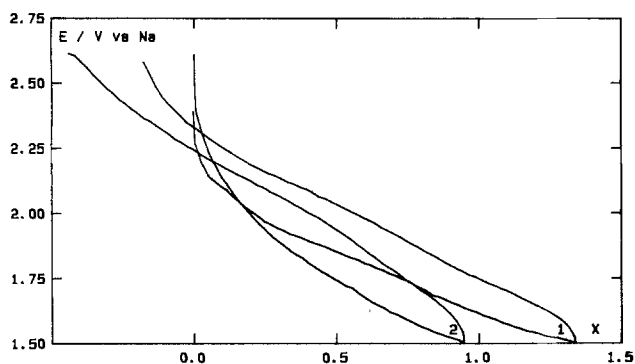


Fig. 1. Initial cycles of the cell Na/NaI-PEO (10:1) / MoS_3 at $15 \mu\text{A}/\text{cm}^2$. Charge recalculated as $X = \text{Na}/\text{Mo}$ based on total Mo-analysis of cell.

and recharged to 2.6 V *vs* Na. It is seen that the coulombic cycling efficiency (the ratio between discharge and charge capacity) is considerably less than unity, possibly due to disproportionation of the electrolyte. An advantage of using iodide-containing electrolytes in alkali metal batteries might be that the iodine liberated during overcharge recombines with the alkali metal and thereby scavenges the negative electrode of developing dendrites.

The discharge curve is smooth as expected for an amorphous electrode material, and 1.4 Na/Mo is inserted during the first discharge. Previously discharge capacities of up to 3 Na/Mo have been achieved (4), but the capacity has been shown to be sensitive to the details of the MoS_3 synthesis (6). The stoichiometric capacity calculated from the first discharge is 290 Wh/kg.

The development of the discharge capacity upon cycling is shown on fig. 2. The charge and discharge current used was $150 \mu\text{A}/\text{cm}^2$ in cycle 3 to 9, and $15 \mu\text{A}/\text{cm}^2$ in the other cycles. Despite the rapid decrease in cell capacity, a total number of 10 Na/Mo have been cycled during the lifetime of this cell, and the available amount of sodium has been cycled 1.5 times. This shows that, even close to its melting point, sodium forms a sufficiently

Manuscript submitted July 11, 1985; revised manuscript received Oct. 3, 1985.

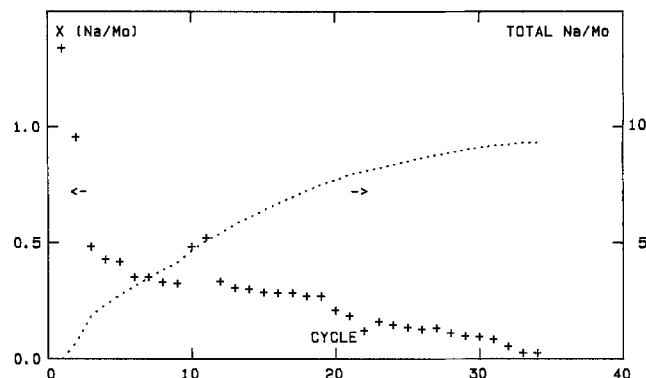


Fig. 2. Discharge capacity as function of cycle number. The total number of Na cycled per Mo is also shown.

stable interface with a PEO-electrolyte to allow reversible operation of this electrode. Possibly the formation of a passive sodium ion conducting film on the interface is responsible for this stability.

It is thus concluded that solid state sodium batteries might be feasible by extension of lithium battery technology, especially when electrolytes with better conductivity and more reversible electrode materials are developed.

REFERENCES

1. D.A. Winn, J.M. Shemilt, and B.C.H. Steele, *Mat. Res. Bull.* **11**, 559 (1976).
2. D. Cherns and G.P. Ngo, *J. Solid State Chem.* **50**, 7 (1983).
3. A.J. Jacobson, R.R. Chianelli, S.M. Rich, and M.S. Whittingham, *Mat. Res. Bull.* **14**, 1437 (1979).
4. G.H. Newman and L.D. Klemann, *J. Electrochem. Soc.*, **127**, 2097 (1980).
5. K.M. Abraham, *Solid State Ionics*, **7**, 199 (1982).
6. R. Williams, D. Shen, S.P.S. Yen, and R.B. Somoano, *Extended Abstract No. 74*, Electrochem. Soc. Meeting, Washington (1983).

The Technical University of Denmark assisted in meeting the publication costs of this article.

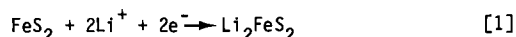
Li-Al/FeS₂ Cell with LiCl-LiBr-KBr Electrolyte

Thomas D. Kaun*

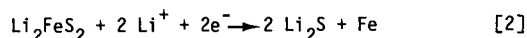
Argonne National Laboratory, Chemical Technology Division, Argonne, Illinois 60439

With its high theoretical specific energy and low resistivity electrolyte, the Li-Al/LiCl-KCl (m.p. 352°C)/FeS₂ cell has long been projected to be capable of very high performance (1). However, the cell, which is operated at temperatures of 425 to 450°C, has an unacceptably high capacity-decline rate of 0.10-0.25%/cycle (2) due to sulfur migrating from the positive electrode into the separator region and depositing there as Li₂S (3). Earlier attempts to reduce this capacity-decline rate concomitantly reduced cell performance (2).

In this study, two major changes from the earlier cells were evaluated: 1) a novel electrolyte, 25 mol% LiCl-37 mol% LiBr-38 mol% KBr (m.p. 310°C) (4), and 2) a higher loading density (2.4 vs. 1.5 Ah/cm²) for the FeS₂ electrode, which was then operated only on its higher-voltage (1.75 avg. V), or "upper-plateau", reaction:



(This reaction is actually a series of three consecutive reactions.) (8) In this mode of operation, the electrode will be designated a dense, upper-plateau (U.P.) FeS₂ electrode. In a conventional "two-plateau (T.P.)" FeS₂ electrode, the lower-voltage (1.33 avg. V) reaction also is used. This reaction is:



Experimental

A sealed prismatic bicell was employed to duplicate earlier test cells that had been used in evaluating the performance of Li-Al/LiCl-KCl/FeS₂ cells (2). The electrodes (8.7cm high x 6.3 cm wide) were contained behind perforated-sheet current collectors--molybdenum for the central FeS₂ electrode and 1008 steel for the two Li-Al electrodes. The electrode area, based on the separator, was 100 cm².

The iron disulfide electrode contained FeS₂ with 15 mol% CoS₂ additive for a total theoretical capacity of 25.2 Ah (on the upper plateau). The slurry-formed LiAl electrode (5) contained 53 at% Li-Al alloy for 35 Ah capacity with 0.9 Ah/cm² loading density. Cells were assembled with a 8N powder feedthrough seal and were subsequently operated in an argon glovebox. Cycle-life testing at a 8-h charge rate (25 mA/cm²) and 4-h discharge rate (50 mA/cm²) was controlled between voltage cutoffs of 2.05 and 1.25 V, respectively. A Ni/Ni₃S₂ reference electrode indicated working-electrode potentials during the deep-discharge cycling. Current interrupts of one second duration were used to evaluate electrode and cell resistances. Power measurements were derived by integrating constant-current pulses (10-100 A) of 15-s duration.

Results and Discussion

The Li-Al/U.P.-FeS₂ cell having LiCl-KBr-LiBr electrolyte and operated at 397°C + 5°C had 50% higher energy and power density than Li-Al/T.P.-FeS₂ cells having LiCl-KCl electrolyte and operated at 427°C. The voltage-capacity curves of the two cells (each of 25.2 Ah capacity) are presented in Fig. 1. Energy density at 50 mA/cm² was

enhanced as a result of approximately 50% higher utilization of the capacity and a 10% higher average discharge voltage. The energy density at higher discharge rates, 100 and 150 mA/cm², showed even greater improvement with the utilization of theoretical capacity ranging from 85 to 65% (Fig. 2). The specific power at 80% depth of discharge (DOD) was also enhanced by approximately 50% for the new cell because the voltage at that point in the discharge was about 0.3 V higher than that of a cell with a T.P.-FeS₂ electrode. (Six cells of 1-Ah capacity have confirmed these improvements.)

The improved power and energy densities of the iron disulfide electrode at the reduced operating temperatures of 388 to 427°C are believed to be caused by two factors. One is improved electronic conductivity of the electrode. According to the Bruggeman equation (6)

$$K_m = (1 - f)^{3/2} \quad [3]$$

where K_m = bed conductivity/dense body conductivity and f = electrolyte fraction, the increased electrode loading density (from 32 to 50 vol %) would double electronic conductivity of the iron disulfide electrode. The second factor is an increased "dynamic range" with the LiCl-LiBr-KBr electrolyte. At 400°C, this electrolyte has a liquidus that extends over a Li⁺/K⁺ ratio of 1.25 to 2.6; for LiCl-KCl, the range is only 1.25 to 1.81. The broader liquidus for the LiCl-LiBr-KBr electrolyte would tend to prevent salt crystallization; it has been postulated that the crystallization of LiCl-KCl impedes operation (7).

The capacity utilization vs. cycle number for U.P. FeS₂ cell is shown in Fig. 3 (the coulombic efficiency of the cell is 99+%). Its utilization is 89% at 50mA/cm², based on a revised cell capacity (24 Ah) from a lower than assumed CoS₂ purity. The cell capacity has been constant through more than 230 cycles and 3000 hours, and the cell voltage vs. capacity curve has remained unchanged (as in Fig. 1) during this time. In this test, the cell was charged at 25 mA/cm² to a charge cutoff voltage of 2.05V. These values are greater than those that could be used with the Li-Al/LiCl-KCl/T.P.-FeS₂ cell while maintaining stable capacity (2). Electrode potentials (vs. the Ni/Ni₃S₂ reference electrode) indicate that both electrodes, LiAl and FeS₂, mutually attain full charge. The discharge capacity is limited by the upper-plateau capacity of the positive electrode.

Apparently, both time-related and cycle-related capacity-loss mechanisms have been overcome in this cell. Considerable attention has been given to gaining understanding of these mechanisms for FeS₂ in LiCl-KCl. Preto et al. (8) indicated that capacity loss for FeS₂ in LiCl-KCl is due to its complex electrochemistry involving formation of non-equilibrium species. Additionally, thermal decomposition and solubility in LiCl-KCl of discharge reaction species have also been found to be causes of capacity loss in the disulfide electrode (9). For the dense U.P.-FeS₂ electrode in LiCl-LiBr-KBr, the reduced operating temperature and increased electrode-bed conductivity would promote capacity stability according to these understandings.

*Electrochemical Society Active Member

Key Words: fused salt, lithium cell, disulfide electrode

Conclusion

The use of the dense U.P.-FeS₂ electrode and LiCl-LiBr-KBr electrolyte, which allows a cell operating temperature of 397°C, has eliminated disulfide electrode capacity loss and increased cell performance significantly. Based on a 250 Ah multiplate cell, we expect a specific energy greater than 150 Wh/kg at the 4-h rate and specific power of greater than 150 W/kg at 80% DOD. The expected cycle life of greater than 1000 cycles is comparable to that of the LiAl/FeS cell (10).

Acknowledgments

This work was conducted under the auspices of the U.S. Department of Energy. The author is grateful to M. F. Roche, J. E. Battles, and J. P. Ackerman for their support.

References

1. E. J. Cairns and R. K. Steunenberg, "High-Temperature Batteries: Progress in High Temperature Physics and Chemistry", C. A. Rouse, ed., Pergamon Press, New York (1973).
2. F. J. Martino, W. E. Moore, and E. C. Gay, Argonne National Laboratory Report ANL-83-62, pp. 29-38 (1983).
3. J. E. Battles, F. C. Martino, N. C. Otto, Argonne National Laboratory Report ANL-80-130 (1980).
4. A. G. Bergman and A.S. Arabadzhan, Russ. J. Inorg. Chem. (English Trans.), **8**, 369 (1963).
5. T. D. Kaun, U.S. Patent No. 4,358,513 (1983) and U.S. Patent No. 4,446,212 (1984).
6. D. A. Bruggermann, Ann. Physik, **24**, 636 (1935).
7. C. E. Vallet and J. Braunstein, *This Journal*, **125**, 1193 (1978).
8. S. K. Preto, Z. Tomczuk, S. von Winbush, and M.F. Roche, *This Journal*, **130**, 264 (1983).
9. D. Warin, Z. Tomczuk, and D. R. Vissers, *This Journal*, **130**, 64 (1983).
10. E. C. Gay et al., Extended Abstracts, 166th Electrochem. Soc. Meeting, New Orleans, LA, October 7-12, 1984, Vol. 84-2, pp. 167-168, 1984.

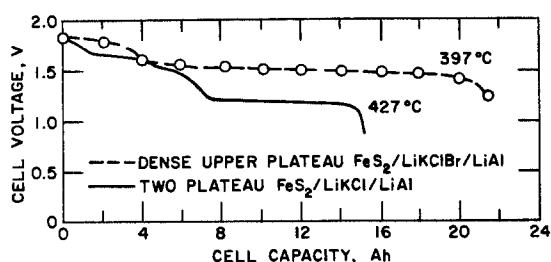


Fig 1. Voltage/Capacity Curves at Discharge Rate of 50 mA/cm² (Each Cell had a 25.2 Ah Theoretical Capacity).

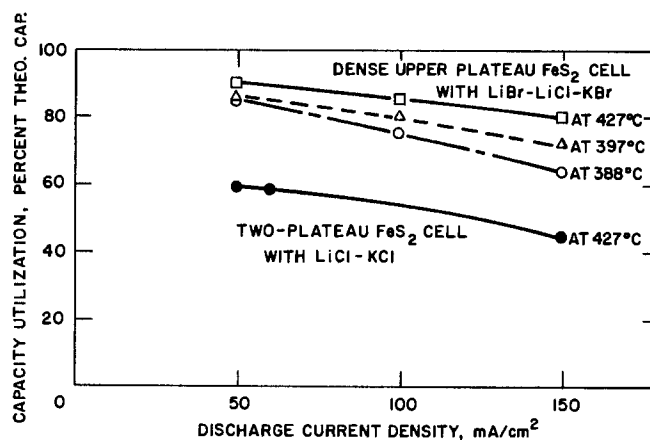


Fig. 2. Utilization vs. Discharge Current Density for U.P.-FeS₂ Cell at Temperatures of 388-427°C.

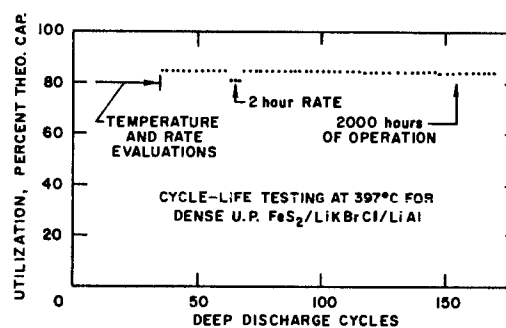


Fig. 3. Discharge Capacity Over Repeated Cycling and Long Operational Time.

Manuscript received Sept. 5, 1985.

Argonne National Laboratory assisted in meeting the publication costs of this article.

The Extent of the Phenomenon of Oscillatory Anion Incorporation in Alumina Barrier Films

D. L. Cocke,* C. A. Polansky, D. E. Halverson, S. M. Kormali, C. V. Barros-Leite, O. J. Murphy,* E. A. Schweikert, and P. Filipus-Luyckx

Department of Chemistry, Texas A&M University, College Station, Texas 77843

The recent observation of oscillatory incorporation of tungstate into anodically grown alumina films (1) has now been extended to include several other anions, such as MoO_4 , MnO_4 , and CrO_4 . This confirms the general nature of the phenomenon, which is the first electrochemically produced oscillation in the solid state. The observation has extremely important ramifications to electrochemical studies on passivity, general electrochemicals and anodic growth mechanisms.

Incorporation of anions into electrochemically grown alumina films is being studied in an effort to determine their effect on the structure (2,3,4), electronic properties (5,6) and stability (2) of the alumina formed. The determination of the distribution of anions in these films is currently being unraveled (2,7). It has been shown through the use of electron microscopy (STEM) that initially the entire film is amorphous, and incorporation of anions into the alumina stabilizes the amorphous structure to the process of dehydration and subsequent crystallization by the electron beam (4). The general structure of electrochemically grown barrier alumina films has been reported to consist of an inner region, which is relatively pure (7), and an outer region, which is thought to be a uniform structure, containing species from the anions present in solution (8,9).

Sharp, et al. (6), have established that the properties of the films are dramatically affected by these anion residues. The incorporation of tungsten species into anodic alumina films resulted in a surprising structure (1). Through the use of alpha and argon backscattering, the tungstate species were found (1) to be incorporated periodically in the alumina structure, suggesting an oscillatory mechanism for formation of the film. This communication de-

scribes the incorporation of three additional anionic species into alumina films.

The anodic oxide films were grown galvanostatically at various current densities on highly polished aluminum discs in 0.15 M borate buffer solutions (pH = 8.4), which also contained either 0.5 M $\text{Na}_2\text{MoO}_4 \cdot 2\text{H}_2\text{O}$, 0.5 M $\text{Na}_2\text{WO}_4 \cdot 2\text{H}_2\text{O}$, 0.5 M $\text{Na}_2\text{CrO}_4 \cdot 4\text{H}_2\text{O}$ or 0.5 M KMnO_4 . The film growth was stopped when the cell voltage reached 72 V. The film thicknesses were calculated to be approximately 1000 Å, using a growth rate of 14 Å/V (5). Two types of Rutherford backscattering data were taken on the films exposed to MoO_4 or WO_4 species; a variable energy cyclotron with a collimated 40 MeV Ar^{4+} ion beam (Texas A&M University) and a Van de Graff accelerator employing a collimated beam of 2 MeV He^{2+} ions (Rio de Janeiro). Only the latter was used on the CrO_4 and MnO_4 exposed films.

In Figure 1, the Ar^{4+} spectra of molybdate and tungstate species incorporated into alumina films grown on ultrapure aluminum samples are shown. In both cases, the anionic species concentration is seen to decay as one moves from the oxide surface into the alumina film. This decay is not monotonic, but exhibits a periodic structure, which is slightly more pronounced for the tungstate than for the molybdate. In Figure 2, the alpha backscattering spectra are shown for tungstate, molybdate, manganate and chromate species incorporated into alumina films. The first three species again exhibit periodic concentration decay, as found in the Ar^{4+} backscattering spectra. Furthermore, a complementary periodic structure was evident in the aluminum oxide spectra (not shown), in that minimums in concentration were found for the aluminum which correspond to maximum concentrations for the anionic species. Even though the periodic structure is not seen on the chromium peak, the oscillatory alumina variation was seen, due to better counting statistics. This is additional evidence to support the presence of a layered concentration profile for the outer region of the alumina films. These spectra also show for the tung-

*Electrochemical Society Active Member.

Key Words: alumina barrier films, anion incorporation, oscillatory phenomena

state and molybdate species that the anion-containing layer penetrates less than half the thickness of the alumina films. However, the chromate and manganate species appear to be more evenly distributed throughout the alumina. A reason for this difference may be linked to the ionic radii of the metal cations, the Cr^{+6} and Mn^{+7} being closer in size to Al^{3+} than the W^{+6} or Mo^{+6} but is more likely to be related to the anions' ease of charge removal.

As a result of this investigation, it appears that incorporation of anionic species into anodic barrier oxide films takes place by an oscillatory mechanism, resulting in characteristic growth patterns. Current work is investigating the mechanism of this incorporation, where it is believed that local space charge growth control is involved. This phenomenon, in addition to providing a means of dramatically altering the structure and properties of the anodic films, may provide a means of studying local space charge phenomena in these films.

REFERENCES

1. D. L. Cocke, et al., J.C.S., Chem. Comm., (1984) 1560.
2. D. L. Cocke, et al., Catal. Rev. Sci. Eng., 26 (1984) 163.
3. S. Soled, J. Catal., 81 (1983) 252.
4. K. Shimizu, et al., Thin Solid Films, 77 (1981) 313.
5. J. W. Diggle, et al., Chem. Rev., (1969) 365.
6. D. J. Sharp, et al., Thin Solid Films, 111 (1984) 227.
7. P. Skeldon, et al., Surf. Interface Anal., 5, 6 (1983) 252.
8. K. Shimizu, et al., Thin Solid Films, 81 (1981) 39.
9. G. E. Thompson, et al., Electrochim. Acta, 26 (1981) 951.

Manuscript received Sept. 9, 1985.

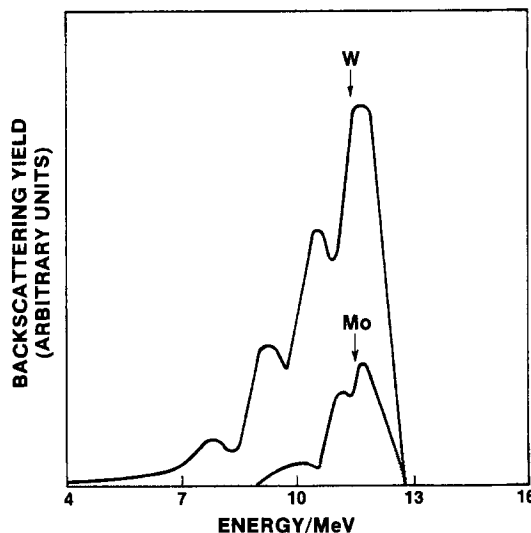


FIGURE 1. 40 MeV Ar^{4+} backscattering spectra of alumina films grown at a current density of 150 mA cm^{-2} in 0.5 M $\text{Na}_2\text{WO}_4 \cdot 2\text{H}_2\text{O}$ and 0.5 M $\text{Na}_2\text{MoO}_4 \cdot 2\text{H}_2\text{O}$ borate buffered solutions (pH = 8.4) at 25°C . The energy scale shown applies only to the alumina film with incorporated tungsten species.

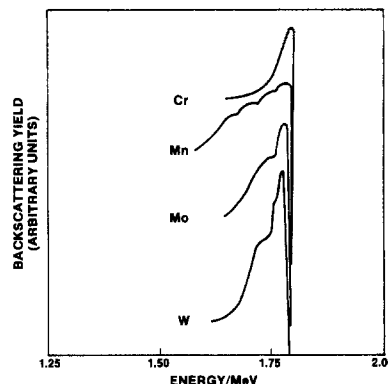


FIGURE 2. 2 MeV He^{2+} backscattering spectra of alumina films grown at a current density of 10 mA cm^{-2} in 0.5 M $\text{Na}_2\text{WO}_4 \cdot 2\text{H}_2\text{O}$, 0.5 M $\text{Na}_2\text{MoO}_4 \cdot 2\text{H}_2\text{O}$, 0.5 M $\text{Na}_2\text{CrO}_4 \cdot 4\text{H}_2\text{O}$ and 0.5 M KMnO_4 , all borate buffered at pH = 8.4, with a solution temperature of 27°C . The energy scale shown applies only to the alumina film with incorporated tungsten species.

Morphology of Defects in GaAs Revealed by Eutectic Etch

W. F. Tseng, H. Lessoff, and R. Gorman

Naval Research Laboratory, Washington, DC 20375-5000

Recently a new eutectic (KOH + NaOH) (1) has been developed to reveal defects in gallium arsenide (GaAs) for evaluating the wafer quality. The etched surface shows additional, distinct patterns other than the features formed by the commonly used molten KOH etchant(2). The purpose of this paper is to identify the defects which cause the formations of such different etched patterns.

The GaAs samples used in this study were semi-insulating 3-inch (100) wafers, grown by Liquid Encapsulated Czochralski method. The eutectic etchant with a melting point ($T_{m.p.}$) of 170°C was a mixture of KOH ($T_{m.p.} \approx 360^{\circ}\text{C}$) and NaOH ($T_{m.p.} \approx 318^{\circ}\text{C}$) in equal mole concentration. The etch procedure is described in ref 1. There is a modification to the procedure described in ref. 1 to insure an oxide free surface after removal of the wafer from the hot etchant. The wafers are immediately placed in ethylene glycol upon removal from the hot etchant. The residual hydroxides are soluble in the ethylene glycol and the surface of the etched wafer is left stain and oxide free. After the approximately 20 minutes in the ethylene glycol, the etched wafers are cleaned as described in ref. 1. To investigate the development of etched patterns, the GaAs samples were etched at 350°C for 15, 30, 45 and 60 min. individually. For comparison, another set of GaAs samples was etched in a molten KOH. The etched surfaces were then investigated by SEM, followed by TEM observation. TEM thin foils were prepared by a standard jet-polishing technique from the backside of GaAs samples using Br_2 -methanol solution.

Typical KOH etched surface is shown in Fig. 1. The etched patterns are in the shapes of hexagonal pyramid pits, and smaller-shallower dimples on the background. The side-walls of etched pits are smooth. On the other hand, for the

new eutectic (KOH + NaOH) etch, the side-walls of etched pits show stair-step structure as shown in Figs. 2a and 2b. The etched pyramids started with a square-shape, then, developed into hexagonal shape as the etch time increased. Most inverted pyramids have sharp pits, however, few of them have a flat bottom as shown in Fig. 2a. Another typical etched pattern is nearly rectangular in shape with its long edge perpendicular to the (110) cleavage edge. The depth is shallower than the depth of the pyramid pattern, as shown in Fig. 2b.

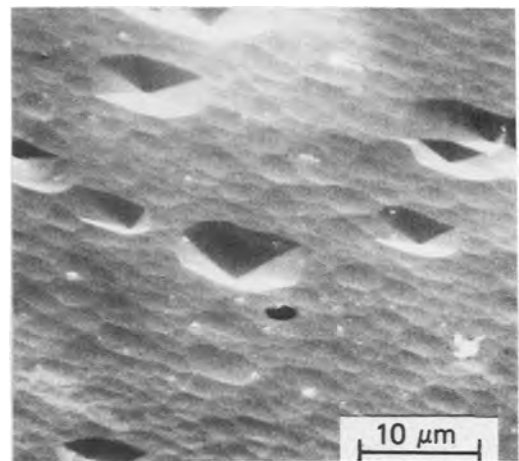


Fig. 1 SEM micrograph of GaAs surface etched by molten KOH etchant.

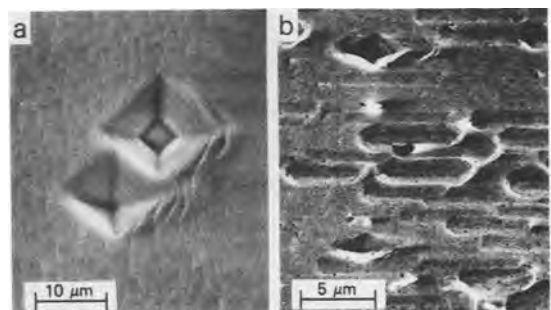


Fig. 2 SEM micrographs of GaAs surfaces etched eutectic (KOH + NaOH) etchant. (a) Pyramid pattern; (b) Rectangular pattern.

The etched pits in Fig. 2a, correlate to dislocations directly. The pyramid with a sharp pit has a dislocation connecting to the tip of etched pit, as shown in the TEM micrograph of Fig. 3. However, the pyramid with flat bottom, shown in Fig. 2a, does not have dislocations attached to it. This can be explained by the dislocation movement (3). The movement of the dislocation may be related to the residual stress in the wafers produced during the crystal growth. There is a large thermal differential at the solid-liquid interface during LEC growth, also the thermal conductivity of GaAs is such that large radial temperature differences will occur on cooling after growth. During the eutectic (KOH + NaOH at 350°C) etching, the dislocations can migrate at the speed of sound. A new pyramid pit with the dislocation attached to it was formed as a result of dislocation movement. The pyramid, now without the dislocation attached to it, was further etched. The (100) surface at the tip of the pyramid was flat in shape due to the slower etch rate on (100) surface than that on the side wall of pyramid. Reference 1 has shown that the rates of etching at 350°C for (100) and (111) GaAs are 0.09 and 0.22 $\mu\text{m}/\text{min}$, respectively.

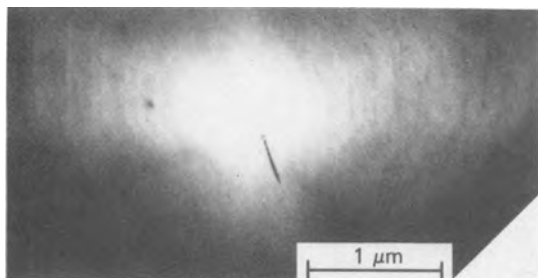


Fig. 3 TEM micrograph of pyramid pattern attached with a single dislocation.

As for the rectangular shape etched pattern shown in Fig. 2b, TEM observation indicates that most shallow patterns are free of dislocations and the deep patterns contain tangled dislocations as shown in Fig. 4. Formation of these rectangular shape patterns may be explained in the following way: During 350°C etching, the residual stress from LEC GaAs growth caused the tangled dislocations to generate new dislocations, and the generated dislocations to glide (on (111) planes). As evidence, Fig. 4 shows an array of generat-

Manuscript submitted Nov. 8, 1984; revised manuscript received Aug. 9, 1985.

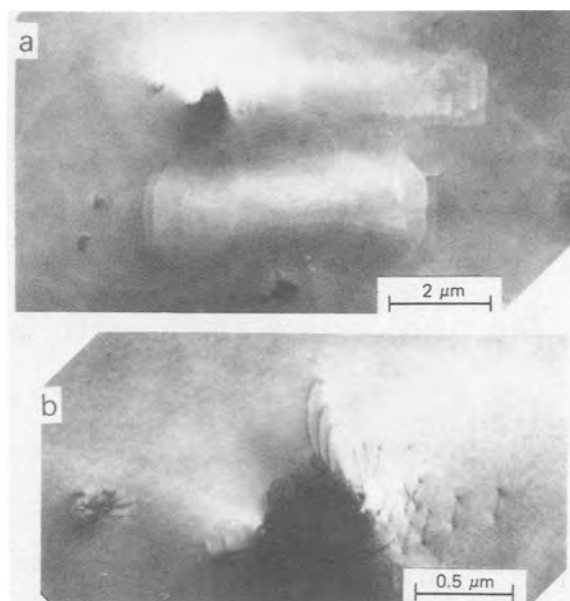


Fig. 4 TEM micrograph of rectangular pattern attached with tangled dislocations and generated dislocations.

ed dislocations aligned along a projected $\langle 110 \rangle$ direction. Regular pyramid shape etched patterns form when the generated dislocations reached the (100) sample surface. The array of these generated and aligned dislocations was revealed by etching. Due to this alignment of dislocation lines along the $\langle 110 \rangle$ projected direction and the slow etch rate on (100) GaAs (same argument as for Fig. 2a), a rectangular shape etched pattern was formed.

In conclusion, the defects, which result in the formation of pyramid and rectangular-shaped patterns as revealed by the eutectic (KOH + NaOH) etchant, have been identified. The pyramid pattern is caused by a single dislocation, whereas the rectangular pattern is caused by tangled dislocations.

REFERENCES

1. H. Lessoff and R. Gorman, *J. Electronic Materials*, **13** 733 (1984).
2. J. G. Grabmaier and C. G. Watson, *Phys. Status Solidi*, **32** K13 (1969).
3. W. G. Johnston and J. J. Gilman, *J. Appl. Phys.*, **31**, 632 (1960).

The Naval Research Laboratory assisted in meeting the publication costs of this article.

Effect of Axial Ligand on the Catalytic Activity of Heat-Treated Tetraphenylporphyrinatoiron (III) Halides for the Cathodic Reduction of Oxygen

O. Ikeda, H. Fukuda, T. Kojima, and H. Tamura

Department of Applied Chemistry, Faculty of Engineering, Osaka University, Suita, Osaka 565, Japan

Metal complexes of the macrocycles such as porphyrin, phthalocyanine, and tetraazaannulene are promising electrocatalysts for the cathodic reduction of oxygen. It is worth noting that the heat treatment of metalloporphyrins in an inert atmosphere improves not only the stability, but also the catalytic activity (1-4). As the heat treatment gives polymeric products insoluble in any solvents, however, it is not easy to determine the true active site and the cause for the improvement of the catalytic activity. Thus far the active site for heat-treated metalloporphyrins has been ascribed to: (a) metal in the N_4 center (4,5), (b) carbonaceous structure formed by the degradation of the N_4 center (6), and (c) an intermediate structure between (a) and (b), namely, metal coordinated to a partially degraded N_4 center (7). However, these three types of active site may be differentiated by the heat-treatment temperature.

Recently, we found that heat-treated *meso*-tetraphenylporphyrinatoiron(III) chloride ($Fe^{III}(TPP)Cl$) showed an anomalously high magnetic moment for a Fe unit, consisting of one porphyrin unit per iron ion, and observed that the increase in the magnetic moment was closely correlated with the improvement of catalytic activity for the cathodic reduction of oxygen, especially, of the capability of reducing oxygen to water (4-electron reducibility) (8). We speculated a participation of chloride ion as an axial ligand in the above anomalous magnetic property of heat-treated $Fe^{III}(TPP)Cl$. In order to clarify such a participation of a ligand and the presumption that the active site is metal, *meso*-tetraphenylporphyrinatoiron(III) with different axial ligands ($Fe^{III}(TPP)X$, $X=F^-, Cl^-, Br^-, I^-$) was heat-treated, and the effect of axial ligand on the so-called 4-electron reducibility of oxygen was studied using the rotating ring-disc electrode technique.

The $Fe^{III}(TPP)X$ -coated disc electrode was prepared by loading 3×10^{-7} mol cm^{-2} of $Fe^{III}(TPP)X$ onto the top surface of a glassy carbon

rod (0.28 cm^2 , Tokai Carbon GC 20), and then heating it in an Ar atmosphere at 700°C for 10 min. After cooling in Ar, the rod was installed in the disc cavity of the ring-disc electrode. $Fe^{III}(TPP)X$ powder was also heat-treated and its molar magnetic susceptibility, χ_M , was measured as described before (8). The presence of halide ions was confirmed by ESCA, although the ratio of X to Fe was somewhat lower than unity.

Figure 1 shows voltammograms at the rotating ring(Pt)-disc(glassy carbon coated with the heat-treated $Fe^{III}(TPP)X$) electrode in O_2 -saturated 1 M KOH. The disc current at lower overpotentials decreases in the order $F^- > Cl^- > Br^- > I^-$, indicating the relative catalytic activity of heat-treated $Fe^{III}(TPP)X$ for the cathodic reduction of oxygen.

The apparent number of electrons consumed in the oxygen reduction n_{app} , which is a measure of the 4-electron reducibility, was evaluated at several potentials between the onset potential and the potential in the diffusion limiting region in Fig. 1. In the evaluation of n_{app} , it is assumed that the O_2 reduction at the disc consists of a mixed reaction of the 2-electron pathway ($O_2 + H_2O + 2e^- \rightarrow HO_2^- + OH^-$), and the 4-electron pathway ($O_2 + 2H_2O + 4e^- \rightarrow 4OH^-$). Thus, n_{app} was estimated by the next relation: $n_{app} = 4I_{Disc} / (I_{Disc} + I_{Ring} / N_{corr})$, where I_{Disc} and I_{Ring} are the disc and ring currents at a potential, respectively, and N_{corr} is the collection efficiency for HO_2^- , corrected for a deviation from coplanarity between the Pt ring and the $Fe^{III}(TPP)X$ -coated disc. Figure 2 shows a correlation between the mean of n_{app} estimated in the above way and the effective magnetic moment μ_{eff} calculated from χ_M . It is obvious from Fig. 2 that n_{app} is closely correlated with μ_{eff} for a Fe unit.

The fact that the effect of axial ligand is clearly reflected in both the n_{app} and μ_{eff} values suggests that the active site for the electrocatalytic reduction of oxygen in $Fe^{III}(TPP)X$ heat-treated at 700°C is not the carbonaceous structure (b), but the metal (a) or (c). The magnetic moment of the Fe unit in all heat-treated $Fe^{III}(TPP)X$ was higher than

Key words: Porphyrin, Heat-treatment, Axial Ligand, Oxygen Reduction

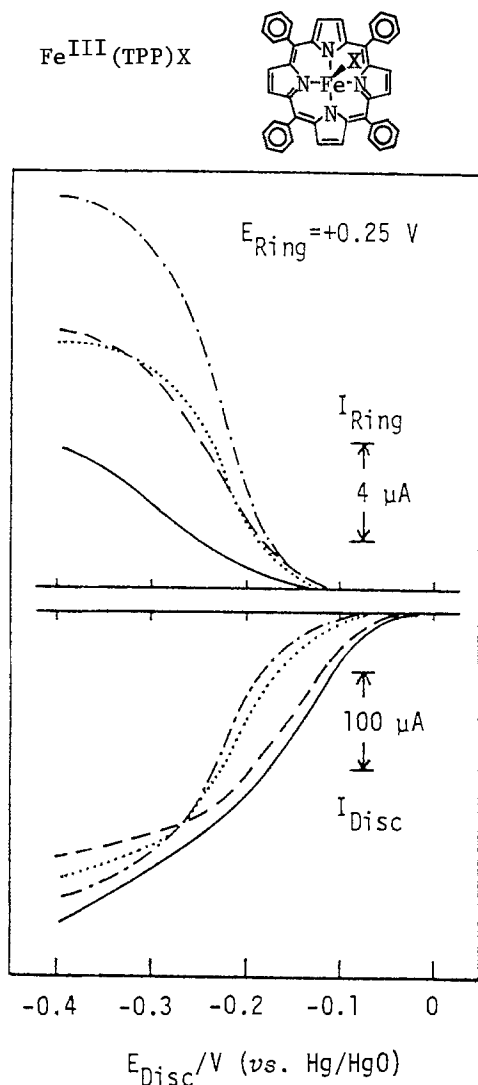


Figure 1 - Voltammograms at the rotating ring (Pt)-disc(glassy carbon coated with $\text{Fe}^{\text{III}}(\text{TPP})\text{X}$ heat-treated at 700°C) electrode for the cathodic reduction of oxygen in O_2 -saturated 1 M KOH. $\text{Fe}^{\text{III}}(\text{TPP})\text{X}$: $\text{X}=\text{F}^-$ (—); Cl^- (---); Br^- (.....); I^- (-·-·-). Potential of the reference electrode: Hg/HgO in 1 M KOH, 0.098 V vs. normal hydrogen electrode (NHE). Ring potential, 0.25 V vs. Hg/HgO; sweep rate at the disc, 1 mV s^{-1} ; rotation rate, 1000 r.p.m.

that of unheated compound, about $5.9 \mu_B$ (Bohr Magnetron). This anomalously high magnetic moment of the Fe unit in the heat-treated $\text{Fe}^{\text{III}}(\text{TPP})\text{X}$, which varies depending on the axial ligand, might be due to a metal-metal interaction based on a structure of two Fe sites bridged by halide ion. This interaction seems to be a ferromagnetic superexchange interaction,

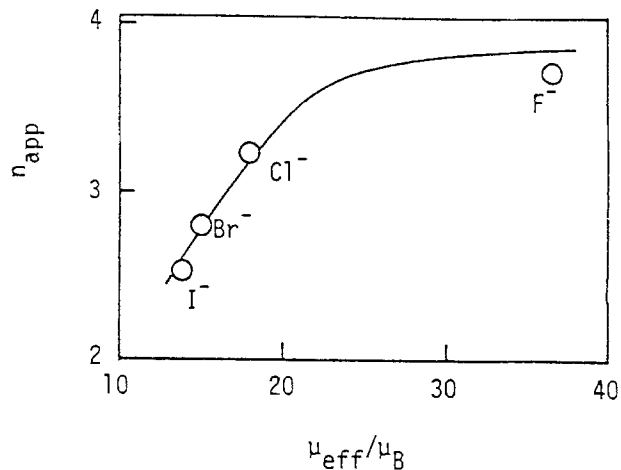


Figure 2 - Correlation between n_{app} and μ_{eff} .

because both the orders of the bond energy between Fe^{III} and X, and the electron donating strength of the axial ligands (9) are as follows: $\text{F}^- > \text{Cl}^- > \text{Br}^- > \text{I}^-$. Such a two-Fe site may act as an active center for the 4-electron pathway in the cathodic reduction of oxygen.

Acknowledgement: We thank Professor Dr. Jiro Shiokawa and his staffs for their helpful suggestions and discussions on the measurement and interpretation of the magnetic moment.

REFERENCES

- H. Jahnke, M. Schönborn, and G. Zimmerman, *Fortsch. Chem. Forsch.*, **61**, 133 (1976).
- V. S. Bagotzky, M. M. Tarasevich, K. A. Radyushkina, O. A. Levina, and S. I. Andrusyova, *J. Power Sources*, **2**, 233 (1977/78).
- K. Wiesener and A. Fuhrman, *Z. Phys. Chem. (Leipzig)*, **261**, 411 (1980).
- J. A. R. van Veen, J. F. van Baar, and K. J. Kroese, *J. Chem. Soc., Faraday Trans. 1*, **77**, 2827 (1981).
- R. W. Joyner, J. A. R. van Veen, and W. M. H. Sachtler, *J. Chem. Soc., Faraday Trans. 1*, **78**, 1021 (1982).
- A. Fuhrman, K. Wiesener, I. Iliev, S. Gamburgzev, and A. Kaisheva, *J. Power Sources*, **6**, 69 (1981).
- E. Yeager, *Electrochim. Acta*, **29**, 1527 (1984).
- O. Ikeda, H. Fukuda, and H. Tamura, *J. Chem. Soc., Chem. Commun.*, **1984**, 567.
- G. N. La Mar and F. A. Walker, *J. Am. Chem. Soc.*, **97**, 5103 (1975).

Manuscript submitted July 29, 1985; revised manuscript received Sept. 25, 1985.

Osaka University assisted in meeting the publication costs of this article.

ized SO₂ electrolyte environment or the reduction process plays a role in the chemistry. The interrelationship among the electrolyte-dithionite-carbon matrix in an ever changing temperature and pressure environment of the cell is complex and warrants additional investigation.

ARC studies on cathodes depleted of electrolyte, taken from discharged Li/SO₂ cells, reveal that the major exothermic reactions arise solely from the thermal decomposition of lithium dithionite, regardless of the complexity of sulfur products present. This adiabatic decomposition is characterized by a rapid self-heating process, a sudden generation of SO₂ gas pressure, and is catalyzed by carbon black. Further studies are planned.

Hazards previously observed during overdischarge, especially at low temperature, occur primarily from a rapid and very exothermic reaction involving lithium with lithium dithionite. This triggers additional reactions involving carbon black producing additional gas pressure in the form of carbonaceous gases. This mechanism of almost synchronous reactions is capable of causing explosive venting in commercial Li/SO₂ cells.

Acknowledgments

I wish to express my appreciation to D. Oglesby for many informative discussions concerning dithionite chemistry. I am especially grateful to L. Van Rouckel for her contributions to the ARC study. This study was funded by the U.S. Navy High Energy Batteries for Weapons Block Program. Part of this paper was presented at the 2nd International Meeting on Lithium Batteries,

Paris, France, April 26, 1984. Travel expenses to the meeting were provided by the National Science Foundation.

Manuscript submitted May 23, 1984; revised manuscript received Jan. 16, 1985.

The Naval Surface Weapons Center assisted in meeting the publication costs of this article.

REFERENCES

1. W. P. Kilroy, W. Ebner, D. L. Chua, and H. V. Venkatasetty, *This Journal*, **32**, 274 (1985).
2. D. M. Oglesby, R. L. Ake, and W. P. Kilroy, in "Proceedings of the 30th Power Sources Symposium," Atlantic City, NJ, June 7-12, 1982, The Electrochemical Society, Inc., p. 127 (1983).
3. S. Dallek, S. D. James, and W. P. Kilroy, *This Journal*, **128**, 508 (1981).
4. W. P. Kilroy and C. R. Anderson, *J. Power Sources*, **9**, 397 (1983).
5. R. L. Ake, D. M. Oglesby, and W. P. Kilroy, *This Journal*, **131**, 968 (1984).
6. W. L. Bowden, L. Chou, L. DeMuth, and R. W. Holmes, *ibid.*, **131**, 449 (1984).
7. S. D. James, P. H. Smith, and W. P. Kilroy, *ibid.*, **130**, 2037 (1983).
8. K. Goodhead, I. K. O'Neill, and D. F. Wardleworth, *J. Appl. Chem. Biotechnol.*, **24**, 71 (1974).
9. W. P. Kilroy, *Talanta*, **30**, 419 (1983).
10. D. I. Townsend and J. C. Tou, *Thermochim. Acta*, **37**, 1 (1980).
11. J. C. Tou and L. F. Whiting, *ibid.*, **48**, 21 (1981).
12. K. Buijs, *J. Inorg. Nucl. Chem.*, **24**, 229 (1962).

The Oxide Film on Steel and Cathodic Disbondment of a Protective Organic Coating

E. L. Koehler*

Niles, Illinois 60648-2653

ABSTRACT

Cathodic disbondment of an oleoresinous organic coating on steel with an air-formed oxide film has been investigated in 0.1N sodium borate solution (pH 9.2) and in pH 7.6 borate buffer solution. This is compared with oxygen reduction and with oxide film reduction for uncoated steel surfaces. The rate of oxygen reduction on the steel surface is found to increase as Fe⁺³ in the oxide film is reduced. The rate of cathodic delamination of the organic coating is a function of the oxygen reduction rate as determined by the oxide film properties. Reduction of Fe⁺³ in the oxide film may result in either soluble Fe⁺² or in intermediate film compositions from Fe₂O₃ to Fe₃O₄, dependent upon pH and potential. At sufficiently negative potentials, once a portion of the Fe⁺³ in the oxide film is reduced, the steel substrate becomes active, yielding soluble or insoluble oxidation product, dependent upon pH and potential. This explains observed surface roughening and oxide film thickening beneath disbonded organic coatings.

Cathodic disbondment is caused by high pH at the coating/substrate interface, generally resulting from the reduction of atmospheric oxygen. Several hypotheses exist to explain the means by which the high pH condition causes the disbondment. These include: (i) cohesive failure within the polymeric material at the interface as the result of hydrolysis of bonding groups (1, 2), (ii) displacement of the coating by a film of high pH water at the interface (3), and (iii) disbondment by dissolution of the oxide film beneath the coating (4, 5). Whatever the mechanism, susceptibility to disbondment is markedly influenced by the oxide film, as indicated by differences displayed by different metals or by different surface treatments of the same metal. In this paper, we will consider the influence of an air-formed oxide film on untreated steel.

Primarily by ellipsometric measurements, Ritter has shown that disbondment is accompanied by roughening of the metal surface and by an increase in the thickness of the oxide film (6, 7). Simultaneous pH measurements be-

neath the coating indicated a change of from 6 to 13.5. Ease of the oxygen reduction process may be important for disbondment. For example, organic coatings on aluminum are not subject to disbondment under corrosion conditions (8). Leidheiser has related such differences between metal surfaces to relative ease of oxygen reduction (9).

Consideration is to be given here to the reduction of the ferric component of the oxide film on steel. Such reduction should occur during cathodic disbondment, but this has been given scant attention. Gonzalez *et al.* have investigated disbondment caused by autoreduction of ferric oxide beneath the coating and dissolution of the resulting ferrous iron (10). This requires a medium in which ferrous iron is appreciably soluble, i.e., a pH < 4 or presence of a complexing agent, unlike the disbondment at elevated pH being considered here. Castle and Watts (11) have indicated some reduction of oxide only at the disbondment front, but they did not consider subsequent oxide film thickening, as reported by Ritter (6, 7).

The effects of the oxide film during cathodic disbondment should be related to the behavior of the film on the

* Electrochemical Society Active Member.

uncoated metal when it is made a cathode. Electrochemical reduction/oxidation methods are used here on both bare steel and on organic-coated steel to tie together the oxide film influences on cathodic disbondment. Most work on cathodic disbondment uses a corrosive solution, usually NaCl. This medium is unsatisfactory in the present work, where effects at relatively positive potentials are investigated. Borate solutions appear ideal, especially in view of the experience with these solutions in oxide film investigations (12-14).

The aim here is to study the effects of the oxide film, its properties, and its cathodic reduction on cathodic disbondment.

Experimental

The steel base used was uncoated and untreated low carbon steel plate, such as used in the can industry. It was desired to work with a well-developed, air-formed oxide film. The material used had been in storage at least 10 yr. It was unruled. Prior to organic coating, it was vapor degreased. It was roll coated to an 8 μm thickness with an unpigmented oleoresinous enamel and baked for 8 min at 213°C.

Responses of the coated specimens were compared with those for the uncoated under conditions of applied cathodic potentials. Galvanostatic methods were unsatisfactory for such work. Both potentiostatic and potentiodynamic methods were used. A number of scanning rates were tried for the potentiodynamic experiments, and a scanning rate of 300 mV/h was selected. Borate solutions were used as test media. A pH 7.6 boric acid/sodium borate buffer was selected as a near-neutral solution. In this case, a soluble ferrous reduction product is expected. For a higher pH, a 0.1N $\text{Na}_2\text{B}_4\text{O}_7$ solution at pH 9.2 was used. While the solubility of ferrous iron is still not negligible at this pH, as a practical matter magnetite is produced. Considerable work was also done with a 0.1N Na_2HPO_4 solution at pH 9.1. Such results were found to be in substantial agreement with those for the sodium borate solution and will not be reported here. To avoid confusing the results for cathodic disbondment with possible simple diffusion effects, higher pH test media were not desired.

The cell shown in Fig. 1 was used for cathodic reduction on uncoated steel in pH 7.6 borate buffer solution. The counterelectrode was platinum. The specimen, 31.8 mm long by 6.4 mm wide (1.25 \times 0.25 in.), was masked with cellophane tape to give an exposure of 12.7 \times 6.4 mm (0.5 \times 0.25 in.), or 0.81 cm^2 on each side. Edges were not masked. The exposed edge area was only 0.05 cm^2 . Specimens

were cut about two weeks before use. Exposed edges had no significant effect on the results.

The solution was preflushed with purified nitrogen and flushed throughout testing. In operation, the specimen was held in the space above the solution. It was then dropped into the solution and instantly polarized to the desired potential. The current was recorded as a function of time. In preliminary work, using this test method, it was determined that vapor degreasing the plate had no evident effect on the response of the oxide.

Other testing was done in cells consisting of half of a spherical O-ring joint, sealed against the specimen by a buna N O-ring. A plastic back-up plate of suitable thickness was used, and the assembly was held together with a joint clamp. Two sizes of cells were used: the large cell had a test area of 22.1 cm^2 ; the small cell had a test area of 3.5 cm^2 . It was not possible to use the small cell in comparative tests requiring continuous nitrogen flushing. In tests on the organic coated plate, test cells were filled 24h before running the test. On uncoated specimens, testing started immediately after filling. For the air-free tests, cells were flushed with purified nitrogen before filling; they were filled with a preflushed solution; nitrogen flushing continued through the test.

In plotting the results, reduction currents are indicated as positive and oxidation currents are indicated as negative.

Results

pH 7.6 borate buffer solution.—Three specimens were potentiostatically treated at each potential, every 50 mV from -0.150 to -1.100V vs. SCE. Typical results are shown in Fig. 2. From -0.150 to -0.350V , the curves were of the form indicated for the -0.300 potential and leveled out at zero current. Coulombic equivalents were determined by measuring the areas under the curves with a planimeter and are shown in Table I.

For all potentials positive to the equilibrium potential for iron, iron would be oxidized except for the existence of the Fe_2O_3 film. At the positive potentials indicated in Table I, iron is completely passivated (15). Reducing the ferric oxide, or some significant part of it, permits oxidation of iron to proceed, as shown for the -0.550V curve (Fig. 2). The -0.750V curve again levels out at zero current and represents the reduction of all of the Fe_2O_3 to the ferrous state. Averaging the values obtained by integration gives a coulombic equivalent of 1.3 mC/cm^2 . At more negative potentials, hydrogen evolution commences and the curves do not level out at zero current. At still more negative potentials, Fe_3O_4 is reduced, resulting in a hump in the curve. The -1.000V curve is indicative of these last two features. Such potentials, negative to the equilibrium

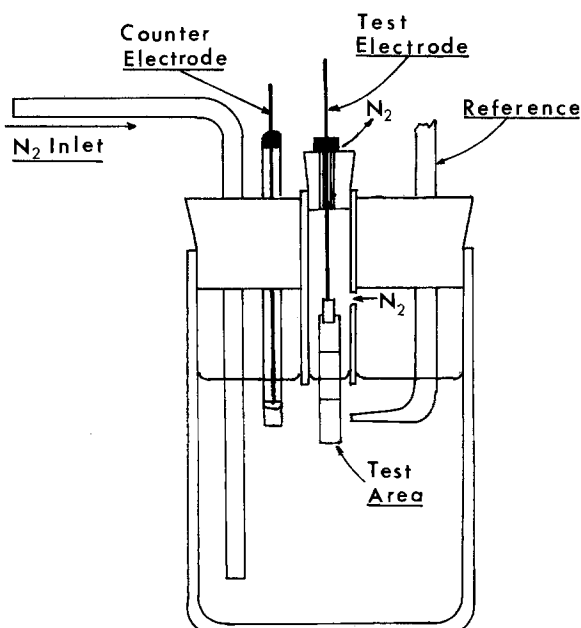


Fig. 1. Cell used for potentiostatic reduction of oxide film on uncoated steel in pH 7.6 borate buffer solution.

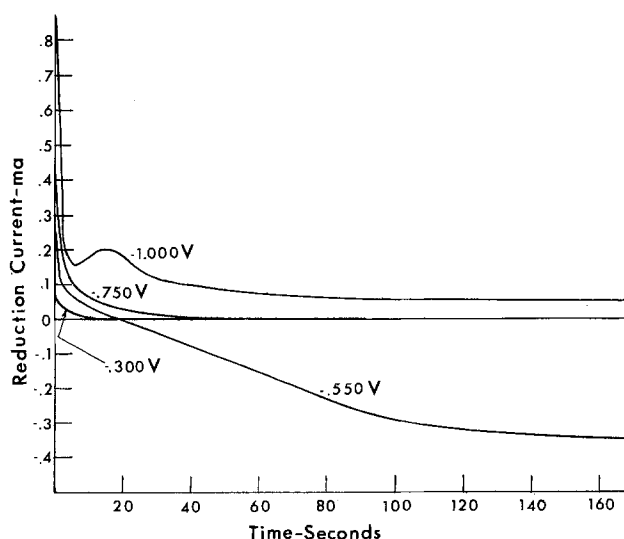


Fig. 2. Potentiostatic reduction of oxide film on uncoated steel in pH 7.6 borate buffer solution.

Table I. Cathodic charge for the potentiostatic reduction of ferric oxide on uncoated steel in pH 7.6 borate buffer solution at the more positive potentials

Potential vs. SCE (volts negative)	Q (mC/cm ²)
0.150	0.001
0.200	0.003
0.250	0.04
0.300	0.11
0.350	0.20

potential for iron, have no relevance to cathodic disbondment produced in corrosion situations.

It was confirmed that even with this well-developed, air-formed oxide film, reduction of oxygen is necessary for cathodic disbondment, at least at potentials positive to hydrogen evolution. Figure 3 shows the response for the organic-coated plate, potentiodynamically polarized in the cathodic direction at 300 mV/h in the pH 7.6 borate buffer solution, with just a trace of air present. This illustrates that oxidation of iron takes place beneath the coating in the appropriate potential range. While this was going on, cathodic disbondment was occurring, starting from a number of cationic ingress points in the coating. For most purposes, potentiodynamic polarization is not ideal for studying cathodic disbondment of coated metal, as too many processes are happening simultaneously.

0.1N sodium borate solution.—The potentiodynamic method was selected to illustrate the response of the uncoated steel to cathodic polarization in 0.1N Na₂B₄O₇ solution. Typical results are shown in Fig. 4. The light curve represents the response under air-free conditions; the heavy curve indicates the response in the presence of air. For the air-free curve, a considerable amount of cathodic reduction takes place at potentials which the Pourbaix diagram for iron indicates should be well within the range of Fe₂O₃ stability (16). The transition to Fe₃O₄ would be expected at about -0.590V vs. SCE, which corresponds to the potential at which Fe oxidation commences according to Fig. 4. For the air-free curve, there is a small hump in the oxide reduction curve, centered at -0.400V. The equivalent of the reduction in this hump is only about 0.03 mC/cm². It is to be noted how closely the reduction of oxygen follows the oxide reduction curve. In particular, the oxygen reduction rate is very low until oxide reduction commences; after that, it increases dramatically.

Figure 5 shows the results of the potentiostatic polarization of the uncoated steel at -0.650V in the presence and in the absence of air. At this potential, oxidation of Fe occurs. In the absence of air, the oxidation rate is seen to decrease as the Fe₃O₄ layer builds up. This is in contrast to the -0.550V curve in Fig. 2, in the pH 7.6 borate buffer

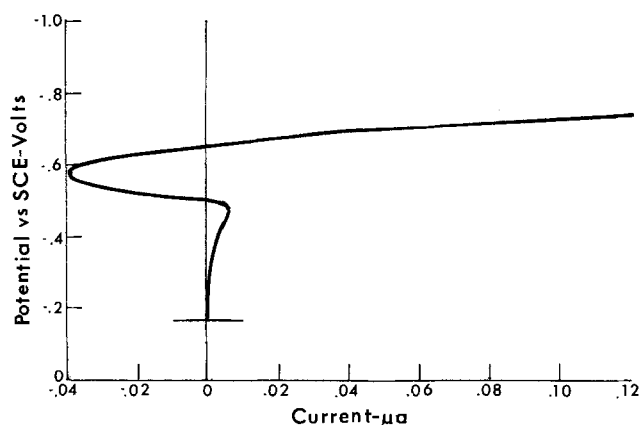


Fig. 3. Test area 3.5 cm². Potentiodynamic current response for oleoresinous-coated steel in pH 7.6 borate buffer solution with trace of oxygen in cell.

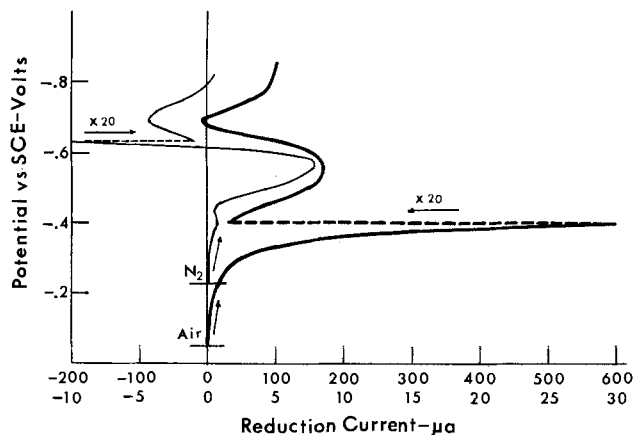


Fig. 4. Test areas: 22.1 cm². Potentiodynamic current responses for uncoated steel in 0.1N Na₂B₄O₇ solution, nitrogen flushed and with air present. Note scale changes at dotted lines; lower curve sections correspond to the lower abscissa scale.

solution, where Fe²⁺ is soluble. The oxide produced on the specimen in the air-free solution after 5h was barely visible. The oxide produced in the presence of air was much greater in amount and greenish-black in color. This should be considered a layer, rather than a film. It is evident that at this potential reduction of oxygen is occurring simultaneously with the oxidation of iron. At potentials positive to the peak potential in Fig. 4, potentiostatic reduction curves in the absence of oxygen level out at zero current.

In Fig. 6, are shown results for nine specimens of the oleoresinous-coated plate, potentiostatically polarized for 14h at 50 mV levels from -0.300 to -0.700V vs. SCE. The open-circuit potential of such specimens was usually around -0.125V vs. SCE. At -0.300V, there is only a very slight disbondment current, due to the restriction on the oxygen reduction process, as has been illustrated in Fig. 4. At -0.350 to -0.450V, the effects of the slight hump (Fig. 4) are noted. At -0.500 and -0.550V, there are greatly increased disbondment currents, as greatly increased oxygen reduction rates corresponding to the peak in the Fe₂O₃ reduction rate (Fig. 4) are attained. The disbondment currents increase further at -0.650V and more negative potentials, but slow down as disbonded areas start to run together.

Actual coating disbondment for these specimens is shown in Fig. 7. Immediately after the test, the specimens were quickly rinsed in distilled water, dried with a towel, and taped with a "super-stick" cellophane tape to remove the disbonded coating. It is noted that there was some disbondment for all of these potentials. There was even slight disbondment for the -0.300V polarization, which is not shown because it was too meager to photograph.

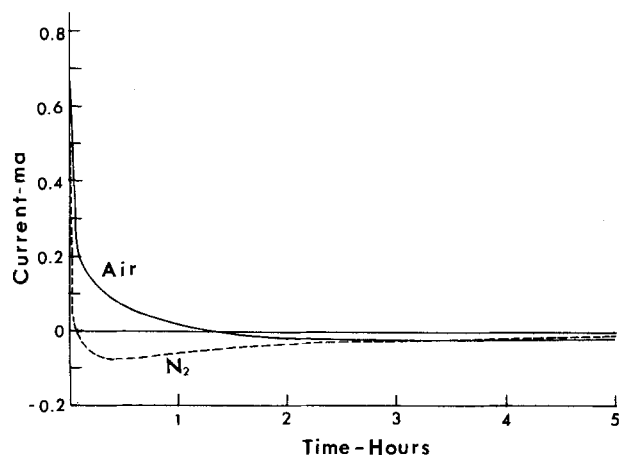


Fig. 5. Test areas, 22.1 cm². Potentiostatic current responses for uncoated steel in nitrogen flushed and air-saturated 0.1N Na₂B₄O₇ solutions, polarized to -0.650V vs. SCE for 5h.

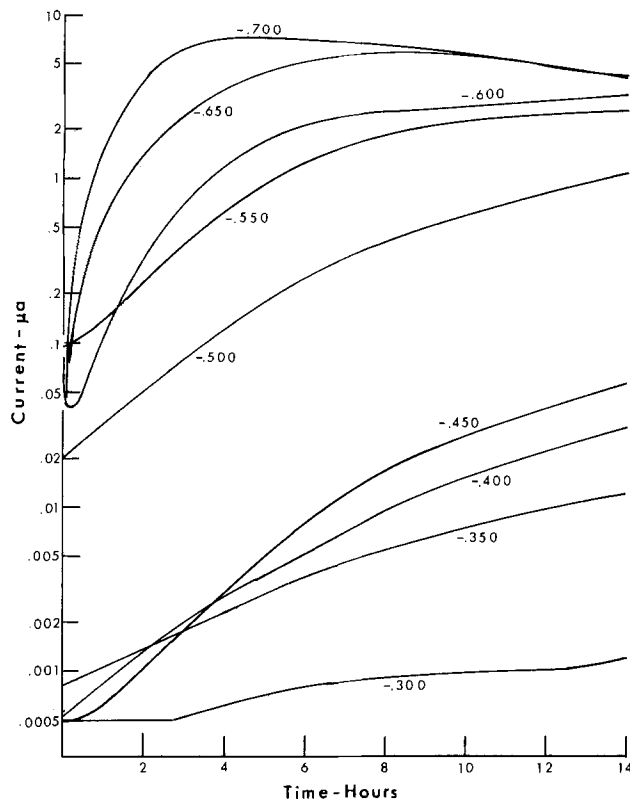


Fig. 6. Potentiostatic reduction current responses for aleoresinous-coated steel specimens, polarized to potentials vs. SCE as indicated, for 14h in air-saturated, 0.1N $\text{Na}_2\text{B}_4\text{O}_7$ solution.

Discussion

As noted earlier, the high pH generated by the reduction process is instrumental in cathodic disbondment. For electrical neutrality, a cation must be transported to the site of OH^- production beneath the coating. The pH required for cathodic disbondment in any particular case is a function of both the coating and the substrate. In general, a strongly basic condition such as provided by KOH or NaOH is required. Other common cations, such as Ca^{+2} , provided only weak bases; therefore, the pH will not rise to the value required for disbondment (17). Cathodic disbondment is characterized by the establishment of an aqueous film or layer between the organic coating and the substrate. The water layer is visible on the surface of the substrate immediately after removal of the coating from the disbonded area by taping. From a comparison with the 8 μm organic coating thickness and the fact that the water layer evaporated in seconds, it is estimated that the water layer was less than 1 μm thick.

In a corrosive situation, such as in NaCl solution, metal exposed at a defect in the coating develops into an anode. Being freely exposed to the corrosive medium, such an area assumes a potential more negative, or active, than the coated areas, which, at least initially, maintain their oxide film. Disbondment starts from a cationic ingress point, which may be a thin spot in the coating, and spreads. It may also spread from the cathodic area around an exposed metal anode. In the disbonded area, the Fe_2O_3 originally existing in the oxide film is shown to be at least partially reduced. The fact that Ritter observed surface roughening of the metal and oxide film thickening indicates that the potential of the metal beneath the disbonded coating in his experiments was in the potential range where Fe oxidation to Fe_3O_4 should occur.

In spite of the fact that the disbonded coating remains intact, reduction of oxygen in the disbonded area is greatly increased. In fact, it is apparent from the results of Fig. 6, plus the results of supplementary experiments not reported here, that at any given potential the "disbondment current" is a direct function of the area disbonded. It follows that the oxide film or surface treatment film

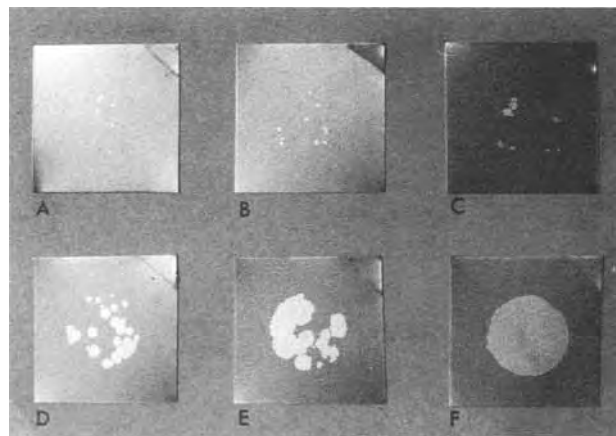


Fig. 7. Test areas: 3.5 cm^2 . Cathodic disbondment for specimens of Fig. 6, polarized for 14h in air-saturated 0.1N $\text{Na}_2\text{B}_4\text{O}_7$ solution at potentials indicated. A: -0.350 . B: -0.400 . C: -0.450 . D: -0.500 . E: -0.550 . F: -0.650 .

beneath the organic coating is actually part of the protective coating system from the standpoint of limiting corrosion currents. Experiments involving a protective organic coating as a detached membrane can only be expected to tell part of the story.

The potentiodynamic curve for Fe_2O_3 reduction at pH 9.2, indicated in Fig. 4, suggests that Fe_2O_3 is not reduced directly to Fe_3O_4 , but that there is a continuous change between these two extremes. Hubbard and Anson have reported the reduction of Fe^{+3} to Fe^{+2} in thin layers of solution to yield a bell-shaped curve, obeying the Nernst equation, with the peak potential at E° . Oxide films represent a thin layer. The slow scan speed used in Fig. 4 should allow time for equilibrium conditions to be approached. Except for the early peak centered at about -0.400V vs. SCE, a bell-shaped curve is apparent for potentials positive to the current maximum. If a soluble reduction product were produced, it would diffuse away, and such a relationship would not be obtained. In conformity, the Pourbaix diagram for iron indicates that a soluble reduction product is not to be expected and that layerwise reduction of Fe_2O_3 to Fe_3O_4 should not occur at potentials positive to the current maximum (16). It would appear, therefore, that the results can be explained on the basis of a potential-dependent reduction of Fe_2O_3 to produce intermediate compositions between Fe_2O_3 and Fe_3O_4 , in a manner similar to the reduction of Fe^{+3} in thin films of solution. As closely as can be discerned, the potentiodynamic current maximum does occur at E° for $\text{Fe}_2\text{O}_3/\text{Fe}_3\text{O}_4$ at pH 9.2. This is also the potential below which the oxidation of iron to magnetite occurs.

The small peak at about -0.400V could represent a higher oxidation state than Fe^{+3} , as has been suggested for the outer layer on passivated iron (15, 19). However, since this is low carbon steel rather than pure iron, there could be other possibilities. The continuing influence of this portion of the curve on oxygen reduction would seem to favor its representing an oxidation state of iron. An increased resistance for such an outer layer on passivated iron has been indicated (20).

For pH 7.6, soluble Fe^{+2} should not be expected as the reduction product over the entire range of potentials considered. At the more positive potentials, the equilibrium solubility is too low (16). This is substantiated by the experimental results for the potential range covered in Table I. The potentiostatic reduction curves for this potential range, as indicated for the -0.300V curve in Fig. 2, all level out at zero current, which would not be expected if soluble Fe^{+2} were the reduction product. The potential-dependent reduction in this potential range is again indicative of reduction to a nonstoichiometric oxidation state in the film, tending to an equilibrium at the reduction potential. At reduction potentials more negative than those indicated in Table I, soluble Fe^{+2} is produced. This results

in a potentiostatic "reduction" curve of the type indicated at -0.550V in Fig. 2, where continuous oxidation of Fe to Fe^{+2} occurs after a preliminary partial reduction of Fe^{+3} .

There is much work in the literature concerning electrochemical formation and reduction of passive films on iron in borate buffer solution at pH 8.4. It has been demonstrated that, in the main, Fe_2O_3 is reduced directly to Fe^{+2} in galvanostatic reduction (21). The present work, however, is concerned with what happens in the limited range of potentials which might exist beneath the organic coating in a corrosion situation. The data presented in the literature at pH 8.4 are in agreement with the present indications at pH 7.6 in that at potentials representing the positive end of the galvanostatic reduction range, (i) there is an amount of cathodic reduction charge which does not result in soluble Fe^{+2} , (ii) Fe^{+2} in solution at the 10^{-4} level, and presumably at lower concentrations, is oxidized to ferric oxide, rather than the reverse reaction, and (iii) charge is passed at identical potentials when going either in the passivating direction or in the reverse direction (15, 22). Other investigations have indicated the existence of nonstoichiometric compositions between the Fe_2O_3 and the Fe_3O_4 layers in passive films and have indicated the high electronic resistance of Fe_2O_3 is decreased with increasing Fe^{+2} in the film (19, 23, 24).

Manuscript submitted Dec. 14, 1983; revised manuscript received Jan. 16, 1985.

REFERENCES

1. J. S. Hammond, J. W. Holubka, and R. A. Dickie, *J. Coatings Technol.*, **51**, 45 (1979).
2. J. S. Hammond, J. W. Holubka, J. E. DeVries, and R. A. Dickie, *Corros. Sci.*, **21**, 239 (1981).
3. E. L. Koehler, *Corrosion*, **40**, 5 (1984).
4. J. J. Ritter, Personal communication (1982).
5. H. Leidheiser, Jr., *Corrosion*, **38**, 374 (1982).
6. J. J. Ritter and J. Kruger, in "Corrosion Control by Organic Coatings," H. Leidheiser, Jr., Editor, p. 28, National Association of Corrosion Engineers, Houston, TX (1981).
7. J. J. Ritter and M. J. Rodriguez, *Corrosion*, **38**, 223 (1982).
8. E. L. Koehler, in "Localized Corrosion," R. W. Staehle, B. F. Brown, J. Kruger, and A. Agrawal, Editors, p. 117, National Association of Corrosion Engineers, Houston, TX (1974).
9. H. Leidheiser, Jr., Preprint of Paper no. 81 presented at Corrosion/81, April 6-10, 1981, Toronto, CA, National Association of Corrosion Engineers, Houston, TX (1981).
10. O. D. Gonzalez, P. H. Josephic, and R. A. Oriani, *This Journal*, **121**, 29 (1974).
11. J. E. Castle and J. F. Watts, in "Corrosion Control by Organic Coatings," H. Leidheiser, Jr., Editor, p. 78, National Association of Corrosion Engineers, Houston, TX (1981).
12. H. G. Oswin and M. Cohen, *This Journal*, **104**, 9 (1957).
13. C. D. Stockbridge, P. B. Sewell, and M. Cohen, *ibid.*, **108**, 928 (1961).
14. N. Sato, T. Noda, and K. Kudo, *Electrochim. Acta*, **19**, 471 (1974).
15. M. Nagayama and M. Cohen, *This Journal*, **109**, 781 (1962).
16. M. Pourbaix, "Atlas of Electrochemical Equilibria in Aqueous Solutions," National Association of Corrosion Engineers, Houston, TX (1974).
17. E. L. Koehler, *Corrosion*, **33**, 209 (1977).
18. A. T. Hubbard and F. C. Anson, *Anal. Chem.*, **33**, 58 (1966).
19. B. D. Cahan and C. Chen, *This Journal*, **129**, 921 (1982).
20. S. Haruyama and T. Tsuru, *Corros. Sci.*, **13**, 275 (1973).
21. M. Cohen and K. Hashimoto, *This Journal*, **121**, 42 (1974).
22. M. Nagayama and M. Cohen, *ibid.*, **110**, 670 (1963).
23. M. C. Bloom and L. Goldenberg, *Corros. Sci.*, **5**, 623 (1965).
24. R. V. Moshtev, *Electrochim. Acta*, **16**, 2039 (1971).

Simultaneous Raman Spectroscopy and Electrochemical Studies of Corrosion Inhibiting Molecules on Copper

D. Thierry and C. Leygraf*

Swedish Corrosion Institute, S-114 86 Stockholm, Sweden

ABSTRACT

Surface-enhanced Raman scattering (SERS) has been used as a complementary *in situ* technique for electrochemical measurements in order to investigate five structurally related N-heterocyclic molecules on copper. Their different abilities to act as corrosion inhibitors are discussed in view of structural information obtained from SERS. It is concluded that the molecules investigated do not dissociate upon adsorption and that different functional groups result in different orientation of the adsorbed molecules on copper.

Since the early detection of anomalously intense Raman scattering from pyridine adsorbed on silver electrodes (1), surface-enhanced Raman scattering (SERS) has become a promising *in situ* tool for studies of reactions at metal/electrolyte interfaces.

The great enhancement of Raman scattering up to a factor of 10^6 for molecules adsorbed on rough Ag, Cu, or Au surfaces has resulted in successful efforts to use SERS as a surface-sensitive *in situ* method in corrosion science. Hence, during the last years, several investigations have been published on SERS experiments with corrosion inhibiting molecules, such as mercaptobenzothiazole ad-

sorbed on Ag (2), benzotriazole adsorbed on Cu (3-5), and thiourea on Cu (5). These results have shown that SERS is an extremely surface sensitive *in situ* technique for studies of inhibitor complexes formed on Ag and Cu surfaces under potentiostatic control.

N-heterocyclic compounds have been used as corrosion inhibitors on copper for several decades. Benzotriazole (BTA) is the most widely used corrosion inhibitor for copper and copper-based alloys and has been the subject of many investigations. Poling (6) attributed the inhibiting effect of BTA to a compact film of a Cu-benzotriazolate (Cu-BTA) complex polymer, which would act as a physical barrier against the corrosive media. Mansfeld *et al.* (7) suggested that the chemisorption of BTA^- on Cu pre-

* Electrochemical Society Active Member.

vents the adsorption of oxygen and the formation of a prenucleation layer, which is the essential condition for oxide formation. For these authors, the chemisorption of BTA^- plays the predominant role in the inhibition mechanisms.

Although BTA has been studied more extensively than other N-heterocyclic compounds, the structural nature of films formed upon adsorption on Cu is not well determined. In order to further examine the role played by BTA and other heterocyclic compounds as corrosion inhibitors for Cu, we report in this work SERS and electrochemical (polarization resistance and ac impedance) studies of BTA and, for the first time, of four other molecules structurally related to BTA.

Experimental

Electrochemical measurements.—The electrochemical measurements were performed using a potentiostat and a standard three-electrode electrochemical cell with a saturated calomel electrode as reference electrode and a platinum electrode as counterelectrode.

The working electrodes were cut from a 99.99% pure polycrystalline Cu rod, resulting in an exposed surface area of 1 cm^2 . The circular Cu samples were diamond polished down to a particle size of $1 \mu\text{m}$, rinsed with distilled water, and degreased with acetone before immersion under potentiostatic control in the electrochemical cell. The polarization resistance results were obtained by monitoring the current as a function of electrode potential in steps of 1 mV (5 mV/min) from -30 to $+30 \text{ mV}$ relative to the corrosion potential. All values of polarizing potentials are given relative to the saturated calomel electrode (SCE).

AC impedance experiments were performed using the same cell and electrodes as for the polarization resistance experiments. A frequency response analyzer (Solatron 1170) was used for measuring the impedance over the frequency range of 100 kHz – 10 mHz . Electrolytes were prepared by mixing 5 mM of inhibitors in 0.01 or 0.1 M NaCl . In all cases, triply distilled water and pure reagents were used as ingredients.

Surface Raman measurements.—The Raman Spectrometer, consisting of a Dilor RTI 30 triple monochromator and a photon counting system, has been described in more detail elsewhere (8). Oxidation-reduction cycling (ORC) in the electrolyte studied was performed in order to increase the amplitude of surface Raman signals. It consists of triangular sweeps from a cathodic potential where Raman spectra later were taken to some anodic potential in the range of 100 – 120 mV/SCE (corresponding to a total charge passed of 10 mC/cm^2). The ORC surface pretreatment was done under simultaneous laser illumination because this was found to increase the surface Raman signals further (8). An Ar laser (5140 \AA) was used for normal bulk Raman measurements, whereas a Kr laser (6470 \AA) operating at a power of 100 mW was necessary for obtaining detectable SERS signals (4, 5).

Results

Electrochemical measurements.—Tables I and II show the molecular structure of the investigated molecules, their polarization resistance, and their inhibiting efficiency in 0.01 and 0.1 M NaCl , respectively, obtained at the actual corrosion potentials. The inhibiting efficiency is defined as

$$I \% = \left(1 - \frac{i_i}{i_0}\right) \times 100$$

with i_i and i_0 the measured currents with and without inhibitor added. According to both electrochemical measurements and to separate weightless measurements, the molecules investigated exhibit the same order of inhibiting ability. In the less aggressive solution, the inhibiting efficiency varies from 75% for hydroxybenzimidazole to 99% for mercaptobenzimidazole (Table I). In the more aggressive solution, the inhibiting efficiency varies from no

Table I. Molecular structure, polarization resistance, and inhibiting efficiency of investigated molecules in 0.01 M NaCl

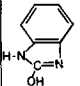
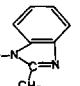
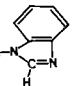
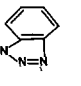
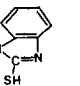
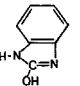
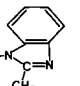
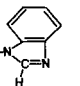
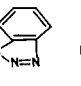
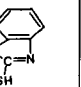
0.01 M NaCl					
Molecule	Hydroxy-benzimidazole	Methyl-benzimidazole	Benzimidazole	Benzotriazole	Mercapto-benzimidazole
Structure					
Polarization-resistance, $\Omega \text{ cm}^2$	54	45	87	245	1775
% Inhibition	75	80	86	90	99

Table II. Molecular structure, polarization resistance, and inhibiting efficiency of investigated molecules in 0.1 M NaCl

0.1 M NaCl					
Molecule	Hydroxy-benzimidazole	Methyl-benzimidazole	Benzimidazole	Benzotriazole	Mercapto-benzimidazole
Structure					
Polarization-resistance, $\Omega \text{ cm}^2$	5	14	15	42	59
% Inhibition	0	32	65	69	83

inhibition at all for hydroxybenzimidazole to 83% for mercaptobenzimidazole (Table II). Hence, under present conditions, the inhibiting ability of mercaptobenzimidazole is significantly higher than that of benzotriazole in 0.01 as well as 0.1 M NaCl .

Surface Raman measurements.—The normal bulk Raman spectra of concentrated benzimidazole and benzotriazole solutions have been reported and discussed elsewhere (3, 9–11). Frequency shifts and tentative assignments of six main Raman lines taken from the literature are shown in Table III for benzotriazole and in Table IV for benzimidazole. The Raman lines shown for benzimidazole were found to be present for all benzimidazole derivatives. Hence, although no assignments of Raman lines have been published for mercapto-, methyl-, and hydroxybenzimidazole, the structural resemblance of these molecules suggests the same assignments for all benzimidazole derivatives.

Figure 1 illustrates the Raman lines of normal Raman spectra (lower part) of benzotriazole in ethanol (used as solvent) and of SERS spectra obtained at different applied potentials in 0.1 M NaCl . Figure 2 illustrates the same spectra for benzimidazole.

The surface-enhanced character of the SERS spectra was verified by a marked potential dependence of the Raman line intensities. This is illustrated in Fig. 1 and 2,

Table III. Frequency shifts and assignments of Raman lines of bulk benzotriazole

Raman frequency (cm^{-1})	Assignment	Ref.
785	Benzene ring breathing	(3, 9, 10)
1010	Benzene in plane ring bending	(9, 10)
1125	Triazole	(11, 12)
1210	Triazole ring breathing	(3, 9, 11)
1385	Triazole ring stretching	(3, 9, 10)
1455	Benzene ring stretching	(3, 9, 10)

Table IV. Frequency shifts and tentative assignments of Raman lines of bulk benzimidazole

Raman frequency (cm ⁻¹)	Assignment	Ref.
775	Benzene	(9, 10)
1010	Benzene in plane ring bending	(9, 10)
1135	Imidazole ring stretching	(9, 12, 22)
1255	Imidazole	(9, 10, 12, 22)
1370	Imidazole	(9, 12, 22)
1455	Benzene ring stretching	(9, 10)

from which it is further concluded that normal Raman and SERS spectra exhibit approximately the same Raman peaks (except those originating from ethanol). This suggests that the benzotriazole and benzimidazole molecules, with exception of a possible loss of protons, are not dissociated upon adsorption on copper. This is in agreement with previous IR (6) and SERS (3) studies of the same system, suggesting that benzotriazole is adsorbed as an ion (BTA⁻) rather than as a neutral molecule (BTAH).

Furthermore, a comparison of Raman line intensities of normal Raman and SERS spectra reveals that peaks from vibrational modes of the triazole ring and the imidazole ring, respectively, increase in intensity more than peaks from vibrational modes of the benzene ring when going from normal Raman spectra to SERS spectra.

Figures 3-5 illustrate the same studies as in Fig. 1 and 2 for, respectively, mercaptobenzimidazole, methylbenzimidazole, and hydroxybenzimidazole. Again, normal Raman and SERS spectra exhibit similar features with Raman peaks at approximately the same positions. As for benzotriazole and benzimidazole, this suggests that the investigated molecules are not dissociated upon adsorption on Cu. For these molecules, however, no preferential enhancement of Raman intensities is observed, for neither the imidazole ring nor the benzene ring, when going from normal Raman to SERS spectra.

Figures 6 and 7 illustrate the potential dependence of the six Raman lines given in Tables III and IV for

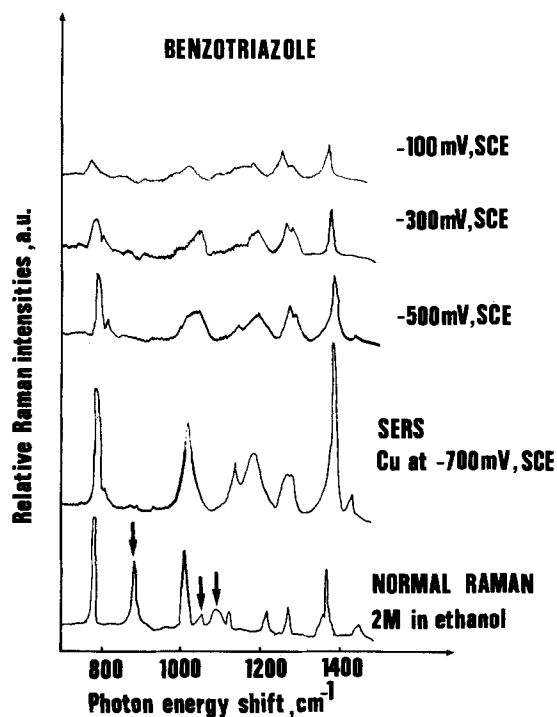


Fig. 1. Normal Raman and SERS spectra of benzotriazole in ethanol and in 0.1M NaCl. SERS spectra were obtained at different electrode potentials. Arrows indicate normal Raman peaks of ethanol used as solvent.

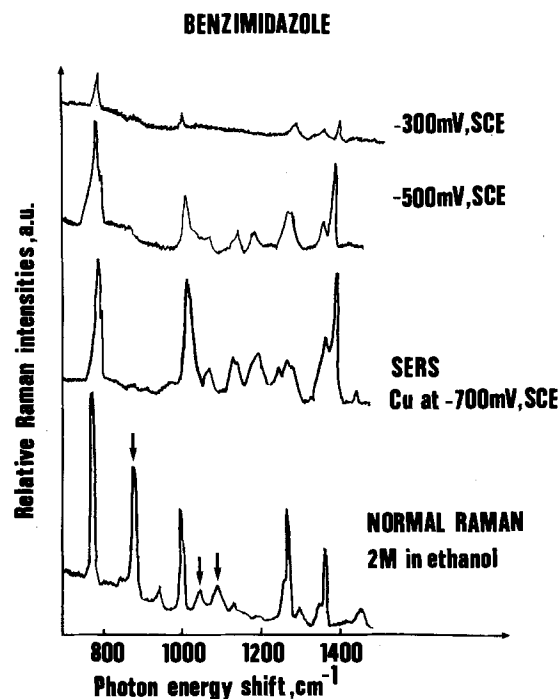


Fig. 2. Normal Raman and SERS spectra of benzimidazole. See caption of Fig. 1 for further explanations.

benzotriazole and benzimidazole, respectively. Raman intensities of peaks originating from vibrational modes of the triazole or imidazole ring, on one hand, and peaks originating from vibrational modes of the benzene ring, on the other, change approximately uniformly in the potential interval from -700 to -100 mV/SCE. In agreement with (13), the maximum in Raman intensity is found at around -700 mV/SCE.

Discussion

General.—Following established procedures values of polarization resistance and inhibiting efficiency given in the previous section were obtained at the actual corrosion potential (around -150 mV/SCE). Raman spectra, on the other hand, were obtained at more cathodic potentials because of Raman line intensity problems at the corrosion

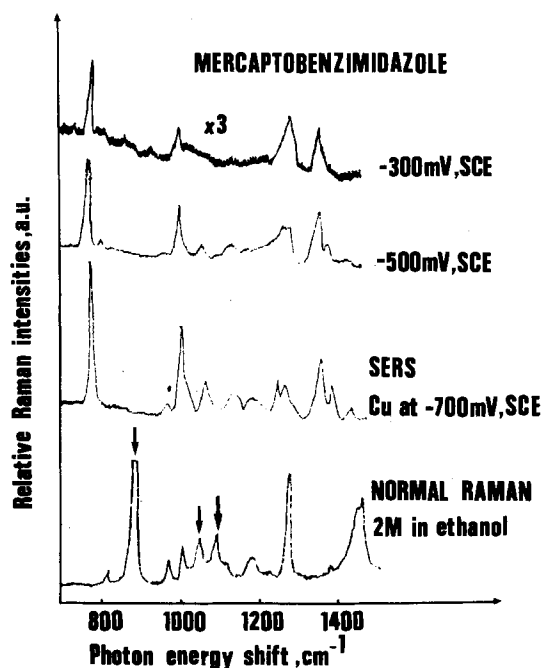


Fig. 3. Normal Raman and SERS spectra of mercaptobenzimidazole. See caption of Fig. 1 for further explanations.

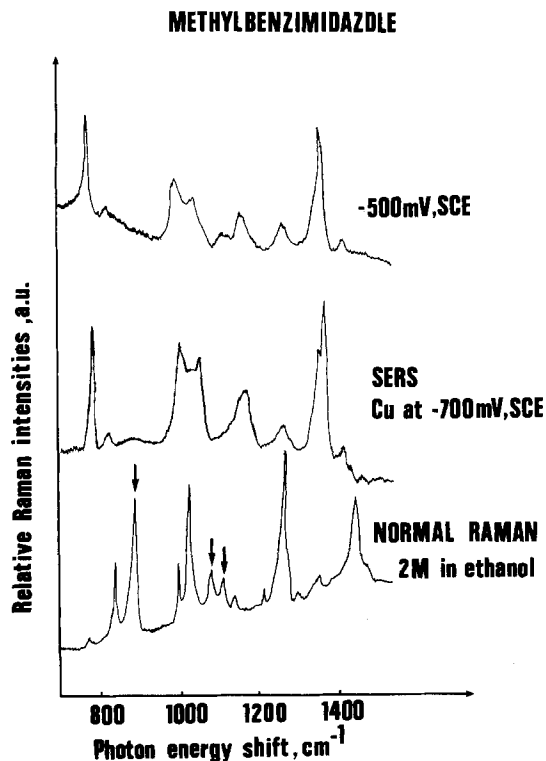


Fig. 4. Normal Raman and SERS spectra of methylbenzimidazole. See caption of Fig. 1 for further explanations.

potential and an observed maximum in intensity at around -700 mV/SCE (Fig. 6 and 7). Hence, before combining results from electrochemical measurements with structural information from Raman measurements, it is first necessary to establish that no major structural changes occur in the interval from -700 to around -150 mV/SCE. Evidence for this is given in Fig. 1 for benzotriazole, which exhibits strong similarities in peak positions of the SERS spectra obtained in the interval between -700 and -100 mV/SCE. The same tendency is

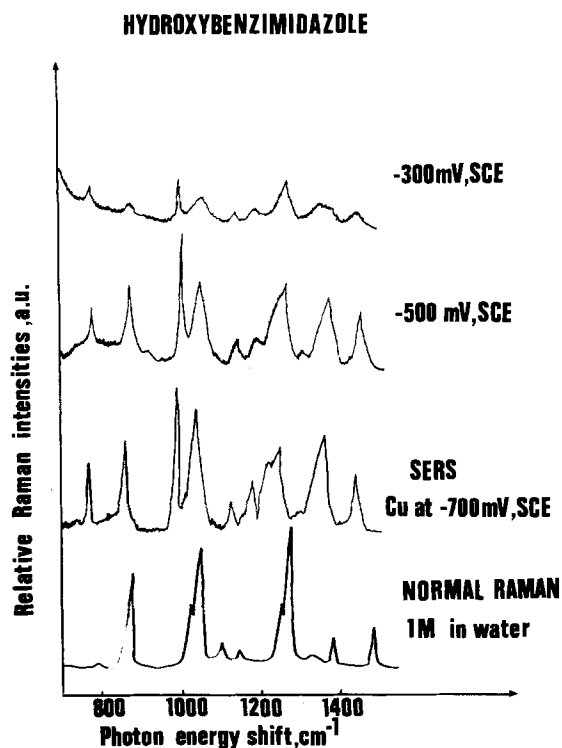


Fig. 5. Normal Raman and SERS spectra of hydroxybenzimidazole. SERS spectra were obtained at different electrode potentials.

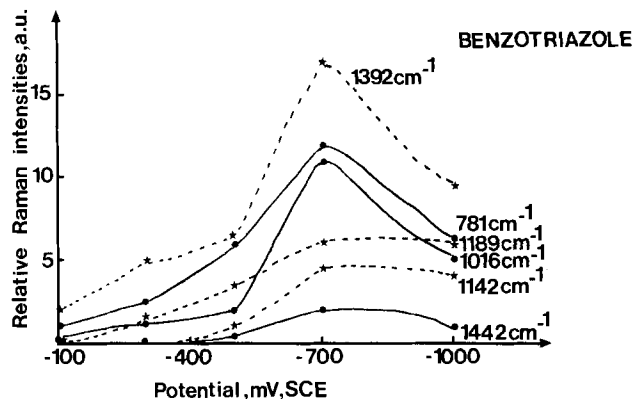


Fig. 6. Variation in amplitude of main Raman lines for benzotriazole with electrode potential.

found for the other molecules investigated, showing strong resemblance in peak positions between different potentials up to the most anodic potentials where surface Raman spectra could be obtained (Fig. 2-5). These results suggest that no major structural changes occur in the investigated potential region.

Further evidence is given by ac impedance measurements of the same components adsorbed on copper in 0.1M NaCl at different potentials. All ac impedance spectra exhibit characteristic hemicircles from which the total capacitance of the solid/liquid interface can be calculated (14). In Fig. 8, numerical values of capacitances are given at different potentials between -100 and -700 mV/SCE in 0.1M NaCl and with benzimidazole, benzotriazole, or mercaptobenzimidazole added. The curves exhibit a continuous decrease with applied potential. In qualitative agreement with ellipsometry measurements obtained elsewhere (7), this is consistent with a continuous growth in adsorbed film thickness when going from -700 mV/SCE to more anodic potentials. Any major change in adsorbed film structure would have resulted in more dramatic changes in capacitance in that particular potential region than those actually observed.

From Fig. 8 it is further concluded that the capacitance at any given potential decreases with inhibiting ability for the molecules investigated. This observation is in agreement with work reported elsewhere and interpreted as being due to the formation of a protective layer with adsorbed inhibitors (15).

To summarize, both Raman spectra and ac impedance measurements suggest that similar inhibition reactions occur at -700 mV/SCE (where the maximum of intensity in SERS is obtained) and around -100 to -200 mV/SCE where the polarization resistance measurements were performed.

Polarization resistance measurements.—Tables I and II clearly show that small variations in molecular structure

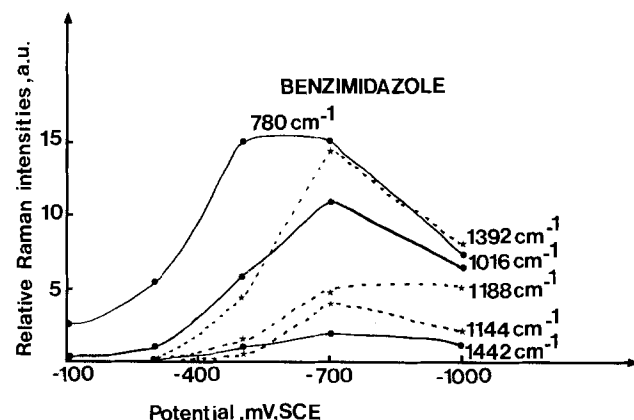


Fig. 7. Variation in amplitude of main Raman lines for benzimidazole with electrode potential.

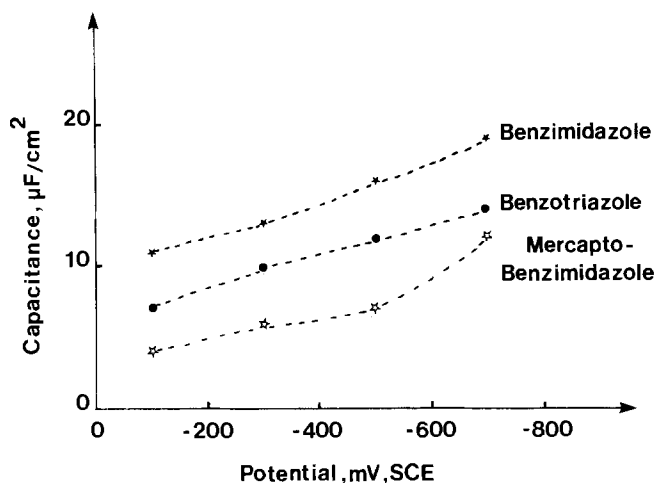
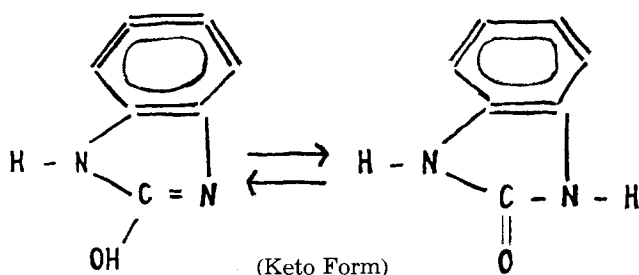


Fig. 8. Capacitance values calculated from ac-impedance spectra of Cu in 0.1M NaCl at different potentials and with various inhibitors added.

can result in noteworthy differences in inhibiting efficiency. The replacement of the middle nitrogen atom in the triazole ring of benzotriazole by a hydrocarbon group leads to a significant decrease in inhibiting ability. This is consistent with observations reported elsewhere (16) that the inhibitive properties of benzimidazole and structurally related molecules such as indole and indazole are inferior to benzotriazole in near-neutral solutions. It suggests further that all three nitrogen atoms in the triazole ring may be involved in the adsorption process.

As further inferred from Tables I and II, the substitution of a proton or a methyl group in the imidazole ring by a mercapto group results in a notable increase in inhibiting efficiency, and mercaptobenzimidazole seems under present conditions to be a better corrosion inhibitor than benzotriazole. Functional groups such as the mercapto group are, for most organic corrosion inhibitors, reaction centers for adsorption processes, which becomes evident also from the present results.

The poor inhibiting ability shown by hydroxybenzimidazole is most likely due to the molecule being in equilibrium with its keto form according to the reaction scheme shown below



From this follows that adsorption on copper mainly occurs through one of the nitrogen atoms in the keto structure.

Considering all molecules investigated in this work, the inhibiting efficiency of various atoms in functional groups follows the generally observed order (16) sulfur > nitrogen > oxygen.

SERS results.—The enhancement of Raman scattering has been described as a contribution of short-range enhancement which applies to the first chemisorbed layer and long-range enhancement which includes many molecular layers away from the surface (18, 19). The short-range contribution is attributed to an increase in the molecule polarizability caused by changes in the electronic charge density distribution near the surface. This effect occurs only for the first adsorbed layer. The long-range contribution is attributed to the enhancement of electromagnetic fields which may arise from excitations of surface plasmon polaritons. The effect is very sensitive to

surface morphology. The exact contribution of these two effects remains uncertain (20, 21).

The difference in contribution of long-range electromagnetic and short-range chemical effects occurring at different distances from the metal surface can be used when interpreting the difference in Raman line intensities between normal and SERS spectra (Fig. 1-5). The increase in Raman line intensities of the triazole part in benzotriazole as compared to that of the benzene part (Fig. 1) may arise from short-range contributions of the total enhancement of Raman scattering. The same holds true for the corresponding increase in Raman line intensities of the imidazole part in benzimidazole as compared to that of the benzene part (Fig. 2). This, together with the appearance of the same peaks in SERS and normal Raman spectra, suggests that benzotriazole and benzimidazole are nondissociatively chemisorbed on Cu and that the triazole and the imidazole part, respectively, are more affected by the Cu surface than the benzene part of the molecules and therefore presumably bonded directly to Cu in the first adsorbed layer.

Further evidence is given by a comparison between frequency shifts from bulk and surface Raman spectra, respectively. This shows that there is a significantly larger difference in frequency shifts for vibrational modes originating from the triazole or imidazole part than for vibrational modes originating from the benzene part. Hence, SERS results suggest that adsorption of benzotriazole and benzimidazole occurs solely via the triazole and imidazole part, most likely through interaction of all three nitrogen or carbon atoms with the Cu substrate.

On the other hand, mercaptobenzimidazole, hydroxybenzimidazole, and methylbenzimidazole exhibit neither any preferential enhancement in Raman intensity nor any preferential shifts in Raman peak positions originating from the imidazole part (Fig. 3-5). Consequently, when adsorbed on copper, these molecules exhibit a different orientation than benzotriazole and benzimidazole as a result of other atoms or functional groups in the imidazole ring taking part in the adsorption process. Hence, the presence of two polar functions in mercaptobenzimidazole may result in adsorption on Cu via sulfur and one of the nitrogen atoms, which results in a different orientation of adsorbed mercaptobenzimidazole than of adsorbed benzotriazole or benzimidazole. Similarly, the presence of a methyl group in methylbenzimidazole and the keto form of hydroxybenzimidazole suggest that the different orientations of these molecules are caused basically via interaction of only one of the nitrogen atoms of the imidazole ring and the Cu surface.

Hence, the difference in inhibiting ability of all five molecules investigated can tentatively be explained by the number and type of functional groups or atoms in the triazole or imidazole ring that interact with Cu according to interpretations of SERS results.

However, even if structural information concerning the first adsorbed layer of inhibiting molecules as obtained by SERS suggests some explanations for their difference in inhibiting ability, it should be emphasized that, also, other parameters have to be considered in the design of an efficient corrosion inhibitor for Cu. Among such parameters should be mentioned possible polymerization of chemisorbed molecules, their acid strength, and surface film thickness. Their possible influence is the subject of further investigations of these and other corrosion inhibiting molecules structurally related to benzotriazole.

Conclusions

Polarization resistance studies of organic molecules on Cu, namely benzotriazole and four derivatives, show marked differences in their ability to act as corrosion inhibitors for Cu. These differences have been combined with structural information concerning chemisorbed films as obtained by SERS.

The results of polarization resistance have been obtained at the corrosion potential (ranging from -100 to -200 mV/SCE), while those of SERS have been obtained

at more cathodic potentials (ranging from -100 to -700 mV/SCE). SERS as well as ac impedance measurements, however, suggest a similar structure for each molecule in the whole investigated potential range from -700 to -100 mV/SCE. Consequently, results from present polarization resistance measurements can be directly combined with SERS measurements.

With the exception of possible losses of protons, SERS results show the molecules investigated not to be dissociated upon adsorption.

Bonding between the molecules investigated and the Cu surface is suggested to involve the N—N—N and N—C—N chain in the case of benzotriazole and benzimidazole, N and S from the N—H and S—H groups in the case of mercaptobenzimidazole, and only N from the N—H group in the case of hydroxy- and methylbenzimidazole.

The change in inhibiting ability of the molecules investigated is reflected in the number and type of functional groups or atoms that interact with the Cu surface.

Acknowledgment

We wish to thank Dr. J. Bergman, Royal Institute of Technology in Stockholm, for fruitful discussions. The financial support of the Swedish Board for Technical Development (STU) is gratefully acknowledged.

Manuscript submitted Oct. 22, 1984; revised manuscript received Dec. 26, 1984. This was Paper 430 presented at the Cincinnati, Ohio, Meeting of the Society, May 6-11, 1984.

Swedish Corrosion Institute assisted in meeting the publication costs of this article.

REFERENCES

1. M. Fleischmann, P. J. Hendra, and A. J. McQuellan, *Chem. Phys. Lett.*, **26**, 163 (1974).
2. M. Ohsawa and W. Suetaka, *J. Electron Spectrosc. Relat. Phenom.*, **30**, 221 (1983).
3. J. Rabim, G. R. Gutz, O. Sala, and W. J. Orville-Thomas, *J. Mol. Struct.*, **100**, 571 (1983).
4. J. J. Kester, T. E. Furtak, and A. J. Bevolo, *This Journal*, **129**, 1716 (1982).
5. B. H. Loo, Annual report, INCRA project no. 341 (1982).
6. G. W. Poling, *Corros. Sci.*, **10**, 359 (1970).
7. F. Mansfeld, T. Smith, and E. P. Parry, *Corrosion*, **27**, 289 (1971).
8. D. Thierry and C. Leygraf, *Surf. Sci.*, **52**, 149, 592 (1985).
9. F. R. Dollish, W. G. Fateley, and F. F. Bentley, "Characteristic Raman Frequencies of Organic Compounds," John Wiley and Sons, New York (1974).
10. M. H. Cordes and J. L. Walter, *Spectrochem. Acta*, **24A**, 1421 (1968).
11. J. J. Kester, *J. Chem. Phys.*, **78**, 12 (1983).
12. D. Thierry and C. Leygraf, Unpublished results.
13. R. P. Van Duyne, in "Chemical and Biological Applications of Lasers," Vol. 4, C. B. Moore, Editor, p. 101, Academic Press, New York (1979).
14. I. Epelboin, M. Keddam, and J. Lestrade, *Faraday Discuss. Chem. Soc.*, **56**, 264 (1973).
15. P. Kirkov and J. Arsov, *Corros. Sci.*, **13**, 707 (1973).
16. J. B. Cotton and I. R. Scholes, *Br. Corros. J.*, **2**, 1 (1967).
17. N. Hackerman, *C. R. Symp. Eur. Inhibit. Corros., Ann. Univ. Ferrara, N.S. Sez. V.*, Suppl. No. 3, 111 (1961).
18. S. S. Jha, J. R. Kirtley, and J. C. Tsang, *Phys. Rev. B.*, **22**, 3973 (1980).
19. R. P. Van Duyne, Private communication.
20. A. Otto, I. Pockrand, J. Billmann, and C. Pettenkofer, in "Surface Enhanced Raman Scattering," T. E. Furtak and R. K. Chang, Editors, p. 147, Plenum Press, New York (1982).
21. C. A. Murray, in "Surface Enhanced Raman Scattering," T. E. Furtak and R. K. Chang, Editors, p. 203, Plenum Press, New York (1982).
22. D. Garfinkel and J. T. Edsall, *J. Am. Chem. Soc.*, **80**, 3807 (1958).

Computation of Pourbaix Diagrams Using Virtual Species: Implementation on Personal Computers

John C. Angus*

Department of Chemical Engineering, Case Western Reserve University, Cleveland, Ohio 44106

Charles T. Angus

Hawken School, Gates Mills, Ohio 44040

ABSTRACT

Computation of the equilibrium composition in complex, multiphase redox systems is accomplished by treating the active element as a virtual species. For ideal solutions, the equation set may be solved sequentially, rather than simultaneously, for the concentrations of all species. For nonideal solutions, the method provides the basis for an efficient iterative solution. The procedure gives a simple test for phase stability and an algorithm for defining the boundaries of the regions of dominance of the dissolved species which is independent of concentration. Examples of Pourbaix diagrams generated on a small personal computer are given.

Since their introduction (1), Pourbaix diagrams have proven to be of great value in describing the complex phase chemistry of aqueous redox systems. Automated generation of Pourbaix diagrams by computer has been receiving increasing attention in recent years (2-7). Computational methods have been reviewed by Linkson (8).

In this paper, we describe a computational approach in which the active element undergoing redox transitions is treated as a virtual species. The resulting formalism is particularly simple and permits rapid solution on small desktop computers or even hand calculators.

The particular procedures described here are restricted to systems involving only one redox element, M, and to

pure solid phases containing only M, H, and O. No other solids, such as carbonates, or complexes, such as chlorides, are considered. The method is, however, completely general and can be extended to these cases.

Thermodynamic Analysis

Phase rule analysis.—Consider a system comprised of k species which contain the active element undergoing redox transitions. For example, for sulfur, these species could include among others: S^{-2} , HS^{-1} , H_2S , S^0 , SO_3^{-2} , HSO_3^{-1} , etc. In addition, there are the species H_2O , H^+ and the electrons, e^- , which are a virtual species. Among these species one can write $k - 1$ independent redox reactions.

The phase rule for reacting systems may be written as

*Electrochemical Society Active Member.

$$f = (s - r) - P + 2 \quad [1]$$

where s is the total number of species, r the number of independent reactions, and P the number of phases. Substituting $s = k + 3$, $r = k - 1$, and fixing both temperature and pressure, the phase rule reduces to

$$f = 4 - P \quad [2]$$

If OH^- ions appear in the reactions, there is an additional species; however, there is another equilibrium equation between the OH^- and H^+ . Furthermore, no provision was made to ensure electroneutrality. Again, adding an equation for electroneutrality and adding an inert counterion leaves the phase rule the same. Equation [2] indicates that a maximum of three independent intensive variables can be chosen, e.g., E , pH , and $[\text{M}]_T$, the total dissolved concentration of active element, M . Therefore, a three-dimensional space is required to truly represent the phase equilibria. It is customary, however, to construct a two-dimensional representation of the three-dimensional diagram by projection onto the E - pH plane.

The full three-dimensional diagram for the copper system is shown in Fig. 1. Figure 1 was obtained by solving the simultaneous equilibrium equations assuming ideal solutions ($\gamma_i = 1$) and pure, immiscible solid phases. In the three-dimensional E - pH - $\log_{10} [\text{Cu}]_T$ space, a two-phase region appears as a surface. The intersection of two two-phase surfaces is a line corresponding to a three-phase region (two solid phases plus the aqueous phase).

In Fig. 2, the three-dimensional diagram of Fig. 1 is plotted in conventional form as a projection onto the E - pH plane. The projections of the three-phase lines are shown as solid lines; lines of constant total dissolved concentration, $[\text{Cu}]_T$, are shown as dashed lines.

In the absence of any standardized nomenclature, we will call diagrams of the type shown in Fig. 2 "Pourbaix diagrams." These differ from so-called "predominance diagrams" in which the regions in which single species are dominant are also plotted on the E - pH field. The two types of diagrams are often superimposed on the same plot.

Calculation of equilibrium compositions: Virtual species.—There are very well-developed techniques for determining the minimum number of independent reactions required to describe the stoichiometry of a reacting system (9). For systems involving many chemical species, many different sets of mathematically independent reactions can be written. However, some sets may have great computational and conceptual advantages. We use the set obtained by writing the $k - 1$ formation reactions in the standard form

$$\text{M} = \nu_i \text{M}_i + h_i \text{H}^+ + w_i \text{H}_2\text{O} + z_i e^- \quad [3]$$

For example, for $\text{S}_2\text{O}_3^{2-}$, one has

$$\text{S} = 1/2 \text{S}_2\text{O}_3^{2-} + 3\text{H}^+ - 3/2 \text{H}_2\text{O} + 2e^- \quad [4]$$

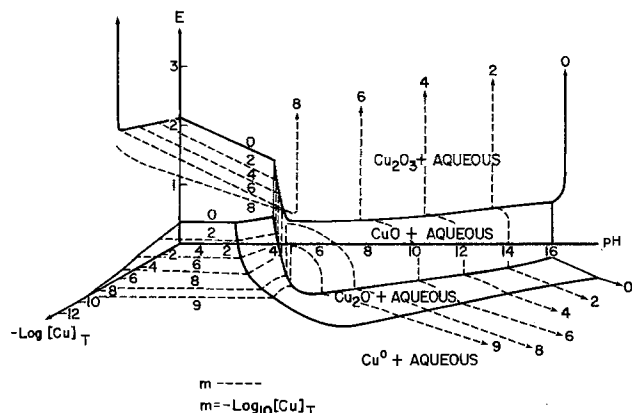


Fig. 1. Three-dimensional Pourbaix diagram for the copper system

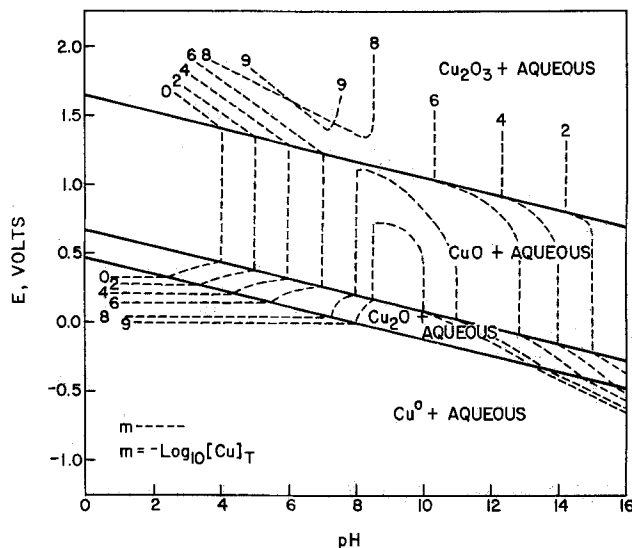


Fig. 2. Two-dimensional Pourbaix diagram for the copper system obtained by projection onto the E - pH plane.

where $\text{S} = \text{M}$, $\text{S}_2\text{O}_3^{2-} = \text{M}_i$, $\nu_i = 1/2$, $h_i = 3$, $w_i = -3/2$, and $z_i = 2$. Equation [3] can be shown to describe the equilibria even if the pure element, M , is not physically present in the equilibrium mixture.

From Eq. [3], one has the equilibrium equations

$$\mu_{\text{M}} = \nu_i \mu_i + h_i \mu_{\text{H}^+} + w_i \mu_{\text{H}_2\text{O}} + z_i \mu_e \quad [5]$$

The relationship between the chemical potential and concentration of species M_i is

$$\mu_i = \mu_i^0 + RT \ln \gamma_i [\text{M}_i] \quad [6]$$

We define a standard chemical potential per atom of active element by

$$\mu_i^{\Delta} \equiv \mu_i^0 / \alpha_i \equiv \mu_i^0 \nu_i \quad [7]$$

where α_i ($\equiv 1/\nu_i$) is the number of atoms of the active element per molecule of species i . Combining Eq. [5]-[7], one finds

$$[\text{M}_i] = \frac{1}{\gamma_i} \exp \frac{[\mu_{\text{M}} - \mu_i^{\Delta} - h_i \mu_{\text{H}^+} - w_i \mu_{\text{H}_2\text{O}} - z_i \mu_e]}{\nu_i RT} \quad [8]$$

The term μ_{M} is the chemical potential of the active element. If the pure element is not physically present in the reactive mixture, μ_{M} still has meaning. In this case, the element is a virtual species.

Virtual species have been used before to simplify equilibrium calculations (10). The most common example is, however, the separation of redox reactions into two half-cells. The electrons which appear in the half-cell reactions are not present as physically distinct species in the reaction mixture. It is nevertheless customary to treat them as virtual species and to use their chemical potential as one of the thermodynamic variables.

Further insight can be obtained by summing Eq. [8] over all dissolved species containing the active element and solving for μ_{M}

$$\mu_{\text{M}} = -RT \ln Q + RT \ln \sum_i (\gamma_i [\text{M}_i])^{\nu_i} \quad [9]$$

where

$$Q \equiv \sum_i \exp \left[\frac{-\mu_i^{\Delta} - h_i \mu_{\text{H}^+} - w_i \mu_{\text{H}_2\text{O}} - z_i \mu_e}{RT} \right] \quad [10]$$

Equations [9] and [10] are of considerable interest. First note the resemblance of the function Q to a partition function. The summation is over dissolved species rather than allowed quantum states. Further note that Eq. [9] can be cast into the standard form for the chemical potential

$$\mu_M = \mu_M^* + RT \ln a_M \quad [11]$$

with

$$a_M = \Sigma (\gamma_i [M_i])^{v_i} \quad [12]$$

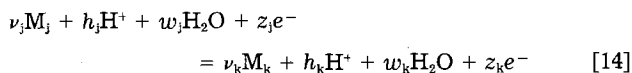
and

$$\mu_M^* = -RT \ln Q \quad [13]$$

The sum $\Sigma(\gamma_i [M_i])^{v_i}$ can be interpreted as the overall activity of the active element in the solution. Note that this quantity is well defined even if the active element does not exist as the elemental form in the reaction mixture.

Stability criteria.—Consider any two species, *j* and *k*, which can either be dissolved species or solid phases. Assume the species coexist at some fixed pH and *E*, i.e., fixed values of μ_{H^+} and μ_{e^-} , but are not necessarily at thermodynamic equilibrium with each other. We examine the criterion which determines which is the stable species.

First write the formal expression for the stoichiometry of the transformation between *j* and *k* using Eq. [3]



The free energy change for this transition is just

$$\begin{aligned} \Delta G = v_k \mu_k - v_j \mu_j + (h_k - h_j) \mu_{H^+} \\ + (w_k - w_j) \mu_{H_2O} + (z_k - z_j) \mu_{e^-} \end{aligned} \quad [15]$$

But from Eq. [5]

$$(\mu_M)_k = v_k \mu_k + h_k \mu_{H^+} + w_k \mu_{H_2O} + z_k \mu_{e^-} \quad [16]$$

$$(\mu_M)_j = v_j \mu_j + h_j \mu_{H^+} + w_j \mu_{H_2O} + z_j \mu_{e^-} \quad [17]$$

Combining Eq. [15]-[17]

$$\Delta G = (\mu_M)_k - (\mu_M)_j \quad [18]$$

Equation [18] shows explicitly that the ΔG for a transformation between any species, dissolved or solid, is just equal to the difference in chemical potential of the active element in these two species. If $\Delta G < 0$, i.e., $(\mu_M)_k < (\mu_M)_j$, the transformation [14] proceeds to the right; if $\Delta G > 0$, to the left. In equilibrium $\Delta G = 0$ for all pairs, *j*, *k*

$$(\mu_M)_k = (\mu_M)_j \quad [19]$$

For any solid phase, one can obtain μ_M directly by writing Eq. [5] for the solid

$$(\mu_M)_s = v_s \mu_s + h_s \mu_{H^+} + w_s \mu_{H_2O} + z_s \mu_{e^-} \quad [20]$$

For the aqueous phase, μ_M can be computed from Eq. [9]. Therefore, Eq. [18] can be used to provide a simple algebraic test for stability. The stable phase will be the one with the lowest μ_M . A solid will dissolve in an aqueous solution if $(\mu_M)_s > (\mu_M)_{aq}$. Furthermore, since μ_M increases monotonically with a_M (see Eq. [11]), the solid phase with the lowest solubility is stable. This is in agreement with the well-known behavior of nonelectrolytes.

Predominance diagrams.—In addition to plotting the two- and three-phase boundaries, it is customary to divide the *E*-pH field into regions corresponding to the dominant dissolved species. The criterion used for determining the boundaries of these regions is usually

$$\gamma_j [M_j] = \gamma_k [M_k] \quad [21]$$

On the other hand, the criterion

$$(\gamma_j [M_j])^{v_j} = (\gamma_k [M_k])^{v_k} \quad [22]$$

may be easily shown to be independent of μ_M and hence concentration by using Eq. [8]. Since the boundaries determined by Eq. [22] are independent of concentration, they may be properly superimposed on the two-dimensional projection of a Pourbaix diagram.

Application of Theory

Conventions.—In this section, the working forms of the equations are developed. The equations are cast into the

form which is used when the free energy data are given as standard electrode potentials.

We assume that the electrode potentials are available for reactions [3] with all species in their standard states. If the standard potentials are not tabulated for all of the formation reactions, they can be obtained by making linear combinations of the tabulated reactions in the normal manner. There is, of course, no guarantee that a complete data set is available for each active element.

The relationship between the standard chemical potentials for the half-cell reaction given by Eq. [3] is

$$\mu_i^\Delta = \mu_M^\circ - h_i \mu_{H^+}^\circ - w_i \mu_{H_2O}^\circ - z_i \mu_{e^-}^\circ \quad [23]$$

Note that $\mu_{e^-}^\circ$ is the chemical potential of electrons in equilibrium with chemical species M_i , H^+ , and H_2O , all in their standard states. The standard-state free energy data for M_i , H^+ , and H_2O are encoded in tabulated values of $\mu_{e^-}^\circ$, which are reported as standard electrode potentials.

The following conventions are used to relate chemical potentials to the practical variables pH and *E*

$$\mu_{H^+} - \mu_{H^+}^\circ = -2.30259RT (\text{pH}) \quad [24]$$

$$(\mu_{e^-} - \mu_{e^-}^\circ) = -F(E - E_i^\circ) \quad [25]$$

Potentials only appear in the equations as the difference, $E - E_i^\circ$. Therefore, any consistent choice of reference electrode is permissible.

The chemical potential of H_2O in the solution, μ_{H_2O} , must be governed by the dictates of the Gibbs-Duhem equation and the chemical potentials of all other species. It appears customary, however, to ignore the influence of the other species and to replace the Gibbs-Duhem equation with the simple equality

$$\mu_{H_2O} = \mu_{H_2O}^\circ \quad [26]$$

It is assumed that all solid phases are pure and that

$$\mu_s = \mu_s^\circ \quad [27]$$

Equation [27] is an assumption about the nature of the system of interest and is not a convention for tabulating standard thermochemical data. If, for example, the pressure in the system of interest were not the standard-state pressure, then a Poynting-type correction would be necessary. Furthermore, if the solid phase were a solid solution, then one would have to introduce the properties of this solid solution.

General working equations.—The total dissolved concentration of active element, $[M]_T$, is used as the practical measure of concentration

$$[M]_T = \Sigma \alpha_i [M_i] \quad [28]$$

where the sum is over all dissolved species. The concentrations of the individual dissolved species are obtained by substitution of Eq. [23]-[27] into Eq. [8]

$$\begin{aligned} [M_i] = \frac{1}{\gamma_i} \exp \alpha_i \left\{ \frac{\mu_M - \mu_M^\circ}{RT} \right. \\ \left. + 2.30259 h_i (\text{pH}) + \frac{F}{RT} z_i (E - E_i^\circ) \right\} \end{aligned} \quad [29]$$

An expression for $\mu_M - \mu_M^\circ$ can be obtained by summing Eq. [29] over all dissolved species. One finds

$$\begin{aligned} \left[\frac{\mu_M - \mu_M^\circ}{RT} \right]_{aq} = - \ln \Sigma \exp \left\{ 2.30259 h_i (\text{pH}) \right. \\ \left. + \left(\frac{F}{RT} \right) z_i (E - E_i^\circ) \right\} + \ln \Sigma (\gamma_i [M_i])^{v_i} \end{aligned} \quad [30]$$

Equation [30] is the working form of Eq. [9].

The expression for the chemical potential of the active element in a pure solid phase, *s*, is obtained from Eq. [23]-[27] and Eq. [20]

$$\left[\frac{\mu_M - \mu_M^\circ}{RT} \right]_s = -2.30259 h_s (\text{pH}) - \left(\frac{F}{RT} \right) z_s (E - E_s^\circ) \quad [31]$$

Two-phase lines.—Eliminating $\mu_M - \mu_M^0$ between Eq. [31] and [29] one has

$$[M_i] = \frac{1}{\gamma_i} \exp \alpha_i \left[2.30259(h_i - h_s)(pH) + \left(\frac{F}{RT} \right) [z_i(E - E_i^0) - z_s(E - E_s^0)] \right] \quad [32]$$

Equation [32] gives the concentration of any dissolved species, M_i , in equilibrium with a pure solid phase, s . Using Eq. [32] in Eq. [28] one obtains the implicit algebraic relationship between E and pH along a two-phase line for any concentration $[M]_T$. These are the dashed lines in Fig. 2.

Three-phase lines.—The criterion of phase equilibrium for a pair of solids, u, v is

$$\left[\frac{\mu_M - \mu_M^0}{RT} \right]_u = \left[\frac{\mu_M - \mu_M^0}{RT} \right]_v \quad [33]$$

Using Eq. [33] and [31] gives the expression for the potential *vs.* pH along a three-phase line

$$E = \frac{z_v E_v^0 - z_u E_u^0}{(z_v - z_u)} - \frac{2.30259RT}{F} (pH) \quad [34]$$

In deriving Eq. [34], the general result that $h_s = z_s$ for all uncharged solids containing only H, O, and M was used.

Substituting Eq. [34] into Eq. [31], one obtains the chemical potential along a three-phase intersection

$$\left[\frac{\mu_M - \mu_M^0}{RT} \right]_{u,v} = - \left(\frac{F}{RT} \right) \left(\frac{z_u z_v}{z_u - z_v} \right) (E_u^0 - E_v^0) \quad [35]$$

Note that $(\mu_M - \mu_M^0)/RT$ is constant along the intersection.

The concentration of any species, M_i , in equilibrium with two solid phases, u and v , can be obtained from Eq. [34], [35], and [8]. One finds after some manipulation

$$[M_i] = \frac{1}{\gamma_i} \exp \left\{ \left(\frac{F}{RT} \right) \left(\frac{\alpha_i}{z_u - z_v} \right) [z_u(z_i - z_v) E_u^0 + z_v(z_u - z_i) E_v^0 + z_i(z_v - z_u) E_i^0] + 2.30259\alpha_i(h_i - z_i)(pH) \right\} \quad [36]$$

Another very useful result is obtained by differentiation of Eq. [31]. Using the fact that for uncharged solids, $h_s = z_s$, one finds

$$\left[\frac{\partial E}{\partial (pH)} \right]_{\mu_M} = -2.30259 \left(\frac{RT}{F} \right) \quad [37]$$

In other words, the chemical potential of any solid phase remains constant along a line of constant slope given by Eq. [37].

By comparison with Eq. [34], one sees that the chemical potential of any other solid, s , remains constant along a three-phase line where two solids, u and v , are in equilibrium.

Implementation

Pourbaix diagrams.—Computations were done on an Apple II+ computer. The stoichiometric coefficients, ν_i , h_i , z_i , and the standard electrode reduction potential, E_i^0 , were stored permanently on the program disk. No further computations of free energies or balancing chemical reactions are required. The sign convention for E_i^0 , embodied in Eq. [25], is consistent with previous published Pourbaix diagrams. The data used to construct the diagrams are given in Tables I and II. Data were obtained from standard sources (11, 12). No claim is made for these data sets, and they are included only as a reference for the diagrams.

The first step in constructing a Pourbaix diagram is to determine the relative stability of solid pairs. This is done

Table I. Copper data

Species	ν_i	h_i	z_i	E_i^0
Solid				
Cu	1	0	0	0
Cu ₂ O	0.5	1	1	0.470
CuO	1	2	2	0.570
Cu ₂ O ₃	0.5	3	3	0.929
Cu(OH)	1	1	1	0.568
Cu(OH) ₂	1	2	2	0.609
Dissolved				
Cu ⁺	1	0	1	0.520
Cu ⁺⁺	1	0	2	0.337
CuO ₂ ⁻⁻	1	4	2	1.515
HCuO ₂ ⁻	1	3	2	1.127
Cu ⁺⁺⁺	1	0	3	1.049
CuO ₂ ⁻	1	4	3	1.250

Table II. Sulfur data

Species	ν_i	h_i	z_i	E_i^0
Solid				
S	1	0	0	0
Dissolved				
S ⁻⁻	1	0	-2	-0.445
HS ⁻	1	-1	-2	-0.062
H ₂ S	1	-2	-2	0.144
S ₂ O ₃ ⁻⁻	0.5	3	2	0.465
HS ₂ O ₃ ⁻	0.5	5/2	2	0.440
H ₂ S ₂ O ₃	0.5	2	2	0.436
SO ₃ ⁻⁻	1	6	4	0.583
HSO ₃ ⁻	1	5	4	0.476
H ₂ SO ₃	1	4	4	0.450
SO ₄ ⁻⁻	1	8	6	0.353
HSO ₄ ⁻	1	7	6	0.333

by first computing $(\mu_M - \mu_M^0)/RT$ of a solid pair, u, v , from Eq. [35]. Next, compute E for this pair at any convenient pH , e.g., $pH = 0$, using Eq. [34]. Then, at this value of E and pH , compute $(\mu_M - \mu_M^0)/RT$ for all other solid phases, s , using Eq. [31]. The pair u, v is stable if for all other solids, s

$$\left[\frac{\mu_M - \mu_M^0}{RT} \right]_{u,v} < \left[\frac{\mu_M - \mu_M^0}{RT} \right]_s \quad [38]$$

Because the chemical potential of any uncharged solid is constant along a three-phase line, it is not necessary to repeat the test at any other pH . The above procedure is then repeated for all possible pairs of solids.

End points of the three-phase lines are found by using Eq. [36] in Eq. [28]. The resulting equation is solved, for fixed $[M]_T$, by the Newton-Raphson technique. Note that if $(\mu_M)_s > (\mu_M)_{aq}$ for all pH , no end points will be found. The two-phase boundaries are then traced out by a simple routine which follows the contour of constant $[M]_T$. The program displays the Pourbaix diagram on the video monitor. Labeling is accomplished by entering from the key board the coordinates of a point approximately in the center of each region. The program determines the stable phase at these coordinates and displays the name of the stable solid (or aqueous phase) at the point selected. Type fonts were obtained using Beagle Brothers software. The final plot is sent to a dot matrix printer using a commercial screen dump program (Advanced Grafpak, Smartware). Examples of several diagrams obtained in this way are shown in Fig. 3-6.

The program automatically handles the situation where a solid phase becomes unstable with respect to the aqueous phase, e.g., note the absence of Cu₂O₃ in Fig. 5. The case of a single stable phase is also covered; see Fig. 6 for sulfur.

The program was written in BASIC. Typical run times are 5 min, most of which is required to trace out the two phase boundaries. Use of a commercial BASIC compiler program could reduce this time by approximately a factor of three.

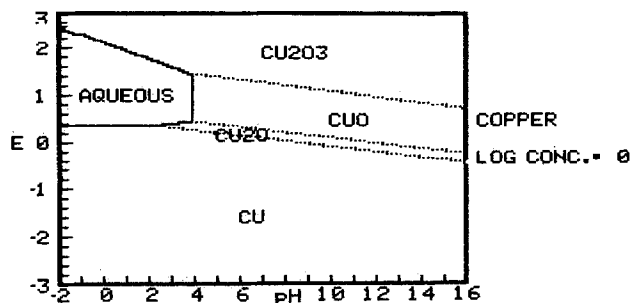


Fig. 3. Computer-generated Pourbaix diagram for copper. $[Cu]_T = 1m$.

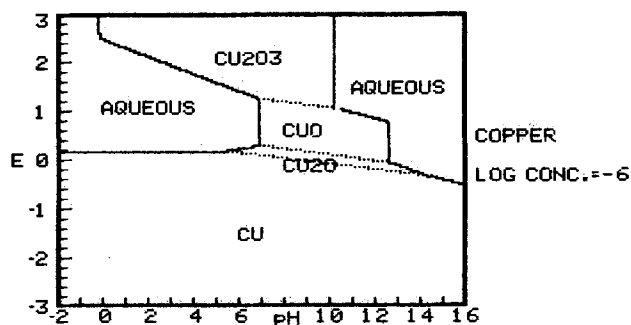


Fig. 4. Computer-generated Pourbaix diagram for copper. $[Cu]_T = 10^{-6}m$.

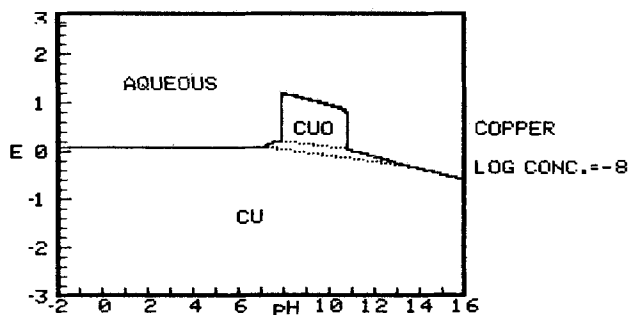


Fig. 5. Computer-generated Pourbaix diagram for copper. $[Cu]_T = 10^{-8}m$.

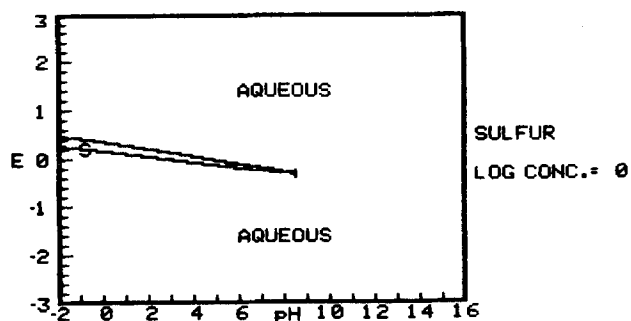


Fig. 6. Computer-generated Pourbaix diagram for sulfur. $[S]_T = 1m$. Triangular area is stability field for solid sulfur.

Predominance diagrams.—Consider any pair (j, m) of dissolved species. We are interested in determining the relationship between E and pH that guarantees

$$(\gamma_j[M_j])^{z_j} = (\gamma_m[M_m])^{z_m} \quad [39]$$

Using Eq. [29] in Eq. [39], one finds

$$E = -2.30259 \left(\frac{RT}{F} \right) \left[\frac{h_j - h_m}{z_j - z_m} \right] (pH) + \left[\frac{z_j E_j^0 - z_m E_m^0}{z_j - z_m} \right] \quad [40]$$

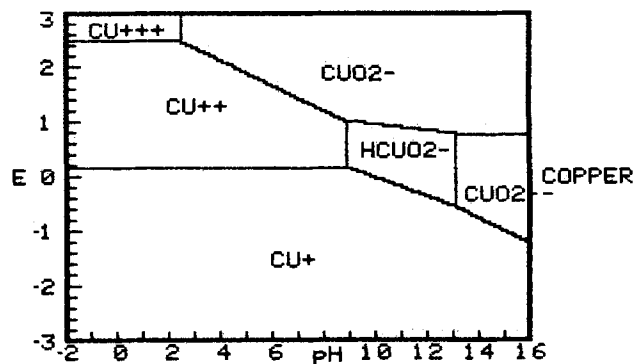


Fig. 7. Predominance diagram for dissolved copper species

Equation [40] is the equation of the lines that appear on predominance diagrams. Note that Eq. [40] is independent of concentration. Intersections of these lines determine the points where three species have equal values of $(\gamma_i[M_i])^{z_i}$. Writing Eq. [40] for the two pairs (j, m) and (k, m) and solving, one obtains the coordinates of the intersection

$$E = \frac{z_j E_j^0 (h_k - h_m) + z_k E_k^0 (h_m - h_j) + z_m E_m^0 (h_j - h_k)}{z_j (h_k - h_m) + z_k (h_m - h_j) + z_m (h_j - h_k)} \quad [41]$$

$$pH = \frac{[(z_j - z_m)z_k E_k^0 + (z_m - z_k)z_j E_j^0 + (z_k - z_j)z_m E_m^0] \left[\frac{F}{RT} \right]}{[h_k(z_j - z_m) + h_j(z_m - z_k) + h_m(z_k - z_j)]2.30259} \quad [42]$$

It can be shown from Eq. [40] that two lines are parallel if

$$h_j(z_m - z_k) + h_k(z_j - z_m) + h_m(z_k - z_j) = 0 \quad [43]$$

The above equations provide a very simple algorithm for construction of a predominance diagram. First, compute the coordinates of all possible intersections using Eq. [41] and [42]. Intersections falling outside the desired range, e.g., $-3 < E < +3$ or $-2 < pH < 16$, are discarded. At each remaining intersection, compute the value of $(\gamma_i[M_i])^{z_i}$ for all other dissolved species using Eq. [29]. The intersection (j, k, m) appears on the predominance diagram if for all other dissolved species, n, one has

$$(\gamma_j[M_j])^{z_j} > (\gamma_n[M_n])^{z_n} \quad [44]$$

This procedure is repeated for all possible intersections. The result is the coordinates of all intersections which should appear within the predominance diagram. Straight lines are drawn between all points which share a common pair of species.

The above procedure joins only those intersections (j, k, m) which are within the interior of the diagram. To complete the construction, one must connect some of these points to the boundaries of the diagram. Specifically, those interior points which are connected to only one or two other interior points must be connected to two or one boundaries, respectively. The appropriate boundary intersections are easily found using Eq. [40] and the equations for the boundaries, which in the present case were $E = -3V$, $E = +3V$, $pH = -2$, and $pH = 16$. All but one of the multiple intersections are discarded by demanding that the intersection be within the above ranges and by application of the criterion given by Eq. [44].

The predominance diagram for copper shown in Fig. 7 was obtained using this method.

Acknowledgments

This work was supported in part by the U.S. Army Research Office and Martin Marietta Energy Systems (Oak Ridge, Tennessee) under contract to the Department of Energy.

Manuscript received Sept. 17, 1984. This was Paper 210 presented at the New Orleans, Louisiana, Meeting of the Society, Oct. 7-12, 1984.

Case Western Reserve University assisted in meeting the publication costs of this article.

LIST OF SYMBOLS

a_M	overall activity of active element in the solution
E	electrochemical potential
F	Faraday's constant
f	degrees of freedom
h_i	stoichiometric coefficient for H^+
k	number of species containing active element
M	symbol for the active element
M_i	symbol for i th species containing element M
$[M_i]$	molal concentration of species M_i
$[M]_T$	total dissolved concentration of active element
P	number of phases
Q	defined by Eq. [10]
r	number of independent reactions
R	gas constant
s	number of species
w_i	stoichiometric coefficient for H_2O
z_i	stoichiometric coefficient for electrons
α_i	atoms of active element in species M_i ($\alpha_i = \nu_i^{-1}$)
γ_i	activity coefficient of species M_i
μ_e	chemical potential of electrons
μ_i	chemical potential of species M_i
μ_i°	standard chemical potential of species M_i
μ_i^Δ	μ_i°/α_i
μ_M	chemical potential of active element
μ_M°	standard chemical potential of element M
μ_M^*	a standard chemical potential defined by Eq. [13]
ν_i	stoichiometric coefficient for species M_i ($\nu_i = \alpha_i^{-1}$)

REFERENCES

1. M. Pourbaix, "Thermodynamics of Dilute Aqueous Solutions: Graphical Representation of the Role of pH and Potential," Thesis, Delft (1945); CEBELCOR Publication F. 227, reprinted 1963 (French).
2. A. D. Pelton, C. W. Bale, and W. I. Thompson, in "Applications of Phase Diagrams in Metallurgy and Ceramics, Proceedings of a Workshop held at Gaithersburg, MD, Jan. 10-12, 1977," pp. 1077-1089, National Bureau of Standards SP-496, National Bureau of Standards, Washington, DC (1977).
3. B. H. Rosof, in "Applications of Phase Diagrams in Metallurgy and Ceramics, Proceedings of a Workshop held at Gaithersburg, MD, Jan. 10-12, 1977," pp. 1090-1092, National Bureau of Standards SP-496, National Bureau of Standards, Washington, DC (1977).
4. B. G. William and W. J. Patrick, *J. Chem. Ed.*, **54**, 107 (1977).
5. P. A. Brook, *Corros. Sci.*, **11**, 389 (1971).
6. M. H. Froning, M. E. Stanley, and E. D. Verink, *ibid.*, **10**, 371 (1976).
7. T. I. Barry, in "The Thermodynamics of Aqueous Systems with Industrial Applications," S. A. Newman, Editor, pp. 681-699, ACS Symposium Series, American Chemical Society, Washington, DC (1980).
8. P. B. Linkson, B. E. Phillips, and C. D. Rowles, *Miner. Sci. Eng.*, **11**, 65 (1979).
9. R. Aris, "Introduction to the Analysis of Chemical Reactors," p. 10, Prentice Hall, Englewood Cliffs, NJ (1965).
10. W. B. White, *J. Chem. Phys.*, **46**, 4171 (1967).
11. D. Dobos, "Electrochemical Data," p. 250, Elsevier, New York (1975).
12. "Handbook of Chemistry and Physics," 55th ed., R. C. Weast, Editor, p. D120, CRC Press, Cleveland, OH (1974).

Long-Term Atmospheric Oxidation of High Purity Iron

R. P. Frankenthal,* P. C. Milner,* and D. J. Siconolfi*

AT&T Bell Laboratories, Murray Hill, New Jersey 07974

ABSTRACT

High purity iron, cast and rolled more than 20 years ago and stored without special precautions in the laboratory, has largely maintained its bright surface finish over this period of time, showing that iron is stably passivated by air. Since long-term (>1 yr) oxidation studies of iron do not exist and since iron is usually thought to rust in air at moderate relative humidities, the thickness of the passivating oxide film was measured by Auger electron spectroscopy and depth profiling. After corrections for an adsorbed carbonaceous layer, the thickness was estimated to be 5-6 nm. This is in reasonable agreement with extrapolations of short-term (<24h) oxide film thickness data from gaseous and anodic oxidation studies in the literature.

There have been numerous investigations of the oxidation of iron at or near room temperature by air and by oxygen from low pressures to about 1 atm for times ranging from a few seconds to a maximum of several weeks (1-10). A summary of the results up to 1961 (7) indicates that the oxide film thickness lies in the range of 1-4 nm, depending on surface pretreatment, oxygen pressure, moisture content, and time of exposure. Later studies (8-10) agree with these findings. The various results imply that iron is stably passivated by oxygen and by air. However, there have been no reports of the passivation of iron when exposed to oxygen or air for long periods of time, i.e., for one or more years.

Andreeva (4) reported that after three years in a humid atmosphere rust centers developed at grain boundaries and spread radially over part of the surface. The surface not covered by rust retained its original brightness, and the thickness of the oxide film on those areas remained constant at the thickness it had after 30 days. Ali and Wood (10) reported that oxidation became rapid after about 60 days of exposure to laboratory air at room temperature at 44-46% relative humidity. After 120 days, the thickness of the oxide was greater than 50 nm, and it con-

sisted primarily of α - Fe_2O_3 . They attributed the increased oxidation rate to impurities in the atmosphere.

One of the present authors (RPF) has some strips of high purity (99.9+%), zone-refined iron (11) that was made in late 1963 or early 1964. These strips were stored in a glass bottle with a polyethylene stopper at the E. C. Bain Laboratory of the U.S. Steel Corporation in Monroeville, Pennsylvania, until 1972 and since then at AT&T Bell Laboratories in Murray Hill, New Jersey. No effort was made to protect these strips or to keep them from rusting, other than to keep the bottle stoppered. Recently (March 1984), we examined the strips and found most to be shiny and free from any visible tarnish or rust. A few pieces were partially discolored (gray), indicating that some tarnishing had occurred on them. Since we know of no really long-term (>1 yr) studies of the oxidation of iron in air and since it is generally assumed that iron will rust in air at moderate relative humidities, we thought it would be of scientific and technological interest and importance to measure the thickness of the oxide film that had formed on the surface of the iron strips that had remained shiny for a period of 20 years. We report here the results of that analysis and of calculations that extrapolate existing short-term gaseous and anodic oxidation data to 20 years.

*Electrochemical Society Active Member.

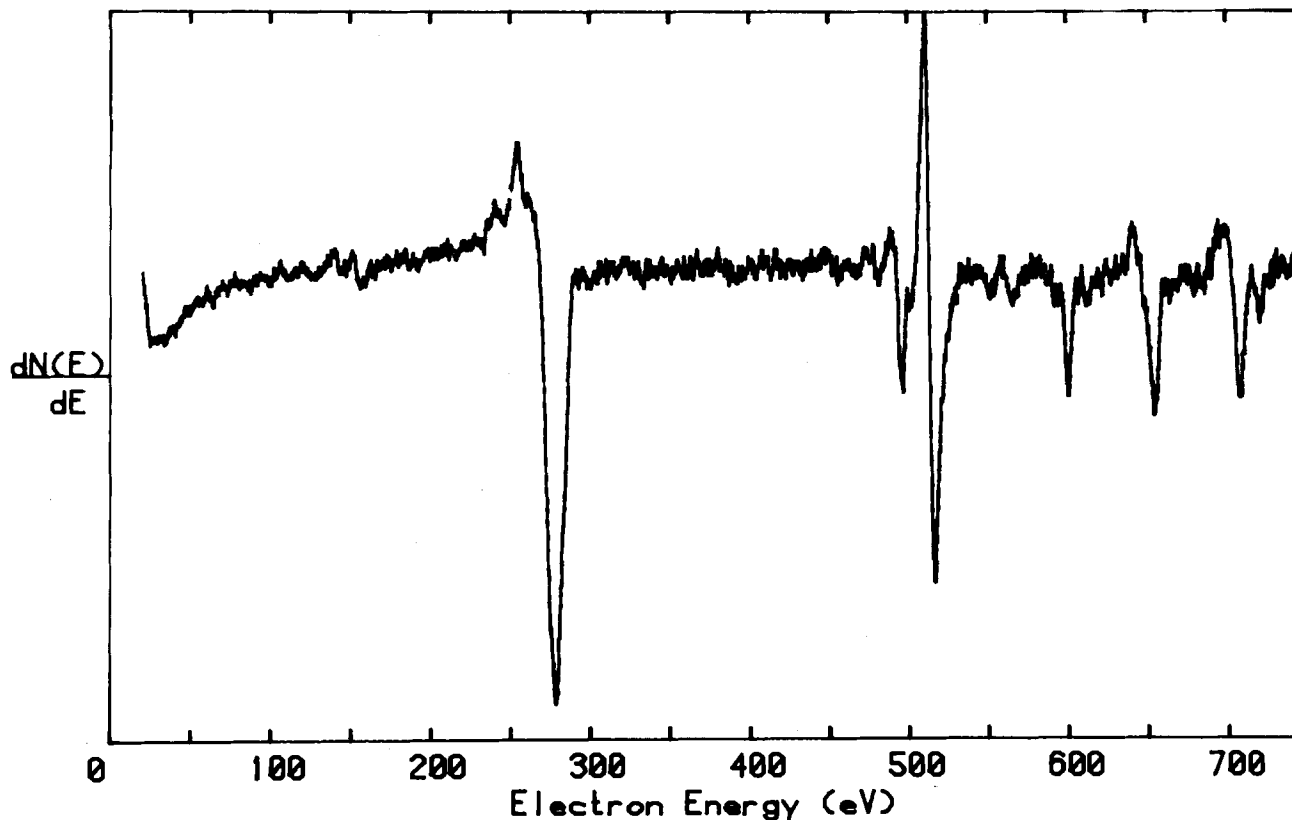


Fig. 1. Auger electron spectrum of surface of high purity, zone-refined iron strip after 20 yr exposure to air at room temperature

Experimental

The preparation and typical analyses of the zone-refined iron are given in Ref. (11). The procedure used to roll the iron ingots is not known. However, the strips, which were not handled during the intervening 20 years, are shiny and free from any lubricant, rolling oil, or inhibitor, as evidenced by Auger electron analysis (see below).

The iron strips were introduced into the vacuum system of the Auger electron spectrometer without any cleaning or unnecessary handling. Surface analysis was performed with a Physical Electronics Industries Thin Film Analyzer system (TFA) using a single-pass cylindrical mirror analyzer. Spectra were recorded in the derivative mode. Operating conditions were 5 kV electron gun voltage, 10 μ A beam current, and 3 eV modulation amplitude. The spectral data were digitized with a TransEra 752 A/D converter that was the interface between a Tektronix 4052 microcomputer and the TFA. Depth profiles were obtained by argon ion sputter etching with a Perkin Elmer no. 04-303 differential ion gun. The ion gun voltage was 3 kV, and the beam was rastered over a 4 \times 4 mm area.

Results

The initial spectrum, before any sputtering, is shown in Fig. 1. The iron peaks between 550 and 720 eV are clearly visible, while the low energy peak at about 50 eV is barely visible above the noise. The oxygen peak is at 510 eV. All the peaks have been attenuated by a layer of adsorbed "dirt" from the atmosphere, as evidenced by the large carbon peak at 270 eV. Since all the iron peaks, including the one at low energy, are visible, the layer is probably no thicker than 1-2 nm, which indicates that no lubricant or rolling oil is present on the surface. The absence of a corrosion inhibitor is evidenced by the fact that the only extraneous peak in the spectrum is that from carbon. Most organic inhibitors contain nitrogen, whose peak at 380 eV is not evident. The most likely inorganic inhibitors are chromates and phosphates, and neither chromium nor phosphorus appears in the spectrum.

Sputter profiles through the 20 year oxide are shown in Fig. 2 for two strips. The initial rise in the oxygen signal,

I_{0s} , results from the sputter removal of the adsorbed carbonaceous layer. The carbon signal decreases rapidly as the oxygen signal increases.

To calibrate the sputter rate, a clean, sputtered area was exposed to air for 24h, after which a depth profile was obtained (Fig. 2). Since the thickness of a film grown for 24h in air or in O_2 containing a trace of water vapor is about 2 nm (4, 8) and the time to sputter through the film is 25s, the sputter rate is about 0.08 nm/s. The two 20 year oxide films, therefore, appear to be about 7-8 and 9-10 nm thick.

The apparent difference in film thickness between the two specimens is attributed to the thicker carbonaceous layer on c, as evidenced by the longer time needed to remove it, i.e., to reach the maximum in the curve. If the effect of this layer can be subtracted out, curves b and c should be the same, and the oxide thickness would be significantly less than the apparent thickness of 7-10 nm. The true thickness may be estimated as follows. We as-

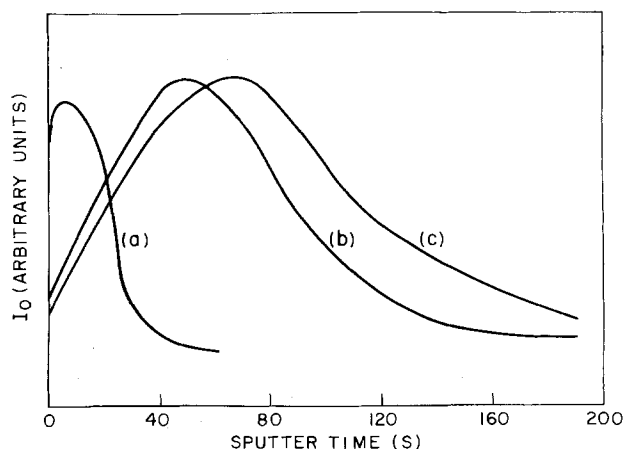


Fig. 2. Sputter depth profiles (intensity of O 510 eV peak vs. sputter time) of oxide film on high purity, zone-refined iron. Curve a: After 24h exposure to air at room temperature. Curves b and c: After 20 year exposure to air at room temperature.

sume that the sputter time to reach the maximum of each curve in Fig. 2 is the time needed to remove the carbonaceous layer. Subtracting this time from the total time to sputter through the layers gives the time to sputter through the oxide. The oxide sputter rate calculated from the specimen exposed to air for 24h is 0.1 nm/s after this correction. Making the correction for the two 20 year specimens and using the corrected sputter rate, the films on these specimens are estimated to be about 5-6 nm thick.

Discussion

The results show that high purity iron is passivated by oxidation in air at or near room temperature and that it can maintain its passivity for more than 20 years. The thickness of the passivating film formed in 20 years (5-6 nm) is only two or three times that formed in 24h. Rusting or the formation of thicker films at long times (4, 10), as well as the tarnishing observed on bits of the iron used in the present study, is most likely caused by contamination from the atmosphere or from handling.

To determine whether the observed 20 year air oxidation of iron is consistent with short-term measurements, we sought studies in the literature that gave well-defined rate laws or sufficient tabulated data to allow extrapolation to 20 years. The data of Kruger and Yolken for the gaseous oxidation of iron yield the rate law (8)

$$d = 0.13 \ln t + C \quad [1]$$

in which d is the oxide film thickness in nanometers, t is the time, and C is a constant. The data of Sato and Cohen for the anodic oxidation of iron in pH 8.43 borate buffer yield the rate law (12)

$$i_t = k' \exp(\beta E - Q_T/B) \quad [2]$$

in which i_t is the faradaic current, E is the electrode potential, Q_T is the total faradaic charge accumulated in the oxide, and k' , β , and B are constants at a given temperature.

From the data in Fig. 6 of Ref. (8) for the oxidation of iron in 1 atm of O_2 at 27°C, one obtains $C = 2$ at time $t = 1$ min. Then, from Eq. [1], one calculates that the oxide film should grow to a thickness of 4.1 nm in 20 years.

To calculate the thickness of an anodically grown oxide film after 20 years from Eq. [2], it must be integrated to obtain the charge passed. Assuming that atmospheric exposure is equivalent to anodization at a constant potential E_2

$$\frac{dQ_T}{dt} = i_t = k' \exp(\beta E_2 - Q_T/B) \quad [3]$$

Rearranging

$$\int_{Q_{T,1}}^{Q_T} \exp(Q_T/B) dQ_T = k' \exp(\beta E_2) t \quad [4]$$

in which $Q_{T,1}$ is the initial amount of oxide. It follows that

$$Q_T = Q_{T,1} + B \ln \left[1 + \frac{k'}{B} \exp(\beta E_2 - Q_{T,1}/B) t \right] \quad [5]$$

The oxide film thickness, d , in nanometers, is obtained from Eq. [5], assuming that the film is $\gamma\text{-Fe}_2\text{O}_3$ with a density of 5 g/cm³ (13), by

$$d = 0.566 Q_T \quad [6]$$

when Q is given in millicoulombs per square centimeter. An analysis of the data of Sato and Cohen (12) and of Nagayama and Cohen (13) gives $k' = 17.0 \text{ A/cm}^2$, $B = 0.181 \text{ mC/cm}^2$, and $\beta = 1/2 \text{ F/RT}$ at 25°C. The oxide film thickness is then calculated from Eq. [5] and [6], assuming that $Q_{T,1}$ is 0 and that the potential is maintained at the reversi-

Table I. Calculated thicknesses as a function of time and temperature

Time	Anodic oxide thickness (nm)	
	20°C	25°C
1 min	2.52	2.54
1h	2.92	2.96
1 day	3.23	3.29
10 day	3.45	3.52
100 day	3.67	3.76
1 yr	3.79	3.89
5 yr	3.95	4.06
10 yr	4.02	4.13
20 yr	4.08	4.20
25 yr	4.10	4.22

ble oxygen potential in air, *i.e.*, at +477.1 mV *vs.* SCE at 25°C and at +486.5 mV *vs.* SCE at 20°C. The calculated thicknesses as a function of time and temperature are given in Table I.

The almost identical values calculated from Eq. [1] and from Eq. [5] and [6] for an oxidation time of 20 years are probably fortuitous, since the equations represent different rate laws and oxidation mechanisms (8, 12). However, this does strongly suggest that iron is passivated equivalently by either gaseous or anodic oxidation and that the passivating films prepared in these different manners grow at comparable rates.

The experimentally determined oxide film thickness, without correcting for the thickness of the adsorbed carbonaceous layer, is about twice that calculated from Eq. [1] or from Eq. [5] and [6]. The approximate correction yields an oxide thickness only about 1-2 nm greater than the extrapolated values. Differences between the experimental and calculated values may be attributed to one or more of several factors, including atmospheric impurities, residual surface impurities from rolling and handling, the many changes in relative humidity and temperature experienced by the iron over the 20 year period, and the length of the extrapolation.

Conclusions

The results show that high purity iron is passivated by air oxidation. The long-term stability of the passivating film has been demonstrated. Over a 20 year period, the film grew to a thickness of no more than 5-6 nm, in reasonable agreement with the values calculated by extrapolating short-term gaseous and anodic oxidation data to 20 years. Rusting of high purity iron apparently requires the presence of impurities and/or very high relative humidities or liquid water.

Manuscript submitted Oct. 23, 1984; revised manuscript received Jan. 28, 1985.

AT&T Bell Laboratories assisted in meeting the publication costs of this article.

REFERENCES

1. E. A. Gulbransen, *Trans. Electrochem. Soc.*, **81**, 327 (1942).
2. E. A. Gulbransen, *ibid.*, **82**, 375 (1942).
3. A. B. Winterbottom, *J. Iron Steel Inst.*, **165**, 9 (1950).
4. V. V. Andreeva, *Trudy Inst. Fiz. Khim., Akad. Nauk SSSR, Novye Metody Fiz. Khim. Issledovaniy*, **1957**, (2), 79 (C.A.).
5. P. Hancock and J. E. O. Mayne, *J. Chem. Soc.*, **1958**, 4167.
6. M. W. Roberts, *Trans. Faraday Soc.*, **57**, 99 (1961).
7. P. B. Sewell, C. D. Stockbridge, and M. Cohen, *This Journal*, **108**, 933 (1961).
8. J. Kruger and H. T. Yolken, *Corrosion*, **20**, 29t (1964).
9. M. J. Graham, S. I. Ali, and M. Cohen, *This Journal*, **117**, 513 (1970).
10. S. I. Ali and G. C. Wood, *Br. Corros. J.*, **4**, 133 (1969).
11. B. F. Oliver and F. Garofalo, *Trans. Met. Soc. AIME*, **233**, 1318 (1965).
12. N. Sato and M. Cohen, *This Journal*, **111**, 512 (1964).
13. M. Nagayama and M. Cohen, *ibid.*, **109**, 781 (1962).

Modification of the Electrochemical and Corrosion Behavior of Stainless Steels with an Electroactive Coating

David W. DeBerry*

SumX Corporation, Austin, Texas 78758

ABSTRACT

Electroactive polyaniline coatings have been deposited on ferritic stainless steels. The coatings appear to be deposited over the passive metal oxide film but can undergo electron transfer with the metal. Polyaniline immobilized on the alloys imparts a form of anodic protection which stabilizes the materials in mineral acids. Electrochemical and SEM characterization results are presented, and effects of coating application techniques are discussed. Oscillations in the open-circuit voltage occur in solutions containing a high enough concentration of chloride ion to initiate pitting at potentials dictated by the coating. Inhibition of localized corrosion may also be obtainable for favorable systems.

There has been a great deal of interest for the past few years in electrodes chemically modified with electroactive materials (1-3). Most of these studies have been performed using nominally inert substrate materials such as Pt, Au, SnO₂, and various forms of carbon. Recently, interest has been shown in application of electroactive materials to relatively reactive substrates (4-6). Modification of active substrates appears to offer unique opportunities for investigation of the substrate itself, as well as any intervening "passive" films which may occur between the metal and electroactive material (4). The composite materials may also have practical applications in corrosion prevention. For example, a form of anodic protection may be obtained by coating an active/passive metal with a redox species capable of maintaining the native passive film on the metal.

This paper is concerned with electroactive coatings, which are shown to protect relatively low alloy 400 series stainless steels in corrosive acid media. The preparation techniques important to their effectiveness are discussed along with possible mechanisms for the observed behavior. Polyaniline (PA) was the primary electroactive material used in this study. Its use is advantageous in acidic environments since hydrogen ion is the preferred counterion for maintaining PA electroneutrality during electron transfer. Aqueous solutions of sulfuric acid have been the major corrosive media in this work, but results obtained in chloride-containing dilute acid are also present.

Experimental

Conventional electrochemical equipment was used for electrode modification and characterization. Solutions were prepared from analytical reagent-grade chemicals and type I water obtained from a Milli-Q (Continental Water Systems) water purifier equipped with an Organex cartridge for removal of trace organic compounds. The atmosphere in the airtight glass cells was maintained using either presaturated zero-grade air or prepurified nitrogen. All potentials were recorded and are reported *vs.* saturated calomel electrodes (SCE). Particularly during long-term experiments, the SCE was separated from the main cell solution by two frits, one being a porous Vycor frit. Platinum auxiliary electrodes were used.

Metal specimens were fabricated into 4-6 cm² "flag"-shaped samples with the integral "flagpole" or handle extending out of the solution and used to make electrical connection. This configuration was chosen to minimize anomalous effects at the metal/gas/solution interface without using insulating coatings, which can also cause irreproducible crevice effects, particularly on long exposure to solution. The electroactive coatings were generally applied to a portion of the flagpole as well as the main flag area, and the samples were then inserted in the corrosion test solution with 2-5 mm of the coated part of the pole extending out of solution. Except as noted,

samples were finished to 600 grit SiC on a Buehler polishing table and then degreased with methanol and thoroughly rinsed with water before use. The composition of the metals (obtained from Metal Samples, Incorporated, Munford, Alabama) are given in Table I.

In general, electroactive polyaniline coatings were obtained on the metals of interest by electrochemical treatment in a 1.0M aniline, pH 1.0 perchloric acid solution (7). The coating was usually applied by cycling the working electrode potential between *ca.* -0.2 and +1.1V at a scan rate of 50 mV/s. Detailed descriptions of the deposition variables and results are given in the next section.

The quantity of charge in the electrode coating was obtained by integration of the appropriate portion of the linear scan or cyclic voltammogram. Slow (0.5 mV/s) linear potential scans were used for determining the corrosion properties of the bare metals in the various environments, particularly the chloride containing solutions. These runs were generally done in deaerated solution with a 1h immersion of the sample prior to starting the scan. No solution agitation was used in the electrochemical treatments or tests unless otherwise specified.

Samples were routinely inspected with a stereomicroscope up to a magnification of 45 times. The scanning electron microscope work was done with a JEOL-JSM 35C operated at 25 kV and equipped with a KEVX elemental detection system.

Results and Discussion

Deposition and characterization of PA films.—Electroactive polyaniline coatings were obtained on types 410 (11.6% Cr) and 430 (16.2% Cr) stainless steels (SS) by electrochemical treatment in a 1.0M aniline, pH 1.0 perchloric acid solution. Typical voltammograms observed during cycling of type 430 SS in the deposition solution are shown in Fig. 1. If the electrode is allowed to become active in the pH 1.0 deposition solution, an active-to-passive current peak is observed at about -0.27V on the first anodic scan from open circuit. Note that this peak is not observed again on repeated scanning through the same potential region. The current decreases rather slowly past this peak on the first scan, with some indication of a postpassivation maximum at +0.12V, until a sharp increase begins at *ca.* +1.0V, signaling the start of polyaniline deposition. The anodic current on the second scan is much lower than the first until +1.0V is reached once again and more PA is deposited. The cathodic current does not show a clear increase until the third cycle. On the fifth cycle, the oxidation peak for deposited polyaniline at +0.12V starts to become significant, and it ultimately becomes the dominant peak. Also on the fifth cycle, three separate oxidation and three corresponding reduction peaks become discernable. These peaks then increase rather uniformly with continued cycling as more PA is deposited.

The effect of this treatment is the apparent buildup of PA film which increases in thickness with each cycle.

*Electrochemical Society Active Member.

Table I. Nominal compositions of metals

Metal	Fe	Cr	Ni	C	Mo	Composition (w/o)						
						Mn	S	Si	P	Cu	N	Other
Type 410 SS	Bal.	11.62	0.19	0.122	0.06	0.54	0.002	0.50	—	—	0.048	0.005 Sn
Type 430 SS	Bal.	16.20	0.41	0.05	0.08	0.50	<0.01	0.46	0.02	0.09	—	—

Following the initial passivation peak, the deposition behavior on the active/passive alloys studied is similar to that for deposition of polyaniline on platinum or other "inert" metals (7-9). The redox reactions occurring in polyaniline on cycling are most likely quite complex. The results obtained on the first few scans seem to indicate that a passive metal oxide film is formed first on the stainless steel surface, with deposition of polyaniline occurring on top of it. Even a small amount of polyaniline appears to stabilize the passive film to some degree against dissolution and/or reduction. Once the surface is passivated and the initial layer of polyaniline is deposited, the cyclic voltammetric response is quite similar to an inert metal. However, the actual situation may be more complicated than indicated by these experiments, and the possibility of polyaniline being incorporated into the metal oxide passive film when initially formed cannot be ruled out.

The initial peak passivation current in the PA deposition solution is higher for type 410 stainless steel than for type 430. Following this, the major part of the scan response for PA deposition on type 410 is very similar to that for type 430.

The reversible electroactivity of the PA-coated stainless steel electrodes is demonstrated by cyclic voltammetric results in sulfuric acid solutions free of added redox couples. A typical response is shown in Fig. 2 for a PA-coated type 410 specimen in 0.2M H₂SO₄. This electrode had been exposed to this solution for 19h on open circuit and was still passive at the time it was potentiostatically reduced then cycled once before recording the cycle shown. A similar response is observed for PA-coated type 430 electrodes, and for both materials in 1.0M H₂SO₄. The cyclic voltammetric results show little change with time of exposure on open circuit, but do change somewhat with repeated cycling. The responses observed are quite similar to those seen for platinum coated with PA. This is noteworthy in view of the likelihood that electron transfer between the stainless steel metal phase and polyaniline is being mediated by a metal oxide passive film (4). This

facile electron-transfer exchange with the metal may be partially responsible for the ability of polyaniline to maintain the passivity of the specimen. It is quite likely that a high repassivation rate is important in "healing" the cracks and ruptures (which continually occur in the passive film) before the damage spreads and the metal becomes active.

Scanning electron microscope (SEM) examination of polyaniline-modified type 410 SS was done to further characterize the material. Typical photomicrographs for samples with no conductive overcoat are shown in Fig. 3a and 3b. As observed for PA on Pt, the coating is continuous and fairly smooth (7), although a number of small nodules can be observed extending out of the surface. A 400Å gold overcoat and somewhat higher magnification reveals more of the porous structure of the film, as shown in Fig. 4a. Both samples which had received a final cycle in sulfuric acid and those which had not were examined. They had practically the same appearance except at the highest magnification, where the cycled sample appeared somewhat "sharper" than the sample which had not been cycled. One edge of the electrode was abraded and then examined, as shown in Fig. 4b. Starting from the metal on the left-hand side of the photograph, the base of the polyaniline appears practically continuous, but then a layered structure becomes apparent, which is topped by the nodular growth. Although speculative, it seems possible that the layers are a result of the cyclic deposition procedure. From this photograph the polyaniline film appears to be about 3-4 μm thick, exclusive of the nodules. The nodules may be a residue from the nonadherent, inactive material described below. Many dark patchy areas can often be observed optically in ordinary light on the polyaniline surface, but these were not differentiated in the SEM photographs. These areas may be locally thicker than the rest of the film, or belong to portions of the film trapped in a higher oxidation state.

Effect of PA film on corrosion in chloride-free solutions.—Weight-loss corrosion measurements for bare type 410 flag samples showed an average equivalent penetration rate of $3.1 \times 10^4 \mu\text{m/yr}$ for a 64h exposure in 1.0M

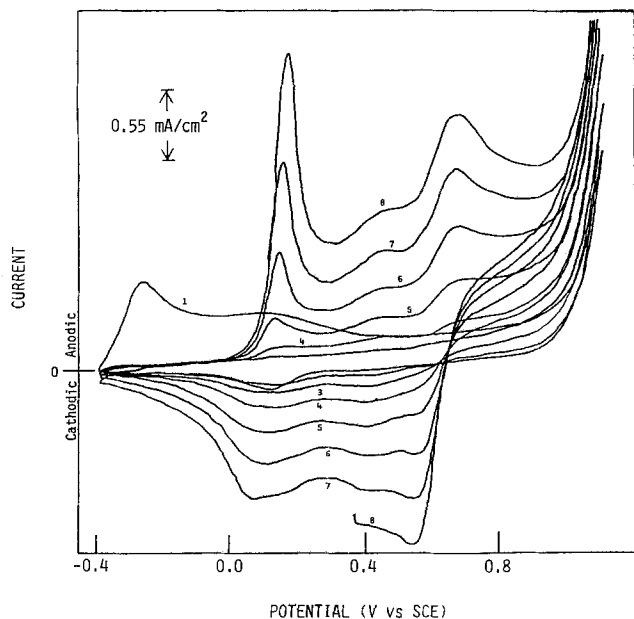


Fig. 1. Cyclic voltammograms at 50 mV/s for deposition of polyaniline on type 430 stainless steel from 1.0M aniline, pH 1.0 perchlorate solution.

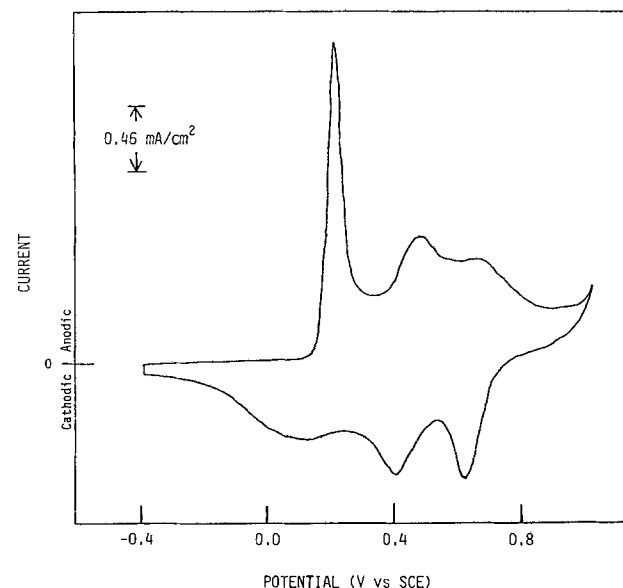


Fig. 2. Cyclic voltammogram at 20 mV/s for polyaniline-coated type 410 SS in 0.2M H₂SO₄ after 19h exposure.

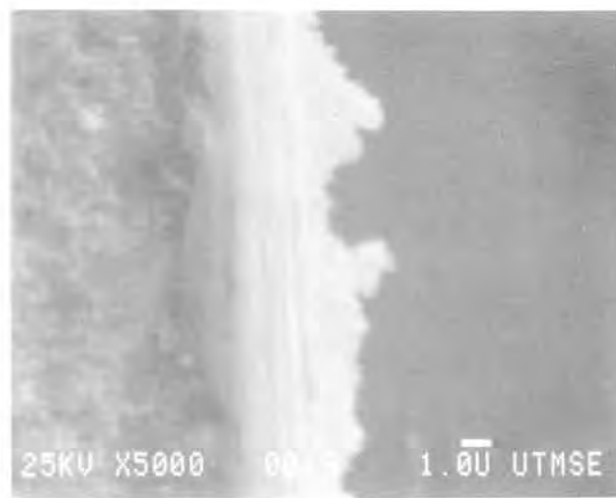
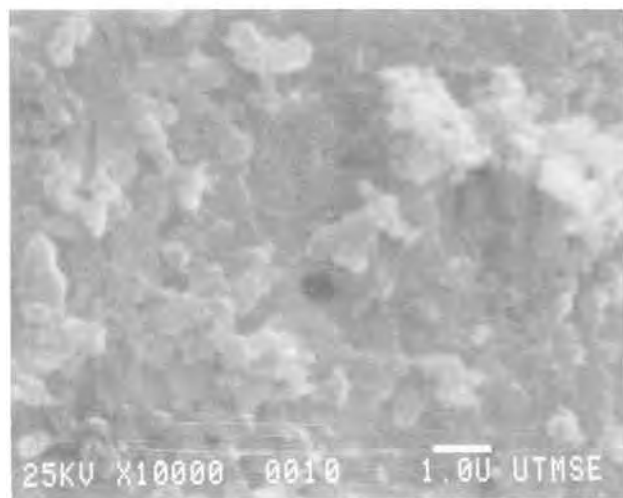
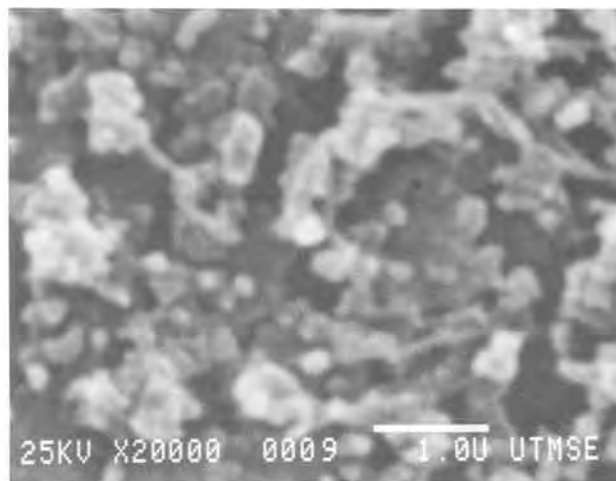
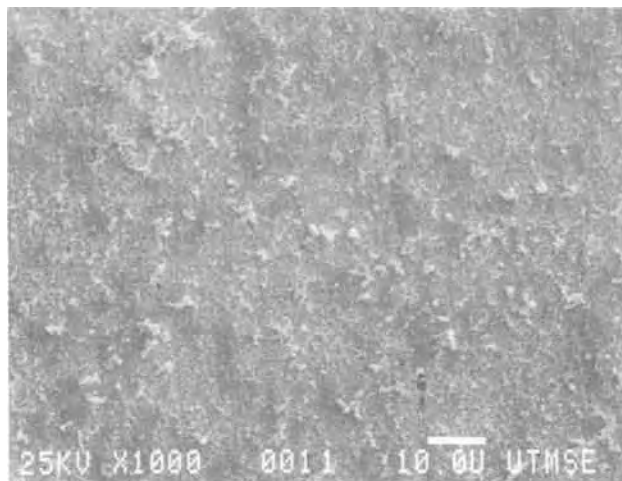


Fig. 3. SEM photographs for polyaniline-coated type 410 SS. a (top): 1000 times magnification 1000. b (bottom): 10,000 times magnification.

Fig. 4. SEM photographs for polyaniline-coated type 410 SS. a (top): After application of 400Å gold overcoat; 20,000 times. b (bottom): Edge view; 5000×.

H_2SO_4 at 25°C. This rate corresponds to the active corrosion state at ca. -0.5V . Similar weight-loss measurements for PA-coated type 410 in the same environment showed rates of less than $25\ \mu\text{m}/\text{yr}$ as long as the coating maintained the open-circuit voltage more positive than ca. $+0.0\ \text{V}$. Therefore, the open-circuit voltage measurement provides an adequate measure of the corrosion rate in this system. Continuous open-circuit voltage monitoring was accompanied by post-test sample examination for judging the effectiveness of a given coating technique.

Visual examination of the PA-coated samples *in situ* provides information on their corrosion status. Samples are ordinarily removed from the deposition bath in their most oxidized state and are then dark blue/black in color. Some extraneous loosely adherent black material is generally present on the electrode and is removed by a stream of wash water. Tests show that this material does not contribute to the electroactivity of the electrode. On placing in the acidic corrosion test solution, the OCV generally decreases fairly rapidly from about $+0.6\text{V}$. This is accompanied by a change in color to a dark green. On further exposure, a lighter, more metallic appearing green color is seen at a potential of ca. $+0.2\text{V}$, and this is usually the most stable state of the electrode. If the electrode begins to fail, this color becomes a lighter green, and finally becomes transparent in the fully reduced state and the electrode becomes active. The coating will persist on the electrode for some time after that, but extended exposure in the active state leads to disbonding, probably because of undermining of the coating by vigorous hydrogen evolution.

Bare or anodically passivated type 410 or 430 stainless steel specimens become active within minutes of being placed on open circuit in either of the dilute sulfuric acid solutions employed. Polyaniline-coated type 410 or 430 samples remained passive from several hours to at least 1200h after immersion. The breakdown time (time of exposure before passive-to-active transition occurs on open circuit) appears to be a function of metal pretreatment and coating application techniques, acid concentration in the corrosion medium, metal substrate properties, and solution aeration. Postapplication treatment affects the protectiveness of the film. With no further pretreatment, PA-coated ($28\ \text{mC}/\text{cm}^2$) type 430 stainless steel begins to fail after about 60 min in deaerated $0.2\text{M}\ \text{H}_2\text{SO}_4$. If the same electrode is cycled several times in the sulfuric solution, and then put on open circuit, there is no sign of breakdown after almost 17h.

Application techniques become more critical when $1.0\text{M}\ \text{H}_2\text{SO}_4$ is used at the test solution and the lower alloy type 410 as substrate. Results obtained for three different PA coating procedures are shown in Fig. 5, and the application methods are summarized in the caption. Similar to the type 430 results, cycling PA-coated type 410 in the dilute acid test solution appears to increase stability. Trials with various treatment techniques indicated that the three most important steps are: (i) an initial active-state open-circuit exposure to the PA deposition solution (5 min), (ii) cycling the potential during deposition, and (iii) cycling in sulfuric acid solution (three cycles) following deposition. A type 410 SS electrode treated in this way alone (and initially degreased) was found to be stable in

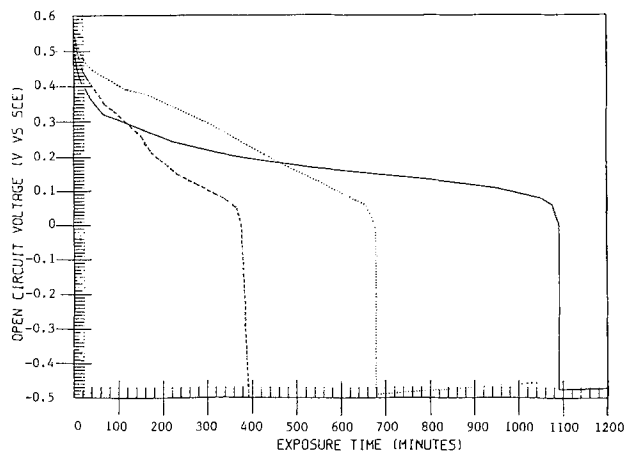


Fig. 5. Open-circuit voltage vs. exposure time in 1.0M H_2SO_4 for polyaniline-coated type 410 SS electrodes prepared in following ways. Dashed line: active for 5 min in PA deposition solution, then cycled seven times and taken out at +0.82V. Dotted line: active for 3 min in PA deposition solution, then passivated and held at +0.96V for 3 min, then cycled six times between -0.2 and 1.15V, then removed at 1.02V. Solid line: etched in 1.0M H_2SO_4 for 8 min, then passivated and cycled in same solution before cycling in PA deposition solution eight times (always positive of 0.0 V) then removed at +0.84V.

aerated 1.0M H_2SO_4 for at least 50 days without breakdown. Part of this exposure run is shown in Fig. 6. The initial cycling in 1.0M H_2SO_4 indicated that the polyaniline on this electrode had a total charge capacity of 25.1 mC/cm². The electroactive form of polyaniline appears to be continuously regenerated by oxygen, producing the observed long term stability.

A quantitative description of the corrosion protection offered by the coatings is difficult due to the interactions of the variables involved and the complexity of the passivation process itself. A major complication is that the properties of the passive film vary with exposure time. In particular, the anodic passive current density is often found to gradually decrease at a given potential in the passive region, presumably due at first to an increase in thickness of the passive metal oxide film and then to repair of defects in its structure. These processes probably explain the increased breakdown time with passivation time recently reported for type 440C SS (10). The second complicating factor is that coating coverage is a somewhat nebulous quantity, difficult to determine experimentally, which may depend on the coating technique in rather subtle ways. Thus the postdeposition cycling in H_2SO_4 solutions which was found to be advantageous for PA-coated electrodes could be explained by a

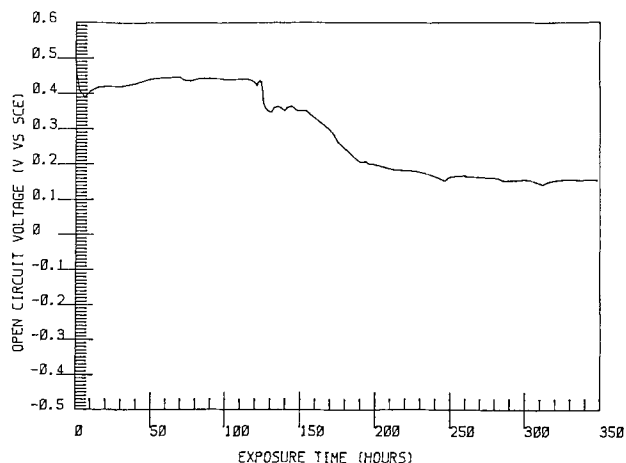


Fig. 6. Open-circuit voltage vs. initial exposure time for polyaniline modified type 410 SS in 1.0M H_2SO_4 . Application method described in text. Note that the time scale is in hours for this run.

restructuring of the film which decreases the effective exposed area.

Polyaniline-modified metals in chloride containing solutions.—Performance of the coated stainless steels in the presence of chloride ion is of interest since it is well known that application of ordinary anodic protection measures to such metals must be done with caution when chloride is present because of the possibility of localized corrosion. Results obtained for the initial part of an exposure of PA-coated 430 to a solution of 0.2M NaCl + 0.2M H_2SO_4 (pH = 0.8) are shown in Fig. 7. The unusual oscillations in the open-circuit voltage continued in a similar manner for over 30h. At this time the solution was changed to 0.2M H_2SO_4 without chloride ion, and the oscillations abruptly ceased. No pits were apparent at up to 45 times magnification on this particular electrode after the run. However, an 18 day exposure of a fresh specimen to the same conditions did result in the formation of about ten small (0.1 mm diam) pits on each side of the electrode. The solution was continuously aerated during this test. Oscillations occurred throughout the test, until the electrode finally became active about 7h before the run was terminated. A weight loss was observed, but, since it was the same as would be expected for the 7h active period, it is quite likely that there was practically no uniform corrosion during the 18 day period preceding breakdown.

These results can be interpreted in part by considering the localized corrosion properties of the bare electrode. A potentiodynamic scan obtained for bare type 430 stainless steel in the same 0.2M NaCl/0.2M H_2SO_4 solution is shown in Fig. 8. It can be seen that the oscillations occur primarily in the potential region between the pit initiation potential (+0.24V) and the so-called protection potential (+0.01V) below which pits are repassivated (11, 12). For the coated electrode, it appears that the passive film is periodically undergoing partial breakdown in the acid chloride solution and is then being reformed with the aid of the polyaniline. The polyaniline is partially reduced during the more negative part of the cycle before the electrode is completely repassivated. This can be observed visually as the electrode becomes clear to pale green. Once the electrode is repassivated, the polyaniline is reoxidized by the oxygen in the system, as evidenced by a return to a green to dark green color and positive open-circuit voltage. However, even though the polyaniline maintains the majority of the surface passive, since the oxidized state of the polyaniline is positive of the pitting potential, pits can be initiated and grow during the positive part of the cycle.

In a somewhat less aggressive environment, polyaniline was able to both maintain a type 430 SS electrode in the passive state and stabilize the open-circuit voltage at a value where pitting did not occur. The test solution contained 0.15M Na_2SO_4 /0.05M H_2SO_4 + 0.1M NaCl (pH = 1.5)

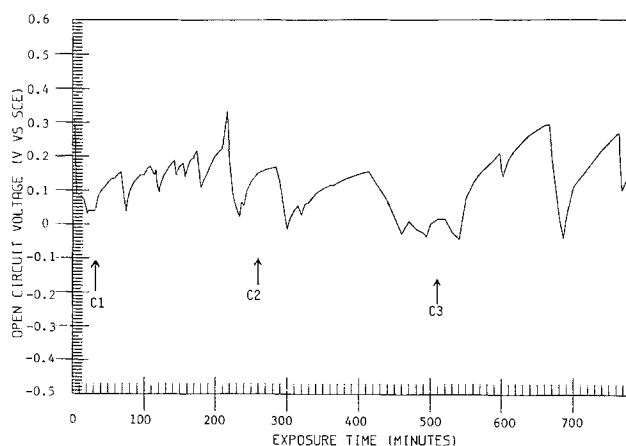


Fig. 7. Initial period of open-circuit exposure for polyaniline modified type 430 SS in 0.2M H_2SO_4 + 0.2M NaCl (initially deaerated); C1, solution aerated; C2, solution deaerated; C3, solution aerated.

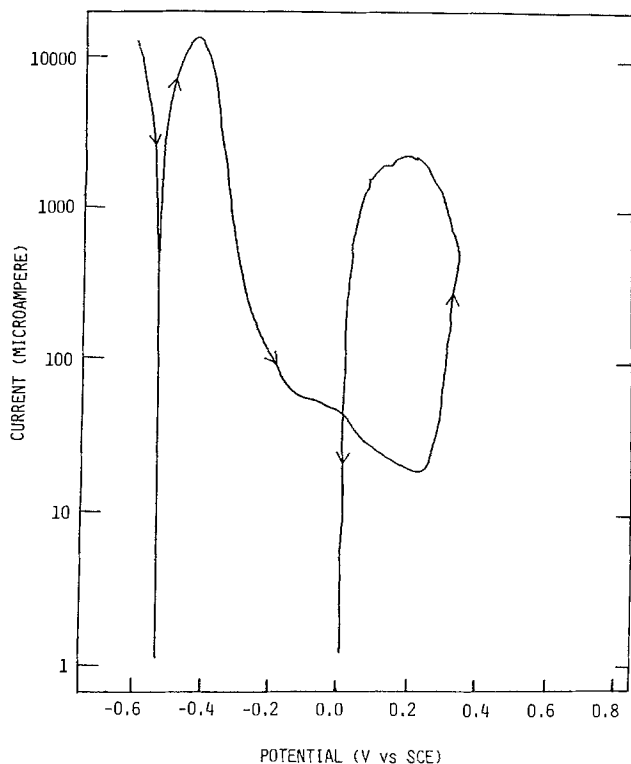


Fig. 8. Potentiodynamic response for type 430 SS in 0.2M H_2SO_4 + 0.2M NaCl at 0.5 mV/s. Electrode area: 3.9 cm^2 .

and was aerated. The pitting potential for a bare type 430 SS sample in this solution is 1.18V. The coating was applied following a 5 min active stand in the polyaniline deposition solution. The electrode was cycled ten times to apply the polyaniline, then removed at a potential of +0.30V, rinsed, and placed in the test solution. No oscillations as such were noted, but the open-circuit voltage did undergo two rather abrupt drops during the first 20h period. After that, the electrode stabilized and the open-circuit voltage remained near +0.14V until the run was terminated after a 30 day exposure. No pits were visible on the electrode at 45 times magnification after the run. The electrode was still quite electroactive at the end of this run, as the remaining charge was 5.9 mC/cm^2 and the cyclic voltammograms were quite similar to those of a freshly immersed sample.

During the run described above, the sample was removed after 310h immersion and a deep scratch was administered with the point of a sharp knife. On reinserting the electrode in the test solution after this scratch, the potential decreased about 15 mV but the remainder of the 30 day run was completed with very little additional decrease. In contrast, a bare type 430 SS electrode was held passive potentiostatically in a similar test solution for 9 days to obtain a passive film stable enough to maintain open-circuit passivity for 2 days. It was then removed and scratched in the same fashion as the PA-coated sample. This specimen became active immediately upon re-immersion in the test solution. These results emphasize

the effect of the electroactive coating as far as preventing the breakdown of passivity and acting as an active adjunct to the passive oxide film.

Conclusions

Stainless steel electrodes coated with thin films of polyaniline remain passive for long periods of time in acid solutions in which they are normally active and subject to high rates of corrosion. The polyaniline-modified steels assume many of the electrochemical characteristics of inert metals coated with polyaniline. The stability of the coated materials is strongly dependent on the treatment method, but scratching has little effect once a favorable coating is deposited. Initiation of pitting of the coated substrate materials in chloride solutions is predictable from the pitting characteristics of the uncoated metal. Pronounced oscillations of the open-circuit voltage of the modified electrode are noted in solutions in which pitting can occur.

Acknowledgments

This work was supported in part by the Naval Air Systems Command. Dr. Al Viehbeck offered valuable consultations, and Mr. Dean Meldrum assisted with the experimental work. Dr. Michael Schmerling of The University of Texas at Austin performed the SEM work.

Manuscript submitted Aug. 13, 1984; revised manuscript received Jan. 15, 1985.

SumX Corporation assisted in meeting the publication costs of this article.

REFERENCES

1. R. W. Murray, *Acc. Chem. Res.*, **13**, 135 (1980); P. G. Pickup, K. M. Kuo, and R. W. Murray, *This Journal*, **130**, 2205 (1983); J. B. Kerr, L. L. Miller, and M. R. Van DeMark, *J. Am. Chem. Soc.*, **102**, 3383 (1980).
2. H. S. White, J. Leedy, and J. J. Bard, *ibid.*, **104**, 4811, 1982; F. C. Anson, T. Ohsaka, and J. M. Saveant, *ibid.*, **105**, 4883 (1983).
3. K. M. O'Connell, E. Waldner, L. Roullier, and E. Laviron, *J. Electroanal. Chem.*, **162**, 77 (1984); G. C. Calabrese, R. M. Buchanan, and M. S. Wrighton, *J. Am. Chem. Soc.*, **105**, 5594 (1983).
4. D. W. DeBerry and A. Viehbeck, in "Fundamental Aspects of Corrosion Protection by Surface Modification," E. McCafferty, C. R. Clayton, and J. Oudar, Editors, p. 308, The Electrochemical Society Softbound Proceedings Series, Pennington, NJ (1984).
5. A. B. Bocarsly and S. Sinha, *J. Electroanal. Chem.*, **137**, 157 (1982).
6. S. Sinha, B. D. Humphrey, and A. B. Bocarsly, *Inorg. Chem.*, **23**, 203 (1984).
7. A. F. Diaz and J. A. Logan, *J. Electroanal. Chem.*, **111**, 111 (1980).
8. R. Noufi, A. J. Nozik, J. White, and L. F. Warren, in "Photoelectrochemistry: Fundamental Processes and Measurement Techniques," W. L. Wallace, A. J. Nozik, S. K. Deb, and R. H. Wilson, Editors, p. 266, The Electrochemical Society Softbound Proceedings Series, Pennington, NJ (1982).
9. T. Ohsaka, Y. Ohnuki, N. Oyama, G. Katagiri, and K. Kamisako, *J. Electroanal. Chem.*, **161**, 399 (1984).
10. T. L. Walzak and J. S. Sheasby, *Corrosion*, **39**, 502 (1983).
11. Y. M. Kolotyrkin, *ibid.*, **19**, 261 (1963); H. P. Leckie and H. H. Uhlig, *This Journal*, **113**, 1262 (1966).
12. M. Janik-Czachor, *ibid.*, **128**, 513C (1981); B. C. Syrett, *Corrosion*, **33**, 221 (1977).

The Critical Geometry for Initiation of Crevice Corrosion

Richard Alkire,* Thor Tomasson, and Kurt Hebert

Department of Chemical Engineering, University of Illinois, Urbana, Illinois 61801

ABSTRACT

The critical crevice dimensions for which initiation of crevice corrosion occurs spontaneously was determined experimentally for Al in 0.05M NaCl. An artificial crevice at room temperature and pressure was employed to permit controlled variation of the crevice length and crevice gap over the ranges 5-15 and 0.1-0.6 mm, respectively. The range of conditions which led to corrosion initiation was compared with theoretical predictions based on a mathematical model of the concentration and the potential distribution within the crevice. It was found that the critical condition for initiation of crevice corrosion could be predicted in this system.

The onset of crevice corrosion occurs when the metal oxide film protecting the metal from general corrosion breaks down as a result of transport restrictions between the crevice and the external solution. These restrictions lead to concentration of aggressive species within the crevice, to eventual breakdown of protective surface films, and to accelerated rates of corrosion attack. Once crevice corrosion has initiated, it is often difficult to stop.

Because crevices are invariably present in engineering structures, it is of interest to develop the ability to predict which geometries will, or will not, lead to crevice corrosion. The purpose of this investigation was to determine by both experimental and theoretical methods the critical crevice geometry which separates the regions between those where crevice corrosion initiates and those where corrosion initiation does not occur (1).

The study of crevice corrosion is commonly divided into two main areas, the preinitiation period prior to breakdown, and the postinitiation period when accelerated attack occurs. During the preinitiation period, the metal surface is passive and corrodes at the low rates associated with such conditions. Owing to transport restrictions, the products of the corrosion process accumulate and cause modification of the crevice solution composition in comparison to that external to the crevice. These changes may include depletion of oxygen, lowering of pH, buildup by migration of species such as chloride ions, and accumulation of dissolved metal species. If these changes cause any of these components to exceed some critical condition, then the passive metal oxide may be caused to break down, leading to rapid dissolution of the unprotected metal. In general, the detailed mechanism of breakdown remains unknown for most structural alloys.

Because the behavior of structural alloys is complex, fundamental studies have emphasized use of model systems which consist of pure metals and simple electrolytes. Thus, Siitari and Alkire (2, 3) investigated crevice corrosion of pure Al in 0.05M NaCl. By assuming tentatively that breakdown occurred as a result of acidification in the crevice, they developed theoretical calculations which, when compared with experimental data, gave agreement with some but not all observations. They emphasized that their theoretical model was highly sensitive to the events associated with breakdown.

Hebert and Alkire (4, 5), therefore, investigated in further detail the three mechanisms commonly accepted as causes of breakdown of passivity: differential aeration, localized acidification, and accumulation of chloride ions. They found that none of these was operative in the model Al system. Rather, accumulation of dissolved aluminum species within the crevice to above a critical value was operative. This conclusion is supported by the recent work of Foley *et al.* (6) which indicated that the weight loss of Al in AlCl₃ solutions was substantially higher than that in NaCl solutions.

While the classic studies of Rosenfeld (7, 8) were influential, more recent studies have emphasized more quantitative treatment of both experimental and theoretical aspects. Artificial crevice assemblies have been

widely exploited (8-15) since these offer controlled and reproducible geometries from which local samples of solution composition may be obtained. Theoretical analysis of alloy systems is complicated by uncertainty about the dissolution kinetics involved as well as by complex multi-component transport processes in the solution phase. Thus, Oldfield and Sutton (13) adopted semiempirical methods for estimating transport processes, while Turnbull (14) emphasized the limiting approximation of differential aeration as well as the steady-state active condition (15). These analyses represent substantial contributions which provide benchmarks for advanced theoretical developments.

From a practical point of view, it is straightforward to distinguish between a crevice which breaks down and corrodes and a crevice which does not. In this investigation, theoretical and experimental methods are directed toward identifying the critical zone between these two types of behavior based on the model system of Al in 0.05M NaCl.

Experimental

The equipment used in this study was described previously by Siitari (2) and Hebert (4) and is only summarized briefly here. A sectioned flat aluminum electrode surface was prepared by machining a set of concentric cylinders from an Al rod (99.9%, 4.45 cm diam, Research Organic/Inorganic) and assembling them with epoxy resin as illustrated in Fig. 1. There are eight sections numbered sequentially from the innermost, no. 1, to the outermost,

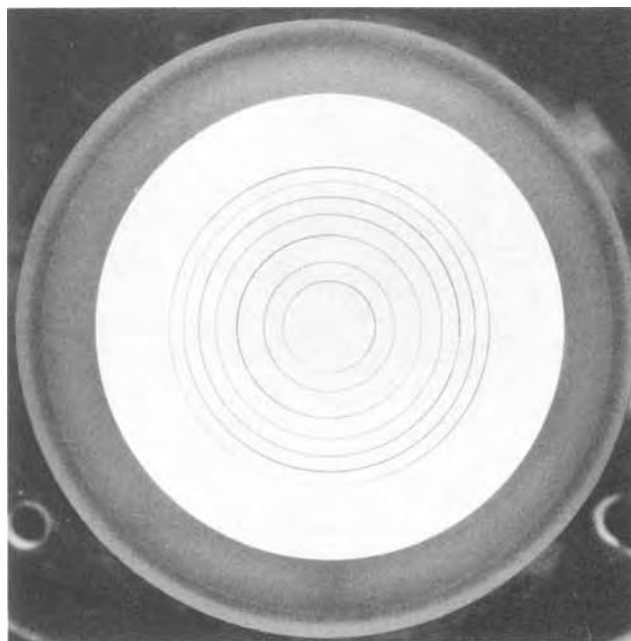


Fig. 1. Sectioned electrode, showing concentric sections separated by insulating rings. Diameters of the sections are: 7.19, 10.2, 14.4, 17.7, 20.4, 22.9, 25.1, and 41.9.

*Electrochemical Society Active Member.



Fig. 2. Experimental crevice corrosion cell described in detail in Ref. (2).

no. 8. Electrical connections were made to each section on the back side. The electrode was mounted in the corrosion cell, illustrated in Fig. 2, in which optically flat quartz disk could be positioned precisely to form a crevice of a preset geometry. The quartz disk shielded only the inner sections of the Al electrode; the outer sections became cathodes during crevice corrosion. As the corrosion proceeded, electrical currents between the sections were measured with a multichannel zero-resistance operational amplifier circuit (based on Analog Devices amplifiers no. 233 K). The output from the current followers was recorded on strip chart recorders.

The 0.05M NaCl solution was prepared by combining analytical reagent-grade NaCl with deionized distilled water. The metal surface was prepared by wet sanding to 600 grade silicon carbide on a flat granite block (DO-ALL Rockford Company, no. 501045967), and then polishing with an 0.3 μm alumina suspension (Buehler, Alpha Polishing Alumina).

The corrosion experiments were conducted by first pouring approximately 80 ml of electrolyte into the cell while the quartz disk was in a raised position. After about 20 min, the quartz disk was lowered to its preset position, thus creating the crevice.

Theoretical

Since the present investigation was based upon the theoretical model of Hebert and Alkire (5), the interested reader is advised to consult that reference for background to the following discussion.

The sequence of events leading to initiation of crevice corrosion begins with the formation of the crevice, which is shown schematically in Fig. 3. Prior to the formation of the crevice, the Al surface corrodes uniformly at a low rate associated with passivity; the corresponding cathodic reactions are oxygen reduction and/or hydrogen evolution. Once the crevice is formed, these corrosion processes continue except that transport restrictions within the crevice set in to an extent determined by the crevice geometry. Thus, deaeration occurs, the pH and chloride concentration become altered from the bulk values, and the concentration of dissolved Al builds up. Eventually, if the Al concentration exceeds the critical level of concentration needed for activation, breakdown occurs and crevice corrosion initiates.

In modeling the foregoing sequence of events, Hebert and Alkire used a one-dimensional transport analysis of the crevice region based upon dilute solution theory. They further assumed that the dissolved aluminum ions

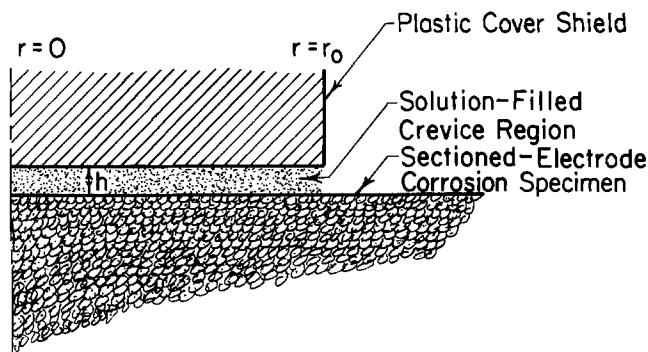


Fig. 3. Schematic of model system showing geometry and coordinate system.

underwent hydrolysis to the first step only, and that the breakdown of the Al passivity led to a step change in the dissolution kinetics.

In predicting the critical crevice geometry for initiation, it is important to realize that it is only the steady-state transport problem that is significant. That is, the critical geometry corresponds to that geometry for which the maximum value of the total concentration of dissolved aluminum in the crevice solution, at steady state, equals the critical value. Thus, the transient part of the analysis of Hebert and Alkire was not included in the treatment which follows. Moreover, these authors also showed that the crevice became deaerated well before attaining the critical condition for initiation. That is, any effect that oxygen has would run its course long before initiation occurs; it is thus appropriate to neglect the presence of oxygen when evaluating the steady state. Also, they showed that both migration of chloride ions and reaction of hydrogen ions within the crevice play a minor role in the initiation phenomenon on Al. For these reasons, the analysis of Hebert and Alkire can be substantially simplified when used to predict the critical geometric conditions for initiation.

In the steady state, the concentration of dissolved aluminum species builds up owing to metal dissolution at the wall, and dissipates by diffusion along the crevice, so that the one-dimensional species balance is

$$D \left(\frac{d^2c}{dr^2} + \frac{1}{r} \frac{dc}{dr} \right) + \frac{\nu}{nFh} j = 0 \quad [1]$$

The dissolution rate of aluminum in the passive state j is assumed to have the linear form

$$j = \begin{cases} A(\phi - \phi_{R1}); & \phi \geq \phi_{R1} \\ 0 & ; \phi < \phi_{R1} \end{cases} \quad [2]$$

where ϕ_{R1} is the pitting potential, and the parameter A is

Table I. Summary of experiments

Run no.	Crevice radius (mm)	Crevice height (mm)	Breakdown time (h)	Comment
33	6.35	0.10	2-3	
34	6.35	0.16	4	
37	6.35	0.17	5	
48	6.35	0.19	6	
40	6.35	0.20	8	
38	6.35	0.22		No rise in current
35	6.35	0.30		No rise in current
25	9.52	0.22	4-5	
50	9.52	0.30	5-6	
24	9.52	0.36		Gradual rise in current
44	9.52	0.40		No rise in current
23	9.52	0.50		No rise in current
21	11.11	0.10	3-4	
22	11.11	0.30	4-5	
46	11.11	0.40		Gradual rise in current
43	11.11	0.50		No rise in current
26	12.70	0.4	6-7	
28	12.70	0.6		No rise in current
27	12.70	0.7		No rise in current

found from experimental polarization curves. The current flowing through the solution between the interior anode and the exterior cathode, obeys Ohm's law

$$i = -\kappa \frac{d\phi}{dr} \quad [3]$$

and the one-dimensional conservation of charge

$$\frac{1}{r} \frac{d}{dr} (ri) = -\frac{1}{h} j \quad [4]$$

so that the potential distribution within the crevice is

$$\frac{d^2\phi}{dr^2} + \frac{1}{r} \frac{d\phi}{dr} = \frac{1}{\kappa h} j \quad [5]$$

Equations [1], [2], and [5] constitute the steady-state model equations to be solved subject to boundary conditions. At the center of the cylindrical crevice, the potential and concentration fields are symmetric

$$\left. \begin{array}{l} \frac{d\phi}{dr} = 0 \\ \frac{dc}{dr} = 0 \end{array} \right\} \text{ at } r = 0 \quad [6]$$

and at the edge of the crevice, adjacent to the bulk solution, the concentration and the potential have values which are characteristic of the bulk solution outside the crevice

$$\left. \begin{array}{l} \phi = \phi_0 \\ c = c_0 \end{array} \right\} \text{ at } r = r_0 \quad [7]$$

The bulk potential ϕ_0 corresponds to the mixed potential of aluminum in the passive state, while the bulk concentration of Al species would be obtained from the equilibrium solubility product.

The foregoing equations are made dimensionless by introducing the following variables

$$\Phi = \frac{\phi - \phi_{li}}{\phi_0 - \phi_{li}} \quad C = \frac{c - c_0}{c_0} \quad R = \frac{r}{r_0} \quad [8]$$

Upon elimination of the local reaction rate j , the dimensionless model equations become

$$\frac{d^2\Phi}{dR^2} + \frac{1}{R} \frac{d\Phi}{dR} - \sigma_1\Phi = 0 \quad [9]$$

$$\frac{d^2C}{dR^2} + \frac{1}{R} \frac{dC}{dR} + \sigma_2\Phi = 0 \quad [10]$$

where

$$\sigma_1 = \frac{r_0^2 A}{\kappa h} \quad [11]$$

$$\sigma_2 = \frac{\nu A r_0^2}{n F h c_0 D} (\phi_0 - \phi_{li}) \quad [12]$$

The parameter σ_1 contains the ratio A/k and thereby denotes the ratio of the electrolyte solution resistance along the crevice to the charge transfer resistance associated with the anodic dissolution process. A value of σ_1 greater than unity would indicate that the electrolyte resistance is the dominant factor, so that anodic dissolution would tend to occur near the outer edge of the crevice. The parameter σ_1 is analogous to the polarization parameter or the Wagner number, which appears in electrochemical engineering analyses of current and potential distribution phenomena.

The parameter σ_2 contains the ratio A/D and thereby denotes the relative importance of the diffusion resistance along the crevice and the charge transfer resistance associated with the anodic dissolution process. A value of σ_2 greater than unity would indicate that diffusion resistance dominates so that substantial buildup of dissolution products would be expected to occur within the crevice.

The solution of Eq. [9] is

$$\Phi = \frac{I_0(\sigma_1^{1/2} R)}{I_0(\sigma_1^{1/2})} \quad [13]$$

where I_0 is a modified Bessel function of the first kind of order zero. By substituting Eq. [13] into Eq. [10] and integrating, one finds

$$C = \frac{\sigma_2}{\sigma_1} \left[1 - \frac{I_0(R\sigma_1^{1/2})}{I_0(\sigma_1^{1/2})} \right] \quad [14]$$

To obtain the maximum value of concentration, this expression is differentiated with respect to distance and set equal to zero

$$\frac{dC}{dR} = -\frac{\sigma_2}{\sigma_1^{1/2}} \frac{I_1(R\sigma_1^{1/2})}{I_0(\sigma_1^{1/2})} = 0 \quad [15]$$

Since I_1 has no real zeroes except at $R = 0$, the maximum steady-state concentration always occurs at the center of the crevice; by setting the maximum concentration equal to the critical concentration required for crevice initiation, one has

$$C_{cr} = \frac{\sigma_2}{\sigma_1} \left[1 - \frac{1}{I_0(\sigma_1^{1/2})} \right] \quad [16]$$

which may be rearranged to the form

$$I_0(\sigma_1^{1/2}) = \frac{1}{1 - \frac{\sigma_1}{\sigma_2} C_{cr}} \quad [17]$$

The right-hand side of Eq. [17] is independent of geometry, and contains only parameters which can be found by experimental measurement. The left-hand side of Eq. [17] contains a function of σ_1 in which the ratio r^2/h appears for the critical conditions associated with crevice corrosion initiation.

Results and Discussion

Table I summarizes conditions for 19 experiments carried out with crevices ranging in height from 0.1 to 0.7 mm, and in radius from 6.35 to 12.70 mm. Table I also indicates that about half of the crevices experienced breakdown within 2-8h, while the remainder did not.

Figure 4 illustrates typical results on an 11.1 mm radius crevice upon variation in the crevice height from 0.1 to 0.5 mm. For this geometry, the quartz disk shielded all of the five interior electrode sections and about half of section 6. The anodic currents flowing from typical interior sections are seen to depend strongly upon the crevice width. For the narrowest crevice (0.1 mm), the current in section 5 increases by more than an order of magnitude within 4-5h, for the widest crevice (0.5 mm), no appreciable in-

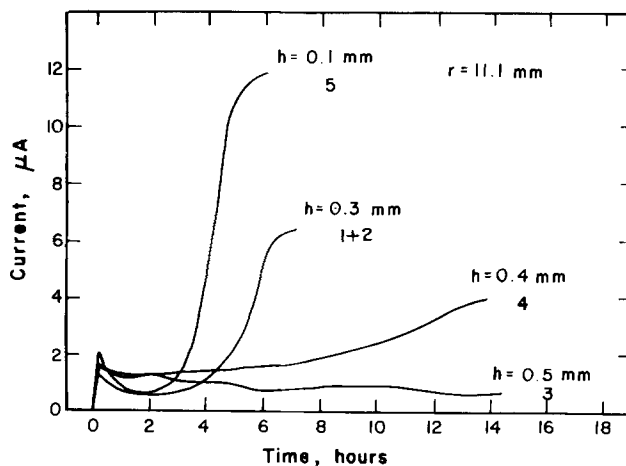


Fig. 4. Typical current vs. time behavior for crevice radius of 11.1 mm for four different crevice heights: 0.1, 0.3, 0.4, and 0.5 mm.

Table II. Value of model parameters

Parameter	Value
A	$1.0 \times 10^{-3} \text{ A/V-cm}^2$
ϕ_{M}	-0.440 V NHE
ϕ_0	-0.437 V NHE
n	3
ν	1
D	$1.0 \times 10^{-5} \text{ cm}^2/\text{s}$
C_0	$1.0 \times 10^{-7} \text{ M}$
κ	$5 \times 10^{-3} \text{ mho/cm}$

crease occurred in over 70h of observation. These data indicate clearly that there is a critical crevice geometry associated with this model system which separates regions where initiation of crevice corrosion occurs from regions where it does not occur.

Figure 5 provides a summary of the experiments carried out. The filled points indicate that for those crevice radius crevice height combination crevice corrosion did initiate, whereas the open points indicate that no breakdown of passivity occurred. As expected, breakdown occurred where crevice radius was larger and the crevice height smaller.

Theoretical calculations were carried out by setting the system equal to values reported in the literature, as summarized in Table II, except for the critical concentration. The three lines in Fig. 5 represent the predicted geometry required for crevice corrosion initiation by Eq. [17] for three different values of the concentration of aluminum required for breakdown. These values are in the lower half of the range which had been identified for the critical aluminum concentration by Hebert and Alkire (4), namely, 2-8 mM. These results show that a value of about 3 mM can now be used for the critical crevice concentration of aluminum. Based on this value, the general criterion for determining whether crevice corrosion will occur in this system is, following Eq. [17]

$$I_0(\sigma_1^{1/2}) = \frac{1}{1 - \frac{\sigma_1}{\sigma_2} (3 \times 10^4)} \quad [18]$$

These theoretical predictions indicate that the geometry required for corrosion initiation is sensitive to the values used for the physical parameters of the system, especially the critical device concentration.

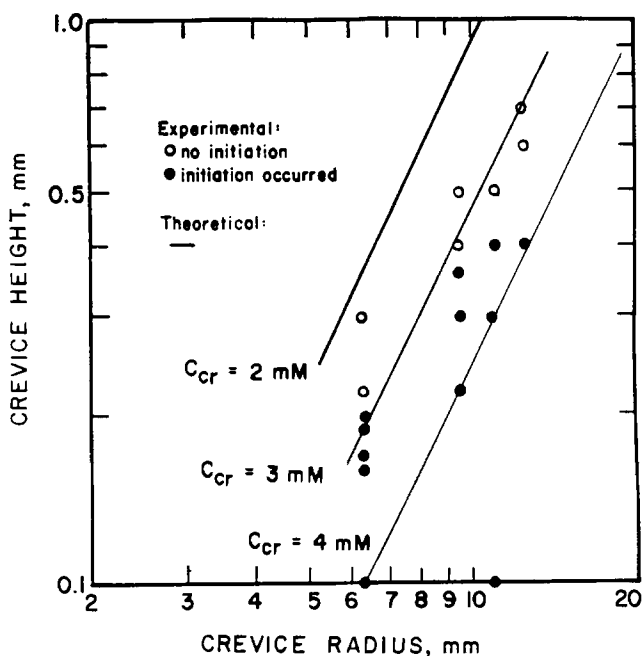


Fig. 5. Summary of experimental data and theoretical comparisons for three values of the critical aluminum concentration: $C_{\text{cr}} = 2 \text{ mM}$; $C_{\text{cr}} = 3 \text{ mM}$; $C_{\text{cr}} = 4 \text{ mM}$.

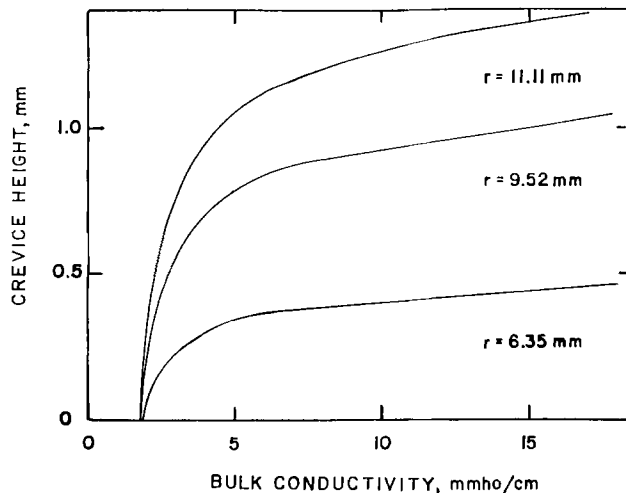


Fig. 6. Effect of bulk conductivity on the critical crevice dimensions

Figure 6 summarizes theoretical calculations of the influence of bulk conductivity upon the critical crevice dimensions for the Al system. The figure contains three curves corresponding to a particular value of the crevice radius. These curves identify the critical conditions; for crevice height above the curve, breakdown will not occur. The region below the curves corresponds to that crevice height that corrosion initiation will occur. These results show that for conductivity above 5 mmho/cm, the critical crevice geometry is relatively insensitive to the value of the conductivity. Below that value, the dependency is strong. It should be noted, however, that the assumption of supporting electrolyte may not be valid for very low conductivity, as the increase in the ionic strength owing to the dissolution of aluminum may cause significant changes in the crevice conductivity.

Conclusions

This investigation demonstrated that understanding of certain features of the mechanism of initiation permits prediction of the geometries under which crevice corrosion will initiate on Al in 0.05N NaCl. The prediction is made by analysis of transport processes which occur during the preinitiation period during which crevice composition becomes altered by comparison with solution external to the crevice. The analysis identified groupings of the system variables, Eq. [11] and [12], which can be used to evaluate the most important physical processes which controlled a given situation. For the model system under study, a criterion was identified, Eq. [18], which describes the boundary between the region of parameter space where initiation occurs and the region where it does not.

Experimental investigations were carried on the Al/0.05 NaCl system over a region of operation which straddled the boundary. By comparison with the foregoing theory, it was found that agreement was excellent when the critical concentration was set at a value of 0.003M. This value falls within the range (0.002-0.008M) previously suggested by Hebert and Alkire (5), and serves, therefore, to improve their estimate.

Even for the model system under study, there remain questions of mechanism about the phenomena which establish the value of critical concentration at which initiation occurs. Even in the presence of such unresolved scientific understanding, however, it is possible to make fundamentally sound engineering predictions by limited use of empirical knowledge combined with a mathematical model of the corrosion process.

Acknowledgment

This work was supported by the National Science Foundation (Grant NSF DMR 82-00781).

Manuscript submitted July 2, 1984; revised manuscript received Jan. 17, 1985.

The University of Illinois assisted in meeting the publication costs of this article.

LIST OF SYMBOLS

A	Kinetic parameter of aluminum dissolution reaction
C	concentration of aluminum, dimensionless
C_{cr}	critical concentration of dissolved aluminum, dimensionless
c	concentration of aluminum (M)
c_0	bulk concentration of aluminum (M)
D	diffusion coefficient (cm ² /s)
F	Faraday's constant (C/eq)
h	height of the crevice gap (mm)
I_0	modified Bessel function of the first kind of order zero
I_1	modified Bessel function of the first kind of order one
i	current density in solution (A/cm ²)
j	electrode current density of aluminum dissolution (A/cm ²)
n	number of electrons involved in Al dissolution (gmeg/gmol)
R	radial position, dimensionless
r	radial position (mm)
r_0	crevice radius (mm)
κ	conductivity (mho/cm)
ν	stoichiometric coefficient
σ_1	dimensionless polarization parameter
σ_2	dimensionless parameter for kinetics and diffusion

Φ	electrode potential, dimensionless
ϕ	electrode potential (V NHE)
ϕ_0	potential of initial uniform corrosion (V NHE)
ϕ_{R1}	rest potential of aluminum dissolution (V NHE)

REFERENCES

1. T. Tomasson, M.S. Thesis, University of Illinois, Urbana, IL (1983).
2. R. C. Alkire and D. W. Siitari, *This Journal*, **129**, 481 (1982).
3. R. C. Alkire and D. W. Siitari, *ibid.*, **129**, 488 (1982).
4. R. C. Alkire and K. R. Hebert, *ibid.*, **130**, 1001 (1983).
5. R. C. Alkire and K. R. Hebert, *ibid.*, **130**, 1007 (1983).
6. K. Sotoudeh, T. H. Nguyen, R. T. Foley, and B. F. Brown, *Corrosion*, **37**, 363 (1981).
7. I. L. Rosenfeld, in "Localized Corrosion," R. W. Staehle *et al.*, Editors, p. 373, NACE, Houston, TX (1974).
8. I. L. Rosenfeld and I. K. Marshakov, *Corrosion*, **20**, 115 (1964).
9. S. Zakipour and C. Leygraf, *ibid.*, **37**, 363 (1981).
10. E. McCafferty, *This Journal*, **121**, 1007 (1974).
11. J. W. Oldfield, *Met. Corros. Ind.*, **56**, (n688), 134 (1981).
12. D. F. Taylor and C. A. Caramihas, *This Journal*, **129**, 2458 (1982).
13. J. W. Oldfield and W. H. Sutton, *Br. Corros. J.*, **13**, 13 (1978).
14. A. Turnbull, *ibid.*, **15**, 162 (1980).
15. A. Turnbull and J. G. N. Thomas, *This Journal*, **129**, 1412 (1982).

Film Formation and Current Oscillations in the Electrodeposition of Cu in Acidic Chloride Media

I. Experimental Studies

H. P. Lee¹ and Ken Nobe*

Department of Chemical Engineering, University of California, Los Angeles, California 90024

Arne J. Pearlstein

Department of Aerospace and Mechanical Engineering, University of Arizona, Tucson, Arizona 85721

ABSTRACT

Oscillatory behavior of Cu electrodeposition in various acidic chloride solutions was studied with rotating disk electrodes. Oscillations were not observed in the apparent Tafel region. However, for 0.5 and 1M Cl⁻, nonsustained oscillations were found in the peak-current, current-minimum, and current-plateau regions. At potentials above the current-plateau region, apparent sustained oscillations were observed. Oscillatory behavior disappeared at sufficiently high rotation rates. Film dissolution studies indicate that the CuCl film begins to form at potentials near the peak current and suggest that oscillations only occur with the formation of a sufficiently thick film. A model based on the diffusion of chloride ions through the porous CuCl film to account for oscillatory behavior is proposed.

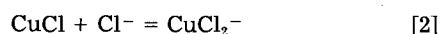
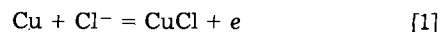
Observations of periodic electrochemical phenomena have been reported for over a century (1, 2). There have been numerous reports of oscillatory behavior of metals such as iron, chromium, copper, etc., in different aqueous media [e.g., see Ref. (3-6)]. Although oscillatory behavior occurs in both anodic and cathodic processes, most of the reported cases are directly associated with anodic polarization of metals and the instability of the anodic films formed.

Bonhoeffer and Gerischer (7) apparently were the first to develop a mathematical model to describe the periodic behavior of Cu dissolution in chloride solutions. Their explanation of the periodicity involved the formation and dissolution of CuCl and Cu₂O films. Cooper and Bartlett (8) studied Cu dissolution in 2N HCl under natural convection conditions and interpreted the observed oscillations in terms of the formation and instability of the CuCl film.

* Electrochemical Society Active Member.

¹ Present address: IBM General Products Division, San Jose, California 95193.

In chloride media, Cu electro-oxidizes to cuprous chloride complexes and the rate is dependent on the chloride concentration but independent of pH (9); the electrodeposition rate has also been shown to be strongly affected by the rate of mass transfer (8-12). The mechanism of Cu dissolution in Cl⁻ media (< 1M) is generally expressed as



At chloride concentrations > 1M, concentrations of higher cuprous chloride complexes, such as CuCl₃⁻², become significant.

In the present study, the dependence of oscillatory anodic behavior of Cu on chloride concentration, potential, and hydrodynamic conditions is examined with rotating ring-disk electrodes.

Experimental

Electrodes were made from a 1.270 cm (0.5 in.) rod of pure Cu (99.9%). The rod was first turned down and pol-

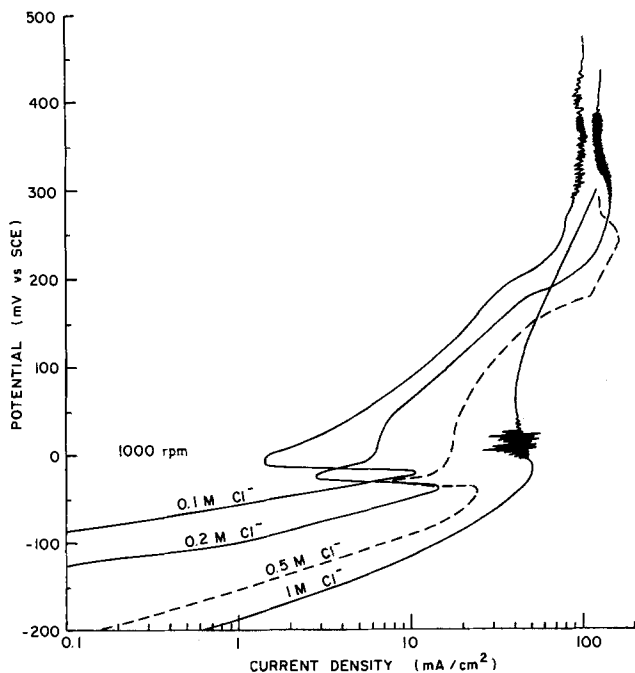


Fig. 1. Anodic polarization of Cu in 0.1M NaCl + 1N H₂SO₄, 0.2M NaCl + 1N H₂SO₄, 0.5M NaCl + 1N H₂SO₄, and 1M HCl. Sweep rate: 0.5 mV/s.

ished on a lathe to a diameter of 1.128 cm, which provided a surface area of approximately 1 cm². The rod was then cut into 1 cm lengths. Smaller surface area electrodes were also prepared from the same Cu rod. The disk electrode surfaces were polished with waterproof alumina paper of various grit sizes (240, 400, and 600), washed thoroughly with distilled water, degreased with hot benzene in a Soxhlet column for 4h, annealed under vacuum ($\approx 10^{-5}$ torr) at 560°C for 4h, and allowed to cool slowly to room temperature. The counterelectrode was a platinum sheet (surface area ≈ 14 cm²). The reference electrode was a saturated calomel electrode.

The hydrochloric acid, sulfuric acid, and sodium chloride were reagent grade. The water was deionized and then distilled from permanganate solutions. Solutions were deoxygenated with prepurified nitrogen before (for 10h) and during each run.

The rotating ring-disk electrode assembly used in this work has been described elsewhere (13). The polarization experiments were carried out with a PAR potentiostat (Model 173) and a universal programmer (Model 175).

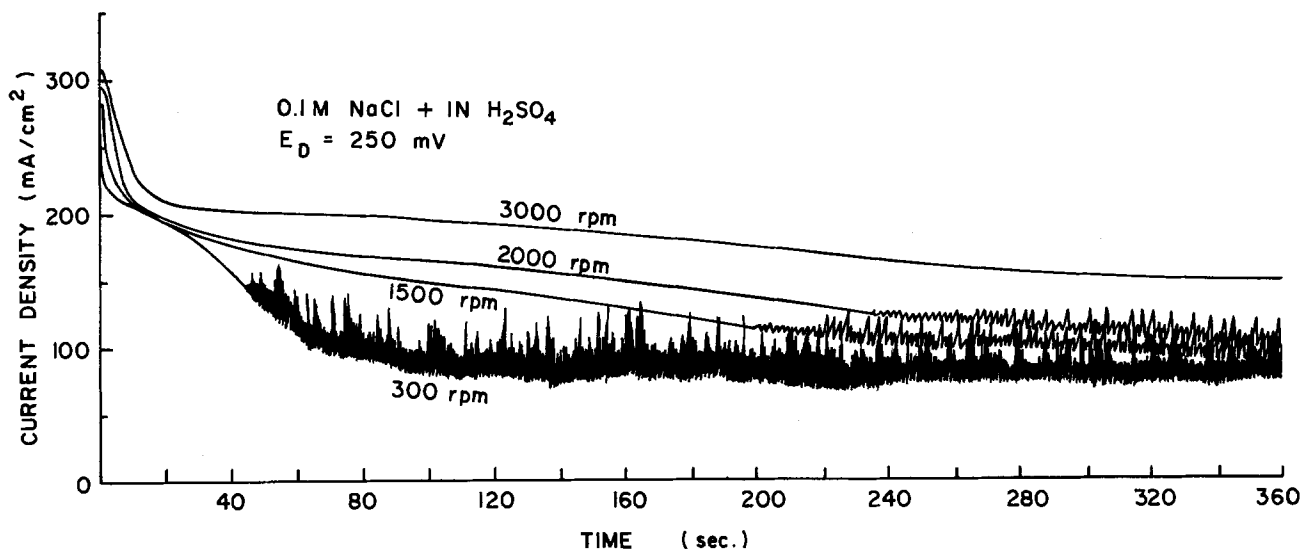


Fig. 2. Oscillations during Cu dissolution in 0.1M NaCl + 1N H₂SO₄. E_D : 250 mV

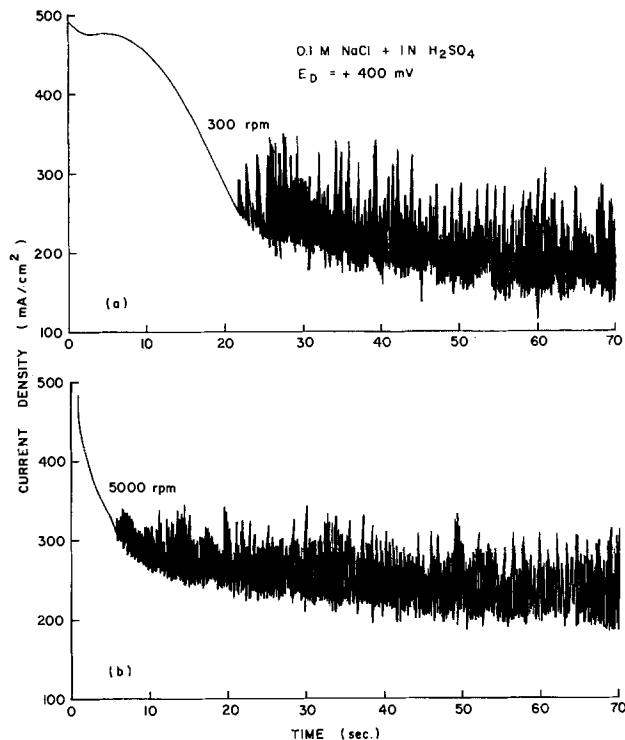


Fig. 3. Typical oscillations during Cu dissolution in 0.1M NaCl + 1N H₂SO₄. E_D : +400 mV.

Potential-current and current-time measurements were made with an H.P. (Model 7040A) X-Y recorder.

Potentiostatic experiments were performed to determine the current-time behavior of Cu in deoxygenated acidic chloride solutions. Unless otherwise noted, the electrode was first lightly polished with fine alumina paper followed by a rinse in distilled water before immersion in the acidic chloride solution; the electrode was then set at a rotation rate of 300 rpm. After steady-state rest potential was achieved (≈ 0.5 h), the anodic potential step was imposed, and the current-time behavior at 300 rpm recorded for several minutes before the potential step was terminated; occasionally, the time duration of the potential step ranged from a low of 1 min to a high of 2-3h. Then, while at open circuit, the electrode was set to a higher rotation rate. When steady-state rest potential was again attained, the potential step was reimposed. This same procedure was followed for each rotation rate run.

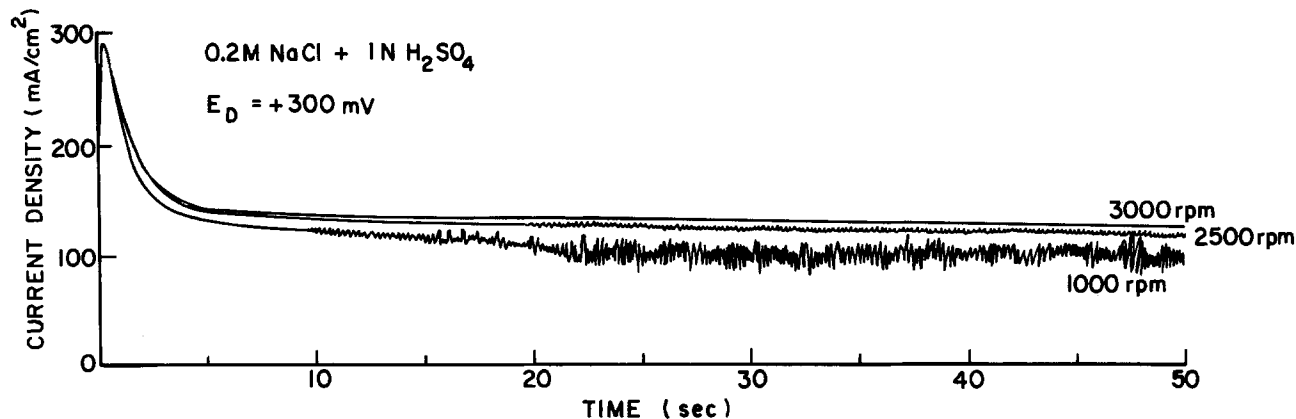


Fig. 4. Oscillations during Cu dissolution in 0.2M NaCl + 1N H₂SO₄, E_D: +300 mV

Results

Oscillatory behavior of Cu was observed during anodic potential sweeps, as shown in Fig. 1. The general polarization characteristics of Cu in acidic chloride solutions show a peak current and a current minimum at potentials above an apparent Tafel region (linear E -log i relationships are obtained when IR drop corrections are made). There is a small current plateau directly above the current minimum. The polarization results in Fig. 1 were obtained at a sweep rate of 0.5 mV/s; lower sweep rates provided essentially the same polarization behavior in the apparent Tafel region.

Figure 1 shows that for low concentrations (0.1 and 0.2M), the oscillatory behavior started at potentials greater than about 200 mV. At 0.5M Cl⁻, oscillations were not observed, but at 1M Cl⁻, oscillations were seen in the peak-current, current-minimum, and current-plateau regions. These potentiodynamic experiments show that oscillations occur in different potential regions at different chloride concentrations.

The dependence of oscillatory behavior on rotation rate, potential, and chloride concentration was examined further by a series of potentiostatic experiments. In these experiments, the current-time behavior of Cu in acidic solutions containing Cl⁻ ranging from 0.1 to 1.0M was recorded at various rotation rates and fixed potentials.

For 0.1M Cl⁻, oscillations were not observed at potentials less than +150 mV. However, at +150 mV, oscillatory behavior was recorded at a rotation rate of 300 rpm but not at 3000 rpm. The oscillations appear to be sustained and periodic with a frequency of 5.4 Hz and amplitude of about 1 mA/cm² [see Appendix of Ref. (13)]. Figure 2 shows that chaotic and apparently sustained oscillations occurred at +250 mV with an induction period that increased as the rotation rate increased from 300 to 2000 rpm. However, at the higher rotation rate of 3000 rpm, oscillations were not observed during a 760s recording period. Sustained and chaotic oscillations were observed at +400 mV for all rotation rates between 300 and 5000 rpm;

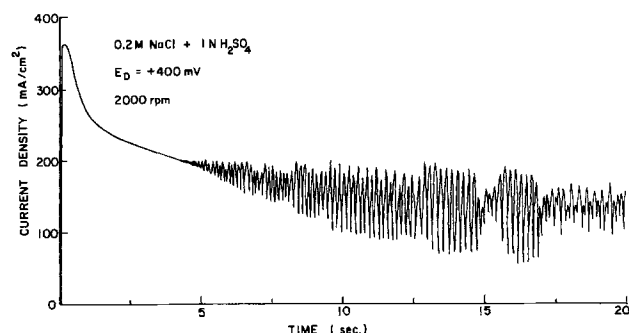


Fig. 5. Typical oscillations during Cu dissolution in 0.2M NaCl + 1N H₂SO₄, E_D: +400 mV.

Fig. 3 shows the oscillating behavior for 300 and 5000 rpm.

For 0.2M Cl⁻, oscillations occurred at +200 mV and higher potentials. At +200 mV and 300 rpm, nonsustained oscillations were recorded for about 30s beginning about 60s after the potential step was imposed (13); the frequency and amplitude were about the same as 0.1M Cl⁻ at +150 mV and 300 rpm. Oscillations were not observed at rotation rates of 600 rpm and above. At an anodic potential of +300 mV, sustained oscillations were found for rotation rates from 300 to 2500 rpm but not at 3000 and 4000 rpm. Figure 4 shows the rotation rate runs for 1000, 2500, and 3000 rpm. At +400 and +500 mV, sustained oscillations were observed for rotation rates from 300 to 4000 rpm. Typical runs at these potentials are shown in Fig. 5 and 6, respectively. For 0.1 and 0.2M Cl⁻, the amplitude of the oscillations increased with increase in potential.

For 0.5M Cl⁻, oscillations were not obtained below 0 mV. However, at 0 mV, nonsustained oscillations were observed at rotation rates from 1000 to 5000 rpm, but not below rotation rates of 1000 rpm (Fig. 7). When the electrode was removed from the cell after each rotation rate run and the electrode surface repolished and then reimmersed in the solution, oscillations were not obtained during any of the nine rotation rate runs between 300 and 5000 rpm (13). This experiment provides a tentative indication of a relationship between oscillatory behavior and the thickness of the CuCl film. At higher potentials of +200 and +400 mV, sustained oscillations were obtained for all rotation rates between 300 and 4000 rpm regardless of whether or not the electrode was removed and repolished after each rotation rate run. Figure 8 shows typical current-time behavior at these two potentials.

For 1M HCl, oscillations were not found below potentials of -40 mV. However, at -40 mV, sustained oscillations were observed for rotation rates of 300, 600, and 800 rpm but not for 1000 rpm and higher rotation rates (13). At -20 mV, nonsustained oscillations were recorded for rotation rates between 300 and 3000 rpm but not for 4000 rpm (Fig. 9); these oscillations were obtained even when the electrode was removed and repolished after each rotation rate run. At +100 mV, nonsustained oscillations were found at all rotation rates between 300 and 4000 rpm; a typical run is shown in Fig. 10. However, at 200 mV and higher potentials, no oscillations were observed for any of the 12 rotation rate runs between 300 and 7000 rpm (13).

For potentials of +300 mV and above, a white film was clearly visible at the end of each rotation rate run; others have also observed the presence of the film and reported it to be CuCl (8, 14-18). With termination of the potential step, the open-circuit potential abruptly dropped to a potential arrest region, the time duration of which decreased as the rotation rate increased as shown in Fig. 11 for 0.1M Cl⁻; the arrest potential was dependent on the Cl⁻ concentration, e.g., -55 mV (0.1M Cl⁻) and -72 mV (0.2M Cl⁻). After the potential arrest, the open-circuit potentials

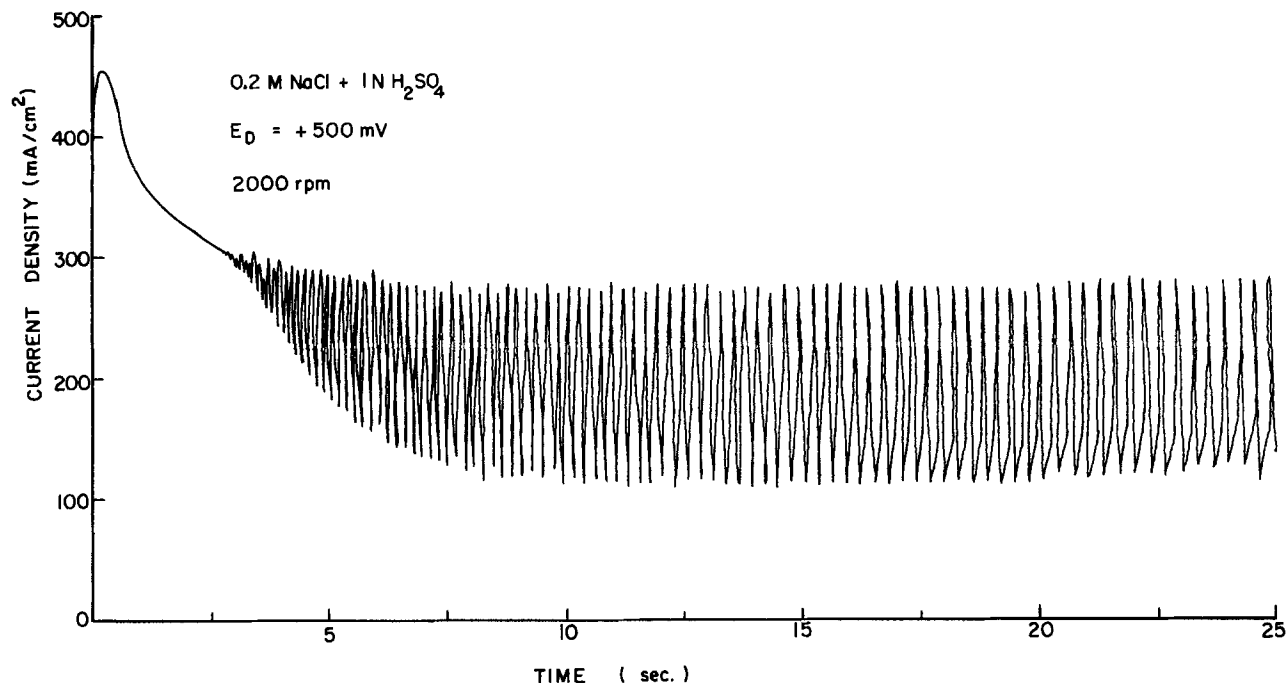
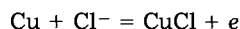


Fig. 6. Typical oscillations during Cu dissolution in 0.2M NaCl + 1N H₂SO₄. E_D : +500 mV

decreased fairly rapidly to a steady-state value, which was approximately the initial rest potential.

The potential arrest approximates the equilibrium potential of Eq. [1], *i.e.*



where

$$E^e = -0.105 - 0.059 \log [\text{Cl}^-] \quad (\text{V vs. SCE})$$

For 0.1M Cl⁻, $E^e = -46$ mV, and for 0.2M Cl⁻, $E^e = -63$ mV. These calculated equilibrium potentials are fairly close to the experimental arrest potentials. These results and the observed dependence of the potential decay profile on the rotation rate (Fig. 11) indicate that the dissolution rate of the CuCl film (Eq. [2]) is affected by the mass-transfer rate.

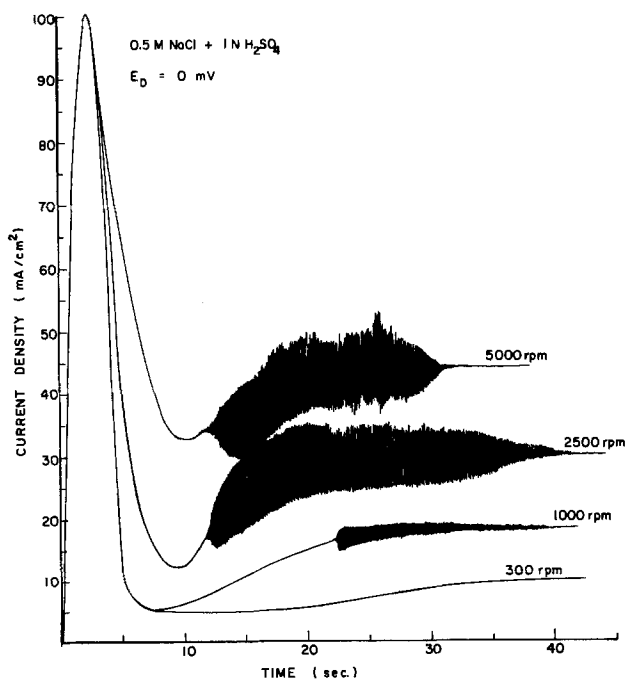


Fig. 7. Oscillations during Cu dissolution in 0.5M NaCl + 1N H₂SO₄. E_D : 0 mV.

Experiments were performed to obtain a measure of the thickness of the CuCl film and its dependence on the potential and rotation rate. The Cu disk electrode was first set at a specific potential for a fixed time to allow the CuCl film to form and grow. The ring electrode was set at +600 mV to measure the dissolution rate of cuprous species from the disk [the collection efficiency of the ring, N_o , was determined to be 0.58, see Ref. (13)]. During the potential step, the formation (Eq. [1]) and dissolution (Eq. [2]) of the CuCl film occur simultaneously. However, when anodic polarization is cut off at the end of the po-

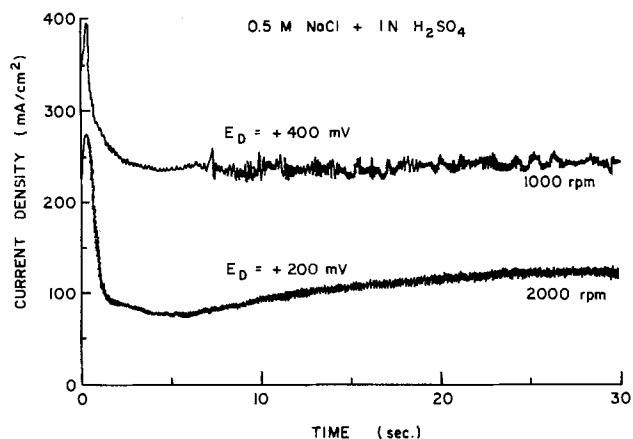


Fig. 8. Typical oscillations during Cu dissolution in 0.5M NaCl + 1N H₂SO₄.

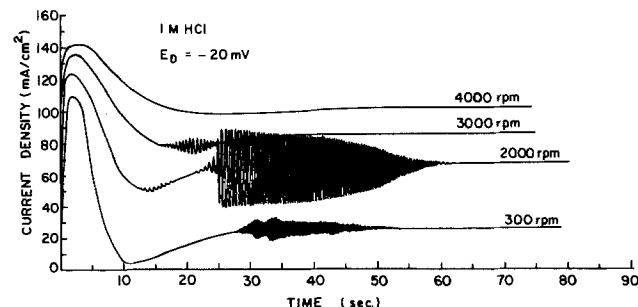


Fig. 9. Oscillations during Cu dissolution in 1M HCl. E_D : -20 mV.

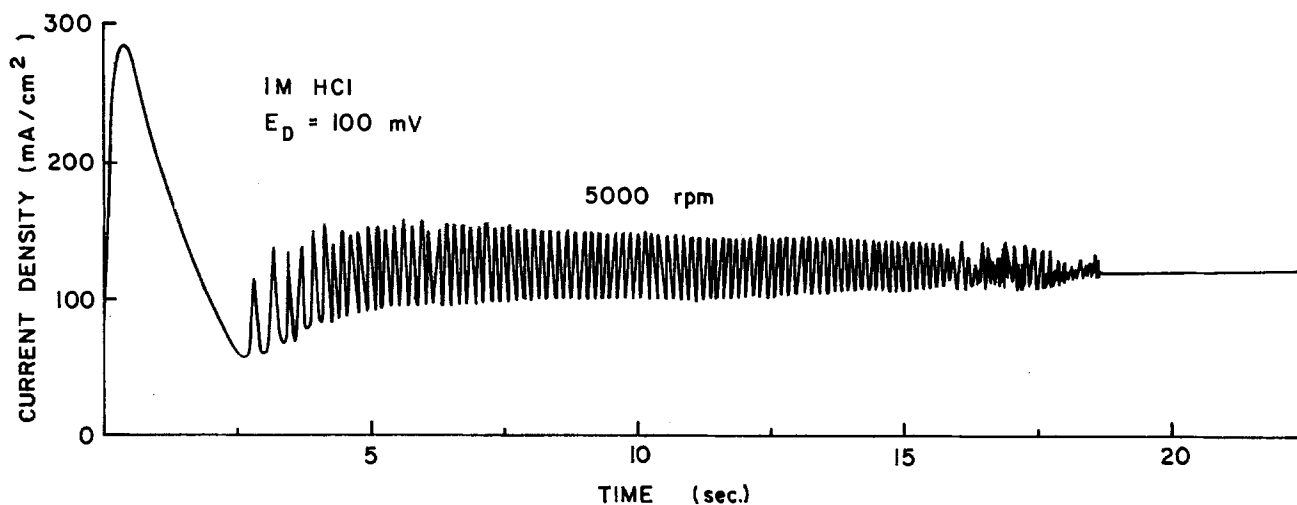


Fig. 10. Typical oscillations during Cu dissolution in 1M HCl. E_D : +100 mV

tential step, film dissolution (Eq. [2]) is essentially the sole process since the Cu disk is at open circuit. At this point, the ring current is recorded as a function of time to determine the amount of film dissolved. Thus, the area under the ring current-time plot to the background ring current provides a relative measure of the film thickness at the end of the potential step.

Figure 12 shows that there is essentially no film buildup in the apparent Tafel region since the ring current rapidly falls back to the background current when the disk polarization is shut off. However, at a potential step of -50 mV, which is just below the peak current (Fig. 1), formation of a thin but finite film is evident, as shown in Fig. 12. Significantly thicker films are formed at potentials above the current-plateau region (Fig. 13); the thicknesses of the films are shown to increase with increasing anodic potential. Since the rate of film growth (Eq. [1]) increases with anodic potential while the rate of film dissolution (Eq. [2]) remains constant at fixed rotation rates, higher anodic potentials should lead to thicker films as indicated by the experimental results shown in Fig. 13. The buildup of the CuCl film is also dependent on the rotation rate. Comparison of the areas under the ring current-time curves for each rotation rate (correcting for the background current) indicates that the film thickness decreases with increase in rotation rate (Fig. 14).

Higher rotation rates should lead to thinner films because the dissolution rate increases with increasing rotation rate.

The kinetics of the film dissolution reaction (Eq. [2]) were investigated by measuring film dissolution rates (ring current) at various chloride concentrations and rotation rates. In this series of experiments, the Cu disk was polarized at $+200$ mV for 1 min. Then, the ring current was recorded at the end of the potential step when the disk was at open circuit. The ring currents plotted in Fig. 15 are corrected for the collection efficiency and based on disk surface area (a different Cu disk electrode was used for each experiment). Figure 15 shows that the rate of the film dissolution reaction (Eq. [2]) is first order with respect to Cl^- (Fig. 15a) and is completely mass-transfer controlled, as indicated by the dependence of the dissolution rate on the square root of the rotation rate (Fig. 15b).

Discussion

The experimental rotating ring-disk results indicate the following: (i) the presence of a sufficiently thick CuCl film on the Cu surface is required for oscillatory behavior, (ii) oscillations are not observed in the apparent Tafel region where there is either no film or it is too thin, (iii) an increase in chloride concentration decreases the poten-

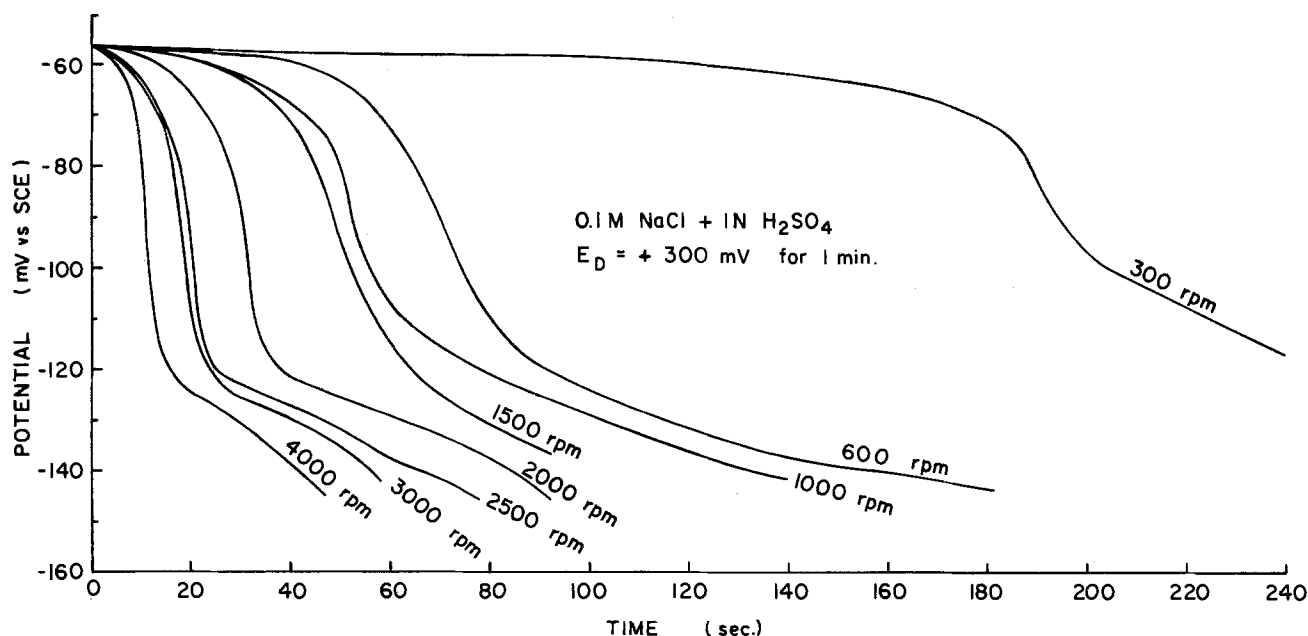


Fig. 11. Open-circuit potential-time behavior after polarization ($+300$ mV for 1 min) of Cu in 0.1M NaCl + 1N H_2SO_4

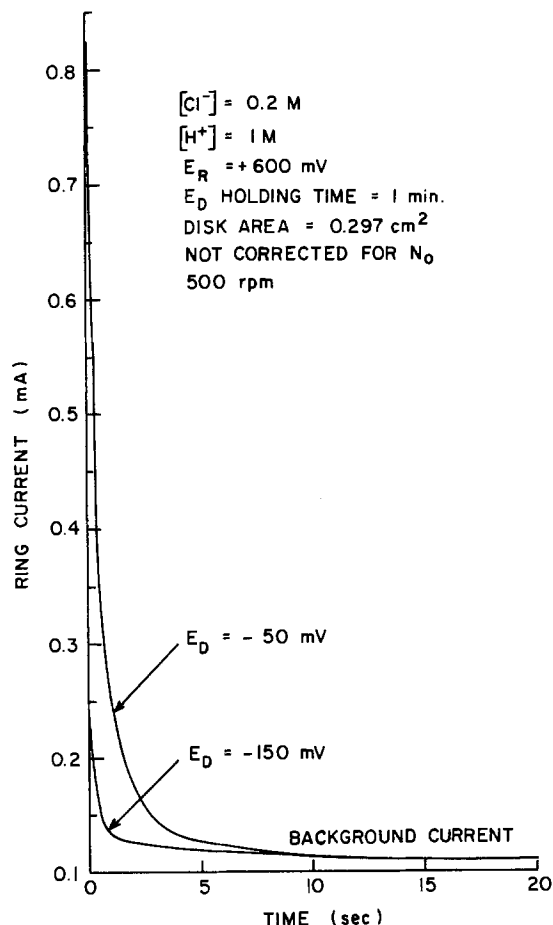


Fig. 12. Dissolution of the CuCl film formed after anodic polarization (1 min) of Cu in the apparent Tafel region.

tial at which oscillatory behavior begins, (iv) oscillations do not occur at sufficiently high rotation rates, and (v) the dissolution rate of the CuCl film is mass-transfer controlled.

A model to explain oscillatory behavior is proposed based on a formation-dissolution mechanism of the porous CuCl film

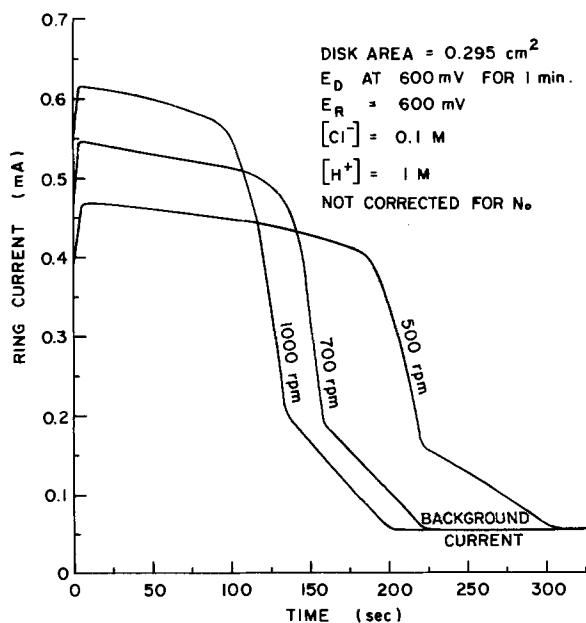
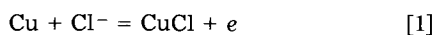


Fig. 14. Dissolution of the CuCl film formed after anodic polarization (+600 mV for 1 min). Effect of rotation rate.

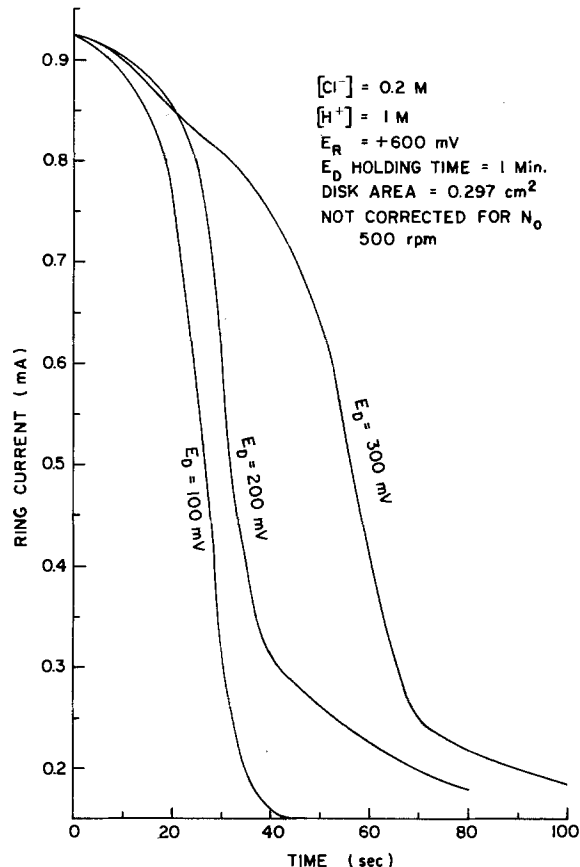
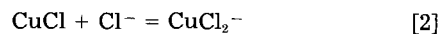


Fig. 13. Dissolution of the CuCl film formed after anodic polarization (1 min) of Cu at potentials above the current-plateau region.



At low potentials (apparent Tafel region), the rate of formation of CuCl (Eq. [1]) is slow compared to the rate of film dissolution (Eq. [2]). Therefore, CuCl will be dissolved (Eq. [2]) as fast as it is formed by Eq. [1], and buildup of film will not occur. As the potential is increased further, the rate of film formation, which is potential dependent, will increase until a CuCl film begins to build up on the surface of the Cu electrode. As the film thickens, it is increasingly difficult for Cl^- to reach the Cu metal surface; thus, the rate of film formation (Eq. [1]) decreases, while film dissolution (Eq. [2]) occurs at a rate that is independent of film thickness. Oscillations are not observed when there is a stable, steady balance between the rates of film formation and film dissolution. The film thickness, the dissolution and formation rates, and the current are then constant and do not vary with time.

The observed oscillations, however, are surmised to correspond to situations for which this steady balance is unstable. In these cases, it is proposed that, when the nominally steady balance just described gives rise to a film that is too thick, a time-periodic balance between the rates of film formation and film dissolution is observed in which the film periodically thickens when the film formation reaction is faster than the dissolution reaction, and thins when the dissolution rate exceeds the film formation rate.

The stability of this periodic balance in preference to the steady balance can be explained as follows. Normally, small changes in film thickness are promptly corrected for by small changes in the chloride ion concentration at the film-metal interface as a result of increased (or decreased) resistance of the porous film to the diffusion of chloride ions from the electrolyte to the metal surface. For instance, an increased diffusion resistance results in a lower chloride ion concentration at the film-metal interface, which in turn gives rise to a decrease in the film formation rate, and hence to a thinning of the film until a

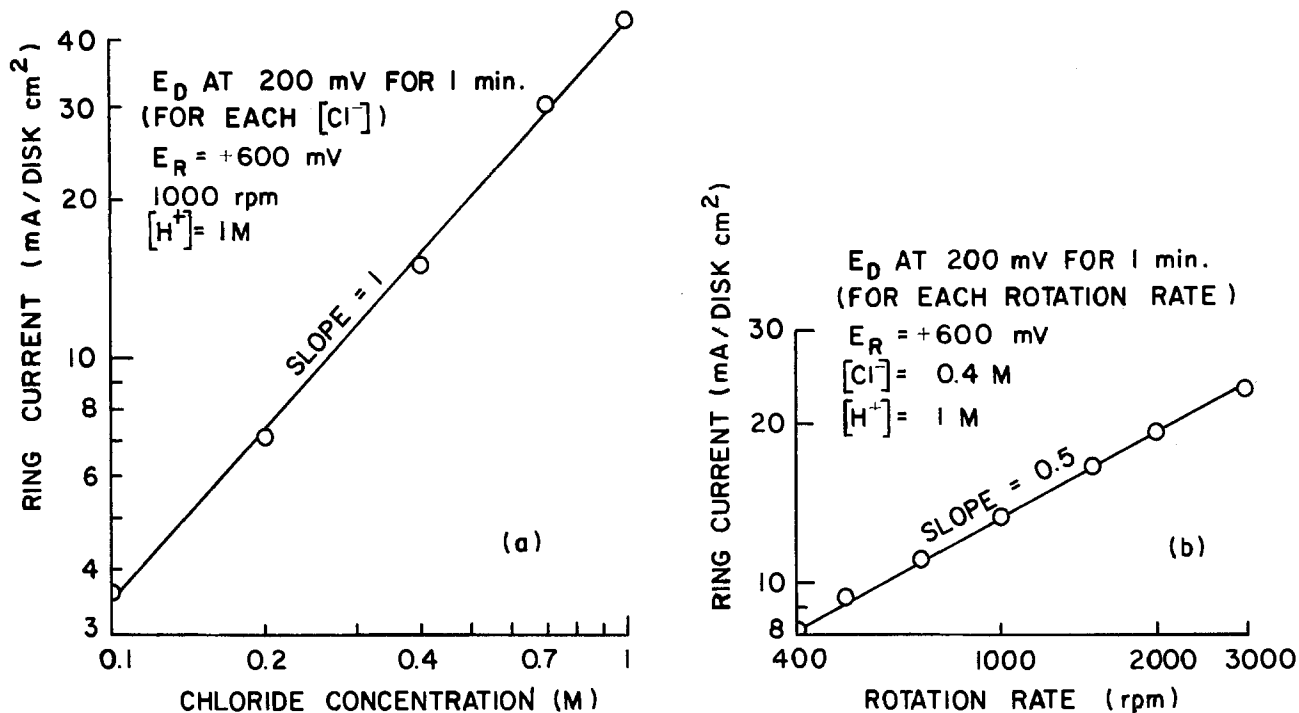


Fig. 15. a(left): The Cl^- reaction order for CuCl film dissolution. b(right): Mass-transfer effects during CuCl film dissolution

steady balance between the film formation and dissolution rates is achieved.

When the film thickness exceeds some critical value, however, there is a large time lag associated with diffusive communication between the electrolyte and the metal. This diffusive communication is so slow that the corrective decrease in the film formation rate continues past the nominally steady value. Eventually, the film has thinned so much that diffusion through the film increases the chloride ion concentration at the film-metal interface to the point that the film formation rate (temporarily) balances the dissolution rate, and the film thickness reaches a minimum. The chloride ion concentration elsewhere in the porous film is now higher than that in the nominal steady state, so that as chloride diffuses to the metal surface the film thickens. Again, diffusive communication is very slow, so that the film thickness overshoots its nominal value, returning to the original condition (an overly thick film). Thus a cycle is completed, and it is readily apparent how an initially infinitesimal disturbance can grow and result in oscillations of finite amplitude. This loss of stability by the steady state is known as "overstability" because it involves an overshoot by a mechanism that normally serves to restore (or stabilize) the steady state when it is disturbed from its nominal value.

This model predicts that oscillations can occur only for those combinations of rotation rate, potential, and chloride ion concentration for which a film of sufficient thickness exists on the Cu surface. Furthermore, the model predicts that oscillations can be suppressed by increasing the rotation rate sufficiently so that the film dissolution rate increases to the point where there is either no film or a very thin film. These predictions of the model are in accord with the experimental findings.

The mathematical development of the model will be presented in a subsequent paper.

Acknowledgment

This work is part of the University of California Water Resource Center's Saline Water Conversion program.

Manuscript submitted Jan. 17, 1984; revised manuscript received Jan. 7, 1985.

The University of California assisted in meeting the publication costs of this article.

REFERENCES

1. G. T. Fechner, *J. Chemie u Physik*, **23**, 131 (1928).
2. J. P. Joule, *Philos. Mag.*, **24**, 106 (1844).
3. E. S. Hedges and J. E. Myers, "The Problem of Physicochemical Periodicity," Arnold, London (1926).
4. E. S. Hedges, "Protective Films on Metals," Longmans, London (1933).
5. J. Wojtowicz, in "Modern Aspects of Electrochemistry," Vol. 8, J. O. Bockris and B. E. Conway, Editors, pp. 47-120, Plenum Press, New York (1972).
6. J. F. Cooper, R. H. Muller, and C. W. Tobias, *This Journal*, **127**, 1733 (1980).
7. K. F. Bonhoeffer and H. Gerischer, *Z. Elektrochem.*, **52**, 149 (1948).
8. R. S. Cooper and J. H. Bartlett, *This Journal*, **105**, 109 (1958).
9. T. Hurlen, *Acta Chem. Scand.*, **15**, 1231 (1961).
10. L. Kiss, J. Farkas, and A. Korosi, *Acta Chim. Acad. Sci. Hung.*, **67**, 179 (1971).
11. A. L. Bacarella and J. C. Griess, *This Journal*, **120**, 459 (1973).
12. M. Braun and K. Nobe, *ibid.*, **126**, 1666 (1979).
13. H. P. Lee, Ph.D. Thesis, University of California, Los Angeles (1983).
14. C. H. Bonfiglio, H. C. Albaya, and O. A. Cobo, *Corros. Sci.*, **13**, 717 (1973).
15. L. Stephenson and J. H. Bartlett, *This Journal*, **101**, 571 (1954).
16. R. S. Cooper, *ibid.*, **103**, 307 (1956).
17. A. Moreau, J. P. Frayret, F. Del Rey, and R. Pointeau, *Electrochim. Acta*, **27**, 1281 (1982).
18. R. L. Brossard, *This Journal*, **130**, 1109 (1983).

The Mechanism of Aluminum Electrodeposition from Solutions of AlCl_3 and LiAlH_4 in THF

M. W. M. Graef

Philips Research Laboratories, 5600 JA Eindhoven, The Netherlands

ABSTRACT

Aluminum coatings on metallic substrates can be made by electrodeposition from a nonaqueous solution such as LiAlH_4 and AlCl_3 dissolved in tetrahydrofuran. Raman spectroscopy has been used to identify the chemical constituents of the plating bath. A quantitative analysis of the equilibrium composition is given. The electrode reactions have been studied by means of chronoamperometry. The catalytic behavior of hydride and the role of neutral and ionic aluminum containing species in the faradaic and chemical processes are elucidated. The influence of variations in the composition of the solution on the properties of the plating bath is explained in terms of the mechanism of the electrodeposition process.

Aluminum has a wide range of applicability, due to a combination of three outstanding properties: it is inexpensive, it has a low density, and it is resistant towards corrosion because it is always covered with a passivating native oxide film. Only in recent years, however, has it become possible to coat metallic objects with aluminum by means of a galvanic process. The difficulties encountered in the electrodeposition of aluminum are related to its being a base metal, with a standard electrode potential of -1.71V vs. NHE in aqueous solutions. This fact precludes the use of aqueous solutions for aluminum plating.

Bulk aluminum can be produced by electrowinning from molten salts at high temperature. The deposition of thin films on metallic substrates can be performed by the use of aluminum complexes in organic solvents. The choice of a suitable plating bath is governed by the following conditions.

1. The solvent has to be electrochemically stable in order to permit the reduction of an Al(III) compound without electrolysis of the solvent. This requires in the first place that the Nernst potential which characterizes the electrochemical equilibrium between metallic Al and the solution lie within the existence regime of the solvent. Second, the electrode reaction has to be kinetically feasible (low overpotential), and mass-transport phenomena have to be in favor of a controllable surface morphology.

2. The solute which is used as an aluminum source should exhibit a high solubility in this solvent. A stable metal complex has to be formed in the plating solution.

3. For some applications, it is desirable that the composition of the bath not change during operation. This implies that the electrode process has to be chemically reversible. In this case, aluminum consumption at the cathode can be compensated by the dissolution of an aluminum anode. This permits long-term operation of the bath without changes of the electrodeposition characteristics.

4. The ionic conductivity of the solution should be sufficient to permit the electrodeposition of aluminum at a considerable rate. A cathode current density of 1 A/dm^2 should be possible without excessive heat evolution.

The first successful aluminum plating bath based on organic solvents was reported by Couch and Brenner in 1952 (1). These authors dissolved lithium aluminum hydride (LiAlH_4) and aluminum trichloride (AlCl_3) in diethylether (Et_2O). The technological application of this bath was hindered by its instability and extreme flammability. Later, improvements were made with the choice of a less volatile solvent such as tetrahydrofuran (THF) (2, 3). By adjustment of the bath composition, an electrode efficiency of 100% was attained by Daenen *et al.* (4). It was found that the conductivity and the stability of the THF-type plating bath could be enhanced by the addition of lithium aluminum tetrachloride (LiAlCl_4) (5). The $\text{AlCl}_3/\text{LiAlH}_4/\text{THF}$ bath is presently known as the REAL (room temperature electroplated aluminum) process (6), and has been developed into a technical process. Other investigators studied organometallic aluminum com-

pounds (7) or used aromatic solvents (8). At present, a considerable amount of work is being conducted on the development of aluminum plating solutions (9-11).

In the present study, the hydride-type THF plating bath is analyzed with respect to several phenomena that are relevant for the electrodeposition process. The quantities of interest are the chemical composition, the electrochemical potential, the electrode process and its kinetic characteristics, the conductivity of the solution, and the morphology of the electroplated metal.

Experimental

All reagents used for the preparation of the solutions were purified by distillation or recrystallization. The adducts $\text{AlH}_3 \cdot 2\text{THF}$ (12), $\text{AlH}_2\text{Cl} \cdot 2\text{THF}$ (13), $\text{AlHCl}_2 \cdot 2\text{THF}$ (13), and $\text{AlCl}_3 \cdot 2\text{THF}$ (14) were prepared by methods reported in the literature. The hydride content of the compounds was determined by means of iodometry (15). Solutions of LiAlH_3Cl , $\text{LiAlH}_2\text{Cl}_2$, LiAlHCl_3 , and LiAlCl_4 were prepared by the addition of a stoichiometric amount of anhydrous LiCl to the corresponding solutions of the aforementioned compounds. All manipulations and all measurements were performed in an argon atmosphere.

Raman spectra were recorded for 1M solutions of these compounds, using a $19,436\text{ cm}^{-1}$ and a $20,489\text{ cm}^{-1}$ laser beam. The positions of the vibrational lines were calibrated with respect to the $\nu_{(\text{CC})}$ band (A_1) of THF at 1029 cm^{-1} .

For the EMF measurements, the electrochemical couple ferrocene/ferricenium picrate ($\text{FeCp}_2/\text{FeCp}_2^+$) (16) in contact with a platinum wire served as a reference electrode. The configuration of the measuring cell was

$\text{Al}/\text{LiAlH}_4, \text{AlCl}_3(\text{THF})/0.5\text{M LiAlCl}_4(\text{THF})/1\text{ mM FeCp}_2,$

$1\text{ mM FeCp}_2\text{pic}, 0.5\text{M LiClO}_4(\text{THF})/\text{Pt}$

The presence of buffer vessels and the separation of the solutions by glass frits prevented reaction between the test solution (left) and the reference solution (right). The working electrode consisted of freshly deposited Al on Pt wire. Polarization curves were recorded using a solid Al counterelectrode in the left vessel. A Luggin capillary was used in order to minimize the ohmic drop between the working electrode and the reference electrode.

Chronoamperograms were recorded with the aid of a PAR 173 potentiostat, a 175 function generator, and a 4101 scan recorder. For these measurements, a different electrochemical cell was used. The working electrode was a 1 cm^2 polished platinum disk plated with aluminum prior to each measurement. An Al-plated platinum wire was situated behind the working electrode (17) and served as a quasi-reference electrode (QRE). The QRE compartment was electrically connected with the bulk solution by way of a Teflon tube fitted in the working electrode. The uncompensated resistance of this construction was determined by measurement of the ohmic drop by means of current interruption, for which a Clare PRME 15005 B

Table I. Raman spectra for species in the $\text{AlCl}_3/\text{LiAlH}_4/\text{THF}$ system

Species Point group Assignment	$\text{AlH}_3 \cdot 2\text{THF}$ Pseudo- D_{3h}			$\text{AlH}_2\text{Cl} \cdot 2\text{THF}$ Pseudo- C_{2v}			$\text{AlHCl}_2 \cdot 2\text{THF}$ Pseudo- C_{2v}			$\text{AlCl}_3 \cdot 2\text{THF}$ Pseudo- D_{3h}		
	Γ	ν	$\Delta\nu_{1/2}$	Γ	ν	$\Delta\nu_{1/2}$	Γ	ν	$\Delta\nu_{1/2}$	Γ	ν	$\Delta\nu_{1/2}$
$\nu_1[\text{Al-H}]$	E'	?	—	B_1	?	—	—	—	—	—	—	—
$\nu_2[\text{Al-H}]$	A_1'	1773	48	A_1	1803	58	A_1	1846	72	—	—	—
$\nu[\text{CO}]$	—	887	sh	—	875	sh	—	867	sh	—	856	sh
$\delta[\text{AlH}_2]$	E'	733	—	A_1	711	—	—	—	—	—	—	—
$\nu_1[\text{Al-Cl}]$	—	—	—	—	—	—	B_1	417	13	E'	507	—
$\nu_2[\text{Al-Cl}]$	—	—	—	A_1	411	30	A_1	347	9	A_1'	327	18

Species Point group Assignment	AlH_4^- T_d			AlH_3Cl^- C_{3v}			$\text{AlH}_2\text{Cl}_2^-$ C_{2v}			AlHCl_3^- C_{3v}			AlCl_4^- T_d		
	Γ	ν	$\Delta\nu_{1/2}$	Γ	ν	$\Delta\nu_{1/2}$	Γ	ν	$\Delta\nu_{1/2}$	Γ	ν	$\Delta\nu_{1/2}$	Γ	ν	$\Delta\nu_{1/2}$
$\nu_1[\text{Al-H}]$	—	—	—	E	1789	sh	B_1	1836	sh	—	—	—	—	—	—
$\nu_2[\text{Al-H}]$	A_1	1756	65	A_1	1759	90	A_1	1797	48	A_1	1844	42	—	—	—
$\nu[\text{CO}]$	—	—	—	—	—	—	—	—	—	—	—	—	—	—	—
$\delta[\text{AlH}_2]$	E	762	—	E	777	—	B_1	765	—	—	—	—	—	—	—
$\nu_1[\text{Al-Cl}]$	—	—	—	—	—	—	B_1	?	—	E	394	10	T_2	494	—
$\nu_2[\text{Al-Cl}]$	—	—	—	A_1	401	19	A_1	396	11	A_1	343	—	A_1	346	8

Frequencies are given in cm^{-1} . Γ : Normal mode of vibration. $\Delta\nu_{1/2}$: Peak width at half-height.

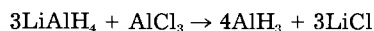
sh : Shoulder.

Reed relay was used. The uncompensated resistance R_u amounted typically to 1.5Ω . The iR_u drop was compensated by the positive feedback method (18).

The specific conductivities of the solutions were determined with a Philips PW9501 conductivity meter and a PW9510 conductivity cell.

Thermodynamics of the Plating Solution

The chemical composition of a plating bath prepared by the reaction of LiAlH_4 and AlCl_3 in THF is of importance for an understanding of the electrochemical properties of the solution. Recently, the results were published of a ^{27}Al NMR study which showed the presence of a number of Al containing species in this plating bath (19). In the present study, a detailed analysis is given of the chemical composition of $\text{AlCl}_3/\text{LiAlH}_4/\text{THF}$ solutions for different hydride/chloride ratios. The preparation of these solutions is based essentially on the Schlesinger reaction (20), i.e., the reaction of LiAlH_4 with AlCl_3 in diethylether, which is used for the synthesis of alane (AlH_3)



Lithium chloride is insoluble in diethylether. The conductivity of the diethylether-type plating bath is determined by the presence of alanate ions, AlH_4^- . Although "mixed hydrides," or chloroalanes (AlX_3 , with $X = \text{H}, \text{Cl}$), have been observed in diethylether solutions (20), chloroalanes (AlX_4^-) do not appear to be stable in this ambience. The situation is more complicated if THF is used as a solvent. In order to identify the chemical species that may be present in THF-type plating solutions, a set of solutions was prepared, each of which contained the stoichiometric composition of a hypothetical compound. Raman spectra of these solutions were recorded and interpreted. The results are shown in Table I. The spectra of $\text{AlH}_3 \cdot 2\text{THF}$ (21, 22), $\text{AlCl}_3 \cdot 2\text{THF}$ (23), AlH_4^- (24), and AlCl_4^- (25) were compared with the Raman and IR data reported in the literature. The vibrational spectra for the other solutions were found to be consistent with the postulation of two series of species with homologous configurations, viz., $\text{AlX}_3 \cdot 2\text{THF}$ and AlX_4^- with $X = \text{Cl}, \text{H}$. The presence of a shoulder on the CO stretching band (A_1) of THF (C_{2v} symmetry) indicates solvation of the aluminum compound via the oxygen atom. The magnitude of the shift with respect to the position of this band in the uncoordinated THF molecule at 912 cm^{-1} allows a classification of the relative strength of the Al-O bond (cf. Table II). The largest shift indicates the strongest Al-O bond. This order reflects the Lewis acidity of the mixed

alanes (20); the nucleophilic character is enhanced by the presence of chloride and decreases if a chloride group is substituted with hydride. The negative ions did not exhibit a CO shift of the solvent, which means that there is no significant solvent addition in this case. This is consistent with the fact that Cl^- is a stronger Lewis base than THF (25).

The absence of dimers of the type Al_2X_6 may be inferred from the fact that no peaks have been observed in the region for $\mu\text{-H}$ bonds around 1550 cm^{-1} (21); neither have Cl bridges been observed for AlCl_3 in THF (23). The formation of solvent-separated aggregates may occur at higher concentrations, but this does not alter the principal symmetries and will cause only minor shifts in the vibrational spectra (26). Ions of the type $\text{AlX}_3 \cdot \text{AlX}_2^+$, formed by association (27), were not detected. Raman spectra gave no positive evidence for the presence of ions such as AlX_2^+ , but concentrations of these species may have been below the detection limit. The existence of the species $\text{AlCl}_2^+ \cdot 4\text{THF}$ could be inferred from the ^{27}Al -NMR spectrum, recorded for solutions of AlCl_3 in THF. This is in agreement with observations reported by Derouault *et al.* (23). The existence of $\text{AlH}_2^+ \cdot 4\text{THF}$ seems to be implied by the fact that solutions of AlH_3 in THF exhibit a notable conductivity.

These considerations lead to the conclusion that three classes of aluminum containing compounds can be discerned in THF (cf. Fig. 1): tetrahedral univalent negative ions, bipyramidal neutral molecules, and octahedral univalent positive ions. This makes up 12 species in total. Lithium is present in the form of tetrahedral $\text{Li}^+ \cdot 4\text{THF}$ (26). Finally, the possible presence of LiH and undissociated LiAlH_4 should also be taken into account.

In commercial plating baths, an excess of AlCl_3 with respect to LiAlH_4 is used (3, 4). The most important features of a Raman spectrum recorded for such a bath are summarized in Table III. A comparison with the data in Table I makes it clear that the bath contains the species $\text{AlHCl}_2 \cdot 2\text{THF}$ and AlCl_4^- ; this is consistent with the preparative

Table II. Shift of the $\nu_{\text{CO}}(A_1)$ band of THF in aluminum complexes

Species	$\Delta\nu_{\text{CO}}(\text{cm}^{-1})$
$\text{AlH}_3 \cdot 2\text{THF}$	-25
$\text{AlH}_2\text{Cl} \cdot 2\text{THF}$	-37
$\text{AlHCl}_2 \cdot 2\text{THF}$	-45
$\text{AlCl}_3 \cdot 2\text{THF}$	-56

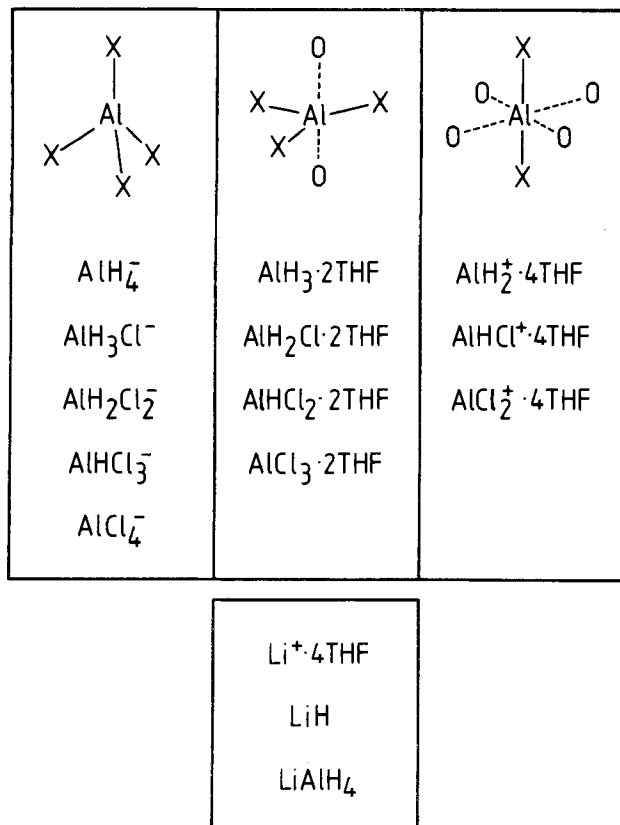
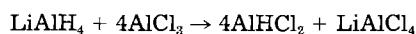


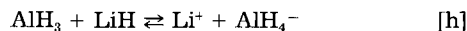
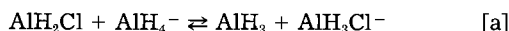
Fig. 1. Species present in $\text{AlCl}_3/\text{LiAlH}_4/\text{THF}$ plating solutions

reaction



Characterization of the solutions with Raman spectroscopy does not allow an accurate quantitative and qualitative description of the plating bath. In the remainder of this section, the chemical properties of the bath constituents will be discussed in the light of experimental data derived from EMF measurements.

The chemical equilibrium in a solution prepared by dissolving AlCl_3 and LiAlH_4 in THF may be represented by a set of eight arbitrary individual reactions [a]-[h]



The reactions describe the transfer of a chloride or hydride ligand between two particles. For the sake of clarity, THF as a ligand has been omitted (*cf.* Fig. 1). Furthermore, AlH_3^+ , AlHCl^+ , and LiAlH_4 have been ignored, since their respective concentrations are presumably negligible

Table III. Raman spectrum for aluminum hydride plating bath. Composition: 0.32M LiAlH_4 and 1.20M AlCl_3 in THF.

Assignment	ν (cm^{-1})	$\Delta\nu_{1/2}$ (cm^{-1})
$\nu_{(\text{Al-H})}$	1844	75
$\nu_{(\text{CO})}$	871	sh
$\nu_{(\text{Al-Cl})}$	341	10

and do not affect the final result. In the set [a]-[h], 13 species participate; consequently, 13 equations are required to describe the equilibrium. These are supplied by the definition of eight equilibrium constants K_a, \dots, K_h , associated with the equilibria [a]-[h]; four mass balances, for aluminum, hydride, chloride, and lithium, respectively, and one "input condition." If the input concentrations of aluminum trichloride and lithium aluminum tetrahydride are denoted by $[\text{AlCl}_3^0]$ and $[\text{LiAlH}_4^0]$, respectively, the input condition may be defined as a single parameter, *viz.* the molar fraction of LiAlH_4 , denoted by x

$$x = [\text{LiAlH}_4^0]/([\text{LiAlH}_4^0] + [\text{AlCl}_3^0]) \quad [1]$$

The total aluminum concentration in the solutions prepared for the EMF measurements was kept constant (C). Thus, the mass balances can be written as

$$[\text{Al}] = C \quad [2]$$

$$[\text{H}] = 4xC \quad [3]$$

$$[\text{Cl}] = C(3 - 3x) \quad [4]$$

$$[\text{Li}] = Cx \quad [5]$$

For the determination of the equilibrium constants, the equilibrium potentials for a series of solutions were measured against the ferrocene-ferrocenium reference couple (*cf.* experimental section). If a solution is brought into contact with metallic aluminum, an equilibrium potential is established. The measured equilibrium potential E as a function of the composition parameter x (*cf.* Fig. 2) can be used to generate a set of equilibrium constants, with the aid of the Nernst equation. The results are presented in Table IV. With these constants the composition of a solution, prepared by dissolving LiAlH_4 and AlCl_3 in THF, can be calculated as a function of x . This is shown in Fig. 3. It is seen that the initial ratio of AlCl_3 and LiAlH_4 has a great influence on the chemical composition. In chloride-rich solutions, chemical species such as AlCl_3 , AlHCl_2 , and AlCl_4^- are stable, whereas in hydride-rich solutions the more important species are AlH_4^- , AlH_3Cl^- , and AlH_3 . The cation AlCl_2^+ and LiH are relatively unstable and are present only in very low concentrations.

The most typical feature of the E vs. x diagram is the fact that the Nernst potential shifts to more negative

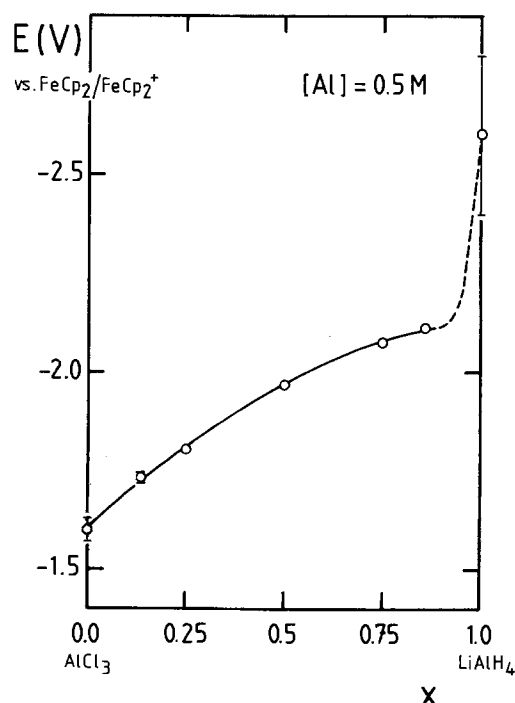


Fig. 2. Equilibrium electrode potential of Al in $\text{AlCl}_3/\text{LiAlH}_4/\text{THF}$ solutions as a function of the initial composition. The total aluminum (III) concentration is kept constant.

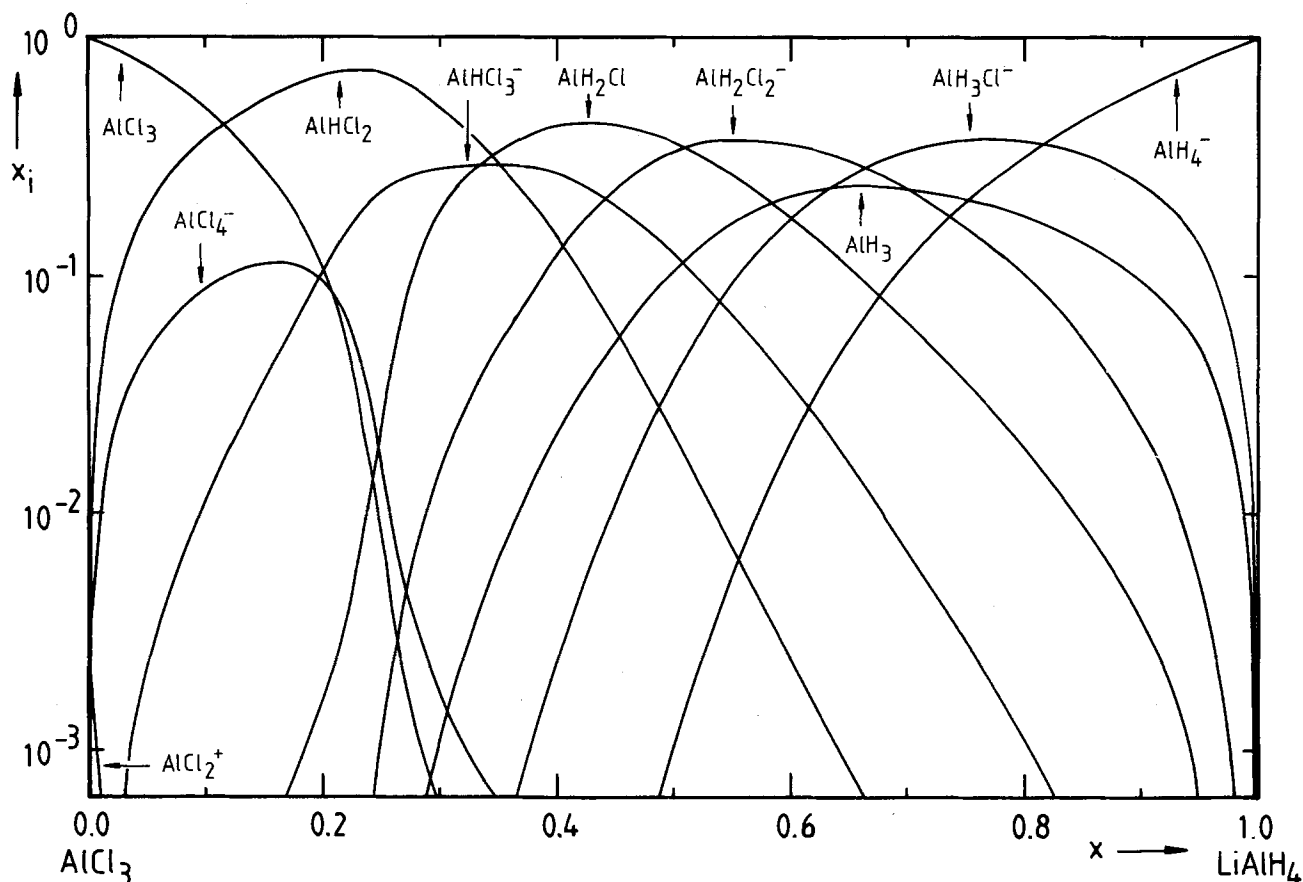
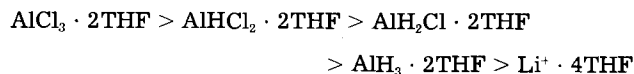


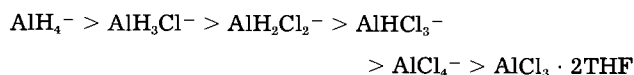
Fig. 3. Calculated equilibrium composition of $\text{AlCl}_3/\text{LiAlH}_4/\text{THF}$ solutions as a function of the initial composition. The mole fraction of each species, defined as $x_i = [i]/[A]$, is plotted on the ordinate.

values as the hydride content of the solution increases. This is equivalent to the consideration that the hydride group has a tendency to reside on neutral molecules or that the chloride group has a tendency to reside on univalent negative ions. This fact is also illustrated, implicitly, by the relative magnitudes of the equilibrium constants. Consider, for instance, the chloride transfer process described by reaction [f]. The mechanism of this reaction may be envisaged as the interaction between a chloride acceptor (*i.e.*, a Lewis acid) and a chloride donor (a Lewis base). Another way of representing the results of the equilibrium analysis is to arrange a list of species according to their electrophilic or nucleophilic character, respectively.

The Lewis acidity decreases in the order



The Lewis basicity decreases in the order



It should be remarked that this result is consistent with the relative strength of the Al-H and Al-Cl bonds in the respective complexes, which can be deduced from the Raman spectra. The replacement of a hydride group by the more electronegative chloride group results in an increased strength of the remaining covalent Al-H bonds. This, again, causes a shift of the Al-H stretching vibration to larger wave numbers.

Table IV. Equilibrium constants for the $\text{AlCl}_3/\text{LiAlH}_4/\text{THF}$ system at 25°C

$\log K_a = 1.02$	$\log K_c = 4.21$
$\log K_b = 0.41$	$\log K_f = 0.76$
$\log K_e = 2.18$	$\log K_g = 5.25$
$\log K_d = 0.82$	$\log K_h = 13.45$

These results can be used to elucidate the observed solvent effect. The apolar diethylether molecule is insufficiently nucleophilic for the creation of a stable $\text{Li}^+ \cdot 4\text{Et}_2\text{O}$ complex. Therefore, the attempted reaction of LiCl with AlCl_3 in diethylether results in precipitation of the former, whereas in THF the stable AlCl_4^- is formed. This explains why the conductivity of solutions of AlCl_3 and LiAlH_4 in Et_2O is relatively low compared to analogous THF solutions (28).

Kinetics of the Electrode Process

Figure 4 depicts a cyclic voltammogram for a platinum disk coated with freshly deposited aluminum in contact with a $\text{AlCl}_3/\text{LiAlH}_4/\text{THF}$ plating solution. The diagram shows that the cathodic/anodic peak/peak separation is 620 mV (corrected for the iR_u drop) at a scan rate of 100 mV/s. Thus, kinetic measurements are meaningful on a time scale of less than 10s. Also, only a single (though possibly complicated) electrode process takes place for cathodic or anodic overvoltages less than 500 mV. These observations permit an interpretation of potential-step experiments in terms of redox processes involving the aluminum electrode and the solution.

The chronoamperometric technique can be used for obtaining information on the mechanism of the electrode process by means of analysis of the extrapolated time-zero current. Mass transport phenomena can be studied by observation of the transient behavior of the current. The method consists of recording the faradaic current response caused by the implementation of a potential step by means of a potentiostat (29).

The charge-transfer mechanism.—The rate-determining step (rds) of the electrode process may be either mass transport towards the surface, surface diffusion, nucleation, or electron transfer, depending on experimental conditions and transient time. In the case where the rds is contained within the overall charge-transfer reaction, the relationship between current and overpotential is gov-

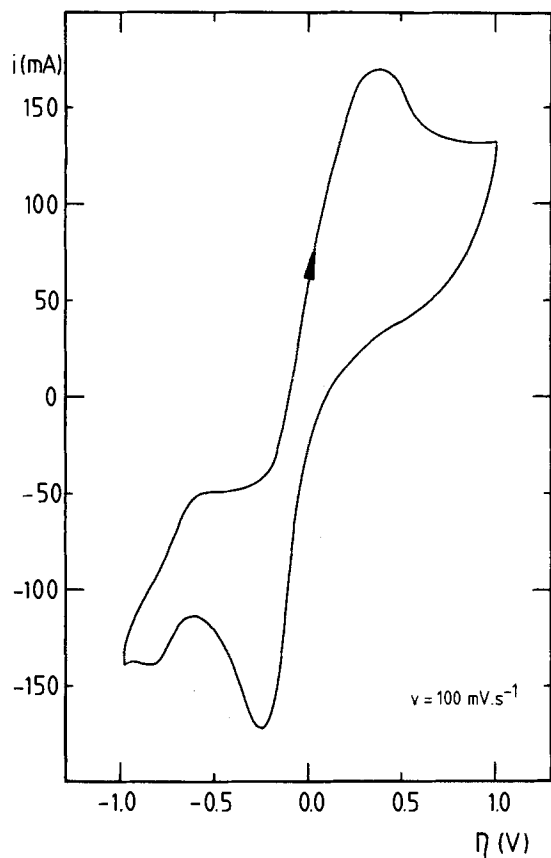


Fig. 4. Cyclic voltammogram of Al immersed in a solution containing 0.52M AlCl_3 and 0.29M LiAlH_4 in THF. The electrode area was 1.0 cm^2 . The potential was measured vs. a quasi-reference electrode.

erned by the general Butler-Volmer equation (30)

$$i = i_0 \{ \exp(\alpha_a F \eta / RT) - \exp(-\alpha_c F \eta / RT) \} \quad [6]$$

where i is the current as measured by a current follower, i_0 is the exchange current, and η is the overpotential. The notation has been chosen in agreement with the IUPAC recommendations (31). By convention, the anodic current has a positive sign and the cathodic current has a negative sign. The transfer coefficients α_a for the anodic and α_c for the cathodic reaction are defined by

$$\alpha_a = \bar{\gamma} / \nu + (1 - \beta)r \quad [7]$$

$$\alpha_c = \bar{\gamma} / \nu + \beta r \quad [8]$$

Here, $\bar{\gamma}$ is the number of electrons transferred in the steps preceding the rds, γ is the number of electrons transferred in the steps after the rds, and r is the number of electrons transferred in the rds. ν is the stoichiometric number of the rds, and β is the symmetry factor in the rds. The total number of transferred electrons n is given by

$$n = \bar{\gamma} + \nu r + \gamma \quad [9]$$

In Fig. 5, examples are given of chronoamperograms for reductive and oxidative processes occurring at an aluminum electrode immersed in a solution of 0.29M LiAlH_4 and 0.52M AlCl_3 in THF at 25°C. Qualitatively, both processes are comparable. An accurate analysis of the chronoamperometric transients may be rather complicated (32), but an extrapolation of the current to $t = 0$ for a series of values of η can be used to study Eq. [6], which is clearly time independent. The effects of mass transfer and nucleation are excluded in this way, and the overall charge-transfer reaction can be studied. The extrapolation is carried out graphically (Fig. 6), using the approximated linear relationship between i and $t^{1/2}$ for short times. The cathodic branch, for instance, is described by

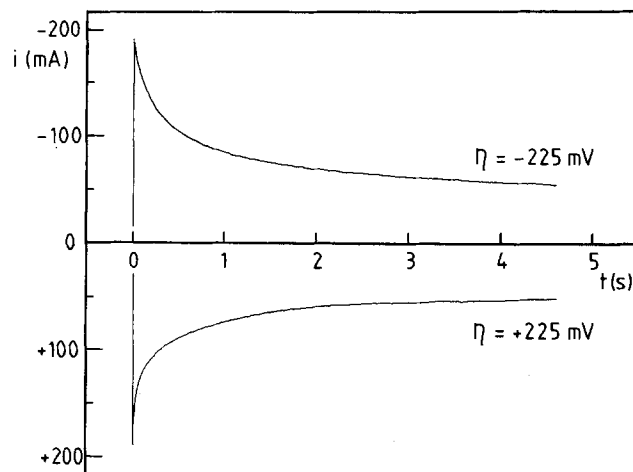


Fig. 5. Chronoamperograms for the cathodic deposition (negative overpotential) and for the anodic dissolution (positive overpotential) of aluminum.

$$\frac{i(t)}{i(t=0)} = 1 - \frac{2i_0 t^{1/2} \exp(-\alpha_c F \eta / RT)}{\pi^{1/2} \eta F A C_0^* D_0^{1/2}} \quad [10]$$

(C_0^* is the concentration at the electrode surface of the species that is consumed by reduction; D_0 is its diffusion coefficient; A is the electrode area.) Graphs showing the relationship between the time-independent part of the current and the overpotential are presented in Fig. 7 for the reductive and for the oxidative process. The exchange current density is found by extrapolation of these Tafel lines to $\eta = 0$. This gives $i_0/A = 20 \text{ mA/cm}^2$ for both the cathodic and the anodic data. The transfer coefficients are determined from the slopes of the Tafel lines. They are roughly equal: $\alpha_c = \alpha_a = 0.3$. Since the sum of α_c and α_a should be equal to or larger than unity, the experimental values are obviously too low. This may be due to an error in the extrapolation caused by the decrease of the slope

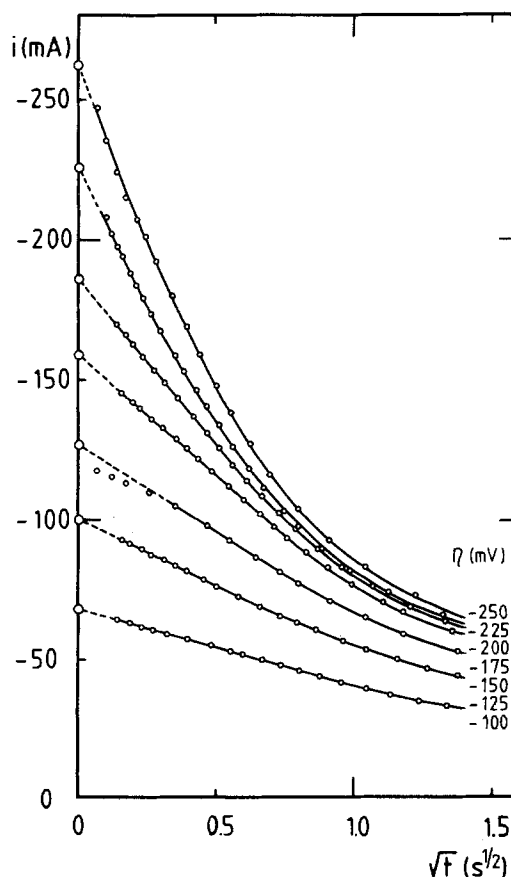


Fig. 6. Linearization of cathodic chronoamperograms for short times

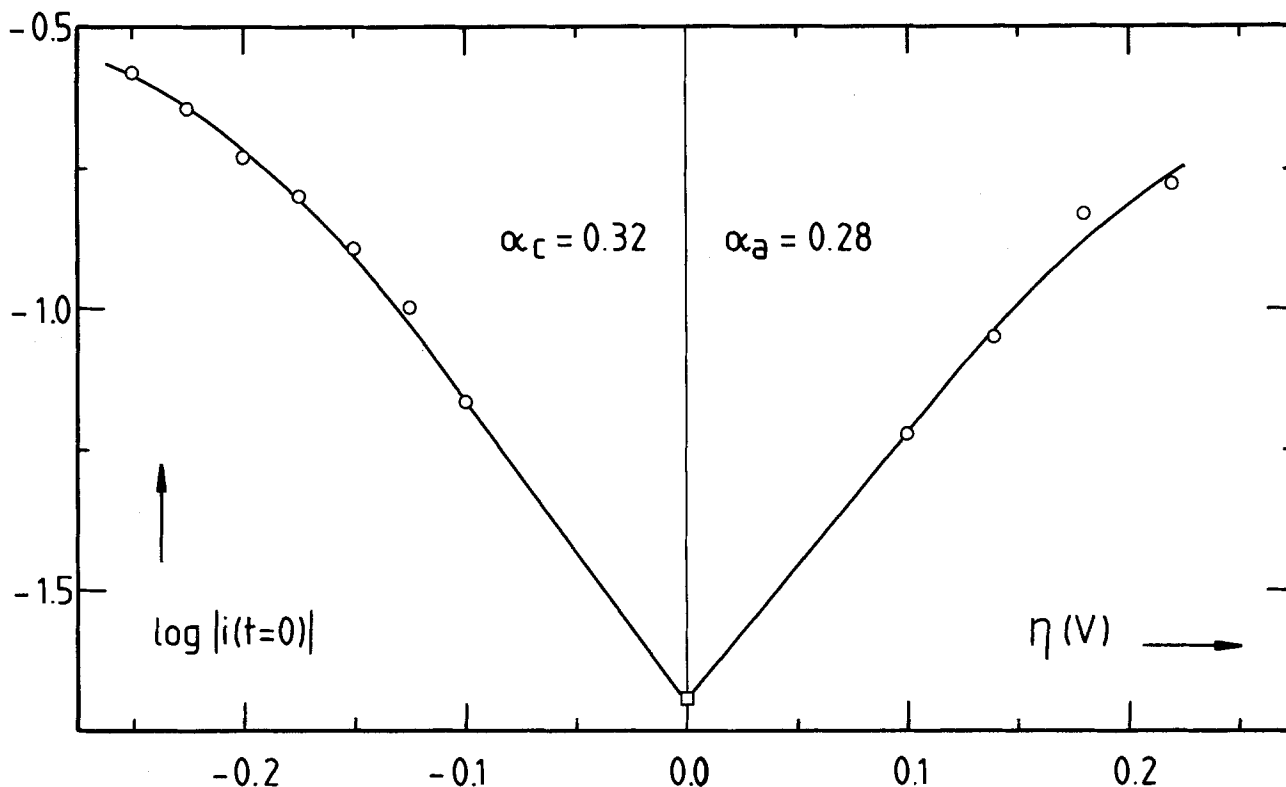
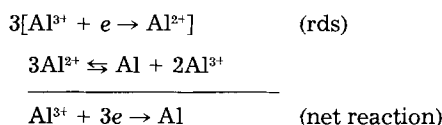
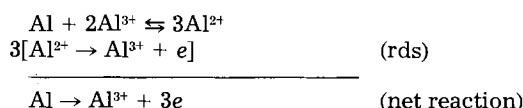


Fig. 7. Tafel lines for Al in a solution of 0.52M AlCl_3 and 0.29M LiAlH_4 in THF

for large overpotentials. This deviation cannot be accounted for completely by the possible influence of uncompensated resistance on the applied voltage. A tentative explanation may run as follows. Since no nonelectroactive supporting electrolyte was available, the conductivity of a solution is largely determined by the presence of aluminum containing anions which participate in the electrode process. A relatively large concentration is required in order to obtain a conducting solution. This implies that relatively high currents and potentials are encountered in the measurements. At large overpotentials the symmetry factor is affected, and this will cause nonlinearity of the i vs. η relationship (33). If allowance is made for this, the only physically meaningful solution in agreement with the experimental data requires that the values for the transfer coefficients are corrected to $\alpha_a = \alpha_c = 0.5$. With $\beta = 0.5$, Eq. [7], [8], and [9] give $r = 1$ and $\nu = 3$, which means that the rds is executed thrice during the reaction sequence. This is consistent with the following model for the charge-transfer mechanism. The cathodic process is described by



Since the process is symmetrical, the anodic process is a mirror image of the cathodic process



The influence of the bath composition on the electrode kinetics was studied qualitatively by measuring the polarization curves for different solutions (Fig. 8). These curves make it clear that the electrode process is facilitated by the presence of hydride, which lowers the polarization resistance. The observation that the reaction mechanism is influenced by the $\text{LiAlH}_4/\text{AlCl}_3$ molar ratio has been reported by Eckert and Galova, who studied the

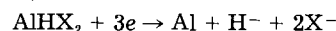
$\text{AlCl}_3/\text{LiAlH}_4/\text{THF}$ system using a rotating disk electrode (34).

The overall reaction.—On a relatively long time-scale the electrochemical reaction rate becomes limited by mass transport to and from the electrode surface. The limiting case is described by the Cottrell equation

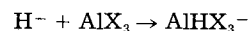
$$i_d = nFAD_0^{1/2}C_0\pi^{-1/2}t^{-1/2} \quad [11]$$

where i_d denotes the diffusion-limited current. Theoretically, i vs. $t^{-1/2}$ yields a straight line. In practice, the current is limited by the kinetics of the electrode process for short times, and is influenced by the onset of natural convection at longer times. In the intermediate region, Eq. [11] is more or less valid. Figure 9 shows the experimental data for the cathodic process. The slope of the asymptote (Eq. [11]) is determined by C_0^* . If the value $10^{-5} \text{ cm}^2\text{s}^{-1}$ is taken for D_0 , the experimental results appear to be in agreement with line b in Fig. 9, where C_0^* is equal to 1/4 times the concentration of AlX_3 (with $X = \text{H}, \text{Cl}$). Apparently, only a fraction of the Al containing species arriving at the electrode surface is actually reduced: four AlX_3 molecules are consumed for the creation of only one aluminum atom. The reason for this is the fact that, together with the Al atom, three unstable ligands of the type X^- are created. These are bonded to other AlX_3 molecules. This observation leads to the following general scheme for the electrode process

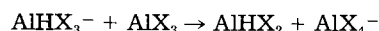
Charge transfer



Ligand transfer



Regeneration



The overall reaction is



It should be noted that the hydride group does not occur

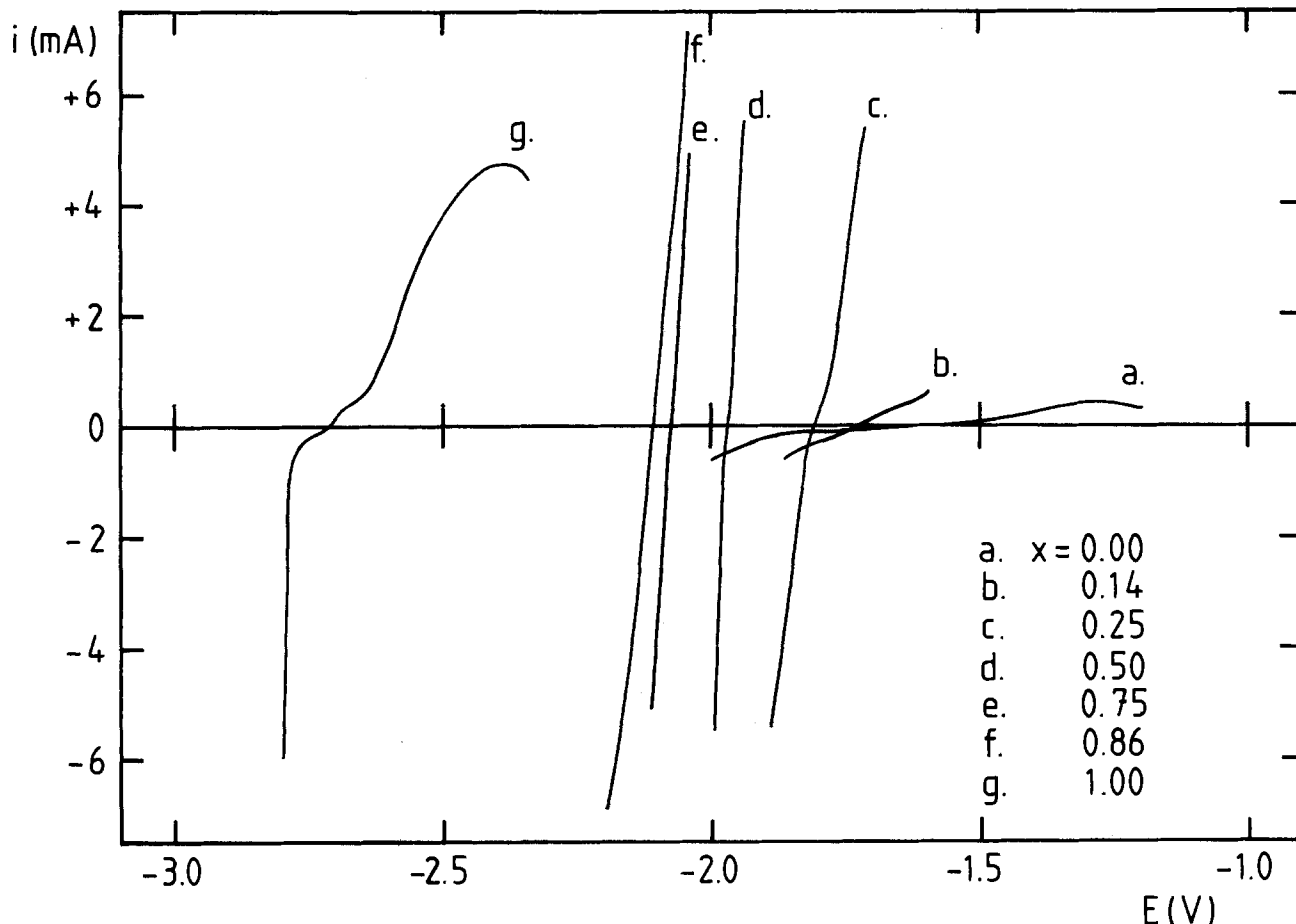


Fig. 8. Polarization curves for an aluminum electrode in several solutions of AlCl_3 and LiAlH_4 in THF. The potential is defined with respect to a ferrocene/ferricenium reference couple. For the composition parameter x , refer to Fig. 2 and text.

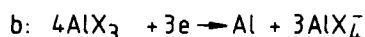
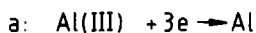
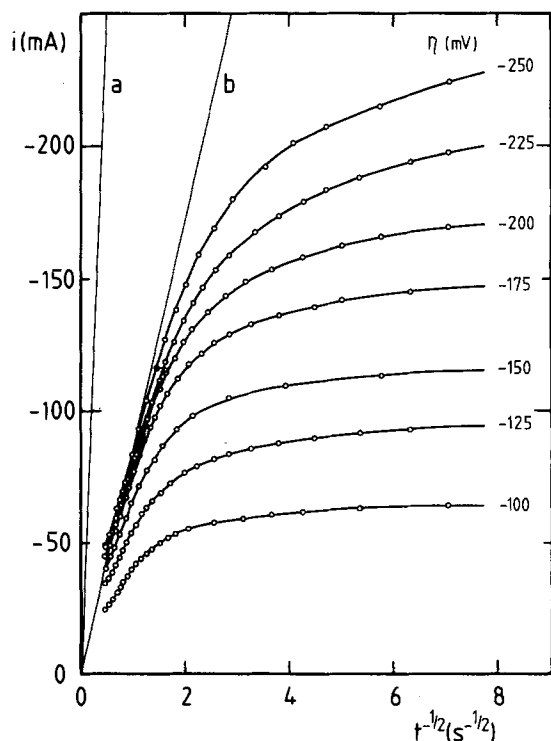


Fig. 9. Cathodic current measured as a function of $t^{-1/2}$, for several overpotentials. The straight lines represent the diffusion-limited transients for the case in which aluminum containing species are reduced at the working electrode (a) and for the case where ligand transfers are taken into account (b).

explicitly in the overall reaction. However, the participation of H^- in the electrode process has been established by Daenen (35), who concluded correctly that the reaction is characterized by a cyclic pattern. It is seen that the hydride group is not consumed in the electrode reaction and serves as a catalyst for the charge-transfer step. For the electrode reaction, it is not important whether the active species is AlHCl_2 , AlH_2Cl , or AlH_3 , as long as at least one hydride group is present.

The functions of the bath constituents in the plating process are summarized in Table V.

Physicochemical Properties of the Plating Bath

The conductivity κ of the $\text{AlCl}_3/\text{LiAlH}_4/\text{THF}$ solutions as a function of the composition parameter x is shown in Fig. 10. It is seen that the conductivity increases with increasing lithium alanate content. This result should be compared with Fig. 8, from which it can be deduced that the polarization resistance decreases with increasing lithium alanate content. These results can be combined to obtain the polarization parameter k (36), defined as

$$k = \kappa |d\eta/d(i/A)| \quad [12]$$

The polarization parameter is plotted as a function of the composition in Fig. 11. This current distribution function is of importance for the throwing power of the plating bath (37). A sharp maximum is visible near the point

Table V. Aluminum hydride plating bath

Constituent	Function
$\text{AlHCl}_2 \cdot 2\text{THF}$	H^- : Catalyst
$\text{AlCl}_3 \cdot 2\text{THF}$	AlX_3^- : Acceptor for X^-
$\text{LiAlCl}_4 \cdot 4\text{THF}$	AlX_4^- : Donor for X^-
	Charge carrier
	Li^+ : Charge carrier.

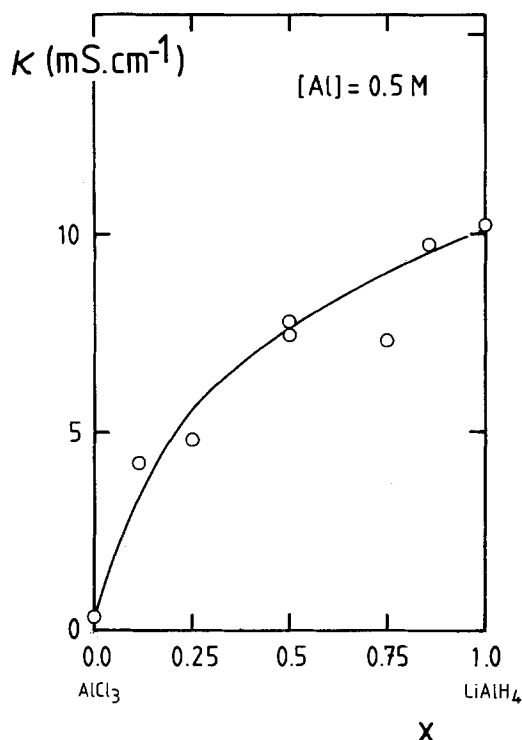


Fig. 10. Conductivity of $\text{AlCl}_3/\text{LiAlH}_4/\text{THF}$ solutions vs. the bath composition.

where the molar ratio of $[\text{AlCl}_3^0]$ to $[\text{LiAlH}_4^0]$ is about 5. If a plating bath is prepared in this way, a very homogeneous Al deposit can be obtained on complicated structures (38).

The kinetic results can also be used for a consideration of the influence of the bath composition on the average grain size of the electrodeposit. Bockris and Razumney (39) defined the following relationship between the critical nucleus size r_c in the initial stage of electrodeposition and the overpotential η

$$r_c = a\gamma/nF\rho_s\eta \quad [13]$$

where a denotes atomic weight, γ is the edge free energy, and ρ_s denotes the surface density of a two-dimensional nucleus. Equation [13] is valid for the case of crystal growth governed by surface diffusion. This is expected to be the case for low overpotentials (40). If the bath is operated galvanostatically (as is usually the case in plating processes), the overpotential is only small during the nu-

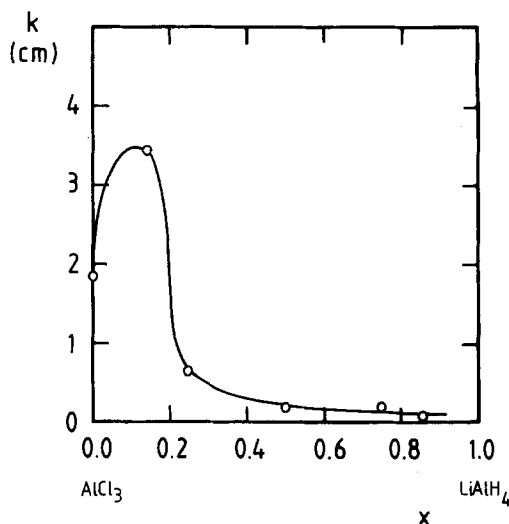


Fig. 11. Current distribution function of $\text{AlCl}_3/\text{LiAlH}_4/\text{THF}$ solutions vs. the bath composition.

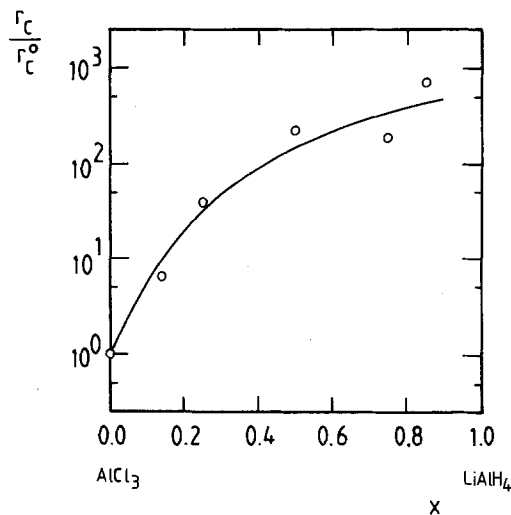


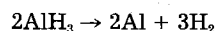
Fig. 12. Grain size parameter as a function of the bath composition under similar plating conditions.

cleation stage. Then, for a constant current, the critical nucleus size is proportional to the inverse of the polarization resistance. This model is rather unsophisticated for the present complicated case of heterogeneous nucleation, and the absolute value of r_c is without significance, but it may be assumed that the tendencies of this quantity under the influence of process conditions reflect the variations in the average grain size of galvanic layers produced in different baths. The relationship between the grain size and the initial concentration of nuclei is inferred from the columnar structure of the grains. Hence, the arbitrary quantity r_c/r_c^0 (where r_c^0 is defined as the theoretical critical nucleus size for a pure AlCl_3 solution under standard conditions) may be used as a grain-size parameter. The variation of r_c/r_c^0 with the bath composition is shown in Fig. 12. According to these data, the average grain size will increase as the hydride content of the plating bath increases. This can be understood by noticing that the presence of hydride enhances the rate of the plating process and also gives rise to a low density of large nuclei under similar plating conditions. This behavior is in fact observed, as Fig. 13 makes clear. Two baths, having comparable conductivities and operated at the same current density, produced different electrodeposited-aluminum layers. Indeed, the grain size was found to increase with increasing hydride concentration. If smooth layers are to be deposited, the plating bath should contain only a small amount of LiAlH_4 .

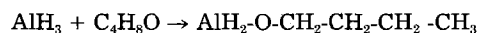
Concluding Remarks

The properties of the aluminum hydride plating solutions are determined by three parameters.

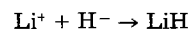
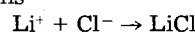
The first is the total hydride concentration $[\text{H}]$. Hydride is present as a catalyst for the electrode reaction. An excess of hydride gives rise to instability of the plating bath. In this case, reactions of the type



occur slowly if the solution is left to stand. Also, ether cleavage is possible in hydride-rich solutions (41), according to the reaction



The second is the total concentration of ligand acceptors $[\text{AlX}_3]$. If an insufficient amount of acceptors is present, the ligand X^- , created in the cathodic process, cannot be stabilized via addition towards AlX_3 . The lithium complex $\text{Li}^+ \cdot 4\text{THF}$ is the only Lewis acid available. This leads to the reactions



These products precipitate at the cathode.

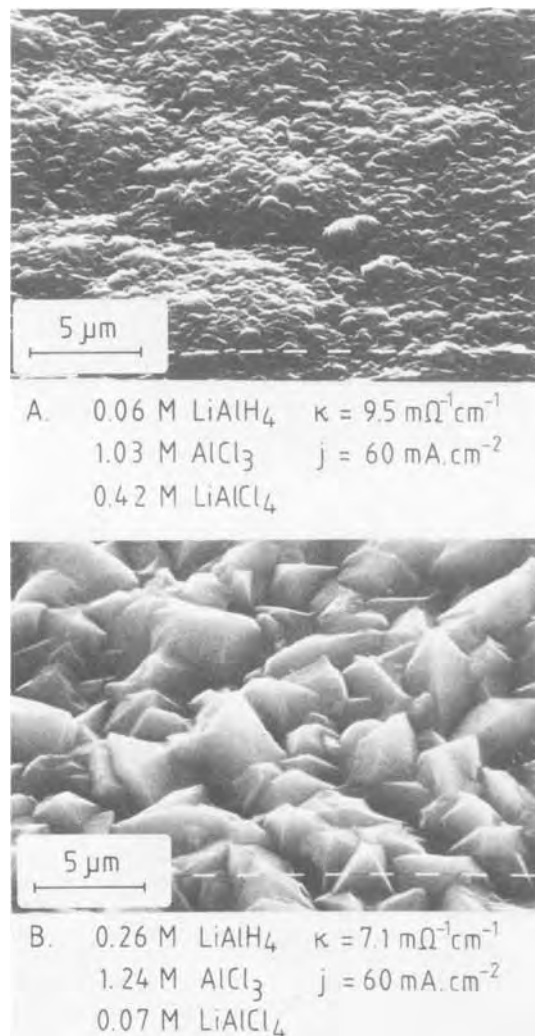


Fig. 13. Scanning electron micrographs of the surfaces of aluminum deposited in different plating baths under similar conditions.

The third is the total concentration of ligand donors [AlX₄⁻]. At the anode, the ligands X⁻ are necessary for the creation of stable AlX₃ · 2THF molecules. These ligands are supplied by AlX₄⁻ anions. If the latter are absent, the activation overpotential for dissolution of aluminum increases. This may cause oxidation of the solvent.

Acknowledgment

The author wishes to thank H. van den Boom and F. J. J. Verschuren for the recording of the Raman spectra, and G. A. R. van Dijk for the preparation of aluminum samples. He also acknowledges the helpful discussions with T. E. G. Daenen.

Manuscript submitted July 2, 1984; revised manuscript received Jan. 15, 1985.

Philips Research Laboratories assisted in meeting the publication costs of this article.

REFERENCES

- D. E. Couch and A. Brenner, *This Journal*, **99**, 234 (1952).
- N. Ishibashi and M. Yoshio, *Electrochim. Acta*, **17**, 1343 (1972).
- M. Yoshio and N. Ishibashi, *J. Appl. Electrochem.*, **3**, 321 (1973).
- J. F. M. van de Berg, T. E. G. Daenen, G. Krijl, and R. E. van de Leest, *Philips Tech. Rev.*, **39**, 87 (1980).
- T. Daenen, G. van Dijk, and S. Stolk, Netherlands Patent Application (1981).
- "Aluminium Taschenbuch," 14th Printing, W. Hufnagel, Editor, Aluminium Verlag Düsseldorf, Germany (1983).
- K. Ziegler and H. Lehmkuhl, *Z. Anorg. Allg. Chem.*, **283**, 414 (1956).
- E. Peled and E. Gileadi, *Plating*, **62**, 342 (1975).
- First International Symposium on Electrodeposition of Aluminum, held at the 68th Annual Technical Conference of the American Electroplaters' Society, Inc., Boston, MA (1981).
- Symposium on Nonaqueous Electrodeposition Processes, held at the 164th Meeting of The Electrochemical Society, Inc., Washington, DC, Oct. 9-14, 1983; Abstracts 233-246, pp. 368-388, The Electrochemical Society Extended Abstracts, Vol. 83-2, Washington, DC, Oct. 9-14, 1983.
- T. Garai, *Mater. Chem. Phys.*, **8**, 399 (1983).
- E. Wiberg and W. Gösele, *Z. Naturforsch., B*, **11**, 485 (1956).
- D. L. Schmidt and E. E. Flagg, *Inorg. Chem.*, **6**, 1262 (1967).
- R. L. Richards and A. Thompson, *J. Chem. Soc. A*, 1244 (1967).
- H. Felkin, *Bull. Soc. Chim. France*, **18**, 347 (1951).
- D. W. Johnson and G. W. Rayner-Canham, *J. Chem. Educ.*, **49**, 211 (1972).
- C. Yarnitzky and Y. Friedman, *Anal. Chem.*, **47**, 876 (1975).
- D. Britz, *J. Electroanal. Chem.*, **88**, 309 (1978).
- G. A. R. van Dijk and H. C. A. M. Smoorenburg, *This Journal*, **131**, 345 (1984).
- E. C. Ashby and J. Prather, *J. Am. Chem. Soc.*, **88**, 729 (1966).
- R. Dautel and W. Zeil, *Z. Elektrochem.*, **64**, 1234 (1960).
- R. Ehrlich, A. R. Young, B. M. Lichstein, and D. Perry, *Inorg. Chem.*, **2**, 650 (1963).
- J. Derouault, P. Granger, and M. T. Forel, *ibid.*, **16**, 3214 (1977).
- A. E. Shirk and D. F. Shriver, *J. Am. Chem. Soc.*, **95**, 5904 (1973).
- D. E. H. Jones and J. L. Wood, *Spectrochim. Acta*, **23A**, 2695 (1967).
- E. C. Ashby, F. R. Dobbs, and H. P. Hopkins, *J. Am. Chem. Soc.*, **95**, 2823 (1973).
- G. G. Evans, J. Kevin, and F. P. Del Greco, *J. Inorg. Nucl. Chem.*, **4**, 40 (1957).
- M. Yoshio, N. Ishibashi, H. Waki, and T. Seiyama, *ibid.*, **34**, 2439 (1972).
- D. D. Macdonald, "Transient Techniques in Electrochemistry," Chap. 4, Plenum Press, New York (1977).
- J. O'M. Bockris and A. K. N. Reddy, "Modern Electrochemistry," 6th Printing, Chap. 9, Plenum Press, New York (1977).
- R. Parsons, *Pure Appl. Chem.*, **52**, 233 (1979).
- A. J. Bard and L. R. Faulkner, "Electrochemical Methods, Fundamentals and Applications," Chap. 11, John Wiley and Sons, New York (1980).
- A. R. Despic and J. O'M. Bockris, *J. Chem. Phys.*, **32**, 389 (1960).
- J. Eckert and M. Galova, *Electrochim. Acta*, **26**, 1169 (1981).
- T. E. G. Daenen, *Nature*, **280**, 378 (1979).
- C. Wagner, *This Journal*, **98**, 116 (1951).
- O. Kardos and D. G. Foulke, "Advances in Electrochemistry and Electrochemical Engineering," Vol. 2, (1962).
- T. E. G. Daenen and S. A. Stolk, U.S. Pat. 4,145,261 (1979).
- J. O'M. Bockris and G. A. Razumney, "Fundamental Aspects of Electrocrystallization," p. 61, Plenum Press, New York (1967).
- A. Damjanovic and J. O'M. Bockris, *This Journal*, **110**, 1035 (1963).
- W. J. Bailey and F. Marktscheffel, *J. Org. Chem.*, **25**, 1797 (1960).

Effects of Thiourea and Guanidine Hydrochloride on Electroless Copper Plating

Aina Hung

Department of Chemical Engineering, Ming-Hsin Engineering College, Hsin-Feng, Hsin-Chu, Taiwan, China

ABSTRACT

The effects of thiourea and guanidine hydrochloride on electroless copper plating were studied by voltammetric and gravimetric methods. Thiourea stabilizes the plating bath and simultaneously decreases the plating rate. The effect of stabilization is attributed to the strong complexing ability of thiourea with Cu(I) and the surface adsorption of thiourea on copper. The surface adsorption is the main reason for the decrease in plating rate. In the case of guanidine hydrochloride, the plating rate is maximum when its concentration is approximately 5 mg/liter. The occurrence of the maximum is interpreted in terms of the interplay of the delocalized π electron effect of guanidine hydrochloride and its surface adsorption on copper.

Since ABS was plated with metals successfully in 1960 (1), the technology of plastics plating has been improving continuously (2, 3). Numerous parts for industrial and household products formerly made with metals were replaced by plated plastics (4-6). The demand for plated plastics has been increasing rapidly; hence, the technique of preparing more stable electroless plating baths with improved plating rates has become one of the main concerns in research. Reported improvements in this regard include optimizations in the nature and concentration of complexing (7) and reducing agents (8), bath temperature (9), pH (10), and, most interestingly, additives (11, 12). Certain additives, such as pyridine and cytosine, enhance the plating rate of electroless copper plating. Small amounts of other additives such as HIQSA (8-hydroxy-7-iodo-5 quinoline sulfonic acid) not only enhance the plating rate, but also stabilize the bath (13). However, high concentrations of some additives such as thiourea result in the undesirable effect of decreasing the plating rate (14, 15). The mechanism of the effect of additives in electroless copper bath was discussed by Schoenberg (13), Nuzzi (9), and Paunovic (16, 17). The correlation between the plating rate and the electronic structure of additives has been discussed. It has been speculated that the change in plating rate results from the surface adsorption of additives and its effect on polarization characteristics of anodic or cathodic partial reactions.

In this paper, the effects of thiourea and guanidine hydrochloride on electroless copper plating were studied using both voltammetric and gravimetric methods. The polarographic method was also used to investigate the complexing ability of the additives and sodium potassium tartrate with copper ions at pH 12.5, an optimized pH suggested for practical plating (9, 10).

Experimental

The voltammetric experiments were performed at room temperature with an electroless copper plating bath recommended by Pearlstein and Baudrand (18). The bath contained 13.8 g/liter $\text{CuSO}_4 \cdot 5\text{H}_2\text{O}$, 69.2 g/liter sodium potassium tartrate, 38 ml/liter formaline (37% by weight), and sodium hydroxide to give a pH of 12.50. Oxygen was removed by bubbling nitrogen through the solution for a few minutes. 50 ml of the solution was put in a glass cell equipped with three electrodes. The working electrode was a 99.5% pure copper wire 1.74 cm long and of 0.165 cm diam. The counterelectrode was a platinum wire 2.14 cm long and of 0.085 cm diam. A saturated calomel electrode (SCE) was used as a reference electrode. The cyclic voltammetric instrument was made by Sun-Light Corporation of Taiwan. It includes a 9028 programmer and a 9627 potentiostat. The scan rate was fixed at 0.1 V/s for all measurements. First, the voltammogram of static electroless copper plating solution without additive was taken in the range of -0.8 to 0 V. Then the voltammograms of the same bath with various amounts of additives were taken in the same potential range.

The same plating bath was used for the gravimetric experiment. 250 ml of the plating solution was used for each gravimetric plating rate measurement. Prior to immersion into the plating solution, a copper plate with specific dimensions was cleaned, weighed, and activated in PdCl_2 . Oxygen was removed by bubbling nitrogen through solution before plating. During plating, nitrogen gas was allowed to flow over the loosely sealed plating bath to keep oxygen away. After 30 min of deposition at room temperature, the copper plate was removed from the bath, dried, and weighed to determine the amount of copper deposited.

A Model 384 polarographic analyzer with Model 303 static mercury drop electrode from EG&G PAR was used for measuring the reduction half-wave potential of copper ion at room temperature. The blank solution contained 10 ml of sodium hydroxide solution at pH 12.5. The reduction half-wave potential of copper was first measured when only copper ions were present at $10^{-3}M$ in the blank. Various amounts of tartrate, thiourea, or guanidine hydrochloride were then added, and the reduction half-wave potentials of copper were recorded.

Results

The effect of thiourea on the anodic peak of the voltammogram is shown in Fig. 1. The peak in the range of -0.67 to -0.45V is due to the oxidation of HCHO. The current decreased gradually with the addition of thiourea. The zero current potential shifted to more positive values as the amount of thiourea was increased. The peak at -0.43V resulted from the oxidation of copper electrode. The peak shifted to more positive values (-0.35V) when the amount of thiourea was increased in the bath. In Fig. 2, the oxidation of HCHO can be considered separately in two ranges: the current in the range between zero current potential and -0.67V increased with the increase of guanidine hydrochloride; however, the current in the range between -0.67 and -0.45V decreased with the increase of guanidine hydrochloride. Figure 2 also shows that the zero current potential was shifted to more negative values when the amount of guanidine hydrochloride was increased. The peak current for the oxidation of copper electrode (-0.43V) decreased with the amount of guanidine hydrochloride added.

The gravimetric study showed that the addition of thiourea caused a decrease in the rate of electroless copper deposition (Fig. 3). On the other hand, the plating rate showed a maximum with the addition of guanidine hydrochloride at about 5 mg/liter (Fig. 4).

In the polarographic study using the procedure described by Lingane (19), it was found that Cu(II) and tartrate form a strong 1:2 complex. The stability constant calculated was 3.2×10^8 . In actual electroless copper solution, there are various other possible strong complex ions of Cu(II)-tartrate (20). However, the complex between Cu(I) and tartrate was found to be relatively weak. On the

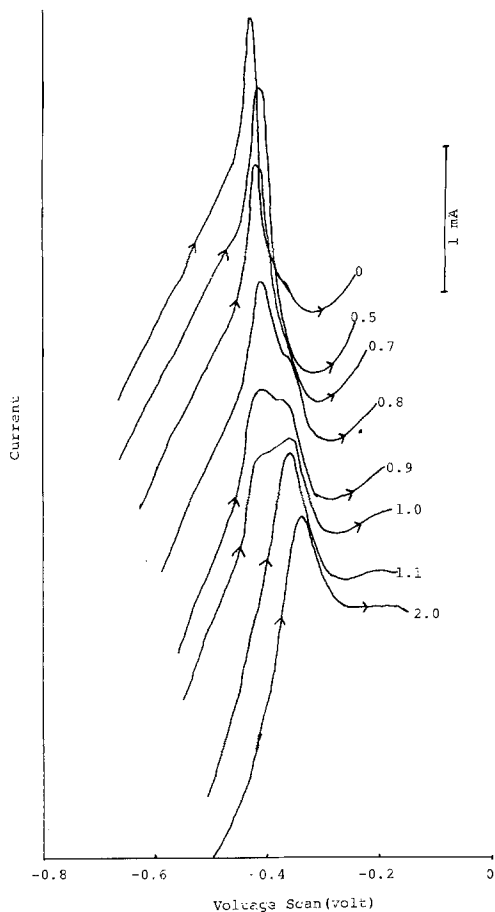


Fig. 1. Effects of thiourea on the anodic oxidation of formaldehyde shown on voltammograms of copper electrode in electroless copper solution. The numbers indicate the concentration of thiourea added in milligrams per liter. The I-V curves were shifted along the current (I) axis for clarification. Each curve was started to draw from zero current potential.

other hand, thiourea was found to form a very strong 1:4 complex with Cu(I). The stability constant calculated was 2.7×10^{11} , whereas the complex formed between thiourea and Cu(II) was relatively weak. For guanidine hydrochloride, there was no evidence of complex formation with copper ions from the polarographic study carried out at pH 12.5.

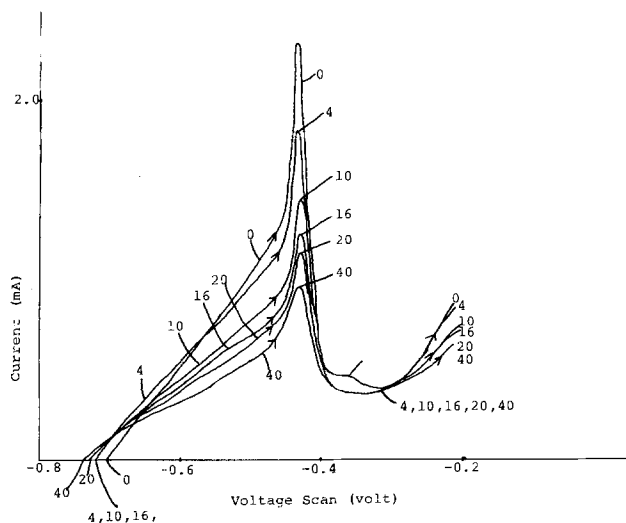


Fig. 2. Effects of guanidine hydrochloride on the anodic oxidation of formaldehyde shown on voltammograms of copper electrode in electroless copper solution. The numbers indicate the concentration of guanidine hydrochloride added in milligrams per liter.

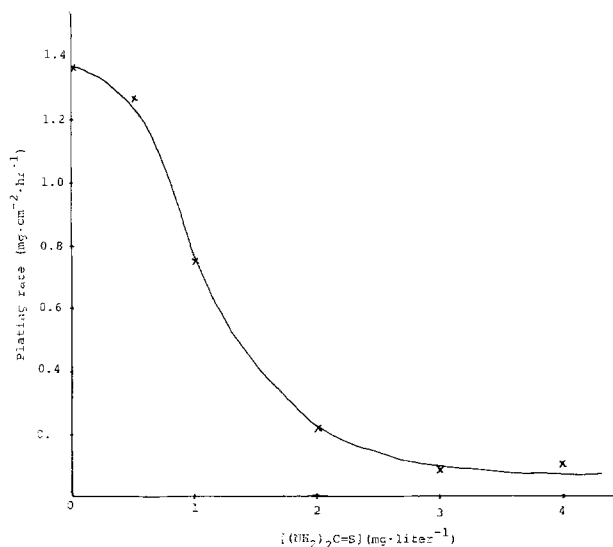


Fig. 3. Effect of thiourea on electroless copper plating rate, determined by gravimetric method.

Discussion

The disappearance of the peak for the oxidation of HCHO in Fig. 1 on addition of thiourea can be explained by the adsorption of thiourea to copper surface. This interpretation is supported by the gravimetric result that the plating rate decreases with the increase of the addition of thiourea. Suppose that the adsorption of thiourea on copper follows the Langmuir isotherm; then, the fractional surface coverage of thiourea is given by

$$\theta = \frac{KC_t}{1 + KC_t} \quad [1]$$

where C_t denotes the concentration of thiourea and K is the adsorption constant.

If the copper deposition is inhibited by the adsorption of thiourea on the copper surface, the fractional surface coverage of the adsorbed species should be reflected in the measured rates of deposition. Thus, if the plating rates measured in the presence and absence of thiourea are r_t and r_o , respectively, then the fractional surface coverage may be computed by

$$\theta = 1 - \frac{r_t}{r_o} \quad [2]$$

Equations [1] and [2] can be combined and rearranged to give

$$\frac{1}{r_t} = \frac{1}{r_o} + \frac{K}{r_o} C_t \quad [3]$$

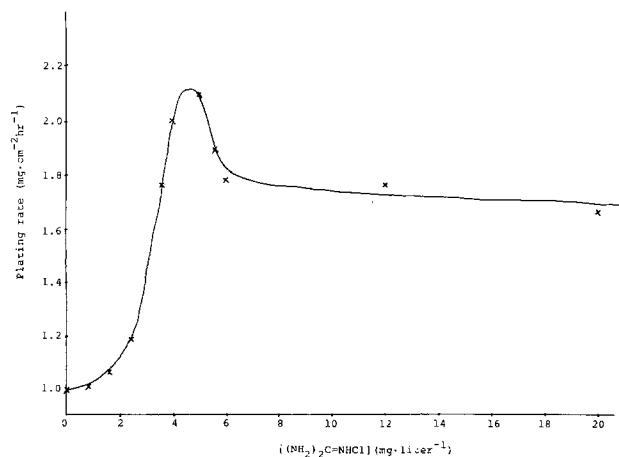


Fig. 4. Effect of guanidine hydrochloride on electroless copper plating rate, determined by gravimetric method.

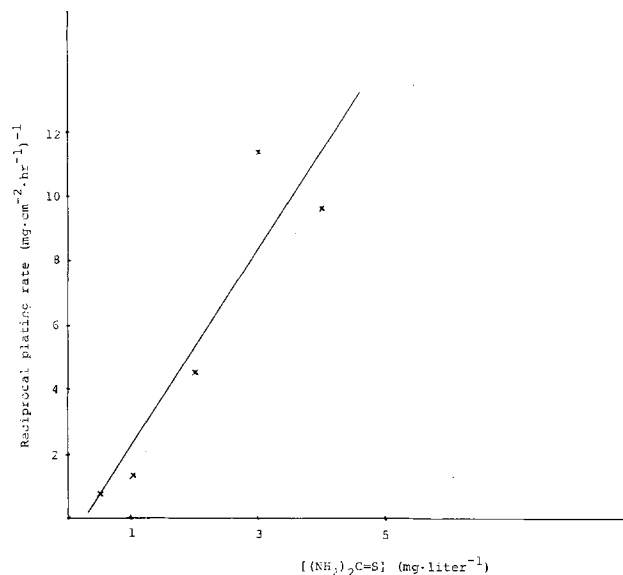


Fig. 5. Test of Eq. [3] for thiourea

The plot of reciprocal plating rate vs. concentration of additive (Fig. 5) was linear, as expected from Eq. [3]. However, the scattering of data should not be neglected. It implies that there are some other factors influencing the plating rate. Nevertheless, from the straight line drawn in Fig. 5, the adsorption equilibrium constant was estimated to be $3.14 \times 10^6 M$. The large K value shows that thiourea strongly adsorbs on copper surface. Hence, it is clear that the plating rate is controlled predominantly by the adsorption of thiourea on copper surface.

Small amounts of Cu(I) present in the plating bath may exist as Cu_2O precipitate. It tends to disproportionate readily to form Cu(O). The Cu_2O particles or Cu(O) particles randomly dispersed in solution can act as nuclei for uncontrolled deposition of copper, leading to bath decomposition (22). From the stability constant, it is evident that thiourea forms a strong complex with Cu(I). The voltammograms in Fig. 1 show that the peak for the oxidation of copper electrode shifted from -0.43 to $-0.35V$ with the addition of thiourea from 0 to 2.0 mg. It is speculated that a new slow reaction pathway was introduced because of the adsorption of thiourea on copper (17, 21). The adsorption of thiourea on copper and the formation of a strong complex between thiourea and Cu(I) explain why a small amount of thiourea stabilizes the electroless copper plating bath.

Voltammograms of plating solutions with various amounts of guanidine hydrochloride are shown in Fig. 2. Four phenomena were observed: (i) the zero current potential shifted to more negative values as the concentration of guanidine hydrochloride was increased; (ii) the current for the oxidation of HCHO in the range between zero current potential and $-0.67V$ increased concomitantly; (iii) the current for the oxidation of HCHO in the range between -0.67 and $-0.45V$ decreased as the amount of guanidine hydrochloride was increased; and (iv) the peak current for the oxidation of copper electrode decreased with the increase of guanidine hydrochloride. The first and the second phenomena are interpreted as a consequence of rate enhancement by the delocalized π electron of guanidine hydrochloride (17). The third is believed to result from the decrease in the number of active sites for the oxidation of HCHO caused by the adsorption of guanidine hydrochloride to the copper surface. The peak for the oxidation of copper electrode does not shift with the addition of guanidine hydrochloride. It shows that there is no new pathway for the oxidation of copper electrode with the addition of guanidine hydrochloride. However, the peak current did decrease as the amount of guanidine hydrochloride was increased. This result con-

firms the decrease of free copper surface by the adsorption of guanidine hydrochloride. The effect of delocalized π electron and surface adsorption work simultaneously at the copper surface, resulting in the appearance of a maximum plating rate at about 5 mg/liter of added guanidine hydrochloride.

With further additions of guanidine hydrochloride up to 40 mg/liter, the plating rate decreased only slowly. This indicates that the surface adsorption of this compound is not as strong as that of thiourea. Instead, the effect of delocalized π electron plays a much more important role in determining the plating rate in the presence of guanidine hydrochloride.

Another additive, urea, whose molecular structure is similar to thiourea and guanidine hydrochloride, was studied for comparison. The addition of urea had no observable effect on voltammogram and plating rate. The result implies that neither surface adsorption nor complex formation with Cu(I) had any significant effect on the rate of electroless copper plating.

In conclusion, it has been discussed that there are three different effects of additives in electroless copper plating: (i) the surface adsorption of additive on copper surface decreases the plating rate; (ii) delocalized π electron of additive enhances the plating rate; and (iii) the stronger complexing ability of additive with Cu(I) than with Cu(II) stabilizes the solution. Besides the three additives studied, the effects of other additives reported in the literature, such as 2-mercaptobenzothiazole, pyridine, adenine, 2,2'-biquinoline, and cystine, may also be explained in terms of the same arguments.

Acknowledgments

This material is based upon work supported by Ming-Hsin Engineering College. I am pleased to thank Professor Chi-Chao Wan and Professor Hwa Sheng Cheng of National Tsing Hua University for permitting me to use some of their laboratory equipment. I also wish to express my gratitude to Professor Cheu-Pyeng Cheng for valuable comments during the preparation of the manuscript.

Manuscript submitted Sept. 6, 1984; revised manuscript received Dec. 10, 1984.

Ming-Hsin Engineering College assisted in meeting the publication costs of this article.

REFERENCES

1. F. A. Lowenheim, "Modern Electroplating," McGraw-Hill Book Co., New York (1978).
2. M. Murphy, *Met. Finish.* **82**, 17 (1984).
3. M. Murphy, *ibid.*, **81**, 21 (1983).
4. L. Streeter, *Electroplating. Met. Finish.* **27**, 8 (1974).
5. J. Hulme and N. H. Jordan, *Finish. Industries*, 15 (1977).
6. A. M. Poskanzer and S. C. Davis, *Plating Surf. Finish.*, 94 (1982).
7. M. Paunovic, *This Journal*, **124**, 349 (1977).
8. R. R. Brookshire, U.S. Pat. 3,046,159 (1962).
9. F. J. Nuzzi, *Plating Surf. Finish.*, 51 (1983).
10. J. Duffy, L. Pearson, and M. Paunovic, *This Journal*, **130**, 876 (1983).
11. J. L. Morico and H. W. Pender, U.S. Pat. 3,595,684 (1971).
12. J. F. McCormack and F. J. Nuzzi, U.S. Pat. 4,301,196 (1981).
13. L. N. Schoenberg, *This Journal*, **119**, 1491 (1972).
14. E. B. Saubestre, *Plating*, **59**, 563 (1972).
15. F. W. Schneble, Jr., R. J. Zeblicky, J. F. McCormack, and J. D. Williamson, U.S. Pat. 3,361,580 (1968).
16. M. Paunovic, *Plating*, **55**, 1161 (1968).
17. M. Paunovic and R. Arndt, *This Journal*, **130**, 794 (1983).
18. F. Pearlstein and D. Baudrand, "Electroless Deposition of Metals," American Electroplater's Society, Inc. (1972).
19. J. J. Lingane, *Chem. Rev.*, **29**, 1 (1941).
20. L. N. Schoenberg, *This Journal*, **118**, 1571 (1971).
21. R. H. Wopschall and I. Shain, *Anal. Chem.*, **39**, 1514 (1967).
22. P. Malathy and B. A. Sheno, *Finish. Industries*, 26 (1977).

Factors That Affect Uniformity of Plating of Through-Holes in Printed Circuit Boards

I. Stagnant Fluid in the Through-Holes

Timothy Sullivan and Stanley Middleman

Department of AMES/Chemical Engineering, University of California, San Diego, La Jolla, California 92093

ABSTRACT

Solutions are presented to a mathematical model that accounts for mass-transfer effects on the rate of plating of through-holes in circuit boards. The assumption is made that the liquid in the through-hole is stationary. Results indicate that even for aspect ratios as low as 3:1, very nonuniform plating occurs along the axis of the through-hole, unless flow within the through-hole can be induced.

Printed circuit board design is moving in a direction leading to increased aspect ratios for plated through-holes that connect parallel layers of circuits. A plating process must be designed to achieve deposition rates that are high enough to yield acceptable productivity in a plating line while maintaining uniformity of deposition consistent with quality considerations. These criteria will be increasingly difficult to achieve as aspect ratios increase for through-holes.

Figure 1 suggests the nature of the physical problems that must be dealt with. We consider a cylindrical through-hole of diameter D , connecting a pair of plane layers separated by a distance L . We define L/D as the aspect ratio of the through-holes. Aspect ratios of 5:1 are common today, and ratios of 20:1 are in the prototype stage in many board shops. Under most industrial circumstances, the rate of plating is controlled by mass-transfer resistances between the plating bath and the board surface. Bath agitation can promote the delivery of electrolyte to the board, but ultimately it is diffusion that controls the delivery of the metal ions or compounds to the sites of deposition. The fundamental question of concern here is this: to what degree can control of the external hydrodynamics in the bath be used to promote diffusion into the relatively stagnant through-holes?

In this paper, we examine the nature of the problem at hand by developing a mathematical model for the non-uniformity to be expected in the plating of through-holes that are filled with stagnant liquid. Part II of this series will present the effect of flow through the through-holes on deposition rate and uniformity.

Mathematical Model

We consider, as in Fig. 2, the region that includes a representative through-hole and the surrounding bath. A diffusion boundary layer, of thickness δ , separates the

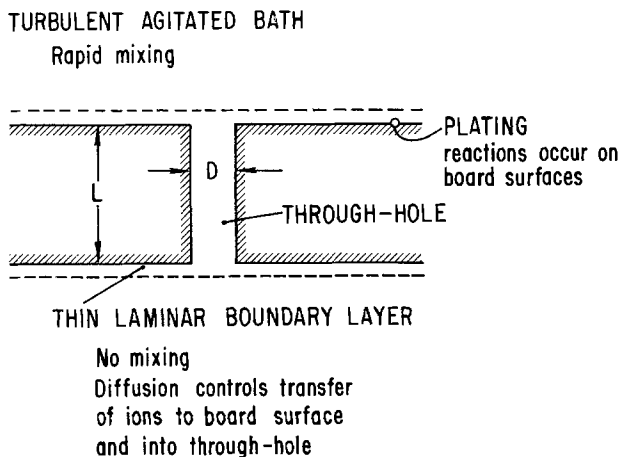


Fig. 1. Phenomena that affect plating within and near the surfaces of a through-hole.

well-agitated bath from the board surface. Fluid within this region is not necessarily stagnant. There could be flow parallel to the board surface, for example. However, we assume that such a flow cannot contribute to the transport of any dissolved species in the direction normal to the board. In other words, external hydrodynamics in the bath, due to agitation, can control the magnitude of the diffusion boundary layer, but ultimately it is diffusion across this layer that delivers a chemical species to the site of plating. In this model, we do assume that fluid in the through-hole is stagnant.

A metallic species is in solution at a concentration C_b in the bath. This species must diffuse through the stagnant solution until, upon achieving contact with the solid surface of the board or through-hole, a reaction occurs which leaves a metal film on the solid.

Within the diffusion layer and through-hole, the concentration of the metallic species, C , is a function of time and position, governed by the diffusion equation

$$\frac{\partial C}{\partial t} = \mathcal{D} \left(\frac{\partial^2 C}{\partial r^2} + \frac{1}{r} \frac{\partial C}{\partial r} + \frac{\partial^2 C}{\partial z^2} \right) \quad [1]$$

For simplification of the mathematics, it is assumed here that the concentration field has angular symmetry about the axis of the hole.

Boundary conditions express the following physical elements of the model

$$C = C_0 \text{ for } t \leq 0 \quad [2]$$

The board has entered the plating bath from a prior clean-

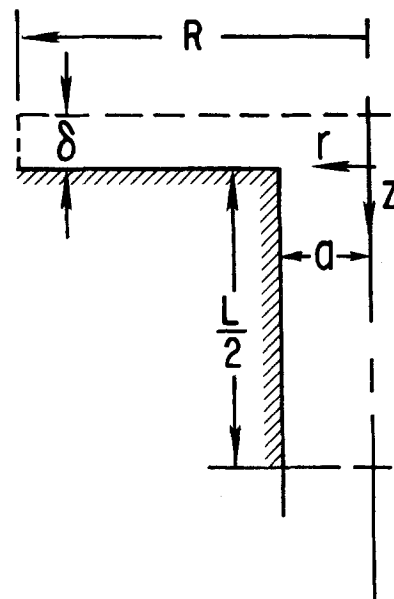


Fig. 2. Definition sketch for the mathematical analysis

ing bath, and the through-holes and the board have entrained a liquid film whose concentration in the metallic species is C_o , different from the concentration C_b in the plating bath. This is an initial condition on the solution of Eq. [1]

$$C = C_b \text{ at } z = -\delta \tag{3}$$

This reflects our assumption that the bath is of uniform concentration to within a distance δ of the board.

$$\frac{\partial C}{\partial z} = 0 \text{ at } z = \frac{1}{2}L \tag{4}$$

We assume symmetry of agitation on both sides of the board. Hence, at the midpoint along the axis of the hole, the concentration gradient vanishes.

$$\frac{\partial C}{\partial r} = 0 \text{ at } r = R, -\delta \leq z < 0 \tag{5}$$

We assume that at some distance R from the axis of the hole, in the diffusion layer above the board, the influence of the hole vanishes and C is no longer a function of r

$$\frac{\partial C}{\partial r} = 0 \text{ at } r = 0 \tag{6}$$

This expresses angular symmetry about the axis of the hole.

The final boundary conditions require some assumptions regarding the rate of deposition of the metallic species on the surface. Whatever factors control the deposition process, we know that the deposition rate (per unit of surface area), \mathcal{R} , must be balanced by the diffusion flux to the surface. In general, then, the boundary conditions take the form

$$\mathcal{R} = -\mathcal{D} \frac{\partial c}{\partial r} \text{ at } r = a, 0 \leq z \leq L/2 \tag{7}$$

$$\mathcal{R} = -\mathcal{D} \frac{\partial c}{\partial z} \text{ at } z = 0, a \leq r \leq R$$

These conditions require that we have kinetic data sufficient to permit a relationship to be written between \mathcal{R} and C . For example, if the reaction is first order

$$\mathcal{R} = kC \tag{8}$$

where k is the rate coefficient. Of course, more complex reaction schemes could be envisioned. In this study, we will adopt Eq. [8].

It is convenient to nondimensionalize Eq. [1] in the following manner. Define a dimensionless time and a radial and axial variable as

$$\theta \equiv \frac{\mathcal{D}t}{a^2} \quad s \equiv \frac{r}{a} \quad x \equiv \frac{z}{a}$$

Define a dimensionless concentration as

$$\phi \equiv \frac{C}{C_b}$$

Then, Eq. [1] takes the form

$$\frac{\partial \phi}{\partial \theta} = \frac{\partial^2 \phi}{\partial s^2} + \frac{1}{s} \frac{\partial \phi}{\partial s} + \frac{\partial^2 \phi}{\partial x^2} \tag{9}$$

Initial and boundary conditions take the forms

$$\phi = \phi_o \equiv \frac{C_o}{C_b} \text{ for } \theta \leq 0 \tag{10}$$

$$\phi = 1 \text{ at } x = -\Delta = -\delta/a \tag{11}$$

$$\frac{\partial \phi}{\partial x} = 0 \text{ at } x = A = \frac{1}{2} \frac{L}{a} \tag{12}$$

$$\frac{\partial \phi}{\partial s} = 0 \text{ at } s = B = \frac{R}{a}, -\Delta \leq x \leq 0 \tag{13}$$

$$\frac{\partial \phi}{\partial s} = 0 \text{ at } s = 0 \tag{14}$$

$$-\frac{\partial \phi}{\partial s} = K_D \phi \text{ at } s = 1, 0 \leq x \leq \frac{1}{2}A \tag{15}$$

$$-\frac{\partial \phi}{\partial x} = K_D \phi \text{ at } x = 0, 1 \leq s \leq B \tag{16}$$

where $K_D = ka/\mathcal{D}$.

We note that this nondimensionalization removes all parameters from the diffusion equation, and introduces, into the boundary and initial conditions, the dimensionless parameters Δ, A, B, K_D , and ϕ_o .

Solution Method

Equation [9] is solved by a finite difference method, using the alternating direction implicit (ADI) procedure (1). The spatial (s, x) discretization is refined until the solution becomes insensitive to mesh size. The advantage of the ADI method is that it is convergent and stable for any time step, although too large a time step gives inaccurate results. A few numerical "experiments" using various time steps and mesh resolution lead to determination of a solution method that represents a good compromise between accuracy, memory requirements, and machine time.

Two test problems, for which analytical solutions are available, were used as an aid to assessing the accuracy of the computational procedure. In each case, Eq. [9] was solved under a set of simplified boundary and initial conditions.

Test Case 1.—Transient diffusion into a through-hole in the absence of reaction.—We solve Eq. [9] with the following conditions

$$\phi_o = 0 \text{ at } \theta \leq 0 \tag{10'}$$

$$\phi = 1 \text{ at } x = -\Delta = 0 \tag{11'}$$

$$\frac{\partial \phi}{\partial x} = 0 \text{ at } x = A = 3 \tag{12'}$$

$$\frac{\partial \phi}{\partial s} = 0 \text{ at } s = 0 \tag{14'}$$

$$\frac{\partial \phi}{\partial s} = 0 \text{ at } s = 1 \tag{15'}$$

From the exact analytical solution (2), we may write

$$1 - \phi = \frac{4}{\pi} \sum_{n=0}^{\infty} \frac{(-1)^n}{m} \cos \left[\frac{m\pi(A-x)}{2A} \right] \exp \left(-\frac{m^2\pi^2}{4A^2} \theta \right) \tag{17}$$

where $m = 2n + 1$.

Test Case 2.—Reaction on the walls of a through-hole isolated from the external bath.—We solve Eq. [9] with the following conditions

$$\phi_o = 1 \text{ at } \theta \leq 0 \tag{10''}$$

$$\frac{\partial \phi}{\partial x} = 0 \text{ at } x = -\Delta = 0 \tag{11''}$$

$$\frac{\partial \phi}{\partial x} = 0 \text{ at } x = A = 3 \tag{12''}$$

$$\frac{\partial \phi}{\partial s} = 0 \text{ at } s = 0 \tag{14''}$$

$$-\frac{\partial \phi}{\partial s} = K_D \phi \text{ at } s = 1 \tag{15''}$$

The exact analytical solution (2) may be written

$$\phi = \sum_{n=1}^{\infty} e^{-\lambda^2 \theta} \frac{2K_D J_0(\lambda_n s)}{(\lambda_n^2 + K_D^2) J_0(\lambda_n)} \tag{18}$$

where the λ_n are the roots of

$$K_D J_0(\lambda_n) = \lambda_n J_1(\lambda_n)$$

Figure 3 shows the transient approach to equilibrium of the concentration at a point on the axis of the hole ($s = 0$), midway between the top and middle of the hole (i.e., at $x = 1/2 A = 3/2$). The spatial mesh and the time step used in the numerical solution are shown in the figure as well.

It is apparent that the mesh and time step used give accurate solutions over most of the approach to equilibrium. It is also apparent that the time scales characteristic of the approach to equilibrium differ markedly depending upon whether radial or axial diffusion dominates, for an aspect ratio of $A = 3$. This observation suggests that it does not matter much if the through-hole has plating solution in it initially (Eq. [10']), or whether it is free of plating solution (Eq. [10'']). Any initially available metal ion will quickly diffuse to the wall, and subsequent plating will depend upon supply of metal ion from the external bath.

Results

Figure 4 shows isoconcentration lines for a given set of geometric parameters, at two different times. The times are selected to be at steady state, and at the half-time. Some remarks on the definition of steady state are necessary.

Figure 5 shows the approach to equilibrium (steady state) for several cases. An arbitrary definition of steady state is always necessary in diffusion problems. Since the approach to equilibrium is asymptotic, an infinite time is required to achieve steady state, and, of course, this does not yield a useful time scale for the process. We have used the concentration at the position $s = 0$, $x = 1/2 A$, as a "tracer" for the approach to steady state. Thus, in Fig. 5, we plot $1 - \phi(0, 1/2 A, \theta) / \phi(0, 1/2 A, \infty)$ against θ . By $\theta = \infty$, we mean a time long enough that $\phi(0, 1/2 A)$ no longer changes. As Fig. 5 shows, for the specific parameter values illustrated, half-times are of order $\theta = 1$, but depend on K_D and Δ .

Figure 6 gives an indication of the reduction in the plating rate to be expected within the through-hole. The results of the numerical simulation are normalized to the plating rate on the plane-exposed surface of the board, far from the hole (i.e., at $s = B$). Results are shown for times beyond that required for achievement of steady plating. In effect, Fig. 6 displays the plating thickness at various positions, relative to the thickness that would be achieved

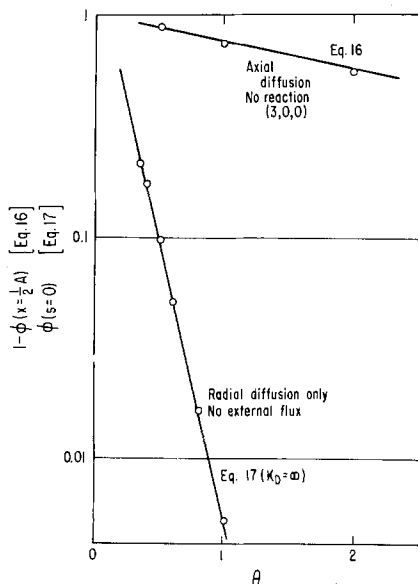


Fig. 3. Transient approach to equilibrium for two test cases. Comparison of exact solutions (—) and numerical results (○). Values of A , K_D , Δ appended to the upper curve. A uniform mesh is used, with $\Delta x = \Delta s = 0.125$. A time step of $\Delta \theta = 0.1$ is used.

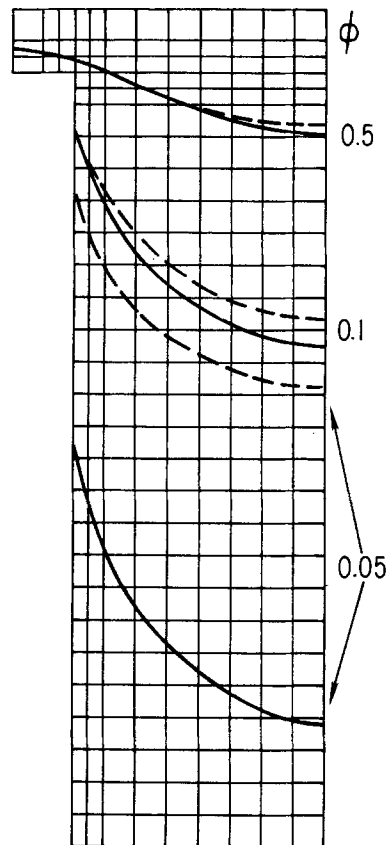


Fig. 4. Concentration profiles at steady state (—) and at the half-time (---), for the case $A = 3$, $\Delta = 0.25$, $\phi_0 = 0$, $K_D = 10$, $R = 1.25$.

on the board if the through-hole were absent. Note that the uniformity of plating is improved at smaller values of K_D . Under no circumstances, for the range of parameters examined, is the plating rate uniform. In the cases studied, the plating rate falls below half of the exposed-surface rate at a depth of less than one diameter of the hole. Thus one can anticipate highly nonuniform plating in through-holes of aspect ratios of 3 or greater, unless one operates at very low plating rates ($K_D \ll 1$), under conditions consistent with the assumptions of this simulation. In particular, of course, these results hold on the assumption that the liquid in the through-hole is stag-

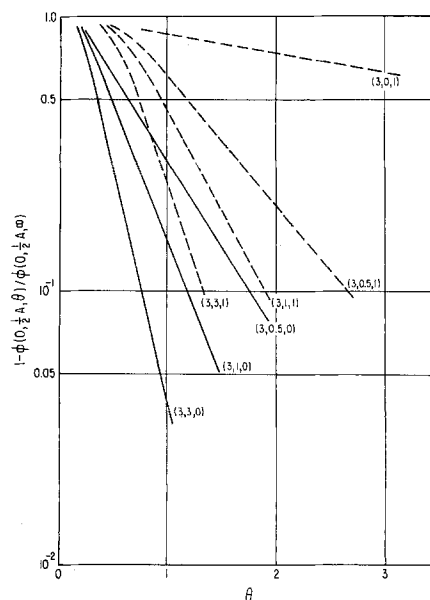


Fig. 5. The approach to steady state, under various conditions. Values of A , K_D , Δ appended to each curve. In all cases, $\phi_0 = 0$.

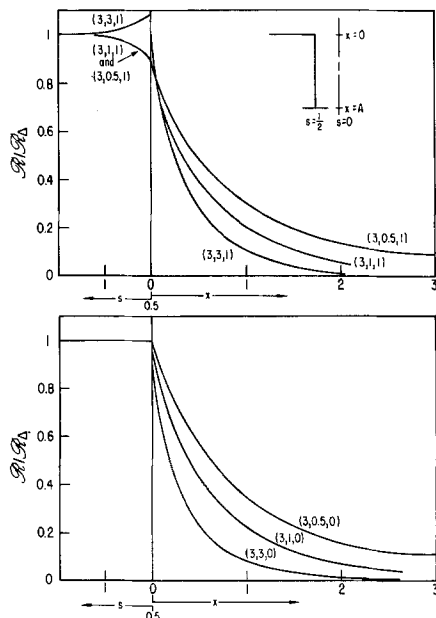


Fig. 6. Plating rate as a function of position, for various parameters, at steady state, normalized to the rate on the exposed surface far from the hole.

nant. (Flow within the through-hole will be addressed in part II of this series.)

In addition to the nonuniformity of plating, our results also illustrate the effect of diffusion resistance on the magnitude of the plating rate, relative to what one would achieve in the absence of any mass-transfer resistance. The nonuniformity is a consequence of the mass-transfer resistance of the stagnant fluid in the through-hole. The magnitude of the plating rate is further reduced by a finite external mass-transfer resistance, controlled by the value of Δ and K_D .

In the absence of a through-hole, plating occurs via one-dimensional diffusion to the planar surface of the board. In this case, the diffusion equations simplify to the form (at steady state)

$$\frac{d^2\phi}{dx^2} = 0 \quad [19]$$

$$\phi = 1 \text{ at } x = -\Delta$$

$$-\frac{d\phi}{dx} = K_D\phi \text{ at } x = 0$$

One easily finds $\phi(x)$, and from the surface value, $\phi(0)$, the plating rate is found to be

$$\mathcal{R}_\Delta = K_D\phi(0) = \frac{K_D}{1 + \Delta K_D} \quad [20]$$

Under conditions of efficient agitation, where the surface of the board is at the bath concentration ($\phi = 1$), that is, at $\Delta = 0$, the maximum plating rate is

$$\mathcal{R}_{\max} = K_D \quad [21]$$

Hence, the reduction in rate, due to the presence of Δ alone, is given by

$$\frac{\mathcal{R}_\Delta}{\mathcal{R}_{\max}} = (1 + \Delta K_D)^{-1} \quad [22]$$

As a typical example, we find that for $\Delta = 0.25$ (efficient agitation) and $K_D = 10$ (rapid reaction, relative to the diffusion rate), Eq. [22] predicts that the plating rate is only 30% of the value that would be achieved in the limiting case of $\Delta = 0$, despite the fact that Δ is so small. This reflects the strong interplay of reaction with diffusion. A large K_D value can lead to significant mass-transfer inhibition, even though Δ itself may be quite small. This is because the factor ΔK_D may be written as

$$\Delta K_D = \frac{k\delta}{\mathcal{D}} \quad [23]$$

and it is the magnitude of this particular combination of parameters, rather than Δ and K_D individually, that controls the importance of external mass-transfer effects on plating rate.

Some comments on the time required to achieve steady plating are in order. As Fig. 5 shows, half-times are of order one for the $\Delta = 1$ cases examined, and about half that magnitude for the $\Delta = 0$ cases. Half-times will be longer or shorter for larger or smaller aspect ratios, respectively. Since dimensionless variables are used, it is worthwhile to examine what these results mean in terms of real times.

From the definition of θ , the real half-time is

$$t_{1/2} = \frac{a^2}{\mathcal{D}}\theta_{1/2} \quad [24]$$

Under typical conditions (3), we might have a board of thickness $L = 0.092$ in. with a through-hole of diameter $2a = 0.031$ in. ($A = 3$). The diffusivity of copper ion in aqueous solution is of order 10^{-5} cm²/s. Converting a to centimeters, we find

$$t_{1/2} = 123 \theta_{1/2} \text{ (s)} \quad [25]$$

Hence, for half-times of order one (in θ), we anticipate that the transient period of plating is only of a duration of a few minutes. Since plating times are typically of the order of tens of minutes, we expect that the steady-state results for plating rate are of most interest to us.

Since these simulations, and the conclusions drawn from them, are strongly dependent upon the magnitude of K_D , it is important to estimate the range of K_D to be expected in commercial plating operations. Plating baths are often "rated" in terms of microinches of copper deposited over a specific time interval. A plating rate of 30 microinches in 10 min is regarded as a fast rate in an electroless process in a bubble-agitated bath (4).

Unfortunately, it is rarely possible to estimate the magnitude of the diffusion layer thickness, δ , in commercial systems. An upper limit can be estimated on the assumption that the deposition is completely mass-transfer controlled. [In electrolytic plating, this is just the condition of plating at the limiting current (6).] We assume, then, that the flux of metal ions, which is just the deposition rate per unit area, may be written as

$$\dot{H} \rho_m / MW = \mathcal{D} C_b / \delta_{\max} \quad [26]$$

where \dot{H} is the rate of growth of the metallic layer, and ρ_m / MW is the molar density of the metal. Under the conditions that

$$\begin{aligned} \dot{H} &= 3 \mu\text{in./min} = 1.27 \times 10^{-7} \text{ cm/s} \\ C_b &= 18.7 \text{ g Cu/liter (3)} \\ \mathcal{D} &= 10^{-5} \text{ cm}^2/\text{s} \\ \rho_m / MW &= 6.9/63.5 \end{aligned}$$

we find $\delta_{\max} = 0.2$ cm.

In a bath operating such that δ is smaller, so that there is a finite resistance associated with the reaction at the surface, we may calculate k from an assumed value of $\delta < \delta_{\max}$. We begin with

$$k = \mathcal{R}/C = \frac{\dot{H}(\rho_m / MW)(1 + \Delta K_D)}{C_b} \quad [27]$$

Note that we use Eq. [22] to correct the bath concentration C_b to the value C that is actually in contact with the board surface.

Using Eq. [26], we may write

$$\frac{k\delta}{\mathcal{D}} = \frac{\delta/\delta_{\max}}{1 - \delta/\delta_{\max}} \quad [28]$$

Obviously, any value of $k\delta/\mathcal{D}$ in the range $(0, \infty)$ follows from a guess of δ/δ_{\max} in the range $(0, 1)$, respectively. Sonin (5) presents a discussion of a plating system which

utilizes liquid jets which impinge on the board surface and provide very efficient agitation. From the information which he presents, we have calculated a value of $\delta = 5 \times 10^{-4}$ cm for his "B-1 manifold." Clearly, this leads to a very small value for $k\delta/\mathcal{D}$. However, it is K_p which controls nonuniformity of plating in the hole, and for this case we find

$$K_p = \frac{ka}{\mathcal{D}} = \frac{k\delta}{\mathcal{D}} \frac{a}{\delta} \approx \frac{a}{\delta_{\max}} = 0.19 \quad [29]$$

Based on this value of K_p , and our simulations, one would expect uniform plating of through-holes in Sonin's laboratory system. However, one could easily imagine, in a bubble-agitated bath, a value of δ considerably greater than that in Sonin's jet-agitated system. Hence, one would expect difficulty in achieving uniformity of through-hole plating under such conditions, unless the bath were agitated in such a way as to induce the flow of plating fluid directly through the holes. A discussion of the effect of such flow is the topic of the next paper in this series.

Manuscript received Sept. 24, 1984.

The University of California, San Diego, assisted in meeting the publication costs of this article.

NOMENCLATURE

a	radius of through-hole (m)
A	aspect ratio of through-hole ($L/2a$)
B	(R/a)

C	molar concentration of metal ion (mol/m^3)
\mathcal{D}	diffusion coefficient of metal ion (m^2/s)
k	first-order rate constant for the plating reaction (m/s)
K_p	(ka/\mathcal{D})
L	axial length of through-hole (m)
R	distance from the hole axis, along the board surface, at which the effect of the hole on diffusion disappears (m)
r	radial variable (m)
\mathcal{R}	surface reaction rate ($\text{mol}/\text{m}^2\text{-s}$)
s	(r/a)
t	time variable (s)
x	(z/a)
z	axial variable (m)

Greek

δ	diffusion layer thickness (m)
Δ	(δ/a)
θ	($\mathcal{D}t/a^2$)
ϕ	(C/C_b)

REFERENCES

1. C. F. Gerald, "Applied Numerical Analysis," 2nd ed., Addison-Wesley, Reading, MA (1978).
2. H. S. Carslaw, and J. C. Jaeger, "Conduction of Heat in Solids," Oxford University Press, Oxford, England (1947).
3. G. Peterson, *PC Fab*, 50, July 1984.
4. C. B. Chapman, II, Hewlett-Packard Corp., Personal communication.
5. A. A. Sonin, *This Journal*, **130**, 1501 (1983).
6. J. S. Newman, "Electrochemical Systems," Prentice-Hall, Englewood Cliffs, NJ (1973).

Electrode Materials for Hydrobromic Acid Electrolysis in Texas Instruments' Solar Chemical Converter

J. D. Luttmer,* D. Konrad,* and I. Trachtenberg*

Texas Instruments Incorporated, Dallas, Texas 75265

ABSTRACT

Texas Instruments has developed a solar chemical converter (SCC) which converts solar energy into chemical energy via the electrolysis of hydrobromic acid. Various materials were evaluated as anodes and cathodes for the electrolysis of the acid. Emphasis was placed on obtaining low overvoltage electrodes with good long-term stability. Sputtered platinum-iridium thin films were identified as the best choice as the cathode material, and sputtered iridium and iridium oxide thin films were identified as the best choice as anode materials. Electrochemical measurements indicate that low overvoltage losses are encountered on these materials at operating current densities in the SCC. Accelerated corrosion tests of the materials predict acceptable electrode stability for 20 years in an environment representative of on-the-roof service.

The solar chemical converter (SCC) in Texas Instruments' solar energy conversion system converts solar energy into chemical energy via the electrolysis of hydrobromic acid into hydrogen and bromine (1-6). The choice of this electrolyte was dictated by several considerations, including electrolysis product separability, ionic conductivity, electrode kinetics, optical transmission, and reasonable load matching to the silicon solar cells. Selection of the hydrobromic acid electrolyte system required identification, characterization, and selection of appropriate materials to use as anodes and cathodes for HBr electrolysis in the SCC.

The primary requirements for SCC electrode materials are that they have low overvoltage for HBr electrolysis and sufficient stability to achieve 20 years of service in an on-the-roof environment. Additionally, the electrode should be low in cost and be readily manufacturable. For optimum SCC performance, the electrodes should also be transparent, although the SCC electrode structure can be designed to minimize light losses associated with the electrodes (3, 5, 6).

* Electrochemical Society Active Member.

The electrodes on the individual solar cells of the SCC experience a wide range of operating conditions over their 20 year service life. Wide variations in operating temperature, electrolyte composition, and electrochemical current density are anticipated. The investigations reported here were designed to encompass these variations and predict SCC operating characteristics.

The electrochemical and corrosion behavior of numerous materials were investigated as candidates for SCC electrodes. The most promising electrode candidates included platinum and iridium and their alloys and oxides. The results of the investigations with the most promising candidates are given here.

Experimental

Thin film electrodes and corrosion samples were prepared by sputter deposition using a MRC 822 sputter system incorporating 8 in. diam targets of iridium and platinum/iridium (7:3) alloys. Silicon wafer (n^+ and p^+) and quartz substrates were cleaned in boiling nitric acid, dried, and sputter etched at 500W for 30s with the sputter chamber containing 6 μm argon. Platinum/iridium and

iridium thin films were sputtered at 500W and 6 μm argon. Iridium oxide thin films were prepared by reactive sputter deposition at 500W using the iridium target with the chamber containing 100 μm oxygen. Iridium oxide thin film electrodes on silicon substrates included a thin (3 nm) barrier layer of iridium to prevent formation of a passivating layer (silicon dioxide) between the silicon and the iridium oxide. A 0.1 μm iridium film was deposited on the back side of the thin film/silicon electrodes to facilitate formation of an electrical contact to the electrode.

Tafel plots of the thin film electrodes were obtained with a single-compartment three-electrode cell. The thin film/silicon test electrode was spaced 1 in. from a parallel thin film iridium counterelectrode. A bromine/HBr (1.0M/6.9M) reference electrode was used with a Luggin capillary positioned approximately 1 mm from the test electrode. Tafel plots were obtained with PAR 173/175 potentiostat/waveform generator and HP 7004B X-Y recorder at a scan rate of 2 mV/s. The plots were corrected for test cell resistance, which was determined by current interruption.

Corrosion studies of the thin films were completed to evaluate electrode stability under SCC array operating conditions (light) and nonoperating conditions (dark). The corrosion rates of the electrode materials were measured both with and without an applied potential bias. Accelerated testing was performed in 48% HBr and in various HBr/bromine solutions containing 8.9 eq/liter bromine + bromide. Tests were made at electrolyte temperatures ranging from 20° to 100°C. Arrhenius plots were made of log corrosion rate as a function of (temperature)⁻¹ to obtain the activation energy of the corrosion reaction.

Corrosion rates and materials losses for nonoperating electrode materials were determined by optical transmission measurements and by electrolyte analysis. The optical transmission of thin films on quartz substrates was measured at 600 nm using a Varian SuperScan 1BE spectrophotometer with 4 nm bandwidth. The corrosion rate of the electrode materials on silicon substrates was determined by measuring the buildup of corrosion products in the electrolyte. Electrolyte analysis for platinum and iridium was done with an ARL 35000 ICP spectrometer. The resolution of the transmission measurements is 0.2% T. The sensitivity is indicated in Fig. 5. The detection limits for Pt and Ir by ICP was 50 ppb.

Operating thin film electrode corrosion rates were determined by monitoring the overvoltage losses as a function of time at fixed current densities and operating temperatures. Cathode tests were accomplished with a single-compartment cell with 48% HBr, a HBr/bromine (6.9M/1.0M) reference electrode, and a Pt/hydrogen (HBr saturated, 1 atm) counterelectrode. Anode tests were also made with a single-compartment cell which contained 1M bromine + 6.9M HBr, a HBr/bromine reference electrode,

SOLAR CHEMICAL CONVERTOR

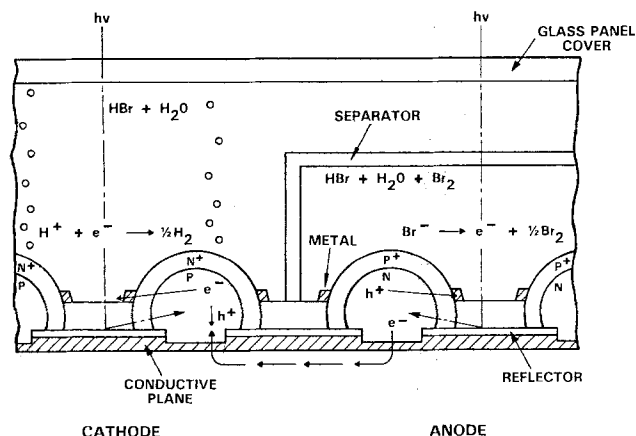


Fig. 1. Texas Instruments' solar chemical converter

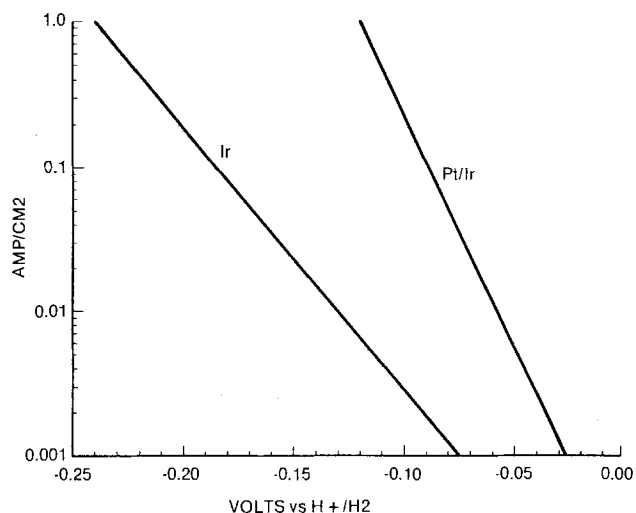


Fig. 2. Reduction of 48% HBr on iridium and platinum/iridium (7:3) thin films at 23°C. Film thickness is 6 nm.

and a large iridium foil counterelectrode. The electrolytes are comparable to those encountered in the SCC during peak outdoor operation. The overvoltage-time behavior was continuously monitored with a Fluke 1720/2400 data acquisition system. Disassembly of the test cell structures after observation of large sudden increases in overvoltage revealed total loss of the thin electrode films. The corrosion rates are calculated from the initial film thickness and the electrolysis time to total loss of the film.

Results and Discussion

The electrochemical activity of thin sputtered films of iridium and platinum/iridium (7:3) alloy on silicon substrates in 48% HBr is shown in Fig. 2. The overvoltage losses encountered on the platinum/iridium alloy cathodes are comparable to those found with bulk platinum electrodes, as shown in Table I. The activity of pure thin film iridium cathodes is considerably lower than that of platinum or platinum/iridium alloy. At the average current density, overvoltage losses on iridium and platinum/iridium cathodes are typically -200 and -95 mV, respectively.

Overvoltage losses encountered on thin film anodes of iridium, platinum/iridium alloy, and iridium oxide at the average SCC operating current density are given in Table I. The average current density anticipated for operational SCC electrodes is 150 mA/cm² (6). The platinum/iridium alloy and iridium oxide electrodes have comparably high electrochemical activity as anodes for HBr oxidation relative to the iridium anodes.

Some improvement in the performance of iridium electrodes was observed when the electrodes were electrochemically activated. Cycling the electrode potential of iridium film electrodes between hydrogen evolution and

Table I. Electrochemical overvoltage at 150 mA/cm²

Material ^a	Electrode	Over-voltage ^b (mV)	Over-voltage ^c (mV)	Conditions
Pt/Ir (7:3)	Cathode	-95	-80	8.9M HBr
Ir	Cathode	-200	-140	8.9M HBr
Pt	Cathode	-85	-70	8.9M HBr
Pt/Ir (7:3)	Anode	40	35	1M Br ₂ /6.9M HBr
Ir	Anode	160	120	1M Br ₂ /6.9M HBr
Ir oxide ^d	Anode	65	40	1M Br ₂ /6.9M HBr

^a Electrode films on n⁺ silicon or p⁺ silicon substrates. Film thickness is 6-15 nm.

^b Typical values at 23°C.

^c Best values at 23°C.

^d Includes a 3 nm barrier layer of iridium between the iridium oxide and the silicon substrate.

bromine generation in 48% HBr at 2 Hz for 10s momentarily increased the activity of the electrodes. The iridium activity for both HBr oxidation and HBr reduction was increased by this technique. However the electrodes resumed their initial activity after several hours of operation at 150 mA/cm². Cycling the electrode potential had no apparent effect on the activity of platinum/iridium electrodes. Total loss of iridium oxide thin films was observed upon identical potential cycling in 48% HBr.

The variation in electrochemical activity of very thin (<10 nm) electrode films with film thickness was examined to determine SCC electrode thickness requirements. Films in excess of 6 nm were found to have electrochemical activity equivalent to thick films or bulk metal, but the activity of films less than 6 nm decreased with film thickness.

The stability of the thin films was determined by measuring the corrosion rates of the films in various HBr/bromine mixtures encountered in the SCC. Measurements were made at various elevated temperatures representative of and in excess of the average operating temperatures anticipated for the SCC. Arrhenius plots of the corrosion rate-temperature data were used with a knowledge of the operating temperature anticipated for the SCC to predict the total corrosion for 20 years of on-the-roof service under operating or nonoperating conditions.

Typical Arrhenius plots of the corrosion data under nonoperating conditions are given in Fig. 3 and 4. The corrosion rates of all the films examined increase both with the temperature and with the bromine concentration in the electrolyte. Iridium and iridium oxide thin films have comparable, very low corrosion rates in HBr/bromine mixtures. The corrosion rate of platinum/iridium alloy films was considerably larger than the rates of iridium or iridium oxide films and was found to increase with the platinum content in the alloy. The corrosion rate of pure Pt was found to be more than 100 times larger than that of Pt/Ir (7:3) alloy for the HBr/bromine mixtures evaluated. The corrosion rate of pure platinum is unacceptable for its use as an SCC electrode material.

The corrosion rates measured for iridium and iridium oxide thin films on quartz substrates were larger than the rates measured on silicon substrates. For these samples, the corrosion rate appeared to be determined by the stability of the metal film/quartz interface or by the stability of the quartz itself. The films evaluated by optical transmission were sufficiently thin (<20 nm) to allow corrosion of the quartz substrate through pinholes in the electrode material. In these cases, small metallic particles were often visible in the electrolyte after several days or weeks at elevated temperature. The optical transmission of platinum/iridium, iridium, and iridium oxide thin films on quartz as a function of film thickness is shown in Fig. 5. All but the iridium oxide film is essentially opaque for film thickness greater than 20 nm.

In the case of platinum/iridium alloy films, the corrosion rate measured by optical transmission on quartz or

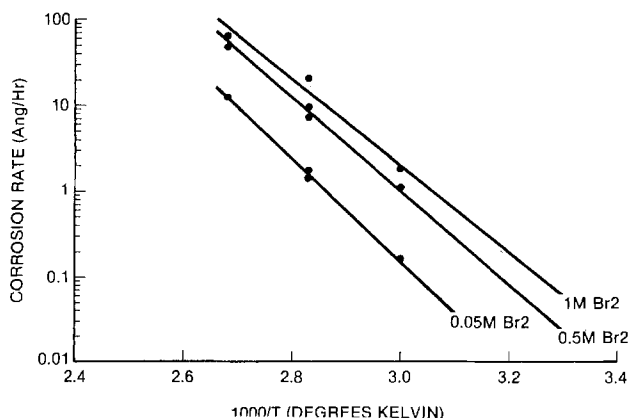


Fig. 3. Platinum/iridium (7:3) film corrosion in HBr/bromine mixtures. Total bromine + bromide content is 8.9 eq/liter.

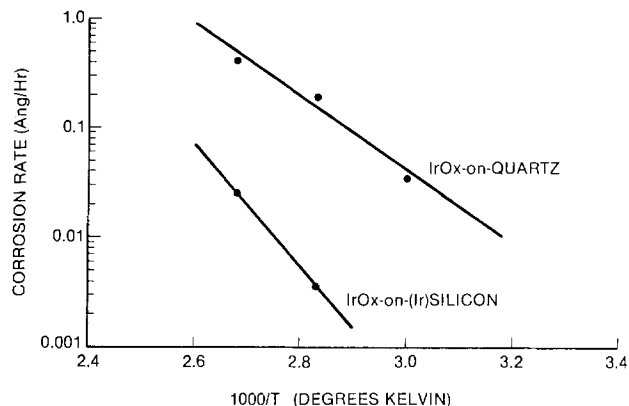


Fig. 4. Iridium oxide film corrosion in 1M Br₂/6.9M HBr

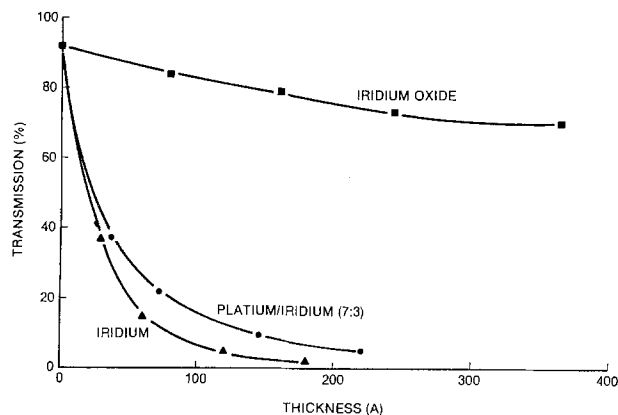


Fig. 5. Optical transmission of platinum/iridium (7:3), iridium, and iridium oxide films on quartz at 600 nm.

by electrolyte analysis on silicon substrates were identical. The corrosion of the platinum/iridium films was limited by the stability of the electrode material rather than by the stability of the substrate or electrode film/substrate interface in this case.

A knowledge of the SCC electrolyte operating temperatures is required to determine the corrosion of SCC system components. The electrolyte temperatures anticipated for the SCC were obtained with a SCC thermal management computer model and hourly weather data obtained from a SOLMET typical meteorological year (7). The simulated 20 year time/temperature histogram for the SCC electrolyte in the Dallas/Fort Worth region was used in predicting the corrosion stability of the thin electrode films. The histogram is given in Fig. 6. The operating temperature of the SCC varies between 0° and 60°C, the cooler temperatures during the nonoperating hours and warmer temperatures during the operating hours.

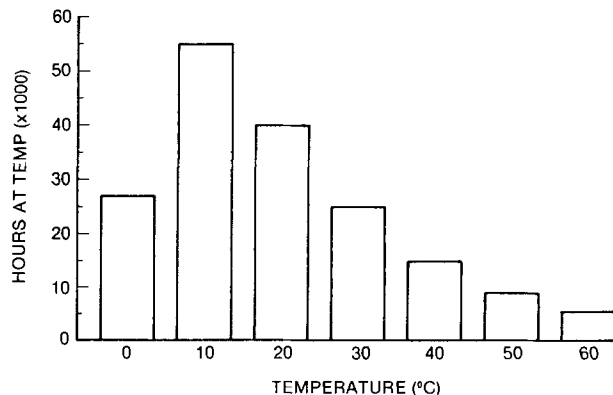


Fig. 6. Simulated 20 year time/temperature histogram for solar chemical converter in Dallas/Ft. Worth region.

Table II. Projected corrosion for 20 years on-the-roof service under nonoperating conditions^a

Material ^b	Electrode	Corrosion (μm)	Conditions
Pt/Ir (7:3)	Cathode	0.14	0.05M Br ₂ /8.8M HBr
Pt/Ir (7:3)	Anode	2.4	1M Br ₂ /6.9M HBr
Ir	Anode	0.0015	1M Br ₂ /6.9M HBr
Ir oxide	Anode	0.0003	1M Br ₂ /6.9M HBr

^a Current density = 0 mA/cm².

^b Electrode films on n⁺ and p⁺ silicon substrates, 6-25 nm.

The projected total corrosion of the electrode films for 20 years on-the-roof service under nonoperating conditions is given in Table II. The worst-case predictions assume that the anodes are immersed in a 1M bromine + 6.9M HBr anolyte and the cathodes are immersed in 0.05M bromine + 8.8M HBr catholyte for the entire 20 year period. Bromine at low concentration may occur in the catholyte during nonoperating periods in the SCC.

The potential bias imposed on the electrodes during operation of the SCC has a significant effect on the stability of those materials. An anodic bias imposed on the anode materials in HBr/bromine electrolytes results in decreased stability, whereas a cathodic bias imposed on the cathode materials results in increased stability. Consequently, it was necessary to determine the stability of the materials under both operating (biased) and nonoperating (nonbiased) conditions.

The corrosion rates of the electrode materials under operating conditions were determined by biasing the electrodes to the average current density anticipated for SCC electrodes, 150 mA/cm², and monitoring the electrochemical overvoltage. The overvoltage observed with the electrodes reflected the integrity of the thin films.

A typical overvoltage-time plot observed for a corrosion test which models active SCC electrode operation is given in Fig. 7. A marked increase in the electrochemical voltage on the iridium anode after 5400h of anodic bias at 150 mA/cm² signaled the loss of the electrode film. The observed corrosion rate for this material under anodic bias was five times larger than that observed for the material in the nonoperating mode without bias. A similar increase in corrosion rate was observed for other anode materials under anodic bias.

Iridium and platinum/iridium materials under cathodic bias in HBr/bromine electrolytes displayed enhanced corrosion stability relative to the nonoperating tests. No dissolution of these materials was observed at temperatures to 80°C for test times in excess of 4500h. However, iridium oxide electrodes rapidly decomposed under cathodic bias in these electrolytes.

The total projected corrosion for the electrode materials after 20 years of on-the-roof operation is given in Table

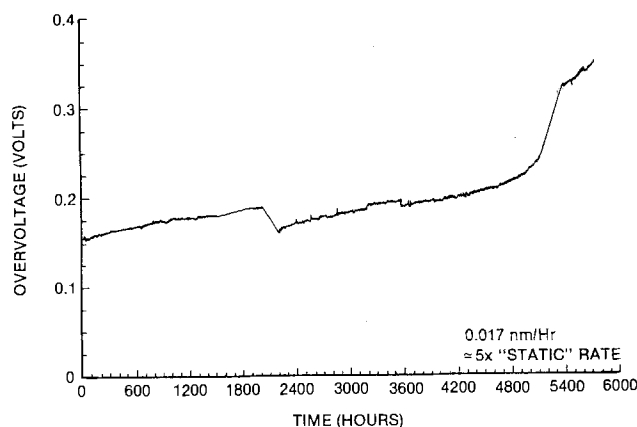


Fig. 7. Overvoltage vs. hours of operation for 9 nm iridium film on p⁺ silicon at 80°C. Anodic current density is 150 mA/cm² in 1M Br₂/6.9M HBr.

Table III. Projected corrosion for 20 years on-the-roof service under operating conditions^a

Material ^b	Electrode	Corrosion (μm)	Conditions
Pt/Ir (7:3)	Cathode	0.0048	48% HBr
Pt/Ir (7:3)	Anode	8.3	1M Br ₂ /6.9M HBr
Ir	Anode	0.0066	1M Br ₂ /6.9M HBr
Ir oxide	Anode	0.0042	1M Br ₂ /6.9M HBr

^a Current density = 150 mA/cm².

^b Electrode films on n⁺ silicon substrates, 6-25 nm.

III. The projected corrosion rates assume continuous electrolysis at 150 mA/cm². The corrosion rates reported for the platinum/iridium cathode under operating conditions is considerably less than that reported for the material under nonoperating conditions and represents the platinum/iridium corrosion detection limit in the former case. The corrosion rates for the iridium and iridium oxide anodes under operating conditions are larger than observed under nonoperating conditions.

The total corrosion predicted for iridium and iridium oxide anodes and for platinum/iridium cathodes is small for both operating and nonoperating conditions. The total anode material lost for 20 years of on-the-roof service is less than 0.15 and 0.02 mg for each square meter of array anode area for iridium and iridium oxide, respectively. Likewise, the projected loss for platinum/iridium is less than 3.2 mg from each square meter of array cathode area.

Conclusions

Electrochemical and corrosion investigations of thin film iridium, platinum/iridium, and iridium oxide materials in HBr/bromine electrolytes reveal that the materials have adequate activity and stability as SCC electrodes for 20 years of on-the-roof service. Overvoltage losses less than 95 and 65 mV are predicted for platinum/iridium cathodes and iridium oxide anodes, respectively, at the average SCC operating current density. Iridium and iridium oxide anodes and platinum/iridium cathodes have shown excellent stability for simulated 20 year on-the-roof service conditions. Currently the performance of the Texas Instruments SCC which incorporates the hydrogen/HBr/bromine system is limited by electrical characteristics of the individual solar cells and not by the electrochemical behavior of the anodes or cathodes.

In the final analysis, the electrode materials selected are the result of many trade-offs, such as cost, manufacturability, activity, and total expected corrosion. Electrodes can be constructed which ensure adequate activity and continued operation for the entire lifetime of the SCC system.

Acknowledgment

The authors gratefully acknowledge the support of this work in part under the Department of Energy/Texas Instruments Cooperative Agreement DE-AC01-79ER10000.

Manuscript submitted Dec. 15, 1983; revised manuscript received Feb. 4, 1985.

Texas Instruments, Incorporated, assisted in meeting the publication costs of this article.

REFERENCES

1. E. L. Johnson, in IEEE Proceedings of the International Electron Devices Meeting, December 1982," pp. 2-5, IEEE, New York (1982).
2. I. Trachtenberg, Paper presented at the AS/ISES Conference, Houston, TX, June 1982.
3. J. D. Luttmner and I. Trachtenberg, Paper 448 presented at the Montreal, Que., Canada, Meeting of the Society, May 9-14, 1982.
4. W. R. McKee, K. R. Carson, and J. D. Levine, Paper presented at the 16th IEEE Photovoltaic Specialists Conference, San Diego, California, September 1982.

5. J. D. Luttmmer and I. Trachtenberg, Submitted to *This Journal*.
 6. J. D. Luttmmer and I. Trachtenberg, Submitted to *This Journal*.

7. R. L. Dawes and G. B. Hotchkiss, in "Proceedings of the ASME Solar Energy Division 5th Annual Conference, Orlando, Florida, April 1983," pp. 420-427, ASME, New York (1983).

Chemical and Electrochemical Behavior of the Cr(III)/Cr(II) Half-Cell in the Iron-Chromium Redox Energy Storage System

David A. Johnson*

Department of Chemistry, Spring Arbor College, Spring Arbor, Michigan 49283

Margaret A. Reid*

National Aeronautics and Space Administration, Lewis Research Center, Cleveland, Ohio 44135

ABSTRACT

The Cr(III) complexes present in the acidified chromium solutions used in the iron-chromium redox energy storage system have been isolated and identified as $\text{Cr}(\text{H}_2\text{O})_6^{+3}$ and $\text{Cr}(\text{H}_2\text{O})_5\text{Cl}^{+2}$ by ion-exchange chromatography and visible spectrophotometry. The cell reactions during charge-discharge cycles have been followed by means of visible spectrophotometry. The spectral bands were resolved into component peaks and concentrations of the Cr(III) species calculated using Beer's law. During the charge mode, $\text{Cr}(\text{H}_2\text{O})_5\text{Cl}^{+2}$ is reduced to $\text{Cr}(\text{H}_2\text{O})_6^{+3}$, and during the discharge mode $\text{Cr}(\text{H}_2\text{O})_6^{+3}$ is oxidized back to $\text{Cr}(\text{H}_2\text{O})_5\text{Cl}^{+2}$. Electrode potential measurements also support this interpretation. Hysteresis effects in the charge-discharge curves can be explained by the slow attainment of equilibrium between $\text{Cr}(\text{H}_2\text{O})_6^{+3}$ and $\text{Cr}(\text{H}_2\text{O})_5\text{Cl}^{+2}$.

Redox flow cells are electrochemical storage devices that utilize the oxidation and reduction of two soluble redox couples for charging and discharging. The active electrode materials, separated by a highly selective ion-exchange membrane, are pumped through a stack of redox flow cells, where the electrochemical reactions take place at porous carbon felt electrodes. Since the redox flow cell concept was first proposed by Thaller in 1974 (1), a number of redox couples have been investigated. More recently, acidified solutions of chromium [Cr(III)/Cr(II)] and iron [Fe(III)/Fe(II)] have been successfully used as redox couples, both as unmixed reactants (2) and as premixed solutions (3), i.e., both the anolyte and catholyte contain both iron and chromium. This study, however, was performed on a system containing unmixed reactants.

A schematic diagram of a single iron-chromium redox cell and the associated electrode reactions is shown in Fig. 1. An ion-exchange membrane separates the compartments and prevents the cross-mixing of the reactive cations. Electrodes consist of carbon felt catalyzed on the chromium side by trace amounts of gold and lead. The catalyst is required on the chromium side because the rate of reduction of Cr(III) to Cr(II) is slow on most surfaces (4, 5). The catalyst must also have a high overvoltage for hydrogen, since, from a thermodynamic standpoint, hydrogen is evolved before chromium is reduced. Trace amounts of gold (12-25 $\mu\text{g}/\text{cm}^2$) and lead (100-200 $\mu\text{g}/\text{cm}^2$) deposited on the carbon felt meet the requirements for an effective catalyst (6). Trace amounts of gold seem to be necessary to produce a surface on which lead deposits uniformly during the charging cycle. The catalyst also improves the cell discharge rate (7). No catalyst is required on the iron side.

During discharge, chloride ions move from the cathode compartment to the anode compartment, and hydrogen ions move in the opposite direction. On charge, all reactions are reversed. Since all species are fully soluble, there are no life limiting factors such as shape changes, inactive forms of reactants, and dendrite formation. There are also many advantages in system sizing and control (2, 8).

Semipermeable membranes have been developed that are sufficiently conductive and selective for use for photovoltaic and wind energy storage applications (9). Methods of keeping the iron-chromium redox system in balance have been developed. Flow characterization and analysis of shunt currents have been carried out, and hardware has been scaled up with little difficulty (10).

The open-circuit voltage behavior of a typical iron-chromium redox cell is shown in Fig. 2, wherein the open-circuit voltages during charge and discharge modes are plotted as a function of state of charge for a complete cycle. There is a distinct difference in the open-circuit voltage of the system at the same state of charge, depending on whether the cell is in the charge or discharge mode. In addition, when charging the cell, a much greater polarization is observed after the open-circuit voltage

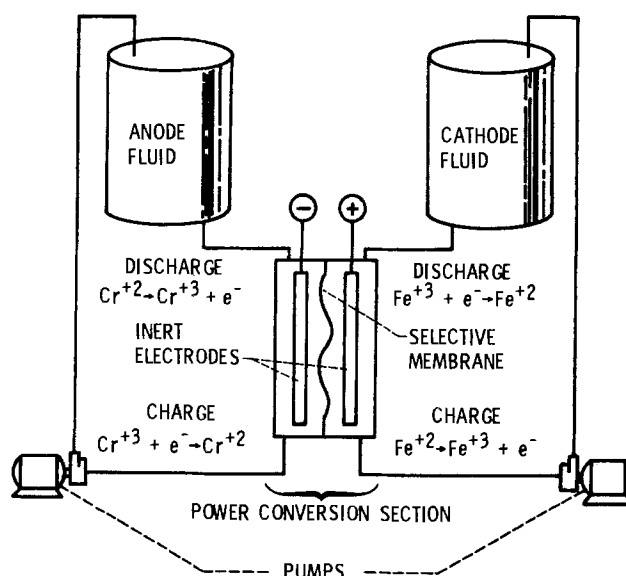


Fig. 1. Schematic showing the principles of operation of an iron-chromium redox energy storage system.

* Electrochemical Society Active Member.

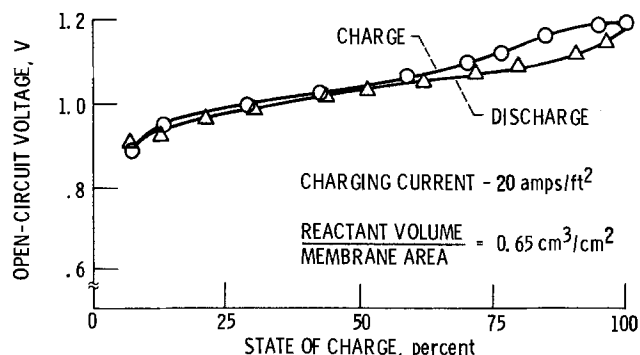


Fig. 2. Open-circuit voltage behavior of an iron-chromium redox cell at 25°C. 1M CrCl₃ in 2M HCl and 1M FeCl₂ in 2M HCl.

risers. Charging must then be done at either a higher voltage or at a much lower charging rate.

Since these effects contribute to lower energy storage efficiency, it seemed critical to undertake a thorough study of the processes occurring at the chromium electrode during the charging and discharging of the system.

It was observed that, during charging, the color of the chromium solution changes from a deep blue-green to a blue color at about 50% state of charge, about the same time that the open-circuit voltage rises and the rate of charging falls. During discharge, the color of the chromium solution changes back to the blue-green color at around 90% state of charge.

It has been demonstrated conclusively (11) that in aqueous solutions containing Cr(III) and chloride ion three inner-sphere complex ions are present: Cr(H₂O)₄Cl₂⁺¹ (green), Cr(H₂O)₅Cl⁺² (blue-green), and Cr(H₂O)₆⁺³ (blue). These ions are relatively "inert", i.e., they are very slow to exchange ligands in their coordination sphere. The electrochemical effects are apparently related to the concentrations of these ions and to the fact that equilibrium between them is reached very slowly.

This paper describes the results of spectrophotometric studies and measurements of electrode potential of the chromium solutions during complete charge-discharge cycles of a single subscale redox cell.

Experimental

A laboratory subscale flow cell with an active electrode area of 14.5 cm² was used for all studies. A schematic diagram of the cell is shown in Fig. 3. An ion-exchange membrane (CD1L series) supplied by Ionics Incorporated, Watertown, Massachusetts, was used in the cell. Electrodes were made from nominally 1/8 in. thick carbon felt. The electrode on the iron side was uncatalyzed, while the electrode on the chromium side was catalyzed with 12.5 μg/cm² of gold (6, 12). Lead was electrochemically deposited at 0.3 mA/cm² onto the electrode from the chromium solution which contained 6 × 10⁻⁵M Pb²⁺. One set of experiments was carried out using 1M CrCl₃ and FeCl₂ solutions in 2M HCl. Because of the high absorbancies of the Cr⁺³ ions, it was difficult to make accurate measurements at low states of charge. Another set of experiments was run with 0.45M CrCl₃ and 0.55M FeCl₂, so that the absorbancies would be less than 1.0 for all states of charge.

A 1 mm quartz flow cell was connected in parallel with the chromium side of the redox cell and placed in a Beckman DK-2A spectrophotometer. The spectrum was then recorded at selected states of charge from 350 to 1000 nm. Chromium half-cell potentials were measured at the same states of charge using a wax-filled graphite rod and a Ag/AgCl (4M KCl) reference electrode placed in the chromium reservoir.

In order to analyze the spectra of the redox solutions, the complexes Cr(H₂O)₆⁺³, Cr(H₂O)₅Cl⁺² and Cr(H₂O)₄Cl₂⁺¹ were prepared by established procedures (13) and the spectra recorded. Solutions of Cr(H₂O)₆⁺³ and Cr(H₂O)₅Cl⁺² in 1M HClO₄ follow Beer's law up to at least 0.70 and 0.40M, respectively, which were the highest concentra-

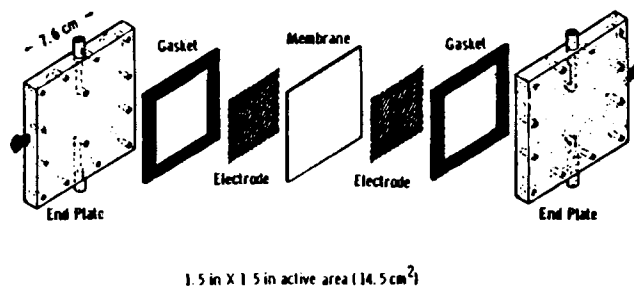


Fig. 3. Laboratory redox cell. Wax-impregnated graphite end plates with bolts for current collection, polyethylene gaskets, carbon felt electrodes catalyzed on chromium side, ion-exchange membrane.

tions studied and are in agreement with literature values (14) (Fig. 4). Maxima for the Cr(H₂O)₅Cl⁺² ion are at 430 and 650 nm and maxima for Cr(H₂O)₆⁺³ are at 407 and 575 nm.

Cr(II) species were generated by reduction with amalgamated zinc in a nitrogen atmosphere (15). Cr(H₂O)₆⁺² was prepared by reducing Cr(ClO₄)₃ in 1.0M HClO₄. The spectrum was then recorded from 350 to 1000 nm using a 1 mm quartz flow cell which was filled directly from the reaction flask. The use of a flow cell was necessary because of the rapid oxidation of Cr(II) in air. The absorption maxima was at 714 nm, identical to that reported in the literature (16). Cr(II) was also prepared by reducing CrCl₃ by ZnO in 6.0M HCl. The absorption maxima was at 750 nm. Reduction of CrCl₃ · 6H₂O in lower concentrations of HCl gave maximum absorption peaks between 714 and 750 nm.

The spectra measured during the charge and discharge cycles were analyzed using a du Pont 310 Curve Resolver. The spectra of the highest charged solution was examined first. The solution consisted mainly of Cr(H₂O)₆⁺³ and Cr(II) as indicated by absorption maxima. Once the curves due to Cr(H₂O)₆⁺³ and Cr(II) were established, the curves for other states of charge were resolved by reducing the curves for these species and adding the contribution of Cr(H₂O)₅Cl⁺². The relative absorbancies of the two peaks of the Cr(III) species were always kept in the ratio of the molar absorptivities (14). The concentrations of the Cr(III) species were then calculated from the resolved curves using Beer's law.

The Cr(III) species present in the uncharged cell solution were also separated by ion-exchange chromatography and the fractions were identified by spectrophotometry. Approximately 10 ml of cell solution were placed on

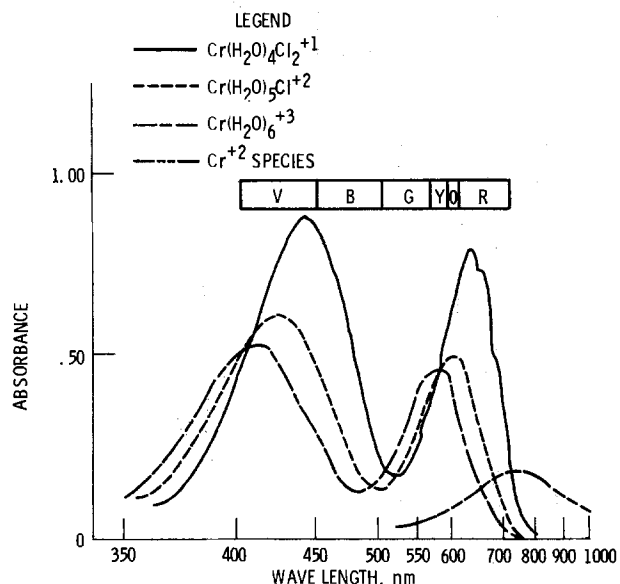


Fig. 4. Spectra of chromium complex ions likely to be present in the acidified chromium solutions of the iron-chromium redox cells. 1 mm path length of cell, 0.3M concentration.

a column of Dowex 50X8-100 cation exchange resin (50-100 mesh H^+ form). The sample was eluted with 0.1, 1.0, and 3.0M $HClO_4$, respectively, and spectra of the resulting fractions recorded (13, 14, 17).

Results and Discussion

The spectra of the chromium solutions of the redox cell were characterized by two broad absorption bands with maxima of 408-430 nm and 575-610 nm. In the highly charged state, a band with a maximum at 750 nm was also observed. Figure 5 is a typical spectrum.

The cell solution was analyzed prior to and immediately after taking it through two complete charge-discharge cycles using ion-exchange chromatography and spectrophotometry. The results indicated that only $Cr(H_2O)_6^{+3}$ and $Cr(H_2O)_5Cl^{+2}$ were present in completely discharged solutions in detectable amounts under normal operating conditions of the cell. This is in agreement with equilibrium constants reported in the literature, which indicate that $Cr(H_2O)_5Cl^{+2}$ and $Cr(H_2O)_6^{+3}$ should be the dominant existing species once equilibrium has been achieved (18, 19). It was also found that the spectra of the solution during charge and discharge could be resolved satisfactorily without assuming the presence of $Cr(H_2O)_4Cl_2^+$.

The band with a maximum at 750 nm is obviously due to the presence of Cr(II). Since $Cr(H_2O)_6^{+3}$ has a maximum at 714 nm (16), other Cr(II) species must be present. Preparation of Cr(II) in environments containing chloride ion at increasing concentrations shows a shift in the maximum to longer wavelengths reaching a maximum at 750 nm. The species identified with this peak are obviously chloride containing Cr(II) complexes. Since there is rapid equilibration among Cr(II) ions, it is not possible to identify the peak with an individual Cr(II) complex. The shift to longer wavelengths is in agreement with the decreased ligand field strength of chloride as compared to water (20).

The results of the second set of experiments with 0.55M $FeCl_2$ and 0.45M $CrCl_3$ in 2.0M HCl are presented in Fig 6 and 7. (The results from the first experiments in which the solutions were 1.0M $FeCl_2$ and 1.0M $CrCl_3$ in 2.0M HCl are similar.) These figures show the concentrations of $Cr(H_2O)_6^{+3}$ and $Cr(H_2O)_5Cl^{+2}$ at selected states of charge and discharge.¹ Differences between the two cycles are due to the different ratios of the species in the initial solutions and the different modes of cycling. The important features of both figures are the large decrease in $Cr(H_2O)_5Cl^{+2}$ concentration and a rather small change in

¹ The error in the spectrophotometric measurements is believed to be less than 1%, and the maximum error in resolving the curves is about 1%.

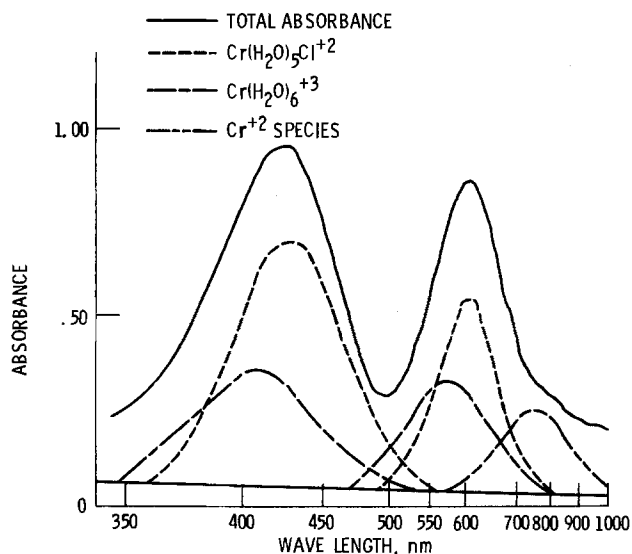


Fig. 5. Spectrum of 1M chromium chloride solution during discharge of iron-chromium redox cell (42.0% charged, 58.0% discharge).

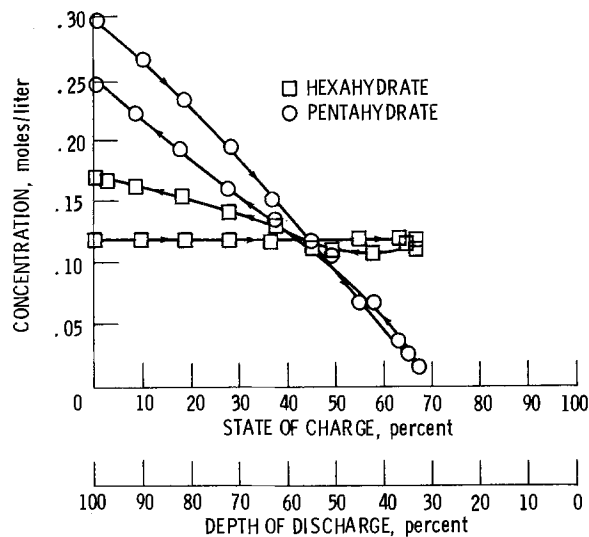


Fig. 6. Concentration of Cr(III) species in iron-chromium redox cell, first cycle, taper current charge (0.45M $CrCl_3$ and 0.55M $FeCl_2$ in 2.0M HCl).

$Cr(H_2O)_6^{+3}$ concentration with increasing state of charge. The decrease of $Cr(H_2O)_5Cl^{+2}$ concentration to a minimal value at high states of charge coupled with the constancy of the $Cr(H_2O)_6^{+3}$ concentration suggests that $Cr(H_2O)_5Cl^{+2}$ is the predominant species involved in the reduction reaction at the electrode surface.

A similar argument applied to the discharge cycle indicates that the oxidation process involves the production of $Cr(H_2O)_5Cl^{+2}$ rather than $Cr(H_2O)_6^{+3}$. In addition, the fact that the $Cr(H_2O)_6^{+3}$ concentration changes only after the $Cr(H_2O)_5Cl^{+2}$ concentration has reached an appreciable level indicates a slow equilibrium step involving $Cr(H_2O)_6Cl^{+3}$ and $Cr(H_2O)_5Cl^{+2}$. This is in agreement with Gates and King, who have found the equilibrium quotient for the reaction $Cr(H_2O)_6^{+3} + Cl^- = Cr(H_2O)_5Cl^{+2} + H_2O$ to be 0.27 at 30°C (11). (Concentrations are used in the equilibrium quotient instead of activities.) The equilibrium state is achieved very slowly in the absence of Cr(II) ion, but the hydration of the $Cr(H_2O)_5Cl^{+2}$ to $Cr(H_2O)_6^{+3}$ is catalyzed by Cr(II) (21, 22).

The electrode potentials in the chromium solution with respect to a Ag/AgCl reference are plotted in Fig. 8 against the log of the ratio of concentration of Cr(II) to the concentrations of the different Cr(III) species. It can be seen that the curve for $Cr(H_2O)_5Cl^{+2}$ is linear and has a slope close to the Nernst slope, in contrast to the

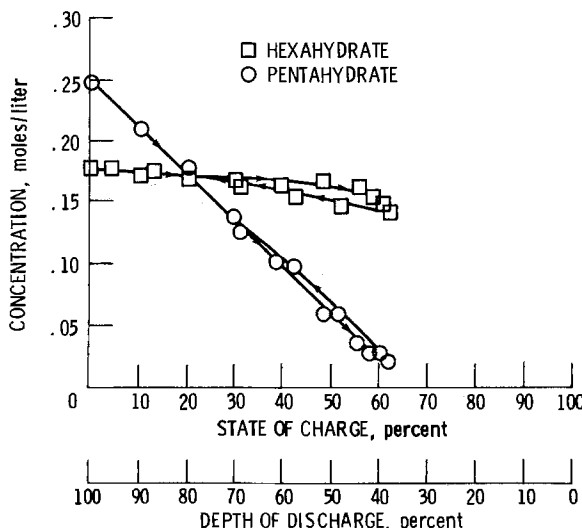


Fig. 7. Concentrations of Cr(III) species in iron-chromium redox cell, second cycle, constant current density, 0.22 A/cm² (0.45M $CrCl_3$ and 0.55M $FeCl_2$ in 2.0M HCl).

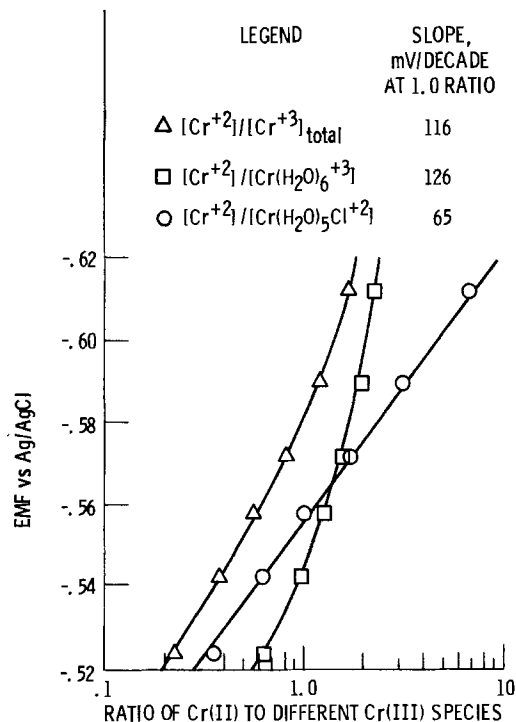


Fig. 8. Plot of EMF of chromium solution during charge against ratios of Cr(II) to Cr(III) concentrations. Reference electrode Ag/AgCl. First charge, taper current (0.45M CrCl₃ and 0.55M FeCl₂ in 2.0M HCl).

curves for the total Cr(III) concentration and Cr(H₂O)₆⁺³. This Nernstian behavior, together with the formation of Cr(H₂O)₅Cl⁺² in the discharge mode and the disappearance of Cr(H₂O)₅Cl⁺² in the charge mode, indicates that the reaction pathway will most likely involve Cr(H₂O)₅Cl⁺². The electroactive species of Cr(II) is presumably Cr(H₂O)₅Cl⁺, since the Frank-Condon principle predicts that the geometry of the reacting species will be retained upon both oxidation and reduction, and since the spectra of the Cr(II) species show the presence of chloride complexes as shown by the shift in the absorption maxima in these solutions from the spectra of Cr(H₂O)₆⁺³.

Weaver and Anson (5) have carried out extensive studies of the electrode reactions of Cr(H₂O)₅X⁺² complexes at mercury electrodes. The formal potential for the Cr(H₂O)₆⁺³/Cr(H₂O)₅X⁺² couple was found to be -0.413 vs. H₂, while that for the Cr(H₂O)₅Cl⁺²/Cr(H₂O)₅Cl⁺ couple was -0.347V. They found electrode reaction rate constants of 2.2 × 10⁻⁵ and 5.60 × 10⁻³ for Cr(H₂O)₆⁺³ and Cr(H₂O)₅Cl⁺², respectively, evaluated at -700 mV vs. SCE (-452 mV vs. H₂). If we assume that the rate constants on the redox catalyst are in the same relative order as on the mercury electrode, the electrochemical behavior of the cell as shown in Fig. 2 can be explained by assuming that when the more electroactive pentahydrate is depleted, the equilibrium potential rises, since the standard potential of the hexahydrate couple is more negative than that of the pentahydrate couple. The greater difficulty in charging the redox cell after the pentahydrate is depleted is due to the slower kinetics of the hexahydrate reduction. Upon discharge the pentahydrate is rapidly regenerated and the equilibrium potential falls.

Weaver and Anson have also found that the oxidation of Cr(II) takes place by means of a chloride-bridged inner-sphere pathway at a mercury electrode, and they suggest that a more efficient reaction pathway is provided by the presence of chloride ion (5). It is likely that a similar mechanism is involved on the Pb/Au on carbon felt electrodes, since all the results here are in qualitative agreement with the results of Weaver and Anson on mercury electrodes.

Conclusions

The complex ions Cr(H₂O)₆⁺³ and Cr(H₂O)₅Cl⁺² have been isolated and identified by ion-exchange chromatog-

raphy and visible spectrophotometry in acidified chromium solutions of the discharged iron-chromium redox energy storage system. The reactions at the catalyzed carbon felt electrode can be followed spectrophotometrically during charge-discharge cycles. The spectra can be resolved and used to determine the concentrations of Cr(H₂O)₆⁺³ and Cr(H₂O)₅Cl⁺², which have been demonstrated to follow Beer's law up to at least 0.7 and 0.4M, respectively.

The spectral data indicate that the concentration of Cr(H₂O)₅Cl⁺² decreases much more rapidly with increasing state of charge than does the concentration of Cr(H₂O)₆⁺³, indicating that Cr(H₂O)₅Cl⁺² is the predominant species being reduced during the charging cycle. There is a rapid rise in Cr(H₂O)₅Cl⁺² concentration as discharge takes place, and the concentration of Cr(H₂O)₆⁺³ rises only after appreciable Cr(H₂O)₅Cl⁺² is produced. This is in agreement with other studies that show that equilibration between Cr(H₂O)₆⁺³ and Cr(H₂O)₅Cl⁺² takes place slowly. The predominant electroactive species in the discharge cycle is probably Cr(H₂O)₅Cl⁺. The electrode potentials also indicate that the main electroactive species in the charging mode is Cr(H₂O)₅Cl⁺². The electrochemical behavior of the redox cell can be explained on the basis of the different equilibrium potentials for the hexahydrate and pentahydrate couples and the different rates of reduction of the hexahydrate and pentahydrate species. The conclusions are consistent with other studies at mercury electrodes.

Acknowledgments

This work was funded by the U.S. Department of Energy under Interagency Agreement DE-A104-80AL12726.

Manuscript submitted Oct. 27, 1982; revised manuscript received Jan. 24, 1985. This was Paper 252 presented at the Detroit, Michigan, Meeting of the Society, Oct. 17-21, 1982.

NASA assisted in meeting the publication costs of this article.

REFERENCES

- L. H. Thaller, in "Proceedings of the 9th Inter-Society Energy Conversion Engineering Conference," pp. 924-928 (1974).
- L. H. Thaller, in "Proceedings of the 14th Inter-Society Energy Conversion Engineering Conference," pp. 715-719, American Chemical Society, Washington, DC (1979).
- R. F. Gahn, N. H. Hagedorn, and J. S. Ling, in "Proceedings of the 18th Inter-Society Energy Conversion Engineering Conference," pp. 1647-1652, American Institute of Chemical Engineering, New York (1983).
- J. E. Earley and R. Cannon, *Transition Met. Chem.*, **1**, 33 (1965).
- M. J. Weaver and F. C. Anson, *Inorg. Chem.*, **15**, 1871 (1976).
- J. Giner and K. Cahill, U.S. Patent 4,192,910 (1980); U.S. Pat. 4,270,984 (1981).
- M. A. Reid, R. F. Gahn, J. S. Ling, and J. Charleston, Abstract 350, p. 871, The Electrochemical Society Extended Abstracts, Vol. 80-1, St. Louis, MO, May 11-16, 1980.
- M. A. Reid and L. H. Thaller, in "Proceedings of the 15th Inter-Society Energy Conversion Engineering Conference," pp. 1471-1476, American Institute of Aeronautics and Astronautics, New York (1980).
- S. A. Alexander, R. B. Hodgdon, and W. A. Waite, "Anion Permselective Membrane," NASA CR-159599, National Aeronautics and Space Administration, Washington, DC (1979).
- J. C. Acevedo, N. H. Hagedorn, P. R. Prokopius, and L. H. Thaller, Paper 170, p. 446, The Electrochemical Society Extended Abstracts, Vol. 79-2, Los Angeles, CA, Oct. 14-19, 1979.
- H. S. Gates and E. L. King, *J. Am. Chem. Soc.*, **80**, 5011 (1958).
- V. Jalan, M. A. Reid, and J. A. Charleston, U.S. Pat. 4,454,649 (1984).
- R. Angelici, "Synthesis and Technique in Inorganic Chemistry," W. B. Saunders, Philadelphia (1968).
- P. J. Elving and B. Zemel, *J. Am. Chem. Soc.*, **79**, 1281 (1957).
- H. Taube and H. Myers, *ibid.*, **76**, 2103 (1954).

16. O. G. Holmes and D. S. McClure, *J. Chem. Phys.*, **26**, 1686 (1957).
17. T. W. Swaddle and E. L. King, *Inorg. Chem.*, **4**, 532 (1965).
18. M. Magini, *J. Chem. Phys.*, **73**, 2499 (1980).
19. L. G. Sillen and A. E. Martell, "Stability Constants of Metal-Ion Complexes," p. 276, The Chemical Society, London (1964).
20. F. A. Cotton and G. Wilkinson, "Advanced Inorganic Chemistry," 3rd ed., Interscience Publishers, New York (1972).
21. D. L. Ball and E. L. King, *J. Am. Chem. Soc.*, **80**, 1091 (1958).
22. A. Adin and A. G. Sykes, *J. Chem. Soc. A*, 1518 (1966).

Ternary Chalcogenide-Based Photoelectrochemical Cells

IV. Further Characterization of the n-CuInS₂/and n-CuInSe₂/Aqueous Polysulfide Systems

David Cahen, Geulah Dagan, and Yehudith Mirovsky¹

Department of Structural Chemistry, The Weizmann Institute of Science, Rehovot 76100, Israel

Gary Hodes*

Department of Material Research, The Weizmann Institute of Science, Rehovot 76100, Israel

Witold Giriat

Centro de Fisica, IVIC, Caracas, Venezuela

Margot Lubke

Fritz Haber Institut der Max Planck Gesellschaft, D-1000 Berlin 33, Germany

ABSTRACT

The photoelectrochemistry of n-CuInS₂ and CuInSe₂ in polysulfide electrolyte is studied with particular emphasis on the pretreatments of the electrodes and on their output stability. The use of Cd doping, (photoelectro)chemical etching, and mild air oxidation all were found to improve electrode performance. The effect of air oxidation was reproducible only for the diselenide, where it improved the fill factor and, because of a negative shift of the flatband potential, the open-circuit voltage. Optimized cells showed, at elevated temperatures, conversion efficiencies around 5 and 7.5% for the sulfide and selenide, respectively. The positive temperature dependence of the photo-I-V characteristics at both low and high illumination intensities, the existence of optimal polysulfide solution compositions, the linear dependence of the photocurrent on the light intensity, and the effects of temperature, solution composition, and initial current density on the photocurrent decrease during the first minute of operation of the cells, are ascribed to limitations of the charge-transfer process across the solid/liquid interface. Thermally activated rates of ad- and desorption of sulfur containing solution species on the semiconductor surface and/or the presence of adsorption-induced electronic states in the bandgap are postulated as causes for this behavior. Notwithstanding these limitations the cells are resistant to photocorrosion, after the initial decrease is arrested, in contrast to what is known for similar Cd-chalcogenide-based systems. We suggest that this stability, which persists under load and at high light intensities, is due to the strength and character of the bonds in CuIn-dichalcogenides, or to the presence of a top layer of indium oxide in which recombination will take place, or to both.

Ternary chalcogenides (and pnictides) with tetrahedral coordination and the general formula ABC₂ can be derived from the corresponding II-VI, e.g., CdSe, (and III-V) binary compounds by cation substitution. They can be thought of as resulting from proton exchange between two cations in the corresponding binary compound (1). Most of these materials are semiconductors and several of them exhibit interesting optoelectronic behavior (2). The partial Cu d character of the top of the valence band in these compounds, which gives bandgap excitation less of a bond breaking character, has been noted (2). To date, CuInSe₂ is probably the most studied of these compounds, by virtue of the very promising photovoltaic activity of thin film solar cells containing this semiconductor as the photoactive material (3). Both n-CuInS₂ (4, 5) and n-CuInSe₂ (6) can be used as photoanodes in a polysulfide containing photoelectrochemical cell (PEC). Such cells show respectable photovoltaic activity and very good output stability, as reported previously (4-6). Here we present results of our characterization of these cells. They show the importance of surface treatments to optimize photovoltaic conversion efficiency of these PEC's, and the occurrence of charge-transfer limitations in them, whose causes we attempt to assess. The time de-

pendence of the output of the cells is studied under a variety of conditions, and possible reasons for their stability are given. Some of the results described here and the conclusions drawn from them aided in the recent development of improved PEC's with a polyiodide electrolyte (7).

Experimental

CuInS₂ crystals were prepared by chemical vapor transport, using halogen transport agents, as described before (2). CuInSe₂ crystals were obtained by melt growth from the purified elements (8). As-grown crystals were generally semi-insulating, p-type, with 10⁵-10⁶ Ω-cm resistivities. They did not exhibit any photoelectrochemical activity. Hence, they were doped to obtain useful n-type material. Cd was found to be a suitable dopant. From various experiments, optimum doping conditions were found (Fig. 1). The dopant and the crystals were sealed in evacuated (10⁻⁶ torr) silica ampuls and heated for several days. For both compounds, In doping was found to be less satisfactory than Cd doping. The doping mechanism probably involves the introduction of Cd on Cu sites, Cd_{Cu}, where it acts primarily as a donor (9, 10).

The crystals were analyzed by electron beam-induced energy or wavelength dispersive x-ray fluorescence. In one case, the incorporation of Cd was verified by secondary ion mass spectroscopy. In addition, some samples were analyzed by Auger and/or x-ray photoelectron spec-

* Electrochemical Society Active Member.

¹ Present address: Israel Aircraft Industries, Ben-Gurion International Airport, Lod, Israel.

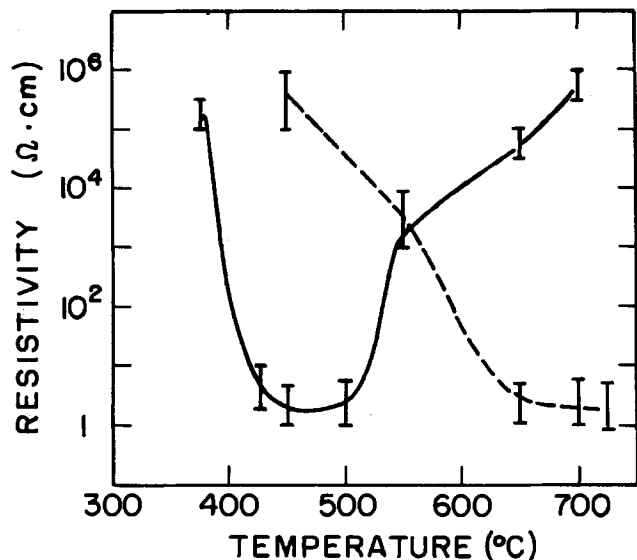


Fig. 1. Effect of temperature of Cd-doping on resistivity of CuInS_2 (solid line) and CuInSe_2 (dashed line). Samples and dopant were placed in a silica ampul, which was evacuated and heated, at the temperatures indicated, for several days.

troscopy. Electrodes were prepared as described previously (5). The etching procedure was as follows: a sequence of 2-3 times 60s immersion in aqua regia, H_2O rinse, 60s immersion in 10% (w/v) KCN at 50°C and H_2O rinse. In some cases, a $\text{HNO}_3\text{:H}_2\text{O}$ mixture (55:100, v/v) was used instead of aqua regia. Photoelectrochemical etching was done in a 1:10 (v/v) diluted solution of 3% NH_3 in HCl (v/v) at reverse bias voltages (*vs.* the potential of the etching solution) between 0.3 and 1.0V. For CuInS_2 , optimum electrode improvement was obtained when this procedure was done at +1.0V. Air heating of electrodes (in addition to heating at 50°C to cure the silver epoxy, used as part of the ohmic back contact) was carried out in conventional laboratory furnaces.

Electrochemical measurements, including spectral response and output stability experiments, were done as described previously (5, 11). Capacitance measurements were carried out as outlined elsewhere (12), using frequencies up to 5 kHz. Concentrations of polysulfide solutions are expressed as follows: $X/Y/Z$, where X, Y, and Z give the molar concentrations for OH^- , S^- , and S, as added. Na and K were used as cations for S^- and OH^- , respectively, except where noted otherwise.

Results and Discussion

Surface treatments.—Previously, photoelectrochemical etching has been found to improve the photoelectrochem-

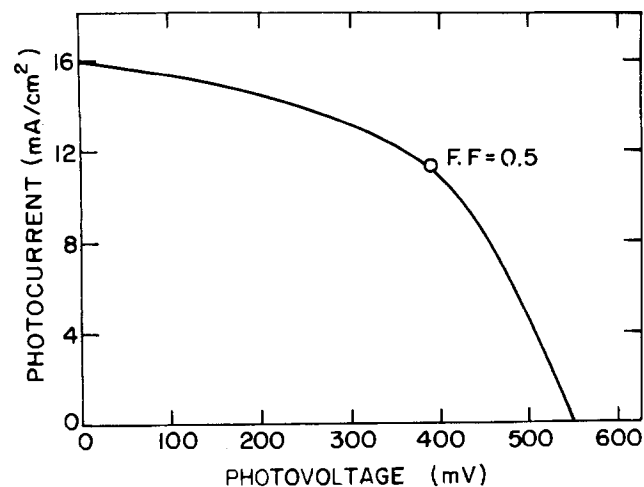


Fig. 2. Potentiostatic I-V curve for $n\text{-CuInS}_2$ in 3/3/4 polysulfide solution at 49°C . Illumination intensity: 89 mW/cm^2 simulated sunlight. Electrode area: 5.5 mm^2 . Electrode efficiency: *ca.* 4.9%.

Table I. Effects of photoelectrochemical etching on CuInX_2 photoanode performance under simulated AM1 illumination at room temperature. Potentiostatic measurements

Electrode	Surface treatment	J_{sc} (mA/cm^2)	V_{oc} (mV)	FF ^a
CuInS_2 ^b	Etched	8.5	390	0.32
CuInS_2 ^{b,c}	Photoetched	11.7	465	0.34
CuInSe_2 ^d	Etched and air-heated	29.7	312	0.38
CuInSe_2 ^{c,d}	Photoetched and air-heated	37.5	312	0.33

^a Fill factor.

^b In 2/1.5/3 polysulfide solution.

^c Photoetching was done on the same electrode after the first treatment.

^d In 0/1.8/3 Cs-polysulfide solution.

ical performances of Cd chalcogenides (13), as well as that of $n\text{-CuIn}_3\text{S}_8$ photoanodes (14). We found that this treatment improves the I-V characteristics of $n\text{-CuInX}_2$ PEC's, although it is less effective if the electrode performs well already before photoetching (after dark etching). Figure 2 shows the photocurrent-photovoltage plot for one of the better, as-etched electrodes. Table I compares the performance of two chemically and photoelectrochemically etched CuInS_2 and CuInSe_2 photoanodes, for which the latter treatment was effective.

Figure 3 shows the surface of a CuInS_2 photoanode, that was photoelectrochemically etched and, subsequently, chemically etched. On the surface of the photoelectrochemically etched electrode, we see the etch pit pattern, familiar from photoetched surfaces of other chalcogenide semiconductors (13). The rather irregular shape of the etch pits can be explained by the fact that a randomly oriented surface was used. Parts of the surface of photoelectrochemically etched CuInSe_2 electrodes showed similar etch pits, while other parts were less affected by the treatment.

The differences between the two compounds are also expressed in their behavior after air-heating. While this treatment was invariably found to improve the performance of CuInSe_2 PEC's (Fig. 4) this was not the case for CuInS_2 ones, where it mostly led to a poorer performance.

In the following paper (15), we present results of detailed surface analyses, on the basis of which we can attribute the effect of the air heating step to the formation of an indium oxide layer on the surface of these semiconductors, or, rather, to the increased homogeneity of a partially existing layer. [In_2O_3 is the native oxide on these materials; *cf.* Ref. (16).] The difference between CuInS_2 and CuInSe_2 may be due to the larger thermodynamic

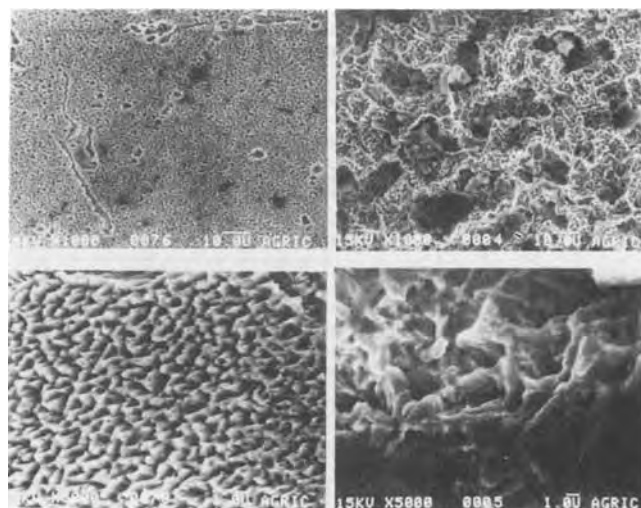


Fig. 3. Scanning electron micrographs of $n\text{-CuInS}_2$ crystal (random orientation) at 1000 (top) and 5000 (bottom) times magnification. Right: chemically etched surface. Left: photoelectrochemically etched surface.

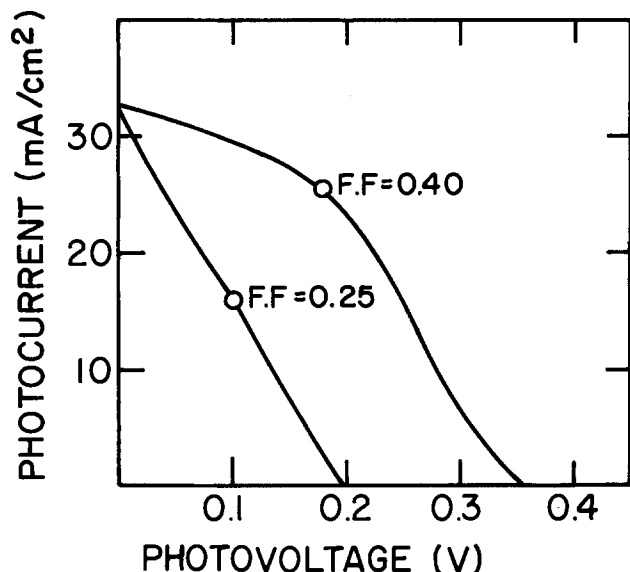


Fig. 4. Photo I-V characteristics of n-CuInSe₂ in 3/3/4 polysulfide electrolyte, before (FF = 0.25) and after (FF = 0.40) heating the electrode, for 60 min at 100°C in air. Illumination intensity: 90 mW/cm² simulated sunlight.

driving force for oxide formation on the disulfide, compared to the diselenide.

We also measured the flatband potential (fbp) of the electrodes as function of surface treatment. Capacitance-voltage measurements were, in many cases, complicated by the relatively narrow potential range over which the C⁻²-V plots were linear, by large frequency dispersion that was encountered, and by hysteresis in the curves. After an etched electrode was either left standing in air overnight, or used for some time in polysulfide solution (*i.e.*, some photocharge was passed), better behavior was observed, suggesting the occurrence of chemical changes in the near-surface region and/or at the surface. Although the dark forward currents for several samples were high in the region of the fbp, measurements of the potential of onset of photocurrent is often an alternative way to obtain a lower limit (in terms of absolute potential) for the fbp. Table II summarizes the results. From it we see that, for most cases where both types of measurements were done on CuInSe₂, the agreement is reasonable. The situation for CuInS₂ electrodes is not so satisfactory; there, the onset potential appears to be the more reliable measurement. We note that these values for the n-CuInS₂ fbp in

Table II. Comparison of fbp's estimated from capacitance-voltage and onset of photocurrent, with measured open-circuit voltages, for CuInX₂ in polysulfide solution after various surface treatments

Semiconductor	Treatment	From C-V ^a (mV)	From onset ^d of photocurrent (mV)	V _{oc} ^e (mV)
CuInS ₂ ^b	Acid etch ^c	640-980	540	490
	H ₂ O ₂ etch	995-1050	570	518
CuInSe ₂ ^b	Acid etch ^c	390-450	490	390
	H ₂ O ₂ etch	465-600	510	410
	Overnight in air	530-555	525	450
CuInSe ₂ ^d	Acid etch ^c	580-620	600	—
	Air-heated	600-620	—	—
	After use in polysul- fide	400	400	—

^a Values given are negative w.r.t. polysulfide solution potential.

^b In 2/2/2 solution.

^c Includes KCN rinse, as described in Experimental section. The treatments were done sequentially.

^d In 3/3/4 solution.

^e Under simulated AM1 illumination.

polysulfide, even though they are quite approximate ones, are between 1 and 1.5V more negative than those found for p-CuInS₂ in polysulfide (5), or in 1M NaOH as reported by McCann and Pezy (17), suggesting that this semiconductor/electrolyte interface behaves reasonably ideally.

The effect of pH of a nonsulfide solution and of polysulfide concentration on the fbp of n-CuInS₂ was briefly investigated. The importance of such an investigation stems from the expectation that if CuInSe₂ behaves as CdS or CdSe, there will be little shift of the fbp as a function of pH over most of the pH range, while if an In-oxide layer on the surface of the CuInSe₂ is in equilibrium with the electrolyte, there would be a 59 mV/pH unit fbp dependence.

The results (obtained by C⁻²-V measurements) show an irregular dependence of the fbp on pH, which is, on the average, less than the 59 mV/pH expected from a simple oxide-electrolyte junction. Still, it is considerably greater than that shown by CdS or CdSe. This indicates that the In-oxide/electrolyte interface is electronically active, and that in sulfide-free electrolyte this oxide layer is involved in charge transfer between CuInSe₂ and the electrolyte, rather than serving merely as a porous interlayer.

Because this result in itself does not prove that a similar situation holds in polysulfide, fbp measurement as function of nominal polysulfide concentration were done as well. Solutions of equimolar concentrations of added hydroxide, sulfide, and sulfur, between 10⁻² and 1M (pH 12-14) were used, and a change of nearly 100 mV/decade of concentration was found. Of this, some 50 mV can be ascribed to the effect of pH. The remainder of the change must be due to sulfur containing species.

After optimization of the surface treatments, it was possible to study the photoelectrochemistry further. Before presenting the results of these measurements, the results of the photoelectrochemical characterization of the CuInS₂ samples, which differed considerably from those of crystals used earlier (5), are given.

Photoelectrochemical characterization of CuInS₂ crystals.—Wavelength dependence of the photocurrent.—Previously, we reported spectral response data for n-CuInS₂ (5), in arbitrary units, and for CuInSe₂ (6), in terms of absolute quantum efficiencies. Therefore, we will show here only the wavelength dependence of the absolute, external, quantum efficiency for n-CuInS₂ (Fig. 5). These results are similar to those obtained previously for single crystals (5), for polycrystalline films (18), and for p-CuInS₂ polycrystalline samples (19), in that they show optimal response at higher wavelengths. The quantum efficiencies are less than those obtained for CuInSe₂ (6).

Monochromatic current-voltage behavior.—As discussed in Ref. (5), we can obtain the fbp from the voltage depen-

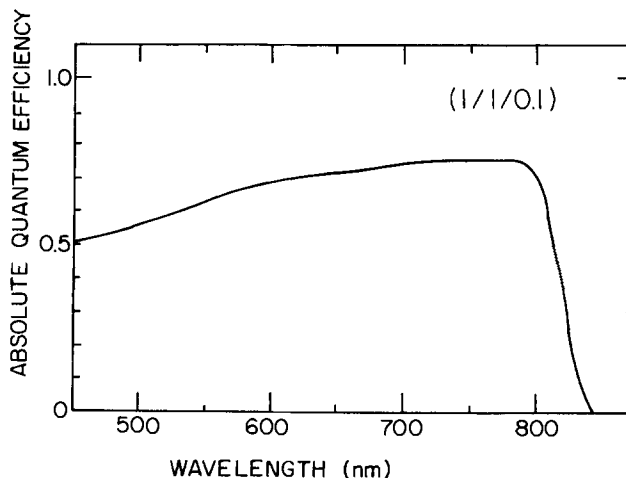


Fig. 5. Wavelength dependence of the absolute external quantum efficiency for a n-CuInS₂/(1/1/0.1) polysulfide cell.

dence of the monochromatic photocurrent (at reverse bias). In the sulfur-poor solution of Fig. 5, we find a value of -750 mV vs. the solution potential, which is similar to that reported earlier, for samples with poorer performance [cf. Fig. 3 with the I-V curve in Ref. (5)]. This difference is expressed mainly in the effective minority carrier diffusion length obtained from these data [cf., Ref. (5)], which is ca. $0.65 \mu\text{m}$ vs. $0.2 \mu\text{m}$ for the inferior crystals. The effective net doping density, obtained from monochromatic I-V plots in the range of strong depletion [cf. Ref. (5)], is similar for both cases: $2.1 \times 10^{16} \text{ cm}^{-3}$ vs. $2.8 \times 10^{16} \text{ cm}^{-3}$ for the inferior crystals.

Photoelectrochemical performance of $\text{CuInX}_2/\text{polysulfide}$ PEC's.—Light-intensity dependence of I-V characteristics.—For both CuInS_2 and CuInSe_2 , plots of the logarithm of the short-circuit currents vs. the open-circuit potential were quite linear from ca. 10 mW/cm^2 up to 100 mW/cm^2 . Saturation sets in only well above this (normal insolation) level. From the slope of these plots values for n , the diode quality factor for the illuminated semiconductor-electrolyte interface could be calculated. Values around 2.4 for CuInS_2 and 1.7 for CuInSe_2 were found, indicating the nonideality of the Schottky barrier. A similar situation was found for Cd-chalcogenides (20). Both types of electrodes show a linear dependence of the short-circuit current on the incident white light intensity between 5 and 100 mW/cm^2 . This suggests the absence of kinetic limitations due to simple solution or interfacial charge transfer processes up to ca. AM1 illumination at least. To investigate this point, which has obvious implications for PEC performance, we studied the effects of solution composition and temperature on the photocurrent-photovoltage characteristics.

Effect of polysulfide composition on I-V characteristics.—The actual composition of aqueous polysulfide solutions is a strong function of the relative and absolute concentrations of the added components (21). Therefore, we investigated the effect of nominal polysulfide composition on the I-V characteristics of $n\text{-CuInS}_2/\text{polysulfide}$ cells. Figure 9 illustrates the marked differences for CuInS_2 in two solutions. From systematic studies, we found that optimal power conversion efficiencies are obtained for solutions with $[\text{S}]/[\text{S}^-]$ between ca. 1.5 and 3. For CuInSe_2 , the optimum value for this ratio was found to be around 1. The solution redox potential decreases with increasing $[\text{S}]/[\text{S}^-]$ ratio, but no systematic correlation between open-circuit voltages and redox potentials was seen, for either of the two types of photoanodes. Because no significant variations in dark currents were measured in different polysulfide solutions, it is likely that the solution composition dependence of the I-V characteristics is attributable to changes in relative concentrations of the oligosulfide species in the solutions, and especially their availability near the surface and their adsorption-desorption equilibria.

Temperature dependence of I-V characteristics.—Robbins *et al.* (4) first noted the strong positive temperature dependence of the $n\text{-CuInS}_2/\text{polysulfide}$ system. Their results were confirmed by us (5), and a similar behavior was found for the diselenide system (16). Figures 6 and 7 and Table III show for CuInS_2 that the temperature dependence is less pronounced if an electrode with better room temperature I-V characteristics is used. The same situation exists for CuInSe_2 , as shown in Fig. 8 and Table IV. This behavior is quite different from that found for solid-state photovoltaic cells, where the increase in short-circuit current is generally more than offset by decreases in open-circuit voltage and fill factor. It is also different from the temperature dependence of single-crystal and thin film $\text{CdSe}/\text{polysulfide}$ cells (22-24), where the power output goes through a maximum at temperatures slightly above room temperature. There the initial strong increase in short-circuit current was attributed to the temperature dependence of sulfur dissolution from the photoanode. Such an effect should depend on the current densities involved, as sulfur is the product of the oxidation reaction

Table III. Temperature dependence of $n\text{-CuInS}_2$ photoanodes

Sample A					
In 1/1/1 polysulfide; 98 mW/cm^2 illumination intensity					
T(°C)	J (mA/cm ²)	V (mV)	FF	P_{max} (mW/cm ²)	$\eta(\%)$
23	9.6	617	0.39	2.31	2.36
30	12.0	588	0.42	2.96	3.02
40	13.3	583	0.44	3.41	3.48
50	14.1	555	0.45	3.52	3.59
60	15.0	524	0.46	3.62	3.69
Increase (%)	56	-15	18	57	57
Sample B					
In 3/3/4 polysulfide; 89 mW/cm^2 illumination intensity					
19	14.2	540	0.41	3.14	3.53
29	14.8	550	0.44	3.58	4.02
39	15.3	550	0.47	3.95	4.44
49	15.9	540	0.50	4.29	4.82
59	16.1	535	0.50	4.30	4.83
69	16.3	530	0.51	4.40	4.95
Increase (%)	15	-2	24	40	40

occurring at the photoanode. Therefore, we checked the temperature dependence of the short-circuit current at low light levels. For CuInS_2 , experiments at 0.75 mW/cm^2 gave results similar to those obtained at 85 mW/cm^2 . At 55°C , the photocurrent was 0.11 mA/cm^2 ; at 23°C , it was 0.072 mA/cm^2 . Experiments on a number of CuInS_2 electrodes gave comparable results. The same holds for CuInSe_2 electrodes, where, for example, the same 40% increase in short-circuit current was found between 15° and 52°C , at 1, 5, 12, 36, and 100 mW/cm^2 light intensities. For polycrystalline CdSe electrodes, however, the temperature dependence of the short-circuit current decreases when lower light intensities are used.

It is interesting to note that a slightly negative temperature dependence is found for the $n\text{-CuIn}_3\text{S}_7/\text{polysulfide}$ (14) and the $n\text{-CuInSe}_2/\text{polyiodide}$ systems (7). A possible explanation may be the temperature dependence of specific adsorption processes involving oligosulfides or HS^- (21) occurring on the chalcopyrite surface in polysulfide electrolyte, but to a much smaller extent on spinel (CuIn_3S_7) surfaces, which are predominantly oxide free (14). With iodide solutions, completely different adsorption processes are expected. The very occurrence of a

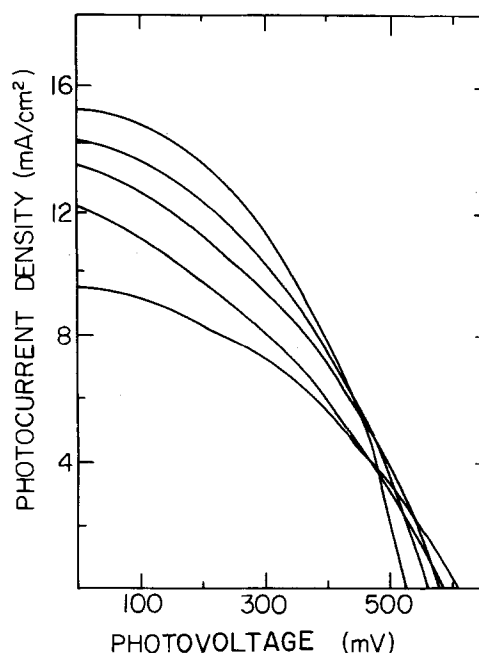


Fig. 6. Temperature dependence of the photo-I-V curves of 2.4% efficient (at room temperature) $n\text{-CuInS}_2$ electrode in 1/1/1 polysulfide solution. The temperatures used are, in order of increasing short-circuit current: 23° , 30° , 40° , 50° , and 60°C . Illumination intensity is 98 mW/cm^2 (cf. Table III).

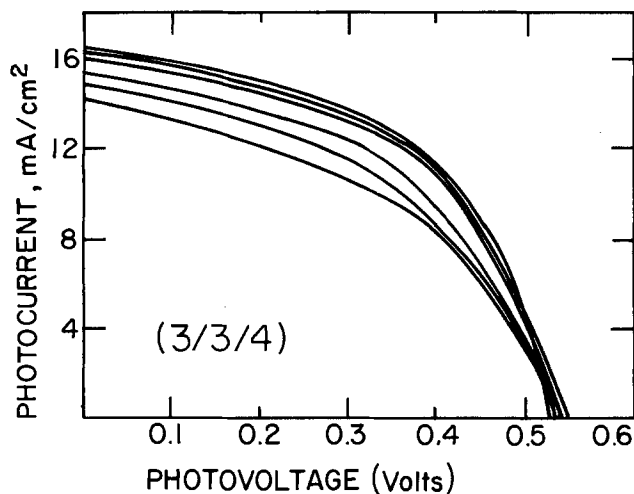


Fig. 7. Temperature dependence of 3.5% efficient (at room temperature) $n\text{-CuInS}_2$ electrode in 3/3/4 polysulfide solution. The temperatures are, in order of increasing short-circuit current, 19°, 29°, 39°, 49°, 59° and 69°C. The light intensity is 89 mW/cm^2 (cf. Table IIIb).

positive temperature dependence of the short-circuit photocurrent indicates that not all photogenerated holes are used for oxidation of sulfide. In the case of Cd chalcogenides, it was argued that such a mismatch between hole flux and electrochemical reaction flux will lead to self-oxidation of the semiconductor and thus to instability (25, 26). As we will see in the following section, this is not so for the $\text{CuInX}_2/\text{polysulfide}$ systems.

Output stability.—One of the most remarkable features of the $\text{CuInX}_2/\text{polysulfide}$ systems is their stability (4, 5). Previously, we reported results of initial experiments for both semiconductors. Further work showed the CuInS_2 system to be stable, even in a poorly stabilizing solution [cf. Ref. (5)] at various initial current densities (Fig. 10). The initial photocurrent density was regulated by changing the incident light intensity. While there is some decrease, which increases with increasing initial current density, the cell stabilizes after a short time rather than exhibiting the catastrophic decreases known for Cd-chalcogenide systems. The initial decrease is also a function of the efficiency of the electrode used (Fig. 12). Here, we compare two electrodes with optimal quantum yields, at 750 nm, of 0.7 and 0.4. Again, the situation is quite different from that known for CdSe, for example, where low efficiency electrodes will corrode more readily. Here only an initial decrease is found. Longer-term experiments, comparing an optimally prepared CdSe single-crystal electrode (27) with CuInS_2 bear out the differences clearly

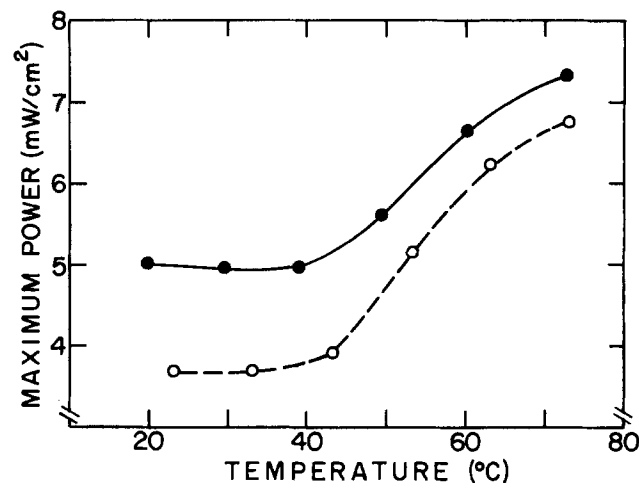
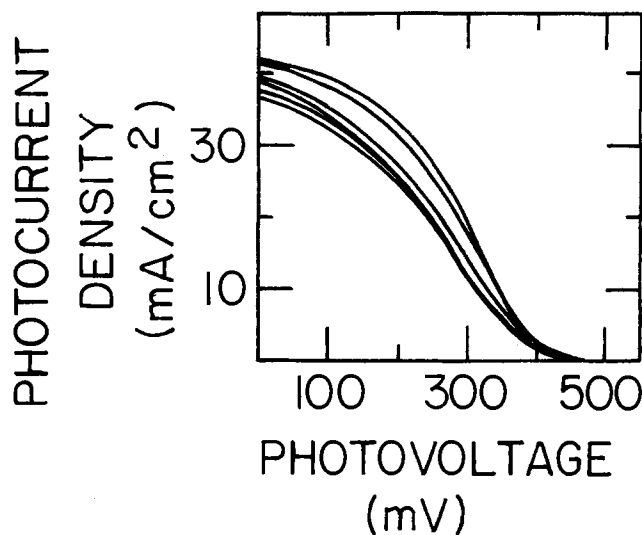


Fig. 8. a(top): Temperature dependence of photo-I-V characteristic of $n\text{-CuInS}_2$ in polysulfide (3/3/4) solution. Temperatures used, in order of increasing short-circuit current: 19.5°, 29°, 39°, 49°, 60°, 73°C. b(bottom): Plot of maximum output power vs. temperature for the electrode of Fig. 8a (solid line) and for less efficient electrode (dashed line). Illumination intensity: 98 mW/cm^2 .

Table IV. Temperature dependence of $n\text{-CuInS}_2$ photoanodes in 3/3/4 polysulfide solution. Illumination intensity: 98 mW/cm^2

Sample A Less-efficient electrode						
T(°C)	J (mA/cm^2)	V (mV)	FF	P_{max} (mW/cm^2)	$\eta(\%)$	
23	32.5	410	0.29	3.86	3.94	
33	33	405	0.29	3.87	3.95	
43	33	405	0.31	4.04	4.22	
53	37	400	0.35	5.18	5.28	
63	40	395	0.39	6.16	6.29	
73	40.5	395	0.41	6.56	6.70	
Increase (%)	25	-4	42	70	70	
Sample B More efficient electrode						
19.5	37	430	0.32	5.09	5.20	
29.5	37	425	0.32	5.03	5.14	
39	36.5	420	0.325	4.98	5.09	
49	39	415	0.34	5.50	5.60	
60	41	410	0.39	6.56	6.69	
73	41.5	410	0.43	7.32	7.47	
Increase (%)	12	-5	34	43	43	

(Fig. 13). From detailed surface analyses, described elsewhere (15), we find that the CuInS_2 surface is at least partially covered with an indium oxide layer. This layer may well prevent direct contact between sulfide ions and the semiconductor, which could lead to further photocurrent deterioration. The initial decreases, observed here, might then be due to chemical changes of the surface or to the relative inability of the electrolyte to dissolve off S, the product of the photo-oxidation (28) (*vide infra*). Surface analyses show that for CuInS_2 in polysulfide solution no Se/S exchange is found (15). While at first sight this may not seem surprising, it should be remembered that this type of exchange takes place on CdSe, where it indicates the occurrence of semiconductor self-oxidation, *i.e.*, breaking of Cd—Se bonds. Also, the CuInS_2 initial decreases in photocurrent output are found at high light intensities (Fig. 14b) and in dilute solutions (Fig. 14c). For comparison, results for CdSe are shown as well (Fig. 14a), indicating apparent total stability at low photocurrent densities, but steady decreases at higher photocurrent densities, even for photoetched samples, *i.e.*, the most stable types of electrodes (27). In this case, the quantum efficiency of the CuInS_2 electrodes was deliberately kept low (0.4) by using electrodes whose surfaces were only partly optimized. This provided photocurrents of 16-18 mA/cm^2 at 100 mW/cm^2 , thereby allowing comparison with the structurally similar CdSe electrodes, which gave 13-15 mA/cm^2 under the same illumination. Here, as in the case of CuInS_2 , the photocurrent will return to its initial

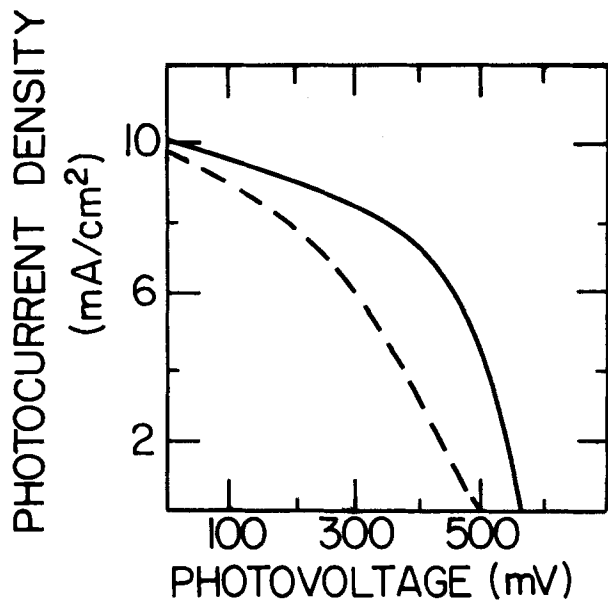


Fig. 9. Photo-I-V characteristics of n-CuInS₂ in 3/3/4 (solid line) and 0.8/0.8/0.8 (dashed line) polysulfide solutions under ca. 80 mW/cm² white light illumination.

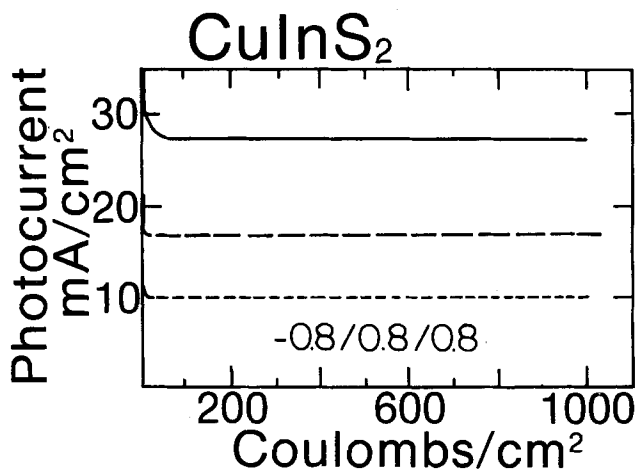


Fig. 10. Short-circuit current density as function of photocharge passed at three different light intensities, for n-CuInS₂ in 0.8/0.8/0.8 polysulfide solution at 47°C.

value if illumination is interrupted. The initial periods of decreasing photocurrents lasted from a few seconds, in solutions poor in S, to ca. 60s in S-rich solutions. Licht has shown (21) that the main difference between such solutions is the higher concentration of free hydroxide in the S-poor ones. For very dilute solutions (e.g., 0.8/0.8/0.8),

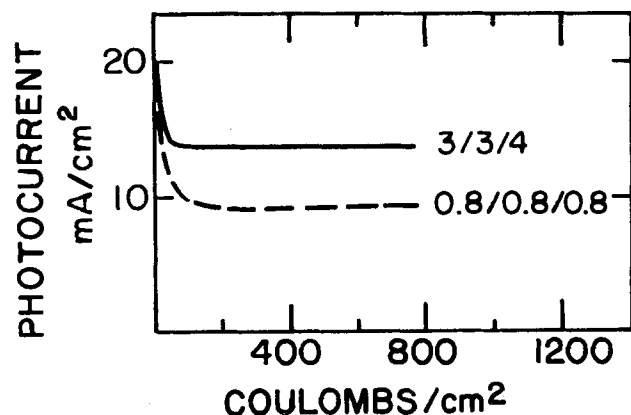


Fig. 11. Short-circuit current density as function of photocharge passed for n-CuInS₂ in two different polysulfide solutions at 35°C.

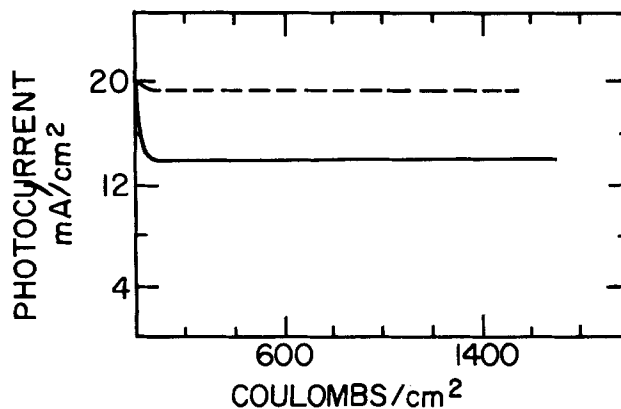


Fig. 12. Short-circuit photocurrent density as function of photocharge passed for two different n-CuInS₂ photoanodes in 1/1/1 polysulfide solution at 34°C. The solid line gives results for the less efficient electrode. The dashed line for the more efficient one.

this initial decline was followed by a much smaller decrease, lasting from 0.5 to 1h, after which the output current stabilized.

The initial output decrease was investigated in a systematic fashion, as it was found to be influenced by initial current density, solution temperature, solution composition, and initial quantum efficiency of the CuInSe₂ electrode. We can define a ratio J_s/J_i where J_s stands for the steady-state value of the photocurrent, reached after 1 min or less, and J_i stands for the initial photocurrent. Figure 15 shows the dependence of this ratio and of J_s on J_i . A linear decrease of J_s/J_i with increasing J_i is found for both electrodes, but the initial photocurrent at which the decrease (from 1.0) starts is higher for the more efficient electrode. The value of J_s/J_i increases with increasing temperature and with increased concentration of the solution. By varying only the concentration of added sulfur, a maximum value for J_s/J_i around $[S] = 1-1.5M$ was found for 1/1/[S] solutions. This value was still somewhat lower than that obtained for solutions containing higher concentrations of added OH⁻ and S⁻, e.g., 3/3/4. This behavior is reminiscent of that found for CdSe (28), where it was explained by the varying dissolving power, for sulfur, of the polysulfide solutions, as S could form a blocking layer on the electrode. It was shown, there, that this phenomenon occurs also at metal/polysulfide interfaces. It is likely that, at the high photocurrent densities encountered with CuInSe₂, a similar explanation holds. For some of the experiments at CuInS₂, the current densities would seem to be sufficiently low to minimize this effect. It is likely that there, and possibly also at CuInSe₂, the above explanation is too simplistic and the previously mentioned processes, i.e., surface adaptation to the solution, for example by forma-

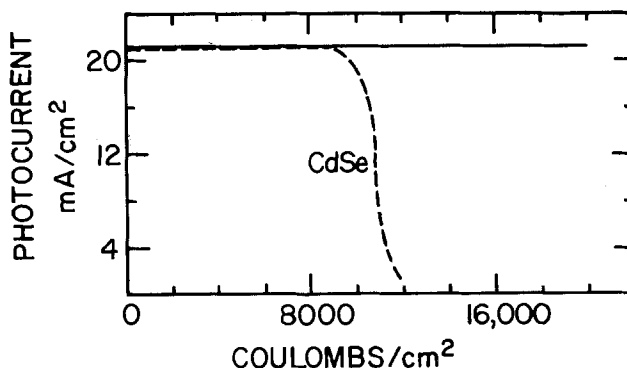


Fig. 13. Short-circuit photocurrent density as function of photocharge passed for n-CuInS₂, (112) face exposed, and for n-CdSe, (1120) face exposed to the 3/3/4 polysulfide solution at 50°C. The CdSe crystal was photoetched to obtain the best possible output stability characteristics (24). The (1120) face of CdSe is more stable than the (0001) or (1000) faces.

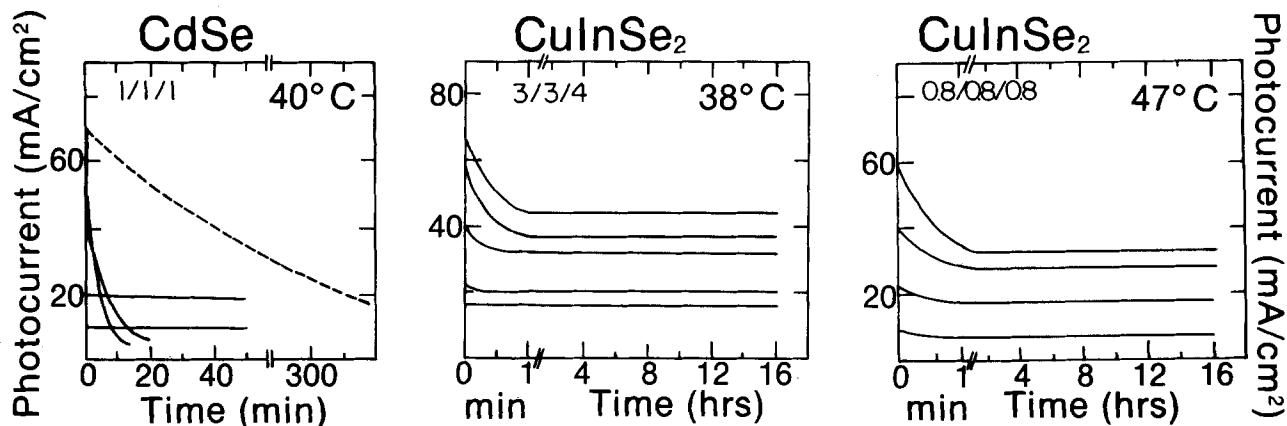


Fig. 14. Short-circuit photocurrent density as function of time, for various initial current densities. Left: n-CdSe in 1/1/1 polysulfide solution at 40°C. The dashed line gives the behavior of a photoetched electrode. Note the difference in time scales between A, and B or C. Center: n-CuInSe₂ in 3/3/4 polysulfide at 38°C. Right: n-CuInSe₂ in 0.8/0.8/0.8 polysulfide at 47°C.

tion of hydrated indium oxide (In(OH)₃, for example), and varying ad- and desorption of sulfides, need to be considered as well.

All the output stability tests described up to this point were carried out under short-circuit conditions, *i.e.*, no electrical power was extracted from the system. In the case of CdSe, it was shown that PEC is less stable at maximum power than at short-circuit, under identical illumination intensity (29). Therefore, it was imperative to check the output stabilities of n-CuInS₂ and n-CuInSe₂ under load conditions, and compare them to that of CdSe from which a comparable amount of electrical power was obtained. Table V summarizes these experiments. Except for the CuInSe₂ entry explained in footnote e, no systematic decrease in performance was found for CuInX₂ photoanodes. Whenever a lower final than initial photocurrent density is shown, the decrease occurred during the initial stages of the experiments (*cf.* Fig. 10-12, 14). In two cases, a higher final than initial photocurrent is indicated. Then an increase occurred during the initial stages of the experiments, and could be due to some "auto-etching" of the electrodes which were, apparently,

not treated optimally before starting the experiments. A similar phenomenon is, at times observed for Cd-chalcogenide photoanodes (27). The results shown in Table V indicate that the CuInX₂ photoanodes are stable against photocorrosion, even when they are used at potentials corresponding to their optimal power points, and when they are subjected to high light intensities. For example, the third entry for CuInSe₂ was run under an illumination intensity that corresponded roughly to 2-2.5× AM1 solar intensity.

General Discussion and Conclusions

The salient features of the work reported here are the apparent crucial role of the electrode surface in determining cell behavior, the involvement of the surface in the occurrence of kinetic limitations on the charge-transfer process, and the stability of these PEC's, notwithstanding those limitations.

To elucidate the role of the electrodes' surface, we carried out detailed surface analyses (15), which show that the top layer of electrodes, used in polysulfide, is composed mainly of indium oxide and is depleted in Cu. They also show that no Se/S exchange takes place for CuInSe₂. The effect of air oxidation can then be connected with the formation of a more complete, more stoichiometric indium oxide layer. Our fbp measurements show this layer to be an active participant in the charge-transfer process.

A central question concerns the nature of the processes that give rise to kinetic limitations on the charge transfer, as expressed in the positive temperature dependence. The effect of solution composition on PEC I-V characteristics and on the initial decrease in photocurrent suggests the involvement of the HS⁻ and/or oligosulfide species [S₃⁻ and S₄⁻ are those present in the highest concentrations in most of our polysulfide solutions; *cf.* Ref. (21)]. Because the optimal concentration ratios are similar to those found for CdSe (28), these effects can be interpreted in terms of the dissolving power (for the oxidized oligosulfide) of the polysulfide solution. Still, the different temperature dependences of CdSe and CuInX₂/polysulfide PEC's indicate that other factors are involved as well. The linear dependence of the photocurrent on the light intensity and the persistence of the positive temperature dependence of the I-V characteristics at low light levels show that the problem is not the availability of the oligosulfides near the surface. We suggest that the main additional factor is, rather, the thermally activated ad- and/or desorption of sulfides, as fbp measurements are consistent with adsorption of such species. The occurrence of chemisorption implies creation or annihilation of electronic states or changes in the population of existing ones, of the solid state. Thus, when we discuss (de)sorption processes, this includes such electronic effects in the solid itself.

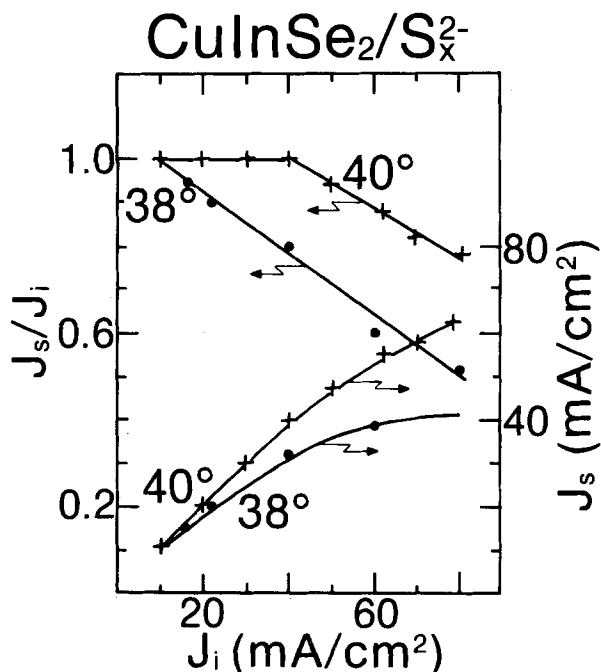


Fig. 15. Dependence of steady-state photocurrent density (J_s) (lower curves) and of the ratio of J_s and J_i , the initial photocurrent density (upper curves), on J_i , for two different n-CuInSe₂ electrodes in 3/3/4 polysulfide. (●—●): 2% efficient electrode. (+—+): 6% efficient electrode.

Table V. Output stability tests under optimal load conditions

Electrode ^c	Temperature (°C)	Potential ^a (mV)	J_{in}^b (mA/cm ²)	J_{fin}^b (mA/cm ²)	Photocharge passed (kC/cm ²)	Power (Wh/cm ²)
CuInS ₂	40	200	20	22	9	0.5
CuInS ₂	40	200	15.5	15.2	5.4 ^d	0.3
CuInS ₂	40	200	30	22	8.4 ^d	0.5
CuInSe ₂	53	100	33	32	8.2 ^d	0.2
CuInSe ₂	45	100	34	38	40	1.2
CuInSe ₂	50	150	45	68	37	1.5
CuInSe ₂	45	100	33	23	42 ^e	1.2
CdSe	50	400	22	8	9	1.3

^a Negative of the solution redox potential.

^b Initial and final photocurrent densities.

^c All CuInS₂ experiments were done in 1/1/1 solutions. All CuInSe₂ experiments and that with CdSe were done in 3/3/4 solutions.

^d Experiment was stopped because a leak in the protective epoxy occurred.

^e Auger analyses showed the presence of Cd on the surface, after the experiment. From scanning Auger microprobe maps, it appears that the presence of Cd is connected with that of S and O, i.e., it may occur as CdS and CdO. This phenomenon probably explains the steady, very small decrease in photocurrent shown by this electrode.

The initial, reversible decrease in photocurrent could be due to a diffusion-limited process in the electrolyte (including slow dissolution and/or desorption of the oxidized sulfide species, as for CdSe). Another possibility which can explain the slow shift in fbp of etched electrodes is that a solution-induced chemical change of the surface, e.g., to a hydrated oxide, In(OH)₃, takes place. The faster initial change in S-poor solutions can then be connected with the higher concentration of free hydroxide in them, as compared to S-rich solutions. The absence of S on surfaces of CuInX₂ electrodes, used in polysulfide, argues against the formation of mixed oxysulfides. The adsorption and desorption process will occur on this modified surface. The lack of a positive temperature effect for CuIn₃S₉/polysulfide PEC's can be understood from the absence of an indium oxide layer on CuIn₃S₉ electrodes.

The fact that the positive temperature dependence is less pronounced for more efficient electrodes indicates that other processes play a role, too. For example, the normal solid-state photovoltaic effect may have a negative temperature dependence that is stronger for more efficient systems, although no strong temperature dependence is encountered with the CdS/CuInSe₂ solar cell. Another possibility which might explain the positive temperature dependence is that the charge transport through the top indium oxide (hydroxide) layer is thermally activated; however, the fact that no positive temperature dependence is found with the CuInSe₂/polyiodide cell argues against this.

Summarizing, we can list three probable reasons for the kinetic limitations on the CuInX₂/polysulfide cells: (i) the S-dissolving power of the polysulfide solutions (as for CdSe); (ii) (near) surface adaptation, to In(OH)₃, for example; and (iii) thermally activated adsorption of HS⁻ and/or oligosulfides (S₃⁻, S₄⁻) and/or thermally activated desorption of their oxidized forms from the adapted surface.

Notwithstanding these limiting factors, both systems showed reasonable photovoltaic performances with 5 and 7.5% efficiencies at elevated temperatures for the disulfide and the diselenide, respectively.

We can ask now how the remarkable stability of these ternary chalcopyrite PEC's can be understood. On the basis of thermodynamic calculations, we expect less susceptibility to photoanodic corrosion for them than for CdSe, because of the position of their decomposition potentials with respect to the solution redox potential. Another factor may be the presence of the native indium oxide layer on the electrode surface. Such a film was found to provide improved performance and improved resistance against photocorrosion also for the n-CuInSe₂/polyiodide system (7). The role of the oxide layer can be to provide a phase where those photogenerated holes that are not transferred to the solution can recombine without causing decomposition. It is unlikely that all these photo-

generated holes will recombine in the oxide layer, which is rather thin [50-100Å, cf. Ref. (15)]. The bond strengths of the Cu—X and In—X bonds and the Cu d orbital character of the top of the valence band can be additional factors. Another aspect of the oxide layer is that it can stop field-assisted migration of positive ions from the bulk. The possibility exists, furthermore, that a photovoltaic solid-state junction forms at the oxide/chalcogenide interface; however, preliminary experiments have not yielded conclusive evidence for this, as yet.

Finally, we note the sensitivity of the performance of these photoelectrodes to surface treatment. It should be stressed that no complete reproducibility has yet been achieved and the effect of the various treatments described here becomes less pronounced the better the initial performance of the electrode. This is usually the case because any such surface treatment will be most effective for an electrode with a severely damaged surface, where there is much room for improvement.

It is obvious from our results that improved PEC's can be obtained with these materials, if solution-related limitations can be overcome. However, when attempting use of alternative or modified solutions, thought should be given to possible causes for photocorrosion. Such a line of action has recently proved effective for the iodide system, and, with increased knowledge of these materials and related ones, other systems should be achievable.

Acknowledgments

We thank the Ministry of Research and Technology of Germany for partial support, through the Israel National Council for Research and Development, and H. Gerischer for his hospitality to one of us. This work was initiated under a grant from the U.S.-Israel Binational Science Foundation, Jerusalem, Israel. Part of the work reported here is based on the Ph.D. thesis of Y. Mirovsky, submitted to the Feinberg Graduate School of the Weizmann Institute of Science in 1983.

Manuscript submitted May 14, 1985; revised manuscript received Jan. 16, 1985.

The Weizmann Institute of Science assisted in meeting the publication costs of this article.

REFERENCES

1. B. R. Pamplin, *Prog. Cryst. Growth Charact.* **1**, 331 (1979).
2. J. L. Shay and J. H. Wernick, "Ternary Chalcopyrite Semiconductors: Growth, Electronic Properties and Applications," Pergamon Press, Oxford, England (1975).
3. R. A. Mickelsen and W. S. Chen, in "Proceedings of the 16th IEEE Photovoltaics Specialists Conference," pp. 781-785, IEEE, New York (1983).
4. M. Robbins, K. J. Bachmann, V. G. Lambrecht, F. A.

- Thiel, J. Thomson, Jr., R. G. Vadimsky, S. Menezes, A. Heller, and B. Miller, *This Journal*, **125**, 831 (1978).
5. Y. Mirovsky, D. Cahen, G. Hodes, R. Tenne, and W. Giriat, *Solar Energy Mater.*, **4**, 169 (1981); J. Manassen, G. Hodes, and D. Cahen, U.S. Pat. 4,064,326 (1977).
 6. Y. Mirovsky and D. Cahen, *Appl. Phys. Lett.*, **40**, 727 (1982).
 7. D. Cahen and Y. W. Chen, *ibid.*, **45**, 746 (1984); S. Menezes, H.-J. Lewerenz, and K. J. Backmann, *Nature (London)*, **305**, 615 (1983).
 8. J. L. Shay, B. Tell, H. M. Kasper, and L. M. Schiavone, *Phys. Rev. B.*, **7**, 4485 (1973).
 9. B. Tell and J. L. Shay, *J. Appl. Phys.*, **43**, 2469 (1972).
 10. H. Neumann, *Cryst. Res. Technol.*, **18**, 483 (1983).
 11. R. Tenne, Y. Mirovsky, Y. Greenstein, and D. Cahen, *This Journal*, **129**, 1506 (1982).
 12. H. J. Lewerenz, H. Gerischer, and M. Lubke, *ibid.*, **131**, 101 (1984).
 13. R. Tenne and G. Hodes, *Surf. Sci.*, **135**, 453 (1983).
 14. G. Dagan, S. Endo, G. Hodes, G. A. Sawatzky, and D. Cahen, *Solar Energy Mater.*, **11**, 57 (1984).
 15. Y. Mirovsky, G. A. Sawatzky, R. Tenne, M. Polak, and D. Cahen, *This Journal*, **132**, 1070 (1985).
 16. L. L. Kazmerski, O. Jamjoum, P. J. Ireland, S. K. Deb, R. A. Mickelsen, and W. Chen, *J. Vac. Sci. Technol.*, **19**, 467 (1981).
 17. J. F. McCann and J. Pezy, *This Journal*, **128**, 1735 (1981).
 18. R. N. Bhattacharya, D. Cahen, and G. Hodes, *Solar Energy Mater.*, **10**, 41 (1984).
 19. H.-J. Lewerenz, H. Goslowsky, and F. A. Thiel, *ibid.*, **9**, 159 (1983).
 20. R. Tenne, *Ber. Bunsenges. Phys. Chem.*, **85**, 413 (1981).
 21. D. Lando, Ph.D. thesis, the Feinberg Graduate School of the Weizmann Institute of Science, Rehovot, Israel (1981); S. Licht, G. Hodes, and J. Manassen, submitted to *J. Phys. Chem.*; S. Licht, Personal communication.
 22. J. F. McCann, M. Skyllas-Kazacos, and D. Haneman, *Nature (London)*, **289**, 780 (1981).
 23. N. Muller, R. Tenne, and D. Cahen, *J. Electroanal. Chem.*, **130**, 373 (1981).
 24. N. Muller and D. Cahen, *Solar Cells*, **9**, 229 (1983).
 25. D. Cahen, J. Manassen, and G. Hodes, *Solar Energy Mater.*, **1**, 343 (1979).
 26. R. Tenne, N. Muller, Y. Mirovsky, and D. Lando, *This Journal*, **130**, 852 (1983).
 27. G. Hodes, J. Manassen, and D. Cahen, *ibid.*, **128**, 2325 (1981).
 28. D. Lando, J. Manassen, G. Hodes, and D. Cahen, *J. Am. Chem. Soc.*, **101**, 3969 (1979).
 29. R. Tenne, D. Lando, Y. Mirovsky, N. Muller, J. Manassen, D. Cahen, and G. Hodes, *J. Electroanal. Chem.*, **143**, 103 (1983).
 30. Y. Mirovsky and D. Cahen, *J. Phys. Chem.*, To be published.

Ternary Chalcogenide-Based Photoelectrochemical Cells

V. Surface Analyses of the $\text{CuInX}_2/\text{Aqueous Polysulfide Interface}$ ($X = \text{S}, \text{Se}$) by X-Ray Photoelectron Spectroscopy; Absence of Se/S Exchange in the $\text{CuInSe}_2/\text{S}_n^{=}$ System

Yehudit Mirovsky,¹ Reshef Tenne, and David Cahen

The Weizmann Institute of Science, Rehovot 76100, Israel

George Sawatzky

Laboratory for Physical Chemistry, University of Groningen, Groningen, The Netherlands

Micha Polak

Department of Materials Engineering, Ben-Gurion University of the Negev, Beer Sheva, Israel

ABSTRACT

$n\text{-CuInS}_2$ and $n\text{-CuInSe}_2$ were subjected to surface analyses by x-ray photoelectron and Auger electron spectroscopy, after their use as photoanodes in polysulfide solutions. For CuInS_2 samples that had a poor (ca. 2%) conversion efficiency, a rather heterogeneous surface was found, with patches rich in In, which is probably present mainly as oxide. Some CuO was found as well, although the top layer was depleted in Cu, compared to a reference sample. More efficient (ca. 5%) samples showed a more homogeneous surface and even stronger Cu depletion. These changes are ascribed to additional surface treatments, viz., dipping in hot KCN solution and thermal oxidation of the resultant etched surface. For CuInSe_2 samples, no significant exchange of lattice Se by S from the polysulfide solution is seen, in sharp contrast to what is observed for CdSe or CdIn_2Se_4 . If sulfur is found, its presence could be correlated with the spurious occurrence of Cd (used as dopant) or Ag (used for the ohmic back contact). Cu depletion also occurs near the surface of the diselenide after use in polysulfide solution. Most of the remaining In seems to occur in indium oxide and/or indium selenide. Cu^{2+} was found neither here nor on the surface of the more efficient disulfide sample. It is suggested that the occurrence of an indium oxide top layer, aided by thermal oxidation of the electrode in the case of CuInSe_2 , has a beneficial effect on electrode performance.

One of the most remarkable aspects of photoelectrochemical cells (PEC's) of the type $\text{CuInX}_2/\text{aqueous polysulfide}$ ($X = \text{S}$ or Se) is their excellent output stability, even under high light intensities and near their maximum power point (1-4). In this, they defy the often accepted rule of thumb that only high bandgap semiconductors can be stable under the conditions of an operating PEC. Indeed, we can compare the CuInX_2 -based PEC's to those using CuIn_5S_8 (5), CdIn_2Se_4 (6), CdS (7), or CdSe (7) as photoanodes. For all of these systems, instability has been observed, either with simulated solar illumination or

in accelerated tests (cf. Fig. 1). For CdSe and CdIn_2Se_4 , this instability could be connected with the occurrence of Se/S exchange at the semiconductor surface (7). For CuIn_5S_8 , it was found to correlate to some extent with both Cu depletion from the surface and the presence of Cu-S-like phases at the surface, while for CdS (and CdSe) it could be connected with the formation of a rather disordered, microcrystalline, top layer. In all of these cases, these phenomena can be explained by breaking of chemical bonds (between Cd, Cu, or In and X) by photogenerated holes that reach the surface of the photoanode and which prefer to attack the semiconductor itself, rather than to oxidize the sulfide species present at the surface.

¹Present address: Israel Aircraft Industries, Ben Gurion International Airport, Lod, Israel.

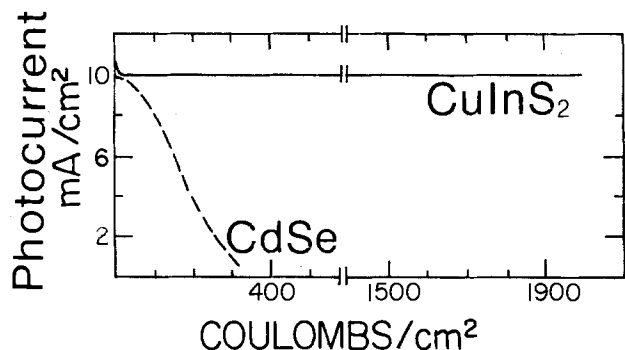


Fig. 1. Comparison of the output stability of CuInS_2 and CdSe photoanodes in polysulfide electrolyte (1M KOH, 1M Na_2S , and 1M S^0 added reagents).

In the case of Cd chalcogenides, it was found that improved sulfur dissolution from the surface of the electrode (where S is formed as the product of sulfide oxidation), improves output stability of this system (7). The reason for this is probably that in such a case the probability of the hole attack on the semiconductor itself is decreased because of the increased probability of hole transfer to the solution species. For n- CuInSe_2 , transient photocurrent measurements indicated the existence of some imbalance between hole flux to the surface and hole transfer to the solution (8), which is exactly the criterion for instability of Cd-chalcogenides. With CuInSe_2 , however, no output deterioration could be observed.

This would seem to imply that hole attack on the bonds in CuInSe_2 is not successful under the normal conditions of operation for a photoelectrochemical cell. Indeed, the argument has been forwarded that participation of d orbitals of Cu in the top of the valence band of CuInSe_2 and CuInS_2 and of anion s and/or p orbitals in the bottom of the conduction band leads to some degree of localization of the bandgap photoexcitation on the Cu site and the anion sublattice (9). This implies that it weakens the chemical bonds less than in, for example, CdSe . This would explain the ineffectiveness of hole attack, as such a localization of the photogenerated electron-hole pairs would increase the probability that those that are not transferred to the solution will simply undergo recombination. However, it is well known from the studies of Kazmerski and co-workers that CuInSe_2 , at least, has an indium oxide film as the native oxide on its surface (10). It could thus be argued that this oxide layer fulfills some protective role, for example, by serving as a region with high probability for recombination which could decrease the quantum efficiency. The very high (0.9)-quantum efficiencies observed for CuInSe_2 (3), argue against this explanation. Another possibility is that the oxide film spatially prevents solution species from reaching the semiconductor proper, thus preventing them from stabilizing possible products of hole attack (e.g., Cu_2S or In_2S_3 , analogous to the formation of CdS on CdSe). The fact that in sulfide-less aqueous electrolyte some pH dependence of the flatband potential is seen (8) indicates that the oxide is not a completely passive element. A third explanation could be that the oxide serves to passivate defects, which would serve as centers for corrosion. At present, insufficient evidence is available to decide between these or other functions of this oxide film.

Notwithstanding the excellent output stability of the CuInX_2 photoanodes, scanning electron micrographs reveal that some surface restructuring occurs during their use in polysulfide electrolyte (Fig. 2). Therefore, we felt that analyses of the surfaces of CuInX_2 photoelectrodes that had been used in polysulfide solutions was needed to try to reach some understanding of the causes for their resistance to photocorrosion. Here we report on our results of such analyses, mainly by x-ray photoelectron spectroscopy. In future reports, we will deal with more detailed surface analyses of clean and etched CuInSe_2 , with analyses of the surface of electrodes used in polyo-

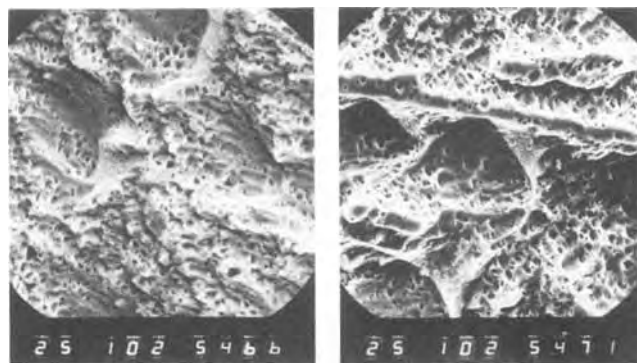


Fig. 2. Scanning electron microscopy pictures of the surface of n- CuInSe_2 . Left: after stable passage of 36 kC/cm^2 at -150 mV vs. polysulfide solution potential, at 45 (initial) to 68 (final) mA/cm^2 , i.e., under illumination equivalent to several times AM1. The increase in photocurrent density occurred during the initial stages of the experiment and is not uncommon in this system (8). Right: after subsequent acid etching of the surface, i.e., restoration to its initial state.

dide solutions, and with thermodynamic analyses of possible decomposition pathways.

Experimental

CuInS_2 and CuInSe_2 electrodes were prepared from Cd-doped crystals, as described previously (4, 8). They were etched in aqua regia, and, after rinsing with water, dipped in KCN solution to remove oxidation products. The CuInSe_2 electrodes were subsequently heated in air for 1 h at ca. 100°C . Polysulfide solutions were prepared from analytical-grade reagents: KOH, $\text{Na}_2\text{S}_2\text{H}_2\text{O}$, and S. Large area brass gauze counterelectrodes were used for two-electrode experiments. Some experiments were done under potentiostatic control, using a Pt wire as the reference electrode. All solutions were prepared and kept under inert atmosphere. X-ray photoelectron spectroscopy (XPS) spectra were obtained mostly on an AEI ES 200 B spectrometer, using Mg K_α (1253.6 eV) radiation, with $\sim 0.7 \text{ eV}$ linewidth. The samples were handled in a glove box attached to the spectrometer, which was made free of oxygen and water by cooling a Cu coil, situated in the glove box, with liquid N_2 , until condensation stopped. Both wide scans (1-1000 eV binding energy [BE]) and narrow scans (20-40 eV) were made. Ar ion sputter etching was done using an ion beam, situated at 60° with respect to the sample surface, operating with a beam current of 3-6 μA and 1 kV.

Some XPS and Auger (including scanning Auger microscope) analyses on less efficient samples, were performed on a PHI 549 spectrometer, using Mg K_α radiation for the XPS experiments and a 15 μm focused electron beam operated at 3 kV for the AES experiments. Some of the results on other samples, mentioned here for comparison, were obtained using PHI 550 or 590 (XPS or Auger) spectrometers.

Generally, the C_{1s} peak at 284.6 eV was used as an internal reference. From time to time, the calibration of the spectrometer was checked using the 4f lines of a Au sample.

Results

CuInS_2 .—Low efficiency electrodes.—The photoelectrochemical characteristics of these electrodes resembled those reported earlier by us (1). A typical sample yielded a photovoltage of 550 mV, a short-circuit photocurrent of 9 mA/cm^2 , and a fill factor of 0.36 under 86 mW/cm^2 white light illumination, corresponding to a 2.2% conversion efficiency. A sample was used for several hours as a photoelectrode under short-circuit conditions, in polysulfide electrolyte, and after it was rinsed in aqueous sulfide and water was inserted in the sample chamber (of a PHI 549 spectrometer). After measurement, the sample was sputter etched using an Ar ion beam. For comparison, a clean sample that had not been in contact with polysulfide so-

Table I. Auger parameters (eV) of In and Cu, for CuInS₂ photoelectrode and reference, and for some binary Cu and In compounds

Compound	$(\alpha + h\nu)$	
	In ^a	Cu ^a
CuInS ₂ (reference)	852.0 (1.4)	1849.9 (1.9)
CuInSe ₂ (photoelectrode) ^b	850.8 (1.6)	1849.9 1851.6 } (3.0)
CuInS ₂ (Ar ⁺ sputtered) ^c	851.9 (1.4)	1850.0 (2.1)
In ₂ S ₃	852.3	—
InS ^d	852.8	—
In ₂ O ₃	850.3	—
In(ox) ^e	850.6	—
In	854.4	—
Cu ₂ S ^d	—	1849.9
Cu ₂ O ^d	—	1849.5
CuO ^d	—	1851.6

^a Numbers in parentheses give full widths at half maximum (FWHM) of the In 4d 5/2 and Cu 2p 3/2 peaks.

^b Used, after chemical (acid) etching, in polysulfide solution.

^c As in second footnote but after 200s Ar ion sputter etching.

^d From Ref. (11).

^e In metal, as received, i.e., with a native oxide layer.

lution was measured as a reference. In Table I, we present the In and Cu Auger parameters for these samples, as well as for some binary In and Cu compounds. The Auger parameter, α , defined as the difference between a photoelectron energy and the corresponding Auger electron energy, is given here, because in this way uncertainty about the C_{1s} photoelectron energy for some samples is avoided. When both energies are measured in a normal XPS scan, where they will be expressed as "binding energies," $\alpha = \text{BE}(\text{photoelectron}) - \text{BE}(\text{Auger electron})$. It is customary to use $\alpha + h\nu$ (the x-ray photon energy), which equals the sum of the kinetic energy of the Auger electron (KE_A) and the binding energy of the photoelectron (BE_p) (11, 12).

In addition to the data presented in Table I, Auger microprobe analyses were done to obtain information on the spatial distribution of the constituent elements on the electrode surface. For the nonsputtered electrode, a heterogeneous surface was found, with oxygen-rich and sulfur-deficient regions a few tenths of a millimeter wide. These regions contained both Cu and In. Some correlation was found also between In and S. Thus it appears that the surface of this electrode had undergone some rearrangement, resulting in patches of Cu + In + O and In + S. This large-scale decomposition resembles the effect induced by 3 kV electron bombardment of a CuInS₂ surface, where residual oxygen was found to substitute for S in the areas exposed to the electron beam, yielding a composition formulated as Cu₂O · In₂O₃ (13). In our experiments, the surface heterogeneity was limited to the outer atomic layers only as the surface presented a much less varied composition after only ca. 40s Ar ion sputtering. After ca. 200s, it became essentially homogeneous, without any oxygen being present.

The XPS results given in Table I provide additional evidence for the difference in composition between the surface of a used electrode and its bulk. The In Auger parameter of the surface corresponds closely to that of oxidized In metal, i.e., a native oxide, while the Cu Auger parameter indicates the presence of Cu¹⁺ and Cu²⁺. The presence of divalent copper was verified by observing the Cu 2p spectral region, which contained the shake-up satellite lines, characteristic for this paramagnetic species (11, 12). In binary copper sulfides and selenides, the formal valence of copper remains fixed at +1 and that of the chalcogen varies (14). Therefore, we can conclude that the divalent Cu species is associated with an oxygen environment such as CuO or possibly Cu₂In₂O₅ (2CuO · In₂O₃). The Auger parameters and relative peak intensities after 200s Ar ion sputter etching agree with the values expected for CuInS₂. Thus only a very thin surface layer (estimated at some 20Å) has been affected, in contrast to what is the situation for CdS and CdSe electrodes that un-

derwent similar treatment (7). There, no appreciable deviation from stoichiometry or significant amount of oxides could be detected (7). Further clues to what might be happening at the surface of this latter type of electrode are found in results obtained from combined reflection electron diffraction, low angle x-ray diffraction, and scanning electron microscopy analyses on electrodes that had passed between 100 and 2500 C/cm² of photocharge. They show the formation of a highly polycrystalline top layer, surface roughening, and some charging in the electron beam. This behavior is consistent with the formation of an insulating polycrystalline phase on the electrode surface [cf. Ref. (1, 15)].

These results provide a ready explanation for the poor performance of these electrodes as they indicate a highly defect surface, which is expected to lead to low currents and fill factors, because of the presence of intra-bandgap states that will enhance recombination.

More efficient electrodes.—Surface analyses by XPS on these electrodes essentially bear out the conclusions obtained from the less efficient ones. The improved performance was the result of better control over the doping process and optimized surface treatments, which involved, after acid etching, dipping in hot (ca. 50°C) KCN solution (10% w/v) and mild heating in air at 70°-100°C for 1h. Such electrodes, when used in 3/3/4 polysulfide solution, gave the following "best" characteristics: 15.9 mA/cm² short-circuit current, 550 mV open-circuit voltage, and 0.5 fill factor at 49°C under 89 mW/cm² simulated solar illumination. This translates into a 4.9% conversion efficiency, i.e., a more than two-fold improvement over the samples described above. Table II summarizes XPS results for this type of electrode. Again, we include, for comparison, data on binary Cu and In chalcogenides. In addition, Table II contains some data on related ternary sulfides. Because data obtained on more than one instrument are included, and the In MNN Auger line was not always resolved well enough to allow a proper determination of the Auger parameter, we have chosen here to present the data mainly as the differences in binding en-

Table II. Binding energies and their differences of Cu, In, and S, for efficient CuInS₂ samples and related materials

Sample	$\Delta(\text{Cu-S})$	$(\text{eV})^a$		$\Delta(\text{In-S})$	FWHM (eV)		
		$\Delta(\text{Cu-S})$	$\Delta(\text{In-S})$		Cu	In	S ^c
CuInS ₂							
Reference	770.3	(931.7)	283.2	(444.6)	1.2	1.2	2.4
Etched ^d	770.1	(931.3)	282.9	(444.1)	1.4	1.3	2.2
Used ^e	770.2	(931.6)	282.6	(444.1)	1.4	1.2	2.0
Thin film	770.2	(930.8)	282.8	(443.4)	~2.5	2.4	2.5
CuIn ₂ S ₈							
Reference	770.3	(930.9)	283.0	(443.6)	1.7	1.4	2.3
Used	769.8	(931.0)	282.3	(443.5)	1.9	1.3	2.5
CuFeS ₂ ^h	770.1	(932.1)	—	—	—	—	—
Cu ₂ S ⁱ	770.2	(932.0)	—	—	1.1	—	(2.4)
CuS ⁱ	≤769.6	(931.4)	—	—	1.3	—	(2.2)
Cu ₂ O ^j	—	(932.2)	—	—	—	—	—
CuO ^j	—	(933.5)	—	—	—	—	—
In ₂ S ₃	—	—	283.3	(444.8)	—	1.9	2.5
InS ⁱ	—	—	—	(444.3)	—	—	—
In ₂ O ₃	—	—	—	(444.0)	—	2.3	—
In(ox) ^k	—	—	—	(444.4)	—	2.2	—

^a Difference in BE's between Cu 2p 3/2 and S 2p peaks. Cu 2p 3/2 peak position given in parentheses, referred to C_{1s} = 284.6 eV.

^b Difference in BE's between In 3d 5/2 and S 2p peaks. In 3d 5/2, peak position given in parentheses, referred to C_{1s} = 284.6 eV.

^c For the unresolved S 2p peak.

^d Etched in aqua regia and dipped in hot KCN solution.

^e After passage of 1.4 kC/cm² at short-circuit current.

^f From Ref. (25).

^g From Ref. (5); used after passage of 6 kC/cm² at short circuit.

^h From Ref. (16).

ⁱ From Ref. (14).

^j From Ref. (12).

^k Indium metal, exposed to air at room temperature.

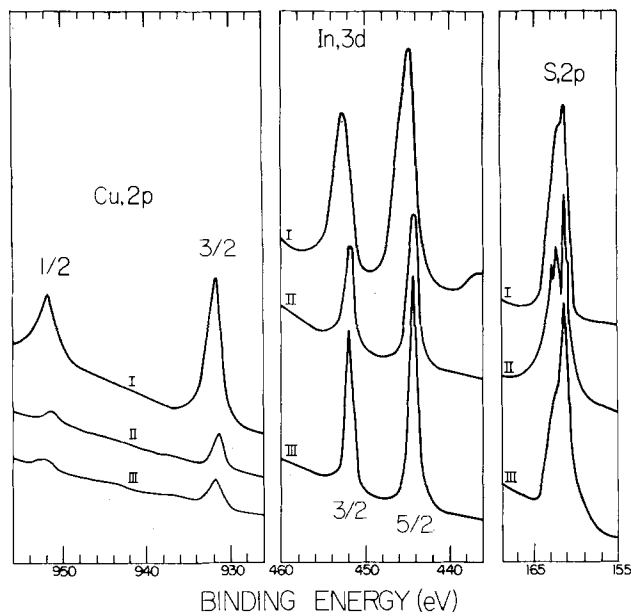


Fig. 3. XPS spectra of Cu 2p, In 3d, and S 2p in CuInS_2 . I: Reference. II: After etching in aqua regia, dipping in hot KCN solution, and heating in air at 100°C . III: after passage of 1340 C/cm^2 of photocharge at short circuit in polysulfide solution. The poorly resolved Cu 2p_{1/2} lines in traces II and III are a result of the low (II) to very low (III) Cu concentration on the surfaces of these samples.

ergies. For completeness' sake, the Cu 2p 3/2 and In 3d 5/2 BE's, referred to C_{15} at 284.6 eV, are given also. For CuInS_2 , these peaks and the S 2p ones are shown in Fig. 3.

Etched as well as polysulfide-used CuInS_2 electrodes differ from the clean CuInS_2 mainly in their In 3d 5/2 BE's, something that can be seen also from their values for $\Delta(\text{In-S})$. The rather small In 3d peak widths (cf. Tables I and II) suggest that for all these CuInS_2 samples only one type of In is present on the surface, although the similarity between In_2S_3 and CuInS_2 in terms of In and S BE's is such that the presence of In_2S_3 cannot be excluded. Because some broadening of peaks would be expected if both CuInS_2 and In_2S_3 were present, due to the occurrence of both tetrahedral and octahedral In coordination in In_2S_3 and only tetrahedral coordination in CuInS_2 , the presence of more than ~5% In_2S_3 is unlikely. In a way similar to the less efficient material, In_2O_3 or some type of oxidized In seems to be the dominant In containing species on the surface of etched or polysulfide-used samples.

The results for copper show that this element is now present in mainly one valence state only, namely Cu^+ , albeit at very low concentrations after etching and especially after use, in polysulfide, of the electrode (cf. Fig. 1). The widths of the peaks of used and of etched samples show more than one type of Cu^{2+} species on or near the surface. The presence of Cu_xS and/or Cu_2O can cause this peak broadening. For all etched samples that were studied, a high BE peak some 7 eV from the main S peak was observed. It is attributed to a SO_4^{2-} species, present only on the very surface as it disappeared after a short time of sputter etching. On samples that had been used in polysulfide, this peak could be discerned as well, though at lower relative intensity. Not only as regards the formation of sulfate does CuInS_2 resemble CuIn_3S_8 (5). Also, the Cu environment, with respect to sulfur, is similar in these two materials, as well as in CuFeS_2 and Cu_2S , and remains fairly constant for the different CuInS_2 surfaces.

Thus, while the two types of CuInS_2 electrodes studied (Tables I and II) behave similarly with respect to use in polysulfide solution, the higher efficiency ones are characterized by a better surface homogeneity, especially as far as Cu species are concerned. The absence of Cu^{2+} on this latter type of electrode may well be due to the action of the hot KCN solution, which will dissolve Cu^{2+} com-

pounds. Indeed, the overall amount of Cu on the surface was found to be less for the more efficient electrodes. Interestingly, this seems to boost electrode performance, or at least, to be connected with it. The decrease in Cu content, which is found also for other CuIn -chalcogenide photoanodes [cf. Ref. (5)] can be understood from the solubility of Cu sulfides in polysulfide solutions with the formation of CuS_4^{2-} salts (17, 19). This ability of Cu to dissolve as copper sulfide in polysulfide solutions was noted also by Hodes *et al.*, who found CuS , originating from the brass counterelectrode, on the CdSe photoanode in a PEC (19).

CuInSe_2 .—In view of the well-documented Se/S exchange on CdSe in polysulfide, especially when they are used as photoelectrodes (7), it was obvious to check if a similar process occurs on CuInSe_2 electrodes. Figure 4 shows the Se 3s and 3p peak regions for a clean CuInSe_2 electrode and for one that passed over 13 kC/cm^2 at ca. 35 mA/cm^2 short-circuit current after washing off the solution and of the same electrode after 10 min of Ar ion sputter etching. For comparison, the S 2s and S 2p peak regions from a clean sample of CuInS_2 are included as well. Clearly, no evidence for Se/S exchange is found. The very small amount of S that may be present on the surface (ca. 5%) is probably due to adsorbed species that were not removed by washing the electrode in sulfide (to dissolve off any sulfur) and in water. It is much smaller than that found for the "clean" reference sample, which probably contained some adsorbed sulfur as well. Thus no bond breaking appears to take place during operation of CuInSe_2 in polysulfide solution, in contrast to what is found for Cd-chalcogenides and for $n\text{-CdIn}_2\text{Se}_4$ (6). A short sputter-etch treatment (10 min) produces sharp Se 2s and Se 2p peaks, confirming our suggestion that only

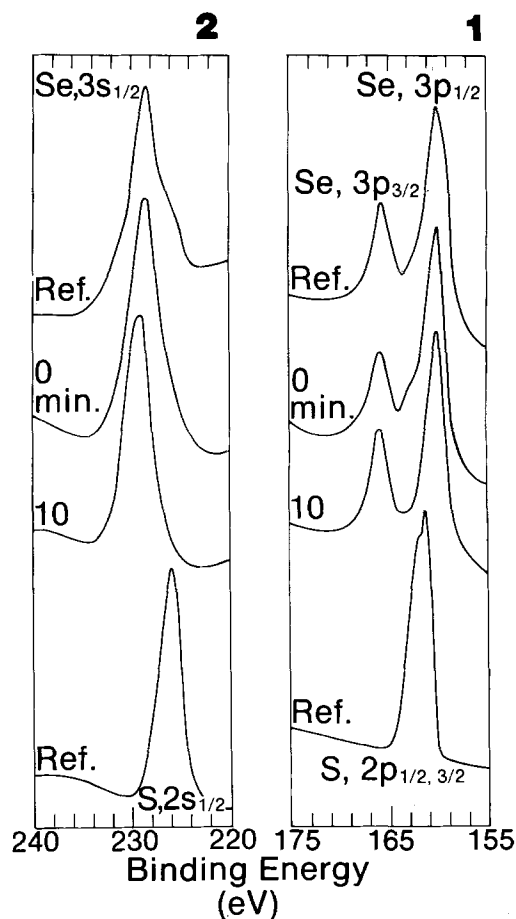


Fig. 4. XPS spectra of Se 3s and Se 3p regions of CuInSe_2 samples. Ref.: clean sample. 0 min: After passage of 13 kC/cm^2 of photocharge at short circuit in polysulfide solution. 10 min: After 10 min of Ar ion sputter etching. The bottom spectra are the S 2s and S 2p regions of clean CuInS_2 .

a slight amount of adsorbed sulfur species is present on the surface of the used electrode. Some experiments on additional samples did show more S on the surface, but this was always accompanied by a foreign metal, Cd or Ag. In one case, the Cd used to dope the crystal appeared to have migrated to and segregated on the surface, where it, obviously, reacted with sulfide from the solution. Indeed, for that electrode some decrease in photocurrent (at -150 mV vs. the sulfide solution potential) was observed, while 42 kC/cm² of photocharge passed. On another sample which showed S on the surface, Ag was found as well. This comes from the Ag paint used in the back contact, and creeping of the Ag through defects in the epoxy/crystal contact is a problem that is, unfortunately, not uncommon during long-term experiments of this type. In that case, it is likely that the sulfur on the surface came from Ag₂S. In both these instances, sputter etching removed the Cd (or Ag) at a rate similar to the disappearance rate of S.

Figure 3 shows the Cu 2p and In 3d regions for the reference sample and the one that passed 13 kC/cm². In Table III, we summarize results for two samples of CuInS₂ and compare them to those of the related binary chalcogenides. The results for Cu indicate that it exists only in the +1 valence state, i.e., that CuO is absent. After use in sulfide, the results for the first sample show Cu depletion, which disappears after sputter etching. The shift in the indium peak may correspond to the presence of indium oxide, although the very small full width at half maximum (FWHM) shows that, if such oxide is present, it covers the surface completely and homogeneously. Sputter etching then restores the normal CuInSe₂ surface. Because of the similarity in $\Delta(\text{In-Se})$ between In₂Se₃ and cleaned CuInSe₂, it is not possible to exclude the presence of this binary selenide, after use of the electrode in polysulfide. This situation is different from that described for the disulfide, because the common form of In₂Se₃ contains tetrahedrally coordinated In, as in CuInSe₂. They differ only in the stacking arrangement of the Se layers, which is hexagonal, rather than cubic, for In₂Se₃.

On the second sample, for which results are given in Table III, some S was found on the surface. This was correlated with the presence of Ag (see above). However, the data for $\Delta(\text{In-O})$, $\Delta(\text{Cu-O})$, and $\Delta(\text{Se-O})$ (not shown) as well as the In 3d 5/2 BE values also suggest the presence of indium oxide here. After prolonged sputter etching, only adsorbed oxygen seems to occur on the surface and the CuInSe₂ surface is restored. The differences between the

$\Delta(\text{Cu-Se})$ values of the clean samples are due to the fact that the first, the reference, sample had been exposed to air for some days before measuring, and they indicate the presence of a fully formed native oxide (23). The values of $\Delta(\text{Cu-Se})$ and $\Delta(\text{In-Se})$ for the used, the second, sample are given for completeness' sake only, as they are influenced by the presence of S (cf. Se FWHM).

These analyses thus indicate that the (near) surface of used CuInSe₂ electrodes do not have the bulk stoichiometric composition; rather, there is a Cu-deficiency and probably some indium oxide.

General Discussion

The observed changes in the (near) surface region of the Cu-In dichalcogenides, after etching, after use in polysulfide solution, or even after prolonged exposure to the ambient at room temperature may be understood from the fact that three constituent elements are involved. All of the treatments described here are oxidizing ones, and, therefore, we have to consider what may happen to CuInX₂ in such oxidizing environments. While it is true that the acid etching, for example, will remove recombination centers, which did affect cell performance adversely, such a treatment will also lead to chemical changes on the surface, and these can lead to heterogeneity. We then can ask the question: what are the factors controlling the formation of the oxidation products, such as In₂O₃, CuO, Cu₂O, SeO₂, S, Se and Cu₂S, Cu₂Se, In₂Se₃, In₂S₃? The final composition of the top layer will be dictated not only by the chemical thermodynamics and kinetics of the preferred oxidation reactions, but also by the mutual solid solubility of oxidation products and ternary compound, the diffusion constants of the different elements in these compounds, evaporation rates and solubility of products in the acid etching, and basic polysulfide environments. Obviously, not enough information is available to allow a firm prediction as to what we can expect to happen. However, we can get some idea from known data, such as the enthalpies of formation, solubility in acid and in basic polysulfide, and ease of evaporation at low temperatures. Some of these are given in Table IV. The possible oxidation products of the chalcogen constituents, S or Se, and SO₂ or SeO₂ were not observed. The latter ones are quite volatile, while the former

Table IV. Some properties of binary chalcogenides and possible oxidation products of CuInS₂ and CuInSe₂

Compound	ΔG_f° (ΔH_f°) ^a (kJ/mol)	Aqueous solubility ^{b,c}		Ease of decomposition/ evaporation at room temperature
		In acid	In basic polysulfide	
In ₂ O ₃	-415	-	-	-
In(OH) ₂ ⁻	-525	+	-	-
In ₂ S ₃	-206	+	+	-
In ₂ Se ₃	(-172)	+	-	-
In ₂ (SO ₄) ₃	-1220	+	+	-
CuO	-130	+	-	-
Cu ₂ O	-73	+	-	-
CuS	-54	-	-	+
Cu ₂ S	-43	-	-	+
CuSe	(-40)	+	-	-
Cu ₂ Se	(-30)	+	-	-
CuSO ₄	-661	+	+	-
CuSeO ₄	(-478)	+	+	-
SO ₂ (g)	-300	-	-	+
SeO ₂ (s)	(-225)	+	+	+
SO ₂ ⁻	-744	+	-	-
SeO ₄ ⁻	-441	+	-	-

Table III. Binding energies and their differences of Cu, In, and Se, for CuInSe₂ samples and related binaries

Sample	$\Delta(\text{Cu-Se})^a$ (eV)		$\Delta(\text{In-Se})^b$ (eV)		FWHM (eV)		
					Cu	In	Se
	CuInSe ₂						
Used ^c	771.5	(931.7)	283.9	(444.1)	1.4	1.1	2.6
Ar etched ^d	771.7	(931.8)	284.5	(444.6)	1.4	1.3	2.4
Reference	771.4	(931.7)	284.2	(444.5)	1.8	1.1	2.6
	CuInSe ₂						
Used ^e	[770.4]	(932.2)	[282.4]	(444.2)	1.4	2.0	>3.0
Ar etched ^f	771.6	(932.6)	283.6	(444.6)	1.7	1.6	3.0
Reference ^g	772.2	(932.6)	284.3	(444.7)	1.6	1.4	2.4
Cu ₂ Se ^h	772.1	(932.2)	—	—	2.0	—	3.2
In ₂ Se ₃	—	—	284.5	(444.3)	—	1.8	3.3

^a Difference in BE of Cu 2p 3/2 and Se 2p 3/2; Cu 2p 3/2 BE in parentheses referred to C_{1s} = 284.6 eV.

^b Difference in BE of In 3d 5/2 and Se 2p 3/2; In 3d 5/2 BE in parentheses referred to C_{1s} = 284.6 eV.

^c After passage of 13 kC/cm² at ca. 35 mA/cm² short-circuit current.

^d For 10 min, corresponding to removal of ca. 50 Å.

^e After passage of 36 kC/cm² (at -150 mV vs. the polysulfide solution potential) and ca. 60 mA/cm² photocurrent; some S was present.

^f For 12 min, corresponding to removal of 50-100 Å.

^g After repolish and chemical etching.

^h Cleaned by Ar ion sputter etching.

^a From Ref. (26). Where values for the free energy of formation were not available, those for the enthalpy of formation are given in parentheses. All values are per mol of metal (or chalcogen, if no metal is present) atoms.

^b Only a qualitative indication is given, where applicable and where the information was available. These table entries are based on data from Ref. (27, 28).

^c No distinction between acid and basic medium is made for compounds that are easily soluble in aqueous solutions.

ones would dissolve in polysulfide and would be further oxidized in acid or dissolved in hot KCN. The only chalcogen oxidation product that was observed was SO_4^{2-} , which could have precipitated as a basic sulfate.

Recently, Wager *et al.* (20) have considered the oxidation of CuInS_2 from a thermodynamic point of view, using the heats of reaction per gram-atom of the reagents or products as their guideline. They concluded that, when no kinetic limitations exist, the oxides or other oxidation products with the most negative heat of formation per gram-atom are indeed the most likely products. These are CuSeO_4 , In_2O_3 , and SeO_2 , with the formation of CuO and Cu_2O being only slightly less likely. They also noted that the very formation of oxidation products should impose kinetic limitations on the process, particularly with respect to Cu out-diffusion. [A recent study by Becker and Wagner shows Cu^+ to be the major diffusing species in CuInX_2 (21).] If this is taken into account, the likely products become Cu, In_2O_3 , and SeO_2 , with the probability of Cu_2Se or CuSe formation being somewhat lower. The formation of Cu_2Se has been reported (10) for CuInS_2 crystals and films that were thermally oxidized at temperatures between 150° and 300°C , but only in a thin interfacial layer between the surface film (of several hundreds of angstroms, composed mainly of indium oxide) and the bulk, *i.e.*, not in the surface film itself.

Under the conditions prevalent in a polysulfide PEC, CuSeO_4 should dissolve, Cu should react to give Cu sulfides (which can dissolve as alkali thiocuprates), and SeO_2 will dissolve. This leaves In_2O_3 as the oxidation product that is most likely to remain on the surface. Similar conclusions can be drawn for CuInS_2 , by repeating the calculations of Wager *et al.*, using S rather than Se oxidation products. Table V shows the six most probable reactions for the disulfide and the free energy changes per gram-atom in them. Thus, it is likely that during the oxidative etch, the mild air heating step, or during use of the electrode as photoanode, oxidation products of In will be formed. This is consistent with results from our surface analyses, and also with results obtained by Kazmerski *et al.* (10). It can explain the heterogeneity of the top layer and the high In/Cu ratios found for all samples, except those that were cleaned by sputter etching. Of all the possible In containing products, In_2O_3 is the only one that, at least in crystalline form, will not dissolve in acid. While the formation of Cu-oxides cannot be excluded, and evidence for CuO was actually seen for the low efficiency CuInS_2 electrodes, even if they are formed, they are likely to be removed from the surface during the acid etching step. As we noted in the Results section, the presence of binary sulfides or selenides [cf. Ref. (10)] cannot be excluded. If they would form during operation of the photo-

anode, they too could dissolve off as thiocuprates (17, 18). Finally, we cannot exclude the formation of mixed oxo-chalcogenides. If a heterogeneous top layer forms on the surface of these electrodes, either during etching or during their use in polysulfide solution, how will the presence of such a layer affect the performance of the photoelectrochemical cell containing these electrodes? A comparison of the surface analyses for the two types of CuInS_2 electrodes studied indicates that increased homogeneity, as expressed mainly by a lower Cu content, is related to increased efficiency. This increase is affected primarily through an increase in fill factor and short-circuit current. Thus, it is likely that heterogeneity introduced traps that led to recombination of photogenerated charge carriers. Clearly, the mere presence of a top layer different from the bulk material is not sufficient to cause a degradation in performance. Indeed, if this layer is thin enough and insulating, it may even increase the device performance (22). Apparently, in the case of the Cu-In-dichalcogenides, an air oxidation step or another type of mild oxidation affecting the whole surface is needed to create some kind of order in the mixture of possible initial oxidation products. The high quantum yields at short circuit, obtained for $\text{CuInS}_2/\text{S}_n^-$ and for $\text{CuInSe}_2/\text{S}_n^-$ (0.7 and 0.9, respectively) indicate that, when a sufficiently strong electric field is present, the charge carriers can pass the top layer. An additional or alternative explanation for the effect of the air oxidation step can be that a barrier forms between indium oxide and the bulk, and that this has a beneficial effect on the cell performance. Preliminary results on indium oxide/n- CuInS_2 structures (24) suggest that the magnitude of such a barrier is insufficient to account for the total photovoltaic effect observed here.

Summary

CuInS_2 .—XPS and Auger analyses on CuInS_2 photoelectrodes revealed heterogeneous patches, rich in In, on

Table V. Possible oxidation reactions of CuInS_2 and the corresponding free energy changes [after Ref. (20); data from Table IV (Ref. 29)]

Reaction Fully oxidized CuInS_2	ΔG_r° (kJ/gram-atom)
$\text{CuInS}_2 + \frac{15}{4} \text{O}_2 - \text{CuSO}_4 + \frac{1}{2} \text{In}_2\text{O}_3 + \text{SO}_2$	-101
$\text{CuInS}_2 + \frac{13}{4} \text{O}_2 - \text{CuO} + \frac{1}{2} \text{In}_2\text{O}_3 + 2\text{SO}_2$	-88
$\text{CuInS}_2 + 3 \text{O}_2 - 1/2 \text{Cu}_2\text{O} + 1/2 \text{In}_2\text{O}_3 + 2\text{SO}_2$	-87
Reactions limited by Cu diffusion	
$\text{CuInS}_2 + \frac{11}{4} \text{O}_2 - \text{Cu} + 1/2 \text{In}_2\text{O}_3 + 2\text{SO}_2$	-84
$\text{CuInS}_2 + \frac{9}{4} \text{O}_2 - 1/2 \text{Cu}_2\text{S} + 1/2 \text{In}_2\text{O}_3 + \frac{3}{2} \text{SO}_2$	-81
$\text{CuInS}_2 + \frac{7}{4} \text{O}_2 - \text{CuS} + 1/2 \text{In}_2\text{O}_3 + \text{SO}_2$	-73

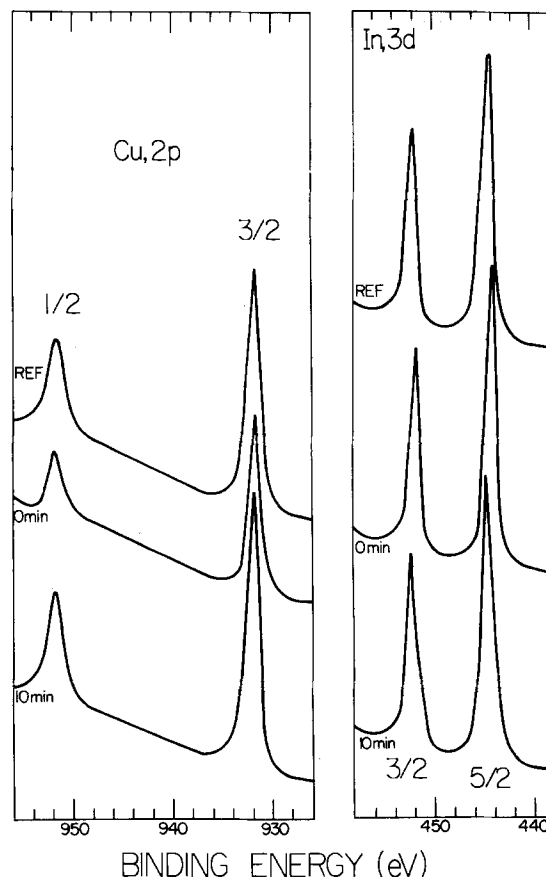


Fig. 5. XPS spectra of the Cu 2p and In 3d regions of CuInSe_2 . Ref.: clean CuInSe_2 . 0 min: After passage of 13 kC/cm^2 of photocharge at short circuit in polysulfide solution. 10 min: After 10 min Ar ion sputter etching.

the surface of low efficiency photoanodes. These patches probably contain mainly oxidized In. Some Cu compounds, such as Cu_2S , Cu_2O , and CuO , may be present as well. On the surface of higher efficiency electrodes, a decrease in Cu content is found together with a better homogeneity of the top layer.

CuInSe₂.—No significant Se/S exchange is found in CuInS_2 photoanodes operated in polysulfide solution. If S is present, it can be correlated with Cd or Ag, the former a dopant, the latter one from the back contact.

The surface of CuInSe_2 electrodes used in polysulfide is depleted in Cu, and the remaining In may be present mainly as an indium oxide.

Acknowledgments

We thank the U.S.-Israel Binational Science Foundation, Jerusalem, Israel, for support of this research. We thank P. J. Ireland, J. R. Pitts (Solar Energy Research Institute, Golden, Colorado), for some of the XPS and Auger analyses on CuInSe_2 samples. We are grateful to W. Giritat (I.V.I.C., Caracas, Venezuela) for providing crystals of CuInS_2 and CuInSe_2 . Part of this work was carried out under the auspices of the Dutch-Israeli Cultural Exchange agreement.

Manuscript submitted May 18, 1984; revised manuscript received Jan. 16, 1985.

REFERENCES

1. Y. Mirovsky, D. Cahen, G. Hodes, R. Tenne, and W. Giritat, *Solar Energy Mater.*, **4**, 169 (1981).
2. M. Robbins, K. J. Bachmann, V. G. Lambrecht, F. A. Thiel, J. Thomson, Jr., R. G. Vadimsky, S. Menezes, A. Heller, and B. Miller, *This Journal*, **125**, 831 (1978).
3. Y. Mirovsky and D. Cahen, *Appl. Phys. Lett.*, **40**, 727 (1982).
4. Y. Mirovsky, Ph.D. thesis, Feinberg Graduate School of The Weizmann Institute of Science, Rehovot, Israel (1983).
5. G. Dagan, S. Endo, G. Hodes, G. Sawatzky, and D. Cahen, *Solar Energy Mater.*, **11**, 57 (1984).
6. R. Tenne, Y. Mirovsky, Y. Greenstein, and D. Cahen, *This Journal*, **129**, 1506 (1982).
7. G. Hodes, in "Energy Resources Through Photochemistry and Catalysis," M. Gratzel, Editor, Chap. 13, Academic Press, New York (1983).
8. D. Cahen, G. Dagan, W. Giritat, G. Hodes, M. Lubke, and Y. Mirovsky, *This Journal*, **132**, 1062 (1984).
9. J. Jaffe and A. Zunger, *Phys. Rev. B*, **28**, 5822 (1983); *ibid.*, **29**, 1882 (1984). J. L. Shay and J. H. Wernick, "Ternary Chalcopyrite Semiconductors: Growth, Electronic Properties and Applications," Pergamon Press, Oxford, England (1975).
10. L. L. Kazmerski, O. Jamjoum, P. J. Ireland, S. K. Deb, R. A. Mickelsen, and W. Chen, *J. Vac. Sci. Technol.*, **19**, 467 (1981); L. L. Kazmerski, O. Jamjoum, J. F. Wager, P. J. Ireland, and K. J. Bachmann, *J. Vac. Sci. Technol. A*, **1**, 668 (1983).
11. "Handbook of X-ray Photoelectron Spectroscopy," C. D. Wagner, *et al.*, Editors, Perkin-Elmer Corp., Eden Prairie, MN (1979).
12. "Handbook of X-ray and Ultra-violet Photoelectron Spectroscopy," D. Briggs, Editor, Heyden, London (1977).
13. M. Polak, *Thin Solid Films*, **27**, 910, 345 (1982).
14. J. C. W. Folmer, Ph.D. thesis, University of Groningen, The Netherlands (1981).
15. D. Cahen, B. Vainas, and J. M. Vandenberg, *This Journal*, **128**, 1484 (1981).
16. J. A. Tossell, D. S. Urch, D. J. Vaughan, and G. Wiech, *J. Chem. Phys.* **77**, 77 (1982).
17. H. Biltz and P. Herms, *Ber. Dtsch. Chem. Ges. A*, **40**, 974 (1907).
18. G. Gattow and O. Rosenberg, *Z. Anorg. Allg. Chem.*, **332**, 269 (1964).
19. G. Hodes, J. Manassen, and D. Cahen, *This Journal*, **127**, 544 (1980).
20. J. F. Wager, O. Jamjoum, and L. L. Kazmerski, *Solar Cells*, **9**, 159 (1983).
21. K. D. Becker and S. Wagner, *Phys. Rev. B*, **27**, 5240 (1983).
22. H. C. Card, *Solid State Electron.*, **20**, 971 (1977).
23. D. Cahen *et al.*, To be published.
24. R. Ahrenkiel *et al.*, Solar Energy Research Institute, Golden, CO, Unpublished results.
25. G. Hodes *et al.*, To be published.
26. D. Wagman *et al.*, *J. Phys. Chem. Ref. Data*, **11**, Suppl. 2 (1982).
27. "Handbook of Chemistry and Physics," 61st ed., R. C. Weast, Editor, CRC Press, Cleveland, OH (1980).
28. "Merck Index," 8th ed., P. G. Stecher, Editor, Merck and Co., Inc., Rahway, NJ (1968).
29. Y. Mirovsky and D. Cahen, To be published.

The Effect of Hydroxide Ion on Cd-Chalcogenide/Aqueous Polysulfide Photoelectrochemical Cells

Stuart Licht and Joost Manassen

Department of Materials Research, The Weizmann Institute of Science, Rehovot 76100, Israel

ABSTRACT

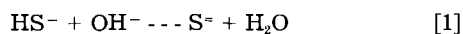
Alkali hydroxide, added to the aqueous polysulfide electrolyte in n-Cd chalcogenide/ S_x^{2-} photoelectrochemical solar cells (PEC's), is shown to be detrimental to cell performance. It is demonstrated that the added hydroxide increases visible light absorption in the polysulfide solution and decreases the solution lifetime. Even after compensation for the decrease in light transmission by the electrolyte, added hydroxide is shown to decrease the PEC photocurrent, photovoltage, and optical-to-electrical conversion efficiency. In a cell of 1 cm path length, the transmittance at 580 nm, for solutions containing 2*m* K_2S , 3*m* sulfur, and 0, 2, 6, or 12*m* KOH, was, respectively, 66, 55, 44, and 37.5%. Analysis of the distribution of ionic species reveals a shift from S_4^{2-} to S_3^{2-} with increasing hydroxide. Compared to S_4^{2-} , the peak absorbance of S_3^{2-} is shifted 50 nm toward the visible, causing the variation in solution spectral response with hydroxide. K^+ activity measurements were interpreted as indicative of increasing ion pairing with increased added hydroxide which may adversely effect charge-transfer kinetics. A measured negative shift in polysulfide redox potential with increasing hydroxide is evidently not paralleled by a comparable shift in Cd(SeTe) flatband potential, resulting in the observed decrease in open-circuit voltage. Relative conversion efficiency for an electroplated thin film $\text{CdSe}_{0.65}\text{Te}_{0.35}$ electrode was 36% less in polysulfide with 12*m* KOH compared to the PEC without added KOH. The electrode immersed in 2/2/2, 2/2/3, 0/2/3, or 0/1.3/2 (molality KOH/ $\text{K}_2\text{S}/\text{S}$) exhibited conversion efficiencies of 4.72, 4.80, 5.24, and 5.44, respectively, at 100 mW/cm² tungsten-halogen lamp illumination.

Cadmium-chalcogenide/aqueous polysulfide photoelectrochemical solar cells ($\text{CdX}/\text{S}_x^{2-}$ PEC's) were introduced as a potentially inexpensive method for solar-to-

electrical energy conversion. Yet, since their early inception, neither single-crystal (1) nor polycrystalline thin film (2) $\text{CdX}/\text{S}_x^{2-}$ PEC's have achieved solar-to-

electrical conversion efficiencies higher than 7-8%. Furthermore, CdX/S_x⁻ PEC operating lifetimes of greater than one year have yet to be proven. Little attention has been paid to the solution chemistry aspect of these cells, possibly due to the complexity of the aqueous polysulfide system. The aqueous alkali polysulfide system is known to contain, in addition to H₂O and alkali cations, OH⁻, H⁺, H₂S, HS⁻, S⁼, S₂⁼, S₃⁼, S₄⁼, and S₅⁼ (and perhaps HS_x⁻, x = 2-5). Nevertheless, the equilibria relationships for many of these species are known (3, 4). Recently, a computer model which incorporated these equilibria constants was developed to predict the distribution of ionic species in polysulfide solution upon input of the nominal sulfur, sulfide, and hydroxide concentrations in solution (5). The model provides simultaneous solution of the 11 equations which relate the species in solution. As exemplified in this paper, knowledge of the various species in solution allows for a systematic modification of the polysulfide electrolyte, and significant PEC improvements can result.

In addition to sulfide and sulfur, alkali hydroxide had been added, in molar quantities, to the aqueous polysulfide electrolyte preparation for CdX/S_x⁻ PEC's. This had been done in order to maintain a large concentration of sulfide in the solution according to the equilibrium



which has the equilibrium constant

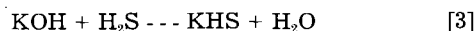
$$K' = (a_{\text{S}^{=}} a_{\text{H}_2\text{O}}) / (a_{\text{HS}^-} a_{\text{OH}^-}) = K_2 / K_w \quad [2]$$

where K_2 is the aqueous second acid dissociation constant for H₂S and K_w is the water dissociation constant. Spectroscopic (6, 7) and potentiometric (8) studies indicate that K_2 is less than 10⁻¹⁷, which is many orders of magnitude smaller than previously thought. Therefore, little divalent sulfide will exist in solution, even upon sufficient hydroxide addition to increase the solution pH from 14 to 15.

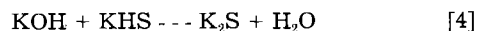
Recently, we reported on the effect of alkali cations on CdX/S_x⁻ PEC performance (9, 10). This cation effect, combined with an optimization of the polysulfide electrolyte sulfur-to-sulfide ratio (11) and the effect of added alkali hydroxide reported here, has led us to the one of the highest sustained solar-to-electrical conversion efficiencies reported to date for a photoelectrochemical solar cell—12.7% (12).

Experimental

Electrolyte preparation.—Analytical-grade potassium hydrosulfide and sulfide are not available. Potassium hydrosulfide solutions were prepared by saturation of aqueous potassium hydroxide solution with H₂S



The reaction is exothermic and results in an increase in volume, a proportional mass increase, and a pH decrease, all consistent with Eq. [3]. Saturation with H₂S was monitored by mass change yielding 98.5 (±1)% reaction. Potassium sulfide is then nominally formed upon addition of equimolar hydroxide



Polysulfide solutions were obtained by addition of sulfur. Solutions were prepared with analytical-grade reagents and deionized, doubly distilled water and were prepared, stored, and utilized under argon to prevent solution oxidation.

Bulk electrolyte measurements.—Potassium ion activities were determined by measuring the potential response in solution of a cation responsive electrode couple (pM). The electrode couple consisted of a Beckman 39137 cationic selective electrode and a Radiometer K401 saturated calomel electrode (SCE). The pM cell potential, E_{M^+} , exhibits a nernstian potential response to cationic activity, a_{M^+} . In alkaline solutions containing only potassium salts, the pM cell responds only to cationic potassium (13)

$$E_{\text{K}^+} = E_{\text{K}^+}^0 + (RT/F) \log (a_{\text{K}^+}) + E_j \quad [5]$$

E_j represents the liquid junction potential arising over the solution/SCE interface. The pM cell was thermostatically maintained at 25.0° ± 0.1°C. The mean solution activities of aqueous potassium chloride and potassium hydroxide solutions are known (14) and were used for calibration of the pM cell. These measurements are summarized in Fig. 1.

Spectroscopic measurements were made in a UVIKON 810 spectrometer using a cell of path length 1 cm. Thermostatically controlled specific conductivity measurements were made at 25.0° ± 0.1°C using a Radiometer CDC304 immersion conductivity cell and a Radiometer CDM 2d conductivity meter, as calibrated with solutions of known conductivity.

Electrode preparation.—Thin films of CdSe_{0.65}Te_{0.35} were prepared by electrodeposition. A previous method for the electrodeposition process (15) resulted in electrodes which occasionally evidenced good light conversion performance, although the results were irreproducible. A more reproducible method was obtained by optimization of the experimental parameters. This modified procedure, described here, has reproducibly produced 1-20 cm² electrodes of 4-5% conversion efficiency, as measured in a 2*m* KOH, 2*m* Na₂S, 2*m* S electrolyte. The electrodeposition bath, prepared with deionized, doubly distilled water using analytical-grade reagents, is 1*m* in sulfuric acid, 0.0654*m* in 3CdSO₄ · 8H₂O, 0.02*m* in SeO₂, and 0.0058*m* in TeO₂. Upon dissolution of the SeO₂ and TeO₂, which takes several hours with stirring at 40°C, 2 cm²/liter of 10% Triton X solution is added.

The deposition substrate is prepared from a section of 0.67 mm thick Ti sheet which has been cleaned and immersed in 5% aqueous HF, until the sheet is uniformly corroded. On the sheet, a gray layer can be observed which is not removed, but only scratched with 220 mesh sandpaper. A substrate thus treated turns clear blue when heated for 2 min in an argon stream containing 0.5% oxygen at 630°C.

The blue substrate is immersed into the plating solution between a Pt auxiliary electrode and the SCE. The solution is not stirred, and at 40°C the potential is switched on at -700 mV vs. SCE and brought down to -650 mV within 30s. Plating is continued at this voltage for 40 min at a current density of approximately 7.5 mA/cm².

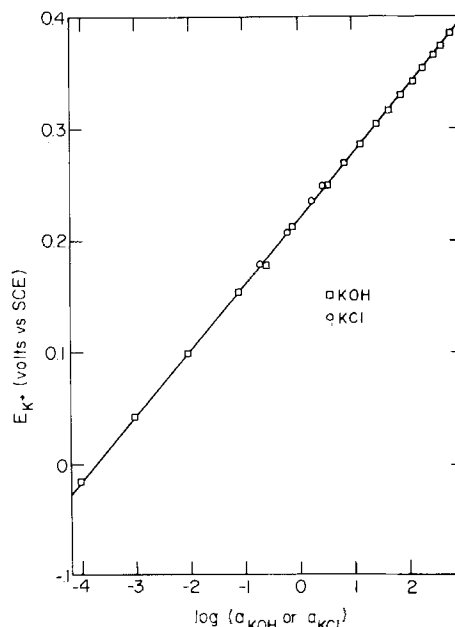


Fig. 1. The voltage response, as a function of solution activity, of a Beckman 39137 cationic selective electrode, measured vs. a Radiometer K401 SCE, in aqueous potassium hydroxide and potassium chloride solutions at 25°C. Solution activities are calculated from Ref. (9).

Electrode treatments.—The plated CdSeTe electrode is immersed in polysulfide solution to dissolve excess Se or Te and then annealed for 10 min in an argon stream containing 0.5% oxygen at 630°C. The electrode is photoetched (16) under 80 mW/cm² illumination at -1V reverse bias in (i) 0.1N HCl and then in (ii) 10N HCl, until the measured photoetching current decreases slowly. The photoetching procedure increases the photocurrent, as measured in polysulfide electrolyte, by up to fivefold.

PEC measurements.—Standard electrochemical equipment was used for obtaining the photocurrent vs. applied potential (I-V) curves data and redox potentials. A constant distance (5 mm) from the front wall of the test cell to the photoelectrode, and also a constant distance from the stabilized tungsten/halogen lamp to the photoelectrode, was maintained during the experiments. To insure that the observed I-V changes were reproducible and reversible, each I-V curve measurement was both preceded and followed by an additional I-V curve measured using the same electrode but in a polysulfide solution set aside for this standardization. The I-V measurements reported here represent the average of repeated results on two or more photoelectrodes.

Results and Discussion

The cation electrode couple response in a variety of potassium sulfide and polysulfide solutions is presented in Fig. 2. Accurate theoretical calculation or experimental measurement of the variation of the liquid junction potential in concentrated aqueous solutions is not available, although Licht has indicated that it is small in concentrated KOH solutions (13). Using the calibration provided by Fig. 1, potassium ion activities were calculated from Eq. [1], using the data in Fig. 2 and assuming zero liquid junction potential variation. The results are presented in Fig. 3 along with several other bulk properties measured in these solutions.

Activity coefficients larger than one in concentrated aqueous solutions result from immobilization of water within the sphere of ionic hydration. This decrease in free solvent concentration acts to raise activities. This is evident for potassium hydroxide in Fig. 3, in which activity coefficients of up to 25 are measured. In this figure, it can be seen that the measured potassium activities in sulfide and polysulfide solutions are depressed compared to the potassium activities in the hydroxide solutions. We attribute this, in part, to considerable ion pair-

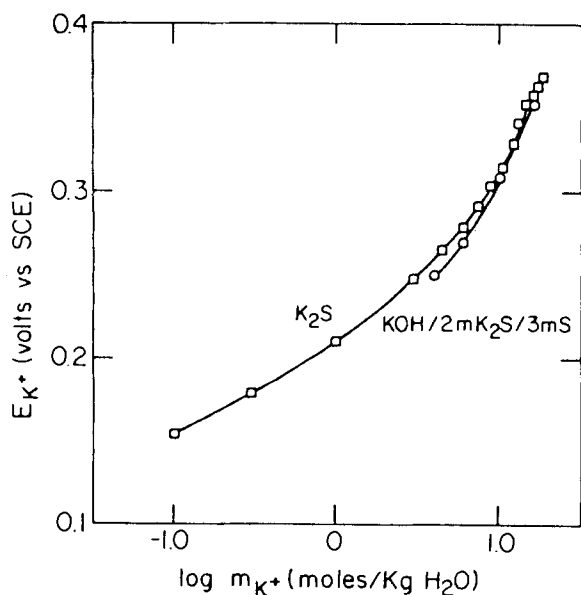


Fig. 2. The voltage response, as a function of potassium ion concentration, of a Beckman 39137 cationic selective electrode, measured vs. a Radiometer K401 SCE, in aqueous potassium sulfide and polysulfide solutions at 25°C. The polysulfide solutions contain 2m potassium sulfide, 3m sulfur, and either 0, 2, 6, or 12m potassium hydroxide.

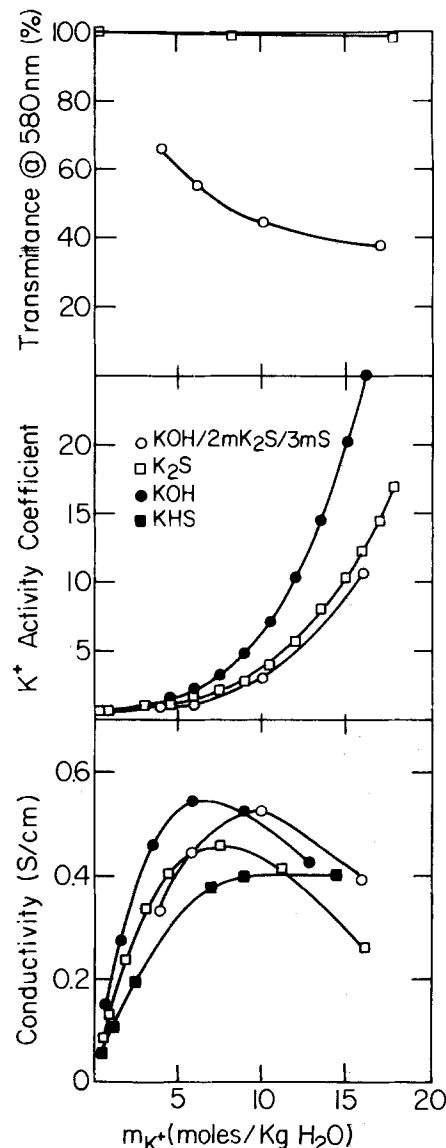


Fig. 3. The specific conductivity, potassium ion activity, and transmittance at 580 nm for various aqueous potassium hydroxide, potassium sulfide, and potassium polysulfide solutions. The activity results are at 25°C and were determined from data in Fig. 1 and 2. Spectral data were measured at room temperature. The specific conductivity results for polysulfide were measured at 25°C; those for KHS and K₂S are at 18°C and are from Ref. (22) and (23); those for KOH are at 15°C and are from Ref. (22). The polysulfide solutions contain 2m potassium sulfide, 3m sulfur, and either 0, 2, 6, or 12m potassium hydroxide.

ing in solution, similar to that observed in Ref. (10). Hence, it appears that the addition of potassium hydroxide to solution, by increasing the cation concentration in solution, increases the probability of sulfide or polysulfide ion pairing.

The specific conductivities of a variety of potassium hydroxide, hydrosulfide, sulfide, and polysulfide solutions are presented in Fig. 3. The high conductivity of the KOH solutions reflects the known high mobility of the hydroxide species (17). In all solutions, a near maximum conductivity is found at a 10m concentration of ionic potassium. In a polysulfide solution containing 2m K₂S and 2m S, the maximum specific conductivity occurs upon the addition of 6m KOH.

Polysulfide solutions absorb light strongly at near-UV and visible wavelengths. Therefore, concentrated polysulfide solutions act as cutoff filters for shorter wavelength light. This will diminish the amount of solar irradiation incident on the photoelectrode in aqueous polysulfide-based PEC's and thereby reduce conversion efficiencies. Surprisingly, it is seen in Fig. 3 that the relative transpar-

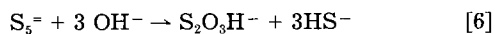
Table I. The calculated distribution of species within a polysulfide solution containing 2*m* potassium sulfide, 3*m* sulfur, and various concentrations of potassium hydroxide. The calculation is based on equilibria constants in Ref. (3) and (4) according to the method presented in Ref. (5). The activity coefficient of all species in solution is considered unity except for *F*, the activity coefficient for OH⁻ and K⁺, and *A_w*, the activity coefficient of water. *F* and *A_w* are the values for potassium hydroxide solutions of the same ionic strength (18)

Temperature (°C) and nominal concentration (mol/Kg H ₂ O)					
T	60	25	25	25	25
KOH	0	0	2	6	12
Assumed activity coefficients					
<i>F</i>	1.15	1.34	2.22	6.27	25.0
<i>A_w</i>	0.826	0.818	0.700	0.447	0.187
Calculated activities					
H ₂ S	3.41 × 10 ⁻⁷	5.98 × 10 ⁻⁸	8.60 × 10 ⁻⁹	6.06 × 10 ⁻¹⁰	1.12 × 10 ⁻¹¹
HS ⁻	0.877	0.872	0.773	0.571	0.186
S ⁼	0.000658	0.00109	0.00595	0.0460	0.266
S ₂ ⁼	0.00998	0.0109	0.0358	0.130	0.305
S ₃ ⁼	0.354	0.368	0.594	0.889	1.03
S ₄ ⁼	0.749	0.741	0.587	0.363	0.209
S ₅ ⁼	0.00838	0.00789	0.00307	0.000782	0.000223
OH ⁻	1.01	1.17	6.15	41.2	304
H ⁺	7.64 × 10 ⁻¹⁴	7.27 × 10 ⁻¹⁵	1.18 × 10 ⁻¹⁵	1.13 × 10 ⁻¹⁶	6.37 × 10 ⁻¹⁸
K ⁺	4.62	5.35	13.3	62.7	400
H ₂ O	45.9	45.5	38.8	24.8	10.4

ency of polysulfide solutions is a strong function of the added potassium hydroxide in solution. The 580 nm light transmittance, through a 1 cm path-length cell containing 2*m* sulfide and 3*m* sulfur, drops by half when 12*m* KOH is added to the solution. Similarly, these polysulfide solutions containing 0, 2, 6, or 12*m* KOH, exhibited 90% light transmittance at 615, 620, 635, and 640 nm, respectively.

Known equilibria constants (3, 4) and the known variation of aqueous potassium hydroxide mean solution activity (18) were incorporated into an iterative computer model (5). This was used to calculate the distribution of species in polysulfide solutions, containing 2*m* K₂S and 3*m* S, as a function of added hydroxide in solution. The results of these calculations, presented in Table I for 25° and 60°C, show that the main ionic components of these solutions are K⁺, OH⁻, HS⁻, S₃⁼, and S₄⁼, and, additionally in the polysulfide solutions with concentrated KOH, S⁼ and S₂⁼. The distribution of species is not a strong function of temperature. It also is seen in the tables that a primary effect of the addition of hydroxide is an increase in the S₃⁼-to-S₄⁼ ratio with increasing hydroxide. The S₄⁼ species displays peak absorbance at 368 nm, the S₃⁼ species, at 417 nm (19). The transmission measurements in Fig. 3 reflect the long wavelength shoulders of these peaks. Hence, as an increasing hydroxide concentration is added to these polysulfide solutions, the concentration of S₃⁼ increases, which shifts the solution transmission spectra from the near-UV toward the visible and significantly decreases the transparency of the solution.

Thermodynamically, aqueous polysulfide solutions are unstable. Giggenbach observed that polysulfide spontaneously disproportionates in solution according to the reaction (20)



The half-life of a polysulfide solution may be defined as the time for half of the free sulfur (as polysulfide) to disproportionate. This time, *t_h* (s), is given by (20)

$$t_h = 0.173c_s(a_{HS^-})^2[(10.9 - 5600/T)a_{OH^-} - a_{S_5^{=}}]^{-1} \quad [7]$$

where *c_s* is the concentration of sulfur initially added to the solution and *a_{HS⁻}*, *a_{OH⁻}* are the activities of HS⁻ and OH⁻ in solution, and *T* is the temperature in degrees Kelvin. Temperatures over 60°C have been measured for CdX/S_x = PEC's operating under normal insolation (21). At these temperatures, the calculated useful half-life of polysulfide solutions is seen in Table II to be strongly limited by adding hydroxide, decreasing from 442 to 12 days in solutions with 0 and 12*m* KOH, respectively.

Potentiostatic current-voltage measurements were made for illuminated 1 cm² CdSe_{0.65}Te_{0.35} electroplated thin film electrodes immersed in a variety of polysulfide solutions. These results are presented in Fig. 4, in which a cutoff filter was used to eliminate light of wavelengths below 665 nm, and also in Fig. 5, in which the full spectral output of the lamp was incident on the cell. Use of the cutoff filter negated differences in light absorbance by the different polysulfide solutions.

Redox potentials of polysulfide electrolytes prepared with 2*m* K₂S and 2*m* S, as a function of added KOH concentration, are also included in Fig. 4 and 5. It is seen that the redox potential of the bulk electrolyte becomes increasingly negative with increasing hydroxide. If one makes the assumption that the flatband potential of the Cd(SeTe) photoelectrode remains approximately the same in each of these solutions, then this should be reflected in an open-circuit voltage, *V_{OC}*, which decreases with increasing concentration of added hydroxide. In Fig. 4, this is indeed seen to be the case.

In Fig. 4, the variation of short-circuit photocurrent, *I_{SC}*, is shown to decrease as a function of increasing added KOH in the potassium polysulfide solution. This depression of *I_{SC}* with increasing hydroxide may be attributed to one or more of the following effects. (i) The activity results presented indicate that ion pairing increases with hydroxide concentration. This will remove photo-oxidizable species from solution, and thereby diminish the rate of charge-transfer kinetics and the measured current. (ii) As we have shown, increasing hydroxide will decrease S₄⁼ concentration in solution. If we hypothesize that the kinetically preferred photo-oxidized species is S₄⁼, then suppression of this species will decrease the rate of adsorption and again diminish charge transfer and the cur-

Table II. The calculated time for half the free sulfur to disproportionate to thiosulfate and hydrosulfide in polysulfide solutions containing 2*m* potassium sulfide, 3*m* sulfur, and various concentrations of potassium hydroxide. The half-life, *t_h*, is calculated from Eq. [7] using data from Table I

KOH	Nominal concentration (mol/Kg H ₂ O)			
	0	2	6	12
Calculated time of 50% sulfur disproportionation (days)				
<i>t_h</i> (25°C)	37,800	14,500	4,640	235
<i>t_h</i> (60°C)	442	179	68.9	11.9

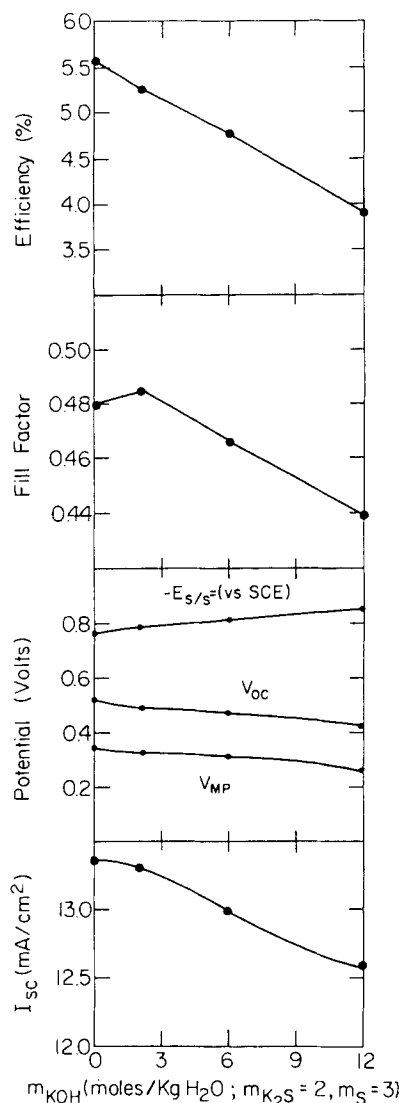


Fig. 4. The variation, with potassium hydroxide concentration, of polysulfide redox potential and of various current- and voltage-related properties of an illuminated 1 cm^2 electroplated thin film $\text{CdSe}_{0.65}\text{Te}_{0.35}$ electrode in aqueous polysulfide solution at room temperature. $E_{S/S^{2-}}$, V_{OC} , V_{MP} , and I_{SC} refer to the polysulfide redox potential, the open-circuit voltage, the voltage at the I-V point of maximum power, and the short-circuit current, respectively. The light source was a tungsten halogen lamp with a cutoff filter to eliminate radiation below 665 nm . Illumination intensity was approximately 60 mW/cm^2 .

rent. (iii) An increase in OH^- species in solution may have some direct negative effect on charge transfer.

As seen in Fig. 4, the fill factor, calculated as the ratio of the maximum measured photopower to the product $V_{OC}I_{SC}$, shows a slight increase from 0 to $2m$ added KOH in the polysulfide electrolyte and then exhibits a sharp decrease with increasing hydroxide. Hence, the measured variations in V_{OC} and I_{SC} with hydroxide are expected to be generally additionally enhanced by the fill factor. This is reflected in Fig. 4 by the sharp optical-to-electrical energy conversion efficiency gains, for the CdSeTe photoelectrode, when a diminishing amount of potassium hydroxide is added to the polysulfide electrolyte. Note that there is no correlation between the specific conductivity of the electrolyte, presented in Fig. 3, and the variation in efficiency in Fig. 4.

In order to roughly simulate real operating conditions for these PEC's, performance was tested under nonfiltered artificial illumination at an intensity approximating peak insolation. These measurements are compiled in Fig. 5. As expected, the increasing light transmittance by the polysulfide electrolyte, with decreasing added KOH, produces an additional increase in relative I_{SC} . It can be seen, upon comparison to Fig. 4, that the relative increase

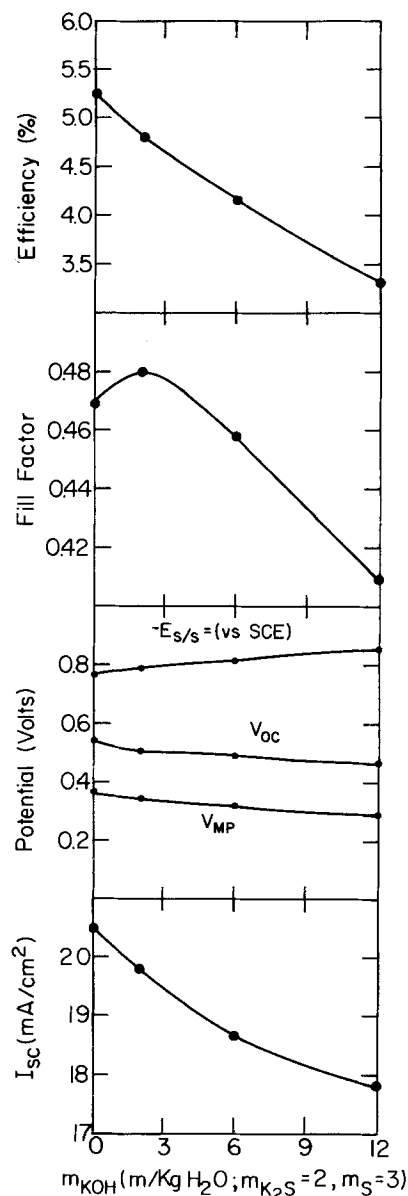


Fig. 5. As in Fig. 4, but the light source was a tungsten halogen lamp (without cutoff filter) providing an illumination intensity of approximately 100 mW/cm^2 .

in efficiency, with decreasing hydroxide, is also additionally enhanced. We point out that the magnitude of this additional enhancement is dependent on the proximity of the photoelectrode to the cell wall. The I-V curves for a 1 cm^2 electroplated CdSeTe electrode, at approximately 100 mW tungsten halogen illumination, immersed in polysulfide electrolytes, containing $2m \text{ K}_2\text{S}$, $3m \text{ S}$, and either 0 or $12m \text{ KOH}$, are presented in Fig. 6. There is a 36% relative increase in efficiency upon comparing the electrode in the polysulfide electrolyte with and without the added hydroxide.

Initial tests indicate that by not adding alkali hydroxide to the polysulfide solution, not only are solution lifetimes improved and CdX/S_x PEC efficiencies increased (and electrolyte costs reduced), but also the operating lifetime of the photoelectrode is extended. These results will be presented in a future publication.

An aqueous solution containing $2m \text{ KOH}$, $2m \text{ K}_2\text{S}$, and $2m \text{ S}$ is typical of electrolytes previously used in CdX/S_x PEC's. Some of the measured improvements, gained upon modification of this polysulfide electrolyte, are presented in Table III. Increasing the sulfur-to-sulfide ratio to 1.5 increases charge-transfer kinetics but decreases solution transparency (11). The first effect is evidently dominant; a relative improvement in electrode conversion efficiency is measured. However, the extent of this

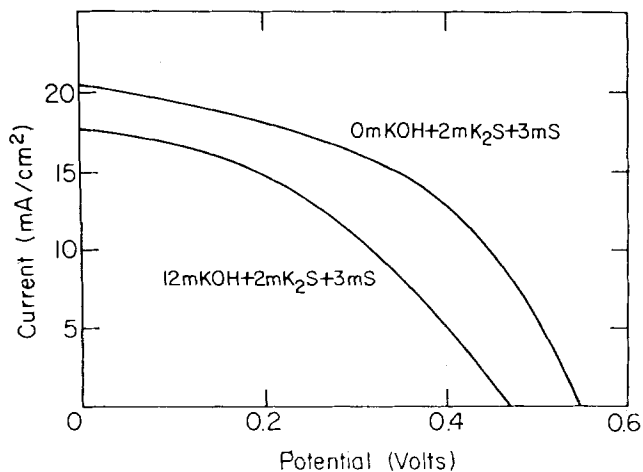


Fig. 6. Current/potential curves of an illuminated 1 cm² electroplated thin film CdSe_{0.65}Te_{0.35} electrode in solutions 2m in potassium sulfide, 3m in sulfur, and containing either 0 or 12m potassium hydroxide, at room temperature. Scan rate: 10 mV/s. Tungsten halogen lamp illumination intensity approximately 100 mW/cm².

improvement depends on the proximity of the electrode to the front wall of the cell. An additional 9.2% relative efficiency improvement is gained employing an electrolyte without added hydroxide. As has been shown, this is a result of a decrease in solution transparency and an increase in both current and voltage light response of the photoelectrode. In situations where higher current densities are to be maintained by the electrode, the relative importance of improved charge-transfer kinetics should increase. Therefore, if the PEC were to be illuminated under concentrated light, or if electrodes of higher conversion efficiencies were employed, the relative increase in efficiency by removal of hydroxide is expected to be even higher. As can be seen in Table III, an additional 3.8% relative efficiency improvement is gained by maintaining the sulfur-to-sulfide ratio but removing total sulfur from solution. It should be noted, however, that this final efficiency gain is accomplished by decreasing the concentration of oxidizable polysulfide in solution, which may decrease mass transport in the solution and diminish photoelectrode lifetime.

Conclusions

Removal of the alkali hydroxide, which had always been added in the preparation of the alkali polysulfide electrolyte for CdX/S_r PEC's, has been shown to (i) decrease the solution absorbance of light, (ii) positively shift the redox potential, and (iii) increase the calculated disproportionation-limited lifetime of the solution. If alkali hydroxide is not added to the polysulfide electrolyte, improvements in PEC current, voltage, and efficiency are observed. These improvements are shown to be related to the calculated change in distribution of the species in the solution and to apparent ion pairing in the solution.

Manuscript submitted July 6, 1984; revised manuscript received Nov. 27, 1984.

Table III. The measured efficiencies of an electroplated thin film CdSe_{0.65}Te_{0.35} electrode immersed in various polysulfide solutions at room temperature and under approximately 100 mW/cm² tungsten halogen lamp illumination. Also presented is the effect of electrolyte variation on solution transparency and PEC performance; each PEC is compared to the PEC described in the column to its immediate left

Nominal solution composition (mol/Kg H ₂ O)				
KOH	2	2	0	0
K ₂ S	2	2	2	1.33
S	2	3	3	2
H ₂ O	55.51	55.51	55.51	55.51
Measured thin film CdSeTe efficiency				
Efficiency	4.72%	4.80%	5.24%	5.44%
Effect of solution change on I-V and light transmittance				
Photovoltage	—	Increase ^a	Increase	Decrease ^a
Photocurrent	—	Increase ^a	Increase	Decrease ^a
Transmit hv	—	Decrease	Increase	Increase

^a After compensation for variation in solution transparency.

REFERENCES

- A. Heller, G. P. Schwartz, R. G. Vadimsky, S. Menezes, and B. Miller, *This Journal*, **125**, 1156 (1978).
- G. Hodes, *Nature*, **285**, 29 (1980).
- W. Giggenbach, *Inorg. Chem.*, **13**, 1724 (1974).
- A. Iverson, *J. Phys. Chem.*, **68**, 515 (1964).
- S. Licht and J. Manassen, Submitted to *J. Phys. Chem.*
- W. Giggenbach, *Inorg. Chem.*, **10**, 1333 (1971).
- B. Meyer, K. Ward, K. Koshlap, and L. Peter, Abstract 9 presented at the American Chemical Society National Meeting, Seattle, Washington, March 20-25, 1983.
- S. Licht and J. Manassen, To be published.
- S. Licht, R. Tenne, H. Flaisher, and J. Manassen, *This Journal*, **131**, 950 (1984).
- S. Licht, R. Tenne, H. Flaisher, and J. Manassen, Submitted to *This Journal*.
- S. Licht and J. Manassen, Submitted to *This Journal*.
- S. Licht, R. Tenne, G. Hagan, J. Manassen, G. Hodes, D. Cahen, R. Triboulet, J. Rioux, and C. Levy-Clement, Submitted to *J. Appl. Phys. Lett.*
- S. Licht, *Anal. Chem.*, To be published.
- B. E. Conway, "Electrochemical Data," pp. 65-105, Elsevier Publishing Co., New York (1968).
- G. Hodes, D. Cahen, J. Manassen, and M. David, *This Journal*, **127**, 2252 (1980).
- R. Tenne and G. Hodes, *Surf. Sci.*, **135**, 453 (1983).
- J. O'M. Bockris and A. K. N. Reddy, "Modern Electrochemistry," Vol. 1, p. 366, Plenum Press, New York (1970).
- G. Akerlof and P. Bender, *J. Am. Chem. Soc.*, **70**, 2366 (1948).
- W. Giggenbach, *Inorg. Chem.*, **11**, 1201 (1972).
- W. Giggenbach, *ibid.*, **13**, 1730 (1974).
- N. Muller and D. Cahen, *Sol. Cells*, **9**, 220 (1983).
- N. A. Lange, "Handbook of Chemistry," 10th ed., p. 1208, Handbook Publishers, Inc., Sandusky, OH (1957).
- J. W. Mellor, "A Comprehensive Treatise on Inorganic and Theoretical Chemistry," Vol. II, p. 626, Longmans, London (1960).

Analysis of the Transient Response of a Semiconductor-Electrolyte Circuit to a Short Light Pulse: Application to CdSe Electrodes

R. H. Wilson,^{*,1} T. Sakata, T. Kawai, and K. Hashimoto

Institute for Molecular Science, Myodaiji, Okazaki 444, Japan

ABSTRACT

A model to describe the transient response to a short light pulse of a circuit containing a semiconductor-electrolyte interface is presented. It is applicable to the case where charge separation across the depletion layer is fast compared to other processes. Rate constants for charge transfer and carrier recombination at the interface are introduced in the model, and the conditions necessary for measuring these are discussed. Experimental results using 10 ns light pulses on n-CdSe electrodes are used to demonstrate the validity of the model for properly prepared electrodes and to illustrate the role of semiconductor defects in masking interface reactions in improperly prepared electrodes.

The phototransient response of a circuit with a semiconductor-electrolyte interface has been investigated in a number of previous reports (1-4). Attempts have been made to use the experimental observations to obtain information about the rate constants for various charge-transfer processes at the interface. There is a need to describe these processes with a quantitative model that can be used as a guide in the interpretation of the experimental results. In this report, such a model is developed and applied to experimental measurements using an n-type CdSe electrode.

The model treats the system as a RC circuit with rate constants for charge-transfer processes. A short light pulse creates minority carriers in the semiconductor which rapidly move across the depletion region to change the potential across the depletion capacitance in a process faster than other processes in the circuit. Charge transfer across the Helmholtz capacitance, recombination of the photoexcited carriers, or charge redistribution through the external circuit then occur with their own rates. Information available in the resulting external signal depends on the relative values of these rates and the relative size of the depletion and Helmholtz capacitance.

Measurements with n-CdSe electrodes are used to support the applicability of the model. With a properly prepared sample, the transient decay is dominated by the circuit RC time constant at potentials more than about 0.5V positive of the flatband potential. Some of the properties of poorly prepared electrodes that can interfere with the interpretation of the observations are illustrated. Nearer the flatband potential, the transient decay is dominated by an interface recombination process. Light pulses that cause fewer than 10^{11} hole/cm² to be transferred across the depletion region are used so that the small signal approximation used in the analysis is appropriate.

Analytical Model

The circuit used is shown in Fig. 1a. No potentiostat is used. The potential is applied to R_v through a power supply (a battery circuit is used to avoid noise pickup through the power line), and the potential between the semiconductor and the reference electrode is read with a voltmeter using an isolated dc power supply.

A simplified circuit with the essential elements used in the analysis is shown in Fig. 1b. C_s is the capacitance across the depletion region of the semiconductor, and C_H is the Helmholtz capacitance at the semiconductor-electrolyte interface. R_i is the total, unknown series resistance internal to the cell, and R_e is the total, known series resistance external to the cell. Current generators across the two capacitors are labeled with k_s and k_H which will be used as rate constants and defined in the equations describing the charge-transfer processes. This circuit differs from those in Ref. (3) by the inclusion of the Helmholtz capacitance and the use of rate constants in place of re-

sistances. This allows physical interpretation of the observed rates.

The assumption is that a fraction of the minority carriers generated by the photons from a short light pulse incident on the semiconductor are moved across the depletion region in a time short compared with other processes to be measured. The remaining minority carriers recombine within the semiconductor. The time for this transport process is the shorter of the minority carrier lifetime or $(\alpha^2 D)^{-1}$ where α is the absorption coefficient of the semiconductor for the wavelength of light used and D is the diffusion coefficient of the minority carriers. Field-driven transport across the depletion region of the semiconductor occurs in a time on the order of $2\epsilon\epsilon_0/N_d u$, where $\epsilon\epsilon_0$ is the permittivity of the semiconductor, N_d is its doping density, and u its minority carrier mobility. This is generally much faster than the diffusion times discussed above.

For purposes of the analysis only deviations from the steady-state condition that existed before the light pulse will be considered. Thus, the initial condition will be a charge, Q_{SO} , on the depletion capacitance caused by the motion of the minority carriers across the depletion layer. Q_{HO} is zero. Due to the resulting potential, Q_{SO}/C_s , a current will flow through the external circuit with a consequent buildup of Q_H so that the magnitude of the current is determined by

$$\frac{Q_s}{C_s} + \frac{Q_H}{C_H} = i(R_e + R_i) = iR \quad [1]$$

Simultaneously, the excess minority carriers at the semiconductor electrolyte interface will begin to react to produce charge transfer across the capacitors so that

$$\frac{dQ_s}{dt} = -i - k_s(Q_s - Q_H) \quad [2]$$

and

$$\frac{dQ_H}{dt} = -i + k_H(Q_s - Q_H) \quad [3]$$

To avoid conceptual difficulties, it should be pointed out that the charge on the right side of C_s in Fig. 1b may be indistinguishable from that on the left side of C_H ; it is the difference in these two charges that is related to the photoinduced minority carrier density at the interface. Equations [2] and [3] can be combined to give

$$\frac{d(Q_s - Q_H)}{dt} = -k_s(Q_s - Q_H) - k_H(Q_s - Q_H) \quad [4]$$

It should further be noted that the charge transfer processes may be more complex than shown in Eq. [2] and [3]. It may be necessary to distinguish between holes in the valence band and holes in localized surface states. Furthermore, the availability of conduction band electrons is an important consideration in the value of k_s , and the availability of reducing agents in solution is an impor-

^{*}Electrochemical Society Active Member.

¹Permanent address: General Electric Company, Corporate Research and Development, Schenectady, New York 12301.

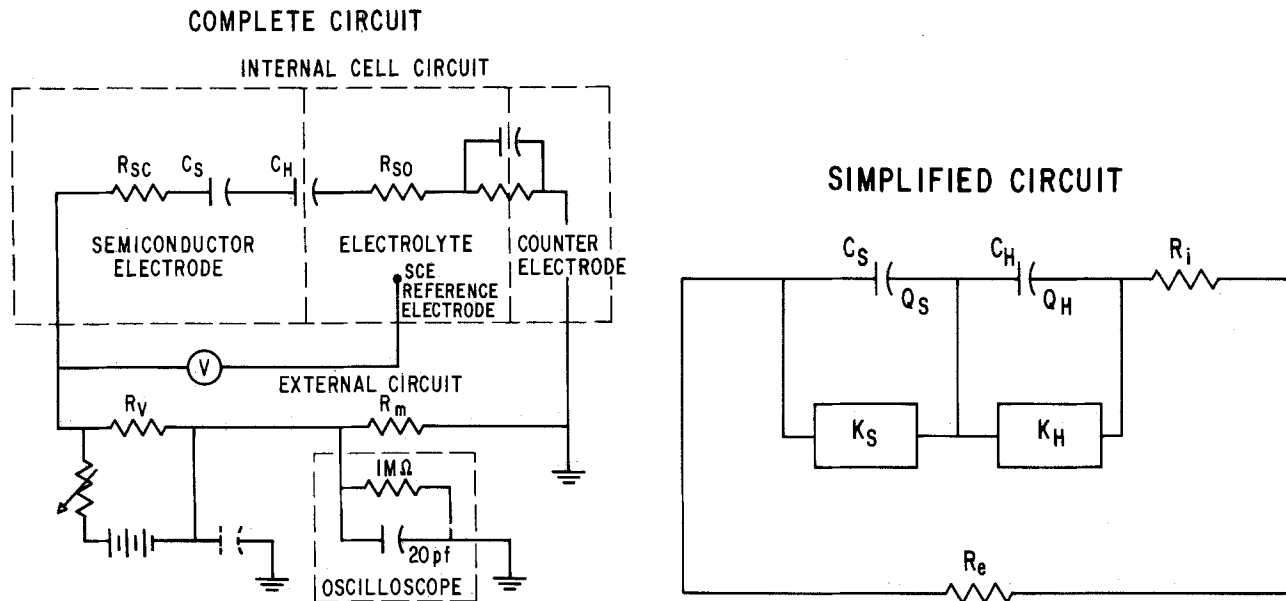


Fig. 1. a: Complete circuit for a semiconductor-electrolyte cell . b: Simplified circuit used in model

tant factor in k_H . Such refinements can be made as needed. The objective here is to illustrate the competition between the internal charge transfer rates and the external RC time constant for charge transfer through the external circuit.

Using Eq. [1]-[3], the initial conditions $Q_s = Q_{s0}$ and $Q_H = 0$, and the final conditions for large t of $Q_s = Q_H = 0$, the expression for the current in the external circuit becomes

$$i = Q_{s0} \left[\left(\frac{k_s}{RC_s} - \frac{k_H}{RC_H} \right) e^{-kt} + \left(\frac{k_H}{RC} - \frac{1}{R^2CC_s} \right) e^{-t/RC} \right] \quad [5]$$

where $k = k_s + k_H$ and $1/C = 1/C_s + 1/C_H$. The potential change across the depletion layer is assumed small enough so C_s can be considered a constant at a given applied voltage.

Equation [5] fulfills all of the intuitive expectations. In addition, it gives insights into the experimental conditions necessary to measure the rate constants. The initial value of the current is Q_{s0}/RC_s . For $kRC \gg 1$, i.e., a long time constant for relaxation through the external circuit (approximating a coulostatic condition), the internal charge transfer controls the current decay. If in that case $k_H \gg k_s$, the current will increase to $[1 + (C_s/C_H)]$ times its

original value, as the charge is now across a smaller capacitance, C , than it was originally. This can be seen in Fig. 2a for $C_s = C_H$. (For this change to be significant, C_s must be made comparable to C_H by low voltage across the depletion region, a high doping density, high dielectric constant, or a combination of these.) The current would eventually decrease through the external circuit with time constant RC. This case is also shown in Fig. 2a. As the RC time constant is decreased, it dominates the decay, leaving a small tail dominated by k_H .

If, however, $k_s \gg k_H$ and $kRC \ll 1$, the current would simply decay with time constant RC as shown in Fig. 2b. As k_s increases, however, the current decays to a negative value depending on the relative size of k_s and RC. This current then decays to zero with a time constant RC, as shown in Fig. 2b. This is the case that is addressed experimentally in this report.

Experimental Considerations

CdSe is a material widely studied for use in solar photoelectrochemical applications. Its transient response has been investigated previously (3) in the presence of sulfide ions. In the absence of sulfide or selenide ions in solution, the dominant photoelectrochemical reaction is a two or more electron process leading to cadmium ions in solution and a selenium layer on the surface of the electrode. An investigation of the kinetics of the corrosion process and the factors that affect it seemed appropriate. The CdSe crystals available (obtained from Cleveland

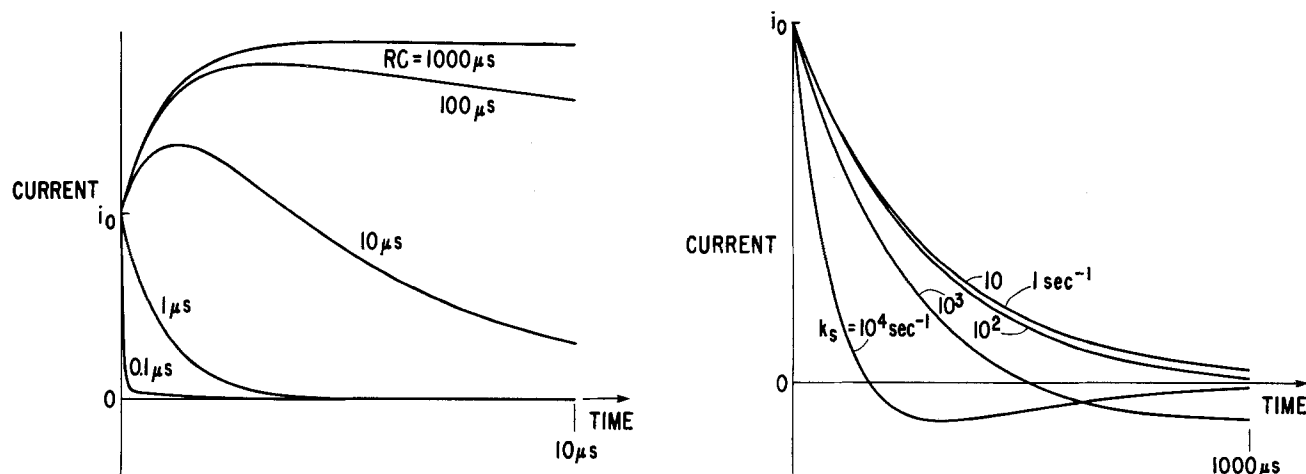


Fig. 2. Calculated response based on Eq. [5]. a: With $C_s = C_H$ for various values of RC. b: With $C_s \ll C_H$ and $k_s \gg k_H$ for various values of k_s

Crystals, Incorporated) were doped at about $10^{17}/\text{cm}^3$, making it difficult to achieve a C_j/C_H ratio large enough to study the charge-transfer process across the Helmholtz layer. Furthermore, the surface recombination process involved in the rate constant, k_s , can yield important information about intermediates of multielectron reactions (5). Therefore, the experimental conditions chosen approximated those of Fig. 2b.

The internal resistance of the cell is not readily measured directly. Assuming good ohmic contact, the electrode resistance for the samples used was expected to be about 2Ω . The electrolyte resistance was calculated to be few tens of ohms for the geometry used. As is discussed below, the total internal resistance was inferred experimentally to be about 10Ω .

Intensity of the light pulse is another important consideration. Pulses producing 10^{19} minority carriers per square centimeter have been shown to produce results that are not proportional to the number of photons. The model used here is not appropriate for that case. Light pulses of a few times 10^{11} photons per square centimeter were found to produce currents proportional to the number of photons. The size of the signal is 100 mV or less, so the change in sample bias is not excessive but the signal is still measurable. (At low band bending potentials, the signal was maintained even lower to avoid excessive perturbations of the applied potential.) Furthermore, by using a small number of photons, the minority carriers produce so few reaction intermediates at the surface that a second oxidation reaction can probably be neglected.

Finally, the importance of the quality of the semiconductor electrode should be mentioned. Several electrode related factors can affect the time response measurements.

Minority carrier traps.—If these are present at a density high enough, the risetime will be delayed by the rate of emptying of these traps. If this rate is very slow, it can also affect the decay time of the signal.

Recombination centers in the depletion region.—The photogenerated minority carriers are not all at the semiconductor surface. They are distributed some distance into the depletion region. A high rate of recombination in the depletion region can control the decay of the signal. An experimental example is presented later.

Nonuniform doping.—If the doping of the semiconductor is not uniform, then linear Mott-Schottky plots are not expected and it is difficult to separate surface and bulk effects.

High leakage current.—If a localized low resistance path exists in parallel to other parts of the semiconductor, both the chemical and potential distributions can be different than assumed in the model and thereby can change the observed effects. The point to be emphasized here is that these electrode characteristics must be evaluated by independent measurements to assure that they do not interfere with the surface reactions effects that are being investigated.

In the experiments reported here, single-crystal CdSe wafers about 0.1 cm thick had GaIn contacts mechanically applied to one side and a copper wire attached with silver cement. The wire was fed through a glass tube, and the wire, tube, and semiconductor were potted in epoxy to make a seal leaving one surface of the electrode exposed. The exposed area was about 0.25 cm^2 . This assembly was mounted in a quartz cuvette with a platinum counterelectrode and a saturated calomel reference electrode mounted in a separate holder connected by a plastic tube.

The electrodes were connected in the circuit in Fig. 1a or to a potentiostat system for steady-state dark and photocurrent measurements. For capacitance measurements, a phase sensitive detector at 1000 Hz was used.

Experimental Results

The samples were first checked for dark-current, capacitance, and quantum efficiency in the potentiostatic

systems. If a dark current of more than about $1\ \mu\text{A}$ was observed, the phototransient measurements were erratic. Most samples gave quantum efficiencies of about 10-40% at the dye laser wavelength of 520 nm. An exception was a sample that had been baked for 10 min at 300°C in air to improve the GaIn contact. This sample gave a much lower quantum efficiency, and capacitance measurements indicated a very lightly doped surface layer. After a 6 min etch in aqua regia, however, this sample showed a good quantum efficiency, a linear Mott-Schottky plot and well-behaved, consistent phototransient results. Figure 3 shows Mott-Schottky plots for this electrode in 1N KCl and 1N KI. There is a negative shift of 200 mV in the intercept of the KI data compared to the KCl results. The slope indicates a doping density of $7 \times 10^{16}\text{ cm}^{-3}$. Under some conditions with continuous illumination, the Mott-Schottky plots shifted to more positive potentials. During pulse illumination, however, no shift was observed, so it is presumed that Fig. 3 gives the capacitance for the phototransient measurements.

When the sample was illuminated with a light pulse from a nitrogen laser pumped dye laser at 520 nm [the system has been described previously (2)], the voltage developed across R_m in Fig. 1a showed a single exponential decay when the sample was biased at potentials more positive than 0 V vs. the SCE. The voltage decay constant, τ , determined from $\exp(-t/\tau)$ was measured for different values of R_e with the electrode biased at $1.2\text{ V}_{\text{SCE}}$ in 1N KCl. Results for several of the lower values of R_e are shown in Fig. 4. The linearity shown there continues up to $20,000\Omega$. [The nonlinearity reported in Ref. (3) suggests that their decay was affected by the semiconductor itself.] Assuming that τ is determined by the RC time constant of the circuit, the slope shown gives a value of $C = 0.017\ \mu\text{F}$ compared to the value determined from capacitance measurements of $0.016\ \mu\text{F}$. The negative intercept on the R axis indicates an internal cell resistance of 10Ω .

Values of τ were measured as a function of electrode potential with an external resistance of $20,000\Omega$. The results of 1N KCl and 1N KI are shown in Fig. 5, where $1/\tau^2$ is plotted in analogy with a Mott-Schottky plot. The solid curves are calculated for $\tau = RC$ using the slopes and intercepts of Fig. 3 and the $20,000\Omega$ external resistance. It

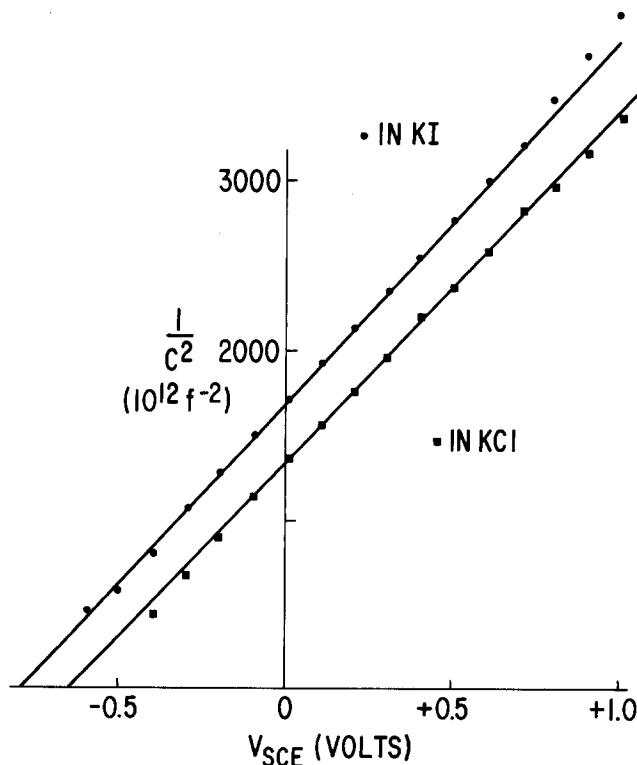


Fig. 3. Mott-Schottky plots for properly prepared n-CdSe electrode in 1N KI and 1N KCl. Capacitance measured at 1000 Hz.

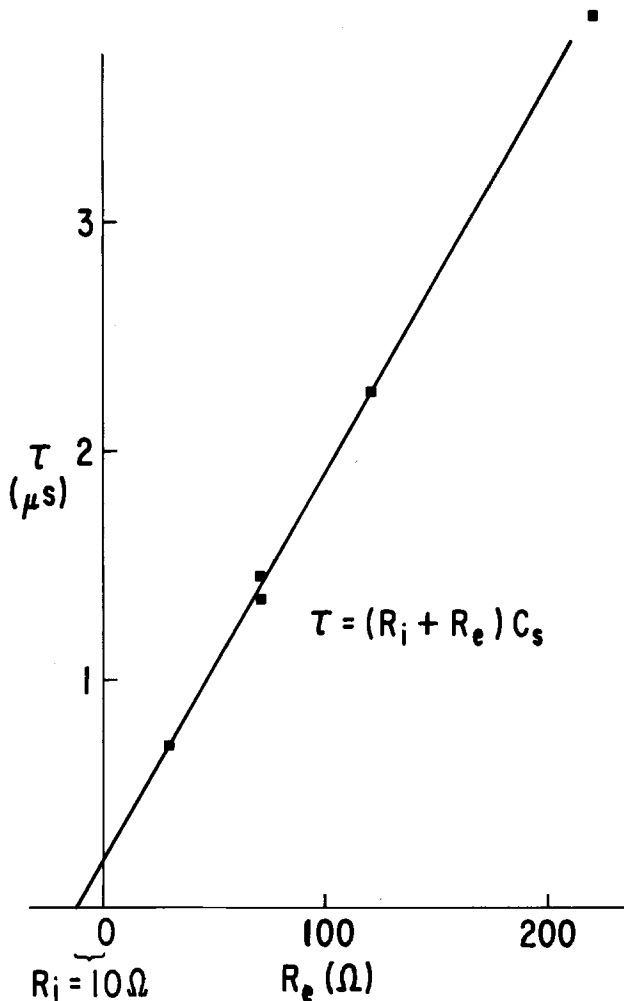


Fig. 4. Measured decay constant, τ , as a function of external series resistance, R_e .

can be seen that after some deviation at high potentials the data points fall on the predicted curve within experimental error until the potential is about 0.6V positive of the flatband potential. Examples of the observed signals are shown in Fig. 6. At the lower potentials, there is a dramatic increase in the decay rate and an accompanying departure from a single exponential decay curve. Figure 6b shows the negative current obtained with some samples reminiscent of the calculated behavior in Fig. 2. The behavior of the decay at low potentials depends on the history of the electrode surface and the electrolyte used in the observation. The investigation of these effects is incomplete and will be reported in a later publication.

Another electrode was prepared in the same manner except it was not baked and not etched. It showed quite different behavior. Its internal resistance was estimated to be 40Ω possibly indicating some contact resistance in the back contact. A calculated $1/\tau^2$ plot based on measured capacitance is shown in Fig. 7. Under illumination, there is a change in slope of this curve to about one-third of the dark slope. A plot of measured $1/\tau^2$ is also shown in Fig. 7. Significant discrepancies are apparent. The τ values plotted are slopes taken from the longer time constant after an initial, faster decay. These effects are believed to be due to trapping and recombination in the depletion region, as suggested earlier and discussed below. This difference between samples that were baked and not baked was reproduced in other samples. If an unbaked sample is etched, it does not give a single exponential decay, but the longer decay constant is that predicted by the measured capacitance and known resistance.

Discussion

The good agreement between predicted and observed values of τ shown in Fig. 5 suggests that at potentials

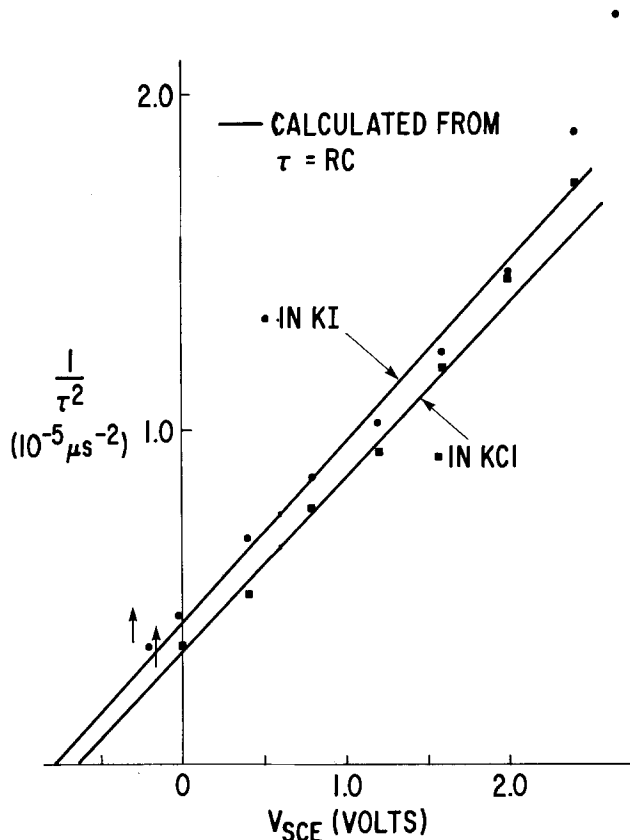


Fig. 5. Reciprocal of the square of the measured decay constant, τ , plotted (in analogy to a Mott-Schottky plot) vs. voltage (referred to a saturated calomel electrode) applied to the same electrode as Fig. 3 for 1N KI (circles) and 1N KCl (squares). The solid lines are calculated from Fig. 3 and 20,000Ω external resistance.

more positive than 0 V SCE the decay is determined by the RC time constant of the circuit. This is not surprising since for our samples $C_H \gg C_s$, so that even for large k_{H1} no effect of charge transfer across the Helmholtz layer would be observed. Furthermore, at these potentials, the

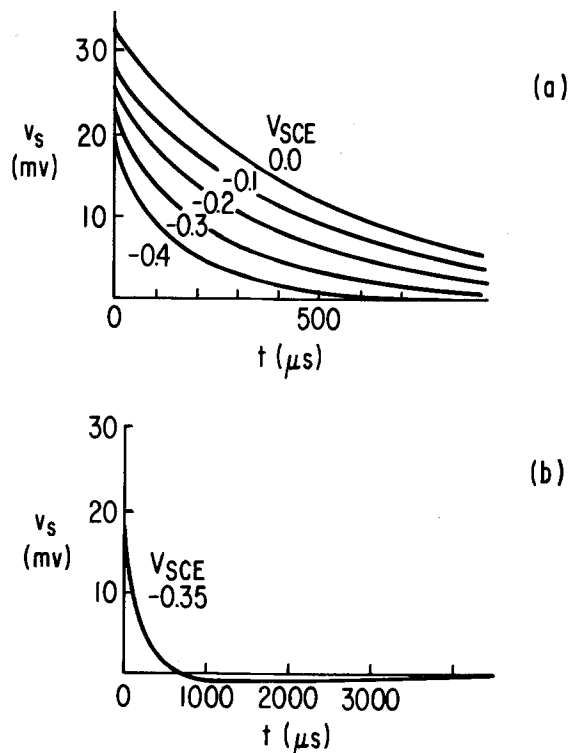


Fig. 6. Signal as a function of time after 10 ns light pulse as read on the oscilloscope of the circuit in Fig. 1a with $R_m = 20,000\Omega \gg R_v$.

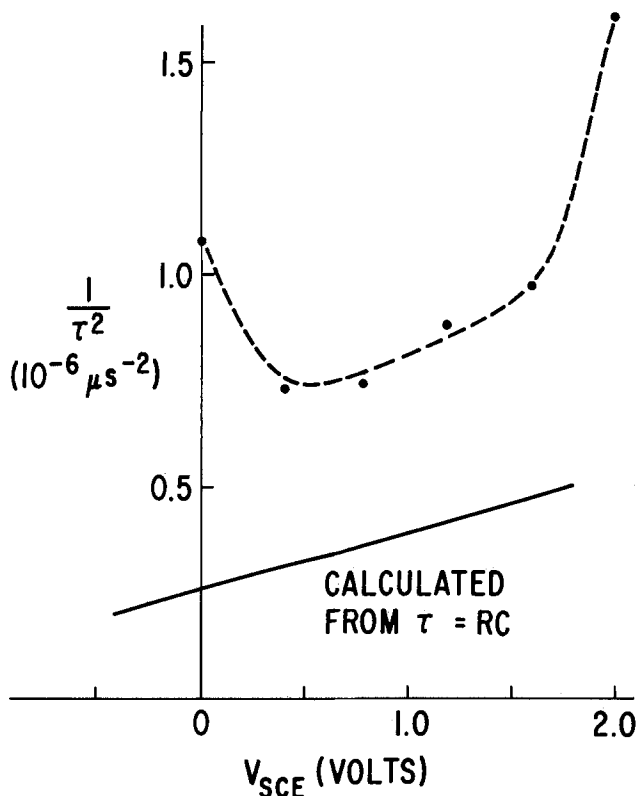


Fig. 7. Plot similar to Fig. 5 for an n-CdSe electrode that was not adequately etched after polishing.

density of electrons in the conduction band at the interface, n_s , would be small so k_s would also be small, as will be discussed later. In addition, the lifetime of holes in CdSe is less than 10 ns, *i.e.*, less than the length of the light pulse. In other words, under these circumstances the model described earlier is applicable and predicts $\tau = RC$ as in Fig. 2b. As n_s increases at more negative potentials, however, k_s increases and the decay is no longer determined by RC. The model prediction of this is seen in Fig. 2b, and experimental observation of it shown in Fig. 6. Thus, in a properly prepared sample, transient measurements at low potentials can be used to obtain information about rate constants for reactions at the semiconductor-electrolyte interface through measurement of k_s . The relationship between k_s and rate constants is discussed in the Appendix.

If, however, the electrode is not properly prepared, substantial deviation from the model can occur. For our unbaked, unetched sample, not only is the decay faster than predicted, as seen in Fig. 7, but the decay is not a single exponential. At least two causes for these observations are possible. One is a nonohmic contact to the electrode which introduces another, unknown circuit element. Another possible cause is traps and/or recombination centers in a layer of the electrode near the electrolyte interface. Recombination at centers away from the interface can occur at potentials where the interface density of electrons is very small. Such recombination could cause a fast decay of the phototransient signal.

As mentioned before, the slope of the Mott-Schottky plot for the electrode of Fig. 7 changes slope under illumination. The change is consistent with a larger positive charge density in the depletion region. This could be due to photoexcited holes trapped in defects that could also give rise to recombination and consequently faster decay of the signal. While these measurements could be used to study defects in CdSe, they are included here to illustrate some of the effects that can interfere with using phototransient measurements to study surface reactions.

Appropriate criteria for samples to be used in phototransient measurements would be a single exponential decay and approximate agreement with predicted RC de-

cah times at potentials more than several tenths of a volt positive of the flatband potential for n-type electrode (or negative for p-type). Since this implies an independent measurement of the capacitance, a word of caution concerning frequency-dependent capacitance is needed. If a strong frequency dependence is observed, then the capacitance should be measured at a frequency on the order of reciprocal of the decay times being measured. (In some cases, such a frequency dependence itself could imply defects in the semiconductor.)

Conclusions

Within the constraints discussed, the model developed for the response of a semiconductor-electrolyte circuit to short light pulses correctly describes the observed photovoltage decay if the semiconductor itself is sufficiently free of defects. At low band bending, the majority carrier density at the surface is high enough so that a back reaction or recombination controls the decay. An approach to analyzing this process is developed in the Appendix, thus providing the basis for future use of these methods to study the kinetics of the process.

Manuscript submitted June 29, 1984; revised manuscript received Jan. 3, 1985.

General Electric Company assisted in meeting the publication costs of this article.

APPENDIX

The general relationship between k_s and the physical parameters at the interface between the semiconductor and the electrolyte can be very complicated. A simplified relationship is developed here to illustrate the approach. The simplifying assumptions used may be appropriate for some experimental circumstances but must be evaluated before being used to interpret experimental results in detail.

Starting with Eq. [4], using $Q = Q_s - Q_H$ and assuming $k_H \ll k_s$ gives

$$\frac{dQ}{dt} = -k_s Q \quad [\text{A-1}]$$

Under these circumstances, however, the only mechanism for changing Q is the flux of electrons, F_n , in the conduction band of the semiconductor reacting at the interface, consequently

$$\frac{dQ}{dt} = -qAF_n \quad [\text{A-2}]$$

where q is the magnitude of the electronic charge and A is the area of the electrode.

Assume that there are interface states with an area density, N_0 , capable of capturing a hole from the valence band and that the area density of these states that have captured a hole is N_1 . The photogenerated charge is then distributed between holes in the valence band and holes in these interface states

$$\frac{Q}{qA} = Hp_s + N_1 \quad [\text{A-3}]$$

where p_s is the volume density of valence band holes at the semiconductor surface, and $H \approx WkT/2q$, where W is the width of the depletion region, k is Boltzmann's constant, and T is the absolute temperature. The value for H is obtained from

$$H = \int_0^\infty \frac{p dx}{\rho_s} = \int_0^\infty \exp\left(-\frac{qV(x)}{KT}\right) dx \quad [\text{A-4}]$$

Ignoring other possible electron reactions at the interface, F_n can be written

$$F_n = N_1 n_s \sigma_e v_e \quad [\text{A-5}]$$

where n_s is the volume density at the surface of electrons in the conduction band, σ_e is the cross section for capture of electrons by the interface states, and v_e is the thermal velocity of the electrons. Combining Eq. [A-1], [A-2], [A-3], and [A-5] gives

$$k_s = \frac{N_1 n_s \sigma_e v_e}{H \rho_s + N_1} \quad [\text{A-6}]$$

N_i is determined by kinetic expressions such as

$$\frac{dN_i}{dt} = (N_0 - N_i)p_s\sigma_h v_h - N_i n_s \sigma_e v_e - N_i p_s \sigma_p v_h - N_i k_r C_r \quad [A-7]$$

The first term of the right-hand side is the rate of hole capture by the unfilled interface states giving rise to the filled state; the second term is the rate of electron capture by these filled states; the third term is the rate of a second hole capture by the filled states, e.g., the second step in a corrosion process; and the fourth term is the rate of electron capture from a reducing species in the electrolyte with concentration, C_r .

These expressions can be used to interpret the transient decay measurements at low potentials.

REFERENCES

1. S. P. Perone, J. H. Richardson, S. B. Deutscher, J. Rosenthal, and J. N. Ziemer, *This Journal*, **127**, 2580 (1980); *J. Chem. Soc. Faraday Discuss.*, **70**, 35 (1980); J. H. Richardson, S. B. Deutscher, and S. P. Perone, *J. Phys. Chem.*, **85**, 341 (1981).
2. T. Kawai, H. Tributsch, and T. Sakata, *Chem. Phys. Lett.*, **69**, 336 (1980); *ibid.*, **56**, 541 (1978).
3. Z. Harzion, N. Croitoru, and S. Gottesfeld, *This Journal*, **128**, 551 (1981).
4. A. Frippiat, A. Kirsch-DeMesmaeker, and J. Nasielski, *ibid.*, **130**, 239 (1983).
5. R. H. Wilson, *ibid.*, **127**, 228 (1980).

Electrorefining of Zirconium Metal in Alkali Chloride and Alkali Fluoride Fused Electrolytes

G. J. Kipouros*

Department of Materials Science and Engineering, Massachusetts Institute of Technology, Cambridge, Massachusetts 02139

S. N. Flengas*

Department of Metallurgy and Materials Science, University of Toronto, Toronto, Ontario, Canada M5S 1A4

ABSTRACT

The electrorefining of zirconium metal in alkali halide melts has been investigated. Variables affecting the electrodeposition process such as the composition of the electrolyte, the current density, and the configuration of the electrodes were studied. Two types of electrolytes were used: the alkali chloride-rich and the alkali fluoride-rich electrolytes. The various electrolytes are considered in terms of their ability to complex the soluble zirconium ions, a property which is important for the electrodeposition of coherent metal deposits from these melts. Crystalline zirconium metal of good quality has been obtained from fluoride melts containing NaF, LiF, and either ZrF₄ or K₂ZrCl₆ at about 750°C.

Nuclear-grade, hafnium-free zirconium metal is used in nuclear reactors for structural purposes and for containing the nuclear fuel. Zirconium is an irreplaceable component because of its very low neutron capture cross section.

With the expected depletion in the supplies of fossil fuels throughout the world, a shift toward nuclear energy seems inevitable and the demand for nuclear-grade zirconium is expected to increase dramatically. The metal is produced today exclusively by the reduction of zirconium tetrachloride with magnesium metal by the well-known Kroll process (1). In this method, the tetrachloride is reduced to zirconium sponge in closed reactors. Magnesium is particularly suitable, since it is readily available in an oxygen-free condition. The oxygen content is critical as 0.7% oxygen makes zirconium metal unworkable (2) and the specifications for reactor-grade zirconium call for a maximum oxygen content of 1000 ppm. In this sense, the closed reactor in the Kroll process ensures purity and the oxygen carried into the metal product depends on impurities present in the magnesium and the zirconium tetrachloride reagents. The latter must be anhydrous and freshly distilled.

High temperature electrolysis from molten salt baths containing ZrCl₄ has been proposed as an alternative to the Kroll process. For an electrolytic process to become truly competitive, however, it should be continuous, contamination from oxygen should be avoided at all cost, and the metal produced should be in the form of dense, coherent deposits with very low salt content. In this respect, electrolytic deposition of zirconium from aqueous solvents appears to be impossible (3), owing to the hydrolysis of all zirconium salts by water and to the high chemical reactivity of the finely divided zirconium metal.

* Electrochemical Society Active Member.

Electrodeposition from fused-salt baths is promising, although all efforts to date have yielded poorly defined dendritic or microcrystalline powdery deposits at low current efficiencies. A comprehensive review of the work prior to 1953 has been given by Steinberg and co-workers (4).

Mixtures of ZrCl₄ and ZrF₄ dissolved in alkali fluoride and alkali chloride melts were electrolyzed and produced a zirconium metal (5) deposit which was a nonadherent granular metal-salt agglomerate. Current efficiencies were about 50%. The granules in this deposit had a particle size of about 100 mesh and a large electrolyte "pull-out" factor—"one-third metal and two-thirds salt" (5). Thus, elaborate crushing and leaching procedures had to be adopted to remove the entrapped solidified electrolyte.

Tablets of zirconium oxide and carbon dissolved in a fluoride bath (6) upon electrolysis yielded a deposit that contained 2% oxygen.

Recently, Martinez *et al.* (7, 8) of the U.S. Bureau of Mines reported that ductile zirconium dendrites had been produced at 800°C from an electrolyte that contained NaCl-NaF-ZrCl₄. The current density used was about 3230 A/m², and 93% of the deposit granules had a particle size greater than 100 mesh. This deposit also contained salt and had to be leached. The average cathode efficiency was 76%. At such high current densities and high voltages (5.34V), it is likely that metallic sodium was also produced and that some of the sodium metal could have reacted with tetravalent zirconium to produce powdery zirconium metal.

Lebedeva and Baraboshkin (9-11) have also reported that Zr deposits could be obtained from chloride melts. Again, these deposits were in the form of coarse loose crystals.

In all of the preceding efforts, zirconium was deposited on a solid cathode. Attempts have also been made to deposit Zr on a liquid cathode, such as molten tin, copper, or zinc (12) from electrolyte containing fluorides. With the tin cathode, only a black amorphous powder was formed, which was dispersed throughout the electrolyte; also, a ZrSn alloy was produced. Similarly, powders and alloys were produced when a copper cathode was used. With a liquid zinc cathode, the deposit was an alloy of zirconium as well as unidentified lower-valency zirconium species.

A promising electrolytic process for the deposition of coherent zirconium metal was reported by Mellors and Senderoff (13, 14), who conducted the electrolysis in a melt of ZrF_4 dissolved in alkali fluorides. Most of the work was conducted in the NaF-KF-LiF ternary solvent, to which was added 10 weight percent (w/o) ZrF_4 . The most efficient plating conditions were at 750°C with the cathode current density at 100-300 A/m². However, the exact nature of the deposit has not been described.

In all-chloride melts, zirconium was electrodeposited as a powder mixed with a large amount of dark colored salt, and recoveries were very low (4, 7, 13). It was also noted that recoveries from fluoride melts were far from satisfactory.

In the case of electrodeposition from molten chloride baths that contain $ZrCl_4$, the entire electrolytic process is affected by the thermodynamic stability of the $ZrCl_4$ in solution and the related properties of solubility and volatility. Previous investigations (15-23) have established that the state of $ZrCl_4$ dissolved in alkali chloride melts is determined by the thermodynamic stability of complex compounds of the general formula A_2ZrCl_6 , where A is an alkali metal. These compounds melt congruently.

In the present study, an electrorefining cell was used to investigate the deposition characteristics of zirconium metal in molten alkali halide electrolytes. Electrorefining was chosen in preference to electrowinning mainly because the cathodic process, which is of primary interest in the deposition of the metal, is expected to be the same during electrorefining as during electrowinning. Also, electrorefining is becoming more important to industry, particularly in the treatment of the zirconium scrap metal. Finally, during electrorefining, complicating factors, such as depletion of the melt in zirconium, chlorine, or fluorine evolution at the anode, and technical problems

related to the separation of the anode from the cathode compartments are absent.

The research work was focused on two types of electrolytes: the alkali chloride-rich melts with small additions of alkali fluoride containing zirconium bearing compounds of the type A_2ZrCl_6 and the alkali fluoride-rich melts with small additions of alkali chlorides. By studying these two extreme cases, the behavior of the intermediate melts should be predictable.

Variables affecting the electrodeposition process, such as the composition of the electrolyte, current density, and electrode configuration were studied.

The structural characteristics of the deposits were determined by means of scanning electron microscopy and by optical methods. The purity and hardness of some deposits were also determined. Reducibility experiments in which zirconium metal is allowed to react with tetravalent zirconium in solution in a number of solvent electrolytes were also conducted.

Experimental

Zirconium tetrachloride used in this work was obtained from two sources: as spectrographic-grade $ZrCl_4$ available from Puratek MC/B Manufacturing Chemists and supplied in glass containers loaded under argon, and as reactor-grade $ZrCl_4$ purchased from the Teledyne Wah Chang Corporation. The later required further purification by the vacuum sublimation technique through molten tin, as described earlier (16).

Zirconium tetrafluoride of purity better than 99% was obtained from the Research Organic/Inorganic Chemical Corporation and was treated in a vacuum oven.

Cesium chloride of purity better than 99.9% was obtained from Cerac, Incorporated, and from the British Drug House Limited. All other alkali chlorides were of analytical grade and were dehydrated by heating under vacuum to 400°C. The alkali-metal fluorides were also of reagent grade and were treated in a similar way as the chlorides.

Zirconium metal rods of about 6 mm diam were of reactor-grade quality and, prior to use, were etched with a solution containing by volume 45% HNO_3 , 45% H_2O , and 10% HF (24).

Spectroscopic-grade graphite was used for electrodes. They were purified by heating in a silica glass tube under vacuum for about 12h at 900°C, followed by chlorination at 800°C, and then cooling under vacuum. A small amount of an oily impurity product was observed at the ends of the silica tube after completing the purification cycle.

Stoichiometric Cs_2ZrCl_6 and K_2ZrCl_6 were prepared by a method previously developed in this laboratory (15). K_2ZrF_6 and ZrF_4 were the commercially available compounds described earlier.

The furnace-cell assembly used in these experiments is shown in Fig. 1. The furnace was a resistance type with a Chromel wire element. The temperature was maintained constant with a Honeywell proportionating controller connected to a Chromel-Alumel thermocouple. The temperature in the furnace was constant to within $\pm 2^\circ C$, and a hot zone of about 15 cm could be established. This furnace could accommodate an electrolysis cell provided with a nickel crucible of about 10 cm diam having a capacity of 750 ml.

Special care was taken to exclude nitrogen and oxygen, for which zirconium metal is an excellent getter, from the environment of the cell, along with moisture which causes hydrolysis of the electrolyte components. Dehydrated and oxygen-free helium was used in all of the experiments for purging and as a blanket gas.

The cell assembly consisted of the following three main parts: the Inconel cell-crucible system, the upper quartz part, and the electrode cover assembly.

The cell-crucible system was made of an Inconel tube 60 cm long and 10 cm id. A brass fitting, furnished with an O-ring for vacuum-tight sealing, was attached to the top of the Inconel tube for connecting the two sections of the cell. The upper part of the cell was a quartz tube, both

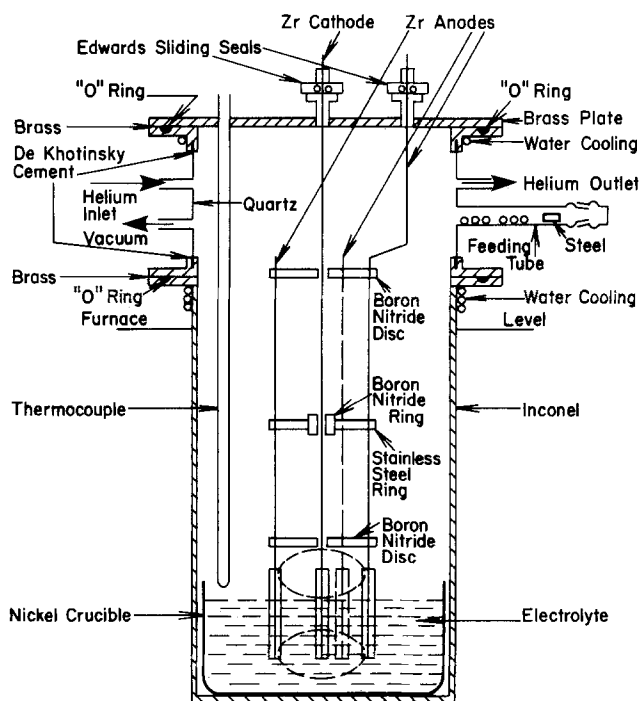


Fig. 1. Furnace-cell assembly for the electrorefining of zirconium in alkali chloride-rich electrolytes.

ends of which were fitted with water-cooled brass plates and O-ring-type seals for vacuum-tight connections with the other parts of the cell. The cell was equipped with a sidearm feeding tube from which additions of solute to the cell could be made using a magnetically operated piston without opening the cell.

The electrode assembly consisted of the zirconium cathode surrounded symmetrically by three zirconium anodes. Electrical connections were provided by means of threaded 3 mm Inconel leads, onto which the electrodes could be attached. The cathode assembly was electrically insulated from the anode assembly by means of boron nitride spacers and it could be independently rotated to provide stirring of the melt. The electrode assembly could be lifted or lowered through sliding seals attached onto the cover plate. A spare plain cell cover plate bearing only an opening for loading the materials into the crucible was used during the initial stage of a run alternatively with the cover plate containing the electrode assembly.

The assembled cell was checked prior to use for leaks with a Veeco MS-9 mass spectrometer leak detector using helium as a tracer fluid.

Prior to a run, the assembled cell, except for the electrode-cover assembly, was heated under vacuum at about 400°C for approximately 12h and then cooled to room temperature under helium gas. The solid solvent salt mixture was loaded through the opening in the spare plain cover into the crucible, and the cell was quickly evacuated. The temperature was slowly increased over a 24h period to 450°C, when the salts were melted under vacuum and cooled to room temperature under flow of helium gas.

The electrode assembly was quickly positioned into the upper part of the cell, and the solute zirconium salt, which was either Cs_2ZrCl_6 , K_2ZrF_6 , or ZrF_4 , in the form of pellets was placed into the feeding tube. The cell was again evacuated with the electrode assembly raised into the upper cold section of the cell, and the temperature was increased until the salts were melted under vacuum. Purified helium was then introduced into the system, and the solute was introduced into the crucible. The addition of the zirconium bearing compound was done at this stage in order to avoid any thermal decomposition or losses of ZrCl_4 due to prolonged evacuation. The electrodes were then lowered to the desired depth and electrolysis was started.

At the end of the experiment, the electrodes were withdrawn from the melt, left for about 1h in the hot section of the cell in order to drain the entrapped salt, and then lifted to the upper part of the cell to cool.

A much simpler cell design was used for electrorefining zirconium metal in alkali fluoride-rich electrolytes. The cell assembly is shown in Fig. 2 and consists of a nickel tube closed at one end with a brass cover plate. This cell could accommodate a zirconium or nickel crucible of about 12 cm diam, having a capacity of about 250 ml.

The cell was checked for leaks prior to its use, and its ability to hold vacuum for extended periods of time was tested. The experimental procedure involved loading the crucible with the appropriate amounts of salts in the dry box and then lowering it into the electrolysis cell, which was immediately covered and evacuated. With the electrodes kept in the cold part of the cell, the salts were melted under vacuum. Purified helium was introduced into the cell, and the heating continued until the temperature of the melt reached the desired level. Then the electrodes were lowered to the desired depth and electrolysis was started.

At the end of the experiment, the electrodes were pulled over the melt level and left there to drain the entrapped salt. Then the electrodes were withdrawn to the cold part of the cell and the cell was cooled down to room temperature.

All experiments were performed using a constant current-constant voltage direct current power source,

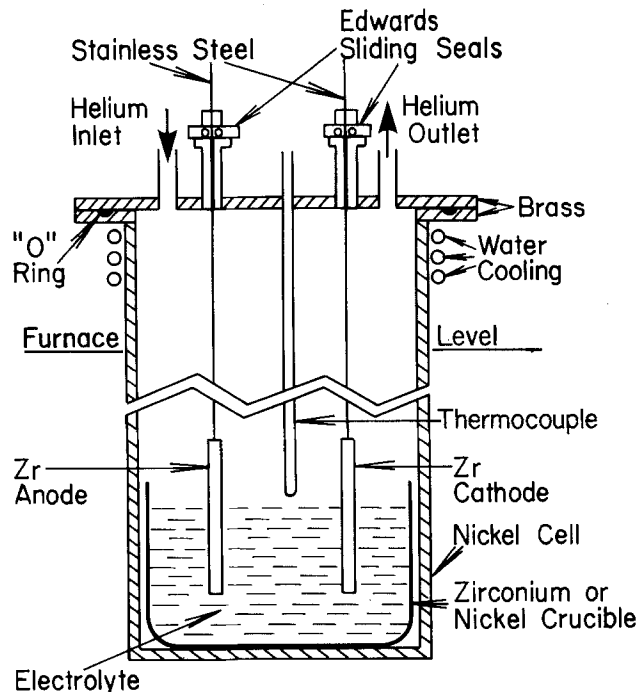


Fig. 2. Electrorefining cell for zirconium in alkali fluoride-rich electrolytes.

having a voltage range of 0-15V and a corresponding current range of 0-10A.

At the end of a series of experiments the electrodes were cleaned in water and alcohol, air dried, and stored in stoppered test tubes. Sectioning of the electrodes was done by means of a low speed diamond saw using kerosene as lubricant. The specimens were mounted with "Koldmount" self-curing resin and polished in the conventional manner.

The microhardness of the polished samples was determined on the Krenton microhardness tester using a 100g load. Debye-Scherrer x-ray powder patterns were taken on electrodeposited zirconium using a copper target and a nickel filter. Energy dispersive analysis was also used to record the x-ray emission spectra of electrodeposited zirconium samples. A 20 kV accelerating voltage source and a current of 120 mA were applied.

The zirconium content of the deposits was determined by conventional wet chemical analysis. The metal was not analyzed for nitrogen or oxygen, but the content of the metal deposits in these elements could be deduced approximately from the microhardness measurements. The solubilities of zirconium metal in alkali chloride melts containing zirconium tetrachloride were investigated directly.

The experiments involved the measurement of the weight loss of zirconium metal which was reacted with alkali chloride melts as well as with alkali chloride melts containing known amounts of tetravalent zirconium added in the form of stable hexachlorozirconate compounds, A_2ZrCl_6 .

The cell used for the experiments is shown in Fig. 3; it consisted of a closed quartz tube separated into two compartments. A boron nitride, or an Inconel crucible, located in the lower compartment, constituted the reaction chamber. The two compartments were separated by a quartz porous fritted disk which allowed filtering of the melt and separation of any solid reaction product. Zirconium metal and the salt mixture containing Cs_2ZrCl_6 or K_2ZrCl_6 were loaded into the reaction cell in a dry box, the cell was evacuated, and its side arms were flame-sealed under vacuum. After heating for about 48h in a furnace at constant temperature, the cell was inverted inside the furnace and the melt was allowed to filter through the fritted disk. After solidification, the cell was opened in a dry box and the zirconium metal was weighed to

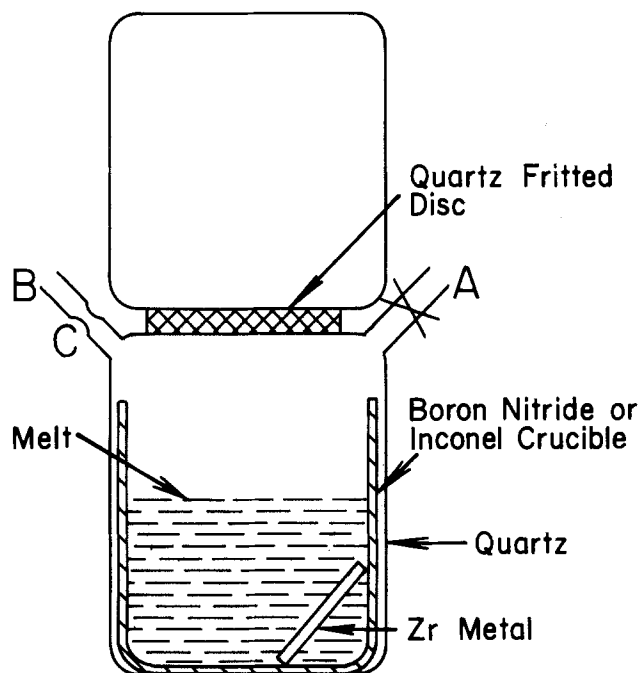


Fig. 3. Reaction cell for the determination of solubilities of zirconium metal in alkali chloride melts containing Zr^{IV} as an alkali-hexachlorozirconate compound.

establish the solubility. In all cases, the reacted electrolyte was found to be reactive toward water and to evolve hydrogen.

Results

The results of the investigations on the electrorefining of zirconium in alkali chloride-rich electrolytes and in alkali fluoride-rich electrolytes are summarized in Tables I and II, respectively. The tables contain information on melt composition, temperature, cell voltage, current density, coulombic efficiency, and type of deposit.

The experiments were conducted using the following electrolytes: (i) CsCl-KF with soluble zirconium added in the form of the stable Cs_2ZrCl_6 compound; (ii) NaF-LiF in which the soluble zirconium was added as ZrF_4 ; (iii) NaF-LiF with addition of zirconium in the form of K_2ZrCl_6 or Cs_2ZrCl_6 ; (iv) NaF-LiF-KF eutectic, also called FLINAK, with additions of zirconium as K_2ZrF_6 ; and (v) NaF-LiF-KF (1:1:1 mole) and zirconium additions as K_2ZrF_6 .

The current densities shown were calculated on the basis of the initial geometric surface area of an immersed

electrode. However, as the deposit grows, the surface area increases substantially. Thus the current densities listed represent initial apparent current density values.

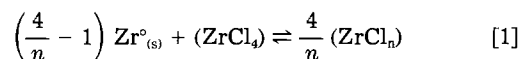
The evaluation of the quality of the deposits was based on external characteristics, as well as by the analytical techniques already mentioned. An excellent deposit would be smooth, shiny, and continuous, having a considerable thickness. This kind of deposit would be superior to the metal produced by the conventional Kroll process (25). Coherent, coarse dendritic deposits and the noncoherent fine crystalline portion of a deposit which could be collected separately on a diaphragm would also be acceptable (25).

The Table I summarizes the results obtained with solutions rich in CsCl. These melts also contained KF in amounts corresponding to KF/ Cs_2ZrCl_6 ratios from 4 to 12, respectively.

The zirconium metal obtained from run 2-a, shown in Fig. 4, is the best of this series and should be described as coarse dendritic, not too coherent, and rather reactive towards water. This deposit was similar to those obtained previously (26) from solutions of similar compositions. Contrary to expectations, the presence of fluoride ions appears to be detrimental to the quality of the deposited zirconium. As shown in Table I, higher KF/ Cs_2ZrCl_6 ratios in the electrolyte yielded powdery and noncoherent deposits. Previous investigators (10) attributed the adverse effect of the fluoride ions in mixed chloride-fluoride melts to their ability to inhibit the growth of large crystals.

Solidified electrolyte recovered at the end of electrolysis contained significant amounts of a black precipitate, which is indicative of the presence of zirconium species of lower valence. This electrolyte also reacted with water, and vigorous evolution of hydrogen was observed.

Reduced zirconium species may form either electrochemically or by the direct chemical reaction of tetravalent zirconium with the metal, following reactions of the type



where $4 > n > 1$. Anodic current efficiencies higher than 100% are clear indications of such chemical reactions.

The reducibility of tetravalent zirconium by zirconium metal and the presence of reduced zirconium species were confirmed in a separate series of experiments. These results are given in Fig. 5, as plots of moles of dissolved zirconium metal vs. the initial number of moles of $ZrCl_4$ present in a reaction cell. Some of our previous solubility measurements conducted in similar closed con-

Table I. Zr electrolysis experiments in alkali chloride-rich electrolytes

Run no.	Melt composition (w/o)	Temp. (°C)	Cell voltage (mV)	Current density (A/m ²)	Coulombic efficiency*		Evaluation of deposit	Comments	Mole ratio KF/ Cs_2ZrCl_6
					Cathode	Anode			
1-a	CsCl:89.01 KF:6.21 Cs_2ZrCl_6 :4.78	700	80	50	35	128	Loose powdery	Nickel crucible. No alkali metal evolution	12.74
1-b	Same melt as above	700	140	110	42	46	Loose powdery	Same as in run 1-a	
1-c	Same melt as above	700	180	190	31	71	Loose powdery	Same as in run 1-a	
2-a	CsCl:79.45 KF:6.30 Cs_2ZrCl_6 :14.25	700	140	300	27	177	Dendritic	Excessive dissolution of anode	4.34
2-b	Same melt as above	700	220	560	36	39	Very poor	Same as in run 2-a	
	Same melt as above	700	160	320	33	56	Powdery		
3-a	CsCl:83.88 KF:6.12 Cs_2ZrCl_6 :10.00	700	240	340	67	108	Black Poor	Excessive dissolution of anode	6.00
3-b	Same melt as above	700	330	600	52	47	Black		

Table II. Zr electrolysis in alkali fluoride-rich electrolytes

Run no.	Melt composition	Temp. (°C)	Cell voltage (mV)	Current density (A/m ²)	Coulombic efficiency* (%)		Type of deposit	Comments
					Cathode	Anode		
1-a	(NaF-LiF) _{eut.} :95.0 ZrF ₄ :5.0	750	180	300	2	132	Nodules	Zr crucible No alkali metal evolution
1-b	Same melt as above	750	160	300	25	113	Nodular	Excessive dissolution of anode
1-c	Same as in run 1-a	750	140	300	35	30	Crystalline	No alkali metal evolution
1-d	Same as in run 1-a	750	350-300	900	27	33	Thin shiny film	Same as in run 1-c
1-e	Same as in run 1-a	750	420-380	1200	32	3	Coarse dendritic. Plate	Anode almost intact
2-a	(NaF-LiF) _{eut.} :90.0 K ₂ ZrCl ₆ :10.0	750	140-120	300	0	81	No deposit	No alkali metal evolution
2-b	Same melt as above	750	160-140	500	76	108	Coarse crystalline. Plates	Same as in run 2-a
2-c	Same as in run 2-a	750	200-180	1000	85	97	Massive. Plates	Same as in run 2-a
2-d	(NaF-LiF) _{eut.} :90.0 K ₂ ZrCl ₆ :10.0	750	250-200	1200	92	93	Massive, crystalline. Large plate	Ni crucible alkali metal evolution
3-a	(NaF-LiF) _{eut.} :95.0 Cs ₂ ZrCl ₆ :5.0	750	420	1000	0	53	No deposit	No alkali metal evolution
3-b	Same melt as above	750	700	2000	0	124	No deposit	Same as in run 3-a
4-a	(KF-NaF-LiF) _{eut.} :97.5 K ₂ ZrF ₆ :2.5	750	620-320	1170	0	82	No deposit	Ni crucible Potassium metal evolution
4-b								
4-c	Same melt as above	750	900-780	2170	18	72	Average	Same as in run 4-a
5-a	(KF-NaF-LiF) _{eut.} :94.3 K ₂ ZrF ₆ :5.7	750	140-120	250	46	104	Average	Ni crucible Potassium metal evolution
5-b	Same melt as above	750	160-150	490	46	104	Massive, nodular	Same as in run 5-a
6-a	(KF-NaF-LiF) (1:1:1 mole):95.0 K ₂ ZrF ₆ :5.0	750	160	200	6	129	Fine	Ni crucible Excessive potassium evolution. Pre-electrolysis for 12h
6-b	Same melt as above	750	130	200	32	175	Dendritic	Same as in run 6-a
6-c	(KF-NaF-LiF) (1:1:1 mole):95.0 K ₂ ZrF ₆ :5.0	750	200-170	500	69	187	Massive	Ni crucible Excessive potassium evolution. Pre-electrolysis for 12h
6-d	Same melt as above	750	300-360	1000	80	155	Good, long large coherent dendrites	Same as in run 6-c
6-e	Same as in run 6-c	750	400-370	2000	85	69	Very good. Large, coherent flowerlike deposit	Same as in run 6-c
7-a	(KF-NaF-LiF) (1:1:1 mole):97.5 K ₂ ZrF ₆ :2.5	750	240	2000	—	—	Excellent. Large coherent crystals	Zr crucible

tainers (26) are also included in Fig. 5. Dashed lines represent theoretical solubilities in accordance with various possible reaction mechanisms. The results indicate that the solubility of zirconium metal is related to the degree of reduction of the tetravalent zirconium in solution. The latter appears to be related to the size of the alkali chloride ion present in these melts. For example, solutions of ZrCl₄ in mixtures of NaCl-KCl, or in molten KCl, appear to have been reduced to monovalent zirconium, with a corresponding high solubility of zirconium metal.

Solutions of ZrCl₄ in molten CsCl are reduced approximately to divalent zirconium. The addition of KF or CsF further reduces the solubility of zirconium metal and the zirconium in solution appears to be in a trivalent state. It

should be noted that some of our previous solubility experiments (26) in the presence of either KF or KF and CsF were conducted in open-reaction cells for which equilibrium conditions could be doubtful.

The loss of metal due to the reducibility of tetravalent zirconium has also been observed elsewhere (27).

Alkali fluoride-rich electrolytes.—Table II shows the results obtained with the alkali fluoride-rich electrolytes. Deposits from this series of electrorefining experiments were of much better quality than those obtained from the alkali chloride-rich electrolytes. Metallic deposits were generally coherent and of nodular or dendritic morphologies. Dendrites, however, were quite large, and in some

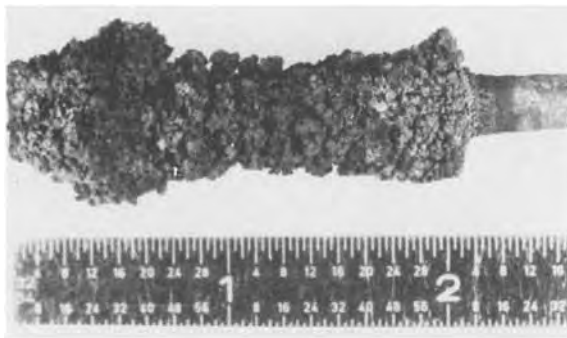


Fig. 4. Dendritic zirconium deposit from run 2-a (Table I). The electrolyte was CsCl-KF-Cs₂ZrCl₆, the current density was 3.0 A/dm², and the temperature was 700°C.

cases "plates" or "flower"-like deposits of pure crystalline metal were obtained, indicating that the deposition of dense and coherent electrolytic zirconium is possible. It should be emphasized that this is the first time that such truly metallic large electrolytic deposits have been reported in the literature.

The observations from the experiments with the alkali fluoride-rich electrolytes with respect to the characteristics of the deposition process are summarized below.

Experiments 1-a to 1-e in Table II constitute a series in which the electrolyte was the eutectic NaF-LiF (40% mole NaF, melting temperature of 652°C) and zirconium tetrafluoride was the zirconium bearing solute. The container was a zirconium crucible, and no evolution of alkali metal during electrolysis was observed.

The applied potentials were in the range of only 140-420 mV, depending on the apparent cathode current density, which was in the range of 30-120 mA/cm or 3-12 A/dm². The solute concentration was the same for all the experiments, namely 5 w/o ZrF₄.

Each of the deposition experiments in the 1-a to 1-e series was conducted using new zirconium electrodes which were introduced into the same melt after the completion of a run. This was necessary, as it was observed that conditioning of the melt was a prerequisite for obtaining good deposits. Thus, in a series of experiments, the first two or three successive experiments yielded deposits of lower quality and low current efficiency.

However, after the melt had been conditioned, all subsequent deposition runs produced metal of higher quality. For example, in the 1-a to 1-e series, the quality of the deposits improved from coarse dendritic or nodular, for run 1-a to 1-c, to the type of deposit shown in Fig. 6 (for run 1-d). This deposit is continuous, appears to be dense and microcrystalline, and represents shiny metal of good quality.

Cathodic current efficiencies for these experiments were very low, and the anodic current efficiencies higher than 100%. Solidified salt samples after electrolysis reacted violently with acidified water and evolved hydrogen gas. The behavior indicates that reducibility reactions had taken place.

Runs in the 2-a to 2-d series in Table II corresponded to experiments having the same electrolyte as in series 1, except that the solute was the complex K₂ZrCl₆.

The deposits obtained from these experiments consisted of massive crystalline zirconium and of large plates of pure metal. These plates grew from the electrode surface as in experiment 2-d and are shown in Fig. 7a and 7b. In the case of experiments 2-b and 2-d, the plates originate from the dendrites which cover the parent electrode, as shown in Fig. 7a. The plates consisted of large crystals of zirconium metal and probably acted as a secondary surface for electrodeposition. The amount of entrapped salt in this part of the deposit was also insignificant. The formation of the plates may indicate field-oriented preferred electrodeposition, which is common in the electrodeposition of the refractory metals and has also been

observed recently by Schulze (28) during the electrorefining of niobium.

The well-defined crystalline nature of this deposit is seen in Fig. 8a and 8b, which include photographs of the cathodic deposit taken on the scanning electron microscope. The hexagonal zirconium crystals from experiment 2-d have well-defined faces and a columnar character which is characteristic for the unidirectional electrodeposition process. X-ray diffraction pattern obtained from a sample of this deposit were compared with patterns produced from a sample of reactor-grade zirconium metal and were identical.

Microhardness tests were also conducted. The mean Vickers hardness of the deposit (162 VHN) is comparable to the mean Vickers hardness of the parent electrode (160 VHN). This may indicate that the deposit contains acceptable levels of oxygen and nitrogen impurities.

From the viewpoint of melt conditioning, the following observations are pertinent.

The cathode current efficiencies vary from 0, as in experiment 2-a, which gave no deposit, to the highest value of about 92% for experiment 2-d. The anodic current efficiencies varied from 81 to 108%. The current densities were in the range 30-120 mA/cm² or 3-12 A/dm².

The calculation of metal recovery for individual runs may be misleading, since run 2-a gave no deposit while the anodic current efficiency was 81%. It appears that the dissolved metal was used either for the purification of the electrolyte from oxygen or for bringing the mean valence of zirconium in the melt to the proper value for electrodeposition. At the completion of the series of experiments, the metal recovery, calculated as the ratio of the amount of the electrodeposited metal to the amount of the metal dissolved, was of the order of 72%. Recoveries of zirconium metal in the range of 60-75% have also been reported recently (25) from an electrolyte consisting of NaCl-K₂ZrF₆.

In conclusion, the results of this series of experiments indicate that crystalline zirconium metal of acceptable purity may be obtained by electrolysis of fluoride solutions containing potassium hexachlorozirconate as solute. The potassium hexachlorozirconate can be easily prepared by reaction of zirconium tetrachloride vapors with solid or molten potassium chloride, thus making the electrorefining in these melts compatible with the presently employed zirconium extractive cycle. Furthermore, electrolysis in chloride-fluoride melts containing potassium ion is free of any alkali metal evolution as opposed to the all-fluoride melts to be discussed subsequently.

In experimental runs 3-a to 3-b, the electrolyte was again the NaF-LiF eutectic, but K₂ZrCl₆ was replaced with Cs₂ZrCl₆ as the zirconium bearing solute. The concentration of Cs₂ZrCl₆ in the melt was 5 w/o. As shown in Table II, no deposit was obtained. The applied current densities were 100 mA/cm² and 200 mA/cm², respectively. No alkali metal evolution was observed. In experiment 3-a, both electrodes lost weight.

It appears that melts containing Cs₂ZrCl₆ needed more time to be "conditioned" for successful electrodeposition to begin, although this was not understood at the time this system was investigated.

The final series of experiments were conducted in all-fluoride melts. For runs 4 and 5, the electrolyte was the eutectic of the ternary system KF-NaF-LiF, which is also called FLINAK. This electrolyte, containing 10% mole NaF, 45% mole KF, and 45% mole LiF, has a very low melting temperature of only 454°C. The zirconium bearing solute was potassium hexafluorozirconate.

The deposits obtained from run 4 were coarse dendritic with salt inclusions, as shown in Fig. 9, representing run 4-c. As shown in Fig. 10, representing run 5-a, the quality of the deposit improves as the concentration of the potassium hexafluorozirconate solute increases and the applied cathode current density decreases. The cathode current efficiency varied in the range of 18-97%, with the lower values associated with very high cathode current

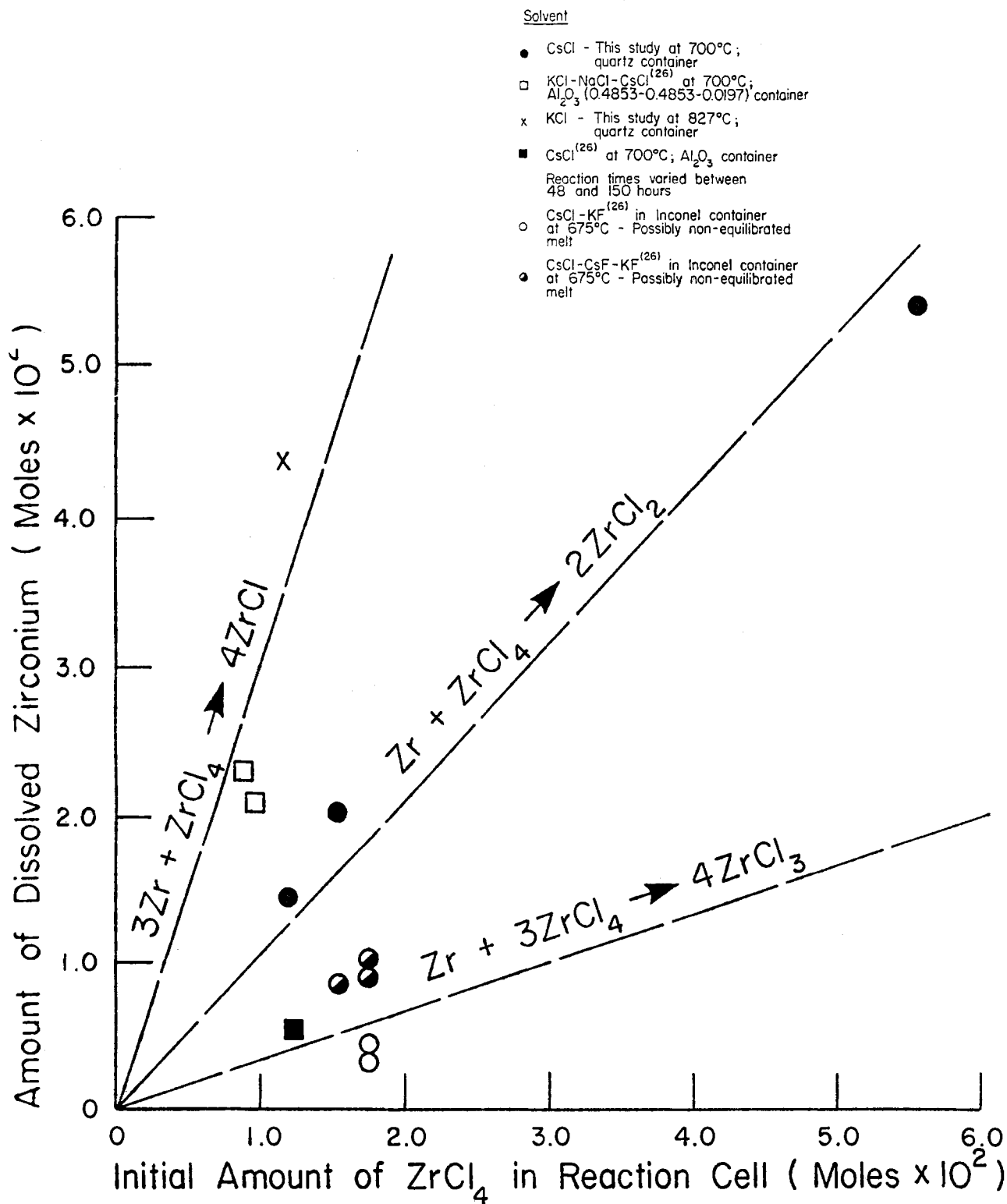
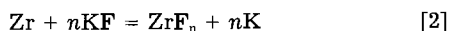


Fig. 5. Solubility of zirconium metal in alkali halide melts containing Zr^{4+} as an alkali-hexachlorozirconate compound

densities. Again, cathodic deposition required the conditioning of the melt.

Potassium evolution was observed during these experiments. Potassium evolution during electroplating of zirconium in FLINAK has also been reported previously by Mellors and Senderoff (13) and was attributed to the exchange reaction



with the value of n close to 4. Their conclusion that the potassium evolution is not due to electrolysis is supported by the results in the present work. Thus in experiments where potassium fluoride is absent, as in runs 1-3, there was no evolution of an alkali metal. Also, in an at-

tempt to electrodeposit the metal from an electrolyte consisting of the KF-LiF eutectic, contained in a zirconium crucible, the evolution of potassium metal occurred as soon as the salt melted at 492°C with simultaneous total disintegration of the zirconium crucible.

The effect of the potassium metal evolution on an electrolytic process, as well as on the possibility of its industrial application, should not be underestimated. Apart from making the process difficult and dangerous to operate, it consumes valuable metal by eroding the anode and the cathodic deposit.

Excessive potassium evolution was also observed in runs 6 and 7, which utilized the equimolar ternary KF-NaF-LiF system having a melting temperature of about

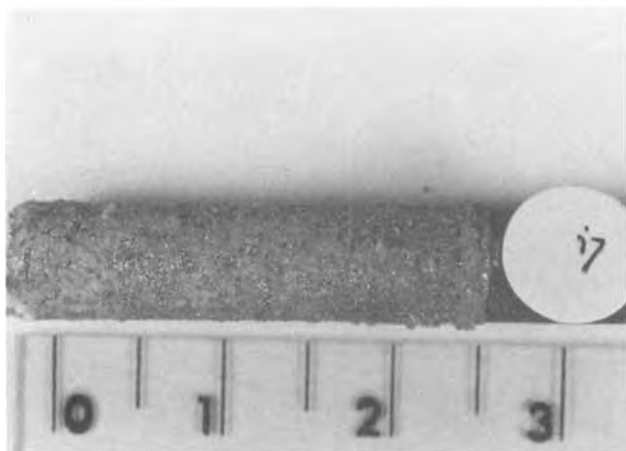


Fig. 6. Dense, microcrystalline zirconium deposit from run 1-d (Table II). The electrolyte was NaF-LiF-ZrF and the current density was 9.0 A/dm². Temperature was 750°C.

670°C. Excessive dissolution of the anodes took place due to reaction [2], while the cathodic current efficiency was very low at the initial runs of this series. However, for run 6-d, the current efficiency had increased to its maximum value of 85% and the quality of the deposit improved following the same pattern. For this run, pre-electrolysis was also carried out with two graphite electrodes for 12h prior to the commencement of the actual electrolysis.

The scanning electron microscope photograph of a smaller "flower" type of deposit obtained in run 6-e is given in Fig. 11, and it indicates a columnar structure. With respect to purity, the results of the energy dispersive analysis on this deposit did not indicate the presence of

any other metal except zirconium. The mean Vicker hardness of the deposit was 156 VHN, which was even better than in the starting electrode materials, which had a mean Vicker hardness value of 163 VHN. This appears to indicate that by purifying the melt by pre-electrolysis, the oxygen level of the deposit is reduced.

Finally, run 7-a also gave an excellent, coarse, crystalline zirconium deposit which is shown in Fig. 12a, 12b, and 12c. The cross section of this deposit reveals the formation of a continuous coherent crystalline deposit of limited thickness. The smooth interface between the electrodeposited zirconium metal and the parent electrode is shown in Fig. 12c. The electrodeposition is interrupted, however, probably due to the evolution of potassium metal because of chemical reaction [2] between zirconium and potassium fluoride in the electrolyte. A well-grown large zirconium crystal from this deposit is shown in Fig. 12b. Unfortunately, because of the disintegration of the zirconium crucible, used as container in this experiment, it was not possible to determine current efficiencies. The present results can only be compared with the recent work at the U.S. Bureau of Mines (8) and with that on previous deposition work in this laboratory (26).

It should be noted that both studies were directed toward obtaining zirconium metal from all chloride salt baths. The deposits, however, were dendritic or powdery, loosely adhered to the cathode, and contained an excessive amount of salts. Deposits of better quality were obtained from cesium chloride-rich electrolytes. Small additions of fluoride have shown positive effect, although the quality of a deposit did not improve significantly (26). Additions of larger amounts of fluoride salt (up to 20 w/o) resulted (8) in the formation of flakes containing entrapped salt. Current efficiencies and metal recovery was of the same order as in the results obtained in this study.

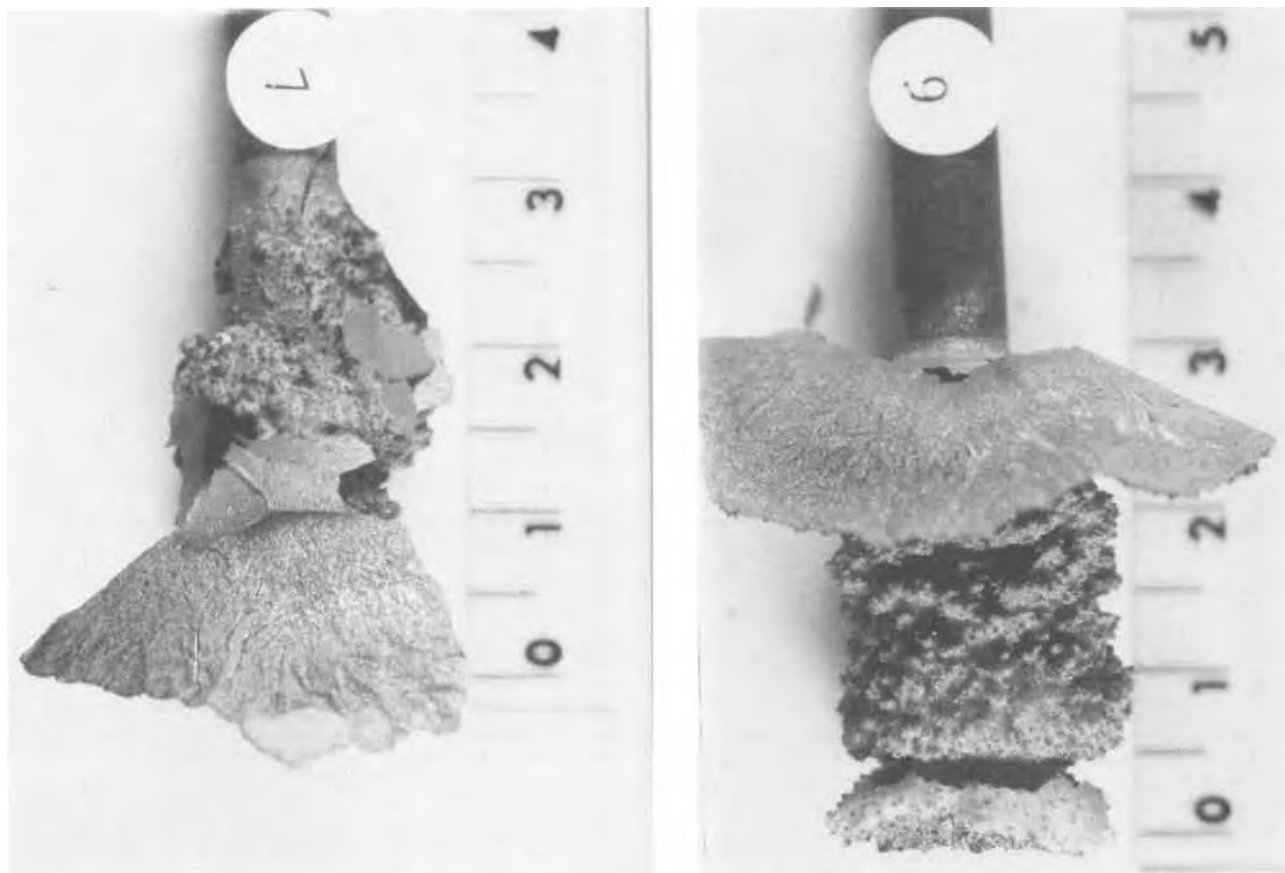


Fig. 7. a: Large platelike zirconium deposit from run 2-b. Plates originate from dendrites in deposit. Current density was 5.0 A/dm². Electrolyte was a mixture of (NaF-LiF)_{eutectic} containing 10 w/a ZrF₄ at 750°C. b: Same melt as in a, except for current density, which was 12.0 A/dm². Massive platelike crystalline deposit from run 2-d (Table II).

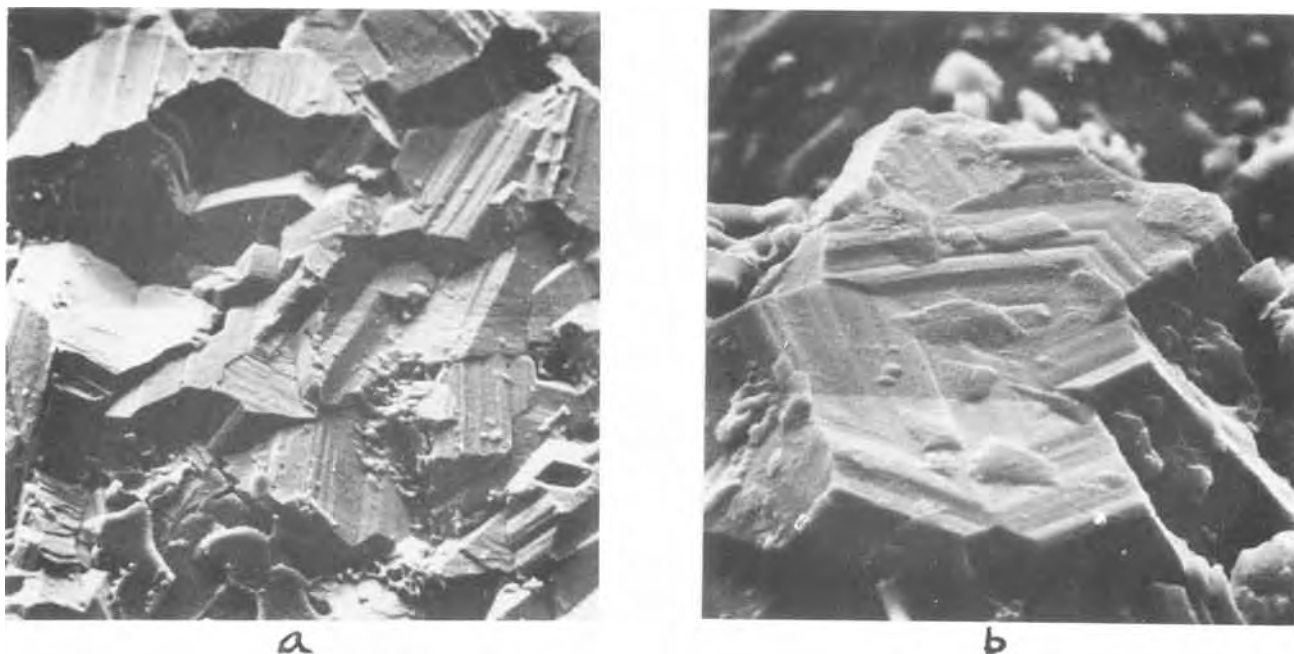


Fig. 8. a: Microphotograph of zirconium deposit (X510) taken on the scanning electron microscope. This crystalline deposit from run 2-d is columnar and shows well-defined faces. b: The same as in a, except taken at a magnification of 3000. Well-defined hexagonal crystal growth is evident.

The results of the present study indicate that the fluoride-rich electrolytes are most promising as electrolytes for electrorefining of zirconium metal.

Discussion

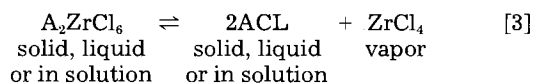
With respect to electrodeposition from alkali chloride baths, the mechanism of the electrolytic process is affected by the solubility and the thermal stability of the solutions of $ZrCl_4$ in these melts, and particularly by the thermodynamic behavior of the complex compounds of the general formula A_2ZrCl_6 , where A is an alkali metal cation. The latter form when $ZrCl_4$ reacts with an alkali chloride in the bath.

The alkali metal hexachlorozirconates represent stable compounds in which the activities of the corresponding tetrachloride are particularly low. This is manifested by the dramatic reduction in the pressures of $ZrCl_4$ over the pure A_2ZrCl_6 compounds, shown in Fig. 13, which represents the temperature dependence of the partial pressure of $ZrCl_4$ in equilibrium with alkali hexachlorozirconates. As shown in Fig. 13, the vapor pressure of pure $ZrCl_4$, at $450^\circ C$, is about 25 atm (29), as compared to the partial

pressure of $ZrCl_4$ of 0.01 atm over the pure Cs_2ZrCl_6 at $450^\circ C$.

The thermodynamic stability of the A_2ZrCl_6 compounds, where A represents an alkali metal, may be related to the size of the alkali cation A^+ . In Fig. 13, the decomposition temperature of the alkali metal hexachlorozirconate compounds, which is defined as the temperature at which the partial vapor pressure of $ZrCl_4$ over the pure compound becomes 1 atm, increases as in the sequence $Li_2ZrCl_6 \rightarrow Na_2ZrCl_6 \rightarrow K_2ZrCl_6 \rightarrow Cs_2ZrCl_6$, i.e., as the size of the alkali metal cation increases.

The thermodynamic properties of these solutions were also investigated by vapor-pressure (15-23) measurements in the composition range that represented the subsystems $ACL-A_2ZrCl_6$. In this range, the equilibrium pressures of $ZrCl_4$ over the melts are determined by equilibria of the type



Any composition within an $ACL-A_2ZrCl_6$ subsystem may be realized if the applied tetrachloride pressure over the system is kept at the corresponding equilibrium value. It

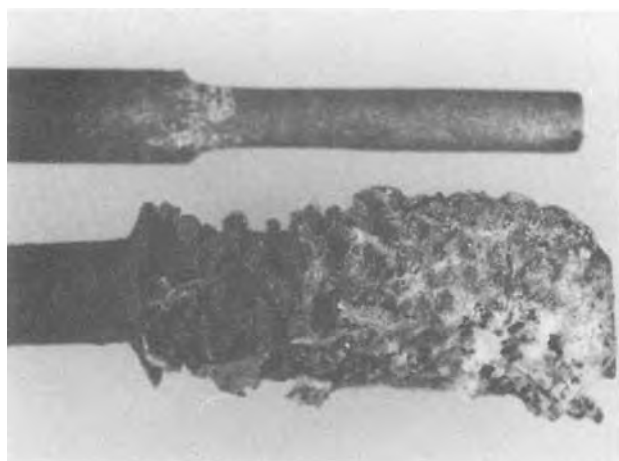


Fig. 9. Condition of anode and cathode, respectively, after completion of run 4-c. Uniform wear of anode is indicated. Zirconium deposit on cathode is coarse dendritic with salt inclusions. Electrolyte was the $(KF-NaF-LiF)_{eutectic}$ containing K_2ZrF_6 (2.5 w/o). Current density was $21.7 A/dm^2$ at $750^\circ C$.

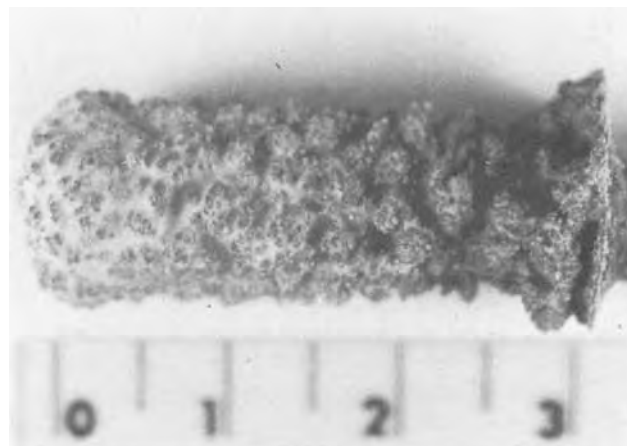


Fig. 10. Massive coarse dendritic deposit from run 5-a, at a high current density of $2.5 A/dm^2$. Electrolyte same as Fig. 9, except for K_2ZrF_6 content, which was 5.7 w/o.

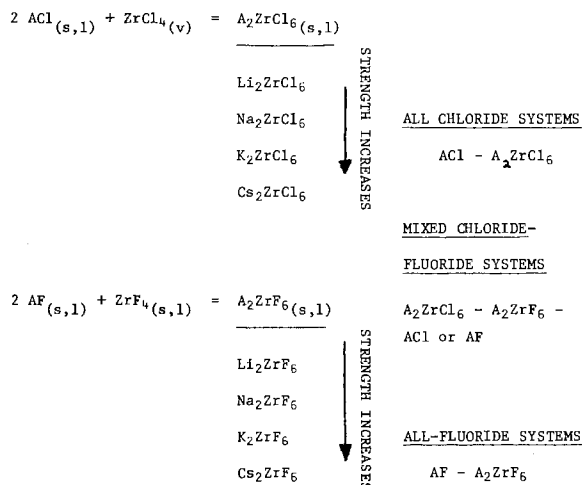
was also shown that solutions that contain $ZrCl_4$ in excess of the amount required to form A_2ZrCl_6 , i.e., in the composition range that represented the subsystem A_2ZrCl_6 - $ZrCl_4$, are extremely unstable and cannot be considered as potential electrolytes for zirconium electrolysis. The volatility of $ZrCl_4$ from such melts is excessively high.

The thermal stability of the pure A_2ZrCl_6 compounds and of the solutions of A_2ZrCl_6 and ACl at comparable concentrations increases with the size of the alkali-metal cation. In this sense, the solutions of $ZrCl_4$ in $LiCl$ are the least stable, and the solutions of $ZrCl_4$ in $CsCl$ are the most stable in this series. It should also be noted that the solutions of $ZrCl_4$ in alkaline-earth chlorides are even less stable than those in $LiCl$.

It is evident that in high temperature electrolytic cells in which the parts outside the furnace are at room temperature and act as a condenser, equilibrium conditions cannot be maintained, and industrially useful electrolytic solutions should have escaping pressures of $ZrCl_4$ of no more than 1-2 mm Hg. This requirement restricts the optimum bath compositions to those that contain less than 10 mole percent (m/o) A_2ZrCl_6 and to solvent melts that contain alkali-metal cations such as K^+ , Rb^+ , and Cs^+ .

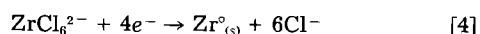
The thermodynamic stability of the A_2ZrCl_6 complex compounds in solution also affects the solubility of zirconium metal. In consideration of the possible equilibria between Zr metal and Zr^{4+} species in solution, such as those given in reaction [1], it is reasonable to expect that the position of equilibrium for each reaction will be determined primarily by the state of the zirconium species having the highest valency. Melts that contain $ZrCl_4$ at low activity levels should also be expected to contain the least amounts of zirconium of lower valency. This is in agreement with the trends indicated by the reducibility results where solutions containing cesium chloride, in which the activity of $ZrCl_4$ is very low, were reduced to a lesser extent than those containing $NaCl$ or KCl .

With regard to melts containing fluoride salts, the latter introduce an additional element of stability. Again, within the alkali fluoride salt series, the thermodynamic stability of the compounds A_2ZrF_6 where A is an alkali metal cation should increase as in the order $Li^+ \rightarrow Cs^+$. From such considerations, the expected sequence of thermodynamic stability of Zr^{4+} ions in solution in alkali halide melts should be as follows



The probable anodic and cathodic reactions in an electrorefining cell may be written as follows.

1. For a chloride type electrolyte, the cathodic reaction is



and side reactions which could lower current efficiencies may be written schematically as

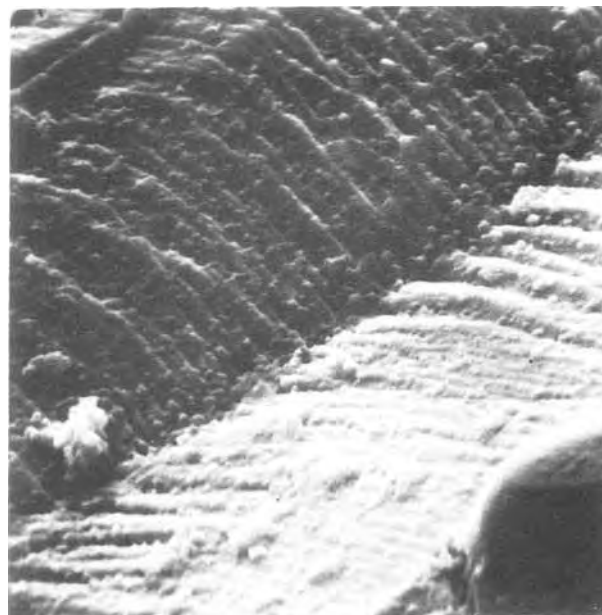
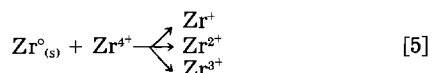
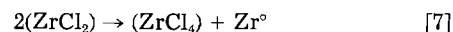


Fig. 11. Columnar structure of a zirconium deposit obtained from run 6-e. Microphotograph taken on the scanning electron microscope represents a magnification of 3300. Melt consisted of equimolar $KF-NaF-LiF$ and 5 w/o K_2ZrCl_6 . Current density was $20 A/dm^2$, at $750^\circ C$.

Redox electrode reaction causing lower current efficiencies could also be considered, such as



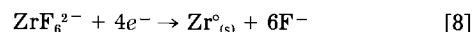
and so on. Disproportionation reactions of the type



which are thought to be responsible for producing metal powders, could also be part of the overall equilibration process.

The anodic reactions are the opposite of the cathodic processes. In the absence of diaphragms, mass transfer of reduced zirconium species should be taking place and could result in their oxidation to tetravalent zirconium at the anode. In this manner, electrons are consumed without gaining any useful metallic deposit, creating a "redox loop."

2. For a fluoride-type electrolyte, the main cathodic reaction may be written as

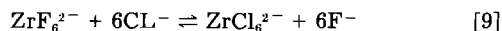


and the side reaction, in addition to possible Zr metal solubility and other redox schemes, should include the potassium evolution reaction [2].

All these equilibria depend upon the activity levels of the zirconium species in solution and could be controlled through choice of a solvent electrolyte having the appropriate salt components.

The potassium metal producing reaction is predominant in the all-fluoride electrolytes, containing potassium ions, as in runs 6-a and 6-d, because in such electrolytes Zr^{4+} are present at a very low activity state in the form of ZrF_6^{2-} .

To avoid potassium metal evolution, it is necessary to add some alkali chloride, which, in effect, increases the activity of Zr^+ ions, probably by an exchange reaction mechanism representing the equilibrium



which, however, introduces some zirconium metal reducibility side reactions. Thus, the conditioning of the electrolyte prior to electrodeposition is necessary for obtaining good zirconium metal deposits.

It appears that conditioning contributes to the purification of the melt and allows the formation of zirco-

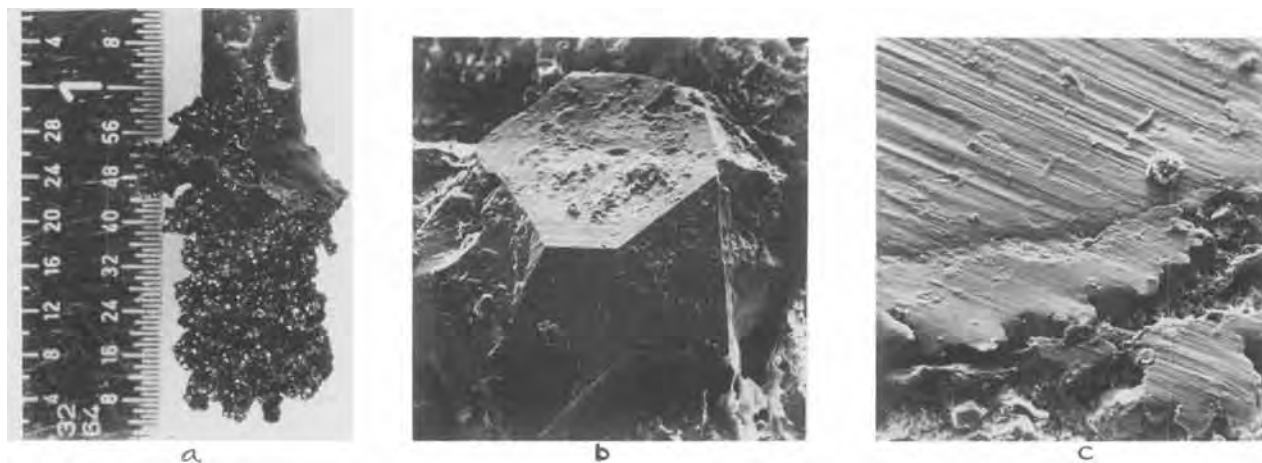


Fig. 12. a: Coarse, crystalline, coherent and shiny deposit obtained from run 7-a. The electrolyte consisted of the equimolar mixture of KF-NaF-LiF containing 2.5 w/o K_2ZrF_6 . Current density was 20 A/dm² at 750°C. b: Microphotograph (280 \times) of the above deposit, obtained on the scanning electron microscope showing crystalline nature of deposit. c: Microphotograph showing the interface between the electrodeposited zirconium metal and the parent electrode.

nium species having a mean valence, from which successful electrodeposition becomes possible.

The present results and, particularly, the chemical and electrochemical behavior of the molten salt electrolytes investigated in our laboratory appear to be consistent with these general comments.

Conclusions

The observations regarding the electrodeposition of zirconium metal from the alkali chloride and alkali fluoride melts used in the present study may be summarized as follows.

1. Zirconium deposits obtained from $CsCl$ - Cs_2ZrCl_6 melts, to which small additions of potassium fluoride were made, are dendritic in nature and highly oxidized.

The current efficiencies for the applied cathode current densities are very low. Although the melts contained potassium fluoride as a component, no potassium metal evolution occurred. The deposits, however, are of no commercial value. It is doubtful that crystalline zirconium metal can be obtained from these melts due to the formation of lower valence zirconium chlorides.

2. Truly crystalline zirconium deposits of very good quality were obtained from all-fluoride melts containing potassium ions. Unfortunately, the presence of potassium fluoride in the electrolyte, which is helpful to the electrodeposition process, is undesirable from the operation point of view, as it is thought to cause the evolution of potassium metal.

3. Crystalline zirconium may be obtained from fluoride melts to which potassium hexachlorozirconate

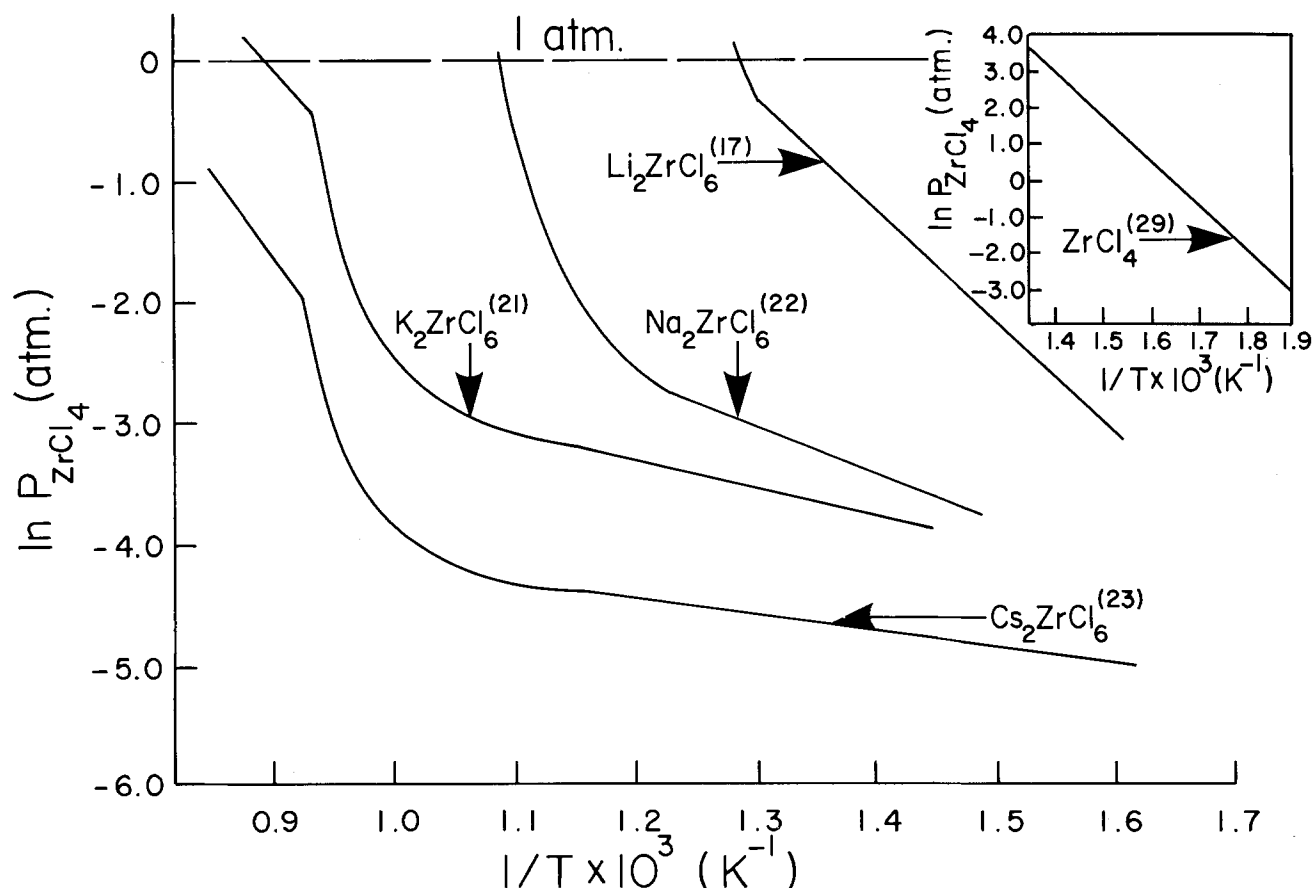


Fig. 13. Temperature dependence of the partial pressure of $ZrCl_4$ in equilibrium with the various alkali hexachlorozirconate compounds

has been added as a solute, such as those containing NaF-LiF-ZrF₄ or NaF-LiF-K₂ZrCl₆. Alkali metal is not generated from these melts, and the quality of the obtained deposits could be further improved.

It was found that the metal dissolves in significant amounts in melts that contain zirconium tetrachloride. In the presence of tetravalent zirconium, the degree of zirconium metal solubility depended on the type of the alkali chloride present, on temperature, and on the concentration of zirconium tetrachloride in the melt. The addition of fluoride salts generally reduced metal solubility, and appears to increase the average valence of zirconium in these melts.

Acknowledgment

The authors are grateful to the Natural Sciences and Engineering Research Council of Canada for a grant in support of this work.

Manuscript submitted June 15, 1984; revised manuscript received Jan. 30, 1985.

The University of Toronto assisted in meeting the publication costs of this article.

REFERENCES

1. A. J. Kauffman, Jr. and E. D. Dilling, in "The Metallurgy of Zirconium," B. Lustman and F. Kerze, Jr., Editors, pp. 66-101, McGraw-Hill, New York (1955).
2. W. B. Blumenthal, "The Chemical Behavior of Zirconium," p. 398, Van Nostrand, Princeton, NJ (1958).
3. M. L. Holt, *This Journal*, **98**, 33C (1951).
4. M. A. Steinberg, M. E. Sibert, and E. Wainer, "Zirconium and Zirconium Alloys," pp. 37-72, American Society for Metals, Cleveland, OH (1953).
5. M. A. Steinberg, M. E. Sibert, and E. Wainer, *This Journal*, **101**, 63 (1954).
6. P. A. Sheikh, R. Winand, and A. Fontana, *J. Nucl. Mater.*, **39**, 84 (1971).
7. G. M. Martinez and D. E. Couch, *Metall. Trans.*, **3**, 571 (1972).
8. G. M. Martinez, D. E. Shanks, J. R. Woodyard, and M. M. Wong, US Bureau of Mines, RI. 8125 (1976).
9. K. P. Lebedeva and A. N. Baraboshkin, *Electrochem. Molt. Sol. Electrol.*, **3**, 83 (1966).
10. K. P. Lebedeva and A. N. Baraboshkin, *ibid.*, **3**, 91 (1966).
11. A. N. Baraboshkin and A. N. Lebedeva, *ibid.*, **4**, 55 (1967).
12. O. S. Petenev and L. E. Ivanovskii, *ibid.*, **8**, 55 (1970).
13. G. W. Mellors and S. Senderoff, *This Journal*, **113**, 60 (1966).
14. G. W. Mellors and S. Senderoff, Canadian Pat. 688,546 (1964).
15. R. L. Lister and S. N. Flengas, *Can. J. Chem.*, **43**, 2947 (1965).
16. J. E. Dutrizac and S. N. Flengas, *ibid.*, **45**, 2312 (1967).
17. J. E. Dutrizac and S. N. Flengas, in "Advances in Extractive Metallurgy," p. 572, IMM, London (1968).
18. S. N. Flengas, J. E. Dutrizac, and R. L. Lister, *Can. J. Chem.*, **46**, 495 (1968).
19. S. N. Flengas and P. Pint, *Can. Metall. Q.*, **8**, 151 (1969).
20. D. Asvestas, P. Pint, and S. N. Flengas, *Can. J. Chem.*, **55**, 1154 (1977).
21. G. J. Kipouros and S. N. Flengas, *ibid.*, **56**, 1549 (1978).
22. G. J. Kipouros and S. N. Flengas, *ibid.*, **59**, 990 (1981).
23. G. J. Kipouros and S. N. Flengas, *ibid.*, **61**, 2183 (1983).
24. D. J. McPherson and M. Hansen, "Zirconium and Zirconium Alloys," p. 222, American Society for Metals, Cleveland, OH (1953).
25. P. L. Vijay, J. C. Sehra, and C. V. Sundaram, in "Extractive Metallurgy of Refractory Metals," H. Y. Sohn, O. N. Carlson, and J. J. Smith, Editors, p. 361, AIME, New York (1981).
26. P. Pint and S. N. Flengas, *Trans. IMM*, **87**, C29 (1978).
27. F. Basile, E. Chassaing, and G. Lorthoir, *J. Appl. Electrochem.*, **11**, 645 (1981).
28. K. K. Schulze, *J. Metals*, **33**(4), 33 (1981).
29. A. A. Palko, A. D. Ryon, and D. W. Kuhn, *J. Phys. Chem.*, **62**, 319 (1958).

Liquid-Line Corrosion of Nickel in Molten Sodium Carbonate

Venkatraman R. Iyer and Owen F. Devereux*

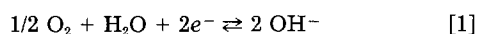
Department of Metallurgy and Institute of Materials Science, University of Connecticut, Storrs, Connecticut 06268

ABSTRACT

Liquid-line corrosion of nickel in molten sodium carbonate at 1000°C under reduced air pressures was measured as a function of time and of air pressure. The observed attack profile approached a circular arc whose depth increased parabolically with time. Attack depth increased with air pressure from zero under an inert environment, passed through a maximum, and decayed approximately hyperbolically at higher (subatmospheric) pressures. These observations are shown to be quantitatively consistent with rate control by the electron-transfer step of the cathodic process, reduction of peroxide.

During the course of a study of the polarization characteristics of the nickel electrode in molten sodium carbonate (1, 2), we observed marked liquid-line attack on a specimen that had been only partially immersed in the melt. The striking feature of this attack was the remarkably circular nature of the attack profile shown in Fig. 1. The study reported herein was initiated to determine whether such a profile was a reproducible feature characteristic of this process and to investigate the mechanism by which it was created.

Liquid-line corrosion is generally understood in aqueous systems in terms of an oxygen concentration, or differential aeration, cell in the meniscus region, in which ready access of oxygen to the electrode surface near the meniscus renders that region cathodic and, thereby, the electrode surface immediately below becomes anodic via reactions typified by

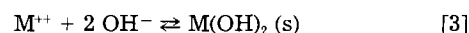


*Electrochemical Society Active Member.

and



The restricted geometry of the region of meniscus-electrode intersection, together with the close proximity of the anodic and cathodic regions, encourages hydrolysis of the reaction products



which may further isolate the anolyte, forming an "occluded cell" of low pH which continues to experience active anodic dissolution (3, 4). Similarly, the catholyte remains basic, allowing the cathodic region to be passive and enhancing the rate of dissolution in the anodic region (4). Pourbaix (5) has reviewed in detail the electrochemical features of such occluded cells in the general context of localized corrosion.

The partially immersed electrode has also served as a model for the gas diffusion electrodes of interest in fuel cell technology. Studies of hydrogen oxidation (6, 7) and

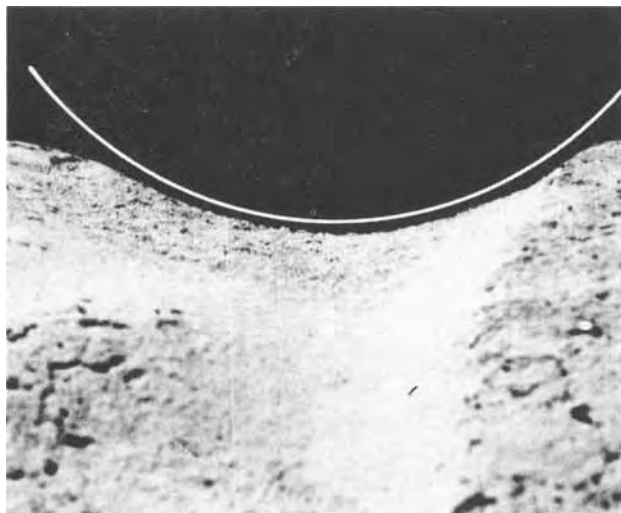


Fig. 1. Circular arc superposed on typical attack profile

of oxygen reduction (8) on platinum electrodes partially immersed in sulfuric acid have shown the electrode reactions to occur almost exclusively at a narrow region of the electrode surface just above the visible meniscus, presumed to be coated with a thin film of electrolyte. Similar results were found for oxygen reduction on silver and nickel electrodes partially immersed in aqueous potassium hydroxide (9). The rates of these electrode reactions were found to be dependent upon molecular and ionic transport processes in the thin film region and on charge transfer. Similar interfacial effects are seen in molten salts; Rahmel (10) observed enhanced dissolution of silver specimens partially immersed in neutral alkali sulfate melts, and attributed the effect to rapid oxygen transport through a thin electrolyte film coating the exposed portion of the specimens.

Experimental Program

All of our studies were conducted using nickel specimens partially immersed in reagent-grade sodium carbonate at 1000°C under partial vacuum (reduced air pressure). Specimens 1.5 cm long were prepared from Ni-200 (99% Ni) rod of nominal 1/4 in. diam (0.635 cm) and mounted to 1/4 in. (0.635 cm) od alumina support tubes with an alumina cement (Ultrabond 552, Aremco Products, Incorporated). Surface preparation consisted of grinding with 600 grit SiC paper, washing, and drying. The test cell was similar to that previously described for electrode polarization studies (1), consisting of a vertical 3 1/2 in. (8.9 cm) od closed-end mullite tube with a vacuum-tight closure from which the specimens were suspended. The melt was contained in a recrystallized alumina crucible also supported by the top flange. The cell was evacuated continuously by a mechanical pump; cell pressure was regulated by an air bleed valve and measured with a mercury manometer. Two sets of experiments were conducted: one to establish the effect of cell pressure, P , at a constant immersion time of 48h, and the other to establish the effect of immersion time at a constant cell pressure of 667 Pa (5 torr). At the end of each experiment, the melt was cooled and then dissolved in water to permit removal of the specimen. The specimen was then immersed in a saturated mercuric chloride solution for 48h to remove the oxide scale without further dissolution of metal. Following rinsing and drying, the profile of the attacked region was recorded as a scanning electron micrograph. Depth of attack as a function of position was measured directly on the scanning electron micrograph. In one exception to this procedure, the solidified carbonate was left intact, and the crucible containing the carbonate and specimen was sectioned vertically to establish the profile of the meniscus and its relationship to the region of corrosive attack. This specimen had been partially immersed for 24h at a cell pressure of 667 Pa.

Experimental Results

Specimens showed reasonably uniform attack around their circumference; however, there was significant variation in attack depth from specimen to specimen at the same pressure. Figure 2 shows typical profiles obtained at cell pressures of 667, 10,000, 20,000, and 40,000 Pa (5, 75, 150, and 300 torr), while Fig. 3-6 depict measured attack profiles for the several specimens tested at each pressure. The abscissa on these plots is a relative height, in that position relative to the melt meniscus could not be fixed with certainty save for the one test in which a section was made through the solidified carbonate. Several tests were performed in air at 1 atm and in nitrogen (Matheson Extra Dry, >99.9%) at 1 atm. Attack was slight in each case; a profile typical of the meniscus region of a specimen tested in nitrogen is shown in Fig. 7. The maximum depth of attack observed thus increases very rapidly from essentially nil in nitrogen to its maximum value at the lowest cell pressure tested, then decays to a small value in air at 1 atm. Attack profiles for specimens tested for various times at a cell pressure of 667 Pa are shown in Fig. 8-10, and Fig. 3, showing a somewhat less than linear increase in attack depth with time and the development of an approximately circular attack profile. The section prepared through the specimen and solidified melt is shown in Fig. 11, and Fig. 12 shows the measured meniscus profile superposed on the measured attack profile (the scale of the latter exaggerated) for that specimen. It is clear in this figure that anodic activity is confined to the upper portion of the meniscus, but that the anodic region does not extend to the top of the meniscus. There is no visual indication of a thin electrolyte film above the meniscus.¹

The tested specimens invariably displayed a black oxide scale, even in the region of anodic activity. The scale formed on the immersed portion of the specimen, however, was thinner than that on the portion not immersed. This thinning was found to be associated with dissolution of the oxide in the melt in the following experiment. Three specimens were oxidized in air at 1000°C for 6h. One of these specimens was subsequently immersed in a carbonate melt under vacuum for 24h at 1000°C, and a second immersed in a similar melt exposed to atmospheric air. Following this, all three specimens were cleaned, but not descaled, and then electroplated with nickel to provide mechanical support for the scale, sectioned, and polished. Average scale thicknesses, determined by SEM examination of the polished sections, were observed as follows: as-oxidized was 24 μm ; immersed in air-saturated melt, 4.4 μm ; and immersed in melt under vacuum, 0.5 μm . These observations indicate that the nickel oxide scale is dissolved to a limited extent by molten sodium carbonate, and that dissolution is enhanced by reduced air pressure. This is consistent with the existence of a nickelate species, e.g., NiO_2^- , soluble in the basic environment afforded by carbonate decomposition at low CO_2 pressures. A similar examination was made of a specimen that had been partially immersed in a melt under a reduced pressure for 24h without prior oxidation. On the nonimmersed portion of the specimen, the scale thickness was 14 μm ; on the fully immersed portion, it was 8.3 μm ; and at the site of maximum attack, 5.5 μm . This, together with the aforementioned observations on fully immersed oxidized specimens, suggests that scale thinning is enhanced at the liquid line by increased basicity

¹The line through the meniscus profile data is drawn according to the theoretical form (11)

$$\frac{x}{h} = \frac{1}{\sqrt{2}} \left[\cosh^{-1} \left(\frac{\sqrt{2}h}{z} \right) - \cosh^{-1}(\sqrt{2}) + 1 - \sqrt{2 - \left(\frac{z}{h} \right)^2} \right] + \delta$$

where x and z are the horizontal and vertical coordinates, respectively, $h^2 = 2\gamma/(\Delta\rho g)$ is the capillary constant, and δ is the thickness of a thin liquid film above the meniscus. The data in Fig. 12 correspond to $h = 3.756$ mm and $\delta = 0.08$ mm, whereas the expected value of h is 4.674 mm (12). The discrepancy is most obviously attributable to a lowering of the surface tension of the melt by adsorption of the various additional species present in the meniscus region, e.g., O^- , O_2^- , and Ni^{+2} .

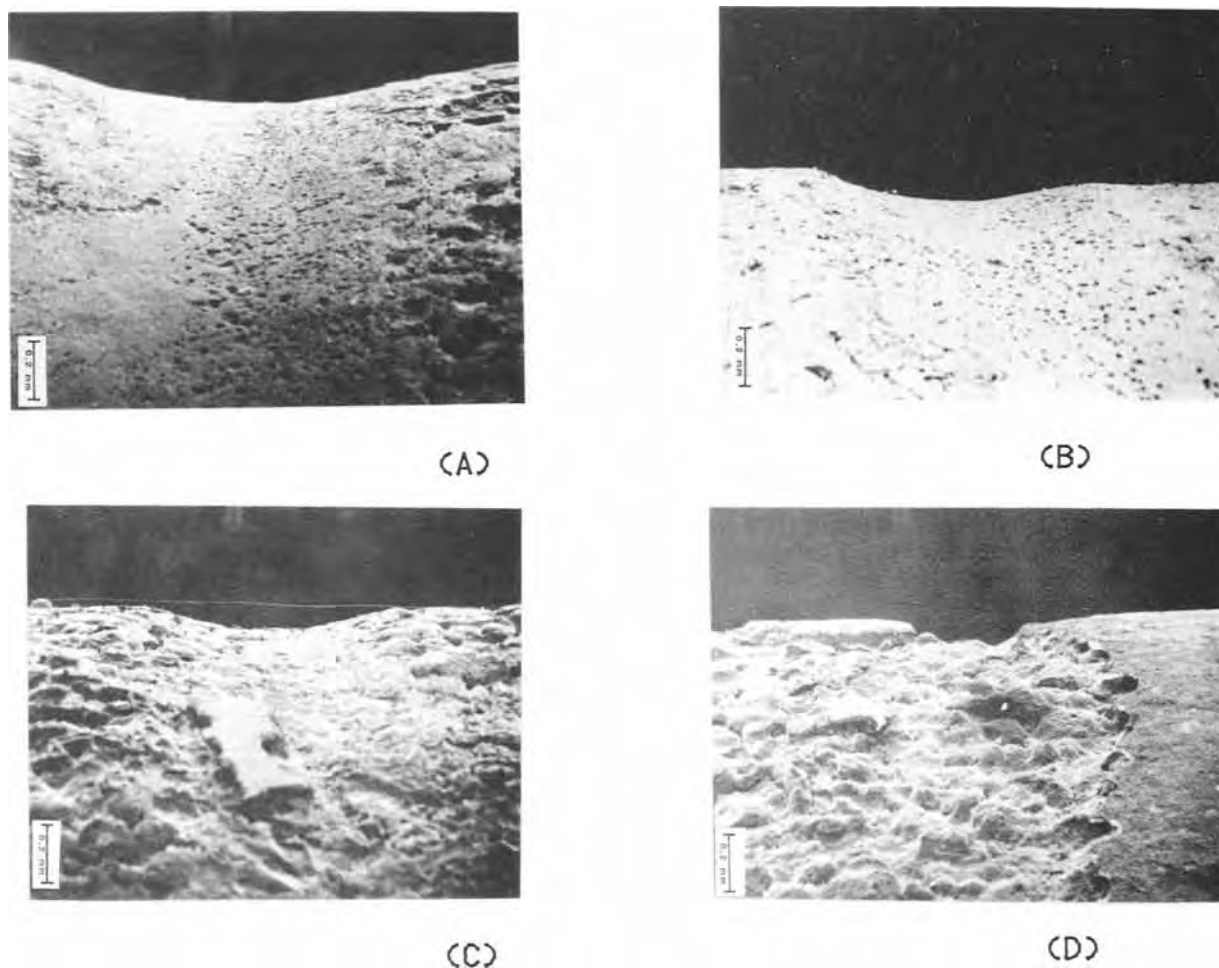


Fig. 2. Pressure dependence of liquid line attack after 48h partial immersion. A: 667 Pa. B: 1×10^4 Pa. C: 2×10^4 Pa. D: 4×10^4 Pa

in that region due to cathodic production of oxide ion. The scale, as shown in Fig. 13, was observed to be bilayered; the outer layer was columnar and compact, while the inner layer was finer grained and porous. Wavelength

dispersive x-ray analysis (WDX) in the scanning electron microscope revealed that the scales contained nickel and oxygen; no sodium was detected. Similar observations

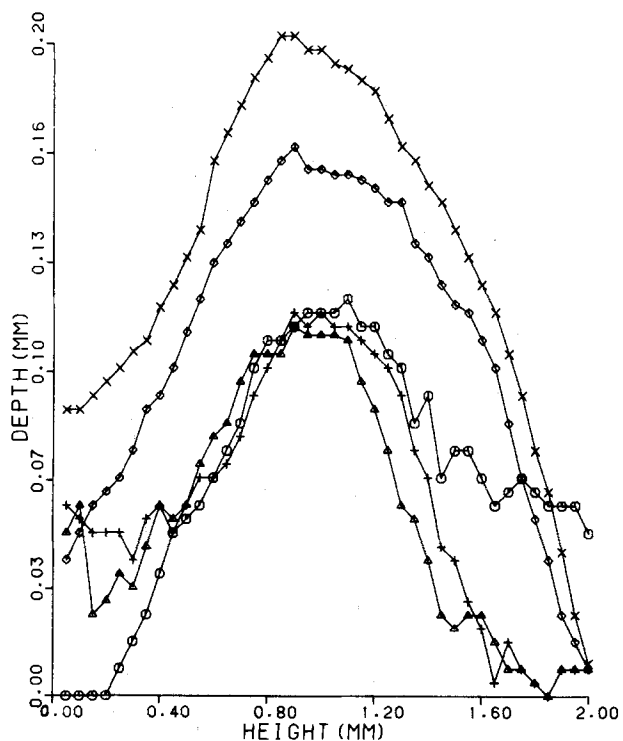


Fig. 3. Measured attack profiles for different specimens after 48h partial immersion at 667 Pa.

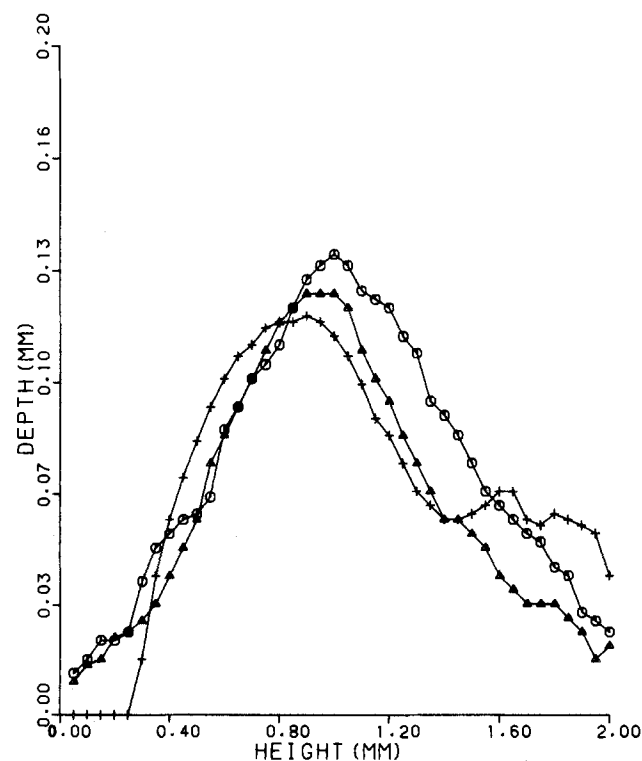


Fig. 4. Measured attack profiles for different specimens after 48h partial immersion at 1×10^4 Pa.

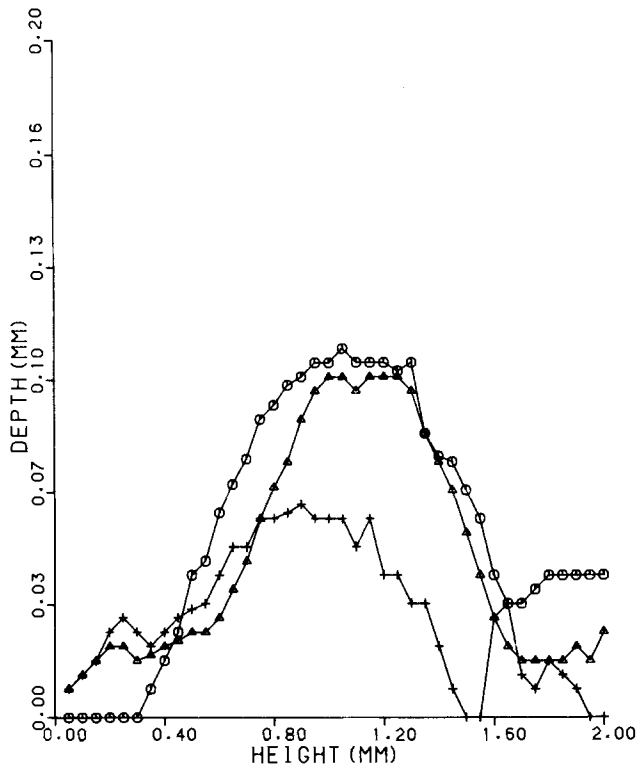


Fig. 5. Measured attack profiles for different specimens after 48h partial immersion at 2×10^4 Pa.

were made by Douglass on the structure of air-formed films on dilute alloys of chromium in nickel (13). The sectioned specimens also revealed considerable grain boundary attack; this is evident in Fig. 13 and also in Fig. 2.

Discussion

Three distinct forms of attack were seen in this study: a generalized attack above the liquid-line region (gaseous ambient), a generalized attack below the liquid-line region (liquid ambient), and a localized attack at the liquid-line region (liquid ambient). The first of these is mani-

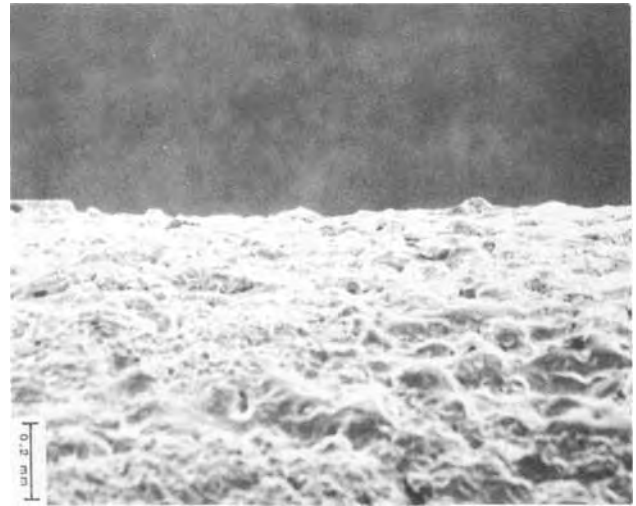


Fig. 7. Specimen profile after 48h partial immersion under nitrogen atmosphere.

festes simply in a scale formation, but the latter two must, in general, be regarded in terms of both scale formation and scale dissolution in order to explain the occurrence of the thinnest scale at the site of the greatest metal loss. Such simultaneous scale formation and dissolution processes have been discussed previously (14, 15). The data reported in Fig. 3-6 and 8-10 represent the extent of localized liquid-line attack relative to general attack, the base line of these figures representing the postexperiment metal surface above and below the meniscus. Examination of the figures indicates that the extent of generalized attack is approximately the same in these two regions, the one immersed in the melt and the other in the gaseous ambient above the melt. The extent of scale formation above the melt is consistent with data reported by Philips (16) for gas phase oxidation of impure nickel. He reports a parabolic constant at 1000°C of $1.5 \text{ mg}^2\text{cm}^{-4}\text{h}^{-1} = 57 \text{ } \mu\text{m}^2\text{h}^{-1}$, which corresponds to the formation of an oxide layer $7.5 \text{ } \mu\text{m}$ thick after 1h and $52 \text{ } \mu\text{m}$ thick after 48h, and to a metal losses of 5 and $34 \text{ } \mu\text{m}$, respectively.

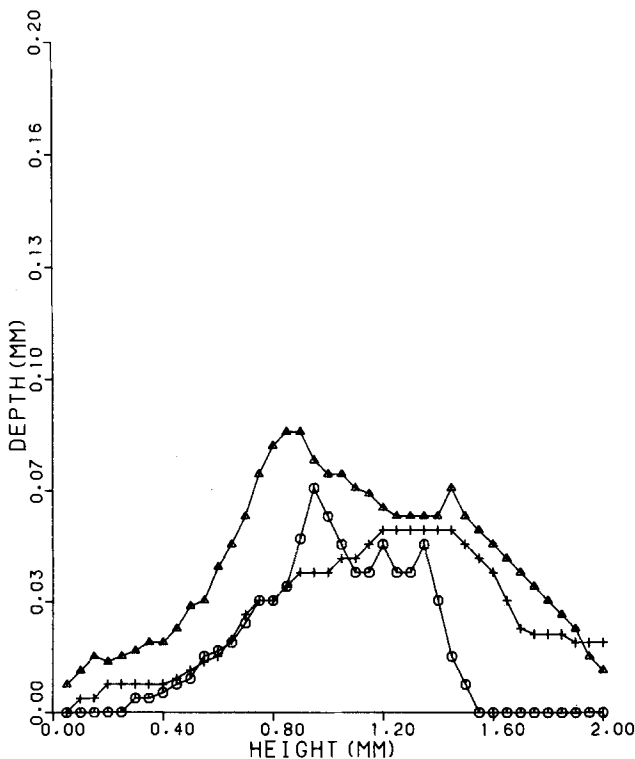


Fig. 6. Measured attack profiles for different specimens after 48h partial immersion at 4×10^4 Pa.

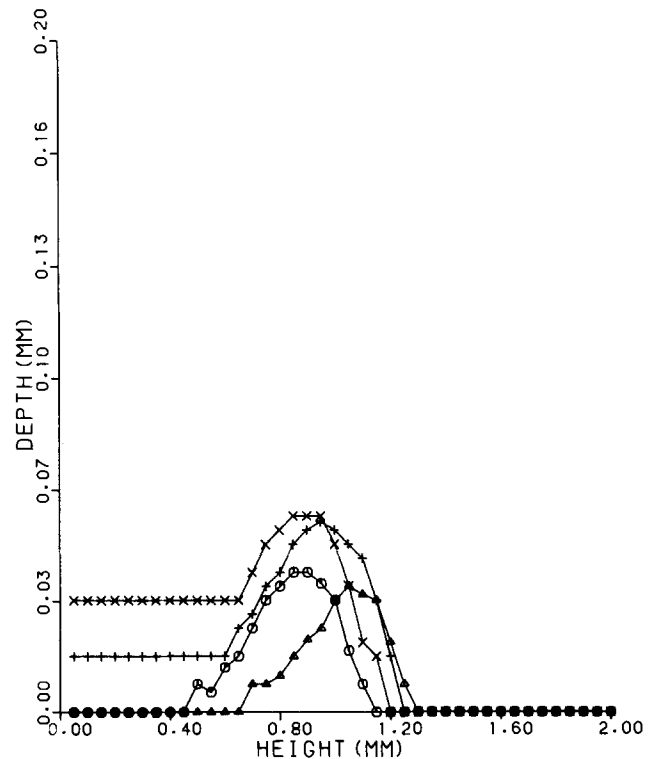


Fig. 8. Measured attack profiles for different specimens after 6h partial immersion at 667 Pa.

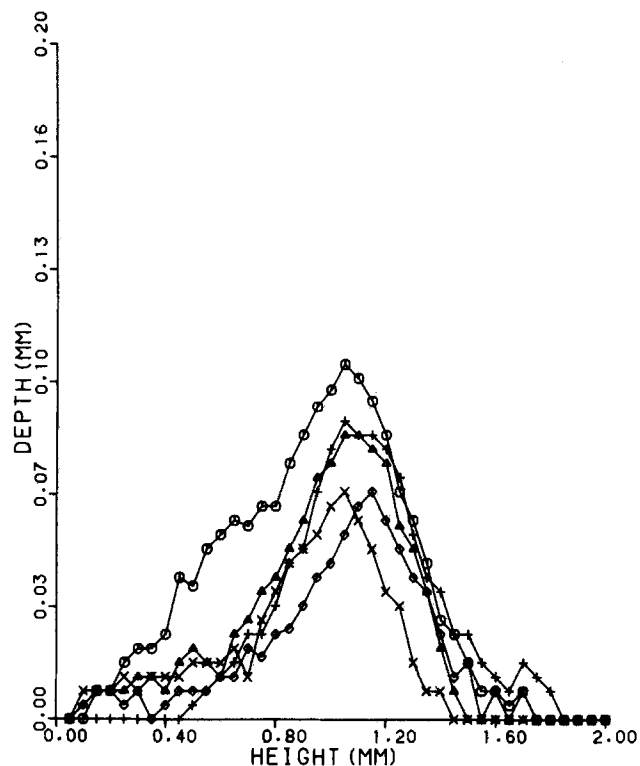


Fig. 9. Measured attack profiles for different specimens after 12h partial immersion at 667 Pa.

The observed $1/6$ power dependence of the parabolic constant on oxygen pressure (17) would cause only a variation of a factor of two over the cell pressures studied quantitatively in this investigation (667-101,325 Pa).

Given the p-type nature of NiO (18) and the ubiquity of scale formation in this system, it is likely that anodic oxidation in the liquid-line and subliquid-line regions is preceded by injection of cation vacancies at the oxide/melt interface

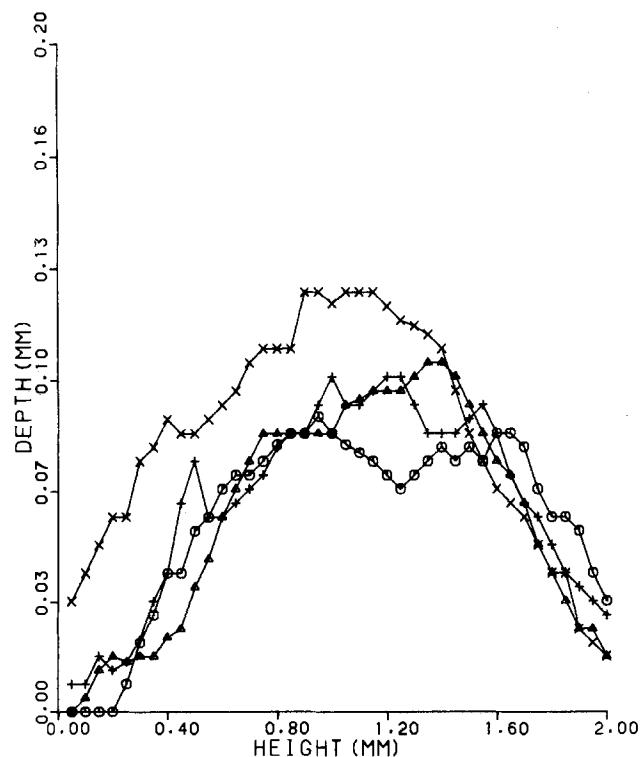
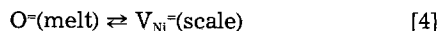


Fig. 10. Measured attack profiles for different specimens after 24h partial immersion at 667 Pa.

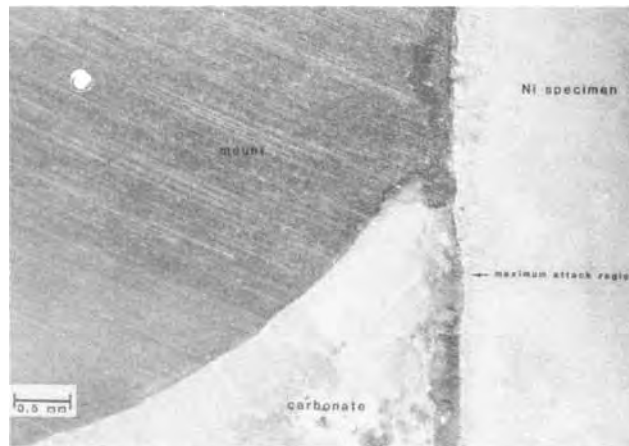
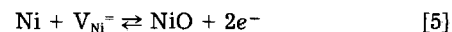


Fig. 11. Metallographic section through solidified interfacial region, showing region of maximum attack in relation to the line of three phase contact.

followed by their diffusion to the metal/oxide interface, where they are consumed in the anodic reaction



Scale dissolution in the basic melt may be represented by



again postulating the existence of NiO_2^{\ominus} in basic solutions, and may be presumed to be essentially independent of the anodic process. However, the rate and extent of such dissolution processes may, in general, be regarded as a function of the electric field at the scale/solution interface as well as of solution parameters such as basicity (14, 15).

The absence of significant attack under oxygen-free environments indicates that the cathodic reaction is reduction of dissolved oxygen, and the dependence of the extent of attack upon cell pressure further implies that the overall process is rate limited by the cathodic reaction. Dissolution of oxygen in carbonate melts has been observed to be non-Henrian, with formation of peroxide according to the reaction (19-23)



or

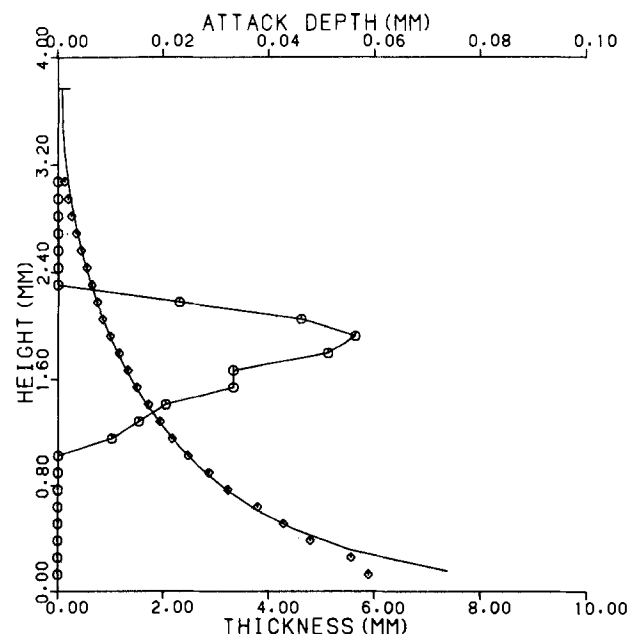
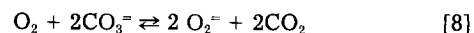


Fig. 12. Measured attack profile superposed on measured meniscus profile from Fig. 12 (not to scale).

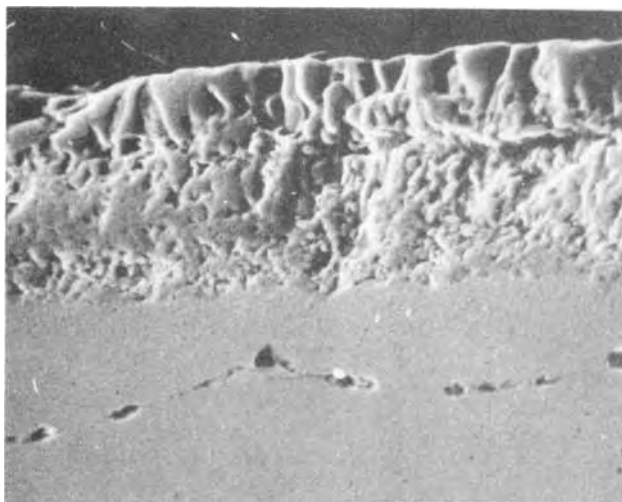
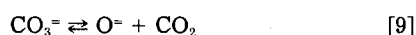


Fig. 13. Section through scale, showing two-layer structure and grain boundary attack in substrate.

if the equilibrium



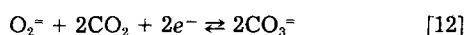
is assumed, and superoxide according to the reaction (19, 21-23)



Reduction in carbonate cells is attributed to (20, 22)



or, assuming equilibrium [9]



and, at more negative potentials (22)



Although the dependence of the extent of liquid-line attack upon air pressure within the cell indicates control by the cathodic reaction on the overall process, it is difficult to argue that the localized nature of the attack is due to diffusion control by the cathodic reactants within the melt. We lack specific data concerning the diffusivities of peroxide or superoxide ions in molten carbonates; however, Turkdogan (24) notes that the diffusivities of foreign ions in molten salts are similar to the self-diffusivities, and that the latter fall in the range of 1×10^{-5} to 8×10^{-5} cm^2s^{-1} . These values correspond to a diffusion distance, $x = 2\sqrt{Dt}$, ranging from 1.6 to 7.4 cm, *i.e.*, a value of the order of the melt depth, for the maximum exposure time of 48h. However, significant corrosive attack is confined to a band of ~ 2 mm width in the vicinity of the meniscus, and a logical explanation is that the major part of the flux of cathodic reactants is through the thin electrolyte film just above that region postulated by Rahmel (10). In their careful potentiostatic investigation involving the gold electrode in carbonate melts, Appleby and Nicholson (22) found cathodic oxygen reduction to be rate limited by electron-transfer processes, *i.e.*, reactions [12] and [13] with the latter dominant at high $P_{\text{O}_2}/P_{\text{CO}_2}$ ratios.

The rate of the cathodic electron transfer process, J , is proportional to the corresponding exchange current density, expressed by Vetter as (25)

$$J \propto i_0 = k_- c_0 \exp\left(\frac{\alpha F}{RT} \epsilon_0\right) \quad [14]$$

where k_- is a rate constant incorporating the electronic charge, c_0 is the concentration (or, more properly, the activity) of the oxidized species at the reaction site, α is the transfer coefficient, and ϵ_0 is the equilibrium potential of the half-cell reaction. For peroxide reduction, assuming reaction [8] to be at equilibrium, c_0 may be expressed as

$$c_0' = a_{\text{O}_2^-} = \frac{K_1^{1/2} P_{\text{O}_2}^{1/2} a_{\text{CO}_3^{2-}}}{P_{\text{CO}_2}} \quad [15]$$

where K_1 is the equilibrium constant for reaction [8]. The equilibrium potential for reaction [12] may then be expressed

$$\epsilon_0' = \frac{RT}{nF} \ln K_2 = \frac{RT}{2F} \ln \frac{a_{\text{CO}_3^{2-}}}{P_{\text{CO}_2} P_{\text{O}_2}^{1/2} K_1^{1/2}} \quad [16]$$

where K_2 is the equilibrium constant for half-cell (12). Substituting

$$J' \propto i_0' = k_-' K_1^{(1/2-\alpha/4)} P_{\text{O}_2}^{(1/2-\alpha/4)} P_{\text{CO}_2}^{-(1-\alpha/2)} a_{\text{CO}_3^{2-}}^{(1+\alpha/2)} \quad [17]$$

If we assume that the partial pressures of oxygen and carbon dioxide are simply proportional to pressure (*i.e.*, their mole fractions in the cell environment remain constant), Eq. [17] becomes

$$J' \propto i_0' \propto P^{-(1/2+3\alpha/4)} a_{\text{CO}_3^{2-}}^{(1+\alpha/2)} \quad [18]$$

Comparable expressions for superoxide reduction are

$$c_0'' = a_{\text{O}_2^-} = \frac{K_1^{1/4} K_3^{1/2} P_{\text{O}_2}^{3/4} a_{\text{CO}_3^{2-}}^{1/2}}{P_{\text{CO}_2}^{1/2}} \quad [19]$$

where K_3 is the equilibrium constant for reaction [10]

$$\epsilon_0'' = \frac{RT}{nF} \ln K_4 = \frac{RT}{F} \ln \frac{K_1^{1/4} a_{\text{CO}_3^{2-}}^{1/2}}{K_3^{1/2} P_{\text{O}_2}^{1/4} P_{\text{CO}_2}^{1/2}} \quad [20]$$

where K_4 is the equilibrium constant for half-cell (13), and

$$J'' \propto i_0'' = k_-'' K_1^{(1+\alpha)/4} K_3^{(1-\alpha)/2} P_{\text{O}_2}^{(3-\alpha)/4} P_{\text{CO}_2}^{-(1+\alpha)/2} a_{\text{CO}_3^{2-}}^{(1+\alpha)/2} \quad [21]$$

which, on assuming constant cell gas composition, becomes

$$J'' \propto i_0'' \propto P^{(1-3\alpha)/4} a_{\text{CO}_3^{2-}}^{(1+\alpha)/2} \quad [22]$$

Note that in Eq. [15]-[22], the superscripts ' and '' refer to peroxide reduction and superoxide reduction, respectively. In developing expressions similar to Eq. [17] and [21], Appleby and Nicholson assumed $a_{\text{CO}_3^{2-}}$ to be constant (22).

The cathodic reaction rate is related to the depth of liquid-line attack by a simple model which is consistent with our observations. We presume that initial anodic action is quite localized, occurring only at a narrow band or line just below the intersection of the meniscus with the specimen surface. Once attack has started, the profile of the corroding surface recedes radially from the initial point of attack as seen in the time progression of Fig. 8-10 and Fig. 3, thus creating the circular attack profile of Fig. 1. Since the total rate of dissolution is determined by the rate of the cathodic reaction, which is constant with time, the depth of attack is described by a simple parabolic expression of the form

$$X^2 = \alpha v n J t \quad [23]$$

where α is a geometric factor, v is the molar volume of the metal ($v_{\text{Ni}} = 6.6 \text{ cm}^3/\text{mol}$), and n is a stoichiometric factor (2 mol Ni/mol O_2). If the rate of cathodic reaction is expressed per length of meniscus/specimen contact, the constant α is given by the ratio of the attack depth squared to the area of the sector representing metal loss in the specimen profile, approximately 0.12 as estimated from Fig. 3-6. Thus

$$J = 0.63 X^2/t \quad \text{mol O}_2 \text{ cm}^{-1} \text{h}^{-1} \quad [24]$$

or for constant J , attack depth is proportional to (exposure time)^{1/2}. This parabolic correlation is shown in Fig. 14 using data from Fig. 8-10 and 3.

Figure 15 is a log-log plot of the average cathodic reaction rate, calculated from average maximum attack depth by means of Eq. [24] vs. cell pressure. The plotted line

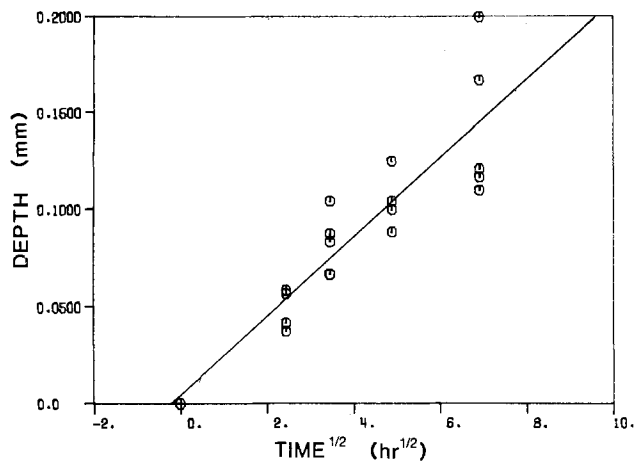


Fig. 14. Plot of attack depth at 667 Pa vs. $t^{1/2}$. Line is least squares fit through all points.

represents a least squares fit of the data for $P \geq 10^4$ Pa to the relation

$$\log J = \log b + m \log P \quad [25]$$

where b and m are constants with the values of 1.047×10^{-2} mol O_2 $cm^{-1}h^{-1}Pa^{-m}$ and -0.925 , respectively. The correlation factor, $R = 0.9992^2$ shows excellent correspondence of the higher pressure data to Eq. [25], which itself is consistent with either Eq. [18] or [22] for constant carbonate activity. Agreement with the latter, however, would require a transfer coefficient of 1.567, while assumption of the former, rate limitation by reduction of peroxide, leads to a transfer coefficient of 0.603, in agreement with Appleby and Nicholson, who noted values "close to 1/2" (20).

The equilibrium constant for reaction [9], assumed to be at equilibrium in the above argument, is 1.41×10^{-6} atm at 1000°C (26). Using the average CO_2 content of air, 0.033% (27), and assuming this to be representative of the cell environment independent of pressure, at a cell pressure of 10^4 Pa the equilibrium value of the ratio $a_{O_2}/a_{CO_3^{2-}}$ is 0.0433; i.e., at this and higher pressures very little dissociation of the carbonate occurs and $a_{CO_3^{2-}}$ is essentially independent of pressure. This is consistent with the simple power relationship between cathodic reaction rate and cell pressure observed in this pressure range. However, at the lowest controlled cell pressure, 667 Pa, the equilibrium value of the ratio $a_{O_2}/a_{CO_3^{2-}}$ is 0.649, indicating considerable decomposition of the melt and suggesting a substantial change in the value of $a_{CO_3^{2-}}$. In order for the cathodic reaction rate determined at this pressure to be consistent with Eq. [18], the value of the carbonate activity would have to be 0.17 (vs. a standard state of pure sodium carbonate), a value not inconsistent with the equilibrium activity ratio. At very low pressures, a simple proportionality between $a_{CO_3^{2-}}$ and pressure (or P_{CO_2}) is expected. For transfer coefficients less than 2, Eq. [18] predicts a cathodic reaction rate approaching zero, in accord with observation.

Conclusions

Liquid-line corrosion of nickel in molten sodium carbonate under reduced air pressures is rate limited by the cathodic reaction. Initial attack occurs just below the line of three-phase contact and appears to be quite localized. Subsequent metal loss occurs at a uniform rate along the surface of the attacked region; the attack profile thus approximates a circular arc whose radius increases with time. Inasmuch as the rate of the cathodic reaction is not affected by the progress of corrosive attack while the area of anodic activity (the attack profile) increases in propor-

$$^2R = \left[1 - \frac{\sum (J_{exp} - J_{calc})^2}{\sum (J_{exp} - \bar{J})^2} \right]^{1/2}$$

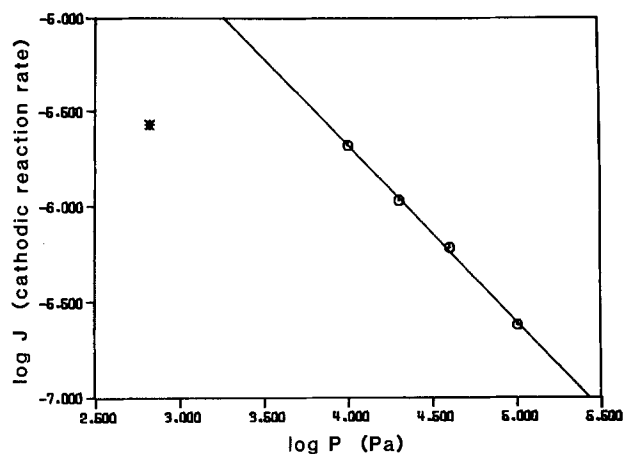


Fig. 15. Plot of cathodic reaction rate, calculated from attack depth, vs. pressure after 48h partial immersion. Points are average values for the several specimens tested at each pressure. Line is least squares fit of Eq. [25] to open points.

tion to attack depth, the attack depth displays a parabolic dependence upon time. Corrosive attack is nil in the absence of oxygen, increases very rapidly to a maximum value at the lowest controlled air pressure studied (667 Pa), and again decreases to approximately nil in atmospheric air. Higher (subatmospheric) pressure data follow a simple power relationship that is consistent with control by the electron-transfer step of peroxide reduction. Deviation from this behavior at low cell pressures is attributed to a decrease in carbonate activity.

Acknowledgment

The authors are pleased to thank the U.S. Department of Energy for its support through Contract no. DE-AC02-76ER02960.

Manuscript submitted July 5, 1983; revised manuscript received July 27, 1984.

The University of Connecticut assisted in meeting the publication costs of this article.

REFERENCES

1. K. Y. Kim and O. F. Devereux, *Corros. Sci.*, **22**, 21 (1982).
2. O. F. Devereux, K. Y. Kim, and K. S. Yeum, *ibid.*, **23**, 205 (1983).
3. U. R. Evans, "Corrosion and Oxidation of Metals," Edward Arnold Publishers, London (1960).
4. L. L. Schreir, "Corrosion," 2nd ed., Vol. 1, Newnes-Butterworths, London (1976).
5. M. Pourbaix, in "Localized Corrosion," R. W. Staehle, et al., Editors, p. 12, NACE, Houston (1974).
6. F. G. Will, *This Journal*, **110**, 145 (1963).
7. F. G. Will, *ibid.*, **110**, 152 (1963).
8. H. J. R. Maget and R. Roethlein, *ibid.*, **112**, 1034 (1965).
9. D. N. Bennion and C. W. Tobias, *ibid.*, **113**, 589 (1966).
10. A. Rahmel, *Corros. Sci.*, **13**, 833 (1973).
11. F. P. Buff, "Structure of Liquids," Vol. X in "Encyclopedia of Physics," S. Flugge, Editor, Springer-Verlag, Berlin (1960).
12. G. J. Janz, "Molten Salts Handbook," Academic Press, New York (1967).
13. D. L. Douglass, *Corros. Sci.*, **8**, 665 (1968).
14. K. Y. Kim, R. D. Smith, and O. F. Devereux, *This Journal*, **123**, 1789 (1976).
15. Y. H. Choo and O. F. Devereux, *ibid.*, **122**, 1645 (1975).
16. W. Philips, *ibid.*, **110**, 1014 (1963).
17. K. Fueki and J. B. Wagner, *ibid.*, **112**, 384 (1965).
18. N. Birks and G. H. Meier, "Introduction to High Temperature Oxidation of Metals," Edward Arnold Publishers, London (1983).
19. A. J. Appleby and S. Nicholson, *J. Electroanal. Chem.*, **38**, 13 (1972).
20. A. J. Appleby and S. Nicholson, *ibid.*, **53**, 105 (1974).
21. B. K. Andersen, *Acta Chem. Scand.*, **A31**, 242 (1977).
22. A. J. Appleby and S. Nicholson, *J. Electroanal. Chem.*, **83**, 309 (1977).
23. R. E. Andresen, *This Journal*, **126**, 328 (1979).

24. E. T. Turkdogan, "Physical Chemistry of High Temperature Technology," Academic Press, New York (1980).
25. K. J. Vetter, "Electrochemical Kinetics," Academic Press, New York (1967).
26. R. A. Cooke and O. F. Devereux, *Corrosion*, **36**, 167 (1980).
27. "Handbook of Chemistry and Physics," 44th ed., R. C. Weast, Editor, Chemical Rubber Publishing Co., Cleveland, OH (1961).

Optimization of Electrolytic Cells

Richard Alkire,* See-Aun Soon,** and Mark Stadtherr

Department of Chemical Engineering, University of Illinois, Urbana, Illinois 61801

ABSTRACT

A methodology was developed for optimizing electrolytic cells described by a potential field distribution along with material, voltage, and economic balance equations. In the present study, the cell consisted of two flow-through porous electrodes separated by a membrane. The model consisted of two nonlinear differential equations, 19 variables, eight equality constraints, and five inequality constraints. The optimum solutions were obtained for simple economic objectives with use of a successive quadratic programming method. The sensitivity of the optimum to operating variables and design constraints was found with the use of Lagrange multipliers. The method may be applied to any electrolytic cell which can be modeled by a combination of differential, algebraic, and polynomial (curve-fit) equations.

A central goal of engineering design practice is to predict the optimal configuration of a system on the basis of economic and scientific principles. Until recently, electrochemical cell and process design have depended largely on intuition, empirical relationships, and rules of thumb based on past experience. As a consequence, large margins of safety were required in design and optimization, especially of new systems.

The modeling of electrochemical systems based on fundamental principles has advanced to a high degree of sophistication in recent years. Rigorous electrochemical models based on current and potential distribution phenomena within the cell have been developed for the more common cell configurations (1). These models pave the way for the use of improved techniques for optimizing electrochemical processes. In the present study, a flexible and robust method is used to optimize an electrolytic cell modeled by a set of differential and nonlinear algebraic equations.

The literature on electrochemical optimization studies has recently been reviewed (2). Published works on optimization have generally used an analytical technique in which a cost equation is differentiated with respect to the variable of interest, the derivative set to zero, and the equation solved to obtain the optimum value. Another commonly reported approach is use of a graphical technique where the trade-off curves were plotted and the optimum determined by inspection.

With the advent of the digital computer, the field of optimization has been completely revolutionized. Within the past two decades, there has been a rapid growth in the literature on optimization. There are available several reviews of nonlinear optimization methods (3), applications (4, 5), as well as algorithms and software (6, 7). Lasdon (6) has identified the four most promising nonlinear optimization algorithms as the augmented lagrangian (AL), successive linear programming (SLP), generalized reduced gradient (GRG), and successive quadratic programming (SQP). Recent comparative studies (8, 9) have found that GRG and SQP seemed to be the most promising of the four methods. Schittkowski (9) ranked SQP methods first in efficiency and reliability, followed closely by GRG methods.

Modern techniques of optimization have not penetrated the electrochemical literature to any significant extent. To date, there have been few efforts directed towards incorporating state-of-the-art optimization techniques as an engineering design tool (10). Alkire *et al.* (10) implemented a state-of-the-art algorithm for the optimization of

an electrolytic cell. They used the GRG method of Lasdon (11) to optimize profit for a chlor-alkali cell based on a model of a diaphragm cell by MacMullin (12). The model consisted of a system of nonlinear algebraic constraint equations which included 42 variables, 37 equality constraints, and two inequality constraints. In addition, sensitivity to certain design and operating variables was also explored. Current and potential distribution phenomena in the cell, however, were not taken into account because the optimization method used in that study did not lend itself efficiently to applications which involve differential equations. This limitation is removed in the present study.

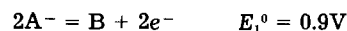
Models of current and potential distribution within cells have increasingly served as guides in the design, scale-up, and optimization of electrochemical cells (13). Models of electrolytic cells generally include both nonlinear algebraic and differential equations. In the present work, a general methodology was developed that incorporate state-of-the-art optimization techniques with a model of the current and potential distribution within an electrolytic cell (14). The goal was to optimize efficiently all cell parameters simultaneously. In this study, a divided cell containing two flow-through porous electrodes was chosen for investigation.

Theoretical

The following text is divided into three subsections that involve developing the porous electrode model, establishing the additional criteria necessary to identify the optimum, and carrying out the optimization.

Formulation of porous electrode model.—An electrolytic cell having two flow-through porous electrodes separated by a membrane and operated under steady, continuous conditions in a flow-by configuration was investigated. Figure 1 illustrates the cell configuration. The model of the reactor is an extension of that of Alkire and Ng (15, 16), and also includes multiple reaction terms following procedures established by Alkire and Gould (17-19). The porous electrodes were of uniform porosity, thickness, and specific surface area throughout, and were assumed to be made up of a packed bed of spheres. Dilute solution theory was used to describe the transport of species in solution. The kinetic behavior of the electrochemical reactions was represented by the Tafel form of the Butler-Volmer equation.

The main reaction at the anode represents a hypothetical oxidation reaction involving a two-electron transfer process



*Electrochemical Society Active Member.

**Electrochemical Society Student Member.

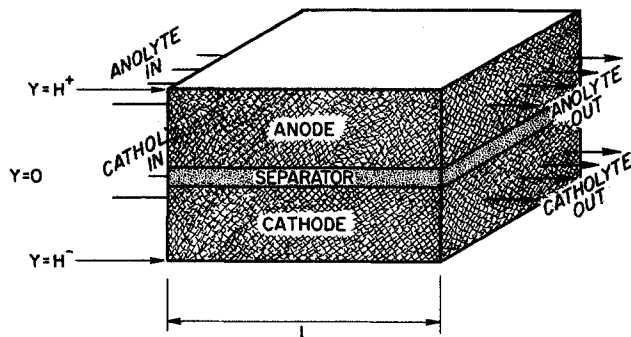
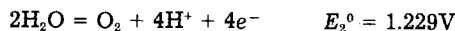


Fig. 1. Schematic diagram of electrolytic cell

The thermodynamic voltage for the above reaction is given by the following equation

$$E_1^+ = E_1^0 + \frac{RT}{n_1 F} \ln \frac{\alpha'_1}{(\alpha_1)^2} \quad [1]$$

The side reaction at the anode is oxygen evolution and is given by



The thermodynamic voltage for this half-cell reaction is given by

$$E_2^+ = E_2^0 + \frac{RT}{n_2 F} \ln \frac{\alpha'_2 (\alpha_{H^+})^4}{(\alpha_2)^2} \quad [2]$$

In this case, the activity of oxygen, α'_2 was taken to be the partial pressure of oxygen and the activity of water; α_2 was taken to be unity.

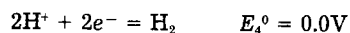
The main reaction at the cathode represents a hypothetical reduction reaction involving a two-electron transfer process



The thermodynamic voltage for the half-cell reaction is given by

$$E_3^- = E_3^0 + \frac{RT}{n_3 F} \ln \frac{(\alpha_3)^2}{\alpha'_3} \quad [3]$$

The side reaction on the cathode is hydrogen evolution and is given by



The thermodynamic voltage for the half-cell reaction above is given by

$$E_4^- = E_4^0 + \frac{RT}{n_4 F} \ln \frac{(\alpha_4)^2}{\alpha'_4} \quad [4]$$

In this case, the activity of hydrogen, α'_4 is the partial pressure of H_2 at the cathode and may be calculated from the total pressure of the system minus the cathode vapor pressure of water.

The equations representing the system were based on several assumptions: (i) the electrode phase was isopotential; (ii) the pores of the electrode were large with respect to the double layer; (iii) convection through the porous electrodes occurred by plug flow with no channeling effects; (iv) transport through axial diffusion and dispersion were negligible compared to axial convection; (v) conduction through bulk electrolyte obeys Ohm's law, and migration effects were negligible due to a large excess of supporting electrolyte; (vi) mass transfer from the bulk stream to the electrode surface may be characterized by an average mass transfer coefficient which was independent of position; (vii) the system was operated isothermally; and (viii) the conversion per pass was low.

The stoichiometry of the reaction to the porous electrode can be defined in the general form

$$\sum_i s_{ij} M_i^{z_i} = n_i e^- \quad [5]$$

The flux of species i due to migration, diffusion, and convection is given by

$$\underline{N}_i = -z_i u_i c_i F \nabla \Phi - D_i \nabla c_i + c_i \underline{v} \quad [6]$$

The current density in the solution is defined by

$$\underline{i} = F \sum_i z_i \underline{N}_i \quad [7]$$

A material balance on species i gives

$$\frac{\partial c_i}{\partial t} = -(\nabla \cdot \underline{N}_i) + R_i \quad [8]$$

The source term, R_i , for each species may be written as

$$R_i = -\sum_j \frac{\alpha_{sj}}{n_j F} f_j^e \quad [9]$$

The solution phase is electrically neutral

$$\sum_i z_i c_i = 0 \quad [10]$$

Combining Eq. [7]-[10] gives the current balance equation

$$\nabla \cdot \underline{i} = -a \sum_j f_j^e \quad [11]$$

The rate expression for the main anodic reaction is

$$f_1^e = i_{01} \frac{c_1^s}{c_1^0} \exp \{ \alpha n_1 F \Phi^+ / RT \} \quad [12]$$

For the side reaction at the anode, the reaction kinetics is given by

$$f_2^e = i_{02} \frac{c_2^s}{c_2^0} \exp \{ \alpha n_2 F (\Phi^+ + \phi_{r1}) / RT \} \quad [13]$$

In the above two equations, Φ^+ is the potential with respect to the thermodynamic rest potential of the main anodic reaction, while ϕ_{r1} is the thermodynamic rest potential of the main anodic reaction with respect to the thermodynamic rest potential of the side reaction at the anode. The reaction kinetics for the main cathodic reaction is given by

$$f_3^e = -i_{03} \frac{c_3^s}{c_3^0} \exp \{ -\beta n_3 F \Phi^- / RT \} \quad [14]$$

For the side reaction at the cathode, the reaction kinetics is given by

$$f_4^e = -i_{04} \frac{c_4^s}{c_4^0} \exp \{ -\beta n_4 F (\Phi^- + \phi_{r2}) / RT \} \quad [15]$$

In the above two equations, Φ^- is the potential with respect to the thermodynamic rest potential of the main cathodic reaction, while ϕ_{r2} is the thermodynamic rest potential of the main cathodic reaction with respect to the thermodynamic rest potential of the side reaction at the cathode.

The local concentration difference between the surface of the electrode and the concentration of the bulk electrolyte is related through the mass-transfer coefficient

$$f_j^e = \frac{n_j F k_{1j}}{s_{ij}} (c_i - c_i^0) \quad [16]$$

In the electrolyte phase, Ohm's law is obeyed

$$\underline{i} = -\kappa \nabla \Phi \quad [17]$$

Combining Eq. [11] and [17], the differential equation for the potential distribution in solution is obtained

$$\nabla^2 \Phi = \frac{a}{\kappa} \sum_j f_j^e \quad [18]$$

From the assumptions of the model, particularly in that it was a differential reactor, the differential equation

is one-dimensional and in Cartesian coordinates is given by

$$\frac{d^2\Phi}{dy^2} = \frac{a}{\kappa} \sum_j f_j^e \quad [19]$$

Equation [19] is applicable to both the anode and the cathode. By combining Eq. [12], [13], and [16], the differential equation for the anode is

$$\frac{d^2\Phi^+}{dy^2} = \frac{a}{\kappa_1} \left[\frac{i_{01} \exp\{\alpha n_1 F \Phi^+ / RT\}}{1 + \frac{i_{01} S_{11}}{n_1 F k_1 C_1^0} \exp\{\alpha n_1 F \Phi^+ / RT\}} + i_{02} \exp\{\alpha n_2 F (\Phi^+ + \phi_{r1}) / RT\} \right] \quad [20]$$

Similarly, combining Eq. [14]-[16] gives the following differential equation for the cathode

$$\frac{d^2\Phi^-}{dy^2} = \frac{a}{\kappa_2} \left[\frac{i_{03} \exp\{-\beta n_3 F \Phi^- / RT\}}{1 + \frac{i_{03} S_{33}}{n_3 F k_3 C_3^0} \exp\{-\beta n_3 F \Phi^- / RT\}} + \frac{i_{04} \exp\{-\beta n_4 F (\Phi^- + \phi_{r2}) / RT\}}{1 + \frac{i_{04} S_{44}}{n_4 F k_4 C_4^0} \exp\{-\beta n_4 F (\Phi^- + \phi_{r2}) / RT\}} \right] \quad [21]$$

The model for the porous electrode was completed by the following boundary conditions. For the anode

$$\text{at } y = O^+, \frac{d\Phi^+}{dy} = -\frac{i}{\kappa_1} \quad [22]$$

$$\text{at } y = H^+, \frac{d\Phi^+}{dy} = 0 \quad [23]$$

For the cathode

$$\text{at } y = O^-, \frac{d\Phi^-}{dy} = \frac{-i}{\kappa_2} \quad [24]$$

$$\text{at } y = H^-, \frac{d\Phi^-}{dy} = 0 \quad [25]$$

Formulation of objective function and constraints.—

The objective function represents the goal of the optimization. For example, return on investment, discounted cash flow rate of return on investment, and profit are frequently used as objective functions. Two objective functions were formulated in this study. The first objective was that of maximizing a profit function consisting of total revenue minus total cost on an annual basis. The profit function was chosen to demonstrate methodology because of its simplicity. More complex economic models may be incorporated, provided that investment cost data are available. The second objective function was that of maximizing current per unit volume. This is equivalent to maximizing the space-time yield. In order to relate these objectives to the behavior of the porous electrode modeled in the previous section, it is necessary to introduce additional equations in the form of material balances, energy balances, mass-transfer correlations, and voltage balances.

The applied current density is

$$i = I/xz \quad [26]$$

A material balance on the anode for species A is

$$C_1^0 Q_1 = C_1 Q_1 + \frac{2IU_1}{n_1 F} \quad (\text{mol/s}) \quad [27]$$

A material balance on the anode for water is

$$\frac{M_1^0}{m_1^0} Q_1 = \frac{M_1}{m_1} Q_1 + \frac{36I(1 - U_1)}{1000n_2 F} \quad (\text{kg/s}) \quad [28]$$

A material balance on the cathode for species C is

$$C_3^0 Q_2 = C_3 Q_2 + \frac{2IU_2}{n_3 F} \quad (\text{mol/s}) \quad [29]$$

A material balance on the cathode for H⁺ is

$$C_4^0 Q_2 = C_4 Q_2 + \frac{2I(1 - U_2)}{n_4 F} \quad (\text{mol/s}) \quad [30]$$

The anode volumetric flow rate is

$$Q_1 = v^+ yz \quad [31]$$

The cathode volumetric flow rate is

$$Q_2 = v^- yz \quad [32]$$

There are also a number of inequality constraints. Anode and cathode conversion are constrained to be less than or equal to 10%, because of the assumption of low conversion per pass. The membrane area is set not to exceed a maximum area of 4500 cm (45 × 100 cm). A cell with a maximum electrode size of 45 × 100 cm allows for maximum membrane interchangeability since availability of ion-exchange materials is a size limiting factor for various applications (20). Upper bounds on the anode and cathode pressure drops are also imposed. The pressure drop is correlated using the Ergun equation (21)

$$\frac{\Delta p}{L} = 4.2 \frac{\mu v a^2}{\epsilon^3} + 0.29 \frac{\rho v^2}{\epsilon^3} \quad (\text{g/cm}^2 \text{s}^2) \quad [33]$$

The vapor pressure of water in solution is calculated with an equation which fits the data (22)

$$\ln p_w = 0.01621 - 0.1380m + 0.1933m^{1/2} + 1.024 \ln p_w^0 \quad [34]$$

The pure vapor pressure may be estimated to within 1% by (22)

$$\ln p_w^0 = 37.04 - 6276/T - 3.416 \ln T \quad [35]$$

Equations [34] and [35] are valid for the temperature range 25°-300°C.

The mass-transfer correlation of Wilson and Geankoplis (23) is used in this study

$$k_i = 1.09 \left(\frac{\rho D_i}{d_p} \right)^{2/3} G^{1/3} \quad [36]$$

The spheres are assumed to be packed in a hexagonal close-packed (hcp) arrangement. For a hcp arrangement, $\epsilon = 0.26$ and the specific surface area is given by

$$a = \frac{6(1 - \epsilon)}{d_p} \quad [37]$$

The activity of species *i* is given by

$$a_i = f_i c_i \quad [38]$$

The activity coefficient, f_i , may be calculated using a Debye-Huckel equation

$$-\log_{10} f_i = 0.5 z_i^2 (\Lambda)^{0.5} \quad [39]$$

where

$$\Lambda = 0.5 \sum_i M_i z_i^2$$

The conductivity of the solution has to be corrected for the porous media. The effective conductivity for the porous media is given by (24)

$$\kappa = \left(\frac{2\epsilon}{3 - \epsilon} \right) \kappa_0 \quad [40]$$

The voltage drop across the membrane is calculated by taking into account the resistivity of the membrane, the conductivities of the anolyte and catholyte, as well as the thickness of the membrane. The voltage balance is given by

$$V = E_1^+ + \Phi^+|_{y=0^+} + V_M - E_3^- - \Phi^-|_{y=0^-} \quad [41]$$

Table I. Description of variables in optimization

Variables	Description
X(1)	Total cell current (A)
X(2)	Applied current density (A/cm ²)
X(3)	Thickness of porous electrode (cm)
X(4)	Length of porous electrode (cm)
X(5)	Width of porous electrode (cm)
X(6)	Anodic volumetric flow rate (cm ³ /s)
X(7)	Anodic superficial velocity (cm/s)
X(8)	Initial concentration of species 1 (mol/cm ³)
X(9)	Final concentration of species 1 (mol/cm ³)
X(10)	Cathodic volumetric flow rate (cm ³ /s)
X(11)	Cathodic superficial velocity (cm/s)
X(12)	Initial concentration of species 3 (mol/cm ³)
X(13)	Final concentration of species 3 (mol/cm ³)
X(14)	Initial concentration of species 4 (mol/cm ³)
X(15)	Final concentration of species 4 (mol/cm ³)
X(16)	Particle diameter (cm)
X(17)	Specific surface area (1/cm)

The final model consisted of two nonlinear differential equations, 19 variables, eight equality constraints, and five inequality constraints. The two differential equations were used to solve for the potential distributions Φ^+ and Φ^- . The remaining 17 variables used in the optimization are presented in Table I. Upper and lower bounds are imposed on all these 17 variables. The number of degrees of freedom was determined by the number of variables minus the number of equality constraints. In this study, the total number of degrees of freedom was nine.

Method of solution.—The nonlinear differential equations were solved with a finite difference numerical technique. The nonlinear differential equations were first linearized about a trial solution, and the equations were then written in finite difference form by employing central difference operators. The resulting tridiagonal matrix was then inverted by a modified Gauss-Jordan elimination method (25) with the use of CDC Cyber 175. Solutions of the equation were obtained when a convergence of 0.01% was achieved by the mesh points during successive iterations.

The optimization problem was solved using a successive quadratic programming method as implemented in the program SQPHP (26, 27). Successive quadratic programming was chosen because of its need for fewer function and gradient evaluations, efficiency, ease of use, and reliability. In general, the optimization problem can be written in the following standard form

Minimize $F(\mathbf{X})$

$$\text{Subject to: } \begin{array}{ll} h_i(\mathbf{X}) = 0 & i = 1, 2, \dots, P \\ h_i(\mathbf{X}) \geq 0 & i = P + 1, \dots, Q \end{array}$$

where \mathbf{X} is a vector of variables, $F(\mathbf{X})$ is a nonlinear objective function, and $h_i(\mathbf{X})$ are nonlinear equality and inequality constraints. This is the standard problem solved by SQPHP. Maximization problems can be easily transformed into standard minimization problems by multiplying by -1 ; hence, there is no loss in generality in considering maximization problems.

In SQPHP, the P equality constraints are used to eliminate some of the variables. This is tantamount to reducing the dimensionality of the problem from N to $N - P$. The code then solves the original problem by solving a sequence of reduced quadratic programming (QP) subproblems.

The code handles bounds on the variables directly in the QP subproblems. There are several options available in the code. There is an option to restrict the initial step size during the initial first three iterations, and there is an option providing for automatic scaling of the objective function as well as for user-selected scaling of the variables.

Reverse communication is used to provide SQPHP with values for $F(\mathbf{X})$, $h_i(\mathbf{X})$, $\partial F/\partial x_i$, and $\partial h_j/\partial x_j$, $i = 1, 2, \dots, Q$; $j = 1, 2, \dots, N$. This means that computer instructions for their calculation must be present in the user's pro-

gram that calls SQPHP initially. When the subroutine requires the values of these terms, it sets the appropriate values of the variables in the vector \mathbf{X} and it returns to the user's program with a flag variable, called INF, which is set to a negative value that indicates whether the evaluation of functions and derivatives is required. The user's program then sets the values of the required terms and, without altering any of the other arguments of SQPHP, calls SQPHP again with INF unchanged. The initial call of SQPHP is indicated by setting $\text{INF} = 0$, and the final return from SQPHP was indicated by $\text{INF} > 0$. Before the initial call, it is necessary to calculate $F(\mathbf{X})$, $h_i(\mathbf{X})$, $\partial F/\partial x_i$, and $\partial h_j/\partial x_j$, $i = 1, 2, \dots, Q$; $j = 1, 2, \dots, N$ for the initial value \mathbf{X} . Figure 2 is the flow diagram illustrating reverse communication.

In the execution of the optimization runs, a large number of different starting points were used, in an attempt to ensure that a global rather than local optimum was found. A total of 68 optimization runs were made for each objective function. The final program required 32.25K words of core on the CDC Cyber 175.

Results and Discussion

The methodology by which the following results were obtained was general enough for it to be applied to any electrolytic cell which can be modeled by a combination of differential and algebraic equations. Hence, the results below are presented to illustrate the types of considerations that can be made with the optimization method presented here. The particular results obtained with the model system were not intended to correspond to a particular application.

A series of case studies was carried out in order to evaluate optimization methodology as well as to explore electrochemical aspects of the problem. The 17 variables in the optimization problem are listed in Table I. Table II summarizes model parameters used, including physical property data, thermodynamic and kinetic rate constants, mass-transfer correlation, as well as economic data. For the case studies here, values of parameters were chosen to be representative of a paired synthesis from aqueous solution of two organic compounds, one valued at about \$4/kg and the other about \$5/kg.

The simple profit objective function took into consideration power costs as well as market prices of feedstocks and products. Table III shows the optimal values together with the initial guesses. These initial guesses represent the starting point in the search for the optimum and they are needed to initialize the program. A total of 68 starting points were tried, and several local maxima were found. The best of these local maxima has a maximum profit of \$63,419.45/yr with a production rate of 10.1 mol/h, and corresponds to the optimal values and starting point given in Table III. Since a large number of different starting points were tried, making it likely that all local maxima were found, one can be reasonably confident, though not absolutely certain, that this is the global maximum.

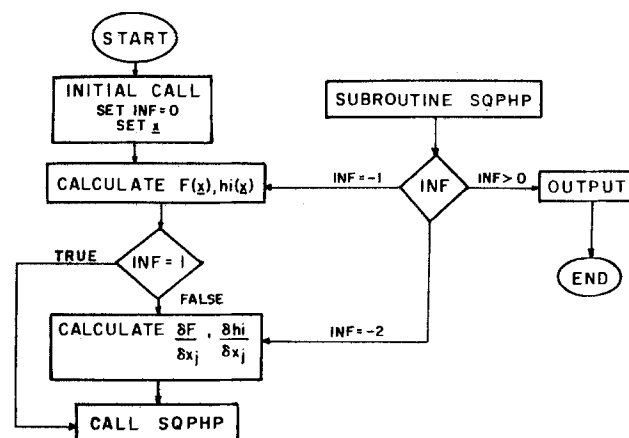


Fig. 2. Flow diagram illustrating reverse communication

Table II. Summary of model parameters

Input data		
	Anolyte	Catholyte
ρ	1.0056 g/cm ³	1.0061 g/cm ³
μ	0.0114 g/cm s	0.01115 g/cm s
κ	0.0515 (Ω -cm) ⁻¹	0.0552 (Ω -cm) ⁻¹
	Anode reaction	Cathode reaction
i_0	2.0×10^{-6} A/cm ²	1.4×10^{-6} A/cm ²
Other parameters		
α	= 0.5	
β	= 0.5	
P_1	= \$0.72	
P_2	= \$0.53	
S_1	= \$5.00	
S_2	= \$3.70	
ϵ_R	= 0.97	
W_1	= 100 g/mol	
W_2	= 78 g/mol	
W_3	= 50 g/mol	
W_4	= 39 g/mol	
Selected upper bounds		
x	≤ 100 cm	
y	≤ 45 cm	
z	≤ 4 cm	
Δp	1×10^6 g/cm s ² (1 atm)	

It is seen from the optimal results in Table III that the dimensions x , y , and z of the porous electrode cell were forced to their upper bounds; this was expected since the objective function did not take into account capital costs. Increasing the dimensions of the cell would mean an increase in production rate and, hence, profit. However, as the dimensions of the cell increase, the capital costs associated with the cell also increase. To account for this trade-off between increasing production rate and capital cost, a capital cost term incorporating the costs of the material and the labor required for the fabrication of the cell needs to be taken into consideration. Provided estimated or actual cost data are available, this can be incorporated into the optimization scheme with modest effort.

The optimum anodic volumetric flow rate Q_1 was found to exist at the upper bound of the range, while the cathodic volumetric flow rate Q_2 was not. It was more profitable to increase the throughput of the anode since the anodic product was more valuable than the cathodic product.

With the simple profit objective function, the effect of an increase in energy costs was examined. Alkire *et al.* (10) had used a different optimization problem to explore how changes in the price of electricity impact on profit and on optimum production rate. As the price increases, the profit and the production rate were found to decline. In the present study, the major impact of increasing energy costs was decreasing profits. In the study of Alkire *et al.* (10), it was found that changes in market prices affect only the optimum value of the objective function and not the optimal operating conditions. The same effect was observed in the present study.

Table III. Optimal solution obtained with simple profit as objective

Variable	Initial guess	Optimal value	Unit
I	1172.5056	543.0	A
i	0.2513	0.12	A/cm ²
x	28.75	100.0	cm
y	1.3125	4.0	cm
z	1.5	45.0	cm
Q_1	1.5125	270.0	cm ³ /s
v^+	0.4375	1.5	cm/s
C_1^0	2.5002×10^{-4}	9.10×10^{-4}	mol/cm ³
C_1^-	2.2502×10^{-4}	9.0×10^{-4}	mol/cm ³
Q_2	1.5125	37.98	cm ³ /s
v^-	0.4375	0.21	cm/s
C_3^0	2.5002×10^{-4}	9.74×10^{-4}	mol/cm ³
C_3^-	2.2502×10^{-4}	9.0×10^{-4}	mol/cm ³
C_4^0	1.0×10^{-10}	2.35×10^{-9}	mol/cm ³
C_4^-	9.0×10^{-11}	2.28×10^{-9}	mol/cm ³
d_p	1.0×10^{-3}	9.05×10^{-3}	cm
α	220	491	cm ⁻¹

Table IV. Optimal solution obtained with current per unit volume as objective

Variable	Initial guess	Optimal value	Unit
I	4.5×10^{-3}	1.13	A
i	1.0×10^{-3}	0.25	A/cm ²
x	3.0	3.0	cm
y	0.25	0.25	cm
z	1.5	1.5	cm
Q_1	1.88×10^{-2}	0.56	cm ³ /s
v^+	5.0×10^{-2}	1.5	cm/s
C_1^0	1.9×10^{-8}	9.10×10^{-4}	mol/cm ³
C_1^-	1.7×10^{-8}	9.0×10^{-4}	mol/cm ³
Q_2	1.88×10^{-2}	5.86×10^{-2}	cm ³ /s
v^-	5.0×10^{-2}	0.16	cm/s
C_3^0	1.9×10^{-8}	1.0×10^{-3}	mol/cm ³
C_3^-	1.7×10^{-8}	9.0×10^{-4}	mol/cm ³
C_4^0	1.0×10^{-10}	9.68×10^{-10}	mol/cm ³
C_4^-	9.0×10^{-11}	9.32×10^{-10}	mol/cm ³
d_p	1.0×10^{-3}	2.0×10^{-2}	cm
α	220	222	cm ⁻¹

To test the consistency of the methodology further, an objective function was chosen which maximized the current per unit volume. Table IV shows the optimal values of the variables together with initial guesses. It was found that the optimum value was 0.5 A/cm³, or 14,000 A/ft³. Again, because a large number of starting points were tried, it is likely that this is the global maximum.

The major differences in the optimal results obtained from the two different objectives as shown in Tables III and IV are in the dimensions of the cell and in the applied current density. In the case of the current per unit volume as objective, the cell dimensions are smaller and the applied current density higher in comparison to the profit as objective case. This is because the energy cost in production is not taken into account in the current per unit volume case.

For the cases investigated, the total CPU time needed to arrive at the optimum depended on the starting point and ranged from 1.7 to 40s on a CDC Cyber 175. Of this, the time spent in the optimization code ranged from 0.5 to 1.5s, the remainder was spent in solving the differential equations. These results suggested that efficient numerical methods for the solution of the differential equations is critically important. These results also suggested that adroit selection of starting point is important, but that the computational costs of the present model are modest in all cases.

The results of the optimization runs may be reformulated into information such as current efficiency, selectivity, space-time yield, and energy consumption. Table V compiles optimal results for the two objectives investigated in this study.

It was found that a temperature rise of about 1.5°C occurred in both cases. Hence, heat transfer was not an important consideration.

The sensitivity of the operating variables was investigated by evaluation of the Lagrange multipliers associated with the optimal solution. The Lagrange multipliers are sensitivity coefficients and are therefore capable of giving an indication of sensitivity. The Lagrangian multipliers are determined as a byproduct of the optimization code. They provide a relative measure of the sensitivity of

Table V. Optimal electrochemical figures of merit

	Objective function	
	Profit	Current per unit volume
Current efficiency of anode	100%	100%
Current efficiency of cathode	100%	100%
Selectivity of anode	100%	100%
Selectivity of cathode	100%	100%
Space-time yield	1,105 mol/liter-h	1,041 mol/liter-h
Energy consumption	126.5 kWh/kmol	197.3 kWh/kmol

Table VI. Lagrange multipliers for select variables with simple profit as objective

Constraints	Lagrangian multipliers	Units	Change	Expected change in optimal objective
Current density	-5.19×10^{-21}	\$/A/cm ²	1.2×10^{-3} A/cm ²	—
Anodic volumetric flow rate	2.35×10^2	\$/cm ³ /s	2.7 cm ³ /s	\$634.20
Initial concentration of anodic reactant	-6.39×10^9	\$/mol/cm ³	9.1×10^{-6} mol/cm ³	-\$58,169.00
Cathodic volumetric flow rate	2.27×10^{-13}	\$/cm ³ /s	0.38 cm ³ /s	—
Initial concentration of cathodic reactant	-2.48×10^7	\$/mol/cm ³	9.7×10^{-6} mol/cm ³	-\$240.16
Specific surface area	-2.01×10^{-15}	\$/cm ⁻¹	4.9 cm ⁻¹	—

Table VII. Lagrange multipliers for select variables current per unit volume as objective

Constraints	Lagrangian multipliers	Units	Change	Expected change in optimal objective
Current density	-1.26×10^{-14}	A/cm ³ /A/cm ²	2.5×10^{-3} A/cm ²	—
Anodic volumetric flow rate	0.89	A/cm ³ /cm ³ /s	5.62×10^{-3} cm ³ /s	0.005
Initial concentration of anodic reactant	-4.82×10^4	A/cm ³ /mol/cm ³	9.1×10^{-6} mol/cm ³	-0.439
Cathodic volumetric flow rate	-2.19×10^{-16}	A/cm ³ /cm ³ /s	5.86×10^{-14} cm ³ /s	—
Initial concentration of cathodic reactant	2.42×10^{-8}	A/cm ³ /mol/cm ³	1.0×10^{-5} mol/cm ³	—
Specific surface area	6.75×10^{-15}	A/cm ³ /cm ⁻¹	2.2 cm ⁻¹	—

the objective function with respect to small changes in the constraints. If the objective function is in terms of dollars of profit, then the Lagrange multiplier λ_i may be interpreted as dollars of profit per unit of the i th constraints.

Tables VI and VII show the Lagrange multipliers for selected variables for the two objectives investigated in this study. The changes were based on a 1% perturbation of the variables at the optimum. The expected changes in optimal value were calculated by multiplying the Lagrange multipliers by the magnitudes of the change. By this method, it is possible to identify the more sensitive features of the cell from among the large list of input parameters and constraints. This capability should be particularly helpful in the early stages of engineering assessment and development. In the cases studied in this investigation, it was found that the sensitive variables were the anodic flow rate and the initial concentration of the anodic reactant, with the latter being the most sensitive.

Conclusions

In this study, a successive quadratic programming technique was used to optimize a model of a porous electrode cell that incorporated current and potential distribution phenomena. The model was prepared for optimization by formulating an objective function as well as a system of equality and inequality constraints that included material balances, charge balances, physical property, and physical limitations.

The model used in this study consisted of two nonlinear differential equations, 19 variables, eight equality constraints, and five inequality constraints. The methodology described here gave the optimal value of all the variables required for optimization of two different objectives: maximum profit based on the prices of chemicals and electrical energy and maximum current per unit volume. Lagrangian multipliers were used to determine the sensitivity of the constraints to the optimal solution.

The model required the use of certain physical property data such as mass-transfer coefficients, density, viscosity, conductivity, vapor pressure, activity, and pressure drop. Membrane transport properties were needed to calculate cell voltage. Physical property data correlations were incorporated wherever possible for determining pressure drop, vapor pressure of water, and correcting

conductivities for the effect of porosity. A lack of availability of such auxiliary data may limit the accuracy of any optimization model.

It is recognized that to optimize a process an entire flowsheet needs to be considered rather than a single cell. It is also recognized that in process optimization the objective function normally consists of maximizing a rate of return on investment or maximizing venture profit. While rate of return is the final criterion in the assessment of a process, it is sometimes convenient, especially in electrochemical processes, to develop a criterion which pertains more closely to the electrolytic process. Hence, for electrolytic processes in the preliminary design stages, high selectivity, space-time yield, chemical yield, or energy yield may be the desired objective. However, in a first-generation study such as this, the simple profit function served adequately to illustrate the usefulness and feasibility of the methodology.

Tremendous advances in the modeling of electrochemical systems have been made in recent years. Rigorous electrochemical models based on current and potential distribution phenomena within the cell have increasingly served as guides in the design, scale-up, and optimization of electrochemical cells. The development of digital computers and numerical methods for optimization, as well as the recent progress in the thermodynamics of electrolyte solutions, has paved the way for the use of improved optimization techniques for electrochemical processes. This study attempted to show how state-of-the-art optimization techniques can be applied to cell models to obtain optimal conditions and to provide an estimate of the sensitivity of operating variables. Optimization methods can assist in implementing wise technological changes in the electrochemical process industry.

Acknowledgments

This work was supported by a grant-in-aid from the Monsanto Company.

Manuscript submitted Aug. 27, 1984; revised manuscript received Jan. 21, 1985.

The University of Illinois assisted in meeting the publication costs of this article.

LIST OF SYMBOLS

- a specific surface area (cm⁻¹)
 a_i activity of species i

c	concentration (mol/cm ³)
D	diffusion coefficient (cm ² /s)
d_p	characteristic particle diameter (cm)
E^0	standard electrode potential (V)
E^+	anode thermodynamic reversible potential (V)
E^-	cathode thermodynamic reversible potential (V)
E_c	energy consumption (kWh/kmol)
e	symbol for electronic charge
F	Faraday's constant (96,487 C/g-eq)
$F(\mathbf{X})$	nonlinear objective function
f^e	intrinsic reaction rate (A/cm ²)
f_i	activity coefficient of species i
G	liquid flow rate (g/cm ² s)
H^+	thickness of anode (cm)
H^-	thickness of cathode (cm)
$h_i(\mathbf{X})$	nonlinear constraints
I	total cell current (A)
i_0	exchange current density (A/cm ²)
i	applied current density (A/cm ²)
k	mass transfer coefficient (cm/s)
L	total electrode length (cm)
M	molarity (mol/liter)
M_i	symbol for species i participating in reaction
m	molality (mol/kg H ₂ O)
N	species flux (mol/cm ² s)
\bar{n}	number of electrons in reaction (g-eq/mol)
N	total number of variables
P	number of equality constraints
Δp	pressure drop (g/cm s ²)
p_w^0	pure vapor pressure of water (atm)
p_w	vapor pressure of water (atm)
Q_1	anode volumetric flow rate (cm ³ /s)
Q_2	cathode volumetric flow rate (cm ³ /s)
Q	total number of constraints
R	molar gas constant (8.3143 J/mol-K)
R_i	reaction source term (mol/cm ³ s)
s_i	stoichiometric coefficient
T	temperature (K)
t	time (s)
U_1	current efficiency of anodic reaction
U_2	current efficiency of cathodic reaction
u	mobility of species (cm ² mol/J s)
V	cell voltage (V)
V_M	membrane voltage drop (V)
\bar{v}	velocity of fluid (cm/s)
\bar{v}^+	anolyte velocity (cm/s)
\bar{v}^-	catholyte velocity (cm/s)
\mathbf{X}	vector of variables
x	length of porous electrode (cm)
y	thickness of porous electrode (cm)
z	width of porous electrode (cm)
z_i	symbol of electronic charge of species i

Greek characters

α	anodic transfer coefficient
β	cathodic transfer coefficient
ϵ	void fraction (cm ³ void space/cm ³ reactor volume)
κ	electrolyte conductivity [(Ω -cm) ⁻¹]
κ_1	anolyte conductivity [(Ω -cm) ⁻¹]
κ_2	catholyte conductivity [(Ω -cm) ⁻¹]
κ_0	specific conductivity [(Ω -cm) ⁻¹]
ρ	density of solution (g/cm ³)
μ	viscosity of solution (g/cm s)
ϕ_r	potential (V)
D	potential (V)
λ	Lagrange multiplier
Λ	ionic strength

Superscripts

o	value at reactor inlet
s	surface value
$'$	products of reaction

Subscripts

i	species i
j	reaction j
r	reference value

REFERENCES

- G. A. Prentice and C. W. Tobias, *This Journal*, **129**, 72 (1982).
- T. R. Beck, in "Techniques of Electrochemistry," Vol. 3, E. Yeager and A. J. Salkind, Editors, p. 1, John Wiley and Sons, New York (1978).
- R. W. H. Sargent, in "Computer Applications to Chemical Engineering," G. V. Reklaitis and R. G. Squires, Editors, p. 37, ACS Symposium Series 124, American Chemical Society, Washington, DC (1980).
- A. W. Westerberg, in "Foundations of Computer-Aided Process Design," R. S. H. Mah and W. D. Seider, Editors, Vol. 1, p. 149, Engineering Foundation, New York (1981).
- L. S. Lasdon, and A. D. Waren, *Oper. Res.*, **28**, 1029 (1980).
- L. S. Lasdon, in "Foundations of Computer-Aided Process Design," R. S. H. Mah and W. D. Seider, Editors, Vol. 1, p. 185, Engineering Foundation, New York (1981).
- A. D. Waren and L. S. Lasdon, *Oper. Res.*, **27**, 431 (1979).
- E. Sandgren and R. M. Ragsdell, *J. Mech. Des.*, **102**, 540 (1980).
- K. Schittkowski, *Lect. Notes Control Info. Sci.*, **30**, 109 (1981).
- R. C. Alkire, G. D. Cera, and M. A. Stadtherr, *This Journal*, **129**, 1225 (1982).
- L. Lasdon, A. D. Waren, A. Jain, and M. Ratner, *ACM Trans. Mathem. Software*, **4**, 34 (1978).
- R. B. Macmullin, *Denki Kagaku*, **38**, 570 (1970).
- R. C. Alkire, in "Tutorial Lectures in Electrochemical Engineering and Technology," AIChE Symposium Series 204, Vol. 77, R. C. Alkire and T. R. Beck, Editors, p. 121, New York (1981).
- S. A. Soon, M. S. Thesis, University of Illinois, Urbana, IL (1983).
- R. C. Alkire and P. K. Ng, *This Journal*, **121**, 96 (1974).
- R. C. Alkire and P. K. Ng, *ibid.*, **124**, 1220 (1977).
- R. C. Alkire and R. M. Gould, *ibid.*, **123**, 1842 (1976).
- R. C. Alkire and R. M. Gould, *ibid.*, **127**, 605 (1980).
- R. M. Gould and R. C. Alkire, *ibid.*, **126**, 2125 (1979).
- K. B. Keating and V. C. Sutlic, in "Electroorganic Synthesis Technology," AIChE Symposium Series 185, Vol. 75, M. Krumpelt, E. Y. Weissman, and R. C. Alkire, Editors, p. 76, New York (1979).
- R. B. Bird, W. E. Stewart, and E. N. Lightfoot, "Transport Phenomena," p. 200, John Wiley and Sons, New York (1960).
- R. L. Leroy, C. T. Bowen, and D. J. Leroy, *This Journal*, **127**, 1954 (1980).
- E. J. Wilson and G. C. Geankoplis, *Ind. Eng. Chem. Fund.*, **5**, 9 (1966).
- G. Neale and W. Nader, *AIChE J.*, **19**, 112 (1973).
- J. S. Newman, "Electrochemical Systems," p. 414, Prentice Hall, Englewood Cliffs, NJ (1973).
- H. S. Chen, PhD. Thesis, University of Illinois, Urbana, IL (1983).
- H. S. Chen and M. A. Stadtherr, *Comput. Chem. Eng.*, To be published.

Voltammetric Studies of Electrodes in Contact with Ionomeric Membranes

James McBreen*

Brookhaven National Laboratory, Department of Applied Science, Upton, New York 11973

ABSTRACT

Cyclic voltammetry studies were carried out on platinum and gold screen electrodes in contact with Nafion ionomeric membranes. In addition, experiments were carried out on multiple combinations of platinum screens with either graphite felt or gold screen electrodes, with only one of the electrodes in direct contact with the membrane. In the case of platinum and gold screens, it was found that the voltammograms were almost identical to that found for the same screens in acidic aqueous electrolytes. When two platinum screens were used, the adsorption charges on the platinum doubled. Obviously, adsorption can occur on sites remote from the membrane/electrode contact, provided the metal is wetted with water. In the case of platinum, a mechanism based on rapid mobility of adsorbed hydrogen and hydroxyl species is proposed. The implications of these findings regarding solid polymer electrolyte electrolyzers and fuel cells are discussed.

In the past 25 years, ionomeric membranes have been used in many electrochemical applications. These include water electrolyzers (1, 2) fuel cells (2-4), electrochemically regenerative energy storage systems (2), and various electrochemical reactors. The latter include brine electrolyzers (2), ozone generators (5), and reactors for organic synthesis (6-8). In the case of water electrolyzers and fuel cells, the electrodes are bonded to the membrane surface. This is accomplished by pressure bonding an electrocatalyst (e.g., Pt or RuO₂) on to the membrane surface (8) or by direct reduction of platinum on to the membrane (9). The structure (10, 11) and transport properties (12, 13) of these membranes have been characterized by most of the sophisticated techniques of materials science. However, there have been very few studies of electrodes in contact with ionomeric membranes.

In fuel cells with ionomeric membranes, it is well known that good performance can be obtained only with prehumidified reactants. This has been attributed to maintenance of water content and conductivity of the membrane (4). In the case of electrolyzers, corrosion problems have been observed on bipolar separator plates in regions that are remote from the membrane electrocatalyst interface. The mechanisms of this are not understood.

Stucki and Menth (14) reported the first cyclic voltammograms for a platinized platinum screen in contact with a Nafion ionomeric membrane. They found that the cyclic voltammograms for the same screens in 1N H₂SO₄ were almost identical. No explanation was given for this. More recently (15), investigations were made on chemically reduced platinum on Nafion membranes. Cyclic voltammograms were found to be the same irrespective of whether the working electrode was exposed to nitrogen or flooded with nitrogen purged 1M HClO₄.

The electrochemical oxidation of hydrogen on platinum in contact with an ion exchange membrane has been investigated (16). However, interpretation of the results is difficult because of residual H₂SO₄ in the membranes and the effects of organic materials from the membrane on hydrogen oxidation (17).

Chernyshov has examined the catalyst/solid polymer electrolyte both experimentally and in terms of porous electrode theory (18). He concluded that increases in electrode activity can be achieved by dispersing a powder of the finely divided ionomeric material in the catalyst (19).

At present, the current-generation mechanism and the factors controlling catalyst utilization at electrodes in contact with ionomeric membranes are poorly understood. This is the subject of the present investigation. Cyclic voltammetry results for platinum and gold screens in contact with Nafion membranes are presented. Initial studies with platinum screens confirmed the results of Stucki and Menth (14). The hydrogen adsorption charge was

identical for a platinum screen pressed against a Nafion membrane and for the same screen in 0.5M trifluoromethanesulfonic acid. Obviously, all of the screen was utilized for hydrogen adsorption even though only approximately one third of the screen was in contact with the membrane. Two hypotheses were advanced to explain this: one was fast mobility of adsorbed hydrogen on the platinum metal surface; the other was an ionic pathway through the water surrounding the Nafion membrane. To test these hypotheses, several experiments were carried out. These included use of multiple platinum screens one on top of the other and the interposition of graphite felt or a gold screen between the platinum and the membrane. It is known that hydrogen neither adsorbs nor is mobile on either of these materials. By means of these tests, it was possible to elucidate the relative contributions of fast surface mobility and ionic pathways in the water.

Experimental

The cell.—The cell used in these investigations is shown schematically in Fig. 1. The cell body was machined from two blocks of PTFE. The overall dimensions of the machined blocks were 6.5 × 6.5 × 2.0 cm. When the cell was assembled, the Nafion membrane and the electrodes were clamped between both PTFE blocks, which were bolted together. Provisions were made for having the electrodes and membrane under a slight compression during a run. A number of holes and grooves were machined in the PTFE to ensure ready access of water to the electrodes and membrane.

The reference electrode.—The reference electrode was a dynamic hydrogen electrode (DHE) and is shown in Fig. 1. The electrode was in a glass tube containing 0.5M trifluoromethanesulfonic acid (TFMSA). The salt bridge consisted of a 1.25 mm Nafion tubing (du Pont no. 815X) inside a PTFE tube. The tubing was wetted with triply distilled water prior to cell assembly. To prevent siphoning of the TFMSA, several knots were tied on the tubing. Electrolytic contact was made by pressing the tubing against the membrane.

Working and counterelectrodes.—The counterelectrode was a circular disk of 52 mesh platinum screen (2.4 cm diam) with a spotwelded platinum lead. The working electrodes were similar circular electrodes with wire leads. The graphite electrode was a 0.25 mm thick graphite felt (Fiber Materials, Incorporated, GH Graphite Felt).

Experimental procedures.—Particular care was given to cleaning the cell, the membrane, and the electrodes.

The cell was cleaned by immersion in concentrated HNO₃ for three days and then washed repeatedly in triply distilled water for an additional three days.

The membranes (du Pont Nafion 125) had a yellowish tinge which has been ascribed to some unknown impurity (20). The membranes were cut to size and boiled for

* Electrochemical Society Active Member.

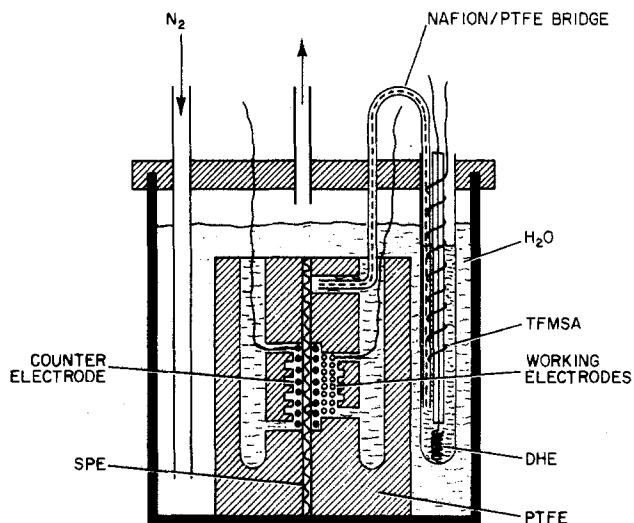


Fig. 1. Schematic of cell for cyclic voltammetry studies. This shows the electrode arrangement when one platinum and two gold electrodes were used as the working electrode.

4h in triply distilled water. The water was changed four times during the boiling operation. After that the membranes were soaked for five days in triply distilled water. The water was changed twice each day. The washed membranes were clear.

The platinum electrodes were cleaned by a method described by Hoare (21). Gold electrodes were cleaned by soaking for three days in concentrated HNO_3 and were then subjected to repeated washings in triply distilled water for three days. The graphite felt was cleaned by repeated washings in triply distilled water.

Prior to a run, the Nafion membrane was placed in 300 ml of triply distilled water in a covered container. Nitrogen was bubbled through the water for 30 min to remove oxygen from the membrane. Meanwhile the beaker cell container (Fig. 1) was filled with triply distilled water, and the water was purged with nitrogen for 30 min. The cell was quickly assembled and transferred to the beaker cell. The cell was immediately evacuated to remove air bubbles, thus ensuring complete flooding of the electrodes with water. The bell jar was backfilled with nitrogen. The cell was then immediately connected to the potentiostat (Stonehart Associates BC 1200), and cyclic voltammetry measurements were started.

Results

Platinum screens on Nafion and in 0.5M TFMSA.—Figure 2 shows cyclic voltammograms for a platinum screen in contact with Nafion and in 0.5M TFMSA. The results are similar to those of Stucki and Mentz, in that the cyclic voltammograms are very similar. One salient aspect of the cyclic voltammograms on platinum in contact with Nafion is the reversibility of the peaks. Peak shifts with sweep rate (10-200 mV/s) were very similar to those reported for platinum in 1M H_2SO_4 (22).

Results with platinum electrodes that were not flooded with water were similar. However, it was necessary to carefully prehumidify the nitrogen gas to get reproducible results. Therefore, in the remainder of the experiments the simple expedient of flooded electrodes was used.

When two screens, one on top of the other, were placed against the Nafion membrane, the amount of charge in the hydrogen and oxide region was doubled (Fig. 3a). Even though only one screen was in direct contact with the Nafion, the surfaces of both screens were utilized for hydrogen and hydroxyl adsorption. Introduction of the second screen did not introduce any irreversibilities in the cyclic voltammogram.

When a graphite felt disk was interposed between the two platinum screens and the membrane, the cyclic voltammogram in Fig. 3b was obtained. This cyclic

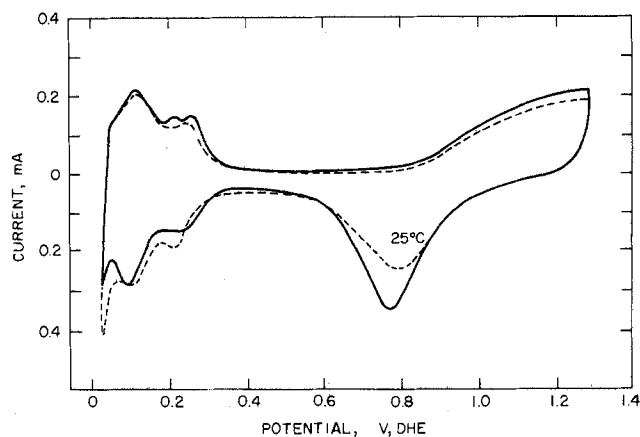


Fig. 2. Cyclic voltammograms for a 2.4 cm diam, 52 mesh platinum screen electrode in contact with Nafion (solid line) and the same electrode in 0.5M TFMSA (broken line). Platinum wire diameter was 0.1 mm; sweep rate was 50 mV/s.

voltammogram differed from that for the graphite felt alone in contact with the membrane (Fig 3c). The results in Fig. 3b would indicate that there is double-layer charging of the platinum as well as some hydrogen adsorption and reduction of platinum oxide. The shape of the cyclic voltammogram is consistent with these processes occurring through a highly resistive electrolyte pathway (23, 24).

A gold screen on Nafion and in 1M H_2SO_4 .—Figure 4 shows cyclic voltammograms for a gold screen in contact with a Nafion membrane and for the same screen in 1M H_2SO_4 . Even though there was some shift in the peaks the cathodic oxide stripping charge was identical for both voltammograms. This indicates that, as with platinum, all of the screen is utilized for oxide formation. In the case of the screen in contact with the Nafion membrane, the

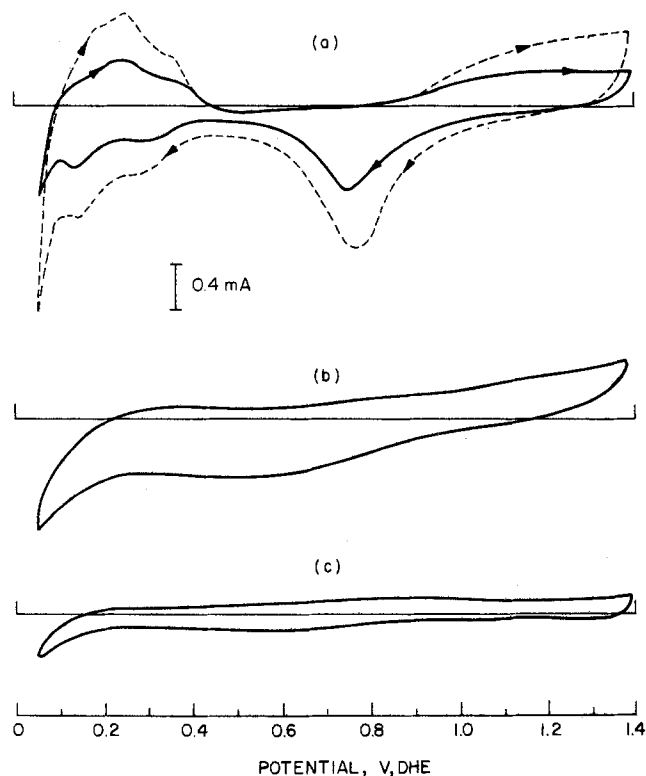


Fig. 3. a: Cyclic voltammograms for one and two 2 cm diam, 100 mesh platinum screen electrodes in contact with Nafion; platinum wire diameter was 0.076 mm. b: The same two screens with a 2.8 cm diam 0.25 mm graphite felt between the two platinum electrodes and the membrane. c: The graphite felt alone with a gold wire contact. Sweep rate was 50 mV/s.

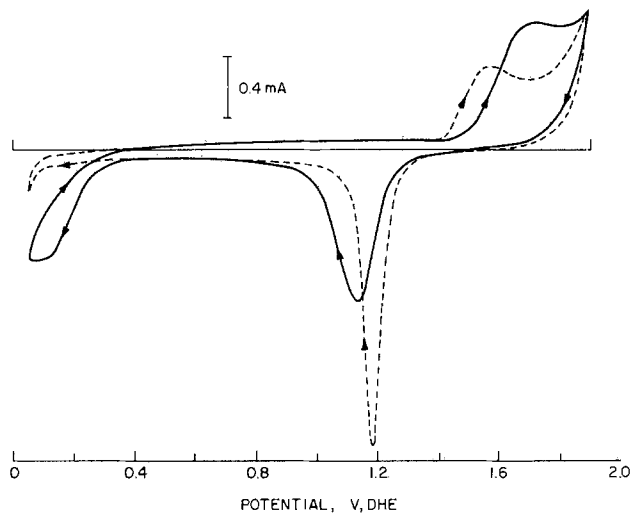


Fig. 4. Cyclic voltammograms for a 2.8 cm diam, 80 mesh gold screen electrode in contact with Nafion (solid line) and the same electrode in 1M H_2SO_4 ; the gold wire diameter was 0.1 mm. The sweep rate was 50 mV/s.

peak shifts with sweep rate (10-200 mV/s) were similar to that observed for gold in 1M $HClO_4$ (25). There was no evidence of hydrogen adsorption.

Combinations of gold and platinum screens on Nafion.—Figure 5 shows cyclic voltammograms for a combination of one gold and two platinum screens, with the gold screen in contact with the Nafion membrane. The reversible reduction peaks for the oxide on gold can be seen at ≈ 1.1 V. The peaks for hydrogen desorption and reduction of platinum oxide are distorted. However, they can be seen more clearly than in the case where graphite felt was interposed between the platinum and the membrane. Once again, processes occurring through a highly resistive electrolyte pathway are indicated. The results were reproducible. After minor changes in the cyclic voltammogram in the first few cycles, the pattern remained stable over a 6h period of cycling between 0.05 and 1.8V.

On increasing the sweep rate from 10 to 100 mV/s, the gold oxide reduction peak shifted from 1.14 to 1.09V. The corresponding potentials for the platinum oxide reduction peak were 0.6 and 0.32V.

Figure 6 shows a cyclic voltammogram for a combination of one platinum and two gold screens with the platinum screen in contact with the Nafion membrane. Also shown is a cyclic voltammogram for the two gold screens alone. All of the oxide reduction, hydrogen adsorption, and hydrogen desorption peaks are at the expected po-

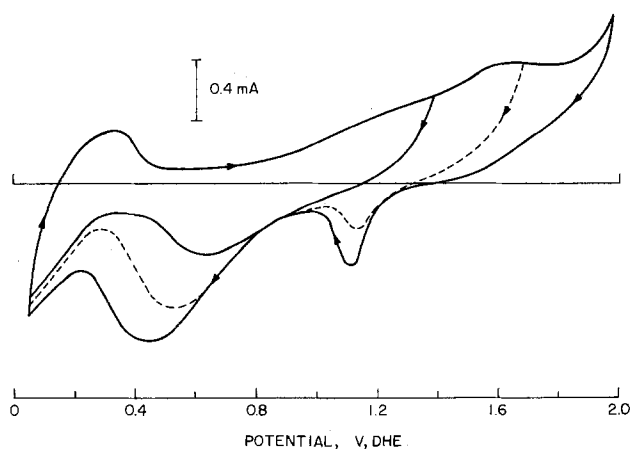


Fig. 5. Cyclic voltammogram for a combination of a 2.8 cm diam, 80 mesh gold electrode and two 2 cm diam, 100 mesh platinum electrodes, with the gold electrode in contact with the membrane; sweep rate was 50 mV/s.

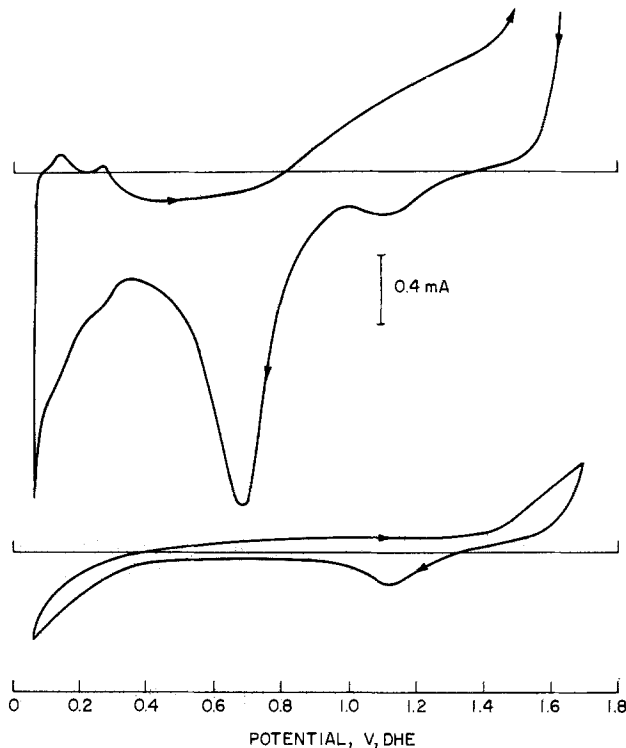


Fig. 6. Cyclic voltammograms for a combination of a 2.8 cm diam, 100 mesh platinum electrode and two 2 cm diam, 80 mesh gold electrodes, with the platinum electrode in contact with the membrane; sweep rate was 50 mV/s. Also shown is a cyclic voltammogram for the two gold screens alone.

tentials. There are no distortions in the cyclic voltammograms, other than those that can be ascribed to reduction of oxygen that is dissolved in the membrane. This shifts the current in a negative direction at potentials less than 0.9V.

Discussion

General features of the cyclic voltammograms.—The results in Fig. 2-4 indicate that the cyclic voltammograms on either platinum or gold screens in contact with Nafion are very similar to those found for the same screen in aqueous acid electrolyte. Slight negative shifts in the current in the hydrogen region can be ascribed to reduction of dissolved oxygen in the membrane. Differences in the oxide region can be explained in terms of anion adsorption (26). The doubling of the adsorption charges when a second screen is introduced (Fig. 3a) confirms the fact that parts of the electrode that are remote from the membrane surface are electrochemically active. The results indicate that, provided the nitrogen gas humidity is sufficiently high, flooding of the electrode with water is not necessary to achieve complete utilization of the electrode surface.

If either graphite felt (Fig 3b) or a gold screen (Fig. 5) is interposed between the platinum electrode and the membrane, there is considerable distortion of the platinum oxide reduction peaks and the peaks for hydrogen adsorption and desorption. The results are consistent with the effects of a resistive electrolyte path. However, interposition of a platinum screen between the gold electrodes and the membrane does not affect the oxidation or reduction behavior at the gold electrodes.

Mechanism of current generation.—Three possible mechanisms for current generation at sites remote from the membrane surface are (i) fast surface mobility of adsorbed species on the electrodes, (ii) conduction through the water because of dissolved Nafion fragments, or (iii) surface conductance effects.

If material leached from the Nafion into the water, one would expect a decrease in the water pH with time. No such pH change was observed. The stability of the cyclic

voltammogram in Fig. 5 over a 6h period would tend to exclude this mechanism.

The most likely mechanism for the highly reversible behavior with platinum and gold screens is rapid surface mobility of adsorbed hydrogen and hydroxyl species. Adsorbed hydrogen on platinum is undoubtedly a very mobile species (27), and recent studies show that adsorbed hydroxyl species on platinum are reactive, even at very low temperatures (28). This would imply a rapid surface mobility, so the mechanism appears reasonable.

Hydrogen does not adsorb on gold or graphite. This would explain the absence of reversible behavior in the hydrogen region (Fig. 3b and 5). Reduction of platinum oxides occurs in a potential region where oxide species are not adsorbed on gold or graphite. This would account for the irreversible behavior found for oxide reduction (Fig. 5). However, in the case where the platinum is interposed between the gold and the membrane, gold oxide formation and reduction occurs in a potential domain where hydroxyl groups are adsorbed on the platinum. Rapid migration of these on platinum yield the reversible behavior for reduction of the gold oxide species (Fig. 6).

Surface conductance effects are the most plausible explanation for the resistive conductance path which yields the irreversible behavior in the cyclic voltammograms in Fig. 3b and 5. It is well known that, when glass is immersed in water, ionization of the silicate groups will alter the water conductivity at the glass surface (29). Similar effects will occur when Nafion is immersed in water. These surface protons can provide a conductive pathway along the surface of the gold or graphite and transmit current to the platinum. In the hydrogen region, the gold will be negatively charged and the protons at the membrane surface can rearrange themselves over the gold surface to provide a conductive pathway. At more positive potentials, conduction can occur via adsorbed water and a Grotthus mechanism. A mechanism such as this would explain the reproducibility of the effects and the invariance of the cyclic voltammograms in Fig. 5 over several hours.

Implications regarding electrolyzers and fuel cells.—Solid polymer electrolyte electrolyzers use platinum black hydrogen electrodes and noble metal oxides (e.g., IrRuO₂) as oxygen electrodes (30, 31). The adsorbed intermediates for both reactions are mobile on their respective electrocatalysts. Therefore, a high degree of electrocatalyst utilization is expected.

In a solid polymer electrolyte electrolyzer, the oxygen electrocatalyst is in contact with an anode support such as porous titanium foil. This, in turn, contacts the bipolar current collector which is usually made from a carbon-plastic composite (1). Because of corrosion problems, it has been necessary to coat this with a thin foil of titanium or platinum. Carbon oxidation can occur either via fast hydroxyl mobility on the porous titanium surface or via the surface conductance mechanism.

Solid polymer electrolyte fuel cells use platinum black as the electrocatalyst for both electrodes. Hydrogen can dissociate anywhere on the platinum and migrate to the membrane. Catalyst utilization is expected, therefore, to be high. In the presence of water, oxygen can interact with platinum to form adsorbed hydroxyl species (28). Fast mobility of the latter would yield high electrocatalyst utilization. A carbon-supported platinum catalyst would preclude such mobilities and would result in a low electrocatalyst utilization. Only the resistive surface conductance pathway would be available. There are no reports of the use of carbon-supported platinum electrocatalysts in solid polymer electrolyte fuel cells. Supported catalysts would require pathways for ionic conduction in the electrode structure (8, 18, 19) or catalyst supports that would permit surface mobility of adsorbed hydrogen or hydroxyl intermediates.

Conclusions

Cyclic voltammograms on platinum and gold screen electrodes pressed against Nafion membranes are almost

identical for those obtained for the same screens in aqueous acid electrolytes. This indicates that the various electrochemical adsorption and desorption processes can occur on parts of the screen that are not in direct contact with the membrane. A set of critical experiments was devised which indicated that two pathways can exist for the occurrence of electrochemical adsorption reactions on parts of the metal not in contact with the membrane. One is a fast process involving fast mobility hydrogen or hydroxyl species on the metal; the other is a resistive pathway involving surface conductance effects. This has important implications regarding the performance of electrochemical devices with Nafion membranes.

Acknowledgment

This research was performed under the auspices of the U.S. Department of Energy under Contract no. DE-AC02-76CH00016.

Manuscript submitted July 10, 1984; revised manuscript received Dec. 14, 1984. Part of this article was presented as Paper 131 at the Washington, DC, Meeting of the Society, Oct. 9-14, 1983.

Brookhaven National Laboratory assisted in meeting the publication costs of this article.

REFERENCES

- P. W. T. Lu and S. Srinivasan, *J. Appl. Electrochem.*, **9**, 269 (1979).
- T. G. Coker, A. B. LaConti, and L. J. Nuttall, "Membranes and Ionic and Electronic Conducting Polymers," E. B. Yeager, B. Schumm, K. Mauritz, K. Abbey, D. Blankenship, and J. Akridge, Editors, pp. 191-213, Electrochemical Society Softbound Proceedings Series, Pennington, NJ (1983).
- W. T. Grubb and L. W. Niedrach, *This Journal*, **107**, 131 (1960).
- H. A. Liebhafsky and E. J. Cairns, "Fuel Cells and Fuel Batteries," pp. 587-619, John Wiley & Sons, Inc. New York (1968).
- S. Stucki and G. Thies, Abstract 573, p. 866, The Electrochemical Society Extended Abstracts, Vol. 83-1, San Francisco, CA, May 8-13, 1983.
- J. Sarrazin and A. Tallec, *J. Electroanal. Chem.*, **137**, 183 (1982).
- Z. Ogumi, K. Nishio, and S. Yoshizawa, *Electrochim. Acta*, **26**, 1779 (1981).
- V. A. Grinberg, V. N. Zuravleva, Yu. B. Vasil'ev, and V. E. Kazarinov, *Elektrokhimiya*, **19**, 1447 (1983).
- H. Takenaka and E. Torikai, *Kokai Tokyo Koho*, **55**, 38934 (1980).
- R. S. Yeo and A. Eisenberg, *J. Appl. Polym. Sci.*, **21**, 875 (1977).
- M. Pineri, E. Roche, B. Rodmacq, and F. Volino, in "Ion Exchange: Transport and Interfacial Properties," R. S. Yeo and R. P. Buck, Editors, pp. 210-222, The Electrochemical Society Softbound Proceedings Series, Pennington, NJ (1981).
- R. S. Yeo and J. McBreen, *This Journal*, **126**, 1682 (1979).
- Z. Ogumi, Z. Takehara, and S. Yoshizawa, *ibid.*, **131**, 769 (1984).
- S. Stucki and A. Mentz, in "Industrial Water Electrolysis," S. Srinivasan, F. J. Salzano, and A. R. Landgrebe, Editors, pp. 180-185, The Electrochemical Society Softbound Proceedings Series, Pennington, NJ (1978).
- A. Katayama-Aramata, H. Nakajima, K. Fujikawa, and H. Kita, *Electrochim. Acta*, **28**, 777 (1983).
- A. B. Khanin, N. A. Aladzhalova, and N. A. Fedotov, *Elektrokhimiya*, **3**, 59 (1967).
- A. B. Khanin, N. A. Aladzhalova, and N. A. Fedotov, *ibid.*, **4**, 107 (1968).
- S. F. Chernyshov, *J. Res. Inst. Catal. Hokkaido Univ.*, **30**, 179 (1982).
- V. S. Bagotsky, A. G. Pschenichnikov, and S. F. Chernyshov, *Inventions of USSR No. 2959729/2G* (1981).
- C. R. Martin, T. A. Rhoades, and J. A. Ferguson, *Anal. Chem.*, **54**, 1639 (1982).
- J. P. Hoare, *Electrochim. Acta*, **27**, 1751 (1982).
- H. Angerstein-Kozłowska, B. E. Conway, and W. B. A. Sharp, *J. Electroanal. Chem.*, **43**, 9 (1973).
- R. S. Nicholson, *Anal. Chem.*, **37**, 667 (1965).
- W. T. deVries and E. van Dalen, *J. Electroanal. Chem.*, **10**, 183 (1965).
- D. Dickertman, J. W. Schultze, and K. J. Vetter, *ibid.*, **55**, 429 (1974).

26. H. Angerstein-Kozłowska, B. E. Conway, B. Barnett, and J. Mozota, *ibid.*, **100**, 417 (1979).
 27. R. Lewis and R. Gomer, *Surf. Sci.*, **17**, 333 (1969).
 28. G. B. Fischer and B. A. Sexton, *Phys. Rev. Lett.*, **44**, 683 (1980).
 29. J. F. Davies and E. K. Rideal, "Interfacial Phenomena," pp. 108-114, Academic Press, New York (1963).
 30. J. L. Weininger and R. R. Russell, *This Journal*, **125**, 1482 (1978).
 31. R. S. Yeo, J. Orehotzky, W. Visscher, and S. Srinivasan, *ibid.*, **128**, 1900 (1981).

Open-Circuit Photopotentials and Photoelectrochemical Behavior of the Si-Doped α -Fe₂O₃ Semiconductor Electrode in Acetonitrile Solutions

Saeed Sahami and John H. Kennedy*

Department of Chemistry, University of California, Santa Barbara, California 93106

ABSTRACT

The photoelectrochemical behavior of Si-doped sintered polycrystalline α -Fe₂O₃ was investigated in acetonitrile solutions containing the redox couples ferrocene, Cl⁻, Br⁻, I⁻, Ru(bpy)₃²⁺, Fe(bpy)₃²⁺, and Fe(phen)₃²⁺. There was no oxidation in the dark at the iron oxide electrode for these couples, but they all showed photo-oxidation at potentials negative of their oxidation potential at Pt. Cathodic back reactions of all couples, except halides, were observed. This indicates that surface states capable of mediating electron transfer from the conduction band to the oxidized forms of the couples exist in the bandgap region of the iron oxide. In addition, open-circuit photovoltages were found to increase with increasing redox potentials of these couples. An open-circuit photopotential as high as 0.8V was obtained for Ru(bpy)₃^{2+/1+}.

Iron oxide (α -Fe₂O₃) has been widely investigated as a semiconductor electrode material for photoassisted electrolysis of water. This is due to the following facts: (i) it has high stability, (ii) it is inexpensive and electrode fabrication is easy, and (iii) it has a relatively small bandgap of 2.2 eV. Although photochemistry of variously prepared iron oxide electrodes has received considerable attention in aqueous media (1-26), little work has been performed in nonaqueous solvents (27-29). Fredlein and Bard have reported the behavior of iron oxide electrodes in acetonitrile (27) using Pb-doped single-crystal, Ti-doped sintered polycrystal, and chemical vapor deposited films of Fe₂O₃.

Since it has been shown by Kennedy and co-workers (13) that silicon is a better dopant for α -Fe₂O₃ than titanium (*i.e.*, higher photocurrents were observed for Si-doped α -Fe₂O₃ at less positive potentials), we decided to examine the behavior of Si-doped iron oxide in acetonitrile. In the present work, we report the properties of Si-doped α -Fe₂O₃ in acetonitrile solutions containing various redox couples, including polypyridine complexes and halides. In addition, open-circuit photovoltage measurements helped to understand the energetics of the α -Fe₂O₃/liquid junction interface.

Experimental

Preparation of sintered polycrystalline α -Fe₂O₃ electrodes doped with 1 atomic percent (a/o) SiC (n-type Fe₂O₃) have been previously described (22, 25). The electrodes were about 0.37 cm² area and 0.1 cm thick. Electrical contact to the α -Fe₂O₃ was made by sputtering gold film on one side. A Cu wire was attached to the sputtered gold using silver epoxy (Epoxy Technology Incorporated). The electrode and Cu wire were sealed in a glass tube with ordinary epoxy, leaving only one face of the α -Fe₂O₃ exposed. The resistances of the electrodes measured at 1 kHz in aqueous solution were 60-350 Ω .

A three-compartment electrochemical cell with α -Fe₂O₃ photoanode, a coiled Pt wire counterelectrode, and a silver quasi-reference electrode was used. The reference and counterelectrode compartments were separated from the main compartment by medium porosity fritted-glass disks. The main compartment (containing the working electrode) had an optically flat quartz window. The potential of silver electrode was determined during each ex-

periment from cyclic voltammograms of each couple at the Pt measured with respect to both silver and aqueous saturated calomel electrode (SCE). All potentials are reported *vs.* SCE. The cell was kept under a N₂ gas blanket which was passed through acetonitrile. All measurements were carried out at ambient temperature.

Cyclic voltammograms and photocurrent-voltage curves were obtained using an EG&G PAR 174A, and a Houston Omnigraphic Model 2000 X-Y recorder. Open-circuit photovoltages were measured with a multimeter (Keithley Model 179).

The light source was an Oriel 150W Xe lamp. The light path included a shutter (1 in.), an infrared filter, and a quartz lens. The light intensity was measured with an EG&G Model 450-1 radiometer/photometer and light absorbing neutral density filters. Light intensity at the electrode surface was \sim 450 mW/cm². Screen-type neutral density filters were used to reduce the light intensity when desired.

Spectroscopic-grade acetonitrile (Mallinckrodt) was used without further purification. Tetra-n-butylammonium perchlorate (TBAP) purchased from Alfa was dried in a vacuum oven at 80°C and used as the supporting electrolyte. Fe(bpy)₃(ClO₄)₂, Fe(phen)₃(ClO₄)₂, and Ru(bpy)₃Cl₂·6H₂O (where bpy = 2,2'-bipyridine and phen = 1,10-phenanthroline) were obtained from G. F. Smith Chemical Company. To eliminate the interference of chloride electrochemical oxidation (at both Pt and illuminated α -Fe₂O₃ in acetonitrile), Ru(bpy)₃(ClO₄)₂ was prepared from its chloride salt, using a previously published method (30). Ferrocene and anhydrous salts of LiCl, LiBr, and LiI were purchased from Alfa. The halide salts were dried in a vacuum oven prior to their use. For photovoltage measurements, the oxidized form of each couple was generated in solution by means of either constant potential or constant current coulometry.

Results and Discussion

Open-circuit photopotential measurements.—In order to determine the effect of the redox potential and chemical nature of the individual redox system on the energetic situation at the α -Fe₂O₃/electrolyte interface, the photovoltages of several redox couples dissolved in acetonitrile were measured. The ideal semiconductor/liquid junction model (31) predicts that the bandedges, E_{cb} and E_{vb} , are

*Electrochemical Society Active Member.

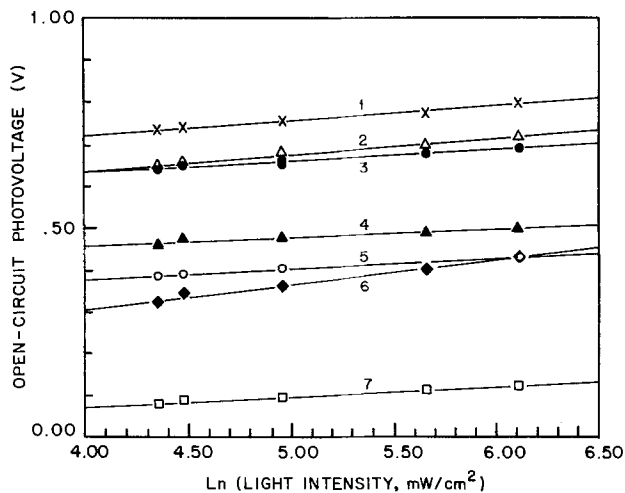


Fig. 1. Open-circuit photovoltage as a function of light intensity for various redox couples in 0.1M TBAP/acetonitrile solutions. 1: Ru(bpy)₃^{3+/2+}. 2: Fe(bpy)₃^{3+/2+}. 3: Cl₃⁻/Cl⁻. 4: Br₃⁻/Br⁻. 5: I₃⁻/I⁻. 6: Fe(phen)₃^{3+/2+}. 7: Ferricinium/ferrocene.

fixed and the amount of band bending depends on the redox potential of the couple. According to the model, the maximum open-circuit photovoltage, E_{oc} (max) for an n-type semiconductor is given by

$$E_{oc}(\text{max}) = E_{\text{redox}} - E_{\text{FB}}$$

where E_{FB} and E_{redox} are the flatband potential of the semiconductor and redox potential of the couple in the solution, respectively. Thus, in the absence of changes in the double layer or surface reaction, the photovoltage should increase proportionally with E_{redox} (32).

Plots of the open-circuit photovoltages of various redox couples in 0.1M TBAP in acetonitrile as a function of logarithm of light intensity are shown in Fig. 1. The slopes of the lines are in the range of 24–27 mV, except for polypyridine couples, where larger slopes were observed. The slopes for Ru(bpy)₃^{3+/2+}, Fe(bpy)₃^{3+/2+}, and Fe(phen)₃^{3+/2+} are 36, 38, and 58 mV, respectively. According to a simplistic model at 25°C a slope of 25.7 mV (*i.e.*, kT/e) is expected (31, 33). Although slopes close to this value have been observed in several previous cases (21, 33), larger slopes have also been reported (31, 33). Slopes greater than kT/e have been attributed to a nonequilibrium distribution of electrons and holes in the space-charge layer of the semiconductor electrode (31, 33).

In Fig. 2, the dependence of the photovoltages on redox potentials is represented. Values of E_{oc} are obtained at α -Fe₂O₃ electrodes using the highest light intensity available (~450 mW/cm²). Values of E_{redox} are the average of the cathodic and anodic peak potentials obtained from cyclic voltammograms at a Pt electrode. Tabulations of E_{oc} , E_{redox} , and anodic peak potentials at both Pt and illuminated α -Fe₂O₃ are presented in Table I. As can be seen from Fig. 2, the open-circuit photopotential generally rises with increasing E_{redox} . Although variation of E_{oc} for the polypyridine couples is less pronounced, it is obvious that the Fermi level pinning model (that predicts an E_{redox} independent photovoltage) is not entirely applicable to this system. However the behavior is far from the ideal expectation where a straight line with slope of 1 is anticipated. In addition to some Fermi level pinning, the negative deviation from the straight line for polypyridine complexes might also be due to their high molar absorptivity. High absorptivity (in addition to h^+e^- recombination processes) limits the light absorption by α -Fe₂O₃ which in turn prevents achieving the highest possible E_{oc} . The positive deviation of I₃⁻/I⁻ from the theoretical line may be partly due to its more negative E_{FB} , as discussed later.

It has been suggested by Wrighton and co-workers (34, 35) that the extent to which the photoanodic peak (at n-type semiconductors) is more negative than the anodic peak at Pt is a measure of the E_{oc} for fast redox couples.

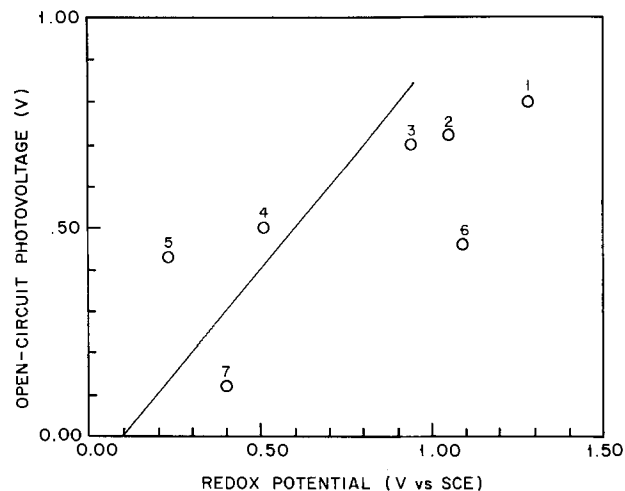


Fig. 2. Open-circuit photovoltage vs. the redox potential in 0.1M TBAP/acetonitrile. 1: Ru(bpy)₃^{3+/2+}. 2: Fe(bpy)₃^{3+/2+}. 3: Cl₃⁻/Cl⁻. 4: Br₃⁻/Br⁻. 5: I₃⁻/I⁻. 6: Fe(phen)₃^{3+/2+}. 7: Ferricinium/ferrocene. Solid line is a theoretical line of slope one, starting from the flatband potential.

Comparison of the values of E_{oc} and ΔE_{pa} in Table I indicates that there is a relatively good agreement between these values for electrochemically reversible couples such as Ru(bpy)₃^{3+/2+}, Fe(bpy)₃^{3+/2+}, and ferricinium/ferrocene. The behavior of Fe(phen)₃^{3+/2+} is an exception. Although the redox potential of Fe(phen)₃^{3+/2+} is very similar to its analog bipyridine complex, its E_{oc} is smaller than that of Fe(bpy)₃^{3+/2+}. This indicates that surface energetics are sensitive not only to the E_{redox} but also to the chemical nature and electrochemical kinetics of the couple.

Voltammetric measurements.—In Fig. 3, current-potential scans for 0.1M TBAP in acetonitrile at α -Fe₂O₃ both in the dark and under illuminated polychromatic light are shown. The anodic currents in Fig. 3 are due to the oxidation and photo-oxidation of the supporting electrolyte (*i.e.*, ClO₄⁻) (27). The cathodic currents correspond to the reduction of iron oxide.

Flatband potentials were measured in separate acetonitrile solutions containing different couples, using the previously described transient photocurrent technique (25). E_{FB} in I⁻ solutions was found to be somewhat more negative (~0.1V) than those measured in other solutions. In general, though, E_{FB} for all acetonitrile solutions was 0.1 ± 0.1V vs. SCE. Knowing E_{FB} and E_{bg} , one can locate the valence and conduction bandedges, E_{vb} and E_{cb} , respectively, by recognizing that for a highly doped n-type semiconductor, E_{FB} is within 0.1V of E_{cb} . This means that for couples with E_{redox} between ~0.1 and 2.2V vs. SCE, Si-

Table I. Open-circuit photopotentials and cyclic voltammetric parameters for various redox couples at Pt and illuminated α -Fe₂O₃ in 0.1M TBAP/acetonitrile

Redox couple	E_{oc}^a	E_{redox}^b	$E_{\text{pa}}^{\text{Pt}c}$	$E_{\text{pa}}^{\alpha\text{-Fe}_2\text{O}_3d}$	ΔE_{pa}^e
Ru(bpy) ₃ ^{3+/2+}	0.80	1.28	1.31	0.59	0.72
Fe(bpy) ₃ ^{3+/2+}	0.72	1.05	1.10	0.43	0.67
Fe(phen) ₃ ^{3+/2+}	0.46	1.09	1.14	0.92	0.22
Ferricinium/ferrocene	0.12	0.4	0.45	0.33	0.12
I ₃ ⁻ /I ⁻	0.43	0.23	0.30	0.49	-0.19
Br ₃ ⁻ /Br ⁻	0.50	0.51	0.69	0.54	0.15
Cl ₃ ⁻ /Cl ⁻	0.70	0.94	1.06	0.93	0.13

^a E_{oc} is the difference between the open-circuit potential of Pt vs. SCE and the open-circuit photopotential of α -Fe₂O₃ vs. SCE.

^b E_{redox} is the average of the cathodic and anodic peak potentials measured at a Pt electrode vs. SCE.

^c $E_{\text{pa}}^{\text{Pt}}$ is the anodic peak potential measured at Pt vs. SCE, with scan rate of 200 mV/s.

^d $E_{\text{pa}}^{\alpha\text{-Fe}_2\text{O}_3}$ is the anodic peak potential measured at an illuminated α -Fe₂O₃ electrode vs. SCE with scan rate of 200 mV/s.

^e ΔE_{pa} is the difference between $E_{\text{pa}}^{\text{Pt}}$ and $E_{\text{pa}}^{\alpha\text{-Fe}_2\text{O}_3}$.

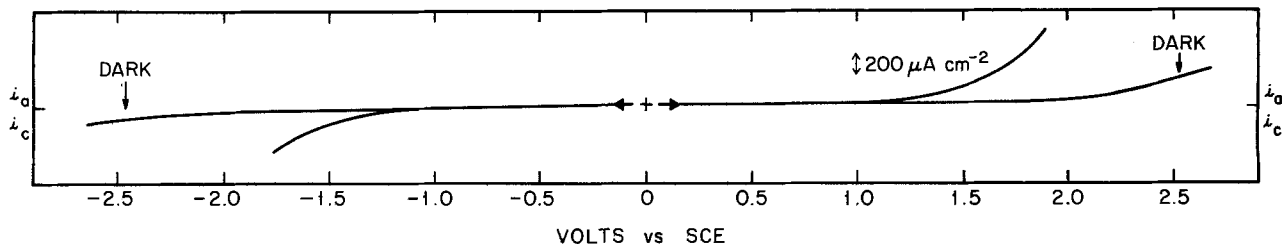


Fig. 3. Linear scan voltammograms for Si-doped $\alpha\text{-Fe}_2\text{O}_3$ in 0.1M TBAP/acetonitrile in the dark and under illumination. Scan rate = 20 mV/s.

doped $\alpha\text{-Fe}_2\text{O}_3$ should be blocked to oxidation in the dark. However, upon illumination with light of energy ≥ 2.2 eV, their photo-oxidation should take place.

Linear and cyclic voltammograms at both dark and illuminated $\alpha\text{-Fe}_2\text{O}_3$ were obtained for a number of compounds that exhibit reversible or quasireversible behavior at Pt. Some of these voltammograms are shown in Fig. 4-8. All the redox couples studied have E_{redox} situated in the bandgap of iron oxide. As expected, there was no oxidation peak for the experiments performed in the dark while under illumination; photo-oxidations of all reduced forms of the redox couples began at potentials negative of their oxidation potentials at Pt.

Polypyridine complexes and ferrocene.—In Fig. 4-6, cyclic voltammograms of $\text{Ru}(\text{bpy})_3^{2+}$, $\text{Fe}(\text{phen})_3^{2+}$, and ferrocene at Pt and n-type $\alpha\text{-Fe}_2\text{O}_3$ are shown. In addition, their

linear sweep voltammograms with chopped illumination are presented. The polypyridine complexes studied all have high molar absorptivity in the visible region. Due to this absorbance, only low concentrations ($\sim 0.5\text{-}1$ mM) of the complexes were used. The photoanodic currents were all diffusion controlled. Cyclic voltammetric results at illuminated iron oxide and Pt for polypyridine complexes and ferrocene in 0.1M TBAP/acetonitrile are given in Table I. As was mentioned before, the photo-oxidations of all these couples occur at potentials negative of their reversible potentials. The magnitude of this negative shift increased as the standard potential of the redox couple increased.

Chopped illumination of all couples showed anodic current spikes decaying with time. During the dark period, cathodic spikes in the potential ranges of 0.5-0.9V for polypyridines and 0.2-0.3V for ferrocene were observed.

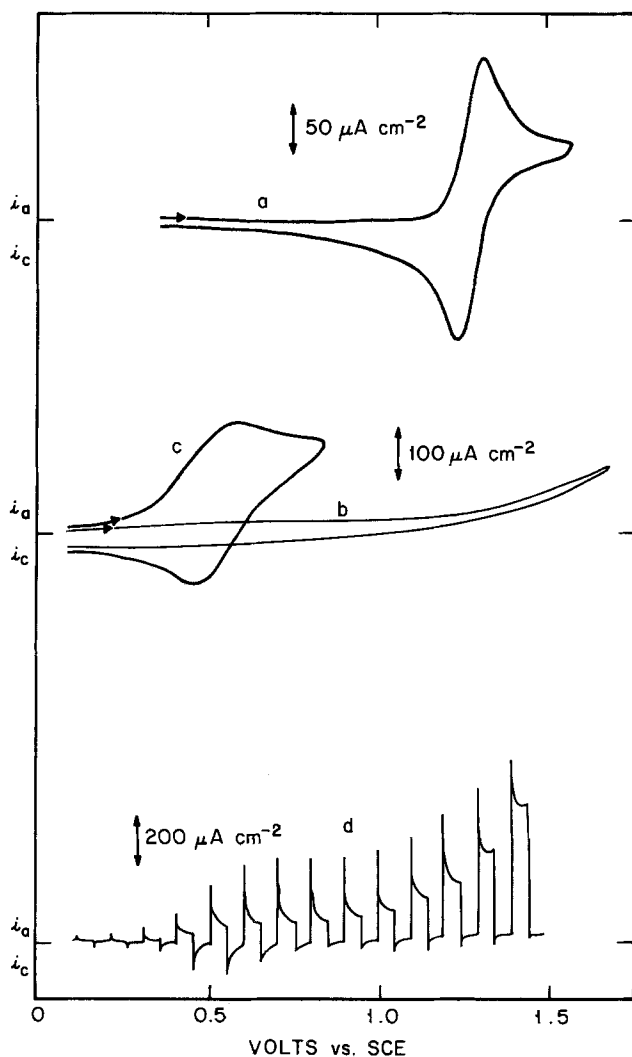


Fig. 4. Cyclic and linear sweep voltammograms of 0.5 mM $\text{Ru}(\text{bpy})_3(\text{ClO}_4)_2$ in 0.1M TBAP/acetonitrile. a: Pt electrode at 50 mV/s. b: dark $\alpha\text{-Fe}_2\text{O}_3$ at 200 mV/s. c: Illuminated $\alpha\text{-Fe}_2\text{O}_3$ at 200 mV/s. d: Transient photocurrent for $\alpha\text{-Fe}_2\text{O}_3$ of 20 mV/s and 0.2 Hz (i.e., light and dark periods = 2.5s each).

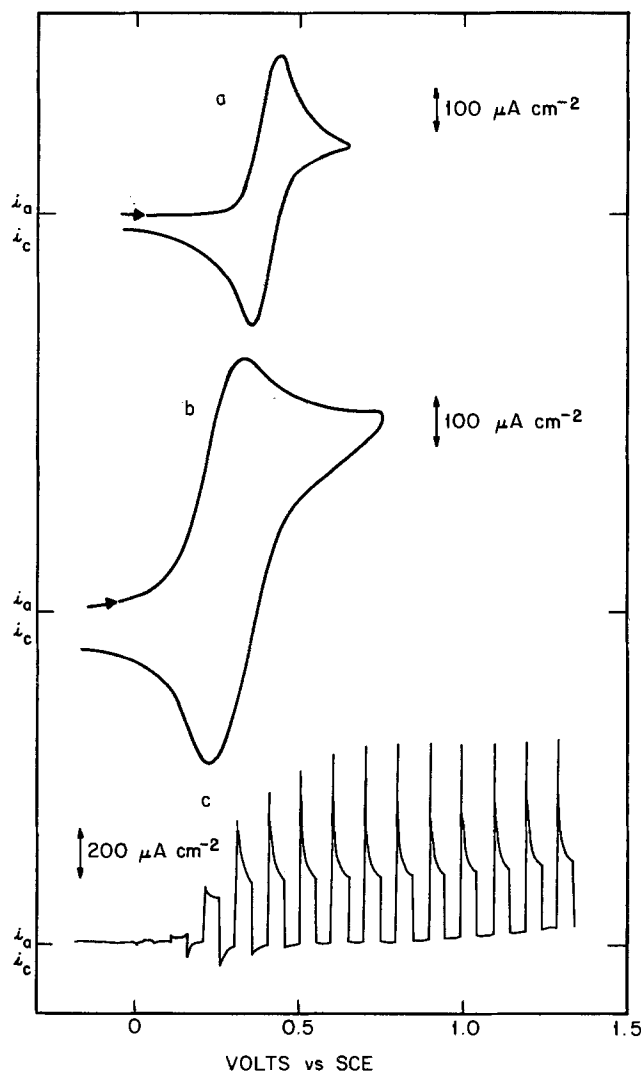
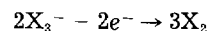
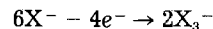


Fig. 5. Voltammograms of 1 mM $\text{Fe}(\text{phen})_3(\text{ClO}_4)_2$ in 0.1M TBAP/acetonitrile. Cyclic voltammograms at 200 mV/s: Pt electrode (a), illuminated $\alpha\text{-Fe}_2\text{O}_3$ (b) and transient photocurrent for $\alpha\text{-Fe}_2\text{O}_3$ at 20 mV/s and 0.2 Hz (c).

This behavior has been observed previously in acetonitrile solutions containing Ru(bpy)₃²⁺ and other species and was attributed to the back reduction of the product of the photo-oxidation (27). The reduction of the photo-oxidized species in the potential region positive of the E_{FB} is inconsistent with the ideal semiconductor/liquid electrolyte model (31, 36). These results, coupled with small variation observed in the open-circuit photovoltage measurements for the polypyridine complexes, imply that surface states, capable of mediating charge transfer, exist between E_{vb} and E_{cb} .

A comparison of our results for Ru(bpy)₃²⁺ with those of Fredlein and Bard (27), reveals that steady photocurrents observed in this work are at least four times more than the transient photocurrents obtained at 0.2% Ti-doped α -Fe₂O₃ for the same concentration of the complex. Any meaningful comparison requires the knowledge of the irradiation power at the electrode surfaces. Fredlein and Bard (27) have not mentioned the intensity of the light in their study. However, since they used a 250W lamp, one can assume that the light intensity at the electrode surface was not less than the light intensity used in the present work. This enhancement is due to the fact that Si is a better dopant for α -Fe₂O₃ than Ti (13). We observed that, upon increasing the concentration of ferrocene, the photoanodic current also increased. It reached a saturation value of ~ 2.8 mA/cm² at 1.0V vs. SCE for ~ 15 mM ferrocene.

Halides.—Acetonitrile solutions of LiI, LiBr, and LiCl were also investigated at iron oxide electrodes. Cyclic and linear sweep voltammograms for LiBr and LiI at illuminated α -Fe₂O₃ are shown in Fig. 7 and 8, respectively. Cyclic voltammograms at a Pt electrode are shown for comparison. It is known that halides (X⁻) give two anodic waves at Pt in acetonitrile solutions, producing X₃⁻/X₂ mixtures by the following reactions (37)



Our results at illuminated α -Fe₂O₃ also show two oxidation waves for halides of low concentrations (~ 20 mM or less). The position of peak potentials for the oxidation of halides at both Pt and illuminated iron oxide are not very reproducible, but they generally all show photoanodic currents at potentials negative of their anodic currents at Pt. In Table I, differences between the anodic peak potentials at Pt and illuminated α -Fe₂O₃, ΔE_{pa} , for X₃⁻/X⁻ halide couples are presented. Oxidation peaks of Br₃⁻/Br⁻ and Cl₃⁻/Cl⁻ at illuminated α -Fe₂O₃ occurred ~ 0.15 and ~ 0.13 V, respectively, negative of that at the Pt electrode. Although the photo-oxidation peak for I₃⁻/I⁻ is somewhat more positive than in oxidation peak at Pt, the onset of the photoanodic current is ~ 0.3 V more negative.

As can be seen from cyclic voltammograms and transient current behavior of halides at illuminated iron oxide, unlike the polypyridine and ferrocene couples, neither reduction peaks nor cathodic spikes are observed. This is probably due to the less reversible nature of the halides and would be expected for the ideal model for n-type semiconductors. However, the observation of two oxidation waves for halides at the illuminated iron oxide

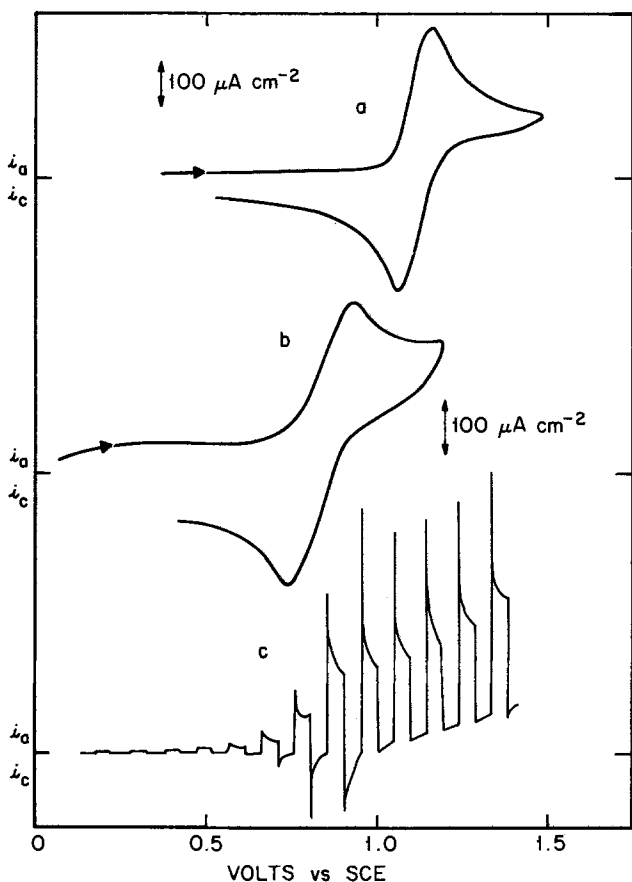


Fig. 6. Voltammograms of 1 mM ferrocene in 0.1M TBAP/acetonitrile. a: Pt electrode at 50 mV/s. b: Illuminated α -Fe₂O₃ at 200 mV/s. c: Chopped illumination of α -Fe₂O₃ at 20 mV/s and 0.2 Hz.

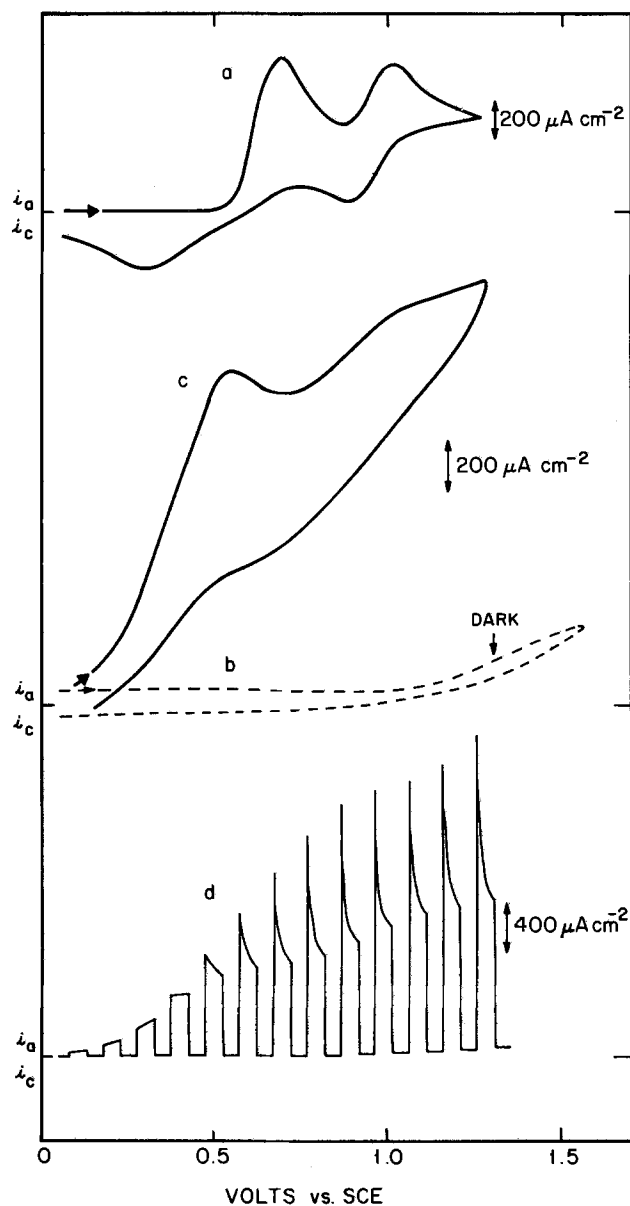


Fig. 7. Voltammograms of 6 mM LiBr in 0.1M TBAP/acetonitrile. a: Pt electrode at 50 mV/s. b and c: Dark and illuminated α -Fe₂O₃ at 200 mV/s. d: Chopped illumination of α -Fe₂O₃ at 20 mV/s and 0.2 Hz.

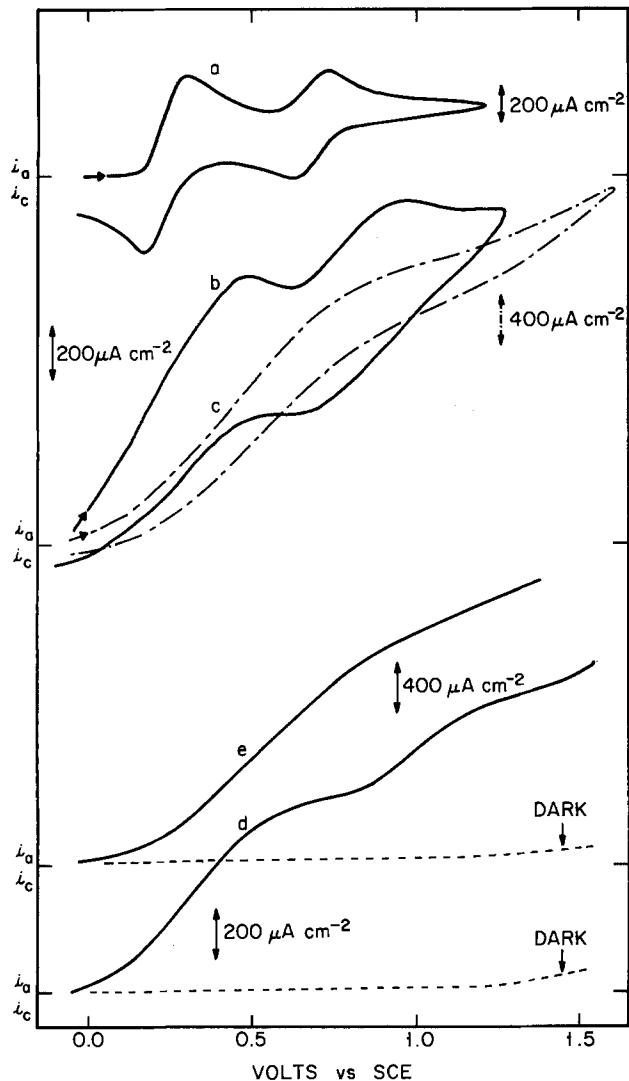


Fig. 8. Cyclic voltammograms and steady-state photocurrent-potential curves of LiI in 0.1M TBAP/acetonitrile. a: Pt electrode in 6.7 mM LiI at 50 mV/s. b: Illuminated α -Fe₂O₃ in 6.7 mM LiI at 200 mV/s. c: Same as b, except in 25 mM LiI. d: Linear sweep at illuminated α -Fe₂O₃ in 6.7 mM LiI at 20 mV/s. e: Same as d, except in 25 mM LiI.

as found at Pt is in contrast to the ideal expectations. Within the ideal frame of semiconductor model (31, 32), one would expect a single wave for the total oxidation of X⁻ to X₂, rather than two separate waves for oxidation to X₃⁻ and X₂. This is because the photogenerated holes should thermodynamically be able to oxidize X⁻ to X₂. Similar results (*i.e.*, two peaks rather than one) have been found for biferrocene and tetramethyl-*p*-phenylenediamine (TMPD) at illuminated n-type CdTe and n-type MoSe₂ in acetonitrile solutions (34, 35). If, as suggested earlier, cathodic transients are caused by back reduction of photogenerated intermediates, we must conclude halide oxidation does not involve intermediates that are easily reduced or that are sufficiently long-lived to exhibit cathodic spikes.

As the concentration of halides increased above ~20 mM, the double waves at the illuminated iron oxide were replaced by a single wave. This is shown in Fig. 8 for I⁻, and the same behavior was observed for Br⁻. Apparently, at higher concentrations, the photocurrents are not diffu-

sion controlled and they are limited by photogenerated holes in the valence band. Therefore, a single wave, rather than two, is observed.

Acknowledgment

Support from the University Energy Research Group is acknowledged.

Manuscript submitted, July 16, 1984; revised manuscript received Dec 10, 1984.

REFERENCES

1. K. L. Hardee and A. J. Bard, *This Journal*, **123**, 1024 (1976).
2. R. K. Quinn, R. D. Nasby, and R. J. Baughman, *Mater. Res. Bull.*, **11**, 1011 (1976).
3. K. L. Hardee and A. J. Bard, *This Journal*, **124**, 215 (1977).
4. L. S. R. Yeh and N. Hackerman, *ibid.*, **124**, 833 (1977).
5. H. H. Kung, H. S. Jarrett, A. W. Sleight, and A. Ferretti, *J. Appl. Phys.*, **48**, 2463 (1977).
6. J. H. Kennedy and K. W. Frese, Jr., *This Journal*, **125**, 709 (1978).
7. J. H. Kennedy and K. W. Frese, Jr., *ibid.*, **125**, 723 (1978).
8. J. S. Curran and W. Gissler, *ibid.*, **126**, 56 (1979).
9. A. F. Sammells and P. G. P. Ang, *ibid.*, **126**, 1831 (1979).
10. S. M. Wilhelm, K. S. Yun, L. W. Ballenger, and N. Hackerman, *ibid.*, **126**, 419 (1979).
11. K. G. McGregor, M. Calvin, and J. W. Otvos, *J. Appl. Phys.*, **50**, 369 (1979).
12. M. Gori, H.-R. Gruniger, and G. Calzaferri, *J. Appl. Electrochem.*, **10**, 345 (1980).
13. J. H. Kennedy, R. Shinar, and J. P. Ziegler, *This Journal*, **127**, 2307 (1980).
14. J. H. Kennedy, M. Anderman, and R. Shinar, *ibid.*, **128**, 2371 (1981).
15. H. Mettee, J. W. Otvos, and M. Calvin, *Solar Energy Mater.*, **4**, 443 (1981).
16. M. V. C. Sastri and G. Nagasubramanian, *Adv. Hydrogen Energy*, **2**, 597 (1981).
17. P. Iwanski, J. S. Curran, W. Gissler, and R. Memming, *This Journal*, **128**, 2128 (1981).
18. R. Shinar and J. H. Kennedy, *Solar Energy Mater.*, **6**, 323 (1982).
19. H. L. Sanchez, H. Steinfink, and H. S. White, *J. Solid State Chem.*, **41**, 90 (1982).
20. C. Leygraf, M. Hendewerk, and G. A. Somorjai, *ibid.*, **48**, 357 (1983).
21. R. Shinar and J. H. Kennedy, *This Journal*, **130**, 392 (1983).
22. J. H. Kennedy and M. Anderman, *ibid.*, **130**, 848 (1983).
23. R. Shinar and J. H. Kennedy, *ibid.*, **130**, 860 (1983).
24. M. P. Dare-Edwards, J. B. Goodenough, A. Hamnett, and P. R. Trevellick, *J. Chem. Soc. Faraday Trans. 1*, **79**, 2027 (1983).
25. M. Anderman and J. H. Kennedy, *This Journal*, **131**, 21 (1984).
26. M. Anderman and J. H. Kennedy, *ibid.*, **131**, 1565 (1984).
27. R. A. Fredlein and A. J. Bard, *ibid.*, **126**, 1892 (1979).
28. S. Miyoshi and A. Kunugi, *Denki Kagaku*, **48**, 476 (1980).
29. J. H. Kennedy and D. Dunnwald, *This Journal*, **130**, 2013 (1983).
30. N. E. Tokel, R. E. Hemingway, and A. J. Bard, *J. Am. Chem. Soc.*, **95**, 6582 (1973).
31. H. Gerischer, *J. Electroanal. Chem.*, **58**, 263 (1975).
32. A. J. Bard, A. B. Bocarsly, F.-R. Fan, E. G. Walton, and M. S. Wrighton, *J. Am. Chem. Soc.*, **102**, 3671 (1980).
33. H. Tributsch, *Solar Energy Mater.*, **1**, 257 (1979).
34. A. Aruchamy and M. S. Wrighton, *J. Phys. Chem.*, **84**, 2848 (1980).
35. L. F. Schneemeyer and M. S. Wrighton, *J. Am. Chem. Soc.*, **102**, 6964 (1980).
36. A. B. Bocarsly, E. G. Walton, M. G. Bradley, and M. S. Wrighton, *J. Electroanal. Chem.*, **100**, 283 (1979).
37. I. M. Kolthoff and J. F. Coetzee, *J. Am. Chem. Soc.*, **79**, 1852 (1957).

Electrodes Modified by a Thick Deposit of an Organic Compound

Mechanism of Electron Transfer

Loïc Roullier, Eric Waldner, and Etienne Laviron

Laboratoire de Synthèse et d'Electrosynthèse Organométalliques associé au CNRS (LA 33), Faculté des Sciences, 21100 Dijon, France

ABSTRACT

Electrodes modified by a thick crystalline deposit of an organic compound (phenazine, chloranil, azobenzene, benzo(c)cinnoline, 2,6-diaminoanthraquinone) are studied in aqueous medium by cyclic voltammetry and by the potential step method. When the deposit is thick enough, only a fraction of it is electroactive, and the loss of material by dissolution is small. The voltammograms have approximately the shape for a process controlled by diffusion in a confined space. It is shown that during the cathodic cycle, the process consists in a dissolution of the crystals of the oxidized form O, induced by the reduction of O at the electrode, followed by a crystallization of the reduced form R; the reverse process takes place during the oxidation cycle. The theoretical laws for diffusion in a confined space are approximately obeyed, because the system behaves as a thin layer placed near the electrode surface.

A large number of electrodes modified by redox polymers have been described (1); the diffusion-like transmission of the electrons through the coating can be limited by the hopping of electrons between redox sites, by diffusion of the counterion or of the solvent, or by the movements of the polymeric chain.

By contrast few studies concern electrodes covered by a thick deposit of a redox monomer, which can be organic [benzo(c)cinnoline (2), azobenzene, phenazine (3), chloranil (3, 4), phenoxazine (4), catechols (5), flavine adenine dinucleotide (6), tetrathiafulvalene (7)], organometallic [metal phthalocyanines (8)], or mineral [Prussian blue (9, 10), ruthenium purple (10), ferric ruthenocyanide (11), cupric hexacyanoferrate (12)].

We report and analyze in this paper results obtained with crystalline deposits of organic substances: phenazine (P), chloranil (QCl), azobenzene (AB), benzo(c)cinnoline (BC), and 2,6-diaminoanthraquinone (QNH₂). We have already briefly described the behavior of P, QCl, and AB in a preliminary note (3). On the basis of our results, we discuss the possible mechanisms of the reduction or oxidation of these films.

Experimental

Materials.—Phenazine, azobenzene, chloranil, and 2,6-diaminoanthraquinone were commercial products and were used without further purification.

Apparatus.—All electrochemical experiments were carried out on a Tacussel Instrument (potentiostat PRT 30-01, differential amplifier, and GSTP function generator). The *i*-E curves were drawn on a SEFRAM TGM 164 X-Y recorder, and the *i*-t curves were recorded on a NICOLET 2090-III digital oscilloscope. The measurements were carried out in water (Britton-Robinson buffers 0.2M KNO₃ or NaCl), in 2M HClO₄, 5M NH₄Cl, or in 1M NaOH at 20°C. The potentials refer to the saturated calomel electrode.

Electrodes.—A platinum disk electrode (0.8 or 2 mm diam) or a glassy carbon disk electrode (Carbone Lorraine V 25, 3 mm diam) sealed in a glass tubing were employed. Prior to use, the electrodes were polished successively on abrasive disks (ESCIL, grain 400-1200) and on alumina (ESCIL A3, grain 0.5 μm), and then ultrasonically cleaned in acetone or dimethylformamide.

The modified electrodes were prepared by dipping the electrodes in CH₂Cl₂, C₂H₅OH, CH₃COCH₃, or CF₃CO₂H solutions containing 1-10 mg ml⁻¹ of electroactive product or by micropipetting a few microliters of the solutions onto the platinum or the carbon disk and allowing the solvent to air dry.

No significant difference has been found in the stability of the electrodes or in their electrochemical properties when the supporting electrolyte was changed (LiClO₄, NaCl, or KBr instead of KNO₃, for example).

Results

Cyclic voltammetry.—Examples of voltammograms are given in Fig. 1-3. At slow sweep rates, the peak is symmetrical and resembles that obtained in a thin layer cell (13). At higher sweep rates, a tailing appears, as for a diffusion-limited process (14). The sweep rate ν at which the tailing begins to develop is different for each peak; for phenazine at pH 2, it can already be seen for peak A' (Fig. 1a) for $\nu = 45 \text{ mV s}^{-1}$ whereas much larger rates are needed for other peaks (Fig. 1b). In the case of azobenzene at pH 2 (Fig. 3), the cathodic peak already has a tailing for $\nu = 20 \text{ mV s}^{-1}$, but the anodic peak remains symmetrical even for higher sweep rates. For chloranil, the limits are much lower ($\nu < 0.4 \text{ mV s}^{-1}$).

The peaks obtained during the first cycle are often different from those of the subsequent cycles; a typical example is shown in Fig. 4.

Another characteristic feature is the marked hysteresis of the curves. The cathodic and anodic peaks are often widely separated, even at slow sweep rates. The difference ΔE_p between the peak potentials is about 170 mV for peaks A/A', and 250 mV for peaks B/B' of phenazine at pH 2 (Fig. 1); it reaches 500 mV in the case of azobenzene at pH 2 (Fig. 3). It must be noted that a smaller system of peaks, less separated, is often observed at the foot of the main peaks (Fig. 3). These peaks might be attributed to monolayer adsorption.

Generally speaking, at slow sweep rates, the peak current i_p varies linearly with ν , whereas it becomes proportional to $\nu^{1/2}$ at higher sweep rates (Fig. 5). The rate for which the transition occurs depends on the substance; no transition, for example, is observed in the case of phenazine at pH 14 (Fig. 5b) or for chloranil (Fig. 5d).

With thick deposits, the electrodes are quite durable; for phenazine at pH 2, the loss of active material after ten consecutive cycles between +0.43 and -0.47V at 10 mV s⁻¹ is less than 3%; with azobenzene at pH 2, after ten cycles at 17 mV s⁻¹ between +0.9 and -0.8V, it is about 2%. The loss with chloranil is even smaller. The amount of electricity Q involved during the reduction or the oxidation, measured by integration of the voltammetric peak, is then always much smaller than the charge Q_t which would correspond to the reduction or oxidation of all the deposit; some values are given in Table I. The charge Q tends to increase slightly when ν decreases, but always remains much smaller than Q_t .

When the deposit is too thin, the voltammograms are not stable, and the peaks disappear after a few cycles.

***i*-t Curves at constant potential.**—The current obtained when the potential is stepped from a value where no electrochemical reaction occurs to a value well past the reduction (or oxidation) potential decreases with time. A few examples of the transform $i = f(t^{-1/2})$ are shown in Fig. 6.

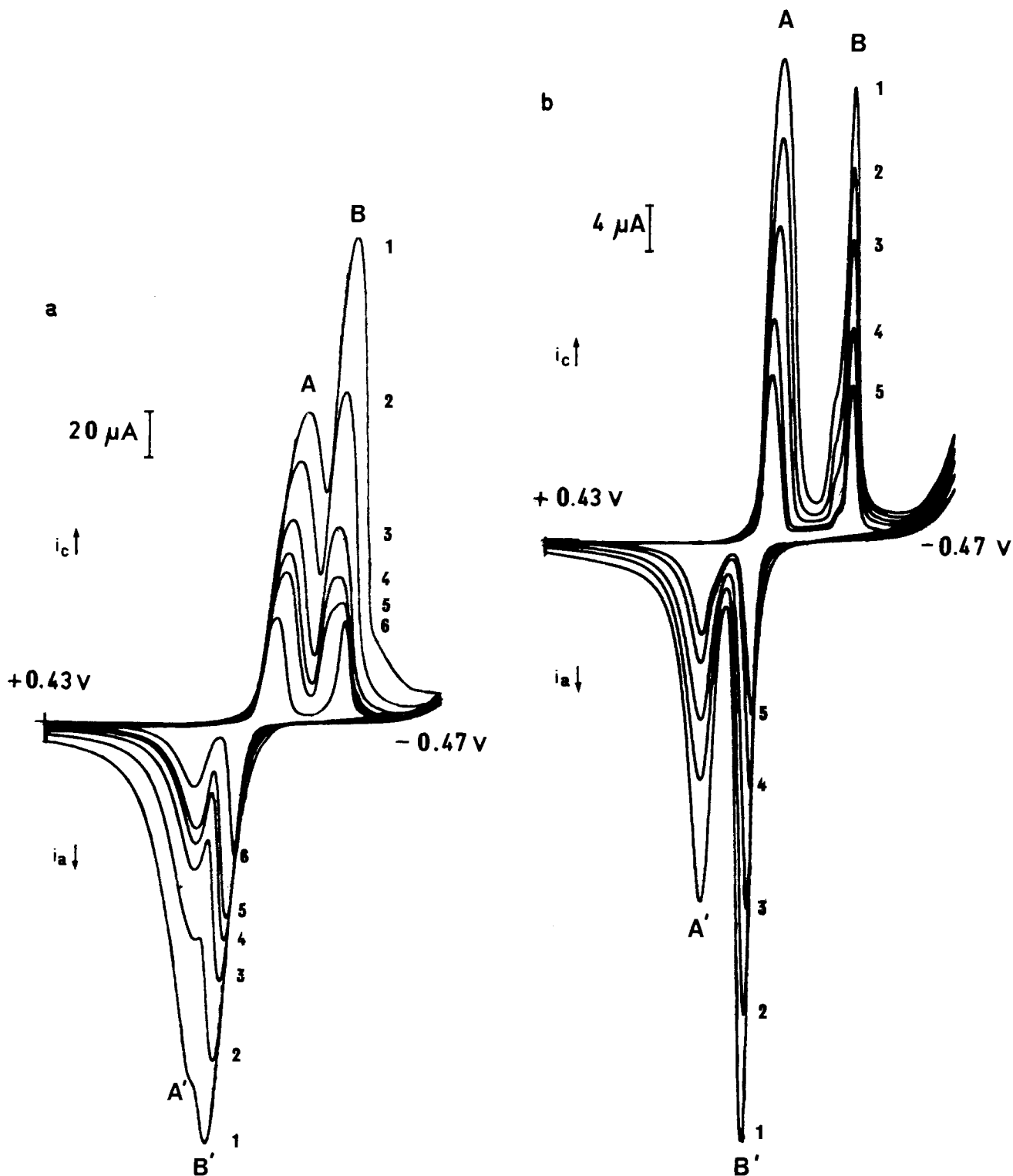


Fig. 1. Cyclic voltammograms of phenazine on a platinum electrode (electrode area $S = 5 \times 10^{-3} \text{ cm}^2$) at pH 2 (0.2M KNO_3). v (mV s^{-1}) in a: curve 1, 300; curve 2, 225; curve 3, 150; curve 4, 112; curve 5, 90; curve 6, 45. v (mV s^{-1}) in b: curve 1, 45; curve 2, 30; curve 3, 22; curve 4, 15; curve 5, 11.

The curves have the general shape expected for a process limited by diffusion in a confined space (15), when

$$i = nFAD^{1/2}C_s\pi^{-1/2}t^{-1/2} \left[1 + 2 \sum_{k=1}^{k=\infty} (-1)^k \exp\left(\frac{-k^2l^2}{Dt}\right) \right]$$

D being the diffusion coefficient, C_s the concentration, and l the thickness of the layer. However, if a value of $D^{1/2}C_s$ is calculated from the slope of the linear part (15), and if the whole curve is simulated, by using this value, discrepancies appear (Fig. 6a, 6c). In certain cases, moreover, the curve does not show the characteristic dip of

current at long times (Fig. 6b). Also, the first curve usually differs from the following (Fig. 6a).

Visual observation of the deposit.—We have observed visually under a microscope the evolution of crystals of phenazine at pH 2 when the potential is stepped from +0.3 to -0.7V by using the cell described in Fig. 1 of Ref. (16), in which the carbon particles were replaced by glassy carbon fibers. Phenazine is present initially under the form of small yellow crystals. When the potential is applied, they dissolve, while other long blue green crystals of dihydrophenazine appear in the solution between the fibers.

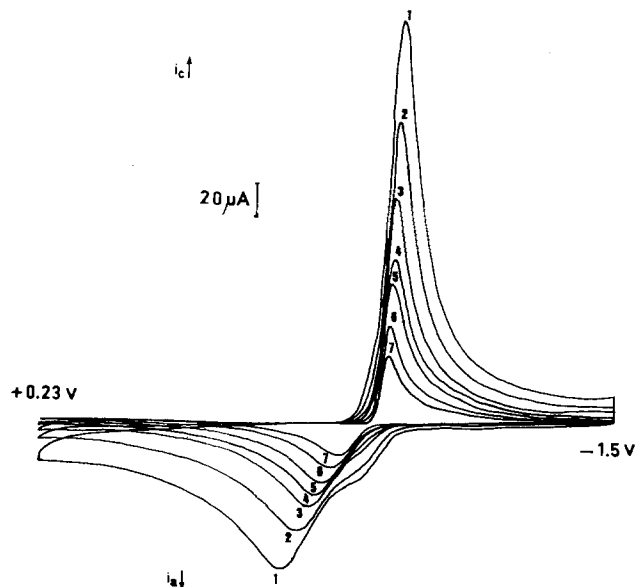


Fig. 2. Cyclic voltammograms of phenazine on a glassy carbon electrode ($S = 0.07 \text{ cm}^2$) in 1M NaOH . v (mV s^{-1}): 1, 175; 2, 87.5; 3, 43.7; 4, 29.2; 5, 17.5; 6, 8.75; 7, 4.37.

Dissolution of the deposit in a thin layer cell.
 —Experiments were carried out with P, AB, QCl, and QNH_2 , as described below. A few microliters of a solution containing the compound were micropipetted onto the glass plate forming one of the walls of the thin layer cell [cf. Ref. (17) and Fig. 7] and allowed to air dry. The cell was then filled with the electrolytic solution, and a sheet of very thin paper was placed between the spacer and the electrode (Fig. 7), to ensure that the crystals would not be in contact with the electrode. The potential was scanned repetitively at a slow sweep rate ($v < 50 \text{ mV s}^{-1}$) between two potentials situated on either side of the redox peaks. A system of anodic/cathodic peaks appears gradually (Fig. 8) until a steady-state system is obtained; the same system is still observed when the electrode is lifted into the bulk of the solution. This shows that an electrochemically induced dissolution of the deposit followed by a crystallization on the electrode has taken place. Such experiments can be used to prepare the modified electrodes electrochemically. Besides, electrodes can also be coated by successive scans in a saturated alcoholic solu-

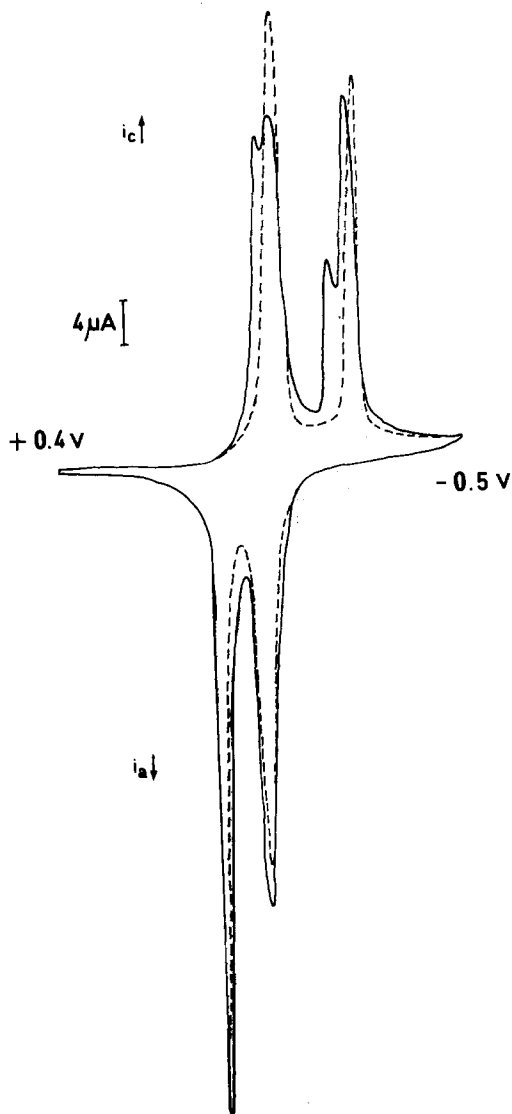


Fig. 4. Cyclic voltammograms of phenazine on a glassy carbon electrode at $\text{pH } 2$ (0.2M KNO_3). v : 18 mV s^{-1} . (—): First scan. (---): Second scan. Apparent coverage $\Gamma = 2.2 \times 10^{-8} \text{ mol cm}^{-2}$.

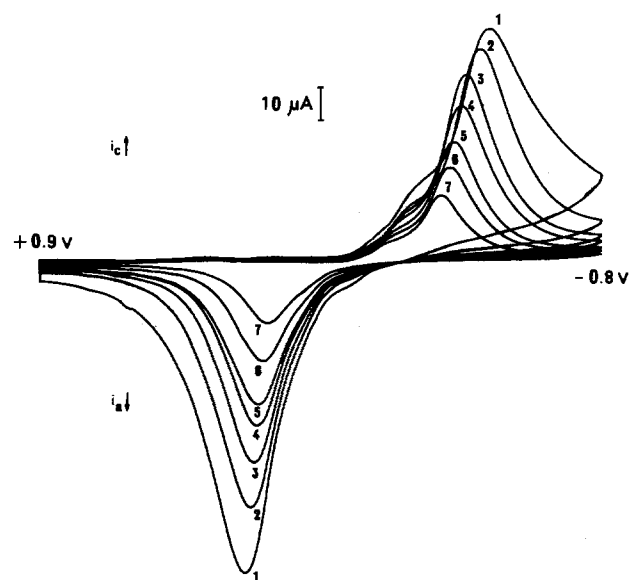


Fig. 3. Cyclic voltammograms of azobenzene on a glassy carbon electrode at $\text{pH } 2$ (0.2M KNO_3). v (mV s^{-1}): 1, 42; 2, 28; 3, 21; 4, 17; 5, 11; 6, 8.5; 7, 5.7.

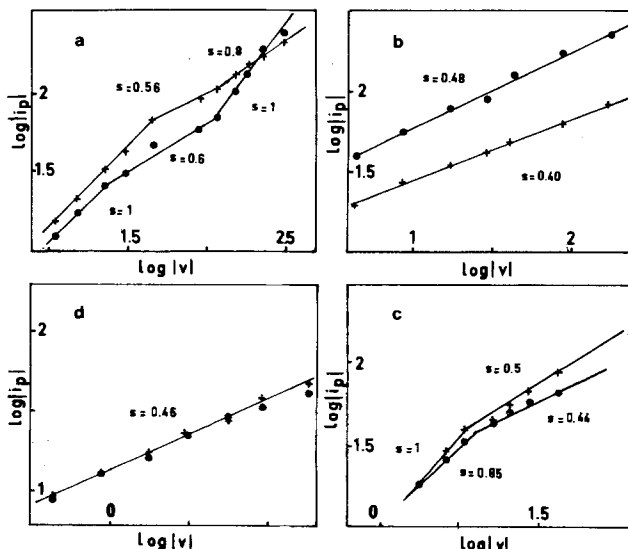


Fig. 5. Variations of $\log i_{p,a}$ ($i_{p,a}$: anodic peak current in microamperes) and $\log i_{p,c}$ ($i_{p,c}$: cathodic peak current in microamperes) with $\log |v|$ (v in millivolts per second). +: $i_{p,a}$; \bullet : $i_{p,c}$. a: Phenazine; peaks B and B' in Fig. 1. b: Phenazine; same conditions as in Fig. 2. c: Azobenzene; same conditions as in Fig. 3. d: Chloranil; on a glassy carbon electrode in 2M HClO_4 . The slope S is indicated on each curve.

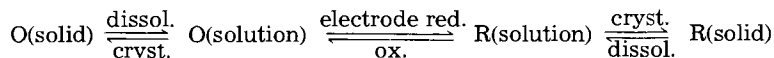
tion of the compound. A typical example of such an electrochemically modified electrode is given in Fig. 9.

Discussion

Two types of mechanisms can be considered for the reduction or oxidation of a crystalline deposit.

The first consists in a direct electron transfer between neighboring sites in the crystal. This is similar to the process observed in the case of redox polymer electrodes with fixed sites (1, 18). The electron transfer must be accompanied here also by the transport of a counterion in the crystal lattice.

The second mechanism involves an intermediate electrochemically induced dissolution of the solid, followed by a crystallization, according to



If the two mechanisms can coexist, as suggested to one of us (19), with possible redox exchanges between the ions in solution and in the lattice, a situation similar to that observed with polymer electrodes when the redox centers are electrostatically bound to the polymeric chain could be found. The theory developed for that case could eventually be applied (20).

It has been demonstrated conclusively that in the case of Prussian blue (9b) and its analogs (12), the first mechanism is operating. The crystal lattice of the reduced and oxidized forms are very similar, and the size of the counterion is critical; transport occurs if it is small enough to enter the lattice.

With crystalline deposits of organic compounds, on the contrary, the redox process takes place exclusively ac-

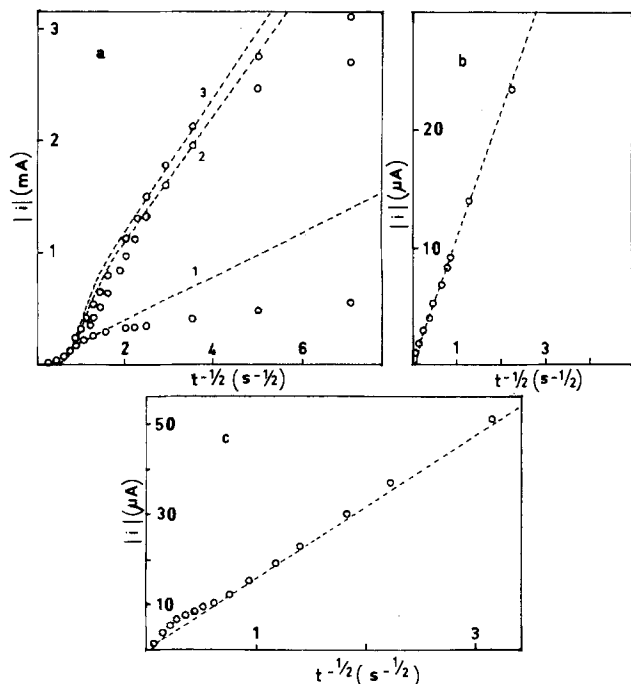


Fig. 6. $i-t^{-1/2}$ transforms of the current-time curves. Values of $D^{1/2}C_s$ are calculated from the slope $nFAD^{1/2}C_s/\pi^{1/2}$. O: Experimental values. (---): Curves from the finite-diffusion theory calculated from the $D^{1/2}C_s$ values. a: Phenazine on a glassy carbon electrode at pH 2 (0.2M KNO_3). Three successive curves on the same deposit. Potential stepped from +0.3 to -0.7V. Curve 1: apparent coverage $\Gamma = 6.7 \times 10^{-9}$ mol cm^{-2} ; $D^{1/2}C_s = 2.6 \times 10^{-8}$ mol $\text{cm}^{-2} \text{s}^{-1/2}$. Curve 2: $\Gamma = 9.33 \times 10^{-8}$ mol cm^{-2} ; $D^{1/2}C_s = 7.3 \times 10^{-8}$ mol $\text{cm}^{-2} \text{s}^{-1/2}$. Curve 3: $\Gamma = 10^{-7}$ mol cm^{-2} ; $D^{1/2}C_s = 7.9 \times 10^{-8}$ mol $\text{cm}^{-2} \text{s}^{-1/2}$. b: Curve for chloranil after the steady state is obtained ($\Gamma = 1.46 \times 10^{-8}$ mol cm^{-2}) on a glassy carbon electrode in 0.1M HClO_4 . Potential stepped from +1 to -0.4V. $D^{1/2}C_s = 1.48 \times 10^{-9}$ mol $\text{cm}^{-2} \text{s}^{-1/2}$. c: Curve for azobenzene after the steady state is obtained ($\Gamma = 4.3 \times 10^{-8}$ mol cm^{-2}) on a glassy carbon electrode at pH 2 (0.2M KNO_3). Potential stepped from +0.9 to -0.8V. $D^{1/2}C_s = 2.1 \times 10^{-9}$ mol $\text{cm}^{-2} \text{s}^{-1/2}$.

Table I. Comparison between the experimental (Q) and theoretical (Q_t) quantity of electricity

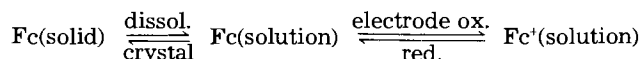
Substance	ν (mV s^{-1})	Q (C)	Q_t (C)
QNH_2^a	40	0.93×10^{-4}	7.16×10^{-2}
AB^b	10.15	7×10^{-4}	2.29×10^{-2}
QCl^c	21.5	4.82×10^{-4}	1.48×10^{-2}

^a At pH 3.8 (0.2M KNO_3).

^b At pH 2 (0.2M KNO_3).

^c In 5M NH_4Cl .

According to the second mechanism, as shown by the experimental findings. No difference is found when the size of the counterion is changed. The visual observation that the crystals of the reactant dissolve while those of the reduced product grow in a different place and under a different form is a direct proof of the mechanism. The same direct observation of the dissolution process has been reported (16) in aqueous medium in the case of the oxidation of particles of ferrocene Fc to the ferricinium ion Fc^+ , which is soluble



This scheme, in which the formation of Fc^+ is not followed by a crystallization, is simpler, and can be treated mathematically (21). The experimental results obtained with ferrocene are in good agreement with the theory (16). That a direct electron transfer from one site to the other in the crystal cannot take place is also in keeping with the fact that the crystalline forms of the oxidized and reduced species are usually very different [see, e.g., the case of azo/hydrazobenzene (22)]. It also tallies with theoretical (23) and experimental (24, 25) results which show that in the case of quinones (24) and azobenzene (25) the transfer of electrons between the reduced and oxidized forms is

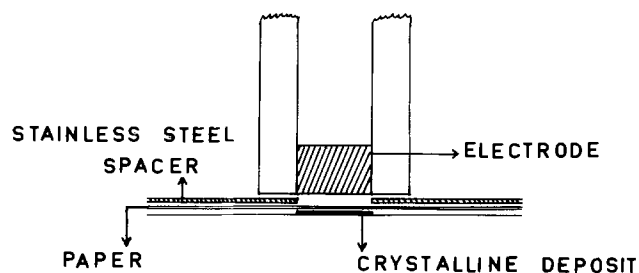


Fig. 7. Electrochemical cell for the thin layer potential sweep voltammetric experiments.

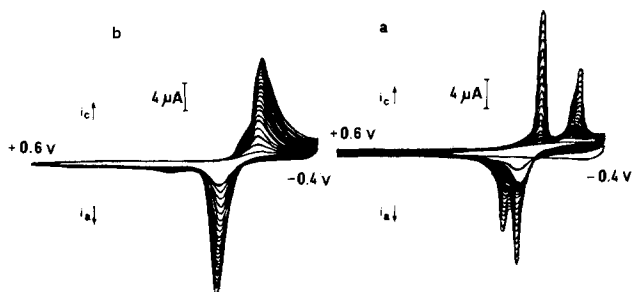


Fig. 8. 50 successive cyclic voltammograms of phenazine in the thin layer cell (see text) with a platinum electrode ($S = 0.03 \text{ cm}^2$); $\nu = 9.3 \text{ mV s}^{-1}$. a: pH 2 (0.2M KNO_3). b: pH 2.85 (0.2M KNO_3).

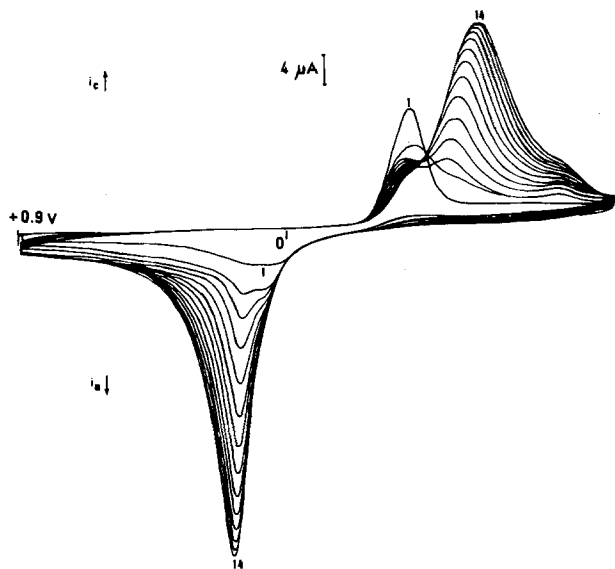


Fig. 9. 14 successive voltammetric curves in a saturated solution of azobenzene (pH 3.7; 0.2M NaCl; 20% C₂H₅OH) on a glassy carbon electrode at 10 mV s⁻¹. Apparent coverage $\Gamma = 6.4 \times 10^{-8}$ mol cm⁻² (calculated from the fourteenth curve).

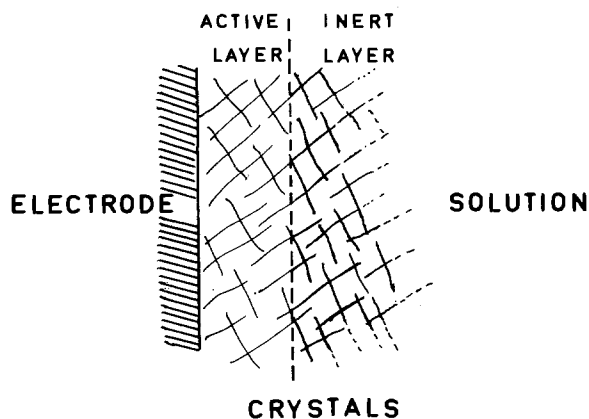


Fig. 10. Schematic representation of the electrode modified by a thick deposit.

very slow in solution, due to the participation of protons in the global exchange; it is likely that the same reaction would also be slow in the crystal. A last proof of the mechanism is given by the dissolution experiments in the thin layer cell (*vide supra*).

The characteristics of the voltammetric peaks (variations of i_p with v , shape of the peak) and of the $i-t$ curves point to a diffusional transport in a confined space. This can be explained schematically as shown in Fig. 10. Two zones can roughly be distinguished in the deposit, an inert part which is too far from the electrode to play a role in the process, and a layer near the electrode, where the dissolution and recrystallization take place. This active zone is similar to a thin layer cell (17), the inert part playing the role of the wall of the cell. The inert layer protects the active zone from dissolution into the bulk solution during the redox process, as shown by the fact that the deposit dissolves after a few cycles when it is too thin. This insulating role of the crystalline outer deposit has already been illustrated in the case of the deposition of ferrocene from a solution of ferricinium salt, which ceases when the thickness of the crystalline layer has attained a certain value (16).

The diffusional process follows only approximately the laws for a thin layer, because of the approximate (nonplanar crystalline) nature of the wall of the cell. The fact that the transition from a thin layer to a semi-infinite diffusional behavior depends on the substance is certainly linked with the shape and the size of the crystals, which determine the equivalent thickness of the thin layer.

Manuscript submitted June 29, 1984; revised manuscript received Jan. 20, 1985.

CNRS assisted in meeting the publication costs of this article.

REFERENCES

1. See, for example, R. W. Murray, in "Electroanalytical Chemistry," Vol. 13, A. J. Bard, Editor, p. 191, Marcel Dekker, New York (1984).
2. E. Laviron, L. Roullier, and C. Degrand, *J. Electroanal. Chem.*, **112**, 11 (1980).
3. L. Roullier and E. Laviron, *ibid.*, **134**, 181 (1982).
4. H. Huck and H. L. Schmidt, *Angewand. Chem.*, **20**, 402 (1981); H. Huck, *Z. Anal. Chem.*, **313**, 548 (1982).
5. H. Jaegfeldt, T. Kuwana, and G. Johansson, *J. Am. Chem. Soc.*, **105**, 1805 (1983).
6. L. Gorton and G. Johansson, *J. Electroanal. Chem.*, **113**, 151 (1980).
7. T. P. Henning, H. S. White, and A. J. Bard, *This Journal*, **130**, 613 (1983).
8. J. M. Green and L. R. Faulkner, *J. Am. Chem. Soc.*, **105**, 2950 (1983); F. Van den Brink, W. Visscher, and E. Barendrecht, *J. Electroanal. Chem.*, **157**, 283 (1983); C. A. Melendres and X. Feng, *This Journal*, **130**, 38 (1983).
9. (a) V. D. Neff, *ibid.*, **125**, 886 (1978); D. Ellis, M. Eckhoff, and V. D. Neff, *J. Phys. Chem.*, **85**, 1225 (1981); K. Itaya, T. Ataka, S. Toshima, and T. Shinohara, *ibid.*, **86**, 2415 (1982); (b) K. Itaya, T. Ataka, and S. Toshima, *J. Am. Chem. Soc.*, **104**, 4767 (1982); (c) K. Itaya, H. Akahoshi, and S. Toshima, *This Journal*, **129**, 1498 (1982); K. Itaya, I. Uchida, and S. Toshima, *J. Phys. Chem.*, **87**, 105 (1983); R. M. C. Goncalves, H. Kellawi, and D. R. Rosseinsky, *J. Chem. Soc. Dalton Trans.*, 991 (1983); R. J. Mortimer and D. R. Rosseinsky, *J. Electroanal. Chem.*, **151**, 133 (1983).
10. K. P. Rajan and V. D. Neff, *J. Phys. Chem.*, **86**, 4361 (1982).
11. K. Itaya, T. Ataka, and S. Toshima, *J. Am. Chem. Soc.*, **104**, 3751 (1982).
12. L. M. Siperko and T. Kuwana, *This Journal*, **130**, 396 (1983).
13. A. T. Hubbard and F. C. Anson, in "Electroanalytical Chemistry," Vol. 4, A. J. Bard, Editor, p. 129, Marcel Dekker, New York (1970).
14. P. Delahay, "New Instrumental Methods in Electrochemistry," p. 115, Interscience, New York (1954).
15. D. M. Oglesby, S. H. Omang, and C. N. Reilley, *Anal. Chem.*, **37**, 1312 (1965); P. Daum, J. R. Lehnard, D. Rolison, and R. W. Murray, *J. Am. Chem. Soc.*, **102**, 4649 (1980).
16. R. Gavasso and E. Laviron, *J. Electroanal. Chem.*, **102**, 249 (1979).
17. A. Vallat and E. Laviron, *ibid.*, **74**, 177 (1976).
18. E. Laviron, *ibid.*, **112**, 1 (1980); C. P. Andrieux and J. M. Savéant, *ibid.*, **111**, 377 (1980); P. J. Pearce and A. J. Bard, *ibid.*, **114**, 89 (1980).
19. J. M. Savéant, Personal communication.
20. F. C. Anson, J. M. Savéant, and K. Shigehara, *J. Phys. Chem.*, **87**, 214 (1983); *J. Am. Chem. Soc.*, **105**, 1096 (1983).
21. E. Laviron, *J. Electroanal. Chem.*, **90**, 33 (1978).
22. "A. S. T. M. Files," J. C. P. D. S., International Center for Diffraction Data, Swathmore, PA (1981).
23. E. Laviron, *J. Electroanal. Chem.*, **169**, 29 (1984).
24. E. Laviron, *ibid.*, **164**, 213 (1984).
25. E. Laviron and Y. Mugnier, *ibid.*, **111**, 337 (1980).

On Ionic Association in Ambient Temperature Chloroaluminate Molten Salts

Analysis of Electrochemical and Conductance Data

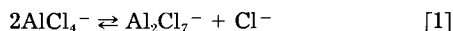
Marek Lipsztajn and Robert A. Osteryoung*

Department of Chemistry, State University of New York at Buffalo, Buffalo, New York 14214

ABSTRACT

A simple model based on the validity of the Nernst-Einstein equation and a constant $u_i\eta$ product was applied to the interpretation of conductance data for $\text{AlCl}_3\text{-RCl}$ [$\text{R} = \text{N-(1-butyl)pyridinium}$ or $\text{1-methyl-3-ethylimidazolium}$] ambient temperature ionic liquids. The dissociation constants of RAlCl_4 and RAl_2Cl_7 were calculated, and the experimental values of specific conductivity were reproduced with an error not exceeding 5% from ionic mobilities calculated from electrochemically measured diffusion coefficients. This calculation suggests that about 50% of the ions are associated into ion pairs. For very basic melts ($\text{MC} \leq 0.6$), the formation of ion aggregates is postulated.

In the past several years, low temperature molten salt systems composed of aluminum chloride and either $\text{N-(1-butyl)pyridinium}$ chloride (BuPyCl) or $\text{1-methyl-3-ethylimidazolium}$ chloride (ImCl) have been found to be useful solvents for electrochemical and spectroscopic investigations of both organic and inorganic species (1-4). Certain physical and chemical properties of these ionic liquids have been found (5, 6) to be very dependent on the melt composition, defined here as the mole ratio of AlCl_3 to RCl taken for preparation of the melt ($\text{MC} = n_{\text{AlCl}_3}/n_{\text{RCl}}$). Here R^+ is either BuPy^+ or Im^+ . Because of this strong dependence of physical and chemical properties on melt composition, it is difficult to compare the results obtained in the melts of different values of the MC. Since the equilibrium reaction



occurs over the entire range of melt composition (3), the chemical properties of these melts have been related to the acidity function defined as the logarithm of chloride ion concentration, $p\text{Cl}$. This treatment, however, assumes that the $\log[\text{Cl}^-]$ is the only essential variable (like pH in aqueous solutions), which is satisfying only in some cases, e.g., the complexation of metal ions with chloride ions (7, 8).

In this paper, we will consider the binary molten salts as mixtures of two or three compounds: RCl , RAlCl_4 , and RAl_2Cl_7 ($\text{R}^+ = \text{BuPy}^+$ or Im^+). This treatment, supported by spectroscopic studies (9) indicating that only R^+ , Cl^- , AlCl_4^- , and Al_2Cl_7^- ions are present in the melts in significant quantities, will be used for the interpretation of electrochemical and conductance data. Each melt characterized by a different MC will be treated as a different ionic liquid.

Let one consider the reactions occurring during mixing of RCl and AlCl_3

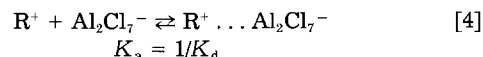


for $\text{MC} = y/x \leq 1$, and



for $1 \leq \text{MC} \leq 2$. Reaction [2] corresponds to the formation of so-called "basic" melts, reaction [3] to the formation of so-called "acidic" melts. A very special case is when $\text{MC} = 1.00$, which corresponds to the formation of the "neutral" melt (10), i.e., pure, molten RAlCl_4 . If $\text{MC} = 2$, we obtain pure, molten RAl_2Cl_7 . These considerations will be now applied to the interpretation of conductance data in the literature (5, 6).

Let us consider the 2:1 $\text{AlCl}_3\text{-RCl}$ melt, as molten RAl_2Cl_7 , consisting of R^+ and Al_2Cl_7^- ions, partially associated into ion pairs



The degree of association of ions (or dissociation of ion pairs) can be estimated from an analysis of the specific conductance (κ) and electrochemical data (diffusion coefficients of R^+ and Al_2Cl_7^-) by using two rather simple equations

$$\kappa = F \sum_i u_i c_i \quad [5]$$

and

$$u_i = |z_i|FD_i/RT \quad [6]$$

where u_i , D_i , z_i , and c_i denote ionic mobility ($\text{cm}^2 \text{s}^{-1} \text{V}^{-1}$), diffusion coefficient ($\text{cm}^2 \text{s}^{-1}$), charge and concentration of ion i (mol cm^{-3}), respectively, and F , R , and T have their usual meanings. The controversial problem of the applicability of Eq. [6], the Nernst-Einstein equation, to molten salts will be discussed in the next section.

For pure, molten $\text{BuPyAl}_2\text{Cl}_7$, we obtain

$$\kappa/F = u_{\text{BuPy}^+} c_{\text{BuPy}^+} + u_{\text{Al}_2\text{Cl}_7^-} c_{\text{Al}_2\text{Cl}_7^-} \quad [7]$$

with $c_{\text{BuPy}^+} = c_{\text{Al}_2\text{Cl}_7^-}$. Experimental values of the diffusion coefficients and calculated mobilities are collected in Table I. Substituting the experimental and related values into Eq. [7] [the specific conductivity, κ , for 2:1 $\text{AlCl}_3\text{-BuPyCl}$ melt at 40°C is equal to $0.0104 \Omega^{-1} \text{cm}^{-1}$ (5, 11), the value of the total concentration of $\text{BuPyAl}_2\text{Cl}_7$ (c_0), calculated by use of the molecular weight of this salt and its density (5) is $c_0 = 3.034 \text{ mol dm}^{-3}$], we obtain $\alpha_{\text{diss}} = c_i/c_0 \approx 0.47$, and K_d of an assumed ion pair is equal to 1.3 mol dm^{-3} .

Unfortunately, the conductance data for $\text{AlCl}_3\text{-BuPyCl}$ melts are very incomplete [the specific conductance was measured for 2:1 (5) and 1:1 (11) melts]. Therefore, we will analyze conductance data as measured for $\text{AlCl}_3\text{-ImCl}$ melts (6).

Table I. Transport properties of 2:1 $\text{AlCl}_3\text{-BuPyCl}$ melt

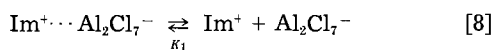
Ion	Diffusion coefficient ^a at 313 K and $\eta = 0.145\text{P}$ ($\text{cm}^2 \text{s}^{-1}$)	$D\eta/T$ ($\text{g cm s}^{-2}\text{K}^{-1}$)	Ionic mobility calculated from Eq. [6] ($\text{cm}^2 \text{s}^{-1}\text{V}^{-1}$)
BuPy^+	1.15×10^{-6}	5.3×10^{-10}	4.26×10^{-5}
Al_2Cl_7^-	8.85×10^{-7}	4.1×10^{-10}	3.28×10^{-5}

^a The diffusion coefficients were measured (14) in almost neutral $\text{AlCl}_3\text{-ImCl}$ melt at 303 K. The value of the viscosity, $\eta = 0.156\text{P}$ (6), was recalculated to conditions of the 2:1 $\text{AlCl}_3\text{-BuPyCl}$ melt, $\eta = 0.145\text{P}$ at 313 K (5), under the assumption that the $D\eta/T$ product is constant and independent of the concentration of electrolyte (see Discussion section).

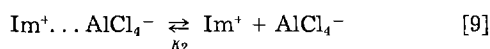
* Electrochemical Society Active Member.

Acidic Melts

The acidic $\text{AlCl}_3\text{-ImCl}$ will be considered as a mixture of ions and ion pairs of ImAlCl_4 and ImAl_2Cl_7 involving two equilibria



and



To find the concentrations of the ionic components (Im^+ , AlCl_4^- , and Al_2Cl_7^-) at a particular melt composition, the following system of equations is considered

$$\begin{aligned} K_1 &= [\text{Im}^+][\text{Al}_2\text{Cl}_7^-]/(c_{\text{ImAl}_2\text{Cl}_7} - [\text{Al}_2\text{Cl}_7^-]) \\ K_2 &= [\text{Im}^+][\text{AlCl}_4^-]/(c_{\text{ImAlCl}_4} - [\text{AlCl}_4^-]) \\ [\text{Im}^+] &= [\text{AlCl}_4^-] + [\text{Al}_2\text{Cl}_7^-] \end{aligned} \quad [10]$$

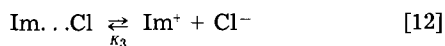
The parameters are equilibrium constants K_1 and K_2 , as well as the total concentration of salts in a mixture, $c_{\text{ImAl}_2\text{Cl}_7}$ and c_{ImAlCl_4} are obtained from the stoichiometry of the melt in the acid composition. We obtain a cubic equation in the form

$$\begin{aligned} &[\text{Im}^+]^3 + (K_1 + K_2)[\text{Im}^+]^2 + (K_1K_2 \\ &\quad - K_1c_{\text{ImAl}_2\text{Cl}_7} - K_2c_{\text{ImAlCl}_4})[\text{Im}^+] \\ &\quad - K_1K_2(c_{\text{ImAl}_2\text{Cl}_7} + c_{\text{ImAlCl}_4}) = 0 \end{aligned} \quad [11]$$

Introducing various values of K_1 and K_2 , which were, however, not very different from the value estimated for pure $\text{BuPyAl}_2\text{Cl}_7$, we were able to calculate the concentrations of ionic species across the range of acidity ($1 < \text{MC} < 2$). Fortunately, only one root of this cubic equation was positive, and no problem of choosing the proper root appeared. The calculated concentrations of ionic components were subsequently introduced into Eq. [5] formulated for each experimental value of specific conductivity measured for acidic melts and reported in Ref. (6) ($\text{MC} = 1.00, 1.04, 1.08, 1.27, 1.38, 1.50, 1.56, 1.78, 1.94, 2.0$, see Table II). Since our purpose was to find the best fit of the parameters of Eq. [5] but since the mobilities of ions are dependent on melt viscosity, we have used the values of specific conductivity normalized to the same viscosity, assuming the constancy of the Walden product. As a reference point, we have chosen the viscosity of the neutral $\text{AlCl}_3\text{-ImCl}$ melt at 25°C [$\eta = 0.178 \text{ P}$ (6)]. That is $\kappa_{\text{normalized}} = \eta \cdot \kappa_{\text{expt.}}/0.178$. Based on this normalization, ten separate equations were formulated (one for each MC), similar to Eq. [5], in which five parameters were involved; the three mobilities, u_{Im^+} , $u_{\text{Al}_2\text{Cl}_7^-}$, $u_{\text{AlCl}_4^-}$ and two equilibrium constants, K_1 , K_2 determining the concentrations of ions. (A more detailed explanation of this procedure is offered in the Appendix). The best fit was found by using the following set of parameters: $K_1 = 1.3 \text{ mol dm}^{-3}$, $K_2 = 1.2 \text{ mol dm}^{-3}$, $u_{\text{Im}^+} = 4.37 \times 10^{-5} \text{ cm}^2 \text{ s}^{-1} \text{ V}^{-1}$, $u_{\text{Al}_2\text{Cl}_7^-} = 2.65 \times 10^{-5} \text{ cm}^2 \text{ s}^{-1} \text{ V}^{-1}$, and $u_{\text{AlCl}_4^-} = 8.0 \times 10^{-5} \text{ cm}^2 \text{ s}^{-1} \text{ V}^{-1}$. The largest difference between experimental and calculated value of specific conductivity did not exceed 5% (Fig. 1).

Basic Melts

The same procedure was used for basic melts, which were treated as mixtures of ImCl and ImAlCl_4 . Additionally, the equilibrium



was assumed. Using the value of $K_2 = 1.2 \text{ mol dm}^{-3}$ (for ImAlCl_4), the mobilities of Im^+ and AlCl_4^- , as in acidic melts, and the mobility of Cl^- ($u_{\text{Cl}^-} = 3.2 \times 10^{-5} \text{ cm}^2 \text{ s}^{-1} \text{ V}^{-1}$) calculated according to Eq. [6] from a recently measured value of D_{Cl^-} ($D_{\text{Cl}^-} = 9.55 \times 10^{-7} \text{ cm}^2 \text{ s}^{-1}$ in 1:1 $\text{AlCl}_3\text{-ImCl}$ melt at 303 K , $\eta = 0.156 \text{ P}$) (12), the best fit for three points ($\text{MC} = 0.92, 0.72$, and 0.67) was found with $K_3 = 0.5 \text{ mol dm}^{-3}$. For two other, very basic melts ($\text{MC} = 0.56$ and 0.45), the values of normalized specific conduc-

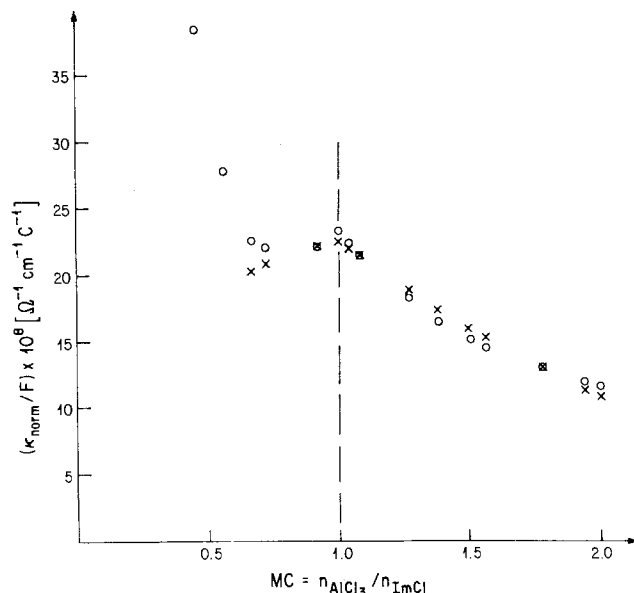


Fig. 1. The dependence of normalized specific conductivity on melt composition for $\text{AlCl}_3\text{-ImCl}$ melts at 298 K . o: Experimental values taken from Ref. (6). x: Values calculated in this paper.

tivity were very high (even higher than that for the neutral melt). We assume this is due to an increase of the number of charge carriers, possibly because of the formation of charged ion aggregates.

Discussion

To initiate this section, we will summarize and discuss the assumptions of the calculations presented in the previous section. First, we assumed (i) a constant ionic mobility-viscosity product, *i.e.*, $u_1\eta = \text{constant}$, (ii) the independence of u_1 on the concentration of electrolyte, and (iii) no change of transport mechanism across the entire range of melt compositions. Second, we assumed the validity of the Nernst-Einstein equation (Eq. [6]). Third, we assumed the independence of ion pair dissociation constants on melt composition.

The assumption that the viscosity of the melt is the only factor influencing the mobilities of ions and the constancy of the Walden product in the form $u_1\eta = \text{const.}$ is supported by numerous electrochemical measurements performed in the low temperature molten salts. For example, Nanjundiah *et al.* (13) found adherence to the Stokes-Einstein relation for diffusion coefficients of Fe(III) and Fe(II) in $\text{AlCl}_3\text{-BuPyCl}$ melts, and the constancy of $D\eta/T$ value was subsequently extended to the $\text{AlCl}_3\text{-ImCl}$ melts (12). $D\eta/T$ was found to be constant for BuPy^+ reduction in basic and neutral $\text{AlCl}_3\text{-ImCl}$ melts (14). Angell *et al.* (15) have carried out physicochemical measurements and computer simulations on the role of cation coordination numbers on melt physical properties for ambient temperature $\text{AlCl}_3\text{-}\alpha\text{-picolinium chloride}$ melts. They reported that ionic mobilities generally scale with the melt fluidity (reciprocal viscosity), except near glass-transition temperature. The relation between transport properties of ions (diffusion coefficients) and the viscosity of ionic liquids has also been discussed in the literature in terms of the applicability of the Stokes-Einstein equation [see, *e.g.*, Ref. (16)], and the applicability of this equation was also found in $\text{AlCl}_3\text{-BuPyCl}$ ambient temperature melts (13).

The change of the total concentration of electrolyte in going through the entire range of melt compositions is not very large (*e.g.*, for $\text{AlCl}_3\text{-ImCl}$ melts the total concentration changed from 4.6 mol dm^{-3} to 3.35 mol dm^{-3} for 1:1 and 2:1 $\text{AlCl}_3\text{-ImCl}$ melts, respectively), and should not significantly influence the mobilities or diffusion coefficients in the solvent. The most controversial question in our treatment of the problem is the applicability of the Nernst-Einstein equation (Eq. [6]) to the molten salt data. This problem has often been discussed in the litera-

ture, and it is not our purpose to present a review of this subject; a short discussion is in order.

The values of conductivity calculated from the Nernst-Einstein equation using experimental diffusion coefficients, usually measured by radiotracer methods, were found to be higher than experimentally determined values, and these positive deviations from the Nernst-Einstein equation usually increased with increasing temperature (17). Various interpretations of these facts have been given, both in terms of phenomenological and molecular theories.

Most important is a statement by Bockris and Hooper (18) that the Nernst-Einstein equation does not necessarily involve the laws of dilute solutions. This limitation is avoided in the conclusions of Mott and Gurney (19) and Carman and Stein (20).

The phenomenological "explanation" of deviations from the Nernst-Einstein equation can be derived from an irreversible thermodynamic approach [see, e.g., Ref. (21, 22)]. Using the Onsager phenomenological equations, it was found that the Nernst-Einstein equation is obeyed when the cross coefficients L_{\pm} and L_{\mp} , governing the influence of the driving force (\bar{F}_{\pm}) on the flow of the positive ions (J_{\pm}) and vice versa, are both equal to 0, i.e., when the flow of each species is unaffected by the driving forces on the other species. Since phenomenological treatments cannot throw light on the molecular mechanism responsible for the deviations from the Nernst-Einstein equation, several molecular explanations have been given. The common conclusion in all these explanations is that the extent to which the Nernst-Einstein equation holds is a measure of the similarity of the frictional interactions for the different modes of motion. If the frictional force in electrical conductance is taken to be the same as that in diffusion, the Nernst-Einstein relation results [see, e.g., Ref. (23)].

According to Borucka *et al.* (24), the measured diffusion includes displacements of entities which do not contribute to conduction (so-called "vacancy pair" or "molecule" diffusion). These authors apparently assumed that the Nernst-Einstein equation is applicable to molten salts if the "true" diffusion coefficients of ionic components, after subtraction of the noncontributing diffusion term corresponding to the displacement of entities which have a zero net charge during jumps and thus do not contribute to conduction, are used. Similar conclusions also have been given by Hansen and McDonald (25) in a molecular-dynamic study of a model in which the interionic pair potential consists of the coulombic term and an inverse-power repulsion, which is assumed to be the same for all ions. The relation between the self-diffusion coefficient and the electrical conductivity is discussed, and the observed deviations from the Nernst-Einstein equation are explained in terms of short-lived cross correlation and formation of ionic complexes which contribute to the diffusion flux but not to the electrical current. In both these papers, it was suggested that deviations from the Nernst-Einstein equation are not necessarily the result of a permanent association of ions of opposite charge.

The possibility of partial association of molten salts and its influence on transport properties was also considered (26-29). For example, Chemla and Lantelme (27), in discussing the validity of the Nernst-Einstein equation in molten salts, introduced the polyionic motion model. According to these authors, any experimental transport property should be the result of the motion of several species, i.e.

$$D_c = \sum x_i D_i \quad [13]$$

where x_i denotes the molar fraction of species i containing element c . These authors also found that the Nernst-Einstein equation is strictly obeyed in ionic single crystals.

Summarizing all these treatments one can see that the main problem is to find the proper value of the diffusion coefficients, or, in other words, to extract from the measured value of self-diffusion coefficients the diffusion

coefficients which could be attributed to the charged particles involved both in diffusion and conduction. We assume that the experimental values of the diffusion coefficients measured by using rotating disk electrode voltammetry as employed in this paper do not exceed the "true" values of ionic components, as was the case of self-diffusion coefficients measured by use of radiotracer method (24). If one considers the possibility that both the free ions and short-lived ion pairs contribute to diffusion, the diffusion coefficients measured here would be a weighted average of the respective values for free ions and ion pairs and thus would be smaller than the values for the free ion.

The assumption of the independence of the estimated equilibrium constants on melt composition (and concentration of electrolyte) is not new in the field of thermodynamics of reactions in molten salts. Similar assumptions have been implicit in all studies regarding the estimation of any other equilibrium constants, like that of reaction [1] (4) or complexation reactions (7, 8).

It is also worth mentioning that all the data taken to our analysis were measured at temperatures below the temperature $2T_0$, i.e., in the range of temperatures where the deviations from the Nernst-Einstein equation, according to Angell (30), are rather small. [T_0 is the temperature of configurational ground state for liquids, corresponding to the experimental value of the glass transition temperature; these parameters were reported by Wilkes *et al.* (6); the values of T_0 were estimated according to the Vogel-Tammann-Fulcher equation (31).]

Consequently, using all these assumptions, we were able to reproduce the conductivity data in the whole range of melt compositions, except in the very basic $\text{AlCl}_3\text{-ImCl}$ melts. As follows from Fig. 1, in this region of acidity a very significant increase of normalized conductivity is observed, presumably corresponding to a distinct increase of charge carriers. As follows from our calculations of concentrations of associated entities, $\text{Im}^+ \dots \text{AlCl}_4^-$ and $\text{Im}^+ \dots \text{Cl}^-$ (see Fig. 2 and Table II), the minimum of normalized conductivity is located at $[\text{Im}^+ \dots \text{Cl}^-]/[\text{Im}^+ \dots \text{AlCl}_4^-]$ ratio close to 1. For $r = [\text{Im}^+ \dots \text{Cl}^-]/[\text{Im}^+ \dots \text{AlCl}_4^-] > 1$, the steep increase of normalized conductivity is observed [the normalized equivalent conductance (κ_{norm}/c_0) is changing qualitatively in the same way (see Table II)]. This "strange" behavior of the conductivity can be explained if we consider the possibility of weak dipole-dipole-type interactions between $\text{Im}^+ \dots \text{Cl}^-$ and $\text{Im}^+ \dots \text{AlCl}_4^-$ at $r < 1$ and interactions $\text{Im}^+ \dots \text{Cl}^- - \text{Im}^+ \dots \text{Cl}^-$ accompanied with ion aggregate formation for $r > 1$. The hypothesis of ion aggregate formation in basic melts was considered by Wilkes *et al.* (32) in magnetic resonance studies of $\text{AlCl}_3\text{-ImCl}$ ionic liquids.

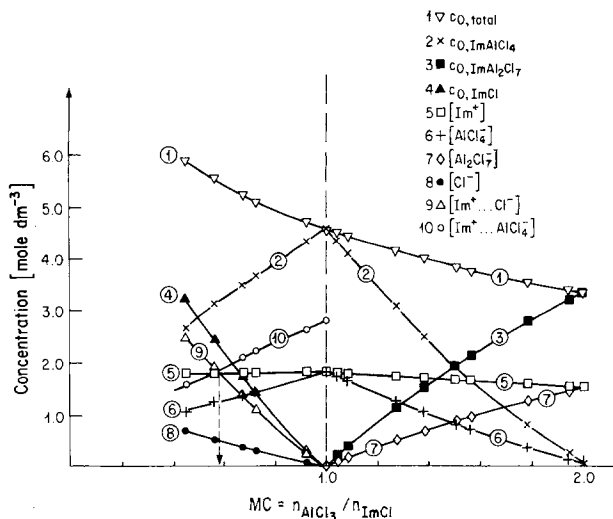


Fig. 2. The concentrations of different entities calculated in this paper for $\text{AlCl}_3\text{-ImCl}$ melts. The arrow at $MC = 0.58$ corresponds to $r = [\text{Im}^+ \dots \text{AlCl}_4^-]/[\text{Im}^+ \dots \text{Cl}^-] = 1$.

Table II. Physicochemical properties of AlCl₃-ImCl melts^a

Mole fraction of AlCl ₃ N_{AlCl_3}	Melt composition MC = $\frac{N_{AlCl_3}}{N_{ImCl}}$	Equivalent weight of melt $M_E = \frac{M_{ImCl} + M_{AlCl_3} [N_{AlCl_3} / (1 - N_{AlCl_3})]}{(g)}$	Total concentration of electrolyte; c_0 (mol dm ⁻³)	Analytical concentration of ImCl - $c_{0, ImCl}$ (mol dm ⁻³)	Analytical concentration of ImAlCl ₄ - $c_{0, ImAlCl_4}$ (mol dm ⁻³)	Analytical concentration of ImAl ₂ Cl ₇ - $c_{0, ImAl_2Cl_7}$ (mol dm ⁻³)	Density at 298 K; (g cm ⁻³)	Viscosity at 298 K; η (P)	Specific conductivity at 298 K; $\kappa \times 10^3$ ($\Omega^{-1} \text{cm}^{-1}$)	Specific conductivity; $\kappa_{norm} \times 10^3$ Normalized to $\eta = 0.178 \text{P}$ ($\Omega^{-1} \text{cm}^{-1}$)	Equivalent conductance normalized on $\eta = 0.178 \text{P}$; $\Lambda = \frac{\kappa_{norm}}{c_0} (10^{-3} \Omega^{-1} \text{cm}^{-1} \text{mol}^{-1})$	[Im ⁺]	[Al ₂ Cl ₇ ⁻]	[AlCl ₄ ⁻]	[Cl ⁻]	[Im ⁺ ...AlCl ₄ ⁻]	[Im ⁺ ...Cl ⁻]	[Im ⁺ ...AlCl ₄ ⁻]/[Im ⁺ ...Cl ⁻]
0.31	0.45	206.6	5.89	3.24	2.65	—	1.217	2.68	2.48	37.34	6.34	1.78	1.07	0.71	1.58	2.53	0.62	
0.36	0.56	221.6	5.59	2.45	3.14	—	1.239	1.236	3.88	26.94	4.82	1.79	1.26	0.53	1.88	1.92	0.98	
0.40	0.67	235.5	5.27	1.76	3.51	—	1.240	-0.58	6.51	21.88	4.03	1.79	1.41	0.38	2.10	1.38	1.5	
0.42	0.72	243.2	5.13	1.42	3.71	—	1.247	0.475	8.0	21.34	4.16	1.80	1.49	0.31	2.22	1.11	2.0	
0.48	0.92	269.7	4.74	0.37	4.37	—	1.278	-0.20	18.2	21.47	4.53	1.82	1.74	0.08	2.63	0.29	9.1	
0.50	1.0	280.0	4.60	—	4.60	—	1.288	0.178	22.6	22.6	4.86	1.82	1.82	—	2.78	—	—	
0.51	1.04	285.4	4.53	—	4.34	0.19	1.293	0.175	22.03	21.66	4.78	1.81	0.08	1.73	—	—	—	
0.52	1.08	291.1	4.47	—	4.09	0.38	1.300	0.172	21.46	20.74	4.65	1.80	0.16	1.64	—	—	—	
0.56	1.27	316.3	4.19	—	3.05	1.14	1.325	0.162	13.5	17.64	4.21	1.74	0.51	1.23	—	—	—	
0.58	1.38	330.8	4.03	—	2.50	1.53	1.334	0.156	18.20	15.95	3.95	1.70	0.67	1.03	—	—	—	
0.60	1.50	346.6	3.87	—	1.935	1.935	1.346	0.151	17.3	14.63	3.78	1.66	0.85	0.81	—	—	—	
0.61	1.56	355.2	3.80	—	1.66	2.14	1.351	0.148	16.85	14.01	3.68	1.65	0.95	0.70	—	—	—	
0.64	1.78	383.7	3.57	—	0.79	2.78	1.370	0.143	15.57	12.51	3.50	1.59	1.25	0.34	—	—	—	
0.66	1.94	405.5	3.41	—	0.20	3.21	1.382	0.141	14.70	11.60	3.40	1.55	1.46	0.09	—	—	—	
0.667	2.0	413.3	3.35	—	—	3.35	1.384	0.140	14.2	11.17	3.33	1.54	1.54	0	—	—	—	

^a Values of density, viscosity, and specific conductivity are taken from Ref. (6); all concentrations are calculated in this paper.

The interpretation of normalized specific conductivity in the acidic and slightly basic region seems to be rather straightforward. Going from 2:1 AlCl₃-ImCl melt (pure, molten ImAl₂Cl₇) to 1:1 melt (pure, molten ImAlCl₄), the increase of normalized specific conductivity (as well as of normalized equivalent conductivity) can be related to the replacement of the less mobile anion (Al₂Cl₇⁻) with the more mobile one (AlCl₄⁻). By analogy, the small decrease of conductivity in going from neutral to basic melts can be explained in terms of dilution of the high conducting neutral melt with molten ImCl, containing chloride ions which are less mobile than AlCl₄⁻.

An example of the usefulness of this treatment is the analysis of the differences of normalized conductivities measured for 1:1 and 2:1 AlCl₃-RCl melts. Assuming that the degree of association for all these melts is similar, we can write Eq. [5] for each of these melts

$$\kappa_{norm}^{BuPyAl_2Cl_7} / \{\alpha F c_{0, BuPyAl_2Cl_7}\} = u_{BuPy^+} + u_{Al_2Cl_7^-} \quad [14]$$

$$\kappa_{norm}^{BuPyAlCl_4} / \{\alpha F c_{0, BuPyAlCl_4}\} = u_{BuPy^+} + u_{AlCl_4^-} \quad [15]$$

$$\kappa_{norm}^{ImAl_2Cl_7} / \{\alpha F c_{0, ImAl_2Cl_7}\} = u_{Im^+} + u_{Al_2Cl_7^-} \quad [16]$$

$$\kappa_{norm}^{ImAlCl_4} / \{\alpha F c_{0, ImAlCl_4}\} = u_{Im^+} + u_{AlCl_4^-} \quad [17]$$

Subtracting Eq. [14] from [15] and Eq. [16] from [17], we get expressions for the difference of mobilities of AlCl₄⁻ and Al₂Cl₇⁻ in the melts containing either BuPy⁺ or Im⁺ cations. Introducing experimental values, we find that these differences are almost exactly the same in both melts. The constant difference between $u_{AlCl_4^-}$ and $u_{Al_2Cl_7^-}$ calculated for both melts, which is in accord with chemical intuition, seems to indicate that the assumptions in our paper are reasonable.

Some comments can be made regarding the very high mobility of tetrachloroaluminate anion. This observation cannot be explained from the viewpoint of ionic radii of this ion, and we still do not have any reasonable explanation. However, a very high mobility of AlCl₄⁻ ion was postulated by Angell *et al.* (15) in a paper dealing with ambient temperature AlCl₃- α -picolinium chloride melts.

In view of the probable uncertainties inherent in the estimation of ionic mobilities, especially in the case of AlCl₄⁻ and Im⁺ (no corresponding diffusion coefficients were measured), no detailed analysis of these data will be

presented; however, it is difficult to avoid, for example, the problem of transference numbers in molten salt chemistry. However, for cases like the 2:1 AlCl₃-BuPyCl melt, where both diffusion coefficients were measured and the ratio of $D_{BuPy^+}/D_{Al_2Cl_7^-}$ was found to be about 1.26, one cannot expect that only cations are the charge carriers and $t_{M^+} = 1$. If we formally calculate the transference numbers in this particular case, we obtain the respective value for cation equal to 0.56. This result is supported by data for other molten salts containing large organic cations (5, 33) [see also Ref. (34)]. Recently, Hussey and Øye (35), by use of the Hittorf method, determined the external and internal transport numbers for the AlCl₃-ImCl ionic liquid in acidic melt compositions. The Im⁺ external and internal transport numbers were found to be 0.71 and 1.0, respectively, in the acidic range. This result is consistent with our findings only in the case of more acidic melts (MC close to 2).

Finally, we must emphasize that our very simple treatment, based on considering the mobilities of ions, seems to be more fruitful and predictable than the traditional treatment based on the analysis of changes of equivalent conductance with concentration. In our opinion, this latter treatment can be successfully used only for electrolyte solutions in "normal" solvents where no significant change of viscosity and composition occurs. The sense of equivalent conductance in binary molten salts is not very clear, however formally this property can be defined (5, 6).

Acknowledgment

This work was supported by the Air Force Office of Scientific Research.

Manuscript submitted July 20, 1984; revised manuscript received Dec. 10, 1984.

The State University of New York assisted in meeting the publication costs of this article.

APPENDIX

In the first step, we calculate from Eq. [10] the concentrations of ionic components: Im⁺, AlCl₄⁻, and Al₂Cl₇⁻ assuming 20 different sets of dissociation constants K_1 and K_2 . We assume these constants are (i) not very different from the value calculated for BuPy⁺...Al₂Cl₇⁻ ($K = 1.3 \text{ mol dm}^{-3}$) and (ii) smaller than that value (since the ra-

dus of Im^+ is smaller than of BuPy^+). We expect more pronounced ion pairing in the case of imidazolium salts and hence smaller dissociation constants.

In the next step, the concentrations calculated for the ionic components were introduced into Eq. [5] formulated for ten different melt compositions: MC = 1.00, 1.04, 1.08, 1.27, 1.38, 1.50, 1.56, 1.78, 1.94, 2.0. Before specific conductivities were introduced into Eq. [5], they were normalized to the same viscosity; the value of the viscosity of the neutral $\text{AlCl}_3\text{-ImCl}$ melt at 25°C was chosen arbitrarily. This normalization permitted the use of the same set of mobilities, u_{Im^+} , $u_{\text{AlCl}_4^-}$, and $u_{\text{Al}_2\text{Cl}_7^-}$, in all ten equations (one equation for one melt composition). A fixed set of dissociation constants, K_1 , K_2 , determined the concentrations of ions. At this point, we fitted the ten equations with three parameters (three mobilities) for 20 separate cases (various sets of K_1 and K_2). The initial value of $u_{\text{Al}_2\text{Cl}_7^-}$ employed was as calculated from the corresponding diffusion coefficient (see Table I), and the initial value of u_{Im^+} was assumed slightly greater than u_{BuPy^+} for the same reason as above (size of radius, see also Table I). The minimized sum of squares of the difference between calculated and experimental normalized specific conductivities was used to establish the "best" value for the mobilities and equilibrium constants.

In addition, the case of large K_1 and K_2 values (no ion pairing) was considered. We assumed $\alpha = 1$ and applied similar procedures to those described by Eq. [14]-[17]. That is, we considered the differences of normalized specific conductivities between 1:1 and 1.5:1 as well as between 1.5:1 and 2:1 melts. In these simple cases, we can rewrite Eq. [5] as

$$\kappa_{(1:1)}/c_{(1:1)} = u_{\text{Im}^+} + u_{\text{AlCl}_4^-} \\ = 4.91 \times 10^{-3} \Omega^{-1} \text{cm}^{-1} \text{mol}^{-1} \quad \text{for MC} = 1.0 \quad \text{[A-1]}$$

$$\kappa_{(1.5:1)}/c_{(1.5:1)} = u_{\text{Im}^+} + 0.5(u_{\text{AlCl}_4^-} + u_{\text{Al}_2\text{Cl}_7^-}) \\ = 3.78 \times 10^{-3} \Omega^{-1} \text{cm}^{-1} \text{mol}^{-1} \quad \text{for MC} = 1.5 \quad \text{[A-2]}$$

$$\kappa_{(2:1)}/c_{(2:1)} = u_{\text{Im}^+} + u_{\text{Al}_2\text{Cl}_7^-} \\ = 3.33 \times 10^{-3} \Omega^{-1} \text{cm}^{-1} \text{mol}^{-1} \quad \text{for MC} = 2 \quad \text{[A-3]}$$

Subtracting Eq. [A-2] from [A-1] and Eq. [A-3] from [A-2], we obtain

$$\text{[A-1]} - \text{[A-2]} = 0.5(u_{\text{AlCl}_4^-} - u_{\text{Al}_2\text{Cl}_7^-}) \\ = 1.12 \times 10^{-3} \Omega^{-1} \text{cm}^{-1} \text{mol}^{-1} \quad \text{[A-4]}$$

while

$$\text{[A-2]} - \text{[A-3]} = 0.5(u_{\text{AlCl}_4^-} - u_{\text{Al}_2\text{Cl}_7^-}) \\ = 0.45 \times 10^{-3} \Omega^{-1} \text{cm}^{-1} \text{mol}^{-1} \quad \text{[A-5]}$$

This significant discrepancy between Eq. [A-4] and [A-5] indicates that the "no ion pairing" model is not acceptable.

REFERENCES

- H. L. Chum, V. R. Koch, L. L. Miller, and R. A. Osteryoung, *J. Am. Chem. Soc.*, **97**, 3264 (1975).
- J. Robinson and R. A. Osteryoung, *ibid.*, **101**, 323 (1979).
- R. J. Gale and R. A. Osteryoung, *Inorg. Chem.*, **18**, 1603 (1979).
- J. S. Wilkes, J. A. Levisky, R. A. Wilson, and C. L. Hussey, *ibid.*, **21**, 1263 (1982).
- R. A. Carpio, L. A. King, R. E. Lindstrom, J. C. Nardi, and C. L. Hussey, *This Journal*, **126**, 1644 (1979).
- A. A. Fannin, D. A. Floreani, L. A. King, J. S. Landers, B. J. Piersma, D. J. Stech, R. L. Vaughn, J. S. Wilkes, and J. L. Williams, *J. Phys. Chem.*, **88**, 2614 (1984).
- T. M. Laher and C. L. Hussey, *Inorg. Chem.*, **21**, 4079 (1982).
- T. M. Laher and C. L. Hussey, *ibid.*, **22**, 1279 (1983).
- R. J. Gale, B. Gilbert, and R. A. Osteryoung, *ibid.*, **17**, 2728 (1978).
- M. Lipsztajn and R. A. Osteryoung, *This Journal*, **130**, 1968 (1983).
- J. Robinson, R. C. Bugle, H. L. Chum, D. Koran, and R. A. Osteryoung, *J. Am. Chem. Soc.*, **101**, 3776 (1979).
- M. Lipsztajn and R. A. Osteryoung, *Inorg. Chem.*, **23**, 1735 (1984).
- C. Nanjundiah, K. Shimizu, and R. A. Osteryoung, *This Journal*, **129**, 2474 (1982).
- M. Lipsztajn and R. A. Osteryoung, *Electrochim. Acta*, **29**, 1349 (1984).
- C. A. Angell, I. M. Hodge, and P. A. Cheeseman, in "Molten Salts," J. P. Pemsler, J. Braunstein, K. Nobe, D. R. Morris, and N. E. Richards, Editors, pp. 138-149, The Electrochemical Society Softbound Proceedings Series, Princeton, NJ (1976).
- J. O'M. Bockris and A. K. N. Reddy, in "Modern Aspects of Electrochemistry," Vol. 1, pp. 550-553, Plenum Press, New York (1977).
- H. Bloom and J. O'M. Bockris, in "Fused Salts," B. R. Sundheim, Editor, p. 20, McGraw-Hill, New York (1964).
- J. O'M. Bockris and G. W. Hooper, *Discuss. Faraday Soc.*, **32**, 218 (1961).
- N. F. Mott and R. W. Gurney, in "Electronic Processes in Ionic Crystals," p. 63, Oxford University Press, New York (1957).
- R. C. Carman and L. H. Stein, *Trans. Faraday Soc.*, **52**, 619 (1956).
- B. R. Sundheim, in "Fused Salts," B. R. Sundheim, Editor, pp. 239-245, McGraw-Hill, New York (1964).
- J. O'M. Bockris and A. K. N. Reddy, in "Modern Aspects of Electrochemistry," Vol. 1, pp. 413-415, 557-560, Plenum Press, New York (1977).
- B. R. Sundheim, in "Molten Salts," J. P. Pemsler, J. Braunstein, K. Nobe, D. R. Morris, and N. E. Richards, Editors, p. 126, 127, The Electrochemical Society Softbound Proceedings Series, Princeton, NJ (1976).
- A. Z. Borucka, J. O'M. Bockris, and J. A. Kitchener, *J. Phys. Chem.*, **24**, 1282 (1956).
- J. P. Hansen and I. R. McDonald, *Phys. Rev. A*, **11**, 2111 (1975).
- S. Zuca and M. Constantinescu, *Rev. Roumaine Chim.*, **17**, 385 (1972).
- M. Chemla and F. Lantelme, in "Molten Salts," J. P. Pemsler, J. Braunstein, K. Nobe, D. R. Morris, and N. E. Richards, Editors, pp. 155-158, The Electrochemical Society Softbound Proceedings Series, Princeton, NJ (1976).
- P. L. Spedding, *J. Phys. Chem.*, **76**, 1348 (1972).
- B. Cleaver, in "Advances in Molten Salts Chemistry," Vol. 4, G. Mamantov, J. Braunstein and C. B. Mamantov, Editors, p. 127, Plenum Press, New York (1981).
- C. A. Angell, *J. Phys. Chem.*, **69**, 399 (1965).
- G. S. Fulcher, *J. Am. Ceram. Soc.*, **8**, 339 (1925).
- A. A. Fannin, L. A. King, J. A. Levisky, and J. S. Wilkes, *J. Phys. Chem.*, **88**, 2609 (1984).
- D. S. Newman, W. Rohr, D. Kirklin, and H. D. Frame, *This Journal*, **119**, 797 (1972).
- H. A. Øye and L. A. King, *Inorg. Nucl. Chem. Lett.*, **16**, 547 (1980).
- C. L. Hussey and H. A. Øye, *This Journal*, **131**, 1621 (1984).

Magnetic and Transport Properties of Electrochemically Oxidized Polyacetylene

John R. Reynolds,* Joseph B. Schlenoff,* and James C. W. Chien

Department of Chemistry, Department of Polymer Science and Engineering, Materials Research Laboratories, University of Massachusetts, Amherst, Massachusetts 01003

ABSTRACT

The magnetic and transport properties of polyacetylene electrochemically oxidized in the presence of perchlorate ion have been determined. Room temperature dc conductivity is unaffected by doping between $10^{-6} < y \leq 10^{-3.5}$. A rapid conductivity increase occurs with increasing dopant level having a midpoint of transition at $ca. y \sim 8 \times 10^{-3}$. By comparison, the change in thermopower *vs.* y is sharper taking place within a tenfold increase in y with a midpoint at $ca. y \sim 3 \times 10^{-3}$. The unpaired spin concentrations remain constant as dopant concentration increases before the onset of a Dysonian lineshape at $ca. y = 10^{-2}$. The results are interpreted as the melting of a glassy carrier state causing the sharp change of transport properties. A phase separation into metallic domains occurs at $y = ca. 10^{-2}$. Side reactions involving the electrolyte complicate the electrochemistry of polyacetylene.

Polyacetylene, $[CH]_x$, can be doped to the highly conductive state by chemical, photochemical, or electrochemical processes (1). The last of the three (2) is the most versatile, since the level of doping can be controlled by the applied potential and the approach to equilibrium (3) can be monitored by the current. This technique has been used to study *cis-trans* isomerization (4) and changes in the midgap states (5). However, even though the magnetic and transport properties of chemically doped polyacetylene have been extensively investigated, especially in regard to the effect of dopant uniformity (6), the same cannot be said about the electrochemically doped materials. Studies on the electrochemical process have been confined up to now to high dopant concentration. The central purpose of this paper is to report the magnetic and transport properties of electrochemically oxidized *trans*- $[CH]_x$ from ppm to percent dopant level.

Experimental Techniques

Film preparation.—Free standing films of polyacetylene, approximately 100 μm thick, were prepared by the method of Ito *et al.* (7) at 195 K. The resulting *cis*-rich films were thermally isomerized to *trans*- $[CH]_x$ by heating at 453 K for 1 h *in vacuo*. Films were handled under N_2 in a Vacuum Atmospheres dry box and stored at 195 K under argon.

Doping method.—Electrochemical oxidation of *trans*- $[CH]_x$ was performed by loading a 1 cm diam circular specimen (*ca.* 10 mg) into a cell constructed from a Teflon stopcock (Fig. 1). The working electrode makes pressed contact with the film, which can be subsequently removed for characterization of the doped polymer. Lithium wire counter and reference electrodes were scraped clean under 1M LiClO_4 in propylene carbonate immediately prior to use. LiClO_4 was melt dried under dynamic vacuum; propylene carbonate was distilled under vacuum from anhydrous sodium carbonate and potassium permanganate. Potential was controlled (with IR compensation) by a Princeton Applied Research (PAR) 173 potentiostat/galvanostat. Charge was recorded with a PAR 179 digital coulometer. Open-circuit potential, V_{oc} , was measured with a Keithley 616 electrometer.

Oxidation of $[CH]_x$ was carried out by stepping the applied potential of the working electrode just high enough to pass 0.02–0.05 mA mg^{-1} of polymer. After each potential step, the low current, which assures a slow doping rate, was allowed to decay to less than 10% of the initial current before another potential increase was applied. The dopant level per CH unit, y , was determined coulometrically.

After doping to the desired level, the film was immersed in 5 ml of electrolyte for 5 or 10 days to study the interaction between doped $[CH]_x$ and the electrolyte. The

film was then washed thoroughly in distilled, degassed CH_2Cl_2 , and dried *in vacuo*. Alternatively, the doped film after washing and drying was allowed to stand in N_2 or argon atmosphere and changes in V_{oc} and room temperature dc conductivity (σ_{RT}) followed.

Measurement methods.—Conductivity was measured using the four-probe technique and the thermoelectric power coefficient (\mathcal{E}) was measured as described previously (6). EPR spectra were recorded with a Varian X-band spectrometer; the unpaired spin concentration was obtained by double integration of the EPR spectra and compared with a standard solution of tetramethylpiperidinoxyl free radical in hexadecane. However, EPR

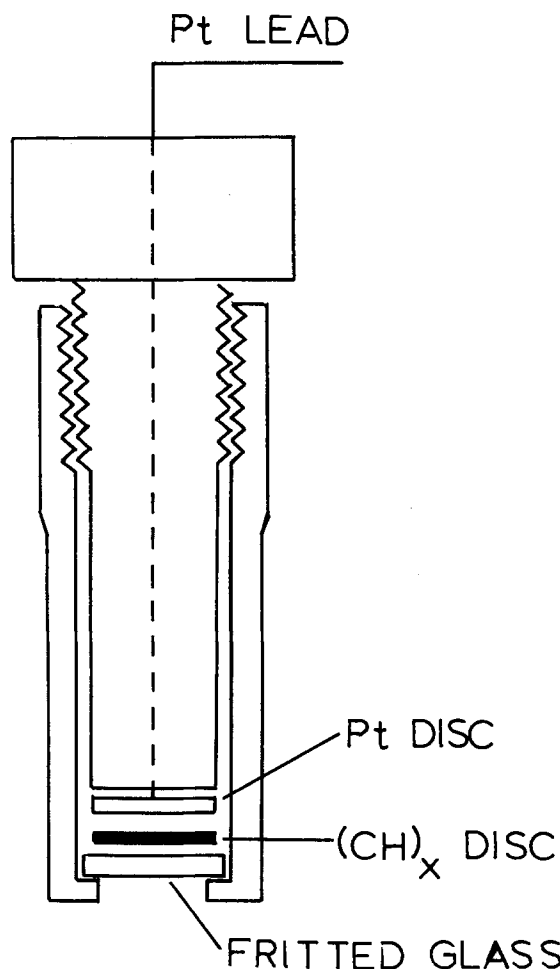


Fig. 1. Schematic drawing of the electrochemical cell constructed from a Teflon stopcock.

* Electrochemical Society Student Member.

spectra with Dysonian lineshapes cannot be integrated in the same way. V_{oc} 's of dried films were measured vs. Li/1M LiClO₄.

Experimental Results

Open-circuit potential.—It has been reported (3) that V_{oc} is linearly dependent on the degree of oxidation by

$$V_{oc} (24h) = 3.43 + 0.14 \ln y \quad [1]$$

where $5 \times 10^{-4} \leq y \leq 6 \times 10^{-2}$. It was observed that the values of V_{oc} decrease with time of contact between doped [CH]_x and the electrolyte. We extended this experiment to $10^{-6} < y < 9 \times 10^{-2}$ and increased the time of equilibration to 5 and 10 days (Fig. 2). The results showed that Eq. [1] is valid only for the range of y studied by Kaneto *et al.* (3). The shape of the V_{oc} vs. $\log y$ plot resembles, to a certain extent, the $\log \sigma$ vs. $\log y$ plots.

Figure 3 shows that a [CH(ClO₄)_{0.05}]_x film retains its initial conductivity when stored in nitrogen after rinsing and removal of solvent, whereas a similar film in contact with electrolyte loses conductivity steadily.

Transport properties.—The variation σ_{RT} with dopant level is shown in Fig. 4. There is no significant change in σ for $10^{-6} < y < 10^{-3.5}$ above which there is a 10⁷-fold increase in σ between $10^{-3.5} < y < 10^{-1.5}$. If one takes the midpoint of this transition at $\sigma = 10^{-2} (\Omega\text{cm})^{-1}$, this corresponds to a y value of ca. 8×10^{-3} .

The open squares in Fig. 4 are those of specimens equilibrated with the electrolyte for 21 days. They have, in general, much lower conductivities than those equilibrated for a shorter time.

There is a small decrease of the thermopower coefficient, \mathcal{S} , between $10^{-6} \leq y \leq 10^{-3}$ (Fig. 5). A precipitous drop in \mathcal{S} occurs between $10^{-3} \leq y \leq 10^{-2}$ with the midpoint of the transition at $y \sim 3 \times 10^{-3}$. Therefore, without the interfibril contribution to resistance observed by dc conductivity, the intrinsic transition in transport property according to \mathcal{S} occurs over a narrower range and at a lower value of y .

Magnetic properties.—The unpaired spin concentrations of electrochemically doped polyacetylene remain virtually constant for $10^{-6} \leq y \leq 10^{-2}$ (Table I), over which range the EPR spectra can be doubly integrated. The Cu-

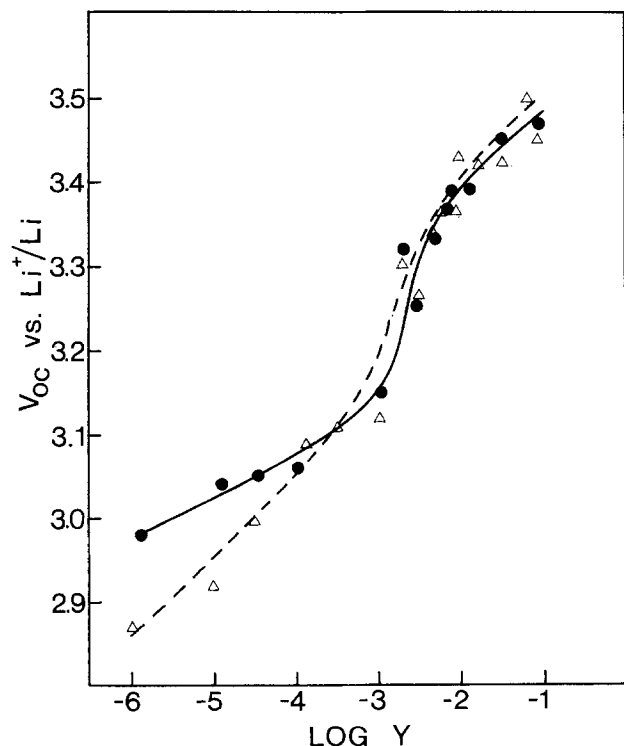


Fig. 2. Variation of V_{oc} with $\log y$ measured on film immersed in electrolyte for 5 days (solid circles) and 10 days (triangles).

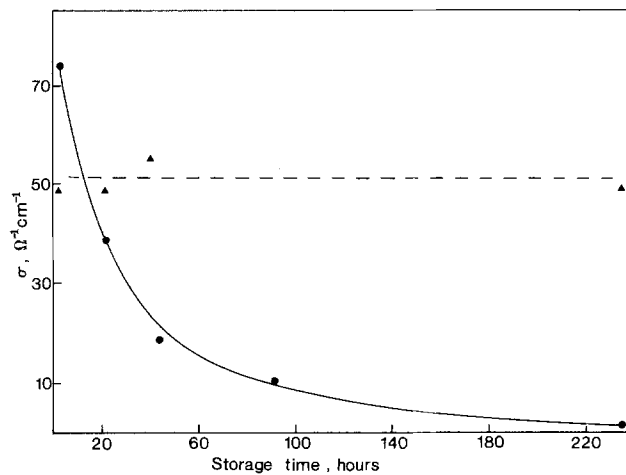


Fig. 3. Variation of conductivity of electrochemically oxidized [CH(ClO₄)_{0.05}]_x film with time (solid circles) film immersed in electrolyte with 150 ppm H₂O. Solid triangles: film rinsed, dried, and stored under nitrogen.

rie dependence decreases with increasing y (Fig. 6) as determined by spin concentration vs. T^{-1} between 133 and 278 K. When the films attain a $\sigma > 10 (\Omega\text{cm})^{-1}$ at $y > 10^{-2}$, the EPR spectra assumed a Dysonian lineshape (Fig. 7).

Discussion

The questions of homogeneity in doping and semiconductor to "metal" transition have been the subjects of numerous publications. We have proposed several criteria for homogeneity in the case of chemical doping (6). In the case of electrochemical doping, the process can be monitored continuously. Due to the nature of electrochemical doping, one must consider the homogeneity of dopant ion

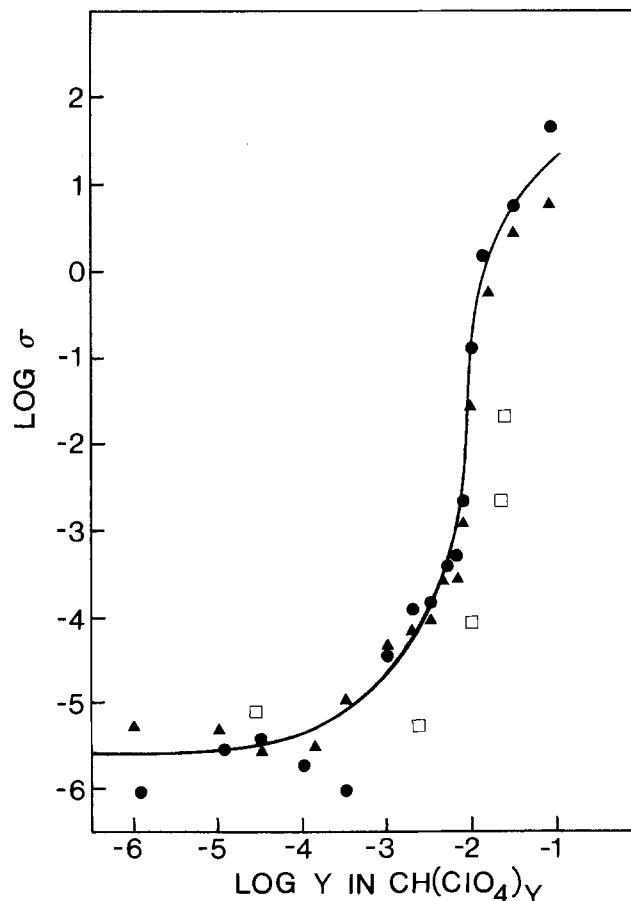


Fig. 4. Variation of $\log \sigma$ with $\text{trans-}[\text{CH}]_x$ electrochemically oxidized in LiClO₄ electrolyte for samples immersed in electrolyte for 5 days (solid circles), 10 days (solid triangles), and 21 days (squares).

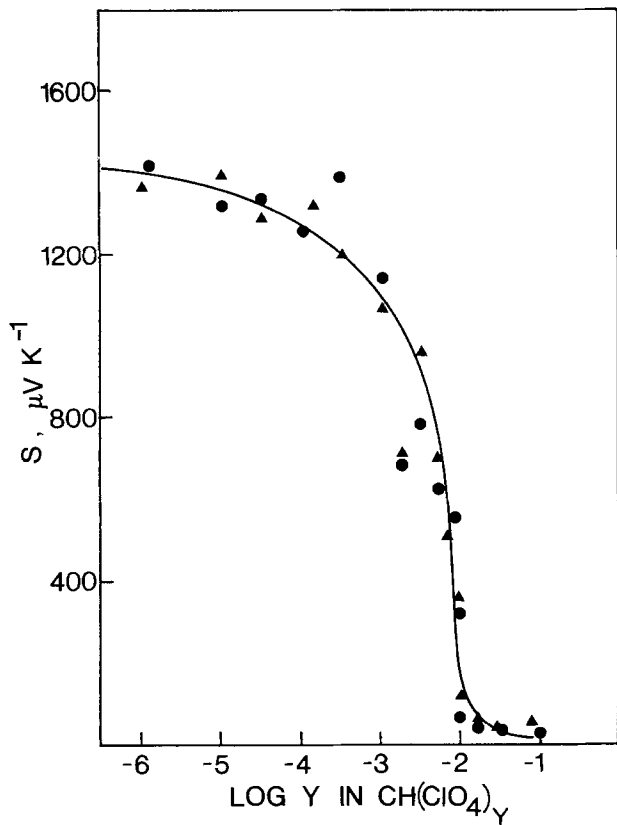


Fig. 5. Variation of S with $trans\text{-}[\text{CH}]_x$ electrochemically oxidized in LiClO_4 electrolyte.

distribution at two morphological levels. The first is the macroscopic distribution across the thickness of the 100 μm film and the second is that across the $[\text{CH}]_x$ fibrils from its surface to the core.

For the macroscopic $[\text{CH}]_x$ film, initial oxidation will occur at the Pt-polymer contact. Further removal of electrons proceeds across the thickness of the film. To study this process, an experiment was carried out with two $[\text{CH}]_x$ films sandwiched together and placed into a doping vessel. A potential of 3.7V was applied for 24h, and the

Table I. Unpaired spin concentrations in electrochemically oxidized $[\text{CH}]_x$

Equilibration time	y in $[\text{CH}(\text{ClO}_4)_y]_x$	Spins CH unit ($\times 10^4$)
5 days	1.3×10^{-6}	4.78
	1.1×10^{-5}	6.58
	3.2×10^{-5}	7.41
	1.0×10^{-4}	6.25
	3.0×10^{-4}	3.89
	1.0×10^{-3}	3.65
	3.0×10^{-3}	6.76
	1.3×10^{-2}	3.64
	3.2×10^{-2}	4.27
	Average	
Relative standard deviation		28.6%
10 days	3.1×10^{-5}	3.82
	1.3×10^{-4}	4.78
	3.0×10^{-4}	3.33
	1.0×10^{-3}	3.08
	3.1×10^{-3}	3.65
	1.5×10^{-2}	3.39
	3.2×10^{-2}	3.91
	Average	
Relative standard deviation		14.9%
21 days	Undoped	3.82
	2.9×10^{-5}	4.33
	2.3×10^{-3}	3.88
	9.5×10^{-3}	4.30
	2.3×10^{-2}	3.60
	3.0×10^{-2}	3.25
	Average	
Relative standard deviation		10.7%

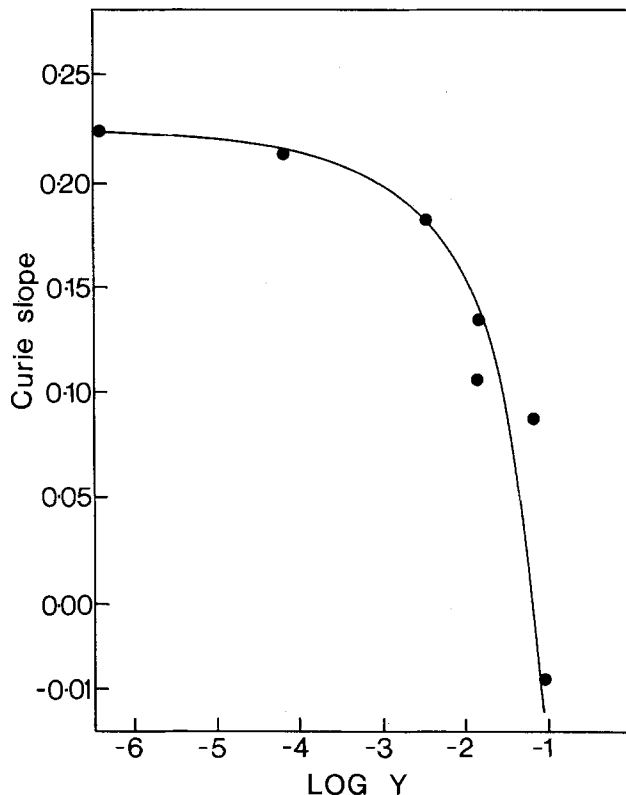


Fig. 6. Variation of Curie dependency of EPR with $\log y$

two films were separated, washed, and dried. We found compositions of $[\text{CH}(\text{ClO}_4)_{0.04}]_x$ and $[\text{CH}(\text{ClO}_4)_{0.03}]_x$ by elemental analysis with respective conductivities of 11 and 9 $(\Omega \text{ cm})^{-1}$. This small difference was similar to that observed by Castaing microprobe studies (8).

With regard to the microscopic homogeneity of electrochemical doping, Kaneto *et al.* (3) attributed the voltage

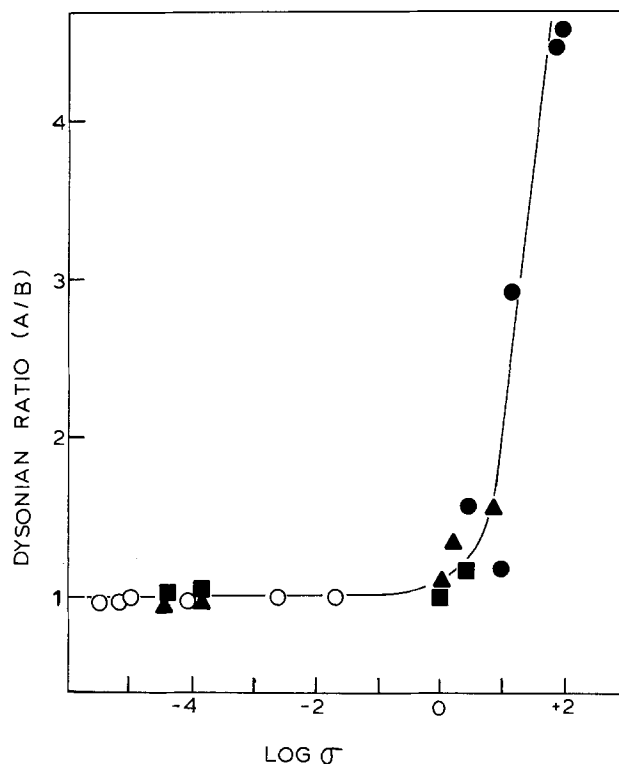


Fig. 7. Change of EPR asymmetry with $\log \sigma$; A/B ratio defines the Dysonian lineshape. Sample equilibrated in electrolyte for 5 days (solid triangles), 10 days (solid squares), and 21 days (open circles). Closed circles represents no equilibration.

decrease of $[\text{CH}(\text{ClO}_4)_y]_r$, on standing after doping, to the diffusion of dopant ions from the exterior to the interior of the ca. 20 nm diam polymer fibrils. This process is said to be slow and a diffusion-limited equilibrium attained after 24h (3). Since the V_{oc} is determined by that portion of the $[\text{CH}(\text{ClO}_4)_y]_r$ in contact with the electrolyte, its value will decrease with time on standing as the extent of oxidation at the exterior of the fibrils decreases while the degree of oxidation in the fibril interior increases by the diffusion of the ClO_4^- ion. A theory of electric field enhancement of diffusion was proposed (9) to explain how high power and current densities can be generated by a $[\text{CH}]_r$ battery cell despite the postulated slow diffusion and low ionic mobility in polyacetylene. We have found (10) that for ultrathin $[\text{CH}]_r$ films (~ 100 nm) complete and uniform electrochemical doping took only a few seconds. In these samples, there are an abundance of microfibrils only 2-3 nm in diameter. For the more conventional $[\text{CH}]_r$ film, *i.e.*, prepared by the procedure of Ito *et al.* (7) comprised of thicker fibrils of 20-30 nm in diameter, we found equilibrium electrochemical doping to take 1.5-2h.

The following results show definitively that side reactions involving the electrolyte present complications to the electrochemical behavior of $[\text{CH}]_r$. For instance, if $[\text{CH}]_r$ is doped to $V_{oc} = 3.67\text{V}$, washed, dried, and kept in argon, there is only a 0.05V drop in V_{oc} after 400h. However, if the same film remains immersed in the electrolyte, the V_{oc} drops rapidly and asymptotically to 3.5V. There is little further decrease of V_{oc} after 24h as reported and V_{oc} is virtually unchanged after 5 and 10 days, as shown in Fig. 2 for $y \geq 3 \times 10^{-4}$. This result is best interpreted as reactions of doped $[\text{CH}]_r$ at high potential occurring with electrolyte until all the doped surface sites have reacted. The same behavior was found for conductivity. In Fig. 3, a $[\text{CH}(\text{ClO}_4)_{0.05}]_r$ sample, rinsed, dried, and kept under nitrogen, shows no decrease of σ_{RT} after 230h. But, a similar sample immersed in electrolyte has exponential decay in conductivity. Figure 4 shows that, even though σ_{RT} (5 days) $\approx \sigma_{RT}$ (10 days), longer contact with electrolyte can reduce σ_{RT} further, indicating slow but further reaction between doped $[\text{CH}]_r$ and the electrolyte.

The side reaction occurs more slowly for $[\text{CH}]_r$ doped to lower $V_{oc} < 3.05\text{V}$ (*i.e.*, $y < 10^{-4}$). Figure 2 shows that at a given dopant concentration the V_{oc} is smaller for samples immersed in electrolyte for 10 days than after 5 days. In other words, side reactions with electrolyte are still progressing between 5 and 10 days. The slower side reaction may be mainly due to the fact that the $[\text{CH}]_r$ is at lower oxidation potential. An additional factor may be that decay of V_{oc} continues until the surface is covered with species formed in the reaction with the electrolyte.

One observation we have made is that, following the doping of $[\text{CH}]_r$ and removal of the electrode, the electrolyte solution turned very dark in color after about 3 weeks. Electrolyte which was not used in the doping process remains clear indefinitely. Therefore, there are oxidation products dissolved in the electrolyte which were formed during the doping process.

Finally, Eq. [1] is applicable only to a limited range of high dopant concentrations. Figure 2 shows that the V_{oc} vs. $\log y$ is sigmoidal in shape, which reflects the change of $\log \sigma_{RT}$ vs. $\log y$ (Fig. 4). Our results cannot be reconciled with the conclusion of Kaneto *et al.* (3) that the drop of V_{oc} with time is due to diffusion of dopant ions from the surface to the interior of the $[\text{CH}]_r$ fibrils.

The changes in σ and \mathcal{E} vs. y observed here (Fig. 4 and 5) are nearly as sharp as those reported for $[\text{CH}]_r$ very slowly doped with I_2 and AsF_5 (6). This large increase of transport properties, commonly referred to as the semiconductor-metal transition, occurs at a much lower dopant concentration than the few percent suggested previously. The term semiconductor-metal transition is a misleading one. Lightly doped $[\text{CH}]_r$ is not a classical intrinsic or extrinsic semiconductor. Heavily doped $[\text{CH}]_r$ is not a true metal, though the conductivity approaches that of metals having low conductivity. It does not exhibit the

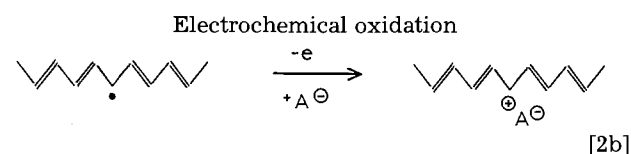
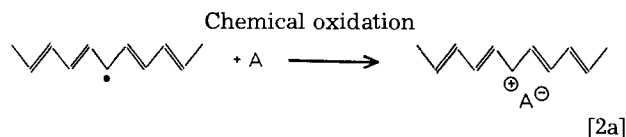
metallic properties of increasing conductivity with decreasing temperature.

We tend to view the sharp conductivity changes with y reported here and previously (6) as a phase transition. At low dopant concentrations the carriers are strongly pinned by the coulombic potential of the counterions. They are rather immobile and can hop only with significant activation. One can speak of a "glassy" state for the charge carriers. At high dopant concentrations, the pinning potentials are screened and the mobility of the carriers increases greatly. One can think that the carriers are in a "liquid" state. Thus, the sharp increase of transport properties with y may be considered to be a "glass" transition of the carriers in a frozen state to a melt state. Above this transition, any further increase of conductivity is largely due to an increase in the number of carriers.

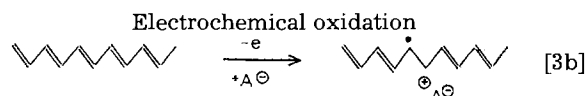
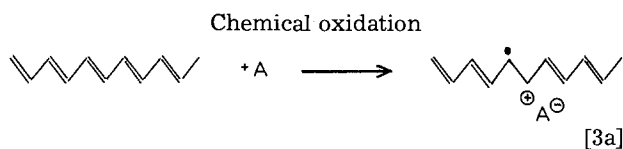
Comparison of the EPR and conductivity results of *trans*- $[\text{CH}]_r$ chemically doped with I_2 and AsF_5 (6) very slowly and homogeneously and that of electrochemically doped materials (Fig. 6 and 7) show similarities as well as significant differences. The midpoint of the large decrease in thermopower occurs at $y \sim 8 \times 10^{-4}$ for I_2 and AsF_5 doped $[\text{CH}]_r$ (6); it occurs at a higher dopant concentration of $y \sim 3 \times 10^{-3}$ for $[\text{CH}(\text{ClO}_4)_y]_r$. According to the above interpretation of the "carrier glass transition," there should be some dependence on the size, charge density, and polarizability of the counterion. The EPR intensity of unpaired spins in I_2 - and AsF_5 -doped $[\text{CH}]_r$ decreases precipitously in the vicinity of y for the carrier glass transition (6, 14). However, the unpaired spin concentration of electrochemically doped $[\text{CH}]_r$ did not show any decrease over the entire dopant range studied. With increasing extent of oxidation, the EPR intensity becomes less temperature dependent, *i.e.*, the Curie susceptibility decreases (Fig. 6). At high doping levels, the EPR is temperature independent indicative of Pauli susceptibility.

There are several ways oxidation of $[\text{CH}]_r$ can occur.

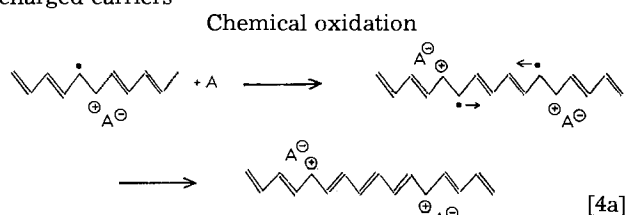
First, it can occur by direct oxidation of a neutral defect (there are ca. 10^{-3} unpaired spins/CH in *trans*- $[\text{CH}]_r$)



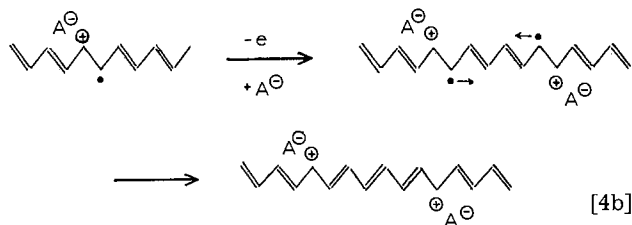
Second it can occur by oxidation of a C=C double bond; formation of a polaron



Third it can occur by bipolar doping resulting in two charged carriers

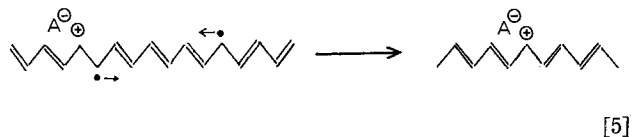


Electrochemical oxidation



Feldblum *et al.* (5) have interpreted optoelectrochemical oxidation and reduction of $[\text{CH}]_x$ data as doping by polaron injection and undoping by soliton removal.

In case [2] above, if the chain contains a neutral defect, then it can interact with the polaron to form a positive carrier annihilating two spins



At low dopant levels, $y < 10^{-3}$, the changes in unpaired spin concentrations are small because of the intrinsic spin concentration of about 10^{-3} in pristine *trans*- $[\text{CH}]_x$. For $y > 10^{-3}$, the changes in unpaired spin concentration would depend upon which of the above doping pathways dominate. The present electrochemical doping results appear to be consistent with predominance of production of bipolaron pairs by successive oxidations of nearby chains or segments of a chain. Increased doping produces domains of metallic electrons which may or may not include the initial neutral defects of the pristine polymer. The other mechanism, found previously in I_2 and AsF_5 doping (6, 15), reactions [2a], [3a], and [5] are probably dominant, resulting in the disappearance of Curie susceptibility with the increasing y .

The decrease of the Curie susceptibility with chemical p doping has been widely reported for other systems: SbF_5 doping of *cis*- $[\text{CH}]_x$ (16), Br_2 doping of *trans* $[\text{CH}]_x$ (17), NOHSO_4 doping of $[\text{CH}]_x$ (18), and electrochemical reduction of *cis*- $[\text{CH}]_x$ (19). Furthermore, Dysonian EPR lineshapes are obtained in saturation chemically doped samples such as Li-benzophenone doping of *cis*- $[\text{CH}]_x$ (19), $\text{Fe}(\text{ClO}_4)_3$ doping of *trans*- $[\text{CH}]_x$ (20), and NOHSO_4 doping of *trans*- $[\text{CH}]_x$ (21). Therefore, phase separation into metallic domains occurs in chemical as well as electrochemical oxidation of $[\text{CH}]_x$. In the case of $[\text{CH}]_x$ cyclically doped with I_2 and AsF_5 (6, 15) to saturation levels which show no Dysonian EPR, it is likely that the carriers are homogeneously distributed without a phase separation.

Acknowledgment

This study was supported by NSF and ONR. The authors appreciate discussions with Professors F. E. Karasz, C. P. Lillya, and D. J. Curran, and J. S. Choo for help with initial experiments.

Manuscript submitted May 29, 1985; revised manuscript received Oct. 26, 1984.

The University of Massachusetts assisted in meeting the publication costs of this article.

REFERENCES

- J. C. W. Chien, "Polyacetylene—Physics, Chemistry and Material Science," Academic Press, New York (1984).
- P. J. Nigrey, A. G. MacDiarmid, and A. J. Heeger, *J. Chem. Soc. Chem. Commun.*, 594 (1979).
- K. Kaneto, M. Maxfield, D. P. Nairns, A. G. MacDiarmid, and A. J. Heeger, *J. Chem. Soc. Faraday Trans.*, **78**, 3417 (1982).
- A. Feldblum, A. J. Heeger, T. C. Chung, and A. G. MacDiarmid, *J. Chem. Phys.*, **77**, 5114 (1982).
- A. Feldblum, J. H. Kaufman, S. Etemad, A. J. Heeger, T. C. Chung, and A. G. MacDiarmid, *Phys. Rev. B.*, **26**, 815 (1982).
- J. C. W. Chien, J. M. Warakowski, F. E. Karasz, W. L. Chia, and C. P. Lillya, *ibid.*, **28**, 6937 (1983).
- T. Ito, H. Shirakawa, and S. Ikeda, *J. Polym. Sci. Polym. Chem. Ed.*, **13**, 1943 (1975).
- M. Rolland, M. Aldissi, M. Cadere, J. F. Bresse, and C. Benoit, *Rev. Phys. Appl.*, **17**, 373 (1982).
- J. H. Kaufman, E. J. Mele, A. J. Heeger, R. Kaner, and A. G. MacDiarmid, *This Journal*, **130**, 571 (1983).
- J. C. W. Chien and J. E. Schlenoff, *Nature*, **311**, 362 (1984).
- F. E. Karasz, J. C. W. Chien, R. Galkiewicz, G. E. Wnek, A. J. Heeger, and A. G. MacDiarmid, *Nature*, **282**, 286 (1979).
- K. Shimamura, F. E. Karasz, J. A. Hirsch, and J. C. W. Chien, *Macromol. Chem. Rapid Commun.*, **2**, 473 (1981).
- J. C. W. Chien, F. E. Karasz, and K. Shimamura, *Macromolecules*, **15**, 1012 (1982).
- J. C. W. Chien, G. E. Wnek, F. E. Karasz, J. M. Warakowski, L. C. Dickinson, A. J. Heeger, and A. G. MacDiarmid, *ibid.*, **15**, 614 (1982).
- J. M. Warakowski, Ph. D. Thesis, University of Massachusetts, Amherst, MA (1984).
- P. Bernier, M. Rolland, M. Galtier, A. Montaner, M. Regis, M. Candille, C. Benoit, M. Aldissi, C. Linaya, F. Schue, J. Sledz, J. M. Fabre, and L. Giral, *J. Phys. Lett.*, **40**, L-297 (1979).
- F. Rashdi, P. Bernier, D. Billaud, A. Pron, and J. Przulski, *J. Polym.*, **22**, 1605 (1981).
- P. Bernier, A. El-Khodary, and F. Rachdi, *J. Phys. (Paris) Colloq.*, **44**, C3-307 (1983).
- F. Rachdi, P. Bernier, E. Faulques, S. Lefraut, and F. Schue, *Polym. Commun.*, **23**, 173 (1982).
- J. R. Reynolds, J. C. W. Chien, F. E. Karasz, C. P. Lillya, and D. J. Curran *J. Chem. Soc. Chem. Commun.*, 1358 (1982).
- F. Rachdi, P. Bernier, D. Billaud, A. Pron, and J. Przulski, *Polym. Commun.*, **22**, 1605 (1981).

Characterization of Low Oxidation States of Tungsten and Tungsten Electrodes in $\text{AlCl}_3\text{-NaCl}$ Melts by X-Ray Photoelectron Spectroscopy

A. G. Cavinato, G. Mamantov,* and X. B. Cox III[†]

Department of Chemistry, University of Tennessee, Knoxville, Tennessee 37996-1600

ABSTRACT

The ultimate products of the electroreduction of WCl_6 in acidic $\text{AlCl}_3\text{-NaCl}$ melts at tungsten and platinum electrodes were investigated by x-ray photoelectron spectroscopy (XPS). The XPS analysis reveals the presence of tungsten species, having formal oxidation state between 0 and +2, on electrode surfaces. Evidence for the formation of metallic tungsten at platinum electrodes was also obtained. An XPS study performed on tungsten electrodes electrolyzed in acidic chloroaluminates at the chlorine evolution potential revealed no protective polymeric tungsten chloride film.

The chemistry of tungsten is among the most complex of the transition elements. Tungsten exhibits a variety of oxidation states. The lower oxidation states of tungsten are characterized by metal-metal bonding and the formation of metal atom clusters, such as the octahedral $\text{W}_6\text{Cl}_8^{4+}$ (1).

The electrochemistry and chemistry of several refractory group metals (groups IVB-VIB) in molten $\text{AlCl}_3\text{-NaCl}$ have been investigated previously by our group (2-6) and others (7). For several metals, such as niobium, tantalum, and tungsten, formation of metal clusters was found to occur in acidic (AlCl_3 -rich) melts. In the case of tungsten (6), the cluster $\text{W}_6\text{Cl}_8^{4+}$ is formed by the electroreduction of WCl_6 and several other solute species. The electrochemical reaction sequence is very complex and not fully understood. It was found (6) that $\text{W}_6\text{Cl}_8^{4+}$ can be reduced further electrochemically; the essentially insoluble product of this reduction was not characterized in this early study.

In this paper, we report on the x-ray photoelectron spectroscopic (XPS) studies of the final products of the electroreduction of WCl_6 in acidic chloroaluminate melts at tungsten and platinum electrodes.

In addition, since tungsten is a very good electrode in chloroaluminate melts for studies of reactions occurring at very positive potentials, such as the oxidation of sulfur to tetravalent sulfur (a process that occurs close to the anodic limit of the melt) (8), we examined, using XPS, tungsten electrodes which were employed for chlorine evolution. It was thought that this unusual resistance of tungsten to oxidation may be due to the formation of a protective halide cluster layer.

Other electrochemical studies of tungsten in molten salts have been performed by Senderoff and Mellors in molten fluorides (9), Johnson and Mackenzie in molten LiCl-KCl (10), Sabbatini *et al.* in molten nitrates (11), and, most recently, by Scheffler and Hussey in the basic AlCl_3 -methylethylimidazolium chloride melt (12).

Experimental

Dry box system.—Because of the air- and moisture-sensitive nature of the compounds used, all handling of materials was performed under a nitrogen atmosphere inside a Vacuum Atmospheres dry box equipped with a dry train/oxygen removal column. The moisture level of the atmosphere was monitored with a Panametrics Model 700 hygrometer. The moisture level was typically less than 3 ppm.

Materials.—The chloroaluminate melts were prepared from aluminum chloride (Fluka, anhydrous), purified twice by sublimation at $\approx 210^\circ\text{C}$ and from sodium chloride (Fisher) dried under vacuum at 400°C . The melt preparation has been described previously (13). Tungsten foil (0.127 mm thick), 99.99% purity (Alfa Products), and platinum foil (0.0254 mm thick), 99.99% purity (Fisher), were used.

*Electrochemical Society Active Member.

[†]Permanent address: Department of Chemistry, University of North Carolina, Chapel Hill, North Carolina 27514.

num foil (0.0254 mm thick), 99.99% purity (Fisher), were used. Tungsten (VI) chloride, resublimed, 99% (Alfa Products), was purified by heating at 180°C under vacuum in a Pyrex tube to allow the more volatile tungsten oxychlorides (WOCl_4 , WO_2Cl_2) to sublime off. The Pyrex tube was then sealed and the temperature raised to 210°C , at which point WCl_6 sublimed to the cool portion of the Pyrex tube.

Sulfur dioxide, anhydrous, 99.98% (Matheson), and prepurified nitrogen (MG Scientific Gases) were used for the removal of the melt from the electrode surfaces (*vide infra*).

Electrochemical measurements.—Current-voltage curves were recorded using a Princeton Applied Research Model 174 Polarographic Analyzer coupled with a PAR 175 Universal Programmer. Controlled potential electrolyses were performed with a PAR 173 Potentiostat/Galvanostat. The electrochemical cell was a Pyrex vessel equipped with threaded glass connectors and Teflon bushings with Teflon ferrules (Ace Glass, Incorporated) to position the electrodes. The working electrodes were tungsten (0.75 mm diam) or platinum (0.5 mm diam) wires sealed in glass tubes; the reference electrode was an aluminum wire (0.75 mm diam), and the counterelectrode was a tungsten spiral. Both counter and reference electrode compartments were separated from the working compartment by means of fine porosity (4.5-5 μm pore size) frits. Samples prepared for examination by XPS employed a working electrode made of tungsten or platinum foil with an area approximately 0.4 cm^2 . The platinum foils were cleaned in concentrated HCl; the tungsten foils were cleaned as described below, and sealed under vacuum to avoid contamination during transport to the spectrometer.

XPS measurements.—All of the spectra were obtained using an XPS/Auger spectrometer, Physical Electronics Model 548, operated in the Fixed Analyzer Transmission (FAT) mode, using $\text{MgK}\alpha$ x-ray radiation. The operating pressure in the sample chamber varied from 10^{-8} to 10^{-9} torr. Preliminary XPS studies on the cleaning of tungsten, as well as the characterization of $(\text{H}_2\text{O})_2[(\text{W}_6\text{Cl}_8)\text{Cl}_6] \cdot 6\text{H}_2\text{O}$, were carried out at the Oak Ridge National Laboratory (Oak Ridge, Tennessee), while the studies of cluster films on electrodes were performed at the University of North Carolina (Chapel Hill, North Carolina). The spectra were calibrated with respect to the $\text{W } 4f_{7/2}$ metal peak (31.0 eV) and to the $\text{Au } 4f_{7/2}$ peak (84.0 eV). Spectra are plotted to express the photoelectron binding energy of the tungsten compounds relative to that of the tungsten metal (*i.e.*, the chemical shift of the photoelectrons). Powders were analyzed by pressing them on an indium foil; the $3d_{5/2}$ (443.6 eV) peak of indium was also used as a standard in the calibration of these spectra. To determine the contribution of different oxidation states of tungsten to the $\text{W } 4f$ photoelectron peak shape, data obtained at UNC were

subjected to curve fitting by means of an iterative least squares curve fitting computer program (14), which, with interactive feedback from the operator, determines the best fit of gaussian-lorentzian peaks with S-shaped base lines to the data.

In this study, the inherent (instrumentally limited) peak width is 0.50 eV (25 eV pass energy), and the gaussian-lorentzian peak components are 40% gaussian and 60% lorentzian. The computer used was an in-house built microcomputer based on a Z-80 microprocessor.

To prevent possible contamination of the tungsten clusters, special care was taken in introducing the samples into the spectrometer. A glove bag was mounted around the sample introduction rod, sealed carefully, and maintained under a constant flow of nitrogen (ultrapure grade).

SO₂ cleaning apparatus.—A prior removal of the relatively thick layer of the chloroaluminate melt without introducing moisture contamination must be performed before the XPS analyses of the electrode surfaces. Liquid sulfur dioxide is a very good solvent for covalent substances; aluminum chloride has a very high solubility in liquid SO₂, while sodium chloride is completely insoluble (15). However, in the case of a ternary system (16), the solubility is enhanced by the formation of compounds of the type NaAlCl₄ · nSO₂. The apparatus for melt removal is shown in Fig. 1. It consists of a vessel (g) that can be opened for sample introduction at clamp (f). Kimax process pipes with beaded ends linked with a coupling assembly (stainless steel outer band with T-bolt and hex nut, Viton liner, and a TFE seal ring from Laboratory Glass, Incorporated) were used. The vessel also contains a medium porosity (10-20 μm pore size) frit (k) on which the sample (h) is positioned. The vessel is connected to three independent lines: one for SO₂, the second for nitrogen, the third to vacuum, and, on the other side, to a trap (n) filled with concentrated sulfuric acid which converts SO₂ into H₂SO₄. All the joints between the glass and the stainless steel tubing were made using ultra-torr Swageloks (a). A safety valve (d) is placed between the vessel and the

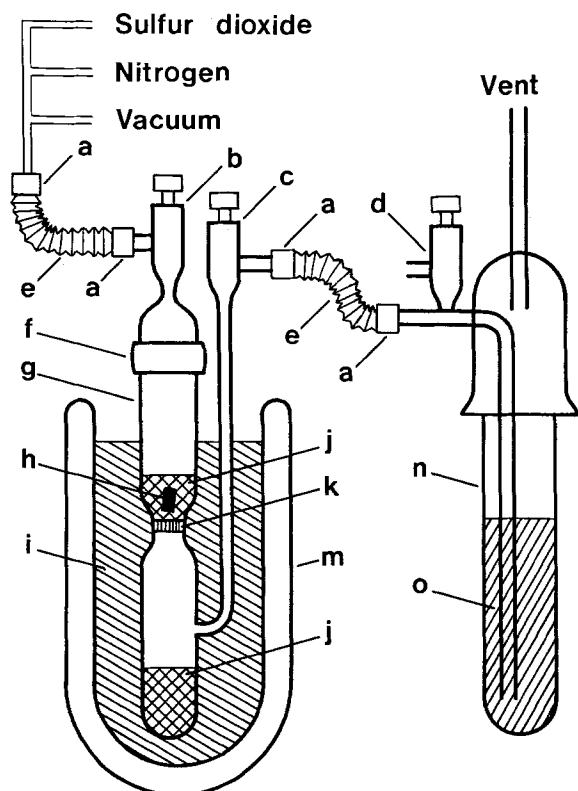


Fig. 1. SO₂ cleaning apparatus. a: Ultratorr fitting. b: Inlet stopcock. c: Outlet stopcock. d: Safety release valve. e: Stainless steel flexible tubing. f: Clamp. g: Vessel. h: Tungsten. i: Bath. j: Liquid SO₂. k: Frit. m: Dewar. n: Trap. o: H₂SO₄.

trap. During the cleaning operation, the vessel was maintained at -25° to -20°C in an ethanol-Dry Ice bath. The system is designed for samples that cannot be exposed to air; the main vessel can be sealed with two Teflon stopcocks (b, c) and transferred into a dry box for loading. After the sample is positioned, all the lines up to the inlet stopcock (b) in the vessel are evacuated below 10⁻² torr; prepurified nitrogen is flushed through the system before the sulfur dioxide is allowed to flow. The sulfur dioxide pressure is kept below 5 psi. After the sulfur dioxide has condensed above the frit and been in contact with the sample long enough to dissolve the melt covering the surface, a pressure of nitrogen (about 3 psi) is used to force the liquid through the frit. This operation can be repeated several times. Finally, nitrogen is passed through the system and the temperature is allowed to reach the room temperature value so that the sulfur dioxide slowly evaporates and is carried away by the nitrogen. After the cleaning operation, the vessel is transferred into a dry box and the samples are sealed under vacuum.

Results

XPS characterization of (H₃O)₂[(W₆Cl₈)Cl₆] · 6H₂O.—An XPS study of the products of the electroreduction of WCl₂ (or [W₆Cl₈]Cl₄) involves the knowledge of the binding energy for the unit W₆Cl₈⁴⁺ (formal oxidation state W⁺²). For the W-Cl system, no XPS data on W⁺² have been previously reported.

The binding energy for the W 4f peaks (split by spin-orbit splitting) for the unit W₆Cl₈⁴⁺ was determined on the cluster (H₃O)₂[(W₆Cl₈)Cl₆] · 6H₂O. The hydrate form instead of (W₆Cl₈)Cl₄ was used because of the high moisture sensitivity of the anhydrous cluster which also showed some decomposition to higher oxidation states as shown by the XPS spectra. The synthesis of (H₃O)₂[(W₆Cl₈)Cl₆] · 6H₂O was performed according to Dorman and McCarley (17); the product was characterized by x-ray powder diffraction. The chemical shift for the W₆Cl₈⁴⁺ unit, as compared to tungsten metal, is 1.8 eV (see Fig. 2). Spectra recorded in the chlorine 2p region show two different chlorine contributions, in accordance with the structure of the cluster, in which at least two different kinds of chlorine should be detected (18).

XPS studies of tungsten-surface cleaning techniques.—Particular care was taken to provide very clean tungsten surfaces to use as the electrode material in the elec-

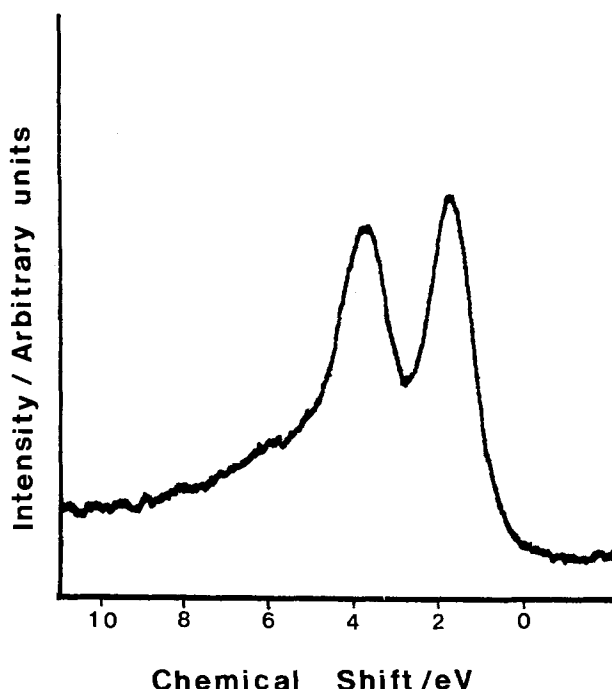


Fig. 2. Tungsten 4f XPS spectra of (H₃O)₂[(W₆Cl₈)Cl₆] · 6H₂O.

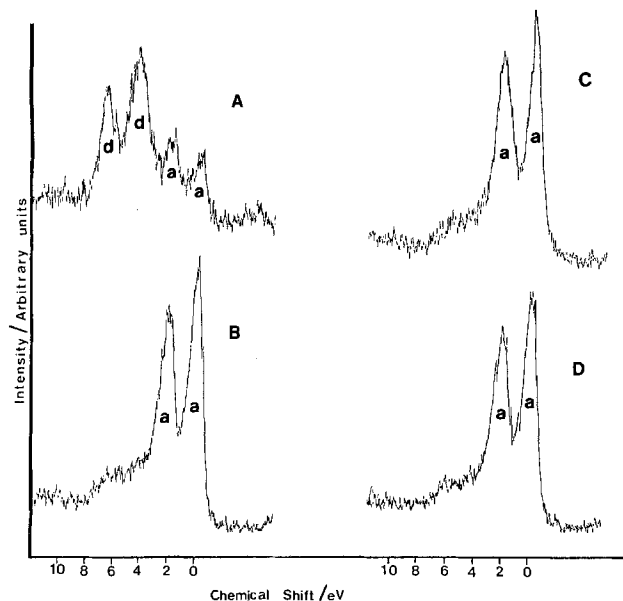


Fig. 3. Tungsten 4f spectra for samples cleaned using different techniques: A: "as received." B: Electrolyzed in 50% NaOH solution containing 5% NaNO₂ at ~200 mA/cm² for 2h. C: Electrolyzed in the same solution at ~200 mA/cm² for 30 min and at 330 mA/cm² for 1h. D: Reduced under hydrogen at 500°C for 24h. Peak assignments: (a) tungsten (O) doublet, (b) tungsten(VI) doublet.

trochemical study of the tungsten cluster film. A tungsten surface is usually covered by a layer of oxides, particularly WO₃, that would limit the XPS detection of lower oxidation state tungsten species. Figure 3A shows the spectrum for the W 4f region for tungsten foil "as received." The spectrum shows the presence of oxide (doublet d) on the left of the metal peaks (doublet a) that, on the basis of the chemical shift of 4.5 eV, can be attributed mainly to W(VI) oxide (19). Figures 3B-3D show results obtained with different cleaning procedures. The spectrum shown in Fig. 3B was recorded on the sample WA electrolyzed in 50% NaOH solution containing 5 weight percent NaNO₂ at ~200 mA/cm² for 2h. The metal doublet is now very sharp while a small shoulder on the left is still present, which, on the basis of the chemical shift, can be attributed mainly to W(VI) oxide. Similar results were obtained by electrolyzing sample WB for a longer period of time (Fig. 3C). Figure 3D shows the W 4f doublet for the sample WC reduced in hydrogen at 500°C. In Table I, the percentage amounts, calculated as areas, of the tungsten species detected, are reported. It may be seen that both cleaning techniques result in clean metal tungsten surfaces. The similarity in the results suggests that the residual oxide still detected is formed after the cleaning operation, possibly during the introduction of the sample in the XPS spectrometer.

XPS studies of the sulfur dioxide cleaning technique.—The cleaning power of the method was tested by analyzing with x-ray photoelectron spectroscopy the surface of two tungsten samples. The samples were also checked for possible surface modifications due to the contact with liquid sulfur dioxide. The two samples, initially cleaned

Table I. Percentage amounts of tungsten species detected by XPS

Sample	Percentage of W(O) ^a (%)	Percentage of W(VI) (%)
W "as received"	34	66
WA	96	4
WB	95	5
WC	97	3

^a The areas were measured manually; the differences between samples WA, WB, and WC are not significant.

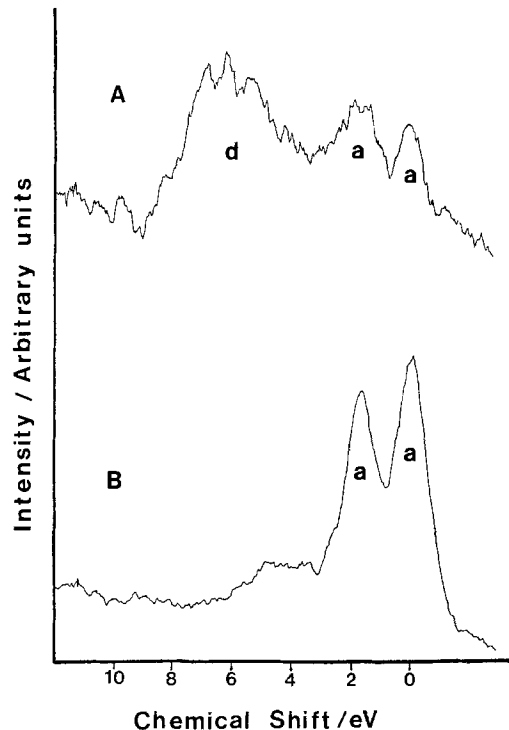


Fig. 4. Tungsten 4f spectra. A: Before SO₂ cleaning procedure. B: After SO₂ cleaning procedure. Peak assignments: (a) tungsten (O) doublet, (b) tungsten (VI) doublet.

by electrolysis as described previously, were dipped for a short time in an AlCl₃-NaCl (63-37 mole percent) melt. One sample was sealed under vacuum while still covered with the melt; the other was cleaned according to the procedure described in the Experimental section. Figures 4A and 4B show a comparison of the W 4f spectra recorded on the two samples. A sharp signal due to metallic tungsten is clearly present in the cleaned sample. The liquid sulfur dioxide does not affect the tungsten surface; the relative percentage of oxide and metal is the same as in cleaned tungsten surfaces not exposed to sulfur dioxide

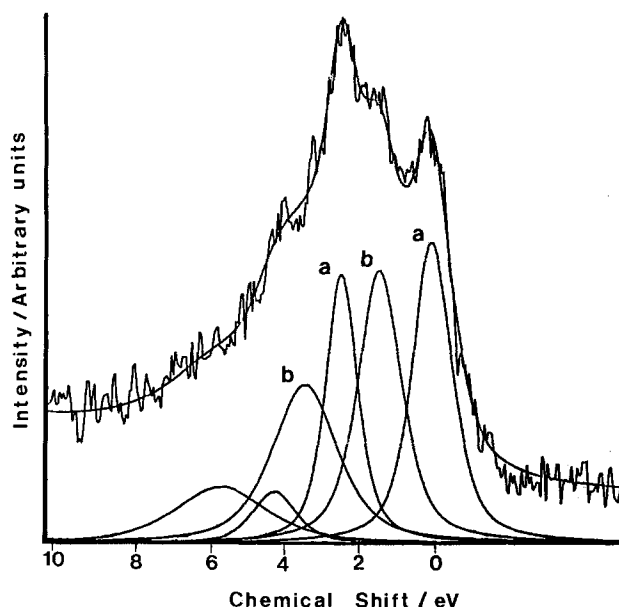


Fig. 5. Tungsten 4f spectrum of a tungsten sample electrolyzed at 0.10V for 60 min. Initial [WCl₆] = 7.9·10⁻³M. Peak assignments: (a) tungsten (O) doublet, (b) reduced cluster doublet. In this figure and Fig. 6-8, the "erratic" curve represents experimental data; the smooth curve is the result of the calculated curve fit. The curve fit doublets are based on initially assigned parameters consistent with values derived from analysis of pure compounds.

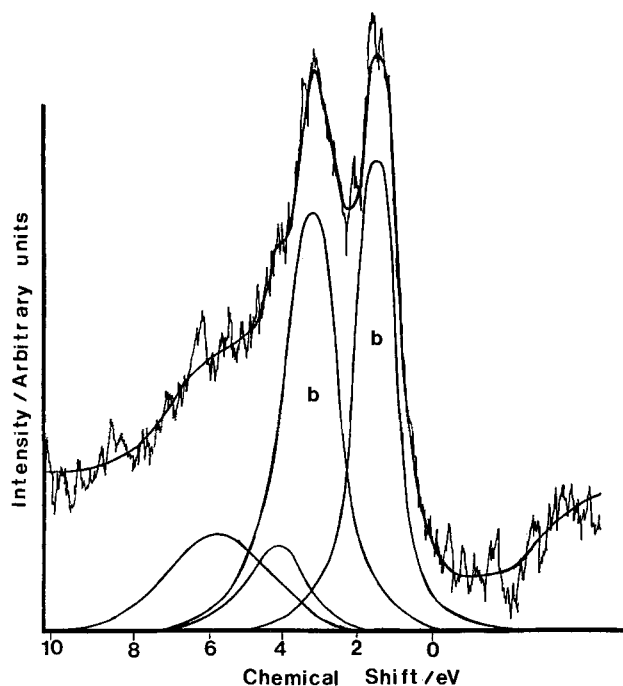


Fig. 6. Tungsten 4f spectrum of a tungsten sample electrolyzed at 0.10V for 35 min. Initial $[WCl_6] = 2 \cdot 10^{-2}M$. Peak assignments: (b) reduced cluster doublet.

(compare Fig. 3B and 4B). A survey spectrum shows that the amount of sulfur contamination on the surface is very low.

XPS study of cluster films on tungsten and platinum electrodes.—When W(VI) chloride is added to an $AlCl_3$ -rich chloroaluminate melt, four reduction waves can be detected; the last wave, occurring at +0.30V vs. the Al(III)/Al reference electrode, has been attributed to the electroreduction of $(W_6Cl_8)Cl_4$ to an insoluble product (6). XPS analyses were performed on tungsten electrodes electrolyzed at this and more negative potentials in order to define the nature of the product formed on the electrode surface. An example of an XPS spectrum for such a sample and curve fitting is shown in Fig. 5. The doublet a is due to the tungsten metal of the substrate, while the doublet b at a binding energy 1.13 eV higher may be attributed to a “reduced cluster” with tungsten oxidation

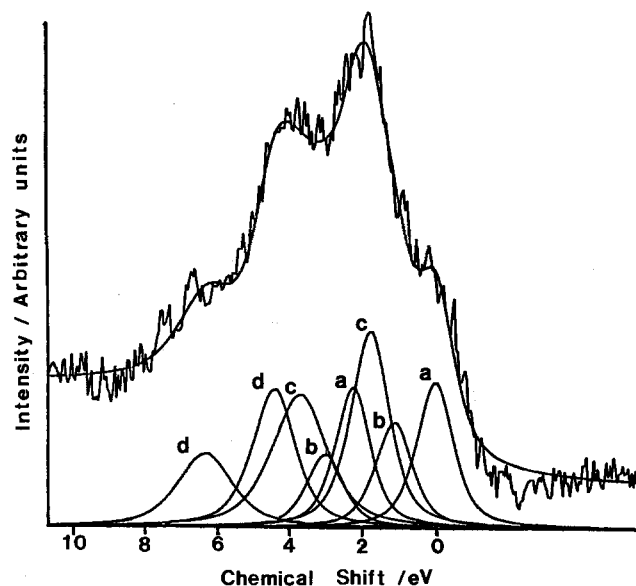


Fig. 7. Tungsten 4f spectrum of a platinum substrate electrolyzed at 0.10V for 25 min. Initial $[WCl_6] = 1.99 \cdot 10^{-2}M$. Peak assignments: (a) tungsten (O) doublet, (b) reduced cluster doublet, (c) $W_6Cl_8^{4+}$ doublet, and (d) tungsten (VI) doublet.

Table II. Parameters from the curve fitting of the W 4f peaks of tungsten species on a platinum substrate

Peak	Position (B.E.) (eV)	FWHM 4f (eV)	Separation from W(O) (eV)
a	$4f_{7/2}$	31.06	1.22
	$4f_{5/2}$	33.33	1.17
b	$4f_{7/2}$	32.19	1.23
	$4f_{5/2}$	34.09	1.24
c	$4f_{7/2}$	32.86	1.28
	$4f_{5/2}$	34.81	1.84
d	$4f_{7/2}$	35.52	1.43
	$4f_{5/2}$	37.42	1.83

state less than +2, formed electrochemically on the tungsten electrode. Attempts to fit an oxide component were unsuccessful; however, the high binding energy tail may include shake-up peaks overlapping with a tungsten oxide component. Figure 6, obtained for a more concentrated sample electrolyzed for a shorter time, only shows the presence of the reduced cluster and a possible tungsten oxide component. At longer times, some peeling of the film was observed which explains the detection of the underlying metal in some of the samples.

The presence of the reduced cluster was also detected on a different substrate (namely, platinum), as shown in Fig. 7. Curve fitting indicates the presence of four oxidation states: (a) the metal, (b) the reduced cluster, (c) W(II), and (d) tungsten oxide. Table II lists some XPS parameters for these species.

XPS study of tungsten anodization in chloroaluminate melts.—Figure 8 shows the XPS spectrum and the curve fitting for a tungsten sample electrolyzed at the chlorine evolution potential for 60 min. The analysis of the parameters shows only the presence of metallic tungsten; the higher binding energy peak represents energy loss features, probably shake-up peaks, and a small contribution of tungsten oxide.

Discussion

The XPS results show that the reduction of tungsten (VI) chloride in acidic chloroaluminate melts leads ultimately to the formation of a cluster film in which tungsten has a very low oxidation state, between W(II) and the metal. The same product is obtained at either platinum or tungsten electrodes. At platinum, evidence for metallic

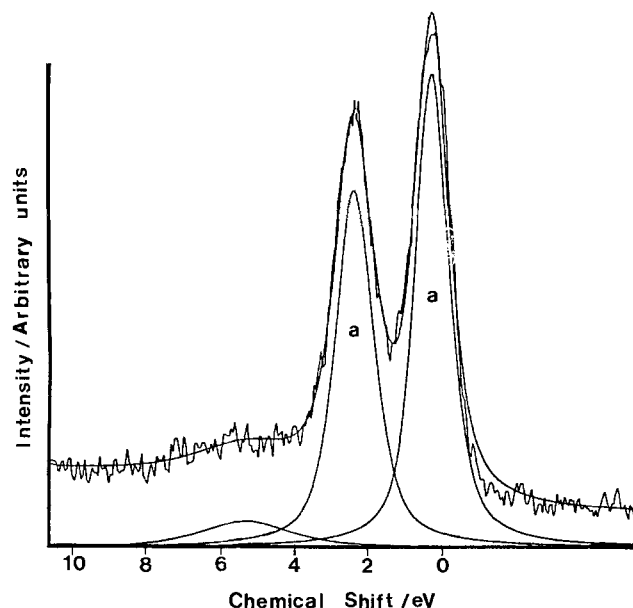


Fig. 8. Tungsten 4f spectrum of a tungsten sample electrolyzed at +2.5V for 60 min. Peak assignments: (a) tungsten (O) doublet.

tungsten was also obtained. No evidence for the formation of the metal was obtained from purely electrochemical studies (6), although Phillips and Osteryoung (7) assume Mo(O) to be the final oxidation state of the reduction of molybdenum chloride in basic chloroaluminates. It was found that the chlorine-evolution reaction occurs at a metallic tungsten surface. The hypothesis of the formation of an insoluble polymeric tungsten chloride that protects the tungsten surface is not supported by these results.

Acknowledgments

This research was supported by the Department of Energy through the University of California Subcontract 4502810 and the Atlantic Richfield Company. Initial studies on this problem were undertaken by J. S. Ledford and O. R. Melroy. We are grateful to R. E. Clausing and L. Heatherly, Jr., for the use of their XPS/Auger spectrometer at the Oak Ridge National Laboratory and to R. W. Linton for access to the XPS/Auger spectrometer at the University of North Carolina. A useful discussion with L. Sabbatini, University of Bari, Bari, Italy, is acknowledged.

Manuscript submitted Dec. 26, 1984; revised manuscript received Jan. 8, 1985.

REFERENCES

1. F. A. Cotton and G. Wilkinson, "Advanced Inorganic Chemistry," 4th ed., pp. 844-883, Wiley-Interscience, New York (1980).
2. B. Gilbert, G. Mamantov, and K. W. Fung, *Inorg. Chem.*, **14**, 1802 (1975).
3. G. Ting, K. W. Fung, and G. Mamantov, *This Journal*, **123**, 624 (1976).
4. L. E. McCurry, G. Mamantov, N. J. Bjerrum, F. W. Poulsen, and J. H. von Barner, in "High Temperature Metal Halide Chemistry," D. Cubicciotti, Editor, pp. 421-427, The Electrochemical Society Soft-bound Proceedings Series, Princeton, NJ (1978).
5. M. Katabua, P. Rolland, G. Mamantov, and L. Hulett, *Inorg. Chem.*, **21**, 3569 (1982).
6. D. L. Brotherton, PhD. Dissertation, University of Tennessee, Knoxville, TN (1974).
7. J. Phillips and R. A. Osteryoung, *This Journal*, **124**, 1465 (1977).
8. R. Marassi, G. Mamantov, M. Matsunaga, S. E. Springer, and J. P. Wiaux, *ibid.*, **126**, 231 (1979).
9. S. Senderoff and G. W. Mellors, *ibid.*, **114**, 586 (1967).
10. K. E. Johnson and J. R. Mackenzie, *Anal. Chem.*, **41**, 1483 (1969).
11. L. Sabbatini, P. M. A. Sherwood, and P. G. Zambonin, *This Journal*, **130**, 2199 (1983).
12. T. B. Scheffler and C. L. Hussey, *Inorg. Chem.*, **23**, 1926 (1984).
13. G. Torsi and G. Mamantov, *ibid.*, **10**, 1900 (1971).
14. D. F. Smith, PhD. Dissertation, University of North Carolina, Chapel Hill, NC (1978); also see P. M. A. Sherwood, in "Practical Surface Analysis by Auger and X-Ray Photoelectron Spectroscopy," D. Briggs and M. P. Seah, Editors, pp. 445-475, John Wiley & Sons, New York (1983).
15. T. C. Waddington, Editor, "Non-Aqueous Solvent Systems," pp. 253-284, Academic Press, New York (1965).
16. von H. Kühnl, A. Strumpf, and M. Gladziwa, *Z. Anorg. Allg. Chem.*, **449**, 145 (1979).
17. W. C. Dorman and R. E. McCarley, *Inorg. Chem.*, **13**, 491 (1974).
18. von H. Schafer, H. G. von Schnering, J. Tillack, F. Kühnen, H. Wohrle, and H. Baumann, *Z. Anorg. Allg. Chem.*, **353**, 281 (1967).
19. G. K. Wertheim, M. Campagna, J. N. Chazalviel, and D. N. E. Buchanan, *Appl. Phys.*, **13**, 225 (1977).

Surface Potential Difference of Anodized Al₂O₃ Electrets

J. J. Bernstein*,¹ and R. M. White

Department of Electrical Engineering and Computer Sciences, University of California, Berkeley, California 94720

ABSTRACT

The surface potential difference (SPD) across barrier-type anodic Al₂O₃ films is much larger than previously thought. SPD's as high as 60V have been measured across these anodized electrets, using an improved SPD measuring apparatus and a new rinsing procedure which removes compensating ions from the Al₂O₃ surface. The intense electric field at the surface of these films has been used to make air-gap electret ultrasonic transducers with a sensitivity of 1.5 × 10⁸ V/m. Theoretical and experimental results are presented on the decay of SPD by surface and volume conduction.

This paper is a study of charge retention in Al₂O₃ electrets formed by anodization. These thin film electrets have been used to make transducers for bulk ultrasonic waves (1-3). Previously reported values for the surface potential difference (SPD) across anodic oxide films ranged from 0.5 up to 10V (4-6), however, we have measured SPD's as high as 60V across barrier-type Al₂O₃ films by using a new rinsing procedure which completely removes compensating ions left on the oxide surface by the anodizing electrolyte.

In the Theory section of this paper, we analyze the charge decay in a thin film electret due to surface and volume conduction. Using conductivity data from the literature, volume conduction is predicted to be negligible after a brief initial transient. This is confirmed in the Results section, where surface conduction is shown to be the dominant decay mechanism. In the Experimental Procedures section, a new rinse procedure which removes compensating ions from the anodic oxide surface is described. An improved apparatus for measuring SPD is also described, and data taken with this apparatus are used to follow the decay of SPD as a function of the

anodizing electrolyte, atmospheric humidity, temperature, and the surface roughness of the film.

Theory of Charge Decay in an Anodized Electret

In this section, we consider the decay of charge in a thin barrier-type anodic oxide film following anodization. We examine first volume conduction, solving for both the instantaneous decay time-constant and the explicit time evolution of the electric field. We then look briefly at the surface conduction problem. The bulk of the mathematical derivations are confined to the Appendixes in order to clarify the presentation.

Figure 1 shows the evaporated aluminum films on glass used in this investigation. For the volume conduction problem, the current flow is assumed to be parallel to the film normal; hence, the problem is one-dimensional and the shape and size of the anodized area are unimportant. However, for the surface conduction problem, the size and shape of the anodized region are important because the boundary conditions are applied at the edge. Because the aluminum samples were chosen to be disk-shaped, the surface conduction problem is also one-dimensional (in r), but the length of the surface conduction path increases with increasing sample size.

*Electrochemical Society Active Member.

¹Present address: Solavolt International, P.O.B. 2934, Phoenix, Arizona 85062.

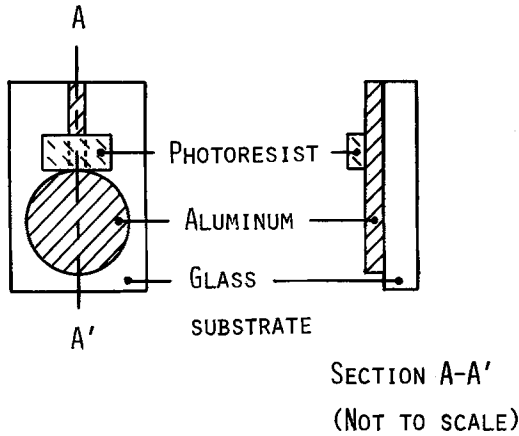


Fig. 1. Configuration of the anodization samples. Aluminum pattern formed by evaporation through shadow mask onto glass slides. Photoresist stopoff is then applied at waterline to prevent arcing.

The relation between current density (J) and electric field (E) in the anodic film at constant temperature is (7)

$$J(t) = J_0(e^{E(t)/E_0} - 1) \quad [1]$$

where J_0 and E_0 can be derived from various atomistic models (7) but are considered here to be simple empirical constants. Although other, more complicated current-field relations have been derived, Eq. [1] fits the experimental data very well, and in the low electric field regime of primary interest here ($E \leq E_0$), most of the more complicated equations reduce to Eq. [1].

From Eq. [1], the conductivity σ of the oxide is

$$\sigma(t) = \frac{J(t)}{E(t)} = \frac{J_0}{E(t)} (e^{E(t)/E_0} - 1) \quad [2]$$

Under the conditions of the anodization (high electric field), the conductivity is large and ionic currents flow. After anodization, the electric field decays to lower values, and the conductivity decreases to a low field limiting value $\sigma_{\min} = J_0/E_0$ for $E \ll E_0$. Under these low field conditions, the anodic oxide is a very good insulator and can hold charge and serve as an electret.

We now extend the concept of dielectric relaxation time constant, which is strictly applicable only when the conductivity is constant, to the instantaneous decay time, which is shown in Appendix A to be

$$\tau_{\text{inst}}(t) \equiv \frac{-\rho}{(\partial\rho/\partial t)} = \frac{\epsilon E_0}{J_0} e^{-E/E_0} \quad [3]$$

As the charge density and the electric field decay, the instantaneous decay time increases, approaching asymptotically a low field value

$$\tau_{\text{max}} = \frac{\epsilon E_0}{J_0} \quad [4]$$

Qualitatively, then, we expect the initial decay of the electric field to be rapid, gradually approaching an exponential decay with time constant τ_{max} . These expectations are confirmed both by the experimental data and by the explicit solution for the time evolution of the electric field, derived in Appendix B. The equation for the electric field $E_2(t_2)$ is (from Appendix B)

$$E_2(t_2) = -E_0 \ln [1 - e^{-t_2/\tau_{\text{max}}}(1 - e^{-E_1/E_0})] \quad [5]$$

where E_1 is the electric field at $t = 0$. For large t_2 , $\ln(1+x) \approx x$ gives

$$E_2 = E_0(1 - e^{-E_1/E_0})e^{-t_2/\tau_{\text{max}}} \quad [6]$$

confirming our earlier conclusion that the decay is a simple exponential for long times. For very short times, assuming $E_1 \gg E_0$, we have

$$E_2(t_2) \approx -E_0 \ln(1 - e^{-t_2/\tau_{\text{max}}}) \approx -E_0 \ln\left(\frac{t_2}{\tau_{\text{max}}}\right) \quad [7]$$

The initial rapid decay should be logarithmic.

We would like to rewrite (5) in terms of SPD (surface potential difference) because this is what our experiments measure. This can be done if we make the simplifying assumption that the electric field and polarization are constant throughout the film. This assumption is equivalent to assuming that the space charge is zero in the film, (i.e., surface charge only, no volume charge), which probably is not true. The effect of this approximation is to underestimate the decay of SPD, because the decay rate increases exponentially with electric field, and the average field is lower than the peak field.

Proceeding under the assumption of uniform field, Eq. [5] becomes

$$V(t) = -dE_0 \ln [1 - e^{-t/\tau_{\text{max}}}(1 - e^{-V_0/dE_0})] \quad [8]$$

where d is the film thickness and V_0 is the surface potential difference at time $t = 0$ (assumed equal to the peak anodizing voltage). In the Results section, we will examine this equation using values of E_0 and J_0 from the literature.

Charge Decay by Surface Conduction

We analyze here the decay by surface conduction of a disk-shaped anodic oxide film charged to a voltage V_0 with respect to a conducting substrate. The analogous problem for heat conduction has been solved (8). The problem can be stated mathematically as follows

$$\frac{\partial V(r, t)}{\partial t} = \frac{\sigma_{\text{surf}}}{C_A} \frac{1}{r} \frac{\partial}{\partial r} \left(r \frac{\partial V(r, t)}{\partial r} \right) \quad [9]$$

Initial condition

$$V(r, 0) = V_0$$

Boundary condition

$$V(a, t) = 0$$

where $V(r, t)$ is the voltage at a distance r from the center of a disk of radius a , σ_{surf} is the surface or sheet conductivity of the anodic oxide film (Ω^{-1}), and C_A is the capacitance per unit area of the film. C_A is also the constant of proportionality between the surface voltage $V(r, t)$ and the surface charge density. The solution is

$$V(r, t) = \frac{2V_0}{a} \sum_{n=1}^{\infty} \exp\left(-\frac{\sigma_{\text{surf}}}{C_A} \alpha_n^2 t\right) \frac{J_0(r\alpha_n)}{\alpha_n J_1(\alpha_n a)} \quad [10]$$

where $J_0(J_1)$ is the Bessel function of the first kind of order zero (one), and α_n is the n th positive root of the equation $J_0(\alpha a) = 0$. The average potential over the entire disk is

$$V_{\text{avg}} = \frac{4V_0}{a^2} \sum_{n=1}^{\infty} \frac{\exp\left(-\frac{\sigma_{\text{surf}}}{C_A} \alpha_n^2 t\right)}{\alpha_n^2} \quad [11]$$

which, because of the large probe size of our SPD measuring equipment, was the potential actually measured.

For large t , the higher-order terms drop out, leaving only the first term. We conclude that surface conduction, like volume conduction, will lead to an initial rapid voltage decay followed by a slow exponential decay with time constant

$$\tau_{\text{max}} = \frac{C_A}{\alpha_1^2 \sigma_{\text{surf}}} = \frac{a^2 C_A}{5.78 \sigma_{\text{surf}}} \quad [12]$$

We can use Eq. [12] to calculate σ_{surf} from τ_{max} obtained from SPD decay measurements

$$\sigma_{\text{surf}} = \frac{a^2 C_A}{5.78 \tau_{\text{max}}} \quad [13]$$

This is a possible way to measure surface conductivities too small to be measured by other means.

In the Results section, we will compare the voltage decay predicted by volume and surface conductivity with

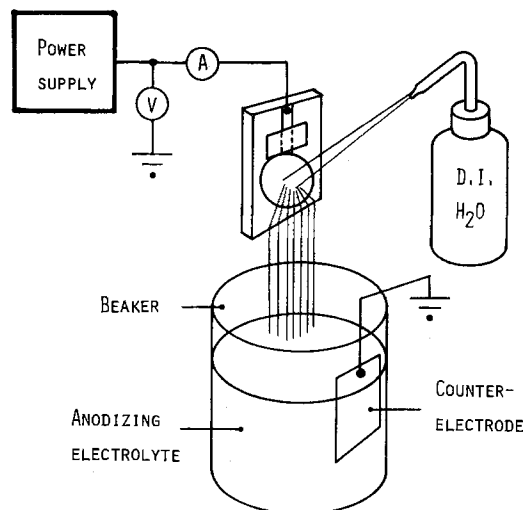


Fig. 2. Sketch showing rinse with voltage on, which removes compensating ions from anodic oxide film surface.

the measured voltage decay. From the sensitivity of voltage decay to atmospheric humidity and surface roughness, it will be concluded that surface conduction is the dominant decay mechanism.

Experimental Procedures

Aluminum films 300 nm thick and 99.999% pure were evaporated through a shadow mask onto clean glass microscope slides, giving the pattern shown in Fig. 1. These films were then anodized at 50 A/m² to 180V, using photoresist (Shipley AZ1350J) as a stopoff and an aluminum foil counterelectrode. The electrolytes used were 4.0, 2.0, 1.0, and 0.1 weight percent (w/o) H₃PO₄ and 1.0 and 0.1 w/o APB. All anodizations were done at 4° ± 0.1°C.

To avoid charge compensation, the anodic oxide is rinsed with a stream of deionized water from a plastic squeeze bottle and dried before the voltage is turned off (Fig. 2). This rinsing with voltage on procedure results in a factor of ten higher surface charge than rinsing with voltage off. During this rinse procedure, the water draining from the anodic film into the electrolyte bath below completes an electrical circuit, and a current of several microamperes can be observed. As the ions are washed away, the current decreases, which could be used for process end-point detection.

Measurements of SPD (surface potential difference) were made by the vibrating electrode method (6). In this

method, a vibrating electrode (voltage biased through a large resistor) is brought near the unmetallized surface of an electret. The bias voltage is varied to achieve a null in the ac signal (at the frequency of vibration) between the vibrating electrode and the electret back metallization. When the null is achieved, the electric field between the vibrating electrode and the electret surface is zero, and the bias voltage is therefore equal to the SPD. In our apparatus, an aluminum foil vibrating electrode was fastened to the end of a plastic tube, and forced to vibrate by a small loudspeaker in a funnel at the other end of the tube. The ac signal was buffered by a JFET input op-amp and amplified by an HP 415B SWR meter, which has a narrow bandpass filter at 1 kHz, the frequency of vibration.

The effective surface charge was measured by pressing an aluminum foil top electrode against the oxide film, and using the resulting air gap electret transducer to detect a known acoustic signal. An electrical pulser (Panametrics 5052 PR) connected to a 10 MHz resonant piezoelectric transducer produced a known displacement δ (1.6 nm). The electric field was computed as the output voltage V divided by the displacement δ . The surface effective charge is related to the surface field by Gauss's law. Electric fields as high as 1.5×10^8 V/m have been measured this way on anodic Al₂O₃ films, corresponding to surface charges of 1.3×10^{-3} C/m².

Results

Figure 3 shows the decay of SPD with time for anodic Al₂O₃ films produced in a variety of electrolytes. Included are various concentrations of ammonium-pentaborate (APB), which forms a nearly ideal barrier-type film, and phosphoric acid, which forms films with an interior barrier layer and a porous surface layer (9, 10). It is clear that the anodic films formed in H₃PO₄ solutions retain their charge far longer than those formed in APB. This may be due to the greater surface roughness of the more porous phosphate films, which leads to a much longer surface conduction path in comparison to a smooth barrier film. Another possible explanation for the different charge retention properties of the films is the incorporation of phosphate or borate ions into the film, which would be expected to modify the surface and volume conductivity of the film.

To predict τ_{\max} from the volume conduction theory developed earlier (Eq. [4]), we need values of E_0 and J_0 . Values for barrier-type films taken from the literature vary widely. For example, Ref. (11) gives $E_0 = 2.33 \times 10^7$ V/m and $J_0 = 3.87 \times 10^{-16}$ A/m², yielding $\tau_{\max} = 1.42 \times 10^5$

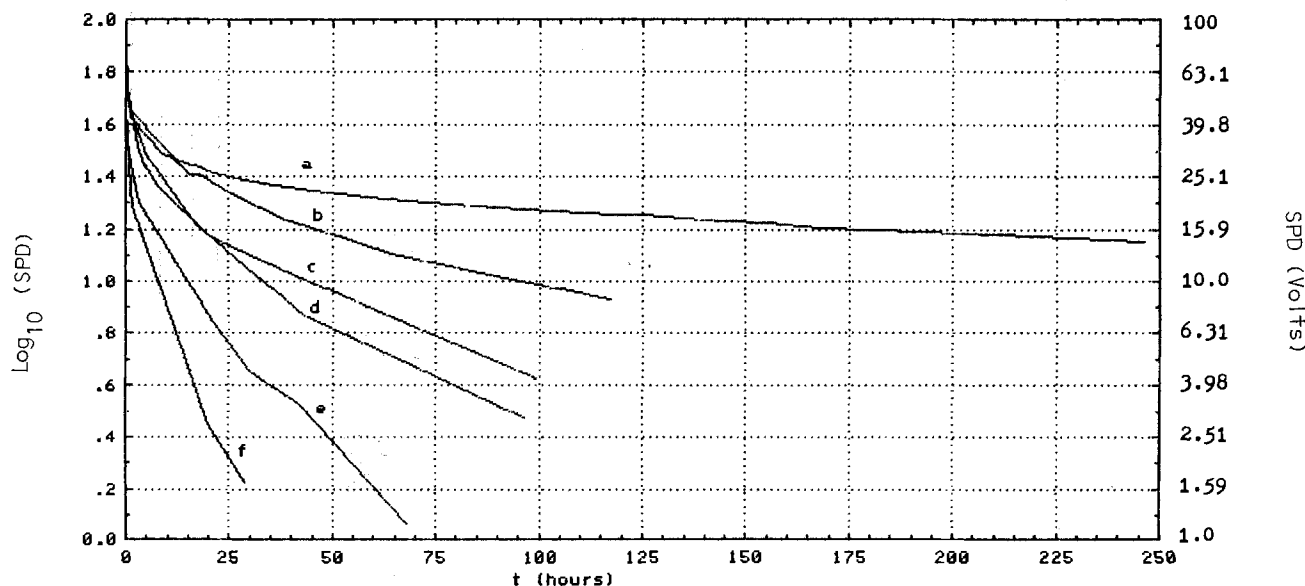


Fig. 3. Decay of surface potential difference (SPD) for Al₂O₃ films formed to 180V in the following electrolytes: 1.0 w/o H₃PO₄ (curve a), 2.0 w/o H₃PO₄ (curve b), 4.0 w/o H₃PO₄ (curve c), 0.1 w/o H₃PO₄, 1.0 w/o ammonium penta-barate (APB) (curve e), and 0.1 w/o APB (curve f).

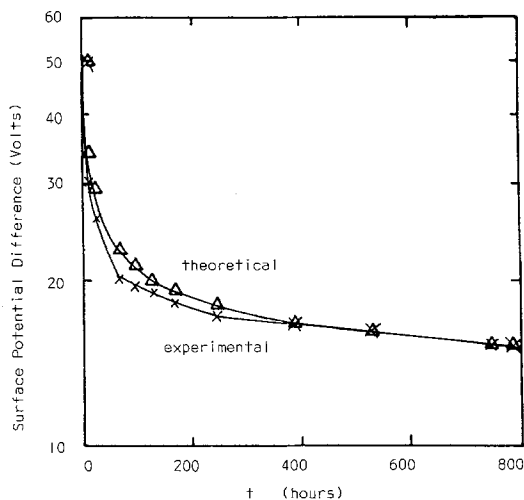


Fig. 4. Variation of surface potential difference (SPD) with time after anodization for Al_2O_3 electret stored in air. Theoretical curve is a plot of Eq. [4].

yr. Reference (13) gives $E_0 = 2.9 \times 10^7$ V/m and $J_0 = 2.46 \times 10^{-11}$ A/m², giving $\tau_{\text{max}} =$ only 2.78 yr. In the absence of reliable numbers, one can regard Eq. [4] as a two-parameter equation to be fit to the experimental data, as we have done in Fig. 4. We do not regard the good fit as proof of the validity of Eq. [4], but we note that the general shape of the decay curve is matched by the equation.

The effect of ambient humidity was investigated by preparing two identical films and storing one in a petri dish at atmospheric pressure and humidity, and storing the other in a desiccator with Drierite (CaSO_4) desiccant and air at a pressure of 3.1×10^4 Pa (0.3 atm). The decay of the SPD for the two samples is shown in Fig. 5. The change from humid air to dry air at 1/3 atm increased the lifetime dramatically from 72 to 1068h. This indicates that surface conduction is the dominant contribution to charge decay.

To further investigate the effects of atmosphere on the decay of SPD, an anodic film was sealed in a glass ampul at a pressure of 10^{-4} Pa and stored for 6 months. A very small change in SPD was detected after storage (30 mV), which yielded an extrapolated lifetime of 18 yr for the anodic Al_2O_3 electret in vacuum.

The effect on SPD of heating an Al_2O_3 electret to 100°C for 1h in air is shown in Fig. 6. During the 1h, the SPD dropped from 22.4 to 8.4V, after which the decay paralleled the decay of an identically prepared sample which was not heated. Presumably, both surface and volume conductivity increase with temperature and, therefore, heating did not help elucidate the decay mechanism.

The effect of increasing surface roughness on SPD decay was investigated without changing the chemical com-

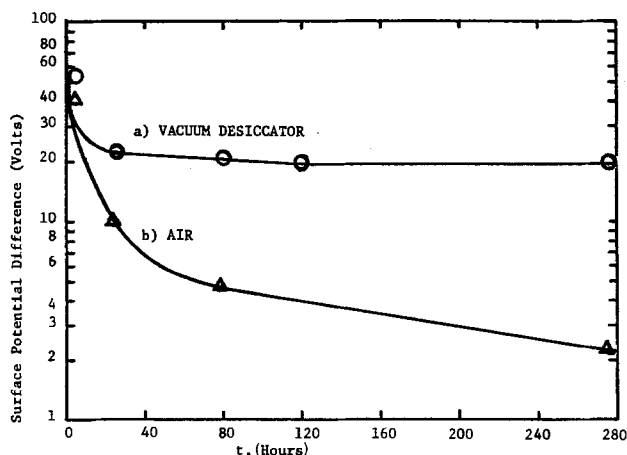


Fig. 5. Decay of SPD for two identical Al_2O_3 electrets stored in desiccator at 1/3 atm (a) and air at atmospheric pressure (b).

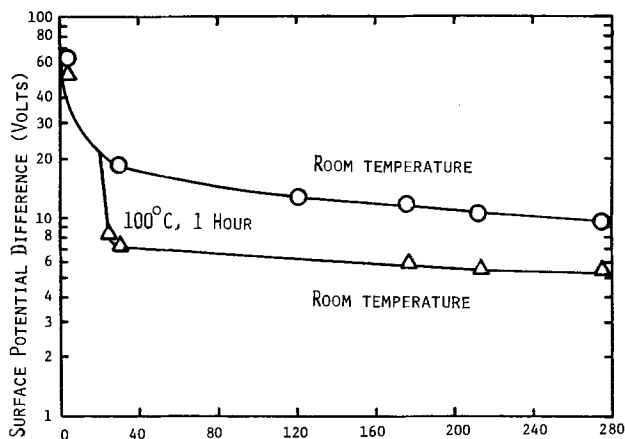


Fig. 6. Effect of heating to 100°C for 1h on SPD of an Al_2O_3 electret. Control was kept at room temperature.

position of the anodization electrolyte by anodizing aluminum films that had been lightly abraded with cotton prior to anodization. Pores are known to nucleate preferentially at surface irregularities such as scratches (13). Hence, surface roughness of the anodic film was greatly increased by the abrasion process. Charge retention was observed to increase in the anodic films formed on the abraded aluminum films.

Discussion

The strong dependence of charge decay on surface roughness and humidity indicate that surface conduction is the dominant decay mechanism, although theory predicts that volume conduction contributes to the initial rapid decay from the peak anodizing voltage (180V in our experiments) to the values measured several minutes after anodization and rinsing (about 60V in our experiments). Equation [12] predicts that τ due to surface conduction is proportional to the square of the disk radius (conduction path), which for a rough film may be much greater than the apparent disk radius. The experiment with abraded films removes the oxide-composition variable by comparing decay on oxide films of identical chemical composition but different surface roughnesses. The dependence of charge decay on humidity also points towards surface conduction, because it seems unlikely that atmospheric humidity would have a strong effect on the bulk conductivity of the Al_2O_3 . Because of this humidity sensitivity, any devices made from anodic oxide electrets [such as air-gap or polymer-gap ultrasonic transducers (3)] would need to be hermetically encapsulated with water-impervious material.

The new rinse-with-voltage-on technique is superficially similar to the electrochemical charging technique (14), but there are several important differences. Electrochemical charging of uncharged polymer sheets is done with electrolytic solutions such as HCl containing ions which are injected into the polymer surface to create the electret. Our rinsing procedure is only successful with high resistivity deionized water, because we are removing charge compensation ions from the surface of a charged anodic oxide film.

It is interesting to compare anodized aluminum electrets to commercial state-of-the-art Teflon polymer electrets. The thin film electrets produced by anodization (typically 200 nm thick) have a higher surface charge and hence higher surface field than Teflon sheet electrets (typically 20 μm thick) precisely because they are so thin and can, therefore, achieve high electric fields at relatively low voltages. This higher electric field results in higher sensitivity for transducers made from thin film electrets compared to transducers made from thick film Teflon electrets.

A common limit to the voltage to which an electret can be charged is Paschen breakdown (15). When a counter-electrode is brought near the surface of an electret, an

electrical breakdown can occur if the voltage across the gap is greater than a certain breakdown value. This breakdown voltage is a function of the product of gas pressure and gap separation (Paschen's law). For air, the minimum breakdown voltage is 380V at a pressure times gap product of 0.54 Pa m. Although this limits the voltage to which Teflon sheet electrets can be charged, Paschen breakdown is not a limitation on anodized aluminum electrets because the voltage across the anodized electret (the SPD) is usually less than 380V, even during anodization.

Manuscript submitted Jan. 3, 1984; revised manuscript received Nov. 5, 1984.

APPENDIX A

Derivation of Instantaneous Decay Time

In this appendix, we derive the instantaneous decay rate as a function of the residual field in an anodic oxide film. Gauss's law in one dimension is

$$\nabla \cdot E = \frac{\partial E}{\partial x} = \frac{\rho}{\epsilon} \quad [\text{A-1}]$$

Conservation of charge yields

$$-\frac{\partial \rho}{\partial t} = \nabla \cdot J = \frac{\partial J}{\partial x} \quad [\text{A-2}]$$

Substitution of Eq. [1] into [A-2] gives

$$-\frac{\partial \rho}{\partial t} = \frac{J_0}{E_0} e^{E/E_0} \frac{\partial E}{\partial x} = \frac{J + J_0}{E_0} \nabla \cdot E \quad [\text{A-3}]$$

Substituting Eq. [A-1] for $\nabla \cdot E$ gives

$$-\frac{\partial \rho}{\partial t} = \frac{J + J_0}{\epsilon E_0} \rho = \frac{\rho}{\tau} \quad [\text{A-4}]$$

where τ is the instantaneous decay time and is given by

$$\tau = \frac{\epsilon E_0}{J_0} e^{-E/E_0} \quad [\text{A-5}]$$

APPENDIX B

Open-Circuit Decay of Electric Field in an Exponentially Conducting Dielectric

The electric field as a function of time can be derived as follows. Differentiating Eq. [A-1] with respect to time and using Eq. [A-2] yields

$$\frac{\partial^2 E}{\partial x \partial t} = \frac{-1}{\epsilon} \frac{\partial J}{\partial x} \quad [\text{B-1}]$$

Rearranging this, we have

$$\frac{\partial}{\partial x} \left(\frac{\partial E}{\partial t} + \frac{J}{\epsilon} \right) = 0 \quad [\text{B-2}]$$

Since $E = J = 0$ for $x < 0$, $(\partial E/\partial t + J/\epsilon)$ must be 0 everywhere. Substituting for J from Eq. [1], we have

$$\frac{\partial E}{\partial t} = -\frac{J_0}{\epsilon} (e^{E/E_0} - 1) \quad [\text{B-3}]$$

This equation can be solved exactly by separation of variables. Let $Y = E/E_0$, $u = (1 - e^{-Y})$ and $du = e^{-Y} dY$. Then Eq. [B-3] becomes

$$\frac{dE/E_0}{(e^{E/E_0} - 1)} = -\frac{J_0}{\epsilon E_0} dt = -\frac{dt}{\tau_{\max}} = \frac{du}{u} = -\frac{dt}{\tau_{\max}} \quad [\text{B-4}]$$

Integrating from t_1 to t_2 gives

$$\ln \left(\frac{1 - e^{-E_2/E_0}}{1 - e^{-E_1/E_0}} \right) = \frac{t_1 - t_2}{\tau_{\max}} \quad [\text{B-5}]$$

Letting $t_1 = 0$ and solving for E_2 , we have

$$E_2(t_2) = -E_0 \ln [1 - e^{-t_2/\tau_{\max}}(1 - e^{-E_1/E_0})] \quad [\text{B-6}]$$

This is the explicit expression for the decay of the electric field as a function of time under open-circuit conditions.

REFERENCES

1. A. W. Davies and R. E. Collins, *Electron. Lett.*, **5**, 462 (1969).
2. A. R. Champion, *J. Appl. Phys.*, **40**, 3766 (1969).
3. J. J. Bernstein and R. M. White, Thin Film Condenser and Electret Ultrasonic Transducers, IEEE Ultrasonics Symposium, San Diego, 1982.
4. T. Smith, "Nondestructive Evaluation of Phosphoric Acid Anodized Aluminum Panels For Contamination," Air Force Report no. AFML-TR-77-42 (1977).
5. I. Tatsuyo, K. Futoshi, S. Joichi, and M. Takao, *J. Jpn. Inst. Light Metals*, **25**, 237 (1975).
6. J. Siejka, A. Morawski, J. Lagowski, and H. C. Gatos, *Appl. Phys. Lett.*, **38**, 552 (1981).
7. L. Young, "Anodic Oxide Films," pp. 13-20, Academic Press, New York (1961).
8. H. S. Carslaw and J. C. Jaeger, in "Conduction of Heat in Solids," 2nd ed., pp. 198-199, Oxford University Press, Oxford, England (1959).
9. L. Young, in "Conduction of Heat in Solids," 2nd ed., pp. 193, 211, Oxford University Press, Oxford, England (1959).
10. G. E. Thompson, R. C. Furneaux, J. S. Goode, and G. C. Woode, *Trans. Inst. Metal Finish.*, **56**, 159 (1978).
11. C. G. Dunn, *This Journal*, **115**, 220 (1968).
12. C. J. Dell'Oca and P. J. Fleming, *ibid.*, **123**, 1491 (1976), information from graph.
13. G. E. Thompson, R. C. Furneaux, and G. C. Wood, *Trans. Inst. Metal Finish.* **57**, 123 (1979).
14. P. W. Chudleigh, *Appl. Phys. Lett.*, **21**, 547 (1972).
15. G. M. Sessler, "Electrets," p. 22, Springer-Verlag, New York (1980).

Measurement of Concentration Profiles of Cu^{2+} Ion and H^+ Ion near a Plane Vertical Cathode by Two-Wavelength Holographic Interferometry

K. Denpo, T. Okumura, Y. Fukunaka, and Y. Kondo*

Department of Metallurgy, Faculty of Engineering, Kyoto University, Sakyo-ku, Kyoto, Japan

ABSTRACT

A technique of two-wavelength holographic interferometry was applied to simultaneously measure the concentration profiles of Cu^{2+} ion and H^+ ion near a plane vertical cathode placed in an unstirred aqueous solution containing CuSO_4 and excess H_2SO_4 . It was revealed that the measured concentration profiles of Cu^{2+} ion and H^+ ion are approximated with the parabolic equations of horizontal distance from cathode surface and that the concentration gradient of Cu^{2+} ion at the cathode surface is larger in $\text{CuSO}_4\text{-H}_2\text{SO}_4$ solution than in CuSO_4 solution at the same cathodic current density and vertical distance. The following matters were also clarified: (i) the nondimensional rate of ionic mass transfer is shown as a function of Rayleigh number based on the boundary layer theory, and (ii) the effect of the addition of excess H_2SO_4 is expressed by a parameter f which is the ratio of Rayleigh numbers in $\text{CuSO}_4\text{-H}_2\text{SO}_4$ solution and in CuSO_4 solution under the conditions of the uniform distribution of cathodic current density and an excess of H_2SO_4 .

The measurement of cathodic concentration profile of ion is important for elucidating not only the ionic mass transfer itself, but also the effect of supporting electrolyte (1, 2). The optical methods such as Jamin (3), Mach-Zehnder (4), and holographic interferometry (5, 6) are effective for the measurement in the single-component aqueous solutions because of the proportionality between the ionic concentration and the refractive index of the solution.

In the industrial electrolysis, such as the electrolytic refining of copper, for example, an excess of sulfuric acid is added. In the multicomponent aqueous solutions, the above proportionality no longer holds and the measurement of concentration profiles of ions becomes more difficult.

An experimental technique using an image sensor of one-dimensional photodiode array was developed in order to measure the concentration profile of Cu^{2+} ion in aqueous $\text{CuSO}_4\text{-H}_2\text{SO}_4$ solution (7). In this measurement of the light absorbance distribution, however, a noise caused by the light diffraction near the cathode surface was superimposed on the output signal, and the concentration of Cu^{2+} ion on the cathode surface was estimated by extrapolating the profile toward the cathode surface. The estimation of the concentration of H^+ ion on the cathode surface was tried by subtracting the light absorbance due to Cu^{2+} ion from the refractive index of the solution measured by the conventional holographic interferometry (5). Due to the error of the measurements and the extrapolation, however, the precision and accuracy of the estimated H^+ ion concentration was relatively poor.

It is the intent of the present work to carry out the simultaneous measurement of concentration profiles of Cu^{2+} ion and H^+ ion in the cathodic boundary layer by using a technique of two-wavelength holographic interferometry which is based on the dispersion effect of refractive index of the solution. The problem due to diffraction pattern appearing near the cathode surface can be avoided in this measurement, because the interference pattern is set up as being at right angles with the diffraction pattern.

The principle of the two-wavelength holographic interferometry is shown in Fig. 1. The profiles of refractive index in the cathodic boundary layer are measured simultaneously at two different wavelengths, and the phase differences S_i ($i = \text{I, II}$) at a horizontal distance $y = y$ from the cathode surface are calculated. Then the differences in the refractive index Δn_i ($i = \text{I, II}$) are calculated at both wavelengths by using the ideal interferometer equation (8-11). When the regression equations of the difference in the refractive index upon the concentration of CuSO_4 and H_2SO_4 are given at each wavelength, both concentration profiles of Cu^{2+} ion and H^+ ion are obtained.

* Electrochemical Society Active Member.

Experimental Arrangement

The optical arrangement for the two-wavelength holographic interferometry is schematically illustrated in Fig. 2. An argon ion laser emitter (Lexel 95-2) and a helium-neon gas laser emitter (Nihon Kagaku Engineering NEO-20M) were used as the light sources. The laser beams were mixed at a half-mirror B_1 to form a single beam with the same optical axis. The mixed beam was split into two beams of objective and reference waves, respectively, by another half-mirror B_2 , after it passed through a half-wavelength plate $\lambda/2$ and a shutter S . The objective wave was collimated to a beam of 1.2 cm diam by an objective lens E_1 (magnification: 10 times) and a lens LE_1 ($f = 200$ mm). After passing through the vicinity of cathode surface in the electrolytic cell C , it was projected on a holographic plate H , on which the image of the cathode surface was recorded.

The center line of the cathode surface was focused on the holographic plate by a lens LE_2 ($f = 135$ mm) which removes the chromatic aberration caused by the different color of the laser beams. The reference wave was collimated to a beam of 50 mm diam by a lens E_2 (magnification: 40 times) and a lens LE_3 ($f = 200$ mm). It was superimposed with the objective wave on the same holographic plate. In order to improve the contrast of the interferogram, it was required to adjust the relative intensity of both waves. Two polarizers P_1 and P_3 were installed for this purpose, while the other polarizers P_2 and P_4 were used to maintain the same polarization plane as the emitted laser beam from the light source. The recon-

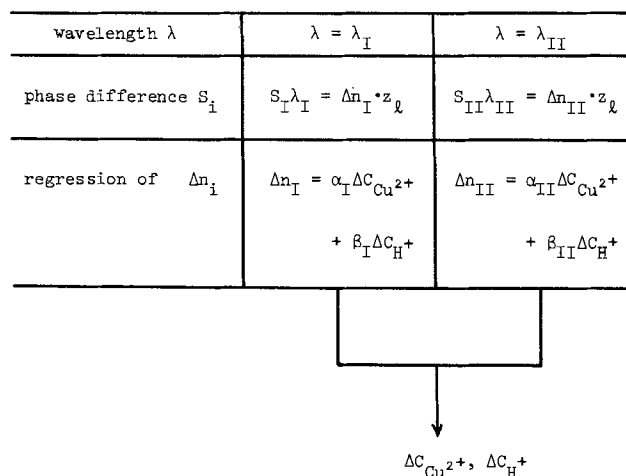


Fig. 1 Principle of two-wavelength holographic interferometry ($\lambda_I, \lambda_{II}, \alpha_I, \alpha_{II}, \beta_I, \beta_{II}$: known)

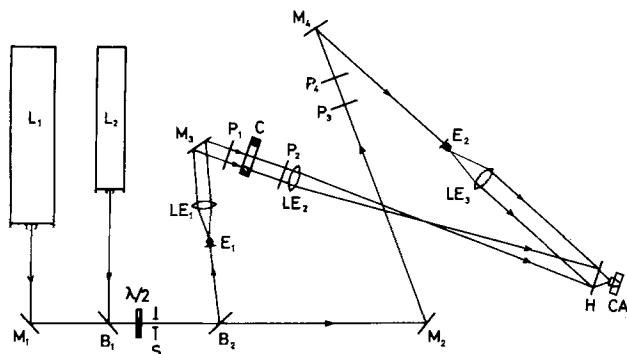


Fig. 2. Optical arrangement for two-wavelength holographic interferometry

L₁: Ar laser. L₂: He-Ne laser. M₁, M₂, M₃, M₄: Mirror.
 B₁, B₂: Beam splitter. E₁, E₂: Spatial filter.
 LE₁, LE₂, LE₃: Lens. P₁, P₂, P₃, P₄: Polarizer.
 S: Shutter. C: Electrolytic cell. H: Hologram.
 CA: Camera. λ/2: Half-wavelength plate.

structured interferograms were taken with a camera. In order to eliminate any mechanical vibration during the measurement, all optical instruments shown in Fig. 2 were mounted on a vibration-free table.

A real-time technique was used for producing a holographic interferogram. In order to assure the optical reproducibility of measurement at these two wavelengths, the profile of refractive index formed during a steady electrolysis under the respective experimental conditions was first recorded on a holographic plate. It was then reconstructed and interfered with the objective wave of a uniform profile of refractive index which was obtained after interrupting the electrolysis. It is thought that by this technique the profile of refractive index is recorded on a holographic plate for each wavelength under exactly the same optical configuration.

The copper rod electrodes were 0.5 cm square, and the effective electrode area was 0.5×8.0 cm². The distance between both electrodes was maintained at 4.8 cm. The details of the electrolytic cell and experimental conditions were already described in the previous paper (7).

Experimental Results

A few examples of the interferogram obtained by the two-wavelength holographic interferometry are demonstrated in Fig. 3. Electrolysis was carried out at a cathodic current density of 0.946 mA/cm². Figure 3a is the holographic interferogram reconstructed simultaneously by both argon ($\lambda_I = 488$ nm) and helium-neon ($\lambda_{II} = 633$ nm)

laser beams. The dispersion effect is clearly shown. Figures 3b and 3c are the interferograms separately reconstructed by argon and helium-neon laser beam, respectively.

The apparent phase differences S in the cathodic boundary layer in these interferograms were obtained from the measured profiles of refractive index. Then the true phase differences were calculated for both wavelengths according to the correcting procedures similar to Hauf *et al.* (8) and Mayinger *et al.* (10). Then the concentration profiles of Cu²⁺ ion and H⁺ ion were obtained by using the ideal interferometer equation and the regression equations (12) of refractive index upon the concentration of Cu²⁺ and H⁺ ions at the two wavelengths. The regression equations were obtained as

$$\Delta n_I = 0.023718\theta_1 - 0.010912\theta_2 \quad (\lambda_I = 488 \text{ nm}) \quad [1]$$

$$\Delta n_{II} = 0.023257\theta_1 - 0.010118\theta_2 \quad (\lambda_{II} = 633 \text{ nm}) \quad [2]$$

Different numerical coefficients in Eq. [1] and [2] are due to the dispersion effect (see Appendix).

A few examples of the concentration profile of Cu²⁺ ion at a vertical distance of $x = 4$ cm from the lower edge of cathode in 0.05M CuSO₄ solution are shown in Fig. 4. It is seen that the concentration difference between cathode surface and bulk electrolyte and the concentration gradient at the cathode surface are larger at higher current densities. It is also shown that the concentration profiles of Cu²⁺ ion at a current density of 0.946 mA/cm² measured by the conventional holographic interferometry (5), by the light absorbance distribution (7), and by the two-wavelength holographic interferometry are compared, and the agreement is satisfactory.

The concentration profiles of Cu²⁺ ion at various current densities in 0.05M CuSO₄-1.85M H₂SO₄ solution are demonstrated in Fig. 5. It is seen that the concentration difference between bulk electrolyte and cathode surface and the concentration gradient at the cathode surface increase and the thickness of the concentration boundary layer decreases with the increase of the current density. The limiting current density was obtained from a current-potential curve shown in Fig. 6 at 1.96 mA/cm², and it is seen that the surface concentration of Cu²⁺ ion is zero at this current density.

The concentration profiles measured under the same electrolytic conditions in 0.05M CuSO₄ and 0.05M CuSO₄-1.85M H₂SO₄ solutions are compared in Fig. 7. The concentration difference between bulk electrolyte and cathode surface and the concentration gradient at the cathode surface in 0.05M CuSO₄-1.85M H₂SO₄ solution are far larger than in the 0.05M CuSO₄ solution.

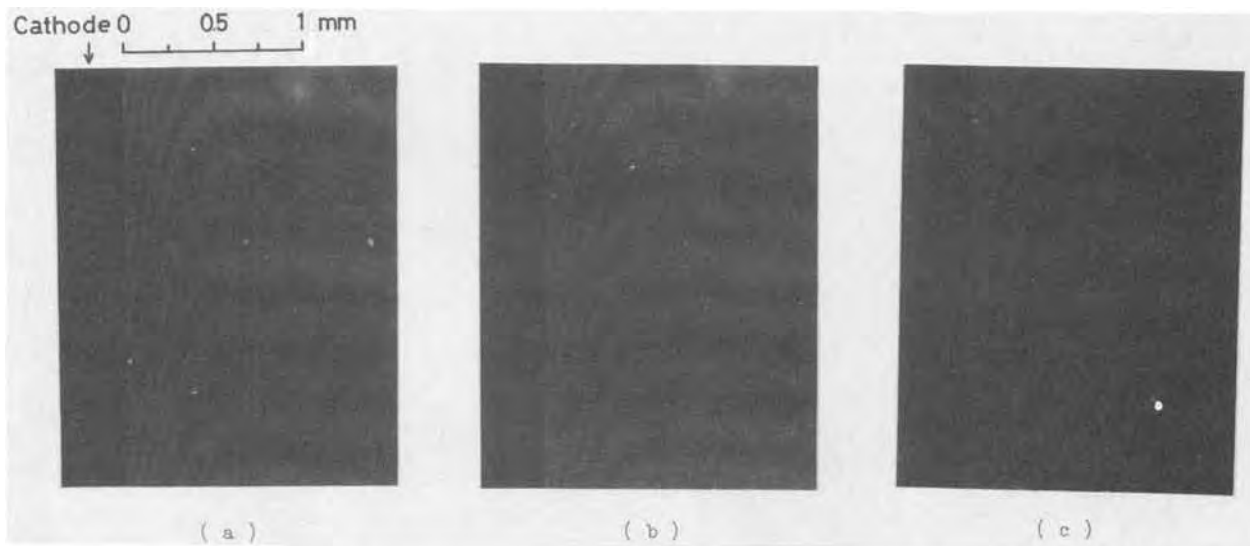


Fig. 3. Holographic interferograms of cathodic diffusion layer (0.05M CuSO₄-1.85M H₂SO₄, $x = 4$ cm, $i = 0.946$ mA/cm²). a: Reconstructed by both Ar laser and He-Ne laser. b: Reconstructed by Ar laser. c: Reconstructed by He-Ne laser.

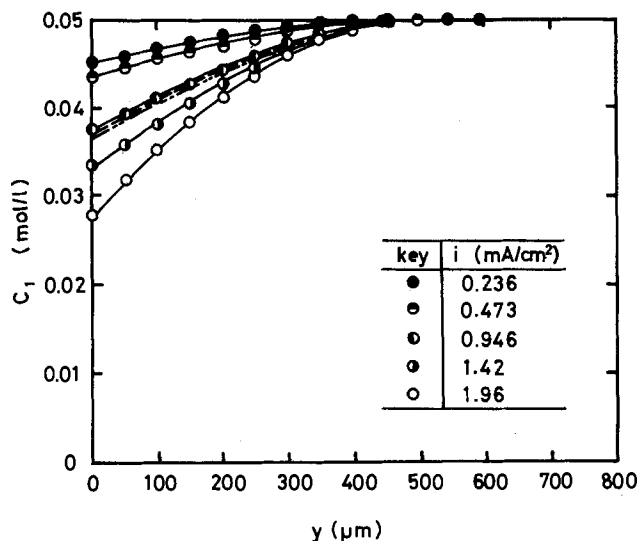


Fig. 4. Concentration profiles of Cu^{2+} ion in the cathodic diffusion layer (0.05M CuSO_4 solution, $x = 4$ cm).

(---): Measured by conventional holographic interferometry (5).
 (---): Measured by light absorbance distribution (7).

Since the cathodic polarization curves with the same copper reference electrode in both solutions are virtually identical at the lower current densities as shown in Fig. 6, the overpotential for electrodeposition of Cu^{2+} ion is not influenced by the presence of H_2SO_4 . The transference number of Cu^{2+} ion in the solution containing CuSO_4 and excess H_2SO_4 is remarkably lowered due to the high mobility of H^+ ion, and the prevailing mechanism of mass transfer of Cu^{2+} ion in the CuSO_4 - H_2SO_4 solution is diffusion and convection. Then the increase of concentration difference and concentration gradient at the cathode surface is expected in order to maintain the same overall rate of electrodeposition as in the CuSO_4 solution. At the same time, hydrogen ion is accumulated near the cathode surface, and the concentration profile is due to the mass balance among the fluxes of migration, diffusion, and convection.

A few examples of the measured concentration profile of H^+ ion are shown in Fig. 8. It is seen in this figure that the concentration of H^+ ion increases from the bulk electrolyte toward the cathode surface. It is also seen that the concentration difference between cathode surface and bulk electrolyte and the absolute value of the concentration gradient at the cathode surface are larger, while the thickness of the concentration boundary layer of H^+ ion is smaller at higher current densities.

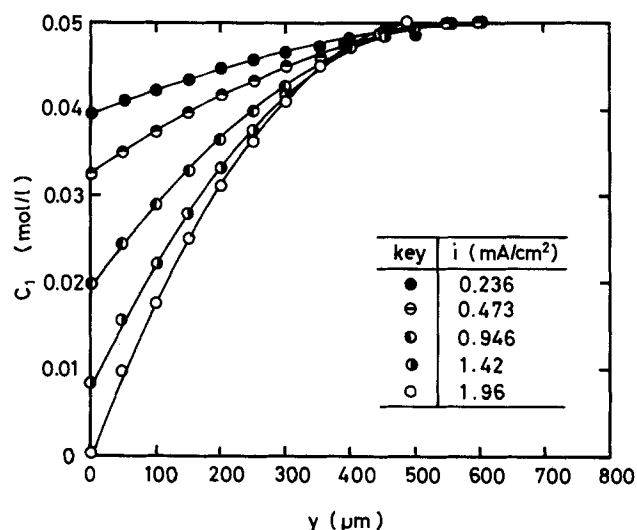


Fig. 5. Concentration profiles of Cu^{2+} ion in the cathodic diffusion layer (0.05M CuSO_4 -1.85M H_2SO_4 solution, $x = 4$ cm).

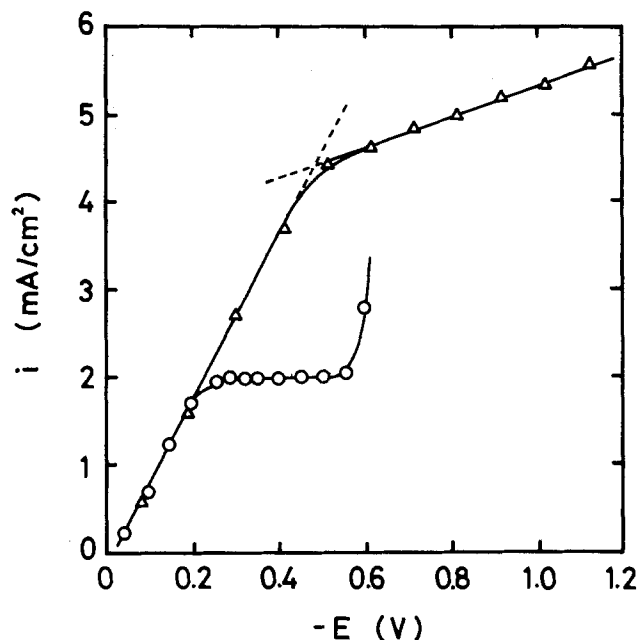


Fig. 6. Current-potential curves. Δ : 0.05M CuSO_4 solution. \circ : 0.05M CuSO_4 -1.85M H_2SO_4 solution.

Discussion

It was shown that the concentration profile of Cu^{2+} ion in the cathodic boundary layer is affected by the addition of H_2SO_4 . The effect of H_2SO_4 on the concentration profile of Cu^{2+} ion and the concentration profile of H^+ ion itself in the cathodic boundary layer are considered below.

The concentration profiles of Cu^{2+} ion and H^+ ion in the cathodic boundary layer are expressed as

$$\theta/\Theta = (1 - y/\delta)^\omega \quad [3]$$

The numerical value of parameter ω was estimated in both 0.05M CuSO_4 and 0.05M CuSO_4 -1.85M H_2SO_4 solutions: the logarithm of θ'/Θ' in 0.05M CuSO_4 solution¹ was plotted against $\log(1 - y/\delta')$ in Fig. 9, and the ω' value for Cu^{2+} ion was obtained to be 1.80 by the least squares method. Similarly, ω_1 and ω_2 values (for Cu^{2+} ion and H^+ ion, respectively) in 0.05M CuSO_4 -1.85M H_2SO_4 solution were obtained at 1.98 and 2.00, respectively. No significant difference was detected by the statistical test

¹Quantities specified with prime are defined for aqueous CuSO_4 solution.

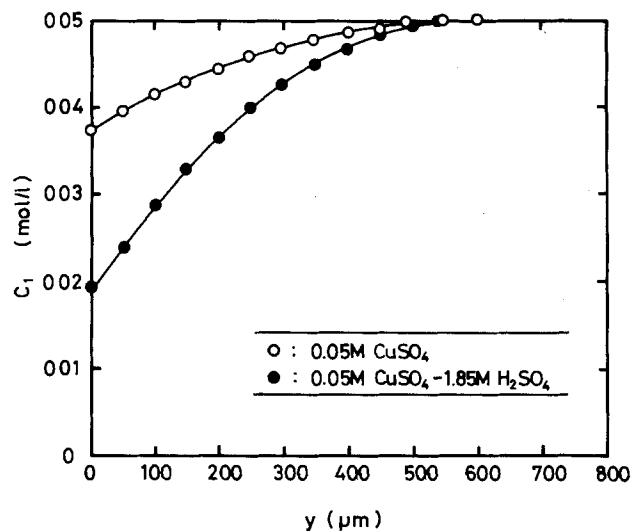


Fig. 7. Comparison of Cu^{2+} ion concentration profiles in the cathodic diffusion layer of aqueous 0.05M CuSO_4 solution and 0.05M CuSO_4 -1.85M H_2SO_4 solution ($i = 0.946$ mA/cm², $x = 4$ cm).

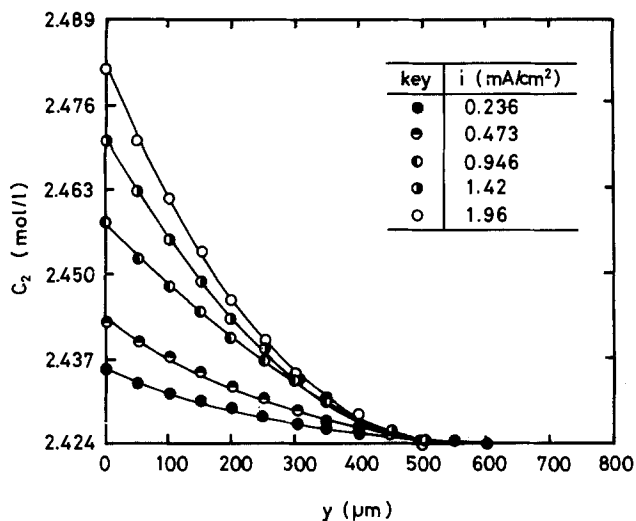


Fig. 8. Concentration profiles of H^+ ion in the cathodic diffusion layer (0.05M $CuSO_4$ -1.85M H_2SO_4 solution, $x = 4$ cm).

among the obtained numerical values of ω' , ω_1 , and ω_2 . These values are lower than 2.3 obtained for Cu^{2+} ion in aqueous $CuSO_4$ solution by Ibl and Müller (3). It is known, however, that the results of calculation by the von Kármán-Pohlhausen integral method are not very sensitive to the numerical value of parameters. Then it can be presumed that the above-mentioned ω values are virtually the same and that the concentration profiles of Cu^{2+} ion in these two solutions are similar.

The velocity profile of natural convection is written as (7)

$$u/u_m = \left(\frac{1}{\lambda - 1}\right) \left\{ \lambda \left(\frac{y}{\tau}\right) - \left(\frac{y}{\tau}\right)^\lambda \right\} \quad 0 \leq y \leq \tau \quad [4]$$

$$u/u_m = 1 - \frac{y - \tau}{\epsilon \tau} \quad \tau \leq y \leq (\epsilon + 1)\tau \quad [5]$$

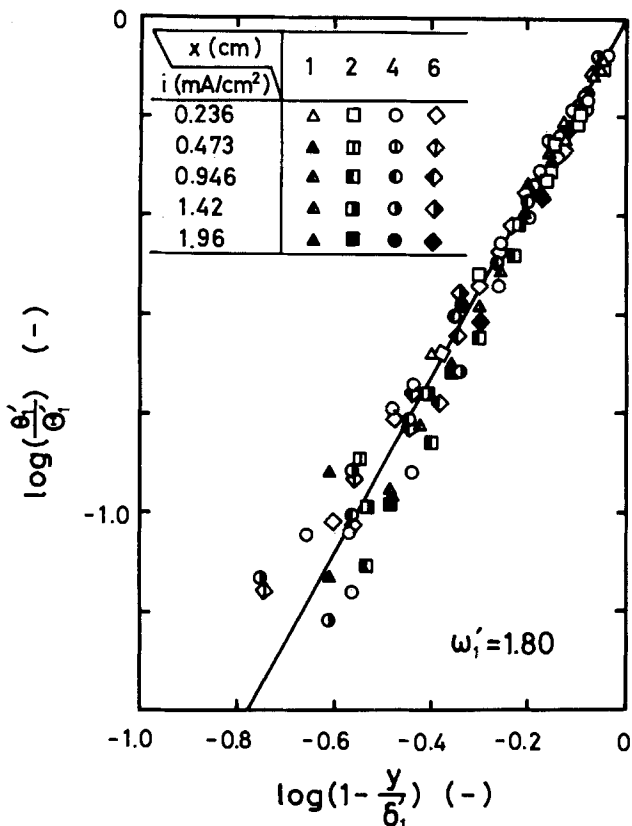


Fig. 9. Plot of $\log(\theta'_1/\theta'_1)$ vs. $\log(1 - y/\delta'_1)$ with aqueous 0.05M $CuSO_4$ solution.

It is assumed that the values of numerical parameters ϵ , λ , τ which determine the velocity profile of natural convection are similar in the two solutions.

Fundamental equations describing laminar natural convection along the cathode surface in a solution containing $CuSO_4$ and excess H_2SO_4 are the momentum balance equation and ionic mass balance equations regarding a volume element of height dx and length $\delta_u(x)$ and the ionic mass flux equation at the cathode surface (7). They are as follows

$$\frac{d}{dx} \int_0^{\delta_u(x)} u^2 dy = -\nu \frac{\partial u}{\partial y} \Big|_{y=0} + \alpha_1 g \int_0^{\delta_u} \theta_1 dy + \alpha_2 g \int_0^{\delta_u} \theta_2 dy \quad [6]$$

$$\frac{d}{dx} \int_0^{\delta_u} u \theta_1 dy = \frac{i(1 - t_1)}{z_1 F} \quad [7]$$

$$\frac{d}{dx} \int_0^{\delta_u} u \theta_2 dy = -\frac{i t_2}{z_2 F} \quad [8]$$

$$k_1 \frac{\partial \theta_1}{\partial y} \Big|_{y=0} = \frac{i(1 - t_1)}{z_1 F} \quad [9]$$

$$-k_2 \frac{\partial \theta_2}{\partial y} \Big|_{y=0} = \frac{i t_2}{z_2 F} \quad [10]$$

respectively. These equations were solved by the von Kármán-Pohlhausen integral method (7), and the following nondimensional rate equations for $CuSO_4$ solution and $CuSO_4$ - H_2SO_4 solution were derived

$$Sh'_x = A' \cdot (Ra^*_{x'})^{1/5} \quad [11]$$

$$Sh_x = A \cdot (Ra^*_{x})^{1/5} \quad [12]$$

where

$$Sh_x = \frac{i(1 - t_1)x}{z_1 F k_1 \theta_1} \quad [13]$$

$$Ra^*_{x} = \frac{g \alpha i (1 - t_1) x^4}{z_1 F \nu k_1^2} \quad [14]$$

Under the assumptions of higher Schmidt number and the similar profiles of velocity and concentration, numerical coefficients A' and A become equal and

$$Sh_x/Sh'_x = f^{1/5} \quad [15]$$

The parameter f is defined as

$$f = \frac{Ra^*_{x'}}{Ra^*_{x}} = \left(\frac{\alpha_1 - \gamma \sigma^2 \alpha_2}{\alpha'_1} \right) \cdot \left(\frac{1 - t_1}{1 - t'_1} \right) / \left(\frac{k_1}{k'_1} \right)^2 \cdot \left(\frac{\nu}{\nu'} \right) \quad [16]$$

When effective diffusivity of Cu^{2+} ion is regarded as being the same as the diffusivity of $CuSO_4$ since each Cu^{2+} ion is surrounded by SO_4^{2-} ions to satisfy the electroneutrality principle in the solution containing $CuSO_4$ and excess H_2SO_4 , the f value is obtained from Eq. [16]. The numerical coefficients A' and A in Eq. [11] and [12] were calculated to be 0.628 at Schmidt number of 3000 from the similarity principle described elsewhere (7, 12). Thus the rate of ionic mass transfer in $CuSO_4$ and $CuSO_4$ - H_2SO_4 solutions is given by

$$Sh'_x = 0.628(Ra^*_{x'})^{1/5} \quad [17]$$

$$Sh_x = 0.628(Ra^*_{x})^{1/5} \quad [18]$$

respectively. Logarithmic Sh'_x and Sh_x were plotted against $\log(Ra^*_{x'})$ and $\log(Ra^*_{x})$, respectively, for both

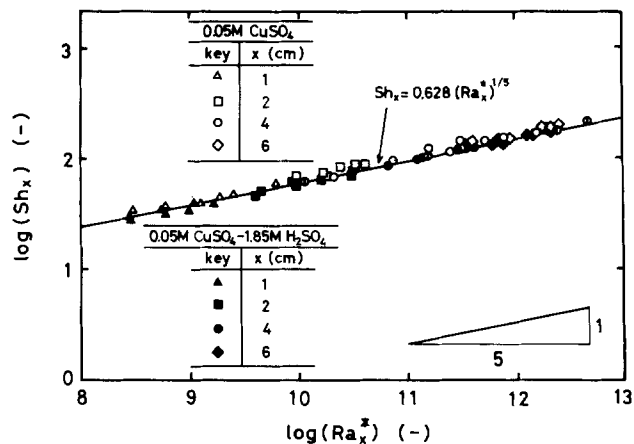


Fig. 10. Relationship between $\log (Sh_x)$ and $\log (Ra_x^*)$. \odot : Measured by light absorbance distribution (7).

solutions in Fig. 10. It is seen that the agreement between the theoretical correlations in the form of Eq. [17] and [18] and the obtained experimental results is satisfactory.

In the same figure, the experimental results obtained by the measurement of light absorbance distribution (7) were also plotted. It is again seen that the agreement is excellent.

From this agreement between the theory and the two kinds of independent measurements, it can be said that the correlation Eq. [17] and [18] are valid and that the parameter f defined by Eq. [16] is meaningful to reveal the effect of added H_2SO_4 on the cathodic ionic mass transfer. Once f value is obtained from the property constants of the solutions, the rate of mass transfer of Cu^{2+} ion in $CuSO_4-H_2SO_4$ solution can be estimated from the rate of ionic mass transfer in $CuSO_4$ solution, so far as the assumptions of uniform distribution of current density and the presence of excess H_2SO_4 are satisfied.

With regard to the concentration of Cu^{2+} ion and H^+ ion at the cathode surface, the ratio of Θ_1 and Θ_2 is given as

$$\Theta_2/\Theta_1 = -\gamma\sigma \quad [19]$$

which was derived from the electroneutrality principle (7). The γ and σ values were calculated as

$$\gamma = \frac{1+a}{1+2a} = 0.809 \quad [20]$$

$$\sigma = \delta_2/\delta_1 = 1.27 \quad [21]$$

respectively (7). With these γ and σ values

$$\Theta_2/\Theta_1 = -1.03$$

However, it was obtained from the experimental results of Fig. 5 and 8 that

$$\Theta_2/\Theta_1 = -1.07$$

The standard deviation of this experimental value is 0.10. Again, the agreement is satisfactory.

Summary

Though it is possible to obtain the cathodic concentration profile of ion in a single-component solution by measuring the distribution of refractive index of the solution, it cannot be applied for obtaining the ionic concentration profiles in the multicomponent solutions such as the aqueous solution containing $CuSO_4$ and excess H_2SO_4 , because the refractive index of the solution is a function of all ionic concentrations. A new technique of two-wavelength holographic interferometry was developed to measure the concentration profiles. In this technique, the dispersion effect of refractive index is utilized.

After the optical distortions in the cathodic concentration boundary layer were corrected, the concentration profiles of Cu^{2+} ion and H^+ ion were obtained from the re-

gression equations of refractive indexes measured at each wavelength upon the concentration of Cu^{2+} and H^+ ions.

It was elucidated from the electrolysis of 0.05M $CuSO_4-1.85M H_2SO_4$ solution that the concentration difference of Cu^{2+} ion between bulk electrolyte and cathode surface and the concentration gradient at the cathode surface increase and the thickness of concentration boundary layer decreases with the increase of the current density. It was also revealed from a comparison of the concentration profiles of Cu^{2+} ion in $CuSO_4$ and $CuSO_4-H_2SO_4$ solutions under the same electrolytic conditions that the concentration difference between bulk electrolyte and cathode surface and the gradient at the cathode surface are larger in $CuSO_4-H_2SO_4$ solution. This effect was explained by the reduced contribution of migration of Cu^{2+} ion in the $CuSO_4-H_2SO_4$ solution to the total current density. The concentration difference of H^+ ion between cathode surface and bulk electrolyte is larger at higher current densities. The numerical values of a parameter ω of the concentration profile of cations were found similar. They were about 2.0.

Based on the experimental results with the two-wavelength holographic interferometry and the light absorbance measurement, the rate of mass transfer of Cu^{2+} ion in $CuSO_4$ solution and $CuSO_4-H_2SO_4$ solution was represented by the correlation equation of

$$Sh'_x = 0.628(Ra_x^*)^{1/5}$$

and

$$Sh_x = 0.628(Ra_x^*)^{1/5}$$

respectively. They are based on the similarity principle applied to the present laminar natural convection. Furthermore, these two equations are mutually related by a parameter f , which is the ratio of the Rayleigh numbers in both solutions. This parameter is predictable from the physical properties of the electrolytes. The concentration difference of H^+ ion in the cathodic concentration boundary layer is estimated from the relationship of

$$\Theta_2/\Theta_1 = -\gamma\sigma$$

which is based on the electroneutrality principle.

Acknowledgments

The authors wish to thank Dr. J. Tsujiuchi, Dr. S. Ueha, and Dr. T. Honda, Tokyo Institute of Technology, and Dr. R. Nagata and Dr. K. Iwata, University of Osaka Prefecture, for their valuable discussions on the optical measurement. Their thanks are also extended to Dr. Y. Nishijima and Dr. T. Fujimoto, Kyoto University, and Mr. K. Kobayashi, Leonix Company, Limited. Further, they express their appreciation to Dr. F. Mayinger and Dr. W. Panknin, Hannover Technical University, Hannover, Germany. Part of this work was carried out under the financial aids given to the authors by the Ministry of Education, Science and Culture (Project no. 57470045), and by the Kurata Foundation, to which the authors are grateful.

Manuscript submitted April 6, 1984; revised manuscript received July 25, 1984.

Kyoto University assisted in meeting the publication costs of this article.

APPENDIX

The following procedure has been carried out to obtain the concentration profiles of Cu^{2+} and H^+ ion from the interferograms (12).

1. The location of cathode surface is determined from the theory of Fresnel diffraction pattern (7).

2. The distance, y , from cathode surface and the number of fringe shift, S_i^M , at that position are simultaneously measured on each picture to obtain the regression equation in a form of

$$S_i^M = a_i y^2 + b_i y + c_i \quad (i = I, II) \quad [A-1]$$

The ratio of sum of squares due to regression to the total sum of squares was calculated to be 0.998.

3. In the present measurement, the focal plane is set up at the center of effective cathode surface whose width is $2b$. The interference equation is thus given by

$$S_1^M \lambda_i = S_1 \lambda_i + \Delta S_1^D \lambda_i + \Delta S_1^E \lambda_i \quad [\text{A-2}]$$

where

$$\Delta S_1^D \lambda_i = -\frac{n_{\infty 1}}{12} \left(\frac{\lambda_i}{b} \right)^2 z_1 \quad [\text{A-3}]$$

and

$$\Delta S_1^E \lambda_i = \frac{2}{z_1} S_1 \sqrt{\delta^2 - y^2} \lambda_i \quad [\text{A-4}]$$

The first term in Eq. [A-2] is the ideal shift, and the second represents the phase difference due to the light deflection in the concentration boundary layer. The last term is due to the end effect of the concentration boundary layer, which extends over the effective cathode surface to the electrolytic cell wall. Roughly speaking, the ratios of ΔS_1^D and ΔS_1^E to the true phase difference are about 0.1 and 0.3, respectively.

All other errors due to chromatic aberration, spherical aberration, parallelness of laser beam, and glass effect of electrolytic cell are negligibly small in comparison with ΔS_1^D and ΔS_1^E .

LIST OF SYMBOLS

A	numerical value
a	degree of dissociation of bisulfate ion
c	concentration (mol/cm ³)
$*c$	concentration in bulk electrolyte (mol/cm ³)
c^s	concentration at cathode surface (mol/cm ³)
E	electrode potential (V)
f	parameter defined by Eq. [16]
i	current density (A/cm ²)
k	diffusivity (cm ² /s)
Δn	difference of refractive index
Ra^*_r	Rayleigh number
Sh_r	Sherwood number
$*t$	transference number
x	vertical distance from the lower edge of cathode (cm)

y	horizontal distance from the cathode surface (cm)
z_1	geometrical path length of reference beam (cm)

Greek Letters

α_1	densification coefficient of CuSO ₄ (cm ³ /mol)
α_2	densification coefficient of H ₂ SO ₄ (cm ³ /mol)
γ	ratio of concentration gradients of H ⁺ ion and Cu ²⁺ ion at cathode surface
δ	thickness of diffusion layer (cm)
Θ	concentration difference between bulk-electrolyte and cathode surface (mol/cm ³)
θ	= $*c - c$ (mol/cm ³)
λ	wavelength (cm)
ν	kinematic viscosity (cm ² /s)
σ	ratio of the thickness of concentration boundary layer of H ⁺ ion and Cu ²⁺ ion
ω	numerical parameter of the concentration profile

Subscripts

1	Cu ²⁺ ion
2	H ⁺ ion
I	488 nm
II	633 nm

REFERENCES

1. C. Wagner, *This Journal*, **95**, 161 (1949).
2. N. Ibl and U. Braun, *Chimia*, **21**, 395 (1967).
3. N. Ibl and R. H. Müller, *Z. Elektrochem.*, **59**, 671 (1955).
4. A. Tvarusko and L. S. Watkins, *This Journal*, **118**, 248 (1971).
5. Y. Awakura and Y. Kondo, *ibid.*, **123**, 1184 (1976).
6. Y. Fukunaka, N. Nishioka, T. Minegishi, and Y. Kondo, *ibid.*, **128**, 1274 (1981).
7. Y. Fukunaka, K. Denpo, M. Iwata, K. Maruoka, and Y. Kondo, *ibid.*, **130**, 2492 (1983).
8. W. Hauf and U. Grigull, "Advances in Heat Transfer," Vol. 6, p. 113, Academic Press, New York (1970).
9. R. H. Müller, "Advances in Electrochemistry and Electrochemical Engineering," Vol. 9, p. 281, John Wiley and Sons, New York (1973).
10. F. Mayinger and W. Panknin, *J. Combust. Meas. Mod. Tech. Instrum.*, 270 (1976).
11. K. Denpo, PhD. Dissertation, Kyoto University, Kyoto, Japan (1984).
12. T. Okumura, M. Eng. Thesis, Kyoto University, Kyoto, Japan (1983).

Technical Notes



Electrocatalytic Activity of Phthalocyanines in Secondary Lithium Cells¹

D. Wöhrle and M. Kirschenmann

Organische und Makromolekulare Chemie, FB 2-Chemie, Universität Bremen, D-2800 Bremen 33, Germany

N. I. Jaeger*

Angewandte und Physikalische Chemie, Angewandte Katalyse, FB 2-Chemie, Universität Bremen, D-2800 Bremen 33, Germany

The feasibility of cathodes containing low molecular unsubstituted phthalocyanines (Pc, I) in secondary lithium cells was studied by Yamaki and Yamaji (1). They reported values of discharge capacities of more than 17 electrons per molecule of phthalocyanine requiring the intercalation of the equivalent number of charge compensating lithium cations. The extensive literature

¹ Part IX of "Polymeric Phthalocyanines and Their Precursors."

* Electrochemical Society Active Member.

concerning the properties of phthalocyanines (2-5), namely, electrochemical and chemical redox equilibria (6-8), suggests a reversible reduction of up to four electrons per molecule. The apparent discrepancies gave rise to a more detailed investigation of the electrochemistry of the cell. At the same time, the properties of low molecular copper octacyanophthalocyanine 2 (9) and copper polyphthalocyanine 3 (10, 11) were tested in the same cell reaction. The structures of the compounds are given in Fig. 1.

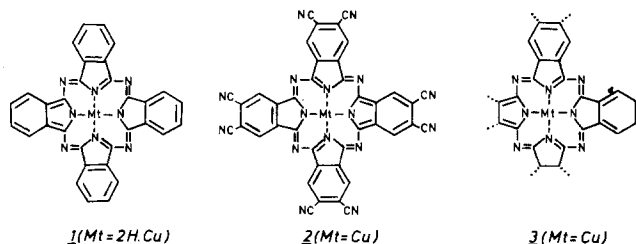


Fig. 1. Structure of Mt-phthalocyanine **1** with Mt = H₂, Cu; copper octacyanophthalocyanine **2** and copper polyphthalocyanine **3**.

Experimental

β -H₂Pc **1**, β -CuPc **1**, **2**, and **3** used in the experiments were synthesized following procedures given in Ref. (2, 3, 9, 10). The compounds **1** were purified by sublimation (12). Test cells were constructed in analogy to the method described in Ref. (1). The lithium anodes (3.14 cm²) were punched from Li foil (99%, Goodfellow Metals). The cathode material contains 0.1g acetylene black (Fa. Hoechst, Germany) acting as a current collector and different amounts of phthalocyanine. The powders were thoroughly mixed in a ball mill for several hours and used directly without further treatment. A polypropylene separator foil (Freudenberg, Weinheim, Germany) soaked with the electrolyte for several days was used to prevent contact between cathode material and the anode. The separator foil was clamped on the powder at the bottom of the cell by means of a PTFE stamp, which was screwed finger tight into the cell. Otherwise, no pressure was exerted on the cathode. The electrolyte was found to soak the cathode material completely.

The electrolyte was 1M LiClO₄ in propylenecarbonate, which had been dried over a molecular sieve (Linde 3 A) and distilled several times under vacuum. The experiments were carried out in a dry box under dry oxygen-free argon.

The stability of the electrolyte during discharge was followed by gas chromatography and mass spectroscopy taking samples from a test volume into which the cell could be vented. The phthalocyanines were tested by infrared spectroscopy before and after discharge.

Results and Discussion

The discharge capacity of a cell for a given amount of β -H₂Pc **1** could be optimized by the amount of acetylene black in the cathode mixture. Figure 2 depicts results obtained for acetylene black to phthalocyanine ratios (by weight) ranging from 0.2 to 10.0. The highest absolute discharge capacities are obtained at the ratio 1.0, since for lower ratios (higher amounts of **1**) the conductivity of the mixture and for higher ratios (higher amounts of acetylene black) the amount of **1** is too low. The corresponding specific discharge capacities are listed in Table I. A blank test run without the cathode active material yielded no capacity. The absolute cell capacity is highest for the acetylene black to β -H₂Pc ratio of 1.0. The specific energy based on H₂Pc weight, however, increases with decreasing amounts of β -H₂Pc in the mixture. The capacities are higher than those reported in Ref. (1).

Table I. Specific discharge capacities of β -H₂Pc **1** in dependence on the ratio of acetylene black to β -H₂Pc in the cathode mixture (0.1g acetylene black in each case). Discharge current 3.14 mA, 1V cutoff.

Ratio acetylene black to β -H ₂ Pc	Specific discharge capacity of β -H ₂ Pc (Ah/kg)	Specific energy related to β -H ₂ Pc (Wh/kg)	Cell capacity (mAh)
0.2	190	285	95
1.0	1014	1521	101
2.0	1193	1789	60
10.0	1256	1884	13
0 (blank)	0	0	0

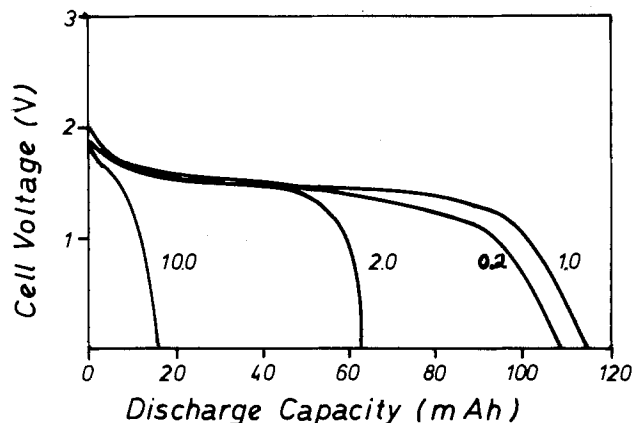


Fig. 2. Discharge capacities *V* of Li- β -H₂Pc **1** cells in dependence on the ratio (by weight) of acetylene black (0.1g) to cathode active material; discharge current 3.14 mA.

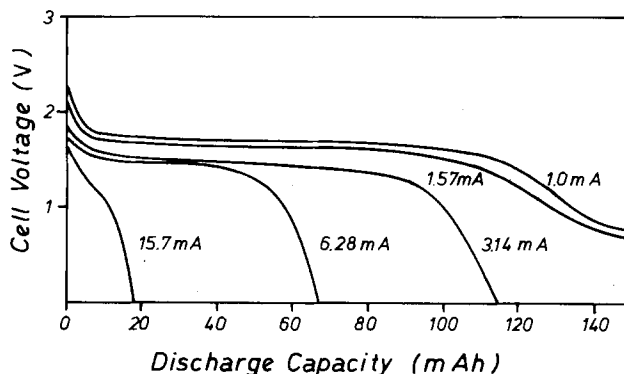
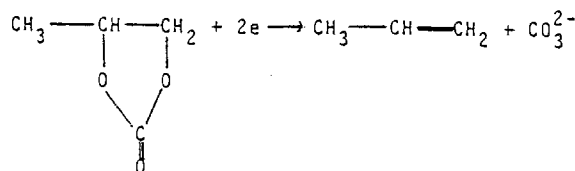


Fig. 3. Discharge capacities of Li- β -H₂Pc **1** cells in dependence on the discharge current. Cathode composition: 0.1g **1**, 0.1g acetylene black.

Cell characteristics and discharge capacity in dependence on the discharge current are given in Fig. 3. For a 1V cutoff, a specific discharge capacity of up to 1340 Ah kg⁻¹ could be achieved corresponding to about 26 electrons per molecule of phthalocyanine.

Since the reversible reduction of phthalocyanines exceeding four electrons per molecule can be ruled out (6-8), the electrocatalytic activity of the material toward the decomposition of propylene carbonate was held responsible for the high discharge capacity of the cell. No irreversible changes in the phthalocyanine structure could be detected by IR spectroscopy following the discharge of the cell. Quantitative analysis by gas chromatography (using standard mixtures of different hydrocarbons) and also the determination of the gaseous reaction products by mass spectrometry shortly after start of the discharge procedure led to the following results: ~70% propene (m/e 42), ~30% mixtures of butenes (m/e 56), and ~0.5% of unidentified hydrocarbons. Therefore, the phthalocyanines exhibit electrocatalytic activity in the decomposition of the electrolyte mainly under formation of propene (13)



CuPc **1** also shows high specific capacities (Table II) in analogy to Ref. (1). Considerably lower capacities were obtained for **2** and **3**. From these results, a drop in the electrocatalytic activity in the order β -H₂Pc **1** > β -CuPc **1** > **3** > **2** can be inferred quite in contrast to the electrocatalytic activity of these compounds (**1**, **3** containing Co or Fe as metal atom) in the reduction of dioxygen (14,15).

Table II. Specific discharge capacities of cathode materials containing β -CuPc 1, copper octacyanophthalocyanine 2, and copper polyphthalocyanine 3

Compound	(g)	Acetylene black (g)	Discharge current (mA)	Specific discharge capacity (Ah/kg)	Specific energy (Wh/kg)	Cell capacity (mAh)
1	0.1	0.1	1.00	1008	1512	101
	0.1	0.1	3.14	455	637	46
	0.2	—	1.00	168	218	34
2	0.1	0.1	1.00	260	364	26
	0.1	0.1	3.14	55	72	6
	0.2	—	1.00	98	157	20
3	0.1	0.1	1.00	350	490	35
	0.1	0.1	3.14	251	301	25
	0.2	—	1.00	100	110	20

Even though Li-SOCl₂ cells are superior to Li-propylene carbonate cells in theoretical charge density by about 20% and in theoretical energy density by about 30%, it could be worthwhile to look into the electrocatalytic activity of the phthalocyanines in more detail.

Acknowledgment

Financial support by Eltech Electrosearch S.A., Geneva, Switzerland, is gratefully acknowledged.

Manuscript submitted Oct. 22, 1984; revised manuscript received Jan. 15, 1985.

Universität Bremen assisted in meeting the publication costs of this article.

REFERENCES

- J. Yamaki and A. Yamaji, *This Journal*, **129**, 5 (1982).
- F. H. Moser and A. L. Thomas, "Phthalocyanine Compounds," Reinhold Publishing Corporation, New York (1963).

- F. H. Moser and A. L. Thomas, "The Phthalocyanines," CRC Press, Incorporated, Boca Raton, FL (1983).
- A. B. P. Lever, *Adv. Inorg. Chem. Radiochem.*, **7**, 27 (1965).
- K. Kasuga and M. Tsutui, *Coord. Chem. Rev.*, **32**, 67 (1980).
- R. Taube, *Z. Chem.*, **6**, 8 (1966).
- D. W. Clack, N. S. Hush, and I. S. Woolsey, *Inorg. Chim. Acta*, **19**, 129 (1976).
- A. P. B. Lever, S. Licocchia, K. Magnell, P. C. Minor, and B. S. Ramaswamy, *Adv. Chem. Ser.*, **201**, 237 (1982).
- D. Wöhrle, G. Meyer, and B. Wahl, *Makromol. Chem.*, **181**, 2127 (1980).
- R. Bannehr, G. Meyer, and D. Wöhrle, *Polym. Bull.*, **2**, 841 (1980).
- D. Wöhrle, *Adv. Polym. Sci.*, **50**, 45 (1983).
- H. J. Wagner, R. O. Loutfy, and C.-K. Hsiao, *J. Mater. Sci.*, **17**, 2781 (1982).
- A. N. Dey and B. P. Sullivan, *This Journal*, **117**, 222 (1970).
- H. Jahnke, *Chimia*, **34**, 58 (1980).
- H. Jahnke, M. Schönborn, and G. Zimmermann, *Top. Curr. Chem.*, **61**, 133 (1976).

Cyclic Voltammogram of SnCl₂ and SnCl₂ + PdCl₂ Sensitizing Solution

Thomas M. Tam*

Lockheed Missiles and Space Company, Incorporated, Sunnyvale, California 94086

A mixed SnCl₂/PdCl₂ sensitizing solution is commonly used to initiate dielectric surface for subsequent metal deposition (1, 2). The catalytic activity of this mixed solution depends upon several parameters: temperature (100°F), specific gravity (1.12 minimum); concentration of Sn²⁺ (50-63 mM) and Pd (1.0-3.8 mM). The most frequently changing parameters are the concentration of Sn and Pd, and these must be adjusted periodically. In order to control these two parameters, it is important to design an *in situ* analytical sensor to monitor the concentration of Sn and Pd.

This communication describes a cyclic voltammetric method for analyzing a Sn-Pd sensitizing solution. Quantitative data will be presented to verify that the technique is simple, rapid, and easily adaptable to automation.

Experimental

Chemical and solutions.—The solvent used in this study was prepared by dissolving 270g of Cataprep 404 salt (Shipley Company, Newton, Massachusetts) into 1 liter of deionized water. The resulting solution is highly acidic and has a high chloride ion concentration. As the Cataprep 404 salt used here is a proprietary salt, the exact composition of other ingredients are not known. This solution is used (i) as a prep solution to activate a noncon-

ducting material for subsequent treatment and (ii) to dilute concentrated Sn-Pd catalyst provided by the vendor (Cataprep 44, Shipley Company, Newton, Massachusetts). The procedure below was used to prepare solutions for this study. The chloride salts of tin (II, IV) and palladium (II) were obtained from Alfa Products. The Sn and Pd content of the salts were determined by Inductive Couple Plasma Atomic Spectrophotometer (Instrument S. A.) and were used to calculate their concentrations in the solutions.

Solutions containing tin were prepared by dissolving known weight of tin salts into Cataprep 404. The tin-palladium (Sn-Pd) solutions were prepared by dissolving known weight of SnCl₂ · 2H₂O and PdCl₂ in separate Cataprep 404 solutions. The two solutions were mixed and left to stand overnight before being used in measurements. Color changes of the solution after being mixed were similar to that reported in the literature (1, 2). These color changes are due to the formation of Sn-Pd colloid suspended in the solution. The catalyst prepared in this manner may not have the optimum activity required, but it is adequate for evaluating the analytical technique described herein.

Cyclic voltammetric measurements.—A 250 ml Brinkmann titration vessel was used to hold the platinum working, auxiliary (copper wire), and Ag/AgCl reference

* Electrochemical Society Active Member.

electrodes. This working electrode was prepared by pressing a 0.32 cm diam platinum rod into 0.953 cm diam stainless steel rod. The electrode body was sealed by using Microstop (Michigan Chrome and Chemical Corporation), and the exposed platinum surface was polished with 600 grit silicon carbide paper. The surface area of the electrode was 0.08 cm². The electrode was rotated at 3000 rpm using a Dietzen Motor equipped with a rotating mercury contact (Mercota, Incorporated). The potential was driven by an in-house built cyclic voltammetric unit (3). A Soltec X-Y recorder (U. P. 64325) was used to record the voltage and current change. The potential was scanned between -0.8 and +0.65V¹ at a rate of 80 mV/s. All voltammograms were run at room temperature (21° ± 1°C).

The peak intensity is defined as area under the peak, which can be converted into total number of coulombs, *I*, by using a proportioning factor. The cyclic voltammetric system currently used does not have an area integrator. Therefore, to obtain the area, the voltammogram obtained from the X-Y chart recorder is photocopied. On the photocopied voltammogram, base lines were drawn under the peaks. The peaks were then cut out along the trace and weighed. Using a proportionality factor, the weight was then converted to *I*.

Results and Discussion

Voltammograms of SnCl₂/SnCl₄ + PdCl₂ in Cataprep 404.—The cyclic voltammetric technique has been used by Osaka *et al.* (4) and Horkans (5) for studying the chemistry of Sn-Pd mixed catalyst. Each of the authors used different electrodes and solutions in their studies, which are quite different from the present work. In this work, the voltammograms are obtained *in situ* by immersing the three electrodes into solution containing SnCl₂, SnCl₄, and SnCl₂ + PdCl₂.

Voltammograms of Sn²⁺ and Sn⁴⁺ in Cataprep 404 are characterized by a set of anodic and cathodic peaks (Fig. 1A); the anodic peak (SnA) is at -0.41V and the cathodic peak is at -0.53V (SnC). As SnC is easier for analysis, it is used for obtaining quantitative data. When PdCl₂ is added to the Sn²⁺ solution, an anodic peak (Pd1) at -0.21V is also observed (Fig. 1A). This peak can be used for the analysis of Pd²⁺ quantitatively.

An additional palladium peak (Pd2) can be observed by treating the platinum electrode as follows. (i) The platinum electrode is immersed in a Sn-Pd containing solution and is cycled three times between -0.8 and +0.65V.

¹All potentials are measured against Ag/AgCl reference electrode.

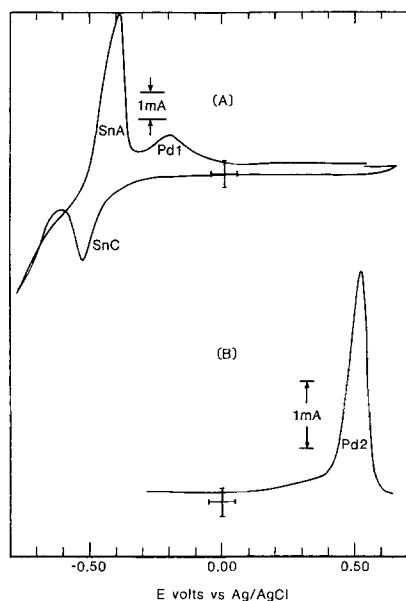


Fig. 1. Cyclic voltammogram of Sn²⁺ + Pd²⁺ in Cataprep 404. Temp. = 21°C. Scan rate = 80 mV/s. C_{Sn²⁺} = 54 mM; C_{Pd²⁺} = 9.3 mM.

Table I. Parameters of the straight line plot shown in Fig. 2 and 3

	Slope (C/mM)	Intercept (C)	Coeff. of DTM. (r ²)	Figure no.
<i>I</i> _{SnC} vs. C _{Sn²⁺/Sn⁴⁺}	5.69 × 10 ⁻⁵	-3.3 × 10 ⁻⁴	0.98	2
<i>I</i> _{Pd1} vs. C _{PdII}	1.45 × 10 ⁻⁴	-2.22 × 10 ⁻⁵	0.97	3
<i>I</i> _{Pd2} vs. C _{PdII}	4.44 × 10 ⁻⁴	-2.87 × 10 ⁻⁴	0.99	3

(This peak intensity increases with the number of cycles scanned). (ii) Rinse the electrode, immerse the electrode into Cataprep 404 solution, and scan the voltage anodically while rotating the platinum electrode at 3000 rpm. A single anodic peak is observed at +0.51V (Pd2, Fig. 1B). This procedure was followed in our experiments on Pd²⁺ because of its reproducibility to obtain quantitative data for the Pd2 peak.

Intensity of SnC Peak (*I*_{SnC}).—The linear dependence of *I*_{SnC} vs. C_{Sn²⁺} and C_{Sn⁴⁺} is shown in Fig. 2, and the properties of the straight line plot are shown in Table I. The behavior of *I*_{SnC} vs. C_{Sn²⁺} and C_{Sn⁴⁺} is identical and therefore can be considered as one plot. In order to identify the SnC peak, Joisson and Devand's (6) work was repeated using a differential polarography technique to study Sn²⁺ and Sn⁴⁺ in 0.1M HCl/4M NH₄Cl solution. We found that the reduction of Sn⁴⁺ and Sn²⁺ appeared at -0.286V and -0.482V, respectively. The peak intensity measured from the Sn⁴⁺ solution is approximately one-tenth that of Sn²⁺, although the concentrations of the two species are approximately equal (10 ppm). The reason for this is not yet clear. Based upon these results, SnC was designated as the reduction of Sn²⁺ to Sn⁰, and SnA as the dissolution of Sn⁰ in Cataprep 404. For a Sn⁴⁺ solution, the peak at -0.286V due to the reduction of Sn⁴⁺ should be observed. However, the peak in this region could be relatively small and broad so that we are unable to observe it. As a result, only the SnC peak is observed. The data points for *I*_{SnC} vs. C_{Sn²⁺} with constant amount of PdCl₂ added are also shown in Fig. 2. At low C_{Sn²⁺}, the data points can be fitted onto the straight line. As the C_{Sn²⁺} increases, the data points begin to deviate from the straight line.

The effect of Pd²⁺ on *I*_{SnC} was measured by using solutions containing an approximately constant amount of Sn²⁺ (60 ± 1.5 mM) and varying amounts of Pd²⁺ (0.7-17 mM). The apparent peak intensity, *I*_{SnC}/C_{Sn²⁺}, remains relatively constant, 4.0 ± 0.4 × 10⁻⁵ C/mM.

Intensity of Pd1 peak (*I*_{Pd1}).—When PdCl₂ is added to the Sn²⁺ containing solution, a small anodic peak at -0.21V is also observed. The intensity of this peak (*I*_{Pd1})

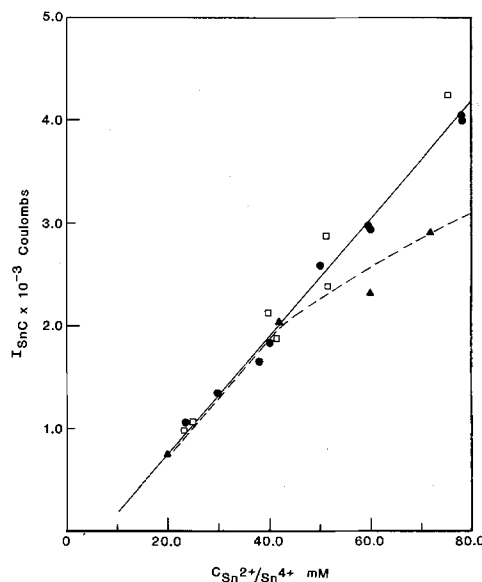


Fig. 2. *I*_{SnC} vs. C_{Sn²⁺/Sn⁴⁺}. Experimental conditions, see Fig. 1. ●, Sn²⁺; □, Sn⁴⁺; ▲, Sn²⁺ + Pd²⁺.

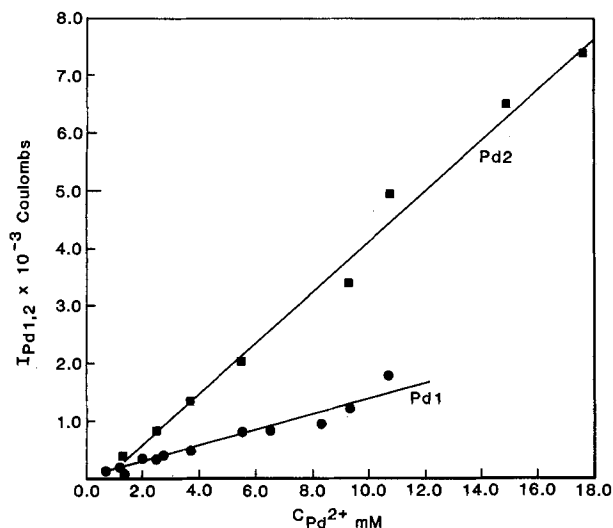


Fig. 3. I_{Pd1} and I_{Pd2} vs. $C_{Pd^{2+}}$. Experimental conditions, see Fig. 1. $C_{Sn^{2+}} = 60$ mM.

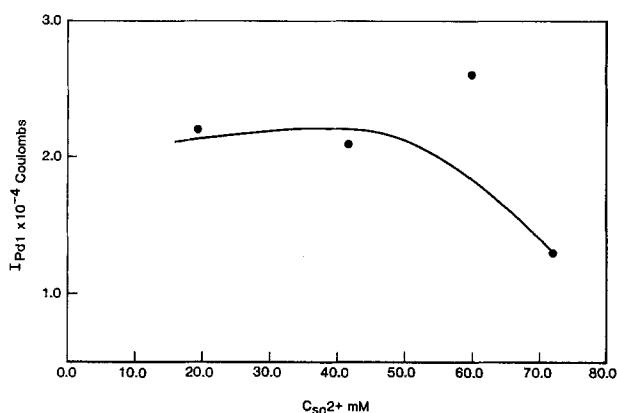


Fig. 4. I_{Pd1} vs. $C_{Sn^{2+}}$. Experimental conditions, see Fig. 1. $C_{Pd^{2+}} = 1.64$ mM.

increased linearly with respect to $C_{Pd^{2+}}$ (Fig. 3). The parameters of the straight line are shown in Table I. The effect of Sn^{2+} on I_{Pd1} is shown on Fig. 4. Notice at low $C_{Sn^{2+}}$ (20-40 mM) the effect of Sn^{2+} is negligible, but at higher concentrations the intensity of the peak decreases. It is apparent that this peak can be directly related to the $C_{Pd^{2+}}$ in solution. It is unlikely that this peak is due to the dissolution of palladium deposited on the electrode surface. Both Osaka *et al.* (4) and Horkans (5) suggested that in this region the observed anodic current is due to the desorption of hydrogen (7). Another hypothesis is that, as the Pd-Sn colloid is deposited onto the electrode surface during cathodic scan, quantitative amounts of hydrogen are absorbed on the palladium surface. During the anodic scan, the desorption of hydrogen gives rise to the anodic current. But as the concentration of Sn^{2+} increases, it competes with hydrogen for the coordinate site of palladium, causing the peak intensity to drop.

Intensity of Pd2 peak (I_{Pd2}).—Interestingly, this peak is not observed in a Sn-Pd sensitizing solution. It will show when the electrode is treated by the steps described in the experimental section. The peak intensity I_{Pd2} increases linearly with respect to the concentration of Pd in solution (Fig. 3, Table I). Using a different procedure, Osaka *et al.* (4) observed a similar peak. There is little doubt that Pd2 is due to the dissolution of Pd^0 (4, 8). The metallic palladium can be produced on the electrode in two ways: (i) activation, the result of a reaction between

Sn^{2+} and Pd^{2+} on the electrode; or (ii) electroposition, as the result of pretreatment by potential cycling.

In a Sn-Pd sensitizing solution, it is likely that Pd is well protected, or insulated by the excess Sn^{2+} (stabilizing Sn^{2+}) (9, 10). As the electrode is immersed into a pure Cataprep 404 solution, the stabilizing Sn is dissolved and Pd is then exposed to the high chloride solution. As a result, the dissolution process is possible.

The following two experiments were done to test the above hypothesis.

1. The Sn-Pd colloid is deposited onto the electrode surface as described, rinsed, and anodically stripped in a Sn^{2+} containing Cataprep 404 solution. The Pd2 peak does not show up. If the same electrode is further stripped in a pure Cataprep 404 solution, the expected Pd2 peak shows up.

2. Six 1×1 cm² platinum plates were coated with Sn-Pd complex similar to the technique used above. Three of the plates were rinsed with deionized water (set 1), and the rest were rinsed with Cataprep 404 (set 2). The surface of the Sn-Pd coat was investigated using Auger electron spectroscopy. We have found the atomic ratio of Pd and Sn on the surfaces are: set 1, Pd:Sn = 0.17:0.83; set 2, Pd:Sn = 0.37:0.63. The standard deviation of these values is ± 0.03 .

Experiment 1 shows that Sn^{2+} in Cataprep 404 will inhibit the dissolution of Pd^0 . Experiment 2 shows that significant amount of Sn^{2+} on the electrode surface can be leached (stabilizing Sn^{2+}) by rinsing it with high chloride containing solution. The remaining Sn could be the complexed Sn.

Conclusion

The cyclic voltammetric technique described in this communication can be used in monitoring the concentration of Sn and Pd in Sn-Pd sensitizing solution. The advantages of this sensing system are (i) measurement of Sn and Pd *in situ*; (ii) measurement of Sn and Pd simultaneously in one scan cycle (SnC , PdI); and (iii) two measurements on Pd ($Pd1$, $Pd2$).

The system used in the laboratory has an accuracy of $\pm 10\%$. Improvement is possible by automation of the system. The system cannot measure specifically the Sn^{2+} and Sn^{4+} concentrations.

Acknowledgment

The author would like to express his gratitude to Hugh A. Six and Tim W. Rodgers for their technical assistance.

Manuscript submitted Aug. 21, 1984; revised manuscript received Dec. 17, 1984.

Lockheed Missiles and Space Company, Incorporated, assisted in meeting the publication costs of this article.

REFERENCES

1. E. D. D'Ottavio, U.S. Pat. 3,532,518 (1970); 3,650,913 (1972).
2. R. J. Zeblysky, U.S. Pat. 3,672,938 (1972).
3. A. M. Bond, "Modern Polarographic Methods in Analytical Chemistry," p. 47, Marcel Dekker Inc., New York (1980).
4. T. Osaka, H. Takematsu, and K. Nihei, *This Journal*, **127**, 1021 (1980).
5. J. Horkans, *ibid.*, **130**, 311 (1983).
6. A. Joissin and M. Devand, *C. R. Acad. Sci. Paris*, **275**, 1363 (1972).
7. J. Horkans, *J. Electroanal. Chem.* **106**, 245, (1980).
8. J. A. Harrison, *Electroanal. Chem. Interf. Electrochem.* **41**, 415 (1973); *ibid.*, **47**, 431 (1973); *ibid.*, **53**, 145 (1974).
9. R. L. Cohen and K. W. West, *Chem. Phys. Lett.*, **16**, 128 (1972); *This Journal*, **119**, 433, (1972); *ibid.*, **120**, 502 (1973).
10. N. Feldstein, M. Schlesinger, N.E. Hedgecock, and S. L. Chow, *This Journal*, **121**, 738 (1974).

Potentiostatic High Overpotential Studies of Copper Deposition from Electroless Copper Solutions

Milan Paunovic*

Kollmorgen Corporation, PCK Technology Division, Melville, New York 11747

The mechanism of electroless metal deposition has been studied so far from two aspects: electrochemical and structural. First, some mechanistic aspects of charge transfer processes in electroless metal deposition were studied by transient and quasi-steady-state electrochemical techniques (1-6); second, the mechanistic aspects of lattice formation processes were studied by scanning and transmission electron microscopy (7-9). One unsolved problem is a correlation between the electrochemical and structural kinetic parameters.

The purpose of this study is to initiate work on the elucidation of the above unsolved correlation problem. For these studies, we have chosen the potentiostatic transient method (10-13).

In this communication, we report potentiostatic current-time transients obtained in the studies of the cathodic partial reaction in electroless copper deposition using palladium and platinum electrodes. Results obtained using a copper electrode were reported previously (13). These measurements are the first applications of the potentiostatic current-time technique to the study of processes in electroless metal deposition.

Experimental

The solutions were prepared with analytical-grade reagents and distilled water. The electroless copper solution used for these studies contained 0.05M CuSO_4 , 0.15M EDTA (ethylene-diaminetetraacetic acid), 0.25M Na_2SO_4 , 0.074M CH_2O , $3.0 \times 10^{-4}\text{M}$ NaCN, and NaOH to give a pH of 12.50. The formaldehyde was a 37% solution of an analyzed reagent grade. Oxygen was removed by bubbling argon. The temperature was 25°C.

An all-glass, three-compartment cell with three electrodes with 500 ml of solution was used. The reference electrode compartment was connected to the test electrode compartment via a Luggin capillary. The test electrode was either (i) a platinum disk, 0.442 cm^2 in area, or (ii) a palladium disk, 0.500 cm^2 in area. The auxiliary electrode was a platinum cylinder (1 cm^2 in area) electroplated with copper in an acid copper solution (1), and a saturated calomel electrode (SCE) was used as a reference electrode. The test electrode was polished to a mirror finish using 0.05 μm alumina powder. Between tests, deposited copper was stripped in a persulfate solution ($\text{Na}_2\text{S}_2\text{O}_8$ 40 g/liter and H_2SO_4 to give a pH of 2.5) and the electrode was polished with 0.05 μm alumina powder. The test electrode was introduced into the solution at the test potential and recording of the current-time curves was started simultaneously with establishment of the electrode-solution contact.

Potentiostatic current-time transients were obtained with a PAR (Princeton Applied Research, Princeton, New Jersey) Model 173 potentiostat-galvanostat. The current-time (i-t) curves were recorded on a Hewlett-Packard 7004 recorder.

Results and Discussion

Two typical sets of potentiostatic current-time transients for the reduction of cupric ions in the absence of formaldehyde are shown in Fig. 1. Figure 1 shows that these curves exhibit a maximum (i_m) and that the height and the position of this maximum on the time coordinate (t_m) are a function of the potential. These potentials are relatively high. The rest potentials for Pt and Pd were -50 and -200 mV vs. SCE, respectively.

* Electrochemical Society Active Member.

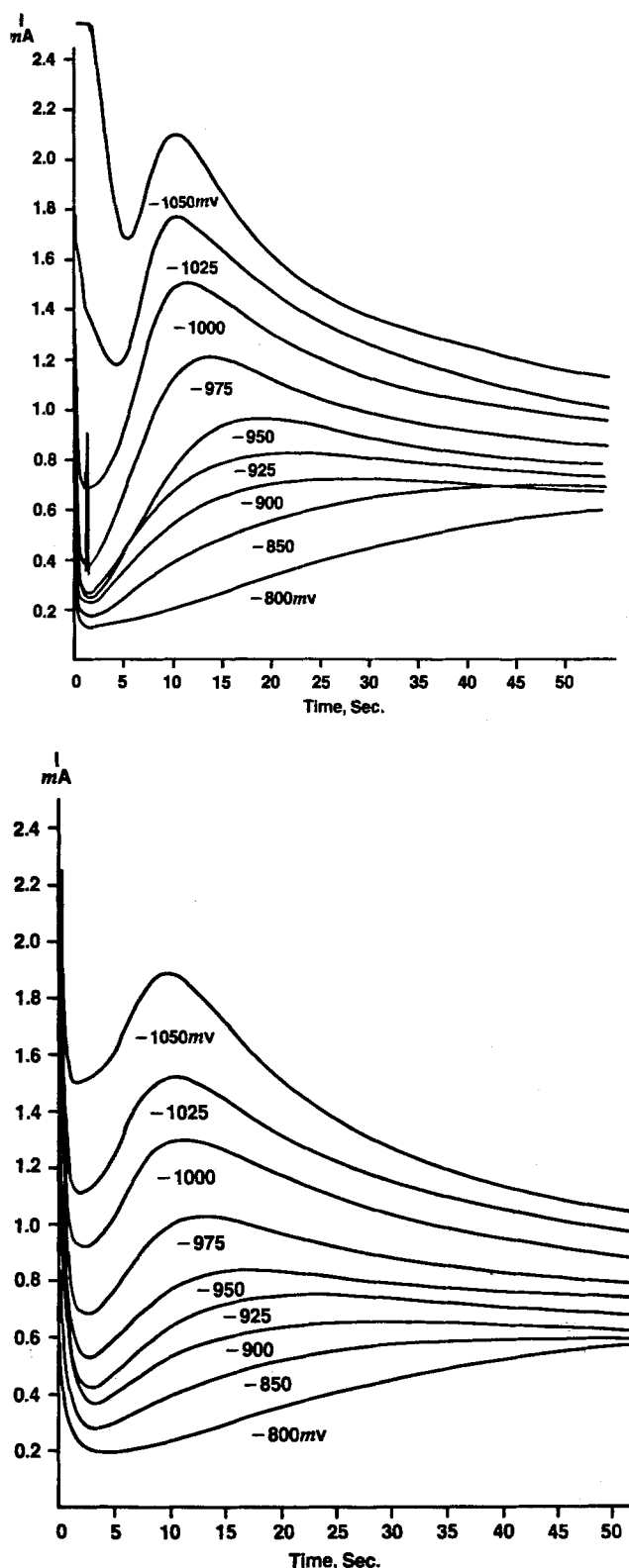


Fig. 1. Potentiostatic current-time transients for the deposition of copper from the solution containing 0.05M CuSO_4 , 0.15M EDTA, 0.25M Na_2SO_4 , $3.0 \times 10^{-4}\text{M}$ NaCN, and NaOH to give a pH of 12.50. Absence of CH_2O . a (top): A platinum electrode. b (bottom): A palladium electrode.

Two sets of current-time transients for the deposition of copper from the electroless copper solution, in the presence of formaldehyde, are shown in Fig. 2. Figures 1 and 2 show that the curves recorded at the Pt and Pd electrodes in the solution in the absence of formaldehyde exhibit essentially the same shape as those in the presence of formaldehyde. One significant difference is that, at certain

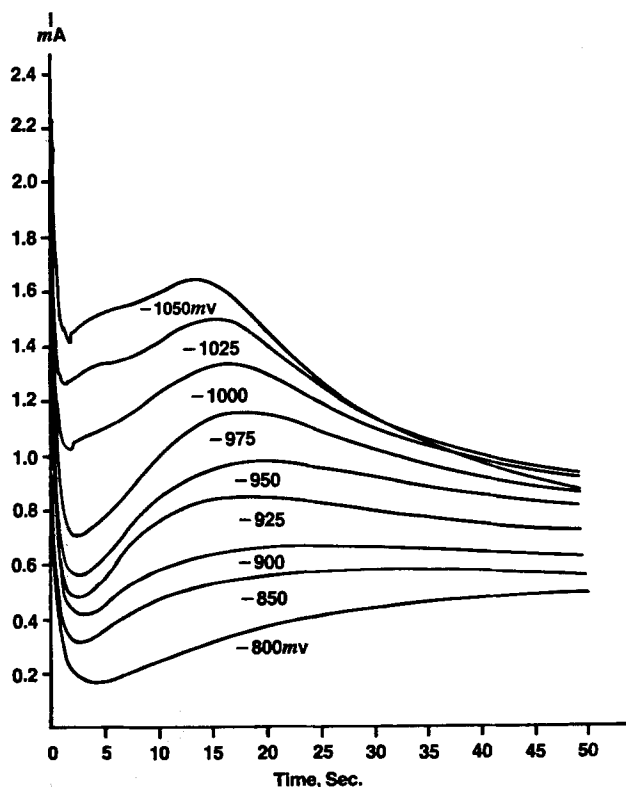
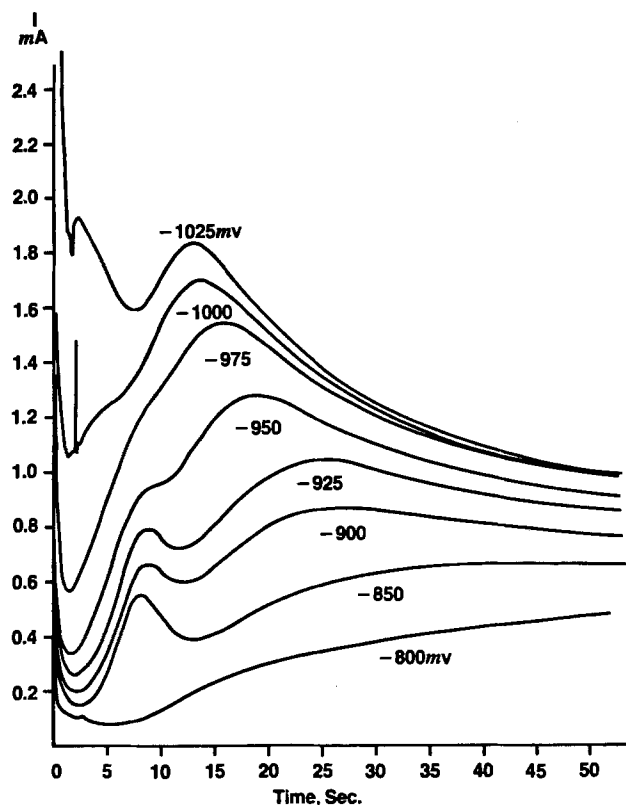


Fig. 2. Potentiostatic current-time transients for the deposition of copper from the electroless copper solution. a (top): A platinum electrode. b (bottom): A palladium electrode. The mixed potential of a copper electrode in this solution is -720 mV vs. SCE. The composition of the solution is given in the Experimental section.

potentials in the presence of formaldehyde, two maxima are clearly visible; the analysis of these maxima will be published elsewhere.

A comparison between Fig. 1 and 2 shows that the height and the position of the maxima are in the same current and time range for the both types of solutions (the presence and the absence of formaldehyde). Figure 3 shows that the height and the position of this maximum on the time coordinate depend on the additive present in the solution.

Plots of $\log i_m$ vs. overpotential are linear and, when extrapolated to $\eta = 0$, they yield intercepts ($i_{m,0}$) of 3.0×10^{-5} and 3.5×10^{-5} A/cm², for Pd and Pt, respectively (Fig. 4). The intercept $i_{m,0}$ is analogous to that in the classical Tafel relation, i_0 , and the reversibility parameter $i_{m,0}$ observed for the case of the nucleation and growth process control (14). At the present, there is no theoretical equation for the diffusion-controlled processes giving $i_{m,0}$ in terms of the nucleation rate constant, diffusion coefficient, and overpotential.

Slightly different values of $i_{m,0}$ for different substrates (e.g., Fig. 4) are due to differences in the interaction energies between the substrate and the first layer, which are different for different substrates (14).

It was shown earlier (6), using a rotating disk electrode, that reduction of complexed copper ions in an electroless copper solution, at the Cu²⁺ ion concentration of 0.05M, is diffusion controlled. Also, in the preliminary experiments in this work, we have found that the height of the potentiostatic i - t maxima depend on the rate of rotation of the test electrode; thus, these maxima are diffusion controlled, and are the result of two opposing effects: first, an increase in the current due to the increase in the surface area of growing nuclei, and second, a decrease in the current due to (i) overlap and (ii) an increase in the thickness of the Nernst diffusion layer δ , $\delta(t) \propto t^{1/2}$ (12) and $i \propto (1/\delta)$.

If diffusion of electrodepositing ions from the solution to the nuclei is rate-determining, and if the overlap effect is taken into account (10-12), then the theoretical values of the product $i_m^2 t_m$ for hemispherical diffusion are given for instantaneous nucleation by (11)

$$i_m^2 t_m = [0.163 (nFc)^2 D] = 1.52 \times 10^{-4}$$

and for progressive nucleation by

$$i_m^2 t_m = [0.260 (nFc)^2 D] = 2.42 \times 10^{-4}$$

for $c = 5 \times 10^{-5}$ M/cm³, $n = 2$, and $D = 1 \times 10^{-5}$ cm²/s,

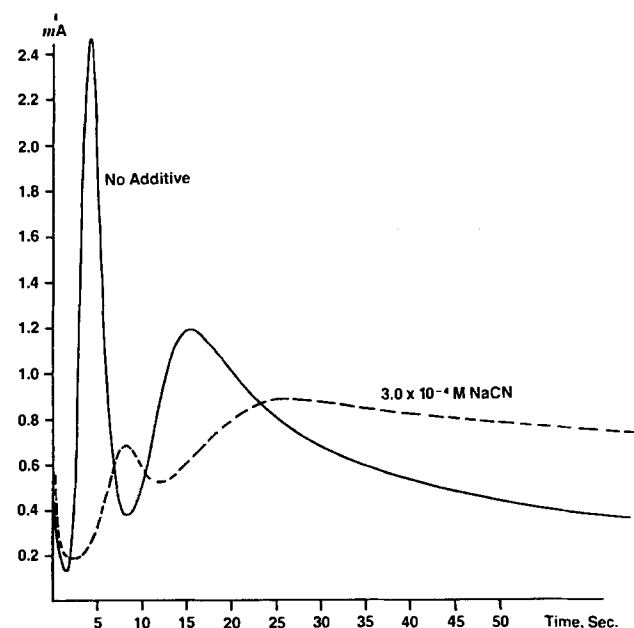


Fig. 3. Potentiostatic current-time transients of a Pt electrode in electroless copper solution showing effect of NaCN. $E = -900$ mV.

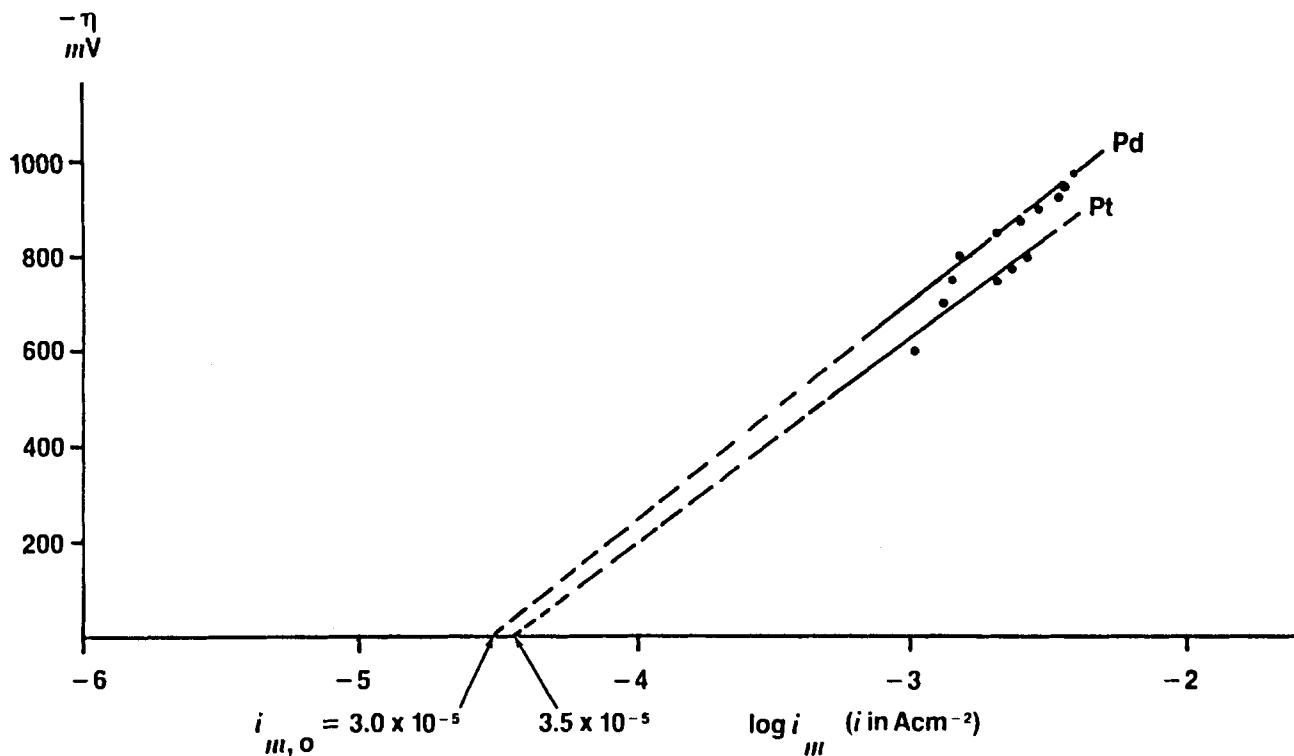


Fig. 4. Plot of η vs. $\log i_m$ of Pd and Pt electrodes in electroless copper solution

where c is the concentration of copper ions, n the number of electrons, F the Faraday constant, and D the diffusion coefficient.

The experimental values at -1000 mV vs. SCE, for the electroless solution, are 1.98×10^{-4} and 1.18×10^{-4} for Pt and Pd electrodes, respectively. This relatively good agreement between the experimental and theoretical (instantaneous nucleation) values can be taken as a confirmation of the diffusion control.

Other types of analysis of the current-time curves and correlation of these to our structural studies (7) will be published elsewhere. Also, by changing, the concentration of copper ions, controls other than diffusion will be studied.

The current-time curves (and the above-mentioned correlation) are of great theoretical and practical significance since they enable us to determine (i) number of nuclei N , from $i = F(D, t, N)$ for the instantaneous nucleation, (ii) the nucleation rate constant k , from $i = F(D, t, k)$, for the case of the progressive nucleation, and (iii) geometry of nuclei by electrochemical methods. The electrochemical methods are much faster than methods used in structural studies (7) and are capable of being computerized for the continuous monitoring of quality of metal deposition.

Conclusions

It was shown that the potentiostatic transient technique using high overpotentials can be used to study (i) processes comprising electroless copper deposition and (ii) the effect of additives on these processes. The use of high overpotentials in the potentiostatic step functions is a limitation when this technique is applied to the studies of electroless copper deposition. The dependence of $i = f(t)$

transients on (i) the type (morphology, geometry) and (ii) the number of nuclei is an advantage of the potentiostatic technique over electrochemical techniques used previously. This advantage enables one to establish a correlation between the electrochemical and structural kinetic parameters and provide a new method for copper quality control.

Manuscript submitted Aug. 2, 1984; revised manuscript received Dec. 13, 1984.

Kollmorgen Corporation assisted in meeting the publication costs of this article.

REFERENCES

1. M. Paunovic, *Plating*, **55**, 1161 (1968).
2. M. Paunovic, *Plat. Surf. Finish.*, **70**, 62 (1983).
3. F. Donahue, *Oberflaeche-Surf.*, **13**, 301 (1972).
4. M. Paunovic and R. Arndt, *This Journal*, **130**, 794 (1983).
5. L. Schoenberg, *ibid.*, **119**, 1491 (1972).
6. D. Vitkavage and M. Paunovic, *Plat. Surf. Finish.*, **70**, 48 (1983).
7. M. Paunovic and C. Stack, in "Electrocrystallization," R. Weil and R. G. Barradas, Editors, p. 205, The Electrochemical Society Softbound Proceedings Series, Pennington, NJ (1981).
8. R. Sard, *This Journal*, **117**, 864 (1970).
9. S. Nakahara and Y. Okinaka, *Acta Metall.*, **31**, 713 (1983).
10. G. J. Hills, D. J. Schiffrin, and J. Thompson, *Electrochim. Acta*, **19**, 657 (1974).
11. G. Gunawardena, G. Hills, I. Montenegro, and B. Scharifker, *J. Electroanal. Chem.*, **138**, 225 (1982).
12. B. Scharifker and G. Hills, *Electrochim. Acta*, **28**, 879 (1983).
13. M. Paunovic, in "Extended Abstracts of the 35th I.S.E. Meeting," Berkeley, CA, August 1984.
14. H. Angerstein-Kozłowska, B. E. Conway, and J. Klinger, *J. Electroanal. Chem.*, **87**, 321 (1978).

Electrocatalytic Oxidation of Demineralized Oil Shale

Patrick M. Dhooge and Su-Moon Park*

Department of Chemistry, University of New Mexico, Albuquerque, New Mexico 87131

K. M. Jeong

Gulf Research & Development Company, Pittsburgh, Pennsylvania 15230

Electrochemical oxidation of coal slurries has recently been suggested as a means of gasifying coal at low temperatures by Coughlin *et al.* (1-3). Subsequent studies by other investigators (4, 5) indicated that electrolytic currents observed from the coal slurry in 1M sulfuric acid were attributed to the oxidation of iron(II) leached out from the coal. We (6-8) and Lalvani *et al.* (9) have more recently shown through various experiments that coal slurries are catalytically oxidized by iron(III); the reduced ion, iron(II), produced in the electron-transfer process is then oxidized back to Fe(III) at the anode, completing a catalytic cycle. The oxidation products for this reaction were carbon dioxide and hydrogen, and oxygen atoms in the product, CO₂, were shown to be derived from water. Thus, the overall reaction resembles that of the coal gasification reaction. This electrochemical reaction, however, has the advantages that hydrogen is produced as a pure gas product suitable for use in fuel cells or synthetic processes and that high temperature operations are not necessary to produce hydrogen from the coal. Peat has also been shown to oxidize to produce a good yield of regenerated humic acids in alkaline media (10), and we have suggested the possibility that other organic matrices and wastes might be oxidized by this process to produce hydrogen as a useful product (6).

Experimental

In our current communication, we report our recent results on electrochemical oxidation of oil shale. Similar results to those shown with coal were obtained with lower reaction rates than shown by New Mexico subbituminous coal.

The Colorado Green River oil shale taken from the Mahogany Zone (C-a tract) was reduced to 50 × 100 mesh samples (44 GPT, density = 1.65 g cm⁻³) by a mechanical pulverizing and sieving procedure. The shale was washed first with 6N HCl and then with a (1:3) mixture of 6N HCl and 50% HF at room temperature under the nitrogen atmosphere to minimize or eliminate air oxidation. This washing procedure was made to remove minerals and to concentrate kerogen. Elemental analysis of this sample showed 58.4% C, 7.65% H, 4.96% O, 1.64% N, and 4.12% S. The experimental apparatus and various reagents used have been described elsewhere (6, 7). Cyclic voltammograms were recorded using a Bioanalytical Systems (West Lafayette, Indiana) Model CV-1 voltammetry unit as a function generator along with a Princeton Applied Research Model 173 as a potentiostat. All the experiments were run in 1M sulfuric acid solution using platinum working and counterelectrodes, and the Hg-mercury sulfate (saturated) electrode as a reference electrode. The potentials shown in current-potential curves were all calibrated to give values against the normal hydrogen electrode (NHE).

Results and Discussion

Cyclic voltammograms (CV) recorded from an oil shale slurry in 1M H₂SO₄ solution (unstirred) are shown in Fig. 1. The CV recorded from the initial slurry (Fig. 1, curve a) shows peaks attributable to the oxidation/reduction of the Fe(II)/Fe(III) pair. Peaks shown at lower potentials are attributed to reduction/oxidation of protons in acidic solution. After this solution was stirred for about 50h (Fig. 1, curve b), we notice that the former peaks grew significantly,

indicating that electroactive material was being built up. This is because a reversible, stable redox pair was leached out by the acid solution. The redox pair was identified by a standard addition method as shown in Fig. 1, curve c. This CV was recorded after the addition of 1.0 × 10⁻²M Fe(III). This procedure not only helps confirm the identity of the electroactive materials, but also allows the determination of its concentration. The amount of iron extracted after about 50h was thus estimated to be 1.2 × 10⁻³M, or approximately 0.27% by weight in the oil shale used here. This was confirmed by analyzing the electrolyte with atomic absorption methods.

The source of iron leached out should be pyrite, which survived the HF-HCl treatment. The iron content was down to 0.96% after the acid enrichment from 3.7% for the untreated sample.

Figure 2 gives the current-voltage characteristics for the oil shale slurry under steady-state conditions. That is, the current-potential measurements were made while the solution was stirred. Steady-state measurements were made to determine the oxidation state of iron ions extracted. Curve b gives the *i*-*E* characteristics for the oil shale slurry, whereas curve a is for the acid solution alone. These figures show that part of the iron leached from the oil shale is in the +2 state, indicating that iron(III) extracted is already in the +2 state or has been reduced in the oxidation of organic materials as in coal oxidation. After oxidation of this solution overnight at +1.0V *vs.*

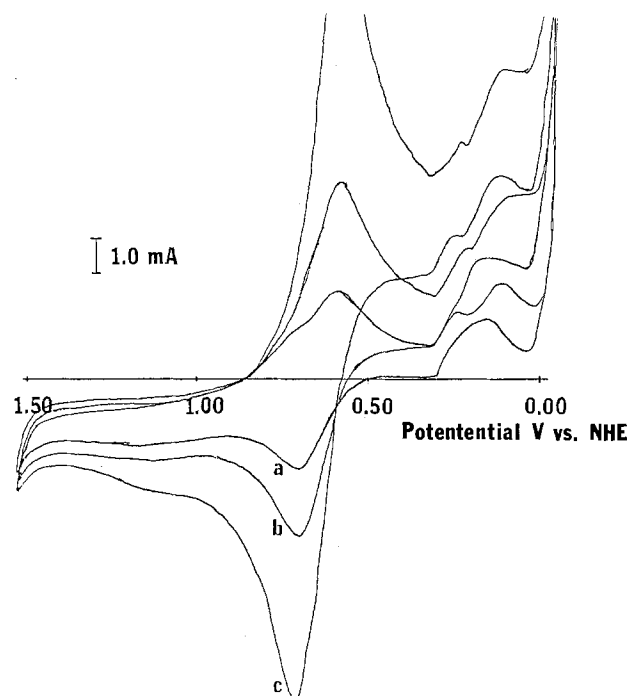


Fig. 1. Cyclic voltammograms (CV) of oil shale slurries. CV's were recorded in a slurry containing 5.0g of oil shale in 200 ml of 1.0M H₂SO₄ at a platinum electrode (area = 10 cm²) with a scan rate of 20 mV/s. These were recorded from a freshly prepared slurry (curve a), after 50h in the 1.0M H₂SO₄ solution (curve b), and with 1.0 × 10⁻²M Fe(III) added (curve c).

*Electrochemical Society Active Member.

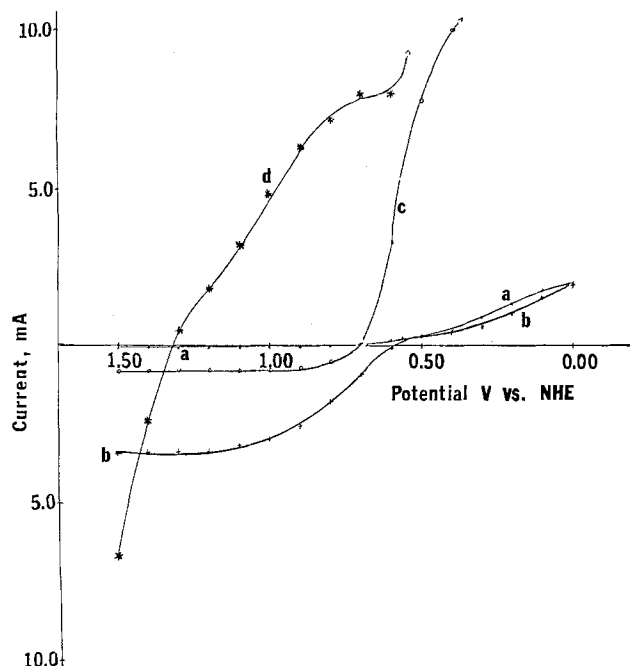


Fig. 2. The steady-state current-voltage characteristics. a: 1.0M H_2SO_4 solution without shale added. b: 5.0g oil shale in 200 ml of 1.0M H_2SO_4 solution. c: After oxidation overnight at +1.0V. d: After addition of 1.0×10^{-2} Ce(IV) was added to the solution of curve c.

NHE, curve c is obtained. The oxidation current level has dropped considerably, and some of the iron is still in the +3 state. This observation indicates that the rate of oxidation of iron(II) at the electrode is faster than the reaction to regenerate the iron(II) in the solution. Addition of cerium(IV) to this solution gives the i-E characteristics shown in curve d, where both anodic and cathodic currents are observed for the Ce(IV)/Ce(III) pair around its reversible redox potential. This indicates that cerium(IV) oxidizes both iron(II) and organic functional groups quickly.

The electrocatalytic nature of the oil shale oxidation is also shown by the time dependency of the electrolytic current. If the oxidation of iron(II) extracted is the only source of the anodic current, the current should approach to zero upon complete depletion of iron(II). This was not the case, however, as shown in Fig. 3, curves a and b. The anodic current leveled off after about 15h of electrolysis, maintaining the same current level for a few days until the cell was disconnected. The solution was continuously stirred while the measurements were made. This observa-

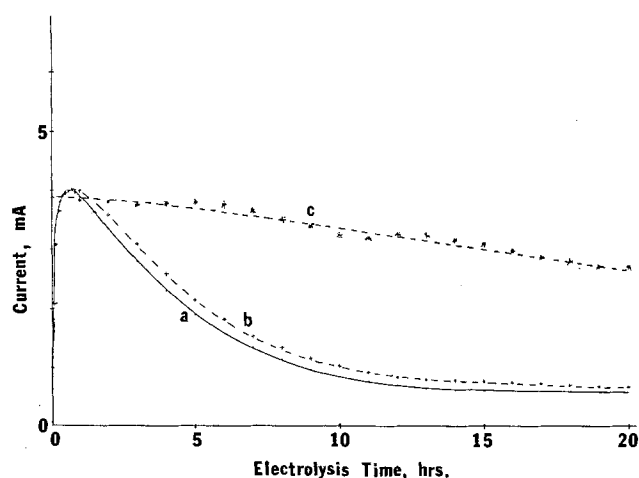
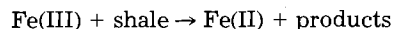


Fig. 3. a: Current level vs. time for 5.0g oil shale in 200 ml of 1.0M sulfuric acid at +1.0V vs. NHE at the Pt electrode (area = 10 cm^2). b: Same as in curve a, except at 1.5V vs. NHE. c: With 1.0×10^{-2} M Ce(IV) added at 1.5V.

tion indicates that iron(II) was continuously regenerated through the process



as was shown in the oxidation of coal (6, 7). When Ce(IV) was added to the solution (Fig. 3, curve c), essentially similar processes occurred but with higher steady-state currents observed, indicating a higher catalytic reaction rate with Ce(IV) than with Fe(III). The same was shown to be the case for coal oxidation. This would be expected because the oxidation potential of Ce(IV) is higher than that of Fe(III). Many organic functional groups that are not oxidized by Fe(III) can be oxidized by Ce(IV).

The catalytic current increased with the amount of catalyst ions added, as can be seen in Fig. 4. The addition of iron(III) did not increase the current as much as with the addition of Ce(IV). The case shown here resembles that shown by the electrocatalytic oxidation of Norit A (6) (amorphous carbon used as an organic decolorizing agent). In the case of Norit A oxidation, we surmised that there were very few functional groups oxidizable with Fe(III). Cerium(IV), however, is a strong enough oxidant to oxidize many more resistant functionalities.

The results shown here indicate that electrocatalytic oxidation of oil shale resembles that of coal in many respects. Oxidizable functional groups on oil shale are electrocatalytically oxidized by iron(III) leached from the shale, as was found for coals. The reason for the lower catalytic current with oil shale is perhaps due to the fraction of aliphatic hydrocarbons (*i.e.*, shale kerogen), which is higher than that in coal. Many of these compounds require an oxidant with more positive standard electrode potentials to get oxidized. Oxidation currents might be from alcohol, aldehyde, phenolic, quinone, or some carboxylic acid functional groups, which were shown to be present in the oil shale used in this study (11). Iron(III) should account for most of the catalyst ions, since other major minerals present are shown to be Al, Ca, K, Mn, and Si. Manganese is present in a trace amount, approximately 100 ppm in an untreated, original sample. Further, oxidation of Mn(II) to its higher oxidation state, Mn(VII), for example, requires higher potentials than +1.0V, which was the potential applied in most of our experiments.

Also, the large enhancement in catalytic current, when Ce(IV) is added, is consistent with the results obtained from coal oxidation. As pointed out, Ce(IV) has a higher oxidation potential than Fe(III) and therefore is capable of oxidizing many organic functional groups indiscriminately (12).

Current densities observed in our experiments with oil shale may not be high enough to justify the use of oil shale as an anodic depolarizer for the electrolytic produc-

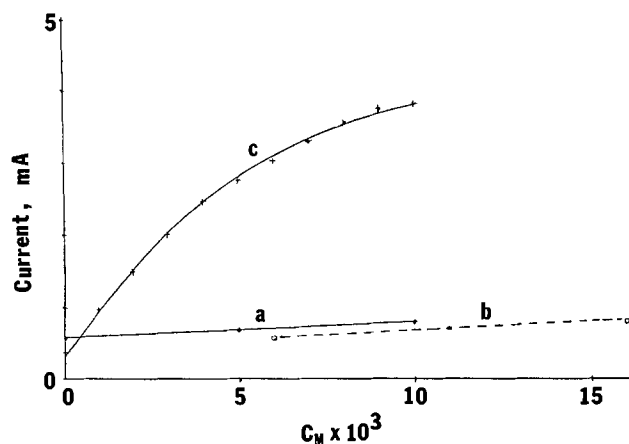


Fig. 4. a: Current level vs. concentration of added Fe(III) at +1.0V vs. NHE at 10 cm^2 Pt electrode, 5g oil shale in 200 ml of 1.0M H_2SO_4 . b: Same as in curve a, but corrected for the amount of iron leached from the oil shale. c: Current level vs. concentration of added Ce(IV) at +1.5V vs. NHE, 10 cm^2 Pt electrode, 5g oil shale in 200 ml of 1.0M H_2SO_4 solution.

tion of hydrogen. Electrolytic procedures, however, may turn out to be useful for washing and concentrating oil shale, and the hydrogen gas produced at the cathode would be a useful byproduct. Further work is in progress along these lines in our laboratory.

Manuscript submitted Oct. 26, 1984; revised manuscript received Jan. 16, 1985.

REFERENCES

1. R. W. Coughlin and M. Farooque, *Nature (London)*, **279**, 301 (1979).
2. M. Farooque and R. W. Coughlin, *ibid.*, **280**, 666 (1979).
3. M. Farooque and R. W. Coughlin, *Fuel*, **58**, 705 (1979).

4. R. P. Baldwin, K. F. Jones, J. T. Joseph, and J. L. Wong, *ibid.*, **60**, 739 (1981).
5. G. Okada, V. Gruswamy, and J. O'M. Bockris, *This Journal*, **128**, 2097 (1981).
6. P. M. Dhooge, D. E. Stilwell, and S.-M. Park, *ibid.*, **129**, 1719 (1982).
7. P. M. Dhooge and S.-M. Park, *ibid.*, **130**, 1029 (1983).
8. P. M. Dhooge and S.-M. Park, *ibid.*, **130**, 1539 (1983).
9. S. Lalvani, M. Pata, and R. W. Coughlin, *Fuel*, **62**, 427 (1983).
10. M. H. Khundkar and M. M. Kamal, *ibid.*, **45**, 9 (1966).
11. K. M. Jeong and T. P. Kobylinski, in American Chemical Society Symposium Series 230, F. P. Miknis and J. F. McKay, Editors, pp. 493-512, American Chemical Society, Washington, DC (1983).
12. S.-M. Park, *This Journal*, **131**, 363C (1984).

Oxygen Reduction Kinetics in Deuterated Phosphoric Acid

M. M. Ghoneim,¹ S. Clouser,* and E. Yeager*

Case Center for Electrochemical Sciences and Department of Chemistry, Case Western Reserve University, Cleveland, Ohio 44106

Despite the substantial research on the reduction of O₂ on platinum in phosphoric acid, the mechanistic aspects still remain very uncertain. The situation has become even more in question with the recent observation that the Tafel slope is almost independent of the temperature over the range 298–500 K, indicating that the apparent transfer coefficient is proportional to the temperature (1). In an attempt to gain further insight into the mechanistic aspects, polarization measurements for O₂ reduction on Pt have been carried out in deuterated and undeuterated 85% H₃PO₄ at 25°C. This article reports the preliminary results.

Experimental

The most critical aspect of such isotope studies is that of reproducibility of surface and electrolyte conditions between the deuterated and undeuterated acid solutions. A major effort has been made to reproduce conditions and to eliminate impurity effects.

The O₂ reduction measurements have been made with the rotating disk electrode technique. The measurements were carried out in two identical Teflon cells, each consisting of a main working electrode compartment and two separate compartments for the reference and counterelectrodes (2). The working electrode was a disk electrode (Pine Instruments Company) with an area of 0.46 cm². The reference electrodes were reversible H₂/H⁺ and D₂/D⁺, using a platinized-platinum surface. The counterelectrode was bright Pt.

The working electrode surface was first polished with alumina (0.05 μm) to a mirror finish, submerged in distilled water for 15 min with ultrasonic vibrations, and then rinsed in distilled water, followed by purified H₃PO₄. The distilled water used in this work was prepared by reverse osmosis of tap water followed by distillation with a counterflow of N₂ to purge volatiles such as CO₂ and organics. The reverse osmosis-distillation system was assembled by B. D. Cahan at Case Western Reserve University and is based on a design developed by Gilmont and Silvis (3).

A Pine Instruments RDE-3 bipotentiostat with input impedance of 10¹²Ω in the reference circuit and built-in triangular sweep generator was used for all measurements. The current-potential curves were recorded on a Yokagawa Electric Works Type 3086 X-Y recorder. Prior to electrochemical measurements, the Pt disk electrode was cycled several times between potentials of 1.0 and 0.3V vs. a reversible hydrogen or deuterium electrode (p = 1 atm) at a sweep rate of 10 mV/s.

For preparation of the D₃PO₄ and H₃PO₄ electrolytes, Mallinckrodt 85% H₃PO₄ was first purified with H₂O₂ ac-

cording to the procedure of Ferrier *et al.* (4). Two samples of this purified H₃PO₄, each 120 ml, were then placed in Teflon containers and concentrated by boiling out the H₂O until the acid samples became concentrated to ~96% at 150°C while passing N₂ gas through the boiling acids. After cooling, 50g of D₂O (99.8% D, Stohler Isotope Chemicals) were added to one acid sample (A). At the same time, 50g of distilled H₂O were added to the other sample (B). The two samples were reconcentrated by boiling until they reached 150°C while bubbling purified D₂ gas and H₂ gas through samples A and B, respectively. The additions of D₂O or H₂O were repeated ten times. The last step was dilution of each sample with D₂O and H₂O to the original volume (120 ml each). Proton NMR measurements indicated that the deuterated acid sample was 98% D. The deuterated and undeuterated acids were further purified by adding 4g of Na₂O₂ (Fisher certified ACS reagent) to each, then heating to 50°C for 3h until the H₂O₂ and D₂O₂ produced from Na₂O₂ were completely decomposed. This procedure is similar to that of Ferrier *et al.* (4), except that Na₂O₂ is added instead of H₂O₂ in the present work, to avoid introduction of H into the D₃PO₄ solution. Earlier work has shown that sodium phosphate has no appreciable effect on O₂ reduction on Pt in 85% H₃PO₄ (5). The two acid solutions were next deoxygenated by passing purified N₂ through them. The O₂ was removed by passing the gas over heated copper turnings while trace organics in the N₂ were removed with molecular sieves at Dry Ice-ethanol temperatures. To each acid, 0.2g of Pt black (Engelhart fuel cell-grade) were added and H₂ or D₂ bubbled through the acid for 48h. Finally, purified N₂ was bubbled through the acids to remove the H₂ or D₂ gas.

Results and Discussion

The voltammetry curves for Pt in the deuterated and undeuterated acids (Fig. 1) are similar but not identical in the double-layer and anodic film regions. The voltammetry curves differ significantly in the hydrogen region. Two sets of principal adsorption/desorption peaks are present in both curves. The peaks are shifted anodically for the deuterated acid by ~30 mV and are more pronounced, particularly for the weaker bound H/D peaks I and I'. The hydrogen oxidation peak III appears more reversible in the D₃PO₄ than in the H₃PO₄. The conditions for the D₃PO₄ and H₃PO₄ differ in temperature (30° and 25°C) and slightly in acid concentration (86 vs. 85%), but prior experience with H₃PO₄ indicates that these factors are not the principal source of the differences in the hydrogen region of the voltammetry curves. The authors believe that the principal factor responsible for the difference in the voltammetry curves is the isotopic difference and not impurity effects.

*Electrochemical Society Active Member.

¹Permanent address: Tanta University, Tanta, Egypt.

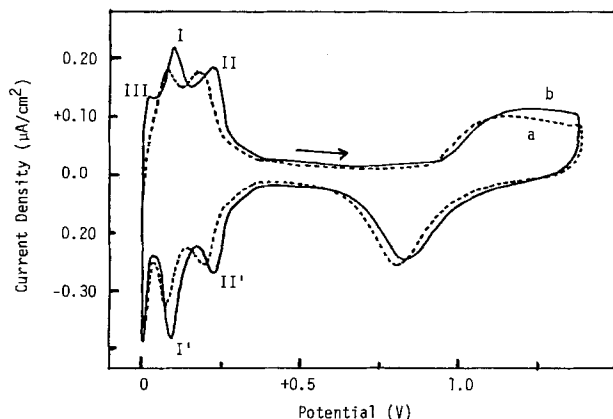


Fig. 1. Voltammogram for Pt disk in purified 85% H_3PO_4 at 25°C (curve a) and 86% D_3PO_4 at 30°C (curve b). Sweep rate: 100 mV/s; N_2 saturated. Reference electrodes for curve a: H_2 (1 atm)/ H^+ ; for curve b: D_2 (1 atm)/ D^+ .

The polarization curves for O_2 reduction using the rotating disk electrode are shown in Fig. 2 for 400 and 1600 rpm. The Pt electrode was first cycled between 1.0 and +0.3V vs. RHE or RDE and then held for a few seconds at $\sim 1.0\text{V}$ before sweeping the potential in the cathodic direction at 10 mV/s. The rise in the curves at $\sim 0.3\text{V}$ is due to the H/D adsorption region. The apparent difference in the limiting current densities in Fig. 2 may not be significant since it is difficult to saturate the solution with O_2 to the same degree. The corresponding Tafel plots are shown in Fig. 3 with a correction for mass transport using the diffusion limiting current evaluated from the dotted section of each curve at $\sim 0.3\text{V}$ in Fig. 2. The O_2 reduction appears to proceed about two times faster in the deuterated acid than in the undeuterated acid at the same potential vs. the reversible deuterium and hydrogen reference electrodes. The Tafel slope differences are small. At a given current density in the middle of the Tafel linear region, the potential for the O_2 electrode in the deuterated specimen is $\sim 0.055\text{V}$ more positive than that in the undeuterated acid at a given current density.

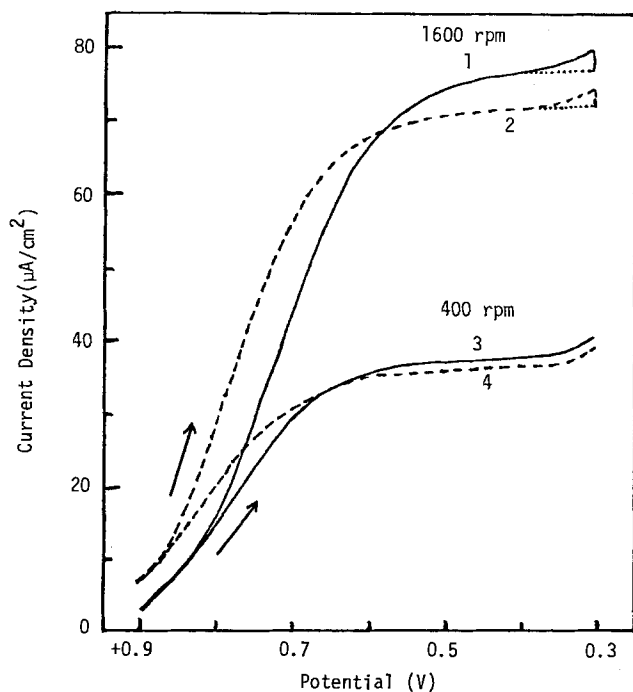


Fig. 2. Rotating Pt disk data for O_2 reduction at 400 and 1600 rpm in purified Mallinckrodt 85% H_3PO_4 at 25°C (curves 1, 3) and 86% D_3PO_4 at 30°C (curves 2, 4). Sweep rate: 10 mV/s; O_2 saturated. Reference electrodes for curves 1, 3: H_2 (1 atm)/ H^+ ; for curves 2, 4: D_2 (1 atm)/ D^+ .

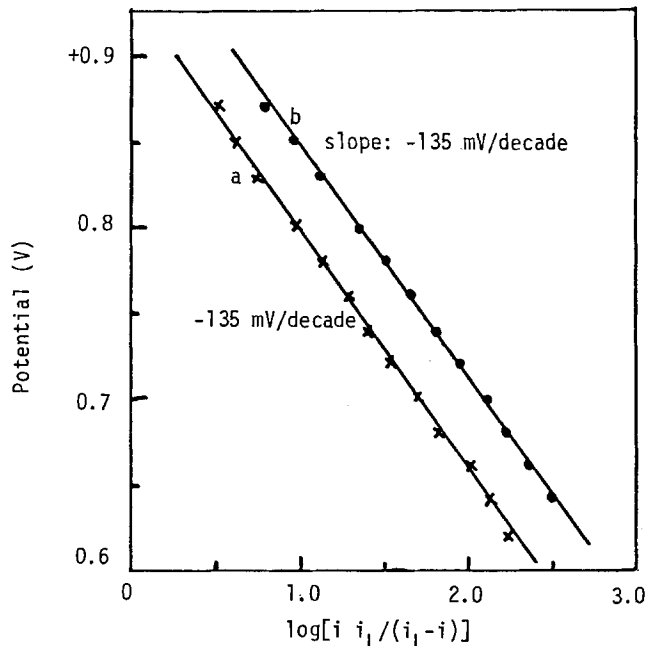
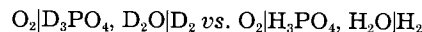


Fig. 3. Tafel plots obtained for rotating Pt disk data in purified Mallinckrodt 85% H_3PO_4 at 25°C (curve a) and 86% D_3PO_4 at 30°C (curve b). Rotation rate: 1600 rpm. Reference electrodes for curve a: H_2 (1 atm)/ H^+ ; curve b: D_2 (1 atm)/ D^+ . Current is in microamperes per centimeter.

To obtain the difference in the overpotentials in the deuterated and undeuterated acids at a given current density, it is necessary to take into account the difference in the reversible potentials of the O_2 electrode vs. the reversible deuterium and hydrogen electrodes, i.e., the potential difference of the cells



The potential for each is given by

$$E_{\text{D}} = E_{\text{D}}^{\circ} - \frac{RT}{4F} \ln \frac{(a_{\text{D}_2\text{O}})^2}{(p_{\text{D}_2})^2(p_{\text{O}_2})} \quad [1]$$

and

$$E_{\text{H}} = E_{\text{H}}^{\circ} - \frac{RT}{4F} \ln \frac{(a_{\text{H}_2\text{O}})^2}{(p_{\text{H}_2})^2(p_{\text{O}_2})} \quad [2]$$

where the activities of the gases have been taken as equal to their pressures and the activities of D_2O and H_2O are referred to the pure liquids as 1. Thus the difference in the potentials of the reversible O_2 electrode in the two acid samples vs. the reversible deuterium and hydrogen electrodes is

$$E = E_{\text{D}} - E_{\text{H}} = E_{\text{D}}^{\circ} - E_{\text{H}}^{\circ} - \frac{RT}{2F} \ln \frac{(a_{\text{D}_2\text{O}})}{(a_{\text{H}_2\text{O}})} \quad [3]$$

The value of $E_{\text{D}}^{\circ} - E_{\text{H}}^{\circ}$ corresponds to the difference in the standard free energy of formation of liquid D_2O and H_2O , which is $\Delta G_{\text{D}_2\text{O}}^{\circ} - \Delta G_{\text{H}_2\text{O}}^{\circ} = -1.51 \text{ kcal/mol}$ (6) at 25°C. The calculated value for $(E_{\text{D}}^{\circ} - E_{\text{H}}^{\circ})$ is then +0.033V at 25°C. Since the boiling points of the 86% D_3PO_4 and 85% H_3PO_4 were virtually identical, this provides evidence that the ratio $(a_{\text{D}_2\text{O}}/a_{\text{H}_2\text{O}})$ is ~ 1 and hence $\Delta E = +0.033\text{V}$. Thus the overpotential for the O_2 reduction reaction is $\sim 0.02\text{V}$ less in the deuterated vs. undeuterated acid and the reaction at the same overpotential is $\sim 40\%$ faster in the deuterated acid.

This relatively small factor can be explained on the basis of the 5°C higher temperature of the deuterated acid during the polarization measurements. Using an apparent Arrhenius energy of $A = 10 \text{ kcal/mol}$ (2) for O_2 reduction on Pt in 85% H_3PO_4 , the Arrhenius equation yields

$$(k_{303}/k_{298}) = \exp \frac{A}{R} \left| \left(\frac{1}{298} - \frac{1}{303} \right) \right| = 1.32$$

where k_{303}/k_{298} is the ratio of the rate constants at the indicated absolute temperature at constant overpotential and R is the perfect gas constant. Thus the observed ratio of 1.4 is mostly due to the temperature difference and the kinetic isotope effect is negligible.

The lack of any appreciable kinetic isotope effect provides evidence that the rate-controlling step in concentrated phosphoric acid does not involve the making or breaking of any bonds involving protons (or deuterons). For the situation to be otherwise would require the coincidence of virtually completely compensating isotope effects. This observation has important mechanistic implications.

Acknowledgment

The authors are pleased to acknowledge financial support from EPRI for this research. One of the authors (MMG) acknowledges support from the Faculty of Science, Tanta University of Egypt through a sabbatical leave.

Manuscript submitted Dec. 30, 1982; revised manuscript received Nov. 14, 1983.

Case Western Reserve University assisted in meeting the publication costs of this article.

REFERENCES

1. S. J. Clouser, J. C. Huang, and E. Yeager, Abstract 348, p. 572. The Electrochemical Society Extended Abstracts, Vol. 82-1, Montreal, Que., Canada, May 9-14, 1982.
2. J. C. Huang, R. K. Sen, and E. B. Yeager, *This Journal*, **126**, 487 (1979).
3. P. Gilmont and S. J. Silvis, *Am. Lab.*, **6**, 46 (1974).
4. D. Ferrier, K. Kinoshita, J. McHardy, and P. Stonehart, *J. Electroanal. Chem.*, **61**, 233 (1975).
5. S. Clouser, PhD. Thesis, Case Western Reserve University, Cleveland, OH, (1980); see also E. Yeager, P. Bindra, S. Clouser, and S. Sarangapani, Electric Power Research Institute Project 634-1-2, Report EPRI EM-1814, April 1981.
6. D. D. Wagman, W. H. Evans, V. Parker, I. Halow, S. M. Baily, and R. H. Schumm, NBS Technical Note 270-3, Table 2(2), p. 13, National Bureau of Standards, Washington, D.C. (1965).



Effects of Corona-Discharge Induced Oxygen Ion Beams and Electric Fields on Silicon Oxidation Kinetics

I. Ion Beam Effects

Douglas N. Modlin*

Department of Electrical Engineering, Stanford University, Stanford, California 94305

William A. Tiller

Department of Materials Science and Engineering, Stanford University, Stanford, California 94305

ABSTRACT

At temperatures between 500° and 950°C, in an oxygen ambient, a flux of either negative or positive oxygen ions, generated via a point-to-plane corona discharge, is directed to the front side of a silicon wafer. Electrical contact to the wafer was made via the back side. Both ion beam polarities lead to oxidation enhancement, but with very different oxide thickness profiles, even though the ion beam current density profiles in the gas phase at the surface are almost identical. Wafer orientation, P_{O_2} , current, temperature, and time dependences have been studied.

Abundant studies have been conducted on the thermal oxidation of silicon which manipulate the conventional thermodynamic state variables of the system (concentration, temperature, and pressure). Studies have also been conducted to investigate the electrochemical nature of the oxidation process, and this has led to extensive controversy over the charge state of the oxidant species (1-16). The plasma oxidation studies being pursued in many quarters today are a measure of the generally recognized benefits to be derived from control of the electrochemical state of the oxidizing species. However, in plasma oxidation, one has the intermixing of (i) oxygen ion species effects, (ii) neutral diatomic and monatomic oxygen species effects, (iii) electric field effects, and (iv) UV radiation effects. In an attempt to understand these effects more fully and to learn more about oxidation at low temperatures, we have investigated some effects on thermal oxidation associated with isolated studies of these individual factors. In this paper, we restrict our attention to only negatively and positively charged oxygen ion beam effects since studies involving only electric field effects (11) and only laser light (12) are described elsewhere.

In the present study, at temperatures between 500° and 950°C in an oxygen ambient, a flux of either negative or positive oxygen ions, generated via a corona discharge, is directed to the upper surface (the front side) of a silicon wafer. Here, the combined effects of both electric fields and ion beam species on the oxidation rate are manifest. The effects of the electric field alone are manifest on the opposite side of the wafer (the back side) (11). Both polarities of oxygen ion beams lead to oxidation rate enhancement, but, because we have used a point-to-plane discharge technique (13, 14) which produces a nonuniform (bell-shaped) ion flux profile in the gas near the surface, the oxide thickness profile on the wafer is quite different in the two cases even though the ion beam current density profiles in the gas phase at the surface are believed to be almost identical.

*Electrochemical Society Student Member.

Experimental Techniques

A complete description of the apparatus used for positive and negative ion beam processing has been published elsewhere (13, 14); therefore, only a few necessary details will be given here. The ion beams are generated by applying a negative or positive voltage of ± 0.05 to ± 2.0 kV to a platinum needle (the point) relative to a silicon wafer (the plane), as illustrated in Fig. 1a. The ions are generated in a narrow zone close to the needle because of the strong field enhancement at that location. The polarity of the ions generated is the same as the sign of the voltage applied to the point, and these ions are repelled from the point by the local field. The ions spread out as they travel from the point to the plane and form a bell-shaped ion beam current density profile on the surface of the plane.

A portion of the ion beam generating apparatus is shown in Fig. 1b. A platinum needle with a tip diameter of 0.003 in. is suspended 0.5 cm above the silicon wafer which rests upon a 63.5 mm diam, 1.6 mm thick quartz disk. The bottom of the quartz disk is coated with a 1 μ m thick sputter-deposited layer of platinum. In addition to providing electrical contact to the back side of the wafer, the quartz disk acts as a diffusion barrier between the Pt and the Si wafer. The quartz has a sufficiently high electrical conductivity at 900°C to cause a voltage drop of < 100 V at a beam current of ~ 10 μ A (14). The entire assembly rests on a 0.002 in. Pt sheet which is connected to the high voltage power supply via Pt lead-in wires (14).

The Pt lead-in wires are separated by sapphire rods to minimize electrical leakage between them. Since a portion of this leakage current is picked up by the sample lead-in wire, it produces an error in the measurement of the ion beam current. It was observed that this leakage current is at its maximum value when the discharge is first switched on and decays to a value ≤ 0.25 μ A after ~ 10 min. It is believed that this is due to electrical polarization effects in the sapphire standoffs. Thus, in order to minimize the current measurement error during the oxidation experiments, the discharge was initially switched

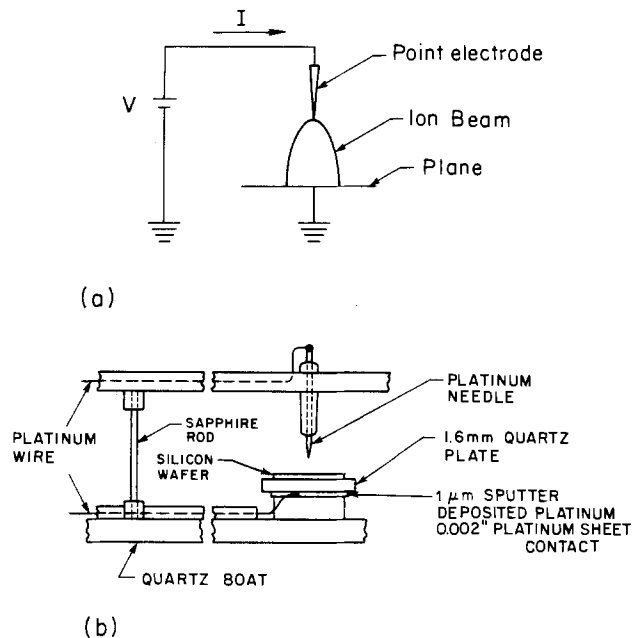


Fig. 1. a: Schematic diagram of the point-to-plane ion beam generator. b: An illustration of the experiment setup.

on in nitrogen for a period of 10 min before changing the ambient gas from N_2 to O_2 . For oxidation temperatures less than 800°C , a more suitable contact technique involving platinum silicide formation was utilized (13, 14).

Silicon samples were first given a 15 min ultrasonic clean in warm soap and deionized (DI) H_2O to degrease and remove particles, followed by a 5 min rinse in DI H_2O . The wafers were then cleaned according to the following schedule: (i) boil for 10 min in (5:1:1) H_2O : H_2O_2 : NH_4OH , (ii) rinse in DI H_2O for 3 min, (iii) boil for 10 min in (5:1:1) H_2O : H_2O_2 : HCl , (iv) rinse in DI H_2O for 3 min, (v) 30s dip in (50:1) H_2O : HF , and (vi) rinse in DI H_2O for 5 min.

After the above cleaning, the wafers were hydrophobic and were "pulled dry" and placed directly in the wafer boat. This eliminated the need to blow the wafers dry with N_2 . The larger pieces of quartz apparatus, *i.e.*, diffusion tubes, wafer boats, etc., were cleaned using a soap and DI H_2O degrease followed by a 10 min etch in (10:1) HF : (DI) H_2O ($\rho \geq 18 \text{ M}\Omega \text{ cm}$). Platinum parts were degreased by an ultrasonic soap and warm DI H_2O bath, then by boiling in TCE, acetone, and methanol, followed by a DI H_2O rinse.

Experimental Results

Negative point.—Oxide thickness profiles.—Oxide thickness profiles on $\langle 111 \rangle$ Si substrates for a range of oxidation times at 900°C in 100% O_2 with a constant needle current of $-5 \mu\text{A}$ are shown in Fig. 2. The bell-shaped profiles, which were measured via ellipsometry, mimic those of the ion beam density such that the peak oxide thickness lies directly below the tip of the point electrode and the constant background level occurs where the beam intensity has fallen to zero. Figure 3 shows that the $\langle 111 \rangle$ and $\langle 100 \rangle$ Si substrate results are similar but with the $\langle 100 \rangle$ being below the $\langle 111 \rangle$ by a constant offset which, for the case of an oxidation at 900°C for 1h at $-5 \mu\text{A}$, is about 100\AA .

Peak oxide thickness variations.—In Fig. 4 and 5, the peak oxide thickness, X_p , is plotted as a function of time, t , for a range of temperatures, T , beam currents, I , and the substrate orientations $\langle 111 \rangle$ and $\langle 100 \rangle$. Each data point is the average of several experiments. The data are presented on a background of the conventional $I = 0$ data for $\langle 111 \rangle$ Si. We note a marked difference in the $I < 0$ data from the $I = 0$ data.

In the $600^\circ\text{--}800^\circ\text{C}$ range, the peak oxide thickness, for a constant beam current, I , is relatively insensitive to

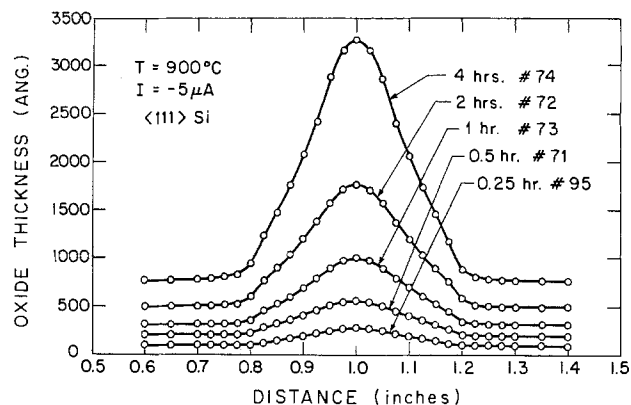


Fig. 2. Oxide thickness profiles for Si $\langle 111 \rangle$ wafers oxidized in 100% oxygen at 900°C with $I = -5 \mu\text{A}$ for various times.

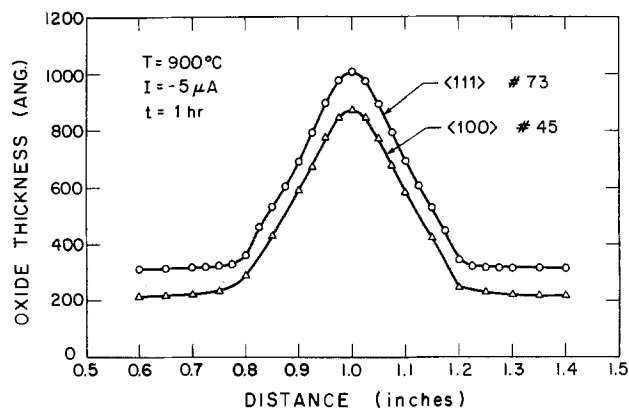


Fig. 3. Oxide thickness profiles for Si $\langle 111 \rangle$ and Si $\langle 100 \rangle$ wafers with $I = -5 \mu\text{A}$ oxidized at $T = 900^\circ\text{C}$ for 0.5h with $P_{O_2} = 1 \text{ atm}$.

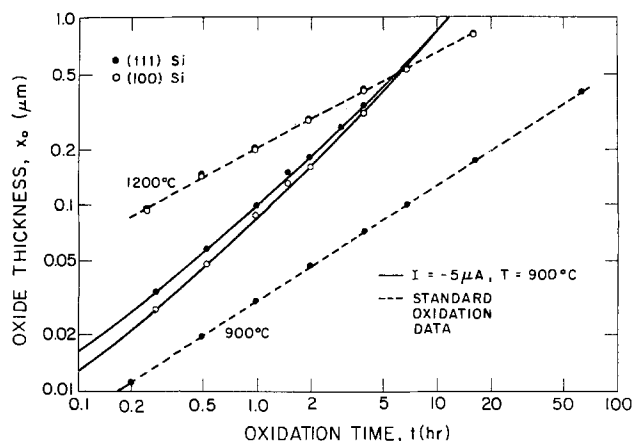


Fig. 4. Oxide thickness at the profile peaks for Si $\langle 111 \rangle$ and Si $\langle 100 \rangle$ wafers for $T = 900^\circ\text{C}$ with $I = -5 \mu\text{A}$ and $P_{O_2} = 1 \text{ atm}$. Each datum is the average of several experiments. The $I = 0$ data are shown for reference.

changes in temperature and begins to increase markedly only in the $900^\circ\text{--}1200^\circ\text{C}$ range (see Fig. 6). At temperatures lower than $\sim 600^\circ\text{C}$, it became difficult to produce a stable discharge in 100% oxygen. The datum at 500°C represents an experiment carried out despite the fact that significant instability or "flicker" was present in the ion beam.

As has been stated earlier, in the experiments carried out at temperatures below 800°C , a PtSi contact to the back side of the wafer was used instead of the quartz contact because of the greatly reduced electrical conductivity of the quartz and the relatively slower silicide formation rate at these temperatures. A cross-check of these two contact schemes was performed to insure consistent results. Samples were oxidized at 900°C with a beam current of $-5 \mu\text{A}$ for 1h, and the resulting oxide thickness

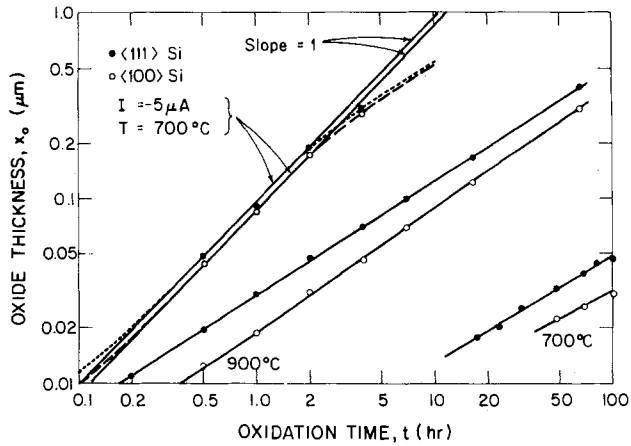


Fig. 5. Oxide thickness at the profile peaks for Si $\langle 111 \rangle$ and Si $\langle 100 \rangle$ wafers for $T = 700^\circ\text{C}$ with $I = -5 \mu\text{A}$ and $P_{\text{O}_2} = 1 \text{ atm}$. The $I = 0$ data is shown for reference. Each datum is the average of several experiments.

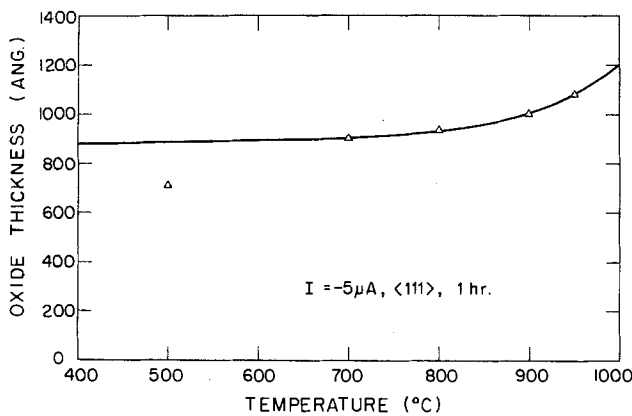


Fig. 6. Oxide thickness at the profile peaks for Si $\langle 111 \rangle$ wafers with $I = -5 \mu\text{A}$ for $t = 1 \text{ hr}$ at a number of temperatures and $P_{\text{O}_2} = 1 \text{ atm}$.

profiles were found to be identical regardless of which technique was used to contact the back side of the wafer.

Oxygen partial pressure dependence.—An investigation of the effects associated with a reduced oxygen partial pressure, P_{O_2} , was carried out at 700°C using an admixture of O_2 in P_{O_2} argon. In Fig. 7, values of the peak oxide thickness at $I = -10 \mu\text{A}$ for 1 hr are shown for a range of P_{O_2} . We note that a reduction of P_{O_2} by a factor of ten leads to a reduction in X_p of only $\sim 18\%$.

Substrate doping dependence.—A series of experiments was conducted on $\langle 111 \rangle$ Si substrates doped with either boron or phosphorus at $I = -5 \mu\text{A}$ and $t = 1 \text{ hr}$. The substrate resistivity was varied from 0.5 to 20 $\Omega \text{ cm}$ with no observable differences in the resulting oxide thickness profiles.

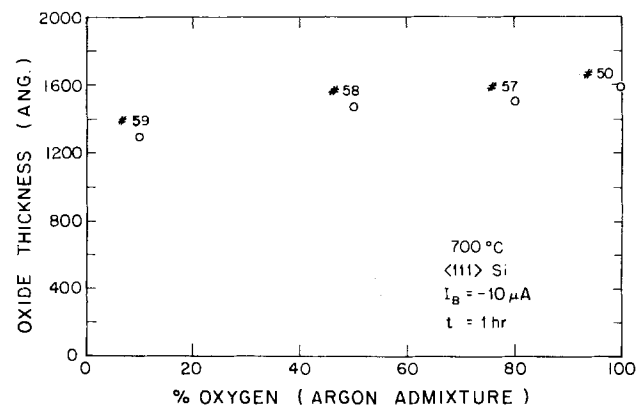


Fig. 7. Oxide thickness at the profile peaks for Si $\langle 111 \rangle$ wafers with $I = -5 \mu\text{A}$ at 700°C for 1 hr at a range of P_{O_2} in argon ($P_{\text{total}} = 1 \text{ atm}$).

Positive point.—Oxide thickness profiles.—In Fig. 8, oxide thickness profiles for Si $\langle 111 \rangle$ wafers at 900°C and $I = +5 \mu\text{A}$ for dry O_2 are shown as a function of position on the wafer. The profiles are seen to have a bimodal shape with a crater appearing directly beneath the needle. In Fig. 9, the 2h $I = +5 \mu\text{A}$ profile is compared with that obtained with a negative point at $I = -5 \mu\text{A}$ for 2h. The reference markers at 0.725 and 1.275 in. indicate the half-width of both the positive and negative ion beams measured at low temperatures. While there is a clear correspondence between the ion beam current density and the oxide thickness profile for the negative ion case, there appears to be virtually none for the positive ion case.

The manner by which the back side of the wafer was contacted did not influence the front-side oxide thickness profile since virtually identical profiles were obtained with or without a silicide back-side contact.

Crater effects.—The normal sample, which was a quarter section of a 3 in. wafer placed on the quartz plate beneath the needle, exhibited the type of oxide profile sketched in Fig. 10a. The dark and light areas correspond to regions of thick and thin oxide, respectively. Figure 8 was generated by plotting the oxide thickness found along the line $Y_1 Y_2$ from point A to point B. From Fig. 10a, we note that the oxidation-enhancement effect disappears completely between the contour Q_1 and the edge of the sample. In addition, the region between the center of the crater C_1 and the contour Q_1 is nonuniformly enhanced; e.g., the oxide is somewhat thicker in the lower right-hand portion of the enhanced region.

To investigate a possible sample edge effect, a whole 3 in. wafer instead of a quartz wafer was used. From Fig. 10b, we see that the enhanced area does, in fact, expand, whereas the total beam current was held constant at +5

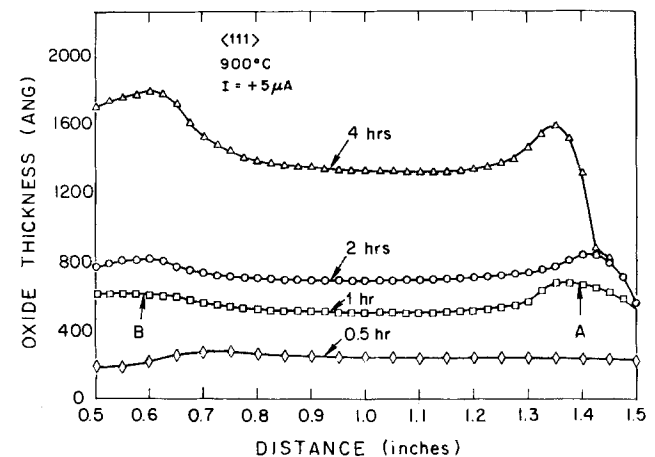


Fig. 8. Oxide thickness profiles for Si $\langle 111 \rangle$ wafers obtained at 900°C for $I = -5 \mu\text{A}$ and $P_{\text{O}_2} = 1 \text{ atm}$.

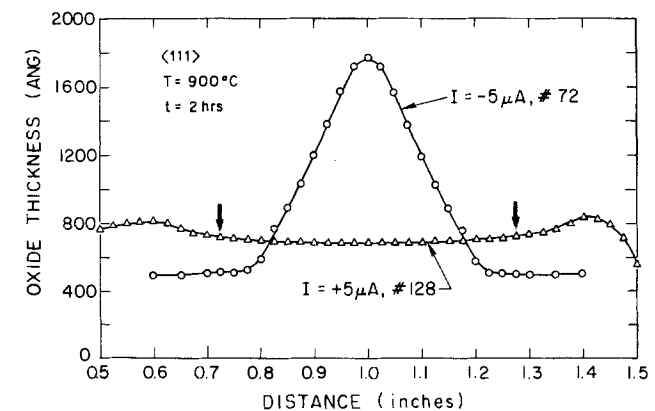


Fig. 9. Comparison of oxide thickness profiles for Si $\langle 111 \rangle$ wafers at 900°C for 2h at $I = +5$ and $-5 \mu\text{A}$. The vertical arrows indicate the half-width of the positive ion beam at room temperature.

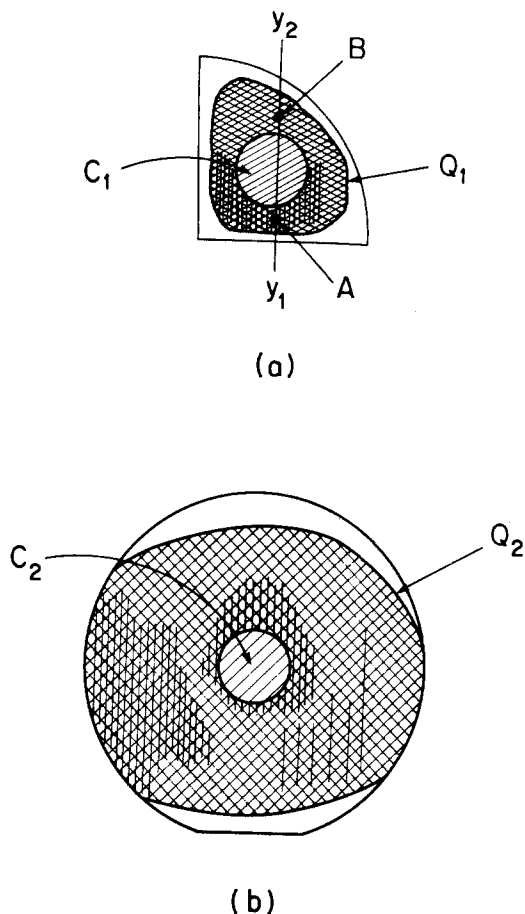


Fig. 10. Illustration of Si<111> wafer surfaces oxidized at 900°C for 1h at $I = +5 \mu\text{A}$. The light and dark areas correspond to thinner and thicker oxides, respectively.

μA . Under identical oxidation conditions, the craters C_1 and C_2 are the same size, while the contour Q_2 is much larger than the contour Q_1 . The elongation of Q_2 was found to be along the direction taken by the Pt needle lead-in wire inside its quartz conduit above the wafer.

As a check to see if the crater effect could be due to electrolytic thinning of the SiO_2 layer (15, 16), several wafers with different oxide thickness were subjected to positive ion beams of up to $+20 \mu\text{A}$ for 1h in argon at 900°C. For wafers with oxides about 1000Å thick, a change of less than 5-10Å was observed. This is considered to be an insignificant effect; therefore, electrolytic thinning does not seem to be responsible for the cratering.

Because of the nonuniform nature of the positive point results and the fact that the oxide thickness profiles tended to vary somewhat from experiment to experiment, a detailed investigation of the temperature, time, and ion beam current density dependence was not attempted.

Discussion

Negative point.—Thickness as a function of time.—Figure 4 shows that the oxide growth curves for $I = 5 \mu\text{A}$ are concave upward with the <100> data falling below the <111> data at short times while, for long times, the two sets of data are essentially identical. These phenomena can be understood in terms of a simple interpretation of the interaction between the ion beam and the native growth process. We assume that the flux of oxidant due to the ion beam and due to the native growth process add linearly at the Si/SiO₂ interface. Thus, for short times, the ion beam-enhanced data approach those of the native process because the rapid native oxidation rate in the thin oxide regime is much greater than that due to the ion flux at low values of I . For long times, the growth rate becomes dominated by the ion flux. As the oxide thickness approaches 1 μm , the growth curves tend toward a slope of unity. If the ion flux had not been present, the growth

curves would have tended towards a slope of 1/2, corresponding to diffusion-limited growth. Freedom from diffusion-limited growth, via the agency of the ion beam, strongly enhanced the overall oxidation rate.

If the temperature is low enough ($T \leq 700^\circ\text{C}$), so that the contribution of the native oxidant to the growth rate is negligible, then the growth rate is dominated by the ion beam flux (see Fig. 5). In this case, we have

$$X_p \approx X_N + \frac{J_p t}{qN_o} \quad [1]$$

where X_p is the peak oxide thickness with an ion beam, X_N is the native oxide thickness, J_p is the peak current density, t is the oxidation time, q is the magnitude of the electronic charge, and N_o is the density of network oxygen atoms in vitreous SiO_2 .

In Eq. [1], the value of J_p is related to I via the low temperature measurements (13, 14). It is assumed to be independent of temperature although first-order analysis predicts that it will decrease slightly as T increases. Assuming a value for X_N of $\sim 20\text{Å}$ at low temperatures, one calculates $X_p = 820\text{Å}$ for $I = -5 \mu\text{A}$, $t = 1\text{h}$, and $N_o = 4.5 \times 10^{22}$ atom/cm³. This agrees fairly well with the extrapolated value of 875Å given in Fig. 6. As the temperature is increased above 700°C, X_N accounts for a thickness increase of $\sim 30\%$ above that due solely to the ion beam at $T \leq 700^\circ\text{C}$. Thus, at $T \leq 700^\circ\text{C}$, the ion beam flux essentially dominates the growth process.

Independence of native oxidant species and ionic fluxes.—Figure 11 shows the results of two experiments wherein profiles for samples oxidized at -10 and $-5 \mu\text{A}$ for 1 and 2h, respectively, are overlaid upon each other. We note that the $-10 \mu\text{A}$ profile has a reduced peak and a broadened base and question whether this is due to differing beam shapes for the two current levels and corresponding voltages or it, instead, reveals an interaction between the native and ionic fluxes of the oxidant species.

Considering the beam shape factor, we have found (3) that, for the apparatus shown in Fig. 1a with a gap of a 0.5 cm at room temperature in air, the beam width is given by

$$W_B = 1.3 + 0.05I \quad [2]$$

where W_B is the beam width in centimeters and I is the beam current in microamperes. Thus, the beam width increases by 16% in going from -5 to $-10 \mu\text{A}$ at room temperature. This is due to the enhanced electrostatic repulsion associated with the increased ion density and is consistent with the $\sim 16\%$ oxide profile width change of Fig. 11. The corresponding decrease in oxide peak height, X_p , on increasing the total beam current from -5 to $-10 \mu\text{A}$ should then be due to the reduced value of the peak current density. Again, a 1:1 correlation with the room temperature results was found. Since the beam-shape factor is able to account for the data of Fig. 11, it appears reasonable to assume that little, if any, interaction occurs be-

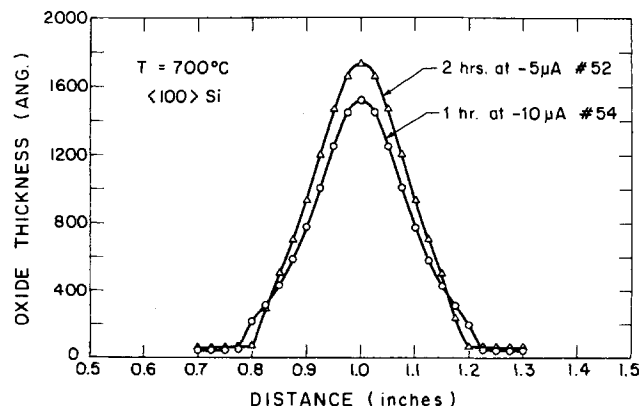


Fig. 11. Oxide thickness profiles for Si<100> wafers at 700°C for 1h at $I = -10 \mu\text{A}$ and 2h at $I = -5 \mu\text{A}$.

tween the native oxidant and ionic fluxes at these temperatures and that they act independently.

Temperature dependence.—One of the most striking features of the negative point results is the apparent insensitivity of the oxide thickness profile to changes in temperature. The smooth curve in Fig. 6 has been linearly extrapolated to 400°C without regard to the datum at 500°C. This implies that, if one controls the beam flicker which sets in at $T < 650^\circ\text{C}$, the corrected data will lie on the projected curve. It is also likely that, due to the greatly reduced ionic mobility, at lower temperatures, the large voltages needed across the SiO_2 to sustain a constant beam current result in sufficiently strong electric fields in the SiO_2 such that electrons would dissociate from the O. Thus, the current becomes increasingly electronic as T is decreased.

To test this hypothesis, samples of Cu, Ni, Al, and Si were subjected to a current of $-10\ \mu\text{A}$ for 1h at room temperature in air under a laminar flow hood. By visual observation of the interference patterns, it was determined that the greatest amount of oxide formed on the Cu sample with successively less oxide forming on the Ni and Al samples. Virtually no oxide was observed to form on the Si sample. This ordering of the relative oxide thicknesses is consistent with the relative magnitudes of both anion and cation diffusion coefficients measured in the corresponding oxides (16-24), i.e., D^+ and D^- are highest for Cu_2O and least for SiO_2 . Thus, in SiO_2 , because the diffusion coefficients and solubilities of anions and cations are relatively low, very large electric fields ($> 10^7\ \text{V cm}^{-1}$) (25) are necessary to induce ionic motion and hence form an anodic oxide. Because of these high fields, electron and hole injections into the conduction and valence bands, respectively, become likely. The consequence is that many electrons and holes cross the oxide layer, whereas few cations and anions move. Thus, for Si at room temperature, anodic oxidation via corona discharge is a very inefficient process, and under the present experimental conditions we do not expect to be able to readily form an anodic oxide of appreciable thickness.

From the foregoing, we can conclude that, in the low temperature regime, $25^\circ < T < 600^\circ\text{C}$, the ionic transport efficiency, η , defined as the ratio of ionic to total current, increases from $\sim 3 \times 10^{-2}$ (25) at 25°C to ~ 1.0 at 600°C . Thus it is likely that the combined effects of the ion beam "flicker" and the reduced transport efficiency are responsible for the reduced values of X_p for $T < 600^\circ\text{C}$. In the intermediate temperature regime, $600^\circ < T < 800^\circ\text{C}$, $\eta \approx 1$, and the native oxidant flux plays a minor role compared to the ion beam flux in the overall growth rate. In the temperature regime $T \geq 800^\circ\text{C}$, $\eta = 1$, and both the native oxidant flux and the ion beam flux contribute significantly to the growth rate and hence to X_p .

P_{O_2} dependence.—From the results of Fig. 7, we can infer that, with 100% O_2 gas, the concentration of free electrons is very small since X_p decreases by only $\sim 2\%$ per percent decrease in P_{O_2} content of the argon. The explanation for this behavior is related to the strong electron affinities of O (1.75 eV) and O_2 (0.4 eV) (26). Because of the relatively large electron collision cross section and the large number of collisions to be made between the needle electrode and the SiO_2 surface, very few electrons will cross the gap without attaching to oxygen molecules in the 100% oxygen case. For $T \geq 200^\circ\text{C}$, once O_2^- ions have formed they will readily dissociate to generate O plus O^- (27). Because the electron affinity for O^- is $\sim 1.75\ \text{eV}$, there is very little chance that O^- species will deionize before crossing the gap. Thus, even in the 10% oxygen case, the number of electrons surviving to reach the SiO_2 surface is only $\sim 18\%$.

Positive point.—Unlike the negative point case, it is clear that the positive point results cannot be explained simply by a flux of interstitial ions (positive in this case) injected into the oxide by the ion beam which are transported across the oxide in parallel with the native oxidant species. First, in contrast with the negative point results,

the oxide thickness profiles obtained with a positive point bear little, if any, resemblance to the ion beam current density profile (see Fig. 9). Second, the crater-shaped oxide thickness profiles imply that multiple interactions affecting the oxidation rate are present in the positive point case. A simple explanation for the crater-shaped oxide-thickness profiles involving a growth-enhancement factor due to the positive ions and a retardation factor due to electrolytic thinning of the oxide can be ruled out since a pregrown oxide was not found to thin after being subjected to a positive ion beam treatment in an inert ambient. Furthermore, as seen in Fig. 10, the spatial extent of the enhanced area increased when the wafer size was increased even though the ion beam current was held constant. From the above, we conclude that more work will be necessary in order to fully explain the positive point results.

Conclusions

Oxidation enhancement occurs for both the negative point and positive point cases with the negative point case providing the larger effect. In the negative point case, (i) the geometry of the oxidation enhancement mimics the ion beam profile in the gas, (ii) the effect seems to be independent of the native oxidant, (iii) the effect decreases slowly with decrease in P_{O_2} content of the gas, and (iv) the effect is linearly proportional to the product of the local ion beam current density and the time. The above results imply that the native oxidant species is/are electroneutral since the negative ion enhancement effects appear to be independent of the presence of the native oxidant species.

In the positive point case, a shallow crater develops under the ion beam. This crater is surrounded by a ridge of oxide thickness enhancement which falls off radially as the outer edge of the wafer is approached. Although no explanation for these results is provided, we conclude that electrolytic thinning of the oxide due to the positive voltage developed across the oxide is not a significant factor. Additional work is currently in progress to provide an explanation of the positive point results.

Acknowledgments

This work was supported by the Defense Advanced Research Projects Agency, Contract no. MDA903-79-C-0257. The authors would like to thank Les Landsberger for helpful discussions and timely experimental assistance.

Manuscript submitted May 17, 1984; revised manuscript received Nov. 24, 1984.

Stanford University assisted in meeting the publication costs of this article.

REFERENCES

1. P. J. Jorgensen, *J. Chem. Phys.*, **37**, 874 (1962).
2. B. E. Deal and A. S. Grove, *J. Appl. Phys.*, **36**, 3770 (1965).
3. D. O. Raleigh, *This Journal*, **113**, 782 (1966).
4. P. J. Jorgensen, *ibid.*, **114**, 820 (1967).
5. D. O. Raleigh, *ibid.*, **115**, 111 (1968).
6. S. J. Laverty and W. D. Ryan, *Int. J. Electron.*, **26**, 519 (1969).
7. T. G. Mills and F. A. Kroger, *This Journal*, **120**, 519 (1969).
8. J. K. Srivastava, M. Prasad, and J. B. Wagner, Jr., Abstract 305, p. 478, The Electrochemical Society Extended Abstracts, Vol. 83-2, Washington, DC, Oct. 9-14, 1983.
9. F. C. Collins and T. Nakayama, *This Journal*, **114**, 167 (1967).
10. R. H. Doremus, *J. Phys. Chem.*, **80**, 1773 (1976).
11. D. N. Modlin and W. A. Tiller, Submitted to *This Journal*.
12. E. M. Young and W. A. Tiller, *Appl. Phys. Lett.*, **42**, 63 (1983).
13. D. N. Modlin, Ph.D. Thesis, Stanford University, Stanford, CA (1983).
14. D. N. Modlin and W. A. Tiller, *Rev. Sci. Instrum.*, **55**, 1433 (1984).
15. P. J. Jorgensen, *J. Chem. Phys.*, **49**, 1594 (1968).
16. J. W. Hinze, J. A. Baker, and J. W. Patterson, *This Journal*, **121**, 1328 (1974).
17. W. J. Moore and B. Selikson, *J. Chem. Phys.*, **19**, 1539

- (1951); *ibid.*, **20**, 927 (1952).
18. M. O'Keefe, Y. Ebisuzaki, and W. J. Moore, *J. Phys. Soc. Jpn.*, **18**, Suppl. II, 131 (1962).
 19. K. Fueki and J. B. Wagner, Jr., *This Journal*, **112**, 284 (1965).
 20. M. O'Keefe and W. J. Moore, *J. Phys. Chem.*, **65**, 1438 (1961).
 21. A. E. Paladino and W. D. Kingery, *J. Chem. Phys.*, **37**, 957 (1962).
 22. Y. Oishi and W. D. Kingery, *ibid.*, **33**, 480 (1960).
 23. E. L. Williams, *J. Am. Ceram. Soc.*, **48**, 190 (1965).
 24. F. J. Norton, *Nature*, **191**, 701 (1961).
 25. G. C. Jain, A. Prasad, and B. C. Chakravarty, *This Journal*, **126**, 1, (1979).
 26. L. B. Loeb, "Electrical Coronas, Their Basic Physical Mechanisms," p. 18, University of California Press, Berkeley, CA (1965).
 27. L. B. Loeb, in "Advances in Geophysics," H. E. Landsberg and J. Van Miegheem, Editors, pp. 223-255, Academic Press, New York (1969).

Resist Materials Utilizing Oxygen Plasma Resistance of Iodine Compounds

Takumi Ueno, Hiroshi Shiraishi, Takao Iwayanagi,* and Saburo Nonogaki

Hitachi, Limited, Central Research Laboratory, Kokubunji, Tokyo 185, Japan

ABSTRACT

Relative rates were measured for polymer film loss in an oxygen plasma environment. Both polymers doped with iodine compounds and iodinated polymers show high resistance to the oxygen plasma. Our ESCA studies on iodinated polystyrenes indicate that the oxygen plasma converts the iodo-substituent to iodine oxides. Through taking advantage of the oxygen plasma resistance of iodine compounds, we have been able to come up with a two-layer photolithography system for microfabrication. In the context of this two-layer process, evaluations were made of a positive photoresist formulated from OFPR-800 (Tokyo Ohka Kogyo Company) and 2,4,6-triiodophenol, as well as a negative deep-UV resist composed of iodinated poly(vinyl phenol) and 3,3'-diazidodiphenyl sulfone.

Resist system requirements for modern IC fabrication are becoming more and more difficult to meet as the minimum feature size is reduced. One of the most serious problems in conventional single-layer resist systems is that it is very difficult to control resolution and linewidth control over high steps in different parts of the wafer topography. This problem can be alleviated by using a multi-layer resist system (1-3). Utilizing a thick planarizing layer at the bottom and a thin imaging layer on top, multilayer resist systems offer improved linewidth control and height-to-width aspect ratio of the resist image. Since an oxygen plasma etching is used for transferring the pattern to an underlying planarizing layer, an understanding of the factors leading to polymer resistance to an oxygen plasma environment is important in a multilayer system.

Here, we report on measurements of oxygen plasma removal of polymer film, and on high oxygen-plasma resistance of polymers doped with iodine compounds and iodinated polymers. We apply this high oxygen-plasma resistance of iodine compounds to develop a novel two-layer photolithography system which uses resists containing iodine compounds as a top image layer.

Experimental

Materials.—*Iodinated polystyrene (IPS)*.—IPS was prepared by iodination of polystyrene using the previously described method (4). While the reaction vessel was kept at a temperature of $90 \pm 2^\circ\text{C}$, polystyrene was dissolved in nitrobenzene. Iodine, iodine pentaoxides, carbon tetrachloride, and sulfuric acid were added to the polystyrene solution. From the infrared spectrum, it is confirmed that iodination takes place at the *para* position. The iodination degree was defined as the mole fraction of 4-iodostyrene monomer units in IPS and evaluated using elementary analysis with a Hitachi 026 CHN analyzer.

Chlorinated polystyrene and brominated polystyrene.—Chlorinated polystyrene was prepared by polymerization from a mixture of the freshly distilled 4-chlorostyrene and styrene monomers using α,α' -azobisisobutyronitrile as a catalyst. Brominated polystyrene was polymerized from a mixture of 4-bromostyrene and styrene monomers in the same manner. The chlorination degree and bromination

degree were defined as mole fractions of 4-chlorostyrene and 4-bromostyrene monomer units in chlorinated polystyrene and brominated polystyrene, respectively.

Iodinated phenolic resin (IP).—Poly(vinyl phenol) obtained from Maruzen Oil Company and morpholin were dissolved in ethanol. While stirring the solution at room temperature, ethanol solution of iodine was added dropwise. The polymer precipitated after stirring for 2h. It was purified by precipitation using dioxane and water. From NMR analysis, it was ascertained that the polymer obtained was poly(3,5-diiodo-4-hydroxystyrene).

Poly(styrene sulfone).—Poly(styrene sulfone) was prepared by copolymerization of styrene with sulfur dioxide according to the previously reported method (5).

Other polymers and resists.—Most polymer and resist samples were obtained from external suppliers, i.e., Scientific Polymer Products Incorporated, Tokyo Ohka Kogyo Company, Maruzen Oil Company, Hoechst AG, Daikin Kogyo Company, and Mead Associates.

Oxygen plasma etching.—All oxygen plasma etching in our study on relative removal rates was carried out using an LFE Company, Model PDE/EDS-301 etcher which was modified to make it into a diode-coupling plasma etcher. Operating conditions were 0.5 torr and 55W. The diameter of the aluminum electrode was 60 mm. Several sections of silicon wafers spin coated with polymer films were etched on the lower-grounded electrode. A silicon wafer section coated with polystyrene was etched on the electrode as a standard for checking the oxygen plasma condition. Film thicknesses were measured with an interferometer both before and after etching.

Surface analysis.—ESCA spectra measurements were made with a VG Company Model ESCA-1 spectrometer.

Oxygen Plasma Removal of Polymer Films

Removal rates for polymer and resist films.—Absolute rates, for oxygen plasma removal were obtained from the slope of film thickness vs. etching time plots, as shown in Fig. 1. The oxygen plasma removal rates for polymers and resists relative to polystyrene, k_r , are summarized in Table I. Taylor and Wolf (6) have measured the rates of oxygen plasma removal for 40 polymer samples, and dis-

*Electrochemical Society Active Member.

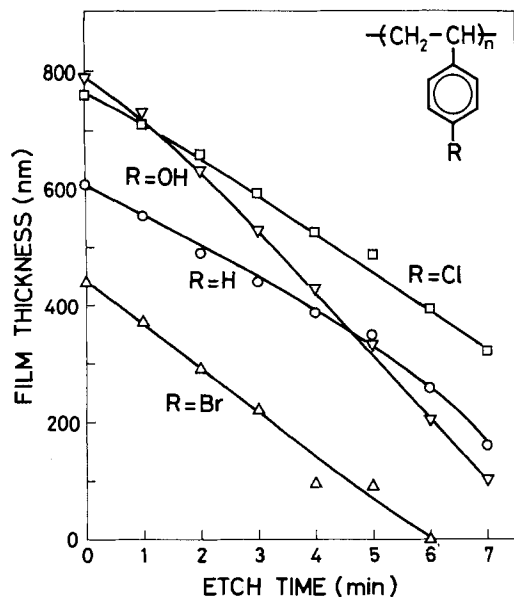


Fig. 1. Thickness remaining vs. oxygen plasma etching time at 55W and 0.55 torr.

cussed the mechanism of polymer film removal by an oxygen plasma. Our results do not completely agree with those reported by Taylor and Wolf. This discrepancy may be due to differences between the oxygen plasma etchers used: we used a diode coupling system, whereas they used an inductive coupling system.

The most striking result in Table I is that iodinated polystyrenes (IPS) (4) have remarkably small values of k_r , while the k_r values for other polymers and resists are in the range of 0.7-3.5. We measured in some detail the k_r values for IPS having various iodine percentages. Plots of k_r as a function of iodine content are shown in Fig. 2. This figure indicates that the oxygen removal rate for IPS decreases as the iodination degree increases.

Table I. Relative rates (k_r) of oxygen plasma removal for polymers and resists

Polymer	MW (10 ⁶)	k_r
Polystyrene	2.7	1.0
Iodinated polystyrene		
2% I ^a	2.7	0.89
4% I	2.8	0.86
13% I	3.1	0.72
27% I	3.6	0.51
61% I	4.5	0.10
85% I	5.5	0.04
Chlorinated polystyrene		
10% Cl	9.4	1.25
100% Cl	11	1.15
Brominated polystyrene		
10% Br	10	1.12
100% Br	20	0.98
Poly(α -methyl styrene)	0.39	0.95
Poly(vinylbenzylchloride)	75	1.12
Poly(styrene sulfone)	4.1	0.71
Poly(styrene-co-maleic anhydride)	0.5	1.20
Poly(epichlorohydrin)	7.0	3.5
Novolac resin		1.0
Poly(vinylphenol)	0.07	1.1
Brominated poly(vinylphenol)	0.14	1.65
AZ 1350J		0.84
Poly(methyl methacrylate)	6.8	1.69
Poly(glycidyl methacrylate)	1.4	1.69
Poly(methyl methacrylate-co-acrylonitrile)	6.3	1.61
Poly(glycidyl methacrylate-co-ethyl acrylate)		1.44
Poly(hexafluorobutyl methacrylate)	5.3	1.82
Poly(methyl isopropenyl ketone)	3.13	1.8
Cyclized poly(isoprene)		1.33
OMR-83 ^b		1.0
Polyimide ^c		0.83

^a The halogenation degree is defined in the Experimental section.

^b A negative photoresist composed of cyclized poly(isoprene) with a bisazide manufactured by Tokyo Ohka Kogyo Company.

^c Polyimide was prepared by baking spin-coated PIQ (obtained from Hitachi Chemical Company) at 200°C.

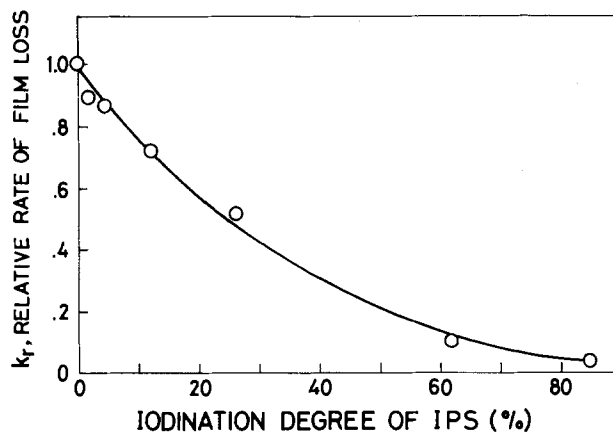


Fig. 2. Dependence of relative rates of iodinated polystyrene film loss on iodination degree.

To confirm that iodinated compounds have inherent properties of high resistance to oxygen plasma, we measured the removal rates for mixtures of polystyrene and such iodinated compounds as iodoform and 1,4-diiodobenzene. The results for mixtures of iodoform and polystyrene are shown in Fig. 3. This figure indicates that the removal rate decreases with an increase of iodoform concentration in the polystyrene matrix. A sample baked at 80°C over 10 min gives the same removal rate as for polystyrene. This is due to the volatilization of iodoform from the polymer matrix during the baking process. Similar results were obtained for mixtures of diiodobenzene and polystyrene. These results make it evident that polymers doped with iodine compounds and iodinated polymers have high resistance to an oxygen plasma.

The removal rate for IPS with reactive ion etching (RIE) was also measured as shown in Fig. 4. Here it can be seen that the IPS rate is smaller than that for polystyrene. The RIE process is less selective in terms of etching speed than the oxygen plasma etching process (7).

Surface analysis.—We analyzed the polymer surface using ESCA, so as to elucidate the reason for oxygen plasma resistance by iodine compounds. ESCA spectra for IPS (83% iodination), both before and after the oxygen plasma treatment, are shown in Fig. 5 and 6. Those figures, respectively, show wide-band spectra and I_{3d} core level signals for IPS, taking the carbon signal C_{1s}

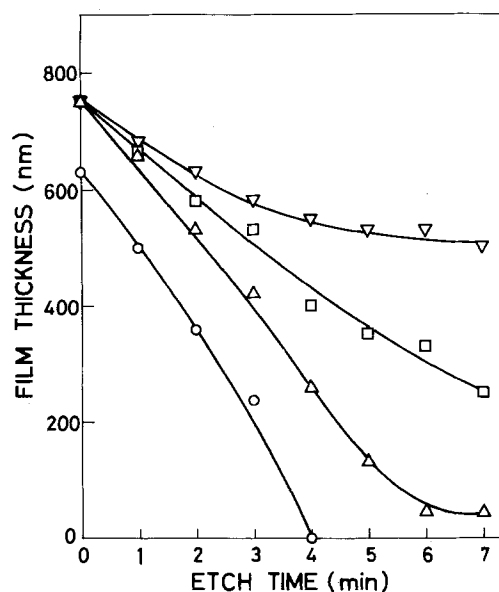


Fig. 3. Thickness remaining vs. oxygen plasma etching time at 55W and 0.55 torr for polystyrene as well as mixtures of polystyrene and iodoform. Molar ratios of iodoform to polystyrene monomer units: 0%, \circ ; 6%, Δ ; 13%, \square ; 24%, ∇ .

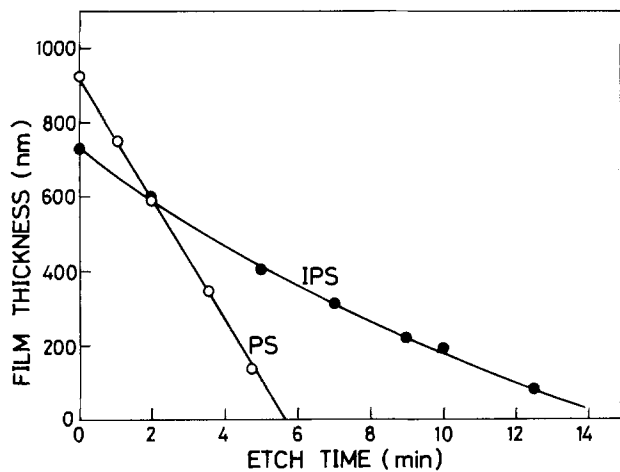


Fig. 4. Thickness remaining for IPS (83% iodination) and polystyrene, shown vs. reactive ion etching time at 24W and 20 mtorr.

(284.6 eV) as an internal standard. It is clear from Fig. 5 that the oxygen core level signal appears after oxygen plasma treatment. In Fig. 6, the I_{3d} core level signals after oxygen plasma treatment shift to larger binding energies than those before treatment.

It is known that the binding energy of an oxide is larger than that of a pure element. In fact, the value of I_{3d} binding energy for diiodo pentaoxide (I_2O_5) is 3.4 eV larger than that for IPS. The above results suggest that a thin layer of iodine oxide is formed on the surface of the polymer during the initial stage of oxygen plasma treatment and that this thin surface layer protects the bulk polymer from further etching.

Two-Layer Photolithographic System

Through utilizing the oxygen plasma resistance of iodine compounds, we were able to produce a two-layer resist system. Resists containing iodine compounds, after exposure and development, act as an etch mask for pattern transfer to the underlying planarizing polymer in an oxygen plasma.

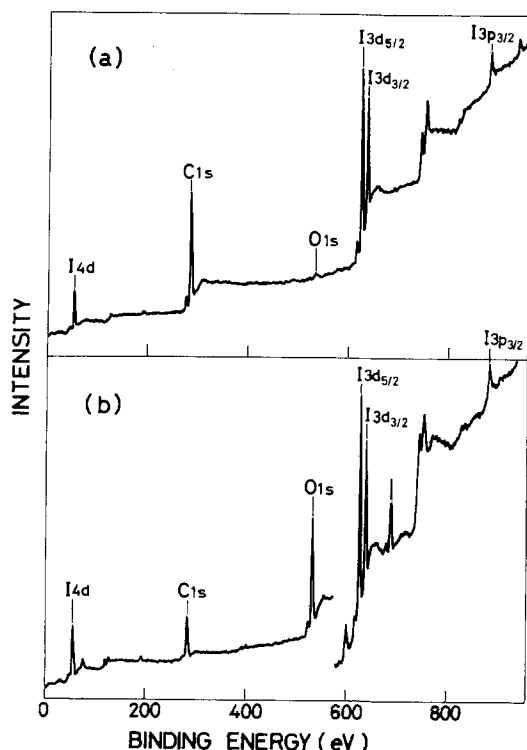


Fig. 5. Wideband ESCA spectra for IPS (83% iodination): (a) before and (b) after oxygen plasma treatment.

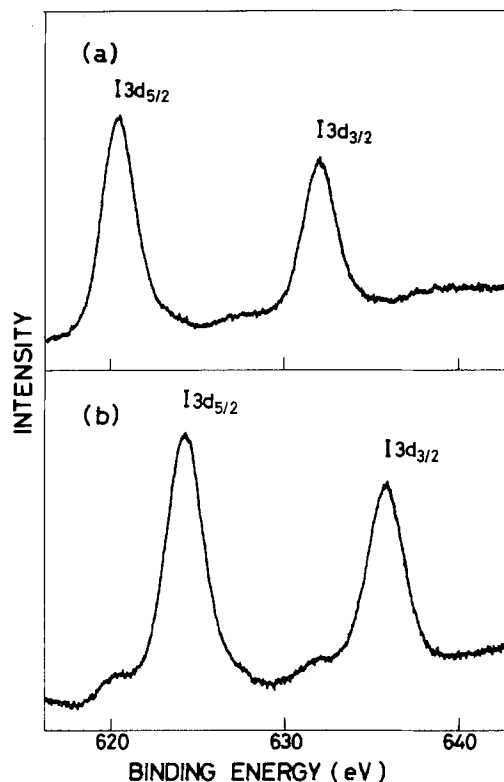


Fig. 6. I_{3d} core level ESCA signal of IPS (83% iodination): before, a, and after, b, oxygen plasma treatment.

Top imaging layer.—Resists evaluated as the top imaging layers were a positive photoresist applicable to the reduction projection aligner and a negative deep-UV resist.

Positive photoresist.—Investigations were made of a phenolic resin-quinone diazide photoresist mixed with various kinds of iodine compounds. A resist comprised of 2,4,6-triiodophenol (TRIP) and OFPR-800 (Tokyo Ohka Kogyo Company, a quinone diazide photoresist) was used.

Twelve parts of TRIP by weight were dissolved in an OFPR-800 resist solution. The rate of oxygen plasma removal for OFPR-TRIP was measured as shown in Fig. 7. The etching ratio of OFPR-800 to OFPR-TRIP was 4 to 1. OFPR-TRIP sensitivity was almost the same as that for OFPR-800.

Negative deep-UV resist.—A deep-UV negative resist composed of an iodinated phenolic resin and an azide compound was studied. Iodinated phenolic resin (IP) was synthesized by iodination of poly(vinyl phenol). 3,3'-Diazidodiphenyl sulfone (DS), which was used as an azide compound for deep-UV resist (8), was selected. The IP-DS resist was prepared by dissolving the IP and DS [20 weight percent (w/o) based on the resin] in cyclohexanone. The etching ratio of OFPR-800 to IP-DS was 5 to 1.

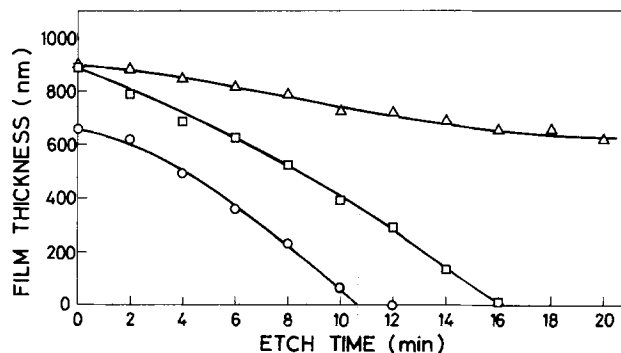


Fig. 7. Thickness remaining vs. oxygen plasma etching time at 55W 0.55 torr for polystyrene, \circ , OFPR, \square , and a mixture of OFPR and triiodophenol, \triangle .

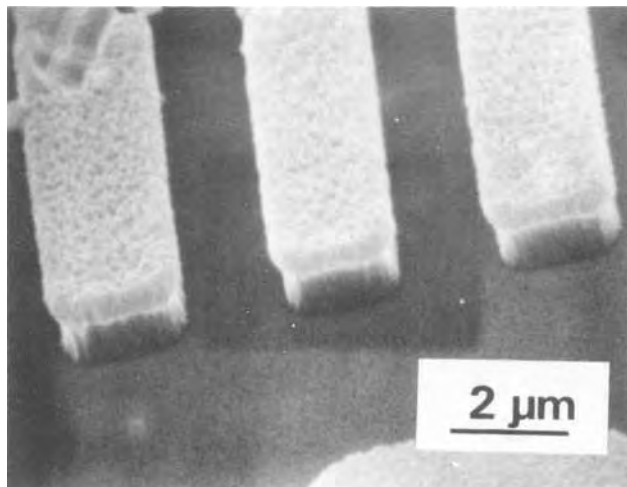


Fig. 8. SEM photograph of two-layer patterns generated by a Hitachi RA-101 Reduction Projection Aligner. A positive photoresist formulated from OFPR, and triiodophenol was used as the top imaging layer.

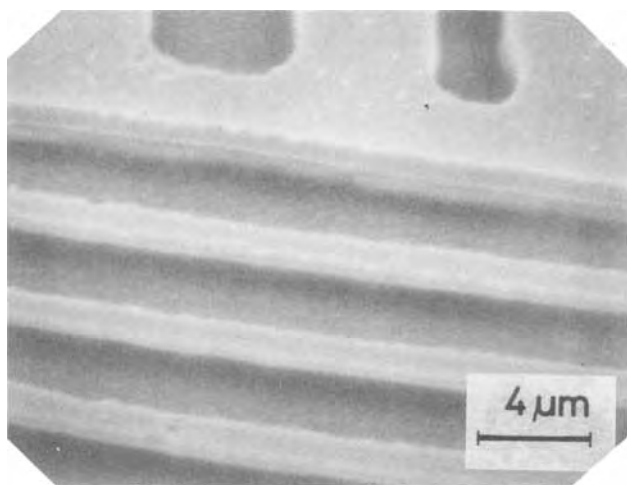


Fig. 9. SEM photograph of two-layer patterns transferred by deep-UV exposure. A negative deep-UV resist formulated from iodinated poly(vinyl phenol) and 3,3'-diazidodiphenyl sulfone was used as a top imaging layer.

Bottom polymer layer.—Requirements for the underlying polymer layer were the following: the underlying layer should be free from any mixing with the top layer; it should not dissolve in the top-layer developer; and it is desirable that it show resistance to dry etching of the substrate. OFPR-800 baked at 200°C meets these requirements.

Lithographic characteristics of the two-layer system.—OFPR-800 was spin cast on a silicon wafer to a thickness

of 1-2 μm , and hard baked at 200°C for 20 min. The top imaging layers described above were coated over the underlying layer and baked at 80°C for 20 min. After exposure and development of the top layer in an aqueous base solution, the resulting pattern was transferred to the bottom OFPR layer by oxygen plasma etching. The results for OFPR-TRIP used as a top imaging layer are shown in Fig. 8. The optical exposure was carried out with a Hitachi RA-101 Reduction Projection Aligner. IP-DS results are shown in Fig. 9. Deep-UV light was exposed through the test pattern mask which was in contact with the resist. It is clearly demonstrated in these photographs (Fig. 8 and 9) that the top layer formed by photolithography was transferred to the OFPR layer by oxygen plasma etching.

Conclusion

Iodinated polymers and polymers doped with iodine compounds are found to have a high resistance to an oxygen plasma. Our ESCA studies indicate that thin surface layer iodine oxides are formed during the early stage of oxygen plasma etching. Utilizing the oxygen plasma resistance of iodinated compounds, we propose a two-layer photolithographic system. Two resists, a positive photoresist containing triiodophenol and a deep-UV resist comprised of an iodinated phenolic resin as well as an azide compound, were evaluated for use as a top imaging layer. Good quality patterns are obtained as a result of a sequence starting with exposure followed by development of the top imaging layer and transferring the image by means of oxygen plasma etching to the bottom layer.

Acknowledgments

We thank Masatoshi Nakazawa for his measurement of ESCA spectra, and Toshiharu Matsuzawa and Hiroshi Yanazawa for making optical exposure experiments. We also thank Dr. Gary N. Taylor, of AT&T Bell Laboratories, for discussions and his oxygen RIE measurement data (Fig. 4).

Manuscript submitted June 22, 1984; revised manuscript received Jan. 11, 1985.

Hitachi, Limited, assisted in meeting the publication costs of this article.

REFERENCES

1. M. Hatzakis, *Solid State Technol.*, **24**, 74 (1981).
2. B. J. Lin, *ibid.*, **26** (5), 105 (1983).
3. E. Ong and E. L. Hu, *ibid.*, **27** (6), 155 (1984).
4. H. Shiraishi, Y. Taniguchi, S. Horigome, and S. Nonogaki, *Polym. Eng. Sci.*, **20** (8), 1054 (1980); T. Ueno, H. Shiraishi, and S. Nonogaki, *J. Appl. Polym. Sci.*, **29**, 223 (1984).
5. M. J. Bowden and L. F. Thompson, *This Journal*, **121**, 1620 (1974).
6. G. N. Taylor and T. M. Wolf, *Polym. Eng. Sci.*, **20**, 1087 (1980).
7. G. N. Taylor, T. M. Wolf, and J. M. Moran, *J. Vac. Sci. Technol.*, **19**, 872 (1981).
8. T. Iwayanagi, T. Kohashi, S. Nonogaki, T. Matsuzawa, K. Dota, and H. Yanazawa, *IEEE Trans. Electron Devices*, **ed-28**, 1306 (1981).

Diffusivity of Implanted Chlorine Atoms in Thermal Oxides on Silicon

A. S. Vengurlekar, K. V. Ramanathan, and V. T. Karulkar

Tata Institute of Fundamental Research, Bombay 400 005, India

V. P. Salvi

Department of Physics, University of Bombay, Bombay 400 098, India

ABSTRACT

It is well known (1-4) that substantial amounts of chlorine can be incorporated in HCl grown thermal oxides on silicon to effectively passivate sodium ions. It has been of interest to find out if similar effects can be obtained for oxides chlorinated by implanting Cl ions at the surface of SiO₂ films on Si. It appears (5, 6), however, that when these films are annealed at temperatures in excess of 700°C, no Na neutralization property is evident. In this paper, we show with the help of ⁴He ion Rutherford backscattering (RBS) experiments on chlorine implanted into a thermal oxide film on Si that the oxide loses about 10 (50) percent of the implanted Cl during annealing at 600°C (1100°C) in nitrogen for 30 min. We obtain the diffusion coefficient *D* of Cl in SiO₂ at various temperatures with the help of a process simulation program (SUPREM II) and show that for $D \sim D_0 \exp(-E_a/kT)$, $D_0 = 10^{-12}$ cm²/s and $E_a \sim 0.5$ eV. Corrections for system resolution and energy straggling effects are made to obtain the actual Cl density profiles in the SiO₂ film. It is seen that Cl at 50 keV has a range of 440Å in SiO₂ with a standard deviation of 220Å for a gaussian form.

It is a well-established fact that small addition of a chlorine containing species (such as HCl, Cl₂, C₂HCl₃) to the oxidizing atmosphere (oxygen) during thermal oxidation of silicon can lead to several beneficial effects on the stability of the oxide, quality of the interface, dielectric breakdown properties, etc. (1, 2). The basic physicochemical mechanisms of many of the phenomena associated with chlorinated oxidations, however, are not fully understood. Mention in this regard may be made of thresholds observed for chlorine incorporation and for sodium ion passivation in the HCl to O₂ volume ratio, and in the oxidation temperature (3, 4). Convincing explanations also remain to be given as to the precise role of Cl in Na⁺ neutralization. Elimination of the use of a corrosive gas like HCl for chlorination of oxides has been recently attempted with the help of the chlorine-implantation technique (5-7). This idea, however, has the following problems. First, since rather large amounts ($> 10^{15}$ cm⁻²) of incorporated chlorine ions are required to achieve appreciable Na passivation (4), the resulting radiation damage in the oxide as well as at the interface is rather severe. It is necessary to anneal the implanted samples at temperatures in excess of 800°C in order to achieve adequate recovery of the damaged oxide and of the deteriorated Si/SiO₂ interface (8). Second, no Na passivation property is exhibited by chlorine implanted oxides annealed at temperatures in excess of 700°C (5-7). These observations may imply that the sodium neutralization mechanisms which operate in the case of HCl oxides are absent in the chlorine-implanted oxides. The recent work on x-ray microanalysis and electron microscopy of HCl oxides (9-11) has established that a Cl containing separate amorphous phase is formed at the Si/SiO₂ interface during HCl oxidation in the Na passivation regime. This result has received further support from x-ray photoelectron spectroscopy study of chlorine incorporation in HCl oxides (12). Formation of such a phase is possible when reactions of Si both with Cl and O are competing as they are at the O-deficient oxidation front at the interface. The correlation of formation of this phase with significant Na neutralizations has been demonstrated (9-11). It is not clear whether a similar phenomenon is possible in the case of Cl-implanted oxides in view of the larger Si-O bond energy as compared to the Si-Cl energy. There is also the possibility that a considerable loss of Cl takes place during thermal annealing of Cl-implanted oxides at temperatures exceeding 700°C, in contrast to the observations that the amount of Cl incorporated in HCl grown oxides does not reduce appreciably unless the annealing temperatures well exceed 1100°C (13, 14). This, of course, would be the

case if the chemical state of a Cl atom is not the same in the two situations. The purpose of the present paper is to report the result of our nuclear (Rutherford) backscattering (NBS or RBS) experiments on Cl incorporated in SiO₂ by ion implantations. They provide clear evidence that the implanted Cl atoms diffuse away as the annealing temperatures exceed 600°C. We further deduce that the diffusivity of implanted Cl is characterized by a small activation energy of about 0.5 eV.

Experimental

Silicon wafers [(100), n-type, phosphorous-doped, 2.6-3.2 Ω cm, polished] were thoroughly cleaned in standard H₂O₂-based basic and acidic solutions along with dilute HF dips and DI water rinses. They were then oxidized in dry O₂ for 75 min at 1100°C. Ellipsometric measurements made on a Gaertner Scientific Model 117 gave a thickness of 1415.8Å and refractive index 1.46 for these oxides. [The measured value of the thickness increased to about 1450Å on implantation due to the dilation effect (8).] ³⁵Cl ions obtained from a cobalt chloride source were implanted uniformly all over the front side of the oxidized wafers after removing the oxide on the back surface. The implantation dose was 8×10^{15} cm⁻² at an energy of 50 keV. The expected range of Cl in SiO₂ at 50 keV from the plots of calculations based on an improved Lindhard-Sharff-Schiott formulation (15) is about 500Å. The wafers were then cut into four quarters each and collected into four groups called C(1), C(2), C(3), and C(4). Samples C(2), C(3), and C(4) were separately annealed in dry N₂ for 30 min at 600°, 850°, and 1100°C, respectively, while C(1) was left unannealed. The moisture level in the dry oxygen and nitrogen used in these experiments was stated by the suppliers to be about 4 ppm. Samples C(1), C(2), C(3), and C(4) were now cut to obtain pieces with the dimensions 8 × 6 mm, suitable for mounting in the RBS measurement setup. ⁴He ions of energy 2 MeV were incident on the samples at a current of 20 nA to give integrated charge of 10 μC. The surface barrier detector detected the backscattered particles at a scattering angle of 165°. The detector solid angle was 1.9 msterad. The vacuum in the system was about 10⁻⁶ torr. To obtain the channel number to energy conversion, RBS experiments for scattering from Al and Au target films were also carried out.

Results and Discussion

We first briefly discuss the process of Rutherford backscattering (16) and the associated kinematics with the help of Fig. 1 as follows. The scattering cross section in the center of mass (c.m.) frame is

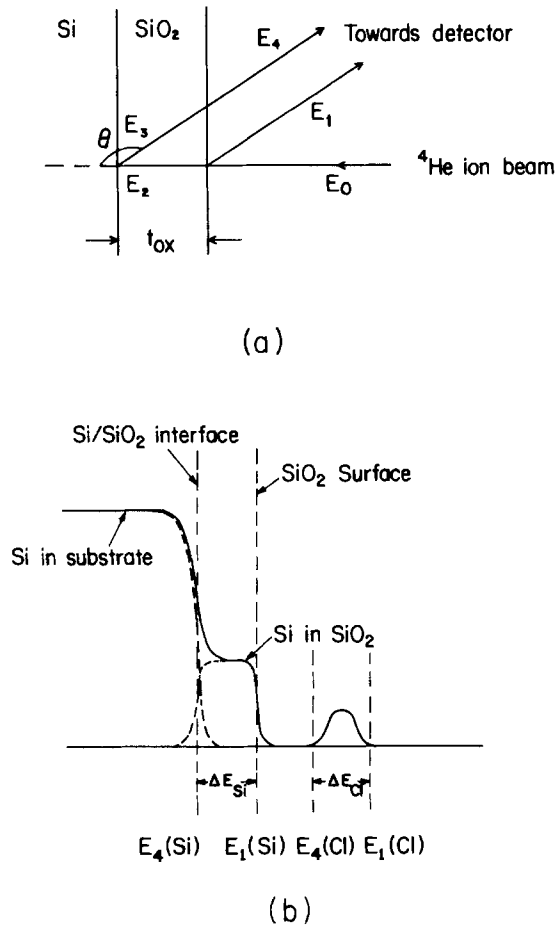


Fig. 1. (a) Kinematics of Rutherford backscattering of ^4He ions from atoms in SiO_2 on Si. (b) The expected energy spectrum of the backscattered ions (schematic).

$$\sigma_c = \frac{1}{16} \frac{zZe^2}{\frac{1}{2}\mu v^2} \sin^4(\theta_c/2) \quad [1]$$

where $z(m)$ and $Z(M)$, respectively, are the projectile and target charges (masses), v is the c.m. velocity, and $\mu = mM/(m + M)$. The laboratory frame cross section is given by

$$\sigma_L = \left(\frac{zZe^2}{4E}\right)^2 \frac{4}{\sin^4 \theta} \frac{\left\{ \left[1 - \left(\frac{m}{M} \sin \theta\right)^2 \right]^{1/2} + \cos \theta \right\}^2}{\left[1 - \left(\frac{m}{M} \sin \theta\right)^2 \right]^{1/2}} \quad [2]$$

$$\approx \left(\frac{zZe^2}{4E}\right)^2 \left[\sin^{-4} \frac{\theta}{2} - 2 \left(\frac{m^2}{M}\right) + O\left(\left(\frac{m}{M}\right)^4\right) \right] \quad [3]$$

where E is the energy before scattering. The energy of particles scattered by the atoms at the surface is related to the incident energy E_0 by

$$E_1 = K_M E_0 \quad [4]$$

where

$$K_M = \left(\frac{m}{M+m}\right)^2 \left[\cos \theta + \left(\frac{M^2}{m} - \sin^2 \theta\right)^{1/2} \right]^2 \quad [5]$$

To convert the RBS data of yield per channel into yield *vs.* energy, the observed spectra due to scattering from Si and O atoms in SiO_2 and from Au and Al films can be used to obtain a plot of the channel number at the high energy edge E_1 of the various peaks *vs.* the corresponding kinematic factors K_M (Eq. [5]). The standard practice (in the case of peaks broader than the resolution width) is to associate the scattering from surface atoms with the half-height points on the leading edge. We found that scattering from O, Al, Si, and Au atoms on the sur-

face occurs at channel no. 183, 289, 299.5, and 500, respectively, whereas the corresponding values of the kinematic factor K_M are given by 0.3635, 0.5555, 0.568, and 0.923. This leads to a straight line plot with a slope of $\psi = 3.53$ keV/channel and an offset of -35 keV. It is now possible to express RBS spectra in terms of yield *vs.* energy. The target atoms inside the surface of a substrate see less energetic ions due to the energy loss in the traversed path. Atoms in a thin SiO_2 film close to the Si/SiO₂ interface, for instance, see ions of energy $E_2 \approx E_0 - (dE/dt) t_{\text{ox}}$, where (dE/dt) is the rate of energy loss at the incident energy. The displacement of detected energy δE from E_1 is related to the depth δt in SiO_2 by

$$\delta E = [S] \delta t \quad [6]$$

where the stopping factor $[S]$ given as

$$[S] = \left[(dE/dt)_{E_{\text{in}}} K_M + (dE/dt)_{E_{\text{out}}} \frac{1}{\cos \theta} \right] \quad [7]$$

is related to the stopping cross section $[\epsilon]$ by $[S] = [\epsilon]N$, where N is the density of SiO_2 units. For thin films and when the E dependence of $[\epsilon]$ is insignificant, one can obtain the energy width ΔE corresponding to the full thickness of the film under the surface energy approximation. Since t_{ox} is given by ellipsometric measurements to be about 1400\AA , $[\epsilon]_{\text{SiO}_2}$ at 2 MeV for scattering from Si in SiO_2 is $2.26 \times 10^{-1} \text{ eV cm}^2$ (16), and, taking N_{SiO_2} to be $2.3 \times 10^{22} \text{ cm}^{-3}$, one obtains $\Delta E(\text{Si})$ to be 72.7 keV. This, using $\psi = 3.53$ keV/channel, can be seen to correspond to about 20 channels. Using $\Delta E(\text{Cl}) = \Delta E(\text{Si})\eta$ where $\eta = [S]_{\text{Cl}}/[S]_{\text{Si}}$ [which is about 1.01 (14)], and Eq. [4] for Cl, one has $K_M(\text{Cl}) = 0.637$, $E_1(\text{Cl}) = 1.2736$ MeV, and $\Delta E(\text{Cl}) \approx 73.4$ keV.

Figure 2 shows the RBS yield against channel number spectra for samples C(1), C(2), C(3), and C(4). The results provide clear evidence for the loss of the Cl atoms during postimplant annealing. This is to be contrasted with the fact that no appreciable loss of Cl incorporated in the HCl-grown oxides occurs unless the annealing temperatures well exceed 1100°C (13, 14). This may be taken as an indication that the physicochemical environment of Cl atoms in the two cases is quite different. The results of Fig. 2 can, to some extent, explain the observed failure (5-7) of Cl-implanted samples in exhibiting Na passivation when annealed at temperatures of 700°C or higher. It must, however, be pointed out on the basis of Fig. 2 that the loss of Cl is not complete even at 1100°C [sample C(4)]. The failure of Na passivation in Cl-implanted samples, therefore, raises questions such as: is the presence of large Cl concentrations alone enough for Na passivation? Since the neutralizing negative charge must come from the silicon substrate, is the vicinity of the Cl containing phase to Si/SiO₂ interface crucial for Na passivation? Further study to clarify these aspects will be necessary.

Coming now to obtaining chlorine density profiles in SiO_2 from the RBS spectra, we note that Eq. [6] can be utilized to obtain the energy to depth conversion. In the ideal case, the ^{35}Cl peak can be well separated from the Si peak provided $E_4(\text{Cl}) > E_1(\text{Si})$ (see Fig. 1) which requires

$$\frac{E_1(\text{Si})}{[S]_{\text{Cl}}^{\text{SiO}_2}} \left(\frac{K_M(\text{Cl})}{K_M(\text{Si})} - 1 \right) > t_{\text{ox}} \quad [8]$$

For $E_0 = 2$ MeV, one can estimate the left-hand side of Eq. [8] to be about 2500\AA . In practice, however, the line shapes show departures from the ideal case (16) due to: (i) system resolution limitations, (ii) energy straggling for the projectile ions inside a target substrate, (iii) background counts due to pulse "pile up" on the high energy side, and (iv) dependence of various cross sections on the energy of the scattering ions, etc. These factors can affect the shapes of both the low and high energy edges and can also lead to slopes in the plateau region. In order to obtain the correct chlorine concentration profiles from the data of Fig. 2, one needs to eliminate the effects of the above factors as far as possible. To estimate the effects of the

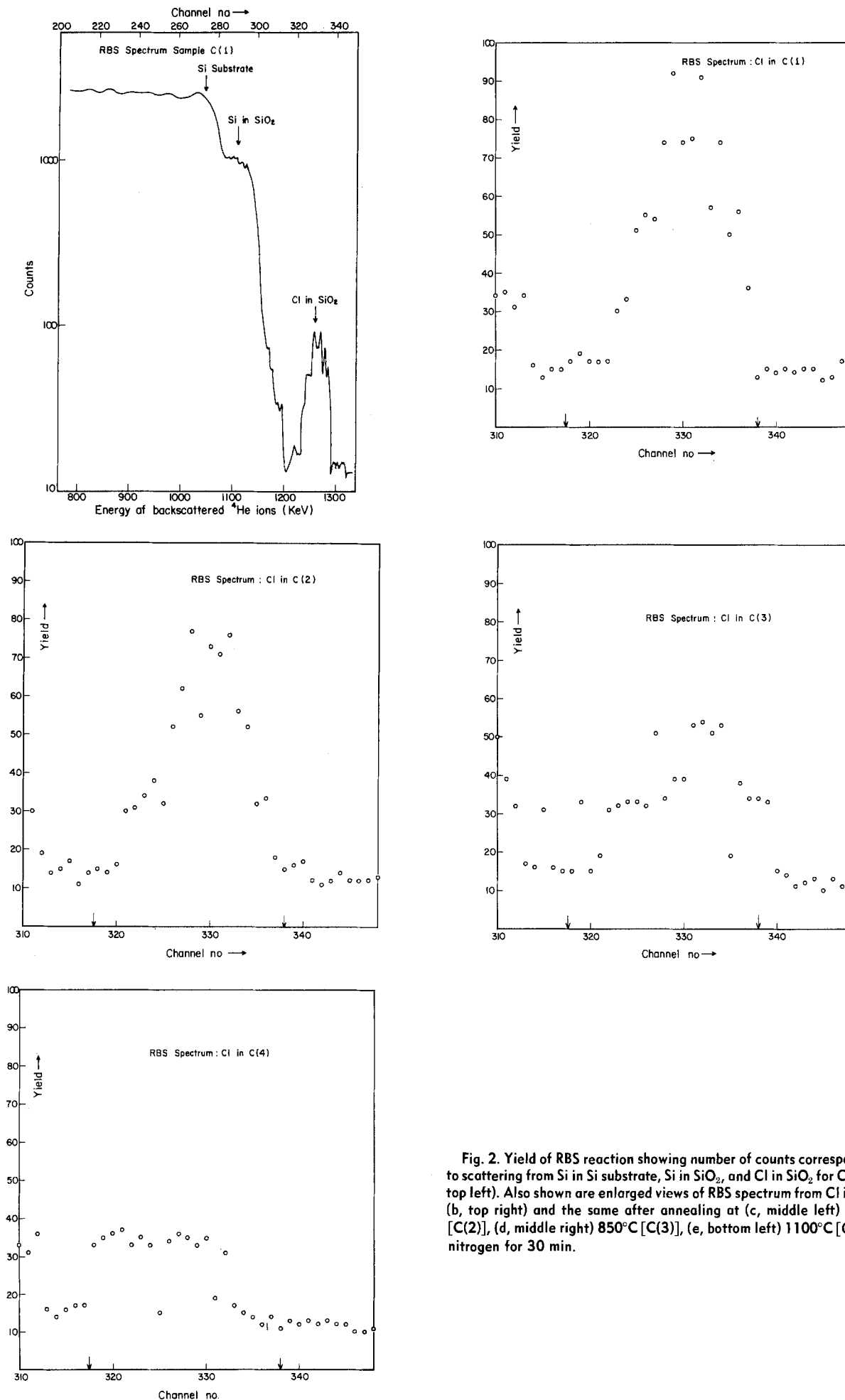


Fig. 2. Yield of RBS reaction showing number of counts corresponding to scattering from Si in Si substrate, Si in SiO_2 , and Cl in SiO_2 for C(1) (a, top left). Also shown are enlarged views of RBS spectrum from Cl in C(1) (b, top right) and the same after annealing at (c, middle left) 600°C [C(2)], (d, middle right) 850°C [C(3)], (e, bottom left) 1100°C [C(4)] in nitrogen for 30 min.

system resolution, it is customary to assume a gaussian form for the detection response function and estimate its full width at half maximum (FWHM) either by obtaining

the energy difference for the points on high energy edge for Si in SiO₂ corresponding to 12% and 88% of the peak height or by measuring FWHM of the peak for a very thin

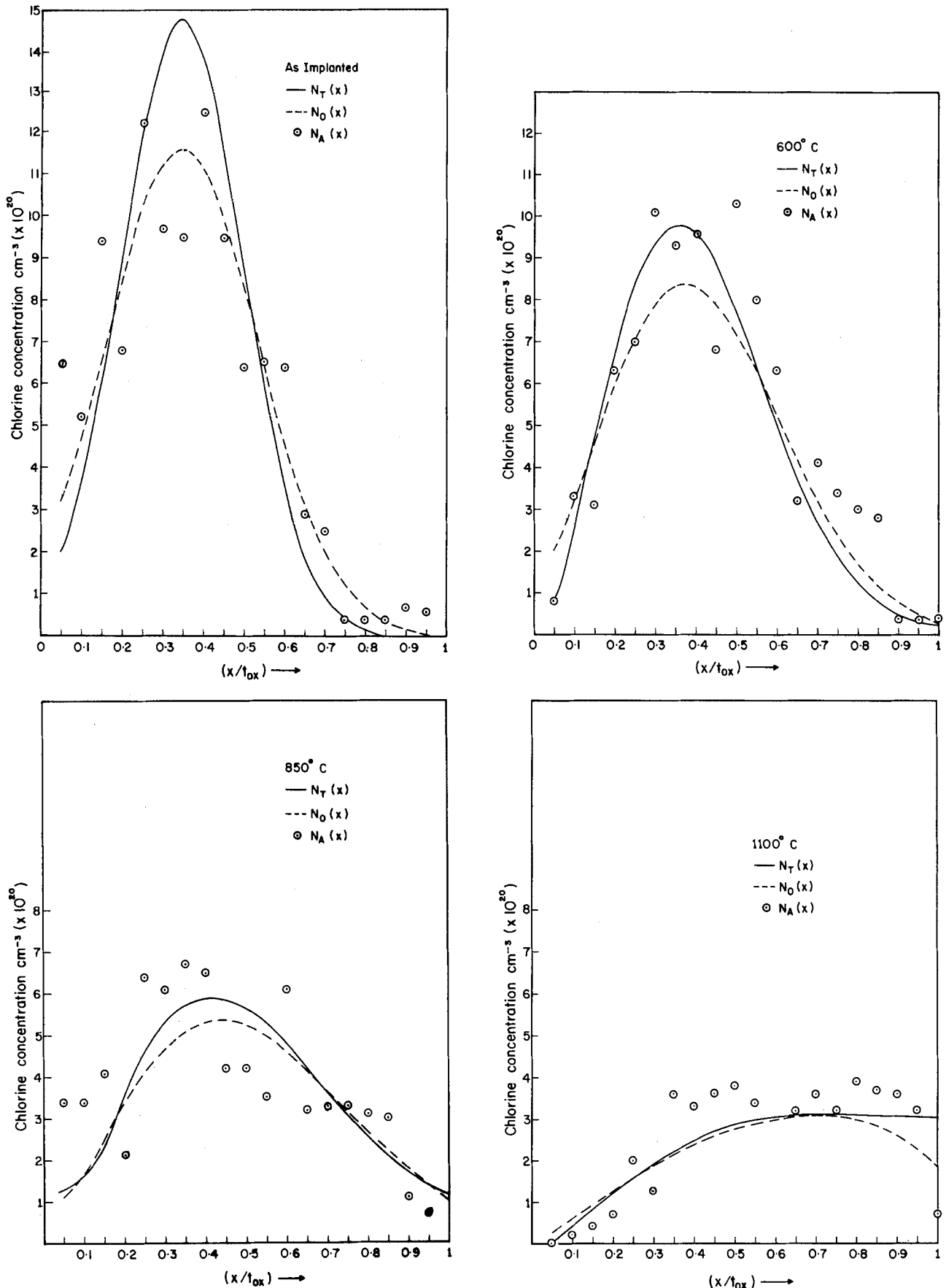


Fig. 3. (a, top left) Chlorine depth profile after implantation in SiO₂ at 50 keV with a dose of $8 \times 10^{15} \text{ cm}^{-2}$ and the profiles for samples C(2) (b, top right), C(3) (c, bottom left), and C(4) (d, bottom right) after annealing. N_O are the fits to the data points N_A , while N_T give the true profiles (corrected for resolution, see text), $(x/t_{\text{ox}}) = 0.0$ is the oxide surface.

Au film. We have obtained from both these methods an estimate for the system resolution FWHM of about 21 keV. The standard deviation Ω_R of the resolution function is to be equated to FWHM/2.355. The second factor, namely, the energy straggling due to fluctuations in the number of collisions (and the energy lost in each) the incident ions experience in traversing a distance inside the substrate, has a smaller effect in the case of a thin film such as the one we have. One usually estimates the energy straggling variance for a thin film with the help of the formula (16)

$$\Omega_S^2 = \Omega_B^2 (K_M + 1/\cos \theta) \quad [9a]$$

where

$$\Omega_B^2 = 4\pi (Ze^2)^2 (ZN)_{\text{SiO}_2} t \quad [9b]$$

as given by Bohr's theory (16), $(ZN)_{\text{SiO}_2} = (Z_{\text{Si}} + 2Z_{\text{O}})N_{\text{SiO}_2}$ and $t =$ traversed depth in SiO_2 . For $t = t_{0x}$, Ω_B can be estimated to be about 3.0 keV, while an average of Ω_S^2 over "t" is about 2.7 keV. (We use this value as an approximation in the analysis to be described presently.) As for the background contribution to the yield due to pulse pile-up, one needs to use pile-up rejection electronics in the detection system. Not having done this, we have corrected the yield for chlorine by subtracting out a constant which is an average of the rather flat background seen for about 20 channels on the high energy side of $E_1(\text{Cl})$. Using the formula

$$(Nt)_{\text{Cl}} = \frac{A_{\text{Cl}}}{H_{\text{Si}}} \frac{\sigma_{\text{Si}}(E_0)}{\sigma_{\text{Cl}}(E_0)} \frac{\psi}{[\epsilon_0]_{\text{SiO}_2}^{\text{Si}}} \quad [10]$$

in the case of C(1), the corrected data points give $(Nt)_{\text{Cl}} = 8.49 \times 10^{15} \text{ cm}^{-2}$, which reproduces the nominal Cl implantation dose of $8 \times 10^{15} \text{ cm}^{-2}$ reasonably well. Here H_{Si} is the height of Si peak (for Si in SiO_2) and $A_{\text{Cl}} = \sum_i H_i(\text{Cl})$ is the area under the Cl peak. [Surface energy approximation is used in Eq. [10] along with $\sigma_{\text{Si}}(E_0)/\sigma_{\text{Cl}}(E_0) = 0.638$.] The chlorine peak density is obtained from

$$N_{\text{Cl}}^{\text{Peak}} = \frac{H_{\text{Cl}}^{\text{Peak}}}{H_{\text{Si}}} \left(\frac{\sigma_{\text{Si}}(E_0)}{\sigma_{\text{Cl}}(E_0)} \right) \frac{[\epsilon_0]_{\text{SiO}_2}^{\text{Cl}}}{[\epsilon_0]_{\text{SiO}_2}^{\text{Si}}} N_{\text{Si}}^{\text{SiO}_2} \quad [11]$$

to be $1.26 \times 10^{21} \text{ cm}^{-3}$, where $N_{\text{Si}}^{\text{SiO}_2} = 2.3 \times 10^{22} \text{ cm}^{-3}$. Now we express the "observed" density profile $N_O(E)$ in terms of the true profile $N_T(E)$ as follows (18)

$$N_O(E) = \int_{\text{all channels}} N_T(E') R(E - E') dE' \quad [12]$$

where R is the resolution function and is assumed to be a gaussian with a standard deviation of $(\Omega_R^2 + \Omega_S^2)^{1/2}$ where Ω_S may take channel number dependent values. To extract $N_T(E)$ from Eq. [12], we have followed the following

procedure. First: $N_T(E)$ is initially obtained from process simulation program SUPREM II (17) using trial input parameters such as implantation dose, range, and standard deviation as well as diffusion, surface transport, and segregation coefficients. Since chlorine diffusion is not considered in SUPREM II, we use As as the dummy name to simulate Cl diffusion in SiO_2 by appropriately varying the above parameters. The second step is to use Eq. [12] to obtain $N_O(E)$, which is a smooth function and is expected to serve as a fit to the actual data points $N_A(E)$. We vary the values of the input parameters in $N_T(E)$ until Eq. [12] obtains a least χ^2 fit $N_O(E)$ to $N_A(E)$. Here $\chi^2 = \sum_i ([N_O(E_i) - N_A(E_i)]/\delta N_A(E_i))^2$ and δN_A is the error in N_A given by $\sqrt{N_A}$ for Poisson statistics. A reasonable, simplifying approximation is made by restricting the integration in Eq. [12] to those channels which correspond to Cl in SiO_2 . The procedure outlined earlier is used to obtain the energy to depth scale conversion. Figure 3 shows the data points $N_A(x)$ along with the fit $N_O(x)$ to those points and the corrected line shapes $N_T(x)$. It may be noticed that the 50 keV Cl implantation in SiO_2 [sample C(1)], Fig. 3a, follows a gaussian form with a range of 440Å and a standard deviation of 220Å. These may be compared with the predicted values of 500 and 160Å, respectively, based on Lindhard-Shorff-Schiott theory (15). Table I summarizes the values of the various parameters used to obtain $N_O(x)$ and $N_T(x)$ by allowing SUPREM II to simulate Cl diffusion in SiO_2 during annealing at 600°, 850°, and 1100°C for 30 min in N_2 , given the initial distribution of Fig. 3a. We first reach a minimum χ^2 point by varying $D_{\text{Cl}}(\text{SiO}_2)$. Then all the parameters are varied to obtain smaller χ^2 . We find that the fits and χ^2 are not very sensitive to variations in S_G , S_T , and $D(\text{Si})$. To get an idea of this behavior, Table I shows various values of S_G , S_T , and $D(\text{Si})$ and the corresponding χ^2 . Figure 4 shows the plot of $D_{\text{Cl}}(\text{SiO}_2)$ given by SUPREM II against $1000/T$. From the line shown in Fig. 4 as an attempt to fit these points, one can deduce that $D = D_0 \exp(-E_a/kT)$, where $D_0 \cong 10^{-12} \text{ cm}^2/\text{s}$ and the activation energy $E_a \cong 0.5 \text{ eV}$. This rather small activation energy is comparable to that for H_2 diffusion in SiO_2 (-0.7 eV) (19). The pre-exponent in $D(\text{Cl})$, however, seems to be smaller than that for most impurities in SiO_2 . It may be noted that Greeuw and Hosper (5) had earlier suggested a much larger estimate of $E_a \sim 2 \text{ eV}$ based on their long wavelength x-ray analysis of Cl-implanted oxides, D_0 was given to be $2 \times 10^{-6} \text{ cm}^2/\text{s}$. Their value of D can be found to vary between 10^{-17} and 10^{-13} in the range 600°-1100°C. The orders of magnitude of these numbers are comparable to those of this paper. On the other hand, the value $D = 10^{-11} \text{ cm}^2/\text{s}$ estimated by Schaeffer *et al.* (20) at 750°C from their tracer experiments on radioactive chlorine (^{36}Cl) solution on SiO_2 is much larger. The sources of this discrepancy are not immediately clear. Figure 5, in which we show R ,

Table I. Sensitivity of χ^2 to the values of the fit parameters for $N_T(E)$

Sample	Anneal temp. (°C)	$D_{\text{Cl}}(\text{SiO}_2) \times 10^{-15}$ (cm ² /s)	S_G	$S_T \times 10^{-4}$ (cm ² /s)	$D_{\text{Cl}}(\text{Si})$ (cm ² /s)	$\chi^2 \times 10^{20}$
C(2)	600	1.92	0.1	21.7	1.96×10^{-22}	7.90
		1.92	100	21.7	1.96×10^{-22}	7.84
		1.92	100	3.66×10^{-5}	1.96×10^{-22}	10.50
		1.92	100	21.7	1.159×10^{-18}	7.84
		1.92	100	21.7	3.3×10^{-28}	7.84
		2.2	100	21.7	1.95×10^{-22}	8.07
		1.68	100	21.7	1.95×10^{-22}	7.94
		C(3)	850	5.71	1.0	31.0
5.71	100			31.0	2.7×10^{-17}	15.1
5.71	100			0.95	2.7×10^{-17}	15.1
5.71	100			0.95	8.28×10^{-13}	15.1
5.71	100			0.95	8.79×10^{-22}	15.2
6.33	100			0.95	2.7×10^{-17}	15.2
5.15	100			0.95	2.7×10^{-17}	15.4
C(4)	1100			15.87	100	3.56
		15.87	0.001	3.56	5.0×10^{-14}	7.65
		15.87	0.001	521.0	5.0×10^{-14}	7.66
		15.87	0.001	3.56	2.34×10^{-10}	7.67
		15.87	0.001	3.56	1.067×10^{-17}	7.65
		19.6	0.001	3.56	5.0×10^{-14}	8.16
		8.34	0.001	3.56	5.0×10^{-14}	19.1

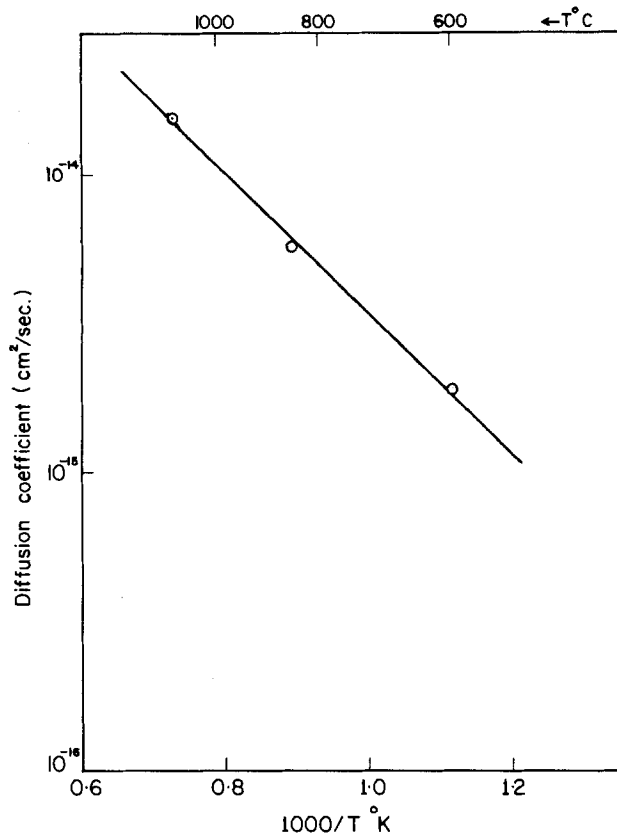


Fig. 4. Chlorine diffusion constant as a function of $1000/T$ (K) obtained by fitting a diffusion model using SUPREM II (17) to be distributions N_T of Fig. 3.

the percentage loss of Cl against temperature T , indicates that about 56% of implanted charge has been lost from SiO_2 after annealing at 1100°C in nitrogen for 30 min. We find that $R \sim bT$, where $b \sim 0.08^\circ\text{C}$.

Conclusion

We have shown in this paper, with the help of our experiments on Rutherford backscattering from Cl ions implanted in a thin thermal SiO_2 film on Si, that: (i) the implanted Cl atoms diffuse away as one anneals the samples at temperatures in excess of 600°C . (ii) the chlorine implantation profile shows a gaussian form ($\sim \exp -((x - R_p)^2/2\Delta R_p^2)$) with $R_p = 440\text{\AA}$ and $\Delta R_p = 220\text{\AA}$ after corrections for system resolution and energy straggling effects. We have also obtained the chlorine profiles (corrected for system resolution and projectile energy straggling effects) after diffusion in SiO_2 during annealing at 600° , 850° , and 1100°C in nitrogen. An estimate based on the process simulation program SUPREM II indicates an Arrhenius relation $D = D_0 \exp(-E_a/kT)$ for the Cl diffusion coefficient in SiO_2 with $D_0 \sim 10^{-12} \text{ cm}^2/\text{s}$ and $E_a = 0.5 \text{ eV}$. The results show that the implanted Cl has a diffusivity different from that of Cl in HCl-grown oxides.

Acknowledgments

We wish to express our gratitude to Professor S. C. Jain, Director, Solid State Physics Laboratory, New Delhi, Dr. K. K. Laroia and other staff for providing the Cl implantation facility in their laboratory. We gratefully acknowledge the help of Mr. Animesh Jain of Bhabha Atomic Research Centre, Bombay, where the RBS measurements were carried out. We thank Mr. P. R. Apte for his help in use of SUPREM II.

Manuscript submitted Aug. 6, 1984; revised manuscript received Feb. 8, 1985.

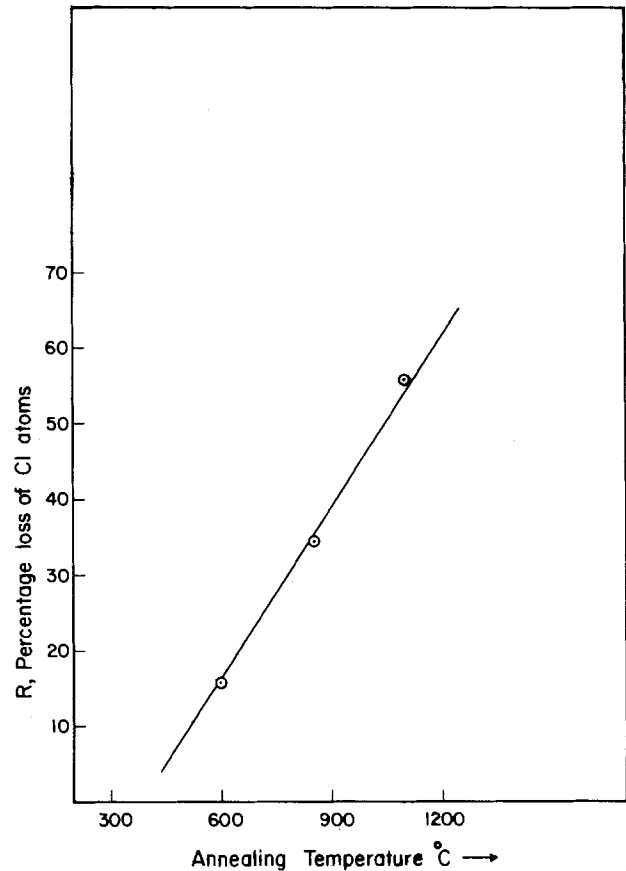


Fig. 5. Percentage loss of Cl ions implanted in SiO_2 as a function of annealing temperature.

REFERENCES

1. B. R. Singh and P. Balk, *This Journal*, **128**, 453 (1978).
2. J. Monkowski, *Solid State Technol.*, **22**, 58, 113 (1979).
3. R. J. Kriegler, *Thin Solid Films*, **13**, 11 (1972).
4. A. Rohatagi, S. R. Butler, F. J. Feigl, N. W. Kraner, and K. W. Jones, *Appl. Phys. Lett.*, **30**, 104 (1971).
5. G. Greeuw and H. Hosper, in "Insulating Films on Semiconductors," M. Schulz and G. Pensl, Editors, p. 203, Springer-Verlag, New York and Heidelberg (1982).
6. W. Wronski, *Phys. Status Solidi A*, **53**, 659 (1979).
7. A. S. Vengurlekar and A. N. Chandorkar, Unpublished.
8. A. N. Chandorkar, V. T. Karulkar, A. S. Vengurlekar, and K. V. Ramanathan, *Phys. Status Solidi A*, **81**, 407 (1984).
9. A. Rohatagi, S. R. Butler, F. J. Feigl, H. W. Kraner, and K. W. Jones, *This Journal*, **126**, 143 (1979).
10. J. Monkowski, J. Stach, and R. E. Tressler, *ibid.*, **126**, 1129 (1979).
11. H. L. Tsai, R. O. Gale, D. B. Williams, S. R. Butler, H. W. Kraner, and K. W. Jones, *ibid.*, **131**, 411 (1984).
12. A. S. Vengurlekar, A. N. Chandorkar, and K. V. Ramanathan, *Thin Solid Films*, **114**, 285 (1984).
13. R. L. Meek, *This Journal*, **120**, 308 (1973).
14. Y. J. Van der Meulen, C. M. Osburn, and J. F. Ziegler, *ibid.*, **122**, 284 (1975).
15. R. G. Wilson and G. R. Brewer, "Ion Beams," John Wiley & Sons, New York (1973).
16. For a review, see, e.g., W. K. Chu, J. W. Mayer, and M. A. Nicolet, "Backscattering Spectrometry," Academic Press, New York (1978).
17. D. A. Antoniadis, S. E. Hansen, and R. W. Dutton, Stanford Univ. Tech. Rept. no. 5019-2, Stanford University, Stanford, CA (1978).
18. J. F. Ziegler and J. E. E. Baglia, *J. Appl. Phys.*, **42**, 2031 (1971).
19. H. F. Wolf, "Silicon Semiconductor Data," Pergamon Press, Elmsford, NY (1969).
20. H. A. Schaeffer, J. Mecha, and J. Steinmann, *J. Am. Ceram. Soc.*, **62**, 343 (1979).

Oxygen RIE-Resistant Deep-UV Positive Resists: Poly (trimethylsilylmethyl methacrylate) and Poly (trimethylsilylmethyl methacrylate-co-3-oximo-2-butanone methacrylate)

E. Reichmanis and G. Smolinsky

AT&T Bell Laboratories, Murray Hill, New Jersey 07974

ABSTRACT

The polymer, P(SiMA), derived from trimethylsilylmethyl methacrylate and the copolymer, P(SI-OM), with 3-oximino-2-butanone methacrylate are resistant to oxygen reactive ion etching in the pressure range 20-100 μm and thus are effective patterning masks for planarizing layers such as hard-baked HPR-204. At 100 μm of O_2 , the latter material is etched about 40 times faster than either methacrylate resin. P(SI-OM) is sensitive to short wavelength (≤ 260 nm) radiation. A resin containing 25% oxime requires an exposure dose of 0.25 J/cm^2 to delineate 0.75 and 1.0 μm lines and spaces. These materials are potentially useful in a bilevel resist system.

Incorporation of silicon into organic polymers generates materials which are resistant to oxygen reactive ion etching (RIE) and thus are potentially useful in two-level photoresist processes. The effects of silicon were first reported by Taylor and Wolf (1), who suggested that a protective layer of SiO_2 was formed when the polymers were exposed to an oxygen discharge. These findings laid the basis for the development of resist systems which could be employed in a multilevel RIE pattern-transfer process as depicted in Fig. 1. Specifically, the chemical incorporation of silicon into a novolak-base polymer (2) has proved effective in enhancing the oxygen RIE resistance of these polymers. Several silicon-substituted, negative, deep-UV resists have also been reported. The trimethylsilyl group has been used to lower the oxygen discharge erosion rate of styrene-chlorostyrene (3) and styrene-chloromethylstyrene (4) copolymers, and thin films of dialkylsiloxane polymers have themselves proved useful as deep-UV negative resists (5).

Since a positive deep-UV resist is desirable to ensure high resolution capabilities, we previously investigated the efficacy of siloxane substitution on methacrylate polymers for improving the oxygen RIE resistance of poly(methyl methacrylate) (PMMA) without destroying its high resolution properties (6). Terpolymers of methyl methacrylate, methacrylic acid, and pentamethyldisiloxypropyl methacrylate are high resolution, RIE-resistant materials, which, however, lack photosensitivity. While improvements in resist sensitivity should obtain upon incorporation of such photoreactive chromophores as the α -keto-oxime in 3-oximino-2-butanone methacrylate (7-9) preparation of the four-component polymers may be complicated.

Sensitive, high resolution, oxygen RIE-resistant, deep-UV resists have been prepared using trimethylsilylmethyl methacrylate and 3-oximino-2-butanone methacrylate as components. Etching rate ratios relative to hard-baked HPR-204 (novolac-quinonediazide conventional photoresist) of 12 to 45:1 have been observed, and it is demonstrated that these resists are useful as oxygen RIE masks in two-level photoresist systems employing dry etching pattern-transfer techniques.

Experimental

Materials.—3-Oximino-2-butanone methacrylate was prepared as described in the literature (7). Trimethylsilylmethyl methacrylate was obtained from Petrarch Systems, Incorporated. High molecular weight ($M_w \sim 250,000$) poly(methyl methacrylate) was obtained from the Aldrich Chemical Company and used without further purification. HPR-204 photoresist was obtained from the Philip A. Hunt Chemical Company. Hexane, cyclohexane, cyclopentanone (Gold Label spectroquality solvents), and methyl isobutyl ketone were obtained from the Aldrich

Chemical Company. Ethyl acetate and toluene were obtained from MCB, Incorporated.

Poly (trimethylsilylmethyl methacrylate) and copolymers of trimethylsilylmethyl methacrylate and 3-oximino-2-butanone methacrylate were prepared and purified by standard techniques. Conversions were carried out to $<20\%$. Molecular parameters for these polymers are given in Table I.

Processes.—Under typical processing conditions, the polymer (10 weight percent [w/o]) was dissolved in cyclopentanone, filtered through a 0.5 μm membrane, applied with a spin coater (Headway Research Spinner, Model EC101) operated at 4000 rpm, to either silicon, hard-baked HPR-204 on silicon, or NaCl substrates and baked at 150°C for 60 min. HPR-204-coated silicon substrates were prepared in the same manner to give nominal 1 μm thick films which were baked at 250°C for 60 min.

The oxygen RIE resistance of each polymer was determined by etching the appropriately coated silicon substrate in a Cooke Vacuum Products, Incorporated, Model C71 RIE system. The etching rates were determined from the slope of the least squares linear fit of points obtained

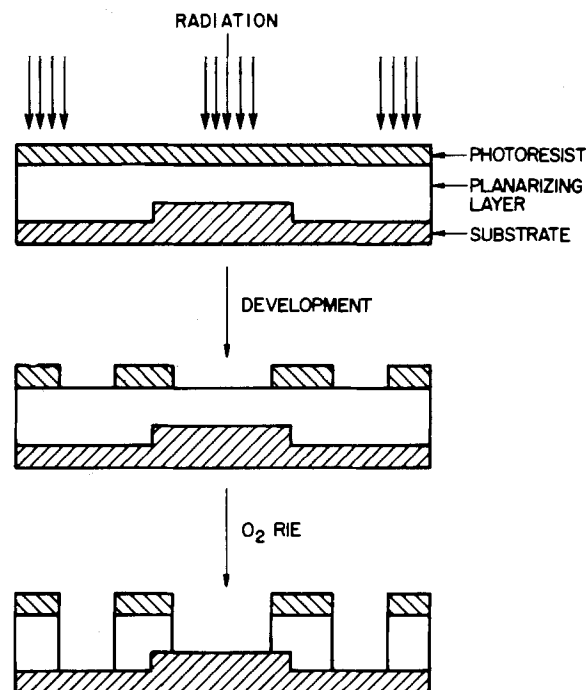


Fig 1. Schematic representation of the two-level resist process in which the top level is a deep-UV sensitive resist.

Table I. Polymer molecular parameters

Polymer	Mole ratio ^a	Weight percent silicon ^b	Molecular weight ^c		T_g	Absorbance ^d	
			$M_w \times 10^{-5}$	M_w/M_n		215 nm (λ_{max})	248 nm
P(SiMA) ^e	—	14.82	2.02	1.78	108°C	0.13	0
P(SI-OM) ^f	90:10	14.33	1.49	2.36	85°C	0.83	0.06
P(SI-OM)	77:23	10.80	1.01	2.23	80°C	>1	0.20
P(SI-OM)	62:38	9.61	1.25	3.46	91°C	>1	0.25

^a This refers to the ratio of the two components as determined by elemental analysis.

^b As determined by elemental analysis.

^c GPC analysis using polystyrene equivalent molecular weights.

^d The absorbance is given for $1 \mu\text{m} \pm 10\%$ thick films.

^e P(SiMA) refers to poly(trimethylsilylmethyl methacrylate).

^f Si refers to trimethylsilylmethyl methacrylate. OM refers to 3-oximino-2-butanone methacrylate.

from a measurement of thickness as a function of elapsed etching time. The rates are essentially linear with time.

Resist sensitivity and contrast were ascertained by contact/proximity printing the coated substrates through a quartz Multidensity Resolution Target (Model B, Opto-Line Corporation) with a deep-UV exposure system (Model 29DH, Optical Associates, Incorporated) optimized for use at 260 ± 20 nm.

Infrared spectra of resist films coated on NaCl substrates were obtained with a Nicolet Model 5DX FT-IR spectrophotometer.

Results and Discussion

Poly(trimethylsilylmethyl methacrylate) [P(SiMA)] was examined for its physical properties and ability to withstand oxygen RIE treatment. The relatively high glass transition temperature (T_g) of this material (108°C) obviates the need for enhancement via copolymerization. It is possible to increase the photosensitivity of the system

through incorporation of such monomers as 3-oximino-2-butanone methacrylate. To this end, three different compositions of poly(trimethylsilylmethyl methacrylate-co-3-oximino-2-butanone methacrylate) [P(SI-OM)] were prepared. In all cases, the amount of silicon actually incorporated into the polymer was lower than that anticipated from the monomer ratios. While this may result partially from solvent trapped in the resin, it also implies that the reactivity ratios (r) for the two components are unequal. A higher value for the α -keto-oxime would explain the increased incorporation of the nonsilicon containing species.

Examination of Table I reveals that the absorbance of (nominal) $1 \mu\text{m}$ films of P(SI-OM) increases with increasing keto-oxime content. Absorbance values are listed for 248 nm and for the maximum at 215 nm. Figure 2 compares the absorption spectra of P(SiMA) and P(SI-OM)

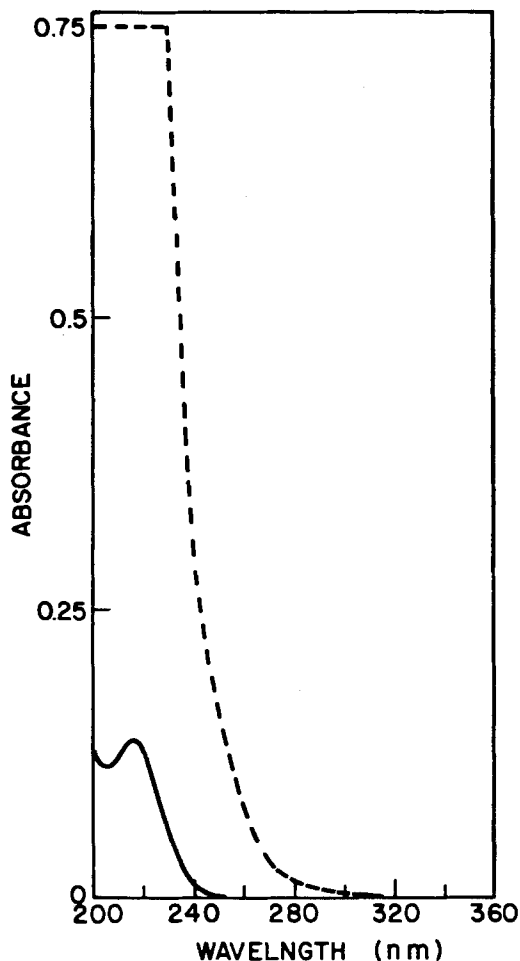


Fig. 2. The absorption spectra of nominal $1 \mu\text{m}$ films of P(SiMA) (—) and P(SI-OM) (77:23) (---).

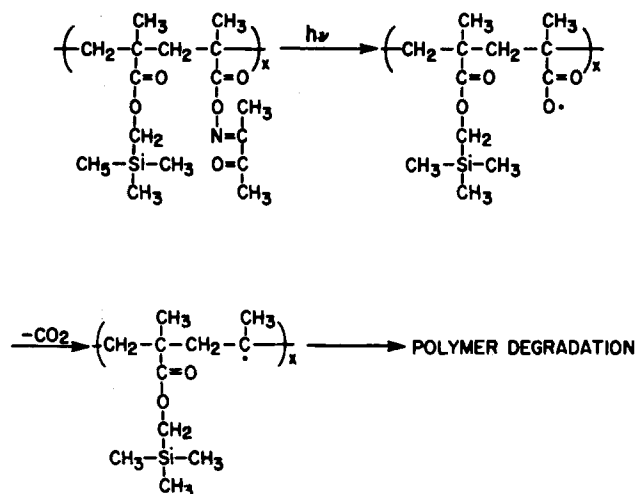


Fig. 3. Scheme depicting the photodegradation of P(SI-OM).

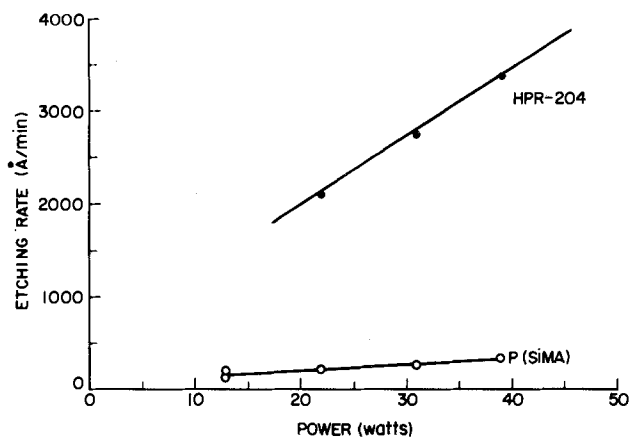


Fig. 4. A comparison of the etching rates of HPR-204 (•) and P(SiMA) (○) as a function of power (the power density ranged from ~ 0.15 to 0.6 W/cm^2).

(77:23). The degradation mechanism of these materials should be similar to that observed for PMMA and copolymers of methyl methacrylate and 3-oximino-2-butanone methacrylate, and is outlined in Fig. 3.

Oxygen RIE behavior.—The oxygen RIE rates of P(SiMA) and P(SI-OM) at a pressure of 20 μm are given in Table II. The values for PMMA and HPR-204 are included as reference points. As expected from the study of etching rate vs. silicon content in the series of pentamethyldisiloxypropyl methacrylate polymers (6) (where only small incremental reductions in etching rate were observed with increased silicon content above about 8-10%), only minor variations in the oxygen RIE rate are observed for the polymers investigated in the current study.

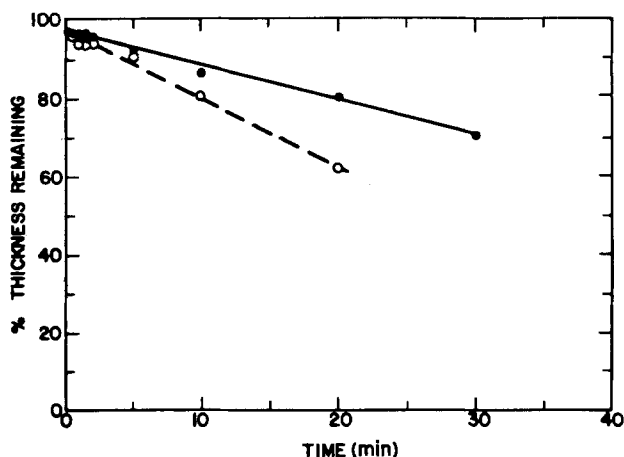


Fig. 5. A plot of the etching rate of P(SiMA) vs. time at oxygen pressures of 20 (O) and 100 μm (•) (RF power \approx 20W).

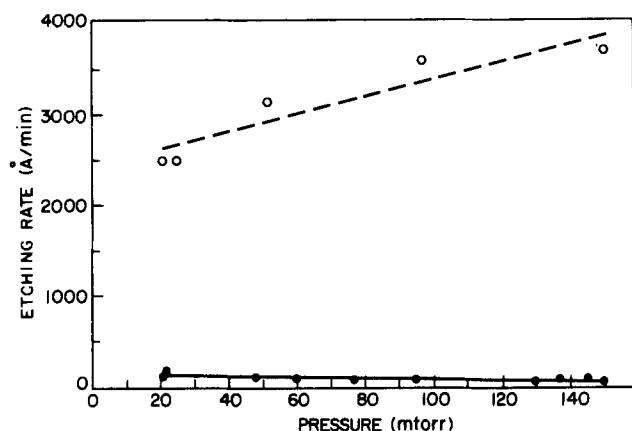


Fig. 6. A comparison of the RIE rates of HPR-204 (---) and P(SiMA) (—) as a function of oxygen pressure (RF power \approx 20W).

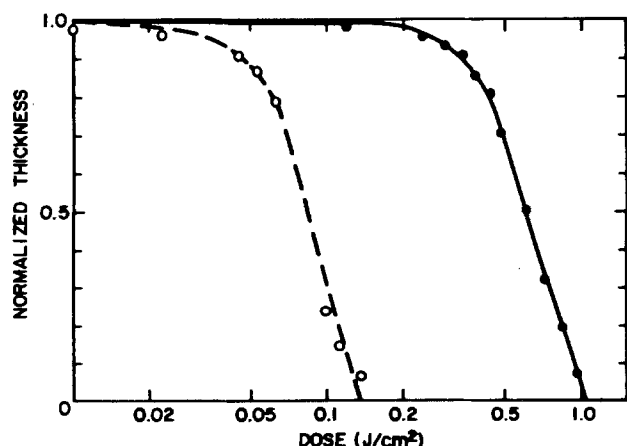


Fig. 7. Contrast curves obtained for P(SiMA) (—) and P(SI-OM) (62:38) (---).

Table II. Etching rate of silicon containing polymers as a function of silicon content and oxygen pressure

Polymer	Mole ratio	Weight percent Si	O ₂ RIE rate ($\text{\AA}/\text{min}$)	
			at 20 μm	at 100 μm
PMMA	—	0.0	3700	—
HPR-204	—	0.0	1750	3250
P(SiMA)	—	14.8	160	80
P(SI-OM)	90:10	14.33	70	(25)
P(SI-OM)	77:23	10.80	125	70
P(SI-OM)	62:38	9.61	150	70

While an increase in power effects an increase in etching rate of both HPR-204 and P(SiMA) (Fig. 4), an increase in oxygen pressure results in a decrease in the etching rate of P(SiMA). Figure 5 depicts the etching rate vs. time for P(SiMA) at low and high oxygen pressure. A comparison of the rates obtained for HPR-204, P(SiMA), and P(SI-OM) at an oxygen pressure of 20 vs. 100 μm is given in Table II. The silicon substituted species generally show a decrease in etching rate with increased pressure, while the converse is true for HPR-204. This effect appears linear with respect to pressure, as seen in Fig. 6, which depicts the RIE rate of HPR-204 and P(SiMA) as a function of oxygen pressure. An etching rate ratio ranging from 12:1 to >40:1 may be obtained for the silylated polymers vs. HPR-204.

The divergence observed in the etching rates of P(SiMA) and HPR-204 vs. oxygen pressure (see Fig. 6) is readily explained. An increase in pressure effects an increase in the concentration of reactive species in the discharge. Thus, a polymer such as HPR-204, which generates only volatile etching products, will erode more rapidly as the pressure rises. However, P(SiMA) represents a situation in which both volatile and nonvolatile (*i.e.*, SiO_2) products result from RIE. Thus, if sufficient silicon is present in the polymer, an increased concentration of reactive oxygen species will more efficiently produce a uniform barrier of silicon oxide which will protect the underlying polymer from further RIE. Concomitantly, the increased pressure causes a decrease in the sputtering efficiency of the discharge which slows the removal of the silicon oxide layer and further enhances the etching rate differential between the HPR-204 and P(SiMA).

Oxygenated silicon species are formed upon oxygen RIE treatment of P(SiMA) and its α -keto-oxime analogs. Although we have been unable to conclusively show the formation of SiO_2 , it is clear from the changes in the IR spectra before and after etching that Si-O bonds have been generated.

Lithographic characteristics.—The silylated polymers are positive working photoresists whose sensitivities are far improved over the parent, PMMA. The exposure dose required for complete development of the irradiated regions with minimum loss of film thickness in the unirradiated areas is given in Table III. It was not possible to

Table III. Polymer lithographic characteristics

Polymer	Mole ratio	Developer ^a	Sensitivity (J/cm^2)		Contrast
			A ^b	B ^c	
PMMA	—	MIBK ^d	—	3.6	\sim 2
P(SiMA)	—	C_6H_{12} -MIBK(5:2)	1.05	1.5	2.1
P(SI-OM)	90:10	—	—	—	—
P(SI-OM)	77:23	C_6H_{14} ^f	0.13	0.30	1.5-2
P(SI-OM)	62:38	C_6H_{12}	0.14	0.25	2.2

^a For 60s.

^b Determined as the exposure required to clear an area of 1 cm^2 (film thickness \sim 0.7 μm).

^c Determined as the exposure required to delineate 1 μm lines and spaces (film thickness \sim 0.7 μm).

^d Methyl isobutyl ketone.

^e Cyclohexane.

^f Hexane.

find a suitable developing solvent for P(SI-OM) (90:10), *i.e.*, the polymer was simply too soluble in all solvents examined. Generally, silylation of methacrylate polymers affords increased solubility in organic solvents. This is evidenced by the need to use the hydrocarbon solvents hexane and cyclohexane for the development of P(SI-OM) (77:23) and P(SI-OM) (62:38), respectively.

The improved absorption characteristics of P(SI-OM) relative to P(SiMA) (see Fig. 2 and Table I) lead to improved sensitivity of these copolymers relative to P(SiMA) and PMMA (Table III). The exposure required to clear an area of 1 cm^2 drops from 1.05 J/cm^2 for P(SiMA) to 0.13 J/cm^2 for P(SI-OM) (77:23). Table III also gives the dose required to delineate 0.75 and $1 \mu\text{m}$ features in the

resists examined. Of interest are the doses required for P(SI-OM) (77:23) and P(SI-OM) (62:38), which are 0.3 and 0.25 J/cm^2 , respectively.

Resist contrast (γ), the rate at which a resist responds to incident light, is given in Table III along with the sensitivity data. Figure 7 depicts the contrast curves for P(SiMA) and P(SI-OM) (62:38). The values are approximately equal to that of PMMA (~ 2).

The high resolution characteristics of PMMA have been retained in the silicon containing analogs. Figure 8 depicts lines and spaces with nominal dimensions of 0.75 , 1.0 , and $0.75 \mu\text{m}$ contact/proximity printed in $\sim 0.7 \mu\text{m}$ of P(SiMA), P(SI-OM) (85:15), and P(SI-OM) (62:38), respectively. The developers employed were those used to determine resist sensitivity and contrast, and are given in Table III. Deviations from the stated feature sizes result primarily from linewidth variations in the mask and imperfect mask to wafer contact.

Two-level photoresist processing.—The high resolution characteristics and oxygen RIE resistance of P(SiMA) and P(SI-OM) combine to produce deep-UV positive resists which act effectively as etching masks for a two-level pattern-transfer process such as that depicted in Fig. 1. Micron and submicron features printed in these resists are readily transferred through a hard-baked HPR-204 planarizing layer to the substrate. Figures 9a and 9b depict, respectively, nominal 0.75 and $1.25 \mu\text{m}$ lines and spaces obtained in P(SiMA) ($\sim 0.7 \mu\text{m}$) after RIE pattern transfer into HPR-204 ($\sim 1.2 \mu\text{m}$) at an oxygen pressure of $25 \mu\text{m}$. The effect of raising the pressure to $95 \mu\text{m}$ is

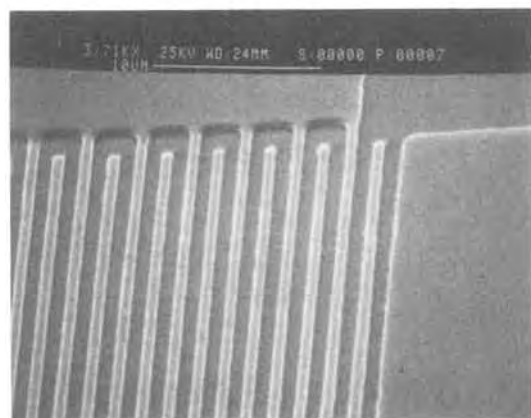
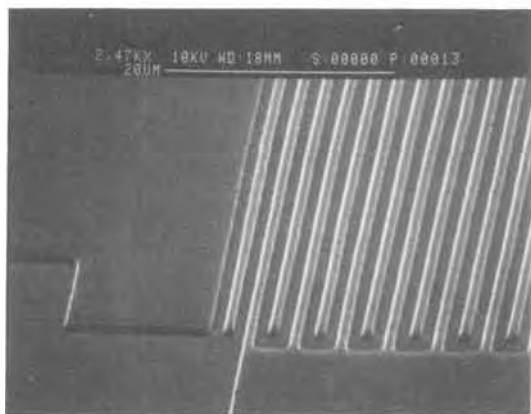
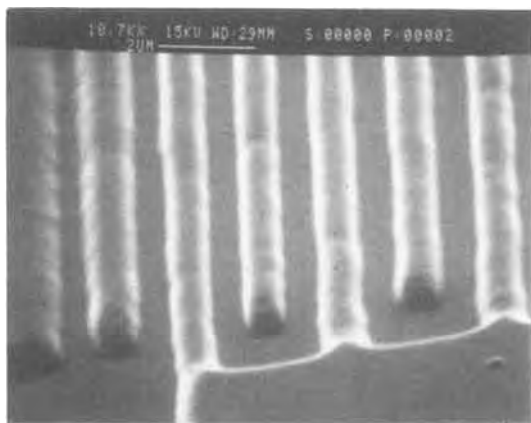


Fig. 8. SEM micrographs depicting nominal $0.75 \mu\text{m}$ lines and spaces printed in P(SiMA) top, $1.0 \mu\text{m}$ lines and spaces printed in P(SI-OM) (77:23), middle, and $0.75 \mu\text{m}$ lines and spaces printed in P(SI-OM) (62:38) bottom.

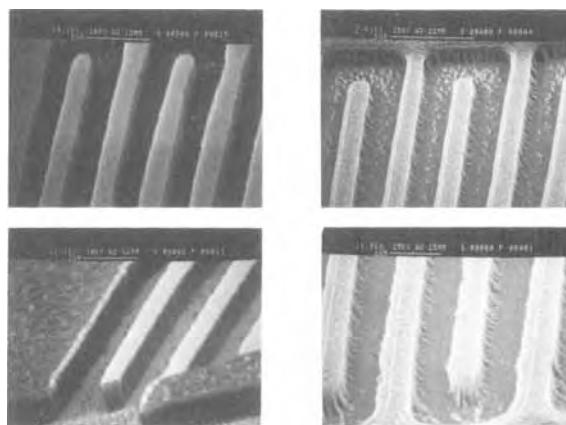


Fig. 9. SEM micrographs depicting nominal (a) 0.75 and (b) $1.25 \mu\text{m}$ lines and spaces printed in P(SiMA) and RIE pattern transfer at $25 \mu\text{m}$ O_2 , and (c) 1.5 and (d) $1.25 \mu\text{m}$ lines and spaces printed in P(SiMA) after RIE pattern transfer at $95 \mu\text{m}$ O_2 .

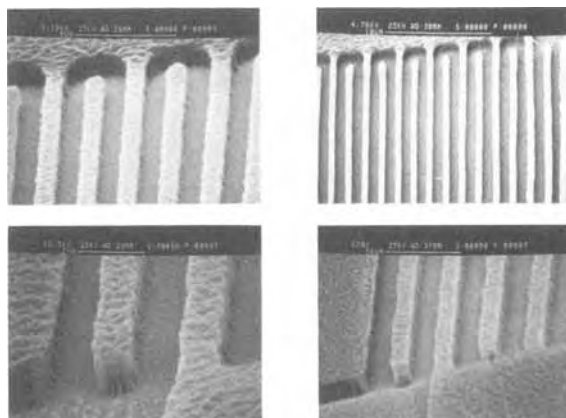


Fig. 10. SEM micrographs depicting nominal (a) 1.0 and (b) $1.25 \mu\text{m}$ lines and spaces printed in P(SI-OM) (77:23) and (c) 0.75 and (d) $1.5 \mu\text{m}$ lines and spaces printed in P(SI-OM) (62:38) after RIE pattern transfer at $95 \mu\text{m}$ O_2 .

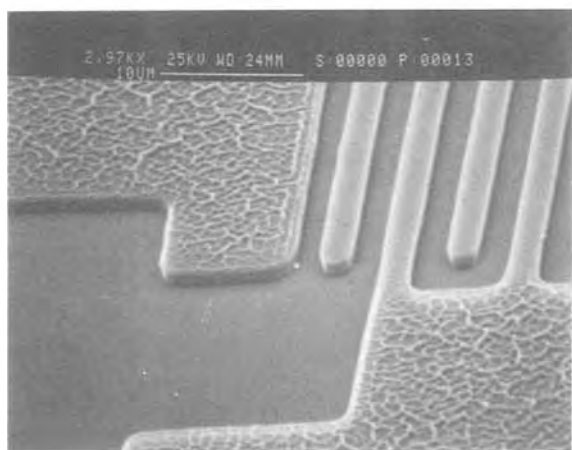
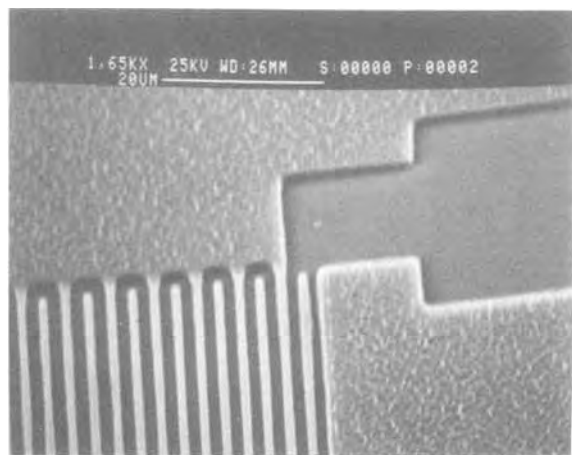


Fig. 11. SEM micrographs depicting nominal 1.25 μm , top, and (b) 2.0 μm , bottom, lines and spaces printed in P(SiMA) after RIE pattern transfer at an oxygen pressure of 25 μm followed by dilute HF rinse.

shown in Fig. 9c and 9d, which depict 1.5 and 1.25 μm lines and spaces, respectively, printed in the same resist. High resolution is observed at both pressures. However, the effects of residual photoresist on the surface of the planarizing layer are more pronounced at the higher oxygen pressure; for example, note the ragged left edge of the 1.25 μm lines shown in Fig. 9d, which is presumably due to both a decrease in sputtering and etching rate of the resist. Also, the surface of the polymer appears less rippled when higher oxygen pressures are employed. Decreased sputtering may result in decreased redeposition of material. Figure 10 depicts nominal 1.0 and 1.25 μm , and 0.75 and 1.5 μm lines and spaces printed in P(SI-OM) (77:23) and P(SI-OM) (62:38), respectively, followed by a 9 μm oxygen RIE pattern transfer. In these cases, the

photodefining layers were clearly delineated. While the increase in oxygen pressure does effect slight isotropic etching (compare, in particular, Fig. 10b with 9b), somewhat less residue is apparent in the larger open spaces because of a decrease in sputtering and consequent redeposition of material (*i.e.*, the effects of backsputtering are alleviated). With either high or low oxygen pressure, the residue appears to be primarily SiO_2 , which can be removed from the substrate by a brief (1 min) rinse with dilute aqueous HF (5%). This is demonstrated in Fig. 11, which depicts 1.25 and 2.0 μm lines and spaces printed in P(SiMA) followed by oxygen RIE pattern transfer and an HF rinse.

Summary

P(SiMA) has been shown to be a high resolution, oxygen RIE-resistant, deep-UV photoresist. Incorporation of 3-oximino-2-butanone methacrylate into this polymer renders it sensitive to short wavelength (≤ 260 nm) radiation without loss of resolution or etching resistance. P(SI-OM) (62:38) requires an exposure dose of 0.25 J/cm^2 to delineate 0.75 and 1.0 μm lines and spaces. The oxygen RIE rate of the polymer is on the order of 100 $\text{\AA}/\text{min}$ and decreases with a rise in pressure. P(SiMA) and P(SI-OM) (77:23) and (62:38) are effective etching masks for such planarizing materials as hard-baked HPR-204. Oxygen pressure-dependent etching ratios relative to the HPR-204 ranging from 12:1 to 45:1 have been observed.

Acknowledgment

The authors gratefully thank M. Y. Hellman for polymer molecular weight determinations.

Manuscript submitted Nov. 10, 1984; revised manuscript received Jan. 21, 1985.

AT&T Bell Laboratories assisted in meeting the publication costs of this article.

REFERENCES

1. G. N. Taylor and T. M. Wolf, *Polym. Eng. Sci.*, **20**, 1087 (1980).
2. C. W. Wilkins, Jr., E. Reichmanis, T. M. Wolf, and B. C. Smith, *J. Vac. Sci. Technol.*, To be published.
3. S. A. MacDonald, A. S. Steinmann, H. Ito, M. Hatzakis, W. Lee, H. Hiraoka, and C. G. Willson, Paper Presented at the 1983 International Symposium on Electron, Ion and Photon Beams, Los Angeles, CA, May 31-June 3, 1983.
4. M. Suzuki, K. Saigo, H. Gokan, and Y. Ohnishi, *This Journal*, **130**, 1962 (1983).
5. J. M. Shaw, M. Hatzakis, J. Parazczak, J. Liutkus, and E. Babich, in "Proceedings of SPE Reg. Technical Conference on Photopolymers, Principles, Processes, and Materials," p. 25, Nov. 8-10, 1982, Society of Plastics Engineers, Ellenville, NY (1982).
6. E. Reichmanis and G. Smolinsky, *Proc. SPIE*, **469**, 38 (1984).
7. C. W. Wilkins, Jr., E. Reichmanis, and E. A. Chandross, *This Journal*, **127**, 2510 (1980).
8. E. Reichmanis, C. W. Wilkins, Jr., and E. A. Chandross, *ibid.*, **127**, 2514 (1980).
9. E. Reichmanis and C. W. Wilkins, Jr., "Polymer Materials for Electronic Applications," E. D. Feit and C. W. Wilkins, Jr., Editors, pp. 29-43, ACS Symposium Series 184 American Chemical Society, Washington, DC (1982).
10. A. I. Yezrielev, E. L. Brokhina, and Y. S. Roskin, *Vysokomol. Soedin.*, **A11**, 1670 (1969).

An Optical Study of the Deposition, Discharge, and Recharge of Manganese Dioxide Films

J. L. Ord* and Z. Q. Huang¹

Department of Physics, University of Waterloo, Waterloo, Ontario, Canada N2L 3G1

ABSTRACT

The galvanostatic electrodeposition of manganese dioxide films onto a platinum substrate is studied over a thickness range from 0 to 2000 nm. At the upper end of the thickness range, optical absorption causes the ellipsometer null settings to approach within 0.02° of the infinite thickness limit, at which the films are indistinguishable from substrates. The optical extinction coefficient increases with film thickness over the range 0-50 nm, but from 50 to 160 nm the films have optical constants which are independent of thickness but which depend on the deposition current density. Beyond 160 nm, the optical data become progressively more difficult to interpret in terms of uniform isotropic or anisotropic film models. When relatively thin films (50 nm) are transferred to alkaline electrolyte and are cycled galvanostatically, optical changes are observed which correlate well with the electrochemical behavior for both reversible partial discharge cycles and irreversible complete discharge cycles.

In a previous ellipsometric study (1), Spricis *et al.* found the optical properties of manganese dioxide films to be quite sensitive to the deposition conditions. The deposition was carried out using a sequence of potentiostatic pulses which enabled the process to be studied using a conventional ellipsometer, and increases in deposition potential and pulse duration were both reported to lower the extinction coefficient of the film by as much as a factor of two. For thicknesses below 40 nm, both the refractive index and the extinction coefficient were reported to vary somewhat with film thickness, and above about 70 nm the optical data were found to deviate from the theoretical curves. The thickness dependences were attributed to insular structure in the thinner films and surface roughening in the thicker films, and the extinction coefficient variation was attributed at least partially to a change in porosity.

In this paper, we use an automated ellipsometer to follow the galvanostatic deposition and charge-discharge cycling of manganese dioxide films. We study deposition over a current density range of 64 for thicknesses up to 2000 nm to see whether the reported dependence on thickness and deposition rate is found also under galvanostatic conditions. In the optical analysis, we use both isotropic and anisotropic film models to see whether or not the dependence of refractive index on film thickness is an artifact resulting from isotropic analysis of an anisotropic system. The objective of the study of charge-discharge cycles in alkaline electrolyte is more to evaluate the usefulness of ellipsometry for such measurements than to provide any definitive statement about the processes involved. Ellipsometry is an effective tool for the study of homogeneous film-conversion processes, but heterogeneous processes can only be studied if the film remains stratified.

This investigation forms part of our continuing study of oxidation and reduction processes which involve ionic transport through thin solid films. Included in this category are both the growth of films of fixed oxidation state by the anodic oxidation of a substrate and the oxidation or reduction without film growth which occurs in batteries and electrochromic displays. Our ellipsometric studies of charge-discharge cycles on nickel hydroxide (2, 3) and color-bleach cycles on tungsten oxide (4) and iridium hydroxide (5) lead us to conclude that all of the processes involve the homogeneous conversion to oxyhydroxide by a mechanism in which hydrogen ions from the electrolyte move into the film and back out again, exactly the same mechanism proposed for the initial reversible stage of the discharge of manganese dioxide (6). DeSmet and co-workers have carried out ellipsometric

investigations of heterogeneous electrochromic processes in the anodic oxides of vanadium (7) and molybdenum (8), but these processes can be reversed and may have little in common with the heterogeneous stage of the discharge of manganese dioxide.

Experimental

The manganese dioxide films were deposited onto a platinum single-crystal electrode from 0.1M MnSO₄ + 0.017M H₂SO₄, the same pH 2 electrolyte used in the earlier potentiostatic study (1). The alkaline electrolyte used for the charge-discharge cycles was 0.05M NaOH. The cell consists of a hollow equilateral glass prism with standard-taper joints for the working electrode holder, a platinum counterelectrode, a gas dispersion tube, and the mercury-mercurous sulfate electrode to which all potentials quoted in this paper are referenced. The electrolyte was maintained at room temperature (22°C), and was air saturated, except in experiments testing for the effect of dissolved oxygen, where it was argon saturated. The working electrode is in the form of a cylinder with a flat on one side for optical measurements, and when it is clamped between Teflon washers in its holder and mounted in the cell, it exposes a vertical surface 1.44 cm² in area to the electrolyte.

The self-nulling ellipsometer uses quadrature Faraday modulation decoded by a two-phase lock-in amplifier and fed back to ministepping drives through voltage-to-frequency converters. Under typical operating conditions, the instrument has a response time of a few tenths of a second and a resolution of a few thousandths of a degree. The angle of incidence is set at 60° to accommodate the equilateral cell, and refractive index values quoted here are for a wavelength of 632.8 nm, the wavelength of the helium-neon laser source.

A process-control computer operates the circuitry used with the cell and records current and potential along with polarizer and analyzer settings at specified time intervals. Potentials are digitized by a 16-bit analog-to-digital converter with a 25 μs conversion time. The operation of the ellipsometer is monitored on a four-trace oscilloscope, and progress of the experiment is followed on two storage displays and an X-Y plotter which are updated by the computer.

Results and Discussion

Figure 1 shows results from a deposition experiment at a current density of 44 μA/cm². Aside from a minor initial overshoot, the potential-time plot in the lower portion of the figure is featureless. However, the polarizer *vs.* analyzer (P-A) plot of the ellipsometer null settings in the upper portion of the figure shows a great deal of structure, spiraling outward from point A to form open loops, then spiraling inward toward a different point as the film becomes quite thick. P-A curves of this type are characteris-

*Electrochemical Society Active Member.

¹ Permanent address: Department of Chemistry, Chongqing University, Chongqing, Sichuan, China.

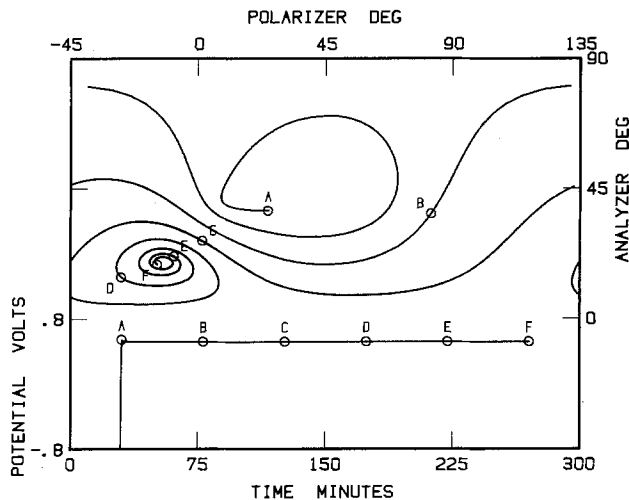


Fig. 1. Galvanostatic deposition onto a platinum substrate at $44 \mu\text{A}/\text{cm}^2$.

tic of the growth of a film which absorbs some of the light passing through it. An ellipsometer measures the change in polarization resulting from interference between light reflected at the electrolyte-film and film-substrate interfaces, and growth of a transparent film produces a P-A "loop," which closes when the product of film thickness and the cosine of the angle of refraction is equal to half the wavelength of light in the film. If the film is partially absorbing, the loop does not close, and an outward spiral results. Light reflected at the substrate interface traverses the film twice before superimposing on light reflected at the electrolyte interface, and hence its amplitude becomes progressively smaller as the film grows if the film is optically absorbing. When film growth reaches the point where the amplitudes are greatly different, interference can have only a small effect on the polarization of the reflected light, and the P-A locus spirals rapidly inward. The point toward which it spirals is the point at which the film becomes the substrate as far as optical measurements are concerned. For the deposition experiment in Fig. 1, this point (not shown in the figure) is reached by the end of a 6h deposition.

Deposition experiments at the other current densities give optical results which are similar in their general character, but different in specific detail. The P-A curves all start at the same point (determined by the platinum substrate) and have a spiral structure, but they differ in the number of loops in the inward and outward spirals, and the asymptote of the inward spiral. Figure 2 shows the first-loop data for current densities ranging from 11 to $704 \mu\text{A}/\text{cm}^2$ (the loop at $704 \mu\text{A}/\text{cm}^2$ overlaps the loop at $176 \mu\text{A}/\text{cm}^2$). The ten points at fixed charge interval used in the analysis are identified on each curve. In the analysis, a value is first chosen for the film index N , then the P-A data are used to calculate a set of values for the film thickness L and extinction coefficient K . The value of N is then varied to minimize the standard deviations in the values of K and L/Q , the film thickness to accumulated charge ratio (9). This analysis procedure implicitly assumes that the composition and structure of the film do not vary appreciably as the film grows, and hence N and K are independent of film thickness. Since this may not be true here, the thickness range over which deviations are minimized is also varied in the analysis.

Analysis of the data from Fig. 2 using this procedure shows that the films have well-defined properties over the thickness range of 50-160 nm. The value of N , 1.9, does not depend on deposition current density, but the values of K decrease from 0.187 at $11 \mu\text{A}/\text{cm}^2$ to 0.096 at $704 \mu\text{A}/\text{cm}^2$, and the standard deviations in K and the L/Q ratio are approximately 4 and 2%, respectively. Figure 3 shows the dependence of film thickness on accumulated charge at each deposition current density (the $44 \mu\text{A}/\text{cm}^2$ results overlap the $176 \mu\text{A}/\text{cm}^2$ results and are not

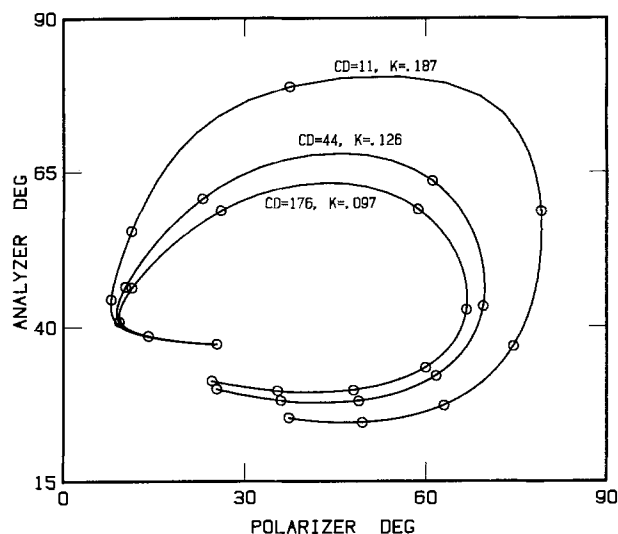


Fig. 2. First-cycle optical data for galvanostatic deposition onto a platinum substrate at current densities from 11 to $704 \mu\text{A}/\text{cm}^2$. The optical analysis uses a common value of 1.9 for N and finds the value of K which gives the best fit to the data. The cycle at $704 \mu\text{A}/\text{cm}^2$ (with $K = 0.096$) overlaps the cycle at $176 \mu\text{A}/\text{cm}^2$ and is not shown.

plotted). Least squares lines fitted to the results have slopes of 2.62, 2.97, 3.00, and $2.78 \text{ nm}/\text{mC}/\text{cm}^2$ in order of increasing deposition current density.

If we know the composition of the film and the number of electrons transferred to the electrode per molecule deposited, we can use the slopes in Fig. 3 to calculate values for the film density (assuming roughness and efficiency factors of unity). If we assume that the films are entirely manganese dioxide deposited by transferring two electrons per molecule (10), we calculate density values which range from 1.50 to $1.72 \text{ g}/\text{cm}^3$ and bracket the $1.65 \text{ g}/\text{cm}^3$ found under potentiostatic deposition conditions (1). If we assume that the film contains some MnOOH and that deposition requires the transfer of only 1.9 electrons per molecule on average (11), we get slightly higher values, but the average is still only about one-third the density of a compact film of manganese dioxide. This low a density value does not appear to be consistent with a refractive index as high as 1.9.

Since neither roughness nor efficiency factors can account for a density value which is unreasonably low, we were forced to consider other possibilities. We ruled out effects due to dissolved oxygen when deposition in

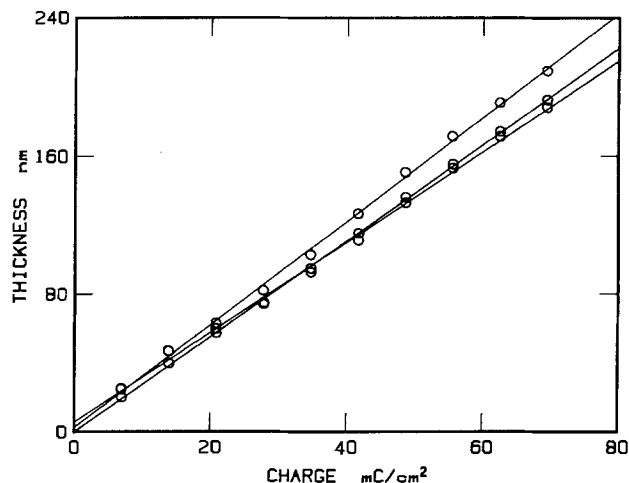


Fig. 3. Dependence of film thickness on accumulated charge for the data from Fig. 2. The slope is steepest at a deposition current density of $176 \mu\text{A}/\text{cm}^2$, shallowest at $11 \mu\text{A}/\text{cm}^2$, and intermediate at $704 \mu\text{A}/\text{cm}^2$. The data at $44 \mu\text{A}/\text{cm}^2$ overlap the data at $176 \mu\text{A}/\text{cm}^2$ and are not shown.

deaerated electrolyte gave a density value which agreed with the value in air-saturated electrolyte at the same current density to within half a percent. We tested for the presence of other deposition processes by tracking film growth optically after opening the circuit, and found that at a deposition current density of $44 \mu\text{A}/\text{cm}^2$ perhaps 10% of the film growth could be attributed to nonelectrochemical processes. The only alternative left is to assume that manganese dioxide is deposited by a one-electron process similar to the solid phase oxidation of MnOOH . If we make this assumption, and assume further that the 10% MnOOH content of the film is not electrochemically deposited, we calculate density values which are on the order of three quarters of the density of a compact film. We will test these assumptions later when we compare the deposition charge with the charge passed on charge-discharge cycles in alkaline electrolyte

Films thinner than 50 nm appear to have extinction coefficients which are lower than those fitted over the 50-160 nm thickness range. This is most likely due to the fact that the film nucleates in an insular structure and grows into a uniform film by the time its thickness reaches 50 nm. The 160 nm upper limit of the fitting range, on the other hand, appears to be due to a limitation of the optical model, not to a change in film structure. The model assumes homogeneous films of uniform thickness, and, although nonideal films may fit such a model over a reasonable thickness range, the deviation of the experimental data from theoretical curves generated by the model becomes progressively larger as the thickness increases. This point is illustrated in Fig. 4. The optical data in the lower portion of the figure are from the same experiment as the data in Fig. 1. Deposition on a bare platinum substrate begins at point A, and the film thickness reaches 1000 nm at point B if the proportionality between thickness and charge determined in Fig. 3 remains valid throughout the deposition. Point C, reached after 6h of deposition, marks the infinite thickness limit, the point at which the film behaves optically as if it were a substrate. Two theoretical curves for 1000 nm of film growth are shown in the upper portion of the figure. Curve A-B has $N = 1.9$ and $K = 0.126$, the values fitted to the first loop data in Fig. 2, and A-C has $N = 1.548$ and $K = 0.689$, the values obtained by treating the infinite thickness limit as a substrate. The high extinction coefficient causes growth curve A-C to approach within 0.01° of the infinite thickness limit by the time the thickness reaches 500 nm. Clearly, theoretical curve A-C does not fit the

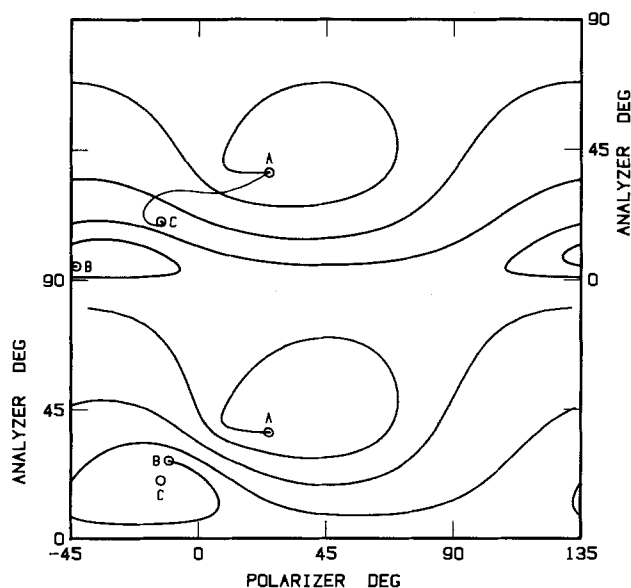


Fig. 4. Lower portion: optical data from Fig. 1 for deposition from 0 to 1000 nm (A-B) and at the infinite thickness limit (C). Upper portion: theoretical 0-1000 nm curves for films with $N = 1.9$, $K = 0.126$ (A-B) and $N = 1.548$, $K = 0.689$ (A-C).

experimental data in either the thin film or thick film regions, whereas A-B fits the data in the thin film region and describes the shape of the curve in the thick film region fairly accurately, although it spirals about a different infinite thickness limit.

We initially thought that the "tilt" between the theoretical and experimental curves in Fig. 4 was due to optical anisotropy, and we spent a great deal of time developing procedures to deal with the parameters involved in the analysis of absorbing anisotropic films. We found, however, that even for anisotropic films the measured P and A values at the infinite thickness limit require that the extinction coefficient be so high that the growth curve cannot spiral appreciably as it approaches this point. We regard the N and K values fitted to the first-loop data in Fig. 2 as characteristic of the film right through to the infinite thickness limit, and attribute the deviation between the theoretical and experimental curves in Fig. 4 to the inhomogeneous codeposition of oxide and oxyhydroxide, even though we have no quantitative model to support this viewpoint.

The results of an experiment in which the deposition is followed by cycling in 0.05M NaOH are shown in Fig. 5. The optical results in the upper portion of the figure include the deposition data (A-B), but the potential-time plot in the lower portion of the figure shows only the cycles in the alkaline cell. The current density was $44 \mu\text{A}/\text{cm}^2$ throughout, and the duration of the deposition was 405s. To avoid overlap of the cycling data, segments E-H and J-K are omitted from the optical plot.

The optical cycling data exhibit many qualitative features which correlate well with features in the electrochemical data. The optical changes on the first anodic cycle are consistent with oxidation of the MnOOH in the deposited film, and the changes on the initial restricted range cycles which reverse completely with no residual offset are consistent with reversible MnO_2 to MnOOH conversion. The first complete discharge cycle (D-E) is an inflection in the optical data at the x, which marks the beginning of a second change in the structure of the film, a change which appears irreversible. Further cycling produces progressive optical changes which correlate well with changes in the structure of the potential-time plot.

Quantitative optical analysis of the cycling data is complicated by inhomogeneity problems which are encountered when thicker films are cycled in alkaline electrolyte. Ideally, we would like to base the optical analysis on data from cycles which span a wide range of film thickness, but here our thicker film data are not reliable. To

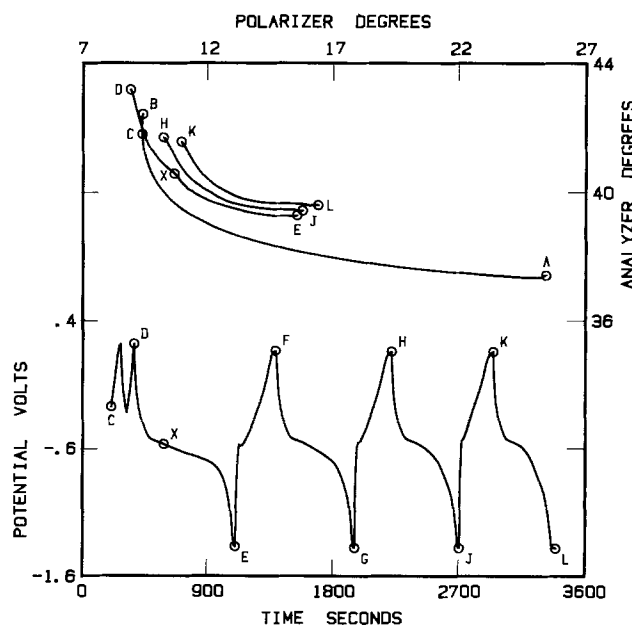


Fig. 5. Deposition at $44 \mu\text{A}/\text{cm}^2$ (A-B, optical data only) followed by cycling at $44 \mu\text{A}/\text{cm}^2$ in 0.05M NaOH.

the unaided eye, thicker films appear transparent in the reduced state and highly absorbing in the oxidized state, and they give the sharpest ellipsometric nulls in the fully reduced state. If we assume that $K = 0$ for fully reduced films, we can determine values for N and film thickness at point E in Fig. 5 without using thicker film data. However, if we take point E from Fig. 5 and a similar point obtained by cycling a thicker film, we can find common values of N and K which fit both points. The first approach gives $N = 1.64$ with an assumed $K = 0$, and the second gives $N = 1.57$, $K = 0.02$. No matter which approach we follow, we find that both N and K are significantly lowered by reduction, and that there is a corresponding 10% increase in film thickness. We do not have sufficiently reliable data on thicker films to enable us to calculate optical constants at the point x , the inflection point on the first discharge cycle, but the shape of the optical curve between D and x indicates that the conversion is a homogeneous process.

The electrochemical aspects of the conversion process can be studied by comparing the cycling time intervals with the deposition time, since the same constant current density is used throughout. The initial cycling between C and D is designed to determine the charge required to oxidize any MnOOH in the deposited film to MnO₂. The cathodic time interval required to return the film to its initial optical state, 45s, is a more reliable charge indicator than the anodic charging time because it avoids oxygen evolution corrections. The 45s interval is one-ninth of the 405s deposition time, a result which is consistent with our earlier assumption of a one-electron deposition process and a 10% MnOOH content in the deposited film. With this assumption, a 450s time interval produces a unit change in the oxidation state of the film, or in the more common nomenclature, a change of 0.5 in the value of x in MnO _{x} (6). In terms what happens to the value of x , the cycling in Fig. 5 begins from 1.95 at C, goes to 2.00, 1.95, back to 2.00 at D, then to 1.75 at x , and finally 1.19 at E. These x values appear reasonable, and it is worth noting that a change in the conversion process has been reported at $x = 1.75$, the midpoint of the MnO₂ to MnOOH conversion (11). What is more worthy of note is the fact that un-

reasonably low x values (0.54 at E) result from assuming that deposition is a two-electron process, and hence the cycling results support the conclusion we reached initially on the basis of the refractive index of the deposited film.

As we stated at the outset, the primary objective of the cycling study was to see whether the film-conversion processes in alkaline electrolyte are suitable for study by ellipsometry, and the answer appears to be a qualified yes. There is scope for further profitable ellipsometric study of the system, but problems with inhomogeneity may eventually limit the amount of useful information which can be obtained.

Acknowledgment

This work received partial support from the Natural Sciences and Engineering Research Council Canada under Grant no. A-1151.

Manuscript submitted Oct. 29, 1984; revised manuscript received Jan. 9, 1985. This was Paper 79 presented at the New Orleans, Louisiana, Meeting of the Society, Oct. 7-12, 1984.

The University of Waterloo assisted in meeting the publication costs of this article.

REFERENCES

1. A. A. Spricis, G. J. Slaidins, J. J. Abele, and J. R. Dzelme, *Elektrokhimiya*, **18**, 339 (1982).
2. M. A. Hopper and J. L. Ord, *This Journal*, **120**, 183 (1973).
3. J. L. Ord, *Surf. Sci.*, **56**, 413 (1976).
4. J. L. Ord, *This Journal*, **129**, 767 (1982).
5. J. L. Ord, *ibid.*, **129**, 335 (1982).
6. A. Kozawa and J. F. Yeager, *ibid.*, **112**, 959 (1965).
7. J. C. Clayton and D. J. DeSmet, *ibid.*, **123**, 174 (1976).
8. D. J. DeSmet, *Electrochim. Acta.*, **21**, 1137 (1976).
9. J. L. Ord, *J. Phys. (Paris)*, **44**, C10-221 (1983).
10. M. Fleishmann, H. R. Thirsk, and I. M. Tordeillas, *Trans. Faraday Soc.*, **58**, 1865 (1962).
11. F. L. Tye, Abstract 82, p. 94, The Electrochemical Society Extended Abstracts, Vol. 84-2, New Orleans, LA, Oct. 7-12, 1984.
12. W. C. Maskell, J. E. A. Shaw, and F. L. Tye, *J. Appl. Electrochem.*, **12**, 101 (1982).

Gallium Contamination of InP Epitaxial Layers in InP/InGaAsP Multilayer Structures Grown by Hydride Transport Vapor Phase Epitaxy

S. N. G. Chu,* F. A. Stevie,¹ A. T. Macrander, R. F. Karlicek, C. C. Chang,² C. M. Jodlauk, K. E. Strege, D. L. Mitcham, and W. D. Johnston, Jr.*

AT&T Bell Laboratories, Murray Hill, New Jersey 07974

ABSTRACT

Gallium contamination of InP epitaxial layers grown in CVD reactors designed for InGaAsP/InP multilayer structures was observed by secondary ion mass spectrometry (SIMS). Defect characterization of gallium-contaminated InP buffer layers by the damage-free grooving and etching technique showed misfit dislocations and an interfacial layer containing a high density of saucer pits. Cross-sectional transmission cathodoluminescence further indicated that these defects are nonradiative recombination centers. Results from x-ray double-crystal diffractometry on a successively chemically stripped InP buffer layer indicated that the misfit was confined to the region near the interfacial layer which was consistent with the SIMS profile where the gallium content peaked near the interfacial layer. By presaturating the reactor with PH_3 , the amount of the gallium which was incorporated into the InP was found to be reduced. SIMS profiles of gallium on layers grown after the withdrawal of the gallium source from the reactor indicated that the indium melt was cross contaminated even though the reactor was designed to physically exclude the gallium source from the indium source. Small amounts of As, Fe, Si, Cr, and Zn were also found. The possible mechanisms which lead to the cross contamination are discussed. The evidence seems to support the suggestion that Ga is incorporated preferentially in the growth of ternary and quaternary compounds. In a four-layer laser structure consisting of n-InP(buffer)/InGaAsP(active)/p-InP(cap)/p⁻-InGaAsP(contact) layers, both gallium and arsenic contamination were observed in p-InP and n-InP regions by Auger spectroscopy.

Hydride transport vapor phase epitaxy has been demonstrated (1, 2) to be a viable technique for the fabrication of low threshold InGaAsP/InP heterostructure laser diodes operating in the wavelength region of 1.3-1.5 μm . The high throughput and large area uniformity possible via vapor phase epitaxy render the technique particularly attractive for large-scale production. However, because of the large number of input gases involved and the complication of the gas phase reaction chemistry, the reactor design has to take into consideration various factors such as the flexibility and rapidity of switching gas types, the requirement of separate source tubes to prevent reactive gas mixing before reaching the deposition zone, and the degree of turbulence for reactive gas mixing before deposition, etc. Although we have successfully demonstrated the growth of low threshold heterostructure lasers (2), a systematic investigation of the defect structure associated with the VPE layers has only been performed recently. In this work, we report the observation of gallium contamination of InP epitaxial layers grown in a reactor designed to produce InGaAsP/InP multilayer structures. The defect structure associated with the contaminated layers has been characterized, and various factors leading to the contamination will be discussed. Results for contaminants other than gallium will also be presented.

Experimental

Undoped InP buffer layers were grown on S-doped (100) InP substrates by hydride transport vapor phase epitaxy using a computer-controlled vapor phase epitaxial reactor described previously (2, 3) and designed to grow InGaAsP/InP multilayer structures. Briefly, the VPE reactor made out of quartz tubes consisted of two temperature zones, i.e., the source zone at 800°-840°C and the deposition zone at 700°C, as shown in Fig. 1. The source zone was constituted of four separate small quartz tubes: two of the tubes were used for the metal sources (In and Ga contained in the graphite boats), the third supplied AsH_3 (4% in H_2) and PH_3 (5% in H_2), and the fourth tube was used to add dopants. The Group III metals were transported in the form of chlorides by reacting the molten metals with input HCl (5% in H_2 over In and 1.5% in H_2 over Ga) at high temperature (800°-840°C). All

the input gases were controlled by mass flow controllers interfaced with a minicomputer. The reactor had a continuous flow of purified hydrogen at 4 liter/min all the time to prevent air from leaking in. An overnight bake out period at the operating temperature was utilized each time when the reactor was restarted from shutdown for service. Since each source tube has a constant flow of H_2 at 1 liter/min, cross contamination of the elements in different source tubes was not expected. For the growth of epitaxial layers, Group III chlorides emerging from a large nozzle were mixed and reacted with Group V hydrides in front of the substrate wafer, and deposition of the III-V compound then occurred on the surface of the substrate at 700°C. The four-layer laser structure used in this study was grown by manually retracting the substrate wafer to the loading zone after the growth of each individual layer. The reactive gases were then turned off and the reactor was flushed with hydrogen. The reactive gas flow controllers were then reset for the succeeding layer and turned on after the wafer was reinserted into the deposition zone. The elapsed time between the growth of individual layers is ~5 min. No preheating and cooling of the wafer was incorporated. Prior to the growth of a multilayer structure, the melts were presaturated with chlorides. For InP, only In was presaturated with chloride, while if the structure involved both In and Ga compounds both melts were presaturated with chlorides. A typical growth condition of a four-layer structure is given in Table I.

Analysis of the laser structure was made by SIMS, Auger spectroscopy, double-crystal x-ray diffractometry, a damage-free grooving and etching technique, and cross-sectional transmission cathodoluminescence.

SIMS mass spectra and depth profiles were obtained with a Cameca IMS-3F ion microanalyzer. An O_2^+ primary

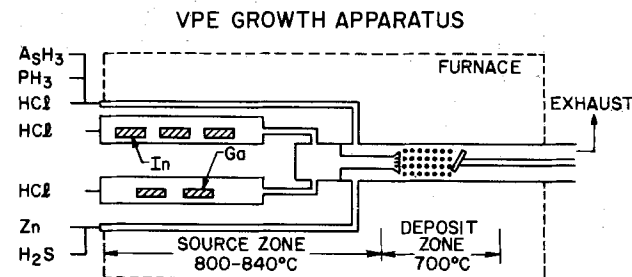


Fig. 1. Schematic diagram of computer-controlled VPE reactor

*Electrochemical Society Active Member.

¹Present address: AT&T Bell Laboratories, Allentown, Pennsylvania 18103.

²Present address: Bell Communications Research, Murray Hill, New Jersey 07974.

Table I. Typical growth condition of a four-layer structure

Reactive gases	Reactive gas mole fraction			
	n-InP	Q	p-InP	p ⁺ -Q
InCl (5% HCl/H ₂)	3.4 × 10 ⁻³	5 × 10 ⁻³	3.4 × 10 ⁻³	5 × 10 ⁻³
GaCl (1.5% HCl/H ₂)		1.5 × 10 ⁻⁴		0.7 × 10 ⁻⁴
PH ₃ (5% in H ₂)	3.4 × 10 ⁻³	1.0 × 10 ⁻³	3.4 × 10 ⁻³	4.0 × 10 ⁻³
AsH ₃ (4% in H ₂)		1.0 × 10 ⁻³		0.6 × 10 ⁻³
Typical growth rate	10 μm/h	15 μm/h	10 μm/h	15 μm/h

ion beam at a net energy of 6.1 keV was used at a current of 2000 nA. The primary beam was rastered over a 500 μm square area from which only ions from a 150 μm diam circle at the center were detected. Sputter rates were in the range of 5-25 Å/s. Only positive secondary ions were analyzed. Crater depths were measured with a profilometer. The background pressure in the sample chamber was approximately 5 × 10⁻⁹ torr with the primary beam off and 5 × 10⁻⁸ torr with the beam on.

The composition profile of the four-layer laser structure was determined by Auger spectroscopy using a Physical Electronics 590A system. Data were taken from a nominally 5° angle-lapped sample and by direct depth profiling. These two methods provided complementary data that were necessary for correctly interpreting the results. The angle-lapped sample provided data with a good signal-to-noise ratio as well as an expanded depth scale, while the depth profile data provided good depth resolution. The angle-lapped sample could be cleaned by ion milling away only about 100 Å of the surface; in fact, if more than 1000 Å was milled off, the depth scale became distorted due to differing ion milling rates of the various layers. The Auger vacuum system is pumped by ion pumps; therefore, Ne ions were used for depth profiling to avoid the Ar instabilities.

The actual lattice mismatch was measured using an x-ray double-crystal diffractometer. The first crystal of the double-crystal diffractometer was (100) LEC InP, and rocking curves were made for the (400) reflection with Cu Kα radiation.

The defect morphology of the InP epilayer was characterized using a damage-free grooving and etching technique described previously (4). This method exposes the multilayer structure on a cylindrically lapped surface by chemical means. The defect structure was revealed via a dislocation etch (5).

The distribution of the defects associated with the non-radiative recombination centers was imaged using transmission cathodoluminescence (TCL) on both grooved and cross-sectioned samples. Details for the preparation of thin cross-sectional samples containing the multilayer structure was similar to that for preparing the cross-sectional samples for TEM (6). TCL was performed inside an ETEC Autoscan SEM using a silicon photodetector.

Results and Discussion

InP buffer layer.—Gallium contamination was first examined on buffer layers grown during the initial runs after the start-up of a new reactor where the gallium source was never exposed to the input HCl. The reactor was baked out in H₂ overnight before the first run to remove oxide films on the metal sources. The as-grown surface morphology of undoped buffer layers grown during the initial runs were highly specular and revealed a typical wavy structure for VPE layers under the Nomarski interference contrast microscope. The layer thickness of sample run number 4 was around 10 μm. Although gallium was not expected to be present, SIMS mass spectra showed strong *m/e* 69 and *m/e* 71 ion intensities in the correct isotopic abundance for Ga. SIMS depth profiles indicated the Ga was concentrated in the buffer layer. X-ray wavelength dispersive analysis gave an estimated

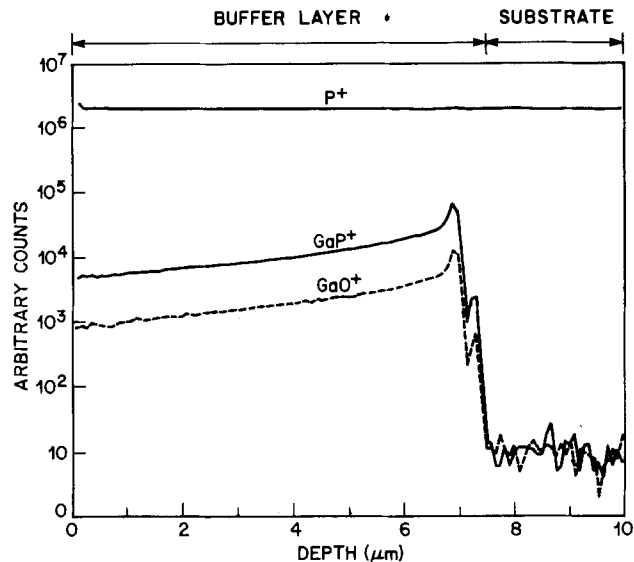


Fig 2. SIMS depth profile of ³¹P⁺, ¹⁰⁰GaP⁺, and ⁸⁵GaO⁺ in the InP buffer layer run no. 4.

concentration in the order of 1.0 atomic percent (*a/o*). The Ga⁺ ion current was excessive, and, therefore, the depth profiles were made for GaO⁺ and GaP⁺ because these ions are less intense than Ga⁺ but would have a similar depth profile. Figure 2 shows the ⁸⁵GaO⁺ and ¹⁰⁰GaP⁺ distributions *vs.* the depth from the surface of the buffer layer. The two profiles conform to each other and are around three orders of magnitude higher in the epilayer as compared to the substrate. Furthermore, the profile contains two peaks as it approaches the interface. These peaks are not due to secondary ion yield enhancement caused by the presence of some other possible species, such as oxygen, because the P matrix ion current is constant from the surface to the substrate. The exact cause of high Ga concentration near the interface is not clear. However, it does reflect an initial transient behavior of the source of contaminant. Defect characterization using a damage-free grooving and etching technique revealed an interfacial layer containing a high density of saucer pits, as shown in Fig. 3. The origin of the saucer pits is believed to be associated with point defect clusters. The cross-grid pattern oriented along the <110> directions in-

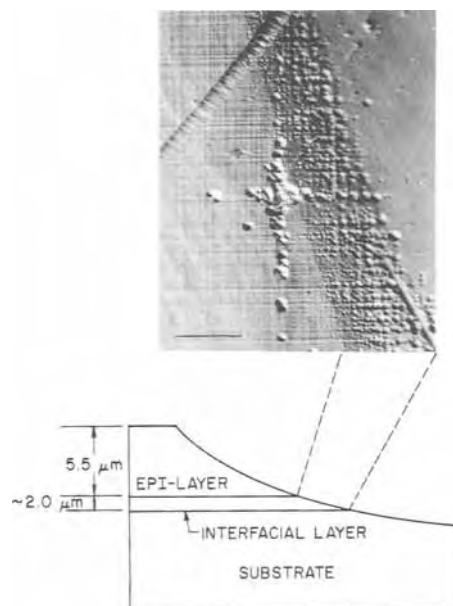


Fig. 3. Interfacial layer of the InP buffer layer (sample no. 4) revealed by a damage-free grooving and etching technique. The marker represents 50 μm.

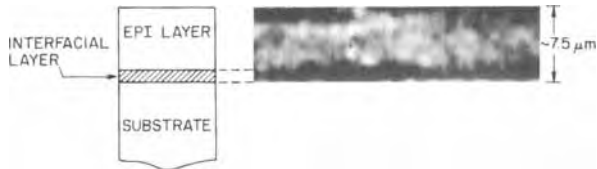


Fig. 4. Cross-sectional transmission cathodoluminescence of a [110] cross section of InP buffer layer (sample no. 4). The thickness of the cross section is less than $50 \mu\text{m}$.

indicates the existence of misfit dislocations near the interfacial layer, which is consistent with the high concentration of gallium in the buffer layer.

Cross-sectional transmission cathodoluminescence on a $50 \mu\text{m}$ thick [110] cross section showed a dark interfacial layer as seen in Fig. 4. The irregularity of the dark contrast indicates that it is composed of overlapping dark spots which were observed before in a layer containing a high density of saucer pits (4). The dark spots distributed over the buffer layer are believed to be the dislocations.

The width of the interfacial layer as revealed by chemical etching and measured by Dektak is usually larger than the width of the peaks measured from the SIMS profile.

X-ray double-crystal rocking curves for sample no. 4 are shown in Fig. 5a. The linewidth of the as-grown wafer was 62 arcseconds, which is twice as large as that measured for the substrate alone. Such a broad linewidth is attributed to the defect structure described above. The mismatched layer near the epitaxial interface was further demonstrated by etching away $8 \mu\text{m}$ of the $10 \mu\text{m}$ epitaxial InP layer and making another rocking curve. This rocking curve is shown in Fig. 5b. The major rocking curve is from substrate InP, while the shoulder on the right indicates that the remaining $2 \mu\text{m}$ were mismatched with $\Delta a/a = -4.3 \times 10^{-4}$, where the minus sign indicates that the $2 \mu\text{m}$ layer had a smaller lattice parameter than that of the substrate. An application of Vegard's law (7) yields 0.6% for the Ga concentration.

By presaturating the reactor with PH_3 (at mole fraction of 2×10^{-3} in 5 liter/min H_2 flow) for 5 min prior to the growth of InP, the incorporation of the gallium into the InP buffer layer was found to be greatly reduced. Figure 6 shows a SIMS profile of $^{31}\text{P}^+$, $^{85}\text{GaO}^+$, and $^{100}\text{GaP}^+$ of

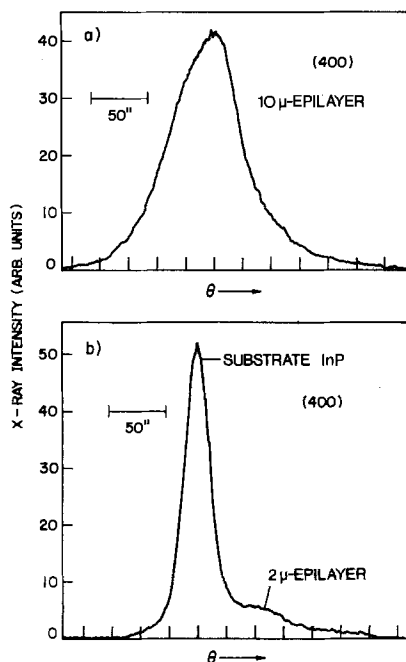


Fig. 5. X-ray double-crystal diffractometer measurements of, a, rocking curve of $10 \mu\text{m}$ InP buffer layer (run no. 4) and b, rocking curve of substrate InP with $\sim 2 \mu\text{m}$ buffer layer after etching.

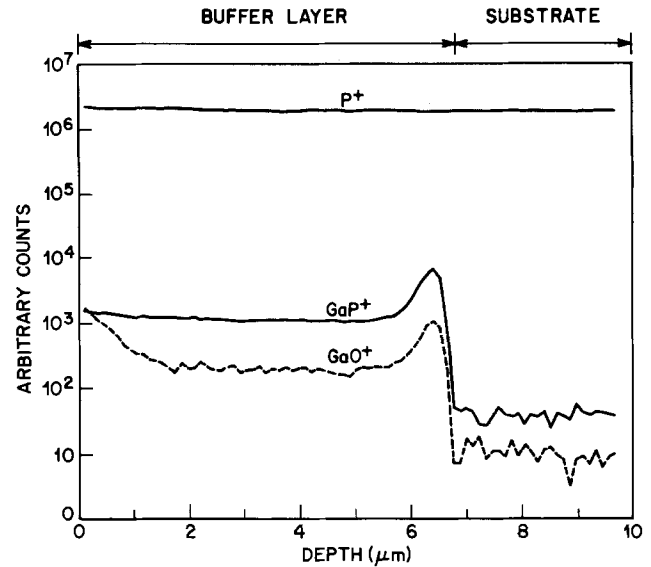


Fig. 6. SIMS depth profile of $^{31}\text{P}^+$, $^{100}\text{GaP}^+$, and $^{85}\text{GaO}^+$ in buffer layer (run no. 16).

sample number 16, for which this was done. The gallium content is only two orders of magnitude higher in the buffer layer than in the substrate and has only one peak at the interface between the buffer layer and substrate. The defect structure of the buffer layer was found to be greatly improved. Defects revealed by the damage-free growing and etching technique did not show misfit dislocations and saucer pits. This is shown in Fig. 7. However, an interfacial layer is still present. Furthermore, cross-sectional TCL revealed a uniform luminescence intensity across the entire buffer layer as shown in Fig. 8. The overall low luminescence efficiency of the buffer layer compared to that of the substrate is attributed to the undoped nature of the buffer layer.

In order to determine the cause of the gallium contamination, the gallium source was completely removed from the reactor just prior to run number 127. Between run numbers 16 and 127, the reactor was occasionally used to grow InGaAs. Figure 9a shows SIMS profiles of a buffer layer grown during the tenth run after the removal of the gallium source. The amount of gallium observed inside

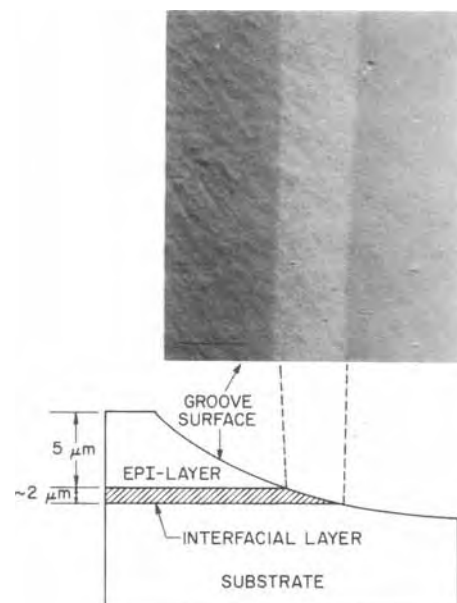


Fig. 7. Interfacial layer of sample no. 16 revealed by a damage-free grooving and etching technique does not show misfit dislocation and saucer pits. The marker represents $50 \mu\text{m}$.



Fig. 8. Cross-sectional transmission cathodoluminescence of a [110] cross section of sample no. 16.

the buffer layer was similar to that found for run number 16.

Figure 9b shows SIMS profiles of $^{69}\text{Ga}^+$, $^{100}\text{GaP}^+$, and $^{85}\text{GaO}^+$ for the same sample as in Fig. 9a, but at reduced sputter rate in order to show the similarity of the shapes of the profiles and the relative intensity of the three ions. Since the reactor was cleaned thoroughly after each run by passing HCl through the deposition zone, the remaining possibility which leads to the contamination of the InP buffer layer is that the indium melt was cross contaminated. This was confirmed later by examining the buffer layer grown during run 410, which is more than 200 runs after the removal of the gallium source. Because of the consumption of the indium metal, the indium had been replenished in the meantime. A SIMS profile of $^{69}\text{Ga}^+$ ion in sample 410 (Fig. 9c) showed that the gallium content had dropped to a level only slightly higher than that of the substrate, and the GaO^+ and GaP^+ were reduced almost to background levels. The Ga peak at the interface has been totally eliminated. We conclude that the indium source for the early runs had indeed been contaminated with gallium.

n-InP/InGaAsP/p-InP/p⁺-InGaAsP laser structure.—Gallium contamination of InP epilayers was also examined in a four-layer laser structure. Figures 10a and 10b show the Ga and As profiles from a four-layer structure obtained by scanning Auger spectroscopy on a 2°-5° beveled surface. The presence of Ga on both sides of the active Q layer is clearly visible. The As line scan will be discussed in the next section.

Figure 10c shows Auger depth profiles for all four elements. The abscissa is the milling time and therefore is a distorted depth scale. The relative thickness of the various layers do not agree with those of Fig. 11 (see below); this disagreement is probably due to ion milling artifacts, but the detailed explanations are not yet understood. The concentration profiles are normalized to 100 a/o using approximate sensitivity factors. It is clear that gallium is present in both n- and p-InP regions as indicated by the arrows. A complementary lowering of the In concentration is also observed. A similar situation is observed for As and P.

Defect characterization using damage-free grooving and etching revealed an orange peel morphology in both InP regions, as seen in Fig. 11. High magnification photographs show that they are composed of a high density of saucer pits which is similar to that observed previously in Fig. 3. Furthermore, TCL imaging of the buffer layer region also indicates a high density of dark spots as shown in Fig. 12. These results indicate that the gallium contained in the buffer layer is probably on the order of 1 a/o. The orange peel morphology in the p-InP region is less distinct because of the difference in etching rate of the defect revealing etchant on p-type InP. A similar amount of the gallium is believed to be present in the p-InP, as indicated by the Auger profile.

Other contaminants.—Besides the gallium contamination observed, small amounts of arsenic were found in the InP epilayer. Figure 13 is a SIMS profile of $^{31}\text{P}^+$ and $^{75}\text{As}^+$ obtained from run number 4. The arsenic concentration in the epilayer is around an order of magnitude higher than that found in the substrate. The same amount of arsenic was observed in most of the single layers. For a

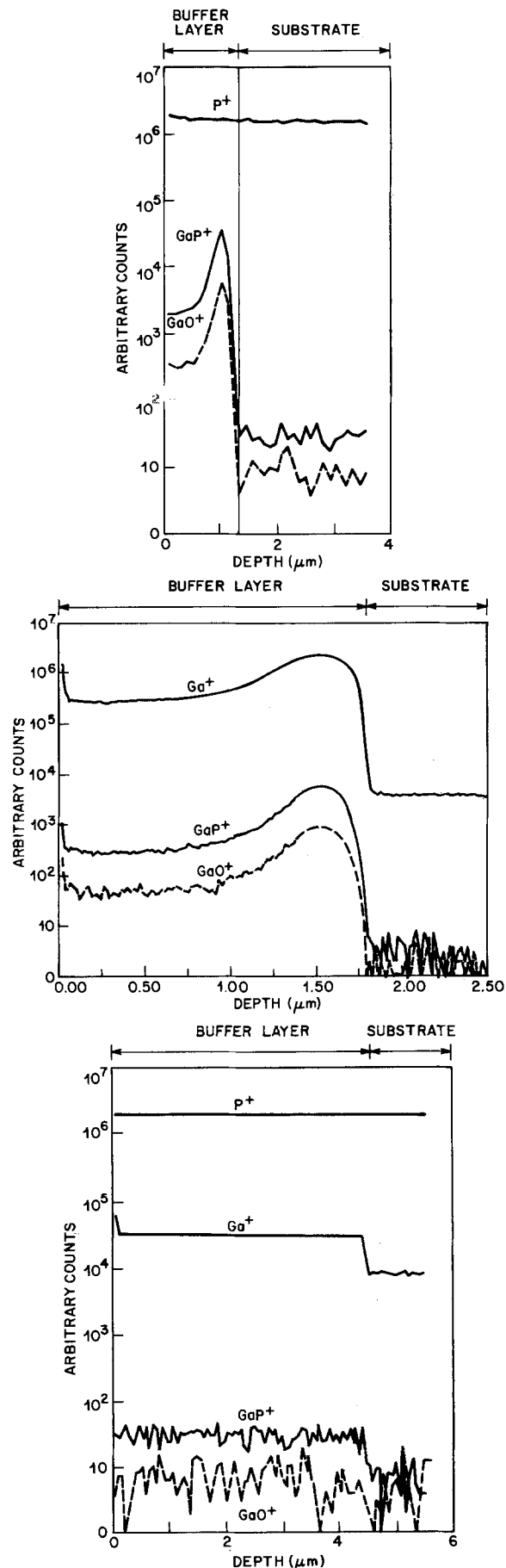


Fig. 9. (Top): SIMS depth profile of $^{31}\text{P}^+$, $^{100}\text{GaP}^+$, and $^{85}\text{GaO}^+$ in a buffer layer grown in the tenth run after the removal of the gallium source. (Middle): SIMS depth profile of $^{69}\text{Ga}^+$, $^{100}\text{GaP}^+$, and $^{85}\text{GaO}^+$ in a buffer layer grown in the tenth run after the removal of the gallium source. (Bottom): SIMS depth profile of $^{31}\text{P}^+$, $^{69}\text{Ga}^+$, $^{100}\text{GaP}^+$, and $^{85}\text{GaO}^+$ in buffer layer (run no. 410).

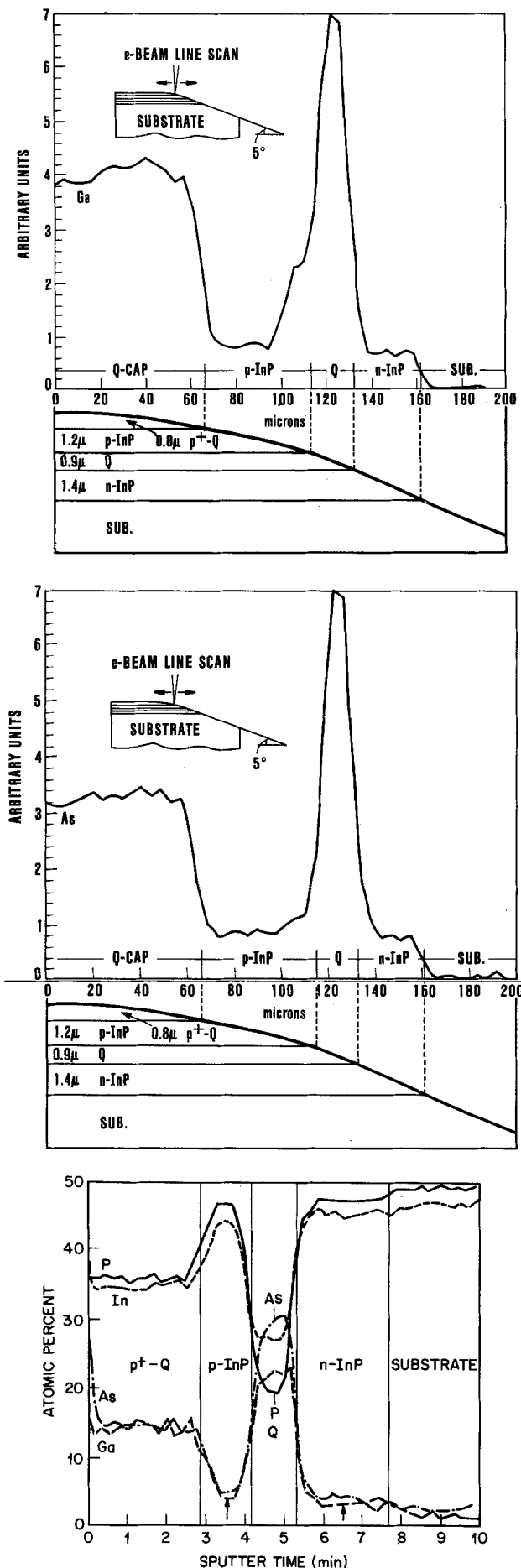


Fig. 10. (Top): Ga and (Middle) As profiles of a n-InP/InGaAsP/p-InP/p⁺-InGaAsP four-layer structure obtained by scanning Auger spectroscopy on a 2°-5° chemically beveled surface. (Bottom): Auger depth profiles for all four elements.

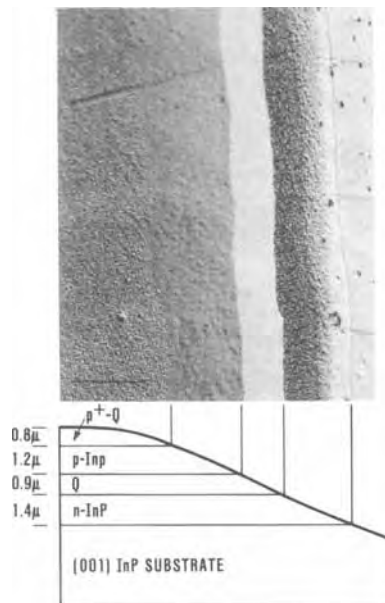


Fig. 11. Defect structures of a four-layer laser structure revealed by the damage-free grooving and etching method. The marker represents 50 μm.

four-layer laser structure, scanning Auger spectroscopy on 2°-5° beveled surface also detected arsenic in both InP buffer and cap layers, as seen in Fig. 10b.

SIMS profiling of InP single layers also indicated that small amounts of Fe, Si, Cr, and Zn accumulated at the substrate-epilayer interface. These contaminants are believed to have come from the reaction of HCl with the steel cylinder or with the stainless steel gas handling system.

Possible factors leading to contamination.—Gallium contamination.—Gallium contamination of InP buffer layers which have been studied may be ascribed either to transport of Ga from a contaminated In₍₁₎ source or to transport of volatile Ga containing compounds from the Ga₍₁₎ source. Assuming that Ga contamination of the In₍₁₎ source was accidental (loss of H₂ flow while the reactor was hot, or cross contamination during preparation of the metal sources), only transport of Ga from the Ga₍₁₎ source will be considered. Three aspects of the Ga contamination in the samples studied above require explanation: (i) the source of Ga in InP epilayers grown without

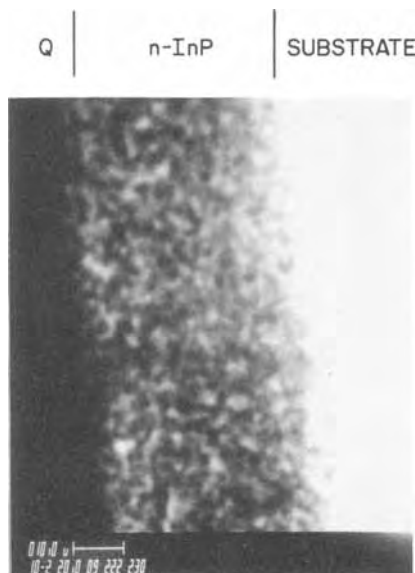


Fig. 12. Transmission cathodoluminescence imaging of a n-InP buffer layer on as-grooved sample.

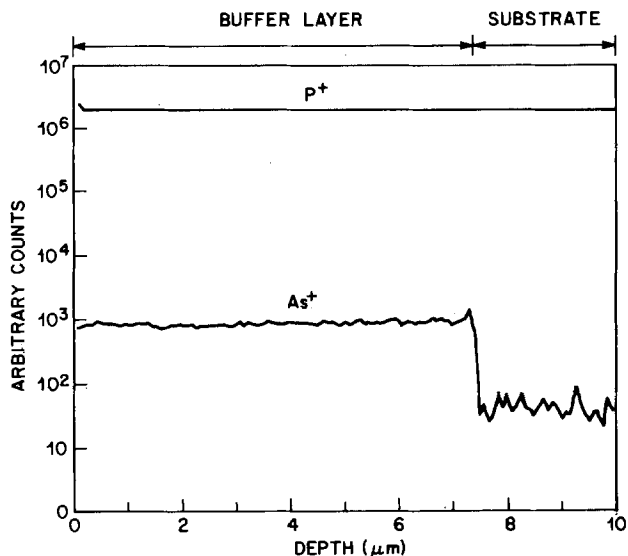
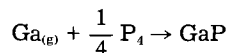


Fig. 13. SIMS depth profile of $^{31}\text{P}^+$ and $^{75}\text{As}^+$ ion in a single buffer layer.

exposure of the $\text{Ga}_{(l)}$ source to HCl; (ii) the effect of passing PH_3 through the reactor immediately prior to growth on suppressing Ga contamination; and (iii) Ga contamination of InP in multilayer structures with at least one layer containing Ga.

Several of the InP buffer layers examined contained large amounts of Ga even though the $\text{Ga}_{(l)}$ source was not exposed to HCl (run numbers 4-15). The two most likely sources of Ga transport in the absence of HCl include atomic Ga ($P_{\text{Ga}} \sim 10^{-10}$ atm at 700°C) (8) and Ga_2O formed by reaction of trace O_2 or H_2O contained in the H_2 carrier gas. For growth of InP, the InCl partial pressure (P_{InCl}) is on the order of 3.4×10^{-3} atm at a total flow rate of 4 liter/min. Assuming that Ga contamination from atomic Ga occurs according to



with P_{P_4} at 5×10^{-4} atm typical for InP growth, the equilibrium P_{Ga} is calculated (9, 10) to be $\sim 10^{-12}$ atm. Since this is much less than P_{Ga} expected from evaporation of $\text{Ga}_{(g)}$ from the liquid source, it is unlikely that this source could account for contamination levels as high as $\sim 1\%$.

A more plausible source of Ga contamination involves the formation of Ga_2O , which has been used as the transport agent in epitaxial growth of GaP (11). Although the H_2 used for growth is purified using commercial Pd diffusers, it is possible that contamination with O_2 occurs in the gas manifold (valves, mass flow controllers) or connections to the reactor. This may be particularly true for the early runs owing to the possibility of outgassing of new components which constitute the growth system. Assuming an upper limit of ~ 10 ppm H_2O over the $\text{Ga}_{(l)}$ source at 800°C , thermodynamic data for Ga_2O predicts a $P_{\text{Ga}_2\text{O}}$ of 5×10^{-7} atm (8). Based on calculations by Seki and Minagawa (12) for the system $\text{In}_x\text{Ga}_{1-x}\text{P}$ and substituting $\text{Ga}_2\text{O}/\text{H}_2\text{O}$ for GaCl/HCl as the transport system, the assumed level of H_2O contamination is thermodynamically sufficient for the incorporation of 1% Ga in InP.

The effect of PH_3 presaturation on Ga incorporation in InP buffer layers may be due to the deposition of GaP on the reactor walls prior to layer growth. The presence of such deposits may serve to getter Ga and prevent its incorporation into the growing InP layer. By nucleating such deposits prior to growth, both high Ga content at the interface of the grown layer and the substrate, as well as the Ga content in the remainder of the layer, would be reduced.

The growth of multiple layer structures which include at least one ternary or quaternary layer require transport

of Ga using HCl. In order to assure stable conversion of HCl to GaCl (InCl) in the reactor source zone, the $\text{Ga}_{(l)}$ ($\text{In}_{(l)}$) source is usually saturated with HCl prior to growth of any layers. Recent optical absorption studies of InCl and GaCl formation in these reactors have demonstrated that transport continues for over 10 min after the HCl in the reactor is turned off because of evaporation of GaCl (InCl) dissolved in the $\text{Ga}_{(l)}$ ($\text{In}_{(l)}$) sources (13). This effect is responsible for the high Ga content observed in both InP buffer and cap layers of the four-layer laser structure described above.

Additional contaminants.—The presence of additional contaminants, with the exception of As, is probably due to the reaction of HCl with the steel components of the growth system. Since AsH_3 and PH_3 pass through the same lines in the manifold, outgassing of these lines during InP growth may contribute to the presence of As in InP buffer layers. Another possibility is due to the presence of trace amounts of AsH_3 in the PH_3 used for growth. In multiple-layer structures which involve at least one As containing layer, contamination may also be due to evaporation of As_4 from deposits formed on the reactor walls during ternary or quaternary growth, or from elemental As deposited in the source end of the reactor due to the extremely rapid pyrolysis of AsH_3 at the point where the reactor enters the furnace (14). If the wall deposit contains As containing compounds, the reaction with unreacted HCl can also form As_4 .

Conclusions

We have observed the gallium contamination of InP epitaxial layers grown in a hydride transport VPE reactor designed for InP/InGaAsP multilayer laser structures by secondary ion mass spectrometry and Auger spectroscopy. Despite the fact that the Ga and In sources are physically excluded from each other, the initial InP layers grown from a new reactor were found to contain Ga at levels as high as ~ 1 a/o. Defect structure characterization of the InP epitaxial layer revealed misfit dislocations and an interfacial layer containing a high density of saucer pits. Cross-sectional transmission cathodoluminescence further confirmed that these defects were nonradiative recombination centers. Results from x-ray double-crystal diffractometry indicated that the mismatch was confined to the region near the interfacial layer which is consistent with the SIMS profile of Ga which showed a peak in the same region. Since the Ga source had not been exposed to HCl, the exact cause leading to the Ga contamination was not clear. A plausible transport agent for Ga was suspected to be the formation of Ga_2O due to a trace amount of O_2 or H_2O in the H_2 carrier gas.

For a four-layer laser structure, the Ga contamination of InP is further complicated by the evaporation of the GaCl dissolved in the Ga source after the turn-off of HCl. This delay turn-off of GaCl contributes to the major Ga contamination of InP in multilayer laser structure.

A small amount of As was also present in the single buffer layer. This can be attributed to the outgassing of AsH_3 absorbed on the walls of the input tubing and to trace amounts of AsH_3 in the PH_3 gas used for growth. However, in a four-layer laser structure, considerable amounts of As were present in both the InP buffer and cap layers. A possible explanation is the evaporation of As containing deposits formed on the reactor walls during the growth of ternary or quaternary layers. The fact that the InP buffer layer contains the same amount of As as those in the subsequent InP cap layer indicates that these deposits were formed in the previous runs. The small amounts of Fe, Si, Cr, and Zn found at the substrate-buffer layer interface are believed to derive from the reaction of HCl with the steel cylinder or gas handling system.

Acknowledgment

The authors are grateful for the support and encouragement of J. V. DiLorenzo.

Manuscript submitted April 30, 1984; revised manuscript received Oct. 29, 1984.

AT&T Bell Laboratories assisted in meeting the publication costs of this article.

REFERENCES

1. G. H. Olson, C. J. Nuese, and M. Ettenberg, *Appl. Phys. Lett.*, **34**, 262 (1979).
2. W. D. Johnston, Jr., and K. E. Sturge, IEEE 38th Device Research Conference, Abstract Vol. IV B-3, Ithaca, New York (1980).
3. G. H. Olson, in "GaInAsP Alloy Semiconductors," T. P. Pearsall, Editor, Chap. 1, John Wiley and Sons, New York (1982).
4. S. N. G. Chu, *This Journal*, **129**, 2082 (1982).
5. S. N. G. Chu, C. M. Jodlauk, and A. A. Ballman, *ibid.*, **129**, 352 (1982).
6. S. N. G. Chu and T. T. Sheng, *ibid.*, To be published.
7. R. E. Nahory, M. A. Pollack, W. D. Johnston, Jr., and R. L. Barns, *Appl. Phys. Lett.*, **33**, 659 (1978).
8. C. N. Cochran and L. M. Foster, *This Journal*, **109**, 144 (1962).
9. D. Shaw, *J. Phys. Chem. Solids*, **36**, 111 (1975).
10. C. D. Thurmond, *ibid.*, **26**, 785 (1965).
11. M. Gershenzon and R. H. Mikulyak, *This Journal*, **108**, 548 (1961).
12. A. Koukitsu and H. Seki, *J. Cryst. Growth*, **49**, 325 (1980).
13. R. F. Karlicek, Jr., and A. B. LaRoe, Unpublished work.
14. V. M. Donnelly and R. F. Karlicek, *J. Appl. Phys.*, **53**, 6399 (1982).

Resistance Switching Characteristics in Polycrystalline Silicon Film Resistors

Chih-Yuan Lu*

AT&T Bell Laboratories, Reading, Pennsylvania 19603-0856; Institute of Electronics, National Chiao-Tung University, Hsin-Chu, Taiwan, 300, China; Department of Electrical and Computer Engineering, North Carolina State University, Raleigh, North Carolina 27695-7911

Nicky Chau-Chun Lu

IBM T.J. Watson Research Center, Yorktown Heights, New York 10598

Chih-Ching Shih

Institute of Electronics, National Chiao-Tung University, Hsin-Chu, Taiwan 300, China

ABSTRACT

Both reversible and irreversible resistance switchings have been investigated in boron- and arsenic-doped LPCVD polycrystalline silicon film resistors. The effects of film thickness and doping concentration on the transition voltage and current have been characterized for different length resistors having film thickness from 0.1 to 1.2 μm and doping concentration ranging from 5×10^{16} to $1 \times 10^{20} \text{ cm}^{-3}$. Under a large voltage bias, the resistor can be switched to a conductive "on" state or to a "short" state having resistance reduction by a factor of 10^3 - 10^6 , or it can be blown "open". The transition voltage and current and the resistance after switching depend strongly on film thickness, doping concentration, and applied power. A simple qualitative model is proposed to explain these resistance switching phenomena.

Polycrystalline silicon (polysilicon) films have been widely used as solar cell and integrated-circuit elements, and such applications have stimulated extensive studies of the electrical properties of this material. Both reversible and irreversible resistance switching phenomena have been reported (1-3). The irreversible resistance switching has been extensively applied to integrated-circuit applications, such as a memory element in fusible-link PROM's (3-5) and a fuse or antifuse in redundancy circuits in high density RAM's (6). However, there are a limited number of papers in the literature systematically studying resistance switching properties of polysilicon resistors. Greve studied the programming mechanism of heavily doped polysilicon resistor fuses and showed that formation of a second-breakdown state is necessary to blow open the fuses (1). He also studied n^+ - p - n^+ polysilicon devices and showed that the dopant migration and the aluminum penetration in molten filaments through polysilicon devices are the mechanisms for resistance switching (7, 8). On the other hand, Mahan reported a reversible switching phenomenon in undoped polysilicon resistors having high value resistance (2).

This work reports new experimental results on the effects of film thickness, doping concentration, and device dimensions on resistance switching behavior in polysilicon resistors. The resistances before and after switching, the switching I-V curves, and the transition voltage

and current beyond which the switching occurs were characterized extensively. Different switching patterns have been clearly identified from this systematic study, and a better physical understanding of the switching behavior in polysilicon resistors has been obtained from a qualitative model.

Sample Preparation and Measurements

A 0.80 μm thick oxide was grown at 1100°C on top of N-type (100) silicon wafers with resistivity of 4 ~ 7 $\Omega\text{-cm}$. Undoped polysilicon films with thickness ranging from 0.1 to 1.2 μm were deposited in a low pressure CVD reactor at 620°C with deposition rate of 80 $\text{\AA}/\text{min}$. Either boron or arsenic dopants were then implanted with various doses to yield doping concentrations from 5×10^{16} to $1 \times 10^{20} \text{ cm}^{-3}$ for arsenic and from 5×10^{16} to $2 \times 10^{18} \text{ cm}^{-3}$ for boron. After polysilicon resistors were patterned by plasma etching, an 8000 \AA CVD oxide layer was deposited at 430°C to avoid dopant evaporation during subsequent thermal steps. For p-type samples, the contacts were either undoped or heavily doped with boron. For n-type samples, the contacts were all heavily doped with arsenic to avoid Schottky barrier formation. All samples were annealed at 900°C for 60 min to activate and uniformly redistribute the dopants, as well as to remove the implantation damage. A 1.0 μm thick aluminum layer was deposited and etched to form the contact pattern. The contacts were sintered in N_2 at 450°C for 20 min.

*Electrochemical Society Active Member.

The thickness of polysilicon films was measured by an optical method (Nanospec Model Axp-010-0180) and an α -step profiler. Measured electrical properties of polysilicon resistors include zero bias resistance and I-V characteristics. The measurement systems were: (i) an HP 4140B picoampere meter with dc programmable voltage source, coupled to an HP-85 microcomputer to measure the zero bias resistance, and (ii) a Tektronix 576 curve tracer to observe I-V characteristics and to trigger polysilicon-resistance switching. The surface of resistors after switching was studied by an optical microscope and a scanning electron microscope (SEM).

Results

The general behavior of the I-V characteristics of polysilicon resistors is illustrated in Fig. 1. The I-V curve of polysilicon resistors before switching follows the predicted hyperbolic sine function (curve 1) (9, 10) to a certain point A. It was found that the high voltage part of curve 1 was not stable for most device configurations. The resistivity drastically decreases with increasing voltage, and would contract to a stable curve 2 ("off" state) (2).

When voltage increases along curve 2, a negative resistance behavior may appear. When the voltage further increases, the I-V curves of devices of light doping concentration and short dimensions were switched to a more conductive "on" state (curve 3). When the power of the curve tracer was limited below a certain value, the negative resistance characteristic is stable and the switching between curve 2 and 3 is reversible. This reversible switching in polysilicon film was reported by Mahan as "threshold switching" (2). When more power was added into the resistor, a sudden change from "on" state (curve 3) to the "short" state (curve 4) occurred for thick film devices. However, for thin film devices, more power can cause the resistor to "open" (curve 5). Both switchings from curve 3 to 4 and from 3 to 5 are irreversible. For medium and heavily doped polysilicon resistors, the switching always jumps directly from "off" state to either "open" or "short" state without going through the "on" state. For example, in boron-doped samples with $N_A \geq 5 \times 10^{17} \text{ cm}^{-3}$, no switching to "on" state has been observed. However, for short and lightly doped samples ($N_A \leq 1 \times 10^{17} \text{ cm}^{-3}$, and nominal length less than $15 \mu\text{m}$), reversible switching was observed.

Similar observations were made on arsenic-doped polysilicon resistors, and the same conclusions were obtained. These various switching patterns are summarized in Fig. 1. The reversible switching is more likely to occur for short and lightly doped samples. No reversible switching has been observed for our samples with doping level higher than $1 \times 10^{17} \text{ cm}^{-3}$ and/or longer than $15 \mu\text{m}$.

Along the stable curve 2, the voltage beyond which the switching occurs is defined as "transition voltage," V_T , and the corresponding current as "transition current," I_T . The zero bias resistance before switching is defined as R_b and after switching as R_a .

Figure 2 shows the transition voltage and resistance vs. doping concentration for boron-doped resistors with lengths of 10 and $5 \mu\text{m}$ before and after switching. The resistance before switching strongly depends on the doping concentration, especially around a critical doping concentration N^* where most of the grains change from total depletion into partial depletion, thus causing a drastic change of resistance (10). An interesting phenomenon is that the transition voltage has shown a maximum around N^* . Away from N^* on the heavily doped side, the transition voltage generally follows the decreasing pattern of R_b . It was also found that the transition voltage scales proportionally to the resistor length. Resistance after switching decreases by a factor of 10^3 - 10^6 . For the short and lightly doped samples, the resistor mostly switched first to "on", then to "open" rather than "short".

As the maximum power of the curve tracer was raised from 0.5 to 2.2W, the resistance after switching (already "short") can be further reduced by a factor of 10^2 - 10^4 . Fi-

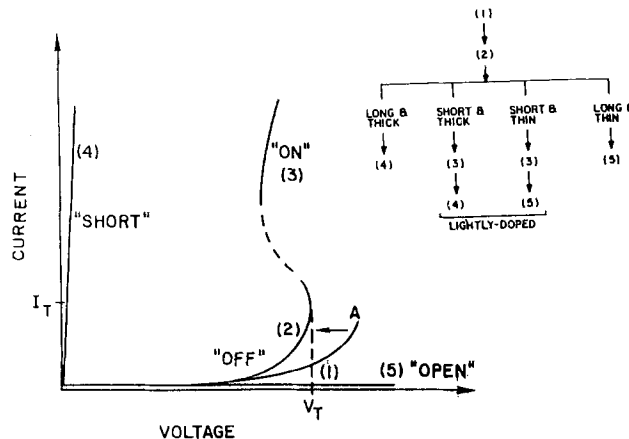


Fig. 1. The general I-V switching behavior of polysilicon resistors

nal resistance is approximately several ohms and relatively independent of doping concentration (Fig. 3). Shiny aluminum penetration path was found in these further "short" state resistors, which accounts for the low resistance.

Figure 4 shows the relationship between film thickness and measured resistances before and after switching for two doping concentrations of 1×10^{17} and $2 \times 10^{18} \text{ cm}^{-3}$. The resistance before switching decreases drastically as the film thickness increases for resistors at doping concentration of $2 \times 10^{18} \text{ cm}^{-3}$, but not so much for resistors at doping concentration of $1 \times 10^{17} \text{ cm}^{-3}$. The details of effect of doping effect on resistivity vs. film thickness was investigated by Lu *et al.* (12). Almost all the devices with film thickness less than 2000\AA were switched to "open" state, and R_a is infinite.

The behavior of V_T vs. film thickness is shown in Fig. 5. It is similar to the relationship of R_b vs. film thickness in Fig. 4, except that for the thinnest sample at doping level of $2 \times 10^{18} \text{ cm}^{-3}$, the transition voltage decreases and the postswitching was an "open" state instead of a "short" state. The similar behavior between V_T and R_b suggests that Joule heating plays an important role in the switching mechanism (1, 2).

Figure 6 shows the V_T and I_T of boron-doped resistors at doping level of $2 \times 10^{18} \text{ cm}^{-3}$ for various film thicknesses. There is no significant difference whether the contacts have been heavily doped or not (12). It is found that over the observed range of film thickness, I_T and V_T obey an

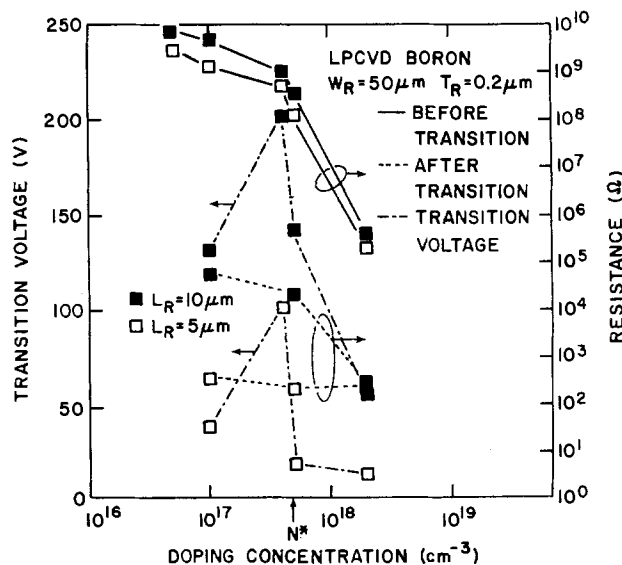


Fig. 2. Transition voltage and resistance vs. doping level before and after switching (power $\leq 0.5\text{W}$).

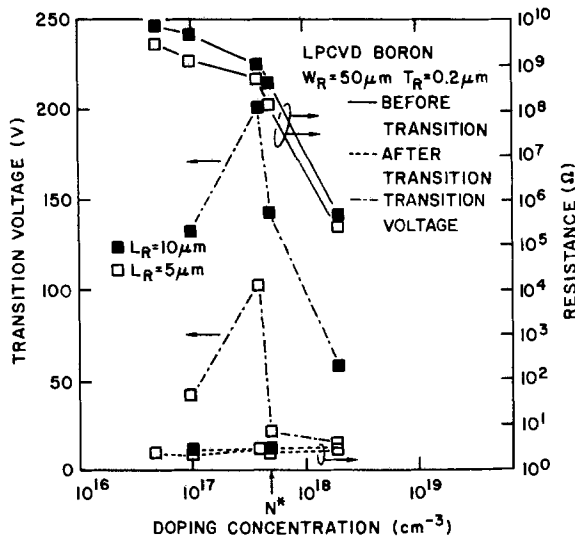


Fig. 3. Transition voltage and resistance vs. doping level before and after switching (power $\leq 2.2W$).

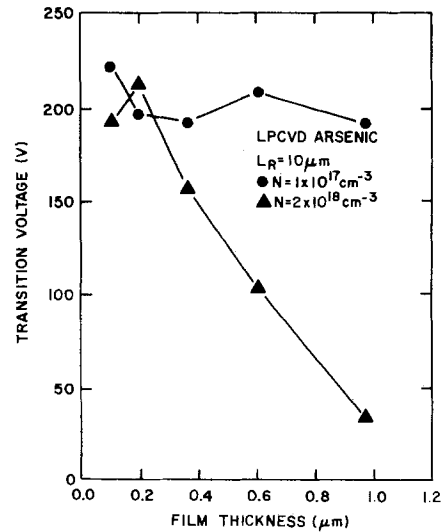


Fig. 5. Transition voltage vs. film thickness

empirical expression

$$I_T = I_0[\exp(V_0/V_T)]$$

where I_0 and V_0 are empirical parameters.

Discussion

A simple qualitative model is proposed to understand the above observations. When the applied voltage is below the transition voltage, the I-V characteristics of polysilicon resistor can be described by the carrier trapping and dopant-segregation models (9-13). According to these models, the active dopant concentration can be obtained by subtracting the inactive segregated dopant concentration from the actual doping concentration (10, 11), and the grain-boundary trapping states can trap free carriers from the ionized active dopants and act as recombination centers (14, 15). This trapping process reduces the number of free carriers and creates built-in potential barriers surrounding the grain boundary, which impede carrier motion from one crystallite to another. The carrier transport across the grain boundary and the built-in potential barriers by thermionic emission and tunneling processes show a hyperbolic sine function I-V characteristic (13).

As the applied voltage further increases, the forward-biased space-charge barrier can eventually be flattened

and a great number of carriers is then injected into the resistors. Once this happens, bulk resistance of silicon crystallite becomes dominant, and the I-V characteristic exhibits a transition from "grain-boundary limited" to "bulk-limited" condition. Thus the observation that transition voltage reaches a maximum value around the critical doping concentration can be understood by the fact that the highest built-in potential barrier exists at this doping concentration (10) and, therefore, a higher voltage is needed to flatten the forward-biased built-in potential barrier.

For lightly doped polysilicon films, the crystallites are totally depleted by the grain-boundary trapping states, and hence the films are nearly intrinsic. The resistivity of totally depleted polysilicon films is very high, and this semi-insulating property is mainly due to carrier depletion rather than mobility degradation (10). If a finite voltage which is large enough to flatten the built-in potential barrier is applied across the resistor, a large number of electrons and holes can be injected at the cathode and the anode, respectively. Because there are more unfilled grain-boundary traps for capturing minority carriers than for majority carriers, the lifetime of minority carriers is shorter.

If the resistor is long compared to the mean free path of minority carriers, the minority carriers are not able to transverse the resistor, and this condition results in single injection. Under a high current level, majority-carrier single injection is space-charge limited (16). However, as the bias is further increased, the field across the resistor eventually becomes high enough to allow the minority

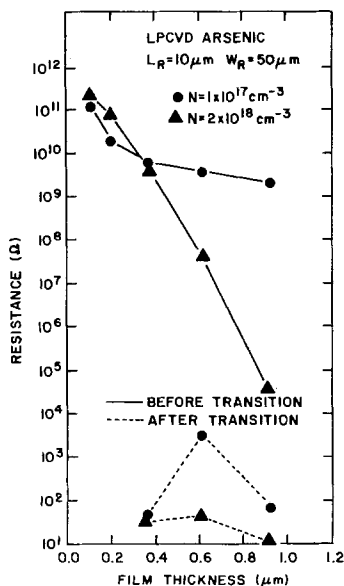


Fig. 4. Resistance vs. film thickness before and after switching

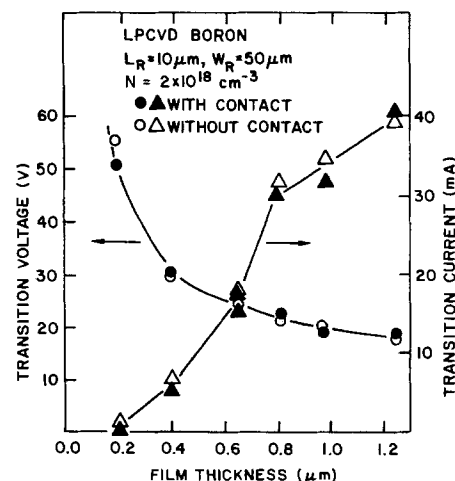


Fig. 6. Transition voltage and transition current vs. film thickness

carriers to reach the other end of the resistor. This double injection process causes the majority space-charge barrier to be lowered and minority carrier lifetime (mobility) to increase, permitting more carriers to transit the resistor; as a result, a lower voltage is required to provide the current for maintaining the condition. This positive feedback process results in negative resistance characteristics. The condition causing this negative resistance behavior is that the minority carrier transit time is equal to their lifetime. It is clear that in a shorter resistor it is easier to reach this condition. Eventually, the high level injection condition will be reached when the lifetimes of minority and majority carriers are equal. At this point, two-carrier recombination-limited current flow prevails and the negative resistance behavior terminates; the polysilicon resistor can then switch to the "on" state. This double injection mode is much more likely observed for small grain and/or lightly doped polysilicon films which have plenty of recombination centers for both majority and minority carriers (17).

Similar phenomena have been observed in many amorphous semiconductors where the initiation of switching and the maintenance of the "on" state in threshold switching can be satisfactorily explained as a double injection electronic process (18, 19). Undoped or lightly doped polysilicon films of small grain size have many properties close to amorphous films. Just like any electronic transport process, heat will be generated by current, and thermal effects will accompany this electronic injection process. For short polysilicon resistors, however, the high field induced carrier generation is more likely to occur before thermal effects take over the major role. Therefore, if the double injection process and positive feedback mechanism occur before Joule heating makes any microstructure change, a reversible threshold switching occurs. However, if more power is fed into the "on" state resistor, the Joule heating will finally become large enough to cause an irreversible switching from "on" state to "short" or "open" state.

For heavily doped polysilicon films, although the grain-boundary trapping states are completely filled up with majority carriers, the concentration of free majority carriers is still substantially larger than the intrinsic carrier concentration and of the same order of magnitude as the active doping concentration (10, 11). The lifetime of minority carrier is much shorter than that of majority carrier. This majority carrier transport process is not space-charge limited. The double injection condition is hardly reached even under a relatively large bias. Usually, the thermal process will then prevail to induce current filamentation (20). Thermal current filamentation results in irreversible switching to either "short" or "open" state, depending on the configuration of resistor and programming conditions. For thick and short resistors, thermal filamentation can induce either dopant migration or aluminum penetration through the molten filament to form "short" state (1). For thin and long resistors, Joule heating can simply evaporate the polysilicon film to leave a void (21), or the applied field can be strong enough to sweep the molten silicon ions to form an "open" gap (1).

It should be noted that the coexistent electronic and thermal processes always compete and influence each other. Therefore, the device configuration, composition of the resistor, and the programming conditions all have their roles and become a control parameter in some particular stage of this complex switching phenomenon.

Conclusion

Several distinct patterns of polysilicon resistance switching have been observed for both arsenic- and

boron-doped materials over a wide range of doping concentration and film thickness. The transition voltage reaches a maximum value around the critical doping concentration, which separates the totally depleted and partially depleted cases. Beyond this point, toward higher doping levels, the transition voltage generally follows the variation of R_b . As applied power increases, resistance after switching to "short" state can be further decreased and becomes less dependent on film thickness and doping level and, finally, aluminum penetration occurs, causing a resistance of only a few ohms.

Lightly doped resistors are more likely to show reversible threshold switching, probably due to their abundant recombination centers. Short and thick resistors are more likely to switch to "short" state, and the aluminum penetration path can be easily observed. Long and thin resistors are more likely to switch to "open" state, and a physical gap is observed. These distinct patterns have been understood by a qualitative model.

Acknowledgments

The authors wish to thank Dr. Ming-Kwang Lee of ERSO, Industrial Technology Research Institute, ROC, for sample preparation, and Professor Si-Chen Lee of National Taiwan University for many valuable discussions. C. Y. Lu wishes to thank Dr. A. Reisman for his encouragement and support during his stay in NCSU and MCNC. We also would like to thank Dr. L. M. Terman for helpful comments and C. Winston for typing this paper.

Manuscript submitted June 11, 1984; revised manuscript received Dec. 7, 1984.

IBM Corporation assisted in meeting the publication costs of this article.

REFERENCES

1. D. W. Greve, *IEEE Trans. Electron Devices*, **ed-29**, 719 (1982).
2. J. E. Mahan, *Appl. Phys. Lett.*, **41**, 479 (1982).
3. M. Tanimoto, J. Murota, Y. Ohmori, and N. Ieda, *IEEE Trans. Electron Devices*, **ed-27**, 517 (1980).
4. R. K. Wallace, *ISSCC Dig. Tech. Papers*, 148 (1980).
5. L. R. Metzger, *IEEE J. Solid-State Circuits*, **sc-18**, 562 (1983).
6. T. Mano, K. Takeya, T. Watanabe, N. Ieda, K. Kiuchi, E. Arai, T. Ogawa, and K. Hirata, *ibid.*, **sc-15**, 865 (1980).
7. D. W. Greve and L. V. Trans, *IEEE Trans. Electron Devices*, **ed-29**, 1313 (1982).
8. M. E. Lunn and D. W. Greve, *J. Appl. Phys.*, **54**, 3270 (1983).
9. G. J. Korsh and R. S. Muller, *Solid-State Electron.*, **21**, 1045 (1978).
10. N. C. C. Lu, L. Gerzberg, C. Y. Lu, and J. D. Meindl, *IEEE Trans. Electron Devices*, **ed-28**, 818 (1981).
11. M. M. Mandurah, K. C. Saraswat, C. R. Helms, and T. I. Kamins, *J. Appl. Phys.*, **51**, 5755 (1980).
12. N. C. C. Lu, C. Y. Lu, M. K. Lee, C. C. Shih, C. S. Wang, W. Reuter, and T. T. Sheng, *This Journal*, **131**, 897 (1984).
13. N. C. C. Lu, L. Gerzberg, C. Y. Lu, and J. D. Meindl, *IEEE Trans. Electron Devices*, **ed-30**, 137 (1983).
14. H. C. Card and E. S. Yang, *ibid.*, **ed-24**, 397 (1977).
15. W. Hwang, E. Poon, and H. C. Card, *Solid-State Electron.*, **26**, 599 (1983).
16. M. A. Lampert and P. Mark, "Current Injection in Solids," Academic Press, New York (1970).
17. M. Braustein, A. I. Braustein, and R. Zuleeg, *Appl. Phys. Lett.*, **10**, 313 (1967).
18. D. Adler, M. S. Shur, M. Silver, and S. R. Ovshinsky, *J. Appl. Phys.*, **51**, 3289 (1980).
19. D. Adler, H. K. Henisch, and N. Mott, *Rev. Mod. Phys.*, **50**, 209 (1978).
20. D. H. Pontius, W. B. Smith, and P. P. Budenstein, *J. Appl. Phys.*, **44**, 331 (1973).
21. R. J. Smith, *IEEE IEDM Tech. Dig.*, 608 (1982).

Molecular Layer Epitaxy

Jun-ichi Nishizawa* and Hitoshi Abe

Research Development Corporation of Japan, Semiconductor Research Institute, Kawauchi, Sendai 980, Japan

Toru Kurabayashi

Research Institute of Electrical Communication, Tohoku University, Sendai 980, Japan

ABSTRACT

We report, for the first time, the success of GaAs molecular layer epitaxy (MLE) using AsH₃ as an As containing gas and trimethyl-gallium (TMG) as a Ga containing gas. Growth conditions for a single layer by layer deposition process were investigated as a function of the substrate temperature, the pressure in the growth chamber, the admittance quantity per cycle, and photoirradiation. The substrate temperature of 500°C fulfilled the conditions for a monolayer growth, where the film thickness per one cycle is saturated with the admittance quantity, at the higher temperature that increased with the TMG admittance quantity. The electrical properties of the film grown by MLE method strongly depended on the gas admittance rate, *i.e.*, pressure in the growth chamber. The carrier density of the film proportionally decreased with increasing AsH₃ pressure and decreasing TMG pressure. However, all growth films show p-type behavior with a carrier density of 1×10^{18} - 10^{20} cm⁻³. Photoirradiation during the growth by a high pressure Hg lamp, Ar laser (514.5 nm), and with a doubler (257.3 nm) largely improved the surface morphology and electrical properties of the films by MLE.

In recent years, there has been an increasing demand for high speed integrated circuits, micro- and millimeter wave devices, optical devices, and optoelectronic integrated circuits. Nishizawa proposed an ideal static induction transistor (ISIT) and estimated the maximum gain bandwidth product as 780 GHz for GaAs. Tunnel injection types of SIT may operate in the region of Tera Hz (1, 2). For such high speed devices, the control of epitaxial layer thickness to within single atomic dimension becomes necessary. Molecular layer epitaxy can afford such demands. In this paper, we report for the first time the success of GaAs molecular layer epitaxy (MLE).

The halide-transport vapor phase epitaxy (VPE), the metalorganic chemical vapor deposition (MO-CVD), and molecular beam epitaxy (MBE) are well known as vapor phase epitaxial techniques for III-V compound semiconductors. Very recently, atomic layer epitaxy (ALE) has appeared in the academic publications (3, 4).

VPE and MO-CVD, however, are not available techniques for preparing semiconductor thin films with an atomic-order accuracy. MBE is a widely used technique for producing semiconductor thin films with an atomic-order control, which is based on the vacuum deposition technique in UHV region (5). Typical problems, however, appear owing to the vacuum deposition. Out gassing due to heating the source cell, evacuation of evaporants, and complicated replenishment of the source material become considerable problems for a vacuum system. Furthermore, growth-rate control has been achieved by the evaporation rate monitored by a quartz microbalance oscillator or mass spectrometer. As a result of the complexity of controlling the evaporation rate, epitaxial films with an accuracy of a single molecular layer have been difficult to prepare and confirming the achievement of a stoichiometric film is equally difficult.

Very recently, Suntola *et al.* reported ALE (6, 7) producing II-VI compound films like CdTe and ZnTe using conventional MBE equipment. Since the film grows by a monolayer per reactant pulse in the ALE method, the film thickness is exactly determined by the number of cycles of the reactant pulses.

We define molecular layer epitaxy (MLE) as follows. MLE is a crystal-growth method using chemical reaction of adsorbates on the semiconductor surface, where gas molecules containing one of the semiconductor elements are introduced alternately into the growth chamber by which a single layer of film growth develops. ALE is the crystal-growth method where a specific atomic element is alternately deposited on the substrate. Suntola also tried MLE preparing ZnS polycrystalline films and Ta₂O₅,

amorphous films, but no single-crystal films were obtained (8). Furthermore, Si and GaAs, the most popular semiconductor materials, which are widely used for VLSI circuits today, have not been investigated.

Photoepitaxy was proposed by the author (J. Nishizawa) in 1961 and has been applied to Si and GaAs vapor phase epitaxy, resulting in higher crystal quality at lower epitaxial temperatures (9-12). A combination of MLE and photoepitaxy may increase the film quality by MLE at even lower temperatures, and photostimulated processes of the crystal growth can be better controlled.

We report here the MLE method applied to GaAs using AsH₃ as an As containing gas and TMG as a Ga containing gas.

Experimental Procedure

A main part of the experimental setup used here, shown in Fig. 1, consists of a gas-admittance system, a mass spectrometer for reaction species determination, a heating lamp system, a temperature controlling unit with a pyrometer, and a pumping system. After the substrate is etched by a usual treatment, the substrate is set in the preparation chamber and evacuated to 1×10^{-5} Pa. The substrate is transported from the preparation chamber to the growth chamber ($p \leq 5 \times 10^{-6}$ Pa). The growth chamber is evacuated for as long as 30 min. The substrate is heated by the lamp system situated outside of the growth chamber. The temperature measurement is achieved by the pyrometer, and the power of the heating lamp is controlled by an automatic controlling unit coupled to the output signal of the pyrometer. The substrate temperature could be stabilized within $\pm 1^\circ\text{C}$ during the epitaxial growth.

After heating the substrate up to 600°C for evacuating the surface contaminants mainly consisting of oxides, AsH₃ gas is admitted for 2-200s at the pressure of 10^{-1} - 10^{-5} Pa and evacuated; then TMG is admitted for 0.5-20s at the rate of 10^{-3} - 10^{+1} Pa-liter/s and evacuated. Such a periodic gas admittance cycle is repeated up to the desired film thickness. Figure 2 shows the dependence of the growth chamber pressure on time during gas admittance.

No deposition on the insulating material was observed in the case of MLE. Using a mask pattern of an insulating film, the film thickness was measured by the alpha step. GaAs substrates (100) and off-angle were etched more than 2 μm deep by H₂SO₄ etchant (H₂SO₄:H₂O₂:H₂O = 4:1:1 and 10:1:1). Thereafter, a Si₃H₄ film was deposited by plasma CVD \sim 200 nm, and mask patterns were made on the substrate. Furthermore, the liftoff area of the substrate was etched by Cica TMK-1 (Kantokagaku, Tokyo) 150Å deep, producing a contamination-free surface.

*Electrochemical Society Active Member.

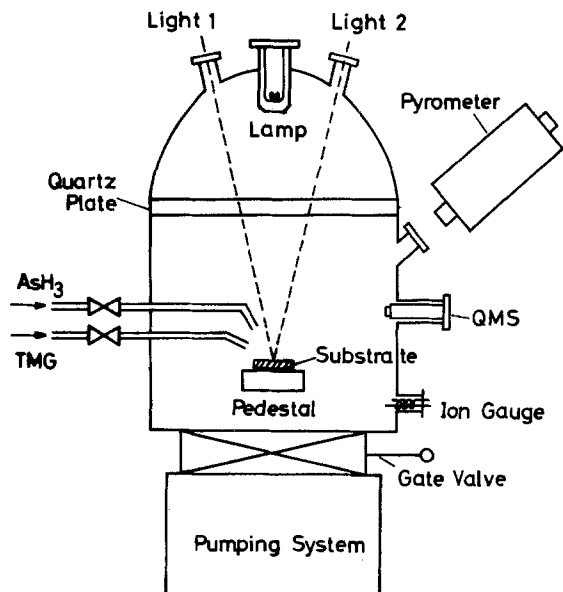


Fig. 1. A main part of the experimental setup consisted of a gas admittance system, a mass spectrometer for reaction species determination, a heating lamp house with two ports for light beam irradiation, a pyrometer, and pumping units.

Results and Discussion

Monolayer film growth.—The diffraction pattern of a film of GaAs grown by MLE is shown in Fig. 3, which was prepared by alternately introducing AsH_3 and TMG at the inlet pressure of 7×10^{-3} and 1.3×10^{-3} Pa for a gas admittance mode (20", 1", 2", 1") at the growth temperature of 500°C. A beautiful spot pattern clearly indicates the single-crystal nature of the growth film.

For a purpose of finding out the growth condition of monolayer epitaxial growth, film thickness per cycle was measured as a function of TMG admittance quantity at the substrate temperature of 500°C. The admittance time of TMG was kept constant for the measurements only, except for the maximum quantity for which it was varied. Therefore, the transverse axis of Fig. 4 represents also the admittance rate corresponding to the inlet pressure. As the admittance rate of TMG increased from 1.0×10^{-2} to 0.6 Pa-liter/s, the film thickness per cycle was nearly saturated and indicated 2.2–2.3 Å/cycle. When the admittance rate decreased to 0.33×10^{-2} Pa-liter/s, the thickness reduced to 1.2 Å/cycle, nearly one-half of the saturated value. As the admittance quantity becomes lower than 2.7×10^{-2} Pa-liter, the supplied quantity is no longer suffi-

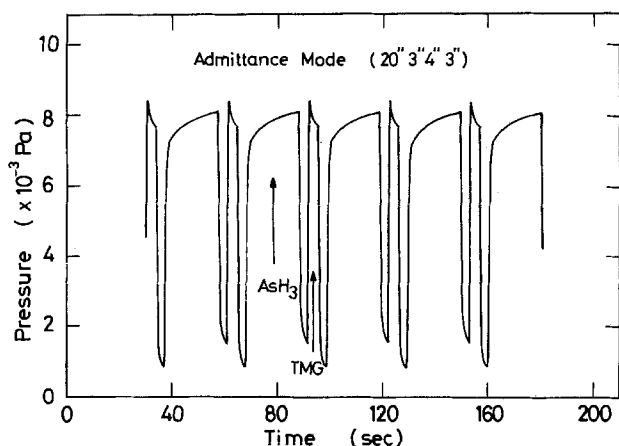
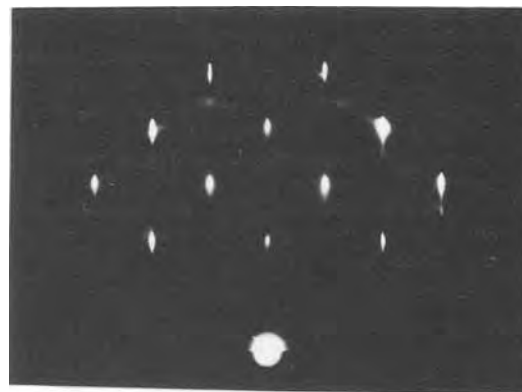


Fig. 2. The pressure in the growth chamber during the gas admittance. AsH_3 is introduced 20s and evacuated 3s, then TMG is introduced 4s and evacuated 3s (20", 3", 4", 3"). This is a standard gas admittance mode in this paper. Such a periodic cycle preparing one monolayer film growth is repeated up to the desired film thickness.



Reflection electron beam diffraction pattern of epi-layer ($T_{\text{sub}} = 500^\circ\text{C}$)

Fig. 3. The diffraction pattern of GaAs growth film by MLE, which is prepared by alternately introducing AsH_3 and TMG at the inlet pressures of 7×10^{-3} and 1.3×10^{-3} Pa for a gas admittance mode (20", 1", 2", 1") at $T_{\text{sub}} = 500^\circ\text{C}$.

cient for monolayer adsorption coverage. So, the film thickness per cycle was dropped. The dashed and dotted line indicates 2.83Å corresponding to a single monolayer of GaAs (100) surface.

At the growth temperatures of 600°, 550°, and 450°C, the film thickness per cycle was also investigated, and the data, along with those at 500°C, are shown in Fig. 4 in semilog scale. At the substrate temperature of 600°C, the film thickness increases with increasing TMG admittance rate, which is quite different compared with the growth at 500°C. In the case of $T_{\text{sub}} = 500^\circ\text{C}$, a mirrorlike surface is maintained during the growth, even as the admittance quantity per cycle is increased up to 2.4 Pa-liter, while at $T_{\text{sub}} = 600^\circ\text{C}$, the film surface becomes white at the admittance quantity of 0.7 Pa-liter/cycle. It indicates that decomposed products from adsorbed TMG on the

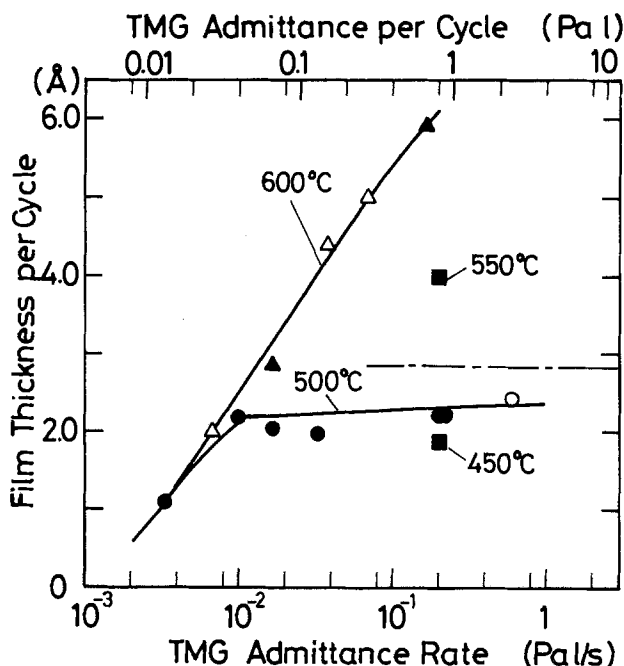


Fig. 4. Film thickness per cycle as a function of TMG admittance rate (closed circle) and quantity (open circle) at the substrate temperature of 600°, 550°, 500°, and 450°C with a gas admittance mode (20", 3", 4", 3") (closed circle) and other modes (open circle). AsH_3 pressure is always kept 7×10^{-3} Pa. The film thickness is nearly saturated at 2.2–2.3 Å/cycle at $T_{\text{sub}} = 500^\circ\text{C}$. The dashed and dotted line indicates 2.83Å corresponding to a single monolayer of GaAs (100) surface.

substrate may supply more than is consumed by chemical reaction with AsH_3 to film growth.

At the lower temperature, TMG is deposited on the substrate as some kind of Ga complex, and monolayer adsorption may take place as a character of the chemical adsorption. With increasing the substrate temperature, CH_3 radical can be released from the Ga complex, which becomes adsorbed in the form of a single Ga element, so at higher pressures a condensation of Ga takes place to multiple layer adsorption. Now we suppose N molecules of TMG adsorbed on the substrate may be divided into two parts

$$N(\text{TMG})_{\text{ad}} = (1 - \alpha)N(\text{Ga-complex})_{\text{ad}} + \alpha N(\text{Ga})_{\text{ad}}$$

where α is the ratio of adsorbed TMG as a single Ga element, which is written as a function of the substrate temperature, surface state, adsorption time, and so on. If one chooses the condition $\alpha \ll 1$ and the vapor pressure of TMG to be not too high, as a typical result of a chemisorption the saturated value is independent of the admittance quantity of TMG and monolayer growth is able to be realized. The substrate temperature of 500°C fulfills the conditions for such a monolayer growth.

The influence of AsH_3 pressure on the film growth has been investigated at the substrate temperature of 500°C, a TMG admittance rate of 0.2 Pa-liter/s, and a gas admittance mode (20", 3", 4", 3"). With increasing AsH_3 pressure, the film thickness per cycle increased nearly one monolayer, corresponding to 2.83Å, which is indicated as a dashed and dotted line in Fig. 5. The AsH_3 pressure, however, influences the film thickness less than the TMG pressure under these experimental conditions. The measured values are gradually saturated at first in the pressure region of $p \approx 2 \times 10^{-2}$ Pa, which corresponds to the AsH_3 admittance quantity of 10^3 L. It is worthwhile to note that, with increasing AsH_3 pressure, the surface morphology of the growth film is improved.

Photo MLE.—During the film growth by MLE, the substrate has been irradiated by a high pressure Hg lamp (500W), Ar laser (514.5 nm), and Ar laser plus Doubler (257.3 nm). Irradiation light is injected through the two ports of the heating lamp house in Fig. 1 onto the substrate. It is worthwhile to note that the temperature increase of the substrate is determined by a pyrometer to be less than 1° under any photoirradiation. This means that any changes of the film quality or the growth behavior by irradiation are purely influenced by photons and are not due to the temperature increase. The photon flux levels at the substrate were about 3 mW/cm², 0.1 W/cm², and 0.1

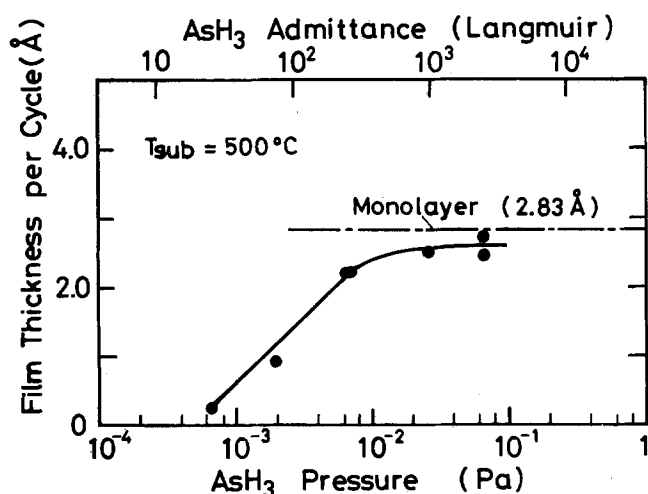


Fig. 5. Film thickness per cycle as a function of AsH_3 pressure in the growth chamber. With a gas admittance mode (20", 3", 4", 3") and a TMG admittance rate of 0.2 Pa-liter/s at the substrate temperature of 500°C. The dashed and dotted line indicates 2.83Å corresponding to a single monolayer of GaAs (100) surface. With increasing AsH_3 pressure, the film thickness per cycle becomes close to that of one monolayer.

Table I. Electrical properties of films prepared by MLE and photo-MLE under the same gas-admittance conditions

T_{sub}	Light source	μ_n (cm ² /V-s)	Carrier density (cm ⁻³)	Type
600°C		56	1.9×10^{19}	p
600°C	Hg lamp	103	1.3×10^{18}	p
700°C		68	1.2×10^{19}	p
500°C	Hg lamp	103	3.1×10^{18}	p
500°C	Laser (257.3 nm)	84	4.6×10^{18}	p
500°C	Laser (257.3 + 514.5 nm)	110	2.4×10^{18}	p

mW/cm² for a Hg lamp for 514.5 and 257.3 nm, respectively.

The surface morphology of grown films by MLE at $T_{\text{sub}} = 500^\circ\text{C}$ without photoirradiation and with photoirradiation by a Hg lamp are shown in Fig. 6a and 6b, respectively. The film surface with a Hg lamp irradiation is smoother than that without irradiation. At $T_{\text{sub}} = 350^\circ\text{C}$, film growth was observed with the Hg lamp irradiation, while at $T_{\text{sub}} = 400^\circ\text{C}$ film growth was not observed without irradiation under the same experimental conditions. An electron diffraction pattern of this growth film at $T_{\text{sub}} = 350^\circ\text{C}$ clearly indicates single-crystal nature. This growth temperature is the lowest value ever reported for MO source and AsH_3 . MO-MBE reported by Takahashi *et al.* needed a growth temperature of more than 500°C (13). This demonstrates that photo-MLE growth largely decreases the growth temperature and improves the surface morphology.

Electrical properties of the growth film.—In the case of MO-CVD, electrical properties of the films are strongly influenced by the AsH_3 and the TMG flow rate and the ratio during the growth. We found that the carrier density of the films grown by MLE are strongly dependent on



(a) without irradiation



(b) with irradiation

100 μm

Surface morphology of epi-layer
($T_{\text{sub}} = 500^\circ\text{C}$)

Fig. 6. Optical photos of the growth film by MLE without photoirradiation (a) and with irradiation by a Hg lamp (b) at $T_{\text{sub}} = 500^\circ\text{C}$. The film surface with irradiation by a Hg lamp is smoother than that without irradiation.

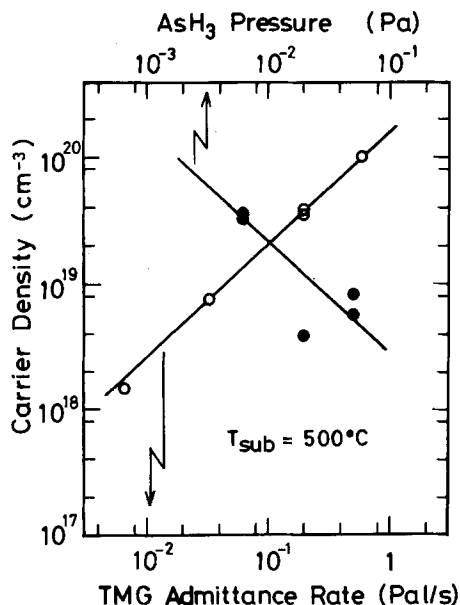


Fig. 7. Carrier density of growth film (~ 200 nm) by MLE as a function of TMG admittance rate (open circle) and AsH_3 pressure (closed circle) at the substrate temperature of 500°C with a gas admittance mode (20", 3", 4", 3").

the gas admittance rate, *i.e.*, TMG and AsH_3 pressure. Figure 7 shows the carrier density of these films as a function of the TMG admittance rate at the constant AsH_3 pressure of 6.7×10^{-3} Pa and as a function of the AsH_3 pressure at the constant TMG admittance of 0.2 Pa-liter/s at the substrate temperature of 500°C . All films for these measurements were grown only ~ 200 nm on the n^+ Si-doped substrates of (100) and of (100) misoriented 4° to $\langle 110 \rangle$ faces. All growth films show p-type behavior. Carrier densities were calculated by including a correction of depletion layer widths. A depletion layer width of an abrupt approximation is estimated to be about 400\AA for GaAs at the carrier density of 10^{18} cm^{-3} .

With decreasing TMG admittance rate from 1 to 10^{-2} Pa-liter/s, the carrier density proportionally decreased from 10^{20} to 10^{18} cm^{-3} , while with decreasing AsH_3 pressure the carrier density increased. It demonstrates that the quality of the film grown by MLE can be tremendously improved with slower TMG admittance rate and higher AsH_3 pressure. However, under these experimental conditions, all growth films are p-type with a carrier density in the order of $10^{18}\text{--}10^{20}\text{ cm}^{-3}$. Such a high impurity level suggests the existence of a deviation from the stoichiometry and contaminations, such as carbon doped in the film during the growth. At the moment, we will not comment in detail on such a marked influence of TMG and AsH_3 pressure during the film growth. Those will be discussed in another paper. The influence of the photoirradiation on the electrical properties was studied and is summarized in Table I. Photoirradiation significantly improved the Hall mobility and decreased the carrier density.

Selective film growth by MLE.—An observation of the growth film surface by an optical microscope indicates no deposits on the Si_3N_4 film used for a mask pattern.

Auger electron spectroscopy shows neither Ga nor As components on the Si_3N_4 mask film. On the contrary, film growth occurred only on the region of GaAs surface without Si_3N_4 film. These facts indicate that the selective adsorption and selective reaction for crystal growth of TMG and AsH_3 took place on the substrate. We can conclude that MLE is a crystal-growth technique that progresses by a chemical adsorption reaction, *i.e.*, surface catalysis.

It is quite interesting to note that the substrate orientation does not influence the film growth by MLE. No significant differences between (100) and (100) misoriented 4° to $\langle 110 \rangle$ substrates have been observed on the growth rate and on the electrical properties of the film. However, films on the (100) substrate have a better surface morphology than those on the (100) misoriented 4° to $\langle 110 \rangle$.

Conclusion

For the first time, single-crystal GaAs films were prepared by MLE using TMG and AsH_3 and monolayer growth conditions were determined as a function of the gas admittance mode and substrate temperature. At the substrate temperature of 500°C , monolayer film growth was realized. The electrical properties of the film were strongly influenced by the TMG and AsH_3 pressure. Those were improved by increasing AsH_3 pressure and decreasing TMG pressure at the gas admittance. Photoirradiation improved the surface morphology and the electrical properties of the growth film by MLE. At the substrate temperature of 350°C , single-crystal film growth was realized by the irradiation of a Hg lamp.

Manuscript submitted Sept. 24, 1984; revised manuscript received Dec. 17, 1984.

Research Development Corporation of Japan assisted in meeting the publication costs of this article.

REFERENCES

- J. Nishizawa, in "Proceedings of the 11th Conference on Solid State Devices," (1979); *Jpn. J. Appl. Phys. Suppl.*, **19-1**, 3 (1980).
- J. Nishizawa, in "Technical Digest of Conference Microwave Solid State Devices," p. 28, Gdansk, Poland (1980).
- J. Nishizawa *Oyo Butsuri*, **53**, 516 (1984).
- M. Ahonen, M. Pessa, and T. Suntola, *Thin Solid Films*, **65**, 301 (1980).
- A. Y. Cho, *J. Vac. Sci. Technol.*, **16**, 257 (1979).
- T. Suntola and M. Antson, U.S. Pat. 4,058,430 (1977); T. Suntola, in "Extended Abstracts of 16th Conference on Solid State Devices and Materials," p. 647, Kobe, Japan (1984).
- M. Pessa, O. Jylha, P. Huttunen, and M. A. Herman, *J. Vac. Sci. Technol. A*, **2**, 418 (1984); M. Pessa, P. Huttunen, and M. A. Herman, *J. Appl. Phys.*, **54**, 6047 (1983).
- M. Pessa, R. Makela, and T. Suntola, *Appl. Phys. Lett.*, **38**, 131 (1981).
- J. Nishizawa *J. Metall. Soc. Jpn.*, **25**, 149, 177 (1961).
- M. Kumagawa, H. Sunami, T. Terasaki, and J. Nishizawa, *Jpn. J. Appl. Phys.*, **7**, 1332 (1968).
- J. Nishizawa and Y. Kokubun, in "Extended Abstracts of 16th Conference on Solid State Devices and Materials," p. 1, Kobe, Japan (1984).
- H. Beneking, A. Escobosa, and H. Krautle, *J. Electron. Mater.*, **10**, 473 (1981); N. Putz, H. Heinecke, E. Veuhoff, G. Arens, M. Heyen, H. Luth, and P. Balk, *J. Cryst. Growth*, **68**, 194 (1984).
- E. Tokumitsu, Y. Kudou, M. Konagai, and K. Takahashi, *J. Appl. Phys.*, **55**, 3163 (1984).

Effect of Furnace Preanneal and Rapid Thermal Annealing on Arsenic-Implanted Silicon

R. Kwor,* D. L. Kwong, and C. C. Ho**

Department of Electrical Engineering, University of Notre Dame, Notre Dame, Indiana 46556

B. Y. Tsaur

Lincoln Laboratory, Massachusetts Institute of Technology, Lexington, Massachusetts 02173

S. Baumann

Charles Evans and Associates, San Mateo, California 94402

ABSTRACT

In this paper, the effect of low temperature preanneal followed by rapid thermal annealing on arsenic-implanted Si is studied. The electrical properties and impurity distribution of the annealed Si are discussed. Sheet mobility and dopant activation of the implanted Si (100) samples (As⁺: 80 keV, 1×10^{15} and 1×10^{16} cm⁻² doses) as functions of annealing temperature are reported. TEM measurements on samples with and without preanneal (550°C, 1h) are presented. RBS and channeling results on samples with and without preanneal are also included. It is found that the dopant diffusion during RTA of 1×10^{15} cm⁻² dose As implants can be reduced somewhat by employing a 550°C, 1h furnace preanneal prior to RTA. However, the preanneal does not have significant effect on the carrier profiles of the 1×10^{16} cm⁻² dose implants. In some cases, the preanneal increases the dopant activation slightly.

In the fast developing VLSI technology, the trend is to have smaller device dimensions and shallower junctions. More stringent requirements have thus been imposed on the annealing of ion-implantation damage. One promising technique is rapid thermal annealing (RTA), during which the implanted wafer is heated by a short exposure to an incoherent light. The wafer is usually thermally isolated, and its maximum temperature is limited by a balance between absorbed and radiated power. Compared with furnace annealing, RTA is found to be capable of more efficient dopant activation with minimal diffusion. In the past two years, many researchers have reported their findings on the RTA of ion-implanted Si. Being a well-behaved dopant for Si, arsenic is of special interest; its RTA behavior has been studied extensively (1-6). Hodgson *et al.* used ion backscattering, channeling, and TEM to study the As-implanted (100) Si rapidly annealed with an arc lamp (1). Wagner *et al.* did research on photoluminescence from rapidly annealed, As-implanted Si (2). Kalish *et al.* reported their SIMS results of As implants annealed with a tungsten halogen RTA system (3). Fair *et al.* have modeled the As diffusion during RTA and suggested the possibility of enhanced diffusion for As during RTA (4). Wilson *et al.* reported the RTA results of As implants using a Varian IA-200 graphite annealing system (5). Recently, Seidel presented a paper in which he reported the absence of enhanced diffusion during RTA for arsenic implants (6).

In this paper, the two-stage annealing process using a low temperature furnace preanneal and a high temperature rapid thermal anneal for high dose As⁺ implants is investigated. Emphasis has been given to the electrical properties and the damage removal of the annealed samples.

Experimental

Si wafers of (100) orientation and 7 Ω-cm p-type resistivity were implanted with As⁺ ions at an energy of 80 keV to a dose of 1×10^{15} or 1×10^{16} cm⁻². The implantation was performed at room temperature with the substrate tilted 7° off the direction of the incident beam to minimize channeling. Some of the samples were preannealed in a quartz-tube furnace at 550°C for 1h in a flowing N₂ ambient. Both the preannealed and unannealed samples were then exposed to radiation from high intensity tungsten

lamps in a flowing N₂ ambient. The annealing time was 2s, and the annealing temperatures were about 1000°, 1050°, and 1100°C. The temperature of each sample was measured during the irradiation using a thermocouple contacted to the back of the same sample. The sample heating rate was 150°C/s, and the initial cooling rate was 90°C/s. Hall effect measurements using the van der Pauw method in conjunction with anodization and layer removal were used to determine the carrier concentration, sheet resistance, and mobility. The microstructures of the samples were studied by transmission electron micros-

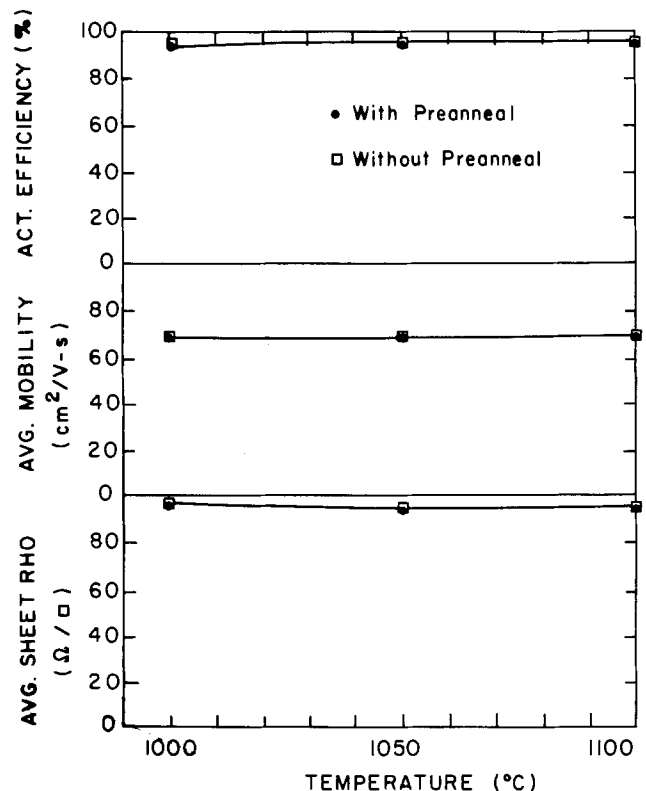


Fig. 1. Dopant activation efficiency, sheet mobility, and sheet resistivity as functions of RTA temperature for 1×10^{15} cm⁻² dose sample, both with and without preanneal (550°C, 1h).

* Electrochemical Society Active Member.
** Electrochemical Society Student Member.

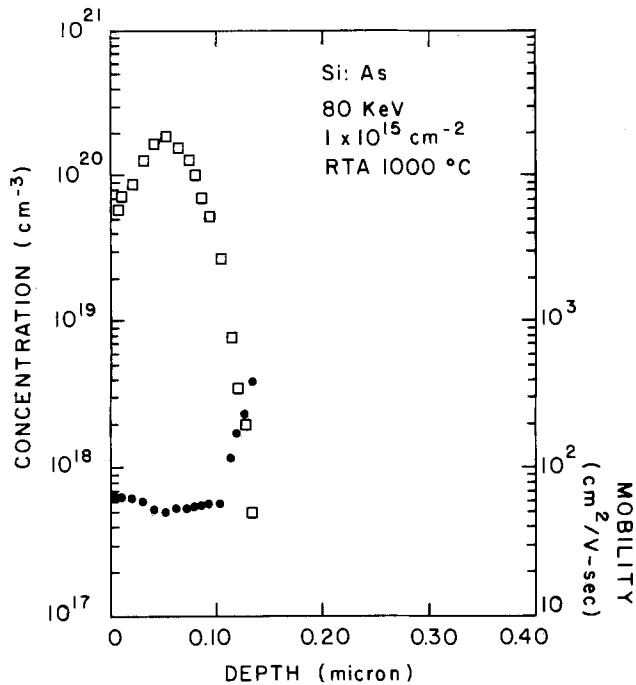


Fig. 2. Carrier concentration and mobility profiles for 80 keV, $1 \times 10^{15} \text{ cm}^{-2}$ dose arsenic implants rapidly annealed at 1000°C for 2s.

copy (TEM). Channeled RBS measurements were also taken from a group of unannealed and annealed samples with and without furnace preanneal. The results obtained are discussed and correlated to those from TEM and Hall measurements.

Results

Hall and TEM Measurements.—Figure 1 shows the dopant activation efficiency, sheet mobility, and sheet resistivity as functions of RTA temperature for the $1 \times 10^{15} \text{ cm}^{-2}$ samples (both with and without preanneal). Nearly complete electrical activation was achieved for all the samples with or without preanneal. Figure 2 shows the carrier concentration and mobility profiles for the 1000°C RTA sample without preanneal, and the results for the

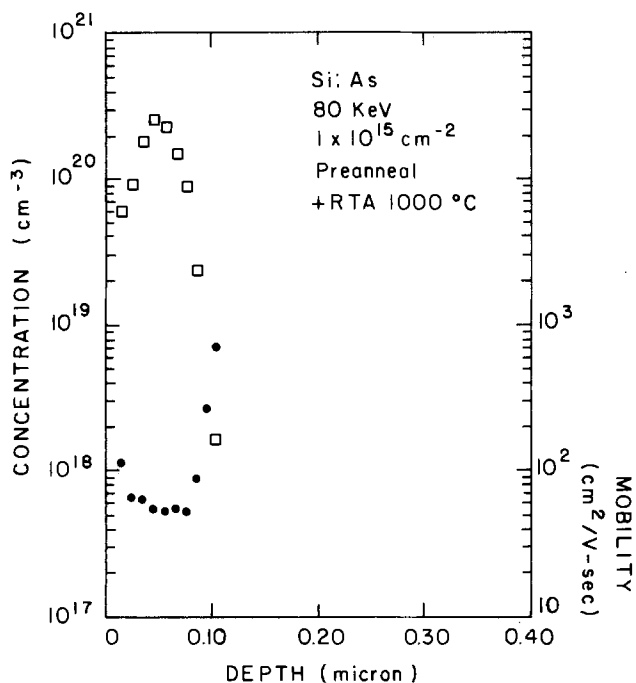


Fig. 3. Carrier concentration and mobility profiles for 80 keV, $1 \times 10^{15} \text{ cm}^{-2}$ dose arsenic implants preannealed at 550°C in furnace, followed by RTA at 1000°C for 2s.

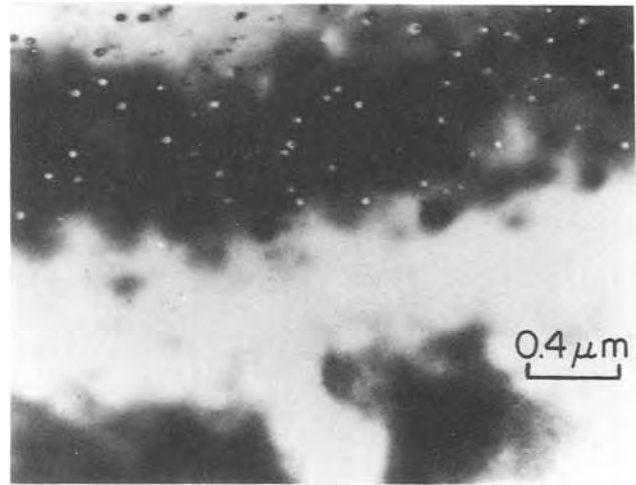


Fig. 4. Planar TEM micrograph of 80 keV, $1 \times 10^{15} \text{ cm}^{-2}$ dose arsenic implants preannealed (550°C , 1h), followed by RTA at 1000°C for 2s.

preannealed, 1000°C RTA sample are shown in Fig. 3. The sample with the preanneal has a shallower concentration profile and higher peak carrier concentration than the sample without preanneal. This result indicates that the preanneal may have some effect on the dopant diffusion during RTA, resulting in a shallower junction. Figure 4 is a planar TEM micrograph of the preannealed, 1000°C RTA sample. The regrown layer (lower portion of the micrograph) is defect free, although defects (dislocations) are observed underneath this layer. The depth of the defects was evaluated from the number of thickness fringes produced by the dynamical diffraction conditions in the wedge-shaped sample. The defects were found to be about $0.13 \mu\text{m}$ deep, roughly corresponding to the position of original amorphous-crystalline interfaces.

The activation efficiency, sheet mobility, and sheet resistivity for the $1 \times 10^{16} \text{ cm}^{-2}$ samples without and with preanneal are shown in Fig. 5, respectively, as a function of RTA temperatures. The activation efficiency increases with temperature, while the mobility and sheet resistivity

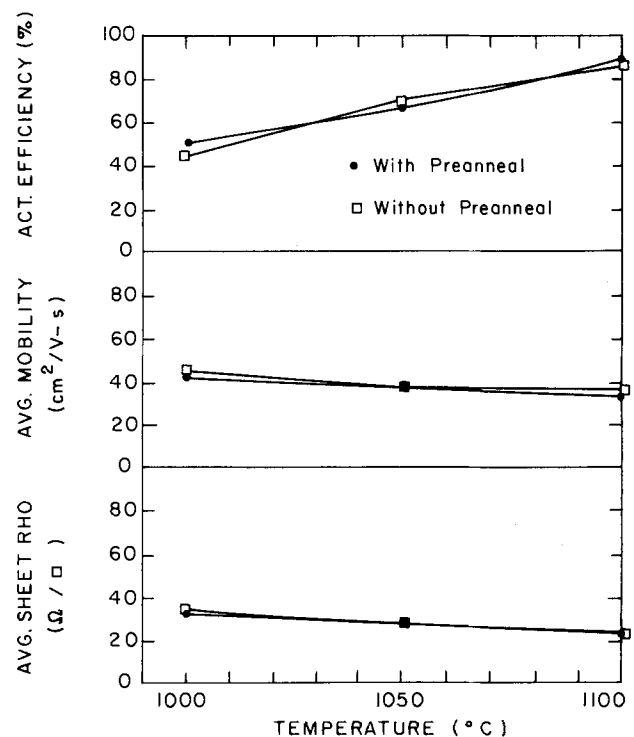


Fig. 5. Dopant activation efficiency, sheet mobility, and sheet resistivity as functions of RTA temperature for $1 \times 10^{16} \text{ cm}^{-2}$ dose samples both with and without preanneal (550°C , 1h).

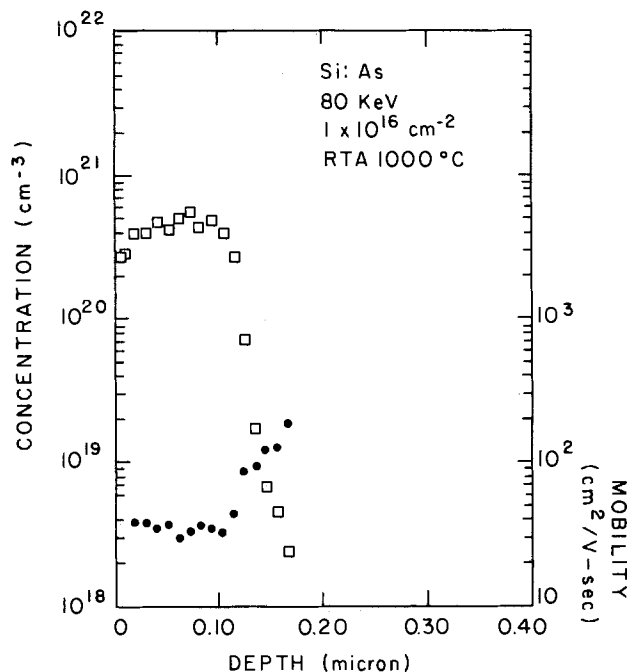


Fig. 6. Carrier concentration and mobility profiles for 80 keV, $1 \times 10^{16} \text{ cm}^{-2}$ dose arsenic implants annealed at 1000°C for 2s.

decrease slightly with temperature. This is probably due to the effect with a high As dose. Figures 6 and 7 show the carrier concentration and mobility profiles for the non-preannealed samples with RTA temperatures of 1000°C and 1100°C , respectively. The carrier concentration profiles are relatively flat in comparison with the gaussian profiles for the $1 \times 10^{15} \text{ cm}^{-2}$ samples shown in Fig. 2 and 3. This difference is observed because the As concentration for the $1 \times 10^{16} \text{ cm}^{-2}$ samples exceeds the equilibrium solid solubility near the peak of the implanted dopant distribution, and the As near that region is only partially activated.

The 1100°C RTA sample (Fig. 7) shows a much deeper profile due to better activation and dopant diffusion. Figures 8 and 9 are the carrier concentration and mobility profiles for the preannealed samples with RTA tempera-

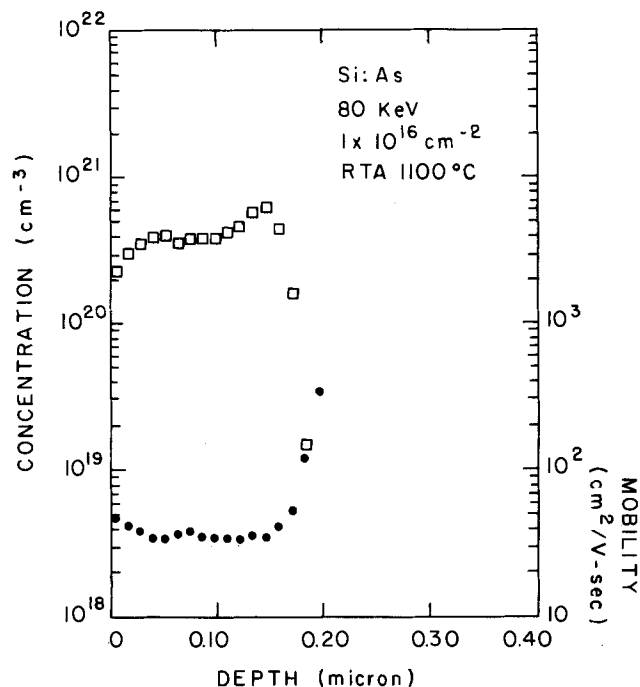


Fig. 7. Carrier concentration and mobility profiles for 80 keV, $1 \times 10^{16} \text{ cm}^{-2}$ dose arsenic implants rapidly annealed at 1100°C for 2s.

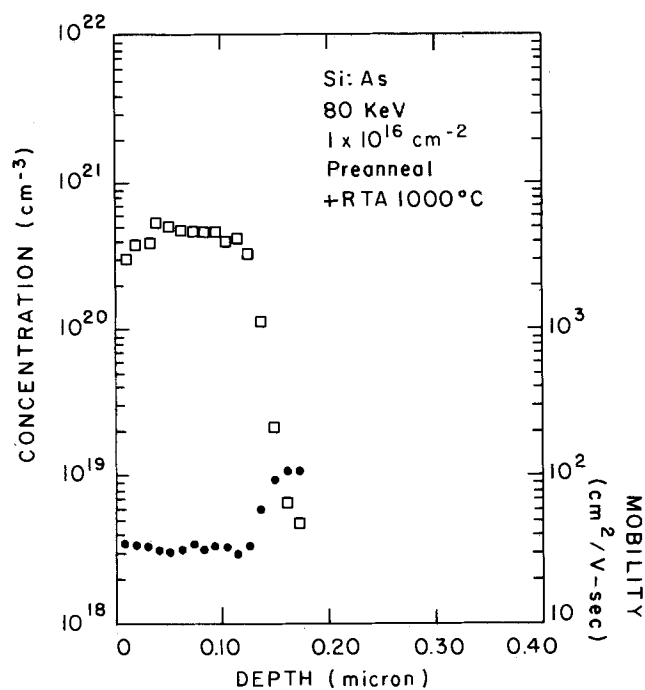


Fig. 8. Carrier concentration and mobility profiles for 80 keV, $1 \times 10^{16} \text{ cm}^{-2}$ dose arsenic implant preannealed at 550°C in furnace, followed by RTA at 1000°C for 2s.

tures of 1000° and 1100°C , respectively. Higher activation efficiency ($\sim 50\%$) is observed for the preannealed 1000°C sample of Fig. 8 compared to the sample of Fig. 6, which was not preannealed. For the 1100°C sample, shown in Fig. 9, higher carrier concentrations are achieved, giving rise to higher activation efficiency compared to that of 1000°C sample of Fig. 8. The profile is slightly shallower than that of the sample without preanneal in Fig. 7. Since this difference is within the experimental uncertainty of the Hall measurement, as far as the carrier concentration profile is concerned, the preanneal did not seem to have very much effect. This contrasts with the results reported by Fair *et al.* (4), who found a significant reduc-

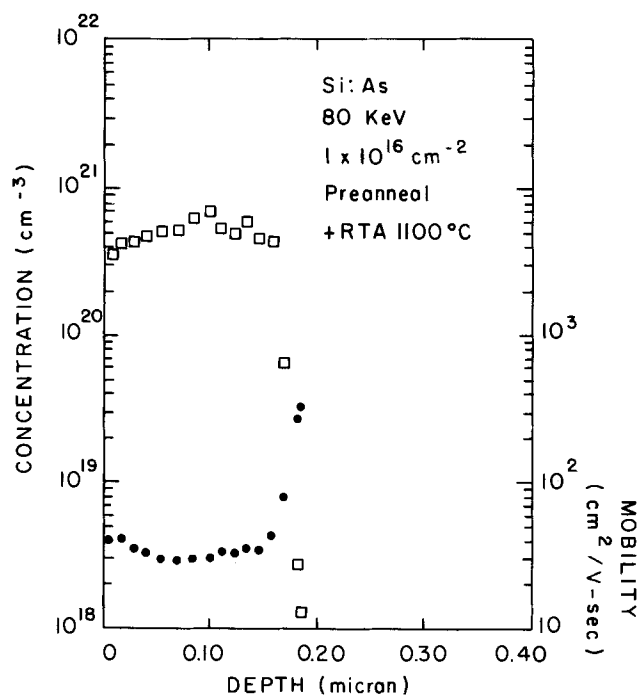
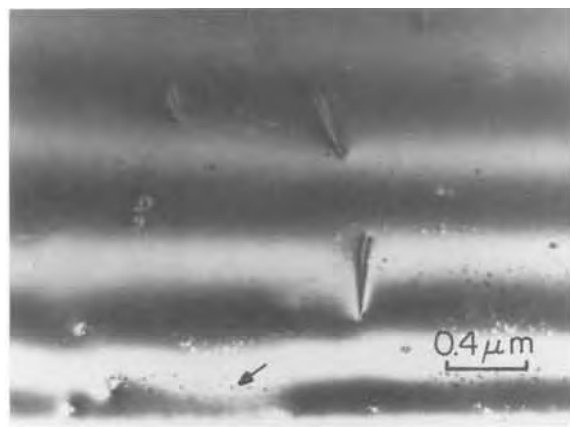
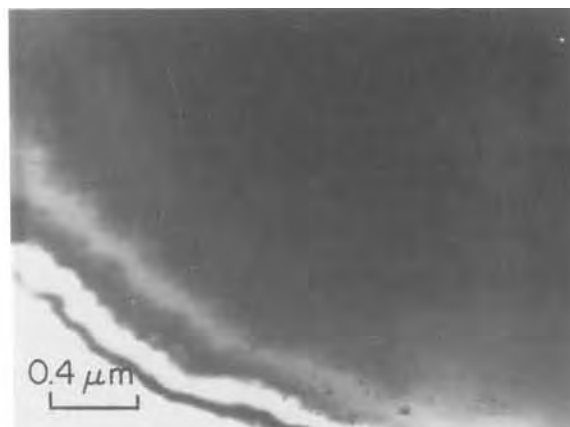


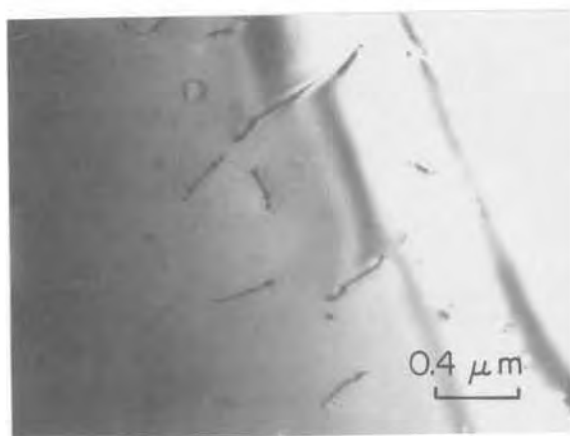
Fig. 9. Carrier concentration and mobility profiles for 80 keV, $1 \times 10^{16} \text{ cm}^{-2}$ dose arsenic implants preannealed at 550°C in furnace, followed by RTA at 1100°C for 2s.



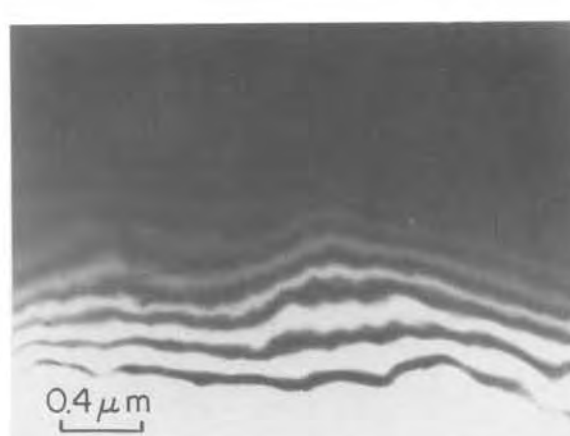
(a)



(a)



(b)



(b)

Fig. 10. Planar TEM micrograph of 80 keV, $1 \times 10^{16} \text{ cm}^{-2}$ dose arsenic implant rapidly annealed at 1000°C for 2s. The arrow indicates a precipitate. a: Without 550°C, 1h furnace preanneal. b: With preanneal.

Fig. 11. Planar TEM micrograph of 80 keV, $1 \times 10^{16} \text{ cm}^{-2}$ dose arsenic implant rapidly annealed at 1100°C for 2s. a: Without 550°C, 1h furnace preanneal. b: With preanneal.

tion of atomic profile broadening in preannealed samples.

Figure 10 shows the TEM micrographs of the 1000°C RTA samples without (Fig. 10a) and with (Fig. 10b) preanneal. "Hairpin" dislocations are present in the regrown layers for both samples. However, the sample without preanneal has a higher density of As precipitates, resulting in poorer activation. Figure 11 shows the TEM mi-

crographs for the 1100°C RTA samples without (Fig. 11a) and with (Fig. 11b) preanneal. No dislocations are observed for either sample.

RBS/channeling measurements.—Rutherford backscattering (RBS) and channeling measurements of 2.275 MeV He ions were made at Charles Evans Associates. The "rotating random" orientation technique was used when measuring the total As dose in each of the samples. The sample was continuously moved through all crystal orientations during the data acquisition phase so that an average or "random" crystal orientation is obtained. The description of the samples analyzed is summarized in Table I.

Figures 12-17 present the backscattering spectra in <100>-aligned and random directions for the samples. The channelled spectra are denoted with the suffix "CC," while random spectra are denoted with the suffix "RR." The aligned backscattering yield is identical to the yield

Table I. All samples were <100>, 10 Ω-cm Si implanted with 80 keV arsenic

Sample no.	Description	Arsenic dose from RBS (A/cm^2)
1	Dose $1 \times 10^{15} \text{ cm}^{-2}$, unannealed	8.2×10^{14}
2	Dose $1 \times 10^{16} \text{ cm}^{-2}$, unannealed	8.6×10^{15}
3	Dose $1 \times 10^{15} \text{ cm}^{-2}$, RTA 1100°C	8.9×10^{14}
4	Dose $1 \times 10^{15} \text{ cm}^{-2}$, preanneal + RTA 1100°C	8.1×10^{14}
5	Dose $1 \times 10^{16} \text{ cm}^{-2}$, RTA 1100°C	8.1×10^{15}
6	Dose $1 \times 10^{16} \text{ cm}^{-2}$, preanneal + RTA 1100°C	9.0×10^{15}
7	Dose $1 \times 10^{16} \text{ cm}^{-2}$, preanneal + RTA 1050°C	8.9×10^{15}

Table II. Arsenic substitutionality

Sample	$\chi_{\text{min}} \text{ Si}$	$\chi_{\text{min}} \text{ As}$	S
3	0.04	0.21	0.82
5	0.03	0.19	0.83
6	0.04	0.16	0.88
7	0.04	0.24	0.79

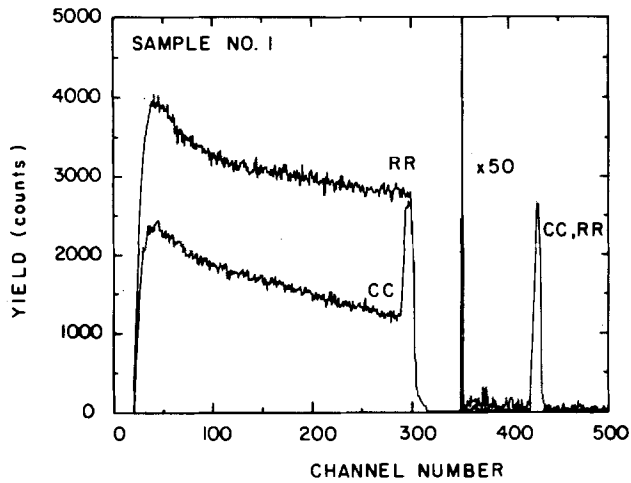


Fig. 12. Rutherford backscattering spectra in $\langle 100 \rangle$ aligned and random directions for unannealed, 80 keV, $1 \times 10^{15} \text{ cm}^{-2}$ dose arsenic implant.

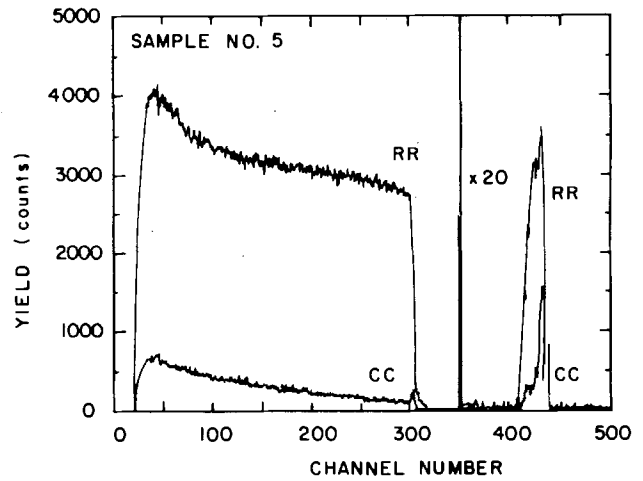


Fig. 15. Rutherford backscattering spectra in $\langle 100 \rangle$ aligned and random directions for 80 keV, $1 \times 10^{15} \text{ cm}^{-2}$ dose arsenic implant preannealed (550°C, 1h), followed by RTA at 1100°C for 2s.

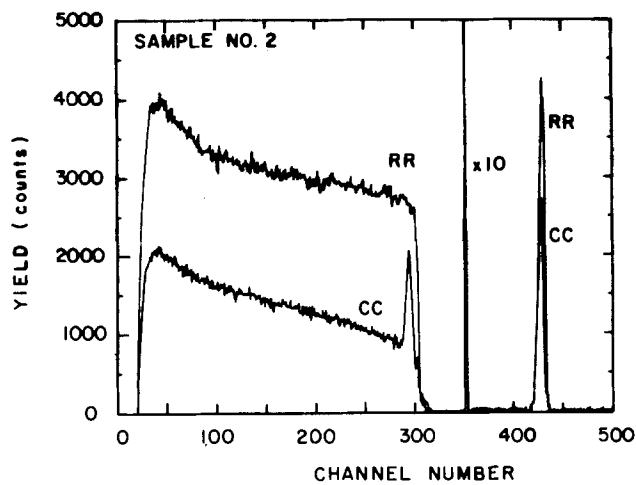


Fig. 13. Rutherford backscattering spectra in $\langle 100 \rangle$ aligned and random directions for unannealed, 80 keV, $1 \times 10^{16} \text{ cm}^{-2}$ dose arsenic implant.

in Table II. The following equation was used to calculate the values of S

$$S = \frac{1 - X_{\text{impurity}}}{1 - X_{\text{host}}}$$

These S values are only first estimates (7). However, they do correlate well with the values from Hall measurements.

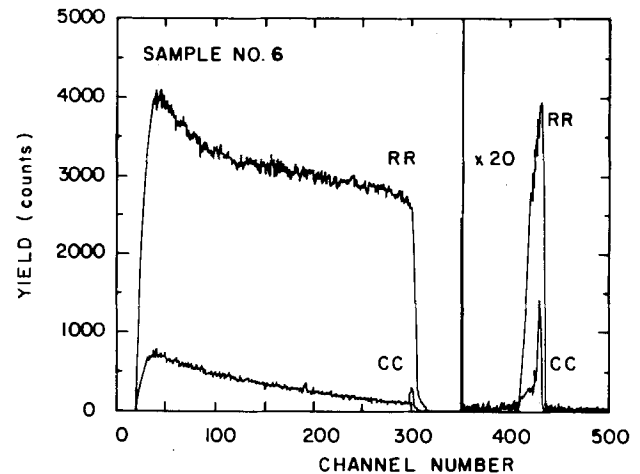


Fig. 16. Rutherford backscattering spectra in $\langle 100 \rangle$ aligned and random directions for 80 keV, $1 \times 10^{16} \text{ cm}^{-2}$ dose arsenic implant preannealed (550°C, 1h), followed by RTA at 1100°C for 2s.

from a virgin crystal for all the annealed samples (with or without preanneal). The minimum scattering yields (X_{min}) for the annealed samples are around 0.03-0.04, indicating that the recovery of the crystal is nearly perfect. The total arsenic dose measured in each sample is shown in Table I, and the first-order substitutional fractions S are shown

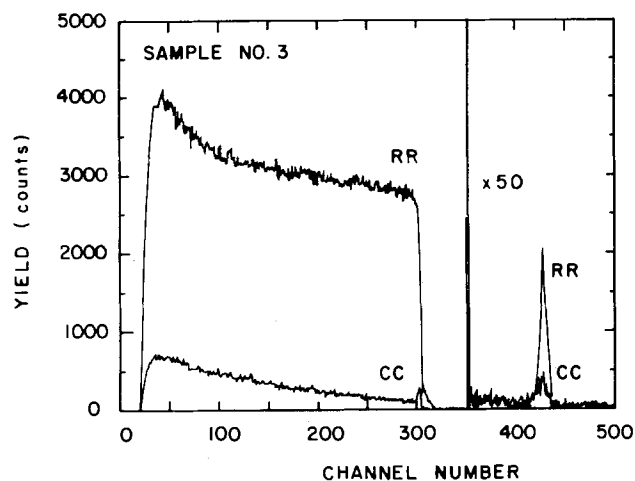


Fig. 14. Rutherford backscattering spectra in $\langle 100 \rangle$ aligned and random directions for 80 keV, $1 \times 10^{15} \text{ cm}^{-2}$ dose arsenic implant rapidly annealed at 1100°C for 2s.

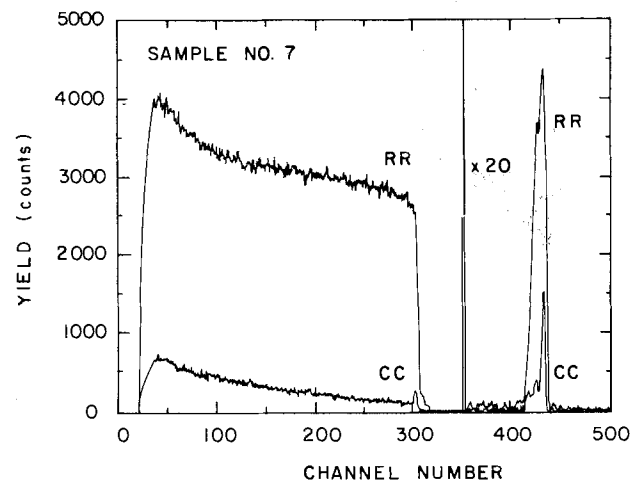


Fig. 17. Rutherford backscattering spectra in $\langle 100 \rangle$ aligned and random directions for 80 keV, $1 \times 10^{16} \text{ cm}^{-2}$ dose arsenic implant preannealed (550°C, 1h), followed by RTA at 1050°C for 2s.

Summary and Discussion

For arsenic implants with $1 \times 10^{15} \text{ cm}^{-2}$ dose, a 1000°C RTA results in nearly complete activation, but many residual defects still exist even after a 550°C , 1h furnace preanneal prior to RTA. Higher temperature ($> 1050^\circ\text{C}$) is needed for better defect removal. For a dose of $1 \times 10^{16} \text{ cm}^{-2}$, a 1000°C RTA results in $\sim 50\%$ activation, and many residual defects still exist even after a 550°C furnace preanneal, which seems to increase the activation slightly. An 1100°C RTA, with or without preanneal, removes most of the residual dislocations and results in an activation better than 80% . We have found that dopant diffusion during RTA of $1 \times 10^{15} \text{ cm}^{-2}$ dose As implants can be reduced somewhat by employing a low temperature furnace preanneal prior to RTA. For $1 \times 10^{16} \text{ cm}^{-2}$ dose, there is no significant difference between the carrier concentration profiles with and without preanneal. However, the preanneal treatment in some cases increases the dopant activation efficiency.

Acknowledgments

This work was partially supported by Semiconductor Research Corporation under Contract no. 83-01-008. The

Lincoln Laboratory portion of this work was sponsored by the Department of the Air Force.

Manuscript submitted Oct. 1, 1984; revised manuscript received Jan. 25, 1985. Part of this article was presented as Paper 114 at the Cincinnati, Ohio, Meeting of the Society, May 6-11, 1984.

The Semiconductor Research Corporation assisted in meeting the publication costs of this article.

REFERENCES

1. R. T. Hodgson, J. E. E. Baglin, A. E. Michel, S. Mader, and J. S. Gelpey, *Mater. Res. Soc. Symp. Proc.*, **13**, 355 (1983).
2. J. Wagner, J. C. Gelpey, and R. T. Hodgson, *Appl. Phys. Lett.*, **45** 47 (1984).
3. R. Kalish, T. O. Sedgwick, S. Mader, and S. Shatas, *ibid.*, **44**, 107 (1984).
4. R. B. Fair, J. J. Wortman, and J. Liu, *This Journal*, **131**, 2387 (1984).
5. S. R. Wilson, W. M. Paulson, R. B. Gregory, A. H. Hamdi, and F. D. McDaniel, *J. Appl. Phys.*, **55**, 4162 (1984).
6. T. E. Seidel, Paper A5.1 presented at the Materials Research Society 1984 Fall Meeting, Nov. 26-30, Boston, MA.
7. L. Feldman, J. Meyer, and S. Picraux, in "Materials Analysis by Ion Channeling," p. 59, Academic Press, New York (1982).

Fluence (Dose) Monitoring of Energetic H^+ , B^+ , N^+ , P^+ , and As^+ Ions Using Ionization in a Radiachromic Film

Kranti V. Anand and Myron Cagan^{*1}

Fairchild Research Center, Palo Alto, California 94304

ABSTRACT

We have measured the increase in optical density vs. ion fluence (dose) of H^+ , B^+ , N^+ , P^+ , and As^+ ions implanted at 80 and 150 keV energies using a radiachromic dye in a nylon matrix. The technique, with some modification to the substrate, would be suitable for automatic, routine monitoring of low ion implant doses in the range of about 10^{11} to 10^{13} cm^{-2} . The data have been theoretically analyzed, and a model for optical density saturation (or bleaching) at high doses is proposed.

In this paper, we describe a method for monitoring the implant fluence² (dose) for H^+ , B^+ , N^+ , P^+ , and As^+ ions at 80 and 150 keV. These species are commonly used in the silicon integrated circuit industry, and the energies cover the values typically encountered. The method is particularly suitable at low doses (typically in the range of about 10^{11} cm^{-2} - 10^{13} cm^{-2} , depending on the ion species) which are at least an order of magnitude lower than the other commonly employed method such as sheet resistivity (ρ_s) (1). However, the technique of threshold voltage measurement using either MOSFET's or MOS structures (2) suffers from the disadvantage that complete wafer processing is required. This new technique to be described has the advantage, because it is rapid, that it can be used for routine monitoring of implanter performance. The measured dose is accurate and absolute in the sense that, unlike ρ_s measurement, it does not depend on mobility and free carrier concentration after a high temperature anneal. It is also capable of being automated, so that a dose map of each wafer can be obtained. It should be pointed out that a system similar to the one proposed, but relying on optical changes in photoresist, is commercially available (3). Though that system has the advantage of a wider dose range capability (5×10^{12} - $5 \times 10^{15} \text{ cm}^{-2}$), the low end of the range is approximately an order of magni-

tude higher than that observable with the proposed method.

Experimental Details

The ions were implanted into a sample of $1 \text{ cm} \times 1 \text{ cm} \times 40 \mu\text{m}$ thickness of radiachromic dye (RCD) using an implanter³ with a hot cathode ion source. The RCD was originally developed by McLaughlin and Chalkley (4, 5) and is commercially available as self-supporting flexible films as thin as about $8 \mu\text{m}$ (6, 7). The films consist of a nylon matrix containing a dye of hydroxyethyl-substituted aminotriphenyl methane nitrile. Such materials are used mostly for x-ray, gamma ray, and electron dosimetry in radiation processing and medical fields. Shaw *et al.* (8) have used this material⁴ for lithographic applications and have given details of its sensitivity to UV radiation, x-rays, electron beams, and, to a smaller extent, H^+ and Ga^+ ion beams. During implantation, the sample is held on a stainless steel backing fixture, and a circular area of 7.5 cm diam is exposed to the beam. The measured beam currents with and without the RCD sample were found to be essentially the same, indicating that there were no anomalies in charge collection due to the presence of the RCD. Similar conclusions were reached by Rosenstein and co-workers (9) for the same material when bombarded with 1.5 MeV electrons and with 3 MeV protons. Hansen *et al.* (10) have also exposed it to 3 and 16 MeV protons, 10 MeV α particles, 21 MeV Li^+ ions, 42 MeV N^+

^{*}Electrochemical Society Active Member.

¹Present address: Philips Research Laboratories Sunnyvale, Sunnyvale, California 94086.

²Fluence is defined as the number of incident ions per unit area (cm^{-2}). However, since in the semiconductor industry this is referred to as dose, we shall call it by that name from now on.

³High Voltage Engineering, Model 300 keV/LS5.

⁴Far West Technology, Incorporated, Goleta, California 93117.

ions, and 64 MeV O^+ ions. Since the RCD is sensitive to UV and normal fluorescent light, all operations are carried out under yellow light. The optical density (OD) was calculated from transmission data measured using a UV spectrometer⁵ at 610 nm wavelength. The minimum transmission actually occurs at 600 nm, but we found better repeatability at 610 nm.

Analysis of Experimental Results

As can be seen in Fig. 1a and 1b, the response data for this dye to the various ions consists of an initial regime in which the OD increases with dose. It is followed by a saturation and a bleaching regime. The dose at which the maximum in OD occurs we shall refer to as D_{max} .

We find (solid lines in Fig. 1a and 1b) that the initial regime can be fitted to a theoretical curve of the form of Eq. [1]

$$OD = K[1 - \exp(-D/D_0)]^m \quad [1]$$

This equation results from the "one or more hit" theory (11, 14) and was shown to apply to a wide range of detectors. Though in the past this treatment has been applied to megaelectron volt gamma rays and protons, Sharma *et al.* (11) have discussed its applicability to heavy ions as well. The theory uses Poisson statistics to work out the probability of photoionization events as a function of the radial distance from the particle track. The model assumes that it is the energetic secondary electrons which cause the radiolytic ionization process and that the direct particle contribution is negligible.

Table I gives the calculated values of the three constants k , D_0 , and m ; m is called the "target" or "extrapolation" number. We note that for H^+ , the value of m is 1, implying that it is a one-hit detector as referred to by Sharma and Katz (11). This has also been observed by Rosenstein *et al.* (9) with 3.0 MeV protons and by Hansen *et al.* (10). However, as seen in Table I for the other ions, $m \neq 1$. For this reason, the ionization process appears to be more complex. In spite of this, the theory gives a satisfactory fit to the ions and energies which were used.

We proceed now to calculate the saturation dose, D_{max} , from a different set of theoretical considerations. In the discussion above, we have neglected the nuclear energy

loss of the penetrating ion. We calculate the parameter E_{TN} (defined below), together with the projected range R_p , using a range theory developed by one of us (K.V.A.) using a semi-Monte Carlo technique (12, 13). The theory uses a Thomas-Fermi screening potential for calculating the nuclear energy loss. The values of E_{TN} and R_p are also given in Table I. If we were to assume that bleaching occurs when the total nuclear energy absorbed by the RCD reaches a constant value, which is independent of the type of ion or its initial energy, then for the best fit to our experimental data, this constant is as given by Eq. [2].

$D_{max}E_{TN} = \text{total nuclear energy absorbed (const.)} = 2.3 \times 10^{14} \text{ keV-cm}^{-2}$ [2] where E_{TN} is total nuclear energy loss in [keV-(ion)⁻¹] over its stopping track length. Table I shows the theoretical (using Eq. [2]) and experimental values of D_{max} . As can be seen, the correspondence is good, implying that our assumption that bleaching is caused by nuclear energy loss is correct.

It should be noted that, as expected, the highest calculated range (10,350Å) is that of the lightest ion, H^+ , at 150 keV and the lowest calculated range (930Å) is for the heaviest ion, As^+ . However, the total nuclear energy loss when bleaching occurs is the same for each ion, *i.e.*, $2.3 \times 10^{14} \text{ keV-cm}^{-2}$. This means that the average nuclear energy loss per unit volume for As^+ is an order of magnitude higher than for H^+ . This suggests that bleaching is not due to the primary reaction between the incoming ion and the material. Instead, it is caused by secondary processes which distribute the nuclear energy loss over a much wider range. Since H makes up 60% of the atomic density of the dye matrix and has the requisite long range, it is proposed that it is primarily responsible for the bleaching action by directly disrupting the dye molecule.

Measurement of Ion Dose Using the Dye

The experimental data given in Fig. 1a and 1b can obviously be used to calculate dose from the measured value of OD on any given sample. The accuracy with which the dose can be measured using this data depends on the accuracy of the OD measurement. Our spectrometer is capable of measuring the transmission through the dye with a maximum error of $\pm 0.1\%$. Using the functional relationship between OD and dose as given by Eq. [1], we calculate the dose that can be measured with an accuracy of

⁵Perkin-Elmer UV spectrophotometer (Model 320).

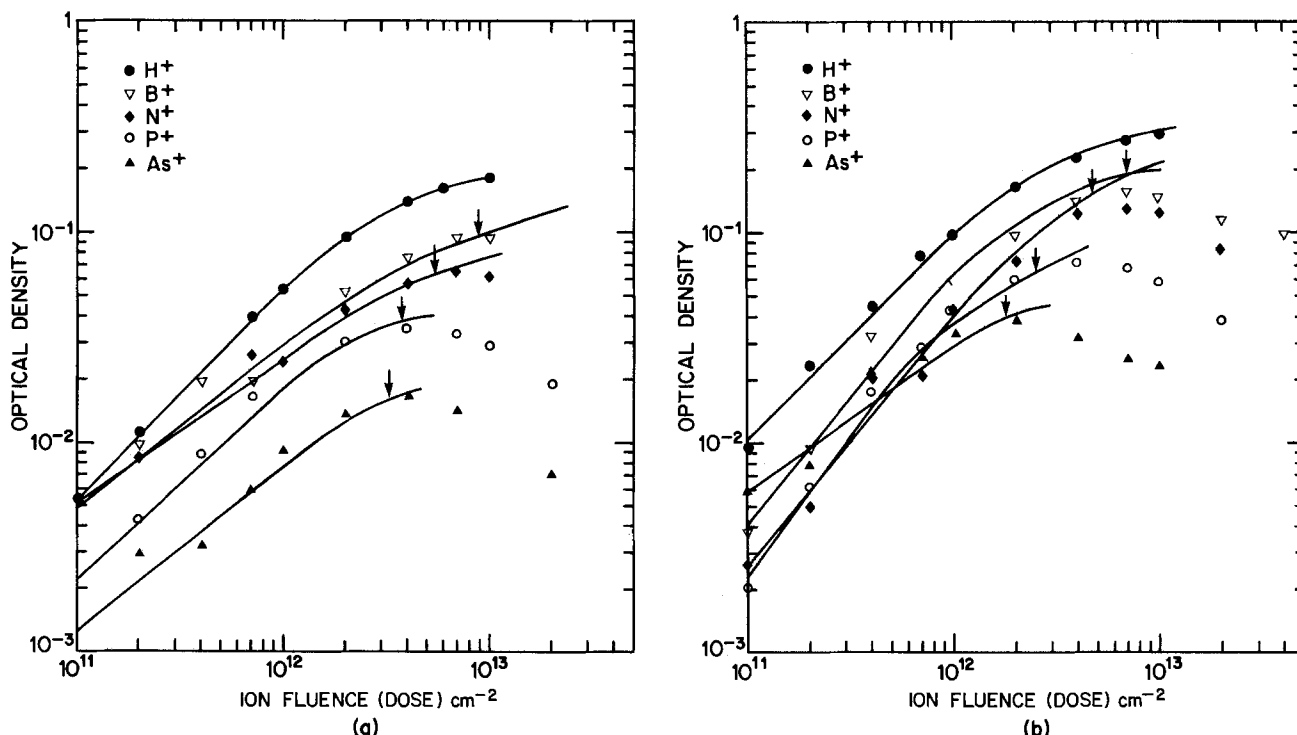


Fig. 1. The experimental data (points) and the best theoretical fit (in solid lines) for optical density increase at 610 nm as a function of ion fluence (dose) using Eq. [1] for 80 keV (a) and 150 keV (b) for the various ions. Arrows indicate the values of D_{max} as calculated by Eq. [2].

Table I. This shows for H⁺, B⁺, N⁺, P⁺, and As⁺ the various parameters defined in the text associated with the ions at the two implant energies of 80 (columns 2-9) and 150 keV (columns 10-17)

Ion	m	80 keV							150 keV							
		D_0 ($\times 10^{12}$)	k	E_{TN} (keV)	D_{max} (theor.) ($\times 10^{12}$)	D_{max} (expt.) ($\times 10^{12}$)	D_{min} ($\times 10^{11}$)	Range (Å)	m	D_0 ($\times 10^{12}$)	k	E_{TN} (keV)	D_{max} (theor.) ($\times 10^{12}$)	D_{max} (expt.) ($\times 10^{12}$)	D_{min} ($\times 10^{11}$)	Range (Å)
H	1.00	4.5	0.23	1.2	192	>50	2.0	7,470	1.00	2.9	0.32	1.1	209	>50	0.8	10,350
B	0.81	5.8	0.13	25.7	8.9	8.7	2.6	4,860	1.23	2.3	0.20	32.7	7.0	7.4	1.8	7,695
N	0.70	5.8	0.09	35.5	6.5	6.5	3.5	3,450	1.23	3.8	0.23	48.2	4.8	5.5	2.7	5,875
P	0.97	3.5	0.07	59.1	3.9	4.4	5.0	1,625	1.33	1.5	0.09	95.5	2.4	3.0	2.7	3,075
As	0.81	3.8	0.03	71.1	3.2	3.2	12	930	0.78	2.0	0.06	128.1	1.8	1.6	3.1	1,650

$\pm 5.0\%$. This dose, D_{min} , is also shown in Table I. D_{min} ranges from $8.0 \times 10^{10} \text{ cm}^{-2}$ for the light ion H⁺ at 150 keV to $1.2 \times 10^{12} \text{ cm}^{-2}$ for As⁺ at 80 keV. For doses above D_{min} , the accuracy will be better than $\pm 5.0\%$ up to a dose close to D_{max} , where accuracy drops again due to the maximum in the response curve. Hence, for implant monitoring purposes, a dose value should be chosen within this range to give the best dose precision depending on the energy and ion type. We calculate that, using this method, the precision of the dose measurement would be $\pm 0.5\%$.

It should be pointed out that the experimental scatter in the measured OD in comparison to the smooth curve shown in Fig. 1a and 1b is occasionally greater than the instrument OD error. This is because the standard deviation of the OD of the unexposed material is specified by the RCD manufacturer is $\pm 5\%$. In order to realize the best accuracy for dose measurement, an OD map of the RCD detector should be obtained prior to implantation (a reference check). Then the implanted sample would be mapped and corrected using the reference measurement on a point-by-point basis. With this technique, it will be possible to realize the dose measurement accuracies discussed above.

In principle, it should be possible to use this technique for doses larger than D_{max} (when OD begins to go down due to the bleaching action). However, since our interest was primarily in low dose monitoring, this was not investigated. It should, however, be noted that dose error near D_{max} will be very large. Hence, measurement near that region should be avoided.

It is envisaged that, in a semiconductor manufacturing facility, the dye would be deposited on a glass or quartz plate whose dimensions conform to silicon wafer specifications. After implantation in the usual way, the RCD containing wafer would be mapped automatically on a spectrophotometric dosimeter (at 610 nm) with a computer-controlled X-Y stage. Such a system would produce an X-Y map of the ion implantation dose distribution using the calibration data shown in Fig. 1a and 1b.

Conclusions

We have shown that for a wide mass range of ions such as H⁺, B⁺, N⁺, P⁺ and As⁺ implanted into RCD at energies of 80 and 150 keV the relationship between OD and dose at the low doses can be modeled on the basis of Eq. [1]. The three constants associated with this model equation have been calculated from our experimental data and allow dose calibration to be made from OD data. As the dose increases, a bleaching action causes a maximum in OD to be reached. Our detailed calculations of the energy-

loss mechanism suggests that this bleaching action is primarily due to the hydrogen-assisted nuclear energy loss disrupting the dye molecule.

We estimate that this technique can be successfully used for dose monitoring in ion implantation systems with an accuracy of better than $\pm 5.0\%$ down to very low doses of about 10^{11} cm^{-2} for most ions and typical acceleration potentials in the 50-200 keV range used in the semiconductor industry.

Acknowledgments

We are indebted to J. C. Elliott and L. Kennedy for the implants and the spectrophotometer measurements. One of us (K. V. A.) would like to thank Dr. D. G. Ashworth and Dr. M. Moulavi-Khakhi of the University of Kent, Kent, England, for doing the energy-loss calculations. K. V. A. would also like to acknowledge the help and information supplied by W. L. McLaughlin of the National Bureau of Standards and K. C. Humphreys and A. D. Kantz of Far West Technology. We appreciate the helpful comments of the reviewers.

Manuscript submitted April 25, 1984; revised manuscript submitted July 10, 1984.

Fairchild Research Center assisted in meeting the publication costs of this article.

REFERENCES

1. D. S. Perloff, J. N. Gen, and F. E. Wahl, *Solid State Technol.*, **24** (2), 112 (1981).
2. P. L. F. Hemment, *Rad. Effects*, **44**, 31 (1979).
3. J. C. Cheng and G. R. Tripp, *Solid State Technol.*, **26**, 143 (1983).
4. W. L. McLaughlin and L. Chalkley, *Photo. Sci. Eng.*, **9**, 159 (1965).
5. W. L. McLaughlin, *Int. J. Appl. Radiat. Isotopes*, **17**, 85 (1966).
6. K. C. Humphreys and A. D. Kantz, *Rad. Phys. Chem.*, **9**, 737 (1977).
7. A. D. Kantz and K. C. Humphreys, *ibid.*, **18**, 937 (1981).
8. J. M. Shaw and M. Hatzakis, *J. Vac. Sci. Technol.*, **19**, 1343 (1981).
9. M. Rosenstein, H. Eisen, H. L. Roush, and J. Silverman, *Int. J. Appl. Rad. Isotopes*, **26**, 423 (1975).
10. J. W. Hansen and K. J. Olsen, *Radiat. Res.*, **97**, 1 (1984).
11. S. C. Sharma and R. Katz, in "Euratom," Vol. II, p. 655 (1974).
12. M. Moulavi-Khakhi, Ph.D. Thesis, University of Kent, Canterbury, England (1982).
13. M. Moulavi-Khakhi, D. G. Ashworth, and K. V. Anand, *J. Phys. C.*, **17**, 2449 (1984).
14. R. Katz, S. C. Sharma, and M. Homayoonfar, *Nucl. Inst. Method.*, **100**, 13 (1972).

Low Pressure Metalorganic Vapor Phase Epitaxy of InP in a Vertical Reactor

Mamoru Oishi* and Koichi Kuroiwa¹

Nippon Telegraph and Telephone Public Corporation, Atsugi Electrical Communication Laboratory, 1839 Ono, Atsugishi, Kanagawa 243-01, Japan

ABSTRACT

InP growth characteristics in low pressure metalorganic vapor phase epitaxy (MOVPE) in a vertical reactor were studied. A maximum mobility of 32,000 cm²/V s at 77 K was obtained. Selective epitaxy was also investigated, and completely selective epitaxy was realized for 15 μm wide SiO₂ masks at 40 torr. Preliminary results are shown for a hybrid LPE/MOVPE-grown distributed-feedback laser diode. Single longitudinal mode operation under pulsed current injection was achieved at room temperature.

Recently, InP has become increasingly important because of its applications to optoelectronic devices and to monolithic integration of lasers, detectors, and FET's. For such device integration, ultrafine lithography and larger surface areas with smooth specular layers will be required. Large-area epitaxial films can be obtained fairly easily by metalorganic vapor phase epitaxy (MOVPE) or metalorganic chemical vapor deposition (MOCVD) (1). MOVPE has proven its suitability for GaAs and GaAlAs epitaxial growth and for device applications (2, 3). The principles of MOVPE operation and reactor design are comparatively simple, and materials with uniform device quality over large areas are readily obtained, particularly for GaAs.

Application of the MOVPE technique to the growth of InP has been investigated through a variety of approaches (4-13); triethylindium (TEI) + phosphine (PH₃) (4-8), adducts (9, 10), trimethylindium (TMI) + PH₃ (11, 12), and TMI + trimethylphosphine (TMP) (13). Early problems encountered for the MOVPE growth of In containing compounds are attributed to the parasitic reaction between TEI and PH₃ in the gas phase to form nonvolatile polymeric liquids upstream from the substrate. To solve these problems, some groups have adopted the use of adducts, such as TMI-TMP (9) or TMI-triethylphosphine (TEP) (10), as sources. These molecules do not themselves form nonvolatile polymers, hence the disadvantages of this approach are the low vapor pressures of the adducts, which necessitates heating the tubing and reactor walls upstream from the substrate, and the difficulty for growing multicomponent systems. The other approach is to use TMI instead of TEI. TMI was observed to participate in the gas phase reactions less than TEI. A disadvantage of this method is the low melting point of TMI; precisely controlled transport to a reactor is difficult because TMI is solid at near room temperature. At the present stage, therefore, the conventional sources, TEI and PH₃, have fewer problems. In using TEI and PH₃, effective approaches are to adopt the low pressure growth technique (5), to pyrolyze PH₃ (5), or to keep the reactants separated until the last possible moment in the growth process using a special guide which also plays a role of the oven for PH₃ pyrolysis (6). There have been some successes with these approaches.

Note that these studies have used horizontal reactor (HR) systems. Although successful results were obtained using vertical reactor (VR) systems for GaAs MOVPE (14, 15), no successful results have yet been reported concerning the InP growth using a VR system. The reasons for this may arise from difficulties involved in a VR system: (i) parasitic reaction problem, or (ii) thermal convection problem. These problems are more crucial in a VR system than in an HR system. In fact, the radiation from the heated susceptor in a VR system directly promotes the premature decomposition of MO molecules far from

the substrate and accelerates the parasitic reaction. Moreover, some turbulent gas flow is liable to develop in a VR system, because the pronounced thermal convection due to the heated susceptor impedes the smooth stream of the source gases. So, finding a way out of the difficulties mentioned above and applying a VR system to MOVPE of InP is worth investigating.

In addition, a highly selective epitaxy technique, once accomplished, can extend the design flexibility of integrated devices and reveal the growth mechanism. In many cases, MOVPE is carried out over the entire area of planar substrate surfaces. Selective MOVPE has been investigated for application with GaAs (16-19), but very little attention has been paid to InP (20).

The authors investigated the promising application of a vertical reactor system to MOVPE of InP and selective epitaxy using TEI and PH₃. The techniques of low pressure MOVPE and separate introduction to source gases are adopted to overcome the problems mentioned above. As a test of the quality of the films produced and their applicability to devices, a hybrid liquid phase epitaxy (LPE)/MOVPE technique was used to fabricate distributed-feedback buried-heterostructure (DFB-BH) lasers.

In this paper, the growth and properties of InP films produced by low pressure MOVPE in a vertical system are reported. Selective epitaxy is also investigated to establish the necessary conditions for completely selective epitaxy. An application to distributed-feedback buried-heterostructure (DFB-BH) laser fabrication together with LPE (a hybrid LPE/MOVPE technique) is also reported.

Experimental

Growth system.—The growth system used in this study is similar to one previously reported (21), a schematic diagram of which is shown in Fig. 1. The reactor gas manifold and mixing system were constructed of stainless steel, and all gases were controlled by mass flow controllers. Triethylindium [TEI, In(C₂H₅)₃] was used as the indium source, and PH₃ diluted to 10% in hydrogen was used as the phosphorus source. TEI was contained in a stainless steel bubbler and maintained at constant temperature with a thermostat. PH₃ was contained in a commercially supplied high pressure gas cylinder. The carrier gas was palladium-diffused high purity hydrogen. PH₃ flow-rate values refer to the flow rates of diluted gases.

The cold-walled growth reactor was a quartz tube 40 cm long. It was of 4 cm diam for its upper one-quarter, 10 cm for the lower three-quarters, and had O-ring seals for separation at the base. Two lines for TEI and PH₃, respectively, are separately connected to the reactor to suppress the parasitic reaction. TEI is introduced via a fine tube to the vicinity of the pedestal, while PH₃ flows down from the reactor top end. A rotatable pedestal made of high purity graphite is inductively heated (300 kHz). Temperature is measured by a thermocouple inserted into this pedestal within the quartz tube. All temperature values given refer to readings of this thermocouple.

*Electrochemical Society Active Member.

¹Present address: Tokyo University of Agriculture and Technology, Koganei, Tokyo, Japan.

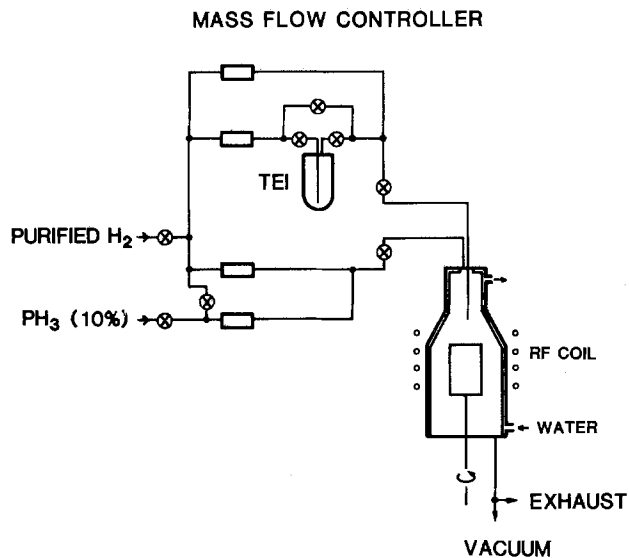


Fig. 1. Schematic diagram of vertical MOVPE growth system

Growth at reduced pressure was carried out by incorporating a rotary pump at the outlet of the reactor tube. To monitor the pressure within the reactor and the gas manifold, diaphragm pressure gauges were used. A molecular sieve was used to impede oil back-diffusion at the input of the pump. The working pressure was adjusted by varying the line conductance using a valve.

Epitaxial growth was carried out (i) on iron-doped semi-insulating InP substrates to facilitate subsequent electrical evaluation, (ii) on masked InP substrates for the study of selective epitaxy, and (iii) on p-type InP substrates for fabricating DFB-BH lasers. The substrates were obtained commercially and had one side polished. The orientations of the substrates were (100) and 3° off the (100) plane toward [110]. Identical results were obtained for both substrate orientations.

Growth procedures.—The substrates were cleaned with trichloroethylene, acetone, and isopropyl alcohol. They were etched first in an $\text{H}_2\text{SO}_4\text{-H}_2\text{O}_2\text{-H}_2\text{O}(3:1:1)$ mixture and then in 10% Br-methanol just prior to growth, then rinsed in deionized water, and finally dried.

Substrates for the study of selective epitaxial growth were also prepared. First, an SiO_2 layer about 300 nm thick was RF sputtered on the cleaned surface of the substrates. Five different types of masks (patterns A-E shown in Fig. 2) were formed along the [110] or $[\bar{1}\bar{1}0]$ directions with conventional photolithography techniques and using buffered HF as the etchant. Prior to loading in the growth system, the substrates were cleaned again in organic solvents.

The substrates were placed perpendicular to the gas stream on the quartz susceptor which was set on the graphite pedestal. After loading the substrates, the reac-

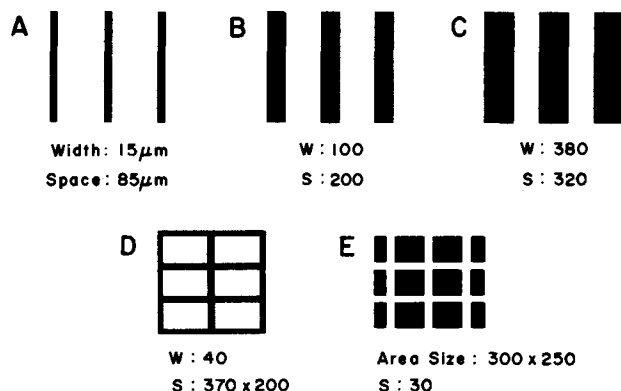


Fig. 2. Five mask patterns for the study of selective epitaxy

tor was purged with a hydrogen flow of 5 liter/min for 60 min, and the pressure was brought down to the working level. After the pressure had stabilized, heating was begun. The PH_3 flow was maintained as long as the temperature stayed above 450°C . Typical growth parameters are listed in Table I.

Sample evaluation.—The samples grown in this study were evaluated using van der Pauw-Hall effect measurements. The measurements were taken on rectangular samples by placing Sn dots around each sample periphery. The Hall effect was measured in 1 kG magnetic fields. To measure the thickness of the epitaxial layers, staining technique was applied to cleaved sections.

Photoluminescence (PL) was excited with the 530.8 nm line of a Kr⁺ laser. The excitation intensity was typically 5 W/cm^2 .

InP epitaxial layers on Fe-doped InP substrates were studied by x-ray diffraction using a double-crystal monochromator, in which the first crystal was a (100) InP wafer and the (400) (+, -) parallel arrangement was used. The x-ray beam size incident on a sample surface was less than 1 mm in diameter. The extinction distance of the (400) reflection of an InP crystal is $1.2 \mu\text{m}$ (22). This is shorter or the same as the thicknesses of the InP epitaxial layers grown here. For this reason, the x-ray diffraction is considered to be mainly from the InP epitaxial layers with only a negligible contribution from the substrates themselves.

DFB laser fabrication by the hybrid LPE/MOVPE technique.—MOVPE was applied to distributed-feedback buried-heterostructure (DFB-BH) laser fabrication. In the fabrication of DFB lasers, the melt-back or deformation of the corrugated layers has often been observed during LPE growth (23). However, MOVPE is expected to keep the shape of the corrugation.

MOVPE was applied to grow the on-corrugation layer and the other layers were made by LPE (hybrid LPE/MOVPE technique) because at the stage of this work doping was not investigated. Figure 3 shows the schematic diagram of a DFB-BH laser grown by this hybrid LPE/MOVPE technique. It was fabricated by the following process. A three-layer structure, composed of a Zn-doped InP buffer and a lower cladding layer ($5 \mu\text{m}$ thick, $p = 3 \times 10^{17} \text{ cm}^{-3}$), an undoped InGaAsP active layer ($0.25 \mu\text{m}$ thick, $\lambda = 1.55 \mu\text{m}$), and a Sn-doped InGaAsP waveguide layer ($0.25 \mu\text{m}$ thick, $n = 2 \times 10^{18} \text{ cm}^{-3}$, $\lambda = 1.3 \mu\text{m}$), was grown on a Zn-doped (100) InP substrate ($p = 5 \times 10^{17} \text{ cm}^{-3}$) by the conventional LPE technique (Fig. 4a). A second-order corrugation was then formed on the InGaAsP waveguide layer by holographic photolithography and chemical wet etching (24) (Fig. 4b). The pitch and the depth of the corrugation were typically 460 and 160 nm, respectively. The direction of the corrugation was [110].

The corrugated surface was overgrown with an undoped InP layer formed by MOVPE (Fig. 4c). Prior to the loading of the wafer into the MOVPE reactor, the corrugated surface was cleaned in hot acetone, concentrated H_2SO_4 , and HF. The growth temperature and the reactor pressure were 600°C and 90 torr, respectively. Doping was not utilized at this stage of the MOVPE study.

After the MOVPE growth, a buried-heterostructure was formed by the selective LPE technique (25) (Fig. 4d). First, reverse-mesa stripes were formed in the [110] direction with the SiO_2 masks. Next, successive n- and p-type InP layers were grown. The width of the active region was $19 \mu\text{m}$. Ohmic contacts were made by evaporating

Table I. List of typical growth conditions

Substrate temperature	$600^\circ\text{-}660^\circ\text{C}$
Total flow rate	2-3 liter/min
TEI flow rate	$120 \text{ cm}^3/\text{min}$
H_2 flow rate through TEI at 21°C	600 torr
PH_3 flow rate (10% in H_2)	$150 \text{ cm}^3/\text{min}$
Growth time	60 min

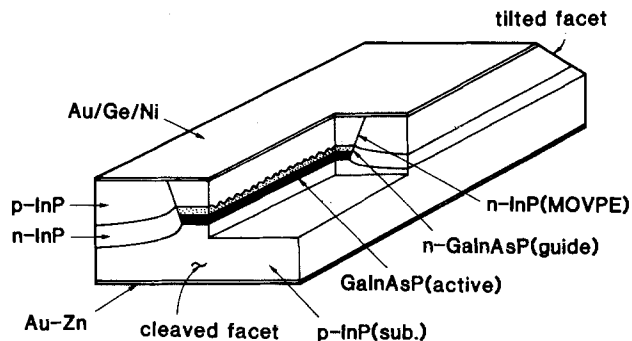


Fig. 3. Schematic diagram of an InGaAsP/InP DFB-BH laser grown by hybrid LPE/MOVPE.

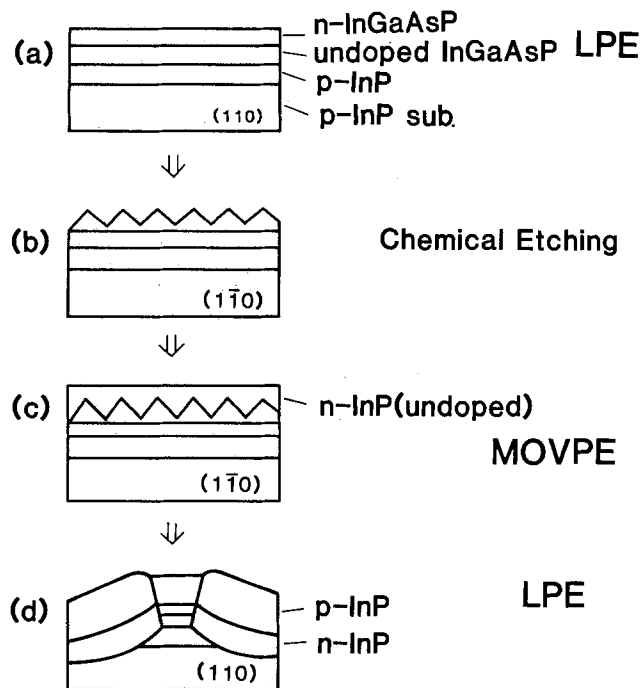


Fig. 4. Fabrication procedures for hybrid LPE/MOVPE-grown DFB-BH laser.

Au-Zn on the p side, and Au-Ge-Ni on the n side. One facet of the laser was formed by cleavage and the other was tilted by the etching technique to suppress oscillation in the Fabry-Perot modes. The length of the laser fabricated was 500 μm .

Results and Discussion

Study of growth.—The layers grown showed good surface quality over a wide range of growth conditions. Furthermore, the morphology was found to be essentially independent of the TEI or PH_3 flow rates as long as the mole ratio introduced, PH_3/TEI , was greater than 1. Figure 5 shows a surface feature of the epitaxial layers. Figure 6 presents a roughened surface grown under the PH_3 -depleted condition. Indium droplets were formed on the rectangular pits which had been the result of thermal damage.

Figure 7 shows the growth rate of the epitaxial layers as a function of TEI flow rate. The linear variation in the growth rate with the TEI flow rate and the independence of the growth rate from the PH_3 flow rates, which had been widely reported in the MOVPE literature (26), was also observed here. Other parameters, such as substrate temperature and PH_3/TEI ratio had no effect on growth rates. The growth rate was, thus, mass-transport limited as long as plane substrates were used.

The undoped InP layers are n-type with carrier concentrations of $(0.5\text{--}10) \times 10^{15} \text{ cm}^{-3}$. The electron mobilities typically ranged from 3000 $\text{cm}^2/\text{V s}$ at room temperature

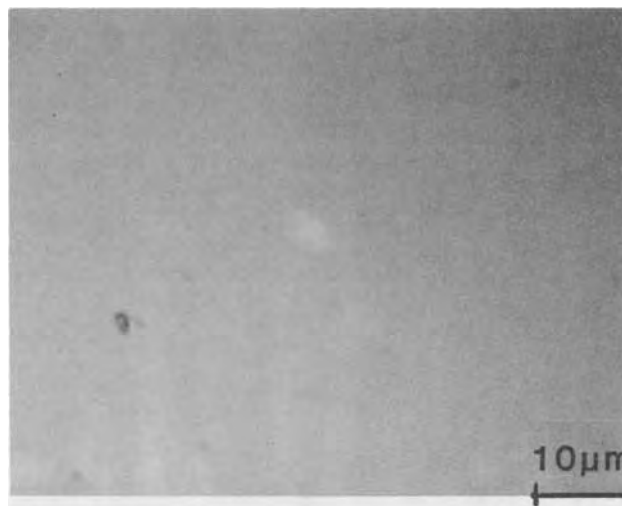


Fig. 5. Photomicrograph of the surface of an epitaxial layer grown

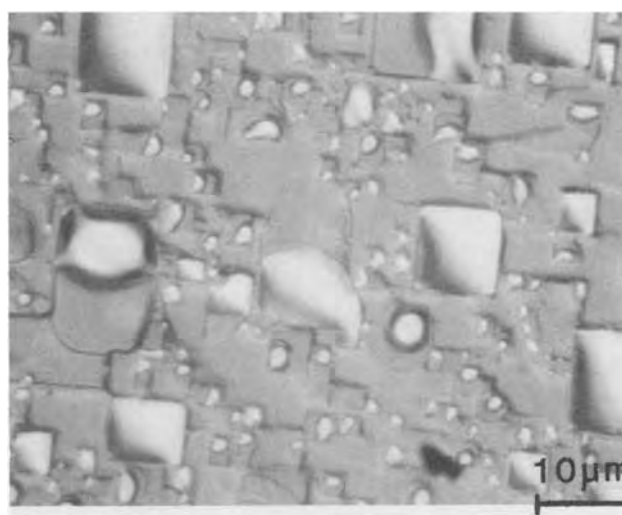


Fig. 6. Micrograph of a roughened surface grown under PH_3 depleted condition.

to 30,000 $\text{cm}^2/\text{V s}$ at 77 K. The lowest carrier concentration and the highest mobilities are $5 \times 10^{14} \text{ cm}^{-3}$, 4100 $\text{cm}^2/\text{V s}$ (room temperature), and 32,000 $\text{cm}^2/\text{V s}$ (77 K), respectively. These values are comparable to the epitaxial layers grown from TEI and PH_3 using an HR system (6, 8) and from adducts (9, 10).

The photoluminescence (PL) spectrum of undoped InP epitaxial layers at 77 K is shown in Fig. 8. PL intensity is

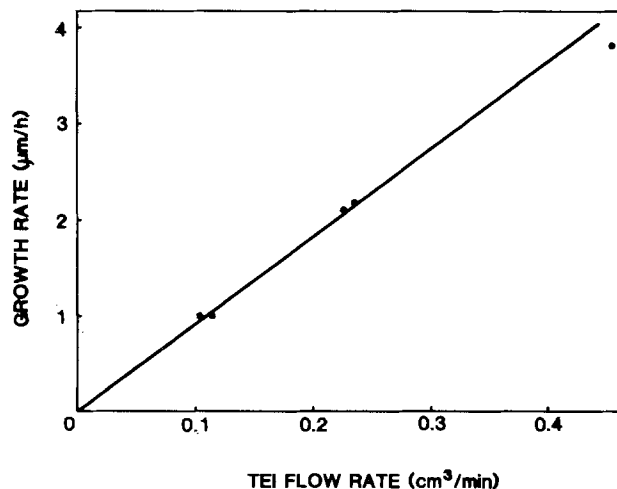


Fig. 7. Growth rate as a function of TEI flow rates

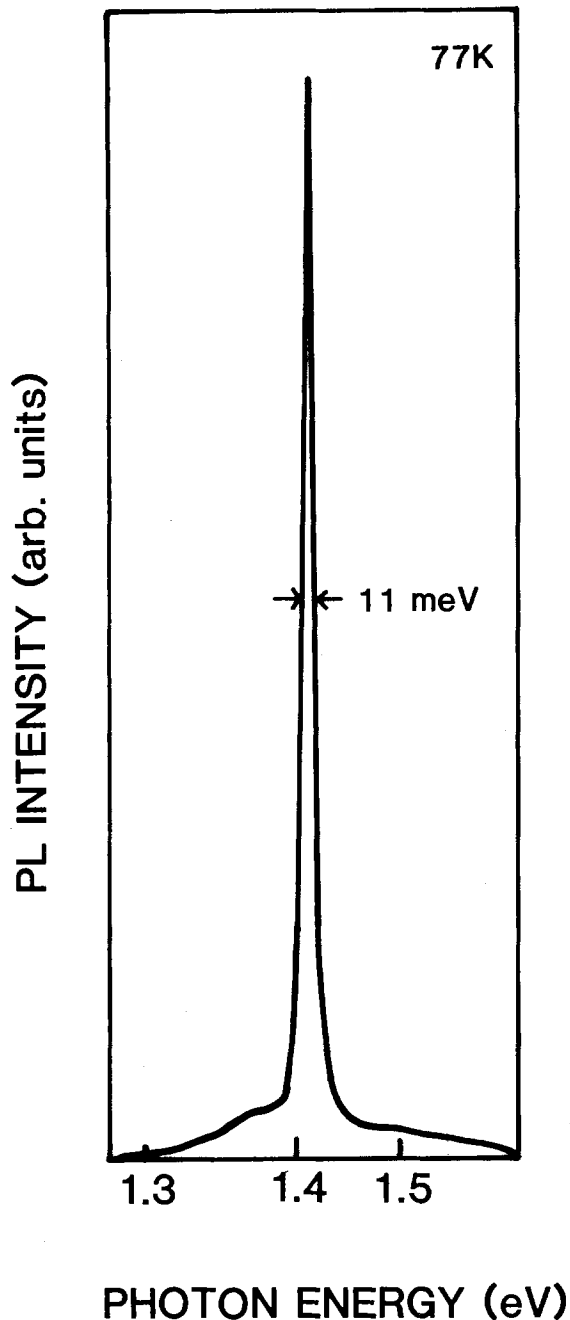


Fig. 8. PL spectra of undoped InP epitaxial layer at 77 K

as high as that of the best sample of MBE-grown InP (22). It has only one peak and a trace of a second peak; the peak is centered at 1.41 eV with a full width at half maximum (FWHM) of 11 meV, which is a near band-edge emission, and the trace is near 1.38 eV. The peak intensity ratio of the 1.38 eV peak to the 1.41 eV peak has often been reported as 1/10 or more (6, 7). In this case, however, the ratio was as small as 1/100. Assuming that the 1.38 eV peak results from the transition due to the acceptors (6), this difference can be attributed to the concentrations of the residual acceptor-like impurities in the unintentionally doped layers.

The FWHM of the x-ray rocking curve of the epitaxial layer is as small as 20s. This value is comparable with those of the substrates used in the study.

Application to DFB-BH laser fabrication.—Figure 9 shows SEM photographs of the corrugated structure before (Fig. 9a) and after (Fig. 9b) MOVPE overgrowth. The shape of the corrugation was hardly affected during MOVPE overgrowth.

Figure 10a shows light output/current characteristics at 25°C under pulsed operation (pulse width = 5 μs; duty cy-

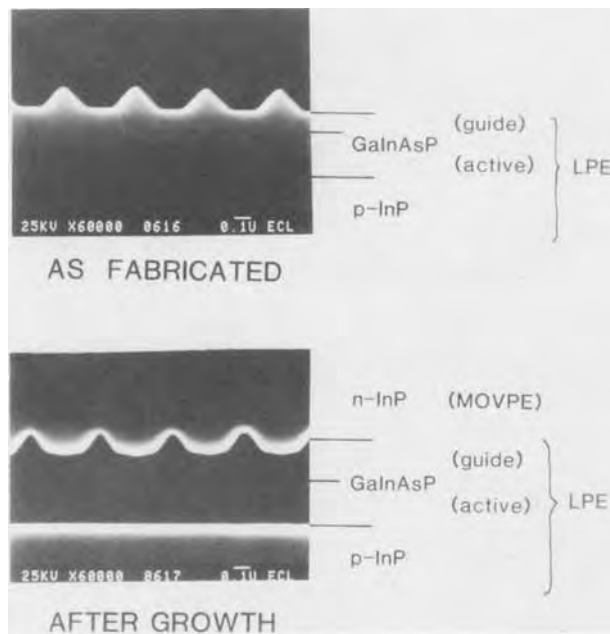


Fig. 9. SEM photographs of the corrugated structure before (a, top) and after (b, bottom) MOVPE overgrowth.

cle = 3 kHz). The threshold current I_{th} was 400 mA, which corresponds to a current density of 6.8 kA/cm². Figure 10b shows the emission spectra. Single longitudinal mode operation was achieved. The lasing wavelength was 1.55 μm (at 25°C), and the temperature dependence of the lasing wavelength was 0.11 nm/K.

In the present diode structure, doping was not utilized for the MOVPE-grown InP cladding layer and the width of the active layer was not so narrow as that of the conventional BH lasers. These factors are considered to cause low injection efficiency and high I_{th} . Therefore, further reduction of I_{th} can be achieved by optimizing the structure.

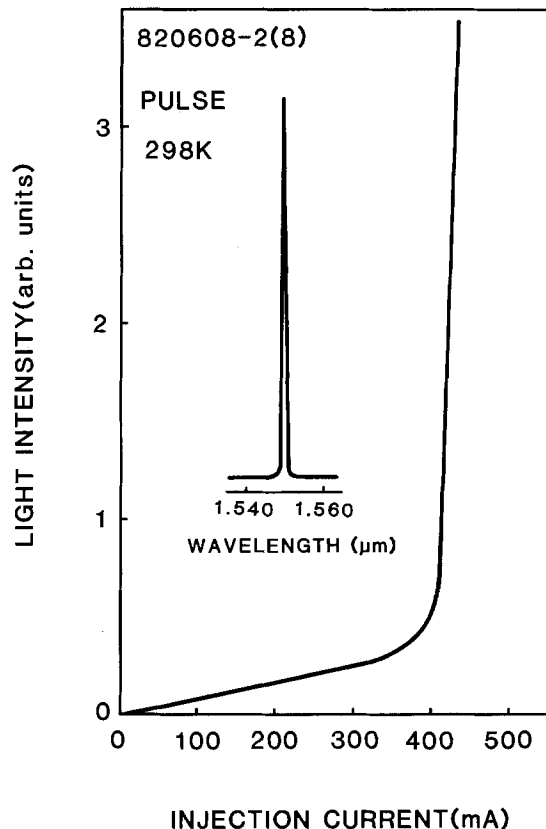


Fig. 10. Light output/current characteristics and emission spectra (inset) of a hybrid LPE/MOVPE grown InGaAsP/InP DFB-BH laser.

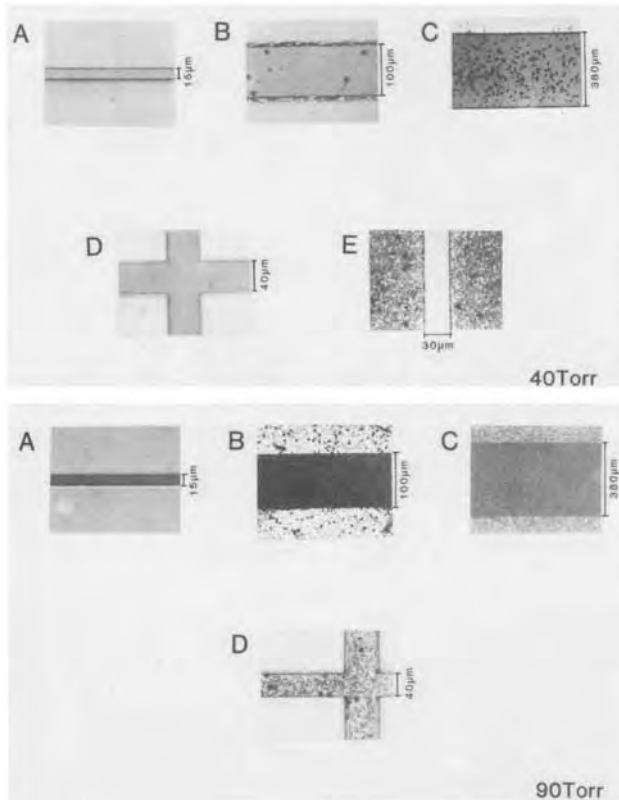


Fig. 11. Epitaxial InP on SiO₂ masked substrates. Pressure is 40 and 90 torr.

Selective epitaxy.—InP was grown on SiO₂-masked substrates under 90 and 40 torr. Figure 11 shows photographs of the surfaces grown. Results are summarized in Table II from the viewpoint of selectivity. Here the symbol O indicates “completely selective epitaxy,” that is, no deposition was observed on the SiO₂ masks and mirror-smooth InP was grown on the InP region. The symbol Δ shows that mirror-smooth InP was obtained on the InP region and polycrystalline InP was partly deposited on the masks. The symbol × shows that polycrystalline InP was obtained over the entire area of the masks and mirror-smooth InP was grown on the InP region. Finally, ×× means that polycrystalline InP was deposited both on the masks and on the InP region.

“Completely selective epitaxy” was achieved for 15 μm wide stripes at 40 torr. The selectivity became more effective with the narrowing of the stripes and the lowering of the working pressure. It can be supposed from this result that the surface mobility of In decomposed from TEI is higher on the SiO₂ masks than on the InP region, which makes it possible for InP nucleation or growth on the InP region to be larger than that on the SiO₂ masks.

Typical growth features on the mesa and reverse-mesa structures are shown in Fig. 12. For GaAs, Azoulay *et al.* demonstrated single-layer growth on a mesa-etched substrate without the use of masks (19). In their report, one layer grown covers the entire mesa structure (25 μm wide), and straight edges perpendicular to the substrate are obtained after growth over a long period. In this experiment, however, the sidewall of the layers grown coincided with the reverse-mesa edges when the reverse-mesa was fabricated. When the mesa structure was fabricated,

Table II. Summary of selective epitaxy results (see text)

Pressure (torr)	Mask patterns				
	A	B	C	D	E
90	Δ	×	× ~ × ×	×	—
40	O	Δ	×	Δ	×

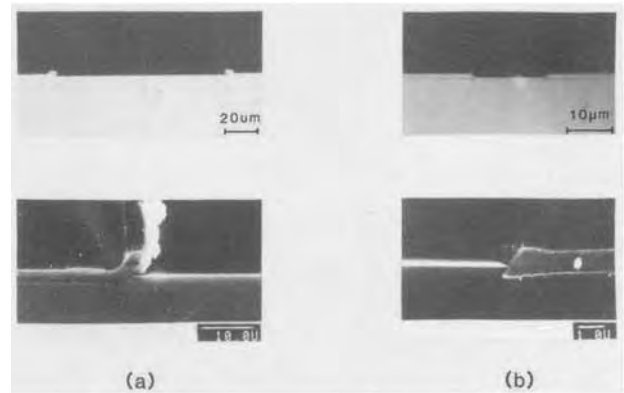


Fig. 12. Growth features on mesa, a, and reverse-mesa, b, structures

the growth front climbed over the SiO₂ masks. The lateral growth rate in the direction of [110] is larger than that in the direction of [110], or, rather, (111) planes on reverse-mesa have the function of limiting the growth towards [111].

This technique for the growth of epitaxial layers on SiO₂ masked substrates, and especially on reverse-mesa substrates, will be useful in obtaining buried structures with flat surfaces.

Conclusion

We have investigated the low pressure MOVPE of InP in a vertical reactor. Without making any special considerations, InP epitaxial layers with free carrier concentrations of as low as $5 \times 10^{14} \text{ cm}^{-3}$ have been obtained. The highest mobility is $4100 \text{ cm}^2/\text{V s}$ at room temperature and $32,000 \text{ cm}^2/\text{V s}$ at 77 K.

Selective epitaxy by this technique has also been studied. The conditions for completely selective epitaxy have been established. It has also been demonstrated that we can achieve completely selective MOVPE of InP on 15 μm wide SiO₂-striped InP substrates. This technique is promising for the fabrication of integrated devices.

DFB-BH lasers have been fabricated by a hybrid LPE/MOVPE technique. Room temperature pulsed operation has been achieved. These devices operated stably in a single longitudinal mode at room temperature under pulsed operation.

Acknowledgments

The authors would like to thank Y. Itaya and Y. Noguchi for LPE growth, T. Matsuoka for the fabrication of the corrugation, Y. Suzuki for laser chip fabrication, and N. Shibata for assistance in sample evaluation. They are also grateful to T. Ikegami, K. Kurumada, and H. Nagai for their fruitful discussions and comments and to M. Fujimoto for his continuous encouragement throughout the course of this work.

Manuscript submitted March 7, 1984; revised manuscript received Dec. 1, 1984.

Nippon Telegraph and Telephone Public Corporation assisted in meeting the publication costs of this article.

REFERENCES

- H. M. Manasevit and W. I. Simpson, *This Journal*, **116**, 1725 (1969); R. D. Dupuis and P. D. Dapkus, *Appl. Phys. Lett.*, **32**, 406 (1978).
- R. D. Dupuis, P. D. Dapkus, R. D. Yingling, and L. A. Moudy, *ibid.*, **31**, 201 (1977).
- E. J. Thrush, P. R. Selway, and G. D. Henshall, *Electron. Lett.*, **15**, 156 (1979).
- H. M. Manasevit and W. I. Simpson, *This Journal*, **120**, 135 (1973).
- J. P. Duchemin, M. Bonnet, G. Beuchet, and F. Koelsch, in “Proceedings of the 7th International Symposium on GaAs and Related Compounds, St. Louis, 1978,” p. 10, Institute of Physics Conference Series 45, Institute of Physics, London (1979).
- T. Fukui and Y. Horikoshi, *Jpn. J. Appl. Phys.*, **19**, L395 (1980).
- M. Ogura, K. Inoue, Y. Ban, T. Uno, M. Morikoshi, and

- N. Hase, *ibid.*, **21**, L548 (1982).
8. M. Razeghi and J. P. Duchemin, *J. Cryst. Growth*, **64**, 76 (1983).
 9. H. Renz, J. Weidlein, K. W. Benz, and M. H. Pilkuhn, *Electron. Lett.*, **16**, 228 (1980).
 10. R. H. Moss and J. S. Evans, *J. Cryst. Growth*, **55**, 129 (1981).
 11. C. C. Hsu, R. M. Cohen, and G. B. Stringfellow, *ibid.*, **63**, 8 (1983).
 12. M. Sacilotti, A. Mircea, and R. Azoulay, *ibid.*, **63**, 111 (1983).
 13. S. J. Bass, *ibid.*, **64**, 68 (1983).
 14. P. D. Dapkus, H. M. Manasevit, K. L. Hess, T. S. Low, and G. E. Stillman, *ibid.*, **55**, 10 (1981).
 15. T. Nakanisi, T. Udagawa, A. Tanaka, and K. Kamei, *ibid.*, **55**, 255 (1981).
 16. P. Rai-Choudhury and D. K. Schroder, *This Journal*, **118**, 107 (1971).
 17. Y. Nakayama, S. Ohkawa, and H. Ishikawa, *Fujitsu Sci. Tech. J.*, **13**, 53 (1977).
 18. J. P. Duchemin, M. Bonnet, F. Koelsch, and D. Huyghe, *J. Cryst. Growth*, **45**, 181 (1978).
 19. R. Azoulay, N. Bouadma, J. C. Bouley, and L. Dugrand, *ibid.*, **55**, 229 (1981).
 20. P. N. Favennec, M. Salvi, M. A. Di Forte Poisson, and J. P. Duchemin, *J. Appl. Phys.*, **43**, 771 (1983).
 21. M. Oishi and K. Kuroiwa, *Jpn. J. Appl. Phys.*, **20**, 203 (1981).
 22. H. Asahi, Y. Kawamura, M. Ikeda, and H. Okamoto, *J. Appl. Phys.*, **52**, 2852 (1981).
 23. A. W. Nelson, L. D. Westbrook, and J. S. Evans, *Electron. Lett.*, **19**, 34 (1983).
 24. T. Matsuoka, H. Nagai, Y. Itaya, Y. Noguchi, Y. Suzuki, and T. Ikegami, *ibid.*, **18**, 27 (1982).
 25. H. Nagai, Y. Noguchi, K. Takahei, Y. Toyoshima, and G. Iwane, *Jpn. J. Appl. Phys.*, **19**, L218 (1980).
 26. H. M. Manasevit and W. I. Simpson, *This Journal*, **116**, 1725 (1969).

An Optical Imaging Method for Wafer Warpage Measurements

K. H. Yang

IBM East Fishkill Facility, General Technology Division, Hopewell Junction, New York 12533

ABSTRACT

A simple optical imaging method is developed for quick evaluation of wafer surface quality and warpage. Surface irregularities 50-100Å deep can be detected by this method. The detection limit is about 270m for the radius of curvature. The sense of curvature can be unambiguously determined by image contrast and image size. The principle of this method for warpage measurements is described. A comparison of this method with the optical interference method and the x-ray method is given and discussed.

Wafer warpage can lead to serious degradation in device yield. The warpage, in general, is generated by excessive thermal stresses during hot processings, or by elastic stresses due to thin film deposition. At present, measurement of wafer warpage and film stresses relies mainly on techniques such as the surface profiling method (1), the Newton-ring method (2), the x-ray method (3-6), and the optical interference method (7, 8). The first three methods can only produce a single scan of surface profile or measure warpage at two reference points. Recording a warpage map of an entire wafer through these methods is difficult and time consuming. The optical interference method is the only one that can provide a contour map of an entire wafer. The contour map is represented by fringes at equal height. For severely warped wafers and rough surfaces, the contour map sometimes becomes too complex and difficult to be recognized. Availability of a simple method capable of examining the warpage of an entire wafer surface is therefore most desirable.

Recently, Kugimiya (9) reported an optical method that allows one to examine irregularities and warpage of an entire wafer surface. In this method, a projection lens is used to form a defocused image of a wafer surface. The use of the projection lens, however, imposes some restrictions on the flexibility and sensitivity of this method. Namely, the wafer size has to be smaller than the size of the projection lens, and the sensitivity is limited by the magnification power of the lens. As a result, this method has a relatively low sensitivity, about 500Å for surface irregularities and 100m for the radius of curvature. Because of the low sensitivity, it can hardly be used to measure thin film stresses. In 1980, we developed a similar optical method, which required no projection lens. With elimination of the lens, our method is capable of examining wafers of any size and has a greater sensitivity. The detection limit is 50-100Å for surface irregularities, and 270m for the radius of curvature.

In this paper, we first describe the experimental setup and principle of our optical imaging method. The results of our measurements are expressed in measurable parameters, which can be used to calculate radius of curvature,

wafer warpage, and film stresses. Optical imaging photographs of warped wafers and surface irregularities are also given as examples.

Experimental

82 mm (100) wafers processed through MOS processings or deposited with Si₃N₄ thin film were used as samples for warpage measurements. The MOS processed wafers were covered with 0.5 μm thermal SiO₂ and 1.5 mm Al dots on the wafer front side and with 1 μm Al contact film on the back side. The deposition temperatures were 1000°C for atmospheric pressure CVD (APCVD) Si₃N₄ and between 200° and 300°C for plasma Si₃N₄. Wafer warpage due to the MOS processing on the film deposition was measured by the optical imaging method.

The experimental setup of the optical imaging method is shown schematically in Fig. 1. A collimated beam (divergence of about 1.4°) is used as a light source. The beam passes through a transparent square grid. The lines of the square grid are projected onto a wafer surface. The wafer is mounted on a goniometer, which provides a three-dimensional rotation. The square lines on the wafer surface are reflected back horizontally at an angle of 2α, which is approximately 12°, and vertically at nearly 0°. A matt-glass image screen intercepts the reflected beam to produce an image that can be photographed. For practical purposes, the angle, α, between the incidence beam and the wafer surface normal is kept as small as possible. Thus, the difference in image size between the vertical and the horizontal directions is kept to a minimum. For the present setup with α = 6°, the image difference is only 0.5%.

The image distortion produced by a warped surface is schematically shown in Fig. 2. Figure 2 shows that two beams A and B (with a small divergence of 2β) incident at positions W₁ and W₂ on an optically flat wafer surface W will reflect and form a magnified image I₁, I₂ in the image plane I. For the convex surface W', the image formed is I', I'₂. From simple geometry, the size of the image is

$$I_1 I_2 = W_1 W_2 + 2L \tan \beta \quad [1]$$

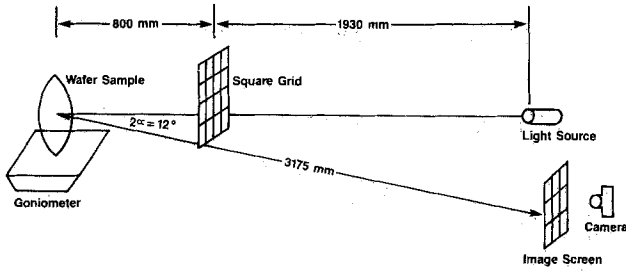


Fig. 1. Experimental setup of the optical imaging method

and

$$I'_1 I'_2 = W_1 W_2 + 2L \tan(\beta + 2\Theta) \quad [2]$$

where L is the distance between the image plane and the wafer surface, and 2Θ is the angle of bending for the convex wafer. The image distortion due to the convex surface is

$$d = I'_1 I'_2 - I_1 I_2 = 2L(2\Theta) \quad [3]$$

for small Θ and β .

The magnification factor m , defined as the ratio of reference image $I_1 I_2$ and reference spacing $W_1 W_2$, $m = I_1 I_2 / W_1 W_2$, can be measured from an optically flat mirror or obtained from Eq. [1].

The images $I_1 I_2$ and $I'_1 I'_2$ are reduced by a factor of n in the recorded picture. The image size in the recorded picture becomes $I_p = I_1 I_2 / n$, $I'_p = I'_1 I'_2 / n$, and the image distortion, $d_p = d/n$.

Knowing the values of m and n , the angle of bending can be readily obtained from a recorded picture as

$$2\Theta = nd_p / 2L \quad [4]$$

The radius of curvature is

$$R = \text{arc } W_1 W_2 / 2\Theta \cong 2L I_p / m d_p \quad [5]$$

The wafer warpage of a wafer diameter D is calculated from simple geometry as

$$h = 2R \times \sin^2[(2\Theta)/4] \cong D^2 / 8R \quad [6]$$

For $m = 2.3$, $n = 2.8$, $D = 82$ mm, $I = 49$ mm (obtained from a flat mirror), and $L = 3175$ mm, Eq. [4]-[6] reduce to

$$2\Theta = 91.6 d_p \text{ (seconds)} \quad [7]$$

$$R = 135 / d_p \text{ (meters)} \quad [8]$$

$$h = 6.21 d_p \text{ (micrometers)} \quad [9]$$

where d_p in millimeters can be measured from the difference in I_p between the sample and an optically flat mirror.

The sense of warpage can be determined unambiguously. A convex surface will produce a magnified image with a dark contrast, while a concave surface will give a demagnified image with a bright contrast.

The film stress is calculated from R according to

$$\sigma_f = \pm 1/6 (t_s^2 / t_f R) E / (1 - \nu) \quad [10]$$

where $+$ and $-$ denote tensile and compressive stresses, respectively, t_s is the wafer thickness, t_f is the film thickness, E is the Young modulus of the wafer, and ν is the Poisson ratio of the wafer. For (100) Si wafers, the value of $E/(1 - \nu)$ is 1.85×10^{12} dyn/cm² (6).

The results of the optical imaging method were compared with those obtained by both the x-ray method and the optical interference method. In the x-ray method, the angle of bending was measured from the difference in the Bragg angle between two reference points (6). Both transmission and reflection arrangements were used. In the transmission arrangement, the difference in the (220) Bragg angle between two points at a spacing of 50 mm was measured through an x-ray topographic camera using MoK α radiation. In the reflection arrangements, the (444) Bragg angles at a spacing of 20 mm were mea-

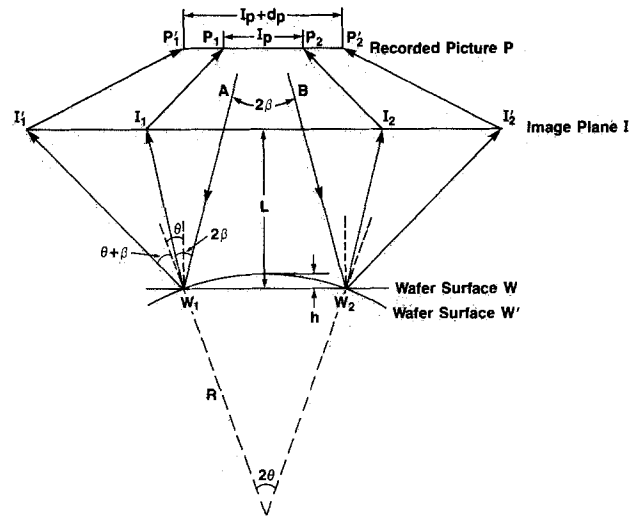


Fig. 2. The principle of the optical imaging method

sured by the Bond technique (10) using CuK α radiation. The reflection x-ray method is more sensitive to lattice distortion in the surface layer, while the transmission method is more sensitive to internal lattice distortion. The application of the optical interference method for film-stress measurements has been described by Irene (7).

Results

Si₃N₄ film stress.—Figure 3a shows the optical imaging photograph of an 82 mm wafer covered with 4000Å plasma Si₃N₄ on the front side. Measurements of the spacing between nine lines indicate that the I'_p is 60 mm. The reference spacing I_p is 49 mm. Therefore, the image distortion is +11 mm. The positive sense of the image distortion indicates that the curvature of warpage is convex. This implies that the plasma Si₃N₄ film is under a compressive stress and that the substrate at the Si₃N₄/substrate interface is under a tensile stress.

The film stress of as-deposited plasma Si₃N₄, as measured by the optical imaging method, the optical interference method, and the x-ray method, is plotted as a function of film thickness in Fig. 4. Note that the optical imaging method and the optical interference method yield almost identical profiles. The film stress increases gradually as the film thickness increases. The agreement obtained by these two methods is within 30%. On the other hand, transmission x-ray measurements yield a completely different profile. The film stress decreases as the film thickness increases. The discrepancy between the transmission x-ray method and the other two methods is substantial, especially at low values of film thickness.

We further investigated the effect of thermal annealing on the film stress. The annealing is carried out at 1000°C in H₂ for 15 min. As shown in Fig. 3b, the curvature of the substrate reverses from convex in the as-deposited state to concave after annealing. This results in a tensile stress in the plasma Si₃N₄ film. The tensile stress probably arises from a densification of the plasma Si₃N₄ during annealing. As a result of densification, holes and cracks are generated in the wafers deposited with 0.2 and 0.4 μm thick plasma Si₃N₄ films. The film stresses measured by the optical imaging method and the transmission x-ray method are shown in Fig. 4. Again, both methods show substantial discrepancies.

The film stress for LPCVD and APCVD Si₃N₄ films is also measured by the optical imaging method. The film stress is $(15.8 \pm 6.0) \times 10^9$ dyn/cm² for LPCVD Si₃N₄ and $(10.2 \pm 3.0) \times 10^9$ dyn/cm² for APCVD Si₃N₄. Both films are in tension. The value of the film stresses is in good agreement with that obtained by the optical interference method (7) and by the Newton-ring method (2).

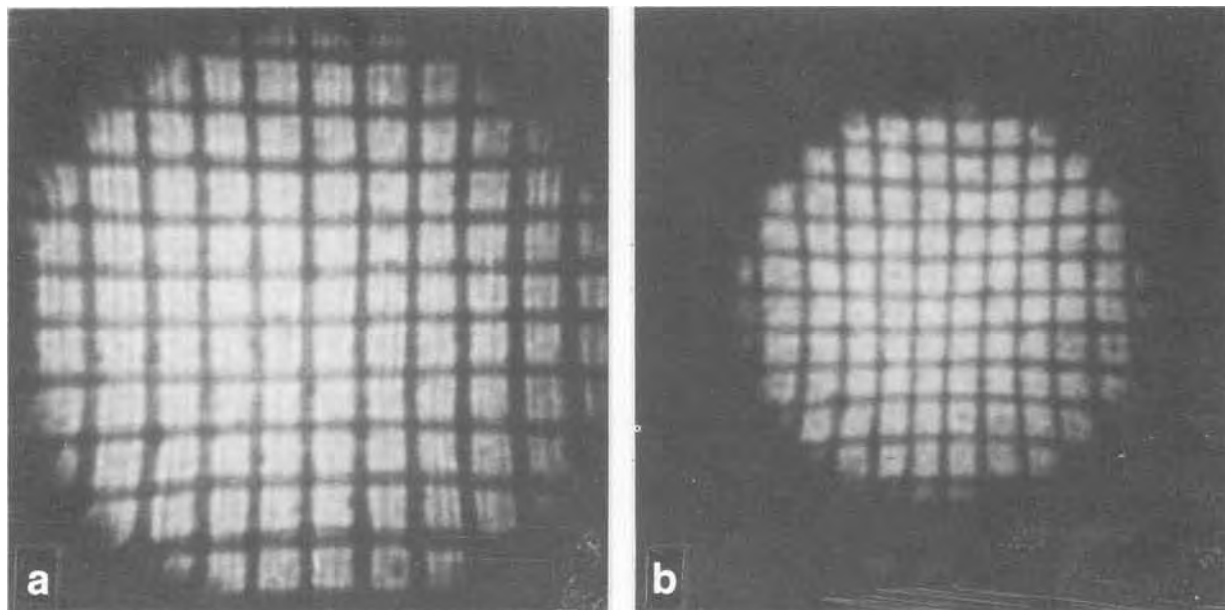


Fig. 3. Optical imaging photographs of a wafer front-side deposited with 4000Å plasma Si_3N_4 . a: As deposited. b: After annealing. (Note: I_p' is reduced through reproduction).

Process-induced warpage.—Wafer warpage induced by hot processings can be easily monitored through this technique. Figure 5a shows a severely convex wafer, while Fig. 5b shows a severely concave wafer induced by MOS processings. The convex wafer exhibits a magnified image with a dark contrast, while the concave wafer exhibits a demagnified image with a bright contrast. The process-induced warpage in general has a nonuniform curvature across the wafer. This can be seen from the variation in line spacings. In some cases, the shape of warpage is very complex. The advantage of this optical imaging method is that the shape of warpage can be immediately visualized.

The elastic and plastic deformations in a warped wafer can be measured by successive removal of surface thin films. For example, these MOS-processed wafers are covered with 5000Å thermal oxide and 1.5 mm Al dots on the front side and with 1 μm Al contact film on the back side. As shown in Fig. 6, removal of Al film and dots has negligible change in image distortion, thus indicating negligible Al film stresses. However, removal of thermal oxide shows a decrease of d_p in convex wafers or an increase of

d_p in concave wafers. The value of d_p is very consistent, even though two of these wafers, shown in Fig. 5, are severely warped. The average of d_p is 2.25 ± 0.22 mm. From Eq. [10], the SiO_2 film stress is calculated as $(2.23 \pm 0.21) \times 10^9$ dyn/cm² in compression. The film stress is in good agreement with published values of $2 \sim 3 \times 10^9$ dyn/cm² (1, 3, 5). The results of transmission x-ray measurements as shown in Fig. 6 are less consistent, and the SiO_2 film stress so obtained is $(1.30 \pm 0.78) \times 10^9$ dyn/cm² with a standard deviation of more than 50%. After removal of elastic film stresses, the residual warpage due to plastic deformation is obtained. It is given in Fig. 6.

Damage-induced warpage.—As will be shown later, mechanical damage in a wafer back side tends to generate a concave front surface. Various degrees of mechanical damage were introduced in the wafer back sides. Subsequently, the bending in the front surface was measured by both the optical imaging method and the reflection x-ray method using the Bond technique (10). The degree of bendings 2θ , at a spacing of 60 mm, is shown in Fig. 7. Figure 7 shows that the agreement between these two methods is very good for $2\theta > 500''$. The agreement becomes relatively poor for small bending. The bending obtained by the optical imaging methods tends to be higher than that obtained by the x-ray method. For 2θ between $100''$ and $500''$, the agreement is within 20%. At the detection limit of the optical imaging method (about $46''$), the disagreement increases to 50%.

Surface irregularity.—In addition to stress and warpage measurements, the optical imaging method is very sensitive in detecting irregularities on a wafer surface. For investigation of surface irregularity, the square grid in Fig. 1 is removed in order to improve the image resolution.

Figure 8a shows the front surface of an 82 mm wafer. Three irregularities are noticed. First, residual saw marks run nearly vertically across the wafer. Second, a bright spot at the left corner results from laser-scribed serial numbers on the wafer front surface. Third, bright letters and numbers, A, B, C, 1, 2, and 3, result from hand-scribed letters and numbers on the wafer back surface. The bright and dark contrast of the saw marks corresponds to the valleys and ridges, respectively. The valleys are locally concave surfaces, which gives stronger intensity in the reflected light. The ridges are locally convex surfaces, which give weaker intensity. For the same reason, the brightness of laser-scribed serial numbers and hand-scribed letters and numbers indicates that they are

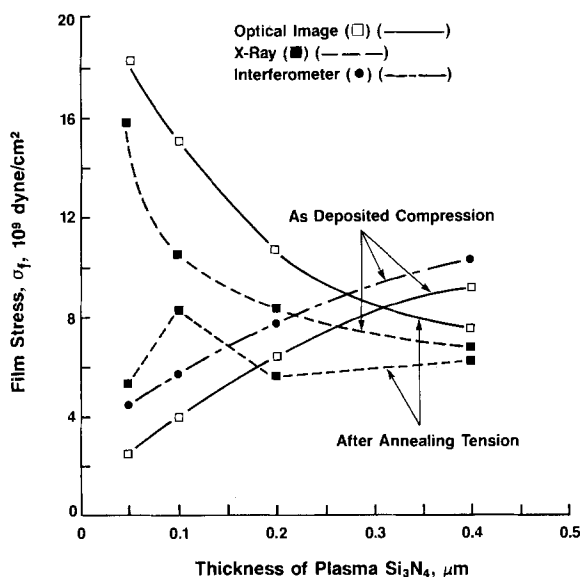


Fig. 4. Film stress of as-deposited and annealed plasma Si_3N_4 as measured by the optical imaging method, the transmission x-ray method, and the optical interference method.

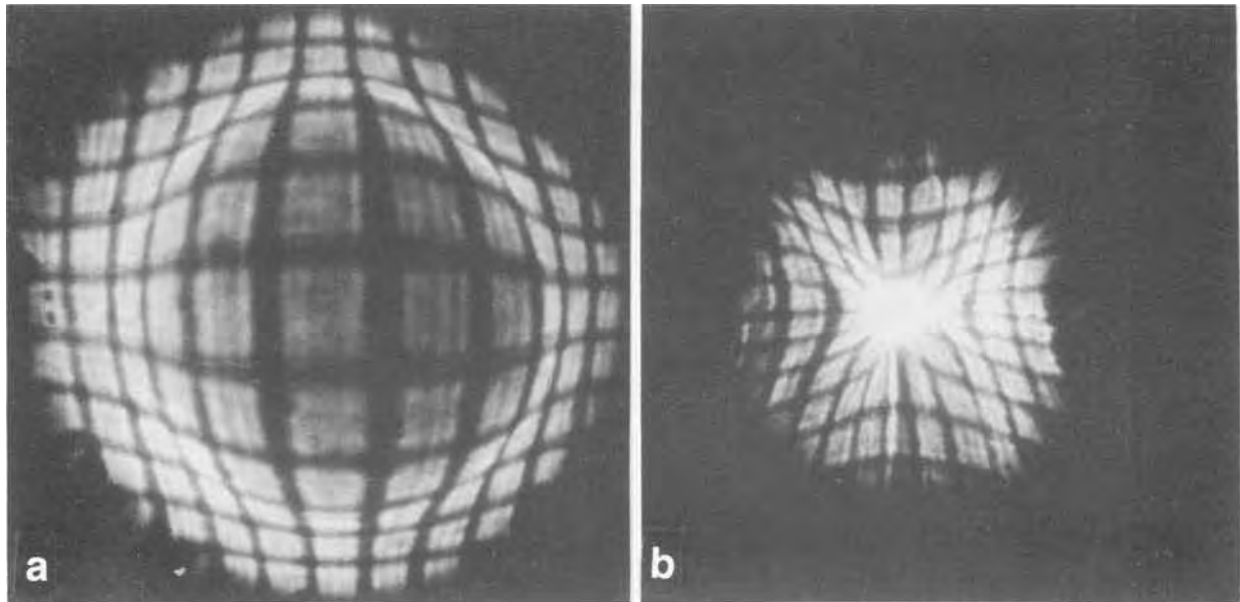


Fig. 5. Optical imaging photographs of severely warped wafers induced by MOS processing. a: Convex surface. b: Concave surface

surface depressions. It is interesting to note that the serial numbers are laser scribed on the wafer front surface, while the letters and numbers are hand scribed on the wafer back surface. The same bright contrast obtained from two opposite surfaces indicates that laser scribing and hand scribing produce stresses of opposite sense in the wafer. Laser scribing generates a compressive stress due to surface contraction and causes a locally concave surface. Hand scribing generates a tensile stress due to surface tension and causes a locally convex surface.

This is further confirmed by examining the back side of the wafer, as shown in Fig. 8b. Figure 8b shows that the contrast of the laser-scribed serial numbers and the hand-scribed letters becomes dark, in contrast to the bright contrast observed on the front side, Fig. 8a. The dark contrast indicates a locally convex surface. The size of the dark contrast area resulting from a convex surface is larger than that of the bright contrast area obtained from a concave surface. This is evident by comparing the size

of laser-scribed serial numbers in Fig. 8a and 8b. These results indicate again that the sense of the stresses introduced by laser scribing and hand scribing are opposite. Laser scribing generates a compressive stress, and the hand scribing generates a tensile stress. When the stresses are large enough, they propagate to the opposite side of the wafer and result in local bending of opposite sense. This method unambiguously displays this effect.

In order to appreciate the sensitivity of this method, two surface profiles, 1 and 2 in Fig. 8a, are measured by a Sloan surface profile unit. Profile 1 measures the profile of saw marks only. Profile 1, Fig. 8c, shows that the height of saw marks varies from 100 to 350Å. The variation of the height correlates with the contrast in Fig. 8a. The valley corresponds to the bright contrast area, and the ridge corresponds to the dark contrast area. In addition to the saw marks, profile 2 intersects once the bottom of letter B and three times the number 2. The intersections at the number 2 clearly give three dips, as indicated by the arrows in Fig. 8c. The depth of the dips is about 50-100Å. The dip is consistent with the bright contrast of a locally concave surface introduced by hand scribing on the wafer back side.

This method is extremely valuable in the evaluation of the surface quality of chem-mech polished wafers. Wafers

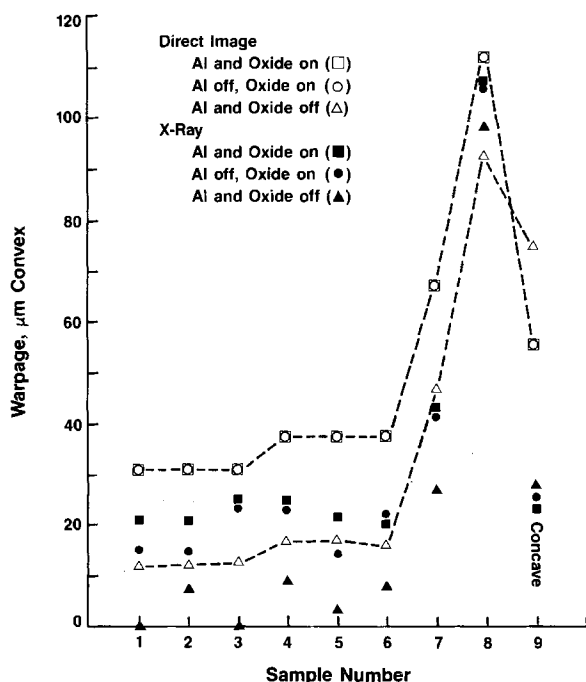


Fig. 6. A comparison of the optical imaging method and the transmission x-ray method for warpage induced by MOS processing.

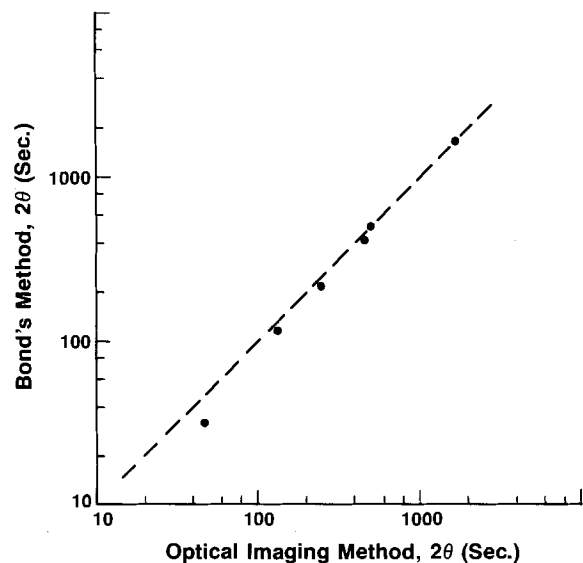


Fig. 7. A comparison of the optical imaging method and the reflection x-ray method for bending induced by back-side damage.

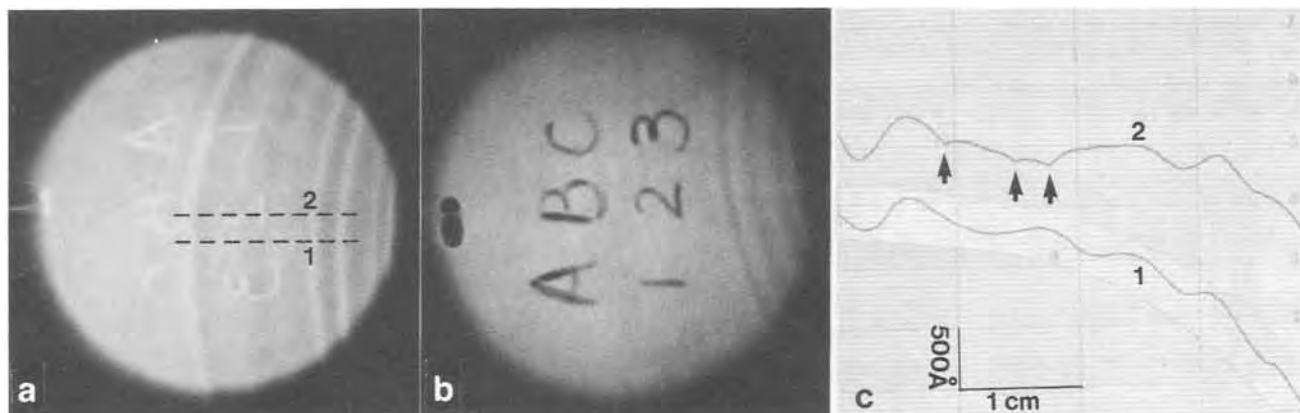


Fig. 8. Optical imaging photographs showing (a) the front surface and (b) the back surface of an 82 mm wafer. c: Surface profiles 1 and 2 in (a)

obtained from different vendors usually show different characteristics in surface finish.

Discussion

This optical imaging method uses the image distortion of a reflected beam from a warped surface as a means to detect surface irregularities and wafer warpage. This allows one to examine surface irregularities and wafer warpage simultaneously. The technique can be used as a tool for quality control. Several examples for the measurement of surface irregularities, process-induced warpage, and thin film-induced warpage have been given.

The sensitivity of this method, as indicated in Eq. [2], depends on L . For the present setup, $L = 3175$ mm, and with a measurable d_p of 0.5 mm, the detection limit is 270m for R , 45.8" of arc for 2θ , and $3.1 \mu\text{m}$ of warpage h for 82 mm wafers. This sensitivity is sufficient for most practical purposes. The detection limit can be improved through the use of more sophisticated optics or simply by the increase of L . For examination of extremely rough surfaces and severely warped wafers, the sensitivity should be decreased by decreasing L . This approach can also be used to examine saw masks after slicing.

Measurements of plasma Si_3N_4 film stresses indicate that the agreement between the optical imaging method and the optical interference method is within 30%. This agreement is considered to be good in consideration of the errors involved in these two methods. For example, the optical interference method has a relatively poor accuracy for highly warped wafers, while the accuracy for the optical imaging method is relatively poor for low warpage.

A comparison of the optical imaging method with the reflection x-ray method (Bond's technique) also shows a reasonable agreement of 20% for a wafer bending larger than 100". However, the agreement between the optical imaging method and the transmission x-ray method is poor, especially at low film stresses. The poor agreement arises probably from a difference in the principle of measurements. The optical imaging method and the optical interference method use the curvature of a wafer surface for warpage measurements. The reflection x-ray method measures the lattice distortion in a surface layer. These three methods are more sensitive to the curvature change and the lattice distortion in a wafer surface. As a result, a reasonable agreement among these three methods is observed.

On the other hand, the transmission x-ray method, which uses a transmission diffracted beam for the warp-

age measurements, is sensitive not only to external film stresses, but also to internal lattice distortion. At low film stresses, the contribution of internal lattice distortion is significant in comparison with film stresses. This results in a substantial disagreement between the optical imaging method and the transmission x-ray method.

Summary

A simple optical imaging method was developed for quick evaluation of wafer surface quality and warpage. Surface irregularities of 50-100Å can be detected by this method. The detection limit for the radius of curvature is about 270m. The agreement between this method and the optical interference method is within 30%. A comparison of this method with the reflection x-ray method also shows a reasonable agreement of 20%. A substantial discrepancy exists between this method and the transmission x-ray method. The discrepancy arises mainly from the fact that the transmission x-ray method is also sensitive to internal lattice distortion. The film stress obtained by this method is $(2.23 \pm 0.21) \times 10^9$ dyn/cm² in compression for thermal SiO_2 , $(15.8 \pm 6.0) \times 10^9$ dyn/cm² in tension for LPCVD Si_3N_4 , and $(10.2 \pm 3.0) \times 10^9$ dyn/cm² in tension for APCVD Si_3N_4 .

Acknowledgments

The author thanks Dr. J. A. Engelbrecht and Dr. G. H. Schwuttke for valuable discussions, Mr. C. Hoopendoorn for x-ray measurements, and Mr. W. James for technical assistance.

Manuscript submitted May 18, 1984; revised manuscript received Feb. 1, 1985.

IBM Corporation assisted in meeting the publication costs of this article.

REFERENCES

1. R. J. Jacondine and W. A. Schlegel, *J. Appl. Phys.*, **37**, 2429 (1966).
2. M. Tamura and H. Sunami, *Jpn. J. Appl. Phys.*, **11**, 1097 (1972).
3. G. H. Schwuttke and J. K. Howard, *J. Appl. Phys.*, **39**, 1581 (1967).
4. G. A. Rozgonyi and T. J. Ciesielka, *Rev. Sci. Instrum.*, **44**, 1053 (1973).
5. J. R. Patel and N. Kato, *J. Appl. Phys.*, **44**, 971 (1973).
6. E. W. Hearn, *Adv. X-Ray Anal.*, **20**, 273 (1977).
7. E. A. Irene, *J. Electron. Mater.*, **5**, 287 (1976).
8. C. E. Synborski, *Soc. Photo-Opt. Instrum. Eng., J.*, **135**, 104 (1978).
9. K. Kugimiya, *This Journal*, **130**, 2123 (1983).
10. W. L. Bond, *Acta Crystallogr.*, **13**, 814 (1960).

Dry Etch-Back of Overthick PSG Films for Step-Coverage Improvement

J. S. Mercier,* H. M. Naguib,*¹ V. Q. Ho, and H. Nentwich

Northern Telecom Electronics Limited, Semiconductor Components Group, Ottawa, Ontario, Canada K1Y 4H7

ABSTRACT

In this article, we present the results of a study initiated to improve the step coverage of phosphosilicate glass (PSG) obtained with a low temperature LPCVD process and intended for use in VLSI multilevel interconnect structures. It is shown that increasing the PSG film thickness leads to a substantial improvement in the PSG step-coverage profile, but could create problems for subsequent patterning steps. We have alleviated these problems through the use of dry etching to reduce the thickness of these films to values more compatible with VLSI multilevel interconnect technology, while successfully maintaining the superior step-coverage profile obtained with the thicker PSG films.

A very important requirement of interlayer dielectric films in multilevel interconnect structures is smooth and conformal coverage of the underlying topography (1-9). For the intermetal dielectric level, the need for compatibility with an underlying aluminum alloy interconnect also precludes any high temperature treatments. The dry etching techniques required for the fine line lithography of VLSI chips produce features that can be much sharper than the wet etching methods used in LSI technology. As a consequence, with currently available dielectric deposition techniques, it has become very difficult to obtain satisfactory as-deposited coverage over these sharp features, thereby leading to poor overlying metallization. To overcome this difficulty, work was initiated in our laboratory to investigate methods of improving the step-coverage characteristics of phosphosilicate glass (PSG) films obtained using low temperature oxidation of silane and phosphine in a low pressure chemical vapor deposition (LPCVD) system.

Preliminary experiments included varying the deposition parameters and increasing the ratio of PSG film thickness (t) to underlying step height (h) (9). It was found that variations of the deposition conditions, within the parameter ranges investigated, did not result in any appreciable step-coverage improvement, while a significant improvement could be obtained by increasing the ratio of t/h . In the present study, the deposition of overthick PSG films is followed by a dry etch-back cycle to reduce the glass film thickness to values compatible with VLSI multilevel interconnect technology, while preserving the superior step-coverage profile obtained with the thicker PSG films.

Experimental Procedure

The test structure used for step-coverage evaluation is shown schematically in Fig. 1. A thin (100 nm) silicon dioxide layer was first thermally grown at 1000°C over a (100) Si substrate. An LPCVD polysilicon film was then deposited at 625°C, phosphorus doped with a POCl_3 cycle at 900°C, and patterned into sharp steps using plasma etching.

The PSG films were deposited in a conventional horizontal tube, hot-wall, LPCVD system using the following typical hydride oxidation conditions: gas flow ratios of 6/5 for O_2/SiH_4 and 1/10 for PH_3/SiH_4 , total gas flow rate of 335 sccm, deposition temperature of 410°C, and pressure of 0.4 torr. These conditions resulted in a deposition rate of 26 nm/min and a nominal phosphorus concentration in the PSG films of 4 weight percent (w/o).

A layer of Al-Si alloy was sputtered over the PSG films to evaluate the effect of the PSG film step coverage on subsequent metallization. The deposition was performed in an MRC DC-Magnetron sputtering system (Model 603), using a double-pass procedure under the following condi-

tions: target composition of Al-(1%)Si, Ar pressure of 0.01 torr, power of 8 kW, wafer preheat temperature of 300°C, and dc bias voltage of 50V. The deposition rate was approximately 700 nm/min.

Scanning electron microscopy (SEM) was used to examine the step-coverage profile of all test samples. The SEM cross-sectional micrographs were taken near the center of the cleaved wafers. The polysilicon-PSG interface was delineated with a $\text{CF}_4\text{-O}_2$ plasma etch of the cross section. Figure 2 shows an SEM micrograph of a 1.1 μm thick PSG film deposited over a 0.9 μm high polysilicon step having a step angle $\psi = 70^\circ$, for a t/h ratio of approximately 1.2. A 1.2 μm Al-Si layer was sputtered over the PSG film. In this case, the PSG step-coverage profile is characterized by an acute reentrant angle θ of about 75° and a sidewall thickness ratio t_{sw}/t of approximately 0.75. Such a difficult topography resulted in even poorer step coverage of the Al-Si metallization, as shown in Fig. 2, where the metal step-coverage angle ϕ is approximately 70° and its sidewall thickness ratio T_{sw}/T is about 0.2. In the present study, we have used the PSG profile of this control sample as a reference for comparison with later experimental results to determine step-coverage improvement.

Reactive ion etching (RIE) of the overthick PSG films was performed in an AMT 8110 system which uses a hexagonal cathode configuration. Typical RIE conditions were as follows: gas flow ratio of 5/3 for CHF_3/O_2 , total gas flow rate of 83 sccm, pressure of 0.05 torr, and discharge power of 1350W. These conditions yielded an etch rate of approximately 50 nm/min. The amount of PSG removed was determined with laser interferometry.

Plasma etching was also tested in a Perkin-Elmer Omni-Etch system. The etching conditions were as follows: gas flow ratios of 2/1 for CF_4/CHF_3 and 5/1 for $\text{Ar}/(\text{CF}_4 + \text{CHF}_3)$, total gas flow rate of 364 sccm, pressure of 1.8 torr, and discharge power of 255W. An etch rate of approximately 12.5 nm/s was obtained under these conditions. This value was used to calculate the duration of the etch cycle for control of the amount of PSG removed.

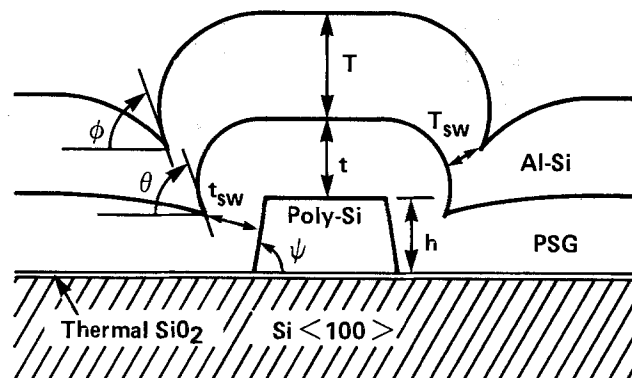


Fig. 1. Step-coverage test structure

*Electrochemical Society Active Member.

¹Present address: Fairchild Camera and Instrument Corporation, Mountain View, California 94039.

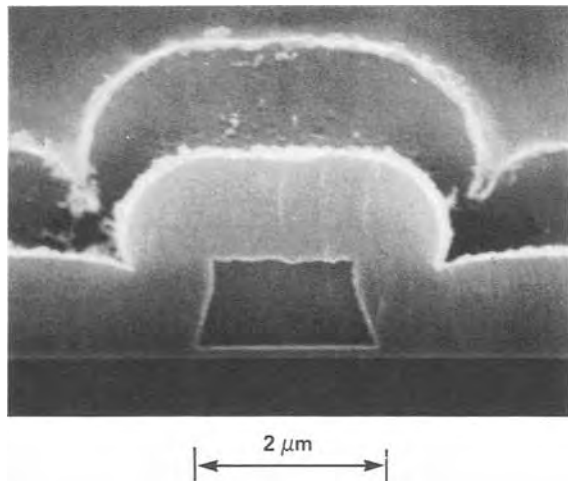


Fig. 2. SEM micrograph showing the step coverage of a control sample. A sputtered Al-Si layer can also be seen on top of the PSG film.

Results and Discussion

Effect of film thickness.—In the first series of experiments, PSG films ranging in thickness from 0.6 to 2.3 μm were deposited over polysilicon steps with height varying from 0.3 to 1.2 μm , and the ratio of t/h was varied from 0.6 to 4.7. The results are shown in Fig. 3, where the dependence on the ratio of t/h for the PSG step-coverage angle θ and the sidewall thickness ratio of t_{sw}/t are plotted.

The scatter of the results in these graphs can be attributed partly to our measurement accuracy for θ , which is $\pm 5^\circ$. Furthermore, the angle ψ at the bottom of the polysilicon steps defined in Fig. 1 varied from 65° to 75° and has been modeled to have a direct influence on the PSG step-coverage angle θ (10). Finally, in most cases, the corners at the bottom and at the top of the polysilicon steps were quite sharp. Indeed, the top corners of most of the steps were actually acute, displaying a "dog-ear" feature. The radius of curvature of these corners, although quite small, could not be controlled very well and may have had an influence on the reproducibility of our results. Modeling of small variations in these radii of curvature has shown that they are likely to be amplified by subsequent PSG film deposition (11).

Despite the sources of variation discussed above for our results, a definite trend emerges from the plots in Fig. 3,

namely, that significant improvement in PSG step coverage results from an increase in the ratio of t/h . This can be clearly seen in the micrograph of Fig. 5a, where the step angle ψ is about 67° and the ratio of t/h has a value of approximately 3.0. The angles θ (PSG) and ϕ (Al-Si) have both increased to more than 125° , as compared to a value of about 75° for θ and 70° for ϕ , for $t/h \approx 1.2$ (Fig. 2). Also, the sidewall thickness ratio of t_{sw}/t (PSG) has increased from approximately 0.75 to almost 0.95, while the sidewall thickness ratio of T_{sw}/T (Al-Si) went from about 0.2 to more than 0.75, a substantial improvement.

It should be pointed out that a test structure step angle ψ of approximately 70° does not constitute the worst-case topography that an angle ψ close to 90° would offer to the deposition of glass films. Nevertheless, it can represent a realistic situation for VLSI applications, since tapered etching techniques are being actively developed in many laboratories.

Various studies involving atmospheric pressure chemical vapor deposition (APCVD) reported that the PSG film coverage exhibited a more pronounced reentrant profile (*i.e.*, a decrease in θ) with an increase of t/h (1, 3, 4, 12-14). In other APCVD studies (5, 7), the step-coverage angle θ was reported to increase up to 90° as t/h was increased to unity, but remained at 90° when t/h was increased further.

For LPCVD, an improvement in step coverage with an increase in t/h was observed for the pyrolysis of tetraethyl orthosilicate (TEOS) (1). This improvement has been attributed to the inherent conformality of the TEOS process which minimizes the self-shadowing effect that initiates a reentrant profile in other processes. In effect, good initial step coverage should get better, while poor initial step coverage should get worse.

Since the initial step coverage obtained in our experiments was not conformal, but improved with an increase in the ratio of t/h , this explanation does not apply to our results. Therefore, further work is required to understand the mechanisms involved in the improvement of step coverage obtained with increasing the thickness of PSG films produced with low temperature LPCVD.

This film growth from a diffuse deposition source has recently been modeled by Ross and Vossen (10). In addition to the effect of the ratio of t/h on the sidewall thickness ratio t_{sw}/t , the influence of the underlying step angle ψ has been taken into account. The impact of the proximity of closely spaced steps, represented by the ratio of the spacing between steps w to the step height h , was also in-

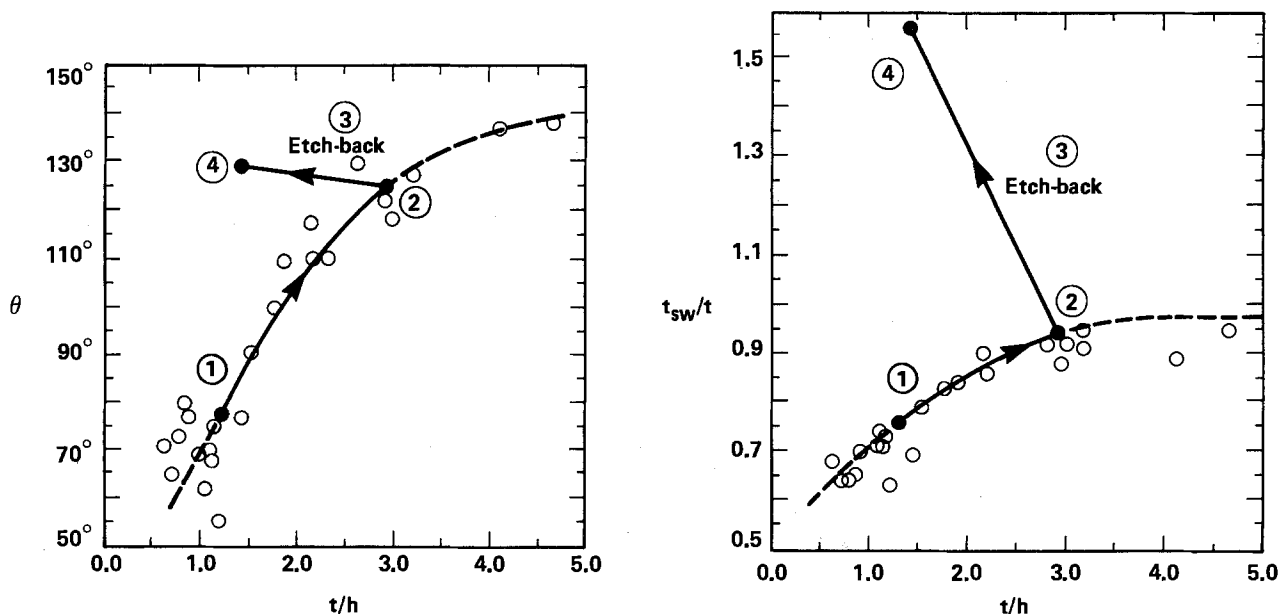


Fig. 3. Effect of ratio of PSG film thickness t over underlying step height h on step-coverage angle θ , (a, left), and sidewall thickness ratio of t_{sw} over t , (b, right). The underlying step angle ψ varied between 65° and 75° . Points 1-4 correspond to the process steps explained in the diagram of Fig. 4.

corporated in the model. In effect, the step-coverage test structure used in Ref. (10) is a groove of width w and of depth h . The overlap with our experimental results is minimal, since the highest value considered in their calculations for t/h is unity. Nevertheless, for isolated steps and for all values of the step angle ψ considered, one of their findings was that the sidewall thickness ratio t_{sw}/t becomes independent of t/h , for $t/h \leq 1$. Our experimental findings, shown in Fig. 3b, appear to contradict these theoretical results. Furthermore, for $t/h = 1$, $\psi = 75^\circ$, and $w/h \rightarrow \infty$, the value calculated in Ref. (10) for t_{sw}/t is below 0.5, while our experimental results for $\psi \approx 65^\circ\text{--}75^\circ$ are grouped around 0.7, as shown in Fig. 3b. More theoretical work is therefore required to resolve these discrepancies.

A conclusion of this theoretical study indicates the possibility that unacceptable step coverage would be obtained for narrow, deep and vertical trenches (*i.e.*, small values of w/h and ψ close to 90°). This conclusion can also be reached intuitively from geometrical shadowing considerations. As the glass films on opposing vertical sides of each groove get closer and closer, it becomes increasingly difficult for a fresh supply of reactant gases to reach the bottom of the trench and this results in a lower local deposition rate. Furthermore, opposing vertical PSG walls will eventually touch and at that point, the glass step-coverage angle Θ must be at least 90° because the top part will touch before the bottom part and a triangular void will be formed (1).

For $\Theta > 90^\circ$, a minimum value of $t/h \approx 1.5$ can be derived from Fig. 3a and a corresponding value of $t_{sw}/t \approx 0.8$ is obtained from Fig. 3b. For this case, the vertical glass film has a uniform thickness equal to t_{sw} and the minimum step separation w is equal to $2t_{sw}$. After the proper substitutions, a minimum value of approximately 2.5 is derived for the step spacing ratio w/h .

It must be noted that, since the results of Fig. 3a and 3b are for isolated steps ($w/h \approx 10$), the shadowing effect of a neighboring step is not taken into account in the above deduction although it is not expected to be dominant for $w/h \approx 2.5$. The specific minimum value for w/h would, of course, increase with the underlying step angle ψ .

Etch-back of overthick PSG films.—The use of overthick PSG films may present problems in subsequent patterning steps for VLSI multilevel interconnection structures, especially if sloped-wall vias are to be dry etched through the glass layer. Accordingly, in a second series of experiments, we explored the use of dry etching techniques to reduce the ratio of t/h to a value more suitable for VLSI processing. This concept of anisotropic etch-back of overthick PSG films is illustrated in the diagram of Fig. 4, where the step-coverage profile of an as-deposited PSG film with t/h near unity is also shown for

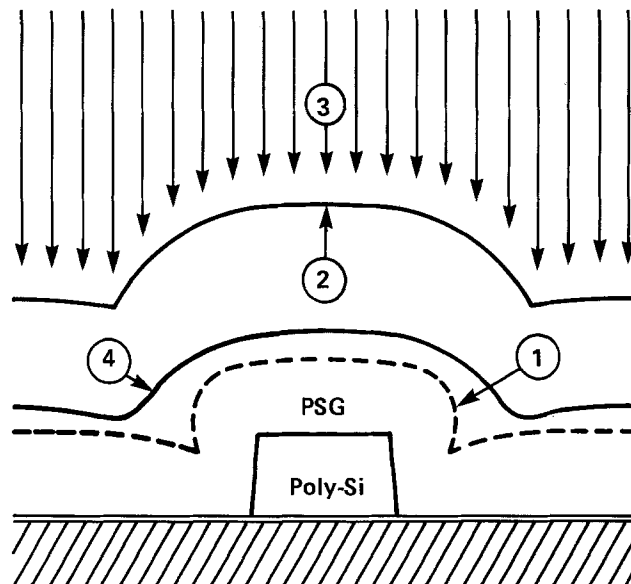


Fig. 4. Dry etch-back of overthick PSG film. 1: Thin as-deposited film. 2: Thick as-deposited film. 3: Dry etch-back. 4: Final etched-back film.

comparison purposes. The micrographs of Fig. 5 show the cross section of a $2.1 \mu\text{m}$ thick PSG film, as deposited over a $0.7 \mu\text{m}$ step ($\psi \approx 67^\circ$) and after an etch-back cycle, using RIE, down to a thickness of about $1.0 \mu\text{m}$ ($\psi \approx 75^\circ$). Similar results were obtained with plasma etching.

The superior step-coverage profile obtained with the thick as-deposited PSG film was clearly conserved during the etch-back cycle. As t/h decreased from approximately 3.0 down to 1.4, the step-coverage angle Θ (PSG) actually increased slightly from 125° to almost 130° , while the step-coverage angle ϕ (Al-Si) remained close to 125° . The changes in Θ during the etch-back procedure are illustrated in the graph of Fig. 3a (closed circles). The etch-back cycle also resulted in rounding of the bottom of the PSG step-coverage profile. Furthermore, Fig. 3b shows that the sidewall thickness ratio of t_{sw}/t (PSG) increased from less than 0.95 to almost 1.6 during the etch-back cycle, while the sidewall thickness ratio of T_{sw}/T (Al-Si) remained close to 0.75. It should be noted that the above improvements were observed despite the fact that the step angle ψ was larger under the etched-back film (75°) than under the overthick film (67°).

An attractive feature of the etch-back method, aside from its being a low temperature technique, lies in its simplicity as compared to more elaborate step-coverage

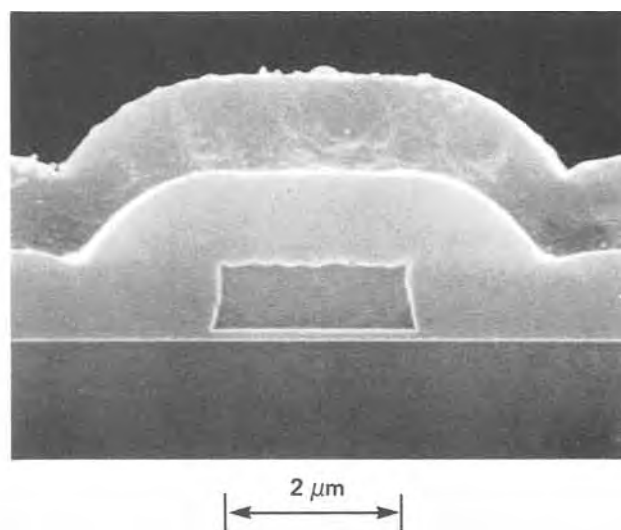
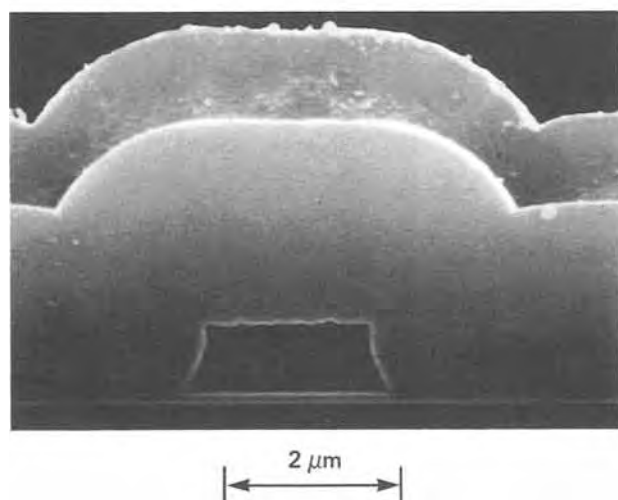


Fig. 5. SEM micrograph showing the step coverage of an overthick PSG film before ($t/h \approx 3.0$), (a, left), and after ($t/h \approx 1.4$) the etch-back procedure, (b, right). An Al-Si layer has been sputtered on both PSG films.

improvement schemes reported elsewhere (15-20). The etch-back technique does not need sacrificial planarization layers, such as resists (15, 16) or silicon nitride (17, 18), where precise characterization and control of differential etch rates are essential. It is very simple compared to complicated lift-off procedures where low temperature directional deposition processes, such as electron cyclotron resonance plasma deposition, are needed to obtain a suitable SiO₂ layer (19). In other methods, RF-bias sputtering is used in a complex technique involving simultaneous deposition and resputtering of SiO₂ to obtain self-planarized as-deposited films (20). Indeed, for the etch-back procedure described in this work, deposition and dry etching equipment readily available in most production lines can be used directly, with minimal optimization needed.

However, the creation of triangular voids during the deposition of overthick PSG films over closely spaced steps would limit the applicability of the etch-back method to cases where the step separation ratio w/h is sufficiently large. In our case (*i.e.*, $\psi = 70^\circ$), if we apply the criterion derived above ($w/h \geq 2.5$), 0.8 μm thick interconnect lines could not be closer than about 2.0 μm . Since for more vertical steps (*i.e.*, $\psi \approx 90^\circ$) this minimum required separation would be even larger, some taper etching of the underlying steps would be needed.

Conclusion

This study demonstrates the feasibility of a procedure designed to improve the step coverage of LPCVD phosphosilicate glass films over sharp, dry-etched steps. A dry etching technique was successfully applied to overthick PSG films to reduce the ratio of the PSG film thickness to underlying step height towards unity while preserving the superior step-coverage profile obtained with the thicker PSG films. The low temperature feature of this method makes it compatible over aluminum alloy interconnections in multilevel metallization structures. However, in this experiment, the applicability of the procedure over closely spaced vertical steps appears to be limited to step separation over step height ratios (w/t) larger than approximately 2.5.

Acknowledgments

The authors would like to acknowledge the technical help received from P. Leung, M. Brown, B. Tait, J. Saeki, R. Leblond, and T. Abraham during the course of this work.

Manuscript submitted Sept. 13, 1984; revised manuscript received Jan. 4, 1985.

Northern Telecom Electronics Limited assisted in meeting the publication costs of this article.

REFERENCES

1. R. M. Levin and K. Evans-Lutterodt, *J. Vac. Sci. Technol. B*, **1**, 54 (1983).
2. E. W. Sabin and C. Ramiller, Abstract 250, p. 559, The Electrochemical Society Extended Abstracts, Vol. 81-2, Denver, CO., Oct. 11-16, 1981.
3. W. Kern, J. L. Vossen, and G. L. Schnable, in "11th Annual Proceedings of Reliability Physics of IEEE," p. 214, IEEE, New York (1973).
4. D. L. Tolliver and C. J. Santoro, *Solid State Technol.*, **14**, (4), 32 (1971).
5. C. J. Santoro and D. L. Tolliver, *Proc. IEEE*, **59**, 1403 (1971).
6. J. L. Vossen, G. L. Schnable, and W. Kern, *J. Vac. Sci. Technol.*, **11**, 60 (1974).
7. C. J. Santoro, D. L. Tolliver, and J. R. Devaney, in "8th Annual Proceedings of Reliability Physics of IEEE," p. 281, IEEE, New York (1971).
8. C. J. Santoro and D. L. Tolliver, Abstract 15, p. 44, The Electrochemical Society Extended Abstracts, Vol. 71-1, Washington, DC, May 9-13, 1971.
9. J. S. Mercier, H. M. Naguib, V. Q. Ho, H. Nentwich, and P. Leung, in "Proceedings of the First International IEEE VLSI Multilevel Interconnection Conference," p. 99, IEEE, New York (1984).
10. R. C. Ross and J. L. Vossen, *Appl. Phys. Lett.*, **45**, 239 (1984).
11. I. A. Blech, *Thin Solid Films*, **6**, 113 (1970).
12. M. M. Schlacter, E. S. Schlegel, R. S. Keen, Jr., R. A. Lathlaen, and G. L. Schnable, *IEEE Trans. Electron Devices*, **ed-17**, 1077 (1970).
13. M. M. Schlacter, R. S. Keen, Jr., and G. L. Schnable, *IEEE J. Solid State Circuits*, **se-6**, 327 (1971).
14. T. C. Tisone and J. B. Bindell, *J. Vac. Sci. Technol.*, **11**, 72 (1974).
15. A. C. Adams, *Solid State Technol.*, **24**, (4), 178 (1981).
16. E. R. Sirkin and I. A. Blech, *This Journal*, **131**, 123 (1984).
17. H. Hazuki, T. Moriya, and M. Kashiwagi, in "Digest of Technical Papers, 1982 Symposium on VLSI Technology," Paper no. 2-1, p. 18, IEEE, New York (1982).
18. M. O. Aboelfotoh, *IBM Tech. Disclos. Bull.*, **26**, 4115 (1984).
19. K. Ehara, T. Morimoto, S. Muramoto, and S. Matsuo, *This Journal*, **131**, 419 (1984).
20. M. Morimoto, T. Mogami, H. Okabayashi, and E. Nagasawa, in "Digest of Technical Papers, 1983 Symposium on VLSI Technology," Paper no. 7-8, p. 100, IEEE, New York (1983).

Preparation and Characterization of Boron- and Phosphorus-Doped Hydrogenated Amorphous Silicon Nitride Films

Y. K. Fang, C. F. Huang, C. Y. Chang,* and R. H. Lee

Semiconductor and System Laboratories, National Cheng Kung University, Tainan, Taiwan, China

ABSTRACT

Hydrogenated amorphous silicon nitride (a-SiN) films were deposited on silicon wafers by plasma-enhanced chemical vapor deposition and *in situ* doped with boron or phosphorus. Film properties, including both wet and dry etching rate, refractive index, dielectric constant, breakdown strength, dc resistivity, and pinhole density vs. doping percentage were systematically investigated and compared with the undoped films. It has been found that the films with doping concentrations around 2-3% exhibit the best film quality, which drastically deteriorate when the doping concentrations are beyond 6%.

Plasma-enhanced chemically vapor-deposited hydrogenated amorphous silicon nitride SiN films are useful for semiconductor passivation and for diffusion or oxida-

tion barriers (1-7). However, plasma-deposited SiN films are extremely sensitive to the deposition conditions, including the reactant gas composition, RF power, substrate temperature, gas flow rate, and reactor pressure (6, 7).

* Electrochemical Society Active Member.

Efforts have been made to investigate the relationship between deposition conditions and the properties of these films, and it has been found a SiN film with lower chemical etch rate and higher optical refractive index can be obtained by tailoring the process conditions (6, 8). Nevertheless, in real fabrication process, due to diffusion or auto-doping, the SiN films may be incorporated with the dopant impurities (*i.e.*, P or B) and change the properties.

Little research about this phenomenon has been reported. In 1976, Bind and Bigger reported that suitable addition of impurities (*i.e.*, boron carbide, boron, or alumina) can make the silicon carbide more dense and resistive. It is the purpose of this study to investigate the change of doped SiN film properties as a function of dopant impurities (*i.e.*, P or B) with various doping concentrations. The properties include etch rate in 49% HF, buffered HF, 180°C H₃PO₄, and CF₄ + O₂ plasma, dc resistivity, dielectric breakdown strength, pinhole density, dielectric constant, and deposition rate. The chemical composition and doping traces in SiN film were examined by Auger electron spectroscopy and infrared (IR) spectroscopy.

Film Preparation

The samples used in this study were prepared by RF glow discharge both silane gas and doping gas on silicon wafers with an Anelva PECVD 301 plasma CVD system. The stainless steel reaction chamber of the system possesses one pair of capacitive electrodes, which can create the RF glow-discharged plasma by a 13.56 MHz RF high voltage power supply. Also, the chamber contains a rotary susceptor equipped heating elements.

First, the (100)-oriented, 4-7 Ω-cm n-type silicon wafers were cleaned sequentially by acetone, deionized (DI) water, H₂SO₄/H₂O mixture, and HNO₃ solutions, then rinsed thoroughly in DI water and blown dry with nitrogen (N₂) gas. After the cleaning process was completed, the wafers were placed on the susceptor and we began to pump down the chamber. At the same time, the substrate was heated up to 350°C.

When the total pressure in the chamber was pumped down to 1.33×10^3 Pa (10 torr), diluted silane (25% SiH₄ + 75% N₂), ammonia (NH₃), and diluted diborane (1% B₂H₆ + 99% N₂) or phosphine (1% PH₃ + 99% N₂) were introduced into the chamber and adjusted the valves of the system to obtain a 133 Pa (1 torr) reaction pressure in chamber.

During the deposition of SiN films, the flow rates of diluted SiH₄ and NH₃ were kept at 60 and 20 sccm, respectively, and those of B₂H₆ and PH₃ were varied from 15 to 100 sccm, according to the doping percentage desired.

The RF power was kept at 150W (which is a power density of about 4.34 kW/m²). The cathode voltage was kept at 2.6 kV.

Film Analysis

To identify the quantities of doping impurities P or B in the doped SiN films, the Auger spectroscopy (AES) was employed. Infrared (IR) spectroscopy was used to examine the structure of doped SiN films.

Auger analysis.—From the Auger spectrum (with Anelva AAS-200 Auger Spectroscopy) of phosphorus- or boron-doped SiN films, the films were found to contain Si, N, O, C, B, or P. The existence of boron or phosphorus identifies the effectiveness of the doping processes, and their related peak amplitudes were used to calculate the individual doping concentration in the films. However, the doping concentrations of P or B are dependent on the PH₃ or B₂H₆ flow rate during film deposition and will be discussed in the next section. The presence of oxygen and carbon may be due to the residues from cleaning process or surface contamination during exposure to the air.

IR analysis.—IR spectroscopy gives information on the type and nature of the chemical bonds.

To prepare for IR analyzing, the SiN films were deposited on 1000 Ω-cm, (100)-oriented silicon wafers. The higher intrinsic property of silicon eliminates auto-doping

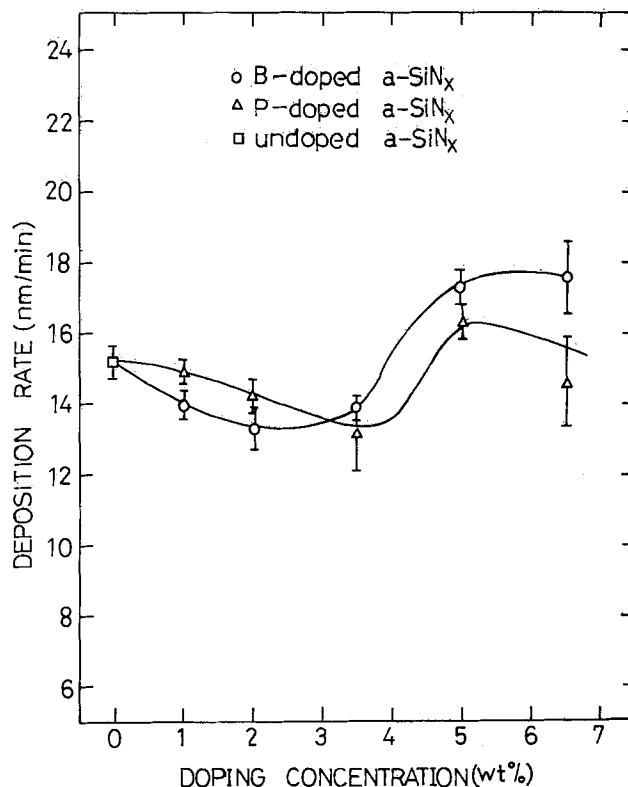


Fig. 1. The measured deposition rate of phosphorus- or boron-doped plasma-deposited silicon nitride films as a function of doping concentration in weight percent.

effect. The IR spectrum shows N-H absorption at 3300 cm⁻¹, a Si-H bond at 2100 cm⁻¹, a Si-O bond at 1120 cm⁻¹, and a Si-N bond at 870 cm⁻¹. The N-H bond at 3300 cm⁻¹, Si-H bond at 2100 cm⁻¹, and Si-N bond at 870 cm⁻¹ show

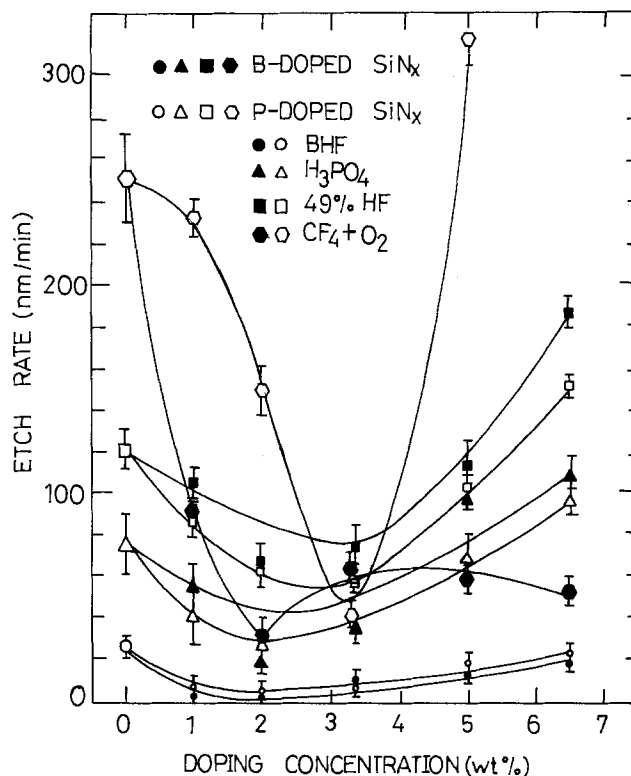


Fig. 2. The measured etch rate of phosphorus- or boron-doped SiN films by various etching solutions or methods as a function of doping concentration in weight percent. The black dots indicate the B-doped films, and the blank dots P-doped films. The circles, triangles, squares, and hexagles indicate the etching by BHF, H₃PO₄, 49% HF, and CF₄ + O₂, respectively.

the structure of doped SiN, which is the same as the undoped one. The Si-O bond at 1120 cm^{-1} indicates the incorporation of O and coincides with the results from the AES analysis.

Deposition Rate vs. Doping Concentration

Deposition rate vs. doping concentration is shown in Fig. 1. For undoped films, the deposition rate is around 15 nm/min . However, it decreases with increasing boron or phosphorus concentration to a minimum around 3% doping and then increases again to 5% doping. The lower deposition rate at 3% doping concentrations causes the more dense SiN film with better bonding scheme, as seen from the higher dielectric constant and lower etch rate of films with 3% P- or B-doped as presented in the following sections. The reason why 3% B- or P-doped SiN films get lower deposition rate is not clear. More studies should be made in the future.

Chemical Etching Properties

Various kinds of etching solutions, including wet etching in 180°C of H_3PO_4 , 49% HF, buffer HF(BHF), and 96% $\text{CF}_4 + 4\% \text{O}_2$ plasma dry etching are used to investigate the etching rate of doped SiN films. Figure 2 shows the results. It is interesting to note that the 2-3% B- or P-doped SiN films possess the lowest etching rate in these various etching solutions, except the etching rate of films in 49% HF solution is higher and lower in BHF and H_3PO_4 solutions, respectively. For dry etching in 96% $\text{CF}_4 + 4\% \text{O}_2$ plasma (with Plasmaline Plasma Etcher) as indicated with hexangular dots in Fig. 2, the tendency is also similar to the previous wet etchings, i.e., in both P- or B-doped SiN films, the etch rate decreased to a minimum at 2 or 3% doping concentration (2% for B-doped, 3% for P-doped) and then increased again with increasing doping concentration. However, in general, the etching rate of doped films with dry etching is higher than the wet etching, except in the case of the 2% B-doped or 3% P-doped films, where the etching rate of 49% HF wet etching is larger than that of the dry etching.

Electrical Properties

The effect of doping P or B on the electrical properties of plasma-deposited nitride films could be found from

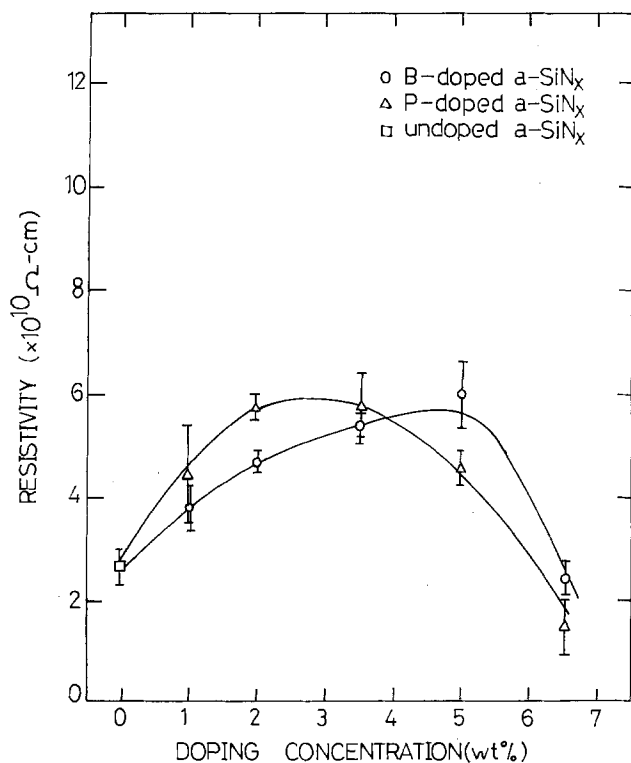


Fig. 3. The measured resistivities of P- or B-doped SiN as a function of doping concentration in weight percent.

the change of resistivity, breakdown field strength, and dielectric constant of the doped SiN film as a function of doping concentrations, as described below.

Resistivity vs. doping concentration.—The doped films were measured with a six-point probe (Four-Dimension, Incorporated). As shown in Fig. 3, the resistivities of both P- and B-doped films increase to a maximum of $6 \times 10^{10}\ \Omega\text{-cm}$ at 3%P doped or 5%B doped, then decrease with increasing the doping concentration. In this measurement, it is noteworthy that both the P- and B-doped SiN films possess higher resistivities than the undoped ones. This is a positive performance for these films used as passivation layer of devices.

Breakdown field strength vs. doping concentration.—A Tektronix 577 curve tracer was applied for evaluation of the breakdown field strength of both P- and B-doped films by measuring the breakdown voltage of Al-SiN-Si MIS diodes.

Figure 4 shows the breakdown field strength as a function of doping concentration. The tendency is also similar to that of resistivity. The maximum breakdown field strengths are $9 \times 10^5\ \text{V/cm}$ and $8 \times 10^5\ \text{V/cm}$ for 2-3% phosphorus and boron doped, respectively. The maximum field strength of doped films is almost 2-3 times larger than that of undoped ones.

Dielectric constant vs. doping.—With measuring the capacitance of Al-SiN-Si MIS diodes biased with reverse constant voltage, the dielectric constant of SiN film was calculated, as shown in Fig. 5. Again, the dielectric constant increases to a maximum at a doping concentration of 2-3% both for P and B and then decreases with further increasing the doping. The maximum dielectric constant value for the P-doped film is 8.3, whereas it is 7.6 for the B-doped one.

Pinhole Density

The pinhole density of doped SiN was measured by the copper decoration method (10). The samples were inserted into copper plating solution first, and then the silicon substrate was plated with copper through the pinhole. The pinhole density is calculated with the aid of microscopy. Figure 6 shows the measured results.

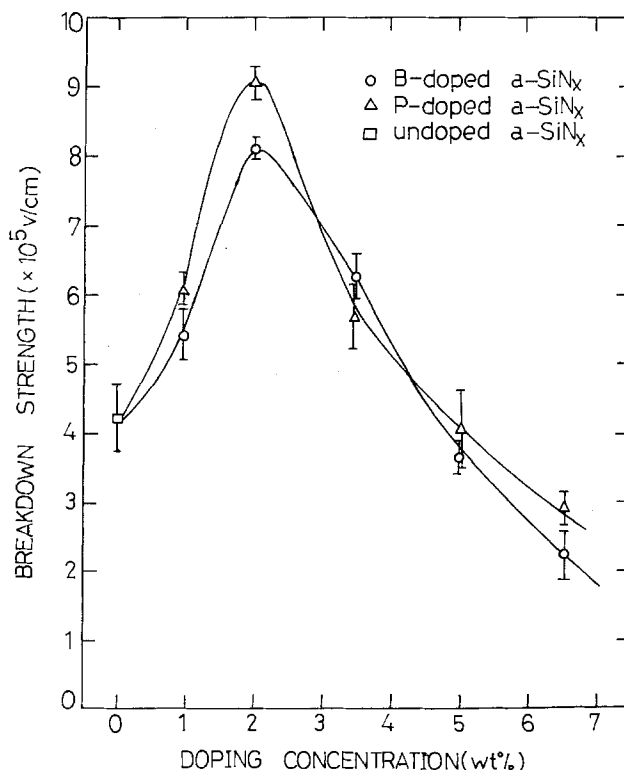


Fig. 4. The measured breakdown field strength of P- or B-doped SiN films as function of doping concentration in weight percent.

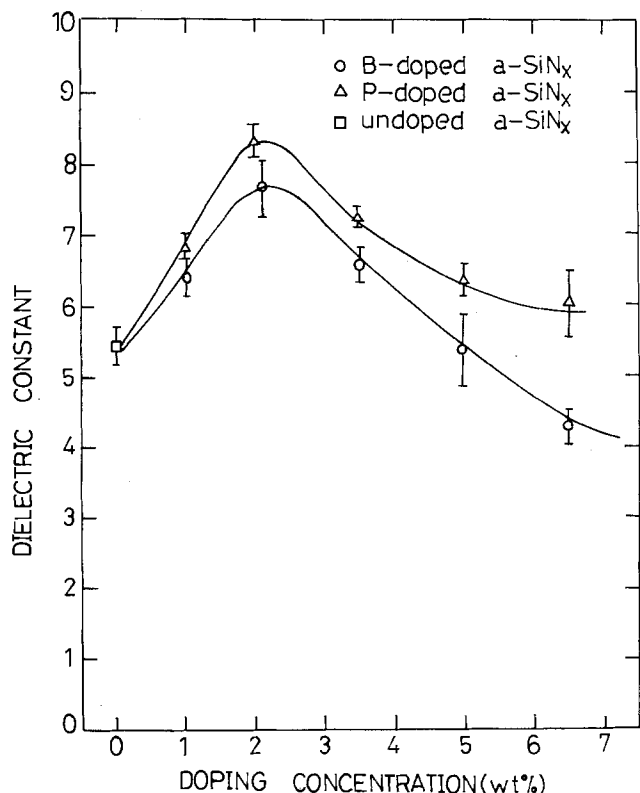


Fig. 5. The measured dielectric constant of P- or B-doped SiN films as a function of doping concentration in weight percent.

For phosphorus-doped films, the lowest pinhole density was found at 2% doping. For boron-doped ones, it occurred beyond 5% doping. The thickness of these SiN films is around 100 nm.

Discussion and Conclusions

In general, the resistivity, dielectric constant, and breakdown field strength of both P- and B-doped film increase to a maximum value at 2-3% of doping, and then decrease with increasing doping concentration. The deposition rate, pinhole density, and etching rate show an opposite tendency.

These results show that film quality is enhanced with P or B doping of 2-3%, but deteriorates for higher doping. The cause of enhancement is considered to be the correct slow growth rate in deposition of 2-3% P- or B-doped films. The slower growth rate provides a better bond scheme of the film and thus higher film quality. However, the mechanism of lower growth rate in deposition of these P- or B-doped films is still not clear. More experiments are required to understand this doping effect and

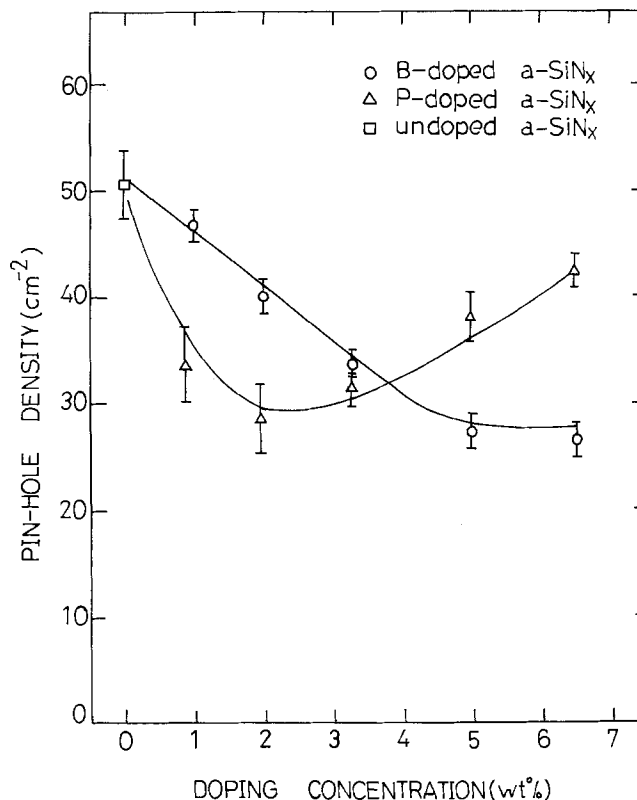


Fig. 6. The measured pinhole density of P- or B-doped SiN films as a function of doping concentration in weight percent.

the application of these doped films, e.g., passivation, diffusion, or impurity barriers in device fabrication.

Manuscript submitted July 16, 1984; revised manuscript received Jan. 10, 1985.

The National Cheng Kung University assisted in meeting the publication costs of this article.

REFERENCES

1. L. V. Geogor, *Solid State Technol.*, **14**, 37 (1971).
2. A. L. Armirrotto, *ibid.*, **11**, 43 (1968).
3. G. L. Schnable, W. Kern, and R. B. Comizzoli, *This Journal*, **122**, 1092 (1975).
4. K. M. Mar and G. M. Samuelson, *Solid State Technol.*, **23**, 137 (1980).
5. F. H. P. M. Habraken, A. E. T. Kuiper, A. V. Oostrom, and Y. Tamminga, *J. Appl. Phys.*, **53**, 404 (1980).
6. R. S. Rosler, W. C. Benzing, and J. Baldo, *Solid State Technol.*, **19**, 45 (1976).
7. A. K. Sinha, H. J. Levinstein, T. E. Smith, and S. E. Haszko, *This Journal*, **125**, 601 (1978).
8. K. M. Mar and G. M. Samuelson, *ibid.*, **129**, 1773 (1982).
9. J. M. Bind and J. V. Bigger, *J. Appl. Phys.*, **47**, 5171 (1976).
10. W. J. Shannon, *RCA Rev.*, **31**, 431 (1970).

Sulfidation Properties of Fe-Al Alloys (6-28 a/o Al) at 1173 K in Sulfur Vapor at $P_{S_2} = 1.45 \times 10^{-3}$ Pa

P. C. Patnaik* and W. W. Smeltzer**

Institute for Materials Research and Department of Metallurgy and Materials Science, McMaster University, Hamilton, Ontario, Canada L8S 4M1

ABSTRACT

Sulfidation properties of Fe-6, 9, 18, and 28 atomic percent (a/o) Al alloys were investigated at 1173 K in sulfur vapor at the dissociation pressure of FeS. The Fe-6 Al alloy exhibited internal sulfidation; the Fe-9 and 18 Al alloys exhibited internal sulfidation along with formation of an external $FeAl_2S_4$ scale. Compositions of the internal sulfide precipitates corresponded to $FeAl_2S_4$ in the Fe-6 Al alloy and to $FeAl_2S_4$ - Al_2S_3 in the alloys containing 9 and 18 a/o Al. The Fe-28 a/o Al alloy upon sulfidation only formed an Al_2S_3 external scale. The apparent permeability of sulfur in the alloy of the internal sulfidation zone as defined by $N_s^{(S)}D_s$ product increased linearly with alloy composition. Growth of the sulfide precipitates which extended as plates across the internal sulfidation zones is satisfactorily interpreted by a model involving enhanced sulfur diffusion along the interfaces between the internal sulfides and alloy matrix. Transition from internal sulfidation to internal sulfidation plus external scale formation and finally to only external scale formation based upon the alloy aluminum composition is discussed.

The sulfidation resistance of iron in sulfur as well as H_2S bearing atmospheres is improved considerably by addition of aluminum as an alloying element (1-7). The reaction kinetics of these alloys are generally complex due to growth of a multilayered scale and internal sulfidation (7). The present paper is concerned with obtaining an understanding of the sulfidation properties of Fe-Al alloys with respect to internal sulfidation and of the transition to external sulfide scale formation. Accordingly, Fe-Al alloys containing up to 28 atomic percent (a/o) Al have been sulfidized at 1173 K in sulfur vapor at the dissociation pressure of FeS (1.45×10^{-3} Pa) to prevent formation and influence of this rapid growing phase on the reaction mechanism.

Experimental

Alloys of nominal compositions 6, 9, 18, and 28 a/o Al were prepared by electric arc melting of iron (99.99% pure) and aluminum (99.98% pure) in an argon atmosphere gettered of oxygen by titanium chips. Chemical analyses for impurities in the pure metals are given in Table I. Actual compositions of these ferritic solid solution alloys were 5.8, 8.8, 18.2, and 27.8 a/o Al. The alloy ingots were annealed at 1473 K for 12h in a furnace equipped with a continuous ultrapure argon flow system. The average grain size of any alloy was usually large; it varied from 0.1 mm to about 0.8 mm. Small cylindrical plates approximately 1-3 mm thick and of 10 mm diam were prepared from the alloy ingots using silicon carbide cutting blades. These specimens were polished on all sides through a series of silicon carbide papers using water as a lubricant. Final polishing was carried out on napless cloths impregnated with 6 and 1 μm diamond paste with kerosene as the lubricant.

Sulfidation of the alloys was carried out at 1173 K in sulfur vapor set at the dissociation pressure of FeS equal to $P_{S_2} = 1.45 \times 10^{-3}$ Pa (8) by means of the reaction cell assembly shown in Fig. 1. Two alloy specimens suspended in open-ended alumina tubes by platinum wires and a pressed Fe + FeS porous compact were encased in an evacuated quartz tube. The alloys were sulfidized for periods extending up to 20 ks. Metallographic examination of the Fe + FeS compacts after sulfidation runs demonstrated that these compacts retained their porosity without any evidence of a protective iron layer.

Sulfide phases were identified by x-ray diffraction powder analyses using Ni-filtered $Cu-K\alpha$ radiation. Optical microscopy was used to study the morphology of the reaction products and to measure the depths of internal sulfidation zones. Electron probe microanalyses (EPMA) were used to determine composition profiles within the sulfidation zones.

*Electrochemical Society Student Member.

**Electrochemical Society Active Member.

Table I. Chemical analyses of iron and aluminum

Impurities	Iron (ppm)	Aluminum (ppm)
C	18	—
Cu	30	<1
Si	50	—
Cr	30	—
Mo	30	—
Mg	<10	10
Ca	<10	—
Ti	<10	—
S	40	—
Al	60	By difference
Fe	By difference	2

Results

Sulfidation kinetics.—These kinetics for the alloys containing 6, 9, and 18 a/o Al were determined by measuring the depths of internal sulfidation and the sulfur uptakes. As demonstrated by the plots of these results in Fig. 2 and 3, these reaction kinetics were of parabolic type. The depths of internal sulfidation in the alloys after corresponding exposures decreased with aluminum content only up to 9 a/o Al; the alloy containing 18 a/o Al exhibited the largest penetration depth. This is also indicated by the corresponding parabolic rate constants for internal sulfidation (see Table II). A scale on the Fe-9 Al alloy was only observed at isolated small areas over the alloy surface. The scale on the Fe-18 Al alloy which sulfidized both internally and externally was continuous and grew parabolically at $8.9 \times 10^2 \mu m/s^{1/2}$. Sulfidation led only to growth of a scale on the Fe-28 Al alloy which grew at $7.2 \times 10^{-2} \mu m/s^{1/2}$.

Scale morphological development.—The internal sulfide precipitates formed in the Fe-6, 9, and 18 Al alloys were acicular in morphology, and they extended as plates across the internal sulfidation zones largely oriented normal to the alloy surface, with the exception of some alloy

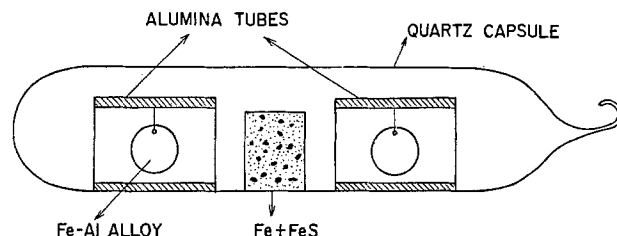


Fig. 1. The reaction cell assembly for Fe-Al alloys in S_2 vapor at the dissociation pressure of FeS.

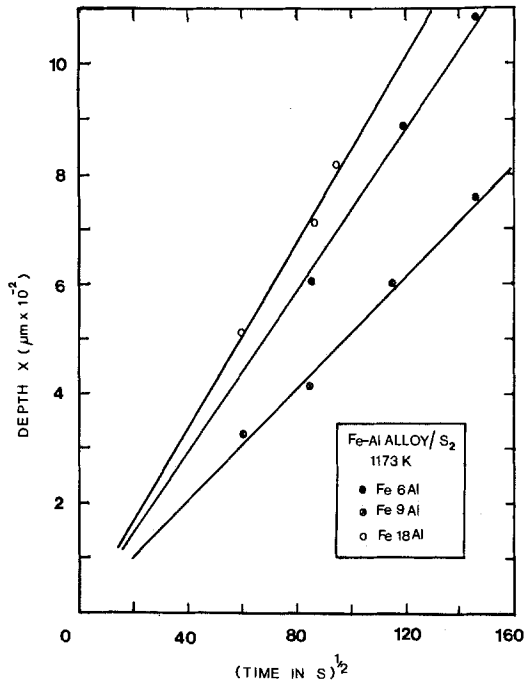


Fig. 2. Plots of internal sulfidation depth vs. $(\text{time})^{1/2}$ for various Fe-Al alloys.

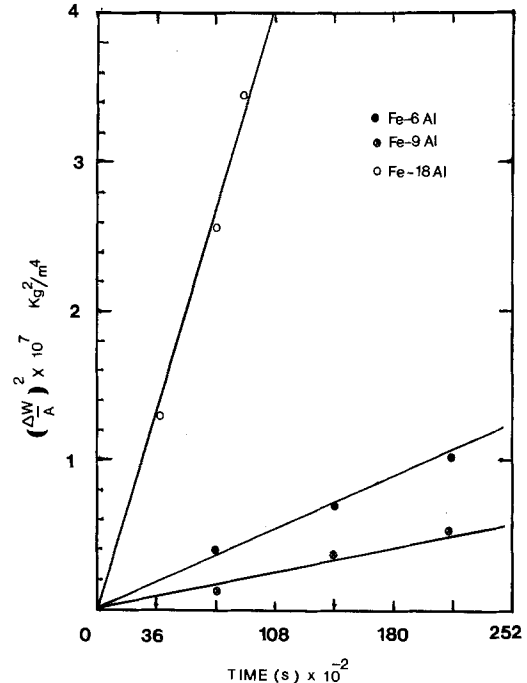


Fig. 3. Plots of sulfur uptake $(\Delta W/A)$ vs. $(\text{time})^{1/2}$ for various Fe-Al alloys.

grains in which they were oriented at an angle slightly less than 90° . Figure 4 illustrates these features. The advancing front of an internal sulfidation zone was quite uniform, although slight irregularities were found occasionally at the corners of the specimens. Preferential intergranular sulfidation was not observed in these alloys.

Figure 5 shows transverse sections of the internal sulfides at different depths from the surface of the alloy

containing 9 a/o Al. The sulfide platelets are oriented in several crystallographic directions. Those platelets existing deep within the internal sulfidation zone near its advancing front in this alloy contained more than one phase, one enveloping the other (Fig. 5, bottom), apparently due to conversion of Al_2S_3 into FeAl_2S_4 . The sulfide precipitates right at the internal sulfidation front were composed of only the Al_2S_3 phase.

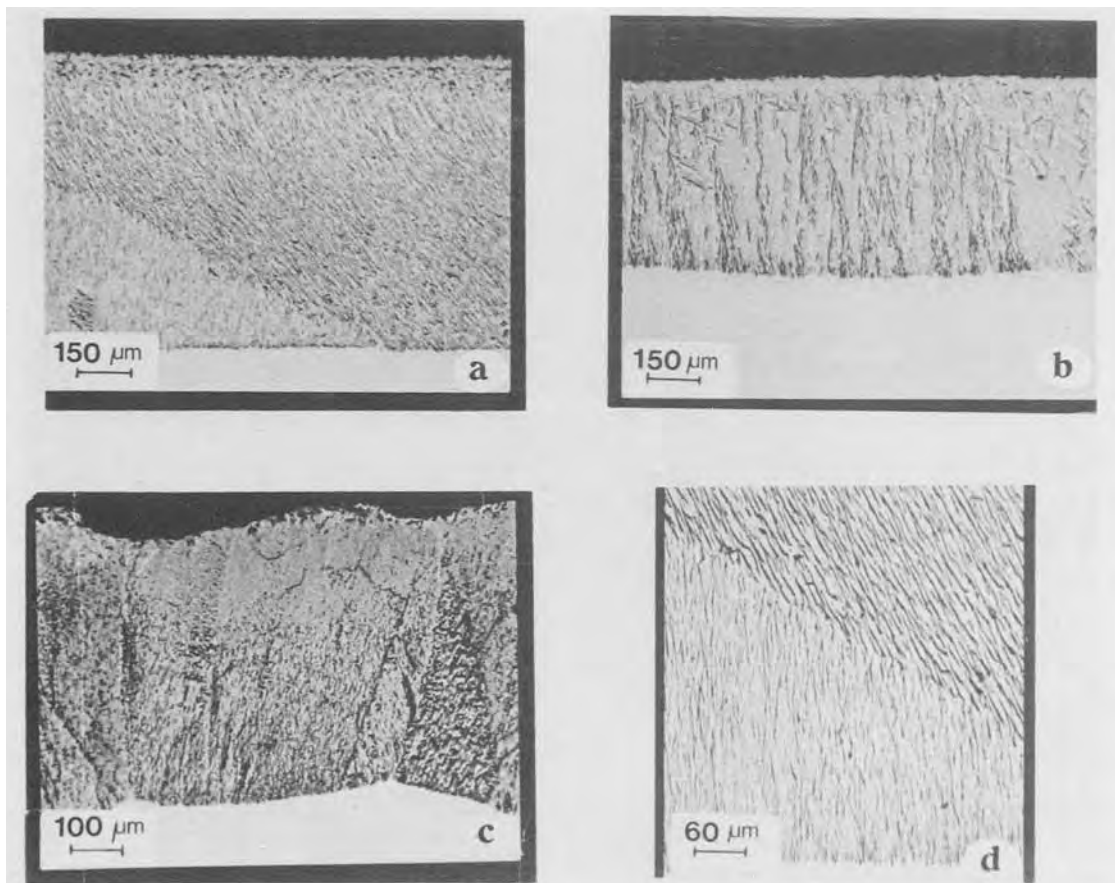


Fig. 4. Photomicrographs of the polished cross section of the internal sulfidation zones in (a) Fe-6 a/o Al, (b) Fe-9 a/o Al, and (c) Fe-18 a/o Al alloys. d: The change in orientation of internal sulfide platelets at a grain boundary.

Table II. The parabolic rate constants for internal sulfidation of Fe-Al alloys in S_2 (Fe/FeS) at 1173 K

Alloy composition	Parabolic rate constant k_p ($\mu\text{m}^2/\text{s}^{1/2}$)
Fe-6 a/o Al	7.4
Fe-9 a/o Al	5.1
Fe-18 a/o Al	8.5

In all the alloys, the platelike internal sulfide precipitates ranging from 0.5 to 2 μm thickness and 10 to 20 μm widths extended either from just below the gas/alloy interface or from the external scale/subscale interface across the internal sulfidation zone as shown in Fig. 6. As shown in Fig. 7, the spacing between sulfide platelets within the internal sulfidation zones decreased with increasing aluminum content in the alloy. Table III presents the variation of this spacing with alloy composition. These spacings are average values of measurements carried out at various depths in the internal sulfidation zone for each alloy. It was not possible by this measurement technique to distinguish any variation in spacing at various depths within the internal zone.

An external scale without any associated internal sulfidation was observed to grow on the Fe-28 Al alloy. This compact adherent scale spalled off the alloy during cooling. Its morphology is shown in Fig. 8.

Sulfide compositions and structures.—Compositions of the internal sulfide precipitates corresponded most closely to FeAl_2S_4 in the Fe-6Al alloy and $\text{FeAl}_2\text{S}_4\text{-Al}_2\text{S}_3$ platelets in the alloys containing 9 and 18 a/o Al. The FeAl_2S_4 phase appeared to be at least 80-90% of a sulfide

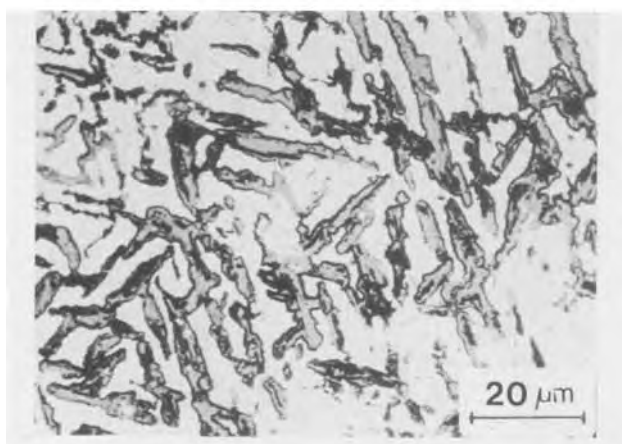
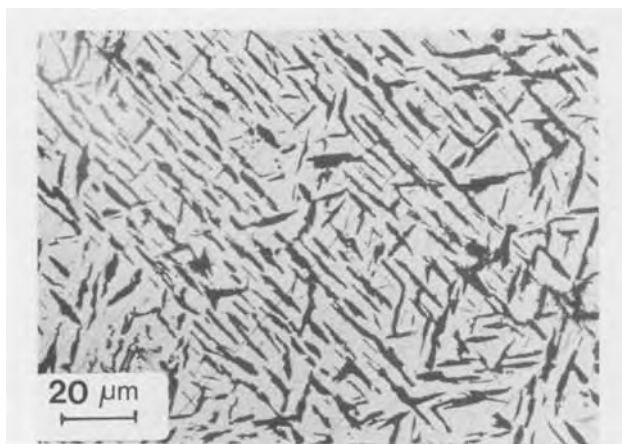


Fig. 5. Photomicrographs of the Fe-9 a/o Al alloy depicting the morphology of the internal sulfides at various depths in a transverse section. Top: close to the external surface. Bottom: close to the alloy/internal sulfidation front.

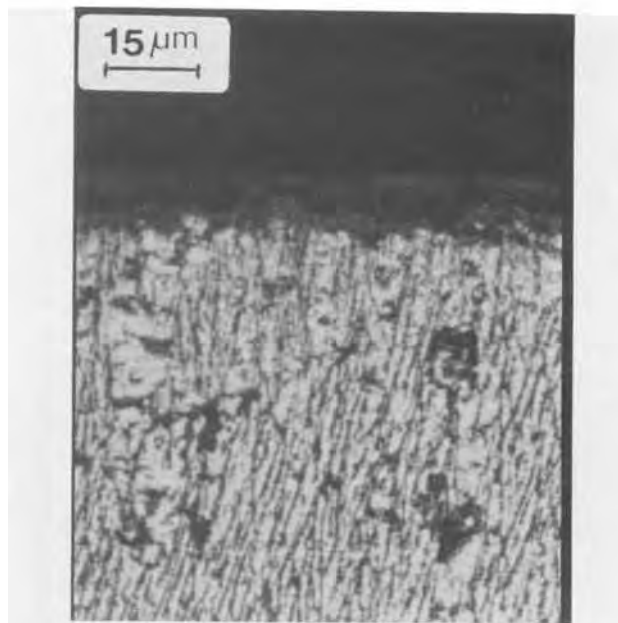


Fig. 6. Photomicrographs illustrating the cross section of an internal sulfidation zone near the alloy and external scale/alloy interface for (top) Fe-9 a/o Al and (bottom) Fe-18 a/o Al alloys.

platelet, based upon the metallographic observations; in particular, the Al_2S_3 precipitates were present toward the internal sulfide/alloy interface. In the case of Fe-9 and 18 Al alloys, the internal sulfidation zones of $\text{FeAl}_2\text{S}_4\text{-Al}_2\text{S}_3$ were overgrown by FeAl_2S_4 external scales. Figure 9 shows microprobe traces for iron and aluminum across the internal sulfidation zone of the Fe-9Al alloy. The alloy is depleted of aluminum near the internal sulfidation zone interface which caused a slight enrichment of aluminum in the sulfidation zone. The x-ray diffraction pattern from the internal sulfidation zone of the Fe-9Al alloy corresponding to the presence of FeAl_2S_4 is illustrated in Fig.

Table III. Intersulfide spacings for Fe-Al alloys at 1173 K in S_2 (Fe/FeS)

Alloy composition	Spacing (μm)
Fe-6 a/o Al	7.9 ± 0.5
Fe-9 a/o Al	3.8 ± 0.6
Fe-18 a/o Al	2.6 ± 0.5

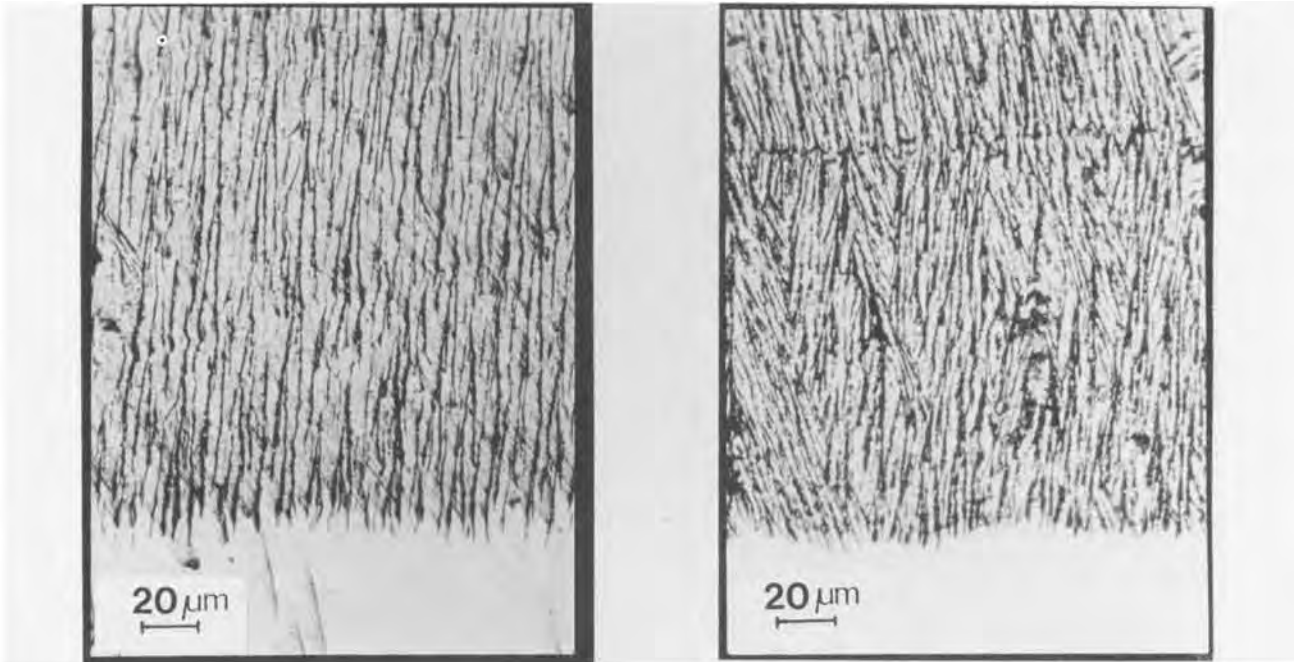


Fig. 7. Photomicrographs revealing the cross section of internal sulfide precipitates and their spacings in (left) Fe-9 a/o Al and (right) Fe-18 a/o Al alloys.

10a. The external scale on the Fe-28Al was identified to be Al_2S_3 , as illustrated in Fig. 10b.

Discussion

In order to present a diffusion model for growth of the internal sulfide platelets in the Fe-6, 9, and 18 a/o Al alloys, a comparison is made of the permeabilities ($N_s^{(s)}D_s$)

for these alloys calculated from the classical diffusion model for internal sulfidation (9-12). According to this latter model, the depth, ξ , of the internal sulfidation zone is a parabolic function of time. It can be shown that for the Fe-Al alloys

$$\frac{N_s^{(s)}}{N_{\text{Al}}^0} \ll \frac{D_{\text{Al}}}{D_s} \sim 0.1-1 \quad [1]$$

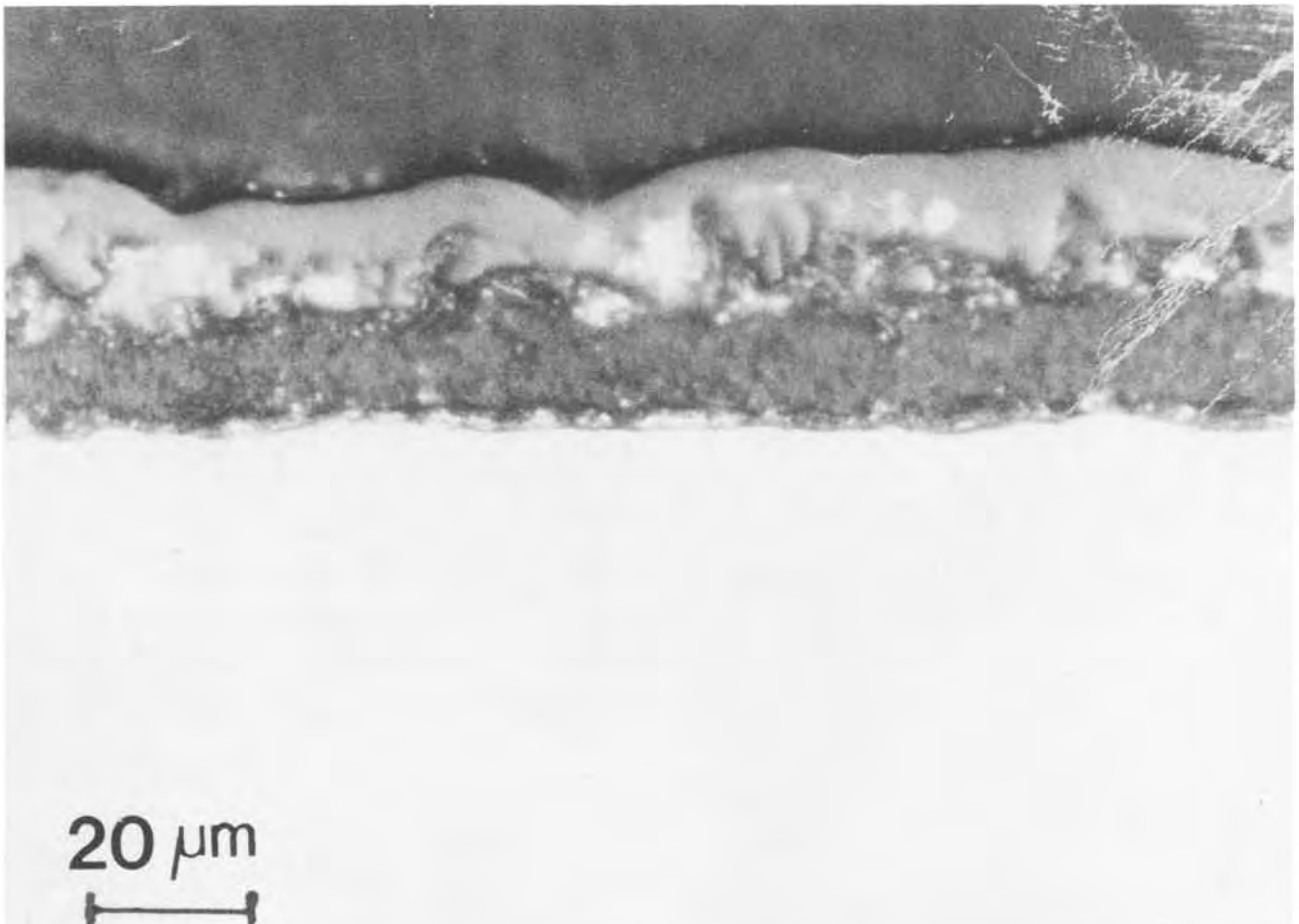


Fig. 8. Photomicrograph of the cross section of the sulfide scale (Al_2S_3) formed on the Fe-28 a/o Al alloy

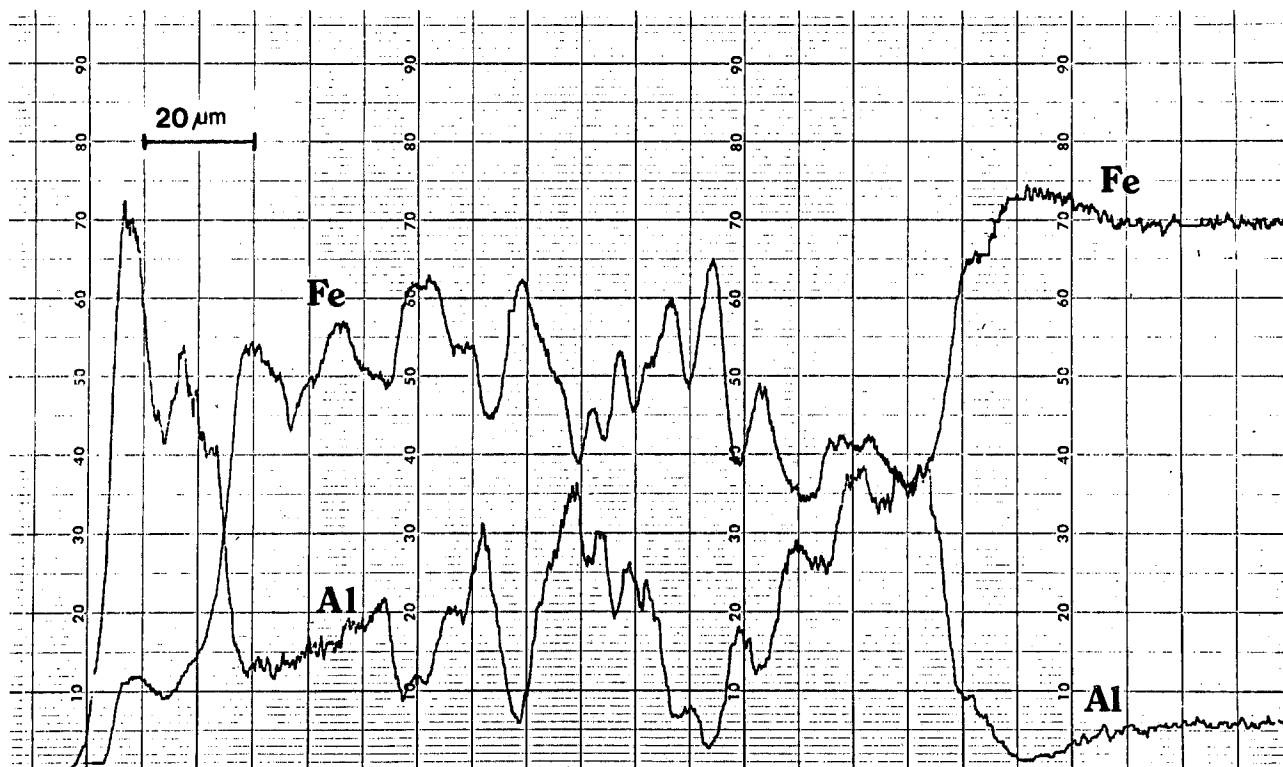


Fig. 9. Electron microprobe traces for iron and aluminum in the internal sulfidation zone of Fe-9 a/o Al alloy

Therefore, the depth of the internal sulfidation is described as (9)

$$\xi = \frac{N_S^{(S)}}{\nu N_{Al}^0} (\pi \phi D_S t)^{1/2} \quad [2]$$

where $N_S^{(S)}$ and N_{Al}^0 are the atomic fractions of dissolved sulfur at the alloy surface and of aluminum in the bulk alloy, respectively, and $\phi = D_S/D_{Al}$ is the ratio of diffusivities of sulfur and aluminum in the alloy. The limiting case in Eq. [2] corresponds to significant diffusion of aluminum, hence its enrichment within the internally sulfidized zone. In the presence of an external receding scale as the source of sulfur, the depth of internal sulfidation zone is given by (13, 14)

$$\frac{\xi(\xi - \xi')}{2t} = \frac{N_S^{(S)} D_S}{\nu N_{Al}^0} F(\eta) \quad [3]$$

where the auxiliary function $F(\eta)$ is defined as

$$F(\eta) = \pi^{1/2} \eta \exp(\eta^2) \operatorname{erfc}(\eta) \quad [4]$$

with

$$\eta = \xi/2 (D_{Al} t)^{1/2} \quad [5]$$

and ξ' is the position coordinate of the alloy/scale interface at any time. Equations [3] and [4] were used, respectively, to calculate the apparent permeabilities¹ of sulfur in the Fe-6, 9, and 18 a/o Al alloys (see Table IV).

A linear increase in the apparent permeability with alloy composition is observed, as illustrated in Fig. 11. In order to account for this behavior, a model involving sulfur diffusion within the internal sulfidation zone in the alloy matrix and along the boundaries between the sulfide and the alloy matrix is considered. The model which we employ corresponds to that advanced by Whittle and co-workers (15) to account for enhanced diffusion of oxygen in the internal oxidation of Ni-Al alloys.

The effective sulfur flux through the internal sulfidation zone is expressed as the sum of sulfur fluxes through the alloy lattice, J_1^S , the internal sulfide/alloy interface, J_i^S , and the internal sulfide particles, J_{sulf}^S , as illustrated schematically in Fig. 12. Thus

$$J_{eff}^S = J_1^S A_1 + J_i^S A_i + J_{sulf}^S A_{sulf} \quad [6]$$

where A_1 , A_i , and A_{sulf} are the area fractions of alloy phase, alloy/sulfide interfaces, and sulfide, respectively, in a unit cross section cut parallel to the external surface. Sul-

¹In the subsequent text, the product $N_S^{(S)} D_S$ is termed as the apparent permeability.

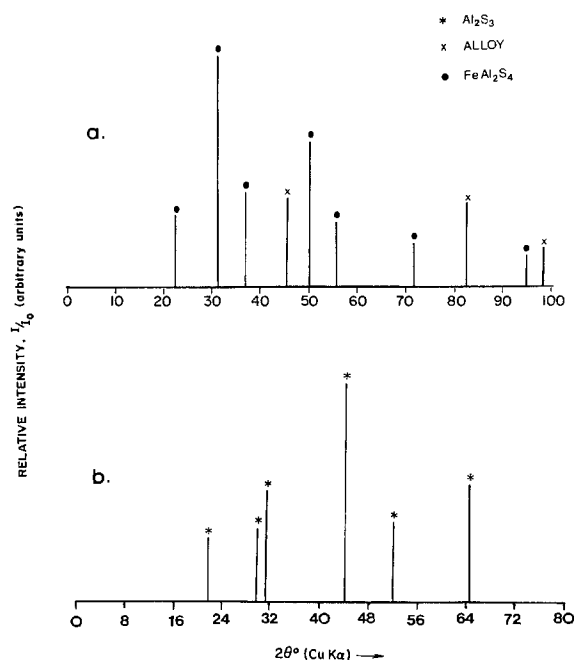


Fig. 10. Reflection x-ray diffraction of sulfides from (a) internal sulfidation zone of Fe-9 a/o Al alloy and (b) external scale on the Fe-28 a/o Al alloy.

Table IV. Apparent permeability of sulfur in Fe-Al alloys at 1173 K

Alloy composition	Apparent $N_S^{(S)} D_S$	Equation used
Fe-6 a/o Al	5.7×10^{-10}	[3]
Fe-9 a/o Al	9.7×10^{-10}	[4]
Fe-18 a/o Al	18.3×10^{-10}	[4]

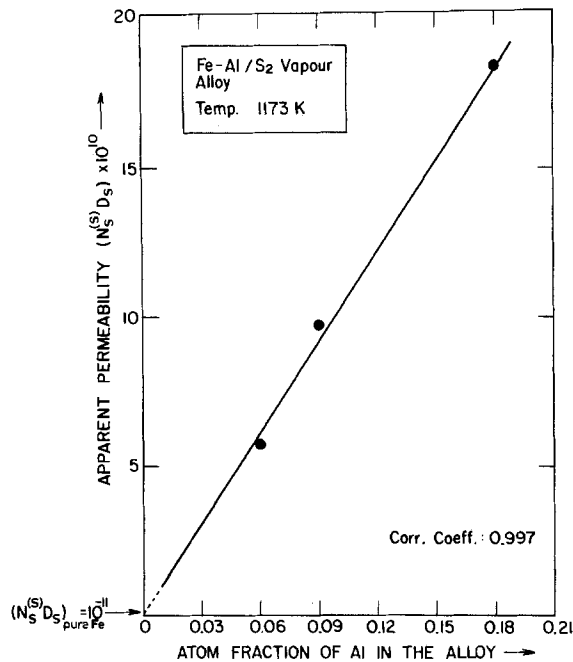


Fig. 11. Plot of apparent permeability of sulfur as a function of alloy aluminum content.

fur diffusion in the sulfide can be neglected in comparison to diffusion in the alloy lattice and along the interfaces. Assuming a common sulfur concentration gradient, the effective sulfur diffusion coefficient in the internal sulfidation zone is given by

$$D_{s,eff} = D_{s,l}A_1 + D_{s,i}A_i \quad [7]$$

where $D_{s,l}$ is the lattice diffusion coefficient for sulfur, and $D_{s,i}$ the interfacial or boundary diffusion coefficient.

The area fractions A_1 and A_i are calculated as follows. The thickness and width of the platelets are designated as d and w (Fig. 12), and it is assumed that they extend continuously through the internal sulfidation zone up to its depth, ξ , below the metal surface. If the mole fraction of the sulfide is expressed as $N_{(AlFe)S_2}$, the number of sulfide platelets z per unit cross-sectional area is calculated to be

$$\frac{N_{(AlFe)S_2}\xi}{V_{alloy}} = z \frac{wd\xi}{V_{sulf}} \quad [8]$$

assuming that no volume expansion has occurred due to internal sulfidation. In this equation, V_{sulf} and V_{alloy} are the molar volumes of sulfide and alloy phase, respectively. The fractional area of the interface is given by

$$A_i = 2(w + d)zb_1 \approx 2wzb_1 \quad [9]$$

since $d \ll w$ for thin plates and b_1 is the width of the in-

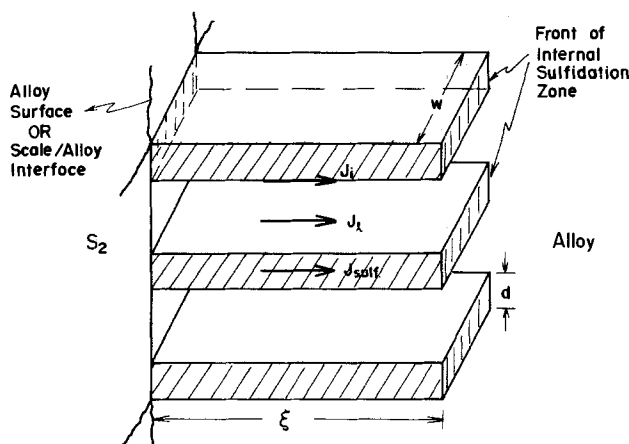


Fig. 12. Schematic internal sulfidation model for Fe-Al alloys sulfidized in S_2 vapor at the dissociation pressure of FeS .

terface. Therefore, the fractional cross-section area available for lattice diffusion is given by

$$A_1 = 1 - A_i - A_{sulf} = 1 - 2wzb_1 - zwd \quad [10]$$

Substituting Eq. [8]-[10] into Eq. [7] with the restriction that $b_1 \ll d$ gives upon rearrangement

$$\frac{D_{s,eff}}{D_{s,l}} = 1 + \left[2 \frac{b_1}{d} \frac{D_{s,i}}{D_{s,l}} - 1 \right] \frac{V_{sulf}}{V_{alloy}} N_{(AlFe)S_2} \quad [11]$$

Thus, the effective diffusion coefficient in the internal sulfidation zone is a linear function of the mole fraction of internal sulfide precipitate. This parameter is proportional to the original atom fraction of aluminum in the alloy, N_{Al}^0 if one assumes that aluminum enrichment into the internal sulfidation zone by diffusion can be expressed by a factor α independent of alloy composition (11)

$$\frac{N_{s}^{(S)}D_{s,eff}}{N_{s}^{(S)}D_{s,l}} = 1 + \left[2 \frac{b_1}{d} \frac{D_{s,i}}{D_{s,l}} - 1 \right] \frac{V_{sulf}}{V_{alloy}} \alpha N_{Al}^0 \quad [12]$$

The sulfur solubility at the interface does not depend upon alloy aluminum composition, since the alloy matrix is virtually pure iron due to the selective sulfidation of aluminum. The ratio on the left-hand side of Eq. [12] corresponds to the ratio of the apparent $N_{s}^{(S)}D_s$ product obtained by extrapolating to pure iron. A plot of Eq. [12] is shown in Fig. 13; a linear fit is obtained with 0.997 correlation coefficient. The slope of the linear plot in Fig. 13 corresponds to

$$\left(2 \frac{D_{s,i}}{D_{s,l}} \frac{b_1}{d} - 1 \right) \frac{V_{sulf}}{V_{alloy}} \alpha = 1030 \quad [13]$$

The ratio $D_{s,i}/D_{s,l}$ was calculated using Eq. [13] to examine whether the parameters in Eq. [13] are physically reasonable. Since the internal sulfide precipitates were largely composed of $FeAl_2S_4$, $V_{sulf} = 8 \times 10^{-5} \text{ m}^3$, $V_{alloy} = 7.2 \times 10^{-6} \text{ m}^3$, $\alpha = 2$, $b_1 = 1 \text{ nm}$, and the thickness of the internal sulfide precipitates ranged from 0.5 to 2 μm , the calculated $D_{s,i}/D_{s,l}$ ratio has values in the range $1.2-8.4 \times 10^4$. These values compare well to a calculation of the ratio from independently determined values for sulfur grain boundary diffusion (16) and lattice diffusion in iron (17, 18), $D_{s,i}/D_{s,l} = 8.3 \times 10^3$.

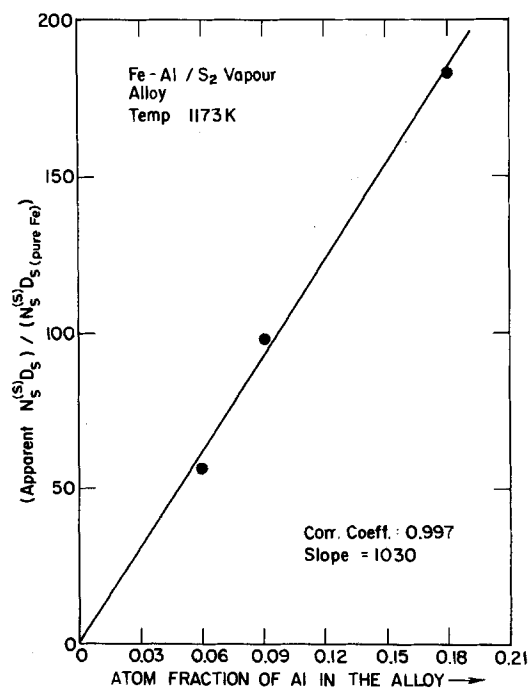


Fig. 13. Plot of the ratio of apparent sulfur permeability in Fe-Al alloys to that in pure iron as a function of alloy aluminum content (Eq. [15]).

The average intersulfide spacing decreased from $7.9 \pm 0.5 \mu\text{m}$ for Fe-6Al alloy to $2.6 \pm 0.5 \mu\text{m}$ for Fe-18Al alloy, but the dependence of platelet size with distance into a specific alloy could not be quantitatively assessed. It is not possible, therefore, to give a more complete analysis to account for the diverse internal sulfidation phenomena involving an unusual dependence of the reaction rate which does not decrease regularly with alloy composition presumably caused by different properties of the alloy/sulfide boundaries with respect to sulfur diffusion.

Three modes of sulfidation were exhibited by the alloys dependent upon their aluminum composition: internal sulfidation, internal-external sulfidation, and sole growth of an external sulfide scale. The sequence of the stability of FeAl_2S_4 and Al_2S_3 with increasing Al contents of the alloy is consistent with the ternary thermodynamic properties (20). The growth of the Al_2S_3 scale on the alloy of high aluminum content of 28 a/o proceeded at a very slow rate. It would appear that this transition from internal sulfidation to sole growth of an external scale is determined by the criterion that the diffusion path in this alloy phase contacts without crossing the sulfur solubility curve into the two-phase alloy-sulfide phase field at an alloy composition determined by solid solution thermodynamics and diffusion (10, 19). It is necessary to postpone an analysis of this sulfidation behavior to a subsequent paper in which the internal-external sulfidation transition is analyzed with respect to positive interactions which occur between sulfur and aluminum alloying solutes in the Fe-Al-S ternary system (21).

Summary

High temperature sulfidation properties of Fe-Al alloys at the dissociation pressure of FeS were investigated at 1173 K, with special interest given to the microstructure and growth of internal sulfide precipitates and the transition from internal sulfidation to external scale formation. The alloys sulfidized parabolically and the alloy of highest Al content (27.8 a/o) only exhibited growth of a protective external scale.

The Fe-6 a/o Al alloy exhibited growth of FeAl_2S_4 acicular platelets which extended into and across the internal sulfidation zone. In the cases of Fe-9 and 18 a/o Al alloys, the internal sulfidation zones containing FeAl_2S_4 - Al_2S_3 platelets were overgrown by external FeAl_2S_4 scales. A diffusion model was advanced to describe the sulfidation behavior of these alloys involving enhanced sulfur diffusion along the interfaces between the internal sulfides

and the alloy matrix. In the internal sulfidation zones of these alloys, the apparent permeability of sulfur $N_s^{(SD)}$ increased with increasing alloy aluminum content. The ratio of boundary to lattice diffusivities of sulfur in iron estimated from this model were in satisfactory agreement with the values available in the literature.

Acknowledgments

This research was carried out by P. C. Patnaik as part of the requirements for award of the Ph.D. degree at McMaster University. Financial support from the Natural Sciences and Engineering Research Council of Canada for this research is gratefully acknowledged.

Manuscript submitted Oct. 22, 1984; revised manuscript received Jan. 14, 1985.

McMaster University assisted in meeting the publication costs of this article.

REFERENCES

1. R. B. Sutherland and G. R. Prescott, *Corrosion(Houston)*, **18**, 277t (1961).
2. E. B. Backensto, J. E. Prior, J. W. Sjooberg, and R. W. Manuel, *ibid.*, **18**, 253t (1962).
3. F. J. Burns, *ibid.*, **25**, 119 (1969).
4. K. N. Strafford and R. Manifold, *Oxid. Met.*, **1**, 221 (1969); **5**, 85 (1972).
5. K. Nishida, *Trans. Iron Steel Inst. Jpn.*, **10**, 421 (1970).
6. K. Nishida and T. Narita, *ibid.*, **12**, 422 (1972).
7. P. C. Patnaik and W. W. Smeltzer, *Oxid. Met.*, **23**, 53 (1985).
8. K. T. Jacob, D. B. Rao, and H. G. Nelson, *ibid.*, **13**, 25 (1979).
9. C. Wagner, *This Journal*, **63**, 772 (1959).
10. C. Wagner, *Corros. Sci.*, **8**, 889 (1968).
11. R. A. Rapp, *Corrosion(Houston)*, **21**, 382 (1965).
12. J. H. Swisher, in "Oxidation of Metals and Alloys," D. L. Douglass, Editor, p. 235, ASM, Metals Park, OH (1970).
13. F. N. Rhines, *Trans. AIME*, **137**, 246 (1940).
14. F. Maak, *Z. Metallk.*, **52**, 545 (1961).
15. D. P. Whittle, Y. Shida, G. C. Wood, F. H. Stott, and B. D. Bastow, *Philos. Mag. A*, **46**, 931 (1982).
16. P. L. Gruzin, V. V. Mural, and A. P. Fokin, *Fiz. Met. Metalloved.*, **34**, 1326 (1972).
17. N. G. Ainslie and A. U. Seybolt, *JISI*, **3**, 341 (1960).
18. N. G. Ainslie, R. E. Hoffman, and A. U. Seybolt, *Acta Metall.*, **8**, 523 (1960).
19. W. W. Smeltzer and D. P. Whittle, *This Journal*, **125**, 1116 (1978).
20. P. C. Patnaik and W. W. Smeltzer, *ibid.*, **131**, 2688 (1984).
21. G. K. Sigworth and J. F. Elliot, *Met. Sci.*, **8**, 298 (1974).

Transition from Internal Sulfidation to External Scale Growth on Fe-Al Alloys at 1173 K

W. W. Smeltzer* and P. C. Patnaik**

Institute for Materials Research and Department of Metallurgy and Materials Science, McMaster University, Hamilton, Ontario, Canada L8S 4M1

ABSTRACT

The transition from internal sulfidation to exclusive growth of an external scale on Fe-Al alloys sulfidized at 1173 K in sulfur vapor at the dissociation pressure of iron sulfide was studied using the criterion that the diffusion path in the alloy contacts the sulfur solubility curve without crossing into the alloy-sulfide phase field. This analysis based upon a vacancy mechanism for diffusion of aluminum and sulfur and repulsive interaction between sulfur and aluminum is used to show the effect of diffusion coefficients, the parabolic scaling rate constant, and the Wagner sulfur-aluminum interaction coefficient on the relationship between the diffusion path and the sulfur solubility curve in the alloy. It is demonstrated that the critical atom fraction of aluminum required for exclusive growth of an Al_2S_3 scale can only be defined when account is given to positive values of the sulfur-aluminum interaction coefficient.

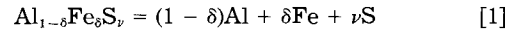
In our preceding paper (1), an investigation was reported on the sulfidation properties of Fe-Al alloys at 1173 K in sulfur vapor at the dissociation pressure of iron sulfide. Emphasis was given to examining the growth and morphologies of the $FeAl_2S_4$ scale and $FeAl_2S_4$ - Al_2S_3 internal precipitates and to the transition for exclusive growth of an external protective Al_2S_3 scale. A diffusion model was employed to account for internal-external sulfidation.

In this paper, a diffusion analysis is carried out to account for the transition from internal sulfidation to external scale formation by a model in which account is given to sulfur diffusion by a vacancy mechanism and to repulsive interaction between sulfur and aluminum in the alloy. The problem is posed in terms of ternary diffusion and solution thermodynamics, and equations are deduced for describing the sulfidation phenomena based on assertions relating to the locus of the virtual diffusion path on the Fe-Al-S phase isotherm. Since the methodology corresponds closely to that previously introduced by Smeltzer and Whittle (2) to define the criterion for onset of internal oxidation beneath the oxide scale on binary alloys, direct reference is made whenever possible to equations employed in that paper.

The Ternary Sulfidation Model

Placement of representative diffusion paths on the Fe-Al-S isotherm determined at 1173 K (3) is shown in Fig. 1. Diffusion path (1 in Fig. 1) corresponds to exclusive growth of an Al_2S_3 scale. Here, the virtual diffusion path contacts, or, in the limit, tangents, the sulfur solubility curve and corresponds to the actual diffusion profile in the alloy sulfidizing by parabolic kinetics. This sulfidation behavior was exhibited by the Fe-28 atomic percent (a/o) Al alloy (1). Path 2 in Fig. 1, corresponds to the case for Al_2S_3 scale formation and Al_2S_3 internal precipitation in the alloy by relief of sulfur supersaturation. Consequently, the criterion for the absence or presence of internal sulfidation during scaling is based upon the relationship between the locus of the virtual diffusion path and the sulfur solubility curve in the alloy. If path 2 in Fig. 1, was to cut across the alloy- $FeAl_2S_4$ - Al_2S_3 field into the alloy- $FeAl_2S_4$ field before contacting the alloy sulfur solubility curve, sulfidation would lead to precipitation of $FeAl_2S_4$ - Al_2S_3 precipitates in the alloy beneath the $FeAl_2S_4$ scale as encountered for the alloys containing 9-18 a/o Al (1).

Ternary solution thermodynamics determine the shape of the sulfur solubility curve as a function of metal solute alloy content, as illustrated in Fig. 2. Sulfur solubility over a region of alloy composition is determined by the following reaction equilibrium



where Al, Fe, and S refer to the alloy components, and $\nu = 1.5$ and $\delta \ll 1$ represent the small iron solubility of 0.3 a/o in Al_2S_3 (3). If the non-Henrian solution behavior of sulfur in this alloy is interpreted by Wagner interaction coefficients, equilibrium of reaction [2] can be represented by Eq. [32] of Ref. (2)

$$(N_S)_{NH} = \left(\frac{K}{N_A \gamma_{Al}^0 \gamma_S^{\nu}} \right)^{1/\nu} \exp - \epsilon_S^A N_A$$

$$= \left(\frac{K_H}{N_A} \right)^{1/\nu} \exp - \epsilon_S^A N_A \quad [2]$$

where $(N_S)_{NH}$ is the non-Henrian sulfur solubility, K and K_H are the actual and Henrian equilibrium constants, respectively, γ^0 is a Henrian activity coefficient, and ϵ_S^A is the Wagner interaction coefficient for sulfur with aluminum. The sulfur solubility curves exhibit minima with negative values of ϵ_S^A at larger sulfur concentrations and smaller alloy contents with increasing negative values of this interaction coefficient.

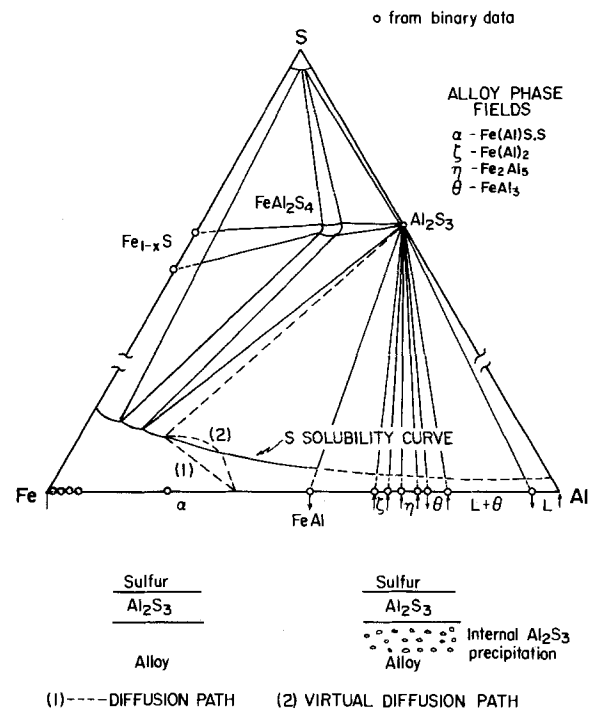


Fig. 1. Diffusion paths for metal and sulfur superimposed on the A-B-S ternary isotherm. Diffusion path, 1, corresponds to exclusive growth of an external Al_2S_3 scale. Virtual diffusion path, 2, leads to internal-external sulfidation.

* Electrochemical Society Active Member.

** Electrochemical Society Student Member.

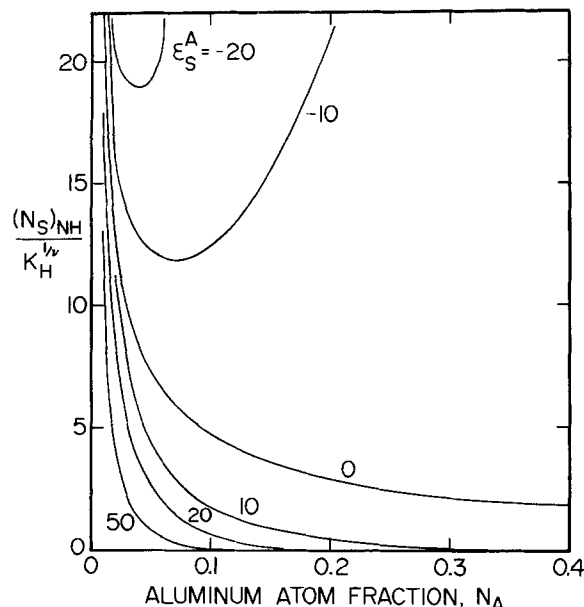


Fig. 2. The shape of the sulfur solubility curve in the Fe-Al alloy as a function of alloy aluminum atom fraction for Henrian ($\epsilon_S^A = 0$) and nonideal ($\epsilon_S^A \neq 0$) solid solution behavior.

In the previous analysis for internal-external oxidation of a binary alloy (2), account was given to oxygen diffusion in the alloy by an interstitial mechanism and oxygen interaction with the alloying solute element of an attractive kind (negative Wagner interaction coefficient). These properties, however, do not apply to the Fe-Al-S system. Sulfur diffusion in bcc iron proceeds by a vacancy mechanism (4-6), and the thermodynamics of liquid Fe-Al alloys containing dissolved sulfur are determined by a repulsive interaction between sulfur and aluminum (positive Wagner interaction coefficient) (7, 8) even though Al_2S_3 is a relatively stable compound (3). Consequently, the diffusional analysis for sulfidation in contrast to oxidation of the Fe-Al alloys must take into account a different type of diffusion mechanism and of thermodynamic behavior. We are able to demonstrate, notwithstanding, that this analysis is similar to that previously carried out and gives a more detailed general understanding of internal-external oxidation phenomena.

The scale-alloy diffusion model is shown schematically in Fig. 3. Then, equations describing diffusion in the alloy when the gaseous solute element is regarded as diffusing on both its own and metal gradient are as follows

$$j_A = -D_{AA} \frac{dN_A}{dx} \quad [3]$$

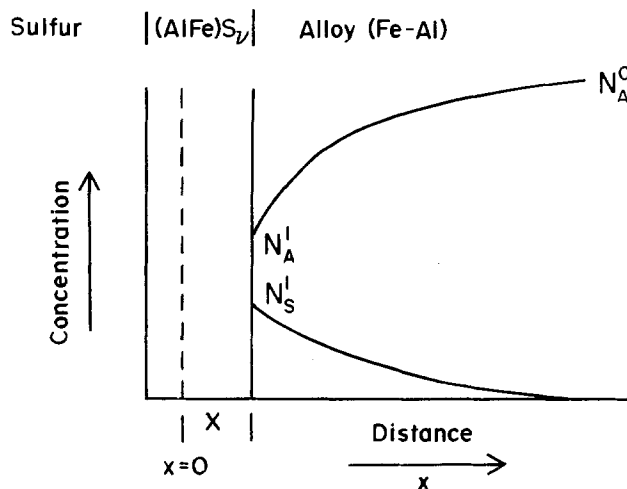


Fig. 3. The ternary scale-alloy sulfidation model

$$j_S = -D_{SS} \frac{dN_S}{dx} - D_{SA} \frac{dN_A}{dx} \quad [4]$$

where D is a diffusion coefficient for aluminum and sulfur and D_{SA} is the off-diagonal diffusion coefficient. For the ternary dilute substitutional solid solution approximation and a solute vacancy diffusion mechanism (9)

$$D_{SA} = D_{SS} N_S \left\{ \epsilon_S^A - N_S \left(\frac{D_{AA}}{D_{SS}} - N_B \frac{D_{BB}}{D_{SS}} \right) \right\} \quad [5]$$

Since $N_S \ll 1$; $D_{SS} \sim 10 D_{AA}$ or D_{BB}

$$D_{SA} = \epsilon_S^A D_{SS} N_S \quad [6]$$

in exact correspondence to the previous case for interstitial oxygen diffusion in a binary alloy, Eq. [36] of Ref. (2). Thus we may utilize Eq. [1] and [39] of Ref. (2) to define the atom fraction of aluminum and sulfur at any distance x within the alloy

$$N_A = N_{A0} - (N_{A0} - N_A) \frac{\text{erfc } x/2 \sqrt{(D_{AA}t)}}{\text{erfc } \sqrt{(k/2D_{AA}t)}}; x \geq X \quad [7]$$

$$N_S = \frac{D_{SA}}{D_{SS}} (N_{A0} - N_A) \frac{\text{erfc } [x/2 \sqrt{(D_{AA}t)}]}{\text{erfc } (k/2D_{AA}t)^{1/2}} + N_S \frac{\text{erfc } [x/2 \sqrt{(D_{SS}t)}]}{\text{erfc } (k/2D_{SS}t)^{1/2}} - \frac{D_{SA}}{D_{SS}} (N_{A0} - N_A) \frac{\text{erfc } [x/2 \sqrt{(D_{SS}t)}]}{\text{erfc } (k/2D_{SS}t)^{1/2}}; x \geq X \quad [8]$$

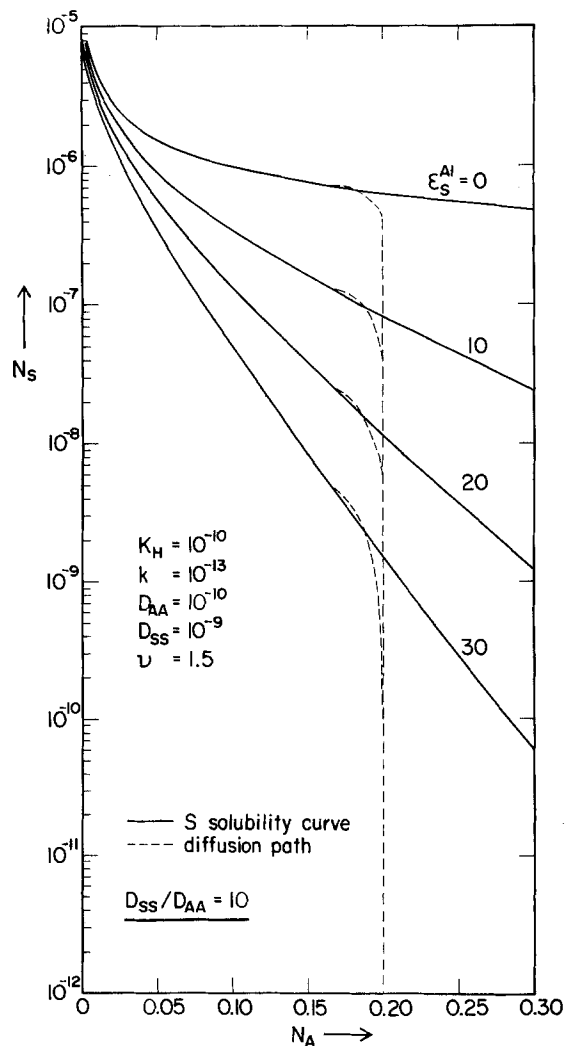


Fig. 4. Sulfur solubility curves calculated according to Eq. [2] with diffusion paths calculated by means of Eq. [7]-[9] superimposed for an Fe-20 at% Al alloy. The region above a solubility curve corresponds to the alloy-sulfide phase field.

$$X = \sqrt{2kt} \quad [9]$$

Diffusion paths are determined from Eq. [7]-[9] by calculating the metal and sulfur profiles and then eliminating the variable x/\sqrt{t} . In Fig. 4, calculated diffusion paths have been superimposed on alloy sulfur solubility curves for an alloy of composition $N_{A_0} = 0.2$ and Henrian ($\epsilon_s^A = 0$) and non-Henrian ($\epsilon_s^A > 0$) sulfur solution behavior. The values of the equilibrium constant, diffusivities, and the parabolic sulfidation rate constant correspond to those for growth of Al_2S_3 on the Fe-Al alloy at 1173 K. As was emphasized earlier, the solubility curves with positive interaction coefficients did not exhibit minima but they decreased markedly in value with increase in the positive value of ϵ_s^A . Moreover, the calculated diffusion paths in all cases cut into the two-phase alloy and sulfide phase field (region above each solubility curve) in a manner such that the interfacial aluminum concentrations do not practically depend on the value of ϵ_s^A even though the sulfur interfacial concentration decreases by several orders of magnitude. It also is to be noted that a decrease in the value of ϵ_s^A decreases the slopes of both the diffusion path and the sulfur solubility curve; it is the relationship between these two parameters which governs the critical atom fraction of aluminum necessary for prevention of internal oxidation.

Transition from Internal Sulfidation to External Sulfide Scale Growth

For scale growth only, one has the relationship (2)

$$\left(\frac{dN_s}{dN_A}\right)_{x=X}^{DP} \leq \left(\frac{dN_s}{dN_A}\right)_{x=X}^{Sol} \quad [10]$$

where the slopes of the sulfur diffusion and solubility profiles in the alloy are designated as DP and Sol, respectively. Since the diffusional analysis for sulfidation has been shown to correspond to that for oxidation, Eq. [26a], [42], and [57] of Ref. (2) can be utilized to define the expressions in Eq. [10] and the critical atom fraction of aluminum, $N_{A_0^*}$, for suppression of internal sulfidation and exclusive growth of the Al_2S_3 scale.

$$\epsilon_s^A (N_{A_0^*})^2 + \left\{ \frac{1 - F(u)}{F(u)} \left[1 + \frac{u}{v} \left(\frac{\pi D_{SS}}{D_{AA}} \right)^{1/2} \right] - \epsilon_s^A [1 + F(u)] \right\} (N_{A_0^*}) + \left\{ \epsilon_s^A F(u) - [1 - F(u)] - \frac{u}{v} \left(\frac{\pi D_{SS}}{D_{AA}} \right)^{1/2} \frac{1 - F(u)}{F(u)} \right\} = 0 \quad [11]$$

where u replaces $k/(2D_{AA})^{1/2}$ and $F(u)$ represents the auxiliary function

$$F(u) = \sqrt{\pi} u \exp u^2 \operatorname{erfc} u \quad [12]$$

Thus, $N_{A_0^*}$ depends on the two diffusion coefficients D_{SS} and D_{AA} , the alloy/sulfide interfacial recession rate as given by the parabolic scaling rate constant k and the thermodynamics of sulfur solubility in the alloy dependent upon the interaction coefficient ϵ_s^A .

Equation [11] was used to calculate $N_{A_0^*}$ as a function of negative and positive values of ϵ_s^A , several values of k/D_{AA} , $K_H = 10^{-10}$ (10, 11), and $D_{SS}/D_{AA} = 10$ (4, 12). These results are shown in Fig. 5. An increase in the metal diffusivity or decrease in the parabolic sulfidation rate constant decreased the initial bulk atom fraction of aluminum required for exclusive scale formation. $N_{A_0^*}$ may be larger or smaller than the concentration given by Henrian or ideal solution behavior ($\epsilon_s^A = 0$). With increasing negative values of ϵ_s^A corresponding to stronger attractive interactions between the alloy solutes, $N_{A_0^*}$ becomes of smaller value. The converse is valid under solute repulsive interactions: $N_{A_0^*}$ increases with increasing positive values of ϵ_s^A . Moreover, the variation in $N_{A_0^*}$ is largest in the range $-50 < \epsilon_s^A < +50$ if $k/D_{AA} > 10^{-3}$.

It is appropriate here to consider sulfidation of the Fe-Al alloys at 1173 K in sulfur vapor at the dissociation pressure of FeS. The Fe-18 a/o Al alloy exhibited internal-external sulfidation giving rise to $FeAl_2S_4$ - Al_2S_3 internal

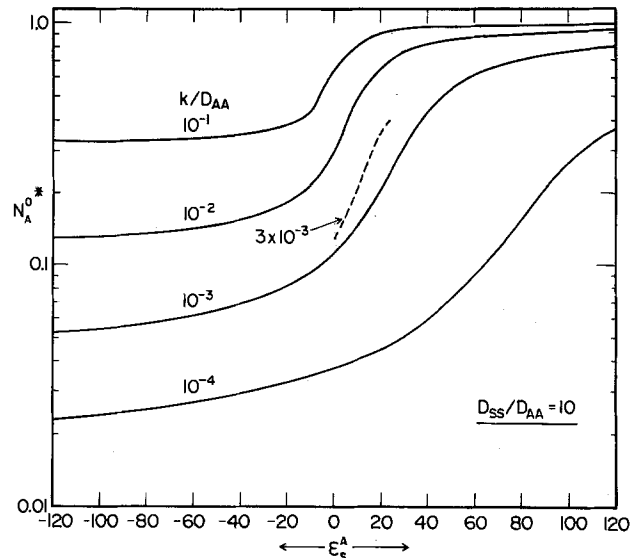


Fig. 5. The critical atom fraction of aluminum in the Fe-Al alloy, $N_{A_0^*}$, for exclusive external oxidation as a function of k/D_{AA} and the interaction parameter ϵ_s^A , $D_{SS}/D_{AA} = 10$. The region above the calculated $N_{A_0^*}$ represents alloy compositions for external scale formation only.

precipitates and an $FeAl_2S_4$ scale, whereas the Fe-28 a/o Al alloy exhibited exclusive growth of an Al_2S_3 scale. The values $k = 1.9 \times 10^{-12}$ cm/s^{1/2} for scale growth (1), $D_{AA} = 5.8 \times 10^{-10}$ cm²/s (12), and $D_{SS} = 1.3 \times 10^{-9}$ cm²/s (4) were used in these calculations. If $\epsilon_s^A = 0$, the initial alloying concentration is 12.7 a/o Al. Thus, a $\epsilon_s^A > 0$ must be considered. Under this condition of an aluminum-sulfur repulsive interaction, more aluminum alloy content is necessary to take up the sulfur and to permit the transition from internal sulfidation to external scale growth. $N_{A_0^*}$ was determined as a function of positive values of ϵ_s^A by Eq. [11], and these results are shown in Fig. 5. Values of $9 < \epsilon_s^A < 15$ correspond to aluminum alloy contents 18 a/o $< N_{A_0^*} < 28$ a/o Al. Thus, positive interaction coefficients must be considered for suppression of internal sulfidation. These values, however, can only be compared to values presently available for liquid Fe-Al alloys, $\epsilon_s^A = 4.4$ -6.7 at 1823 K (7, 8), which, upon extrapolation to 1173 K, yield $\epsilon_s^A = 12$ -18 (8).

This analysis has demonstrated that repulsive interactions between sulfur and aluminum ($\epsilon_s^A > 0$) must be taken into account to define the critical atom fraction of aluminum to prevent internal sulfidation of Fe-Al alloys. A consideration of this interaction coefficient was reasonable even though values of $\epsilon_s^S = -3.3$ and $\epsilon_A^A = 5.3$ have been reported for liquid alloys at 1823 K (7). The sulfur solute interaction coefficient only occurred as a factor $\epsilon_s^S N_s$ in the diffusion and sulfur solubility equations, and this factor is negligible, since $N_s \ll 1$ in the solid alloys. ϵ_A^A only occurred in the equations as a factor $(\epsilon_A^A + \epsilon_s^A) N_A$ and therefore did not alter the form of the equations within the approximations carried out to obtain expressions in analytical form.

Acknowledgment

This work was carried out under the auspice of the Natural Sciences and Engineering Council of Canada.

Manuscript submitted Oct. 22, 1984; revised manuscript received Jan. 14, 1985.

McMaster University assisted in meeting the publication costs of this article.

REFERENCES

1. P. C. Patnaik and W. W. Smeltzer, *This Journal*, **132**, 1226 (1985).
2. W. W. Smeltzer and D. P. Whittle, *ibid.*, **125**, 1116 (1978).
3. P. C. Patnaik and W. W. Smeltzer, *ibid.*, **131**, 2688 (1984).
4. W. H. Herrstein III, F. H. Beck, and M. G. Fontana, *Trans. AIME*, **242**, 1049 (1968).

5. N. G. Ainslie, R. E. Hoffman, and A. U. Seybolt, *Acta Metall.*, **8**, 523 (1960).
6. N. G. Ainslie, V. A. Phillips, and D. Turnbull, *ibid.*, **8**, 528 (1960).
7. G. K. Sigworth and J. F. Elliot, *Met. Sci.*, **8**, 298 (1974).
8. S. Hayashi and T. Uno, *Bull. Nagoya Inst. Technol.*, **27**, 249 (1975).
9. J. S. Kirkaldy and G. R. Purdy, *Can. J. Phys.*, **40**, 208 (1962).
10. M. J. Ferrante, J. M. Stuyve, H. C. Ko, and R. R. Brown, *High Temp. Sci.*, **14**, 91 (1981).
11. S. V. Radcliffe, B. L. Averbach, and M. Cohen, *Acta Metall.*, **9**, 169 (1961).
12. H. C. Akuezue and D. P. Whittle, *Met. Sci.*, **17**, 27 (1983).

Kinetics of the Hydrogenation of Silicon Tetrachloride

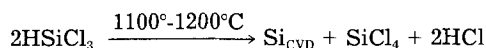
William M. Ingle and Marilyn S. Peffley

Motorola, Incorporated, Semiconductor Products Sector, Phoenix, Arizona 85008

ABSTRACT

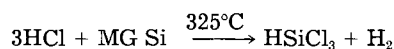
The hydrogenation of SiCl_4 in the presence of silicon, was investigated at temperatures between 525° and 650°C and at various pressures. It was found that increasing the temperature increased the HSiCl_3 conversion efficiency and throughput. Increasing the pressure increased the conversion efficiency at the expense of the reaction rate and adding CuCl catalyst enhanced the HSiCl_3 conversion efficiency and throughput. An energy of activation of 10-15 kcal/mol was found for the SiCl_4 hydrogenation with CuCl catalyst and 20-25 kcal/mol without catalyst. A HSiCl_3 throughput rate of 2578 $\text{kg/m}^3 \text{ h}$ was observed at 5.1 atm with a residence time of ~0.5s and conversion efficiency of 18.5%. Finally, the effect of HCl being added to the reactants and products was examined and a reaction mechanism was proposed. Without CuCl catalyst, the addition of HCl slightly enhances the concentration of HSiCl_3 in the products; with CuCl catalyst, the addition of HCl slightly reduces the concentration of HSiCl_3 in the products. When HCl is added to the effluents of the hydrogenation reaction in a cooler zone (~325°C) above the first stage, then HSiCl_3 conversion efficiencies and throughputs are markedly increased. Virtually 100% of the HCl is converted into HSiCl_3 .

The majority of all of the high purity silicon used for manufacturing of semiconductor devices is produced by the chemical vapor deposition (CVD) of silicon from HSiCl_3 onto hot filaments in a bell jar-type reactor



The molar SiCl_4 to HCl ratio of approximately 1:2 is typical of the effluents for hot-filament reactors.

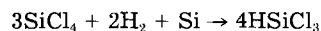
The HCl can be reacted with metallurgical-grade silicon (MG silicon) to regenerate HSiCl_3 , which, when purified, is suitable for high purity silicon production



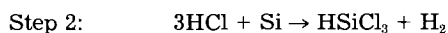
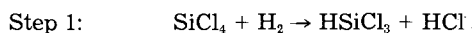
In the reaction of HCl with MG silicon, anhydrous HCl is injected into a bed of silicon particles in a fluidized bed-type reactor. The reaction is highly exothermic and requires heat exchange to minimize overheating. However, hot spots do occur which reduce HSiCl_3 conversion efficiency and degrade the reactor.

The recycling of the SiCl_4 by-product, which accounts for approximately 70% by weight of the HSiCl_3 feed, is an important consideration in the overall economics of the silicon-production process. One process currently used is to hydrolyze or burn the by-product SiCl_4 in a O_2/H_2 mixture to recover HCl and by-product SiO_2 .

Investigations at Union Carbide Corporation (1), Massachusetts Institute of Technology (2), Solar Electronics (3), and Dow Corning Corporation (4) have examined the hydrogenation of SiCl_4 in the presence of silicon at high temperatures and intermediate to high pressures



The hydrogenation of SiCl_4 in the presence of silicon is suggested as a combination of two reactions



In this work, the combined reaction is referred to as STH (an acronym for SiCl_4 hydrogenation), which differentiates the combined reaction from the SiCl_4 hydrogenation reaction (step 1) and the silicon hydrochlorination reaction (step 2).

Typically, a SiCl_4/H_2 mixture was passed through a heated vertical tubular reactor containing silicon particles with catalyst. Reactor temperature, pressure, residence time, H_2 to SiCl_4 ratio, and presence of catalyst dictate the SiCl_4 to HSiCl_3 conversion efficiency and HSiCl_3 throughput rate.

The purposes of the present investigation were as follows: (i) to study process parameters affecting HSiCl_3 throughputs and conversion efficiencies, (ii) to obtain kinetic data and postulate a reaction mechanism, and (iii) to study the effect of the addition of HCl on conversion efficiencies, HSiCl_3 throughputs, and reaction rates of the STH reaction.

Experimental Apparatus

The STH reactor was constructed of Incoloy 800H after the basic design of Mui (2). Incoloy 800H was chosen because of its superior corrosion resistance and mechanical strength at high temperatures. Mui's reactor design was modified to include a heat-exchange coil to preheat the incoming H_2/SiCl_4 mixture. This preheater helped to provide a more uniform temperature distribution over the entire reactor length and ensure that the reactor inlet was at reaction temperature.

Near the completion of the STH experiments, the reactor was modified to allow for HCl to be mixed with incoming H_2/SiCl_4 or injected into the effluents of the STH reaction in a cooler zone (stage 2) as depicted in Fig. 1.

The H_2/SiCl_4 mixture was formed by bubbling hydrogen through two SiCl_4 cylinders arranged in series to ensure a saturated SiCl_4/H_2 gaseous mixture. The SiCl_4/H_2 ratio was set by controlling the temperature and pressure in the two SiCl_4 cylinders. Internal temperatures were monitored at three points in each cylinder and pressures were monitored at each cylinder. As the SiCl_4 was consumed, the level in the first cylinder would drop and the liquid level could be determined at the point where the sharp temperature gradient occurred. A rapid increase in temperature was observed when the liquid level dropped below each of the three thermocouple points. When the liquid level in the first cylinder dropped below the level of the lowest thermocouple, positioned about one-quarter of the way up from the bottom, the reactor and apparatus would be shut down for emptying and recharging SiCl_4 in the cylinders and the silicon and catalyst in the reactor.

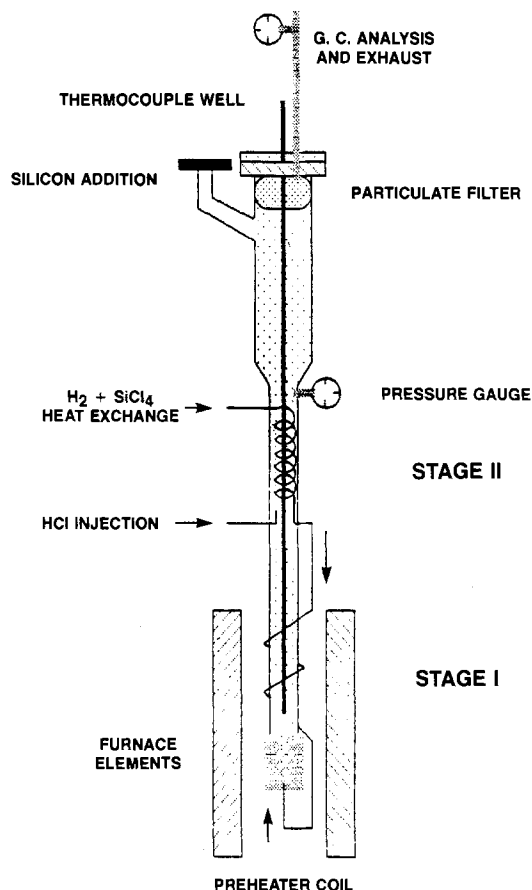


Fig. 1. Two-stage STH reactor

Analysis of the reaction products was accomplished via a Hewlett-Packard 5880A gas chromatograph with level four logic and in-line automated injection and with a Finnigan 3300 GC/MS with data system equipped with a heated six portal manual GC sampling valve. Reaction products were diluted with nitrogen and passed through a heat-traced line to the GC sampling valves. Sampling in this manner assured that a representative sample would be analyzed for accurate determination of reaction product concentration. The unanalyzed portion of the reactor effluent was scrubbed in a continuous-spray water scrubber.

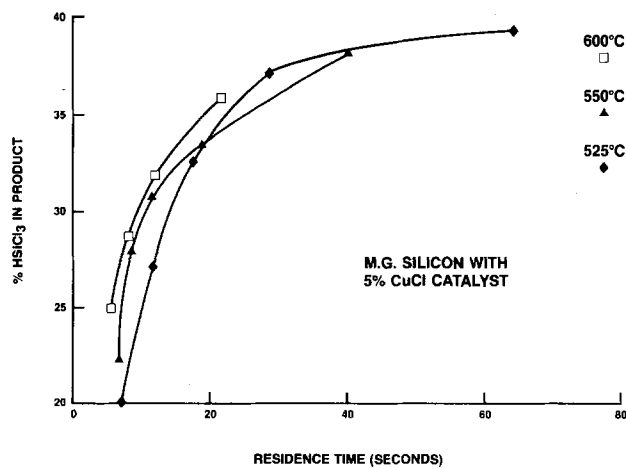
The SiCl_4 utilized in the experiments was of semiconductor-grade (SG) quality and contained $<0.1\%$ HSiCl_3 . The H_2 , HCl , N_2 , and other gases utilized in these experiments were of "Ultrahigh Purity" grade. The SG and MG silicon used in these experiments had been crushed in a jaw crusher and sieved to a particle size smaller than 10 mesh. The CuCl catalyst was in the form of a fine powder and of A.C.S. reagent grade.

Results

Residence times and HSiCl_3 production throughput rates were calculated for each of the various pressures, temperatures, and flow rates. Typically, the 200g silicon charge would occupy a volume 181.8 cm^3 with a bed density 1.1 g/cm^3 . This is 50% of the solid silicon density of 2.2 g/cm^3 , which yields a free bed volume of 90.9 cm^3 for the nominal 200g charge in a static bed.

The high pressure studies (35 atm) were conducted at 525° , 550° , and 600°C at a H_2 to SiCl_4 ratio of 2 to 1 on SG silicon with CuCl catalyst. H_2/SiCl_4 flow rates were varied to yield varying residence times with corresponding SiCl_4 to HSiCl_3 conversion efficiencies and HSiCl_3 production rates [e.g., see Ref. (2)].

In Fig. 2 is depicted the high pressure reaction rate data generated by plotting the mole fraction of the HSiCl_3 in the product vs. the residence time. The highest conversion efficiencies were observed at higher temperatures

Fig. 2. Percentage of HSiCl_3 product at $\text{H}_2:\text{SiCl}_4$ ratio of 2:1 at 35 atm.

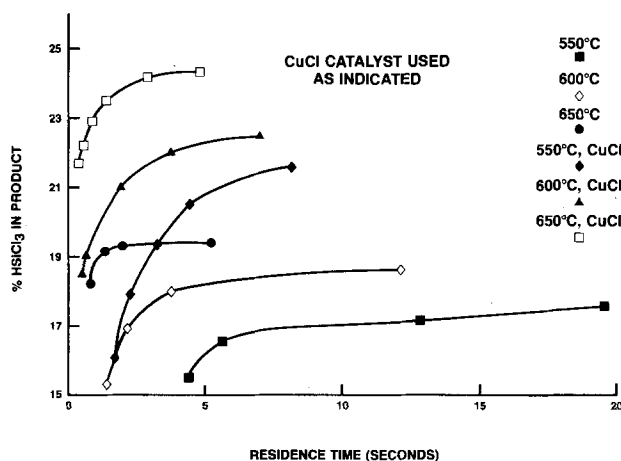
($600^\circ > 550^\circ > 525^\circ\text{C}$), longer residence times, and with a CuCl catalyst.

The intermediate pressure studies (5.1 atm) were conducted at 550° , 600° , and 650°C , at a 2 to 1 H_2/SiCl_4 ratio on MG silicon, with and without CuCl catalyst. Again, H_2/SiCl_4 flow rates were varied to generate throughput and rate data. A plot of the mole fraction of the HSiCl_3 in the chlorosilane product vs. residence time is depicted in Fig. 3. Again, highest conversion efficiencies were observed at higher temperatures, with longer residence times and CuCl catalyst.

The low pressure studies (2.7 atm) were conducted at 600° and 650°C , with a 2 to 1 H_2/SiCl_4 ratio on MG silicon with and without catalyst and with and without HCl injected into the H_2/SiCl_4 feed mixture. In Fig. 4 is depicted a plot of reaction rate data at 600° and 650°C with and without catalyst. Higher temperatures and presence of CuCl catalyst enhanced the conversion efficiency.

In Table I are listed HSiCl_3 production rates for the CuCl catalyzed STH reaction at 35, 5.1, and 2.7 atm. It is worth noting that even though the equilibrium conversion efficiencies continued to drop with decreasing pressure ($35 > 5.1 > 2.7 \text{ atm}$), the enhanced reaction rates at lower pressures had compensating effects and therefore similar HSiCl_3 production rates were observed over this wide pressure range.

In Table II, the effect of variable HCl concentrations on HSiCl_3 conversion efficiency at 2.7 atm with and without CuCl catalyst is found. It was observed that without CuCl catalyst the addition of HCl slightly increased the HSiCl_3 concentration in the product mixture. However, increasing concentrations of HCl in the presence of CuCl catalyst apparently diminished the HSiCl_3 concentration in the

Fig. 3. Percentage of HSiCl_3 product at $\text{H}_2:\text{SiCl}_4$ ratio of 2:1 at 5.1 atm.

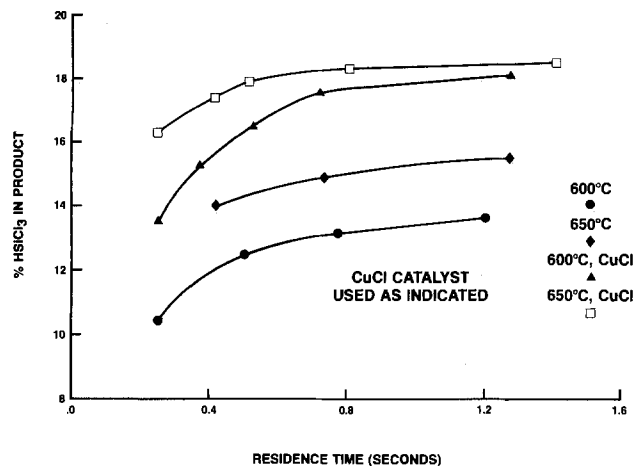


Fig. 4. Percentage of HSiCl_3 product at H_2/SiCl_4 ratio of 2:1 at 2.7 atm.

product mixture. The addition of 25 mole percent (m/o) HCl shortened the residence time about 0.4s with a corresponding reduction in conversion efficiency of 1.0%. Even though these increases and decreases in HSiCl_3 conversion efficiency were quite small, the method of data collection suggests that the trends are reproducible. Specifically, the data for the uncatalyzed and catalyzed sets of experiments were collected in a continuous manner on one silicon charge for each with the HCl flow rate being varied from 0 to 33 m/o two or three times. During this collection period, the data were very reproducible.

In a final series of experiments, varying amounts of HCl were added to stage 2 of the STH/HCl (Fig. 1) reactor, while the H_2/SiCl_4 flow rate remained constant. In these experiments, stage 1 of the reactor was set at 650°C and stage 2 was set at 325°C with an inlet pressure of 5.1 atm. The results of these experiments are depicted in Table III. The addition of 25 m/o HCl ($\text{H}_2/\text{HCl}/\text{SiCl}_4$ ratio equaled 2/1/1) resulted in a marked increase of the percent HSiCl_3 in the product from 20.5 to 33.3%. Calculations contrasting theoretical *vs.* observed yields suggest that under these reaction conditions, 100% of the HCl reacts to form HSiCl_3 .

A critical reaction temperature of about 325°C was required in stage 2 over a length of about 40-45 cm to obtain these results. Under these experimental conditions, this volume and flow rate suggest a minimum residence time of about 0.5s for the HCl to react with the silicon. When part of the stage 2 reaction zone was below approximately 300°C, HCl was detected in the reactor effluents accompanied by a decrease in percent HSiCl_3 in the effluent. When the temperature of part of the zone drifted above approximately 350°C, SiCl_4 was formed from the HCl reacting with the HSiCl_3 with a corresponding loss of percent of HSiCl_3 .

At the completion of the HCl addition experiments, the reactor was dismantled and inspected for corrosion

Table I. HSiCl_3 production rates calculated for the STH reaction

Pressure (atm)	Residence time (s)	Catalyst	HSiCl_3 concentration in product (%)	Calculated HSiCl_3 production rate ($\text{kg}/\text{m}^3\cdot\text{h}$)
5.1	1.4	none	15.3	785
2.7	0.25	none	10.4	15.24
35	5.6	CuCl	25.0	1695 ^a
5.1	0.51	CuCl	18.5	2578
2.7	0.25	CuCl	13.5	1730

Experimental conditions: temperature of 600°C, H_2/SiCl_4 ratio of 2:1, MG silicon, with and without CuCl catalyst.

^a 35 atm HSiCl_3 production rate limited by heat-exchange capacity of the H_2/SiCl_4 preheater.

Table II. Effect on mole fraction of HSiCl_3 in effluent through the addition of HCl to H_2/SiCl_4 feed

HCl (m/o)	No CuCl catalyst	
	HSiCl_3 in product (%)	Residence time (s)
0	13.3	1.1
6-7	13.4	1.0
20-21	13.9	0.8
33-34	14.0	0.7
CuCl catalyst (5%)		
0	17.4	1.1
2-3	17.4	1.1
5-6	17.4	1.1
11-12	17.4	0.9
16-17	16.8	0.85
20-21	16.7	0.8
32-33	16.4	0.7

Experimental conditions: 600°C, H_2/SiCl_4 ratio of 2:1, MG silicon, with and without CuCl catalyst at 2.7 atm.

and/or "hot spots." No evidence of corrosion or hot spots was observed in the cooler second stage of the reactor. This correlates with observations made during the actual HCl addition experiments. In the presence of a H_2/SiCl_4 mixture, moderation of the hydrochlorination reaction occurs which results in a more uniform temperature distribution without "hot spots."

Discussion

Previous publications on the investigations of the STH reaction (1-4) have focused mainly on the data collection for HSiCl_3 conversion efficiency calculations and engineering design for scaled-up HSiCl_3 production facilities. In a recent report, Mui (3) demonstrated that the reaction of H_2 with SiCl_4 in the presence of CuCl catalyst was not the rate-limiting step.

The following discussion will serve to integrate the results of the previous experiments. Rate constants and energies of activation will be calculated as in previously reported data. A mechanism will be suggested which is more consistent with the body of knowledge defining the STH reaction.

One of the initial goals of the conversion enhancement studies was to identify the reaction parameters which led to enhanced conversion efficiency and increased HSiCl_3 throughput. In Table IV are summarized the trends which were observed during the current investigation.

In order to generate rate data, temperatures and flow rates continued to be varied even though higher temperatures and flow rates yielded greatest HSiCl_3 throughputs. Experiments were conducted at high pressure (35 atm), intermediate pressure (5.1 atm), and low pressure (2.7 atm) to generate conversion efficiency data and to evaluate the feasibility of operating the STH process at considerably reduced pressure.

A simple first-order rate equation of the form

$$\ln \frac{X_e}{X_e - X} = \frac{K_1 a}{X_e} t$$

Table III. Effect on mole fraction of HSiCl_3 in effluent through the addition of HCl to two-stage STH/HCl reactor

HCl (m/o)	Two-stage STH/HCl reactor	
	HSiCl_3 in product (%)	Residence time (s)
0.0	20.5	0.69
8.3	23.5	0.69
16.6	25.3	0.69
25.0	33.3	0.69

Experimental conditions: Temperatures of 650°C for stage 1 and 325°C for stage 2; H_2/SiCl_4 ratio of 2:1; MG silicon with CuCl catalyst at 5.1 atm.

Table IV. Summary of effects of process parameters on conversion efficiency, HSiCl₃ throughputs, reaction rates, and energy of activation for the STH reaction

Process parameters	Conversion efficiency	HSiCl ₃ throughput	Reaction rate	Energy of activation
Increased temperature	Increases	Increases	Increases	No measurable effect
Reduced pressure	Decreases	Compensating effects	Increases	No measurable effect
CuCl catalyst	Increases	Increases	Increases	Decreases
Increased H ₂ /SiCl ₄ ratio	Increases	Compensating effects	No measurable effects	—
Particle size	No measurable effect	No measurable effect	No measurable effect	No measurable effect
Increased residence time	Increases	Decreases	—	—
HCl addition				
Stage 1	Minor	Increases	Compensating effects	Insufficient data
Stage 2	Increases	Increases	—	—

was applied to the STH reaction (2). In solving the pseudo-first-order kinetics for the rate of conversion of SiCl₄ to HSiCl₃, X is the concentration of HSiCl₃ at time t , X_e is the equilibrium concentration of HSiCl₃, and a is the initial concentration of SiCl₄.

The pseudo-first-order rate equation was applied to each set of the 35, 5.1, and 2.7 atm data. Individual partial pressures of HSiCl₃ (P_{HSiCl_3}), initial SiCl₄ partial pressures (P_{SiCl_4}), and equilibrium partial pressure of HSiCl₃ (P_{eHSiCl_3}) were calculated at each residence time from conversion efficiency and flow data. Plots of $\ln P_{\text{eHSiCl}_3}/P_{\text{HSiCl}_3} - P_{\text{HSiCl}_3}$ vs. residence times yielded straight lines with slopes equal to $K_1 P_{\text{SiCl}_4}/P_{\text{eHSiCl}_3}$. Multiplying the slope by P_{eHSiCl_3} and dividing by P_{SiCl_4} yielded the rate constant K_1 for various reaction conditions.

Table V contains the rate constants calculated from data depicted in Fig. 2, 3, and 4. It is interesting to observe the inversely proportional effect of reaction pressure on rate constant K_1 . Specifically, as the pressure is reduced from 35 to 5.1 to 2.7 atm, the rate constant is observed to increase from 0.07 to 1.0 to 5.0 (600°C with CuCl catalyst).

The activation energy, E , was determined by plotting the log of K_1 vs. the inverse temperature $1/T$, in the Arrhenius equation

$$k_1 = Ce^{-\Delta E/RT}$$

$$\ln K_1 = \ln C - \frac{\Delta E}{RT}$$

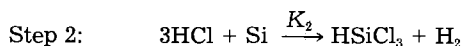
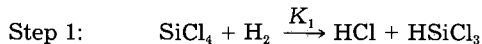
where R is the gas constant (1.987 cal/mol°C) and C is a constant. Values calculated for energies of activation are also found in Table V.

The fluctuations that were observed in the calculated activation energy values for the STH reaction were due in part to the variations in the reaction conditions that occurred as the flow rates were increased and in part to the simplicity of the pseudo-first-order rate treatment. At

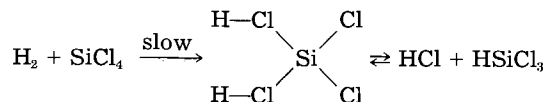
low flow rates (*e.g.*, residence times of $\geq \sim 10$ s), the silicon particle bed behaved as a packed bed, at intermediate flows (*e.g.*, residence times of 1-10s) as a fluidized particle bed, and at high flows (residence times of ≤ 1 s) the bed behaved as a turbulent flow bed (5). These changing conditions dramatically affect free volume, catalyst distribution, pressure drops, and gas/solid interaction within the silicon particle bed.

In Table II, the effect of the addition of HCl on the STH reaction with and without CuCl catalyst are contrasted. The interpretation of the significance of these results was a key factor in the postulation of a mechanism for the STH reaction.

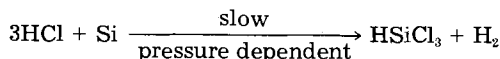
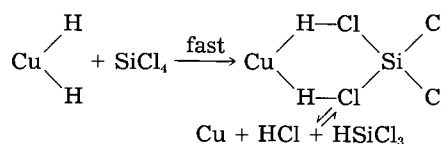
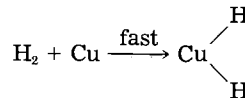
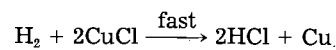
Previous experimental studies have suggested a plausible reaction pathway involving the following stepwise reaction



Furthermore, the assumption has been made that step 1 is slow and step 2 is fast (*i.e.*, $K_2 > K_1$). If step 2 is faster than step 1, then the addition of HCl to the reaction should increase the concentration of HSiCl₃ via step 2. This was indeed the case when CuCl was not present. Apparently, without CuCl catalyst H₂ reacts slowly with SiCl₄, possibly in the following manner (step 1)



However, in the presence of a CuCl catalyst, step 1 could proceed through a previously identified, labile, low energy route (6) as follows



Thus it is postulated that step 1 reaction rate is considerably enhanced by the addition of Cu (CuCl). This is consistent with the lower activation energies associated with the CuCl-catalyzed STH reaction (Table II).

Table V. Comparison of rate constants and energies of activation under various process conditions

Reaction parameters	Rate constants	Energies of activation (kcal/mol)
35 atm/MG silicon		
CuCl 5%, 600°C	0.07	10-15
CuCl 5%, 500°C [Ref. (2)]	0.007 s ⁻¹	13.2
5.1 atm/MG silicon		
CuCl 5%, 600°C	1.0	15-20
No catalyst, 600°C	0.26	25-30
2.7 atm/MG silicon		
CuCl 5%, 600°C	5.0	~10
No catalyst, 600°C	1.6	~15

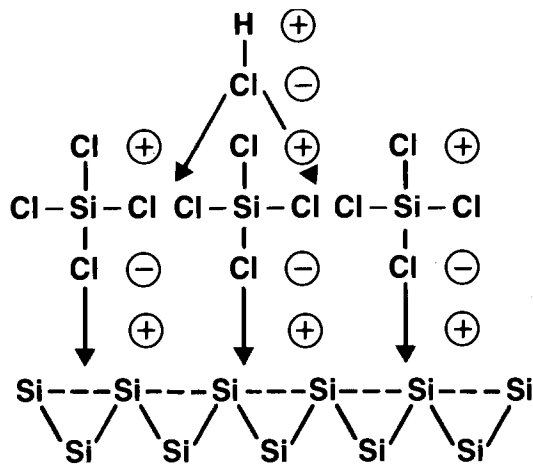
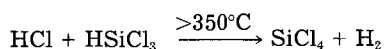


Fig. 5. Blockage of reactive sites by SiCl_4 .

A plausible explanation for the retarded reaction rate of HCl with silicon and consequently the inverse dependency of the reaction rate on pressure is as follows: (i) SiCl_4 forms a Si-SiCl_4 dipole-induced dipole bond at the surface of the silicon particles as depicted in Fig. 5, (ii) at high pressures the density of these groups is greatly enhanced (*i.e.*, more SiCl_4 molecules per unit area), and (iii) HCl has to diffuse through the SiCl_4 to react with the silicon (step 2). The enhanced density of these SiCl_4 groups at high pressure greatly retards this reaction rate of HCl with silicon. Consequently, the reaction rate of HCl with silicon in the presence of SiCl_4 would be expected to be reduced as the pressure is increased.

Observations made while conducting experiments on the two-stage STH/HCl reactor are also consistent with the two-step mechanism. Previous investigators studying the direct reaction of HCl with silicon (step 2) have found that the highest HCl to HSiCl_3 conversion efficiencies are obtained when the reaction is maintained at about 300°C - 325°C (7, 8). Above about 350°C , HCl also reacts with HSiCl_3 to form SiCl_4 , which reduces the HSiCl_3 product as follows



In the current investigation, it was found that a reaction zone about 40-45 cm long was required to completely react the HCl with the silicon particles in the two-stage reactor.

If temperatures in this zone rose above $\sim 350^\circ\text{C}$, SiCl_4 concentrations increased at the expense of the HSiCl_3 . If

the temperature of this zone dropped below $\sim 300^\circ\text{C}$, unreacted HCl was observed at the expense of the HSiCl_3 . The length of this zone suggests that a residence time of about 0.5s is required for the complete reaction of HCl with silicon in the presence of SiCl_4 . This residence time is only a small amount less than the 0.69s required to complete the entire STH reaction which combines steps 1 and 2.

Consequently, if the assumption is made that steps 1 and 2 are mutually independent and if step 2 requires about 0.5s, then step 1 must occur in approximately 0.19s and $K_1 > K_2$. Thus, it would appear that in the presence of CuCl at 5.1 atm that step 1 does occur at a faster rate than step 2. As stated earlier, this observation is considerably different than what is commonly accepted in the literature.

Acknowledgments

The authors extend considerable appreciation to Dr. H. S. N. Setty, Professor Morey Ring (San Diego State University), and Professor James Birk (Arizona State University) for their assistance with the interpretation of the kinetic results. In addition the technical assistance of Robert Darnell, Manu Patel, Sid Palmer, and Roger Nikirk was also appreciated.

Manuscript submitted Aug. 13, 1984; revised manuscript received Jan. 31, 1985.

Motorola, Incorporated, assisted in meeting the publication costs of this article.

REFERENCES

1. Union Carbide Corporation, Final Report, D.O.E./J.P.L. Contract no. 954,334, p. 210, D.O.E. Technical Information Center, Springfield, VA (1979).
2. J. P. Mui and D. Seyferth, Massachusetts Institute of Technology, Final Report, D.O.E./J.P.L. Contract no. 955,382, D.O.E. Technical Information Center, Springfield, VA (1981).
3. J. P. Mui, Solarelectronics, Inc., Final Report, D.O.E./J.P.L. Contract no. 956,061, D.O.E. Technical Information Center, Springfield, VA (1983).
4. J. McCormick, F. Plahutnik, A. Arvidson, D. Sawyer, and K. Sharp, Hemlock Semiconductor Corp., Final Report, D.O.E./J.P.L. Contract no. 955,533, D.O.E. Technical Information Center, Springfield, VA (1982).
5. J. Yershaimi and A. M. Squires, in American Institute of Chemical Engineers Symposium Series, Vol. 161-73, pp. 44-50, American Institute of Chemical Engineers, New York (1977).
6. J. Halpern, G. R. McGregor, and E. Peters, *J. Phys. Chem.*, **60**, 1455 (1956).
7. E. Enk, J. Nickl, and H. Teich, U.S. Pat. 3,148,035 (1964).
8. E. Bonitz, *Angew. Chem. Int. Edit.*, **5**, 462 (1966).

Oxidative Purification of Chlorosilane Silicon Source Materials

William M. Ingle and Robert D. Darnell

Motorola, Incorporated, Semiconductor Products Sector, Phoenix, Arizona 85008

ABSTRACT

At temperatures above $\sim 180^\circ\text{C}$, trace levels of oxygen react with the Si-H bond of HSiCl_3 to form an "Si-OH" species, which in turn complexes impurities in the HSiCl_3 , such as BCl_3 or PCl_3 . Purification occurs during a subsequent distillation step which separates the purified HSiCl_3 from the less volatile complex BCl_3 and PCl_3 . In the laboratory-scale studies, 1 mol of oxygen was found to complex 0.38 mol BCl_3 . In the pilot-scale studies, the addition of 0.025% (mol/mol) oxygen to a $\text{HSiCl}_3/\text{SiCl}_4$ mixture reduced both the acceptor (boron) and donor (phosphorous) concentrations of 1.2 and 1.0 ppb to ≤ 0.05 ppb.

Currently, commercial purification of HSiCl_3 for the semiconductor industry occurs via a combination of repetitive distillation steps and chemical complexing operations. Repetitive distillation steps are capable of rendering HSiCl_3 of suitable purity for semiconductor device fabrication. However, chemical purification can reduce the number of these repetitive steps and offers a higher

level of purification than distillation alone. Furthermore, the introduction of a chemical purification step into a chlorosilane recovery loop can reduce the probability of a potential impurity buildup.

Previous studies (1-6) suggest that boron impurity levels in silicon could be reduced by a number of techniques. The first of numerous patents using partial hy-

drolysis purification of chlorosilanes was that of Rosenberger (6) in 1954. The purified HSiCl_3 is separated from the partially hydrolyzed polysiloxane residue via distillation. If bromine or iodine is added to HSiCl_3 containing elemental boron or phosphorous, Bradley *et al.* (2) also suggest that the respective bromides and iodides can be formed which facilitate separation by distillation.

In the first part of the present investigation, a laboratory-scale apparatus was constructed for the demonstration of the BCl_3 complexation via partial oxidation of HSiCl_3 . The BCl_3 concentration was monitored by low temperature distillation mass spectroscopy. The second part of this investigation was conducted in a pilot-scale silicon production operation. Oxygen was added to a heated $\text{HSiCl}_3/\text{SiCl}_4$ mixture and, after a one-step distillation, the HSiCl_3 was analyzed for boron and phosphorous content.

Experimental

The laboratory-scale purification apparatus was constructed primarily of stainless steel hardware, 6.35 mm tubing, valves, gauges, and tanks due to the corrosive properties of HSiCl_3 . In this apparatus, 0.2 standard liter/min (SLM) of compressed nitrogen at 4.4 atm was bubbled through a 95 liter trap containing semiconductor-grade HSiCl_3 doped to 1.0% with BCl_3 . The $\text{HSiCl}_3/\text{BCl}_3$ mixture was maintained at 26°C to ensure a constant delivery rate and constant BCl_3 concentration. Oxygen was metered through a calibrated mass flowmeter and mixed with the $\text{HSiCl}_3/\text{BCl}_3/\text{N}_2$ mixture just prior to heating. In this way, various oxygen flow rates could be selected to determine the effect of oxygen concentration on the extent of BCl_3 complexation. All desired gases flowed into the reactor, where they were heated to determine the effects of temperature on BCl_3 complexation rate.

Construction materials of the reactor consisted of 50 mm stainless steel tubing, 2m long with Swagelok fittings at each end. Clam-shell heaters were fitted around approximately 70 cm of the lower portion of the vertical reactor tube. Temperatures inside the reactor were monitored by placing a multizone thermocouple in a stainless steel sheath along the center axis of the tube. Regulation of the reactor temperature was controlled manually by variable voltage regulators, one each for the top and bottom heating elements.

Analysis of the reaction products was accomplished with a Finnigan 3300 GC/MS with data system. Exhausting gases passed through a heat-traced line to a heated six-port manual GC sampling valve. Sampling in this manner assured that the same sample size would be analyzed for accurate determination of reaction product concentration. The unanalyzed portion of the reactor effluent was scrubbed in a continuous-spray water scrubber.

Inasmuch as the analysis of BCl_3 on a standard chromatography column was not possible (7), a new analytical technique was adopted. For these experiments, a distillation column was designed and built of 6.35 mm quartz tubing packed with crushed quartz sieved to a size of 10-20 mesh. The crushed quartz had been etched with 5% HF, rinsed, and dried before being packed into the column. The packed column was fitted into the GC/MS and conditioned before experimental runs by injecting $\text{BCl}_3/\text{HSiCl}_3$ samples every 2 min for 1h.

To initiate the analysis of a sample, the distillation column was cooled with liquid N_2 in a Dewar flask for 1 min. Data collection was initiated and a sample was injected via the sampling valve and allowed to freeze onto the column for 1 min. The Dewar flask was then removed, the column would come to ambient temperature, and the individual components would distill into the MS. All laboratory-scale samples were analyzed by this procedure.

The pilot-scale HSiCl_3 oxidative purification facility was designed and engineered to operate 24h per day. Under normal operation, a chlorosilane mixture consisting

mainly of HSiCl_3 and SiCl_4 flowed out of a storage tank, through a particulate filter, and into a small metering pump where the pressure was increased to about 6.8 atm. The chlorosilane mixture then flowed through the first of two heat exchangers, where incoming chlorosilanes were heated at the expense of exhausting chlorosilanes. Oxygen (10.7 sccm) is metered from a regulated cylinder and added to the heated HSiCl_3 . Additional heating occurs in a second heat exchanger located within a small 1600W furnace. The exhausting chlorosilanes are cooled via a water-cooled heat-exchange unit and filtered before entering the distillation unit. Pressure gauges at the inlet and outlets of the filter register pressures.

In addition, internal thermocouples (J type) were located at strategic points throughout the system to monitor and control the purification process temperature. The thermocouples were monitored via a five-channel Doric Trendicator, and the temperature was controlled via a two-channel Doric temperature controller.

Under normal operation, power to the furnace was regulated via a 110V variable transformer set at 90V. The process stream temperature was maintained at $210^\circ \pm 30^\circ\text{C}$. The apparatus was operated 24h/day for the duration of the experiments.

The flow of chlorosilanes through the purification unit averaged about 11.4 liter/h. An oxygen flow rate of 10.3 sccm was utilized which was equivalent to 0.025 mol oxygen/mol chlorosilane.

During the subsequent distillation process, HSiCl_3 was separated from the SiCl_4 which now contained the higher boiling complexed impurities. The purified HSiCl_3 was collected at a rate of about 2.5 liter/h and retained for boron and phosphorous analysis. Analysis included wet chemical analysis for boron and seven-pass float-zone analysis technique for both boron (acceptor) and phosphorous (donor) concentrations.

The minimum detectable limit in the boron wet chemical analysis was approximately 0.050 ppb (mol/mol) with an uncertainty of 5%. The limiting factor was the reproducibility of the spectrophotometer.

In an alternate analysis procedure, acceptor (boron) and donor (phosphorous) concentrations were measured in the HSiCl_3 by growing a small polysilicon rod in a metal analysis reactor followed by a gas pass and seven-pass vacuum float-zone analysis. Wet chemical and float-zone analysis were conducted once a day throughout the experiment.

The HSiCl_3 utilized in the laboratory-scale experiments was of semiconductor-grade quality doped to 1.0% with BCl_3 to facilitate BCl_3 analysis. The $\text{HSiCl}_3/\text{SiCl}_4$ mixture utilized in the pilot scale studies represented a "reclaimed" chlorosilane mixture generally containing 2-3 ppb of combined donor and acceptor impurities. All other gases utilized throughout the experiments were of ultra high purity grade.

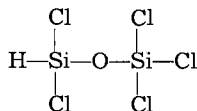
Results

In a series of preliminary experiments, nitrogen was bubbled through separate cylinders of HSiCl_3 and BCl_3 and then mixed. Periodically, samples of the gaseous product mixture were injected into the GC/MS for spectral analysis. Various flows of BCl_3 and HSiCl_3 were utilized. Total separation of the individual products was not always accomplished via low temperature distillation mass spectroscopy. However, calculations of the peak areas of the BCl_3 component peaks was accomplished by monitoring the total BCl_3^+ ion in the single ion mode and comparing it with the total SiCl_3^+ ion. With this technique, it was found that the areas of the BCl_3^+ ion peaks were indicative of the BCl_3 concentration in the gas stream. In this manner, the BCl_3 detection limits were also established for the process.

In the initial laboratory-scale oxidative HSiCl_3 purification experiments, flow rates of both HSiCl_3 and oxygen were set at 3.0×10^{-4} mol/min. Below 170°C no reaction was observed between the oxygen and HSiCl_3 . However, at higher temperatures ($\geq 180^\circ\text{C}$) the oxidation of HSiCl_3 is

rapid and the consumption of oxygen complete. In fact, no trace of oxygen could be detected via GC/MS (< 1 ppm).

The major HSiCl_3 oxidation products were examined, and it was found that at low temperatures one small chain species predominated. For example, the only detectable HSiCl_3 oxidation product found in the $170^\circ\text{--}225^\circ\text{C}$ range had a molecular weight of $m/e = 248$. The following structure is consistent with this molecular weight



At higher temperatures, higher molecular weight species resulted (at the expense of the $m/e = 248$ species). The m/e values were consistent with linear and cyclic compounds containing three and four silicon atoms.

In Fig. 1 are depicted the results from the laboratory-scale studies in which oxygen concentrations were varied. In this series of experiments, the BCl_3 flow rate was set at 3.0×10^{-4} mol/min and the oxygen flow rate was alternately selected between 0.0, 2.0×10^{-4} , and 4.0×10^{-4} mol/min. A straight line with a slope of 0.38 was obtained while varying the oxygen concentration. This indicates that, under these experimental conditions, 1 mol of oxygen reacts with 0.38 mol of BCl_3 . The data depicted in this graph were extracted from more than 4000 spectra and 1.5×10^6 data points. A mean value was then selected for each data point.

It was postulated that during the intra/inter molecular rearrangement that the BCl_3 could possibly react further with the intermediate species or final products. This would result in enhanced purification at higher temperatures. From the results represented in Fig. 2, it was concluded that no additional purification was observed at higher temperatures.

In Fig. 3 is depicted the average daily boron concentration in the HSiCl_3 recovered off the top of the 4 in. distillation column of the pilot-scale purification unit. During the first seven days of operation, no oxygen was added to the chlorosilanes, but analyses were conducted and served as base-line studies. Over the next seven days, oxygen was added to the chlorosilane mixture at a rate of $0.01 \text{ mol O}_2/\text{mol HSiCl}_3$. A 2 day lag time was observed between when the oxygen flow is initiated and when purification was definitely occurring. During an additional 5 days at the conclusion of the experiment, oxygen flow was terminated. Similarly, a 4 day lag time was observed between when the oxygen flow was terminated and when purification ceased.

In Fig. 4 is depicted the daily phosphorous concentration in the HSiCl_3 recovered from off the top of the 4 in. distillation column of the pilot-scale purification unit. The reduction in phosphorous levels parallels those of the boron levels.

Upon completion of the pilot-scale experiments, the purification reactor, heat exchanger, and filters were dis-

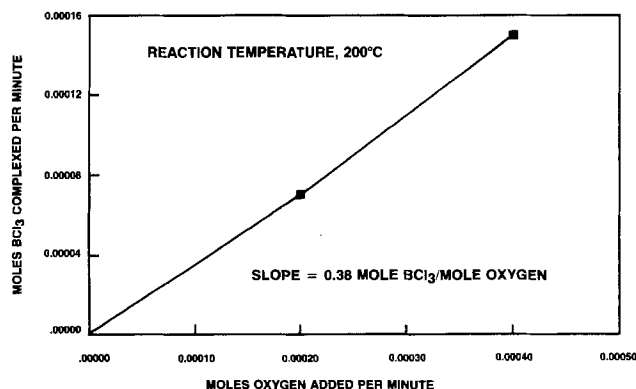


Fig. 1. Rate of BCl_3 complexed via oxidation during laboratory-scale purification of HSiCl_3 .

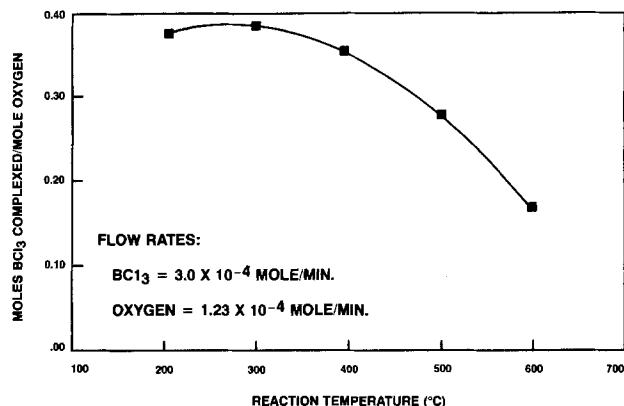


Fig. 2. Effect of reaction temperature on laboratory-scale purification

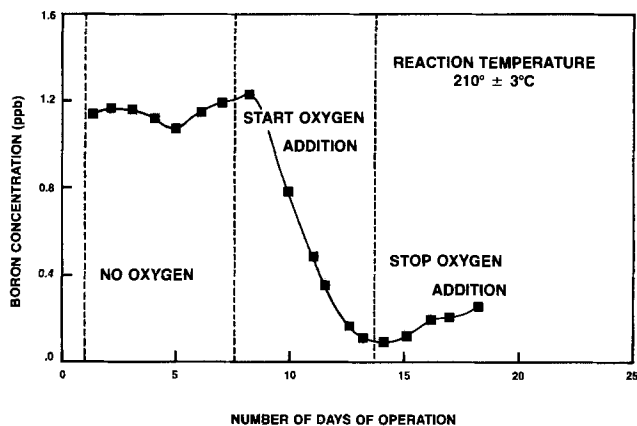


Fig. 3. Average daily boron concentration of HSiCl_3 in pilot facility after distillation.

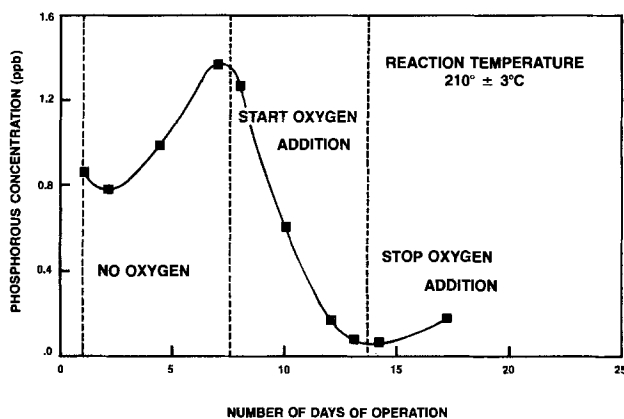
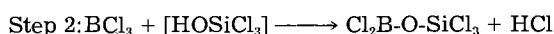
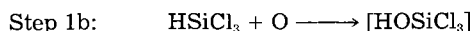
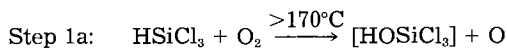


Fig. 4. Daily phosphorous concentration of HSiCl_3 in pilot facility after distillation.

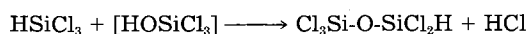
assembled and checked for residues and/or potential problems. In the various filters and tubing were found small quantities of metal flakes and corroded metallics, but no sign of liquid or solid polysiloxane residues was observed.

Discussion

The oxidative purification of HSiCl_3 can be described by the following equations



Competing side reaction:

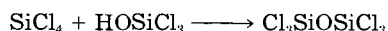


The initial step in this process is written as the formation of an $[\text{HOSiCl}_3]$ intermediate. The justification for this type of species is the formation of only $\text{Cl}_3\text{Si-O-SiCl}_2\text{H}$ during the low temperature oxidation studies. The driving force in this reaction is the thermodynamically favorable formation of strong Si-O and H-Cl bonds.

The addition of SiCl_4 to the HSiCl_3 during oxidative purification can have the following advantages.

1. The oxidative purification process increases the boiling points of most of the unwanted impurities. The subsequent distillation/separation of the SiCl_4 from HSiCl_3 facilitates the separation of these impurities from HSiCl_3 .

2. SiCl_4 will reduce the amount of HSiCl_3 consumed in the competing side reaction as follows

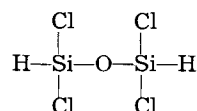


3. The SiCl_4 also undergoes the same degree of purification after subsequent distillation.

The pilot-scale demonstration of the oxidative HSiCl_3 purification process presented some unique problems in data interpretation at the sub-parts per billion levels. For example, (i) typical wet chemical analysis of boron took 8-12h of laboratory work per sample, (ii) a typical float-zone analysis on a silicon rod took 75-95 liter of purified HSiCl_3 , which limited the number of analyses to one per day, (iii) Every 3-4 days, a new shipment of HSiCl_3 would be delivered to the plant which could affect the boron and phosphorous background concentrations, (iv) the turnover rate of HSiCl_3 through the purification system, distillation column, transfer lines, and collection tank was about 1.5 days. Bearing in mind this turnover period, it still appears that purification continued to occur even after the termination of oxygen flow. This effect suggest the presence of an undetectable substance or coating which remains active even after the oxygen flow has stopped.

In order to compare the oxidative HSiCl_3 purification with hydrolysis purification, wet nitrogen was reacted with HSiCl_3 in the laboratory scale reactor at 200°C. During the operation, sizable quantities of solid and semi-solid residues were formed which after a few hours of operation clogged the transfer lines and made smooth con-

tinuous operation of the reactor impossible. GC/MS of the reaction products revealed numerous small polysiloxane species, the most abundant having a $m/e = 214$. The following structure is consistent with this molecular weight



Even though both purification processes (1, 8, 9) are believed to complex boron impurities in a similar manner (for example, the formation of an "Si-O-B" bond), each appears to have advantages. The advantage of the hydrolysis purification process is that it occurs at ambient temperatures, where as the advantage of the oxidative purification process is that no solid residues were observed when the reaction was carried out below ~250°C.

Acknowledgments

The authors are grateful for the assistance from Sandy Buchner, Ron Lenz, Steve Rogers, and Sid Palmer.

Manuscript submitted Aug. 13, 1984; revised manuscript received Jan. 31, 1985.

Motorola, Incorporated, assisted in meeting the publication costs of this article.

REFERENCES

1. H. B. Bradley, P. Ridge, and D. J. Neal, U.S. Pat. 3,540,861 (1970).
2. H. B. Bradley, U.S. Pat. 3,188,168 (1965).
3. S. M. Freund and W. C. Danen, Los Alamos National Laboratory Technical Report La-Ur-78-9, D.O.E. Contract W-7405-ENG, p. 36, D.O.E. Technical Information Center, Springfield, VA (1978).
4. A. Yusa, Y. Yatsurugi, and T. Takaishi, *This Journal*, 122, 1700 (1975).
5. J. Coursier, I. Grenoble, and M. Moutach, U.S. Pat. 3,148,131 (1964).
6. Rosenberger (Siemens; DAS 1,028,543).
7. Union Carbide Corp., Final Report, D.O.E./J.P.L. Contract no. 954,334, D.O.E. Technical Information Center, Springfield, VA (1979).
8. R. Darnell and W. Ingle, U.S. Pat. 4,374,110 (1983).
9. R. Darnell and W. Ingle, U.S. Pat. 4,409,195 (1983).

Structure of Selective Low Pressure Chemically Vapor-Deposited Films of Tungsten

M. L. Green* and R. A. Levy*

AT&T Bell Laboratories, Murray Hill, New Jersey 07974

ABSTRACT

Tungsten films have been selectively deposited (*i.e.*, deposited on Si and TaSi₂ to the exclusion of SiO₂) by LPCVD via the reduction of WF₆ by either Si or H₂. Films formed by H₂ reduction can be unlimited in thickness; however, those formed by Si reduction are self-limited in thickness to about 150Å. The effects of deposition parameters such as temperature and WF₆ and H₂ flow rates on the properties of the W films have been investigated. To prevent excessive erosion of Si in window areas, the volumetric flow ratio of H₂ to WF₆ must be larger than the critical value of about three. Typical films are polycrystalline with an average grain size of 2000Å and exhibit a tensile film stress of about 7 × 10⁹ dyn/cm². W film resistivity is found to be about 13 μΩ-cm for a 1000Å film, resulting in a sheet resistance of 1.3 Ω/□. The W films exhibit good contact resistance to N⁺ and P⁺ Si, and are also found to be excellent diffusion barriers between Al and Si at annealing temperatures up to 450°C.

Tungsten (W) is a very useful metal for VLSI processing. As a diffusion barrier between Al and Si (1, 2), it prevents spiking (interdiffusion of Al and Si), thereby permitting the use of shallow junction contacts. As an alternative to aluminum and aluminum alloys for second-level metallization (3, 4), W has the advantage of superior electromigration resistance due to its high melting point. Therefore, although W has a higher resistivity than Al (5.3

μΩ-cm as opposed to 2.6 μΩ-cm) it may be a useful second-level metallization in circuits with high current densities and/or high operating temperatures.

W can be chemically vapor deposited by the hydrogen reduction of WF₆ or WCl₆ (1-6), or by the pyrolysis of W(CO)₆ (7, 8). For several reasons, the hydrogen reduction of WF₆ has proven to be the most favorable deposition chemistry. First, W can be deposited selectively from WF₆ and WCl₆, *i.e.*, W can be deposited on Si, silicides, and metals to the exclusion of SiO₂ (2, 9). The deposition of W

* Electrochemical Society Active Member.

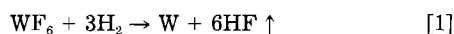
from $W(CO)_6$ does not exhibit such selectivity (8). W films deposited from WF_6 have an advantage over those deposited from WCl_6 : lower contact resistance to Si (4). Finally, WF_6 is a liquid that boils at about room temperature, whereas WCl_6 is a solid that melts at 275°C, making its use as a CVD source more difficult.

Although significant work has been devoted to CVD W, extensive characterization of the structural aspects of the films is lacking.

Deposition Chemistry

W can be chemically vapor deposited by the reduction of WF_6 at temperatures as high as 700°C (4, 6). However, by lowering the deposition temperature to approximately 300°C, one can achieve selective deposition of W on Si (2). This becomes very advantageous for diffusion barrier applications, because the W barrier layer can be deposited exclusively in the windows to N^+ or P^+ Si, as is shown in Fig. 1, thereby bypassing the usual patterning and etching steps.

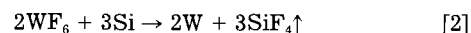
Extensive evaluation of the kinetic literature pertaining to the hydrogen reduction of WF_6 (10)



has led to the conclusion that the rate-limiting step in reaction [1] is the dissociation of H_2 into atomic hydrogen

(H) on the reaction surface. Therefore, selectivity is achieved by depositing at a temperature below which glass (e.g., thermally grown SiO_2 , phosphorus-doped glass grown by CVD, etc.) will not catalyze H_2 dissociation, but Si, with its thin ($\sim 20\text{\AA}$) native SiO_2 layer, will. At temperatures below about 400°C, this is apparently the case and selectivity is observed; above this temperature, W will deposit on both Si and glass simultaneously. In addition, even in the selective temperature regime, the selectivity mechanism is only operative for films of a given thickness. Once the selective W deposit reaches a thickness of about 2500Å, W begins to deposit on thermal SiO_2 . The exact thickness of W that can be deposited selectively on Si before nonselective deposition occurs depends upon the composition of the glass (9). For example, it has been found in this work that phosphorus-doped SiO_2 (PSG) tends to enhance selectivity more than thermal SiO_2 ; therefore, one can deposit thicker selective W films on devices surrounded by PSG than on devices surrounded by thermal SiO_2 . Compositional variations of the glasses lead to variations in selectivity behavior most probably because of differences in the etch rate of the glass by WF_6 (9). Obviously, if a fresh glass surface is being created, W film nucleation will be difficult.

An alternate reduction scheme for WF_6 exists, the so-called displacement reaction



in which Si reduces the WF_6 (3, 5). Displacement will compete with hydrogen reduction, Eq. [1], when hydrogen is present, and will occur exclusively when hydrogen is absent. Both reactions are thermodynamically possible, the free energy being -285 kcal/mol for the hydrogen reduction, Eq. [1], and -364 kcal/mol for displacement, Eq. [2], (both at 327°C).

The displacement of Si by WF_6 imparts some interesting structural features to the W film, with some important consequences for VLSI processing. First, the displacement reaction is self-limiting. Once a substantially thick film of W ($\sim 150\text{\AA}$) is formed by displacement, the reaction stops because the WF_6 can no longer diffuse through the W (product) film to react with the underlying Si. In addition, the reaction of WF_6 with Si causes erosion of the Si. As is demonstrated in the Appendix, about twice as much thickness of Si is consumed for a given thickness of W film formed.

The displacement reaction will not, in general, be self-limiting on a device wafer. This is because a fresh supply of Si, needed to react with WF_6 , is present at the Si/SiO_2 interfaces of the windows. Figure 2 illustrates an effect, called the "halo effect," which results from the erosion, by WF_6 , of the Si at the Si/SiO_2 interface of a device feature, in this case, a window. A self-limiting W film has formed in the center of the window area, (Fig. 2a and 2b), but the displacement reaction has then eroded the Si at the interface. Because the interface is a region of high stress, this erosion is a stress-assisted corrosion reaction reminiscent of many bulk metallurgical phenomena. Haloing can be so extensive that neighboring windows become completely linked under the SiO_2 (Fig. 2c).

The sample illustrated in Fig. 2 was grossly overexposed to WF_6 with no H_2 present, in order to produce a pronounced halo effect. By controlling the ratio of the hydrogen flow rate to the WF_6 flow rate during film deposition, haloing can be prevented. A simple explanation for this is that by controlling $\dot{V}_{H_2}/\dot{V}_{WF_6}$, where \dot{V} is the volumetric flow rate, the ratio of W produced by reduction to that produced by displacement is controlled. Figure 3 illustrates the effect of $\dot{V}_{H_2}/\dot{V}_{WF_6}$ on haloing behavior. In this figure, the extent of the halo effect is followed by optical microscopic investigation of windows on a device. When $\dot{V}_{H_2}/\dot{V}_{WF_6}$ is greater than about 20 (Fig. 3a), no haloing is observable. When H_2 is absent ($\dot{V}_{H_2}/\dot{V}_{WF_6} = 0$), haloing is seen to extend to the window-pad boundaries (Fig. 3c). An intermediate case, $\dot{V}_{H_2}/\dot{V}_{WF_6} \approx 5$, reveals the beginnings of haloing (Fig. 3b).

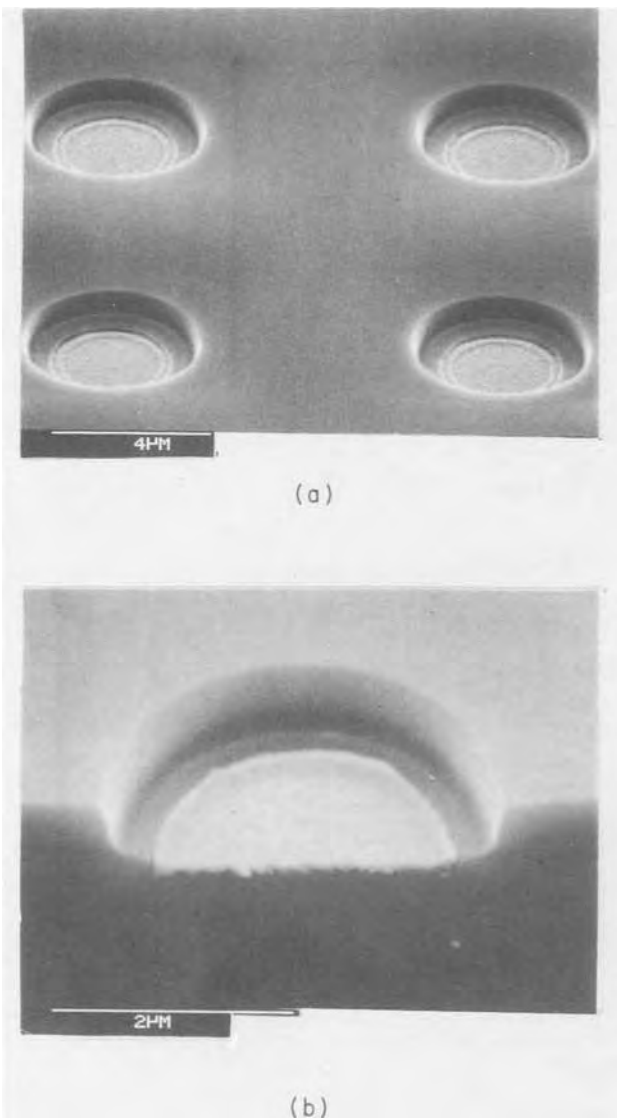


Fig. 1. Two views of CVD W selectivity deposited in windows to Si. Deposition conditions: 290°C, $P = 800$ mtorr; $\dot{V}_{H_2}/\dot{V}_{WF_6} = 20$. Larger opening of phosphorus-doped SiO_2 (thicker upper layer) is due to preferential dry etching of this layer as compared to undoped SiO_2 layer (thinner, lower layer) during opening of window.

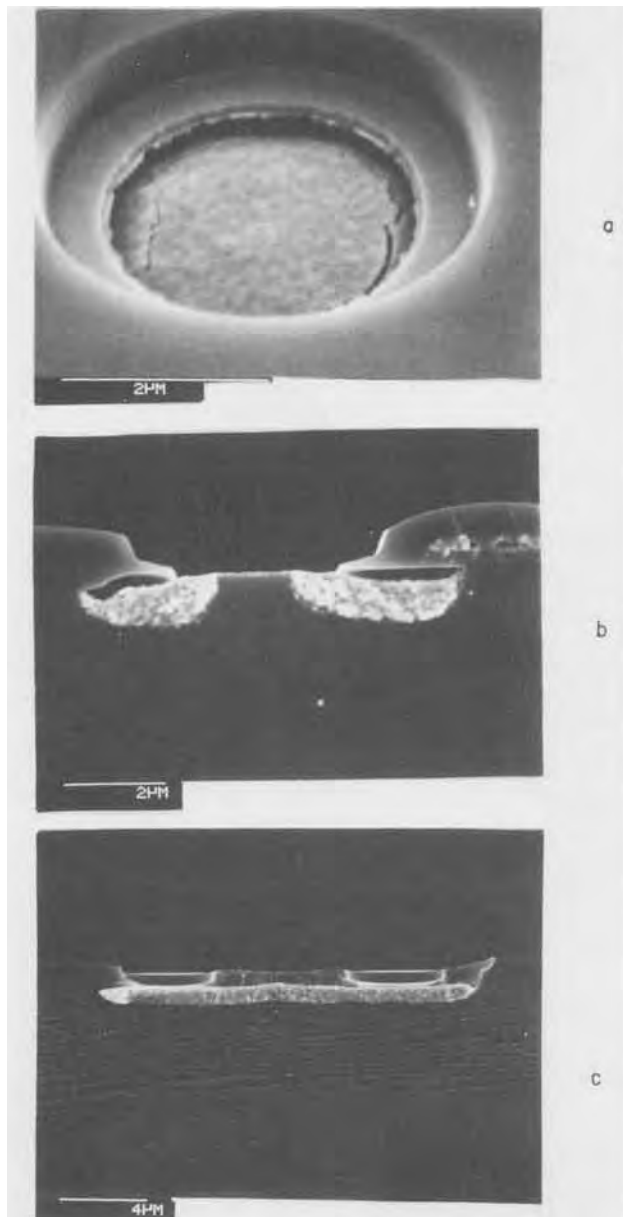


Fig. 2. Three views of the halo effect (stress-assisted corrosion) observed on a typical device wafer. Deposition conditions: 290°C ; $P = 600$ mtorr; $\dot{V}_{\text{H}_2}/\dot{V}_{\text{WF}_6} = 0$.

Film Deposition

The W films were deposited in a hot-wall CVD reactor, depicted in Fig. 4. Many different deposition schemes, based on the reduction and/or displacement reactions, with temperature, pressure, and H_2 and WF_6 flow rates as variables, were studied. All of the deposition schemes can be thought of as variations of the one- and two-step procedures outlined in Fig. 5. One-step processes involve deposition by reduction or displacement only. Two-step processes involve deposition by displacement followed by deposition by reduction.

The substrates consisted of 4 in. diam unpatterned (monitor) Si, SiO_2 , or TaSi_2 wafers, and device wafers. The Si monitors and the device wafers were precleaned by immersion in buffered 30:1 HF for 2 min, followed by a 10 min rinse in H_2O (18 MΩ quality) and spin drying. This resulted in Si surfaces with native oxides of $\sim 20\text{\AA}$, as measured by an ellipsometer. The SiO_2 and TaSi_2 monitors were precleaned in the same way, to remove some surface oxide and contamination. Usually, 40 wafers were placed in the furnace for each run. Depending upon whether a one-step or a two-step deposition procedure was used, the various steps outlined in Fig. 5 were followed. Deposition

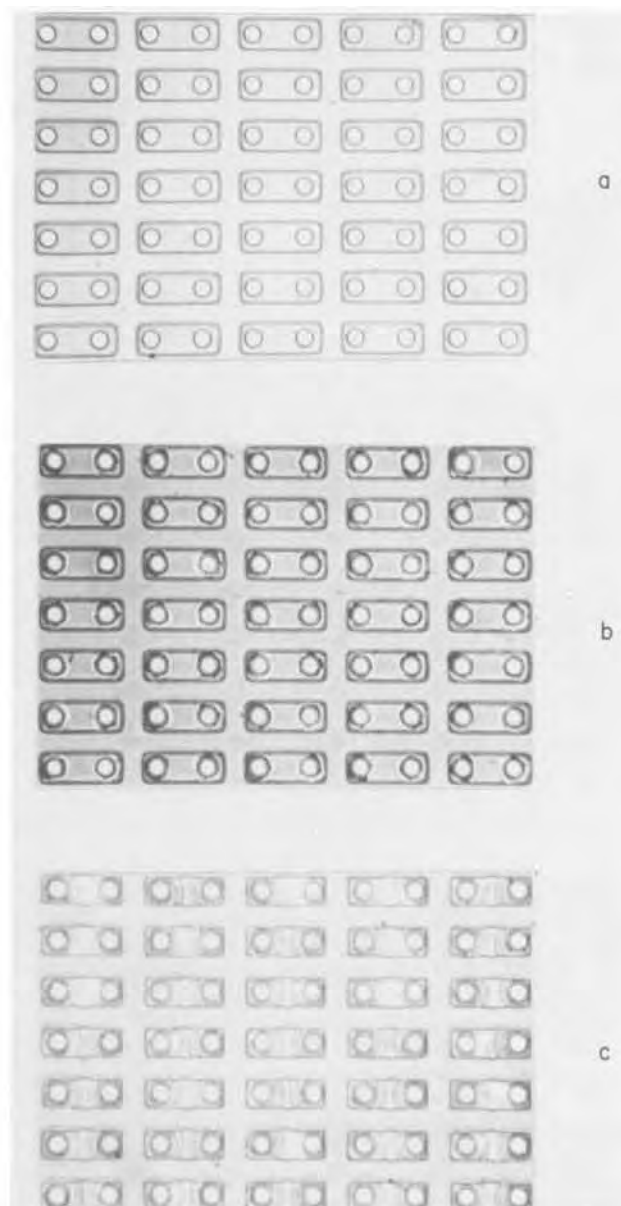


Fig. 3. Halo effect observed optically on a device wafer. Deposition conditions as follows. a: 290°C ; $P = 600$ mtorr; $\dot{V}_{\text{H}_2}/\dot{V}_{\text{WF}_6} \approx 20$. b: 290°C ; $P = 600$ mtorr; $\dot{V}_{\text{H}_2}/\dot{V}_{\text{WF}_6} \approx 5$. c: 290°C ; $P = 150$ mtorr; $\dot{V}_{\text{H}_2}/\dot{V}_{\text{WF}_6} = 0$. Circular features (windows) are $2.5\ \mu\text{m}$ diam.

temperatures were varied between 260° and 400°C . Deposition pressures ranged between 100 and 1000 mtorr. WF_6 , H_2 , and Ar flow rates were varied between 0.5 and 100 sccm, 100 and 2000 sccm, and 500 and 2000 sccm, respectively. Optional heat-treatments after deposition, to evolve gases trapped in the films or cause interdiffusion (silicidation) of W and Si, ranged between 290° and 750°C ,

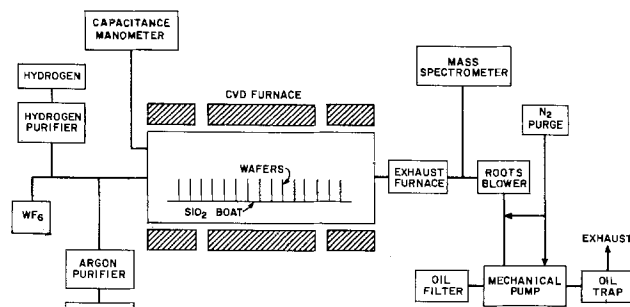


Fig. 4. Schematic diagram of apparatus used to deposit CVD W films

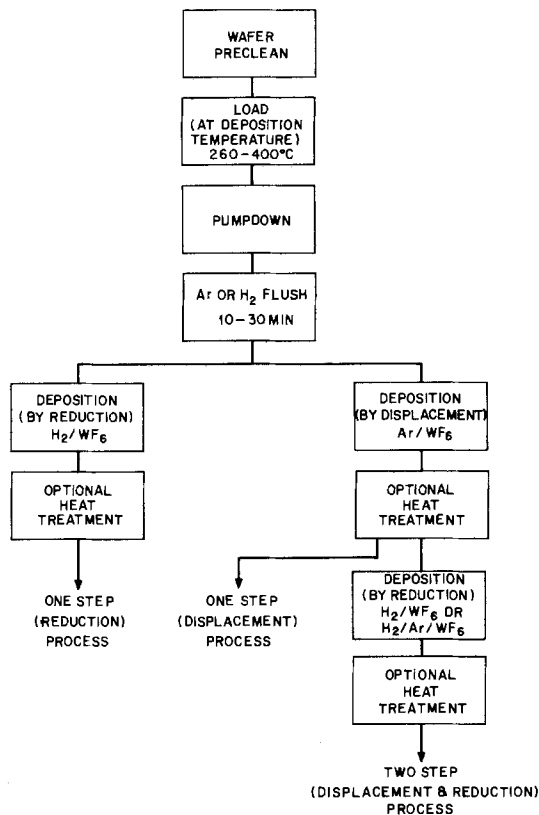


Fig. 5. Process flow diagram for one- and two-step selective CVD W

all for 30 min. The exhaust furnace (see Fig. 4), which was kept at 600°C, prevented unspent WF_6 from entering the pumping system. At the end of the deposition, which usually lasted between 20 min and 3h, depending upon deposition conditions, the wafers were removed.

The thickness of the W films was measured using a mechanical stylus profilometer on steps etched in the film. Steps are readily etched in W using 30% H_2O_2 . Figure 6 is a plot of W film deposition rate as a function of WF_6 flow rate for W films produced by hydrogen reduction. The data of Fig. 6 were gathered for deposition runs at essentially the same total pressures, in the range 600-800 mtorr. The flow-rate ratio, $\dot{V}_{H_2}/\dot{V}_{WF_6}$, is not constant for this data, but there was no satisfactory correlation between this ratio and the deposition rate. Rather, the deposition rate seems to be a function of the WF_6 flow rate only, implying that the deposition rate is controlled by the rate of WF_6 adsorption on the wafer surfaces. Our deposition conditions are therefore characterized as mass-transport limited. Films deposited by displacement (no

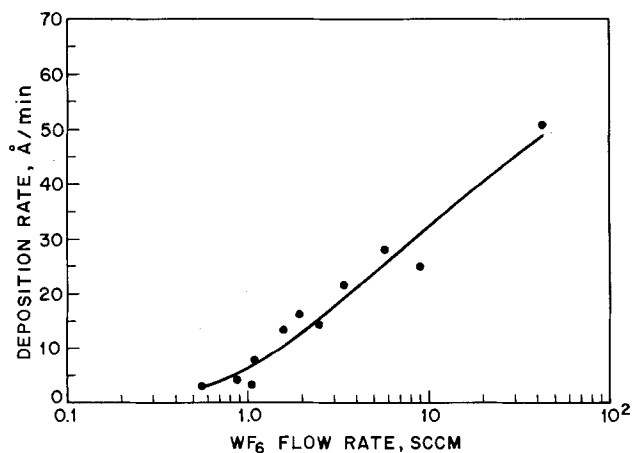


Fig. 6. Deposition rate as a function of WF_6 flow rate, for hydrogen-reduced W films. $P_{total} = 600-800$ mtorr; 290°C.

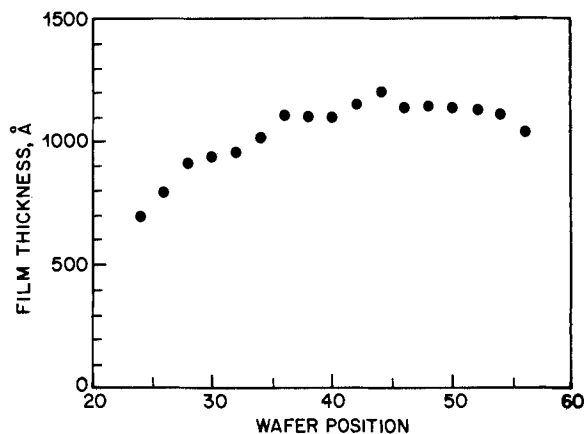


Fig. 7. Wafer-to-wafer uniformity (film thickness vs. wafer position) for a typical CVD W deposition.

hydrogen present) were self-limited to about 150Å in thickness at 290°C, and formed in less than 1 min. The deposition rate for displaced films is, therefore, faster than that of reduced films.

Figure 7 illustrates the wafer-to-wafer uniformity that can be achieved under typical experimental conditions. Forty Si wafers were placed back to back in a wafer boat, the spacing between each pair being 3/4 in. It can be seen from Fig. 7 that the 24 wafers between positions 34 and 56 are within $\pm 10\%$ of each other in thickness. More precise manipulation of the temperature gradient in the three-zone CVD furnace would have further extended the uniformity zone. Thickness variations on each wafer (center to edge) were $< 5\%$. This degree of wafer-to-wafer, as well as center-to-edge uniformity, is sufficient for W barrier technology, since the barrier thickness is not critical as long as it is thicker than about 400Å.

Film Characterization

Electrical resistivity.—The sheet resistance of the CVD W films was measured on a four-point probe. Figure 8 is a plot of sheet resistance, R_s , as a function of film thickness, for films produced by displacement and/or reduc-

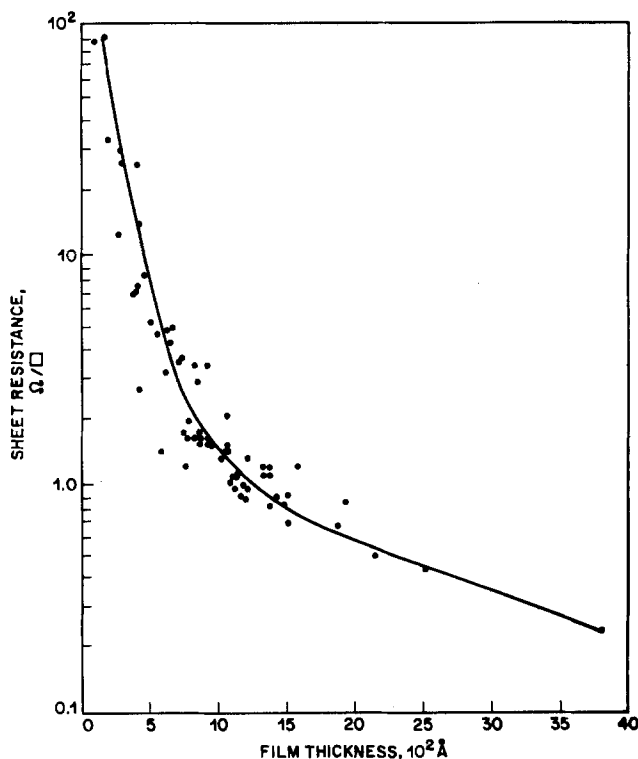


Fig. 8. Sheet resistance of selective CVD W films as a function of film thickness.

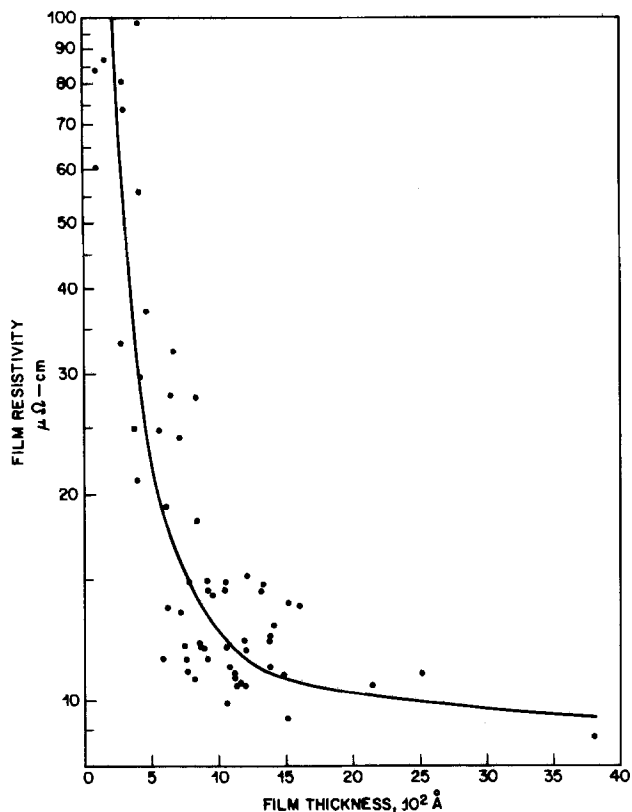


Fig. 9. Resistivity of selective CVD W films as a function of film thickness.

tion. The sheet resistance, when multiplied by the film thickness, is converted to film resistivity, which is plotted in Fig. 9 as a function of film thickness. Several observations can be made from Fig. 9. First, as film thickness increases, the resistivity decreases and tends toward the bulk resistivity of W, $5.3 \mu\Omega\text{-cm}$. Also, it can be seen that for films between about 500 and 1500Å , the film resistivity falls between 10 and $15 \mu\Omega\text{-cm}$, which is in very good agreement with earlier data (4). Finally, film resistivity increases dramatically for films less than 500Å thick. The increase is believed to be due in part to thin film electron scattering effects and due in part to the four-point probe's lack of precision in measuring voltage drops in this thickness range.

Film stress and adhesion.—Figure 10 is a plot of film stress vs. film thickness for selective CVD W on Si. All of the films whose stress data is represented in Fig. 10 were adherent to the Si substrates, *i.e.*, they did not come off when subjected to a transparent adhesive tape peel test. The stress is seen to be a maximum for films less than 400Å , a minimum for films between 500 and 600Å , and at

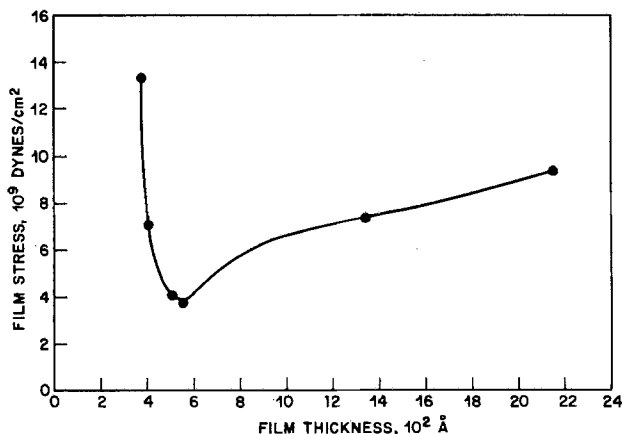


Fig. 10. Film stress vs. film thickness for CVD W films deposited on Si

an intermediate and fairly constant level for thicker films. Figure 10 can be interpreted in terms of an interfacial stress and a volume stress. The largest contribution to the residual film stress usually comes from the interfacial stress. For the thin W films, the stress is dominated by this contribution, which falls off rapidly away from the interface (thicker films), at which point the largest contribution to the stress is the volume-generated stress. The combination of these two stress contributions gives rise to a stress-thickness curve reminiscent of Fig. 10 (11). The observed stress is tensile, which is contrary to that observed in earlier CVD W films (4). However, those films were significantly thicker ($>1 \mu\text{m}$), and were deposited at higher temperatures ($\sim 700^\circ\text{C}$); therefore, the stress state is likely to be different.

Table I is a summary of film adhesion data based on the transparent adhesive tape peel test. It can be seen that displaced films tend to adhere to the Si. Hydrogen-reduced films show an increasing tendency to adhere to the Si as the volumetric flow-rate ratio, $\dot{V}_{\text{H}_2}/\dot{V}_{\text{WF}_6}$ increases. Two-step films tend not to adhere to Si unless they are given a postdeposition anneal at 450°C , or if the second step (reduction) occurs at 350°C . The fact that raising only the first-step (displacement) temperatures $\geq 350^\circ\text{C}$ does not give rise to adhesion implies that the adhesion inhibiting mechanism is active in the reduction step. These results will be explained later in terms of the deposition chemistry.

CVD W films deposited on TaSi_2 were always adherent and generally had lower stress than the films deposited on Si, *i.e.*, 0 to $3 \times 10^9 \text{ dyn/cm}^2$ (tensile). W films on TaSi_2 showed no stress dependence on film thickness.

Film microstructure.—Figure 11 is a TEM photomicrograph of a typical W film, showing that it is composed of grains ranging between 1000 and 3000Å in diameter. Figure 12 is an x-ray diffraction pattern of a typical W film, compared to a stick figure pattern of a randomly oriented W standard. It can be seen that the grains comprising the W film are randomly oriented in the film, as there is a one-to-one correlation between observed and standard intensities.

Figure 13 is a TEM photomicrograph of a W film deposited on a Si window, exhibiting a tunnel-type defect in the Si substrate. That the defects are actually tubular voids has been proven by contrast experiments in the TEM. The tunnels are observed only at the rim of the window, suggesting that the interfacial stress present there has aided in their nucleation. The tunnels are not observed in Si onto which W has been deposited solely by displacement (no hydrogen). Therefore, HF gas, a by-product of W deposition by reduction with hydrogen, is

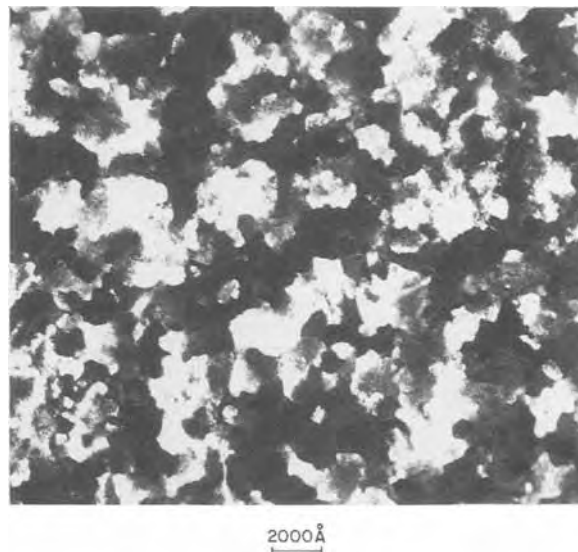


Fig. 11. Darkfield transmission electron photomicrograph of a W film deposited by the two-step procedure at 290°C .

Table I. Film adhesion results

Film	Number of runs for which monitor wafers were adhesion tested	Percentage of these runs for which wafers exhibited 100% adhesion of Si on W ^a	Comments
Single step (displacement), 290°C	9	78%	$\dot{V}_{\text{H}_2}/\dot{V}_{\text{WF}_6} < 20$ $\dot{V}_{\text{H}_2}/\dot{V}_{\text{WF}_6} = 20$ $\dot{V}_{\text{H}_2}/\dot{V}_{\text{WF}_6}$ between 100 and 500 $\dot{V}_{\text{H}_2}/\dot{V}_{\text{WF}_6}$ between 800 and 3000
Single step (reduction), 290°C	2	50%	
	23	57%	
	11	73%	
Two Step			
Displacement 290°C, reduction 290°C	11	9%	
Same, plus 450°C/15 min postdeposition anneal	10	80%	
Displacement $T \geq 350^\circ\text{C}$, reduction 290°C	3	0%	
Displacement 350°C, reduction 350°C	2	100%	

^a Transparent adhesive tape test.

thought to be the agent responsible for attacking the Si and etching out the tunnels.

Silicidation experiments.—Attempts were made to form WSi_2 from the deposited W films by reaction with the Si substrates. As is illustrated in Fig. 14b, a temperature of 750°C is sufficient to cause all of the W to convert to WSi_2 (tetragonal form). Since the W did not react at 675°C (Fig. 14a), the silicide formation temperature is somewhere between 675° and 750°C. This is in good agreement with earlier data (12). We did not observe the hexagonal form of WSi_2 at lower reaction temperatures, as has been reported (12).

Discussion

Our results demonstrate that high quality, selective CVD W films can be grown in a reproducible manner. We would like to discuss the observations of haloing behavior and film adhesion in some detail, as they are very

much related to film processing history and reveal important subtleties of CVD W processing.

Haloing behavior, depicted in Fig. 2 and 3, is the stress-assisted reaction between WF_6 and exposed Si. As such, one would expect the state of stress at the Si/SiO₂ interface to influence the course of this reaction. We believe that this influence is illustrated in Fig. 3c, where haloing behavior is observed to be nearly complete under the SiO₂ pads that contain the windows to Si, but is observed to stop abruptly at the pad boundaries. Whereas the pads are comprised of $\sim 1 \mu\text{m}$ of PSG on top of 1000Å of undoped SiO₂, both deposited by LPCVD at 430°-460°C, the oxide between the pads is field oxide, $\sim 7000\text{Å}$ thick, and is grown at 950°C. The LPCVD film stress is about $3 \times 10^9 \text{ dyn/cm}^2$ (tensile) (13), whereas the thermal oxide stress is approximately zero (14). Therefore, it is believed that the near-zero stress state of the field oxide prevents the WF_6 attack of the underlying Si from spreading.

Adhesion tests, using the transparent adhesive tape peel method, were carried out on at least one Si monitor wafer placed in every run. Variables such as room humidity, change of gas cylinders, and slight unintentional variations in wafer cleaning procedure resulted in less than 100% predictability of film adhesion. However, as the adhesion data of Table I reveal, there are several interesting

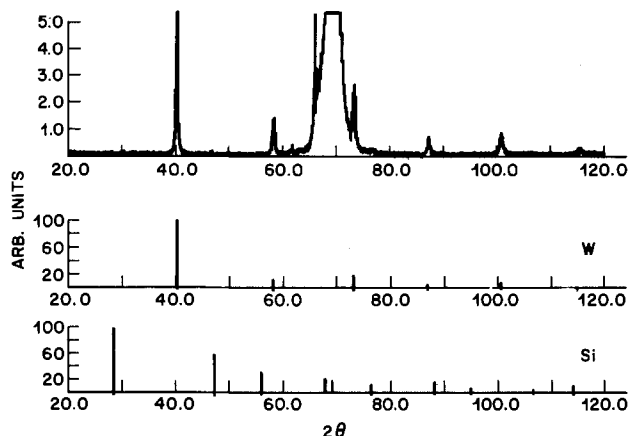


Fig. 12. X-ray diffraction pattern of a typical selective CVD W film, deposited on (100) Si at 290°C. The one-to-one intensity correlation between the observed pattern and the W standard (stick figure), indicates that the film is composed of randomly oriented grains.



Fig. 13. TEM of a W film deposited on a window to Si on a tester device (wet-etched window). Note tunnels in the Si emanating from the window edges.

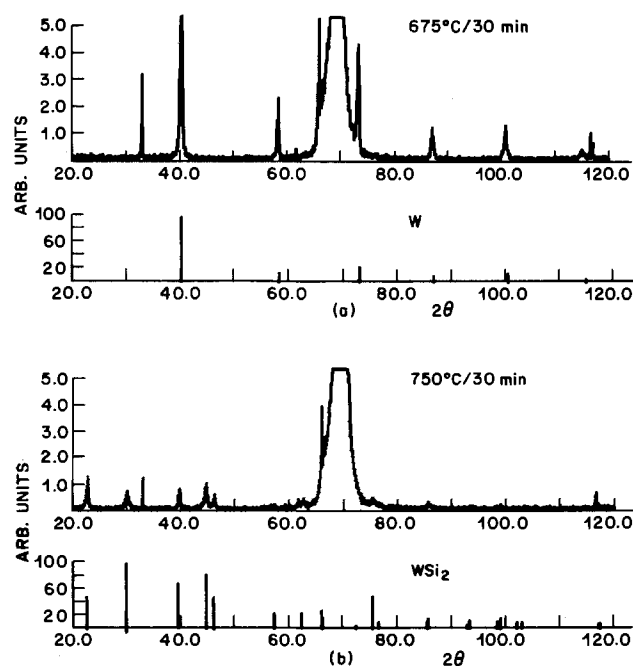


Fig. 14. X-ray diffraction patterns of typical selective CVD W films, deposited on (100) Si at 290°C, and reacted with Si substrate at 675°C for 30 min (top) and 750°C for 30 min (bottom) both in hydrogen.

trends in adhesion behavior that are related to deposition processing.

The data in Table I suggest that a chemical species causes lack of adhesion. This is most strikingly demonstrated for the two-step films, where it can be observed that films deposited at 350°C, or postdeposition annealed at 450°C after 290°C deposition, exhibit good adhesion. However, two-step films deposited at 290°C rarely exhibit adhesion in the as-deposited state. Although information is lacking regarding low temperature interactions between W and Si, it is likely that there is no significant interdiffusion between the two at temperatures less than about 500°C. Therefore, the effect of the higher deposition temperature and postdeposition anneal is most probably the evolution of the chemical species, thereby restoring adhesion.

There is much circumstantial evidence to support this hypothesis. First, Table I shows, for the case of single-step reduced films, that adhesion is possible at 290°C, if $\dot{V}_{H_2}/\dot{V}_{WF_6}$ is large enough, further suggesting that lack of adhesion is due to some sort of interfacial film. That the adhesion improves as $\dot{V}_{H_2}/\dot{V}_{WF_6}$ increases indicates that the species causing lack of adhesion might be a reaction by-product, which is diluted and pumped out to a greater extent when this ratio is high. Furthermore, in some 40-wafer runs, the films in the front of the reactor (furthest from pumps, upstream of flowing gases, see Fig. 4), adhered, whereas those near the back did not. Again, the reason may be the preferential incorporation of larger amounts of by-products in wafers positioned in the back of the reactor, as that is where their concentration will be highest.

Some recent work on the computer analysis of the thermodynamics of CVD W on a variety of substrates has rationalized the adhesion behavior in terms of the formation of reaction by-products (15). Poor adhesion of W is observed on substrates that form nonvolatile fluorides during reduction of WF_6 . Therefore, the lack of adhesion observed for certain W films deposited on Si can be due to the presence of, for example, WF_4 , which has previously been identified as the cause of porosity in CVD W thermionic emitters (16). WF_4 melts at 502°C and boils at 627°C, and therefore becomes increasingly volatile as temperatures increase; however, it would be nonvolatile at our deposition temperatures. As many subfluorides (*i.e.* WF_3 , WF_2 , etc.) probably exist (17), others of them can be invoked to explain the lack of adhesion. The existence of partially reduced WF_6 compounds is even more likely as the concentration of H_2 is decreased; therefore, it is not surprising that adhesion gets worse as $\dot{V}_{H_2}/\dot{V}_{WF_6}$ decreases. Finally, since the free energy for Si reduction of WF_6 exceeds that of the H_2 reduction at 327°C (-364 *vs.* -285 kcal/mol), one would expect there to be more reduction of WF_6 , and, therefore, less incorporation of W subfluorides in displaced films. This is supported by the observation from Table I that single-step displaced films almost always adhere. Indeed, lack of adhesion is determined during the hydrogen reduction step, as two-step films, even those whose displacement step has occurred at $T \geq 350^\circ\text{C}$, do not adhere after a 290°C reduction step, as is indicated in Table I.

Conclusions

W films have been chemically vapor deposited by the reduction of WF_6 , and extensively characterized. W films can be deposited selectively, *i.e.*, on Si and TaSi₂ to the exclusion of SiO₂, thereby eliminating the need for patterning and etching of a diffusion barrier layer. Whereas W films of unlimited thickness can be deposited by H_2 reduction of WF_6 , W films formed by Si reduction (displaced films), are self-limited to about 150Å in thickness. However, on actual device wafers, uncontrolled displacement reaction (haloing) can occur if the volumetric flow-rate ratio, $\dot{V}_{H_2}/\dot{V}_{WF_6}$, is between zero and approximately 15. Haloing behavior is aggravated by a high stress state at the Si/SiO₂ interface of device features.

W films were deposited by H_2 and/or Si reduction of WF_6 , under a variety of temperatures and pressures. The hot-wall, horizontal CVD reactor was mass-flow limited, *i.e.*, the W growth rate was proportional to the WF_6 flow rate. The films were specular, with resistivity of $\sim 13 \times 10^{-6} \Omega\text{-cm}$, and a sheet resistance of 1.3 Ω/\square for a 1000Å thick film. The films are composed of grains averaging 2000Å diam, and have a tensile film stress of about 7×10^9 dyn/cm². Film adhesion was almost always observed if any of the following steps were taken: deposition at 350°C, deposition at 290°C followed by a 450°C postdeposition anneal, or the use of very high H_2 to WF_6 volumetric flow-rate ratios. That these steps lead to adhesion suggests that the incorporation of nonvolatile WF_x (W subfluoride) into the W at the 290°C deposition temperature is the cause of the lack of adhesion sometimes observed.

CVD W films are excellent diffusion barriers between Al and Si. In view of the physical attributes of the films reported here and the convenience of depositing selective W, these films are good candidates for diffusion barriers in shallow junction VLSI technologies.

Acknowledgments

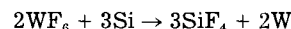
The authors would like to acknowledge the help of P. K. Gallagher (evolved gas analysis), R. Knoell (TEM), L. Lecheler (preparation of substrates), and T. McGahan (SEM). Helpful discussions were had with S. Hillenius, W. Lai, and L. Parrillo.

Manuscript submitted Nov. 27, 1984; revised manuscript received Jan. 7, 1985. This was Paper 416 presented at the New Orleans, Louisiana, Meeting of the Society, Oct. 7-12, 1984.

AT&T Bell Laboratories assisted in meeting the publication costs of this article.

APPENDIX

During the displacement reduction of Si by WF_6



what thickness of Si is consumed in forming a W film of a certain thickness?

$$V_w = A_w t_w = \frac{m_w}{\rho_w} = \frac{n_w MW_w}{\rho_w}$$

where V_w is the volume of W film, A_w the area of W film, t_w the thickness of W film, m_w the mass of W film, ρ_w the density of W (19.3 g/cm³), n_w the number of moles of W in the film, and MW_w the molecular weight of W (183.85 g/mol). Therefore

$$n_w = \frac{A_w t_w \rho_w}{MW_w}$$

similarly

$$n_{Si} = \frac{A_{Si} t_{Si} \rho_{Si}}{MW_{Si}}$$

where n_{Si} is the moles of Si displaced by W, A_{Si} the area of Si displaced by W, t_{Si} the thickness of Si displaced by W, ρ_{Si} the density of Si (2.33 g/cm³), and MW_{Si} the molecular weight of Si (28.09 g/mol). For every mole of W formed, 3/2 mol of Si are required. Therefore

$$n_{Si} = \frac{3}{2} n_w$$

or

$$\frac{A_{Si} t_{Si} \rho_{Si}}{MW_{Si}} = \left(\frac{3}{2}\right) \frac{A_w t_w \rho_w}{MW_w}$$

but

$$A_{Si} = A_w$$

Therefore

$$\frac{t_{Si}}{t_w} = \left(\frac{3}{2}\right) \left(\frac{\rho_w}{\rho_{Si}}\right) \left(\frac{MW_{Si}}{MW_w}\right) = \left(\frac{3}{2}\right) \left(\frac{19.3}{2.33}\right) \left(\frac{28.09}{183.85}\right)$$

$$\frac{t_{Si}}{t_w} = 1.90$$

The thickness of Si consumed to form a W film of thickness t_w by displacement is, therefore, about twice t_w .

REFERENCES

1. N. E. Miller and I. Beinglass, *Solid State Technol.*, **25** (12), 85 (1982).
2. P. A. Gargini, *Ind. Res. Dev.*, **25**, 141 (1983).
3. J. M. Shaw and J. A. Smith, *RCA Rev.*, **31**, 306 (1970).
4. C. M. Melliar-Smith, A. C. Adams, R. H. Kaiser, and R. A. Kushner, *This Journal*, **121**, 298 (1974).
5. C. R. Crowell, J. R. Sarace, and S. M. Sze, *Trans. Met. Soc. AIME*, **233**, 478 (1965).
6. N. E. Miller and I. Beinglass, *Solid State Technol.*, **23** (12), 79 (1980).
7. G. J. Vogt, *J. Vac. Sci. Technol.*, **20**, 1336 (1982).
8. M. Diem, M. Fisk, and J. Goldman, *Thin Solid Films*, **107**, 39 (1983).
9. J. J. Cuomo, in "Proceedings of the 3rd International Conference on Chemical Vapor Deposition," F. A. Glaski, Editor, p. 270, American Nuclear Society, LaGrange Park, IL (1972).
10. W. A. Bryant, *This Journal*, **125**, 1534 (1978).
11. R. W. Hoffman, in "Physics of Nonmetallic Thin Films," C. H. S. Duprey and A. Cachard, Editors, pp. 273-354, Plenum Press, New York (1974).
12. S. P. Murarka, M. H. Read, and C. C. Chang, *J. Appl. Phys.*, **52**, 7450 (1981).
13. A. C. Adams, Private communication (1984).
14. L. E. Katz, Private communication (1984).
15. M. Boman and J. Carlsson, in "Chemical Vapor Deposition," McD. Robinson, G. W. Cullen, C. H. J. van den Brekel, and J. M. Blocher, Jr., Editors, p. 150, The Electrochemical Society Softbound Proceedings Series, Pennington, NJ (1984).
16. F. A. Glaski, in "IEEE Conference Record: 1970 Thermionic Conversion Specialists Conference, "Miami Beach, Fla., 1970," p. 72, IEEE, New York (1970).
17. A. Glassner, Argonne National Laboratory Report ANL-5750, Argonne, IL.

Hydration and Carbonation of Beta Alumina Powders

A. Marini, G. Flor, and V. Massarotti

Dipartimento di Chimica Fisica, Universita di Pavia, Pavia, Italy

A. R. McGhie and G. C. Farrington*

Laboratory for Research on the Structure of Matter, University of Pennsylvania, Philadelphia, Pennsylvania 19104

ABSTRACT

The absorption of water by powders of sodium, potassium, and lithium beta alumina was observed using thermogravimetric analysis (TGA), differential scanning calorimetry (DSC), and x-ray powder diffraction. For samples derived from Union Carbide beta alumina, no water absorption/adsorption was observed for potassium beta alumina, about 2.1 molecules of water per unit cell for sodium beta alumina, and about 4 molecules per unit cell for lithium beta alumina. All of these results are at 25°C with the composition at 400°C as a base line. Some samples also were observed to react with CO₂ in the presence of water to form complex hydrated carbonates, which underwent multistage decomposition reactions upon heating.

Since the rediscovery of the beta aluminas (1, 2), it has been widely recognized that various compounds of this family react with water. The effects of hydration vary greatly. Water absorption by sodium beta alumina, for example, decreases its Na⁺ ion conductivity (3). In contrast, a high water content is essential for high conductivity in various protonic beta⁺ aluminas (4). Hydration reactions of powders of the beta aluminas can influence their behavior during forming and sintering into polycrystalline ceramics.

Over the past few years, the absorption of water by various beta aluminas has been investigated extensively. A complete picture of the phenomenon does not yet exist. It is complicated by the many ions which can substitute for sodium in the beta aluminas, their nonstoichiometric compositions, and the fact that their hydration reactions may be influenced by particle size.

Beta (typically M_{1.24}Al₁₁O_{17.12}) and beta⁺ alumina (typically M_{1.67}Mg_{0.67}Al_{10.33}O₁₇) in which M is Na⁺, Li⁺, (4, 5) or H⁺ (6) are known to hydrate in air at room temperature. Most experimental evidence indicates that water is not localized in cracks or micropores but enters the conduction planes and is bulk rather than surface water. The extent of hydration is strongly influenced by the identity of the mobile ion. Na⁺ beta alumina absorbs less water than Li⁺ beta alumina. In contrast, even with powder samples, we have been unable to measure any water uptake for Ag⁺, K⁺, Tl⁺, and Rb⁺ beta aluminas (7). To our knowledge, a phase diagram for a water/beta alumina system has only been explored for Li⁺ beta alumina above 200°C (8), a temperature range in which water diffuses more rapidly in the compound but in which the hydration equilibrium is

shifted toward a lower bulk water content. The study, by Dudney *et al.* (8), found the maximum hydration state of Li⁺ beta alumina single crystals to be 1.6 water molecules per unit cell at 235°C.

The hydration reactions of the beta aluminas are quite complex. Considerable spectroscopic evidence indicates that water can dissociate in the compounds and that a number of different water complexes can exist (8-10). Kuhns *et al.* (11), Hayes *et al.* (12), and Dunn (3) have suggested that, during hydration, the sodium in beta⁺ alumina ceramics is replaced by protonic species. They suggested that the sodium migrates to the surface to form hydroxides, which can react with CO₂. These reactions can be reversed by heating.

This paper reports the results of our recent investigations of the hydration and carbonation of Na⁺ and Li⁺ beta alumina powders. It demonstrates that the hydration reactions of beta alumina are strongly influenced by the

Table I. Rapid hydration of Li beta alumina at various temperatures (particle size <44 μm, sample prepared by exchange in LiNO₃)

T (°C)	Water uptake % (weight) increase
20	1.2
60	3.2
96	3.0
130	3.1
178	1.9
208	1.2
230	0.6

*Electrochemical Society Active Member

source of the material, that powder samples absorb more water than single crystals, and that carbonation reactions occur readily with various powdered beta and beta' aluminas.

Experimental Description

Beta aluminas from four sources were examined.

1. *Melt-grown Na⁺ beta alumina obtained as single crystals from the Union Carbide Corporation.*—The composition of the crystals was determined to be Na_{1.22}Al₁₁O_{17.12} by measuring the weight change after complete substitution of Na⁺ by Ag⁺. Single-crystal samples were ground to fine powders, and a set of sieves from 40 to 400 mesh was used to select powder fractions. Powders with average grain sizes of about 20 and 10 μm were obtained by further grinding of the finest fraction. The particle size distributions were determined with a Coulter (TM) Counter particle analyzer.

1. *Mg-stabilized Na⁺ beta alumina crystals grown by the flux evaporation method (13).*—Crystals were grown at several different temperatures between 1650° and 1700°C and had compositions of Na_{1.67}Mg_{0.67}Al_{10.33}O₁₇ based on the weight change observed after Na⁺ exchange with Ag⁺.

3. *Monofrax Na⁺ beta alumina from the Carborundum Corporation.*—This had a particle size of 44-105 μm.

4. *Na⁺ beta alumina that was synthesized as a powder from sodium carbonate and alumina.*—Powder x-ray diffraction analysis detected no phases other than sodium beta alumina. The particles nearly all passed through a 44 μm sieve. This material was by no means as well characterized as the previous three. Because it was not derived from a well-analyzed single crystal, its behavior cannot be considered to define the intrinsic properties of sodium beta alumina. Nevertheless it is included here because it is an example of the kind of beta alumina from which polycrystalline tubes are prepared.

Beta alumina containing ions other than Na⁺ was synthesized by ion exchange. Li⁺ beta alumina was prepared from large single crystals of Union Carbide sodium beta alumina by ion exchange in either LiCl at 650°C or LiNO₃ at 350°C. K⁺ beta alumina was prepared from the same Union Carbide starting material by ion exchange in molten KNO₃ at 350°C. All salts were greater than 99.99% pure, and the molten salt baths were changed three or four times in order to maintain a low Na⁺ concentration. The weight change measured on large single crystals was that expected for the complete replacement of Na⁺.

Thermal analysis was carried out with du Pont 990 and 1090 systems. The crystallographic parameters of the samples were obtained with an x-ray powder diffractometer equipped with a thermal attachment which permitted control of both temperature (−180° and 900°C) and atmosphere.

Results and Discussion

Union Carbide Na⁺ beta alumina.—A TGA for a sample of Na⁺ beta alumina with grain size 44 μm < d < 63 μm in dry nitrogen is shown in Fig. 1, along with a DSC analysis for the same material. The DSC plot includes a base-line trace observed with a sample of K⁺ beta alumina. Both the Na⁺ and K⁺ beta alumina powders had been exposed to air for one year at room temperature after grinding.

The TGA results indicate that water desorption occurs by a process which is well described by first-order kinetics. No further weight loss was observed from 300° to 1000°C. In the DSC trace, the expected endotherm was seen in the same temperature region as the dehydration in the TGA plot. A small but reproducible deviation in the exothermic direction sometimes occurred near 250°C. The endothermic peak in the DSC plot gives an enthalpy of dehydration of 14.5 kcal/mol H₂O. Similar values of dehydration enthalpies were obtained for samples which were exposed to air for shorter times and contained less water than that of Fig. 1.

A previous report (5) indicated that water uptake in powder samples of this type occurs in two steps: a fast

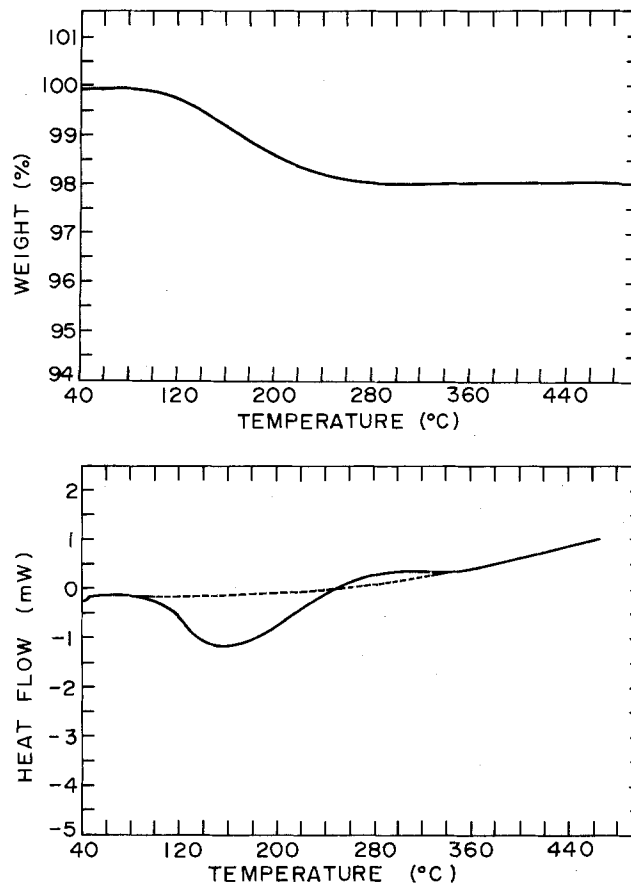


Fig. 1. TGA (top) and DSC (bottom) results for Union Carbide Na⁺ beta alumina powder in nitrogen. Particle size distribution: 44 μm < d < 63 μm.

one which may affect only a narrow band near the surface, and a slow one which is controlled by two-dimensional diffusion into the bulk. The previous work obtained a good fit of the grain size dependence for the fast uptake process by assuming that it involved a 3.3 μm wide band at the crystal surface which was uniformly filled with one water molecule for each sodium ion. We have checked this model by measuring the weight lost during heating of Na⁺ beta alumina samples having an average grain size of 10 μm. Samples which were allowed to stand for a few hours in air after grinding had a weight loss that corresponded to 2.8 weight percent (w/o) water (1.9 H₂O/unit cell), which agrees well with the model. After several weeks or months in air, samples gained slightly more water, 3.10-3.15 w/o (2.10-2.13 H₂O/unit cell).

The chemical diffusion coefficient of water in Na⁺ beta alumina was estimated from the rate of weight increase of the Na⁺ beta alumina powder with particle diameter (d) < 44 μm and was found to be 2 × 10⁻¹³ cm²s⁻¹ at 27°C and 1 × 10⁻¹² cm²s⁻¹ at 50°C. These data correspond to an activation energy for diffusion of 0.56 eV, a figure which is clearly quite uncertain, because only two points were used to obtain it.

The chemical diffusion coefficients are also average values. They were calculated assuming a uniform particle radius of d = 33 μm, even though the actual sample had a distribution of particle sizes. The radius of 33 μm was chosen because it yielded the best fit to the data. In addition, during the portion of the diffusion-controlled uptake that was analyzed, the overall water content changed from 1 to 2.5% by weight. There is no reason to assume that the diffusion coefficient of water is independent of its concentration.

Monofrax Na⁺ beta alumina.—The total weight loss of a sample of particle size d < 45 μm which had been exposed to air for two months at room temperature after grinding was 2.6% (see Fig. 2), about the same as for the

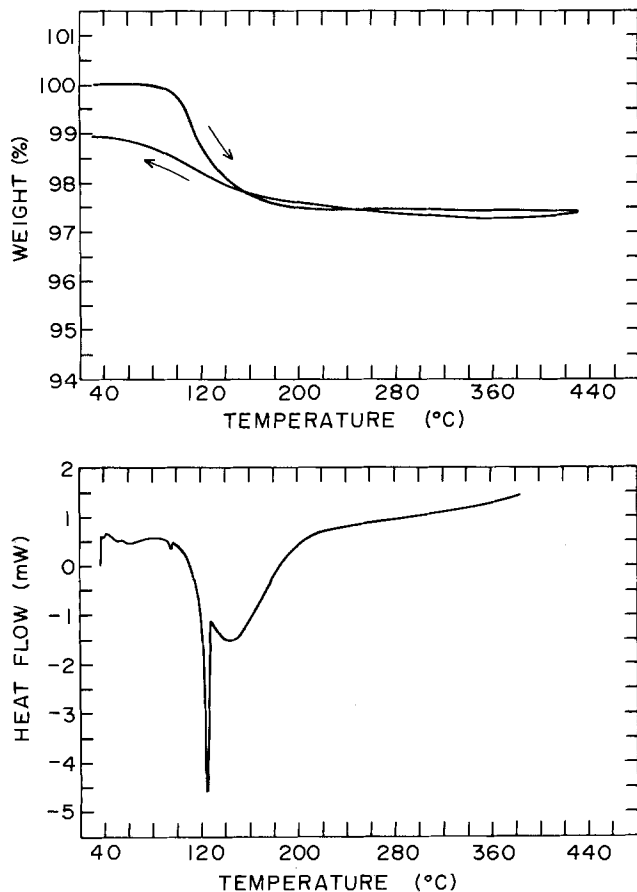


Fig. 2. TGA (top) and DSC (bottom) results for Monofrax Na⁺ beta alumina powder in nitrogen. Particle size distribution $d < 44 \mu\text{m}$.

Union Carbide material described in the previous section. However, as Fig. 2 shows, the TGA and DSC plots for the dehydration of this sample are very different from those for the Union Carbide material. The sharp peak in the DSC plot corresponds to the rapid weight loss of about 1% which occurs at 115°C. Sharp peaks around 100°C have also been observed with beta^{''} alumina and type 4 beta alumina. They are believed to be due to the decomposition of products formed on the surface of powders exposed to ambient air for extended periods of time. Possible products are discussed later in this paper.

Union Carbide K⁺ beta alumina.—No evidence of hydration or dehydration reactions was observed with TGA and DSC analysis of finely ground powders of K⁺ beta alumina prepared by ion exchange from Union Carbide Na⁺ beta alumina crystals.

Union Carbide Li⁺ beta alumina.—The general phenomena of water absorption/desorption in Li⁺ beta alumina are qualitatively similar to the parent sodium compound. However, preparation conditions appear to influence the hydration reactions of Li⁺ beta alumina. Fine powders of Li⁺ beta alumina prepared by ion exchange in molten LiNO₃ and equilibrated in air lost considerably more water, 6.2-6.3 w/o (4.2 H₂O/unit cell) vs. 3.0-3/2 w/o (2.1 H₂O/unit cell), than comparable powders of Na⁺ beta alumina when heated from 100° and 400°C. Weight losses observed with samples prepared by ion exchange in LiCl were systematically lower, typically 5.1-5.2 w/o (3.4 H₂O/unit cell).

We also have observed that the amount of water absorbed by Li⁺ beta alumina depends on grain size. Figure 3 illustrates the water lost upon heating of freshly ground powders of LiCl-exchanged beta alumina as a function of grain size. TGA analysis of the crystals before crushing showed about 1.5% weight loss to 400°C. After grinding, samples were exposed to air for about 12h, then heated to 400°C at 1°C/min and held at 400°C until constant weight was attained.

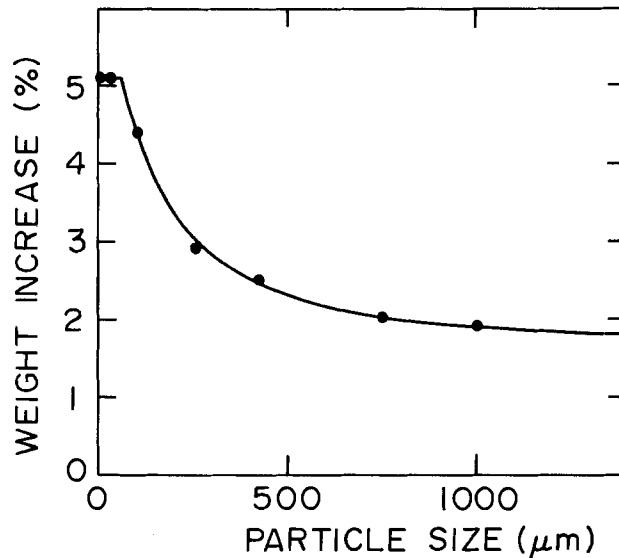


Fig. 3. Weight loss of Li⁺ beta alumina powders upon heating from 25° to 400°C, as a function of particle size. Samples prepared by ion exchange in LiCl.

The solid curve in Fig. 3 has been drawn according to a model which assumes that the grains homogeneously hydrate to a level of 1.5 w/o (1 H₂O/unit cell) and that those portions of the grains within 30 μm of the surface hydrate to a maximum water content of 5.1 w/o (3.4 H₂O/unit cell). The penetration depth and maximum hydration level were chosen to give a best fit to the data. The data actually do appear to reach a limiting hydration level of about 5.2 w/o for particle sizes less than 50 μm, which is consistent with this model. A similar experiment and model for sodium beta alumina gave a penetration depth of 3.3 μm and no background water in the crystals (5).

Changes in the c-lattice parameter for a Li⁺ beta alumina powder exchanged in LiNO₃ ($d < 45 \mu\text{m}$) were measured during heating/cooling cycles. The data are plotted in Fig. 4 along with the results of parallel TGA experiments. Regardless of the water content, the c-axis expands as the sample is heated from 60° to 140°C. It contracts from 140° through 300°C, the region in which most of the water is lost, and then expands again above 300°C. When a sample is then cooled to 160°C in dynamic vacuum, only the expected thermal contraction is observed. Although it was possible to cool samples to 160°C without significant water uptake, it was never possible to prepare anhydrous Li⁺ beta alumina powders ($d < 45 \mu\text{m}$) at room temperature. Weight increases were always observed when samples were cooled below about 60°C, even if the experiment was carried out under dynamic vacuum (10^{-3} torr or lower) or under a flow of dry gas.

The Li⁺ beta alumina samples lost no weight between 400° and 750°C, but they lost about 0.5% between 750° and 850°C. The source of this weight loss is not known, but it is irreversible and accompanied by a number of changes in the sample. X-ray powder diffraction patterns were taken for a sample before and after being held for 16h at 850°C. After heating, the formerly transparent crystals were opaque and no longer reacted with water. These results are consistent with an earlier report (14), which indicated that Li⁺-Na⁺ beta alumina decomposes in this temperature range by a process that involves the irreversible migration of Li⁺ into the spinel blocks of the structure.

Na⁺ beta alumina synthesized as powder.—This material, which had a particle size of $d < 44 \mu\text{m}$, had been in contact with air for several years. Its x-ray pattern before heating showed several weak reflections which do not belong to beta alumina. Immediately after annealing at 600°C, the positions and intensities of these foreign reflections had changed. The original spectrum was eventually restored after months of exposure to air. A very reasonable explanation for the extra reflections is that

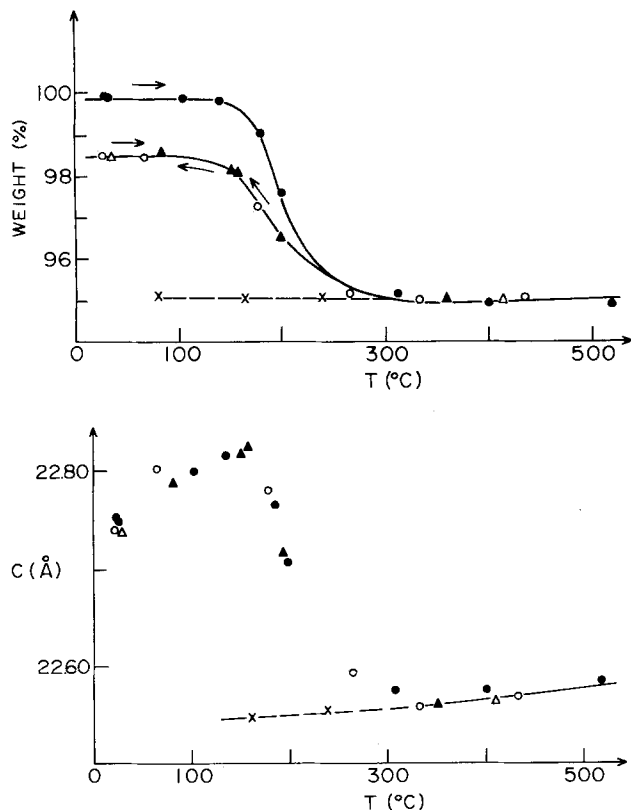


Fig. 4. Weight change (top) and corresponding change in *c*-lattice parameter (bottom) function of temperature for Li^+ beta alumina powder. Li^+ beta alumina prepared by exchange in LiNO_3 . [●]: First heating in air. [○]: First cooling in air. [▲]: Second heating in air. [△]: Second cooling in air. [x]: Cooling in vacuum.

they arose from the hydration and, possibly, carbonation reactions which these powders underwent upon prolonged standing in air. The formation of carbonates and bicarbonates on the surface of beta alumina powders was previously reported by Garbarczyk *et al.* (15-17) and Harbach (18).

A TGA, taken under dynamic vacuum, of a sample of this powder more than two years old is shown in Fig. 5. Various steps are apparent in the weight-loss process. However, the steps are not clearly distinguished even at very slow heating rates ($1^\circ\text{C}/\text{min}$). Although the exact weight lost in each step is uncertain, the total weight lost from room temperature to 700°C is reproducibly 9-10%.

During cooling at $0.5^\circ\text{C}/\text{min}$ from 700°C to room temperature in air, the weight increased about 3%. After five months of exposure to air, the powders reproduced the thermal behavior of Fig. 5.

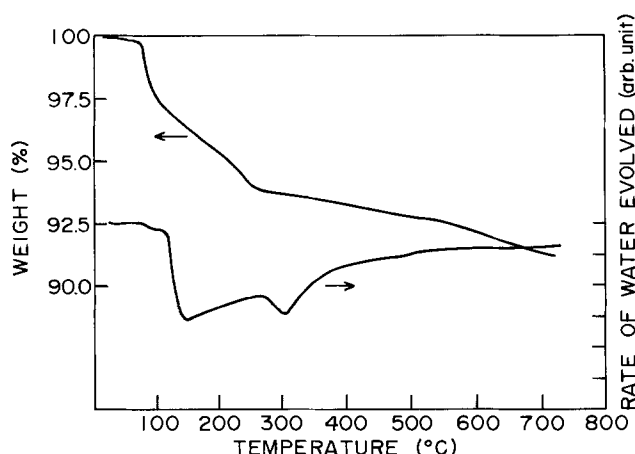


Fig. 5. TGA results and humidity detector output during heating of sample of Na^+ beta alumina powder (type 4) in dry nitrogen at $10^\circ\text{C}/\text{min}$.

To determine whether all of the weight losses in Fig. 5 actually correspond to the evolution of water a P_2O_5 humidity detector was connected in series with the gas stream exiting the TGA chamber. Its output is also plotted in Fig. 5. A downward trace represents an increased water signal. What is most interesting is that only the high temperature weight loss ($> 600^\circ\text{C}$) is not accompanied by water evolution. A reasonable explanation is that it is the result of the decomposition of carbonates on the surface of the powder.

To explore this possibility, a series of TGA analyses were carried out in various atmospheres. Fresh samples of Na^+ beta alumina were heated to 800°C and then cooled to room temperature at $0.5^\circ\text{C}/\text{min}$. Gas flows of 8 liter/h were maintained over the samples. The total weight increases from 800°C to room temperature were 1.4% for a wet nitrogen atmosphere with no CO_2 , 0.4% for dry CO_2 , and 5.5% for wet CO_2 . These results demonstrate that simultaneous carbonation/hydration can be responsible for considerable weight increase in these beta alumina samples.

Moist CO_2 presumably leads to the formation of bicarbonate and carbonate species on the surface of the beta alumina powders. Separate TGA analyses on sodium bicarbonate and sodium carbonate show that the former decomposes to the carbonate between 100° and 200°C , and the carbonate begins to decompose above 800°C . The decomposition of bicarbonate/carbonate species can therefore account not only for the high temperature weight loss in these powders, but also for some of the complexity of the low temperature weight losses.

To further corroborate the role of CO_2 in these reactions, infrared spectroscopy (IR) measurements using a Nicolet FTIR spectrometer with a HgCdTe detector were carried out on powder samples. The results were consistent with the presence of various sodium carbonates, bicarbonates, and their hydrates.

Additional evidence for carbonate formation was obtained by bubbling the effluent from the TGA into a water trap and measuring the pH as a function of weight loss. Distinct acidic peaks were observed to correspond with weight loss regions. The largest occurred above 500°C , the temperature range in which CO_2 evolution is expected from carbonate decomposition. The second largest peak was observed at 100°C and correlates well with bicarbonate decomposition.

The high temperature weight loss signaling the presence of carbonates did not appear with all samples. It was absent with those prepared from Union Carbide crystals. Some weight loss which could indicate the presence of carbonation was observed with Monofrax Na^+ beta alumina. It was observed with sodium beta alumina powders prepared from single crystals of Mg-stabilized material and also with Li^+ beta alumina crystals prepared from Union Carbide crystals.

Summary and Conclusion

We have studied the hydration reactions of various beta aluminas under conditions that were intentionally quite different from those of several previous investigations that used large single-crystal samples. The prior work yielded considerable insight into the nature of the hydration processes at high temperatures and over long diffusion pathlengths. We have emphasized the other extreme—low temperatures and short diffusion pathlengths. Our conditions required powder samples, which made it more difficult to obtain structural insight into the process of water intercalation in these compounds. Nevertheless, the data obtained from powder samples are quite important. They highlight reactions that may be too slow to be observed with larger crystals, and the short hydration pathlengths of powders reveal reactions that occur in regions very near the surface. Understanding reactions of this type is especially important in the study of interfacial ion transfer.

Our results underscore that the beta alumina hydration reactions are strongly influenced by the ion present in

the conduction plane. The behavior of K^+ beta alumina is one extreme. Even in fine powder form, it neither adsorbs nor absorbs significant amounts of water. In contrast, at 100°C , Na^+ beta alumina intercalates the equivalent of about 2.1 H_2O molecules per unit cell. At the same temperature, Li^+ beta alumina absorbs about 4 H_2O molecules per unit cell, which is considerably greater than the maximum of 1.6-1.8 H_2O molecules per unit cell reported by Dudney *et al.* (8) from studies of single crystals.

The fact that fine powders of K^+ beta alumina do not hydrate indicates that surface hydration reactions and the condensation of water in microcracks probably are minor mechanisms for the trapping of water by this material. Assuming that the physical characteristics of powders of other beta aluminas are similar to those of K^+ beta alumina, microcrack condensation can be generally ignored. In addition, if general surface adsorption is invoked to help explain the greater water uptake by powders of Na^+ and Li^+ beta alumina, it must be strongly influenced by the ion in the conduction plane.

On the basis of these results, we suggest that the near-surface region of beta alumina hydrates more rapidly and to a greater extent than the interior. As shown previously (5) and confirmed here, the hydration behavior of Na^+ beta alumina powders is well explained by assuming that regions $3.3\ \mu\text{m}$ wide around the edges of each particle hydrate rapidly to a level of about two H_2O molecules per unit cell. The interior region hydrates to a lower water content. The behavior of Li^+ beta alumina powders can be explained by assuming regions $30\ \mu\text{m}$ wide which hydrate to about four H_2O molecules per unit cell. Since Li^+ beta alumina is an extremely powerful desiccant, it is not clear whether a truly anhydrous form has ever been prepared.

Our results indicate that some beta aluminas react with CO_2 , especially in the presence of water, to form bicarbonates and carbonates. These are presumably surface reactions. We have no evidence to indicate that CO_2 penetrates the conduction planes near the surface. The extent of carbonation varies greatly. Powders of Union Carbide Na^+ beta alumina show no evidence of carbonation. But, Na^+ beta alumina powders synthesized as powders and Mg-stabilized Na^+ beta alumina both have high temperature weight losses that are not the result of the loss of water vapor. IR analyses with the beta alumina samples reveal multiple absorptions characteristic of bicarbonates/carbonates. Felsche (18) has identified x-ray diffraction lines as being due to sodium sesquicarbonate, $Na_3H(CO_3)_3 \cdot 2H_2O$. The decomposition of such a species is probably responsible for the sharp weight losses observed in the $70^\circ\text{--}115^\circ\text{C}$ temperature range. Li^+ beta alumina powders from Union Carbide crystals also have a high temperature weight loss that may be the decomposi-

tion of carbonates, although we have no clear evidence that it is.

Acknowledgment

The authors thank Dr. T. Zerlia for carrying out the IR measurements mentioned in this paper. This research was supported by M.P.I., CNR (Italy), and the U.S. Department of Energy. Additional support came from the National Science Foundation, M.R.L. Program, Grant no. DMR 82-16718.

Manuscript submitted April 25, 1984; revised manuscript received Feb. 4, 1985.

The University of Pennsylvania assisted in meeting the publication costs of this article.

REFERENCES

1. Y-F. Y. Yao and J. T. Kummer, *J. Inorg. Nucl. Chem.*, **29**, 2453 (1967).
2. J. T. Kummer, *Prog. Solid State Chem.*, **7**, 141 (1972).
3. B. Dunn, *J. Am. Ceram. Soc.*, **64**, 125 (1981).
4. J. B. Bates, R. Frech, H. Engstrom, J. C. Wang, and T. Kaneda, *Solid State Ionics*, **1**, 15 (1980).
5. G. Flor, A. Marini, V. Massarotti, and M. Villa, *ibid.*, **2**, 195 (1981).
6. W. L. Roth, M. W. Breiter, and G. C. Farrington, *J. Solid State Chem.*, **24**, 321 (1978).
7. G. Flor, J. L. Bjorkstam, and M. Villa, *Z. Naturforsch.*, **35**, 951 (1980).
8. N. J. Dudney, J. B. Bates, J. C. Wang, G. M. Brown, B. C. Larson, and H. Engstrom, *Solid State Ionics*, **5**, 225 (1981).
9. L. J. Richter, P. L. Kuhns, and M. S. Conradi, *ibid.*, **5**, 229 (1981).
10. N. J. Dudney, J. B. Bates, and J. C. Wang, *Phys. Rev. B*, **24**, 6831 (1981).
11. P. L. Kuhns, L. J. Richter, and M. S. Conradi, *J. Chem. Phys.*, **76**, 6 (1982).
12. C. E. Hayes and D. C. Ailion, *Solid State Ionics*, **5**, 233 (1981), and references therein.
13. J. L. Briant and G. C. Farrington, *J. Solid State Chem.*, **33**, 385 (1980).
14. R. R. Dubin, J. S. Kasper, J. B. Bates, and T. Kaneda, in "Fast Ionic Transport in Solids," P. Vashishta, J. N. Mundy, and G. K. Shenoy, Editors, p. 361, North-Holland, Amsterdam (1979).
15. J. Garbarczyk, M. Wasiucioneck, W. Jakubowski, and A. Grodzinski, *Phys. Stat. Solidi A*, **70**, K163 (1982).
16. J. Garbarczyk, M. Wasiucioneck, W. Jakubowski, and A. Grodzinski, *ibid.*, **73**, K97 (1982).
17. J. Garbarczyk, W. Jakubowski, and M. Wasiucioneck, in "Proceedings of the 4th International Conference on Solid State Ionics," M. Kleitz, B. Sapoval, and Y. Chabre, Editors, p. 249, North-Holland, Amsterdam (1983).
18. F. Harbach, in "Proceedings of the 4th International Conference on Solid State Ionics," M. Kleitz, B. Sapoval, and Y. Chabre, Editors, p. 231, North-Holland, Amsterdam (1983).

COMMENTS



Each issue of the **Journal** will have a section of "Comments." In this section, we provide a means via short pieces, *i.e.*, one column or less, to applaud, dispute, or otherwise discuss the papers published in the **Journal**. Space will be provided for one response by the paper's author(s) to each comment.

Since space available in each issue for the "Comments" section is limited, it is important to be concise.

Comments should be sent to the Editor, Dr. Norman Hackerman, President's Office, Rice University, P.O. Box 1892, Houston, TX 77251.

Norman Hackerman
Editor

Martensitic Transformation of Gd

S. Yamaguchi

(pp. 1145-1146, Vol. 129, no. 5)

A. E. Curzon¹ and **M. Gasgnier**²: The paper by Yamaguchi³ reporting martensitic transformations in Gd and Dy is open to criticism because it does not take into account numerous well-known results of other workers. Space restrictions preclude a full discussion. Important points are as follows.

1. As pressure is increased, the rare earths follow the structure-sequence hcp, Sm-type, dhcp, fcc.^{4,5,6,7} Sometimes, unstable structures can be "frozen in."⁴ Because the hcp and Sm-types of Gd and Dy have not been observed to coexist, it is even less likely that the hcp and fcc forms which are at opposite ends of the sequence should coexist.

2. Yamaguchi reports fcc Gd is paramagnetic and not ferromagnetic like the bulk phase. This is attributed to change in bond length but could be due to impurities.

3. The polytype sequence gives $a_0 = 5.10\text{\AA}$ ⁴ for fcc Gd. Yamaguchi obtains 5.51\AA , indicating that other elements are present.

The above points strongly suggest that impurities should be considered. The rare earth metals react readily with oxygen and hydrogen.^{4,8,9,10,11,12,13,14} The plane spacings of the strong reflections from Gd₂O₃ [bcc, space group T_h⁷ (Ia3)] agree to ~2% with those reported by Yamaguchi. The lattice parameter of fcc Gd calculated from the individual reported reflections³ ranges from 5.41 to 5.60Å, indicating an error of about 2%. Thus, the likely explanation of the results is that the reported fcc Gd and Dy are due mainly to strong reflections of the oxide R₂O₃ with the possibility of the presence of some hexagonal metal or of the dihydride RH₂ (fcc). Similar arguments apply to results for fcc Tb.¹⁵

¹Department of Physics, Simon Fraser University, Burnaby, British Columbia, Canada V5A 1S6.

²ER 210, Elements de Transition dans les Solides, CNRS Bellevue, 92915 Meudon Principal Cedex, France.

³S. Yamaguchi, *This Journal*, **129**, 1145 (1982).

⁴M. Gasgnier, *Phys. Status Solidi A*, **57**, 11 (1980).

⁵L. G. Liu, *J. Phys. Chem. Solids*, **36**, 31 (1975).

⁶A. R. Verma and P. Krishna, "Polymorphism and Polytypism in Crystals," John Wiley and Sons, New York (1966).

⁷W. A. Grosshans, Y. K. Vohra, and W. B. Holzapfel, *J. Magnet. Mater.*, **29**, 282 (1982).

⁸J. Müller, B. Singh, and N. A. Surplice, *J. Phys. D*, **5**, 1177 (1972).

⁹A. E. Curzon and O. Singh, *ibid.*, **8**, 1703 (1975).

¹⁰M. Gasgnier, A. E. Curzon, and N. A. Surplice, *Thin Solid Films*, **52**, L1 (1978).

¹¹J. Dexpert-Ghys, Ch. Loier, Ch. Henry la Blanchetais, and P. Caro, *J. Less-Common Met.*, **41**, 105 (1975).

¹²A. E. Curzon and H. G. Chlebek, *ibid.*, **32**, 365 (1973).

¹³C. Boulesteix, P. E. Caro, M. Gasgnier, Ch. Henry la Blanchetais, B. Pardo, and G. Schifmacher, *Phys. Status Solidi A*, **23**, 597 (1974).

¹⁴A. E. Curzon, *J. Less-Common Met.*, **98**, 149 (1984).

¹⁵S. Yamaguchi, *J. Phys. D*, **15**, 347 (1982).

Physicochemical Effects of Heating Gold Thin Films on Gallium Arsenide

S. Leung, L. K. Wong, D. D. L. Chung, and A. G. Milnes

(pp. 462-468, Vol. 130, no. 2)

A. J. McEvoy¹⁶ In the report by Leung *et al.*¹⁷ on interface effects on heating between a gallium arsenide substrate and an evaporated gold overlayer, etching of the substrate, dissociation of the semiconductor, diffusion of the dissociated species through the overlayer and consequent evolution of arsenic, and formation of a gold-gallium intermetallic were all noted. However, by scanning Auger spectroscopy, the presence of gallium and arsenic on the gold surface prior to heating was also established. While the dissociation may be initiated by the condensation of gold on the semiconductor surface, an effect of particular relevance for device structures in that it determines the Fermi level pinning in the initial stages of Schottky barrier formation^{18,19}, it does continue at ambient temperatures, as verified in the time-dependance measurements of Hiraki *et al.*²⁰ There it was established that ambient temperature interdiffusion eventually produces a non-abrupt interface between the semiconductor and the metal overlayer, extending over a depth of some 200Å.

In Schottky barrier photovoltaic devices, the metallization is limited to 100Å if it is to be sufficiently transparent. It is therefore thinner than other of those reported,^{7,20} and thin relative to the interdiffusion depth. It is known empirically that the deliberate introduction of an oxide layer between semiconductor and metal gives a higher Schottky barrier, and the resulting MOS solar cell is a more efficient device.²¹ Optimum oxide thickness is some 35Å, *i.e.*, significantly thinner than the interdiffusion layer formed at an intimate metal-semiconductor junction.²² The oxide does not completely suppress interdiffusion, however, and gallium and arsenic species have been detected by ESCA on the surface of a MOS cell. Nonetheless, the thermodynamic data²³ does establish the relative stability of the oxides of gallium and arsenic in contact with gold, so some inhibition of interdiffusion must occur.

In the literature on photovoltaic devices, the consistent approach is to consider the MOS cell as a planar sequence

¹⁶Institute for Physical Chemistry, University of Hamburg, Hamburg, Germany.

¹⁷S. Leung, L. K. Wong, D. D. L. Chung, and A. G. Milnes, *This Journal*, **130**, 462 (1983).

¹⁸W. E. Spicer, P. W. Chye, C. M. Garner, I. Lindau, and P. Pianetta, *Surf. Sci.*, **86**, 763 (1979).

¹⁹I. Lindau, P. W. Chye, C. M. Garner, P. Pianetta, C. Y. Su, and W. E. Spicer, *J. Vac. Sci. Technol.*, **15**, 1332 (1978).

²⁰A. Hiraki, S. Kim, W. Kammura, and M. Iwami, *Surf. Sci.*, **86**, 706 (1979).

²¹H. J. Hovel, "Solar Cells," Academic Press, New York (1975).

²²G. T. Wrixon, Report EYR 6933 EN, Commission of the European Communities, Luxembourg (1980).

²³S. P. Kowalczyk, J. R. Waldrop, and R. W. Grant, *J. Vac. Sci. Technol.*, **19**, 611 (1981).

of layers, with interfaces abrupt on the atomic scale. It is now suggested that the experimental evidence does not allow of such models. The role of the oxide may be the better to define the interface, so that the barrier characteristics are not unduly degraded by the ambient temperature interdiffusion process. It is noted that for silicon, where the MOS structure also displays superior photovoltaic behavior, a similar interdiffusion has been observed.²⁴

The conclusion is drawn that there is still a need for careful comparative microanalytical profiling of intimate Schottky barrier and MOS structures to determine the consequences of the presence of the oxide layer in the latter case, for the interfacial reactions and consequent interdiffusion. From those data, a more definitive theoretical understanding could arise, with consequences for device design.

I. Mojzes and R. Veresegyházy:²⁵ Gold and gold-based alloys are frequently used as contact materials to compound semiconductors. Contact technology involves high temperature heat-treatment. During this technological step, an interaction of the metallization with the semiconductor material to be contacted takes place. The investigation of this interaction is of high interest from point of view of the device parameters and the reliability of devices.

In the cited paper,¹⁷ the physicochemical effects taking place in the system Au-GaAs were investigated using the evolved gas analysis (EGA) technique, completed by various analytical methods. These techniques mentioned later were applied *ex situ*.

The character of the As₂ ion-temperature profile presented in the cited paper is in good agreement with our results^{26,27} published partly during the edition period of the cited paper.¹⁷ The giant peak, observed in both laboratories, found for the Au contact could be completely eliminated by coevaporating Ga with the gold contact material. The same effect was observed for other contact materials²⁷ and for the InP-Au system.²⁸ It should be noted that Ga in this relation could not be replaced by In.²⁸

Based on our earlier experiments, we concluded that the temperature belonging to these giant peaks does not depend on the heating rate or the thickness of the metal layer.²⁶ Concerning the effect of the heating rate Leung and co-workers found that it is smaller than the systematic error of temperature measurement. During the last year, we studied the role of the layer thickness. A definite dependence on the layer thickness was found. Some of our results are shown in Fig. 1. For comparison, results from the work of Leung *et al.* are also shown. These results are in good agreement. Based on these experimental results, one should conclude that the arsenic evolution temperature also depends on the heating rate. The effect of heating rate on the arsenic yield was also investigated.²⁶ Our results show that the arsenic yield depends on the heating rate. A higher heating rate causes lower arsenic yield for both the first and second heat cycle. During the EGA experiments, the evaporation of Ga was also monitored. In the case of GaAs, no Ga evolution was detected by us, either.²⁶ In the case of InP, a small evaporation of In was registered.²⁹ This is in good agreement with Guthbier's earlier results³⁰ obtained for the thermal decomposition of pure, *e.g.*, uncovered compounds.

Surface morphology and microstructural changes are also to be investigated. To investigate these phenomena, practically the same experiments have been carried out in our laboratory as are described by Leung *et al.* Au-GaAs

²⁴Y.-S. Wang, H. Yu, C. Hsu, B. W. Lee, and W. A. Anderson, *Solar Energy Mater.*, **7**, 291 (1982).

²⁵Research Institute for Technical Physics, Hungarian Academy of Sciences, H-1325 Budapest, Hungary.

²⁶I. Mojzes, T. Sebestyén, and D. Szigethy, *Solid-State Electron.*, **25**, 449 (1982).

²⁷T. Sebestyén, I. Mojzes, and D. Szigethy, *Electron. Lett.*, **16**, 504 (1980).

²⁸I. Mojzes, D. Szigethy, and R. Veresegyházy, *ibid.*, **19**, 117 (1983).

²⁹I. Mojzes, R. Veresegyházy, and V. Malina, To be published.

³⁰H. Guthbier, *Z. Naturforschung A*, **16**, 268 (1961).

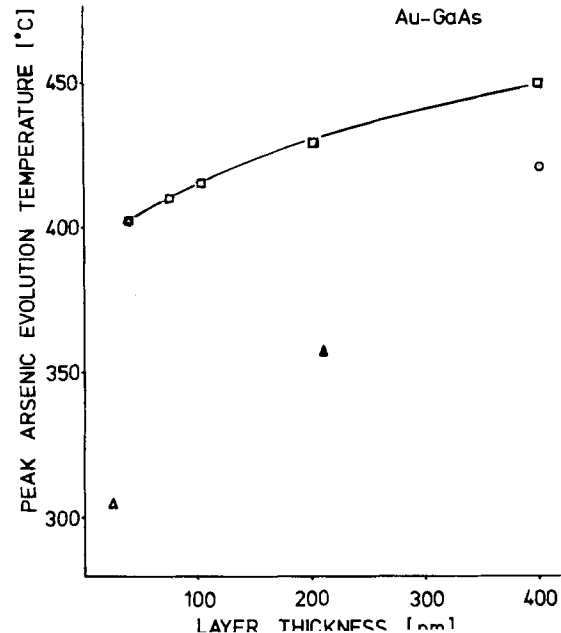


Fig. 1. Peak arsenic evolution temperature vs. layer thickness for Au-GaAs system. The points are averages of several measurements, the scattering was approximately $\pm 10^\circ\text{C}$. \square : Present work; heating rate $150^\circ\text{C}/\text{min}$. \circ : Present work; heating rate $50^\circ\text{C}/\text{min}$. \triangle : Results of Leung *et al.*; heating rate $25^\circ\text{C}/\text{min}$.

samples were quenched at several points of the heat cycle. Typical dendritic structures were obtained, when the samples were quenched at the peak arsenic evolution temperature (Fig. 7B of the work of Mojzes *et al.*²⁶). Surface morphology observed during our study was slightly different from those described by Leung *et al.* Different layer thicknesses, different sample preparation techniques, and different heat-treatment parameters are or may be responsible for this inconsistency. It should be noted that rectangular protrusions were also observed by us in the case of contact system with additional Ga.^{26,31} It may be that in the case of Leung *et al.* this amount of Ga originates from the decomposition of GaAs, because of the longer heat-treatment cycle used in their work. It is of technological interest to investigate the electrical characteristics of the processes taking place during the annealing. For this purpose, the *in situ* electrical resistance measurement,^{32,33} and the control of the barrier height³⁴ could be used. The heating rates which have to be used to obtain good quality ohmic contacts make the electrical measurements almost impossible. By using these techniques in the future, useful new information may be obtained. That is to say, no single technique provides a complete description of the processes that take place during the heat-treatment.

Summarizing our results, we conclude that the peak arsenic evolution temperature depends on the heating rate and layer thickness. The effect causes the giant As₂ peak which is not yet identified. Further experiments with other compounds and layer structures are in progress in our laboratory.

Fabrication of Via Holes in 200 μm Thick GaAs Wafers

S. P. Yenigallo and C. Z. Gosh

(pp. 1377-1378, Vol. 130, no. 6)

H. Beneking:³⁵ It should be mentioned that the fabrication of via holes is used for through connections of GaAs MESFET's since 1972 and was first presented in 1973.³⁶

³¹I. Mojzes, T. Sebestyén, P. B. Barna, G. Gergely, and D. Szigethy, *Thin Solid Films*, **61**, 27 (1979).

³²I. Mojzes, *Phys. Status Solidi A*, **47**, K183 (1978).

³³I. Mojzes, *Acta Phys. Hung.*, **48**, 131 (1980).

³⁴A. Diligenti and P. Terreni, *J. Phys. E.*, **14**, 1441 (1981).

³⁵Institute of Semiconductor Electronics, Technical University Aachen, 5100 Aachen, Germany.

³⁶H. Beneking and E. Kohn, "X-Band GaAs MESFET's," paper presented at the European Specialist Seminar on Active Microwave Semiconductor Devices, Calvi/Corsica, Nov. 1973.

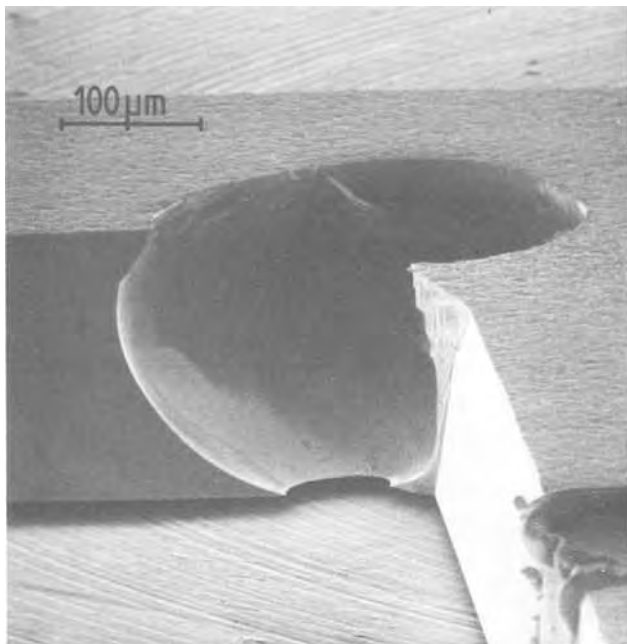


Fig. 2. Etched hole in a GaAs-substrate, rear side on top, after Beneking and Kohn.

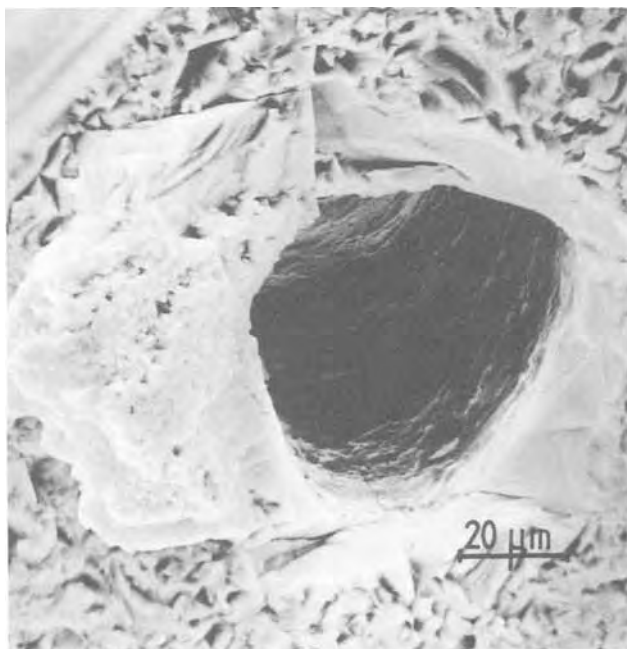


Fig. 3. Laser bore in a GaAs-substrate, after Beneking and Kohn

Figure 2 shows a via hole chemically etched through a 300 μm thick wafer.³⁶ The chemical etch we used consists of $\text{NaOCl} + \text{H}_2\text{O}$ (1:7), temperature 70°C. The procedure is described in more detail in the thesis of Kohn.³⁷

Also, laser processing can be used as demonstrated in 1973.³⁶ Using a CW laser (He-Ne), the material is stressed very strongly, resulting sometimes in destroyed crystals. Applying a pulsed ruby laser (50 Ws/1 mS) can also result in satisfying holes, also without added chemical etching. The control of geometry is as good as with combined chemical etching favored by Tucker and Birnbaum³⁸ (see Fig. 3).

Applying a special time-domain measurement setup,³⁹

³⁷E. Kohn, Thesis Aachen Technical University, Aachen, Germany (1975).

³⁸A. W. Tucker and M. Birnbaum, *IEEE Trans. Electron. Devices Lett.*, **ed1-4**, 39 (1983).

³⁹U. Piller, Thesis, Aachen Technical University, Aachen, Germany (1973).

we were able to measure the impedance of the via contact itself, the value being less than $\text{pH } 13$ and 0.2Ω , depending on the thickness of the gold covering.

Phosphorus-Doped Polycrystalline Silicon via LPCVD

I. Process Characterization

B. S. Myerson and W. Olbricht

(pp. 2361-2365, Vol. 131, no. 10)

A. Learn:⁴⁰ In the paper listed above, data are presented for the radial variation of growth rate of polycrystalline silicon phosphorus-doped during growth. Film growth was performed under low pressure (LPCVD) conditions using SiH_4 and PH_3 source gases. Similar growth rate variations were observed for semi-insulating polysilicon⁴¹ (SIPOS) and silicon dioxide⁴² grown at low pressure from $\text{SiH}_4/\text{N}_2\text{O}$ and SiH_4/O_2 reactions, respectively. The SIPOS growth rate characteristics were interpreted⁴¹ on the basis of the following sequence: reduction of SiH_4 to $\text{SiH}_2 + \text{H}_2$ at an oxygen containing site on the substrate surface, adsorption of SiH_2 on a silicon containing site where growth would normally occur, and reaction of SiH_2 with SiH_4 to form Si_2H_6 . The net effect of the SiH_2 is, therefore, to reduce the growth rate. If the SiH_2 concentration varies radially, then the growth rate will vary correspondingly. Slight modification to the SIPOS model leads to quantitative agreement with growth rate data for oxide.⁴² In this case, a proportionality for growth rate, GR, is derived as follows

$$\text{Gr} \propto d \frac{r_c^2 - r^2}{r_c d + r_w^2 - r^2} \quad [1]$$

where d is wafer-wafer spacing, r_c is the inner radius of the tube surrounding wafers, r_w is the wafer radius, and r is the radial position on a wafer. Wafer-center growth rate data for polycrystalline silicon from the subject paper are plotted in Fig. 4 as a function of wafer spacing. The solid line represents relationship [1], where $r_c = 2.0$ in., $r_w = 1.125$ in., and $r = 0$. The proportionality constant was determined by fitting the curve to the data point at $d = 0.15$ in. The correlation coefficient between theoretical and experimental points is near unity (0.997). A second test of relationship [1] is shown in Table I where observed and predicted radial variations near the wafer edge are compared.

⁴⁰Anicon, Incorporated, San Jose, California 95134.

⁴¹M. L. Hitchman and J. Kane, *J. Cryst. Growth*, **55**, 485 (1981).

⁴²A. J. Learn, *This Journal*, **132**, 390 (1985).

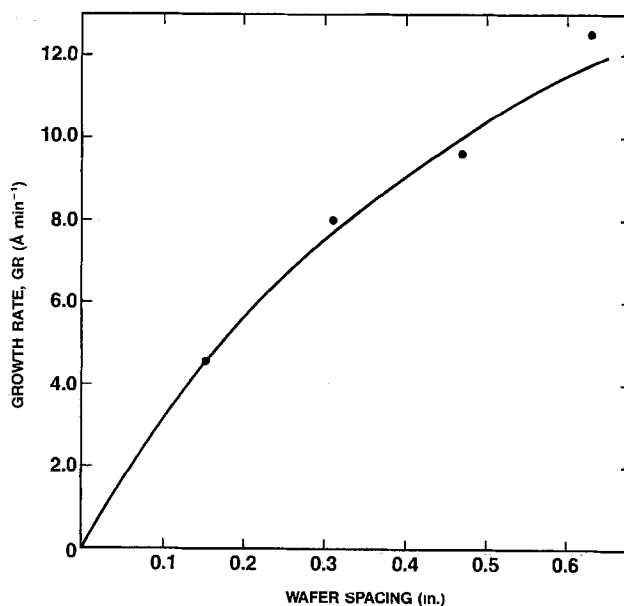


Fig. 4. Doped-polycrystalline-silicon growth rate at wafer center as a function of wafer spacing. The solid line is a plot of relationship [1].

Table I. Ratio of GR at wafer edge and center

Wafer spacing, d (in.)	Observed	Predicted at $r = r_w$
0.15	1.98	3.58
0.31	1.71	2.08
0.47	1.54	1.61
0.63	1.37	1.37

Agreement between predicted and observed values is good, particularly for the large d values. Part of the difference at small d may be accounted for by the inability to measure precisely at the wafer edge. As a matter of interest, relationship [1] predicts no radial variation for d equal to 1.37 in. For larger d , a lower GR at wafer edge than at wafer center is predicted. The reasonably close agreement between theory and experiment suggests that the models used for SIPOS and oxide may also be relevant to doped-polycrystalline silicon growth. Adsorbed-phosphorus sites could thus play the same role as oxygen containing sites. The fact that observable amounts of Si_2H_6 were detected, as reported in this paper, lends additional credence to the type of mechanism discussed above.

B. S. Meyerson:⁴³ There are several aspects of radical chemistry that must be discussed to properly respond to this comment. First, the overall reaction



is derived from observations⁴⁴ of chemistry in the gas phase, and is an insertion reaction of the SiH_2 diradical into SiH_4 . The two unbound electrons of the diradical insert across an Si-H bond in the silane molecule to produce Si_2H_6 . Our experiments have shown that silane, when adsorbed on the silicon surface, bonds to that surface via a dissociative adsorption, where a hydrogen is transferred to the surface, and the silane then bonds across the now free orbital to another site. Thus, although written as "bound" SiH_x , where $x < 4$, there are not $4 - x$ unbound and active electrons on the bound SiH_x . Chemisorbed SiH_2 is thus quite distinct from the gas phase spe-

⁴³IBM Corporation, Thomas J. Watson, Research Center, Yorktown Heights, New York 10598.

⁴⁴P. John and J. H. Purnell, *J. Chem. Soc., Faraday Trans.*, **69**, 1455 (1973).

cies as it is unlikely that an unbound and active electron pair exists.

Although one can propose this bound SiH_2 reacts with incoming SiH_4 to give Si_2H_6 , many other steps for Si_2H_6 formation are possible, such as the surface recombination of adsorbed SiH_3 . There is no *a priori* reason to assume SiH_2 is involved in the chemistry, if any occurs, that would take place on the surface.

Second, the rate of insertion of SiH_2 into phosphine has been measured by Blazejowski and Lampe⁴⁵ and was found to be roughly four times the rate of insertion of SiH_2 into silane. Were there silylene present on the surface, as argued in the comment, it would preferentially insert into and likely remove the phosphine from the surface, reacting to a lesser degree with silane. Thus, any SiH_2 present would serve to primarily interact with adsorbed phosphine. This directly contradicts our observation that the presence of silane near a phosphine saturated silicon surface fails to produce any effect. Were phosphine acting as an active site for the production of SiH_2 from SiH_4 , as argued in the comment, rapid insertion of SiH_2 into the P-H bond of adsorbed phosphine would be expected, yet was not observed. It was found⁴⁶ that with phosphine present on the Si surface, no silane adsorption or decomposition occurred. However, with a bare Si surface, silane dissociated and adsorbed even at room temperature, until saturation coverage by resulting molecular fragments was obtained. Thus, in fact, the silicon surface itself promoted silane decomposition, while phosphine suppressed it. Furthermore, as the comment argues that phosphine promotes the decomposition of SiH_4 , eventually producing Si_2H_6 , it predicts an increase in silane consumption (forming Si_2H_6 rather than film) as phosphine on the surface should promote silane pyrolysis. The opposite of this is observed, as noted in Fig. 5 of our work. When phosphine is added to the silane LPCVD process, silane consumption decreases significantly.

Finally, the presence of Si_2H_6 as reported in our paper is attributed by us to the homogeneous, gas phase pyrolysis of silane.⁴⁴ As SiH_2 insertion into SiH_4 is well known to produce Si_2H_6 in the gas phase, its presence is expected. In summary, we find the deposition mechanism proposed in the comment at odds with numerous aspects of our experimental data, and thus implausible.

⁴⁵J. Blazejowski and F. W. Lampe, *J. Photochem.*, **20**, 9 (1982).

⁴⁶B. S. Meyerson and M. L. Yu, *This Journal*, **131**, 2366 (1984).

ERRATUM

In the paper titled "Electrodeposition and Characterization of Cu_xS Films," by R. D. Engleken and H. E. McCloud [*This Journal*, **132**, 567 (1984)], the caption to Fig. 9 (p. 572) was omitted. The correct caption and the figure are at the right.

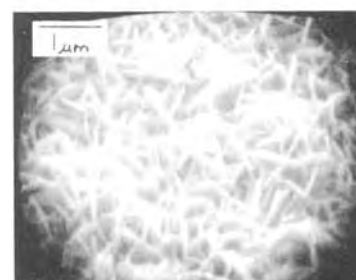


Fig. 9. Micrographs for sample E79 ($\text{Cu}_{1.90}\text{S}$) after annealing



Polydithienothiofene: A Novel Polymer Electrode for Lithium Batteries

M. Mastragostino

Istituto Chimico "G. Ciamician," University of Bologna, Bologna, Italy

B. Scrosati*

Dipartimento di Chimica, University of Rome, "La Sapienza," Rome, Italy

The recent discovery that conductive polymers can be doped electrochemically has opened the possibility of using these materials as electrodes in rechargeable batteries. In this respect, polyacetylene has been the most studied polymer and various papers have been published on the behavior of p-doped (cathode) or n-doped (anode) polyacetylene in lithium batteries (1-4). The most of the results indicate that polyacetylene suffers of poor coulombic efficiency and of instability and thus the possibility of its use as a cathode in high-energy, long-life lithium batteries, is now somewhat doubtful (4-6). However, the interest in polymer electrodes remains high and various new electrochemically active polymers are presently under investigation.

In this paper we report preliminary results on the electrochemical behavior of doped polydithienothiofene (pDTT), whose chemical structure is shown in Figure 1.

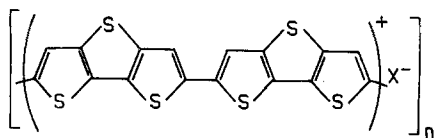


Figure 1- Chemical structure of polydithienothiofene.

As previously described (7,8), this conductive polymer can be prepared electrochemically on a Pt or on a SnO₂-coated glass support, by constant current electrolysis of a methylene

chloride solution containing the monomer dithieno (3,2-b:2',3'-d) thiofene (DTT) and MX (M⁺=N(Bu)₄⁺, X⁻=ClO₄⁻, PF₆⁻) as the supporting salt. The oxidation of the monomer starts at 1.2V vs. SCE with the growth on the electrode support of an electroactive adherent film. The polymer so formed may be repeatedly reduced to the neutral state and oxidized to the conducting state with a cycling regime which involves about 20% of the total charge consumed in the initial electrochemical preparation. The electrochemical doping-undoping process is accompanied by a color change since the oxidized film is black and the neutral film is red (7,8).

The good cyclability and the color change of the electrochemical reaction open the possibility of using pDTT as electrode in rechargeable batteries and in electrochromic displays (8). In this prospective, we have examined the behavior of pDTT in a cell having a Li counter electrode, a Li reference electrode and a solution of lithium perchlorate in propylene carbonate (LiClO₄-PC) as the electrolyte.

In Figure 2 are shown the 1st and the 9th consecutive cyclic voltammograms of a pDTT electrode in the LiClO₄-PC electrolyte. The pDTT electrode used for these voltammograms was electrosynthesized on Pt in the oxidized form for a total charge of 450 mC and then reduced to the neutral state, in a N(Bu)₄⁺ClO₄⁻, CH₂Cl₂ solution.

The voltammograms of Figure 2 reveal that the polymer may be doped both anodically (presumably with ClO₄⁻ as the p-doping specie) and cathodically (presumably with Li⁺ as the n-doping specie).

However, while the p-doping process shows a narrow separation and a good reproducibility of the oxidation and reduction waves, the peaks of the n-doping process are different in shape and far apart. This indicates that favourable kinetics are to be expected for the p doping-undoping process only.

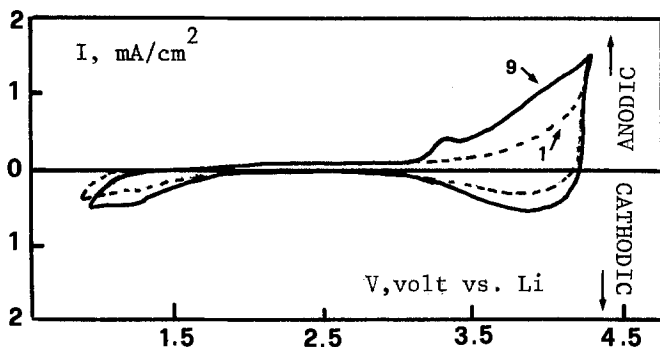


Figure 2-Cyclic voltammograms of a pDTT electrode in the LiClO_4 -PC electrolyte. Cycle 1 starts with a neutral pDTT electrode from 2.5V vs. Li in the anodic direction. Scan rate: 40 mV/s.

This suggests that pDTT might be considered as a good cathode material in lithium, organic electrolyte batteries. Some preliminary results obtained in our laboratories confirm this suggestion since cells of the type $\text{Li}/\text{LiClO}_4\text{-PC/pDTT}$ may be cycled at a constant current of the order of $50 \mu\text{A}/\text{cm}^2$ with charge-discharge coulombic efficiencies of the order of 75%.

*Electrochemical Society Active Member.

Manuscript received Jan. 21, 1985.

The University of Rome assisted in meeting the publication costs of this article.

Work is in progress to further characterize the electrochemical properties of pDTT and to fully evaluate the performance of this novel polymer cathode material in lithium, rechargeable batteries.

ACKNOWLEDGEMENTS.

This work has been carried out with the financial support of the Consiglio Nazionale delle Ricerche, Progetto Finalizzato Energetica 2.

REFERENCES.

- 1)-P.J.Nigrey, D.McInnes, D.P.Nairns, A.G.MacDiarmid and A.J.Heeger, *This Journal*, 128, 1651 (1981).
- 2)-D.McInnes, M.A.Druy, P.J.Nigrey, D.P.Nairns, A.G. MacDiarmid and A.J.Heeger, *J.Chem. Soc. Chem. Commun.*, 317 (1981).
- 3)C.K.Chang, *Polymer*, 22, 1454 (1981).
- 4)G.C.Farrington, B.Scrosati, D.Frydrych and J.DeNuzzio, *This Journal*, 131, 7 (1984).
- 5)A.Padula, B.Scrosati, M.Schwarz and U.Pedretti, *This Journal*, 131, 2761 (1984).
- 6)A.Padula and B.Scrosati, *J.Power Sources*, 14, 31 (1985).
- 7)P.G.DiMarco, M.Mastragostino and C.Taliani, *Mol. Cryst. Liq. Cryst.*, Conf. Proc. ICSM 84, in press.
- 8)M.Biserni, A.M. Marinangeli and M. Mastragostino, *This Journal*, submitted.



Interpretation of Sodium-Sulfur Cell Characteristics Using an Alternating Current Resistance Technique

Bradley R. Karas*

General Electric Company, Corporate Research and Development, Schenectady, New York 12301

ABSTRACT

An alternating current (ac) resistance technique for sodium-sulfur cells is described. The method has been applied to central sodium and central sulfur cells with between 16 and 650 Ah capacity. The shape of the ac charge resistance-capacity plot has been correlated with resistive layer composition. Anomalies in direct current (dc) resistances for oriented-mat sulfur electrode cells are explainable in conjunction with ac analysis. The increased sensitivity of ac compared to dc measurements has been utilized to identify incipient electrolyte failure and sodium electrode problems not discernable by the latter technique.

The sodium-sulfur (beta) cell is comprised of liquid sodium and sulfur electrodes separated by a solid sodium beta- or beta"-alumina electrolyte. Interest in this secondary battery arises from its high energy density, efficiency, achievable current densities, and the availability and cost of the electrode components. Since it was first described by Kummer and Weber in 1967 (1), the beta cell has reached a fairly advanced state of development (2). Typical cells are tubular, and both central sodium (sodium contained within the beta" electrolyte) and central sulfur designs exist. Considerable development effort has been devoted not only to the sodium-sulfur cell itself, but also to the individual cell components (2). For example, alternating current (ac) impedance techniques have been applied to the electrolyte (3), sodium-electrode in sodium-sodium cells (4), and the sulfur electrode (5). Although ac impedance or resistance methods have been utilized in other battery systems (6), little work in this area has been performed on beta cells (13). This paper describes such an ac technique developed to analyze and evaluate sodium-sulfur cell performance.

Cell Operation and Description

During cell discharge, sodium is oxidized at the anode (negative electrode). The sodium ions are transported through the electrolyte to the cathode compartment where sulfur is reduced. Electrons flow from the sodium to the sulfur electrode via an external circuit. The low electronic conductivity of sulfur is overcome by incorporating a conductive carbon mat in the sulfur-electrode compartment. It is generally accepted that the initial reaction product is Na_2S_3 (2). At the cell operating temperature of 330°C, sulfur and Na_2S_3 are immiscible liquids. Thus, a "two-phase" region yielding a constant cell open-circuit voltage (OCV) of 2.08V is defined and exists until all the sulfur has reacted. Continued discharge produces lower polysulfides, which are miscible. At this point, the cell potential begins to drop and a "one-phase" region is created. A polysulfide composition corresponding to Na_2S_3 represents complete discharge. The existence or absence of Na_2S_3 as a discrete species in polysulfide melts is disputed. The formulation is used here simply to refer to a quantity of charge passed, sufficient to produce an overall sodium to sulfur ratio of 2:3 in

the cathode compartment (7). Discharge much beyond this point produces insoluble polysulfides at the temperatures normally employed for cell operation (2, 7a, 8).

The electrode processes are reversed during cell charging. If sodium polysulfide oxidation occurs directly at the solid electrolyte/conductive mat interface, then the beta"-alumina electrolyte becomes passivated with a layer of elemental sulfur when the cell enters the two-phase region. The high sulfur resistivity hinders further recharge (2). This problem can be circumvented by the use of a high resistivity, porous matrix adjacent to the electrolyte surface (9). This matrix is commonly referred to as the "resistive mat" or "barrier layer."

Most of the cells utilized in this study were 16 Ah with respect to Na_2S_3 , central-sodium laboratory cells. The letter preceding the cell number indicates the type of seals employed, and the last letter designates the sodium-fill technique. The cells were either filled electrolytically (10) from reagent-grade NaNO_3 , or via vacuum filling of the liquid metal. For example, B800L contained two thermo-compression bonded seals and was vacuum filled with liquid sodium. The "800" refers to the cell number. The sulfur electrode was cast and contained sulfur purified by the Bacon-Fanelli process (11). Union Carbide Thornel VMA® carbon fiber as the conductive mat, and a carbon- or ceramic-based resistive layer. Carbon-based resistive layers were made from 0.006 in. thick nonresilient paper, hereafter referred to as NRP-6, purchased from Fiber Materials, Incorporated (Biddeford, Maine). Two types of ceramic-based resistive layers were used, Saffil® alumina fiber (Imperial Chemical Industries, England), and alumina-based papers (F. K. Fiber, Incorporated, Wilmington, Delaware) designated Al-2 and Al-4 which were nominally 0.020 and 0.040 in. thick, respectively. The electrolytes were 99% beta"-alumina and had an ~3 $\Omega\text{-cm}$ 330°C specific resistivity.

A Hewlett-Packard 9825B minicomputer was used to control an automated test system. Laboratory cells were cycled at 330°C and a constant direct current (dc) of 108 mA/cm^2 with respect to the electrolyte area. Each cell operated between individually preset voltage limits. The system monitored each cell voltage every 3 min. Every 27 min, the cells were removed from load and placed on open circuit. At the conclusion of the 3 min open-circuit period, the voltage was again recorded and the cell returned to test. The difference between the OCV and load

* Electrochemical Society Active Member.

voltage at the same depth of discharge (or charge) divided by the current yielded the dc resistance. The dc resistance calculated in this manner will contain a contribution from concentration polarization effects. This fact should be borne in mind.

Alternating Current Resistance Technique

Alternating current resistance measurements were performed concomitantly with dc testing. The experimental arrangement is depicted in Fig. 1. An ac signal was generated by a Princeton Applied Research (PAR) Model 121 lock-in amplifier/phase detector or a Model 5204 lock-in analyzer. This signal flowed across an in-series, 1 k Ω carbon-film resistor to the cell. The 1 k Ω resistor fixed the ac current and prevented direct current from passing through the ac circuit. Two voltage probes were connected between the cell and the lock-in amplifier. The lock-in amplifier output was fed to a Houston Instrument Superscribe 4950, dual-pen, strip chart recorder. The PAR Model 5204 has analog outputs for both the signal-phase and magnitude, whereas the Model 121 has only a magnitude output. In the latter case, the phase was read off a front-panel meter. Measurements performed at 1000 Hz on a 100 Ω resistor yielded almost no phase shift between the reference signal and measured ac voltage. Thus, the dc output from the lock-in amplifier was proportional to the ohmic portion of the ac impedance. Both lock-in amplifiers were checked in a similar manner.

To prevent disruption of dc testing and measurements, the ac signal was maintained at less than 2 mA_{rms}. This implies that the ac voltage between the probes was typically less than 100 μ V_{rms}. The automated recording system has a 1 mV sensitivity. Further, the 10 Ω limiting resistor used in the dc circuit is at least 100 times larger than the measured cell resistance. Thus, the ac signal flowing through the dc circuit should be minimal. Ideally, the ac resistance, R_{ac} , should be insensitive to dc effects or flow. Most cells display little difference in R_{ac} whether under load or open-circuit conditions (*vide infra*). If, however, dc effects are present, it is expected that R_{ac} will increase when the cell is removed from load during discharge and decrease under similar circumstances during charge.

The above technique has been applied to nonlaboratory central sodium (100-650 Ah) and central sulfur (25-150 Ah) cells as well. Measurements on these cells were made similarly, except the low, \sim 1-3 m Ω , resistance of the 650 Ah utility cell required a PAR Model 124A lock-in amplifier. The Model 124A has an increased ac reference signal and enhanced detector sensitivity relative to both the Model 121 and 5204.

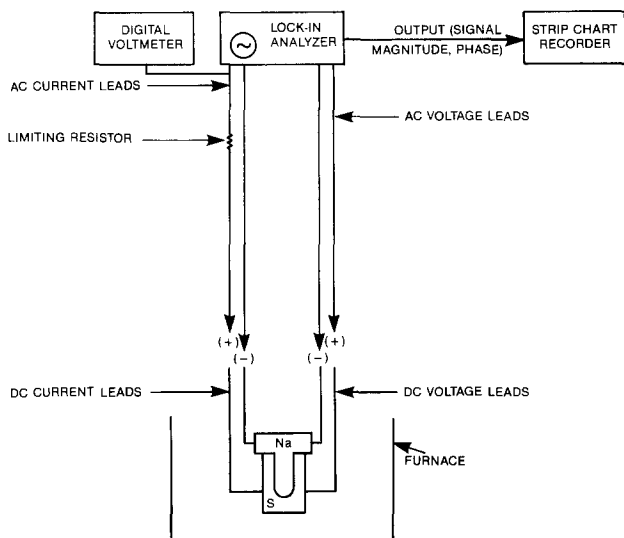


Fig. 1. Apparatus for four-probe ac resistance measurements. In measurements on laboratory cells, the dc current leads are connected to a Hewlett-Packard 9825B minicomputer-controlled power controller. The 9825B is interfaced to a digital voltmeter which monitors cell voltage every 3 min.

Results and Discussion

The sections below detail the effects of cell components and quality on the resistance fingerprint.

Laboratory cell B800L was examined in half-decade frequency increments between 10 and 100,000 Hz at 1 Ah intervals during both charge and discharge. In these experiments, the PAR Model 121 was used as both the signal generator and detection device between 10 and 1000 Hz, and the signal generator for the Model 5204 detector between 1000 and 100,000 Hz. Data obtained from both instruments at 1000 Hz generally agreed to within 10%. The experimental setup was checked out by measuring the resistance and phase dependence of 1 and 0.1 Ω resistors. Measured resistances were within 10% of the actual values and phase shifts less than 10 $^\circ$ were detected. More precise phase shifts are difficult to obtain with a lock-in amplifier. Crossover from the Model 121 to the 5204 was necessitated by inductance in the Model 121, the effects of which became evident at \sim 10,000 Hz.

Load measurements on cell B800L were performed at 10, 100, and 1000 Hz in the 3 min interval preceding an open-circuit period. The depth of discharge varies only 0.1 Ah per 3 min. The open-circuit period was extended to 9 min in order to examine the desirable frequency range. Less than 5% deviation was detected between the load and open-circuit impedance values. Figures 2 and 3 present frequency vs. impedance plots for charge cycle number 266 and discharge cycle number 267, respectively. Little phase shift, $< 10^\circ$, was observed in these experiments except at high depths of discharge, $> 80\%$, and even then it was only 15 $^\circ$ -20 $^\circ$ at 100,000 Hz. When present, the phase shifts were capacitive; however, the general flatness of these curves indicates that capacitive and inductive contributions to the impedance are minimal. Therefore, single frequency measurements at any frequency between 10 and 3000 Hz can be utilized to probe cell performance.

The discharge-charge resistance behavior for cell B800L is shown in Fig. 4. Data were recorded in cycle 353. The time increment between each datum is 30 min, and the ac frequency was 1000 Hz. The drop in resistance at the beginning of discharge (Fig. 4a) is attributed to removal of sulfur deposited during the previous charge cycle (*vide infra*). Alternating current and dc resistance values differ due to electrode polarization effects and the inclusion of concentration polarization effects to the dc value. These arise because the dc measurement is not made rapidly enough, *i.e.*, electrochemical changes occur during the measurement time interval. Although no discernable break was seen in the dc data during charge (Fig. 4b), a sharp increase was detected at \sim 60% depth of discharge by the ac measurement. The resistance rise coincides with recharge into the two-phase region and oxi-

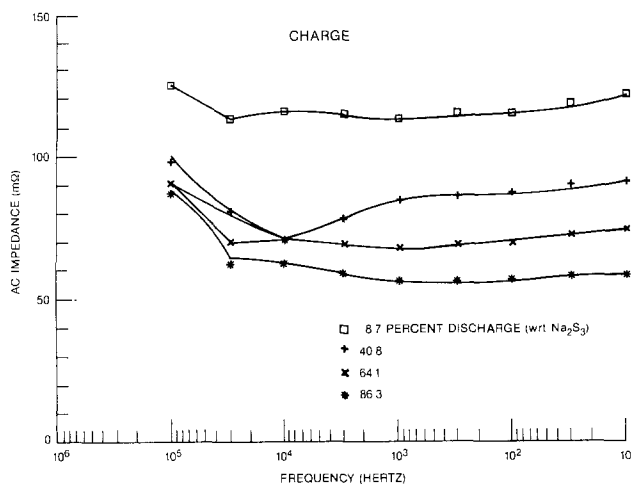


Fig. 2. Plots of ac impedance vs. frequency for cell B800L. The cell operated at 330 $^\circ$ C and 108 mA/cm 2 . Data were recorded during charge cycle 266.

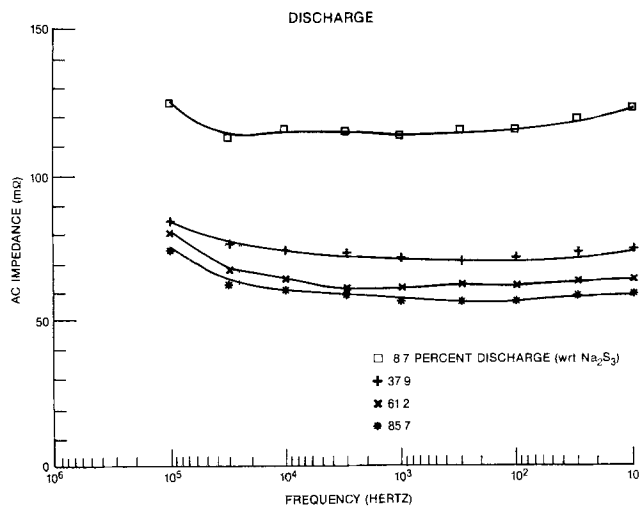


Fig. 3. Alternating current impedance-frequency graphs for cell B800L. Operating conditions same as those in Fig. 2. Data were collected during discharge cycle 267.

dation of sodium polysulfide to sulfur. The resistance break indicates that the resistive layer is not completely effective in preventing sulfur deposition on the beta"-alumina electrolyte surface.

Resistive layer materials.—Examination of ac charge resistance vs. depth of discharge plots indicates that the "hump" or "break" which occurs during cell charging is more pronounced, *i.e.*, greater in magnitude and narrower in breadth, in cells containing a NRP-6 resistive mat (Fig. 5a), and flatter and broader in cells with Saffil- or alumina-resistive layers (Fig. 5b). A possible explanation is afforded by the equivalent-circuit model of Brennan (12). Brennan divided the sulfur electrode compartment into 1000 annular segments, and then calculated the effect of varying felt resistance on electrochemical activity. He found that when r_2 , the resistive mat resistivity, equaled r_1 , the conductive mat resistivity, that the reaction rate was greatest at the electrolyte/resistive mat interface. As r_2/r_1 increased, the percent reaction occurring at the solid electrolyte/resistive mat interface decreased, and a reaction spike formed at the resistive mat/conductive mat interface.

When the resistive and conductive mats are NRP-6 and Thornel VMA, respectively, r_2/r_1 is ~ 600 (9). One might presume that very little reaction should occur at the NRP-6/beta"-alumina interface. However, NRP-6 has a finite electrical conductivity; therefore, some reaction still occurs at the electrolyte surface. During charge, sulfur coats the beta"-alumina surface, and an abrupt change in ac resistance occurs. Whether or not this phenomenon is de-

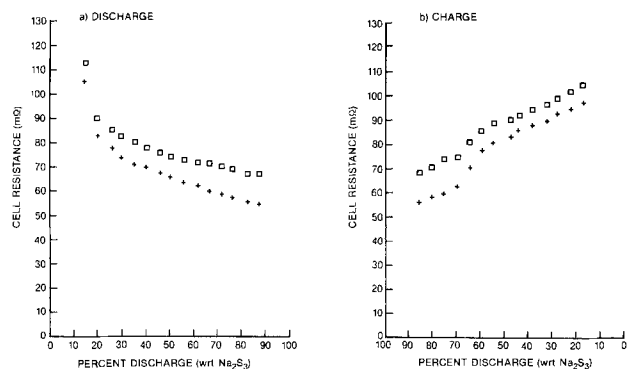


Fig. 4. Cell resistance vs. percent discharge (with respect to Na_2S_3) for cell B800L. The cell contains an unoriented-sulfur electrode and a NRP-6 resistive layer. Data from cycle 353. a: Discharge-alternating current resistance (+) at 1000 Hz. See text for dc resistance. (\square): calculation technique. b: Same as in a, except charge cycle.

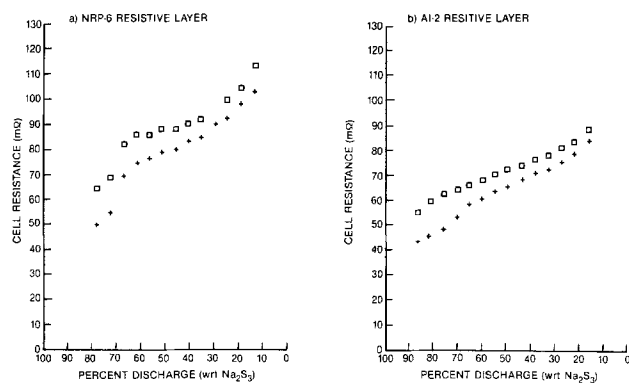


Fig. 5. The effect of resistive layer composition on charge resistance. a: DC (\square) and ac (+) resistance for cell containing carbon-based resistive layer. b: Same as in a, except alumina-paper resistive layer cell. Alternating current resistances measured at 1000 Hz.

tected in the dc calculation is dependent on the severity of sulfur deposition (*cf.* Fig. 4b and 5a).

In contrast, when a Saffil- or alumina-resistive layer is employed, r_2/r_1 approaches 10^{10} . These resistive layers act as electronic insulators. In effect, the electrochemical reaction takes place at the resistive mat/conductive mat interface. The increased surface area of this interface compared to the electrolyte surface area makes it much more difficult to deposit a continuous sulfur blocking layer the entire length of the cell. Therefore, the charge resistance increase should be more gradual (Fig. 5b). The ideal curve shape is one in which no break and no resistance increase occurs. Although cells have been constructed and tested which display only a minimal break, such as B857L shown in Fig. 5b, all cells display a gradual resistance increase during cell charging.

Conductive mat orientation.—The standard laboratory cell sulfur electrode was manufactured by shredding the Thornel VMA conductive mat, twisting the mat fibers together, adding the resistive layer, and molding. Each electrode consisted of three sections in which the mat fibers were randomly oriented. A new electrode was developed which consisted of oriented-mat segments. Mat orientation within each segment was radial and axial. Orientation was achieved by proper manipulation of the layered bulk mat. Cells containing the new electrode had lower resistance, improved chargeability, and increased efficiency, *e.g.*, 91% vs. 87% for oriented- and non-oriented-sulfur electrode containing cells, respectively, operating at 330°C and 108 mA/cm².

Figure 6 presents resistance vs. percent capacity plots for cell B888L. This cell contained an oriented-sulfur electrode and a Saffil-resistive layer. The improved chargeability of cells with oriented electrodes can be seen by comparing the discharge inception points in Fig. 4a and 6a and the final charge depths. Further, the improved chargeability was achieved with an ~ 140 mV lower cutoff

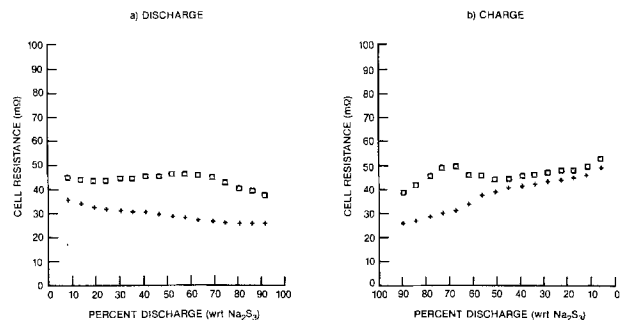


Fig. 6. Cell resistance vs. percent discharge for cell B888L. The sulfur electrode was comprised of oriented-conductive mat fibers and a Saffil-resistive layer. Data from cycle 26. a: Discharge; DC (\square) and ac (+) resistances. b: Charge; symbols have same meaning as in a. Alternating current resistances measured at 1000 Hz.

voltage in cell B888L than in cell B800L. Also note the reduced sulfur polarization effect in cell B888L at the beginning of discharge and end of charge compared to cells B800L (Fig. 4) or A834L (Fig. 5a, charge only). Both of these latter two cells contained nonoriented-sulfur electrodes.

Other than magnitude, the ac resistance plots for cell B888L were similar to those presented for cell B800L. The dc behavior, however, has been considerably altered. Cell B800L displays a gradually declining discharge resistance. In contrast, as cell B888L neared the two-phase/one-phase transition and then entered the one-phase region, the dc resistance increased, displayed a broad maximum, and then declined again. A similar type of behavior has been reported by Mennicke on metal-oxide containing electrodes (13). Although the resistance increase reported herein was not as great as that discussed by Mennicke, increases as large as ~25% have been observed. A more perplexing situation is shown in Fig. 6b, where the dc charge resistance decreased upon nearing the one-phase/two-phase transition. Declines up to ~20% have been observed. In contrast to the decreasing dc resistance, the ac charge resistance continued to increase throughout this period.

The sodium-sulfur cell resistance contains contributions from the leads, carbon-fiber to sulfur canister contact resistance, sulfur electrode, beta" electrolyte, and a polarization resistance due to electrochemical processes. If contact resistances are lumped together with the sulfur-electrode resistance, the major contributors to cell resistance are the sulfur electrode and beta" electrolyte (14). Therefore, a crude ac sulfur-electrode resistance can be calculated by subtracting the electrolyte resistance from the overall cell resistance. Aging studies and pre- and post-test resistivity measurements on RS-1 electrolytes substantiate the validity of this type of approach (15).

Breiter and Dunn developed a sulfur electrode model which allows direct calculation of a sulfur electrode resistance (16). Manipulation of their equations and utilization of Cleaver *et al.* sulfur/polysulfide data (17) allow calculation of the conductive mat resistivity. A 330°C resistivity value of 2.8 and 0.45 Ω -cm was obtained for the standard- and oriented-sulfur electrode, respectively. Out-of-cell resistivity measurements employing Pt electrodes confirmed these values (18).

Brennan studied the effects of fiber orientation on cell recharge characteristics, in particular, mat resistivity and reaction zone thickness (19). Using Le Carbone RVC 4000® carbon felt, he found an ~2.5-fold increase in resistivity between parallel and perpendicular mat orientations. Orientations are referenced to the direction of current flow. The discrepancy between his value and the factor of ~6-7 reported herein results from the use in this study of an oriented and a completely unoriented electrode. In contrast, both Brennan's electrodes had oriented fibers. Further, differences in carbon fiber-sulfur canister and interfiber contact resistances exist between the present electrodes and Brennan's electrodes (18, 20). Brennan also stated that the lower the mat resistivity, the greater the percentage reaction located adjacent to the electrolyte. The high electronic resistivity of Saffil- or alumina-resistive layers implies that conduction through these porous matrices is via parallel ionic paths (16). The resistive layers can, therefore, be considered extensions of the solid electrolyte.

Based on these considerations, more reaction should occur at the electrolyte/conductive mat interface in cells with oriented-sulfur electrodes. At the current density employed in this study, mass-transport limitations exist. During cell discharge, melt adjacent to the electrolyte becomes overreduced, "overdischarged," with respect to the bulk melt. Overreduction refers to a condition in which polysulfides lower than Na_2S_5 are formed when sulfur still exists within the melt. This lowers the working voltage. In the open-circuit periods, the melt reequilibrates. The calculated dc resistance is thus larger than expected and increases with time near the two-phase/one-phase

transition. This is because the potential of Na_2S_x ($x < 5$) is lower than the constant two-phase potential of 2.08V (21). In the one-phase region, the potential difference between the various polysulfides formed decreases, and R_{dc} , the dc resistance, declines.

Upon charge inception, R_{dc} increases as expected. Again, however, diffusional limitations are present and the melt near the electrolyte surface becomes overoxidized. When Na_2S_5 first forms, the OCV jumps abruptly to near the two-phase value of 2.08V. Sudden increases as large as ~60-70 mV have been observed between two successive open-circuit periods. The working voltage remains relatively constant, however. This causes a drastic reduction in R_{dc} . Direct current resistance plots are relatively flat in the two-phase charge region, whereas ac resistance curves continue to increase. This is because the ac measurement is sensitive to changes in melt composition. The ac resistance behavior of cells containing oriented- and unoriented-sulfur electrodes is similar. The disparate dc resistance traits are an artifact of the manner in which the dc resistance is calculated.

Electrolyte related phenomena.—Since the lock-in amplifier output is recorded on a strip chart recorder, R_{ac} can be determined for any point during the discharge/charge cycle. This capability is unaffected whether or not direct current flows. Changes in R_{ac} within a cycle, between cycles, or during open-circuit periods are easily detected and most informative. Figures 7a and 7b display discharge and charge, respectively, ac resistance behavior for a typical sodium-sulfur cell containing an unoriented-sulfur electrode. Resistance is presented on the ordinate and time on the abscissa. The $|x|$ symbols represent open-circuit periods and were separated by 30 min or 0.9 Ah. As can be seen in the figures, passage of direct current had little effect on the ac measurement. Furthermore, the ac changes which did occur

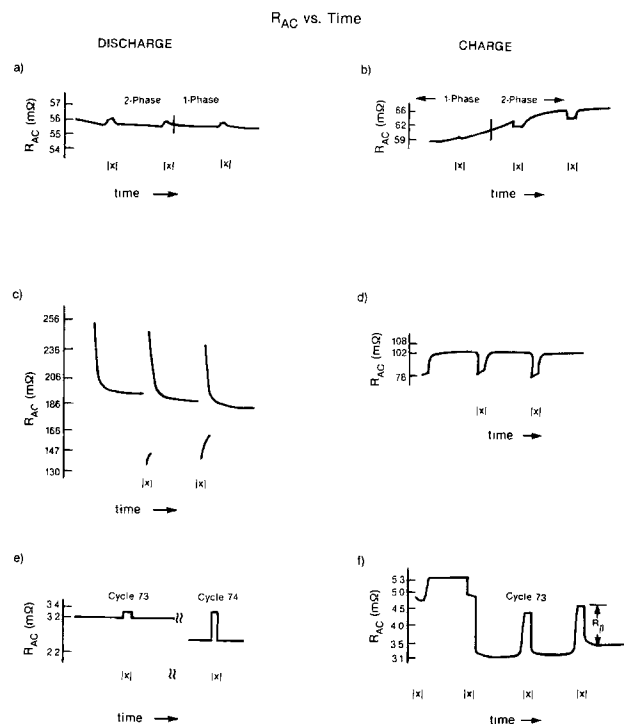


Fig. 7. Alternating current resistance-time response traces. Discharge depicted in a, c, and e, and charge in b, d, and f. Traces shown in a and b are for a typical laboratory cell with an unoriented electrode. Cell operated at 330°C, 108 mA/cm². The $|x|$ delineate open-circuit periods and are separated by 0.9 Ah. The effect of a sodium-side electrolyte film on ac-cell resistance is shown in c and d. Operating conditions were the same as in a and b. Figures e and f are data collected on a 650 Ah utility cell. This cell operated at 350°C and 150 mA/cm² discharge, 105 mA/cm² charge rate. The $|x|$ are separated by 37.8 Ah during discharge and 27.0 Ah during charge. The discharge data were recorded at ~66% depth of discharge. f: Cycle 73 charge.

during the open-circuit periods were abrupt, *i.e.*, ohmic in nature.

Asymmetric behavior has been observed in sodium-sulfur cells and is characterized by a greater discharge than charge resistance (10, 22). This phenomenon depends upon ceramic electrolyte composition, its phase, and previous handling, and has been attributed to film formation on the sodium side of the solid electrolyte. The presence and level of certain impurities within the beta' electrolyte or sodium can induce asymmetry. Recently, the distribution and composition of the film has been determined (23).

Alternating current resistance measurements on asymmetric cells also showed enhanced discharge resistances. In contrast to "normal" cell behavior, however, a large dc effect was observed, *i.e.*, passage of direct current affected the ac resistance value. During discharge open-circuit periods, R_{ac} varied by as much as 50% from the load value. An ~30% decrease is depicted in Fig. 7c for a cell with unusually high calcium species present in the sodium electrode (15). The resistance was not constant and displayed diffusional limitations. Similar trends were seen during charge, as shown in Fig. 7d. Differences in the discharge load-resistance behavior are also readily apparent (cf. Fig. 7a and 7c). These arise from changes in the electrolyte surface film and changes in sodium wetting, which may or may not be related to the surface film (10, 22, 23).

Frequency dependence of the ac resistance has been detected in asymmetric cells; however, the resistance time-dependent nature makes quantification difficult (22). Although the magnitude of the dc effect varied, cells with sodium-side problems were characterized by the ac-resistance traits depicted in Fig. 7c and 7d. This is in sharp contrast to "normal" cell behavior and to cells with sulfur-electrode problems. The latter situation is discussed elsewhere (8).

Alternating current resistance measurements on 25-650 Ah central sulfur or central sodium cells were very similar to those described above on laboratory sodium-sulfur cells. The same discharge/charge characteristics, *e.g.*, electrode orientation effects, were found regardless of cell size or configuration.

Examination of utility cell F09115, 650 Ah capacity, was conducted between cycles 72 and 75. This cell operated at 350°C and was discharged and charged at 150 and 105 mA/cm², respectively. The ac resistances at the end of cycles 72D and 72C (D represents discharge, C charge) were ~3.2 and ~4.7 mΩ, respectively. The next discharge cycle was relatively uneventful until ~65% depth of discharge was reached (discharge limit was 90%). At this point, R_{ac} began to fluctuate. No dc effect was apparent and R_{ac} at the end of the cycle was ~3.4 mΩ. Alternating current resistance oscillations of the sort detected are usually associated with cell failure. This is evidenced by abnormalities in the dc load voltage-time relationship and/or a decrease in cell voltage to zero. In the present example, however, the voltage appeared normal.

The subsequent charge cycle began normally. However, at ~33% depth of discharge (charge limit was 18%), R_{ac} dropped drastically (Fig. 7f). A dc effect was apparent and opposite in direction to that previously observed. Interestingly, for a given depth of discharge, R_{ac} was approximately the same in this cycle, 73C, when no direct current flowed as in previous charge cycles. In fact, during an extended open-circuit period at the conclusion of the cycle, R_{ac} was ~4.7 mΩ. The next discharge cycle, 74D, was initiated, and a large dc effect was noted (Fig. 7e). Again, as in the preceding charge cycle, the resistance increased during open-circuit periods and at the same depth of discharge matched previous discharge cycle resistances.

Specific resistivity measurements on similar ceramics yielded an electrolyte resistance of ~1.1 to ~1.3 mΩ. This value corresponded to the magnitude of the dc effect. It is felt that the electrolyte underwent a noncatastrophic failure which was detected in the ac, but not the dc, measurement. When direct current flowed, sodium was pushed

through the flaw and the beta' electrolyte was partially shorted from the sodium side. Hence, R_{ac} dropped. Interruption of dc flow broke the sodium short and reintroduced the electrolyte resistance into the ac measurement. Another indication of a beta'-alumina ceramic fracture would be a reduction in cycle-to-cycle capacity. During this period, however, the capacity did not follow any specific trend. Comparison of R_{dc} at a particular depth of discharge in this and 10-15 cycles previous revealed a decrease in R_{dc} . This is also an indication of a short.

Conclusion

An alternating current resistance technique for sodium-sulfur cells has been described. The trends observed were independent of size (16-650 Ah), configuration (central sodium or central sulfur), and seal type. Except for severely asymmetric cells, no frequency dependence was observed in 16 Ah laboratory cells between 10 and 100,000 Hz. Alternating current resistance analysis has proven most useful in identifying resistive mat and electrode orientation effects on cell performance. Furthermore, ac measurements are more sensitive to electrolyte failure, asymmetric contributions, and changes in cycle-to-cycle behavior than traditionally used techniques. The method has been applied to the investigation of current density, temperature, and polysulfide composition effects on cell performance and life (8).

Acknowledgments

The author is grateful to R. N. King for experimental assistance in conducting these tests, J. L. Briant for aiding in the laboratory cell multifrequency measurements, and M. D. Thomas for his assistance in conducting tests on nonlaboratory cells. Dr. R. W. Powers is acknowledged for many helpful discussions and critical review of this manuscript. This work was supported by the Electric Power Research Institute under Contract RP-128-7; this support is gratefully acknowledged.

Manuscript submitted Oct. 14, 1984; revised manuscript received Jan. 28, 1985.

General Electric Company assisted in meeting the publication costs of this article.

REFERENCES

1. J. T. Kummer and N. Weber, in "Proceedings of the SAE Congress of 1967," Paper 670179, pp. 1-6, SAE (1967).
2. J. L. Sudworth and A. R. Tilley, in "The Sulfur Electrode—Fused Salts and Solid Electrolytes," R. P. Tischer, Editor, p. 235, Academic Press, New York (1983), and references therein.
3. (a) F. Harbach and W. Bansemir, *J. Appl. Electrochem.*, **13**, 79 (1983). (b) R. D. Armstrong and R. A. Burnham, *J. Electroanal. Chem.*, **72**, 257 (1976), and references therein. (c) W. Jakubowski and D. H. Whitmore, *J. Am. Ceram. Soc.*, **62**, 381 (1979). (d) R. D. Armstrong and D. P. Sellick, *J. Appl. Electrochem.*, **9**, 623 (1979). (e) R. W. Powers and S. P. Mitoff, *This Journal*, **122**, 226 (1975).
4. R. D. Armstrong, T. Dickinson, and J. Turner, *J. Electroanal. Chem.*, **44**, 157 (1973).
5. R. D. Armstrong, T. Dickinson, and M. Reid, *Electrochim. Acta*, **21**, 935 (1976).
6. (a) S. Sathyanarayana, S. Venugopalan, and M. L. Gopikanth, *J. Appl. Electrochem.*, **8**, 479 (1978); (b) J. H. Sluyters, *Rec. Trav. Chim.*, **79**, 1092 (1960), and subsequent articles in series.
7. (a) B. Cleaver, in "The Sulfur Electrode—Fused Salts and Solid Electrolytes," R. P. Tischer, Editor, p. 35, Academic Press, New York (1983); (b) D.-G. Oei, *Inorg. Chem.*, **12**, 435 (1973); (c) D.-G. Oei, *ibid.*, **12**, 438 (1973).
8. B. R. Karas and R. N. King, *This Journal*, **132**, 1266 (1985).
9. M. W. Breiter and B. Dunn, *J. Appl. Electrochem.*, **9**, 291 (1979).
10. M. W. Breiter, B. Dunn, and R. W. Powers, *Electrochim. Acta*, **25**, 613 (1980).
11. R. F. Bacon and R. Fanelli, *Ind. Eng. Chem.*, **34**, 1043 (1942).
12. M. P. J. Brennan, *Electrochim. Acta*, **24**, 473 (1979).

13. S. Mennicke, Abstract 100, p. 160, The Electrochemical Society Extended Abstracts, Vol. 83-2, Washington, DC, Oct. 9-14, 1983.
14. New York State Energy Research and Development Authority Report no. 447-ET-AES-82 prepared by the General Electric Company.
15. D. S. Park and R. N. Singh, Private communication.
16. M. W. Breiter and B. Dunn, *J. Appl. Electrochem.*, **9**, 671 (1979).
17. (a) B. Cleaver, A. J. Davies, and M. D. Hames, *Electrochim. Acta*, **18**, 719 (1973); (b) B. Cleaver and A. J. Davies, *ibid.*, **18**, 727 (1973).
18. R. W. Powers, Private communication.
19. M. P. J. Brennan, *Electrochim. Acta*, **24**, 529 (1979).
20. R. W. Powers and B. R. Karas, Manuscript in preparation.
21. N. K. Gupta and R. P. Tischer, *This Journal*, **119**, 1033 (1972).
22. M. W. Breiter and B. Dunn, *J. Appl. Electrochem.*, **11**, 685 (1981).
23. R. N. Singh, Private communication.

The Effects of Current Density, Temperature, and Discharge Beyond Na_2S_3 on Sodium-Sulfur Cell Performance and Life

Bradley R. Karas* and Randall N. King

General Electric Company, Corporate Research and Development, Schenectady, New York 12301

ABSTRACT

The effects of current density (54-865 mA/cm²), temperature (330°-355°C), and discharge depth (Na_2S_3 to $\text{Na}_2\text{S}_{2.4}$) on sodium-sulfur cell efficiency, resistance, capacity, and longevity are presented. Equal discharge and charge cycle times obtained on 16 Ah laboratory cells at 865 mA/cm² and 335°C demonstrated the resistive layer effectiveness in preventing sulfur passivation of the beta"-alumina electrolyte surface during cell charging. Elevated temperatures increased cell efficiency ~3%/10°C, decreased resistance, and increased capacity. A group of cells operating at 216 mA/cm², twice the standard current density, and 330°C have obtained ~700 cycles, ~900 Ah/cm², with little performance deterioration. The cells are ~82% efficient and display ~80% of theoretical capacity. Alternating current resistance analysis of typical laboratory cells revealed an increase in discharge resistance occurred when cells were cycled between Na_2S_3 and Na_2S_2 . Correlations with the sodium-sulfur phase diagram indicate the resistance rise was due to precipitation of Na_2S_2 . Upon subsequent charge inception, the ac resistance dropped. However, an increased two-phase charge resistance was recorded. This suggested that Na_2S_2 deposition occurred at the resistive-mat/conductive-mat interface.

The sodium-sulfur (beta) cell has a myriad of potential uses, for example, load leveling, vehicle propulsion, or satellite power. The exact application determines the cell size, power requirements, and cycling conditions. Circumstances will arise, however, which will necessitate aggressive cell operation. The effects of current density (54-865 mA/cm²), temperature (330°-355°C), and discharge level (between Na_2S_3 and $\text{Na}_2\text{S}_{2.4}$) on sodium-sulfur cell performance and life are discussed herein.

Experimental

Tubular, central-sodium cells of nominally 14-16 Ah capacity were utilized in this study. The sulfur electrode contained a Union Carbide Thornel VMA® carbon-fiber conductive-mat and either a Saffil® or alumina-fiber paper resistive layer. Incorporation of a porous, high resistivity layer adjacent to the beta"-alumina electrolyte prevents deposition of a passivating sulfur layer on the solid electrolyte during cell charging (7, 11). Saffil, an alumina-based material, was obtained from Imperial Chemical Industries (England), and the alumina-fiber papers from F.K. Fiber, Incorporated (Wilmington, Delaware). Two styles of sulfur electrode were employed: oriented and nonoriented. Unoriented-sulfur electrodes were formed by shredding the conductive mat, twisting the mat fibers together, adding the resistive layer, and finally casting with sulfur. This process yielded an electrode comprised of three randomly oriented sections. Oriented-fiber electrodes were produced by appropriate manipulation of the layered bulk mat (1). The fiber orientation within the sulfur electrode was both radial and axial.

The electrolyte was polycrystalline beta"-alumina (99%), with an ~3 Ω-cm 330°C specific resistivity. The cells utilized in this study contained thermocompression-bonded seals and were vacuum filled with liquid sodium.

Cells were cycled under constant current conditions between individually preset voltage limits at 330°-355°C. Current densities are referenced to the 18.5 cm² β'-

alumina electrolyte. An automated test system monitored cell voltage every 3 min. Cells were placed on open circuit for 3 min every 0.5h. Cycles performed at current densities ≥400 mA/cm² employed a 15 min interval between open-circuit periods. Direct current (dc) resistances were calculated from the difference in open-circuit voltage (OCV) and load voltage at the same depth of discharge divided by the load current (1).

Simultaneous alternating current (ac) resistance measurements were performed with a lock-in amplifier. Details of the experimental arrangement were described previously (1), and will therefore only be briefly summarized herein. Appropriate precautions were taken to prevent interaction of the dc and ac systems. The alternating current signal, generated by the lock-in amplifier, flowed across an in-series limiting resistor to the cell. Two voltage probes were connected between the cell and lock-in amplifier. Single frequency measurements between 10 and 100,000 Hz on 16 Ah cells revealed that, except for severely asymmetric cells, no frequency dependence of impedance was observed (1). This indicated that capacitive and inductive contributions to cell impedance were minimal. Therefore, ac measurements were conducted at 1 kHz.

Efficiencies were the quotient of energy out during cell discharge and energy in during cell charge. Capacities were determined by dividing the ampere-hours removed during discharge by the theoretical capacity. An effective polysulfide composition corresponding to Na_2S_3 was the theoretical limit. Oei (2, 3) and Janz *et al.* (4) have shown that, at temperatures greater than ~100°C, Na_2S_3 is a eutectic mixture of Na_2S_2 and Na_2S_4 . While this is generally accepted, there remains some controversy over the exact polysulfide ion composition and distribution within the melt (5, 6). The sodium trisulfide formulation used herein simply refers to a quantity of charge passed sufficient to produce an overall sodium-to-sulfur ratio of 2:3 in the sulfur-electrode compartment. Likewise, similar chemical symbolizations, for example, $\text{Na}_2\text{S}_{3.4}$ or $\text{Na}_2\text{S}_{2.6}$, indicate

* Electrochemical Society Active Member.

sodium-sulfur ratios, not necessarily discrete polysulfide species.

Results and Discussion

Current density and temperature.—The intent of this study was to evaluate cell quality, and in particular, to assess resistive layer performance and durability vis-à-vis aggravated cycling regimens. Identical discharge and charge current densities were utilized in each test. Current densities from 54 to 865 mA/cm² were examined between 330° and 355°C; normal operating conditions were 330°C and 108 mA/cm². The highest cycle rate, 865 mA/cm², was tested only at 335°C. When operated at current densities ≥ 400 mA/cm², the cells were placed on open circuit every 15 min to increase the number of open-circuit data points. A 16 Ah cell operating at 108 mA/cm² requires ~12-14h per complete cycle (both charge and discharge), and typically yields 14 or 15 open-circuit voltage points per half-cycle, i.e., for the discharge or charge half-cycle. Operation at 432 mA/cm² was completed within 4h, which would have resulted in only 3 or 4 OCV readings per half-cycle without the extra open-circuit periods. The paucity of OCV points was further manifested at 865 mA/cm². These measurements were performed on sodium-sulfur cells with both oriented- and nonoriented-sulfur electrodes. Unless otherwise stated, the results were independent of sulfur electrode type.

Charge-discharge plots as a function of current density at 335°C are presented in Fig. 1. Further details are contained in Table I. As can be seen in Table I, high efficiencies were maintained at current densities ≤ 250 mA/cm². Efficiency declines at 432 and 865 mA/cm² resulted from increased IR drop and enhanced concentration polarization effects. The latter resulted from growing reaction heterogeneity caused by an inability of the melt to diffuse rapidly enough. Reaction nonuniformities are particularly evident in the rapid drop in discharge load voltage at ~80% capacity during the 865 mA/cm² measurement (Fig. 1). An attendant increase in dc and ac resist-

Table I. Current density effects on sodium-sulfur cell performance at 335°C^a

Cycle no.	Current density ^b (mA/cm ²)	Efficiency ^c (%)	Capacity ^d (%)	AC cell resistance ^e (mΩ)
75	54	91.4	82.5	36.6
12	108	89.6	78.8	35.1
14	216	82.2	72.6	33.8
18	432	68.4	77.6	29.2
48	865	58.9	80.1	24.3

^a Cell contained oriented sulfur-electrode and Saffil-resistive layer.

^b Current density referred to the electrolyte log mean area, 18.5 cm².

^c (Energy out during discharge/energy in during charge) $\times 100$.

^d (Ampere-hours removed during discharge cycle/theoretical capacity) $\times 100$. This cell contained 28.7g sulfur, which yields a theoretical capacity of 16.0 Ah.

^e Alternating current resistance measured during discharge at a polysulfide composition corresponding to Na₂S_{3.6}.

ance was noted. A lesser increase in ac resistance was observed at 432 mA/cm². No change in the 432 mA/cm² dc resistance was detected because of the 15 min interval between open-circuit, hence, resistance points.

Small, intercycle capacity fluctuations may have resulted due to "limit" errors. These errors have more impact at higher current rates. For a given temperature, voltage cutoff limits were calculated from the limits employed at 108 mA/cm². The data in Table I indicate that, except for the 216 mA/cm² case presented, the limits were reasonably correct. Similar agreements were retained at the other temperatures studied. At a given temperature, decreased resistances at elevated current densities may have resulted from heating effects. A thermocouple laid on the thermocompression bond registered only a 3°C change during the 432 mA/cm² cycle. Fluctuations in the thermocouple reading may not accurately reflect internal cell variations. However, thermocouple insertion directly into the cell is difficult from an engineering viewpoint. Direct attachment of several thermocouples to the sulfur canister of a 120 Ah, central-sodium cell revealed that the cell temperature changed from 373° to 375°, 377° to 385°, and 373° to 403°C when the cell was cycled at 96, 192, and 383 mA/cm², respectively.

During cell charging, sodium polysulfides are oxidized, eventually to sulfur. This latter reaction occurs at the resistive-mat/conductive-mat interface (1). Except for specially designed cells, sodium-sulfur cells with a poorly performing or no resistive layer cannot be charged at appreciable rates, ≥ 100 mA/cm², much beyond the one-phase/two-phase border (7). This results from formation of a blocking layer of sulfur on the solid electrolyte surface. The two-phase region extends between ~60 and 0% depth of discharge, and derives its name from the immiscibility of the sulfur and Na₂S₃ present. One measure of the resistive-mat effectiveness in preventing sulfur deposition on the beta"-alumina electrolyte surface, is the degree of charge acceptance. This is the number of ampere-hours returned to the cell during charging, expressed as a percentage of the theoretical capacity. A charge acceptance of 0% corresponds to a sodium trisulfide melt, i.e., the fully discharged state, and a charge acceptance of 100% represents a pure sulfur melt, i.e., a completely charged state.

The Saffil-resistive layer efficacy in preventing sulfur deposition on the beta"-electrolyte surface is depicted in Fig. 1. Note the relative flatness of the 108-432 mA/cm² two-phase charge curves and the high, ~85-90%, charge acceptance achieved at all current densities. An alternate analysis method is to compare the discharge and charge cycle times. It was expected that the larger current densities, 432 and 865 mA/cm², would cause excessive sulfur deposition during charge and inhibit the time of the charge cycle. In fact, the discharge/charge times agreed to within 6 min or less. The automated test system moni-

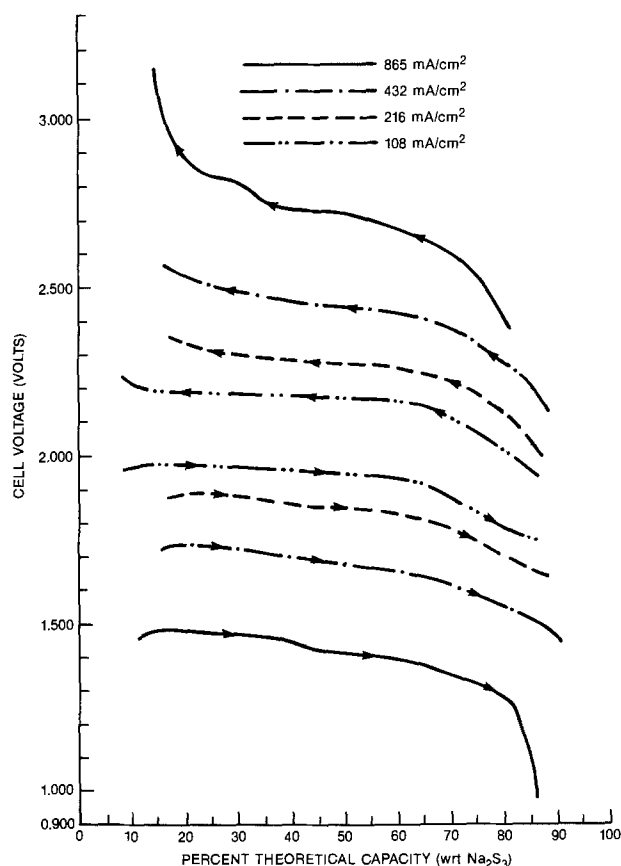


Fig. 1. Charge-discharge characteristics of a 16 Ah laboratory cell operating at 335°C.

tored cell voltages every 3 min. No changes in cycling conditions, *i.e.*, whether a cell is charging or discharging, can be made in shorter time intervals. Thus, charge/discharge time agreement to within two clock periods is considered excellent. Apparent discrepancies shown in Fig. 1 arose from current density effects. At 108 mA/cm², only 0.1 Ah (0.63% with respect to depth of discharge) were passed per 3 min clock period, whereas 0.8 Ah (5.00%) were passed at 865 mA/cm².

The humps observed in the 865 mA/cm² charge curve were reminiscent of those seen in sodium-sulfur cells with a carbon-based resistive layer (1). This material has a moderate electrical resistivity (11) and thus allows some passivation of the solid electrolyte surface by sulfur (1). Cyclic voltammetric studies on oxidation of Na₂S₄ to sulfur by Tischer and Ludwig (6) demonstrated that sulfur was removed from their electrode surface by a chemical reaction which followed the electron transfer step. At low enough charge rates, <100 mA/cm², resolubilization by chemical reaction is faster than sulfur deposition and no passivation occurs. At intermediate rates, ~100-250 mA/cm², a balance between sulfur deposition and removal is maintained, and the large resistive-mat/conductive-mat interfacial area precludes formation of a continuous blocking layer. The sulfur deposition and removal imbalance becomes further aggravated at elevated current densities. Net sulfur deposition occurs and a blocking layer forms. This causes an erratic and rapid increase in cell voltage.

Temperatures between 330° and 355°C influenced the data listed in Table I. For the cells examined, temperature increased efficiency by ~3% per 10°C. The increase became less at the lower current densities as the efficiency approached the IR-limited value. For a given current density, resistance decreased with increasing temperature in a nonsystematic manner. Capacities increased with temperature. Increases were more apparent at elevated current densities, 432 mA/cm². This was not unexpected since diffusional limitations were less at higher operating temperatures. Therefore, more ampere-hours could be removed before reaction nonuniformities depressed the cell voltage beyond the cutoff limit.

A group of cells containing various sulfur electrode types was placed on test at 216 mA/cm² and 330°C to assess the effects of more rapid cycling on cell performance. This current density was selected based on lifetime expectations and experimental ease. These cells have accumulated ~900 Ah/cm² (~700 cycles) with only minimal changes in cell characteristics. The efficiencies and capacities remain about 82 and 80%, respectively.

Discharge between Na₂S₃ and Na₂S₂.—The theoretical capacity of a sodium-sulfur cell is calculated from the quantity of sulfur loaded into the cell during assembly, referenced to the number of coulombs required by Faraday's law to convert all the sulfur to Na₂S₃. Capacities are typically expressed in terms of ampere-hours or percentages of the theoretical capacity. Based on this definition, values in excess of 100% are possible when the final discharge depth is such that the effective polysulfide composition is Na₂S_x, and where $x < 3$. Full charge, 0% depth of discharge, corresponds to a pure sulfur melt.

The terms "overdischarge" or "deep discharge" are used herein to refer to situations in which polysulfides lower than Na₂S₃ were formed. Lowering or decreasing the discharge cutoff voltage limit, *e.g.*, changing the limit from 1.7 to 1.6V, allows more discharge time, and is termed "increasing the discharge depth." Increasing or raising the discharge cutoff voltage limit produces shorter discharge times, and implies that the discharge depth was "decreased." These conventions are shown diagrammatically in Fig. 2, and are used throughout the remainder of this paper.

While typical laboratory cells were constructed with electrochemically equivalent sodium and sulfur weights, the effects of overdischarge on cell performance were studied in cells specially designed to be sulfur limited.

The cells utilized in this part of the study were filled with excess sodium and underfilled with sulfur. Sulfur weight reduction not only decreased the theoretical capacity, but also served to increase the volume available for polysulfide formation within the sulfur-electrode compartment. Deep discharge experiments were conducted on these 14.2 Ah, 25.5g sulfur cells at 108 mA/cm² and 330°C. Although the discharge voltage limit was varied, a constant charge cutoff voltage was employed. No dependence of the results on sulfur-electrode orientation, *i.e.*, whether the cell contained an oriented- or unoriented-sulfur electrode, was observed.

Alternating current resistance measurements were performed several times on cell B878L during the first 28 cycles. The results indicated that performance had stabilized. The lower limit, *i.e.*, discharge cutoff voltage, had been set at 1.80V. A dc cell resistance of 50 mΩ at the end of discharge implies that the IR-corrected voltage corresponds to a 1.90V potential. Interpolation of Gupta and Tischer's (8) open-circuit voltage data indicates that Na₂S_{3.6} has this potential. The cell cycled to ~Na₂S_{3.7} and ~Na₂S_{3.6} in cycles 5 and 28, respectively. Based on further interpolation of Gupta and Tischer's data, a new lower limit was chosen, and the cell should have discharged 14.2 Ah to Na₂S₃. The data in Table II indicate that this was indeed the case, *cf.* cycle 33. In examining the polysulfide composition column of Table II, one might think, that the capacity for this cycle should have been 100%. The capacity was not 100% because the cell had not recharged completely to sulfur at the end of the previous cycle. This fact should be borne in mind when utilizing this table. The cell was cycled in this manner a total of nine cycles. A very slight increase in ac resistance at the end of discharge was observed in these cycles, although no overall increase in resistance was evident.

Two unsuccessful attempts were made to cycle the cell to Na₂S_{2.6}, *cf.* Table II, cycles 41 and 43. The lower limit was decreased further and the cell cycled to Na₂S_{2.6}. Surprisingly, the cell resistance, both ac and dc, was higher at the end of discharge than at the beginning (Table II, cycle 44). One should not presume that the resistance rose the entire cycle. Rather, it increased at the end only. In fact, the ac resistance climbed from ~33 mΩ at 13.2 Ah depth of discharge to ~96 mΩ at the end of discharge. The effects of discharge depth on the cell ac resistance behav-

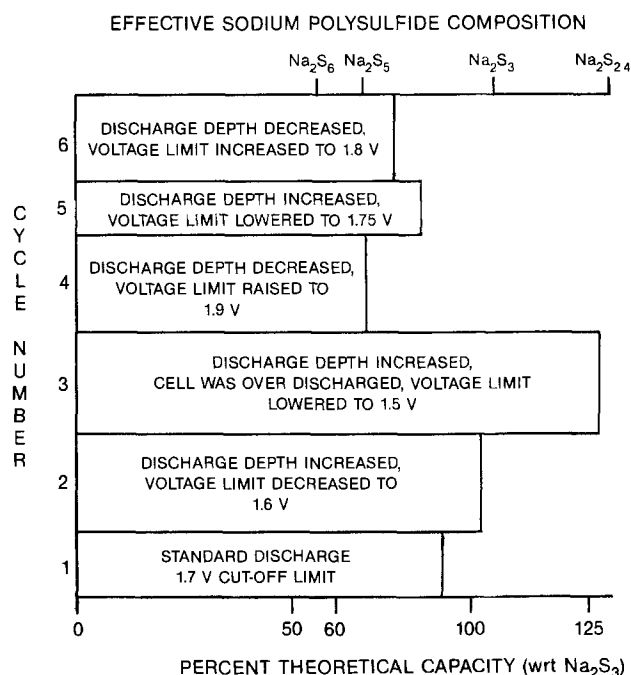


Fig. 2. Bar graphs demonstrating definition of terms. As the percent theoretical capacity increases, the discharge cutoff voltage is lowered or decreased. Conversely, a decrease in theoretical capacity results from raising or increasing the discharge cutoff voltage.

Table II. The effects of discharge depth on laboratory cell B878L Performance

Cycle no.	Lower limit ^a (V)	Capacity ^b (%)	Efficiency ^c (%)	Ah ^e	Polysulfide composition ^d	Weight percent sulfur ^e	R _{ac} ^f (mΩ)
5	1.80	76.8	89.9	11.4	Na ₂ S _{3.7}	72.3	34.5 (74.6)
28	1.80	76.1	90.4	11.7	Na ₂ S _{3.6}	71.6	33.5 (73.2)
33	1.69	93.7	90.2	14.2	Na ₂ S _{3.0}	67.7	33.6 (74.6)
39	1.69	91.6	88.7	14.0	Na ₂ S _{3.0}	68.0	35.3 (73.9)
41	1.64	100.0	90.4	15.1	Na ₂ S _{2.8}	66.3	36.2 (72.5)
43	1.60	101.4	88.1	15.2	Na ₂ S _{2.8}	66.2	35.0 (73.2)
44	1.50	110.6	— ^h	16.4	Na ₂ S _{2.6}	64.2	34.7 (73.9)
45	1.50	102.1	89.3	15.2	Na ₂ S _{2.8}	66.2	36.0 (70.4)
53	1.50	98.6	88.1	14.9	Na ₂ S _{2.9}	66.6	34.4 (73.9)
56	1.75 ⁱ	77.5	89.4	11.9	Na ₂ S _{3.6}	71.4	35.5 (73.9)

^a Discharge cutoff voltage.

^b Discharge capacity. Based on sulfur loading of 25.5g, which yields Na₂S₂ at 14.2 Ah. Note: capacity may not be 100% even though final composition is Na₂S₃ because previous charge cycle did not charge to 0 Ah depth of discharge (cf. text).

^c Energy out during discharge/energy in during charge.

^d Average polysulfide composition at end of discharge.

^e Weight percent sulfur in melt at end of discharge. Based on average composition and assumes no solid deposition occurred.

^f Alternating current discharge resistance at percentage of theoretical discharge listed parenthetically.

^g Discharge depth in ampere-hours.

^h No value obtainable due to equipment malfunction.

ⁱ Direct current resistance increase from ~50 to ~57 mΩ occurred between cycles 41 and 53. The resistance increase was partially offset by utilization of a lower cutoff voltage.

ior are shown in Fig. 3. When cell charging was initiated, the ac resistance plummeted to ~39 mΩ. Other than an increase in the two-phase charge resistance, there were no apparent effects of overdischarging the cell on the charge curve (*vide infra*). The data in Table II demonstrate the overall consistency in discharge performance throughout these measurements.

Although the discharge cutoff voltage limit remained fixed for ten cycles, the discharge depth decreased. Note, for example, that the next cycle depth of discharge, cycle 45, was the same as in cycle 43, even though the cycle 43 cutoff voltage was 100 mV higher. Figure 4 presents an overlay of cycle 28 and 45 discharge/charge behavior. The rapid resistance increase at the end of discharge in cycle 45 is evident in the figure. During these ten deep cycles, the dc resistance rose from ~50 to ~57 mΩ and the depth of discharge reached a plateau at ~Na₂S_{2.8}. The importance of this composition is discussed below.

The discharge voltage was raised in cycle 55. The cell was reexamined in cycle 56. The data for cycle 56 in Table

II imply a return to normalcy occurred. As in previous cycles over a similar polysulfide composition regime, no resistance increase was detected at the end of discharge. The two-phase charge resistance was lower than in cycles 44 to 54; however, it was elevated with respect to the cycles 5 to 28 values. The cell failed two cycles later. Therefore, it was not possible to determine if the cell would completely return to its original performance.

At the time cell B878L failed, it was unclear whether or not the failure was related to the overdischarge experiments. Therefore, a second cell, B890L, was constructed. These two cells were identical with respect to sodium and sulfur weights and resistive layer materials. They differed only in the design of the sulfur electrode. Cell B890L contained an oriented-sulfur electrode. This cell was broken in for ~35 cycles before the deep discharge experiments were initiated. A rise in the discharge resistance was ob-

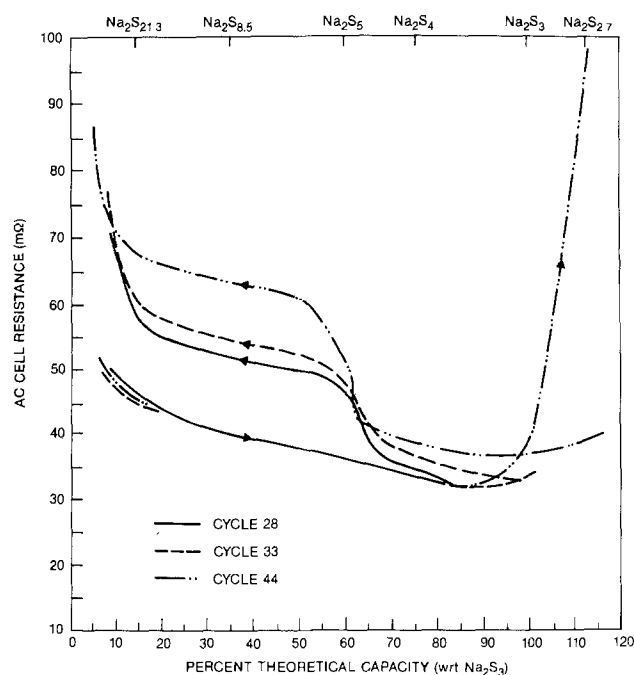


Fig. 3. Alternating current cell resistance vs. percent theoretical capacity for laboratory cell B878L. Cell operated at 108 mA/cm² and 330°C.

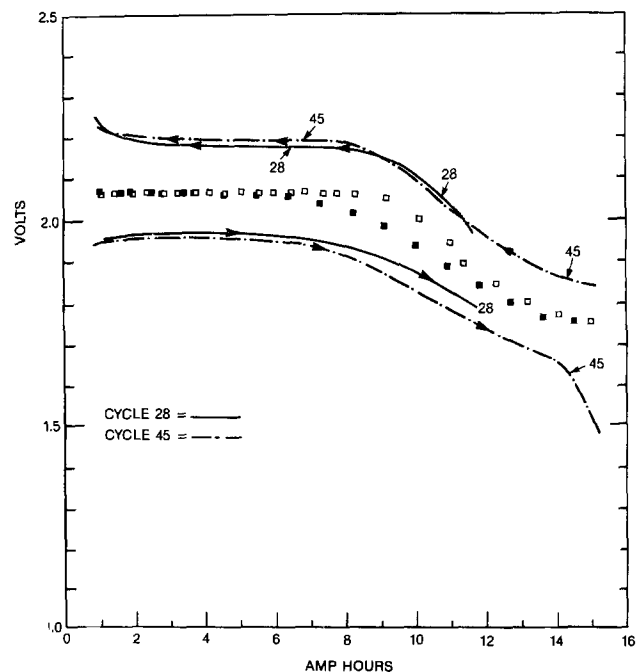


Fig. 4. Charge-discharge characteristics for cell B878L obtained in cycles 28 and 45. Abscissa referenced to discharge state. Filled and open squares represent discharge and charge open-circuit voltages, respectively. Note the precipitous drop in discharge voltage and the open-circuit voltage plateau beyond 14 Ah in cycle 45. No open-circuit voltage data are displayed for cycle 28. Theoretical capacity is 14.2 Ah.

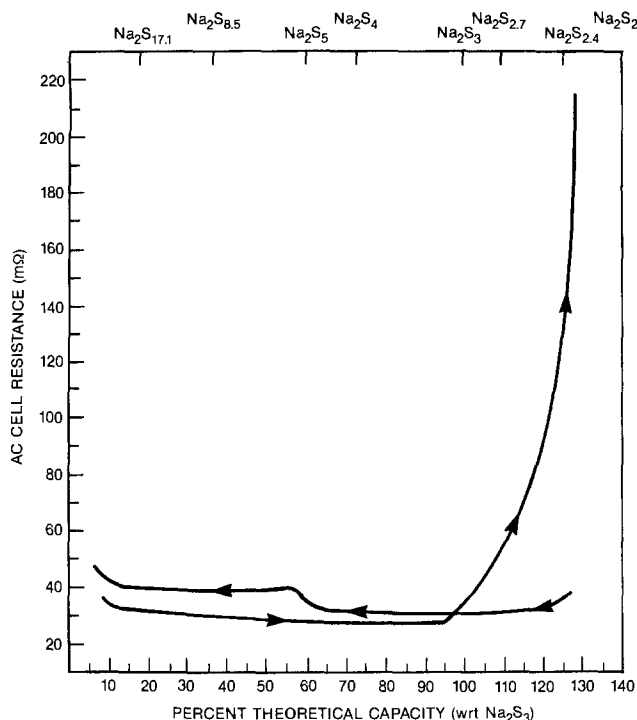


Fig. 5. Alternating current cell resistance vs. percent theoretical capacity for cell B890L. Data recorded during cycle 41 at 108 mA/cm² and 330°C.

served when the cell was cycled at or below Na₂S₃. The magnitude of the resistance rise was dependent on the final discharge depth. Figure 5 displays the ac resistance behavior obtained when cell B890L was discharged to an effective polysulfide composition corresponding to Na₂S_{2.4}. The current was reversed at this point for several reasons. First, the load voltage had dropped to ~0.6V.

Second, the ac discharge resistance increased from ~28 to ~210 mΩ. The initially lower ac resistance of cell B890L compared to cell B878L results from sulfur-electrode orientation effects (1). Interestingly, upon charge initiation, the ac cell resistance was ~34 mΩ. Cell B890L behavior further mimicked that of cell B878L, in that only the two-phase charge resistance increased (as discussed above and shown for cell B878L in Fig. 3).

In contrast to the regimen employed for cell B878L, the lower voltage limit for cell B890L was returned to its original value after only one deep discharge cycle. After ~30 invariant cycles, the lower voltage limit was once again decreased to permit discharge beyond Na₂S₃. Within approximately ten cycles, the discharge depth began to decrease (Fig. 6). The upper curves in the figure display the charge and discharge capacity limits vs. cycle number. Changes in the discharge cutoff voltage are marked. Although the depth of discharge was limited with respect to the "very deep" cycles, the charge-discharge plots displayed characteristics reminiscent of severe overdischarge, cf. curve for cell B878L cycle 45 in Fig. 4. Alternating current resistance analysis revealed that extreme overdischarge was indeed occurring. The decline in discharge depth and its erratic nature were very similar to the behavior observed in cell B878L just before its failure. Therefore, cell B890L was removed for examination (9).¹

The cause of the resistance rise at the end of discharge is explained with the aid of Table II and Figs. 3, 5, and 7. Figure 7 presents a sodium sulfur phase diagram (2, 5, 8). An isothermal line has been drawn at 330°C, the cell operating temperature, and several key points labeled. During discharge, sodium is injected into the sulfur compartment and sodium polysulfides of various compositions form. The exact composition is dependent on the amount of sodium injected and the quantity of sulfur present. Until the sulfur content in the polysulfides reaches ~78 weight percent (w/o), an immiscible mixture

¹ Post-test examination of sodium-sulfur cells is part of an ongoing research effort. Results obtained on cell B890L will be reported separately.

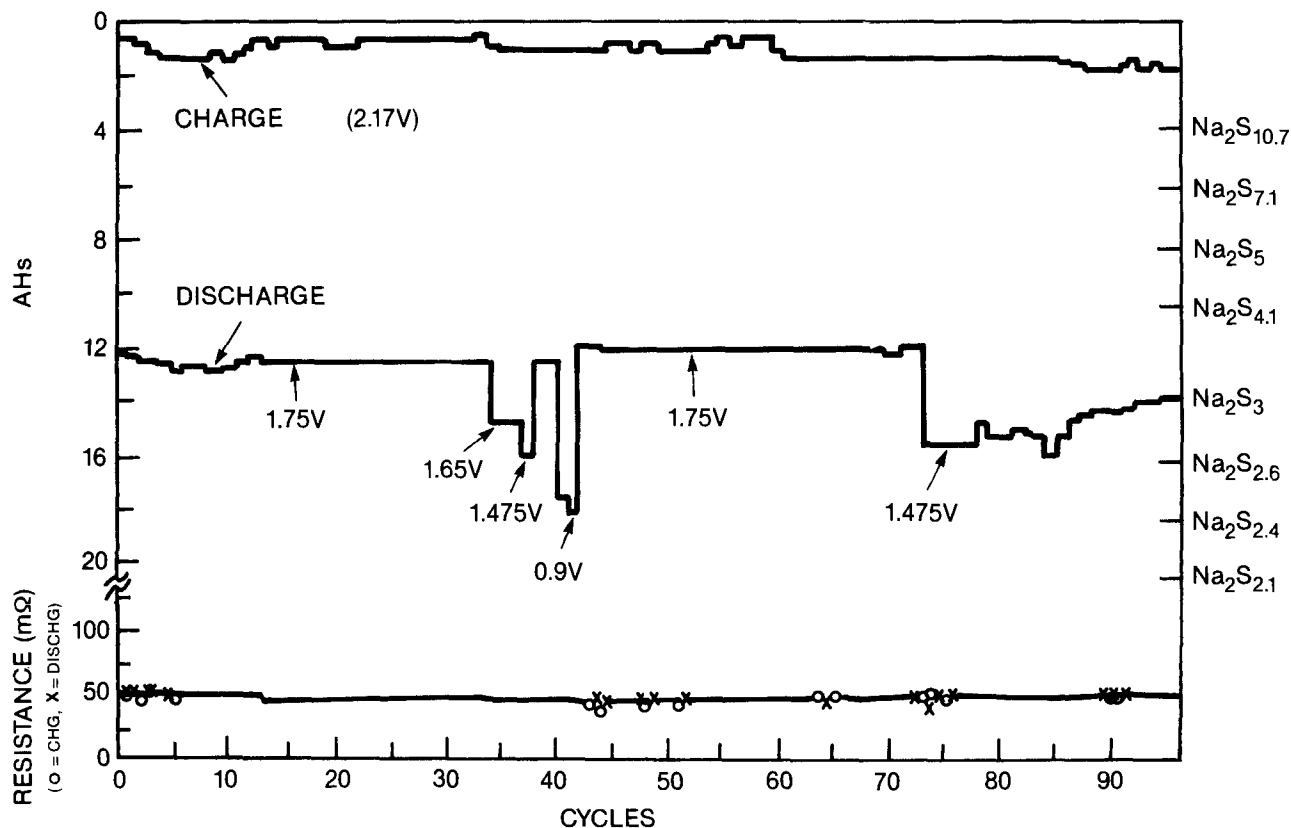


Fig. 6. Cycle limits (upper) and resistance (lower) vs. cycle number for laboratory cell B890L. Ampere-hours are referenced to discharge state. The corresponding effective polysulfide compositions are listed on the right-hand vertical axis. Cell operated at 108 mA/cm² and 330°C. Changes in the discharge cutoff voltage limit are marked.

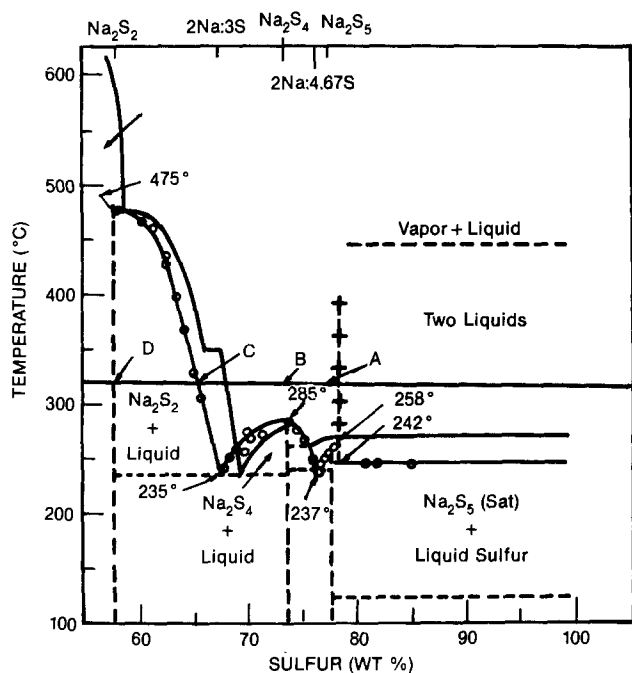


Fig. 7. Sodium-sulfur phase diagram (2, 5, 8)

of sulfur and Na_2S_5 results. This area is to the right of A in Fig. 7. Point A represents pure Na_2S_5 . Further discharge results in the formation of a homogeneous mixture of Na_2S_5 and Na_2S_4 , A to B. The exact composition of the mixture varies with depth of discharge. As the sulfur content drops below $\sim 74\%$, point B in Fig. 7, increasing amounts of Na_2S_2 form (5, 6). At the cell operating temperature, Na_2S_3 is really an equimolar mixture of Na_2S_2 and Na_2S_4 (2-5) both of which remain in solution. A slight resistance increase at the end of discharge, cycle 33 in Fig. 3, for example, indicates that the Na_2S_2 solubility was exceeded. An equilibrium exists between solid and liquid Na_2S_2 . As the discharge depth increases, the amount of Na_2S_2 present increases. If the quantity of Na_2S_2 present is greater than the solubility limit, solid Na_2S_2 will precipitate and the resistance is expected to rise. Local current nonuniformities can affect the "calculated" composition at which solid Na_2S_2 forms. This implies that just because the coulombs passed indicate a particular polysulfide composition exists, regions of the cell may be overdischarged unknown amounts. This was demonstrated by a resistance rise at the end of discharge during the 432 and 865 mA/cm^2 cycles discussed above.

Point C in Fig. 7 is critical. To the right exists a homogeneous solution of Na_2S_2 and Na_2S_4 ; to the left is solid Na_2S_2 and a solution of composition C. This point corresponds to $\text{Na}_2\text{S}_{2.8}$, which contains ~ 66 w/o sulfur. Discharge leading to precipitation of Na_2S_2 with an overall resultant composition in the BC region should be reversible. However, little is known about discharge into the CD region. If the morphology of the deposited Na_2S_2 changes, it may not be possible to resolubilize the solid. The studies of Tischer and Ludwig (6) and South *et al.* (10) indicate that electrochemically formed Na_2S_2 may be more effective than chemically formed Na_2S_2 in producing a blocking layer within the cell. Chemically formed Na_2S_2 is sodium disulfide produced by disproportionation of Na_2S_3 or in a chemical reaction following an electron-transfer step. Electrochemically formed Na_2S_2 results from the reduction of higher polysulfides.

Examination of cell B878L data in Table II reveals that the cell was discharged more deeply than point C during cycles 41 to 53. Figures 3 and 5 clearly demonstrated the effect of solid precipitation on cell resistance. It is extremely important to note that the ac discharge resistance remained virtually unchanged in the two-phase region and in the one-phase region until solid deposition occurred. Further, the ac discharge resistance increased

more rapidly during subsequent cycling. Interestingly, the resistance rise stabilized and the capacity leveled out at point C.

The OCV data for the cycles listed in Table II were plotted against percent discharge. Some of these curves are shown in Fig. 8. The solid line represents the "ideal" curve generated from the original cell sulfur weight and Gupta and Tischer's data (8). The horizontal line represents the constant two-phase voltage, and the sloped line the varying one-phase values. Data from cycles 28 and 33 (Fig. 8a) closely follow the ideal curve and indicate that the sulfur weight was reasonably accurate. Deviations from ideality within these two cycles result from concentration polarization effects. Cycle 41 was the first cycle conducted to $\text{Na}_2\text{S}_{2.8}$. As can be seen in Fig. 8a, a very small shift relative to previous cycles and ideality towards lower percent discharge occurred. Additional shifts were seen during cycles 43 and 45 (Fig. 8b). The OCV percent discharge performance stabilized and did not return to its original relationship even when the discharge cutoff voltage was returned to its starting value. This can be seen by comparing cycle 28 (Fig. 8a) to cycle 56 (Fig. 8b). The cycle 56 data was coincident with that from cycles 45 to 53. Although not shown, similar trends were seen in cell B890L.

These curves imply that cycling at or below $\sim \text{Na}_2\text{S}_{2.8}$, point C in Fig. 7, results in permanent sulfur loss. For a given number of ampere-hours removed, utilization of a corrected, *i.e.*, decreased, sulfur weight would yield a greater percentage discharge and shift the OCV curves to the right in Fig. 8. Further these curves serve to illustrate the difference between electrochemically and chemically formed Na_2S_2 (6). Resolubilization of electrochemically formed Na_2S_2 was not accomplished under the conditions of these tests. In contrast, chemically formed Na_2S_2 did not result in permanent sulfur loss, *cf.* Fig. 8a, cycle 33. This concept was tested in a sodium-sulfur cell. Following break in, the discharge limit was lowered and a cell cycled to $\text{Na}_2\text{S}_{2.95 \pm 0.05}$ for ~ 30 cycles. A small resistance rise was observed at the end of discharge. The cutoff voltage limit was then returned to its original value. Comparisons to the initial cell performance indicated that the cell continued to operate with no change in performance, shift in the OCV-percent discharge plot, or resistance increase, ac or dc, for ~ 200 cycles before it was lost due to an oven failure. Although it was possible to discharge cells below $\text{Na}_2\text{S}_{2.8}$ as computed from the initial sulfur weight, it seems that repeated discharge beyond this point resulted in permanent sulfur loss and decreased cell life.

Severe overdischarge like that shown in Fig. 5 or for cycle 44 in Fig. 3 was observable by both ac and dc resistance techniques. Evidence of overdischarge discernible in dc measurements was a rapid drop in cell voltage, cycle 45 in Fig. 4, and a leveling out of the OCV at $\sim 1.76\text{V}$, cycle 45 in Fig. 4 and cycles 43 and 45 in Fig. 8b. The latter phenomenon is consistent with Gupta and Tischer's open-circuit voltage data (8). More mild overdischarge, cycle 33 in Fig. 3, was usually only detected in ac measurements. This was due to the 30 min interval between dc resistance points.

The effect of deep discharge on the charge resistance was extremely enlightening. Examination of Fig. 3 indicates that the one-phase ac resistance was affected minimally by the depth of discharge. However, the two-phase resistance increased substantially. Comparison of cycle 44 and either cycle 28 or 33, reveals that a slight increase occurred in the one-phase region in cycle 44. The effect on the two-phase charge resistance was not as benign. For example, an $\sim 30\%$ increase was observed in cycle 44 relative to cycle 28 at $\sim 42\%$ depth of discharge. This strongly suggests that Na_2S_2 precipitates at the conductive-mat/resistive-mat interface. If solid deposition occurred on the beta' electrolyte or in the bulk of the sulfur electrode, both charge and discharge resistances would be affected. During charge, reentry into the two-phase region is when the resistive-mat performance is

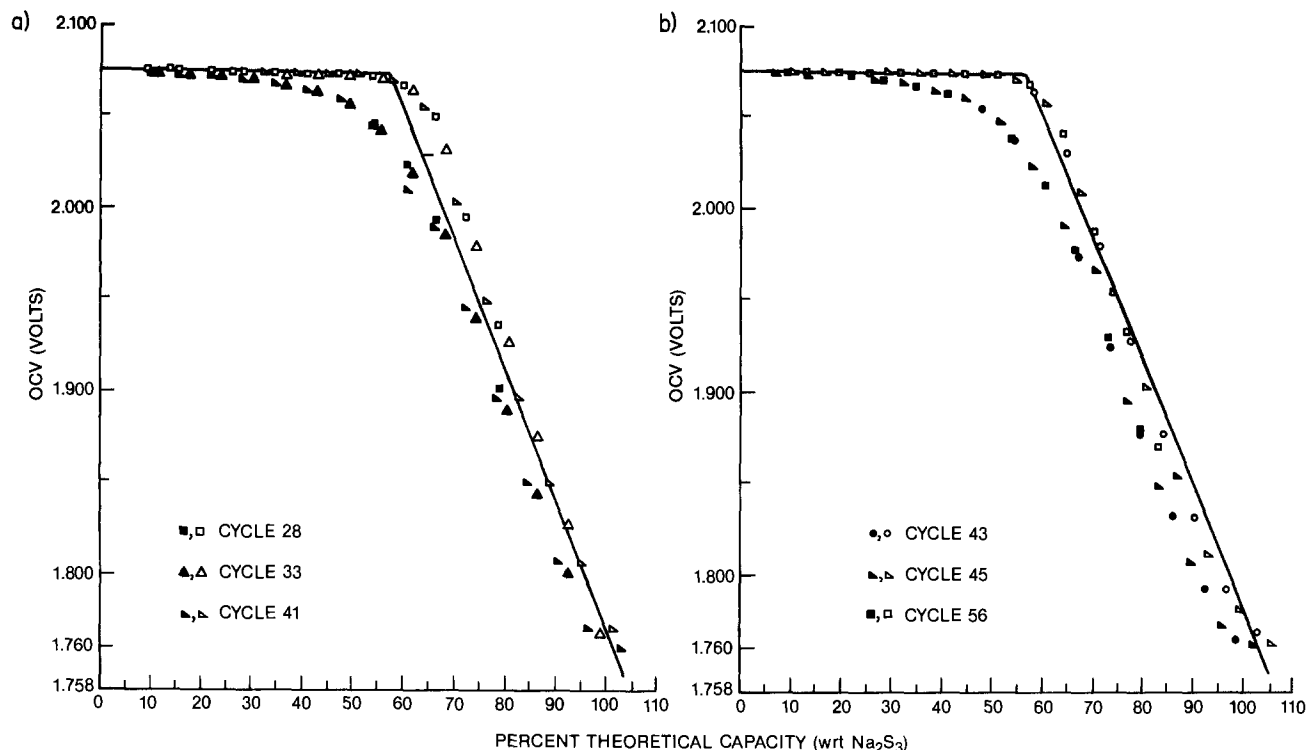


Fig. 8. Plots of open-circuit voltage vs. percent theoretical capacity for cell B878L. Curves obtained at 330°C. Empty and filled data points represent charge and discharge, respectively. Solid-line curve represents ideal curve (8).

most crucial. Solid Na_2S_2 formation in this area should hinder sulfur formation and further aggravate the normally observed resistance rise.

Conclusions

An ac resistance technique has been applied to the study of current density and depth of discharge effects on sodium-sulfur cell performance and life. 16 Ah laboratory cells were discharged and charged at current densities between 54 and 865 mA/cm². The equality of the charge and discharge cycle times demonstrated the extreme effectiveness of ceramic-based resistive layers in preventing sulfur passivation of the beta"-electrolyte surface. Temperatures between 330° and 355°C increased cell efficiency, ~3% per 10°C, and capacity, and decreased cell resistance. Cells operated at twice the normal current density have achieved ~700 cycles, ~900 Ah/cm², while remaining ~82% efficient. The capacities were ~80% of theoretical.

The effects of overdischarge, *i.e.*, formation of polysulfide species Na_2S_x where $x < 3$, on cell performance were studied in cells specially constructed so as to be sulfur limited. Final effective compositions of $\text{Na}_2\text{S}_{2.6}$ and $\text{Na}_2\text{S}_{2.4}$ were achieved in separate cells. An ac resistance rise was detected when either cell was discharged at or below Na_2S_3 . The magnitude of the rise was dependent on the final discharge depth. Direct current measurements are less sensitive and showed abnormal behavior only in the case of severe overdischarge. The resistance rise was attributed to having exceeded the Na_2S_2 solubility limit, thus causing solid Na_2S_2 deposition. The one-phase ac charge resistance and subsequent discharge resistance were unaltered. In contrast, the two-phase charge resistance increased. This implied that precipitation of Na_2S_2 occurred at the resistive-mat/conductive-mat interface. The results of these tests indicated that severe overdischarge can be tolerated in laboratory cells to a very limited degree and for a very limited number of cycles. Whether this limit is one or two cycles has not been deter-

mined. On a recurring or repeated basis, however, discharge beyond $\text{Na}_2\text{S}_{3-x}$, where $x \geq 0.2$, shortened life. Discharge "to" Na_2S_3 appeared satisfactory; this is attributed to the differences in behavior of chemically and electrochemically formed Na_2S_2 .

Acknowledgments

The authors appreciate the assistance of T. M. Evenden in constructing the cells utilized in this study and Dr. R. W. Powers for critical review of this manuscript. The support of the Electric Power Research Institute under Contract RP 128-7 is gratefully acknowledged.

Manuscript submitted Oct. 24, 1984; revised manuscript received Jan. 28, 1985.

General Electric Company assisted in meeting the publication costs of this article.

REFERENCES

1. B. R. Karas, *This Journal*, **132**, 1261 (1985).
2. D.-G. Oei, *Inorg. Chem.*, **12**, 435 (1973).
3. D.-G. Oei, *ibid.*, **12**, 438 (1973).
4. G. J. Janz, J. R. Downey, G. J. Wasilczyk, J. W. Coutts, and A. Eluard, *ibid.*, **15**, 1759 (1976).
5. B. Cleaver, in "The Sulfur Electrode—Fused Salts and Solid Electrolytes," R. P. Tischer, Editor, p. 35, Academic Press, New York (1983).
6. R. P. Tischer and F. A. Ludwig, in "Advances in Electrochemistry and Electrochemical Engineering," Vol. 10, H. Gerischer and C. W. Tobias, Editors, p. 391, John Wiley and Sons, New York (1977).
7. J. L. Sudworth and A. R. Tilley, in "The Sulfur Electrode—Fused Salts and Solid Electrolytes," R. P. Tischer, Editor, p. 235, Academic Press, New York (1983).
8. N. K. Gupta and R. P. Tischer, *This Journal*, **119**, 1033 (1972).
9. D. S. Park, Unpublished results.
10. K. D. South, J. L. Sudworth, and J. G. Gibson, *This Journal*, **119**, 554 (1972).
11. M. W. Breiter and B. Dunn, *J. Appl. Electrochem.*, **9**, 291 (1979).

Mathematical Modeling of the Chlorine Flow-Through Porous Graphite Electrode in the Zinc-Chloride Battery

Emad Roayaie¹ and Jacob Jorné

Department of Chemical Engineering, University of Rochester, Rochester, New York 14627

ABSTRACT

A mathematical model which includes mass transfer within the pores has been applied to the flow-through porous graphite electrode during the discharge of the zinc-chloride battery. The purpose of the model is to obtain key design parameters such as potential distribution, concentration distribution of dissolved chlorine and zinc chloride, and local reaction rate distribution within the porous electrode. The resultant coupled nonlinear differential equations have been solved numerically for the galvanostatic operation. Potential, concentration, and reaction-rate distributions have been obtained for various operating conditions such as specific area of the porous electrode ($100\text{-}1000\text{ cm}^{-2}$), electrolyte flow velocity ($0.5\text{-}3.0\text{ cm/min}$), discharge current density ($30\text{-}100\text{ mA/cm}^2$), electrode thickness ($0.2\text{-}0.4\text{ cm}$), and direction of flow. The results can be used in the optimization of the energy efficiency of the zinc-chloride battery.

The zinc-chloride battery, presently being developed for load leveling and electric-vehicle applications, incorporates porous electrodes. Porous electrodes accommodate the heterogenous nature of electrochemical reactions by providing large reaction rates per unit volume. The effectiveness of the porous electrodes is restricted by the ohmic resistance of the electrolyte in the pores and mass-transfer limitations on the supply of reactants to the porous matrix. To overcome these difficulties, new reactor designs and methods of predicting reactor performance have become increasingly popular (1, 2). The purpose of this study is to apply a mathematical model (3, 7) for improving the porous-graphite chlorine electrode employed in the zinc-chloride battery.

Figure 1 shows the flow configuration of the chlorine electrode in the zinc-chloride battery. The ZnCl_2 electrolyte solution, containing dissolved Cl_2 and KCl and NaCl supporting electrolyte, enters at $x = 0$, flows through the porous graphite, and exits at $x = L$. During discharge, dissolved chlorine is reduced to chloride ion (Cl^-) in the porous electrode $\text{Cl}_2 + 2e \rightarrow 2\text{Cl}^-$ and zinc ion species are produced at the downstream zinc counterelectrode. A mathematical model is developed to evaluate the concentration distribution of dissolved Cl_2 , potential distribution, and local reaction rate within the porous electrode region during discharge.

Mathematical Model

The porous graphite is considered to be of uniform porosity and specific area throughout. The porous electrode is assumed to behave in a one-dimensional manner in which mass transfer within the pores is included. The hydrodynamic motion is assumed to be a plug flow, transport parameters are assumed constant, and activities can be replaced by concentrations. External diffusion resistances are negligible.

Scanning electron micrographs of porous graphite (Union Carbide, PG-60) are shown in Fig. 2. The specific macroarea can be estimated from Fig. 2a to be around $100\text{-}600\text{ cm}^{-2}$. A 500 times magnification of a single pore is shown in Fig. 2b, from which the pore diameter is estimated at 10^{-2} cm ($100\text{ }\mu\text{m}$). It is assumed that only the macroarea is being used since the reaction of chlorine is quite fast and diffusion within the micropores is limited.

In the absence of electrical migration, the following mass-conservation equation can be written for dissolved chlorine (3)

$$-\epsilon D \frac{d^2 c_R}{dx^2} + v \frac{dc_R}{dx} = a j_{Rn} \quad [1]$$

where c_R is the dissolved chlorine concentration, ϵ is the porosity, D is the effective diffusion coefficient, v is the

superficial velocity, and a is the specific interfacial area (cm^{-1}). J_{Rn} is the local flux of dissolved chlorine between the solution and the pore wall, and can be expressed by the average mass-transfer coefficient k_m

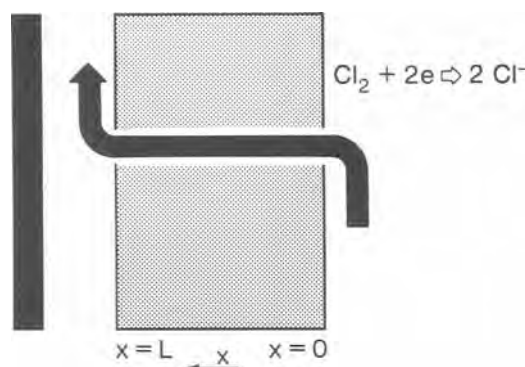


Fig. 1. Flow configuration of the flow-through porous chlorine electrode during discharge.

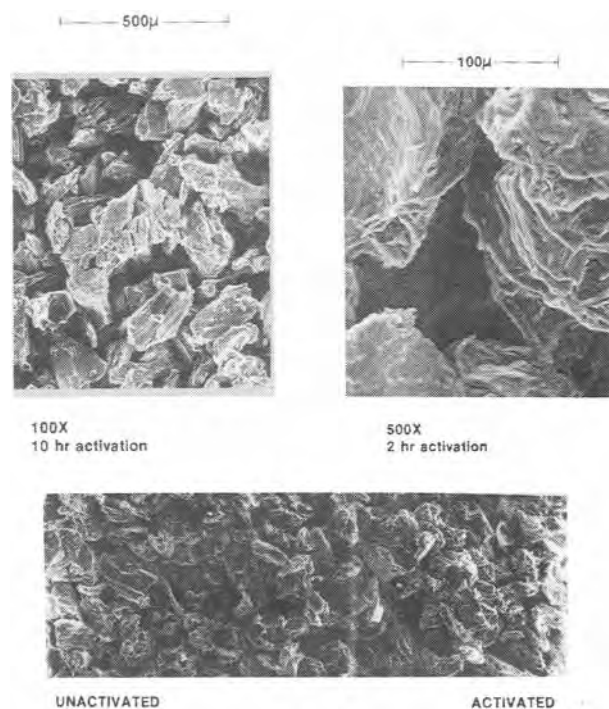


Fig. 2. Scanning electron microscope of porous-graphite (Union Carbide PG-60). A (top left): After 10h activation in H_2SO_4 . B (top right): Close-up of a single pore. C (bottom): Cross-sectional view of 0.15 cm thick porous graphite activated on one side.

¹Present address: Department of Chemical Engineering, Wayne State University, Detroit, Michigan 48202.

$$j_{Rn} = -k_m(c_{Rf} - c_{Rw}) \quad [2]$$

where c_{Rw} is the concentration of dissolved chlorine at the wall.

The local flux can be also expressed by the Butler-Volmer equation

$$J_{Rn} = \frac{S_R i_{0R,ref}}{nF} \left\{ \exp \left[\frac{\alpha_a F}{RT} (\phi_1 - \phi_2) \right] - \frac{c_{Rw}}{c_{Rf}} \exp \left[- \frac{\alpha_c F}{RT} (\phi_1 - \phi_2) \right] \right\} \quad [3]$$

where the dependence of the exchange current density on the concentration of the reduced specie (Cl^-) is neglected, since its concentration is much higher (100-1000 times) than that of the oxidized specie (Cl_2). Thus, Eq. [3] is identical to the Butler-Volmer equation for metal deposition.

The local pore-wall flux j_{Rn} is obtained by eliminating the wall concentration from the mass-transfer equation and the Butler-Volmer equation (3)

$$j_{Rn} = \frac{\frac{c_{Rf}}{c_{Rf}} - \exp[(\alpha_a + \alpha_c)F\eta/RT]}{\frac{1}{k_m c_{Rf}} - \frac{nF}{S_R i_{0R,ref}} \exp[\alpha_c F\eta/RT]} \quad [4]$$

where c_{Rf} is the feed concentration, k_m the mass-transfer coefficient, $S_R = -1$ is the stoichiometric coefficient, and $i_{0R,ref}$ is the exchange current density which is assumed to have a nonlinear composition dependence, according to Trainham and Newman (3). The overpotential $\eta = \phi_1 - \phi_2$, where ϕ_1 and ϕ_2 are the potentials in the matrix and the solution, respectively, measured vs. a reference electrode of the same kind at the feed conditions. The equation for the potential is given by

$$\frac{d^2 \eta}{dx^2} = \left(\frac{1}{\kappa} + \frac{1}{\sigma} \right) \left(\frac{nF}{S_R} \right) \alpha j_{Rn} \quad [5]$$

because in the presence of large excess of supporting electrolyte the current density in the solution is governed by Ohm's law. κ is the effective conductivity in the solution, and σ is the effective conductivity of the solid matrix.

The following boundary conditions must be satisfied (1, 3)

$$\text{At } x = 0 \quad c_{Rf}v = c_{Rf}v - \epsilon D_a \frac{dc_R}{dx} \quad \frac{d\eta}{dx} = -\frac{i}{\sigma} \quad [6]$$

$$\text{At } x = L \quad \frac{dc_R}{dx} = 0 \quad \frac{d\eta}{dx} = \frac{i}{\kappa} \quad [7]$$

where i is the applied current density. The above boundary conditions apply for the case of a downstream counterelectrode and galvanostatic discharge conditions. The downstream boundary condition for dissolved chlorine is the Dankwerts, Wehner-Wilhelm condition, where the axial diffusion and dispersion are included. Since the conductivity of graphite is high, $\sigma \gg 0$, the second boundary condition in Eq. [6] is practically $d\eta/dx = 0$.

Results and Discussion

The coupled nonlinear differential equations were first linearized about a trial solution and then put into finite difference form. The trial matrix was then inverted, and a solution was obtained by an iteration process resulting in a successive improvement of the trial solution, until convergence was achieved, which corresponds to the applied current density (1-3).

Results have been obtained for the following operating discharge conditions: $i = 0.03-0.10$ A/cm²; $v = 0.5-3.0$ cm/min (5); and $\alpha_c = \alpha_a = 0.5$ (4). The exchange current density was measured on pyrolytic graphite, $i_0 = 10^{-5}$ A/cm² (7). The specific area $a = 500$ cm⁻¹ has been estimated from the SEM pictures (Fig. 2). The length of the

electrode is $L = 0.2$ cm and the inlet chlorine concentration is $c_{Rf} = 0.028M$. The mean mass-transfer coefficient k_m is calculated according to Wilson and Geankoplis (1)

$$k_m = \frac{1.09}{\epsilon[6(1-\epsilon)]^{2/3}} (v)^{1/3} (aD_0)^{2/3} \quad [8]$$

where ϵ is the porosity, v is the superficial flow velocity, a is the specific area, and D_0 is the diffusion coefficient for dissolved chlorine. The solution is taken as 2.5M ZnCl₂, 4.0M KCl, and 1.0M NaCl for which the specific conductivity at room temperature is $\kappa = 0.3$ Ω⁻¹ cm⁻¹. The solubility of chlorine is taken as 2 g/liter (5).

The distribution of dissolved chlorine for two electrolyte velocities is shown in Fig. 3. For the given conditions, the difference between the bulk and wall concentrations is very small. At a low velocity of 0.5 cm/min, the reaction proceeds to a higher degree of completion and the outlet chlorine concentration is lower in comparison to that at a higher electrolyte velocity of 2.0 cm/min.

The overpotential distribution is shown in Fig. 4. The overpotential at the downstream, $x/L = 1$, represents the total overpotential contribution of the chlorine electrode. By increasing the velocity from 0.5 to 2.0 cm/min, the overpotential drops from -71 to -66 mV. At higher velocity, the effect of increasing velocity on the overpotential is negligible.

The dimensionless reaction rate can be defined as

$$J = \frac{j_{Rn} a L}{i} \quad [9]$$

The calculated distribution of J is shown in Fig. 5. The reaction rate is higher downstream due to the potential distribution. The increase in the upstream side is due to the higher chlorine concentration. The reaction-rate distribution inside the electrode depth is somewhat interesting. For the case of low flow rate, 0.5 cm/min, the reaction rate declines steadily. Even though the higher overpotential at the outlet portion of the electrode should result in higher reaction rates at the outlet, the low chlorine concentration there dominates the effect of higher overpotential. On the other hand, for higher flow rates such as 2.0 cm/min, the effect of higher overpotential at the electrode outlet results in higher reaction rates at that position.

The effect of electrode thickness.—The effect of increasing the electrode thickness from 0.2 to 0.4 cm is shown in Fig. 6. Increasing the thickness results in a substantial de-

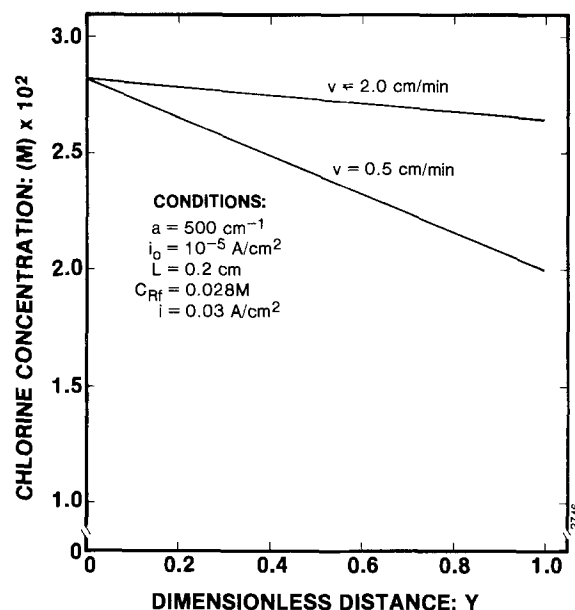


Fig. 3. Distribution of dissolved chlorine for the different flow-through velocities.

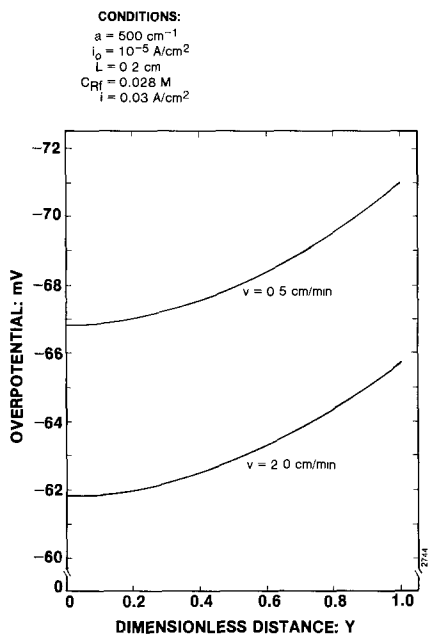


Fig. 4. Overpotential distribution during discharge for two different flow-through velocities.

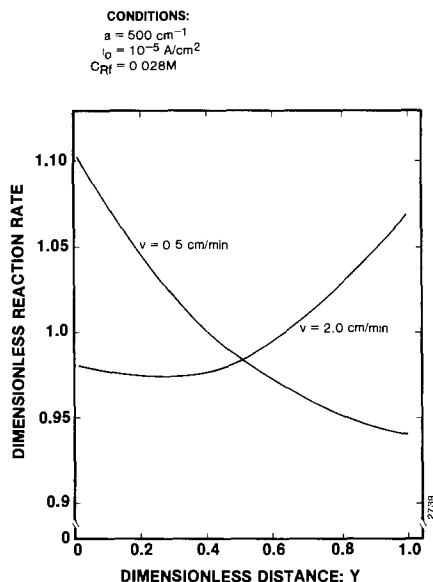


Fig. 5. Dimensionless reaction-rate distribution during discharge for two different flow-through velocities.

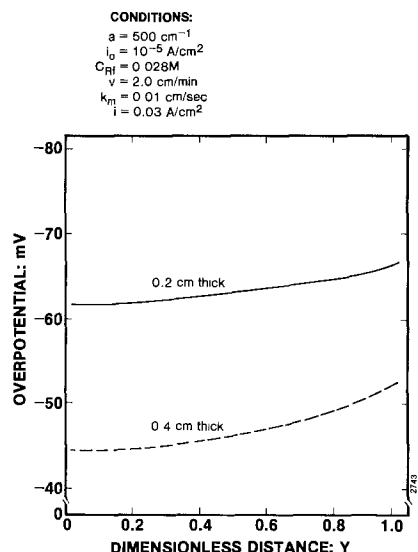


Fig. 6. The effect of electrode thickness on the overpotential distribution.

crease in the overpotential and a corresponding improvement in the voltaic efficiency of the battery during charge.

The effect of discharge current density.—The effect of discharge current density on the overpotential of the flow-through porous chlorine electrode is shown in Fig. 7 in the form of a polarization curve. For example, by increasing the current from 0.03 to 0.10 A/cm², the overpotential increases by about 50 mV.

The effect of increasing the current density from 0.02 to 0.10 A/cm² on the current distribution is shown in Fig. 8, where the dimensionless reaction rate is plotted vs. the dimensionless distance. By increasing the current density, the current distribution becomes less uniform and the depth of penetration is higher.

The effect of reversing the flow.—The results above are referred to the case where the counterelectrode (the zinc electrode) is located in the downstream position (see Fig. 1). By reversing the flow in the battery, a situation in which the counterelectrode is located in the upstream position can be achieved. This flow is represented schematically in Fig. 9.

The boundary conditions for this situation are given by the boundary conditions presented in Eq. [6] and [7], except $x = 0$ is located at the edge facing the zinc electrode and $x = L$ corresponds to the far face of the porous electrode.

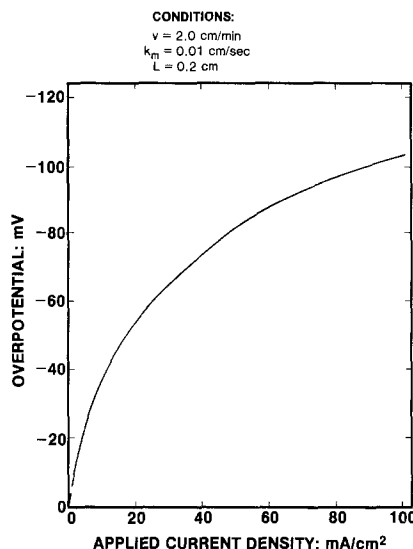


Fig. 7. Polarization curve for flow-through porous graphite under chlorine reduction.

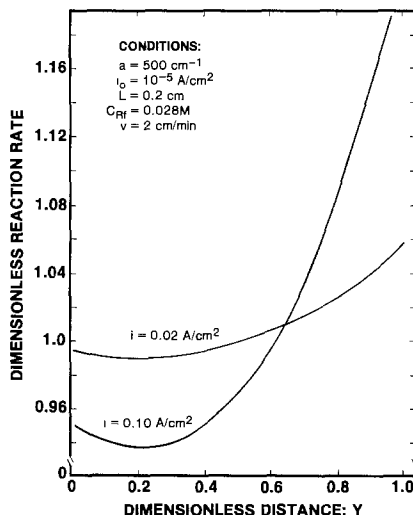


Fig. 8. The effect of discharge current density on the distribution of the dimensionless reaction rate.

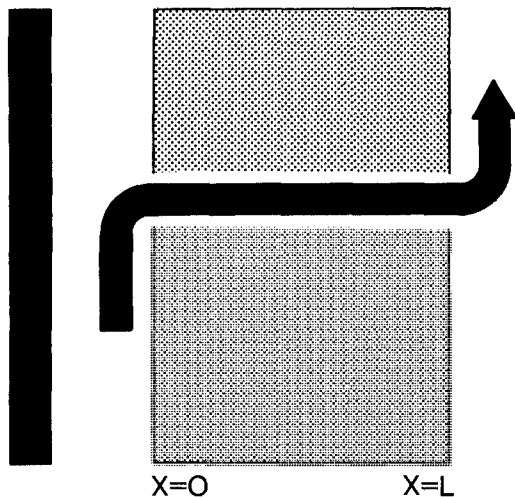


Fig. 9. Flow configuration of the flow-through porous chlorine electrode for upstream location of the counterelectrode.

The distribution of dissolved chlorine concentration is very similar (see Fig 1) to the distribution for the case of a downstream position of the counterelectrode.

The overpotential distributions for upstream and downstream positions of the counterelectrode are compared in Fig. 10. It appears that under the practical operating conditions of the battery, reversing the flow makes very little difference from a voltaic efficiency point of view.

The effect of reversing the flow on the current distribution is shown in Fig. 11, where the dimensionless reaction rate is plotted vs. the dimensionless distance from the zinc facing edge of the porous electrode. As can be seen, the reaction rate is higher at the entrance for the upstream counterelectrode because both the overpotential and the chlorine concentration are higher there. For the case of a downstream counterelectrode, the reaction rate is also nonuniform. A minimum can be observed due to the opposing effects of the overpotential distribution and chlorine concentration distribution. This behavior is in agreement with the analysis of Trainham and Newman (8) concerning the effect of the counterelectrode placement.

Conclusions

The mathematical model suggests the following conclusions.

CONDITIONS:
 $a = 500 \text{ cm}^{-1}$
 $i_0 = 10^{-5} \text{ A/cm}^2$
 $v = 2.0 \text{ cm/min}$
 $k_m = 0.01 \text{ cm/sec}$
 $i = 0.03 \text{ A/cm}^2$
 $L = 0.2 \text{ cm}$

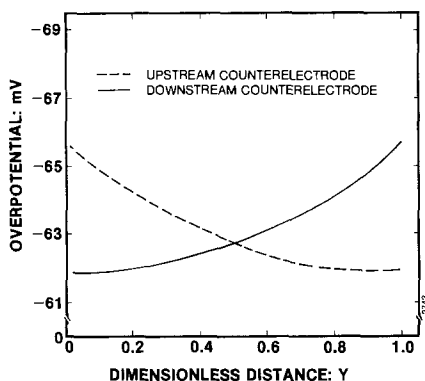


Fig. 10. Comparison of overpotential distribution for upstream and downstream location of the counterelectrode.

CONDITIONS:
 $a = 500 \text{ cm}^{-1}$
 $i_0 = 10^{-5} \text{ A/cm}^2$
 $L = 0.2 \text{ cm}$
 $C_{Cl} = 0.028 \text{ M}$
 $v = 2.0 \text{ cm/min}$
 $i = 0.03 \text{ A/cm}^2$

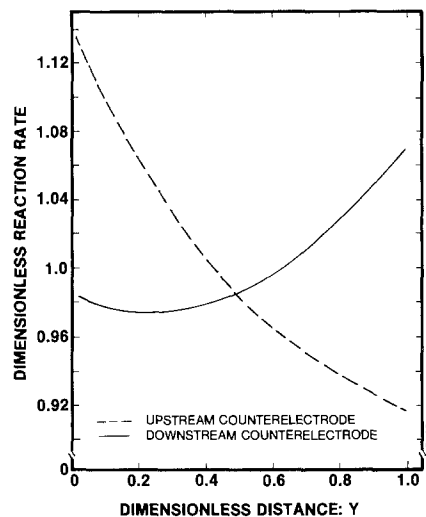


Fig. 11. Comparison of distribution of dimensionless reaction rate for upstream and downstream location of the counter distribution of the dimensionless reaction rate.

1. The macroarea is the most important since the actual area available for the electrochemical reaction is based on the macropores.

2. It appears that mass transfer within the pores is of no importance under the practical operating conditions where the flow-through velocity is greater than 2 cm/min.

3. The lower limit of the flow depends on the mass transfer of dissolved chlorine to the wall.

4. The reaction rate distribution is quite uniform. For an electrode thickness of 0.2 cm the entire electrode participates in the reaction.

Acknowledgments

This work was jointly supported by the Electric Power Research Institute and Energy Development Associates (Gulf+Western Industries). Discussions with J. Newman, S. Argade, A. Shah, and C. J. Warde are gratefully acknowledged.

Manuscript submitted June 15, 1984; revised manuscript received Jan. 3, 1985.

REFERENCES

1. J. S. Newman and W. Tiedemann, in "Advances in Electrochemistry and Electrochemical Engineering," Vol. 11, H. Gerischer and C. W. Tobias, Editors, p. 353 (1978).
2. J. Newman, "Electrochemical Systems," Prentice Hall, Englewood Cliffs, NJ (1973).
3. J. A. Trainham and J. Newman, *This Journal*, **124**, 1528 (1977).
4. J.-T. Kim and J. Journé, *ibid.*, **124**, 1473 (1977).
5. "Development of the Zinc-Chloride Battery for Utility Applications," EM-1417, Electric Power Research Institute, Palo Alto, CA (1980).
6. J. A. Trainham and J. Newman, *Electrochim. Acta*, **26**, 455 (1981).
7. E. Roayaie, Ph.D. Thesis, Wayne State University, Detroit, MI (1984).
8. J. A. Trainham and J. Newman, *This Journal*, **125**, 58 (1978).

Effect of Reinforcement on the Pitting Behavior of Aluminum-Base Metal Matrix Composites

Denise M. Aylor* and Patrick J. Moran**

David Taylor Naval Ship Research and Development Center, Bethesda, Maryland 20084 and Department of Materials Science and Engineering, Johns Hopkins University, Baltimore, Maryland 21218

ABSTRACT

This paper examines the effect of graphite and silicon carbide reinforcements on the pitting behavior of graphite/aluminum (Gr/Al) and silicon carbide/aluminum (SiC/Al) metal matrix composites. Electrochemical corrosion tests were performed on both Gr/Al and SiC/Al composite specimens. Identical tests were completed on powder metallurgy processed aluminum and wrought aluminum of the same composition. The electrochemical behavior of the SiC/Al composites was essentially identical to that of the powder processed and wrought aluminum alloys; however, the pitting attack on the SiC/Al composites was distributed more uniformly across the surface, and the pits penetrated to significantly less depths. The presence of graphite in the Gr/Al composites did not cause an electropositive shift in corrosion potential as anticipated, but caused a substantial decrease in resistance to passive film breakdown. This effect is the predominant reason for the poor performance of Gr/Al composites in marine environments.

Interest in implementation of metal matrix composites (MMC) in marine applications is rapidly expanding due to the materials' higher strength and modulus than that which can be attained by conventional alloying. Utilization of MMC in marine environments requires adequate corrosion resistance. To date, composites considered for marine application are typically aluminum-based, specifically 5000 series or 6061 Al, with reinforcements of graphite (Gr) and silicon carbide (SiC). It has been reported that aluminum alloys suffer localized attack by pitting in chloride environments (1, 2). A reinforcement of Gr or SiC added to the aluminum matrix could potentially decrease the corrosion resistance as compared to an unreinforced alloy due to the structure of the composite. Continuous graphite/aluminum (Gr/Al) composites typically consist of Gr/Al wires (graphite multifilament tows infiltrated with aluminum) diffusion bonded between aluminum foils. This composite configuration could promote wicking of the electrolyte (thereby increasing the corrosion rate) at the foil-to-wire and wire-to-wire interfaces once pitting corrosion progresses through the aluminum foils. The structure of the discontinuous silicon carbide/aluminum (SiC/Al) composites, that of silicon carbide whiskers or particles blended into a powder aluminum matrix could increase the probability of pitting/crevice corrosion at exposed SiC-Al interfaces in the composite.

Dull *et al.* (3, 4) studied the Gr/Al system in 3.5% NaCl. They concluded that the corrosion rate was slightly higher for Gr/Al relative to 6061 aluminum alloy controls. The explanation for this increased corrosion rate was galvanic corrosion at the graphite fiber-aluminum interface. Trzaskoma *et al.* (5) studied the SiC/Al system in 0.1N NaCl. They concluded that the SiC whiskers did not influence the susceptibility of 6061 aluminum to pit initiation, but promoted the development of a smaller size pit morphology relative to 6061 aluminum controls.

In this research, both SiC/Al and Gr/Al composites were evaluated in the laboratory utilizing an electrolyte of ASTM ocean water, which simulates the inorganic constituents of marine environments more closely than sodium chloride. Also, a series of exposures was conducted in two natural marine environments. The results of the laboratory tests are correlated with actual exposure behaviors.

Background

Pitting corrosion involves two stages: pit initiation and propagation. Initiation of pitting occurs at local discontinuities or flaws in the natural oxide film on the aluminum surface (6). Numerous investigators (7-11) have shown evidence of flaws in aluminum passive films,

attributing the defects to voids, inclusions, or other impurities. At each initiated pit site, a high local anodic current density is created with a very low oxygen concentration due to limited access into the pit. The high concentration of aluminum cations within each pit encourages chloride ion migration to maintain charge balance. Precipitation of $Al(OH)_3$ occurs once the solution inside the pit is adequately concentrated with aluminum cations. This lowers the pH within the pit and creates a solid corrosion product. A low pH and a high chloride ion concentration accelerates the anodic dissolution reaction, thereby facilitating the aluminum corrosion process (12, 13). Work by Trzaskoma *et al.* (5) states that in addition to the localized corrosion from structural flaws in the aluminum passive film, surface variations due to the presence of ceramic reinforcements in the matrix could also promote increased corrosion.

Both potential- and current-controlled electrochemical techniques have been utilized to study the pitting mechanism in aluminum alloys (5, 14-30); however, controversy still exists among researchers as to which electrochemical method accurately assesses the pitting corrosion mechanism. Characteristic potentials determined from these methods are E_p , the breakdown or pitting potential, and E_{prot} , the protection or repassivation potential. E_p is defined as the critical potential at which pitting will initiate and propagate, and E_{prot} is the potential at which propagating pits repassivate.

In this investigation, cyclic anodic potentiodynamic polarization was used to determine E_p and E_{prot} values on graphite/6061 aluminum (Gr/6061 Al), silicon carbide (whisker)/powder metallurgy 6061 aluminum ($SiC_w/6061$ Al), silicon carbide (whisker)/powder metallurgy 6061-T6 aluminum ($SiC_w/6061-T6$ Al), 6061-T6 aluminum (6061-T6 Al), and powder metallurgy 6061 aluminum (PM6061 Al) specimens. The anodic potentiodynamic polarization test was chosen because both the susceptibility to initiation, estimated by E_p , and the potential below which pitting would not occur, E_{prot} , could be readily determined and compared. While the significance and reproducibility of E_p by this technique is debated, it can be adequately employed to compare the susceptibility to pit initiation for a variety of materials. Also, potentiostatic tests were conducted on specimens held between E_p and E_{prot} in order to compare the extent and morphology of pitting between SiC/Al and Al materials.

Experimental Procedure

Gr/Al composites, containing approximately 30 volume percent (v/o) graphite, were fabricated by first forming Gr/Al wires. The wires were then stacked and hot-press diffusion bonded between 6061 aluminum surface foils to a 3.8 mm (0.150 in.)¹ final plate thickness. The $SiC_w/6061$

¹Imperial dimensions are actual and stated to appropriate precision; derived metric dimensions are approximate.

*Electrochemical Society Student Member.

**Electrochemical Society Active Member.

Al composites were fabricated from atomized 6061 Al powder and 25 v/o discontinuous silicon carbide whiskers (approximately 0.1 to several microns in diameter, 1-50 μm in length). The 6061 Al powder and SiC whiskers were consolidated into plate form, and the plate was vacuum hot pressed and then forged to its final 2.5 mm (0.1 in.) thickness. SiC_w/6061-T6 composites were additionally tempered to a T-6 condition after forging. PM6061 Al material was fabricated using the same procedures as for the SiC_w/6061 Al MMC but without the added SiC reinforcement. The 6061-T6 Al alloy was conventional wrought, T-6 tempered material in the form of a 6.4 mm (0.25 in.) thick plate.

Marine environment testing.—Corrosion test panels of Gr/6061 Al, SiC_w/6061 Al, SiC_w/6061-T6 Al, 6061-T6 Al, and PM6061 Al were exposed at the LaQue Center for Corrosion Technology in environments of (i) quiescent, filtered natural seawater controlled at $30^\circ \pm 2^\circ\text{C}$ ($86^\circ \pm 3.6^\circ\text{F}$) (full immersion), and (ii) marine atmosphere, 25m (80 ft) from the ocean. The test panels, with surface areas ranging from 77 cm² (12 in.²) to 168 cm² (26 in.²), were exposed for 1-12 months and some exposures are still in progress. Panels are periodically inspected during exposure to assess the pitting corrosion behavior.

Electrochemical testing.—Electrochemical testing included corrosion potential (E_{corr}) monitoring, cyclic anodic polarization, and potentiostatic holds. All electrochemical tests were conducted in ASTM ocean water, prepared according to ASTM Standard D1141-75 (31). Composite specimens of Gr/6061 Al, SiC_w/6061 Al, and SiC_w/6061-T6 Al were mounted to mutually expose both the Gr or SiC reinforcement and the aluminum matrix. Corrosion potentials were monitored for 30 days on specimens of Gr/6061 Al, SiC_w/6061 Al, SiC_w/6061-T6 Al, 6061-T6 Al, and PM6061 Al immersed in aerated ocean water.

Cyclic anodic polarization testing was carried out on Gr/6061 Al, SiC_w/6061 Al, SiC_w/6061-T6 Al, 6061-T6 Al, and PM6061 Al materials. These tests were conducted to make a qualitative assessment of the susceptibility to breakdown for both composite and control materials. Specimens were mounted to expose a 2 cm² area. A Princeton Applied Research (PAR) system was utilized in these tests (Model 173 Potentiostat, Model 175 Programmer, and Model RE0074 X-Y Recorder). Each specimen was allowed to reach a stable corrosion potential in partially deaerated, ambient temperature (21-27°C) ocean water before testing began. Partial deaeration was necessary to clearly observe the breakdown and repassivation potentials. Testing was initiated at the stabilized corrosion potential and a scan carried out in the electropositive direction at a rate of 0.1 mV/s until a breakdown potential (E_p) was reached. This potential is marked by a rapid increase in the current. Once E_p was reached and the current density increased to approximately 1-5 mA/cm², the scan was reversed and continued at the same rate until this electronegative direction scan crossed the original electropositive direction curve. This crossover point was taken as the repassivation potential (E_{prot}), where active pits are repassivated.

Potentiostatic tests were also conducted on SiC_w/6061 Al, SiC_w/6061-T6 Al, 6061-T6 Al, and PM6061 Al materials. The test began by imposing potentiostatic control of each specimen at the previously stabilized corrosion potential. The potential was then shifted in the electropositive direction at a rate of approximately 50 mV/s to 0 mV vs. a saturated calomel reference electrode (SCE) to initiate pitting, and then immediately reversed at the same rate to -700 mV vs. SCE. Each specimen was held at -700 mV vs. SCE, and the currents were monitored for approximately one week. This potential was chosen, based on the anodic polarization tests, as the potential at which pits would continue to propagate for all specimens. In other words, the -700 mV potential is between E_p and E_{prot} for all specimens tested. The specimens were cleaned after testing according to ASTM Standard G1-81 (32).

Results and Discussion

Marine exposures.—A thorough review of the marine exposures for Gr/6061 Al, SiC_w/6061 Al, and 6061-T6 Al is covered elsewhere (33). The major results of the above panel exposures as well as exposures of SiC_w/6061-T6 Al and PM6061 Al are described in this section.

6061-T6 Al and PM6061 Al panels exposed in filtered seawater exhibited more accelerated corrosion than the aluminum alloy panels exposed in the marine atmosphere. For both marine environments, the quantity of pitting was similar between the two 6061 alloy processing forms, but the depth of attack was slightly greater for the PM6061 Al specimens. Corrosion of the SiC_w/Al panels also proceeded by pitting on the surfaces, with the 6061 Al controls exhibiting superior corrosion resistance to the composites. Figure 1 exemplifies the increased corrosion resistance of the 6061-T6 Al controls relative to the SiC_w/6061 Al after 60 days in filtered seawater. The surface deposits observed on the panels are corrosion products resulting from pitting processes beneath. SEM analysis of a metallographically polished cross section through the aforementioned SiC_w/6061 Al panel (Fig. 2) revealed that the pitting corrosion was concentrated around the silicon carbide whiskers, suggesting that the crevices formed at each SiC-Al interface are preferential sites for pitting corrosion.

Marine exposures of the Gr/6061 Al panels in filtered seawater exhibited severe attack for exposure periods of 1-4 months. Figure 3 presents a typical failure of a Gr/6061 Al MMC, which occurred after 60 days in filtered seawater. Severe blistering of the aluminum surface foil along one edge is evident, which exemplifies the accelerated corrosion which takes place when the aluminum surface foil is penetrated and the graphite fibers and the aluminum are mutually exposed to the environment. The severity of attack observed in these field exposures is significantly more severe than that reported by other investigators (3, 4).

It should be emphasized that the corrosion resistance of Gr/Al composites is highly dependent on the integrity of the aluminum surface foils. For example, Gr/6061 Al panels from another phase of this program were exposed in the marine atmosphere and other marine environments for up to 20 months and revealed no severe attack. Only light surface pitting of the foils and no penetration into the Gr/Al matrix occurred. Corrosion of the aluminum surface foils will proceed at a rate typical for marine aluminum alloys until the foils are penetrated, whereby both graphite and aluminum are exposed to the environment

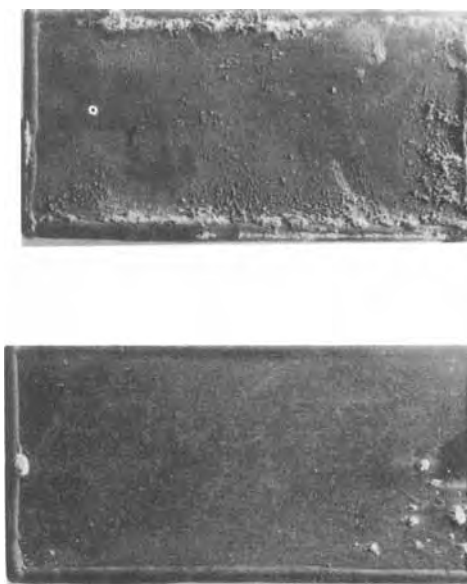
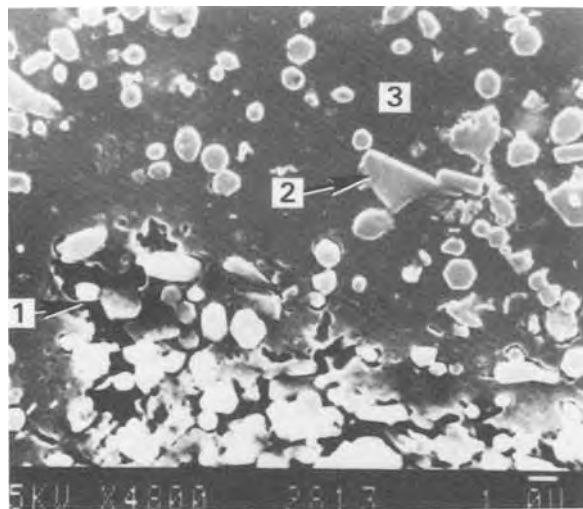


Fig. 1. SiC_w/Al and Al control panels after 60 day filtered seawater exposure. Top: SiC_w/6061 Al. Bottom: 6061-T6 Al.



1 PITTING CORROSION
2 SILICON CARBIDE WHISKERS
3 ALUMINUM MATRIX

Fig. 2. Cross section through SiC_w/6061 Al panel after 60 days in filtered seawater.

and accelerated corrosion of the Gr/Al occurs. Thus, the service life of Gr/Al composites is determined solely by the corrosion resistance of the aluminum surface foils. This has also been reported by other researchers (33, 34), who suggested that the accelerated corrosion following penetration is due to anodic polarization of the aluminum by the graphite, *i.e.*, classical galvanic corrosion.

Stabilization of corrosion potentials.—Average corrosion potentials for three specimens each of Gr/6061 Al, SiC_w/6061 Al, SiC_w/6061-T6 Al, 6061-T6 Al, and PM6061 Al immersed in aerated ASTM ocean water are shown in Table I. The average E_{corr} value listed for Gr/6061 Al is more electronegative than the average E_{corr} for the unreinforced Al controls in the same solution, indicating that the graphite fibers do not polarize the composite in the electropositive direction (as would be expected in normal galvanic corrosion). An explanation of this shift in E_{corr} will be discussed below. The similarities seen in the corrosion potentials between the SiC/Al and Al specimens suggest that the E_{corr} of the SiC/Al composites is not affected by the presence of the silicon carbide. This is not

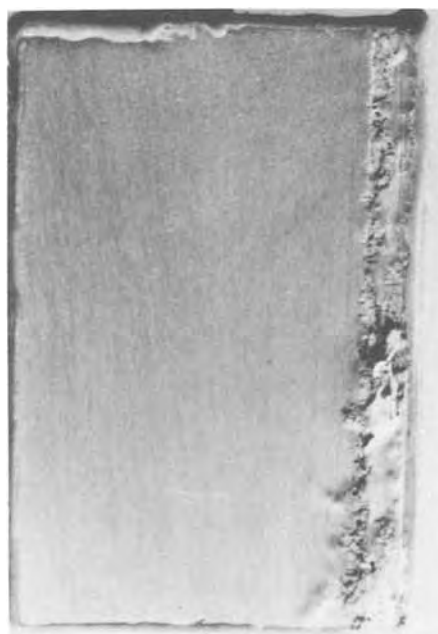


Fig. 3. Gr/6061 Al MMC panel after 60 day filtered seawater exposure

Table I. Average corrosion potentials for Gr/Al, SiC/Al, and Al immersed in aerated ASTM ocean water for 30 days

Material	Average E_{corr} (mV vs. SCE)
Gr/6061 Al	-840
SiC _w /6061 Al	-740
SiC _w /6061-T6 Al	-735
6061-T6 Al (Control)	-750
PM6061 Al (Control)	-720

an unexpected result because of the known poor electrical conductivity of silicon carbide.

Potentiodynamic tests.—Figure 4 shows the cyclic anodic polarization results for 6061-T6 Al and PM6061 Al. The solid curves represent a range of potential and current density values based on four PM6061 Al specimens tested. The dashed curves represent a range of values for four 6061-T6 Al specimens. The shaded areas represent the range of E_p and E_{prot} values for both 6061 Al alloy forms. The measured corrosion potentials exhibited a large amount of scatter because the extent of deaeration was not carefully controlled.

A wide range of breakdown potentials is evident for both 6061-T6 Al and PM6061 Al, yet the most electronegative values for each material are identical. Further, the repassivation potentials for both materials tend to fall within a narrow band, showing good reproducibility for the E_{prot} parameter. The E_{prot} range for the PM6061 Al is somewhat electronegative to the E_{prot} values for the 6061-T6 Al. In general, though, the similarities seen in the pitting scans between 6061-T6 Al and PM6061 Al suggest that the differences in the processing forms of 6061 Al alloy do not significantly affect the anodic polarization characteristics.

Potentiodynamic polarization curves generated for SiC_w/6061 Al and SiC_w/6061-T6 Al specimens are included in Fig. 5. These curves also represent a range of values based on four specimens evaluated for each material. Again, a large scatter in E_{corr} is evident and is due to differences in the extent of deaeration of the solution. As in the 6061 Al alloy specimens, the breakdown potentials for the SiC/Al composites extend over a wide range of values, demonstrating the difficulty in reproducibility of the E_p parameter. However, the lowest detected breakdown potentials for both SiC_w/6061 Al and SiC_w/6061-T6 Al composites are electropositive relative to the lowest breakdown potentials for the aluminum alloys. Therefore, the presence of the SiC in the composite does not increase the susceptibility of the aluminum surface film to breakdown. This result is consistent with the work of Trzaskoma *et al.* (5). In addition, the repassivation potentials for both SiC/Al composites were quite reproducible (as with the Al alloys) and general similarities in these potentiodynamic scans suggest that heat-treating does not

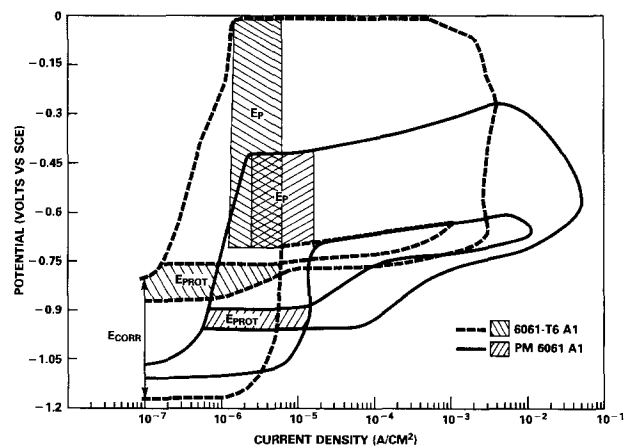


Fig. 4. Cyclic anodic polarization of 6061-T6 Al and PM6061 Al

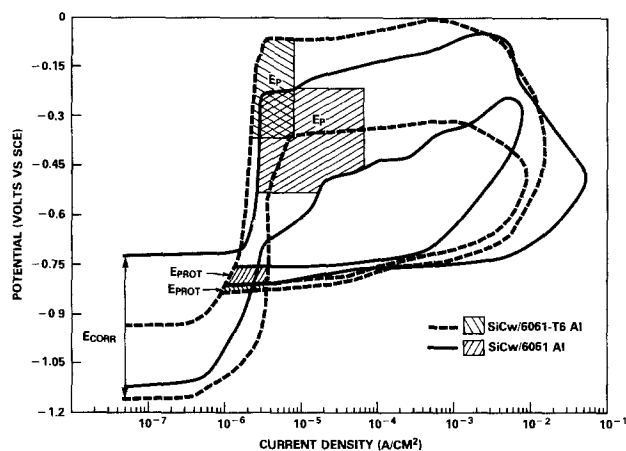


Fig. 5. Cyclic anodic polarization of SiC_w/6061 Al and SiC_w/6061-T6 Al

significantly influence the anodic polarization behavior of the SiC/Al composites.

SEM examination of all specimens after cyclic anodic polarization revealed irregular pitting scattered over the surfaces. The maximum pitting size on the SiC/Al specimens was generally an order of magnitude smaller than on the Al specimens, ranging in the 10-50 μm size for the SiC/Al and in the 100-500 μm size for the Al. Although the maximum pitting size range was smaller on the SiC/Al composites as compared to the Al alloys, there were a larger number of pits on the SiC/Al specimens. An explanation for this phenomenon is that the SiC/Al interfaces are preferred sites for passive film breakdown and are more numerous than preferred sites on the unreinforced alloy.

Cyclic anodic polarization curves for the Gr/Al MMC are presented in Fig. 6. Again, this figure represents a range of potential and current density data based on four specimens tested. Both E_p and E_{prot} values are quite reproducible. The E_{prot} values are similar to those reported for the SiC/Al and Al materials, but the Gr/6061 Al E_p values are significantly more electronegative than those materials, indicating that the passive film of the Gr/Al composite is more susceptible to breakdown compared to the other materials tested. This result, coupled with the fact that this composite does not exhibit an electropositive shift in corrosion potential, suggests that classical galvanic corrosion is not the predominant cause of the accelerated corrosion. The diffusion of carbon into the aluminum matrix and the possible formation of aluminum carbides at the reinforcement-matrix interface may change the properties of the aluminum surface film in these localities, rendering it more susceptible to breakdown. This theory, also postulated by Pfeifer (35), explains the electronegative shift in corrosion potential of Gr/Al composites which is presumably caused by active

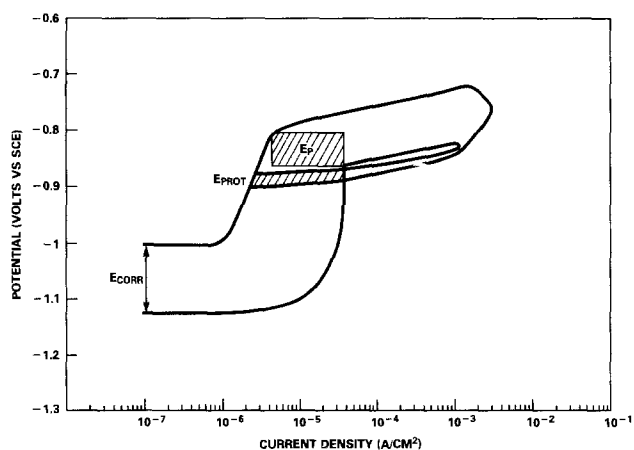


Fig. 6. Cyclic anodic polarization of Gr/6061 Al

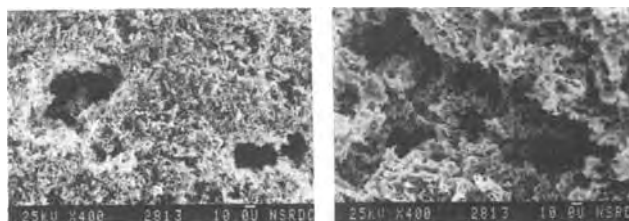


Fig. 7. Representative pitting of SiC/Al and Al surfaces after potentiostatic testing. Left: SiC_w/6061-T6 Al. Right: 6061-T6 Al.

dissolution at such sites, the observed decrease in the breakdown potential, and the concentration of attack at the graphite fiber-aluminum interfaces. Further, if mechanical disturbance alone was responsible for the lowering in E_p , it would have been expected to cause similar behavior for the SiC/Al composites, which it did not. These results and explanations contradict those of previous investigators (3, 4).

Pitting morphology tests.—Potentiostatic testing of SiC_w/6061 Al, SiC_w/6061-T6 Al, 6061-T6 Al, and PM6061 Al consisted of holding each specimen at -700 mV, a potential between E_p and E_{prot} where the pitting propagated, as previously described. The resultant currents, monitored over a one week period, ranged from 5 to 8 mA/cm² for all specimens. SEM photomicrographs showing typical pitting on the specimen surfaces after the potentiostatic testing are seen in Fig. 7. The pitting morphology of the potentiostated specimens generally correlated with the size range and extent of pitting seen on the composite and Al control specimens after cyclic anodic polarization testing. The size and distribution of pitting was similar between SiC_w/6061 Al and SiC_w/6061-T6 Al specimens and between 6061-T6 Al and PM6061 Al specimens, with the composites exhibiting a maximum pit size generally an order of magnitude smaller than that seen on the Al surfaces. These results agree with the work of Trzaskoma *et al.* (5). The potentiostated specimens were held at approximately the same current densities, indicating that the overall corrosion rates were similar for all specimens. Since there are more active sites on the SiC/Al as compared to the Al alloys, the pitting on the SiC/Al will be more uniformly distributed on the surface and the depths of pitting attack will be less. An interpretation of this result is that the silicon carbide whiskers present in the aluminum matrix distribute the pitting corrosion across the surface and subsequently limit the depths of attack.

Conclusions

1. Breakdown potentials as determined from cyclic anodic polarization testing on both SiC/Al and Al materials exhibit a wide range of values; however the repassivation potentials are highly reproducible.
2. Utilization of different 6061 Al processing forms (wrought *vs.* powder metallurgy) and SiC/Al composite heat-treating (as-fabricated *vs.* T-6 temper) does not affect the anodic polarization characteristics of SiC/Al and Al.
3. The presence of SiC in the 6061 Al matrix does not alter the corrosion potential in aerated ocean water. Further, the SiC does not increase the pitting susceptibility of the SiC/Al composite.
4. The morphology and extent of pitting differs between SiC/Al and Al materials. SiC/Al composites exhibit pitting concentrated predominantly at the SiC/Al interfaces, with the pitting being greater in number, smaller in size, and more shallow in penetration depth relative to the unreinforced aluminum alloys.
5. Accelerated corrosion of Gr/Al occurs when the aluminum surface foils are penetrated and the graphite and the aluminum are mutually exposed to the marine environment. Electrochemical test results indicate that the accelerated Gr/Al corrosion is not predominantly due to classical galvanic corrosion. The suggested explanation for the corrosion is that carbon diffuses into the alumi-

num at the reinforcement-matrix interfaces during fabrication, which causes a decrease in the surface film integrity at these localities and renders the composite more susceptible to breakdown.

Manuscript submitted Aug. 24, 1984; revised manuscript received Nov. 26, 1984. This was Paper 155 presented at the Washington, DC, Meeting of the Society, Oct. 9-14, 1983.

The U.S. Department of the Navy assisted in meeting the publication costs of this article.

REFERENCES

- H. H. Uhlig, "Corrosion and Corrosion Control," pp. 335-338, John Wiley & Sons, New York (1971).
- W. K. Boyd and F. W. Fink, "Corrosion of Metals in Marine Environments," pp. 57-67, 85-87, Metals and Ceramics Information Center, Columbus, OH (1978).
- D. L. Dull, W. C. Harrigan, Jr., and M. F. Amateau, "1974 Tri-Service Corrosion Conference," Vol. 1, F. H. Meyer, Editor, p. 399, U.S. Government publication.
- D. L. Dull, W. C. Harrigan, Jr., and M. F. Amateau, Aerospace Report ATR-76 (7564)-1, El Segundo, CA (1977).
- P. P. Trzaskoma, E. M. McCafferty, and C. R. Crowe, *This Journal*, **130**, 1804 (1983).
- S. C. Britton, and U. R. Evans, *J. Chem. Soc.*, 1773 (1930).
- G. E. Thompson, P. E. Doherty, and G. C. Wood, *This Journal*, **129**, 1515 (1982).
- G. E. Thompson and G. C. Wood, *Corros. Sci.*, **18**, 721 (1978).
- D. R. Arnott, W. J. Baxter, and S. R. Rouze, *This Journal*, **128**, 843 (1981).
- R. S. Alwitt and C. K. Dyer, *ibid.*, **129**, 711 (1982).
- G. C. Wood, W. H. Sutton, J. A. Richardson, T. N. K. Riley, and A. G. Malherbe, in "Localized Corrosion," pp. 526-546, NACE, Houston, TX (1974).
- C. Edeleanu and U. R. Evans, *Trans. Faraday Soc.*, **47**, 1121 (1951).
- H. Kaesche, *Corros. Trait. Port. Fintion*, **17**, 389 (1969).
- R. Baboian and G. S. Haynes, in "Electrochemical Corrosion Testing," F. Mansfeld and U. Bertocci, Editors, pp. 274-282, American Society for Testing and Materials, Philadelphia (1981).
- S. T. Hirozawa, *This Journal*, **130**, 1718 (1983).
- W. D. France and N. D. Greene, *Corrosion*, **26**, 1 (1970).
- Ph. Gimenez, J. J. Rameau, and M. C. Reboul, *ibid.*, **37**, 673 (1981).
- A. Broli and H. Holtan, *ibid.*, **30**, 427 (1974).
- I. L. Rozenfeld, *Korroz. Zash. Metall. Moscow* (1970).
- E. Brauns and W. Schwenk, *Arch. Eisenhüttenwes.*, **32**, 387 (1961).
- W. Schwenk, *Corrosion*, **20**, 129 (1964).
- A. Broli and H. Holtan, *Corros. Sci.*, **17**, 59 (1977).
- J. R. Galvele, S. M. de Micheli, I. L. Muller, S. B. de Wexler, and I. L. Alanis, in "Localized Corrosion," pp. 580-598, NACE, Houston, TX (1974).
- B. E. Wilde and E. Williams, *Electrochim. Acta*, **16**, 1971 (1971).
- B. E. Wilde, *Corrosion*, **28**, 283 (1972).
- B. E. Wilde and E. Williams, *This Journal*, **117**, 775 (1970).
- B. E. Wilde and E. Williams, *ibid.*, **118**, 1058 (1971).
- N. Pessall and C. Liu, *Electrochim. Acta*, **16**, 1987 (1971).
- D. Sinigaglia, B. Vicentini, G. Taccani, G. Salvago, and G. Dallaspezia, *This Journal*, **130**, 991 (1983).
- B. C. Syrett, *Corrosion*, **33**, 221 (1977).
- ASTM Standard D1141-75, "Substitute Ocean Water," American Society for Testing and Materials, Philadelphia (1984).
- ASTM Standard G1-81, "Standard Practice for Preparing, Cleaning, and Evaluating Corrosion Test Specimens," American Society for Testing and Materials, Philadelphia (1984).
- D. M. Aylor and R. M. Kain, "Assessing the Corrosion Resistance of MMC in Marine Environments," ASTM Special Technical Publication, To be published.
- M. G. Vassilaros, D. A. Davis, J. P. Gudas, and G. L. Steckel, in "Proceedings of the 1980 Tri-Service Corrosion Conference," Vol. 2, pp. 21-53, Nov. 1980, U.S. Government publication (1980).
- W. H. Pfeifer, in "Hybrid and Select Metal Matrix Composites: A State of the Art Review," W. J. Renton, Editor, pp. 231-252, American Institute of Aeronautics and Astronautics, New York (1977).

Establishment of the Zn Corrosion Rate in NaHSO₃ Aqueous Solutions

Blanca M. Rosales and S. L. Granese

Departamento de Investigaciones en Corrosion, CITEFA/CONICET, Buenos Aires, Argentina

ABSTRACT

By means of electrochemical techniques, the corrosion of Zn in NaHSO₃ aerated and deaerated aqueous solutions at 25°C was studied. The kinetic equations proposed from values obtained in the Tafel region were in good agreement with those provided by computer program POLCURR (1) developed by Gerchakov *et al.* for overpotentials of ±20 mV. On those bases and analyzing by x-ray, the corrosion products formed an overall reaction was proposed which would be controlled by an adsorption-oxidation step.

The aim of this paper is to contribute to establishing the mechanism of corrosion of Zn in aqueous NaHSO₃ solutions.

Usually, corrosion rates are determined by an electrochemical technique, originally described by Wagner and Traud (2) and by Stern *et al.* (3), designed herein as the Stern-Geary or polarization resistance technique.

In this work, the POLCURR computer program was used to obtain some kinetic parameters controlling the corrosion of Zn in NaHSO₃ solutions. It accepts initial estimates for all parameters and applies the Gauss-Newton method to generate a new set of parameter estimates. This process is repeated until the nonlinear residual error fails to change by more than a preset value. The initial estimated values for these parameters are provided by CORFIT (4) program, which was incorporated as a subroutine into POLCURR.

The CORFIT program is based on an expansion in a Taylor series of the expression

$$I = \frac{1}{2.303 R_p} \left(\frac{1}{\frac{1}{B_a} + \frac{1}{B_c}} \right) \left[\exp \left(\frac{2.303(\phi - \phi_c)}{B_a} \right) - \exp \left(\frac{-2.303(\phi - \phi_c)}{B_c} \right) \right] \quad [1]$$

which is derived from a combination of the theoretical expression of the polarization curves (2) proposed by Wagner and Traud and of the definition of the polarization resistance (R_p) (3)

$$I = I_c \left[\exp \left(\frac{2.303(\phi - \phi_c)}{B_a} \right) - \exp \left(\frac{-2.303(\phi - \phi_c)}{B_c} \right) \right] \quad [2]$$

$$\left(\frac{\partial i}{\partial \phi}\right)_{\phi=\phi_c} = \frac{1}{R_p} = 2.303I_c \left(\frac{1}{B_a} + \frac{1}{B_c}\right) \quad [3]$$

I_c and ϕ_c being the corrosion current and potential and B_a , B_c the anodic and cathodic, respectively, Tafel constants used for mechanistic considerations. Truncating Eq. [1] and providing an initial estimate of one of the unknown parameters, an expression results which is linear with respect to the unknown parameters and may be solved by the usual method of linear least squares.

The electrochemical parameters were estimated introducing the experimental results for overpotentials in the mixed potential range ($|\Delta\phi| < 20$ mV) obtained from the polarization curves in deaerated solutions.

A subroutine CORFIT on the POLCURR program was applied. POLCURR reelaborates the data and calculates the estimates of the parameters with a high level of statistical significance. The program was adapted to the Fortran IV plus language and processed in a Digital PDP11 computer.

Experimental

The test samples were 99.99% Zn sealed in a polyester orthophthalate methacrylate resin, catalyzed by MEK, leaving exposed areas of 0.2 cm². For each test, the sample was polished with 0.25 μ m diamond paste washed with water, followed by an alcohol polish, and was finally dried with a jet of air. The aqueous solutions were prepared with pure reagents and bidistilled water over alkaline permanganate. The tests were all performed at 25°C.

Open-circuit potentials were measured with respect to the saturated calomel electrode (SCE) in NaHSO₃, NaCl, and Na₂SO₄ (10⁻⁵-1.0M) in oxygenated solutions during 24h. This was also done in phthalic-phthalate buffered solutions, at pH = 4, in the concentration range 10⁻⁴-10⁻¹M in NaHSO₃ (Fig. 1).

Polarization curves in the absence of oxygen, in the buffered solutions, were collected after deaerating by 99.99% N₂ bubbling for 2h and cathodic cleaning at -1.300 mV (SCE) for 30 min. Potentiostatic polarization curves were measured after maintaining the potential at each given current density for 15 min. For the oxygenated solutions, air bubbling and magnetic stirring were maintained during the polarizations (Fig. 2 and 3).

Results and Discussion

The results shown in Fig. 1 correspond to the behavior described by Brasher (5), where $E = a - b \log c$, with $b = 40$ mV for NaCl, Na₂SO₄, and in diluted NaHSO₃ nonbuffered solutions.

According to Brasher *et al.* (6), the potential decrease with the concentration increase would be due to the predominance of the film rupture by the anion over its repair by oxygen, as can be proposed for Cl⁻ and SO₄²⁻ over the whole range of concentrations tested. For HSO₃⁻ concentrations above 5 × 10⁻³M, the potential is independent of concentration. This effect is associated with competi-

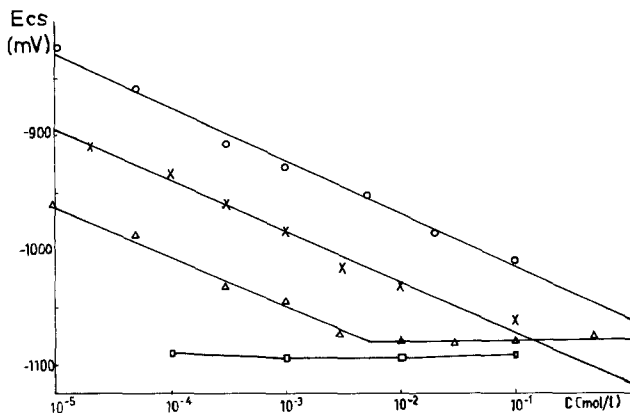


Fig. 1. Stationary open-circuit potentials of Zn. pH = 4. Circles: NaCl. X: Na₂SO₄. Triangles: NaHSO₃. Squares: NaHSO₃.

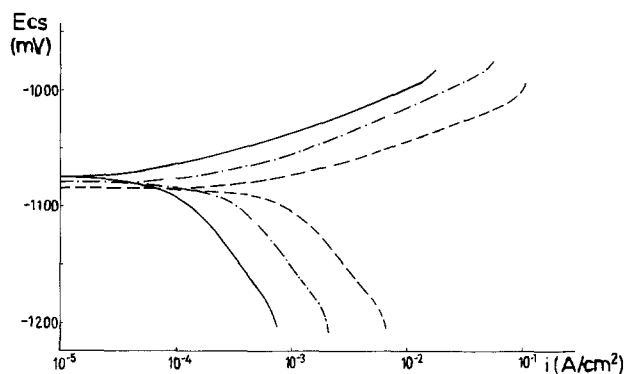
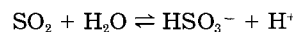


Fig. 2. Polarization of Zn in deaerated NaHSO₃ solutions. Solid lines: 10⁻²M. Dot-dashed line: 10⁻³M. Dashed line: 10⁻¹M.

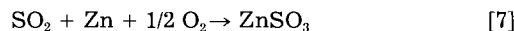
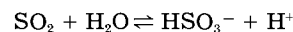
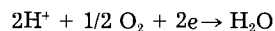
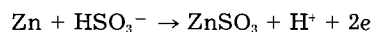
tive adsorption (7) between SO₂ and HSO₃⁻, being pH dependent, as can be seen from the following equilibrium



$$\log \frac{[\text{HSO}_3^-]}{P_{\text{SO}_2}} = -1.82 + \text{pH} \quad [6]$$

At low concentrations, the HSO₃⁻ anion presents a similar behavior to species SO₄²⁻ and Cl⁻, as can be seen in Fig. 1. Its adsorption would cause the oxide film rupture, while SO₂ exhibits a protective effect strongly dependent on the pH of the solutions (8-10). Two distinct behaviors are observed depending on the anion concentration. For HSO₃⁻ concentrations lower than 5 × 10⁻³, the same slope as for aggressive Cl⁻ and SO₄²⁻ ions can be associated to [HSO₃⁻]/P_{SO₂} > 100, introducing in Eq. [6] the pH values 7-4 produced by the salt dissolution.

For HSO₃⁻ concentrations 5 × 10⁻³M or higher, the pH value obtained is approximately 4. The opposite effects associated to both species seem to compensate to each other due to the constant relation [HSO₃⁻]/P_{SO₂} ~ 100 for constant pH value produced. To confirm that interpretation, stationary potentials of Zn, in buffered solutions at pH = 4, were measured. They were independent of the salt concentration over the whole range, as is shown in Fig. 1. The overall reaction proposed for [HSO₃⁻] > 5 × 10⁻³M is



The stoichiometric HSO₃⁻ coefficient ν can be calculated from the variation of the corrosion potential of Zn with its concentration

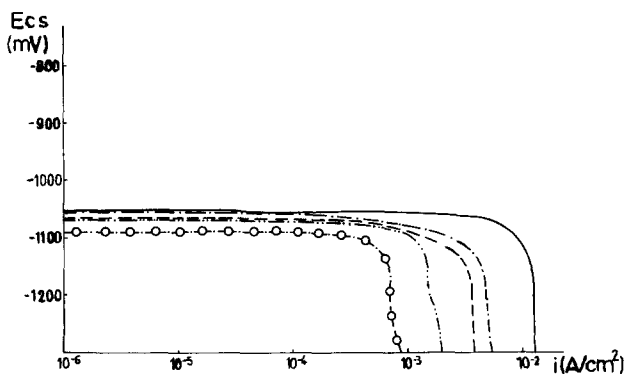
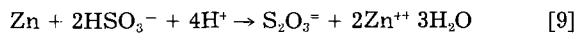
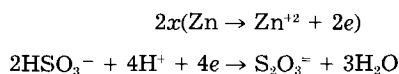


Fig. 3. Polarization of Zn in aerated NaHSO₃ solutions. Solid lines: 10⁻¹M. Dot-dashed line: 2 × 10⁻²M. Dashed line: 10⁻²M. Dash-two dots line: 5 × 10⁻³M. Dash-circle line: 10⁻³M.

$$\frac{\partial E_c}{\partial \log C_{\text{HSO}_3^-}} = \frac{2.303RT}{nF} \nu_{\text{HSO}_3^-} \quad [8]$$

The slope ($\partial E_c / \partial \log C_{\text{HSO}_3^-}$) of the respective curve in Fig. 1 is 0; in Eq. [8], $n = 2$ (total number of exchanged electrons), then $\nu_{\text{HSO}_3^-} = 0$, in good agreement with the Eq. [7] proposed. The corrosion products show the presence of S, O, and Zn. Their presence was determined by electron probe microanalysis. By x-ray diffraction, $\text{ZnSO}_3 \times 2\frac{1}{2} \text{H}_2\text{O}$ was determined.

The overall reaction for $[\text{HSO}_3^-] < 5 \times 10^{-3} \text{M}$ is



Following the same scheme from Eq. [8] as $n = 4$ and the $\partial E_c / \partial \log C_{\text{HSO}_3^-} = 40 \text{ mV}$, then $\nu_{\text{HSO}_3^-} = 2$, in agreement with Eq. [9]. In dilute solution, nonprotective corrosion products are formed. It was not possible to confirm the presence of the reduced specie $\text{S}_2\text{O}_3^{2-}$, owing to its low concentration and to the interference by other sulfur compounds (11) produced during the reduction of SO_3H^- .

In order to get mechanistic information about the corrosion of Zn, polarization curves were recorded in buffered solutions at pH 4 of ionic strength high enough to act as support electrolyte for solutions as diluted as 10^{-3}M in NaHSO_3 . The results are shown in Fig. 2.

Using the computer program POLCURR previously described, the Tafel slopes B_a and B_c , the polarization resistance R_p , and the corrosion current I_c were calculated from the experimental data obtained for $|\Delta\phi| < 20 \text{ mV}$. The results are summarized in Table I.

B_a and B_c were also determined from the Tafel region of the overall polarization curves, and were found in good agreement with those determined by the computer method in the vicinity of ϕ_c . The kinetic parameters were calculated from the expressions

$$B_a = 2.303 \frac{RT}{\alpha F}$$

and

$$B_c = 2.303 \frac{RT}{\alpha F}$$

with $\bar{\alpha}$ and $\vec{\alpha}$ being the transfer coefficients for the anodic and cathodic reactions. The electrochemical anodic and cathodic reaction orders with regard to HSO_3^- were obtained from the Tafel region in order to avoid the reverse reactions. We plotted $\log i$ vs. $\log [\text{HSO}_3^-]$ for different potentials

$$\left(\frac{\partial \log |i|}{\partial \log [\text{HSO}_3^-]} \right)_\phi = n_{a,c}$$

with

$$\phi > \phi_c \pm \frac{RT}{F}$$

n_a and $n_c = 0.5$ were obtained.

The kinetic equations consistent with the results summarized in Table II are

$$i_a = K_a [\text{HSO}_3^-]^{0.5} \exp \left[1.62 \frac{F\phi}{RT} \right] \quad [10]$$

Table I. Electrochemical results from the POLCURR program

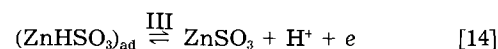
$[\text{HSO}_3^-]$ (M)	$-\phi_c$ (mV SCE)	I_c (A cm ²)	R_p (Ω)	B_a (mV)	B_c (mV)
10^{-3}	1076	2×10^{-5}	674.2	36	125
10^{-2}	1080	2.8×10^{-4}	237.1	40	130
10^{-1}	1083	8.2×10^{-4}	71.8	35	120

Table II. Kinetic parameters

Polarization	B	$\bar{\alpha}$	$\vec{\alpha}$	n_a	n_c
Anodic	37	1.62	—	0.5	—
Cathodic	125	—	0.48	—	0.5

$$i_- = K_- [\text{HSO}_3^-]^{0.5} \exp \left[-0.48 \frac{F\phi}{RT} \right] \quad [11]$$

The corrosion product formed by immersion in NaHSO_3 solutions buffered at pH = 4 was $\text{ZnSO}_3 \times 2 \frac{1}{2} \text{H}_2\text{O}$. The dependence of the potential-current curves on the surface state of the test sample indicates that the process contains a heterogeneous reaction. These facts enabled us to understand the role of HSO_3^- on the corrosion of Zn through an adsorption-oxidation mechanism with the following possible steps for the anodic reaction



From Eq. [11], applying the Frumkin isotherm

$$\frac{\Theta_{(\text{ZnHSO}_3)_{\text{ad}}}}{1 - \theta} = K_I C_{\text{HSO}_3^-} e^{-g\theta} \quad [15]$$

with $K_I = k_I/k_{-I}$ and g the variation in the apparent adsorption free energy with the coverage: $g = \partial \Delta G_{\text{ad}}^\circ / \partial \theta$.

For intermediate values of θ , applying the Temkin approximation

$$e^{g\theta} = K_I C_{\text{HSO}_3^-} \quad [16]$$

For reaction [13] in quasi-equilibrium state

$$\Theta_{(\text{ZnHSO}_3)_{\text{ad}}}^{-} k_{\text{II}} \exp \frac{(1 - \beta)F\Delta\phi}{RT} \\ = k_{-II} \Theta_{(\text{ZnHSO}_3)_{\text{ad}}} \exp \frac{-\beta F\Delta\phi}{RT}$$

$$\Theta_{(\text{ZnHSO}_3)_{\text{ad}}} = K_{\text{II}} \exp \frac{F\Delta\phi}{RT} \Theta_{(\text{ZnHSO}_3)_{\text{ad}}}^{-} \quad [17]$$

where $K_{\text{II}} = k_{\text{II}}/k_{-II}$ with equation (14) as rds

$$v_{\text{III}} = k_{\text{III}} \Theta_{(\text{ZnHSO}_3)_{\text{ad}}} \exp \frac{\beta F\Delta\phi}{RT} e^{g\theta} \quad [18]$$

Neglecting the pre-exponential $\Theta_{(\text{ZnHSO}_3)_{\text{ad}}}^{-}$ in Eq. [17] and replacing Eq. [16] and [17] in Eq. [18]

$$v_{\text{III}} = k_{\text{III}} K_{\text{II}} K_I^\alpha C_{\text{HSO}_3^-}^\alpha \exp \frac{F\Delta\phi}{RT} \exp \frac{\beta F\Delta\phi}{RT} \\ = K_{\text{III}} C_{\text{HSO}_3^-}^\alpha \exp \frac{(1 + \beta)F\Delta\phi}{RT}$$

with $K_{\text{III}} = k_{\text{III}} K_{\text{II}} K_I^\alpha$.

Considering the symmetry coefficients α and $\beta = 0.5$

$$v_{\text{III}} = K_{\text{III}} C_{\text{HSO}_3^-}^{0.5} \exp 1.5 \frac{F\Delta\phi}{RT} \quad [19]$$

The stoichiometric coefficient of the anodic process is

$$\nu = \frac{n}{\bar{\alpha} + \vec{\alpha}} = 1$$

Using $n = 2$, Eq. [13], [14], $\bar{\alpha} = 1.62$, and $\vec{\alpha} = 0.48$ were calculated (Table II).

The theoretical expression (12) of the transfer coefficients enabled us to verify the consistency of the proposed steps with the experimental results

$$\bar{\alpha} = \bar{\gamma} / \nu + \beta r = 1.5$$

and

$$\vec{\alpha} = \vec{\gamma} / \nu + r - r\beta = 0.5$$

with $\bar{\gamma}$ being the number of steps previous to the controlling one, $\vec{\gamma}$ the number of steps after the controlling one, r the number of electrons transferred in that step, and β the symmetry coefficient.

Derivation of log of Eq. [19] for high anodic overpotentials leads to

$$B_a = \left(\frac{\partial \log E}{\partial \log i} \right)_{C_{\text{HSO}_3^-}} = \frac{2.303}{1.5} \frac{RT}{F} = 40 \text{ mV}$$

which is in good agreement with the experimental value of the Tafel slope. Equation [19] also fits the anodic reaction order in HSO_3^- .

Cathodic curves in the presence of O_2 were also determined to complete the analysis of the reactions occurring during the atmospheric corrosion of Zn. The limiting current for the O_2 reduction increased with the concentration of the salt, as can be seen in Fig. 3, indicating the positive effects of the anion, as it was also observed for NO_3^- for the O_2 reduction on Zn (13). The variation of the limiting current i_L for O_2 reduction with the anion concentration

$$\frac{\partial \log i_L}{\partial \log [\text{HSO}_3^-]} = 0.65$$

indicates that the reaction is under diffusion control at which a reaction overpotential is superposed with a heterogeneous reaction order 0.65 in the anion concentration.

For this reason, mechanistic conclusions cannot be obtained. The O_2 reduction would depend on the coverage of the electrode by the adsorption complex formed.

Conclusions

From the results presented here, the following can be concluded.

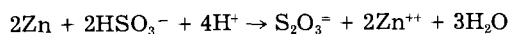
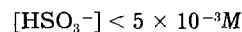
1. The Tafel constants and corrosion rate obtained from the POLCURR program in the vicinity of the corrosion potential are in good agreement with those extrapolated in the Tafel region.

2. In the absence of O_2 , the Tafel constants and the reaction orders experimentally obtained for the anodic reaction, shown in Eq. [10] and [11], are in good agreement with the electrochemical parameters of the theoretical Eq. [19] derived on the base of an adsorption-oxidation sequence of reactions.

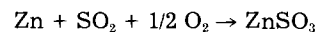
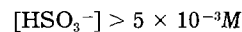
3. The controlling step in the oxidation of Zn is the charge transfer reaction [14] giving as final product $\text{ZnSO}_3 \times 2 \frac{1}{2} \text{H}_2\text{O}$.

4. The O_2 reduction implies a heterogeneous reaction depending on the adsorption complex.

5. The overall reactions proposed, in aerated solutions are for



and for



Manuscript submitted Jan. 6, 1984; revised manuscript received Feb. 18, 1985.

Instituto de Investigaciones Cientificas assisted in meeting the publication costs of this article.

REFERENCES

1. S. M. Gerchakov, L. R. Udey, and F. Mansfeld, *Corrosion*, **37**, 696 (1981).
2. C. Wagner and W. Traud, *Z. Elektrochem.*, **44**, 391 (1938).
3. M. Stern and A. L. Geary, *This Journal*, **104**, 56 (1957).
4. F. Mansfeld, *Corrosion*, **29**, 397 (1973).
5. D. M. Brasher, *Nature (London)*, **193**, 868 (1962).
6. D. M. Brasher, J. G. Beynon, A. D. Mercer, and J. E. Rhoades-Brown, in "Proceedings of the 2nd European Symposium on Corrosion Inhibition," p. 61, Ferrara, Italy (1965).
7. P. Berge, V. Jovancevic, D. Noel, and P. Saint-Paul, *This Journal*, **129**, 2194 (1982).
8. E. T. Seo and D. T. Sawyer, *Electrochim. Acta*, **10**, 239 (1965).
9. A. Q. Contractor and H. Lal, *J. Electroanal. Chem. Interfacial Electrochem.*, **93**, 99 (1978).
10. V. K. Gouda, M. G. A. Khedr, and A. M. Shams el Dim, *Corros. Sci.*, **7**, 221 (1967).
11. E. Pouillard and J. P. Chiola, *Rev. Metall.*, **65**, 603 (1968).
12. J. O'M. Bockris and A. K. N. Reddy, "Modern Electrochemistry," Vol. 2, Plenum Publishing Corp., New York (1978).
13. B. M. Rosales, *Corros. Protec.*, **10**, 19 (1979).

Mechanical and Current Oscillations in Corroding Electrodes

O. Teschke,* F. Galembeck, and M. A. Tenan

Instituto de Fisica and Instituto de Química, Universidade Estadual de Campinas, 13100 Campinas, SP, Brasil

ABSTRACT

Mechanical oscillations of the solution meniscus risen around a corroding wire electrode were observed in synchronism with electrical current oscillations. Scanning electron microscopy coupled to microprobe analysis was used to investigate the topochemistry of the system under study. Solution capillarity effects on iron and on iron compounds are related to the oscillations detected in this system.

Iron corrosion by acids is a rather complex phenomenon (1-5), involving many steps of chemical and physical transformation of the system constituents. A recent work (6) shows that anodically polarized electrodes made of pure iron, immersed in sulfuric acid, are covered with ferrous salts; oxide formation occurs underneath these. The oscillatory phenomena observed during passivation of iron seems to be related to the formation and dissolution of salt films (7).

During experiments on the behavior of iron immersed in sulfuric acid solution, we have observed mechanical oscillations (i.e., oscillatory vertical movement of sulfuric acid solution touching an iron tip, anodically polarized) coupled to electrical current oscillations. This observation suggests that capillary phenomena may be relevant to understand the behavior of passivating systems, at least in the case of incompletely immersed metal. The interpretation of capillary effects requires information on the topochemistry of the system under study, for which reason we have used scanning electron microscopy cou-

* Electrochemical Society Active Member.

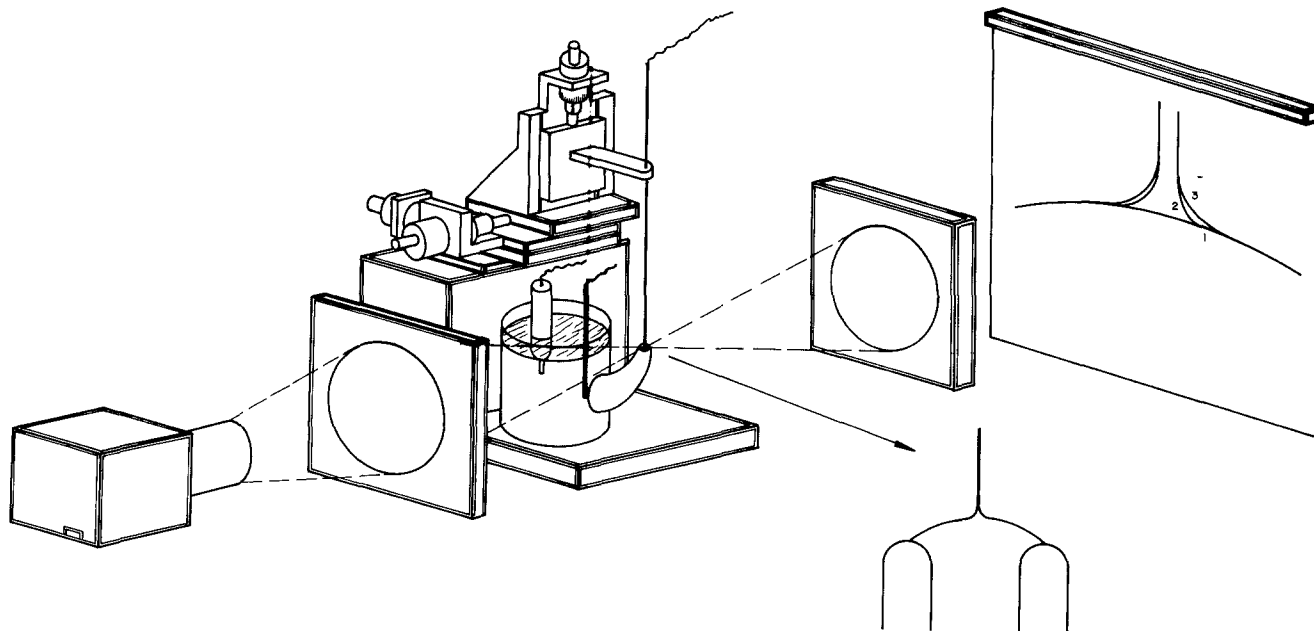


Fig. 1. Experimental setup

pled to microprobe analysis to examine corroding iron electrode. Results of these experiments are reported in this paper.

Experimental

The apparatus in which oscillations were observed consists of a borosilicate glass cylinder (8 cm diam, 15 cm height) as shown in Fig. 1. There is a lateral tubing (5 mm id at its top) exiting the cylinder. The cylinder volume is at least 100 times bigger than the capillary tube volume. A convex meniscus at the wetted capillary end (see detail in Fig. 1) was obtained by keeping the liquid level in the main cylinder a few millimeters above the meniscus level.

Reagent-grade chemicals were used without further purification. 1N aqueous H_2SO_4 was prepared using twice-distilled water. A 99.99% pure (C. Erba) iron wire 0.3 mm thick, cleaned with methanol and rinsed with twice-distilled water, was used as anode.

The iron electrode was grounded. Voltage was applied between the counterelectrode, a platinum wire with a downed area of at least 20 times larger than the area of the iron tip, and a saturated calomel electrode (SCE). An operational amplifier-based potentiostat kept the electrode voltages at the desired level, independent of the current. A constant voltage of +300 mV was applied between the iron electrode and the SCE. The current-time curves were recorded on a 7100 BM Hewlett-Packard Strip Chart Recorder. The photographs of the liquid level changes were taken using a Nikon F-2 reflex camera fitted with extension tubes for greater magnification. In order to obtain reproducible current-time curves, it was necessary to use a fresh solution and a new iron electrode tip for each experiment.

The topography and composition of deposits formed during iron corrosion were examined using a scanning electron microscope. The pictures were obtained by secondary electron imaging, and the composition by x-ray microanalysis using a beam energy of 20 keV. The data reduction was made by a computer correction program. Since the x-rays producing regions in the sample are about $2 \mu m$ wide, it was possible to characterize different regions of the surface. The results obtained were then related to the most likely compounds of iron, sulfur, and oxygen to identify the substance in each point analyzed.

Results

A typical current-time oscillation is given in Fig. 2. It was observed that the oscillation period depends on the applied voltage, the diameter of the iron tip, and the ra-

dus of curvature of the liquid surface. Oscillation periods for other radii of curvature of the liquid surface were measured, but the results reported here are for a tube diameter of 5 mm (id).

It was found that the peak maximum was affected by a number of physical factors including magnetic stirring of the solution, concentration, shape of the conducting (iron) tip, and the exact placement of the iron tip with respect to the liquid interface. In the experiments reported here, the iron wire was cut normal to its axis. The iron tip was placed approximately at the center of the liquid meniscus, and it was positioned to touch the liquid surface gently by using micromanipulators. By capillary action, the liquid rises immediately, wetting the lower part of the iron electrode.

After an induction period of a few minutes, mechanical oscillations of the liquid level around the iron electrode are observed. The oscillation occurs between the levels shown in Fig. 3a and 3b. These oscillations are sustained for periods of up to 1h with changes of frequency and pulse amplitude.

The measured solution electrolyte contact angle on a surface covered with iron sulfate is approximately 30° , and for an oxide-covered metallic iron surface this is approximately 83° (measured directly from photograph prints). This change in the contact angle for the initial and final product of the electrode reaction indicates a considerable change in the iron tip wetting ability as it is cor-

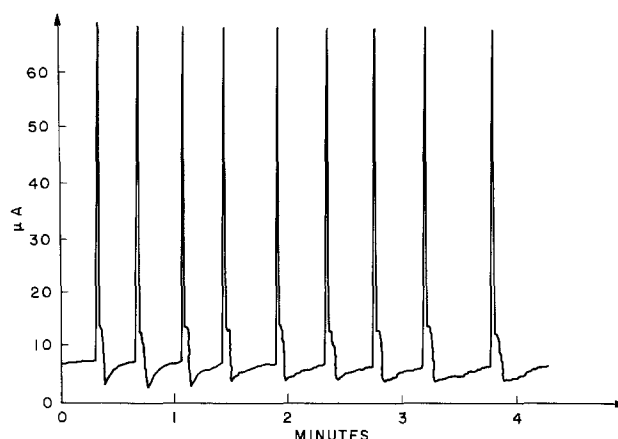


Fig. 2. Current-time profile for an iron electrode in a solution 1N of H_2SO_4 at constant external potential (300 mV SCE).

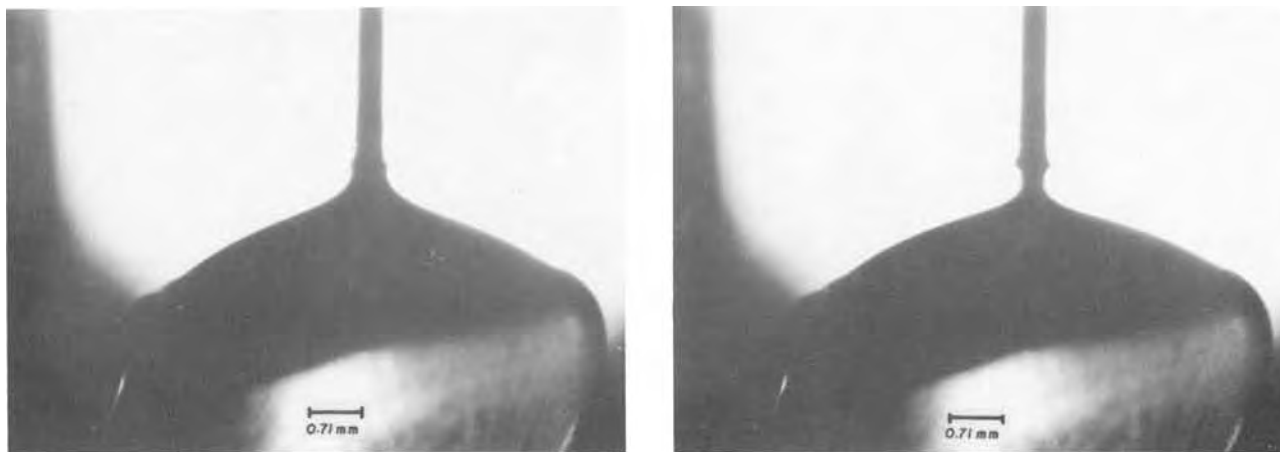


Fig. 3. Photograph of the liquid level changes at the iron electrode tip. a(left): Lower level. b(right): Upper level

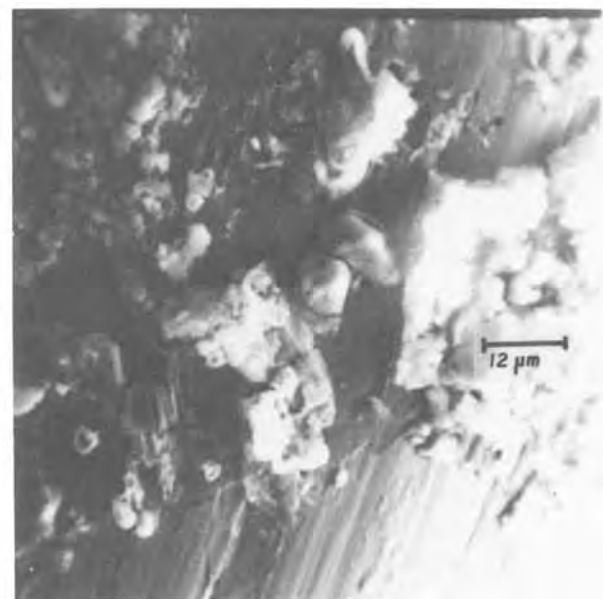
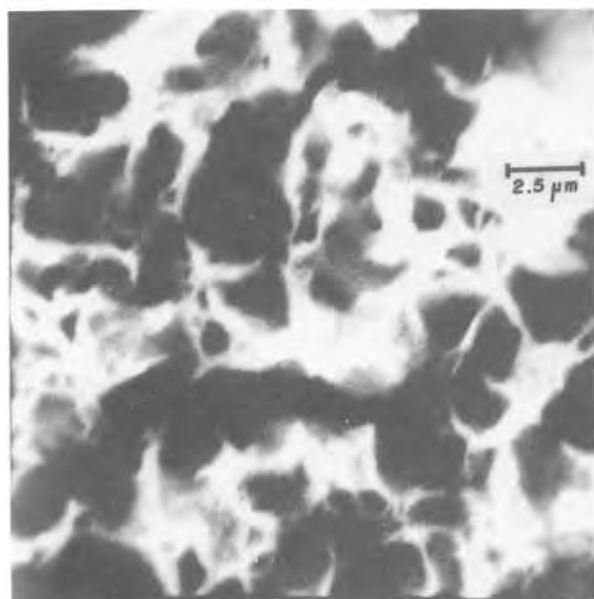
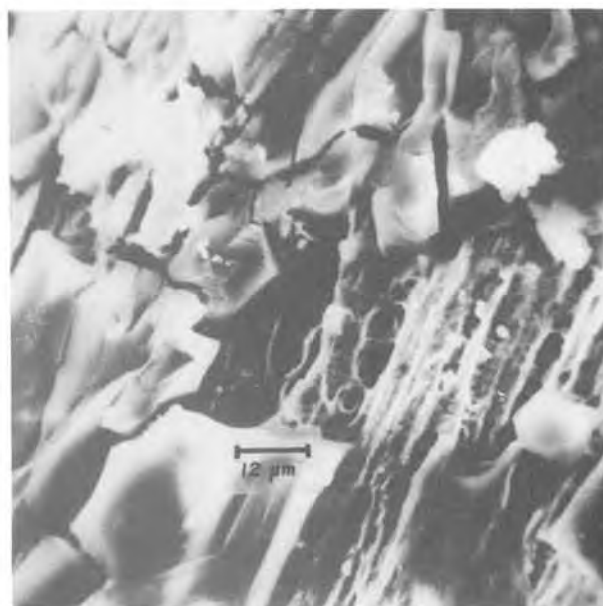


Fig. 4. SEM photograph of an iron tip. a(top left): Low amplification photograph showing the base iron (or oxide covered iron) as dark regions covered by a lighter overlayer of iron sulfate. b(top right): A detailed view of the drowned area of iron wire. c(bottom left): Oxide layer found under a crystal of iron sulfate removed in the SEM. d(bottom right): A detailed view of iron wire surface above the meniscus upper level.

roded by sulfuric acid. Note that these angles cannot be observed in Fig. 3 because the shape of the iron tip is being continuously altered by corrosion.

After some oscillations, the iron tip was gently removed from the solution and dried in air. SEM photographs were taken from these samples showing in detail the microstructure of the product formed at the movable air-liquid-metal interline.

A corroded iron tip is pictured in Fig. 4a. It is partly covered with thick pieces of light material appearing as bright, white areas. This material is also spread along the iron wire which was in contact with the solution, as shown in Fig. 4b. Microprobe analysis showed this material to contain iron and sulfur in different proportions: 9.52 atomic percent (a/o) Fe and 10.72 a/o S (Fe:S ratio ~ 1), and 19.32 a/o Fe and 12.70 a/o S (Fe:S ratio ~ 3:2). These two different measured Fe:S ratios may correspond to $\text{FeSO}_4 \cdot n\text{H}_2\text{O}$ and $\text{Fe}_3(\text{OH})_2(\text{SO}_4)_2$, respectively, or could be attributed to the different compactness presented by the sample in different regions. This is a low conductivity solid which acquires charge under the SEM beam. It is possible to remove chunks of this material by allowing the sample to stay for some time under the beam. Under the iron sulfate pieces, we find the material shown in Fig. 4c, appearing as white, patched areas. From microprobe analysis, we obtained a composition of 52 weight percent (w/o) Fe and only ca. 1 w/o S. This material has a composition corresponding to that of hydrous iron (III) oxide. The dark product below this oxide layer is pure iron (95+ %, perhaps covered with an oxide layer much thinner than the microprobe sampling depth).

Examination of another area which corresponds to a point above the liquid-iron-air line, shown in Fig. 4d shows three main features: (i) bright spots which contain 20.73 a/o Fe and 13.27 a/o S (Fe:S ratio ~ 3:2), (ii) dark, rough areas (24 w/o Fe, 0.88 w/o S), and (iii) dark, even areas (100% Fe). From the microprobe analysis data, it is clear that the flat areas are made of bare metal. The highly reflecting areas are rich in iron sulfate, and the dark, rough areas contain less sulfate than the former; their composition corresponds to that of an hydrous iron oxide contaminated with some sulfate mixture. The features described above were found in other samples, but in many instances bare metal was not detected. Varying Fe:S ratios were frequently observed, indicating the occurrence of phases containing different proportions of oxide and sulfate.

Figure 5 shows a SEM photograph of the morphology of an area of the iron wire produced by the movement of the liquid-iron-air boundary. The iron wire was removed from the solution a few minutes after the mechanical oscillations started. The dark region (iron or iron oxide) surrounded by the lighter overlayer of iron sulfate was located just on the triple-phase boundary for the meniscus upper level. The dark area shown had its layer of iron sulfate removed by the liquid fall.

Discussion

From the results reported here, some conclusions may be drawn: (i) iron sulfate precipitates on mechanically oscillating iron electrodes, forming rather large crystals which tend to bulge out of the surface, instead of making films; (ii) other deposits are found which still contain some sulfate (perhaps as the result of adsorption or absorption in amorphous iron hydroxide); these are neither as prominent, nor as strongly insulating (at least regarding their ability to acquire electrostatic charge in the SEM beam); (iii) bare metal may also be detected, contiguous to areas covered with salt and oxide. However, this occurs less frequently than the other features found. Oxide films were found to form a porous layer under the iron sulfate in agreement with another recent report (6); (iv) the liquid-iron-air line movement removes the iron sulfate layer from the iron wire lateral surface, producing a region of bare metal.

The following mechanism is then proposed to justify the mechanical oscillations of the liquid level.



Fig. 5. SEM photograph of an iron tip removed from the solution a few minutes after mechanical oscillations started. The dark region (iron or iron oxide) surrounded by the lighter overlayer of iron sulfate was located just on the triple-phase boundary for the meniscus upper level.

1. Fe^{2+} ions are generated at the surface of the corroding positive electrode.

2. Metal oxidation is accompanied by a slow rise of the liquid level because the reaction products deposited on the metal surface are more hydrophilic than the metal itself. This resulting change in the contact angle for the initial and final product at the electrode surface plays an important role in the oscillation phenomenon. As can be seen from the equation for the total weight W of a liquid column rising above a flat liquid surface

$$2\pi r g \int_r^{\infty} h(x) x dx = W = 2\pi r \gamma \cos \theta \quad [1]$$

(where the integration variable x represents the radial distance from the wire axis), the static equilibrium height $h(x=r)$ attained by the meniscus above the liquid surface is expected to be (i) an increasing function of both the wire radius r and the liquid-air surface tension γ and (ii) a decreasing function of the solid-liquid contact angle θ . According to Eq. [1], a change in the wettability conditions of the solid wall corresponding to a contact angle change from 80° to 30° leads to a fourfold increase in the weight of the liquid column supported by capillary action. The change in the exposed area of the electrode wire as suggested by this considerable weight increase can thus be responsible for the current rise prior to the current pulse. Figure 2 shows this increase of ca. 125% measured from the minimum current at the end of the sharp peak to the beginning of the next one. In analogy to liquid flow in cylindrical capillaries (8, 9), we can estimate for the conditions found in our experiments a time of a few seconds for the meniscus to attain its maximum height. This corresponds to the time of the slow rise of the current before the current pulse (see Fig. 2). Consequently, meniscus oscillations and current oscillations fit into the same time frame.

3. The liquid level oscillates between lower level and upper level shown in Fig. 3a and 3b. The liquid is at the upper level at the beginning of the current pulse. The liquid level stays at this position only for a very short period. Then the liquid falls rapidly, removing from the iron metal surface the iron solid compounds and forming a visible stream of solid products. As the solid layer falls off, the new bare metal surface reacts with the draining solution generating a current pulse. Figure 2a (lower

level) shows the position corresponding to the current minimum.

4. The time of the slow rise of the meniscus determines the spacing between current pulses, as shown in Fig. 1, and it increases after each oscillation. This is a consequence of the removal of the lateral cylindrical surface material by corrosion. The removal is faster at the tip in contact with the liquid. The iron corroded surface is gradually cone shaped in the successive motion steps until, finally, the liquid loses contact with iron electrode. At this point, the iron tip diameter has decreased so much that the surface tension forces are unable to stop the liquid downward movement (*cf.* Eq. [1]).

Conclusion

The meniscus oscillations described herein are induced by the combined action of three phenomena: capillarity of the liquid on the wire wall, wetting changes on the wire surface due to chemical reaction, and gravity. The iron oxidation reaction produces changes in the physical and chemical characteristics of the substrate solid surface, making the electrode wall more hydrophilic, up to the moving triple-phase boundary of the meniscus. Capillarity is thus responsible for the meniscus rise around the vertical wire. Gravity, on the other hand, is responsible for the liquid fall when, due to the poor wetting character of the iron surface at which oxide was converted to sulfate, the liquid-metal adhesion force is not sufficient to hold the liquid column.

Mechanical oscillations and current oscillations at an anodically polarized iron tip are thus interdependent for

the system described. They are related to the formation and destruction of passivating oxide films. We believe that these findings should be relevant to the understanding of metal corrosion at liquid-air-metal intersection lines.

Manuscript submitted Sept. 12, 1984; revised manuscript received Jan. 23, 1985.

Universidade Estadual de Campinas assisted in meeting the publication costs of this article.

REFERENCES

1. D. A. Vermilyea, in "Advances in Electrochemistry and Electrochemical Engineering," Vol. 3, P. Delahay and C. W. Tobias, Editors, John Wiley and Sons, New York (1963).
2. T. P. Hoar, in "Modern Aspects of Electrochemistry," Vol. 2, J. O'M. Bockris, Editor, Butterworths, London (1959).
3. H. S. Isaacs and R. C. Newman, in "Corrosion and Corrosion Protection," R. P. Frankenthal and F. Mansfeld, Editors, p. 121, The Electrochemical Society Soft-bound Proceeding Series, Pennington, NJ (1981).
4. G. Kortum, "Treatise on Electrochemistry," 2nd ed., Elsevier, New York (1965).
5. J. R. Galvele, in "Treatise on Materials Science and Technology," Vol. 23, J. C. Scully, Editor, Academic Press, London (1983).
6. T. R. Beck, *This Journal*, **129**, 2412 (1982).
7. J. Wojtowicz, in "Modern Aspects of Electrochemistry," Vol. 8, B. E. Conway and J. O'M. Bockris, Editors, Chap. 4, Plenum Press, New York (1972).
8. E. W. Washburn, *Phys. Rev.*, **17**, 273 (1921).
9. G. Beni and M. A. Tenan, *J. Appl. Phys.*, **52**, 6011 (1981).

Current and Potential Transients during Localized Corrosion of Stainless Steel

Hugh S. Isaacs* and Yuichi Ishikawa¹

Brookhaven National Laboratory, Upton, New York 11973

ABSTRACT

The currents flowing from a localized corrosion site (LCS) on passive stainless steel in air-saturated 0.25M NaCl have been studied using a vibrating probe electrode. The potential behavior during applied currents was analyzed by assigning equivalent circuits to the passive surface and the localized site so that the paths of the current across the passive surface and the LCS could be calculated and compared with the measured values. The equivalent circuit of the passive surface without active localized corrosion was determined from potential transients and was found to be dependent on the prior history of the electrode. The LCS was equated to a resistance with an EMF which were calculated from the LCS current and specimen potential. The variations of this resistance were attributable to changes in solution resistance adjacent to the LCS. It was found that the capacitance of the passive surface played a major role during potential transients and the initiation of pitting.

Potential fluctuations, observed during open-circuit exposure of stainless steels (1-5) and other passive metals (6-8) have been associated with the onset of chloride-induced localized corrosion. The potential of the passive metal depends on the behavior of both the freely exposed surface and the growing localized corrosion site (LCS). Under freely corroding conditions with rapid cathodic kinetics, for example, in ferric chloride solutions, the potential variations are determined by the polarization of this reaction. When these cathodic polarization currents are known, the corrosion rate can be determined directly from the potential (5). The potential has been observed to decrease relatively slowly when pits initiate and grow, but increase almost immediately when they repassivate in these solutions (4, 5). In contrast, when the cathodic reaction is slow, as with dissolved oxygen, the behavior becomes more complex. The potential then drops rapidly

during the onset of pitting and increases slowly following repassivation (1-3, 6). The causes of the potential variations have not been presented in detail.

This work describes an approach to this problem which also closely resembles the exposures to which stainless steels are generally subjected. The approach developed from an analysis of results obtained with a scanning vibrating probe which has been used to monitor current from a LCS and leads to a number of interesting conclusions and possible applications.

Experimental

The location and monitoring of the currents from localized corrosion sites was accomplished using a scanning vibrating electrode. This technique was developed by biologists to overcome the noise interfering with amplification by masking small dc voltages (9, 10). The specific frequency of vibration enabled other signals associated with the noise to be filtered out and signals of the order of a few nanovolts to be measured (10). The design used

* Electrochemical Society Active Member.

¹ Visiting Scientist from Hitachi Limited, Mechanical Engineering Research Laboratory, Tsuchiura 300, Japan.

in this and other studies (11-13) was based on the work of Jaffe and Nuccitelli (10). The vibrating electrode was a coated platinum wire of 0.12 mm diam and coated with an insulation layer, having only the tip of the wire exposed to the solution. The tip scanned above the steel surface at a height of 0.1 mm. A similar wire was positioned well above the surface and was incorporated to reduce noise. The wires were attached to a piezoelectric bimorph reed and vibrated perpendicular to the steel surface. Generally, the frequency was about 600 Hz and the vibration amplitude about 0.03 mm, which could be adjusted by changing the voltage to the piezoelectric reed.

A schematic of the apparatus is shown in Fig. 1. The (Vibrating Probe Company) Probe Vibrator Power Supply activated the reed and also supplied a reference signal for the (Princeton Applied Research, Model 5204) Lock-in Amplifier. The experiments were computer controlled (Hewlett-Packard Desktop Computer, Type 9845T and Control and Data Acquisition Unit, Type 2240). The stage on which the vibrating probe was held was positioned with computer-activated stepping motors giving a single-step distance of 0.005 mm.

Samples of Type 304 stainless steel (Cr 18.88, Ni 8.61, Si 0.68, Mn 1.58, C 0.07, P 0.026, S 0.007 weight percent) with one 20×13 mm face exposed to the solution. The samples with insulated leads were mounted in epoxy resin (Buehler Type Epo Quick). The exposed surface was wet abraded down to a 600 grade silicon carbide finish. A series of samples with known crevice sizes was also prepared, but, as corrosion generally initiated at the interface with the epoxy, the carefully characterized crevices were discarded. The polarization measurements were made on samples with the edges coated with lacquer to reduce the initiation of localized corrosion leaving an area of 10×15 mm exposed.

All measurements were made at room temperature in 0.25M NaCl solutions prepared from deionized water and analytical-grade salt. The solutions were aerated before use and held in an open square flat-faced glass cell to allow observation of the probe from the side with a stereoscopic microscope. The cell also contained a calomel reference electrode and a platinum counter electrode.

Results

Localized corrosion was initiated and maintained by applying currents of about $1 \mu\text{A}$. When the potential continued to drop for a few minutes after its initial rapid increase, the position of the localized corrosion was located by scanning the entire sample to ensure only one localized corrosion site (LCS) was present. If more than one site did initiate, it was repassivated by washing with a jet of solution or the sample was cathodically polarized below the protection potential and the process repeated. When only a single LCS was found, the scanning was repeated around the site on a finer scale to more accurately determine the position of the maximum current density over its center. The vibrating probe was then positioned at this place and the effects of applied currents on the potential and the current from the LCS were studied. No effect of the vibrating probe on the behavior of the LCS was observed.

The output from the lock-in amplifier was calibrated against the applied current. When the potential showed only slow changes (<1 mV/s) and the LCS current approached a constant value, it was considered that a very small fraction of applied current flowed across the passive surface and the currents from the LCS were equal to the applied current. The calibration was linear and gave a slope of $4.3 \mu\text{V}/\mu\text{A}$ with an accuracy for the currents from the LCS of $\pm 0.1 \mu\text{A}$. The linear calibration also implied the LCS behaved as a point source, because the current density measured was proportional to the current.

Figure 2 shows the variations of the potential and the LCS current following step changes in the applied current. Immediately following the step, they both changed linearly with time for a short period. The linear change in the potential was indicative of no significant series resist-

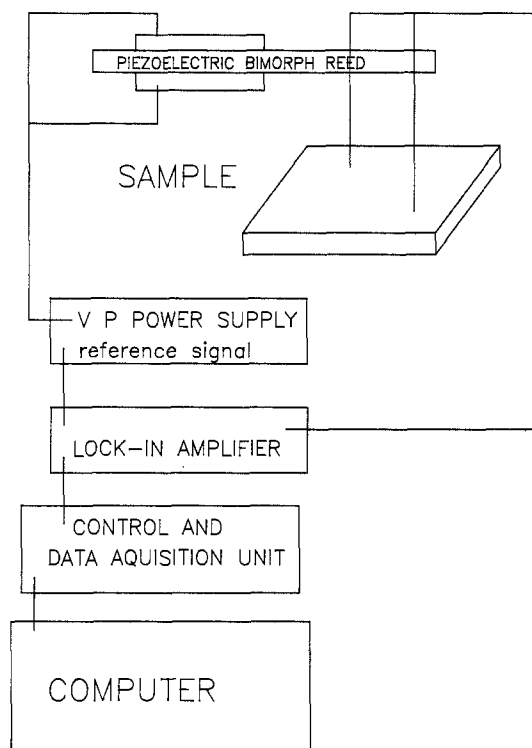


Fig. 1. Schematic of the vibrating electrode instrumentation

ance and a dominant capacitance. The value of the effective capacitance (C) was calculated from the equation

$$C = \frac{\Delta i}{dE/dt} \quad [1]$$

where Δi was the change in applied current and dE/dt the linear slope of the potential curve. The value of the capacitance was $95 \pm 15 \mu\text{F}$ ($36 \mu\text{F}/\text{cm}^2$). On increasing the applied current, the potential initially increased and if the current change was relatively large ($>0.5 \mu\text{A}$) the potential reached a maximum before decreasing. The opposite effect was seen on decreasing the potential. If the current changes were small ($<0.5 \mu\text{A}$), no maxima or minima were observed. The LCS currents approached constant values when the applied currents were above $0.6 \mu\text{A}$, but below this value the LCS currents generally decreased until the LCS repassivated. Following repassivation, the potential increased rapidly until a new LCS initiated. After the results shown in Fig. 2 were recorded and the sample was at open circuit, the potential rose to a steady value of -110 mV, following repassivation of the LCS. This potential was taken as the EMF of the passive surface.

The behavior of passive surfaces was studied without any localized corrosion occurring on the surface. The open-circuit potential and the impedance derived from potential or current transients, as well as the polarization behavior, all depended on the history of the electrode. At open circuit, a freshly abraded surface initially increases in potential and reaches around -120 mV after a few hours and about -75 mV after a few days. During these exposures, there were very few indications of LCS initiation events. If, however, the sample was anodically polarized repeatedly in the chloride solution to potentials above 250 mV, the long-term open-circuit potential was about 200 mV (the applied potential was turned off immediately after any initiation), and repeated initiation events having similar shapes were observed at open circuit. An example of such an initiation event is shown in Fig. 3. The potential dropped rapidly as the initiated site grew and after its repassivation the potential rose slowly over a period of 1000s. This behavior is typical of initiation and repassivation events in solutions containing only oxygen as the cathodic reactant.

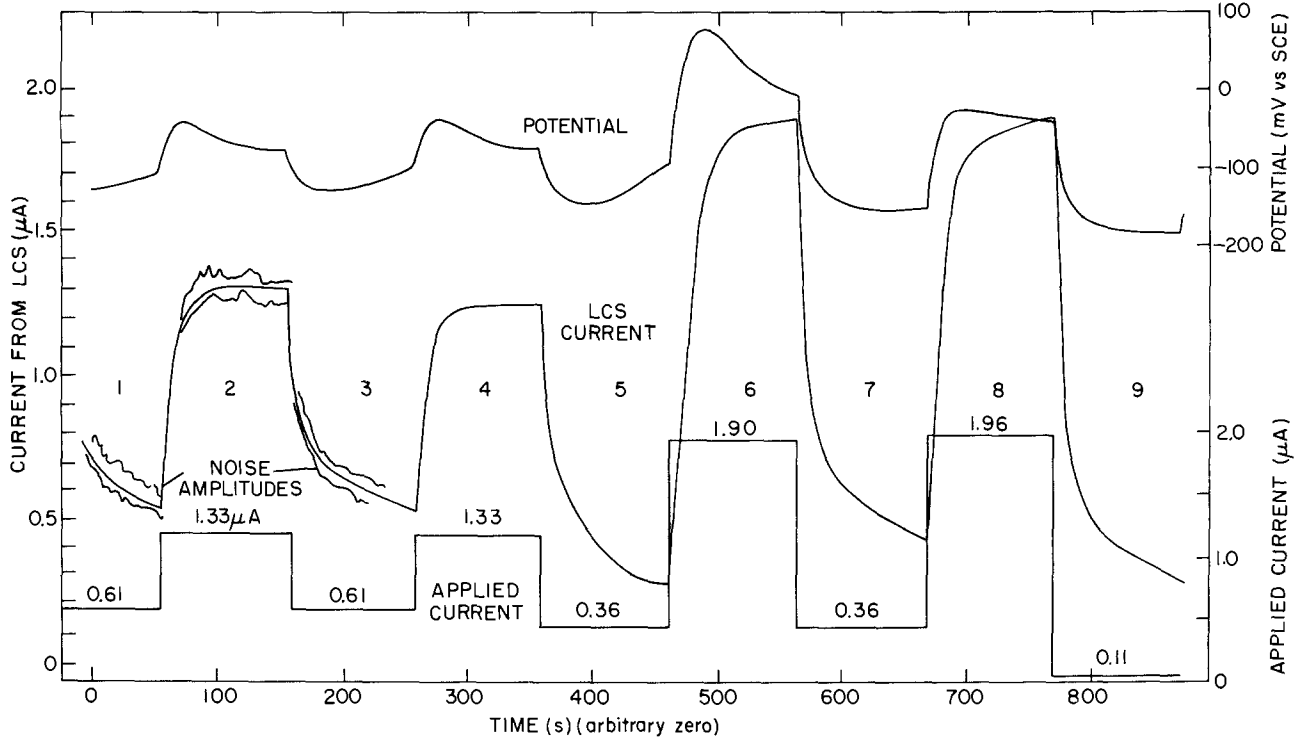


Fig. 2. Variation of potential and LCS current following step changes in applied current

Polarization measurements of the passive surface were carried out both potentiodynamically and, essentially, galvanostatically. Figure 4, taken after 20h cycling at 0.1 mV/s, shows the currents depended on the potential direction. Over the range of -200 to 50 mV, the polarization curves had a greater slope (or impedance) on increasing the potential. The increased polarization impedance was also observed when a "square" current wave was stepped between two fixed values of -15 and -165 nA/cm² at 1 mHz. The magnitude of the potential response increased with time, indicating an increased electrochemical impedance. It was about 24 mV after 0.5h and 160 mV after about 21h. This change was less rapid than expected from the inverse current-time dependence at more positive potentials with passive metals (14, 15).

The potential response to a square current wave was analyzed at 5 mHz, as this frequency correlated with the changes in the applied current when a LCS was active (see Fig. 2). Figure 5 shows the potential response to a step current wave of -125 and 75 nA/cm². The asymmetric response again indicated a higher impedance on increasing the potential. The equivalent circuit for each of these half cycles was determined graphically (16) in terms

of a series of resistances (R_n) with parallel capacitances (C_n). The equation representing the response is

$$V = 0.5I \sum_{n=1}^n R_n [1 + \tanh(T/C_n R_n)] [1 - \exp(-t/C_n R_n)] \quad [2]$$

where I is the peak-to-peak current (200 nA/cm²), T is half the period of the cycle (100s), and t the time. The results with $n = 2$ are given in Table I and have an accuracy of about 10%.

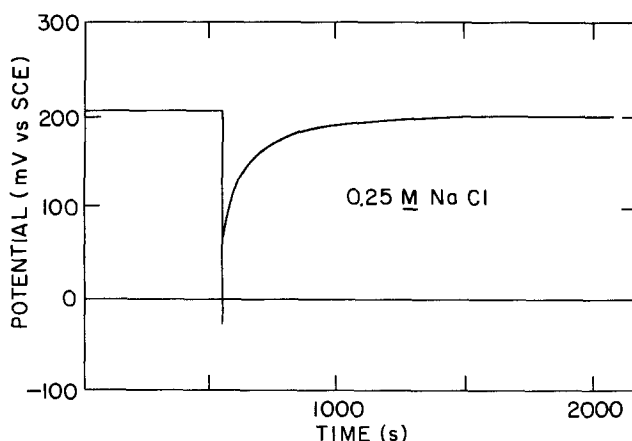


Fig. 3. The open-circuit potential of abraded and anodically pre-treated surfaces.

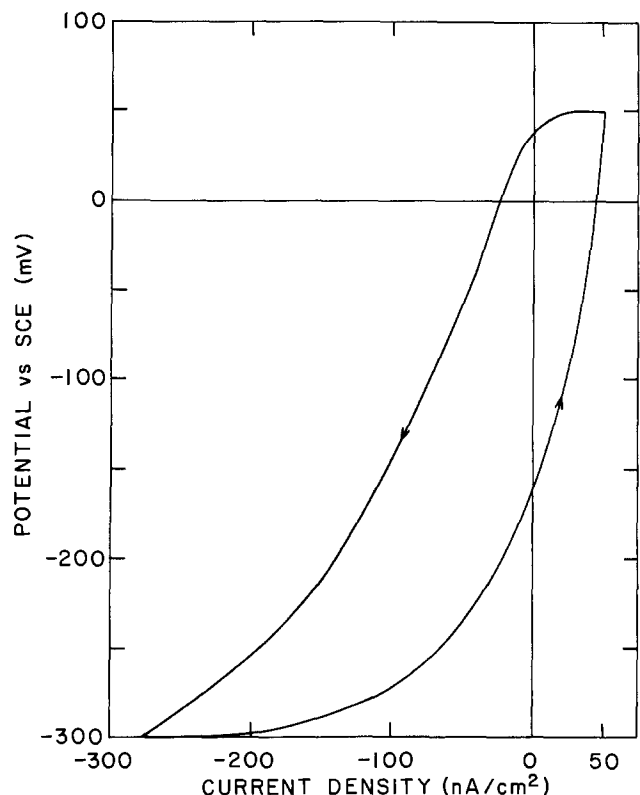


Fig. 4. Polarization curve for abraded stainless steel after potential cycling for 20h at 0.1 mV/s.

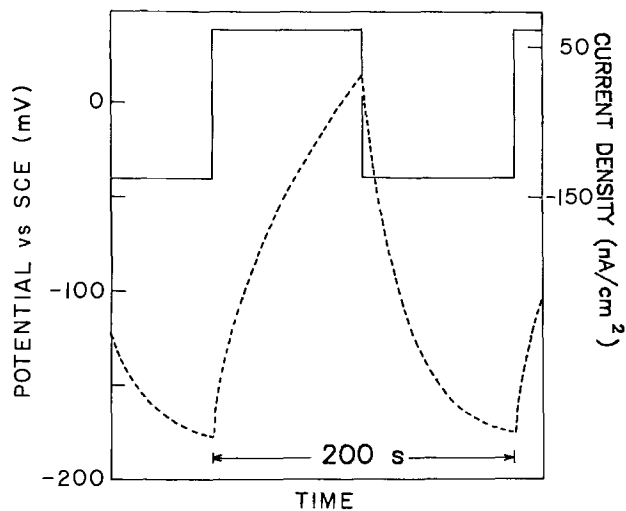


Fig. 5. Potential response to a 5 mHz current wave stepped from -125 to 75 mA/cm².

Discussion

The analysis of the behavior of the passive surface with an active localized corrosion site (LCS) has been carried out by considering the electrical analogue of the steel/solution interface shown in Fig. 6a. Z_a represents the LCS, Z_c the passive surface with both metal oxidation and oxygen reduction taking place, I the externally applied current, i_a the LCS current measured with the vibrating probe electrode, and E the potential measured against a calomel reference electrode. Because of their electrochemical nature, Z_a and Z_c must also incorporate a potential generator or EMF.

The impedance of a passive surface has been attributed to the dielectric, resistive, and space-charge properties of the oxide (17) or to the presence of adsorbed species on the surface (18). Neither of these models has been unequivocally demonstrated, and an equivalent circuit based on either model will be controversial. In view of this, we chose an analogue for convenience of analysis of the response of the systems rather than attempt to confine to a particular model. The analysis of the potential response was in terms of capacitors with parallel resistors and offered sufficient accuracy for the present results and the time frame of minutes for the purposes of these discussions.

Table I shows the magnitude of the capacitors and resistors obtained from Fig. 5 and were used to partly replace Z_c . An EMF source having the value of the open-circuit potential observed after the LCS had repassivated (i.e., $E_c = -110$ mV) was added to complete the analogue of the passive surface. The polarization curve in Fig. 4 shows curvature, indicating that the equivalent circuit changed with potential direction. The derived equivalent circuit was therefore an approximation covering the potential over which the LCS measurements were made and was also dependent on the direction of potential change. The open-circuit potential also depended on the potential history, as was shown by the effects of anodic pretreatment and the results in Fig. 3, which led to higher potentials than observed with the specimen following the LCS current measurements. The value of -110 mV was taken because it was representative of the particular sample for

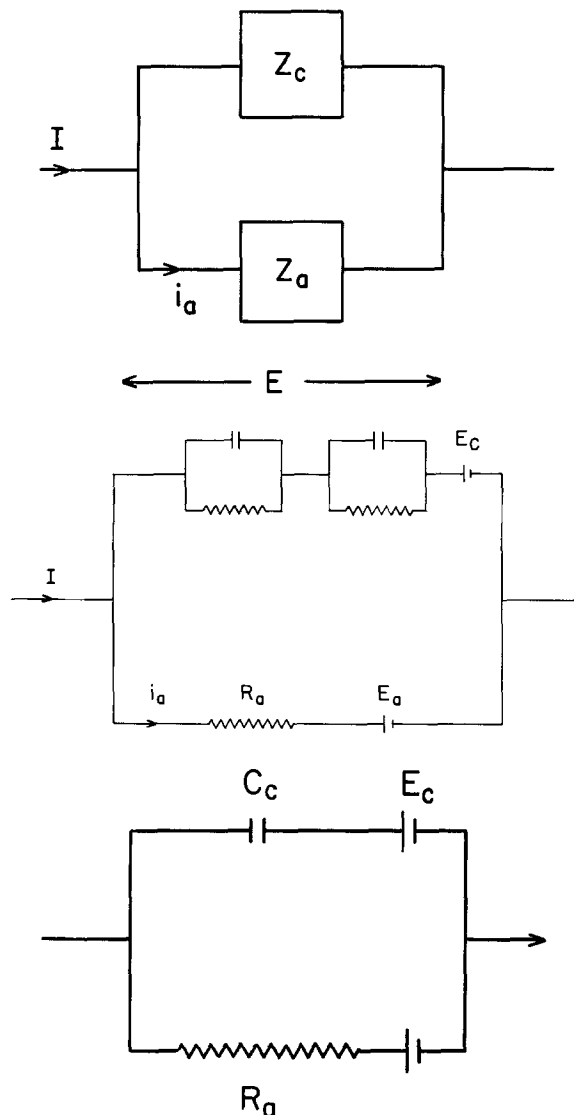


Fig. 6. a (top): An equivalent circuit showing the impedance of the LCS, Z_a , the passive surface, Z_c , the applied current, I , and the LCS current, i_a measured using the vibrating electrode. b (center): An equivalent circuit showing the experimentally derived analogue components. c (bottom): The simplified equivalent circuit during the early stages of pit initiation.

which a simulation of the potential variations and LCS current were carried out.

The equivalent circuit of the LCS was determined from the analysis of the current flowing through the LCS (i_a) and the potential in Fig. 2 and does not incorporate the passive surface. In order to characterize the behavior of the LCS, the LCS current was plotted against the potential of the specimen in Fig. 7. These plots indicated that there was a linear relation between LCS current and the potential immediately following the changes in the applied current. The linear relation was indicative of a resistive response having a resistance equal to the slope of this line. A second observation was the extrapolations of these lines all intersected the ordinate at close to -230 mV, as emphasized by their inclusion in Fig. 7 for the various applied currents. It is clear from the results in Fig. 7 that the value of the resistance varied with time. There is obviously a representational difficulty involved with this approach. Generally, inductances and capacitances are invoked to account for time variations, and indeed an added inductance and series resistance, placed in parallel with a resistance, could possibly be used to fit the potential responses. However, a single inductance could not fit the results. In addition, when small changes in applied current were made (<0.5 μ A), there was no in-

Table I. Calculated values of the equivalent circuit of the passive surface from analysis of a stepped current wave of 5 mHz

Potential	Parallel capacitances (μ F/cm ²)		Parallel resistances (k Ω -cm ²)		Time constants (s)	
	C_1	C_2	R_1	R_2	T_1	T_2
Increasing	80	29	558	153	45	4.4
Decreasing	35	44	879	137	31	6.1

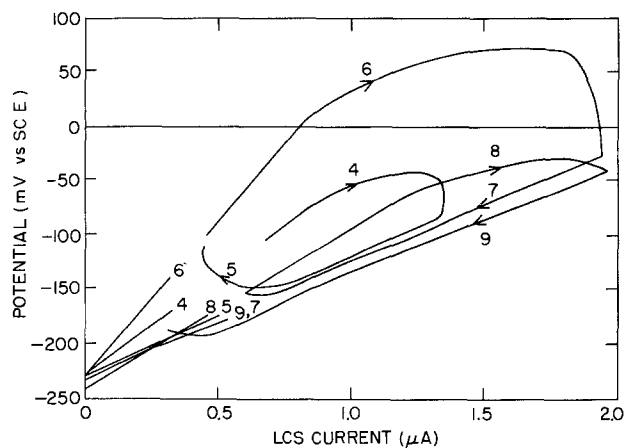


Fig. 7. Variation of the LCS current with potential taken from Fig. 4 with number corresponding to the particular half-cycles.

dication of inductive behavior, and trials with inductances led to resonances not observed experimentally.

Potentials close to that of the constant intercept in Fig. 7 have also been observed in other studies (19, 20) and result from the localized corrosion cell consisting of the active metal and the concentrated chloride electrolyte with dissolved corrosion products within the LCS. The open-circuit potential for this cell, and the Type 304 alloy used in these experiments, has been observed to be about -250 mV and was dominated by the presence of copper corrosion product from the alloy (19).

The above consideration led to an equivalent circuit for the LCS consisting of a resistor (R) and an EMF (E_a) in parallel with that of the passive surface giving an equivalent circuit shown in Fig. 6b. The LCS resistance was calculated from the results in Fig. 2 or 7 from the equation.

$$R = (E - E_a)/i_a \quad [3]$$

Graphically, this was the slope of the line between the intercept on the potential axis and the point on the curve obtained at the time of interest.

The results of Fig. 2 and 7 are related to the dissolution characteristics of the LCS as the applied current was changed. The best measure of the state of the LCS was the resistance R , which generally decreased after the current was increased and vice versa. This was obviously caused not by changes in size of the LCS because a particular resistance could be obtained repeatedly on cycling, but rather by a result of the changes in the localized environment. One explanation could be the effect of changes in the concentration of dissolution products, chlorides, and pH on the conductivity in and around the LCS. The conductivity range of the solution that could possibly be present varies from that of 0.25M NaCl having a resistivity of about 45 Ω -cm to that within the LCS with a resistivity of around 5 Ω -cm. Similar effects have been discussed by Newman (21). The difference in solution conductivity of, say, nine times is adequate to account for the observed changes in R which from Fig. 7 and Eq. [3] were calculated to vary from 75 to 275 k Ω .

In order to confirm the equivalent circuit, the potential changes and LCS currents were computer calculated. The changes in R were used as input to the calculation. The passive surface impedance which depended on the direction of potential was taken from Table I, and the values of E_c and E_a were fixed at -110 and -230 mV (SCE), respectively. A comparison of the observed and calculated values are shown in Fig. 8, showing good agreement between the observed and the calculated potentials and LCS currents with time. This clearly demonstrates the validity of the analogue circuit requiring only the resistance of the LCS to change fairly rapidly with time and shows a consistent split of the current between the passive surface and the LCS. It also shows that if the behavior of the anode and cathode during localized corrosion can be de-

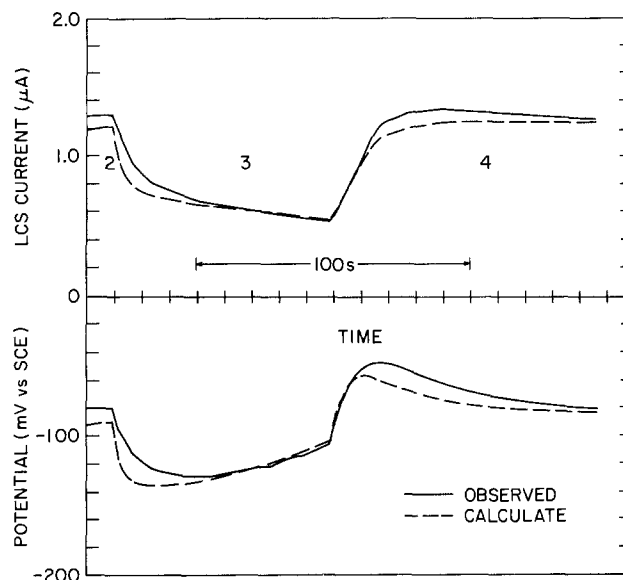


Fig. 8. Comparison between the observed and calculated LCS currents and specimen potential for transients 3 and 4 are shown in Fig. 2.

scribed in sufficient detail, the potential behavior can be predicted.

The equivalent circuit in Fig. 6b can also be used to analyze the open-circuit potential changes following initiation of the pit in Fig. 3. It becomes clear from the equivalent circuit that the capacitance of the passive surface is the component of major importance when the potential varies rapidly either immediately following changes in applied current or when pitting initiates. The equivalent resistances of the passive surface then play a minor role because of their high values. During the potential decrease in Fig. 3, the passive surface can be represented by a single capacitor. The equivalent circuit of the stainless steel is shown in Fig. 6c. The capacitance markedly retards the potential changes, with virtually no faradaic or net electrochemical reaction taking place. This was also noted when the applied currents were turned off and the current flowing from the LCS were far greater than those that could be produced by the oxygen reduction reaction.

The role of the capacitance is also extremely important during freely corroding conditions when pitting initiates. Considering Fig. 6c prior to pit initiation, the value of R is infinite. On initiation of localized corrosion, the presence of R leads to charging the capacitance. The amount of charge involved, Q , is given by the product of the potential change ΔE , and the capacitance, *i.e.*

$$Q = C\Delta E \quad [4]$$

In other words, the potential change observed in Fig. 3 when pitting initiated can, on one's knowing the magnitude of the capacitance, be used to estimate the amount of charge passed through the pit. From the charge, the amount of metal dissolved or the size of the pit can be calculated. Taking the capacitance as 25 μ F/cm², which is representative of the passive surface over a period of less than a few seconds, and a surface area of 1 cm², the transient in Fig. 3 of 230 mV results in a hemispherical pit size of about 5 μ m.

This approach can be extended to give information about the rate of growth of pits. Differentiation of Eq. [2] gives

$$i = C dE/dt \quad [5]$$

and indicates that the rate of pitting or pit growth can be determined from the shape of the rapidly decreasing portion of the curve in Fig. 3. This approach requires that the capacitance remains constant or its dependence with time be known. This approach was not developed in the present work but will be used in the future.

Following the repassivation of the pit, the value of R is again infinite and the potential changes are then controlled by the slow discharging of the capacitance via the high parallel resistances which are determined by passive surface polarization currents.

It may also be of interest to note that, because the capacitance increases with surface area of the stainless steel, this must have a bearing on pit propagation. From Eq. [5] and [4], increasing the capacitance decreases both the magnitude and rate of potential change. For both these reasons, increasing the surface area increases the likelihood of a pit's remaining active and not repassivating. Because of the greater charge available, the potential does not drop below any protection potential for the very small pits and the pit remains active. This analysis strongly suggests that the probability of forming a stable pit increases with area of stainless steel. The cause is related not to the statistics of initiation, as has been suggested, but to stabilizing propagation after initiation. The critical stages in producing a stable pit occur relatively rapidly and hence appear to be essentially independent of the rate of oxygen reduction and dependent on factors determining the interfacial capacitance.

Acknowledgments

The authors wish to thank D. Becker for his experimental expertise and R. C. Newman for bringing Ref. (9) to our attention. This work was funded by the U.S. Department of Energy, Office of Basic Energy Sciences under Contract no. DE-AC02-76CH00016.

Manuscript submitted July 23, 1984; revised manuscript received Feb. 22, 1985.

Brookhaven National Laboratory assisted in meeting the publication costs of this article.

REFERENCES

1. S. Ito, M. Yabumoto, H. Omata, and T. Maruta, in "Passivity of Metals and Semiconductors," M. Froment, Editor, p. 637, Elsevier Science, New York (1983).
2. A. Atrens in "Passivity of Metals and Semiconductors,"

- M. Froment, Editor, p. 631, Elsevier Science, New York (1983).
3. B. C. Syrett, R. Viswanathan, S. S. Wing, and J. E. Wittig, *Corrosion*, **38**, 273 (1982).
4. N. D. Tomashov, G. P. Cernova, and O. N. Marcova, in "Localized Corrosion," R. W. Staehle, B. F. Brown, J. Kruger, and A. Agrawal, Editors, p. 363, National Association of Corrosion Engineers, Houston, TX (1974).
5. H. S. Isaacs, in "Localized Corrosion," R. W. Staehle, B. F. Brown, J. Kruger, and A. Agrawal, Editors, p. 158, National Association of Corrosion Engineers, Houston, TX (1974).
6. T. Hagyard and M. J. Pryor, *Trans. Faraday Soc.*, **57**, 2295 (1971).
7. J. A. Richardson and G. C. Wood, *Corros. Sci.*, **10**, 313 (1970).
8. F. J. Cornwell, G. Wildsmith, and P. T. Gilbert, *Brit. Corros.*, **8**, 202 (1973).
9. D. Mackenzie, *New Scientist*, p. 217, Jan. 28, 1982.
10. L. F. Jaffe and R. Nuccitelli, *J. Cell Biol.*, **63**, 614 (1974).
11. Y. Ishikawa and H. S. Isaacs, *Boshoku Gijutsu*, **33**, 147 (1984).
12. Y. Ishikawa and H. S. Isaacs, Paper presented at the Conference on Corrosion and Exploitation of Aluminum Alloys, Branfield, England, 1983.
13. H. S. Isaacs and R. Jackson, in "Fundamental Aspects of Corrosion Protection by Surface Modification," E. McCafferty, C. R. Clayton, and J. Oudar, Editors, p. 339, The Electrochemical Society Softbound Proceedings Series, Pennington, NJ (1984).
14. B. MacDougall, *This Journal*, **130**, 114 (1983).
15. R. C. Newman, Y. C. Lu, R. Bandy, and C. R. Clayton, Paper presented at the 9th International Congress on Metallic Corrosion, Toronto, Ontario, Canada, June 1984.
16. H. S. Isaacs and J. S. L. Leach, *This Journal*, **110**, 680 (1963).
17. B. D. Cahan and C-T. Chen, *ibid.*, **129**, 921 (1982).
18. R. D. Armstrong and K. Edmondson, *Electrochim. Acta*, **18**, 937 (1973).
19. R. C. Newman and H. S. Isaacs, in "Passivity of Metals and Semiconductors," M. Froment, Editor, p. 269, Elsevier Science, New York (1983).
20. H. S. Isaacs, *This Journal*, **120**, 1456 (1973).
21. R. C. Newman, *Corros. Sci.*, **23**, 1045 (1983).

Kinetics of the Low Temperature Hot Corrosion of Co-Cr-Al Alloys

Krishan L. Luthra*

General Electric Company, Corporate Research and Development, Schenectady, New York 12301

ABSTRACT

Hot corrosion rates have been measured on many Co-Cr, Co-Al, and Co-Cr-Al alloys coated with 2.5 mg/cm² of Na₂SO₄ and exposed in O₂-0.15%(SO₂ + SO₃) at 750°C. The hot corrosion resistance of the binary alloys increases with the chromium and aluminum content of the alloys. However, the additions of aluminum to Co-Cr and of chromium to Co-Al alloys have deleterious effects. These results can be explained on the basis of a mechanism similar to one previously proposed in the literature (1, 2). Additional experiments have been conducted as a function of temperature and the (SO₂ + SO₃) content of oxygen to extend the proposed mechanism.

Sodium sulfate-induced hot corrosion problems have plagued the gas turbine industry for more than 30 years. Until about the mid nineteen-seventies, it was believed that these problems occurred only when liquid salts deposited on the surface of gas turbine components. However, since then, severe degradation of cobalt containing alloys and coatings has been observed at temperatures below the melting point of Na₂SO₄ (884°C). This corrosion is believed to be caused by formation of an Na₂SO₄-CoSO₄ eutectic and is identified in the literature as low temperature hot corrosion.

Many publications in the literature have been concerned with various aspects of low temperature hot corrosion (1-8). In earlier papers, we described the morphology

and mechanism of corrosion of cobalt-base alloys (1-3). While attempting to quantify further the corrosion rates of Co-Cr-Al alloys, some rather strange interactions were observed between the effects of chromium and aluminum, which ultimately led to the development of new coatings (9). This paper discusses these results and correlates them with the mechanism proposed earlier (1, 2).

Experimental

Hot corrosion studies were conducted on coupons of several cobalt-base alloys listed in Table I' by using laboratory-accelerated oxidation tests with 2.5 mg/cm² of Na₂SO₄. The coupon specimens (~12.5 × 6.3 × 1.0 mm) were obtained by machining small chill cast ingots pre-

* Electrochemical Society Active Member.

' All alloy compositions in this paper are in weight percent.

Table I. Compositions of alloys used for corrosion study

Nominal composition (w/o)	Actual composition ^a (w/o)	
	Cr	Al
Co-20Cr	18.5	—
Co-30Cr	29.6	—
Co-35Cr	34.6	—
Co-40Cr	38.5	—
Co-10Al	—	9.7
Co-12Al	—	11.9
Co-15Al	—	14.8
Co-20Al	—	19.5
Co-40Cr-1Al	39.1	1.1
Co-40Cr-2Al	39.9	1.9
Co-40Cr-5Al	40.0	4.3
Co-15Al-2Cr	1.8	13.7
Co-15Al-5Cr	4.5	16.3
Co-15Al-20Cr	19.9	14.7

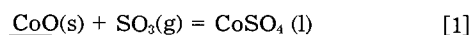
^a As measured by Chemical Analysis and Balance Company.

pared from 99.9% pure elements. The salt coatings were obtained by spraying an aqueous solution of Na_2SO_4 with an air brush on prewarmed ($\sim 150^\circ\text{C}$) specimens. These samples were then exposed at 1 atm total pressure in an O_2 -0.15%($\text{SO}_2 + \text{SO}_3$) gas mixture at 750°C to simulate low temperature hot corrosion conditions present in engines. A platinum catalyst was used to ensure equilibrium in the gas mixture. During the course of the experiments, which usually lasted for about 24-72h, the samples were continuously weighed using a Cahn 1000 microbalance. Further details of the experimental arrangement are given elsewhere (1, 10).

Thermochemical Considerations

Thermodynamic calculations were performed to determine the minimum p_{SO_3} for which an Na_2SO_4 - CoSO_4 liquid can form on various cobalt oxides; the results are shown in Fig. 1. The details of calculations for CoO and Co_3O_4 , including the required minimum activity of CoSO_4 , were described in earlier publications (1, 10). These calculations will be extended to other oxides here.

The sulfation of any cobalt oxide can be considered as that of CoO existing at an activity of less than or equal to unity. Thus, the reaction for the formation of an Na_2SO_4 - CoSO_4 liquid can be represented by

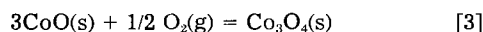


where the underline indicates that CoO and CoSO_4 can exist at less than unit activity. From reaction [1], at any temperature

$$\frac{a_{\text{CoSO}_4}}{a_{\text{CoO}}p_{\text{SO}_3}} = \text{const.} \quad [2]$$

Thus, the SO_3 pressure needed to stabilize a liquid will increase inversely with a_{CoO} .

The equilibrium CoO activity in Co_3O_4 can be calculated from the equilibrium constant of the following reaction



Calculations based on JANAF Tables (11) show that at $P_{\text{O}_2} = 1$ atm Co_3O_4 is the stable cobalt oxide and the CoO activity in Co_3O_4 is less than unity below 947°C . Consequently, the SO_3 pressure required to form liquid Na_2SO_4 - CoSO_4 from Co_3O_4 in Fig. 1 is higher than that for CoO . The CoO activity may be even lower and the required SO_3 pressure even higher if cobalt exists only as CoCr_2O_4 or CoAl_2O_4 , which is possible on cobalt-based alloys containing high chromium or high aluminum, respectively. Under these conditions, the CoO activity can be calculated from the equilibrium constants of the following reactions

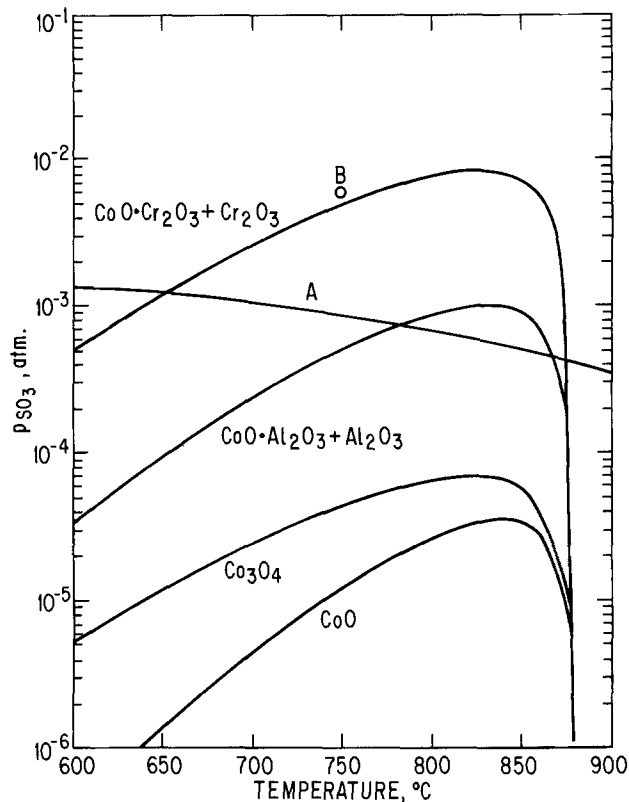
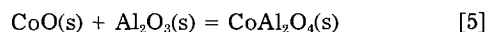


Fig. 1. Plots of the calculated SO_3 needed to form an Na_2SO_4 - CoSO_4 liquid from CoO , Co_3O_4 , a $\text{CoCr}_2\text{O}_4/\text{Cr}_2\text{O}_3$ mixture, and a $\text{CoAl}_2\text{O}_4/\text{Al}_2\text{O}_3$ mixture. The SO_3 values for Co_3O_4 decrease with $P_{\text{O}_2}^{1/6}$, and the values shown here are for $P_{\text{O}_2} = 1$ atm; all other curves are P_{O_2} independent. Also shown are the SO_3 pressures of an O_2 -0.15%($\text{SO}_2 + \text{SO}_3$) mixture at 1 atm (curve A) and of an O_2 -1%($\text{SO}_2 + \text{SO}_3$) mixture at 1 atm and 750°C (point B) (1, 10).



These calculations were performed using the free energy data for reactions [4] and [5] from Kubaschewski (12). The corresponding SO_3 pressures needed to stabilize the liquid phase are shown in Fig. 1. At present, it is not possible to ascertain errors associated with these SO_3 values because the errors associated with the SO_3 pressures for CoO in Fig. 1 and with the free energy data for reactions [4] and [5] are unknown.

Results and Discussion

Hot corrosion studies were conducted on several Co-Cr and Co-Al alloys. As shown in Fig. 2, the corrosion rates decreased with an increase in the chromium content of Co-Cr alloys. Macroscopic examination of the reacted samples showed that the Na_2SO_4 salt had melted on all alloys except on Co-40Cr, which corroded very slowly. Similar results were obtained on Co-Al alloys. As shown in Fig. 3, corrosion rates decreased with an increase in the aluminum concentration; again, the macroscopic examination of the reacted samples showed that the Na_2SO_4 salt did not melt on Co-15Al and Co-20Al, alloys that reacted very slowly.

An unexpected result was observed when aluminum was added to Co-40Cr. As shown in Fig. 4, even 1% aluminum significantly increased the corrosion rate. A purple Na_2SO_4 - CoSO_4 liquid was observed on the surface of the corroded samples containing aluminum. The detrimental effect of aluminum was also observed on other Co-Cr alloys, such as Co-35Cr (see Fig. 5), that normally formed a liquid and corroded significantly. However, comparison of Fig. 4 and 5 shows that the effect was less pronounced on Co-35Cr than on Co-40Cr. The detrimental effect of aluminum has been reported before (5). However, what has not been appreciated is that at a high enough chromium concentration (e.g., $\geq 40\%$ Cr) the liquid may not

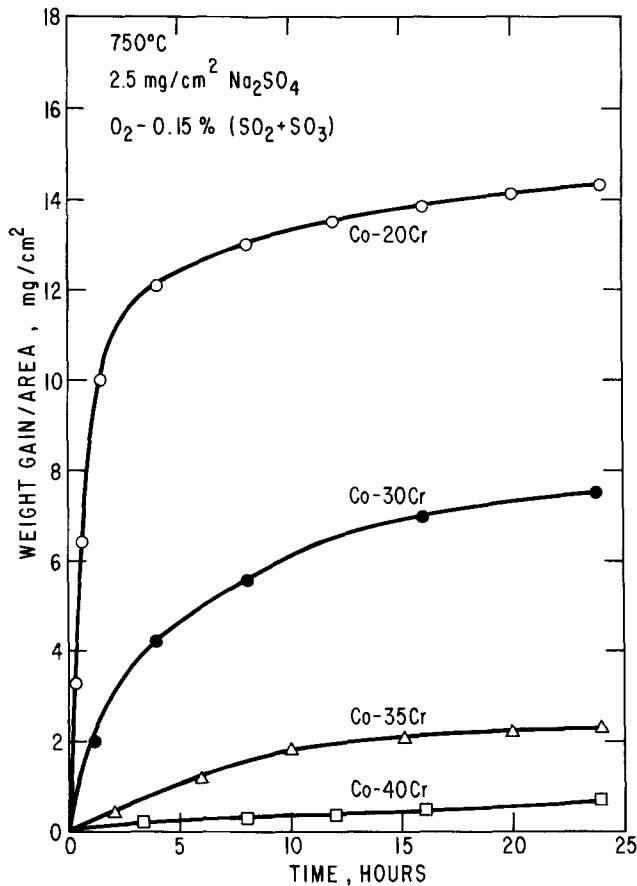


Fig. 2. Effect of chromium concentration on the hot corrosion of binary Co-Cr alloys.

form and that under these conditions even a small amount of aluminum promotes the liquid formation and severely degrades the alloy. Figure 6 shows that the addition of 2, 5, and 20%Cr to Co-15Al, an alloy with excellent corrosion resistance at 750°C, also produced a detrimental effect.

These results show that the simultaneous presence of chromium and aluminum accelerates low temperature hot corrosion. The coatings used in industry (e.g., CoCrAlY) contain both of these elements because they

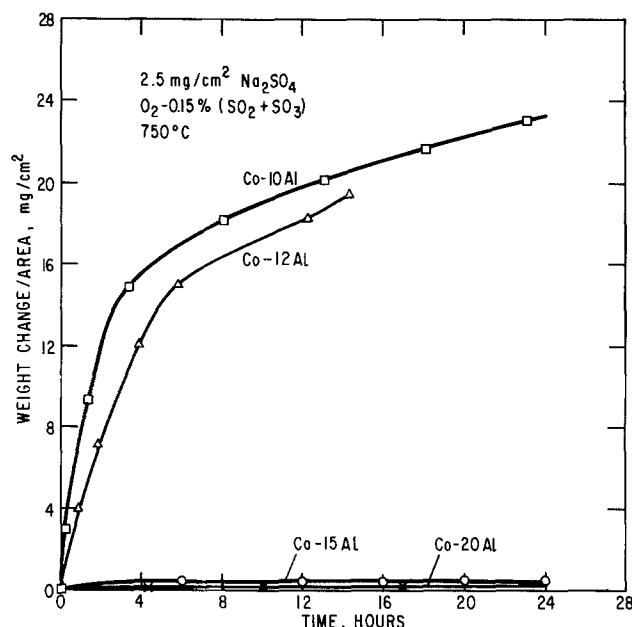


Fig. 3. Effect of aluminum concentration on the hot corrosion of binary Co-Al alloys.

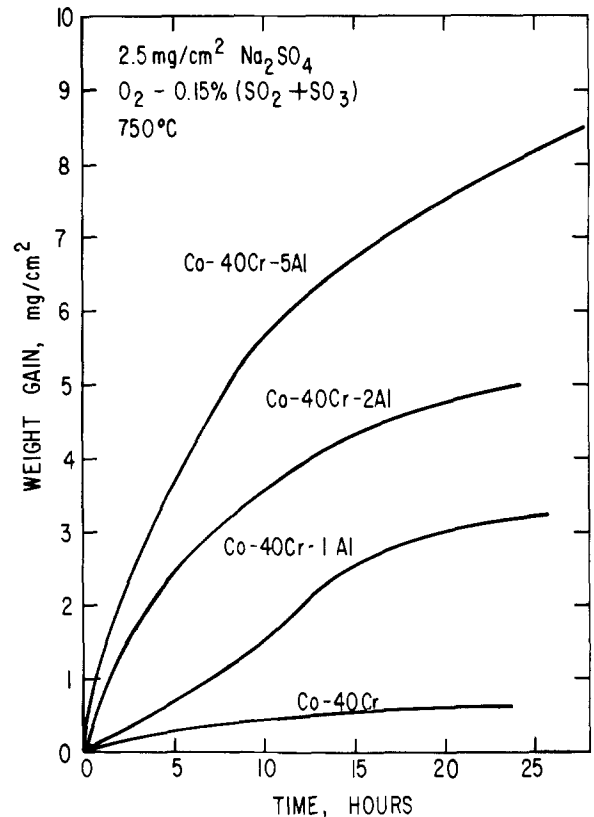


Fig. 4. Effect of aluminum addition on the hot corrosion of Co-40Cr at 750°C.

are believed to be beneficial from the standpoint of hot corrosion at higher temperatures. Indeed, as shown in Fig. 7, chromium addition to Co-15Al and aluminum addition to Co-40Cr have beneficial effects at 900°C.

These results can be explained on the basis of an earlier mechanism (1, 2) that is based on the rapid dissolution of the more noble metal or metal oxide in liquid salts. An Na₂SO₄-CoSO₄ liquid forms on the surface of cobalt containing alloys by interaction of cobalt oxide, formed dur-

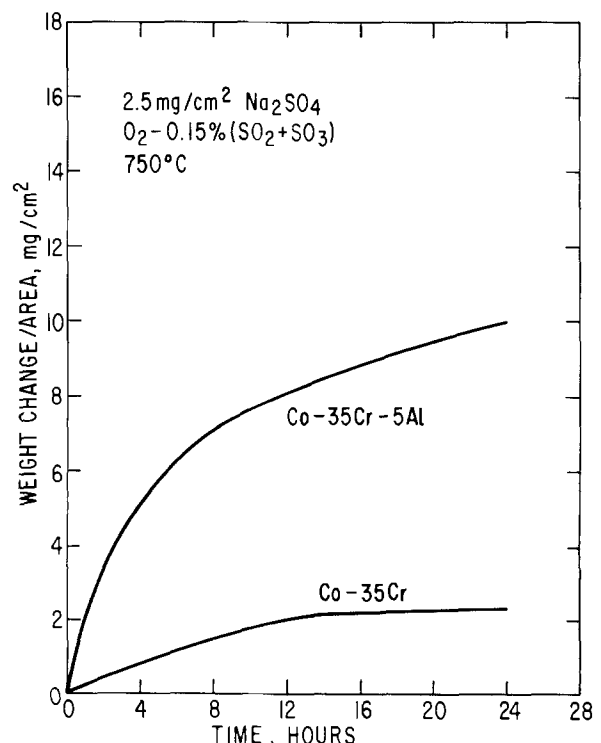


Fig. 5. Effect of aluminum addition on the hot corrosion of Co-35Cr at 750°C.

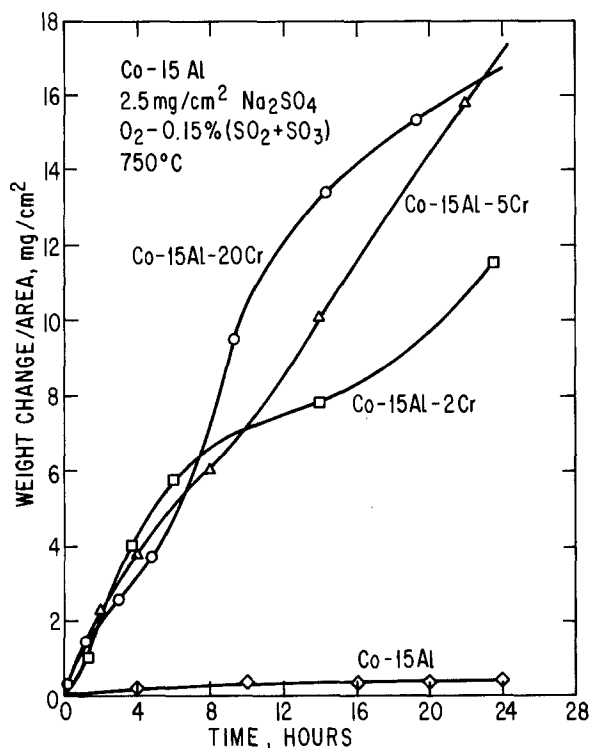


Fig. 6. Effect of chromium addition on the hot corrosion of Co-15Al at 750°C.

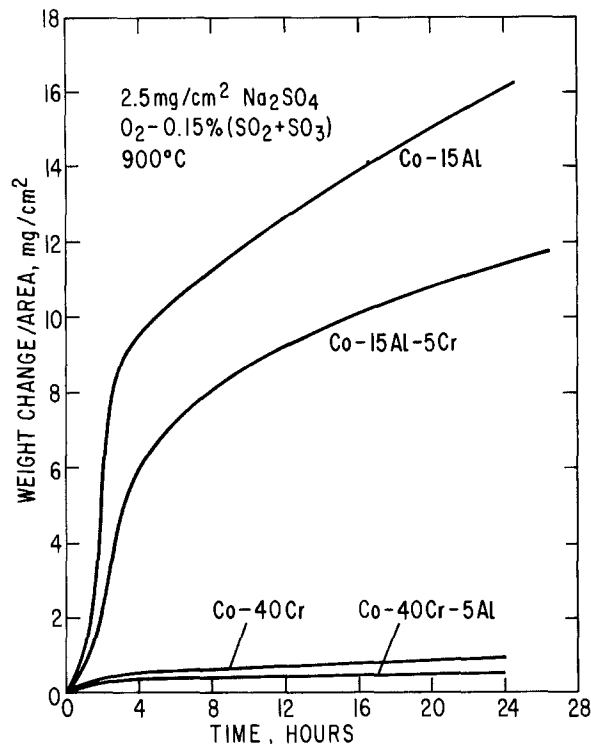


Fig. 7. Effect of chromium addition on the hot corrosion of Co-15Al and of aluminum addition on the hot corrosion of Co-40Cr at 900°C.

ing the transient oxidation, with the Na_2SO_4 salt and SO_3 present in the gas. Subsequent to the liquid formation, degradation is caused by the dissolution of cobalt and cobalt oxide.

Consider first the corrosion of Co-Cr alloys. The protection against corrosion is offered by formation of a $\text{CoCr}_2\text{O}_4/\text{Cr}_2\text{O}_3$ film and the exclusion of CoO and Co_3O_4 . With an increase in chromium content, the rate of growth of CoCr_2O_4 and Cr_2O_3 increases, in competition with CoO and Co_3O_4 formation, which thereby increases the corrosion resistance of alloys. For chromium levels $\geq 40\%$, the growth rate is presumably so fast that for all practical purposes the salt is in contact with only a $\text{CoCr}_2\text{O}_4/\text{Cr}_2\text{O}_3$ mixture; consequently, as expected from Fig. 1, the liquid phase would not form at 750°C in O_2 -0.15% ($\text{SO}_2 + \text{SO}_3$) and corrosion would not occur. The addition of aluminum must increase the corrosion rate of binary alloys by retarding the rate of growth of Cr_2O_3 and CoCr_2O_4 , which therefore makes the scales less protective. For alloys containing high chromium on which the liquid does not normally form ($\geq 40\%$ Cr), the effect would be most pronounced. If aluminum oxidation lowers the growth rates of Cr_2O_3 and CoCr_2O_4 , some cobalt may exist as Co_3O_4 during transient oxidation which would then promote the degradation of alloys by formation of an Na_2SO_4 - CoSO_4 liquid. The liquid formation was indeed observed on aluminum containing Co-40Cr alloys reported in Fig. 4.

The proposed mechanism of corrosion of Co-Al alloys is similar. With an increase in the aluminum content of alloys, the rates of growth of Al_2O_3 and CoAl_2O_4 increase, thereby making the oxide film more protective. At aluminum levels above about 15 weight percent, the protection is presumably markedly improved because cobalt exists only as CoAl_2O_4 which prevents the formation of the liquid phase. For such high-aluminum alloys, the chromium addition may retard the growth rate of an $\text{Al}_2\text{O}_3/\text{CoAl}_2\text{O}_4$ film and, thus, may promote the formation of the liquid, thereby increasing the corrosion rate. Indeed the liquid was observed on chromium containing Co-15Al alloys reported in Fig. 6. At present, it is not known whether the detrimental effect of chromium observed here is limited to the Co-Al alloys on which the liquid film does not form normally or whether it extends to lower aluminum alloys also.

A new conclusion in the mechanism proposed here compared to that previously proposed (1, 2) is that liquid formation on binary alloys containing high chromium and aluminum concentrations can be prevented by spinel formation. However, the presence of spinels has not been confirmed experimentally. The only oxide identified by x-ray diffraction on the Co-40Cr sample in Fig. 2 was Cr_2O_3 . This, however, provides no information about the formation of CoCr_2O_4 during the early stages of oxidation. The available literature on oxidation is also not helpful. At steady state, the formation of CoCr_2O_4 and CoAl_2O_4 has been reported on binary and ternary alloys in the Co-Cr-Al system at 1000°-1200°C (13-15). However, there have been no studies on transient oxidation of binary alloys containing high chromium and aluminum used in this study at 600°-800°C. According to the current theories of oxidation, some cobalt containing oxide should form on the surface during transient oxidation. It is, therefore, reasonable to expect that this oxide is a spinel on binary cobalt-base alloys containing high chromium and aluminum.

At present, it is not clear why additions of even small amounts of aluminum in Co-Cr alloys and of chromium in Co-Al alloys have such marked effects on the growth rate of $\text{Cr}_2\text{O}_3/\text{CoCr}_2\text{O}_4$ and $\text{Al}_2\text{O}_3/\text{CoAl}_2\text{O}_4$ films, respectively. These detrimental effects seem particularly surprising because at 1000°-1200°C addition of Cr to Co-Al promotes the formation of an Al_2O_3 film and addition of Al to Co-Cr alloys promotes a Cr_2O_3 film (15-16). As discussed above, these detrimental effects may be related to the oxides formed during transient oxidation. A more quantitative explanation is not possible without extensive studies on the transient oxidation of Co-Cr-Al alloys as a function of Cr and Al concentration at 600°-800°C, which are beyond the scope of this work.

Additional experiments were conducted to further prove the formation of spinels. Figure 1 shows that the SO_3 content of an O_2 -0.15% ($\text{SO}_2 + \text{SO}_3$) gas mixture at 750°C is slightly higher than the calculated value for formation of the liquid on a $\text{CoAl}_2\text{O}_4/\text{Al}_2\text{O}_3$ film. However, due to uncertainties associated with the calculated values, higher SO_3 values than in O_2 -0.15% ($\text{SO}_2 + \text{SO}_3$) or lower temperatures than 750°C might be necessary to form the liquid. Experiments were, therefore, conducted

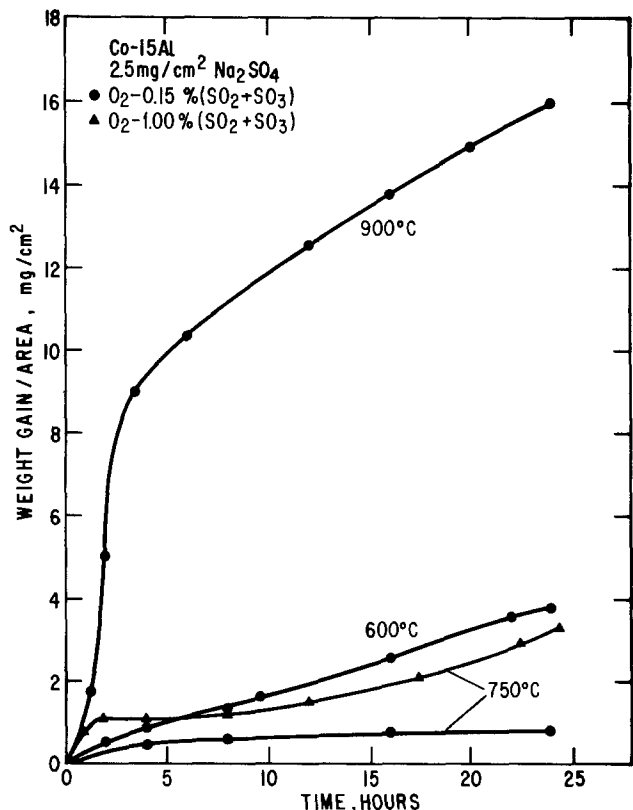


Fig. 8. Hot corrosion of Co-15Al in O_2 -0.15%($SO_2 + SO_3$) at 600°C and in O_2 -1%($SO_2 + SO_3$) at 750°C, two conditions under which an Na_2SO_4 - $CoSO_4$ liquid can form even from a $CoAl_2O_4/Al_2O_3$ film. Also shown for comparison are the plots of results in O_2 -0.15%($SO_2 + SO_3$) at 750° and 900°C.

in O_2 -1%($SO_2 + SO_3$) at 750°C and in O_2 -0.15%($SO_2 + SO_3$) at 650°C. Liquid formation was indeed observed, and as shown in Fig. 8, significant corrosion rates were observed on Co-15Al for both sets of conditions. Figure 9 shows a plot of an average hot corrosion rate in O_2 -0.15%($SO_2 + SO_3$) as a function of temperature. A minimum in corrosion rate occurs at 750°C, where the liquid does not form. Higher corrosion rates are observed at 600°C, where low temperature corrosion occurs as a result of the formation of an Na_2SO_4 - $CoSO_4$ liquid, and at 900°C, where normal high temperature hot corrosion occurs.

Whereas a liquid can form at 600°C in O_2 -0.15%($SO_2 + SO_3$) on a $CoAl_2O_4/Al_2O_3$ film, it may not form on a $CoCr_2O_4/Cr_2O_3$ film because the SO_3 content of the mixture

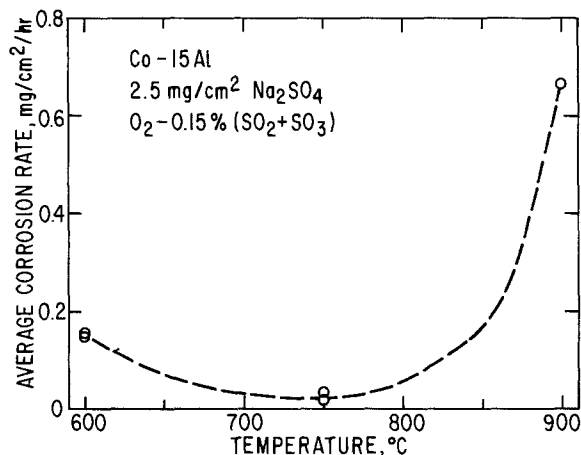


Fig. 9. A plot of an average corrosion rate, obtained by dividing weight gain/area with time, over 24h as a function of temperature for corrosion of Co-15Al in O_2 -0.15%($SO_2 + SO_3$). The Na_2SO_4 - $CoSO_4$ liquid forms at 600° and 900°C, but not at 750°C. The curve connecting data points may not be smooth and is therefore shown dashed.

is close to the minimum required to form the liquid (see Fig. 1). Indeed, the liquid did not form, and the observed corrosion rate was very low on Co-40Cr. A weight gain of 0.6 mg/cm² was observed in 24h at 600°C, which is comparable to that observed at 750°C (0.5 mg/cm²) in Fig. 2.

These results show that, due to differences in the stability of $CoCr_2O_4$ and $CoAl_2O_4$, binary Co-Cr alloys can offer protection against low temperature hot corrosion up to higher SO_3 partial pressures in comparison to binary Co-Al alloys. It is known that due to solid-state diffusion effects the growth rates of Cr_2O_3 films are much higher than of Al_2O_3 films. Therefore, from the standpoint of kinetics also, the Co-Cr alloys should be superior to Co-Al alloys at lower temperatures.

This study shows that the simultaneous presence of Cr and Al is detrimental to low temperature hot corrosion. Traditionally, coatings developed for high temperature hot corrosion have been MCrAlY compositions containing 20-30% Cr, 6-15% Al, and a small amount of an active element, such as Y, to promote scale adhesion. But from the standpoint of low temperature corrosion, coatings of Co-Cr alloys containing $\geq 40\%$ Cr with a small amount of an active element should be good candidates for coating materials. Extensive studies conducted in our company show that coatings containing $\geq 37.5\%$ Cr provide excellent resistance to low temperature corrosion, at least an order of magnitude better than the current CoCrAlY coatings, and provide adequate resistance to normal high temperature corrosion, comparable to current CoCrAlY coatings (9). Figure 10 shows the results of a few such laboratory tests, where Co-40Cr coatings have been compared with CoCrAlY coatings normally used in marine engines. A patent application has been filed for these new, high-chromium cobalt-base coatings.

Conclusions

The degradation of cobalt-base alloys during low temperature hot corrosion is caused by formation of an

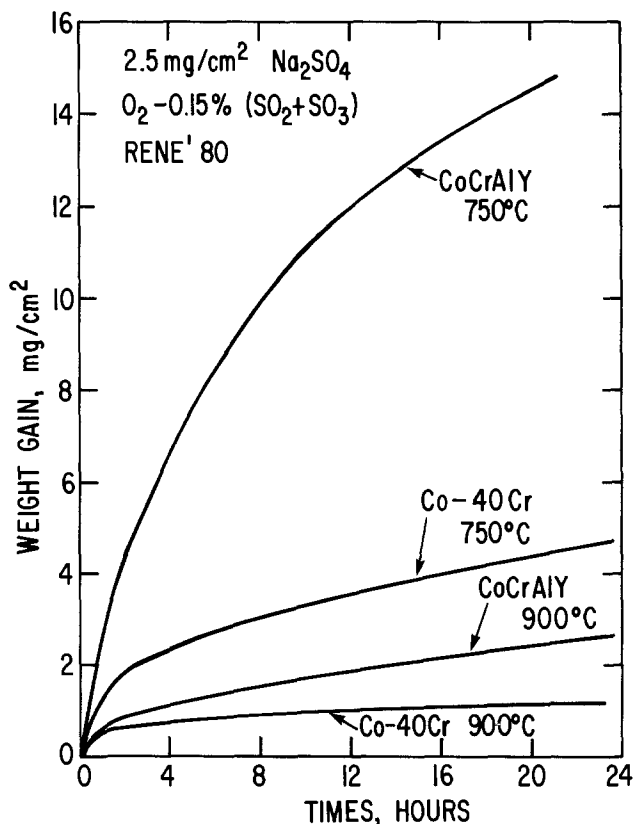


Fig. 10. Comparisons of the hot corrosion behavior of Co-40Cr and Co-22Cr-12Al-0.3Y coatings on Rene 80 substrate at 750° and 900°C. Clearly, the Co-40Cr is superior to the CoCrAlY coating. (The coatings were ~ 0.10 mm thick and were obtained by electron beam vapor deposition).

$\text{Na}_2\text{SO}_4\text{-CoSO}_4$ liquid that forms by interaction of cobalt oxide formed during the transient oxidation of alloys, with SO_3 in gas and Na_2SO_4 salt. Accelerated oxidation tests at 750°C show that the corrosion resistance of binary Co-Cr and Co-Al alloys increases with the Cr and Al content of alloys, respectively. This protection is offered by the rapid growth of $\text{CoCr}_2\text{O}_4/\text{Cr}_2\text{O}_3$ and $\text{CoAl}_2\text{O}_4/\text{Al}_2\text{O}_3$ oxides in comparison to CoO and Co_3O_4 . At high enough chromium ($\geq 40\%$) and aluminum ($\geq 15\%$) concentrations, the growth rates are so fast that the liquid does not even form; consequently, the corrosion rates are very low. The SO_3 pressures below which the formation of a liquid film can be prevented have been calculated.

Contrary to the experience at higher temperatures ($\geq 884^\circ\text{C}$), tests on Co-Cr-Al alloys indicate that the simultaneous presence of chromium and aluminum is deleterious to the resistance against low temperature hot corrosion resistance. It is proposed that the additions of aluminum to Co-Cr and of chromium to Co-Al alloys retard the growth rates of $\text{CoCr}_2\text{O}_4/\text{Cr}_2\text{O}_3$ and $\text{CoAl}_2\text{O}_4/\text{Al}_2\text{O}_3$ films, respectively, thereby reducing their corrosion resistance. Further work is, however, needed on transient oxidation of Co-Cr-Al alloys at $600^\circ\text{-}750^\circ\text{C}$ to confirm the mechanism of these deleterious effects.

Acknowledgments

The author acknowledges Mr. J. F. Fleischer for help in carrying out experiments and Dr. D. A. Shores and Dr. A. W. Urquhart for many useful discussions. This work was partially supported by the Naval Research Laboratory Contract N00173-77-C-0253.

Manuscript submitted Aug. 6, 1984; revised manuscript received Feb. 15, 1985.

General Electric Company assisted in meeting the publication costs of this article.

REFERENCES

1. K. L. Luthra and D. A. Shores, *This Journal*, **127**, 2202 (1980).
2. K. L. Luthra, *Met. Trans. A*, **13**, 1853 (1982).
3. K. L. Luthra, *ibid.*, **13**, 1843 (1982).
4. R. L. Jones, in "High Temperature Corrosion," R. A. Rapp, Editor, p. 513, NACE-6, National Association of Corrosion Engineers, Houston, TX (1983).
5. K. T. Chiang, F. S. Pettit, and G. H. Meir, in "High Temperature Corrosion," R. A. Rapp, Editor, p. 519, NACE-6, National Association of Corrosion Engineers, Houston, TX (1983).
6. K. L. Luthra, in "High Temperature Corrosion," R. A. Rapp, Editor, p. 507, NACE-6, National Association of Corrosion Engineers, Houston, TX (1983).
7. R. H. Barkalow and G. W. Goward, in "High Temperature Corrosion," R. A. Rapp, Editor, p. 502, NACE-6, National Association of Corrosion Engineers, Houston, TX (1983).
8. S. Y. Hwang, G. H. Meir, F. S. Pettit, G. R. Johnston, V. Provenzano, and F. A. Smidt, in "High Temperature Protective Coatings," S. C. Singhal, Editor, p. 121, The Metallurgical Society of AIME, New York (1982).
9. K. L. Luthra and J. H. Wood, *Thin Solid Films*, **119**, 271 (1984).
10. K. L. Luthra, *Met Trans. A*, **13**, 1647 (1982).
11. JANAF Thermochemical Tables, published by Dow Chemical Co., Midland, MI (1971); supplement (1974); supplement (1975).
12. O. Kubaschewski, *High Temp. High Press.*, **4**, 1 (1972).
13. S. Espevik, R. A. Rapp, P. L. Daniel, and J. P. Hirth, *Oxid. Metals*, **20**, 37 (1983).
14. G. C. Wood and F. H. Scott, *ibid.*, **3**, 365 (1971).
15. G. N. Irving, J. Stringer, and D. P. Whittle, *Corrosion (Houston)*, **33**, 56 (1977).
16. C. S. Giggins and F. S. Pettit, *This Journal*, **118**, 1782 (1971).

A Mathematical Model for the Periodic Electrodeposition of Multicomponent Alloys

Mark W. Verbrugge* and Charles W. Tobias**

Lawrence Berkeley Laboratory, University of California, Berkeley, California 94720

ABSTRACT

A mathematical model is presented for the electrodeposition of multicomponent alloys by an arbitrarily specified current source. The model takes into consideration transient, convective mass transfer to a rotating disk electrode, Butler-Volmer kinetics, and individual component activities in the electrodeposits. The model can be used to calculate current-potential relationships, ionic concentration profiles, and electrodeposits composition. Results for square-pulse, pulse-reversal, and triangular current waveforms are presented. An analogous model for potential-controlled electrolysis is also discussed.

The properties of alloys vary over a wider range than those of their parent metals, and thus can often be designed to better fulfill the mechanical and chemical requirements of our civilization. Electrodeposition offers several unique advantages for the formation of alloys. The superior control of the alloy composition, including the formation of nonequilibrium alloys, and the ability to prepare thin films are well documented. Brenner's encyclopedic monograph (1) reviews some practical methods for the electrodeposition of various alloys, and Gorbunova and Polukarov's treatment (2) outlines the fundamental principles involved. Srivastava and Mukerjee (3) review developments in the electrodeposition of binary alloys.

It has long been known that pulsing the current can profoundly affect the nature of single-component electrodeposits. Although the pulsed plating of alloys has re-

ceived comparatively little attention, it has been observed that the phase structure and morphology of alloy deposits can be altered by changing the characteristics of the pulsed-current waveform. This work presents a model for predicting the current-potential relationship and the composition profiles in the electrodeposits and the electrolyte.

Wan *et al.* (4) have presented a literature review dealing with the application of pulsed-plating techniques for single-component metal deposition. Avila and Brown (5) have cited the following advantages of pulsed plating over dc electroplating: (i) extremely dense and highly conductive deposits, (ii) a reduced need for plating additives, and (iii) increased plating rates. In reference to the last advantage, Cheh (6) has shown analytically that pulsed-current plating can never attain a higher average plating rate than dc plating at the diffusion-limited current. However, a higher average current density is often used in pulsed plating, relative to dc plating, since poor quality electrodeposits are often formed under dc condi-

*Electrochemical Society Student Member.

**Electrochemical Society Honorary Member.

tions near the diffusion limiting current. Lamb (7) has investigated the mechanical properties of single-component copper and silver electrodeposits obtained by current pulses in the microsecond range. Puipe and Ibl (8) studied the morphology of pulse-plated cadmium, copper, and gold electrodeposits. The influence of the off time, the pulse-current density, and the length of the pulse time were analyzed. Different morphological trends were observed and discussed for the different chemical systems. Ismail (9) investigated the periodic, reverse-current electroplating of copper from an alkaline-cyanide bath. The maximum brightness occurred at 0.27 Hz with a cathodic-current to anodic-current ratio of 2. Despic and Popov (10) examined the effect of a pulsating potential on the morphology of copper and zinc electrodeposits. Typical results illustrated that increasing the frequency led to a progressively smoother deposit. Popov (11) also has reviewed some approaches to the quantitative modeling of the surface-roughness amplification during an electrodeposition process. Sullivan (12) has reported that high-current-density pulsed plating of cobalt results in significantly stronger and harder electrodeposits.

The pulsed plating of multicomponent electrodeposits has received less attention than pure-component electrodeposition. Gelchinski *et al.* (13) electroplated chromium-cobalt alloys using a pulsed-potential source. Mirror-bright electrodeposits containing supersaturated solid solutions were obtained. It has been observed that the structure and the physical properties of the electrodeposited alloys can be very different from the thermally prepared alloys of similar composition. Gelchinski *et al.* also found that a change in the electrodeposition conditions can cause a marked change in the phase structure of the electrodeposit, even for those deposits of identical chemical composition. Burrus (14) has described various conditions where the pulsed plating of different metals and metal mixtures can be used advantageously. Leidheiser and Ghuman (15) used a pulsed-current setup to electrodeposit silver-tin alloys which could be easily polished to a high luster. Cohen *et al.* (16) have electroplated cyclic, multilayered, alloy coatings of varying silver and palladium composition with square-pulse and triangular current waveforms. They also report on periodic-potential plating studies of various multicomponent electrodeposits.

Mathematical Analysis

In considering the mathematical modeling for the electrodeposition of multicomponent alloys, it is convenient to divide the problem into three interrelated parts: the liquid phase containing the discharging ions, the electrolyte-electrodeposit interface, and the electrodeposited alloy.

The liquid phase.—One of the goals of this work is to quantitatively predict the ionic surface concentrations throughout the electrodeposition process. It has been well established that the ionic surface concentrations can greatly influence the electrodeposit composition and morphology (17, 18).

A theoretical analysis for single-component mass transfer in pulsed electrolysis was recently published by Chin (19). A stagnant (Nernst) diffusion layer was assumed valid in order to develop a comprehensive theory for pulsed electrolysis. Chin's paper includes a brief review of previous theoretical studies in single-component pulsed electrolysis.

Since our treatment uses a current-step solution and the method of superposition to derive a model for multicomponent mass transfer, we shall review some current-step solutions which can be used with this technique. The method of superposition is computationally very efficient, although the differential equations describing the process must be linear for this method to be applied. Therefore, migration effects are not included in this model. Double-layer charging is also not considered. Since practical plating baths usually contain an excess of supporting electrolyte, migration effects can often be ne-

glected. Double-layer charging effects can become important in an electrodeposition process if microsecond current cycles are used (20). Before proceeding, it should be mentioned that attempts have been made to qualitatively describe multicomponent, pulsed-current processes (21-24). Also, Cheng and Cheh have presented finite-difference models for the pulsed-current electrodeposition of copper with hydrogen evolution (25) and of lead-tin alloys (26).

The convective diffusion equation for the one-dimensional mass transport of species *i* is

$$\frac{\partial c_i}{\partial t} + v_y \frac{\partial c_i}{\partial y} = D_i \frac{\partial^2 c_i}{\partial y^2} \quad [1]$$

For high Schmidt numbers, the appropriate expression for the normal component of the fluid velocity to a rotating disk electrode (RDE) is (27, 28)

$$v_y = -0.51023 \omega^{3/2} \nu^{-1/2} y^2 \quad [2]$$

The radial variation of the ionic surface concentration is neglected in this treatment, as it would considerably complicate the problem (29-31). In a rigorous treatment for the RDE system incorporating both radial and axial variations, dimensionless groups arise which include the disk radius (29, 30). For small disks, it is appropriate to neglect radial variations in concentration and potential. Nanis and Klein (32) qualitatively address this assumption in their one-dimensional treatment for transient mass transfer to an RDE in the absence of kinetic resistance.

For the current-step problem, the initial condition and boundary conditions are

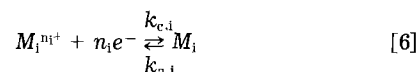
$$c_i(0, y) = c_i^b \quad [3]$$

$$c_i(t, \infty) = c_i^b \quad [4]$$

and

$$\frac{\partial c_i(t, 0)}{\partial y} = -\frac{i(0)}{n_i F D_i} \quad [5]$$

where the electrode reaction for metal deposition is



Krylov and Babak (33) have obtained an analytic series solution for the current-step problem stated by Eq. [1]-[5]. However, the solution does not converge for long times (34). Nisancioglu and Newman (35) numerically calculated an alternate series solution which is valid for long times and can be used in conjunction with a short-time, asymptotic series representation of Krylov and Babak's solution.

Nisancioglu and Newman's long-time solution is

$$c_i = c_i^b + \frac{i_i \delta_i}{n_i F D_i \Gamma(4/3)} \left\{ \int_0^\infty \frac{\Gamma(4/3) y}{\delta_i} e^{-x^3} dx - \sum_{k=1}^{\infty} B_k Z_k \left[\frac{y \Gamma(4/3)}{\delta_i} \right] e^{-\lambda_k D_i t \left[\frac{\Gamma(4/3)}{\delta_i} \right]^2} \right\} \quad [7]$$

The values of B_k , Z_k , and λ_k are given in Ref. (20) and (35).

The first few terms of the short-time, asymptotic series representation of Krylov and Babak's solution are

$$c_i = c_i^b + \frac{2i_i \sqrt{t}}{n_i F \sqrt{\pi} D_i} \left\{ 1 - \frac{\sqrt{\pi}}{16} \left[\frac{D_i t}{\left(\frac{\delta_i}{3^{1/3} \Gamma(4/3)} \right)^2} \right]^{3/2} + \frac{1}{420} \left[\frac{D_i t}{\left(\frac{\delta_i}{3^{1/3} \Gamma(4/3)} \right)^2} \right]^3 + \dots \right\} \quad [8]$$

In Eq. [7] and [8], δ_i is the Levich diffusion-layer thickness (36)

$$\delta_i = 1.612 \left(\frac{D_1}{\nu} \right)^{1/3} \left(\frac{\nu}{\omega} \right)^{1/2} \quad [9]$$

which is the characteristic distance for long times.

More approximate representations for the current-step problem have also yielded relatively accurate results. In a classic treatment, Rosebrugh and Miller (37) derived an analytic solution for the current-step problem by replacing Eq. [1] with the equation representing Fick's second law of diffusion and Eq. [4] by

$$c_i(t, \delta_i) = c_i^b \quad [10]$$

This solution is presented in the Appendix.

Rosebrugh and Miller used the method of superposition on their current-step solution to describe single-component mass transfer with a periodic current source (37). Cheh *et al.* (6, 38, 39) have made use of this solution by comparing it with some experimental results. Visawanathan and Cheh (40) and Hale (41) have presented numerical solutions to Eq. [1]-[5] and compared their solutions to that of Rosebrugh and Miller. [Hale actually compared his solution to Siver's solution (42), which Siver had in turn referenced to Rosebrugh and Miller.] The error was always less than 4%. Visawanathan *et al.* (43) numerically solved the system of Eq. [1]-[4], with a pulsed-current boundary condition in place of Eq. [5], and compared this to Rosebrugh and Miller's analytic solution for a pulsed-current source. The agreement between the two solutions was excellent.

Thus far, we have reviewed one analytical current-step solution (that assumes a Nernst diffusion layer) and three numerical solutions. For the problem we address in this paper, we require a current-step solution for short and long times. There is very little extra numerical effort involved in using Eq. [7] instead of Eq. [A-2], especially if only the surface concentrations of the discharging ions are required. For this reason, we have chosen to use Eq. [7] and [8], along with the method of superposition, to model the ionic mass transfer. This restricts our treatment to a RDE. The procedure to be used for other systems which can be modeled accurately with a Nernst diffusion layer is presented in the Appendix. A comparison between the two methods is shown in Fig. 2 for the RDE system.

Using the method of superposition on Eq. [7], the concentration expression for an arbitrarily specified current source is

$$c_i = i_{i,n} \Theta_{i,n} + \Psi_{i,n} \quad [11]$$

where

$$\Theta_{i,n} = \frac{\delta_i}{n_i F D_i \Gamma(4/3)} \left\{ \int_0^\infty \frac{y \Gamma(4/3)}{\delta_i} e^{-x^3} dx - \sum_{k=1}^{\infty} B_k Z_k e^{-\lambda_k D_i \left[\frac{\Gamma(4/3)}{\delta_i} \right]^2 (t-t_{n-1})} \right\} \quad [12]$$

and

$$\Psi_{i,n} = c_i^b + \frac{\delta_i}{n_i F D_i \Gamma(4/3)} \left\{ \sum_{j=1}^{\infty} i_{i,j} \sum_{k=1}^{\infty} B_k Z_k \left[e^{-\lambda_k D_i \left[\frac{\Gamma(4/3)}{\delta_i} \right]^2 (t-t_{j-1})} - e^{-\lambda_k D_i \left[\frac{\Gamma(4/3)}{\delta_i} \right]^2 (t-t_j)} \right] \right\} \quad [13]$$

The current source has been expressed as n discrete current steps. The method of superposition has been used previously for single-component, pulsed-current chronopotentiometry by Andricacos and Cheh (44), and there are a number of references in the literature which can be consulted to derive Eq. [11]-[13] (37, 45, 46).

For short times, the series in Eq. [12] and [13] will not converge. Equation [8] can then be used to express $\Theta_{i,n}$ and $\Psi_{i,n}$. For very short times, only the first term in Eq. [8] need be retained. Equation [8] then becomes the fam-

ilar Sand equation and δ_i drops out of the problem since there is no characteristic length for the semi-infinite linear diffusion problem. Equations [12] and [13] are then replaced by

$$\Theta_{i,n} = \frac{2\sqrt{t-t_{n-1}}}{n_i F \sqrt{\pi D_i}} \quad [14]$$

and

$$\Psi_{i,n} = c_i^b + \frac{2}{n_i F \sqrt{\pi D_i}} \sum_{j=1}^n i_j [\sqrt{t-t_{j-1}} - \sqrt{t-t_j}] \quad [15]$$

Equations [14] and [15] can also be used to solve the analogous problem of multicomponent mass transfer to a stationary electrode.

The liquid-electrode interface.—While a relatively accurate liquid-phase transport model can be developed, such an exacting and general approach is not as easily accomplished for the interface. In multicomponent electrolysis, the potential distribution across the double layer will be affected by the various discharging ions. However, in well-supported solutions, the discharging ions will not significantly influence the double-layer structure. The crystallization kinetics can also be changed, although this will not be considered in this paper. An excellent treatment of this problem can be found in the work of Fleischmann and Thirsk (47).

For the electrode reaction of component i , given by Eq. [6], a Butler-Volmer expression will be used to describe the electrode kinetics. Specific adsorption and chemisorption are not taken into account. Thus (48)

$$\frac{i_{i,n}}{n_i F} = k_{a,i} \alpha_{i,n} e^{(1-\beta) n_i f E_n} - k_{c,i} \frac{c_{i,n}^s}{\rho_0} e^{-\beta n_i f E_n} \quad [16]$$

where

$$E_n = V_n + \left[U_{re}^\theta - \frac{1}{n_{ref}} \sum_i s_{i,re} \ln \frac{c_{i,re}}{\rho_0} \right] - i_n r \quad [17]$$

The bracketed term in Eq. [17] represents the open-circuit potential difference between the reference electrode and a standard hydrogen electrode. The potential difference between the working electrode and the reference electrode is V_n . The last term in Eq. [17] accounts for the ohmic drop between the reference electrode and the working electrode. Hence, E_n is the potential difference between the working electrode and a standard hydrogen electrode, corrected for ohmic drop.

The individual currents can be obtained by substituting for $c_{i,n}^s$ in Eq. [16] using Eq. [11], evaluated at the surface, and solving for $i_{i,n}$

$$i_{i,n} = \frac{k_{a,i} \alpha_{i,n} e^{(1-\beta) n_i f E_n} - \frac{1}{\rho_0} k_{c,i} \Psi_{i,n}^s e^{-\beta n_i f E_n}}{\frac{1}{n_i F} + \frac{1}{\rho_0} k_{c,i} \Theta_{i,n}^s e^{-\beta n_i f E_n}} \quad [18]$$

The total imposed current must equal the sum of the m individual currents

$$\left(\sum_{i=1}^m i_{i,n} \right) - i_n = 0 \quad [19]$$

Equations [18] and [19] can be combined to yield a nonlinear equation in E_n , the electrode potential. The second-order Newton-Raphson algorithm (49) is used to solve the resulting equation for an arbitrary number of depositing metal ions.

Using Eq. [18] and [19], the function H_n is defined as

$$H_n = \left(\sum_{i=1}^m i_{i,n} \right) - i_n \quad [20]$$

For the correct value of the electrode potential, H_n will be equal to zero. H_n is given by

$$H_n = \left[\sum_{i=1}^m \frac{k_{a,i} a_{i,n} e^{(1-\beta)n_f E_n} - \frac{1}{\rho_0} k_{c,i} \Psi_{i,n}^s e^{-\beta n_f E_n}}{\frac{1}{n_i F} + \frac{1}{\rho_0} k_{c,i} \Theta_{i,n}^s e^{-\beta n_f E_n}} \right] - i_n \quad [21]$$

The value of E_n is found by iteration

$$(E_n)_{\text{new}} = (E_n)_{\text{old}} - \left[\frac{H_n}{\left(\frac{\partial H_n}{\partial E_n} \right)} \right]_{\text{old}} \quad [22]$$

The value of the derivative in Eq. [22] is

$$\frac{\partial H_n}{\partial E_n} = \sum_{i=1}^m \frac{\frac{k_{a,i} a_{i,n} (1-\beta)}{RT} e^{(1-\beta)n_f E_n} + \frac{k_{c,i} \Psi_i^s \beta_i}{\rho_0 RT} e^{-\beta n_f E_n}}{\left(\frac{1}{n_i F} + \frac{1}{\rho_0} k_{c,i} \Theta_i^s e^{-\beta n_f E_n} \right)^2} + \frac{\frac{1}{\rho_0} k_{c,i} \Theta_{i,n}^s k_{a,i} a_{i,n} \beta_i n_f e^{(1-2\beta)n_f E_n}}{\left(\frac{1}{n_i F} + \frac{1}{\rho_0} k_{c,i} \Theta_i^s e^{-\beta n_f E_n} \right)^2} \quad [23]$$

For each time step, the iteration scheme outlined in Eq. [20]-[23] must be completed. However, when the previous time step's value of E_n is used to start the iteration in Eq. [22], convergence is generally obtained within three or four iterations.

It should be noted that the partial currents can be obtained explicitly in terms of E_n in Eq. [18] because the electrochemical reaction was assumed to be first order in the concentration of the discharging metal ion concentration. This is usually the case in the electrodeposition of metals. If the reaction were not first order, it would still be relatively easy to solve numerically for the electrode potential and the partial currents.

Equation [18] is also valid for controlled-potential electrolysis. If the ohmic drop is neglected in Eq. [17], Eq. [18] yields the partial current explicitly for controlled-potential electrolysis. Since the ohmic drop can easily be subtracted out in one-dimensional systems, this does not present a major restriction.

The model we have provided for the liquid-phase mass transfer and kinetics could also be used to describe processes for the electrosynthesis of compounds by a periodic current source. Alkire and Tsai (50) have listed a number of references for the synthesis of compounds by a periodic current source.

The electrodeposit.—Two problems must be treated for a complete description of the solid-state alloy. The first problem concerns the dependence of the surface activity on the alloy composition. When experimental data are combined with the judicious choice of an activity model, the activities of the alloy components can be obtained. The second problem involves the actual number of monolayers in the electrodeposit which affect the surface activity, or the relevant surface-activity thickness (RSAT).

The first step in determining component activity coefficients is to choose a model for the molar excess Gibbs energy G^E . The excess properties are taken with reference to an ideal solution wherein the standard state for each component is the pure solid at the temperature and pressure of the mixture. Once the molar excess Gibbs energy is expressed, the activity coefficients γ_i can be found by (51)

$$RT \ln \gamma_i = \left(\frac{\partial(N_T G^E)}{\partial N_i} \right) \quad [24]$$

Since no general treatment has yet been developed to consider repulsion between ion cores or the interaction among cores and electrons at the Fermi surface, a useful approach is to treat the interaction between ions in a mixture by a pairwise model. The properties of such a system

are represented by the sum of interactions between neighboring pairs of ion cores, and the complications due to higher-order interactions are ignored. This quasi-chemical (or lattice theory) approach is outlined by Swalin (52) for regular solutions in which there is no excess entropy creation upon mixing, and any nonideality is considered in an enthalpy of mixing term. For the quasi-chemical approach, the activity coefficients for a binary, regular solution are given by (52, 53)

$$\ln \gamma_A = \frac{(1-x_A)^2 \Omega}{RT} \quad [25]$$

$$\ln \gamma_B = \frac{(1-x_B)^2 \Omega}{RT} \quad [26]$$

where Ω is an adjustable parameter.

Equations [25] and [26] bear close resemblance to the two-suffix Margules equation. Guggenheim (54) has extended the quasi-chemical approach to model systems which exhibit considerable deviation from randomness. For this case, the excess entropy of mixing is no longer zero and a short-range order parameter is introduced which may be determined in some cases by x-ray and neutron diffraction techniques (52).

Two other informative treatments of solid-state thermodynamics should be mentioned before presenting the theoretical aspects for the activity model we have chosen to use in this paper. Darken and Gurry's text (55) contains a great number of references with tabular thermodynamic data for numerous metal systems, as well as an informative description of solid-state physical chemistry. Lumsden's (56) monograph illustrates the usefulness of thermodynamics for the accurate correlation of various equilibrium properties in alloy systems.

Electrodeposited metals usually have a more fine-grained, amorphous structure than their pyrometallurgical counterparts. Hence, the simple quasi-chemical lattice model does not generally represent the true thermodynamic nature of electrodeposited alloys. The activity model proposed by Renon and Prausnitz (57, 58) is well suited to such a morphology. The authors define a local mole fraction x_{ij} representing the mole fraction of i in the vicinity of j . In a treatment similar to Guggenheim's extension of the quasichemical lattice theory, the local mole fractions are related to the overall mole fractions through Boltzmann factors

$$\frac{x_{ji}}{x_{ki}} = \frac{x_j}{x_k} \frac{\exp(-\alpha_{ij} g_{ji}/RT)}{\exp(-\alpha_{ik} g_{ki}/RT)} \quad [27]$$

The parameter α_{ij} ($\alpha_{ij} = \alpha_{ji}$) characterizes the tendency of components i and j to mix in a nonrandom fashion. The parameter g_{ik} ($g_{ik} = g_{ki}$) represents the energy of interaction between an i - k molecular pair. Scott's theory (59) is used to relate the extensive excess properties to the interaction energies and the local mole fractions. For a solution of m components, the molar excess Gibbs energy is

$$\frac{G^E}{RT} = \sum_{i=1}^m x_i \frac{\sum_{j=1}^m \tau_{ji} G_{ji} x_j}{\sum_{k=1}^m G_{ki} x_k} \quad [28]$$

where

$$\tau_{ji} = \frac{(g_{ji} - g_{ii})}{RT} \quad [29]$$

and

$$G_{ji} = \exp(-\alpha_{ij} \tau_{ji}) \quad [30]$$

Using Eq. [24] and [28], the activity coefficient of component i can be calculated (57)

$$\ln \gamma_i = \frac{\sum_{j=1}^m \tau_{ji} G_{ji} x_j}{\sum_{k=1}^m G_{ki} x_k} + \sum_{j=1}^m \frac{x_j G_{ij}}{\sum_{k=1}^m G_{kj} x_k} \left(\tau_{ij} - \frac{\sum_{l=1}^m x_l \tau_{il} G_{il}}{\sum_{k=1}^m G_{kl} x_k} \right) \quad [31]$$

One of the advantages of this activity model is that it can be extended to as many components as desired without any additional assumptions and without adding any constants other than those obtained from binary data. This treatment is applicable to partially miscible as well as completely miscible systems.

Equilibrium-potential measurements of binary solids in contact with an aqueous phase containing the corresponding ions represent a convenient method for obtaining activity data. For some alloy systems, the simpler quasi-chemical treatment may represent the activity data quite well. This approach, outlined by Eq. [25] and [26], can also be extended to model multicomponent systems. When Eq. [25] and [26] cannot be used to fit the data, the computer programs listed in Appendix K of Ref. (60) can be used to fit the parameters of Eq. [31].

For this general treatment, we have chosen to use Eq. [27]-[31] to describe the electrodeposition thermodynamics. However, the overall mole fractions in Eq. [27] must be adjusted to represent the surface, rather than bulk, composition. Though the activity model accounts for local composition, no characteristic length is associated with the range of applicability. Even for single-component electrodeposition systems, the surface plays a major role in the kinetics. Wranglen (61) observed that metals of low overvoltage grow by the lateral extension of layers 0.1-1 μm thick. It was also observed that changing the current density changes the relative growth rates between crystal faces as well as where the deposited layers begin to grow on the respective crystal faces. Wranglen's microphotographic study of growth layers contains results for a periodic current source, although no high frequency results are reported.

Underpotential deposition studies can yield some information about the RSAT. Kolb *et al.* (62) correlated the underpotential shift between the bulk deposit stripping peak and the first deposited monolayer stripping peak as a function of the difference in work functions between the substrate and the deposited material. The authors conclude that the work function of the first deposited monolayer may not differ greatly from that of the bulk electrodeposit, although the optical properties of such a monolayer are usually far from those of the bulk. Adzic *et al.* studied the underpotential deposition of Zn on Ag (63) and Zn on Cu and Au (64). For these reversible systems, the results support the work of Kolb *et al.* Approximately one monolayer of zinc was formed on the polycrystalline substrates prior to bulk deposition.

All of the work mentioned above indicates that the RSAT is about one monolayer. However, this may not be the case for all systems. Cadle and Bruckenstein (65) found that although only one monolayer of Bi is deposited on Pt by underpotential deposition, it is not until approximately five monolayers have been deposited that bulk deposition occurs.

Takamura and Kozawa (66) have reviewed a great deal of literature concerned with the use of optical reflectance methods to investigate an electrode-electrolyte interface *in situ*. They have found that, for a number of systems, the first few atomic layers do not have the same reflectance properties (67).

In general, higher current densities will shorten the RSAT. Setty and Wilman (68) have shown by electron diffraction experiments that high current densities promote the growth of a random, polycrystalline deposit growth which does not reflect the original electrode structure even during the initial stages of electrodeposition. Since most pulse plating processes make use of unusually high current densities, a highly random (or amorphous), polycrystalline deposit typically results. It has also been observed that the influence of a polycrystalline substrate with small crystallite grains ceases to exist at much earlier stages of deposition than that of the surface of a large single-crystal substrate (69).

Although there is a wealth of literature concentrating on epitaxy and morphology of electrodeposits, there is no clear *a priori* approach to estimate the RSAT. The work

reviewed in this paper dealt only with the early stages of electrodeposition. In pulse plating processes, the deposit usually has a random, polycrystalline structure, and the RSAT is probably much less than that of the initially deposited monolayer.

Optical studies seem to indicate that the RSAT can be greater than a monolayer. Conversely, the high current-density pulses often used in practical plating operations may lower the RSAT to about a monolayer. In light of the above considerations, it may be advantageous to weight the substrate's influence on the newly forming surface with a function that decays with depth (70, 71). For the purposes of this work, the following heuristic treatment will be used in estimating a relevant surface composition

$$x_i = \frac{\sum_{ml} \left[1 - \exp\left(-\sigma \frac{\text{RSAT} - d_{ml}}{\text{RSAT}}\right) \right] x_{i,ml}}{\sum_{ml} \left[1 - \exp\left(-\sigma \frac{\text{RSAT} - d_{ml}}{\text{RSAT}}\right) \right]} \quad [32]$$

where $d_{ml} \leq \text{RSAT}$.

In Eq. [32], the subscript ml refers to a monolayer, d_{ml} is the monolayer's distance from the surface, σ is a system-specific proportionality constant, $x_{i,ml}$ refers to the monolayer mole fraction of component i, and the bracketed terms are weighting functions for each monolayer. Monolayers that are deep below the surface make only a small contribution to the relevant surface composition. For $d_{ml} > \text{RSAT}$, no effect on the surface composition is taken in account. Equation [32] assures that the sum of the overall mole fractions is unity. It can also be seen that if σ is set to a very high value, then the weighting function for each monolayer within the RSAT will essentially be unity.

We can now formalize in the following algorithm the procedure for the implementation of the mathematical model.

For $t = t_1, t_2, \dots, t_n$, the procedure is as follows.

1. Obtain the total current i_n .
2. Solve for $\Theta_{1,n}^s$ and $\Psi_{1,n}^s$ (Eq. [12]-[15]).
3. Solve for H_n (Eq. [21]).
4. Solve for $(\partial H_n / \partial E_n)$ (Eq. [23]).
5. Solve for E_n by iteration (Eq. [22]).
6. Obtain the new surface composition from the individual currents according to Faraday's law (Eq. [18] and [32]).
7. Determine the new surface activity (Eq. [31]).

Results

We have chosen to model a three-component system to illustrate the flexibility of the algorithm. It is not possible to obtain the necessary parameters required for the model from the literature; for this reason, we are presently working on experiments that should yield the necessary data. We will discuss the experimental investigation and make a model comparison in a future publication.

The model inputs are listed in Table I. The values of the standard electrode potentials U_i^θ can be calculated from the rate constants. The values of U_i^θ are 0.3, 0.1, and -0.1V for components 1, 2, and 3, respectively. For each reaction, the rate constants have been chosen to yield an exchange-current density of 2 mA/cm² for $a_i = 1$ and $(c_i/\rho_0) = 1$ mol/kg. The transport properties for all components are equivalent since the diffusion coefficient and the characteristic length δ_i , which has been used to nondimensionalize the mass-transfer problem, were set equal for all ionic species.

For the base case, the current is pulsed to the total dc limiting current of the system. This current program is displayed in Fig. 1. In Fig. 2, the dimensionless surface concentrations are plotted for a system in which a Nernst diffusion layer is applicable (the dotted curves) and for the more rigorous solution outlined by Eq. [12] and [13] (the unbroken curves). It can be seen that the two solution techniques yield very similar answers, as would be expected from the close agreement of the respective current-step solutions. Due to the low bulk concentration

Table I. Model inputs^a

Quantity				Units
c_i^b	1×10^{-6}	1×10^{-5}	1×10^{-4}	mol/cm ³
d_m	3			Å
$k_{a,i}$	8.741×10^{-14}	2.109×10^{-10}	5.091×10^{-7}	mol/cm ² ·s
$k_{c,i}$	1.229×10^{-3}	5.092×10^{-7}	2.110×10^{-10}	kg/cm ² ·s
n_i	2	2	2	—
r	0			Ω·cm ²
RSAT	9			Å
x_i^o	1.0	0.0	0.0	mol i/mol
β_i	0.5	0.5	0.5	—
γ_i	1.0	1.0	1.0	—
δ_i	0.001014	0.001014	0.001014	cm
ρ_o	0.001			kg/cm ³
ρ_i	0.073	0.073	0.073	mol/cm ³
σ	1.0			—

^a For component entries, component 1 is at the far left, followed by components 2 and 3, respectively.

and more noble character of component one, its surface concentration remains negligible throughout the electrodeposition process. The least-noble component 3 has the highest bulk and surface concentration. Figure 2 illustrates that the process reaches a uniform and sustained periodic state after about the fourth cycle.

The electrode-potential profile is portrayed in Fig. 3. The lower portions of the curve correspond to the on time. While deposition is occurring, the electrode potential is forced to more cathodic (negative) values since the discharging ion concentrations are decreasing. During the off times, the potential drifts in the anodic direction as corrosion reactions take place and metal ions are transported to the electrode surface by convection and diffusion.

One of the more practical aims of this work is to obtain the electrodeposition composition. A plot of the deposit composition is shown in Fig. 4. Though component 1 is the most noble component, its low bulk concentration limits its rate of mass transfer, thereby suppressing its deposit concentration. The opposite is true for component 3. About ten monolayers are deposited during the on time; thus, there is a considerable variation in the electrodeposition concentration during the on time. The corrosion currents also cause a change in the deposit mole fractions during the off time. At higher frequencies, there would be less variation in the deposit composition during a pulse.

In order to obtain the deposit mole fractions, the partial currents must be known. A plot of partial currents is

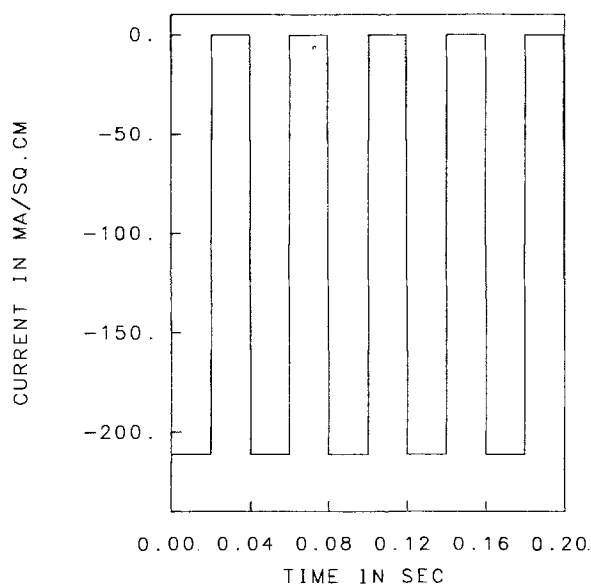


Fig. 1. Current source for the base case. The maximum cathodic current is the sum of the dc limiting currents of the discharging ions (-211 mA/cm^2).

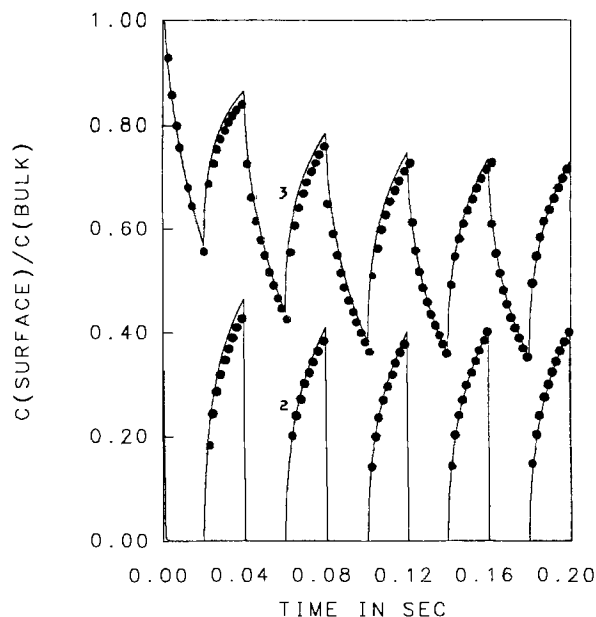


Fig. 2. Dimensionless surface concentrations for the first five cycles. The current source is shown in Fig. 1. The dotted curve was obtained using the Nernst diffusion layer approximation. The surface concentration of component 1 remains near zero throughout the deposition process.

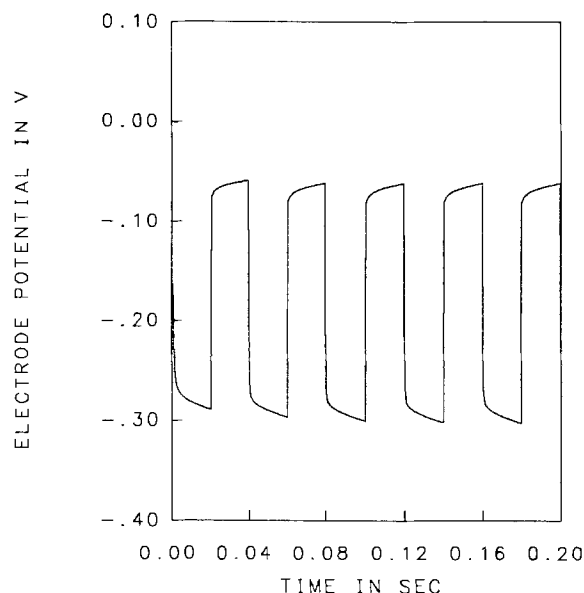


Fig. 3. Electrode potential relative to a SHE for the base case. The lower portion of the curve represents the on time.

shown in Fig. 5 for a pulse-reversal current source. A pulse-reversal current source is often used to produce smooth deposits, and it has a significant effect on the alloy composition and ionic surface concentrations. Due to the high bulk concentration of component 3, it carries most of the cathodic current. Figure 5 shows that components 1 and 2 incur mass-transport limitations during the on time. Component 3 also carries most of the anodic current due to its more negative standard electrode potential. At the end of the fifth cycle, the total deposit mole fractions are 0.028, 0.222, and 0.750 for components 1, 2, and 3, respectively. For the base case (Fig. 1-4) the analogous values are 0.021, 0.175, and 0.804. In addition, the pulse-reversal current source supports higher ionic surface concentrations due to the periodic deposit dissolution. A comparison of Fig. 2 and 6 illustrates this.

Some insight into multicomponent electrodeposition can be gained by examining the case of a triangular current source. The triangular current waveform in Fig. 7 reaches a cathodic current density 1.7 times the total dc

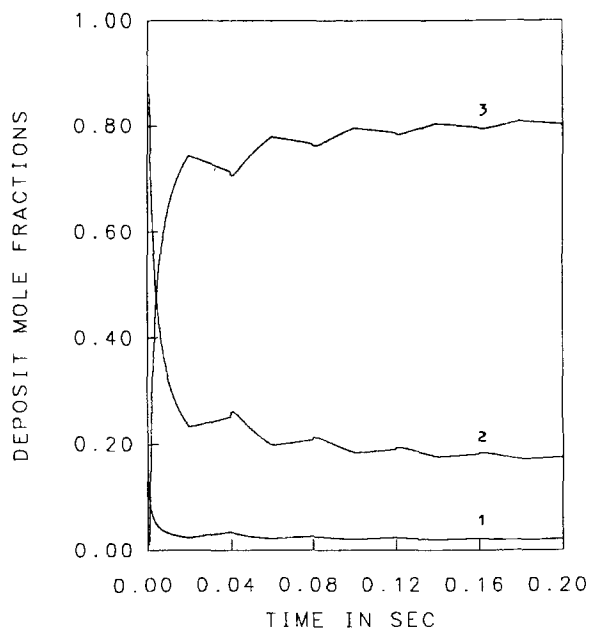


Fig. 4. Deposit mole fraction variation for the base case. Upper curve: component 3. Middle curve: component 2. Lower curve: component 1. At time zero, the electrode is pure 1.

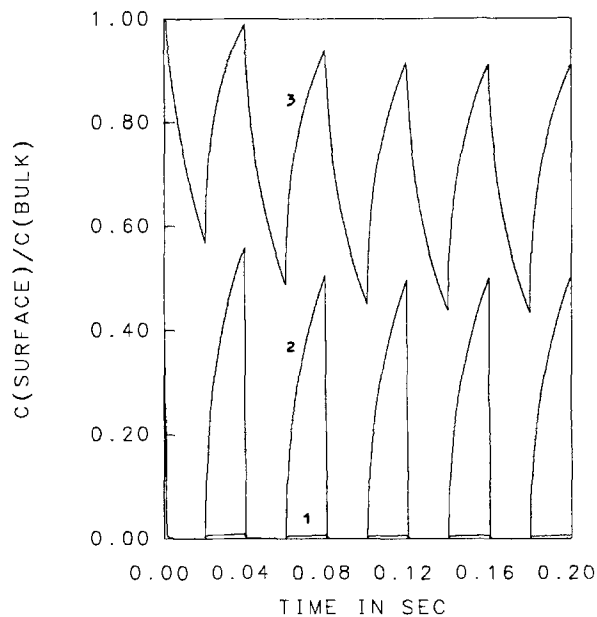


Fig. 6. Dimensionless surface concentrations for the pulse-reversal current source. The surface concentrations are higher than those for the pulsed-current source depicted in Fig. 2.

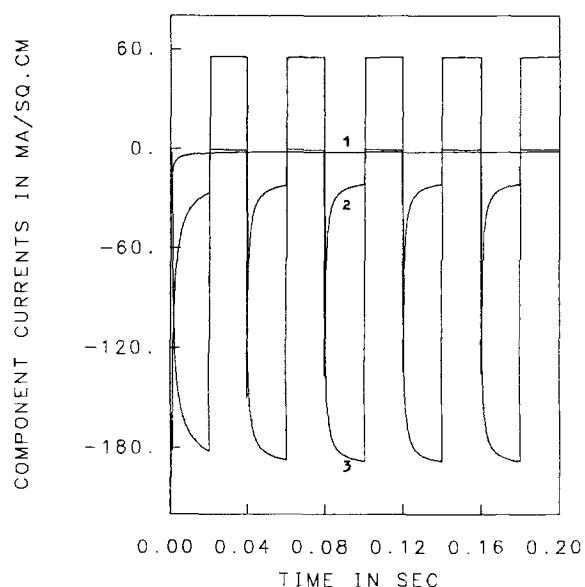


Fig. 5. Component currents for a pulse-reversal current source. The current is reversed to 52.8 mA/cm^2 . The maximum cathodic current is the same as that shown in Fig. 1 (211.2 mA/cm^2).

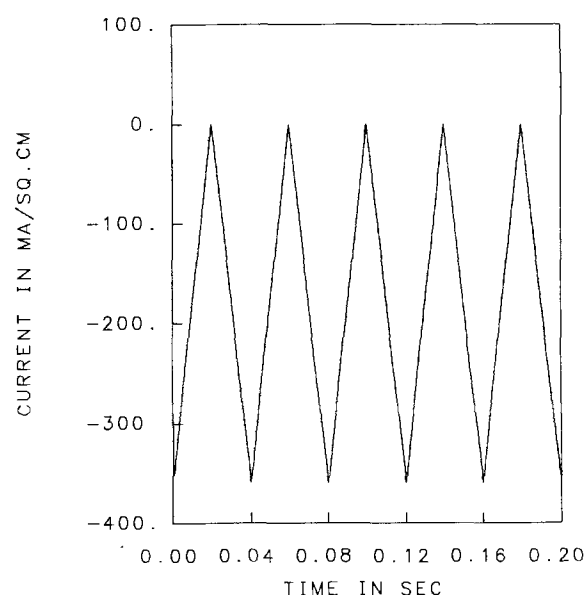


Fig. 7. Triangular current source. The maximum current is 1.7 times the base case maximum cathodic current source shown in Fig. 1.

limiting current density displayed in Fig. 1. The nonlinear nature of the electrode kinetics is manifest in the electrode-potential profile in Fig. 8. The waveform in Fig. 7 was constructed to disallow the achievement of a periodic state. In Fig. 8, it can be seen that the minima reach more cathodic values for each succeeding period. At 0.20s, all three discharging metal ions reach a zero surface concentration. Directly after this another reaction would be forced to take place, such as solvent decomposition.

The influence of the individual solid-state activities can be seen by comparing Fig. 9 and 10 for the last off time displayed in Fig. 1. The partial currents for the base case are shown in Fig. 9. Component 1 carries its dc limiting current density throughout the process. Component 2 is also depositing during the off time, whereas component 3 dissolves. The partial currents sum to zero during the off time.

When the energy of interaction between components 1 and 3 and components 2 and 3 is attractive, the corrosion currents are reduced and the deposit is more stable dur-

ing the off time. This is depicted in Fig. 10. These concepts are important to the understanding of the corrosion of alloys. In particular, elements can be chosen to form a more corrosion resistant alloy. Though the partial currents are relatively low in Fig. 9 and 10, and the overall deposit composition will not change greatly because of the surface free-energy changes, situations can occur in which the individual solid-state activities could be very important. For instance, in pulse-reversal electrodeposition, where the magnitude of the anodic current is high, the surface activities will play an important role in determining the electrodeposit composition and the ionic surface concentrations.

Conclusions

This paper presents a mathematical model for the periodic electrodeposition of multicomponent alloys by an arbitrarily specified current source. An analogous model for potential-controlled electrolysis is also discussed. The method of superposition is used to solve this problem with an efficient numerical algorithm. This treatment ex-

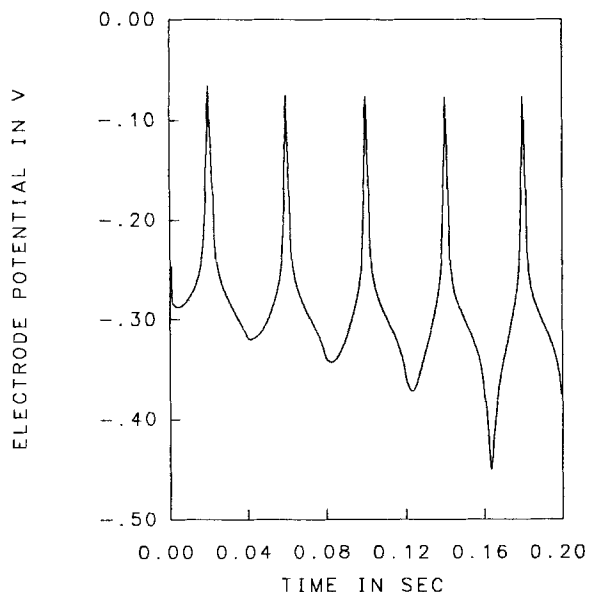


Fig. 8. Electrode potential relative to the SHE for the triangular current source displayed in Fig. 7. For the specified conditions, a periodic state will not be achieved.

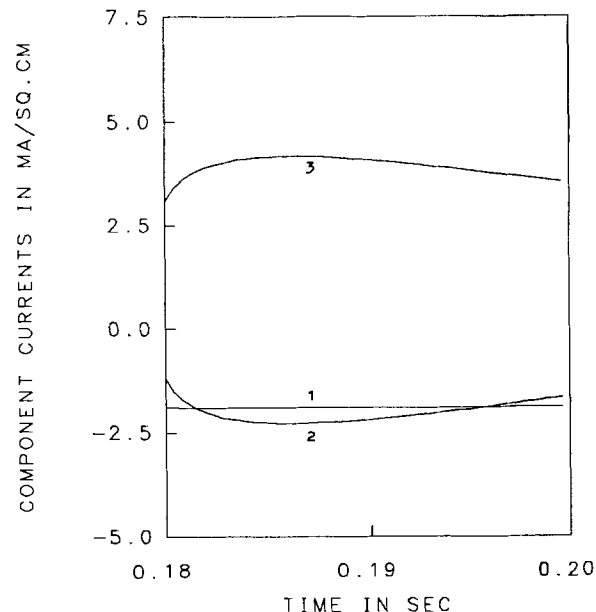


Fig. 10. Component currents during the fifth off time of the current source shown in Fig. 2. For this case, the activity coefficients deviate from unity. $G_{3,1} - G_{3,3} = G_{3,2} - G_{3,3} = -20,000$ J/mol. Component 3 is attracted to components 1 and 2 in the electrodeposit.

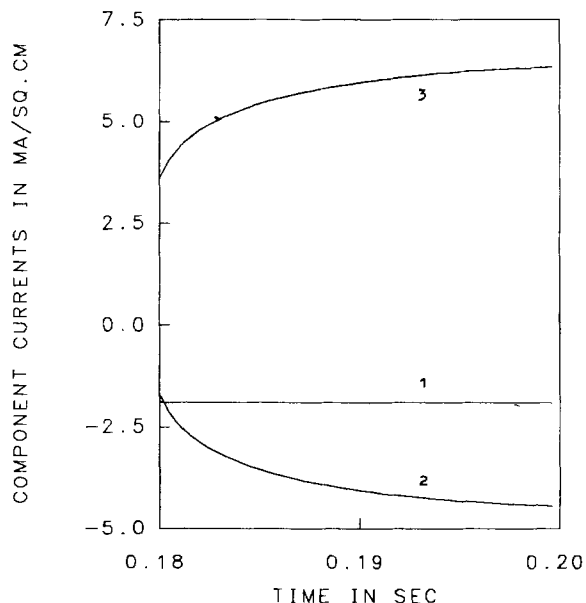


Fig. 9. Component currents during the fifth off time for the base case. The activity coefficients are all unity.

poses the large number of parameters the electroplater must consider for obtaining thin alloy films with the desired properties. If an accurate model is used by the electroplater, the different plating parameters can be intelligently varied to assist in manufacturing the desired electrodeposit.

Acknowledgments

Our modeling efforts were benefited by insightful discussions with Professor John Newman. This work was supported by the Director, Office of Energy Research, Office of Basic Energy Sciences, Materials Sciences Division of the Office of the U.S. Department of Energy, under Contract no. DE-AC03-76SF00098.

Manuscript submitted Aug. 31, 1984; revised manuscript received ca. Feb. 11, 1985.

The University of California assisted in meeting the publication costs of this article.

APPENDIX

Rosebrugh and Miller's solution can be used to derive alternate expressions for Eq. [12] and [13]. The current-step solution is first required. Fick's second law

$$\frac{\partial c_1}{\partial t} = D_1 \frac{\partial^2 c_1}{\partial y^2} \tag{A-1}$$

with the initial condition and the boundary conditions given by Eq. [3], [5], and [10] outline the current-step problem. The solution is (37)

$$c_1 = c_1^b + \frac{i_1 \delta_1}{n_1 F D_1} \left[1 - \frac{y}{\delta_1} - \frac{8}{\pi^2} \sum_{j=1}^{\infty} \frac{\cos(m g_1 y)}{m^2} e^{-m^2 \alpha_1 t} \right] \tag{A-2}$$

where $m = 2j - 1$, $g_1 = \pi/2\delta_1$, and $\alpha_1 = \pi^2 D_1/4\delta_1^2$.

The similarity between Eq. [7] and [A-2] is evident. Retention of the velocity term in Eq. [1], the convective diffusion equation, tends to change slightly the eigenfunctions and the eigenvalues. The form and the behavior of the two current step solutions are very similar.

For short times, Eq. [A-2] can be reduced to the Sand equation. Thus, Eq. [8] bears a close resemblance to the asymptotic expression of Eq. [A-2] evaluated for short times and at the electrode surface.

When the method of superposition is used to obtain an expression for a varying current source, the concentration can be expressed by Eq. [11] and

$$\Theta_{1,n} = \frac{\delta_1}{n_1 F D_1} \left[1 - \frac{y}{\delta_1} - \frac{8}{\pi^2} \sum_{j=1}^{\infty} \frac{\cos(m g_1 y)}{m^2} e^{-m^2 \alpha_1 (t-t_{n-1})} \right] \tag{A-3}$$

and

$$\Psi_{i,n} = c_i^b + \frac{\delta_1}{n_i F D_i} \left\{ \frac{8}{\pi^2} \sum_{j=1}^{n-1} i_{i,j} \sum_{k=1}^{\infty} \frac{\cos(m g_i y)}{m^2} \left[e^{-m^2 \alpha_i (t-t_k)} - e^{-m^2 \alpha_i (t-t_{k-1})} \right] \right\} \tag{A-4}$$

The similarity between Eq. [12], [13], [A-3], and [A-4] is evident. This is especially true at the electrode surface where Z_k is unity. Equations [A-3] and [A-4] and Eq. [14] and [15] were used to model the solution-side mass transport in order to obtain the dotted curves in Fig. 2.

LIST OF SYMBOLS

- $a_{i,n}$ surface activity of component i at time step n
- $c_{i,n}$ concentration of species i during time step n (mol/cm³)
- c_i^b bulk concentration of species i (mol/cm³)
- $c_{i,n}^s$ surface concentration of species i during time step n (mol/cm³)

$c_{i, \text{re}}$	reference electrode compartment concentration of species i (mol/cm ³)
d_{ml}	monolayer thickness of electrodeposit (cm)
D_i	diffusion coefficient of species i (cm ² /s)
f	F/RT , (mol/V-eq)
F	Faraday's constant (96,487 C/eq)
g_{ij}	energy of interaction between components i and j (J/mol)
G^E	molar excess Gibbs energy (J/mol)
H_n	zeroing function (mA/cm ²)
$i_{i,n}$	current density carried by species i at time step n (mA/cm ²)
i_n	total current density at time step n (mA/cm ²)
$k_{a,i}$	anodic rate constant of component i (mol/cm ² -s)
$k_{c,i}$	cathodic rate constant of species i (kg/cm ² -s)
m	number of deposit components
M_i	symbol for chemical formula for species i
n	time step
n_i	number of electrons in the deposition reaction of species i
n_{re}	number of electrons in reference-electrode reaction
N_i	moles of component i
N_T	total moles
r	cell ohmic resistance (Ω -cm ²)
R	universal gas constant (8.314 J/mol-K)
RSAT	relevant surface-activity thickness (cm)
$s_{i,\text{re}}$	stoichiometric coefficient of species i in reference electrode reaction
t	time (s)
T	absolute temperature (K)
U_i^θ	standard electrode potential for reaction involving species i (V)
U_{re}^θ	standard electrode potential of the reference electrode reaction (V)
V_n	electrode potential referred to the reference electrode, during time step n (V)
v_y	normal velocity component to a rotating disk electrode (cm/s)
x_i	mole fraction of component i
y	normal distance from the electrode surface (cm)

Greek Symbols

α_{ij}	species interaction constant characteristic of the nonrandomness of the mixture
β_i	symmetry factor for component i
γ_i	activity coefficient of component i
$\Gamma(4/3)$	0.89298, the gamma function of 4/3
$\Theta_{i,n}$	concentration function (mol/A-cm)
$\Theta_{i,n}^s$	surface-concentration function (mol/A-cm)
$\delta_{i,n}$	Nernst diffusion layer thickness of species i (cm)
σ	exponential proportionality constant for the RSAT mole fraction
ν	kinematic viscosity (cm ² /s)
ρ_0	solvent mass density (kg/cm ³)
ρ_i	species i molar density (mol/cm ³)
ω	disk rotation speed (rad/s)
$\Psi_{i,n}$	concentration function (mol/cm ³)
$\Psi_{i,n}^s$	surface concentration function (mol/cm ³)

REFERENCES

- A. Brenner, "Electrodeposition of Alloys, Principles and Practice," Academic Press, New York (1963).
- K. M. Gorbunova and Yu.M. Polukarov, in "Advances in Electrochemistry and Electrochemical Engineering," Vol. 5, C. W. Tobias, Editor, p. 256, Interscience, New York (1967).
- R. D. Srivastava and R. C. Mukerjee, *J. App. Electrochem.*, **6**, 321 (1976).
- C. C. Wan, H. Y. Cheh, and H. B. Linford, *Plating*, **61**, 559 (1974).
- A. J. Avila and M. J. Brown, *ibid.*, **57**, 1105 (1970).
- H. Y. Cheh, *This Journal*, **118**, 551 (1971).
- V. A. Lamb, *Plating*, **56**, 909 (1969).
- J. Cl. Puipe and N. Ibl, *ibid.*, **67**, 68 (1980).
- M. I. Ismail, *J. Appl. Electrochem.*, **9**, 407 (1979).
- A. R. Despic and K. I. Popov, *ibid.*, **1**, 275 (1971).
- K. I. Popov, in "Modern Aspects of Electrochemistry," Vol. 7, B. E. Conway and J. O'M. Bockris, Editors, p. 304, Plenum Press, New York (1972).
- W. Sullivan, *Plating*, **62**, 139 (1975).
- M. H. Gelchinski, L. Gal-Or, and J. Yahalom, *This Journal*, **129**, 2433 (1982).
- C. A. Burrus, *ibid.*, **118**, 833 (1971).
- H. Leidheiser, Jr., and A. R. P. Ghuman, *ibid.*, **120**, 484 (1973).
- U. Cohen, F. B. Koch, and R. Sard, *ibid.*, **130**, 1987 (1983).
- A. Kindler, PhD. Thesis, University of California, Berkeley, CA (1981).
- N. Ibl and K. Schadegg, *This Journal*, **114**, 54 (1967).
- D.-T. Chin, *ibid.*, **130**, 1657 (1983).
- K. Nisancioglu, PhD. Thesis, University of California, Berkeley, CA (1973).
- R. Haynes, *This Journal*, **126**, 881 (1979).
- P. Radhakrishnamurty, *ibid.*, **127**, 1320 (1980).
- R. Haynes, *ibid.*, **127**, 1321 (1980).
- H. Y. Cheh, *ibid.*, **127**, 1321 (1980).
- T. Cheng and H. Y. Cheh, Abstract 414, p. 681, The Electrochemical Society Extended Abstracts, Vol. 82-1, Montreal, Que., Canada, May 9-14, 1982.
- T. Cheng and H. Y. Cheh, Abstract 248, p. 390, The Electrochemical Society Extended Abstracts, Vol. 83-2, Washington, DC, Oct. 9-14, 1983.
- W. G. Cochran, *Proc. Cambridge Philos. Soc.*, **30**, 365 (1934).
- J. S. Newman, "Electrochemical Systems," Prentice-Hall, Inc., Englewood Cliffs, NJ (1973).
- J. S. Newman, *This Journal*, **113**, 1235 (1966).
- J. S. Newman, *ibid.*, **117**, 198 (1970).
- P. Appel, PhD. Thesis, University of California, Berkeley, CA (1976).
- L. Nanis and I. Klein, *This Journal*, **119**, 1683 (1972).
- V. S. Krylov and V. N. Babak, *Sov. Electrochem.*, **7**, 626 (1971).
- D. A. Scherson, P. F. Marconi, and J. S. Newman, *This Journal*, **127**, 2603 (1980).
- K. Nisancioglu and J. S. Newman, *J. Electroanal. Chem.*, **50**, 23 (1974).
- V. G. Levich, "Physicochemical Hydrodynamics, p. 69, Prentice-Hall, Englewood Cliffs, NJ (1961).
- T. R. Rosebrugh and W. L. Miller, *J. Phys. Chem.*, **14**, 816 (1970).
- H. Y. Cheh, *This Journal*, **118**, 1132 (1971).
- K. Visawanathan and H. Y. Cheh, *ibid.*, **125**, 1616 (1978).
- K. Visawanathan and H. Y. Cheh, *J. Appl. Electrochem.*, **9**, 537 (1979).
- J. M. Hale, *J. Electroanal. Chem.*, **6**, 187 (1963).
- Yu. G. Siver, *Russ. J. Phys. Chem.*, **34**, 274 (1960).
- K. Visawanathan, M. A. Farrell, and H. Y. Cheh, *This Journal*, **125**, 1772 (1978).
- P. C. Andricacos and H. Y. Cheh, *J. Electroanal. Chem.*, **121**, 133 (1981).
- W. M. Kays and M. E. Crawford, Convective Heat and Mass Transfer," pp. 117-129, McGraw-Hill, New York (1980).
- F. B. Hildebrand, "Advanced Calculus for Applications," pp. 463-467, Prentice-Hall, Englewood Cliffs, NJ (1976).
- M. Fleischmann and H. R. Thirsk, in "Advances in Electrochemistry and Electrochemical Engineering," Vol. 3, P. Delahay, Editor, p. 124, Interscience, New York (1963).
- K. J. Vetter, "Electrochemical Kinetics," p. 140, S. Bruckenstein and B. Howard, Translation Editors, Academic Press, New York (1967).
- L. Lapidus, "Digital Computation for Chemical Engineers," p. 288, McGraw-Hill, New York (1962).
- R. C. Alkire and J. E. Tsai, *This Journal*, **129**, 1157 (1982).
- E. A. Guggenheim, "Thermodynamics," p. 215, North-Holland, Amsterdam (1959).
- R. A. Swalin, "Thermodynamics of Solids," pp. 141-153, John Wiley and Sons, New York (1972).
- J. M. Prausnitz, "Molecular Thermodynamics of Fluid-Phase Equilibria," pp. 279-292, Prentice-Hall, Englewood Cliffs, NJ (1969).
- E. A. Guggenheim, "Mixtures," pp. 215-242, Oxford Press, London (1952).
- L. S. Darken and R. W. Gurry, "Physical Chemistry of Metals," R. F. Mehl, Consulting Editor, McGraw-Hill, New York (1953).
- J. Lumsden, "Thermodynamics of Alloys," Institute of Metals, London (1952).
- H. Renon and J. M. Prausnitz, *AIChE J.*, **14**, 135 (1968).
- J. M. Prausnitz, "Molecular Thermodynamics of Fluid-Phase Equilibria," pp. 309-314, Prentice-Hall, Englewood Cliff, NJ (1969).
- R. L. Scott, *J. Chem. Phys.*, **25**, 193 (1956).
- H. M. Renon, PhD. Thesis, University of California, Berkeley, CA (1966).
- G. Wranglen, *Electrochim. Acta.*, **2**, 130 (1960).
- D. M. Kolb, M. Prazasnyski, and H. Gerischer, *J. Electroanal. Chem.*, **54**, 25 (1974).
- G. Azdic, J. McBreen, and M. G. Chu, *This Journal*, **128**, 1691 (1981).
- J. McBreen and M. G. Chu, and G. Azdic, *ibid.*, **128**, 2281 (1974).

65. S. H. Cadle and S. Bruckenstein, *Anal. Chem.*, **44**, 1993 (1974).
66. T. Takamura and K. Takamura, in "Surface Electrochemistry, Advanced Methods and Concepts," T. Takamura and A. Kozawa, Editors, pp. 222-234, Japan Scientific Societies Press, Tokyo, Japan (1978).
67. T. Takamura, F. Watanabe, and K. Takamura, *Electrochim. Acta.*, **19**, 933 (1974).
68. T. H. V. Setty and H. Wilman, *Trans. Faraday Soc.*, **51**, 984 (1955).
69. J.O'M. Bockris and A. Damjanovic, in "Modern Aspects of Electrochemistry," Vol. 3, J. O'M. Bockris and B. E. Conway, Editors, p. 329, Butterworth London (1964).
70. K. H. Z. Brainina, D. P. Synkova, and I. G. Yudelevich, *J. Electroanal. Chem.*, **35**, 165 (1972).
71. K. H. Z. Brainina, N. K. Kiva, and V. B. Beliavskaia, *Elektrokhimiya*, **1**, 311 (1965).

Electrolytic Recovery of Gallium from Dilute Solutions Employing Microelectrodes

R. C. Paciej*

Naval Air Development Center, Warminster, Pennsylvania 18974

G. L. Cahen, Jr.,* and G. E. Stoner*

Department of Materials Science, University of Virginia, Charlottesville, Virginia 22901

E. Gileadi*

Department of Chemistry, Tel Aviv University, Ramat Aviv 69978, Israel

ABSTRACT

The recovery of gallium from dilute solutions is known to be slow and inefficient due to competing hydrogen evolution and the limitations of mass transport. Methods used to improve the process include pulse plating, inhibition of hydrogen evolution by suitable additives, increasing the pH, and conducting the process at temperatures above the melting point of gallium. In the present work, an alternative approach was taken employing microelectrodes to enhance the rate of mass transport and thus to increase the rate of gallium recovery. Potentiostatic plating and stripping experiments were performed using electrodes ranging in diameter from 1 cm down to 45 μm . The effect of electrode diameter on the rate and efficiency of the plating of gallium was studied at different potentials and under different conditions of mass transport. The effect of plating time was also determined, and the conditions for the optimum recovery of gallium in terms of the overall rate as well as the current efficiency were evaluated. Carbon fiber epoxy composites can serve as ensembles of microelectrodes. It was shown that, with a typical radius of 3-5 μm for the individual fibers, considerable enhancement of the rate of recovery of metals from dilute solutions can be expected.

Novel electrode designs have been suggested in recent years for the recovery of metals from dilute solutions, either as a means for purifying industrial waste, or as a method of primary recovery of the metal from low grade ore. Some well-known designs include the "Swiss roll" (1), the fluidized bed (2), the so-called "Eco cell" (3), as well as various types of porous electrode flow-through cells (4). Most of the above designs cannot be used efficiently for the recovery of gallium due to the low current efficiency caused by hydrogen evolution and because gallium tends to be soluble in the electrolyte used after it has been detached from the electrode surface and is no longer cathodically protected. An alternative electrode design, which has so far not been studied for this purpose, is a microelectrode or an ensemble of microelectrodes on a planar surface.

Recent interest in the electrochemical properties of microelectrodes is due to several possible applications of such systems. They can be considered for implantation in living organisms to follow the changes in concentration of biologically active molecules. The various future applications of microelectrodes were discussed in a recent symposium devoted to this subject (5). A number of theoretical papers have dealt with the calculation of the rate of mass transport to a microelectrode (6-11). In two recent studies (12, 13), the rate of mass transport to ensembles of microelectrodes was calculated, taking into account the interaction of the diffusion layers of adjacent electrodes. It was shown (13, 14) that an added advantage of ensembles of microelectrodes, as compared to large continuous electrodes, is the reduced ohmic potential drop. A number of experimental studies employing microelectrodes of

various types have been reported in recent years (15-23). Further possibilities for such experimental studies are enhanced by the advent of modern techniques of microelectronics and by the introduction of carbon fiber epoxy matrix composite materials as electrodes in certain applications (19, 24-26).

The inherent advantage of ensembles of microelectrodes for the recovery of metals from dilute solutions is the enhancement of mass transport, as compared to planar electrodes of equal total area. Since the partial current for metal recovery from dilute solutions will usually be limited by mass transport, enhancing the rate of mass transport should increase both the rate of metal recovery and the current efficiency for recovery (assuming that the competing reaction, which is typically hydrogen evolution, is not limited by mass transport). A possible drawback of microelectrodes is their tendency to be easily blocked by impurities and specifically by minute gas bubbles formed in the accompanying reaction of hydrogen evolution. This may lead to a significant scatter of experimental results in laboratory experiments, but should be of lesser importance in large-scale industrial operations in which flow rates of the solutions are typically high and large ensembles of microelectrodes will be used in any one reactor.

Theory

The limiting current density on a planar electrode following a potential step was given (8) for $(\pi Dt)^{1/2} \leq r$ as

$$I = nFCD \left[\frac{A}{\sqrt{\pi Dt}} + \frac{P}{2} \right] \quad [1]$$

*Electrochemical Society Active Member.

in which C is the bulk concentration, A is the area, and P is the circumference of the electrode. By setting $A = \pi r^2$ and $P = 2\pi r$, for a disk electrode this equation reduces to the well-known equation of the limiting current to a spherical electrode

$$I = nFCDA \left[\frac{1}{\sqrt{\pi Dt}} + \frac{1}{r} \right] \quad [2]$$

The first term in the brackets represents the classical Cottrell equation and is valid at short times when the diffusion layer thickness $\delta = (\pi Dt)^{1/2}$ is small with respect to the radius r of the microelectrode. If diffusion is the only mode of mass transport, the time-dependent term in Eq. [1] and [2] will approach zero at long times and the current will be governed by the radius of the microelectrode. This, however, is not a case of practical interest, since in any electrochemical reactor the diffusion layer thickness at steady state is governed by the conditions of flow near the electrode surface. Such steady state is reached when the naturally growing diffusion layer reaches the thickness enforced by electrolyte flow. If the latter is known, the time to reach steady state can readily be estimated from the relationship $t = \delta^2/\pi D$.

In the present work, the case studied was that in which the diffusion layer was determined by the method of stirring of the solution. In this case, one can define a capture area, shown in Fig. 1, as the envelope within which the concentration of the reactants and products significantly deviate from their respective bulk values. From simple geometrical considerations, it can be seen that the "capture area" A_c defined above is related to the diffusion layer thickness and the radius of the microelectrode. The ratio between the capture area and the area of the microelectrode is given by

$$A_c/A_e = 1 + \pi\delta/r + 2\delta^2/r^2 \quad [3]$$

This ratio may serve as a qualitative measure of the enhancement of mass transport to a microelectrode or to an ensemble of microelectrodes. For an infinitely large planar electrode, the above ratio is, by definition, equal to unity. As the ratio between the diffusion layer thickness and the radius of the microelectrode increases, the second and the third terms in the above equation become predominant. When the ratio is very large, the term involving the square of this ratio is most important. With this concept, the enhancement of the rate of diffusion is to an extent proportional to the ratio of areas of a circle having a radius equal to the diffusion layer thickness to the area of the microelectrode. A similar result was reached for an ensemble of microelectrodes assuming that the rate of mass transport was controlled only by diffusion, with no convective flow (13, 14).

Experimental

The cell and electrodes.—A rectangular cell constructed of polymethylmethacrylate was employed. The distance between the working and counterelectrodes was 8.5 cm, and a saturated calomel reference electrode (SCE) was situated in the compartment with and at a distance of 3.5 cm from the working electrode. All potentials shown in this

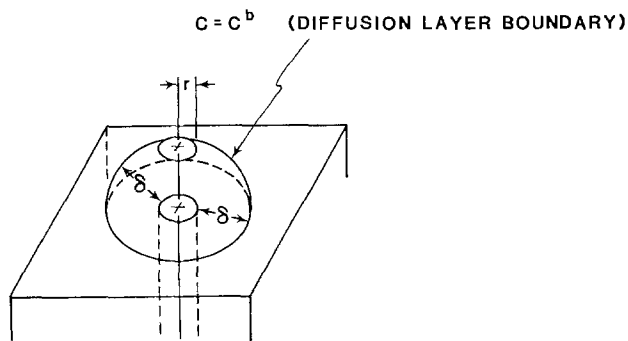


Fig. 1. The capture envelope

paper are with respect to the saturated calomel electrode. The counterelectrode and working electrode compartments were separated by a 125 μm Tyvek separator in order to prevent oxygen from getting to the working electrode when it was polarized cathodically. A 1 cm^2 copper plate was used as the continuous or plate electrode. Copper wires embedded in an epoxy matrix were used as the microelectrodes. The diameters of these electrodes were 1000, 510, 250, 100, 67, and 45 μm . For the three larger sizes, single electrodes were used. For the three smaller sizes, ensembles of electrodes having 6, 13, and 15 electrodes, respectively, were employed. The electrodes were situated at a relatively large distance from each other to ensure that their diffusion layers would not overlap during the experiment. Bonding of the microelectrodes to the embedding polymer initially posed some problems. These were overcome by the use of a silane coupling agent prepared by mixing 5 ml of organosilane ester (Union Carbide, A 176) with 5 ml acetic acid and diluting with 5 ml of distilled water.

After imbedding the copper wires into the polymer, the electrodes were polished to be flush with the surface. Polishing was performed with successively finer polishing materials, starting with 180, 320, 400, and 600 grit papers (3M Company), followed by 10 and 5 μm SiC papers (Mager Scientific Company). In the final polishing stage, 6 and 1 μm diamond pastes were used, followed by 0.05 μm alumina powder (Buehler).

Electrolyte and methods of stirring.—The electrolyte was prepared from reagent grade NaOH (Fisher Scientific, 283 g/liter) and anhydrous $\text{Ga}_2(\text{SO}_4)_3$ (Alfa Products, 2 g/liter, dissolved in distilled water). The molar concentrations were 7.07M hydroxide and 9.4 mM gallium, in the form of the gallate ion GaO_3^{3-} . The pH of the solution was 15.1 (27).

Two methods were used to agitate the solution. In initial measurements, a magnetic stirrer was employed. This was found to be unsatisfactory, since hydrogen bubbles sticking to the electrode surface were not removed. Much more efficient stirring was achieved by the use of an impinging jet of electrolyte, which was positioned 1.5 cm above and 0.5 cm away from the working electrode. The effective value of the diffusion layer thickness, estimated from measurements on the plate electrode (see Results and Discussion) was 68 and 19 μm for the two methods of stirring, respectively. The great advantage of the impinging jet was that it helped remove most of the hydrogen bubbles from the surface of the microelectrodes.

Procedure and apparatus.—At the start of each set of experiments, the solution was deaerated with pure nitrogen for 30 min. The working electrode was maintained at a potential of -1.4V to protect it cathodically. All experiments were conducted potentiostatically using a PAR Model 173 potentiostat. Plating was conducted for 10, 30, and 50s at potentials ranging from -1.70 to -1.90V . Anodic stripping was performed at a potential of -0.75V , until the anodic stripping current decayed to zero. The charge during plating and anodic stripping was measured with a bipolar computing coulometer (Electrosynthesis Company, Model 680). The amount of gallium stripped off was also measured in some of the experiments by determining the weight loss which varied from the coulometric determinations by no more than $\pm 5\%$.

A peristaltic pump (Cole-Palmer Instruments Company) was used to form the impinging jet. It provided a volume flow rate of 9.6 ml/s and a linear flow velocity of ca. 5m/s.

Results and Discussion

The rate of gallium deposition.—The average rate of gallium deposition is shown in Fig. 2 as a function of potential for microelectrodes of different size. In this figure, the current densities are based on the electrode conductors' apparent area with the data for the 1 cm^2 plate electrode shown for comparison. The results for the two largest microelectrodes studied here are not included in

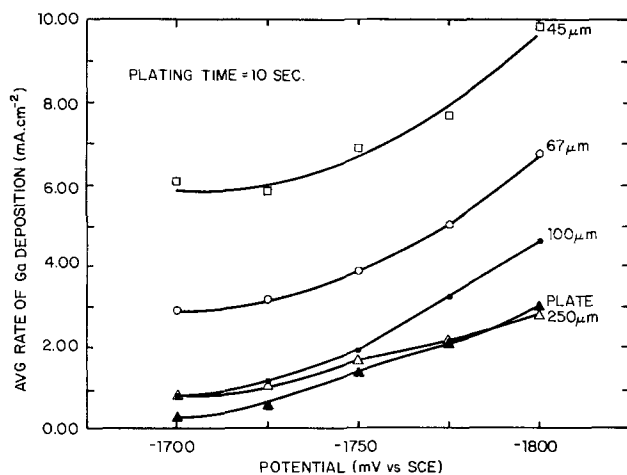


Fig. 2. The effect of the diameter of the electrodes and the potential on the rate of deposition of gallium.

Fig. 2, since they are the same as for the plate electrode. The diffusion-limited current density for gallium deposition was estimated from the current density and the current efficiency measured in the range of potentials of -1.8 to -1.9 V. On the plate electrode, the value obtained in this manner was $i_L = 4.5$ mA/cm². This value was used to calculate the diffusion layer thickness δ , given here. The viscosity of the solution is approximately 6.0 cP, and the diffusion coefficient for the gallate ion is $D = 3 \times 10^{-6}$ cm²/s, significantly lower than in dilute aqueous solutions. Thus, the rate of gallium deposition was under mixed activation/mass-transport control on the plate electrode up to a potential of -1.80 V and switched to fully mass-transport control at more negative potentials. Due to significant enhancement of the rate of mass transport on the microelectrodes, the rate of gallium deposition was probably under mixed control throughout the range of potentials studied.

If we were to assume that the reaction is under mass-transport control for all electrodes at all potentials measured, it would be easy to calculate the difference between the current densities on the plate and on the microelectrodes, since

$$i_L(\text{micro}) - i_L(\text{plate}) = nFDC \left[\left(\frac{1}{\delta} + \frac{1}{r} \right) - \frac{1}{\delta} \right] = nFDC \left(\frac{1}{r} \right) \quad [4]$$

The differences calculated in this way amount to 3.8, 2.5, 1.7, and 0.7 mA/cm² for the 45, 67, 100, and 250 μm diam electrodes, respectively. The average values observed at the less negative potentials are 3.7, 2.5, and 1.7 mA/cm², respectively, the values for the 250 μm electrode being within experimental error of the value for the plate electrode. It is noteworthy, however, that this difference increases at more negative potentials. It is reasonable to assume that in this region the plate electrode is already completely under mass-transport control, while the rate of gallium deposition still increases slightly with increasing negative potential on the microelectrodes.

The solution resistance may play an important role in determining the rate of gallium deposition at the less negative potentials. Since the reversible potential for the deposition of gallium in the solvent is close to -1.70 V, a small difference in the potential across the interface, caused by an IR drop, may effect the rate of deposition of gallium in a major way. As pointed out above (13, 24), the solution resistance (for a fixed value of the current density) decreases with decreasing radius of the microelectrode. This may explain the relatively large difference in current density between the plate electrode and the smallest microelectrode observed in Fig. 2.

It should be noted that the condition $r \ll \delta$ did not exist even for the smallest microelectrodes employed in this

study. It was shown (12, 13) that for electroanalytical applications the radius of the microelectrodes in the ensemble should be 3 μm or less to have a significant advantage over large electrodes. However, the comparison in that case was done with pulse polarography, which is in itself one of the most sensitive electroanalytical techniques. The present results clearly show that when the radius is decreased below 50 μm , a definite advantage over large electrodes is observed and this advantage increases sharply with decreasing radius. Extrapolating the data in Fig. 2 to a radius of 3-5 μm would indicate a possible increase in the rate of recovery of gallium by one to two orders of magnitude compared to large continuous electrodes. This may be very significant technologically, since the radii of the fibers in graphite fiber epoxy composites are in that range. Thus, graphite fiber composites with relatively low graphite fiber loading may turn out to be very useful as ensembles of microelectrodes for the recovery of metals from dilute solutions.

Anodic stripping and alloy formation.—Anodic stripping was conducted following each plating experiment. The potential was held at -0.750 V until the anodic current decayed to zero, and the charge passed in this period was determined with the aid of a coulometer. Some typical anodic stripping curves are shown in Fig. 3. The longer the plating time, the longer the plateau during stripping. It should be noted that a Cu/Ga alloy was formed during longer periods of plating, leading to a somewhat complex form of the anodic stripping transient.

The formation of an alloy is indicated in Fig. 4. The lines shown represent consecutive cathodic plating transients, each followed by anodic stripping, as outlined above. The current density increases after each plating cycle and the current efficiency decreases, showing that the increase in current density is due to an enhancement of the rate of hydrogen evolution. The surface could be restored to its original form (*i.e.*, all the alloy could be removed) by setting the potential at a much more positive value of 0.00 V for a short time following anodic stripping at -0.75 V. It was not maintained at this potential for any length of time, since some anodic dissolution of copper could occur.

Current efficiency.—Plots of the average current efficiency for gallium deposition as a function of potential are shown in Fig. 5 for different sized microelectrodes. For the plate and the two largest microelectrodes, the efficiency is low at -1.70 V, has a broad maximum between -1.75 and -1.80 V, and decreases somewhat at higher negative potentials. This behavior is easy to understand. At the lowest negative potentials, one is close to the reversible potential of gallium deposition, and its rate is low and rising slowly (in a linear rather than exponential form) with potential. As the potential reaches -1.75 V, both the gallium deposition and the hydrogen evolution are in the Tafel region and the two partial currents increase to the same extent with potential, leaving their ratio, which is proportional to the current efficiency, essentially constant. It should be noted that the size of the

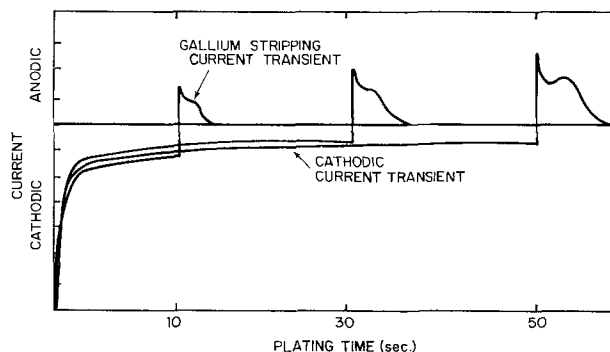


Fig. 3. Three cathodic deposition and following anodic dissolution transients.

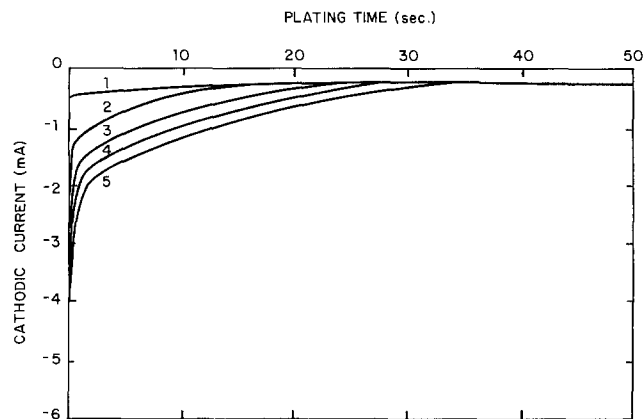


Fig. 4. Consecutive cathodic deposition transients, each followed by anodic stripping. The average current efficiencies (%) were 1-27.6, 2-21.4, 3-17.4, 4-14.7, and 5-13.0.

electrodes has no effect in this range since their radii are large compared to the diffusion layer thickness under the present experimental conditions. The results shown for the smaller microelectrodes ($250 \mu\text{m}$ or less) are more difficult to reconcile with theory. *A priori*, one might have expected the efficiency to increase with decreasing radius of the microelectrode, since gallium deposition is under partial mass-transport control and its rate should increase with decreasing size, while hydrogen evolution is under activation control and hence should not be effected by the size of the electrode. This view, however ignores the effect of IR drop in solution. This can be estimated by considering the partial current densities for hydrogen evolution shown in Fig. 6. The apparent Tafel slopes observed are quite high, in the range of 0.20-0.25V. If one assumes that the correct Tafel slope should be 0.12V, the experimental data can be corrected by making $R_{\text{soln}} = 4.5 \Omega \text{ cm}^2$ for the plate electrode and $0.3 \Omega \text{ cm}^2$ for the microelectrode. While these numbers should only be considered as approximate, they show clearly the important effect of decreasing IR at microelectrodes. It should also be noted that a preliminary estimate of R_{soln} , based on the known geometry of the cell and the conductivity of the solution (0.38 mho cm^{-1}), yielded a value of $9.0 \Omega \text{ cm}^2$ for the plate electrode. For a spherical electrode of the same diameter as the microelectrode used here, a value of $0.011 \Omega \text{ cm}^2$ is calculated, significantly lower than found for the flat disk microelectrode, as expected.

The rate of gallium deposition is partially diffusion controlled and is hence little effected by the decrease in solution resistance. As the radius of the microelectrode is decreased, both partial current densities increase, although for different reasons. The diffusion-limited cur-

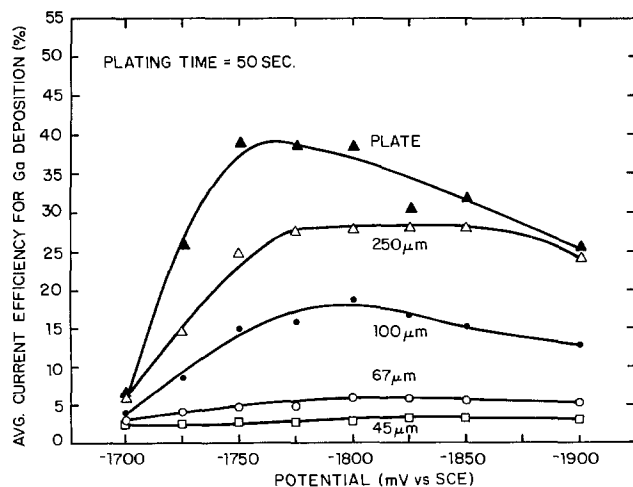


Fig. 5. The effect of the diameter of the electrodes and the potential on the average current efficiency for gallium deposition.

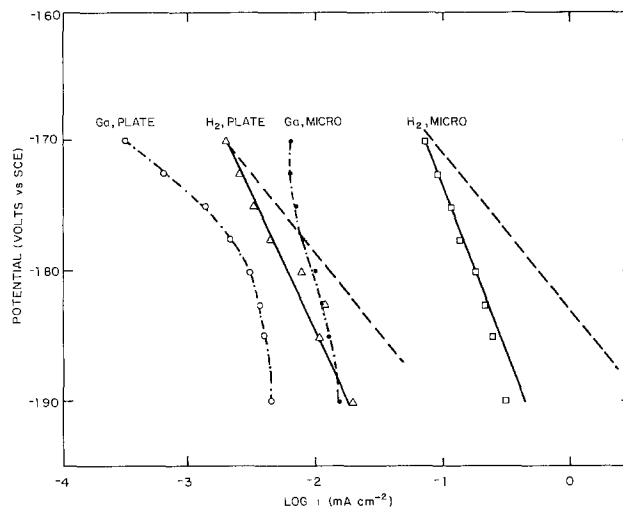


Fig. 6. Partial current densities for hydrogen evolution and for gallium deposition on a plate electrode and on the smallest microelectrodes used in this study ($r = 22.5 \mu\text{m}$). Dotted lines are obtained by assuming $R = 4.5$ and $0.30 \Omega \text{ cm}^2$ for the plate and the microelectrode, respectively.

rent density for gallium deposition increases as expected according to Eq. [1] and [2]. At the same time, the IR drop in solution is decreased (13, 14), leading to an increased rate of hydrogen evolution. The latter can depend on a number of factors, including cell geometry and the conductivity of the electrolyte. The results shown in Fig. 5 evidently indicate that in the present experiment the latter effect was predominant.

The large increase of current density for hydrogen evolution for the microelectrodes shown in Fig. 6 cannot be explained on the basis of the change in solution resistance alone. It is probably a catalytic effect occurring at the boundary between the metal and the surrounding epoxy matrix and silane binder. (It could be, for example, that gallium cannot wet this region, leaving a free copper surface on which hydrogen evolution can occur much faster). This effect has not been studied quantitatively.

It is of interest to consider the way in which the two partial current densities would change with a further decrease in the size of the microelectrode. When δ/r is very large, the partial current for gallium deposition increases as $1/r$ without limit, according to Eq. [2]. The solution resistance for unit area tends to zero under these conditions, but this can increase the hydrogen evolution rate only to the value corresponding to the Tafel line in Fig. 6. Thus one would expect that the current efficiency would go through a minimum at a certain value of the diameter of the microelectrode, and then increase with further decreases in diameter. The size of the microelectrode for which this minimum will occur depends on experimental conditions, as pointed out above. It is indeed possible that the smallest microelectrodes used in this study fall in the region of this minimum, since the radius of $22.5 \mu\text{m}$ was not sufficiently small, compared to the diffusion layer thickness, to cause a very large increase in diffusion-limited current density, as seen from Eq. [2].

Conclusions

Electrolytic recovery of gallium from dilute solutions in concentrated alkaline has been demonstrated experimentally. The rate of recovery (*i.e.*, the partial current density for gallium deposition) was found to be higher on microelectrodes than on large plate electrodes. This result is particularly significant in view of the fact that the microelectrodes were not really very small, the radius of the smallest being only $22.5 \mu\text{m}$, about the size of the diffusion layer thickness. It was shown recently (13, 27) that ensembles of microelectrodes would become very effective, compared to large electrodes, only when the radius of each microelectrode was of the order of $3 \mu\text{m}$ or even less. This is true when the ensemble is considered for

electroanalytical applications and its performance is compared to pulse polarography, which is itself a powerful tool in electroanalytical chemistry. For metal recovery, it was shown in the present work that the advantage of ensembles of microelectrodes becomes apparent already when the radius of each microelectrode is $50\ \mu\text{m}$ and their relative efficiency increases sharply as the radius decreases further. Carbon fibers used in fiber epoxy composites have radii in the range of $3\text{--}5\ \mu\text{m}$. Thus, a carbon fiber epoxy matrix composite with low fiber loadings (to comply with the requirement that the diffusion layers of adjacent electrodes will not overlap) could serve as a very good and relatively inexpensive ensemble of microelectrodes, which would be highly effective for the recovery of metals from dilute solutions. An effort to fabricate such composite electrodes or other types of ensembles of microelectrodes having even smaller radii of the individual microelectrodes is fully justified in view of their possible application for the recovery of metals and for the purification of industrial effluents containing heavy metal contaminants.

The decrease in current efficiency with decreasing diameter needs further investigation. If this is indeed due to a decrease of the IR drop in solution, as suggested above (12, 13), the current efficiency should reach a minimum, dependent on cell configuration and specific conductivity of the solution, and rise thereafter steadily with decreasing radius, after solution resistance has become insignificant. If the hydrogen evolution reaction is enhanced on the microelectrodes for some other reason (e.g., due to the reduction in the nucleation overpotential associated with hydrogen bubble formation at the edges of the microelectrodes), then an increase of the current efficiency with decreasing radius of the microelectrode may not be observed. In such event, one may still take advantage of the enhanced rate of gallium deposition on ensembles of microelectrodes, combined with suitable highly effective hydrogen inhibitors, to further identify conditions for high rate, high efficiency recovery of the metal from dilute solutions.

Acknowledgment

This work was supported in part by the National Science Foundation under NSF Grant CPE-8119765.

Manuscript submitted Dec. 10, 1984; revised manuscript received Feb. 11, 1985.

The University of Virginia assisted in meeting the publication costs of this article.

REFERENCES

1. P. M. Robertson, B. Scholder, G. Theis, and N. Ibl, *Chem. Ind.*, 459 (1978).
2. G. Van Der Heiden, C. M. S. Rauts, and H. F. Boon, *ibid.*, 465 (1978).
3. F. S. Holland, *ibid.*, 458 (1978).
4. D. Matic, *J. Appl. Electrochem.*, **9**, 15 (1979).
5. Symposium on Ultramicroelectrodes, The Electrochemical Society Meeting, Cincinnati, Ohio, May 6-11, 1984; see Abstracts 382-395, pp. 521-537, The Electrochemical Society Extended Abstracts, Vol. 84-1, Cincinnati, OH, May 6-11, 1984.
6. R. M. Wightman, *Anal. Chem.*, **53**, (9) (1981).
7. O. S. Ksenzhek and G. A. Lobach, *Elektrokhimiya*, **17**, 266 (1981).
8. K. B. Oldham, *J. Electroanal. Chem.*, **122**, 1 (1981).
9. J. B. Flanagan and J. Marcous, *J. Phys. Chem.*, **77**, (8) (1973).
10. K. Aiki and J. Osteryoung, *J. Electroanal. Chem.*, **122**, 19 (1981).
11. T. Gueshi, K. Tokuda, and H. Matsuda, *ibid.*, **89**, 247 (1978).
12. H. Reller, E. Kirowa-Eisner, and E. Gileadi, *ibid.*, **138**, 65 (1982).
13. H. Reller, E. Kirowa-Eisner, and E. Gileadi, *ibid.*, **161**, 247 (1984).
14. H. Reller, Ph.D. Dissertation, Tel-Aviv University, Tel Aviv, Israel (1984).
15. H. A. Laitinen and I. M. Kolthoff, *This Journal*, **61**, 3344 (1939).
16. C. R. Iro, S. Asakura, and K. Nobe, *ibid.*, **119**, 698 (1972).
17. J. C. Myland and K. B. Oldham, *J. Electroanal. Chem.*, **147**, 295 (1983).
18. P. Pint and S. N. Flengas, *This Journal*, **123**, 1042 (1976).
19. L. Nacamulli and E. Gileadi, *J. Appl. Electrochem.*, **12**, 73 (1982).
20. B. Scharifker and J. G. Hills, *J. Electroanal. Chem.*, **130**, 81 (1981).
21. A. J. Bard, *Anal. Chem.*, **33** (1961).
22. T. Pavlopoulos and T. D. H. Strickland, *This Journal*, **104**, 116 (1957).
23. M. A. Dayton, J. C. Brown, K. J. Stutts, and R. M. Wightman, *Anal. Chem.*, **52**, 946 (1980).
24. G. Stafford, Ph.D. Dissertation, University of Virginia, Charlottesville, VA (1981).
25. M. Sachyani, M.Sc. Dissertation, Tel-Aviv University, Tel Aviv, Israel (1980).
26. G. E. Stoner, G. L. Cahen, Jr., M. Sachyani, and E. Gileadi, *Bioelectrochem. Bioenergetics*, **9**, 229 (1982).
27. H. S. Harned and B. B. Owen, "Physical Chemistry of Electrolytic Solutions," ACS Monograph, American Chemical Society, Washington, DC (1958).
28. H. Reller, E. Kirowa-Eisner, and E. Gileadi, Abstract 392, p. 532, The Electrochemical Society Extended Abstracts, Vol. 84-1, Cincinnati, Ohio, May 6-11, 1984.
29. J. O. Howell and R. M. Wightman, Abstract 385, p. 525, The Electrochemical Society Extended Abstracts, Vol. 84-1, Cincinnati, Ohio, May 6-11, 1984.

Performance Predictions for Solar-Chemical Converters Based on Photoelectrochemical I-V Curves

J. D. Luttmmer*

Texas Instruments, Incorporated, Dallas, Texas 75265

Isaac Trachtenberg*

Department of Chemical Engineering, University of Texas, Austin, Texas 78712

ABSTRACT

Texas Instruments' solar energy system contains a solar-chemical converter (SCC) which converts solar energy into chemical energy via the electrolysis of hydrobromic acid (HBr) into hydrogen (H_2) and bromine (Br_2). Previous predictions of SCC performance have employed electrical dry-probe data and a computer simulation model to predict the H_2 generation rates. The method of prediction described here makes use of the photoelectrochemical I-V curves to determine the "wet"-probe parameters of V_{OC} , J_{SC} , FF, and efficiency for anodes and cathodes. The advantages of this technique over the dry-probe/computer simulation method are discussed. A comparison of predicted and measured H_2 generation rates is presented. Solar to chemical efficiencies of 8.6% have been both predicted and measured for the electrolysis of 48% HBr to hydrogen and bromine by a full anode/cathode array. Individual cathode solar to hydrogen efficiencies of 9.5% have been obtained.

Texas Instruments' solar energy system contains a solar-chemical converter (SCC) which converts solar energy into chemical energy via the electrolysis of hydrobromic acid into hydrogen and bromine (1-5). Figure 1 illustrates the various processes which occur in the SCC. Photons from the sun are absorbed by the spherical silicon solar cells either directly or by reflection and scattering from the SCC matrix. Hydrogen and bromine are simultaneously generated at metal electrodes deposited on the n/p (cathode) solar cells and on the p/n (anode) solar cells as electrons flow through the back-side conductor.

Previous evaluations and quality control required fabrication of completed arrays followed by actual hydrogen-generation tests. In most instances, either the anode cells or the cathode cells were limiting the performance of the SCC array. The hydrogen data alone were not sufficient to determine which electrode was in fact limiting. Predictions of SCC performance were then made based on dry probe data (V_{OC} , I_{SC} , and FF) of a small sampling of the cells and a complex computer simulation model (3, 5). The computer model included algorithms which described the relationships between the electrical characteristics of the individual solar cells, the assumed electrochemical behavior of the front-side electrodes, and the resistance parameters associated with the electrolyte, back-side conductor, membrane separator, and SCC panel geometry. This approach toward predicting the SCC performance was complicated by the difficulty encountered in measuring the electrical characteristics of a statistically significant number of solar cells and in estimating or measuring the area and activity of the electrodes on the solar cells. A prediction method is described where photoelectrochemical I-V curves are used with a simplified model to predict hydrogen generation rates and the performance of the SCC. This method also allows for the pairing of individual anode and cathode array sections in order to optimize the performance of a given anode/cathode combination for HBr electrolysis.

Experimental

The SCC arrays used in these experiments consisted of near-single-crystalline silicon spheres, each of 380-400 μm diam. Typically, SCC arrays are fabricated to include only anode cells or only cathode cells. The cells are cast and fired in a glass matrix with a center-to-center sphere spacing equal to 2.2 sphere radii, yielding more than 600 cells for each square centimeter of array area. The thin film electrodes on the front surface of the solar cells con-

sist of platinum/iridium alloy (7:3), sputter deposited as equatorially positioned bands around the individual solar cells. The electrode thickness is 100-400 \AA . The cores of the solar cells are interconnected on the back side of the SCC array with a thick, corrosion-resistant, sputtered tantalum film. For hydrogen-generation measurements, anode and cathode sections with a total area of 38-40 cm^2 were interconnected and mounted on a conductive substrate with conductive adhesive.

Hydrogen generation rate measurements for complete arrays which include both anode and cathode cells were accomplished by immersing the arrays in a quartz fixture which contains 48% hydrobromic acid. The fixture was illuminated with a solar simulator incorporating multiple ELH-type tungsten-halogen lamps. The insolation at the fixture was calibrated with a NBS traceable Si solar cell to air mass 1 (100 mW/cm^2). The spectral mismatch between the solar simulator and air mass 1 is less than 5% as measured with a LICOR 1800 spectroradiometer. Hydrogen was collected for 4 min, and the hydrogen generation rate was calculated from the gas volume.

The photoelectrochemical behavior of SCC array sections was determined with the test cell illustrated in Fig 2. Electrical contact was made to the back-side conductor by a clip along one edge of the array section. Selected areas of the array were masked off with photoresist. Typically, array areas of 5-10 cm^2 containing thousands of solar cells were evaluated with each determination. The three-electrode configuration included a hydrobromic

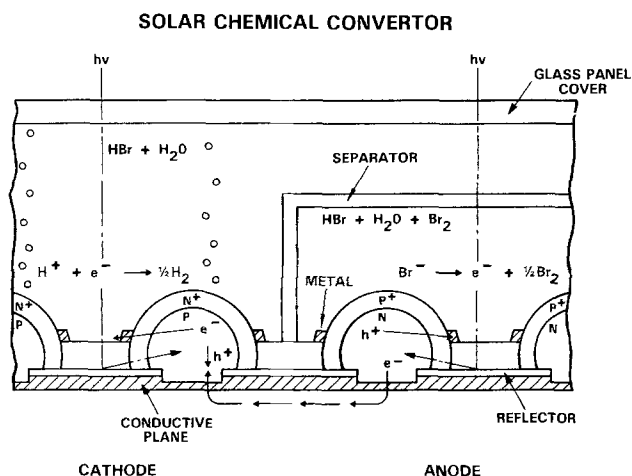


Fig. 1. Texas Instruments' solar-chemical converter

*Electrochemical Society Active Member.

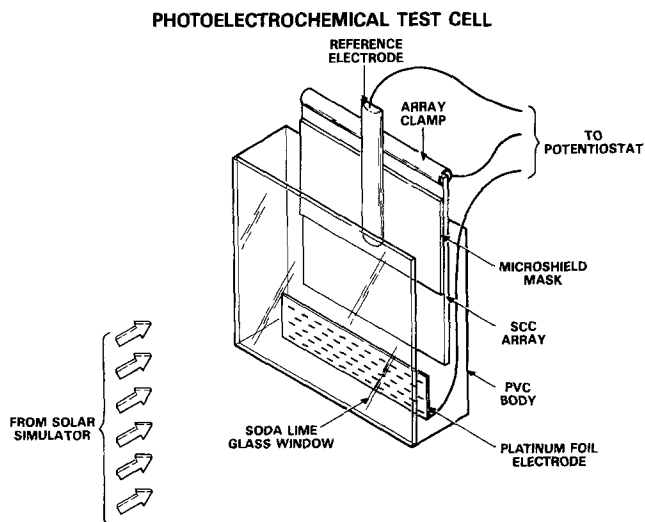


Fig. 2. Photoelectrochemical test cell

acid/bromine (6.9M/1.0M) reference electrode and a large platinum foil counterelectrode placed just outside the optical path of the multiple lamp solar simulator. Current-potential scans were obtained with a computer-driven ECO Model 555/B potentiostat at a scan rate of 40 mV/s in various hydrobromic acid/bromine mixtures (8.9 eq/liter). The electrochemical cell resistance was determined either by current interruption or from the slope of the current-voltage curve when the sections were strongly forward biased in the electrolyte (+10V for cathode cells, -10V for anode cells). Computer-plotted and -stored current-potential data were corrected for the photoelectrochemical cell resistance and normalized to the current density of the array section. The current density on the individual solar cell electrodes is typically ten times larger than the array section current density since the ratio of the electrode area to the projected array section area is approximately 1:10.

The condensed, normalized, and resistance-corrected data were transmitted to a main frame computer system for additional SCC system performance modeling. A simplified computer model calculated the SCC performance from the photoelectrochemical data and various re-

sistance parameters associated with the electrolyte, the back-side conductor, the membrane separator, and the panel geometry.

Results and Discussion

Typical photoelectrochemical behavior of SCC array anode and cathode sections in hydrobromic acid/bromine solutions is given in Fig. 3 and 4. From the photocurrent-potential curves, wet-probe parameters including open-circuit voltage, short-circuit current, fill factor, and efficiency are obtained for separate anode and cathode sections. These values are readily measured relative to the bulk electrochemical potential of the anolyte and catholyte. The potential values in these examples are -81 and -756 mV vs. the reference electrode for the anolyte and catholyte, respectively.

The increase in current observed on the cathode cells at potentials more negative than the electrochemical potential of the bulk catholyte results from a small number of leaky and shorted solar cells among the cathode cells of good quality. Analogous behavior is not observed on photoelectrochemical scans with anode sections. The poor quality anode cells have been selectively passivated. No attempt was made to passivate poor quality cathode cells, since they have little detrimental effect on the performance of the cathode section when used to reduce hydrobromic acid. Shorted or low V_{oc} cells among the anode cells can severely degrade the performance of the anode section, especially at high anolyte bromine concentration (> 300 mM), since they consume rather than generate bromine.

The observed photoelectrochemical response of a typical anode and cathode section is compared with the calculated response in Fig. 5. The calculated response was obtained with the previous computer simulation model which utilized dry-probe data for a multitude of individual solar cells (3, 5). The anode and cathode sections are readily matched to obtain the operating current density of complete arrays, which incorporate both section types. The operating current density is given where the anode and cathode photoelectrochemical response curves intersect. The calculated and observed response are in good agreement, especially along the current-limited regions of the photoelectrochemical curves and at the operating

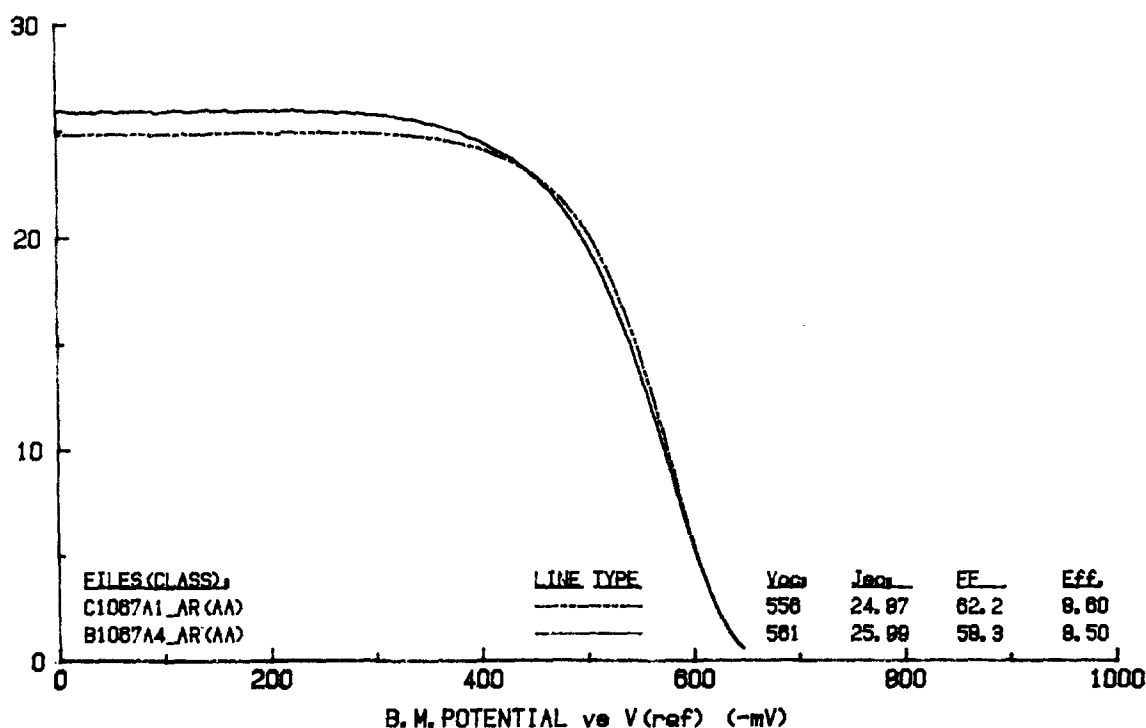


Fig. 3. Photoelectrochemical behavior of anode SCC sections: array current density vs. potential of the back-side metal conductor. Electrolyte contains 0.05M bromine + 8.8M HBr.

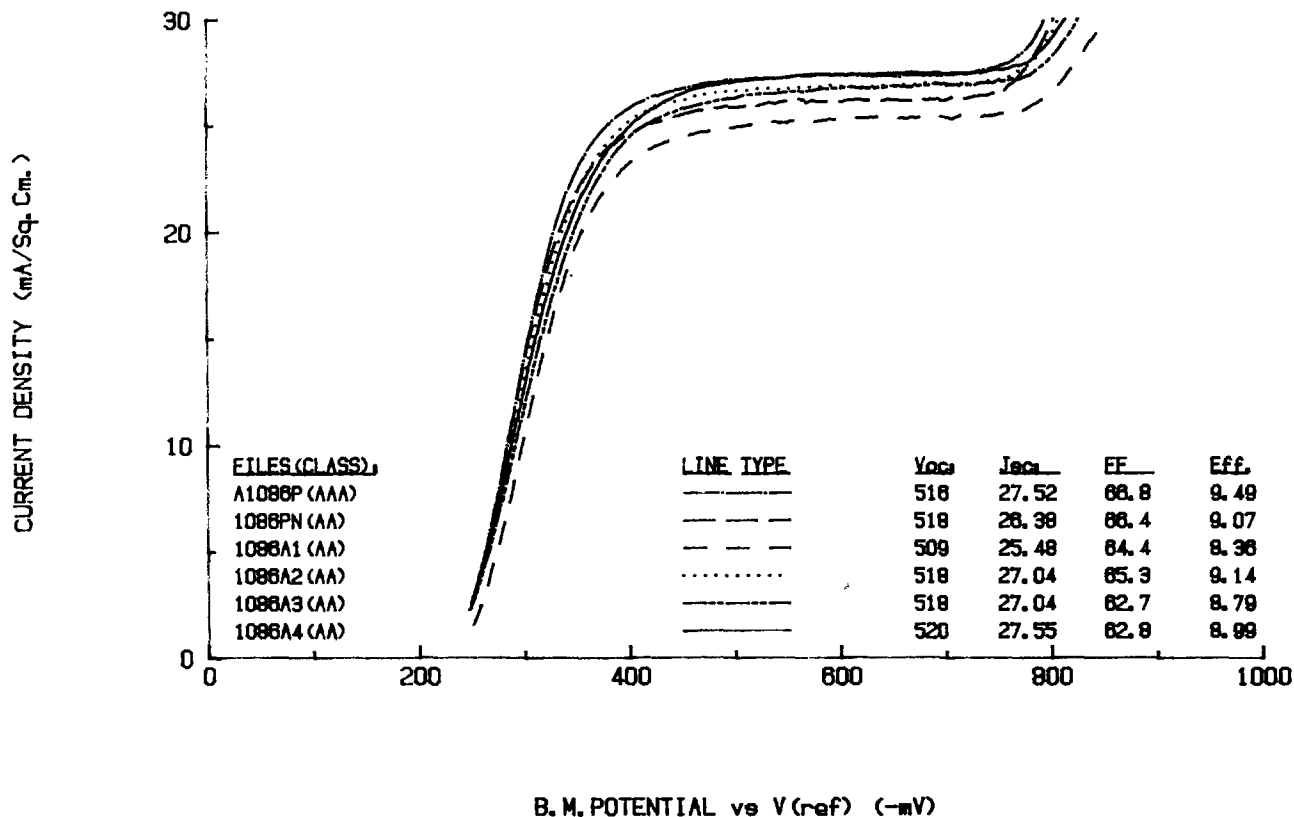


Fig. 4. Photoelectrochemical behavior of cathode SCC sections: array current density vs. potential of the back-side metal conductor. Electrolyte is 8.9M HBr.

point of the combined anode/cathode array. Some small error is observed in the calculated response along the voltage limited regions of the curves. The error primarily arises from two sources: the dry-probe sampling error and the error encountered in estimating the area and activity of the platinum/iridium electrodes on the individual solar cells. Typically, less than 1% of the individual cells are probed to obtain representative values of V_{oc} , I_{sc} , and FF.

Table I compares the hydrogen generation rates of several complete SCC arrays. The table includes the experimentally measured values, the values predicted from the photoelectrochemical behavior of the separate anode and cathode sections, and the values predicted from the dry-probe data/computer simulation model. Excellent agreement is found among the two prediction techniques and the observed SCC array performance. The best individual hydrogen generating cathode section fabricated had a

solar-to-chemical efficiency of 9.5%. The efficiency for individual array sections is defined as the product of the wet-probe J_{sc} , V_{oc} , and FF. In combination with the best bromine generating anode section, the best HBr electrolysis efficiency obtained was equivalent to a solar-to-chemical efficiency of 8.6%. In this case, the efficiency is defined as the product of the operating current density and the difference in the electrochemical potential of the bulk anolyte and the bulk catholyte divided by the incident light power (100 mW/cm^2).

The advantage of the photoelectrochemical method is that it encompasses the actual electrochemical activity of the front-side electrodes and the electrical characteristics of a multitude of individual solar cells in a single measurement. Consequently, sampling errors are reduced by this method. A larger number of solar cells are more readily characterized by the photoelectrochemical method since the dry-probe method requires that individual solar cells be probed. Anode and cathode SCC sections can be

PHOTOELECTROCHEMICAL BEHAVIOR

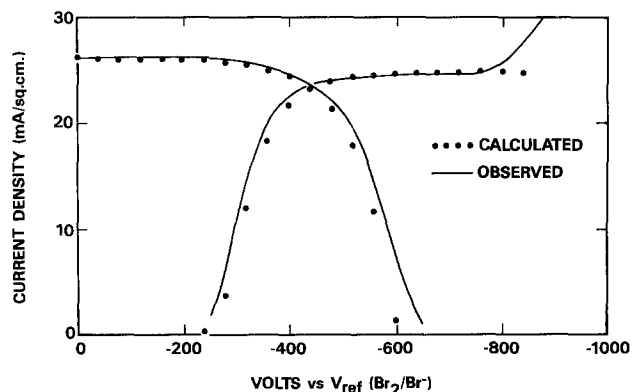


Fig. 5. Comparison of observed and calculated photoelectrochemical response. Anolyte contains 0.05M bromine + 8.8M HBr. Catholyte is 8.9M HBr.

Table I
SCC ARRAY EVALUATION
 H_2 GENERATION RATES (mL/hr)

ARRAY	H_2 QUICK TEST MEASURED	ELECTROCHEMICALLY PREDICTED	DRY PROBE COMPUTER SIMULATION PREDICTION
1015-A2	153	155	151
1015-A3	157.5	149	154
1015-PN	156	159	158
1018-A1	159	158	159
1018-A2	157.5	154	158
1018-A3	154.5	149	N.D.*
1018-A4	150	159	N.D.
1018-PN	148.5	158	N.D.
1028-A1	151.5	148	146
1036-A1	192	194	183

*NOT DETERMINED

fabricated and evaluated separately without the need to fabricate complete arrays incorporating both cell types and to measure the hydrogen-generation rate. Anode and cathode sections are readily matched by their photoelectrochemical behavior to obtain performance-optimized SCC modules. Additionally, the photoelectrochemical method can be used as a diagnostic tool to evaluate alternate SCC fabrication processes.

Although the dry-probe method is more difficult to use, the dry-probe technique itself serves as a useful diagnostic tool. It is particularly useful in distinguishing between array performance limitations associated with the electrical characteristics of the solar cells and those associated with the electrochemical activity of the front-side electrodes and the electrochemical process. In other words, the dry-probe method gives all the solid-state and electrical data and yields considerable information concerning array processing. It is a very good quality-control tool for the array-fabrication process. The photoelectrochemical measurements yield information on the electrode and electrochemical characteristics.

Conclusions

Performance predictions for solar-chemical converters are facilitated by investigations of the photoelectrochemical behavior of separate anode and cathode sections. The photoelectrochemical method encompasses the actual electrochemical activity of the front-side electrodes and the electrical characteristics of thousands of individual solar cells in a single measurement and minimizes sampling errors. This method allows for the separate optimization of the design and processing of anode and

cathode array sections. Anode and cathode sections can be evaluated separately and matched by their photoelectrochemical behavior to obtain performance-optimized SCC modules.

Use of the solar-chemical converter is not restricted to the hydrogen/HBr/bromine system. Different anolytes and catholytes can be examined independently for alternate systems. Likewise, electrodes of other materials can be fabricated on the anode or cathode cells and tailored for performance-optimized array sections. By changing the electrodes, electrolytes, or even the types of solar cell spheres (such as GaAs), a wide variety of photoelectrochemical systems can be investigated.

Manuscript submitted Nov. 7, 1983; revised manuscript received Feb. 4, 1985.

Texas Instruments, Incorporated assisted in meeting the publication costs of this article.

REFERENCES

1. E. L. Johnson, in "IEEE Proceedings of the International Electron Devices Meeting," pp. 2-5, IEEE, New York (1981).
2. I. Trachtenberg, "The Texas Instruments Solar Energy System", presented at the AS/ISES Conference, Houston, TX, June 1982.
3. J. D. Luttmir and I. Trachtenberg, Paper 448 presented at the Electrochemical Society Meeting, Montreal, Que., Canada, May 9-14, 1982.
4. W. R. McKee, K. R. Carson, and J. D. Levine, "Development and Evaluation of the Texas Instruments Solar Energy System," presented at the 16th IEEE Photovoltaic Specialists Conference, San Diego, California, September 1982.
5. J. D. Luttmir and I. Trachtenberg, Submitted to *This Journal*.

Investigation of Electroreduction Kinetics on Modified p-InP in Alkaline Electrolyte

Ronald L. Cook,* Patrick F. Dempsey, and Anthony F. Sammells*

Eltron Research Incorporated, Aurora, Illinois 60505

ABSTRACT

The electroreduction kinetics of surface modified p-InP were investigated. The surface was modified by electro-deposition of Co, Ru, Rh, Pt, Co/Pt, Ru/Pt, and Rh/Pt. Exchange current densities (i_0) for hydrogen evolution were obtained both in the dark and under 100 mW/cm² illumination. For sequentially deposited metals, i_0 values are lower compared to individually deposited metals during hydrogen evolution. Cathodic currents observed positive of the hydrogen-evolution region can be explained by electron-transfer processes involving p-InP surface states. In this latter potential region, i_0 values are higher for the sequentially deposited metals.

In optimizing the efficiency for light to chemical conversion for hydrogen evolving photocathodes such as p-InP, attention must be paid to two surface-related processes which can influence overall photoelectrochemical (PEC) performance. The first of these is the presence of extrinsic surface states which can act as recombination centers for the radiationless recombination of the photo-generated electrons and holes. If appropriate surface modification of the semiconductor is not performed to suppress the activity of such recombination centers, then there will be little opportunity for electron transfer to occur across the semiconductor/liquid junction to promote the desired hydrogen-evolution reaction. The second surface process relates to the electrocatalysis of the hydrogen-evolution reaction.

Clearly, the photogenerated electron, once successfully reaching the liquid junction interface, must find an appropriate catalytic site favoring this reaction. Here, the free energy associated with the formation and cleavage of the metal-hydrogen bond at the catalytic site plays a criti-

cal role in determining overall reaction kinetics. As is well documented, platinum group metals have metal-hydrogen bond strengths in the 15 kJ mol⁻¹ range which permits significant coverage of the catalytic site but does not impede cleavage of the M-H bond (1).

Here, the role of surface modification procedures on photoelectrodes should ideally fulfill the dual role of suppressing surface recombination sites and enhancing the kinetics for the desired photoelectrochemical (PEC) reaction.

For p-InP present in strong aqueous acids, a stable hydrated layer of In₂O₃ is present which can serve to effectively suppress electron-hole recombination (2, 3). Such oxide surfaces are not suited, however, for the promotion of the hydrogen evolution reaction. Hence, introduction of platinum group metals onto the p-InP surface favors the kinetics for this reaction (4). For Rh and Re, hydrogen evolution results in the formation of hydrogen alloys which can serve to increase the barrier of the modified p-InP, resulting in greater photopotentials and consequently larger overall solar efficiencies.

*Electrochemical Society Active Member.

The photoelectrolysis of strongly acidic aqueous solutions might introduce severe materials restraints, particularly at the oxygen evolution site. For this reason, we have recently started to investigate the PEC characteristics of p-InP in strongly alkaline electrolytes (5). For such electrolytes, however, the strategy of suppressing surface states via the *in situ* formation of a hydrated metal oxide, by analogy to the acid electrolyte case, is probably not valid. As a consequence, we have investigated various alternative approaches for both the simultaneous suppression of such surface states and enhancement of the electron-transfer step leading to hydrogen evolution. This work resulted in the identification of a 14.2% efficient p-InP photocathode (as calculated from power savings) after surface modification by the sequential electrodeposition of cobalt and platinum. Similar enhancements in PEC behavior have also been observed by us after surface modification with ruthenium/platinum and rhodium/platinum codeposits. Since in 6M KOH surface oxides can be expected to be largely absent from the p-InP surface, the question remains as to what is the apparent role of such surface modifications on the suppression of surface states. It has recently been shown from photocapacitance measurements (6) that the initial density of interface states present near the valence band can be significantly reduced after the sequential electrochemical deposition of cobalt and platinum and, in addition, introduces a surface state close to the conduction band associated with the metallic absorbate. This latter introduced state probably facilitates the electron-transfer step leading to hydrogen evolution during illumination.

If one of the roles of such bimetallic surface modifications is essentially electrocatalytic in nature for the hydrogen evolution process, then it is to be expected that there should be some correlation between exchange current density (i_0) as measured during hydrogen evolution and the nature of the metal introduced onto the p-InP surface. In addition, further electrode kinetic information relating to the presence or suppression of surface states might be obtained from steady-state measurements made on p-InP at potentials positive of the hydrogen evolution reaction. Such measurements can be made under cathodic bias conditions since the equilibrium potential of p-InP in alkaline electrolyte is significantly positive of that for the hydrogen evolution reaction.

In order to pursue this overall approach, we have measured exchange current densities on p-InP photocathodes both unmodified and modified with Co, Pt, Rh, Ru, Co/Pt, Ru/Pt, and Rh/Pt at potentials both positive and negative of the hydrogen evolution potential. These investigations were performed both with and without 100 mW/cm² ELH illumination. In the hydrogen evolution region, exchange current densities were obtained directly from the Tafel relationship. Cathodic processes occurring at potentials below the inception of hydrogen evolution may well be due to electron transfer via surface states involving metal oxides or hydroxides present at the liquid junction. In this second potential region, kinetic information was obtained via the use of the Allen-Hickling relationship (7)

$$\log \frac{i}{1 - \exp(nF\eta)} = \log i_0 - \frac{anF\eta}{2.3RT} \quad [1]$$

where i_0 is the exchange current density, and the other symbols have their usual significance. Here, by plotting $\log(i/[1 - \exp(nF\eta)])$ vs. η , i_0 can be obtained directly from the current axis intercept.

By comparing i_0 data for these two distinct electrochemical processes, some insight into the respective role of p-InP surface modifications on both the suppression of surface states and enhancement of the electron-transfer step leading to hydrogen evolution can be gained.

Experimental

p-InP was obtained from Varian Associates (VAIPC no. 109, Zn-doped, 1.27×10^{17} cm⁻³). Electrodes typically had

electrode areas of 0.06 cm². The (100) face was used in all experiments. Ohmic contact was performed by initially etching with concentrated HCl followed by rinsing with distilled water. To this was sequentially vacuum-deposited Au, Zn, and Au layers followed by annealing under hydrogen at 400°C for 1h. Current collection was achieved using a nickel wire contacted via silver epoxy and curing. Surface modifications of p-InP were achieved by electrodeposition from 1M solutions of the appropriate acidic chloride salt. Typical current densities varied between 0.09 and 0.11 mA/cm².

The electrolyte was 6M KOH in all experiments. A three-electrode configuration was used with platinized platinum as the counterelectrode and a SCE reference electrode connected via a salt bridge. The light intensity was 100 mW/cm² from a Sylvania 300W ELH bulb. The light intensity was measured with an Eppley 8-48 pyranometer. PEC measurements were made via the use of a Stonehart BC 1200 potentiostat and data recorded on a Linear Instruments 8036XY recorder.

Results and Discussion

Initial equilibrium potentials for single-crystal p-InP both with and without surface modification were initially in the range -500 to -600 mV vs. SCE after introduction into 6M KOH electrolyte. Following hydrogen evolution on the surface modified p-InP, rest equilibrium potentials were generally found to be in the -900 to -950 mV range. The cathodic shift in potential realized here after hydrogen evolution is probably a result of either formation of a metallic hydrogen alloy or surface adsorbed hydrogen species. In the absence of hydrogen evolution, the initial rest potential of ≈ -600 mV was shifted to ≈ -400 mV vs. SCE under 100 mW/cm² illumination. p-InP photocathodes were surface modified with Co, Pt, Rh, Ru, Co/Pt, Ru/Pt, and Rh/Pt by electrodeposition. Deposits were not uniform but more in the form of islands. Their nominal "thickness" was 100Å, however. These surface modified photoelectrodes were subjected to current-voltage measurements up to -1000 mV from the initial rest potential both with and without illumination.

A typical Tafel-type plot under illumination for ruthenium-modified p-InP is shown in Fig. 1. Here, the linear portion of the curve starts at an overpotential of -400 mV and corresponds to the hydrogen evolution region. Figure 2 shows a typical current-overpotential curve for platinum-modified p-InP in the dark. The i_0 data obtained here for these various modified photocathodes in 6M KOH are summarized in Table I. As can be seen, all

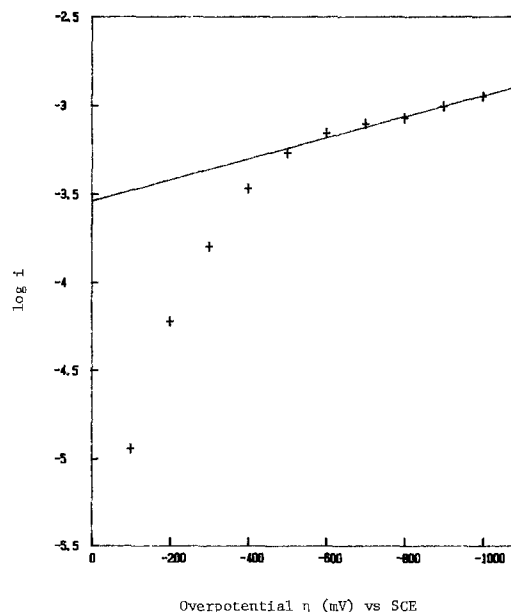


Fig. 1. Current-voltage curve for p-InP surface modified by 100Å ruthenium under 100 mW/cm² ELH illumination.

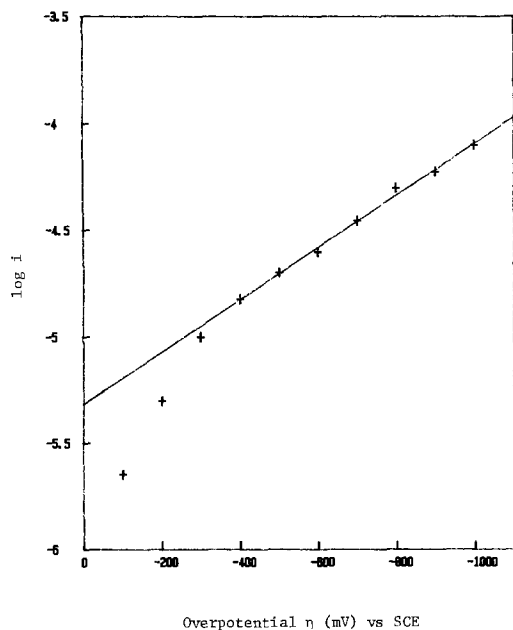


Fig. 2. Current-voltage curve for p-InP surface modified by 100Å Pt in the dark.

metallic surface modifications resulted in increased i_0 values for the hydrogen evolution region.

In the dark, currents were in the microampere per square centimeter range. Upon illumination, the minority carrier concentrations are substantially increased and the observed currents are in the milliampere per square centimeter range.

For p-InP, the increase in i_0 for hydrogen evolution on modification with platinum group metals appears to be essentially electrocatalytic in nature. For p-InP surface modified with individual metals, measured i_0 values for hydrogen evolution were found to be in the order $Rh > Rh \approx Pt > Co > \text{unmodified}$. For the sequentially surface modified p-InP, however, the exchange currents are similar or lower in value than those observed on p-InP modified by the individual metals. This is in contrast to the observed improvement in PEC performance for p-InP surface modified by sequentially deposited cobalt and platinum (5). This suggests that although photoelectrocatalytic phenomena are expected to have a dominant

Table I. Exchange currents for hydrogen evolution on modified p-InP in 6M KOH (Tafel region)

p-InP surface modification	Dark ($\mu\text{A}/\text{cm}^2$)	100 mW/cm ² (mA/cm ²)
Unmodified	3.2	0.025
Co	3.65	0.327
Ru	5.69	5.68
Rh	9.71	8.08
Pt	5.45	6.3
Co/Pt	1.20	0.89
Ru/Pt	1.23	6.68
Rh/Pt	2.56	6.85

Table II. Exchange currents for surface-modified p-InP electrodes in 6M KOH (Allen-Hickling region)

p-InP surface modification	Dark i_0 ($\mu\text{A}/\text{cm}^2$)	100 mW/cm ² i_0 ($\mu\text{A}/\text{cm}^2$)
Unmodified	0.58	5.38
Co	0.485	1.98
Ru	2.65	11.7
Rh	3.22	65.7
Pt	18.7	71.0
Co/Pt	3.47	17.0
Rh/Pt	12.7	136.7
Rh/Pt	10.2	148.7

role in influencing the photocurrent-voltage characteristics for hydrogen evolution on surface-modified p-InP, other factors such as the presence or absence of surface states might also be influential in dictating overall performance.

Differential capacitance studies on surface-modified and unmodified p-InP have indicated that the p-InP flatband potential remains relatively constant. Recent photocapacitance measurements have, however, shown that surface modification of p-InP with Co/Pt appeared to reduce the density of energy levels in the bandgap near the valence band and introduce new states near the conduction band (8). Such an observation could in part explain the improved fill factors found for Co/Pt modified p-InP by suppressing recombination at the semiconductor surface.

For p-InP surface modified with Co/Pt, Rh/Pt, or Ru/Pt, it appears that improved PEC performance may be influenced by both electrocatalytic and surface state recombination effects. Improvements in photocurrent-voltage behavior were observed for p-InP surface modified by Ru/Pt and Rh/Pt where increases of 20% were observed in fill factors on going from p-InP surface modified by single metals to sequential modification by two platinum group metals.

The large overpotential (with respect to the flatband potential) required for hydrogen evolution has been observed by others for p-InP (9), p-GaAs (10), and p-GaP (11). It has been suggested that surface recombination and trapping of electrons in these systems may be responsible for the large observed overpotential for hydrogen evolution (10). In view of photocapacitance results which indicate that surface-state recombination may be significantly suppressed by the sequential deposition of platinum group metals onto the p-InP surface, we have, in addition, investigated the photocurrent-voltage behavior of these electrodes at potentials positive of the inception of hydrogen evolution. In this potential region, cathodic currents may be explained by electron-transfer processes via surface states, possibly involving metal oxides or hydroxides present at the liquid junction.

Figures 3 and 4 show the current-overpotential curves for p-InP surface modified by Ru (illuminated) and Pt (dark). As anticipated from Eq. [1] plotting $\log(i/[1 - \exp(nF\eta)])$ vs. η is linear in the overpotential region 0-100 mV cathodic of the equilibrium potential. Table II gives i_0 values for p-InP modified with Co, Pt, Rh, Ru, Co/Pt, Ru/Pt, and Rh/Pt in this potential region (with respect to the flatband potential).

Here, i_0 values do not follow the same order seen in the hydrogen-evolution region. In general, the sequentially

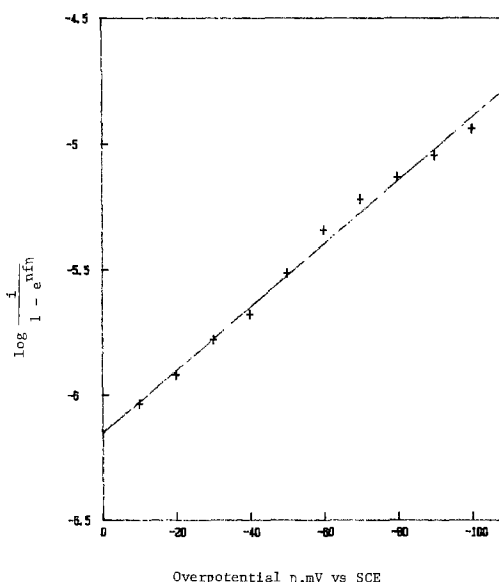


Fig. 3. Allen-Hickling plot for p-InP surface modified by 100Å of ruthenium under 100 mW/cm² ELH illumination.

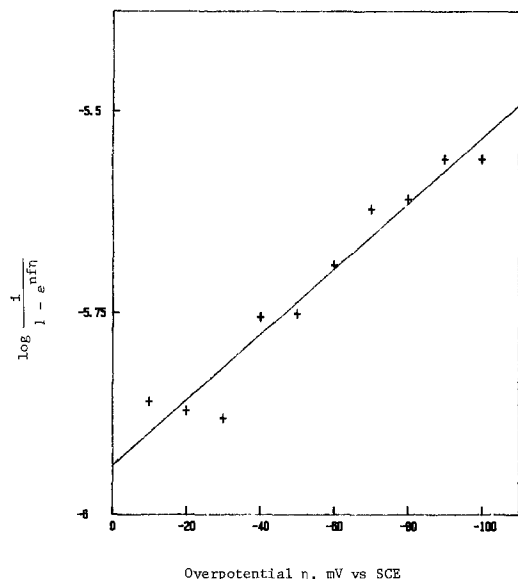


Fig. 4. Allen-Hickling plot for p-InP surface modified by 100Å of platinum in the dark.

deposited metals give higher exchange currents than the respective single metals. The higher exchange currents observed for the sequentially deposited metals are consistent with other results observed on p-InP by us. On going from p-InP modified with Co, Ru, or Rh to the sequentially deposited metals (Co/Pt, Ru/Pt, Rh/Pt) an increase in the fill factor of $\approx 20\%$ can be generally observed. The higher exchange currents, fill factors, and the photocapacitance results are all consistent with an increased suppression of surface-state recombination when p-InP is modified by the sequential deposition of Co/Pt, Ru/Pt, and Rh/Pt.

For electron transfer via surface-state energy levels, the exchange current is given by (10)

$$i_{ss0} = k_s C N_t f \quad [2]$$

where k_s is the rate of electron transfer to the solution from the surface state, C the concentration of redox species in solution, N_t is the total number of surface states, and f the fraction of surface states occupied by electrons. If n_t is defined as the number of electrons in the surface state, then f becomes n_t/N_t , and

$$i_{ss0} = k_s C n_t \quad [3]$$

The change in the number of electrons in the surface state in terms of the schematic energy level diagram shown in Fig. 5 will be determined by (i) the rate of capture of electrons from the conduction band, (ii) the rate of hole capture from the valence band, and (iii) the rate of transfer of electrons to the solution redox species. Thus

$$\frac{dn_t}{dt} = k_n(n_s[N_t - n_t]) - k_p(p_s n_t) - k_s n_t C \quad [4]$$

where k_n is the rate of electron capture from the conduction band, n_s is the surface electron density in the conduction band, k_p and p_s are the rate of hole capture by the surface state and the concentration of holes in the valence band, respectively. At steady state ($dn_t/dt = 0$), Eq. [4] can be solved for n_t to give

$$n_t = N_t \left(\frac{k_n n_s}{k_n n_s + k_p p_s + k_s C} \right) \quad [5]$$

Equation [5] can be inserted into Eq. [3] to give the dependence of the surface state current i_{ss0} on the electron concentration in the conduction band and the hole concentration in the valence band. Thus

$$i_{ss0} = N_t \left(\frac{k_s C k_n n_{s0}}{k_n n_{s0} + k_p p_{s0} + k_s C} \right) \quad [6]$$

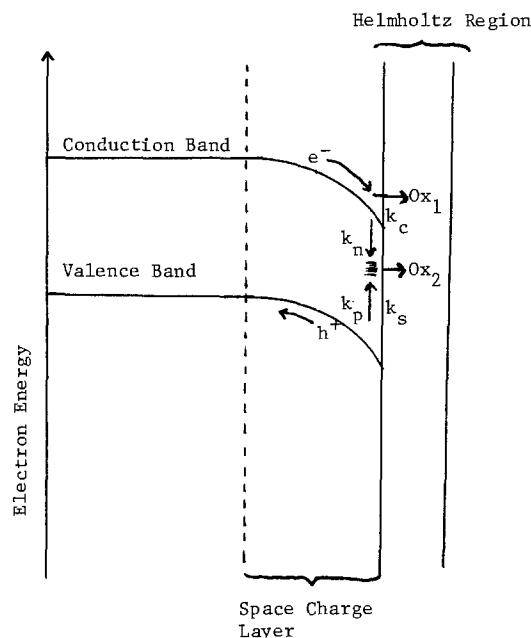


Fig. 5. Schematic energy level diagram representing electron transfer from p-InP to electrolyte via either the conduction band or surface states.

When the surface state is close to the conduction band, recombination may be negligible and the exchange current density would be determined by the electron density present in the conduction band, the concentration of the redox species at the interface, and the relative values of k_s and k_n . For surface modified p-InP in this work, it is not clear how k_s correlates with the observed exchange current in the low overpotential region. It appears, however, that for p-InP modified with Co/Pt, Rh/Pt, and Ru/Pt, the larger i_0 values are due to increases in k_n and a decrease in k_p . This may be due to the suppression of surface states near the valence band edge and introduction of a new surface state near the conduction band edge.

Although the exchange current densities for hydrogen evolution are smaller for the sequentially deposited metals than for the single metals on p-InP, the fill factors are increased for the sequentially deposited metals, leading to an overall increase in efficiency in these cells. It has been concluded (12) that improving the fill factor may play a larger role in increasing the efficiency than reducing the overpotential. Both our results and those obtained separately with a Co/Mo modified p-InP photocathode (13) are consistent with this conclusion.

Acknowledgment

Funding by the Gas Research Institute under Contract no. 5082-260-0671 is gratefully acknowledged.

Manuscript submitted July 30, 1984; revised manuscript received Feb. 14, 1985.

Eltron Research, Incorporated, assisted in meeting the publication costs of this article.

REFERENCES

1. D. Pletcher, "Industrial Electrochemistry," p. 32, Chapman Hall, New York (1982).
2. A. Heller and R. G. Vadimsky, *Phys. Rev. Lett.*, **46**, 1153 (1981).
3. A. Heller, R. Aharon-Shalom, W. A. Bonner, and B. Miller, *J. Am. Chem. Soc.*, **104**, 6942 (1982).
4. E. Aharon-Shalom and A. Heller, *This Journal*, **129**, 2865 (1982).
5. P. G. P. Ang and A. F. Sammells, *ibid.*, **131**, 1462 (1984).
6. C. E. Goodman, B. W. Wessels, and P. G. P. Ang, *Appl. Phys. Lett.*, **45**, 4 (1984).
7. P. A. Allen and A. Hickling, *Trans. Faraday Soc.*, **53**, 1626 (1957).
8. A. F. Sammells, B. W. Wessels, P. M. Raccach, P. G. P.

- Ang, C. E. Goodman, P. F. Dempsey, and S. K. Schmidt, GRI Quarterly Report on Contract no. 5082-260-0671 May 1984.
9. A. A. K. Vervaet, W. P. Gomes, and F. Cardon, *J. Electroanal. Chem. Interfacial Electrochem.*, **91**, 133 (1978).
10. J. J. Kelley and R. Memming, *This Journal*, **129**, 730 (1982).
11. M. P. Dare-Edwards, A. Hamnett, and J. B. Goodenough, *J. Electroanal. Chem. Interfacial Electrochem.*, **119**, 109 (1981).
12. M. F. Weber and M. J. Dignam, *This Journal*, **131**, 1258 (1984).
13. K. Uosaki and H. Kita, *Chem. Lett.*, 301 (1984).

Structural and Solar Conversion Characteristics of the $(\text{Cu}_2\text{Se})_x(\text{In}_2\text{Se}_3)_{1-x}$ System

J. C. W. Folmer,¹ John A. Turner,* R. Noufi,* and David Cahen²

Solar Energy Research Institute, Golden, Colorado 80401

ABSTRACT

Members of the title system were prepared by direct syntheses and studied by means of x-ray diffraction, electron microprobe analyses, and photoelectrochemistry. We found three new hexagonal phases in the low x region ($0.25 < x < 0.09$), all of which can be understood in terms of Se close packing. They provide indications for the occurrence of polytypism. Two of the three previously reported phases with cubic stacking were found in the less Cu-poor part. This region of cubic stacking extends from at least $x = 0.5$ to $x = 0.23$. CuIn_3Se_5 ($x \approx 0.25$) was found to be the end member of the cubic stacking region, and its frequent recurrence in various synthesis attempts indicates its stability. This compound, as well as all others identified in this study (e.g., $x = 0.15$), were photoelectrochemically active with some variability. Their optical bandgaps all fell between 0.9 and 1.3 eV. Two mixed sulfoselenides were prepared as well. One of them with $x = 0.55$ possessed the normal chalcopyrite structure and a direct optical bandgap that corresponded to what one would expect for such a mixed sulfide-selenide. Close to the nominal stoichiometry CuIn_5X_8 , we did not find the spinel phase as found for $X = \text{S}$; instead, we found two different polytype phases for the pure selenide and the sulfoselenide.

The compound CuInSe_2 is often regarded as a ternary analog of elemental Group IV semiconductors (e.g., Si, Ge) and of binary semiconductors (e.g., GaAs, ZnSe) (1). To support this point of view, the close relationship of its chalcopyrite structure to the diamond and sphalerite structures, from which it can be derived by simple unit cell doubling (because of cation ordering), is often mentioned. The promising photovoltaic and photoelectrochemical properties (2) of CuInSe_2 have stimulated extensive structural, optical, and electronic studies of this and related materials.

To some extent, this effort overshadows the fact that the material is also a member of a rather different family of interesting and versatile, but complicated, materials: the chalcogenides of transition metals, in particular, those of copper. This group of materials often displays a number of remarkable characteristics (3), such as broad homogeneity ranges, order-disorder transitions, strong d-p covalent mixing (4, 5), and fast ionic diffusion (6). Concerning the metal atoms, one often finds complicated structural characteristics, in contrast to a rigidly close-packed arrangement of the chalcogen atoms, albeit in various stackings.

This study represents a first step towards understanding the photovoltaic implications of the solid-state chemistry of CuInSe_2 , particularly where deviations from the 1:1:2 stoichiometry along the $\text{Cu}_2\text{Se-In}_2\text{Se}_3$ tie line are concerned. Results of measurements of some photoelectrochemical properties along this tie line are included as well.

The $(\text{Cu}_2\text{Se})_x(\text{In}_2\text{Se}_3)_{1-x}$ Pseudo-Binary System

From simple valence considerations, it is clear that changing the nonmolecularity parameter, x (7), of the $(\text{Cu}_2\text{Se})_x(\text{In}_2\text{Se}_3)_{1-x}$ system does not necessarily undo the semiconducting properties that are known for CuInSe_2 ($x = 0.5$). Rather, it is the nonstoichiometry parameter, y , describing the deviation of the total metal-to-nonmetal ratio from the ideal value of $2/(3 - 2x)$ that

will strongly affect sign and level of doping of a Cu-In-Se ternary (cf. Fig. 1). Although small variations in the parameter y were observed in our study, we shall limit our discussions to the x parameters.³

The phase diagram data that are used exclusively by the workers in the photovoltaic field covered only part of the title system (8), although recently some additional data have become available (9). The latter results refute the existence of a number of distinct stoichiometric phases purported to exist (10). This is in agreement with part of our own findings. The earlier data show that a two-phase region exists between Cu_2Se and the well-known chalcopyrite phase with x values slightly larger than 0.5. Other recent work (11) indicates that at elevated temperatures an additional phase Cu_5InSe_4 ($x = 0.84$) exists in the copper selenide-rich part of the diagram; unfortunately, its structure is unknown.

For the comparable sulfide system, Binsma and co-workers reported a tentative diagram (12) in which one other definite phase besides the chalcopyrite was identified, viz., the spinel phase CuIn_5S_8 ($x = 0.167$). This material has shown some photovoltaic merit (13). A narrow range of stoichiometry for the chalcopyrite phase (nominally $x = 0.5$) was suggested by Binsma *et al.* (12), although no specific experimental evidence was available. Similar inference was applied to the selenide diagrams (8, 9).

It seems clear that the phase relationships along x are not very well elaborated. Improvement of our knowledge on this subject can clearly be beneficial, particularly for the preparation of thin layer cells, where proper control of the x and y parameters is as important as it is difficult.

Experimental

Preparation.—Bulk polycrystalline samples were typically prepared from the elements in evacuated, sealed quartz ampuls. All starting materials used were 5N pure or better obtained from Cerac (Milwaukee, Wisconsin) or Spex (Metuchen, New Jersey) (Cu, In, Se, S). In_2S_3 and In_2Se_3 were 5N pure (Cerac). The reagents were heated to

* Electrochemical Society Active Member.

¹ Present address: Dow Chemical (Nederland) BV, P.O. Box 48, 4530 A A Terneuzen, The Netherlands.

² On Sabbatical leave from the Weizmann Institute of Science, Rehovot, Israel.

³ Note that not all x, y combinations are equally likely from a structural point of view. For example, $x > 0.5$ and $y > 0.5$ are extremely unlikely to be single phase because it would involve overcrowding of the metal sites in the chalcopyrite lattice.

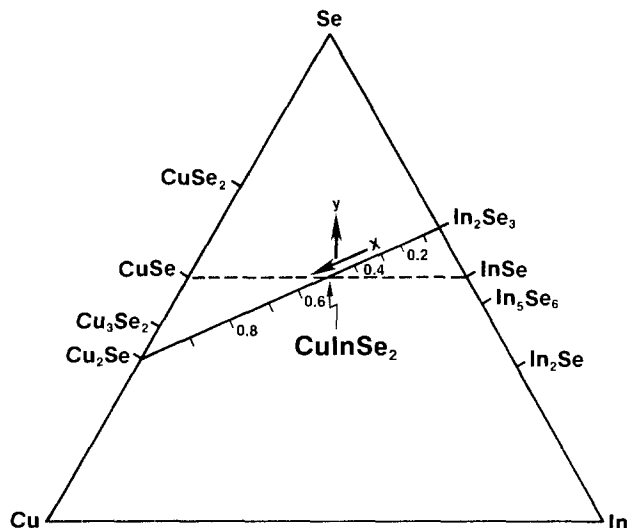


Fig. 1. The ternary Cu-In-Se system indicating the tie-line Cu_2Se_2 - In_2Se_6 along which runs the nonmolecularity (7) parameter x (from 0 to 1) and the nonstoichiometry (nonmetal excess or deficiency) ratio parameter y . Note that the two parameter axes are not perpendicular in this diagram.

temperatures of 600°-800°C, where they were held for several weeks. A pronounced tendency towards chemical vapor transport under their own vapor pressures (a slight excess of chalcogen was usually present) was observed. Even small accidental gradients in an otherwise well-controlled furnace were sufficient to produce this effect. The transport always took place towards the cooler end and the transported material, usually in the form of thin, at times brownish, translucent platelets, of hexagonal habit, always proved to be of significantly lower x than the bulk (x ranging from 0.18 to ~ 0.09). Often, the transported material did, however, contain Cu, which indicates that a species containing both Cu and In must be present in the vapor phase [Cu alone is not known to give this effect (29)]. Due to the transport effect, the samples obtained were often quite inhomogeneous in the sense that a gradient in x was obtained in conjunction with the temperature gradient that had been present. Since this made the information concerning the stoichiometry, as weighed in, worthless, we divided our samples in various parts, determined their stoichiometries by microprobe analyses, and correlated the obtained compositional data with structural data obtained from x-ray powder diffraction for each part.

Polycrystalline thin films were prepared by vacuum evaporation from the elements (2a, 14). The films were deposited on glass substrates. During deposition, the substrate temperature was held at 350°-400°C. The rates of evaporation of the three elements were determined empirically, so that the composition of the deposited films could be controlled by variations in one or more of the rates of evaporation of the elements. Film thicknesses varied between 3 and 5 μm .

Characterization.—X-ray diffraction.—All samples were characterized by powder x-ray diffraction using a powder diffractometer (Rigaku) with a rotating Cu anode source (Cu K_α). In one case, a Guinier-Hägg camera was used as well (Cu K_α).

Electron microprobe analyses.—All samples were analyzed by electron beam-induced wavelength dispersive x-ray fluorescence. A Cameca MBX electron microscope was used. The electron beam voltage was 20 kV; this voltage, which allows detection of the Se K_α line, was chosen because results obtained with it on a CuInSe_2 sample matched those of wet analyses most closely (30). The ZAF correction program (Tracor Northern) plus the following empirically derived multipliers (Cu:0.98; In:1.02; Se:0.99) were used. Except for very smooth samples, a defocused beam with 20 μm spot size and ca. 30 nA beam current

was employed. (We thank C. Herrington for these analyses.)

Optical spectroscopy.—Diffuse reflectance and scattered transmission spectra were obtained using a Beckman 5200 spectrophotometer. Thin film samples were used as prepared. Other samples were spread on a glass plate using double-sided tape or collodion.

Photoelectrochemical studies.—Electrodes were made from suitable crystals or oligocrystalline specimens, where possible, by mounting these on a small copper disk wetted with a liquid In-Ga alloy; a copper wire had been soldered previously to the back of the disk. The metallic parts and all but one face of the specimen were covered by insulating epoxy. In some cases, when only polycrystalline material was obtained, the powder was pressed onto tantalum foil, and a copper wire was attached to the back. A similar sealing procedure using epoxy was followed.

The photoelectrochemical measurements and analyses were accomplished using a computer-controlled apparatus. Its principal components were a 250W tungsten light source, a Jarrel-Ash Mark X monochromator fitted with a TTL-driven stepper motor, a PAR 92 light chopper (operating at 18 Hz), a PAR 174 polarograph, and a lock-in amplifier.

The Model 174 polarograph was used both as potentiostat and as current-to-voltage converter for output to the lock-in amplifier. The computer controlled the wavelength via the monochromator/stepper motor and measured the spectral response via the lock-in amplifier. Typically, a number of averages, ranging from 100 to 200, were taken at each wavelength depending on the sample response. The averaging was done on two time scales; a set of ten points was taken at 50 ms intervals, with each set of ten separated by 0.5s. Appropriate cutoff filters were used to eliminate second-order light from the monochromator. Lamp spectra was taken separately under the same conditions using a Dexter Research Model 2M thermopile with quartz window. The semiconductor response was corrected off line. The nature of the optical transitions was analyzed, as described in Ref. (15c), using a model first presented by Gärtner (15a) and subsequently applied to liquid junctions by Butler (15b). The true photocurrent, J , will be proportional to the absorption coefficient, α , for low values of α , if the conditions for this model are satisfied (15c). Then, if plots of $(Jh\nu)^n$ vs. $(h\nu)$ are linear, they will provide values for the energy of the direct ($n = 2; 2/3$) or indirect ($n = 1/2, 1/3$) transitions (16). Such an analysis can be incorporated in a general photoelectrochemical characterization procedure (31). Part of our goal in applying these analyses was to identify complications. In the course of our present study, two main sources of such complications were identified. The first is the interference of photoconductive effects; the second is the absorption in the IR by the electrolyte (particularly H_2O). A possible remedy for the first one is to apply a bias voltage when the spectral data are taken. This problem is encountered particularly for low doped samples. The second problem is relevant only if bandgap analyses are carried out over a region where the electrolyte absorbs significantly. For H_2O , this effect becomes important if data at wavelengths beyond ca. 925 nm need to be used for analyses. Possible remedies are reducing the optical pathlength through the solution to minimize absorption (in the case of H_2O , this may extend the useful wavelength region to about 1100 nm), correcting for the solution absorption (if the optical pathlength through the solution is known accurately), or using a different solvent (e.g., D_2O will not start to absorb significantly until ca. 1250 nm). Both kinds of complications were encountered, and their implications are discussed below.

The optical-transition analysis routine was written in FORTRAN IV.

Results

Compositions and structures.—For stoichiometries ranging from $x = 0.5$ to ca. 0.23, we typically find

reflections in the powder diffractograms corresponding to the cubic sphalerite sublattice together with superstructure reflections that can be indexed on the basis of a body-centered tetragonal cell with $c \cong 2a_0$. For values around $x = 0.5$, these additional lines obey the extinction rules of the chalcopryrite space group I42d. For $x = 0.23$, however, lines with indexes (114) and (118) are observed, indicating that the structure does not possess a diamond glide. In all cases, the tetragonal distortion c/a is at the edge of or beyond our detection limits. The tetragonal superlines were particularly weak or even absent for thin film samples, especially for those with low x values ($x \sim 0.3$). No stoichiometries between 0.23 and 0.18 were observed, and there appears to be a two-phase region between these limits. For values ranging from $x = 0.17$ to 0.09, we found three different new phases. Except for In₂Se₃, we did not investigate the $x < 0.09$ region. The three new phases were often found in heavily mixed form. Our evidence leads us to believe that their stoichiometries are quite comparable. As indicated above, these materials were often obtained as extremely thin, millimeter-size platelets of hexagonal habit. Their appearance suggests that they may have a layered structure, which is not unreasonable since the structures of α - and β -In₂Se₃ are also layered ones (17). The crystal habit leads to extreme preferential orientation when taking powder diffractometry data. In this particular case, this is helpful in identifying the phases because it reveals the periodicity in the direction perpendicular to the platelets. All three phases have one relatively strong reflection in common with each other and with the chalcopryrite phase. This line is indexed (112) in the latter case [or (111) in the corresponding sphalerite and diamond structures]. It is well known that the direction along which the close-packed Se layers are stacked corresponds to this lattice plane. The structure of the majority of chalcogenides can be described as having such a stacking of close-packed anion layers as its backbone (3). In the chalcopryrite case, the stacking occurs in a cubic fashion with a periodicity of three layers. For the low temperature phases of In₂Se₃, the stacking sequence is hexagonal (based on a twofold sequence). The most obvious approach to structurally identifying the new phases is therefore to treat them as possible mixed cubic/hexagonal stackings, *i.e.*, polytypes. Indeed it is possible to index most strong lines of the three patterns as (00 l) reflections after putting the line they have in common with the chalcopryrite ($d \cong 330$ pm) equal to (005), (006), or (007), respectively. On the one hand, this demonstrates that the new compounds are actually polytypes with stacking sequences of 5, 6, or 7 Se layers and makes it plausible that they are often obtained together. Kinetic effects are known to play an important role in the appearance of polytypes since their thermodynamic differences can be rather small (18). However, the extreme preferential orientation suppresses almost all information concerning directions other than the stacking direction.

Since for CuInSe₂ and In₂Se₃ the prefixes γ , δ , and α , β , γ , δ , respectively, are already in use, we will refer to the new phases as ϵ (7 layers), ζ (6 layers), and η (5 layers). They will be discussed in detail below. Figure 2 shows a tentative phase diagram as amended by integration of our results into the previous ones (8, 9).

The ϵ phase ($x \approx 0.14$ -0.17); [(112) chalcopryrite corresponds to ϵ (007) or (0014)].—We obtained a more complete picture of the lattice periodicity of this phase by combining powder diffractometry data with data from a Guinier-Hägg pattern. The preferential orientation effect for the latter is such that the two data sets are complementary. A hexagonal indexing based on a septuple axis (*i.e.*, seven close-packed Se layers) and an a axis corresponding to *ca.* $2\sqrt{3}$ times the shortest Se-Se distance in a close-packed layer was successful for both patterns. The refinements of the cell parameters were executed separately, and a slightly different c/a ratio was found for the two sets of data. Since the data were collected from adja-

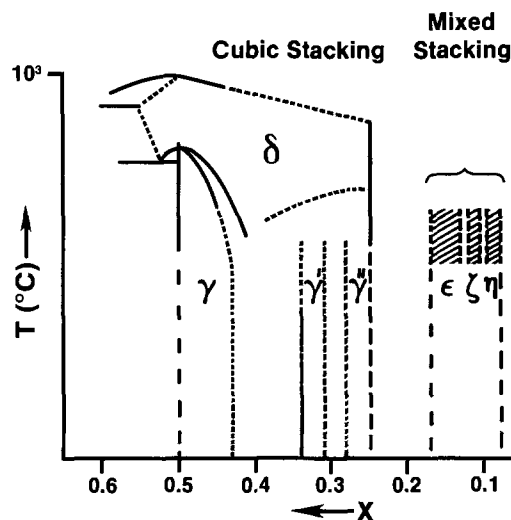


Fig. 2. Tentative T - x diagram for the title system. It is based on our results, as discussed in the text, and data from Ref. (8-10, 18). Two endothermic thermal arrests were observed in a preliminary DTA run on an $x = 0.14$ sample at 610° and 645°C. These may indicate order-disorder transitions in the $\epsilon + \zeta$ mixed phase.

cent parts of the same sample, this could indicate that the phase possesses a certain width of homogeneity. A number of weak lines in both patterns remained unindexed. If we assume, however, that the c axis is double the septuple value, the lines in the diffractogram are easily indexed, mostly again as (00 l) reflections with l being odd. This may mean that a sevenfold stacking periodicity of the Se layers is to be combined with a twofold ordering of the metal atoms between them. Applying this doubling of the axis to the Guinier pattern provides an indexing of all lines, but since the resulting cell is quite big, we cannot consider this as additional evidence. It should be stressed that no attempt was made to find possible indexes with l being odd for lines that were successfully indexed with γ being even previously. Powder x-ray diffraction data for the selenide ϵ phase are given in Table I. These are the observed and calculated d spacings for both diffractometer and Guinier-Hägg data and their (common) indexing. The two patterns were refined independently and gave slightly different axes. The doubling of c explaining the few remaining hkl (l being odd) lines was applied afterwards. It should be noted that we find this phase to be the one closest to a nominal CuIn₂Se₈ stoichiometry ($x = 0.167$). No spinel phase as for the pure sulfide analog is found, while a mixed sulfoselenide with similar stoichiometry adopts another polytype structure (see η phase below).

The ζ phase ($x \approx 0.14$); [(112) chalcopryrite corresponds to ζ (006)].—Powder x-ray diffractometry data for the selenide ζ phase are given in Table II. The sixfold periodicity in the c direction is well documented, but the a axis only corresponds to a value that is comprehensible in terms of short Se-Se distances if we assume it to be $\sqrt{3}$ times the value found from the indexing. The pattern can be indexed on the basis of a hexagonal cell with $a = 913.9(7)$ and $c = 1964(4)$ pm. The c axis corresponds to a sixfold stacking (without doubling), but the a axis only shows a clear relationship to a short Se-Se distance if we take it to be $\sqrt{3}$ times as large. Since the amount of information on this axis contained in the pattern is limited, this assumption is plausible enough, especially since the resulting cell with $a = \sim 1600$ pm is identical to the cell of α -In₂Se₃. It should be noted, however, that no extinctions of (00 l) reflections, as imposed by the 6₃ axis reported for α -In₂Se₃ (17) are observed. A number of lines corresponding to the strongest (00 l) reflections of the ϵ phase are also observed in the pattern. It should also be noted that a phase with a cell like the one described here was reported by Gambarov *et al.* (10c). They claim, however, that its x value is 0.25.

Table I. Powder x-ray diffraction data for selenide ϵ phase

$d_{\text{obs}}^{\text{diff}}$	$d_{\text{calc}}^{\text{diff}}$	$d_{\text{obs}}^{\text{guin}}$	$d_{\text{calc}}^{\text{guin}}$	$hk l^{\text{even}}$	$hk l^{\text{odd}}$	001
766 w [†]	767			00 6		6
655 w	657				00 7	7
574 m	575			00 8		8
511 w	511				00 9	9
460 vw	460			0010		10
418 w	418			11 8	0011	11
		395.7 w	397.0	21 0		
383.4 vw	383.4	384.5 w	385.1	0012		12
353.5 w	353.0/9			21 6	0013	13
		349.6 m	350.2	30 0		
		340.9 m [†]	340.2		21 7	
		336.2 vw	335.1	30 4		
328.7 s	328.6	330.6 w	330.1	0014		14
324.3 w	324.2	325.2 vs	325.1	1112		
		316.8 w	318.8/49	30 6/1014		
306.9 vw	305.8/67	306.1 w	306.7/81		1113/0015	15
		293.2 w [†]	293.3	22 4		
287.6 s	287.6			0016		16
		272.7 vw	272.5	31 6		
255.7 w	255.6			0018		18
		228.5 vw	228.3	4010		
219.1 vw	219.1				0021	21
216.8 vw	216.9			4012		
		213.3 w	213.1	418		
		211.8 w	211.5	2020		
211.3 w	211.4				3115	
209.0 w	209.1			0022		22
202.3 w	202.4	202.2 vvs	191.3	33 0		
196.9 vw	197.0			4112		
		191.2 w	191.3	5010		
		188.3 w	188.3	4114		
187.8 w	187.9			42 8		
183.8 vw	184.0				0025	25
		180.0 w [†]	180.1	3022		
179.1 vw	179.0	179.0 w [†]	179.0	3312		
177.0 w	177.0			0026		26
175.5 vw	175.5			3218		
		175.2m ⁻	175.1/2	60 0/1026		
		173.6 m ⁻	173.5	4020		
172.0 vw	172.2			2222	5111	
		171.7 m	171.6		43 3	
		169.9 vw	169.9	5016		
		166.4 vw	166.5	52 4		
164.3 vw	164.3			0028		28
		162.1 w	162.2	2126		
		158.4 vw	158.3/5	3222/3026		
148.4 vw	148.4				0031	31
		146.4	146.3		70 7	
143.8 vw	143.8			0032		32
		139.0 vw	138.9	6210		
		137.5 vw	137.6		71 5	
135.3 w	135.3			0034		34
		132.3 m	132.3	63 0		
		131.8 m	131.9		54 7	
		131.1 m	131.1/0	80 2/54 8		
		130.1 w	130.1	6216		
		128.5 w	128.6	4324		
127.8 vw	127.8			0036		36
122.1 vw	122.1			8014		
121.1 w	121.1			0038		38
		118.5 w	118.5	2038		
118.2 vw	118.4			73 2		
		116.7 s	116.7	90 0		
		114.5 w	114.4/5	90 8/82 2		
		113.8 w	113.9	5514		
		111.7 w	111.7	9012		
		110.0 w	110.0	9014/0042		42

Diffractometer
 $a = 1214.7(2)$ pm
 $c = 2*2300.5(2)$ pm
 $= 4601.0(3)$ pm

Guinier-Hägg
 $a = 1213.0(1)$ pm
 $c = 2*2310.5(6)$ pm
 $= 4621(1)$ pm

The η phase ($x \approx 0.09$); [(112) chalcopyrite corresponds to η (005) or (0010)].—Just as what is found for the ϵ phase, there is evidence for doubling of the c axis and rather little information on the a axis. The pattern can be indexed successfully by analogy to the epsilon phase using an a axis that is $2\sqrt{3}$ times the shortest Se-Se distance and a tenfold stacking in the c direction. This indexing should be regarded as tentative in the a , b directions. One line corresponding to the strongest line of the zeta phase was also observed as a weak signal. Table III shows the powder x-ray diffractometry data for the selenide η phase. Both the basic fivefold periodicity in c and its doubling (cf. Table I) are well documented. The a , b indexing was adopted in analogy to the ϵ phase and is tentative. A slight

miscalibration rendered a refinement unreliable; instead, the cell parameters were based on an average over the high index reflections ($d < 200$ pm).

It should be mentioned at this point that crystals obtained by spontaneous vapor transport from a $\text{CuInS}_{0.8}\text{Se}_{1.2}$ bulk also proved to have a fivefold periodicity in the c direction. The measured stoichiometry corresponds to $x \sim 0.18$. (The remaining bulk had an x value ranging from 0.55 to 0.48).

The cubic stacking region ($0.5 \leq x \leq 0.24$).—As mentioned above, materials with cubic stacking and a tetragonal ordering were observed in the region $0.5 > x > 0.24$. The cell parameters do not change very much over this broad

Table II. Powder x-ray diffraction data for selenide ζ phase

d_{obs}	d_{calc}	hkl	$00l$	Impurity lines
1898	vvw	1964	00 1	1
812	vvw	791	10 0	
756	vvw	—	—	$\epsilon(003)$
649	m	655	00 3	3
570	w ⁺	—	—	$\epsilon(004)$
506.8	vw	504.6	10 3	
490.1	vvw	491.5	00 4	4
414.3	w	414.2	10 4	
		417.5	11 2	
391.7	vvs	393.2	00 5	5
381.7	s	—	—	$\epsilon(006)$
351.9	vw	352.1	10 5	
327.3	s	327.6	00 6	6
286.7	m	—	—	$\epsilon(008)$
280.5	m ⁺	280.8	00 7	7
255.0	vvw	255.4	21 4	
245.7	w	245.7	00 8	8
218.3	w	218.4	00 9	9
196.4	vw	196.6	0010	10
189.9	vw	189.8	21 8	
178.7	w	178.7	0011	11
176.7	vvw	176.7	40 5	
163.9	vw	163.9	0012	12
151.3	vw	151.2	0013	13
143/6	vvw	143.6	1113/2112	
140.4	w	140.4	0014	14

$$a = 913.9(7) \text{ pm} \cdot \sqrt{3} = 1600 \text{ pm}$$

$$c = 1965.8(4) \text{ pm}$$

range of homogeneity, and the tetragonal splitting remains at the edge of observability by ordinary diffraction means. We observed $a = 574.5(5)$ and $c = 1148(1)$ pm at the low x boundary [compared to 578.5 and 1157 pm for $x = 0.5$ (1)]. Diffractometry of a number of thin film samples deposited by multiple source evaporation according to the method described in Ref. (14) (at 400°C) showed the presence of monoclinic Cu₂Se for compositions with $x > 0.6$, and a tetragonal pattern without lines belonging to monoclinic Cu₂Se, for about $x = 0.6$ to $x = 0.45$; from $x = 0.45$ to $x = 0.3$, only the cubic substructure lines were observed. Obviously, the films do not achieve complete equilibrium under the deposition conditions. The (pseudo-cubic) cell parameter decreases slightly from 579 to 578 pm over this range. The homogeneity range at the high x side seems somewhat metastably broadened, whereas at the low x side the Cu/In or metal/vacancy ordering is not established. An interesting question relevant to photovoltaic applications in this respect is how long such unstable or metastable states may endure at room temperature. The samples we investigated were about one year old. The question is most likely to be answered in terms of years at least. We note that the detailed electron diffraction study by Manolikas *et al.* (19) also mentions freezing of the disordered state by quenching of the high temperature disordered state. It is claimed that above 700°C the symmetry is that of sphalerite (or even Li₂O). Unfortunately, the composition reported by these authors falls outside the range we find to be the region of existence of the cubic stacking. We assume, therefore, that this study was done on a sample corresponding to the lowest x limit (~ 0.24).

The precise nature of the Cu/In and metal/vacancy orderings for lower x values is far from clear. Whereas Manolikas *et al.* (19) claim an I4̄ thio-gallate structure, Djega-Mariadassou *et al.* (20) claim they observed, by careful x-ray work, that between $x = 0.34$ and $x = 0.31$ there is a cubic ordering P4̄3m, with a cell eight times the sphalerite cell and a tetragonal ordering from $x = 0.28$ to $x = 0.25$ with a "paracrystalline" (two-phase) region in between. Since both these and the chalcopyrite ordering stem from the same disordered sphalerite substructure, we have named them γ , γ' , and γ'' , respectively (Fig. 2). A group theoretical treatment showed the three orderings to be very closely related in terms of symmetry (21). Table IV summarizes the structural types encountered in the (Cu₂Se)_x(In₂Se₃)_{1-x} system for $x < 0.6$. (For $x > 0.6$, the monoclinic Cu₂Se is found, mixed with γ or δ .)

Table III. Powder x-ray diffractometry data for selenide η phase

d_{obs}	d_{calc}	hkl	$00l$	Impurity lines
1590	vw	1630	00 2	2
1070	vw	1090	00 3	3
808	w ⁺	816	00 4	4
651	m	653	00 5	5
542	s	544	00 6	6
478.3	w	478.6	10 6	
464.7	m	466.2	00 7	7
434.3	vvw	434.2	11 5	
406.8	vs	407.9	00 8	8
392.6	w	—	—	$\zeta(005)$
377.8	m	378.1/2	21 1/108	
361.9	w	362.6	00 9	9
325.5	s	326.3	0010	10
319.8	w	320.8	30 3	
298.8	s	298.6	30 5	
271.4	s	271.9	0012	12
217.6	w	217.5	0015	15
214.1	w	214.3	40 8	
206.7	w	206.9	40 9	
203.8	vw	203.9	0016	16
201.4	vw	201.5	50 0	
		201.1	32 8/3013	
199.3	vw	199.9	1016	
		199.7	2015	
		199.4	4010	
193.7	vw	193.5	41 8	
192.6	vw	192.0	0017/4011	17
		192.5	50 5/1116	
181.1	w	181.3	0018	18
		181.0	51 0	
		180.7	50 8	
176.2	w	176.3	42 7	
		176.1	50 9/3212	
171.0	vvw	171.0	33 9	
		171.5	5010	
		171.1	4014	
		171.4	2117	
163.1	w	163.2	0020	20
148.2	vw	148.3	0022	22
142.7	vw	142.7	70 3/533	
		142.9	6012	
		142.6	3218	
142.1	w	141.9	0023	23
		142.3	2220/2022	
136.1	w ⁺	136.0	0024	24
		136.2	6014	
125.6	w	125.5	0026	26

$$a = 1163 \text{ pm}$$

$$c = 2 \cdot 1631.5 = 3263 \text{ pm}$$

Photoelectrochemical experiments.—For the application of thin film Cu-In-Se materials to solar energy conversion, it is important to know how the structural complexity of the phase diagram relates to the performance of these materials in photovoltaic or photoelectrochemical cells. Since we obtained in the above structural study a number of samples that met with the rather modest requirements for photoelectrochemical characterization, we report here a number of relevant data obtained using this method.

The cubic stacking region.—Samples of only two of the stoichiometries encountered in this region were suitable for mounting as electrodes [except for the $x = 0.5$ chalcopyrite phases, *cf.* Ref. (2d)]. Figure 3 shows the current-voltage behavior with modulated white illumination for a sample with $x \approx 0.25$ in an acetonitrile solution of Co(bpy)₃(ClO₄) [see legend to Fig. 3 and Ref. (22)]. It is clear that the sample shows mainly a photoconductive effect. Similar results were obtained in aqueous polysulfide electrolyte. No significant photoactivity was detected in aqueous I⁻/I₃⁻. Using a lock-in technique, we were able to detect a small true n-type photoelectrochemical effect, probably superimposed on the photoconductive one. Figure 4 shows the wavelength dependence of what appears to be a true photovoltaic effect in deuterated polysulfide solution. By analyzing these data as explained in the Experimental section, we deduce a direct allowed optical transition of 1.15 eV and an indirect one of 0.87 eV. These numbers are in reasonable agreement with our reflectance data which indicate a lowest bandgap around 0.95 eV. Because the 0.87 eV value is

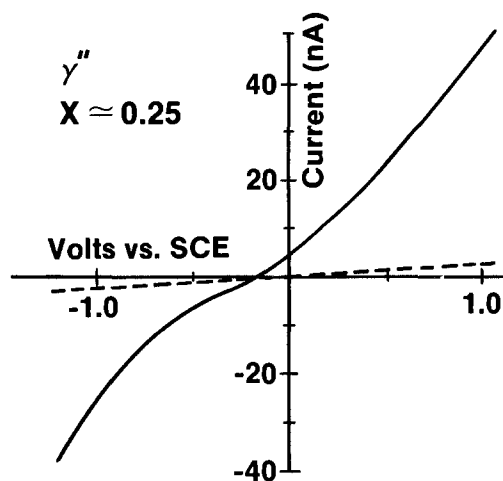


Fig. 3. Current-voltage characteristics in the dark and under illumination for hot-pressed layer of $x = 0.25$ (γ') on Ta foil (see Experimental section). The redox couple used was $0.1M$ $\text{Co}(\text{bpy})_3(\text{ClO}_4)_2$ in acetonitrile with $0.1M$ tetraethylammonium perchlorate as supporting electrolyte. This solution was developed by us for use in diagnostic tests on Cu-In-Se thin films (22).

significantly below the indirect gap values obtained for the other phases studied (see below), we should consider it with some caution, as it may be lowered artificially due to impurity bands. The second sample studied was a mixed sulfide/selenide (2:3) with a rather large x value of 0.55. Its photoelectrochemical effect (also n-type) in polysulfide electrolyte was harder to detect than that of the selenide phase with $x = 0.25$. Its spectral response shows a sharp bandedge at 1.18 eV. This value can be expected on the basis of linear interpolation between the reported values for the pure 1:1:2 ($x = 0.5$) sulfide and selenide (1). The value of 1.18 is also in excellent agreement with the value obtained from diffuse reflectance (1.17 ± 0.1 eV).

Because all thin film samples were on a nonconducting substrate (glass), no photoelectrochemical measurements were possible with them. From optical spectroscopic experiments, we could, however, deduce values for their optical bandgaps. All samples between $x = 0.35$ and $x = 0.84$ showed a bandgap of 1.0 ± 0.02 eV. The most Cu-poor ($x = 0.31$) sample gave a somewhat higher value of 1.05 ± 1.02 eV.

The epsilon phase.—Several platelike crystals of this phase ($x = 0.14$ -0.17) were suitable for use as electrodes. Figure 5 shows the current-voltage behavior under illumination and in the dark for one of these samples in aqueous polysulfide electrolyte. Although they exhibit reasonable n-type photovoltaic activity ($V_{oc} \approx 110$ mV), the figure shows clear evidence for some photoconductivity, too. Experiments in a $6M$ KI, $0.1M$ CuCl_2 solution (2d) showed an open-circuit voltage of some 300 mV, but the photoconductive effect was even more pronounced in

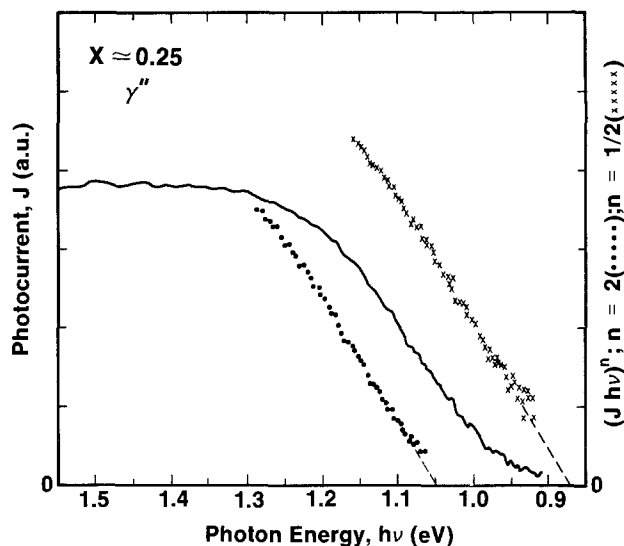


Fig. 4. The wavelength dependence of the photo effect of $x = 0.25$ (γ') at +50 mV bias vs. the redox potential of the deuterated polysulfide solution, $1.2M$ in Na_2S and $2M$ in S^0 , and $(Jh\nu)^n$ vs. $h\nu$ plots of these data to determine value of direct (...) and indirect (xxx) gaps.

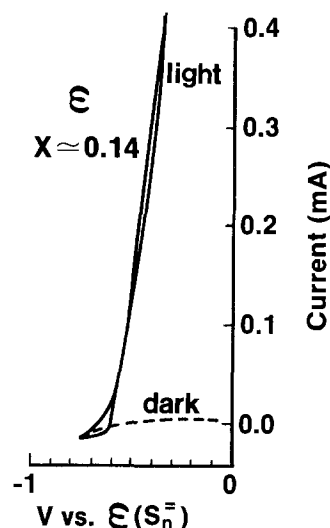


Fig. 5. The current voltage behavior of $x = 0.14$ (ϵ phase) in aqueous polysulfide, $3M$ in KOH, $3M$ in Na_2S , and $4M$ in S . A three-electrode configuration with an SCE reference electrode was used. White illumination corresponding to ca. eight times AM1 was applied. The exposed crystal area was 3 mm^2 .

this solution. Etching the crystal in a 2% Br_2/MeOH solution improved the response in iodide solutions by a factor of ~ 25 . The improvement in polysulfide solutions was much less (some 50%). Nevertheless, the response in the

Table IV. Structural types encountered in the $(\text{Cu}_x\text{Se})_x(\text{In}_2\text{Se}_3)_{1-x}$ system for $x < 0.6$

Composition (x)	Symbol	Type	Symm	Se stacking	Ref.
0.5-0.24 (0.45-0.31) ^a	δ	Sphal.	$F\bar{4}3m$	3	This work, (8), (1)
(0.6-0.45) ^a 0.5-0.47	γ	Chalc.	$I\bar{4}2d$	2×3	This work, (8), (1)
0.34-0.31	γ'	Own	$P\bar{4}3m$	2×3	(20)
0.28-0.24	γ''	?	$I\bar{4}2m$?	2×3	This work, (19)
0.17-0.15	ϵ	?	$> P3$	2×7	This work
~ 0.14	ζ	?	$> P3$	6	This work, (10c)
~ 0.09	η	?	$> P3$	2×5	This work

^a For thin film samples on glass.

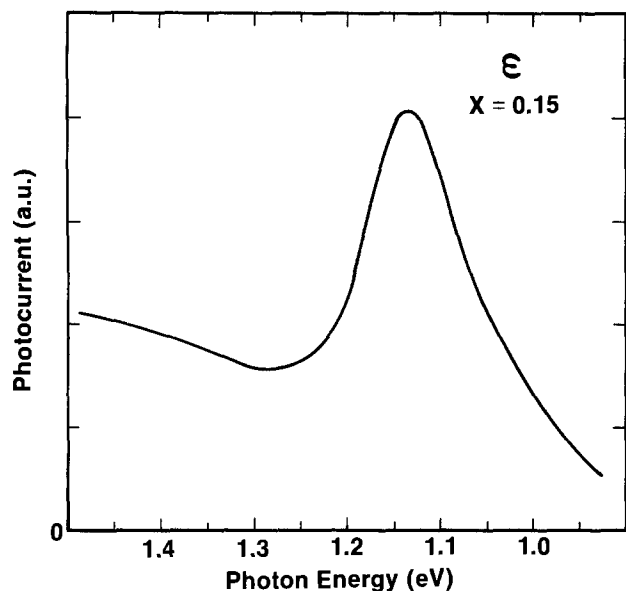


Fig. 6. Photoresponse spectrum of $x \approx 0.15$ (ϵ phase), in deuterated polysulfide, 1.2M in Na_2S , and 2M in S^0 , at +200 mV vs. the solution redox potential.

latter solution was about ten times better than the best response obtained in the former. This is in contrast to results obtained from CuInSe_2 crystals (2). It is likely that the etch removes a partly rectifying layer from the crystal surface. Some of the photovoltaic response shown in Fig. 5 may be due in part to a heterojunction formed by this layer, which might be an indium oxide [cf. Ref. (2d)], as the most pronounced change was observed after a cathodic scan. This conclusion is in agreement with the observed decrease in dark current with time, after immersing a fresh electrode in the solution (suggesting a surface reaction) and the observed slight hysteresis in the C^{-2} -V plots. These plots suggested a donor density of ca. 10^{16} cm^{-3} .

The photoconductivity, alluded to above, was confirmed by spectral response data on a sample with $x \approx 0.15$ in D_2O -based polysulfide solution (cf. Fig. 6), which showed a pronounced peak around 1100 nm. This peak persisted also after etching the electrode, thus making it unlikely that it is due to surface effects such as surface recombination. It became more pronounced, when positive bias was applied and disappeared with sufficiently

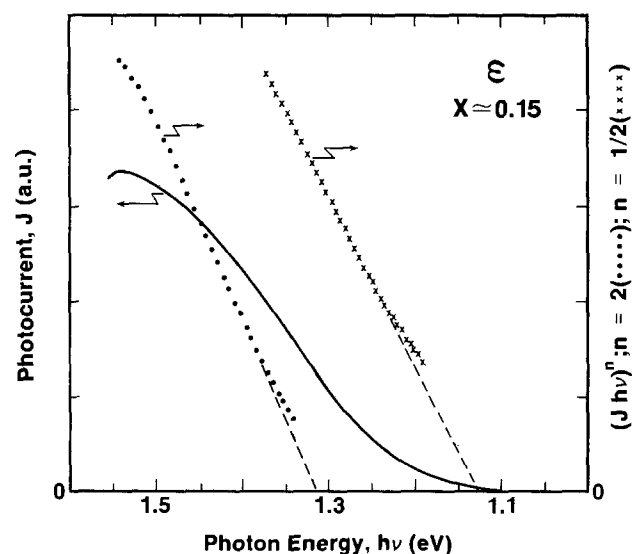


Fig. 7. The photoresponse spectrum of $x \approx 0.15$ (ϵ phase) in the deuterated polysulfide solution of Fig. 6 at -300 mV vs. the solution redox potential. $(Jh\nu)^{1/2}$ vs. $h\nu$ plots to determine direct (...) and indirect (xxx) allowed transitions are shown as well.

Table V. Structural types and estimated optical bandgaps (E_g) of $(\text{Cu}_2\text{X})_x(\text{In}_2\text{X}_3)_{1-x}$

X S:Se	x	Sample ^a form	Structure	E_g^b
1	0.58-0.44	f/cr	γ	1.05(d)
1	0.58-0.44	f/cr	γ	1.55(d)
2:3	0.55	cr	γ	1.20(d)
1	0.35	f	δ	1.10
1	0.31	f	δ	1.00
1	0.25	cr	$\gamma''?$	1.15/0.85(d/i)
1	0.23	cr	γ''/ϵ	—
~4:5	0.18	cr	η	1.35/1.10(d/i)
1	0.17	f/cr	spinel	1.50/1.30(d/i)
1	0.17	cr	ϵ	1.00(df)
1	0.15	cr	ϵ	1.30(d)/1.15(i)
1	~0.15	cr	ζ	1.30/1.10(d/i)
1	0.09	cr	η	—
1	—	cr	β	1.70/1.20(d/i)
1	0	cr	spinel	2.35/2.00(d/i)

^a f = film; cr = crystal.

^b d = direct allowed optical transition; i = indirect allowed optical transition; df = direct forbidden optical transition.

An accuracy of 50 meV is assumed for all data.

negative bias (cf. Fig. 7) (23). Also, the wavelength dependence of the resistivity of the cell showed a severalfold decrease around 1100 nm and the capacitance increased in this wavelength range (phenomena that can be ascribed to optical doping).

The data at -300 mV bias were analyzed for indirect and direct allowed optical transitions, as shown in Fig. 7. In this way, an indirect gap of 1.13 eV (1097 nm) was found, confirming the suggestion that the 1100 nm peak (Fig. 6) is due to photoconductivity. A direct gap of 1.31 eV was identified, as well. A sample with $x \approx 0.17$ showed similar photoconductivity behavior, with a peak at slightly longer wavelengths (1000-1050 nm), which could be suppressed at -100 mV bias. Then analysis of the data was possible only in terms of a direct forbidden transition, yielding a gap value of 1.0 eV. Similar analyses in H_2O -based electrolyte gave "evidence" for indirect and direct allowed transitions at 1.10 and 1.25 eV, respectively, illustrating the effect of H_2O absorption. Analyses of spectra that still showed the photoconductivity peak gave erroneously low results. The marked decrease in response at shorter wavelengths (Fig. 6) may indicate that surface recombination becomes a dominant de-excitation mechanism at higher energies.

The zeta phase.—This phase generally was not obtained in form pure enough to allow further study. The few samples that could be investigated showed complicated behavior, indicative of both bulk photoconductive and surface effects. Capacitance measurements indicate a n-type donor density similar to that observed for the ϵ samples (ca. 10^{16} cm^{-3}). A photoconductivity peak around 950 nm was seen in D_2O -based electrolyte. Note that such a peak would have been obscured in H_2O -based solutions. At slightly negative bias, spectra could be obtained that allowed analyses of the optical bandgaps. In this way, values of ca. 1.3 and 1.1 eV were deduced for direct and indirect gaps, respectively.

The eta phase.—While no pure selenide samples with this structure could be isolated, a mixed sulfoselenide with S/Se ≈ 0.8 , and $x = 0.18$, proved suitable for photoelectrochemical study. Crystals of this phase showed photoactivity of predominantly photovoltaic nature in various electrolytes: aqueous ferro/ferricyanide, in aqueous and deuterated polysulfide, in aqueous polyiodide, and in the previously mentioned (Fig. 4) organic electrolyte. Photovoltages up to 200 mV could be obtained in aqueous ferro/ferricyanide and polysulfide as well as in polyiodide, but in the last electrolyte this phase was grossly unstable. Capacitance-voltage plots in buffered aqueous nitrate solution indicated a donor density of 10^{15} - 10^{16} cm^{-3} and a flatband potential of -0.8V vs. SCE in this solution. Some evidence for surface recombination [from double-

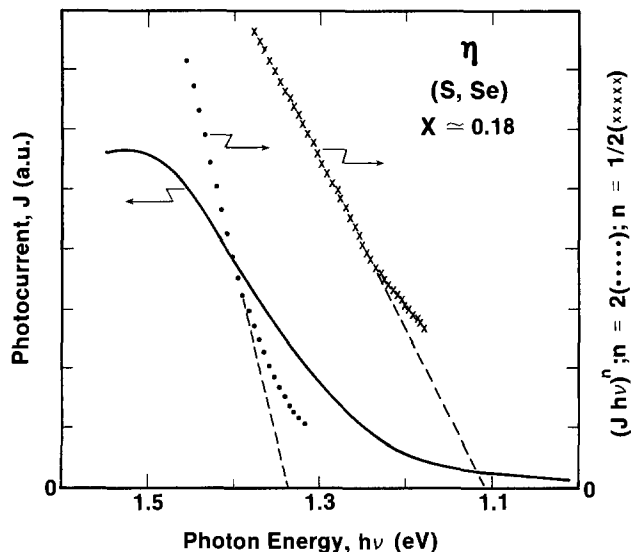


Fig. 8. The photoresponse spectra of $x \approx 0.18$ (η phase) sulfoselenide (solid line) in the deuterated polysulfide solution of Fig. 6 under short-circuit conditions. Plots to analyze for direct and indirect allowed transitions are shown as well. For details, see Fig. 7.

illumination experiments, cf. Ref. (25)] and/or photoconductivity effects was seen in the spectral response data for one sample, but others showed straightforward n-type photovoltaic response (cf. Fig. 8). Analyses of the wavelength dependence of the photocurrent, both at 0 V bias (Fig. 8) and at +200 mV bias yielded values for direct and indirect allowed gaps of 1.34 and 1.11 eV, respectively. These values are surprisingly close to those obtained for the pure selenide, ϵ , and ζ phases discussed above. More experiments on pure samples are needed to confirm this anomaly.

In_2Se (δ).—For completeness' sake, we investigated briefly samples of In_2Se_3 on Ta. These samples were obtained from 5N pure In_2Se_3 which was heated at 780°C for several weeks, and subsequently hot pressed at 10^4 psi (69 MPa) and 350°C in a N_2 atmosphere for 60 min and held at this pressure during the 3h of cooling. Such samples showed appreciable n-type photoresponse in the acetonitrile (Fig. 4) electrolyte.

The wavelength dependence of the photoresponse was measured in aqueous ferro/ferricyanide solution, and its analysis showed the presence of a direct (allowed) transition at 1.7 eV, in fair agreement with the 1.6 ± 0.1 eV value obtained from diffuse reflectance. Further analysis of the photocurrent spectrum showed some evidence for an additional, indirect allowed transition at ~ 1.2 eV, which value agrees with the earlier reported⁴ one, obtained by optical absorption spectroscopy.

In_2S_3 .—We made some attempts to look at the other possible end members of the generalized series $(Cu_2X)_x(In_2X_3)_{1-x}$, where X stands for S or Se, in view of our success in preparing some mixed sulfoselenides and the obvious photovoltaic interest in such mixed chalcogenides. No significant photoelectrochemical activity was observed for Cu_2S or Cu_2Se (prepared as hot pressed pellets or layers on Ta). We had some success, though, with In_2S_3 . The electrode was prepared from 5N pure In_2S_3 powder, which was melted *in vacuo* at $\sim 1100^\circ C$ in an ampul and allowed to cool slowly. A slice was cut off the end of the resulting boule and mounted on a Ti plate. (We thank G. Hodes for this sample.)

This electrode was tested without further treatment, and showed appreciable n-type response in polysulfide electrolyte, extending far beyond the reported bandgap for In_2S_3 [2.03 eV, Ref. (26)], although a distinct discontinuity in the photoresponse was observed at ~ 2.02 eV.

⁴ Rehwald and Harbeke (26a) and Garlick *et al.* (26b) report a bandgap of 2.28 eV. Both these measurements were done on single crystals by optical absorption spectroscopy.

Analyses of this photoresponse revealed a direct, allowed, optical transition at 1.84 eV and an indirect, allowed one at 1.54 eV. (We did not note any photoconductive effect and the solvent absorption effect is minimal around these energy values.) The direct transition corresponds very closely to that reported for InS [27], 1.86 eV, although this value was obtained from thermal activation of electrical conductivity measurements. However, Diehl and Nitsche (28) report absorption edges for p- In_2S_3 (As) and p- In_2S_3 (Sb) of 1.88 and 1.44 eV, respectively, indicating that significant shifts of the absorption edge are possible by incorporation of small amounts of impurities. In view of the high purity starting material, and the likelihood of some S loss during the vacuum anneal, it seems reasonable to assume that the top layer was composed of a S-poorer indium sulfide. Indeed, after polishing off the top layer of the electrode and etching it in $Br_2/MeOH$, no significant photoresponse could be obtained anymore in polysulfide. This is easily understood because of the solution absorption. Subsequently, we tested this electrode in ferro/ferricyanide (0.1M $Fe(CN)_6^{4-}$; 0.01M $Fe(CN)_6^{3-}$) to which 1M K_2HPO_4 buffer was added (pH 8.8). Quantum yields up to 0.04 were obtained at 480 nm and 0.0 V vs. SCE and a photoresponse was obtained (Fig. 9) that yielded, after analyses, an indirect bandgap (allowed) of $1.99 (\pm 0.01)$ eV, in reasonable agreement with the 2.03 eV literature value, and a direct gap (allowed) of 2.33 eV, which corresponds to the 2.28 eV literature value (26).

Discussion

The pseudobinary system $(Cu_2Se)_x(In_2Se_3)_{1-x}$ presents a rich variety of structural complexities like so many chalcogenide systems. We can distinguish one common denominator: the fact that all structures are based on a close packed lattice of chalcogen atoms. Further, we can distinguish two or possibly three complicating structural features.

First of all, with decreasing x there is a change in the stacking of the close packed lattice from cubic via a number of mixed polytype-like stackings to hexagonal while at the same time the structures become more layerlike. Secondly, the Cu *vs.* In *vs.* vacancy ordering is quite varied in the region of cubic stacking. At high temperatures this region is very broad and a disordered structure is established; at lower temperatures there are indications for various types of order and the precise equilibrium phase boundaries are unclear; it is likely that at room

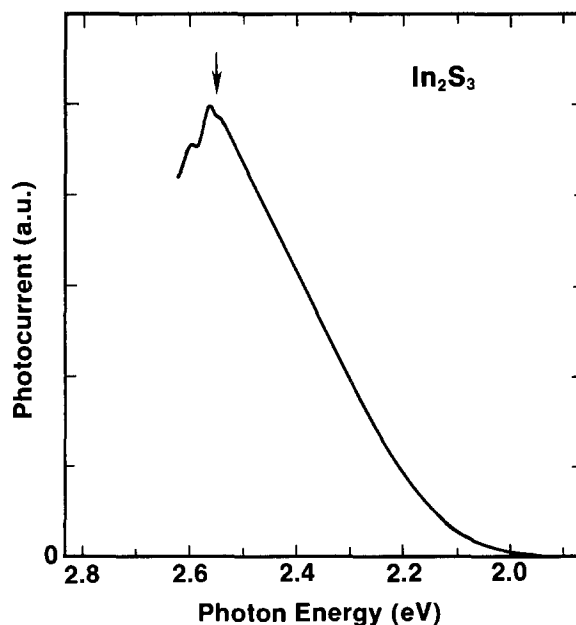


Fig. 9. Wavelength dependence of the short-circuit photocurrent of an etched In_2S_3 electrode (cf. text), in aqueous ferro/ferricyanide solution, phosphate buffered to pH = 8.8. The arrow indicates the onset of solution absorption.

temperature metastable (or unstable) materials can be obtained over the broad homogeneity range of the high temperature phase. A third feature is illustrated in the analogous sulfide system (12) where for lower x values the coordination of In changes from tetrahedral to octahedral. Although a spinel phase is not encountered in the selenide system, partial octahedral coordination is claimed for the α - and β -In₂Se₃ structures (17). Only a complete structure determination of the ϵ , ζ , and η phases can reveal if these structures are purely tetrahedral as the cubic stacked phases seem to be.

Our photoelectrochemical (PEC) survey has shown both the power and a number of complications of the PEC method as a characterization tool in solid-state chemistry. Because it only yields results if materials are obtained that answer to a number of requirements not always in control of the investigator (*e.g.*, specimens of suitable size, appropriate doping levels, mobilities and recombination rates, and suitable chemical behavior with respect to some electrolyte), a survey such as this is likely to be somewhat patchy. Nevertheless, useful information was obtained on a number of (new) materials which would not easily have been obtained otherwise and which allows us the following generalizations. The lowest bandgap of all the Cu-In-Se materials shows values that range only between 1.15 and 0.85 eV, even if the stacking is completely different. However, the rather subtle differences in the ratios of vacancies and Cu and In atoms and their orderings are able to destroy the good photoresponse of the chalcopyrite phase. It seems imperative, therefore, to monitor closely the value of x for any thin film material made and possibly the order parameter of the material can be of equal importance. For the former, x-ray diffraction will be of limited use since the lattice parameters change so little, but the intensities of the superstructure lines as opposed to those of the cubic sublattice may give at least some semiquantitative idea of the latter parameter. Of course, the details of the ordering(s) can only be elaborated on basis of detailed single-crystal x-ray, or, preferably, electron diffraction efforts.

Acknowledgments

We thank Y.-W. D. Chen, C. Herrington, and G. Hodes for assistance with some of the experiments. The Guinier-Hägg data were obtained in the Laboratory for Inorganic Chemistry/Solid State of the University of Groningen, Groningen, The Netherlands. We thank Dr. G. A. Wiegers for giving us access to the equipment and Ms. R. Haange for her support. J. A. T. acknowledges support from the Office of Energy Research, Basic Energy Sciences, Division of Chemical Sciences of the U. S. Department of Energy. This study was performed under the auspices of the Photoelectrochemical Cell Task of the Photovoltaic Program Office of the Solar Energy Research Institute, operated under Contract DE-AC-02-83CH10093 for the United States Department of Energy.

Manuscript submitted Sept. 24, 1984; revised manuscript received Jan. 28, 1985.

Solar Energy Research Institute assisted in meeting the publication costs of this article.

REFERENCES

- J. L. Shay and J. H. Wernick, "Ternary Chalcopyrite Semiconductors Growth, Electronic Properties and Applications," Pergamon Press, New York (1975).
- (a) W. S. Chen and R. A. Mickelsen, *Proc. SPIE*, **248**, 62 (1981); (b) Y. Mirovsky and D. Cahen, *Appl. Phys. Lett.*, **40**, 727 (1982); (c) S. Menezes, H. A. Lewerenz, and K. J. Bachmann, *Nature*, **305**, 615 (1983); (d) D. Cahen and Y.-W. D. Chen, *Appl. Phys. Lett.*, **45**, 746 (1984); *This Journal*, **131**, 433C (1983).
- F. J. Jellinek, in "MTP International Review of Science, Inorganic Chemistry Series," Vol. 5, D. W. A. Sharp, Editor, Butterworths, London (1972).
- J. C. W. Folmer, F. J. Jellinek, and G. Calis, Submitted to *J. Solid State Chem.*
- J. E. Jaffe and A. Zunger, *Phys. Rev. B*, **27**, 5176 (1983); *ibid.*, **28**, 5822 (1983).
- K. Becker and S. Wagner, *ibid.*, **28**, 5822 (1983).
- F. A. Kröger, "The Chemistry of Imperfect Crystals," Vol. 2, 2nd ed., p. 826, North Holland Amsterdam (1974).
- L. S. Palatnik and E. I. Rogacheva, *Sov. Phys. Doklady*, **12**(5), 503 (1967).
- T. I. Koneshova, A. A. Babitsyna, and V. T. Kalinnikov, *Russ. J. Inorg. Chem.*, **18**, 1267 (1983).
- (a) V. I. Tagirov, N. F. Gakhramanov, A. G. Guseinov, F. M. Aliev, and G. G. Guseinov, *Sov. Phys. Cryst.*, **25**, 237 (1980); (b) R. Lesueur, C. Djega-Mariadassou, P. Charpin, and J. H. Albany, in "Ternary Compounds," pp. 5ff, Institute of Physics Conference Series 35, Institute of Physics, London (1977); (c) D. M. Ganbarov, G. G. Guseinov, and Z. Sh. Karaev, *Izv. Akad. Nauk. SSSR, Neorgan. Mater.*, **8**, 2211 (1972).
- K. J. Bachmann, M. I. Fearheily, Y. H. Shing, and N. Tran, *Appl. Phys. Lett.*, **44**, 407 (1984).
- J. J. M. Binsma, L. J. Giling, and J. Bloem, *J. Cryst. Growth*, **50**, 429 (1980).
- G. Dagan, S. Endo, G. Hodes, G. A. Sawatzky, and D. Cahen, *Solar Energy Mater.*, **11**, 57 (1984).
- R. A. Mickelsen and W. S. Chen, U.S. Pat. 4,335,266 (1982); *Appl. Phys. Lett.*, **36**, 371 (1980).
- (a) W. W. Gärtner, *Phys. Rev.*, **116**, 84 (1959); (b) M. A. Butler, *J. Appl. Phys.*, **48**, 1914 (1977); (c) Y. Mirovsky, R. Tenne, G. Hodes, and D. Cahen, *Thin Solid Films*, **91**, 349 (1982); R. Tenne, Y. Mirovsky, Y. Greenstein, and D. Cahen, *This Journal*, **129**, 1506 (1982).
- J. I. Pankove, "Optical Processes in Semiconductors," Chap. 3, Dover, New York (1971).
- S. A. Semiletov, *Sov. Phys. Crystallog.*, **5**(5), 673 (1961); *ibid.*, **6**(2), 158 (1961).
- cf.* D. M. Adams, "Inorganic Solids," Chap. 7.1.4., John Wiley and Sons, Ltd., London (1974).
- C. Manolikas, J. van Landuyt, R. de Ridder, and S. Amelinckx, *Phys. Status Solidi A*, **55**, 709 (1979).
- C. Djega-Mariadassou, A. Rimsky, R. Lesueur, and J. H. Albany, *Jpn. J. Appl. Phys.*, **19**, Suppl. 19-3, 89-93 (1980).
- J. C. W. Folmer and H. F. Franzen, *Phys. Rev. B*, **29**, 6261 (1984).
- Y. W. D. Chen, D. Cahen, R. Noufi, and J. A. Turner, *Solar Cells*, To be published, *This Journal*, **130**, 442C (1983).
- J. A. Turner, M. Bhushan, and B. A. Parkinson, Abstract 357, p. 571, The Electrochemical Society Extended Abstracts, Vol. 83-2, Washington, DC, Oct. 9-14, 1983; *This Journal*, To be published.
- cf.* A. Heller, K. C. Chang, and B. Miller, *ibid.*, **124**, 697 (1977), *J. Am. Chem. Soc.*, **100**, 684 (1978).
- J. C. Bride, P. C. Newman, and H. C. Wright, *Br. J. Appl. Phys.*, **9**, 110 (1958).
- (a) W. Rehwald and G. Harbeke, *J. Phys. Chem. Solids*, **26**, 1309 (1965); (b) G. F. Garlick *et al.*, *Proc. Phys. Soc. London*, **82**, 16 (1963).
- P. G. Rustamov, F. D. Mamedaliev, and M. A. Alidzhanov, *Inorg. Mater.*, **5**, 313 (1967).
- R. Diehl and R. Nitsche, *J. Cryst. Growth*, **28**, 306 (1975).
- J. C. W. Folmer, Unpublished results.
- C. Herrington and D. Cahen, Unpublished results.
- J. A. Turner, To be published.

Gas Permeation Properties of Solid Polymer Electrolyte (SPE) Membranes

Tetsuo Sakai, Hiroyasu Takenaka, Noboru Wakabayashi, Yoji Kawami, and Eiichi Torikai

Government Industrial Research Institute, Osaka Ikeda-shi, Osaka-fu 563, Japan

ABSTRACT

Gas permeation properties for Nafion membranes and their composites were investigated under various conditions. The permeability coefficients of Nafion depended greatly on the water content, the cation form, and the ion-exchange capacity. The gas permeation rate through a same sample varied with temperature, pressure, and membrane thickness. The permeability of hydrogen was about twice as great as that of oxygen. The electrocatalyst plated on the membrane did not serve as a barrier for gas permeation, but the structure of the catalyst layer played an important role in gas permeation during water electrolysis.

Perfluorosulfonic acid membranes (Nafion®), which has excellent chemical stability and high protonic conductivity, have received remarkable attention owing to their importance in electrochemical applications such as hydrogen-air fuel cells (1), chlor-alkali electrolysis (2, 3), and water electrolysis (4-6). In these electrochemical cells, catalytic electrodes are tightly bonded to the both sides of Nafion membrane to form an intimate electrode/electrolyte contact, and the membrane serves as both solid polymer electrolyte (SPE) and cell separator. It is well known that gas permeation through the SPE membrane causes a decrease in current efficiency. Recently, many studies on polymer structure (7-11) and ion transport (12-14) in Nafion membranes have been reported; however, detailed studies on gas permeability of the SPE membranes are few (15-17).

In this work, therefore, the effects of water content, cation form, ion-exchange capacity, and catalyst plating for Nafion membranes were examined on gas permeation. On the basis of the results, gas permeation during water electrolysis (18) was discussed.

Experimental

Membrane materials.—Measurements were made on Nafion 117 and 125 membranes (Plastic Department, du Pont) which have film thickness of 0.0185 and 0.013 cm and equivalent weight (EW) of 1100 and 1200, respectively. The EW is defined as the weight of acid polymer which neutralizes one equivalent of base and is given by

$$\text{IEC} = 1000/\text{EW} \quad [1]$$

where IEC is an ion-exchange capacity expressed in milliequivalents per gram of dry H⁺ form polymer.

Pretreatments of the purchased membranes were made as follows. They were thoroughly washed with acetone, then boiled in 2N HCl solution for 1h, and repeatedly washed with distilled water. The H⁺ form membrane obtained in this way was used as a starting material. Water absorption of the membrane was controlled by changing hydrothermal treatment temperature using an autoclave and expressed in weight percentage of water per 1g of dry polymer. The drying processes at 100°C in an air were repeated until a constant value was obtained. Potassium form membrane was obtained by immersing the H⁺ form membrane in 2N KOH solution for several days.

Nafion-electrocatalyst composites, which load metals in the range of 1-2 mg/cm², were prepared by an electroless plating of noble metal such as Pt, Rh, and Ir onto both sides of membrane (5). In order to improve adhesive property between the membrane and the plated metal, the surface of the membrane was roughened by a sand blasting machine (Daiichi Meteco Company). The thickness of the plated catalyst layer and the extent of the surface roughening were examined by means of a scanning electron microscope (Hitachi, S-430).

Measurement of gas permeation.—Gas permeability was measured with a volumetric method under high pressure

differences. The sample was sandwiched between stainless cells which have permeation area of 15.2 cm². In order to prevent the wet membrane from drying out during the experiment, filter paper soaked in distilled water was placed on the both sides of the membrane and penetrating gas was humidified by passing through distilled water in an autoclave. The penetrating gases such as H₂ and O₂ were introduced into the higher pressure cell after several flushings to replace the air. Gas permeation rate v (expressed in cubic centimeters per second), was measured by a precise gas flowmeter based on soap membrane (Standard Technology Company) in a steady state and converted to a STP (0°C, 1 atm) state of gas volume. The permeation rates under various pressures in the range of 1-30 atm were obtained at a constant temperature and plotted against the pressure differences (Δp). From the slope of the v vs. Δp plot, average permeability coefficient (P_m) expressed in cm³ (STP) · cm/cm² · s · cm Hg was derived from the following equation

$$P_m = \frac{(v/\Delta p)L}{A} \quad [2]$$

where L is the membrane thickness (in centimeters), A the permeating area (in square centimeters), and P the pressure difference (in cm Hg). The permeability values of H₂ and O₂ were obtained in the temperature range of 20°-90°C.

Results and Discussion

Table I shows characteristics of various kinds of Nafion membranes for gas permeation measurements. The water content of the membranes depended greatly on the treatment temperatures, equivalent weight, and salt form, as reported previously (19). Considerable loss of absorbed water occurred during gas permeation measurements for the highly swollen membranes, despite the existence of the wetted filter paper. By measuring permeability after a gas permeation for several hours, reproducible values of permeability coefficients (P_m) were obtained within ±5% on repeated runs. The existence of the wetted filter paper scarcely had influence on the permeation rate. We discussed the P_m values of the membranes on the basis of the values of water content and film thickness after the permeability measurements. Figures 1, 2, and 3 show Arrhenius plots of the P_m values of H₂ and O₂ for Nafion 117 (H⁺ form), 125 (H⁺ form), and 117 (K⁺ form) membranes with various water content, respectively.

Effect of water content.—The P_m values of H₂ and O₂ for all the types of membranes increased with increasing water content, suggesting that water contained in the membranes plays an important role in gas permeation. In order to discuss in more detail the influence of water on the P_m values, the permeabilities for Nafion 117 (H⁺) containing water less than 35 weight percent (w/o) and for Nafion 125 (H⁺) containing water less than 22 w/o were examined as follows. Immediately after the dry membrane was wetted with distilled water, the P_m value at

Table I. Characteristics of Nafion membranes for gas permeation measurements

Type of membrane	Thermal treatment temperature (°C)	Water content ^b (Film thickness) ^c	
		Before ^d	After ^e
N117 H ⁺	Dry ^a		1.7 (0.185)
	100	36 (0.220)	35 (0.220)
	140	60 (0.242)	50 (0.237)
	170	121 (0.280)	102 (0.265)
N125 H ⁺	Dry		1.6 (0.132)
	100	26 (0.152)	22 (0.149)
	140	39 (0.162)	34 (0.159)
	180	63 (0.175)	50 (0.169)
N117 K ⁺	Dry		1.5 (0.185)
	100	22 (0.200)	21 (0.198)
	140	31 (0.220)	27 (0.215)

^a Dried at 100°C in an air for 5h.

^b In weight percent water per 1g of dry polymer.

^c In millimeters. The average deviation is ± 0.003 .

^d Before gas permeability measurements.

^e After gas permeability measurements.

26°C was measured, and thereafter the water content was determined. The water content dependences of the P_m values of H₂ and O₂ at 26°C are shown in Fig. 4 and 5, respectively. The previous data by LaConti *et al.* (15, 16), which exhibited average values for three kinds of Nafion (H⁺ form) membranes with different ion-exchange

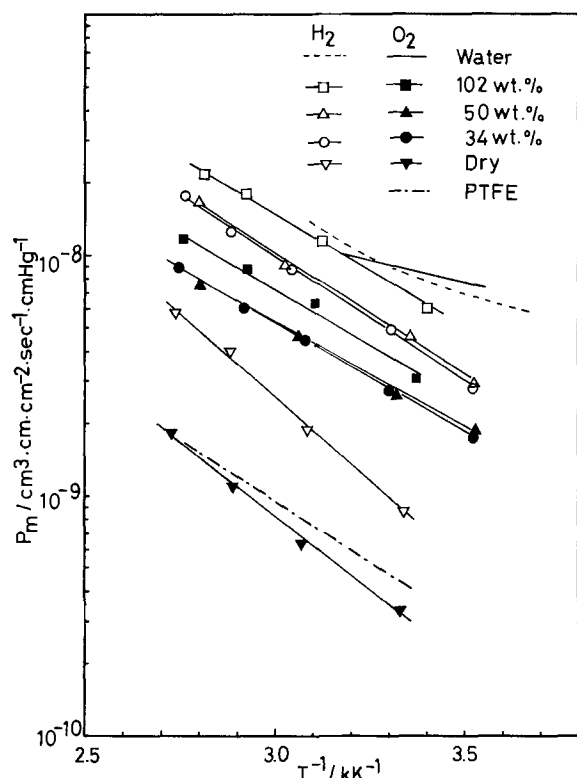


Fig. 1. Arrhenius plots of permeability coefficients (P_m) of H₂ and O₂ for Nafion 117 (H⁺) membranes with various water contents. Estimated values for water and previous values (22) for PTFE were shown for comparison.

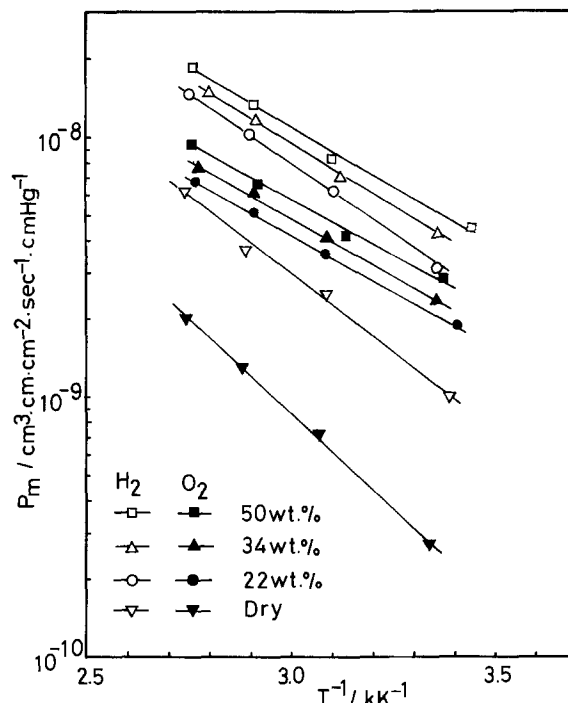


Fig. 2. Arrhenius plots of permeability coefficients (P_m) of H₂ and O₂ for Nafion 125 (H⁺) membranes with various water contents.

capacities (EW = 1640, 1260, and 1090), are shown by the dotted line for comparison. Though both sets of values were very close in the range of low water content, previous values showed a more rapid increase than those in this work with increasing water content.

The water content dependences of permeability ratio, $P_m(\text{H}_2)/P_m(\text{O}_2)$, at 80°C for Nafion 117 (H⁺), 125 (H⁺), and 117 (K⁺) are shown in Fig. 6. The permeability ratio drastically decreased with increasing water content and became almost constant in the higher water content region. The constant $P_m(\text{H}_2)/P_m(\text{O}_2)$ value was approximately 2 at 80°C for Nafion 117 (H⁺) and 125 (H⁺). The $P_m(\text{H}_2)/P_m(\text{O}_2)$ values for the K⁺ form membrane had a tendency to come close to the values for the H⁺ form membranes with increasing the water content.

The structure of Nafion membrane has been proposed by Gierke *et al.* (7) based on the results obtained by small

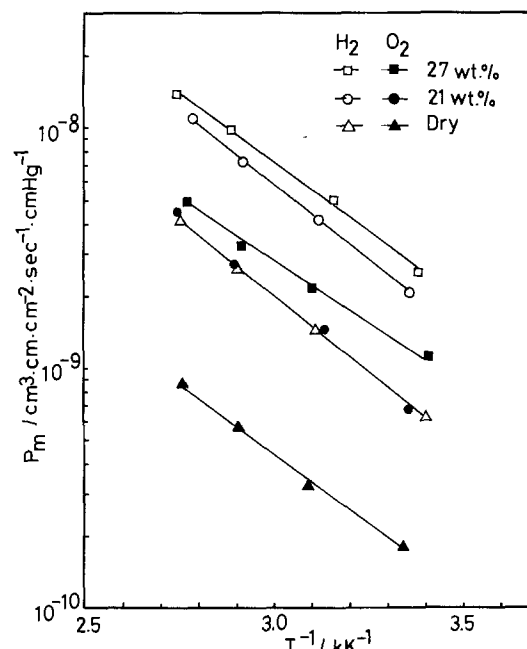


Fig. 3. Arrhenius plots of permeability coefficients (P_m) of H₂ and O₂ for Nafion 117 (K⁺) membranes with various water contents.

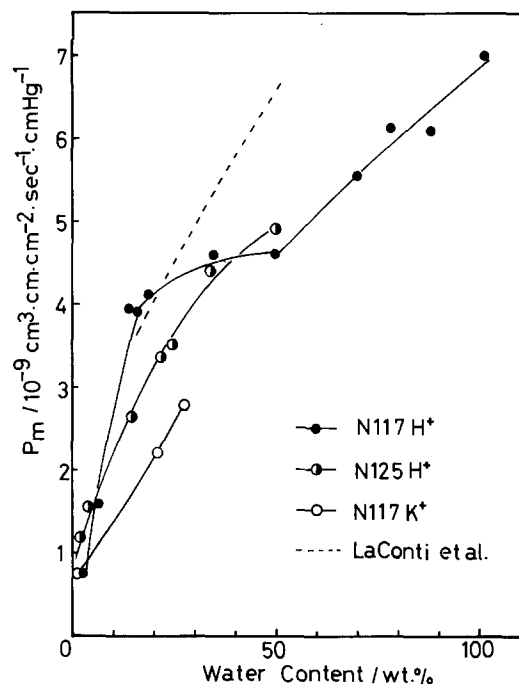


Fig. 4. The influence of water content on permeability coefficients (P_m) at 26°C of H_2 for Nafion 117 (H^+), 125 (H^+), and 117 (K^+) membranes. Previous data by LaConti *et al.* (15, 16) on Nafion (H^+) membrane are shown by the dotted line.

angle x-ray scattering, mass-transfer experiments including hydraulic permeation and water diffusion, and electron microscopy. The structure model, so-called the cluster-network model, is as follows. Polymeric ions and absorbed water exist in approximately spherical domains as ionic clusters, separated from the polytetrafluoroethylene (PTFE) matrix. These clusters are assumed to be connected by short narrow channels which have a diame-

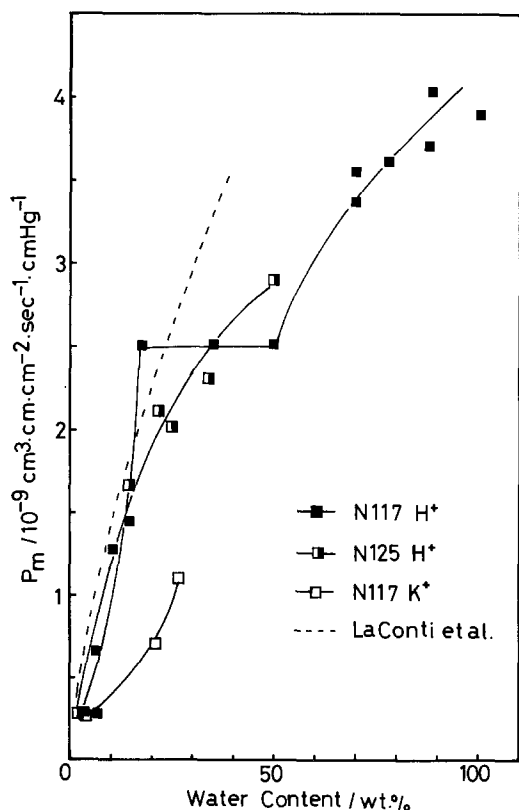


Fig. 5. The influence of water content on permeability coefficients (P_m) at 26°C of O_2 for Nafion 117 (H^+), 125 (H^+), and 117 (K^+) membranes. Previous data by LaConti *et al.* (15, 16) on Nafion (H^+) membrane are shown by the dotted line.

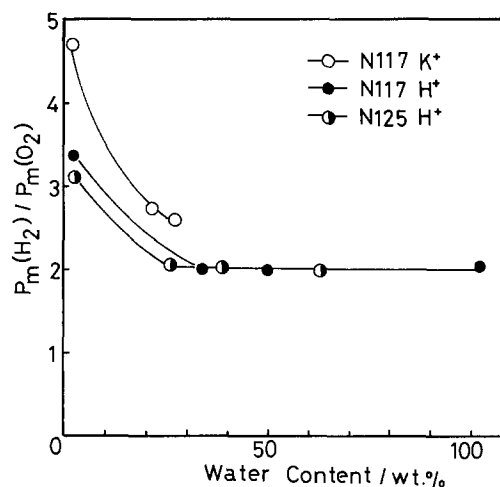


Fig. 6. The influence of water content on permeability ratios, $P_m(H_2)/P_m(O_2)$, at 80°C for Nafion 117 (K^+), 117 (H^+), and 125 (H^+) membranes.

ter of about 10Å. It was revealed that the cluster size grows with increasing amount of absorbed water; for example, a diameter of ionic cluster changed from 25.2 to 40.8Å when a water content increased from 5.4 to 19.4 w/o for 1200 EW membrane (8).

Since the swollen membrane was composed of both the PTFE matrix and the water absorbed in ionic cluster, its permeability properties are expected to depend strongly on those of their materials. The permeability coefficients (P_m) for water were estimated from the previous data (20, 21) of the diffusion coefficients (D) and the solubility (S) on the assumption that the equation $P_m = DS$ was applicable to the gas permeation in water. The P_m values estimated here for water and previously reported for PTFE (22) are plotted in Fig. 1 for comparison. The P_m values for Nafion dry membrane were very close to those for PTFE, while the P_m values for the wet membranes increased and approached those for water with increasing water content.

The water-content dependences of gas permeation properties can be explained in terms of the cluster-network model of Nafion structure. In a dried state, since only small amounts of absorbed water are accommodated in the clusters and these are isolated from each other, the water can scarcely influence the gas diffusion. When the membrane absorbs water and the narrow channels are filled with water, the gas diffusion through water would become predominant, causing the rapid change in the P_m and the $P_m(H_2)/P_m(O_2)$. With an increase of the water content, since an interaction between gas and polymer chains is reduced, the $P_m(H_2)/P_m(O_2)$ value would become almost constant.

Effect of equivalent weight.—A slight decrease of ion-exchange capacity from 0.91 meq/g (Nafion 117) to 0.83 meq/g (Nafion 125) is attended by a significant decrease of water absorption from 36 to 26 w/o (hydrothermal treatment at 100°C). This behavior is ascribed to the decrease in ion-cluster size with decreasing ion-exchange capacity as reported previously (8). When both the membranes were treated at a same temperature, the Nafion 117 had higher P_m values than the Nafion 125. In order to discuss whether the P_m is influenced by only the water content or by both the water content and the ion-exchange capacity, the P_m values of Nafion 117 (H^+) and 125 (H^+) were compared on the P_m vs. water content plots in Fig. 4 and 5. The P_m values of H_2 and O_2 for Nafion 117 drastically increased about six to eight times and then became almost constant in the water content range of 20-50 w/o, followed by a further increase in P_m in the higher water content range. On the other hand, the P_m values for Nafion 125 increased smoothly with the water content. The difference of behaviors of both the membranes may be explained by using the structure model of Nafion. Since the

amount of water which can be accommodated within a cluster in Nafion 117 is considerably greater than that in Nafion 125, their structures at the same water content would be different from each other. If we assume that Nafion 117 has a water content region where absorbed water is used only in the cluster growth and the channel diameter is kept almost constant, the occurrence of the constant P_m region can be understood.

The difference in the P_m values between Nafion 117 and Nafion 125 would be mainly ascribed to the difference in water content. The change in the ion-exchange capacity itself can affect the behavior of the P_m vs. water content plot.

Effect of cation form.—The change in cation forms influences the cluster size and therefore water content (8), resulting in the change in the P_m values. In order to discuss the effect of cation form itself on the permeability, the P_m values of the Nafion 117 (H⁺ form) and (K⁺ form) membranes were compared at the same water content in Fig. 4 and 5. The P_m values of H₂ and O₂ for the H⁺ form membrane were much greater than those for the K⁺ form one, suggesting that the K⁺ ions hinder the gas diffusion. Similarly, the $P_m(\text{H}_2)/P_m(\text{O}_2)$ values for H⁺ form membrane were less than those for the K⁺ form membrane (Fig. 6). Since the values of P_m and $P_m(\text{H}_2)/P_m(\text{O}_2)$ for the K⁺ form membrane have a tendency to come close to the values for the H⁺ form one with increasing water content, the influence of cations on the P_m seems to decrease with an increase of water content.

These results support the gas permeation model that gases diffuse through the part of the channels and the clusters which contain ions and water.

Effect of electrocatalyst plating.—The membrane-electrocatalyst composite, which was formed by plating noble metals on both the sides of Nafion, was used in a SPE water electrolysis cell. In order to discuss the decrease in current efficiency in terms of the gas permeation through the composite during water electrolysis, the permeability properties of the composites were examined and compared with those obtained for the original membrane (nonplating Nafion 117). The results were summarized in Table II. The Arrhenius plots of the P_m showed that the apparent activation energies were almost constant throughout all the samples. By the surface roughening treatment of the original membrane (OM), the surface was etched in the depth of 5-10 μm which corresponds to the 2-5% of the swollen membrane thickness, causing a little increase in the P_m . The OM-electrocatalyst composite with a catalyst thickness of 5-10 μm had a little greater permeability than the OM, indicating that the catalyst layer had a porous structure and did not serve as a gas barrier. The increase in P_m will be due to the effect of metal insertion into the membrane by which the path of

gas permeation is spread out. This behavior became more significant for the surface-roughened membrane (SRM)-electrocatalyst composites, where the maximum crack depth went to 18-22 μm after the metal plating. The increase in P_m , which was almost proportional to the increase in the depth of crack, was attended by an increase in the P_m ratio, $P_m(\text{H}_2)/P_m(\text{O}_2)$, suggesting an increase in the number of fine pores whose size is comparable to the molecular size of hydrogen.

It was revealed that the deposition of the catalyst layer on the membrane surface does not prevent gas permeation, but promotes it because the metal forms porous layer and is deeply inserted into the polymer.

When these composites were used for the water electrolysis, the current efficiencies in the range of 94-97% at 100 A/dm² and very high gas purities (greater than 99.999% for H₂, greater than 99.98% for O₂) were obtained as previously reported (18). The loss of current will be ascribed to the gas permeation through the membrane and recombination reaction of the permeating gas on the electrocatalyst. In terms of mass balance, the current efficiency can be related to the gas permeating rate as follows. When a part of generating hydrogen on the cathode permeates toward the anode at the rate of X_H (cm³/s · cm²) and approximately 100% of it undergoes recombination reaction on the anode, oxygen of 1/2 X_H will be inhibited to evolved. In the same manner, when a part of generating oxygen on the anode permeates toward the cathode at the rate of X_O (cm³/s · cm²) and undergoes recombination reaction on the cathode, hydrogen of 2 X_O will be inhibited to evolved. Therefore, the current efficiency (E) can be given by

$$E \text{ (cathode side)} = E \text{ (anode side)} \\ = (C_H - 2X_O - X_H)/C_H \quad [1]$$

where C_H is the hydrogen evolving rate predicted from the current density. The loss volume at 80°C ($P = 2X_O + X_H$) was plotted against the current density for samples no. 3, no. 4, and no. 6 in Fig. 7. The loss volume varied almost proportionally with the current density, suggesting that the evolved gas is disturbed to escape from the catalyst layer and induces a considerably high local pressure. If an individual permeation rate (X_H, X_O) is estimated, the values of the induced local pressures can be obtained by using the permeation rate vs. pressure difference relation shown in Fig. 8.

The permeation ratio, X_H/X_O , under water electrolysis will be given by

$$X_H/X_O = [P_m(\text{H}_2)/P_m(\text{O}_2)] [\Delta P_H/\Delta P_O] \quad [2]$$

where $P_m(\text{H}_2)/P_m(\text{O}_2)$ is the permeability ratio shown in Table II and $\Delta P_H/\Delta P_O$ the ratio of local pressure of hydrogen to oxygen. Since the local pressure has tendency to increase with increasing the gas generating volume, the $\Delta P_H/\Delta P_O$ is assumed roughly to be 2 according to the volume ratio of generating gases. From the X_H/X_O ratio estimated here and the loss volume ($P = 2X_O + X_H$), hydrogen permeation rate (X_H) was obtained and then the hydrogen local pressure was determined based on the permeation rate vs. pressure difference relation. The hydrogen local pressures at 80°C at 50 and 100 A/dm² for the composites are listed in Table III.

The local pressures of the SRM composites were lower than that of the OM composite by about 30% at 100 A/dm². Since the catalyst plated on the SRM has a more porous

Table II. Permeability coefficients (P_m) at 80°C and their ratios $P_m(\text{H}_2)/P_m(\text{O}_2)$ for Nafion 117 membrane and its electrocatalyst composites

Sample no.	Type of sample	P_m^a (80°C)		$P_m(\text{H}_2)/P_m(\text{O}_2)$
		H ₂	O ₂	
1	OM ^c	144 (4.7) ^b	71 (4.0) ^b	2.0
2	SRM ^d	154	71	2.2
3	Pt-OM-Rh	170 (4.7) ^b	78 (4.1) ^b	2.2
4	Pt-SRM-Rh	191	78	2.4
5	Pt-SRM-Ir(Ru)	203	80	2.5
6	Pt-SRM-Pt	250 (4.8) ^b	92 (3.9) ^b	2.7

^a P_m in 10⁻¹⁰ cm (STP) · cm/cm² · s · cm Hg.

^b Activation energies in kilocalories per mole.

^c Original membrane (35 w/o water content).

^d Surface-roughened membrane.

Table III. The estimated values of local pressure induced by the evolving gas under water electrolysis at 80°C

Current density (A · dm ⁻²)	Local pressure (atm)		
	Pt/OM/Rh (no. 3)	Pt/SRM/Rh (no. 4)	Pt/SRM/Pt (no. 6)
50	29	28	28
100	65	43	50

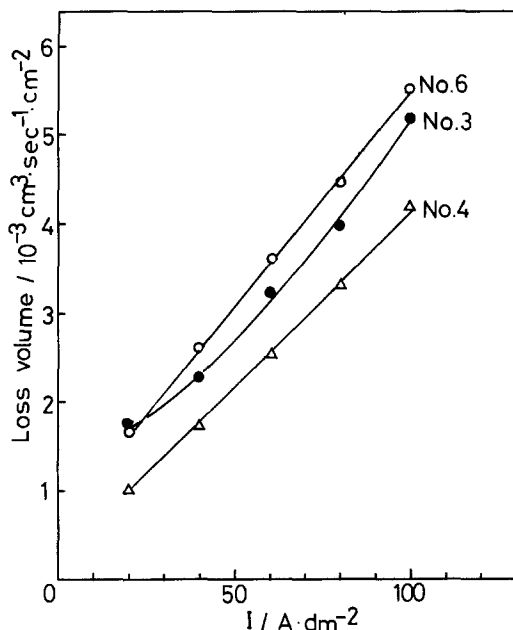


Fig. 7. Current density (I) dependences of loss volume ($P = 2X_{O_2} + X_{H_2}$) at 80°C for samples no. 3, no. 4, and no. 6.

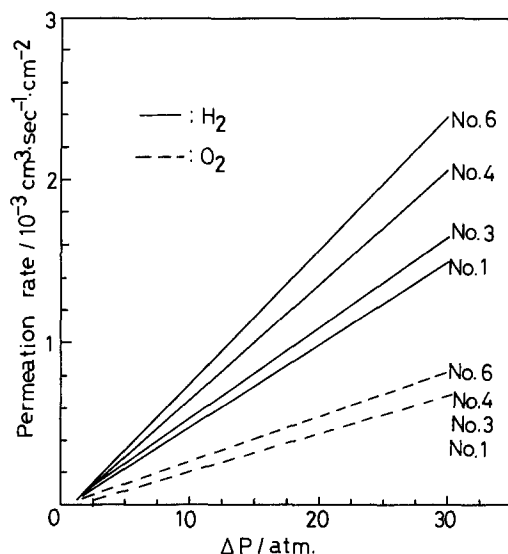


Fig. 8. Permeation rate vs. pressure difference (Δp) relations at 80°C for samples no. 1, no. 3, no. 4, and no. 6.

structure for the evolved gas to escape than that plated on the OM, this result would be explained in terms of the difference in structure of the catalyst layer. On account of the above effects of electrode structure, the loss volume under water electrolysis increased in order of no. 4 (Pt/SRM/Rh), no. 3 (Pt/OM/Rh), and no. 6 (Pt/SRM/Pt), as shown in Fig. 7, despite the fact that the permeability coefficients of H_2 for no. 4 and no. 6 were higher than that for no. 3 by about 12% and 47%, respectively. Therefore, it is concluded that the mild surface roughening treatment, by which porous layer of catalyst is formed, is very effective for suppressing the gas permeation under water electrolysis.

Summary

The gas permeation measurements carried out in this work revealed the following matters. The permeability

coefficients (P_m) of the Nafion depend greatly on the water content, the cation form, and the ion-exchange capacity. The gas permeation rate through a same sample varies with temperature, pressure, and membrane thickness. The permeability of hydrogen is about twice as large as that of oxygen. Though the electrocatalyst plated on the membrane surfaces does not serve as a barrier for gas permeation, the structure of the catalyst layer is very important for gas permeation during water electrolysis. The porous structure facilitates the departure of the evolving gas, leading to the decrease in the induced local pressure and then the decrease in the gas permeating rate.

Further investigations are in progress in order to understand more completely the gas diffusion mechanism through Nafion membranes.

Acknowledgments

The authors are grateful to Dr. H. Ishikawa and Mr. I. Uehara for their useful suggestions in connection with the experimental works. The authors thank Dr. Y. Souma for her help in preparation of manuscript.

Manuscript submitted July 10, 1984; revised manuscript received ca. Feb. 1, 1985.

The Government Industrial Research Institute assisted in meeting the publication costs of this article.

REFERENCES

1. L. J. Nuttall and J. F. McElroy, *Int. J. Hydrogen Energy*, **8**, 609 (1983).
2. W. Grot, *Chem. Ing. Tech.*, **50**, 299 (1978).
3. T. Berzins, Abstract 437, p. 1137, The Electrochemical Society Extended Abstracts, Vol. 77-2, Atlanta, GA, Oct. 9-14, 1977.
4. L. J. Nuttall, *Int. J. Hydrogen Energy*, **2**, 395 (1977).
5. H. Takenaka, E. Torikai, Y. Kawami, and N. Wakabayashi, *ibid.*, **7**, 397 (1982).
6. H. Takenaka, E. Torikai, Y. Kawami, N. Wakabayashi, and T. Sakai, *Denki Kagaku*, **52** (6), 156 (1984).
7. T. D. Gierke, Abstract 438, p. 1139, The Electrochemical Society Extended Abstracts, Vol. 77-2, Atlanta, GA, Oct. 9-14, 1977.
8. Y. H. William and T. D. Gierke, *J. Membr. Sci.*, **13**, 307 (1983).
9. R. S. Yeo, *This Journal*, **130**, 533 (1983).
10. M. Falk, *Can. J. Chem.*, **58**, 1495 (1980).
11. K. A. Mauritz and C. J. Hora, in "Ions in Polymer," A. Eisenberg, Editor, Chap. 8, ACS Advances in Chemistry Series 187, American Chemical Society, Washington, DC (1980).
12. H. L. Yeager and B. Kipping, *J. Phys. Chem.*, **83**, 1836 (1979).
13. H. L. Yeager and A. Steck, *This Journal*, **128**, 1880 (1981).
14. Z. Twardowski, H. L. Yeager, and B. O'Dell, *ibid.*, **129**, 328 (1982).
15. A. B. LaConti, A. R. Fragala, and J. R. Boyack, in "Electrode Materials and Processes for Energy Conversion and Storage," J. D. E. McIntyre, S. Srinivasan, and F. G. Will, Editors, pp. 354-374, The Electrochemical Society Softbound Proceedings Series, Princeton, NJ (1977).
16. J. R. Boyack, Unpublished data.
17. R. S. Yeo and J. McBreen, *This Journal*, **126**, 1682 (1979).
18. H. Takenaka, E. Torikai, Y. Kawami, and T. Sakai, Abstract, p. 17, The Electrochemical Society of Japan: The Chloralkali Industry Association Extended Abstracts, Kyoto, Nov. 18-19, 1982.
19. W. G. F. Grot, G. E. Munn, and P. N. Walmsley, Abstract 154, p. 394, The Electrochemical Society Extended Abstracts, Vol. 72-1, Houston, TX, May 7-11, 1972.
20. D. M. Himmelblau, *Chem. Rev.*, **64**, 527 (1964).
21. "Lange's Handbook of Chemistry," 12th ed., J. A. Dean, Editor, McGraw-Hill, New York (1979).
22. R. A. Pasternak, M. V. Christensen, and J. Heller, *Macromolecules*, **3**, 366 (1970).

Assessment of Polymer-Electrolyte Batteries for EV and Ambient Temperature Applications

M. Gauthier,* D. Fauteux,* G. Vassort,* A. Bélanger,* and M. Duval

Institut de recherche d'Hydro-Québec (IREQ), Varennes, Québec, Canada J0L 2P0

P. Ricoux, J.-M. Chabagno, D. Muller, and P. Rigaud

Direction Recherche, Développement et Innovation, Société Nationale Elf Aquitaine (SNEA), 75739 Paris Cedex 15, France

M. B. Armand* and D. Deroo

Laboratoire d'Énergétique Electrochimique (LEE), 38402 Grenoble, France

ABSTRACT

The feasibility of polyether-based all-solid-state cells has been assessed in a joint research and development program. At 80°-100°C, cells using TiS_2 or V_6O_{13} positive-electrode material and excess lithium show high material utilization at 0.5-1.0 mA/cm² and can be cycled more than 250 times. Furthermore, a new family of polyether electrolytes has been found that allows room temperature (26°C) operation at 3-20 $\mu\text{A}/\text{cm}^2$.

A joint research and development project ("ACEP¹ Project") between Société Nationale Elf Aquitaine (SNEA), Institut de recherche d'Hydro-Québec (IREQ), and ANVAR² acting for Laboratoire d'Énergétique Electrochimique (LEE) has been under way since 1980 to develop thin film solid-state batteries based on polyether complexes. The starting point for this project was Armand's pioneering work, which suggested the use of polymer electrolytes for high energy-density batteries (1). Albeit only slightly conducting, these materials can be obtained in a high surface-to-thickness ratio, and they also maintain a good contact with the electrode materials.

The main interest of SNEA and IREQ in this joint project is to develop a battery for electric vehicle (EV) application. Consequently, the work was organized along the lines of the main technical tasks identified an essential for success (Fig. 1).

Only two of the aspects of the project shown in Fig. 1 are dealt with in the present paper: the performance of TiS_2 and V_6O_{13} positive composite electrodes and their cycling properties vs. an excess-lithium negative electrode, and the ambient temperature project. To meet the power density requirements for EV applications (>80 W/kg sustained power) while using polyethylene oxide (PEO, Mw = 5×10^6 or 5M), the operating temperature was fixed at 80°-100°C for most of the tests. As shown below, PEO electrolytes have a very limited performance at temperatures below 40°C, which precludes their use in electrochemical cells working at ambient temperature. In the course of research, however, a family of improved electrolytes was developed that appears to be useful for ambient temperature applications. Initial results on primary and rechargeable cells at 26°C are presented to give an idea of the potential applications of this emerging technology.

Experimental

The experimental work described here was done using electrolyte and composite-electrode films obtained by solution casting techniques, as previously described (1, 2). Commercial PEO (5M and 0.9M) from Polyscience was used as received. The ratio between the number of monomer units ($\text{CH}_2\text{-CH}_2\text{-O}$) and the number of lithium in the salt (O/Li) was fixed at $\approx 8/1$ for both LiClO_4 (Ventron-Alfa Division) and LiCF_3SO_3 (Ozark-Mahoning) complexes.

The electrolyte thickness varied from 160 to 100 μm for small electrochemical cells and from 80 to 50 μm for

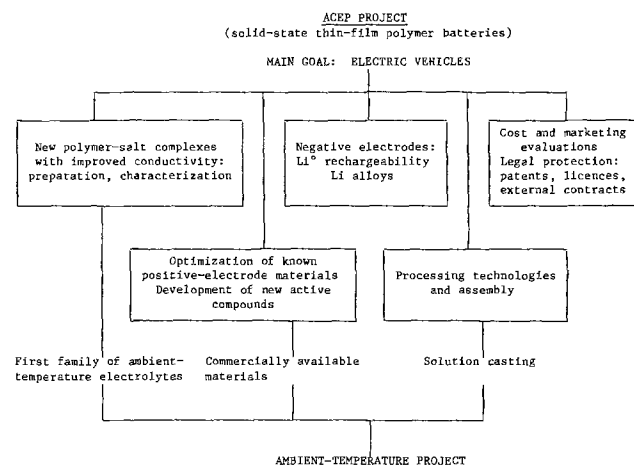
larger surface cells. The anodes were cut from freshly pressed Li° or from $\approx 100 \mu\text{m}$ lithium foils. The TiS_2 and V_6O_{13} (< 37 μm grain size) were prepared by in-house synthesis after adapting published procedures (6, 7).

Electrolytic MnO_2 (Trona Chemicals, Kerr-McGee Chemical Corporation) and MoO_2 (Ventron-Alfa Division) (< 15 μm grain size) were used after drying. The positive composite electrodes included the electrolyte (O/Li = 8/1), the active material (40-50 volume percent [v/o]) and acetylene black (≈ 10 v/o).

The 3.9 cm² cells were crimp-sealed button cells or the cell constituents were housed in containers such as illustrated in Fig. 2 and 3. As shown in Fig. 2a, a central Li° reference electrode was used on one side of the electrolyte, while in the configuration of Fig. 2b a LiAl-Al reference electrode was made by inserting a 10 μm aluminum strip during cell assembly and electrochemically charging it. The EMF of the latter reference electrode ranged from +400 to +360 mV vs. Li° between room temperature and 100°C (3).

Figure 3b shows a larger 70 cm² cell. Cells like this can be stacked in parallel for the scale-up tests described later. This design is convenient for laboratory tests. Optimization in terms of the energy density for future cells is presently under study.

The cycling mode used for this study is based on constant discharge and charge currents with high and low voltage limits.



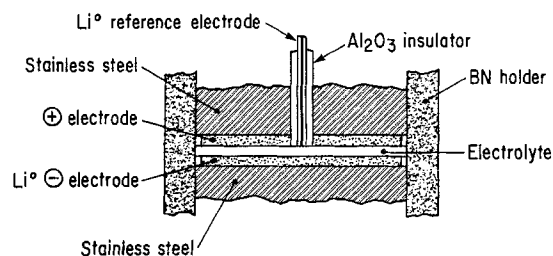
Started January 1983 - reassessed December 1984
Applications: microelectronics; small rechargeable power sources

Fig. 1. ACEP Project organization

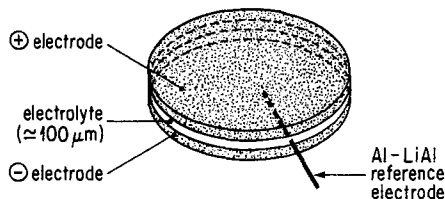
*Electrochemical Society Active Member.

¹Accumulateurs à électrolyte polymère.

²Agence Nationale de Valorisation de la Recherche.



a) Central-type reference electrode



b) Strip-type reference electrode

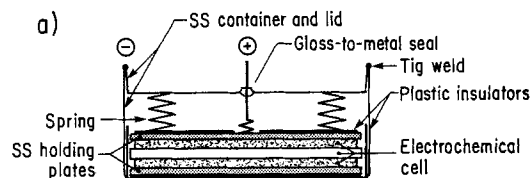
Fig. 2. Electrochemical cells with reference electrodes. a: Central-type Li⁺ electrode. b: Strip-type LiAl-Al electrode.

Results and Discussion

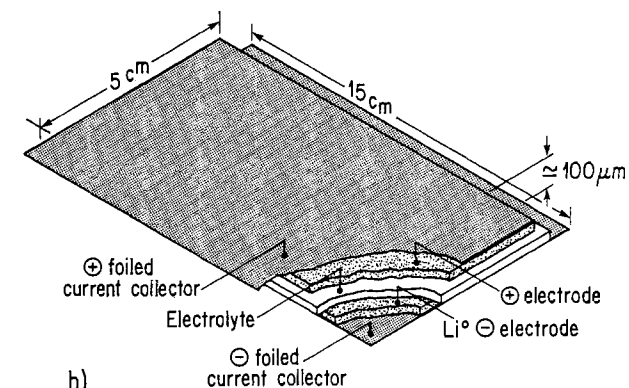
The results presented here serve to establish the characteristics of experimental Li/PEO/TiS₂ and Li/PEO/V₆O₁₃ cells with respect to their performance on cycling. The achieved power and energy densities represent only a first step towards performance optimization based on presently known or commercially available materials. Although the present work is based on the results of a large number of cells, efforts have been made in this presentation to gather most of the studies into a limited number of cells. The results are then considered typical of the technology.

In the discussion of the cycling profiles, unless otherwise indicated, comparison is made between a discharge curve and the subsequent charge curve.

Li/PEO/TiS₂ cell cycling profiles.—Figure 4 illustrates the cycling profile of a 2.9 mAh cell, showing the number of coulombs measured during discharge and charge vs.



b)

Fig. 3. a: Welded stainless steel cells with glass to metal seal. b: 70 cm² capacitor-type cell.

cycling. During the tests, several parameters such as T (°C) or the charge and discharge currents, J_c and J_d , were modified and/or systematically studied.

The changes (a to k on cycle number scale in Fig. 4) observed are listed below. They are also illustrated by additional figures.

a. At this point appears the effect of a lower discharging current on the number of coulombs followed by the effect of lower operating temperatures at constant current (Fig. 5).

b. This point shows charging/discharging at 70°C pursued for 14 cycles.

c. This marks the restorations, at 65°C, of the initial utilization of the TiS₂ electrode (previously observed at 100°C) by the reduction of currents J_d and J_c .

d. Here, cycling is continued at 44°C with a utilization lower than 10%. (Not shown here are some attempts at 26°C where, after a few hours, no current could be drawn from the cell.)

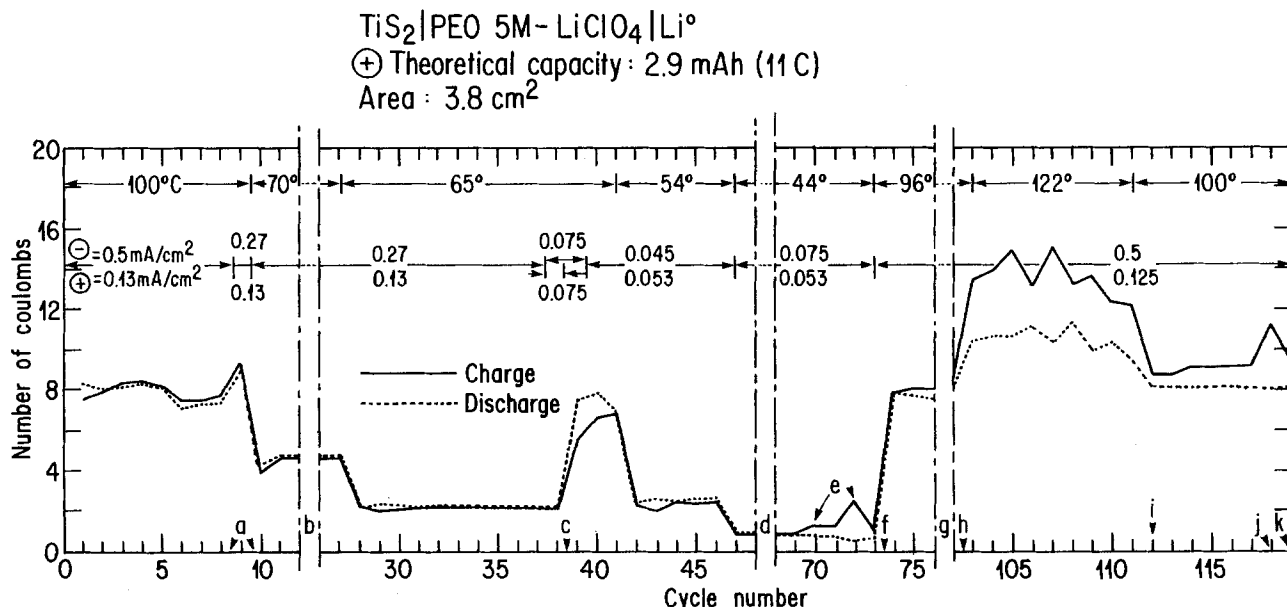


Fig. 4. Cycling profile of a 2.9 mAh TiS₂/Li cell: effect of temperature and cycling conditions on the number of coulombs observed on discharge (full lines) and charge (dotted lines). The discharge and charge currents, J_d and J_c , are represented as - and +, respectively.

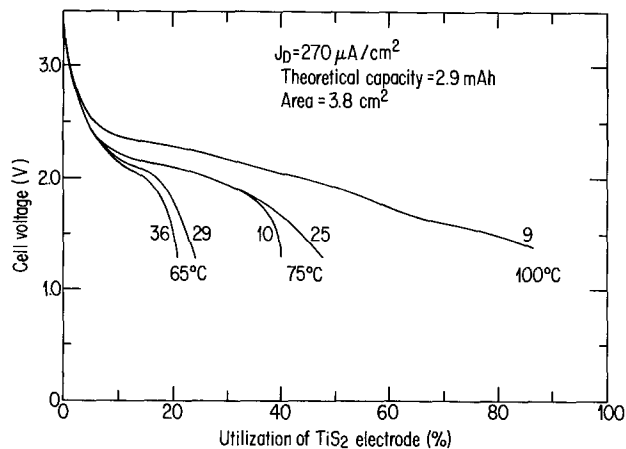


Fig. 5. Effect of the temperature on percentage of utilization of TiS_2 at 0.27 mA/cm^2 during discharge. The number on each curve corresponds to the cycle number.

e. At this point is marked the appearance of dendrites on charge after 24 cycles at 44°C (50h), a phenomenon believed to be related to the onset of crystallization of the PEO/LiClO_4 complex. The test temperature is relatively close to a eutectic temperature in the PEO/LiClO_4 phase diagram presently under study (4).

f. The initial utilization of TiS_2 is restored when the temperature increases to $\approx 100^\circ\text{C}$.

g. This marks continuation of cycling under initial conditions.

h. At this point, the increase of the operating temperature to 122°C results in a high utilization but leads to inefficient and anomalous recharge plateaus (Fig. 6).

i. This point indicates a return to operating temperature of 100°C , which leads to initial utilization on discharge (Fig. 7) but to slightly less efficient recharge. (Possible damage resulted from previous high temperature cycles, (Fig. 6)).

j. A dendrite at the end of the 118th recharge plateau appears here (Fig. 6). This phenomenon was not observed in other experiments, not reported herein, when Li^+ was replaced by an LiAl alloy, which seems to confirm that lithium dendrite formation is involved.

k. This marks the return to stable performance of the cycle observed before the dendrite appearance; this suggests that (i) the dendrite is burnt by the Joule effect and (ii) no permanent damage results from occasional dendrites owing to the self-healing properties of the polymer electrolyte.

The second cycling profile (Fig. 8) also for a Li/PEO/TiS_2 cell with a 3.3 mAh capacity was used princi-

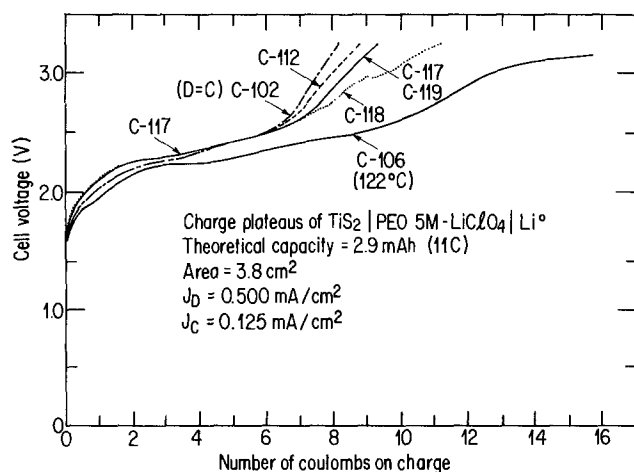


Fig. 6. Typical charge plateaus of TiS_2/Li^+ cell at different cycle numbers. C-102: Efficient charge plateau ($C = D$). C-106: Double-wave charge plateau of TiS_2 at 122°C . C-112: Slightly inefficient charge plateau after 10 cycles at 122°C . C-118: Charge plateau showing a dendrite occurrence. C-117/119: Charge plateaus before and after C-118.

pally to establish the relations between the charge and discharge currents and the utilization of the TiS_2 electrode, especially for power and energy evaluation. The main observations are described below.

Points a, a', and a'' mark the appearance of occasional dendrites observed during charge, similar to cycle C-118 of Fig. 6.

Points b and b' indicate where several cycles are run at 100° and 80°C to establish a relation between the utilization of TiS_2 and the discharge current J_D (mA/cm^2) (Fig. 9 and 10). The results at 100°C (Fig. 9) show very good agreement with the theory of the insertion of an alkali metal in a composite electrode (5), which proves that the limiting mechanism at 100°C is the lithium diffusion in TiS_2 and not the polymer electrolyte conductivity.

Points c and c' mark improved utilization of the TiS_2 electrode at 80°C as a result of the lower charging current.

Point d shows the effect of a time delay (1h) between the end of a discharge and the next charge, indicating the presence of local concentration gradients in the Li/TiS_2 cell at 80°C .

Point e marks drop in utilization of the TiS_2 electrode resulting from a relatively high charging current (1 mA/cm^2).

Point f indicates cycling at $J_D = 0.5 \text{ mA/cm}^2$ and $J_C = 1.0 \text{ mA/cm}^2$ for more than 90 cycles without any evidence of dendrite formation or significant performance degradation.

Point g marks the appearance of a certain inefficiency of the charge half-cycle (5-10%) after 275 cycles (already illustrated for cycle C-112 in Fig. 6). This test was pursued under similar conditions for more than 450 cycles.

A third cycling profile illustrated in Fig. 11 is also based on a Li/PEO/TiS_2 cell of 3.7 mAh capacity. It is a study of the effect of uninterrupted deep-discharge/charge cycles on the cell performance at 100°C .

The area between a and a' is an area of stable performance of the cell and the balanced discharge and charge plateaus over the first 36 cycles.

At point b, $\approx 95\%$ overall energy efficiency (energy out at C/2)/(energy in at C/7) was observed at cycle 16 (Fig. 12).

The span from c to c' encompasses the appearance of a slight inefficiency of the charge half-cycle at cycle 31, increasing to $\approx 10\%$ at cycle 89.

At point d, a temporary reduction in the observed charge inefficiency took place through an increase in the charge current (cycles 90-100).

Point e shows the stabilization of the charge half-cycle inefficiency vs. cycling from cycles 100 to beyond 250.

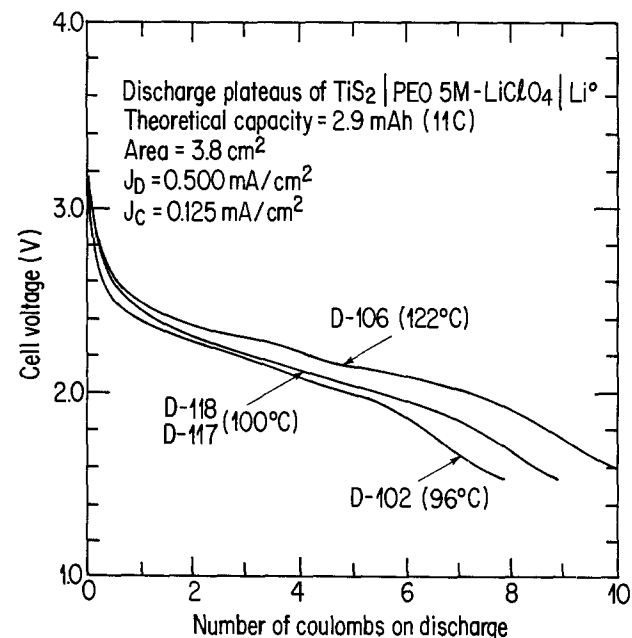


Fig. 7. Discharge plateaus corresponding to the cycle number and charge plateaus of Fig. 6.

TiS₂|PEO 5M-LiClO₄|Li⁺
 ⊕ Theoretical capacity: 3.3 mAh (12.5 C)
 Area: 3.8 cm²

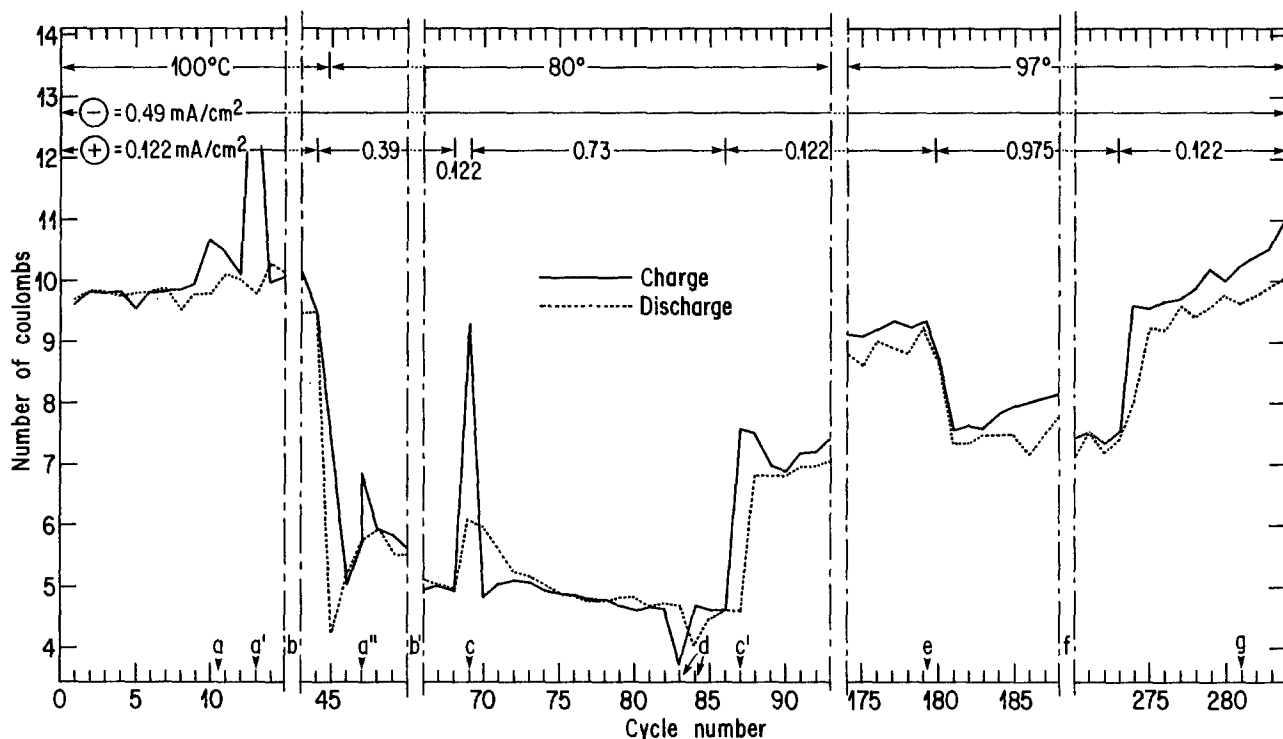


Fig. 8. Cycling profile of a 3.3 mAh TiS₂/Li⁺ cell: effect of discharge current vs. temperature and cycling. The discharge and charge currents, J_D and J_C , are represented as - and +, respectively.

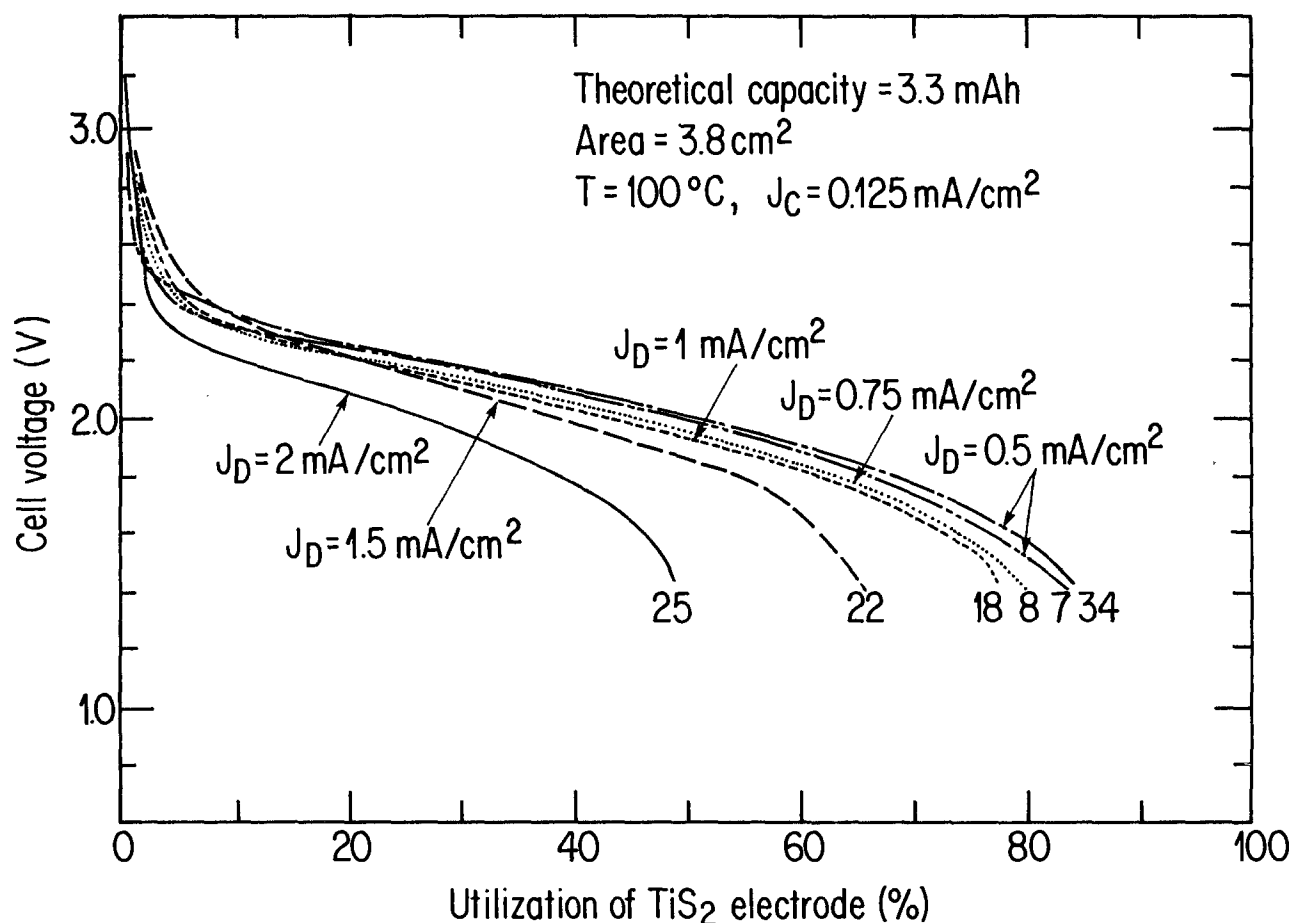


Fig. 9. Utilization of TiS₂/Li cell vs. discharge current densities at 100°C. The number on each curve corresponds to the cycle number

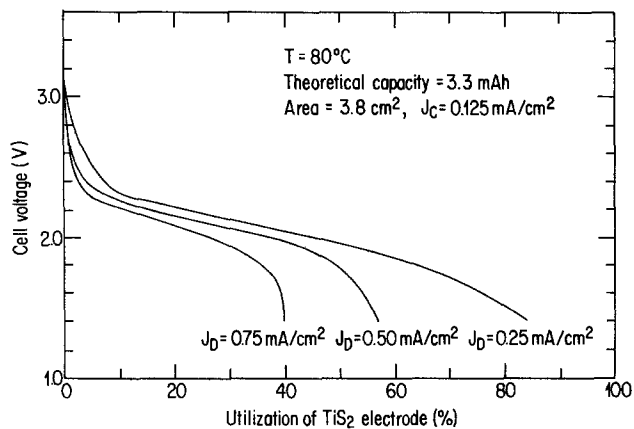


Fig. 10. Utilization of $\text{TiS}_2\text{Li}^\circ$ cell vs. discharge current densities at 80°C .

Nature of the lithium salt.—All cells described so far were prepared with lithium perchlorate complexes (O/Li = 8/1) present in the electrolyte and in the TiS_2 composite electrode. However, other cells were prepared which contained lithium salt only in the electrolyte and not in the composite electrode (where only pure PEO was used) when they were assembled. The results presented in Fig. 13 and 9 (at 100°C and 0.5 mA/cm^2) afford the conclusion that there is no significant difference in performance whichever of the two methods of cell preparation is used.

Furthermore, if for a given cell LiClO_4 was replaced by LiCF_3SO_3 , the utilization of the TiS_2 electrode dropped from 80% to $\approx 15\%$ to 100°C and 0.5 mA/cm^2 . To obtain an equivalent performance with LiCF_3SO_3 , the operating temperature had to be increased to $>130^\circ\text{C}$ and the current density reduced by half. This large difference in the performance of LiClO_4 - and LiCF_3SO_3 -based cells at 100°C is expected considering that the conductivity of LiCF_3SO_3 8/1 complexes is much lower than that of LiClO_4 8/1 complexes (1.9×10^{-5} vs. $1.6 \times 10^{-4} \Omega^{-1} \text{ cm}^{-1}$ at 100°C); furthermore, the LiCF_3SO_3 -PEO phase diagram predicts the presence of crystalline phases in the electrolyte. An additional explanation could be a higher anionic transference number in PEO- LiCF_3SO_3 vs. PEO- LiClO_4 complexes.

Origin of the polarization.—The *in situ* LiAl-Al reference electrode described in Fig. 2b was used (3) on several occasions in the present study in order to determine

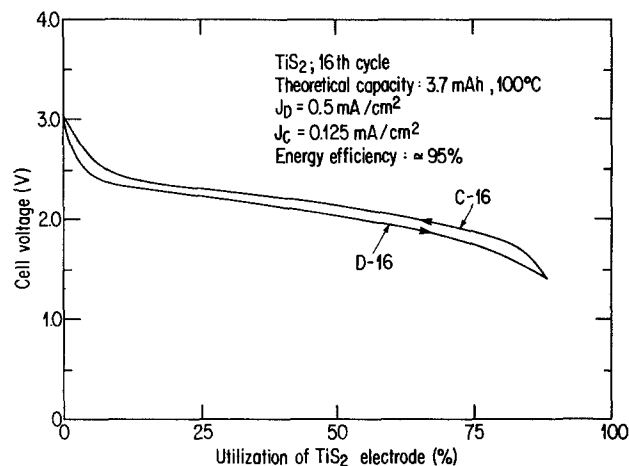


Fig. 12. Energy efficiency of Li/TiS_2 cell at 16th cycle

the origin of the polarization that limits the Li/PEO/TiS_2 cell performance. Figure 14 illustrates a test in which the cell potential is recorded simultaneously with the potential of the TiS_2 electrode vs. the LiAl reference electrode. It is clear from the similarity of the two curves at 100°C that the cell potential is largely controlled by the positive composite electrode. This behavior, typical of most of the present results, was obtained against a negative Li° electrode.

Li/PEO/ V_6O_{13} cells.— V_6O_{13} has many practical advantages as a positive-electrode material for EV application, namely, its light weight, high voltage, and number of lithium inserted per vanadium. These advantages compensate for the relatively sharp decrease in performance during the first few cycles (illustrated in Fig. 15 for a 2.42 mAh cell tested at 80°C). This behavior is typical of a high purity acicular $\text{V}_6\text{O}_{13}\text{-C}$ (x-ray diffraction). Up to 0.5 mA/cm^2 , the initial utilization of this positive-electrode material is close to 90-95% (vs. $\text{Li}_4\text{V}_6\text{O}_{13}$). However, in the subsequent cycles this value decreases and stabilizes at about 60% for a current density of 0.5 mA/cm^2 . These results are in agreement with those obtained by Murphy (6) for liquid organic electrolytes (0.7 Li/V). Under these conditions, V_6O_{13} electrodes appear to compare well with TiS_2 electrodes in terms of energy and power densities.

Larger cells (140 cm^2) made up of two 70 cm^2 units connected in parallel (represented in Fig. 3b) were assem-

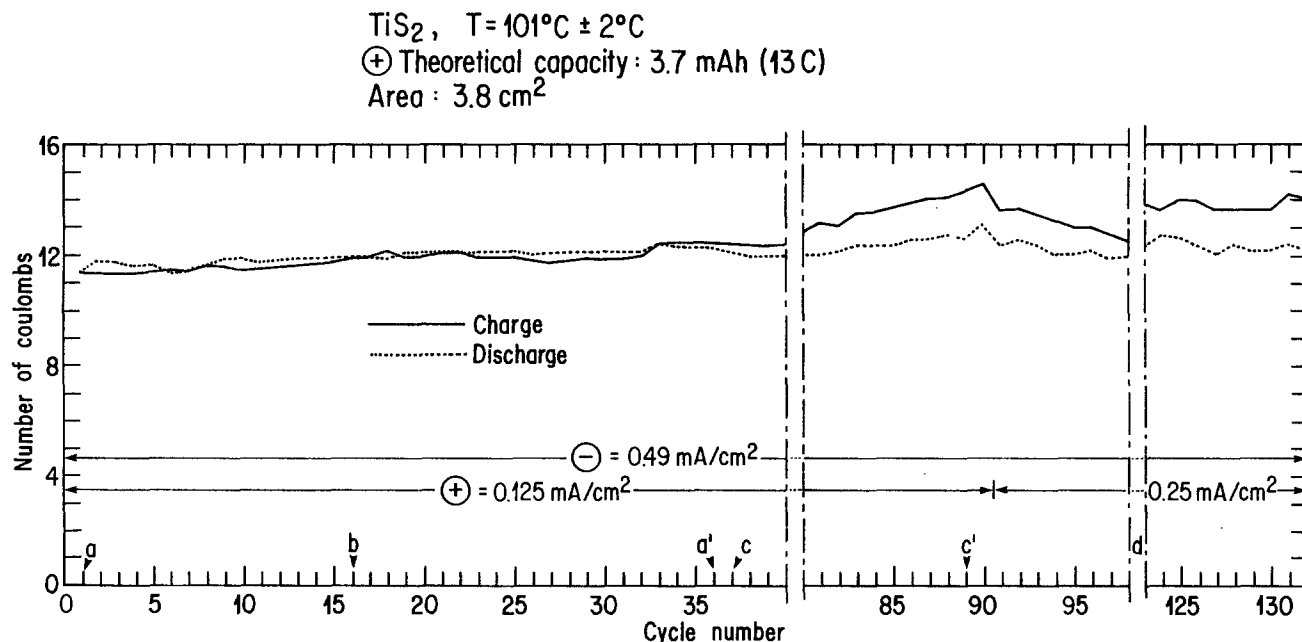


Fig. 11. Cycling profile of a 3.7 mAh $\text{TiS}_2/\text{Li}^\circ$ cell: effect of uninterrupted deep-discharge/charge cycles. The discharge and charge currents, J_D and J_C , are represented as \ominus and \oplus , respectively.

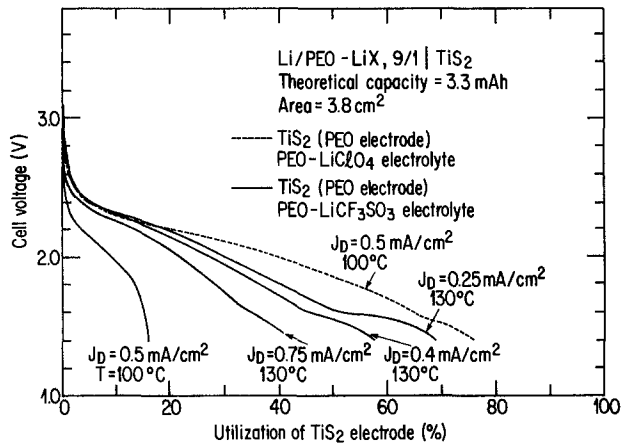


Fig. 13. Utilization of Li/TiS₂ cells prepared without lithium salt in the composite electrode vs. a LiClO₄ (dotted line) or a LiCF₃SO₃ containing electrolyte (full line).

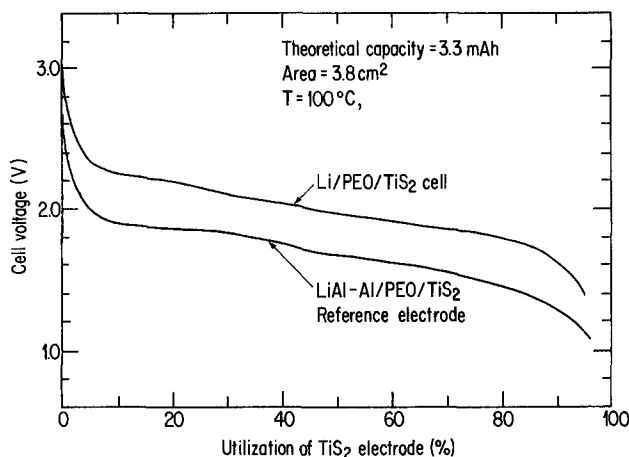


Fig. 14. Comparison of the Li/TiS₂ cell voltage with the signal of the same positive composite electrode vs. LiAl-Al reference electrode.

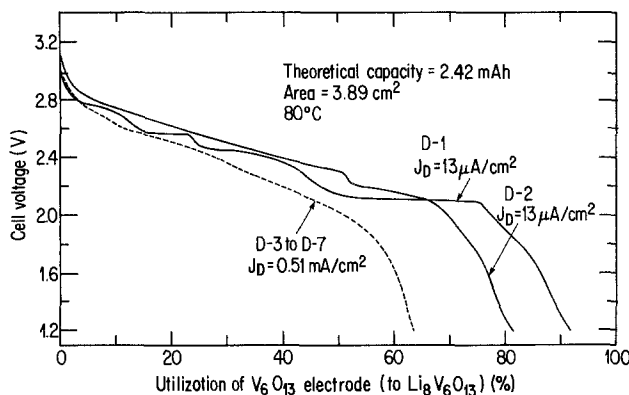


Fig. 15. Evolution of the discharge plateaus of a Li/V₆O₁₃-C cell during cycling at 80°C.

bled, one with V₆O₁₃-C, the other with a lower purity V₆O₁₃-B containing a small percentage of vanadium oxides such as V₂O₅. The performance of the 98 mAh V₆O₁₃-B cell, cycled at 100°C, presented in Fig. 16 is very close to that observed for small cells made with the same batch of V₆O₁₃. Except for the initial cycles, these experiments show a coulombic efficiency of about 100% between discharge and charge without any formation of dendrites.

Stabilized utilization, both for large and small cells, at high current drains (C/2.7 or C/1.5) depends on the quality of the V₆O₁₃: 60-65% for V₆O₁₃-C vs. 40% for V₆O₁₃-B at 0.5 mA/cm² for 140 cm² cells and 60-70% for V₆O₁₃-C vs. 50-60% for V₆O₁₃-B at 0.5 mA/cm² for 3.9 cm² cells.

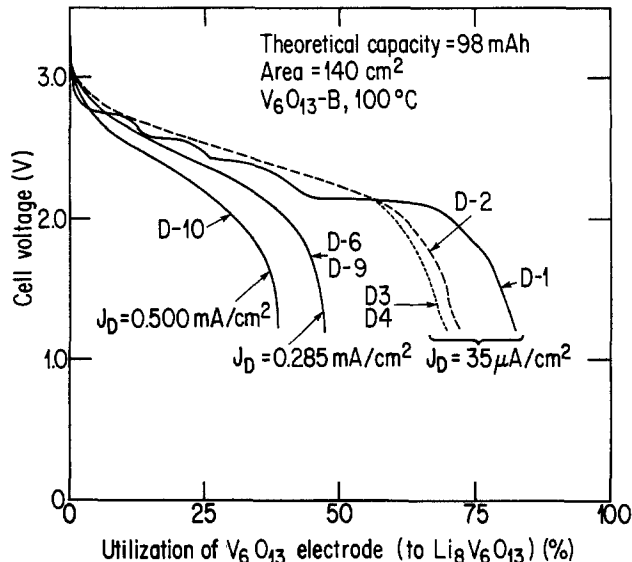


Fig. 16. Behavior of a 140 cm² Li/V₆O₁₃-B cell with cycling at 100°C

ACEP Technology at 80°-100°C

Table I contains estimates of the power and energy densities along with other characteristics deduced from the present results obtained mostly on Li/TiS₂ cells. These estimates are based on experimentally determined values such as the utilization, the electrode thickness, etc. The only arbitrarily fixed values are the negative electrode capacity and a 10 μm provision for the current collector and the electrical insulation.

The power and energy densities presented in Table I correspond to a first step towards the optimization of the positive composite electrodes, but, already, they clearly demonstrate the power density of polymer-electrolyte batteries. This can be attributed to the polymer electro-

Table I. Present performance of ACEP technology based on positive-electrode-limited Li/TiS₂ cells

Calculations are based on 3.1 C/cm² Li/TiS₂ cell characteristics and performance: average discharge plateau voltage V, electrode composition, thickness, and utilization at 2, 1, and 0.5 mA/cm². Electrolyte thickness of 50, 100, and 150 μm. The anode capacity is three times that of the cathode. Provision of 10 μm is made for collectors and/or insulators.

	Energy density		Sustained power		Electrolyte thickness (μm)
	(Wh/kg)	(Wh/liter)	(W/kg)	(W/liter)	
0.5 mA/cm ² (C/1.7)	101	154	68	104	50
	71	103	48	70	100
	55	77	37	52	150
1.0 mA/cm ² (1.2 C)	87	133	130	198	50
	61	89	92	132	100
	47	67	71	100	150
2.0 mA/cm ² (2.3 C)	56	86	260	397	50
	40	58	183	266	100
	31	43	141	199	150

Peak power (5-10s)			
100°C		80°C	
Full charge 1553 W/liter (9 mA/cm ² at 1.7V)	Half-charge 1435 W/liter (9 mA/cm ² at 1.37V)	Full charge 888 W/liter (6.4 mA/cm ² at 1.36V)	Half-charge 431 W/liter (2.6 mA/cm ² at 1.65V)

Cycling performance at 100°C (% Util.)	
Li ² /TiS ₂ ;	250 discharges > 80
Li ² /V ₆ O ₁₃ ;	100 discharges > 60
Energy efficiency at 100°C	
Li/TiS ₂	Wh out (C/2) / Wh in (C/7) = 95%

lyte's unique combination of solid-state characteristics with plastic behavior, which is particularly well suited to the power and cycling performance of positive composite electrodes.

The cycling values presented in Table I were obtained with excess-lithium electrode capacity and constitute indirect evidence of the efficiency of lithium redeposition from polymer electrolytes. However, systematic work with lithium-limited cells is under way and tends to confirm the high efficiency of the electrodeposition process. As for the dendrite problem, it appears to be an occasional phenomenon, dependent on the control of several technological parameters, which does not affect the cycling capacity of small or larger (70-140 cm²) cells built with lithium negative electrodes. Moreover, the polymer electrolyte appears to possess self healing properties since the dendrites do not seem to affect the following cycles.

The projected energy efficiency of large-scale practical Li/PEO/TiS₂ cells is notably higher than that found with existing rechargeable batteries. This will certainly contribute to the thermal management of large installations of thin film batteries.

Ambient Temperature Cells

As mentioned earlier, at room temperature the PEO conductivity is too low for this material to be used in practical cells, even at a very low drain (see first cycling profile in Fig. 4). In the ACEP Project, therefore, new polymer-salt complexes were developed with improved electrochemical and transport properties which allow operation of all-solid-state primary and secondary cells at ambient temperature.

Several cells have already been built and tested at low to moderate current drains. Figures 17 and 18 illustrate typical performances. The primary high voltage MnO₂ electrode and the reversible low voltage MoO₂ electrode both show utilizations in excess of 80% at rates up to C/37. In addition, nonoptimized MoO₂ cells have confirmed the feasibility of a large number of cycles: > 20 cycles at deep discharges (> 75%) have already been demonstrated at C/36, while 400 cycles have been obtained with the same cell but at rates between C/50 and C/10 at 27°C. Figure 20 shows that good electrochemical properties have been maintained at C/50 even after 300 cycles at C/10.

Moreover, the results presented in Fig. 19, based on a MoO₂/Li cell with a larger surface area (70 cm²), suggest that scale-up is possible and that the results obtained with small cells will be repeated.

Although the technology used for the construction of such ambient temperature cells has not reached a high level of development, a first attempt has been made to establish some of the characteristics of ACEP batteries at room temperature (see Table II). At the time these tests

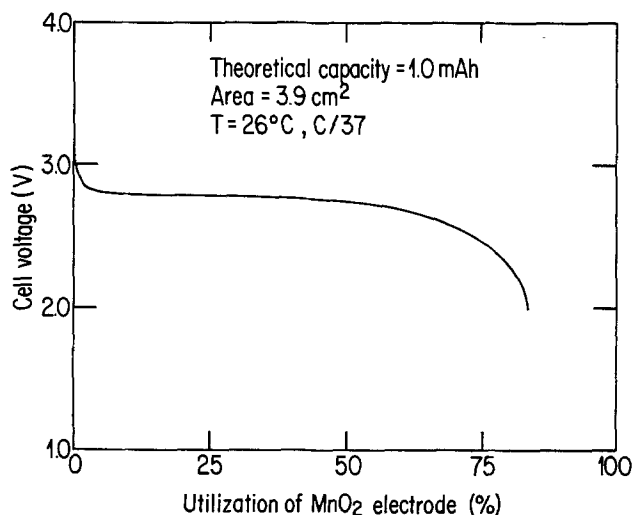


Fig. 17. Utilization of primary Li/MnO₂ cell at 26°C

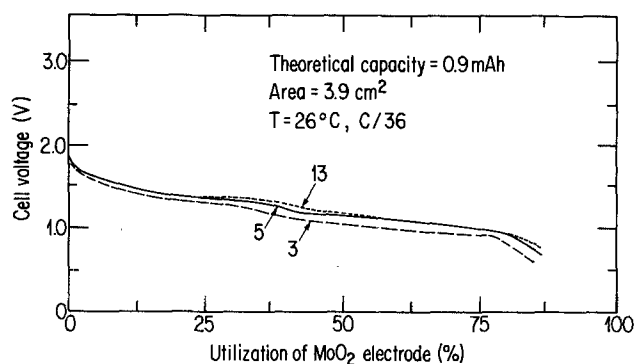


Fig. 18. Utilization of rechargeable Li/MoO₂ cell vs. cycling at 26°C. The number on each curve corresponds to the cycle number.

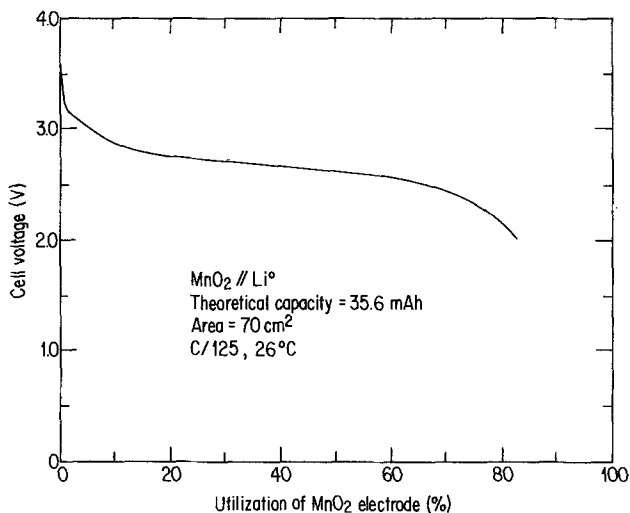


Fig. 19. Discharge plateau of a scaled-up (36 mAh) Li/MoO₂ cell at 26°C.

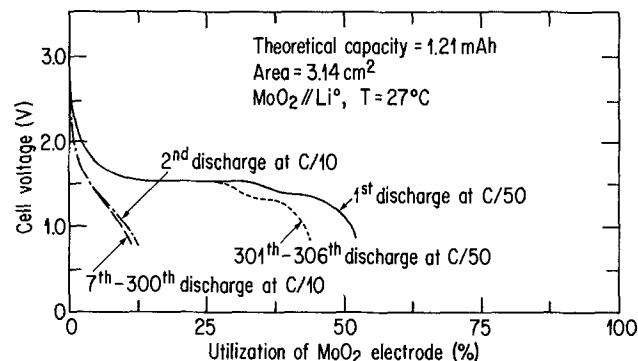


Fig. 20. Discharge plateau of a nonoptimized Li/MoO₂ cell at C/10 and C/50 for more than 300 cycles at 27°C.

were conducted, the temperature observed in the glove box was $\approx 25^{\circ}\text{--}27^{\circ}\text{C}$. Based on more recent results, the authors consider that the performances presented here are still representative of ACEP technology at 20°C, for example.

The authors believe that this emerging technology based on polymer electrolytes is promising for microelectronic and other applications, especially those requiring a rechargeable power source.

Conclusions

In conclusion, the present work, although incomplete, suggests the feasibility of thin film polymer electrolytes in high energy- and power-density batteries for EV applications.

Projected energy densities of ≈ 100 Wh/kg were shown to be possible associated with a sustained power of ≥ 200 W/kg and peak power over 900 W/kg at half-charge and at

Table II. Performance of ACEP technology at ambient temperature

Electrolytes: aprotic polyethers + lithium salt complexes

Calculations based on observed characteristics of positive composite electrodes and electrolyte: V , utilization of positive electrode material thickness, etc. Arbitrarily fixed parameters were (i) the anode capacity is three times that of the cathode, and (ii) provision of 10 μm is made for collectors and/or insulators.

Li/MnO ₂ systems		
0.1-0.17 Wh/cm ³	at C/15-C/40	for 0.3 mAh/cm ² +
0.2-0.4 Wh/cm ³	at C/250-C/600	for 2 mAh/cm ² +
Projected performance of primary cells:		
0.3-0.5 Wh/cm ³ at C/10 to C/400		
Li/MoO ₃ , Li/TiS ₂		
0.5-0.1 Wh/cm ³	at C/15-C/30	for 0.3 mAh/cm ² +
0.1-0.17 Wh/cm ³	at C/60-C/160	for 1 mAh/cm ² +
For 20 cycles (75%), projected performance of secondary cells:		
0.15-0.3 Wh/cm ³ at C/10-C/200 > 100 cycles		
State of the art		
≈ 0.07 Wh/cm ³ for packaged Ni-Cd at C/10		
Other characteristics: (i) no self-discharge or performance losses after storage for 1 month at 71°C or > 6 months at ambient temperature; (ii) no liquid electrolyte (thus reducing sealing problems), and (iii) scale-up demonstrated at 70 and 150 cm ² .		

100°C. Also, an energy efficiency in excess of 90% and a cycling performance of ≥ 250 deep discharges (or 450 medium to deep discharges) have been demonstrated.

In the authors' opinion, the results obtained in the present study, especially in terms of power density, may be attributed mostly to the unique combination of solid-state properties with those of plastic materials, such as the deformability inherent in polymer electrolytes. This appears desirable as a means of maintaining the electrochemical integrity of the electrode/electrolyte interfaces, especially with respect to the cycling properties of composite electrodes.

In addition, it has been shown that polymer electrolyte cells can be operated at room temperature with lower rate capacities (C/15-C/300) for primary and secondary systems. These preliminary results appear very promising for small rechargeable applications.

The fact that recently the performance obtained on small cells has been successfully repeated at 100° and 26°C with cell areas greater than 100 cm² has led to the initiation of a demonstration program. In this program, the large-scale preparation techniques now used at both SNEA and IREQ will be adapted to the present manufacturing procedure in order to build a first generation of cells with capacities of 10-50 Ah. These cells will serve to establish realistic performances for the ACEP technology and to assess the scale-up problems and manufacturing costs.

These activities will be pursued in parallel with the research into new families of electrolytes and electrode materials and on performance optimization in particular by increasing the surface capacities of the positive electrode in order to improve the energy density yet maintain similar power densities.

Acknowledgments

The authors thank M. C. Anerot, R. Bellemare, E. Bon, F. Brochu, R. Gillard, Y. Giguère, P. E. Harvey, B. Kapfer, C. Robitaille, M. Robitaille, S. Sempe, and Y. Tauzy for their valuable contribution to this work. Thanks are due to Hydro-Québec and to Société Nationale Elf Aquitaine for the financial support of this work.

Manuscript submitted June 5, 1984; revised manuscript received Feb. 6, 1985.

Institut de Recherche d'Hydro-Québec assisted in meeting the publication costs of this article.

REFERENCES

1. M. B. Armand, J. M. Chabagno, and M. J. Duclot, in "Fast Ion Transfer in Solids," P. Vashishta, Editor, p. 131, North Holland, New York (1979).
2. A. Hooper and J. M. North, *Solid State Ionics*, **9-10**, 1161 (1983).
3. D. Fauteux, Ph.D. thesis in preparation, INRS-Énergie, Varennes, Québec, Canada.
4. C. Robitaille, Personal communication.
5. S. Atlung, K. West, and T. Jacobson, *This Journal*, **126**, 1311 (1979).
6. D. W. Murphy, P. A. Christian, F. J. Disalvo, J. N. Carides, and J. V. Waszczak, *ibid.*, **128**, 2053 (1981).
7. S. Whittingham, *Prog. Solid State Chem.*, **12**, 41 (1978).

Ionic Conductivity in Solid Solutions of the Na₃YSi₃O₉ Type

Chy Hyung Kim, Bingyi Qiu¹ and Ephraim Banks*

Department of Chemistry, Polytechnic Institute of New York, Brooklyn, New York 11201

ABSTRACT

Samples based on the Na₃MSi₃O₉ structure (M = Sm, Eu, Gd, Dy, Ho, Er, Tm, Yb, Lu, and Y) were prepared. A combination of phosphorus substitution and reduction of M³⁺ content permitted increasing sodium content, the maximum sodium content being 3.3. Conductivity of this sample, measured by pulse and two-terminal ac methods, was about 5.5×10^{-4} ($\Omega\text{-cm}$)⁻¹ at 320°C, compared to 9×10^{-8} ($\Omega\text{-cm}$)⁻¹ for Na₃YSi₃O₉ at the same temperature. Activation energies were slightly lowered with increasing sodium content, from 15 to 14 kcal/mol. In compositions with other rare earths, conductivity increased with increasing ionic radius of the rare earth ion. Lithium ions were introduced by ion exchange in molten LiNO₃. The conductivities were slightly lower than those of the corresponding sodium samples, but decreased with increasing rare earth radius.

The compounds of the type Na₃MSi₃O₉ (M = Y, Dy, Gd) were prepared by Shannon *et al.* (1). The sodium ion conductivity of Na₃YSi₃O₉ was reported to be 6×10^{-6} ($\Omega\text{-cm}$)⁻¹ at 300°C.

In our study of Na₃MSi₃O₉-type compounds, it was found that excess sodium could be introduced into the structure. Also, reduction of M³⁺ content (M = Y, Sm, Eu, Gd, Dy, Ho, Er, Tm, Yb, Lu) and substitution of small amounts of phosphorus for silicon without distortion of the Na₃MSi₃O₉ structure were possible, as evidenced by x-ray analysis. The conductivities of these modified com-

pounds improved with the values being in the range of 10^{-4} ($\Omega\text{-cm}$)⁻¹ at 300°C.

Experimental

Starting materials Na₂CO₃, SiO₂, and M₂O₃ of reagent grade were mixed and fired overnight at 900°-1100°C in covered platinum crucibles. The procedure of grinding and heating each of the samples was repeated to insure that the reactions were complete. The x-ray patterns were obtained on a Philips Diffractometer using CuK α radiation. The x-ray patterns of products obtained by quenching at the reaction temperature and by annealing were essentially the same.

*Electrochemical Society Active Member.

¹Present Address: Peking University, Beijing, China.

Table I. Ionic conductivity ($\Omega\text{-cm}$)⁻¹ $\times 10^5$ at 320°C by pulse and ac method in $\text{Na}_{3+x}\text{Y}_{1-y}\text{Si}_{3-z}\text{P}_{9+(x-3y+z)/2}$

y \ x		0.0	0.1	0.2	0.3
z = 0.0,	0.0(1170°C)	0.90 (0.94)	2.3 (2.3)	6.8 (6.8)	
	0.3(1040°C)		43 (42)	a	
	0.4	a	a	a	a
z = 0.1,	0.0(1100°C)	a		2.0 (2.1)	1.9 (1.9)
	0.1(1070°C)				14 (13)
	0.2(1045°C)	17 (17)	29 (28)	26 (25)	29 (27)
	0.3(1015°C)	31 (30)	40 (40)	58 (55)	60 (55)
	0.4(990°C)	a	a	a	a
z = 0.2,	0.0(1090°C)	a		2.3 (2.4)	4.0 (3.9)
	0.1(1065°C)		10 (10)	a	a
	0.2(1040°C)		17 (15)	a	a
	0.3(1010°C)	a	a	a	a

The value in parentheses is the conductivity by ac method.

^a Does not belong to $\text{Na}_3\text{YSi}_3\text{O}_9$ phase.

To test the effect of each element on the magnitude of the conductivity, the electrical conductivity of the system $\text{Na}_{3+x}\text{Y}_{1-y}\text{Si}_{3-z}\text{P}_{9+(x-3y+z)/2}$ was measured for different values of x , y , and z in the range of existence of the $\text{Na}_3\text{MSi}_3\text{O}_9$ phase. The firing temperatures were decreased with decreasing yttrium and increasing phosphorus to avoid formation of amorphous phases, as described in Table I.

The compositions $\text{Na}_{3.2}\text{M}_{0.7}\text{Si}_{2.9}\text{P}_{0.1}\text{O}_{8.7}$ were selected to compare the conductivity values for different rare earth elements. The firing temperatures were also adjusted depending on the sort of M_2O_3 . After sufficient firing was carried out, x-ray powder diffraction was used for phase analysis.

To synthesize $\text{Li}_{3.2}\text{M}_{0.7}\text{Si}_{2.9}\text{P}_{0.1}\text{O}_{8.7}$, powders of $\text{Na}_{3.2}\text{M}_{0.7}\text{Si}_{2.9}\text{P}_{0.1}\text{O}_{8.7}$ were treated with excess molten LiNO_3 at 300-350°C for about 30 min-1h and washed with warm water, filtered, and dried overnight at 150°C. X-ray diffraction of these phases showed a "halo" in the powder pattern, indicating the existence of amorphous material, probably due to the synthetic technique employed. No $\text{Na}_{3.2}\text{M}_{0.7}\text{Si}_{2.9}\text{P}_{0.1}\text{O}_{8.7}$ could be detected. However, it is assumed that small quantities of impurity (< 5%) may not be detected in x-ray analysis.

Samples for the conductivity measurement were prepared as ceramic pellets. About 0.6g of powder was mixed with about 0.05g of recrystallized naphthalene as binder (more naphthalene was needed for making pellets of lithium compounds) and pressed into pellets at 3500-4000 psi. The pellets were heated at 250°C for 1h to drive off naphthalene, followed first by sintering at 800-1000°C for 15-20 min and then quenching in air. The lithium compounds were not sintered due to its undergoing a phase

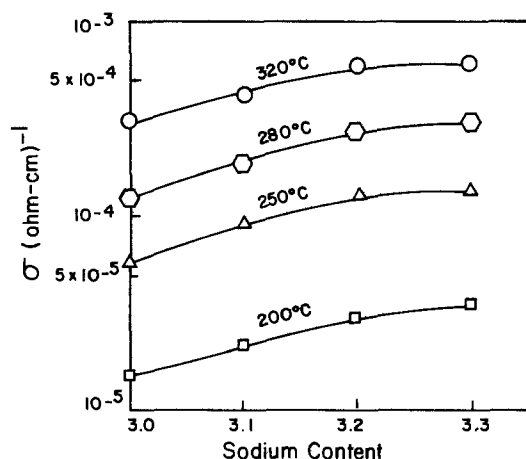


Fig. 1. Variation of ionic conductivity with sodium content at different temperatures for $\text{Na}_{3+x}\text{Y}_{0.7}\text{Si}_{2.9}\text{P}_{0.1}\text{O}_{8.6+x/2}$.

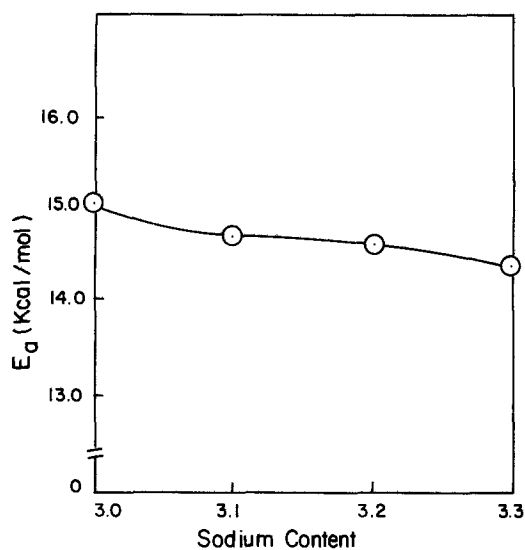


Fig. 2. Variation of activation energy with sodium content for $\text{Na}_{3+x}\text{Y}_{0.7}\text{Si}_{2.9}\text{P}_{0.1}\text{O}_{8.6+x/2}$.

change or reaction around 600-800°C, as evidenced by DTA and x-ray. Relative densities of the pellets were 64-83%.

After sintering, the pellets were coated by vacuum deposition of a thin layer of gold, which acted as electrodes for conductivity measurement (3). These are blocking electrodes, being irreversible to alkali metal decomposition. A thin layer of chromium was intercalated between the surface of the pellet and gold layer because gold itself does not adhere strongly to the surface of the pellet. A pulse method was used in combination with dc measurement, permitting the separation of ionic and electronic components of the conductivity (4). Voltage pulses of 3-7V in magnitude, a pulse width of 80 μs , and pulse repetition time 200 μs were used at 200°, 250°, 280°, and 320°C. For the dc measurement, 0.5V from a constant source was applied, but the electronic contribution was found to be negligible under the condition that the known resistance was 10 k Ω . Also, ac measurements were done at 10^2 - 10^5 Hz and at 1V in all cases; the results at high frequency agreed well with those of the pulse method.

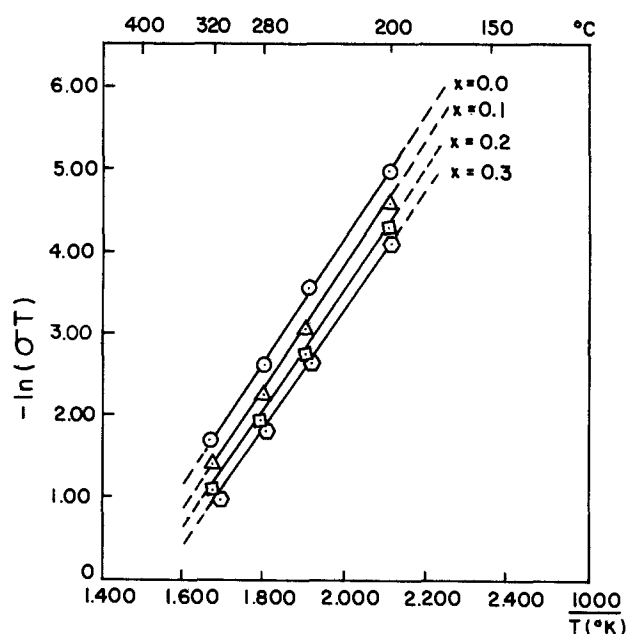


Fig. 3. Arrhenius plots of ionic conductivity for $\text{Na}_{3+x}\text{Y}_{0.7}\text{Si}_{2.9}\text{P}_{0.1}\text{O}_{8.6+x/2}$.

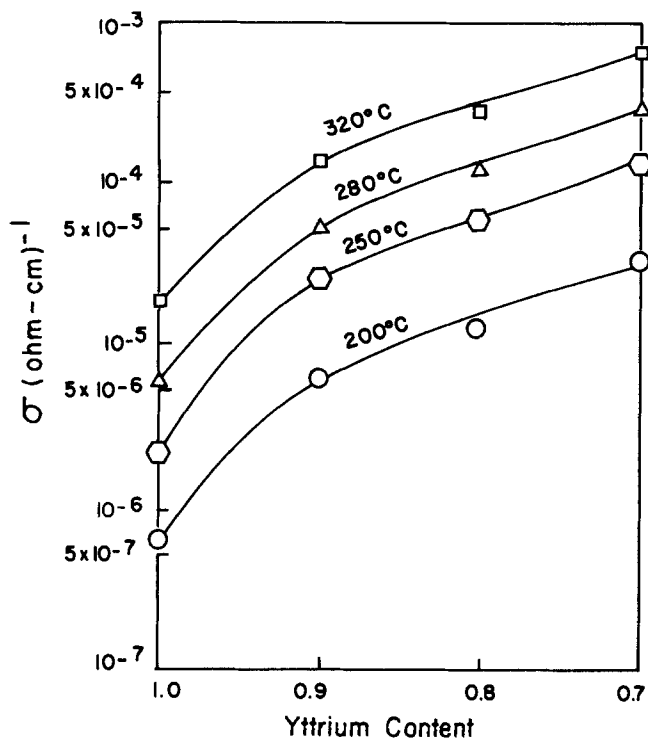


Fig. 4. Dependence of ionic conductivity on yttrium content at various temperatures for $\text{Na}_{3.3}\text{Y}_{1-y}\text{Si}_{2.9}\text{P}_{0.1}\text{O}_{9.2-3y/2}$.

Results and Discussion

Table I shows the range of the $\text{Na}_3\text{YSi}_3\text{O}_9$ -type phase and the ionic conductivities at 320°C by pulse and ac method. The conductivities listed in the table are corrected for porosity under the assumption that the pores inside the sample are in the form of spherical cavities (4). Beyond the range of the $\text{Na}_3\text{YSi}_3\text{O}_9$ phase, one or more other phases such as $\text{Na}_5\text{YSi}_4\text{O}_{12}$, Na_3PO_4 , $\text{Na}_3\text{Y}(\text{PO}_4)_2$, $\text{Na}_3\text{YSi}_2\text{O}_7$, Y_2SiO_5 , and $\text{Y}_2\text{Si}_2\text{O}_7$ appeared. The table also shows the effect of each element on the magnitude of the conductivity. With increasing sodium concentration in the structure, the conductivities are seen to increase. This would appear to be due to the increase of mobile sodium ion concentration. Figures 1 and 2 show the variation in conductivity and activation energy calculated from the equation $\sigma = \sigma_0/T \exp(-E_a/kT)$ as functions of increasing sodium content in the $\text{Na}_{3+x}\text{Y}_{0.7}\text{Si}_{2.9}\text{P}_{0.1}\text{O}_{8.6+x/2}$ series. Figure 3 shows Arrhenius plots of the ionic conductivity as a function of temperature for the same system. The conductivities increase with decreasing yttrium concentration because vacancies in the structure are apparently

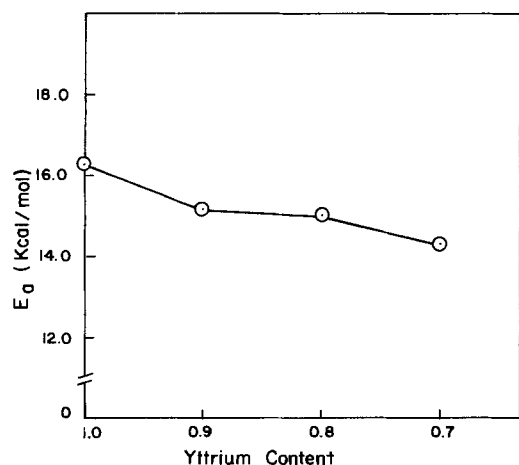


Fig. 5. Variation of activation energy with yttrium content for $\text{Na}_{3.3}\text{Y}_{1-y}\text{Si}_{2.9}\text{P}_{0.1}\text{O}_{9.2-3y/2}$.

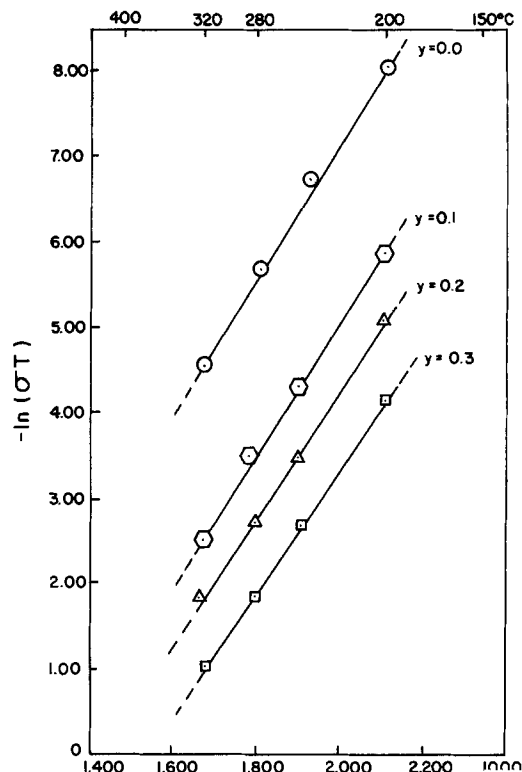


Fig. 6. Arrhenius plots of ionic conductivity for $\text{Na}_{3.3}\text{Y}_{1-y}\text{Si}_{2.9}\text{P}_{0.1}\text{O}_{9.2-3y/2}$.

formed with decreasing yttrium content. Figures 4 and 5 show the dependence of the electrical conductivity and activation energy on yttrium content. Figure 6 shows Arrhenius plots of the conductivity in the $\text{Na}_{3.3}\text{Y}_{1-y}\text{Si}_{2.9}\text{P}_{0.1}\text{O}_{9.2-3y/2}$ system. The influence of yttrium content on the conductivity is larger than that of the sodium content in the same structure. The $\text{Na}_3\text{YSi}_3\text{O}_9$ structure has been

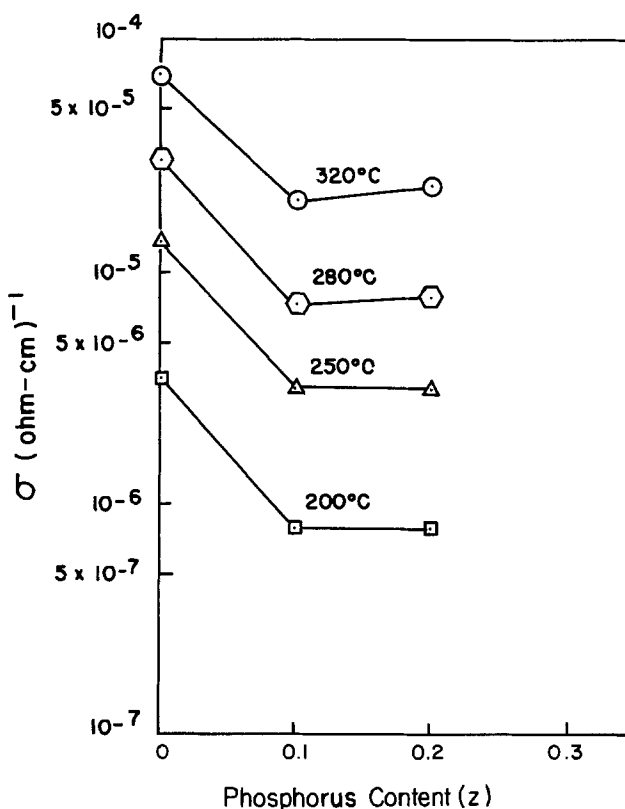


Fig. 7. Variation of ionic conductivity with phosphorus content at different temperatures for $\text{Na}_{3.2}\text{YSi}_{3-2}\text{P}_z\text{O}_{9.1+z/2}$.

Table II. $\text{Na}_{3.2}\text{M}_{0.7}\text{III}\text{Si}_{2.9}\text{P}_{0.1}\text{O}_{8.7}$

Formula	Lattice constants (Å)
$\text{Na}_{3.2}\text{Lu}_{0.7}\text{Si}_{2.9}\text{P}_{0.1}\text{O}_{8.7}$	$a = 15.160 \pm 0.006$ $b = 15.076 \pm 0.004$ $c = 14.989 \pm 0.005$
$\text{Na}_{3.2}\text{Yb}_{0.7}\text{Si}_{2.9}\text{P}_{0.1}\text{O}_{8.7}$	$a = 15.165 \pm 0.001$ $b = 15.103 \pm 0.001$ $c = 15.000 \pm 0.001$
$\text{Na}_{3.2}\text{Tm}_{0.7}\text{Si}_{2.9}\text{P}_{0.1}\text{O}_{8.7}$	$a = 15.192 \pm 0.006$ $b = 15.095 \pm 0.020$ $c = 15.011 \pm 0.015$
$\text{Na}_{3.2}\text{Er}_{0.7}\text{Si}_{2.9}\text{P}_{0.1}\text{O}_{8.7}$	$a = 15.193 \pm 0.008$ $b = 15.108 \pm 0.019$ $c = 15.011 \pm 0.016$
$\text{Na}_{3.2}\text{Y}_{0.7}\text{Si}_{2.9}\text{P}_{0.1}\text{O}_{8.7}$	$a = 15.211 \pm 0.002$ $b = 15.118 \pm 0.001$ $c = 15.017 \pm 0.001$
$\text{Na}_{3.2}\text{Ho}_{0.7}\text{Si}_{2.9}\text{P}_{0.1}\text{O}_{8.7}$	$a = 15.197 \pm 0.003$ $b = 15.124 \pm 0.001$ $c = 15.034 \pm 0.001$
$\text{Na}_{3.2}\text{Dy}_{0.7}\text{Si}_{2.9}\text{P}_{0.1}\text{O}_{8.7}$	$a = 15.218 \pm 0.002$ $b = 15.146 \pm 0.001$ $c = 15.040 \pm 0.002$
$\text{Na}_{3.2}\text{Gd}_{0.7}\text{Si}_{2.9}\text{P}_{0.1}\text{O}_{8.7}$	$a = 15.241 \pm 0.001$ $b = 15.175 \pm 0.002$ $c = 15.064 \pm 0.002$
$\text{Na}_{3.2}\text{Eu}_{0.7}\text{Si}_{2.9}\text{P}_{0.1}\text{O}_{8.7}$	$a = 15.300 \pm 0.004$ $b = 15.201 \pm 0.005$ $c = 15.074 \pm 0.004$

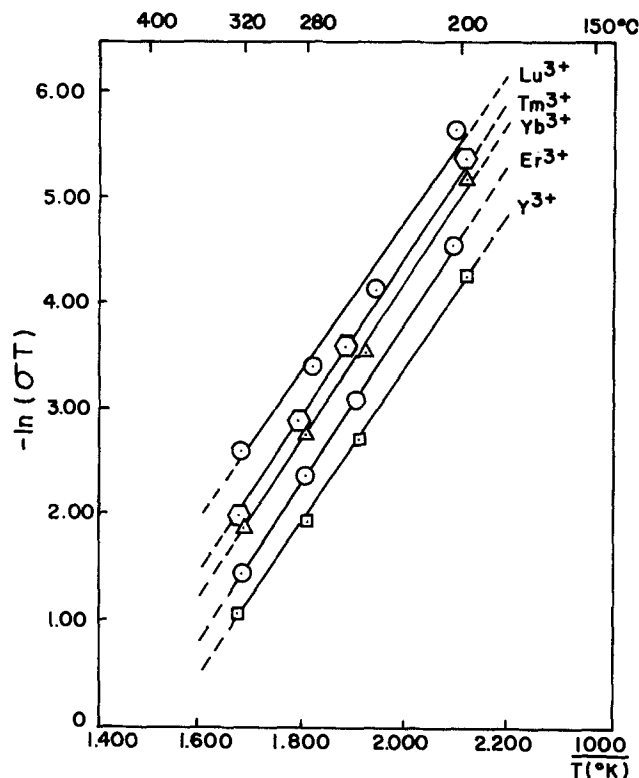
Table III. Cell dimensions of $\text{Na}_3\text{MSi}_3\text{O}_9$

Formula	Lattice constants (Å)
$\text{Na}_3\text{YSi}_3\text{O}_9$	$a = 15.215 \pm 0.001$ $b = 15.126 \pm 0.001$ $c = 15.036 \pm 0.001$
$\text{Na}_3\text{DySi}_3\text{O}_9$	$a = 15.234 \pm 0.002$ $b = 15.165 \pm 0.001$ $c = 15.050 \pm 0.001$
$\text{Na}_3\text{GdSi}_3\text{O}_9$	$a = 15.289 \pm 0.003$ $b = 15.221 \pm 0.002$ $c = 15.084 \pm 0.003$

reported (1) to show similarity to the $\text{Ca}_3\text{Al}_2\text{O}_6$ structure with $a = 15.263\text{Å}$ (5) and $\text{Na}_4\text{CaSi}_3\text{O}_9$ with $a = 15.115\text{Å}$ (6, 7). The orthorhombic $\text{Na}_3\text{YSi}_3\text{O}_9$ phase with $a = 15.215\text{Å}$, $b = 15.126\text{Å}$, and $c = 15.036\text{Å}$ is expected to contain $[\text{Si}_6\text{O}_{18}]$ rings. The substitution of phosphorus for silicon

Table IV. Temperature dependence of the ionic conductivity for $\text{Na}_{3.2}\text{M}_{0.7}\text{III}\text{Si}_{2.9}\text{P}_{0.1}\text{O}_{8.7}$, pulse (ac method), corrected for porosity

M^{III}	Ionic conductivity ($\Omega\text{-cm}$) ⁻¹				E_a (kcal/mol)
	200°C	250°C	280°C	320°C	
Lu	7.10×10^{-6} (7.83×10^{-6})	3.21×10^{-5} (3.63×10^{-5})	5.95×10^{-5} (6.04×10^{-5})	1.75×10^{-4} (1.77×10^{-4})	16.24 ± 0.10 (15.89 ± 0.12)
Yb	1.13×10^{-5} (1.21×10^{-5})	5.50×10^{-5} (5.20×10^{-5})	1.12×10^{-4} (1.10×10^{-4})	2.57×10^{-4} (2.45×10^{-4})	15.47 ± 0.13 (14.97 ± 0.08)
Tm	9.47×10^{-6} (1.01×10^{-5})	5.13×10^{-5} (4.94×10^{-5})	1.00×10^{-4} (9.36×10^{-5})	2.30×10^{-4} (2.32×10^{-4})	15.53 ± 0.03 (15.17 ± 0.10)
Er	2.15×10^{-5} (2.37×10^{-5})	8.64×10^{-5} (8.04×10^{-5})	1.70×10^{-4} (1.71×10^{-4})	3.98×10^{-4} (3.75×10^{-4})	15.27 ± 0.06 (14.62 ± 0.09)
Y	2.94×10^{-5} (3.12×10^{-5})	1.27×10^{-4} (1.23×10^{-4})	2.63×10^{-4} (2.66×10^{-4})	5.83×10^{-4} (5.54×10^{-4})	14.62 ± 0.10 (14.19 ± 0.14)
Ho	2.24×10^{-5} (2.27×10^{-5})	8.25×10^{-5} (7.85×10^{-5})	1.60×10^{-4} (1.52×10^{-4})	3.85×10^{-4} (3.79×10^{-4})	14.55 ± 0.05 (14.39 ± 0.08)
Dy	1.56×10^{-5} (1.70×10^{-5})	6.87×10^{-5} (6.85×10^{-5})	1.57×10^{-4} (1.52×10^{-4})	3.52×10^{-4} (3.27×10^{-4})	15.31 ± 0.03 (14.59 ± 0.04)
Gd	2.78×10^{-5} (3.04×10^{-5})	1.31×10^{-4} (1.35×10^{-4})	2.47×10^{-4} (2.36×10^{-4})	5.71×10^{-4} (4.83×10^{-4})	15.66 ± 0.13 (14.45 ± 0.18)
Eu	3.10×10^{-5} (3.24×10^{-5})	1.19×10^{-4} (1.20×10^{-4})	2.86×10^{-4} (2.68×10^{-4})	6.36×10^{-4} (5.96×10^{-4})	15.14 ± 0.05 (14.57 ± 0.07)
Sm	5.00×10^{-5} (5.02×10^{-5})	1.51×10^{-4} (1.36×10^{-4})	3.31×10^{-4} (3.07×10^{-4})	8.25×10^{-4} (7.34×10^{-4})	14.92 ± 0.07 (14.41 ± 0.06)

Fig. 8. Arrhenius plot of ionic conductivity for $\text{Na}_{3.2}\text{M}^{3+}_{0.7}\text{Si}_{2.9}\text{P}_{0.1}\text{O}_{8.7}$

does not contribute toward improving the conductivity; instead, it decreases the conductivity and increases the activation energy (see Fig. 7). That is, $\text{PO}_{1/2}$ substitution for silicon increases the number of atoms and thereby interferes with ion transport. But experimentally we found that more sodium could be introduced into the structure by substitution of a very small amount of phosphorus ($z = 0.1$) for silicon (see Table D). For example, in $\text{Na}_{3+x}\text{Y}_{0.7}\text{Si}_{3-x}\text{O}_{8.55+x/2}$ and in the $\text{Na}_{3+x}\text{Y}_{0.7}\text{Si}_{2.9}\text{O}_{8.35+x/2}$ series, the x values were lower than 0.2 in spite of regrinding and reheating at 1040°C for 3 days. However, in the $\text{Na}_{3+x}\text{Y}_{0.7}\text{Si}_{2.9}\text{P}_{0.1}\text{O}_{8.6+x/2}$ series, which is the same as the former series except that a small amount of phosphorus is introduced, the x value could be increased (< 0.4) by heating at 1015°C for 24h. It appears that phosphorus has the effect of stabilizing the structure at higher sodium concentration, perhaps by

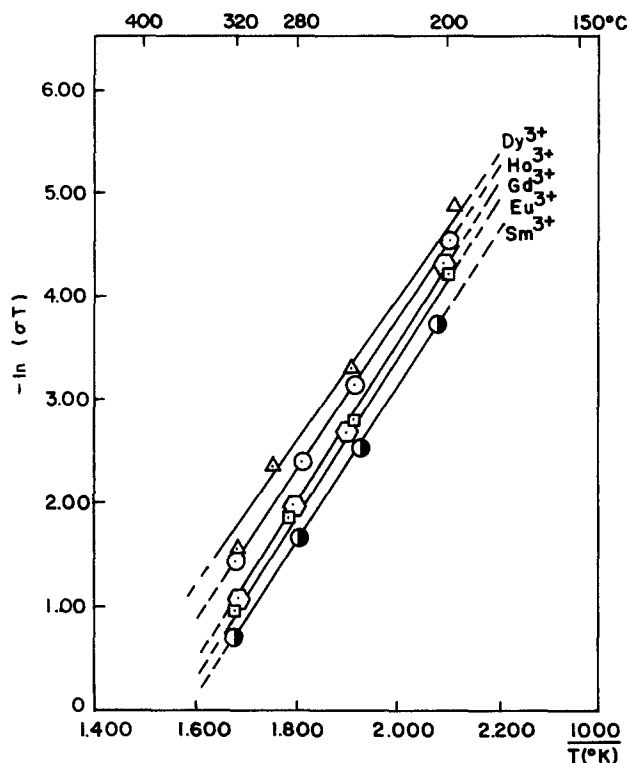


Fig. 9. Arrhenius plot of ionic conductivity for $\text{Na}_{3.2}\text{M}^{3+}_{0.7}\text{Si}_{2.9}\text{P}_{0.1}\text{O}_{8.7}$.

enlarging the available sites, even though the increase of oxygen may induce a decrease in conductivity. At higher phosphorus concentrations, the appearance of other phases like $\text{Na}_3\text{Y}(\text{PO}_4)_2$ and Na_3PO_4 was observed by x-ray analysis.

Other rare earth compounds could be fabricated in the same way as described above for yttrium. In the case of $\text{M} = \text{Sm}$, more regrinding and reheating were needed to complete the reaction. The x-ray patterns of $\text{Na}_{3.2}\text{M}_{0.7}\text{Si}_{2.9}\text{P}_{0.1}\text{O}_{8.7}$ showed that they are isostructural with $\text{Na}_3\text{YSi}_3\text{O}_9$. Only some shifts in the position of the peaks depending on the size of M^{3+} were observed. The orthorhombic $\text{Na}_{3.2}\text{M}_{0.7}\text{Si}_{2.9}\text{P}_{0.1}\text{O}_{8.7}$ lattice constants were estimated using x-ray powder diffraction patterns (see Table II). The cell

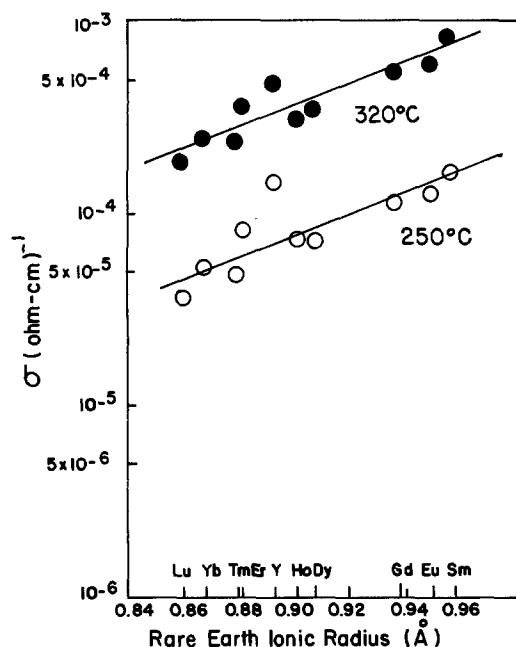


Fig. 10. Variation of ionic conductivity with rare earth ionic radius for $\text{Na}_{3.2}\text{M}_{0.7}\text{Si}_{2.9}\text{P}_{0.1}\text{O}_{8.7}$.

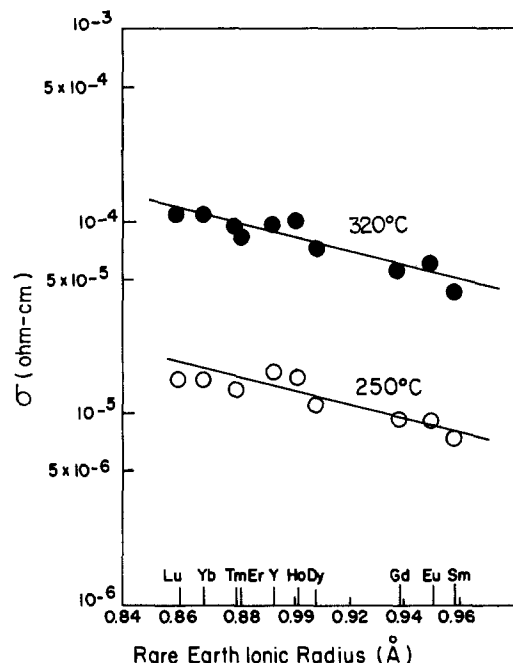


Fig. 11. Variation of ionic conductivity with rare earth ionic radius for $\text{Li}_{3.2}\text{M}_{0.7}\text{Si}_{2.9}\text{P}_{0.1}\text{O}_{8.7}$.

volumes of these modified compounds were less than those of $\text{Na}_3\text{MSi}_3\text{O}_9$, as can be seen in Table III, mainly due to the reduction of M^{3+} and O^{2-} contents even though the sodium content was increased. However, the ionic conductivity was improved in modified compounds. Table IV and Fig. 8 and 9 indicate the conductivities and Arrhenius plots of $\text{Na}_{3.2}\text{M}_{0.7}\text{Si}_{2.9}\text{P}_{0.1}\text{O}_{8.7}$ compounds. In general, with increasing size of the rare earth ion the conductivity increases, as shown in Fig. 10. If it is assumed that the $[\text{Si}_6\text{O}_{18}]$ rings are held together by sodium and rare earth ions, the amount of space between the rings will be influenced by the size of six coordinated M^{3+} . The larger the M^{3+} size, the larger the cell volume, which can probably provide more space in the structure. But in the $\text{Li}_{3.2}\text{M}_{0.7}\text{Si}_{2.9}\text{P}_{0.1}\text{O}_{8.7}$ series, the conductivity decreased with increasing size of the rare earth ion (see Fig. 11). It might be expected that the lithium ion size becomes smaller than the optimum size for ionic motion as the size of M^{3+} becomes larger.

Detailed structural analysis of $\text{Na}_3\text{YSi}_3\text{O}_9$ would help in understanding the mechanism of the conductivity. This will probably require the growth of single crystals, which has not yet been accomplished.

Acknowledgments

The authors thank Mary Eschwei of the Department of Physics, Polytechnic Institute of New York, for the preparation of electrodes on the samples. This research was supported by the Polytechnic Institute of New York via a teaching assistantship of C. H. Kim. Qiu Bingyi was supported by the government of the People's Republic of China. This paper is part of a dissertation submitted to the Polytechnic Institute of New York by C. H. Kim in partial fulfillment of the requirements for the degree of Doctor of Philosophy.

Manuscript submitted March 15, 1985; revised manuscript received Feb. 4, 1985.

The Polytechnic Institute of New York assisted in meeting the publication costs of this article.

REFERENCES

1. R. D. Shannon, T. E. Gier, C. M. Foris, J. N. Nelen, and D. E. Appleman, *Phys. Chem. Miner.*, **5**, 245 (1980).
2. R. D. Shannon, B. E. Taylor, T. E. Gier, H.-Y. Chen, and T. Berzins, *Inorg. Chem.*, **17**, 958 (1978).
3. R. N. Sacks, Ph.D. Thesis, Polytechnic Institute of New York, Brooklyn, NY (1981).

4. H. J. Juretschke, R. Landauer, and J. A. Swanson, *J. Appl. Phys.*, **27**, 838 (1956).
5. P. Mondal and J. W. Jeffrey, *Acta Crystallogr. B*, **31**, 689 (1975).
6. R. P. Gunawardane and F. P. Glasser, *Z. Anorg. Allg. Chem.*, **411**, 163 (1975).
7. I. Maki and T. Sugimura, *Yogyo Kyokai Shi*, **78** (4), 129 (1970).

Solvent Effects on the Electrochemistry of Tetracyanoquinodimethane Polymer Modified Electrodes

Pal Joo¹ and James Q. Chambers

Department of Chemistry, University of Tennessee, Knoxville, Tennessee 37996-1600

ABSTRACT

The electrochemistry of tetracyanoquinodimethane (TCNQ) modified electrodes in contact with simple alcoholic solvents containing lithium salt electrolytes has been studied. Cyclic voltammetric responses characteristic of each alcohol are obtained for 0.1M LiCl/ROH solutions where R = CH₃, CH₃CH₂, CH₃CH₂CH₂, and CH₃CH₂CH₂CH₂. Film stability in the -2 oxidation state and persistence on the electrode were greatly improved in the alcohol solvents relative to the behavior in water. Based on the voltammetric responses, reversible and facile swelling of the polymeric TCNQ films was found when the electrodes were transferred between solvents and electrochemically cycled between the neutral and reduced forms. The effective diffusion coefficient for charge transport (D_{eff}) through the films decreases as the solvent size increases, but the product of the effective diffusion coefficient and viscosity was found to be approximately constant.

The modification of electrode surfaces with polymers has been pursued actively in recent years (1). Materials studied have included conducting metallic polymers such as polyacetylene (2) and poly(pyrrole) (3), ion-exchange polymers such as Nafion (4) and poly(vinylpyridine) (5), and polymers with fixed electron-transfer sites such as poly(vinylferrocene) (6), poly(bipyridine) metal complexes (7), and poly(nitrostyrene) (8). Judging by the many examples reported in a relatively brief time, it is evident that polymeric materials have great versatility for the chemical elaboration of the electrode/solution interface and mediation of concomitant redox processes.

We have recently synthesized a polyester that incorporates the electron-acceptor unit, tetracyanoquinodimethane (TCNQ), into the polymer backbone (9). Thin films of this polymer cast on metal substrates are electroactive and have been studied in contact with aqueous electrolytes. Aside from possible applications, these electrodes are of interest because the electron hopping charge-transport process through the films is markedly affected by chemical reactions in the polymer film phase. The rapid electron-transfer reactions of the TCNQ acceptor renders the films fully electroactive and permits the observation of the effects of coupled chemical reactions on the film electrochemistry. Association (10), protonation (11), and ion pairing (12) of reduced sites in the polymer phase have been documented in previous publications from this laboratory.

Solvent swelling of electroactive polymer films can be extensive, although the role of solvent in the film charge-transport process is difficult to establish. Film thickness increases of approximately 80% were reported by Leddy and Bard for electrodeposited poly(vinylferrocene) films in contact with acetonitrile (13). Earlier, in the case of plasma-polymerized vinylferrocene, Daum and Murray observed that the shapes of the cyclic voltammetric waves are solvent dependent and interpreted the differences by invoking solvent swelling effects (14, 15). A similar observation was reported by Shigehara and by Oyama and Anson for poly(vinylpyridine) ion exchange films (16). It is to be expected that solvent swelling will favor motions of electron donor and acceptor sites, migration of counterions in and out of the polymer film, and, accordingly, will promote electrochemical charge transport.

Herein we report on the electrochemistry of TCNQ polymer films in contact with aliphatic alcohol solvents

(ROH: R = CH₃, CH₃CH₂, CH₃CH₂CH₂, and CH₃CH₂CH₂CH₂). Cyclic voltammograms and spectroelectrochemical data characteristic of each solvent are observed. Since the TCNQ electrochemistry is well understood, both in solution (17) and in the polymer film state (10), the results provide some insight into the role of solvent on the polymer film electrochemistry experiment.

Experimental Section

The preparation of the TCNQ polymer has been described previously (9). Gel permeation chromatography analysis of material synthesized recently indicates that the molecular weight of the polymer is somewhat higher than that prepared initially (9). Voltammetric results in aqueous electrolytes were identical with previous reports. Analytical-grade LiCl and LiClO₄ (Fisher Scientific) were recrystallized and dried under vacuum prior to use. Methanol, ethanol, n-propanol, and n-butanol (all Fisher Scientific) were distilled and stored over 3A, 8-12 mesh molecular sieves (Aldrich).

The film electrode preparation procedures by spin coating and evaporation procedures using saturated tetrahydrofuran (THF) solutions of the polyester have been described (12, 18). Freshly distilled THF was used to prepare the solutions. The coated Pt button (Beckman, $r = 0.25$ cm) and Pt-on-quartz optically transparent disk ($r = 0.65$ cm) electrodes were usually baked for 5 min at 130°C in order to produce a stable, adherent coating.

An Ag/AgCl reference electrode and Pt auxiliary electrode were employed and immersed directly in the alcohol, 0.1M LiCl solutions. In order to correct for variation of the reference electrode potential in the alcohol solvents, the potential of the ferrocene/ferricenium "reference redox system" (19) was also measured at a bare platinum electrode in the solvents studied.

Results

Cyclic voltammetry.—Cyclic voltammograms (CV's) of (TCNQ)_x films adsorbed on platinum substrates in ROH (R = H, CH₃, CH₃CH₂, CH₃CH₂CH₂, and CH₃CH₂CH₂CH₂) are shown in Fig. 1-5. An initial observation is that the solvent markedly influences the qualitative voltammetric wave shapes, although all of the CV's display the basic EE behavior that has been reported previously for TCNQ polyester-modified electrodes. Solvent effects are found on the reversibility for the TCNQ^{0/-} and TCNQ^{-1/2-} processes, the effective diffusion coefficients for charge transport through the film, the film "break-in" process, and the stability of the film in the reduced state.

¹Present address: Department of Chemistry, Kossuth Lajos University, Debrecen, Hungary.

Table I. Voltammetric parameters for tetracyanoquinodimethane modified electrodes in alcoholic solvents containing 0.1M LiCl supporting electrolyte^a

Solvent	E_{p1}^c (V)	E_{p1}^a (V)	E_{pw1}^c (mV)	E_{p2}^c (V)	E_{p2}^a (V)	E_{pw2}^c (mV)
CH ₃ OH	0.110 0.045 $E_{1/2}^1 = 0.05$ (-0.32) ^d	0.055	90 ^b	-0.219	-0.203	73
CH ₃ CH ₂ OH	0.108 $E_{1/2}^1 = 0.13$ (-0.34) ^d	0.150	140	-0.166 $E_{1/2}^2 = -0.15$ (-0.62) ^d	-0.131	66
CH ₃ (CH ₂) ₂ OH	0.11 $E_{1/2}^1 = 0.15$ (-0.34) ^d	0.19	c	-0.19 $E_{1/2}^2 = -0.17$ (-0.66) ^d	-0.14	c
CH ₃ (CH ₂) ₃ OH	-0.02 $E_{1/2}^1 = 0.11$ (-0.40) ^d	0.23	c	-0.27 $E_{1/2}^2 = -0.20$ (-0.71) ^d	-0.14	c

^a Volts vs. Ag/AgCl, unless stated otherwise. Sweep rate: 20 mV/s.

^b Peak width at $i = i_{peak/2}$.

^c Diffusion wave shape, E_{pw} , not measured.

^d Values in parentheses give $E_{1/2}$, volts vs. E_p^c for Fc^{+/0}; see text.

Peak potentials and $E_{1/2}$ values are collected in Tables I and II for the polymer film and TCNQ monomer, respectively. For the first wave in particular, good correspondence is found between the half-wave potentials for the film and monomer in solution. All of the $E_{1/2}$ values are positive relative to the values in water. This is especially true for the second wave, which is probably a reflection of stronger ion association between TCNQ²⁻ and Li⁺ ion in the alcohol solvents relative to water.

The half-wave potential vs. the ferrocene couple does not display any significant trends in the alcohol solvents. The ferrocene reference system was chosen in order to minimize variation of the reference electrode potential between solvents. Cyclic voltammograms were obtained for ferrocene at a bare platinum electrode in each solvent/electrolyte vs. an Ag/AgCl reference electrode. Unfortunately, the cyclic voltammograms of ferrocene in ROH/0.1M LiCl did not have the theoretical shape for a simple reversible one-electron transfer electrode reaction. The reverse cathodic peak was attenuated, indicating that the ferricinium ion was reactive in these alcoholic solvents, and the anodic wave was drawn out. Nonetheless, the ferricinium ion reduction wave was developed to approximately the same extent in all solvents studied and was used as a point of reference for the TCNQ waves.

The most dramatic solvent effect is seen on the stability of the film in the -2 oxidation state where protonation of the TCNQ²⁻ groups occurs in aqueous electrolytes (11). The film instability in water is seen in Fig. 1, which documents the effect of variation of the switching potential in the cyclic voltammetric experiment. When the potential sweep is extended into the region of the second wave in unbuffered aqueous media (on the second cycle in Fig. 1), the film dissolves as evidenced by the irreversible

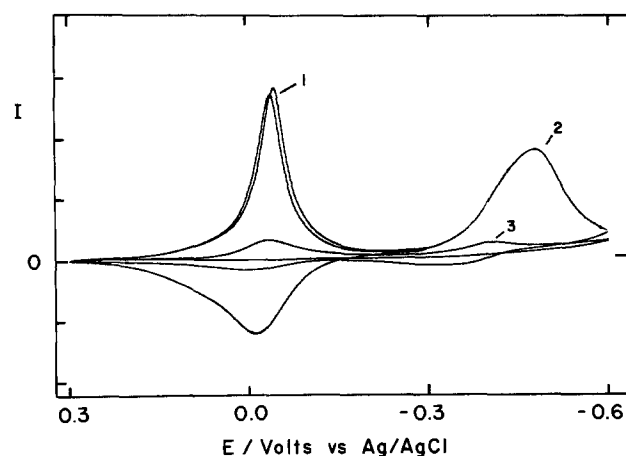


Fig. 1. Cyclic voltammogram of a TCNQ film in contact with aqueous 0.5M LiClO₄. Sweep rate, 10 mV/s; current axis, 10 μ A/division; initial potential, 0.3V vs. Ag/AgCl. Cycles 1-3 are shown.

TCNQ^{-1/2-} wave ($E_p = -0.48$ V vs. Ag/AgCl), the greatly diminished TCNQ^{0/-} wave on subsequent cycles, and the appearance of the characteristic color of TCNQ and TCNQ⁻ in solution. By the third cycle of this voltammogram, only about 10% of the TCNQ sites remain in communication with the platinum substrate based on the charge under the TCNQ^{0/-} cathodic peak. This phenomenon has been ascribed to hydrolysis of the ester links in the TCNQ polyester by the OH⁻ ions formed by hydrolysis of the reduced acceptor sites (11).

In the alcohol solvents, the TCNQ polymer films are much more persistent in the -2 oxidation state. In CH₃OH, for example, well-developed reversible waves are observed for both the first and second electron-transfer steps which persist as the electrode is cycled between the 0 and the -2 oxidation states. With repeated cycling in CH₃OH/0.1M LiCl, however, the solution acquires the color of TCNQ monomer and the peak currents decrease, indicating that film dissolution does occur.

At slow sweep rates, the peak widths ($E_{pw} =$ peak width at $i = i_{p/2}$) and peak separations ($E_p^a - E_p^c$) are typical of reversible surface waves. At very slow sweep rates (less than ca. 5 mV/s), a prewave on the first wave becomes well developed in the CH₃OH voltammograms. This prewave is evident in the voltammogram shown in Fig. 2, where the sweep rate is 20 mV/s; at higher sweep rates, the prewave seems to merge into the first wave. The origin of this prewave is discussed below.

In the higher molecular weight alcohols, the stability and persistence of the TCNQ films increase. In addition, a rather different type of "break-in" phenomenon is observed. For thick films in contact with aqueous electrolytes, several potential sweep cycles are required to activate fully a TCNQ film as documented in the literature (12). In the voltammogram in Fig. 3 obtained in ethanol/0.1M LiCl, the peak current for the first wave decreases and a new wave, assigned to the TCNQ^{-1/2-} process, develops. Absorbance measurements at 720 nm on the TCNQ⁻ radical anion band support this assignment of the

Table II. Voltammetric peak potentials for 2,5-bis(2-hydroxyethoxy) 7,7,8,8-tetracyanoquinodimethane in 0.1M LiCl, alcohol solvents^a

Solvent	E_{p1}^c/V	E_{p1}^a/V	E_{p2}^c/V	E_{p2}^a/V
CH ₃ OH	0.013 $E_{1/2}^1 = 0.045$	0.077	-0.265 $E_{1/2}^2 = -0.21$	-0.155
CH ₃ CH ₂ OH	0.098 $E_{1/2}^1 = 0.13$	0.170	-0.286 $E_{1/2}^2 = -0.25$	-0.219
CH ₃ (CH ₂) ₂ OH ^b	0.099 $E_{1/2}^1 = 0.13$	0.158	-0.304 $E_{1/2}^2 = -0.27$	-0.236
CH ₃ (CH ₂) ₃ OH ^b	0.102 $E_{1/2}^1 = 0.14$	0.173	-0.317 $E_{1/2}^2 = 0.28$	-0.243

^a All potentials are reported vs. Ag/AgCl. Sweep rate: 20 mV/s.

^b IR compensated values.

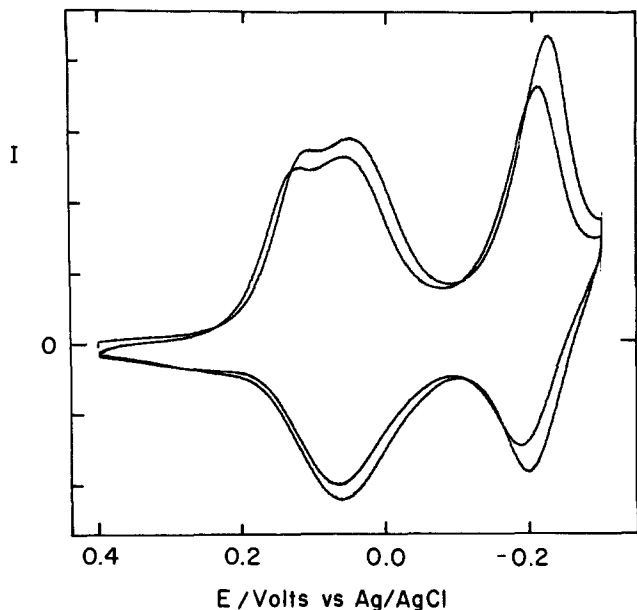


Fig. 2. Cyclic voltammogram of a TCNQ film in contact with 0.1M LiCl/CH₃OH. Sweep rate, 20 mV/s; current axis, 5 μ A/division; initial potential, 0.4V vs. Ag/AgCl. Two cycles are shown.

developing wave to the TCNQ⁻²⁻ process. After several cycles, two waves with approximately equal peak currents are evident in the voltammogram. The value of $dAbs^{720}/dE$ decreases and reaches a minimum in the region of E_p^{cath} for the second wave in the CH₃CH₂OH/0.1M LiCl solution as would be expected for EE behavior (12). Careful inspection for the voltammograms in n-propanol and n-butanol reveals similar behaviors. In n-butanol (see Fig. 5), the current on the first negative going sweep is poorly defined, while subsequent cycles reveal a well-developed first wave and a steadily increasing second wave. The reason for this behavior is not fully understood. Virgin films achieve almost full electroactivity in the initial cycle in methanol and acetonitrile solvents, implying that the solvent swelling process occurs more readily in these solvents than in water.

Other implications of the role of solvent in these "break-in" phenomena can be seen in cyclic voltammograms obtained when a film is cycled in solvent A until a steady-state behavior is obtained and then transferred to solvent B for subsequent voltammetric experiments. For all of the solvents examined, the voltammetric pattern of a given solvent could be regenerated by potential cycling

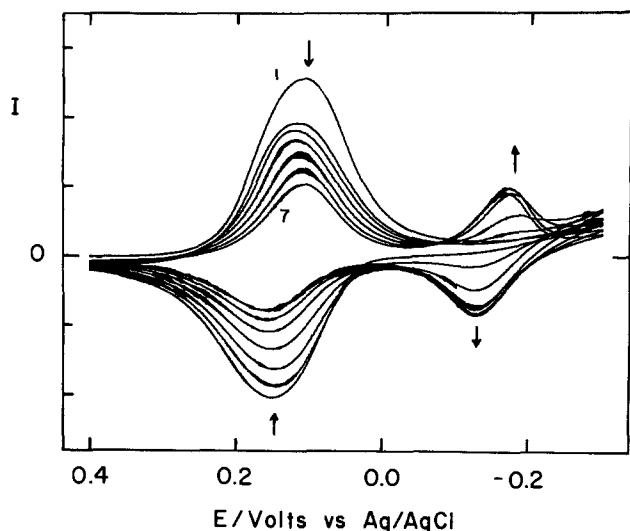


Fig. 3. Cyclic voltammogram of a TCNQ film in contact with 0.1M LiCl/CH₃CH₂OH. Sweep rate, 20 mV/s; current axis, 10 μ A/division; initial potential, 0.4V vs. Ag/AgCl. Seven cycles are shown.

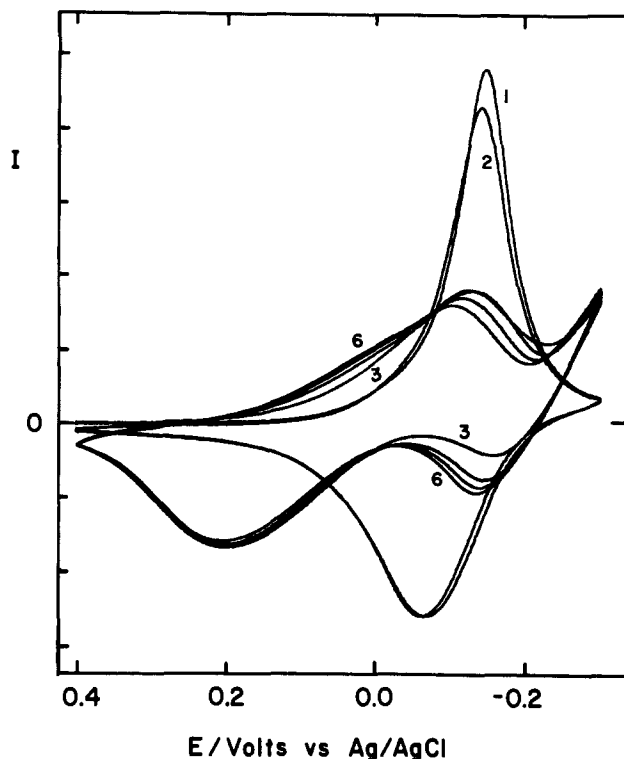


Fig. 4. Cyclic voltammogram of a TCNQ film in contact with 0.1M LiCl/H₂O (cycles 1 and 2) and transferred to 0.1M LiCl/CH₃CH₂CH₂OH (cycles 3-6). Sweep rate, 20 mV/s; current axis, 20 μ A/division; initial potential, 0.4V vs. Ag/AgCl.

through the TCNQ^{0/-} and TCNQ⁻²⁻ redox processes. An example is shown in Fig. 4 for the transfer of a TCNQ film from water to n-propanol. The first two cycles of this voltammogram are typical of the behavior observed in lithium salt electrolytes (9). Cycles 3-6 were obtained when the film was transferred to n-propanol/0.1M LiCl. Even on the first sweep in the alcoholic solvent (sweep number 3), the characteristic voltammetric curve in H₂O/0.1M LiCl is replaced with that in CH₃CH₂CH₂OH/0.1M LiCl. In this experiment, the potential was swept only into the foot of the TCNQ⁻²⁻ wave in n-propanol, but the definition and peak current for the oxidation of TCNQ²⁻ clearly increases as the electrode is cycled. After six cycles, the pattern is almost identical to that obtained on a virgin film that is broken in in CH₃CH₂CH₂OH/LiCl.

The striking feature of these voltammograms, and indeed all of the results of these transfer experiments, is that the voltammetric response characteristic of an alcohol solvent develops on the first cycle. The second wave,

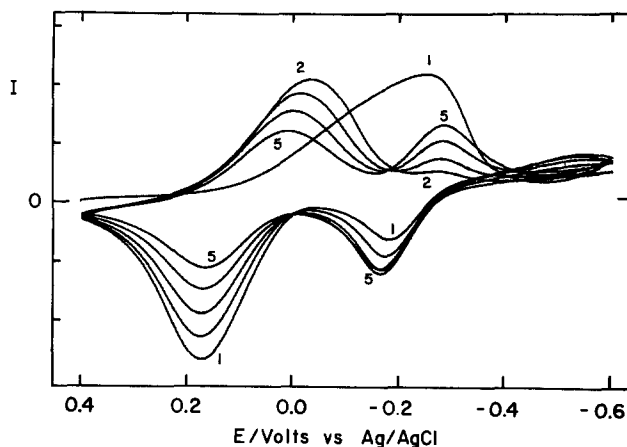


Fig. 5. Cyclic voltammogram of a TCNQ film in contact with 0.1M LiClO₄/CH₃(CH₂)₃OH. Sweep rate, 20 mV/s; current axis, 10 μ A/division; initial potential, 0.4V vs. Ag/AgCl. Five cycles are shown.

in contrast to the observation in water (Fig. 1), has the appearance of a quasi-reversible one-electron surface wave. (The small asymmetry apparent in these voltammograms is probably due to uncompensated resistance in the electrochemical cell.) In water, film electroactivity is lost after the initial potential sweep into the region of the second wave; see Fig. 1.

In *n*-butanol also a noticeable break-in process is observed; see Fig. 5, which displays cycles 1-5 of a virgin film in *n*-butanol/0.1M LiClO₄. The perchlorate, and not the chloride salt, was used in this experiment in order to increase the solution conductivity. In *n*-butanol/0.1M LiCl, the same voltammetric features were evident, but the effect of uncompensated resistance was more evident. In the voltammogram of Fig. 5, the first negative going sweep is considerably drawn out. However, on subsequent cycles, the second wave develops at the expense of the first wave in a manner similar to the ethanol behavior of Fig. 3.

It is also clear that the electrochemical reversibility of the film redox processes is solvent dependent. There is an increase in the TCNQ wave peak separations in the sequence methanol to *n*-butanol. The peak separations, $E_p^a - E_p^c$, and peak widths are significantly larger in the higher molecular weight solvents. Quantitative measurements of "effective charge transfer rate constants" were not made from the peak separations owing to the difficulty of assessing the role of uncompensated resistance artifacts which will also contribute to the observed peak separations.

A final qualitative solvent effect is evident in the voltammograms obtained in methanol. In this solvent, even for virgin films, a split wave is seen for the first electron-transfer step. At even slower sweep rates, the separation and definition of the two components of this split first wave increase. Similar behavior is seen in acetonitrile solvents for the TCNQ films cast using the above procedures (20).

The TCNQ film reduction in CH₃OH/0.1M LiCl was studied in further detail by two spectroelectrochemical techniques, simultaneous electrochemistry and electron spin resonance spectroscopy, SEESR (21), and derivative voltabsorptometry (22). In the latter technique, absorbance measurements at 735 nm on the TCNQ^{•-} radical anion band showed that the prewave in the CH₃OH voltammogram was not due to reduction of the TCNQ units to the radical anion state. This experiment is shown in Fig. 6 for a thin (TCNQ)_x film on a platinum substrate. (Essentially identical patterns were obtained on gold substrates.) The value of dA_{735}/dE reaches a maximum in the region of the symmetrical wave at ca. 0.05V and a minimum at ca. -0.25V in the region of the second wave. This pattern is that expected for the TCNQ^{0/-2} redox chemistry undergoing EE reduction. Unfortunately, partially reduced TCNQ units, or the "mixed-valence species," do not absorb light in the visible or near-infrared spectral regions (12). Thus, it was not possible to monitor this state in a voltabsorptometry experiment. Accordingly, we turned to electron spin resonance techniques to study the process further.

The SEESR signal did not display a maximum in the region of the prewave at ca. 0.1V vs. Ag/AgCl as would be expected for formation of a paramagnetic "mixed-valence" species in a reduced film where extensive dimerization of the radical anion occurs (10). Only a slight increase (ca. 10%) over the residual ESR signal was noted in this potential region. However, stepping the electrode potential through the TCNQ^{0/-} wave at ca. 0.05V greatly increased the magnitude of the ESR signal and slightly increased the peak width from 4.7 to 5.2G. This can be understood if there is less dimerization of the radical anion sites in methanol than in water.

The redox process responsible for the prewave in 0.1M LiCl/CH₃OH is not clear. The addition of trace amounts of water or air to the cell had no effect on the voltammograms. Based on previous studies in water, it is possible that formation of partially reduced TCNQ units

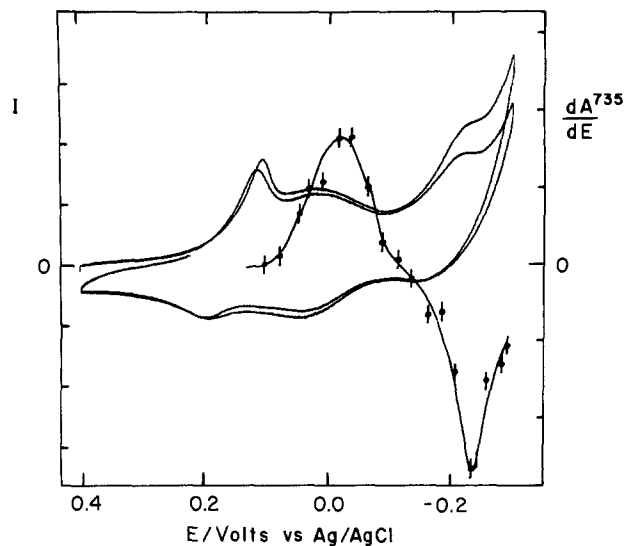
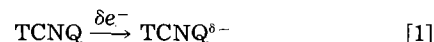


Fig. 6. Cyclic voltammogram and derivative voltabsorptometry (obtained simultaneously) of a TCNQ film in contact with 0.1M LiCl/CH₃OH. Sweep rate, 5 mV/s; current axis, 5 μ A/division; dA/dE axis, 2×10^{-2} absorbance unit/V/division; initial potential, 0.4V vs. Ag/AgCl.



occurs in this region where the electron charge is delocalized into a semiconductor band formed by a superstructure of TCNQ units in the polymer film. Semiconductor and "organic metal" salts of partially reduced TCNQ monomers have been known for some time (23, 24).

Spectroelectrochemistry.—Absorption spectra of fully reduced films in ROH/0.1M LiCl solutions in the wavelength range, 300-750 nm, were qualitatively identical to spectra in aqueous LiCl solution (12). Upon reduction, bands for the radical anion ($\lambda_{\text{max}} = 720$ nm) and dimer dianion ($\lambda_{\text{max}} = 650$ nm) grow in intensity. The radical anion band is distinctly more prominent relative to the dimer band in the alcohol solvents than in aqueous solutions. The degree of dimer dissociation, $\alpha = [\text{TCNQ}^-]/C_T$, where C_T is the total concentration of acceptor sites in the polymer film, was found to be approximately 0.5 for all the alcohol solvents studied. This compares to $\alpha = 0.27$ found previously in aqueous solution. This result is consistent with the above cyclic voltammetric results which show that the anodic segment of the TCNQ^{0/-} process is less drawn out in alcohol than in water, indicating that oxidation of the radical anion dominates the anodic peak current for this process.

Another qualitative difference between the aqueous and alcoholic solvents is that reaction of the reduced film in the -2 oxidation state with oxygen is more rapid in the latter solvents. This is evidenced in the absorption spectra by the irreversible disappearance of all TCNQ bands, the appearance of a new band at $\lambda_{\text{max}} = 480$ nm, and a decrease of film electroactivity. It is likely, in view of the observation of Sushanski and Van Duyne (25), that the 480 nm band is due to the product reaction of the TCNQ²⁻ dianion with O₂.

In the previous studies in water, the potential region for the generation of the dianion was avoided due to the film dissolution process, and as a consequence, the O₂ decay product with $\lambda_{\text{max}} = 480$ nm was usually not observed. Furthermore, the previous derivative voltabsorptometric spectroelectrochemical studies (12) were conducted in the presence of aqueous CaCl₂ where the dianion and the TCNQ polymer films were relatively stable. However, even under these conditions, TCNQ films in the -2 oxidation state will undergo irreversible reaction in the presence of air to give a species with $\lambda_{\text{max}} = 480$ nm. Films that have been held in the -2 oxidation state in alcohol for ex-

tended periods of time ($> ca. 10$ min) no longer display the spectral characteristic of the TCNQ group. Potential sweeps in the region of $+0.4$ to -0.3 only revealed weak TCNQ redox processes and did not indicate the presence of any new waves.

Chronocoulometry.—In order to determine the “effective diffusion coefficient” for charge transport (D_{ct}) in the various solvents, potential step chronocoulometry was performed. Typical results are shown in Fig. 7 for 0.1M LiCl in each of the four alcohols studied. Based on the Cottrell slopes, there is approximately an order of magnitude decrease in D_{ct} in the sequence methanol through n-butanol. The following values ($D_{ct} \times 10^{12}/\text{cm}^2\text{s}^{-1}$) were determined: CH_3OH , 1.0 ± 0.1 ; $\text{CH}_3\text{CH}_2\text{OH}$, 0.4 ± 0.1 ; $\text{CH}_3\text{CH}_2\text{CH}_2\text{OH}$, 0.2 ± 0.1 ; and $\text{CH}_3\text{CH}_2\text{CH}_2\text{CH}_2\text{OH}$, $ca. 0.1$. The values of D_{ct} in n-butanol, and to a lesser extent in n-propanol, were difficult to reproduce, owing in part to the high resistance of the 0.1M LiCl solutions in these solvents. In addition, the D_{ct} values in n-butanol appear to be strongly dependent on the film preparation procedures, i.e., baking time and temperature.

The viscosity of the alcohol solvents increases as the chain length increases (26). Not surprisingly, the product of the effective diffusion coefficient for charge transport and viscosity is approximately constant. At $ca. 25^\circ$, we find the following values for $D_{ct} \times 10^{12}/\text{cm}^2\text{s}^{-1}\text{cp}$: CH_3OH , 0.55 ± 0.06 ; $\text{CH}_3\text{CH}_2\text{OH}$, 0.44 ± 0.11 ; $\text{CH}_3\text{CH}_2\text{CH}_2\text{OH}$, 0.4 ± 0.2 ; $\text{CH}_3\text{CH}_2\text{CH}_2\text{CH}_2\text{OH}$, 0.3 ; average, $ca. 0.4$.

Summary and Conclusions

These experiments have shown that the electrochemical behavior of TCNQ film electrodes is basically the same in a series of alcohol solvents as it is in water. Successive electron-transfer reactions (EE behavior) are observed in all solvents studied, including acetonitrile (20). The natures of the charge transport process, however, and the resulting voltammetric behavior are solvent dependent.

Cyclic voltammograms characteristic of each solvent are observed, and relatively facile transitions from the pattern of one solvent to that of another are found when film electrodes are transferred between solvents con-

taining the same supporting electrolyte. These results imply that solvent uptake by the film and film swelling occur readily. The break-in phenomena observed in these transfer experiments indicate that this solvent swelling process can be electrochemically driven. This conclusion is consistent with our observation (27) that coupling of platinum oxidation with the $\text{TCNQ}^{0/-}$ couple and penetration of water to the polymer/substrate interface take place in films that have been electrochemically cycled.

The approximately constant value of D_{ct}^{xn} suggests, but does not prove, that counterion migration balanced by a Stokes viscous force controls the charge-transport process in these TCNQ polymer films. Approximately constant D^{xn} values are predicted by the Stokes-Einstein relation for diffusion of particles of uniform size in viscous media (28). Polymer backbone segmental motions should also be diminished as the viscosity of the solvent increases. Both effects are likely to be involved in the electron hopping charge-transport process in electroactive polymer films (18).

Regardless of the detailed mechanism of the charge-transport process, however, it can be concluded that the solvent is intimately involved in the polymer film phase. Facile swelling is observed when the TCNQ electrodes are transferred and electrochemically cycled in different solvents. The voltammetric parameters reflect the swelling process. In the sequence from methanol to n-butanol, deviations from reversible surface wave behavior increase.

Acknowledgment

This research was supported by grants from the U.S. Army Research Office and the National Science Foundation.

Manuscript submitted July 20, 1984; revised manuscript received Jan. 18, 1985.

REFERENCES

- R. W. Murray, in “Electroanalytical Chemistry,” Vol. 13, A. J. Bard, Editor, Marcel Dekker, New York (1983).
- D. MacInnes, Jr., M. A. Druy, P. J. Nigrey, D. P. Nairns, A. G. MacDiarmid, and A. J. Heeger, *J. Chem. Soc. Chem. Commun.*, 317 (1981).
- K. K. Kanazawa, A. F. Diaz, R. H. Geiss, W. D. Gill, J. F. Kwak, J. A. Logan, J. F. Rabolt, and G. B. Street, *ibid.*, 854 (1979).
- I. Rubinstein and A. J. Bard, *J. Am. Chem. Soc.*, **102**, 6641 (1980); C. R. Martin, T. A. Rhodes, and J. A. Ferguson, *Anal. Chem.*, **54**, 1639 (1982).
- N. Oyama and F. C. Anson, *J. Am. Chem. Soc.*, **101**, 739 (1979).
- A. Merz and A. J. Bard, *ibid.*, **100**, 3222 (1978).
- H. D. Abruna, P. Denisevich, M. Umana, T. J. Meyer, and R. W. Murray, *ibid.*, **103**, 1 (1981).
- L. L. Miller and M. R. Van De Mark, *ibid.*, **100**, 3223 (1978).
- R. W. Day, G. Inzelt, J. F. Kinstle, and J. Q. Chambers, *ibid.*, **104**, 6804 (1982).
- G. Inzelt, R. W. Day, J. F. Kinstle, and J. Q. Chambers, *J. Phys. Chem.*, **87**, 4592 (1983).
- G. Inzelt, J. Q. Chambers, J. F. Kinstle, and R. W. Day, *J. Am. Chem. Soc.*, **106**, 3396 (1984).
- G. Inzelt, R. W. Day, J. F. Kinstle, and J. Q. Chambers, *J. Electroanal. Chem.*, **161**, 147 (1984).
- J. Leddy and A. J. Bard, *ibid.*, **153**, 223 (1983).
- P. Daum and R. W. Murray, *J. Phys. Chem.*, **85**, 389 (1981).
- P. Daum and R. W. Murray, *J. Electroanal. Chem.*, **103**, 289 (1979).
- N. Oyama and F. C. Anson, *This Journal*, **127**, 640 (1980).
- L. R. Melby, R. J. Harder, W. R. Hertler, W. Mahler, R. E. Benson, and W. E. Mochel, *J. Am. Chem. Soc.*, **84**, 3374 (1962); M. Sharp, *Anal. Chim. Acta*, **85**, 17 (1976).
- F. B. Kaufman, A. H. Schroeder, E. M. Engler, S. R. Kramer, and J. Q. Chambers, *J. Am. Chem. Soc.*, **102**, 483 (1980).
- H. Strehlow, in “The Chemistry of Non-Aqueous Solvents,” J. Lagowski, Editor, Academic Press, New York (1966); A. J. Bard and L. R. Faulkner, “Electrochemical Methods,” p. 702, Wiley-Interscience, New York (1980).
- R. W. Day, Ph.D. Thesis, University of Tennessee, Knoxville, TN (1984).
- I. R. Goldberg and A. J. Bard, *J. Phys. Chem.*, **75**, 3281 (1971).

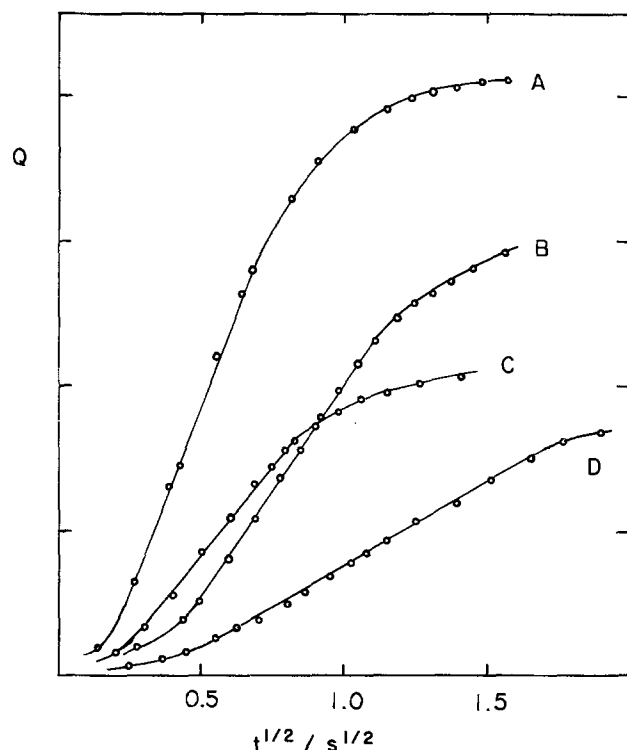


Fig. 7. Chronocoulometric Cottrell plots for reduction of TCNQ films in contact with 0.1M LiCl/(A) CH_3OH , (B) $\text{CH}_3\text{CH}_2\text{OH}$, (C) $\text{CH}_3\text{CH}_2\text{CH}_2\text{OH}$, and (D) $\text{CH}_3\text{CH}_2\text{CH}_2\text{CH}_2\text{OH}$. Charge axis, 1×10^{-4} C/division.

22. E. E. Bancroft, J. S. Sidwell, and H. N. Blount, *Anal. Chem.*, **53**, 1390 (1981).
23. F. Gutmann and L. E. Lyons, "Organic Semiconductors," Wiley, New York (1967).
24. A. F. Garito and A. J. Heeger, *Acc. Chem. Res.*, **7**, 232 (1974).
25. M. R. Suchanski and R. P. Van Duyne, *J. Am. Chem. Soc.*, **98**, 250 (1976).
26. "Handbook of Chemistry and Physics," 14th ed., C. D. Hodgman, Editor, Chemical Rubber Publ. Co., Cleveland, OH (1958).
27. G. Inzelt, J. Q. Chambers, J. F. Kinstle, and M. A. Lange, *Anal. Chem.*, **56**, 301 (1984).
28. J. O'M. Bockris and A. K. N. Reddy, "Modern Electrochemistry," Vol. 1, p. 379, Plenum Press, New York (1970).

Semiconducting Characteristics of Galena Electrodes

Relationship to Mineral Flotation

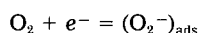
P. E. Richardson* and C. S. O'Dell*

U.S. Department of the Interior, Bureau of Mines, Avondale Research Center, Avondale, Maryland 20782-3393

ABSTRACT

Electrochemical, interfacial capacitance, and surface photovoltage (SPV) measurements have been used in a study of oxygen reduction and xanthate chemisorption on *in situ* cleaved natural and synthetic lead sulfide crystals. Electrodes cleaved in nitrogen-sparged 0.1M sodium tetraborate assume the flatband potential, V_{FBP} , at the instant of cleavage, and thus the cleavage potential decreases with increasing bulk electron concentration. Highly n-type electrodes have a cleavage potential (V_{FBP}) of $\approx -0.6V$ (SCE), and highly p-type electrodes have a value of $\approx -0.2V$ (SCE). The space charge is readily varied by applied potentials in the range -0.2 to $-0.6V$. This Bureau of Mines, U.S. Department of the Interior, report discusses the effect of the variable space-charge layer on oxygen reduction and xanthate chemisorption.

The use of xanthates as flotation collectors for sulfide minerals is one of this century's more successful examples of applied surface chemistry, and their practical significance has stimulated extensive research on the reactions that confer hydrophobicity. The 1950's marked a major milestone when it was discovered by Plaksin (1) that oxygen was an essential reagent in the xanthate flotation of sulfides. Most sulfides are semiconductors, and Plaksin and Shafeev (2) suggested, in the case of galena, that oxygen chemisorption converted the surface from n- to p-type, energetically favoring the oxidation of xanthate anions to produce an adsorbed hydrophobic species



At about the same time, Salamy and Nixon (3) proposed a mixed potential model of sulfide flotation where xanthate oxidation to a hydrophobic surface species is compensated by the reduction of dissolved oxygen. The major difference between these two proposals is that the mixed potential model focuses on the solution side of the interface and assumes that the potential drop, V_h , between the surface and the outer Helmholtz plane, OHP, adjusts to make the rate of the anodic and cathodic reactions equal. In contrast, the semiconductor model focuses on the potential drop across the solid, which is assumed to control collector adsorption by changes in the Fermi level at the surface or by changes in the energetics of xanthate oxidation.

During the past decade, the mixed potential model has gained wide acceptance in flotation research. In the application of this model, semiconducting effects have been neglected by assuming sulfides behave as metals. For galena, it is assumed (4, 5) that there is no varying potential drop across the solid side of the interface so that the transfer coefficient has the same value as at metal electrodes, i.e., ≈ 0.5 . A transfer coefficient of 0.5 suggests that the Fermi level at the surface is pinned at a fixed value. However, Fermi level pinning at galena surfaces is inconsistent with a potential-dependent photovoltage (6), a Tafel slope of 225 mV, which has been reported for oxygen reduction at pH 9.2 (7), the influence of light on xanthate adsorption (8), nonuniform adsorption of xanthate and nonuniform deposition of copper, suggesting areas of

differing electrochemical potential (9), and the dependence of oxidation rate on light and stoichiometry (10).

In an attempt to reconcile the different viewpoints expressed in the two models and the conflicting experimental results, the present study on oxygen reduction and xanthate chemisorption on *in situ* cleaved galena electrodes was undertaken by the Bureau of Mines. *In situ* cleavage was selected to obtain unoxidized electrode surfaces having minimum mechanical damage in the surface region in order to avoid defect states that might pin the surface Fermi energy. Surface photovoltage and capacitance measurements were used to study variations in the space-charge potential.

Experimental

A conventional three-compartment quartz cell was used for xanthate chemisorption studies and a two-compartment cell for oxygen reduction studies. Potentials are reported with respect to a saturated calomel electrode connected via a Luggin capillary to the cells. A constant-current charging pulse with an amplitude of 0.1-1 mA/cm² and width of 15-20 μs was used to determine the capacitance. The electrode response of galena is characterized by a nearly vertical rise and fall in potential when the pulse is applied and terminated, a linear increase in potential during the on time of the pulse, and an exponential decrease in potential after the pulse is terminated. The surface photovoltage (SPV) was excited by illumination from a 200W xenon-arc lamp filtered to pass a 2000Å band near 8000Å, chopped at 86 Hz, and measured by a procedure described previously (6).

The electrolyte was 0.05 or 0.1M sodium tetraborate. The cell was sparged with ultrahigh purity nitrogen or with nitrogen containing known oxygen partial pressures ($pO_2 = 10^{-3}$ and 10^{-2} atm). Separate measurements on a platinum electrode in the cell used for oxygen reduction studies indicated that the diffusion current due to residual oxygen when sparging with nitrogen was $\approx 1 \mu A/cm^2$, which corresponded to a $pO_2 = 10^{-4}$ atm (11).

The electrodes were natural crystals of galena from Galena, Kansas, and Brushy Creek, Missouri, and synthetic crystals obtained from the Naval Surface Weapons Center, White Oak, Maryland. The semiconducting characteristics of the actual electrodes were determined from surface photovoltage (SPV) measurements (12-14), which are discussed in detail in the Results section. Based on the

*Electrochemical Society Active Member.

SPV, all of the natural crystals were highly n-type, possibly degenerate. Hall-effect measurements on a selected natural sample gave a bulk electron density, n_b , of $\approx 2 \times 10^{-18} \text{ cm}^{-3}$. The synthetic samples mounted as electrodes were from several different growth runs, and the SPV showed that they ranged from slightly n-type to highly p-type.

Electrodes were cleaved *in situ* in the electrochemical cell. Figure 1 shows an electrode prior to and after cleavage and illustrates the mounting technique. A platinum wire spot welded to the back surface prior to encapsulation in a nonconductive epoxy provided an ohmic contact. A sharp blow on a glass rod resting on the electrode resulted in (100) cleavage. Usually, the samples cleaved flush with, or just below, the surface of the epoxy so that the entire electrode area after cleavage was that of the freshly cleaved surface.

Results

Electrode potentials and photovoltages at cleavage.—All of the "as-mounted" samples had open-circuit potentials of -0.26 to -0.1V in oxygen-free borate. These potentials were dependent on dissolved oxygen but had no correlation with carrier densities. They are believed to represent the mixed potential of oxidation and/or dissolution reactions occurring on the surface. All electrodes except those found in subsequent studies (next section) to be highly p-type had positive photovoltages, indicating positive (electron-deficient/hole-rich) space charges.

Figure 2 shows the change in electrode potential and SPV for a typical natural mineral electrode as it is cleaved under borate. At cleavage, the electrode potential instantly decreases by several hundred millivolts and then slowly increases with time; simultaneously, the SPV instantly decreases to zero and then becomes increasing positive as the electrode potential increases. The behavior of the other electrodes at cleavage is qualitatively similar to the highly n-type, as shown in Table I. The zero SPV suggests that the electrodes all assume the flatband potential, V_{FBP} , at the instant they are cleaved, which will be substantiated in the next section. Since the flatband potential depends on the bulk carrier concentration through the well-known relationship (14)

$$V_{FBP} = \text{const.} - (kT/q) \ln(n_b/n_i)$$

the progressive increase in the potential at cleavage with decreasing electron concentration is also explicable by the assumption that the potential assumed at cleavage is equal to the flatband potential.

The increase in potential following cleavage represents a slow oxidation process, which gives rise to a positive SPV (upward band bending) on all electrodes except the



Fig. 1. Electrodes before and after cleavage

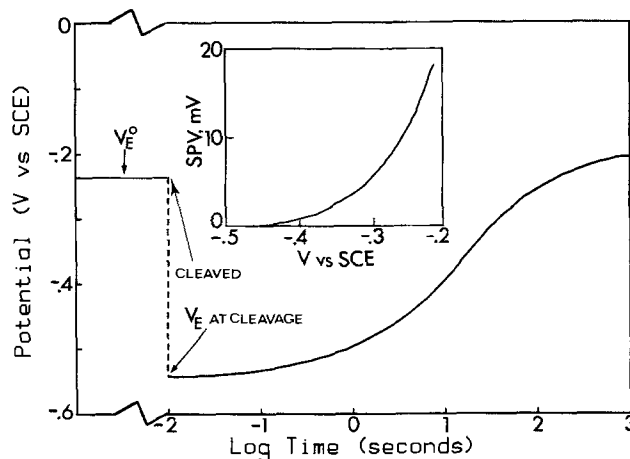


Fig. 2. Changes in electrode potential and surface photovoltage following cleavage of a natural galena electrode in 0.1M sodium tetraborate.

highly p-type. The latter is presumably close to degeneracy, preventing upward band bending at the surface due to an anodic process. Electrodes cleaved in oxygen containing solutions exhibit a much faster increase in electrode potential following cleavage. The increase in potential and the development of a positive space charge, therefore, can be plausibly attributed to an acceptor state associated with oxygen chemisorption. Alternatively, lead vacancies are known to act as acceptors in lead sulfide (15-16) and a dissolution reaction whereby lead is leached from the surface to produce a metal-deficient surface may also account for the development of a positive space following cleavage.

The behavior of the cleaved electrodes is in essential agreement with Plaksin and Shafeev's proposal (2) that an oxidation reaction increases the free hole concentration at the surface of galena, either by their mechanism of oxygen chemisorption or by a dissolution process that produces a lead-deficient surface.

Oxygen reduction and anodic oxidation reactions on cleaved samples.—The bottom and middle curves of Fig. 3-5 show the SPV and interfacial capacitance for two synthetic and one mineral electrodes. The SPV and capacitance curves exhibit the classical shape (12-14) characteristic of semiconductor electrodes, establishing qualitatively the existence of a polarizable space-charge layer. It can also be noted that variations in the SPV and capacitance occur over a potential range greater than the thermal bandgap, $E_g = 0.37 \text{ eV}$ (15), of lead sulfide. Therefore, changes in the Helmholtz potential cannot be neglected, and the usual Schottky-Mott plots (17) cannot be used to determine the flatband potential or the carrier densities of the electrodes. However, V_{FBP} can be determined from the SPV measurements for samples in which both the positive and negative branches are observed (Fig. 3 and 4).

Theoretically, the ratio of the saturation SPV's under strong anodic and cathodic bias should vary as the bulk electron-hole ratio, n_b/p_b (13). The ratio for the synthetic sample in Fig. 3 is close to unity, establishing that the sample is intrinsic. From the zero value of the SPV, the flatband potential, V_{FBP} , is at -0.375V , essentially the potential observed at cleavage. The equality of V_{FBP} deter-

Table I. Electrode potential, V_{E_r} and SPV of cleaved electrodes

Sample	Rest potential before cleavage		Potential at cleavage		Rest potential after cleavage	
	V_{E_r} V(SCE)	SPV	V_{E_r} V(SCE)	SPV	V_{E_r} V(SCE)	SPV
Highly n-type	-0.237	+	-0.540	0	-0.240	+
Slightly n-type	-0.232	+	-0.465	0	-0.225	+
Intrinsic	-0.137	+	-0.380	0	-0.137	+
Highly p-type	-0.260	0	-0.235	0	-0.225	0

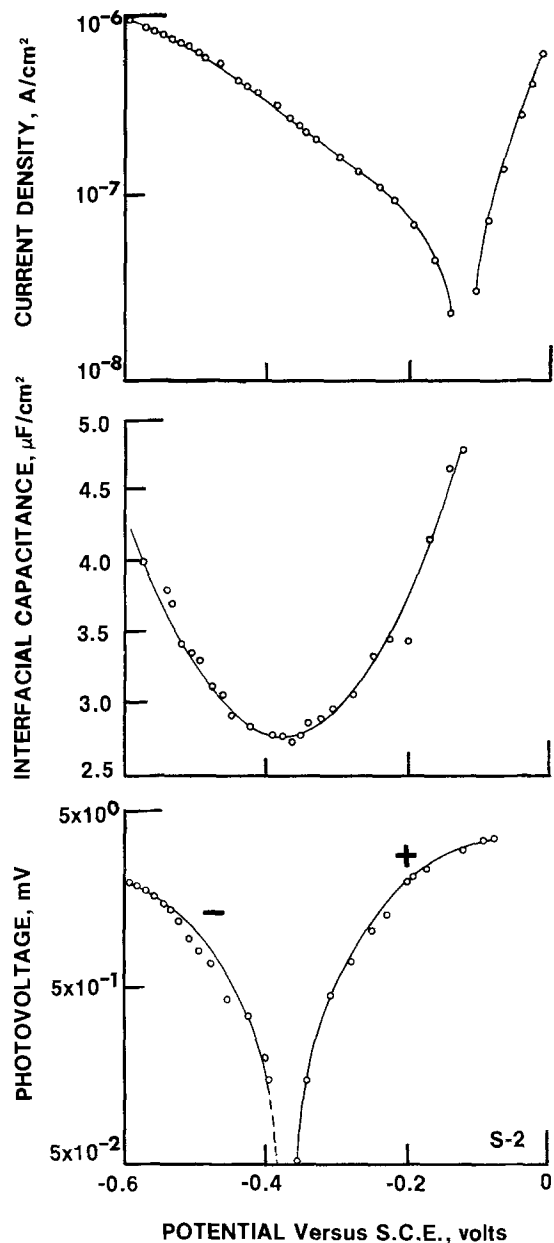


Fig. 3. Surface photovoltage (bottom), interfacial capacitance (middle), and constant current polarization (top) for a synthetic PbS electrode in 0.1M sodium tetraborate.

mined from the SPV with the potential of the capacitance minimum provides further support of the intrinsic nature of this electrode (18).

The flatband potential of the synthetic sample in Fig. 4 is at -0.475V , again in agreement with the cleavage potential. The ratio of the saturation SPV's, after a small extrapolation of the negative branch, suggests this sample is slightly n-type with $5 < n_v/p_b < 10$. The slight shift of the capacitance minimum to potentials more positive than V_{FBP} , i.e., toward depletion, is in agreement with the expected theoretical shift (17) and provides further support for a slightly n-type sample.

Only the positive branch of the SPV is observable on highly n-type mineral electrodes (Fig. 5). Typically, at electrode potentials between -0.5 and -0.6V , the SPV of natural electrodes becomes less than the noise level ($\approx 0.05\text{ mV}$), and no photosignal is observed at potentials as low as -1.0V , suggesting that the bulk is degenerate p-type. Therefore, the surface Fermi level is at the conduction bandedge at V_{FBP} , preventing downward band bending even with strong cathodic polarization. The flatband potential cannot be determined precisely without reversal in the sign of the SPV, but it is apparently located at potentials $< -0.5\text{V}$. From the potential of several

natural electrodes at the instant of cleavage, it is believed to be between -0.54 and -0.69V (SCE). The capacitance minimum (Fig. 5) occurs $0.2\text{--}0.3\text{V}$ positive of the flatband potential, i.e., is shifted farther toward the depletion region, as expected for a highly n-type sample.

The uppermost curves of Fig. 3-5 show the constant-current polarization behavior of the electrodes. The oxygen reduction reaction (Fig. 4-5) is close to first order with respect to $p\text{O}_2$. The Tafel slopes are not constant but have approximate values of $\approx 0.21\text{V}$ for the intrinsic electrode, $\approx 0.16\text{--}0.22\text{V}$ for the slightly n-type electrode, and $\approx 0.2\text{V}$ for the highly n-type mineral electrode. A Tafel slope of 0.059V is usually anticipated (19) for cathodic reactions on semiconductors when the rate is dependent on the surface concentration of electrons, n_s , and changes in

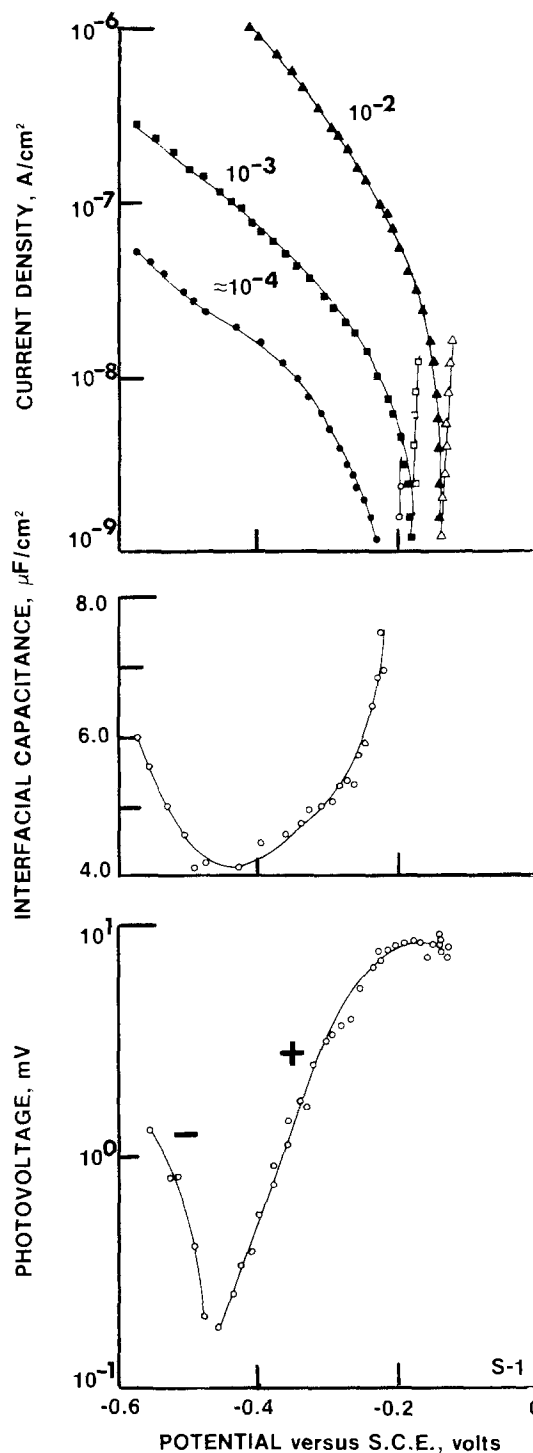


Fig. 4. Surface photovoltage (bottom), interfacial capacitance (middle), and constant current polarization (top) for a synthetic PbS electrode at oxygen partial pressures of 10^{-2} , 10^{-3} , and $\approx 10^{-4}$ atm in 0.1M sodium tetraborate.

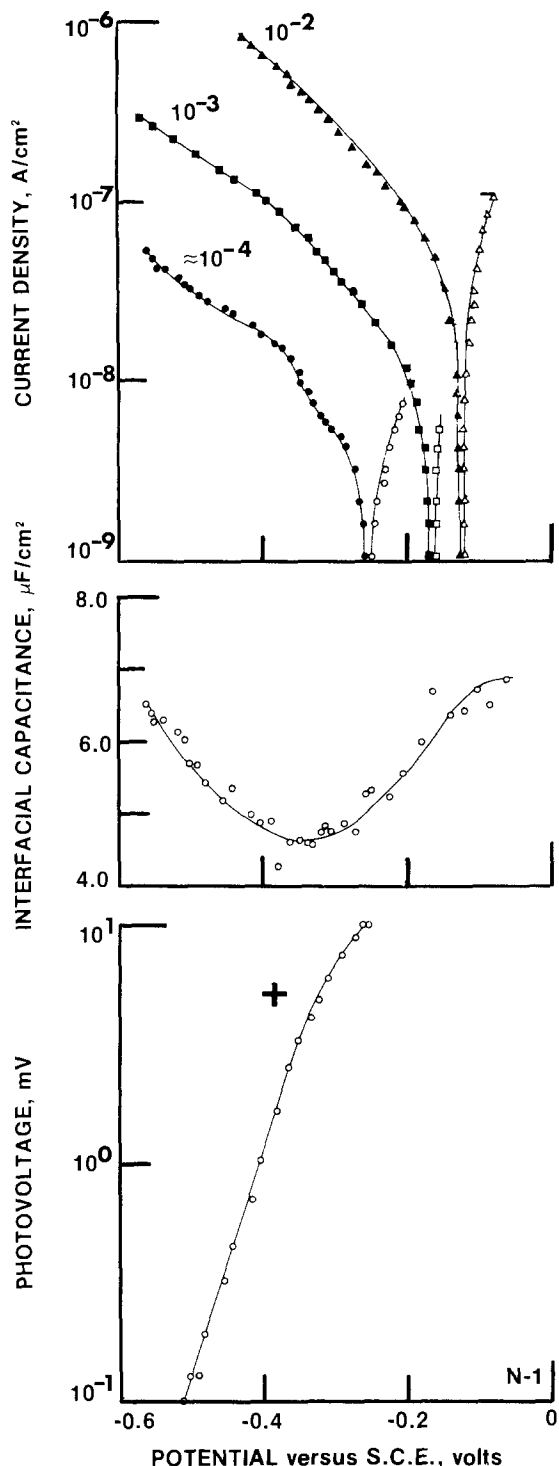


Fig. 5. Surface photovoltage (bottom), interfacial capacitance (middle), and constant current polarization (top) for a mineral galena electrode at oxygen partial pressures of 10^{-2} , 10^{-3} , and $\approx 10^{-4}$ atm in 0.1M sodium tetraborate.

electrode potential occur solely across the space-charge layer; whereas, an ideal Tafel slope of 0.118V is anticipated for the simplest one electron reduction reaction at metal electrodes. For the present electrodes with $n_b \geq n_i$ (n_i = intrinsic concentration), the rate of oxygen reduction is not dependent on n_s . In this case, any changes in potential across the space-charge layer should reduce the changes in overvoltage available in the Helmholtz layer for oxygen reduction, giving rise to the large apparent Tafel slopes. In the Appendix, the SPV has been used to estimate the partition of the potential between the solid and solution phases. The results indicate that over the range of potentials corresponding to the Tafel region for oxygen reduction, the potential is partitioned nearly

equally between the solid and solution phases. This suggests that Tafel slopes referenced to the change in Helmholtz potential have values approximately one-half as large as the experimental values, that is, ≈ 0.08 -0.12V.

These "corrected" Tafel slopes are not sufficiently accurate to warrant their use for a detailed analysis of the mechanism of oxygen reduction. The important point is that independent measurements of the SPV and capacitance establish the existence of a polarizable space-charge layer, which logically accounts for the large Tafel slopes observed experimentally on electrodes with $n_b \geq n_i$. It should also be noted that, on p-type electrodes, the rate of oxygen reduction conceivably could become limited by the rate of diffusion of electrons to the surface (19). However, the rate could only be less than at n-type electrodes. A slower rate is inconsistent with the semiconducting model of flotation reactions where p-type minerals are predicted to react more readily with anionic collectors than are n-type minerals (2). The results and the above argument suggest that a semiconducting limit of the rate of oxygen reduction should not be significant in galena flotation.

Xanthate chemisorption on cleaved electrodes.—

Ethylxanthate is known to chemisorb on galena, possibly as a 1:1 complex with surface lead (4, 20). Chemisorption is limited to a monolayer or less and accordingly does not give rise to steady-state currents but may be studied using transient methods such as voltammetry, after correcting for background effects. Figure 6 shows a background voltammetry curve at high current sensitivity for galena in 0.05M borate. The electrode was cleaved *in situ* while potentiostated near the flatband potential, a procedure selected to inhibit oxidation. The anodic and cathodic limits of the voltammetry scan were then gradually increased until an oxidation wave (O_I) and a reduction wave (R_{II}) became apparent at potentials $\geq -0.2V$ and $\leq -0.9V$, respectively. These waves are believed to produce second solid phases on the electrode, corresponding to $PbO + S^\circ$ at potentials $> -0.2V$ (6, 21) and to Pb° at potentials $< -0.9V$ (22). R_I and O_{II} appear only after prior oxidation at potentials $> -0.2V$ and reduction at potentials $< -0.9V$, respectively. For electrodes cleaved *in situ* and potentiostated in the range $-0.9 < V_E < -0.2V$, no gross compositional changes in the surface occur, and their behavior should be characteristic of lead sulfide and should not be influenced by other solid phases on the surface produced by oxidation or reduction.

In the presence of high concentrations of ethylxanthate, the currents between -0.6 and $-0.2V$ (Fig. 7) are much in excess of those occurring on the background voltammetry curve. The excess currents, therefore, are due to redox reactions between lead sulfide and ethylxanthate. The dotted voltammetry (Fig. 7) is in excellent agreement with voltammograms of Woods (4) and Gardner and Woods (23). The anodic prewave beginning

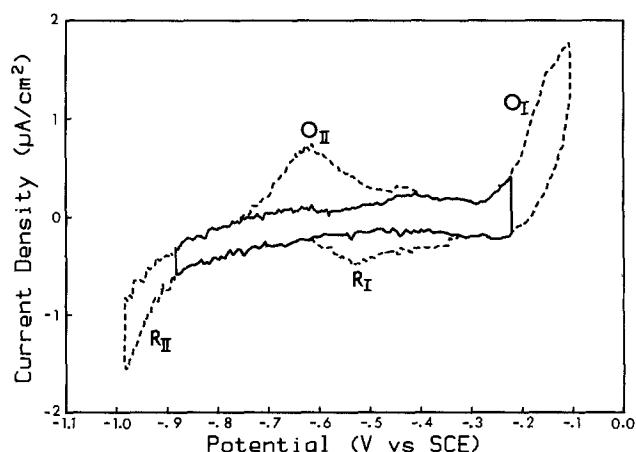


Fig. 6. Cyclic voltammogram of a cleaved natural galena electrode in 0.05M sodium tetraborate at 5 mV/s.

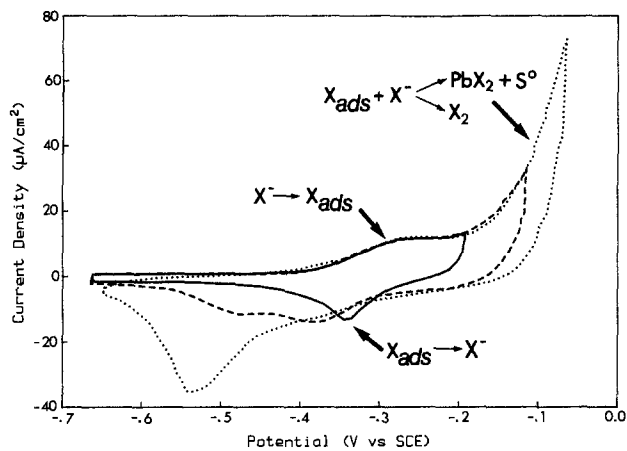


Fig. 7. Cyclic voltammograms of natural galena electrode in the presence of 0.01M sodium ethylxanthate/0.05M sodium tetraborate at 5 mV/s.

at -0.4V has been attributed to xanthate chemisorption to form a surface analogue of lead ethylxanthate (4), the wave at $\approx -0.2\text{V}$ to the formation of a mixed lead xanthate/sulfur/dixanthogen product layer (23, 24), and the reduction peak at $\approx -0.55\text{V}$ to the reduction of the mixed layer and any chemisorbed xanthate (23, 24).

When the anodic limit is kept slightly below the potential of mixed film formation, a distinct cathodic peak is observed at -0.35V that contains the same charge as the anodic chemisorption peak. A cathodic peak at as positive a potential as -0.35V , with distinct separation of this peak from that for $\text{PbX}_2/\text{S}/\text{X}_2$ reduction, has not been reported previously. It clearly represents the reduction and probably desorption of chemisorbed xanthate. It is also apparent that the chemisorption/desorption process is more reversible than reactions leading to $\text{PbX}_2/\text{S}/\text{X}_2$ products on the surface and their reduction. This result is not unexpected, since chemisorbed xanthate is an obvious intermediate in the formation of a $\text{PbX}_2/\text{S}/\text{X}_2$ layer and the formation of PbX_2 requires structural rearrangement at the surface.

From the standpoint of possible semiconducting effects, we are primarily interested in the chemisorption/desorption process occurring between -0.4 and -0.2V . Figures 8 and 9 show the xanthate chemisorption/desorption reaction and the SPV for a synthetic and natural mineral electrode. The SPV was obtained on the freshly cleaved surfaces immediately prior to xanthate addition. Only negative SPV's were observed on the synthetic electrode, establishing this electrode as highly p-type; only positive SPV's were observed on the natural mineral electrode, establishing it as highly n-type.

The flatband potentials of the electrodes (determined as the potentials at cleavage) are also indicated in Fig. 8 and 9. These provide reference potentials where the surface densities of carriers are qualitatively known; that is, the surface of the highly p-type electrode is highly p-type at $\approx -0.2\text{V}$, and the surface of the highly n-type is highly n-type at $\approx -0.6\text{V}$. Since at the semiconductor-electrolyte interface the Fermi level at the surface is independent of the bulk Fermi level (17), it follows that the p-type electrode has a highly n-type surface $\approx -0.6\text{V}$, and the n-type has a highly p-type surface at $\approx -0.2\text{V}$. The band configurations relative to a voltammetry curve are schematically illustrated in Fig. 10. The xanthate chemisorption/desorption process occurs between -0.4 and -0.2V , i.e., over the range of potentials where the space charge changes, suggesting chemisorbed xanthate may be represented by a surface state (donor-like) having an energy within the forbidden gap. The bandgap of PbS (15) is only $\approx 15kT$ (0.37 eV). With such a narrow gap, surface states are anticipated to be in equilibrium (facile charge exchange) with bandedge states, and with their occupancy determined by the location of the Fermi level at the surface. The occupied state corresponds to chemisorbed

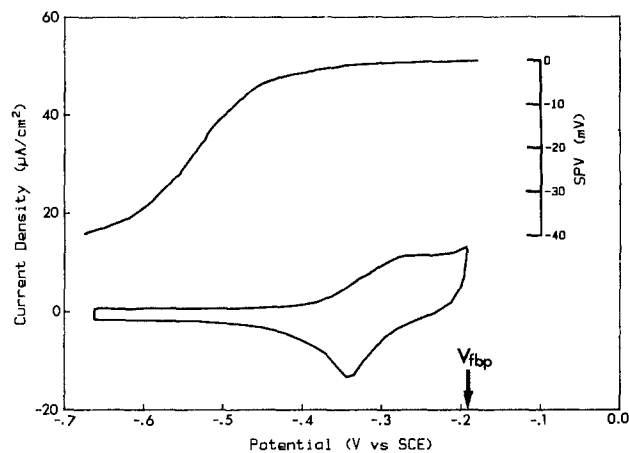


Fig. 8. Cyclic voltammogram and surface photovoltage of a synthetic PbS electrode in 0.01M sodium ethylxanthate and 0.05M sodium tetraborate. V_{FBP} = potential at cleavage. Sweep rate 5 mV/s.

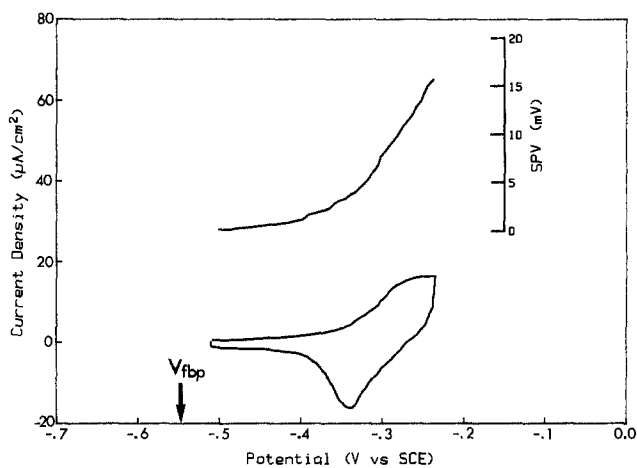


Fig. 9. Cyclic voltammogram and surface photovoltage of a natural mineral electrode in 0.05M sodium ethylxanthate and 0.05M sodium tetraborate. V_{FBP} = potential at cleavage. Sweep rate 5 mV/s.

xanthate, probably in a 1:1 coordination with a surface cation, whereas the unoccupied (or reduced state) is rapidly desorbed to a xanthate anion in solution.

The results from the earlier cleavage experiments are also summarized in Fig. 10. The cleavage experiments establish that fresh surfaces of highly p-type galena assume a potential where ethylxanthate can spontaneously chemisorb; whereas highly n-type galena must undergo an oxidation or oxygen chemisorption reaction to lower the Fermi level at the surface to the point where it is thermodynamically favorable for xanthate to chemisorb. The inversion of the surface from n- to p-type by oxygen chemisorption is essentially in agreement with the original proposal of Plaksin and Shafeev (2) and explains the energetic changes that must occur at the interface before xanthate chemisorption. However, contrary to Plaksin and Shafeev, oxygen chemisorption alone cannot lead to significant, approximately monolayer, xanthate adsorption, for, as pointed out by Woods (25), an isolated surface cannot remain nearly neutral if the only processes are the anodic chemisorption of xanthate and oxygen chemisorption. The charge balance in this case simply represents the transfer of a negative xanthate ion and molecular oxygen to the surface and transfer of an electron from adsorbed xanthate to adsorbed oxygen, a process that would quickly lead to an electric field retarding further xanthate adsorption. To maintain electrical neutrality, it is assumed that oxygen must also be simultaneously reduced, as in a mixed potential model, to obtain a significant coverage with xanthate. The role of oxygen is apparently twofold with (i) oxygen chemisorption initially providing the energetic change that is thermodynamically

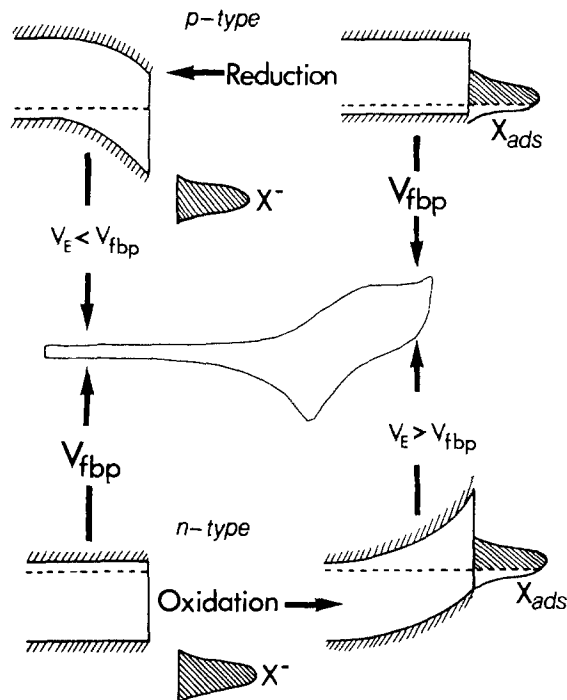


Fig. 10. Band diagrams showing flatband potentials of highly p- and n-type lead sulfide electrodes relative to the xanthate chemisorption/desorption reaction.

necessary before xanthate can chemisorb on n-type galena, in agreement with Plaksin and Shafeev, and (ii) oxygen reduction maintaining a "near"-neutral surface to sustain chemisorption to approximately monolayer coverage, in agreement with the mixed potential of Salamy and Nixon (3).

From the standpoint of flotation, the only significant difference that might be expected between p- and n-type galena is that the flotation of the latter may exhibit an induction period, following grinding, during which the potential increases to the point where xanthate chemisorption can occur. An induction period for the aqueous oxidation of n-type galena has been reported by Eadington and Prosser (10) and is explicable by the present work; that is, the potential of n-type electrodes must increase to the dissolution potential before measurable oxidation occurs. However, sulfide flotation circuits, excepting recent molybdenite practice, are operated with an infusion of air. With the abundant availability of oxygen, any induction period may be unobservable or insignificant.

Conclusions

Interfacial capacitance and surface photovoltage measurements have provided independent evidence of a polarizable space-charge layer on galena electrodes at pH 9.2, with the surface ranging from highly n-type at $\approx -0.6V$ (SCE) to highly p-type at $\approx -0.2V$. The flatband potential of galena decreases with increasing bulk electron concentration, consistent with the expected relation (14)

$$V_{FBP} = \text{const.} - (kT/q) \ln (n_b/n_i)$$

It has also been shown that galena surfaces instantly assume the flatband potential when cleaved in an electrolyte, with highly n-type galena having a cleavage potential (V_{FBP}) of $\approx -0.6V$ and highly p-type a potential of $\approx -0.2V$.

The Tafel slopes for oxygen reduction are larger than would be predicted from simple models of oxygen reduction at semiconductor or metal electrodes. The large slopes have been qualitatively explained by assuming the rate of oxygen reduction is not dependent on the surface concentration of electrons. The partition of changes in electrode potential between the solid and solution phases then simply reduces the Helmholtz overvoltage available for oxygen reduction.

Ethylxanthate has been shown to chemisorb and desorb over a narrow potential range between -0.4 and $-0.2V$. The chemisorption/desorption process is consistent with a semiconducting model in which xanthate chemisorption induces a donor-like surface state in the forbidden gap whose occupancy is determined by the Fermi energy at the surface. Ethylxanthate can spontaneously adsorb on freshly fractured, highly p-type galena, but the surface of freshly fractured, highly n-type galena must oxidize to increase the free hole concentration (lower the Fermi energy at the surface) to the point where xanthate can chemisorb.

Manuscript submitted Nov. 19, 1984; revised manuscript received Feb. 19, 1985.

The U.S. Department of the Interior assisted in meeting the publication costs of this article.

APPENDIX

Taking into account lack of minority carrier effects (approximately equal current density-potential plots for the three electrodes and the negligible influence of steady illumination), the rate of oxygen reduction, I [see, for example, Ref. (18)] on electrodes with $n_b \geq n_i$ may be written

$$I = I_0 e^{-\alpha(F/RT)\Delta V_h} \quad [A-1]$$

where I_0 = exchange current density, α = transfer coefficient, ΔV_h = change in Helmholtz potential, and the other symbols have their usual meaning. Changes in electrode potential, ΔV_e , are assumed to be partitioned between the Helmholtz and space-charge layer, ΔV_{sc} , which can be expressed as

$$\Delta V_h = \gamma(V_e)\Delta V_e \quad [A-2]$$

$$\Delta V_{sc} = -(1 - \gamma)\Delta V_e \quad [A-3]$$

$$\Delta V_e = \Delta V_h - \Delta V_{sc} \quad [A-4]$$

where $\gamma(V)$ describes the partition of the potential across the two phases. The sign conventions are such that ΔV_h and ΔV_{sc} are both measured with respect to their bulk phases. To calculate the appropriate ΔV_h value from Eq. [A-2] for use in Eq. [A-1] a knowledge of $\gamma(V)$ under steady-state polarization conditions is required. Values of γ can be estimated from the SPV with appropriate assumptions.

Following the treatment of Frankl and Ulmer (26), the SPV in the absence of surface traps is given by

$$\text{SPV} = \frac{G_0 \tau (e^{\beta V_{sc}} + e^{-\beta V_{sc}} - 2)}{(1 + \epsilon) (1 + s^*/v) n_i \beta [e^{\beta \phi_b} (e^{\beta V_{sc}} - 1) - e^{-\beta \phi_b} (e^{-\beta V_{sc}} - 1)]} \quad [A-5]$$

where G_0 = light intensity, τ = lifetime, ϵ = absorption coefficient, s^* and v = surface recombination and diffusion velocities, respectively, n_i = intrinsic carrier concentration, $\beta = q/kT = RT/F$, and ϕ_b = bulk potential. If we assume a depletion barrier layer at the surface with $1 \ll |\beta V_s| \ll 2\beta \phi_b$ and that $s^*/v \ll 1$, Eq. [A-5] reduces to

$$\text{SPV} = -G_0 \tau \beta^{-1} n_b^{-1} (1 + \epsilon)^{-1} e^{-\beta V_{sc}} \quad [A-6]$$

which may be written using Eq. [A-4] as

$$\text{SPV} = -G_0 \tau \beta^{-1} n_b^{-1} (1 + \epsilon)^{-1} e^{\beta V_{sc}} e^{(1-\gamma)(F/RT)\Delta V_e} \quad [A-7]$$

If we also assume that $\gamma(V)$ is a slowly varying function of electrode potential, $\delta\gamma/\delta(\Delta V_e) = 0$, it can be shown from Eq. [A-7] that

$$\delta(\Delta V_e)/\delta \ln |\text{SPV}| = (RT/F)/(1-\gamma) \quad [A-8]$$

The $\log |\text{SPV}|$ vs. ΔV_e plots of Fig. 4 and 5 are fairly linear over the depletion region, in agreement with the exponential dependence suggested by Eq. [A-7]. The slopes are 125 and 110 mV per decade change in SPV, respectively. From Eq. [A-8] the slopes yield γ values of 0.53 (Fig. 4) and 0.46 (Fig. 5). These values suggest that Tafel regions for oxygen reduction vs. ΔV_h have slopes $\approx 50\%$ smaller than the experimental values determined from Fig. 4 and 5, i.e., Tafel slopes of 0.08-0.12V for the

slightly n-type electrode (Fig. 4) and 0.092 for the highly n-type electrode (Fig. 5).

REFERENCES

- I. N. Plaksin, *Trans. AIME*, **214**, 319 (1959).
- I. N. Plaksin and R. Sh. Shafeev, *Proc. Acad. Sci. USSR, Phys. Chem. Sect.*, **132**, 421 (1960).
- S. G. Salamy and J. C. Nixon, "Recent Developments in Mineral Dressing," pp. 503-516, Institute of Mining and Metallurgy, London (1953).
- R. Woods, *J. Phys. Chem.*, **75**, 354 (1971).
- K. C. Pillai and J. O'M. Bockris, *This Journal*, **131**, 568 (1984).
- P. E. Richardson and E. E. Maust, Jr., in "Flotation, A. M. Gaudin Memorial Volume," Vol. 1, M. C. Fuerstenau, Editor, pp. 364-392, AIME, New York (1976).
- D. A. J. Rand, *J. Electroanal. Chem.*, **83**, 19 (1977).
- C. Guarnaschelli, *Trans. AIME*, **247**, 324 (1970).
- I. N. Plaksin, *IMPC London*, 253 (1960).
- P. Eadington and A. P. Prosser, *Inst. Min. Metall. Trans. Sect. C*, **78**, 74 (1969).
- S. Schuldiner, T. B. Warner, and B. J. Piersma, *This Journal*, **114**, 343 (1967).
- W. H. Brattain and C. G. B. Garrett, *Bell Syst. Tech. J.*, **34**, 129 (1955); *ibid.*, **35**, 1041 (1956).
- C. G. B. Garrett and W. H. Brattain, *Phys. Rev.*, **99**, 376 (1955).
- P. J. Boddy and W. H. Brattain, *This Journal*, **110**, 570 (1963); *Ann. N.Y. Acad. Sci.*, **101**, 683 (1963).
- W. W. Scanlon, "Solid State Physics," p. 83, Academic Press, New York (1959).
- Y. I. Ravich, B. A. Efimova, and I. A. Smirnov, "Semiconducting Lead Chalcogenides," Plenum Press, New York (1970).
- H. Gerischer, in "Physical Chemistry, An Advanced Treatise," Vol. IXA, "Electrochemistry," H. Eyring, Editor, pp. 463-540, Academic Press, New York (1970).
- A. Y. Many, Y. Goldstein, and N. B. Grover, "Semiconductor Surfaces," Chap. 6, North-Holland Publishing Co., Amsterdam (1965).
- V. A. Myamlin and Y. V. Pleskov, "Electrochemistry of Semiconductors," Plenum Press, New York (1967).
- G. W. Poling, in "Flotation, A. M. Gaudin Memorial Volume," Vol. I, M. C. Fuerstenau, Editor, pp. 334-363, AIME, New York (1976).
- J. R. Gardiner and R. Woods, *J. Electroanal. Chem.*, **100**, 447 (1979).
- C. Gutierrez and A. Navarro, in "Interfacial Phenomena in Mineral Processing," B. Yarar and D. J. Spottiswood, Editors, pp. 19-32, Engineering Foundation, New York (1982).
- J. R. Gardner and R. Woods, *Aust. J. Chem.*, **30**, 981 (1977).
- O. Huynh Thi, M. Lamache, and D. Bauer, *Electrochim. Acta.*, **26**, 33 (1981).
- R. Woods, Personal communication (1984).
- D. R. Frankl and E. A. Ulmer, *Surf. Sci.*, **6**, 115 (1966).

Computer Modeling of Batteries from Nonlinear Circuit Elements

S. Waaben, I. Moskowitz, J. Federico, and C. K. Dyer*,¹

AT&T Bell Laboratories, Murray Hill, New Jersey 07974

ABSTRACT

Circuit analogs for a single battery cell have previously been composed of resistors, capacitors, and inductors. This work introduces a nonlinear circuit model for cell behavior. The circuit is configured around the PIN junction diode, whose charge-storage behavior has features similar to those of electrochemical cells. A user-friendly integrated circuit simulation computer program has reproduced a variety of complex cell responses including electrical isolation effects causing capacity loss, as well as potentiodynamic peaks and discharge phenomena hitherto thought to be thermodynamic in origin. However, in this work, they are shown to be simply due to spatial distribution of stored charge within a practical electrode.

Circuit analog models for the cell of a battery have typically been structured from resistors, capacitors, and inductors (1). This limited set of linear circuit elements cannot simulate many nonlinear cell characteristics such as transients, recovery from deep discharge and gassing effects.

The present work introduces a nonlinear circuit model for cell behavior. It is based on the PIN junction diode, whose time-dependent charge-storage behavior is related to that of electrochemical cells. The integrated circuit simulation computer program, ADVICE (2), is used to "painlessly" predict nonlinear responses from a circuit analog of the cell built directly by simply specifying the interconnection of components available from the circuit simulation program library.

Charge Sourcing, Transport, and Sinking

The basic features of a PIN diode and a cell are similar because their mechanisms of charge dynamics are analogous, as illustrated in Fig. 1. For charging a nickel-cadmium (NiCd) cell, the electrochemical reactions provide sourcing and sinking of charge carriers, OH⁻ ions, at the electrodes. Similarly, in a PIN diode under forward bias, negative charges (electrons) are injected by the N-type side into the I region, and negative charges are removed from the I region by the P side. Thus, there are analogies between the N-type side of the diode and the

negative electrode of the cell, the P-type side and the positive electrode, the I region and the electrolyte, and the diode space-charge regions and the interfacial regions in the cell. In brief, during the forward operation of both the diode and the cell, charge carriers are transported between interfaces; however, the time scales differ by many orders of magnitude (3-7).

Charge-Storage Diode Transients

The dynamic response of a minority carrier PIN junction charge storage diode is summarized in Fig. 2 (6, 7). The stored charge Q_s equals $I_F \bar{\tau}$ for the condition where the forward diode current I_F has been conducted for a period much longer than the minority carrier lifetime $\bar{\tau}$. It is significant to note that, as long as the diode contains substantial numbers of minority carriers, it remains forward biased even under reverse current conduction. Typical integrated circuit analysis packages like ADVICE (2) include minority carrier charge storage in the model for the circuit element "PIN diode." In cell circuit-analog modeling, by choosing an "infinitely" long minority storage lifetime for the diode, the basic charge-discharge cell response is obtained. The diode's minority carriers simulate the charge storage of the cell by chemical transformation and its discharge by the reverse chemical reaction. Changing the direction of the diode current produces a minor modulation of the voltage across the forward biased diode due to the voltage drop across the finite resistance of the diode (4-7). This small voltage ΔE can be expressed by the algebraic symbols $R_{\text{diode}}(I_F + I_R)$. The

* Electrochemical Society Active Member.

¹ Present address: Bell Communications Research, Incorporated, Murray Hill, New Jersey 07974.

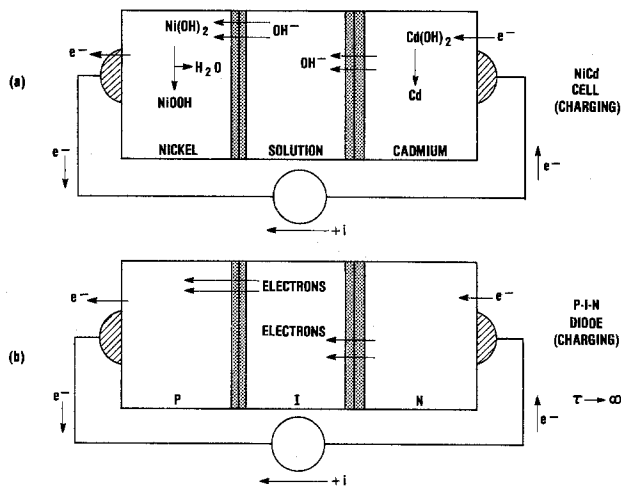


Fig. 1. Ad hoc charge transport and accumulation in NiCd cell and PIN diode. a: NiCd cell. A forward current causes Cd(OH)₂ to produce Cd, injecting OH⁻ ions into the neutral solution across a charged double layer. The OH⁻ ions are transported through the electrolyte and absorbed at another charged double layer at the Ni(OH)₂ side, where NiOOH is formed by oxidation of Ni(OH)₂. Discharge involves the relaxation by reversal of the chemical and transport process that formed the Cd and the NiOOH: OH⁻ ions return to the Cd electrode, forcing current to flow in the external circuit. b: PIN diode. A forward current causes the N-type side to inject electrons into a neutral intrinsic region across a space-charge layer. The electrons are transported through this I region and absorbed across another space-charge layer at the P-type side, where they activate minority carriers. Discharge involves the relaxation reversal of the charge storage and transport process: stored minority carriers are returned to the side where they originated, forcing current to flow in the external circuit.

“double-layer” capacitance at electrode surfaces is here represented by a simple capacitor of constant value in parallel to the charge-storage PIN diode.

Electrochemical Turn-On Transients

After a NiCd cell has been completely discharged for a long period of time, the first application of a charging current produces a “turn-on transient.” This consists of a short-term rise in voltage associated with an initial phase change at the surface of the electrode (8). Similarly, a semiconductor PIN diode has a conductivity turn-on transient (4), but it is 6-8 orders of magnitude faster. In the case of the diode, the conductivity of the semiconductor is modulated by the injection of charge carriers into a previously uncharged region. Circuit simulation methodology using ADVICE circuits used as a function generator rather than sets of equations has been used for

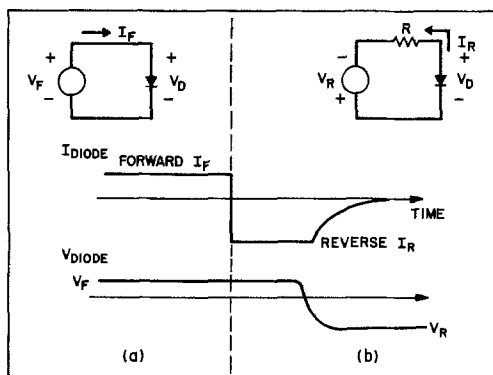


Fig. 2. Standard response of charge storage diode. a: During the forward current (charging) direction, semiconductor regions are filled with minority carriers; stored charge $Q_s = \int i_F dt$ for infinitely long minority carrier lifetime τ . For finite τ and $t \gg \tau$, $Q_s = I_F \tau$. b: During reverse conduction, the diode remains forward biased until the semiconductor regions are emptied of charge; then, the current and voltage decay. A correction ΔE is due to a voltage drop across the internal ohmic diode resistance.

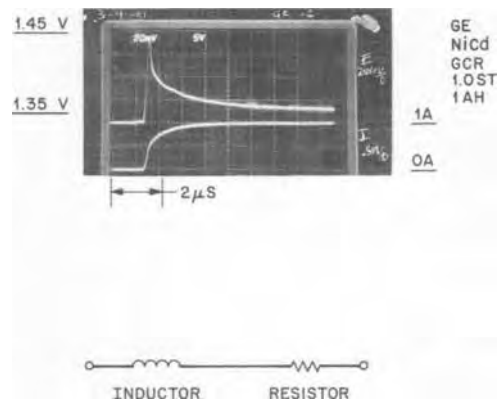


Fig. 3. Response of a charged NiCd battery to a current pulse. Top: Oscilloscope trace of the voltage response (upper curve) of a 1 Ah battery to a current pulse (lower curve) with risetime on the order of microseconds. Bottom: Circuit topology for ADVICE that simulates battery behavior shown in top of Fig. 3.

the simulation of PIN junctions (15). This subcircuit model method will be used for modeling the electrochemical turn-on transient of an electrochemical cell.

Electromagnetic Turn-On Transients: Series Resistance and Inductance

Figure 3 shows the measured two-terminal response of a small, charged, NiCd cell to a current pulse with risetime of about 1 μ s. For fast rising pulses, capacitors behave as short circuits. Therefore, Fig. 3 shows only an inductive spike, $E = L \Delta i / \Delta t$. Eventually, a steady-state voltage is reached which is proportional to the series resistance and the amplitude of the current pulse. The inductance is roughly that of a conductor of the geometrical dimensions of the cell, approximately 10^{-8} H in the present case. The resistance, about 10 m Ω , results from the combination of the metallic resistance of the electrode and the ionic conductance of the electrolyte. Figure 4 shows the basic circuit model for the cell: a PIN diode with a parallel capacitor, in series with an inductor, and a resistor.

Charging and Discharging

The cell overvoltage, η , can be defined as (3)

$$\eta = \text{nonequilibrium voltage} - \text{equilibrium voltage} \quad [3]$$

expressing that while a cell is being charged or discharged, there is a temporary increase or decrease, respectively, in the terminal voltage compared with the

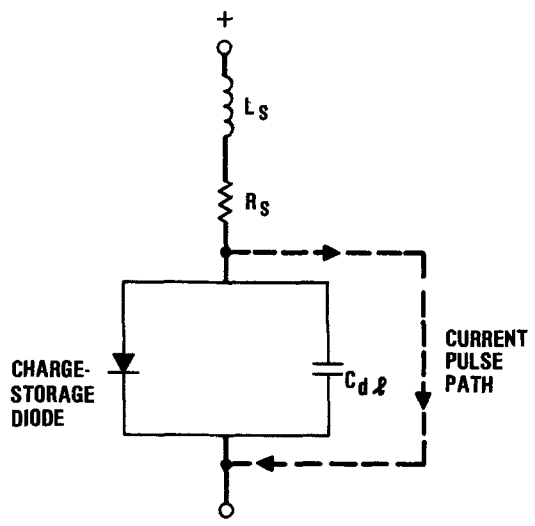


Fig. 4. PIN diode, double-layer capacitance (C_{dl}), series resistance, and series inductance interconnection topology.

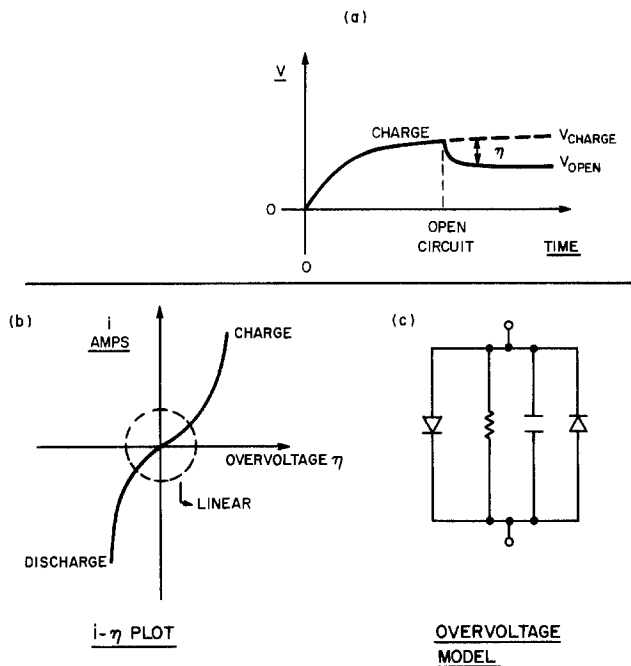


Fig. 5. Overvoltage characteristics and modeling. a: Voltage response of a battery to constant current drive and subsequent open circuit. b: Plot of drive current i vs. η . c: Circuit analog model for overvoltage only.

open-circuit or equilibrium cell voltage. Typical overvoltage characteristics are shown in Fig. 5a (3). The overvoltage response curves are exponential for large currents and are linear for small currents (Fig. 5b). A circuit for implementing these responses is shown in Fig. 5c and consists of two diodes in parallel but in opposite directions, both in parallel with a resistor and a capacitor. These ADVICE model diodes are specified to have a relatively low barrier height of tens of millivolts to simulate typical low-load cell overvoltages.

The cell model with the overvoltage circuit section added is shown in Fig. 6. The internal node, "equilibrium voltage," marked in this figure is not physically accessible in an actual cell. Note that the PIN diode section contributes nearly all of the steady-state voltage developed across the two external terminals. For NiCd, this voltage is about 1250 mV, compared to overvoltages of only tens of millivolts. The measured overvoltage decays rapidly

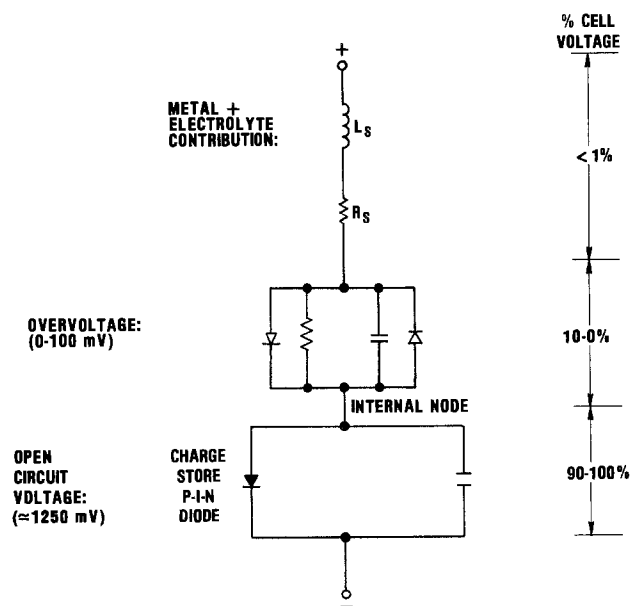


Fig. 6. PIN diode, overvoltage section, and series resistance and inductance interconnection topology. Typical relative contributions to the overall battery voltage are indicated at the right.

when the external cell current flow is set to zero, as shown in Fig. 5a. Hence, in the ADVICE model, the minority carrier charge-storage lifetime for these overvoltage model diodes is short.

The queuing effect of charge carriers in a cell gives rise to a charge cloud at the electrode interfaces which is simplistically simulated by placing a fixed capacitor in parallel with the overvoltage diodes.

Charge Relocation in Grains

The voltage value to which the cell recovers after open circuiting depends in a very complicated way on previous cycling history. The circuit topology shown in Fig. 6 does not reproduce the open-circuit voltage "recovery" from deep discharge, open-circuit "charge loss," or "past history effects." A typical recovery from deep discharge is shown in Fig. 7.

Voltage recovery after deep discharge and "past history effects" are commonly assumed to be due to gradual charge relocation within the granular structure of the active material of the electrodes (9-12). In the case of the nickel electrode of a NiCd cell, for example, the nickel hydroxide grains at the spongy surface are converted to NiOOH by "absorbing" electrical charge. The internal sections of the grains are originally electrochemically uncharged, but can slowly absorb charge (9-12). The nonlinear circuit topology of Fig. 6 has been extended in Fig. 8 to model this relocation of charge by a nonlinear-diffusion mechanism, where the analytically complex responses can be directly computed using the ADVICE simulation program. In Fig. 8, the outermost diode and capacitor sections represent the interfacial reactions fed by exterior charge transport to and from the electrode. The charge storage and transport mechanism for a one-dimensional interior grain is modeled by a parallel combination of nonlinear storage sites represented by capacitors and PIN charge-storage diodes, where the diffusion of charge between the storage sites is modeled by adding 1 k Ω connecting resistors. When the circuit in Fig. 8 is first charged and then rapidly discharged, the overall voltage is mostly determined by the outer diodes and capacitors. The inner diodes and capacitors still retain much of their previous charge state due to the isolation provided by the 1 k Ω resistors; rapidly discharging the outer diodes leaves the charge within internal grains relatively untouched. However, on open circuiting, charge from the internal PIN diodes leaks back into the outer PIN diodes and causes the Fig. 8 circuit voltage to rise again, simulating the cell's recovery characteristic.

The inclusion of this grain model also reproduces the anomalous "bumps" in the final portion of the cell discharge curves observed when the load is a resistor (e.g., on the order of 100 Ω -1 k Ω depending upon the cell type and size). If we qualitatively assume that the internal diodes are all initially charged, say after operating at a continued constant voltage or "float," then, if at the end of a

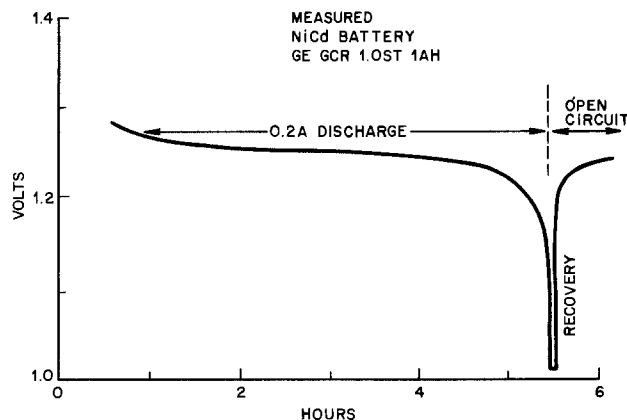


Fig. 7. Measured voltage recovery of a NiCd battery after deep discharge at 200 mA.

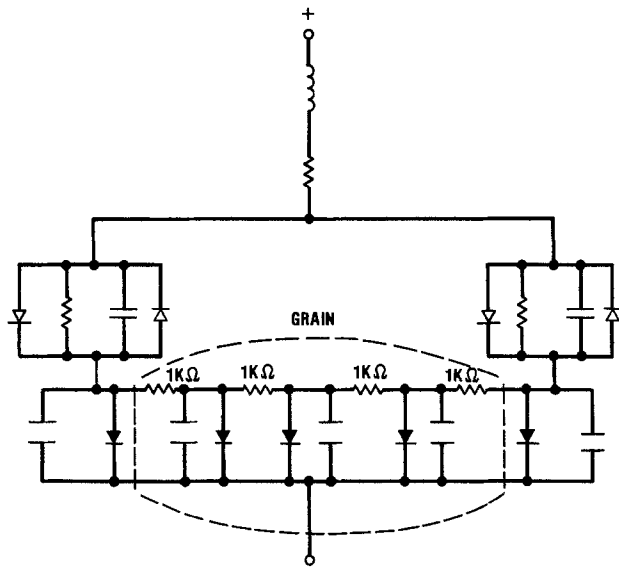


Fig. 8. Circuit topology modeling the behavior of a one-dimensional granular electrode. Outer PIN charge-storage diodes simulate grain surface; internal diodes simulate internal grain charge storage mechanism.

discharge cycle of the outer diodes a resistive load on the order of 1 kΩ is applied, voltage divisions are caused by the progressive discharge of each internal diode through the 1 kΩ connecting resistors. Changing the size of the load resistor produces different plateaus in the simulated cell discharge curve, similar to the experimental observations. One may think of the cell as a nonlinear Thévenin-like source where the impedance of the charge source depends upon the charge state determined by the past history of operation, and Fig. 8 as the circuit model representation of such a distributed Thévenin source.

Gas Evolution during Overcharge

Continued charging to a high voltage triggers a gassing reaction when all active material at the grain surfaces is exhausted (11). For modeling simplicity, assume a constant voltage for the start of the gassing reaction. The circuit shown in Fig. 9 includes a mathematical function generator simulating the voltage climb for a nonsealed cell. The function generator circuit model works as follows. The outer charge storage diodes model the charge stored at the grain surfaces. When the surfaces are fully

charged (i.e., when the surface diode reaches a specified potential), it is disconnected from further charging by operating a switch. In the circuit of Fig. 9, from the beginning of charging, the switches (transistors) are "on," i.e., shorted, and the outer charge storage diodes receive charge. When these outer diodes reach the voltage of the transistor base supplies, the switches (transistors) turn off. The charging current is now routed to the internal diode string as well as to the gassing process; current through the 1 kΩ resistors to the grain causes the voltage to climb. The value of the transistor base supply thus simulates the gassing potential.

For generating the two-terminal response of a sealed cell, it can be of sufficient modeling precision to add the clamping diode shown in Fig. 9, which causes the rising voltage to level off, which occurs in sealed cells upon the buildup of gas pressure.

Computer-Generated Simulation

A variety of responses have been computed with the Fig. 9 circuit. The "user-friendly" ADVICE computer program analyzes circuits described by the node connections of circuit elements and their models. It should be noted that other standard circuit simulation computer programs, such as the commonly available SPICE program (2), can also be set up to compute the response of a given circuit. Since the ADVICE computer program is geared towards silicon integrated circuit simulations, such as 0.7V silicon diode junction drops, some *ad hoc* adjustments are required to scale the computer printout and plotting voltages up to values corresponding to cell voltages. Further, for Pb-acid simulations, a voltage source was for convenience placed in series with each charge storage diode to raise the overall cell voltage above 2V. This additional circuit complexity is due only to the restriction of "mathematical" access for ADVICE users to coefficients in the program's exponential expressions and may not exist for other circuit simulation packages. For NiCd, a judicious choice of the existing basic library diode parameters specified for the ADVICE user was sufficient to achieve the desired voltage magnitudes for plotting by the computer directly.

For "programming" simplicity, the circuit topology used was that of Fig. 9 for both NiCd and Pb-acid cells. There is no fundamental circuit difference in the responses of these two cell types on the level of precision of topology assumed here (14); only the quantitative parameter choices are different. For a particular cell, one set of device parameters was chosen, so that the computer-generated results matched the best available measurements. The NiCd measurements shown were performed on the GE GCR 1.0ST 1.0 Ah cell using an HP87 mini-computer in a laboratory experiment control and data gathering mode. The Pb-acid data were taken from the 1980 Gates Energy Products Battery Application Manual as well as from measurements on the Gates 2V, 5 Ah X-cell, PN 0800-0004.

Figure 10 shows a set of constant-current charge to open-circuit curves for the NiCd cell, starting from an initial equilibrium voltage of 1.290V. The differences between simulated and measured curves are less than 5 mV over a current range of nearly a decade.

Figure 11 shows constant-current charge-discharge open-circuit cycles for the NiCd cell, along with the simulations, for various current levels and initial voltages.

Figure 12 changes the time scale to microseconds and demonstrates the measured and model results for the inductive spike and series resistance.

Figure 13 shows an example of simulated recovery behavior. Values of the model's grain resistors can be selected to match the measured conditions.

Figure 14 shows simulated overcharge behavior after 600s.

Figure 15 exhibits simulated results under potentiodynamic conditions. In this simulation, an applied voltage is slowly ramped to the gassing overvoltage potential and down again. The computed current is plotted against

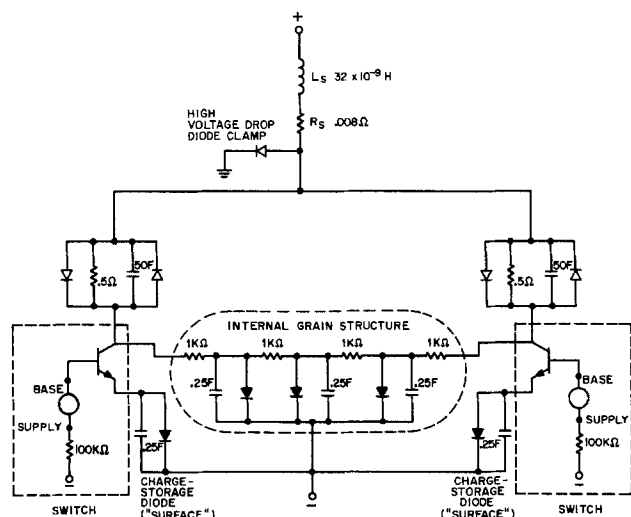


Fig. 9. Circuit analog topology for functional response simulation of gas-generation behavior. The battery's external charging current flow is switched from outer charge-storage PIN diodes to internal PIN diodes when the outer diode voltages reach that of the base supplies. (Simple ADVICE bipolar switches are used.) The clamping diode limits voltage rise to simulate sealed-battery behavior.

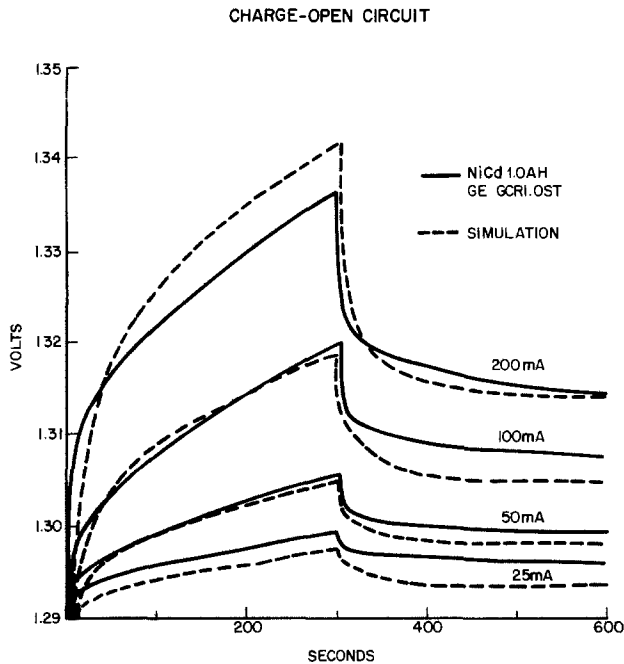


Fig. 10. Measured (solid lines) and simulated (broken lines) curves for constant-current to open-circuit measurements.

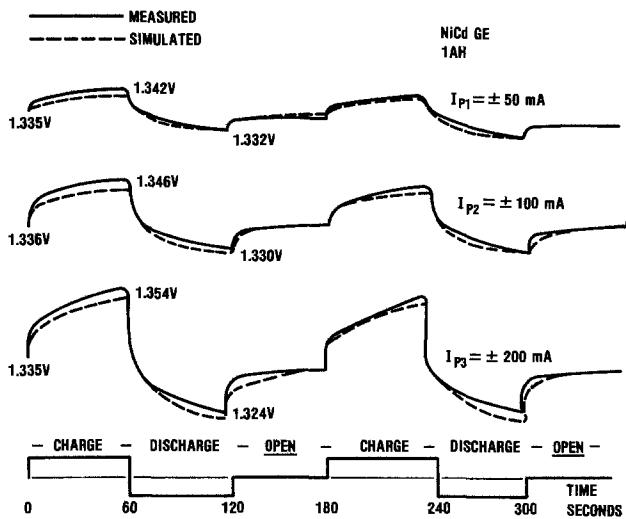


Fig. 11. Measured (solid lines) and simulated (broken lines) curves for charge-discharge open-circuit measurement cycle. Also shown is the simulated voltage recovery after discharge.

the voltage, showing first a major peak due to the charging reaction, then a rise in current due to the gassing reaction, then, on ramp reversal, a second and/or third large peak dependent upon the ramp rate (16).

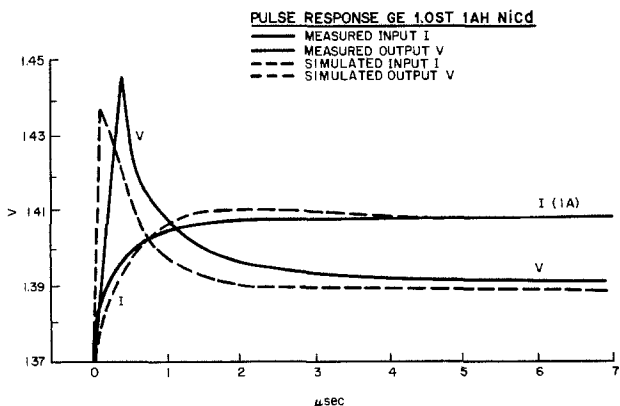


Fig. 12. Measured (solid lines) and simulated (broken lines) results for NiCd response to current pulse.

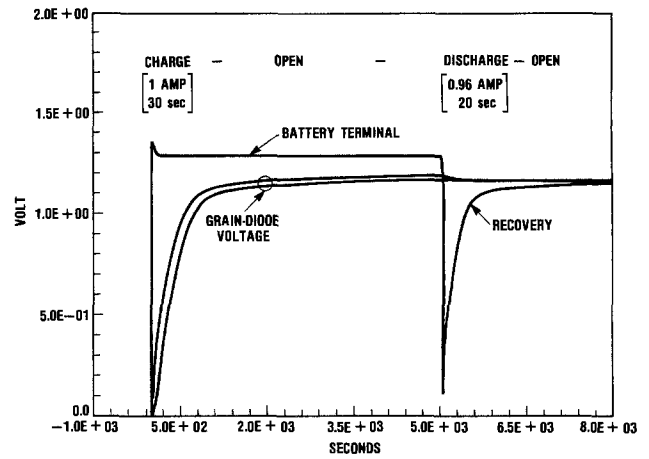


Fig. 13. Simulated voltage recovery after deep discharge of a float-charged battery. Note that the overall cell voltage drops during discharge as the outer diodes lose charge, while the internal diodes retain charge throughout the grain and contribute charge to cause recovery.

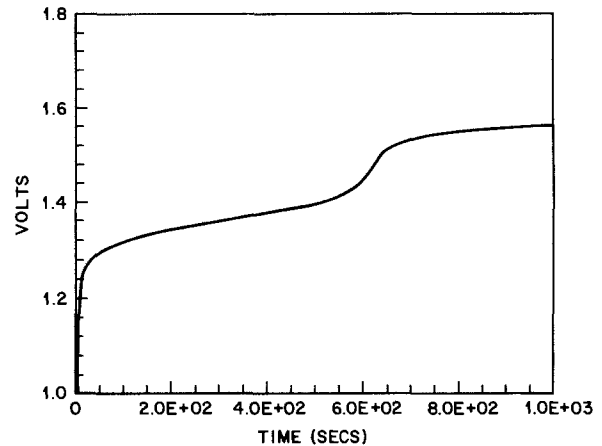


Fig. 14. Oxygen evolution behavior for constant current charge. Simulation result shown is for generic battery, showing features of gas generation reproduced by the circuit model of Fig. 9.

Figure 16 shows an example of the computed frequency response of the two-terminal admittance using the circuit of Fig. 8. Due to the nonlinear properties of the cell, such responses are of ambiguous value.

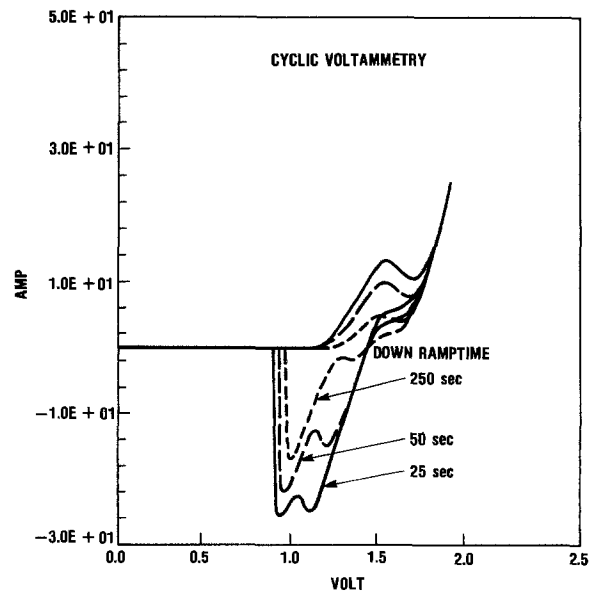


Fig. 15. Cyclic voltammery simulation using Fig. 9 for NiCd battery parameters, showing effect of voltage ramp rate. Shown as time (s) to complete one-half cycle (2.0-0.0V).

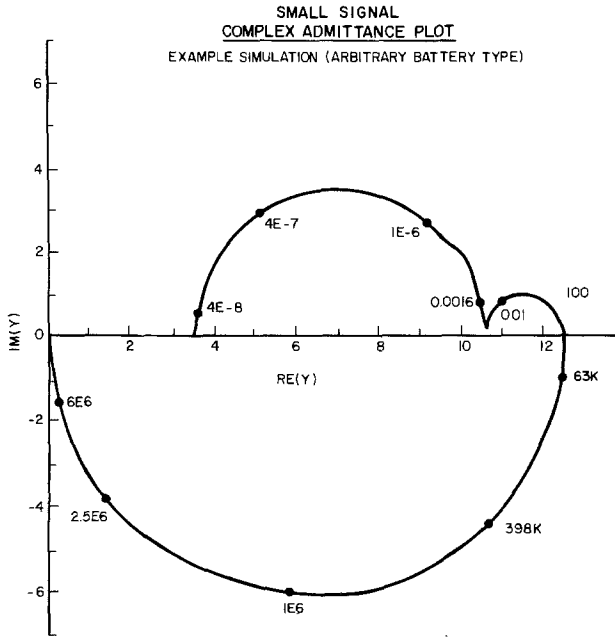


Fig. 16. Admittance simulation, plotted $IM(Y)$ vs. $RE(Y)$, for a generic battery type using the circuit of Fig. 8. Frequencies in Hertz are designated on the plot.

Interpretation of Cell Discharge Plateaus and Potentiodynamic Peaks

Common to several cells is the phenomenon of "capacity loss." That is, the coulombic storage capacity is significantly less than that which is theoretically available from the amount of electrochemically active material in the cell electrodes. In the case of NiCd and NiH₂ cells, a secondary discharge plateau is often measured at a lower voltage than that which is generally associated with the electrochemical couple. The magnitude and duration of the secondary plateau voltage is a very sensitive function of the discharge current such that the higher the current the lower the voltage and the shorter the plateau length. For example, for a threefold increase of discharge current there can be a 0.5V depression in voltage, while the primary plateau is only reduced by 30-50 mV (17). In the published literature, this phenomenon has been attributed to either (i) a different chemical phase, so that the lower voltage discharge plateau is due to different thermodynamics (18), (ii) a change in conductivity (decrease) due to removal of "defects" (17, 19), or (iii) reduction of adsorbed oxygen. The first direct experimental verification in favor of the second mechanism was reported recently (20) and showed undischarged regions of a Ni electrode electrically isolated from the conducting Ni grid by a lower conductivity phase, presumably Ni(OH)₂. Also, an additional mechanism of "capacity loss" has been identified as a loss of contact between the metal grid and the electrochemically active material (21).

The same basic circuit topology used above to simulate the electrical behavior of a single grain will now be used to model the electrically resistive connection of a group of individual grains or charge storage sites to the current collecting metal grid. The modeling of this physical situation involves the addition of resistive elements and a new choice for the value of resistors R_e in Fig. 9. Any of the capacity loss mechanisms mentioned above (20, 21) effectively interpose a resistor between each "internal" diode, representing a grain of active material, and the metallic contact or ground, as shown in Fig. 17. Secondary discharge plateaus similar to those observed in Ref. (17) can be produced from ADVICE by choosing equal values for each of the three resistors, R_b , in the range 0.1Ω (for 3A charges and discharges) to 10Ω (for 0.1A rates = C/10) (Fig. 18). This circuit simulation arrangements also shows high sensitivity to current amplitude. For example, for $R_b = 0.1\Omega$, tripling the current from 3A (3C rate) to 9A (9C rate)

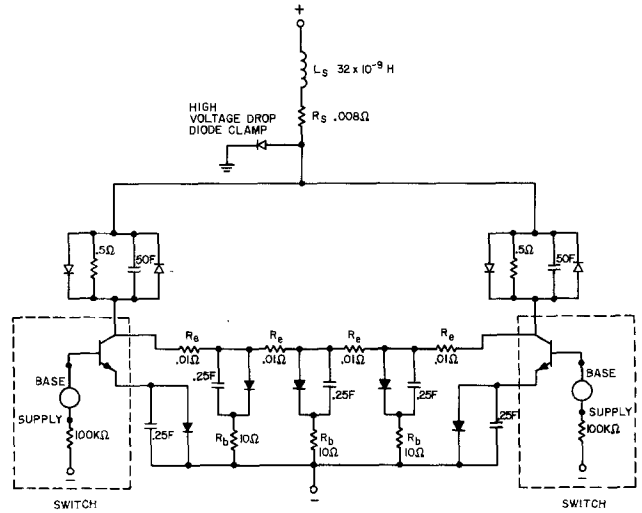


Fig. 17. Circuit analog topology for functional simulation of discharge plateaus.

depresses the secondary plateau from 1.1 to 0.7V. This is similar to the reported cell measurements (18). To calculate the electrolyte resistances R_e within the pore structure the following electrochemical data were used: solution resistivity (ρ) = 1.84 Ω-cm, 1 Ah electrode area (A) = 50 cm², the electrode thickness (t) = 0.030 in., porosity after impregnation (P) = 10%, and

$$R_e = (\rho t)/(4AP) = 0.01\Omega$$

The four series resistances R_e between each "grain" in Fig. 17 were chosen to be 0.01Ω for the computation shown in Fig. 18. Note that ohmic conduction and not a diffusion mechanism is modeled here. For increasing values of R_b , there is a greater depression computed in voltage of the secondary plateau, and for $R_b = 0$ there is no secondary plateau. However, an increase in the value of R_e while $R_b = 0$ can also produce secondary plateaus with similar dependences on current. For instance, a tenfold increase in resistivity or reduction in porosity such that $R_e = 0.1\Omega$ gives two secondary plateaus in the model. Although the general results of such calculations are possibly intuitively obvious, the model gives quantitative information for a particular design choice.

The model demonstrates that the effect of the inclusion of the resistances R_e and R_b is to produce additional potentiodynamic peaks which might otherwise have been misinterpreted as arising from new thermodynamic behavior such as the proposed appearance of new electrochemical phases in the case of the Ni electrode (18). Addi-

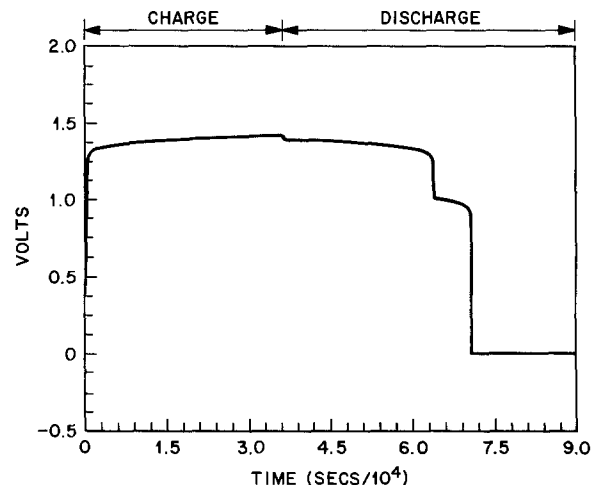


Fig. 18. Simulation of 11h charge at a current of $C/10 = 0.1A$, capacity = 1 Ah, discharge current = 0.1A, $R_e = 0.01\Omega$ and $R_b = 10\Omega$.

tion of R_b elements in the model topology to simulate the electrical isolation (20, 21) produces a second peak on reduction at scan rates lower than that shown in Fig. 15 where otherwise only one reduction peak would have appeared. This work corresponds to the second plateau under constant-current conditions. This second peak appears at lower potentials for higher values of R_b . A third peak appears on raising the scan rate from 0.3 to 3 mV/s. For negligible values of R_b , increasing R_e from 0.01 to 0.1 Ω or more also produces second and third peaks on potentiodynamic reduction.

Similar modeling of the Pb-acid system may also be used to interpret the observed relationship between electrolyte accessibility and composition within the porous electrode structure and the available discharge capacity (22). Recent work (22) shows that higher conductance of the electrolyte in pores gives higher delivered capacities, which is predicted from our model by lowering R_e .

Conclusions

The measured electrical behavior of NiCd and lead-acid cells can be simulated using a nonlinear circuit topology model based on the dynamic properties of the charge storage PIN diode and RLC circuit elements. A circuit-analysis computer program such as ADVICE (similar to SPICE) can be used to compute circuit responses directly from an interconnection description of the components. For a particular cell, one set of parameters accurately simulates a variety of measured data to within the precision of measurements. Charge-discharge, pulse response, deep discharge, turn-on transients, gas generation, cyclic voltammetry, and admittance characteristics all can be simulated by computer from the model. Since suitable circuit components for the cell model can be found to simulate both the spatially distributed electrochemical processes and the physical structure of the cell, the effects of a design change on performance can be simulated.

Application of the model shows that considerable care should be exercised in interpreting additional peaks during potentiodynamic scanning or additional plateaus during constant-current discharge. They may not be thermodynamic in origin, but may simply be the nonequilibrium response of spatially distributed electrochemical processes within the electrode structure.

Cell characteristics missing in the present model can be added by simply developing a physically reasonable circuit analog and including it in the present model through the use of a circuit simulation program.

Acknowledgments

Initial simulation runs on ADVICE were performed by N. Timmerman of Wells College, Aurora, New York. We would like to thank J. Broadhead, D. Maurer, B. Vyas,

and T. Willis of AT&T Bell Laboratories, Murray Hill, New Jersey, for many helpful discussions.

Manuscript submitted May 7, 1984; revised manuscript received Dec. 20, 1984.

AT&T Bell Laboratories assisted in meeting the publication costs of this article.

REFERENCES

1. S. Sathyanarayana, S. Venugopalan, and M. L. Gopikanth, *J. Appl. Electrochem.*, **9**, 125 (1975).
2. L. W. Nagel, in "Proceedings of the 1980 International Symposium on Circuits and Systems," Houston, Texas, April 28, 1980. To acquire original version (SPICE), contact the Department of Electrical Engineering and Computer Science, University of California, Berkeley, CA 94720.
3. J. O'M. Bockris and A. K. N. Reddy, "Modern Electrochemistry," Vol. 2, pp. 718, 880, 886, 877, 936, 994, Plenum Press, New York (1977).
4. M. B. Prince, *Bell Syst. Tech. J.*, **35**, 661 (1956).
5. K.-J. Euler and B. Seim, *J. Appl. Electrochem.*, **8**, 49 (1978).
6. S. M. Sze, "Physics of Semiconductor Devices," p. 127, J. Wiley and Sons, New York (1969); D. A. Hodges and H. G. Jackson, "Analysis and Design of Digital Integrated Circuits," University of California, McGraw Hill, New York (1983).
7. J. L. Moll, S. Krakauer, and R. Shen, *Proc. IRE*, **50**, 43 (1962).
8. D. Berndt and E. Voss, in "Batteries 2," D. H. Collins, Editor, p. 17, Pergamon Press, Glasgow (1965).
9. E. M. Kuchinski and B. V. Ershler, *J. Phys. Chem. USSR (Azhurnal Fiz. Khim.)*, **20**, 539 (1946).
10. J. Labat, *Ann. Chim.*, **9**, 399 (1964).
11. D. Tuomi, *This Journal*, **112**, 1 (1965).
12. P. C. Milner and U. B. Thomas, in "Advances in Electrochemistry," Vol. 5, P. Delahay and C. W. Tobias, Editors, p. 2, Interscience Publishers, New York (1967).
13. H. Bode, "Lead-Acid Batteries," p. 314, J. Wiley and Sons, New York (1977).
14. J. Atkin, R. Bonnaterre, and J. F. Laurent, in "Power Sources 6, Proceedings of the 10th International Symposium, Brighton, Sept. 1976," D. H. Collins, Editor, p. 91, Academic Press, Inc., Ltd., London (1977).
15. C. D. Root, J. Melillo, and S. Sammon, *IEEE Trans. Electron. Devices*, **ed-29**, 3, 461 (1982).
16. R. S. Guzman, J. P. Vilche, and A. J. Arvia, *This Journal*, **125**, 10, 1578 (1978).
17. R. Barnard, G. T. Crickmore, J. A. Lee, and F. L. Tye, *J. Appl. Electrochem.*, **10**, 61 (1980).
18. O. Glemser and J. Einerhand, *Z. Elektrochem.*, **54**, 302 (1950).
19. D. M. MacArthur, *This Journal*, **117**, 422 (1970).
20. C. K. Dyer, in "The Nickel Electrode," R. G. Gunther and S. Gross, Editors, p. 118, The Electrochemical Society Softbound Proceedings Series, Pennington, NJ (1982).
21. C. K. Dyer, To be published.
22. U. Hullmeine and W. Kappus, *Electrochim. Acta*, **27**, 1677 (1982).

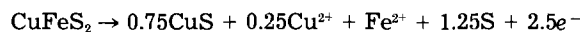
The Electrochemistry of Surface Oxidation of Chalcopyrite

T. Biegler and M. D. Horne

CSIRO Division of Mineral Chemistry, Port Melbourne, Victoria 3207, Australia

ABSTRACT

Linear sweep voltammetry with a freshly renewed surface of a chalcopyrite (CuFeS_2) mineral electrode shows a small anodic prewave in acid electrolytes. The main anodic reaction, with complete dissolution of copper and iron, occurs at more positive potentials. Experiments under nitrogen show that the prewave is not a consequence of atmospheric oxidation during surface preparation. The prewave represents a surface oxidation of chalcopyrite to form a thin passivating film. The charge passed in forming this film is around 2 mC cm^{-2} for a polished surface. The prewave reaction is identified with the initial phase of the oxidative dissolution or leaching of chalcopyrite. Contrary to the reported behavior at 80°C , the surface film is stable at 25°C for long periods at open circuit. Various evidence, including the relative charges passed in forming and then reducing the surface film, and the presence of dissolved copper, leads to the following suggested stoichiometry for the prewave reaction



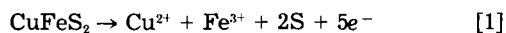
The product layer containing CuS and S is about 3 nm thick.

The main interest in electrochemical studies of the mineral chalcopyrite (CuFeS_2) arises from the information such studies provide concerning the mechanism and kinetics of chalcopyrite dissolution in acidic oxidizing solutions. The dissolution, or leaching, process is a corrosion reaction, with anodic and cathodic half-reactions. The reaction in the oxidizing media most suited to practical use, such as acidic ferric chloride or sulfate solutions, is very slow. Since copper dissolution from chalcopyrite is the primary step in many hydrometallurgical processes for copper extraction, it is important to establish what determines this slow rate, especially from the viewpoint of the anodic process.

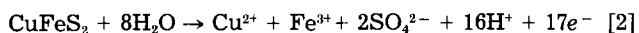
The recent work of Dutrizac (1-3) seems to have resolved some of the controversial issues in the kinetics of chalcopyrite leaching, such as the influence of temperature, iron concentration in chloride or sulfate media, surface area of the chalcopyrite particles, and locality of origin of the mineral sample. However, many different mechanisms have been proposed to explain the observed rates. Chemical leaching and electrochemical studies (4-12) show that a type of passivating surface layer limits the oxidation rate and causes the parabolic kinetics (rate $\propto t^{1/2}$) found under some conditions, particularly in sulfate media. The precise nature of this layer is in dispute. It has variously been described as sulfur (1, 7), a metal-deficient chalcopyrite-like sulfide (5, 12), a polysulfide (10), a solid electrolyte interphase (11), or precipitated iron compounds (1). Its effect on the oxidation kinetics has been explained in terms of physical blockage (1), solid-state diffusion of metal ions (5), electron-transport properties (7), passive film growth (12), or electrolytic conduction of metal ions (11).

How one could distinguish between some of these mechanisms, if indeed a distinction exists, is as yet unclear. An acceptable mechanism should also draw a clear line between reactions which form the passivating film and further reactions, such as film dissolution or transport through the film, which could continue when the film is complete. We believe that electrochemical studies will help to resolve some of these problems and to define these reaction stages.

The passivating reaction is a low potential electrochemical process (e.g., 0.7-0.8V vs. SHE at ambient temperatures) such as would occur when chalcopyrite is oxidized in a ferric solution. At higher potentials (1.0-1.2V vs. SHE), where there is continuous current, a number of studies agree [see Ref. (8)] that the reactions



and



both take place, in the proportion of around 6:1.

In this paper, we wish to present further evidence [see Ref. (8)] that an anodic prewave in voltammetry with a freshly prepared chalcopyrite surface represents the initial stages of chalcopyrite oxidation and gives information concerning the initial product layer. Other authors [e.g., Parker *et al.* (10)] have explicitly discarded "first sweep" results as spurious effects produced by surface oxidation during electrode preparation (grinding, polishing, washing). We are able to show that this view is incorrect and that the electrochemical results are representative of a clean chalcopyrite surface. Obviously, this conclusion has important implications for other kinds of surface studies on chalcopyrite, such as with Auger electron spectroscopy (13) or ESCA (14), where a knowledge of the initial state of the mineral surface is vital to interpretation of results.

Experimental

Electrodes suitable for rotation (Beckman variable-speed rotator) were prepared, as previously described (15), from high quality natural polycrystalline specimens of chalcopyrite showing no foreign inclusions under the microscope. Of the four electrodes used at various times, three (designated as A, B, and C) were cut from the same sample, from Moonta, South Australia, and the fourth (D) was from Mt. Lyell, Tasmania. The exposed areas were: A, 0.41 cm^2 ; B, 0.24 cm^2 ; C, 0.61 cm^2 ; D, 0.35 cm^2 . Two types of surface finish were used: ground surface, finished on fine silicon carbide paper (grit size: $15 \mu\text{m}$) and polished surface finished with $0.3 \mu\text{m}$ alumina on a polishing cloth.

A three-compartment glass electrolysis cell was used, with an isolated gold counterelectrode and a Luggin probe from the reference electrode compartment. Programmed voltammetry was carried out with conventional instrumentation (potentiostat, potential programmer, X-Y recorder). The reference electrode was a saturated calomel electrode (SCE), and all potentials are quoted with respect to the SCE. Measurements were carried out at 25°C in nitrogen-purged solutions prepared from doubly distilled water and reagent-grade chemicals.

Results and Discussion

Prewave shape and charge.—Figures 1 and 2 show the prewaves obtained for one specimen in different acid electrolytes and for different chalcopyrite specimens in the same electrolyte. These curves were all obtained by a similar procedure. The electrode was ground or polished, washed with a jet of distilled water, and quickly inserted into the deoxygenated electrolyte. Then, the potentiostat circuit was closed at or near the rest potential (which was usually drifting slowly at this stage) and the sweep started. The time between ending the surface preparation and starting the voltammogram was around 30-40s.

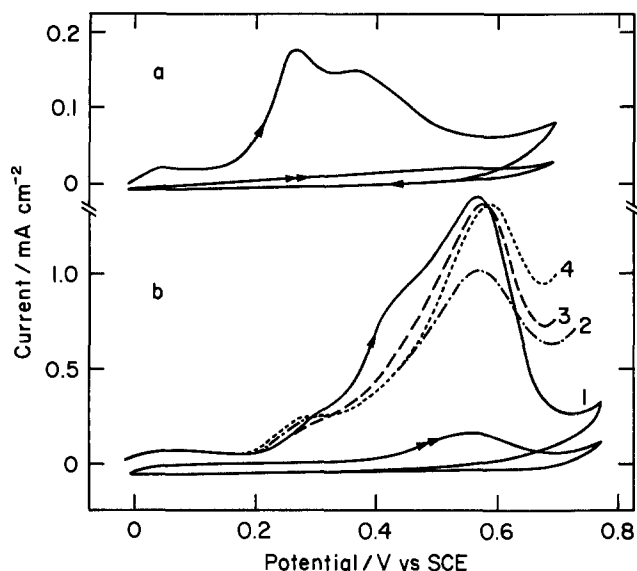


Fig. 1. First-sweep voltammograms on chalcopyrite electrode C; sweep rate 20 mV s^{-1} ; rotation rate 50 Hz . a: Polished surface; 1 M HCl (two cycles). b: Ground surface. Curve 1: 1 M HCl (two cycles). Curve 2: 1 M HNO_3 . Curve 3: $1 \text{ M H}_2\text{SO}_4$. Curve 4: 1 M HClO_4 .

These curves confirm and extend the limited results presented previously (8) for one specimen in $1 \text{ M H}_2\text{SO}_4$. The first anodic sweep shows a prewave, absent or, in 1 M HCl , greatly diminished on subsequent sweeps. The shape, position, and area (*i.e.*, charge) of the prewave depend on the mode of surface preparation (Fig. 1) but not much on the acid (Fig. 1) or the sample origin (Fig. 2). Stirring has little effect on the prewave itself but does influence associated phenomena as described in a subsequent section.

The prewave for a polished electrode (Fig. 1) shows two clear peaks at around 0.28 and 0.38 V vs. SCE . These vary in relative height from run to run and with different specimens. For a ground electrode, the major peak is more positive, at 0.55 – 0.59 V . The presence of two poorly defined shoulders on the rising branch of this peak leads us to suggest that it contains components corresponding to the peaks seen with a polished surface. An electrode which gave the prewave shown in Fig. 3 seems to have been incompletely polished after grinding; it shows the two characteristic peaks for a polished surface, plus a peak at 0.59 V . If we assume that peak position is a function of exposure of different aspects of the chalcopyrite

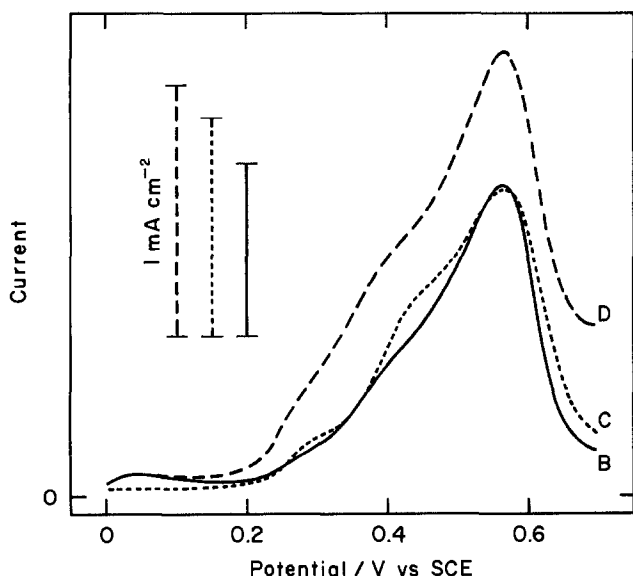


Fig. 2. First-sweep voltammograms for three chalcopyrite electrodes in 1 M HCl . Ground surfaces; sweep rate 20 mV s^{-1} ; rotation rate 50 Hz .

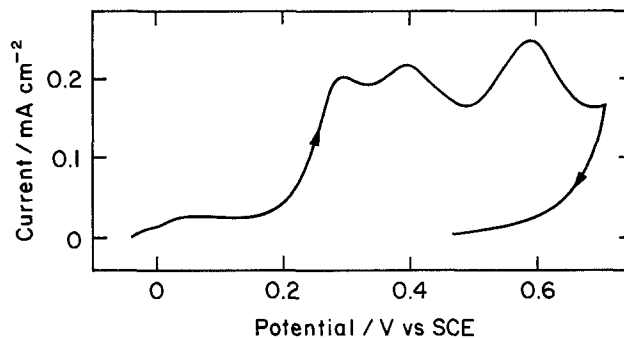


Fig. 3. First-sweep voltammogram on polished electrode C in 1 M HCl , showing residual peak for a ground surface.

lattice, then the surface fractures produced by polishing and grinding must be quite different. This behavior could result from the brittleness of chalcopyrite and its tendency to fracture unevenly. However, the peak shift with grinding is very large, and an explanation based on site exposure may not be adequate.

Prewave charges obtained by integrating the recorded curve from the foot of the prewave (0.15 V) to the current trough at around 0.55 or 0.7 V for polished or ground electrodes, respectively, are given in Table I. Most values represent the mean of several determinations, with a typical range of $\pm 10\%$. Charges for different specimens under the same conditions and for the same specimen in different acids are similar. The ratio between the charges for a ground and a polished surface is about 8. This ratio is a little less than the value of 11 reported previously (8) but still seems rather high to be explained by an increase in surface roughness. The dependence of prewave charge on sweep rate was similar to the previous finding (8), *e.g.*, for a ground surface in 1 M HCl , charges were 15.9 , 17.7 , and 11.3 mC cm^{-2} at sweep rates of 10 , 20 , and 50 mV s^{-1} , respectively.

In general, the observed behavior supports the earlier hypothesis (8) that the prewave represents a surface reaction involving oxidation of a thin layer of chalcopyrite. For complete oxidation to S , Cu^{2+} , and Fe^{2+} (see below for discussion of the oxidation state of iron), chalcopyrite would be consumed at a rate of $1.14 \text{ nm/mC cm}^{-2}$, based on true surface area, so that the prewave product layer can be no more than a few atoms thick (see below). The small dependence of prewave charge on sweep rate implies some influence of the kinetics of the prewave process on the amount of chalcopyrite oxidized.

Prewave in dilute acid electrolyte.—Prewaves in 1 , 0.1 , and 0.01 M HCl (the latter two with added 0.1 M NaCl) are shown in Fig. 4. The prewave seems not to shift with pH, but the main wave moves to less positive potentials with increasing pH and begins to obscure the prewave. This is presumably connected with the pH dependence of reaction [2], which involves protons. The results show that the prewave phenomenon exists at pH levels commonly

Table I. Prewave charges for various chalcopyrite electrodes and electrolytes at sweep rate 20 mV s^{-1}

Electrode	Electrolyte	Surface preparation	Charge (mC cm^{-2})
B	1 M HCl	Polished	2.2
C	1 M HCl	Polished	2.0
D ^a	1 M HCl	Polished	2.0
A	1 M HCl	Ground	16.1
B	1 M HCl	Ground	15.5
C	1 M HCl	Ground	15.6
D ^a	1 M HCl	Ground	17.0
C	$1 \text{ M H}_2\text{SO}_4$	Ground	14.5
C	1 M HNO_3	Ground	12.1
C	1 M HClO_4	Ground	14.3

^a Integrated with a steeper baseline than for other electrodes, with slope estimated from second and subsequent sweeps.

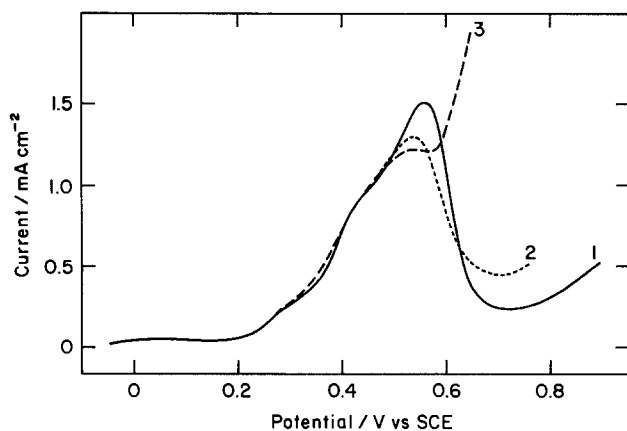


Fig. 4. First-sweep voltammograms on ground chalcopyrite electrode C in chloride electrolytes of different acidity. Sweep rate 20 mV s^{-1} ; rotation rate 20 Hz . Curve 1: 1 M HCl . Curve 2: 0.1 M HCl , 0.1 M NaCl . Curve 3: 0.01 M HCl , 0.1 M NaCl .

found in chalcopyrite leaching processes and is therefore relevant to the mechanism of those processes.

Surface preparation under nitrogen.—In view of the suspicions [e.g., see Ref. (10)] that first-sweep results may be influenced by exposure of the fresh chalcopyrite surface to air and to aerated water during preparation, it is important to establish what effect exclusion of oxygen has. We have attempted to do this by enclosing the cell, electrode assembly, and wash bottle in a glove box purged with nitrogen. No significant effect of the oxygen exclusion procedures was found. Indeed, prewave areas tended to be 10-20% greater than average, although this could easily be attributed to the different grinding technique required in the glove box and the likelihood of a different surface roughness.

We conclude, therefore, that the prewave is not a consequence of surface oxidation during electrode preparation. While this conclusion should be further substantiated under more rigorous conditions (fracturing chalcopyrite under oxygen-free electrolyte would be ideal), it is hard to accept arguments that the prewave is an artifact of prior exposure to oxygen. Preoxidation would surely tend to lower the anodic current, and this is not observed except after long exposure to air (8).

Effects of varying the potential program.—In Fig. 5, the normal prewave (program 1, solid curve) is compared with the voltammogram for an initial short sawtooth cycle to 0.45 V , immediate return to the starting potential, and a triangular cycle extending to 0.9 V (program 2, broken curves). In Fig. 6, a series of sawtooth cycles to 0.55 V is followed by a fifth cycle to 0.9 V . In both sets of curves, the diminishing currents on successive cycles are consistent with an accumulation of a prewave product layer.

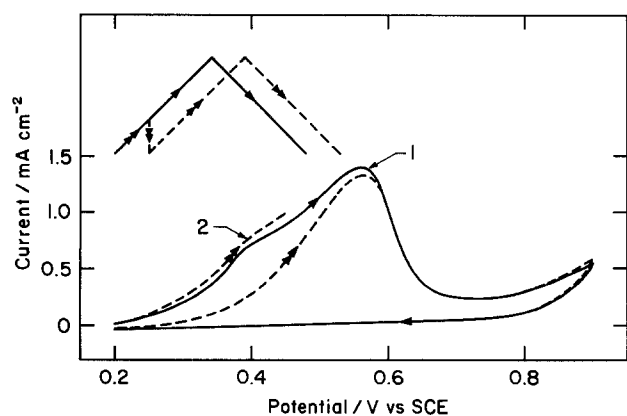


Fig. 5. Initial voltammograms on ground chalcopyrite electrode A in 1 M HCl for the two potential programs indicated. Sweep rate 20 mV s^{-1} ; rotation rate 20 Hz .

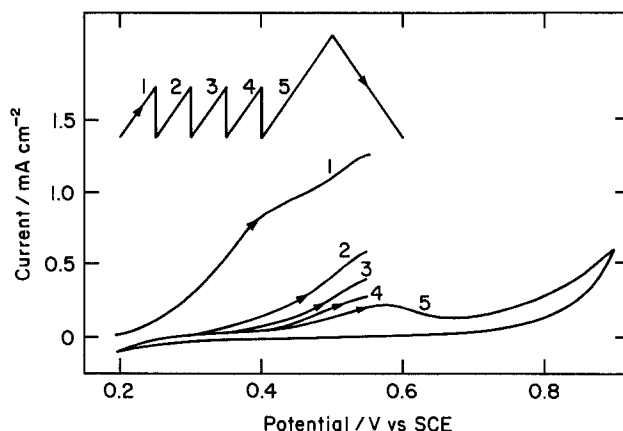


Fig. 6. Initial voltammograms on ground chalcopyrite electrode A in 1 M HCl for the potential program indicated. Sweep rate 20 mV s^{-1} ; rotation rate 20 Hz .

Thus, the charge passed during the four sawtooth cycles in Fig. 6 is 17.9 mC cm^{-2} , of the correct magnitude for a complete prewave. On the fifth cycle, the prewave has essentially disappeared. Similarly, the charge in the second cycle of program 2 (Fig. 5) is diminished by about the charge passed during the first cycle. Note that the shoulder on the rising branch of the prewave appears only on the first cycle in such programs.

Figure 7 shows pairs of curves for potential programs which include a period at open circuit between two potential scans. The first scan for a fresh surface is interrupted at 0.45 , 0.55 , or 0.70 V , the potential decays at open circuit to 0.24 V . At this point, the second scan is started. As the potential of interruption increases, the charge passed on the second scan decreases, but the total charge remains constant; the full prewave charge (solid curve) in Fig. 7 is 13.3 mC cm^{-2} , and the sum of the charges is 13.3 mC cm^{-2} and 12.0 mC cm^{-2} for the pairs of curves with interruption at 0.55 and 0.45 V , respectively. Thus the complete surface layer can be formed in stages, unaffected by interruptions at open circuit.

Further experiments were carried out to test the stability of the prewave product at open circuit. After an initial sweep to give a complete prewave, the various treatments at open circuit were (i) leave electrode in the electrolyte (deoxygenated $1 \text{ M H}_2\text{SO}_4$) for 17h, (ii) withdraw electrode, rinse with water, and keep wet while exposed to air for 4

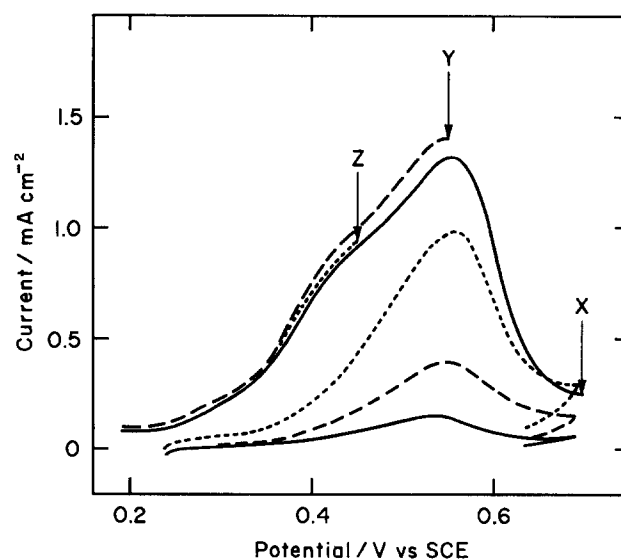


Fig. 7. "Interrupted" initial voltammograms on ground chalcopyrite electrode B in 1 M HCl without rotation. Sweep rate 20 mV s^{-1} . First scan is interrupted at X (0.7 V), Y (0.55 V), or Z (0.45 V). In each case, the potential is allowed to decay at open circuit to 0.24 V (approximate time taken is 5, 4, and 1 min, respectively). Then, a triangular scan from 0.24 to 0.7 V is started.

min, (iii) withdraw electrode, dry, and leave in air for 4 min, and (iv) withdraw electrode, rinse, and leave in deoxygenated water for 6h. In all cases, the first sweep from the new rest potential after returning to the cell gave no prewave.

Thus, the open-circuit reactivation phenomena observed by Parker *et al.* (10) at 80°C, which would be expected to lead to "regeneration" of the prewave, are not seen at 25°C. Any decomposition or solid-state diffusion processes tending to restore the initial surface composition must, therefore, be very slow at 25°C.

Effects of stirring—detection of a soluble product.—As noted above, stirring (by means of electrode rotation) does not significantly affect the prewave itself, but it does produce some interesting changes in other parts of the first and second cycles of triangular cyclic voltammograms (Fig. 8). Without stirring (solid curves), there are two small waves, marked A and B, on return sweep 1, and a peak C on sweep 2, which are all absent when the electrode is rotated (broken curves). The disappearance of these waves on stirring indicates that they involve a soluble species generated by the prewave process and dispersed by stirring.

Analogous results are found in the other acid electrolytes used, 1M H₂SO₄, 1M HNO₃, and 1M HClO₄, except that there is only a single cathodic peak on the first reverse sweep (Fig. 9, solid curve).

The obvious candidates for a reducible dissolved species are Cu²⁺ and Fe³⁺. Copper (5 × 10⁻⁴M) added to the electrolyte clearly enhances the waves shown in Fig. 8 and 9 (see, *e.g.*, the broken curve in Fig. 9). Iron (either Fe²⁺ or Fe³⁺) at a concentration of 5 × 10⁻⁴M has no effect on the voltammograms, consistent with the known irreversible nature, *i.e.*, the slow kinetics, of this redox system on chalcopyrite (10). In other words, iron as a soluble product of the prewave reaction would not be detected in voltammograms covering the potential range in Fig. 8 and 9. The cathodic waves are therefore due to dissolved copper, the presence of two waves A and B in 1M HCl presumably being due to the stability of a Cu(I) intermediate in chloride media. The size of the cathodic waves indicates that only a small amount of Cu²⁺ is released in the prewave reaction.

In establishing the nature of the process in the presence of Cu²⁺, we note that it seems to have a reversible potential (*e.g.*, at 0.16V in Fig. 9) well positive to the Cu²⁺/Cu⁰ potential for this copper concentration (around 0 V vs. SCE). This indicates formation of a sulfide rather than copper metal by reactions such as

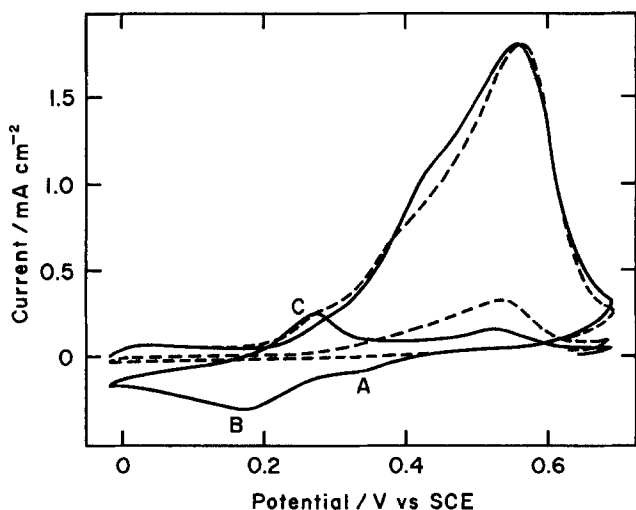
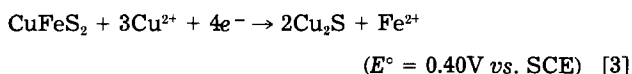


Fig. 8. First and portion of second cyclic voltammograms for ground chalcopyrite electrode B, unstirred (solid curves) and stirred (50 Hz, broken curves), in 1M HCl. Sweep rate; 20 mV s⁻¹.

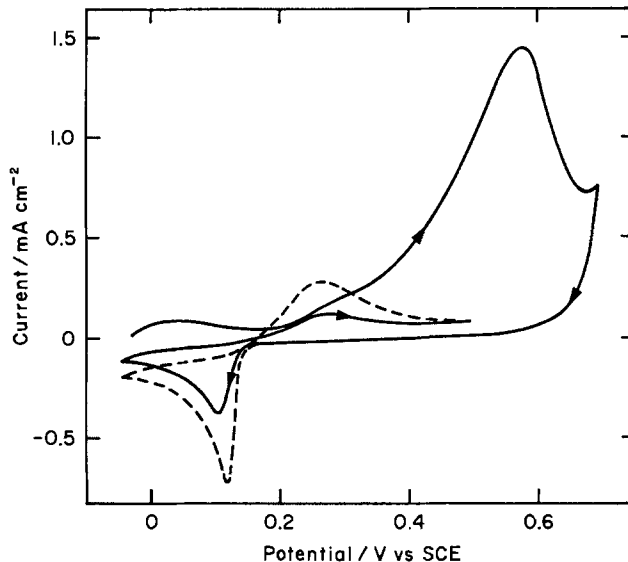
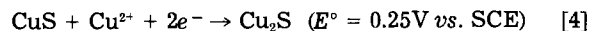
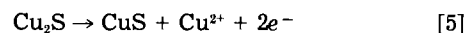


Fig. 9. First and portion of second cyclic voltammograms for ground chalcopyrite electrode C in 1M H₂SO₄ (solid curve) and 1M H₂SO₄ + 5 × 10⁻⁴M CuSO₄ (broken curve). No rotation; sweep rate 20 mV s⁻¹.

which has been demonstrated (16) for chalcopyrite reduction in the presence of Cu²⁺, or



Either of these reactions is feasible in the potential range of interest. If, as seems likely, Cu₂S is the solid product, the anodic peak on the second cycle would then represent reoxidation according to the reverse of reaction [4]



We shall discuss evidence below that the anodic peak position at 0.28V vs. SCE (Fig. 8 and 9) is characteristic for this reaction.

Effects of surface reduction—scanning to negative potentials.—Results considered so far have involved only the potential region positive to the initial rest potential, about 0 V vs. SCE. When cycling covers lower potentials (Fig. 10), the shape of the first cycle depends on the initial scan direction (see below) but subsequent cycles covering the full potential range (*i.e.*, at least +0.6 to -0.3V) give the main features shown in cycle 2 of Fig. 10. These features are a cathodic peak D centered around -0.22V and two anodic peaks, E and F, at 0.27 and 0.56V, the latter coinciding with the anodic prewave. Further cycling causes progressive small changes in these peaks. In each cycle (apart from the first), there is an approximate balance of the total anodic and cathodic charge passed.

The general behavior in 1M H₂SO₄ is similar to that shown for 1M HCl. With polished chalcopyrite, peak D is sharper and has no shoulder. In unstirred solution, extra peaks appear, indicating further reactions involving dissolved products of the main processes.

The first cycle (1a) of Fig. 10 starts in the positive direction from -0.03V and gives the anodic prewave expected with a freshly ground surface. At the positive limit, a surface layer of an as yet undetermined composition is present. The first return sweep (1c) gives the complex cathodic wave G in the region -0.1 to -0.3V. Wave G is found only on cycle 1 and clearly differs from D found from cycle 2 onwards. It also differs from the cathodic prewave (17), a single sharp peak at -0.10V found when the first scan with a fresh surface starts in the negative direction. Since this wave corresponds to the reduction of chalcopyrite itself, we conclude that wave G is characteristic for reduction of the surface layer formed during the anodic prewave.

The surface compositions at the end of the scans 1c and 2c must be very similar as their anodic oxidation characteristics in curves 2a and 3a are virtually identical. Since

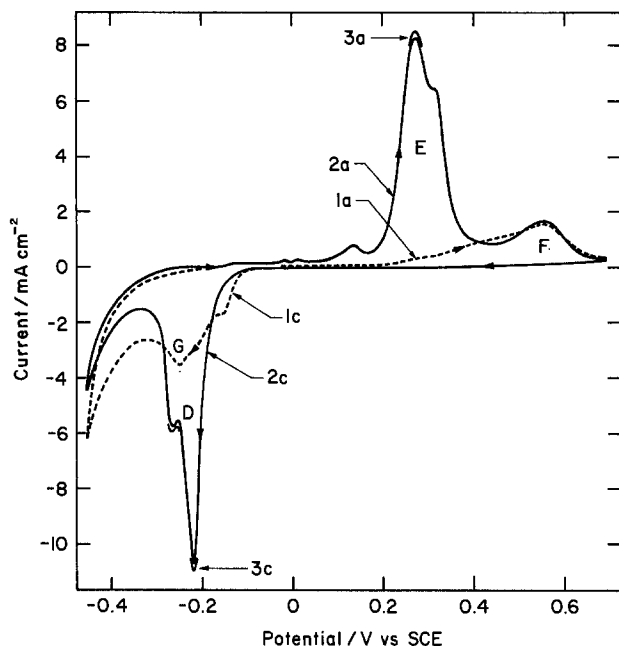
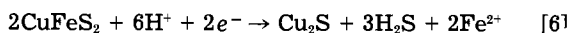
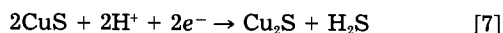


Fig. 10. First (broken curve), second (solid curve), and segments of third cyclic voltammograms for ground chalcopyrite electrode B in 1M HCl, with starting potential $-0.03V$, initial scan in positive direction, and potential limits $+0.70$ and $-0.45V$. Rotation rate 50 Hz; sweep rate 20 mV s^{-1} .

peak E at $0.27V$ is in the region where an anodic peak for chalcocite oxidation is found (18), it can reasonably be assigned to reaction [5]. The reduced surface formed at $-0.45V$ is therefore chalcocite, or a similar sulfide. This is consistent with the known potential region of stability of chalcocite and related sulfide phases, which form through reactions such as



or



Various other phases, e.g., digenite $\text{Cu}_{1.78}\text{S}$, djurleite $\text{Cu}_{1.93}\text{S}$, and bornite Cu_5FeS_4 , are formed (19-21) by similar reactions and could be present with, or in place of, chalcocite in the reduced surface layer.

We now have to decide whether peak F at $0.55V$ on curves 2a, 3a, etc., represents the same reaction as the anodic prewave on curve 1a. The evidence on this point is contradictory. On the one hand, the two waves virtually coincide and are of similar heights. Furthermore, the size of wave E, but not of F, depends on the negative potential limit of the sweep. This is consistent with a surface-limited process of the prewave type and not with the other obvious possibility, that E and F are successive oxidation steps of the chalcocite layer. On the other hand, wave D is clearly different from wave G, which we have suggested is characteristic for reduction of the prewave product layer.

On balance, we favor the prewave process for wave F. This, of course, requires that fresh chalcopyrite surface is available, and we envisage that this occurs through the volume decrease in the solid phases formed during the electrochemical reactions. In the sequence $2\text{CuFeS}_2 \rightarrow \text{Cu}_2\text{S} \rightarrow \text{CuS}$, the total volume decrease is calculated to be about 77%.

At the positive potential limit of curve 2a, the surface contains a layer of CuS (formed in E) and prewave product (formed in F). These are reduced, together with more chalcopyrite, over the potential range -0.1 to $-0.45V$ in the next sweep 2c, and a quantity of Cu_2S is again formed. A charge of $2 F/\text{mol}$ of Cu_2S is passed through either reaction [6] or [7], while $2 F/\text{mol}$ of Cu_2S is also passed when Cu_2S is oxidized according to reaction [5]. This accounts for the observed approximate balance of charges in the

anodic and cathodic branches of these voltammograms from the second cycle onwards. At higher pH, charge balance in cyclic voltammograms is explained (22) by reversible transformations of phases within an immobile surface layer. Such explanations cannot apply here, where soluble products are formed and leave the reaction zone.

In summary, cyclic voltammograms which extend into a region where cathodic processes occur in a stirred solution show that the surface layer formed during the anodic prewave is reduced to Cu_2S (or a related sulfide), that reoxidation of this reduced layer to CuS occurs, that this sequence of reactions exposes fresh chalcopyrite surface, and that these processes continue for numerous cycles.

The prewave process.—The knowledge of the various processes in the voltammograms of Fig. 10 can be used to derive further details of the prewave reaction. We start with several assumptions as follows.

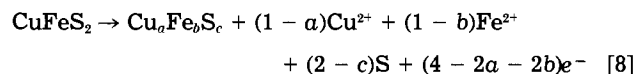
1. The only process occurring within wave G is the reduction of the layer of prewave product. The evidence for the lack of reduction of chalcopyrite itself in this region was discussed above, but is certainly not conclusive.

2. The solid reduction product is Cu_2S (see above); other products of the reduction process are taken to be Fe^{2+} and H_2S .

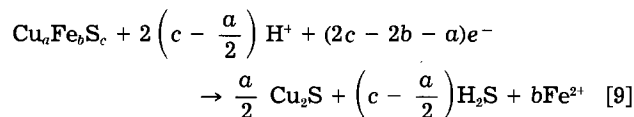
3. In the potential region of the anodic prewave, iron dissolves as Fe^{2+} . Given that the prewave extends over the range $0.2-0.7V$ vs. SCE and the E° for $\text{Fe}^{2+}/\text{Fe}^{3+}$ is $0.52V$ vs. SCE, this is a reasonable assumption for most of the prewave. The slow kinetics of Fe^{2+} oxidation at a chalcopyrite surface (10) would further favor this assumption.

4. The charge in wave G can be obtained by integration from $-0.08V$ to the current minimum at $-0.32V$. On this basis, the cathodic charge in wave G for a rotated electrode (at which any soluble reducible species have been dispersed) is around 1.3 times the anodic prewave charge.

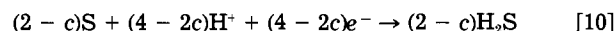
Applying these assumptions, we write general reactions for the anodic prewave



and for cathodic reduction of the solid products



and



We can then determine whether there are stoichiometries consistent with the observed charge ratio 1.3.

Summing the charges in reactions [9] and [10] and taking this sum as 1.3 times the charge in [8], we obtain

$$8a + 3b = 6 \quad [11]$$

The only additional information is that a and b are both positive and no greater than unity. With these restrictions, we can deduce the possible ranges of values as $0.75 \geq a \geq 0.375$ and, correspondingly, $0 \leq b \leq 1$. Hence

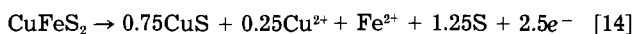
$$4 \geq (1-b)/(1-a) \geq 0 \quad [12]$$

In other words, a series of equations in the form of reactions [8]-[10] can be written which satisfy the measured charge ratio of 1.3. In these equations, the ratio of dissolved iron and copper can lie anywhere in the range 0-4.

The small amount of Cu^{2+} detected as a prewave reaction product (see above) and the evidence from leaching studies (5, 23), that the $\text{Fe}^{2+}:\text{Cu}^{2+}$ ratio is at least 2:1 and perhaps as high as 6.6:1 in the initial stages of chalcopyrite dissolution, both point to an $\text{Fe}^{2+}:\text{Cu}^{2+}$ ratio close to the upper limit given by Eq. [12]. At this limit, the reaction stoichiometry would be



i.e., the product layer contains no iron. $\text{Cu}_{0.75}\text{S}_2$ is not a known phase, but is reminiscent of the metal-deficient polysulfide suggested by Parker *et al.* (10) as the composition of the passivating film on oxidized chalcopyrite. Since there are no restrictions on how sulfur appears on the right-hand side of this equation (c is eliminated when the charges in reactions [9] and [10] are summed), we can equally write reaction [13] in the form



in which the product layer contains the more familiar CuS and S.

With reaction [14] as the basis for the prewave reaction, the thickness of the reaction layer can be calculated from the prewave charge, estimated to be around 2 mC cm^{-2} for a smooth surface in 1 M HCl . This gives the thickness of chalcopyrite reacted as 3.7 nm and, from the molar volumes of CuS and S, a product layer thickness of 2.9 nm .

To summarize, the evidence from iron and copper ratios in chalcopyrite leaching, from copper dissolution during the anodic prewave, and from the charge passed in reducing the prewave product is consistent with a prewave reaction in which the product contains CuS and S, according to reaction [14]. The product layer is estimated to be about 3 nm thick.

Implications for chalcopyrite leaching and related studies.—The evidence from recent electrochemical studies shows that the initial stages of oxidative dissolution (*i.e.*, leaching) involve the formation of a copper-rich surface layer (10-12). The description of this layer is different in each study, depending on how the various authors view the way it inhibits the leaching process. Thus, it is described as a polysulfide layer (10), a solid-electrolyte interphase (11), and a passivating film (12).

The present contribution is to show that the formation of this material occurs in a voltammetrically distinct step, the anodic prewave, which can help characterize the product layer. Study of the prewave has not resolved the views of the inhibition mechanism. However, we see no compelling reason to go past the simplest view of the prewave reaction as an energetically favored process producing an ordered product layer which eventually covers the surface and blocks any further movement of iron and copper atoms. At ambient temperatures, the further reaction of this blocking layer is slow, but as the potential is increased the bulk oxidation process can be nucleated, with sulfate formation as the possible trigger (8). At elevated temperatures, decomposition of the blocking layer occurs at a measurable rate, as evidenced by the "reactivation" of the low potential process at open circuit (10).

Several authors have analyzed decaying current-time transients in the low potential region to derive the inhibition mechanism. Apart from the difficulty that the studies disagree on the experimental form of the transient (9, 11, 12), there seem to be inadequate criteria to allow such analysis to be diagnostic of any particular mechanism. A current decay with $t^{1/2}$ (9, 11) could be indicative of some form of transport control within a thickening product layer, but the conclusion that this passivating layer is an electrolytic and not an electronic conductor (11) seems unjustified. The evidence points to the contrary, as other authors (9, 10) have also concluded. One could also reasonably hope for more convincing $i - t^{1/2}$ data [compare the time scales used in Ref. (9), 0-100 min and Ref. (11), 0-16 ms] and more systematic temperature effects (11). Warren *et al.* (12) attach significance to their finding that the current decays according to $\ln i = b - mQ$ (where Q is the total charge passed and b and m are constants), which is characteristic of some passive film growth kinetics. This is simply the electrochemical form of the Elovich equation which is widely obeyed in surface chemical and electrochemical reactions (24) and reflects a linear increase in the activation energy of a reaction with coverage of the surface. It conveys limited mechanistic information.

Warren *et al.* (12) found large electrochemical reactivity differences between different chalcopyrite specimens which they attributed to the presence of impurities in some of the samples. As the differences they saw were in the same potential region as the prewave studied here, the properties of the prewave (shape, position, dependence on stirring, and sweep rate) established in this work should provide a method of determining whether a particular voltammogram is characteristic of chalcopyrite or contains contributions from, say, a more reactive sulfide impurity. One could then decide whether or not the differences were intrinsic to the chalcopyrite. This is important information in view of the continuing interest in reactivity differences of natural minerals (3, 8).

Two aspects of chalcopyrite electrochemical behavior have implications for spectroscopic studies (*e.g.*, photoelectron spectroscopy) of chalcopyrite surfaces [see, *e.g.*, Ref. (13, 14)]. First-sweep studies, both in the negative (17) and positive directions, show that a freshly prepared chalcopyrite surface is moderately stable to atmospheric oxidation, so that surface preparation in air before transfer to the instrument is feasible. Voltammetric characterization after spectroscopic examination should be a useful auxiliary tool. Further, the layer of initial oxidation product, which is formed during a suitable voltammetric scan, is also stable over periods of minutes or longer after withdrawal from the electrolyte, and this should provide an appropriate method of preparation of samples for studies of the composition of this layer, which has been one of the key problems in interpreting the leaching behavior of chalcopyrite.

Conclusion

The anodic prewave found on linear sweep voltammograms for freshly prepared chalcopyrite electrodes in acid solutions represents a surface oxidation process which is distinct in mechanism from the bulk oxidation of chalcopyrite observed at higher potentials. All indications are that it is a genuine reaction of a clean chalcopyrite surface and not a spurious process attributable to reaction with atmospheric oxygen prior to voltammetry. The significance of the prewave lies in the insight it provides into the mechanism of oxidative dissolution (leaching) of chalcopyrite, a reaction known to be progressively inhibited by formation of a thin surface film. This film is considered to be the same as the layer of product formed by the prewave reaction.

The main characteristic of the prewave is that its area is roughly independent of sweep rate and type of acid electrolyte used. The layer of product can be shown to accumulate progressively with a variety of potential programs and to remain stable for many hours at open circuit, even when the electrode is withdrawn from the cell. The prewave characteristics do not depend on specimen origin, implying that the initial reactivity with leachants such as ferric ion should also not depend on origin. The charge passed in forming the prewave product is about 2 mC cm^{-2} for a polished chalcopyrite surface.

The nature of the prewave reaction is deduced from information on the relative amounts of Fe^{2+} and Cu^{2+} which pass into solution and the relative charges associated with formation and reduction of the product layer. The latter comparison involves an arbitrary separation of the surface-layer reduction from other overlapping processes and an assumption of the composition of the reduced surface layer. A set of reactions is then obtained which satisfy the observations. The most plausible of these indicates a prewave reaction with Fe^{2+} and Cu^{2+} dissolving in the ratio 4:1 and a solid product of stoichiometry $\text{Cu}_{0.75}\text{S}_2$. If the phases in this layer are taken to be CuS and S, the layer is 2.9 nm thick and is formed from a 3.7 nm thick layer of chalcopyrite.

Manuscript submitted Aug. 15, 1984; revised manuscript received Jan. 22, 1985. This was Paper 261 presented at the Cincinnati, Ohio, Meeting of the Society, May 6-11, 1984.

CSIRO assisted in meeting the publication costs of this article.

REFERENCES

1. J. E. Dutrizac, *Metall. Trans. B*, **9**, 431 (1978).
2. J. E. Dutrizac, *ibid.*, **12**, 371 (1981).
3. J. E. Dutrizac, *ibid.*, **13**, 303 (1982).
4. J. E. Dutrizac, R. J. C. MacDonald, and T. R. Ingraham, *Trans. Metall. Soc. AIME*, **245**, 955 (1969).
5. H. G. Linge, *Hydrometall.*, **2**, 51 (1976).
6. L. W. Beckstead, P. B. Munoz, J. L. Sepulveda, J. A. Herbst, J. D. Miller, F. A. Olson, and M. E. Wadsworth, in "Extractive Metallurgy of Copper," Vol. 2, J. C. Yannopoulos and J. C. Agarwal, Editors, p. 611, AIME, New York (1976).
7. P. B. Munoz, J. D. Miller, and M. E. Wadsworth, *Metall. Trans. B*, **10**, 149 (1979).
8. T. Biegler and D. A. Swift, *J. Appl. Electrochem.*, **9**, 545 (1979).
9. M. Ammou Chokrum, P. K. Sen, and F. Fouques, in "Thirteenth International Mineral Processing Congress, Warsaw, 1979, Proceedings," Part A, J. Laskowski, Editor, p. 759, Elsevier and PWN-Polish Scientific Publishers, Warsaw (1981).
10. A. J. Parker, R. L. Paul, and G. P. Power, *Aust. J. Chem.*, **34**, 13 (1981).
11. R. S. McMillan, D. J. MacKinnon, and J. E. Dutrizac, *J. Appl. Electrochem.*, **12**, 743 (1982).
12. G. W. Warren, M. E. Wadsworth, and S. M. El-Raghy, *Metall. Trans. B*, **13**, 571 (1982).
13. P. Eadington, *Trans. Instn. Min. Metall. C*, **86**, 186 (1977).
14. A. Buckley and R. Woods, in "Interfacial Phenomena in Mineral Processing," proceedings of an Engineering Foundation conference, Rindge, New Hampshire, 2-7 August 1981, B. Yarar and D. J. Spottiswood, Editors, p. 3, Engineering Foundation, New York (1982).
15. T. Biegler, D. A. J. Rand, and R. Woods, *J. Electroanal. Chem.*, **60**, 151 (1975).
16. H-J. Sohn and M. E. Wadsworth, *J. Metals*, **32**, (11), 18 (1980).
17. T. Biegler, *J. Electroanal. Chem.*, **85**, 101 (1977).
18. T. Biegler, and D. A. Swift, *Hydrometall.*, **2**, 335 (1976/77).
19. T. Biegler, and D. A. Swift, *J. Appl. Electrochem.*, **6**, 229 (1976).
20. T. Biegler and D. C. Constable, *Inst. Mining Met. Trans. C*, **85**, 23 (1976).
21. I. D. MacLeod and D. M. Muir, *J. Appl. Electrochem.*, **13**, 411 (1983).
22. J. R. Gardner and R. Woods, *Int. J. Min. Process.*, **6**, 1 (1979).
23. J. P. Baur, H. L. Gibbs, and M. E. Wadsworth, "Initial stage sulfuric acid leaching kinetics of chalcopyrite using radiochemical techniques," U.S. Bureau of Mines, Report of Investigation 7823 (1974).
24. T. Biegler and R. Woods, *J. Electroanal. Chem.*, **20**, 347 (1969).

Electrochemistry of Prussian Blue Films on Metal and Semiconductor Electrodes

Alfred Viehbeck* and David W. DeBerry*

SumX Corporation, Austin, Texas 78758

ABSTRACT

The electrochemical properties of Prussian blue films on Pt and spark anodized n-type TiO₂ electrodes were investigated. Evidence for four redox states for Prussian blue was obtained. While the oxidation of Everitt's salt to Prussian blue involves the high spin iron atoms, the oxidation of Prussian blue to Berlin green and Berlin green to Prussian yellow involves the low spin hexacyanoferrate groups. The Prussian blue/Everitt's salt redox system ($E_0 = +0.2V$ vs. SCE) is the most stable and reversible couple. The diffusion coefficients for reduction and oxidation of this redox couple are 5.0×10^{-9} and 2.7×10^{-9} cm²/s, respectively. The photoelectrochromic behavior of Prussian blue on semiconductor TiO₂ electrodes is discussed. The films deposited on TiO₂ have short-circuit memory, and lateral color spreading through the film is slow. A light addressable electrochromic display is described.

In a previous communication, we demonstrated reversible photoelectrochromic imaging using a semiconductor electrode coated with an electrochromic material (1). The system consisted of a thin film of Prussian blue on an n-type TiO₂ electrode (both single crystal and anodized metal). Light absorbed by the semiconductor produced electrochromic reactions in the Prussian blue film at potentials negative of that measured at noble metals. Images resulted that were stable at open circuit but erasable upon reversal of potential bias. Other electrochemical photoimaging systems have been reported (2-6). Abruna and Bard (7) demonstrated the photoreduction of surface-confined poly(benzylviologen) on p-Si electrodes. Inganäs and Lundström (8) investigated the photoelectrochromic properties of poly(N-methylpyrrole) polymer on n-type silicon. And, recently, Itaya *et al.* (9) reviewed the photoelectrochemical properties of Prussian blue on single-crystal n-TiO₂ electrodes.

The present study is concerned with both the redox conductivity of Prussian blue films and their photoelectrochromic characteristics on spark-anodized polycrystalline TiO₂ electrodes. Spark anodization of Ti metal, as first reported by Sato *et al.* (10), yields n-type TiO₂ films with much-improved photoconversion efficiencies compared to anodic oxide films formed at low voltage. The various redox states of Prussian blue films on Pt and

TiO₂ electrodes are discussed. This work also examines the "short-circuit" memory (image retention) properties of the Prussian blue/semiconductor electrode. A prototype light addressable electrochromic display (LAED) device is described and an example of a light-pen-written image is shown.

Experimental

Polycrystalline semiconductor TiO₂ electrodes were made by high current-high voltage sparking of Ti metal (10). The anodic films were formed by applying 103V between a Ti electrode (0.25 mm thick) and a large-area Pt electrode in 1M Na₂SO₄ solution. During the anodization process, the Ti electrode exhibits various interference colors as the oxide film thickens with increasing voltage. Avalanche breakdown of the surface film occurred at ~85V as evidenced by the localized eruption of oxygen bubbles, followed by the visible generation of sparks at the surface. Sparking was maintained at 103V for 2 min. Following complete breakdown of the entire surface, the electrode has a uniform gray appearance. Scanning electron micrographs of the spark-anodized surface showed that the oxide film was quite porous in nature. Cross-sectional views allowed an estimate for the film thickness of ~15 μm. The sparked electrodes were etched in concentrated HCl for 2 min, then reduced at -1.0V for 2 min in 1M KCl solution. The quantum efficiencies of

*Electrochemical Society Active Member.

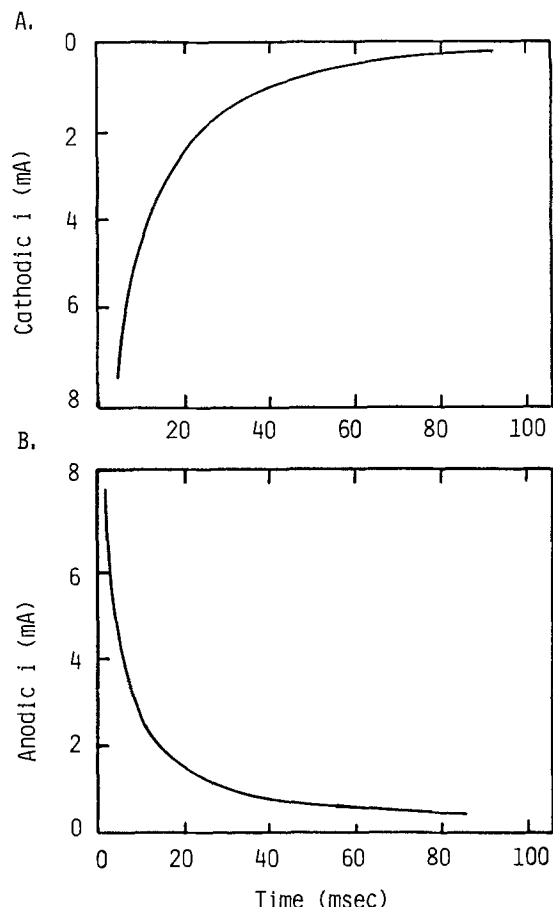


Fig. 2. Negative (A) and positive (B) current transients for the reduction of Prussian blue and oxidation of Everitt's salt, respectively, for a Pt electrode with a 10 mC/cm^2 Prussian blue film in 0.9M KCl solution.

$t^{-1/2}$ to test applicability of the Cottrell equation. Only at very short times, $t < 10 \text{ ms}$, are the plots linear with a zero intercept as expected for a semi-infinite diffusion-controlled process. The apparent diffusion coefficients for

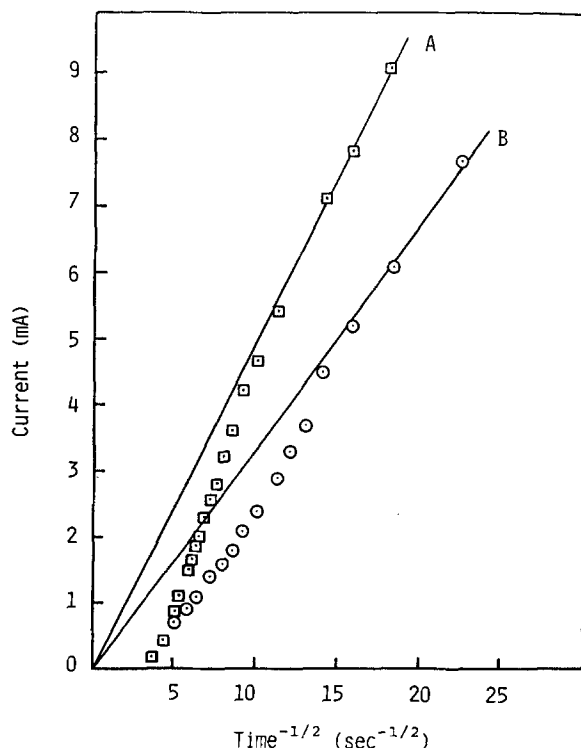


Fig. 3. Cottrell plots for Prussian blue reduction and Everitt's salt oxidation transients of Fig. 2A and 2B, respectively.

the reduction and oxidation redox processes are 5.0×10^{-9} and $2.7 \times 10^{-9} \text{ cm}^2/\text{s}$, respectively. The deviation from Cottrell behavior at longer times indicates the transition from semi-infinite to finite diffusion boundary conditions (22-24). The kinetics of the Prussian blue/Everitt's salt redox process is reflected by the shape, relative position, and potential sweep rate behavior of the voltammetric response (23, 25). The excellent reversibility of this couple demonstrated by the small potential peak separation (see Fig. 1) is indicative of rapid electron-transfer kinetics. The linear relationship found for both the oxidation and reduction peak current density as a function of sweep rate (to 500 mV/s) further indicates that the diffusion-layer thickness quickly approaches the film thickness.

Concentration profiles during Prussian blue reduction are shown schematically in Fig. 4. The permeation of redox charge during the potential pulse is represented by the concentration profiles for Prussian blue sites in the film at time zero (solid line), relatively short time, $< 10 \text{ ms}$ (broken line), and at longer times (dot-dash line). Using the calculated diffusion coefficients and the onset time for thin layer behavior, the film thickness is estimated at 2000 \AA , in good agreement with the predicted thickness. As expected for a diffusion-controlled process, similar overall results are obtained for the experiments carried out in 0.1M KCl.

It is very interesting to note that the Cottrell slope ($D_{\text{app}}^{1/2}C$) for Everitt's salt oxidation is smaller than for Prussian blue reduction. This difference might be due to a change in the film resistance with a change in oxidation state of the film. However, this effect is also possibly the result of a change in the actual site concentration of the film due to film swelling during incorporation of counterions (20). Humphrey *et al.* (26) have recently investigated the charge-transport properties of nickel hexacyanoferrate derivatized nickel electrodes and found that D_{app} for oxidation was greater than for reduction. The redox conductivity of this system was interpreted in terms of time-dependent diffusion coefficients.

Prussian blue/semiconductor properties.—Figure 5 shows i/E curves for a Prussian blue-modified Pt electrode (A) and a Prussian blue-modified TiO_2 electrode (B) for comparing the potential regions of the various surface processes. Under dark conditions, Prussian blue reduction on the TiO_2 electrode occurs at $\sim -0.35\text{V}$ as shown (a), with no corresponding reoxidation of Everitt's salt form on the positive scan (b). Following reduction of the Prussian blue film, it remains in the Everitt's salt form on positive potential scan even at potentials above $+1.0\text{V}$ —in sharp contrast to its facile reoxidation on Pt. Such behavior is expected for an n-type semiconductor electrode on which dark oxidation reactions are inhibited. However, if this electrode, with its "Everitt's salt-coating," is illuminated with light having energy greater than the bandgap separation of the electrode, in this case

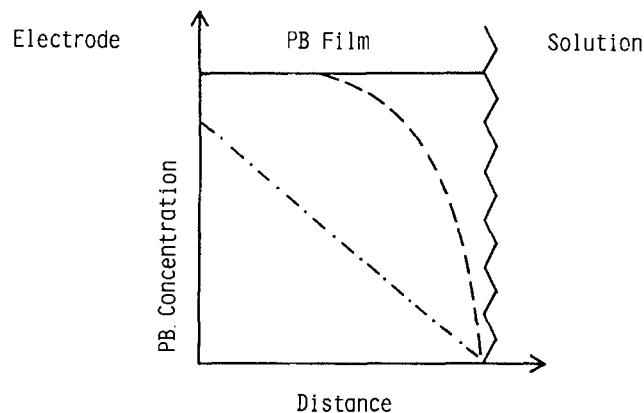


Fig. 4. Schematic representation of the Prussian blue form concentration profiles in the film during reduction at time zero (solid line), $< 10 \text{ ms}$ (broken line), and $> 10 \text{ ms}$ (dot-dash line).

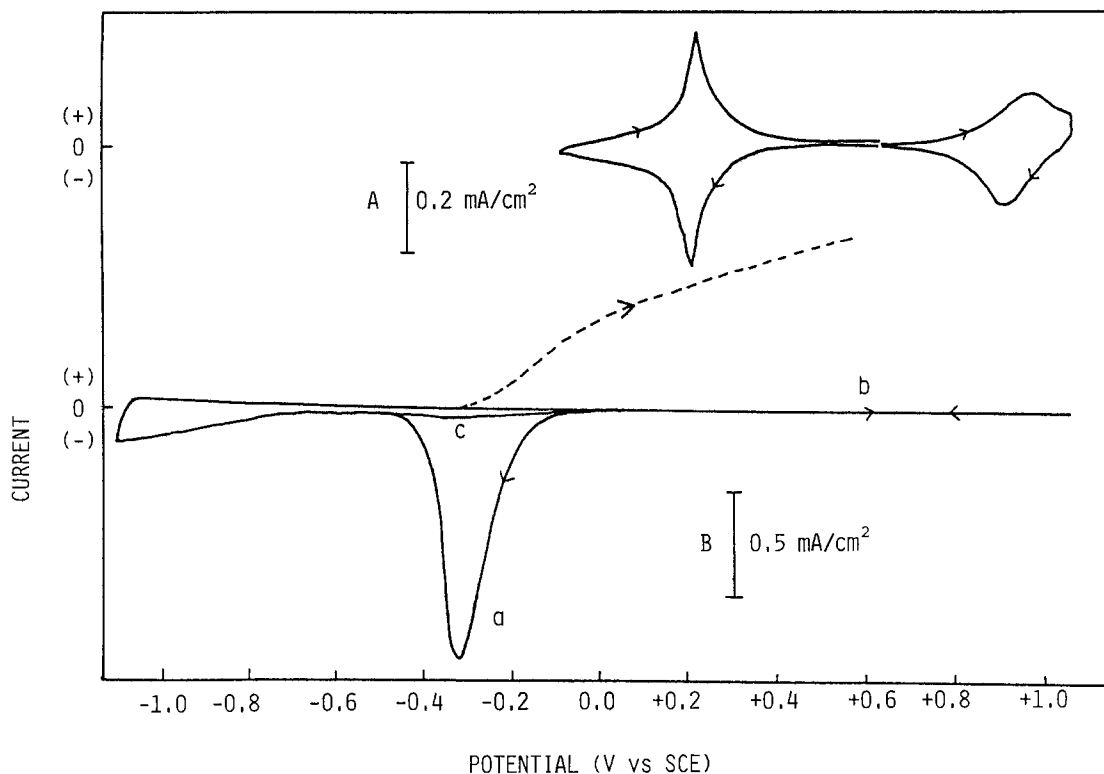


Fig. 5. Cyclic voltammograms for a Prussian blue-modified Pt electrode (A) and a Prussian blue-modified TiO_2 electrode (B). Solid lines represent dark response; the dashed line represents under illumination with UV light. Scan rate = 50 mV/s.

UV ($\lambda < 400$ nm) light, an anodic photocurrent is exhibited on the positive-going scan at potentials above -0.35 V (dashed line). No difference in the photocurrent output was observed between the Prussian blue-modified TiO_2 and the bare TiO_2 electrode. Therefore, the photoresponse of this system is due to light absorption only by the TiO_2 electrode. The negative 0.5 V shift for photo-oxidation of Everitt's salt on TiO_2 as compared to the Pt electrode is due to conversion of light energy to electrochemical energy and consequent decrease in potential needed to drive the reaction. After photo-oxidation of Everitt's salt on TiO_2 , the negative going scan again shows the reduction of Prussian blue.

In our previous communication, we showed that the rate of Everitt's salt photo-oxidation depends on the semiconductor conversion efficiency, electrode potential, and light intensity (1). The ratio of the total quantity of cathodic reduction charge (Q_c) to anodic photocharge (Q_a) shows that the average charge storage efficiency is greater than 95% for Everitt's salt oxidation to Prussian blue. However, once the anodic photocharge exceeds the capacity of the Prussian blue form, the storage efficiency decreases and the subsequent reduction scan exhibits a separate peak at -0.20 V, as seen by comparing curves 2 and 3 in Fig. 6. The excess photocharge is then partially consumed by Prussian blue oxidation to Berlin green. On reduction, this doublet is due to the two-step process from Berlin green to Everitt's salt. Itaya *et al.* (10) recently confirmed the further photo-oxidation of Prussian blue to Berlin green on semiconductor electrodes.

Figure 7 shows the reduction response on TiO_2 following an extended potentiostatic hold at $+0.5$ V and electrode illumination with UV light. We postulate that the additional peak at -0.05 represents the reduction of the completely oxidized form of Prussian blue, *i.e.*, $\text{Fe}^{+3}[\text{Fe}^{\text{III}}(\text{CN})_6]_3$, the so-called Prussian yellow or Prussian brown form. This form seems to be less stable in aqueous solution as compared to the others.

The electrochemical characteristics of the semiconductor system can be explained using an energy-band model (27). For the n-type TiO_2 semiconductor under cathodic bias, the band bending makes electrons available at the electrode/Prussian blue interface for the reduction of any

Prussian blue form in the film. As shown in Fig. 5, the Prussian blue reduction process occurs at ~ -0.35 V. Under anodic bias, however, since no free carriers are available in the valence band, the oxidation process is inhibited. While the anodic photocurrent was linearly related to the UV light intensity, the potential of photocurrent onset was only slightly affected by intensity. The onset potential was used as an approximation for the flatband (E_{FB}) potential of -0.35 V (28, 29). This value for E_{FB} agrees well with those estimates obtained by capacitance mea-

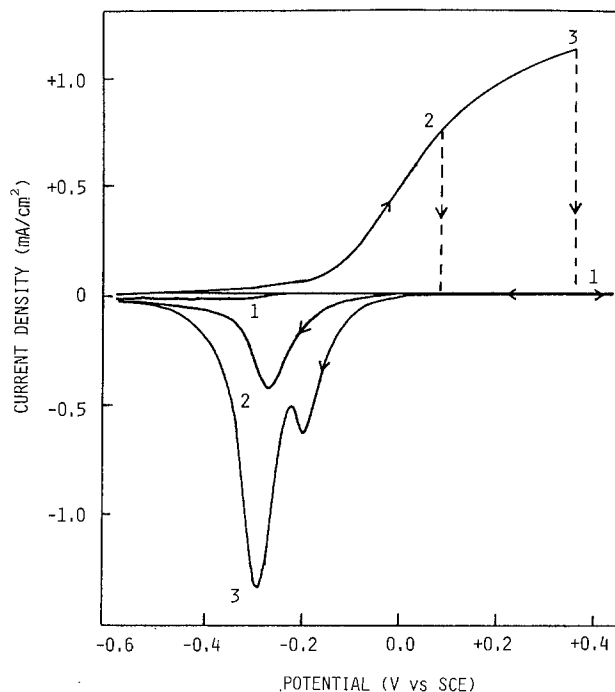


Fig. 6. Cyclic voltammograms for a Prussian blue-modified TiO_2 electrode. Scan 1 done in the dark, scans 2 and 3 under UV illumination. Note: scan to higher positive potential 3, shows Berlin green and Prussian blue reduction peaks on the negative scan.

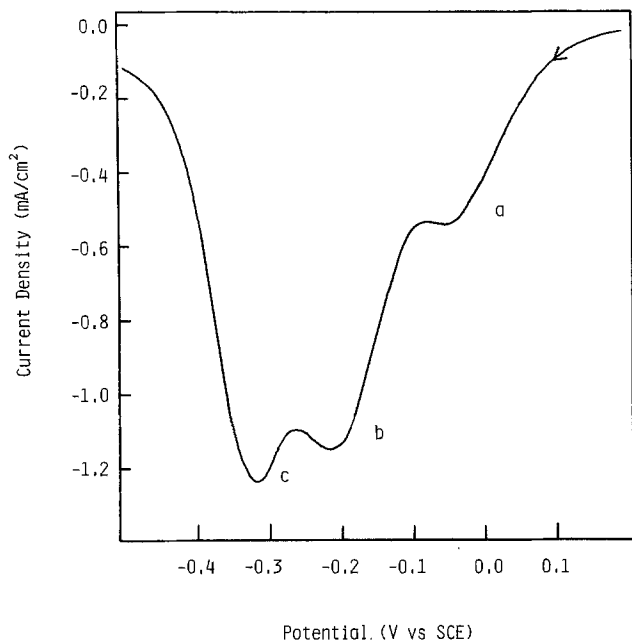


Fig. 7. Voltammogram for reduction of an initially fully oxidized Prussian blue film on Pt. Three-step reduction of Prussian yellow to Everitt's salt shown: Prussian yellow to Berlin green (a), Berlin green to Prussian blue (b), and Prussian blue to Everitt's salt (c). Scan rate = 50 mV/s.

measurements in acidic solutions (30, 31). In this highly doped n-type TiO_2 material, the conduction band is usually within -0.2V of E_{FB} (32). Since the spectral response measurement of the spark-anodized TiO_2 bandgap gave a value of 2.95 eV, the valence band is therefore located positive of 2V. The potential of the photogenerated holes is sufficiently positive to oxidize Everitt's salt. Prussian blue, Berlin green, and electrolyte. The reduction of the more oxidized forms positive of E_{FB} is perhaps due to electron transport via intermediate surface states of the semiconductor to the redox centers in the film (33). The band bending must be reduced before electrons in the

conduction band fill the intermediate states. This accounts for the narrow potential range for the reduction of Prussian yellow, Berlin green, and Prussian blue just positive of the flatband potential as compared to the spacing for the reductions on a Pt electrode.

Electrochromic memory.—The ability to photogenerate a stable image on Prussian blue-modified TiO_2 electrodes indicates short-circuit memory because the imaged region of the electrochromic film is not in equilibrium with the reduced form of the rest of the surface coating. The redistribution of redox charge is suppressed by the semiconductor properties of the electrode substrate. Therefore, the effect of lateral charge transport within the film (involving self-exchange) is almost negligible for practical applications. For instance, if the lateral conduction is similar to the process normal to the surface (diffusion coefficient $\sim 5 \times 10^{-9} \text{ cm}^2/\text{s}$), it would require an estimated $1 \times 10^4 \text{ min}$ for an image to spread about 1 mm.

A metal-semiconductor electrode was fabricated to test the persistence of an image and the low degree of lateral self-exchange. This electrode had both an Au and a TiO_2 surface region with a Prussian blue coating over the combined electrode surface. It was made from a strip of Ti metal, first spark anodized, then partially etched and electroplated with gold. Front and cross-sectional drawings of the electrode are shown in Fig. 8. Figure 8 also gives i/E curves for the TiO_2 -Au/Prussian blue electrode in 1M KCl solution. The first scan (film in Prussian blue form) toward negative potentials (curve a) shows Prussian blue reduction on the Au surface at $\sim +0.2\text{V}$ and on the TiO_2 region at $\sim -0.4\text{V}$. On the following positive scan, only the film on the Au side oxidizes and turns blue, as depicted by the anodic peak at $\sim +0.3\text{V}$. The subsequent negative scan shows only reduction of the Prussian blue coating on Au (curve b). Thus, following total film reduction, the electrochromic process can then only proceed electrochemically (in the dark), on the Au substrate. However, as expected, the Prussian blue coating on TiO_2 can be photoelectrochemically oxidized under illumination with UV light at potentials positive of -0.3V . In this manner, only the TiO_2 side undergoes the electrochromic process, provided the overall electrode potential does not ex-

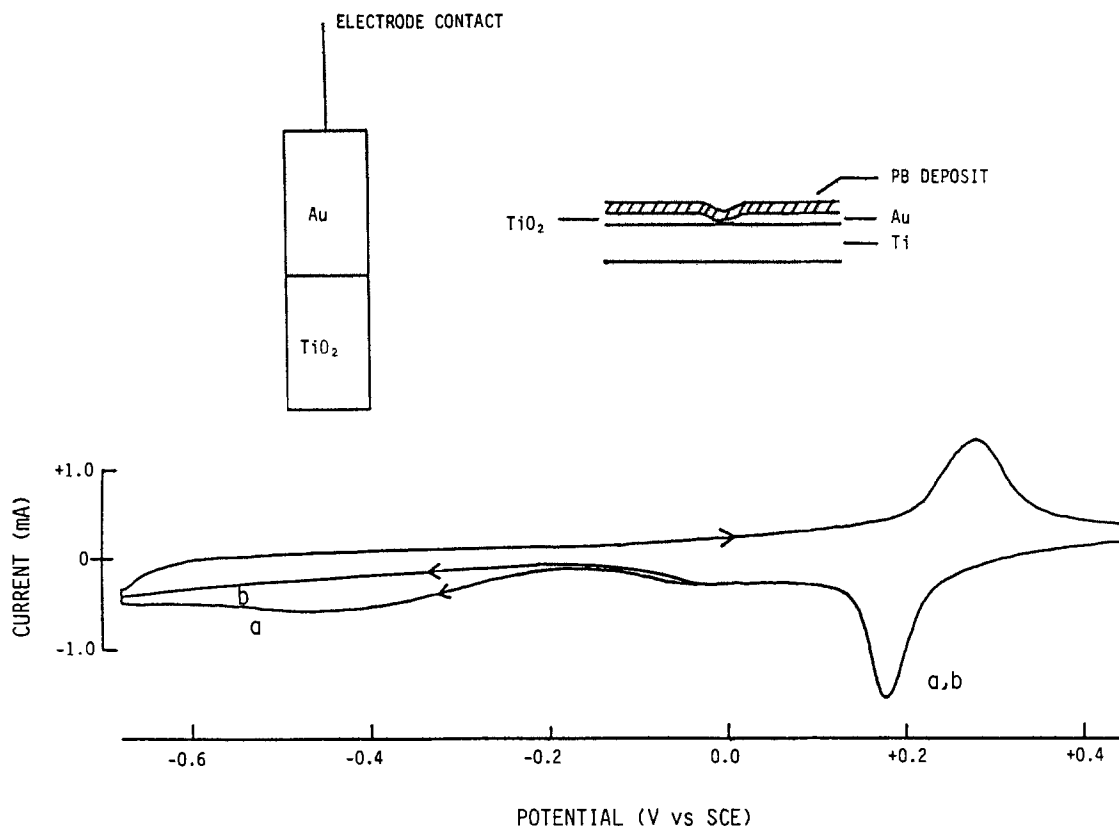


Fig. 8. Illustration of a combination Au/ TiO_2 electrode modified with Prussian blue, and cyclic voltammograms for this system. Scan rate = 50 mV/s

ceed +0.2V. These results illustrate the feasibility of using combination semiconductor/metal electrode segments side-by-side in a multiplexed, light-addressable display device.

Following complete reduction, then polarization to +0.4V, the Au film in the Prussian blue form and the TiO₂ film in the Everitt's salt form are stable at open circuit. However, in this condition, UV illumination of the TiO₂ portion results in a blue image with simultaneous loss of blue color on the Au side. In other words, this "short-circuited" semiconductor/metal system acts as a photobattery with Everitt's salt oxidation at the TiO₂ and Prussian blue reduction at the Au regions. This effect is due to the difference in "reversible potential" for the Prussian blue/Everitt's salt redox couple on these substrates. While photo-oxidation of Everitt's salt to Prussian blue on TiO₂ generates electrons with sufficient energy to reduce Prussian blue on Au, Prussian blue is not reduced by the oxidation of Everitt's salt on Au. A further demonstration involved an all-TiO₂ electrode containing a blue region. The charge (color) in this image can be transferred by illuminating a region containing Everitt's salt while under open circuit. Thus, the Prussian blue portion becomes the electron accepting region for open-circuit photo-oxidation of Everitt's salt at some other location.

Photoelectrochemical display operation.—A light addressable electrochromic display (LAED) based on a three-electrode configuration was developed. The photoelectrochromic electrode consists of a Prussian blue-modified spark anodized Ti sheet. A tin oxide-coated glass plate acts as both the counterelectrode and display window. This laboratory device has an Ag/AgCl reference electrode for allowing potentiostatic control. The display face measures ~30 cm² and the flat panel is ~0.5 cm wide. Figure 9 shows an example of a "light-written" image generated on the LAED. The image was written using the output of a fiber optic cable ("light-pen") connected to a UV light source (200W Hg lamp). The writing rate was ~1 cm/s. No noticeable spreading of the image occurred after 1h on open circuit. The image was completely erased by a cathodic voltage pulse, leaving no "ghost" images.

Conclusion

The photo-oxidation of Everitt's salt to Prussian blue on semiconductor TiO₂ electrodes occurs with better than 95% photocurrent conversion efficiency. The oxidation of the Prussian blue film leads to the Berlin green form involving the incomplete oxidation of the hexacyanoferrate (II) groups. A fourth oxidation stage of the film corresponds to Prussian yellow or iron (III) hexacyanoferrate (III). Cottrell slopes of the reduction of Prussian blue and the corresponding oxidation of Everitt's salt yield diffusion coefficients of 5×10^{-9} and 2.7×10^{-9} cm²/s, respec-

tively. For the PB-modified TiO₂ electrode, surface illumination with UV ($\lambda < 400$ nm) light at potentials positive of the flatband, $E_{FB} = -0.35$ V, can lead to oxidation of Everitt's salt to Prussian blue and Berlin green because of the high potential of photogenerated holes.

Spark anodization provides polycrystalline n-type TiO₂ electrodes with reasonable photoconversion efficiencies (5-15%). The n-type properties of the anodically formed electrodes allow a stable image to be produced since charge transport between different redox forms present in the same surface film via the electrode substrate is inhibited. A stable image further implies that lateral charge transport through electrochromic film itself is quite slow.

Acknowledgment

This research was supported by the Defense Advanced Research Projects Agency.

Manuscript submitted Nov. 5, 1984; revised manuscript received Jan. 8, 1985.

SumX Corporation assisted in meeting the publication costs of this article.

REFERENCES

1. D. W. DeBerry and A. Viehbeck, *This Journal*, **131**, 249 (1983).
2. G. L. McLeod, *Photogr. Sci. Eng.*, **13**, 93 (1969).
3. F. Möllers, H. J. Tolle, and R. Memming, *This Journal*, **121**, 1160 (1974).
4. T. Inoue, A. Fujishima, and K. Honda, *Chem. Lett.*, **11**, 1197 (1978).
5. T. Inoue, A. Fujishima, and K. Honda, *This Journal*, **127**, 1582 (1980).
6. B. Reichman, F.-R. F. Fan, and A. J. Bard, *ibid.*, **127**, 333 (1980).
7. H. D. Abruna and A. J. Bard, *J. Am. Chem. Soc.*, **103**, 6898 (1981).
8. O. Inganäs and I. Lundström, *This Journal*, **131**, 1129 (1984).
9. K. Itaya, I. Uchida, S. Toshima, and R. M. DeLaRue, *ibid.*, **131**, 2086 (1984).
10. Y. Matsumoto, T. Shimizu, A. Toyoda, and E. Sato, *J. Phys. Chem.*, **86**, 3581 (1982).
11. K. Itaya, T. Ataka, and S. Toshima, *J. Am. Chem. Soc.*, **104**, 4767 (1982).
12. K. Itaya, T. Ataka, S. Toshima, and T. Shinohara, *J. Phys. Chem.*, **86**, 2415 (1982).
13. M. B. Robin and P. Day, *Adv. Inorg. Chem. Radiochem.*, **10**, 247 (1967).
14. A. Ludi and H. U. Güdel, *Struct. Bonding (Berlin)*, **1**, 14 (1973).
15. D. Ellis, M. Eckhoff, and V. D. Neff, *J. Phys. Chem.*, **85**, 1225 (1981).
16. R. M. C. Goncalves, H. Kellawi, and D. R. Rosseinsky, *J. Chem. Soc. Dalton Trans.*, 991 (1983).
17. H. J. Buser, D. Schwarzenbach, W. Peter, and A. Ludi, *Inorg. Chem.*, **16**, 2704 (1977).
18. A. B. Bocarsly and S. Sinha, *J. Electroanal. Chem.*, **137**, 157 (1982).
19. L. M. Siperko and T. Kuwana, *This Journal*, **130**, 396 (1983).
20. K. Itaya, T. Ataka, and S. Toshima, *J. Am. Chem. Soc.*, **104**, 3751 (1982).
21. K. P. Rajan and V. D. Neff, *J. Phys. Chem.*, **86**, 4361 (1982).
22. P. Daum, J. R. Lenhard, D. Rolison, and R. W. Murray, *J. Am. Chem. Soc.*, **102**, 4649 (1980).
23. A. J. Bard and L. R. Faulkner, "Electrochemical Methods, Fundamentals and Applications," p. 205, John Wiley and Sons, New York (1980).
24. P. Daum and R. W. Murray, *J. Phys. Chem.*, **85**, 389 (1981).
25. C. R. Martin, I. Rubinstein, and A. J. Bard, *J. Am. Chem. Soc.*, **104**, 4817 (1982).
26. B. D. Humphrey, S. Sinha, and A. B. Bocarsly, *J. Phys. Chem.*, **88**, 736 (1984).
27. H. Gerischer, *J. Electroanal. Chem.*, **58**, 263 (1975); and references therein.
28. J. M. Bolts and M. S. Wrighton, *J. Phys. Chem.*, **80**, 2641 (1976).
29. M. A. Butler, *J. Appl. Phys.*, **48**, 1914 (1977).

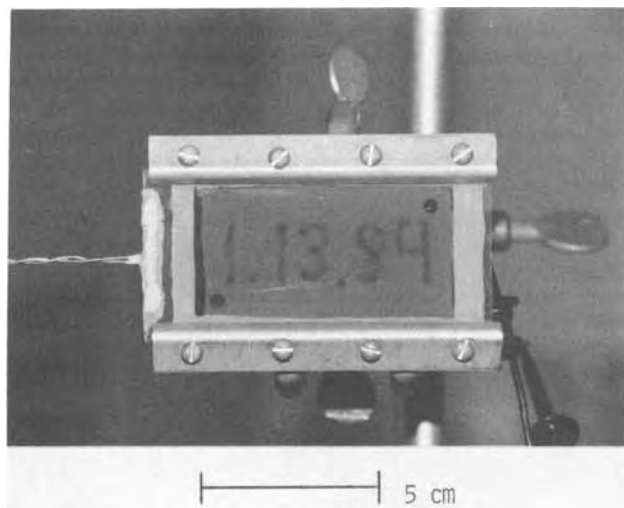


Fig. 9. Photograph of the LAED displaying a light-pen-written image

30. M. Tomkiewicz, *This Journal*, **126**, 1505 (1979).
 31. E. C. Dutoit, F. Cardon, and W. P. Gomes, *Ber. Bunsenges. Phys. Chem.*, **80**, 475 (1976).
 32. S. R. Morrison, "Electrochemistry at Semiconductor

- and Oxidized Metal Electrodes," Plenum Press, New York (1980).
 33. R. N. Noufi, P. A. Kohl, S. N. Frank, and A. J. Bard, *This Journal*, **125**, 246 (1978).

Transport Numbers in Molten Aluminum Chloride-1-Methyl-3-Ethylimidazolium Chloride Mixtures

Chester J. Dymek, Jr.,* and Lowell A. King

The Frank J. Seiler Research Laboratory (AFSC), United States Air Force Academy, Colorado Springs, Colorado 80840

ABSTRACT

The transport numbers of 1-methyl-3-ethylimidazolium (MEI^+), AlCl_4^- , and Cl^- ions were measured in equimolar and AlCl_3 -poor melts of AlCl_3 and 1-methyl-3-ethylimidazolium chloride (MEICl). The moving boundary method and a modified Hittorf method were used. The external transport numbers of the three ions in the equimolar melt were 0.70 ± 0.02 , 0.30 ± 0.02 , and 0, respectively. As AlCl_3 mole fraction decreases, the transport number for AlCl_4^- decreases, while that for Cl^- increases and that for MEI^+ remains the same. The internal transport number of the MEI^+ relative to Cl^- as the reference is 1.00 ± 0.02 .

Chloroaluminate melts have attracted great interest in recent years in connection with battery applications, as solvents for the stabilization of unusual oxidation states, as media for conducting inorganic and organic reactions, and in the Alcoa smelting process. In the most familiar chloroaluminate melts, which contain AlCl_3 in combination with an alkali chloride such as NaCl , the probable but never proven assumption generally made is that the alkali metal cation transports virtually all the charge passed through such a melt (1, 2). The fraction of the charge carried by an individual species during the passage of an electrical current is called the "transport number" of the species. The transport number is an "external" transport number when the flux of the transporting species is measured relative to some physical reference in the electrolytic cell, such as a porous separator or the wall of the cell. It is an "internal" transport number when the flux is measured relative to some other species present in the electrolyte.

If one makes the assumption that the cation is the principal charge carrier, and if charge transport actually is carried out by anions or shared between the cations and anions, serious errors may occur in calculating activities and equilibrium constants and in predicting concentration changes and voltage changes during discharge and charge of batteries utilizing these melts (3). The information on ion transport numbers may also be sufficient to rule out certain battery-design concepts at some electrolyte compositions. Conversely, knowledge of transport numbers may suggest the most promising designs to be investigated.

The assumption that only the cation transports charge may not be valid for a melt with an organic cation, which can be significantly larger than AlCl_4^- . In fact, in recent studies (4-6) of room temperature chloroaluminates, which contain AlCl_3 in combination with an organic salt such as a 1-alkylpyridinium chloride or a 1,3-dialkylimidazolium chloride, there was abundant circumstantial evidence that anions were important charge carriers. These melts with organic cations are liquid at and below room temperature for mixtures with apparent mole fractions of AlCl_3 , N , in the range $0.30 < N < 0.70$. The three most probable anions present in chloroaluminate melts in this mole fraction range are Cl^- , AlCl_4^- , and Al_2Cl_7^- . The anion fractions of all three vary with overall melt composition (see Fig. 1).

The first experimental verification that anions transport significant charge in chloroaluminate melts was made by Hussey and Øye (7). They studied mixtures of

AlCl_3 and 1-methyl-3-ethylimidazolium chloride (MEICl) in the composition range $0.507 < N < 0.670$. They used a classical Hittorf-like procedure, in which current was passed through a three-compartment cell. The compartments were isolated from each other by fine-porosity glass disks.

At the end of each experiment, the melt in each compartment was weighed, then dissolved in water, and the composition determined from absorption spectroscopic analysis of the 1-methyl-3-ethylimidazolium cation (MEI^+) in water. Their method yielded the external transport number of MEI^+ . Anion external transport numbers could also be extracted with lesser precision from the data. They obtained a value of 0.71 ± 0.05 for the cation and composition-dependent values for the two chloroaluminate anions. Chloride ion was present in negligible amounts in their composition range and was assumed to carry no charge.

Hussey and Øye also calculated the internal transport numbers for the MEI^+ cation and for aluminum atoms, relative to chlorine atoms as the internal reference. They found the internal transport number of the cation to be 1.0, and the corresponding value for aluminum to be 0.0. Notice that this result does not imply that the cation carries all the charge. Since in their treatment, by definition, chlorine was assigned a zero internal transport number, a zero value for aluminum atoms indicates that aluminum and chlorine are bound together in the same chemical

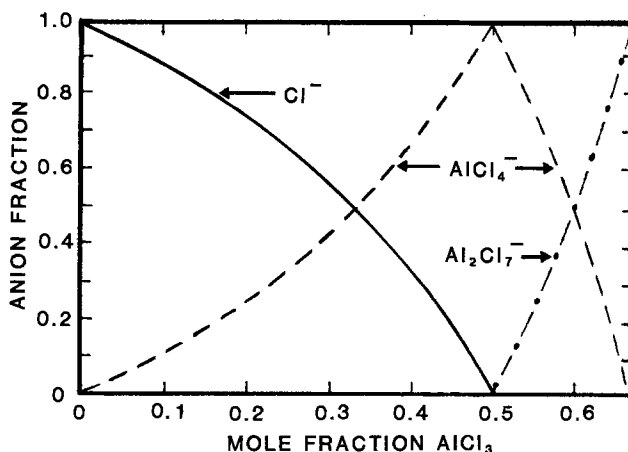


Fig. 1. Anion mole fractions vs. apparent mole fraction of AlCl_3 in $\text{MEICl}_3/\text{AlCl}_3$ melts. The basis for these calculated plots is described in Ref. (11).

* Electrochemical Society Active Member.

species, and the bare chloride ions carry no charge. The latter might be expected, since the concentration of Cl^- is extremely small in the composition range studied.

This report describes work done in equimolar melts using a moving boundary method and also work done in AlCl_3 -poor ($0.37 < N < 0.50$) melts, which do contain significant Cl^- concentrations, using a modified Hittorf method.

Experimental

Sample preparation.—The 1-methyl-3-ethylimidazolium chloride, MEICl , and its binary mixtures with AlCl_3 were prepared as described elsewhere (8). All sample preparation and handling (except in sealed apparatus) was conducted in an argon-filled glove box (Vacuum/Atmospheres Company dry box and Model MO-40 Dri Train) having a combined moisture and oxygen concentration less than 10 ppm. Borosilicate glassware was used.

Apparatus.—In both methods, electric current was supplied and monitored by a Princeton Applied Research Model 173 Galvanostat and Model 179 digital coulometer. The moving boundary cell was immersed in a silicone oil bath maintained at 93°C by a Haake constant-temperature circulator. This temperature is slightly above the melting point of MEICl . The modified Hittorf cell was kept at the ambient glove box internal temperature (ca. 30°C). Weighing was done in the dry box using a Mettler AE 163 electronic balance. Figures 2 and 3 show the main features of the two cells.

Moving boundary method.—The moving boundary technique for determination of transport numbers in molten salts depends on the maintenance of a sharp boundary between two liquid phases. The two phases should possess one common ion, in our case, MEI^+ , and differing counterions, Cl^- and AlCl_4^- . It is most convenient experimentally if hydrostatic flow is eliminated. This was accomplished in our cell by means of a very low porosity fritted disk through which all liquid transport must occur, and by filling the two arms of the cell to about equal heights. Use of such a cell for determination of transport

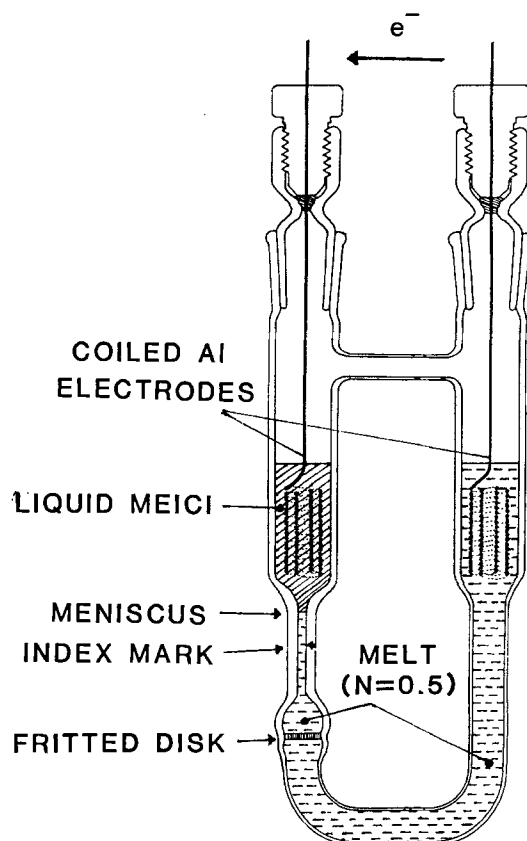


Fig. 2. Moving boundary cell

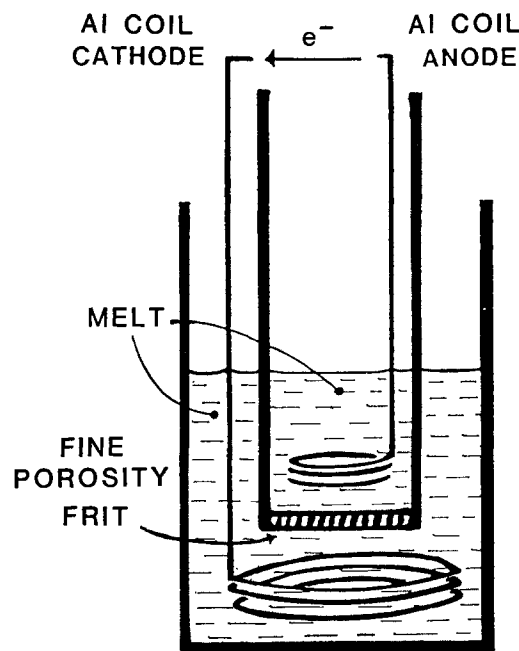


Fig. 3. Modified Hittorf cell

numbers in fused salts was previously reported by Duke and Cook (9).

The charge transporting ions will move when an electric current is passed across the boundary. The direction of electron flow is indicated by the arrow at the top of Fig. 2. If all the charge is carried by the common ion, MEI^+ , no movement of the meniscus will be observed because every MEI^+ crossing the meniscus into the pure MEICl phase will be "replaced" by a MEI^+ crossing the fritted disk. However, if the counterion in the melt in which the porous disk is located, *i.e.*, AlCl_4^- , carries charge, the effect of current passage is for the meniscus to move in the direction of the disk. In this case, an AlCl_4^- moving down through the fritted disk is not "replaced" by another from above the meniscus. As a practical matter, the leading counterion, AlCl_4^- , must possess a higher mobility than the trailing counterion, Cl^- . This will insure the maintenance of a sharp moving boundary between the two phases.

Moving boundary experiments were conducted in cells such as shown in Fig. 2. The fritted disks originally were fine through ultrafine porosity. They were partially fused during cell assembly to further reduce the possibility of significant hydrostatic flow during the course of an experiment. The capillary tubing used in the moving boundary cells was calibrated beforehand in volume per unit length with mercury in the conventional manner. The radius of the capillary we used was 0.104 cm. (We also used capillaries of 0.059 cm and 0.17 cm. The ohmic resistance of the former was too large to permit passage of a convenient current. A sharp meniscus was difficult to maintain in the largest radius capillary at the maximum currents the galvanostat could provide, given the total resistance of the cell.)

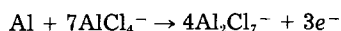
The moving boundary cell was filled inside the glove box in the following manner. Equimolar MEICl-AlCl_3 at ambient temperature was placed in the compartment opposite the capillary. The compartment was filled so that the melt was in contact with the porous separator. A several centimeter head was maintained until liquid could be seen on the capillary side of the disk (this required, as a minimum, 15h and insured that the disk was saturated with the equimolar melt). Then, more of the equimolar melt was added on the capillary side until the capillary was very nearly filled. Thus, the equimolar melt is the electrolyte in contact with both sides of the porous disk and therefore also the electrolyte in which the transport numbers are being measured. The addition was made with a Pasteur pipette inserted through the capillary to

exclude bubbles and to avoid wetting the wall of the compartment above the capillary. With another Pasteur pipette, pure MEICl from a reservoir maintained above its melting point was carefully added on top of the equimolar melt column.

The aluminum coils (Alfa Products, 99.999% Al) were quickly (but carefully, to minimize mixing at the liquid-liquid interface) immersed in the two compartments before the MEICl solidified. The capped cell was then removed from the glove box. When the MEICl was remelted in the oil bath, a distinct meniscus was evident between the two liquids. [The densities at 93°C of MEICl and of the equimolar melt are 1.1120 and 1.2395 g/cm³, respectively (6).] The meniscus became very sharp within a few seconds after the current was turned on. As indicated in Fig. 2, electron flow in the external circuit was from the right electrode to the left, and, consequently, negative ion conduction in the electrolyte would be from the left compartment to the right, or "down the capillary." A constant current of 20-30 mA was most convenient, and no dependence of calculated transport numbers on current was noted between 7.5 and 50 mA. The meniscus fell at about 1.4 cm/h at 20 mA. The meniscus movement was determined by measuring (using a cathetometer) the distance between the meniscus and an index mark on the capillary. Cathetometer readings of the meniscus location and index mark were made to a precision of ±0.05 cm.

When the current was turned on, the meniscus location and the total number of coulombs passed were recorded at periodic intervals. By the time the first reading was taken, the meniscus was sharp; the number of coulombs passed at that point was subtracted from all subsequent values. The corresponding meniscus location thus became the "zero" position for meniscus movement.

We evaluated the electrode reaction products and hydrostatic flow through the fritted disk for their possible effects on the melt composition and the meniscus position. Oxidation of aluminum at the anode (in the $N = 0.5$ melt) can be represented by the reaction



The acidic melt formed at the anode is well removed from the fritted disk. Also, since it is denser than neutral melt and mixes slowly, it is unlikely that significant Al_2Cl_7^- concentration builds up near the fritted disk. The cathode reaction (in the pure MEICl) must involve reduction of MEI^+ , but the products of the reaction have not been identified. The reduction does produce a distinct orange-brown color in the vicinity of the coiled aluminum cathode; however, the colored product does not appear to diffuse into the capillary. This observation, along with the constancy of the transport number obtained during a run (see Fig. 4 and related discussion), strongly support the

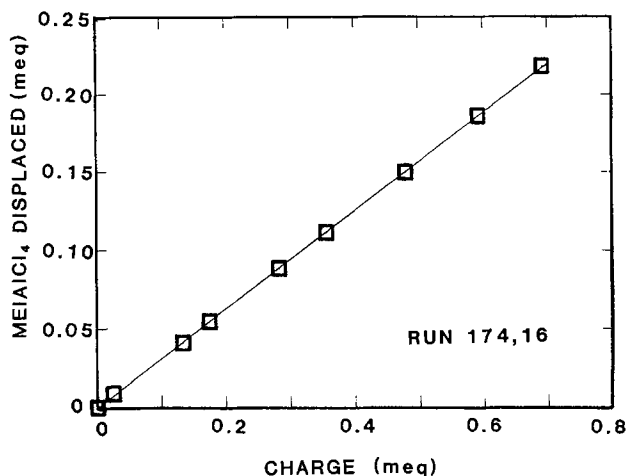


Fig. 4 Experimental results for Run 174,16 of moving boundary method. Equivalents of salt transported across the porous disk vs. charge passed.

assumption that the electrode reaction products do not significantly affect the calculated transport numbers.

In separate experiments (for each different porous disk used), enough equimolar melt was added to the capillary side of the cell to only half fill the capillary section. Motion of the meniscus was followed for 12-24h as a several centimeter head of melt was maintained on the other side of the porous disk. A typical hydrostatic flow rate was about 1% of the total flow rate observed during passage of a 20 mA current. Not even this hydrostatic flow rate would occur in an actual experiment, where the two liquid columns were at about the same height. Furthermore, a connecting tube between the vapor spaces of the two compartments prevented any unequal buildup of gas pressure from the electrode reactions. Accordingly, no corrections to the data for hydrostatic flow or pressure differences in the gas above the columns were deemed necessary.

Modified Hittorf method.—The cell was comprised of two concentric tubes, open at the top, and communicating by a fine-porosity glass disk, which was the bottom of the inside tube (see Fig. 3). Coils of aluminum wire (Alfa Products, 99.999% Al) were placed in each compartment. As with the other cell, the porosity of the glass disk was further reduced by partial fusion to reduce the possibility of hydrostatic flow between the compartments. This cell was filled and operated inside the glove box.

We call this technique a "modified Hittorf method" because there is a region defined by the porous separator in the cell in which the changes in species concentrations are measured and related to transport of ions into and out of the region. The inner compartment is such a region in our cell and it is also the anode, so the expected ionic motion during the passage of current is for MEI^+ cations to migrate out of this compartment and for anions to migrate into it. The composition and mass of the anolyte would be affected by both ion migration and the anodization of the aluminum electrode, i.e., $\text{Al} + 4\text{Cl}^- \rightarrow 4\text{AlCl}_4^- + 3e^-$. Thus, the mass and composition of the anolyte (before and after electrolysis), along with the charge passed through the cell, are required to determine how many moles of each species transported charge across the disk. Because of the unknown cathodic processes in basic ($N < 0.5$) melts (aluminum deposition does not occur to any significant extent), we did not attempt to relate the catholyte composition to any transport properties.

The hydrostatic flow rate was determined by monitoring the change in mass of the anode compartment for several hours while it was filled with sufficient melt to provide a 12 mm hydrostatic head above the frit. The leak rate was found to be 0.0012 g/h per mm of pressure head. In the cell assembly and operation, we estimate that the anolyte and catholyte levels can be maintained to within ± 2 mm, so our leak-rate error did not exceed ± 0.002 g/h. In a typical measurement, this leak-rate uncertainty contributes ± 0.006 to the overall uncertainty in the transport number.

The anode compartment (including the aluminum anode) was weighed empty of melt except for the amount of melt required to saturate the frit. This recorded tare weight also included a beaker used to hold the anode compartment during the weighings. The anode compartment was then filled with melt of a known composition and weighed again to obtain the initial mass of anolyte. Melt of the same composition then was placed in the cathode compartment. Next, the cell was assembled so that the anolyte and catholyte levels were at the same height. Finally, the cell was connected and a known charge passed at constant current of 50 mA. Then the anode compartment was removed, its outside surface was wiped clean, and it was weighed.

Since the method of wiping the outside frit surface can introduce serious error into the weight of the anolyte, the magnitude of this error was determined. The anode compartment containing melt was submerged in the catholyte for several minutes and then removed, wiped, and

weighed. Successive cycles of this process resulted in an uncertainty of $\pm 0.0005\text{g}$ for the more viscous basic melts ($0.33 < N < 0.40$). For the less viscous melts ($0.40 < N < 0.48$), the wiping process had to be done more gently to achieve an uncertainty of $\pm 0.001\text{g}$.

By correcting for the amount of aluminum anodized into the melt using the known anode reaction stoichiometry, the weight change of the melt can be combined with the composition change to obtain the number of moles of ions transported into or out of the anode compartment for a given passage of charge. The anolyte compositions before and after passage of a measured charge were determined by proton nuclear magnetic resonance (NMR) spectroscopy of aliquots removed from the anolyte compartment. Prior to obtaining the aliquots, the anolyte, which had already been weighed, was stirred to insure a uniform composition of melt in the anode compartment. NMR spectra were taken with a JEOL Model FX90Q NMR spectrometer. This procedure is the same as described elsewhere (10), except that a hexamethyldisiloxane external standard was used and the spectrometer was operated at 90 MHz in the present work.

This procedure was performed for several melts in the range $0.33 < N < 0.48$. Prior to each experiment, the frit was saturated with melt to be used in that experiment by placing some of the melt in the anode and letting it diffuse through the frit.

Results and Discussion

Moving boundary method.—For each ion moving in the vicinity of the boundary, a corresponding ion is moving through the porous disk. Thus, this experiment really measures the transport of ions through the disk. It follows that the transport numbers obtained are external transport numbers as described by Hussey and Øye. The transport numbers were calculated from

$$t_-(\text{AlCl}_4^-) = \frac{\text{equivalents of salt transported}}{\text{equivalents of current passed}} \\ = \frac{(\pi r^2 \Delta h) \rho / M}{Q/F}$$

where r is the capillary radius, ρ is the density of equimolar melt, Δh is the distance traveled by the boundary, M is the gram equivalent weight of the equimolar melt, F is the Faraday constant, and Q is the charge passed. The "equivalents of salt transported" down the capillary is equal to the equivalents of AlCl_4^- transported across the porous disk since the MEI^+ is the only cation in the two phases forming the boundary.

The results of the moving boundary experiments are given in Table I. The data from experiment 174,16 are also plotted in Fig. 4. The plotted data should be considered only representative; they are neither the best nor the poorest in terms of experimental scatter.

Since AlCl_4^- is, presumably, the only anion present in significant concentration in the $N = 0.50$ melt, the remainder of the charge will be carried by the imidazolium cation. If one assumes for the transport number of AlCl_4^- the overall value 0.30 ± 0.02 , given in Table I, the imidazolium ion transport number will be 0.70 ± 0.02 . This value is in agreement with the 0.71 ± 0.05 reported by Hussey and Øye (7) for acidic melts. Hussey and Øye claim their value is valid throughout the AlCl_3 composition range, $0.50 < N < 0.67$. The agreement is particularly gratifying in view of the two different experimental approaches taken.

It should be noted that Hussey and Øye worked at 28°C , while the present data were taken at 93°C . It is not known what, if any, effect the temperature has on the observed transport numbers.

Modified Hittorf method.—In this method, the measured mass, m , and mole fraction of AlCl_3 , N , of the anolyte were used to calculate the number of moles of MEICl and AlCl_3 before and after each passage of charge as follows

Table I. Moving boundary data for equimolar AlCl_3 -1-methyl-3-ethylimidazolium chloride

Run no.	I (mA)	$t_-(\text{AlCl}_4^-)$	Number of data	Total charge (meq)
174,14	20	0.258 ± 0.003	3	0.24
174,16	20	0.314 ± 0.001	9	0.69
174,20	20	0.260 ± 0.0008	9	0.68
174,21	20	0.253 ± 0.001	9	0.67
174,23	20	0.256 ± 0.0004	8	0.66
174,31	20	0.330 ± 0.0009	4	0.28
174,33	15	0.343 ± 0.001	7	0.37
	20	0.318 ± 0.002	4	0.20
	15	0.327 ± 0.002	9	0.40
	13	0.336 ± 0.002	4	0.20
174,36	[all]	0.335 ± 0.002	17	0.87
	40	0.333 ± 0.002	9	1.37
	50	0.365 ± 0.0006	4	0.46
174,43	20	0.265	2	0.03
	17.5	0.286 ± 0.005	3	0.10
	15	0.278 ± 0.002	4	0.18
	12.5	0.272 ± 0.002	4	0.14
	10	0.272 ± 0.003	3	0.12
	7.5	0.256 ± 0.004	4	0.14
	[all]	0.272 ± 0.008	20	0.90
175,3	30	0.330 ± 0.002	10	0.62
175,5	30	0.301 ± 0.0006	15	0.79
175,6	30	0.300 ± 0.001	9	0.44
175,7	30	0.291 ± 0.0007	10	0.85
All data		0.299 ± 0.02	143	

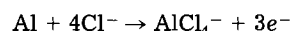
$$\text{mol}(\text{MEICl}) = \frac{(1-N)m}{M_{\text{AlCl}_3}N + M_{\text{MEICl}}(1-N)}$$

and

$$\text{mol}(\text{AlCl}_3) = \frac{Nm}{M_{\text{AlCl}_3}N + M_{\text{MEICl}}(1-N)}$$

where the M is the formula weight of the subscripted species.

Since $\Delta \text{mol}(\text{MEICl})$ is the same as $\Delta \text{mol}(\text{MEI}^+)$ in the anolyte, we can calculate the mols of MEI^+ transported out of the anolyte. Similarly, $\Delta \text{mol}(\text{AlCl}_3) - Q/3F$ gives $\Delta \text{mol}(\text{AlCl}_4^-)$, or the number of moles of AlCl_4^- transported into the anolyte, since AlCl_4^- is the only Al containing anion present in the basic melt. The $Q/3F$ correction is required to account for AlCl_4^- formed by anodization of the Al anode by the reaction



Thus we have

$$t_+(\text{MEI}^+) = \frac{\Delta \text{mol}(\text{MEICl})}{Q/F}$$

$$t_-(\text{AlCl}_4^-) = \frac{\Delta \text{mol}(\text{AlCl}_3) - Q/3F}{Q/F}$$

and

$$t_-(\text{Cl}^-) = 1 - t_-(\text{AlCl}_4^-) - t_+(\text{MEI}^+)$$

The data recorded are tabulated in Table II with the runs listed in order of increasing AlCl_3 mole fraction of the melts used. The results using these data are listed in Table III with the same ordering of the runs. The initial tare weights listed in Table II include the weight of the beaker used to contain the anode compartment for the weighings. In Fig. 5, the transport numbers obtained by this method are plotted against the mole fraction of the melt used. Several runs were performed at $N = 0.37$, and the results at this point reflect the uncertainty in the data. Even considering this fairly large scatter in the results, it is clear that the transport numbers for the Cl^- and AlCl_4^- vary approximately with the concentrations of these species. When the transport numbers for these anions are plotted against their molarities in the melts (Fig. 6), it also becomes clear that the two anions have approximately the same mobilities. This may be rationalized by

Table II. Data from modified Hittorf method experiments

Initial N (± 0.001)	Final N (± 0.001)	Q ($\pm 0.5C$)	Initial m ($\pm 0.0001g$)	Final m ($\pm 0.0001g$)	m (tare) ($\pm 0.0001g$)
0.337	0.348	100	84.6246	84.5882	77.6930
0.338	0.354	100	83.0635	82.9958	77.7058
0.359	0.383	145	82.7495	82.6673	77.7679
0.359	0.382	121	81.9797	81.9125	77.7582
0.371	0.390	247	89.0212	88.9088	77.5058
0.371	0.379	100	87.8270	87.7827	77.5883
0.372	0.387	148	87.2021	87.1366	77.7868
0.372	0.384	151	88.6673	88.6021	77.5810
0.372	0.406	342	85.8085	85.6707	77.2831
0.373	0.388	160	86.7432	86.6697	78.0754
0.373	0.392	194	85.9340	85.8583	77.3232
0.374	0.398	154	83.3548	83.2864	78.3489
0.389	0.420	189	83.4916	83.4020	77.7366
0.405	0.427	132	83.9361	83.8758	78.5722
0.405	0.427	141	84.3962	84.3307	78.5513
0.406	0.418	125	86.7969	86.7439	77.4382
0.424	0.454	147	83.0783	83.0107	78.5441
0.424	0.451	144	83.4627	83.4000	78.5359
0.449	0.474	126	83.7434	83.6919	78.6353
0.450	0.478	159	84.2205	84.1640	78.6213
0.467	0.489	168	85.8426	85.7727	77.7502
0.479	0.496	111	84.7781	84.7265	78.5159

noting that the smaller ionic radius of the Cl^- ions may be offset by its stronger associations with surrounding ions due to its larger charge/volume ratio. This dependence of the strength of ion associations on charge/volume ratio may also explain in part the large transport number of the MEI^+ relative to the smaller anions. However, further work, including molecular orbital calculations on the species in the melts and their interactions, is required for an understanding of the actual transport

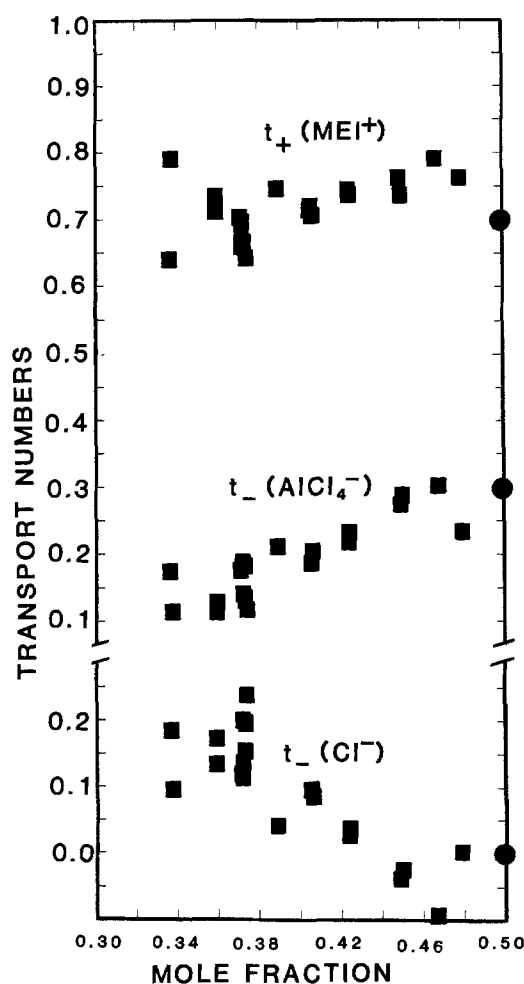


Fig. 5. External transport numbers of the melt species vs. mole fraction $AlCl_3$ in the melt. Squares: Experimental results for modified Hittorf method. Circles: Results for moving boundary method.

Table III. Results from modified Hittorf method experiments

Initial N	$t_+(MEI^+)$	$t_-(AlCl_4^-)$	$t_-(Cl^-)$	t'_R
0.337	0.640	0.175	0.185	0.991
0.338	0.790	0.115	0.096	1.009
0.359	0.735	0.130	0.135	0.979
0.359	0.712	0.115	0.173	0.948
0.371	0.703	0.177	0.120	1.002
0.371	0.700	0.183	0.118	1.006
0.372	0.661	0.140	0.199	0.934
0.372	0.697	0.188	0.115	1.009
0.372	0.677	0.187	0.136	0.995
0.373	0.668	0.136	0.197	0.933
0.373	0.665	0.183	0.153	0.982
0.374	0.643	0.119	0.238	0.899
0.389	0.746	0.212	0.042	1.052
0.405	0.715	0.190	0.095	0.996
0.405	0.719	0.189	0.092	0.997
0.406	0.707	0.205	0.088	1.004
0.424	0.744	0.219	0.037	1.029
0.424	0.739	0.232	0.029	1.038
0.449	0.762	0.276	-0.037	1.071
0.450	0.737	0.288	-0.025	1.063
0.467	0.791	0.303	-0.093	1.099
0.479	0.763	0.235	0.002	1.013

mechanism, and such work is in progress at this laboratory.

Internal transport numbers.—The use of internal transport numbers to relate EMF data from concentration cells using these melts to thermodynamic data was described by Øye and King (3). In their paper on transport numbers in acidic melts, Hussey and Øye (7) reported that the internal transport number of MEI^+ (relative to Cl^- present in the chloroaluminate anions) is 1.00. Their external transport numbers for MEI^+ (t_R) and Al (t_{Al}) can be related to our external transport numbers for MEI^+ and $AlCl_4^-$ as follows

$$t_R = t_+(MEI^+)$$

and

$$t_{Al} = -3[t_-(AlCl_4^-)]$$

We can then use their Eq. [19] to calculate the internal transport number for MEI^+ (t'_R) from our data

$$t'_R = t_R + \frac{1-N}{2N+1}(1-t_{Al}-t_R)$$

The values of t'_R calculated from our data in this way are tabulated in Table III and plotted against N in Fig. 7. The mean value for t'_R in the basic melts we used is 1.00 ± 0.02

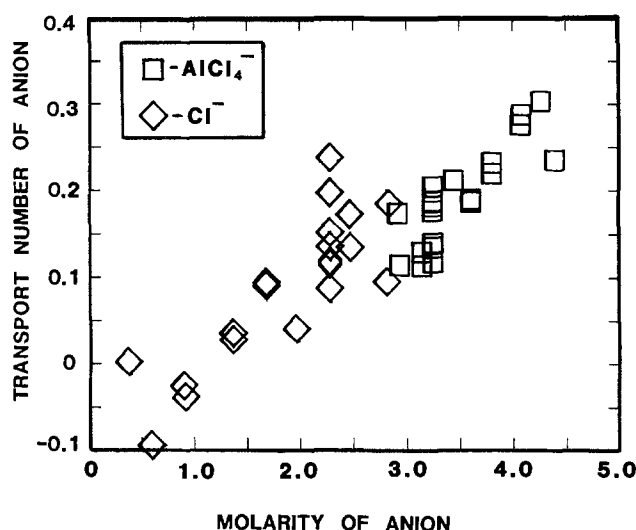


Fig. 6. External transport numbers for Cl^- and $AlCl_4^-$ vs. the molarity of the corresponding anion in the melt.

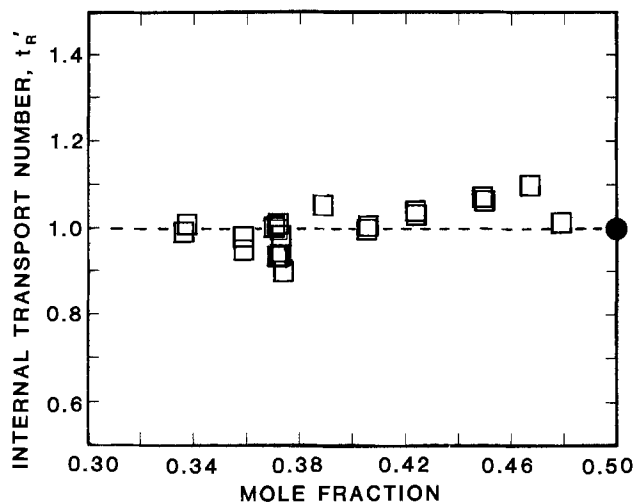


Fig. 7. Internal transport numbers of MEI^+ vs. mole fraction of AlCl_3 in the melt. Open squares: Modified Hittorf method. Circles: Moving boundary method.

(95% confidence limits). It thus appears that, over the entire range in which the $\text{MEICl}/\text{AlCl}_3$ melts are liquid at room temperature ($0.33 < N < 0.67$), the internal transport member for the MEI^+ is 1.00.

Conclusions

The external and internal transport numbers of species in basic and neutral $\text{MEICl}/\text{AlCl}_3$ melts obtained using the two methods reported agree with the values obtained for acidic melts by Hussey and Øye (7). The MEI^+ has external (relative to porous glass disks) and internal (relative to Cl in the melt) transport numbers of 0.70 and 1.00, respectively. The external transport numbers of the anions are roughly proportional to their concentrations in the melts.

Acknowledgments

The authors are grateful to Dr. John S. Wilkes and Dr. Armand A. Fannin, Jr., and to other associates at the Frank J. Seiler Research Laboratory (FJSRL) for many helpful discussions of this work. We are also grateful for the helpful and insightful evaluations of our work by Professors Harald A. Øye and Charles L. Hussey. Mr. Fred Kibler and Mr. Lloyd Pflug of FJSRL provided expert assistance in construction of the cells and in NMR analysis of the melts. Finally, we are grateful to Missy Landess for her expert typing and assistance in editing the manuscript.

Manuscript submitted Nov. 2, 1984; revised manuscript received Jan. 16, 1985.

The Air Force Office of Scientific Research assisted in meeting the publication costs of this article.

REFERENCES

1. G. Torsi and G. Mamantov, *Inorg. Chem.*, **10**, 1900 (1971).
2. L. G. Boxall, H. L. Jones, and R. A. Osteryoung, *This Journal*, **120**, 223 (1973).
3. H. A. Øye and L. A. King, *Inorg. Nucl. Chem. Lett.*, **16**, 547 (1980).
4. D. S. Newman, W. Rohr, and D. Kirklin, *This Journal*, **119**, 797 (1972).
5. R. A. Carpio, L. A. King, R. E. Lindstrom, J. C. Nardi, and C. L. Hussey, *ibid.*, **126**, 1644 (1979).
6. A. A. Fannin, Jr., D. A. Floreani, L. A. King, J. S. Landers, B. J. Piersma, D. J. Stech, R. L. Vaughn, J. S. Wilkes, and J. L. Williams, *J. Phys. Chem.*, **88**, 2614 (1984).
7. C. L. Hussey and H. A. Øye, *This Journal*, **131**, 1621 (1984).
8. J. S. Wilkes, J. A. Levisky, R. A. Wilson, and C. L. Hussey, *Inorg. Chem.*, **21**, 1263 (1982).
9. F. R. Duke and J. P. Cook, *J. Phys. Chem.*, **62**, 1593 (1958).
10. J. S. Wilkes, J. A. Levisky, J. L. Pflug, C. L. Hussey, and T. B. Scheffler, *Anal. Chem.*, **54**, 2378 (1982).
11. C. J. Dymek, Jr., J. L. Williams, D. J. Groeger, and J. J. Auburn, *This Journal*, **131**, 2887 (1984).

Technical Notes



Large-Scaled Polyacetylene Batteries

Takao Nagatomo,* Hidehiko Kakehata, Chiaki Ichikawa, and Osamu Omoto

Shibaura Institute of Technology, Shibaura, Minato-ku, Tokyo 108, Japan

Many detailed investigations on the electronic structure and the physical properties of $(\text{CH})_x$ film have been done since Shirakawa *et al.* proposed the synthetic method in the form of silvery films by a direct polymerization of acetylene on the surface of concentrated soluble catalyst solution in 1974 (1). Polyacetylene, $(\text{CH})_x$ film is the simplest conjugated polymer consisting of parallel chains of CH groups. It has recently been of considerable interest as the electrode active material of secondary batteries, with many superior features: (i) it contains an interwoven network of ca. 200Å $(\text{CH})_x$ fibrils; (ii) the electrical conductivity of $(\text{CH})_x$ films can be varied over 12 orders of magnitude from insulator to metal when suitably doped with donor or acceptor species; (iii) it is very stable chemically; there are other attractive features (2, 3). This battery promises to be lighter and has higher power and energy

densities as compared to conventional batteries such as lead-acid batteries.

We have reported the properties of the polyacetylene batteries (4-6). An $n\text{-(CH)}_x/\text{LiClO}_4 + \text{PC/p-(CH)}_x$ battery was investigated for 2600 charge-discharge cycles, although doping levels were shallow ($y = 0.002$). The maximum energy density obtained was 424 Wh/kg, based on the weight of the electrode active material (both electrodes; ~8 mg) under the charge-discharge conditions of the stored charge of 10.8C and the liberated charge of 4.52C (4-6). In this paper, we describe the charge-discharge characteristics of large-scaled polyacetylene secondary batteries with electrode areas of 20 ~ 54 cm².

The *cis*- $(\text{CH})_x$ films were polymerized by the Shirakawa technique (1). Care was taken to achieve pure $(\text{CH})_x$ starting material through extensive washing to remove all catalyst, with subsequent storage and handling in inert atmosphere to minimize oxygen content. All experiments

*Electrochemical Society Active Member.

for batteries were carried out in the absence of air and moisture in the argon atmosphere of a dry glass vessel as the electrical properties of $(\text{CH})_x$ films degraded on exposure to air and moisture. In our experiments, $(\text{CH})_x$ film on which 1000Å of gold had been evaporated on one side and aluminum foil ($\sim 100 \mu\text{m}$) were employed as the positive and negative electrodes on the doping and charging processes, respectively. Gold wire was attached to one end by pressed mechanical contact, and the $(\text{CH})_x$ with current collector of the evaporated gold film and aluminum foil electrodes were placed at ca. 3 mm distance in a 1.0M solution of LiClO_4 in the mixture of propylene carbonate (PC; 20%) and ethylene carbonate (EC; 80%) through a glass filter. The *cis*- $(\text{CH})_x$ film used as the electrode active material had the film thickness of 50 ~ 100 μm and the areas of 10 ~ 27 cm^2 . The battery was comprised of two $(\text{CH})_x$ cathodes and one Al anode, arranged in an alternating fashion with Al forming the inner electrode in the stack. Two types of batteries were fabricated for use in these studies: the first had a cathode area of 20 cm^2 (2 cm width \times 5 cm length \times 2 sides); the second had a cathode area of 54 cm^2 (3 cm width \times 9 cm length \times 2 sides). If the $(\text{CH})_x$ film and Al foil electrodes were attached to the positive and negative terminals, respectively, of a battery or dc power source (ca. 3.8V), perchlorate ions diffused into the positive electrode in a manner analogous to the way one would dope a semiconductor and lithium ions deposited on the negative electrode. The extent of doping was calculated from the weight of the $(\text{CH})_x$ film employed and the number of coulombs passed.

The course of the cell voltage of a $\text{p}(\text{CH})_x/\text{LiClO}_4 + \text{PC} + \text{EC}/\text{Al}$ battery during charge and discharge is illustrated in Fig. 1. These batteries had a cathode area of 20 cm^2 . A 1.0M solution of LiClO_4 in the mixture of propylene carbonate (PC; 20%) and ethylene carbonate (EC; 80%) was used as the electrolyte. These batteries were charged at constant currents of 10, 15, and 20 mA for 10 min and discharged at constant currents of 10, 15, and 20 mA to 2.5V immediately after charging, respectively. These charge and discharge rates in amperes per kilogram of $(\text{CH})_x$ (35 mg) are 286, 429, and 571, respectively. In these conditions, the charging voltage was gradually raised with an increase in charging current and was in excess of 4.5V at the charging current of 20 mA. The coulombic and power

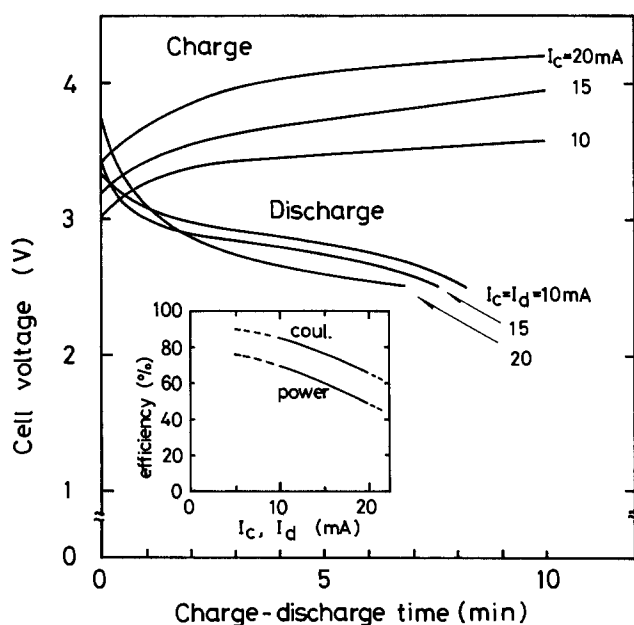


Fig. 1. The course of the cell voltage of $\text{p}(\text{CH})_x/\text{LiClO}_4 + \text{PC} + \text{EC}/\text{Al}$ battery with a cathode area of 20 cm^2 during charging and discharging as a parameter of charge and discharge currents. Charge and discharge rates of $(\text{CH})_x$ (35 mg): 10 mA, 286 A/kg; 15 mA, 429 A/kg; 20 mA, 571 A/kg. The inset shows the coulombic and power efficiencies vs. the charging and discharging currents.

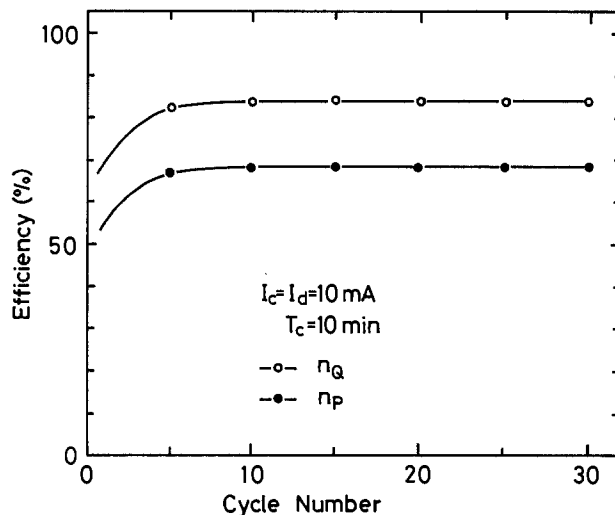


Fig. 2. The coulombic (η_c) and power (η_p) efficiencies of the charge-discharge cycle of $\text{p}(\text{CH})_x/\text{LiClO}_4 + \text{PC} + \text{EC}/\text{Al}$ battery with a cathode area of 20 cm^2 . Charge and discharge conditions: charging at 10 mA (286 A/kg) for 10 min; discharging at 10 mA to 2.5V.

efficiencies vs. the charging and discharging currents are illustrated in the inset. The coulombic and power efficiencies of charge-discharge cycle decreases with an increase in the charging and discharging currents. The loss of charge becomes gradually large, and can be caused by the chemical reaction of the electrolyte or by the reaction of impurities in the electrolyte with $[\text{CH}^+(\text{ClO}_4)_y]^-$ and Al, and by the degradation of $(\text{CH})_x$ and the decomposition of the organic solvent due to the excess amounts of charge and the large charging voltage. In addition, the loss of charge can be caused by the insufficient extraction of charge during the discharge to 2.5V. The problems of the degradations of $(\text{CH})_x$, such as the cross-linking reaction and the replacement of $(\text{CH})_x$ due to charging and discharging processes, and of the decomposition of the solvent are the subjects for a future study.

The coulombic (η_c) and power (η_p) efficiencies of the charge-discharge cycle of $\text{p}(\text{CH})_x/\text{LiClO}_4 + \text{PC} + \text{EC}/\text{Al}$ battery are shown in Fig. 2. This battery was charged and discharged for 30 cycles, each cycle consisting of a 10 min charge at 10 mA (286 A/kg) and a discharge at 10 mA to 2.5V. The coulombic and power efficiencies were 83 and 69%, respectively. No degradation of the charge-discharge characteristics was observed even after 30 successive charge-discharge cycles. This battery has a cathode area of 20 cm^2 as aforesaid. Although this battery had a cathode area ten times as large as that of the 2 cm^2 polyacety-

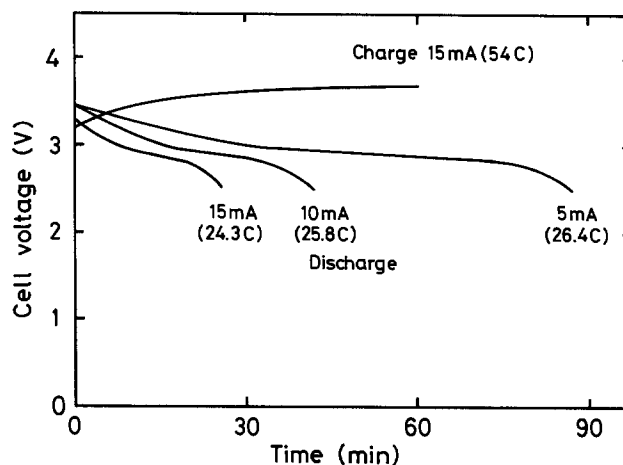


Fig. 3. The course of the cell voltage of $\text{p}(\text{CH})_x/\text{LiClO}_4 + \text{PC} + \text{EC}/\text{Al}$ battery with a cathode area of 54 cm^2 as a parameter of discharging current.

lene battery, the characteristics of the battery were by no means inferior to the 2 cm² battery.

The course of the cell voltage of the polyacetylene battery with a cathode area of 54 cm² during discharging is illustrated in Fig. 3 as a parameter of discharging current. These polyacetylene batteries were initially charged at 15 mA for 60 min (54C, doping level $y = 13.7\%$) and discharged at constant currents of 5, 10, and 15 mA to 2.5V immediately after charging. These discharge rates, in amperes per kilogram of (CH)_x (94.5 mg) are 52.9, 105.8, and 158.7, respectively. The energy density values obtained were: 5 mA, 114 Wh/kg; 10 mA, 110 Wh/kg; and 15 mA, 100 Wh/kg when the battery was discharged to 2.5V. As compared with the charge-discharge characteristics of 2 cm² polyacetylene battery, there was no significant difference between large-scaled polyacetylene battery (cathode area of 54 cm²) and 2 cm² battery. The coulombic efficiencies for the 5, 10, and 15 mA discharges in Fig. 3 are 48.7, 47.8, and 45.0%, respectively. As compared with the charge in short time (10 min) as shown in Fig. 1, the coulombic efficiencies are extremely low. This could be because, as charging time becomes longer, the (ClO₄)⁻ ions diffuse into the interior of the (CH)_x fibrils and the (CH)_x film. It is difficult to release completely their ions diffused into the interior of the (CH)_x fibrils and the (CH)_x film during discharging to 2.5V (6, 7).

Compared to conventional batteries, such as lead-acid battery, the polyacetylene secondary battery promises to be lighter and has high power density and energy density. However, there are several problem areas that must be resolved before use of polyacetylene electrode becomes a reality. Especially, although we did not deal with the polymer salt solvent combinations, these are serious problems. Further work is needed in this area. There is no significant difference between the charge-discharge characteristics of large-scaled polyacetylene battery (cath-

ode area of 54 cm²) and that of 2 cm² battery as mentioned above. Consequently, we consider that scaling up of the battery is not a serious problem.

Acknowledgment

This work was supported by a Grant-in-Aid for Scientific Research from the Hoso-Bunka Foundation of Japan.

Manuscript submitted Sept. 6, 1984; revised manuscript received Jan. 30, 1985.

Shibaura Institute of Technology assisted in meeting the publication costs of this article.

REFERENCES

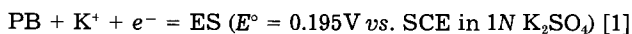
1. T. Ito, H. Shirakawa, and S. Ikeda, *J. Polym. Sci., Polym. Chem. Ed.*, **12**, 11 (1974).
2. P. J. Nigrey, D. MacInnes, Jr., D. P. Nairns, A. G. MacDiarmid, and A. J. Heeger, *This Journal*, **128**, 1651 (1981).
3. C. K. Chiang, Y. W. Park, A. J. Heeger, H. Shirakawa, E. J. Louis, and A. G. MacDiarmid, *J. Chem. Phys.*, **69**, 5098 (1978).
4. H. Seita, T. Honma, C. Yamamoto, T. Nagatomo, and O. Omoto, Reprint of the Meeting of Technical Group on Component Parts and Materials, IECE of Japan, CPM 81-70 (in Japanese) December (1981); K. Negishi, C. Yamamoto, T. Honma, T. Nagatomo, and O. Omoto, Reprint of the Meeting of Technical Group on Component Parts and Materials, IECE of Japan, CPM 82-65 (in Japanese) December (1982).
5. T. Nagatomo, T. Honma, C. Yamamoto, K. Negishi, and O. Omoto, *Jpn. J. App. Phys.*, **22**, L275 (1983).
6. T. Nagatomo, K. Negishi, H. Kakehata, and O. Omoto, in "Advances in Battery Materials and Processes," J. McBreen, D.-T. Chin, R. S. Yao, and A. C. C. Tseung, Editors, p. 34, The Electrochemical Society Softbound Proceedings Series, Pennington, NJ (1984).
7. T. Nagatomo, K. Negishi, H. Kakehata, and O. Omoto, *Trans. IECE Jpn.*, **J67-C**, 413 (1984).

Some Performance Characteristics of a Prussian Blue Battery

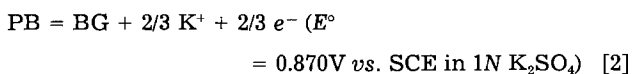
Vernon D. Neff

Department of Chemistry and the Liquid Crystal Institute, Kent State University, Kent, Ohio 44242

In the past, we (1-3) and Itaya *et al.* (4-6) have reported some of the thermodynamic and kinetic characteristics of the electrochemical oxidation and reduction of thin films of Prussian blue (PB) on various substrates. The purpose of this note is to point out the feasibility and to determine some preliminary performance characteristics of a Prussian blue battery. If PB is deposited on a substrate under controlled conditions, it is possible to reduce it to Everitt's salt (ES) according to (2)



or oxidize to Berlin green (BG) according to



In reaction [2] a definite compound is formed when only two-thirds of the ferrocyanide ions in the PB lattice have been oxidized (2). According to the voltammograms, a second oxidation occurs at ca. 1.1V vs. SCE and a yellow film is formed. We shall not be concerned with this second oxidation since the electrochemistry is not well understood and the film gradually deteriorates at potentials above 1.2V.

It is apparent that the two half-cells above could be combined to make a PB battery which, in the uncharged state, would consist of PB as both anode and cathode. The cell reaction would be



with a theoretical voltage of 0.68V.

An obvious disadvantage is the low energy density of such a cell. A pure PB electrode, based on the stoichiometric formula KFeFe(CN)₆, would have an energy density of only 95 mWh/cm³. Even so, there are good reasons for considering such a cell. First of all, the reactions [1] and [2] above are highly reversible (3). Second, the energy density, though small, is about five times greater than that for 1M redox couples in solution (such as the iron-chromium couple) which are being considered for off-peak power storage. Another advantage is that the PB cell requires no separator as do the redox solution cells. Finally, there is the advantage of the high chemical stability of these mixed valence hexacyanides in acid solutions. Judging from our experience (2) and that of others (7) concerning the cycling of carefully prepared thin films, it should be possible to develop a cell which is essentially indefinitely rechargeable.

Experimental

The electrodes consisted of PB electrochemically deposited on highly porous graphite. The graphite (PG-60) was obtained from the Union Carbide Corporation. This material has a density of ca. 1.2 g/cm³. The graphite was cut into blocks 2.5 × 2.5 × 0.6 cm with a volume of 3.75 cm³. The leads into the substrate electrodes were made

from 1/8 in. graphite rods press fit into holes drilled into the graphite blocks.

All chemicals used were reagent grade, and triply distilled water was used throughout. The deposition of PB was carried out from rapidly stirred 1 liter solutions which were 0.01M in $\text{Fe}_2(\text{SO}_4)_3$, $\text{K}_3\text{Fe}(\text{CN})_6$, H_2SO_4 , and 0.1M in K_2SO_4 . Since these bright red solutions are unstable over time, and gradually form a green suspension, they were replaced at 3h intervals. The PB was deposited at constant current of 1 mA with a PAR Model 173 potentiostat. The electrodes were removed periodically and drained on filter paper. During this process, a considerable amount of nonadherent PB came out of the electrodes. Deposition times varied from several hours to several days. After deposition, the electrodes were flushed extensively with 0.01N H_2SO_4 solution and finally with water and were allowed to dry in air for several days.

The amount of active PB on the electrodes was determined from the constant-voltage charging curves. Cathodes were prepared which had approximately one-third more PB (as determined by weighing) than the anodes. The electrodes were inserted in a 100 ml closed cell which could be purged with deoxygenated nitrogen. The cells were charged with a Sola OSV constant-voltage power supply. Cells were tested which had capacities varying between 10 and 40 mAh. The main cell characteristics studied were constant-voltage charging curves, discharge under constant load, and discharge at constant current. Preliminary measurements of voltage retention in the presence and absence of oxygen were also carried out.

Results and Discussion

In terms of oxidation and reduction, the mixed valence transition-metal hexacyanides which have been studied to date behave like solid solutions (2, 3, 8). In this sense, they most closely resemble redox polymeric films like the vinylferrocenes (9). It is instructive to consider the thermodynamic potential of the PB cell as a function of the amount (mole fraction) of PB in the electrodes. We have previously shown that, for the oxidation of PB to BG, the solid solution is approximately ideal so that activities can be set equal to mole fractions. This is apparently not the case for the reduction of PB to ES (2). For carefully prepared thin films, the voltammograms for the reduction are very sharp in 1N potassium ion solutions. One possible explanation of this observation is based on the assumption of a regular solution where the activity of PB is given by (2)

$$\alpha(\text{PB}) = x \exp W(1 - x^2)/RT \quad [4]$$

and that for ES is given by

$$\alpha(\text{ES}) = (1 - x) \exp Wx^2/RT \quad [5]$$

where W is a repulsive energy and x is mole fraction of PB. The general expression for the thermodynamic potential according to Eq. [3] would be

$$E = 0.68 - \frac{RT}{F} \ln \frac{\alpha(\text{PB, anode}) \alpha(\text{PB, cathode})^{3/2}}{\alpha(\text{ES}) \alpha(\text{BG})^{3/2}} \quad [6]$$

Substituting Eq. [4] and [5] for the activities at the anode, and setting activities equal to mole fraction x for ES and $(1 - x)$ for BG at the cathode, we can plot the thermodynamic potential for the discharge of the PB battery, as shown as the solid curve in Fig. 1. For this calculation, the repulsive energy parameter w/RT was set equal to 1.72, which was the value obtained for thin PB films on a platinum substrate (2). The solid circles in Fig. 1 represent the experimental cell voltage for the discharge of a 30 mAh cell at constant current of 1 mA in 1N K_2SO_4 . For these data, the mole fraction x of PB at time t was determined from $x = t/(t_d - t)$, where t_d is the time for complete discharge. Finally, the dashed curve in Fig. 1 represents the calculated potential for a cell in which activities are set equal to mole fractions for both anode and cathode. It is seen that the experimental cell voltages fall between the

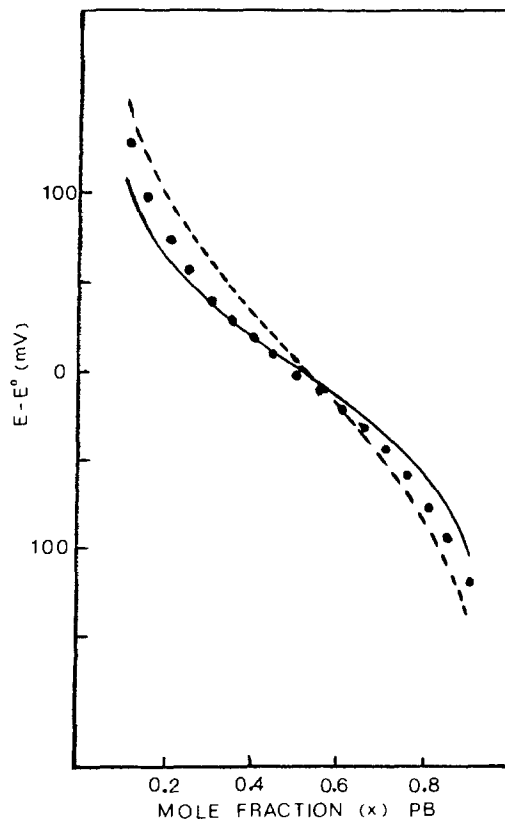


Fig. 1. Solid curve: Calculated difference in potential $E - E^\circ$ as a function of mole fraction x of PB. The ES at the anode is assumed to behave as a regular solid solution with repulsive interaction $W/RT = 1.72$. Dashed curve: Calculated potential difference as a function of mole fraction assuming that both anode and cathode behave as ideal solid solutions. Solid circles: Experimental cell voltage minus E° for the constant current discharge of a 30 mAh capacity PB cell in 1N K_2SO_4 solution. The current was maintained as 1 mA, and the mole fraction x of PB was determined from $t/(t_d - t)$, where t is time and t_d is the time for complete discharge. $E^\circ = 0.68\text{V}$.

two calculated curves, indicating a situation intermediate between the thin film behavior and that for ideal solid solutions. The experimental data clearly illustrate the nernstian behavior and the highly reversible nature of the cell reactions. The underpotential at $x = 0.5$ is only ca. 10 mV below the theoretical value.

In Fig. 2, we have shown the constant voltage charging curve for a 30 mAh capacity cell in 1N K_2SO_4 solution. Under rapid charge, the electrode is subject to the combined effects of ohmic, concentration, and diffusion polarization. From the current in the initial stages of charge, the total ohmic resistance is estimated to be only ca. 3 Ω . The low initial resistance is attributed to the fact that the PB on the outside surface of the electrode is the first to react. Sectioning of the porous carbon showed a distinct gradient in the amount of PB from the outside of the electrode inward. Figure 2 indicates that, as charging proceeds, the current is dominated by the diffusion process. The diffusion process is complicated by the nature of the porous electrodes and by the fact that potassium ions must migrate into or out of the solid PB as well as in the solution. The curve appears to be more exponential than cottrellian, indicating that the diffusion in the PB, rather than in solution, is the primary limiting factor (3). When the cell is charged rapidly at potentials of 1V or greater, a yellow color develops gradually around the anode. The yellow color does not occur under conditions where the cell is charged slowly, and the current does not exceed 5 mA.

We also made some preliminary measurements with regard to the retention of charge. For good charge retention, it is necessary to exclude oxygen from the cell and to make sure that electrodes are well flushed of impurities.

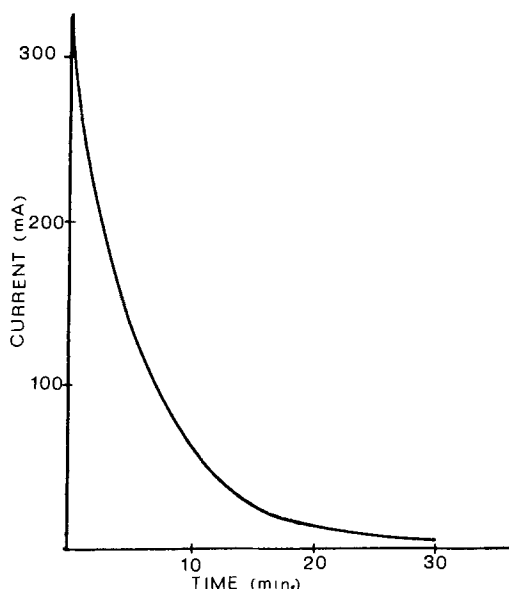


Fig. 2. Constant voltage charging curve at 1.0V for a 30 mAh capacity PB cell in unstirred 1N K_2SO_4 solution.

We epoxy sealed a purged cell with a Lucite cap and slowly charged it to 1.0V. There was an initial voltage drop which leveled out to 0.93V within a few hours and remained constant for 10 days (the duration of the test). A second cell was charged to 1.0V and left open to the air. The voltage dropped to 0.74V within 24h. In this case, the voltage dropped due to the presence of molecular oxygen which reacts chemically with ES to form PB (2). Adsorbed ferric ions will also react with ES.

In these preliminary studies, we make no pretense with regard to having optimized conditions for a practical PB battery. One of the major problems we have encountered is the adherence of the PB deposit on the carbon substrate. In all cases, we observed a gradual loss of PB from

the electrodes after repetitive charging cycles. The PB comes out of the electrodes as a finely dispersed sol. The average rate of loss was ca. 5% capacity per cycle. The nature of the deposition reaction and the conditions for good adherence of the PB deposit are, at present, not well understood (2, 7). It is also obvious that a much more heavily loaded graphite or other substrate should be developed.

Finally, we should point out that it is not necessary to construct both electrodes from PB. There are a large number of insoluble, chemically stable, transition-metal hexacyanides which have not been studied electrochemically. For example, we have recently synthesized manganese blue films $[KFeMn(CN)_6]$ which can be electrochemically reduced to a colorless state at $-0.25V$ vs. the SCE. The details of this reaction will be discussed in a later communication.

Acknowledgment

The author wishes to acknowledge the Union Carbide Corporation for furnishing samples of porous carbon.

Manuscript received Oct. 24, 1984.

Kent State University assisted in meeting the publication costs of this article.

REFERENCES

1. V. D. Neff, *This Journal*, **125**, 886 (1978).
2. D. Ellis, M. Eckhoff, and V. D. Neff, *J. Phys. Chem.*, **85**, 1225 (1981).
3. K. P. Rajan and V. D. Neff, *ibid.*, **86**, 4361 (1982).
4. K. Itaya, H. Akahoshi, and S. Toshima, *This Journal*, **129**, 1498 (1982).
5. K. Itaya, T. Ataka, and S. Toshima, *J. Am. Chem. Soc.*, **104**, 4767 (1982).
6. K. Itaya, K. Shibayama, H. Alahoshi, and S. Toshima, *J. Appl. Phys.*, **53**, 804 (1982).
7. H. Kellawi and D. R. Rosseinsky, *J. Electroanal. Chem.*, **131**, 373 (1982).
8. L. M. Siperko and T. Kuwana, *This Journal*, **130**, 396 (1983).
9. A. Merz and A. J. Bard, *J. Am. Chem. Soc.*, **100**, 3222 (1978).

Direct Observation of Voids and Cracks in the Barrier Oxide Layer of Composite Aluminum Oxide Films

K. Shimizu* and K. Kobayashi

Department of Chemistry, Faculty of Science and Technology, Keio University, 3-14-1 Hiyoshi, Yokohama 223, Japan

Composite aluminum oxide films, formed by the sequential process of the reaction with boiling water followed by anodic oxidation, have been widely used in the fabrication of electrolytic capacitors because of their excellent dielectric properties (1, 2). However, the barrier oxide layer of the composite oxide films frequently exhibits an electrical instability: losing the ability to sustain the original anodizing voltage after anodization. A reformation is needed to restore the barrier oxide to its original state. In an investigation of the electrical instability of the composite oxide films, Alwitt and Dyer (3) suggested that the instability is an intrinsic property of the films that arises from the presence, in the barrier oxide layer, of internal voids or cracks into which water can diffuse when the formation field is removed. A considerable amount of circumstantial evidence (4-6) has been accumulated supporting the mechanism proposed by Alwitt and Dyer. It was hoped that the presence of voids and cracks could be verified independently and directly. Thus, an attempt has been made, by Alwitt *et al.* (7), to detect the voids and cracks by transmission electron microscopy of

the stripped and subsequently ion beam thinned composite oxide films using defocus contrast. Phase objects have been observed in the barrier oxide layer of the composite oxide films and explained as representing discrete voids or cross sections of cracks which are thought to be responsible for the electrical instability of the composite oxide films.

Here, transmission electron microscopy of ultramicrotomed sections has been employed to reveal clearly the existence of voids and cracks in the barrier oxide layer of the composite oxide films.

Electropolished superpure aluminum sheets of dimensions of $50 \times 10 \times 0.2$ mm were immersed in boiling distilled water for 5 min and subsequently anodized to 300V in 0.1M ammonium pentaborate solution at 298 K with a constant current density of $50 A m^{-2}$.

Ultramicrotomed sections of the aluminum substrate and the composite oxide films were prepared in the now usual manner using a du Pont Sorvall MT2B ultramicrotome (8). In short, encapsulated specimens were trimmed initially with a glass knife and suitably thin sections, between 25-50 nm, were obtained finally by sectioning in a direction parallel to the metal/oxide interface with a dia-

*Electrochemical Society Active Member.

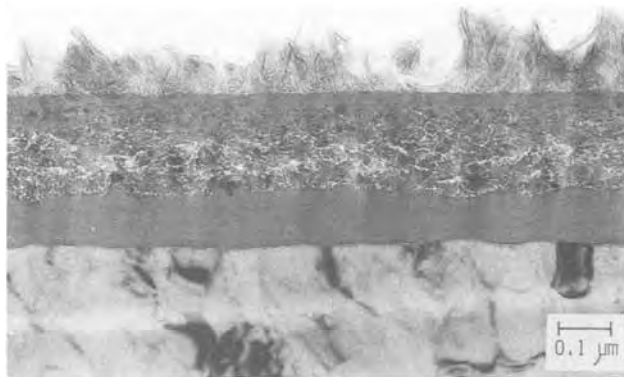


Fig. 1. Transmission electron micrograph of a cross section of the 300V composite oxide film.

mond knife. Ultramicrotomed sections obtained were examined in a Hitachi HU-12AS transmission electron microscope operated at 100 kV.

Transmission electron micrograph of an ultramicrotomed section of the aluminum substrate and the composite oxide film formed to 300V is shown in Fig. 1. The aluminum substrate is observed at the bottom of the micrograph and shows the darker bands or extinction contours that diffract at that particular orientation to the electron beam. Residual hydrous oxide layer is observed at the top of the micrograph as a fibrillar layer of varying thickness.

A barrier oxide layer separating the aluminum substrate and the residual hydrous oxide is clearly observed. The total thickness of the barrier oxide layer is about 290 nm, representing a nanometer-to-volt ratio of 0.97, which is considerably smaller than the 1.18 reported for conventional barrier anodic films formed under similar conditions (9). Within the barrier oxide, an amorphous layer between 70 and 110 nm thick is observed next to the metal. A crystalline region is present adjacent to the amorphous layer and is observed to extend near to the barrier/hydrous oxide interface. An electron diffraction analysis made recently by Alwitt *et al.* (7) has shown that the crystalline oxide within the barrier oxide layer of the composite oxide films formed under a condition similar to ours is γ' - Al_2O_3 . Numerous discrete voids, a few nanometers in diameter, and a network of fine cracks, a few nanometers wide, are observed clearly within the γ' -crystalline region. The voids and cracks could well be artifacts introduced during the sectioning. Our experiences in the ultramicrotomy indicate, however, that the cracks introduced during the sectioning appear generally as lines of differing widths running approximately perpendicular to the direction of the sectioning. In the present case, the

cracks introduced during the sectioning should appear as vertical cracks, since the direction of the sectioning is approximately parallel to the metal/oxide interface. No such cracks are readily apparent in the γ' -crystalline region of the composite oxide barrier layer. Therefore, our view is that the voids and cracks represent largely genuine features, although it is difficult to exclude totally the possibility that the original features of the voids and cracks might have been distorted to some extent during the sectioning operation.

It is interesting to note that the γ' -crystalline region, containing voids and cracks, is seen to be separated from the hydrous oxide layer by a thin barrier oxide layer, about 20 nm thick, which is not penetrated by the cracks and appears relatively featureless. The thin barrier oxide layer appears to prevent the penetration of water into the voids and cracks in the γ' -crystalline region and to also prevent the escape of O_2 gases known to be trapped within the voids and cracks under an extremely high pressure or even as a condensed state (5, 6).

In the fabrication of aluminum electrolytic capacitors, freshly anodized foils are usually given a short-time immersion in a boiling distilled water and then reanodized to the original anodizing voltage to obtain the composite oxide films of stable electrical property. It is readily understood that the role of the boiling water treatment prior to the reformation is to accelerate the complete conversion of the thin protective barrier oxide layer, separating the γ' -crystalline region and hydrous oxide into a nonprotective porous hydrous oxide.

Acknowledgment

Thanks are due to Dr. Y. Fukuda and Dr. T. Fukushima of the National Research Institute for Metals for the provision of time on the du Pont Sorvall MT2B ultramicrotome.

Manuscript submitted Jan. 5, 1985; revised manuscript received Feb. 11, 1985.

Keio University assisted in meeting the publication costs of this article.

REFERENCES

1. R. S. Alwitt, *This Journal*, **114**, 843 (1967).
2. W. J. Bernard, *ibid.*, **124**, 403C (1977).
3. R. S. Alwitt and C. K. Dyer, *Electrochim. Acta.*, **23**, 355 (1978).
4. W. A. Lanford, R. S. Alwitt, and C. K. Dyer, *This Journal*, **127**, 405 (1980).
5. W. J. Bernard and P. G. Russell, *ibid.*, **127**, 1256 (1980).
6. C. Crevecoeur and H. J. deWitt, Paper 174 presented at the Electrochemical Society Meeting, Seattle, Washington, May 21-26, 1978.
7. R. S. Alwitt, C. K. Dyer, and B. Noble, *This Journal*, **129**, 711 (1982).
8. R. C. Furneaux, G. E. Thompson, and G. C. Wood, *Corros. Sci.*, **18**, 835 (1978).
9. A. C. Harkness and L. Young, *Can. J. Chem.*, **44**, 2409 (1966).

In Situ X-Ray Diffraction of Surface Layers on Lithium in Nonaqueous Electrolyte

Gholamabbas Nazri* and Rolf H. Muller*

Lawrence Berkeley Laboratory, Materials and Molecular Research Division, Berkeley, California 94720

X-ray diffraction, combined with electrochemical techniques, has been used for the *in situ* identification of materials on electrode surfaces based on their crystal structure during the progress of electrochemical reactions. This approach avoids some long-recognized problems of *ex situ* measurements, which may not represent the na-

*Electrochemical Society Active Member.

ture of electrode materials because changes can occur upon transfer out of the electrochemical environment, when potential control is not possible (1-3). The combination of different *in situ* techniques has been reviewed by several authors (4-8).

Previous studies with x-ray diffraction from electrodes includes work by Salkind *et al.* (9), who obtained x-ray

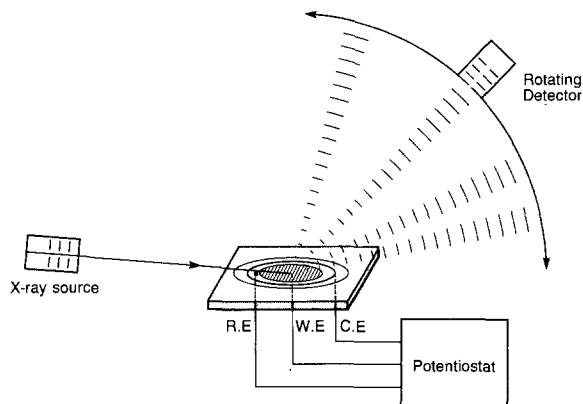


Fig. 1. Arrangement for combined electrochemical technique and x-ray diffractometer for *in situ* x-ray diffraction. X-ray source: Cu $K\alpha$ with Ni filter. The angle of incident x-ray beam with the electrode surface was 6° . Working electrode (WE), counterelectrode (CE) and reference electrode (RE) were connected to a potentiostat for electrochemical studies.

patterns of iron electrodes during cycling in alkali using sealed polyethylene bags. Salkind and Bruins used *in situ* x-ray diffraction to study the Ni electrode in Ni-Cd cells during charge and discharge (10). Falk determined x-ray diffraction patterns of submerged positive and negative electrodes of Ni-Cd cells during charge and discharge (11). Recently, Fleischmann *et al.* used a position-sensitive proportional counter as x-ray detector to study the UPD of Pb on Ag and the adsorption of I_2 on graphite (12, 13). Fleischmann's work indicates that, with use of a sensitive detector, x-ray diffraction is capable to determine diffraction from a monolayer. Unlike LEED, Auger, and ESCA, for which the electrode must be removed

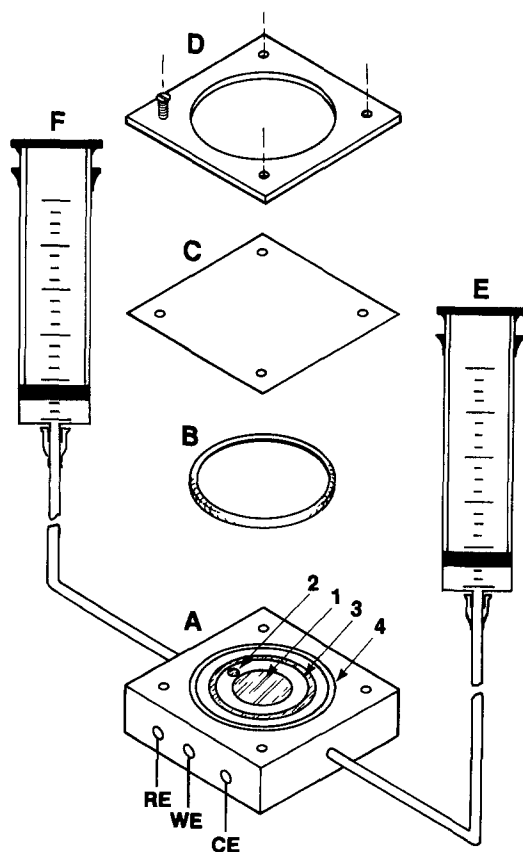


Fig. 2. Electrochemical cell for *in situ* x-ray diffraction. A: Cell body, polypropylene. RE: reference electrode. WE: working electrode. CE: counterelectrode. Leads connected to potentiostat. 1: Working electrode with Li deposited on Ni 1.9 cm diam. 2: Li reference electrode, 0.3 cm diam. 3: Li counterelectrode, 0.3 cm wide. 4: Groove for O-ring. B: O-ring. C: Polyethylene window. D: Cu washer. E: Syringe for electrolyte delivery to cell. F: Syringe for electrolyte removal from cell.

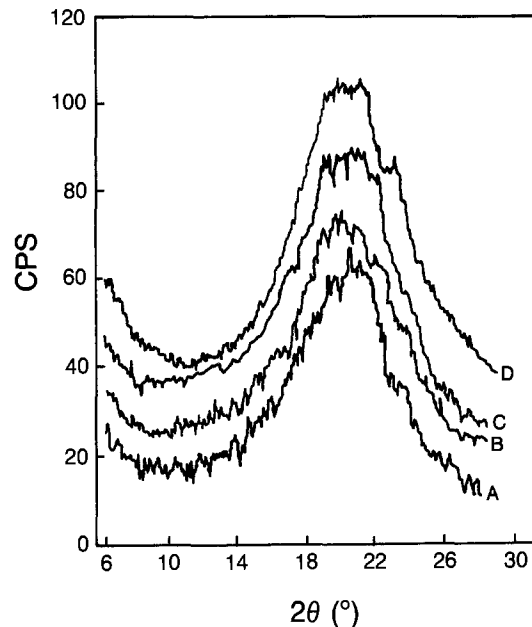


Fig. 3. *In situ* x-ray diffraction from the surface layer formed on Li electrochemically deposited on a Ni substrate at 1 mA/cm^2 , observed during deposition after (A) 5 min, (B) 10 min, (C) 15 min, and (D) 20 min. Electrolyte PC, $1.5M \text{ LiClO}_4$. Peak indicative of polymer formation.

from the electrochemical environment and exposed to ultrahigh vacuum, the specimen can remain under electrochemical control during *in situ* x-ray diffraction. Another *in situ* x-ray technique is represented by the use of high intensity beams, usually provided by an electron storage ring for EXAFS electrode studies (14). EXAFS is able to provide information on short-range order such as distance and number of nearest neighbors and is particularly useful for amorphous compounds and clusters with short-range order.

In this work, *in situ* x-ray diffraction, using a conventional x-ray source and detector, has been applied to the

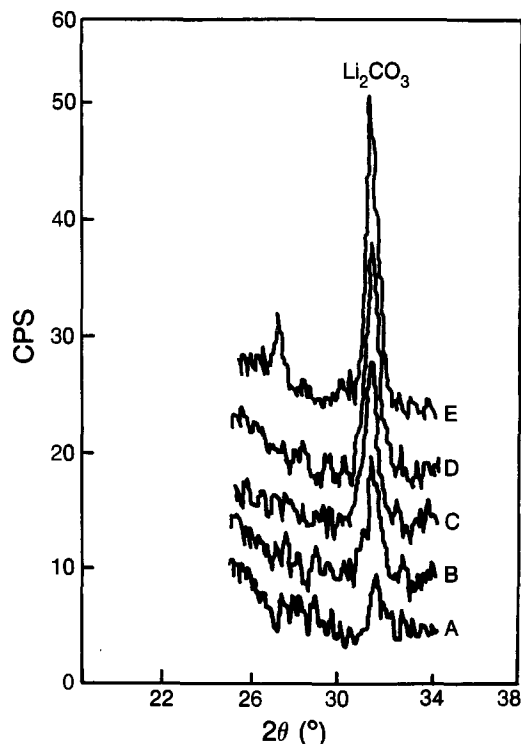


Fig. 4. *In situ* x-ray diffraction from the surface layer formed on Li electrochemically deposited on a Ni substrate observed during deposition, after (A) 5 min, (B) 10 min, (C) 15 min, (D) 20 min, (E) 25 min. Peak indicative of Li_2CO_3 formation.

study of surface layers formed on lithium in nonaqueous electrolytes. The properties of these surface layers are important for the charge and discharge behavior of lithium electrodes in ambient-temperature batteries. Because of the high reactivity of lithium, use of *in situ* techniques for the characterization of surface layers is essential.

Experimental

The arrangement for *in situ* x-ray diffraction from electrode surfaces is illustrated in Fig. 1. A commercial diffractometer (Siemens Model D500) has been used. A collimated x-ray beam is directed toward the electrode surface at a fixed, glancing angle (6° from the surface), and the diffracted x-rays are measured by a rotating detector. In contrast to traditional x-ray diffraction, in which sample and detector are rotated, this arrangement enhances sensitivity for the surface region, although it does not detect monolayer films. The cell containing the electrode is shown in more detail in Fig. 2. The cell body was made of polypropylene and contained the working electrode of 1.9 cm diam in the center, surrounded by a 3 mm wide counterelectrode. A lithium reference electrode of 3 mm diam was located between working and counterelectrodes. Electrolyte could be injected and removed from the cell by the use of two syringes, which were connected to the cell with Teflon spaghetti tubing. Electrodes and electrolyte were separated from the atmosphere by a polyethylene or Mylar window 0.3 mm thick. The x-ray beam enters and exits through this window, which is sealed by use of an O-ring and a washer.

The cell is assembled in an inert atmosphere box where the nonaqueous solution (1.5M LiCl₄ in propylene carbonate) is also prepared. Permeation of water through the cell window in air over the time of the measurements was found to be negligible (no change in water concentration observed by cyclic voltammetry) (15, 16).

Results and Discussion

Results are illustrated by the formation of surface layers on lithium during its cathodic deposition at 1 mA/cm² from 1.5M LiClO₄ on a nickel substrate. Figure 3 shows a broad peak at low diffraction angle (20°), which is characteristic of polymeric compounds. This peak cannot be caused by adsorbed electrolyte because the present arrangement is not sensitive to monolayers. Also, the peak remains after evaporation of the electrolyte in vacuum. Figure 4 shows the much sharper diffraction peak characteristic of lithium carbonate. Both peaks increase with time. The identification of the two film materials agrees with earlier analyses by IR spectroscopy, SIMS, and ESCA (17). In the presence of trace amounts of water, the formation of Li₂O has also been observed. Use of a position-sensitive x-ray detector would make it possible to detect monolayer films and to collect diffraction data on a millisecond time scale, which would be of interest for mechanistic studies of nucleation, film formation,

and phase transformation during the application of potential or current pulses (18-21).

Acknowledgment

This work was supported by the Assistant Secretary for Conservation and Renewable Energy, Office of Energy Systems Research, Energy Storage Division of the U.S. Department of Energy under Contract no. DE-AC03-7600098.

Manuscript submitted Aug. 6, 1984; revised manuscript received Jan. 10, 1985.

Lawrence Berkeley Laboratory assisted in meeting the publication costs of this article.

REFERENCES

1. Gh. Nazri, B. D. Cahan, K. Kuroda, E. Yeager, and T. E. Mitchell, Abstract 5, p. 7, The Electrochemical Society Extended Abstracts, Vol. 82-1, Montreal, Canada, May 9-14, 1982.
2. W. E. O'Grady, *This Journal*, **127**, 555 (1980).
3. H. Shimizu, M. Ono, and K. Nakayama, *Surf. Sci.*, **36**, 817 (1973).
4. R. H. Muller, *Electrochim. Acta*, **22**, 951 (1977).
5. R. Miles, *Surf. Interface Anal.*, **5**, 43 (1983).
6. W. R. Heinman, *Anal. Chem.*, **50**, 390A (1978).
7. E. Yeager, R. Kötzt, and Gh. Nazri, Abstract 354, p. 883, The Electrochemical Society Extended Abstracts, Vol. 81-1, Minneapolis, MN, May 10-15, 1981.
8. G. Blondeau and E. Yeager, *Prog. Solid State Chem.*, **11**, 153 (1976).
9. A. J. Salkind, C. J. Venuto, and S. Uno Falk, *This Journal*, **111**, 493 (1964).
10. A. J. Salkind and P. F. Bruins, "Investigation of the Sintered Plate Nickel-Cadmium Battery," Final Report, Sandia Corp., Nov. 1955-Feb. 1958, Polytechnic Institute of Brooklyn, Brooklyn, NY (1958).
11. S. Uno Falk, *This Journal*, **107**, 661 (1960).
12. M. Fleischmann, P. Graves, I. Hill, A. Oliver, and J. Robinson, *J. Electroanal. Chem.*, **150**, 33 (1983).
13. M. Fleischmann, P. J. Hendra, and J. Robinson, *Nature*, **288**, 152 (1980).
14. L. Bosio, R. Cortes, A. Defrain, M. Fromont, and C. Pallotta, Paper A8-26 presented at the International Society of Electrochemical Meeting, Berkeley, CA, Aug. 5-10, 1984.
15. B. Barrows and S. Kirkland, *This Journal*, **115**, 1164 (1968).
16. S. Sahami and R. A. Osteryoung, *Anal. Chem.*, **55**, 1970 (1983).
17. Gh. Nazri and R. H. Muller, Abstract 61, p. 98, The Electrochemical Society Extended Abstracts, Vol. 83-2, Washington, DC, Oct. 9-14, 1983; Submitted to *This Journal*.
18. E. R. Wölfel, *J. Appl. Cryst.*, **16**, 341 (1983).
19. H. E. Göbel, "Advances in X-Ray Analysis," Vol. 22, p. 255, Plenum Press, New York (1979).
20. C. J. Brokowski and M. K. Ropp, *Rev. Sci. Instrum.*, **39**, 1515 (1968).
21. D. Ortendahl, V. Perez-Mendez, and J. Stoker, *Nucl. Instrum. Meth.*, **156**, 53 (1978).

Kinetic Parameters of the Electro-Oxidation of Adsorbed Methanolic Fragments on Platinum in Acid Solution

D. Brynn Hibbert* and Foo Y. Y. Yon-Hin**

Department of Chemistry, Royal Holloway and Bedford New College, Egham Hill, Egham, Surrey, England

Several workers (1-3) have studied the properties of adsorbed methanol with a view to elucidating the mechanism of this potentially important fuel cell reaction (4). It is thought that the rapid adsorption of methanol occurs giving fragments having the formulas COH or COOH (5-8)

*Electrochemical Society Active Member.

**Electrochemical Society Student Member.

and, eventually, CO (9). The fragment (CHO⁺) has been detected after a platinum emitter was exposed to methanol vapor (10). At potentials below 0.6V (*vs.* SHE), the slow step in the oxidation is thought to be the reaction of the adsorbed fragment with an adsorbed hydroxyl radical (6). The work presented here has measured the rates of oxidation of adsorbed methanol at potentials between 0.6 and

1.0V and temperatures between 0° and 40°C by a potentiostatic step method and by steady-state current-voltage measurements. The oxidation of fragments from fully deuterated methanol has also been studied.

Experimental

Materials.—Spectroscopically pure methanol and 99.5%D CD₃OD were used without further purification. Sulfuric acid (0.5 mol dm⁻³) was prepared from AR-grade sulfuric acid and distilled, deionized water. Platinum foil electrodes (1 cm² Johnson Matthey 99.99% pure) were chemically cleaned (nitric acid, distilled water, tetrachloroethylene, distilled water) and then repeatedly cycled between -0.2 and +2.0V vs. SHE in the sulfuric acid electrolyte until the cyclic voltammogram was reproducible. The electrochemical surface area of the electrodes was measured by constant current charging curves (11).

Apparatus.—All electrochemical measurements were made in a nitrogen-purged, three-electrode cell against a dynamic hydrogen reference electrode (DHE). The DHE was found to be at a potential of -25 mV against a bubbling hydrogen electrode in the same electrolyte.

Method.—A platinum electrode was held at +0.15V vs. DHE in 0.5 mol dm⁻³ sulfuric acid for some minutes, after which it was dipped in methanol, dried for 2-3 min, and reintroduced into the cell, again at 0.15V. All solutions were thermostated ($\pm 0.2^\circ\text{C}$) at the working temperature and purged with nitrogen. The potential was then stepped to the working voltage (0.6-1.0V) and the current measured with time. Steady-state potentiostatic measurements were made on a 0.1 mol dm⁻³ methanol solution in 0.5 mol dm⁻³ sulfuric acid using a Thompson Associates potentiostat. In all cases, blank experiments in the absence of methanol were carried out and, where appropriate, results have had this background component subtracted from them.

Results

Steady-state current voltage data are shown in Fig. 1 for a range of temperatures. The data taken above 0.7V were fitted to an expression of the form

$$\ln i = \ln(A) + (E - \alpha FV)/RT$$

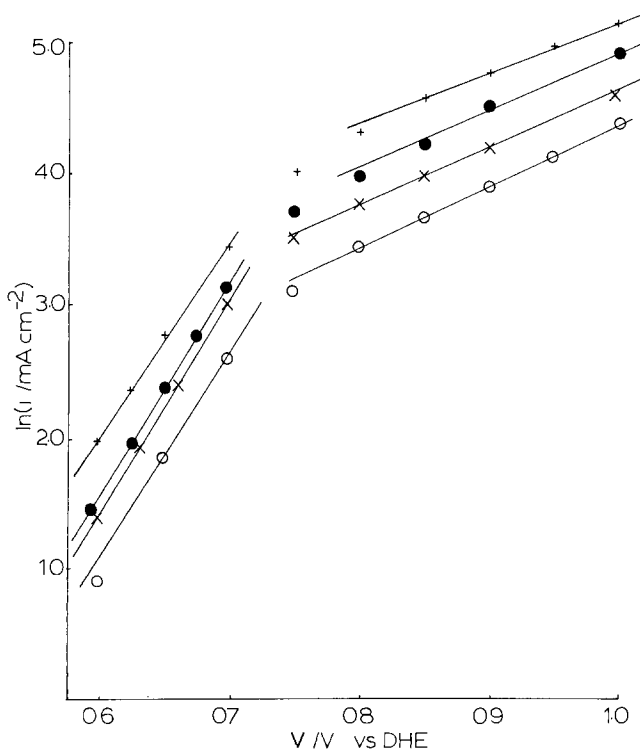


Fig. 1. Tafel plots for the oxidation of methanol (0.1 mol dm⁻³) in sulfuric acid (0.5 mol dm⁻³) at a platinum electrode. Open circles: $T = 290.0$ K. \times : $T = 298.5$ K. Closed circles: $T = 305.0$ K. +: $T = 314.2$ K.

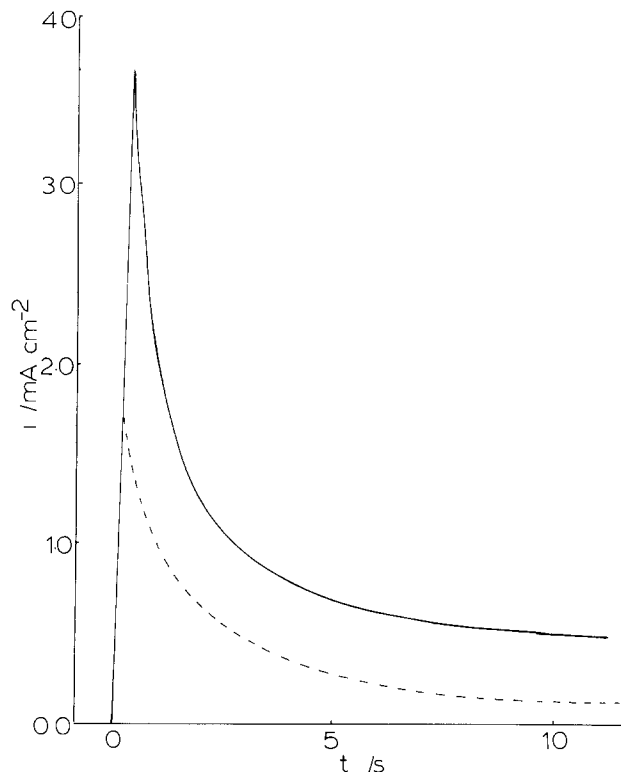


Fig. 2. Current response on stepping a platinum electrode from 0.15 to 0.80V (vs. DHE) in 0.5 mol dm⁻³ sulfuric acid at 291.0 K. Full line: electrode with adsorbed methanol. Broken line: clean electrode.

with $\ln(A/A \text{ cm}^{-2}) = 15.31 \pm 0.07$, $E = 36.1 \pm 0.2 \text{ kJ mol}^{-1}$, $\alpha = 0.10 \pm 0.05$.

A typical transient current response on stepping a methanol-adsorbed electrode from 0.15 to 0.8V is shown in Fig. 2. The data quoted for the higher potentials have been corrected for the small oxidation current on a pure platinum surface. These data are plotted as $\ln(i_t - i_t^{\text{blank}})$ against t (Fig. 3) and the first-order rate constant (k) de-

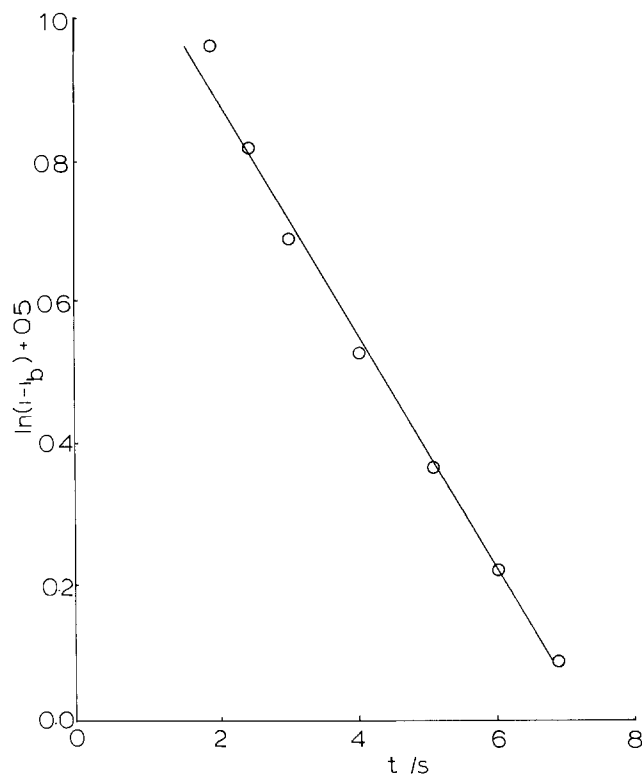


Fig. 3. First-order plot of the transient current response on stepping a methanol-adsorbed electrode from 0.15 to 0.8V in 0.5 mol dm⁻³ sulfuric acid at 297.5 K.

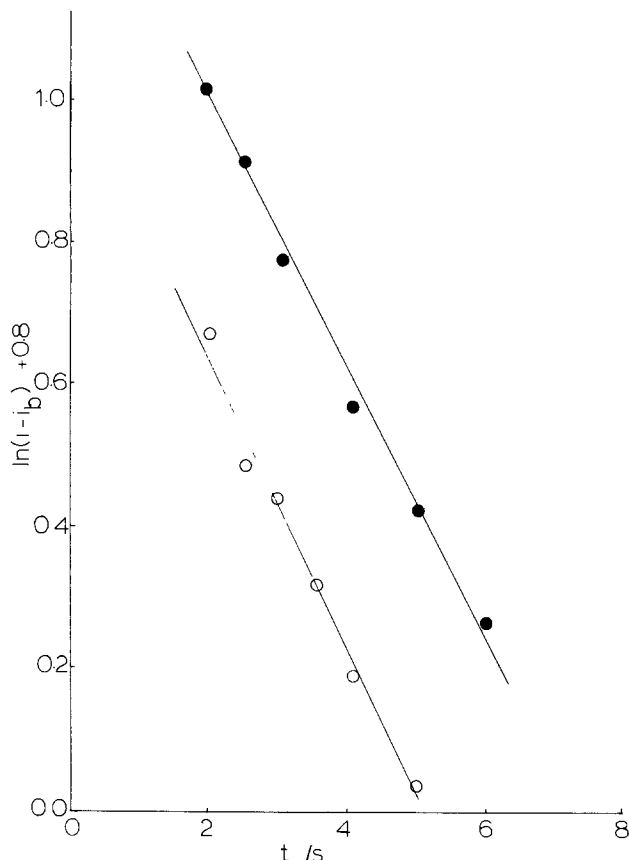


Fig. 4. First-order plots of the transient current response of the oxidation of adsorbed methanolic fragments from CH_3OH (○) and CD_3OD (●). Voltage step 0.15-0.80V, $T = 299.5$ K. Electrolyte 0.5 mol dm^{-3} sulfuric acid.

terminated from the slope of the line. Data from such experiments conducted between 0.7 and 1.1V and 275.0 and 313.3 K (20 experiments in all) were fitted to

$$\ln(k) = \ln(A) - (E - \alpha FV)/RT$$

with $\ln(A) = 10.8$, $E = 39.2 \text{ kJ mol}^{-1}$, and $\alpha = 0.10$. The total charge passed during oxidation of the fragments was measured and compared with the charge required to oxidize the electrode surface in a galvanostatic experiment. In all cases, the coverage of the adsorbed species was less than 0.1. The oxidation of adsorbed deuterated methanol was measured between 0.8 and 1.0V and 292.0 and 311.0 K. No kinetic isotope effects were observed (that is, similar values of the rate constant k were measured at a given temperature and potential), as may be seen in Fig. 4. In all experiments, however, a greater coverage of the deuterated species was observed, the ratio of the coverages of normal and deuterated methanolic fragments being approximately 1:1.5.

Discussion

The current passed when a potential is applied to an electrode with adsorbed methanol shows an exponential decay, indicating a first-order oxidation of the adsorbed species

$$i/nF = dC_{\text{ads}}/dt = kC_{\text{ads}} \quad [1]$$

where C_{ads} is the concentration of the surface species. As-

suming an irreversible oxidation, the current is

$$\begin{aligned} i &= nFC_{\text{ads}}A \exp(-E/RT) \exp(\alpha F\eta/RT) \\ &= nFC_{\text{ads}}A \exp(-E'/RT) \exp(\alpha FV/RT) \end{aligned} \quad [2]$$

where E' is an activation energy at the zero of potential to which V is referenced. Comparison of Eq. [1] with [2] shows

$$k = A \exp(-E'/RT) \exp(\alpha FV/RT) \quad [3]$$

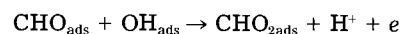
The solution of Eq. [1] is

$$C_{\text{ads}} = C_{\text{ads}}^0 \exp(-kt) \quad [4]$$

and, thus, combining Eq. [2] with Eq. [4]

$$i = nFC_{\text{ads}}^0 k \exp(-kt) \quad [5]$$

A plot of $\ln(i)$ against t yields k , the potential and temperature dependence of which allows the determination of E' and α . The measurement of current transients on stepping the potential gives useful information on the kinetics of the oxidation of surface species. The correspondence between the kinetics of the steady-state oxidation of methanol and the oxidation of adsorbed methanolic fragments suggest a similarity in the rate-determining step. This is consistent with the proposal of Bagotzky and Vassilyev (6) that



is rate limiting. This step is also consistent with the lack of isotope effect between CDO_{ads} (from CD_3OD) and OH_{ads} , the adsorbed hydroxyl coming from the normal electrolyte. Wiekowski (12) has found a kinetic isotope effect in the oxidation of methanol in H_2SO_4 and D_2SO_4 , which is also consistent with the proposed mechanism.

Bewick has shown that the ultimate species which is present at a platinum surface from several precursors is CO (9, 13). The oxidation of CO_{ads} would, of course, show no deuterium isotope effect. Considering the time scale of the experiments presented here, CO may indeed be the fragment which is oxidized. We note, however, that in recent studies of the oxidation of HCOOH and DCOOH on lead adatom covered platinum (14) a deuterium isotope effect of 2.6 was observed suggesting an initial rate-determining step involving the cleavage of the CH bond.

REFERENCES

1. M. W. Breiter, *Discuss. Faraday Soc.*, **79** (1968).
2. A. Wiekowski, *This Journal*, **122**, 252 (1975).
3. V. B. Hughes and R. Miles, *J. Electroanal. Chem.*, **145**, 87 (1983).
4. K. J. Cathro and C. H. Weeks, *Energy Conv.*, **11**, 143 (1971).
5. O. A. Petry, B. I. Podlovchenko, A. N. Frumkin, and H. Lal, *J. Electroanal. Chem.*, **10**, 253 (1965).
6. V. S. Bagotzky and Yu. B. Vassilyev, *Electrochim. Acta*, **12**, 1323 (1967).
7. B. I. Podlovchenko and R. P. Petukhova, *Elektrokimiya*, **10**, 489 (1974).
8. I. E. Wachs and R. J. Madix, *Surf. Sci.*, **76**, 531 (1978).
9. A. Bewick, *J. Electroanal. Chem.*, **150**, 481 (1983).
10. V. B. Labintsev, N. N. Griskin, and A. A. Petrov, *Kinet. Katal.*, **19**, 518 (1978).
11. M. W. Breiter, C. A. Knorr, and W. Volkl, *Z. Elektrochem.*, **59**, 681 (1955).
12. A. Wiekowski, *J. Electroanal. Chem.*, **78**, 229 (1977).
13. B. Beden, A. Bewick, and C. Lamy, *ibid.*, **148**, 147 (1983).
14. A. Razaq and D. Pletcher, *This Journal*, **131**, 957 (1984).



A Cross-Linked Positive Resist Derived from Poly(Methacrylonitrile-co-Methacrylic Acid)

M. Suzuki and Y. Ohnishi

NEC Corporation, Fundamental Research Laboratories, Miyamae-ku, Kawasaki 213, Japan

A. Furuta

Sumitomo Chemical Company, Limited, Takatsuki Research Laboratories, Tsukahara, Takatsuki 569, Japan

ABSTRACT

Cross-linked positive resists derived from copolymers of methacrylonitrile (MCN) and methacrylic acid (MAA) have been developed based on the theoretical formula which shows that a large $M_w \times G_s$ value is essential to improve the cross-linked positive resist sensitivity, where M_w is the weight-average molecular weight and G_s is the main chain scission efficiency. The cross-linked positive resist consists of P(MCN₉₂-MAA₈) with a viscosity-average molecular weight (\bar{M}_v) of 5.7×10^5 and tripropylene glycol diglycidyl ether (TPG) as a cross-linking agent. It has high sensitivity ($3 \mu\text{C}/\text{cm}^2$) and high dry-etch resistance, reflecting the large $M_w \times G_s$ value of the copolymer and the high dry-etch resistance of the MCN component. The resist is applied to a trilayer resist system as the top imaging layer. Submicron fine patterns delineated at $3.4 \mu\text{C}/\text{cm}^2$ are transferred to the thick organic layer, and high aspect ratio patterns are obtained.

Cross-linked positive resists were suggested to attain high sensitivity and good resolution (1-4). In cross-linked positive resists, linear polymers are cross-linked *in situ* on the substrate by heat or light to form an insoluble gel before the exposure. Only the exposed part is changed into a soluble material. The dose Q required to make the exposed part completely soluble is approximately written as

$$Q \cong \frac{200\rho N_A(\delta - 1)}{G_s A M_w}$$

where ρ is the polymer density, N_A is Avogadro's number, δ is the cross-linking coefficient, G_s is the G value for scission, A is the proportionality constant, and M_w is the weight-average molecular weight (5). This formula shows a large $M_w \times G_s$ value is essential to attain high sensitivity in cross-linked positive resists. On the other hand, dry-etch resistance is an inherent property of a resist material. Gokan *et al.* showed that the etch rate of the organic resist materials under ion bombardment condition had a linear dependence on the $N/(N_c - N_o)$ value, where N , N_c , and N_o denote the total number of atoms in a monomer unit, the number of carbon atoms in a monomer unit, and the number of oxygen atoms in a monomer unit, respectively (6). Since the polymers with the smaller $N/(N_c - N_o)$ value have the higher dry-etch resistance, a cross-linked positive resist derived from a polymer with a large $M_w \times G_s$ value and a small $N/(N_c - N_o)$ value is expected to be a positive resist with high sensitivity as well as high dry-etch resistance.

This paper reports the cross-linked positive resist consisting of methacrylonitrile (MCN) as a main constituent. MCN was selected because PMCN has a high G_s value [$G_s = 3.3$ (7, 8)] and high dry-etch resistance (9) because of its small $N/(N_c - N_o)$ value.

Molecular Design

In Table I, G_s values and $N/(N_c - N_o)$ values of well-known positive resists are listed with the qualitative estimates for their dry-etch resistance. PMCN and poly(α -

methylstyrene) (P α MeSt) have small $N/(N_c - N_o)$ values and high dry-etch resistance. Though P α MeSt shows the highest dry-etch resistance among investigated positive resists, its G_s value is too small. On the contrary, PMCN has a large G_s value while keeping high dry-etch resistance. Thus, MCN has been chosen as a main constituent for the cross-linked positive resist. Methacrylic acid (MAA) has been copolymerized with MCN to introduce a functional group which reacts with the cross-linking agent TPG. This cross-linking agent has been mixed with the copolymer so that the mixture contains equivalent quantities of epoxy and carboxyl groups.

Experimental

The copolymer of MCN and MAA has been synthesized by free radical polymerization. The viscosity-average molecular weights (\bar{M}_v) were measured using acetone as a solvent, assuming that the constants values in the Mark-Houwink equation relating η to \bar{M}_v were the same as those for PMCN. MAA content was measured by titration and elemental analysis. The \bar{M}_v values and MAA contents of the copolymers synthesized are shown in Table II.

Table I. G_s values and dry-etch resistance of positive resists

Polymer	G_s	$N/(N_c - N_o)$	Dry-etch resistance	Ref.
PMCN	3.3	2.5	Good	(7, 9)
PMMA	1.3	5.0	Fair	(14)
PMIPK	1.1	3.5	Fair	(15)
PMAAN	2.9	4.2	Fair	(7)
P α MeSt	0.3	2.1	Very good	(16)
PBS	11.0	4.7	Poor	(17)

PMCN: Poly(methacrylonitrile)
 PMMA: Poly(methyl methacrylate)
 PMIPK: Poly(methyl isopropenyl ketone)
 PMAAN: Poly(methacrylic anhydride)
 P α MeSt: Poly(α -methyl styrene)
 PBS: Poly(butene-1-sulfone)

Table II. Viscosity-average molecular weights and MAA contents of MCN-MAA copolymers

Sample no.	Polymer	$\bar{M}_v (\times 10^4)$	MAA content (m/o)
1	P(MCN ₉₁ -MAA ₉)	10	9.1
2	P(MCN ₈₅ -MAA ₅)	1.91	5.3
3	P(MCN ₈₉ -MAA ₁₁)	7.17	11.4
4	P(MCN ₉₂ -MAA ₈)	57.0	7.9
5	P(MCN ₉₁ -MAA ₉)	32.1	9.0

The mixtures of P(MCN-MAA) and TPG were dissolved in cyclohexanone (the polymer was 5-7 weight percent of the solution), spin coated on silicon wafers, and prebaked at 90° to 100°C for 1h in flowing nitrogen. Hiraoka *et al.* reported P(MCN-MAA) as a deep-UV resist (10). As shown in Fig. 1, this copolymer undergoes a cyclization reaction at temperatures over 120°C (11), which gives a broad UV-absorption band with the maximum at 246 nm. In the present experiment, a cross-linking agent TPG was added and prebaking condition was set to form cross-linkages without the formation of ring structures (Fig. 2). No infrared spectral change or color formation was observed by baking even at 110°C for 1h.

Electron beam exposures were carried out at 20 kV accelerating voltage with a JEOL JBX-5A electron beam exposure system. Sensitivity was measured on a 60 × 60 μm square pattern. The cross-linking coefficient δ was calculated from the gel fraction assuming that the molecular weight distribution of polymer follows a Poisson distribution and the weight-average molecular weight approximately equals the viscosity-average molecular weight. The gel fraction was estimated by measuring the thickness of the cross-linked polymer system before and after soaking in acetonitrile (MeCN) for more than 16h to wash out the sol fraction completely.

The resist-layer thicknesses were measured with a Taylor-Hobson Talystep instrument. Fine patterns obtained after the development were checked by an optical microscope and a scanning electron microscope.

Etching rates for P(MCN₉₁-MAA₉), PMCN, polystyrene (PS), polymethylmethacrylate (PMMA), and Shipley photoresist AZ-1350J were measured using Ar ion milling and CF₄ + H₂, CCl₃F + O₂, and CCl₄ + air reactive ion beam etching (RIE).

A Kaufman-type 3 in. ion gun (Veeco) and a 10 in. diffusion pumping system were used in Ar ion beam etching. The etching condition was 2 × 10⁻⁴ torr Ar pressure, 500 eV acceleration energy, and 0.83 mA/cm² ion current density. The RIE system was a parallel-plate reactor. The etching conditions are described in Table III. The target materials were polypropylene, quartz, and stainless steel for CF₄ + H₂, CCl₃F + O₂, and CCl₄ + air RIE, respectively.

Results and Discussion

Sensitivity.—The obtained sensitivity (Q_{exp}) for each molecular weight P(MCN-MAA) + TPG system with its theoretical sensitivity (Q_{theo}) is shown in Table IV. In a fine pattern fabrication, a MeCN and toluene (Tol) solution was used because it was found to be a good developer from the resolution standpoint. Except for the case when a strong developer is used to wash out the sol completely, the sensitivities measured are lower than the theoretical values. The explanation for this phenomenon will be given as follows. The M_w value is infinite at the gel point dose (D_g^1), and the M_w at a dose a little higher than

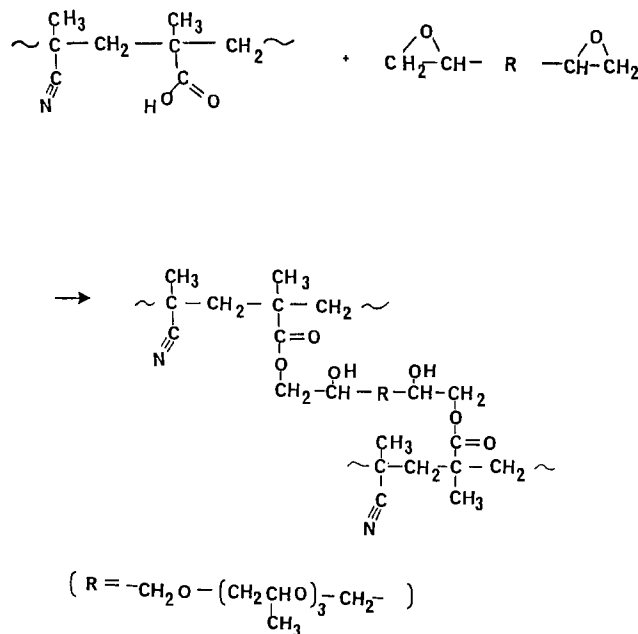


Fig. 2. Cross-linkage formation in a P(MCN-MAA) + TPG system

D_g^1 is quite high. The ultrahigh molecular weight polymer molecules that are almost insoluble in a developer exist in the exposed area. These ultrahigh molecular weight polymer molecules remained after the development in a 1:1 MeCN and Tol solution and are observed as remaining thicknesses. A practical electron exposure requires degradation of not only an insoluble gel but also ultrahigh molecular weight polymer molecules so that the smaller molecular weight molecules can be dissolved by the proper developer. Polymer 4 [P(MCN₉₂-MAA₈), $M_v = 5.7 \times 10^5$] showed the highest sensitivity among the systems developed with the practical developer. The exposure characteristics for the P(MCN₉₂-MAA₈) $M_v = 5.7 \times 10^5$ + TPG system are shown in Fig. 3. These exposure characteristics look unusual because of the surface roughness after development. The gel fraction of this sample is 52%. This means a large amount of sol is washed out in a developer leading to the surface roughness even though the moderate developer is used.

Resolution.—The development of the cross-linked positive resist is similar to that of the negative resist. The most important factor influencing the resolution is the swelling during the soak in a developer; therefore, to find the developer that minimizes the swelling is very important. Dimethylformamide, dimethylsulfoxide, benzonitrile, MeCN, and acetone were selected as good solvents, and Tol and isopropanol (IPA) were chosen as poor solvents. Good solvents and mixed solutions of a good solvent and a poor solvent were tried at various component ratios. As a result, a 1:1 MeCN and Tol solution was found to be a proper developer minimizing the swelling. It has been found that soaking in MeCN for 10 min to wash out the sol fraction before the electron exposure has a favorable effect on the resolution; that is, it prevents scum in the exposed area and improves the surface roughness in the unexposed area. This is because of two favorable effects: the initial resist thickness has been thinned and soluble materials washed out. Though this soaking procedure lessens the resist sensitivity [for example, from 3.0 to

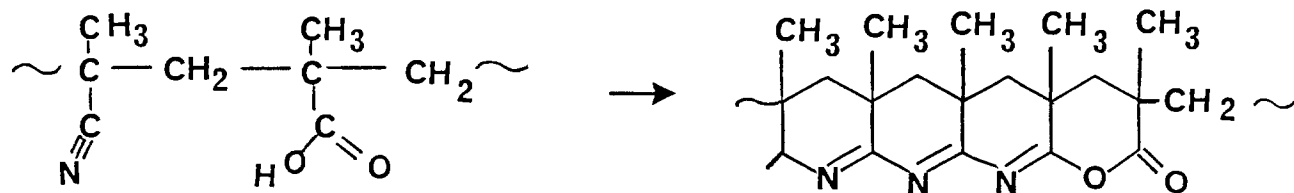


Fig. 1. Ring structure resulting from cyclization reaction

JST

Table III. Etching rates for resist materials under various etching conditions

	Ar ion milling 2×10^{-4} torr 500V; 0.83 mA/cm ² (Å/min)	CF ₄ /H ₂ 100/20 120 sccm 80 mtorr; 0.16 W/cm ² (Å/min)	CCl ₄ /F/O ₂ 40/5 45 sccm 40 mtorr; 0.12 W/cm ² (Å/min)	CCl ₄ /Air 70/80 150 sccm 300 mtorr; 0.33 W/cm ² (Å/min)
P(MCN ₉₁ -MAA ₉)	281	103	1605	285
PMCN	228	104	1325	155
PMMA	400	194	2740	365
AZ-1350J	190	100	925	170
PS	220	— ^a	800	85

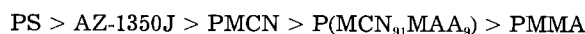
^a Some polymerization occurred.

Table IV. Viscosity-average molecular weights and sensitivities

Sample no.	$\bar{M}_v (\times 10^4)$	Prebake		δ	Development		Sensitivity	
		Temp. (°C)	Time (min)		Solvent	Time	Q_{exp}	Q_{theo}
1	10	100	30	1.4	Acetone	16 h	1.15	1.0
2	1.91	120	60	2.2	MeCN/Tol = 1/1	5 min	25	16
3	7.17	100	60	1.7		5 min	10	2.5
4	57.0	90	60	1.7		5 min	3.0	0.32
5	32.1	100	120	1.7		5 min	4.0	0.56

3.4 $\mu\text{C}/\text{cm}^2$ for P(MCN₉₂-MAA₈) ($\bar{M}_v = 5.7 \times 10^5$) + TPG system] and increases the number of process steps, a fine pattern is delineated at 3.4 $\mu\text{C}/\text{cm}^2$ which is a high sensitivity among positive resists. Patterns obtained with P(MCN₉₂-MAA₈) ($\bar{M}_v = 5.7 \times 10^5$) + TPG are shown in Fig. 4.

Dry-etch resistance.—Etching rates for P(MCN₉₁-MAA₉), PMCN, PS, PMMA, and AZ-1350J under various etching conditions are shown in Table III. Though a quantitative relation between the etching rates and the chemical structures under the RIE conditions is not easily found, the sequences of etching resistance are the same under every etching condition. The sequence from the polymer with higher resistance is



This sequence is paralleled by the corresponding $N/(N_c - N_0)$ values from the lowest value to the highest. This shows that $N/(N_c - N_0)$ value can be taken as a criterion for the polymer's dry etching resistance. Very few positive resists are highly resistant to dry etching and highly sensitive at the same time. The dry-etch resistance of P(MCN₉₂-MAA₈) is almost the same as that of P(MCN₉₁-MAA₉), which is 1.4-1.8 times as high as that of PMMA. This resistance is good for a positive resist, considering the sensitivity of P(MCN₉₂-MAA₈) $\bar{M}_v = 5.7 \times 10^5$ + TPG system is 3.4 $\mu\text{C}/\text{cm}^2$, which is 35 times as high as that of PMMA.

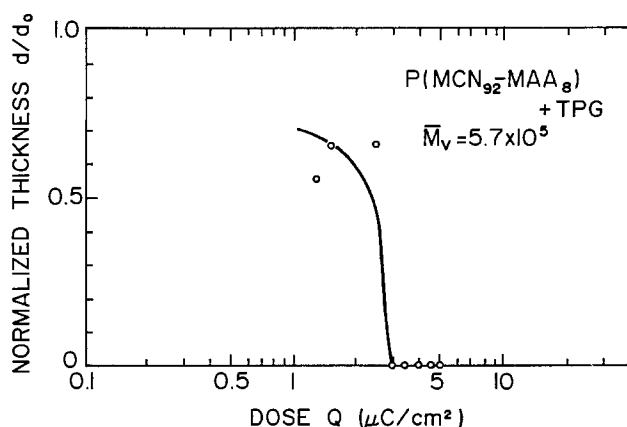


Fig. 3. Exposure characteristics for P(MCN₉₂-MAA₈) + TPG. Development: MeCN/Tol = 1/1; 5 min. Rinse: IPA, 1 min.

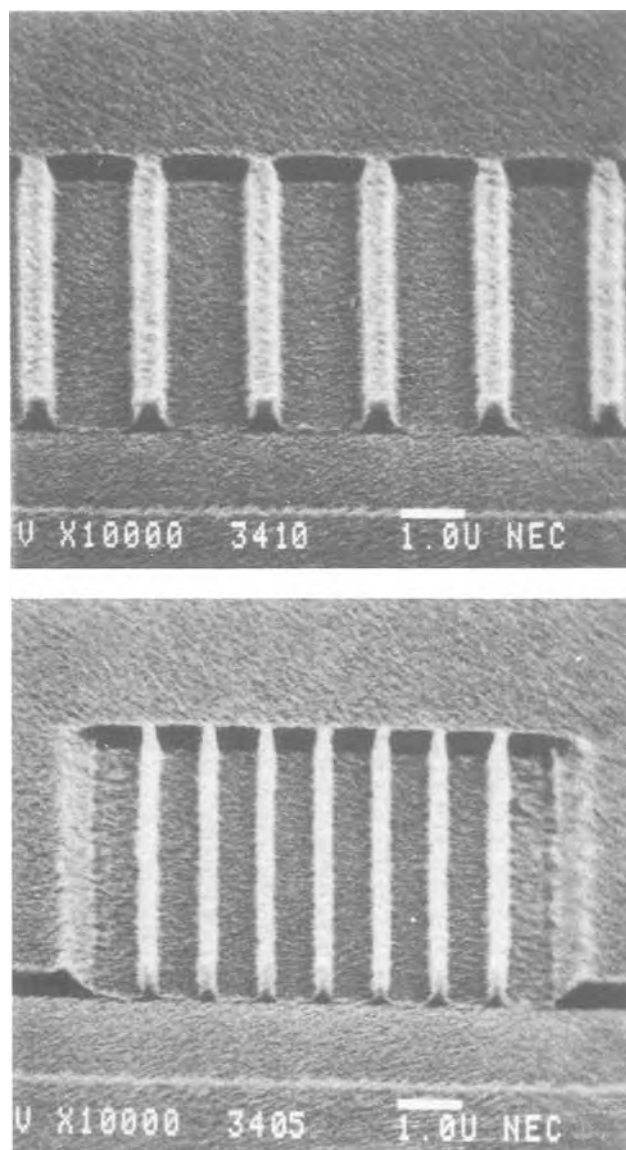


Fig. 4. Scanning electron micrographs of resist profiles delineated in 0.3 μm thick P(MCN₉₂-MAA₈) + TPG as a top imaging layer in a trilayer resist system. The white bar represents 1 μm .

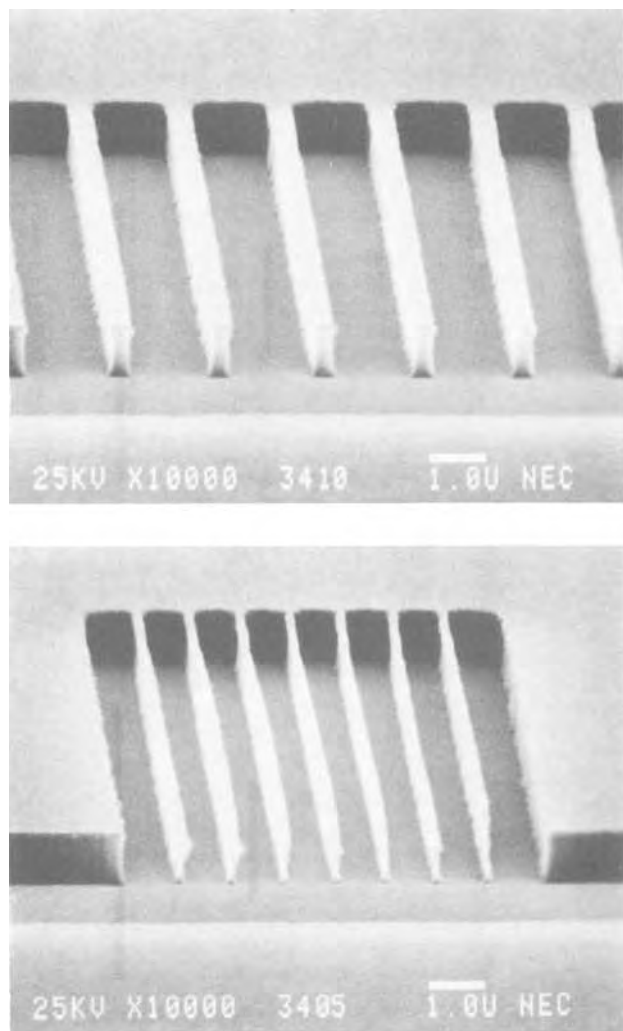


Fig. 5. Scanning electron micrographs of high aspect ratio patterns obtained by successive etching of organosilica film and AZ bottom layer. Fig. 5a (top) and 5b (bottom) correspond to Fig. 4 (top) and 4 (bottom), respectively.

Application to a trilayer resist system.—P(MCN₉₂-MAA₈) is so highly resistive to CF₄/H₂ RIE that it is etched only 60Å (7.5 Å/min), while an organosilica film is etched 2400Å (300 Å/min) when the etching condition is chosen properly (CF₄/H₂ = 10/2, 0.12 W/cm², 80 mtorr, 60 sccm, 8 min). An organosilica film is quite resistive to O₂ RIE and is etched only 163Å (16.3 Å/min), whereas AZ-1350J photoresist is etched 8500Å (850 Å/min) (O₂, 0.08 W/cm², 60 mtorr, 30 sccm, 10 min).

The cross-linked positive resist was applied as the top imaging layer in the trilayer resist system (12, 13). It consisted of a 1.0 μm thick AZ-1350J photoresist as a bottom layer, a 0.1 μm thick spin-coated organosilica film as an intermediate layer, and a 0.3 μm thick top imaging layer. The cross-linked positive resist was soaked in MeCN for 10 min to wash out the sol before exposure. The exposure dose was 3.4 μC/cm². The resist was developed in a 1:1 MeCN and Tol solution for 5 min, then rinsed in IPA for 1 min.

High aspect ratio patterns were obtained by successive etching of the organosilica film and the thick AZ-1350J photoresist layer. (CF₄/H₂ RIE: CF₄/H₂ = 10/2, 0.12 W/cm², 80 mtorr, 60 sccm, 8 min; O₂ RIE: 0.08 W/cm², 60 mtorr, 30 sccm, 12 min). The resultant profiles are shown in Fig. 5.

Conclusion

A highly sensitive cross-linked positive resist with high dry-etch resistance has been developed according to the two theoretical formulas which define the highest sensitivity attainable for cross-linked positive resists and the resist etching rate's linear dependence on the $N/(N_c - N_0)$ value. The resist consists of P(MCN-MAA) and TPG as a cross-linking agent.

A submicron fine-line pattern was obtained at 3.4 μC/cm² using P(MCN₉₂-MAA₈) ($\bar{M}_v = 5.7 \times 10^5$) + TPG cross-linked positive resist. The developed cross-linked positive resist has been applied to a trilayer system as the top imaging layer. High aspect ratio patterns were obtained by successive etching of an intermediate layer and a bottom layer.

Acknowledgments

The authors would like to thank D. Shinoda and S. Fujiwara for their encouragement. They are also grateful to K. Tanigaki, Y. Kurogi, N. Endo, S. Matsui, and H. Tsuge for their helpful discussions.

Manuscript submitted Sept. 10, 1984; revised manuscript received Feb. 11, 1985.

NEC Corporation assisted in meeting the publication costs of this article.

LIST OF SYMBOLS

A	proportionality constant (eV · cm ² /C)
D_g^1	gel point dose (μC/cm ²)
G_s	number of main chain scissions per 100 eV energy absorption
\bar{M}_v	viscosity-average molecular weight
\bar{M}_w	weight-average molecular weight of the polymer
N	total number of atoms in a monomer unit
N_A	Avogadro's number
N_c	number of carbon atoms in a monomer unit
N_o	number of oxygen atoms in a monomer unit
Q	dose (μC/cm ²)
δ	cross-linking coefficient
ρ	density of the polymer (g/cm ³)

REFERENCES

- E. D. Roberts, *Appl. Polym. Symp.*, **23**, 87 (1974).
- T. Kitakohji, Y. Yoneda, K. Kitamura, H. Okuyama, and K. Murakawa, *This Journal*, **126**, 1881 (1979).
- T. Tada, *ibid.*, **126**, 1635 (1979).
- K. Harada, O. Kogure, and K. Murase, *IEEE J. Solid-State Circuits*, **sc-17**, 148 (1982).
- M. Suzuki and Y. Ohnishi, *This Journal*, **129**, 402 (1982).
- H. Gokan, S. Esho, and Y. Ohnishi, *ibid.*, **130**, 143 (1983).
- J. N. Helbert, E. H. Poindexter, G. A. Stahl, C.-Y. Chen, and C. U. Pittman, Jr., *J. Polym. Sci.*, **17**, 49 (1979).
- L. E. Stillwagon, E. M. Doerries, L. F. Thompson, and M. J. Bowden, Abstract 42, 8th International Conference on Electron and Ion Beams in Science and Technology, May, 1978.
- J. N. Helbert, C. F. Cook, Jr., C.-Y. Chen, and C. U. Pittman, Jr., *This Journal*, **126**, 694 (1979).
- H. Hiraoka, W. L. Welsh, Jr., and J. Bargon, *J. Vac. Sci. Technol. B*, **1**, 1062 (1983).
- N. Grassie and I. C. McNeil, *J. Polym. Sci.*, **27**, 207 (1958).
- S. Matsui and N. Endo, *IEDM* **82**, 395 (1982).
- N. Endo and S. Matsui, *Jpn. J. Appl. Phys.*, **22**, L109 (1983).
- E. Gipstein, A. C. Ouano, D. E. Johnson, and O. U. Need, III, *IBM J. Res. Dev.*, **21**, 143 (1977).
- A. R. Shultz, *J. Polym. Sci.*, **47**, 267 (1960).
- J. H. O'Donnell and D. F. Sangster, "Principles of Radiation Chemistry," Arnold, London (1970).
- L. F. Thompson and M. J. Bowden, *This Journal*, **120**, 1722 (1973).

Morphological Clue to a Pyrolytic Thin Film Growth Mechanism

Charles B. Greenberg*

PPG Industries, Incorporated, Glass Research and Development, Pittsburgh, Pennsylvania 15238

ABSTRACT

Methods for forming thin, transition metal oxide films pyrolytically from liquid spray vehicle are well known. On the one hand, there are the uniform and finely crystallized spinel-structured films grown from organic solutions of acetylacetonates; one of these is herein reviewed. A spectrally similar film grown from aqueous solution, of another spinel composition (1), is not so well formed. This film's relatively gross morphology is a clue to its growth mechanism. The morphology can be explained qualitatively by invoking a model for closely associated phenomena characteristic of spray drying (2). By this model, solid or partially molten metal-organic material approaches the hot substrate in the form of roughly spherical, porous, hollow shells. These remain after solvent evaporation from the droplets of the liquid spray. The hollow shells vaporize on the approach to the substrate, and the film grows by a CVD reaction at the substrate. Constituents which do not readily vaporize, such as impurities, impact the substrate and imprint a morphological pattern of collapsed shells. These comprise the rare clue for the analysis and for modeling film growth.

Thin, transparent, transition metal oxide films have been prepared by organic-based pyrolytic spray for many years. They are known to be very uniform and are often quite durable. The latter implies abrasion resistance as well as broad chemical stability. A cobalt-iron-chromium oxide film with these attributes is widely used architecturally in windows for its good solar attenuation (3). The film is grown on a hot, pristine soda-lime-silica float glass surface. It is deposited from a chlorinated hydrocarbon solvent containing acetylacetonates of the transition metal cations (4); a pneumatic spray traverses the moving glass normal to its path. The temperature of the glass $\approx 565^\circ\text{C}$. To preserve both the transparency of the film and its visual uniformity, primarily its freedom from iridescence, the physical thickness must be limited. The upper limit for the high cobalt oxide containing composition of particular interest is about 400\AA . This film is herein reviewed because it sets a standard for preferred morphology. By contrast, a film grown from an aqueous solution containing cobaltous acetate and methyltin chloride is of a less desirable morphology, which suggests the mode of film formation. This constitutes the real focus of discussion herein.

The Organic-Based Film

Film composition and morphology.—A typical composition for the organic-based film, as determined by atomic absorption analysis, is shown in Table I. Assuming a dense oxide structure, the film thickness is 400\AA , which is in agreement with interferometric measurements (5). The averaged composition and standard deviations are, in this instance, for six different 50 cm^2 samples of 3 mm thick glass. The spray solvent was a 1:1 mixture by volume of methylene chloride and trichloroethylene. The solution contained 125, 43, and 32 g/liter, respectively, of the acetylacetonates of trivalent cobalt, chromium, and iron; these were obtained from the Harshaw Chemical Company, Industrial Chemical Department. Figure 1 shows the characteristic microstructure for this film, obtained by using electron microscopy and C/Pt replication. The fine-grained morphology is accompanied by such low grain boundary porosity that the film blocks the otherwise instantaneous dissolution of underlying glass in 0.5% HF solution, at least for 5-10 min at room temperature. The film itself is generally slow to dissolve in various chemical agents, including the HF solution for 5-10 min and hot HCl, H_2SO_4 , NaOH, and NaCl solutions. Based upon the electron diffraction pattern's similarity to that of Co_3O_4 , the most probable film structure is that of a spinel; however, the individual transition metal ion valence states and unit cell sites are unknown.

Optical characteristics.—The curves in Fig. 2 show the reflectance and transmittance for a film in the 400-800 nm spectral range. The reflectance is high generally for an oxide. Values for the index of refraction and extinction

coefficient are given by $n-ik = 2.8 - i(0.5)$ at a wavelength of 550 nm. These values were calculated (6) from the optical data, corrected for substrate, and film thickness. The decimal precision in the calculated values is in large degree governed by film thickness, which is not known with better certainty than about $\pm 75\text{\AA}$.

The Aqueous-Based Film

Solution and film composition.—A Co-Sn-oxide film with virtually the same spectral properties is known from Michelotti and Ohlberg (1). Their spray formulation is an aqueous solution of cobaltous acetate (7) and methyltin chloride with the composition shown in Table II. The solution is acidic, with $\text{pH} = 4.4$, controlled by addition of acetic acid; the latter can be complexing for Co(II) (8). Sn(IV) is known to be very susceptible to hydrolysis with standing (9, 10), although perhaps it is inhibited by the carbon bonding in organotin halides. The possibility of hydrolysis is to be considered again in the interpretation of data. The electron diffraction pattern of the film indicates a spinel structure similar to Co_3O_4 , a result in common with the organic-based film. The ratio Co:Sn in the film is approximately that of the solution.

Cylindrical defect morphology at low magnification.—Generally, there are two ways in which cobalt oxide containing films prepared from aqueous solution, with or without Sn(IV), are of poorer uniformity. Aside from a tendency to be visually textured, they are susceptible to haziness, except where great care is taken to maintain solution purity. At least for the purpose of viewing in conditions that are not overly rigorous, the haze can be avoided. In Fig. 3 is an optical micrograph in pseudo-three-dimensional relief for a cobalt-tin-oxide film which exhibits no qualitatively discernible haze in normal viewing conditions. It was prepared with reagent grade cobaltous acetate and recrystallized methyltin chloride; distilled water was used for both recrystallization and preparation of the solution (11). The cylindrical and nearly cylindrical features, of comparatively low profile here, are projections above the plane of the film. Viguié and Spitz (12) showed a similar cylindrical feature in a pyrolytic iron oxide film prepared from an HCl solution of ferric chloride. While recognizing the spray droplet-to-

Table I. Spinel composition for acetylacetonate-based film

Cation constituent	Film content ($\mu\text{g}/\text{cm}^2$) ^a
Co	10.9 ± 0.7
Fe	3.1 ± 0.2
Cr	2.8 ± 1.0

^a Blanks were used to make allowance for well-known interferences, by cobalt for iron, and by both of these for chromium.

*Electrochemical Society Active Member.



Fig. 1. Typical morphology of the organic solvent-based, Co-Fe-Cr-oxide spinel film at high magnification, showing the low profile structure. The electron micrograph is of a standard replica taken with a JEM-7 microscope.

vapor pathway in general for uniform film growth, they did not expand on the defect's origin.

There are typically many more prominent cylindrical features at low optical magnification in films prepared from solutions of low purity. This is shown by the photo-

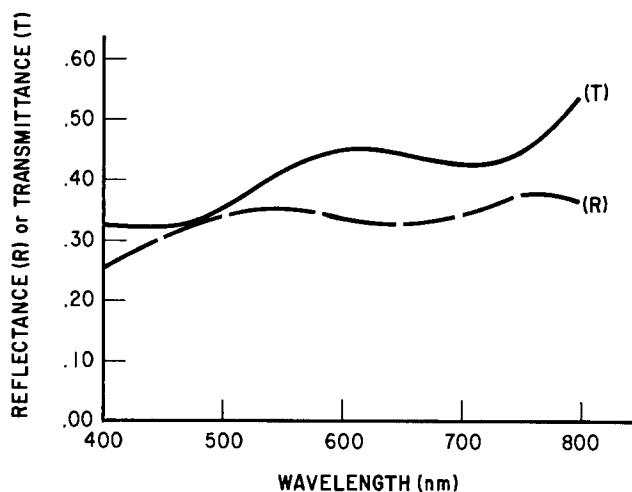


Fig. 2. Characteristic spectral curves for an organic solvent-based, spinel film. Data were obtained with a Beckman DK-2A Spectrophotometer, with an integrating sphere and angle of reflection of 8° . Transmittance was corrected with sufficient approximation by dividing by that for the uncoated glass at each wavelength.

Table II. Michelotti-Ohlberg aqueous solution (I)

Constituent	Concentration (weight percent)	Solute
Co(II)	4.8	$\text{Co}(\text{C}_2\text{H}_3\text{O}_2)_2 \cdot 4\text{H}_2\text{O}$
Sn(IV)	0.5	Methyltin chloride [80% $(\text{CH}_3)_3\text{SnCl}_2$ and 20% CH_3SnCl_3]
CH_3COOH	5.0	Glacial acetic acid

micrograph in Fig. 4, which suggests generally greater defect height above the plane of the film. Haze or light scattering is also very readily visible in the film.

Elevated defect relief is indicated from electron microprobe analysis of a cobalt oxide film that was prepared from aqueous solution of unspecified purity. In solution were cobalt acetate and acetic acid, approximately in the concentrations of Table II. Signal intensities for selected film and substrate constituents were normalized to the signal intensity for cobalt and were compared in and around high projections ($\sim 100\text{\AA}$); the more typical morphological features could not be resolved generally by microprobe counting. The normalized intensity for calcium, a major glass constituent, was typically $\sim 20\%$ less from within a defect than from substrate underlying defect-free film. This suggests in-defect masking of the substrate, that is elevated relief. Positive in-defect identifications were made for compounds of nickel and iron. The normalized in-defect probe signal for nickel impurity was typically approximately four times more intense than that for defect-free film; for iron the intensity was approximately two times greater. In general, nickel is a prin-

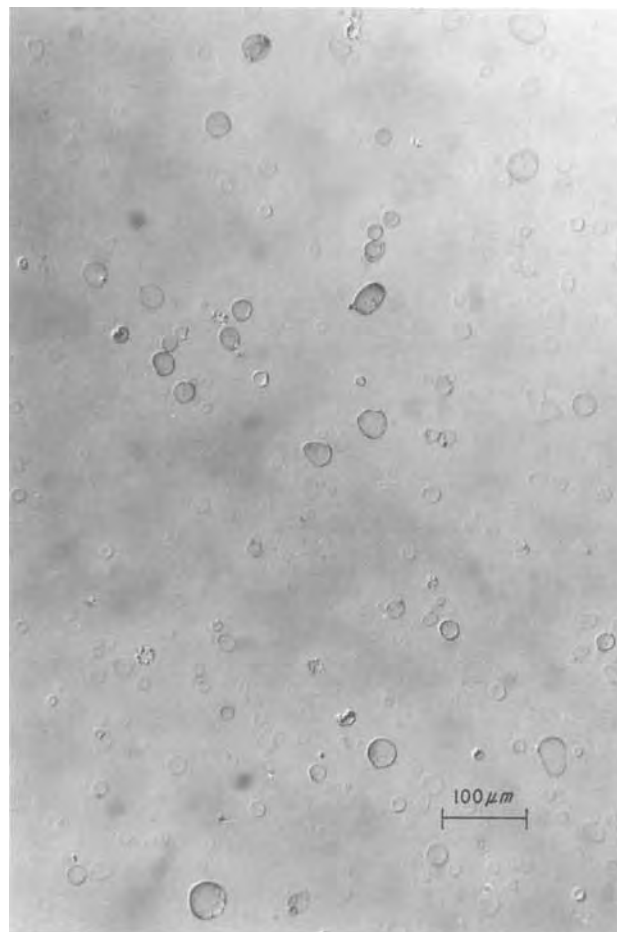


Fig. 3. Typical optical micrograph for the Co-Sn-oxide film prepared on a pristine glass surface from purified aqueous solution, showing characteristic raised features. Zeiss/Nomarski differential interference-contrast microscopy was used with reflected light. Background patchiness is associated with film texture.

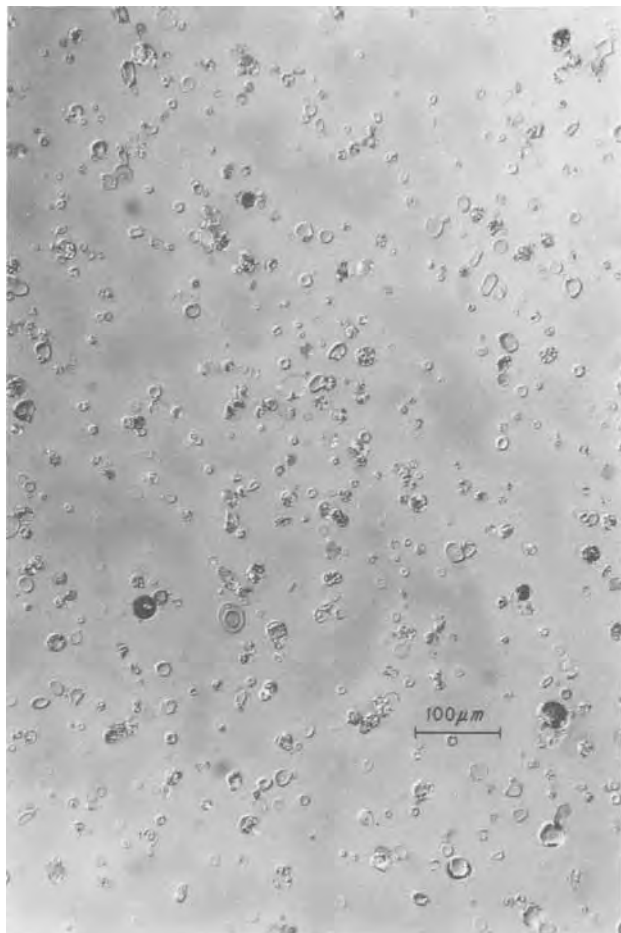


Fig. 4. Typical Zeiss/Nomarski optical micrograph for a Co-Sn-oxide film similarly prepared from impure aqueous solution, showing the characteristic raised features even more distinctly. The metal compounds in solution were industrial grades; nickel is a major noncobalt impurity.

cial impurity in cobalt acetate, and iron is a minor one. In the impure cobalt acetate used for the cobalt-tin-oxide sample of Fig. 4, the nickel content is within 0.2-0.7% by weight. The iron content <0.01%. These are known from emission spectrographic analysis. This impure solution also contains ~0.2% fluoride as HF, an earlier batch constituent (1).

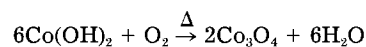
Morphological features such as those in Fig. 3 and 4 are not observable at all at low magnification in a Sn(IV)-free cobalt oxide film made from reagent-grade cobaltous acetate. This indicates that cobalt acetate by itself is not a significant contributor to defects, although the low profile defects in Fig. 3 suggest methyltin chloride may still be. Yet, in the aforementioned microprobe analysis, the signal for cobalt in-defect was greater than that of surrounding cobalt oxide film by about 25%. It is assumed that this is indicative of nonacetate impurities of cobalt. As the cobalt signal was approximately twenty times stronger within the defect than that for nickel, it was used for the indicated estimate of defect height for high projections. Apparently, the height of more typical defects above surrounding film <100Å, which is well below the typically micron-sized diameters in Fig. 3 and 4. These dimensions suggest a model.

The Charlesworth-Marshall model.—It is not necessary to invoke the impact of liquid droplets of aqueous spray to explain these particular features, even though physical appearances of the photomicrographs might suggest it. With such improbable collisions, it is likely that distinctly raised features would always occur at the points of impact, by instantaneous pyrolysis *in situ* (12). They do not occur with reagent-grade cobalt acetate. The same consideration very likely excludes the impact of a molten or

solid cobalt acetate droplet also. Rather, a reasonable explanation is to be found in the spray drying work of Charlesworth and Marshall for dissolved solids (2). These authors concerned themselves with vaporization of the solvent, not the solute. They showed the various configurations which an aqueous spray droplet takes when it is being dried, the most likely one of which is represented in Fig. 5 for the case at hand. Initially, while the coating droplet is in flight, and while receiving radiated energy from the glass, evaporation is from a free liquid surface. The droplet decreases in size at first, but then a solid, smooth, spherical or nearly spherical crust forms, with evaporation of liquid continuing from or through it. The crust is thus porous. In most cases observed by Charlesworth and Marshall, admittedly with relatively large droplets, the final particle was a hollow, thin, and nearly spherical crust. This was the result with a rigid but porous solid, as compared with one pliable and non-porous. By analogy, with the aqueous solution of Table II therefore, metal-organic vaporization and film growth proceed from a hollow solid crust after complete vaporization of the solvent. This situation is most likely to exist late in a droplet's flight, nearest the hot substrate.

If an impurity or a coating constituent, perhaps methyltin chloride, does not vaporize readily, it constitutes a part of a residual spherical skin that impacts the glass. The residual skins of the many spray droplets give the film its characteristic morphology at low optical magnification.

Vaporization and film growth.—It has been suggested that hydrolysis occurs first, and then the film grows by (13)



That, however, is not consistent with bulk simulations of the liquid in the droplet. With regard to the dry crust itself, its temperature will exceed that of the liquid boiling point, and hydrolysis of cobalt acetate is not likely (14). After refluxing a 500 cm³ volume of impure solution at about 90°C for 0.5h, there was no evidence for hydrolysis

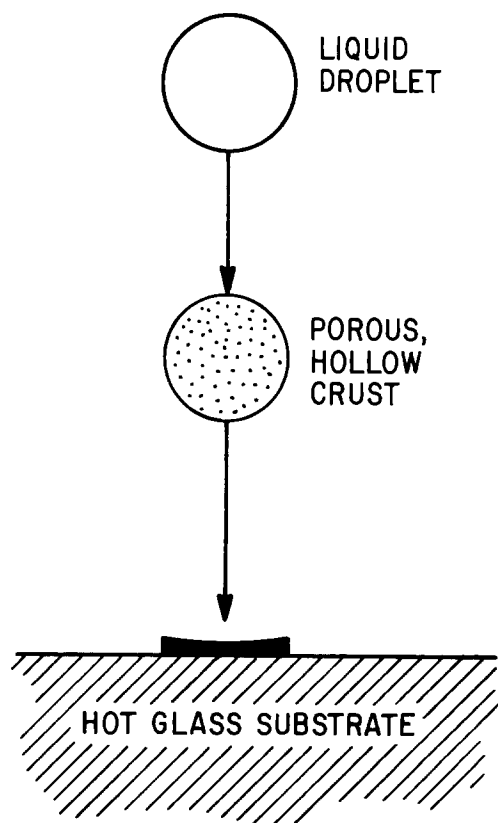
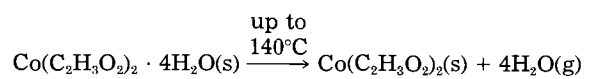


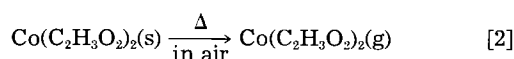
Fig. 5. A Charlesworth-Marshall droplet approaching a hot substrate

beyond solubility limits on a 3 μm Millipore MF-type membrane filter. Not even when heated to dryness to 100°C was there any significant hydrolysis or oxidation of Co(II), nor any unmethylated Sn(IV) hydroxide or oxide. That is, there were no significant formations of insoluble materials left on 3 μm filter paper after redissolving the dried material in water. The metal oxides and hydroxides are generally insoluble in water. One might even speculate that impurity hydroxides present initially could be of shape and size to cause the defects in Fig. 3 and 4 without invoking the drying model. This was, however, not observed when impure solution was filtered in advance of these bulk simulation experiments.

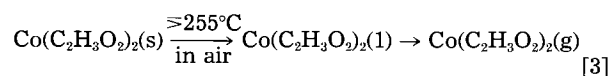
With the loss of bound water at 140°C for $\text{Co}(\text{C}_2\text{H}_3\text{O}_2)_2 \cdot 4\text{H}_2\text{O}$, it is assumed that the crust thereafter contains, aside from impurities, the anhydrous acetate and unidentified methyltin compounds. Judging from the dried bulk, the methyltin compounds are water soluble, and perhaps undecomposed from the original, up to at least 100°C. For the major constituent in the dried solid shell(s)



and there are two possible routes to vaporization (14)



and/or



Sublimation has been reported with relatively slow heating in air and vacuum, and partial melting has been observed with decomposition at temperatures $\geq 255^\circ\text{C}$. Either way, pyrolysis and film growth may proceed on the hot surface from the gas phase, with the evolution of CH_3COOH , H_2O , and CO_2 (14). However, for the purpose of comprehending the morphology in Fig. 3 and 4, it is certainly more consistent to assume the validity of Eq. [2] than that of Eq. [3]. Otherwise, liquid surface tension works against a stable, hollow sphere.

It is appropriate to question whether an acetylacetonate particle is, prior to vaporization and pyrolysis, also in the configuration of a hollow, solid sphere. Even in the presence of known impurities, however, this has not been observed. Perhaps this relates in some way to the generally high vapor pressures of chlorinated hydrocarbons, relative to the less readily evaporated water. On the other hand, perhaps the relatively easy sublimation of acetylacetonate materials in general (15, 16) is an important difference. This matter is unclear in part because films grown from acetylacetonates lack the pronounced morphology that characterizes films prepared from aqueous solution.

Concluding Remarks

The method known as chemical vapor deposition, or CVD, is widely used for the growth of thin films of all sorts, particularly on a laboratory scale. As a typical example, acetylacetonates often are sublimed first and then carried to a hot substrate in a neutral gaseous vehicle. It is much less common, or at least not as well published aside from patent literature, to use a liquid carrier. Yet the latter, for many practical reasons, has lent itself best for coating substrates with thin, transparent films when the

emphasis has been on uniformity over a large area. It is most probable that morphologically good film formation with a liquid carrier, like other CVD, takes place entirely from the gas phase after vaporization. This view was expressed by Vigié and Spitz (12) and is reinforced by our own data. The liquid vehicle is, to a great extent, only a carrier. It is suggested herein that the aqueous vehicle in particular gives the in-flight, to-be-vaporized, metal-organic material its heretofore undisclosed shape as a hollow solid sphere, or nearly so. This follows from photomicrographic data, and microprobe scanning, for aqueous-based pyrolytic films and from a model by Charlesworth and Marshall (2) for spray drying of solutions. Finally, the analysis suggests that morphologically good films can also be grown from very fine metal-organic particles without liquid solvent, given proper dispersion in air and adequate momentum to the hot substrate. Various acetylacetonate-based systems have been described in recent patent literature to support this, which may well presage a technology in transition.

Acknowledgments

Several people have contributed to this work with their fine individual analytical efforts: H. R. Golob for electron microscopy and electron diffraction, J. M. Parsons for electron microprobe data, R. E. Robertson for atomic absorption analyses, and M. E. Helzel for spectrophotometry. I am grateful to J. O. Bookmyer and staff for helping with literature retrieval, and, as usual, to P. P. Harmon and N. Jauhar Seth for careful technical assistance. For the comments and constructive critiques of Dr. J. J. Finley and Dr. C. C. Lin, I am especially appreciative.

Manuscript submitted Oct. 15, 1984; revised manuscript received Feb. 19, 1985.

PPG Industries, Incorporated, assisted in meeting the publication costs of this article.

REFERENCES

1. J. E. Michelotti and S. M. Ohlberg, U.S. Pat. 4,308,319 (1981).
2. D. H. Charlesworth and W. R. Marshall, Jr., *AIChE J.*, **6**, 9 (1960).
3. (a) H. E. Donley, R. G. Rieser, and W. E. Wagner, U.S. Pat. 3,660,061 (1972); (b) H. E. Donley and W. P. Cathers, U.S. Pat. 4,111,150 (1978).
4. J. M. Mochel, U.S. Pat. 3,410,710 (1968).
5. S. Tolansky, "Multiple Beam Interferometry," pp. 8, 147, Clarendon Press, Oxford, England (1948).
6. O. S. Heavens, "Optical Properties of Thin Solid Films," pp. 74-80, Dover, New York (1965).
7. R. F. Raymond, U.S. Pat. 2,688,565 (1954).
8. C. F. Hendriks, H. C. A. van Beek, and P. M. Heertjes, *Ind. Eng. Chem. Prod. Res. Dev.*, **18**, 43 (1979).
9. J. S. Johnson and K. A. Kraus, *J. Phys. Chem.*, **63**, 440 (1959).
10. G. P. Van Der Kelen, E. V. Van Den Berghe, and L. Verdonck, in "Organo-Tin Compounds I," A. K. Sawyer, Editor, pp. 121-123, Marcel Dekker, Inc., New York (1971).
11. Previously unpublished demonstration of successful film preparation by C. B. Greenberg, J. E. Michelotti, and C. C. Lin.
12. J. C. Vigié and J. Spitz, *This Journal*, **122**, 585 (1975).
13. O. K. Botvinkin, I. I. Borissova, and V. A. Riabov, in "Symposium sur la Surface du Verre, et ses Traitements Modernes," p. 265, Union Scientifique Continentale du Verre, Charleroi, Belgium (1967).
14. J. Leicester and M. J. Redman, *J. Appl. Chem.*, **12**, 357 (1962).
15. R. E. Sievers and J. E. Sadlowski, *Science*, **201**, 217 (1978).
16. R. W. Moshier and R. E. Sievers, "Gas Chromatography and Metal Chelates," pp. 1-19, Pergamon Press, Oxford, England (1965).

Thickness Dependence of Transport Properties of Doped Polycrystalline Tin Oxide Films

D. Bélanger* and J. P. Dodelet**

INRS-Energie, Varennes, Québec, Canada J0L 2P0

B. A. Lombos**

Concordia University, Montreal, Québec, Canada H3G 1M8

J. I. Dickson

Ecole Polytechnique, Montréal, Québec, Canada H3C 3A7

ABSTRACT

Tin oxide films were deposited by chemical vapor deposition on borosilicate and fused silica substrates using dibutyltin diacetate (DBTD) as tin feedstock and SbCl_5 or $\text{CCl}_3\text{-CF}_3$ as dopants. The film growth rate was measured as a function of dopant/DBTD ratio, temperature, and film thickness. Scanning electron microscopy and x-ray diffraction spectra of the films were used to determine the grain sizes and the preferential orientations of the crystallites in the film as a function of film thickness. Optical and electrical properties were measured. A model is proposed to elucidate the variation of transport properties of doped SnO_2 as a function of film thickness. It could be shown with this model that the thickness dependence of the conductivity of doped $\text{SnO}_2\text{:Sb}$ and $\text{SnO}_2\text{:F}$ films could be analyzed in terms of carrier concentration taking into consideration deep-level compensation. The number of carriers is decreased by electron trapping at Sb(III) or Sn(II) surface states when antimony or fluorine are used as dopant, respectively. The model based on results of the literature related to a single crystal with (110) orientation is extended in this work to other crystallite orientations. The present analysis indicates that deep levels appear only on the grain boundary surfaces with (110), (211), and (301) orientations, and not on the (200) and (400) ones. The concentration of free carriers can be calculated on the basis of x-ray diffraction spectra indicating an estimate of the relative fraction of the crystallites with each orientation as a function of the film thickness. The conductivities of the films can be computed using this model and taking a single value for the electron mobility of $19 \text{ cm}^2 (\text{V}\cdot\text{s})^{-1}$ for all film thicknesses and a total donor concentration of $2 \times 10^{20} \text{ cm}^{-3}$. All the obtained experimental data can be accounted for exclusively on the basis of film-thickness-dependent carrier concentration.

Tin oxide films have been extensively studied for their wide applications. Among these, they can be used in semiconductor-insulator-semiconductor solar cells (1) as a back contact in either CdS/Cu₂S structures (2) or photoelectrochemical devices (3). As well, such thin films deposited on silicon can protect it from photocorrosion in photoelectrochemical cells (4). For these applications, a high electrical conductivity and a high transparency, in the visible part of the spectrum, are required.

Tin oxide films have been prepared by various techniques. Detailed review papers have recently been published on the preparation and characterization of these layers (5-7). Chemical vapor deposition (CVD) of SnO_2 films using dibutyltin diacetate (DBTD) have been developed, and it was found that films with high conductivity and high transparency could be produced by this method (8-10). In these studies, antimony (V) chloride was used as a dopant. Recently, CVD of fluorine-doped SnO_2 films have been prepared using a Freon as a dopant (11).

The production of $\text{SnO}_2\text{:F}$ films doped with trichlorotrifluoroethane ($\text{C}_2\text{F}_3\text{Cl}_3$) is reported in this work. The latter compound has the advantage of being liquid at room temperature, so it can be transported through a saturator. It is also a cost efficient and noncorrosive chemical.

In the present paper, a systematic investigation for the thickness dependence of optical, structural, and electrical properties of antimony- and fluorine-doped tin oxide is reported. This work shows that structure, grain size, and optical and transport properties of the deposited layers are thickness dependent up to $1 \mu\text{m}$. For thicker films, transport properties become thickness independent, while structure, grain size, and optical properties of these layers undergo a continuous variation.

The electrical properties of the deposited layers were analyzed on the basis of a polycrystalline conduction model. It has been realized that the dominant crystal structure is of major importance in the elucidation of the

transport properties controlled by the grain-boundaries-generated trapping centers.

Experimental Procedures

The CVD setup consists of a resistance-heated Kanthal wire furnace (Lindberg, Model M-200) containing the reaction chamber made of a fused silica tube of 50 mm diam and 1.8 m long. An inner fused silica tube of 20 mm diam was used to bring the reactants in the middle of the reaction chamber separately from oxygen and nitrogen carrier gases. The substrates, being $2.5 \times 7.5 \text{ cm}$ borosilicate slides, were positioned at the downstream side of the reactor starting at about 8 cm from the end of the inner tube. Tin oxide films were prepared following the method of Kane and co-workers (8, 9) using DBTD (Kodak) as the tin feedstock and antimony (V) chloride (Alfa Products) or trichlorotrifluoroethane, Freon 113 (Dupont Canada, Incorporated) as a dopant. Nitrogen was bubbled through the saturators containing the tin feedstock and the dopant. The DBTD, SbCl_5 , and $\text{C}_2\text{F}_3\text{Cl}_3$ sources were maintained at temperatures of 100° , 25° , and 0°C , respectively, in order to obtain the required vapor pressure for each compound. Prior to deposition, the substrate was preheated for 5 min under a nitrogen gas flow which was equivalent to the total flow of the reactants during deposition. The typical deposition flow rates of gases were 400 ml/min nitrogen carrier gas, 550 ml/min oxygen, and 1.14 liter/min nitrogen through the DBTD saturator. Through the dopant saturator, the nitrogen flow rates ranged from 5 to 210 ml/min for SbCl_5 and from 25 to 280 ml/min for $\text{C}_2\text{F}_3\text{Cl}_3$, depending upon the chosen molar ratio.

After deposition, the sheet resistivity of the deposited films was measured with a four-point probe setup for a routine verification of the electrical properties of the deposited layers. Plates of 10 mm width were cut from the SnO_2 -covered slides. The clover leaf sample geometry was defined by photolithography followed by selective etching of the SnO_2 film by a mixture of zinc powder and dilute HCl (6M) (12). This procedure corresponds to the

*Electrochemical Society Student Member.

**Electrochemical Society Active Member.

van der Pauw technique (13). Film thicknesses were determined by a profilometer (Talysurf). Ohmic contacts to SnO₂ layers were obtained using Indium solder no. 3 (Indium Corporation). In the galvanomagnetic measurements, the Hall coefficient was verified to be field independent above 0.05T. Therefore, the reported data in this investigation were measured at 0.5T. The temperature dependence of resistivity and Hall coefficient were determined between 77 and 400 K.

The film structure has been analyzed by conventional x-ray diffraction ($\lambda = 1.544\text{\AA}$) and scanning electron microscopy (SEM). Transmission measurements were performed with a double-beam spectrophotometer using a borosilicate slide in the reference beam for substrate compensation. The transmission spectra were recorded between 400 and 750 nm for each sample. Average transmission in this region was calculated from measurements at every 25 nm.

Results

Film growth rate.—It has been found that the growth rate (film thickness divided by the deposition time) of doped SnO₂ films is a function of temperature, dopant/tin feedstock molar ratio, and film thickness. The maximum growth rates were obtained at 464° and 478°C for SnO₂:Sb and SnO₂:F films, respectively. These temperatures were used for the remainder of this study.

Figure 1 shows the growth rate variation of SnO₂:Sb and SnO₂:F films as a function of dopants/DBTD molar ratio. Growth rates were determined for 1-2 μm thick films. The maxima were found to be at two very different molar ratios: 0.1 for SbCl₅ doping and 27 for Freon doping. In the case of SnO₂:Sb films, the growth rate passes through a minimum at a molar ratio of 0.15. Catalytic effects of dopants on the growth rate of semiconductors have already been reported (14, 15). For example, B₂H₆ increases the growth rate of Si deposited by pyrolysis of SiH₄, but AsH₃ acts as a catalytic poison by impeding the adsorption of silane on the growing film. The decrease of the growth rate for SnO₂:Sb could be interpreted in these terms, but the presence of a minimum in the curve is difficult to understand if there is catalytic

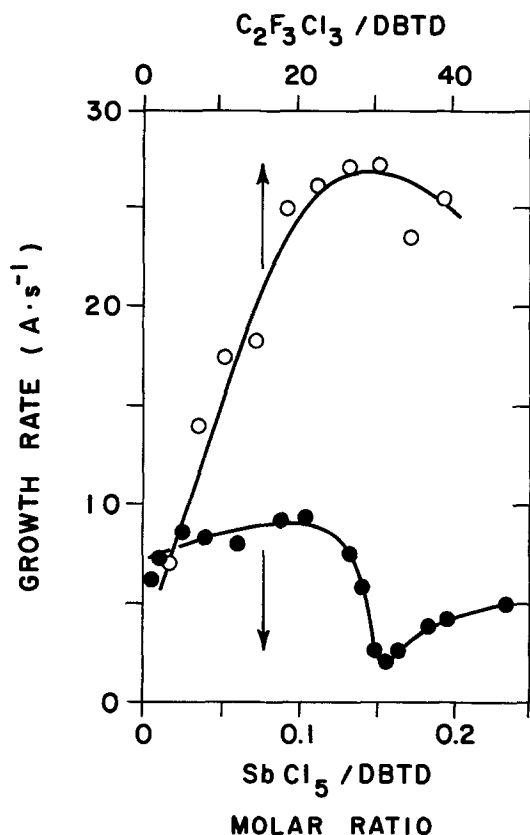


Fig. 1. Growth rate of SnO₂:Sb (dark points) and SnO₂:F (open points) as a function of the dopant/DBTD molar ratio.

poisoning. Another rationalization of the growth rate behavior could be the preferential formation of Sb-O bonds. The formation of preferential P-O bonds was postulated to explain the SnO₂ deposition rate decrease in the case of doped SnO₂ deposited by CVD from tetramethyltin and PH₃ (16). In the present study, however, x-ray diffraction spectra did not reveal any antimony oxide phases in SnO₂:Sb films.

Figure 2 shows the film-thickness dependence of the growth rate. Depositions were made with a SbCl₅/DBTD molar ratio of 0.09 for SnO₂:Sb and with a Freon/DBTD molar ratio of 8 for SnO₂:F. These are also the deposition conditions used for the remainder of this study. Doped SnO₂ films of different thicknesses were obtained by varying the deposition time from 1 to 90 min. For both dopants, the growth rates decrease up to film thicknesses of about 1 μm . For thicker layers, it stabilizes at about 10 and 13 $\text{\AA}\cdot\text{s}^{-1}$ for SnO₂:Sb and SnO₂:F films, respectively. Growth rate was defined as film thickness d divided by the deposition time Δt . In Fig. 2, it can be seen that $d/\Delta t$ varies with the film thickness; therefore, the growth rate values reported in Fig. 1 were determined by the mean value obtained for 1-2 μm thick films.

X-ray diffraction.—X-ray diffraction spectra of SnO₂:F and SnO₂:Sb films, using a beam with $\lambda = 1.544\text{\AA}$, are depicted in Fig. 3 and 4. The deposited layers were found to be composed mostly of cassiterite with a tetragonal rutile structure (17, 18). Additional peaks at $2\theta = 24.5^\circ$ and 31.8° could be assigned to Sn₃O₄ (17, 19), and the peak at $2\theta = 19.0^\circ$ appearing only in SnO₂:F suggests the existence of an unknown tin oxide phase (Sn_xO_y) or a tin fluoride (SnF₂) phase.

These figures clearly show the thickness dependence of the crystallite orientations in the films. It can be seen that, with both dopants, the (110) plane is dominant for films thinner than 1 μm (Fig. 3a and 4a). Above 1 μm , however, the dominant plane becomes (200) (Fig. 3b and 4b). The distribution of the diffraction peaks are different for larger film thicknesses, depending on the dopant. For example, the plane (211) becomes dominant for thick SnO₂:Sb films (Fig. 4c). This peak also appears in the spectrum of SnO₂:F in addition to (301) and (400) ones. The occurrence of the plane (400) as a major crystallographic orientation for SnO₂:F films has previously been observed (6).

This switching from densely populated crystallographic planes for thin films to less densely populated ones for thicker films is reflected in the growth rate. It is indeed known that the fastest growth direction is perpendicular to the plane of the largest atomic density (20). The densely populated (110) crystallites appear to represent the dominant species with both dopants for films thinner

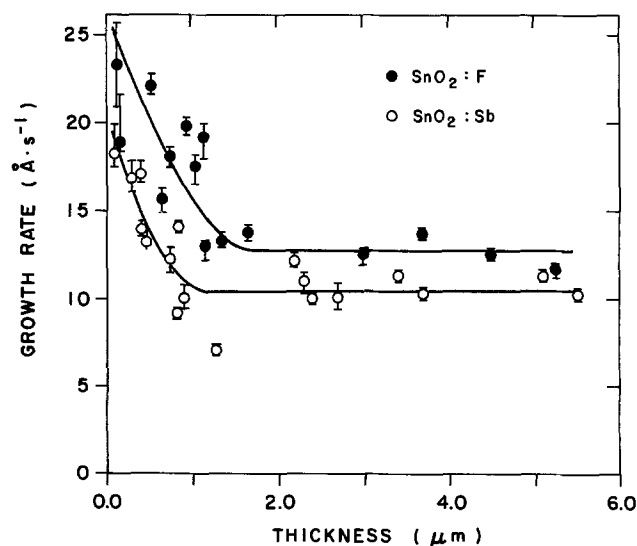


Fig. 2. Growth rate of SnO₂:Sb (open points) and SnO₂:F (dark points) as a function of film thickness.

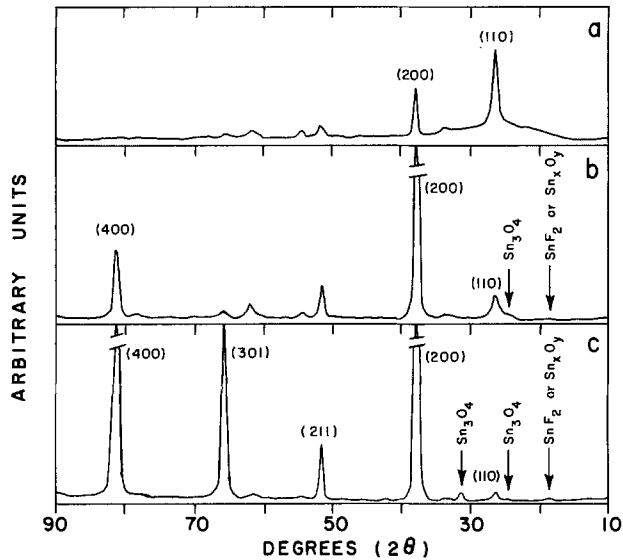


Fig. 3. X-ray diffractograms of three thicknesses of $\text{SnO}_2\text{:F}$ films. a: $0.39 \mu\text{m}$. b: $1.65 \mu\text{m}$. c: $4.5 \mu\text{m}$.

than $1 \mu\text{m}$. The preferential orientation changes for thicker films, to other crystallographic planes such as (200), (211), (301), and (400) which are all characterized by a smaller tin surface density, compared to the one of (110), leads to a reduction of the growth rate.

Scanning electron microscopy.—Grain sizes at the outer surface were determined by scanning electron microscopy (SEM). Two types of grain structures were observed. In one structure (Fig. 5a), grains of different sizes grow either independently or are clustered in a cauliflower-like shape protruding from the surface of the film. For the other structure (Fig. 5b), large grains are surrounded by many smaller grains. Columnar growth structure was revealed from SEM observations of cross sections of thicker films, so the grain sizes measured only refer to those at the outer surface of the film. It is, however, difficult to deduce from cross sections of thicker layers whether they contain small grains, as do thin layers, close to the substrate.

In Fig. 6, the average grain size is plotted as a function of layer thickness. It can be seen that the grain size linearly increases with the film thickness. Such behavior has been observed for indium tin oxide deposited on zirconia in the same thickness range (21). It is usually found that the grain size saturates for a given thickness (22).

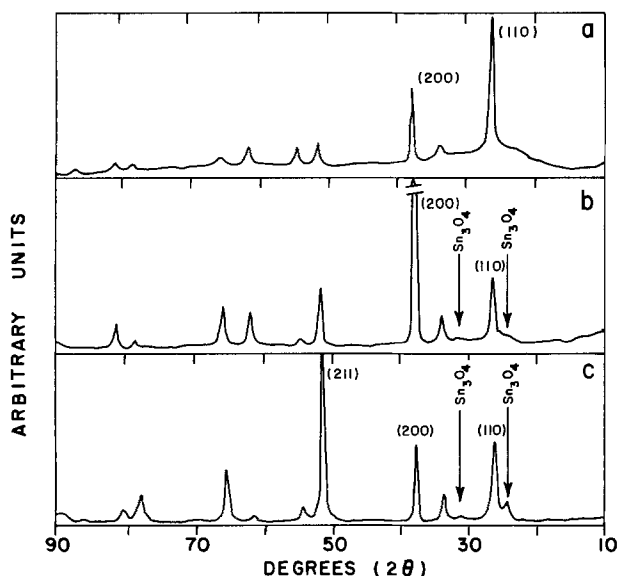


Fig. 4. X-ray diffractograms of three thicknesses of $\text{SnO}_2\text{:Sb}$ films. a: $0.31 \mu\text{m}$. b: $1.28 \mu\text{m}$. c: $5.1 \mu\text{m}$.

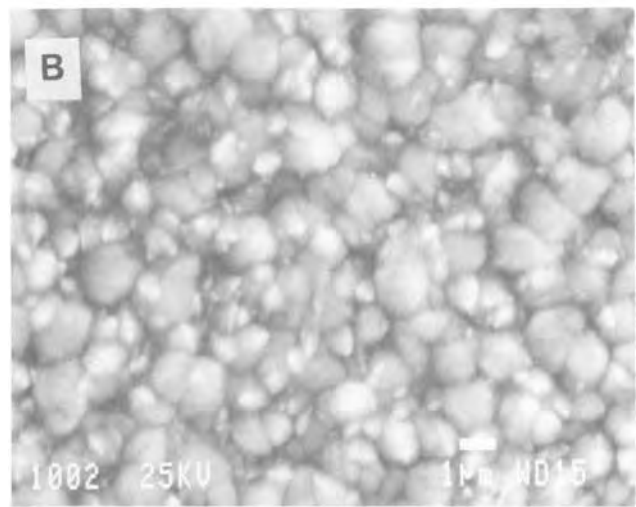
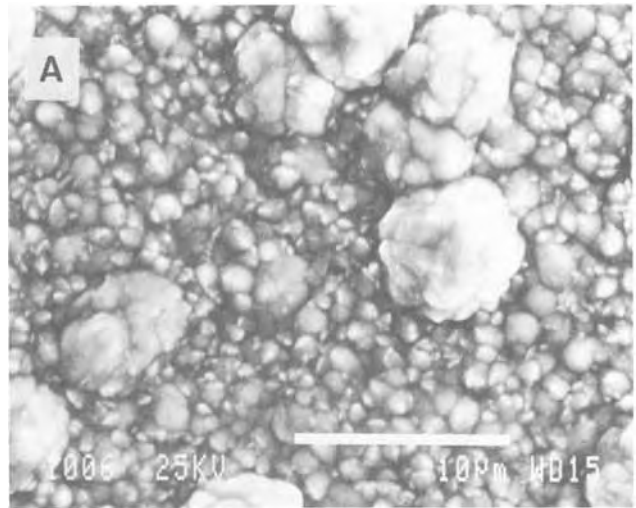


Fig. 5. SEM micrographs of A, $5.1 \mu\text{m}$, and B, $5.3 \mu\text{m}$ thick $\text{SnO}_2\text{:Sb}$ films.

However, in this study, there is no evidence of such a trend, at least up to a thickness of $5 \mu\text{m}$.

Optical properties.—Figure 7 depicts the variation of the optical transmission with the layer thickness. In the wavelength range of 400–750 nm, the transmission decreases as the thickness of SnO_2 layer increases. The ob-

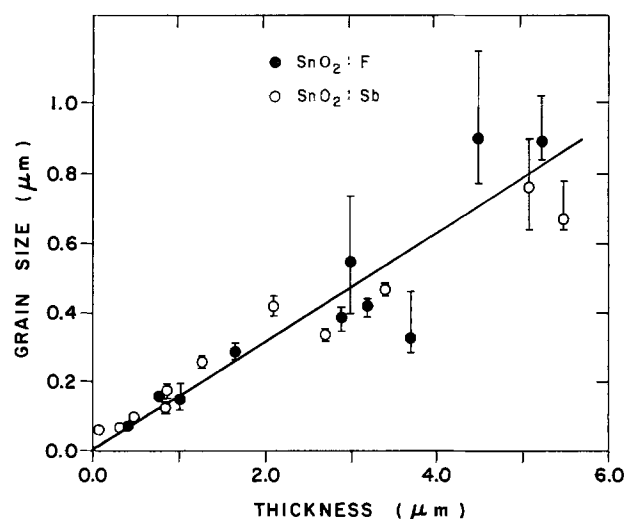


Fig. 6. Grain size of $\text{SnO}_2\text{:Sb}$ (open points) and $\text{SnO}_2\text{:F}$ (dark points) crystallites as a function of film thickness.

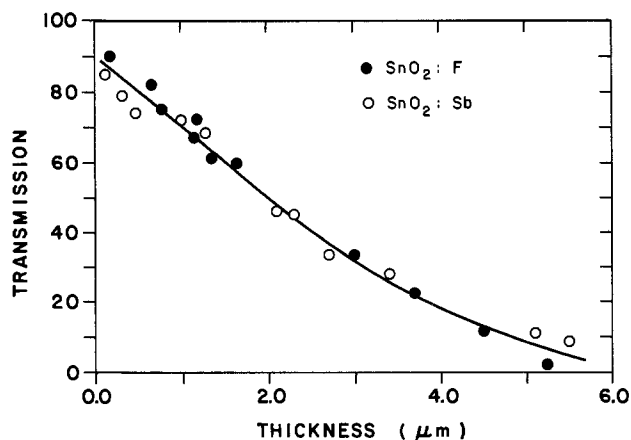


Fig. 7. Transmission in the wavelength range of 400-750 nm for $\text{SnO}_2\text{:Sb}$ (open points) and $\text{SnO}_2\text{:F}$ (dark points) as a function of film thickness.

tained values of the transmission are similar to those reported in the literature for fluorine-doped tin oxide (23, 24). In view of a possible application as transparent conductors, films thicker than $1 \mu\text{m}$ are not to be recommended due to their low transmission of the visible part of the spectrum.

Electrical properties.—Hall effect measurements indicate that $\text{SnO}_2\text{:Sb}$ and $\text{SnO}_2\text{:F}$ are n-type semiconductors. The variations of conductivity, σ , and Hall coefficient, R_H , with film thickness are illustrated in Fig. 8 and 9 for both dopants, respectively. From these data, it can be deduced that above $1 \mu\text{m}$, doped SnO_2 films have a charge carrier concentration $n \sim 2 \times 10^{20} \text{ cm}^{-3}$ and a mobility of $\sim 19 \text{ cm}^2 (\text{V}\cdot\text{s})^{-1}$.

For films thinner than $1 \mu\text{m}$, both carrier concentrations and mobilities decrease with decreasing film thicknesses. Such behavior has already been reported for the conductivity of undoped SnO_2 on Pyrex (25), doped $\text{SnO}_2\text{:F}$ on sheet glass (23, 24) and on Pyrex (23), and doped $\text{SnO}_2\text{:Sb}$ on sheet glass (26). In some instances, however, the conductivity of SnO_2 films remains constant down to very small thicknesses. These were found to be $0.05 \mu\text{m}$ for undoped SnO_2 on Si (27) and $0.1 \mu\text{m}$ for $\text{SnO}_2\text{:Sb}$ on Pyrex and on fused silica (26). The influence of the substrate in the experiments of this investigation

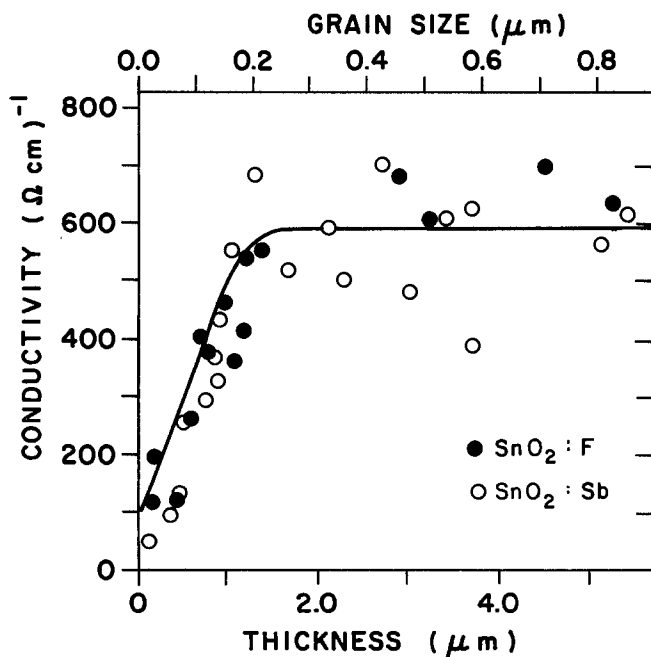


Fig. 8. Conductivity of $\text{SnO}_2\text{:Sb}$ (open points) and $\text{SnO}_2\text{:F}$ (dark points) as a function of film thickness. Calculated curve (solid line) using the model presented in the discussion.

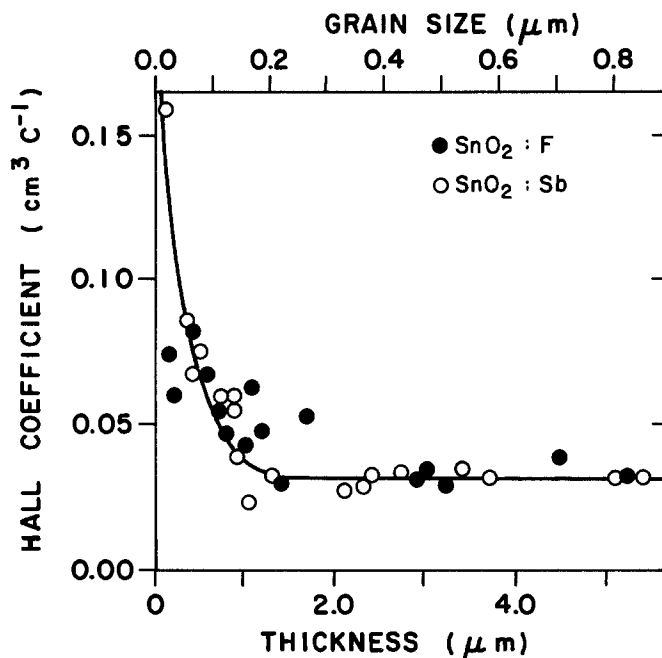


Fig. 9. Hall coefficient for $\text{SnO}_2\text{:Sb}$ (open points) and $\text{SnO}_2\text{:F}$ (dark points) as a function of film thickness. Calculated curve (solid line) using the model presented in the discussion.

has been ruled out, since the same behavior of σ and R_H was obtained on both fused silica and borosilicate substrates.

In Fig. 10, the conductivity of three $\text{SnO}_2\text{:Sb}$ films of different thicknesses is plotted against the reciprocal temperature. Since the carrier concentration, characteristic of each film thickness, remains constant in the investigated temperature range, the change of the film conductivity as a function of the temperature reflects a similar variation of the mobility. The largest activation energy calculated from Fig. 10 is only $\sim 0.01 \text{ eV}$ for a $0.31 \mu\text{m}$ $\text{SnO}_2\text{:Sb}$ film in the high temperature region.

Discussion

Transport properties models.—It can be seen from the above results that SnO_2 films are polycrystalline. They are composed of crystallites joined together by grain boundaries which are transitional regions between differ-

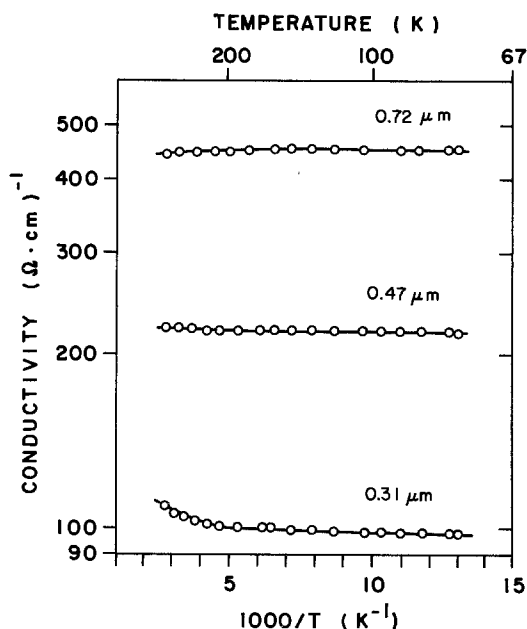


Fig. 10. Conductivity of three thicknesses of $\text{SnO}_2\text{:Sb}$ films as a function of T^{-1} .

ent orientations of neighboring crystallites. Among polycrystalline semiconductors, polysilicon has been the most extensively studied material. Two existing models were employed to analyze the effects of grain boundaries on electrical properties of this material.

The first is a charge trapping model (15, 28-33) where it is assumed that grain boundaries contain lattice-defects-induced trapping states. These states compensate a fraction of the charge carriers of the ionized uniformly distributed dopants. This process creates a potential barrier across the depletion region, impeding the carrier motion from one crystallite to another. The influence of the grain size becomes very important when the depletion layer width becomes commensurable with the grain size of the crystallite. This treatment was applied to SnO_2 as well (34). In this model, the conduction mechanism is based on thermionic emission over the potential barrier. This, of course, requires a barrier energy larger than kT . As has been deduced from Fig. 10, the largest activation energy calculated from this figure is only ~ 0.01 eV for $0.31 \mu\text{m}$ SnO_2 :Sb film in the high temperature region. This is well below kT ; therefore, the model based on thermionic emission of carriers over an energy barrier at the grain boundary is not applicable to doped SnO_2 films.

The second is a dopant segregation model. In this case, the grain boundaries are assumed to act as sinks for preferential segregation of the dopants. Therefore, they become inactive in the boundary layers (35, 36).

In the following discussion, this model will be extended to analyze the conductivity variation of our SnO_2 :Sb or SnO_2 :F films with the layer thickness. In this compound semiconductor, it is to be recognized that the different crystal planes are having characteristic charge distribution to maintain specific neutrality conditions. This was not the case in elemental semiconductor discussed previously in the literature (28-36). In polycrystalline-doped SnO_2 films, based on the x-ray diffraction data (see Fig. 3 and 4), five dominant planes were considered. These are (110), (200), (211), (301), and (400). It will be discussed in the following that only three of these, (110), (211), and (301), are introducing deep lying trapping levels. These result in a compensation of free carriers of the crystallites. Consequently, the thickness dependence of the experimental carrier concentration is analyzed in terms of two factors. On the one hand, the specific effects of the crystalline orientations of the grains are examined. On the other hand, the total surface area of the grains is taken into account.

The extension of the segregation model has been based on the following results obtained from the literature. The maximum solid solubility of antimony in the rutile phase of SnO_2 is limited to an Sb/Sn ratio of $\sim 4\%$ (37). An investigation of polycrystalline material with this critical composition by Mössbauer spectroscopy indicated the presence of antimony (V) ions in the bulk together with antimony (III) ions at the surfaces of the grain boundaries (38). In order to investigate further the surface properties of SnO_2 , Cox *et al.* (39) studied undoped and doped SnO_2 (Sb/Sn = 3%) with surface sensitive techniques such as x-ray photoelectron spectroscopy (XPS) and ultraviolet photoelectron spectroscopy (UPS). Although the results of their investigation will be used in the present discussion, it is important to notice that their preparation method yielded single-crystal material in the (110) orientation for both undoped and doped SnO_2 .

It has been shown by XPS that a dramatic surface enrichment in antimony occurs. This was interpreted by the exchange of Sn cations by Sb at the surface of the bulk rutile structure. The normal $N(\text{Sb})/N(\text{Sn})$ bulk ratio is reestablished immediately beneath this monoatomic surface layer. Their UPS data indicated that the bulk free carrier concentration extends very close to this surface but surface antimony atoms do not contribute to the conduction. This suggests that free carriers may be trapped in these surface states which lie deep below the conduction band. In the literature, the surface states were identified to be Sb(III). These states also exist on the surface of

undoped materials where they are associated with Sn(II). In addition, Cox *et al.* (39) rationalized the stabilization of Sn(II) and Sb(III) on the surface of undoped and doped SnO_2 on the basis of electrical neutrality of the rutile structure. It is to be mentioned that although they recognized the strong tin oxygen covalency in SnO_2 , the ionicity of the covalent bond is used in their model.

Following the results of the literature, Fig. 11a shows the SnO_2 (110) surface without reduction of the top oxygen layer. The sequence of charged planes is $-2, +4, -2$. If the top oxygen plane with two negative charges is removed, the (110) surface terminates on the Sn(IV) containing plane, with four positive charges. To retain electrical neutrality, one Sn(IV) atom of this plane has to be reduced to Sn(II) as is depicted in Fig. 11b. Consequently, the sequence of charged planes at the surface will be $+2, -2$. This represents both undoped and fluorine-doped SnO_2 . In the antimony-doped films, however, the neutrality principle requires that all tin atoms should be exchanged by Sb(III) as is shown in Fig. 11c. Consequently, here as well, the sequence of charged planes at the surface remains $+2, -2$. This argument clarifies why, on doping (110) SnO_2 grains, part of the antimony is first used in the surface plane as Sb(III). Thus, this fraction of the antimony doping does not participate in the conduction mechanism.

The results obtained by Cox *et al.* (39) are used in the present investigation to extend the segregation model to other crystallographic orientations of interest. This is discussed in the following. Figure 12 shows the sequence of charged planes for a (200) surface. In contrast to the above-discussed (110) plane, no top oxygen plane has to be removed in this case in order to terminate the surface of a tin containing plane. Therefore, the (200) SnO_2 surface will only contain Sn(IV) atoms. Doping with antimony will substitute for some Sn(IV) Sb(V), which are acting as donors. Then, according to this treatment, there will not be any surface states as electron traps [e.g., Sb(III)], since surface atoms are either Sn(IV) or Sb(V).

The (211) planes, however, behave like (110) planes. Figure 13a represents the sequence of charged planes of a (211) surface without reduction. The charges are $-4, +16, -4$, and -8 considering four unit cells. If the top oxygen plane is removed (-4), then the (211) surface terminates on a tin containing plane with $+16$ charges. To retain electrical neutrality, two Sn(IV) atoms have to be reduced to Sn(II) as it is shown in Fig. 13b, decreasing the surface charge to $+12$. The sequence of charged planes in this case will be $+12, -4, -8$. This represents the case of undoped and fluorine-doped films. In the antimony-

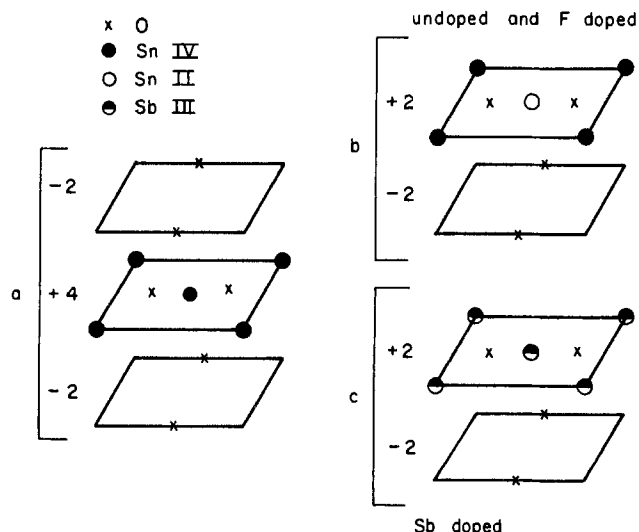


Fig. 11. Crystallite surface of SnO_2 grown according to the (110) plane. a: Undoped SnO_2 with the outside oxygen layer. b: Undoped and F-doped SnO_2 after reduction. c: Antimony-doped SnO_2 after reduction.

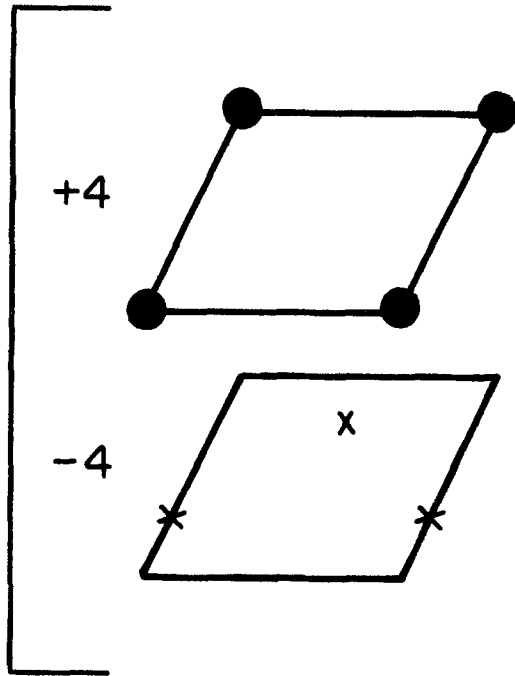


Fig. 12. Crystallite surface of SnO₂ grown according to the (200) plane for undoped SnO₂. The symbols are described in Fig. 11.

doped SnO₂, however, the neutrality requires that all tin atoms in the top layer should be replaced by Sb(III), as it is shown in Fig. 13c, resulting in a surface charge of (+12). Then, the sequence of charged planes remains +12, -4, -8. As in the case of (110) orientation, part of the antimony is first used in the surface plane as Sb(III). This fraction of the antimony doping cannot participate in the conduction mechanism. In the case of undoped and fluorine-doped material, however, the compensating trapping center concentration will be given by the Sn(II) concentration in (110) and (211) grains.

Using this model, based on the crystallographic analysis of the SnO₂:Sb films prepared in this investigation, one can compute the variation of the carrier concentration as a function of film thickness. The results are summarized in Table I. Here, F_{110} , F_{200} , and F_{211} are the fractions of crystallites in the films having (110), (200), and (211) crystallographic orientations, collected for various film thicknesses. These fractions were obtained taking into consideration the relative amplitudes of the (110), (200), and (211) peaks of the x-ray diffraction spectra. It is assumed, as a first approximation, that the peak amplitudes are proportional to the relative amounts of the crystallites of the corresponding orientations. The above-mentioned three orientations are considered for SnO₂:Sb in this analysis.

The Sb(III) densities of the doped (110) and (211) crystallites, N_{110} and N_{211} , can be calculated for various film thicknesses as follows

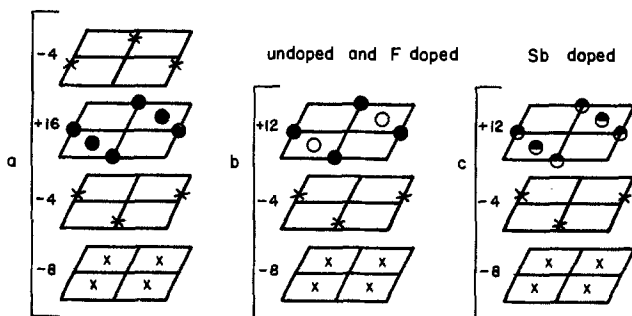


Fig. 13. Crystallite surface of SnO₂ grown according to the (211) plane. a: Undoped SnO₂ with the outside oxygen layer. b: Undoped and F-doped SnO₂ after reduction. c: Antimony-doped SnO₂ after reduction. The symbols are described in Fig. 11.

Table I. SnO₂:Sb film thickness, grain size, fractions of (110), (200), and (211) crystallites, total Sb(III) concentration for (110) and (211) crystallites, and carrier concentration

$d(\mu\text{m})$	$l(\mu\text{m})$	F_{110}	F_{200}	F_{211}	$N_t (\text{cm}^{-3})$ ($\times 10^{20}$)	$n (\text{cm}^{-3})$ ($\times 10^{20}$)
0.11	0.02	0.67	0.18	0.15	15.3	0.38
0.31	0.06	0.57	0.33	0.10	4.26	0.69
0.47	0.08	0.52	0.39	0.09	2.89	0.82
0.86	0.14	0.65	0.30	0.05	1.95	0.74
1.28	0.21	0.16	0.70	0.14	0.446	1.97
2.3	0.37	0.10	0.79	0.11	0.170	2.00
3.4	0.54	0.15	0.45	0.40	0.264	1.96
5.1	0.80	0.21	0.22	0.57	0.253	1.90
5.5	0.87	0.17	0.18	0.65	0.233	1.91

$$N_{t110} = F_{110} \times N_{110} \quad [1]$$

where N_{110} is the number of tin atoms per cubic centimeter on the surface of (110) crystallites. N_{110} is calculated assuming columnar crystallites using the following equation

$$N_{110} = \left(\frac{2}{d} + \frac{4}{l} \right) \times A_{110} \quad [2]$$

where l and d are the diameter and height (film thickness) of the crystallite, respectively. A_{110} is the number of tin atoms per square centimeter on (110) plane. Since the lattice constants for SnO₂ are $a = b = 4.737\text{\AA}$ and $c = 3.185\text{\AA}$ (18), $A_{110} = 9.4 \times 10^{14}$ Sn at./cm². N_{211} can be obtained similarly using $A_{211} = 4.8 \times 10^{14}$ Sn at./cm².

Since Sb(III) replaces all tin atoms on (110) and (211) surfaces, N_{110} and N_{211} represent also the Sb(III) density of their respective crystallographic orientations. Then the total density of Sb(III) in the film, N_s , is given by

$$N_t = N_{t110} + N_{t211} \quad [3]$$

The obtained N_t values are collected in Table I and depicted in Fig. 14 (open triangle). Since, as has been discussed above, the Sb(III) act as trapping centers, the free carrier concentration can be computed as follows. If N_d is the donor concentration, antimony, in this case, the electron density in the conduction band for the (110) and (211) orientations will be $n = (N_d - N_s)$. This corresponds to the number of Sb(V) donors. However, for (200) orientation, the electron concentration in the conduction band will be equivalent to N_d since no Sb(III) are present on the surface of these crystallites. Therefore the total carrier concentration for SnO₂:Sb can be given by

$$n = (F_{200} \times N_d) + [(1 - F_{200}) \times (N_d - N_s)] \quad [4]$$

The calculated values of the free carrier concentration, n , for various film thicknesses are collected in Table I and shown as open circles in Fig. 14. N_d is an adjustable parameter, but its value must be very close to the experimental donor concentration for the largest crystallites. In this case, the effect of surface trapping becomes negligible. Thus, the value of $N_d = 2.0 \times 10^{20} \text{ cm}^{-3}$ has been used in these calculations.

From Fig. 14, it can be deduced that the contribution to charge carrier concentration, n , of the (110) and (211) crystallites begins for SnO₂:Sb films thicker than about 0.5 μm when the surface-state-introduced deep-level trapping center concentration, N_s , becomes less than the doping concentration N_d . For thinner films, all the carriers are coming exclusively from (200) crystallites, and their concentration increases with the increasing fraction F_{200} as a function of film thickness (see Table I). It is implicitly assumed in these calculations that an electric path exists between the (200) crystallites present in these films by direct contact between the (200) grains or, in the case of increasing dilution of these grains, by the formation of preferential conducting path according to the percolation theory (40).

In the case of fluorine doping, the Sn(II) surface states will behave as trapping centers. Therefore, the model can

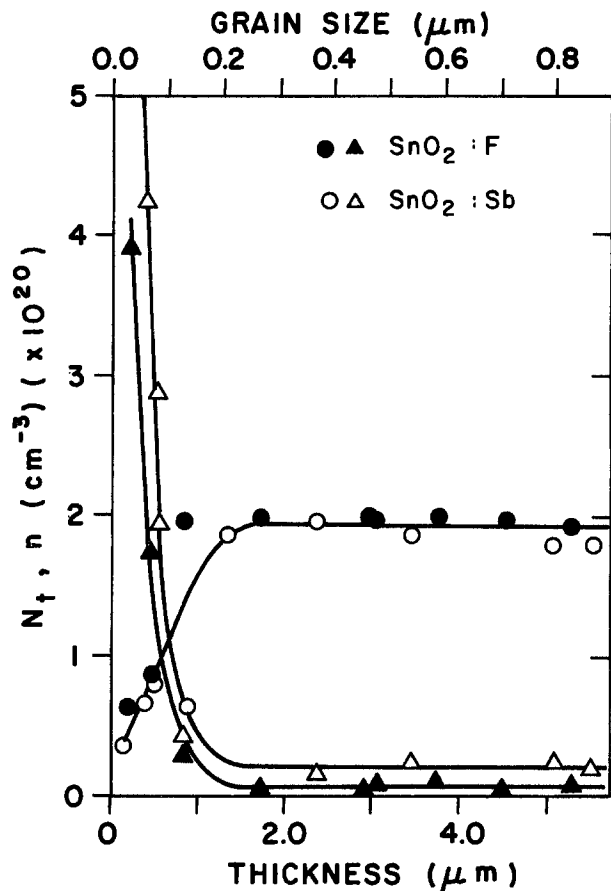


Fig. 14. Total electron trap concentration N_t (Δ , \blacktriangle) and charge carrier concentration n (\circ , \bullet) calculated on the basis of x-ray diffraction spectra, for different thicknesses of $\text{SnO}_2\text{:Sb}$ (open symbols) and $\text{SnO}_2\text{:F}$ (dark symbols). The n curve represents a mean value through the calculated points.

be extended to analyze the transport properties of the fluorine-doped SnO_2 as well. This is treated in the following way. Five crystallographic planes ought to be considered as they become important at different thickness ranges. As far as Sn(II) surface states are concerned, the (400) planes can be treated like (200) planes; similarly, the (301) planes behave like the (110) or the (211) ones. This is shown in Fig. 15. Here, all Sn(IV) (full circles, Fig. 15a) must be reduced to Sn(II) (open circles, Fig. 15b) after the reduction of the oxygen layer to maintain the electrostatic neutrality. The total trapped electron concentration, N_t , corresponds, therefore, in the case of fluorine-doped SnO_2 , to the density of Sn(II). This can be given by the following equation

$$N_t = N_{110} + N_{211} + N_{301} \quad [5]$$

where N_{110} and N_{211} are obtained, as before, from the x-ray diffraction spectra. It is, however, to be noticed that, in this case, only half of the N_{110} and N_{211} concentrations deduced earlier have to be considered. In effect, examin-

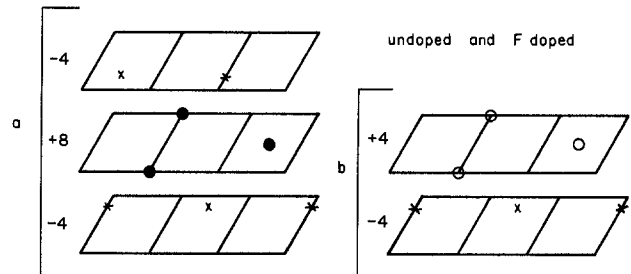


Fig. 15. Crystallite surface of SnO_2 grown according to the (301) plane. a: Undoped SnO_2 with the outside oxygen layer. b: Undoped and F-doped SnO_2 after reduction. The symbols are described in Fig. 11.

ing Fig. 11b and 13b, one can see that only half of the Sn atoms contribute to the trapping density instead of all surface atoms, as in the case of antimony doping shown in Fig. 11c and 13c. For the (301) crystallites, $A_{301} = 4.0 \times 10^{14}$ Sn at./cm² determined from the unit cell parameters, is used to calculate N_{301} .

Finally, the free carrier concentration, in the case of fluorine doping, can be expressed as

$$n = (F_{200} + F_{400}) N_d + [(1 - [F_{200} + F_{400}]) \times (N_d - N_t)] \quad [6]$$

The calculated variation of n vs. the film thickness for $\text{SnO}_2\text{:F}$ is shown in Fig. 14 (full circles), along with N_t (full triangles). A single curve has been drawn through the calculated n values for both dopants. The experimentally determined fractions based on the x-ray diffraction spectra, for all the crystallographic orientations which have been taken into consideration, are collected in Table II.

Values from the calculated carrier concentration curve displayed in Fig. 14 can be used to determine a calculated Hall coefficient curve. This is shown as a full line in Fig. 9. Furthermore, assuming that the drift mobility is equal to the Hall mobility, the conductivity can be calculated. The result is displayed as a full line in Fig. 8. Here, a mobility of $19 \text{ cm}^2 (\text{V}\cdot\text{s})^{-1}$ has been used in the calculation for all film thicknesses. The fit of the calculated curves to the experimental points in Fig. 8 and 9 is quite reasonable.

Conclusion

It has been shown that the thickness dependence of the conductivity of doped SnO_2 films can be elucidated in terms of charge carrier concentration taking into consideration defect-induced deep-level compensation. Independently of the dopants used, the maximum charge carrier concentration in the films is decreased by electron trapping of Sb(III) or Sn(II) surface states when antimony or fluorine are used as a dopant, respectively. These deep lying trapping centers appear only on the surface of crystallites with (110), (211), and (301) crystallographic orientations.

The number of free carriers in the films can be calculated on the basis of x-ray diffraction spectra giving an estimate of the relative fractions of (110), (211), and (301) crystallites as a function of film thickness. The conductivity can be deduced from this model using a single

Table II. $\text{SnO}_2\text{:F}$ film thickness, grain size, fractions of (110), (200), (211), (301), and (400) crystallites, total Sn(II) concentration for (110), (211), and (301) crystallites, and carrier concentration

$d(\mu\text{m})$	$l(\mu\text{m})$	F_{110}	F_{200}	F_{211}	F_{301}	F_{400}	$N_t (\text{cm}^{-3}) (\times 10^{20})$	$n (\text{cm}^{-3}) (\times 10^{20})$
0.14	0.03	0.45	0.32	0.23	0	0	3.92	0.6
0.39	0.07	0.53	0.33	0.09	0.03	0.02	1.75	0.8
0.76	0.13	0.14	0.74	0.05	0.02	0.05	0.290	1.9
1.65	0.27	0.04	0.76	0.06	0.01	0.13	0.059	1.9
2.9	0.46	0.02	0.72	0.02	0.02	0.22	0.021	1.9
3.0	0.48	0.02	0.59	0.17	0.10	0.12	0.080	1.9
3.7	0.59	0.004	0.65	0.01	0.03	0.306	0.012	2.0
4.5	0.71	0.007	0.51	0.06	0.20	0.223	0.059	1.9
5.3	0.83	0.12	0.43	0.28	0.12	0.05	0.088	1.9

value for the electron mobility of $19 \text{ cm}^2 (\text{V}\cdot\text{s})^{-1}$ and a total doping concentration, $N_d = 2 \times 10^{20} \text{ cm}^{-3}$, for all film thicknesses. The computed values are in good agreement with the experimental data.

In this model, it is assumed that in the case of doping with antimony, for example, the dopant first substitutes all tin sites on the surface by Sb(III). This fraction of the antimony does not act as donor, but does introduce deep-lying trapping states. However, it is argued that only some of the crystallites with specific orientations participate in this trapping mechanism.

If this model is correct, very thin films ($\ll 1 \mu\text{m}$) dominated by (200) crystallites should have the same transport properties as thicker films ($> 1 \mu\text{m}$) where this crystallographic orientation prevails. As SnO_2 is used as a transparent electrode, the thinner the film, the better its transmission. Therefore, the production of very thin films with the same conductivity as thicker ones could be an asset if thin film technology of (200) dominant orientation can be developed.

Acknowledgments

This work was partially supported by grants from NSERC and FCAC from the Canadian and Québec governments, respectively. The authors are grateful for the valuable contribution of Dr. M. A. Bartkowski in the transport properties measurements.

Manuscript submitted Nov. 5, 1984; revised manuscript received Feb. 25, 1985.

INRS-Energie assisted in meeting the publication costs of this article.

REFERENCES

- H. P. Maruska, A. K. Ghosh, D. J. Eustace, and T. Feng, *J. Appl. Phys.*, **54**, 2489 (1983).
- S. Martinuzzi, *Solar Cells*, **5**, 243 (1982).
- D. Bélanger, J. P. Dodelet, L. H. Dao, and B. A. Lombos, *J. Phys. Chem.*, **88**, 4288 (1984).
- F. Decker, J. Melsheimer, and H. Gerischer, *Isr. J. Chem.*, **22**, 195 (1982).
- K. L. Chopra, S. Major, and D. K. Pandya, *Thin Solid Films*, **102**, 1 (1983).
- J. C. Manificier, *ibid.*, **90**, 297 (1982).
- J. L. Vossen, *Phys. Thin Films*, **9**, 1 (1977).
- J. Kane, H. P. Schweizer, and W. Kern, *This Journal*, **122**, 1144 (1975).
- J. Kane, H. P. Schweizer, and W. Kern, *ibid.*, **123**, 270 (1976).
- D. Bélanger, M. Bartkowski, J. P. Dodelet, B. A. Lombos, I. Dickson, and L. Dao, *J. Can. Ceram. Soc.*, **52**, 28 (1983).
- R. G. Gordon, U.S. Pat. 4,146,657 (1979).
- D. K. Schroder, *IEEE Trans. Electron. Devices*, **ed-25**, 90 (1978).
- L. J. van der Pauw, *Philips Res. Rpt.*, **13**, 1 (1958).
- Y. S. Hsu and S. K. Ghandhi, *This Journal*, **126**, 1434 (1979).
- P. Rai-Choudhury and P. L. Hower, *ibid.*, **120**, 1761 (1973).
- Y. S. Hsu and S. K. Ghandhi, *ibid.*, **127**, 1592 (1980).
- N. S. Murty and S. R. Jawalekar, *Thin Solid Films*, **100**, 219 (1983).
- Z. M. Jarzebski and J. P. Marton, *This Journal*, **123**, 199C (1976).
- M. Hecq, A. Dubois, and J. Van Cakenberghe, *Thin Solid Films*, **18**, 117 (1973).
- W. L. Runyan, in "Silicon Semiconductor Technology," p. 31, McGraw-Hill, New York (1965).
- M. Privman, J. Berger, and D. S. Tannhauser, *Thin Solid Films*, **102**, 117 (1983).
- C. A. Neugebauer, in "Handbook of Thin Film Technology," L. I. Maissel and R. Glang, Editors, Chap. 8, McGraw-Hill, New York (1970).
- H. DeWaal and F. Simonis, *Thin Solid Films*, **77**, 253 (1981).
- R. Pommier, C. Gril, and J. Marucchi, *ibid.*, **77**, 91 (1981).
- N. Srinivasa Murty, G. K. Bhagavat, and S. R. Jawalekar, *ibid.*, **92**, 347 (1982).
- H. Kaneko and K. Miyaka, *J. Appl. Phys.*, **53**, 3629 (1982).
- W. Badawy, F. Decker, and K. Doblhofer, *Solar Energy Mater.*, **8**, 363 (1983).
- T. I. Kamins, *J. Appl. Phys.*, **42**, 4357 (1971).
- J. Y. W. Seto, *ibid.*, **46**, 5247 (1975).
- G. Baccarani and B. Ricco, *ibid.*, **49**, 5565 (1978).
- N. C. C. Lu, L. Gerzberg, C. Y. Lu, and J. D. Meindl, *IEEE Trans. Electron. Devices*, **ed 28**, 818 (1981).
- N. C. C. Lu, C. Y. Lu, M. K. Lee, C. C. Shih, C. S. Wang, W. Reuter, and T. T. Sheng, *This Journal*, **131**, 894 (1984).
- L. L. Kazmerski, in "5th E. C. Photovoltaic Solar Energy Conference Proceedings," W. Palz and F. Fittipaldi, Editors, p. 40, D. Reidel Publishing Company, Dordrecht (1983).
- M. C. Bost, E. W. Butler, and V. P. Singh, in "Materials and New Processing Technologies for Photovoltaics," J. P. Dismukes, E. Sirtl, P. Rai-Choudhury, and L. P. Hunt, Editors, p. 411, The Electrochemical Society Softbound Proceedings Series, Pennington, NJ (1982).
- M. E. Cowher and T. O. Sedgwick, *This Journal*, **119**, 1565 (1972).
- B. A. Lombos, S. Yee, M. Pietrantonio, and M. Averous, *J. de Phys.*, **43**, C1-199 (1982).
- D. R. Pyke, R. Reid, and R. J. D. Tilley, *J. Chem. Soc. Faraday Trans 1*, **76**, 1174 (1980).
- F. J. Berry and B. J. Laundry, *J. Chem. Soc. Dalton Trans.*, 1442 (1981).
- P. A. Cox, R. G. Edgell, C. Harding, W. R. Patterson, and P. J. Tavener, *Surf. Sci.*, **123**, 179 (1982).
- B. I. Shklovskii, *Sov. Phys. JEPT Engl. Trans.*, **45**, 152 (1977).

LPCVD Oxide/LPCVD Nitride Stacks for Interpoly Dielectrics

Tiao-Yuan Huang,^{*,1} Donald J. Coleman, and James L. Paterson

Texas Instruments Incorporated, Semiconductor Process and Design Center, Dallas, Texas 75265

ABSTRACT

An LPCVD oxide/LPCVD nitride stack has been investigated as a possible substitute for the interpoly oxide in double-level-polysilicon VLSI processes. Results from capacitor lots show that 25 nm LPCVD oxide/25 nm LPCVD nitride stacks yield breakdown voltages greater than 25V with a tight distribution. The breakdown voltage can further be enhanced by depositing an additional LPCVD blocking oxide of 50Å thickness on the stack. Suitable thermal sealing oxides are also shown to be effective in enhancing the breakdown field strength. A further scaling of the stack thickness is also demonstrated.

The thermal oxide grown on polysilicon is known to be much leakier than the single-crystal counterpart. It is also well known that a higher oxidation temperature (> 1100°C) tends to smooth the asperities and yield better polyoxide (1, 2). However, such a high temperature treatment may be prohibitive in future VLSI process flows. On the other hand, the use of lower temperature (less than or equal to 1000°C) oxidation results in surface-reaction-controlled oxidation and, thus, a rougher polysilicon surface and a much leakier resultant polyoxide. An alternative dielectric deposited by LPCVD is a potential substitute for thermal polyoxide in VLSI processes.

Different combinations of thin LPCVD oxide and LPCVD nitride stacks (with equivalent SiO₂ thickness less than 500Å) have been demonstrated to yield good-quality, low defect density interpoly dielectrics suitable for VLSI EPROM/EEPROM applications (3, 4, 7, 8).

Experiments

P-type, (100) silicon slices at resistivity of 12-16 Ω-cm were used as the starting material. After growing a 400Å HCl-oxide, LPCVD polysilicon with nominal thickness of 3000Å was deposited; slices were then saturation POCl₃ doped at 1000°C. After stripping of the PSG grown during POCl₃ predeposition, different LPCVD oxide/LPCVD nitride stacks were then deposited (see Table I). For some splits, the oxide/nitride stacks were subjected to different postdeposition oxidation treatments to grow a suitable sealing oxide. A 4500Å polysilicon film was then deposited and saturation POCl₃ doped to serve as the upper electrode. The polyoxide capacitors were defined by photolithography and plasma etching. An additional 1000°C, 30 min heat-treatment and a 450°C hydrogen sintering were incorporated to simulate a full process flow. Breakdown and I-V characteristics were measured, with breakdown being defined as the voltage at which the current density exceeds 20 μA/cm² when a positive

voltage ramp is applied to the second-level polysilicon gate. The capacitor area is 0.0052 cm².

Results and Discussion

Figure 1 shows the histogram of a 25 nm LPCVD oxide/25 nm LPCVD nitride stack. With an equivalent electrical SiO₂ thickness (the thickness assuming a dielectric constant of 3.9 ε₀) of 37 nm, the stack shows a tight breakdown voltage distribution centered at 27V. The I-V characteristic of a typical 25 nm LPCVD oxide/25 nm LPCVD nitride stack is shown in Fig. 2. It can be seen that the low-field leakage is approximately 1 nA/cm² at 12V. Another feature of the oxide/nitride stack is that the I-V curves of the first (from a virgin sample) and second stresses fall almost upon each other, suggesting that a

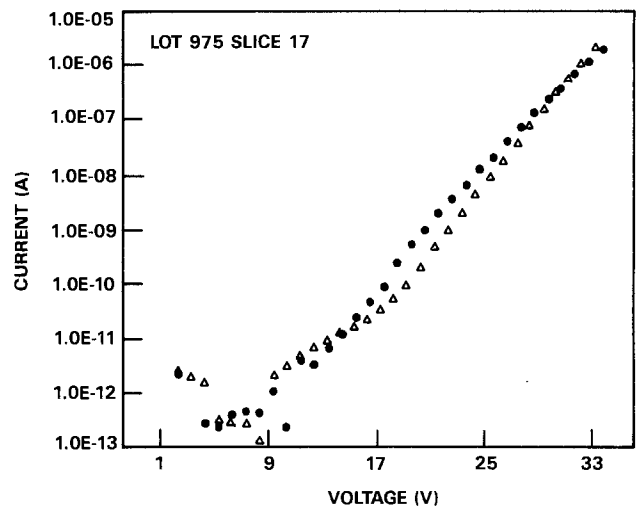


Fig. 2. I-V characteristic for a 25 nm LPCVD oxide/25 nm LPCVD nitride, bilayer film; capacitor area = 0.0052 cm². The solid circle shows the first stress; the solid triangle the second stress.

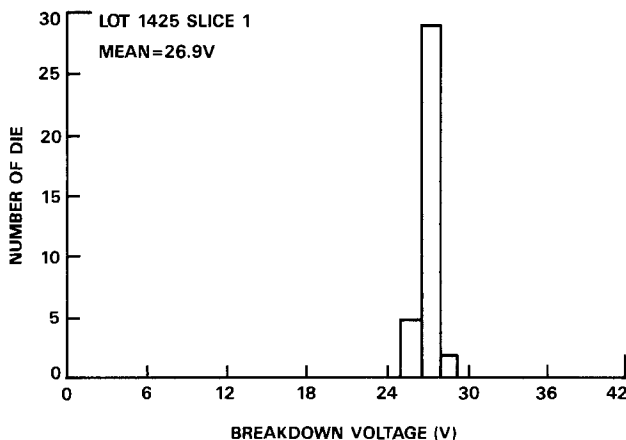


Fig. 1. Histogram of breakdown voltage for a 25 nm LPCVD oxide/25 nm LPCVD nitride, bilayer film.

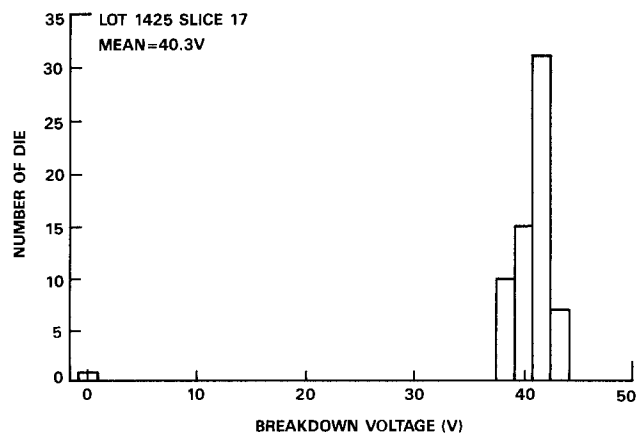


Fig. 3. Histogram of breakdown voltage for a 25 nm LPCVD oxide/25 nm LPCVD nitride/5 nm LPCVD oxide, trilayer film.

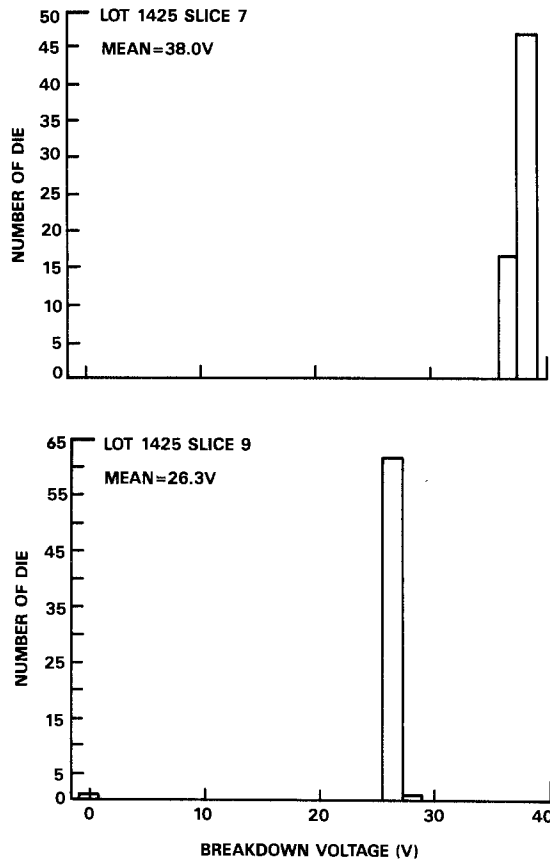


Fig. 4. Histograms of breakdown voltage for 25 nm LPCVD oxide/25 nm LPCVD nitride film annealed at 1000°C in oxygen for 20 min (lower) and 90 min (upper).

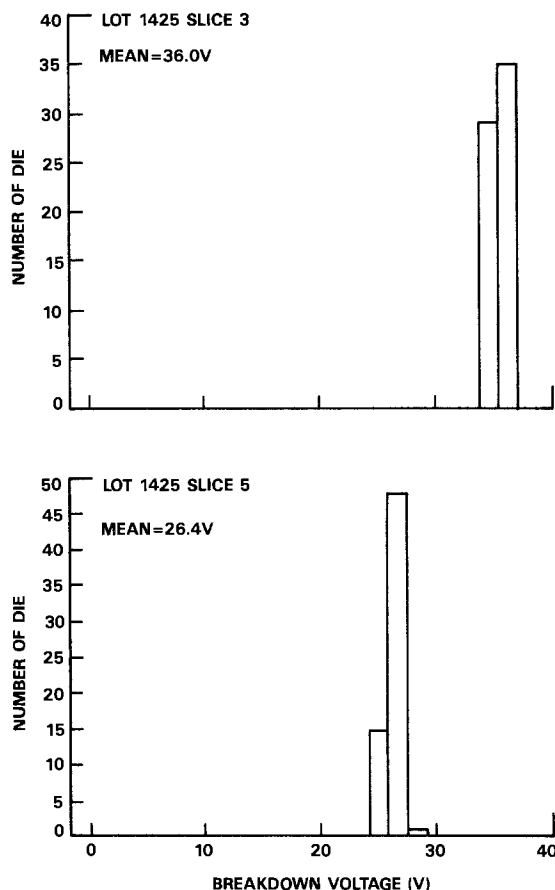


Fig. 5. Histograms of breakdown voltage for a 25 nm LPCVD oxide/25 nm LPCVD nitride film annealed in steam for 65 min at 900°C (lower) and 1000°C (upper).

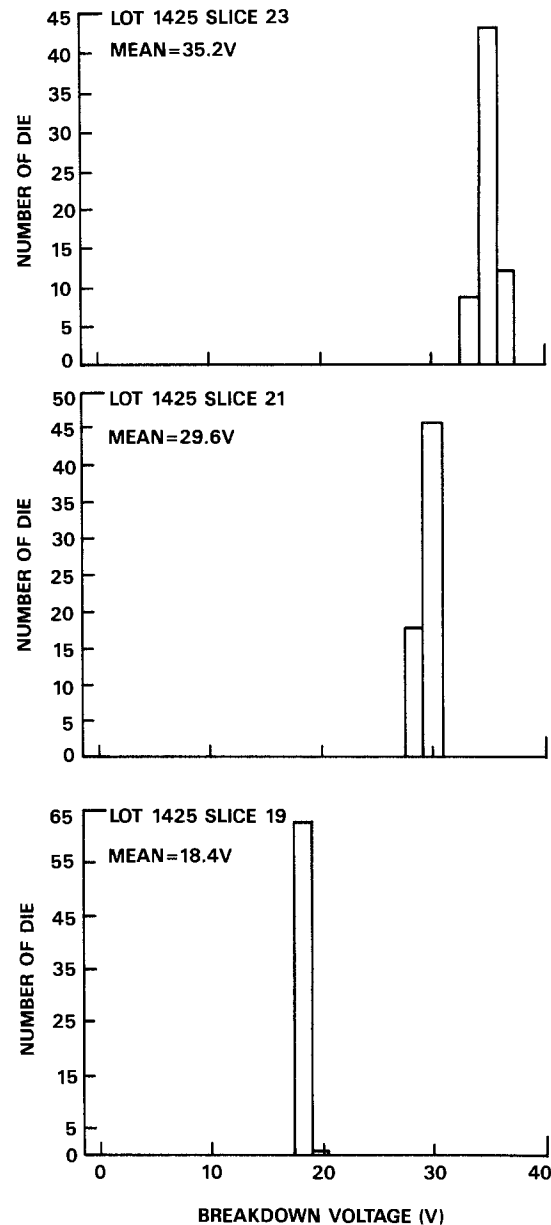


Fig. 6. Histograms of breakdown voltage for 15 nm LPCVD oxide/15 nm LPCVD nitride film as grown (lower), with 1000°C, 90 min anneal in oxygen (middle) and with 5 nm LPCVD cap oxide (upper).

negligible amount of charge trapping occurred during the I-V measurements. This is contrary to what is found with a typical 1000°C, dry O₂ polyoxide that shows a significant shift of the I-V curve to lower values for the second stress, suggesting significant electron trapping.²

Figure 3 depicts the histogram of a 25 nm LPCVD oxide/25 nm LPCVD nitride/5 nm LPCVD oxide trilayer stack. The breakdown voltage is significantly improved to about 40V. This is not surprising, as it is well known in the metal-nitride-oxide-silicon (MNOS) field (5) that a suitable blocking oxide between the nitride and the silicon gate electrode will serve to increase the energy barrier heights (energy barrier height is 2.05 eV for an electron and 1.95 eV for a hole at the silicon nitride interface, while the barrier height is 3.1 eV for an electron and 3.8 eV for a hole at the silicon dioxide interface) between gate electrode and nitride, thus suppressing carrier interface injection from the gate electrode.

The effectiveness of a sealing oxide can also be achieved by treating the oxide/nitride stack in an O₂ or steam ambient, thereby forming a sealing oxide. Figure 4 shows histograms for stacks annealed in O₂ at 1000°C for

²At least an order of magnitude decrease in leakage current at low field (3 MV/cm) was usually observed for the dry thermal interpoly oxide grown at 1000°C, with otherwise the same growth condition.

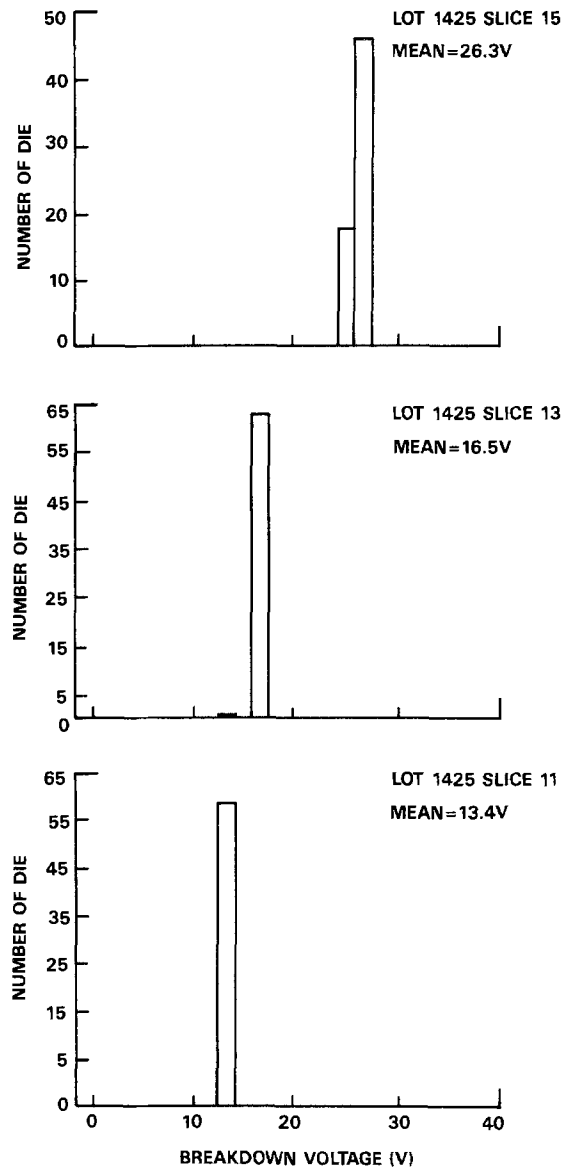


Fig. 7. Histograms of breakdown voltage for 30 nm LPCVD oxide film (lower), 30 nm LPCVD nitride film as deposited (middle), and following 65 min anneal in oxygen at 1000°C (upper).

20 and 90 min. The 20 min anneal produced a mean breakdown voltage of 26.3V, which is comparable to an unannealed stack; the 90 min anneal, however, produced a mean breakdown voltage of 38.0V, a significant improvement. Figure 5 shows histograms for stacks annealed in steam for 65 min at 900° and 1000°C. The 900°C anneal has little effect, producing a mean breakdown

voltage of 26.4V; the 1000°C anneal, however, raises the mean breakdown voltage to 36.0V. The splits that received shorter time or lower temperature heat-treatments do not show any detectable enhancement in breakdown field strength, suggesting that a minimum sealing oxide thickness is required to act as a well-defined Si-SiO₂ energy barrier to enhance the breakdown voltage (6).

The stack has also been scaled in thickness to 15 nm LPCVD oxide/15 nm LPCVD nitride. Figure 6 shows histograms of breakdown voltage for this stack (lower), for a stack annealed in oxygen at 1000°C for 90 min (middle), and for a stack sealed with a 5 nm LPCVD oxide. The mean breakdown voltage increases from a value of 18.4V for the bilayer film to 35.2V for the trilayer film.

The characteristics of single-layer LPCVD films have also been explored. Figure 7 (lower histogram) shows a histogram of breakdown voltage for a 30 nm LPCVD oxide film; the distribution is tight with a mean value of the breakdown voltage of 13.4V. The 30 nm LPCVD nitride film (middle histogram) shows a mean breakdown voltage of 16.5V, and the 30 nm nitride film, annealed in oxygen at 1000°C for 65 min, shows a mean value of 26.3V.

Conclusion

The twelve different interpoly dielectric processes are compared in Table I. The total thickness of the LPCVD films varied from 30 to 55 nm. The anneals listed in the table are done prior to deposition of the second polysilicon film. The capacitors were stressed to 50V; the breakdown voltage was defined as the voltage at which the current density reached 20 $\mu\text{A}/\text{cm}^2$ (100 nA through capacitors of area 0.0052 cm²). A breakdown voltage of 26-27V results from either an unannealed 25 nm oxide/25 nm nitride film or a 30 nm nitride film which is sealed in oxygen at 1000°C. A 25 nm oxide/25 nm nitride film produces a breakdown voltage of > 35V when sealed with a 5 nm LPCVD oxide at 800°C or when sealed at 1000°C in steam for 65 min or in oxygen for 90 min. Note that the thinnest dielectric to achieve a breakdown voltage of 35V is the 15 nm oxide/15 nm nitride/5 nm oxide film, which is roughly equivalent to 28.5 nm of SiO₂.

Acknowledgments

The authors would like to thank the staff of Semiconductor Processing Laboratory for processing the material, especially Bruce Dudley for monitoring the lots, Wayne Caldwell for oxide/nitride stack depositions, and Sarah Poppenhouse for electrical measurements.

Manuscript submitted Oct. 5, 1984; revised manuscript received Jan. 17, 1985.

Texas Instruments Incorporated assisted in meeting the publication costs of this article.

REFERENCES

1. D. J. Dimaria, *Appl. Phys. Lett.*, **27**, 505 (1975).
2. R. M. Anderson and D. R. Kerr, *J. Appl. Phys.*, **48**, 4834 (1977).

Table I. Rank order of dielectric films

Slice number	LPCVD Films			Temp. (°C)	Anneal Ambient	Time (min)	Electrical Parameters		
	Oxide (nm)	Nitride	Oxide (nm)				T ^b (nm)	V ^a (V)	E ^a (MV/cm)
11	30	—	—	—	—	—	31.4	13.4	4.3
13	—	30	—	—	—	—	17.9	16.5	—
19	15	15	—	—	—	—	25.3	18.4	7.3
15	—	30	—	1000	Oxygen	65	20.6	26.3	—
9	25	25	—	1000	Oxygen	20	36.1	26.3	7.3
5	25	25	—	900	Steam	65	35.8	26.4	7.4
1	25	25	—	—	—	—	37.4	26.9	7.2
21	15	15	—	1000	Oxygen	90	29.1	29.6	10.2
23	15	15	5	—	—	—	34.0	35.2	10.4
3	25	25	—	1000	Steam	65	38.3	36.0	9.4
7	25	25	—	1000	Oxygen	90	39.6	38.0	9.6
17	25	25	5	—	—	—	42.8	40.3	9.4

^a At 20 $\mu\text{A}/\text{cm}^2$.

^b Equivalent SiO₂ thickness.

3. R. A. Haken, I. A. Groves, C. S. Wang, W. E. Feger, D. B. Scott, Y. C. See, and R. D. Davies, in "IEEE International Solid State Circuits Conference Digest, ISSCC '83," p. 90, IEEE, New York (1983).
4. R. A. Haken, W. E. Feger, D. J. Coleman, and C. S. Wang, in "IEEE International Conference on Computer Design, ICCD '83," p. 93, IEEE, New York (1983).
5. P. C. Y. Chen, *IEEE Electron. Devices*, ed-24, 584 (1977).
6. L. K. Kasprzak, R. B. Laibowitz, and M. Ohring, *J. Appl. Phys.*, 48, 4281 (1977).
7. S. Mori, M. Sato, Y. Mikata, T. Yanase, and K. Yoshikawa, in "IEEE Symposium on VLSI Technology Digest," p. 40, IEEE, New York (1984).
8. K. Yoshikawa, M. Sato, S. Mori, Y. Mikata, T. Yanase, K. Kanzaki, and H. Nozawa, in "IEEE International Electron Devices Meeting Technical Digest, IEDM," p. 456, IEEE, New York (1984).

Evaluation of Diffusion Coefficients from Nonlinear Impurity Profiles

Dan Anderson and Kjell O. Jeppson

Department of Electrical and Computer Engineering, Chalmers University of Technology, S-412 96 Göteborg, Sweden

ABSTRACT

At high concentrations, impurity diffusion in semiconductors is governed by nonlinear diffusion processes. Using similarity analysis, a general expression for evaluation of the diffusion coefficient from experimental impurity profiles is derived for the case of redistributive diffusion of implanted impurities. This expression corresponds to the Boltzmann-Matano analysis for the case of diffusion with constant surface concentration.

Evaluation of diffusion coefficients from measurements of impurity profiles requires detailed knowledge of the diffusion conditions as well as the expected doping profile. Actually, only very few sources of diffusivity data in literature are reliable (1). For instance, Hu (2) has shown how fictitious diffusion coefficients have been obtained from junction depth and sheet resistivity measurements when the evaluation was based on a theory which was not appropriate for the diffusion conditions. Even when detailed impurity profiles are available from scanning ion mass spectroscopy (SIMS), erroneous diffusion coefficients may be obtained when Arrhenius-type expressions are fitted to diffusivity data that represent the sum of two diffusion mechanisms with different activation energies. Recently, *e.g.*, the diffusion coefficient of arsenic in silicon has been changed by a factor of two (1) after a reevaluation of the diffusion data.

In this paper, we will show that the conditions of diffusion for implanted impurities as arsenic and boron are important and will affect the evaluation of diffusion coefficients at high impurity concentrations. In particular, we demonstrate that for drive-in situations, where a constant predeposited high impurity dose is redistributed by means of nonlinear diffusion, the Boltzmann transformation is not valid. Consequently, diffusion coefficients derived from experiments involving high impurity concentrations of, *e.g.*, arsenic, must be viewed with considerable caution and perhaps even reevaluated.

In analytical studies of impurity diffusion, the use of the Boltzmann transformation (3) plays an important role and has greatly simplified the analysis by reducing the diffusion equation from a partial differential equation to an ordinary equation. This makes it possible to obtain simple explicit solutions for the impurity profile in a variety of different physical situations. Furthermore, it also provides a simple way to infer the diffusion coefficient from the observed impurity profiles. The corresponding Boltzmann-Matano analysis has become a standard procedure for the determination of diffusion coefficients (4).

Analysis

The diffusion of impurities in semiconductors is generally assumed to be governed by the diffusion equation

$$\frac{\partial C}{\partial t} = \frac{\partial}{\partial x} \left(D \frac{\partial C}{\partial x} \right) \quad [1]$$

where $C(x)$ is the impurity concentration and D is the diffusion coefficient. The diffusion of substitutional im-

purities is a result of the interaction with vacant states in the semiconductor. This multiple-charge vacancy model has recently been summarized by Fair (1). The vacancies may be neutral or charged. Since the number of charged vacancies is dependent on the electron concentration, it makes the diffusion coefficient concentration dependent according to

$$D = h[D^0 + D^+(n/n_i) + D^-(n/n_i) + D^{=}(n/n_i)^2] \quad [2]$$

where D^0 , D^+ , D^- , and $D^{=}$ represent the effective diffusivities under intrinsic conditions for the neutral, positive, and negative singly and doubly charged states, n is the electron concentration

$$n = \frac{C}{2} \left\{ 1 + \left[1 + \left(\frac{2n_i}{C} \right)^2 \right]^{1/2} \right\} \quad [3]$$

and h the self electric-field enhancement factor

$$h = 1 + \frac{C}{2n_i} \left[1 + \left(\frac{C}{2n_i} \right)^2 \right]^{-1/2} \quad [4]$$

At low impurity concentrations ($C \ll n_i$), when the diffusion coefficient is independent of concentration, Eq. [1] becomes a linear differential equation and explicit solutions in terms of gaussians or erfc functions are easily found for different diffusion conditions using the Boltzmann transformation, *cf.* (3). However, if $C > n_i$, Eq. [1] becomes nonlinear, and analytical solutions are not as easily available.

In a previous paper (5), we have determined the characteristic impurity profiles, which appear as solutions of Eq. [1] in the case of strongly concentration-dependent diffusion coefficients ($D \sim (n/n_i)^{\gamma}$). This analysis clarified the limitation of the conventional Boltzmann transformation in situations where the nonlinear diffusion process involves a redistribution of a predeposited impurity. In such cases, the proper diffusion variable is not the Boltzmann variable $x/t^{1/2}$, but rather $x/t^{1/(\gamma+2)}$. This point has caused considerable confusion in previous works (6-8).

The purpose of the present work is to consider the important consequences of this result for the evaluation of nonlinear diffusion coefficients from the observed impurity profiles. The conventional interpretation of the diffusion data, in order to infer the diffusion constant, *e.g.*, the Boltzmann-Matano analysis, relies crucially on $x/t^{1/2}$ as the proper diffusion variable.

As shown in Ref. (5), similarity methods are a powerful tool for studying nonlinear diffusion equations. This implies that the solution of the diffusion equation, Eq. [1], is assumed to be of the form

$$C(x,t) = \frac{\phi(\xi)}{t^\alpha} \quad [5]$$

where the similarity variable, ξ , is given by

$$\xi = \frac{x}{t^\beta} \quad [6]$$

The unknown function, $\phi(\xi)$, as well as the parameters α and β , may be determined by insertion of the expressions in Eq. [5] and [6] into the diffusion equation and by using the appropriate boundary or initial conditions.

In the case of diffusion with a constant surface concentration, C_s , it follows that $\alpha = 0$ (cf. Eq. [5]), and by inserting Eq. [5] and [6] into Eq. [1], we obtain

$$-\frac{\beta\xi}{t} \cdot \frac{d\phi}{d\xi} = \frac{d}{d\xi} \left(D \frac{d\phi}{d\xi} \right) \cdot \frac{1}{t^{2\beta}} \quad [7]$$

where D now is a function of ξ . For the powers of t to match, $\beta = 1/2$ is required. (Note that the resulting diffusion variable is then the usual Boltzmann variable $\xi = x/\sqrt{t}$.)

Integration of Eq. [7] results in

$$-\frac{1}{2} \int_0^\phi \xi d\phi = D \frac{d\phi}{d\xi} \quad [8]$$

Substituting back to variables x and t and rearranging yields the diffusion coefficient

$$D(C_1) = \frac{1}{2t} \frac{\int_0^{C_1} x dC}{\left(\frac{dC}{dx} \right)_{x_1}} \quad [9]$$

where $C_1 = C(x_1)$. This is the well-known Boltzmann-Matano (4) expression for evaluation of concentration-dependent diffusion coefficients from experimentally determined impurity profiles. The accuracy of this method has been discussed (9).

However, for drive-in diffusion of a high dose of implanted impurities, the nonlinear character of the diffusion constant has important consequences for the similarity variable, ξ . At high impurity concentrations, one of the charged vacancies dominates the effective diffusivity, making

$$D = 2D_i \left(\frac{C}{n_i} \right)^\gamma \quad [10]$$

where D_i is the intrinsic diffusion coefficient, a good approximation of the concentration dependence of the diffusion coefficient. The parameter γ is equal to one for arsenic and boron diffusion, and γ is equal to 2 for phosphorus diffusion in the "flat region" (1).

In this case, instead of constant surface concentration, a constant amount of implanted impurities redistribute during diffusion. Thus, we require

$$\int_0^\infty C(x,t) dx = T^{\beta-\alpha} \int_0^\infty \phi(\xi) d\xi = Q_0 = \text{const.} \quad [11]$$

This obviously requires that $\alpha = \beta$, and the diffusion equation corresponding to Eq. [7] becomes

$$\frac{1}{t^{\alpha+1}} \alpha \frac{d}{d\xi} (\xi\phi) = \frac{d}{d\xi} \left(2D_i\phi^\gamma \frac{d\phi}{d\xi} \right) \frac{1}{t^{\alpha\gamma+2\beta+\alpha}} \quad [12]$$

Matching powers of t now requires

$$\alpha + 1 = \gamma\alpha + 2\beta + \alpha \quad [13]$$

i.e.

$$\alpha = \beta = 1/(\gamma + 2) \quad [14]$$

Integration of Eq. [12] yields

$$\alpha\xi\phi = 2D_i\phi^\gamma \frac{d\phi}{d\xi} \quad [15]$$

The diffusion coefficient may then be written

$$D = 2D_i \left(\frac{C}{n_i} \right)^\gamma = 2D_i \frac{\phi^\gamma}{t^{\alpha\gamma}} = \frac{\alpha\xi\phi}{t^{\alpha\gamma} \frac{d\phi}{d\xi}} \quad [16]$$

Substituting variables back to x and t yields the following expression for the diffusion coefficient

$$D(C_1) = -\frac{1}{\gamma + 2} \frac{x_1 C_1}{t \left(\frac{dC}{dx} \right)_{x_1}} \quad [17]$$

This equation implies a graphical method for determination of diffusion coefficients from experimentally determined impurity profiles. In this case, the evaluation is simplified as the graphical integration of the Boltzmann-Matano analysis for diffusion with constant surface concentration is eliminated. However, the degree of nonlinearity in the diffusion coefficient must be known in order to perform correct evaluations.

A further integration of Eq. [15] for $\gamma = 0$ yields the well-known gaussian profile. For nonlinear diffusion ($\gamma > 0$), the integration yields, after substitution of variables (5)

$$C(x,t) = C_s(t) \left(1 - \frac{x^2}{x_j^2(t)} \right)^{1/\gamma} \quad [18]$$

where the surface concentration is

$$C_s(t) = \left(\frac{\gamma}{4(\gamma+2)I_\gamma^2} \cdot \frac{Q_0^2 n_i^\gamma}{D_i t} \right)^{1/(\gamma+2)} \quad [19]$$

and the junction depth is

$$x_j = \left(\frac{4(\gamma+2)}{\gamma I_\gamma^\gamma} \cdot \frac{Q_0^\gamma D_i t}{n_i^\gamma} \right)^{1/(\gamma+2)} \quad [20]$$

I_γ is a numerical factor given by $I_1 = 2/3$ and $I_2 = \pi/4$ (5). For $\gamma \rightarrow 0$, this solution (Eq. [18]-[20]) gradually approaches the well-known gaussian profile.

Discussion and Conclusions

The impurity profiles given by Eq. [18]-[20] give excellent agreement with experimental data on impurity profiles for high concentration arsenic diffusion ($\gamma = 1$), see Ref. (5). Some of these data are repeated in Fig. 1.

Two points in relation to Eq. [18]-[20] should be emphasized.

1. The impurity profile is not a function of $x/t^{1/2}$, as was previously believed. Instead, the profile depends on $x/t^{1/3}$ in the case of arsenic and boron ($\gamma = 1$) and on $x/t^{1/4}$ in the case of phosphorus ($\gamma = 2$). The proper diffusion variable in these cases has caused considerable problems in previous investigations on nonlinear diffusion in semiconductors (6-8).

2. The inherent form of the impurity profile changes with increasing nonlinearity and tends to become more "rectangular." The high concentration region becomes more uniform and the descent toward low concentrations is steeper than for the linear profiles, cf. Fig. 1.

To evaluate the concentration dependence of the diffusion coefficient, the Boltzmann-Matano analysis (4) is used when diffusion is performed with constant surface concentration. The diffusion coefficient is then determined by

$$D = \frac{\int_0^{C_1} x dC}{2t \left(\frac{dC}{dx} \right)_{x_1}} \quad [9]$$

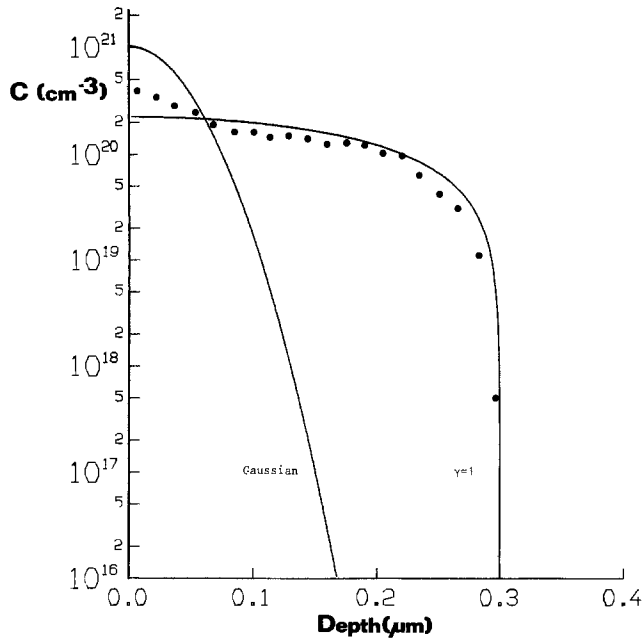


Fig. 1. Doping profile for shallow implanted arsenic ($\gamma = 1$) compared with experimental results from Hill (10). The gaussian profile for linear diffusion ($\gamma = 0$) is given for comparison.

as shown in the analysis. This method has been successfully used to evaluate the diffusion coefficient of several diffusants. The only condition is that the diffusion process must obey Fick's second law, on which the Boltzmann-Matano analysis is based. Hence, the analysis is invalid when other effects are involved, such as precipitation, clustering, or other nonequilibrium complex or vacancy formations. However, there are no restrictions on the concentration dependence of the diffusion coefficient.

In the case of a two-step diffusion process when an implanted or predeposited dose of impurities are redistributed during the drive-in diffusion step, detailed knowledge is needed about the diffusion process before the diffusion coefficient can be evaluated from the doping profile. First of all, as in the Boltzmann-Matano analysis, the diffusion process must obey the diffusion equation. Furthermore, the impurity profile should not contain residues of the originally implanted or predeposited profile, cf. Fig. 1. However, as shown in Eq. [17], detailed knowledge about the concentration dependence of the diffusion coefficient is also required. For arsenic and boron, with $\gamma = 1$, the diffusion coefficient may be evaluated from

$$D = - \frac{C(x_1, t)x_1}{3t \left(\frac{dC}{dx} \right)_{x_1}} \quad [21]$$

A similar expression has been used in the analysis by Fair and Tsai (7) giving the diffusion coefficient as

$$D = - \frac{C(x_1, t)x_1}{2t \left(\frac{dC}{dx} \right)_{x_1}} \quad [22]$$

However, this expression is based on the assumptions that the Boltzmann transformation is the proper variable and that the diffusion coefficient is a function of $C(x, t)/C_s = C(x, t)/C(0, t)$ (7, 8). This assumption is physically not realistic, and the expression is useful only for constant diffusion coefficients and gaussian profiles.

From this point of view, the evaluation in Ref. (7) should give values of diffusion coefficients that are 1.5 times too large. However, great care must be taken with the conditions under which the diffusion was performed. A gaussian profile is a well-known reference assuring that the diffusion was performed under linear conditions.

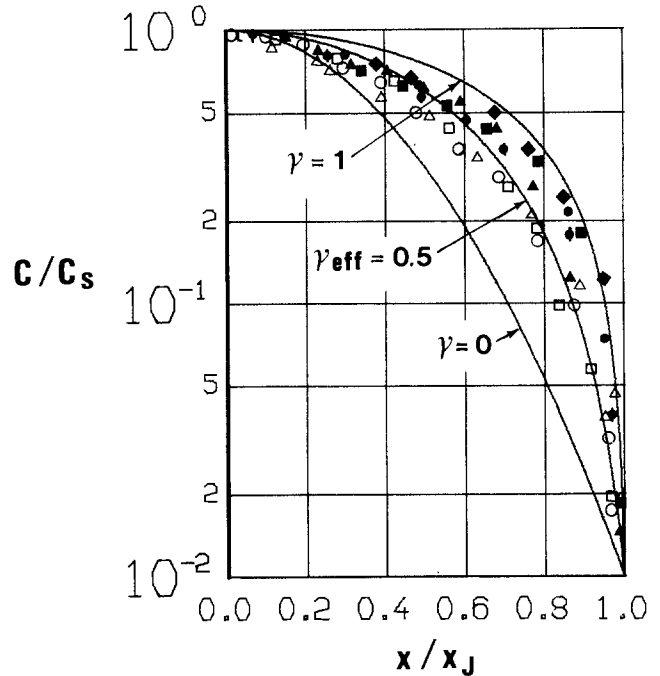


Fig. 2. Normalized impurity profiles for linear ($\gamma = 0$) and nonlinear ($\gamma = 1$) diffusion plotted together with experimental data for arsenic [from Fair and Tsai(7)]. For some lower doses of implanted arsenic an effective γ , $\gamma_{\text{eff}} = 0.5$, is the best approximation.

For nonlinear diffusion involving large doses of arsenic, the impurity profile is given by Eq. [18] as long as the concentration is so high that the nonlinear diffusivity is dominating. These two reference curves are shown in Fig. 2 together with experimental results from previous work by Fair and Tsai. Only the high dose implants agree with the theoretical curve, indicating a mixture of linear and nonlinear diffusion at lower doses. Only for the high dose implants may accurate evaluations of diffusion coefficients be performed using Eq. [21]. For the lower implant doses, approximate diffusion coefficient evaluations may be obtained from

$$D = - \frac{C(x_1, t_1)}{(\gamma_{\text{eff}} + 2)t \left(\frac{dC}{dx} \right)_{x_1}} \quad [23]$$

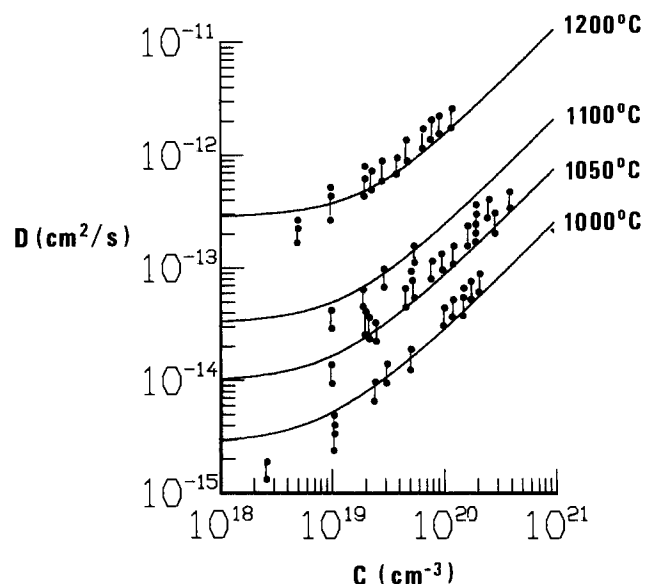


Fig. 3. Arsenic diffusivity vs. total concentration using Eq. [24] and [25]. The upper dots are experimental data from Fair and Tsai (7). The lower dots are the same experimental data reevaluated according to Eq. [21].

where γ_{eff} is an effective nonlinearity coefficient ($0 < \gamma_{\text{eff}} < \gamma$), which empirically accounts for the mixing of linear and nonlinear diffusion effects. Thus, before evaluating the diffusion constant by means of Eq. [17], the appropriate γ_{eff} has to be determined by fitting a curve of the form given by Eq. [18] to the available data points. This is different from the Boltzmann-Matano analysis, which is valid for arbitrary concentration dependence of the diffusion coefficient. In Fig. 2, the theoretical doping profile for diffusion with $\gamma_{\text{eff}} = 0.5$ is also shown.

To illustrate the validity of our theoretical analysis, we have plotted in Fig. 3 the arsenic diffusion coefficient as a function of concentration using the expression

$$D = h \left(D_0 + \frac{C}{n_i} D^- \right) \quad [24]$$

where h is given by Eq. [4] and D_0 and D^- by the today widely accepted (11) values of

$$D_0 = 0.066 \exp(-3.44/kT) \text{ and } D^- = 12 \exp(-4.05/kT) \quad [25]$$

In this figure, the experimental data of Ref. (7) for the diffusion coefficient evaluated from profiles of implanted impurities using Eq. [22] are also shown.

This experimental data generally seem to be too large compared with theoretical curves. On the other hand, if these experimental values are reevaluated using Eq. [21], as shown in Fig. 3, very good agreement with present day theory is obtained, especially for high concentrations when γ truly equals one. At lower concentrations, how-

ever, when γ becomes zero corresponding to linear diffusion, the evaluation of diffusion coefficients from Eq. [21] shows the best agreement with theory, as predicted by Eq. [17].

Manuscript received Dec. 11, 1984.

Chalmers University of Technology assisted in meeting the publication costs of this article.

REFERENCES

1. R. B. Fair, in "Impurity Doping Processes in Semiconductors," F. F. Y. Wang, Editor, Chap. 7, p. 335, North-Holland Publishing Co., Amsterdam (1981).
2. S. M. Hu, in "Atomic Diffusion in Semiconductors," D. Shaw, Editor, Chap. 5, p. 302, Plenum Press, London (1973).
3. J. Crank, "The Mathematics of Diffusion," 2nd ed., Chap. 7, Clarendon Press, Oxford, England (1975).
4. P. G. Shewman, "Diffusion in Solids," p. 28, McGraw-Hill, New York (1963).
5. D. Anderson and K. O. Jeppson, *This Journal*, **131**, 2675 (1984).
6. R. B. Fair, *ibid.*, **122**, 800 (1975).
7. R. B. Fair and J. C. C. Tsai, *ibid.*, **122**, 1689 (1975).
8. M. Ghezzo, *ibid.*, **119**, 977 (1972).
9. T. H. Yeh, in "Atomic Diffusion in Semiconductors," D. Shaw, Editor, Chap. 4, p. 207, Plenum Press, London (1973).
10. C. Hill, Lecture notes, see "Large Scale Integrated Circuits Technology," L. Esaki and G. Soncini, Editors, p. 124, Nato Advanced Study Institutes Series, Vol. E55, Martinus Nijhoff Publishers, The Hague, The Netherlands (1982).
11. C. P. Ho, J. D. Plummer, S. E. Hansen, and R. W. Dutton, *IEEE Trans. Electron. Devices*, **ed-30**, 1438 (1983).

Oxygen Segregation and Microscopic Inhomogeneity in Czochralski Silicon

Wen Lin

AT&T Bell Laboratories, Allentown, Pennsylvania 18103

M. Stavola

AT&T Bell Laboratories, Murray Hill, New Jersey 07974

ABSTRACT

In this paper, the origins of the microscopic impurity inhomogeneity in Czochralski (CZ) silicon are reviewed. The relevance of impurity segregation behavior and microscopic growth rate variations to the impurity microfluctuations are analyzed and discussed. The nature of the oxygen microfluctuations is studied in terms of its segregation behavior and its effects on precipitation. Spatially resolved infrared absorption and spreading resistance are used to study the oxygen microfluctuations induced by the melt thermal asymmetry, isolated by a manually controlled crystal growth. It is shown that oxygen segregates microscopically in the same manner as arsenic in silicon, that is, $K_0 < 1$ for oxygen. A quantitative analysis yields a K_0 value in the neighborhood of 0.3 for oxygen, which agrees well with the previous result based on a macroscopic analysis. Heat-treatment experiments have shown that when CZ silicon exhibits microfluctuations in oxygen concentration the precipitation is not uniform; rather, the precipitation is enhanced in the high oxygen regions of the fluctuations. Such behavior can impede the formation of the denuded zone where the high oxygen regions meet the wafer surface, resulting in nonuniform denuded zone width across the wafer.

The microscopic inhomogeneity of impurity distributions in Czochralski (CZ) silicon crystals is, in general, a result of growth-rate fluctuations during crystal growth. The growth-rate fluctuations cause variations in the impurity incorporation levels. The lattice strain associated with local impurity concentration variations gives rise to the so-called "striation," as may be revealed by chemical etching. Severe microscopic dopant inhomogeneity corresponds to a large variation in carrier concentration, and is not desirable in silicon materials used for device fabrication, especially when such variation is comparable to the device feature size. This is an important consideration in VLSI fabrications. Large local fluctuations in oxygen concentration can result in preferential precipitation, of-

ten observed as concentric ring patterns in etched wafers following heat-treatments.

Several recent works have addressed impurity incorporation in CZ silicon crystals and the effects associated with inhomogeneous impurity distribution (11, 12). Here, we have grown crystals with very regular impurity striation patterns so that a more quantitative analysis of the causes and consequences of microscopic inhomogeneity can be made. The main focus of our work is upon oxygen incorporation and striation.

This paper is organized as follows. First, the sources of impurity concentration fluctuation are reviewed briefly. Next, the growth and characterization of a specially grown crystal with widely spaced, regular impurity stri-

tions are described. From the measured impurity distributions, the segregation behavior of oxygen in silicon is determined. Finally, a number of effects associated with oxygen precipitation in inhomogeneous crystals are shown very clearly in our samples that have regular striation patterns.

Microscopic Inhomogeneity in Czochralski Silicon

In Czochralski silicon growth, there are several sources of microscopic growth rate variations.

Noncentral symmetric thermal distribution in silicon melt.—In large melt silicon growth systems, finite thermal asymmetry exists about the center of the melt. During crystal growth, as the crystal is rotated about the growth axis, the interface will experience slightly different temperatures at different positions of the melt. Therefore, the growth rate of a given crystal element parallel to the crystal axis would fluctuate periodically, as illustrated schematically in Fig. 1. In general, the fluctuation is most pronounced in the crystal elements furthest from the crystal center. The periodicity of the fluctuation is determined by the average growth rate \bar{f} , and crystal rotation rate ω , as \bar{f}/ω . Corresponding to the growth-rate variations, there are variations in the impurity incorporation level. When the equilibrium segregation coefficient (K_0) of the element involved is less than unity, the fluctuation in impurity incorporation level is in phase with the growth rate fluctuation. If $K_0 > 1$, the two fluctuations will be out of phase. This is also illustrated in Fig. 1. The relationship may be realized readily by examining equation of Burton *et al.* (1).

Thermal convection-related temperature fluctuations.—These fluctuations are mostly random in nature and etched striations are characteristically aperiodic (2). When thermal convection is significant, the microstriations would bear the signature of high frequency fluctuations, on the order of tens of hertz.

Automatic diameter control-induced perturbations.—Growth rate fluctuations can be further perturbed by the automatic diameter control mechanism (ADC) commonly employed in silicon growth. The crystal pull rate is slaved by optically monitored crystal diameter variations in order to maintain a preset diameter. The pull rate adjustments are both "instantaneous" (a few seconds) and "long-term" (minutes). The long-term pull rate adjustment determines average growth rate. The instantaneous pull rate adjustment imposes modifications on the microscopic growth-rate fluctuations resulting from thermal asymmetry and thermal convection. The net effect is to smear the periodic nature of the impurity fluctuation resulting from the melt thermal asymmetry.

Microscopic Analyses and Crystal Growth

In this study, the microfluctuations of oxygen were measured directly by spatially resolved infrared absorption near $9 \mu\text{m}$,¹ and indirectly by spreading resistance (SR) following an oxygen donor activation treatment at 450°C .

Our apparatus for making spatially resolved IR measurements is based upon a Hughes Model 3802H-L line tunable CO_2 waveguide laser. The laser could be tuned (4.6) to $9.17 \mu\text{m}$, near the maximum of the well-known $9 \mu\text{m}$ IR absorption band that is used routinely to characterize the concentration of oxygen in silicon. The laser spot diameter (FWHM) at the focus was measured to be less than $200 \mu\text{m}$.

Silicon samples were ground wedge shaped (surfaces 6° off parallel) to eliminate the multiple-reflection interference effects that give rise to large interference fringes for uncoated plane parallel surfaces. Samples were then polished to a mirror finish on both sides. We chose wedge-

¹The earliest microscale measurement of $[\text{O}_i]$ we are aware of was performed by McDonald (3). Recent microscale measurements have been reported by Ohsawa *et al.* (4, 5) and by Rava *et al.* (6). Our measurement system is most like that described by Rava *et al.*

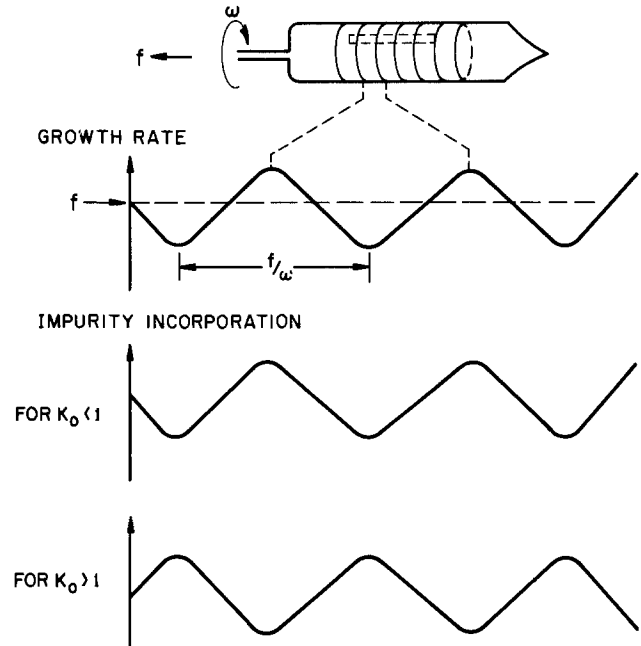


Fig. 1. Schematic illustration of growth-rate fluctuation and its relationship with microscopic impurity fluctuation in CZ crystal. f and ω are growth rate and crystal rotation rates, respectively.

shaped rather than antireflection-coated samples because it was more convenient to perform heat-treatments and remeasure absorption spectra on uncoated specimens. Our system was carefully checked with float-zone (oxygen-free) silicon to ensure that interference effects and surface imperfections had indeed been eliminated. We also measured the spatially resolved IR spectrum for our Czochralski-grown samples at $9.6 \mu\text{m}$ (off the oxygen absorption band) to determine transmission fluctuations not due to oxygen striation. Such nonoxygen-related fluctuations of the transmitted beam were $\sim 0.3\%$ of the transmitted signal.

The spreading resistance measurements were performed on a Solid State Measurement Model ASR210 SR probe. The probe spacing used was $150 \mu\text{m}$.

To understand the nature of the microscopic oxygen inhomogeneity induced by the various mechanisms of growth-rate fluctuations during the crystal growth, it is helpful to isolate the major contribution. For this purpose, a $\langle 100 \rangle$ crystal was grown under a constant pull rate of 90 mm/h to avoid the effect of forced pull-rate variations of the ADC mechanism. The crystal was grown from a relatively small charge, 5 kg , to minimize the thermal convection effect. The crystal was lightly doped with arsenic to serve as a reference. A slow crystal rotation rate of 2 rpm was used in order to maximize the periodicity of the rotational striations and to facilitate SR and IR measurements. After growth, (110) longitudinal slices, 1.4 mm thick, were prepared from near the center of a crystal section 75 mm from the seed. Slices were polished on both sides. The average $[\text{O}_i]$ of these slices were measured by FTIR to be 19 and 17 ppma (7) at the center and near the crystal edge, respectively.

Figure 2 shows IR absorption scans along the growth direction, 8 mm from both crystal edges (labeled sample A and sample B). The observed periodic oxygen concentration fluctuations are well resolved. The average spacing measured is 0.76 mm , consistent with the constant pull rate and crystal rotation rate used. The large absorptions at the ends of the scans are due to reference scratch markers. From the change in transmission, the change in absorption coefficient, about the mean and the percent change in the interstitial oxygen concentration can be deduced. An analysis of ten periods gives an average fluctuation of 4.4% about the mean. Under growth without forced pull-rate variations, these well-resolved fluctuations in microscopic oxygen incorporation rate are due to

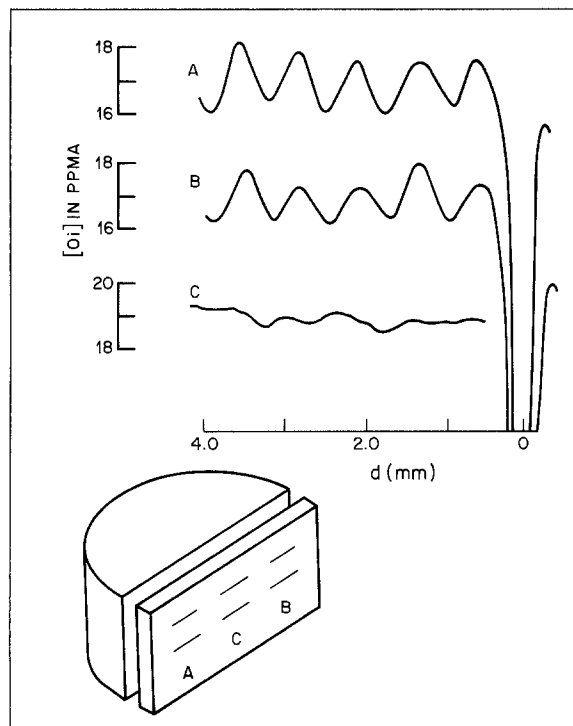


Fig. 2. $9 \mu\text{m}$ IR absorption scans on crystal's longitudinal slice at positions A and B and C, in as-grown condition. Insert shows sample positions with respect to the experimental crystal. Horizontal segments on the sample represent scratch markers.

melt thermal asymmetry. The relatively symmetrical waveform of the fluctuations indicates that the thermal asymmetry consists of hi-lo temperature regions approximately 180° apart across the melt center. Since the "instrument width" of the laser beam was measured to be narrower than $200 \mu\text{m}$, far less than the periodicity of the oxygen fluctuation, the instrument convolution and smearing effect is insignificant. Therefore, the measured amplitude of the oxygen fluctuations are very close to the actual magnitude. However, some details in the microfluctuation are not resolved by the laser beam, but can be detected by high resolution SR measurements.

Variations in oxygen concentration are observed in the IR scans near the crystal center, (such as position C in Fig. 2) along the growth direction. The fluctuations are small ($\leq 3\%$ peak to valley) and are not periodic in nature. They are mainly due to thermal convection-related growth-rate fluctuations.

Microfluctuations of oxygen were also measured by SR after sample A was annealed at 450°C for 4h to convert some of the interstitial oxygen to electrically active donor complexes (8). Figure 3a shows the SR profile measured at the same sample location as the laser scan, 8 mm from

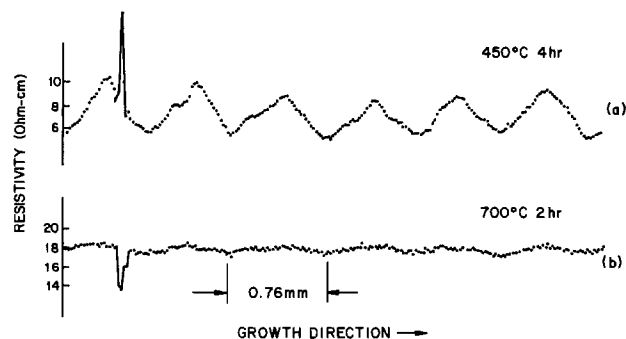


Fig. 3. Spreading resistance profiles measured along growth direction after the as-grown slice was heat-treated at 450°C for 4h (a), and additional 700°C for 2h followed by quenching (b). The spacing of the data points is $20 \mu\text{m}$.

the crystal edge, after the donor heat-treatment. The higher resistance corresponds to lower oxygen concentration. When the scratch marks are aligned in the laser and SR scans, it may be seen that the fluctuations are well matched. It is noted that some of the fine features detected by SR are not resolved by the laser IR. Since the oxygen donor formation kinetics are proportional to fourth power of the $[\text{O}_i]$ (9), the donor profile measured would give a larger fluctuation than the actual magnitude. A SR measurement at the same sample position after an oxygen donor elimination treatment would reveal dopant fluctuations, in this case arsenic, due to exactly the same growth-rate fluctuations that oxygen experienced during the growth. Figure 3b shows such a SR profile after sample A was annealed at 700°C for 2h followed by fast cooling to room temperature. The average arsenic concentration measured is on the order of 2.5×10^{14} . This is in a good agreement with the four-point probe measurement on the neighboring bulk crystal samples after 700°C donor-elimination treatments. The measured arsenic fluctuations can be discerned and have a periodicity of 0.76 mm . With the scratch marks aligned between profiles in Fig. 3a and 3b, it is seen that the periodic fluctuations are in phase. This demonstrates that oxygen segregates in the same manner as arsenic ($K_o = 0.3$) and that K_o for oxygen is also smaller than unity.

Oxygen Segregation

It is realized that under constant-pull-rate growth (or nominally constant average growth rate), the fluctuations in impurity incorporation level, such as have been observed, are the result of impurity segregation and microscopic growth-rate fluctuations about the average growth rate. It is possible to deduce the magnitude of the growth-rate fluctuation when K_o is known, or vice versa. An analysis of the microscopic arsenic fluctuation yields an average of 5.1% about the mean. Figure 4 shows graphically the effect of growth-rate fluctuations on the impurity-incorporation level. In this plot, the percent change in K_{eff} is computed as a function of the percent growth-rate change about the nominal value used in the present experiment, i.e., $\bar{f} = 90 \text{ mm/h}$, for the K_o values of interest. The computation assumes an oxygen diffusion coefficient $D = 10^{-4} \text{ cm}^2/\text{s}$ and a diffusion boundary layer, δ , of 0.04 cm (10). From the figure, the observed $\Delta K_{\text{eff}}^{\text{As}}$ corresponds to a growth-rate fluctuation of 11% about the nominal growth rate. With this range of growth-rate fluctuations, the 4.4% microfluctuation observed in oxygen incorporation would correspond to a K_o value of slightly greater than 0.3. This value may be compared with the previously determined value of ~ 0.25 by a macroscopic

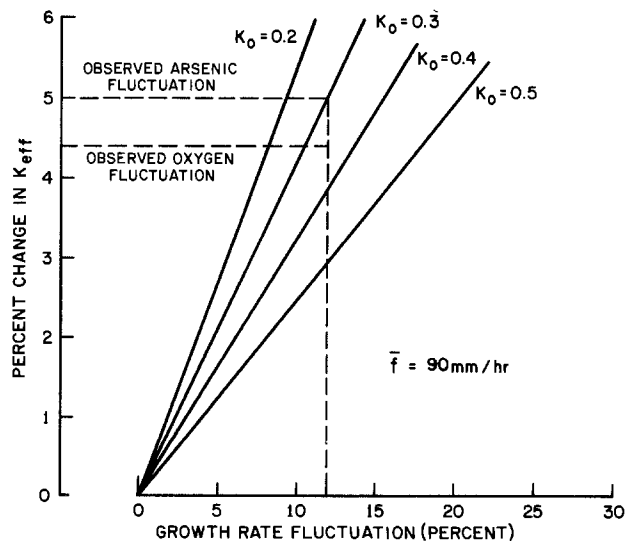


Fig. 4. Percent change in K_{eff} as a function of growth rate fluctuations about a nominal growth rate of 90 mm/h for equilibrium segregation coefficients 0.2-0.5.

analysis (10). Considering the difference in the methods used and the measurement errors involved, the two results are in a good agreement. Our results from direct crystal growth experiments with both macroscopic and microscopic analyses have yielded similar results. The equilibrium segregation coefficient of oxygen in silicon is considerably smaller than unity. The K_0 value is in the neighborhood of 0.3.

Effect on Oxygen Precipitation

In order to examine the effects of microscopic oxygen fluctuations on precipitation behavior, two neighboring samples from the experimental crystal with different thermal history were further heat-treated at 1050°C for 5h. Sample A was previously heat-treated at 450°C for 4h and 700°C for 2h for the study described above. Sample B was in the as-grown condition. After the heat-treatment, the $[O_i]$ measured at 8 mm from the crystal edge in sample A was 10 ppma, a decrease of 6 ppma from the as-grown concentration of 16 ppma. In other words, about 38% of the original interstitial oxygen was precipitated. A similar measurement in sample B showed the corresponding $[O_i]$ decrease was only 2 ppma. The low temperature treatments preceding the 1050°C treatment in sample A clearly enhanced precipitation.

Microstructural analyses of these samples indicate that the precipitation is not uniform. Rather, preferential precipitation takes place in the originally high oxygen regions of the microfluctuations. Figure 5a shows the etched surface of sample A after 1050°C treatment, 8 mm from the crystal edge. The striking microstructure shows periodic bands of oxygen precipitation which extend to the silicon surface. There appears to be no defect-free volume (denuded zone) under the surface in the precipitation band regions. The vertical scratch reference marks are shown at each end. The original SR trails parallel to the growth direction can be vaguely seen among the random scratch damage due to sample handling. With reference to the SR tracks and scratch marks, the precipitation

bands in Fig. 5a may be matched with the SR profile shown in Fig. 3a to show that the heavy precipitation bands correspond to the originally high oxygen regions. The precipitation density in the low oxygen regions appears to be insignificant. However, relatively small precipitates can be seen under high magnification microscopy. These observations suggest that when there are microfluctuations in oxygen distribution, in the present case ~ 4.4% about the mean, enhanced precipitation can occur in the high oxygen regions. Furthermore, the fact that the precipitation occurs at the sample surface suggests that no denudation takes place in the banded precipitation regions. Apparently, the oxygen out-diffusion near the sample surface is suppressed by a fast nucleation/growth mechanism in the high oxygen regions. Such effects are especially pronounced in the case where precipitation was assisted by low temperature nucleation treatments. These preferential precipitation bands would correspond to concentric ring patterns in the crystal's transverse cross sections, *i.e.*, normal wafer slices. It is believed that the preferential oxygen precipitation mechanism associated with microscopic oxygen fluctuations is the cause of the concentric rings often observed in oxidized or heat-treated CZ wafers, following chemical etching. Figure 5b shows etched striated micrograph in sample A near the crystal edge after 1050°C treatment. There is no preferential precipitation taking place due to low oxygen concentration at the crystal edge. The average periodicity of the striations, ~ 25 μm , corresponds to a high frequency fluctuation of 1 Hz associated with melt thermal convection.

Our data indicate that the oxygen precipitation kinetics in CZ silicon with microfluctuations is not strictly proportional to oxygen concentration. Several factors for such preferential precipitation may be speculated. It is likely that the preferential precipitation of oxygen in the high $[O_i]$ regions reflects the number of nuclei formed during the low temperature heat-treatments. Our SR measurements show that, following 450°C heat-treatment, the

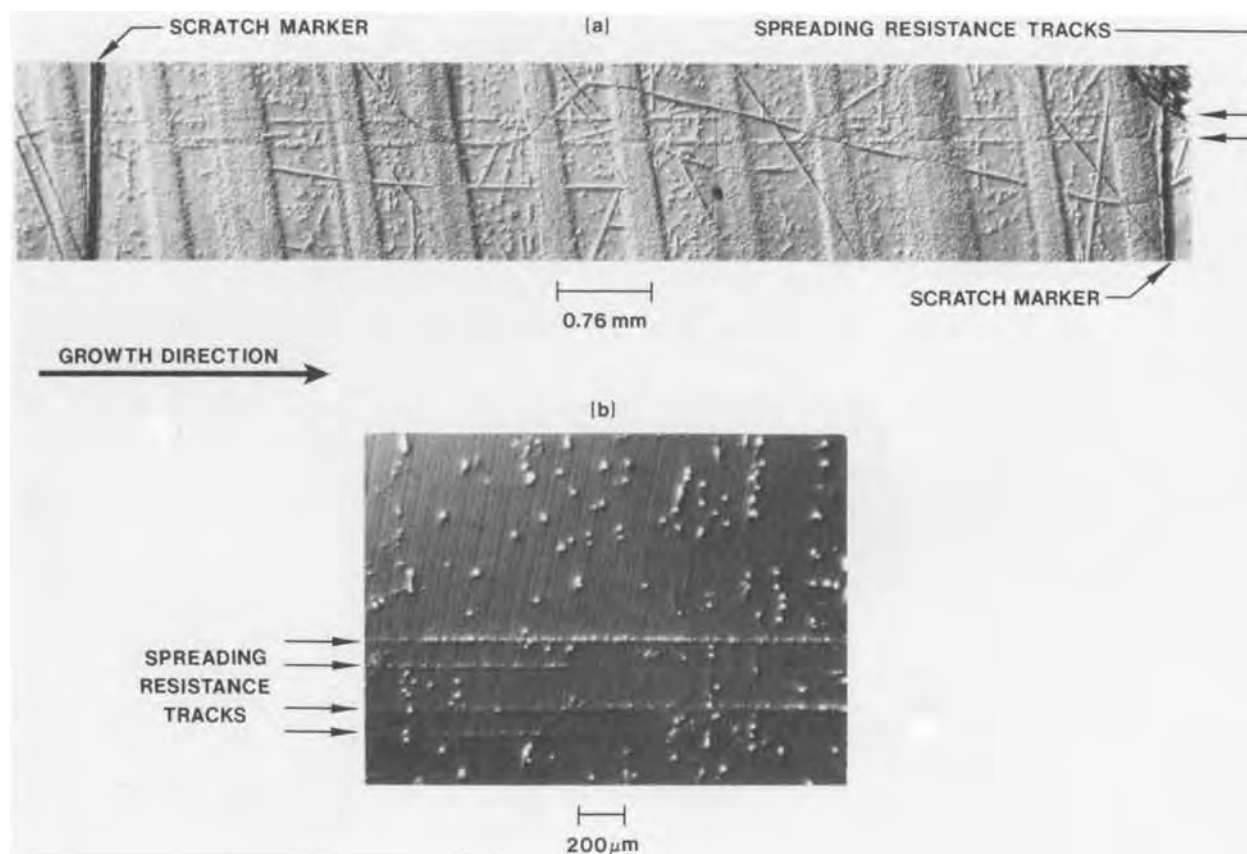


Fig. 5. a: Micrograph of Secco-etched sample A showing preferential oxygen precipitation at high $[O_i]$ regions after 1050°C, 5h treatment. b: Microstriations near the crystal edge (of sample A) showing average periodicity of 25 μm . The heat-treatment condition is same as in a.

distribution of thermal donors reflects $[O_i]$ distribution but with greater fluctuation amplitude. We have not measured directly the distribution of nuclei following 700°C treatment, but the precipitation behavior at 1050°C would seem to indicate a large fluctuation amplitude for the concentration of nuclei also.

Another postulated mechanism for inhomogeneous precipitation behavior involves the preferred nucleation and growth of oxygen precipitation at microdefect centers introduced during crystal growth. Such defects, ranging from several hundred angstroms to tenth of a micron in size, have been related to temperature oscillation and remelting occurring at the growing crystals' solid-liquid interface (13, 14). The defect centers would provide convenient nucleation sites for oxygen precipitations at a preferential rate. The remelting phenomenon is closely related to growth conditions where thermal asymmetry exists.

Remelting can occur when the rotating crystal's interface changes from low to high temperature fields such that a negative instantaneous growth-rate results. In the present sample, this condition would correspond to the low growth-rate portion of the microfluctuations. That is, logically, if remelting-related microdefects exist in the current sample, they are likely to occur in the low oxygen regions, not the high oxygen regions. This is not consistent with the current observation of the enhanced precipitation, which occurs in the high oxygen regions. Furthermore, the present SR measurements and microstructures do not give a sufficient indication that a correlation exists between the microdefects and enhanced precipitation in the present crystal. The possible role of the microdefects in enhanced precipitation needs to be further investigated.

One of the strong characteristics observed in the precipitation band regions is that oxygen outdiffusion at the surface is being suppressed such that precipitation extends to the surface with no "denuded zone." In comparison, much weaker precipitation effects have been observed in CZ silicon with similar $[O_i]$, but much better microscopic uniformity when receiving identical heat-treatments. In the latter case, the precipitation-free depth region near the surface is not zero, but 10 μm or so. Thus, CZ silicon wafers fabricated from crystals with significant microfluctuations would be likely to display nonuniform precipitation and denuded zone width across the wafer. This phenomenon has often been observed (15). The degree of nonuniformity in the denuded-zone width would depend on the amplitude and periodicity of the fluctuations, the crystal's interface curvature, and the thermal history of the wafer prior to the precipitation process. The significant implication of such behavior is that, when the crystal with $[O_i]$ microfluctuations is fabricated into wafers, the formation of the wafer surface-denuded zone may be impeded where high oxygen regions of the fluctuations meet the surface.

Summary and Conclusions

In this paper, the origins of the microscopic impurity inhomogeneity in Czochralski silicon have been reviewed. The relationship of impurity segregation behavior and microscopic growth-rate variations to the impurity microfluctuations is analyzed and discussed. The observed microfluctuations in large diameter CZ silicon crystals are characteristically a result of convoluted growth-rate fluctuations due to melt thermal asymmetry, thermal convection, and forced pull rate variations induced by automatic diameter control.

In general, the effect of the oxygen microfluctuations may be minimized by reducing the periodicity of the fluctuations, via increased crystal rotation rate during crystal growth. However, a more fundamental approach would be to improve the melt thermal symmetry. In a side-heated Czochralski growth system, it is essential that

good contact be maintained between the entire crucible wall and surrounding graphite susceptor for uniform and symmetrical heating. The forced pull-rate variations induced by the automatic diameter control can be reduced by proper adjustment in the control electronics. More recent diameter-control designs based on advanced optical sensors coupled with a microprocessor offer smoother control. Thermal convection-induced temperature oscillations can be suppressed by using either small melt growth, such as a double crucible (16) or low aspect ratio approaches, or by applying magnetic field (17).

The nature of the oxygen microfluctuations is studied in terms of its segregation behavior and its effects on precipitation. High resolution laser IR absorption and spreading resistance are used to study the oxygen microfluctuations induced by the melt thermal asymmetry, isolated by a manually controlled crystal growth. It is shown that, microscopically, oxygen segregates in the same manner as arsenic in silicon, that is, $K_0 < 1$ for oxygen. The quantitative analysis yields a K_0 value in the neighborhood of 0.3 for oxygen, which agrees well with the previous result based on a macroscopic analysis (10).

Heat-treatment experiments have shown that when CZ silicon exhibits microfluctuations in oxygen concentration, the precipitation is not uniform; rather, the precipitation is enhanced in the high oxygen regions of the fluctuations. Such behavior can impede the formation of the denuded zone where the high oxygen regions meet the wafer surface, resulting in nonuniform denuded zone width across the wafer.

Manuscript received Dec. 5, 1984.

AT&T Bell Laboratories assisted in meeting the publication costs of this article.

REFERENCES

1. J. A. Burton, R. C. Prim, and W. P. Slichter, *J. Chem. Phys.*, **21**, 1987 (1953).
2. J. R. Carruthers, A. F. Witt, and R. E. Reusser, in "Semiconductor Silicon 1977," H. R. Huff and E. Sirtl, Editors, p. 61, The Electrochemical Society Softbound Proceedings Series, Princeton, NJ (1977).
3. R. S. McDonald, as reported in W. C. Dash, in "Growth and Perfection of Crystals," R. H. Doremus, B. W. Roberts, and D. Turnbull, Editors, p. 361, John Wiley and Sons, New York (1958).
4. A. Ohsawa, K. Honda, S. Ohkawa, and R. Ueda, *Appl. Phys. Lett.*, **36**, 147 (1980).
5. A. Ohsawa, K. Honda, S. Ohkawa, and K. Shinohara, *ibid.*, **37**, 157 (1980).
6. P. Rava, J. Lagowski, and H. C. Gatos, *This Journal*, **129**, 2844 (1982).
7. ASTM Standard F121-80.
8. C. S. Fuller and R. A. Logan, *J. Appl. Phys.*, **28**, 1427 (1957).
9. W. Kaiser, H. L. Frisch, and H. Reiss, *Phys. Rev.*, **112**, 1546 (1958).
10. W. Lin and D. W. Hill, *J. Appl. Phys.*, **54**, 1082 (1983).
11. T. Abe, K. Kikuchi, S. Shirai, and S. Muraoka, in "Semiconductor Silicon 1981," H. R. Huff, R. J. Kriegler, and Y. Takeishi, Editors, p. 59, The Electrochemical Society Softbound Proceedings Series, Pennington, NJ (1981).
12. A. Murgai, H. C. Gatos, and W. A. Westdorp, *This Journal*, **126**, 2240 (1979).
13. J. Chikawa and S. Shirai, *Jpn. J. Appl. Phys.*, Suppl. 18-1, 165 (1979).
14. S. Shirai, *Appl. Phys. Lett.*, **36**, 156 (1980).
15. F. Secco d'Aragona, R. K. Tsui, H. M. Liaw, and P. L. Fejes, in "Defects in Silicon," W. M. Bullis and L. C. Kimerling, Editors, p. 166, The Electrochemical Society Softbound Proceedings Series, Pennington, NJ (1983).
16. W. Lin and D. W. Hill, in "Silicon Processing," D. C. Gupta, Editor, p. 24, ASTM, Philadelphia (1983).
17. T. Suzuki, N. Isawa, Y. Okubo, and K. Hoshi, in "Semiconductor Silicon 1981," H. R. Huff, R. J. Kriegler, and Y. Takeishi, Editors, p. 90, The Electrochemical Society Softbound Proceedings Series, Pennington, NJ (1981).

Process-Induced Leakage Current in a Low Noise GaAs MESFET

P. A. Folkes, C. C. Chang, and E. Lane

Bell Communications Research, Incorporated, Murray Hill, New Jersey 07974

ABSTRACT

The cause of a process-induced leakage current in low noise GaAs MESFET's has been traced to conduction along the semi-insulating buffer surface surrounding the mesas that contain the active elements of the device. The ion milling process, which we used to define the mesas, is responsible for inducing large, variable increases in surface leakage. For a fixed voltage between the gate and source pads of 1V the induced leakage current ranged from 5 nA to 10 μ A at 23°C. We compared the effects of several commonly used etches for cleaning GaAs. A buffered peroxide solution did not reduce the induced leakage current. By contrast, a concentrated aqueous NH_4OH solution reproducibly reduced the induced leakage current to below 1 nA. Auger analysis revealed a correlation between high surface leakage and the presence of a surface Ga oxide layer. We were unable to definitively identify the cause of the leakage, but suggest two possible mechanisms that are consistent with our data: (i) band bending due to charges in the surface oxide, or surface state effects, and (ii) conduction through a thin layer of elemental As located between the surface oxide and the GaAs.

GaAs MESFET's are receiving increasing attention because of their use as preamplifiers in light wave receivers (1). There is interest in understanding and minimizing the leakage current in GaAs FET's, since at low bit rates the receiver sensitivity is limited by shot noise, which is proportional to the leakage current.

The data shown in Fig. 1 illustrate that, if special precautions are not taken, a tremendous variation is observed in the gate leakage current of GaAs MESFET's from similarly processed wafers. Measurements of the resistivity of the GaAs substrates showed no difference in substrate resistivity, suggesting that the large leakage current variation was induced by processing. We focused on the following aspects of this problem: (i) location of the leakage current, (ii) the processing steps responsible for inducing leakage, (iii) the physical mechanism involved, and (iv) techniques to reduce leakage. We show below that we succeeded with the first, second, and fourth aspects. Although we were unable to definitively identify the third, we suggest two candidates that are consistent with our data.

Experimental

GaAs FET structure.—A schematic cross section of the transistor structure is shown in Fig. 2. The substrate is high resistivity chromium-doped GaAs. An epitaxial high resistivity chromium-doped GaAs buffer layer (3-5 μm thick) separates the substrate from the n-type active layer, which is only 0.4 μm thick. An n^+ layer grown over the active layer facilitates the formation of ohmic contacts. All epitaxial layers were grown by chemical vapor deposition.

Figure 3 shows a top view of the FET. The active region of the device is enclosed by the heavier dashed line. The shorter dashed lines delineate the gate metal. Isolation between different devices is achieved by the creation of mesas using an ion milling process (Ar ions at 300 $\text{\AA}/\text{min}$). Milling is preferred over chemical etching because of undercutting around mesa edges and other problems. The region outside the heavier dashed line in Fig. 3 is the surface of the high resistivity GaAs:Cr buffer that is exposed by the ion milling. The source, drain, and gate bonding pads, which are deposited onto the buffer surface, are indicated in the diagram by the letters S, D, and G, respectively. Typical dimensions are, for mesa length 75 μm , for S and G pads $50 \times 100 \mu\text{m}$, for G to mesa spacing 40 μm , for gate width 250 μm , and for gate length 1 μm .

Electrical measurements.—In order to identify the processing steps responsible for inducing the leakage current, the current-voltage (I-V) characteristics of wafers were monitored at several stages during processing. The I-V characteristics were measured as a function of the applied voltage between the gate and source pads with the drain floating. We demonstrate below that the current being measured was the current flowing between the gate

pad and the entire mesa. Typically, each wafer was characterized by measuring the leakage current of eight devices from different sections of the wafer. Unless otherwise noted, the leakage current was measured at an applied gate voltage of 1V. A computer-controlled measurement system, consisting of a Hewlett-Packard HP-85 computer, an HP Model 3497A Data Acquisition/Control Unit, an HP-6002A programmable power supply, and an HP-7245 plotter/printer, was used. The devices were accessed using an Electroglas Model 131 wafer prober. The processing steps of interest, in sequential order, are: 1, growth of buffer and n-type active layers, 2, mesa definition by ion milling followed by PA etching (using a

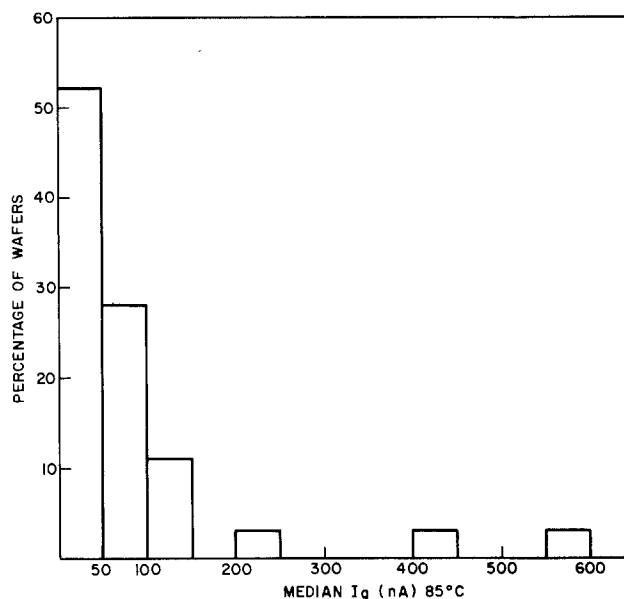


Fig. 1. Distribution of wafer median gate leakage current at 85°C

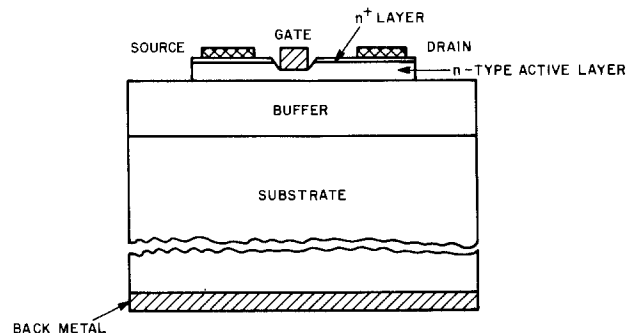


Fig. 2. Schematic cross section of the GaAs MESFET

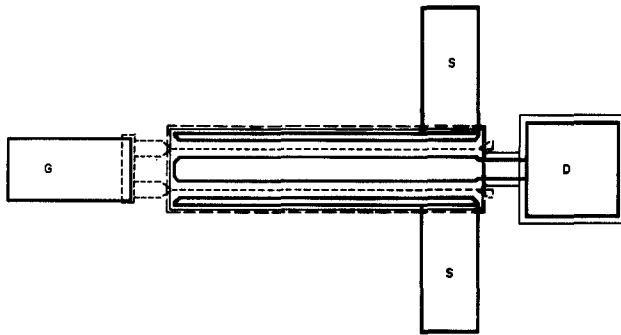


Fig. 3. Top view of the FET structure

solution of 30% hydrogen peroxide in deionized water buffered to a pH 7.2 with ammonium hydroxide), 3, ohmic metal deposition and alloying, 4, gate notch etch and gate metal (Al) deposition, 5, final metal deposition, and 6, dicing. Wafers were evaluated after processing steps 3, 4, 5, and 6, as well as before and after alloying of ohmic metal. Only a small number of devices was measured after dicing, owing to the long sorting time required to find specific devices. In order to investigate the effects of processing steps 1 and 2 on leakage, wafers were grown with no n-type active layer on top of the high resistivity buffer layer. Each wafer was then cleaved into several samples. The surfaces of some of these samples were ion milled in separate runs and had metal deposited on them for ohmic contacts, while others had metal deposited on them without any ion milling. The leakage currents of these samples were then measured.

The ion miller was a Technics Model TLA-20, operated at an ion beam energy of 500 eV with the substrate temperature held at 60°C by use of a water-cooled wafer holder. It is important to note that the machine and the procedure for this ion milling is very different from those used in the Auger apparatus (described below) for depth profiling and surface cleaning.

Surface etching.—The wafers were treated with a variety of etchants to determine whether the leakage current path is at the surface and to develop a technique to reduce the leakage. The PA etch of processing step 2 and an aqueous NH_4OH solution were used primarily in these experiments; however, the effects of a $\text{H}_2\text{SO}_4:\text{H}_2\text{O}_2:\text{H}_2\text{O}$ (1:1:200) and a 0.05% bromine-methanol solution were also investigated.

The NH_4OH etch, when used in conjunction with a prior anodic oxidation of the GaAs surface, can produce an essentially stoichiometric and contaminant-free GaAs surface (2). We used a 1:1 solution of NH_4OH in deionized water with a pH of 12.7. Wafers were etched for 2-10 min, rinsed with deionized water, and blown dry with filtered nitrogen. The etch rates were measured using a Talystep 1 instrument.

Auger electron spectroscopy.—The chemical nature of the GaAs buffer surface was studied by Auger electron spectroscopy (AES) using a PHI 590A system. The experimental system and analysis conditions have been described elsewhere (3). For depth profiling and surface cleaning, a PHI Model 04-303 differentially pumped ion gun was used, operated at an ion energy of 3-4 keV (Ne), and milling rates of 50-100 Å/min. The main objective of the AES analysis was to look for any correlations between the chemical nature of the GaAs surface and the leakage current. This information is important in understanding the mechanism responsible for the leakage current.

Electrical Measurements

Effects of processing steps 3-6 on leakage.—Figure 4 shows typical leakage current vs. voltage curves for two devices from different wafers which were measured after (i) formation of ohmic contacts, (ii) gate deposition, and (iii) deposition of final metal. Most of these data were taken with the gate biased negatively with respect to the

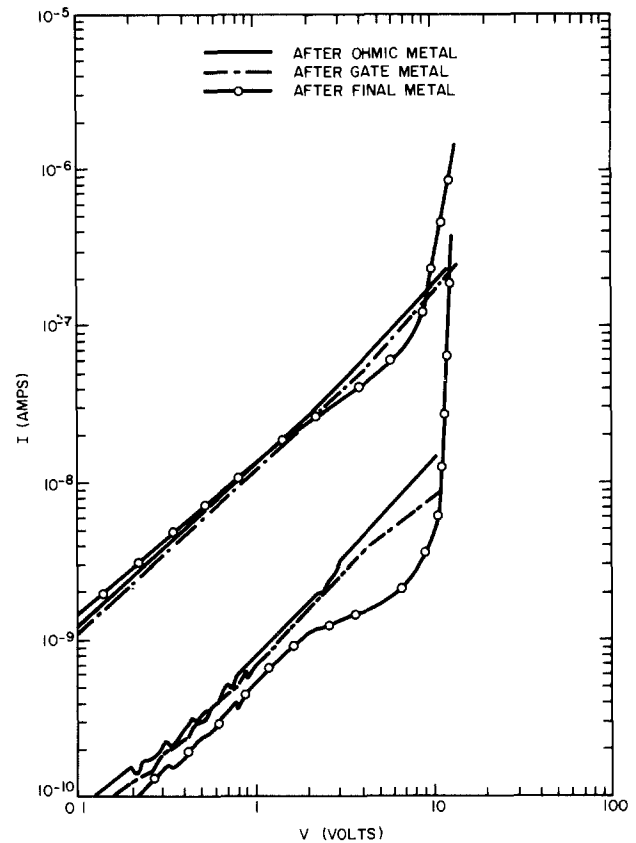


Fig. 4. Typical set of I-V characteristics after ohmic metal, gate, and final metal.

source, after we had established that the leakage current is insensitive to the polarity of the gate. Note that at the ohmic contact and gate formation steps the leakage current varies linearly with voltage over the voltage range 0.1-12V, whereas after final metal the current is ohmic up to 7V and then increases steeply with increasing voltage. This sharp increase in current is indicative of space-charge-limited current flow caused by the injection of electrons into the semi-insulating buffer from the ohmic metal (4). Measurements of over 200 devices showed that the threshold voltage for the transition from ohmic to space-charge-limited current flow lies in the range of 6-10V. The operating voltage of the device is only about 2V, which is well below this space-charge-limited threshold. This fact, along with Fig. 4, indicates that the variation in leakage current is not related to space-charge-limited current flow but is due to variations in the resistivity of a conducting region in the buffer. Figure 5 shows the broad distribution of wafer average leakage current (at 1V) measured at room temperature shortly after formation of ohmic contacts.

Figure 4 also shows that the processing steps subsequent to the formation of ohmic contacts have little effect on the leakage current. Measurements on 40 additional wafers supported this observation. Table I lists the aver-

Table I. Leakage current (nA) at $V_{gs} = 1\text{V}$ after:

Wafer no.	Ohmic metal	Gate	Final metal
CX2028	0.4	0.4	0.6
M3062	0.5	0.4	1.2
CX2523	11	12	11
1196	0.2	0.3	0.6
1197	7	10	6
1338	0.4	0.2	0.4
1403	1.5	2.5	3
1411	0.2	0.2	0.2
1456	9	5.5	9.4
1414	0.1	0.2	0.1
1477	8.4	5.8	6.8
1479	1.7	1	1.2
1001	40	40	—

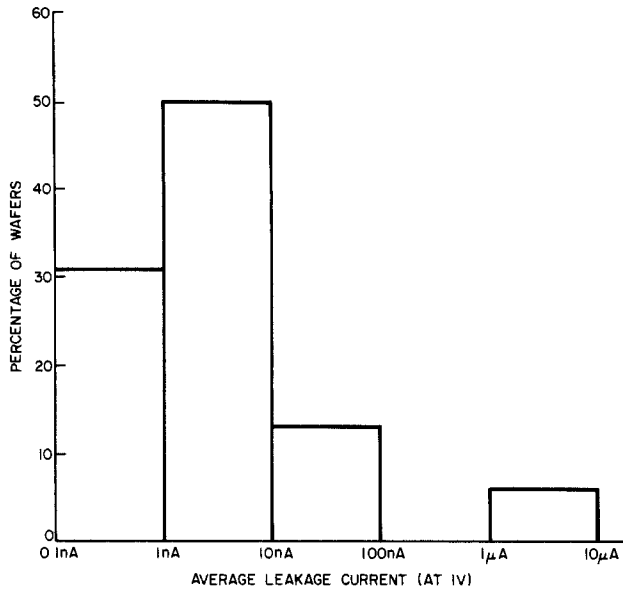


Fig. 5. Distribution of I_g (at 1V) after alloying of ohmic metal

age leakage current at room temperature of some of these wafers after processing steps 3, 4, and 5. Most wafers showed no significant change in leakage, and approximately 20% changed by a factor of 2-3. A limited amount of data from devices measured after dicing showed that this process does not affect leakage. As illustrated by Table II, alloying of the deposited ohmic metal does not increase the leakage. These results suggest that at least one of the processes which precede the deposition of ohmic metal is responsible for inducing an increase in the leakage current.

Effects of ion milling on leakage.—Measurements of the leakage current, I_g , in the unmilled high resistivity buffer were carried out using wafers without any n-type active layer. I_g ranged from 0.1 to 1 nA, as shown in Table III.

The ion-milled samples from these same wafers show a large variable increase in the observed leakage current. In particular, one wafer, labeled "Tester" in Table III, was cleaved into eight samples, three of which were measured as unmilled samples. For the ion-milled samples, I_g ranged from 2 nA to 10 μ A, as shown in Table III; these were milled in separate runs. For the unmilled samples, I_g was consistently equal to 1 nA.

These results prove that the ion milling process is responsible for inducing large variable increases in leakage

Table II. Leakage current ($V_{gs} = 1V$)

Wafer no.	Before alloying (nA)	After alloying (nA)
1346	0.2	0.1
1338	0.2	0.4
1336	1	1.7
1347	6	11
1337	20	21

Table III. Leakage current (nA) at $V_{gs} = 1V$

Wafer no.	Unmilled buffer surface	Ion-milled buffer surface
Tester 1	1	10,000
Tester 2	1	584
Tester 3	1	150
Tester 4	1	2
Tester 5	1	293
1485	0.1	5
V3995	1	51
V3997	0.2	7
V3993	0.2	
V3989	0.1	
V3874	0.1	

Table IV. Evaluation of PA etch

Wafer	PA etched	Leakage current (nA)
1485	No	5
1485	Yes	0.1
1505C	No	0.8
1505H	No	0.5
1505F	No	0.6
1505A	No	1.5
1505B	Yes	1.2
1505D	Yes	1.3
1505G	Yes	0.4
1505E	Yes	2.8
1606B	No	3.6
1606G	No	2.2
1606C	No	2.6
1606E	No	3.1
1606H	Yes	2.2
1606D	Yes	1.1
1606F	Yes	1.4
1606A	Yes	3.1

current. They are also an indication that the leakage current path is located at (or very near) the buffer surface since the 500 eV ion milling process (with the wafer surface temperature maintained at approximately 60°C) is not expected to damage the GaAs material well below the surface (5).

PA etching effects.—An experiment to evaluate the PA etch is shown in Table IV. The wafers were ion milled and then cleaved into several samples. Before the formation of ohmic contacts, half of these samples were PA etched for 1 min using a freshly prepared solution each time, while the other set was not etched. The results show that, except for wafer 1485, there is no significant difference in the measured leakage current of the etched and unetched samples. It should be pointed out that this set of samples happened to have uniformly low leakage currents. Similar results were obtained on samples with higher leakage currents (see Fig. 6 and 7).

Repeated PA etching of the buffer surface can even lead to increased leakage, as shown in Fig. 6. The initial

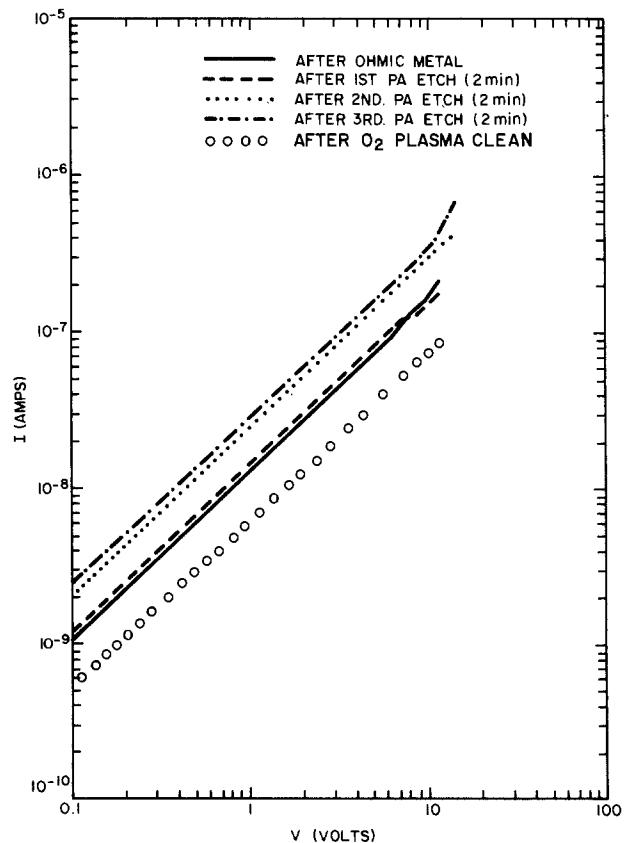


Fig. 6. Effect of repeated PA etching on leakage

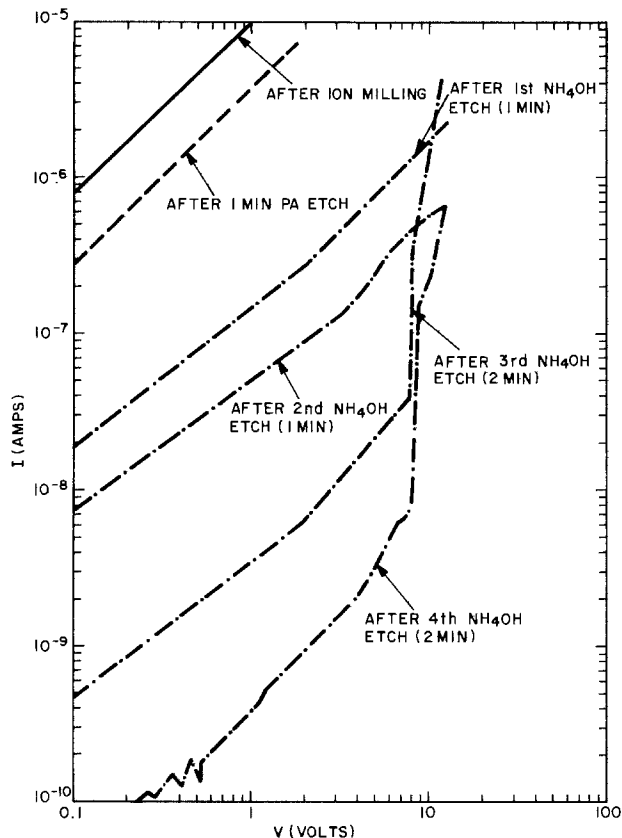


Fig. 7. Effects of NH_4OH and PA etching on the leakage current of the ion-milled sample Tester 1.

I-V curve is shown by the solid line. After three 2 min PA etches the leakage current increased by a factor of 2. A Talystep measurement showed that the PA etch removed 6000\AA from the buffer surface. A subsequent 15 min 100W oxygen plasma "cleaning" of this wafer surface reduced the leakage by a factor of 4. We tried a few more experiments with oxygen plasma cleaning and became convinced that the slight reduction in leakage current did not warrant further investigation of this approach; these surfaces were not Auger analyzed.

Further evidence of the erratic nature of the PA etch can be seen in Fig. 7. The solid line is the leakage I-V curve for the ion-milled sample, Tester 1. This sample was cleaved into two pieces after ion milling. One half was etched with the PA etch for 1 min, while the other was etched with the NH_4OH solution. After the PA etch, the leakage current, which was initially $10\ \mu\text{A}$, decreased to $4\ \mu\text{A}$. A Talystep measurement showed that the PA etch removed less than 30\AA of material from the surface; it appears that, in this case, the PA etch did not remove any GaAs.

The sample which received the PA etch was cleaved in two and each piece etched in either $\text{H}_2\text{SO}_4:\text{H}_2\text{O}_2:\text{H}_2\text{O}$ or the bromine-methanol solution. Both treatments increased the leakage current nonuniformly across the wafer.

NH_4OH etching effects.—Figure 7 shows much more favorable results for the other half of Tester 1, which was etched several times in the NH_4OH solution. The first NH_4OH etch, which lasted for 1 min, reduced the leakage current from $10\ \mu\text{A}$ to $140\ \text{nA}$. Subsequent etches of the same sample resulted in a steady decrease in the leakage current. After the fourth etch, corresponding to a total etch time of 6 min, the leakage current decreased to $0.4\ \text{nA}$. Similar results were observed on all the other ion-milled wafers irrespective of the magnitude of the initial leakage current. Figure 8 shows the leakage current of four different wafers, which were etched in NH_4OH , as a function of etch time.

Talystep measurements of these NH_4OH -etched wafers show that in all cases less than 100\AA of material was re-

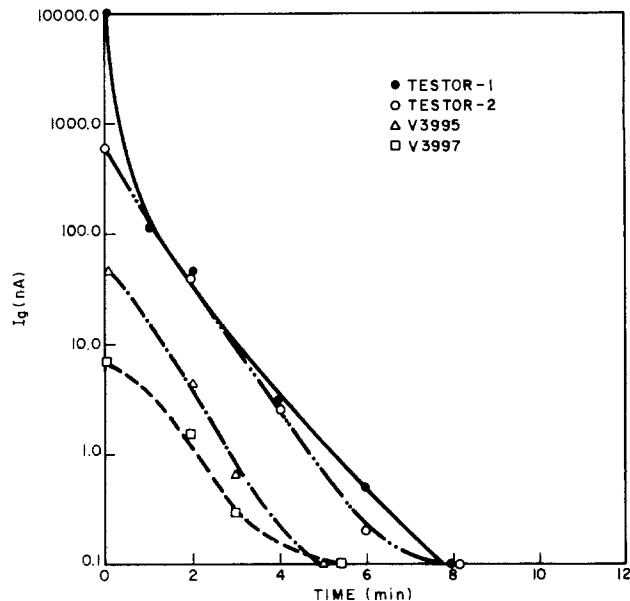


Fig. 8. Leakage current, I_g (at 1V) as a function of length of time of etch in the 1:1 NH_4OH solution for four different samples.

moved from the surfaces after 6-8 min of etching. Because the etch rates are so small, a more careful measurement of the NH_4OH etch rate was made using a wafer on which no active layer was grown. After ion milling, the samples were cleaved from this wafer and etched in the NH_4OH solution for various periods of time using electroplating tape as an etch barrier to create a step. Figure 9 shows that the etch rate of ion-milled buffer surface is approximately $10\ \text{\AA}/\text{min}$. These results confirm that the leakage current path is located at the GaAs buffer surface.

Use of the NH_4OH etch in processing.—Table V shows the average leakage current at room temperature of wafers from nine device lots which received an 8 min NH_4OH etch after mesa definition. The first three wafers were measured after processing steps 3, 4, and 5; the others were measured only after processing steps 3 and 5. The average gate leakage current of devices from three wafers operating at 85°C (with $V_{ds} = 1.5\text{V}$ and $V_{gs} = -0.25 \pm 0.05\text{V}$) were 17, 9, 13 nA, respectively.

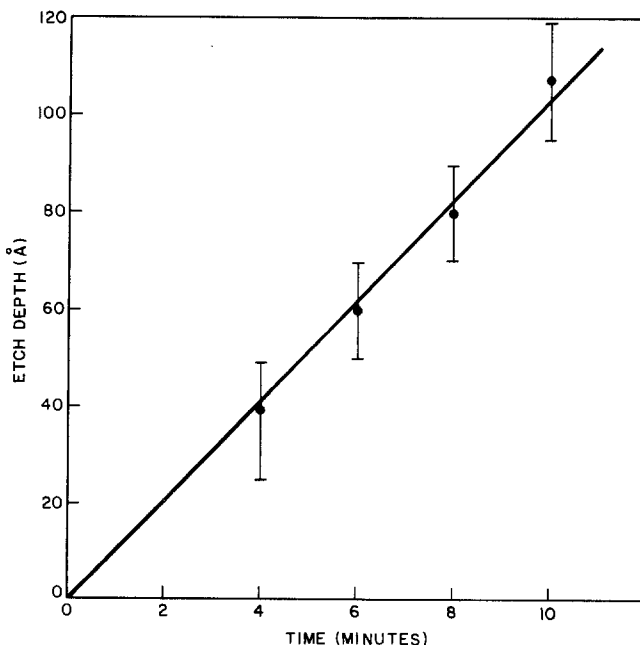


Fig. 9. Etch rate of the ion-milled buffer surface using a 1:1 aqueous solution of NH_4OH .

Table V. Leakage current (nA) at $V_{ds} = 1V$

Wafer no.	Ohmic metal	Gate	Final metal
1684	0.1	0.1	0.4
1876	0.1	0.1	0.3
1877	0.1	0.2	0.3
1859	0.1		0.2
1977	0.2		0.6
1978	0.3		0.3
1979	0.2		0.5
1980	0.4		0.7
1981	0.2		0.3

Surface chemical analysis.—Surface chemical analyses were performed using Auger spectroscopy. Typical Auger spectra are shown in Fig. 10-12; these were taken under identical experimental conditions (3 keV incident electrons at 1 μ A current) and are all displayed at the same vertical magnification scale (except Fig. 11c) so that the relative sizes of the Auger peaks can be directly compared. The Auger data are summarized in Table VI, in which the height of the oxygen Auger peak (labeled O Peak in Table VI in arbitrary units), the As/Ga peak height ratio (As/Ga), the height of the GaAs plasmon loss peak of the Ga spectra (plasmon, normalized to the 1067 eV Ga peak height), and the "symmetry factor" (explained in the table) are shown.

The buffer surface immediately after mesa delineation by ion milling was examined before PA etch (top row of Table VI). Auger data from this surface are shown in Fig. 10a. From these spectra, we estimate that there is a surface Ga oxide containing less than 5 atom percent of As. Note the small value of the GaAs plasmon loss peak height in Table VI, top row, indicating that the surface oxide is sufficiently thick to almost completely attenuate the plasmon loss signal from the GaAs substrate. The oxide was then milled off while monitoring the O, Ga, and As signals, in order to determine the oxide thickness. The oxide was found to be about 60Å thick, as shown by the Auger data in Fig. 10b, which were taken after milling off 60Å. The milled thickness was estimated assuming the milling rate for SiO₂. In the figure, the Ga and As signals from the substrate are strong, and the oxygen signal is almost gone, indicating that the data were taken at the interface between the oxide and the GaAs buffer layer (the rate of oxygen readsorption in our Auger system was negligible).

The escape depth of oxygen Auger electrons (at 507 eV) is about 10Å; we estimate that an oxygen signal of 4 in Table VI should correspond to an oxide 10 ± 5 Å thick. A

Table VI. Analysis of Auger data

Sample	O Peak	As/Ga	Plasmon	Symmetry ^a
Ion milled (mesa)	7.0	0.05	0.05	0.75
High leakage (PA)	5.4	0.40	0.04	0.73
Low leakage (PA)	3.8	0.57	0.12	0.56
NH ₄ OH etched	2.8	0.84	0.15	0.53
"Clean" GaAs ^b	0	0.67 ± 0.07	0.19	0.53 ± 0.03

^a Symmetry = Pos/Neg, where Pos/Neg is the ratio of the positive excursion to the negative excursion of the Ga (1067 eV) peak plotted in the "derivative" mode.

^b Ion mill cleaned in the Auger apparatus.

more quantitative analysis would become somewhat involved, because the peak shape (which affects the peak height) is chemistry dependent (6). The oxide thickness is not linear with the oxygen signal, but increases very rapidly with the oxygen signal above about 4 (6).

The thicknesses of the oxides on both PA etched surfaces are small, about 10Å for the low leakage, and 17Å for the high leakage surface (see Table VI). This thicker-oxide conclusion is supported by the smaller GaAs plasmon loss peak and greater symmetry of the Ga (1067 eV) peak from the high leakage surface than from the low leakage surface. The Auger spectra from these surfaces are given in Fig. 11a and 11b. The plasmon loss peak for the Ga (1067 eV) peak of Fig. 11b is shown more clearly in Fig. 11c. The GaAs plasmon loss peak and the asymmetry of the Ga peak are signatures of the GaAs substrate. Auger data from a thick oxide show no GaAs plasmon loss peak and very symmetric Ga peak shape (symmetry factor about 0.8). The decreasing plasmon signal and increasing Ga peak symmetry with increasing oxygen intensity in Table VI are due to attenuation of signals from the substrate by the surface oxide (6).

The oxide on the high leakage PA etched surface is As deficient because of the small As/Ga peak height ratio (Table VI). The true As deficiency in the high leakage oxide is probably greater than indicated by the As/Ga ratio because the leaky surface should have a thin As-rich layer under the As deficient oxide, according to the literature (2, 7). Because these compositional changes occur in a depth of only about 10Å, useful data can only be generated using the lowest energy (below 100 eV) Auger transitions; unfortunately, such peaks are difficult to quantify. A large amount of such data were taken and analyzed, but the only definitive conclusion we could draw was that we could not exclude the existence of the interfacial As layer.

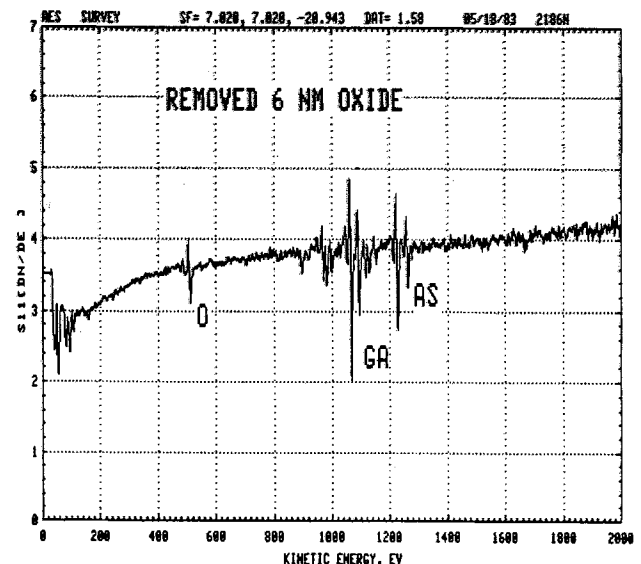
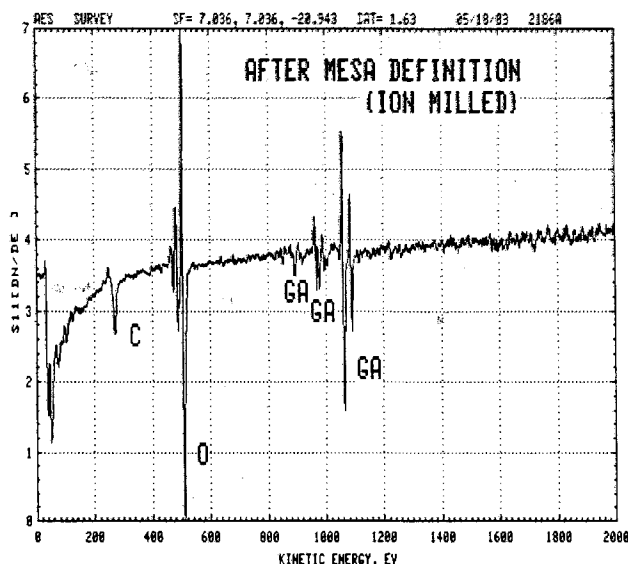


Fig. 10. a (left): Auger spectra from the surface oxide produced after mesa definition by ion milling. The vertical axis is the "derivative" Auger peak intensity in arbitrary units. The same vertical magnification has been maintained in Fig. 10-12 (except Fig. 11c), so that relative intensities can be compared from figure to figure. b (right): Spectra after 60Å were removed from the same sample used in Fig. 10a.

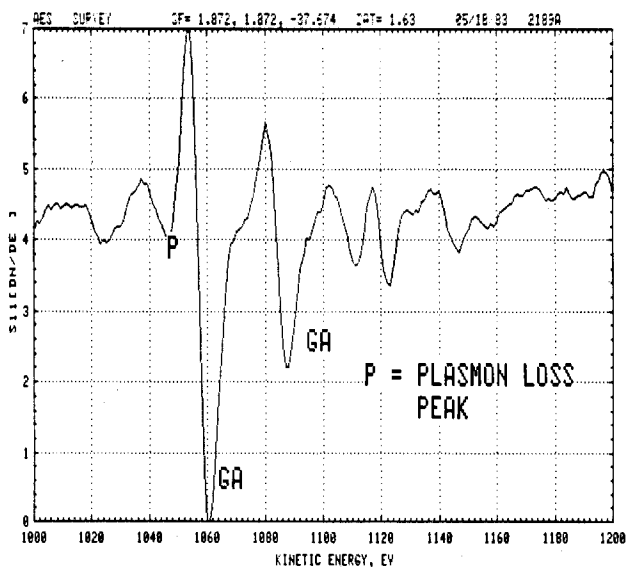
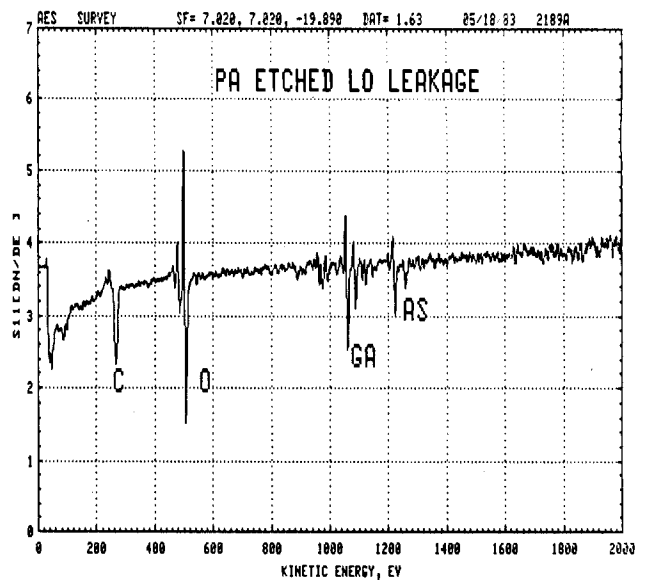
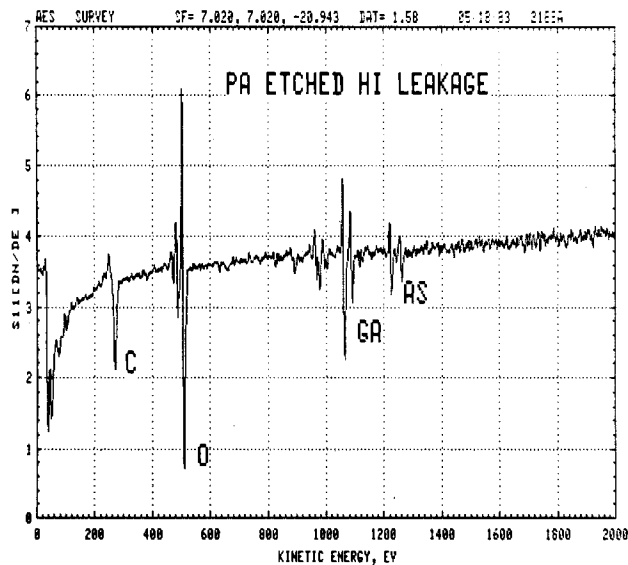


Fig. 11. a (top left): Auger spectra from the buffer surface of a PA-etched, high leakage wafer. b (above): Auger spectra from the buffer surface of a PA-etched, low leakage wafer. c (left): Detail of the Ga Auger peak of Fig. 11b, showing the plasmon loss peak.

We conclude that the high leakage PA-etched surface has a thicker oxide that contains mostly Ga oxide, and that there can be a thin As layer between this oxide and the semiconductor.

Auger data from a surface etched in NH_4OH are displayed in Fig. 12. The O peak is smaller and the As peak is larger than that from the low leakage PA-etched surface; therefore, the NH_4OH etched surface is even closer to the "Clean GaAs" (Table VI) surface than the low leakage PA etched surface. The clean GaAs surface of Table VI was ion-mill-cleaned in the Auger apparatus until no contaminants could be detected. This surface is As deficient (2) by about 7%, a negligibly small quantity compared to the much larger As deficiencies we encountered in this work.

Finally, there are certain perverse situations in which the above quantitative results will not be valid because of diffraction effects in the single-crystal substrates; we did not observe any suspicious variations in our data, but we made no systematic studies of angular dependencies of the peak heights. Possible difficulties from chemical shifts and diffraction are the reasons why we tabulated four properties in Table VI instead of just the oxygen peak height. Since all four columns of data agree, there does not appear to be any significant experimental artifacts.

Discussion

We have found a direct correlation between the amount of surface (As-deficient) Ga oxide and the leakage cur-

rent. The failure of the bromine methanol etch to reduce the leakage is consistent with this correlation because bromine methanol leaves just such a surface oxide (2). A mechanism that would explain the large leakage current variations must take the following factors into considera-

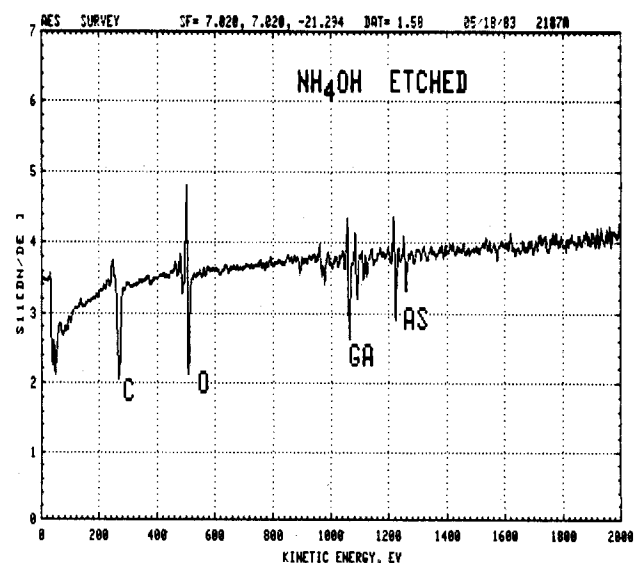


Fig. 12. Auger spectra from an NH_4OH -etched surface

tion: (i) the leakage current is a near-surface phenomenon, (ii) the range of leakage current is large, from 0.5 nA to over 10 μ A, (iii) it operates in the environment of the semi-insulating substrate, and (iv) leakage can be controlled by an oxidized surface layer only about 10-60Å thick.

A mechanism consistent with the above is the surface band bending due to fixed charges in the surface oxide or surface states. Band bending could lead to either accumulation or inversion at the buffer surface with the associated increase in surface conductivity (8). The variation in leakage could then be explained by variations in the buffer surface potential (amount of charge in the oxide) or the type and degree of carrier compensation (buffer layer quality).

Another possible mechanism for current leakage is conduction along an elemental As layer at the interface between the oxide and the semiconductor; the large range of leakage current then results from the thickness variation and degree of continuity of the As layer. It is possible that both mechanisms control the leakage current. The first mechanism is especially interesting because it should be less effective in wide-gap (uncompensated) semi-insulating GaAs.

The composition (almost pure Ga oxide) and thickness (only about 60Å) of the surface oxide created by ion milling for mesa delineation indicate that the poor performance of the PA etch in controlling leakage is caused by the inability of the pH-adjusted PA etch to reproducibly remove this oxide. However, it is not a simple problem of slow or variable etch rate, since, if that were the case, the leakage current should eventually come down after a sufficiently long etch time (which is not the case). We propose that the basic problem is not the oxide etch rate, but rather the competition between the oxide etch rate and growth rate. According to the literature (9), the solubility of Ga oxide is lowest in a neutral solution and increases with both acidity and alkalinity. This is consistent with our finding in this work that the etch rate of GaAs with a Ga oxide surface layer in our neutral PA etch can be very fast or slow (PA etching effects section). It is also known that the oxidation rate of GaAs in the PA etch can be relatively fast because of the presence of the peroxide. Therefore, the slow attack of GaAs can be explained by the growth of a slowly etching oxide during PA etch when the initial surface layer is a passivating oxide. When steady state is established, the surface is covered with a thicker oxide than when the NH_4OH etch is used; in the NH_4OH case, the Ga oxide is dissolved rapidly because of the high pH. However, the PA etch can attack GaAs rapidly if the initial passivating oxide is absent because the rapid oxidation of the unpassivated surface results in the growth of more nonpassivating oxide. According to our data, one criterion of a passivating oxide is its low As content.

Conclusion

We have shown that the leakage current is due to conduction along the semi-insulating buffer surface outside the active area of the device. We have also shown that the ion milling process used to define mesas is responsible for inducing the leakage and that the PA etch does not

consistently reduce the induced leakage current. A concentrated aqueous NH_4OH solution will remove the surface oxide rapidly but will etch the GaAs very slowly and reproducibly reduce the induced leakage current to below 1 nA.

Auger spectroscopy results indicate that ion milling for mesa delineation results in a surface oxide layer which is mostly Ga oxide. Wafers which were ion milled and then PA etched also have an As-deficient surface oxide, probably with a thin As-enriched layer underneath it. We propose that the leakage current phenomenon can be explained by one, or a combination, of the following mechanisms: (i) band bending due to charges in the surface oxide and surface state effects, and (ii) conduction through a thin interface layer of elemental As.

No investigation is ever complete, and neither is this one. A more definitive verdict on the existence of the As layer (perhaps by use of ion scattering spectrometry), electrical measurements of the effect of charges in the Ga oxide layer, and the dependence of the surface etch rate on pH, NH_4OH concentration, solution temperature, As content of the surface oxide, and semiconductor doping level would certainly contribute to better control of the surface leakage problem. Future experiments using pure (uncompensated) semi-insulating GaAs should be especially illuminating with respect to our band bending model. Finally, it is truly surprising that an unpassivated semiconductor surface can be simply etched chemically in such a way that the leakage current can be reproducibly reduced to below 1 nA, and at times by as much as five orders of magnitude.

Acknowledgments

We would like to acknowledge the many informative and helpful discussions with S. H. Wemple, and with H. M. Cox, who was also responsible for the CVD epitaxial growth of the GaAs wafers used in this study. We would also like to thank G. E. Mahoney and P. F. Sciortino for providing processing information and supervision of the experimental wafers in the device processing line.

Manuscript submitted Nov. 8, 1984; revised manuscript received Feb. 27, 1985.

Bell Communications Research, Incorporated, assisted in meeting the publication costs of this article.

REFERENCES

1. T. Li, *IEEE Trans. Commun.*, **com-26**, 946 (1978).
2. C. C. Chang, P. H. Citrin, and B. Schwartz, *J. Vac. Sci. Technol.*, **14**, 943 (1977).
3. R. P. H. Chang, C. C. Chang and S. Darack, *ibid.*, **20**, 45 (1982).
4. M. A. Lampert, *Phys. Rev.*, **103**, 1648 (1956).
5. R. S. Williams, *Solid State Commun.*, **41**, 153 (1982).
6. C. C. Chang, *Surf. Sci.*, **48**, 9 (1975).
7. R. P. H. Chang, T. T. Sheng, C. C. Chang, and J. J. Coleman, *Appl. Phys. Lett.*, **33**, 341 (1978).
8. C. G. B. Garrett and W. H. Brattain, *Phys. Rev.*, **99**, 376 (1955).
9. M. Pourbaix, "Atlas of Electrochemical Equilibria in Aqueous Solutions," Pergamon Press, New York (1966).

Substrate Orientation Dependence of the In-Ga-As Phase Diagram for Liquid Phase Epitaxial Growth of $\text{In}_{0.53}\text{Ga}_{0.47}\text{As}$ on InP

Kazuo Nakajima and Jiro Okazaki

Fujitsu Laboratories Limited, Atsugi Laboratories, 1677 Dannoki, Ono, Atsugi, 243-01 Japan

ABSTRACT

The liquidus isotherms of the In-Ga-As system were determined at 600° and 700°C by the improved seed dissolution technique. From the results of the liquidus isotherms and the lattice-constant measurements, the substrate orientation dependence of solution compositions to grow lattice-matched $\text{In}_{0.53}\text{Ga}_{0.47}\text{As}$ layers on the (100), (111)A, and (111)B InP substrates by liquid phase epitaxy (LPE) was exactly obtained in the temperature range 600°-790°C. The solution compositions of Ga for the (111)A and (111)B faces are always larger than those for the (100) face over the entire temperature range 600°-790°C. The solution compositions of As for the (111)A and (111)B faces are always smaller than those for the (100) face over the entire temperature range 600°-790°C. In order to study effects of the surface free energy on the In-Ga-As phase diagram which was determined by using the LPE method, the In-Ga-As phase diagram was calculated, for the first time, by adding the surface free energy to the chemical free energy of the $\text{In}_{1-x}\text{Ga}_x\text{As}$ solid phase. According to the calculated phase diagram, the composition of Ga in the solution to obtain the (111) oriented $\text{In}_{0.53}\text{Ga}_{0.47}\text{As}$ is smaller than the composition of Ga in the solution to obtain the (100)-oriented $\text{In}_{0.53}\text{Ga}_{0.47}\text{As}$. This tendency of the calculated results is contrary to the experimental results. That is to say, the difference in the surface free energy is not a main reason for the substrate orientation dependence of the In-Ga-As phase diagram.

The liquid phase epitaxial (LPE) growth of lattice-matched $\text{In}_{0.53}\text{Ga}_{0.47}\text{As}$ on InP is important especially for infrared photodetector (1-3) and FET (4-6) applications. It has been reported that the solution composition for the growth of lattice-matched $\text{In}_{0.53}\text{Ga}_{0.47}\text{As}$ strongly depends on the orientation of InP substrates (7-10). However, the growth temperature dependence of the difference of the solution compositions for the growth of lattice-matched $\text{In}_{0.53}\text{Ga}_{0.47}\text{As}$ on (100) and (111)B InP substrates is different according to each author. Antypas *et al.* (7) studied the temperature dependence of the incorporation of Ga during LPE growth of $\text{In}_{0.53}\text{Ga}_{0.47}\text{As}$ on (100) and (111)B InP in the temperature range 621°-650°C, and they reported that there was a cross point at 629°C, at which the solution composition for the growth of $\text{In}_{0.53}\text{Ga}_{0.47}\text{As}$ on both faces of InP are equal. On the other hand, Pearsall *et al.* (8) and Nakajima *et al.* (9) reported that the composition of Ga in the solution for the growth of $\text{In}_{0.53}\text{Ga}_{0.47}\text{As}$ on (111)B InP is always larger than that on (100) InP in the temperature range 600°-670°C. Recently, it was reported by Hsieh (10) that the difference between the solution compositions for the growth of $\text{In}_{0.53}\text{Ga}_{0.47}\text{As}$ on (100) and (111)B InP decreased with increasing temperature, and above about 700°C the solution compositions for both faces were the same. In order to yield clues to these inconsistent results and to understand the LPE growth mechanism of multicomponent systems, it is very important to study the temperature dependence of the solution composition in detail and to make clear the origin of the substrate orientation dependence of the solution composition.

The equilibrium phase diagram is not completely adequate for describing the LPE growth of $\text{In}_{1-x}\text{Ga}_x\text{As}$ on InP because of the strong perturbing effects of the substrate orientation on the phase diagram. It has been generally discussed that these perturbing effects of the substrate orientation presumably result from the attachment kinetics at the growth interface or from a difference in surface energy (8-10). However, the origin of the substrate orientation dependence of the phase diagram has not been made clear until now because no one has calculated the phase diagram by adding these effects to the chemical free energy of the solid phase or confirmed how the phase diagram was influenced by the addition of these effects. Therefore, the influence of these effects on the phase diagram must be investigated in order to develop a theoretical model for calculating the phase diagram which is adapted to the LPE growth.

In this work, the liquidus isotherms of the In-Ga-As system were experimentally determined using an improved seed dissolution technique (9). The results of the

phase diagram and the lattice-constant measurements were used to obtain the solution compositions for the growth of lattice-matched $\text{In}_{0.53}\text{Ga}_{0.47}\text{As}$ layers on the (100), (111)A, and (111)B InP substrates. From these results, the substrate orientation dependence of the solution compositions and the distribution coefficients were exactly obtained in the temperature range 600°-790°C. The surface free energy was obtained for the (100)- and (111)-oriented $\text{In}_{1-x}\text{Ga}_x\text{As}$ layers. The In-Ga-As phase diagram was calculated, for the first time, by adding the surface free energy to the chemical free energy of the $\text{In}_{1-x}\text{Ga}_x\text{As}$ solid phase. The origin of the substrate orientation dependence of the phase diagram was studied by the calculation.

Experiments and Results

Liquidus isotherms.—The accurate liquidus isotherms of the In-Ga-As system were determined at 600° and 700°C by the improved seed dissolution technique, which had been used previously to obtain the 650°C liquidus isotherm of the ternary system (9). A ternary In-Ga-As solution was brought into contact with an InP seed at 600°C (or 700°C) and kept in contact at this temperature for 30 min. If the As concentration in the ternary solution was below the solubility limited at 600°C (or 700°C), the initially undersaturated solution became saturated with P, and the P solubility could be calculated from the weight loss of the seed after removal of the solution. If the As concentration in the solution was just at or above the solubility limit, P could not dissolve from the InP seed, and no weight loss could be detected. Therefore, the accurate ternary solution compositions just saturated at 600°C (or 700°C) could be known by measuring P solubility as a function of As concentration. In this improved seed dissolution technique, a very thin epitaxial film of the ternary alloy was formed on the surface of the InP seed in contact with the saturated ternary solution. The thin film protected the InP seed from further dissolution. Therefore, the ternary solution was in equilibrium with the ternary thin film when the solution was saturated.

The ternary solution was made from semiconductor-grade In, InAs, and GaAs. The InP seeds were semiconductor-grade polycrystals. The experimental apparatus consisted of a horizontal furnace system and a conventional sliding graphite boat. Pd-purified H_2 was flowed through the fused silica tube set in the furnace.

Figure 1 shows the P solubility in solutions at 600°C as a function of X_{As}^1 at several X_{Ga}^1 , where X_i^1 represents the atomic fraction of an element i in the solution. At constant X_{Ga}^1 , X_{P}^1 decreases with increasing X_{As}^1 . X_{P}^1 becomes zero at a certain value of X_{As}^1 , and X_{P}^1 remains zero when X_{As}^1 is above that value. The value of X_{As}^1 at which X_{P}^1 be-

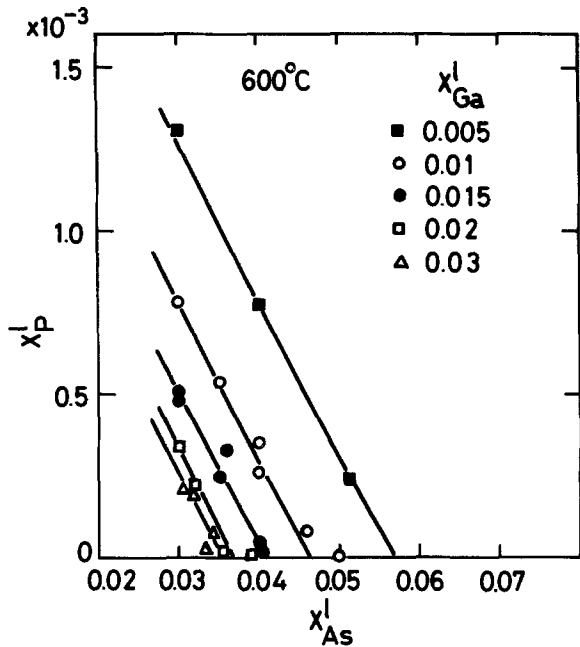


Fig. 1. P Solubility, X_P^I , at 600°C in In-Ga-As-P quaternary solutions as a function of X_{As}^I as determined by the seed dissolution technique.

comes zero is the As solubility in the ternary In-Ga-As solution just saturated at 600°C. Figure 2 shows the P solubility in solutions at 700°C as a function of X_{As}^I at several X_{Ga}^I . The value of X_{As}^I at which X_P^I becomes zero also corresponds to the As solubility in the ternary In-Ga-As solution just saturated at 700°C. From the results shown in Fig. 1 and 2, the accurate liquidus isotherms at 600° and 700°C were determined as shown in Fig. 3. The liquidus isotherm at 650°C was quoted from our previous work (9). The data reported by Wu and Pearson (11) and Liu and Peretti (12) are also shown in Fig. 3. In the temperature range 800°-900°C, much available data have been reported (11-15). Figure 4 shows the liquidus isotherms at 800°, 850°, and 900°C, which were derived from the previously reported data.

Lattice-matching.—In_{1-r}Ga_rAs ternary layers were grown from solutions with compositions on the liquidus isotherms at 600°, 650°, 700°, and 790°C shown in Fig. 3 and 4. The (100), (111)A, and (111)B oriented InP single crystals were used as substrates. No supersaturated solutions were used in the growth. In_{1-r}Ga_rAs layers were grown at a constant cooling rate of 0.5°C/min by the ramp cooling technique. The lattice constants of In_{1-r}Ga_rAs were mea-

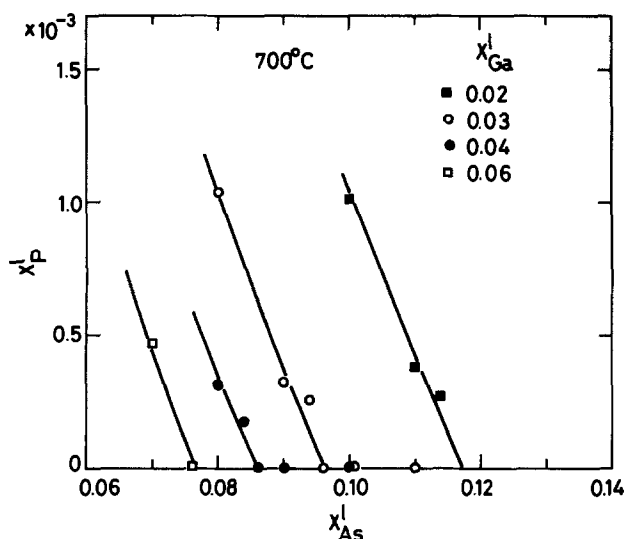


Fig. 2. P Solubility, X_P^I , at 700°C in In-Ga-As-P quaternary solutions as a function of X_{As}^I as determined by the seed dissolution technique.

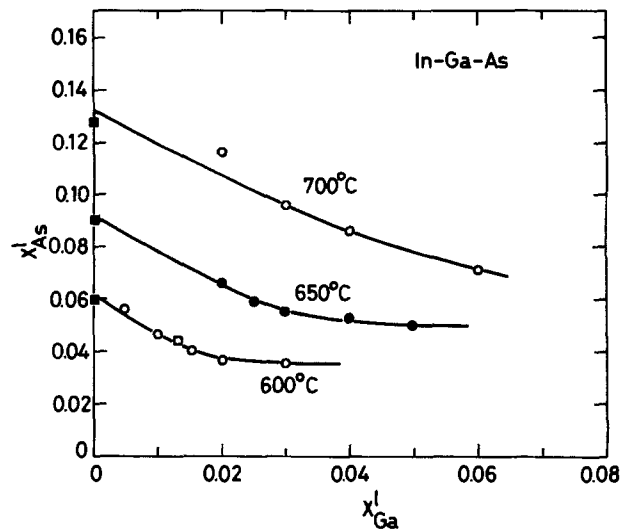


Fig. 3. Liquidus isotherms at 600°, 650°, and 700°C in the In-Ga-As ternary system, including points from this work (○), Ref. (9) (●), Ref. (11) (□), and Ref. (12) (■).

sured by the double-crystal x-ray diffraction technique. The precise diffraction angles of the ternary layers were determined from the (333) Cu-K α_1 or (400) Cu-K α_1 reflection by using the substrate reflection as an internal standard.

The lattice constant is displayed as a function of X_{Ga}^I in Fig. 5 and 6. The dashed line represents the lattice constant of InP. They are lattice constants of the epitaxial lattice perpendicular to the wafer surface. The lattice constant of a layer grown on a (111)A substrate is larger than that of a layer grown on a (100) substrate from a solution with the same composition, and the lattice constant for the (111)A face is smaller than that for the (111)B face. The solution compositions required to grow lattice-matched layers on InP substrates with various orientations can be exactly known from these results.

Substrate orientation dependence of solution compositions and distribution coefficients as a function of growth temperature.—Figure 7 shows the compositions of Ga in the In-Ga-As ternary solutions for the LPE growth of lattice-matched In_{0.53}Ga_{0.47}As on the (100), (111)A, and (111)B InP substrates as a function of the growth temperature, which are derived from Fig. 5 and 6 and our previous work (9, 16). The data reported by other authors are also shown in Fig. 7. The data for the (100) and (111)B faces at 620°C were reported by Pearsall et al. (17) and the data for the (100) and (111)B faces at 600°, 691°, and 714°C

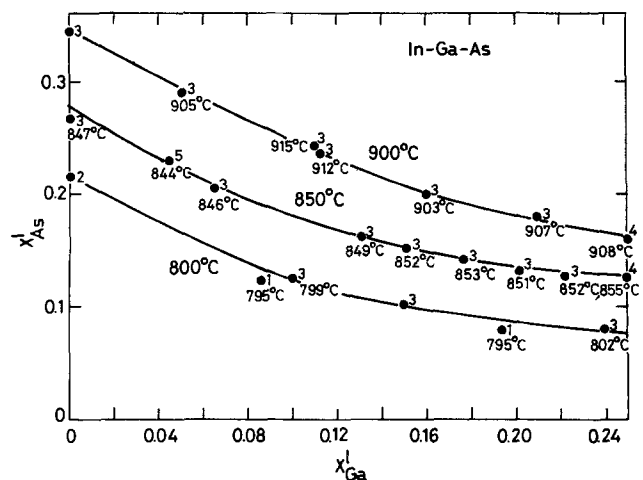


Fig. 4. Liquidus isotherms at 800°, 850°, and 900°C in the In-Ga-As ternary system, including points from Ref. (11) (●), Ref. (12) (●), Ref. (13) (●), Ref. (14) (●), and Ref. (15) (●).

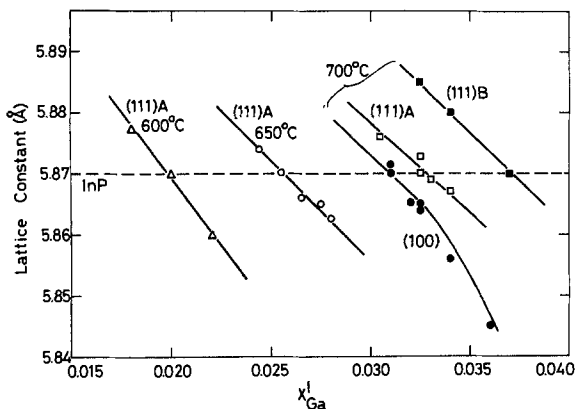


Fig. 5. Lattice constants of the $\text{In}_{1-x}\text{Ga}_x\text{As}$ ternary alloys grown on (100), (111)A, and (111)B InP substrates at 600°, 650°, and 700°C. Broken line represents the lattice constant of InP.

were reported by Hsieh (10). Hsieh's data imply that the solution compositions of Ga for the (100) and (111)B faces are the same above about 700°C. However, it is apparent from our present data in Fig. 7 that the solution compositions of Ga for the (111)B face are always larger than those for the (100) face over the entire temperature range 600°-790°C. It is also apparent that, over the entire temperature range, the solution compositions of Ga for the (111)A face are always somewhat larger than those for the (100) face and are always smaller than those for the (111)B face. These results also make it clear that there are not any cross points as reported by Antypas *et al.* (7).

Figure 8 shows the solution compositions of As in the In-Ga-As ternary solutions for the LPE growth of lattice-matched $\text{In}_{0.53}\text{Ga}_{0.47}\text{As}$ on the (100), (111)A, and (111)B InP substrates as a function of the growth temperature. These results are derived from Fig. 3-6. The data reported by Pearsall *et al.* (17) and Hsieh (10) are also shown in Fig. 8. Hsieh's data show that the solution compositions of As for the (100) and (111)B faces are the same above about 700°C. However, it is apparent from our present data in Fig. 8 that the solution compositions of As for the (111)B face are always smaller than those for the (100) face over the entire temperature range 600°-790°C. It is also apparent that, over the entire temperature range, the solution compositions of As for the (111)A face are always somewhat smaller than those for the (100) face and are always larger than those for the (111)B face. The degree of the difference between the solution compositions for the three orientations is almost constant and is independent of the growth temperature, as shown in Fig. 7 and 8.

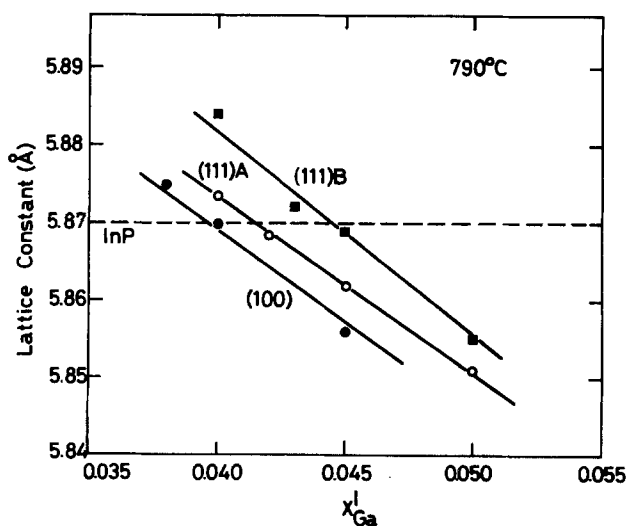


Fig. 6. Lattice constants of the $\text{In}_{1-x}\text{Ga}_x\text{As}$ ternary alloys grown on (100), (111)A, and (111)B InP substrates at 790°C. Broken line represents the lattice constant of InP.

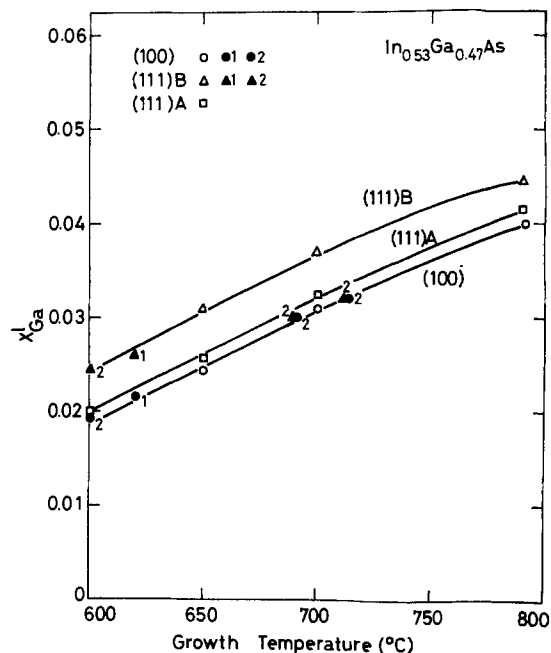


Fig. 7. Compositions of Ga, X_{Ga}^I , in the In-Ga-As ternary solutions for the LPE growth of lattice-matched $\text{In}_{0.53}\text{Ga}_{0.47}\text{As}$ on (100), (111)A, and (111)B InP substrates as a function of the growth temperature, including points from this work (\circ , \triangle , \square), Ref. (17) (\bullet , \blacktriangle), and Ref. (10) (\bullet , \blacktriangle).

Figure 9 shows the distribution coefficient of Ga for the LPE growth of lattice-matched $\text{In}_{0.53}\text{Ga}_{0.47}\text{As}$ on the (100), (111)A, and (111)B InP substrates as a function of the growth temperature. These results are derived from Fig. 7. The distribution coefficient of Ga for the (100) face is always larger than those for the (111)A and (111)B faces over the entire temperature range. Figure 10 shows the distribution coefficient of As for the LPE growth of $\text{In}_{0.53}\text{Ga}_{0.47}\text{As}$ on the (100), (111)A, and (111)B InP sub-

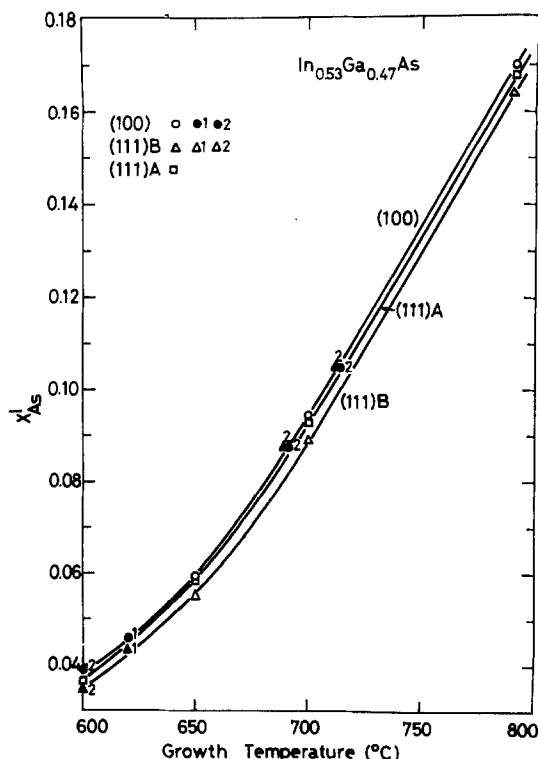


Fig. 8. Compositions of As, X_{As}^I , in the In-Ga-As ternary solutions for the LPE growth of lattice-matched $\text{In}_{0.53}\text{Ga}_{0.47}\text{As}$ on (100), (111)A, and (111)B InP substrates as a function of the growth temperature, including points from this work (\circ , \triangle , \square), Ref. (17) (\bullet , \blacktriangle), and Ref. (10) (\bullet , \blacktriangle).

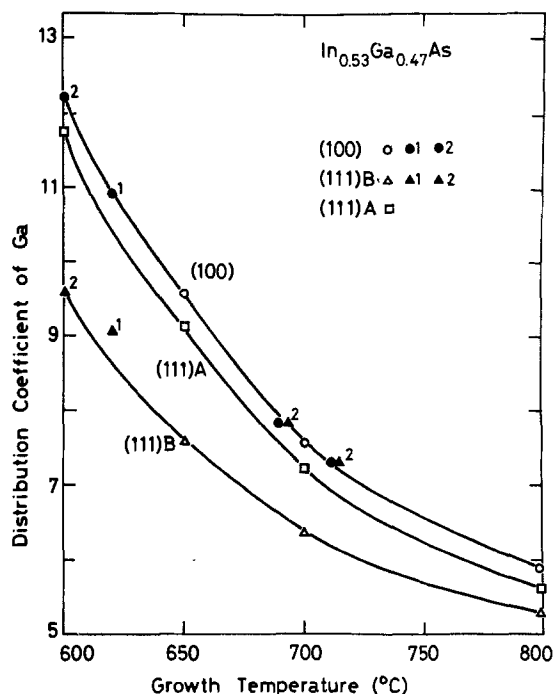


Fig. 9. Distribution coefficient of Ga for the LPE growth of lattice-matched In_{0.53}Ga_{0.47}As on the (100), (111)A, and (111)B InP substrates as a function of the growth temperature, including points from this work (○, △, □), Ref. (17) (●, ▲), and Ref. (10) (●, ▲).

substrates as a function of the growth temperature. These results are derived from Fig. 8. The distribution coefficient of As for the (100) face is always smaller than those for the (111)A and (111)B faces over the entire temperature range.

Substrate orientation dependence of growth rate.—In order to study whether or not the growth rate of In_{1-x}Ga_xAs layers has influence upon the substrate orientation dependence of the liquid-solid phase data for the LPE growth, the substrate orientation dependence of the growth rate was studied over the temperature range 650°–790°C. In_{1-x}Ga_xAs layers were grown on the (100) and

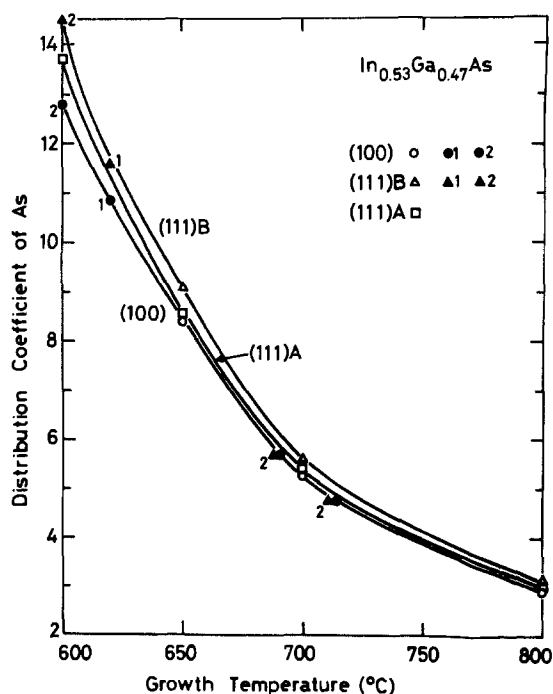


Fig. 10. Distribution coefficient of As for the LPE growth of lattice-matched In_{0.53}Ga_{0.47}As on the (100), (111)A, and (111)B InP substrates as a function of the growth temperature, including points from this work (○, △, □), Ref. (17) (●, ▲), and Ref. (10) (●, ▲).

(111)B InP substrates by the ramp cooling method. Epitaxial layers were grown at the same time on two substrates with different orientations using the same solution. This technique was used in our previous work (18). In the ramp cooling growth, a constant cooling rate of 0.5°C/min was used. The temperature interval cooled from the starting growth temperature, 650°, 700°, and 790°C, was 6°C.

Figure 11 shows the ratio of the thickness on the (100) face, $d_{(100)}$, to the thickness on the (111)B face, $d_{(111)B}$, as a function of the growth temperature. When the growth temperature is 650°C, the ratio, $d_{(100)}/d_{(111)B}$, is about 3, and when the growth temperature is 700° or 790°C, $d_{(100)}/d_{(111)B}$ is less than 2. In spite of the dependence of $d_{(100)}/d_{(111)B}$ on the growth temperature, the degree of the difference between the solution compositions for the (100) and (111)B faces is almost constant and is independent of the growth temperature as shown in Fig. 7 and 8. Therefore, the difference of the growth rate does not play an important role in determining the orientation dependence of the liquid-solid phase data for the LPE growth.

As shown in Fig. 11, the growth rate of In_{1-x}Ga_xAs layers grown on the (100) InP substrates is larger than that on the (111)B InP substrates. Therefore, the depletion of solute Ga in the solution near the interface between the solution and the substrate is stronger for the growth on the (100) face than for the growth on the (111)B face. Because of the different depletion effect on the substrate orientation, the solution composition of Ga, X_{Ga}^l , required to grow In_{0.53}Ga_{0.47}As layers on the (100) face must be larger than that on the (111)B face. However, as shown in Fig. 7, the experimentally determined X_{Ga}^l required to grow In_{0.53}Ga_{0.47}As layers on the (100) face is always smaller than that on the (111)B face. These results indicate obviously that the different growth rates on the different orientations do not have important influence on the orientation dependence of the liquid-solid phase data for the LPE growth. Pearsall *et al.* also reported that kinetic effects in the solution or growth-rate differences played an unimportant role in determining the orientation dependence of the distribution coefficient data (8). Our results are in good agreement with theirs.

Theory and Calculation

Surface free energy.—The effect of substrate orientation on the solidus data cannot be ignored and must be considered in the calculation of the solid composition of epitaxial layers on substrates in equilibrium with the liquid solution. It is considered that this effect presumably results from a difference in surface free energy (9, 10) or from the attachment kinetics at the growth interface (10). However, no one has calculated the phase diagram by

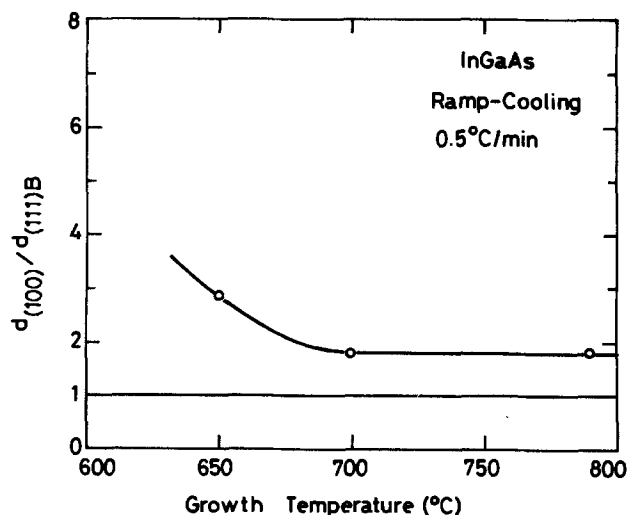


Fig. 11. The ratio of the thickness on the (100) face, $d_{(100)}$, to the thickness on the (111)B face, $d_{(111)B}$, as a function of the growth temperature.

considering the surface free energy or the attachment kinetics and has confirmed how these factors influence the phase diagram until now. In this section, it is described how the surface free energy influences the substrate orientation dependence of the In-Ga-As phase diagram for the LPE growth of $\text{In}_{1-x}\text{Ga}_x\text{As}$ layers.

On the surface between the vapor and solid phases, the surface free energy, $\gamma_{\text{surf}(v,s)}$, can be given approximately by

$$\gamma_{\text{surf}(v,s)} = (1 - w/u)\Delta H_{v0}N_0^{2/3} \quad [1]$$

where u is the number of nearest neighbors of an atom in the bulk of the solid and w is the number of neighbors in the solid of an atom on the face in question, ΔH_{v0} is the enthalpy of evaporation of the material at 0 K, and N_0 is the number of atoms per unit volume (19). The argument used is that the surface free energy is the energy to break all of the nearest neighbor bonds across a given plane. The number of atoms per unit area, N_s , can be related to N_0 as follows

$$N_s = N_0^{2/3} \quad [2]$$

For III-V zinc-blende-type compound, N_s for the (111) and (100) faces can be given by

$$N_s = \frac{4}{\sqrt{3}a^2} \quad [3]$$

for the (111) face, and

$$N_s = \frac{2}{a^2} \quad [4]$$

for the (100) face, where a is the lattice constant of the III-V compound (20).

For growth from solution, such as the LPE growth, however, the enthalpy of dissolution per one atom, ΔH_d , must be used instead of ΔH_{v0} in order to calculate the surface free energy on the surface between the liquid and the solid, $\gamma_{\text{surf}(l,s)}$. ΔH_d is given by the enthalpy of dissolution per mol, ΔH , as follows

$$\Delta H_d = \Delta H/2N_A \quad [5]$$

where N_A is Avogadro's number ($N_A = 6.023 \times 10^{23}$). Therefore, from Eq. [1]-[5], $\gamma_{\text{surf}(l,s)}$ for the (111) and (100) faces can be written as follows

$$\gamma_{\text{surf}(l,s)} = \frac{\Delta H}{2\sqrt{3}a^2N_A} \quad [6]$$

for the (111) face, and

$$\gamma_{\text{surf}(l,s)} = \frac{\Delta H}{2a^2N_A} \quad [7]$$

for the (100) face.

In order to obtain the surface free energy per mol, ΔG_{surf} , it was assumed that all atoms per mol were arranged on the surface. The obtained area, A , on each face is given by

$$A = \frac{\sqrt{3}N_A a^2}{2} \quad [8]$$

for the (111) face, and by

$$A = N_A a^2 \quad [9]$$

for the (100) face. Then, ΔG_{surf} can be written as follows

$$\Delta G_{\text{surf}} = \gamma_{\text{surf}(l,s)} A = \Delta H/4(\text{cal/mol}) \quad [10]$$

for the (111) face, and

$$\Delta G_{\text{surf}} = \Delta H/2(\text{cal/mol}) \quad [11]$$

for the (100) face. The method to derive the equation of ΔH is described in the Appendix.

Surface energy per mol is affected by a solid-liquid interface shape because orientation of interfaces and total

surface area can be varied according to the solid-liquid interface shape. The calculation of the surface energy for the LPE growth which is performed on a surface of substrates is a special case of the calculation of the surface energy. In this case, all atoms per mole grow on the surface of the substrate and then on each surface of each epitaxial layer as they are arranged successively on each surface of each layer. Therefore, the surface energy per mole for the LPE growth just corresponds with the surface energy for arranging all atoms per mole on a wide plane. In this case, the solid-liquid interface shape is considered to be a wide plane.

Expressions to calculate the ternary phase diagram influenced by the surface free energy.—The following expressions can be used to calculate the phase diagram of the III-V A-B-C ternary system in which there are a liquid solution of elements A, B, and C and a solid of the binary compounds AC and BC (22)

$$RT \ln \gamma_{AC} + RT \ln x = RT \ln \frac{\gamma_A \gamma_C}{\gamma_A^{\text{sl}} \gamma_C^{\text{sl}}} + RT \ln 4X_A^{\text{I}} X_C^{\text{I}} + \Delta S_{AC}^{\text{F}}(T_{AC}^{\text{F}} - T) \quad [12]$$

and

$$RT \ln \gamma_{BC} + RT \ln (1 - x) = RT \ln \frac{\gamma_B \gamma_C}{\gamma_B^{\text{sl}} \gamma_C^{\text{sl}}} + RT \ln 4X_B^{\text{I}} X_C^{\text{I}} + \Delta S_{BC}^{\text{F}}(T_{BC}^{\text{F}} - T) \quad [13]$$

where γ_{AC} and γ_{BC} are the activity coefficients of the AC and BC compounds in the solid, respectively, γ_i is the activity coefficient of an element i in the ternary liquid solution, x is the mole fraction of AC in the solid, ΔS^{F} and T^{F} are the entropy of fusion and the temperature of fusion of the indicated pure binary compound, respectively, R is the gas constant, and T is the absolute temperature. The superscript "sl" indicates the stoichiometric liquid. When the surface free energy is considered to calculate the phase diagram, the terms of $RT \ln \gamma_{AC}$ and $RT \ln \gamma_{BC}$ in Eq. [12] and [13] are influenced by the surface free energy. The total excess free energy of the solid, $\Delta G_{\text{total}}^{\text{rs}}$, can be given by

$$\Delta G_{\text{total}}^{\text{rs}} = \Delta G_{\text{m}}^{\text{rs}} + \Delta G_{\text{surf}} \quad [14]$$

where $\Delta G_{\text{m}}^{\text{rs}}$ is the excess free energy of mixing of the solid. On a basis of a simple solution model, $\Delta G_{\text{m}}^{\text{rs}}$ can be written using Eq. [A-8] (see Appendix) as follows

$$\Delta G_{\text{m}}^{\text{rs}} = \Delta H_{\text{m(ABC)}}^{\text{rs}} = \Delta H_{\text{m(ABC)}}^{\text{s}} = x(1-x)\Omega_{AC-BC}^{\text{s}} \quad [15]$$

where $\Delta H_{\text{m(ABC)}}^{\text{rs}}$ is the excess enthalpy of mixing of the ternary solid. $RT \ln \gamma_{AC}$ and $RT \ln \gamma_{BC}$ are given by

$$RT \ln \gamma_{AC} = \Delta G_{\text{total}}^{\text{rs}} + (1-x) \left(\frac{d\Delta G_{\text{total}}^{\text{rs}}}{dx} \right) \quad [16]$$

and

$$RT \ln \gamma_{BC} = \Delta G_{\text{total}}^{\text{rs}} - x \left(\frac{d\Delta G_{\text{total}}^{\text{rs}}}{dx} \right) \quad [17]$$

$RT \ln \gamma_{AC}$ and $RT \ln \gamma_{BC}$ for the (111) and (100) faces can be obtained by using Eq. [10], [11], [14]-[17], and [A-12] (see Appendix) as follows. For the (111) face

$$RT \ln \gamma_{AC} = \frac{3}{4} (1-x)^2 \Omega_{AC-BC}^{\text{s}} + \frac{1}{4} \Delta S_{AC}^{\text{F}} T_{AC}^{\text{F}} - \frac{1}{16} \Omega_{AC}^{\text{I}} - \frac{1}{8} H_A^{\text{I}} - \frac{1}{8} H_C^{\text{I}} + \frac{1}{4} \alpha \quad [18]$$

and

$$RT \ln \gamma_{BC} = \frac{3}{4} x^2 \Omega_{AC-BC}^{\text{s}} + \frac{1}{4} \Delta S_{BC}^{\text{F}} T_{BC}^{\text{F}} - \frac{1}{16} \Omega_{BC}^{\text{I}} - \frac{1}{8} H_B^{\text{I}} - \frac{1}{8} H_C^{\text{I}} + \frac{1}{4} \alpha \quad [19]$$

and for the (100) face

$$RT \ln \gamma_{AC} = \frac{1}{2} (1-x)^2 \Omega_{AC-BC}^s + \frac{1}{2} \Delta S_{AC}^F T_{AC}^F - \frac{1}{8} \Omega_{AC}^l - \frac{1}{4} H_{A^i}^l - \frac{1}{4} H_{C^i}^l + \frac{1}{2} \alpha \quad [20]$$

and

$$RT \ln \gamma_{BC} = \frac{1}{2} x^2 \Omega_{AC-BC}^s + \frac{1}{2} \Delta S_{BC}^F T_{BC}^F - \frac{1}{8} \Omega_{BC}^l - \frac{1}{4} H_{B^i}^l - \frac{1}{4} H_{C^i}^l + \frac{1}{2} \alpha \quad [21]$$

where

$$\alpha = X_A^l X_B^l \Omega_{AB}^l + X_A^l X_C^l \Omega_{AC}^l + X_B^l X_C^l \Omega_{BC}^l + X_A^l H_{A^i}^l + X_B^l H_{B^i}^l + X_C^l H_{C^i}^l \quad [22]$$

The III-V A-B-C ternary phase diagram which is influenced by the surface free energy can be calculated by using Eq. [12], [13], and [18]-[22].

Calculated results.—The parameters to calculate the In-Ga-As ternary phase diagram are listed in Table I. Figure 12 shows the enthalpy of dissolution per mole, ΔH , which was obtained from the phase diagram calculation and Eq. [A-12]. In this calculation, X_{As}^l takes a constant value of 0.5. In Fig. 12, curve a represents ΔH obtained from the phase diagram calculation in which the influence of the surface free energy was not considered, and curves b and c represent ΔH for the (100) and (111) faces, respectively. ΔH of InAs is the smallest, as shown in Fig. 12. When a small amount of InAs is mixed into GaAs, ΔH for the (111) face increases slightly and decreases, but ΔH for the (100) face decreases monotonously. ΔH is nearly in proportion to the strength of bonds in In_{1-x}Ga_xAs solids. Therefore, when the weak bonds of InAs are mixed into the strong bonds of GaAs, the strength of the bonds weakens. ΔH for the (111) face is larger than ΔH for the (100) face, that is to say, the energy to dissolve the In_{1-x}Ga_xAs film from the (111) oriented In_{1-x}Ga_xAs surface into the In-Ga-As solution is larger than the energy to dissolve the film from the (100) oriented In_{1-x}Ga_xAs surface into the solution.

Figure 13 shows the surface free energy of the (111) and (100) oriented In_{1-x}Ga_xAs surface, which was calculated at $X_{As}^l = 0.2$ and 0.5. As a matter of course, the surface free energy depends on the composition of the solutions. The surface free energy for the (100) face is larger than for the (111) face. Therefore, the (111) surface is more stable than the (100) surface. As shown in Fig. 13, the surface free energy of In_{1-x}Ga_xAs which is in contact with the solution of $X_{As}^l = 0.2$ is larger than the surface free energy of In_{1-x}Ga_xAs which is in contact with the solution of $X_{As}^l = 0.5$. That is to say, the surface in equilibrium with the solution of $X_{As}^l = 0.2$ is more unstable than the surface in equilibrium with the solution of $X_{As}^l = 0.5$.

Table I. Thermodynamic input data for the calculation of the In-Ga-As phase diagrams

Input data	
$T_{GAs}^F = 1511$ K	$T_{InAs}^F = 1215$ K
$\Delta S_{GAs}^F = 16.64$ cal/mol K	$\Delta S_{InAs}^F = 14.52$ cal/mol K
$\Omega_{GAs}^l = 5160 - 9.16T$ cal/mol	$\Omega_{InAs}^l = 3860 - 10.0T$ cal/mol
$\Omega_{GAs}^s = 1060$ cal/mol	$\Omega_{GAs-InAs}^s = 3000$ cal/mol
$H_{GAs}^l = -63,353$ cal/mol	$H_{In}^l = -55,909$ cal/mol
$H_{As}^l = -73,166$ cal/mol	

T_{AB}^F and ΔS_{AB}^F are the temperature and entropy of fusion of the AB compound, respectively (22). Ω^l and Ω^s are the interaction parameters in the liquid solution and solid, respectively (22). H_i^l is the enthalpy of the pure i melt (23).

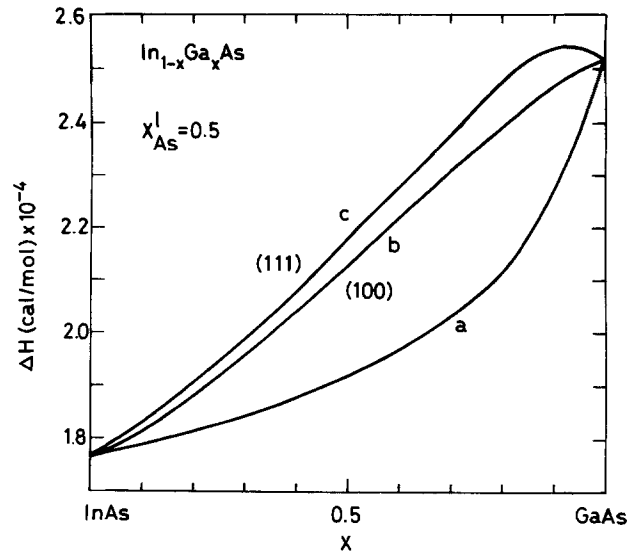


Fig. 12. The calculated enthalpy of dissolution per mole, ΔH (cal/mol), from In_{1-x}Ga_xAs to solutions with $X_{As}^l = 0.5$ as a function of x in In_{1-x}Ga_xAs.

The calculated In-Ga-As phase diagrams which are influenced by the surface free energy are shown in Fig. 14, 15, and 16. Figure 14 shows the solution composition of Ga, X_{Ga}^l , in the In-Ga-As ternary solution in equilibrium with the (100)- and (111)-oriented In_{0.53}Ga_{0.47}As, which are represented by the curves a and b, respectively. The experimental results for the (111) and (100) faces are also shown by the broken lines of curves f and g, respectively. The calculated X_{Ga}^l of the solution in equilibrium with the (100)-oriented In_{0.53}Ga_{0.47}As is larger than the calculated X_{Ga}^l of the solution in equilibrium with the (111)-oriented In_{0.53}Ga_{0.47}As. This tendency of the calculated results is contrary to the experimental results as shown in Fig. 14. Figure 15 shows the solution composition of As, X_{As}^l , in the In-Ga-As ternary solution in equilibrium with the (100)- and (111)-oriented In_{0.53}Ga_{0.47}As, which are represented by the curves a and b, respectively. The experimental results for the (111) and (100) faces are shown by the broken lines f and g, respectively. The calculated X_{As}^l of the solution in equilibrium with the (100) oriented In_{0.53}Ga_{0.47}As is larger than the calculated X_{As}^l of the solu-

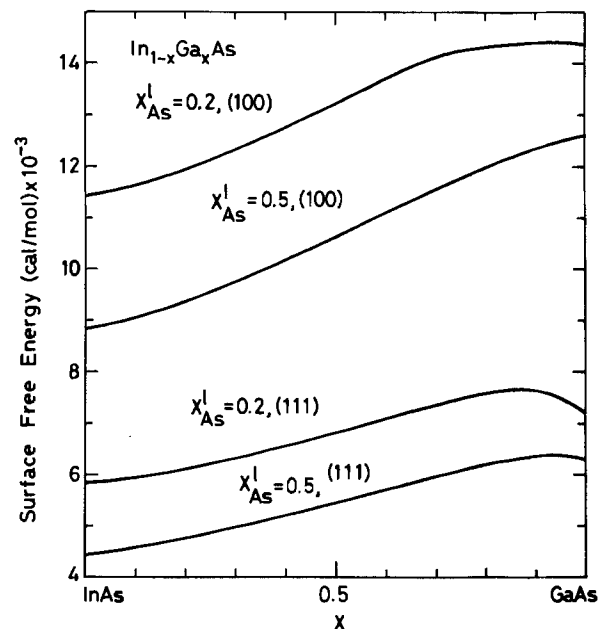


Fig. 13. The calculated surface free energy (cal/mol) of the (111) and (100) oriented In_{1-x}Ga_xAs surfaces in equilibrium with solutions with $X_{As}^l = 0.2$ and 0.5 as a function of x in In_{1-x}Ga_xAs.

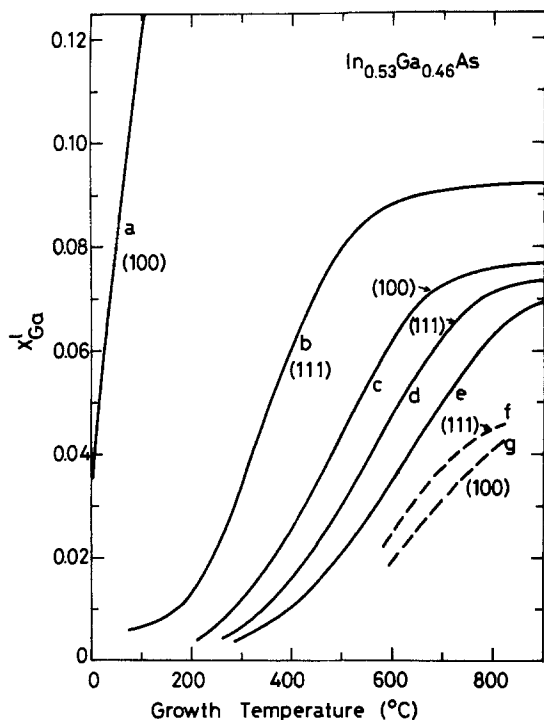


Fig. 14. The solution composition of Ga, X_{Ga}^I , in the In-Ga-As ternary solution in equilibrium with the (100) and (111)-oriented $In_{0.53}Ga_{0.47}As$ as a function of the growth temperature. The solid lines are the calculated results and the broken lines are the experimental results.

tion in equilibrium with the (111)-oriented $In_{0.53}Ga_{0.47}As$. This tendency is in agreement with the experimental results shown in Fig. 15. Figure 16 shows the composition of Ga in $In_{1-x}Ga_xAs$ in equilibrium with solutions of $X_{As}^I = 0.2$ as a function of X_{Ga}^I . The curves a and b show the calculated results for the (100) and (111) faces, respectively. Obviously, X_{Ga}^I of solutions in equilibrium with the (100)-oriented $In_{0.53}Ga_{0.47}As$ is larger than X_{Ga}^I of solutions in equilibrium with the (111)-oriented $In_{0.53}Ga_{0.47}As$.

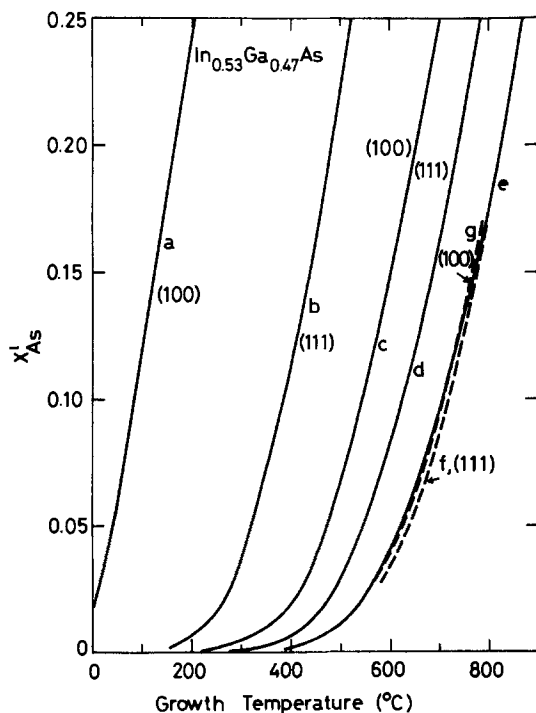


Fig. 15. The solution composition of As, X_{As}^I , in the In-Ga-As ternary solution in equilibrium with the (100)- and (111)-oriented $In_{0.53}Ga_{0.47}As$ as a function of the growth temperature. The solid lines are the calculated results and the broken lines are the experimental results.

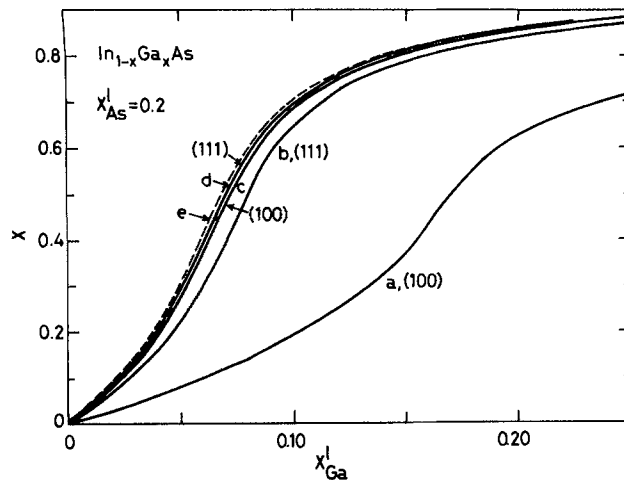


Fig. 16. The composition of Ga, x , in $In_{1-x}Ga_xAs$ in equilibrium with solutions of $X_{As}^I = 0.2$ as a function of X_{Ga}^I , which is calculated by adding the surface free energy effects.

Discussion

The experimental results indicating that the solution compositions of Ga in equilibrium with the (111)-oriented $In_{0.53}Ga_{0.47}As$ are larger than those in equilibrium with the (100)-oriented $In_{0.53}Ga_{0.47}As$ cannot be explained by the effect of the surface free energy only as shown in Fig. 14. The results calculated by adding the surface free energy to the chemical free energy of the solid phase are contrary to the experimental results. These results imply that other effects must be considered to explain the substrate orientation dependence of the In-Ga-As phase diagram for LPE growth of $In_{0.53}Ga_{0.47}As$ on InP.

In Fig. 14, 15, and 16, the curves e show the results calculated by the conventional simple solution model (21), which is not influenced by the surface free energy. The results calculated by adding the surface free energy which are shown by the curves a and b are very much apart from the calculated results shown by the curves e. This is mainly caused by overestimation of the surface free energy per mole, ΔG_{surf} . In order to obtain ΔG_{surf} , it was assumed that all atoms per mole were arranged on the surface. However, in the actual LPE growth, it is naturally considered that, prior to the growth, Ga-As or In-As pairs are made in the liquid solution due to large ionicity of III-V compounds (24, 25). Much of these pairs seems to exist within the region between the grown surface and the liquid solution as shown in Fig. 17, because the crystal structure must be rapidly knitted using the elements in the solution. Therefore, it is only natural that the crystal is grown using these pairs in the solution. That is to say, in order to obtain ΔG_{surf} , it can be assumed that, instead of each atom, Ga-As or In-As pairs per mole were arranged on the surface. Then, ΔG_{surf} can be written under this assumption as follows

$$\Delta G_{surf} = \Delta H/8 \text{ (cal/mol)} \quad [23]$$

for the (111) face, and

$$\Delta G_{surf} = \Delta H/4 \text{ (cal/mol)} \quad [24]$$

for the (100) face. In the actual In-Ga-As ternary solution, it is more natural that bigger pairs (for example, $Ga_2In_2As_4$, $GaIn_3As_4$, or $InAs_4$) than Ga-As or In-As pairs are made and exist within the region between the grown surface and the liquid solution as shown in Fig. 18. Therefore, ΔG_{surf} must be written as follows

$$\Delta G_{surf} = \Delta H/\beta \text{ (cal/mol)} \quad [25]$$

where β is the value which depends on the size of pairs in the solution.

The calculated In-Ga-As phase diagrams which are influenced by the surface free energy of Eq. [25] with $\beta = 16$ for the (111) face and $\beta = 8$ for the (100) face are shown

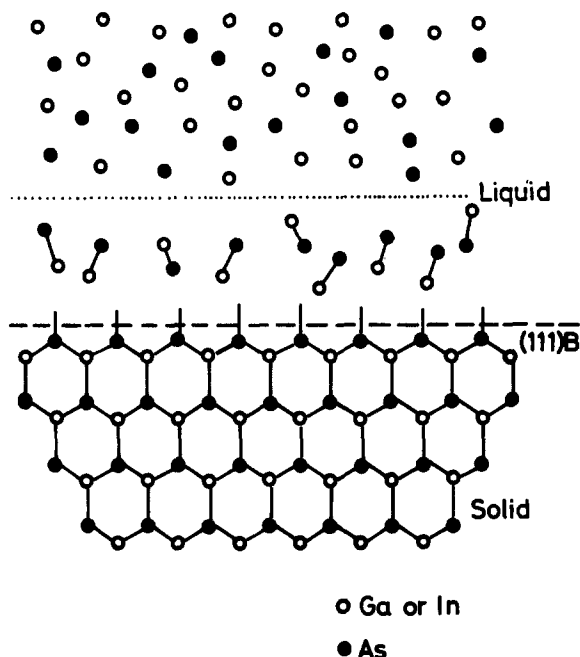


Fig. 17 Schematic representation of the interface between the In_{1-x}Ga_xAs solid and the growth solution with Ga-As or In-As pairs.

in Fig. 14, 15, and 16 by the curves c and d, respectively. This case corresponds to the ternary solution with pairs of Ga₂-In₂-As, Ga-In₃-As, Ga-As₄, and In-As₄ near the growth surface. The curves c and d are closer to the curves e calculated by the conventional simple solution model and the experimental curves f and g than the curves a and b calculated by Eq. [10] and [11]. These results imply that the crystal is grown using some pairs in the solution.

In the calculation of the surface free energy, the difference of the (111)A and (111)B faces cannot be explained. The nature of bonding on (111)A and (111)B surfaces of III-V compounds was qualitatively described by several authors (20, 26). According to them, the Group V atoms of the B surface are triply bonded to the lattice and have an unshared pair of electrons. The (sp³) tetrahedral configuration of the bulk is thus retained. On the other

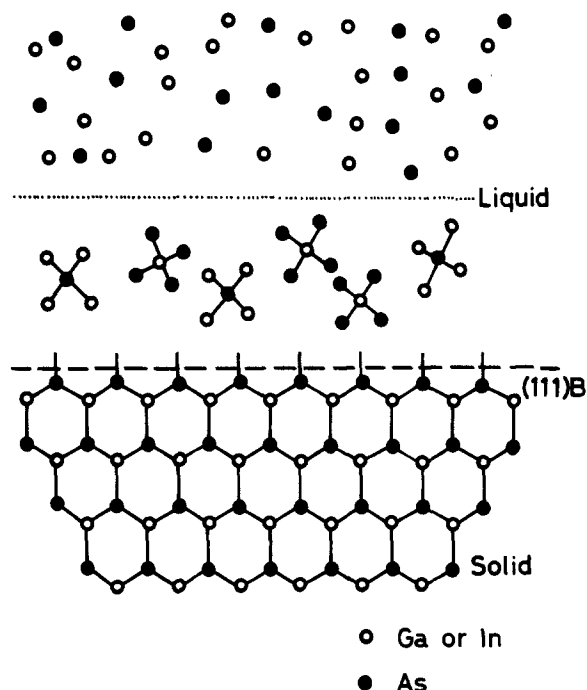


Fig. 18 Schematic representation of the interface between the In_{1-x}Ga_xAs solid and the growth solution with complex pairs.

hand, the Group III atoms of the A surface are also triply bonded to the lattice but have no dangling electrons. Consequently, it is proposed that these atoms tend toward a planar (sp²) configuration. It is not clear how the difference between the configurations reflects the surface free energies of the (111)A and (111)B faces. In order to understand the difference between the phase diagrams for the LPE growth on the (111)A and (111)B faces, it seems that the attachment kinetics at the (111)A and (111)B growth interfaces must also be considered.

Summary and Conclusion

The liquidus isotherms of the In-Ga-As system were determined at 600° and 700°C by the improved seed dissolution technique. From the results of the liquidus isotherms and the lattice-constant measurements, the substrate orientation dependence of the solution compositions to grow lattice-matched In_{0.53}Ga_{0.47}As layers on the (100), (111)A, and (111)B InP substrates was exactly obtained in the temperature range 600°-790°C. The solution compositions of Ga for the (111)A and (111)B faces are always larger than those for the (100) face over the entire temperature range 600°-790°C. The solution compositions of Ga for the (111)A face are always smaller than those for the (111)B face over the entire temperature range. The solution compositions of As for the (111)A and (111)B faces are always smaller than those for the (100) face.

The In-Ga-As phase diagram was calculated, for the first time, by adding the surface free energy to the chemical free energy of the In_{1-x}Ga_xAs solid phase. According to the calculated phase diagram, the compositions of Ga in solutions to obtain the (100)-oriented In_{0.53}Ga_{0.47}As is larger than the compositions of Ga in solutions to obtain the (111)-oriented In_{0.53}Ga_{0.47}As. This tendency of the calculated results is contrary to the experimental results. The difference in the surface free energy for both faces is not a main reason for the substrate orientation dependence of the In-Ga-As phase diagram. Other effects must be considered to explain the experimental results. The surface free energy can be estimated more accurately by considering complex formation in the growth solutions.

Acknowledgments

The authors wish to acknowledge their discussions with Dr. S. Yamazaki and Mr. Y. Kishi and the encouragement of Dr. T. Musugi, Dr. O. Ryuzan, Dr. T. Kotani, and Mr. I. Umebu.

Manuscript submitted Sept. 13, 1983; revised manuscript received Feb. 21, 1985.

Fujitsu Laboratories Limited assisted in meeting the publication costs of this article.

APPENDIX

ΔH corresponds to the enthalpy change accompanying the transfer of one mole of solid A_xB_{1-x}C to the ternary A-B-C solution with which it is in equilibrium at the growth temperature, T . The enthalpy of the ternary solid, H_{ABC}^s , is given by

$$H_{ABC}^s = \Delta H_{m(ABC)}^s + xH_{AC}^s + (1-x)H_{BC}^s \quad [A-1]$$

where $\Delta H_{m(ABC)}^s$ is the enthalpy of mixing of the ternary solid, and H_{AC}^s and H_{BC}^s are the enthalpy of the pure AC and BC binary compounds, respectively. The enthalpy of the ternary solution, H_{ABC}^l , is given by

$$H_{ABC}^l = \Delta H_{m(ABC)}^l + X_A^l H_A^l + X_B^l H_B^l + X_C^l H_C^l \quad [A-2]$$

where $\Delta H_{m(ABC)}^l$ is the enthalpy of mixing of the ternary solution, X_i^l is the atomic fraction of an element i in the ternary solution, and H_i^l is the enthalpy of the pure i melt, that is to say, H_i^l corresponds to the heat of evaporation of the pure i melt. The enthalpies of the pure A-C and B-C binary melts, H_{AC}^l and H_{BC}^l , are given by

$$H_{AC}^l = \Delta H_{m(AC)}^l + H_A^l/2 + H_C^l/2 \quad [A-3]$$

and

$$H_{BC}^l = \Delta H_{m(BC)}^l + H_B^l/2 + H_C^l/2 \quad [A-4]$$

where $\Delta H_{m(AC)}^1$ and $\Delta H_{m(BC)}^1$ are the enthalpies of mixing of the pure A-C and B-C binary melts, respectively. The enthalpies of fusion of the pure AC and BC binary compounds, ΔH_{AC}^F and ΔH_{BC}^F , are given by

$$\Delta H_{AC}^F = H_{AC}^1 - H_{AC}^{s} \quad [A-5]$$

and

$$\Delta H_{BC}^F = H_{BC}^1 - H_{BC}^{s} \quad [A-6]$$

The enthalpy of dissolution per mole, ΔH , can be written using Eq. [A-1]-[A-6] as follows

$$\begin{aligned} \Delta H = & H_{ABC}^1 - H_{ABC}^s = \Delta H_{m(ABC)}^1 \\ & + X_A^1 H_A^1 + X_B^1 H_B^1 + X_C^1 H_C^1 \\ & - \Delta H_{m(ABC)}^s + x \Delta H_{AC}^F + (1-x) \Delta H_{BC}^F - x \Delta H_{m(AC)}^1 - x H_A^{1/2} \\ & - (1-x) \Delta H_{m(BC)}^1 - (1-x) H_B^{1/2} - H_C^{1/2} \quad [A-7] \end{aligned}$$

The enthalpies of mixing can be written using a simple solution model (21, 22) as follows

$$\Delta H_{m(ABC)}^s = x(1-x) \Omega_{AC-BC}^s \quad [A-8]$$

$$\Delta H_{m(ABC)}^1 = X_A^1 X_B^1 \Omega_{AB}^1 + X_A^1 X_C^1 \Omega_{AC}^1 + X_B^1 X_C^1 \Omega_{BC}^1 \quad [A-9]$$

$$\Delta H_{m(AC)}^1 = \Omega_{AC}^1/4 \quad [A-10]$$

$$\Delta H_{m(BC)}^1 = \Omega_{BC}^1/4 \quad [A-11]$$

where Ω_{AC-BC}^s is the interaction parameter in the ternary solid $A_x B_{1-x} C$, and Ω_{ij}^1 is the interaction parameter of the ij pair in the ternary solution. ΔH can be given using Eq. [A-7]-[A-11] as follows

$$\begin{aligned} \Delta H = & X_A^1 X_B^1 \Omega_{AB}^1 + X_A^1 X_C^1 \Omega_{AC}^1 + X_B^1 X_C^1 \Omega_{BC}^1 \\ & - x(1-x) \Omega_{AC-BC}^s + x \Delta H_{AC}^F + (1-x) \Delta H_{BC}^F \\ & - x \Omega_{AC}^1/4 - (1-x) \Omega_{BC}^1/4 \\ & + X_A^1 H_A^1 + X_B^1 H_B^1 + X_C^1 H_C^1 - x H_A^{1/2} \\ & - (1-x) H_B^{1/2} - H_C^{1/2} \quad [A-12] \end{aligned}$$

For the growth from the solution such as the LPE growth, ΔH can be calculated by Eq. [A-12].

REFERENCES

1. T. P. Pearsall, *IEEE J. Quantum Electron.*, **qe-16**, 709 (1980).
2. O. K. Kim, S. R. Forrest, W. A. Bonner, and R. G. Smith, *Appl. Phys. Lett.*, **39**, 402 (1981).

3. T. Shirai, S. Yamazaki, K. Yasuda, T. Mikawa, K. Nakajima, and T. Kaneda, *Electron. Lett.*, **18**, 575 (1982).
4. R. F. Leheny, R. E. Nahory, M. A. Pollack, A. A. Ballman, E. D. Beebe, and J. C. De Winter, *ibid.*, **16**, 353 (1980).
5. A. S. H. Liao, R. F. Leheny, R. E. Nahory, and J. C. De Winter, *IEEE Electron Device Lett.*, **edl-2**, 288 (1981).
6. B. Tell, R. E. Nahory, R. F. Leheny, and J. C. De Winter, *Appl. Phys. Lett.*, **39**, 744 (1981).
7. G. A. Antypas, Y. M. Houng, S. B. Hyder, J. S. Escher, and P. E. Gregory, *ibid.*, **33**, 463 (1978).
8. T. P. Pearsall, M. Quillec, and M. A. Pollack, *ibid.*, **35**, 342 (1979).
9. K. Nakajima, T. Tanahashi, K. Akita, and T. Yamaoka, *J. Appl. Phys.*, **50**, 4975 (1979).
10. J. J. Hsieh, *IEEE J. Quantum Electron.*, **qe-17**, 118 (1981).
11. T. Y. Wu and G. L. Pearson, *J. Phys. Chem. Solids*, **33**, 409 (1972).
12. T. S. Liu and E. A. Peretti, *Trans. ASTM*, **45**, 677 (1953).
13. M. A. Pollack, R. E. Nahory, L. V. Deas, and D. R. Wonsidler, *This Journal*, **122**, 1550 (1975).
14. M. B. Panish, *ibid.*, **117**, 1202 (1970).
15. K. J. Bachmann and J. L. Shay, *Appl. Phys. Lett.*, **32**, 446 (1978).
16. K. Nakajima, S. Yamazaki, and K. Akita, *J. Cryst. Growth*, **61**, 535 (1983).
17. T. P. Pearsall, R. Bisaro, R. Ansel, and P. Merenda, *Appl. Phys. Lett.*, **32**, 497 (1978).
18. K. Nakajima and K. Akita, *This Journal*, **129**, 2603 (1982).
19. J. C. Brice, in "Series of Monographs on Selected Topics in Solid State Physics," E. P. Wohlfarth, Editor, Vol. 12, pp. 78-127, North-Holland, Amsterdam (1973).
20. J. W. Cahn and R. E. Hanneman, *Surf. Sci.*, **1**, 387 (1964).
21. E. A. Guggenheim, in "Thermodynamics," 5th ed., p. 197, North-Holland, Amsterdam (1967).
22. M. B. Panish and M. Ilegems, in "Progress in Solid State Chemistry," Vol. 7, H. Reiss and J. O. McCaldin, Editors, p. 39, Pergamon Press, Inc., Elmsford, New York (1972).
23. G. V. Samsonov, in "Handbook of the Physicochemical Properties of the Elements," G. V. Samsonov, Editor, p. 250, Oldbourne, London (1968).
24. J. C. Phillips, *Rev. Mod. Phys.*, **42**, 317 (1970).
25. K. Osamura and Y. Murakami, *J. Phys. Chem. Solids*, **36**, 329 (1975).
26. H. C. Gatos and M. C. Lavine, *This Journal*, **107**, 433 (1960).

Electrochemical Characteristics of n-Doped Polyacetylene

R. Huq and G. C. Farrington*

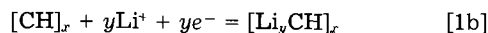
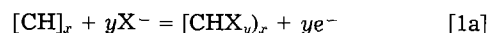
Department of Materials Science, University of Pennsylvania, Philadelphia, Pennsylvania 19104

ABSTRACT

Polyacetylene can be electrochemically reduced in tetrahydrofuran containing dissolved LiClO_4 to form compositions of the type, $(\text{Li}_y\text{CH})_x$. The reduction occurs with high coulombic efficiency for doping levels of $y < 0.10$. Reduced polyacetylene in this composition range appears to be quite stable in this particular electrolyte. The potential of $(\text{Li}_y\text{CH})_x$ is 0.5-1.5V positive of that of Li. Compared with Li as a nonaqueous battery negative electrode, $(\text{Li}_y\text{CH})_x$ has considerably lower gravimetric and volumetric energy densities and a higher electrochemical potential.

Polyacetylene $[(\text{CH})_x]$ is a simple conjugated polymer with unusual electrochemical properties. It can be electrochemically reduced or oxidized to compositions which are n- or p-type electronic conductors (Eq. [1a] and [1b]) (1). Nigrey *et al.* (2) have proposed using polyacetylene as an electrode material for nonaqueous electrolyte batteries. They found that cation-doped (n-type) polyacetylene can function as a negative electrode and anion-doped (p-type) polyacetylene can as a positive electrode. Since their pioneering work, the various forms of polyacetylene have received considerable attention as potential electrode materials (3-7).

*Electrochemical Society Active Member.



MacDiarmid *et al.* (2, 3) have reported that the p doping process is electrochemically reversible with high coulombic efficiency. Other authors (5-7) have confirmed that polyacetylene can be reversibly oxidized to doping levels of $y = 0.09$ and less with near 100% coulombic efficiency. The same researchers (5-7) have also shown that only about 50% of the charge stored in oxidized polyacetylene at a current density of 0.05 mA/cm² can be recovered at a discharge rate comparable to (1-10 times) the charging rate. The remainder of the charge can be recovered, but

only upon extended (10-20h) controlled potential discharge at far lower ($10 \mu\text{A}/\text{cm}^2$) current densities. Several cyclic voltammetry and polarization studies (8, 11) have suggested that electrochemical p doping involves a slow diffusion process, presumably that of the dopant species within the polymer.

The few studies of n doping that have appeared include those of Kaner *et al.* (9) and Shacklette *et al.* (10). Kaner *et al.* (9) concluded that polyacetylene can be reduced to dopant concentrations of $y = 0.06$ with excellent stability and reversibility. The reduction/oxidation coulombic efficiency ($Q_{\text{out}}/Q_{\text{in}}$) was found to be about 99% at Li^+ , Na^+ , and $(\text{Bu}_4\text{N})^+$ dopant concentrations up to $y = 0.06$. Shacklette and co-workers (10) observed considerable swelling of polyacetylene when it was reduced in tetrahydrofuran (THF) with Li^+ as the doping ion. They reported that unreduced, neutral polyacetylene did not swell in the presence of THF.

Our goals in the present work were to examine the general electrochemical characteristics of the n doping reactions of polyacetylene in order to evaluate its attractiveness as a battery electrode. The lithium electrode was chosen as the standard of comparison, since it has received the most investigation as an electrode material for high energy density, nonaqueous electrolyte batteries. Our studies have included measures of the coulombic efficiency, rate capability, stability, and electrode potential as a function of doping level.

Experimental

Electrochemical measurements were carried out in a miniature glass cell having three compartments separated by glass frits. The polyacetylene film electrodes (approximately 1 cm^2 in area and 0.01 cm thick) were sandwiched in Pt mesh and housed in the central compartment of the cell. The lithium reference and counterelectrodes were located in the two side compartments. About 1 ml of electrolyte was required to fill all three compartments. The electrolyte used was $0.8\text{-}1.0\text{M}$ LiClO_4 in THF.

Electrolytes were prepared from Burdick and Jackson tetrahydrofuran, which was distilled and percolated through neutral activated alumina (Woelm). The LiClO_4 (Anderson Physics) was dried at 180°C in vacuum before use. After the salt was dissolved, the electrolyte solution was purified by a second percolation through activated alumina.

All experimental procedures were performed in an argon-atmosphere dry box (Vacuum Atmospheres). Standard electrochemical equipment was used for carrying out the cyclic voltammetry and constant current/potential experiments.

The polyacetylene films used in these experiments were prepared by the technique first described by Shirakawa (12). They were graciously provided to us by the research group of Professor A. MacDiarmid of this university.

Results and Discussion

Controlled potential studies.—Cyclic voltammetry.—Cyclic voltammetry experiments used samples of polyacetylene which had areas of $0.3\text{-}1.0 \text{ cm}^2$ (single side) and weighed approximately $0.00475 \text{ g}/\text{cm}^2$. Cyclic voltammograms were recorded between 0.5 and $2.5 \text{ V vs. Li/Li}^+$ under the following conditions. (i) Pt mesh electrode in fresh electrolyte; (ii) fresh polyacetylene in fresh electrolyte; (iii) reduced polyacetylene; and (iv) polyacetylene after various reduction/oxidation cycles. The results are shown in Fig. 1-3.

Cyclic voltammograms on the Pt mesh electrode without polyacetylene were carried out to monitor the level of background current and the stability of the electrolyte. Fresh electrolyte (Fig. 1a) showed a window of stability from 2.5 to 0.6 V that was interrupted by only a few small peaks. The electrolyte decomposition rate increased at potentials less than 0.5 V . A Pt electrode in the same solvent after 11 reduction/oxidation cycles on a polyacetylene sample (Fig. 1b) showed essentially identical cyclic

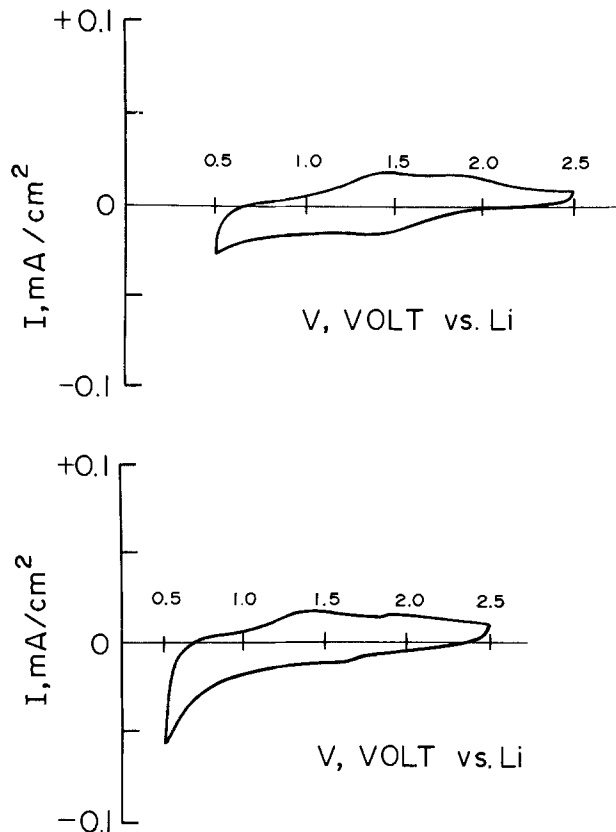


Fig. 1. a (top): Cyclic voltammogram of a Pt mesh electrode in fresh $\text{LiClO}_4\text{-THF}$ electrolyte. Scan rate of 20 mV/s . b (bottom): Voltammogram of same Pt mesh electrode in same solution after eleventh reduction/oxidation cycle of a polyacetylene film. Scan rate of 20 mV/s .

voltammetry behavior. No evidence of soluble electrolyte degradation products was observed over this number of cycles.

The rest potential of fresh polyacetylene was about $2.2 \text{ V vs. Li/Li}^+$. Repeated cyclic voltammograms of a fresh sample of polyacetylene (Fig. 2a) showed that both the reduction and oxidation peaks increased with cycling. For polyacetylene reduced to $y = 0.047$ (Fig. 2b), both the reduction and oxidation peaks were broader and the maximum current densities were $10\text{-}15 \text{ mA}/\text{cm}^2$.

After six cycles (Fig. 3a), the voltammogram was similar to that for fresh polyacetylene, although the peak currents had decreased. After the eleventh cycle (Fig. 3b), the peak current decreased dramatically, and the shape of the voltammogram indicated that the reaction had become less reversible. Since there was no change in the cyclic voltammogram of a Pt electrode in the electrolyte after the eleventh cycle (Fig. 1b), it is reasonable to conclude that the decreased peak current and reversibility were the result of changes in the polyacetylene electrode itself.

Controlled potential reduction of polyacetylene.—Samples of polyacetylene were reduced and then reoxidized in two different controlled potential experiments. In the first, the potential was decreased in 100 mV steps from 2.2 V (approximately the rest potential) to 0.7 V . At each point, the current was allowed to decrease to a steady value of about $20\text{-}25 \mu\text{A}/\text{cm}^2$. When the series of reduction steps was complete, the potential was stepped to 2.5 V to oxidize the film.

The results are shown in Fig. 4, which plots the cumulative doping level, y , as a function of the controlled potential. The points on the curve are not the true maximum doping levels that could be attained, since the current was not allowed to decay below $20\text{-}25 \mu\text{A}/\text{cm}^2$. However, they are quite close to the maxima that would be observed after exhaustive reduction.

As Fig. 4 shows, very little doping took place between 2.2 and 1.3 V ; but, from 1.2 to 1.0 V , the rate of doping in-

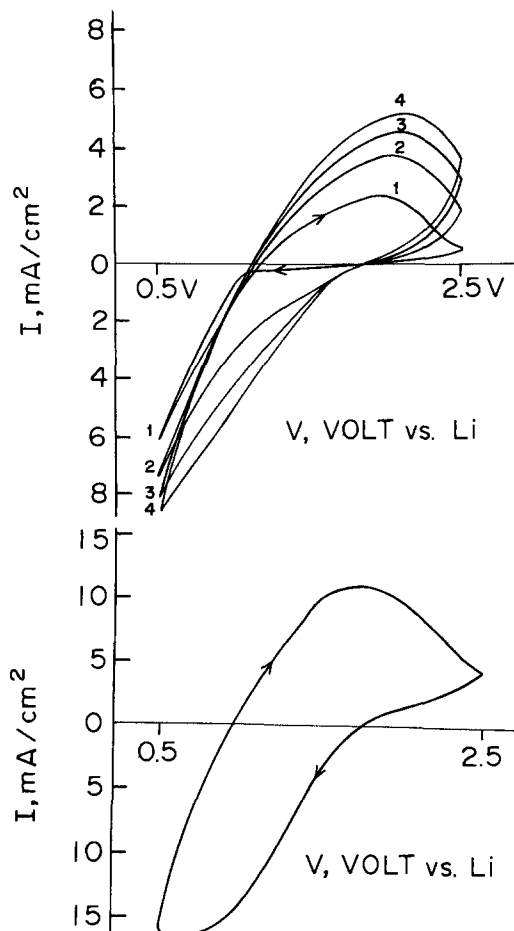


Fig. 2. a (top): Voltammogram of a fresh polyacetylene sample in $\text{LiClO}_4\text{-THF}$ electrolyte. Scan rate of 20 mV/s. The starting potential was the potential of zero current. b (bottom): Voltammogram of polyacetylene sample reduced to $y = 0.047$ in $\text{LiClO}_4\text{-THF}$ electrolyte.

creased rapidly. By 0.7V, the maximum doping level of 0.09-0.10 was reached. It may be possible to achieve higher levels by decreasing the potential below 0.7V. Un-

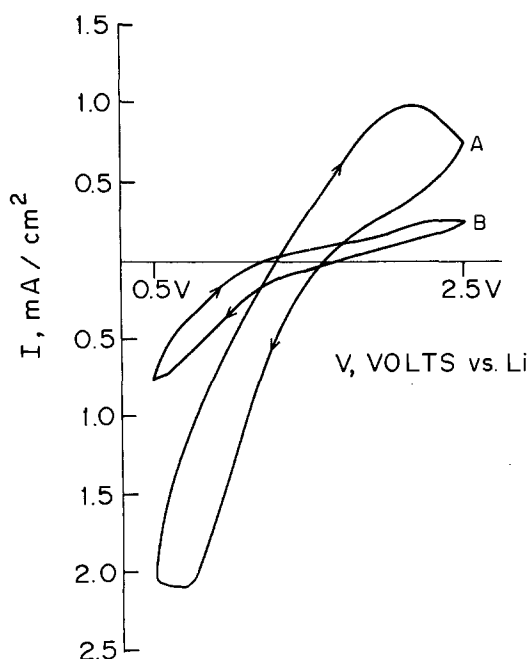


Fig. 3. a (higher): Voltammogram of polyacetylene after sixth reduction/oxidation cycle. Scan rate of 20 mV/s. b (lower): Voltammogram of same electrode after eleventh reduction/oxidation cycle. Scan rate of 20 mV/s.

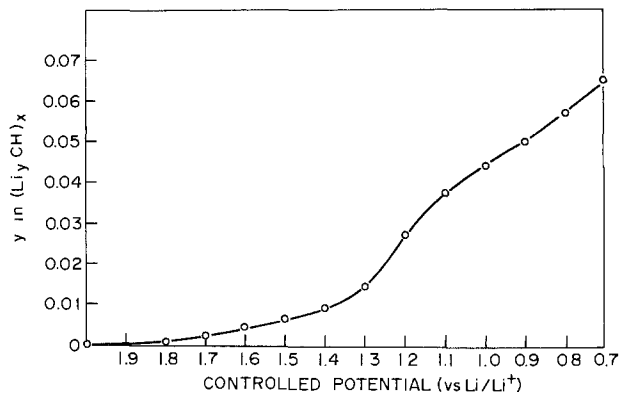


Fig. 4. Reduction level, y , as a function of controlled reduction potential in 100 mV steps.

fortunately, below 0.6V, the electrolyte was increasingly unstable and the reduction process was inefficient.

In the second set of experiments, the polyacetylene was electrochemically cycled by reduction at either 1.1 or 0.7V followed by oxidation at 2.5V. The oxidation was considered complete when the current decayed to about $0.5 \mu\text{A}/\text{cm}^2$. The current decay curves during controlled potential reduction at 1.1V showed an interesting evolution with increasing cycle number (see Fig. 5). The current levels upon initial polarization were typically 4-5 mA/cm^2 , based on the geometric area of one side of the electrode, regardless of the cycle number. In the earlier cycles, the current decreased to a plateau ($0.75\text{-}1.2 \text{ mA}/\text{cm}^2$) after which it decayed to much smaller values. High current densities were only observed in early cycles, and the magnitude of the current plateau decreased steadily with cycling. By the tenth cycle, the current plateau was in the range of $200 \mu\text{A}/\text{cm}^2$.

Because the average reduction current decreased dramatically with cycling, longer and longer times were required to reach the same doping level at a potential of 1.1V. For example, reduction times of 60 min in the second and fifth cycles yielded 3.32 and 3.2% doping, respectively. However, by the tenth cycle, the same reduction time produced only 2% doping. Not only did the doping time increase with cycling, it became necessary to decrease the reduction potential to achieve the same doping levels. For example, 3.8% doping was achieved at 1.1V during the second cycle, but the potential had to be decreased to 0.8V to reach the same doping level during the tenth cycle. All of these results are consistent with the cyclic voltammogram study, which showed a significant decrease in the peak reduction current by the tenth cycle.

Controlled potential oxidation of polyacetylene at 2.5V.—In this series of experiments, polyacetylene was cycled by

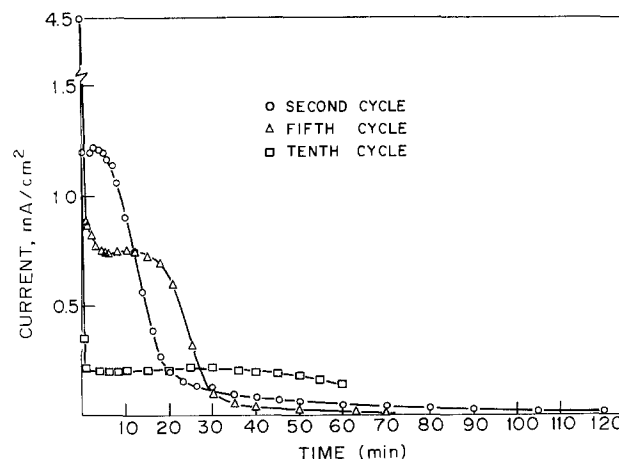


Fig. 5. Curves 1, 2, and 3 are current decay curves for the second, fifth, and tenth constant potential reduction cycles, respectively.

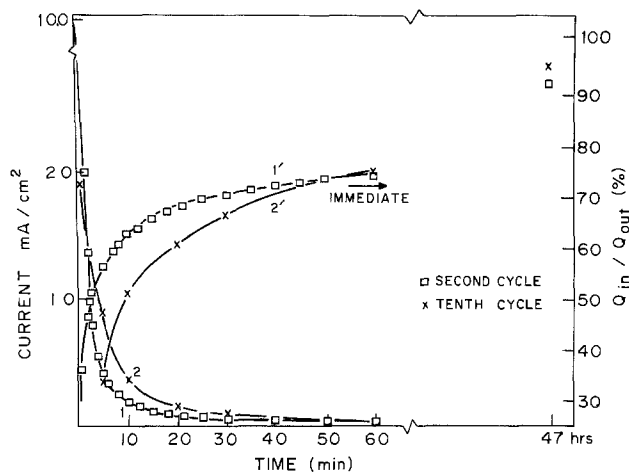


Fig. 6. Curves 1 and 2 are current decay curves for the second and tenth constant potential oxidation cycles, respectively. Curves 1' and 2' show the coulombic efficiencies (Q_{out}/Q_{in}) upon immediate oxidation for 3.8% reduced polyacetylene for the second and tenth cycles, respectively.

first reducing it to $y = 0.038$ under appropriate conditions of controlled potential and then exhaustively oxidizing it at a controlled potential of 2.5V. The variation of the oxidation current with time for the second and tenth cycles is shown in Fig. 6. For each oxidation, a high current in the range of 10 mA/cm² was observed upon initial polarization. The current then decreased at a quasi-exponential rate. Over the first two to ten cycles, about 30-50% of the charge initially passed during reduction was recovered at current densities greater than 1 mA/cm². After 1h, the oxidation current level had decayed to less than 0.1 mA/cm², and the fraction of charge recovered was 60-70%. After exhaustive oxidation until the current level was less than 2 μ A/cm², which typically required 40-60h, the apparent coulombic efficiency, Q_{out}/Q_{in} , was 0.93 or greater.

Controlled current studies.—Constant current reduction.—In these experiments, samples of polyacetylene were reduced at a constant current of 0.1 mA/cm² until a desired doping level was reached. They were then oxidized at 1 mA/cm² until the cell potential reached 2.5V. Oxidation was then continued but at a controlled potential of 2.5V.

Figure 7 shows the cell potential for $(Li_yCH)_x$ during reduction and the open-circuit potential after a 1 min current interruption for the second and eleventh cycles as a function of the doping level, y . The electrode established

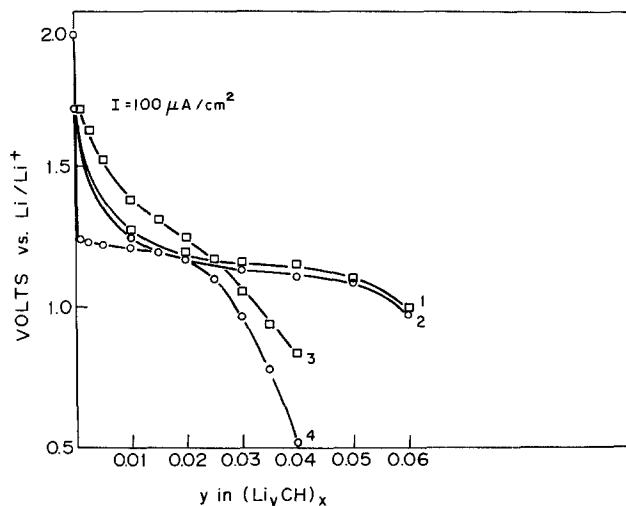


Fig. 7. Open circuit and cell potential of $(Li_yCH)_x$ as a function of y for the second (1, 2) and eleventh (3, 4) reduction/oxidation cycles. See text for more complete description of experimental conditions.

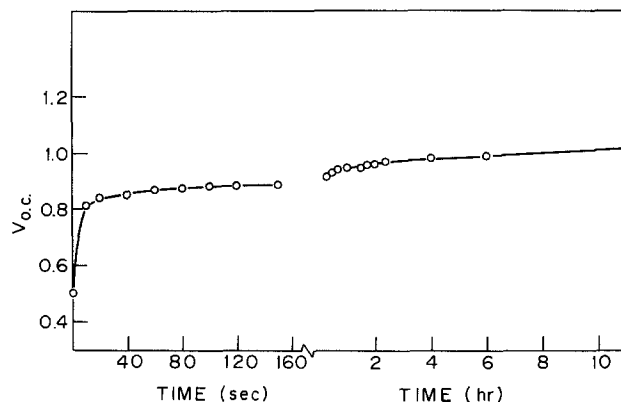


Fig. 8. Change in open-circuit potential with time after the twelfth reduction/oxidation cycle. The polyacetylene was reduced to 3.5%.

a reasonably flat voltage plateau in the second cycle. But, by the eleventh cycle, it decreased sharply with increasing doping level. If 0.5V is considered a cutoff point for efficient reduction, it is clear that the capacity (y) of the polyacetylene electrode that could be efficiently cycled decreased with cycling and was about 0.04 by the eleventh cycle.

In addition, the overvoltage for the reduction process was considerably greater in the eleventh cycle than in the second cycle. The rate at which the open-circuit potential rose after current interruption demonstrates this point. In the third cycle, the current was interrupted at the 4% doping level. The open-circuit potential gradually rose 120 mV over 17h. When the current was interrupted at 4% doping during the twelfth cycle the potential rose about 300 mV within 5s and then gradually rose another 200 mV over 12h.

These observations are consistent with the results of the cyclic voltammetry and constant potential experiments previously discussed. They indicate that the electrochemical characteristics of the polyacetylene electrodes changed upon electrochemical cycling. The behavior of polyacetylene evolved from that which resembles a redox couple with an extended voltage plateau, behavior that is desirable for a battery electrode, to a state in which the potential decreased steeply with increasing charge, a characteristic that is undesirable in a battery electrode. The gradual decrease of the open-circuit potential of polyacetylene doped to 4% as function of cycle number (Fig. 9) severely limits the electrode capacity that can be efficiently cycled.

Constant current oxidation.—Constant current oxidation experiments showed that the rate at which Li⁺-doped

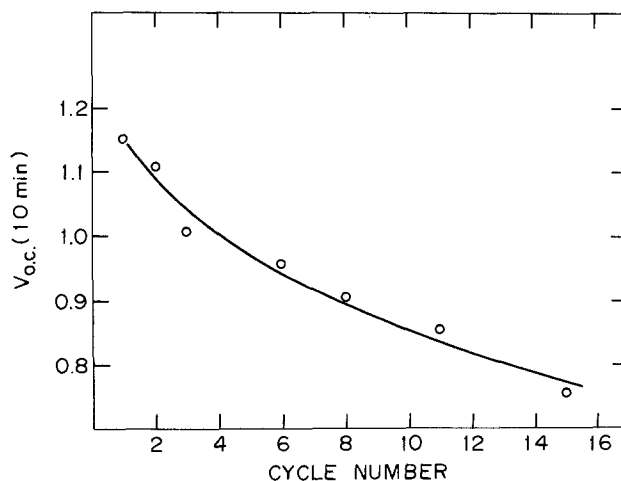


Fig. 9. Open-circuit potential as a function of cycle for a 4% reduced polyacetylene sample.

polyacetylene could be oxidized decreased as the material was cycled. In initial experiments, samples of polyacetylene were cycled by reduction to an n doping level of $y = 0.04$ - 0.06 at 0.1 mA/cm^2 and oxidized at 1 mA/cm^2 until the potential reached 2.5 V . The amount of charge that could be extracted before the potential reached 2.5 V decreased with cycling. In the third and fourth cycles, about 60% of the charge could be extracted before the potential reached 2.5 V . By the eleventh cycle, only about 40% of the charge could be recovered in this way. In each case, the remaining charge could be almost completely recovered by an extended (40-60h) oxidation at a controlled potential of 2.5 V .

The total coulombic efficiency for the reduction/oxidation process was measured by reducing polyacetylene to various doping levels at 0.1 mA/cm^2 , and then reoxidizing, first at a constant current of 1 mA/cm^2 and then exhaustively at a controlled potential of 2.5 V . Table I summarizes the results obtained in one set of experiments over 15 cycles.

Polyacetylene reduced to $y = 0.04$ maintained a coulombic efficiency of nearly 100% to the fifteenth cycle. The reactions were very efficient despite the obvious decrease in the open-circuit potential of the reduced polyacetylene at the $y = 0.04$ doping level. If this gradual decrease in open-circuit potential were to continue, the potential would ultimately enter the region of solvent instability, and the coulombic efficiency of the reduction reaction would decrease.

Reduction to levels higher than $y \approx 0.04$ and allowing the sample to stand on open circuit both decreased the fraction of charge which could be recovered upon oxidation, as Fig. 10 demonstrates. When reduction was followed by immediate oxidation, a coulombic efficiency of nearly 100% was maintained to doping levels of about $y = 0.06$. It then declined sharply, and reached about 80% at $y = 0.09$. An 18-20h stand on open circuit after reduction decreased the overall coulombic efficiency at doping levels above about $y = 0.04$. For example, for polyacetylene doped to $y = 0.07$, the coulombic efficiency dropped from 93% upon immediate discharge to 76% after an 18h delay.

Conclusions

The most important concerns regarding the attractiveness of polyacetylene as an alternative to the lithium electrode for high energy density, rechargeable battery technology are its stability, potential as a function of doping level (y), and volumetric and gravimetric capacity. Our results provide insight into each of these issues.

The stability of Li^+ -doped polyacetylene is quite good. At the reduction levels of $y < 0.10$ investigated in this work, reduced polyacetylene electrodes with Li^+ as the dopant appear to be quite stable in $\text{THF}/\text{LiClO}_4$ toward short-term loss of capacity. Polyacetylene that has been n doped under these conditions is far more tolerant of impurities in the electrolyte and extended storage in contact with the electrolyte than its rather fragile p-doped counterpart (4).

However, we found that the electrochemical characteristics of polyacetylene gradually changed as the material

Table I. Coulombic efficiency for reduction/oxidation of $(\text{CH})_x$

Cycle	y^a	Percentage out at 1 mA/cm^2 ^b	Total percentage out ^c
1	0.040	57	67
2	0.038	75	93
6	0.038	77	100
7	0.085	50	63
8	0.038	78	106
9	0.040	85	105

^a Value of y in $(\text{CHLi}_y)_x$.

^b $Q_{\text{out}}/Q_{\text{in}} \times 100\%$.

^c Same as in footnote b except after exhaustive oxidation at 2.5 V .

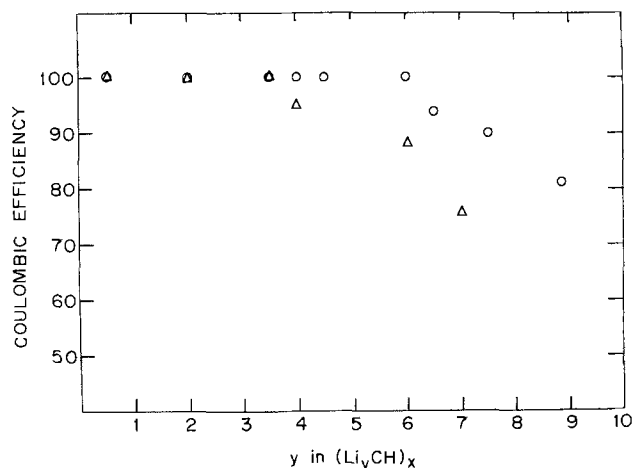


Fig. 10. Coulombic efficiency ($Q_{\text{out}}/Q_{\text{in}}$) as a function of y upon immediate (circles) and delayed (triangles) (18-20h) oxidation.

was cycled from $y = 0$ to $y = 0.04$ - 0.06 ten or 20 times. The electrochemical reduction process grew less reversible, and the cyclic voltammetry peaks corresponding to the reduction/oxidation processes became more diffuse.

The rate capability of polyacetylene electrodes also decreased with cycling. The current levels observed during reduction and subsequent oxidation grew smaller. A careful study of the current/time curves for the reduction of polyacetylene films at 1.1 V showed that a fresh sample had an initial reduction current of 4 - 5 mA/cm^2 , which decayed within 30 - 60 s to a plateau of about 0.7 mA/cm^2 . If the sample was then oxidized to restore the value of y to nearly 0 , and then rereduced at 1.1 V , the initial reduction current was about the same as in the first reduction, but the magnitude of the plateau current decreased. The trend continued through subsequent cycles until the plateau disappeared entirely.

The open-circuit potential of reduced polyacetylene also changed with cycling. At a constant value of y , the potential gradually shifted toward that of Li as the number of cycles increased. For example, during the second reduction/oxidation cycle, the potential of $(\text{Li}_{0.01}\text{CH})_x$ was 1.27 V . It established a plateau of about 1.2 V between $y = 0.01$ and 0.05 and then decreased sharply at higher reduction levels. By the eleventh cycle, the potential at $y = 0.01$ was 1.38 V , but it decreased to 0.84 V at $y = 0.04$. Because the electrolyte was increasingly unstable below 0.5 V , the reduction of polyacetylene to high doping levels was increasingly inefficient.

All of these observations indicate that the electrochemical characteristics of polyacetylene in this electrolyte deteriorate markedly after a few cycles. It becomes increasingly difficult to achieve high reduction levels ($0.06 < y < 0.10$) efficiently. It takes longer to reduce and oxidize the film, because the reduction/oxidation current densities at controlled potential decrease with cycling. Whether this deterioration continues beyond 10 - 15 cycles is not known. It is also not clear whether the degradation is peculiar to the electrolyte used in these experiments. Perhaps more stable behavior would be observed in another electrolyte.

The gravimetric and volumetric energy densities of polyacetylene that has been n doped with Li^+ to the maximum level of $y = 0.10$ that was achieved in this investigation are rather low. The equivalent weight of $(\text{Li}_{0.10}\text{CH})_x$ is 137 g ; that of Li is 6.9 g . The equivalent volume of $(\text{Li}_{0.10}\text{CH})_x$ is about 190 cm^3 ; that of Li is 12.9 cm^3 . In addition, the potential of polyacetylene doped with Li^+ to $y < 0.10$ in $\text{THF}/\text{LiClO}_4$ is 0.5 - 1.5 V positive of that of Li , a substantial penalty in ultimate cell voltage.

All of our results indicate that reduced polyacetylene can serve as a negative electrode in a nonaqueous electrolyte battery in the traditional role of lithium. However, with the $\text{THF}/\text{LiClO}_4$ electrolyte used in this study, it suffers from significant degradation in electrochemical

characteristics upon cycling, a low to moderate gravimetric energy density, low volumetric energy density, and restricted rate capability. Naturally, its performance may be better in other solvent/electrolyte salt combinations.

Our findings do not suggest that n-doped polyacetylene is an attractive alternative to Li for high energy density, rechargeable, nonaqueous battery electrodes. However, it is critical that fundamental studies of the electrochemical reactions of this material be continued. We need to learn whether the electrochemical characteristics observed for n-doped polyacetylene in this study represent ultimate limitations on its performance or are artifacts of, for example, the polymer morphology or the solvent/electrolyte salt combination. If the maximum doping level of $(Li_xCH)_x$ could be increased by a factor of 3-4 and a larger fraction of the stored charge could be recovered at high current densities, n-doped polyacetylene might be an attractive electrode for some applications. However, at present, it appears to be more of an intriguing electrochemical curiosity than a material with immediate technological applications in high energy density batteries.

Acknowledgment

This work was supported by the Assistant Secretary for Conservation and Renewable Energy, Office of Energy Systems Research, Energy Storage Division of the U.S. Department of Energy under Contract no. DE-AC02-76FSF00098.

Manuscript submitted Aug. 20, 1984; revised manuscript received Feb. 20, 1985.

The University of Pennsylvania assisted in meeting the publication costs of this article.

REFERENCES

1. A. G. MacDiarmid and A. J. Heeger, *Syn. Met.*, **1**, 101 (1979/1980).
2. P. J. Nigrey, A. G. MacDiarmid, and A. J. Heeger, *J. Chem. Soc., Chem. Commun.*, 594 (1979).
3. K. Kaneto, M. Maxfield, D. P. Nairns, A. G. MacDiarmid, and A. J. Heeger, *J. Chem. Soc., Faraday Trans.*, **78**, 3417 (1982).
4. G. C. Farrington, B. Scrosati, D. Frydrych, and J. DeNuzzio, *This Journal*, **131**, 7 (1984).
5. R. Huq, D. Frydrych, and G. C. Farrington, in "Membranes and Ionic and Electronic Conducting Polymers," E. B. Yeager, B. Schumm, Jr., K. Mauritz, K. Abbey, D. Blankenship, and J. Akridge, Editors, p. 313, The Electrochemical Society Softbound Proceedings Series, Pennington, NJ (1983).
6. B. L. McKinney and R. G. Burrow, Abstract 559, p. 844, The Electrochemical Society Extended Abstracts, Vol. 83-1, San Francisco, CA, May 8-13, 1983.
7. K. Abe, F. Goto, T. Yoshida, and H. Morimoto, Abstract 553, p. 836, The Electrochemical Society Extended Abstracts, Vol. 83-1, San Francisco, CA, May 8-13, 1983.
8. B. Scrosati, A. Padula, M. Patriarca, M. Schwarz, and G. Lugli, Abstract 70, p. 114, The Electrochemical Society Extended Abstracts, Vol. 83-2, Washington, DC, Oct. 9-14, 1983.
9. R. B. Kaner and A. G. MacDiarmid, Abstract 550, p. 833, The Electrochemical Society Extended Abstracts, Vol. 83-1, San Francisco, CA, May 8-13, 1983.
10. L. W. Shacklette, R. H. Baughman, and J. M. Sowa, Abstract 558, p. 843, The Electrochemical Society Extended Abstracts, Vol. 83-1, San Francisco, CA, May 8-13, 1983.
11. F. G. Will, Abstract 554, p. 838, The Electrochemical Society Extended Abstracts, Vol. 83-1, San Francisco, CA, May 8-13, 1983.
12. T. Ito, H. Shirakawa, and S. Ikeda, *J. Polym. Sci., Polym. Chem. Ed.*, **12**, 11 (1974).

Method for Reducing Metal Salts Complexed in a Polymer Host with a Laser

A. Auerbach

The BOC Group, Incorporated, New Providence, New Jersey 07974

ABSTRACT

We describe a novel method for generating fine metal lines with a laser. The laser radiation is focused onto the surface of a nonconductive silver nitrate-doped polymer film to reduce silver. By translating the surface relative to the laser beam, a highly conductive silver line is formed. The measured resistance agrees well with the computed value for a silver conductor of comparable dimensions.

In the past few years, the application of lasers to a wide variety of technologies has occurred. Among the factors contributing to this are the laser's versatility and ability to provide localized photons and/or heat. In no area is this more evident than microelectronics. Pulsed xenon laser systems have been available for some time as ablation tools for the localized removal of thin metals or polymer films from a substrate (1, 2). Laser machining and welding applications have also been investigated and applied (3).

Recently, lasers have been used to deposit or remove conductors. Applications of these kinds include work done by Raffel *et al.*, who used laser radiation to form carbon conductors in polyimide film by graphitization (4). Since the resistivity of carbon is high compared to metal, these conductors are generally not useful. Another application reported by von Gutfeld *et al.* (5) involves laser-assisted electroplating. The laser makes possible rapid electrodeposition of dense and crack-free gold by providing localized heating of the substrate. Laser-assisted electroless gold and platinum deposition from so-

lution was investigated by Karlicek *et al.* (6). Tsai *et al.* have described an etching application where a laser is used to remove aluminum under an ambient bromine atmosphere (7).

In the area of photochemical metal deposition, UV-visible lasers are being used to enhance the deposition of metals and semiconductors (8-10). While this technique shows good promise for producing thin film conductors, exotic and highly toxic organometallics are often required. Also, to accomplish bond scission with a single photon, large and expensive UV lasers are required.

This paper describes a new approach for generating highly conductive metal lines by laser-assisted thermal reduction of metal salts dissolved in a polymer host. The technique is especially promising, since very low cw laser power (10-30 mW) is required. For the silver system described below, we have achieved conductivities on the order of pure silver. Future publications will describe other metal salt/polymer systems which can be used to form copper or gold conductors.

Experimental

Reagent-grade solvents were used. The polymers were purchased from Amoco Chemical Corporation and du Pont Specialty Coatings Division. The AI-10 polyamic acid (Amoco) came as pellets which had to be dissolved in a suitable solvent. The du Pont materials, PyraLN 2540, 2560, and PyraMIL 5057, are polyamic acid solutions, and were further diluted with either *N*-methyl pyrrolidone or *N,N*-dimethyl formamide.

Silver nitrate salt (AgNO_3 , 99.9%) was purchased from Metron, Incorporated. ULTEM™ sheets (1.5 mm thick) were provided by the Specialty Polymers and Plastics Division of General Electric.

Films were cast from solution with a Headway Research spin coater (Model 1EC101-R485). They were dried and baked in a Blue M oven. A programmable X-Y translator stage (Anorad Corporation Model 170) was used in conjunction with an argon ion laser (Spectra Physics Model 171). The output of the laser was focused through a 10× planar convex microscope objective. The focal region was viewed and displayed with a solid-state camera and television.

Resistance measurements were made with a multimeter. The linearity (I-V) of the conductors and the quality of connection to the contacts were investigated using a curve tracer (Tektronix, Incorporated, Type 576). The curve tracer was also used to determine the electric current carrying capacity of the conductors. A scanning electron microscope (Hitachi Corporation Model 5-520LB) and PGT 4 x-ray analyzer were frequently used.

Results

The present study was undertaken after previous work had shown that highly conductive polymer films result when silver nitrate doped polyamic acid films are processed in an oven at 300°C (11, 12). Resistivities as low as $10^{-3} \Omega\text{-cm}$ (pure silver = $1.6 \times 10^{-6} \Omega\text{-cm}$) were achieved. We decided to investigate the possibility of using a laser to accomplish the reduction in a localized region.

The first attempt at thermal reduction using a laser was successful. A mixture consisting of 1.5g of silver nitrate dissolved in 10g of polyamic acid solution (PyraML 5057) was prepared and cast onto a glass substrate. The film thickness depends both on the viscosity of the solution and the spin speed; for the above formulation and a spin speed of 3000 rpm, a 0.75 μm thick film resulted as measured after a 30 min bake at 150°C. The sample was placed on the Anorad translator stage and translated relative to the laser beam focused onto its surface. Using low output powers, and a 300 $\mu\text{m/s}$ translating speed, conductive silver lines were written. One series of lines formed in this manner is shown in Fig. 1. These conductors were written using laser powers between 10 and 40 mW. Pyrolysis of the undoped polymer, which is transparent in the visible, does not occur at these low powers; it is only after

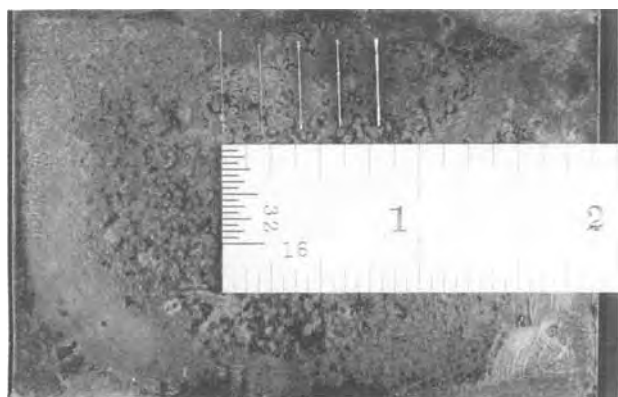


Fig. 1. Laser-reduced silver conductors on glass substrate 10 mW, 20 mW, 30 mW, 40 mW, 40 mW (100 $\mu\text{m/s}$). Film thickness: 0.75 μm .

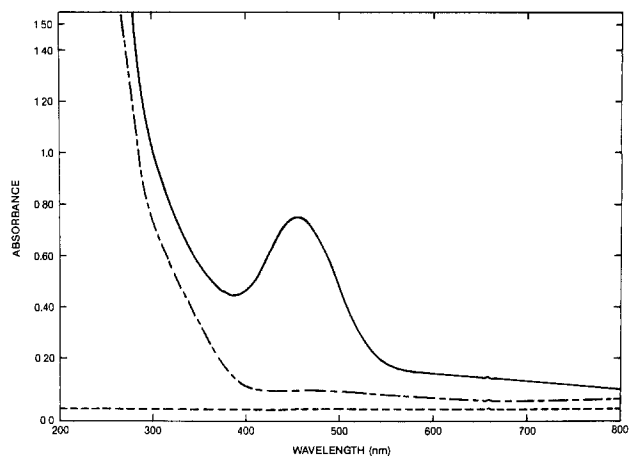


Fig. 2. Absorption spectra. Solid curve: (AgNO_3)-doped AI-10 polymer film. Thickness: 0.75 μm . Middle curve: undoped AI-10 polymer film. Bottom curve: adsorption of Supersil II substrate.

the silver ion is incorporated in the polymer matrix that sufficient absorption occurs to allow the rapid heating and reduction. Figure 2 compares the absorption spectra in the 200-800 nm spectral range for doped and undoped AI-10 polyamic acid films. The prominent adsorption band centered at 450 nm is present only for the doped polymer film. This band results from complexation between the nitrogen containing imide moiety and the silver ion. The rate of complexation is temperature dependent, and the absorbance increases with temperature and time. This is shown in Fig. 3, where the absorbance at 450 nm is plotted against the sample dry temperature. The reason for the high efficiency with which the reduction occurs (as shown below, approximately 100% of the Ag is reduced) is a direct consequence of this temperature dependence. As the laser radiation is adsorbed, heating occurs increasing the absorbance until reduction occurs. Since the polymer is a poor thermal conductor, the reduced volume remains localized.

Initial work using a glass substrate showed that a continuous metal conductor results when the film is translated relative to the focused laser radiation. The resistance of these conductors was measured by forming them between InSnO_2 contacts patterned on glass substrate. Contact metals including aluminum, gold, or silver were

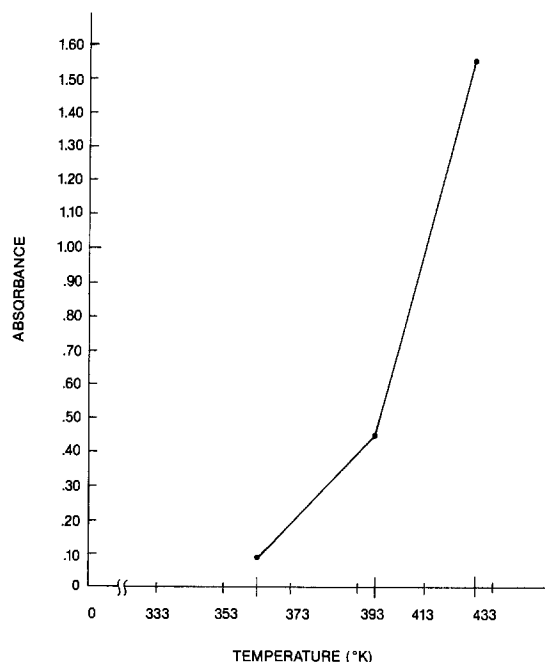


Fig. 3. Adsorbance of doped polymer film with increasing temperature. Film thickness: 1 μm . Drying time: 30 min.

Table I.

Mix	Polyamic acid and quantity (g)	AgNO ₃ (g)	AgNO ₃ /NMP ^b (33%/67%) (g)	AgNO ₃ /NMP (25%/75%) (g)	DMF ^c (g)	Drying time/temp. (min/°C)
	PyraML-5057 ^a					
1	5	0.5				10/180
2	5		3			10/180
3	5		8			10/180
4	10	1.5				10/180
	Al-10 ^d					
5	3	3			7	20/140
6	3	4			7	20/140
	PyraLIN-2530 ^a					
7	3		3			10/180
8	3			6		10/180

^a du Pont.

^b N-Methyl pyrrolidone.

^c Dimethyl formamide.

^d Amoco Chemicals polyamic acid powder.

also evaluated. A variety of AgNO₃ doped polyamic acid solutions (see Table I) were formulated and evaluated. Good connection between the laser-reduced silver and the different contact metals was achieved. As the thickness of the contact metal is increased, higher output powers are required to achieve good electrical connection, since the metal is thermally more conductive than the glass substrate.

A variety of polymer substrates were also evaluated. Among these, the thermoplastic ULTEM worked best because of its high heat deflection temperature (~200°C). Squares (2.54 × 2.54 × 0.120 cm) were cut from ULTEM sheet and laminated with 56g copper foil, (Gould, Incorporated). The copper was patterned using conventional printed circuit board processing. Afterwards, a relaminating step was performed to planarize the surface. This is done to present a uniform surface topography so that no refocusing is required. Figure 4 shows one such patterned substrate coated with mixture no. 3 (see Table I). Also shown is a laser-reduced silver connection between the two copper conductors. The measured resistance between the contacts was 60Ω. This is remarkably low for the silver line 1 cm long by 40 μm wide. As is shown below, the calculated resistivity agrees well with that of pure silver.

Although laser writing directly on a polymer substrate is straightforward, forming good electrical connection to patterned metal laminated on the polymer surface is more difficult, since the metal is inherently thick, and, to achieve good connection, a high laser power is required; too high a power can melt the polymer underneath. Excellent connection between the reduced silver and copper- or gold-plated copper contact metals has been achieved by using one power level for writing on the ther-

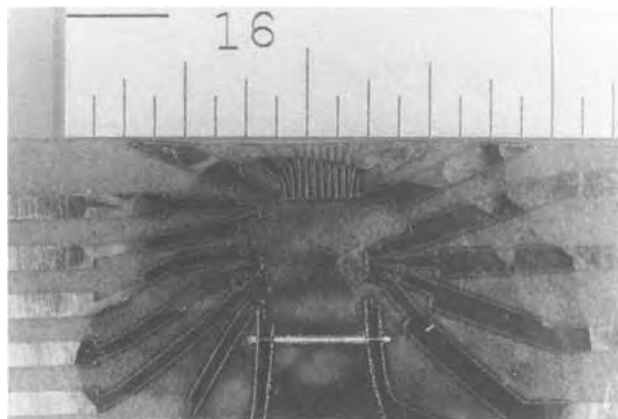


Fig. 4 Laser-written silver connection between two patterned copper conductors on Ultem.

moplastic (10-20 mW) and a power 10 times greater (approximately 100-200 mW) to form connections to the metal. Using this approach, we have formed connections having contact resistance below 1Ω. This is shown in Fig. 5, where the I-V characteristics of one such conductor is investigated with a curve tracer. The trace is linear to 20 mA. The current carrying capacity of the silver line is excellent; a 20 μm by 1 cm long conductor can pass 20 mA (at 3V) continuously. This is equivalent to 1 mA/μm, and agrees with the power-to-width specification for standard VLSI conductors having a comparable thickness (see below). Also shown in the figure is a closeup of the contact region. A higher power was used to form the low resistance connection. These conductors were formed using a scan rate of 1 cm/min (0.2 mm/s). Since scan speed and laser power are interdependent, it is expected that faster scan rates are possible.

Discussion

We have shown that during laser reduction enough silver forms to generate highly conductive lines. The simple calculation which follows predicts almost 100% conversion and agrees both with the measured resistivity and optical SEM results. The calculation is based on mix 5 (see Table I) and a film thickness of 2 μm. Two assumptions are made: first, all solvent evaporates during the casting and oven drying; second, the density of the doped film is approximately double that of undoped film, since

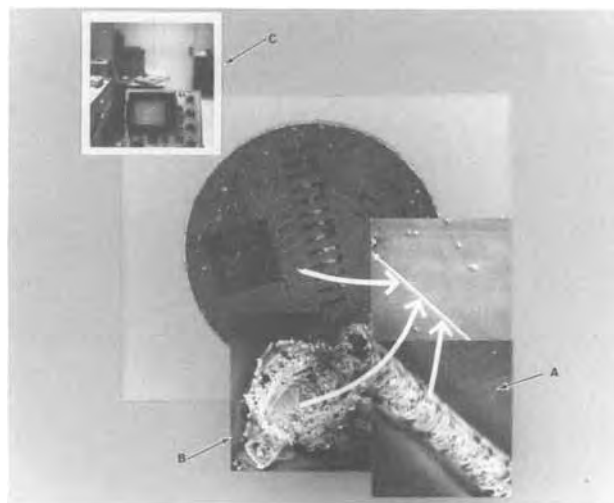


Fig. 5. Laser-written silver lines connecting patterned aluminum conductors to an aluminumized silicon square imbedded in Ultem. A: SEM close-up of silver conductors showing the smooth (not granular) silver deposit. B: The contact region. C: I-V trace of one silver conductor. The linearity is indicative of little contact resistance.

AgNO₃ has a molecular weight comparable to that of an Al-10 unit¹.

The mass of silver nitrate contained in the volume occupied by a typical laser-scribed conductor (1 cm × 20 μm × 2 μm) can be calculated, since the polymer volume is ~4 × 10⁻⁷ cm³ and the density of the doped film is approximately 2.5 g/cm³. The mass of AgNO₃ in this volume is 1 × 10⁻⁶g, and since the mole ratio is approximately 1:1 (Al-10 unit to AgNO₃) the mass of Ag⁺ is 108/200 × 1 × 10⁻⁶g or 5 × 10⁻⁷g. Assuming all the Ag⁺ is reduced to the metal during the laser writing, then the volume of reduced silver is mass (Ag)/density(Ag) or 5 × 10⁻⁸ cm³. For a conductor 1 cm long by 20 μm wide, this implies a silver thickness of ~0.25 μm. Using this value and the tabulated resistivity of silver (1.6 × 10⁻⁶ Ω-cm), the resistance of the 1 cm long by 20 μm by 0.25 μm conductor is

$$R = r \frac{1}{A} \sim 32\Omega \quad [1]$$

Since this value agrees well with resistance values which have been measured, the reduction is very efficient. Also, it is expected that the contact resistance between the reduced silver and the contact metallization is small. This is in agreement with the linear I-V character observed on the curve tracer Fig. 5.²

An important consideration is that these laser-written conductors be durable. Although at the present time no careful study has been undertaken, it has been determined that, once formed, the silver has little tendency to be oxidized if protected with an epoxy or polymer overcoat. This is equally true in the region where the silver contacts the substrate metal. Unprotected contacts tend to open (*i. e.*, electrical connection is lost) with time in the presence of humidity. This is because reaction occurs between the silver, nitrate ion, and substrate metal. The problem is severe with copper; substrate metals such as aluminum, gold, and molybdenum are less reactive. Once encapsulated in epoxy, both the contact region and conductors exhibit good stability under ambient conditions (25°C and 40-80% relative humidity).

Finally, as the silver is reduced on the polymer substrate, it forms in the polymer melt pool, and becomes imbedded into the thermoplastic material as it cools. This means that intimate attachment to the polymer occurs.

¹This assumes that the silver ion occupies a much smaller volume than the polyamic acid repeat unit.

²Contact resistance would appear as nonlinearity in the V-I plot at low voltage (and current).

We have observed that moderate flexing of the substrate does not detrimentally affect the electrical conductivity of the conductor.

Conclusion

It has been shown that, under appropriate conditions, the output of a laser can be used to supply thermal energy for the oxidation reduction reaction between polymer and dopant salt to occur. By translating the substrate relative to the laser beam, highly conductive lines can be generated. Since sufficient heating occurs mainly in the localized region of the focused laser radiation-beam waist 10 μm-fine lines result.

There are a variety of applications for this technique. One which we have begun to investigate is to write connections between the bonding pads on a chip to external conductors on a printed circuit board. Briefly, this involves laminating copper to the surface of a thermoplastic polymer, then patterning and gold plating the copper. A chip is laminated into the thermoplastic so that the patterned conductors surround it. The polymer/salt solution is cast onto the surface, and electrical connection between the bonding pads on the chip to the conductors is made by laser writing. Initial results look very promising (13).

Manuscript submitted Oct. 1, 1984; revised manuscript received Feb. 12, 1985.

General Electric Company assisted in meeting the publication costs of this article.

REFERENCES

1. J. E. Andrew, P. E. Dyer, R. D. Greenough, and P. H. Key, *Appl. Phys. Lett.*, **43**, 1076 (1983).
2. M. A. Saifi and O. J. Masopust, *IEEE J. Quantum Electron.*, **qe-12**, 120 (1976).
3. M. I. Cohen, in "Laser Handbook," Vol. 2, F. Arecchi and E. Schulz, Editors, Dubois, North Holland, Amsterdam (1972).
4. J. I. Raffel, J. F. Freidin, and G. H. Chapman, *Appl. Phys. Lett.*, **42**, 705 (1983).
5. R. J. von Gutfeld, M. H. Gelchinski, and L. T. Roman-kiw, *This Journal*, **130**, 1840 (1983).
6. R. F. Karlicek, V. M. Donnelly, and G. J. Collins, *J. Appl. Phys.*, **53**, 1084 (1982).
7. J. Y. Tsao and D. J. Ehrlich, *Appl. Phys. Lett.*, **43**, 146 (1983).
8. T. F. Deutsch, D. J. Ehrlich, and R. M. Osgood, Jr., *ibid.*, **35**, 175 (1979).
9. R. Solanti, P. K. Boyer, and G. J. Collins, *ibid.*, **41**, 1048 (1982).
10. P. K. Boyer, G. A. Roche, W. H. Ritchi, and G. J. Collins, *ibid.*, **40**, 716 (1982).
11. A. K. St. Clair, V. C. Carver, L. T. Taylor, and T. A. Furtch, *J. Am. Chem. Soc.*, **102**, 876 (1980).
12. A. Auerbach, *This Journal*, **131**, 937 (1984).
13. A. Auerbach, "IEEE Components, Hybrids, and Manufacturing Technology," I.E.E.E., To be published.

Near-Surface Damage and Contamination after CF₄/H₂ Reactive Ion Etching of Si

G. S. Oehrlein,* R. M. Tromp, J. C. Tsang, Y. H. Lee,* and E. J. Petrillo

IBM Thomas J. Watson Research Center, Yorktown Heights, New York 10598

ABSTRACT

Silicon surfaces which had been exposed to CF₄/40%H₂ reactive ion etching have been characterized by x-ray photoelectron emission spectroscopy, He ion channeling, H profiling, and Raman scattering techniques. Plasma exposure of a clean Si surface leads to the deposition of a thin (~30-50Å thick) C,F containing film. The near-surface region (~30-50Å) of the Si substrate is heavily disordered ("amorphized"), as found by ion channeling and Raman scattering. A modified, less damaged Si region extends from about 30-50Å from the surface to a depth in excess of 250Å. This layer contains a high concentration (~5 atom percent) of H as shown by hydrogen profiling techniques. From the observation of Si-H and Si-H₂ vibrational modes by Raman scattering, it has been shown that the H is bonded to the Si lattice. In ion scattering, the extended modified Si layer appears to cause a strongly enhanced background in the energy spectra. Results of Monte Carlo range calculations are reported and compared with the damage depth found experimentally.

Fine-line pattern transfer in very large scale integrated (VLSI) device processing is achieved by anisotropic dry etching techniques (1). Presently, the most widely used directional etching techniques are reactive ion etching (RIE) and ion beam sputtering. The directionality of these etching techniques is based on energetic ion bombardment of the etched surface (2). The low energy ion exposure of electronic materials can result in bombardment damage, which can affect the device applicability of these materials in a detrimental way. Indeed, a large number of reports has appeared in the literature, where detrimental side effects of dry etching techniques on semiconductors were reported and related to dry etching-induced damage in the semiconductor substrates (3-5). In the case of silicon, the following effects have been observed: a degradation of the minority carrier lifetime (6), changes in the barrier height and of the ideality factor of Schottky barriers formed on dry etched Si (7), high contact resistance in contact hole etching (8), and a deterioration of the oxide quality (interface state density, dielectric strength) of thermal SiO₂ films grown on dry-etched substrates (4, 6). The physical and chemical origins of these effects are at this time poorly understood.

An interesting property of the dry etching-induced "damage" is the depth to which it appears to penetrate into the Si substrate. Several investigators report that in order to recover the original electrical properties of a Si wafer, about 500Å of modified Si had to be removed by wet etching techniques (4, 9). This finding was assumed to imply that the "damaged" region would extend 500Å from the free surface into the bulk of the semiconductor.

Another key feature of a dry etching process is the selective etching of one material *vs.* another material. An important problem in Si technology is selective etching of SiO₂ over Si. Addition of H₂ to CF₄ has been found to increase the SiO₂-to-Si etch-rate ratio (10). There are indications that this selectivity is in part due to the deposition of an involatile carbon containing residue onto the Si surface once the SiO₂-Si interface is reached during dry etching (11). It is clear that the formation of surface residues during etching will affect the electrical properties of structures or layers formed on so-contaminated surfaces. By electrical measurements alone, it would be difficult to identify the origin of modified electrical behavior as either surface contamination or displacement damage in the substrate. This differentiation is, however, important in the search for suitable post-RIE cleaning or annealing procedures.

In the present paper (12), we report results of studies aimed at identifying the structural and chemical changes of the surface and near-surface properties of Si caused by reactive ion etching. A number of surface and near-surface sensitive techniques were employed to characterize as-etched room ambient-exposed Si. Although for sur-

face characterization, *in situ* analysis would be more desirable in order to exclude further contamination by room ambient exposure, the results of the present study are of direct technological interest.

Sample Preparation

500Å layers of thermal oxide were grown on chemically cleaned 2 Ω cm, B-doped, <100> 3.25 in. diam Si wafers. The oxide was subsequently completely removed either by dry etching or, in the case of control samples, by wet etching in buffered HF. The dry etching experiments were performed in a single-electrode RIE reactor, *i.e.*, in a configuration where the sample is placed on the powered electrode. The etching conditions were 0.178 W/cm² RF power density applied using a CF₄/40%H₂ gas mixture. A self-bias voltage of about -425V developed at the powered electrode during etching. The gas flow was 40 sccm, and the chamber pressure 25 mtorr. The etch rate of SiO₂ under these conditions was 400 Å/min, while the etch rate of Si was ~15-20 Å/min [see also Ref. (10)].

In order to study the effect of different overetching conditions on the quality of the exposed Si, the etching times were varied. The etch end point was determined by laser interferometry at the center of a Si wafer. In one case, the RIE was stopped once the whole SiO₂ layer had been etched away (denoted by "no" overetching). In other cases, the RIE conditions remained unchanged for various times up to 10 min after complete etching of the SiO₂ film. In those experiments, the Si surface was therefore exposed for the length of the overetching time to the CF₄/40%H₂ plasma.

In reactive ion etching, the maximum energy of impinging ions at the Si surface is given by the difference of the self-bias voltage developed at the powered electrode and the plasma potential [both potentials measured with respect to ground, *i.e.*, in the present case, the numerical values add (1)]. In our experiments, the maximum ion energy was about 450 eV. (We assume that the density of doubly ionized species is negligible.) Collisional processes in the sheath region can lower this energy. As a result, ions and neutrals with a great spread of energies, ranging from the maximum energy listed before to no energy, bombard the etched surface during the discharge.

From the cathode current the ion flux at the Si surface was estimated to be 1.6×10^{15} ion/cm² s (ignoring unknown corrections, such as secondary electron emission). For specimens overetched for 10 min, the total ion dose is therefore of the order of 1.0×10^{18} ion/cm².

After completion of the RIE treatments, the Si specimens were removed from the plasma chamber. The as-etched and room ambient-exposed surfaces were characterized using x-ray photoemission spectroscopy (XPS) and high resolution He ion scattering/channeling techniques. The presence of hydrogen in the near-surface region of the Si specimens was detected by the ¹H + ¹⁵N nu-

*Electrochemical Society Active Member.

clear reaction technique (13). Raman scattering was used to detect the presence of disorder in the Si lattice and to observe vibrational Si-H modes.

Experimental Results

Photoemission measurements.—In Fig. 1 and 2, XPS survey spectra are shown for dry-etched Si samples and Si samples etched in buffered HF (BHF). Magnesium $K\alpha$ radiation was used for the excitation of the photoelectrons. In Fig. 1 (250–800 eV binding energy range), we notice O Auger, O 1s, and C 1s peaks due to the native oxide on the control (BHF-etched) specimen. The native oxide was 20Å thick, as determined by ellipsometry. The carbon contamination is caused by exposure to room atmosphere. A Si sample where the SiO_2 had been dry etched with no overetching shows additional peaks due to F at the surface. The oxygen intensity is decreased, while the C intensity is increased. The changes are more dramatic for a Si specimen which had been 1 min overetched: the F- and C-related peaks are further increased, while the O-related lines are much weaker than those for the control. The F, C, and O photoemission signals of a specimen which had been overetched for 10 min are very similar to the sample which had been overetched 1 min.

The buildup of dry etching-related F, C contamination on the surfaces of processed Si specimens is reflected in the intensity of the photoelectron peaks from the underlying Si substrate. This is shown in Fig. 2. For the dry-etched samples, the Si-related photoelectron peak height is decreased as compared to the BHF control. The peaks are weaker for the 1 min overetched Si than for the no overetched sample, implying a greater amount of surface contamination with longer overetching time. This trend is not continued during prolonged overetching. The 10 min overetched specimen in Fig. 2 shows stronger Si related peaks than the 1 min overetched sample, which can be interpreted as being due to less surface contamination.¹

¹The escape depth of Si 2s and 2p electrons excited with Mg $K\alpha$ x-rays in polymeric materials is about 30Å (14). This XPS-derived thickness of the C, F layer is in agreement with an estimate based on the ion channeling measurements.

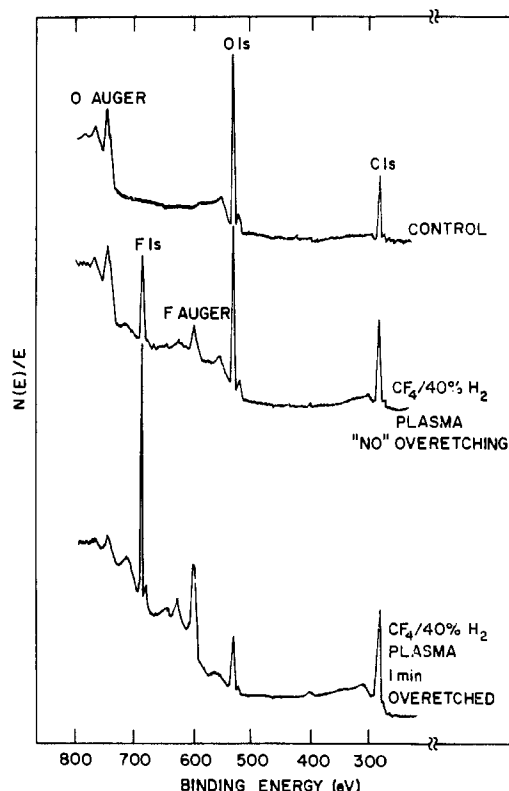


Fig. 1. XPS survey spectra (250–800 eV binding energy range) of control and $\text{CF}_4/40\% \text{H}_2$ dry etched Si samples. With no overetching, a sample is denoted where the RIE was stopped when the SiO_2/Si interface had been reached during etching.

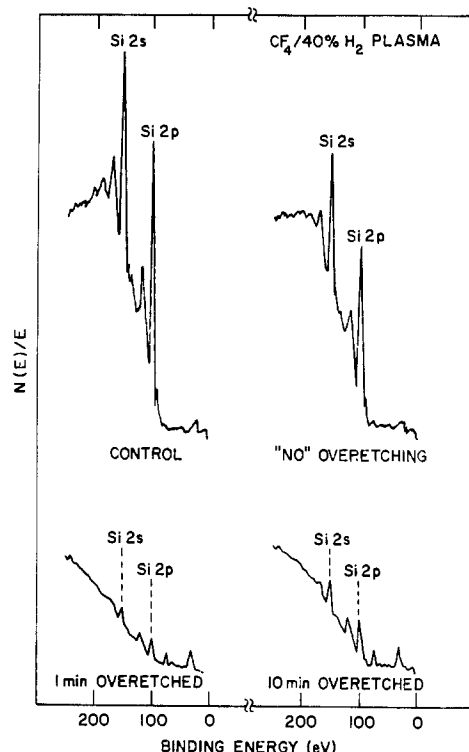


Fig. 2. XPS survey spectra of the 0–250 eV binding energy range of control and dry-etched Si specimens. Note that the Si 2s and 2p peaks are stronger after 10 min overetching as compared to 1 min overetching, indicating less C, F film contamination after 10 min overetching.

The atomic percentage of the surface contaminants for the different Si specimens together with their processing histories is summarized in Table I. The table verifies the trends apparent in Fig. 1 and 2 concerning Si and C. It also shows that there is a monotonic increase in F concentration with longer overetching time.

In Fig. 3 the C 1s fine structure of a sample which had been overetched for 3 min in CF_4/H_2 is shown. On the high binding energy side of the regular C 1s peak, one can recognize three chemically shifted weaker components. A comparison of the binding energy positions of these weaker components with published CF , CF_2 , and CF_3 spectra (15, 16) shows that the energy positions found here agree very well with the literature values. One concludes that the carbon, in addition to being bonded to H and C, is primarily bonded to one, two, or three F neighbors. The relative concentration of the various bonding states depends on the parameters of the particular "etching" process and on the length of the plasma exposure.

Ion scattering and channeling studies.—In order to see whether subsurface damage was introduced by RIE, several samples were studied with He^+ scattering and channeling techniques. The initial energy of the He^+ ions was 120 keV. High surface sensitivity was achieved by performing the experiments in a double-alignment geometry (17). Here the incident and the (detected) scattered particle beam are aligned with respect to channeling and blocking crystal directions, respectively.

In Fig. 4, the intensity of backscattered particles vs. backscattering energy is shown for some representative

Table I. Atomic concentration of Si surface contaminants as measured by x-ray photoelectron emission spectroscopy

Sample	Atomic concentration (%)			
	F	O	C	Si
HF control	—	24.1	20.4	55.4
No overetching	7.3	26.1	31.1	35.6
1 min overetching	15.0	14.8	63.4	6.8
10 min overetching	35.4	11.3	40.8	12.5

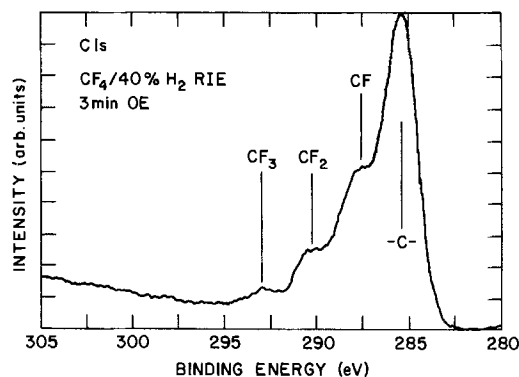


Fig. 3. High resolution XPS spectrum of the C 1s region of a Si sample which had been overetched for 3 min in a CF₄/40% H₂ plasma. The chemically shifted weaker components on the high binding energy side correspond to the indicated bonding states.

experiments. The bottom curve in Fig. 4 is for the wet-etched control sample. At 99 keV, a pronounced random peak due to scattering from Si at the surface is observed. Additional peaks due to oxygen and carbon (from the native oxide layer) occur at 85.5 and 75.9 keV. No other major features appear in the spectrum. The background level is very low.

The second curve from the bottom is for a dry-etched Si specimen where no overetching was applied during RIE, *i.e.*, the plasma was immediately turned off once the SiO₂-Si interface had been reached. The Si surface peak is larger than for the control sample. Furthermore, the background level is higher and an additional F peak at about 90.3 keV is just noticeable. The next curve is for a specimen which had been overetched for 1 min. Strong peaks due to C and F are present in this spectrum. The oxygen peak appears weaker and is shifted to somewhat lower energy. The Si surface peak is also shifted to lower energy, except for a small fraction which remains at 99 keV. The energy shift in the Si and O peaks is caused by the C,F overlayer. The small Si peak remaining at 99 keV indicates that the C,F film is not continuous. The back-

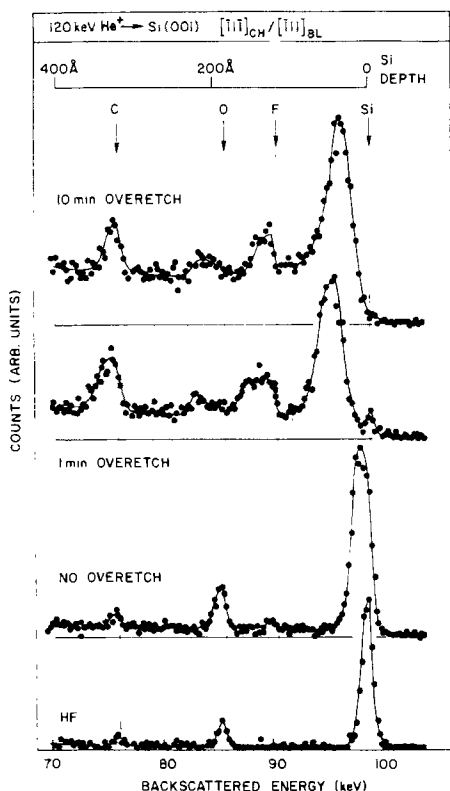
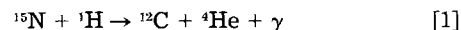


Fig. 4. High resolution He ion scattering and channeling spectra of control and dry-etched Si samples.

ground level is clearly higher than for the HF control in the present case. The upper curve of Fig. 4 is the RBS spectrum for a specimen which had been overetched for 10 min. In this case, most features are similar to the 1 min overetched sample. Notable differences are that no Si peak is remaining at 99 keV (signifying a continuous C,F film) and that the background to the left of the large Si surface peak is about twice that measured for the 1 min overetched sample. For the 10 min overetched sample, the Si surface peak occurs at slightly higher backscattering energy than after 1 min overetching, which is consistent with a thinner C,F layer on top of the Si.

Hydrogen profiling experiments.—The presence of H in the Si lattice was detected using a nuclear reaction profiling technique (13) based on the reaction



A complete description of the application of this technique to the analysis of H in Si can be found in Ref. (19).

Hydrogen concentration depth profiles for the specimens previously studied with XPS and RBS techniques are shown in Fig. 5. For the control (HF-etched) sample, the H concentration close to the surface exceeds 15 atomic percent (a/o). The H arises in this case from a moisture contamination of the native oxide (13). The H concentration drops off rapidly at increasing Si depth, and at about 200Å away from the surface a constant background level is reached. The Si specimens which had been etched in CF₄/H₂ display a much greater H concentration near the surface and deeper into the bulk. The greater H concentration close to the surface is most likely caused by the C,F surface films ("C,F polymer") present on these samples. The 1 and 10 min overetched Si samples, which according to XPS and RBS had about the same thickness of C,F-film contamination, show also nearly the same concentration of H close to the surface. At greater Si depths the H concentration is markedly different for the two samples. The 10 min overetched sample displays consistently a higher H concentration. From this comparison of the 1 and 10 min overetched specimens, it is clear that the substantial H concentration observed in the bulk, *e.g.*, 250Å away from the surface, is not caused by a measurement artifact, *e.g.*, due to a higher H surface concentration, but reflects a H concentration increase in the near-surface region of the 10 min overetched Si caused by the CF₄/H₂ RIE process.

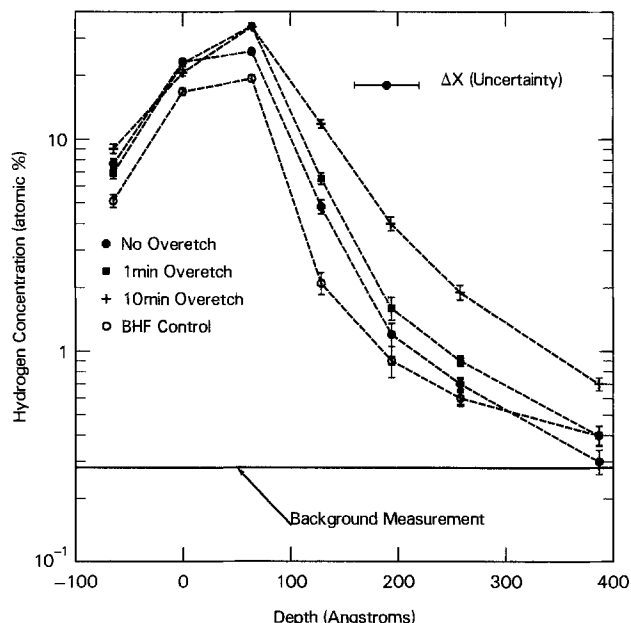


Fig. 5. Hydrogen depth profiles of control (BHF-etched) and dry-etched Si wafers. Note that, for the 1 and 10 min overetched specimens, the H surface peaks are the same (due to similar C,F film contamination), while deeper in the bulk the H concentration of the 10 min overetched sample is higher.

Raman scattering analysis.—Raman spectroscopy can probe several hundred angstroms deep into a Si sample. By observing vibrational excitations of impurities, direct information about the chemical bonding can be obtained (20). The Raman spectrum of amorphous Si shows no sharp lines at frequency shifts larger than 200 cm^{-1} , but does show a broad continuum which peaks at about 480 cm^{-1} (21). The Raman spectrum of crystalline Si consists of a single sharp line at $\sim 520\text{ cm}^{-1}$. The difference arises from the fact that for α -Si no translational symmetry exists as a result of which the selection rules for Raman scattering are relaxed (21). Therefore, all vibrational modes of the amorphous material can take part in the scattering process and a continuum reflecting the density of vibrational states results. These favorable characteristics of Raman scattering have been used to study properties of hydrogenated α -Si (21, 22).

In Fig. 6, Raman spectra of heavily disordered Si which had been produced by several methods are shown. The top curve was obtained with a 60 \AA thick amorphous Si film which had been deposited onto a single-crystal Si substrate at 225°C by decomposition of SiH_4 in a glow discharge. (The contribution of the single-crystal Si substrate has been subtracted, causing the negative excursion of the Raman intensity near 522 cm^{-1} .) The Raman spectrum agrees with the reported spectrum for α -Si (21). The second curve from the top was obtained with a $\text{CF}_4/40\%\text{H}_2$ reactive ion etched Si sample (10 min overetching). The Raman spectrum is similar to the one obtained with the deposited α -Si film. This result demonstrates (in agreement with the RBS findings) that a heavily damaged or amorphized Si layer has been produced by the RIE processing. The two lower curves in Fig. 6 were obtained with single-crystal Si samples which had been implanted with 500 eV Ar^+ ions or 1000 eV H^+ ions to a dose of $1.0 \times 10^{18}\text{ ion/cm}^2$. We notice that these processing steps also introduce Raman scattering similar to the one observed for α -Si.

In Fig. 7, Raman spectra for the same samples are shown at a Raman shift corresponding to Si-H vibrational modes in α -Si ($\sim 2000\text{ cm}^{-1}$) (22). The top curve in Fig. 7

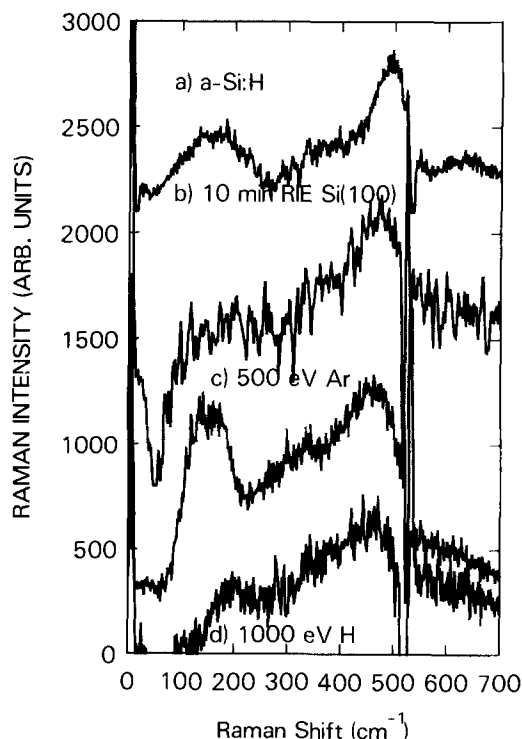


Fig. 6. Raman scattering spectra of amorphous Si layers on top of single-crystal Si. (The Raman spectrum of the crystalline Si substrate has been suppressed in the figure.) The disordered Si layers were either produced by SiH_4 decomposition in a glow discharge, 10 min overetching of a Si sample in a $\text{CF}_4/40\%\text{H}_2$ RIE, 500 eV Ar^+ ion bombardment, or 1000 eV H^+ ion implantation.

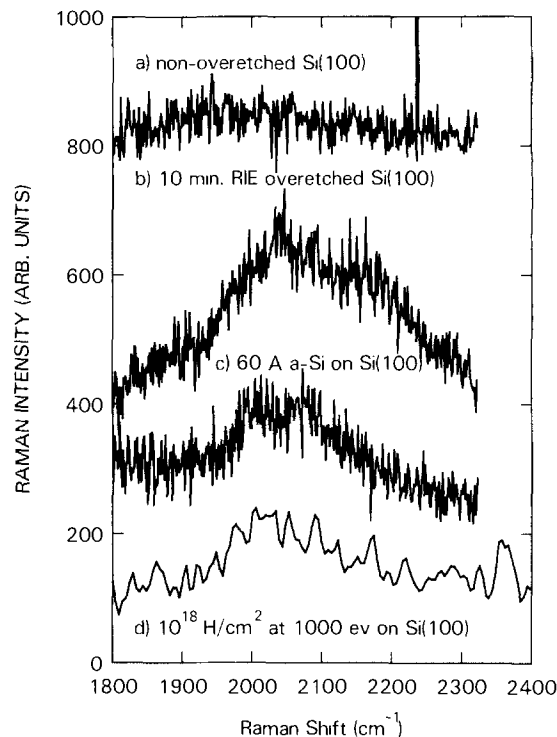


Fig. 7. Raman scattering spectra of Si-H vibrations in $\text{CF}_4/40\%\text{H}_2$ RIE Si (no overetching), a, 10 min $\text{CF}_4/40\%\text{H}_2$ overetched Si, b, 60 \AA of hydrogenated amorphous Si on top of single-crystal Si, c, and 1000 eV H^+ ion-implanted Si, d.

was obtained with a $\text{CF}_4/40\%\text{H}_2$ dry-etched sample without overetching. The spectrum is flat, which indicates a low density of Si-H active modes. The second spectrum from the top was obtained with a sample which had been overetched for 10 min in $\text{CF}_4/40\%\text{H}_2$. In this case a very pronounced double peak is visible. The peak at $\sim 2050\text{ cm}^{-1}$ corresponds to a Si-H vibration, while the band at $\sim 2200\text{ cm}^{-1}$ is due to a vibrational mode of Si-H_2 (22). Figure 7 shows for comparison also Raman spectra of a 60 \AA thick hydrogenated α -Si film on single-crystalline Si and a H^+ -implanted single-crystalline Si target (1000 eV H^+ , $1.0 \times 10^{18}\text{ ion/cm}^2$) in the same wave number region. A more complete description of the Raman scattering experiments and discussion of the results will be published in a separate paper (23).

Monte Carlo range calculations.—We have performed Monte Carlo range calculations utilizing a program developed by Ziegler *et al.* (24). Several elements typically used in RIE (C, F, and H) and an amorphous Si target were employed. The initial energies of the ions were varied from about 100 eV to 2 keV . The following (possibly important) effects were ignored in the range calculation: physical sputtering of the target by the bombarding ions and the influence of damage on the sputter yield; diffusion of already implanted species caused by the high ion flux; and channeling of ions.

The energy dependence of the mean range (projected range) of the ions found in these calculations is displayed in Fig. 8. Despite the many effects which were not considered in the calculation, the following conclusions can be drawn from Fig. 8: (i) the mean range of ions such as F and C is of the order $20\text{--}30\text{ \AA}$ or less for typical ion energies encountered in reactive ion etching; (ii) the mean range of about 150 \AA or less for hydrogen is significantly larger. The depth of the damaged or modified Si layer should roughly correspond to the ion range.²

²In several investigations of H-implanted single-crystal Si, it has been found that the H profile coincided with the damage profile (25a). For electrically active dopant ion implantation, it has often been found that the damage distribution peaks at about 10% closer to the surface than the dopant distribution (25b).

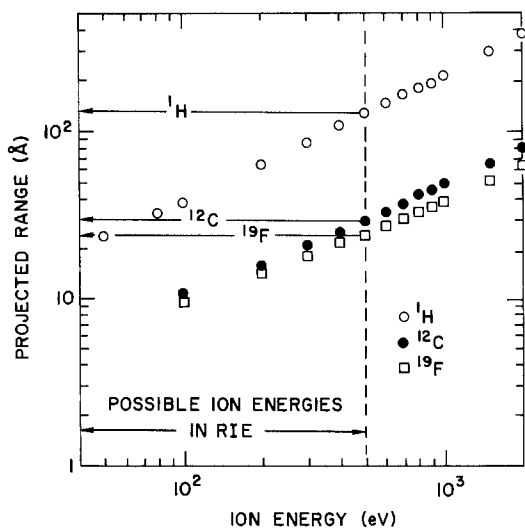


Fig. 8. Projected range of C, F, and H as calculated by a Monte Carlo simulation on an amorphous Si target as a function of the ion energy. Possible ion energies encountered in RIE processing are indicated.

Discussion

Surface contamination.—The surface contamination caused by direct exposure of a Si surface to CF₄/40%H₂ RIE consists mainly of a C,F layer [Ref. (34) describes a similar XPS study of freon-etched Si]. Immediately on top of the Si surface, there is a O-rich transition layer. It is likely that this transition layer is formed upon exposure of the reactive ion-etched sample to room ambient. X-ray photoelectron spectroscopy data (which are not presented here) show that the thickness of the C,F film reaches a maximum after about 3 min overetching and decreases slightly in thickness after overetching times in excess of 3 min. After even longer overetching times (~10 min), it appears that a steady-state situation is reached, where the deposition of new C,F material is equal to the amount removed by the RIE.

We did not verify in our experiments that the Si etch rate of 15-20 Å/min was constant during overetching. However, the quoted etch rate had been determined with the same RIE tool and using the same RIE parameters (10). Silicon etching implies a dynamic 30-50Å thick C,F film on Si, which will change its composition during overetching due to different simultaneous processes: silicon etching and transport of reaction products through the C,F-film; deposition of new C,F-material; physical sputtering of the deposited film; and chemical etching of the C,F-film by F species, which will form C-F bonds, produce volatile fluorocarbon molecules, and desorb. One expects, therefore, that the composition of the C,F film will depend on the overetching duration, which is borne out by Table I.

The C-, F-, and O-related information obtained by the ion scattering experiments is in agreement with the XPS-derived information as regards trends in atomic percentage vs. processing history, C,F layer thickness, etc. The ion scattering results also indicate near-surface damage in the dry-etched Si substrates.

Near-surface disorder.—The increase of the Si surface peak for the no, 1, and 10 min overetched samples indicates that Si atoms close to the surface have been displaced from regular lattice sites as a result of the RIE processing. The width and the area of the surface peak are both a measure of the depth at which the surface damage occurs. The energy resolution in the present experiment of 400 eV for 100 keV ions (31) corresponds to a depth resolution of 6Å and is high enough to enable a determination of the depth of the heavily damaged near-surface layer. In the first two columns of Table II, we list the thickness of the disordered surface region as inferred from the width of the surface peak and the number of Si

Table II. Silicon surface peak width and area (at./cm²), and background intensity (as a percentage of the intensity obtained with random beam incidence) for the He⁺ ion scattering spectra of Fig. 4

Sample	Surface peak		Background (%)	
	Width (Å)	Area (at./cm ²)	Measured	Calculated
HF control	17	4.7 × 10 ¹⁵	0.8	0.0
No overetch	27	8.9 × 10 ¹⁵	2.2	0.1
1 min overetch	34	9.7 × 10 ¹⁵	7.5	0.4
10 min overetch	37	14.4 × 10 ¹⁵	16	0.6

atoms per square centimeter present in this disordered region as determined from the surface peak areas. Both the width of the disordered region and the number of surface atoms displaced from a regular lattice site increase with increasing etching time. Between 1 and 10 min, the width increases less than the number of displaced atoms. This indicates that the surface region gets more heavily disordered, although the depth of the disorder does not change much any more. The thickness of this saturation disorder depth is ~35Å.

This heavily damaged layer is most likely created by the heavier ions in the plasma, which give rise to collision cascades. In particular, polyatomic species such as CF₃⁺ can be critical for damage production since the deposited energy density in the collision cascade has been found to be important in terms of damage creation and retention (29). The extent of the heavily disordered region is roughly in agreement with the maximum projected range of ~25 and ~30Å found for F and C in the Monte Carlo calculations. It is possible that this heavily disordered region contains trapped F and C.

Hydrogen penetration.—One of the surprising results of initial RIE-damage investigations was the "damage depth" of ~500Å (4, 9) caused by the low energy ion bombardment in a glow discharge. The data presented in the previous paragraph showed that there is a heavily disordered region very close to the surface (~35Å). The energy spectra of backscattered He ions, however, do not only show an increase in the surface peak width and area, but also an increase in the background intensity at lower energies and a buildup of a C,F contamination film. The increase in background intensity can be because of two reasons. The first reason is that the ion beam loses its angular definition when it passes through the amorphous film in the surface area before it enters the underlying single crystal. Due to this angular straggling, channeling of the ion beam cannot be as good as for a well-collimated beam, and the background intensity is higher. Alternatively, the region immediately below the heavily disordered surface area may contain a certain concentration of defects, giving rise to an increased background intensity, due either to direct scattering or dechanneling. We have calculated the increase of background intensity caused by dechanneling of the ion beam in the amorphous overlayer, which consists of the heavily disordered Si surface region and the C,F contamination film, if present. These Monte Carlo calculations were performed by following the trajectories of many ions through the amorphous overlayer and the underlying crystal. The background intensity was calculated by evaluation of the nuclear encounter, probability between ion and substrate atoms along the trajectory, and averaging over a large number of trajectories (32). This method only takes dechanneling by nuclear interaction into account. Since the inelastic energy losses are small, we believe this to be a good approximation.

Columns 3 and 4 in Table II show the measured and calculated background intensities as a percentage of the scattering intensity when the beam enters the crystal in a random direction. For the BHF sample, the measured and calculated intensities agree quite well. (A 1% deviation is not surprising, since the calculation assumes the incident beam to be perfectly collimated. In the experiment, the beam has an angular spread of 0.1°-0.15°.) For the RIE-

etched samples, the measured intensities are consistently much higher than the calculated intensities. This can only be explained by the presence of defects. Thus, on the basis of these results and the H profiling experiments, we attribute the increased background (especially observed for the 10 min overetched Si sample) to the presence of H and possibly H-related secondary defects in the Si lattice. The suggested origin of the increased background appears to be in good agreement with a transmission electron microscopy analysis of H₂ plasma-treated Si (3), where centers which compressed the Si lattice and dislocation loops were found in the near-surface region. It is known (18) that dislocations are ineffective in scattering and can be observed primarily by dechanneling effects. Hydrogen-related secondary defects are indicated by the observation of SiH and SiH₂ vibrational modes, since, presumably, the occurrence of SiH bond formation requires that initially broken Si-Si bonds are present, *i.e.*, disorder.

According to the H profiling experiments, even at depths in excess of 250Å there exists a substantial H concentration for the 10 min overetched sample caused by the reactive ion etching. The Monte Carlo calculations found a projected H range of ~150Å for the maximum ion energy possible in our plasma conditions. According to the modeling results, a substantial H concentration can therefore exist at distances in excess of ~200Å from the Si surface for H⁺ ion energies of about 500 eV. We have no experimental data on the actual ion energy distribution at the Si surface for our RIE experiments, and it is possible that due to collision processes the "average" ion energies are much lower than the maximum ion energy and the H range would accordingly be reduced. However, channeling effects can be important, and, additionally, diffusion effects can occur during the ion bombardment. It appears that the diffusion coefficient of H in Si is not well known at room temperature. If diffusivity values determined by tritium diffusion at about 500°C (26) are extrapolated to room temperature, a diffusion distance of ~300Å is obtained. An atomic H diffusivity value determined at about 900°C (27) gives a diffusion distance orders of magnitude larger (~2.0 × 10⁴Å). Recent H diffusion determinations based on compensation of a Au donor level in Si with H by deep level transient spectroscopy (28) gave diffusion values close to the tritium diffusion results. Therefore, the possible H diffusion distances during the plasma processing times used in our experiments should be significant (~300Å). [We ignored here the fact that during reactive ion etching the Si wafer temperature can rise by as much as 30°C (30). The conceivable H diffusion distances could, therefore, be even greater.] We conclude that the observed depth of the H-"modified" layer is not inconsistent with the projected H range and a possible profile redistribution brought about by H diffusion occurring concurrently with the plasma treatment.

Overetch time dependence of damage.—The question arises of how long overetching can proceed before a steady-state damage profile has been reached. Upon exposure of the free Si surface to the CF₄/H₂ plasma, there will be accumulation of damage in the Si substrate. At the same time, reactive ion etching of the Si substrate is occurring which will consume the damaged layer. Initially, the degree of disorder near the Si surface will increase with overetching time. The conditions for obtaining steady state are different for the heavily damaged near-surface layer which has an extent of ~30-50Å and H-modified Si, which has an extent in excess of 250Å.

A simple, approximate³ way to estimate the times to reach steady state in terms of damage production or accumulation of trapped impurities is given here. We assume that the effects of different ions on the Si substrate are in-

dependent and simply add. The erosion of the target and the creation of damage and trapping of ions in the substrate are treated as occurring simultaneously but independently. We assume that the damage profile and the impurity profile coincide (25) and that the impurity profile is given by a gaussian. With $n(x,t')$, the ion concentration at position x introduced in the time interval dt' at time t' is denoted. The surface is located at $x = 0$ initially but moves with a velocity v to the right ($v =$ etch rate). A point in the Si substrate located at a distance x from the original surface will receive an ion density $n(x,t') dt'$ at time t' in the interval dt'

$$n(x,t') dt' = \frac{Q}{\sqrt{2\pi}\Delta R_p} \exp \left[-0.5 \left(\frac{(x - vt' - R_p)^2}{\Delta R_p^2} \right) \right] dt' \quad [2]$$

with Q being the dose rate per square centimeter, R_p the projected range of the impinging ions, and ΔR_p the straggling. The ion (or damage) distributions $n(x,t')$ of all time intervals dt' up to time t will add up to give a resulting ion (or damage) distribution $N(x,t)$

$$N(x,t) = \frac{Q}{\sqrt{2\pi}\Delta R_p} \int_0^t \exp \left[-0.5 \left(\frac{(x - vt' - R_p)^2}{\Delta R_p^2} \right) \right] dt' \quad [3]$$

which gives

$$N(x,t) = \frac{Q}{\sqrt{2\pi}v} \left[\operatorname{erf} \left(\frac{x - R_p}{\sqrt{2}\Delta R_p} \right) - \operatorname{erf} \left(\frac{x - vt - R_p}{\sqrt{2}\Delta R_p} \right) \right] \quad [4]$$

A point x_1 fixed with respect to the actual surface will have coordinates $x_1 + vt$ at time t with respect to the original coordinate system. The ion (or damage) distribution $N(x_1, t)$ is, therefore, given by

$$N(x_1, t) = \frac{Q}{\sqrt{2\pi}v} \left[\operatorname{erf} \left(\frac{x_1 + vt - R_p}{\sqrt{2}\Delta R_p} \right) - \operatorname{erf} \left(\frac{x_1 - R_p}{\sqrt{2}\Delta R_p} \right) \right] \quad [5]$$

For a given location x_1 from the Si surface, $N(x_1, t)$ will have reached its maximum possible value to within 1% after a time t (33)

$$t \geq \frac{2.69\Delta R_p + R_p - x_1}{v} \quad [6]$$

In our experiments, the etch rate of Si was about 15-20 Å/min and the maximum range of C and F are about 30Å. For the sake of simplicity, we assume that the range straggling equals the numerical value of the projected range. The heavily damaged Si (as measured with ion channeling at $x_1 = 0$) will have reached its maximum value after about 5-7 min. Consistent with this time estimate for reaching steady state, the RBS spectra show that the Si surface peak due to displaced Si atoms increases from no overetching to 1 min overetching. However, it is nearly the same for the 1 and 10 min overetched specimens. The intensity (or extent) of the heavily damaged near-surface layer should have reached the maximum possible value possible for the experimental RIE conditions used prior to 10 min overetching.

The overetch time required to measure the maximum H concentration in the H-modified Si is ~18-30 min (taking into account the maximum range and a measurement location x_1 of about 50Å from the surface). Consistent with this much greater time to reach steady state, we measured a large increase in H concentration for the 10 min overetched sample as compared to the 1 min overetched specimen. It is likely that the H concentration obtained after an even longer overetching time, *e.g.*, 20 min, would be greater than the concentration which we measured after 10 min overetching.

Conclusions

Our experimental data allow us to summarize some of the effects which direct exposure of a Si surface to CF₄/40%H₂ RIE has on the Si surface properties as follows (see also Fig. 9): (i) a C,F containing film is deposited

³A full treatment would require knowledge of the energy distribution, mass, and partial flux of the bombarding species, the way in which physical sputtering and chemical reactivity interact and result in a net removal rate of material for each species, the effect of accumulated "damage" and impurities on the various reactive ion sputtering coefficients, etc.

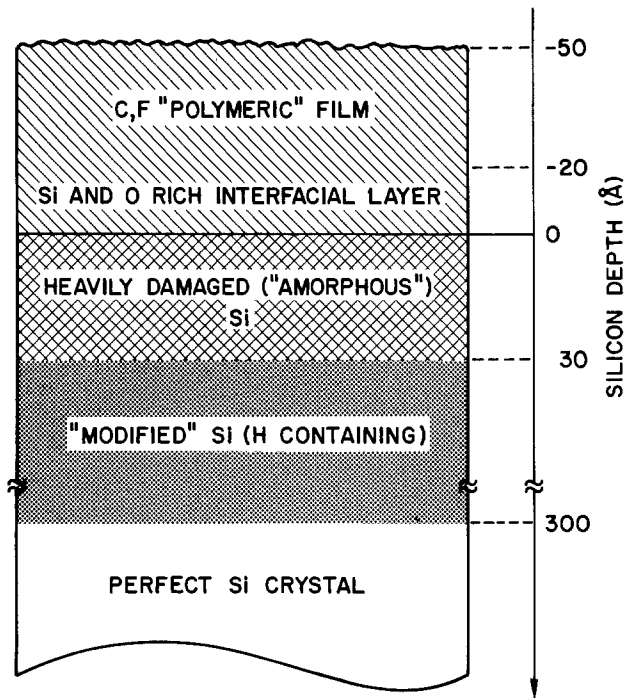


Fig. 9. Schematic diagram of changes of Si near-surface region caused by CF₄/H₂ reactive ion etching.

onto the Si, the thickness of which is limited to less than 50Å; (ii) a layer of ~30-50Å thick heavily damaged Si is formed as a result of the energetic particle bombardment; (iii) hydrogen is implanted to depths in excess of ~200Å. This layer is less damaged than the Si layer immediately adjacent to the surface. In ion channeling studies, these defects give rise to a strongly enhanced background in the energy spectra. At least some of the H bonds to the Si lattice and gives rise to SiH and SiH₂ vibrational modes observable by Raman spectroscopy.

Since, at present, the energy and particle flux distributions impinging upon the Si substrate are unknown, the data were discussed mainly in terms of maximum possible ion energies. The results of Monte Carlo range calculations for F⁺, C⁺, and H⁺ are roughly in agreement with the damage depths or impurity ranges found experimentally.

Acknowledgments

The authors would like to thank Dr. L. E. Gulbrandsen of the Physical Electronics Laboratory for assistance in obtaining some of the XPS data. Professor W. Lanford of SUNY (Albany, New York) is acknowledged for helping us to measure the H depth profiles and stimulating discussions. We are also grateful to Dr. J. F. van der Veen of the FOM Institute for Atomic and Molecular Physics (Amsterdam, The Netherlands), for giving us time and equipment to perform the He ion scattering experiments. We furthermore thank Dr. J. F. Ziegler, Dr. M. R. Polcari, and Dr. R. Kalish for helpful discussions.

Manuscript submitted Nov. 13, 1984; revised manuscript received Feb. 5, 1985. This was Paper 155 presented at the New Orleans, Louisiana, Meeting of the Society, Oct. 7-12, 1984.

IBM Corporation assisted in meeting the publication costs of this article.

REFERENCES

- J. W. Coburn and H. F. Winters, *Ann. Rev. Mater. Sci.*, **13**, 91 (1983).
- J. W. Coburn and H. F. Winters, *J. Vac. Sci. Technol.*, **16**, 391 (1979).
- R. G. Frieser, F. J. Mantillo, B. N. Zingerman, W. K. Chu, and S. R. Mader, *This Journal*, **130**, 2237 (1983).
- S. W. Pang, D. D. Rathman, D. J. Silversmith, R. W. Mountain, and P. D. DeGraff, *J. Appl. Phys.*, **54**, 3272 (1983).
- C. M. Ransom, T. I. Chappell, S. R. Mader, A. Sugarman, and R. W. Young, in "Plasma Processing," G. S. Mathad, G. C. Schwartz, and G. Smolinsky, Editors, p. 93, The Electrochemical Society Softbound Proceedings Series, Pennington, NJ (1983).
- L. M. Ephrath and R. S. Bennett, *This Journal*, **129**, 1822 (1982).
- S. J. Fonash, S. Ashok, and R. Singh, *Thin Solid Films*, **90**, 231 (1982).
- J. S. Chang, in "Plasma Processing," G. S. Mathad, G. C. Schwartz, and G. S. Molinsky, Editors, p. 114, The Electrochemical Society Softbound Proceedings Series, Pennington, NJ (1983).
- N. Yabumoto, M. Oshima, O. Michikami, and S. Yoshii, *Jpn. J. Appl. Phys.*, **20**, 893 (1981).
- L. M. Ephrath and E. J. Petrillo, *This Journal*, **129**, 2282 (1982).
- J. W. Coburn, "Plasma Etching and Reactive Ion Etching," p. 42, American Vacuum Society Monograph Series, New York (1982).
- Several results of this investigation have previously been published in G. S. Oehrlein, R. M. Tromp, Y. H. Lee, and E. J. Petrillo, *Appl. Phys. Lett.*, **45**, 420 (1984).
- W. A. Lanford, H. P. Trautvetter, J. F. Ziegler, and J. Keller, *ibid.*, **28**, 566 (1976).
- See e.g., D. T. Clark, *CRC Crit. Rev. Solid State*, **8**, 1 (1978).
- C. D. Wagner, W. M. Riggs, L. E. Davis, J. F. Moulder, and G. E. Muilenberg, "Handbook of X-Ray Photoelectron Spectroscopy," Perkin-Elmer Corp., Eden Prairie, MN (1978).
- K. Siegbahn, in "Electron Spectroscopy," R. Caudano and J. Verbist, Editors, p. 3, Elsevier, New York (1974).
- W.-K. Chu, J. W. Mayer, and M.-A. Nicolet, "Backscattering Spectrometry," Academic Press, New York (1978).
- L. C. Feldman, J. W. Mayer, and S. T. Picraux, "Materials Analysis By Ion Channeling," Academic Press, New York (1982).
- W. A. Lanford, *Solar Cells*, **2**, 351 (1980).
- See, e.g., J. C. Tsang, Y. Yokota, R. Matz, and G. Rubloff, *Appl. Phys. Lett.*, **44**, 430 (1984), and references therein.
- J. E. Smith, Jr., M. H. Brodsky, B. L. Crowder, M. I. Nathan, and A. Pinczuk, *Phys. Rev. Lett.*, **26**, 642 (1971).
- M. H. Brodsky, M. Cardona, and J. J. Cuomo, *Phys. Rev. B*, **16**, 3556 (1977).
- J. C. Tsang, G. S. Oehrlein, I. Haller, and J. S. Custer, *Appl. Phys. Lett.*, **46**, 589 (1985).
- J. F. Ziegler, J. P. Biersack, and U. Littmark, "The Stopping and Range of Ions in Solids," Vol. 1, Pergamon Press, New York (1984).
- (a) See, e.g., W. K. Chu, R. H. Kastl, R. F. Lever, S. Mader, and B. J. Masters, *Phys. Rev. B*, **16**, 3851 (1977); see, e.g., J. E. Westmoreland, J. W. Mayer, F. H. Eisen, and B. Welch, *Radia. Eff.*, **6**, 161 (1970).
- T. Ichimya and A. Furuchi, *Int. J. Appl. Rad. Isotop.*, **19**, 738 (1968).
- A. Van Wieringen and N. Warmoltz, *Physica*, **22**, 849 (1956).
- W. L. Hansen, S. J. Pearton, and E. E. Haller, *Appl. Phys. Lett.*, **44**, 606 (1984).
- J. A. Davies, G. Foti, L. M. Howe, J. B. Mitchell, and K. B. Winterbon, *Phys. Rev. Lett.*, **34**, 1441 (1975).
- See, e.g., Y. H. Lee and M.-M. Chen, in "Plasma Processing," G. Smolinsky, G. C. Schwartz, and G. S. Mathad, Editors, pp. 78, 88, The Electrochemical Society Softbound Proceeding Series, Pennington, NJ (1985).
- See, e.g., F. W. Saris, *Nucl. Instrum. Meth.*, **194**, 625 (1982); and R. M. Tromp, *J. Vac. Sci. Technol. A*, **1**, 1047 (1983).
- J. H. Barrett, *Phys. Rev.*, **B**, **3**, 1527 (1971).
- See, e.g., J. Crank, "The Mathematics of Diffusion," 2nd ed., Clarendon Press, Oxford (1975), and the table of the error function given there.
- M. Oshima, *Surf. Sci.*, **86**, 858 (1979).

An Empirical Oxidation Rate Law for Thin Oxides

S. Aptekar and M. Fernandes

Department of Metallurgical Engineering and Material Science, University of Notre Dame, Notre Dame, Indiana 46556

D. L. Kwong*

Department of Electrical Engineering, University of Notre Dame, Notre Dame, Indiana 46556

ABSTRACT

An oxidation rate law for thin oxides, as suggested by Hu (2, 3), has been found to correlate very well with experimental data. The growth law, although not based on any interface reaction mechanism, has been formulated to be consistent with the observed power-law pressure dependence of the linear rate constant through the use of a dummy parameter, p . The higher oxidation rate observed at thin oxides has been taken into account by an exponentially decaying term. The analysis assumes that p varies linearly over the thickness of the oxide. Values of the other parameters in the rate law have been taken from available data.

In the process of miniaturization of metal-oxide-semiconductor field-effect transistors (MOSFET's), the gate oxide is being reduced to below 300Å. In case of oxidation under wet oxygen conditions, and for large oxide thickness grown in dry oxygen, the Deal-Grove expression (1) predicts oxide growth accurately. However, oxide growth for thin oxides in dry oxygen conditions has an anomalously high oxidation rate, the mechanism of which is yet not fully understood.

With increasing need to obtain thin oxides, it has become necessary to predict oxide thickness for oxidation in dry oxygen. In this work, therefore, an attempt has been made to correlate an oxidation rate law, suggested by Hu (2, 3), with known experimental values (4). The new law takes into account the power-law dependence of the interface reaction rate. It is therefore not based on any interface reaction mechanism, and is independent of whatever mechanism might give rise to that pressure dependence. In our analysis, we have only assumed an oxide thickness of 700Å over which a dummy parameter $p = p_i/p_o$ (ratio between the oxygen pressure at the Si-SiO₂ interface and that in the ambient) varies linearly over the thickness of the oxide. Values of other parameters in the rate law have been taken from available data. Excellent correlation with experimental values at two different temperatures has been obtained up to 300Å, above which the Deal-Grove expression should be used.

Theory

The classical Deal-Grove relationship, widely used to describe the growth kinetics of oxidation of silicon, is given by

$$X^2/B + X/(B/A) = t + \tau \quad [1]$$

where X is the oxide thickness, t is the oxidation time, B and B/A are the parabolic and linear rate constants, respectively, and τ is a correction parameter for the presence of any initial oxide X_i . The Deal-Grove model suggests that molecular oxygen goes through the gas boundary layer, diffuses through the oxide, and reacts with the silicon substrate. The expression is based on the assumption of three fluxes in steady state: the flux of oxidant from the gas ambient to the gas-SiO₂ interface; the diffusive flux of oxidant through the SiO₂ film; and the flux representing the oxidation reaction at the Si-SiO₂ interface.

By equating the three fluxes and by integrating from time zero to time t , and from an initial thickness X_0 to a final thickness X , one can obtain

$$X = \frac{A}{2} \left[\left(1 + \frac{t + \tau}{A^2/4B} \right)^{1/2} - 1 \right] \quad [2]$$

Equation [2] reduces to

*Electrochemical Society Active Member.

$$X \cong \frac{B}{A} (t + \tau) \cong \frac{KC^*}{N_i} (t + \tau) \text{ for } (t + \tau) \ll \frac{A^2}{4B} \quad [3]$$

where N_i is the number of oxidant molecules to form a unit volume of oxide and C^* is the maximum oxidant concentration for a given pressure. The other limit is

$$X \cong (Bt)^{1/2} \cong \left(\frac{2DC^*t}{N_i} \right)^{1/2} \text{ for } t \gg \frac{A^2}{4B} \quad [4]$$

Hence, for short oxidation times (and therefore for thin oxides), the oxide thickness is linearly proportional to the surface reaction rate constant. For long oxidation times (and hence for thick oxides), oxide thickness is determined by the diffusion constant D . It also follows that B/A , the linear rate constant, is a more important factor for thin oxides than the parabolic rate constant, B .

The oxidation rate can be obtained from Eq. [1]

$$\frac{dX}{dt} = \frac{(B/A)B}{2(B/A)X + B} = \frac{B}{2X + A} \quad [5]$$

The oxidation rate obtained from the Deal-Grove expression is dependent on both the linear rate constant (B/A) and the parabolic rate constant (B). However, by Eq. [3] and [4] it is clear that for very thin oxides the linear rate constant is a more important factor. The growth-rate law suggested by Hu (2, 3) is for very thin oxides and therefore does not depend on the parabolic rate constant B .

To account for the high oxidation rate for thin oxides in dry oxygen, various models have been suggested which differ significantly from each other. Adams *et al.* (5) believe that the best fit for their data is parabolic. Irene (6), Haas and Gray (7), and van der Meulen (8) suggest that thin oxide grows linearly with time. Kamigaki and Itoh (9) show that a different law is obeyed when the oxidation ambient pressure is varied.

Hu's model (2, 3) proposes a general law which encompasses the Deal-Grove linear parabolic growth law and Blanc's law (10) as two special cases. The law assumes that the intermediate step in the oxidation reaction is the chemisorption of oxygen molecules. The chemisorbed molecular oxygen may directly oxidize the silicon or it may dissociate into atomic oxygen, which then rapidly oxidizes the silicon. Hu suggests that the Freundlich isotherm fits data very well and uses this isotherm to derive the general equations for oxide thickness (X) and time (t) (2)

$$X = 1/2 a (p^{-m} - p^{1-m}); 1 > p > 0$$

$$t = 1/4 b (2m - 1)(2m - 1)p^{-2m}$$

$$+ 2(1 - m)p^{1-2m} - 1]; m \neq 1/2$$

$$t = (1/4 b)(p^{-1} - 1 - \log p); m = 1/2 \quad [6]$$

where a and b are related to B/A and B as follows

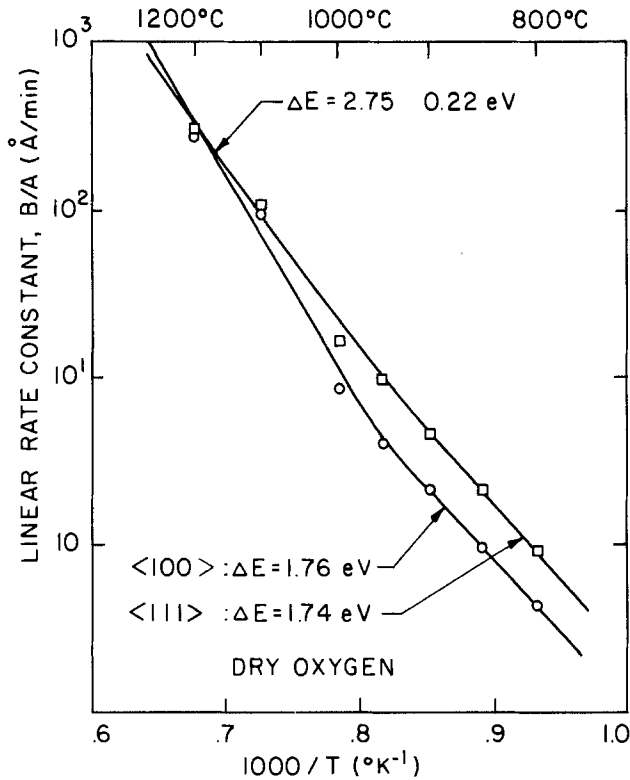


Fig. 1. Temperature dependence of the linear rate constant, B/A , for $\langle 100 \rangle$ and $\langle 111 \rangle$ oriented silicon. See Ref. (11).

$$a = (B/A)/B$$

$$b = (B/A)^2/B$$

m lies between 0.6 and 0.8; p defined as $p = p_i/p_0$ can be regarded as a dummy parameter running from $p = 1$ ($X = 0$) to $p = 0$ ($X \rightarrow \infty$). When $m = 1$, the above set of equations reduces to linear parabolic law, and, when $m = 1/2$, the set reduces to Blanc's growth law (10).

Massoud *et al.* (11) suggest that their data can be fitted by

$$\frac{dX}{dt} = \frac{B}{2X + A} + C_1 e^{-X/L_1} + C_2 e^{-X/L_2} \quad [7]$$

where the characteristic length L_1 slowly increases with temperature and C_1 has a break-in activation energy at $\approx 900^\circ\text{C}$ (11). The first added exponential term represents the fast growth observed at the onset of oxidation and up to about 50\AA (11). By neglecting the first exponential term, one arrives at errors of less than 5% in fitting the experimental data (11). The oxidation rate could therefore be rewritten as

$$\frac{dX}{dt} = \frac{B}{2X + A} + C_2 e^{-X/L_2} \quad [8]$$

The decay length L_2 is approximately independent of temperature and is equal to $\approx 70\text{\AA}$ (12). C_2 is a singly activated function of temperature with an activation energy of 2.35 eV for $\langle 111 \rangle$ and $\langle 100 \rangle$ orientations (12). The physical origin of these parameters is now known, but Ho *et al.* (12) claim that implementation of Eq. [8] in SUPREM III has produced good simulation capabilities for the thin oxide region.

The linear rate constant B/A has been found to have a $p^{0.6} - p^{0.8}$ pressure dependence (4, 8). B/A was also observed to have a $p^{0.7} - p^{0.8}$ pressure dependence in a high pressure oxidation study by Lie *et al.* (13). Massoud's data (11) show that oxidation rate in the thin oxide regime has a high pressure dependence of $\approx p^{0.8}$, which is in agreement with other data.

To take into account this pressure dependence, Hu (2, 3) suggests a different equation for oxidation rate which takes into account this pressure dependence. The

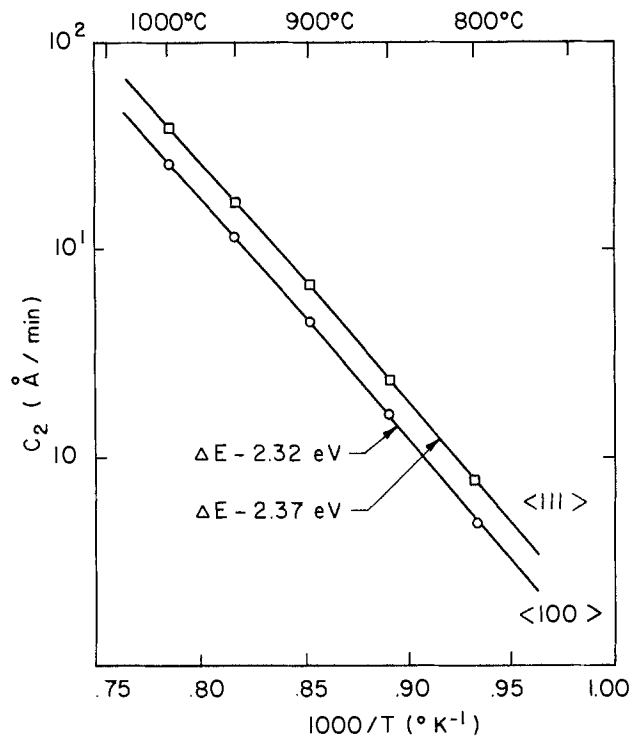


Fig. 2. Temperature dependence of the pre-exponential constant C_2 for the oxidation of $\langle 100 \rangle$ - and $\langle 111 \rangle$ -oriented silicon in dry oxygen. See Ref. (11).

equation is given by

$$\frac{dX}{dt} = \frac{B}{A} p^m + C_2 e^{-X/L_2} \quad [9]$$

where the exponentially decaying term is similar to that in Eq. [8]. Although the equation takes into account the pressure dependence, the physical reason of the non-linear pressure dependence is unknown at this time. It probably reflects the relative contributions of atomic and molecular O_2 reactions at the interface as suggested by van der Meulen and Ghez (8, 14). It should therefore be emphasized again that the new growth law is not based on any interface reaction mechanism.

Results

In our analysis, we have used Eq. [9] to satisfactorily predict the oxidation rate for thin oxides. The calculated oxidation rates have been compared with the data of Hopper *et al.* (4). Hopper *et al.* (4) obtained oxidation rates for $\langle 111 \rangle$ -oriented silicon oxidized at 760 torr oxygen at temperatures of 870° and 930°C . The linear rate constant, B/A , has been determined by Deal and Grove (1), besides oth-

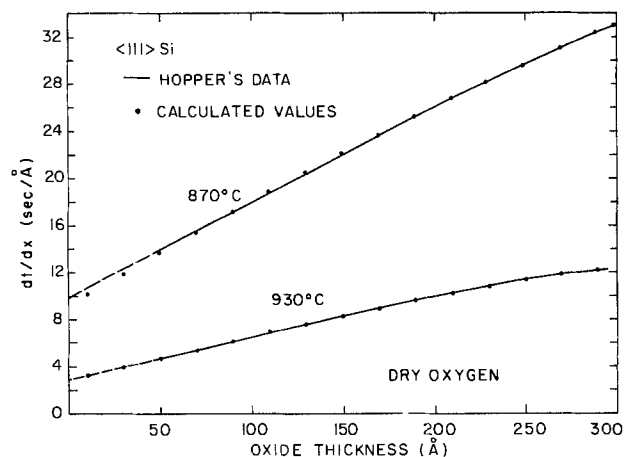


Fig. 3. Fitting of the new growth law (dots) with the data of Hopper *et al.* (4).

Table I. Effects of changing values of m and L_2 on the calculated values of dt/dX (s/Å) at 930°C

	Oxide thickness (Å)	$m = 0.8$ $L_2 = 67\text{Å}$ dt/dX (s/Å)	$m = 0.7$ $L_2 = 67\text{Å}$ dt/dX (s/Å)	$m = 0.6$ $L_2 = 67\text{Å}$ dt/dX (s/Å)	$m = 0.8$ $L_2 = 70\text{Å}$ dt/dX (s/Å)
$T = 930^\circ\text{C}$	10	3.5	3.5	3.5	3.5
	200	10	10	10	10
	300	13	12	12	13
$T = 870^\circ\text{C}$	10	10	10	10	10
	200	26	25	25	26
	300	33	32	31	33

ers, but we have used the values for B/A , C_2 , L_2 , and m as determined by Massoud *et al.* (11).

B/A and C_2 are known to be dependent on temperature. The variations of these parameters as a function of temperature are shown in Fig. 1 and 2 (11). From Fig. 1, the values of B/A at 870° and 930°C are 2.76 and 7.17 Å/min, respectively. The value of C_2 at 870° and 930°C is 3.72 and 11.87 Å/min (see Fig. 2). L_2 has been determined to be independent of temperature (11, 12). We have chosen a value of 67Å which is near to the value of 70Å suggested by Ho *et al.* (12). m lies between 0.6 and 0.8 (4, 8, 11, 13), but in our analysis a value of 0.8 has been used (11).

Although only particular values of m and L_2 have been used, using different reported values of m and L_2 have a small effect on the results. As can be seen in Table I, taking $m = 0.6$ or 0.7 instead of 0.8, and L_2 as 70Å instead of 67Å, changes the results by a small percentage.

Hence, the only parameter which is not available from literature is p . In our analysis, we have assumed that p varies linearly from $p = 1$ ($X = 0$) to $p = 0$ ($X = X$) over an oxide thickness X . Taking $X = 700\text{Å}$, a perfect fit of calculated values with Hopper's data has been obtained at both 870° and 930°C. Taking X to be between 600 and 800Å gives an error of dt/dX (s/Å) of less than 5% up to an oxide thickness of 200Å. The experimental and calculated values of the inverse of oxidation rate *vs.* oxide thickness are shown in Fig. 3.

Calculated values show that a good correlation exists at both temperatures up to an oxide thickness of about

300Å. Beyond 300Å, the calculated and experimental values deviate from each other. Oxide growth can therefore be broken up into two regimes. Up to 300Å, the new oxidation law can be used. For thicknesses greater than 300Å, the Deal-Grove equation (Eq. [1]) is suitable.

Conclusions

An oxidation rate law, which incorporates the pressure dependence of oxidation rate, has been shown to correlate very well with experimental data up to an oxide thickness of 300Å. Values of the various terms in the equation are available from literature. The only assumption made by the authors is that the parameter p varies linearly between 0 and 1 over an oxide thickness of 700Å.

Manuscript submitted Oct. 29, 1984; revised manuscript received Feb. 9, 1985.

The University of Notre Dame assisted in meeting the publication costs of this article.

REFERENCES

1. B. E. Deal and A. S. Grove, *J. Appl. Phys.*, **36**, 3770 (1965).
2. S. M. Hu, *Appl. Phys. Lett.*, **42**, 872 (1983).
3. S. M. Hu, *J. Appl. Phys.*, **55**, 4095 (1984).
4. M. A. Hopper, R. A. Clark, and L. Young, *This Journal*, **122**, 1216 (1975).
5. A. C. Adams, T. E. Smith, and C. C. Chang, *ibid.*, **127**, 1787 (1980).
6. E. A. Irene, *ibid.*, **125**, 1708 (1978).
7. G. A. Haas and H. F. Gray, *J. Appl. Phys.*, **46**, 3885 (1975).
8. Y. J. van der Meulen, *This Journal*, **119**, 530 (1972).
9. Y. Kamigaki and Y. Itoh, *J. Appl. Phys.*, **48**, 2891 (1977).
10. J. Blanc, *Appl. Phys. Lett.*, **33**, 424 (1978).
11. H. Z. Massoud, C. P. Ho, and J. D. Plummer, in "Stanford University Technical Report TRDXG501-82," J. D. Plummer, Editor, ARPA Order no. 3709, July 1982.
12. C. P. Ho, J. D. Plummer, S. E. Hansen, and R. W. Dutton, *IEEE Trans. Electron Devices*, **ed-30**, 1438 (1983).
13. L. N. Lie, R. R. Razouk, and B. E. Deal, *This Journal*, **129**, 2828 (1982).
14. R. Ghez and Y. J. van der Meulen, *ibid.*, **119**, 530 (1972).

Effect of Cu on the Kinetics and Microstructure of Al_3Ti Formation

M. Wittmer,* and F. Le Goues

IBM, T. J. Watson Research Center, Yorktown Heights, New York 10598

H.-C. W. Huang

IBM, General Technology Division, Hopewell Junction, New York 12533

ABSTRACT

Impurities and structural defects have a strong influence on the kinetics of thin film reactions. We have investigated the effect of Cu on the kinetics of formation and microstructure of Al_3Ti in the temperature range of 375°-450°C. We found that the presence of 1 weight percent Cu in the Al changes both the activation energy and the pre-exponential factor of the growth law. At the same time, the Cu influences the microstructure of the growing Al_3Ti phase and smoothens the reaction interface. The results are discussed in terms of possible diffusion mechanisms in Al_3Ti .

There is a continuing interest in the interdiffusion and interaction phenomena of thin metal films for two reasons. First, such phenomena occurring in thin film diffusion couples may be very different from those observed in bulk diffusion couples. In contrast to bulk specimens, thin films contain a lot more interfaces and surfaces. In addition, the film thickness is usually limited to a few thousand angstroms. These structural differences are of

*Electrochemical Society Active Member.

ten responsible for the particular behavior of thin film diffusion couples (1, 2). Second, many areas of thin film technology require a detailed understanding of interdiffusion and interaction in thin metal films. Particularly, microelectronics makes use of multilayer metal films for electrical contacts and interconnects. Aluminum alloys are widely used for metallization of integrated circuits, and, consequently, studies of the reaction of aluminum with transition metals are of great interest.

Interdiffusion and intermetallic compound formation in binary aluminum-transition metal thin film systems have been reviewed by Baglin and Poate (3). In the case of the Al-Ti thin film reaction, it was found that the intermetallic compound Al_3Ti is formed with an activation energy of 1.85 ± 0.05 eV (4). Recently, it has been reported that copper, which is often added to Al for improved electromigration resistance, retards the growth of Al_3Ti and increases the activation energy (5, 6). We have studied the influence of Cu in the Al-Ti thin film reaction in detail by comparing the changes in the kinetics with the concomitant changes in the microstructure of the films.

Experimental

Oxidized silicon wafers were used as a substrate throughout the course of this study. Bilayers of Ti and Al were prepared by sequential deposition of a 1500Å thick Ti layer, followed by a 6300Å thick Al-Cu layer with a Cu content varying from 0 to 4.5 weight percent (w/o) (all percentages are given in weight percent). The layers were evaporated with an electron gun in a diffusion-pumped vacuum system. The base pressure of the system was about 7×10^{-5} Pa. Care was taken to prevent oxygen contamination of the Ti film by first evaporating a thin layer of Ti onto the walls of the vacuum system while the substrates were protected with a shutter. The oxygen content in the Ti film was measured with Auger depth profiling technique and found to be less than 0.1 atom percent (a/o). The Al-Cu films were evaporated from an alloy source of proper composition. Subsequently, the wafers were cleaved and small samples of the thin-film couples were annealed in forming gas ($\text{N}_2:\text{H}_2 = 9:1$) in the temperature range of 375°-450°C for various times.

The kinetics of the Al-Ti reaction were investigated with Rutherford backscattering spectrometry (RBS) and electrical resistivity measurement. A commercially available four-point probe was used for the resistivity measurements. Compound formation was examined with glancing angle x-ray diffraction on selected samples. The microstructure of the films was studied with a Philips scanning transmission electron microscope (STEM) on flat-on as well as cross sections of the bilayer thin films.

Results

Kinetics of phase formation by RBS.—The interaction of Al and Ti was analyzed with RBS at an energy of 2 MeV. The superposition of two RBS spectra from an Al(1%Cu)/Ti sample are shown in Fig. 1. The solid line presents the analysis of the as-deposited sample and the dotted line shows the results of the same sample after a heat-treatment at 400°C for 16h. The vertical arrows in Fig. 1 indicate the energy of $^4\text{He}^+$ particles scattered from the surface position of the corresponding element.

We have chosen to deposit first Ti, the heavier metal, and then the Al alloy, which is the lighter metal. The reason was to protect Ti from oxidation during heat-treatments. As a result, the signals of the Al and Ti overlap in the RBS spectrum because the Ti signal, which would otherwise be at higher energies, is now shifted to lower energies due to the energy loss of the $^4\text{He}^+$ particles in the overlying Al-alloy film. The leading edges of the Al and Ti signal coincide in the spectrum of the as-deposited sample. Shown in Fig. 1 is also the Cu signal which is magnified by a factor of 10. Finally, the RBS signals from the SiO_2/Si substrate make up the low energy part of the spectra in Fig. 1.

The heat-treatment at 400°C caused a partial intermixing of Al and Ti. This can be seen in Fig. 1 from the steps occurring simultaneously at the trailing edge of the Al signal and the leading edge of the Ti signal. The relative composition of the intermixed layer can be calculated from the heights of the Al and Ti signals in that layer, as is shown in Fig. 1. The atom ratio is found to be Al:Ti = 3:1, indicating the formation of the compound Al_3Ti . Positive phase identification was made by glancing-angle x-ray diffraction using a Seeman-Bohlin camera. Figure 2 presents the diffraction pattern obtained

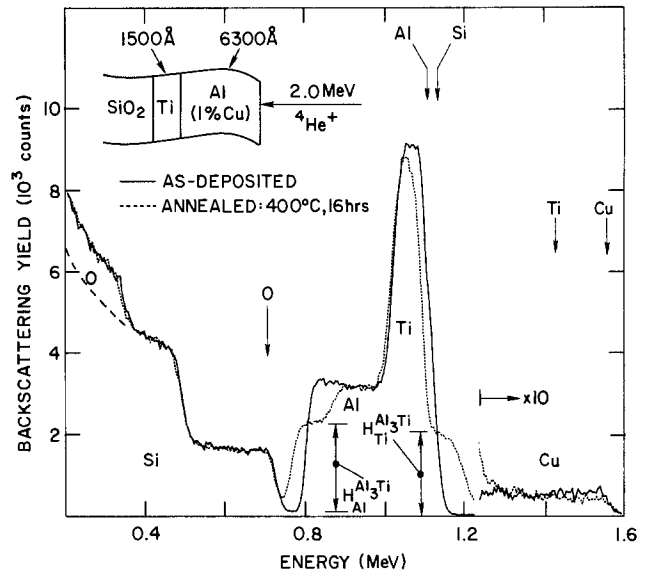


Fig. 1. 2.0 MeV $^4\text{He}^+$ RBS spectra of Al(1%Cu)/Ti samples following deposition of the layers and subsequent heat-treatment at 450°C for 16h. The vertical arrows mark the surface position of the corresponding elements. The heights of the Al and Ti signal near the Al interface indicate a composition of Al:Ti = 3:1 in the intermixed layer.

with Cu $K\alpha$ radiation of an Al(4.5% Cu)Ti sample which has been annealed at 450°C for 6h. The diffraction lines confirm unambiguously the formation of the compound Al_3Ti . This result agrees well with those published in the literature (4-6) and demonstrates that 4.5% Cu dissolved in the Al does not affect the nucleation and growth of the Al_3Ti phase.

The copper distribution observed with RBS in the as-deposited sample is very uniform, as can be seen from Fig. 1. Even after the heat-treatment, the Cu backscattering yield in the Al_3Ti layer is unchanged. A slight reduction of the yield of the Cu signal is observed near the surface at an energy of 1.5 MeV. This is due to the fact that the spectra of Fig. 1 were taken from two different samples which had a slight variation of the Cu content in the surface region of the Al film. In conclusion, we find that the heat-treatment does not disturb the copper distribution in the bilayer thin film. It should be noted that the RBS results present an average over an analysis area of 1 mm². It will be shown that TEM analysis finds many Al_2Cu precipitates. But, from RBS, we know that these precipitates are uniformly distributed in the alloy film.

The thickness of the Al_3Ti layer can be calculated from the width in energy of either the Al or the Ti step in Fig. 1. By assuming bulk density for the compound Al_3Ti and

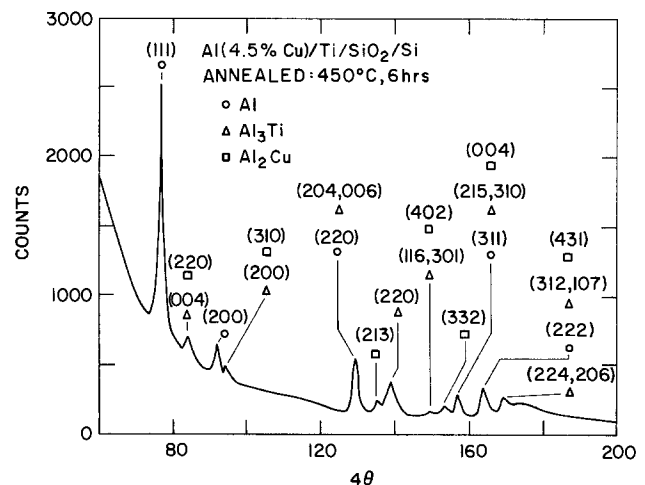


Fig. 2. Glancing angle x-ray diffraction pattern obtained with a Seeman-Bohlin camera and Cu $K\alpha$ radiation of a Al(4.5%Cu)/Ti sample after annealing at 450°C for 9h.

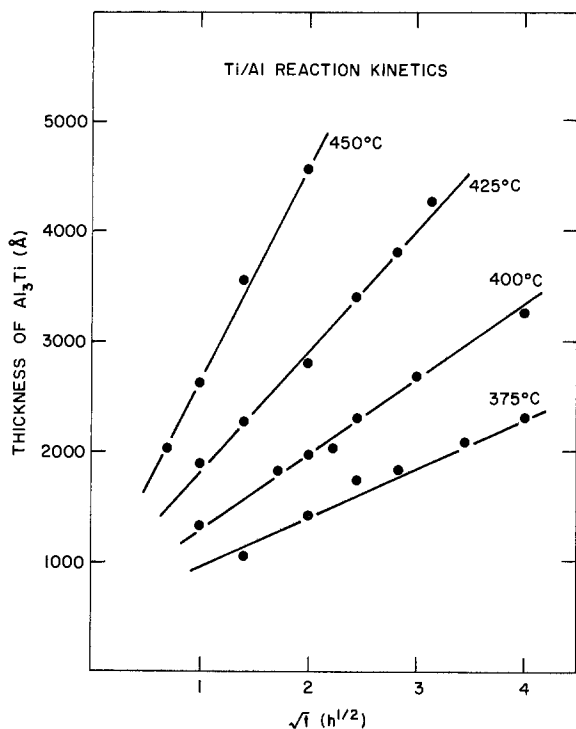


Fig. 3. Growth kinetics of the compound Al_3Ti for pure Al films at four different temperatures.

by using the surface approximation in evaluating the stopping cross sections, we find a thickness of 1950Å. In the same fashion, we analyzed a large number of samples annealed for various times in the temperature range of 375-450°C to obtain the growth kinetics of Al_3Ti . The results are presented in Fig. 3, 4, and 5 for three cases, Al without Cu, with 1% Cu, and with 4.5% Cu, respectively.

A common characteristic of the plots in Fig. 3-5 is that the data points can be fitted to straight lines. It is evident from Fig. 3 that the straight lines do not intercept the origin of the plot. A finite thickness of Al_3Ti exists for zero annealing time. The reason for this peculiarity is twofold. First, the annealing time has been measured as the time

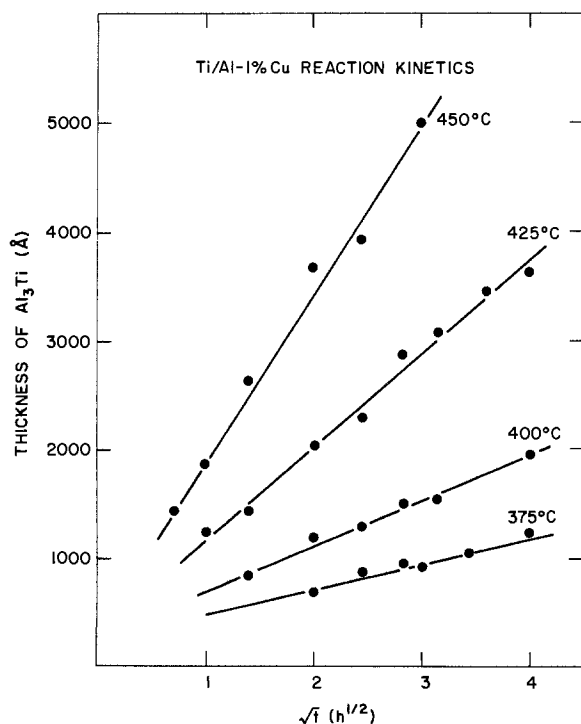


Fig. 4. Growth kinetics of the compound Al_3Ti for Al-1% Cu films at four different temperatures.

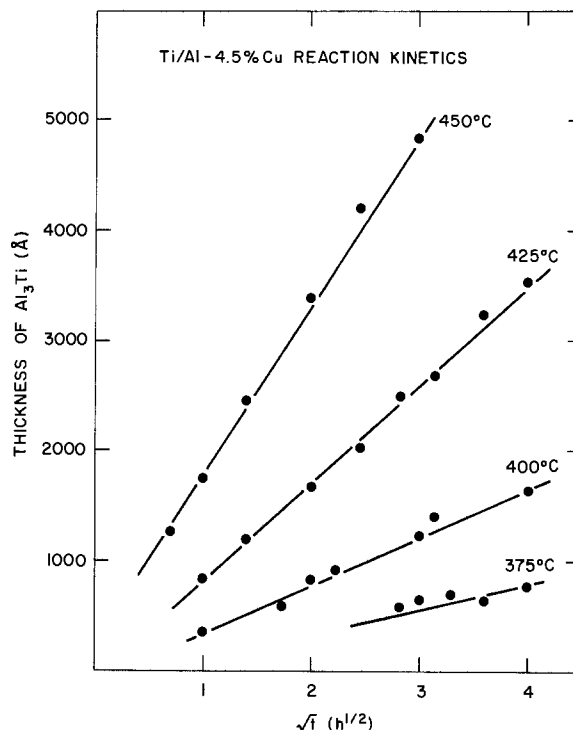


Fig. 5. Growth kinetics of the compound Al_3Ti for Al-4.5% Cu films at four different temperatures.

which the samples spent in the center of the annealing furnace. The time for the manual loading and unloading of the samples has not been taken into account. Thus, the measured annealing time is slightly shorter than the actual annealing time. Second, it will be shown in the Microstructural analysis section that the $\text{Al}_3\text{Ti}/\text{Al}$ interface is rough, which leads to a certain ambiguity in the determination of the actual interface location and, thus, to an uncertainty in the measurement of the Al_3Ti thickness by RBS. The samples with 1% and 4.5% Cu solute have a smooth $\text{Al}_3\text{Ti}/\text{Al}$ interface. Consequently, the straight lines in Fig. 4 and 5 intercept the axes close to the origin of the plot.

Since the abscissa in Fig. 3-5 is calibrated in square root of time, the growth of Al_3Ti obeys a parabolic law. This behavior is independent of Cu solute and characterizes a diffusion-limited reaction process. Thus it is possible to determine the chemical interdiffusion constant from the slopes of the straight lines in Fig. 3-5.

The logarithm of the interdiffusion constant D is plotted as a function of reciprocal temperature $1/T$ (Arrhenius plot) in Fig. 6. Straight lines can be fitted again to the data points. It appears from Fig. 6 that the growth kinetics of Al_3Ti with 1% and 4.5% Cu solute are the same, but differ from those without Cu. Thus the growth of Al_3Ti is thermally activated in all cases, but with different activation energies E_a and preexponential factors D_0 . The parameters E_a and D_0 were obtained from a fit of $D(T) = D_0 \exp(-E_a/kT)$ to the straight lines in Fig. 6 and are listed in Table I. The addition of 1% Cu to the Al increases the activation energy from 1.6 to 2.05 eV and the pre-exponential factor by three orders of magnitude.

Table I. Effect of Cu on the kinetics of Al_3Ti growth as determined from Rutherford backscattering (RBS) and resistivity (Res.) measurements

Cu concentration (%)	E_a (eV)		D_0 (cm ² /s) RBS
	RBS	Res.	
0	1.60 ± 0.10	1.50 ± 0.10	3.4 × 10 ⁻³
1	2.05 ± 0.10	2.00 ± 0.10	2.9
4.5	2.05 ± 0.10	2.00 ± 0.10	2.9

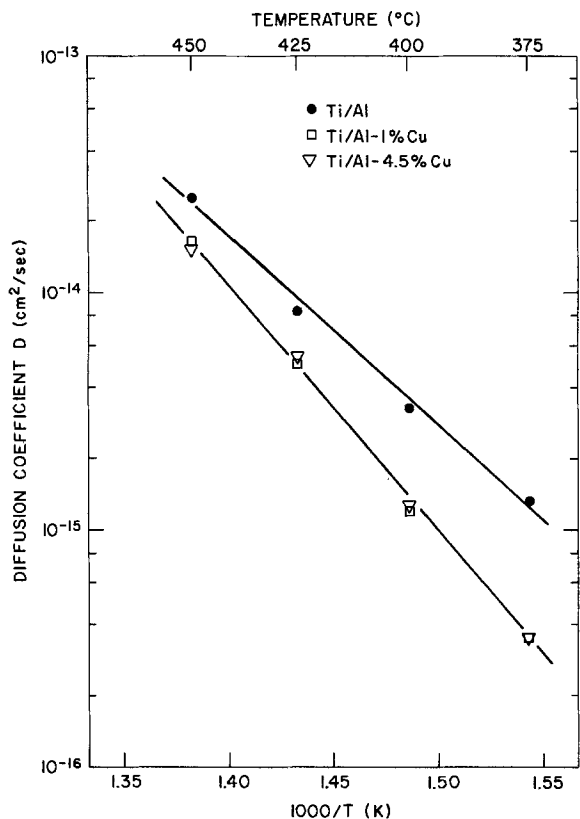


Fig. 6. Arrhenius plots of the chemical interdiffusion coefficients calculated from the data of Fig. 4-6. The addition of Cu to the Al alters both the activation energy and the pre-exponential factor.

Electrical resistivity measurement.—Provided that the Ti has a limited solubility in Al and that the Al film has a low resistivity, then any change in resistivity can be ascribed to the formation of an Al-intermetallic compound layer if the reaction interface is planar. We will show in the next section that this assumption holds in Ti/Al thin film couples. Thus, a time-dependent parameter, β , can be defined which measures the increase in resistivity as a result of the progressing interaction between Al-Cu and Ti, according to

$$\beta \equiv \frac{1}{\rho_0} - \frac{1}{\rho}(t) = \frac{\rho(t) - \rho_0}{\rho_0 \rho(t)}$$

ρ_0 being the electrical resistivity of the as-deposited thin film assembly and $\rho(t)$ the resistivity after annealing the assembly for time t at a given temperature.

It has been shown that the resistivity of a Al(Cu)/Ti bilayer film first decreases rapidly after very short annealing at an elevated temperature, due in large extent to the precipitation of Al_2Cu particles, and then increases monotonically due to the formation of an Al-intermetallic compound (6). Thus, a minimum in resistivity is observed for short anneals of a bilayer film where a certain amount of Cu has been added to the Al. We have chosen this minimum in resistivity to represent the value of ρ_0 .

The parameter β calculated from the measured resistivities of samples with various Cu contents is plotted in Fig. 7 as a function of the square root of the annealing time at 400°C. As shown in Fig. 7, β varies linearly with $t^{1/2}$, except for short annealing times where departure from the parabolic behavior cannot be explained at present. The effect of Cu on the reaction rate is also clearly illustrated in Fig. 7. These results are consistent with those obtained by RBS.

The correlation between the resistivity increments due to compound formation and the compound layer thicknesses measured by RBS is shown in Fig. 8. The results were obtained from samples with pure Al and Al with 1% and 4.5% Cu which were annealed at 400°C for various

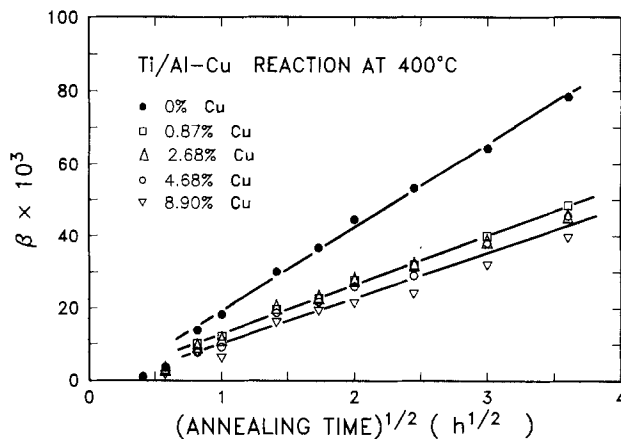


Fig. 7. β vs. annealing time at 400°C for Al(Cu)/Ti bilayer films with various Cu contents.

times. It can be seen in Fig. 8 that the resistivity increments vary linearly with the compound layer thicknesses measured by RBS. The better linear correlation for the Al (1%Cu) and Al (4.5%Cu) samples suggests that the compound layer formed in the presence of Cu has a more planar interface, because the resistivity analysis assumes a planar layer growth. This point has been confirmed by cross-sectional TEM observation as discussed in the next section.

The slopes of the curves in Fig. 7 determine the reaction rate constants, which, if obtained at several annealing temperatures, can be used to calculate the corresponding activation energies. The results are listed in Table I. It is not surprising that, due to the linear correlation, the activation energies determined from the resistivity data are in good agreement with those obtained with RBS.

Microstructural analysis.—It is well known that solutes influence the microstructure of thin metal films. An indication of the effect of Cu on the microstructure of the Al_3Ti compound can be obtained from a careful RBS analysis. In Fig. 9, we present 2.3 MeV RBS spectra of two samples, one with 1% Cu and the other without Cu solute in the Al, following a heat-treatment at 425°C for 2h. The retardation of the Al_3Ti formation can immediately be seen by the difference in widths of the steps at the trailing edges of the Al signals and leading edges of the Ti signals. Besides a difference in widths, there is also a difference in slopes of the signals at these steps. The sample with 1% Cu dissolved in the Al exhibits steeper slopes at these steps than the sample without Cu solute. This points to a smoother and/or laterally more homogeneous interface between the Al_3Ti compound and the Al layer. Since RBS cannot distinguish between the two possibilities, a TEM analysis is needed.

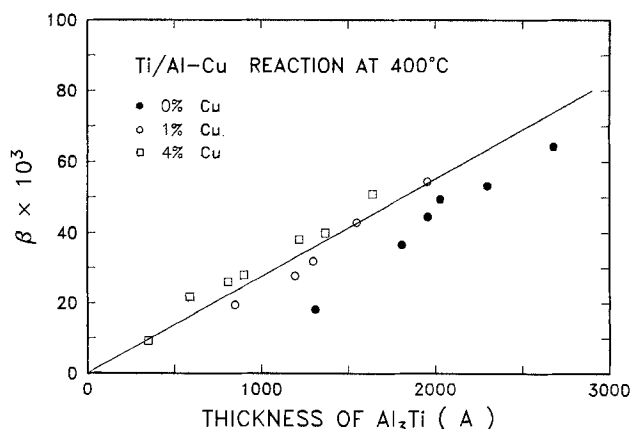


Fig. 8. Correlation between resistivity measurements and thickness of the Al_3Ti compound determined by RBS.

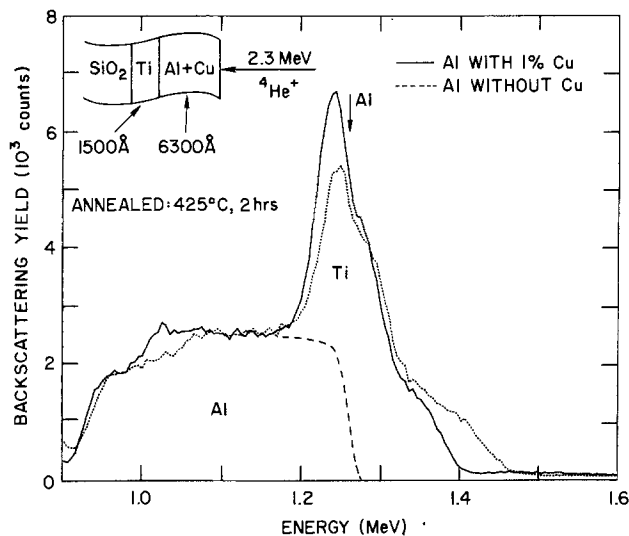


Fig. 9. 2.3 MeV $^4\text{He}^+$ RBS spectra of two samples with Al layers containing 1% Cu and no Cu following simultaneous heat-treatment at 425°C for 2h. The contribution of the Al signal to the overall spectra is indicated by the dashed line.

Figures 10 and 11 show micrographs of cross sections of samples which have been annealed at 450°C for 30 min and 4h, respectively. The micrographs of Fig. 10 were obtained from samples with a pure Al layer, and those of Fig. 11 from samples with a Al-1% Cu layer. The labeling distinguishes the different layers in Fig. 10 and 11. The thickness of the Al_3Ti is much larger for the samples without Cu. Also, without Cu, there is a marked penetration along the Al grain boundaries, where the Al_3Ti compound formation is more advanced. In contrast, the growth of Al_3Ti in the presence of 1% Cu solute in Al is independent of the Al grain boundaries. As a result, the $\text{Al}_3\text{Ti}/\text{Al}$ interface is rough in the samples without Cu, while the samples with Cu exhibit a smooth interface. Finally, it should be noted that the grain size of the Al is larger when Cu is added than without Cu.

Discussion and Conclusion

The above results show that Cu has a significant effect on the formation kinetics and microstructure of Al_3Ti . The presence of 1% Cu in the Al increases the activation energy for the growth of Al_3Ti to 2.05 ± 0.10 eV. This value is in good agreement with that found by Huang and Wittmer (6) and Tardy and Tu (7) but is lower than the value of 2.4 eV published by Krafcsik *et al.* (5). Higher Cu concentrations do not increase the activation energy fur-

ther. Without Cu we found an activation energy of 1.60 ± 0.10 eV, which also agrees well with those published by Huang and Wittmer (6) and Tardy and Tu (7), but is again lower than both the value of 1.8 eV reported by Krafcsik *et al.* (5) and the early value given by Bower (4). A possible explanation for the difference in activation energies found by the different groups could be that in the preceding work Ti was contaminated by some impurities, notably oxygen. Titanium is well known for its oxygen gettering capability, and in many cases Ti thin films contain a small but measurable amount of oxygen.

The growth of Al_3Ti necessitates a continuous supply of Al and Ti atoms to the reaction interface. Each atom species can be supplied by diffusion through the growing Al_3Ti layer. The parabolic growth of the Al_3Ti , which has been observed in all studies on Al-Ti thin film reactions, indicates that the rate-limiting step is the interdiffusion through the growing Al_3Ti layer and not the interfacial reaction at the metal-compound interface. Tardy and Tu (7) have carried out marker experiments to determine which atom species, Al or Ti, is the predominant diffusing species. They found that the diffusivity of Al is about ten times faster than that of Ti in the temperature range of 350°-450°C, irrespective of the presence of a small amount of Cu in the Al. Thus, it appears that the growth kinetics of Al_3Ti are governed mainly by the diffusivity of Al through the growing Al_3Ti layer.

In determining the role of Cu on the microstructure of Al_3Ti , we recall that Cu is known to precipitate as θ -phase particle (Al_2Cu) on surfaces and interfaces of the Al film (8, 9). Without Cu solute in the Al, the Al grain boundaries are preferential nucleation sites for the formation of Al_3Ti , because grain boundary diffusion is faster than bulk diffusion. The presence of Cu in the Al layer causes the formation of θ particles and, probably, Cu segregates at the grain boundaries. Both prevent a significant diffusion of Ti along the Al grain boundaries. Consequently, the growth of Al_3Ti occurs more uniformly at the Al-Ti interface, which results in improved smoothness of the interface.

Other factors influence the smoothness of the Al-Ti interface. In the absence of Cu, the Ti diffusing along the Al grain boundaries impedes the growth of the Al grains. However, in the presence of Cu, not only is the grain boundary diffusion of Ti inhibited, but also the Cu promotes the grain growth of the Al (10). The difference in Al grain size is evident from a comparison of Fig. 10 and 11. With larger Al grains, the Al-Ti interface becomes smoother, independent of the nucleation process of the Al_3Ti .

It is consistently found that the Cu slows the growth of Al_3Ti . With Al being the dominant diffusing species, Krafcsik *et al.* (5) proposed that segregation of Cu on the

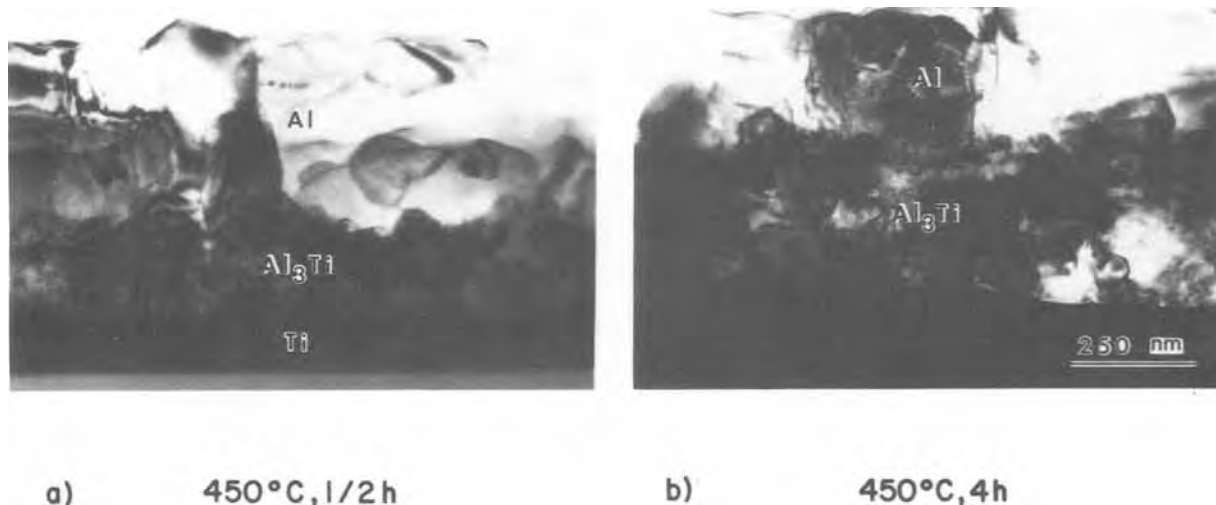


Fig. 10. Cross-sectional TEM micrographs of Al/Ti samples following a heat-treatment at 450°C for (a) 30 min and (b) 4h

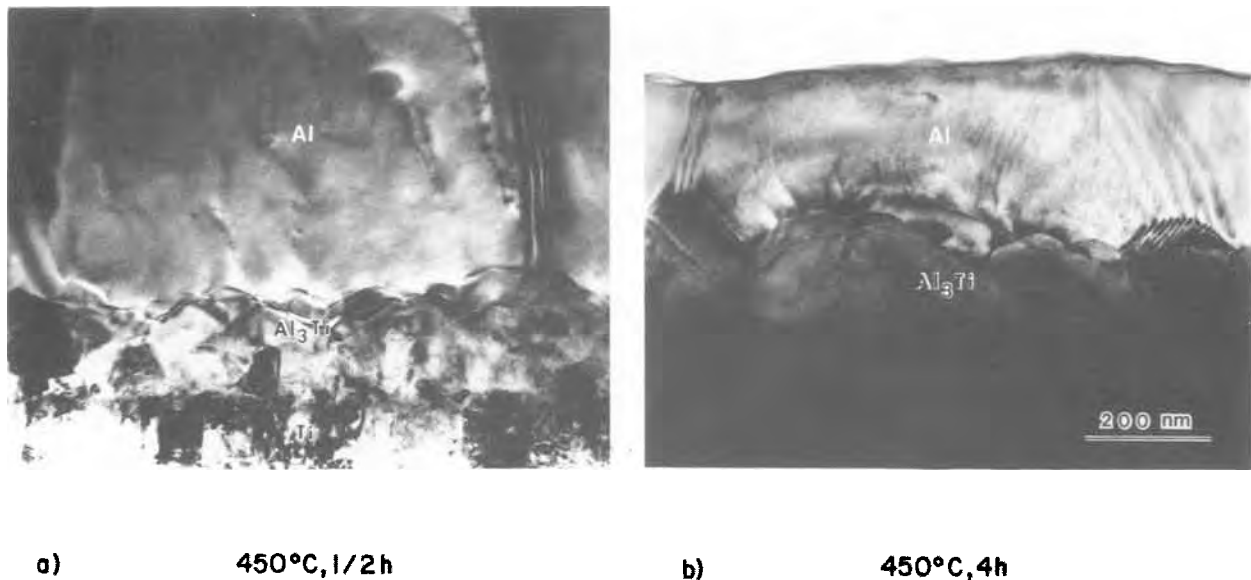


Fig. 11. Cross-sectional TEM micrographs of Al(1%Cu)/Ti samples following a heat-treatment at 450°C for (a) 30 min and (b) 4 h

Al_3Ti grain boundaries retards the diffusion of Al along these fast diffusing paths and shifts the transport of Al atoms more to bulk diffusion. Unfortunately, this segregation model cannot be corroborated with solid solution data of Cu in Al_3Ti because the latter are not known. From our investigation, however, we find an increase in the diameter of the Al_3Ti grains by a factor of 3 to 4 in the presence of Cu, which means that the areas of the fast diffusing paths are reduced by a factor of about 10. This could account for the reduced growth rate of Al_3Ti in the presence of Cu, if grain boundary diffusion is the principle transport mechanism of the Al atoms.

The effect of Cu on the Al-Ti reaction kinetics can also be due to the formation of phases which are different from Al_3Ti . At low Cu concentrations, a (Al_3Ti , Cu) solid solution is likely to be formed. With higher Cu concentrations, however, one may expect from the Al-Cu-Ti ternary phase diagram (11) the formation of $\text{Al}_{23}\text{Ti}_9$ or $\text{Al}_{11}\text{Ti}_5$, whose phase fields extend to ternary alloys of $\text{Al}_{70}\text{Cu}_5\text{Ti}_{25}$ composition. It is also possible that the ternary compound Al_4CuTi_2 forms and is stable in contact with Al(Cu) and Ti. Unfortunately, the crystal structure of $\text{Al}_{23}\text{Ti}_9$, which is the only one known, is so close to that of Al_3Ti that it is difficult to determine unambiguously which one is formed in our Al(Cu)-Ti reaction couples. Therefore, more work is needed to clarify the Al-Cu-Ti ternary system near the Al_3Ti intermetallic compound. In conclusion, the role of Cu in the Al-Ti reaction kinetics is a difficult one and may not be explained by a simple segregation model.

Acknowledgments

The authors are grateful to P. Saunders, S. Colombo, and R. Broadie for technical assistance during the per-

formance of this work and to U. Köster for fruitful comments.

Manuscript submitted Dec. 10, 1984; revised manuscript received Feb. 22, 1985.

IBM Corporation assisted in meeting the publication costs of this article.

REFERENCES

1. D. Gupta, D. R. Campbell, and P. S. Ho, in "Thin Films—Interdiffusion and Reactions," J. M. Poate, K. N. Tu, and J. W. Mayer, Editors, Chap. 7, The Electrochemical Society Series, Wiley-Interscience, New York (1978).
2. U. Gösele and K. N. Tu, *J. Appl. Phys.*, **53**, 3252 (1982).
3. J. E. E. Baglin and J. M. Poate, in "Thin Films—Interdiffusion and Reactions," J. M. Poate, K. N. Tu, and J. W. Mayer, Editors, Chap. 9, The Electrochemical Society Series, Wiley-Interscience, New York (1978).
4. R. W. Bower, *Appl. Phys. Lett.*, **23**, 99 (1973).
5. I. Krafcsik, J. Gyulai, C. J. Palmström, and J. W. Mayer, *ibid.*, **43**, 1015 (1983).
6. H.-C. W. Huang and M. Wittmer, in "Proceedings on the Symposium on Thin Films and Interfaces," J. E. E. Baglin, D. R. Campbell, and W. K. Chu, Editors, pp. 157-162. Elsevier, New York (1984).
7. J. Tardy and K. N. Tu, *Phys. Rev.*, To be published.
8. M. C. Shine and S. R. Herd, *Appl. Phys. Lett.*, **20**, 217 (1972).
9. S. Mader and S. Herd, *Thin Solid Films*, **10**, 377 (1972).
10. A. Gangulee and F. M. D'Heurle, *ibid.*, **12**, 399 (1972).
11. A. Raman and K. Schubert, *Z. Metallkde.*, **56**, 99 (1965).

Silicide-Silicon Interface Degradation during Titanium Silicide/Polysilicon Oxidation

M. Tanielian, R. Lajos, and S. Blackstone

Gould Research Center, Rolling Meadows, Illinois 60008

D. Pramanik*

Gould/American Microsystems Incorporated, Santa Clara, California 95051

ABSTRACT

We have investigated the silicide-silicon interface during the oxidation of titanium silicide on polysilicon. We find that during oxidation the polysilicon layer under the silicide is consumed inhomogeneously and that at the same time the titanium silicide moves into the polysilicon layer. Oxidations were carried out both in wet and dry O_2 with similar results. This nonuniform consumption of the polysilicon layer appears to be related to the condition of the silicide-silicon interface prior to the oxidation step. This effect can result in the reduction of the dielectric breakdown strength of underlying gate oxide in titanium silicide/polysilicon/oxide/Si structures.

The application of refractory metal silicides to interconnects in VLSI has been the subject of many investigations in the last few years (1-6) because of their low resistivity and ability to withstand high temperature processing. Of the four refractory metal silicides, WSi_2 , $TaSi_2$, $MoSi_2$, and $TiSi_2$, that are commonly considered, $TiSi_2$ has the lowest resistivity (15-25 $\mu\Omega\text{-cm}$), and from this point it appears very attractive. However, one of the desired features of any interconnect material which is to be used in place of polysilicon is the ability to grow a passivating layer of oxide over it. Silicides by themselves do not have this feature. Moreover, it is desirable to maintain the work function of the gate at the value for doped polysilicon in order to retrofit existing processes that utilize polysilicon gates. For this reason, the use of a silicide layer on top of a doped polysilicon layer (polycide) has gained wide acceptance. It has been shown that, during oxidation, silicon from the underlying polysilicon layer diffuses through the silicide layer and provides the silicon necessary to grow the silicon dioxide layer (2). It has been found for $MoSi_2^3$ and WSi_2^3 films and $TaSi_2^4$ that the thickness of the polysilicon layer (pad poly) underneath the silicide has to be kept larger than a certain minimum thickness in order to maintain the gate integrity after oxidation of the polycide structures. The requirement of a minimum pad poly thickness may be related to the degradation of the silicide-silicon interface after oxidation. It has been shown in the case of WSi_2 polycides that the presence of a native oxide on the polysilicon can lead to silicon being consumed from only a few points in the polysilicon, thus causing voids to be formed at the silicide-silicon interface (5). These voids, besides affecting the MOS properties, can also cause loss of adhesion between the silicide and polysilicon. In this paper, we report on the effects of oxidation of $TiSi_2$ polycide structures on the gate oxide integrity. We show that this is closely related to the structural changes that occur at the silicide-polysilicon interface during oxidation. The effect of the cleanliness of the initial interface is investigated with the aim of preventing the degradation of the silicide-polysilicon interface and maintaining gate oxide integrity. The consequences of these results on the use of $TiSi_2$ polycides for process applications will be discussed.

Experimental Details

The starting wafers for the MOS capacitor studies were n-type (100) having a resistivity of 3-5 $\Omega\text{-cm}$. Standard 500Å gate oxides were grown and annealed. Polysilicon films with thicknesses ranging from 500 to 2500Å in steps of 500Å were deposited on these oxides by low pressure chemical vapor deposition (LPCVD) and were doped N^+ using $POCl_3$ at 1000°C for 15 min. The sheet resistance of a 2500Å thick polysilicon layer was 28 Ω/\square after the

*Electrochemical Society Active Member.

doping. Two wafers with a 2500Å polysilicon layer were kept as controls; the rest of the wafers were coated with a 2000Å layer of titanium silicide, which was sputtered from a cold-pressed $TiSi_{2.2}$ composite target (Varian, CPVS grade) in a CVC Model 601 sputtering system. In addition, two wafers with only the gate oxide also received the 2000Å layer of titanium silicide. The sheet resistance of the silicide film after deposition was 20 Ω/\square and decreased to 1.2 Ω/\square after an anneal at 950°C in ultrahigh purity (UHP) argon for 30 min corresponding to a resistivity of 24 $\mu\Omega\text{-cm}$. One group of wafers was subsequently oxidized in dry O_2 for 60 min at 950°C. The oxide grown on top of the silicide was removed using a dry plasma etch. In order to simulate realistic devices, both groups of wafers, oxidized and unoxidized, were coated with 1 μm of Al/1% Si and patterned using wet etching into 10 mil diam dots to form capacitors. The back of each wafer was coated with aluminum to ensure good ohmic contact. A voltage ramp of 1 V/s was applied to 100 capacitors on each wafer, and the voltage necessary to reach 1 μA was recorded.

In order to study the oxidation process in more detail, a second set of wafers was also prepared. In this set, the gate oxide was replaced by a 4000Å thermal oxide layer. A 2500Å layer of LPCVD polysilicon was deposited and doped, followed by a 2000Å layer of titanium silicide. Silicide films of the same thicknesses were also deposited on bare Si wafers. This set of wafers was oxidized either in dry O_2 at 950°C or in O_2 bubbled through water at 96°C. This was done to study the growth rate and oxide quality in each case. Prior to turning on the O_2 , the wafers were annealed in dry N_2 for periods of time ranging from 10-60 min.

Auger depth profiles of the annealed samples revealed no detectable oxygen in the films, and the stoichiometry estimated from Auger and x-ray dispersive spectroscopy was that of $TiSi_{2.1}$. X-ray diffraction confirmed that the main phase existing in the films after the anneal was the disilicide.

The oxide thickness on top of the silicide was estimated using values obtained by the sputtering rate in our Auger system, where the oxide sputtering rate was known. The wafers were also examined by SEM. The interface between the silicide and polysilicon film was studied by etching the oxide and silicide film in buffered HF, which does not etch polysilicon or single-crystal silicon substrates.

Results and Discussion

The measured breakdown field strength of the inert ambient-annealed polycide capacitors is plotted in Fig. 1 as a function of the pad polysilicon thickness t_p . The polysilicon thickness was measured prior to doping. The inert ambient annealing was done at 950°C for 30 min in

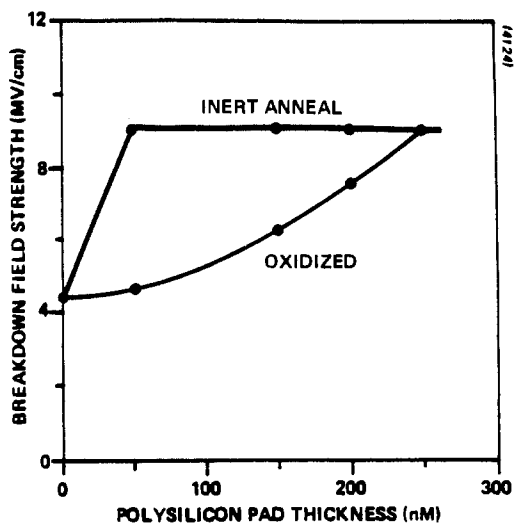


Fig. 1. Breakdown field strength for polycide capacitors as a function of pad poly thickness, when the silicide layer was inert ambient annealed in Ar (not oxidized) and oxidized at 950°C in wet oxygen for 30 min.

UHP Ar. For t_p ranging from 500 to 2500Å, the gate oxide field strength remains at approximately 9 MV/cm, which is the breakdown field strength measured for the control polysilicon capacitors on gate oxide. However, when the silicide is in direct contact with the gate oxide, the field strength drops to about 5 MV/cm. This shows that even for an inert ambient anneal, a TiSi_2 layer cannot be placed directly on the gate oxide without compromising the gate oxide integrity.

This reduction in gate oxide field strength may be the result of an interaction between the titanium silicide film and the SiO_2 layer during which the SiO_2 layer is partially consumed (6). This thinning of the gate oxide may be the cause of the observed lowering of the breakdown voltage.

The polycide films that had been annealed in Ar or N_2 at 950°C for various lengths of time ranging from 10 to 60 min had the top layer of silicide stripped away with BOE to investigate this phenomenon with respect to the silicide-polysilicon interface integrity. The interfaces were examined by SEM and were found to be smooth with no indication of any reaction between the polysilicon and titanium silicide.

In contrast, when the polycide was subjected to either dry or wet oxidation, the gate oxide field strength decreased to approximately 5 MV/cm even with an initial 2500Å thick layer of pad polysilicon underneath (Fig. 1). This indicated that the process of oxidation appeared to cause deterioration of the gate oxide integrity even in a polycide structure. This phenomenon has been observed in other polycide structures using Ta, W, and Mo silicide (3, 4). To further investigate this deterioration of the gate oxide during oxidation of the polycide structure, the silicide-polysilicon and silicide-single-crystal silicon interfaces were examined in detail under various oxidation conditions.

Since wet oxidation of gate structures is common in IC processing, the polycide structures on 4000Å field oxide layers were subjected to wet oxidation at 950°C for various intervals of time. The Auger profiles of the polycide structures which were subjected to wet oxidations for 10, 30, and 60 min at 950°C are shown in Fig. 2. The depth of the profiles extends to the lower portions of the polysilicon layer. As expected, the thickness of the silicon dioxide grown on top of the polycide increases with time and was estimated to be 600, 1500, and 2200Å for 10, 30, and 60 min, respectively, based on Auger sputtering rates. These oxide thicknesses on top of the silicide are consistent with the literature (7, 8). Visually, the films became progressively cloudier as the oxidation time progressed, indicating increasing surface roughness. The Auger profiles show that in all three cases the interface

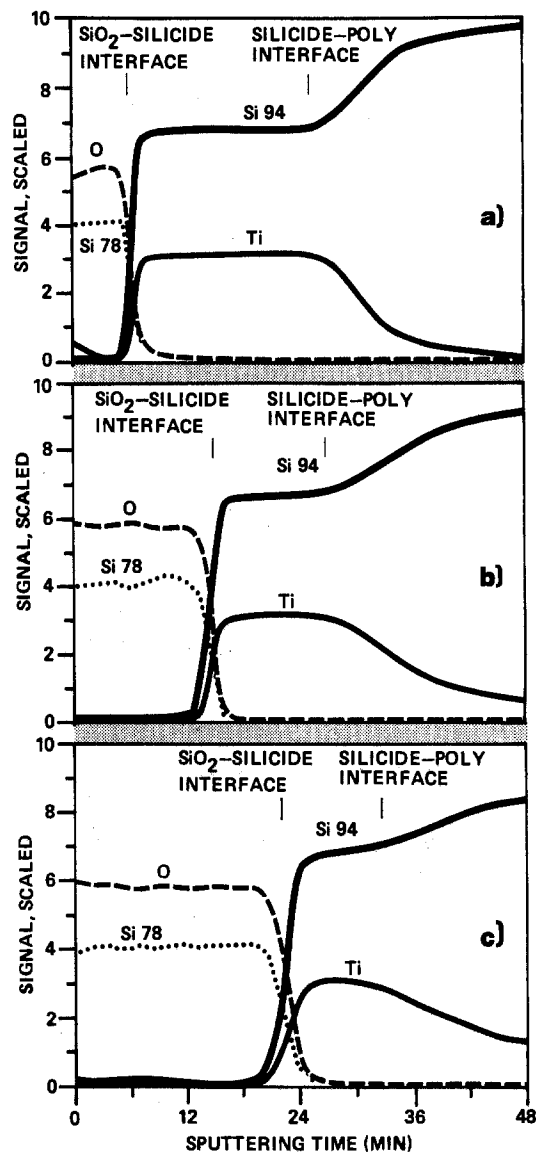


Fig. 2. Auger depth profiles of polycide structures oxidized at 950°C in wet O_2 for 10 min (a), 30 min (b), and 60 min (c).

between the oxide and the silicide is very sharp, that is, the thickness of the oxide layer is uniform over the scanned area, even though the surface morphology is not smooth. In contrast, the interface between the silicide and polysilicon is less sharply defined, with the Ti signal tailing into the polysilicon. This interface broadens with increasing oxidation time such that in the 60 min oxidation case, the silicide and polysilicon are intermixed.

The silicide-polysilicon interface was examined by stripping the oxide and silicide over half the sample using buffered HF. SEM pictures of the samples are shown in Fig. 3. The top half of each micrograph shows the oxide surface, while the lower half shows the exposed surface of the polysilicon. The polysilicon layer, in all cases, is pitted, and the size of the pits increases with increasing oxidation time. The Auger results suggest that these pits were filled with silicide before the HF etch, and confirmation of this is provided by cross-sectional SEM pictures of the 30 min wet oxidized sample shown in Fig. 4. Prior to delineation in BOE, no voids are seen between the silicide and the polysilicon (Fig. 4a). After silicide delineation by dipping the sample in BOE for 10s, the result is shown in Fig. 4b. It is clear that the silicide filled the pits seen earlier in Fig. 3. Note that the oxide layer is very uniform in thickness and that the oxide-silicide interface is abrupt. In contrast, the silicide layer is no longer uniform but is very thick in some places and thin in others. The silicide spiking into the polysilicon reduces the effective pad polysilicon thickness and, therefore, allows the

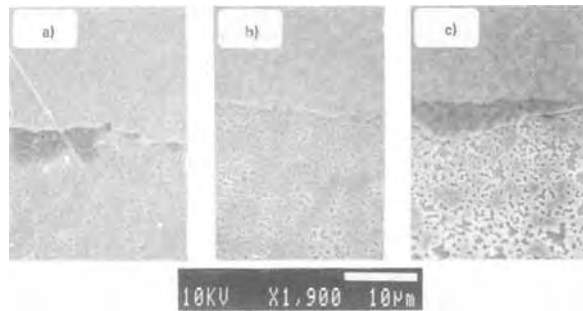


Fig. 3. SEM micrographs of polycide samples that were oxidized at 950°C in wet O₂. The upper half of each picture shows the surface of the oxide film, the lower half the exposed surface of the polysilicon after a BOE etch. a: 10 min oxidation. b: 30 min oxidation. c: 60 min oxidation.

reduction of gate oxide integrity. This is evident in the Auger profiles, where the range over which the silicon and titanium signals are flat (indicating uniform silicide) decreases with increasing oxidation time. On the basis of Auger and SEM results, it is possible to show the progression of the various layers with increasing oxidation, as shown in Fig. 5. This mechanism has also been cited in Ref. (4) as the cause of the gate oxide breakdown field strength reduction in TaSi₂/polysilicon structures.

In order to study the effect of the rate of oxidation, the polycide structure was also oxidized in dry O₂ at 950°C for 30 min to grow about 200Å of oxide. On stripping the oxide and silicide, pits similar in size to the wet oxidation which produced the same oxide thickness were once again observed in the polysilicon layer. Thus the rate of oxidation does not appear to be the critical factor in causing the deterioration of the silicide-polysilicon interface. The 950°C, 30 min dry O₂ oxidation was used as a test for all subsequent attempts to improve the oxidation characteristics of the polycide structures.

The effect of different anneal times in nitrogen prior to oxidation was investigated. The function of the anneal is

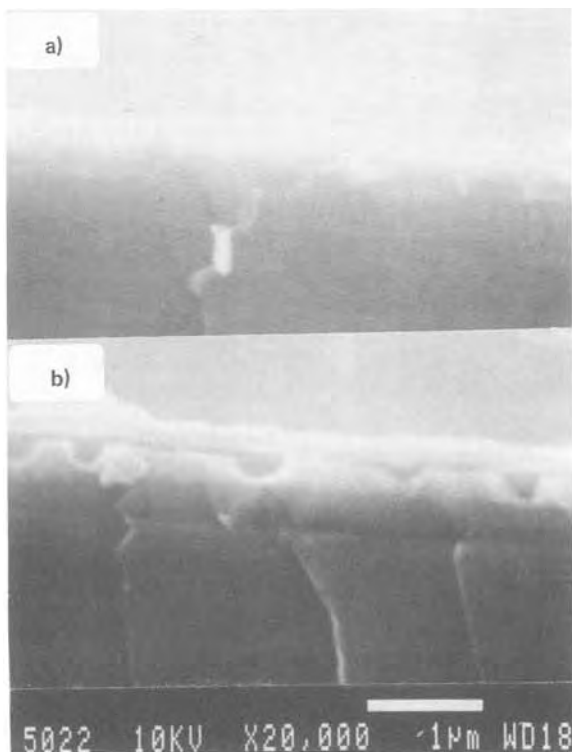


Fig. 4. SEM cross sections of the titanium silicide/polysilicon structure after 30 min oxidation in wet O₂. a: Before delineation of silicide layer. b: After delineation of the silicide layer by dipping the wafer in buffered HF for 10s.

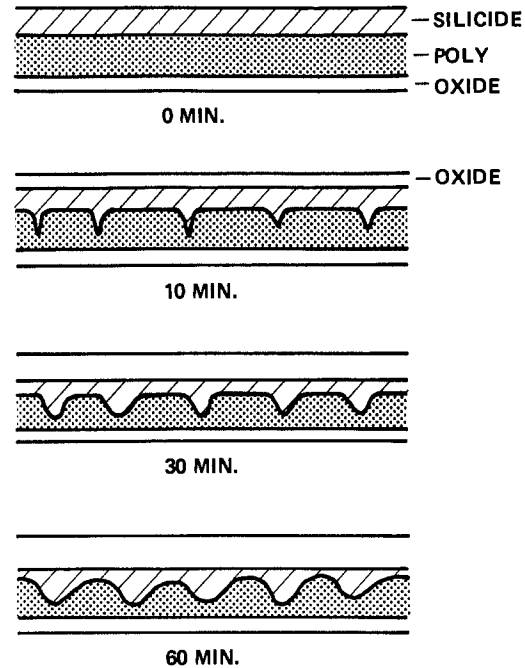


Fig. 5. Schematic representation of the change in the silicide-polysilicon interface with increasing oxidation time.

to crystallize the silicide, to allow it to reach its equilibrium stoichiometry, and to let the silicon distribute uniformly throughout the film so that free Si is readily available at the time of oxidation. The time of the anneal prior to a 30 min dry oxidation at 950°C was varied from 10 to 60 min. Increasing the time of preanneal appeared to decrease the extent of pitting seen in the polysilicon layer but did not remove it entirely.

All the results indicated that the thermal cycle during the oxidation process was not the critical factor causing the silicide penetration into the silicon. In the case of WSi₂⁵, the interfacial oxide between the silicide and polysilicon was shown to be responsible for the formation of voids at the silicide-polysilicon interface during oxidation. The effect of an interfacial oxide that could cause localized consumption of silicon was investigated by trying different cleaning techniques prior to the titanium silicide deposition. The initial technique of cleaning the wafers in HF just prior to silicide deposition was not successful. *In situ* sputter etching of the polysilicon prior to silicide deposition was also attempted but appeared to aggravate the problem, possibly due to redeposition of impurities onto the polysilicon surface. In a third cleaning method, the wafers were given a slight etch in CF₄ + O₂ in a barrel plasma reactor to remove some of the native oxide and about 100Å of polysilicon immediately prior to silicide deposition. The silicon was again consumed nonuniformly, but the pits appeared to be shallower than in the case of an HF dip and rinse prior to deposition. Whenever the pits are shallow, their areal density is higher than when they are deep, which is to be expected because the same amount of Si is consumed in both cases. Finally, high dose ion implantation of heavy ions was considered as a means of dispersing interfacial oxides (9, 10). It has been shown in the case of the direct reaction of Ti films with silicon that the implantation of Si or P ions through the films not only facilitates the diffusion of Si into the Ti, but also leads to the more uniform consumption of silicon (11). Since the oxidation of silicides requires the transport of Si across the silicide-polysilicon interface, ion implantation should prevent localized penetration of the titanium silicide. The thickness of the silicide film was reduced to 1000Å because of the limitations imposed by the highest energy limit of 200 keV in the ion implanter. The film was implanted with 170 keV phosphorus ions to a dose of 1×10^{16} ion/cm². At this energy, the phosphorus penetrates into the polysilicon and the

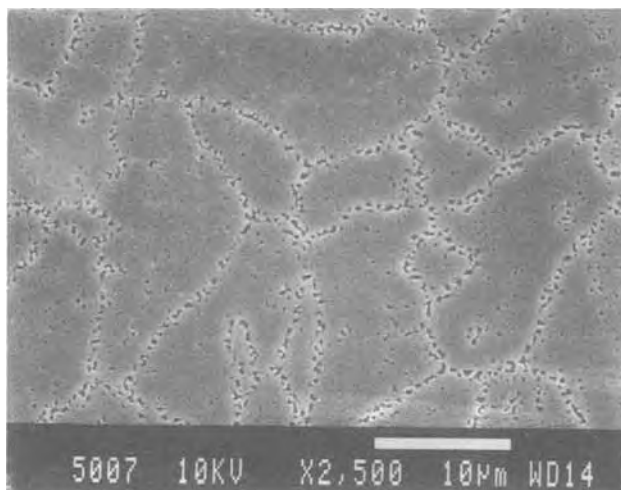


Fig. 6. SEM micrograph of the polysilicon surface after the polycide was implanted with 170 keV P ions at a dose of 1×10^{16} ion/cm², annealed at 950°C in dry O₂ for 30 min, and the oxide and silicide top layers stripped away in BOE.

damage peak should be located at the silicide-polysilicon interface. After oxidation for 30 min in dry O₂ at 950°C and stripping the oxide and silicide, pits were once again observed in the polysilicon layer. However, the pits were more widely distributed and formed a distinctive pattern, as shown in Fig. 6.

It is possible that the doped polysilicon layer may be responsible for the degradation of the interface. Any effect of the polycrystalline nature of the underlying silicon layer and any effect of heavy doping were removed by repeating the oxidation experiments with silicide deposited on undoped single-crystal silicon substrates. Wet oxidations at 950°C were carried out simultaneously with the polycide samples discussed earlier. The oxide thicknesses were the same as for the polycide samples. Figure 7 shows the surface and the silicide-silicon interface of wet oxidized films at 950°C for 10, 30, and 60 min. As in the case of the polycides, nonuniform consumption of silicon occurs from the underlying silicon substrate. Several points of distinction are to be noted between the polycide case and the silicide-single-crystal silicon case. First, the shape of the pits is different. Second, in the case of the single-crystal silicon, the top surface of the oxidized film shows a network which is distinctive of grain boundaries and is not seen on polysilicon. We believe this relates to the titanium silicide grains. The shape of the depressions observed in the silicon substrate match the silicide grains. Numerous voids also appear between the grain-like structures extending into the oxide layer which are not observed in the polycide case (Fig. 4). Similar penetration of

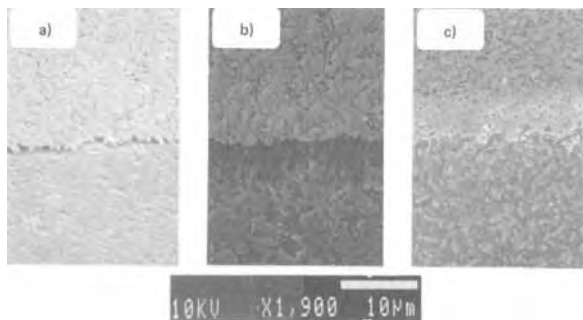


Fig. 7. SEM micrographs of titanium silicide layers on single-crystal silicon that were oxidized at 950°C in wet O₂. The upper half of each picture shows the surface of the oxide film and the lower half of the exposed surface of the polysilicon after the oxide and silicide films were stripped away in BOE. a: 10 min oxidation. b: 30 min oxidation. c: 60 min oxidation.

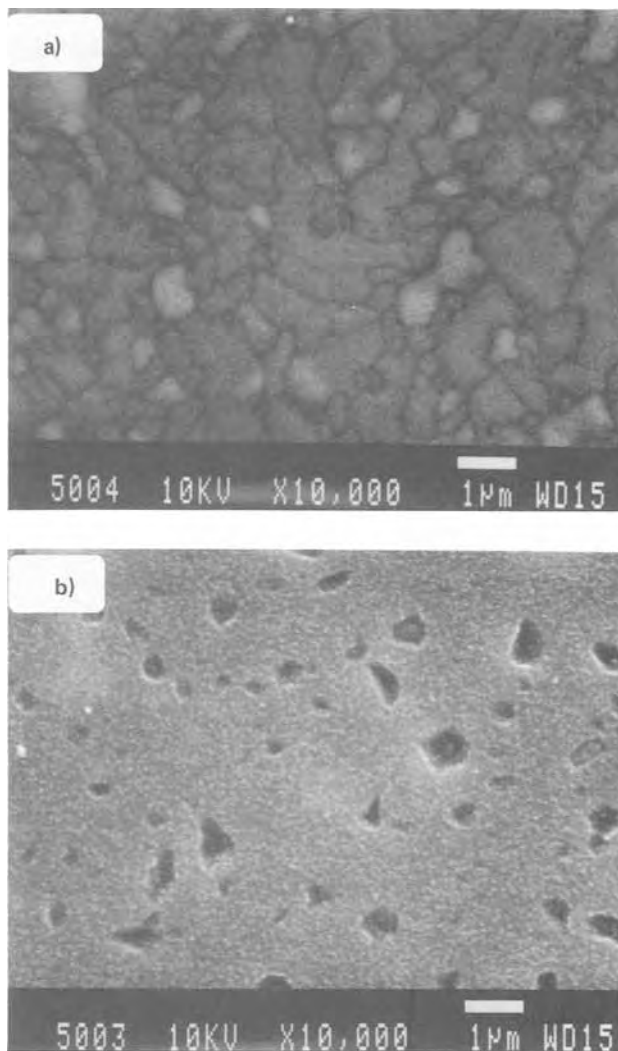


Fig. 8. a: SEM micrograph of the top surface of titanium silicide layer on single-crystal silicon, implanted with 15.0 keV Si to a dose of 1×10^{16} ion/cm² and oxidized in dry O₂ at 950°C for 30 min. b: Same sample as in a, but with the oxide and silicide layer stripped away.

TiSi₂ is noticed when the silicide on single-crystal silicon is oxidized in dry O₂ at 950°C for 30 min.

To further examine the silicide-single-crystal silicon case, the effect of ion implantation interface mixing was also investigated. The implantation consisted of a 150 keV implant of Si ions to a dose of 10^{16} ion/cm². Si was used instead of P to rule out any doping effects, but the masses of the two ions are so close that the ion implantation-related effects should be similar. These films were then oxidized in dry O₂ at 950°C for 30 min following a 15 min N₂ anneal. The top surface of the film (Fig. 8a) shows a pattern resembling grain boundaries and a pitted silicide single-crystal silicon interface (Fig. 8b). It should be noted that some grains appear raised in Fig. 8a and that the distribution and shape of these grains match the pits seen at the interface. This seems to indicate that some of the grains in the silicide film grow perpendicular to the surface both upwards and downwards into the silicon. This takes place only during oxidation, as films annealed in N₂ for the same length of time show a very smooth surface. Faint traces of grain boundaries can be seen in the single-crystal silicon following the anneal with size of the grains being similar to those seen in oxidized films. This grain growth is expected in titanium silicide at 950°C, and the removal of silicon underneath the silicide due to oxidation allows the grains to grow vertically downwards. However, the fact that only some grains of the silicide grow vertically confirms that the silicon is being consumed very nonuniformly from the underlying silicon layer.

Conclusions

It is known that during the oxidation of refractory metal silicides on silicon the silicon required to form the SiO₂ diffuses through the silicide to the top surface from the underlying silicon. As the silicon is consumed, the silicide layer is depressed into the silicon. We have shown that this silicon consumption is nonuniform, as silicon is consumed only from selected sites. In the case of a polysilicide, the uniformity of silicon consumption was shown to be dependent on the condition of the silicide-polysilicon interface. In the case of silicide on single-crystal silicon, the titanium silicide grain boundaries also affected silicon consumption. In addition, we have shown that the titanium silicide fills the areas where the silicon is consumed, and hence, instead of voids, isolated pockets of silicide penetrate into the underlying silicon.

We propose that the presence of a nonuniform silicon diffusion barrier at the silicide-polysilicon interface results in localized silicon consumption. We have attempted to clean this interface by HF etching, plasma etching, *in situ* bias sputter etching, and ion-beam mixing without success. None of the methods described was successful in completely removing the titanium silicide penetration. The best that could be achieved was to reduce the depth of the penetration. The technique that gave the best results was the plasma etching prior to the titanium silicide deposition. Thus, the key to maintaining the gate oxide integrity is to use a pad poly of sufficient thickness to prevent the silicide from spiking through the poly and reaching the gate oxide. This is necessary, since the titanium silicide was shown to have a deleterious effect on

the integrity of the gate oxide when in contact with it. We have shown that the silicide spiking problem is exacerbated with increasing oxidation, and, therefore, a thicker pad poly would be needed with increasing oxidation.

Manuscript submitted Oct. 1, 1984; revised manuscript received Feb. 11, 1985.

Gould Research Center assisted in meeting the publication costs of this article.

REFERENCES

1. S. P. Murarka, "Silicides for VLSI Applications," Academic Press, New York (1983).
2. J. E. Baglin, F. M. d'Heurle, and C. S. Peterson, *J. Appl. Phys.*, **54**, 1849 (1983).
3. H. J. Geipel, N. Hsieh, M. H. Ishaq, C. W. Koburger, and F. R. White, *IEEE Trans. Electron. Devices*, **ed-27**, 1417 (1980).
4. J. M. DeBlasi, R. R. Razouk, and M. E. Thomas, *This Journal*, **130**, 2478 (1983).
5. N. Hsieh and L. Nesbit, *ibid.*, **131**, 201 (1984).
6. M. Berti, A. U. Drigo, C. Cohen, J. Siejka, G. G. Bentini, R. Nipoti, and S. Guerri, *J. Appl. Phys.*, **55**, 3558 (1984).
7. L. N. Lie, W. A. Tiller, and K. C. Saraswat, *ibid.*, **56**, 2127 (1984).
8. J. R. Chen, Y. C. Liu, and S. D. Chu, *J. Electron. Mater.*, **11**, 355 (1982).
9. K. C. Saraswat, D. L. Brors, J. A. Fair, K. A. Monnig, and B. Beyers, *IEEE Trans. Electron Devices*, **ed-30**, 1497 (1983).
10. L. S. Wielunski, C. D. Lien, B. X. Liu, and M. A. Nicolet, *J. Vac. Sci. Technol.*, **20**, 175 (1982).
11. E. Nagasawa, H. Okabayashi, and M. Morimoto, *Jpn. J. Appl. Phys.*, **22**, L57 (1983).

Low Temperature Oxidation of Silicon in a Microwave-Discharged Oxygen Plasma

Shin-ichiro Kimura, Eiichi Murakami, Kiyoshi Miyake, Terunori Warabisako, Hideo Sunami, and Takashi Tokuyama*

Hitachi Limited, Central Research Laboratory, Kokubunji, Tokyo 185, Japan

ABSTRACT

Silicon dioxide growth in an oxygen plasma is investigated using newly developed microwave discharge equipment with electron cyclotron resonance. It is found that the plasma oxidation kinetics can be explained by the Cabrera-Mott model, in which the drift motion of ions is assumed, rather than by the Deal-Grove thermal oxidation model. The drift motion of oxygen ions across the oxide film under the influence of self-bias in the plasma is considered to be the plasma oxidation mechanism. Infrared absorption and etch-rate measurements reveal that the physical properties of plasma oxidized SiO₂ at 600°C are structurally quite comparable to those of thermally oxidized SiO₂.

Low temperature film formation techniques have recently been considered a key process for realizing forthcoming VLSI's. This is because such conventional high temperature processes as thermal oxidation, chemical vapor deposition, or damage annealing of implanted areas have given rise to defect formation and impurity redistribution which seriously damage a VLSI's performance.

Plasma oxidation, utilizing a highly activated oxygen plasma, is one of the low temperature techniques used to grow dielectric films on semiconductor surfaces. This plasma oxidation is usually divided into two categories. One is plasma anodization, in which the specimen to be oxidized is positively biased to enhance the diffusion of oxygen or substrate atom ions through the oxide film, and the other is plasma oxidation without external bias.

The most extensively investigated technique is the former, because with it a considerably higher oxidation rate is obtained. For example, an oxidation rate of about 1 μm/h has been reported (1-3) at 600°C for Si oxidation. This rate is equivalent to that of thermal oxidation in an H₂O atmosphere at 1200°C.

Plasma anodization has several disadvantages, as pointed out by Ray *et al.* (4). For example, since the two electrodes used to apply a bias to the specimen are directly immersed in the plasma, it is difficult to avoid contamination caused by electrode sputtering. Also, heavy damage by irradiation of charged particles and UV light is unavoidable (5).

On the other hand, plasma oxidation has not been as intensively investigated as plasma anodization, since it is difficult to obtain high oxidation rates (6). One of the exceptions is the very thin oxide film formation on lead or niobium for Josephson junctions (7).

However, as the thickness change of the gate oxide in MOS transistors clearly shows, the gate oxide becomes increasingly thinner in accordance with the decrease in device geometry (8). This means that plasma oxidation has potential uses in place of plasma anodization, because the above-mentioned disadvantages of anodization can be avoided.

In this paper, the newly developed plasma oxidation equipment using a microwave discharge is first described (9) along with an investigation of oxygen plasma characteristics. Second, plasma oxidation kinetics are dis-

*Electrochemical Society Active Member.

cussed based on the oxidation mechanisms proposed by Deal and Grove, Tiller, and Cabrera and Mott. The physical properties of the oxide film, such as infrared absorption and etch rate, are also described.

Plasma Oxidation Equipment and Experiments

Several kinds of plasma anodization and/or oxidation equipment have been reported, utilizing dc [Chesler *et al.* (10) and Gourrier *et al.* (11)], RF [Ho, *et al.* (2, 3)] and microwave [Ligenza (1), Kraitchman (12), and Bárdoš *et al.* (13)] discharge plasmas.

The plasma oxidation equipment used in this study is similar to the plasma stream transport system initially proposed by Tsuchimoto (14) for Si_3N_4 film deposition and later developed by Suzuki *et al.* (15) for plasma etching. A schematic diagram of the equipment is shown in Fig. 1.

A 2.45 GHz microwave generated by a magnetron is guided through the waveguide to the quartz discharge tube filled with oxygen gas (99.99%). The vacuum chamber can be evacuated to 6×10^{-6} Pa using a turbomolecular pump.

The diameter of the discharge tube is 100 mm. The oxygen gas is supplied directly from an oxygen cylinder to the discharge tube, and the oxygen pressure in the chamber is controlled by a leak valve. No special purifying system such as a liquid nitrogen trap is provided. The discharge tube is surrounded by three magnetic coils, and the magnetic field is set to meet the electron cyclotron resonance (ECR) condition.

When the electrons rotating spirally absorb the microwave under the ECR condition, a high density oxygen plasma is easily obtained even at a low oxygen pressure ($< 1 \times 10^{-2}$ Pa). This is the characteristic phenomenon of a microwave discharge with a magnetic field which no other discharge system can achieve.

The plasma is then transported to the specimen confined by the magnetic field, as shown in Fig. 2. The silicon substrate to be oxidized is placed on the quartz holder with two halogen lamps to heat it. The oxygen plasma irradiates the specimen at almost normal incidence. The characteristics of this oxidation equipment are summarized as follows.

1. A high density oxygen plasma is easily obtained by ECR discharge.

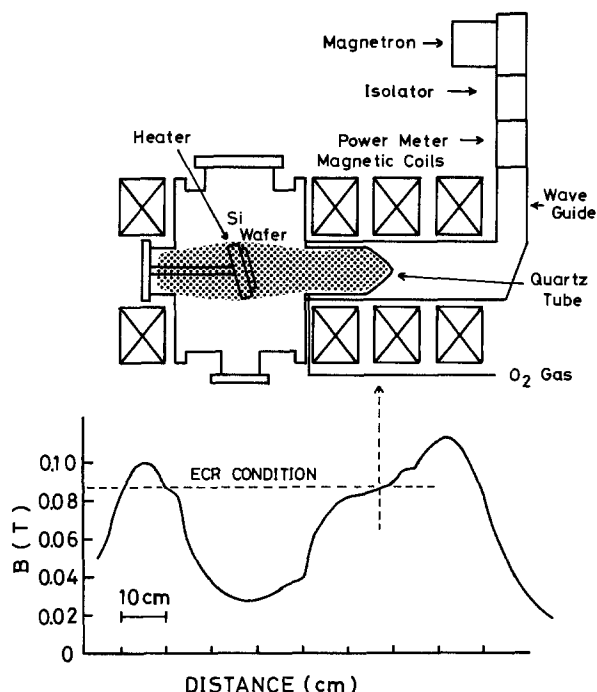


Fig. 1. Schematic diagram of microwave plasma oxidation equipment and distribution of magnetic flux density, B .

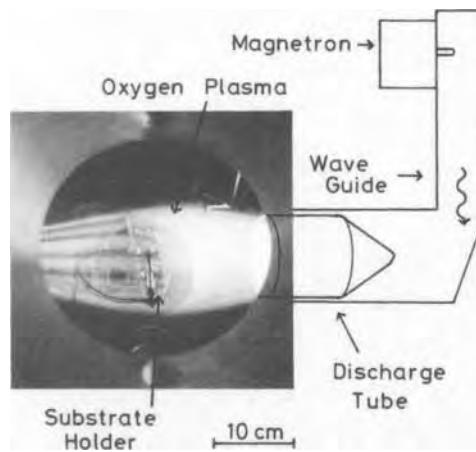


Fig. 2. Side view of oxygen plasma. The plasma is confined by a magnetic field and transported to the specimen.

2. An oxygen plasma with little contamination is obtained, because the plasma is kept away from the chamber wall and sputtering is avoided.

3. Independent temperature control of the specimen is accomplished by separating plasma generation from the specimen.

The physical properties of the oxide film grown using this equipment were investigated. Fourier transform infrared (FTIR) is applied to investigate the IR absorption peak of the oxide. Etch rate measurement using the P etch solution ($\text{HF}:\text{HNO}_3:\text{H}_2\text{O} = 1.5:1:30$) is carried out to evaluate the densification of the oxide film.

Emission Spectrum from Oxygen Plasma

It is well known that plasma characteristics are influenced by factors such as gas pressure and flow rate. The emission spectrum and electron temperature, therefore, were measured to obtain the optimum oxidation condition. The optical emission spectrum from the microwave discharge oxygen plasma is shown in Fig. 3. The ox-

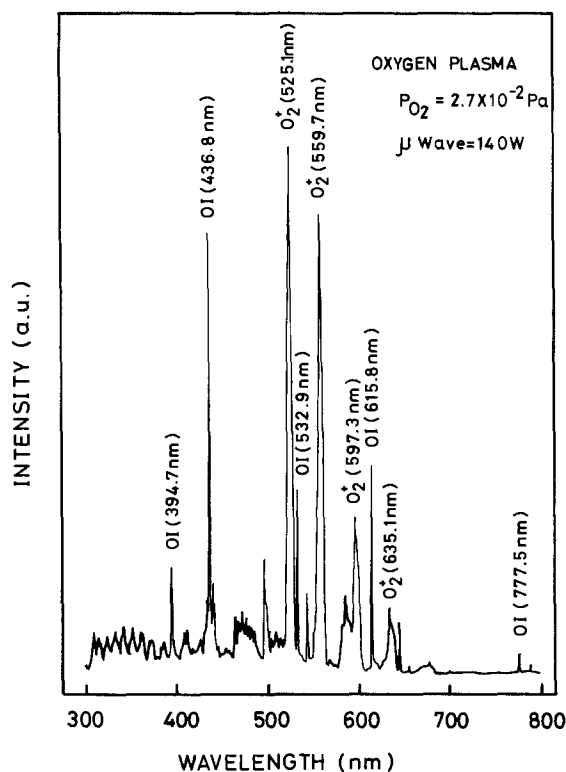


Fig. 3. Emission spectrum from microwave discharge oxygen plasma. The oxygen pressure is 2.7×10^{-2} Pa. The microwave power is 140W. Spectra from oxygen atoms (OI) and molecular oxygen ions (O_2^+) are observed.

xygen pressure is 2.7×10^{-2} Pa, and the microwave power is 140W.

Very sharp spectra from oxygen atoms at 394.7, 436.8, 532.9, and 615.8 nm and somewhat broader spectra from molecular oxygen ions at 525.1, 559.7, 597.3, and 635.1 nm are clearly observed in this figure. These peaks show that highly excited species such as O and O_2^+ exist in the plasma. Dzioba *et al.* (16) have already reported the emission spectra from a microwave (without ECR) oxygen plasma, where the oxygen pressure was 13 Pa. They observed emission not only from O and O_2^+ , but also from O^+ . However, the emissions from O_2^+ were weak compared with the present results. In addition, they observed a peak from Na^+ , which was not observed in this experiment.

Figure 4 shows the oxygen pressure dependence of the relative peak height of O (436.8 nm) and O_2^+ (525.1 nm). The peak height reaches a maximum near 5×10^{-2} Pa. Additionally, in the pressure region below 5×10^{-2} Pa, the O_2^+ peak is higher, while above this pressure, the peak heights are reversed. Taking the dissociation energy (5 eV) and the ionization energy (13 eV) (17) of the oxygen molecule into consideration, it is likely that dissociation rather than ionization occurs in the high pressure region, since the electron energy is low due to frequent collision. However, in the low pressure region, the electron energy is high enough to preferentially give rise to ionization.

Since peak height is related to the concentration of excited species in the plasma, an oxygen pressure of 2.7×10^{-2} Pa, which gives a nearly maximum peak height, was selected for the oxidation experiment.

In order to investigate the electron temperature of the plasma, a probe current measurement was conducted. Figure 5 shows the probe current and applied bias. From the semilog plot of the probe current and positively applied bias, an electron temperature of 5-7 eV was obtained (18). In addition, from the negative bias at which the net current of the probe became zero, the potential of the specimen held electrically floating in the plasma can be evaluated as -15V. The floating potential of the microwave plasma is small compared with that of the conventional dc or parallel-plate-type RF discharge plasma, since the bias is not directly applied to the specimen. This small floating potential in the microwave plasma is one of the advantages useful in the prevention of irradiation damage.

Results and Discussion

Plasma oxidation kinetics.—In order to discuss the plasma oxidation kinetics based on the proposed oxidation model, the time and temperature dependences of oxide growth were investigated. The thickness of the SiO_2 film was measured by an ellipsometer, assuming a re-

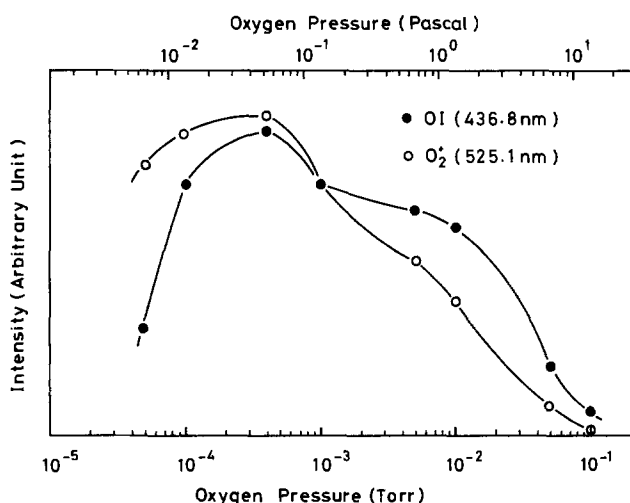


Fig. 4. Oxygen pressure dependence of emission intensity from OI (436.8 nm) and O_2^+ (525.1 nm).

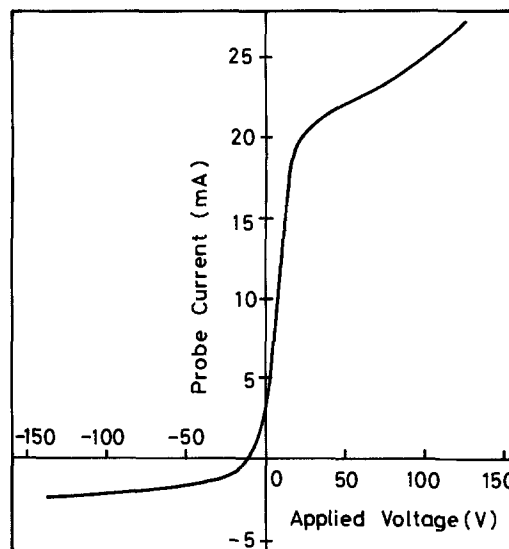


Fig. 5. Current of the probe immersed in the microwave discharge argon plasma. The electron temperature of the plasma is about 6 eV. The floating potential is -15V, which is small compared with that of the conventional dc or parallel-plate-type RF discharge equipment.

fractive index of 1.47. Also, since the thickness varied about 10% from one point to another owing to the plasma distribution, the average of measurements taken at nine points near the center of the specimen was used.

Figure 6 shows the relation between thickness and oxidation time as a function of temperature. The result from thermal dry oxidation (700°C at 1 atm) is shown as a dashed line for comparison. Since an oxide thickness 30 times as large is obtained by plasma oxidation even at 640°C, it is obvious that the oxygen plasma enhances the oxidation considerably.

Fuller *et al.* (19) demonstrated that oxide thickness (x) and oxidation time (t) can be expressed by the power law relation, *i.e.*

$$x^n = kt \quad [1]$$

where n and k are constant. Deal and Grove (20) reported that the constant n varied from 1 to 2 according to a change of the mechanism from the linear rate region in a thin oxide to the parabolic rate region in a thick oxide.

The results in Fig. 6 are replotted according to the power law relationship in Fig. 7. It is obvious that the values of n obtained from the slope of the curves exceed 2, in contrast to Deal and Grove's results.

In the thermal oxidation mechanism of Deal and Grove (DG model) (20), the relation between oxide thickness and

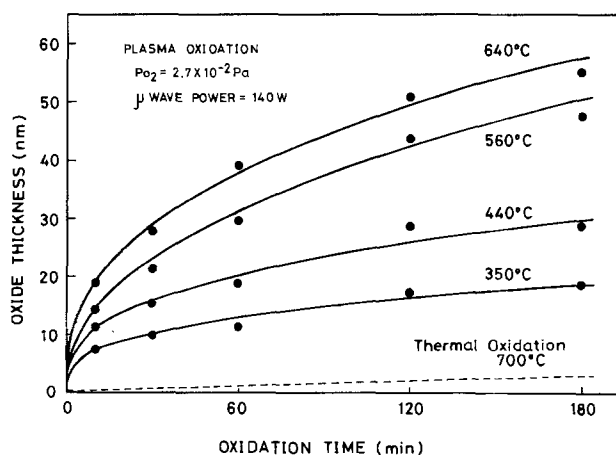


Fig. 6. Oxide growth as a function of oxidation time. The dashed line shows thermal oxidation at 700°C and 1 atm.

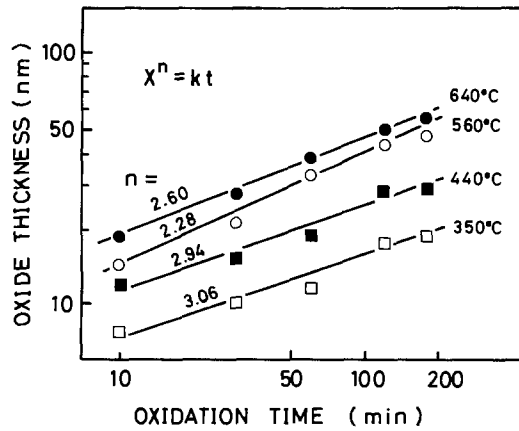


Fig. 7. Plot of oxide thickness (x) and oxidation time (t) using a power law relation. Every n obtained from the slope of the lines exceeds 2.

oxidation time is expressed by the linear-parabolic equation

$$X^2/B + X/(B/A) = t + \tau \quad [2]$$

where B/A , B , and τ are constants which include the reaction rate constant at the Si/SiO₂ interface, diffusion of oxygen through SiO₂, and the time representing oxide thickness present at the beginning of oxide growth, respectively. All the constants can be obtained by fitting the data in Fig. 6 to Eq. [2] by the least squares method. The results are shown in Table I. Every $1/(B/A)$, which contains the reaction rate constant at the Si/SiO₂ interface, becomes negative.

According to a modified DG model proposed by Tiller (21), it is shown that B/A can become negative if migration of oxygen ions is considered. The results shown in Table I indicate that the plasma oxidation mechanism may be explained by a model in which oxygen ion migration is assumed. In Tiller's model, a linear-parabolic oxidation rate equation similar to the DG model is essentially obtained, although the effect of field-aided ion migration enters B/A , B , and τ . The reason why every n in Eq. [1] exceeds 2 in the present experiment is thus not explained by Tiller's model.

However, Fehlner (22) reported that the Cabrera-Mott model (23) (CM model) is valid for explaining the oxidation under low temperature or low pressure conditions. Kamigaki *et al.* (24) and Horiuchi *et al.* (25) reported that the CM model rather than the DG model was adequate for explaining the kinetics of thermal oxidation under low partial pressures, in which diluted oxygen is used to grow very thin oxide films of less than 10 nm for MNOS non-volatile memory devices. Furthermore, Yamasaki *et al.*

Table I. Values of τ , $1/(B/A)$, and $1/B$ from the Deal-Grove thermal oxidation model. Every $1/(B/A)$, even though it includes the reaction rate constant at Si/SiO₂ interface, becomes negative for plasma oxidation

Deal-Grove model	τ	$\frac{1}{B/A}$	$\frac{1}{B}$
Temperature	(min)	(min/nm)	(min/nm ²)
350°C	9.17	-1.42	0.558
440°C	1.05	-2.68	0.308
560°C	-19.40	-1.93	0.104
640°C	-62.63	-4.86	0.122

Deal-Grove model $t + \tau = \frac{1}{B} X^2 + \frac{1}{B/A} X$

(26) proved that the plasma anodization of GaAs was also well explained by the CM model.

In the model, it is assumed that the electric field originating in the contact potential difference between the metal and the adsorbed oxygen ions decreases the activation energy for ion movement, resulting in the rate equation

$$dx/dt = 2U \sinh (X1/x) \quad [3]$$

where $X1$ and U are a characteristic distance and velocity, respectively. $X1$ is linearly proportional to the contact potential difference, and U contains the activation energy. Moreover, Fehlner *et al.* (27) concluded that the same equation could be applied to both cation and anion movement.

When $X1 \gg x$, Eq. [4], which produces the parabolic rate law, can be derived as

$$dx/dt = 2U(X1/x) \quad [4]$$

However, when $X1 \ll x$, Eq. [5], which was discussed above in connection with previous reports, can be derived as

$$dx/dt = U \exp (X1/x) \quad [5]$$

In the present experiment, it is reasonable to directly use Eq. [3] rather than Eq. [5], since the oxide thickness is much larger than the results obtained from Kamigaki *et al.* (24) and Horiuchi *et al.* (25).

The oxidation rate, *i.e.*, dx/dt at an arbitrary oxide thickness, can be estimated by differentiating Eq. [1] ($dx/dt = k/\eta x^{n-1}$) using the n and k obtained in Fig. 7. U and $X1$ from Eq. [3] are determined using this dx/dt , applying the repetition method. The results of the analysis are indicated in Fig. 8, which includes values determined for U and $X1$. The measured oxidation rate (closed circles) coincides well with the calculated curve.

It is found that the present plasma oxidation results can be readily explained by the CM model. However, characteristic distances, $X1$, obtained here (20-40 nm) are much larger than those found in previous results (< 10 nm) (24, 25). These details will be discussed later.

The characteristic velocity, U , in Eq. [3] is closely related to the activated process such as diffusion or solution of substrate atoms in the oxide. The Arrhenius plot of U

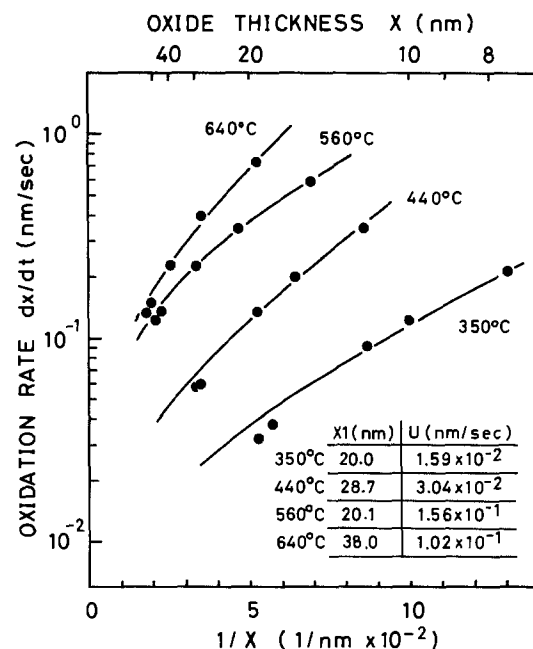


Fig. 8. Plot of reciprocal oxide thickness ($1/x$) vs. oxidation rate (dx/dt) using the Cabrera-Mott equation. Solid lines are calculated curves. The characteristic distance ($X1$) and characteristic velocity (U) are obtained simultaneously by fitting the experimental data to the Cabrera-Matt equation.

is shown in Fig. 9. Although it is peculiar that the data obtained at 560°C are larger than those of 640°C, a very small activation energy (0.40 eV) is obtained. This activation energy is much smaller than the previous results for 1-2 eV (24, 25). In addition, this activation energy is also smaller than the value obtained in thermal oxidation (20).

The kinetics of plasma oxidation can be more readily explained by the CM model and partially by Tiller's modified DG model than by the DG model. It is also found that plasma oxidation is quite similar to low pressure oxidation. Distinguishing differences have appeared, however, between plasma and low pressure oxidation with respect to activation energy and characteristic distance, X_1 .

Since X_1 in the CM model is proportional to the potential across the oxide, the reason it becomes larger in the present experiment as compared with the low pressure oxidation can be considered as follows. The specimen to be oxidized is held electrically isolated in the plasma. Therefore, more mobile electrons can arrive at the specimen surface faster than ions, resulting in a floating potential around the specimen. The electrons on the specimen surface also apply a negative bias across the oxide film. Since this negative bias is considered to be larger than the contact potential assumed in the CM model, it is almost certain that the characteristic distance, X_1 , in plasma oxidation becomes larger.

The second question is the very small activation energy obtained in this experiment. Kamigaki *et al.* (24) obtained 2 eV, which coincided with the bond breaking energy of Si during low pressure oxidation. Additionally, the activation energies obtained by Deal and Grove (20) in the diffusion dominant region were 1.24 eV in a dry atmosphere and 0.71 eV in a wet atmosphere. They concluded that these activation energies were equivalent to the diffusion of O_2 and H_2O in quartz. However, the activation energy (0.40 eV) obtained here is quite small.

The CM model assumes the diffusion of substrate atoms toward the oxide surface in contrast to the oxygen diffusion of the DG model. In order to investigate the diffusing species of this plasma oxidation, oxidation in a tracer ambient and depth profile analysis using SIMS were carried out.

Briefly, the specimen was first oxidized in a $^{16}O_2$ atmosphere at 640°C for 25 min. This oxidation condition grew a 25 nm thick oxide layer, as shown in Fig. 6. Next, the same specimen was reoxidized in a 20% $^{18}O_2$ atmosphere

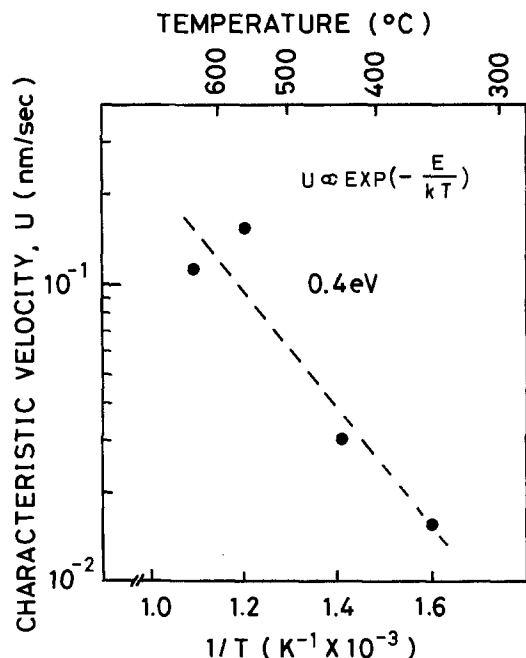


Fig. 9. Arrhenius plot of characteristic velocity (U). The activation energy of plasma oxidation is 0.4 eV.

at the same temperature over 2.5h. The total thickness was therefore 50 nm. Following this oxidation, a depth profile analysis of ^{18}O and ^{16}O was conducted using SIMS with Cs^+ as the primary ion. The results are shown in Fig. 10. The closed circles represent the intensities from ^{18}O and ^{16}O , and the open circles represent the ratio $^{18}O/^{16}O$. In the ratio curve, it is found that ^{18}O exists throughout the oxide film. These results clearly indicate that oxygen diffuses during plasma oxidation, in contrast to the results obtained from plasma anodization of Si (3) and GaAs (26), in which diffusion of substrate atoms is also observed. In addition, the ratio in the bulk of the oxide is equivalent to the tracer content in the atmosphere. Rochet *et al.* (28) report that most of the tracer appears at the Si/SiO₂ interface in the case of thermal oxidation. The existence of the tracer in the bulk of the oxide in Fig. 10 may imply that oxygen exchange takes place during plasma oxidation, similar to oxidation of Si in wet ambient (29) and plasma anodization of silicon through thin ZrO₂ films (30, 31). Studies are in progress to examine such oxygen exchange phenomena during plasma oxidation.

From these results, we can discuss the plasma oxidation mechanism as follows.

As suggested by Hu (32), the diffusing species are considered to be oxygen ions (O^-). The O^- ion is produced in the plasma by dissociation of oxygen molecules followed by electron attachment. Formation on the oxide surface is also possible, since the specimen is covered with electrons from the plasma.

The diffusion process should involve ion drift, since there is a built-in potential across the oxide. This originates in the potential which exists around the specimen held electrically floating in the plasma. Also, since this built-in potential is considered to be larger than the contact potential assumed in the CM model, it is likely that a large X_1 (characteristic distance) can be experimentally obtained.

Moreover, since the O^- ion is smaller than the oxygen molecule in size, the activation energy is expected to be smaller in plasma oxidation. Ray *et al.* (4) also reported a considerably smaller activation energy (0.16 eV) in their RF discharge plasma oxidation. However, the details are subject to further investigation.

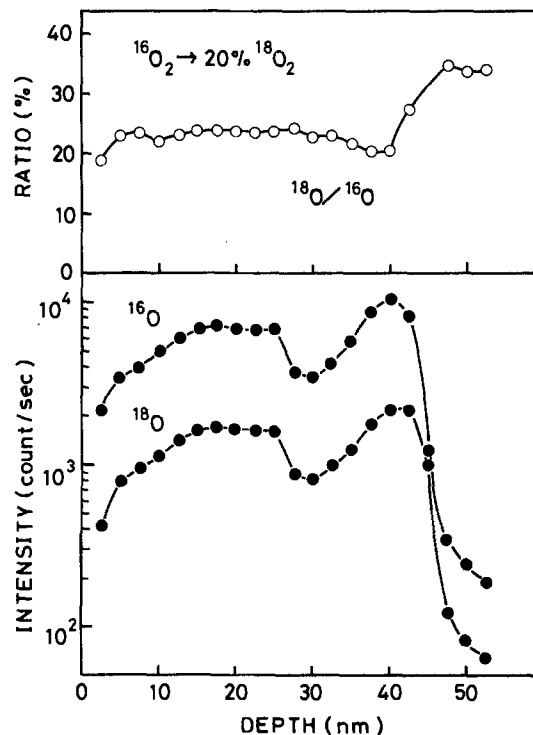


Fig. 10. Depth profiles of ^{16}O and ^{18}O in plasma grown SiO₂. The specimen was first oxidized in $^{16}O_2$ atmosphere and then reoxidized in a 20% $^{18}O_2$ atmosphere. Open circles show the ratio of ^{18}O to ^{16}O .

Physical properties of plasma oxidized SiO₂ films.—Infrared absorption properties.—As there have been several reports concerned with the IR absorption properties of SiO₂ films grown by various methods, it has become well known that absorption peaks vary to a large extent with physical properties such as the density of strains in the film.

Figure 11 shows the IR absorption peaks of microwave-plasma-oxidized SiO₂ films as a function of oxidation temperature. The result from a thermally dry-oxidized films (curve a) is also given for comparison.

The absorption peaks of SiO₂ grown above 500°C (curves b and c) are very similar to that observed in thermally oxidized SiO₂. In addition, the absorption peak coincides well with previous results. On the other hand, the peaks of SiO₂ films grown below 500°C (curves d and e) are shifted slightly (15 cm⁻¹) toward greater wavelengths.

Dylewski *et al.* (33) investigated the properties of SiO₂ films formed by oxygen ion implantation using IR absorption techniques. They reported that the absorption peaks of heavily implanted films shifted toward greater wavelengths. It was concluded that this shift can be attributed to strain in the Si and O bonds. Pliskin (34) observed the same peak shift of SiO₂ films made by a sputtering technique.

These results indicate that SiO₂ films made by a low temperature method, when compared with thermally oxidized films, can differ in structural or physical properties due to large strains in the film. However, since even thermally oxidized SiO₂ films show a peak shift when they are very thin, it is difficult to judge whether the shift IR

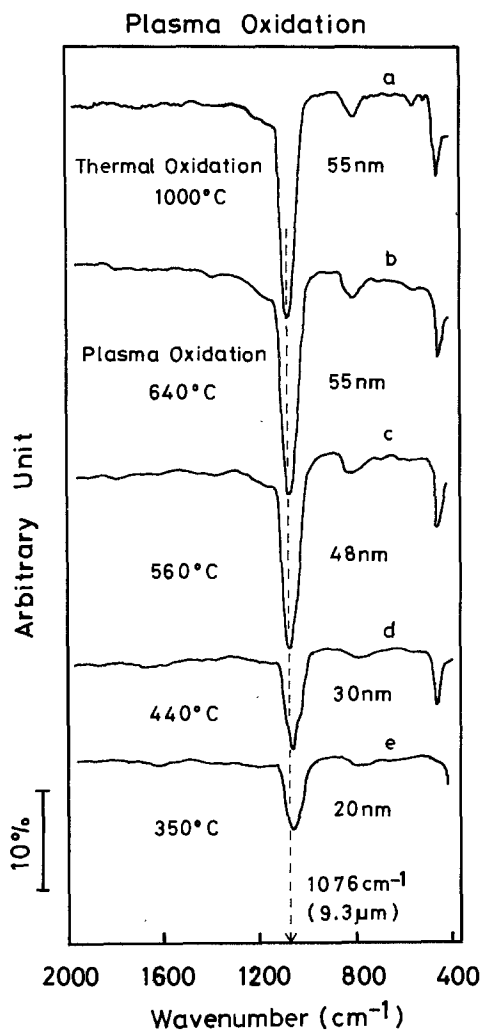


Fig. 11. Relation between infrared absorption peak and plasma oxidation temperature. Curve a is SiO₂ thermally oxidized at 1000°C, which shows the absorption peak at 1076 cm⁻¹.

absorption peaks in the plasma oxidized SiO₂ film below 500°C is attributable to strain.

Etch-rate measurement.—The etch rate using P etch solution (35) has been occasionally used as a parameter to indicate the degree of densification of SiO₂ films. Figure 12 plots the relation between etch rate of the present films and oxidation temperature. The dashed line indicates the etch rate of thermally oxidized SiO₂ at 1000°C for comparison.

Although no peak shift is observed in the plasma-oxidized SiO₂ grown above 500°C, the etch rate is slightly larger than that of the thermally oxidized film. In addition, the lower the plasma oxidation temperature, the larger the etch rate.

Conclusion

Microwave plasma oxidation equipment using electron cyclotron resonance has been developed. An oxygen plasma is ignited under ECR conditions, and optical emissions from oxygen atoms and oxygen molecular ions are observed. The intensities of both emissions depend on the oxygen partial pressure. Below 5×10^{-2} Pa, the emission from the oxygen molecular ion is stronger. However, the emission from the oxygen atom becomes stronger above this pressure.

It is found that plasma oxidation kinetics can be explained using the Cabrera-Mott model rather than the Deal-Grove model. However, there are two differences in the present results compared with previous reports in which the CM model was applied to explain the oxidation kinetics of the low pressure thermal oxidation of Si. One difference is a large characteristic distance (X_1). Since X_1 is proportional to the potential across the oxide film, the floating potential is taken to be the cause of the large X_1 . The other difference is a small activation energy, which may imply that the diffusing species is small in size. Moreover, the depth profile analysis of the oxygen isotope clarifies that the diffusing species is oxygen, similar to the case of thermal oxidation.

From these results, the diffusing species is concluded to be the O⁻ ion produced in the plasma or on the substrate surface. In addition, the O⁻ diffusion is enhanced by the potential across the oxide, which originated in the floating potential existing around the specimen held electrically floating in the plasma.

The physical properties of plasma-oxidized SiO₂ are comparable to those of thermally oxidized SiO₂ with respect to IR absorption. However, the etch rate is a little faster than that of the thermally oxidized SiO₂.

Acknowledgments

The authors express their gratitude to Dr. M. Horiuchi and Dr. M. Naito for useful discussions. They also thank Dr. E. Mitani for his cooperation in the SIMS analysis.

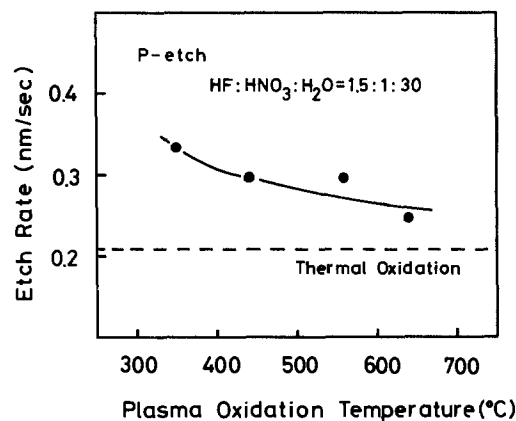


Fig. 12. Relation between etch rate and plasma oxidation temperature. Dashed line is the etch rate of thermally oxidized SiO₂ at 1000°C.

Manuscript submitted Oct. 19, 1984; revised manuscript received March 4, 1985.

Hitachi Limited assisted in meeting the publication costs of this article.

REFERENCES

- J. R. Ligenza, *J. Appl. Phys.*, **36**, 2703 (1965).
- V. Q. Ho and T. Sugano, *Jpn. J. Appl. Phys.*, Supplement 19-1, 103 (1980).
- V. Q. Ho and T. Sugano, *Thin Solid Films*, **95**, 315 (1982).
- A. K. Ray and A. Reisman, *This Journal*, **128**, 2460 (1981).
- D. L. Pulfrey and J. J. H. Reche, *Solid State Electron.*, **17**, 627 (1974).
- J. L. Miles and P. H. Smith, *This Journal*, **110**, 1240 (1963).
- J. H. Greiner, *J. Appl. Phys.*, **42**, 5151 (1971).
- K. Itoh and H. Sunami, *IEEE Proc.*, **130**, 127 (1983).
- K. Miyake, S. Kimura, T. Warabisako, H. Sunami, and T. Tokuyama, *J. Vac. Sci. Technol. A*, **2**, 496 (1984).
- L. A. Chesler and G. Y. Robinson, *J. Vac. Sci. Technol.*, **15**, 1525 (1978).
- S. Gourrier, A. Mircea, and M. Bacal, *Thin Solid Films*, **65**, 315 (1980).
- J. Kraitchman, *J. Appl. Phys.*, **38**, 4323 (1967).
- L. Bárdos, G. Loncar, I. Stoll, J. Musil, and F. Záček, *J. Phys. D.*, **8**, L195 (1975).
- T. Tsuchimoto, *J. Vac. Sci. Technol.*, **15**, 70 (1978).
- K. Suzuki, S. Okudaira, N. Sakudo, and I. Kanomata, *Jpn. J. Appl. Phys.*, **16**, 1979 (1977).
- S. Dzioba, G. Este, and H. M. Naguib, *This Journal*, **129**, 2537 (1982).
- A. T. Bell, in "Techniques and Applications of Plasma Chemistry," J. R. Hollahan and A. T. Bell, Editors, Chap. 1, John Wiley and Sons, New York (1974).
- F. F. Chen, in "Plasma Diagnostic Techniques," R. H. Huddleston and S. L. Leonard, Editors, Chap. 4, Academic Press, New York (1965).
- C. R. Fuller and F. J. Strieter, Abstract 74, p. 180, The Electrochemical Society Extended Abstracts, Vol. 64-1. Toronto, Ont., Canada, May 3-7, 1964.
- B. E. Deal and A. S. Grove, *J. Appl. Phys.*, **36**, 3770 (1965).
- W. A. Tiller, *This Journal*, **127**, 625 (1984).
- F. P. Fehlner, *ibid.*, **131**, 1645 (1984).
- N. Cabrera and N. F. Mott, *Rept. Prog. Phys.*, **12**, 163 (1948).
- Y. Kamigaki and Y. Itoh, *J. Appl. Phys.*, **48**, 2891 (1977).
- M. Horiuchi, Y. Kamigaki, and T. Hagiwara, *This Journal*, **125**, 766 (1978).
- K. Yamasaki and T. Sugano, *J. Vac. Soc. Jpn.*, **23**, 26 (1980).
- F. P. Fehlner and N. F. Mott, *Oxid. Met.*, **2**, 59 (1970).
- F. Rochet, B. Agins, and S. Rigo, *This Journal*, **131**, 914 (1984).
- R. Pfeffer and M. Ohring, *J. Appl. Phys.*, **52**, 777 (1981).
- J. Perriere, J. Siejka, and R. P. H. Chang, *Thin Solid Films*, **95**, 309 (1982).
- J. Perriere, J. Seijka, and R. P. H. Chang, *J. Appl. Phys.*, **56**, 15, 2716 (1984).
- S. M. Hu, *Appl. Phys. Lett.*, **42**, 15, 872 (1983).
- J. Dylewski and M. C. Joshi, *Thin Solid Films*, **37**, 241 (1976).
- W. A. Pliskin and H. S. Lehman, *This Journal*, **112**, 1013 (1965).
- "Fundamentals of Silicon Integrated Device Technology," Vol. 1, R. M. Burger and R. P. Donovan, Editors, Prentice-Hall Inc., Englewood Cliffs, NJ (1967).

Planar Deposition of Aluminum by RF/DC Sputtering with RF Bias

Yoshio Homma and Sukeyoshi Tsunekawa

Hitachi, Limited, Central Research Laboratory, Kokubunji, Tokyo 185, Japan

ABSTRACT

Planarization of multilevel interconnection is most effective for achieving a higher packing density. However, it is shown by computer simulation that degradation of metallization step coverage becomes serious as the via aspect ratio increases. Conventional deposition methods, in which emitted particles flow onto the substrate and usually do not migrate, are shown to be inadequate for maintaining sufficient step coverage. A new deposition technique, RF/dc sputtering with RF bias for metal, is developed and found to provide sufficient step coverage and, moreover, planarity. In an application of the technique to aluminum film deposition, the existence of a resputtering effect was confirmed. Aluminum particles were found to deposit primarily near the bottom of the depressions and to fill up the depressions completely, through sputtering at a high bias. Steep, deep grooves and vias with aspect ratios up to 3 were found to be completely filled with the aluminum film by deposition at resputtering rates higher than 50%. It was also found that substrate biasing has a decisive effect on giving aluminum films an almost complete (111) crystallographic texture.

Highly packed, multilevel interconnection has become one of the most fundamental and indispensable technologies for improving VLSI packing density. Planarization of interlevel insulation layers has been most effective for achieving finer patterns of overlapping metallization layers. For use in interlevel insulation planarization, etchback planarization (1), polyimide insulation (2), and bias sputtering (3, 4) have been developed. Planar SiO₂ films, e.g., those obtained by a planar magnetron bias sputtering technique, have been applied to a two level interconnection for a 1 Mbit dynamic random access memory, and have proved effective in improving the packing density (5).

However, the insulation layer has to be somewhat thicker than in ordinary structures in order to planarize the insulation layer on the very jagged substrate surface produced by fabrication of devices and underlying metallization. This leads to higher aspect ratio vias, through which the upper layer metallization has to be connected with the under layer. This may limit the packing density of interlevel connection in future VLSI's, due to severe degradation of step coverage of the upper layer metallization around the vias.

This paper first discusses step coverage degradation of the metallization layer around such vias. Then a newly developed aluminum film deposition technique is introduced (6). It is shown that this technique can improve aluminum step coverage drastically, and, furthermore, fill up and planarize the fine vias for multilevel interconnection. These effects are obtained by film deposition using RF/dc sputtering with RF bias. The effects of substrate biasing on film quality are also described.

Experimental

Step coverage evaluation.—Coverage of metallization layers around jagged steps on LSI surfaces has been an important measure of reliability. Much research has been reported on improving the metallization step coverage (7, 8). However, it seems that the concept of step coverage has been treated ambiguously.

The step coverage dependence on metal deposition conditions and underlying groove profiles is investigated systematically utilizing a computer simulation which follows Blech's model (9, 10). In the model, particles are assumed to impinge onto the substrate surface isotropically within designated maximum incident angles, $\pm\omega_{\max}$, cor-

responding to the geometrical structure of the deposition systems. The sticking coefficient of the deposited particles is assumed to be 1, and no surface migration effect is taken into account. The step coverage factor was defined as the ratio of the minimum film thickness around the grooves to the nominal film thickness (equal to the groove depth), since the factor changes according to deposited film thickness as well as groove aspect ratio and ω_{\max} .

Aluminum bias sputtering.—A high rate bias sputtering technique, employing both a planar magnetron cathode instead of a conventional cathode and RF substrate biasing during deposition, was developed to deposit planar SiO_2 films at a higher deposition rate (4). This technique was introduced for metal deposition.

The bias sputtering system is shown schematically in Fig. 1. Either dc or RF power can be applied to the cathode, while the application of RF power to the water-cooled substrate electrode causes the resputtering effect necessary to achieve planarization (3). The magnetron cathode was chosen to achieve a high deposition rate of aluminum at low substrate temperatures. The cathode was 122 mm, and the distance between the cathode and the substrate electrode was normally 35 mm. The background pressure of the system was 0.13 mPa.

First, the influence of substrate biasing on the film deposition rate was examined to determine the resputtering effect. Second, the influence of biasing on film quality was investigated by SIMS and x-ray diffractometry. Finally, the effects of substrate biasing on the film step coverage were shown.

Results and Discussion

Step coverage degradation around fine vias.—Customarily, it has been thought that step coverage is mainly determined by film deposition conditions such as maximum incident angles. It is believed that methods for wider deposition incident angles, such as sputtering, provide better step coverage than those with narrow maximum incident angles, such as vacuum evaporation (8, 11). The effects of underlying surface topography have not really been taken into account.

However, these conventional ways of evaluating and improving step coverage were found to be inadequate for future VLSI metallization. For example, the step coverage factor of the second-level metallization layer has been evaluated using isolated steps, as shown in Fig. 2a. The underlying projected line was produced by depositing CVD PSG (phosphosilicate glass by chemical vapor deposition) film on a dry-etched first level metallization. The second-level metallization layer was deposited by a conventional magnetron sputtering system. Around such isolated steps, conventional sputtering technique can achieve good step coverage. On the other hand, Fig. 2b shows an example where the step coverage of the second-

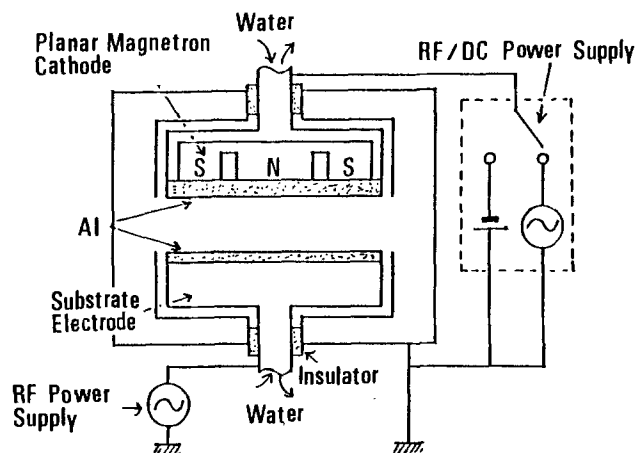


Fig. 1. Aluminum bias sputtering apparatus

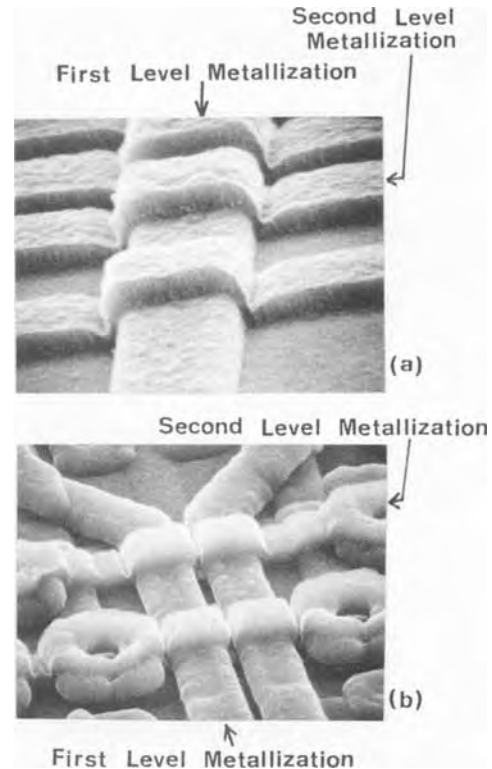


Fig. 2. Influence of underlying step density on second-level metallization step coverage. a: Step coverage around an isolated step. b: Step coverage around dense steps.

level metallization shows extreme degradation around narrow and deep depressions, though the metal deposition conditions are the same as those in Fig. 2a.

The influence of the aspect ratio of vertical grooves on step coverage was investigated by computer simulation. The model is two dimensional and is insufficient for discussing step coverage problems around "three-dimensional" vias. However, the simulation is effective enough for showing qualitatively the seriousness of the problems. The step coverage factor was measured from the calculated figures, as shown in Fig. 3. As shown in Fig. 3, the particles are assumed to flow onto the substrate isotropically through a sliced hemisphere surface within the angular range $\pm\omega_{\max}$. Figures 3b and 3c show examples for a sloped and a vertical groove, respectively. These results are shown together in Fig. 4. The groove aspect ratio was changed from 0.33 to 2.0, i.e., the groove width was changed from three times to one-half of the depth. This figure shows two things. First, the step coverage factor shows extreme degradation as the aspect ratio increases. Second, film deposition under wider ω_{\max} does not necessarily provide better step coverage, especially around grooves of larger aspect ratio. Almost the same results have been reported for steep grooves (slope angle $\theta = 80^\circ$) with dc magnetron sputtering (12).

Next, the effects of maximum incident angles, ω_{\max} , on film step coverages are shown in Fig. 5. The slope angle, θ , of groove side walls is used as a parameter. It can be seen from Fig. 5 that the change of step coverage factor is roughly divided into three parts. The step coverage factor is constant, irrespective of ω_{\max} , and is dependent only on the θ , in region A. In region B, where ω_{\max} exceeds $(90 - \theta)^\circ$, the step coverage factor increases and reaches a maximum. Then, in region C, the step coverage factor decreases as ω_{\max} increases.

As the slope angle, θ , increases, region A becomes narrower, and disappears when θ reaches 90° . Region A corresponds to where there is no shadowing effect. In region B, the effect of step coverage improvement due to ω_{\max} increment is larger than the degradation due to the shadowing effect. In region C, the coverage degradation due to

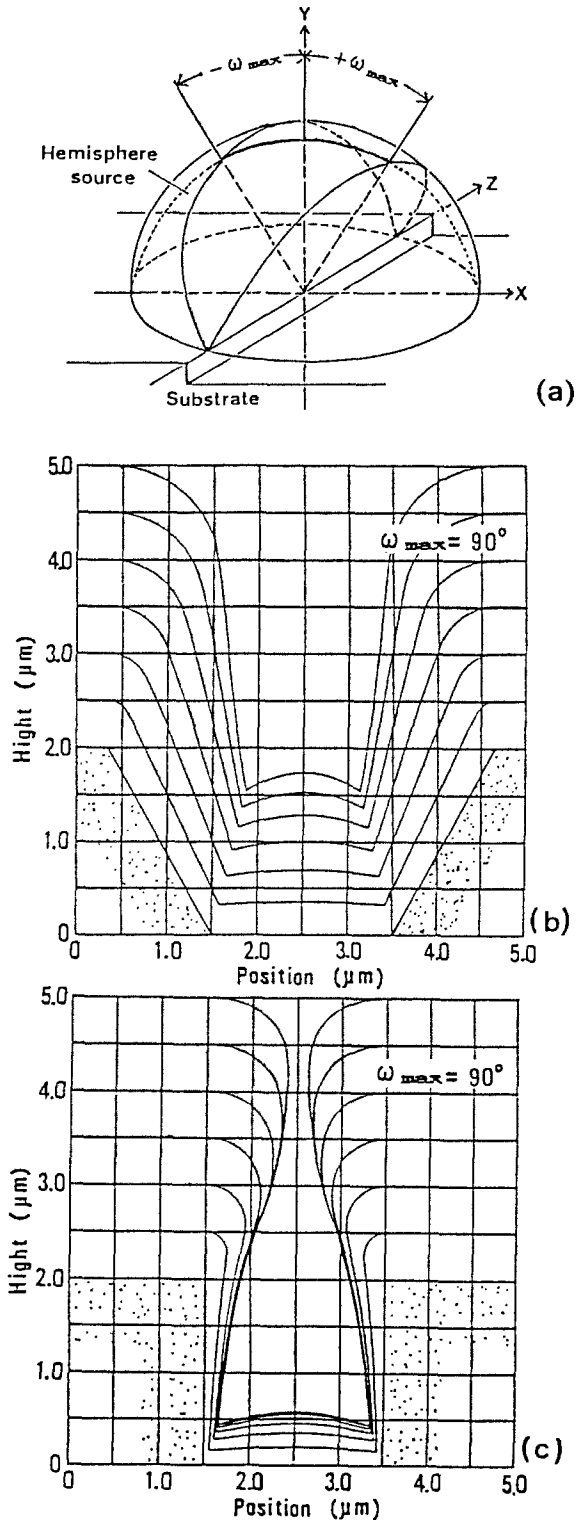


Fig. 3. Examples of calculated figure following Blech's model. a: Definition of the particle incident angle ω_{max} . Particles flow onto the substrate isotropically through a sliced hemisphere surface over the angular range $\pm\omega_{max}$. b: Cross section around a 60° sloped groove. c: Cross section around a vertical groove.

the self-shadowing effect becomes the major effect. The situation for actual vias would become much more severe, since the results are for two-dimensional grooves and the influence of the self-shadowing effect increases more around three-dimensional vias.

It can be concluded from these results that conventional deposition methods, in which particles simply flow on to and stick on the substrate, cannot achieve adequate step coverage around fine vias for future VLSI metallization. Thus, new deposition methods, such as

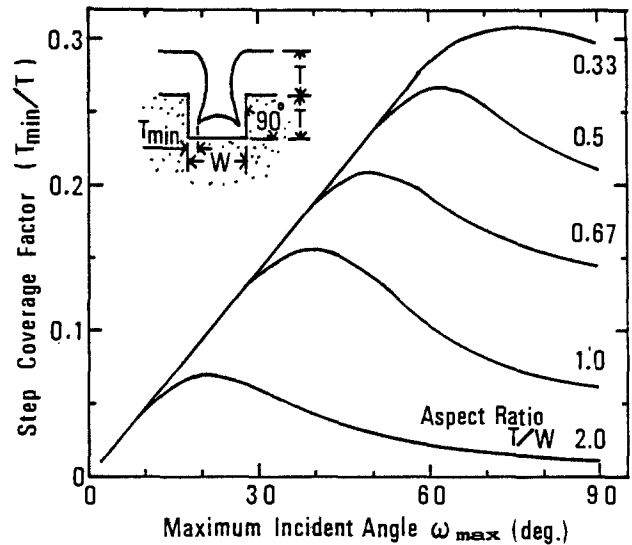


Fig. 4. Influence of groove aspect ratio on film step coverage

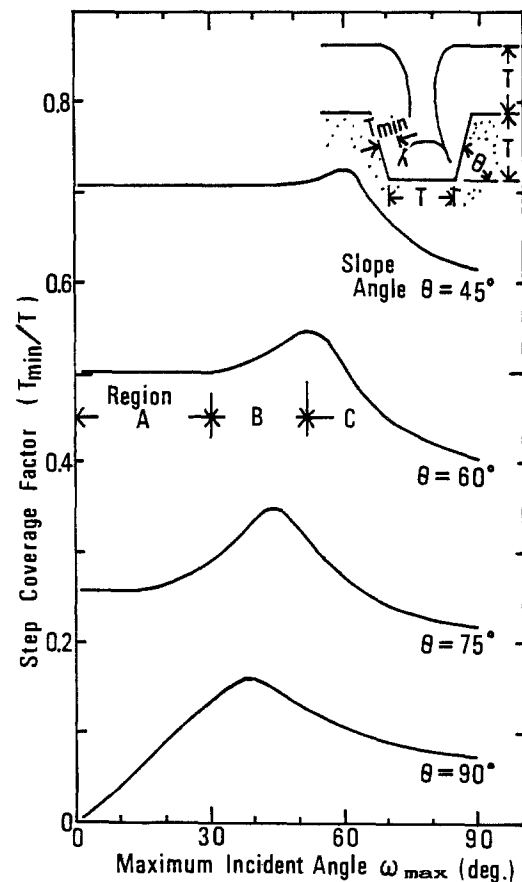


Fig. 5. Influence of groove profile on film step coverage. The aspect ratio of the grooves is 1.

those using surface migration or surface reaction effect, appear to be necessary.

Resputtering effect in aluminum bias sputtering.—Bias sputtering for metals has been mainly used for improving film quality (13). The existence of the planarization effect in metal bias sputtering due to resputtering effect had not been documented (11). We first tried to confirm the existence of the resputtering effect by utilizing the planar magnetron bias sputtering system (6). It was recently reported that the aluminum film step coverage was improved by using an MRC 603 bias sputtering system (14). However, the improvements were slight and it could be argued that the effects were due to surface reflow or a

migration effect caused mainly by an increase in substrate temperature. Such an interpretation is possible because the resputtering effect was not confirmed in the work, and substrate heating as reported in the work could improve surface migration effect and step coverage.

The influence of substrate biasing on the aluminum deposition rate is shown in Fig. 6. Though a strict measurement of the resputtering rate is difficult, it can be defined practically as follows

$$\text{Resputtering rate} = \frac{D_N - D_B}{D_N}$$

where D_N and D_B are deposition rates without and with substrate biasing, respectively, under the same cathode RF power (15).

The figure shows that the aluminum deposition rate decreases when RF power is applied to the substrate electrode. This reduction of the deposition rates corresponds to the resputtering rates from 50 to 70% as the cathode RF power is varied, while the substrate RF power is kept constant. It is reasonable that such an extreme reduction in deposition rate was caused by the resputtering effect rather than the substrate temperature increase due to biasing. The resputtering rates when aluminum films were deposited under Ar pressure of 0.13 Pa were larger than those under 6.7 Pa. Similar effects were observed when the films were deposited with dc power to the cathode and RF power to the substrate electrode.

Effects of deposition conditions on film quality.—The effects of substrate biasing on film crystalline structure were investigated utilizing x-ray diffractometry. It was previously reported that substrate biasing gives aluminum films a (111) texture (16). However, in that report, the influence of substrate temperature increase due to substrate biasing on crystalline structure was overlooked. Therefore, it was not determined whether the texture was the result of the resputtering effect or the substrate temperature increase due to biasing during deposition.

Four kinds of test samples were prepared, as shown in Table I, to clarify this point. Samples a and b were made through normal dc sputtering without substrate biasing, and, in both samples, films were deposited under almost identical sputter conditions with the exception of sub-

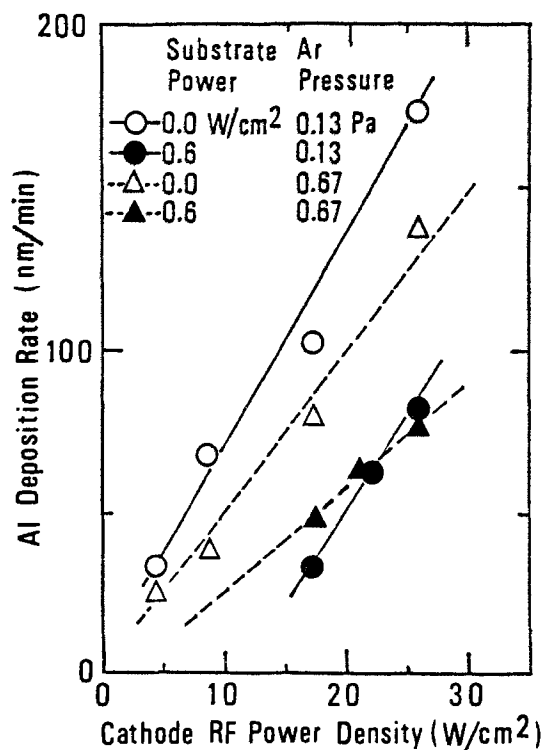


Fig. 6. Effects of substrate biasing on aluminum deposition rate

strate temperature. A comparison of these two samples shows the influence of substrate temperature during deposition on the film crystalline structure. Samples b and c were made under nearly the same deposition rate and substrate temperature conditions but without and with RF substrate biasing, respectively. Thus, a comparison of these two samples shows the influence of substrate biasing on film crystalline structures. Sample d was made with a higher resputtering rate to show the effect of an increment in resputtering rate.

Measurements made with conventional x-ray diffractometry are shown in Fig. 7, and a standard ASTM diffraction pattern is also shown for comparison. The other four figures represent the results for each sample. Sample a, deposited normally at low deposition temperature, shows no special preferred orientations. On the other hand, sample b, deposited normally at a higher temperature, shows a strong (111) texture, although some amount of other orientation textures still remain. Higher deposition temperatures strongly influence aluminum film toward a (111) texture.

However, samples c and d, deposited through bias sputtering, show almost complete (111) texture. Furthermore, although the deposition temperature for sample d was lower than for sample c, there was little difference be-

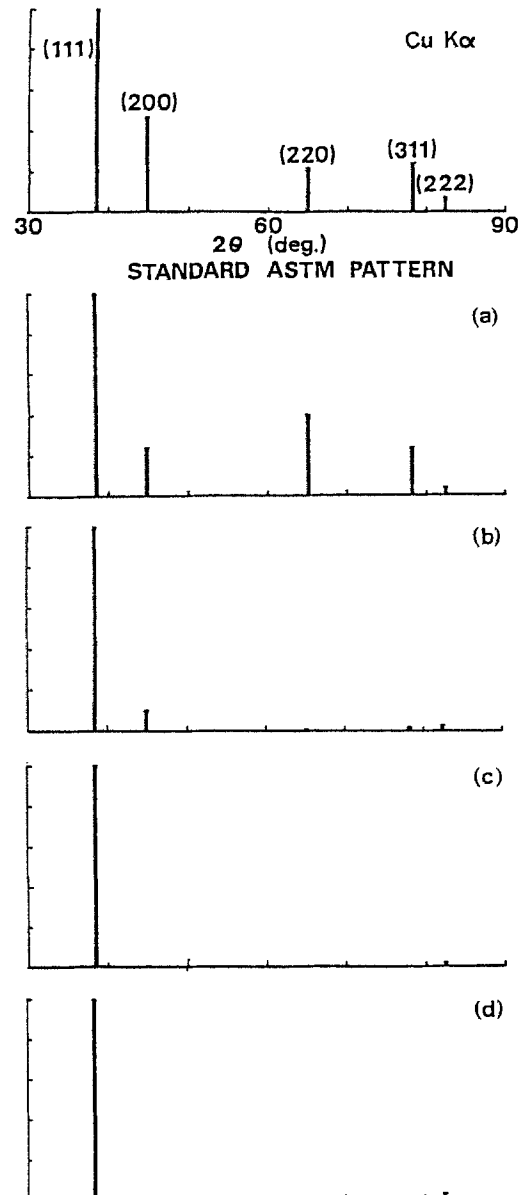


Fig. 7. Influence of aluminum deposition conditions on film crystalline structure. Cu K_{α} x-rays were used.

Table I. Aluminum deposition conditions in crystalline structure evaluation

Sample no.	Ar pressure (Pa)	Cathode dc power (W/cm ²)	Substrate RF power (W/cm ²)	Resputtering rate (%)	Deposition rate (nm/min)	Substrate temperature (°C)
a	0.67	1.74	0	0	176	23
b	0.67	1.73	0	0	175	173
c	0.67	1.88	0.6	17	158	~150
d	0.67	0.82	0.6	38	50	~100

tween results for these two samples. From these results, it can be concluded that substrate biasing has a decisive influence in giving aluminum film structures an almost complete (111) texture, and that this phenomenon is caused by the resputtering effect rather than substrate temperature increase during deposition. The influence of substrate biasing on impurity concentration in the film was also investigated by SIMS, but no significant difference could be observed.

Planarization effect in bias-sputtered aluminum film.—The influence of substrate biasing on aluminum step coverage was evaluated by depositing the films on vertically dry-etched SiO₂ grooves, as shown in Fig. 8. The films were deposited at temperatures lower than 250°C. Both the width and the depth of the grooves are 1.5 μm. The aluminum was deposited on these substrates, and the cross sections were observed by etching the front sides of the aluminum films.

Fig. 8. Cross-sectional comparison of aluminum films deposited on vertical grooves. a: Resputtering rate of 0%. b: Resputtering rate of 40%. c: Resputtering rate of 50%. d: Resputtering rate of 70%. The aspect ratio of the grooves is about 1.

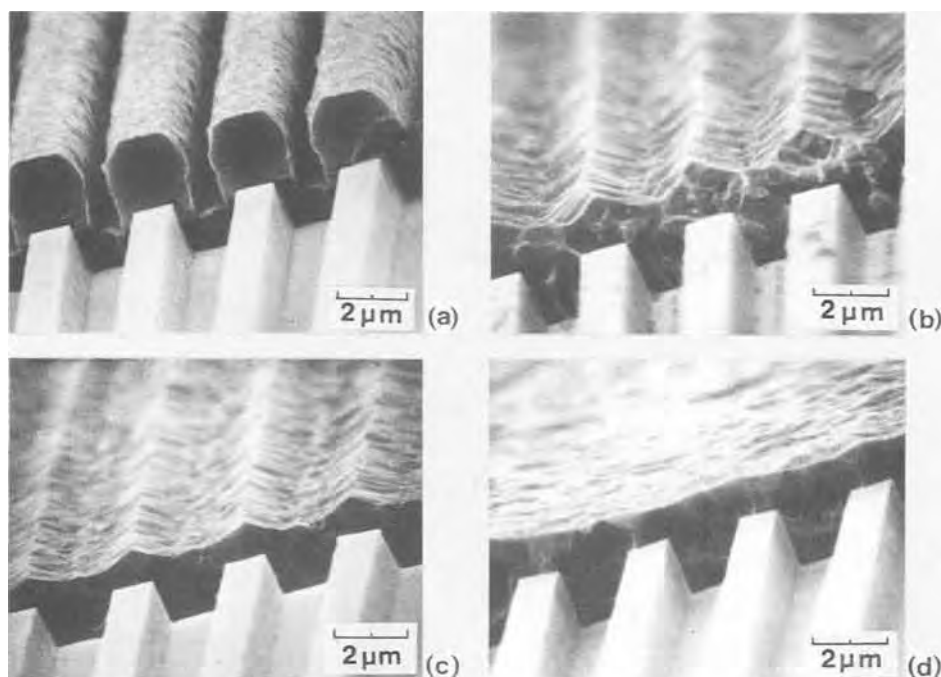
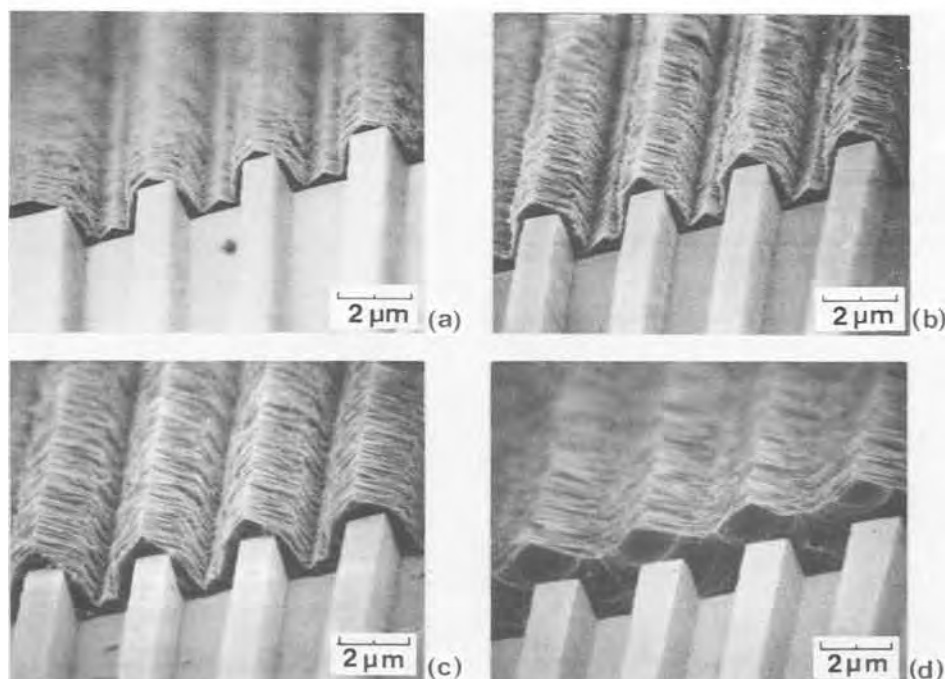


Fig. 9. Change of bias-sputtered aluminum film as a function of deposition time. a: 3 min. b: 6 min. c: 9 min. d: 18 min. The resputtering rate is about 50%.



A cross section of the normally sputtered aluminum film on the vertical grooves is shown in Fig. 8a. The step coverage factor of the film is estimated to be less than 0.2, due to the self-shadowing effect, as shown in the figure. However, the cross sections of aluminum films deposited with substrate biasing show an extreme change. As shown in Fig. 8b, the film deposited at about 40% resputtering rate connects the aluminum film surfaces on top of the grooves to each other, but small crevices can be seen in the middle of the grooves. As the resputtering rate exceeds 50%, the grooves fill up completely with aluminum, and the degree of film surface planarization improves with the rate increase, as shown in Fig. 8c and 8d. The film surface, deposited at about a 70% resputtering rate, was planarized almost completely. In the cases shown in c and d, the conventional term "step coverage" has no meaning. "Filling factor" or "surface planarity" may be more suitable.

The change in film cross section around the grooves as a function of deposition time is shown in Fig. 9. These SEM micrographs illustrate how the bias-sputtered aluminum films fill up the vertical grooves of aspect ratio 1. The resputtering rate in this experiment was about 50%. As can be seen from these micrographs, the bias-sputtered aluminum particles deposit first primarily near the bottoms of the vertical sidewalls. As the film grows, the grooves become shallower and are finally filled up completely. This suggests that some portion of the aluminum particles deposited around the upper edges of the grooves is etched by Ar ions and is deposited inside of the grooves again. Thus, the particles fill up the grooves without the influence of the shadowing effect.

Via filling up with bias-sputtered aluminum.—The aluminum bias sputtering technique was applied to fill up small, high aspect ratio vias. Figure 10a shows an SEM micrograph of $2.5 \mu\text{m}$ deep, $2 \times 2 \mu\text{m}^2$ vias formed in a bias-sputtered SiO_2 film. The aspect ratio of the vias is about 1.2. The SEM micrograph in which the aluminum film was deposited normally is shown in Fig. 10b. In the figure, a significant shadowing effect can be observed which results in poor step coverage. In contrast, by depositing aluminum film at about a 50% resputtering rate, the vias were filled up completely, and only very gently sloped, shallow depressions remained on the film surface, as shown in Fig. 10c.

Cross sections of these test samples were observed utilizing cross-sectional polishing, as shown in Fig. 11. Via sizes in the SEM micrographs are 2×2 , 1.5×1.5 , and $0.8 \times 0.8 \mu\text{m}^2$, respectively. From these micrographs, it

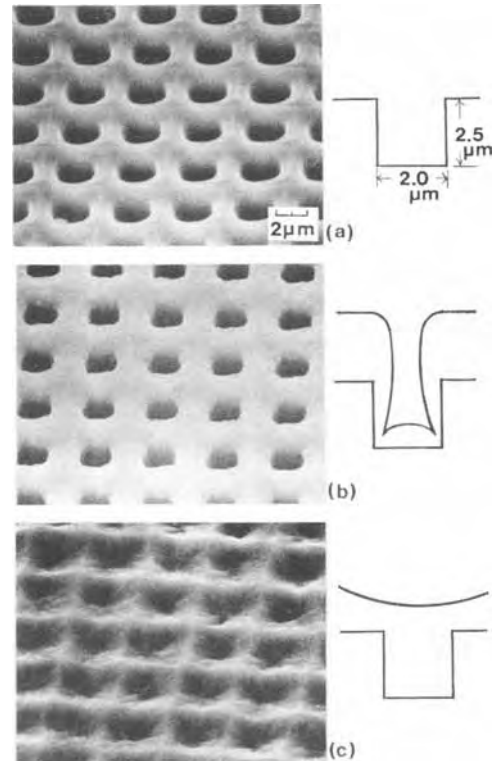


Fig. 10. Via filling with bias-sputtered aluminum film. a: Vias produced through dry etching in bias-sputtered SiO_2 . b: Normally sputtered aluminum surface. c: Surface of bias-sputtered aluminum deposited at about 50% resputtering rate.

can be seen that even a $0.8 \times 0.8 \mu\text{m}^2$ via, whose aspect ratio is about 3, can be completely filled up with aluminum by bias sputtering. It can be seen from these results that bias sputtering for metals should become a very effective technique for near-future VLSI interconnection.

Summary

A new metal deposition technique, i.e., RF/dc sputtering with RF bias for metal, was developed to solve the step coverage problem in VLSI multilevel interconnection. An application of the technique to aluminum film deposition confirmed the existence of the resputtering effect. Through sputtering at a high bias, aluminum

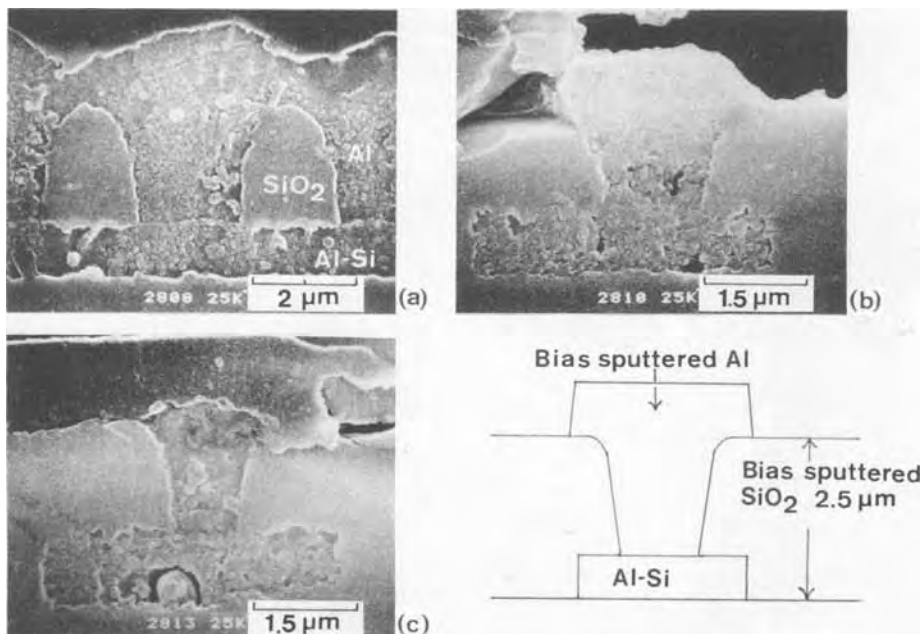


Fig. 11. Cross section of vias filled up with bias-sputtered aluminum. a: Via of aspect ratio 1.2. b: Via of aspect ratio 1.8. c: Via of aspect ratio 3.

particles were found to be deposited primarily near the bottom of the depressions and to fill up the depressions completely. By deposition at resputtering rates higher than 50%, the aluminum film was found to fill up steep, deep grooves and vias, even when the aspect ratio was as high as 3. It was shown that substrate biasing has a decisive effect on giving aluminum films an almost complete (111) crystallographic texture. It was also confirmed that these effects were obtained by the resputtering effect itself rather than by the substrate temperature increase associated with substrate biasing.

Acknowledgments

The authors wish to thank the following members of Hitachi Limited's Central Research Laboratory: Dr. Shojiro Asai, Dr. Kiichiro Mukai, and Dr. Takashi Nishida for their stimulating discussions and encouragement; Akio Yajima of the laboratory, who helped the authors in the computer simulation step coverage evaluation; and Dr. Eisuke Mitani and Dr. Tsutomu Ishiba for their help in supplying the analysis by SIMS and x-ray diffractometry experimental data.

Manuscript submitted Oct. 12, 1984; revised manuscript received Feb. 1, 1985.

Hitachi Limited assisted in meeting the publication costs of this article.

REFERENCES

1. Y. Homma, S. Harada, and T. Kaji, *This Journal*, **126**, 1531 (1979).
2. T. Nishida, A. Saiki, Y. Homma, and K. Mukai, *Tech. Dig. IEEE IEDM*, 552 (1982).
3. C. Y. Ting, V. J. Vivalda, and H. G. Scheafer, *J. Vac. Sci. Technol.*, **15**, 1105 (1978).
4. S. Tsunekawa, Y. Homma, and S. Harada, Abstract 282, p. 436, The Electrochemical Society Extended Abstracts, Vol. 83-2, Washington, DC, Oct. 9-14, 1983.
5. K. Ito, H. Hori, J. Etoh, S. Asai, N. Hashimoto, K. Yagi, and H. Sunami, *ISSCC Dig. Tech. Papers*, 282 (1984).
6. Y. Homma and S. Tsunekawa, Abstract 283, p. 438, The Electrochemical Society Extended Abstracts, Vol. 83-2, Washington, DC, Oct. 9-14, 1983.
7. C. R. Fuller and P. B. Ghate, *Thin Solid Films*, **64**, 25 (1979).
8. P. B. Ghate, *ibid.*, **93**, 359 (1982).
9. I. A. Blech, *ibid.*, **6**, 113 (1970).
10. Y. Homma, A. Yajima, and S. Harada, *IEEE Trans. Electron Devices*, **ed-29**, 512 (1982).
11. J. B. Bindell and T. C. Tisone, *Thin Solid Films*, **23**, 31 (1974).
12. I. A. Blech, *Solid State Technol.*, **26**, (12) 123 (1983).
13. J. Nagano, *ibid.*, **67**, 1 (1980).
14. G. Hughes and C. Ridge, *Vacuum*, **34**, 365 (1984).
15. L. I. Maissel, R. E. Jones, and C. L. Standley, *IBM J. Res. Dev.*, **14**, 176 (1970).
16. J. F. Smith, F. T. Zold, and W. Class, *Thin Solid Films*, **96**, 291 (1982).

Evaluation of the Phosphorus Concentration and Its Effect on Viscous Flow and Reflow in Phosphosilicate Glass

R. A. Levy,* S. M. Vincent, and T. E. McGahan

AT&T Bell Laboratories, Murray Hill, New Jersey 07974

ABSTRACT

This study describes the use of x-ray fluorescence as an analytical tool for determining phosphorus concentration in phosphosilicate glass. By comparison with other available methods, we shall demonstrate that this direct measurement technique is accurate, simple, fast, reproducible, and nondestructive. With the use of this technique, flow and reflow profiles of phosphosilicate glass will be illustrated at different phosphorus concentrations and representative thermal cycles.

Low pressure chemical vapor deposited phosphosilicate glass (PSG) serves a variety of important functions in the fabrication of semiconductor devices (1). It is widely used as a dielectric to insulate gate interconnects from metallization, as a getter of sodium and other rapidly diffusing metal ions, as a material that undergoes viscous flow to provide a planar topography, as a passivation overcoat to provide mechanical protection, and as a solid diffusion source of phosphorus in silicon. Since the properties of the PSG, which make it useful in a given application, are directly related to the phosphorus concentration, a technique which can offer an accurate, nondestructive, fast determination of the composition becomes very desirable in an IC processing line. Many techniques have been used to measure phosphorus concentration in phosphosilicate glass. These include wet chemical analysis (2, 3), neutron activation (4, 5), Auger electron spectroscopy (6), electron microprobe (7), energy dispersive x-ray spectrometry (8, 9), x-ray fluorescence (10-12), infrared absorption (13), refractive index determination (5), etch rate variation (2, 4, 14, 15), and diffusion techniques (4, 16). Although tedious and time consuming, wet chemical analysis, which is independent of film thickness, phosphorus content, or any variation in phosphorus throughout a wafer, is considered by the industry as the primary standard. Neutron activation, Auger electron spectroscopy, electron microprobe, and energy dispersive x-ray spectrometry all require sophisticated and expensive equipment, skilled engineers, lengthy sample preparation procedures, and destruction of the specimens. Infrared absorption, index of refraction determination, etch-rate variation, and diffusion techniques are relatively simple but lack the required accuracy and reproducibility. In this study, we describe the use of x-ray fluorescence as an analytical tool for determining phosphorus concentration in phosphosilicate glass. We shall demonstrate that this direct bulk measurement technique is simple, fast, accurate, reproducible, and nondestructive. However, as is typical of all other analytical techniques which yield relative results, it requires proper standardization. Based on a compilation of x-ray fluorescence data and results gathered on the identical PSG films with electron microprobe and energy dispersive x-ray (EDS) analysis, a correlation among all three techniques will be established. We shall then proceed to examine the effect of phosphorus concentration on the viscous flow and reflow profiles of PSG at representative thermal cycles.

Electrochemical Society Active Member.

Principles of X-Ray Fluorescence Analysis

In the x-ray fluorescence technique, electrons accelerated within the system generate, by collision with a metal target, x-rays which are directed toward the sample. These primary x-rays activate orbital electrons within the sample that cause emission of secondary x-rays which are analyzed. The principles governing the operation of the electron microprobe are quite similar, with the exceptions that no target is used and that the electrons, in this case, are directly accelerated toward the sample. Since x-rays cannot be focused and are more penetrating than

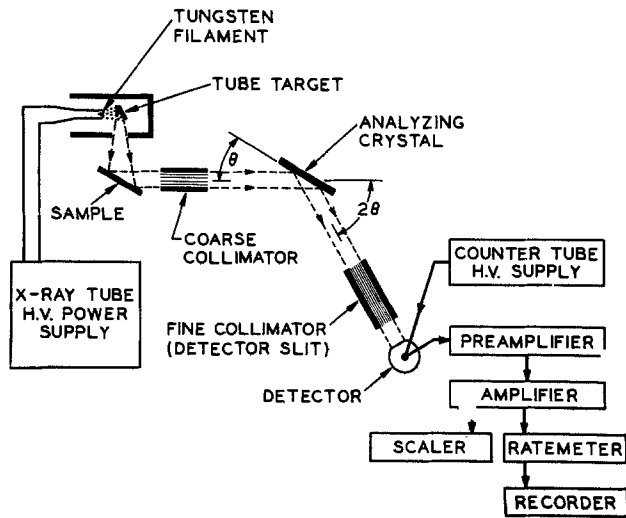


Fig. 1. Schematic representation of the x-ray fluorescence apparatus

electrons, the fluorescence technique represents more of a bulk measurement than the microprobe. That could be an advantage if large local fluctuations in phosphorus concentration exist across the sample.

A schematic representation of the x-ray fluorescence apparatus used throughout this investigation is shown in Fig. 1. The mode of operation includes three basic functions, namely, excitation, detection, and analysis. The excitation system consists of an EA 75 dual target (Cr-W) tube driven by a General Electric XRD-6 power supply operated at 50 kV and 60 mA. The analyzing system utilizes a coarse collimator, a graphite crystal with a 2d spacing of 6.704 Å, and a 250 μm Soller slit. In order for the Bragg equation to be always satisfied for a given x-ray wavelength, the graphite crystal is coupled to the detector and detector slit through a spectrogoniometer which automatically rotates the detector and its associated slit by 2θ while the crystal rotates by θ. The detection system includes an Ar-10%CH₄ flow proportional counter operated at 1480V and assorted electronic modules to amplify the pulses and display the count rate.

For thin films, the observed intensity at a given wavelength is related to film thickness and the concentration

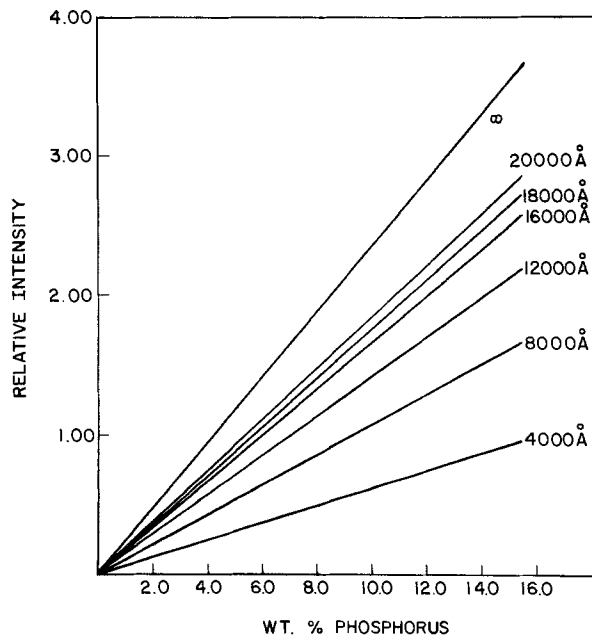


Fig. 2. Calculated curves of relative intensity vs. w/o P for PSG films of constant thickness. Values of A and B used were $4.5874 \times 10^{-26} \text{ cm}^3/\text{at.}\cdot\text{Å}$ and $7.5331 \times 10^{-4} \text{ Å}^{-1}$, respectively.

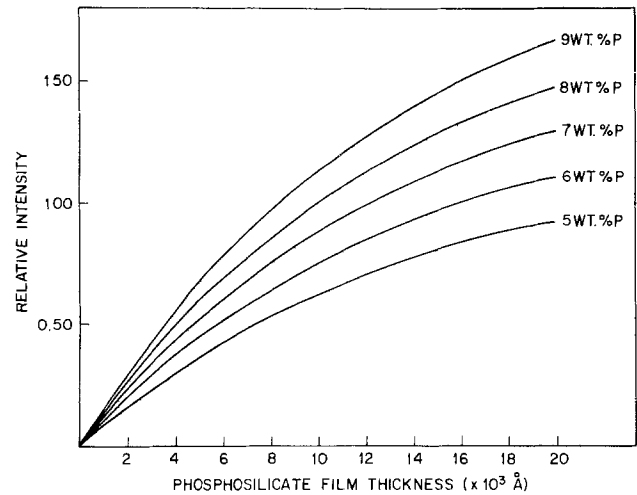


Fig. 3. Calculated curves of relative intensity vs. film thickness for PSG films of constant w/o P. Values of A and B used were $4.5874 \times 10^{-26} \text{ cm}^3/\text{at.}\cdot\text{Å}$ and $7.5331 \times 10^{-4} \text{ Å}^{-1}$, respectively.

of the corresponding element emitting the radiation, through the equation (17, 18)

$$I = \frac{AP}{B} (1 - e^{-BT}) \quad [1]$$

where I is the emitted radiation in normalized counts, T the film thickness in units of angstroms, P is the concentration of the element emitting the radiation (in this case, phosphorus), and A is a parameter that includes the five separate factors involved in the excitation process, which are, as stated by Jenkins and De Vries (17): (i) the number of primary photons striking the sample surface per unit time; (ii) the attenuation of this intensity by the absorbing matrix; (iii) the efficiency of the actual excitation of characteristic radiation; (iv) the proportion of these photons which are accepted by the collimator; and (v) the attenuation of the characteristic radiation by the sample matrix. B is a parameter that depends on the mass absorption coefficient and density of the sample matrix as well as

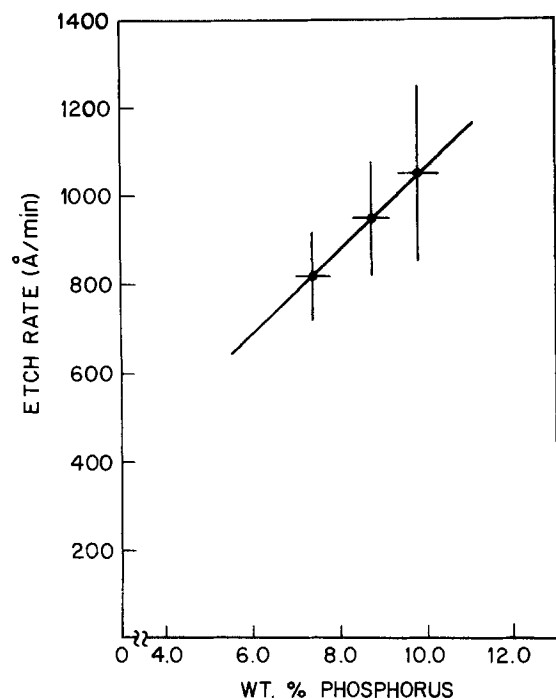


Fig. 4. Plot of average rate for densified PSG films in 30:1 BOE as a function of w/o P. Densification cycle was 1100°C for 20 min in 99% N₂-1% O₂.

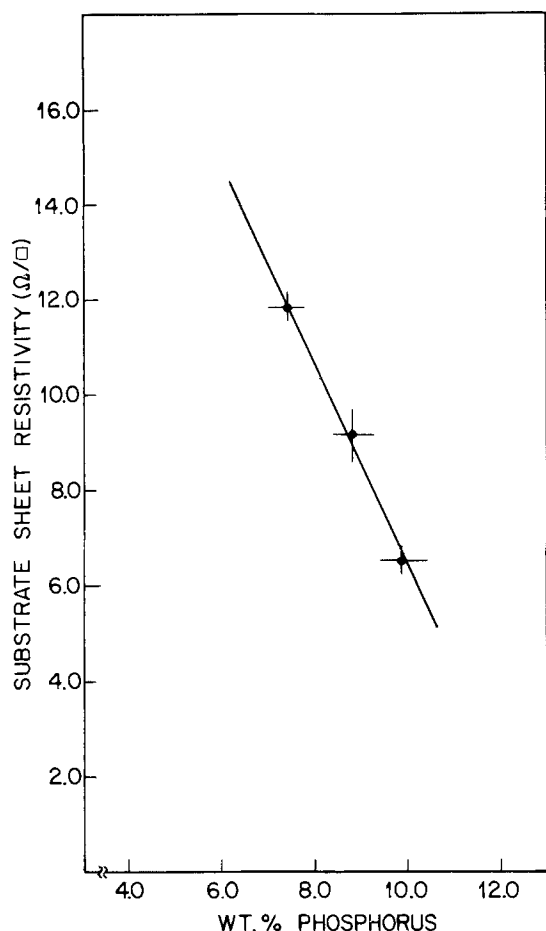


Fig. 5. Plot of average sheet resistivity in (100) p-type silicon (1-10 Ω -cm) as a function of w/o P. Thermal drive was 1100°C for 20 min in 99% N_2 -1% O_2 .

x-ray path correction factors. Since both A and B are functions of the density of the sample matrix, the assumption that these parameters will be constant can only be valid over a limited range of phosphorus concentrations.

Measurement Procedure

With a stabilized power supply to the x-ray tube and proportional counter, and with the goniometer set at an angle of 133.33° to satisfy the Bragg equation for phosphorus $K\alpha$ radiation, the measurement procedure is initiated by placing the standard wafer onto an aluminum mask with a $\frac{1}{4} \times \frac{1}{8}$ in. window in the experimental chamber. The x-ray shutter is open and the ambient gas in the chamber flushed out with He to minimize absorption of phosphorus radiation. After an equilibration time of about 30s, the counter is activated and P $K\alpha$ counts are taken, typically, at a fixed 100s interval. This procedure is repeated after removal of the standard and insertion of the test sample. A sequence of up to ten measurements

Table I. Characterization of standards

Sample	Thickness (Å)	Phosphorus concentration ($\times 10^{20}$ at./cm ³)	Phosphorus concentration (w/o)	Normalized intensity
P03	5,899	28.3	7.28	0.614
P06	10,363	28.8	7.42	0.933
P13	15,784	28.5	7.33	1.237
P31	22,906	35.1	9.03	1.729
P37	8,814	34.3	8.82	1.000
P42	6,127	34.7	8.94	0.797
P53	10,153	38.6	9.93	1.231
P60	14,662	39.8	10.24	1.658
P63	19,902	40.9	10.52	1.939
P68	6,023	39.2	10.08	0.866

Table II. Comparison of calculated and measured values of normalized intensity

Sample	Calculated values of normalized intensity	Measured values of normalized intensity	Residuals	Percentage deviation
P03	0.618	0.614	-0.004	-0.65
P06	0.950	0.933	-0.170	-1.82
P13	1.207	1.237	+0.030	+2.43
P31	1.757	1.729	-0.028	-1.62
P37	1.013	1.000	-0.013	-1.30
P42	0.781	0.797	+0.016	+2.01
P53	1.257	1.231	-0.026	-2.11
P60	1.620	1.658	+0.038	+2.29
P63	1.934	1.939	+0.005	+0.26
P68	0.871	0.866	-0.005	-0.58

Table III. Determination of PSG density

Sample	Thickness (Å)	Area (cm ²)	Volume ($\times 10^{-4}$ cm ³)	Mass ($\times 10^{-3}$ g)	Density (g/cm ³)
P03	5,899	5.36	3.162	0.673	2.128
	5,899	3.96	2.336	0.494	2.115
P06	10,363	2.98	3.088	0.623	2.017
P13	15,784	1.84	2.904	0.600	2.066
P31	22,906	1.72	3.940	0.788	2.000
P37	8,814	2.10	1.851	0.375	2.026
	8,814	1.62	1.428	0.302	2.115
P42	6,127	3.13	1.918	0.393	2.049
P53	10,153	2.31	2.345	0.508	2.166
P60	14,662	2.01	2.947	0.692	2.348
P63	19,902	1.73	3.443	0.785	2.280
P68	6,023	3.11	1.873	0.412	2.200
	6,023	2.30	1.385	0.321	2.318

can be taken before reintroducing the standard wafer for calibration purposes. The elapsed operation time which includes loading, equilibration, and measurement periods has been estimated to amount to less than 3 min/wafer, proving x-ray fluorescence analysis to be one of the fastest available techniques for determination of phosphorus concentration in phosphosilicate glass. Furthermore, the fact that whole wafers can be accommodated in the system with no pre- or postsample preparation qualifies x-ray fluorescence as a nondestructive technique. Possibilities of radiation-induced damage to the device become nonexistent after the subsequent high temperature flow or reflow processing steps. From values of normalized intensity, I , given by the ratio of test wafer count rate to standard wafer count rate, and film thickness, the phosphorus concentration in PSG is determined for known constant values of A and B . These constants were calculated from a systematic investigation of a set of ten PSG samples (to be referred to as "standards") with various phosphorus concentrations and film thicknesses. The PSG films were deposited directly onto p-type (1-10 Ω -cm) silicon wafers in a low pressure CVD (LPCVD) reactor using SiH_4 , O_2 , and PH_3 as source materials. The PH_3 gas flow or deposition time was adjusted in each run to achieve the desirable phosphorus concentration or film thickness, respectively. Half-wafers from this set of standards were forwarded to Balazs Analytical Laboratory¹ for chemical analysis, with the corresponding halves undergoing x-ray fluorescence measurements in adjoining parts of the samples. Table I identifies the samples investigated with their characteristic thickness, phosphorus concentration expressed in at./cm³ and weight percent (w/o) P, and count rate normalized to a selected sample (P37) which was midrange in phosphorus concentration. A computer program with a nonlinear curve fitting routine was then used to calculate the values of A and B from the best fit of the data to Eq. [1]. (A summary of the program logic is described in the Appendix.) The value of A was determined to be equal to

¹ Balazs Analytical Laboratory, Mountain View, California 94043.

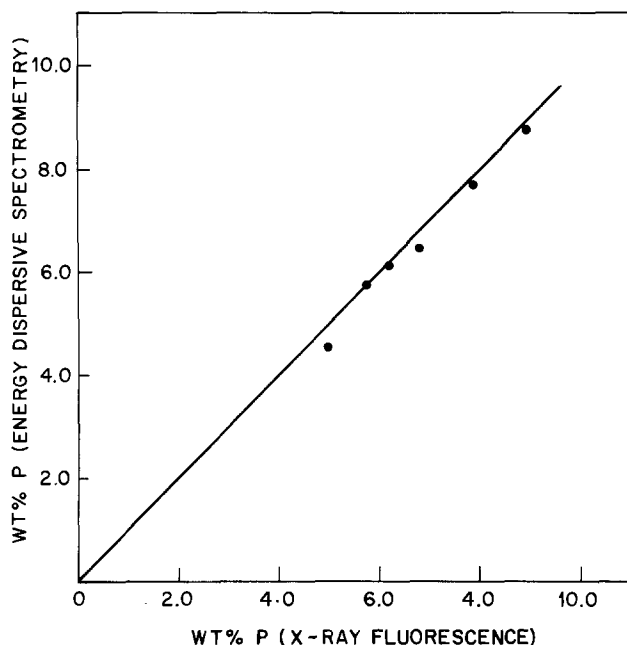


Fig. 6. Graphical representation of degree of correlation between energy dispersive spectrometry and x-ray fluorescence.

$4.5874 \times 10^{-26} \text{ cm}^3/\text{at}\cdot\text{\AA}$ and that of B equal to $7.5331 \times 10^{-4} \text{ \AA}^{-1}$. In Table II, a comparison between calculated and measured values of normalized intensities yielded a percent deviation less than $\pm 2.5\%$, confirming the validity of the theoretical model used in the derivation of Eq. [1].

In wet chemical analysis, the percentage of P in PSG is determined from accurate measurements of the mass of the film. That is accomplished from an evaluation of sample weight loss due to dissolution of PSG in an HF-based mixture. The samples are then run against known standards of the same species using colorimetric spectrophotometry. From measurements of the mass and those of the corresponding test area, the density of PSG has been calculated with the results summarized in Table III. For samples with up to 9 w/o P, the average density, ρ , of LPCVD phosphosilicate glass exhibits a value of $2.06 \pm 0.05 \text{ g/cm}^3$, in excellent agreement with the reported value (10) of 2.00 g/cm^3 for atmospheric pressure CVD films with phosphorus in the range of 1.31-9.00 w/o. At ~ 10 w/o P, our results indicate an increase on the order of $\sim 7\%$ in the value ρ , pointing to a potential loss in accuracy for the x-ray fluorescence technique at these higher concentrations. For consistency's sake, a value of $\rho = 2.0 \text{ g/cm}^3$ has been systematically used in all calculations.

Figure 2 illustrates the calculated curves of relative intensity vs. w/o P for films of constant thickness. As expected, the linear curves intercept the origin and exhibit in the limit as $T \rightarrow \infty$ a slope equal to the ratio A/B . In Fig. 3, the calculated curves of relative intensity vs. film thickness are shown for phosphorus concentrations in the operating range of 5-9 w/o. The results, in this case, convey the message that at film thicknesses as high as $2 \mu\text{m}$, a saturation regime has yet to be reached.

Correlation of Results

From the group of standards, representative samples with phosphorus concentrations of 7.42, 8.32, and 9.93 w/o were selected to investigate the etch-rate and substrate sheet resistivity variations of densified PSG films. Densification of these films was performed in the center zone of a diffusion furnace at 1100°C for 20 min in a $99\% \text{N}_2$ - $1\% \text{O}_2$ ambient. The etching experiments were carried out at room temperature (22°C) in a 30:1 buffered HF solution (30 parts $40\% \text{NH}_4\text{F}$ to 1 part $49\% \text{HF}$ by volume). The film thickness was measured with an interferometer after 1 min intervals in the etch bath. A total of five readings was taken for each of the samples so as to extend the analysis down to depths of over 4000 \AA . Figure

4 exhibits the observed dependence of etch rate ($\text{\AA}/\text{min}$) on w/o P over this investigated range of concentrations. A linear fit through the data emerges with a perfect correlation factor ($R^2 = 1.000$) and a variation in etch rate, as calculated from the slope of the curve, of $92 \text{ \AA}/\text{w/o P}$. However, the scatter in the data, reflecting the slower etch rate at the surface, appears to widen with higher phosphorus concentration. Predictably, as a consequence of Henry's law (19), this is caused by higher phosphorus evaporation, from the surface of samples with a higher phosphorus content, during densification. Following these etch-rate experiments, the samples were stripped in an HF solution down to the bare silicon substrate surface and the sheet resistivity measured with a four-point probe at four sites across each sample. The average sheet resistivity together with its associated standard deviation is plotted in Fig. 5. The substrate sheet resistivity is observed, here, to increase with lower w/o P in the PSG film reflecting the decrease in substrate surface free carrier concentration. The rate of variation, calculated from the slope of a linear fit of the data, yields in this limited range of phosphorus concentration a value of $-2.1 \Omega/\square/\text{w/o P}$.

Since electron microprobe (EM) analysis and energy dispersive x-ray spectrometry (EDS) are routinely used in the determination of phosphorus, a comparative analysis of the standards becomes a prerequisite in establishing a cross correlation among EM, EDS, and x-ray fluorescence. The selected standards for this experiment are listed in Table IV with the corresponding results of chemical analysis, electron microprobe, and energy dispersive spectrometry. The EM analysis was conducted in a Cameca MBX system at a 6 keV accelerating potential with Si, O, and P $K\alpha$ lines being examined. Intensity corrections were made to account for atomic number, fluorescence, and absorption effects. GaP was used as a standard for P and thermal oxide (SiO_2) as a standard for both Si and O₂. Samples coated with carbon yielded, apparently because of poor conductivity, marginal results relative to both chemical analysis and EDS. Other samples coated with Al achieved a better correlation with the chemical analysis results. Each of the EM results represents an average of five data points per sample. The EDS analysis was carried out at 5 keV in a scanning electron microscope interfaced to an Ortec EDS detector. The intensity ratio of P/Si was measured at two points on the carbon-coated samples with the results averaged. Such ratio measurements render the dependence on good conduction to be not as crucial as in case of electron microprobe analysis. The EDS system was calibrated against EM standards. Examination of Table IV reveals excellent agreement between the EDS technique and wet chemical analysis, over the investigated range of P concentrations, with recorded percent deviations typically of the order of $\pm 2\%$ for most samples. The EM results on the carbon-coated samples exhibited strong deviations, from both the chemical analysis and EDS data, most likely caused by surface charging effects. On the other hand, the

Table IV. Comparative results of chemical analysis, electron microprobe, and energy dispersive spectrometry

Sample	w/o P (Chemical analysis)	w/o P (Electron microprobe) ^a	w/o P (Electron microprobe) ^b	w/o P (Energy dispersive spectrometry)
P03	7.28	7.0		7.4
P06	7.42	6.9		7.3
P13	7.33		7.4	
P31	9.03		8.9	
P37	8.82	8.2		9.3
P42	8.94	8.2		8.8
P53	9.93	8.9		9.7
P60	10.24		9.6	
P63	10.52		10.1	
P68	10.08	9.1		9.8

^a Carbon-coated samples.

^b Aluminum-coated samples.

Table V. Comparative analysis of energy dispersive spectrometry and x-ray fluorescence

Sample	w/o P (Energy dispersive spectrometry)	(X-ray fluorescence)	Percentage deviation
RL17 (28F)	4.58 ± 0.07	4.96	+8
RL18 (28F)	5.78 ± 0.14	5.72	-1
RL19 (28F)	6.14 ± 0.08	6.19	+1
RL20 (28F)	6.47 ± 0.01	6.80	+5
RL21 (28F)	7.73 ± 0.19	7.84	+1

results on the Al-coated samples are within $\pm 1.5\%$ of the standards up to 9 w/o P, but start diverging at the higher P concentration, possibly due to the influence of matrix density changes.

These previous results lead to the next step of establishing a direct correlation between EDS and x-ray fluorescence. For that purpose, LPCVD films of phosphosilicate glass typically 10,000Å thick were deposited directly onto p-type Si wafers. The phosphorus concentration was varied from run to run by sole adjustment of the PH_3 gas flow in the LPCVD reactor. X-ray fluorescence measurements were conducted at the center of each of the wafers, followed by EDS analysis in corresponding carbon-coated areas of the sectioned wafer. Table V identifies the run number as of the tested wafer in the reactor and also lists the results and percentage of deviation between these two techniques. It is interesting to note that except for the sample with the lowest P concentration (4.96 w/o) where limitations of the EDS technique have been recognized, the results from all other samples agree to within 5%, with a majority of cases being closer to 1%. A graphical representation of the degree of correlation between these two techniques is shown in Fig. 6 where a slight trend toward systematically lower values for the EDS technique is noted. However, in view of the otherwise excellent agreement achieved, such trends in either direction are judged to be insignificant. Finally, with regard to reproducibility, x-ray fluorescence measurements gathered on the standard wafer (P37) at many interval periods in a lengthy sequence of runs have never been observed to deviate more than $\pm 1\%$.

Having established the viability of x-ray fluorescence as an analytical tool, we shall, now, use it in illustrating the effect of phosphorus concentration on the viscous flow and reflow characteristics of phosphosilicate glass.

Effect of Phosphorus on Viscous Flow and Reflow of PSG

The effect of P concentration on the viscous flow and reflow of PSG has been investigated, by SEM examination of cross sections of both monitor and patterned wafers, at representative thermal cycles. The selected monitor wafers were from runs made to generate the standards and consisted of PSG films with average P concentrations of 7.34, 8.93, and 10.19 w/o deposited directly onto p-type silicon substrates. The patterned wafers used were fabricated with a $\sim 6000\text{\AA}$ TaSi_2 over polysilicon step (20). Preceding PSG deposition, a $\sim 1000\text{\AA}$ LPCVD undoped oxide layer was deposited on all patterned wafers. The PSG deposition proceeded with the PH_3 gas flow adjusted from run to run to yield P concentrations over a range of 6.59-11.83 w/o. The P concentration of each of the product wafers was deduced from x-ray fluorescence measurements of the adjoining monitor wafer. A comparison of P concentrations on several sets of monitors positioned back to back in a given slot yielded the percentage of deviation ($\approx 2\%$) within the accuracy of the measurement technique.

Following deposition, both sets of monitor and patterned wafers underwent several high temperature processing steps. In the case of monitor wafers, samples with the three considered P concentrations were cross sectioned for SEM examination after undergoing reactive sputter etching (RSE) of windows, window reflow, and

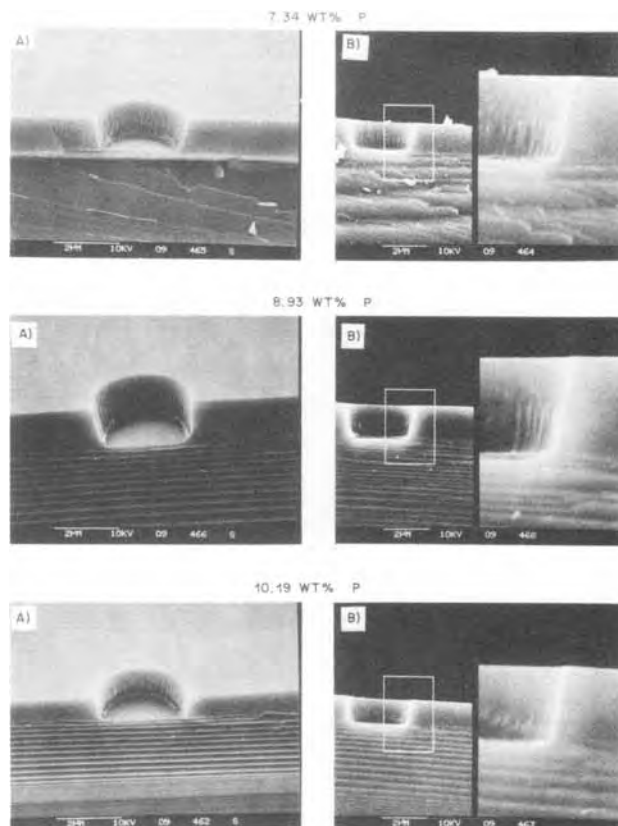


Fig. 7. Series of SEM cross sections of windows at RSE step for PSG films deposited on silicon monitors. Tilt angle was (A) $\sim 60^\circ$, (B) $\sim 90^\circ$.

aluminum metallization. In Fig. 7, a series of SEM micrographs, shot at angles close to 60° and 90° , reveal the window profile at the RSE step, following a high temperature flow ($1000^\circ\text{C}/90 \text{ min}/\text{N}_2$) and phosphorus gettering ($950^\circ\text{C}/30 \text{ min}/\text{PBr}_3$) cycles. The sharp edges and steep walls, characterizing windows of all samples, reflect the anisotropic nature of the plasma etch and are considered, at that stage, unsuitable for metal coverage with present line-of-sight deposition techniques. It is interesting to note in all samples the presence of a step extending $\sim 1000\text{\AA}$ upward from the bottom of the window. There is the possibility that the rounded bottom of the RSE contour can, due to a dry etch-rate difference at the PSG/Si interface, produce that step. A series of micrographs taken, again after window reflow ($1000^\circ\text{C}/30 \text{ min } \text{N}_2$), are shown in Fig. 8. For samples with an average P concentration of 7.34 w/o, the window edges appear adequately rounded and suitable for metal coverage. At 8.93 w/o P, there is a significant change in window geometry reflected here by the excessive rounding of the edges and sloping of the sidewalls. At 10.19 w/o P, the windows are shown to have severely receded, but no signs of a re-entrant angle are noted on any of the windows at this higher P concentration. With a remnant undoped layer on top of the PSG, the reflow is shown in Fig. 9 to be hampered, and, furthermore, due to etch-rate differences between undoped and PSG films in HF, a ledge is formed on the top surface which may disrupt continuity of the metal coverage. SEM micrographs taken on monitor wafers at the aluminum metallization step are shown in Fig. 10. The step coverage, calculated from the ratio of the aluminum thickness along the window sidewalls to that along the PSG top surface, varies, in extreme cases, from $\sim 23\%$ for samples with 7.34 w/o P to $\sim 41\%$ for samples with 10.19 w/o P. Improvements in step coverage of that magnitude for such dramatic differences in window profile emphasizes the inherent limitations, in this case, of In Source Al or similar line-of-sight deposition techniques, in providing the conformal coverage needed for further horizontal or vertical integration of devices.

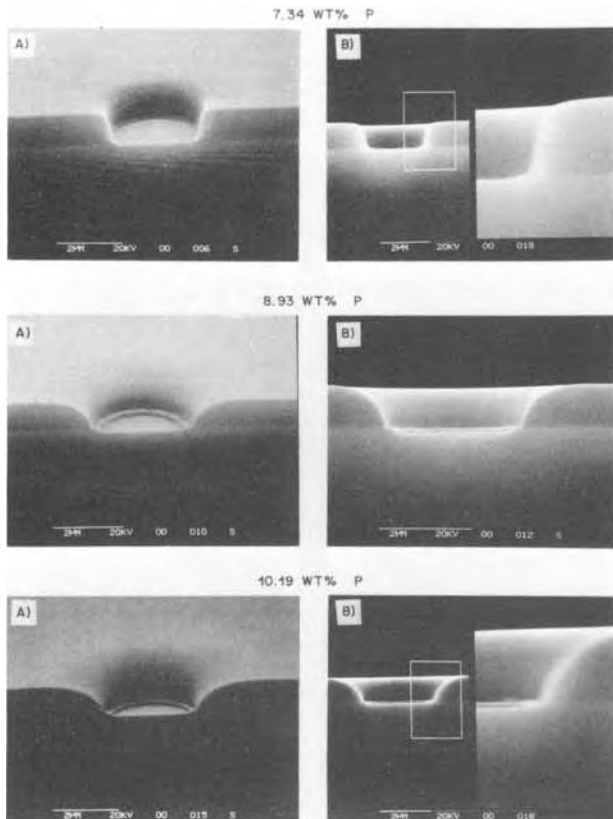


Fig. 8. Series of SEM cross sections of windows at reflow step for PSG films deposited on silicon monitors. Tilt angle was (A) $\sim 60^\circ$, (B) $\sim 90^\circ$.

The effect of bypassing the flow and gettering steps so as to minimize the thermal cycle and achieve shallower junctions was also investigated on monitor wafers with average phosphorus concentrations of 7.34, 8.93, and 10.19 w/o. The wafers were, in this case, patterned directly after PSG deposition and underwent a reflow cycle of 1000°C for 30 min in N_2 . SEM cross sections revealed window profiles similar to those of wafers which received the additional flow and gettering step. The observations emphasize the higher order dependence of viscous flow on phosphorus concentration and temperature over time.

The influence of surface topography on the viscous flow and reflow characteristics of PSG films was determined from examination of SEM cross sections of patterned wafers. The phosphorus concentration was varied, in this case, in steps of typically 0.5 w/o over a range of 6.59–11.83 w/o. Following PSG deposition, these wafers underwent, prior to aluminum deposition, several high temperature steps. Parts of each wafer were cross sectioned after reactive sputter etching the windows, after window reflow, and after a 2 min 30:1 buffered oxide etch. Figure 11 shows a series of SEM micrographs of the combined $\sim 1000\text{\AA}$ undoped oxide and PSG structure over a polycide runner after a flow ($1000^\circ\text{C}/90\text{ min}/\text{N}_2$) and gettering ($950^\circ\text{C}/30\text{ min}/\text{PBr}_3$) cycles for films with phosphorus concentrations of 6.59, 7.07, 7.34, 8.14, 8.48, and 9.09 w/o. The films are observed to exhibit profiles over steps that get progressively smoother with higher phosphorus concentration reflecting the corresponding enhancement in viscous flow. Samples from the same wafers examined after reflow yield, as shown in Fig. 12, a further reduction in topography for films with low phosphorus concentrations; however, at 7.34 w/o P or above the films are notably similar to those at the RSE step (i.e., prior to reflow). Consistent with previous observations on monitor wafers and published results (21), the window edges become, as seen in Fig. 13, progressively rounded with higher phosphorus concentration while the window sidewalls increase correspondingly their tapering angle. Inspection of the same wafers after a 2 min 30:1 buffered oxide etch did

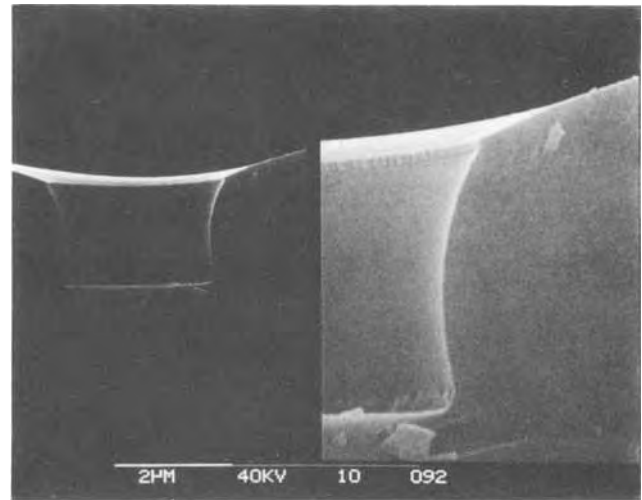


Fig. 9. SEM micrographs revealing window profile at reflow with a remnant undoped oxide on top of the PSG.

not reveal noticeable changes in the step or window profile of any of the considered phosphorus concentrations.

It is interesting in this context to point out that SEM cross sections of a patterned wafer with a measured phosphorus concentration of 11.83 w/o yielded a step and window profile, shown in Fig. 14, characteristic of PSG films with <6 w/o P. This appears to have been common amongst all wafers which exhibited a preponderance of

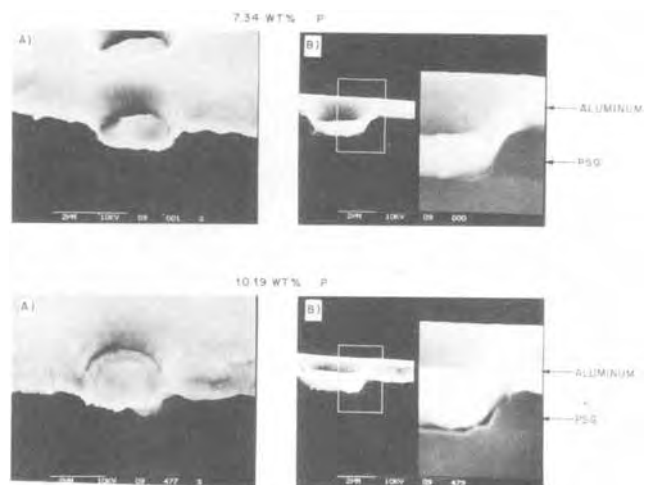


Fig. 10. SEM micrographs illustrating aluminum step coverage on PSG films with phosphorus concentrations of 7.34 and 10.19 w/o. Tilt angle was (A) $\sim 60^\circ$, (B) $\sim 90^\circ$.

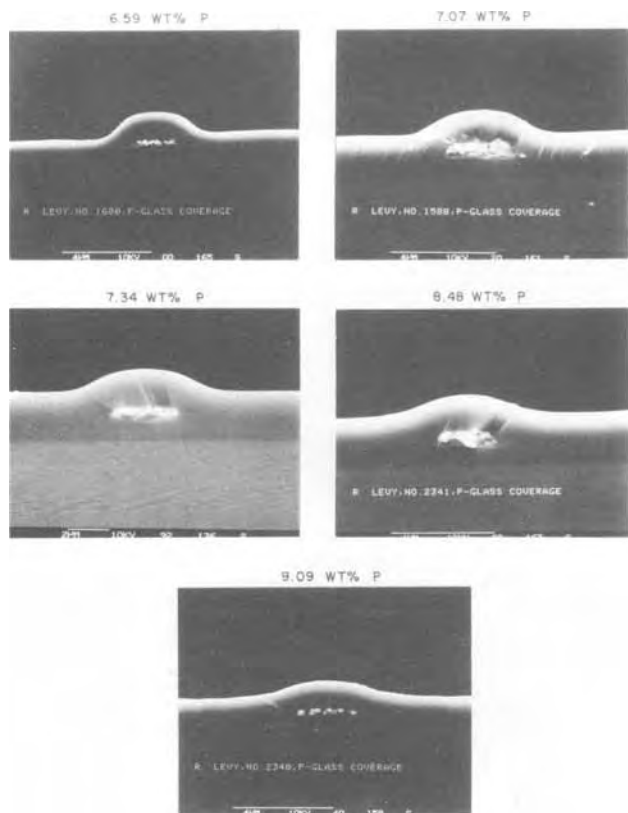


Fig. 11. Series of SEM cross sections of polycide runners at RSE step for PSG films of various phosphorus concentration.

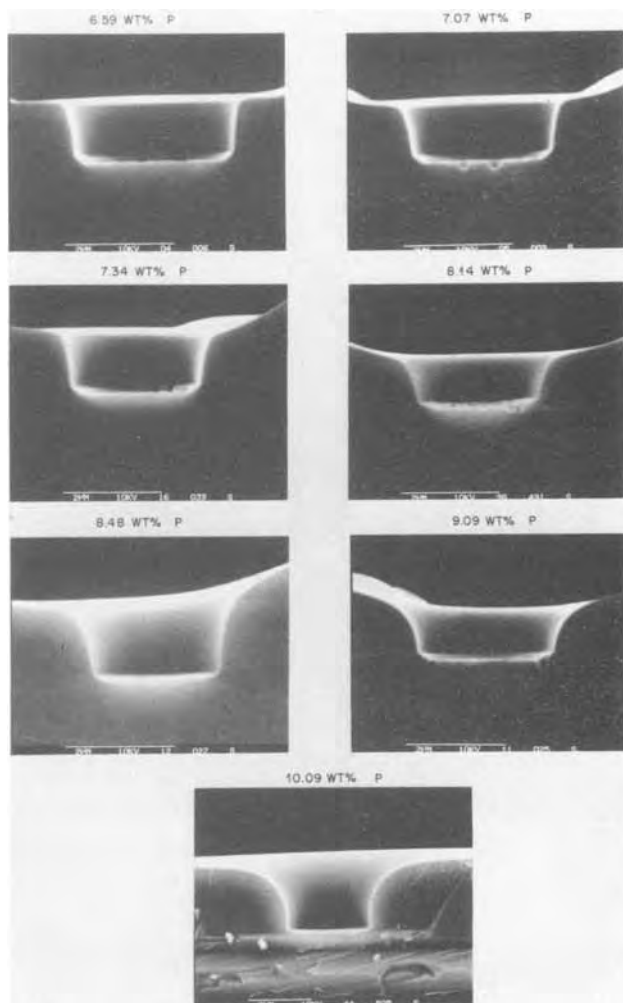


Fig. 12. Series of SEM cross sections of polycide runners at window reflow step for PSG films of various phosphorus concentration.

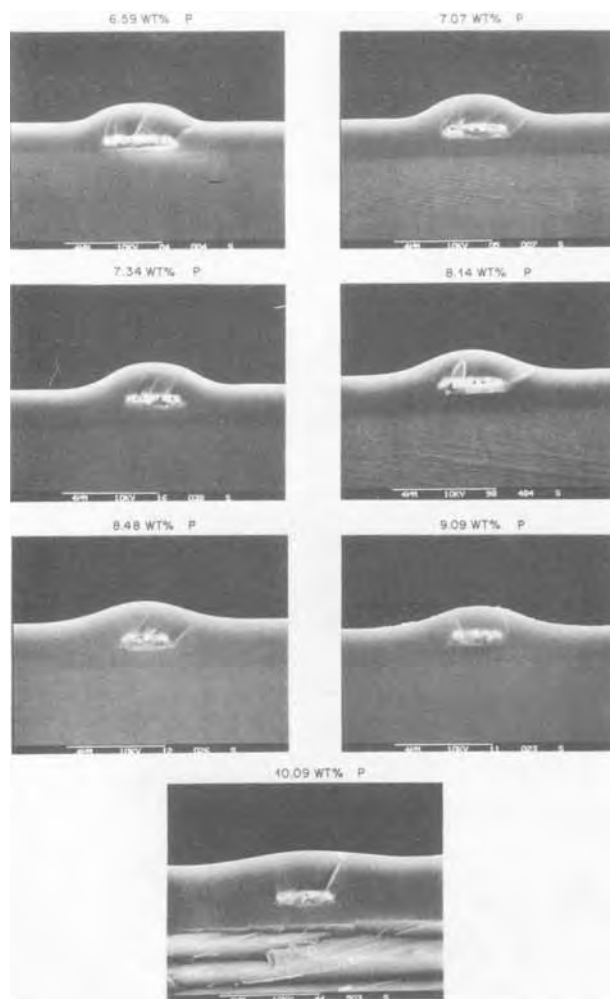


Fig. 13. Series of SEM cross sections of windows at reflow step for PSG films of various phosphorus concentration.

droplets on the wafer surface. A litmus test on these wafers turned in color, confirming the presence of an acid, presumed here to be phosphoric acid. The tendency of as-deposited PSG films with phosphorus concentrations higher than 8 w/o to be hygroscopic has been well documented (22-28) and recognized as the source of aluminum corrosion. However, the work of Nagosima *et al.* (22), as well as that of Levin (23), have also shown that the effect of densification, at temperatures of 700°C or above, is to shift the threshold concentration from ~8 w/o P to ~12 w/o P. The delamination of the PSG film structure over steps at the higher P concentration (11.83 w/o) is assumed to be the result of a phase separation of the glass into a primary $\text{SiO}_2\text{-P}_2\text{O}_5$ (with $P < 6$ w/o) phase and a hygroscopic, water soluble P_2O_5 phase. Since the stress of as-deposited PSG films has been determined to be tensile (1, 29, 30), further increases in thermal stress due to a mismatch in thermal expansion coefficient of the PSG/ SiO_2 film and silicon substrate ($\alpha_{\text{PSG}} < \alpha_{\text{Si}}$) coupled with lack of viscous flow of the low phosphorus primary phase could account for the observed film delamination.

Conclusion

In this study, we have examined the use of x-ray fluorescence as an analytical tool for determining phosphorus concentration in phosphosilicate glass. By comparison with other available methods, we have demonstrated that this direct measurement technique is accurate, simple, fast, reproducible, and nondestructive. Using this technique, we have illustrated the effect of phosphorus concentration on the viscous flow and reflow of PSG at typical thermal cycles. For a given heat-treatment, both

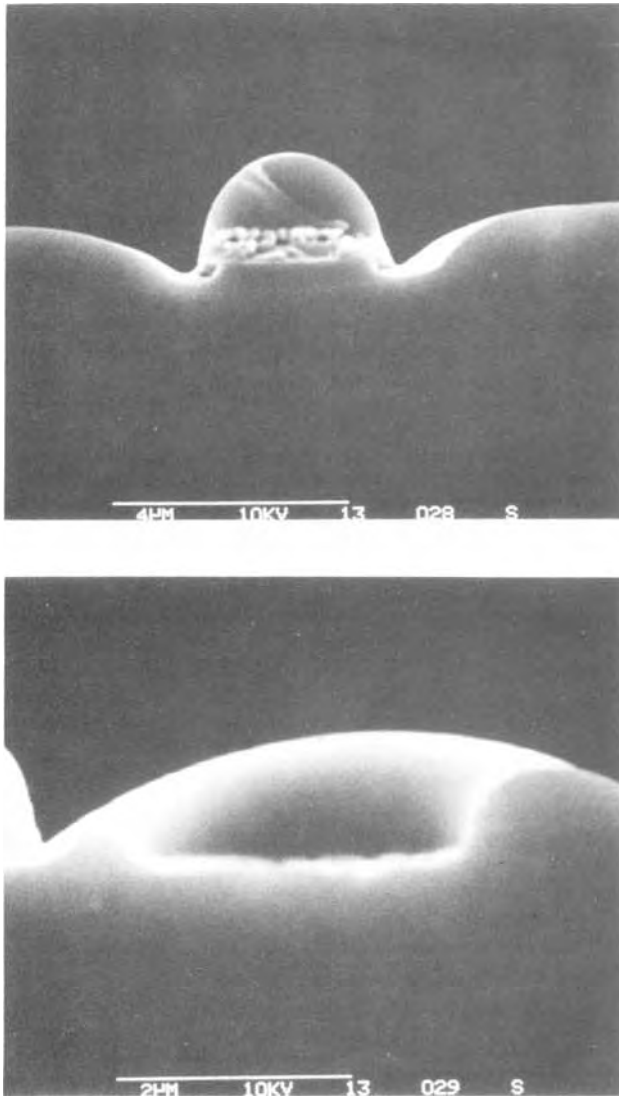


Fig. 14. SEM micrographs of step and window profile of PSG with 11.83 w/o P. Film is presumed to have phase separated.

flow and reflow profiles were observed to be dependent on changes in the phosphorus concentration of the glass.

Acknowledgments

The authors wish to thank J. F. Roberts for deposition of some of the LPCVD PSG films; D. R. Wonsidler and M. D. Patterson for the electron microprobe and energy dispersive spectrometry work; L. Kaufman for aiding with the numerical analysis of the data; B. E. Wilcomb, P. V. Lenzo, K. J. Orłowski, and G. Perez for many helpful interactions; and L. C. Parrillo, J. T. Clemens, and T. C. Loomis for many fruitful suggestions and discussions.

Manuscript submitted Dec. 14, 1984; revised manuscript received Feb. 1, 1985.

AT&T Bell Laboratories assisted in meeting the publication costs of this article.

APPENDIX

Starting from a set of measurements of phosphorus concentration, thickness, and normalized intensity (P_i, T_i, I_i) $i = 1, 2, \dots, n$, the purpose, here, is to fit this data to an equation of the form

$$I = \frac{AP}{B} [1 - e^{-BT}]$$

in a least squares sense to I . Thus, we want to find A and B which minimize

$$R(A, B) = \left[\sum_{i=1}^n \left[\frac{AP_i}{B} (1 - e^{-BT_i}) - I_i \right]^2 \right]^{1/2}$$

By setting $A/B = C$ and the i th component of the vector \bar{M} to

$$M_i = P_i [1 - e^{-BT_i}]$$

then the least squares problem reduces to finding C and B such that

$$R(C, B) = \|\bar{M}(B)C - \bar{I}\|_2$$

[A-1]

is minimized.

In this problem, C appears linearly and B nonlinearly, which means that if the optimal B is known, call it B' , the optimal C is given as

$$C = [\bar{M}(B')^T \bar{M}(B')]^{-1} \bar{M}(B')^T \bar{I} \quad [A-2]$$

It has been shown (31) that Eq. [A-2] can be substituted into Eq. [A-1] and that B' also minimizes the one variable function $S(B)$ defined by

$$S(B) = \|(\bar{M}(B)\bar{M}(B)^T \bar{M}(B))^{-1} \bar{M}(B)^T \bar{I}\|_2$$

where \mathbf{I} is the identity matrix.

A one-dimensional problem that has a unique local minimum in a given interval is much simpler to solve than a two-dimensional problem. We chose to solve Eq. [A-1] by applying Brent's algorithm (32) to minimize $S(B)$ and then use Eq. [A-2] to determine the optimal C . Brent's algorithm does not require derivatives of $S(B)$ and uses a combination of golden section steps guaranteed to yield a terminating algorithm and parabolic interpolation steps to speed convergence. It is superlinearly convergent.

REFERENCES

- G. L. Schnable, W. Kern, and R. B. Comizzoli, *This Journal*, **122**, 1092 (1975).
- W. Kern, *RCA Rev.*, **37**, 78 (1976).
- E. S. Beskova, G. I. Zhurzhevlev, and L. M. Morozova, *Zh. Anal. Khim.*, **31**, 1572 (1976).
- K. Chow and L. G. Garrison, *This Journal*, **124**, 1133 (1977).
- A. C. Adams and S. P. Murarka, *ibid.*, **126**, 334 (1979).
- C. C. Chang, A. C. Adams, G. Quitana, and T. T. Sheng, *J. Appl. Phys.*, **45**, 252 (1974).
- G. DiGiacomo, *This Journal*, **121**, 419 (1974).
- S. E. Omrod and B. P. Richards, *Microelect.*, **8**, 5 (1977).
- G. J. Wolfe, "Proceedings of the Workshop on Microelectronics Device Fabrication and Quality Control with the SEM," O. Johari and R. P. Becker, Editors, p. 587, IIT Research Institute, Toronto (1976).
- P. Durant, in "Chemical Vapor Deposition," J. M. Blocker, Jr., H. E. Hintermann, and L. H. Hall, Editors, p. 421, The Electrochemical Society Softbound Proceedings Series, Princeton, NJ (1975).
- F. X. Pink and V. Lyn, *Electrochem. Technol.*, **6**, 258 (1968).
- C. Grilletto, *Solid State Technol.*, **20**, 27 (1977).
- A. S. Tenney and M. Ghezzi, *This Journal*, **120**, 1276 (1973).
- W. A. Pliskin and R. P. Gnall, *ibid.*, **111**, 872 (1964).
- A. S. Tenney and M. Ghezzi, *ibid.*, **120**, 1091 (1973).
- E. Tannenbaum, *Solid-State Electron.*, **2**, 123 (1961).
- R. Jenkins and J. L. DeVries, "Practical X-Ray Spectrometry," Phillips Technical Library, Eindhoven, The Netherlands (1967).
- J. A. Blokhin, "Methods of X-Ray Spectroscopic Research," Pergamon Press, Ltd., Oxford, England (1965).
- L. S. Darken and R. W. Gurry, "Physical Chemistry of Metals," McGraw-Hill Inc., New York (1953).
- L. C. Parrillo, L. K. Wang, R. D. Swenumson, R. L. Field, R. C. Melin, and R. A. Levy, *IEEE Tech. Dig., Int. Electron Device Meet.* (1982).
- W. E. Armstrong and D. L. Tolliver, *This Journal*, **121**, 307 (1974).
- N. Nagasima, H. Suzuki, K. Tanaka, and S. Nishida, *ibid.*, **121**, 434 (1974).
- R. M. Levin, *ibid.*, **129**, 1765 (1982).
- G. L. Schnable, R. B. Comizzoli, W. Kern, and L. K. White, *RCA Rev.*, **40**, 416 (1979).
- R. C. Olberg and J. L. Bozarth, *Microelectron. Reliab.*, **15**, 601 (1976).
- K. Takahashi, K. Kitajima, and S. Imaoka, *Jpn. J. Appl. Phys.*, **21**, 757 (1982).
- A. T. English and C. M. Melliar-Smith, *Ann. Rev. Mater. Sci.*, 459 (1978).

28. N. Lycondes, *Solid State Technol.*, **21**, 52 (1978).
29. H. Sunami, Y. Itoh, and K. Sato, *J. Appl. Phys.*, **41**, 5115 (1970).
30. R. Lathlaen and D. A. Diehl, *This Journal*, **116**, 620 (1969).
31. G. H. Golub and V. Pereyra, *SIAM J. Numerical Analysis*, **10**, 413 (1973).
32. R. Brent, "Algorithms for Minimization Without Derivatives," Prentice-Hall, Inc., Englewood Cliffs, NJ (1973).

Si Epitaxial Growth of Extremely Uniform Layers by a Controlled Supplemental Gas Adding System

T. Suzuki,* Y. Inoue, T. Aoyama, and M. Maki

Hitachi Limited, Hitachi Research Laboratory, Hitachi, Ibaraki 319-12, Japan

ABSTRACT

A new approach to uniform growth, which directly modulates and controls the reactant gas concentration distribution within a reactor, has been proposed. A rotary disk (pancake) type reactor with a controlled supplemental gas adding system for regions of insufficient epitaxial layer thickness was designed and fabricated after consideration of gas flow patterns and reaction gas concentration distribution within the reactor. Simulation and control methods were developed to optimize the parameters of the multiple supplemental gas nozzles so that a uniform layer thickness distribution over a large range of susceptor radial directions could be achieved. Experiments using three supplemental nozzles showed that this system and control method could achieve deviations in thickness of less than $\pm 1\%$ both within a wafer and within a growth lot.

The chemical vapor deposition of epitaxial layers of silicon is a widely used process in the semiconductor industry. In this process, there is a requirement for better accuracy in growth control of the layer thickness, both to improve device production yield and to allow use of larger diameter wafers. As the diameter of the silicon substrate wafers becomes larger, the size and capacity of the growth reactor are inevitably scaled up to maintain the wafer charge number per growth lot. However, reactor scale-up reduces uniformity in the layer-thickness distribution, since more variation occurs in the growth rate along the gas stream due to depletion of the silicon source gas concentration. Therefore, it is important to consider how high uniformity can be achieved over a large growth area within larger reactors.

Chemical and transport phenomena in the epitaxial reactor have been studied by a number of investigators to obtain the optimal reactor design and operating conditions which ensure higher uniformity. A number of models, describing the growth-rate distribution along the gas stream in horizontal reactors have been studied (1-6). Other groups (7-8) have reported on quantitative models which describe the deposition-rate distribution in vertical cylinder reactors. More recently, another model has been presented which describes growth-rate distribution along the reactor deposition zone (9). Although these models have proven to be useful in optimization of the growth process conditions, they do not give any clue to how to overcome the fundamental problem of reactant gas depletion along the gas stream at reasonable gas flow rates. Unless some basic change is made in the present reactor construction, this problem cannot be avoided and limitations will continue to be placed on realization of extreme uniformity. Therefore, it is necessary to develop a new approach such as direct modulation of gas conditions within a reactor or to utilize a quite different reactor construction. With respect to the latter approach, Ban (6) reported on a novel reactor with a significantly large wafer capacity. This reactor, however, has the disadvantage of mechanical complexity and it has not achieved a thickness uniformity higher than that of conventional reactors.

In this paper, first, gas flow conditions and reaction gas concentration distributions within a rotary disk (pancake) type reactor were observed by means of gas flow pattern visualization and quadrupole mass spectrometric monitoring in order to understand transport and chemical phenomena. After consideration of the observation re-

sults, a practical, new approach to uniform growth, which directly modulates and controls the reactant gas concentration distribution within a reactor, was proposed and investigated. In this approach, supplemental reactant gas is added using multiple auxiliary gas nozzles in regions of poor thickness distribution according to a correction factor supplied from data for the preceding growth lot. The growth results for the extremely uniform layers obtained by using this supplemental gas control method are also shown.

Growth Reactor

Figure 1 is a schematic drawing of the rotary disk-type reactor used in our experiments. The diameter of the graphite susceptor was 12 in. The main gas inlet nozzle, positioned at the center, had an alternating vertical row arrangement of three and two holes for gas emission, spaced at an angle of 60° . A special feature of this reactor was the supplemental gas system used in addition to the conventional main gas system. The former had its own gas control system, inlet nozzle, and position regulator. The reactor had an *in situ* reaction gas concentration measuring system which consisted of a quartz capillary, position regulator, and gas concentration monitor (quadrupole mass spectrometer). This monitoring system and measurement method were the same as used previously (10). Deviations in the concentration measurements were less than $\pm 10\%$ within the concentration range studied.

Figure 2 defines the coordinate axes x and y and angle θ that are used in the following description. The arrows depicted around the center inlet nozzle indicate the direction of gas emission. The thick arrows show the direction of gas emission from the three vertically rowed holes and the smaller arrows show the two holes. The angle θ is defined as the angle from the direction shown by a thick arrow.

The epitaxial films were deposited by the hydrogen reduction of tetrachlorosilane (SiCl_4). Typical growth conditions were as follows: total gas flow rate (F_0) = 27 liter/min; SiCl_4 concentration (C_0) = 2.1 mole percent (m/o); and silicon substrate temperature (T_s) = 1200°C (corrected). The radial temperature distribution of the susceptor surface was almost constant within $\pm 10^\circ\text{C}$. Impurity doping gas was not used. The substrates used were mirror-polished CZ silicon wafers 3 in. in diameter with (111) orientation (off angle: $3^\circ \pm 1^\circ$). The rotation rate of the disk pedestal was kept constant during all experiments at 20 rpm.

*Electrochemical Society Active Member.

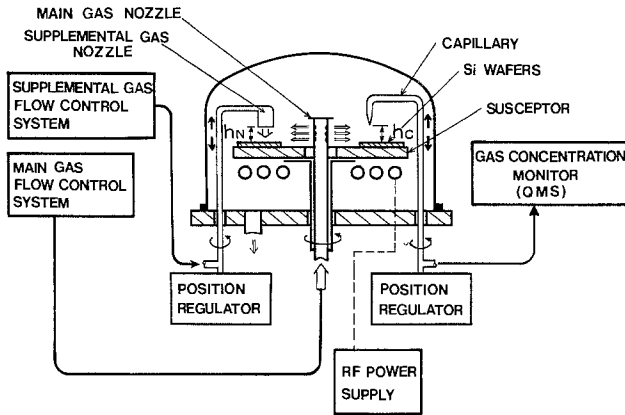


Fig. 1. Schematic representation of rotary disk-type reactor used in this study.

Transport and Chemical Phenomena in Reactor

Deposition and uniformity in CVD reactors are functions of chemical and transport phenomena. Although a few theoretical studies of transport phenomena in rotating disk reactors have appeared previously (11-13), little experimental work using a rotary disk-type, multiwafer reactor has been reported. Only Duchemin (14) has presented results dealing with the mechanism of silicon deposition based on analysis of gas concentration profiles.

In our study, first, gas flow patterns in the reactor were observed. In order to visualize the gas flow, monosilane (SiH_4) gas mixed with helium gas was introduced through the main inlet nozzle to produce a smoke streamline. Flow patterns on a selected reactor cross section were observed by projecting collimated parallel light through a slit onto the transparent quartz reactor. The disk temperature and total gas flow rate in the following two experiments were 800°C and 27 liter/min, respectively. Photographs of the gas flow pattern were taken

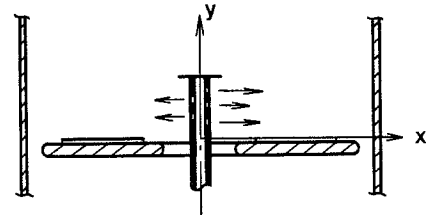
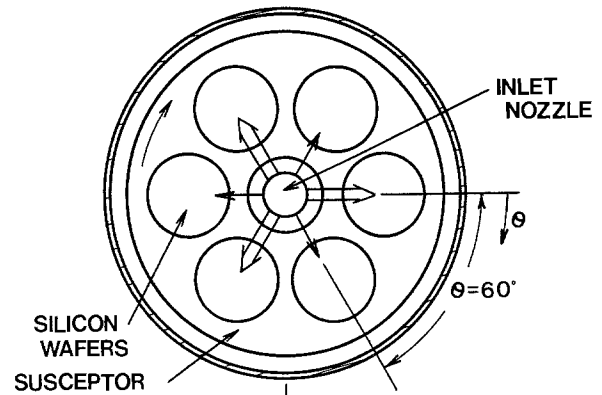


Fig. 2. Definition of coordinate axes x and y and angle θ

1-5s after opening the valve for introduction of tracer gas ($\text{SiH}_4 + \text{He}$) since the pattern became unclear after that.

Figure 3 shows typical streamline results observed on two different vertical cross sections where θ equals (a) 0° and (b) 30° . Streamlines of the emission flow toward the outer circumference of the susceptor, as well as the ascending flow caused by thermal convection, could be seen on the vertical cross section where $\theta = 0^\circ$. Interestingly, streamlines flowing backwards, toward the center nozzle, could also be seen on the vertical cross section where $\theta = 30^\circ$.

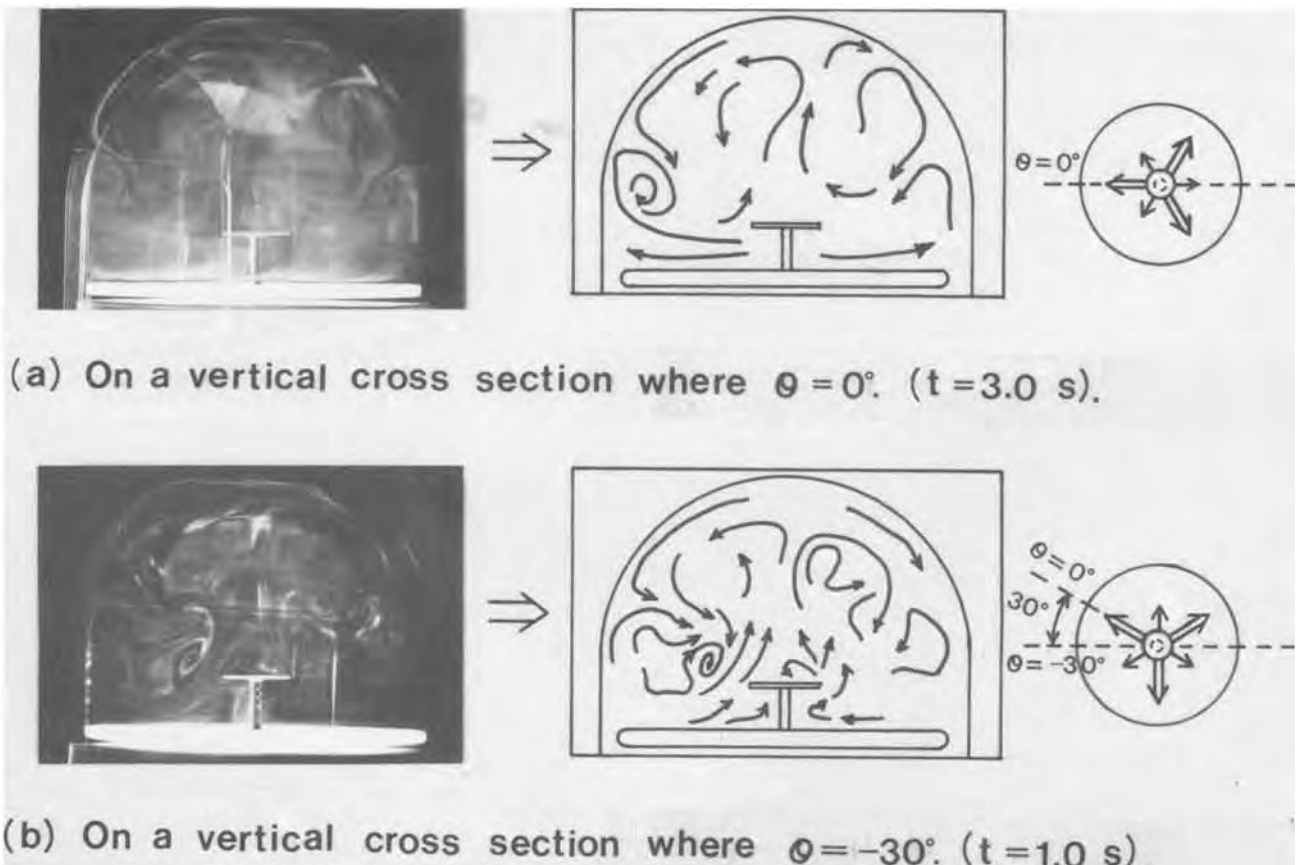


Fig. 3. Typical gas streamlines observed on two different vertical cross sections where (a) $\theta = 0^\circ$ and (b) $\theta = 30^\circ$. $T_s = 800^\circ\text{C}$ and $F = 27$ liter/min.

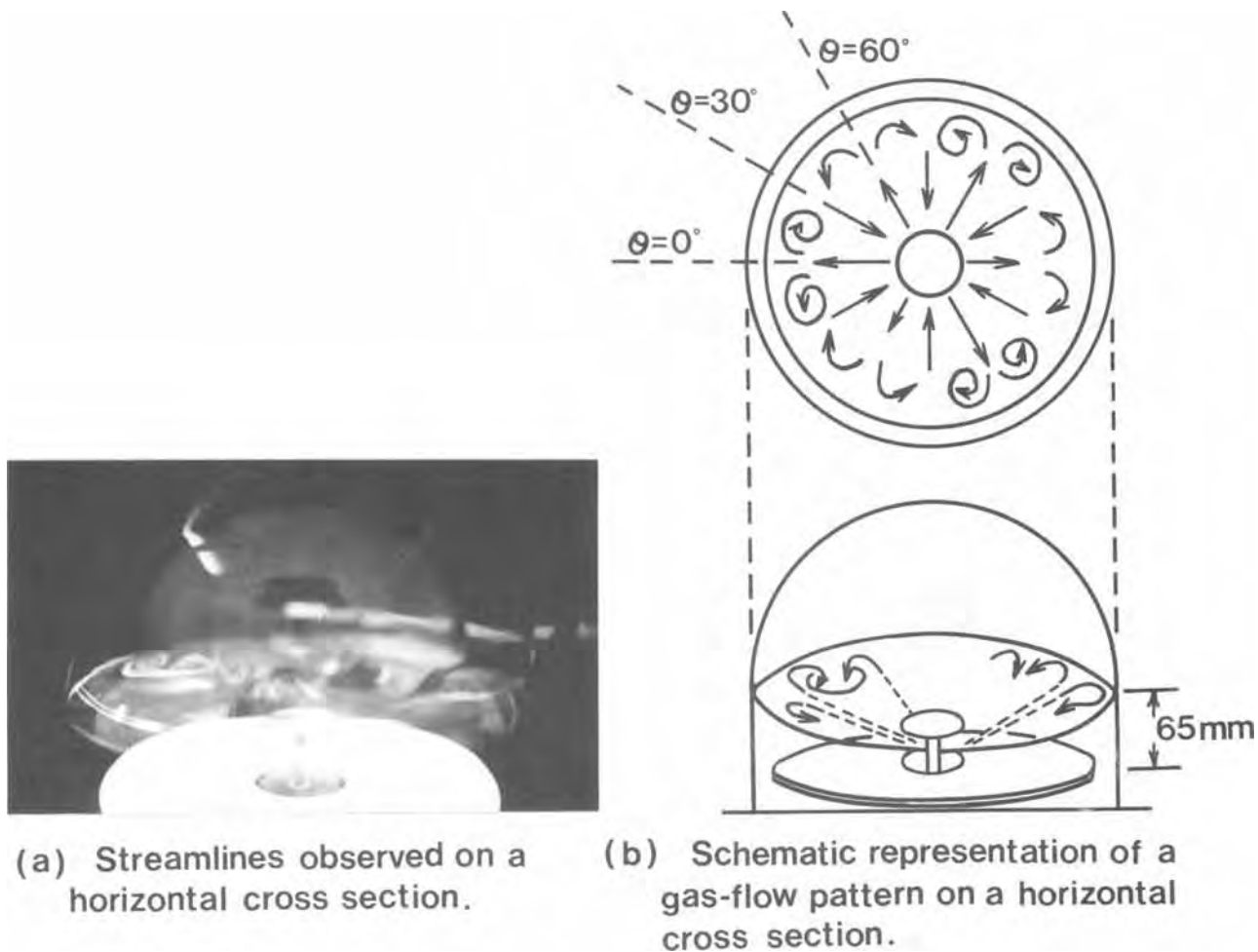


Fig. 4. Typical observed gas flow pattern on a horizontal cross section. $h = 65 \text{ mm}$; $T_s = 800^\circ\text{C}$; and $F = 27 \text{ liter/min}$

Figure 4 shows typical streamline results observed on the horizontal cross section at a height 65 mm above the susceptor. Some gas streams, emitted from the center

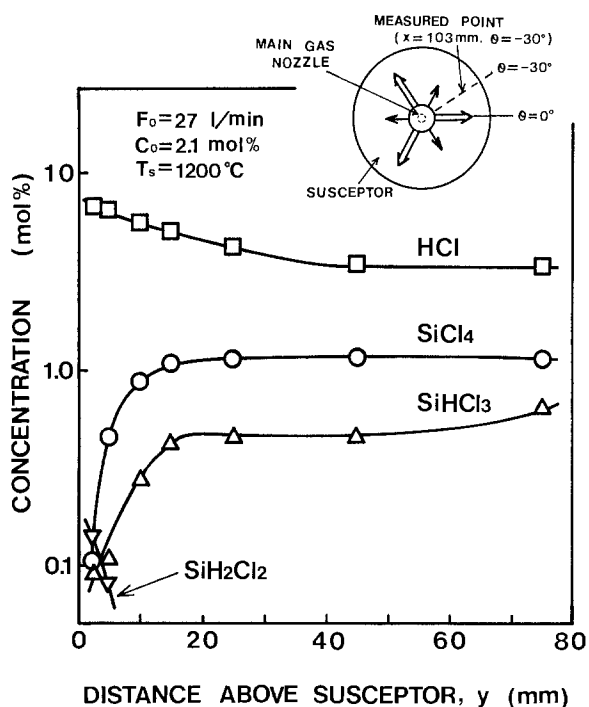


Fig. 5. Concentration profiles for the reactants measured along a distance above susceptor at the position defined by $x = 103 \text{ mm}$ and $\theta = -30^\circ$.

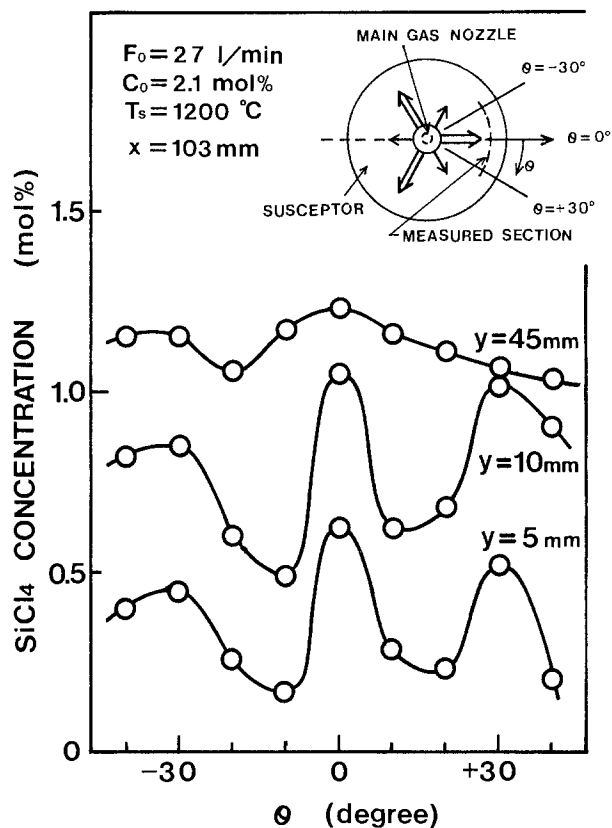


Fig. 6. SiCl_4 concentration profiles measured on a curved plane where the radial distance $x = 103 \text{ mm}$ at various heights of y above the susceptor.

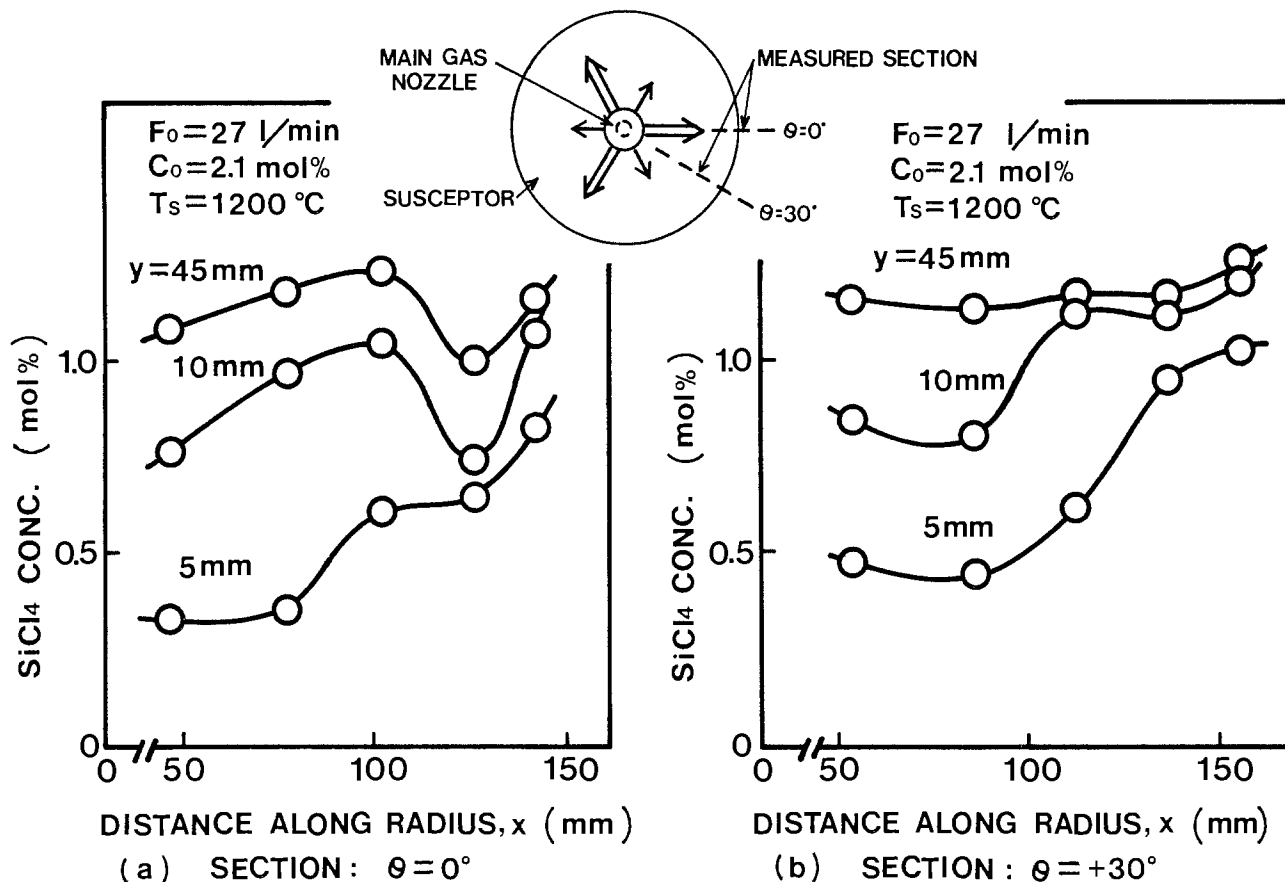


Fig. 7. SiCl_4 concentration profiles measured along the radius of the susceptor at various heights y above the susceptor on two different cross sections where (a) $\theta = 0^\circ$ and (b) $\theta = 30^\circ$.

nozzle which struck the bell jar wall were then turned back in the opposite direction (along the line of the angle $\theta = 30^\circ$) to make an eddy streamline (Fig. 4b). At the same time, the ascending convection flows from the susceptor caused by heating were added to these lateral flows to give a very complicated gas flow pattern.

Next, the gas concentration distribution in the reaction chamber was measured by means of *in situ* mass spectrometry measurements. Figure 5 shows an example of concentration profiles for the reactants measured along a distance above the susceptor at a position defined by $x = 103$ mm and $\theta = -30^\circ$. Trichlorosilane (SiHCl_3), dichlorosilane (SiH_2Cl_2), and hydrogen chloride (HCl) were present, in addition to silicon tetrachloride (SiCl_4) as reactant species. Silicon dichloride (SiCl_2) was not observed. Profiles of SiCl_4 and SiHCl_3 had a concentration gradient in the area between the susceptor surface and a height of about 15 mm, indicating that these species diffused toward the silicon substrate surface and contributed to heterogeneous silicon growth reaction. HCl diffused upwards.

In the upper region of the reactor, the concentration profiles of the reactant gases were fairly constant. The concentration of SiCl_4 at the upper part was about 1.1 m/o, and this value was smaller than the concentration value of 2.1 m/o initially introduced into the reactor as the source gas. This indicated that the SiCl_4 fed into the reactor was extensively decomposed to other chlorosilanes such as SiHCl_3 and SiH_2Cl_2 . From these results, it seemed that the heterogeneous reaction directly related to the deposition of silicon was not only the reduction of SiCl_4 , but also the reduction of other related compounds such as SiHCl_3 . This kind of complicated heterogeneous reaction has also been described for a horizontal reactor by Nishizawa and Saito (1) and the authors, (10).

Figure 6 shows a typical example of SiCl_4 concentration profiles measured on a curved plane at various heights, y , above the susceptor. The radial distance x from the center nozzle to the plane was 103 mm. Although there

was not such a significant variation in SiCl_4 concentration in the upper region of the reactor ($y = 45$ mm), there was a noticeable variation in the lower region near the susceptor surface ($y = 5, 10$ mm). The concentration peak at $\theta = 0^\circ$ corresponded to the gas flow emitted from the center nozzle, and the peaks at $\theta = \pm 30^\circ$ corresponded to the gas flow being turned back towards the center from the bell jar wall.

Figure 7 shows SiCl_4 concentration profiles measured along the radius of the susceptor at various heights y from the susceptor surface. Figure 7a indicates the profiles measured on a section where $\theta = 0^\circ$, and Fig. 7b where $\theta = 30^\circ$. Quite complicated profiles were seen in both cases. The disturbed profiles in the neighborhood of the susceptor circumference could probably be attributed to the gas flow striking the bell jar wall.

As mentioned above, it was seen that the gas conditions in the actual growth reactor were very complicated. The thickness distributions resulted from the interactions of the various gas reactions and gas conditions such as the flow pattern and concentration and temperature distributions. Accordingly, it was thought that, at present, the *in situ* (real time) control of thickness uniformity with such accuracy as $\pm 1\%$ could not be done by a method based on monitoring certain gas parameters within the reactor, especially in a large-scale production facility. Therefore, we took another approach in our investigation.

Supplemental Gas Control Method

It was found in the preliminary experiments that growth rate could be increased locally by adding supplemental reactant gas into the midst of the main gas flow. Using this effect, a new approach for realizing extremely uniform distribution which directly modulated and controlled the reactant gas distribution within a reactor was investigated.

In this approach (Fig. 8), additional reactant gas is introduced through the supplemental gas nozzle to regions of insufficient thickness distribution as determined by a

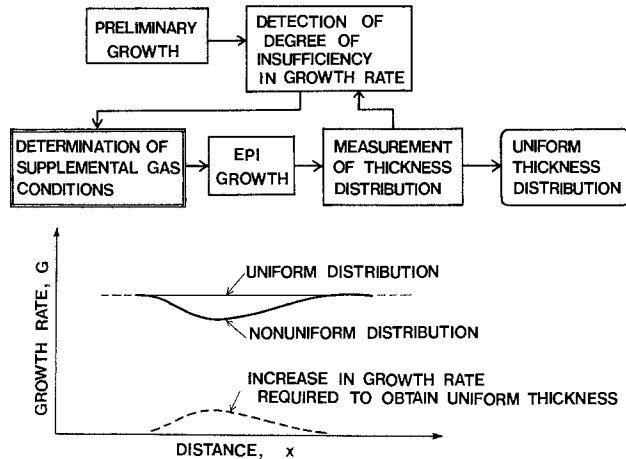


Fig. 8. Concept of thickness uniformity control by supplemental gas addition method.

correction factor supplied from data for the preceding growth lot. That is, preliminary growth is needed first, and then the difference between the uniform and nonuniform distribution is detected. The supplemental gas conditions required to form a uniform distribution are determined. Then, epitaxial layers are grown by applying these conditions to achieve a uniform thickness distribution. If necessary, this revision process can be repeated.

In order to control the uniformity with this method, calculations must be made which simulate the effects of gas supplements on the growth-rate distribution. Therefore, these effects were investigated in detail.

Figure 9 shows the configuration of the supplemental gas nozzles used in the experiments and defines the parameters related to the nozzles (c_i is the SiCl_4 concentration, x_{Ni} the distance from the susceptor center, and h_{Ni} the nozzle height, where i indicates the nozzle number). These supplemental gas nozzles are used to widen the area affected by the supplements. These nozzles are arranged between the emitted streamlines, where the gas velocity is relatively slow, as observed before.

First, the effects of gas supplements using a single nozzle were examined. The nozzle was positioned at $x = 100$ mm. Figure 10a shows the effects of supplemental gas concentration c on the growth-rate distribution along the susceptor radius. As the concentration was increased, the peak height of the growth rate curve increased, although the position and general shape of the peaks were almost unchanged. Figure 10b shows the effect of changes in

nozzle height h_N . As the nozzle height was increased, the peak height of the growth rate curve decreased, while the width of the distribution increased. At the same time, the peak position shifted toward the center of the susceptor. This may be due to the gas flow being turned back towards the susceptor center from the bell jar wall.

As could be seen from these figures, the increase in the growth-rate curve, using a gas supplement, has the same appearance as that of a typical normal distribution function. Therefore, we approximated the increase in growth rate $\Delta G(x)$ as follows

$$\Delta G(x) = A \exp \left\{ -\frac{(x - x_p)^2}{2\sigma^2} \right\} \quad [1]$$

where A is the peak height, σ is the standard deviation corresponding to the width of the peak, and x_p is the distance of the peak from the susceptor center. Using this expression, the effects of supplemental gas parameters, c , h_N , and x_N on the shape and position of the distribution of the increase in growth rate curve, A , σ , and x_p , were examined further and summarized in Fig. 11. These plots showed that the distribution shape could be controlled by using the three nozzle parameters. The shape of the distribution of the increase in growth rate was also influenced by the flow rate f of the supplemental gas. Our experiments showed that, as the flow rate f was decreased, the peak height A decreased, and, at the same time, the peak distance from the susceptor center x_p became less, because the supplemental gas flow was carried away by the main gas stream flowing toward the susceptor center. This fourth nozzle parameter f , however, was kept at a constant value of 1.5 liter/min in the following experiments in order to simplify the supplemental gas control.

Next, we considered a method for calculating the normal distribution functions of the individual supplemental gas nozzles. This was necessary to achieve a uniform distribution from a given nonuniform distribution when multiple supplemental gas nozzles were used. It was assumed that the resultant increase in growth rate using multiple supplemental gas nozzles could be expressed by the simple superposition of the increase in growth-rate curves for individual gas nozzles. Then the normal distribution functions of each supplemental gas nozzle necessary to achieve a uniform distribution from a given nonuniform distribution were obtained as the solution of A_i , σ_i , and x_{pi} in the following equation

$$\sum_j A_j \exp \left\{ -\frac{(x - x_{pj})^2}{2\sigma_j^2} \right\} = T - G_0(x) \quad [2]$$

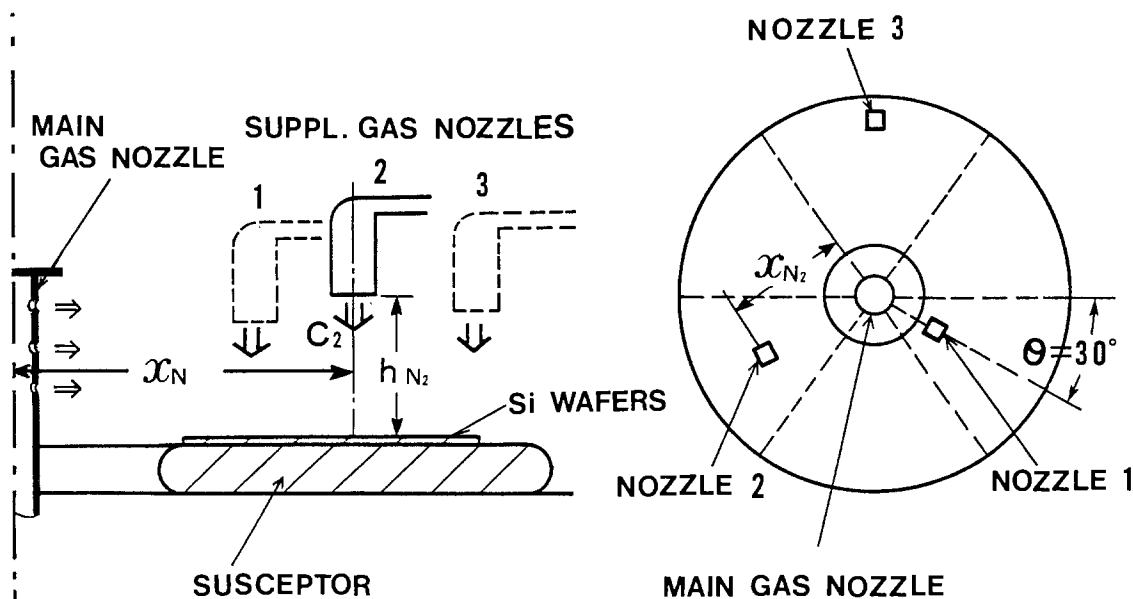


Fig. 9. Configuration of three supplemental gas nozzles and definitions of their parameters

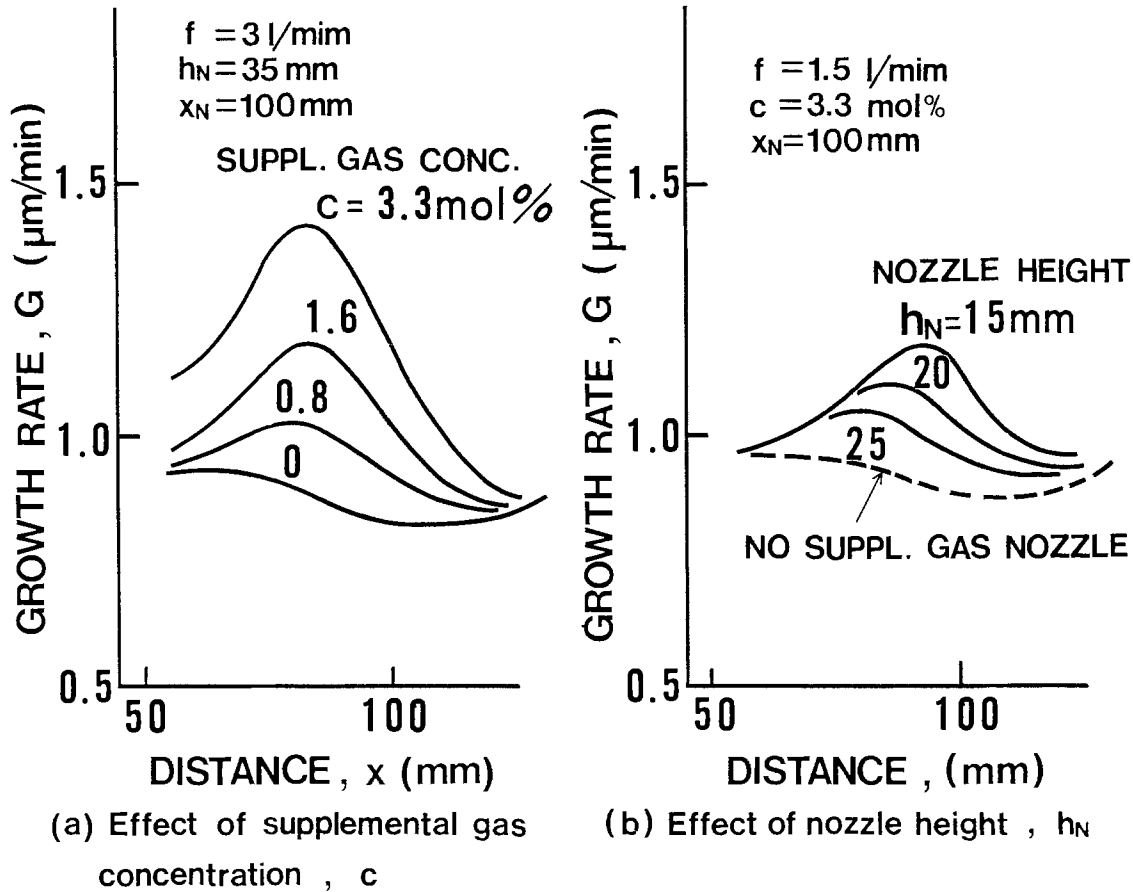


Fig. 10. Effects of changes in supplemental gas conditions on growth rate distribution along the susceptor radius

where j is the number of supplemental gas nozzles, T is the uniform growth rate distribution (constant), and $G_0(x)$ is a given nonuniform distribution of the growth rate. Although an analytical solution of Eq. [2] could not be ob-

tained, an approximate solution was possible using the Newton method in which reasonable values of A_j , σ_j and x_{pj} were given as initial values. Figure 12 shows an example of calculated distribution functions of the growth rate

INCREASE IN GROWTH RATE:

$$\Delta G = A \exp \left\{ - \frac{(x - x_p)^2}{2\sigma^2} \right\}$$

- A : PEAK HEIGHT
- σ : STD. DEVIATION
- x_p : PEAK POSITION

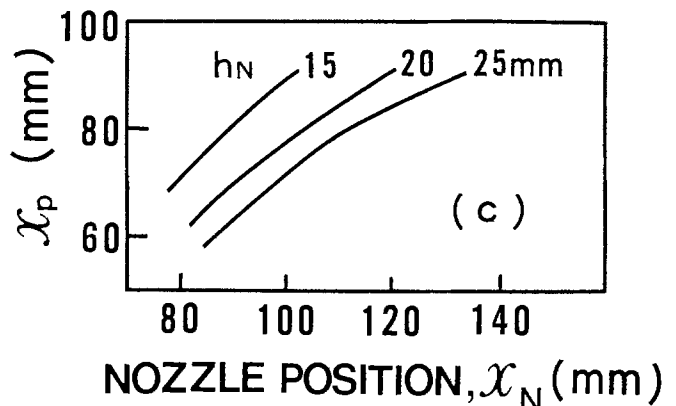
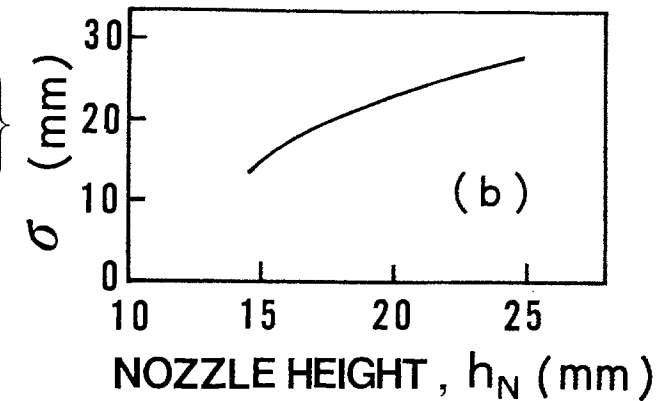
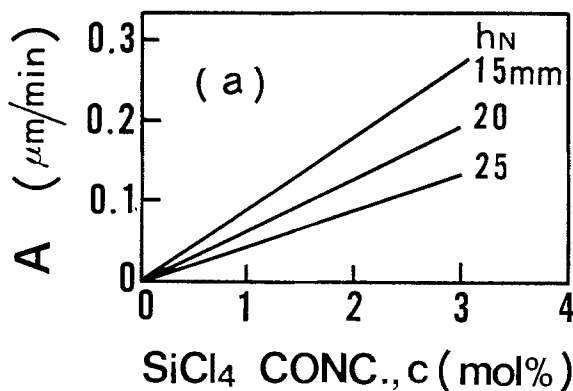


Fig. 11. Relation between supplemental gas conditions and parameters of normal distribution function (increase in growth rate)

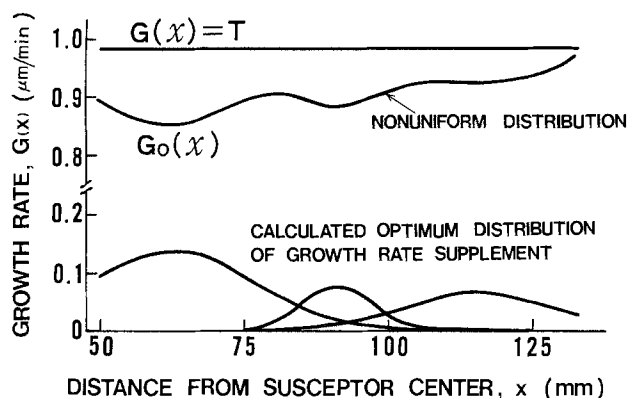


Fig. 12. An example calculation of the distribution functions of the growth rate supplement which are required to make the nonuniform distribution $G_0(x)$ uniform, assuming the use of three nozzles.

supplement which are required to make the nonuniform distribution $G_0(x)$ uniform, assuming the use of three nozzles.

Since the growth-rate distribution functions of each supplemental nozzle could be calculated by solving Eq. [2], it was now possible to control the thickness uniformity by applying the supplemental gas control method shown in Fig. 13. This figure shows a flow diagram for thickness uniformity control by the supplemental gas method. First, preliminary growth was needed to detect the difference between uniform and nonuniform thickness distribution. Then the distribution functions of the growth-rate supplement of each nozzle required to realize a uniform distribution were calculated. After this, the supplemental gas conditions of each nozzle c_i , h_{Ni} , x_{Ni} could be calculated approximately by using calibration data between the distribution functions of the growth-rate supplement and the supplemental gas conditions. Applying these conditions, epitaxial layers were then grown, and the resulting thickness distributions were measured. However, growth rate (or thickness) distribution as uniform as initially planned (for example, $\pm 1\%$) could not always be achieved at once due to errors in the calibration curves and approximations made in the calculations. If the obtained uniformity was insufficient, then the supplemental gas conditions were corrected by comparing the actual distribution functions of each supplemental gas nozzle with the initial ones. The actual supplemented distribution functions after epitaxial growth could be calculated by applying the method which was used for obtaining the distribution of the growth rate supplement required to achieve a uniform distribution. By repeating such growth and correction procedures as needed, the desired uniformity in thickness distribution was achieved.

Results and Discussion

Figure 14 shows an example of the transition to uniform thickness distribution along the susceptor radius on

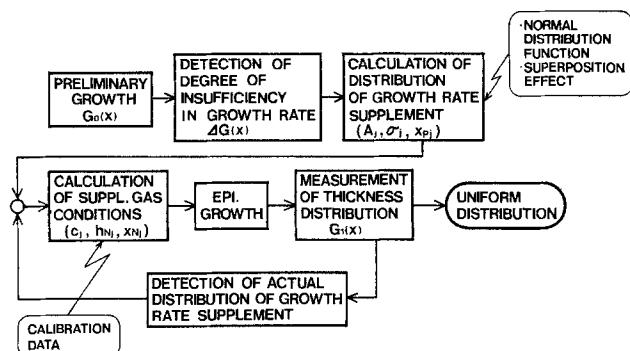


Fig. 13. Flow diagram of thickness uniformity control by supplemental gas method.

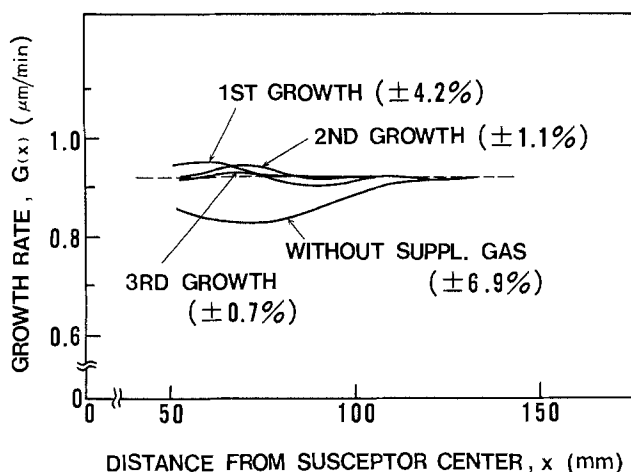


Fig. 14. Example of the transition to uniform thickness (growth rate) distribution along susceptor radius by the application of the supplemental gas control method. Three supplemental gas nozzles were used.

application of the developed supplemental gas control method. Three supplemental gas nozzles were used in this case. The variation in thickness (or growth rate) distribution before the gas supplement was $\pm 6.9\%$. By repeating the correction, the uniformity was enhanced until a deviation of only $\pm 0.7\%$ was achieved, on the third growth, within a 3 in. wafer.

Figure 15 shows an example of the transitions of uniformity within a growth lot when a similar repetition of growth was performed. In this case, six 3 in. wafers were charged per lot. The thickness deviations of less than $\pm 1\%$ were obtained and maintained from the third growth.

Thus, it was demonstrated that a thickness uniformity deviation of less than $\pm 1\%$ both within a wafer and within a growth lot could be obtained by applying the supplemental gas control method. Application of the same control method, it is believed, should make possible the same extremely uniform growth by widening the effect of the gas supplement for each nozzle or by increasing the number of supplemental gas nozzles. Furthermore, automated computer control of the process is possible, since the conditions for the gas supplement can be calculated.

Summary and Conclusions

Gas flow conditions and reaction gas concentration distributions were observed by means of gas-flow-pattern visualization and quadrupole mass spectrometric monitoring in order to understand transport and chemical phenomena of silicon epitaxial growth within a rotary disk-type reactor. After consideration of these observa-

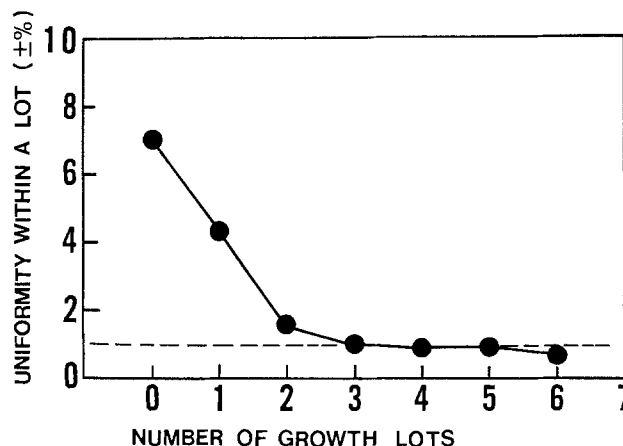


Fig. 15. Example of the transitions of uniformity within a growth lot with the application of the supplemental gas control method. Six 3 in. wafers were charged per lot.

tions, a practical, new approach to uniform growth, which directly modulated and controlled the reactant gas concentration distribution within a reactor, was proposed and investigated.

A rotary disk-type reactor with a controlled supplement gas system for adding reaction gas to regions of insufficient layer thickness distribution was designed and fabricated. Simulation and control methods were developed to optimize the parameters of the multiple supplemental gas nozzles so that a uniform thickness distribution over a large area of the susceptor radial direction could be achieved. In this method, the resultant increase in growth-rate distribution by multiple supplements was simulated by superposition of the individual increase in growth-rate curves, with each single gas supplement being approximated by the normal distribution function. The supplemental gas conditions of each nozzle were determined using calibration data and corrected by comparing resultant distribution functions after growth with the initial ones. Experiments using three supplemental nozzles showed that this system and control method could yield a thickness uniformity deviation of less than $\pm 1\%$, both within a 3 in. wafer and within a growth lot.

It is believed that the same extremely uniform growth can be achieved in a scaled-up reactor and that automated, computer control of the process is possible.

Acknowledgments

The authors wish to express their sincere thanks to Professor J. Nishizawa, Dr. M. Okamura, and Dr. H. Kato for

their guidance and encouragement in this work. They also would like to thank Dr. M. Tanuma for his helpful discussions.

Manuscript submitted Aug. 2, 1984; revised manuscript received Feb. 11, 1985. This was Paper 372 RNP presented at the Detroit, Michigan, Meeting of the Society, Oct. 17-21, 1982.

Hitachi Limited assisted in meeting the publication costs of this article.

REFERENCES

1. F. C. Eversteyn, P. J. W. Severin, C. H. J. v. d. Brekel, and H. L. Peek, *This Journal*, **117**, 925 (1970).
2. F. C. Eversteyn and H. L. Peek, *Philips Res. Rep.*, **25**, 472 (1970).
3. P. C. Rundle, *Int. J. Electron.*, **24**, 405 (1968).
4. P. C. Rundle, *J. Cryst. Growth*, **11**, 6 (1971).
5. V. S. Ban, *J. Jpn. Assoc. Cryst. Growth*, **5**, 119 (1978).
6. V. S. Ban, *J. Cryst. Growth*, **45**, 97 (1978).
7. E. Fujii, H. Nakamura, K. Haruna, and Y. Koga, *This Journal*, **119**, 1106 (1972).
8. C. W. Manke and L. F. Donaghey, *ibid.*, **124**, 561 (1977).
9. J. Juza and J. Cermak, *ibid.*, **129**, 1627 (1982).
10. T. Aoyama, Y. Inoue, and T. Suzuki, *ibid.*, **130**, 203 (1983).
11. K. Sugawara, *ibid.*, **119**, 1749 (1972).
12. P. Pollard and J. Newman, *ibid.*, **127**, 744 (1980).
13. M. L. Hitchman and B. J. Curtis, *J. Cryst. Growth*, **60**, 43 (1982).
14. J. P. Duchemin, *Rev. Thomson CSF*, **9**, 33 (1977).
15. J. Nishizawa and M. Saito, *J. Cryst. Growth*, **52**, 213 (1981).

Physical Properties of Sputter-Deposited Titanium Silicide as a Function of Substrate Temperature

M. Tanielian and S. Blackstone

Gould Research Center, Rolling Meadows, Illinois 60008

ABSTRACT

The resistivity, composition, and microstructure of sputtered titanium silicide films from a composite $\text{TiSi}_{2.1}$ target were investigated as a function of substrate temperature T_s in the range of $T_s \approx 25^\circ\text{--}600^\circ\text{C}$. We find that there are essentially three distinct regimes of properties, for $T_s \approx 25^\circ\text{--}200^\circ\text{C}$, $T_s \approx 200^\circ\text{--}450^\circ\text{C}$, and $T_s \approx 450^\circ\text{--}600^\circ\text{C}$. The oxygen incorporation, oxidation sensitivity, and resistivity of the films decrease as the substrate temperature increases. The most notable observation was that the physical properties of the films in the temperature range of $450^\circ\text{--}600^\circ\text{C}$ are similar to fully reacted titanium disilicide films formed in a furnace anneal at 900°C , and, in addition, they are oxygen free. In order to explain this result, we had to assume that the surface substrate temperature was several hundred degrees higher during sputtering than what the macroscopic measurements of the bulk substrate temperatures would indicate.

The preparation and processing of the refractory metal silicide films such as TiSi_2 , TaSi_2 , MoSi_2 , and WSi_2 have been the topic of many investigations (1). Their importance arises from their usefulness as low resistivity interconnection materials in VLSI circuits. Films of these refractory metal silicides have been deposited using all types of conventional thin film deposition techniques, such as sputtering from a single composite target, co-sputtering, coevaporation, and CVD. Each method provides different advantages in terms of purity, step coverage, and stress. However, one aspect all these methods share in common is that the formation of the fully reacted, low resistivity disilicide phase can only be achieved after a high temperature sinter, typically in the range of $850^\circ\text{--}1000^\circ\text{C}$, subsequent to the thin film deposition. One exception to this process is in the case of plasma-enhanced chemical vapor deposited titanium silicide films where it appears that only a 650°C anneal is necessary to get fully reacted films.

Of all the refractory metal silicides, TiSi_2 has the lowest resistivity, which makes it an attractive candidate as a VLSI interconnection material. However, it also presents

some special problems, since the unreacted (room temperature as-deposited film) has a high affinity for oxygen. For instance, during deposition, some oxygen may be incorporated into the film; also, during sintering, a thick oxide may grow on the film, unless the sintering is done in vacuum or in an inert ambient.

Here, we report that the sintering step is not necessary when the titanium silicide films are sputtered at elevated substrate temperatures, because the high substrate temperature films appear to be fully reacted. In the case of titanium silicide sputtered from a cold-pressed composite target, this range of substrate temperatures (2, 3) is $450^\circ\text{--}600^\circ\text{C}$. In fact, there appear to be three distinct regimes in the properties of sputtered titanium silicide films as they relate to the substrate temperature.

Experimental

The films were sputtered in a small glass bell jar chamber which was fitted with two 2 in. dc magnetron sputter guns. The target was a cold-pressed target from Varian with a nominal composition of $\text{TiSi}_{2.1}$. The system was pumped down to 3×10^{-7} torr before each deposition and

then backfilled with ultrahigh purity argon to a pressure of about 3 mtorr. Before the deposition of the film, the target was presputtered for approximately 1h with the shutter closed, in order to clean the target and getter any background oxygen in the system. The substrates were (111), 10 Ω -cm, bare silicon wafers. The heating of the wafers was done using a Mo resistor fabricated on the oxidized back of the wafers. This heating technique was chosen because it minimized the heating of other parts and fixtures in the sputtering chamber, which could degas and produce unwanted background gases. Using this technique, we could reproducibly heat the wafer between ambient and 650°C. The substrate temperature was measured on the front side of the wafer using a thin wire thermocouple via a spring contact. The sheet resistance of the films was measured using a four-point probe and the thickness was obtained from a Dektak II stylus probe. The Auger signals were calibrated using TiSi_2 powder samples. The sintering step was carried out in a furnace tube in argon at 900°C for 30 min.

Results

The room temperature resistivity of the films both before and after a 900°C, 30 min Ar anneal was measured as a function of substrate temperature over the range of 25°-600°C. The results, shown in Fig. 1, indicate that there are three distinct regions. Presumably, these correspond to three distinct phases of titanium silicide.

Phase I: $T_s \approx 25^\circ\text{-}200^\circ\text{C}$.—This is the range of substrate temperatures conventionally used for sputtering. The Auger analysis of a film deposited at 25°C which is typical of this range (3) is given in Fig. 2. The as-deposited film contains 5-7 atom percent (a/o) oxygen throughout its thickness. No carbon or Ar signals were detected (3).

When annealed, the top third of the film was converted to a mixture of Si, Ti, and their respective oxides. It is worthwhile to observe that the amount of oxygen incorporated in the annealed film decreases to some extent after the high temperature anneal. This effect has been seen before (4) and has to do with the thermodynamic

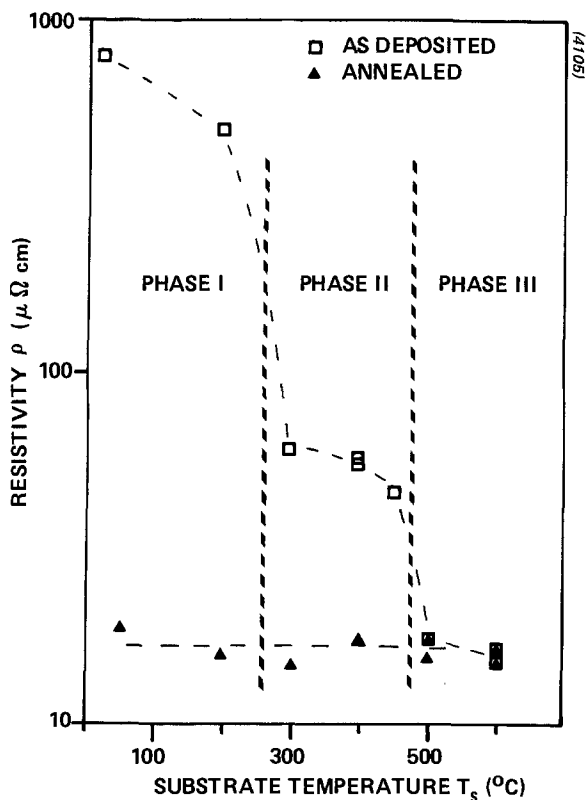


Fig. 1. The resistivity as a function of substrate temperature of titanium silicide films both before and after anneal. As one can see, the resistivity of the films deposited at $T_s > 450^\circ\text{C}$ is unchanged after a 900°C, 30 min argon anneal.

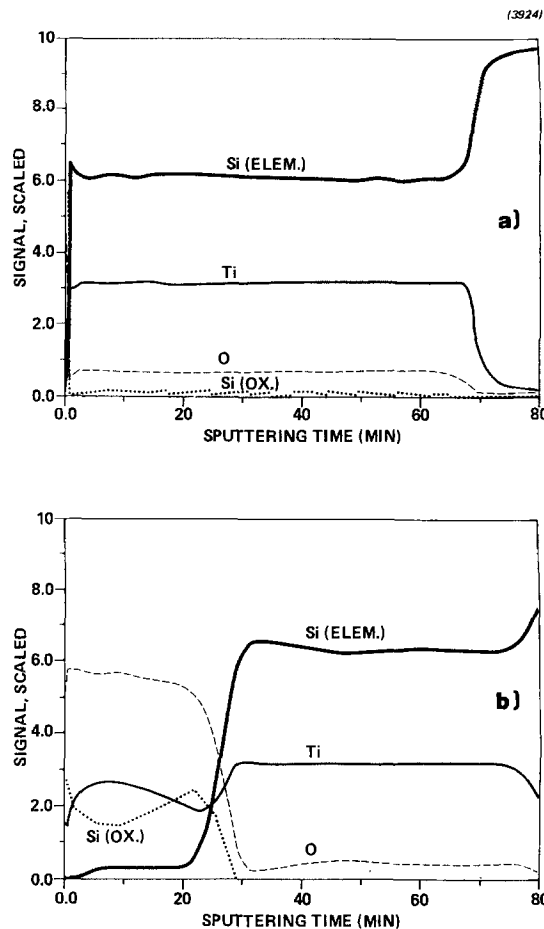


Fig. 2. Auger depth profile of a film deposited at $T_s = 25^\circ\text{C}$. a: As deposited. b: After a 900°C, 30 min argon anneal.

equilibrium of this ternary system (5, 6). The x-ray diffraction trace from this film shows that the as-deposited film is amorphous, and it crystallizes after the high temperature anneal, as shown in Fig. 3. SEM pictures of the surface of the film are shown in Fig. 4. They reveal a grainy structure with a typical grain size of about 1000Å both before and after anneal. These grains cannot be related to the crystallite size in these films, since the x-ray data show that the as-deposited film is amorphous while the annealed film is polycrystalline.

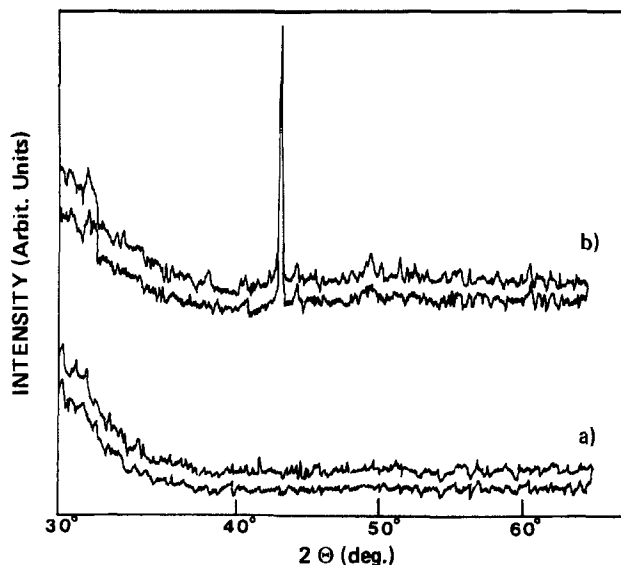


Fig. 3. X-ray diffraction data of a film deposited at $T_s = 25^\circ\text{C}$. a: As deposited. b: After a 900°C, 30 min argon anneal. The peak corresponds to the (004) peak of TiSi_2 .

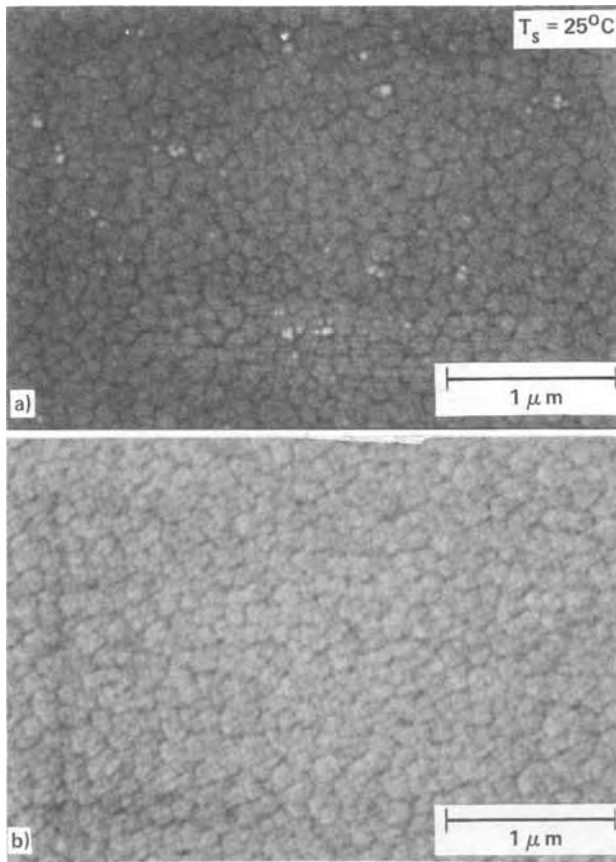


Fig. 4. SEM micrographs of the surface texture of a film deposited at $T_s = 25^\circ\text{C}$. a: As deposited. b: After a 900°C , 30 min argon anneal. The surface morphology remains unchanged although the film crystallized.

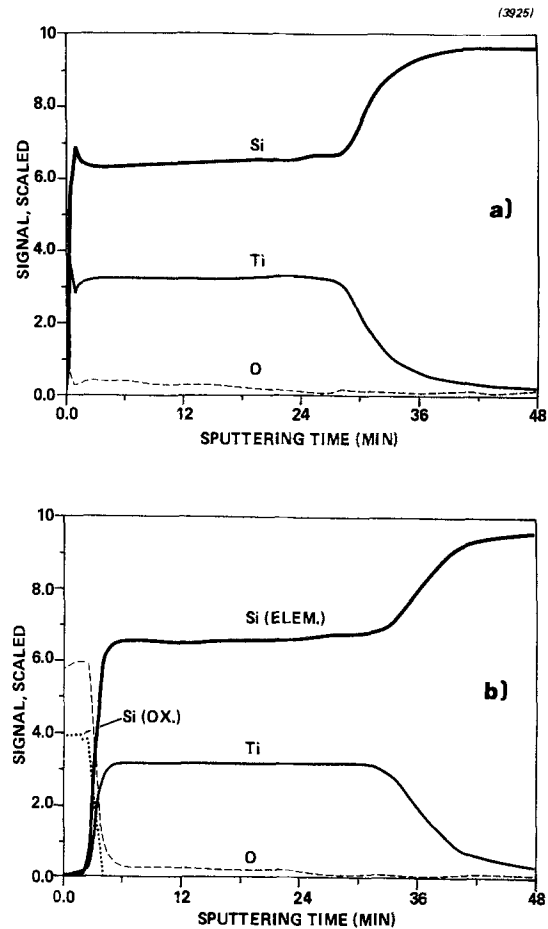


Fig. 5. Auger depth profile of a film deposited at $T_s = 300^\circ\text{C}$. a: As deposited. b: After a 900°C , 30 min argon anneal.

Phase II: $T_s \approx 200^\circ\text{--}450^\circ\text{C}$.—In this range of substrate temperatures, we find that the titanium silicide films are partially reacted. A fully reacted film in this case is defined as a film that has properties similar to a film which has undergone a 900°C , 30 min, argon anneal. This characterization is based on the fact that these films share some features of a fully reacted film. For instance, the surface layer oxide is made of SiO_2 with no Ti or TiO_x species mixed in, which is typical of a fully reacted film. This layer remains unchanged after annealing. The Auger analysis of a film deposited at $T_s \approx 300^\circ\text{C}$ which is typical of this range is shown in Fig. 5. The reason these films are referred to as partially reacted relates to the resistivity of the films in this range which, although lower than the resistivity of the films in Phase I, is still higher than the value of the fully reacted film. Further justification for the term “partially reacted” is based on TEM studies (10) where it was found that the $T_s \approx 300^\circ\text{C}$ film was comprised of two silicide phases, the equilibrium titanium silicide phase (C54 structure), and a metastable TiSi_2 phase (C49, ZrSi_2 structure) which is a precursor to the equilibrium phase. It is interesting to note that the amount of oxygen incorporated into the film in this phase is about 2–4 a/o. This is lower than the amount present in the films deposited in Phase I, and, again, it decreases somewhat after annealing. These films are also less oxidation sensitive than those in Phase I, as seen by a comparison of the Auger depth profile of the as-deposited and annealed films. SEM examination of the surface of these films in Fig. 6 reveals that the grain size is very small. The films appear quite smooth before and after anneal. This is somewhat surprising, since at higher T_s one expects a higher surface mobility and, therefore, larger grains.

Phase III: $450^\circ\text{--}600^\circ\text{C}$.—This range of substrate temperatures is normally unavailable in commercial sputtering systems. Our special heater design allowed us to heat the wafer without heating any other fixtures in the sput-

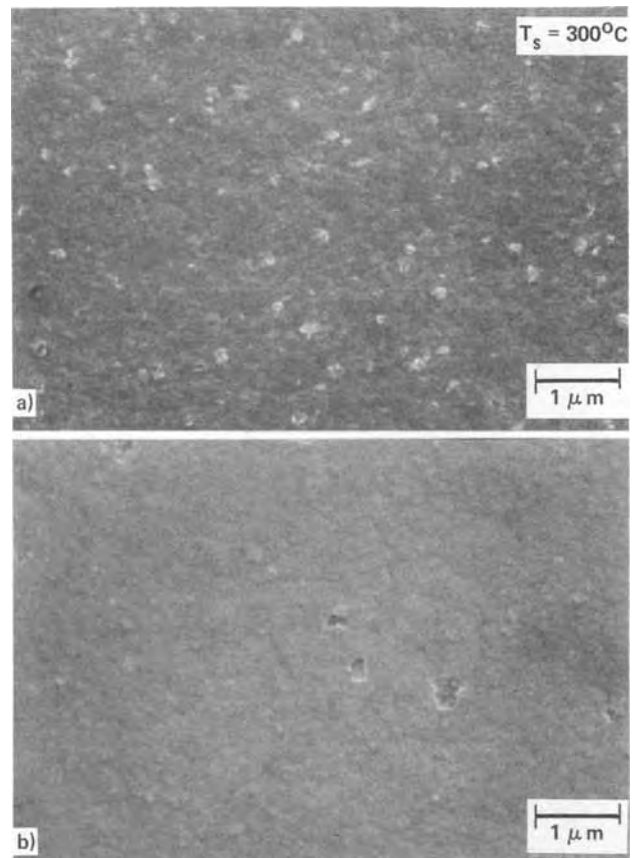


Fig. 6. SEM micrographs of the surface morphology of a $T_s = 300^\circ\text{C}$ film. a: As deposited. b: After a 900°C , 30 min argon anneal.

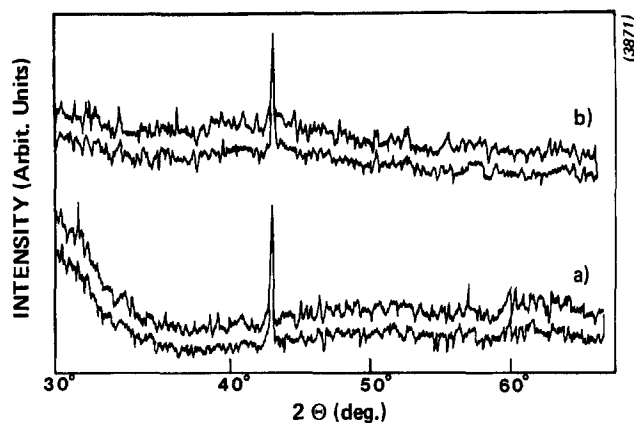


Fig. 7. X-ray diffraction of a film deposited at $T_s = 500^\circ\text{C}$. a: As deposited. b: After a 900°C , 30 min argon anneal. The x-ray diffraction trace remains unchanged. It is interesting to note that the (004) peak present is the same feature present at the $T_s = 25^\circ\text{C}$ film which was annealed (Fig. 3).

tering system and thus reduced the amount of degassing taking place. The resistivity of the as-deposited films in this temperature range is the same as for the fully reacted films as seen in Fig. 1. X-ray diffraction of a film

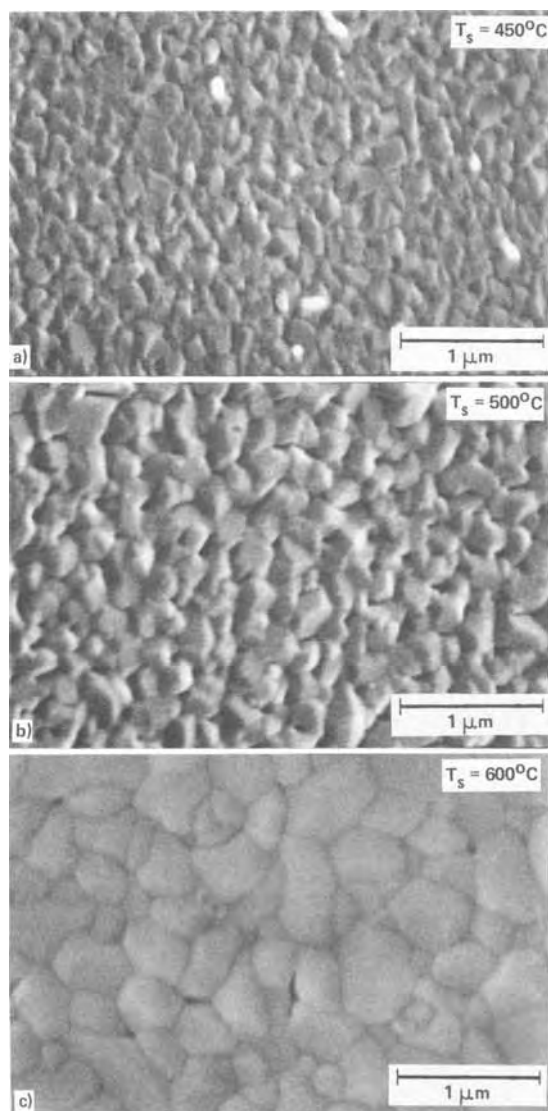


Fig. 8. SEM micrographs of three films deposited at (a) $T_s = 450^\circ\text{C}$, (b) $T_s = 500^\circ\text{C}$, and (c) 600°C . The grain size in this phase is a strong function of substrate temperature.

deposited at $T_s = 600^\circ\text{C}$ in Fig. 7 shows a single peak (004) of the equilibrium type of TiSi_2 (orthorhombic, C54 structure) indicating that the film is crystalline. The absence of other strong peaks suggests that there is a preferred orientation in these films. This feature is unchanged after a 900°C , 30 min argon anneal. TEM studies showed this film to be exclusively of the C54 structure in agreement with the x-ray data. The surface grain size of the films is large, typically $0.6\text{--}0.8\ \mu\text{m}$ and is a strong function of temperature. The higher the temperature, the larger the feature size, as seen in Fig. 8 for $T_s = 450^\circ, 500^\circ,$ and 600°C films. An Auger depth profile of a film deposited at $T_s = 500^\circ\text{C}$ and representative of films in this regime is depicted in Fig. 9. The oxygen incorporation in the as-deposited film is very low and is unchanged after a 900°C , 30 min anneal in argon. The only oxygen present is in the form of SiO_2 on the surface. These films, then, have all the desirable characteristics of a fully reacted film and, in addition, are oxygen free.

Discussion

From the results we have described in the previous section, it is apparent that when we refer to substrate temperatures we are referring to a macroscopic measurement which does not take into account the actual kinetics present on the substrate surface during the sputtering process. The reason is that the formation of fully reacted titanium disilicide films at 500°C is several hundred degrees below typical furnace-reacted, sputter-deposited films. It has been suggested (7) that the high temperature furnace anneals are necessary because of the incorporation of oxygen in the film, which slows down the formation reaction. However, since the system in which these depositions were done had a fairly high oxygen background, as evidenced by the Auger analysis of the low substrate temperature films, the only explanation that could account

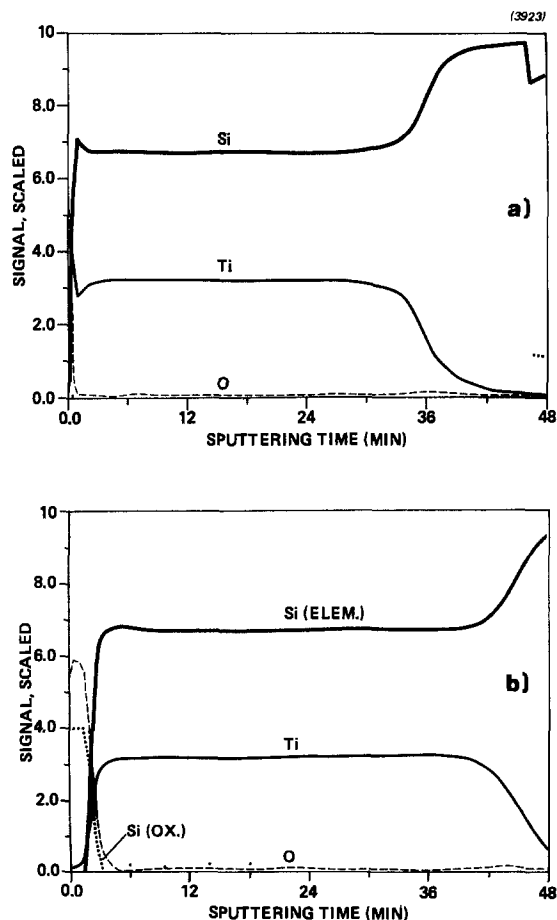


Fig. 9. Auger depth profile of a film deposited at $T_s = 500^\circ\text{C}$. a: As deposited. b: After a 900°C , 30 min argon anneal. The striking feature of these films is the absence of oxygen incorporation in the film.

for the observed results is that the surface temperature of the wafer was actually much higher, perhaps several hundred degrees higher, than the macroscopically measured bulk temperature of the wafer. This hypothesis is supported by experiments done on the direct reaction kinetics of a Ti film on Si. It was found that for partially reacted titanium silicide phases there may be a significant amount of oxygen present in the silicide film. As the film is annealed at about 900°C or above, the oxygen is segregated (6) and pushed to the surface (4), where some of it is lost in the form of SiO₂. The remaining oxygen forms an SiO₂ layer on the surface of the TiSi₂ film. As one can see in a comparison of Fig. 2, 5, and 9, the amount of oxygen incorporated in the as-deposited film decreases with increasing substrate temperature. Assuming that the background amount of oxygen stayed constant, the results can be explained on the basis that *in situ* formation of the TiSi₂ excludes the oxygen from the growing film. This is in accordance with results found by other workers (4-6).

It is well known (8) that the species deposited during sputtering have, on the average, higher kinetic energies than in other vacuum deposition techniques such as evaporation or chemical vapor deposition. Furthermore, this kinetic energy is a function of the forward power applied during sputtering. When the sputtered species arrive at the substrate surface, they will transfer part of that kinetic energy to the substrate surface and the chemical species present there. Increased substrate temperature acts in a similar way by increasing the mobility and diffusivity of the substrate surface species. The combination of the two parameters gives rise to an enhanced surface temperature process which we call TEPSI (thermally enhanced plasma surface interaction), which may have consequences for a number of material systems where high bulk substrate temperatures are not desirable.

Further evidence to support the TEPSI hypothesis comes from a different set of experiments. When a titanium film was deposited onto a Si wafer at a substrate temperature of 515°C in the same system, the results was not a Ti film on Si, but a fully reacted titanium silicide film (9), free of oxygen, with a resistivity of about 15 μΩ-cm. This could only be explained using the above TEPSI model. Similar results were seen for Ta and Mo films deposited at T_s = 600°C. We believe that this technique of sputtering films at high substrate temperatures could be used in a variety of other thin film systems.

Summary and Conclusions

We have studied the substrate temperature dependence of titanium silicide films, sputtered from a composite target in the range of T_s = 25°-600°C. We found that at high substrate temperatures, T_s ≥ 450°C, there is enough energy available to the species on the substrate surface to promote the formation of fully reacted titanium silicide films. To explain these results, we hypothesize that the surface temperature of the wafer, during sputtering, is much higher than what the bulk substrate temperature would indicate, and this effect can be used in other material systems where high bulk temperatures are not desirable.

Acknowledgments

The authors would like to thank R. Lajos for doing some of the sample preparation, A. Brandes for doing the SEM work, and G. Peterson for doing the Auger analysis.

Manuscript submitted Aug. 23, 1984; revised manuscript received Jan. 10, 1985.

Gould, Incorporated, assisted in meeting the publication costs of this article.

REFERENCES

1. S. P. Murarka, "Silicides for VLSI Applications," Academic Press, NY (1983); T. P. Chow, *IEEE Electron Devices*, **ed-30**, 1480 (1983).
2. M. Tanielian, S. Blackstone, and R. Lajos, Abstract 98, p. 145, The Electrochemical Society Extended Abstracts, Vol. 84-1, Cincinnati, OH, May 6-11, 1984.
3. M. Tanielian, S. Blackstone, and R. Lajos, *Appl. Phys. Lett.*, **45**, 444 (1984).
4. P. Merchant and J. Amano, *J. Vac. Sci. Technol. B*, **2**, 762 (1984).
5. R. Beyers, *J. Appl. Phys.*, **56**, 147 (1984).
6. M. Berti, A. V. Drigo, C. Cohen, J. Siejka, G. G. Bentini, R. Nipoti, and S. Guerri, *ibid.*, **55**, 3558 (1984).
7. R. F. Pinizzotto, K. L. Wang, and S. Matteson, Abstract 226, p. 567, The Electrochemical Society Extended Abstracts, Vol. 81-1, Minneapolis, MN, May 10-15, 1981; L. S. Hung, J. Gyulai, J. W. Meyer, S. S. Lau, and M. A. Nicolet, *J. Appl. Phys.*, **54**, 5076 (1983).
8. K. L. Chopra, "Thin Film Phenomena," R. E. Krieger Pub. Co., New York (1979).
9. M. Tanielian and S. Blackstone, *Appl. Phys. Lett.*, **45**, 673 (1984).
10. R. Beyers and R. Sinclair, *J. Appl. Phys.*, To be published.

Photostimulated Luminescence (PSL) and Color Centers in BaFX:Eu²⁺ (X = Cl, Br, I) Phosphors

K. Takahashi* and J. Miyahara

Fuji Photo Film Company Limited, Miyanodai Development Center, Kaiseimachi, Kanagawa 258, Japan

Y. Shibahara

Fuji Photo Film Company Limited, Ashigara Research Laboratories, Minamiashigara, Kanagawa 250-01, Japan

ABSTRACT

Single crystals of BaFX:Eu²⁺ phosphors have been prepared. Optical absorption spectra and stimulation spectra measured with polarized light are in good agreement with each other. The experimental ESR spectra of the F⁻-rich and X⁻-rich undoped BaFX powder phosphors which have been x-rayed coincide with the calculated spectra of F(X⁻) and F(F⁻) centers, respectively. In addition, the decrease of the ESR signal intensity with light exposure is substantially in agreement with the stimulation spectra for each case. It is concluded that the PSL of BaFX:Eu²⁺ phosphors is caused by the liberation of electrons trapped at F centers created by the x-ray exposure.

A new system of computed radiography, Fuji computed radiography (FCR), has been developed. It is based on new concepts and the latest computer technology. This system can eliminate the drawbacks of the conventional film-screen radiography. The basic principle of the system is the conversion of x-ray energy patterns into digital signals utilizing a He-Ne laser scanning of the imaging plate, which consists of photostimulable phosphors (1).

The photostimulated luminescence (PSL) phenomenon was discovered in the middle of the nineteenth century, but it has been almost ignored because of a lack of industrial applications. We have found some materials which exhibit strong PSL (2), of which the europium-activated barium fluorohalide materials, BaFX:Eu²⁺ (X = Cl, Br, I), have the most favorable characteristics for the FCR system. Some characteristics of these are as follows (1).

The PSL emission peaks are located between 385 and 405 nm, while the main peaks of the stimulation spectra are found between 430 and 630 nm. These peaks shift to longer wavelengths as the halogen ion is changed from Cl to I. The response of the PSL intensity to the exposed x-ray energy shows good linearity in the more than 10⁵ range of x-ray dosage.

The lifetimes of these phosphors are listed in Table I. Because of their fast response characteristics, the scanning readout system (like FCR) can be realized.

It is well known that BaFX crystals have the tetragonal structure as PbFCl (P4/nmm;D_{2h}⁷) and that in BaFCl two types of color centers, F(F⁻) and F(Cl⁻), can be created corresponding to trapped electrons in F⁻ and Cl⁻ ion vacancies, respectively (4). The relation of F centers and PSL in these phosphors has not been investigated yet.

In this paper, we show, using the results of optical and ESR measurements, that the PSL of BaFX:Eu²⁺ is caused by the liberation of the electrons trapped at F centers.

Results

Preparation of single crystals.—The single crystals were prepared by the horizontal Bridgman method. Packed in a graphite boat, Eu²⁺-activated BaFX (X = Cl, Br) was heated to 1070°C in a nitrogen atmosphere. The material was then cooled at the rate of 0.2°C/min to 800°C and 1.0°C/min to room temperature. Because of the neighboring halogen ion planes, it is easy to cleave the crystals perpendicular to the c axis, and so it is difficult to make a thick sample. In preparing single crystals, only stoichiometrically F⁻-rich ones were grown well.

Optical measurements.—Optical absorption spectra of an irradiated BaFCl:Eu²⁺ single crystal are shown in Fig. 1a. In the case of the c axis perpendicular to the electric vector **E** of the incident light, the absorption band peaks at about 550 nm. If the c axis is parallel to **E**, the absorp-

*Electrochemical Society Active Member.

Table I. The lifetimes of BaFX:Eu²⁺ phosphors

Sample	Lifetime (PSL) (μs)	Lifetime (UV) (μs)
BaFCl:Eu ²⁺	7.4 ^a	5.7 ^b
BaFCl _{0.5} Br _{0.5} :Eu ²⁺	2.0	1.1 ^b
BaFBr:Eu ²⁺	0.8 ^a	—
BaFI:Eu ²⁺	0.6 ^a	—

^a See Ref. (1).

^b See Ref. (3).

tion peak stands at about 440 nm. These absorption spectra coincide with those of F(Cl⁻) centers in BaFCl single crystals (4). Stimulation spectra of the same sample are given in Fig. 1b, the peaks of which are in good agreement with those of the absorption spectra. In a BaFBr:Eu²⁺ single crystal, the same results have been obtained (see Fig. 2a and 2b).

ESR investigations.—ESR studies on undoped BaFX (X = Cl, Br) powder phosphors have been made to show that color centers created by x-rays are F centers. Undoped materials were used because ESR signals of trapped electric charges become undetectable in the presence of ESR signals of Eu²⁺ ions. The undoped BaFX powder phosphors also show PSL emission whose stimulation spectra are similar to those of BaFX:Eu²⁺ phosphors, although in this case PSL emission was thought to

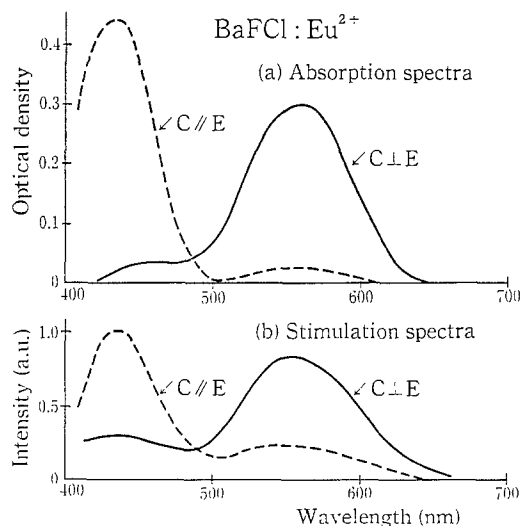


Fig. 1. Optical absorption spectra (a) and stimulation spectra (b) of the x-ray-irradiated BaFCl:Eu²⁺ single crystal.

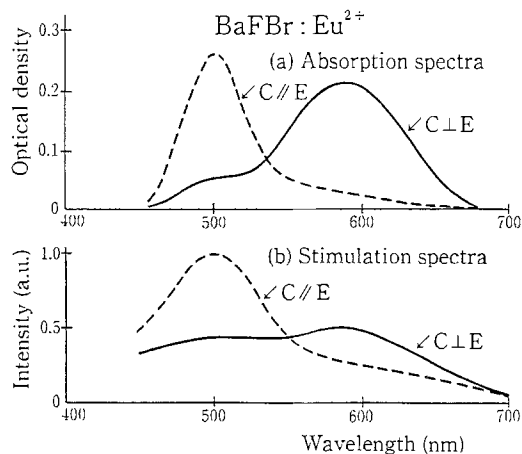


Fig. 2. Optical absorption spectra (a) and stimulation spectra (b) of the x-ray-irradiated BaFBr:Eu²⁺ single crystal.

be due to a trace of contaminated Eu²⁺ ions. Four samples, whose BaF₂/BaX₂ charged ratios are 95/105 and 105/95, X = Cl and Br, respectively, have been prepared to investigate the effect of the chemical composition in BaFX phosphors. In spite of deviating from the 1:1 ratio between BaF₂ and BaX₂ by as much as 10%, the x-ray diffraction patterns of these materials show that they are still substantially single phase (see Fig. 3). The ESR measurements on heavily x-rayed BaFX powder phosphors have been carried out at Q band using a Varian E-109 spectrometer. The ESR spectra of BaFCl (F/Cl = 95/105), BaFCl (F/Cl = 105/95), BaFBr (F/Br = 95/105), and BaFBr (F/Br = 105/95) are shown in Fig. 4 (curves A). These spectra, which decrease under the visible rays, are not observed in BaFX powder phosphors until they are irradiated by x-rays. The decrease of the ESR signal intensity with the light exposure was also measured. The results are shown in Fig. 5 (curves A) for the above samples.

Discussion

In case of F centers in BaFX, only the hyperfine interaction between the electron trapped at the F center and the nearest neighbor barium nuclei should be taken into account. The hamiltonian spin can be written as

$$\mathcal{H} = \beta_e \mathbf{H}(g)\mathbf{S} + \mathbf{I}_k(T_k(\text{Ba}))\mathbf{S}$$

where $(T_k(\text{Ba}))$ and \mathbf{I}_k are the hyperfine tensor and the nuclear spin of the k th Ba nucleus, respectively [k ranges from 1 to 4 for F(F⁻) and from 1 to 5 for F(X⁻)]. Barium has two isotopes of nuclear spins with 3/2, ¹³⁵Ba($g_1 = 0.555$) and ¹³⁷Ba($g_1 = 0.621$), whose natural abundances are 6.6% and 11.3%, respectively. The two other isotopes, ¹³⁶Ba and ¹³⁸Ba, have no nuclear spins (4).

Experimental ESR spectra can be simulated supposing that the hyperfine interaction terms with fluorine and

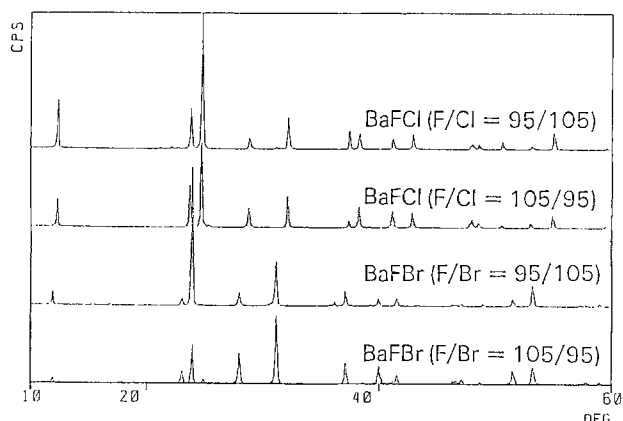


Fig. 3. The x-ray diffraction patterns of BaFCl(F/Cl = 95/105), BaFCl(F/Cl = 105/95), BaFBr(F/Br = 95/105), and BaFBr(F/Br = 105/95), measured with Cu K α .

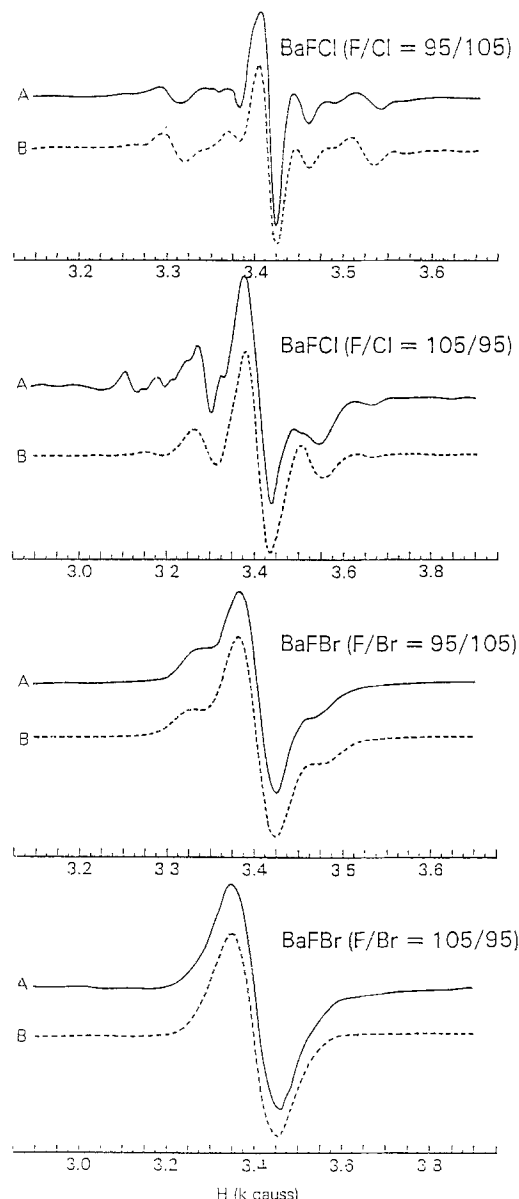


Fig. 4. The experimental ESR spectra of the x-ray-irradiated BaFCl(F/Cl = 95/105), BaFCl(F/Cl = 105/95), BaFBr(F/Br = 95/105) and BaFBr(F/Br = 105/95) powder phosphors (curves A), and the calculated ones of F(F⁻) centers in BaFCl, F(Cl⁻) in BaFCl, F(F⁻) in BaFBr, and F(Br⁻) in BaFBr, respectively (curves B).

other halogen nuclei will only contribute to the broadening of the hyperfine lines and that microcrystals are oriented in all directions with equal probability in powder samples. The results of the calculation are shown in Fig. 4

Table II. The ESR parameters used to calculate the simulated spectra of F(F⁻) and F(X⁻) centers in BaFX (X = Cl, Br)

Parameter	Phosphor F center	BaFCl		BaFBr	
		F(F ⁻) center	F(Cl ⁻) center	F(F ⁻) center	F(Br ⁻) center
g_{\parallel}		1.985	1.983	1.988	1.980
g_{\perp}		1.970	1.970	1.966	1.980
Linewidth		12G	12G	50G	50G
$A_{\parallel} (^{135}\text{Ba}, k = 1 - 4)$		69G	37G	73G	39G
$A_{\parallel} (^{137}\text{Ba}, k = 1 - 4)$		69G	41G	73G	43G
$A_{\perp} (^{135}\text{Ba}, k = 1 - 4)$		78G	34G	82G	30G
$A_{\perp} (^{135}\text{Ba}, k = 1 - 4)$		78G	38G	82G	34G
$A_{\parallel} (^{135}\text{Ba}, k = 5)$		—	41G	—	43G
$A_{\parallel} (^{137}\text{Ba}, k = 5)$		—	45G	—	48G
$A_{\perp} (^{135}\text{Ba}, k = 5)$		—	38G	—	36G
$A_{\perp} (^{137}\text{Ba}, k = 5)$		—	42G	—	40G

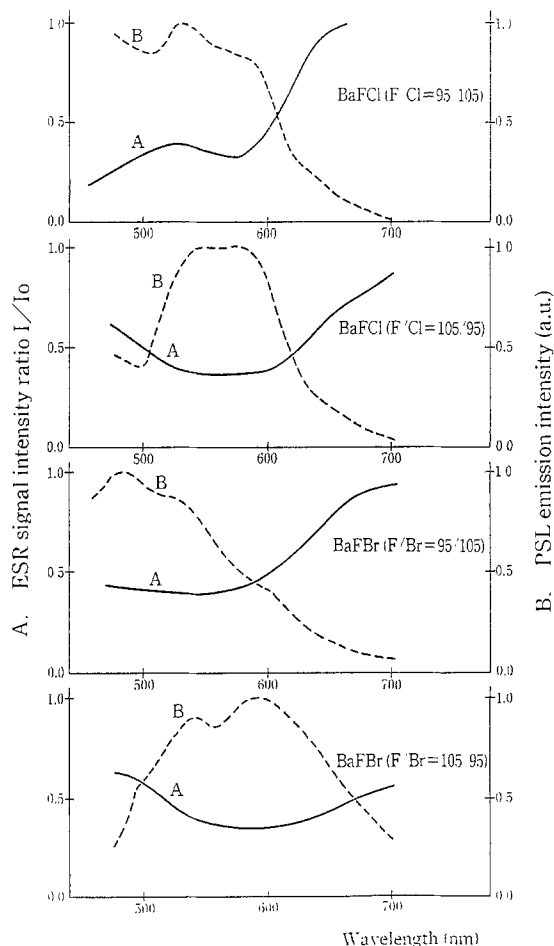


Fig. 5. The decrease spectra of the ESR signal intensity with the light exposure (curves A) and the stimulation spectra (curves B) in the BaFCl(F/Cl = 95/105 and 105/95) and BaFBr(F/Br = 95/105 and 105/95) powder phosphors. I : ESR signal intensity from F centers after the light exposure. I_0 : ESR signal intensity from F centers before the light exposure.

(curves B), and the ESR parameters used in the calculation are listed in Table II, where A_{\parallel} (c axis/magnetic field) and A_{\perp} (c axis \perp magnetic field) represent the hyperfine constant measured at 9.1 GHz. The values for BaFCl were obtained by the simulation based on the data of Yuste *et al.* (4).

Table III. The types of color centers created in BaFX by x-ray exposure

Phosphor	BaFCl (X = Cl)		BaFBr (X = Br)	
	F/X atomic ratio	Color center	F/X atomic ratio	Color center
	95/105	F(F ⁻)	95/105	F(F ⁻)
	105/95	F(Cl ⁻)	105/95	F(Br ⁻)

The coincidence between the experimental spectra and the calculated ones in Fig. 4 implies that color centers created by x-ray exposure in BaFX phosphors are such centers as listed in Table III.

It is shown in Fig. 5 that these centers decrease effectively under the visible radiation that gives rise to efficient PSL. Because of the difference between the exposures of light in the PSL measurement and the ESR, the spectral correlations of these data are not so good. Thus, in BaFX:Eu²⁺ phosphors, PSL emission is caused by the liberation of the electrons trapped at F centers.

Conclusion

In photostimulable BaFX:Eu²⁺ phosphors, F centers can be created by x-ray exposure. When these are irradiated by the visible rays in the F center absorption band, they liberate the electrons and show PSL emission.

Acknowledgments

The authors wish to express their appreciation to Mr. M. Takano for his encouragement, to Dr. T. Tomotsu for his helpful suggestions, to Dr. T. Watanabe, University of Tokyo, for the program for calculating the ESR spectra, and to Dr. H. Kukimoto, Tokyo Institute of Technology, for his suggestion for preparing single crystals. They also thank S. Arakawa, C. Umamoto, and N. Mori for doing much of the experimental work and for rewarding discussions.

Manuscript submitted Oct. 1, 1984; revised manuscript received Feb. 26, 1984. This was Paper 921 RNP presented at the San Francisco, California. Meeting of the Society, May 8-13, 1983.

Fuji Photo Film Company Limited assisted in meeting the publication costs of this article.

REFERENCES

1. M. Sonoda, M. Takano, J. Miyahara, and H. Kato, *Radiology*, **148**, 833 (1983).
2. U.S. Pat. 4,239,968; U.S. Pat. 4,236,078.
3. J. L. Sommerdijk, J. M. P. J. Versteegen, and A. Bril, *J. Lumin.*, **8**, 502 (1974).
4. M. Yuste, L. Taurel, M. Rahmani, and D. Lemoyne, *J. Phys. Chem. Solids*, **37**, 961 (1976).

Automatic End-Point Detection of Spray Etching in Application to Mask Making

Fumio Mizuno, Makoto Kato, Tooru Koizumi, Yoichi Takehana, and Katsuro Sugawara*

Hitachi Limited, Device Development Center, Kodaira, Tokyo 187, Japan

Keiji Mori

Hitachi Limited, Production Engineering Research Laboratory, Totsuka-ku, Yokohama 244, Japan

The development of high performance LSI's has increased the requirement for precise control of mask making in addition to that of wafer processing. One method for obtaining precise control is "in-process" end-point detection. End-point detection methods have previously been devised for thin film formation, such as thickness control of SOS (silicon-on-sapphire) epitaxial layers (1), homoepitaxial layers (2), and for plasma etching (3). In mask making, "wet etching" has been used due to thin Cr film deposited on mask blanks and to flat surface in comparison with the wafer fabrication. In this note, a novel method of the end-point detection used for the mask making will be reported; it is quite different from that used for the "dry etching."

A schematic diagram of the end-point detection apparatus is shown in Fig. 1. The specimen used in this experiment was an electron-beam resist coated mask blank with a Cr film of 800Å thick and was developed by the spray method. This apparatus consisted of (i) a light source, (ii) a reflector, "corner cube," which reflected the incident light, (iii) a photodetector which detected the reflected light and transduced it to the electric signal, (iv) a photosensor which had a disk with a slit in order to generate a timing signal synchronized with the incident light, and (v) a control circuit which decided the end point by receiving the electrical signal converted from the reflected light. The light source and the photodetector were installed above the mask. The corner cube was used as the reflector to separate the incident and the reflected light. The disk with the slit was attached to the mask holder; the slit was adjusted to be located just above the photosensor when the corner cube was rotated just under the light source. The signal from this photosensor produced the timing signal for the control circuit. The reflected light was converted by the photodetector to an electrical signal, synchronized with the timing signal, and the electrical signal was used to detect the end point.

Figure 2 is a block diagram of the control circuit. The signal generated by the reflected light was first amplified, then sampled at the rate of once per revolution, synchronized by the timing signal, and transferred to an A-D converter. The signal was converted to the digital signal through the A-D converter and processed by an 8 bit microcomputer. Thus, the microcomputer, which judged the end point, gave the control signal to the spray etching apparatus and stopped the etching.

There was approximately 10% fluctuation in the output of the A-D converter at the end of the etching unless further signal processing was done. Therefore, a novel algorithm was devised to obtain accurate end-point detection as shown in Fig. 3. The first step was the moving average process. The output value of the signal, TN_n , at a certain time, n , is given by

$$TN_n = \sum_{i=1}^n V_n/i \quad [1]$$

where V_n is the value of the n th signal before the process and i is the sampling number of data to average, ordinarily 16. Thus, the signal of the reflected light became smoothed. The next step was the differential process. The essential object was to increase the judging accuracy. In our method, the end point was defined as the point at which the reflected light signal reached saturation, and was where the signal difference reached 0. That is, the n th signal converted after the differential process, T_n , is expressed as

$$T_n = (TN_n - TN_{n-1})/\Delta t_j \quad [2]$$

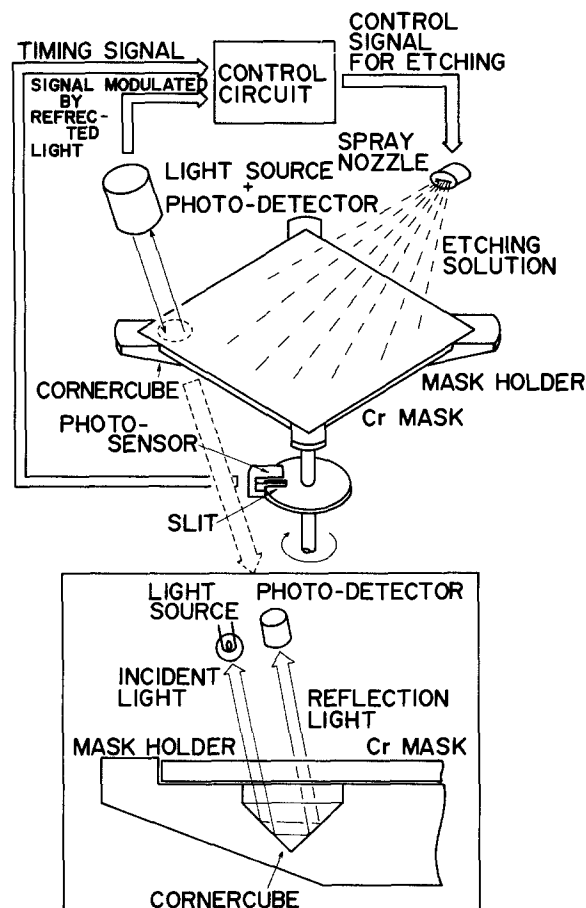


Fig. 1. Schematic diagram of the apparatus to detect the end point during the spray etching of Cr mask.

*Electrochemical Society Active Member.

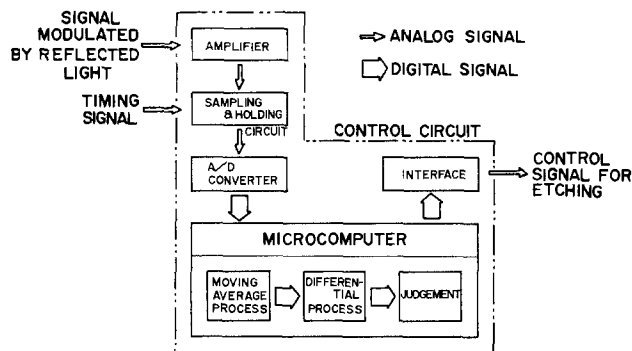


Fig. 2. Block diagram of the control system to judge the end point during the spray etching.

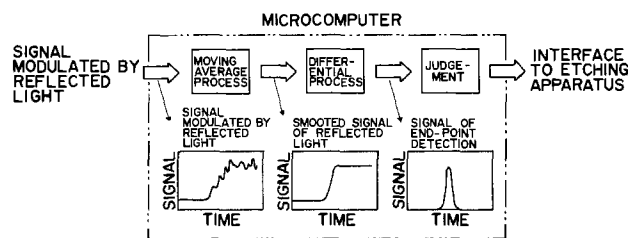


Fig. 3. Data flow to judge the end point during the spray etching

where TN_n and TN_{n-1} are the data after the moving average process at the n th and the $(n-1)$ th signal, respectively; j is the sampling number to be used for the process, and Δt is the interval of the timing signal. Figure 4 shows examples of the data thus treated. Figure 4a is the signal generated by the reflected light, Fig. 4b is the smoothed signal which was treated after Eq. [1], and Fig. 4c is the signal to judge the end point after the differential process using Eq. [2]. The pattern in Fig. 4c shows the sharp peak, which fell to 0 after a few seconds. The spray etching was stopped just after the 0 signal of the end-point detection was sent to the etching apparatus.

For accurate control of mask making using spray etching, a novel method using reflected light from a corner cube to detect the end point of the etching precisely, after smoothing the signal and increasing the accuracy by means of both a moving average process and differential process, was developed. Using this method, the variation of the Cr mask critical dimension after etching could be improved from ± 0.2 to $\pm 0.1 \mu\text{m}$.

MOVING AVERAGE PROCESS

$$TN_n = \frac{\sum_{i=1}^n V_n}{i}$$

TN_n : n -th SIGNAL AFTER PROCESS
 V_n : n -th SIGNAL BEFORE PROCESS
 i : SAMPLING NUMBER TO BE USED FOR PROCESS

DIFFERENTIAL PROCESS

$$T_n = \frac{TN_n - TN_{n-j}}{\Delta t \cdot j}$$

T_n : n -th SIGNAL AFTER PROCESS
 TN_n : n -th SIGNAL BEFORE PROCESS
 Δt : INTERVAL OF TIMING SIGNAL
 j : SAMPLING NUMBER TO BE USED FOR PROCESS

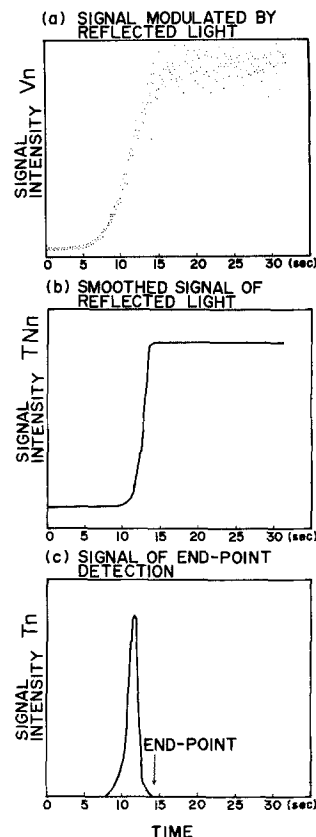


Fig. 4. Example of data treatment to judge the end point during the spray etching.

Acknowledgments

The authors express their sincere gratitude to Dr. Y. Ohya for his encouragement, to Mr. T. Kawanabe and Mr. I. Tanabe for helpful discussion, and to Mr. H. Nakaune, Mr. K. Kamiyama, and Mr. S. Mori for their assistance in the experimental work.

Manuscript submitted June 15, 1984; revised manuscript received Jan. 2, 1985.

Hitachi Limited assisted in meeting the publication costs of this article.

REFERENCES

1. D. J. Dumin, *Rev. Sci. Instrum.*, **38**, 1107 (1967).
2. K. Sugawara, T. Yoshimi, Y. Nakazawa, and K. Itoh, *This Journal*, **123**, 759 (1976).
3. K. Hirobe and T. Tsuchimoto, *ibid.*, **127**, 234 (1980).

Characterization of Epitaxial Layers and Substrate Wafers by Surface Topographic Observation

K. Kugimiya*

Matsushita Electric Industrial Company, Limited, Semiconductor Research Center, 3-15 Yagumonakamachi, Moriguchi, Osaka 570, Japan

The characteristics of polished Si wafer surfaces (1) have been recognized as being very influential to the properties and yields of IC's for a long time. Characterization is carried out by, for instance, Newton ring observation (2), x-ray analyses (3, 4) and optical methods (5, 6). Yet, because of many difficulties, only a few quantitative observations have been made. The optical observation method (7, 8) derived recently from the "Makyo concept" (observation of projected images of mirror surface contours reflecting the surface waviness) has been a very

*Electrochemical Society Member.

powerful tool for the analyses of the topological nature of wafer surfaces. It is a nondestructive, instantaneous, and visual observation method, although a qualitative one. Some of the recent applications, the in-line monitoring of IC processes, and the improvement of the wafer surface quality, are herein briefly summarized.

Experimental

The in-line monitoring (7) was done using a surface monitor ZX-5100 (Matsushita Industrial Equipment Company, Limited) at our laboratory and the production lines. (100) and (111) Si wafers were purchased commercially

from several vendors. After the initial examination of the surfaces, single and cyclic thermal processes (9, 10) were carried out to detect crystal defects hiding behind the apparent deformation at the surfaces. Defects were delineated by the Secco etchant.

The monitor was further applied for optimizing epitaxial Si growth conditions in a barrel-type reactor. Slip lines were observed by the monitor. It was also applied for the improvement of wafer surface quality.

Results and Discussion

Figure 1 shows the various surface deformations of as-received wafers observed by the monitor over a few months. Bright lines and areas correspond to surface concavity and dark lines and areas to surface convexity. Most of observed deformations are polishing/lapping marks (Fig. 1, parts 2, 3, 5, 7, 8), dimples (Fig. 1, parts 1, 5, 9), and back-side damage irregularities (Fig. 1, part 1) and a few scratches (Fig. 1, parts 8, 9), orange peels, protrusions, and some unknown deformations (Fig. 1, parts 2-4, 6, 8). Scratches appearing as dark lines (Fig. 1, parts 8, 9) were made at the front sides (7). The diameters of wafer images indicate the flatness of wafers. A specimen in Fig. 1, part 5 is fairly flat, while a specimen in Fig. 1, part 1 shows concavity and those in Fig. 1, parts 2 and 9 convexity. Skews are also observed in the images. Most of the deformations were clearly made during the processing by wafer vendors, possibly because of the difficulty of achieving perfect process control, *e.g.*, cloths and powders in polishing, dust and air bubbles in pasting, etc. (11).

X-ray topographs of the deformation showed that back-side damage irregularities, scratches, and some of unknown deformations were accompanied by a slight lattice deformation and thus by the residual stresses. However, optical microscopic observation of oxidized and etched wafers showed that most of the deformations were proved to be harmless and some were related with crystal defects (12). A typical example of the stacking fault formation after the dry oxidation at 1000°C for 1h is shown in Fig. 2. Stacking faults revealed by the Secco etching are shown by dots, and their distribution as shown by two gray bands in Fig. 2B is in a fair agreement with lapping marks in Fig. 2A. This clearly indicates that some lapping marks are accompanied by latent mechanical damage. Some specimens with the residual strains, Fig. 1, parts 1, 2, 9 showed an unusual denuded zone formation after cyclic annealing (Fig. 3B). For a wafer with an interstitial oxygen concentration of about $10^{18}/\text{cm}^3$ as used in this

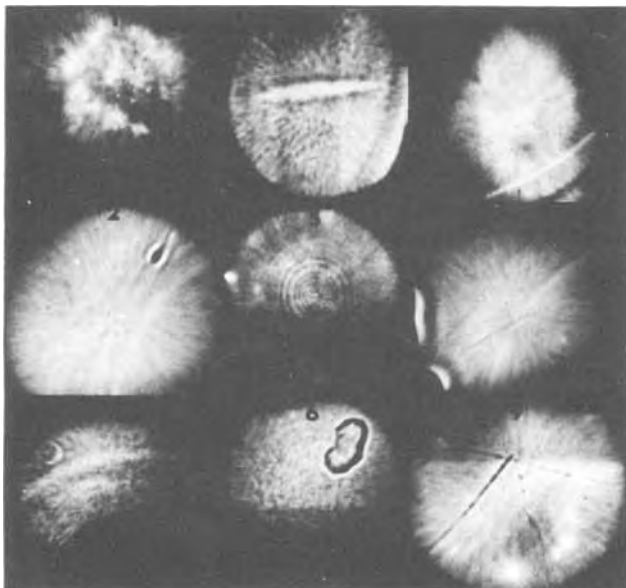


Fig. 1. In-line monitoring of as-received Si wafers. Parts 1-3: left column, top to bottom, respectively. Parts 4-6: middle column, top to bottom, respectively. Parts 7-9: right column, top to bottom, respectively.

experiment, no denuded zone nor microprecipitate formation is usually observed even after the heat cycle of 1100°C O₂ 1% 4h/800°C N₂ 16h/1000°C N₂ 6h (9). Stress-enhanced precipitate formation by Si₃N₄ or poly-Si layers has been observed (13). These stress effects are obviously different and ambiguous, *i.e.*, precipitates are formed with the relaxation of the residual stress in the former while the stresses are present all through the heat cycle in the latter.

The in-line monitoring of the epitaxial Si growth process has been very successful. In a usual technique, slips are, for instance, delineated and observed after etching, a destructive and time consuming process. An abnormal wafer as shown in Fig. 4 clearly reveals the presence of numerous slip lines without destruction. One of the large slip lines is revealed and shown in the circle in Fig. 4 after angle lapping and staining. The surface profiles also shown in the figure clearly point out numerous small steps. Some are of less than 100Å. These small steps of surface curvatures result in dark and bright line images as shown in the figure.

Minor modification and some improvement of polishing and pasting methods in the wafer process resulted in better quality, as shown in Fig. 5. In-line monitoring could still readily pick up any slight change in the wafer process.

GaAs wafers were generally of a very poor surface finish, worse than those shown in Fig. 1. Large residual stresses and distortion were generally observed. The improvement of the wafer process using a surface monitor is now in progress.

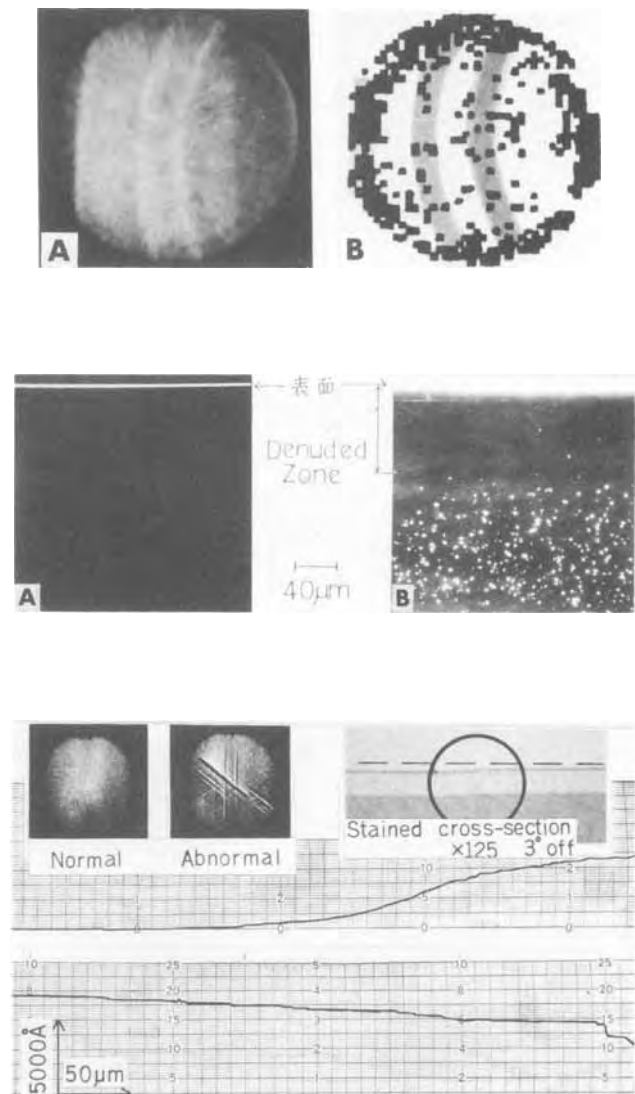


Fig. 4. Monitoring of slip lines formed in the epitaxial process

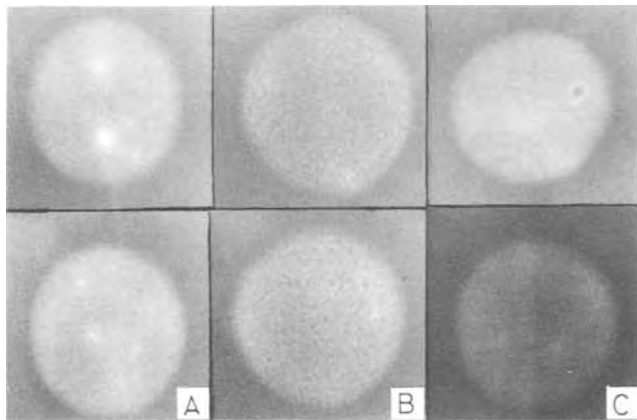


Fig. 5. Surface regularity after the minor modification in the wafer process. Processes A, B, and C.

Conclusion

It has been shown that the optical method derived from the Makyo concept is simple and nondestructive, and thus suitable for the in-line monitoring of wafers and IC processes. The monitoring could effectively stabilize the wafer surface quality and the epitaxial process. It could also eliminate abnormal wafers with unusual residual stresses. The method can be further applied to minimize slip lines in heat processes and also to analyze mirror surfaces and even lenses.

Since the method can pick up surface deformations, which other flatness testers using the scanning laser or Moire methods can barely detect, the method is complementary to the others. Thus, combined analyses will result in the better characterization of the wafer surface.

Acknowledgments

The author would like to express his thanks to A. Nishikawa for the in-line monitoring of as-received wafers and

M. Matsumoto of Matsushita Electric Industrial Company Limited for the wafer and the yield evaluations in the IC production lines.

Manuscript submitted Jan. 7, 1985; revised manuscript received Feb. 25, 1985.

Matsushita Electric Industrial Company Limited assisted in meeting the publication costs of this article.

REFERENCES

1. J. H. Matlock, *Solid State Technol.*, **26**, (11), 111 (1983).
2. M. Tamura and H. Sunami, *Jpn. J. Appl. Phys.*, **11**, 1097 (1972).
3. G. H. Schwuttke and J. K. Howard, *J. Appl. Phys.*, **39**, 1581 (1967).
4. J. R. Patel and N. Kato, *ibid.*, **44**, 971 (1973).
5. E. A. Irene, *J. Electron. Mater.*, **5**, 287 (1976).
6. S. Takasu, Y. Matsushita, H. Kotaka, and T. Wada, in "Semiconductor Silicon 1977," H. R. Huff and E. Sirtl, Editors, p. 456, The Electrochemical Society Softbound Proceedings Series, Princeton, NJ (1977).
7. K. Kugimiya, *This Journal*, **130**, 2123 (1983).
8. S. Kato, H. Mizumaki, and R. Kawanaka, *Inst. Elect. Commun. Engr. Jpn.*, **SSD 77-81**, 33 (1977).
9. K. Kugimiya, S. Akiyama, and S. Nakamura, in "Semiconductor Silicon 1981," H. R. Huff, R. J. Kriegler, and Y. Takeishi, Editors, p. 294, The Electrochemical Society Softbound Proceedings Series, Pennington, NJ (1981).
10. J. H. Matlock, in "Silicon Processing," D. C. Gupta, Editor, p. 332, ASTM Special Technical Publication 804, ASTM, Philadelphia (1983).
11. A. C. Bonora, in "Semiconductor Silicon 1977," H. R. Huff and E. Sirtl, Editors, p. 154, The Electrochemical Society Softbound Proceedings Series, Princeton, NJ (1977).
12. K. Kugimiya and M. Matsumoto, in Proceedings of the 21st Symposium on Semiconductor and IC Technology," p. 12, Electrochemical Society of Japan, Tokyo (1981).
13. K. Inoue, K. Kotera, T. Yonezawa, and K. Kugimiya, *Inst. Elect. Commun. Engr. Jpn.*, **SSD 80-95**, 13 (1981).

Sulfation of CeO₂ and ZrO₂ Relating to Hot Corrosion

R. L. Jones,* S. R. Jones,¹ and C. E. Williams

Naval Research Laboratory, Chemistry Division, Washington, DC 20375-5000

The reactions of SO₂-SO₃ (SO₂ + 1/2 O₂ ⇌ SO₃) with ceria (CeO₂) are of interest in the development of materials for resisting hot corrosion in gas turbine engines. Addition of CeO₂ as a dispersed oxide phase in the metal reduces sulfidation-oxidation attack on nickel-based turbine blade super alloys presumably by reducing the sulfur activity through formation of Ce₂O₃S (1). Ceria appears also to promote hot corrosion resistance in ZrO₂-based ceramics. In material tests for MHD channels, CeO₂-ZrO₂ has shown good resistance to 1200°C K₂SO₄-K₂CO₃ melts (2). And, of more immediate relevance to hot corrosion in gas turbines, plasma-sprayed CeO₂-ZrO₂ has been patented as protecting super alloys against attack by vanadium and SO_x impurities in turbine gas (3).

Ceramic coatings of Y₂O₃-ZrO₂ have been considerably studied as thermal barrier coatings for gas turbines and diesel engines, and reaction with molten vanadates is known to "leach" Y₂O₃ from the ceramic, with resultant rapid degradation of the coatings (4). Perhaps less well known is the fact that the concurrent action of Na₂SO₄ and SO₃ can also cause Y₂O₃ depletion and ceramic degradation under SO₃ partial pressures, e.g., as low as 700 Pa (7 × 10⁻³ atm) at 700°C (5). In a recent investigation of Y₂O₃ and HfO₂ sulfation, we have confirmed the high re-

activity of SO₃ with Y₂O₃ and determined the equilibrium SO₃ partial pressure for the initial sulfation reaction, Y₂O₃(s) + SO₃(g) ⇌ Y₂O₂(SO₄)(s), to be approximately 1.5, 2.5, and 3.5 Pa at 850°, 900°, and 950°C, respectively (6). Mixed sulfates of Y₂(SO₄)₃-Na₂SO₄ were formed when Na₂SO₄ was present, with the system exhibiting a eutectic in the vicinity of 25 mole percent (m/o) Y₂(SO₄)₃ which melted below 800°C. Pure hafnia was strongly resistant to sulfation, and although liquid phase mixed sulfates could be produced by sulfation of 50 m/o HfO₂-Na₂SO₄ mixtures at 700°C, SO₃ partial pressures in excess of 1500 Pa were required.

In the experiments reported here, we have applied the techniques of our Y₂O₃-HfO₂ investigation to study the sulfation behavior of CeO₂ and ZrO₂. Our goals were to determine if CeO₂ is more resistant to SO₃-Na₂SO₄ reaction than Y₂O₃, and if ZrO₂, like HfO₂, is strongly resistant to sulfation (Hf and Zr commonly show similar chemical behavior). The first finding could help to confirm whether CeO₂- or Y₂O₃-stabilized zirconia should be best against molten sulfate hot corrosion, while the second would aid in defining the corrosion resistance of zirconia itself.

Experimental

Our experiments were conducted using controlled gas atmosphere furnaces, described previously (7), wherein

*Electrochemical Society Active Member.

¹Member of the Naval Research Laboratory Ensign Program.

the pure oxides and oxide-Na₂SO₄ mixtures were exposed to low concentrations of SO₂ or equilibrated (over Pt at temperature) SO₂-SO₃ in air at temperatures of 650°-800°C. The incoming SO₂ concentrations were controlled by electronic mass flow controllers, and the furnaces were fitted with analytical trapping systems which allowed determination of the SO₂, SO₃, and SO_x (SO_x = SO₂ + SO₃) concentrations in the exhaust air. Gas control and analyses were within ± 10%, except at high SO₃ partial pressures (> 500 Pa) where sulfuric acid mist formation and SO₃ polymerization reduced accuracy substantially. Furnace temperatures were maintained within ± 5°C.

The specimens were exposed in porcelain boats using 100 mg samples of the oxides and 250 mg samples of the oxide-Na₂SO₄ mixtures which were of 50 m/o composition and taken from thoroughly ground and mixed master stocks. The reagents were of high purity as indicated: CeO₂ (99.9%, Alfa Ventron), ZrO₂ (99.998%, Alfa Ventron Puritronic), Na₂SO₄ (reagent grade, Fisher), and SO₂ (99.98%, Matheson).

Results and Discussion

Catalytic activity of CeO₂.—To understand sulfation reactions, one must know whether the metal oxide reacts predominantly with SO₃, or with SO₂ + 1/2 O₂. Our studies with Co₃O₄, NiO, and ZnO indicate that the 700°C sulfation of these oxides proceeds by reaction with SO₃ (7). This is somewhat difficult to discern with Co₃O₄ and NiO, since both oxides catalyze the reaction, SO₂ + 1/2 O₂ ⇌ SO₃, and sulfation can occur (although at higher SO_x partial pressure) even when the furnace gas contains only SO₂. With ZnO, which is not catalytic, the effect is readily evident, and sulfation occurs essentially only when an external catalyst is present. This can be important, as illustrated, for example, in a study of the sorption of SO₂ from synthetic flue gas by metal oxides where ZnO was found not to sorb SO₂ (*i.e.*, sulfate), even though the thermodynamics were favorable (8).

The catalytic activity of CeO₂ was tested by passing low concentrations (< 30 Pa) of SO₂ in air at 200 ml/min over 100 mg samples of the oxide contained in porcelain boats at 650°C, and analyzing for the SO₂ and SO₃ concentrations in the furnace exhaust air. The SO₃/SO₂ ratio after passing over the CeO₂ was approximately 0.6, whereas with all the conditions the same, except for CeO₂'s absence, the SO₃/SO₂ ratio was near 0.08. Clearly, therefore, CeO₂ catalyzes the SO₃ ⇌ SO₂ reaction.

Equilibrium SO₃ partial pressure for CeO₂ sulfation.—The equilibrium SO₃ partial pressure for the initial sulfation reaction of CeO₂ at 650°, 700°, and 750°C (Fig. 1) was determined following a procedure employed previously (7). By this technique, the weight gain after 24h exposure for individual 100 mg samples of CeO₂ was determined for increasing concentrations of SO₃, and these data points were then plotted and extrapolated to zero weight gain, as shown in Fig. 1, to define the equilibrium SO₃ partial pressure for the reaction. To verify that equilibrium SO₃ was in fact obtained, the sulfated specimens were re-exposed at SO₃ partial pressures below the equilibrium value and shown to revert to the oxide.

The equilibrium P_{SO_3} values obtained in Fig. 1 are 30, 100, and 230 Pa at 650°, 700°, and 750°C, respectively. Assuming the initial sulfation product to be CeOSO₄ (see below), and that there is negligible intersolubility, the standard free energy of the sulfation reaction



can be calculated from $\Delta G^\circ = -RT \ln K$, where taking the solid phase activities as unity, $K = (1/P_{SO_3})$. Estimating the probable error in temperature to be ± 5°, and in SO₃ equilibrium partial pressure to be ± 20%, the standard free energies were calculated as being -62.2 ± 2 , -55.9 ± 2 , and -51.7 ± 2 kJ/mol at 650°, 700°, and 750°C. No standard free energy for reaction [1] exists in the literature for comparison with these values. However, the calculated free energies can be fitted (to within less than the experimental

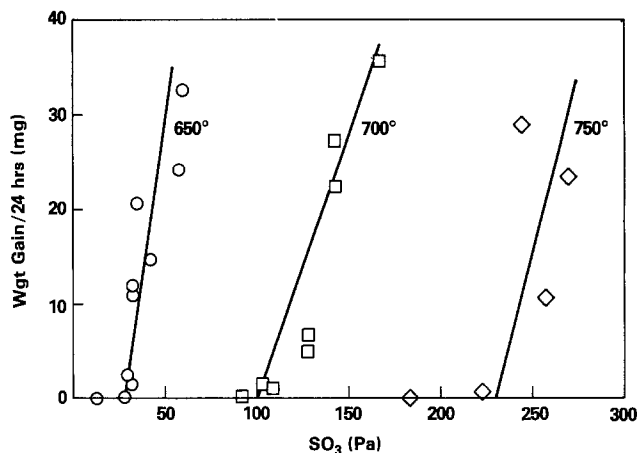


Fig. 1. Determination of the equilibrium SO₃ partial pressure for sulfation of CeO₂ at the temperatures indicated.

error) over the investigated temperature range to the expression $\Delta G = \Delta H - T\Delta S$, where $\Delta H = -160$ kJ/mol and $\Delta S = -0.105$ kJ/mol-deg. The ΔS so derived can then be compared to data compiled, *e.g.*, by Turkdogan (9) where ΔS ranges from -0.105 for $\text{K}_2\text{O}(\text{s}) + \text{SO}_3(\text{g}) \rightleftharpoons \text{K}_2\text{SO}_4(\text{s})$ to -0.186 for $\text{CdO}(\text{s}) + \text{SO}_3(\text{g}) \rightleftharpoons \text{CdSO}_4(\text{s})$. The ΔS in these reactions presumably results mainly from the incorporation of 1 mol of SO₃ that occurs. The agreement in ΔS thus tends to support the postulated CeOSO₄ sulfation reaction and the measured SO₃ equilibrium partial pressures.

Test for the criticality of SO₃ in CeO₂ sulfation.—Although "equilibrium SO₃ partial pressures for sulfation" were determined above, it cannot be unequivocally shown that the reaction involves SO₃ solely. For non-catalytic oxides such as ZnO, the relative roles of SO₂ and SO₃ can be evaluated by comparing the sulfation behavior with and without the platinum catalyst in the gas stream. When the catalyst is removed, the SO₃ concentration at the oxide surface is greatly reduced and, unless the oxide reacts with SO₂, it will not sulfate even though the total SO_x concentration is as high (or higher) as when sulfation occurred when the Pt catalyst was present. This behavior was clearly evident with ZnO (7).

Conversely, the weight gain (sulfation) with CeO₂ could not be seen to be affected by the presence or absence of the external catalyst even at SO_x partial pressures near the equilibrium value (Fig. 2). This implies either that

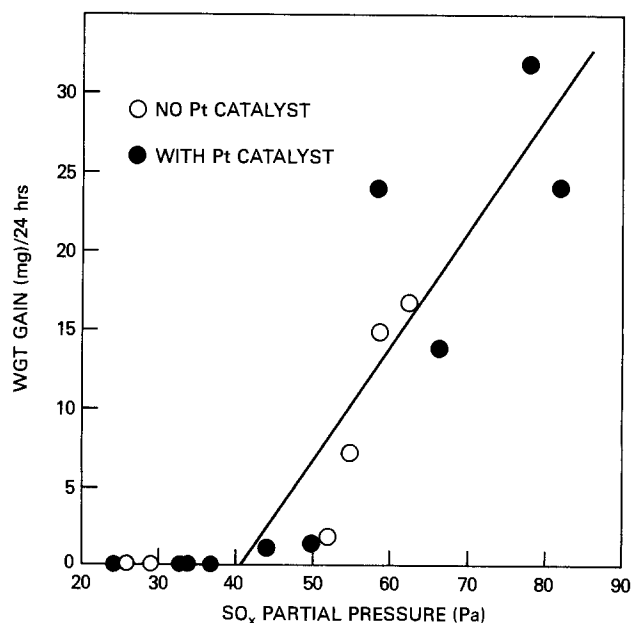
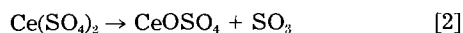


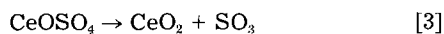
Fig. 2. Sulfation of CeO₂ at 650°C with and without the external Pt catalyst present (as a test of whether the sulfation proceeds principally by SO₂ or SO₃ reaction; see text).

CeO₂ reacts as readily with SO₂ as with SO₃, or more likely, that SO₂-SO₃ equilibrium is achieved at the catalytic CeO₂ surface (at least in the initial stages of sulfation) with sulfation then actually proceeding by SO₃ reaction. Unfortunately, however, neither possibility can be proved within the context of the present investigation.

Identification of the CeO₂ sulfation product.—In studies of CeO₂ for desulfurization of hot gases, the sulfation product has been variously identified as CeO₂O(SO₄)₃ (10) or Ce(SO₄)₂ (8). Cerium sulfate has also been proposed (11) to decompose in eutectic sulfate melts according to



and then at higher temperature



To identify the sulfation product in the present experiments, 500 mg samples of CeO₂ were sulfated over long times, with periodic grinding, at 650° and 750°C under SO₃ partial pressures only moderately above the equilibrium SO₃ pressure for sulfation. In each case, the weight gain approached a limiting value of approximately 220-240 mg, as shown in Fig. 3. The theoretical weight gains for total conversion of the CeO₂ to CeOSO₄, to Ce₂O(SO₄)₃, and to Ce(SO₄)₂ are 233, 349, and 465 mg, respectively. Therefore, the gravimetric data indicate that the initial product in the sulfation of pure CeO₂ is most likely CeOSO₄. At higher SO₃ pressures, of course, other sulfates including Ce₂O(SO₄)₃ and Ce(SO₄)₂ could be formed, which might explain the different CeO₂ sulfation products reported.

The sulfation product produced in these experiments gave a characteristic x-ray diffraction pattern having numerous lines (Table I). The pattern is presumably that of CeOSO₄, but no reference pattern for CeOSO₄ exists in the JCPDS Powder Diffraction File or in other x-ray diffraction literature to our knowledge to allow this to be confirmed. The JCPDS file contains a pattern for CeOSO₄ · H₂O (card 12-89) which, like the Table I pattern, exhibits numerous lines, but there appears to be no simple relationship between the two patterns.

Sulfation of 50 m/o CeO₂-Na₂SO₄ mixtures.—Under hot corrosion conditions, Na₂SO₄ is normally found on turbine blades, and sulfation of CeO₂ in the presence of Na₂SO₄ (50 m/o mixtures were chosen arbitrarily) provides a better measure of the potential hot corrosion performance of CeO₂ containing coatings than simply the sulfation of pure CeO₂. Many sulfates form low melting

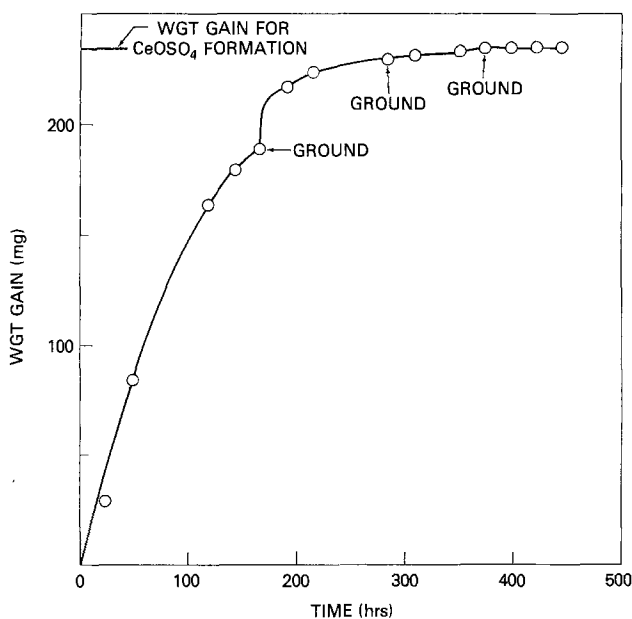


Fig. 3. Long-term sulfation of CeO₂ at 750°C under an SO₃ partial pressure of ~ 300 Pa. (Powder removed from boat and reground in mortar and pestle at points labeled "Ground.")

Table I. X-ray diffraction pattern of CeO₂ sulfation product (presumably CeOSO₄)

dÅ	I/I ₀	dÅ	I/I ₀	dÅ	I/I ₀
8.28	2	2.76	9	1.87	25
7.15	7	2.72	9	1.85	22
6.33	4	2.67	33	1.84	27
6.11	13	2.64	32	1.82	11
5.57	4	2.59	20	1.78	11
4.96	100	2.58	14	1.77	16
4.87	36	2.56	48	1.74	13
4.79	15	2.47	4	1.72	7
4.42	3	2.43	16	1.69	11
4.22	20	2.39	2	1.68	16
4.08	15	2.36	11	1.65	5
4.00	21	2.32	2	1.62	41
3.83	22	2.28	5	1.58	5
3.70	51	2.26	15	1.55	13
3.58	7	2.20	9		
3.42	77	2.17	20		
3.37	59	2.15	16		
3.27	65	2.13	19		
3.12	73	2.11	23		
3.04	8	2.10	17		
2.98	38	2.08	39		
2.94	8	2.04	17		
2.87	19	2.01	20		
2.84	77	1.98	7		
2.79	10	1.90	48		

Plus numerous other weak lines below 1.55Å

Data obtained using a goniometer-equipped Norelco x-ray unit with Cu radiation, diffracted ray monochromation, and a xenon-filled proportional counter.

mixed sulfates with Na₂SO₄, with phase diagrams that show for temperatures above the eutectic melting point and starting at 100 m/o Na₂SO₄, first a single-phase region of MSO₄-Na₂SO₄ solid solution, then a narrow region of solid solution-liquid solution coexistence, and then a single-phase region of MSO₄-Na₂SO₄ liquid solution. The single-phase regions have two degrees of freedom, and therefore, at fixed temperature the solution composition will be a function of the SO₃ partial pressure.

Figure 4 shows representative results from experiments where 50 m/o CeO₂-Na₂SO₄ specimens were exposed over

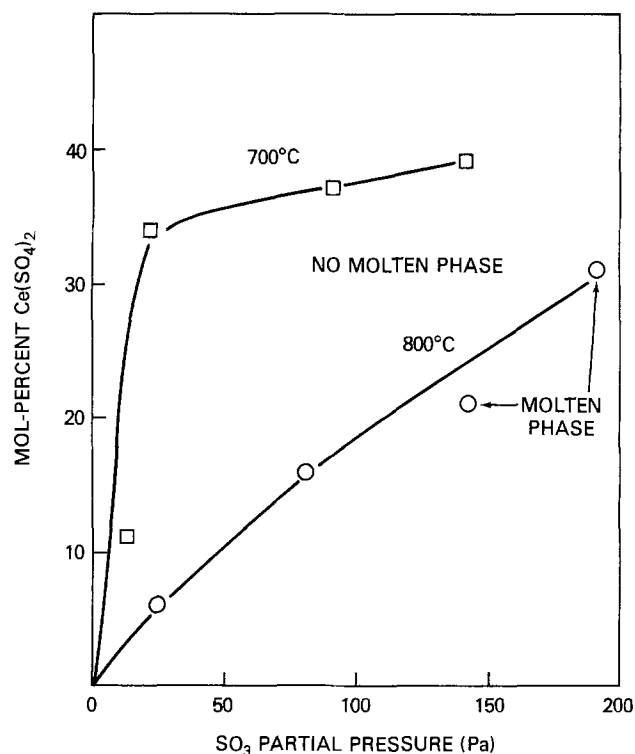


Fig. 4. Equilibrium Ce(SO₄)₂-Na₂SO₄ compositions obtained in the 700° and 800°C sulfation of 50 m/o CeO₂-Na₂SO₄ at the SO₃ partial pressures indicated. Note that liquid sulfate phases were produced at 800° but not 700°C.

long periods (some > 168h) until they reached constant weight (equilibrium composition) at the temperatures and SO₃ partial pressures indicated. Since hot corrosion is generally considered to become aggressive only when molten sulfates are formed, attention was focused on determining the conditions under which molten phases were generated in the CeO₂-Na₂SO₄ sulfation. [Note: although not determined by analysis, Ce(SO₄)₂ is assumed to be the CeO₂ sulfation product in Na₂SO₄ by analogy with other systems (6, 7) where direct oxide sulfation yields the oxysulfate, but sulfation in Na₂SO₄ gives the sulfate.] No molten phases were observed at 700°C for compositions up to 39 m/o Ce(SO₄)₂. The large composition change for small increase in P_{SO₃} shown by the first two 700°C data points may indicate transition across a region of coexistence of two solid phases; there is (at constant temperature) a fixed equilibrium P_{SO₃} for such a region, and even slight increases above this P_{SO₃} will cause the sulfate composition to change from the lower to upper limit of the region. At 800°C, molten phases were clearly visible when the specimen boats were withdrawn from the furnace in the runs giving 21 and 31 m/o Ce(SO₄)₂ formation (Fig. 4). It appears, therefore, that Ce(SO₄)₂-Na₂SO₄ forms a eutectic which melts below 800°C (but probably above 700°C) and has a composition somewhat greater than 20 m/o Ce(SO₄)₂.

The Y₂(SO₄)₃-Na₂SO₄ system exhibits a similar eutectic melting below 800°C and with a composition of ~ 25 m/o Y₂(SO₄)₃ (6). For Y₂O₃ vs. CeO₂ hot corrosion performance, however, the important point is not so much the composition of the eutectic, or even the identity of its components, but rather the SO₃ partial pressure required for molten phase generation. As Fig. 4 shows, this is 100-150 Pa of SO₃ for CeO₂-Na₂SO₄ at 800°C whereas Y₂O₃-Na₂SO₄ forms liquid phases under > 5 Pa of SO₃ at the same temperature (6). Assuming other factors to be equal, CeO₂ thus should be significantly superior to Y₂O₃ as the stabilizer in ZrO₂ coatings intended to withstand SO₃-Na₂SO₄ hot corrosion.

Sulfation of 50 m/o ZrO₂-Na₂SO₄ mixtures.—Zirconia alone, like HfO₂ (6), was found to resist sulfation at 700°C at SO_r partial pressures as high as 3000 Pa (N.B., the partial pressures are reported here as SO_r because of the difficulty in analyzing for SO₃ at such high concentrations; the external Pt catalyst was used, however, and the SO₃ concentrations should presumably be near equilib-

rium, i.e., ~ 1/2 of SO_r). In the presence of Na₂SO₄, ZrO₂ could be sulfated and liquid phases formed, although high SO_r partial pressures were required (Fig. 5). The sulfation behavior in Fig. 5 is very similar to that shown with 50 m/o HfO₂-Na₂SO₄ (6). Both the HfO₂- and ZrO₂-Na₂SO₄ systems are noteworthy in that while they each yield mixed sulfates with eutectic melting below 700°C, the extent of sulfation appears not to become significant (at 700°C) except above SO_r partial pressures of ~ 1000 Pa. This suggests that ZrO₂ (and HfO₂) should have good inherent resistance to hot corrosion by SO₃-Na₂SO₄ attack.

Conclusions

With increasing P_{SO₃}, the first sulfation reaction of CeO₂ with SO₃ is



with ΔG° for reaction over the temperature range 650-750°C given by ΔG° = -160 kJ/mol - T (K) (-0.105 kJ/mol-deg).

Sulfation of CeO₂ in the presence of Na₂SO₄ yields a Ce(SO₄)₂-Na₂SO₄ mixed sulfate system with a eutectic melting below 800°C. An SO₃ partial pressure of 100-150 Pa is required for liquid sulfate phase formation in the Ce(SO₄)₂-Na₂SO₄ system at 800°C.

The sulfation behavior of Y₂O₃ vs. CeO₂ may be compared to indicate their potential 650-850°C hot corrosion resistance when used as stabilizing additives in ZrO₂-based ceramic coatings for gas turbine blades. Extrapolation of the thermodynamic data for Eq. [1] predicts the equilibrium SO₃ partial pressure for sulfation of CeO₂ at 850°C to be ~ 1200 Pa, whereas for Y₂O₃ it is only ~ 15 Pa (6), or nearly 10³ lower. Similarly, the SO₃ partial pressure for liquid phase formation in the sulfation of Y₂O₃-Na₂SO₄ at 800°C is < 5 Pa (6), or approximately 10² lower than for liquid phase production with CeO₂-Na₂SO₄ at the same temperature. Thus, all other factors being equal, CeO₂ should be superior to Y₂O₃ for improving the hot corrosion performance of zirconia coatings.

Zirconia is substantially more resistant to SO₃-Na₂SO₄ attack than either Y₂O₃ or CeO₂ and remains essentially unsulfated at SO_r partial pressures of 1000 Pa (~ 500 Pa of SO₃) at 700°C. The limiting factor in hot corrosion performance appears therefore to lie not with ZrO₂, but rather with the elements used for stabilizing additives.

Acknowledgments

This research was sponsored under the NAVSEA Program for Development of Advanced Marine Gas Turbine Materials, and the support is gratefully acknowledged. We wish also to thank Dr. C. Vold of NRL who aided us in the x-ray diffraction study of the CeO₂ sulfation product.

Manuscript submitted Nov. 26, 1984; revised manuscript received Feb. 27, 1985.

Naval Research Laboratory assisted in meeting the publication costs of this article.

REFERENCES

1. A. U. Seybolt, *Corros. Sci.*, **11**, 751 (1971).
2. T. Sata and K. Kasukawa, *Rev. Int. Hautes Temp. Refract.*, **17**, 174 (1980).
3. P. A. Siemers and D. W. McKee, U.S. Pat. 4,328,285.
4. J. C. Hamilton and A. S. Nagelberg, *J. Am. Ceram. Soc.*, **67**, 686 (1984).
5. R. Barkalow and F. Pettit, in "Proceedings of Conference on Advanced Materials for Alternative Fuel Capable Directly Fired Heat Engines," CONF-790749, J. W. Fairbanks and J. Stringer, Editors, p. 704, NTIS, Springfield, VA.
6. R. L. Jones, D. B. Nordman, and S. T. Gadomski, *Metall. Trans.*, **16A**, 303 (1985).
7. F. G. Foggo III, D. B. Nordman, and R. L. Jones, *This Journal*, **131**, 515 (1984).
8. D. W. DeBerry and K. J. Sladek, *Can. J. Chem. Engr.*, **49**, 781 (1971).
9. E. T. Turkdogan, "Physical Chemistry of High Temperature Technology," Academic Press, New York (1980).
10. R. P. Cahn and J. M. Longo, U.S. Pat. 4,346,063.
11. S. S. Al Omer, D. A. Habboush, and I. Y. Isaac, *Thermochim. Acta.*, **49**, 259 (1981).

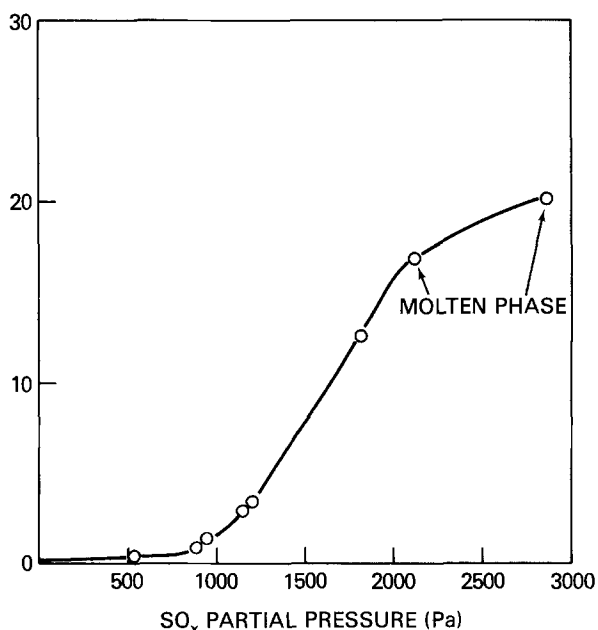


Fig. 5. Equilibrium Zr(SO₄)₂-Na₂SO₄ compositions obtained at 700°C in the sulfation of 50 m/o ZrO₂-Na₂SO₄ under the SO_r partial pressures indicated. Molten phases were clearly formed at SO_r pressures greater than 2000 Pa.

A Novel Scheme for Detection of Defects in III-V Semiconductors by Cathodoluminescence

Jiri Marek

Hewlett-Packard, Optical Communications Division, Palo Alto, California 94304

Roy Geiss

IBM Research, San Jose, California 95193

Larry M. Glassman

GW Electronics, Incorporated, Norcross, Georgia 30092

Martin P. Scott

Hewlett-Packard, Technology Research Center, Palo Alto, California 94304

Interest in III-V compound semiconductors has increased rapidly in recent years due to the advances in both optoelectronics and GaAs IC technology. In contrast to silicon technology, where dislocation-free substrates are available, III-V technology suffers from the lack of homogeneous, dislocation-free substrates. To study the fabrication and growth processes of such materials, it is, therefore, necessary to characterize the distribution of crystalline defects, especially dislocations in the GaAs or InP substrates. Many methods are available for defect characterization, including x-ray topography and preferential etching. However, x-ray topography requires long exposure times, and is, therefore, time consuming. Preferential etching is destructive since it destroys the surface of the substrate and often exhibits artifacts not representative of crystalline imperfections. Another particularly elegant technique to study dislocations is cathodoluminescence (1, 2). Dislocations are revealed by cathodoluminescence due to the presence of nonradiative centers at the dislocation. The cathodoluminescence efficiency varies for the different positions of the electron beam on the sample.

The experimental apparatus usually used for cathodoluminescence (CL) consists of an electron-emission system and a monochromator for analysis of the wavelength of the emitted light, with corresponding photon counting electronics (1, 2). The disadvantage of this experimental setup is that it exhibits poor sensitivity, and therefore requires very high primary beam currents and/or low temperature stage to increase the nonradiative lifetime. Recently, silicon photodiodes have been placed inside the chambers of a scanning electron microscope (SEM) to serve as a wavelength integrating detector (4-6). In this paper, we present an improved detection scheme utilizing a photodiode located in the position usually occupied by a solid-state backscattered electron detector in the SEM. This detection scheme offers very high collection efficiency. Consequently, low primary beam currents can be used at room temperature for satisfactory CL images. These advantages thus make cathodoluminescence easy to use and increase the fields of potential application.

Experimental

The detection arrangement utilized in the present experiment is shown in Fig. 1. A donut-shaped Si detector is positioned on the pole piece of the objective lens in the SEM. The detector consists of a single-crystal silicon wafer with a 5 mm hole drilled in the middle to allow the passage of the electron beam. The wafer is then masked, and a p-n junction is diffused to act as a photodetector. The mask is designed in a way to fabricate four separate diodes in a quadrand arrangement. A similar detector is commercially available from GW Electronics, Incorporated

(Norcross, Georgia), for backscatter imaging. However, the surface of the backscatter detector is coated with aluminum in order to reject cathodoluminescence. A disk-shaped glass cover with a 5 mm hole in the center is attached in front of the cathodoluminescence detector to reject any backscattered electrons. This is necessary, since the backscattered electrons of the primary beam energy would penetrate the silicon, and create a signal by scattering and creation of electron-hole pairs. The backscatter signal would obscure the CL signal. The glass protection is coated with approximately 50 nm of sputtered indium-tin oxide to prevent charging and subsequent deterioration of the resolution. The output of each diode is amplified separately, summed to the other signals, and displayed on the CRT.

For amplification and summation, we used a standard Type 30 Backscatter Electron Detector System manufactured by GW Electronics, Incorporated. The output of the detector is connected directly to the auxiliary CRT input of the microscope. The capacitance of the detector diodes is small enough to allow operation at 2 MHz, half of the TV rate. Due to the geometrical arrangement of the detector, most of the light emitted into the upper hemisphere can be detected.

Results

Figure 2a represents an enlargement of a reflection x-ray topograph of a semi-insulating GaAs wafer grown by the liquid encapsulated Czochralski (LEC) method. Dark regions correspond to disruptions of the periodic lattice, *i.e.*, dislocations or dislocation clusters. Figure 2b is the cathodoluminescence image of the same area imaged with the above-described detector. The image is recorded at a working distance of 15 mm and a sample cur-

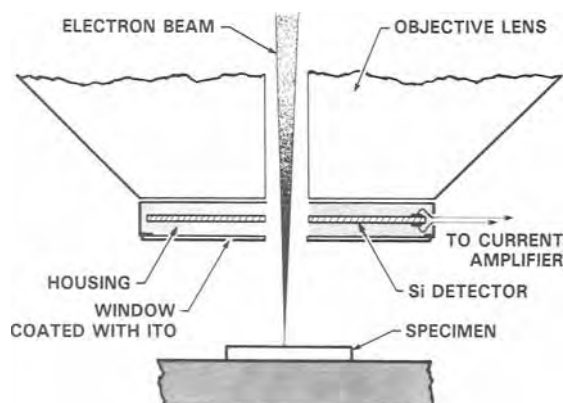


Fig. 1. Geometrical arrangement used for the cathodoluminescence detection.

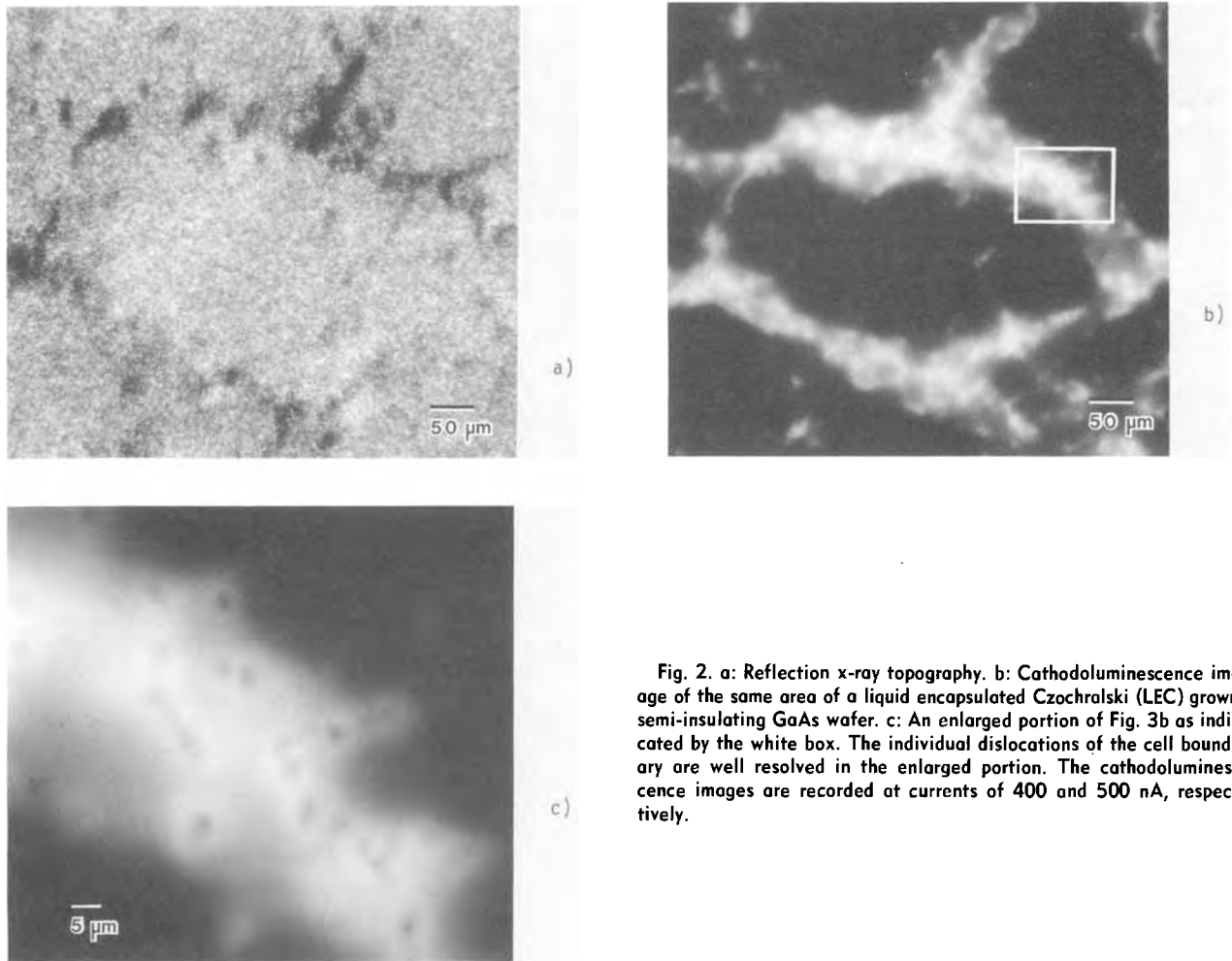


Fig. 2. a: Reflection x-ray topography. b: Cathodoluminescence image of the same area of a liquid encapsulated Czochralski (LEC) grown semi-insulating GaAs wafer. c: An enlarged portion of Fig. 3b as indicated by the white box. The individual dislocations of the cell boundary are well resolved in the enlarged portion. The cathodoluminescence images are recorded at currents of 400 and 500 nA, respectively.

rent of 400 nA. No degradation of the sample is observed at this current level. The cathodoluminescence signal shows excellent correlation to the structure revealed in the topograph. The dislocations are clustered in cell walls, leaving almost dislocation-free cell interior (5, 7). The dislocations in cell walls are clearly resolved, as an enlarged portion of the cell structure reproduced in Fig. 2c demonstrates. These images suggest that the dislocations and dislocation clusters getter the nonradiative impurities through the Cottrell effect in the adjacent volume. Every dislocation is therefore surrounded by a

bright Cottrell cloud (7). For LEC, GaAs cathodoluminescence yields better resolution than reflection x-ray topography. At the same time, the image collection is much more rapid than x-ray topography. SEM images are recorded within minutes, while the x-ray topography technique requires several hours.

As a second example, a cathodoluminescence as well as quasi backscatter image of an AlGaAs double-heterostructure are reproduced in Fig. 3. The quasi backscatter image is obtained by switching off the accelerating voltage of the scintillator. The quasi backscatter image re-

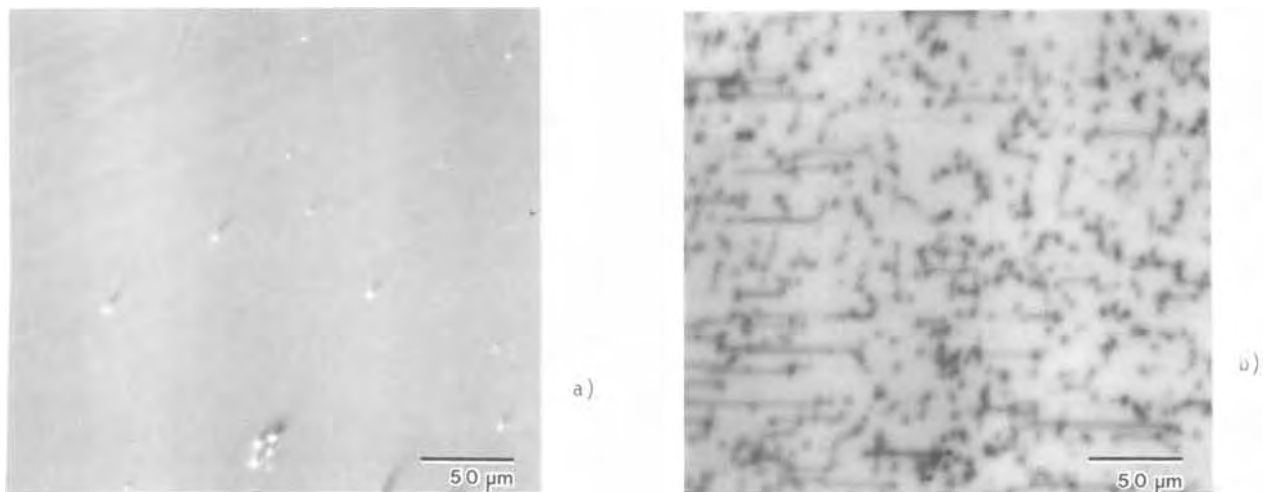


Fig. 3. a: Quasi backscatter electron image of slip dislocations in a AlGaAs heterostructure grown by LPE. b: Cathodoluminescence image of slip dislocations in a AlGaAs heterostructure grown by liquid phase epitaxy. Both images are recorded at the same position of the sample and the same beam conditions. The specimen current is 3 nA.

veals only a diagonal wavy structure of the surface due to the growth by liquid phase epitaxy (LPE) as well as some remaining debris. The cathodoluminescence image in Fig. 3b exhibits a dense array of dislocations. The image pair of Fig. 3 is recorded on a part of the sample close to the wafer edge. Slip dislocations are introduced probably by the thermal stress. The penetration depth of electrons in GaAs at 30 keV is approximately $3 \mu\text{m}$ (8). The cathodoluminescence signal originates in the volume defined by the penetration depth and the diffusion length of the excited carriers in the semiconductor. The dislocations therefore appear diffused. Any surface debris is imaged very sharply in contrast to the defects inside the material. This difference in the image formation mechanism is specially observed in the middle of the lower part of the image, where five particles of debris align very closely. At 30 kV accelerating voltage, a specimen current of only 3 nA is needed to obtain such contrast.

Conclusions

In summary, a new detection scheme for cathodoluminescence has been presented which utilizes a large area photodiode attached to the objective pole piece of the scanning electron microscope. Due to the geometrical arrangement, the emission in almost all of the upper hemisphere is detected. Cathodoluminescence images at room temperature are recorded at specimen currents as low as 3 nA in the case of AlGaAs heterostructures. The detector

operates at half of the TV rate resulting in good visual images. The high collection efficiency should enlarge the application possibilities of cathodoluminescence to include materials with low cathodoluminescence efficiency and/or high electron beam sensitivity.

Manuscript submitted Nov. 23, 1984; revised manuscript received Feb. 12, 1985.

Hewlett-Packard Company assisted in meeting the publication costs of this article.

REFERENCES

1. P. M. Petroff, D. V. Lang, J. T. Strudel, and R. A. Logan, in "Proceedings of the 11th Annual SEM Symposium, p. 325, SEM Inc., AMF O'Hare, IL.
2. L. J. Balk, E. Kubalek, and E. Menzel, in "Proceedings of the 9th Annual SEM Symposium, p. 257, SEM Inc., AMF O'Hare, IL (1976).
3. B. Wakefield, P. A. Leigh, M. M. Lyons, and C. R. Elliott, *Appl. Phys. Lett.*, **45**, 66 (1984).
4. A. K. Chin and W. A. Bonner, *ibid.*, **40**, 248 (1982).
5. A. K. Chin, A. R. von Neida, and R. Caruso, *This Journal*, **129**, 2386 (1982).
6. S. Miyazawa, Y. Ishii, S. Ishida, and Y. Nanishi, *Appl. Phys. Lett.*, **43**, 853 (1983).
7. T. Kamejima, F. Shimura, Y. Matsumoto, H. Watanabe, and J. Matsui, *Jpn. J. Appl. Phys.*, **21**, L721 (1982).
8. R. U. Martinelli and C. C. Wang, *J. Appl. Phys.*, **44**, 3350 (1973).



Lithium Insertion in $V_3Nb_9O_{29}$. A Wadsley-Roth Type Phase

E. Wang, N. Kimura, and M. Greenblatt

Department of Chemistry, Rutgers, The State University of New Jersey, New Brunswick, New Jersey 08903

Compounds which can reversibly incorporate lithium atoms into their structure are of interest because of their potential use as cathode materials in secondary batteries. Recently Cava et al, reported on the lithium insertion reactions of Wadsley-Roth type phases (1-3). These compounds are oxide crystallographic shear structures which form with stoichiometries between MO_3 and MO_2 . The structures can be described in terms of blocks of corner sharing MO_6 octahedra which are finite in two out of three dimension, and are joined to adjacent blocks by edge sharing. Thus there are $n \times m \times \infty$ ReO_3 -type units, where n and m are the length and width of the blocks. The structures display open tunnel like regions (which can accommodate small cations) bound by extensive MO_6 octahedra edge sharing. It has been shown that some crystallographic shear is required to stabilize ReO_3 -type structures upon lithium insertion (4).

$V_3Nb_9O_{29}$ is made up of $4 \times 3 \times \infty$ ReO_3 type blocks (Fig 1) with relatively large

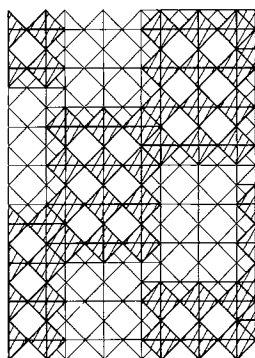


Figure 1. Idealized projection of the $4 \times 3 \times \infty$ block structure of $V_3Nb_9O_{29}$ along the $[010]$ direction. Shaded and unshaded octahedra are centered at $z = 1/2, 0$ respectively, resulting in edge sharing along the block perimeters.

proportion of ReO_3 like regions. This suggested a good combination of structural stability and sufficient interstitial volume for reasonable lithium insertion stoichiometries.

EXPERIMENTAL

$V_3Nb_9O_{29}$ was prepared by heating stoichiometric mixtures of V_2O_5 , VO_2 and Nb_2O_5 powders in sealed, evacuated quartz tubes at $1000^\circ C$ for 1 week. Chemical lithiation of the product was carried out by treatment with $\sim 1.5N$ n -butyllithium (n -BuLi) in hexane. The amount of lithium inserted was determined by acid base titration of the excess n -BuLi and by plasma emission spectroscopy of the lithiated product. Delithiation reactions were carried out on the lithium inserted compound with $\sim 0.1N$ iodine in acetonitrile (I_2/CH_3CN). The amount of I_2 reacted was determined by titration of the excess with standard thio-sulfate solution.

$V_3Nb_9O_{29}$, its lithium-inserted and delithiated analogues were identified by powder X-ray diffraction using Ni filtered Cu radiation.

Small electrochemical test cells (5) were fabricated using $V_3Nb_9O_{29}$ mixed with 15 weight percent graphite as cathode, Li metal foil as anode and $1M LiClO_4$ in propylene carbonate (PC) as electrolyte.

RESULTS AND DISCUSSION

Chemical lithiation of $V_3Nb_9O_{29}$ (brown) by treatment with n -BuLi/hexane for \sim a week with mechanical stirring yielded $Li_{13.6}V_3Nb_9O_{29}$ (black); ~ 1.2 Li/metal. The electrochemical reaction yielded stoichiometries similar to that obtained by the n -BuLi reaction. Open circuit voltages of a test cell as a function of lithium composition (x), is shown in Fig. 2.

Powder X-ray diffraction patterns of the lithiated compound and the starting material are quite similar as shown in Table I, but with substantial changes in the unit cell parameters. The cell parameters of

TABLE I: Powder X-ray Diffraction Patterns of $V_3Nb_9O_{29}$ and $Li_{13.6}V_3Nb_9O_{29}$

$Li_{13.6}V_3Nb_9O_{29}$			$V_3Nb_9O_{29}$			
hkl	d_{obs}	d_{calc}	I/I ₀	d_{obs}	d_{calc}	I/I ₀
400	5.10	5.10	100	5.16	5.16	50
$\bar{4}03$	4.78	4.78	90	4.72	4.72	45
110	4.05	4.04	50	3.752	3.747	90
$\bar{2}03$	3.577	3.577	50	3.521	3.522	100
600	3.402	3.401	60	3.438	3.438	100
112	2.977	2.972	20	2.858	2.863	25
$\bar{7}12$	2.880	2.880	20	2.746	2.744	50
$\bar{1}13$	2.799	2.802	15	2.712	2.701	45
800	2.548	2.551	20	2.576	2.579	20
$\bar{1}006$	2.361	2.353	25	2.301	2.304	20
$\bar{1}007$	2.050	2.050	25	2.058	2.056	40
1000	2.042	2.041	95	2.015	2.013	45

$V_3Nb_9O_{29}$ are: $a = 28.3\text{\AA}$, $b = 3.81\text{\AA}$, $c = 14.1\text{\AA}$ and $\beta = 133.2^\circ$ (Ref.4), compared to that of $Li_{13.6}V_3Nb_9O_{29}$: $a = 28.68\text{\AA}$, $b = 4.118\text{\AA}$, $c = 14.35\text{\AA}$ and $\beta = 134.6^\circ$, which was obtained by least-squares fit to the observed powder x-ray data. There is a significant (8.4%) increase in the b axis, parallel to the infinite dimensions of the ReO_3 type blocks; similar results have been observed in other Wadsley-Roth phases on lithiation (1-3). It is probable that part of the observed unit cell dimension increase on lithiation is associated with increase in the effective ionic radii in reducing Nb^{5+} to Nb^{4+} and V^{5+} to V^{4+} and V^{3+} . The similarity of unit cell dimensions and x-ray powder pattern intensities of the lithiated and host materials respectively, suggest that there has not been extensive distortion of the host lattice on Li insertion. Delithiation of the fully lithiated phase by I_2/CH_3CN restores the

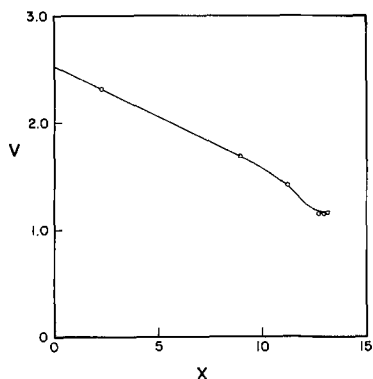


Figure 2. Open-circuit voltage vs x for $Li|1M LiClO_4, PC|Li_xV_3Nb_9O_{29}, graphite$.

original color and X-ray pattern of the host compound. Furthermore, the shape of the emf curve Fig 2. also supports occurrence of topotactic lithium insertion and suggests a continuous homogeneous single phase region at least up to $x = 13$ in $Li_xV_3Nb_9O_{29}$. One cycle of the electrochemical test cell showed very small difference in the emf between charge and discharge curve indicating good reversibility of lithium insertion.

Qualitative measurement of the electrical resistivity at room temperature on pressed powder pellets showed a drastic decrease of resistivity from $\sim 1M\Omega$ for $V_3Nb_9O_{29}$ to $\sim 40\Omega$ for $Li_{13.6}V_3Nb_9O_{29}$. The significant increase in the conductivity of the lithiated phase is most likely due to the presence of small concentrations of mixed valent V^{4+}/V^{5+} , V^{4+}/V^{3+} , Nb^{5+}/Nb^{4+} transition metal ions that facilitate charge hopping.

The theoretical energy density of the $Li/V_3Nb_9O_{29}$ cell based on the n-BuLi stoichiometry of 1.2 Li/metal is approximately 441 Whr/kg which is comparable to those of other cells that are considered for application for lithium secondary batteries.

In summary, $V_3Nb_9O_{29}$ a Wadsley-Roth type phase undergoes lithium insertion reversibly to $Li_{13.6}V_3Nb_9O_{29}$ at room temperature and shows promise as a feasible electrode material for secondary lithium batteries.

ACKNOWLEDGEMENT

This work was supported in part by the Office of Naval Research.

Manuscript received May 8, 1985.

REFERENCES

1. R.J. Cava, D.W. Murphy, E.A. Rietman, S.M. Zahurak and H. Barz, *Solid State Ionics*, 9 & 10, 407 (1983).
2. R.J. Cava, D.W. Murphy and S.M. Zahurak, *This Journal*, 130, 2345 (1983).
3. *Ibid.*, 130, 243 (1983).
4. H. Groh, B. Reitz, R. Guehn and W. Mertin, *Naturwiss.*, 69, 187 (1982).
5. D.W. Murphy, J.N. Carides, F.J. DiSalvo, C. Cros and J.V. Waszczak, *Mater. Res. Bull.*, 12, 825 (1977).

Rutgers University assisted in meeting the publication costs of this article.



A Percolation Model for Electrocatalysis on Microparticle Electrodes

D. C. Wright and D. Stroud

Department of Physics, The Ohio State University, Columbus, Ohio 43210

ABSTRACT

We present a general percolation model for electrocatalysis by microparticles dispersed in a nonconducting film on a conducting substrate. The model addresses the problem of charge transfer between microparticles and the requirement of large effective catalytic surface. A characteristic peaked curve of effective catalytic surface area per microparticle *vs.* the microparticle concentration is found in computer simulations. The behavior of the electrode as a function of various experimental parameters is discussed.

Recent work has shown it is possible to improve significantly the efficiency of certain redox reactions by coating the electrode surface with thin films of microparticles dispersed in a supporting matrix. Examples include platinum and palladium microparticles suspended in nonconducting polymer films or clay colloids on metal and glassy carbon electrodes (1-5) and in polymer films on p-type semiconductor photocathode surfaces (6-10). Because of their high catalytic activity and stability, these systems appear promising for various practical applications, such as fuel cells.

The microparticles in these systems are believed to act as catalytically active centers for the reaction. This means they must be accessible to the electrolyte and be in electrical contact with the electrode supporting the film. An optimum catalytic system would then maximize the surface area of the microparticles, with the constraint that a large fraction of them form part of a conducting pathway to the electrode.

We present here a simple model for microparticle electrodes with nonconductive supporting matrix, based on a variation of the standard percolation picture (11-13), which includes two important aspects of the problem: charge transfer to the microparticles from the electrode and the amount of effective catalytic surface. We investigate the optimum loading of microparticles and the optimum thickness of the film, both of which are important experimentally.

The model does not depend on details of the supporting matrix, and should therefore be generally applicable to a range of systems with minor modifications. We do assume that the microparticles are roughly spherical and are distributed randomly throughout the film, and that the limiting factor for the reaction is the amount of effective catalytic surface area and not the rate of chemical transport through the film. In particular, we are concerned here with the geometrical restrictions imposed by the requirements of electrical conductivity through the microparticles. We believe it is essential to understand these effects before transport effects are considered in detail (although transport effects will doubtless also be important and should be included in a complete theory).

Another, somewhat related example in which connectivity and surface area are important is porous Vycor glass. Porous Vycor is made by embedding small grains of a soluble material in liquid glass and then chemically leaching out the grains after the glass has solidified. This

process leaves a convoluted network of pores throughout the system. If a large fraction of the pores intersect to form a pathway connected to the exterior of the glass, this process results in an extremely large surface area which is available for adsorbing gases, etc. This example is in a sense the complement of the first, since the microparticles in the microparticle electrodes play a similar role to that of the pores in Vycor.

For definiteness, we will specifically consider the case of platinum (Pt) microparticles (or "crystallites"), which provided the original motivation for this work. The ideas underlying the microparticle electrode are quite simple. A nonconducting film of thickness t is laid down on a supporting electrode and is seeded with Pt. The seeding is presumed to occur at random positions throughout the polymer. The seeded regions are then allowed to accrue Pt by electroreduction of platinum salts until the microparticles have grown to the desired size.

The redox reaction can take place only if electrons can reach the Pt from the electrode, and if the reactants can reach the Pt from the electrolyte solution above the film. Electron transfer between the microparticles presumably occurs in two ways: by direct contact between crystallites, and by hopping between crystallites which are sufficiently close. Those crystallites sufficiently near the bottom of the film are in electrical contact with the electrode. All crystallites which are electrically connected to the electrode by at least one route are said to belong to the "effective network." Since electron transfer from the electrode is necessary for the reaction to occur, only the surface area of the Pt crystallites belonging to the connected network is available for catalysis. We shall refer to that surface area simply as the "effective surface" of the system.

The catalytic properties of the system are maximized by maximizing the total effective surface of the platinum. However, since Pt is expensive, the more relevant figure of merit for the electrode is the "effective dispersion," or the effective catalytic surface per particle

$$D = S/M \quad [1]$$

where S is the effective surface and M is the total mass of Pt in the supporting film. D differs from the usual quantity known as "dispersion" only in that S includes only that surface area electrically connected to the electrode, rather than the total surface. Optimum efficiency of the catalyst system is expected near the percolation thresh-

old, since at that concentration of metal a large fraction of the crystallites becomes part of a conducting cluster, while the cluster contains many branches giving a large surface area per volume of Pt added. At higher Pt concentrations, the cluster becomes less branched and D is expected to decrease.

We turn now to the body of the paper. The following section gives a qualitative picture of how the catalytic efficiency is expected to vary with experimental parameters, based on these ideas. We then present a specific lattice model and in the final section describe the results of computer calculations using this model.

Review and Application of Percolation Theory

Some of the main features of the microparticle electrode can be understood from percolation theory, the relevant results of which we briefly review here. [For a more extensive review, see, e.g., Ref. (11) and (12).] We also discuss below how these results are modified when surface area is relevant.

To illustrate the main results of percolation theory, we consider a regular lattice, whose sites can be "occupied" or "unoccupied" at random with probabilities p and $1 - p$, respectively. Each occupied lattice site is considered to be connected to all occupied nearest neighbor sites. (This version is known as "site percolation," to be distinguished from "bond percolation," in which the bonds are occupied or empty at random.) Groups of occupied sites which are connected together are called "connected clusters," and percolation theory is concerned, among other things, with the growth of these clusters as p increases. At low p , the clusters are small and isolated from one another. In the limit of a system which is very large in all directions, the "percolation threshold" p_c is defined by the appearance of a connected cluster which reaches from one edge of the lattice to the opposite edge, the so-called "incipient infinite cluster" (IIC). Various properties associated with the formation of the IIC are characterized by power law dependence (13) on the variable $(p - p_c)$; this behavior accounts for much of the interest in the subject.

For example, $P(p)$, the fraction of all occupied sites which belong to the infinite cluster when the occupation probability is p , is found to vanish at $p = p_c$; while for p just greater than p_c , $P(p)$ is found numerically to vary as

$$P(p) \propto (p - p_c)^\beta \quad [2]$$

where β is a critical exponent which is independent of lattice type and is the same for site and bond percolation. It is also the same for nearest neighbor or farther neighbor percolation models. (It does, however, depend on whether the underlying lattice is two or three dimensional.) The value of β in three-dimensional samples is about 0.2, indicating that just above p_c the fraction of grains belonging to the infinite cluster grows very rapidly from zero.

In contrast to β , the value of the percolation threshold p_c is not universal, but depends on details of the model. For most three-dimensional lattices, p_c is surprisingly low, typically between 0.1 and 0.2; p_c is even lower if connections are allowed between a central site and further neighbors.

The behavior of connectivity described by percolation theory is clearly important in the catalysis problem because of the requirement of electrical connectivity between the Pt microparticles. "Connected" thus translates to "electrically connected" for the electrode case. However, in the catalysis problem, the quantity of interest is not the fraction of Pt particles in the infinite cluster, which connects opposite faces of the sample, but rather the total number of particles connected to one face (the electrode).

The qualitative behavior of the effective surface per microparticle (the effective dispersion D) can be deduced from the percolation results. At low Pt concentrations, most crystallites are isolated and cannot contribute to the effective surface. When the microparticle concentration increases, the crystallites begin to form connected clus-

ters and more of them become connected to the electrode. As the concentration increases above the infinite sample percolation threshold p_c , the effective surface area is expected to increase abruptly as a large fraction of the crystallites becomes part of the connected network. However, the effective surface per crystallite soon begins to decrease for two reasons. First, as p (the filling fraction of metal) increases beyond p_c , more and more grains intersect, obscuring each other's surface area. The connected network, in other words, becomes less and less highly branched. Second, at sufficiently high p , the supporting matrix will begin to form isolated pockets which are entirely surrounded by platinum and therefore cannot be reached by the reactants (that is, the concentration begins to approach the percolation threshold of the matrix). The Pt surface bounding this trapped pocket cannot take part in the reaction and becomes ineffective.

Thus, the Pt concentration must be sufficiently large that many crystallites belong to the connected network, but not so large that the effective surface is decreased by excessive contact between neighboring crystallites, or by the formation of isolated pockets of matrix. The effective surface area per Pt microparticle viewed as a function of Pt concentration is, therefore, expected to be fairly sharply peaked just above the percolation threshold of the crystallites.

Although this picture is constructed for a particular geometry, namely a solid electrode with a microparticle-film catalyst above it, similar effects are expected in quite different contexts. For Vycor, the percolation threshold once again plays an important role in determining the surface activity. Clearly, enough pores must be present to form a large connected network, but if the pore volume fraction is too large, the pore cluster will become less convoluted and the available area of the glass will fall dramatically. For Vycor, however, it is probably the total effective surface area, rather than D , which is relevant.

Lattice Model

To demonstrate the effects just described, we model the supporting matrix as a three-dimensional lattice of N layers, each of $R \times R$ sites, which can be occupied randomly by Pt crystallites (see Fig. 1). While the Pt microparticles in the actual electrode obviously do not sit on a lattice, the presence of the underlying regularity is expected to have little effect on our results (14). In our model, the sites are assumed to be occupied with probability p , and a rule is imposed to determine if nearby occupied sites are to be considered electrically connected. Another rule is neces-

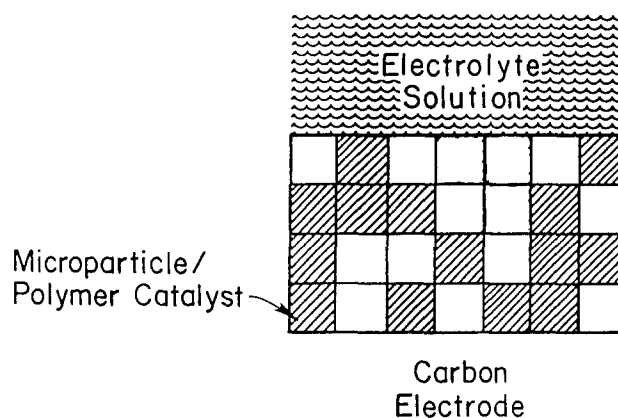


Fig. 1. Schematic of composite film geometry discussed in the text. The film is shown in an edge view. In this schematic, it is four layers thick, and is modeled as a set of cubes, which may be occupied either by Pt (darkened squares) or polymer, randomly distributed on the sites of a periodic lattice, as shown (other models are discussed in the text). The carbon substrate acts as a donor of electrons, which can be transported through those metal particles which are electrically connected to the substrate as discussed in the text. The polymer is assumed permeable to the electrolyte, so that chemical reactions can take place on the polymer-Pt interface.

sary to determine by how much the presence of nearby crystallites reduces the surface available for catalysis. This reduction is assumed to result from direct contact between crystallites. Specifying these rules is equivalent to assuming a size and shape for the crystallites. For convenience we assume that all crystallites throughout the sample have the same size and shape; in particular, we take them to have the shape of the Wigner-Seitz cell for that lattice. (The Wigner-Seitz cell is the polyhedron bounded by planes which perpendicularly bisect lines drawn from a lattice point to all other lattice points). The results of the model are independent of the crystallite size, which is determined by the lattice spacing.

The simplest lattice we have considered is simple cubic (SC), which leads to cubic crystallites (six faces). This is a somewhat unappealing choice for a realistic composite, in which the grains probably more closely approximate spheres, since the number of possible n th nearest neighbors a grain can have is a rather important property in models of connectivity, and is considerably smaller for cubes than for spheres. We have, therefore, carried out most of our calculations on face-centered-cubic (FCC) lattices, whose rhombic dodecahedral crystallites (12 faces) more closely approximate spheres. We have considered connections not only between nearest neighbors, but also, in some of our calculations, between second and third shells of neighbors. These further neighbor connections model the physical fact that electron transfer may occur between microparticles which are sufficiently close to one another but are not in direct physical contact, and which therefore do not reduce the effective surface. While the actual composite is certainly more complicated than our idealized model, the model does include the two effects we believe to be of principal importance: connectivity between microparticles and the reduction of effective surface by the presence of neighbors.

Modeling the crystallites to have flat faces permits us to calculate the reduction of effective surface area in a direct way. If two nearest neighbor sites are occupied, we assume the crystallites are in contact along a face, so that the common faces are rendered unavailable for catalysis. If we allow more distant neighbors to be in electrical contact, we assume that no surface area is obscured by this contact. (The Wigner-Seitz cells of second and further neighbors have, at most, an edge in common.) We shall find that the effective surface area per microparticle is rather insensitive to the assumed crystallite shape.

The occupied sites in the lowest layer of the film are taken to be in electrical contact with the electrode on which the film sits. All microparticles electrically connected to one or more of these sites form the effective catalytic network (the "connected network"). The surface area of the connected network is found by summing up the effective surface areas of all the crystallites in the network.

The relevant figure of merit for this reaction is the quantity D (the lattice version of D), defined as the ratio of the total effective surface of the connected network, S , to the total number of occupied sites, whether or not they are part of the connected network. In addition, it is convenient to divide by the surface area per crystallite. This ratio is clearly appropriate, since the catalytic potential depends on the effective surface, while the cost is proportional to the number of occupied Pt sites.

Results

The results of computer simulations on an FCC lattice with N layers of 40×40 sites are shown in Fig. 2-4. We plot here D , the average fraction of surface area per crystallite which is available for catalysis. In all three cases, the sites of the lattice are occupied at random. These plots show the results of individual runs on the computer; details of the curve shapes may vary slightly from run to run. The size of the lattice was chosen to minimize such statistical fluctuations while giving reasonable run times on the computer. Values of D_{\max} and p_{\max} vary by, at most, a few percent between runs. In Fig. 2, only occupied

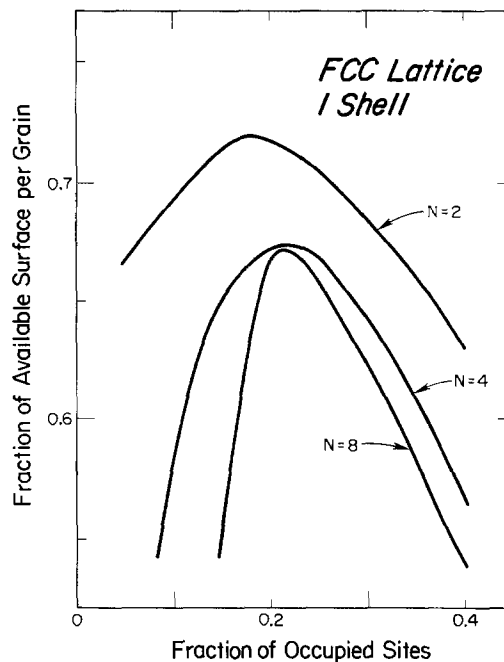


Fig. 2. Computer results on an FCC lattice with $N = 2, 4,$ and 8 layers of 40×40 sites. The horizontal axis is the fraction of sites occupied by Pt grains, and the vertical is the fraction of surface per grain available for catalysis. Electrical connections are only allowed between nearest neighbor sites, i.e., one shell of neighbors.

nearest neighbor sites are assumed to be in electrical contact, while, in Fig. 3 and 4, electrical contact is assumed to extend to second and third nearest neighbors, respectively.

In all three cases shown, the curves have the same characteristic shape. D increases sharply at the percolation threshold, reflecting an abrupt rise in the fraction of particles belonging to the connected network. This increase becomes sharper as the number of layers increases and the percolation transition approaches that of a bulk sample. Little change in the curves occurs as the number of layers N increases above 4, except for some further narrowing of the peak. The curves shown for $N = 8$ are thus probably very similar to those for $N = \infty$ (bulk). Slightly

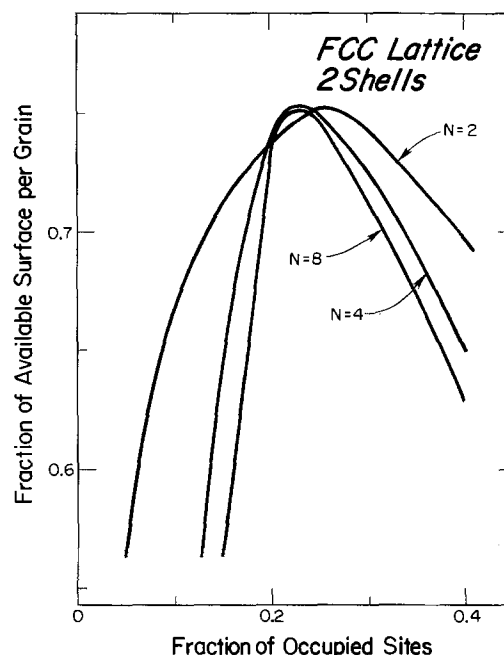


Fig. 3. Results for FCC lattice with electrical connections allowed to first and second nearest neighbor sites, i.e., two shells of neighbors. Other details are the same as in Fig. 1.

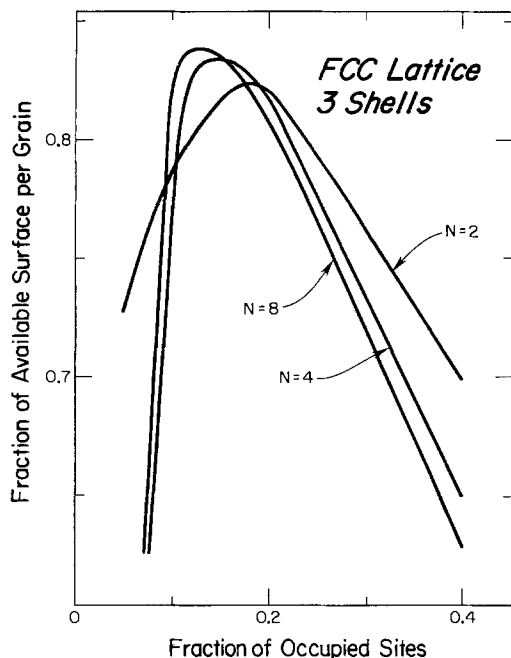


Fig. 4. Results for FCC lattice with electrical connections allowed to first, second, and third nearest neighbor sites, i.e., three shells of neighbors. Other details are the same as in Fig. 1.

above p_c , all the curves reach a maximum and begin to fall as the connected network becomes less extensively branched.

As we increase the number of near neighbor shells assumed to be in electrical contact with a central crystallite, the peak concentration p_{max} decreases. This decrease reflects a decrease in the percolation threshold p_c when second and third neighbors are allowed. Furthermore, the effective surface area per crystallite increases because more electron transport can take place without obscuring surface area.

The results of this model depend on two effects: connectivity, or the total number of neighbors to which a crystallite can be connected; and the obscuring of surface area, which depends only on the number of nearest neighbors. In order to test the model dependence of our calcu-

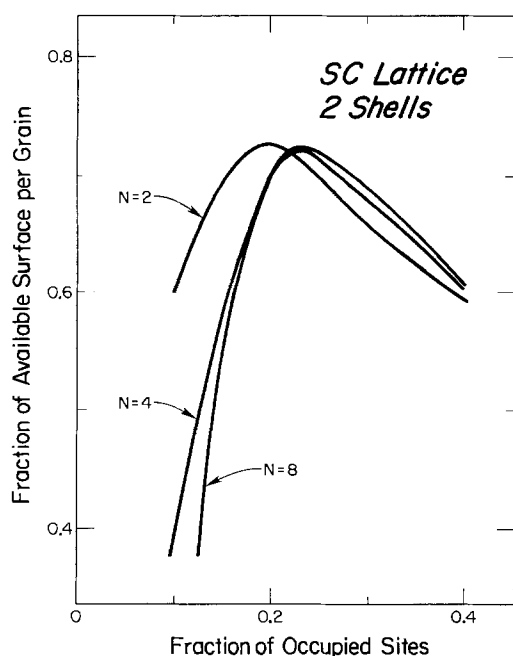


Fig. 5. Results for SC lattice with electrical connections allowed to first and second nearest neighbor sites. Other details are the same as in Fig. 1.

lation of obscured surface, we ran computer simulations for an SC lattice with second nearest neighbor connections (see Fig. 5), since (by coincidence) when second neighbor connections are allowed, a crystallite in both the SC and FCC lattices can be connected to 18 neighbors. Because the number of connections is the same in both cases, we expect the purely connective aspects of the problem to be the same. However, since the number of nearest neighbors is not the same in the two lattices, the degree of surface obscured by nearest neighbors may be quite different in the two cases.

We find that both the models give nearly identical results for $N = 4$ and $N = 8$ layers ($N = 2$ is too far from bulk behavior). In both cases, the maximum efficiency occurs at $p \sim 0.24$, and the fraction of effective surface area per crystallite is 0.74 ± 0.02 . Thus, the most important feature of the model in determining reaction efficiency is the number of possible connections, and not the grain shape. The very weak dependence of the results on details of the grain shape strongly suggests that the results of the simulations presented here are applicable to the physical samples, in which grain shapes may differ from the obviously idealized shapes assumed here.

The correction arising from the presence of isolated pockets of matrix (i.e., a portion of the matrix which is not part of the connected matrix network) can be estimated.¹ It is found to be completely negligible (of order 0.01%) in the neighborhood of the peak in efficiency. This result is reasonable, because the peak occurs at matrix concentrations much above the matrix percolation threshold, so that the fraction of matrix sites which belong to the connected matrix cluster is very nearly unity.

In view of these results, we display in Table I the maximum in effective surface area per grain (\bar{D}) as a function of the principal experimental parameter of importance: the number of potential connections. The value of this

¹If the Pt and matrix are both distributed randomly, the percolation problem for the matrix is the same as that for the Pt, but with p replaced by $(1 - p)$. From our simulations, we therefore automatically know the fraction of matrix sites which are in isolated pockets (i.e., not in the connected matrix network) at any value of p . If we assume that the exposed surface per matrix site is the same in the pockets as in the connected cluster (a quantity we have calculated), then we can estimate the total exposed surface of the matrix in the pockets from the total amount of matrix in pockets. This equals the amount of platinum surface surrounding the pockets, which is therefore available for catalysis.

Table I. Results of computer simulations. N_{conn} is the number of neighbors to which a grain can be connected; it is varied by allowing electrical contact between further neighbors. N_{layer} is the number of layers of points in the lattice. \bar{D}_{max} is the maximum fraction of surface area per microparticle available for catalysis. p_{max} is the critical Pt concentration at which \bar{D}_{max} occurs. The final column tells which lattice was used for the calculation. Most of the values shown are averages over more than one run. Variations in \bar{D}_{max} and p_{max} between runs are, at most, a few percent

N_{conn}	N_{layer}	p_{max}	\bar{D}_{max} (%)	Lattice
6	2	0.38	53	SC
	4	0.44	50	
	8	0.43	50	
12	2	0.29	72	FCC
	4	0.31	68	
	8	0.30	67	
18	2	0.20	72	SC
	4	0.23	72	
	8	0.24	72	
18	2	0.25	76	FCC
	4	0.24	75	
	8	0.24	75	
26	2	0.17	75	SC
	4	0.20	76	
	8	0.18	77	
42	2	0.19	83	FCC
	4	0.15	83	
	8	0.12	84	

maximum increases with the number of connections, as would be expected. The concentration at which the maximum occurs likewise shows a monotonic decrease. For a reasonable number of connections (ten or more) this concentration is surprisingly low, indicating that even at a relatively low filling fraction of Pt, most of the crystallites are indeed able to participate in the chemical reaction.

Our results appear to have several experimental implications. If the percolation model is applicable to a given reaction, then a relatively low filling fraction of microparticles will maximize the catalytic efficiency or effective dispersion (as defined above). Also, it appears that catalytic efficiency mainly depends on the number of potential electrical connections between microparticles, rather than on particle shape. We speculate that the same results would hold for a porous electrode in which the microparticles are characterized by a distribution of shapes (or sizes).

Acknowledgments

This work was supported in part by the National Science Foundation under Grant DMR-14842. It benefited in key ways from ideas exchanged under the auspices of the Materials Research Laboratory at Ohio State University. The authors are grateful to T. Kuwana, R. McCreery, D. Weisshaar, and M. Porter in the Department of Chemistry, Ohio State University, for stimulating interest in this

problem, and for several valuable discussions about the models described in this paper.

Manuscript received Oct. 15, 1984; revised manuscript received March 28, 1985.

The Ohio State University assisted in meeting the publication costs of this article.

REFERENCES

1. K. Doblhofer and W. Durr, *This Journal*, **127**, 1041 (1980).
2. W.-H. Kao and T. Kuwana, *J. Am. Chem. Soc.*, **106**, 473 (1984).
3. D. E. Weisshaar and T. Kuwana, *J. Electroanal. Chem.*, **163**, 395 (1984).
4. C. J. Stalder, S. Chao, D. P. Summers, and M. S. Wrighton, *J. Am. Chem. Soc.*, **105**, 6318 (1983).
5. P. K. Ghosh and A. J. Bard, *ibid.*, **105**, 5691 (1983).
6. D. C. Bookbinder, J. A. Bruce, R. N. Dominey, N. S. Lewis, and M. S. Wrighton, *Proc. Natl. Acad. Sci. U.S.A.*, **77**, 6280 (1980).
7. D. C. Bookbinder and M. S. Wrighton, *J. Am. Chem. Soc.*, **102**, 5123 (1980).
8. D. C. Bookbinder, N. S. Lewis, and M. S. Wrighton, *ibid.*, **103**, 7656 (1981).
9. R. N. Dominey, N. S. Lewis, J. A. Bruce, D. C. Bookbinder, and M. S. Wrighton, *ibid.*, **104**, 467 (1982).
10. J. A. Bruce, T. Murakashi, and M. S. Wrighton, *J. Phys. Chem.*, **86**, 1552 (1982).
11. S. Kirkpatrick, *Rev. Mod. Phys.*, **45**, 574 (1973).
12. D. Stauffer, *Phys. Rep.*, **54**, 1 (1979).
13. A. B. Harris, *Phys. Rev. B*, **28**, 2614 (1983).
14. W. T. Elam, A. R. Kerstein, and J. J. Rehr, *Phys. Rev. Lett.*, **52**, 1516 (1984).

The Passivation of Zinc in Alkaline Solutions

B. Aurian-Blajeni* and Micha Tomkiewicz*

Department of Physics, Brooklyn College, Brooklyn, New York 11210

ABSTRACT

We report on the behavior of zinc electrodes in stirred alkaline solutions saturated with soluble zinc species. Based on the application of the differential effective medium theory for the interpretation of frequency dispersion spectra of the impedance, a mechanism is proposed for the growth of the passive layers on zinc electrodes in batteries. It was concluded that a principal role, during the growth of the passive layer, is played by the diffusion of the electrolyte across a porous layer and that, after passivation, the film becomes more compact, with grains approaching spherical shapes.

Zinc is one of the most important materials being used for electrodes in battery applications. The properties of zinc are the subject of numerous studies. For comprehensive reviews, see Ref. (1-3); many useful references to recent literature are also given in Ref. (4), and recent developments are summarized in Ref. (5).

Under anodic bias, zinc electrodes passivate with formation of zinc oxide layers (4, 6, 7). The mechanism of formation of these layers in alkaline solutions is by a solution-precipitation path. This results in a wide morphological variety, depending on the growth environment. Basically, the passive layers are described in terms of a duplex structure with a thin compact component underneath a porous one, although it was shown that little morphological difference exists between the two layers (8).

Since we shall make use of concepts from the model described in Ref. (7), a short description of that model follows. The passivation of zinc electrodes by a solution-precipitation mechanism occurs by growth and merger of crystallites. The development of an anodic passive film would proceed in a series of steps: a quasiequilibrium state formed immediately after the switching on of the perturbation, which corresponds to a charging of the double layer; and development of a transport region, followed by polymerization. These steps are succeeded by the actual formation of the film by nucleation and growth of

the nuclei, growth of the oxide, and densification. The last stage is a peeling off of the film by buckling and folding.

The aim of the present study is to get some insight about the anodic behavior of zinc electrodes in alkaline solutions by investigating the frequency dispersion of the impedance as a function of various electrochemical parameters such as current density prior to passivation and amount of charge passed after passivation. Although studies using impedance techniques were carried out for zinc electrodes, most of them involved the active regime (9, 10).

Experimental

The experiments were performed in a three-compartment cell. The anodic compartment was separated from the cathodic one by means of a strongly acidic Nafion membrane, in order to repel the zincate ions and to avoid zinc plating on the counterelectrode during discharge. Prior to mounting into the cell, the membrane was soaked in 5M KOH for 24h at room temperature. All the potentials were measured vs. a saturated calomel reference electrode. A 7 cm² platinum foil was used as a counterelectrode. The working electrode was a zinc rod (0.08 cm² exposed area) (Fisher), pressure fitted in a Teflon holder. During the experiments, the exposed area was kept in vertical position. Before each experiment, the exposed area was polished down to 4/0 grid and then etched in concentrated hydrochloric acid for about 10s (9)

* Electrochemical Society Active Member.

and rinsed in purified water (18 M Ω). The 5M KOH solutions were prepared from purified water and analytical-grade potassium hydroxide (Fisher).

The experimental setup is shown in Fig. 1. A typical experiment comprised two kinds of measurements, which were performed alternately. During the experiments, a dc voltage was applied across the whole circuit by means of a dc power supply (Hewlett-Packard HP 6111A). In the first type of measurements, the electrode potential and the current were monitored with a Keithley 192 dmm and a Keithley 177 dmm (measuring the potential drop across a 66.5 Ω resistor), respectively. This type of measurement enabled us to observe the time evolution of the process of passivation of zinc in alkaline solution (Fig 2). At various time intervals (shown by arrows in Fig. 2), impedance measurements were made according to the procedure described in Ref. (11) in order to characterize the layers formed up to a certain moment. The ac source was a Hewlett-Packard HP 3325A synthesizer/function generator, supplying a 5 mV amplitude signal at frequencies between 1 Hz and 1 MHz. The phase angle and the modulus of the ac response were measured with a Hewlett-Packard HP 3575 gain-phase meter. During the impedance measurements, all the voltmeters were disconnected, as was the magnetic stirrer, which was used during the passivation stage of the experiments. Since hydrodynamic control is important in the passivation process (12, 13), the use of a stirrer is the major flaw of our experiments and it is kept responsible for the scatter of the data. Nevertheless, we tried to minimize the errors (or at least make them systematic) by keeping the same stirring regime (except for voltage fluctuations) during all the ex-

periments. The whole setup was controlled by a Hewlett-Packard HP85 desktop computer, which was used also for data collection.

The key feature from the experimental point of view is obtaining a stable layer of zinc oxide. Owing to the high solubility of zinc oxide in alkalis, the passive layers are unstable on smooth electrodes. However, the porous electrodes for which the passivating layer is stable have exceedingly complex impedance characteristics. This problem was overcome by using an extra zinc electrode. Before starting the actual experiments, the solution in the anodic compartment was prepared *in situ* (14). A current was passed between the platinum electrode and this fourth electrode until qualitative turbidimetry showed that the solution was saturated in zinc species. This procedure was necessary to prevent (or slow down) the dissolution of the zinc oxide species formed on the surface of the electrode, based on the fact that electrolytically formed zinc oxide is more soluble than the one externally added [e.g., Fisher (dry process), certified ACS] (1). Moreover, our experimental setup allowed impedance measurements to be performed while the electrode was kept in the passive state.

Results

The layer formed at the surface of the electrode is dark for the first half-hour after exposure to air. It whitens afterwards, and its texture changes. This fact was previously observed and associated with an excess of zinc (15).

The typical behavior of the electrode potential and current density as a function of time is shown in Fig. 2. From Fig. 2, one can see that, following a region of almost constant current and potential, a sudden change occurs. This change is followed by an increase in current density (decrease in electrode potential), and a second, slower, decrease follows. The characteristics of the curves of the type shown in Fig. 2, relevant for the present study, are: the initial current density (I); the initial electrode potential (V_i); the final electrode potential (V_f); and the time of passivation, considered to be the time corresponding to the major change in current density (electrode potential). Passivation experiments were carried out for various values of the initial current density in the range 60-160 mA \cdot cm $^{-2}$.

The impedance measurements reported in this paper are made for the electrode under steady-state conditions, since the frequency dispersion spectra recorded before passivation exhibited no structure in the range of measurement.

In Fig. 3, we show typical experimental results obtained for the impedance of a zinc oxide layer anodically grown.

In Fig. 4, we show the evolution of the frequency dispersion spectrum of the imaginary part of the impedance for the same passivation experiment as a function of the charge passed after passivation.

Discussion

The advantage of using a potentiometric setup is that it is closer to battery operating conditions than a constrained system, in which either constant current or constant electrode potential are imposed. Moreover, it allows the observation of the evolution of the system under charge.

Before passivation, the process is in an ohmic (linear) regime, as shown in Fig. 5, in which the current density is represented as a function of the electrode potential.

Figure 6 shows the change in electrode potential with the total potential drop across the cell. It is noted that the initial electrode potential does not change much with voltage, while the slope of the final electrode potential as a function of voltage is close to one. We interpret this as follows: after passivation, the main potential drop occurs across the passivating layer. In other words, passivation in our case occurs not because a "passivation potential" is reached, but because the overpotential is too small at the reaction interface, because of increased potential drop across the oxide layer. If the potential drop across the cell

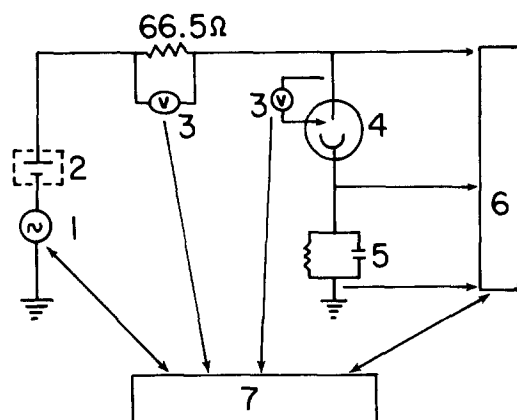


Fig. 1. Schematic diagram of the experimental setup used for the study of the anodic behavior of zinc electrodes. 1: Small amplitude signal generator. 2: Power supply. 3: Voltmeters. 4: Cell. 5: Reference circuit. 6: Gain-phase meter. 7: Desktop computer.

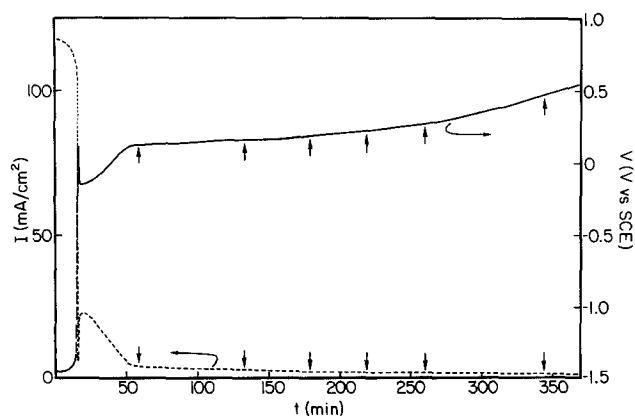


Fig. 2. Time evolution of the current density and electrode potential. The small arrows indicate the times at which impedance measurements were performed. The curved arrows indicate the scale for the plotted quantity.

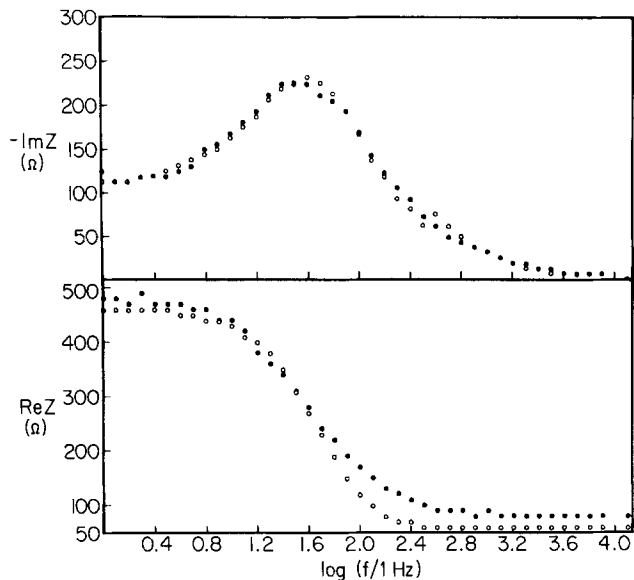


Fig. 3. Typical dispersion spectrum of a passivated zinc electrode. Top: imaginary part of the impedance. Bottom: real part of the impedance. Closed circles: experimental values. Open circles: theoretical values.

is calculated (cf. Fig. 5 and 6), it is observed that, before passivation, the potential drop has a constant value of $0.350 \pm 0.03V$, which compares well with $0.415V$ predicted for the reaction $Zn + H_2O = ZnO + H_2$ (16) and an internal resistance of the cell of $55 \pm 10\Omega$. The value of the series resistance of the cell is consistent with the value obtained from impedance measurements (the high frequency plateau of the real part of the impedance spectrum in Fig. 3b).

The frequency-dependent impedance may be expressed as

$$Z = R + iX = il(\gamma A \omega \epsilon) \quad [1]$$

where l is the thickness, γ is the roughness factor, A the area of the sample of material under consideration (l is parallel to the electric field), ω the angular velocity, and ϵ the complex dielectric constant of the composite. From Fig. 4, one can see that the slope in the low frequency region is not only different from 1 (as for a passive RC element) or $1/2$ (corresponding to a Warburg- or de Levie-type impedance), but increases monotonically as a function of the amount of charge passed.

During the growth of oxide layers at the surface of zinc electrodes, electrolyte solution is also imbedded. The dielectric properties of the resulting layer are not a linear combination of the dielectric characteristics of the components (i.e., oxide and solution), but are affected by other cross-term effects as well (17). One of the ways of describing the dielectric behavior of composites is the effective medium approximation (18, 19). Among the most

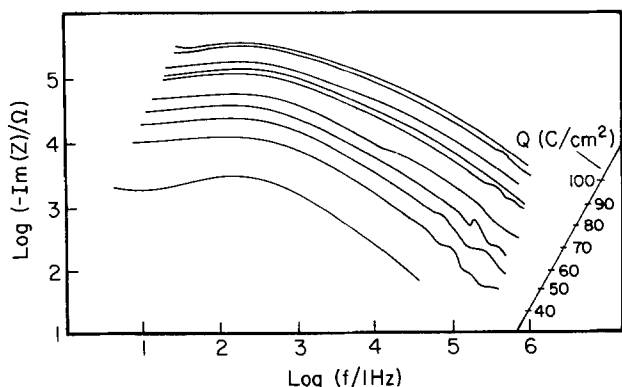


Fig. 4. Change of the dispersion spectrum of the imaginary part of the impedance as a function of the quantity of charge. Data from Fig. 2.

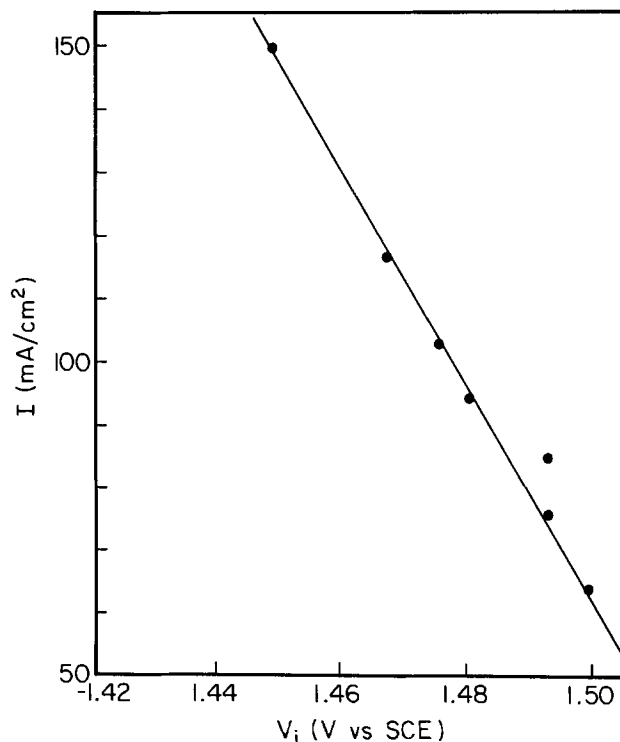


Fig. 5. Initial current density as a function of the initial electrode potential.

used forms of this approximation are the Maxwell-Garnett, the Bruggeman, and the self-similar or differential form. The Maxwell-Garnett approximation for a two-component system is valid whenever a distinction may be made between a "host" and a "guest" component in the composite material. This limitation is not present in the Bruggeman version, which applies for spherical inclusions in a homogeneous medium consisting from the two

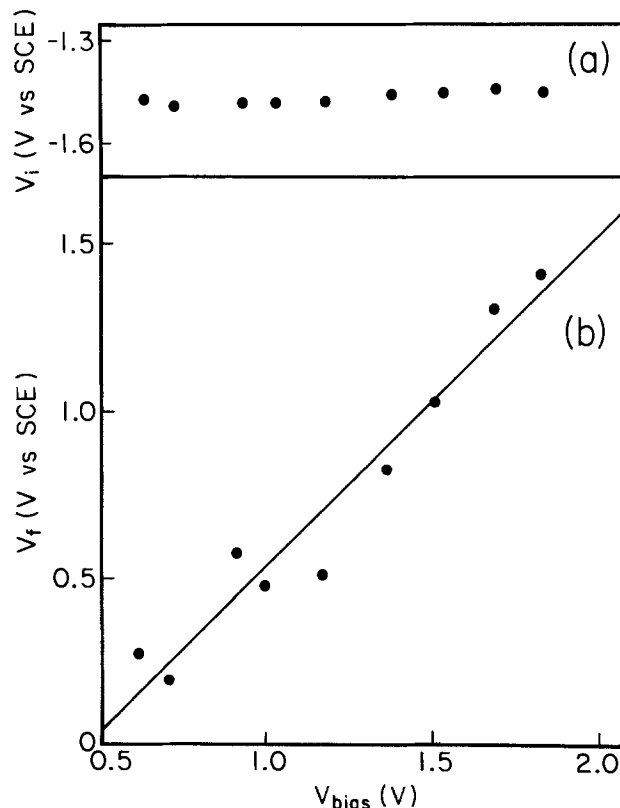


Fig. 6. Variation of the initial electrode potential (V_i) (top) and the final electrode potential (V_f) (bottom) as a function of the potential drop across the cell.

components. The refinement of this latter approximation, the self-similar or differential effective medium theory, allows for any form of inclusions in media in which the conductive phase remains interconnected for any ratio of the components.

We used this interpretation of the frequency dispersion of the impedance based on the SEM data in Ref. (7) and the fact that the behavior of the impedance can be predicted by neither equivalence to a passive circuit nor by Warburg-type impedance (Fig. 4).

The form of the effective medium approximation used by us was developed for the description of the dielectric characteristics of sedimentary rocks (17, 18, 20). In its closed form, for a composite consisting of a porous insulator saturated with electrolyte solution, the equation for the porosity is as follows

$$P = \frac{\epsilon - \epsilon_d}{\epsilon_w - \epsilon_d} \left(\frac{\epsilon_w}{\epsilon} \right)^m \quad [2]$$

where P is the porosity; ϵ , ϵ_w , and ϵ_d the complex dielectric constants of the composite, solution, and insulator, respectively; and $0 < m < 1$ is a screening factor (depolarization factor) dependent on the shape of the grains in the composite (18, 19). The forms encountered in the literature use a limited number of fixed values of the parameter m . We extended the model for the continuous variation of m in the interval $[0, 1]$ (21).

The complex dielectric constant, at frequencies lower than 10^7 Hz, may be written as

$$\epsilon = k + i(4\pi/\omega)\sigma \quad [3]$$

with k is the real dielectric constant, ω the angular velocity, and σ the dc conductivity.

The dissipation spectrum of the impedance will be dependent on the geometric factors of the sample (l , γ , and A), the dielectric characteristics of the components (ϵ_w and especially ϵ_d , their ratio and microstructure (P and m)). The results predicted by the effective medium theory are compared with the experimental values in Fig. 3. Some of the parameters used were taken from the literature as $k_w = 70$ (12), $k_d = 9$ (22), $\sigma_w = 0.500$ ($\Omega\text{-cm}$)⁻¹ (1). The adjustable parameters are the thickness to roughness ratio l/γ (one parameter), the conductivity of zinc oxide σ_d (depending on the nonstoichiometry of the anodically formed zinc oxide), the porosity P , and the depolarization factor m . The adjustable parameters were fit by least mean squares fitting for nonlinear models. Fitting was performed only for the imaginary part of the impedance (Fig. 3, top). As a check for the consistency of the model, the values obtained for the parameters were fed into the expression for the real part of the impedance and the results were compared with the experimental data (Fig. 3, bottom). Thus, some of the characteristics of the passivating layers were derived from impedance measurements: the porosity, the depolarization factor, the thickness to roughness ratio, and the conductivity of the insulating phase.

Figure 7 shows the evolution of the parameters of the system from Fig. 4 and 2 as a function of the quantity of charge passed after passivation. From Fig. 7a, which represents a typical set of data after passivation, a jump in porosity is observed. We associate this jump with the phase transition mentioned by Dirkse (14) and postulated by McKubre and Macdonald (4), probably related to the transformation from polyhydroxide to oxide (7). After this transition is finished, the porous layer considered to comprise zinc oxide and solution becomes more compact, as seen from the decrease in porosity. The decrease of the depolarization factor (Fig. 7b) toward values characteristic for spheres suggests that densification occurs by the grains becoming more and more spherical and, according to Ref. (7), finally merging. This process is accompanied by a decrease in conductivity of the insulating phase (zinc oxide) (Fig. 7c). The number of free carrier concentration derived from conductivity data (10^{16} cm⁻³ as compared to 10^{-11} cm⁻³ for the intrinsic material) is consistent with the

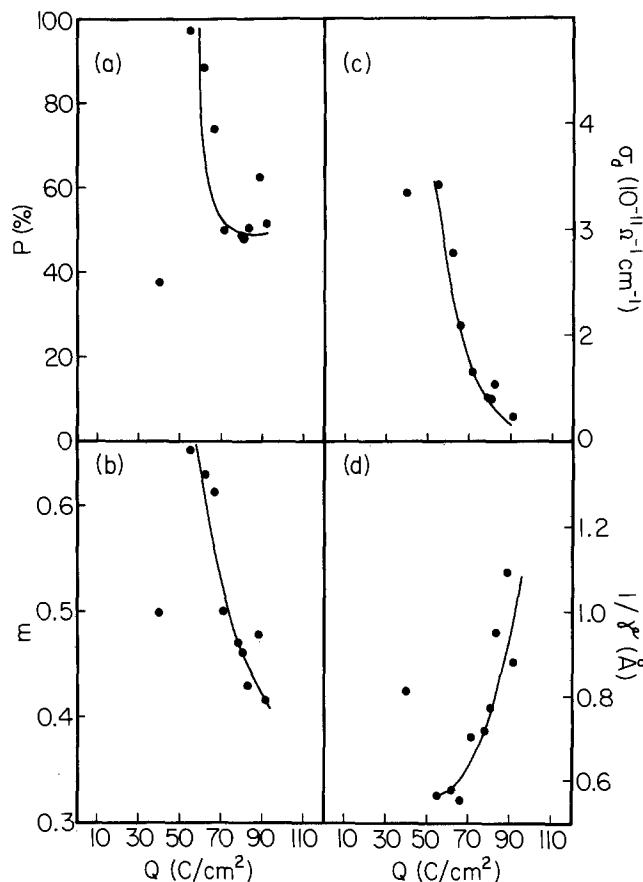


Fig. 7. Change of the parameters derived from the application of the effective medium theory to data in Fig. 4, as a function of charge passed after passivation.

excess of zinc in the passive layer (15). The decrease in conductivity may be due either to migration of impurities in the high field across the layer or to electrochemical reaction inside the layer. After the above parameters reach roughly their steady-state values, the layer continues to grow (Fig. 7d). This conclusion is based on the assumption of constant roughness (the initial decrease in the thickness-to roughness-ratio is probably due to the fact that this assumption is not valid at that stage).

The terms used in Ref. (7) to describe the passivation

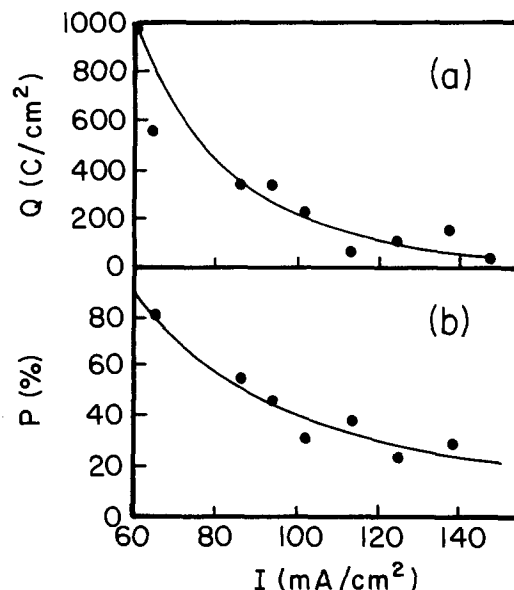


Fig. 8. Variation of the amount of charge passed before passivation (top) and of the initial porosity (bottom) as a function of initial current density.

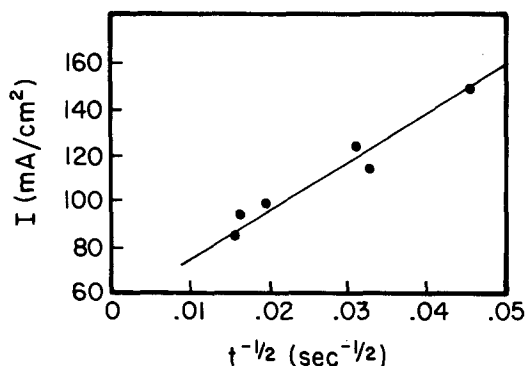


Fig. 9. Initial current density as a function of the reciprocal square root of the passivation time.

are "polymerization" and "densification," where the processes occur successively. We believe that they occur concomitantly and that the ratio of their rates is dependent on the current density. This is better illustrated by Fig. 8, in which are represented the dependence of the amount of charge before passivation (top) and of the initial porosity obtained from impedance measurements (bottom) as a function of the initial current density. The picture suggested by Fig. 8 is that the lower the current density, the "fluffier" the layer formed, since with an increase in current density less charge is necessary for passivation and the passive layer is less porous. In other words, at low current density the polymerization is rapid, while at high current density the densification is rapid. This may be interpreted as a diffusion-controlled mechanism in which the diffusing species is the electrolyte. That the passivation process is a diffusion-controlled one is indicated by Fig. 9, in which the initial current density is seen to be linear with the reciprocal square root of the passivation time. That this is a realistic possibility is also indicated by the observation that, if a passive electrode is left at open circuit, it is "reactivated" after a certain period of time (23). An alternative explanation invokes dissolution. Under the present conditions, we do not believe this to be the case, since the solution is electrolytically saturated in zinc species. Moreover, chemical dissolution would not explain the fact that the time of passivation of the "reactivated" electrode is shorter than that for initially active electrodes. In view of our model, the passivated electrode is just reflooded with electrolyte and again repassivated, with diffusion of the electrolyte becoming more difficult, as the porous layer becomes thicker.

A word about the implicit assumptions involved in this analysis is called for. One is that the passive layer is considered homogeneously porous. The effect of removing this assumption is currently under investigation in our laboratory. Another assumption is that the passivating layer comprises only two components: zinc oxide and solution. Other assumptions are more drastic; namely, that the effects of the high field in the passive layer were neglected, as well as the random orientation of the grains [although the latter assumption is justifiable for an electrolytically grown layer (15)].

Conclusions

The study of vertical flat zinc electrodes in alkaline solutions electrolytically saturated with soluble zinc species has led us to the following conclusions.

1. The passivating layers under these conditions are composite layers comprising both oxide and solution.
2. The growth of the layers and electrical passivity/activity of the electrodes are dictated by the diffusion of the electrolyte across these layers.

3. After passivation, the characteristics of the passive layers change as a function of the amount of charge passed after passivation. These changes are summarized as follows: the passive layer becomes more and more compact with grains approaching a spherical shape; after a certain porosity and conductivity of the insulating layer is reached, the thickness of the layer increases.

Acknowledgments

This work was supported by the Office of Naval Research.

Manuscript submitted Nov. 30, 1984; revised manuscript received March 4, 1985.

Brooklyn College assisted in meeting the publication costs of this article.

REFERENCES

1. J. McBreen and E. J. Cairns, in "Advances in Electrochemistry and Electrochemical Engineering," Vol. 11, H. Gerischer and C. W. Tobias, Editors, p. 273, John Wiley and Sons, New York (1978).
2. R. D. Armstrong and M. F. Bell, in "Electrochemistry," Vol. 4, p. 1, Specialist Periodical Reports, The Chemical Society, London (1974).
3. "Zinc-Silver Oxide Batteries," A. Fleischer and J. J. Lander, Editors, John Wiley and Sons, New York (1971).
4. H. C. H. McKubre and D. D. Macdonald, *This Journal*, **128**, 524 (1981).
5. J. McBreen, *J. Electroanal. Chem.*, **168**, 415 (1984).
6. R. W. Powers and M. W. Breiter, *This Journal*, **116**, 719 (1969).
7. S. Szpak and C. J. Gabriel, *ibid.*, **126**, 1914 (1979).
8. T. Katan, J. R. Savory, and J. Perkins, Abstract 44, p. 120, The Electrochemical Society Extended Abstracts, Vol. 7, Atlanta, GA, Oct. 9-14, 1977.
9. C. Cachet, U. Strode, *Wiart, Electrochim. Acta*, **27**, 908 (1982).
10. R. D. Armstrong and M. F. Bell, *J. Electroanal. Chem.*, **55**, 201 (1974).
11. M. Tomkiewicz, *This Journal*, **126**, 2200 (1979).
12. M. Eisenberg, H. F. Bauman, and D. M. Brettner, *ibid.*, **108**, 909 (1961).
13. T. P. Dirkse and N. A. Hampson, *Electrochim. Acta*, **15**, 1297 (1970).
14. T. P. Dirkse, *This Journal*, **128**, 1412 (1981).
15. K. Huber, *Helv. Chim. Acta*, **26**, 1037 (1943).
16. H. H. Bode, V. A. Oliapuram, D. Berndt, and P. Hess, in "Zinc-Silver Oxide Batteries," A. Fleischer and J. J. Lander, Editors, p. 7, John Wiley and Sons, New York (1971).
17. P. N. Sen, W. C. Chew, and D. Wilkinson, in "Physics and Chemistry of Porous Media," D. L. Johnson and P. N. Sen, Editors, p. 52, AIP Proceedings Series 107, American Institute of Physics, New York (1984).
18. P. N. Sen, C. Scala, and M. H. Cohen, *Geophys.*, **46**, 781 (1981).
19. D. E. Aspenes, *J. Phys. C.*, **44**, 103 (1983).
20. P. Sheng and Callegari, in "Physics and Chemistry of Porous Media," D. L. Johnson and P. N. Sen, Editors, p. 144, AIP Proceedings Series 107, American Institute of Physics, New York (1984).
21. B. Aurian-Blajeni and M. Tomkiewicz, Abstract 96, p. 142, The Electrochemical Society Extended Abstracts, Vol. 84-2, New Orleans, LA, Oct. 7-12, 1984.
22. L. E. Brus, *J. Chem. Phys.*, **79**, 5566 (1983).
23. M. A. Hampson, M. J. Tarbox, J. T. Lilley, and J. P. G. Farr, *Electrochem. Technol.*, **2**, 309 (1964).

Second-Order Harmonic in the Current Response to Sinusoidal Perturbation Voltage for Lead-Acid Battery

An Application to a State-of-Charge Indicator

S. Okazaki, S. Higuchi, and S. Takahashi

Government Industrial Research Institute, Osaka, Midorigaoka 1, Ikeda, Osaka 563, Japan

ABSTRACT

Distortion of the current response to sinusoidal alternating perturbation voltage has been quantitatively measured as a function of state of charge for commercially available lead-acid batteries. The input amplitude adopted here was greater than those used for ordinary impedance measurement. The distortion is represented as a power spectrum. Among higher order harmonics, that of the second one was selected for the parameter of a state-of-charge indicator. Excellent linearity was observed for the state of charge. It was also clarified that, compared to other parameters of the indicator, such as terminal voltage, impedance of fundamental tone, and concentration of sulfuric acid, this parameter is less influenced by other factors during practical operation, such as discharge current and rest time.

Many types of state-of-charge indicators have been proposed for use in primary and secondary batteries. In particular, interests have been directed to lead-acid batteries, which are very popular as SLI batteries, emergency power supplies, and electric vehicle power sources. For the last case, especially, a state-of-charge indicator serves as a fuel meter and plays an important role in the system. As for the SLI batteries, though state-of-charge is presently not monitored, it is hoped that its indication can be incorporated into the car's indicator system for the sake of convenience.

Recently, special efforts have been made to develop various advanced secondary batteries for vehicular and load leveling applications. In consideration of their operational conditions, a correct understanding of the state-of-charge is very important. Consequently, the need for the development of indicators of high accuracy at low cost now becomes greater and greater.

Most indicators proposed so far are based in principle on terminal voltage (1), impedance (2), and especially the concentration of sulfuric acid in the case of lead-acid batteries. Density (3), refractive index (4), and saturated humidity (5) have been studied as physical properties representing the concentration of sulfuric acid. The state-of-charge can also be obtained from integrated current. To measure these physical quantities accurately, simply, and automatically in packed batteries, many devices have been proposed (1-5). Still, many problems remain, and only a few devices have proved good enough to be of practical use. For example, when sulfuric acid concentration is selected as a parameter, a large time delay exists between the change of residual charge and the corresponding concentration at the probe. Thus, real-time monitoring is not possible in this case. Terminal voltage takes different values in the absence and in the presence of a load. If this difference is corrected according to current, the device will be very complicated and costly. Finally, fundamental wave impedance is largely dependent on rest time for lead-acid batteries (6). An attempt is now being made to apply it to primary cells before use (2).

Thus, a new parameter closely correlated to the residual charge of a battery should be proposed. For this purpose, the distortion of output current from a single sinusoid generated by alternating input voltage, represented as a power spectrum quantitatively, has been investigated. Among higher-order harmonics, that of the second one is adopted as such a parameter. The second harmonic was discussed first by Smith with reference to ac voltammetry (7). Using the apparatus stated in the Experimental section, it is possible, in principle, to analyze it more directly. This quantity provides important information about reaction kinetics. Our discussion here is limited to the application of the second harmonic to the state-of-charge indicator, i.e., to phenomenological treatment. More fundamental treatment and application of this pa-

parameter to reaction kinetics will be carried out in the near future.

Experimental

When a sinusoidal alternating voltage

$$V(\omega, t) = V_0 \sin \omega t \quad [1]$$

is superimposed on an inherent terminal voltage, V_b , of a battery as input, the current response is represented as a Fourier series expansion

$$I(\omega, t) = I_0 + \sum_{n=1}^{\infty} I_n \sin(n\omega t + \phi) \quad [2]$$

where $\omega = 2\pi f$ (f : frequency) and ϕ are the angular velocity of the imposed sinusoidal voltage and phase deviation of the response, respectively. The direct current I_0 corresponds to faradaic rectification effect, and I with the subscripts $n = 1, 2, 3, \dots$, are amplitudes of the fundamental tone, second-order harmonic, third-order harmonic, \dots , respectively. In order to evaluate the m -order wave component, $m = 1, 2, 3, \dots$, the distorted wave $I(\omega, t)$ is treated as follows. First, $I(\omega, t)$ is integrated with $\cos m\omega t$ and $\sin m\omega t$ from 0 to the period T . Then

$$I'_m = \int_0^T I(\omega, t) \cos m\omega t dt = \frac{T}{2m} I_m \sin \phi \quad [3]$$

and

$$I''_m = \int_0^T I(\omega, t) \sin m\omega t dt = \frac{T}{2m} I_m \cos \phi \quad [4]$$

The amplitude I_m is obtained from equation

$$I_m = \frac{2m}{T} \sqrt{I'^m{}^2 + I''^m{}^2} \quad [5]$$

Of course, I_0, I_1, I_2, \dots , are functions of ω and V_0 . In the ordinary chemical impedance measurement, V_0 must be selected so that direct current and higher-order harmonics may be neglected. In such a case, a perturbation voltage of a few millivolts is usually employed.

In order to carry out the above measurements, a new system was constructed similar to those used for impedance measurements. This system is controlled by a microcomputer having a potentiogalvanostat to provide a perturbation voltage (or current) to the battery and to charge and discharge it.

The terminal voltage is monitored by a digital multimeter connected to the computer, according to which the offset voltage, V_b , is determined. This device is also used to detect the cutoff voltage of discharge in capacity tests. The main block of the system is FRA S-5720 manufactured by NF Electronic Instruments Company and analyzes distorted waves.

The computer automatically controls charge, discharge, and rest period of the cell, carries out capacity tests according to the defined cutoff voltage, provides perturbation and offset voltage, and performs analysis of response wave forms.

A commercially available pasted-type lead-acid battery with nominal voltage and capacity of 6V and 12 Ah, respectively, was used. The battery was placed within the thermostat at $25 \pm 1^\circ\text{C}$.

The influence of rest time on the parameter was evaluated first. This test concerns not only rest time, but also the difference in behavior of the parameters in the presence and absence of a load. The effect of the discharge current magnitude was then clarified. For this purpose, the battery was treated in the following way.

After a 15-20 min discharge, its terminal voltage was perturbed by an external power supply immediately or after a 15-120 min rest. In the former case, the offset voltage V_t was polarized, *i.e.* a closed-circuit voltage, where three kinds of discharge rates were adopted, *i.e.* 10, 8, and 5 HR, respectively. In the latter case, the rest times were 20 and 120 min for the 10 HR and 15 min for the 5 HR discharge. This procedure was repeated until the terminal voltage dropped to a cutoff voltage defined as 5.4V for the 10 and 8 HR and 5.25V for the 5 HR discharge. The state-of-charge is available from integrated discharge time at each measurement and capacity obtained at the end of discharge.

Results and Discussion

Nonlinear current response.—Rigorously, current response to sinusoidal voltage input does not consist of a single sinusoid as stated in the previous section. It does so only when the low field approximation is valid in the Butler-Volmer equation. Figure 1 shows practical wave forms of current response for a fully charged lead-acid battery with an open-circuit voltage of 6.498V. The ordinate and abscissa scales are arbitrary. When the input is 10 mV rms, the output is nearly sinusoidal and the ratio of the amplitude for the second harmonic to the fundamental tone is less than a few percent. When the amplitude of the input is as much as 30 mV rms, the output wave becomes somewhat distorted and the content of the second harmonic is about 10%. It is evident from the figure that there is a barely distinguishable shoulder at the very center of each of the two sharp peaks for 100 mV rms. This corresponds to the existence of a large second harmonic and the ratio becomes as much as $\sim 20\%$. Thus, the larger

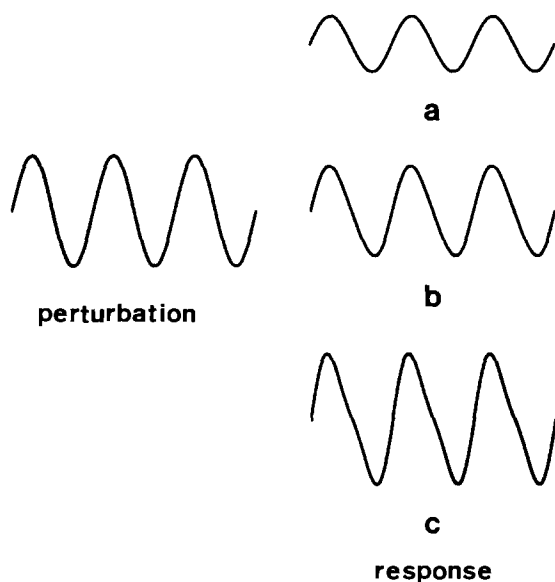


Fig. 1. Wave forms of input perturbation voltage and current responses for fully charged lead-acid battery. The response wave forms are those for three kinds of input magnitudes: a, 10 mV rms, b, 30 mV rms, and c, 100 mV rms. Amplitude scale is arbitrary.

the amplitude of the perturbation voltage, the greater the distortion of the current response.

Wave distortion should be discussed in some detail here. First, we shall consider the ratio as a function of perturbation frequency. The ratio is plotted against the logarithm of frequency in Fig. 2, where $V_0 = 30$ mV rms. It is clear that, although at higher frequencies the system contains only a negligible second harmonic, it increases abruptly at low frequencies less than a few hertz. In spite of the small ratio, 1 or 2% at high frequencies, it is 10% at 1 Hz and exceeds 20% at 0.1 Hz. These frequencies belong to the Warburg region in a usual complex plane analysis for the lead-acid battery. Figure 2 also shows plots against the amplitude of perturbation voltage V_0 , where the frequency is 1 Hz. When V_0 is as small as that used in an ordinary impedance measurement, ~ 3 mV rms, $I_{n=2}/I_{n=1}$ is less than 1%. In this case, even at a lower frequency, the low field approximation may be considered valid.

A linear relation is observed between $I_{n=2}/I_{n=1}$ and small V_0 , < 50 mV rms. This is the case when alternating variation \bar{c} in the reactant concentration in the Taylor expansion of the Butler-Volmer equation is proportional to the perturbation voltage, *i.e.*, the expansion shows that if $\bar{c} \propto V_0$, then $I_{n=1} \propto V_0$ and $I_{n=2} \propto V_0^2$, so $I_{n=2}/I_{n=1}$ must be proportional to V_0 . In Fig. 3, there is a linear relation between $I_{n=1}$ and V_0 and also between $I_{n=2}^{1/2}$ and V_0 at small V_0 . But these three plots deviate from linear lines at similar V_0 . The deviation at large V_0 , > 50 mV rms, may possibly arise from a complicated diffusion process.

A perturbation voltage of 30 mV rms was selected, though this value has no special meaning. At least the second harmonic is large enough to be measured easily at this voltage and the total current is small enough to flow using a common potentiostat. In the following sections, the application of this parameter to the state-of-charge indicator is discussed based on the amplitude, 30 mV rms, and a small number of frequencies.

Relation between second-order harmonic and state-of-charge.—In the previous section, some general features of second-order harmonic in current response were discussed for a lead-acid battery. In this section, the behavior of the second harmonic as a function of state-of-charge is discussed.

The battery was discharged at a constant current, 10 HR, for a certain period. After a 20 min rest, a sinusoidal perturbation voltage, 1 Hz and 30 mV rms, were superimposed on the inherent terminal voltage. Figure 4 shows

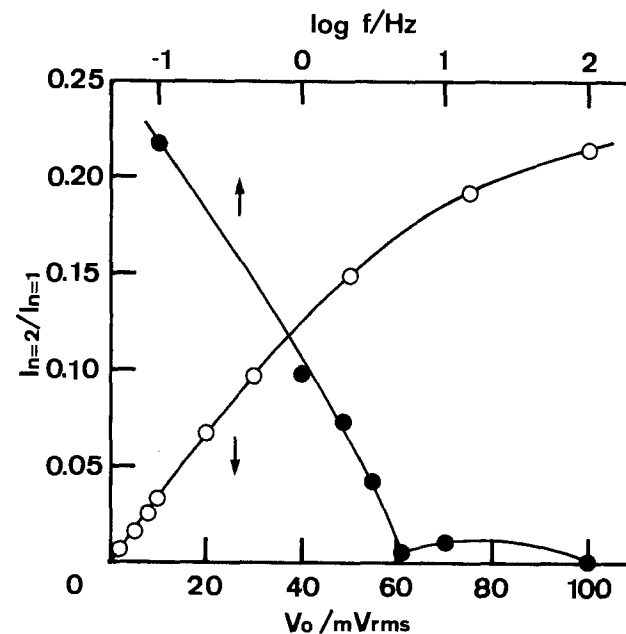


Fig. 2. Ratio of second harmonic to fundamental tone in current response for a fully charged lead-acid battery as a function of amplitude (open circle) or frequency (closed circle) of input.

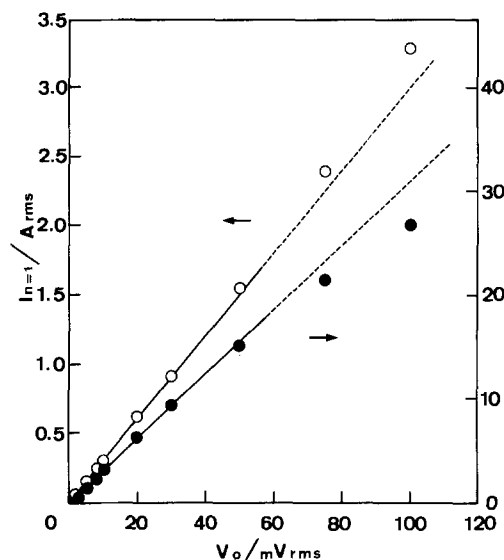


Fig. 3. Amplitude of fundamental tone (open circle) and the square root of the second harmonic (closed circle) in current response as a function of the input voltage for a fully charged lead-acid battery.

the second harmonic in current response, where the abscissa is the residual charge. From the figure, a linear correlation is evident. The residual charge may thus be easily obtained from the value of the second harmonic. Also, measurements of different cycles of the battery (represented by the different shapes at the data points) show good reproducibility of the parameter. Consequently, it may be said that the second harmonic can be applied to the state-of-charge indicator.

However, it should be pointed out that, considering the practical usage of the battery, a rapid and precise measurement is required under various conditions of practical use. But there are many questions in regard to the influence of the discharge rest time, the degree of the parameter change when measured in the presence of a load, and the effect of the magnitude of a load on the value. In other words, only a parameter not influenced by the conditions of measurement or state of the battery except for its charge must be used.

The next section covers these problems, and a comparison is made with classical parameters such as terminal voltage and impedance of the fundamental tone.

Application to the state-of-charge indicator.—The linearity of the relation between the second harmonic in current response and state-of-charge was shown in the previous section. However, it may be influenced by the history of the battery, its environment, and its state, as well as the charge.

We first consider the load. When present, there is a certain concentration gradient in the solution near the electrode. After a sufficient off-load time, there is no concentration gradient, indicating an equilibrium state. Of course, in the former case, there is a deviation of the electrode potential owing to the concentration and reaction overpotential generated by the direct current. These phenomena should be considered in relation to the change in amplitude of the second harmonic as well as fundamental tone. They are influenced by the magnitude of the discharge current itself.

Second, fundamental tone impedance has been reported to depend on the rest time of the battery (6). After load is switched off, concentration gradient decreases and the electrode surface changes slowly, though it is difficult to interpret quantitatively because of its complexity. It is quite probable that the second harmonic is also influenced by the rest time.

The parameters may depend on such factors as ambient temperature, bulk concentration of sulfuric acid, and cycle history, and their effects on the parameters should be clarified. But, at this point, it should be sufficient to say

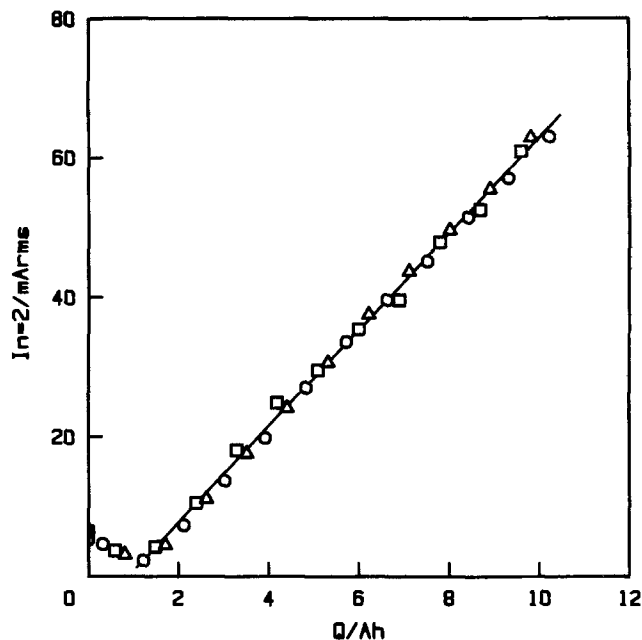


Fig. 4. Second harmonic in current response to perturbation voltage, 1 Hz and 30 mV rms, measured after a 20 min rest in 10 HR discharge for a lead-acid battery as a function of state-of-charge, Q .

that in the course of the work the battery was immersed in thermostat controlled at $25^\circ \pm 1^\circ\text{C}$, the bulk concentration was not strictly controlled, and the charge-discharge cycle of the battery was from about 10 to 60, the discharge or measurement modes being taken arbitrarily.

Measurement was carried out at various frequencies of input. There must be a frequency that is most ideal for application to the indicator. Here the results are shown for three frequencies, 1, 10, and 100 Hz, representative of the diffusion-controlled, both the diffusion- and reaction-controlled, and reaction-controlled regions, respectively. The amplitude of the input was 30 mV rms for all measurements.

In order to determine the differences in parameter behavior arising from the state and conditions of the battery, the second harmonic, fundamental tone in the output wave, and terminal voltage were measured in the presence of a load, 10 HR, and in its absence after 20 and 120 min rests. This measurement was also carried out in the presence of two other loads, 8 and 5 HR.

The apparent total charge or capacity of the battery may vary between continuous discharge and intermittent discharge, but the resulting difference in the capacity is negligibly small. Therefore, no correction was made for the measured capacity.

Measurements for terminal voltage are given in Fig. 5. As expected, the lines are separated into two classes, one for the presence and the other for the absence of a load. The difference is so large that direct application of this parameter to an indicator would not be possible.

The second harmonic and fundamental tone are shown in Fig. 6-8 as a function of state-of-charge for three frequencies, 1, 10, and 100 Hz. In each figure, there are six kinds of plots corresponding to different discharge and measurement modes. The dispersion of the lines or curves in the figure must be a measure of the stability of the parameter toward the state or condition of the battery.

In Fig. 6, larger currents are found in the case without rest of the load than that with it, both for the second harmonic and fundamental tone. This means that $|z|$ probably increases by the rest or load-off and is in good agreement with other observations for similar frequency regions (6). In regard to the fundamental tone, Fig. 6b, the curves spread out like a fan. The dispersion of the plots exceeds about 60% of total battery charge. This means that when this parameter is used as a state-of-charge indicator, it contains an error larger than 60%. Thus, it is im-

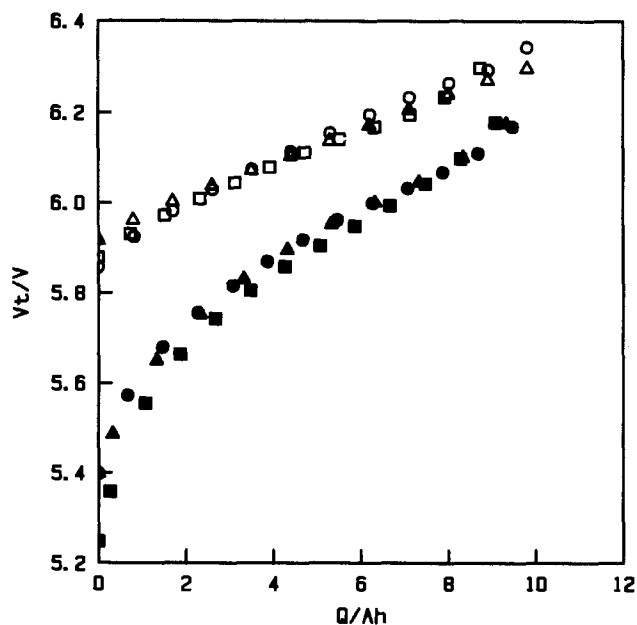


Fig. 5. Terminal voltage of a lead-acid battery for various discharge and measurement modes as a function of the state-of-charge, Q . Open circles: 10 HR and 20 min rest. Open triangles: 10 HR and 120 min rest. Open squares: 5 HR and 15 min rest. Darkened circles: 10 HR without rest. Darkened triangles: 8 HR without rest. Darkened squares: 5 HR without rest.

possible to apply this parameter to a state-of-charge indicator. As for the second harmonic (Fig 6a), however, the line dispersion is remarkably small compared to that of the terminal voltage and fundamental tone at this frequency. It is less than 10% at the first stage of discharge, and increases somewhat at the final, but does not exceed 15%. This satisfies the requirement for accuracy of the indicator as a fuel meter for electric vehicles, *i.e.*, <15%. Thus, the second harmonic is excellent as a parameter for the state-of-charge indicator.

The behavior of the second harmonic is even better at 10 Hz, as shown in Fig. 7a. Although it has a large deviation after a long load-off time, other lines only have errors of less than 10% and are little influenced by the magnitude of the direct current in the case of continuous discharge. Thus, after a small load, at just the initial starting, remarkably accurate information for residual charge of the battery can be obtained and is scarcely influenced by a subsequent short time rest. From Fig. 7b, it is impossible to apply fundamental tone impedance to the indicator, since its dispersion is too large.

The results for fundamental tone measurement are shown in Fig. 8 at 100 Hz. The fraction of the second-order harmonic is within only 0.1% of the total wave at this frequency. It would be difficult to detect such small signals correctly at low cost. The curve of the second harmonic has a minimum in the intermediate region. Consequently, it cannot be applied to an indicator and therefore is not shown here.

The plots for fundamental tone impedance show two separated groups of curves, one with rest time and another without it. The curves within each group are quite similar. The dispersion was about 15% for the former and only a few percent for the latter. However, the groups are somewhat separated and the error exceeds 20%, particularly in the initial region of discharge where the slope of the curves are low. Consequently, it is necessary to construct a device capable of covering this separation.

Concluding Remarks

General pictures have been given for the behavior of the second harmonic, fundamental tone in current response, and terminal voltage as functions of state-of-charge for a lead-acid battery. The frequencies of the input sinusoidal voltage were 1, 10, and 100 Hz, which are representative of the regions where diffusion, both diffu-

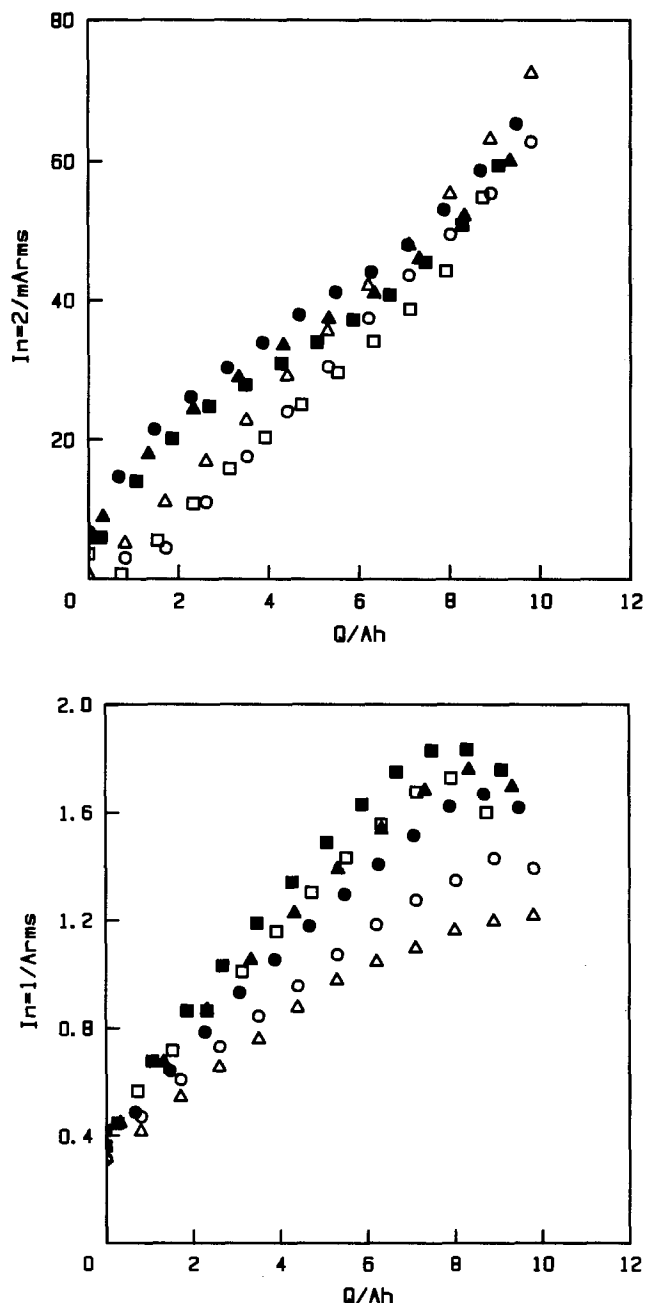


Fig. 6. Second harmonic (a, top) and fundamental tone (b, bottom) in current response to the perturbation voltage, 1 Hz and 30 mV rms, for lead-acid battery for various discharge and measurement modes as a function of the state-of-charge, Q . Symbols are the same as in Fig. 5.

sion and reaction, and reaction play important roles in output, respectively. The second harmonic was found superior to fundamental tone and terminal voltage and to be less influenced by measurement conditions and state of the battery, other than its charge. It satisfies the requirements for electric vehicular use and should find practical application.

In this work, the second harmonic was evaluated by a Fourier transform of the primary wave so as to obtain precise ones. The apparatus is very expensive for state-of-charge indicators. But an ordinary high pass filter is sufficient for the second harmonic, in principle. It is possible to use the electromotive force of the battery itself instead of an external power supply such as a potentiostat. That is, a lower voltage must be used in place of the terminal voltage, and from this direct voltage level, the voltage is perturbed sinusoidally. The final problem is display. This is a rather simple problem. It may be possible to produce the indicator at low cost. Many problems still prevent development of the indicator for practical

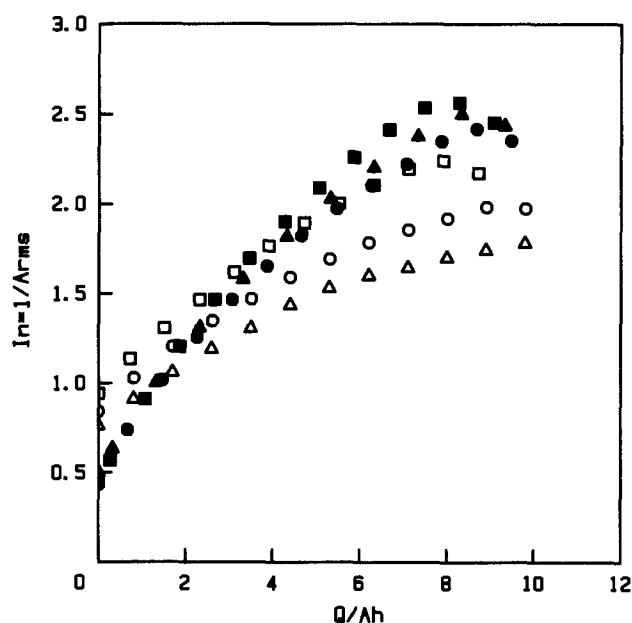
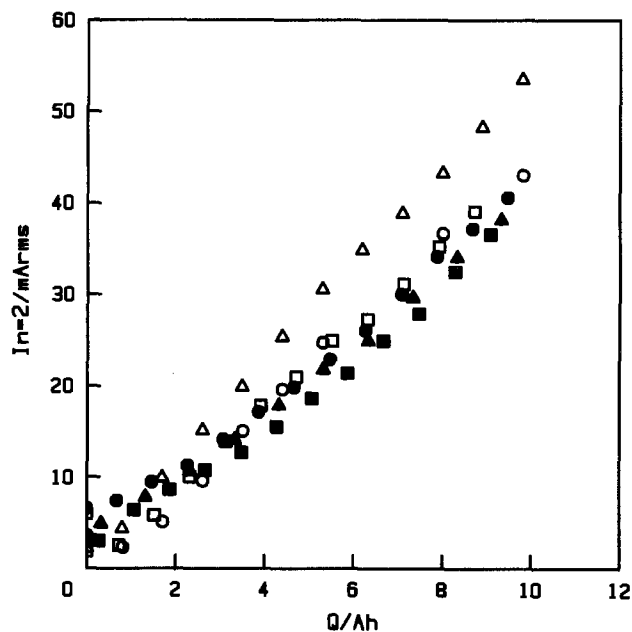


Fig. 7. Second harmonic (a, top) and fundamental tone (b, bottom) in current response to the perturbation voltage, 10 Hz and 30 mV rms, for a lead-acid battery for various discharge and measurement modes as a function of the state-of-charge, Q . Symbols are the same as in Fig. 5.

use, such as comparison with galvanostatic method, determination of the best frequency and amplitude, influence of ambient temperature, charge-discharge cycle history, and battery differences.

It should be mentioned that the parameters discussed here have application only when a battery is discharged. They are not applicable to the case of charging and thus

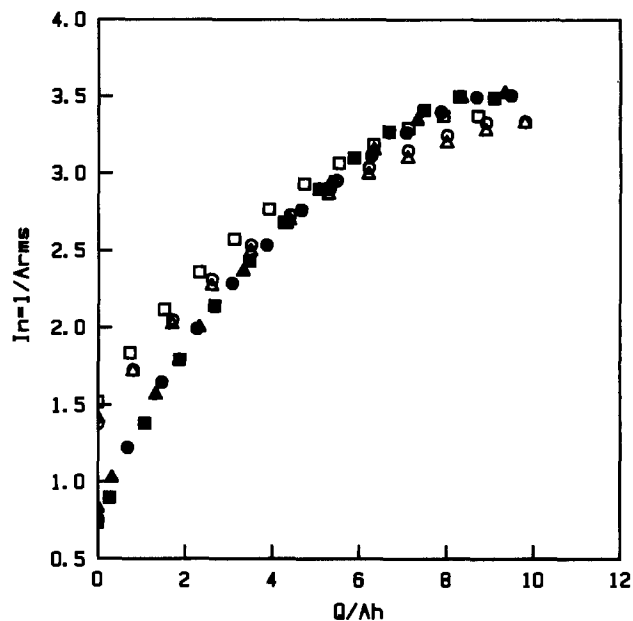


Fig. 8. Fundamental tone in current response to the perturbation voltage, 100 Hz and 30 mV rms, for lead-acid battery for various discharge and measurement modes as a function of the state-of-charge, Q . Symbols are the same as in Fig. 5.

have limited use for SLI batteries. Such an application of these parameters by a technique such as forcing a small discharge current to flow for a short time before measurement may be possible.

Acknowledgment

This work was carried out as part of the project "Research and Development of Advanced Battery Electric Power Storage System," sponsored by the Agency of Industrial Science and Technology, Ministry of International Trade and Industry, Japan.

Manuscript submitted Oct. 18, 1984; revised manuscript received March 30, 1985.

Government Industrial Research Institute, Osaka, assisted in meeting the publication costs of this article.

REFERENCES

1. M. Tanaka and K. Suzuki, *GS News*, **42**, 16 (1983).
2. S. A. G. R. Karunathilaka, N. A. Hampson, M. Hughes, W. G. Marshall, R. Leek, and T. J. Singlair, *J. Appl. Electrochem.*, **13**, 577 (1983).
3. K. W. McElroy, U.S. Pat. 4,192,909 (1980); D. R. Whitford, U.K. Pat. 2,011,698A; S. Uemichi, *Yuasa-Jiho*, **51**, 16 (1981).
4. H. Hattori, T. Matsui, and K. Yamazaki, *ibid.* **49**, 25 (1980).
5. J. L. Weininger and J. L. Briant, *This Journal.*, **129**, 2409 (1982).
6. N. Matsui, in "Complex Plane Analysis for the Electrochemical Studies," A. Kozawa, T. Hirai, and M. Nagayama, Editors, p. 31, U.S. Office of the Japanese Electrochemical Society, Cleveland, OH (1981).
7. A. J. Bard and L. R. Faulkner, "Electrochemical Methods—Fundamentals and Applications," Chap. 9, John Wiley and Sons, New York (1980).

AC Impedance Analysis of Polycrystalline Insertion Electrodes: Application to $\text{Li}_{1-x}\text{CoO}_2$

M. G. S. R. Thomas, P. G. Bruce, and J. B. Goodenough

Inorganic Chemistry Laboratory, Oxford University, Oxford OX1 3QR, England

ABSTRACT

It is argued that a porous insertion electrode can be modeled, for purposes of ac impedance analysis, by a modified Randles equivalent circuit containing a generalized constant-phase-angle impedance in series with the double-layer capacitance. The impedance spectrum of the disintercalation system $\text{Li}_{1-x}\text{CoO}_2$ showed two time-dependent semicircles, indicating the need for a further modification of the equivalent circuit by a physical process that could be represented by a resistor/capacitor combination. An adsorption process and a Li^+ -ion-electrolyte surface layer are each shown to refine to identically low R factors and to be represented by equivalent circuits that transform one into the other, each having circuit values with reasonable values for the physical processes represented. Time-dependent experiments could eliminate the adsorption models, and electron microscopy gave direct evidence for the surface-layer model; further indirect evidence came from constant-voltage experiments and the preparation of electrodes with greater electrode/electrolyte interface area. Although propylene carbonate appears to be kinetically stable in contact with $\text{Li}_{1-x}\text{CoO}_2$ at potentials of up to 4.5V vs. lithium, mixtures of propylene carbonate with oxide particles having $x = 0.34$ produce thick polymer films.

Many successful battery systems, primary as well as secondary, are based on electrodes that utilize insertion compounds. An insertion compound is a mixed electronic/ionic conductor into which atoms may be topotactically inserted over a wide range of solid solution. The mobile species generally enters the host as a cation, donating an electron(s) to the conduction band of the host matrix; it may also enter as an anion, taking an electron(s) from the conduction band of the host matrix. The most successful insertion-compound electrodes now in use are based on mobile H^+ or Li^+ ions in the host matrix, and the search for alternate insertion compounds represents an active area of research.

Although the reversible insertion/removal of mobile Li ions has been extensively studied in layered structures such as Li_xTiS_2 ($0 \leq x \leq 1$) (1) and $\text{Li}_x\text{V}_6\text{O}_{13}$ ($0 \leq x < 7$) (2), fundamental electrochemical investigations have been mostly limited to studies of the ionic diffusion within the insertion compounds, as this has been assumed to be the rate-limiting process. However, other processes, such as charge transfer and adsorption at the surface, are important and could prove rate limiting, especially if new materials provide a high alkali-ion mobility within the host. In this paper, we report an electrochemical investigation of the system $\text{Li}_{1-x}\text{CoO}_2$ ($0 < x < 1$), a system first explored by Mizushima *et al.* (3), in which the interfacial processes prove to be increasingly important as x increases.

The kinetics of insertion-electrode reactions have been most commonly studied by potentiostatic or galvanostatic pulse measurements. However, ac measurements are also applicable; in fact, they have been utilized extensively in classical electrochemistry (4). Whereas, in principle, pulse and ac measurements contain the same information, in practice, ac measurements offer several important advantages over pulse techniques. These advantages are as follows.

1. A cell suffers a significantly smaller perturbation in an ac measurement (< 10 mV) than in a pulse measurement (> 100 mV); therefore, the cell is not displaced so far from equilibrium during the measurement. The severe polarizations induced by a current or voltage pulse may introduce concentration gradients of such a magnitude that the diffusion coefficient can no longer be assumed to be invariant with distance along the diffusion path, making invalid the simple diffusion equation on which analysis of the pulse data is generally based.

2. The cyclic nature of an ac perturbation produces a pseudo steady state within the cell, so no net electrolysis occurs.

3. In an ac experiment, it is possible to obtain a clear separation of the kinetics of the several different electrochemical processes involved by determining the ac re-

sponse as a function of applied frequency; with pulse techniques, the kinetics of the different processes are generally not well resolved.

4. The ac data may be interpreted directly, whereas pulse data must generally be Fourier transformed into the frequency domain before analysis.

The use of ac techniques for classical electrochemical measurements have been reviewed by Sluyters (4), Grahame (5), and Armstrong (6). Ho *et al.* (7) have discussed application of the method to single-crystal and thin film WO_3 insertion electrodes; they focused attention on solution of the diffusion equation in the frequency domain, but they avoided the problem of surface roughness and porosity encountered in pressed-powder insertion electrodes. The latter problem is important because the insertion-compound electrodes used in commercial cells, and many that are tested in the laboratory, consist of finely divided powders pressed so as to ensure electronic conduction between particles, but not so as to eliminate a continuously connected porous space between the particles. The interparticle space allows the electrolyte access to a large surface area. In this paper, we present an equivalent-circuit model for interpreting the ac impedance of a pressed-powder insertion-compound electrode in contact with a liquid electrolyte that penetrates the pores.

The ac results presented below demonstrate that the electrode material $\text{Li}_{1-x}\text{CoO}_2$ in propylene carbonate cannot be characterized in terms of a simple intracomponent Li^+ ion diffusion; more complex electrochemical processes, including the formation of a surface layer on the electrode due to oxidation of the electrolyte, must be considered. A model for the ac impedance of these complex electrochemical reactions, including adsorption and surface-layer formation, is presented and rationalized.

Experimental

Samples of LiCoO_2 were prepared by heating an intimately ground, stoichiometric mixture of Li_2CO_3 (BDH Chemicals Limited, ANALAR purity) and cobalt metal (Koch-Light Laboratories, 1 μm , 99.5% purity) in air initially at 600°C for 12h with subsequent heating at 900°C for 24h. The product was repeatedly ground and reheated at 900°C until x-ray diffraction indicated it was single phase. Atomic absorption analysis confirmed production of a Li:Co ratio of 1:1, and the semiconducting character of the blue-black product indicated an essentially stoichiometric oxide-ion concentration. Lithium-deficient electrodes $\text{Li}_{1-x}\text{CoO}_2$ were prepared by galvanostatic titration of a two-terminal cell constructed as the three-terminal cell described below.

Because the materials used in these studies are air sensitive, the cells were constructed in an argon-filled Vac-

uum Atmospheres glove box in which the dioxygen level was maintained in the region of 3 ppm and the H₂O level in the region of 7 ppm.

A three-terminal cell suitable for kinetic measurements on pressed-powder electrodes is shown in Fig. 1. The working electrode consisted of a 200-mesh stainless steel gauze (N. Greening and Company) current collector shaped as a 13 mm diam disk onto which was pressed (5 ton) about 20 mg of the powdered Li_{1-x}CoO₂ that, in some cases, was premixed with one or two drops of the liquid electrolyte, a 1M solution of LiBF₄ (Ventron GMBH) in propylene carbonate (Aldrich). Nickel gauze was found to be unstable in contact with an oxide containing cobalt in the highly oxidizing Co^{4+/3+} mixed-valence state. Similarly, propylene carbonate was selected for the electrolyte because it appears kinetically stable in contact with Li_{1-x}CoO₂ at potentials of up to 4.5V vs. lithium. The propylene carbonate was distilled under reduced pressure at 80°C and dried over Li chips before preparation of the electrolyte. The pressed-powder compact was placed against one of the two stainless steel spigots, Fig. 1; a freshly cut disk of lithium metal was placed against the other spigot to act as the counterelectrode. The working and counterelectrodes were separated by Whatman glass-fiber pads that had been saturated with electrolyte; one low porosity pad (type GF/F) was placed next to the working electrode and two type GF/D pads next to the counterelectrode. A lithium annulus placed between the two GF/D pads acted as a voltage-reference electrode. The whole cell assembly was compressed by screwing together the stainless steel spigots; pressure on the cell components was increased until a stable and identical voltage was obtained between the working electrode and both counter and reference electrodes.

Impedance measurements were carried out by connecting the cell to a Solartron 1186 Electrochemical Interface that was, in turn, connected to a Solartron 1174 Frequency Response Analyser. The combined system potentiostatically controls the cell voltage and supplies a 10 mV-rms ac perturbation sweeping the frequency range 10⁰-10⁻⁴ Hz. The Model 1186 is a four-terminal device; the two reference leads are provided with driven shielding, which minimizes the stray lead capacitances and inductances, a potential problem with ac measurements. The cell-Solartron system was under the control of an Intertec Superbrain microcomputer; the Superbrain was also used to apply a dc bias to the cell via a digital-to-analog converter and to provide a graphical presentation of the data. The results reported here are presented exclusively in the complex-impedance plane.

The data were analyzed with a complex-nonlinear-least-squares refinement program developed for microcomputers (8). The program allows interactive specification of equivalent-circuit models and their component values. (We are grateful to Dr. B. A. Boukamp for recommending the use of an interactive approach.) The program generates as output the refined component values, the observed and calculated impedance responses and their percentage difference, and a reliability factor *R* calculated as

$$R = \frac{\sum_i [O(\omega_i) - E(\omega_i)]^2}{\sum_i O(\omega_i)^2}$$

where *O*(ω_i) and *E*(ω_i) are the observed and estimated re-

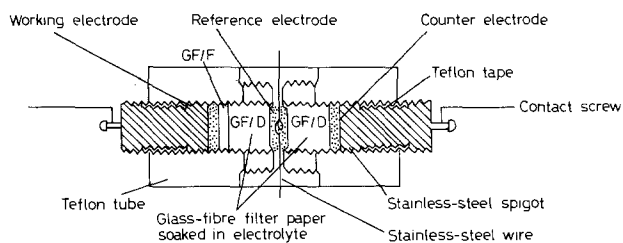


Fig. 1. Electrochemical cell

sponses at the frequencies ω_i . With this program, the optimized component values for a wide variety of different equivalent-circuit models could be rapidly evaluated. This procedure allows comparison of alternative models and an evaluation of the physical interpretation of the components used in any given model.

AC Impedance of a Model Pressed-Powder Electrode

The ac impedance of an electrochemical cell containing a pressed-powder electrode can be described by an equivalent circuit such as that shown in Fig. 2a; a model of the electrode/electrolyte interface is shown in Fig. 2b. The model of Fig. 2a is based on the assumption that the electronic conductivity of the insertion compound is high and that the powder is compacted sufficiently to ensure that each particle is in contact with the aggregate across a solid-solid interface making an ohmic contact of low resistance to electron flow. Under these conditions, the insertion-compound aggregate forms a rough, but continuously interconnected, porous solid of low bulk resistance $R_b \ll R_e$, where R_e is the bulk electrolyte resistance.

The model divides the problem into three segments: the bulk electrolyte, the interface region, and the bulk electrode. The bulk electrode resistance consists of a very low electronic resistance in parallel with a higher insertion-ion resistance. The interface region includes three segments: the interface itself across which insertion-ion transfer and double-layer charging occur, and regions on either side of the interface where these processes introduce insertion-ion concentration gradients in the electrolyte and/or the electrode. In a porous electrode, electronic currents in the solid induce ionic countercurrents in the electrolyte to produce a circuit element analogous to that of a nonuniform RC-transmission line (see Fig. 3). Two

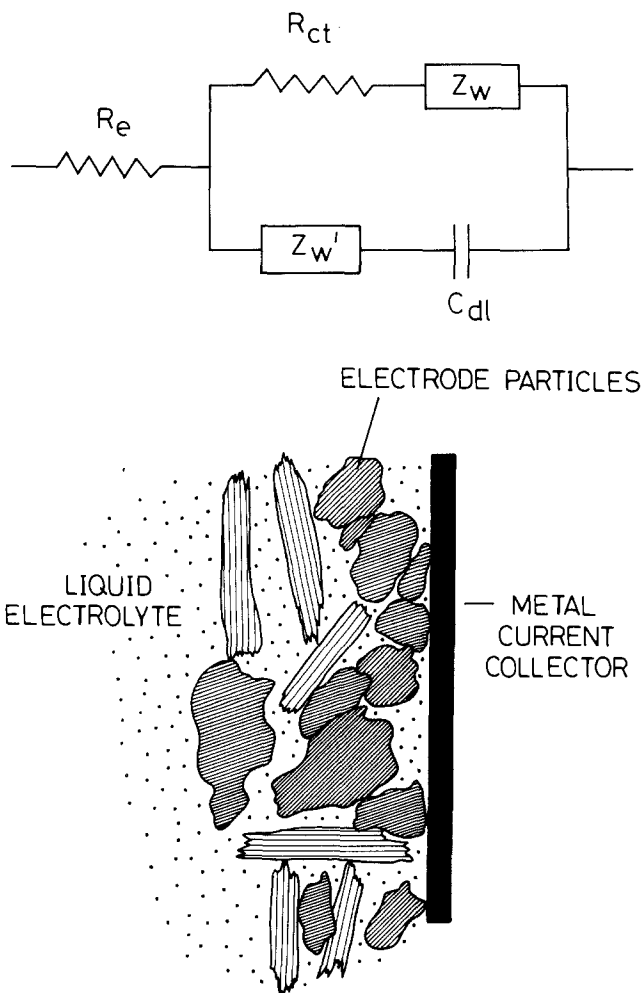


Fig. 2. Modified Randles circuit (a, top) and electrode/electrolyte interface (b, bottom).

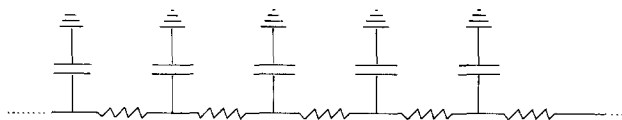


Fig. 3. Transmission-line equivalent circuit

types of currents through the interface must, therefore, be distinguished: that due to insertion-ion and electron migration (faradaic process), and the displacement current due to charge polarization (nonfaradaic process). These two currents flow in parallel branches. We now argue that the faradaic-current branch may be represented by a charge transfer resistance R_{ct} and by a Warburg impedance Z_w , the nonfaradaic-current branch by a generalized Warburg impedance Z'_w and a double-layer capacitance C_{dl} .

Representation of the insertion-ion migration across the interface by a charge transfer resistance R_{ct} is more generally valid, but it may be conveniently derived from the Butler-Volmer equation used in classical electrochemical systems for charge transfer current across an interface of effective area A

$$I = AnFk [a_o \exp(-\alpha\phi) - a_r \exp(\beta\phi)] \quad [1]$$

where reduction currents are defined as positive quantities. In Eq. [1], k is the charge transfer rate constant, $\phi = nF\eta/RT$ (with $n = 1$ for alkali-ion transfer) is proportional to the overpotential η and the Faraday constant F , and the transfer coefficients obey the relation $\alpha + \beta = 1$. The coefficients a_o and a_r represent the insertion-ion activities at the interface in the electrolyte and electrode, respectively. At low overpotentials, linearization of Eq. [1] allows the faradaic current flowing across the interface to be represented by η/R_{ct} , where

$$R_{ct} \equiv RT/nFI_o; \quad I_o \equiv AnFka_o^\beta a_r^\alpha \quad [2]$$

is the charge transfer resistance and I_o is the exchange current. In the case of a layered compound supporting only two-dimensional conductivity, the effective area A across which ions are inserted into or withdrawn from the solid is only a small fraction of the total surface area; this reduction is exaggerated by the tendency of layered-compound particles to form as platelets supporting ion transfer only across an edge interface.

Diffusion-controlled migration, whether in the electrolyte or the solid, may be described by the Warburg impedance (7)

$$Z_w = A_w (1 - j)\omega^{-1/2}; \quad A_w = \frac{V_m}{AnF(2D)^{1/2}} \frac{\partial V_{oc}}{\partial c} \quad [3]$$

provided the applied frequencies are high enough to satisfy the relation $\omega > D/l^2$, where D is the chemical diffusion coefficient and l is the width of the layer supporting a mobile-ion concentration gradient. At lower applied frequencies $\omega < D/l^2$, the impedance may be represented by a resistance and a capacitance in series (7)

$$Z_L = R_L - j(\omega C_L)^{-1} \quad [4]$$

In Eq. [3], V_m is the molar volume of the solid and $\partial V_{oc}/\partial c$ is the slope of the open-circuit voltage V_{oc} vs. mobile-ion concentration c . In the absence of any supporting electrolyte, ionic transport in the electrolyte is not diffusion controlled, and the Warburg impedance in the faradaic branch is related only to the chemical diffusion coefficient D_b of the bulk via Eq. [3]. For an ion blocking electrode, there is no ionic transport in the bulk of the electrode ($l = l_b \rightarrow 0$), and any Warburg impedance in the faradaic branch is related only to diffusion-controlled processes in the electrolyte; this situation has been discussed by Randles (9) for a diffusion-controlled reaction between soluble species at an ion blocking electrode. In the general case, the Warburg impedance in the faradaic branch must be related to the diffusion coefficients of the insertion ion in both the electrolyte and the electrode.

If the concentration of the insertion ion in the electrolyte is low, it may be necessary to introduce a concentration overpotential where there is no supporting electrolyte. In our experiments, a 1M solution of LiBF_4 in propylene carbonate gives a high enough Li^+ ion concentration that any concentration overpotentials may be ignored. However, for a pressed-powder electrode containing a layered insertion compound having only two-dimensional ionic conduction, ion transport between particles is generally difficult; the interfaces are only good electronic conductors. In this case, the width l_b of the mobile-ion concentration gradient in the solid is essentially limited to the radius of the particle in the conducting plane, so we may expect to encounter, at lower applied frequencies, the condition $\omega < D/l_b^2$ where Eq. [3] transforms to Eq. [4]. Although this transformation introduces an effective capacitance into the faradaic branch, it must be appreciated that, as dc conditions are approached, the circuit component transforms further to a simple resistance.

For a smooth electrode or at lower frequencies, uniform charging of the entire electrode surface gives rise to a capacitance C_{dl} , the classical double-layer capacitance, in the nonfaradaic branch. This was the situation in the cell investigated by Randles (9); the Randles circuit has also been used to model the ac response of electrochromic WO_3 films (7). However, in the former case, the Warburg component in the faradaic branch represented diffusion-controlled processes in only the electrolyte; in the latter, the Warburg impedance includes diffusion-controlled processes in the solid.

On the other hand, at higher frequencies with a rough or porous electrode in which the ac signal penetration depth is comparable to the depth of the pores, an in-pore ionic current counter to the in-solid electronic current produces a situation analogous to an RC-transmission-line network (Fig. 3) (10). Current flow in a semi-infinite, uniform transmission line is described by the telegrapher's equation, which has the same form as the diffusion equation since the process taking place in an RC line may be regarded as electronic diffusion into a semi-infinite medium (11). The RC line may therefore be represented by a Warburg impedance. For a porous electrode, the RC-transmission line is nonuniform, and a more general constant-phase-angle impedance is required to represent it (12)

$$Z'_w = A'_w (j\omega)^{-m} = A'_w \omega^{-m} \left[\cos\left(\frac{m\pi}{2}\right) - j \sin\left(\frac{m\pi}{2}\right) \right]; \quad 0 < m < 1 \quad [5]$$

If the nonfaradaic branch of the equivalent circuit of Fig. 2a includes the two components Z'_w and C_{dl} in series, then at low frequencies C_{dl} dominates and at high frequencies Z'_w dominates.

The ac response of the equivalent circuit of Fig. 2a is shown in Fig. 4. This is similar to that for the circuit proposed by Randles (9) except for its modification by Z'_w to include the effect of electrode porosity at higher applied frequencies ω . Inclusion of Z'_w results in the charge transfer semicircle being replaced by a semicircle with a high frequency linear tail.

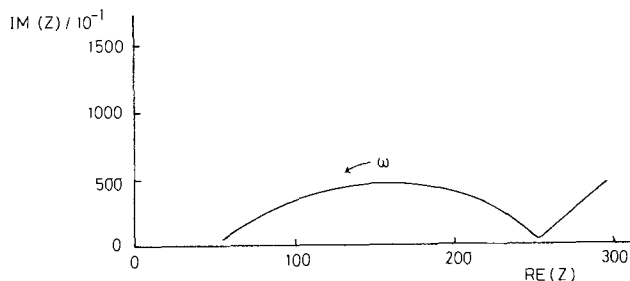


Fig. 4. Simulated ac impedance response for modified Randles circuit: $R_e = 50\Omega$; $R_{ct} = 200\Omega$; $C_{dl} = 10\mu\text{F}$; $A_w = 4\Omega$; $A'_w = 10^5\Omega/\text{s}^{-1/2}$; $m = 0.5$.

Application to $\text{Li}_{1-x}\text{CoO}_2$

A four-probe dc-conductivity measurement was carried out on a $\text{Li}_{0.6}\text{CoO}_2$ pellet fabricated with a pressure (ca. 5 ton) similar to that used to make electrodes. An electronic conductivity (stainless steel electrodes) of $0.2 \Omega^{-1}\text{cm}^{-1}$ confirms that this pressure is sufficient to establish a porous electrode in which the individual particles are making electrical contact. Therefore, the physical model described in the last section should be applicable to our electrodes of $\text{Li}_{1-x}\text{CoO}_2$. However, the observed ac response (see Fig. 5) differs markedly from the response predicted for a modified Randles circuit (Fig. 4); two semicircles are clearly observed. Since each semicircle requires the inclusion of a resistor/capacitor combination in the equivalent-circuit model, the modified Randles circuit is clearly an inadequate model of the electrode reaction.

The appearance of two semicircles proved highly reproducible; of more than 200 impedance-response spectra collected from many different samples of different stoichiometries of $\text{Li}_{1-x}\text{CoO}_2$, every one showed this feature. However, the relative sizes of the semicircles were found to depend on the previous history of the cell; both semicircles were generally found to increase in size with time. The spectrum in Fig. 5 was obtained within one day of construction of the cell; other cells of similar age had impedance spectra of a similar form. Visual inspection of Fig. 5 clearly reveals that at least six circuit components—three resistors, two capacitors, and a Warburg component—are required to produce the basic form of the response.

Two different physical processes may be invoked to account for the addition of a resistor/capacitor pair to the Randles equivalent circuit: (i) adsorption of Li^+ ions or propylene carbonate onto the surface of the electrode without charge transfer and (ii) formation of an ionically conducting but electronically insulating surface layer at the electrode surface. In order to distinguish between these two possibilities, it is necessary first to construct the corresponding equivalent circuits, which are illustrated in Fig. 6.

Adsorption represents a nonfaradaic process that occurs in parallel with the nonfaradaic processes already discussed for the modified Randles circuit of Fig. 4. The adsorption branch of the circuit has two components, one representing the kinetics of formation of the adsorbed species and the other the energy stored by subsequent bond formation (see Fig. 7). The kinetic component may be represented by a resistance (Fig. 6a) or, if diffusion controlled, by a Warburg impedance in series with a resistance (Fig. 6b); the energy-storage component by a capacitance. These two steps occur in series, so they form a single adsorption branch in parallel with the interfacial-region branches of the modified Randles circuit.

A surface-layer electrolyte having a smaller insertion-ion conductivity than the liquid electrolyte is illustrated in Fig. 8. Across the surface layer, the ion transport may be represented by the insertion-ion resistance R_{sl} , and polarization of the surface-layer electrolyte by a capacitance C_{sl} in parallel. The existence of a surface-layer electrolyte modifies the double-layer capacitance, which is associated with the mobile species in the surface layer. Since the double layer is confined to a small fraction of the sur-

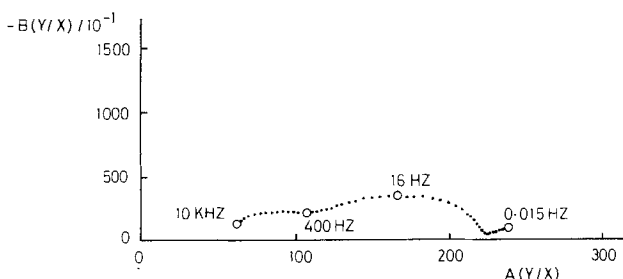


Fig. 5. Measured ac impedance response for $\text{Li}_{0.65}\text{CoO}_2$

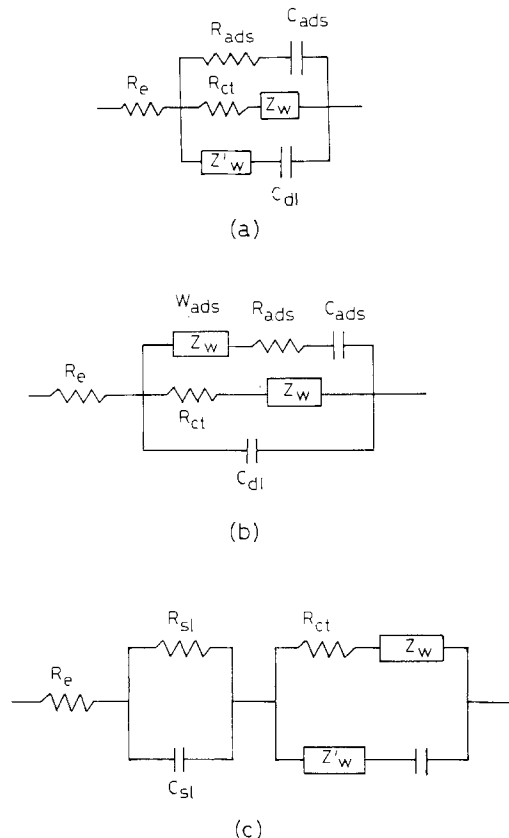


Fig. 6. Equivalent circuits for three models: adsorption (a), diffusion-controlled adsorption (b), and surface layer (c).

face layer, the relation $C_{dl} \gg C_{sl}$ can be anticipated, so we are justified in putting the surface-layer segment in series with the interfacial-region segment as shown in Fig. 6c.

Although the two equivalent circuits given in Fig. 6a and 6c were developed to represent different physical processes, they may be formally transformed one into the other (13), and simulation of the impedance responses for all three circuits of Fig. 6 are indistinguishable from one another with realistic resistor and capacitor values for either the adsorption or surface-layer model. It is therefore not possible to determine which physical model is most applicable to the $\text{Li}_{1-x}\text{CoO}_2$ system simply by least squares refinement of the impedance data. This example demonstrates the danger inherent in any justification for selection of a physical model purely on the grounds of "goodness of fit" between a simulated and an observed

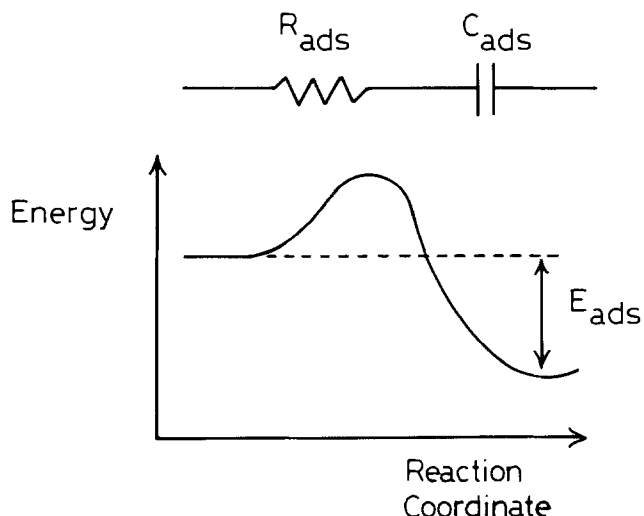
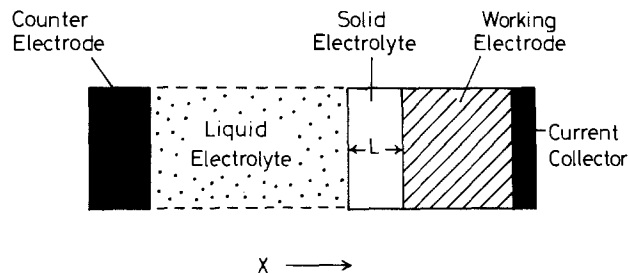


Fig. 7. Modeling of the adsorption process

Fig. 8. Surface layer of thickness L

impedance spectrum; the choice of either the circuit or the physical process it represents need not be unique. The equivalence of at least two superficially different equivalent circuits used to model two distinguishable physical processes demands the establishment of more rigorous criteria upon which to base acceptance of a physical model. The following criteria can be identified.

1. Viable model circuits must contain components that are connected together in the same order as the physical processes they represent.

2. Convergent fits of simulated and observed impedance spectra must be obtained through least squares refinement.

Nonconvergence arises either if the component values are significantly different from those needed for an optimum fit or if two or more of the component values are highly correlated, which indicates that one of them may have no basis in reality. Without a convergent fit, the values of the components in the equivalent circuit may not be determined, in which case the following criteria cannot be met.

3. A low R factor as well as visual inspection of the graphical output produced by the fitting program must verify good agreement between calculated and observed impedance spectra.

4. The optimized values of the individual circuit components produced by the fitting program must correspond to reasonable values for the physical processes they represent. The magnitude of any component value must be significantly greater than the calculated estimated standard deviation.

5. The individual circuit-component values should vary in an explicable and self-consistent manner as the conditions of an experiment are varied.

6. Independent evidence, not based on ac-impedance studies or circuit fitting, should be sought to verify specific conclusions of the fitting procedure.

All three of the equivalent-circuit models shown in Fig. 6 are found to satisfy generally the first four of the above criteria, as can be seen from Fig. 9. However, criterion 3 could not be met for Fig. 9a and 9c without use of the constant-phase element (modified Randles circuit) to parametrize the electrode porosity. It should be noted that the values for the charge transfer resistance and the Warburg prefactor A_w for the intraelectrode diffusion are generally independent of the model used for fitting. This proved reproducibly true for all of the data that were fitted for these three equivalent circuits. In contrast, the values of the double-layer capacitance C_{dl} vary widely with the choice of model.

In order to differentiate between the models, the conditions of the cells were varied systematically. The aim of these experiments was to identify correlations between the variations in the external conditions and the variations in the fitted values of the individual circuit components. Three separate types of experiment were carried out to determine: (i) the time dependence of the ac-impedance response, (ii) the influence of premixing of the electrolyte with the cathode material, and (iii) the variation of the circuit parameters with applied voltage.

As discussed above, the relative sizes of the semicircles characteristic of our $\text{Li}_{1-x}\text{CoO}_2$ electrodes increased with the age of the cell. Impedance-response spectra were recorded at increasing time intervals over a period of seven

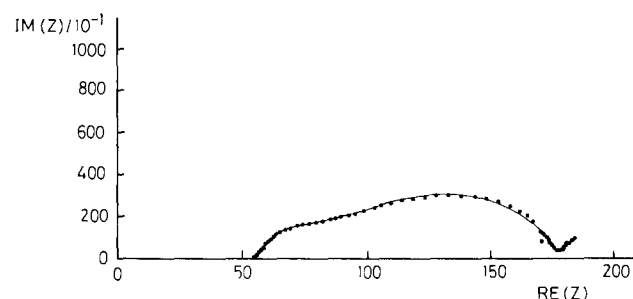
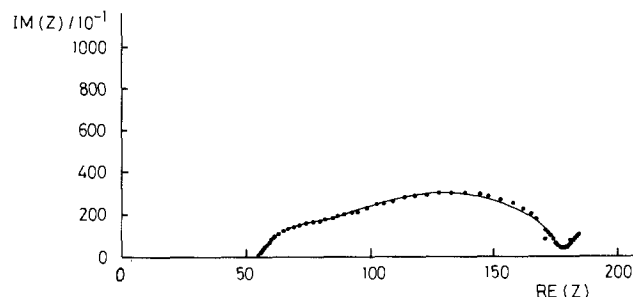
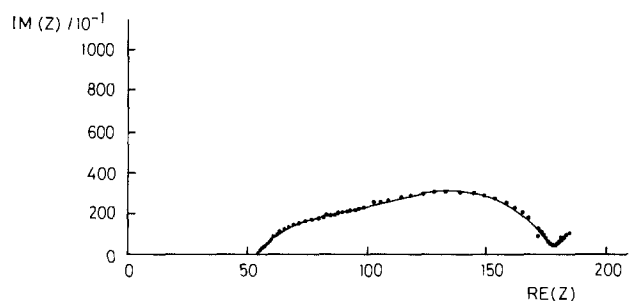


Fig. 9. Fitted ac-impedance response for $\text{Li}_{0.65}\text{CoO}_2$. (a) Adsorption: $R_e = 52.0(2)\Omega$, $R_{ads} = 357(24)\Omega$, $C_{ads} = 15.4(2)\mu\text{F}$, $R_{ct} = 123.3(5)\Omega$, $A_w = 2.8(2)\Omega\text{-s}^{-1/2}$, $C_{dl} = 84(11)\mu\text{F}$, $A'_w = 1803(30)\Omega\text{-s}^{-1/2}$, $m = 0.5$ (b) Diffusion-controlled adsorption: $R_e = 56.0(1)\Omega$, $R_{ads} = 22.7(8)\Omega$, $C_{ads} = 113(5)\mu\text{F}$, $R_{ct} = 119.7(4)\Omega$, $A_w = 2.6(2)\Omega\text{-s}^{-1/2}$, $C_{dl} = 2.62(7)\mu\text{F}$, $A'_w = 1095(22)\Omega\text{-s}^{-1/2}$, $m = 0.5$. (c) Surface layer: $R_e = 53.1(2)\Omega$, $R_{sl} = 12.4(5)\Omega$, $C_{sl} = 10.1(6)\mu\text{F}$, $R_{ct} = 1097(7)\Omega$, $A_w = 2.8(1)\Omega\text{-s}^{-1/2}$, $C_{dl} = 1.13(4)\mu\text{F}$, $A'_w = 682(28)\Omega\text{-s}^{-0.442}$, $m = 0.442(7)$.

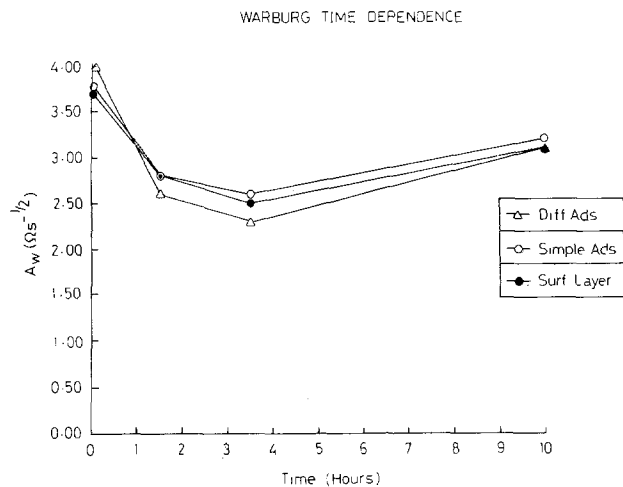
days; the time-dependent behaviors of the optimized equivalent-circuit parameters for each of the three models of Fig. 6 are shown in Fig. 10-18.

Premixing the electrolyte and electrode material together was done to increase the electrode/electrolyte interface area; the results of this experiment are given in Table I.

To investigate the variation in circuit parameters with applied voltage, the high frequency (> 1 Hz) impedance response was monitored during short potentiostatic

Table I. Dependence of resistances and capacitances upon preparation method for two equivalent-circuit models

Parameter	Dry-pressed electrode	Premixed electrode
Surface-layer model		
Electrolyte resistance (R_e)	52(1) Ω	52(1) Ω
Surface-layer resistance (R_{sl})	27(1) Ω	184(1) Ω
Surface-layer capacitance (C_{sl})	7.8(4) μF	0.35(3) μF
Charge-transfer resistance (R_{ct})	136(1) Ω	23(1) Ω
Double-layer capacitance (C_{dl})	128(8) μF	1530(120) μF
Warburg prefactor (A_w)	3.1(1) $\Omega\text{-s}^{-1/2}$	0.93(7) $\Omega\text{-s}^{-1/2}$
Diffusion-controlled adsorption model		
Electrolyte resistance (R_e)	56(1) Ω	57(1) Ω
Adsorption resistance (R_{ads})	43(2) Ω	44(1) Ω
Adsorption capacitance (C_{ads})	127(12) μF	102(34) μF
Charge-transfer resistance (R_{ct})	159(1) Ω	201(1) Ω
Double-layer capacitance (C_{dl})	2.4(1) μF	0.78(2) μF
Warburg prefactor (A_w)	3.1(1) $\Omega\text{-s}^{-1/2}$	0.90(3) $\Omega\text{-s}^{-1/2}$

Fig. 10. Time dependence of A_w for three models

pulses. The voltage dependence of the electrochemical parameters are shown in Fig. 19 for the diffusion-limited adsorption model and the surface-layer model.

It is immediately apparent from Fig. 10 that the Warburg prefactor A_w is essentially independent of both time and the choice of model, as required for bulk diffusion. A slight decrease with time is observed; it is attributable to an electrolyte penetration that increases the effective electrode/electrolyte surface area A .

Adsorption models.—The simple adsorption model of Fig. 7 may be eliminated by inspection of Fig. 11 and 12; inexplicable changes in the adsorption resistance and capacitance over a 24h period are required by this model.

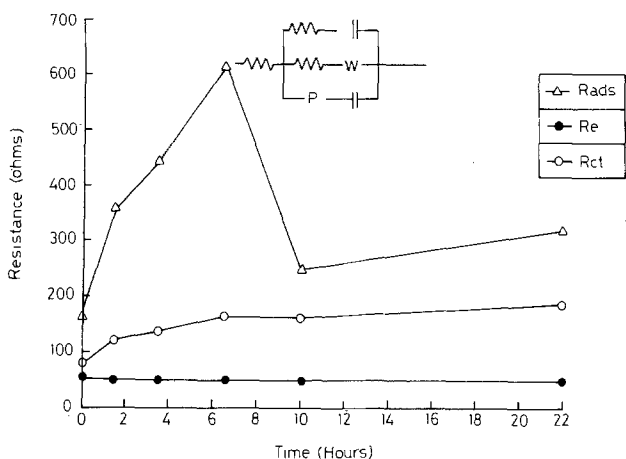


Fig. 11. Time dependence of resistances (adsorption model)

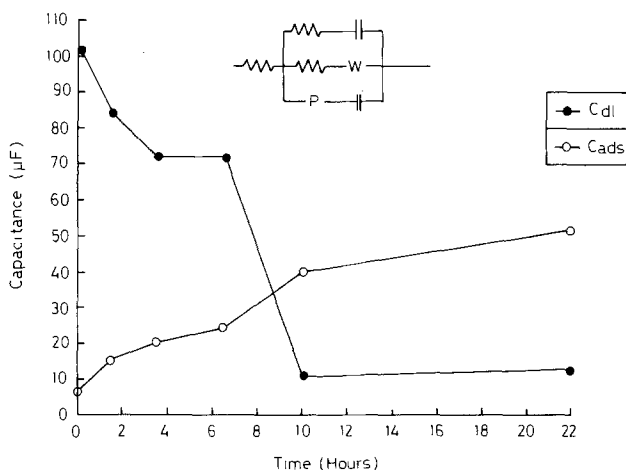
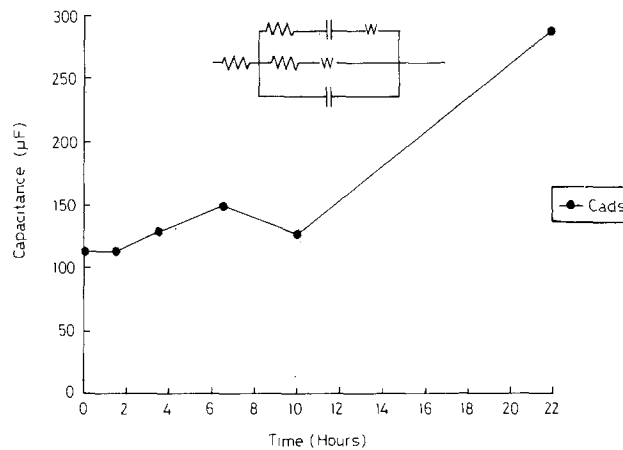
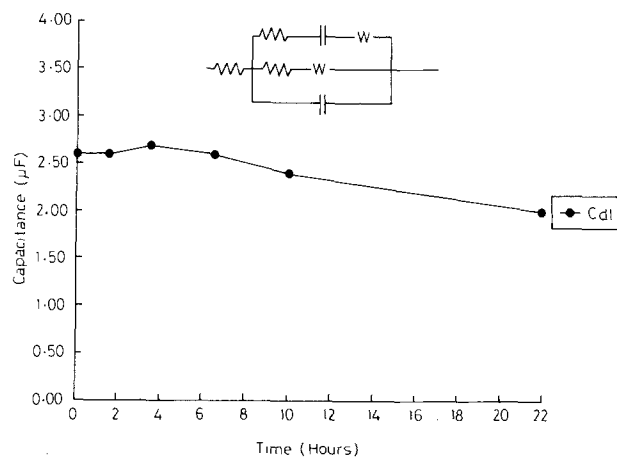


Fig. 12. Time dependence of capacitances (adsorption model)

Fig. 13. Time dependence of C_{ads} (diffusion-controlled adsorption)Fig. 14. Time dependence of C_{dl} (diffusion-controlled adsorption)

Initially, a $C_{dl} > C_{ads}$ is found; this is a physically unreasonable situation. Moreover, it is most improbable that adsorption should cause C_{dl} to decrease with time; rather, increasing electrolyte penetration with time should increase C_{dl} . Therefore, this model was not considered further.

Similarly, the diffusion-controlled adsorption model, Fig. 6b, could be discarded. The irregular increase in C_{ads} with time is peculiar; see Fig. 13. This model gives a C_{dl} , see Fig. 14, that is two to three times smaller than the C_{dl} measured by Bruce (14) for a Li_xTiS_2 electrode in 1M $LiBF_4$ in propylene carbonate. The Li_xTiS_2 system shows only one semicircle; it can be expected to have a similar surface roughness and, hence, a similar C_{dl} value. Moreover, the small decrease in C_{dl} with time, as in the simple-adsorption model, is inconsistent with the rationalization of the decrease in A_w with time as a manifestation of increased electrolyte penetration. To check this rationalization further, the contact surface area was deliberately increased by premixing the cathode material with the electrolyte before pressing the electrode. The resulting decrease in the Warburg prefactor A_w (Table I), which is consistent with a larger effective contact area A , is clearly inconsistent with the tenfold reduction in C_{dl} obtained with the diffusion-controlled adsorption model. Finally, the physical basis for a diffusion-controlled adsorption model does not exist, as all of the experiments were carried out in the absence of any supporting electrolyte. Under our conditions, Li^+ ion transport in the electrolyte is controlled by field migration. Propylene carbonate is the only other species that could be adsorbed on the electrode; it is present in such high concentrations that its movement could not possibly be diffusion controlled.

Surface-layer model.—Having eliminated adsorption as a plausible explanation for the appearance of two semicircles in the impedance plane, we now argue that the

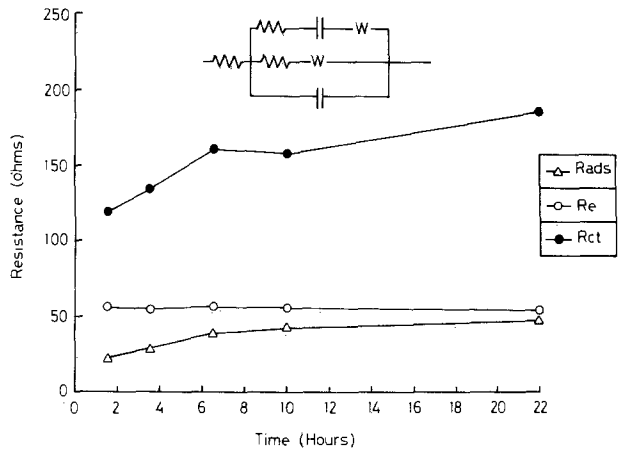


Fig. 15. Time dependence of resistances (diffusion-controlled adsorption).

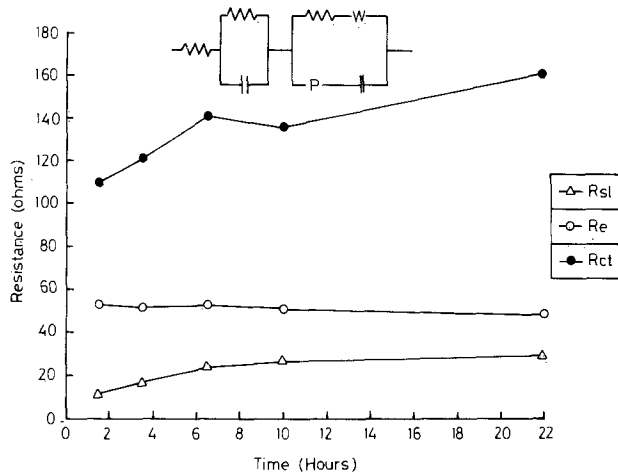


Fig. 16. Time dependence of resistances (surface-layer model)

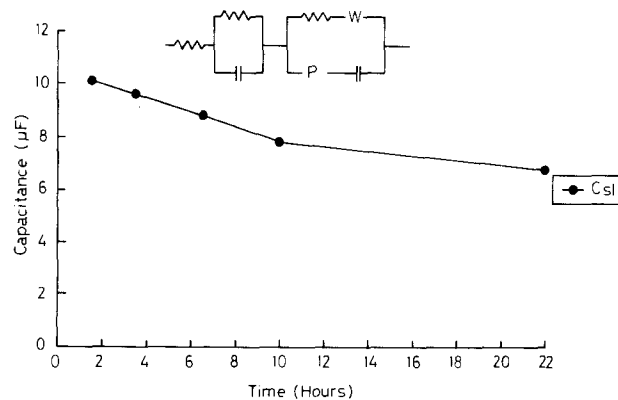


Fig. 17. Time dependence of C_{sl} (surface-layer model)

surface-layer model provides a consistent and physically reasonable interpretation of our experimental data.

According to the model of a Li⁺ ion electrolyte surface layer having a fixed resistivity ρ and permittivity ϵ with thickness L , the resistance $R_{sl} = \rho(L/A)$ should increase with the layer thickness L , and hence with time; the surface-layer capacitance $C_{sl} = \epsilon(A/L)$ should decrease with time. From Fig. 16 and 17, this is just the behavior that is observed. The monotonic increase in R_{sl} and decrease in C_{sl} with time was maintained over a period of at least seven days. The data also imply that the rate of growth of the surface layer is rapid over the first 6h after construction of the cell and thereafter slows continuously with increasing thickness.

According to Fig. 18, the C_{dl} of the surface-layer model increases from 113 to 200 μF over the duration of the experiment. This increase is consistent with an increase in

the total surface area as a result of greater electrolyte penetration even though the relative invariance of the Warburg prefactor A_w indicates that the effective surface area (the particle edges) does not increase significantly over the time scale of the experiment. Since the particles are platelike, this discrepancy can be rationalized.

From Fig. 16, the charge transfer resistance increases by about 30% over the time scale of the experiment. Comparison with Fig. 11 and 15 shows that this variation is model independent. From Eq. [2], the exchange current $I_0 \approx AFka_0^p a_r^q$ decreases with time, *i.e.*, with surface-layer thickness L . Surface-layer formation would tend to trap Li⁺ and BF₄⁻ ions in the same concentration as that in the liquid electrolyte. If the equilibrium concentration of Li⁺ and BF₄⁻ ions in the surface layer is smaller than that in the liquid electrolyte, then a_0 would decrease with time. Thus, the observed increase in R_{ct} with time is understandable with the surface-layer model.

Table I indicates that premixing of the electrode powder with the electrolyte, which must increase the effective surface area A , significantly decreases R_{ct} and A_w while increasing C_{dl} for the surface-layer model. From Eq. [2] and [3], an increase in A is expected to decrease R_{ct} and A_w . The increase in C_{dl} also follows directly from an increase in A . Table I also shows that premixing increases R_{sl} and decreases C_{sl} , indicating an increase in the surface-layer thickness and, hence, initiation of the surface-layer growth in the premixing.

The fitted values derived from the voltage stepping experiments, see Fig. 19 and 20, provide the final evidence for acceptance of the surface-layer model. These data show that R_{sl} and C_{sl} are, as expected, independent of the applied voltage, whereas R_{ads} and C_{ads} vary irregularly.

In conclusion, the surface-layer model—and only the surface layer model—contains equivalent-circuit parameters that vary in a self-consistent manner with the electro-

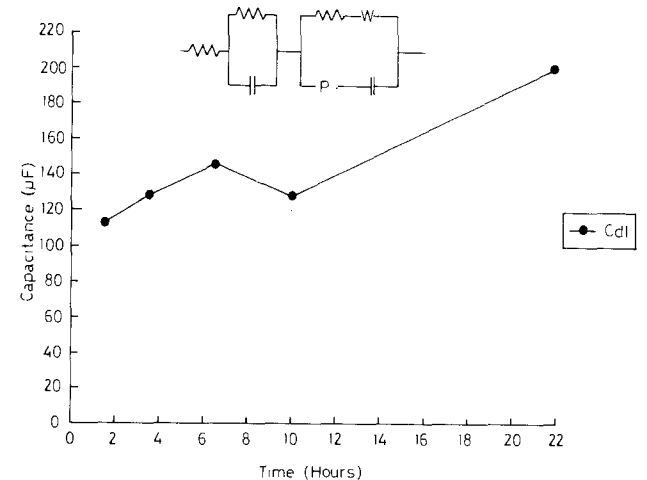


Fig. 18. Time dependence of C_{dl} (surface-layer model)

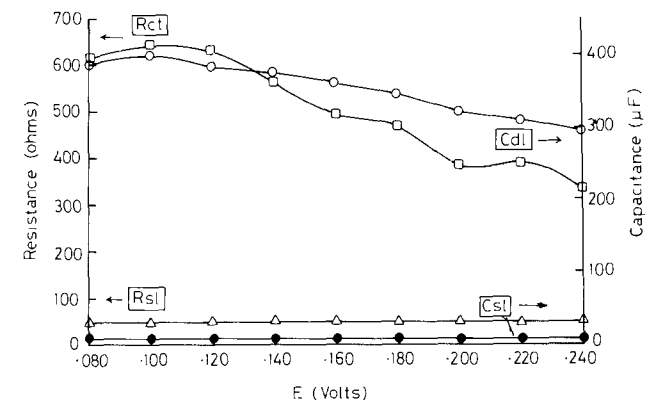


Fig. 19. Voltage dependence of resistances and capacitances (surface-layer model).

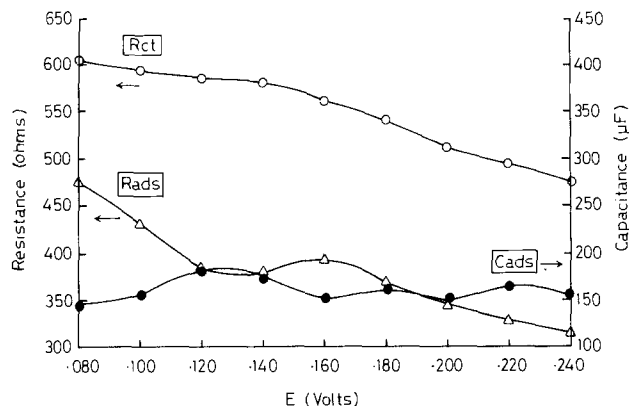


Fig. 20. Voltage dependence of resistances and capacitances (diffusion-controlled adsorption model).

chemical processes they represent as the cell conditions are varied.

Independent support for the surface-layer model is provided by the electron micrograph picture in Fig. 21, which clearly shows an amorphous layer surrounding the crystalline area where lattice-image fringes occur. The sharp boundary between the two regions makes it unlikely that the amorphous region was created by electron-beam reduction in the electron microscope. Electron-beam reduction is generally much more catastrophic,

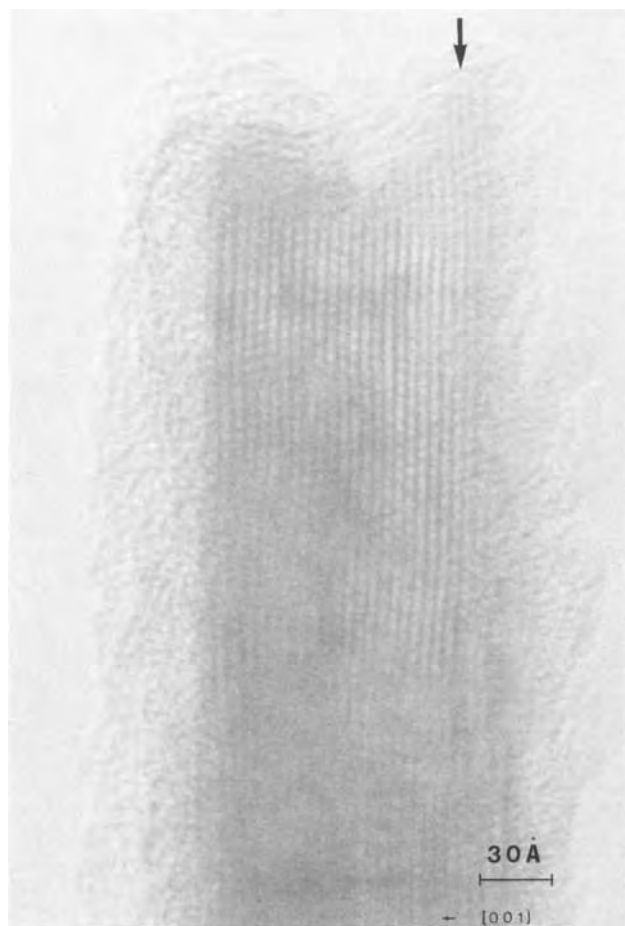


Fig. 21. Lattice image of a $\text{Li}_{0.1}\text{CoO}_2$ crystal showing lattice deformation in the layer planes.

affecting the entire crystalline region rather than the edges alone. With the separation of the (003) lattice fringes as a guide, the surface-layer thickness is estimated to be 30Å , which is in good agreement with values estimated from the surface-layer capacitance.

Studies of the impedance response as a function of composition over the range $0 < x < 0.5$ in the system $\text{Li}_{1-x}\text{CoO}_2$ gave the same form of response as the spectrum of Fig. 5, which indicates that the surface Li^+ ion electrolyte layer forms on the particles of $\text{Li}_{1-x}\text{CoO}_2$ for all values of x . The different stoichiometries were prepared *in situ* by application of a constant-voltage step to the cell. The impedance response of the cell was measured once the cell current had decayed to less than $1\ \mu\text{A}$; the voltage was subsequently stepped to a new value. The compositional ranges studied by this procedure were $0 < x < 0.3$ and $0.2 < x < 0.5$. A steady change from a regime totally dominated by the Warburg component representing bulk diffusion occurred between 3.3 and 3.9V ($0 < x < 0.05$); above 3.9V, the response had the form of that in Fig. 5.

A mixture of propylene carbonate with $\text{Li}_{1-x}\text{CoO}_2$ ($x \approx 0.35$) produces immediately a polymer, which is consistent with the strong oxidizing power of a Co^{4+} cation on the surface of an $\text{Li}_{1-x}\text{CoO}_2$ particle. For $x < 0.35$, polymerization is probably still present, though less extensive. Although we have no direct information on the composition of the surface layer formed on our electrodes, these results are consistent with the formation of a polymeric film on the electrode surface that traps within it Li^+ and BF_4^- ions. Also consistent with such a model are the time dependence of surface-layer formation and growth, the apparent lack of a comparable surface layer on the less oxidizing Li_xTiS_2 particles, and a lowering of the surface-layer time constant $R_{sl}C_{sl} = \rho\epsilon$ for the premixed electrodes; a better LiBF_4 distribution is made possible during premixing.

Acknowledgments

We acknowledge with gratitude the support of the M.O.D. (U.K.), the AFOSR (U.S.), and the S.E.R.C.

Manuscript submitted Sept. 17, 1984; revised manuscript received March 21, 1985.

Oxford University assisted in meeting the publication costs of this article.

REFERENCES

- M. A. Whittingham, *Prog. Solid State Chem.*, **12**, 41 (1978).
- D. W. Murphy, P. A. Christian, F. J. Di Dalvo, and J. N. Carides, *This Journal*, **126**, 497 (1979); P. G. Dickens and G. J. Reynolds, *Solid State Ionics*, **5**, 331 (1981); P. C. Spurdens, J. Drennan, J. R. Owen, and B. C. H. Steele, *ibid.*, **5**, 335 (1981); P. C. Spurdens, Ph.D. Thesis, University of London, London (1982).
- K. Mizushima, P. C. Jones, P. J. Wiseman, and J. B. Goodenough, *Mater. Res. Bull.*, **17**, 785 (1980).
- M. Sluyters-Rehbach and J. H. Sluyters, in "Electroanalytical Chemistry," Vol. 4, A. J. Bard, Editor, p. 1, Marcel Dekker, New York (1970).
- D. C. Grahame, *This Journal*, **99**, 55 (1952).
- R. D. Armstrong, M. F. Bell, and A. A. Metcalfe, *Electrochemistry*, **6**, 98 (1976).
- C. Ho, I. D. Raistrick, and R. A. Huggins, *This Journal*, **127**, 343 (1980).
- J. Roe and M. G. S. R. Thomas, Unpublished.
- J. E. B. Randles, *Discuss. Faraday Soc.*, **1**, 11 (1947).
- R. de Levie, *Electrochim. Acta*, **10**, 113 (1965).
- J. Schrama, Ph.D. Thesis, University of Leiden (1957).
- W. Scheider, *J. Phys. Chem.*, **79**, 127 (1975).
- R. D. Armstrong and M. Henderson, *J. Electroanal. Chem.*, **39**, 81 (1972).
- P. G. Bruce, Unpublished results.

Polyacetylene and Polyphenylene as Anode Materials for Nonaqueous Secondary Batteries

L. W. Shacklette,* J. E. Toth, N. S. Murthy, and R. H. Baughman

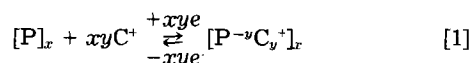
Allied Corporation, Corporate Technology, Morristown, New Jersey 07960

ABSTRACT

The conjugated polymers polyacetylene (PA) and poly(p-phenylene) (PPP) have been examined for their possible use as negative electrode materials in nonaqueous secondary batteries. Cathodically stable electrolytes have been identified which allow high reduction levels for these polymers, and charge-storage capacities of 0.34 Ah/g for PA and 0.15 Ah/g for PPP have been demonstrated. Structural evolution of these polymers during cation insertion and extraction has been shown to have a significant influence on their electrochemical behavior. Several new stoichiometric phases have been identified.

Polyacetylene (PA) (1) and poly(p-phenylene) (PPP) (2, 3) are crystalline conjugated polymers which can be either partially oxidized or reduced electrochemically. This process results in the formation of a highly conducting complex between the reduced or oxidized polymer and the appropriate counterion from the electrolyte. The electrochemical reaction which occurs in a cell containing PA or PPP electrodes involves the removal or addition of electrons through the external circuit and the insertion of ions from the electrolyte into the polymer lattice.

Polyacetylene (1), polyphenylene (2, 3), and other conjugated polymers have been considered for application to nonaqueous-electrolyte secondary batteries, where they may function as either anode or cathode. Recently, the prospects for a particular cell employing polyacetylene as a cathode have been reviewed (4). In this paper, we will discuss the characteristics of polyacetylene and polyphenylene as they relate to the potential use of these polymers as anodes. In this case, we will only be concerned with partially reduced polymers for which the ion-insertion reaction may be represented by



where P denotes the polymer compositional repeat unit, C⁺ the inserted cation, y the fractional charge per repeat unit (frequently called the doping level), and x the degree of polymerization. In this paper, P denotes —CH— for PA and —C₆H₄— for PPP.

Two of the most important considerations relating to use in batteries concern the charge storage capacity (maximum value of y) and the operating voltage of the polymer. To date, there has been a discrepancy in the reported values of y obtainable with Li⁺ for polyacetylene by chemical means (5) (y = 0.3) and by electrochemical means (6) (y = 0.08). We have been able to resolve this discrepancy by performing electrochemical reductions in more cathodically stable electrolytes.

Having found a stable electrochemical system, we have been able to study the intrinsic properties of polyacetylene and polyphenylene at varying degrees of reduction.

Experimental

As we will detail in the following sections, we have found that a variety of organoborate salts offer superior stability to the reduced polymers. Some of these salts, lithium tetraphenyl borate (LiBPh₄), lithium tetrabutyl borate (LiBBu₄), and sodium tetraethyl borate (NaBEt₄), were purchased from Alfa Products. Others, which included lithium tetramethyl borate (LiBMe₄) and potassium tributyl(N-pyrrolyl)borate (KBBu₃Py), were synthesized by methods analogous to those of Ref. (7) and (8), respectively. The LiBMe₄ was prepared by reacting methyl lithium and trimethylborane, (CH₃)₃B, in diethyl ether. The KBBu₃Py was prepared by first reacting po-

tassium hydride and pyrrole in tetrahydrofuran to form KC₄H₉N. A stoichiometric amount of tributylborane, (C₃H₇)₃B, was then added to form the desired salt. Lithium perchlorate was obtained pelletized and sealed under vacuum from Anderson Physics. Lithium tetrafluoroborate and lithium hexafluorophosphate were obtained from Alpha Products, lithium trifluoromethane sulfonate from 3M, and lithium hexafluoroarsenate from U.S. Steel. The solvents used in this study, tetrahydrofuran (THF), 2-methyltetrahydrofuran (2-MTHF), methyl tetrahydrofurfuryl ether (MTFE), and diethyl ether (DEE), were all purified by distillation and storage over sodium benzophenone ketyl.

Since reduced PA and PPP are powerful and even catalytic reducing agents, extreme care was taken in purifying both electrolytes and solvents. The borate salts were typically dissolved in either THF or diethyl ether and crystallized by solvent removal. The salts were then washed with pure pentane and vacuum dried as a final step. After dissolving the salt in the chosen solvent, the electrolytic solution was stirred over a mercury amalgam of the corresponding alkali metal for at least 16h to remove any remaining reductively unstable impurities.

The Lewis acid salts were purified by heating at ca. 100°C under vacuum for 16h, followed by stirring as a solution over Li/Hg amalgam. Where necessary, solutions were centrifuged and recrystallized a final time.

Measurements of potential vs. composition were taken with a computer-controlled incremental-voltage-step (IVS) technique (9). The potential of the polymer electrode vs. an M/M⁺ reference was stepped in 10, 25, 50, or 100 mV increments or decrements between preset voltage limits. The current after each voltage step was allowed to decay to a preset minimum, typically corresponding to 25 μA/cm². Once the minimum current was reached, the circuit was opened for 1 min, and the potential of the polymer was recorded after this wait. A typical insertion and extraction cycle required 30h to complete with the longest high resolution cycles requiring up to 10 days.

Test cells were assembled in glass containers in an argon-filled dry box, degassed under vacuum, and sealed. Each cell contained an alkali metal reference/counter electrode along with the polymer working electrode. The cells contained about 1 ml of electrolyte solution and 8-30 mg of polymer. Polymer electrodes were contacted by expanded nickel screen which was wrapped around the outside surface of the electrode. Polyacetylene was in the form of a film grown by the technique of Shirakawa *et al.* (10). Such PA films were typically 0.01 cm thick, had a density of ca. 0.4 g/cm³, and were composed of 500Å diam fibrils. After synthesis the polyacetylene was stored at -40°C within the dry box. This procedure allowed the film to maintain a high *cis* isomer content (*cis:trans* > 80%). Isomerization to the all *trans* polymer was accomplished during the first cycle to a reduction level greater than 6% (*i.e.*, y > 0.06). This method of isomerization has been shown to produce

* Electrochemical Society Active Member.

longer conjugation lengths (fewer defects) than are produced by thermal isomerization (11).

Poly(p-phenylene) electrodes were fabricated from powdered polyphenylene synthesized from benzene with an $\text{AlCl}_3/\text{CuCl}_2$ catalyst in accordance with the method of Kovacic (12). These electrodes were composed of 80 weight percent (w/o) PPP, 10 w/o carbon black (Shawinigan Black®), and 10 w/o poly(ethylene-chlorotrifluoroethylene) (Halar®). They were compressed and cured at 175°C. Such PPP electrodes were typically 0.025 cm thick and had a density of ca. 0.9 g/cm³.

Results

Compatibility of electrolyte with highly reduced polymer.—The problem with the electrolytes used previously (5) is illustrated in Fig. 1, which shows the reduction (Li^+ insertion) of polyacetylene in an electrolyte solution composed of 1M LiClO_4 in THF. The discharge curve shows a reversible portion for a reduction level of ca. 8% ($y = 0.08$), followed by a large irreversible decomposition of the electrolyte (presumably ClO_4^-) between 0.6 and 0.5V vs. Li/Li^+ on the 8% reduced polyacetylene substrate. The flat (irreversible) portion of the curve was terminated after a fixed amount of charge had passed. The system would not reach an equilibrium at 0.5V vs. Li/Li^+ . The charging of the cell (Li^+ extraction) reoxidized the original 8% reduced polymer. This cycle, as depicted in Fig. 1, was repeated several more times. It exhibited identical behavior each time. Therefore, no significant part of the irreversible portion of the reduction curve involved a degradation of the polyacetylene itself. Any such degradation would have increased the cell resistance and/or decreased the capacity with cycling. The 8% reduced polyacetylene, $[(\text{CH})^{-0.08}\text{Li}_{0.08}]_x$, evidently serves as a catalytic substrate for the reduction of ClO_4^- dissolved in THF. As long as the voltage is maintained above 0.6V, the coulombic efficiency of the reduction and reoxidation process is essentially 100% (3).

At this point, the failure of previous attempts to obtain high reduction levels electrochemically can be associated with the failure of the electrolyte used, LiClO_4 in THF. Other Lewis acid salts were also investigated. Results are summarized in the upper portion of Table I. In this table, "minimum stable voltage" refers to the lowest voltage with respect to an M/M^+ reference where an equilibrium could be obtained. A typical cycle from neutral polyacetylene (at ca. 2.0V vs. M/M^+) to the minimum potential and back over a 10-30h period could be accomplished in each case with at least 95% coulombic efficiency. These criteria determine the definition of the term stability as employed in Table I. As an added caution, the reader should note that less or more rigorous purification procedures may influence the results of Table I. There can also be a solvent dependence to the stability ranges given. For all cases presented in the table, there was no evidence for the

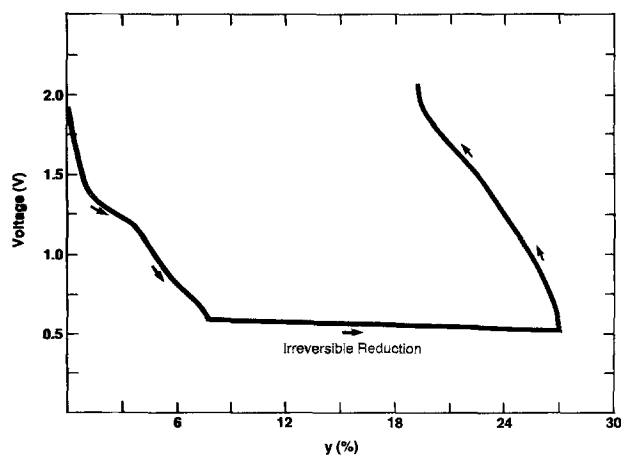


Fig. 1. Reduction of a polyacetylene film in an electrolyte of 1M LiClO_4 in THF. Irreversible reduction of the electrolyte occurs on the partially reduced polyacetylene, $[(\text{CHLi})_y]_x$, when $y > 0.08$.

Table I. Cathodic stability of electrolytes against reduced polyacetylene

Salt, solvent	Minimum stable voltage vs. M/M^+	Maximum reversible y value in CHM _x
LiClO_4 , THF	0.6	0.08
LiCF_3SO_3 , THF	0.6	0.08
LiAsF_6 , THF	1.7	0
LiB_4 , THF	1.3	0.02
LiPF_6 , THF	0.2	0.14
LiBMe_4 , THF	0.07	0.19
NaBET_4 , 2-MTHF	0.0	0.15
KBu_3Py , 2-MTHF	0.1	0.17

Me = Methyl; Et = Ethyl; Bu = Butyl; Py = Pyrrolyl.

formation of any protective (passivating) film on the polyacetylene. We have observed, however, that some solvents can react with the surface of reduced polyacetylene to produce a protective interface which limits further decomposition of either salt or solvent (13). Of all the Lewis acid salts studied here, LiPF_6 exhibits the best performance and LiAsF_6 the worst. Interestingly, this order of performance is the reverse of that observed for the plating and stripping of lithium metal from ether solutions of LiPF_6 (14) and LiAsF_6 (15). The difference between polyacetylene and lithium metal lies with the importance of the formation of a passivating film (or solid electrolyte interface) in the latter case.

In addition to lithium hexafluorophosphate, we have found that various organoborate salts possess even greater cathodic stability against reduced polyacetylene and polyphenylene. As can be seen in Table I and Fig. 2, we have been able to approximately double the previously reported (5) reversible doping levels by going to a more cathodic potential (*i.e.*, to 0.15V vs. Li/Li^+ in Fig. 2) in an electrolyte solution of 1.5M LiBMe_4 in THF. Maximum reduction levels obtained with other alkali-metal counterions (Na^+ and K^+) are comparable as can be seen in Fig. 3 and 4. The maximum electrochemically reversible reduction level for polyacetylene is obtained with lithium counterions in THF and is approximately $y = 0.18 \pm 0.01$. This value is supported by our electrochemical data and by elemental analysis of samples chemically doped with lithium. The remaining discrepancy with the literature (5) probably results from solvent coinsertion, which will raise the apparent lithium content as determined by weight increase. The maximum charge storage capacity of reduced polyacetylene is then 0.34 Ah/g (including the weight of Li^+ but not the weight of coinserted solvent).

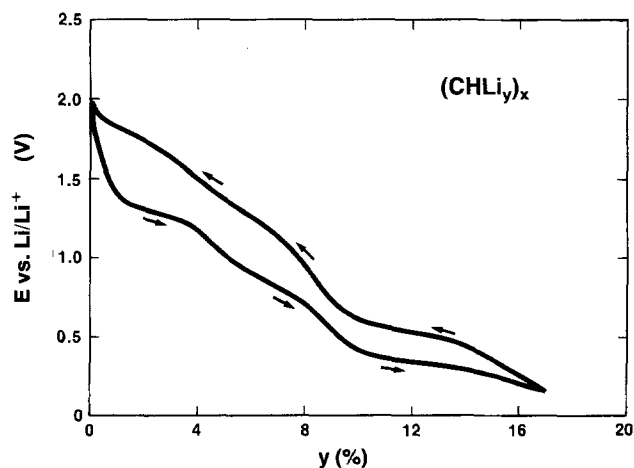


Fig. 2. Lithium ion insertion and extraction in polyacetylene, $[(\text{CHLi})_y]_x$, with an electrolyte of lithium tetramethylborate in THF. The curve shown represents the open-circuit potential after a 1 min wait during the third cycle by the incremental-voltage-step (IVS) method.

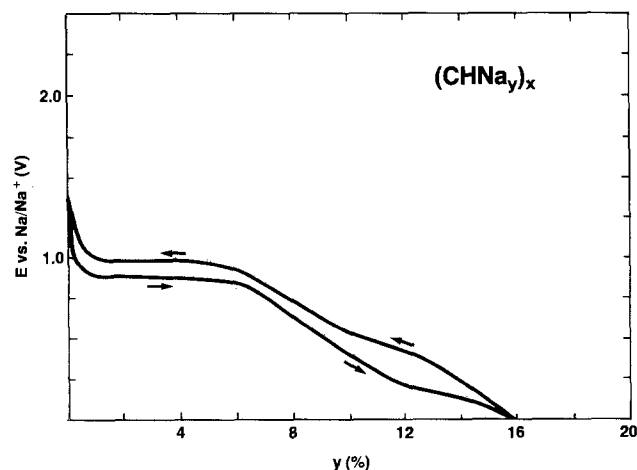


Fig. 3. Sodium ion insertion and extraction in polyacetylene, $[\text{CHNa}_y]_x$, with an electrolyte of sodium tetraethylborate in 2-MTHF. Curve represents the open-circuit potential taken by the IVS method (10 mV steps at a minimum current of $25 \mu\text{A}/\text{cm}^2$).

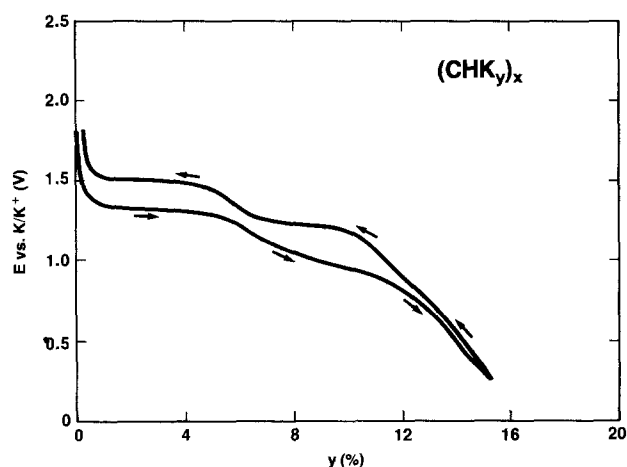


Fig. 4. Potassium ion insertion and extraction in polyacetylene, $[\text{CHK}_y]_x$, with an electrolyte of potassium tributyl (N-pyrrolyl)borate in 2-MTHF. Curves represent open-circuit potential after a 1 min wait during the third cycle with the IVS method (25 mV steps at a minimum current of $25 \mu\text{A}/\text{cm}^2$).

Solvent coinserction.—The weak van der Waals forces which bind polymer chains together also readily allow the coinserction of solvent. Clearly, the charged polymer itself will act to some degree in “solvating” the inserted cation; however, the structural constraints imposed on the polymer may prevent it from achieving a coordination with the cation which has minimum energy. In this latter case, solvation of the inserted cation may be partially accomplished by coinsercted solvent. One expects that solvent coinserction will be the most pronounced for small cations which are the most strongly solvated. The solvating power of the solvent is also important. In this regard, Gutmann (16) has developed the concept of donor number (DN), which may be measured for a given solvent. For our purposes, the magnitude of DN gives an empirical measure of the tendency of the solvent to donate electrons (Lewis base) and hence a qualitative measure for the solvation energy of cations in that solvent. Solvents with high donor numbers will tend to be more readily coinsercted into our polymers. The size and structure of the solvent is also important. For example, tetrahydrofuran (THF) and glyme (DME) have the same relatively high donor number (DN = 20) (16), but the size and bidentate nature of DME allow it to more strongly solvate larger cations such as Na^+ and K^+ .

We have observed that the coinserction of solvent is accompanied by significant changes in the shape of the voltage vs. reduction level curves. Note the marked differ-

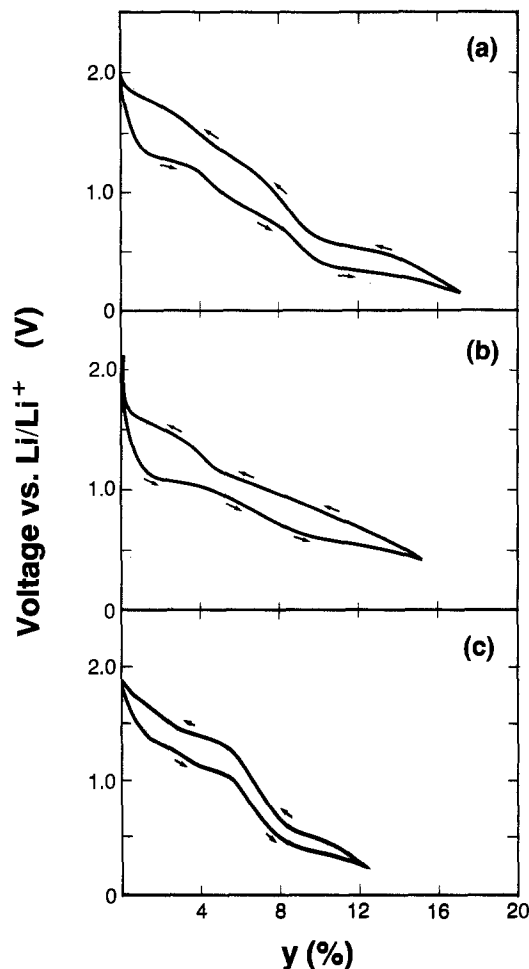


Fig. 5. Comparison of the behavior of polyacetylene during lithium ion insertion and extraction performed in three different solvents: (a) 1M LiBMe_4 in THF, (b) LiBBu_4 in 2-MTHF, and (c) LiBBu_4 in MTFE. Curves were taken with the IVS technique.

ences in the curves presented in Fig. 5 for the solvents tetrahydrofuran (THF), 2-methyltetrahydrofuran (2-MTHF), and methyl tetrahydrofurfuryl ether (MTFE). The potential variation in each solvent is characterized by three plateaus; however, the voltage and extent of each plateau is markedly different. These differences are presumably brought about by the different size and solvating power of each solvent molecule. Other workers (17) have previously shown that THF is reversibly incorporated into lithium-doped polyacetylene by alternate exposure to THF vapor and vacuum.

In this work, we attempted to make a rough quantitative estimate of the solvent coinserction effect during Li^+ ion insertion in polyacetylene by performing a chemical doping experiment in 2-MTHF. We employed lithium biphenyl as the doping agent in order to obtain a very high reduction level of the PA.

Table II gives the history of one sample that was doped, evacuated for 2h at 25°C , and then evacuated for 16h at 60°C .

Electrochemical undoping of half of the PA after the final annealing under vacuum at 60°C determined the doping level to be $y = 0.168$. Elemental analysis of the

Table II. Solvent coinserction in $(\text{CHLi}_y)_x$.

Procedure	Conductivity (S/cm)	Molecules of 2-MTHF/ Li^+
Dynamic vacuum 2h, 25°C	51	0.23
Dynamic vacuum 16h, 60°C	59	0

other half of the sample after this final anneal gave a doping level of $y = 0.177$ and no evidence for incorporated solvent. Solvent content after 2h evacuation at room temperature was calculated from the weight difference between the two entries in the table. This evacuation at 25°C was performed to remove any solvent which might have been simply adsorbed on the surface of the PA or trapped in its pores. Since this procedure might also have removed some of the coinserted solvent as well, the value of 0.23 molecules of 2-MTHF per Li^+ should be considered a lower limit. Similar experiments which were performed with K^+ insertion in 2-MTHF indicated minimal solvent coinsertion with this larger counterion.

The role of structure.—Solvent coinsertion in these polymers is controlled by a complex interplay of electrochemical and structural effects. At this point, we need to enlarge our discussion by considering in more detail certain structural aspects of PA and PPP. In all cases in Fig. 2, 3, and 4, one or more plateaus are evident in the voltage vs. percent reduction curves. The first major plateau (highest voltage) ends in the range 4-6% reduction for all cations, and the second major plateau ends in the range 12-16%. These features may reflect a maximum in the electronic density of states of the polymer, but are more likely to have a structural origin. Sharp plateaus in voltage vs. composition curves are normally indicative of multiphase structural effects as seen in the electrochemical intercalation of graphite (18, 19), TiS_2 (20), and WO_2 (21). For instance, in the electrochemical intercalation of graphite with Me_4N^+ ions (19), a series of plateaus is observed, corresponding to various discrete stoichiometric phases [in particular, $\text{C}_{48}(\text{Me}_4\text{N})$ and $\text{C}_{24}(\text{Me}_4\text{N})$].

Structural modification in crystalline polymers upon ion insertion is expected to be a complex function of ion size and shape. Both polyacetylene and polyphenylene are crystalline polymers which possess similar packing arrangements when in their neutral (undoped) state (22). When inserted with certain cations or anions, these polymers again form crystalline complexes. Since the polymer chains are only weakly bonded to each other, the polymer chains readily reorganize to accommodate the inserted counterion. In general, different crystalline structures appear for different counterions. The particular new structures arising from charge-transfer complex formation are known in some detail only for alkali-metal-doped polyacetylene (23), although staged structures have been found for iodine-doped polyacetylene (24). In the case of polyacetylene heavily doped with an alkali-metal, a channel-like structure is formed in which alkali-metal atoms are inserted into channels formed by four polyacetylene chains (left side of Fig. 6). This tetragonal structure has been identified for polyacetylene chemically doped to saturation with the alkali metals: Na, K, Rb, and Cs (23). The structure is flexible in that the interchain distance expands to accommodate the larger ions, Rb^+ and Cs^+ . The plateaus observed at low levels of reduction

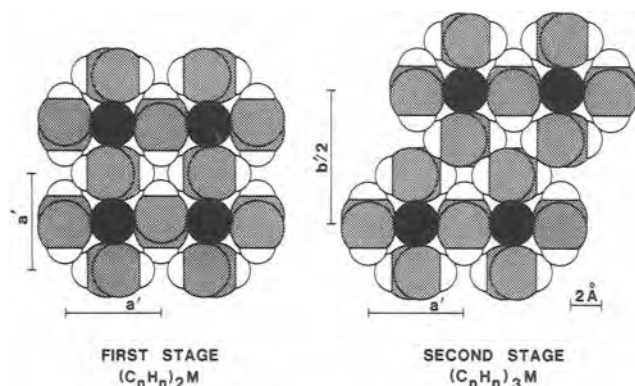


Fig. 6. Proposed first-stage structure, where a' (calc) = 6.04 Å and a' (obs) = 5.98 Å, and second-stage structure, where $b'/2$ (calc) = 8.18 Å and $b'/2$ (obs) = 8.20 Å. View is along the chain direction. K^+ ions (black circles) are arranged in columns.

($y \sim 0.05$) in Fig 2, 3, 4 are indicative of different "higher-stage" structures for these more dilute compositions. A more detailed description of the structure of these different phases based on electrochemical and x-ray diffraction data has been presented elsewhere (25, 26). This study was primarily devoted to the structure of potassium-doped polyacetylene and poly(p-phenylene), since these complexes are the most crystalline and since solvent coinsertion does not occur when either THF or 2-MTHF are used. Polyacetylene film was electrochemically reduced in an electrolyte of $\text{KBBu}_3\text{Py}/\text{THF}$ and samples were removed for x-ray analysis at compositions near $y = 0.06, 0.12,$ and 0.16 . (Electrical conductivities were 170, 220, and 260 S/cm, respectively.) The x-ray data suggest that the organization of K^+ ions in columns is preserved in the more dilute compositions. However, the spacing of ions within columns and the number of chains per column are variable.

At the highest doping levels obtained, the "first-stage" structure of Ref. (23) is observed where the ratio of PA chains to columns of K^+ ions is 2 (Fig. 6). Meridional x-ray data suggest a separation around 3.7 Å between K^+ ions in a given column. Such a spacing leads to a commensurate arrangement of ions along a given polymer chain, as shown in Fig. 7. Since there are three CH units per ion and two chains per ion column in this phase, we denote this composition by $(\text{C}_3\text{H}_3)_2\text{K}$, i.e., $y = 0.167$. Various possible phases are plotted in Fig. 8 according to their particular composition. X-ray data from samples taken at the end of the first plateau ($y = 0.06$) exhibit a long spacing of ca. 8.2 Å, which supports the "second-stage" structure of Fig. 6 where there are three polymer chains per ion column. Other higher-stage compounds are likely to be identified by further study since preliminary evidence suggests a longer spacing (11.7 Å) for samples taken near 5% reduction. Samples taken at $y = 0.12, 0.15,$ or 0.16 all exhibit a long spacing of 6.0 Å and other shorter spacings characteristic of the first-stage structure of Fig. 6. The samples near 16% reduction also exhibit a meridional line corresponding to a 3.72 Å spacing between K^+ ions. As mentioned above, this spacing leads to a theoretical composition of 16.7% for the crystalline regions observable by x-ray diffraction. Amorphous regions of the sample may be doped to a lesser degree.

Electrochemical reversibility.—Another general feature of the electrochemical behavior of polyacetylene which suggests structural transformations over the plateau re-

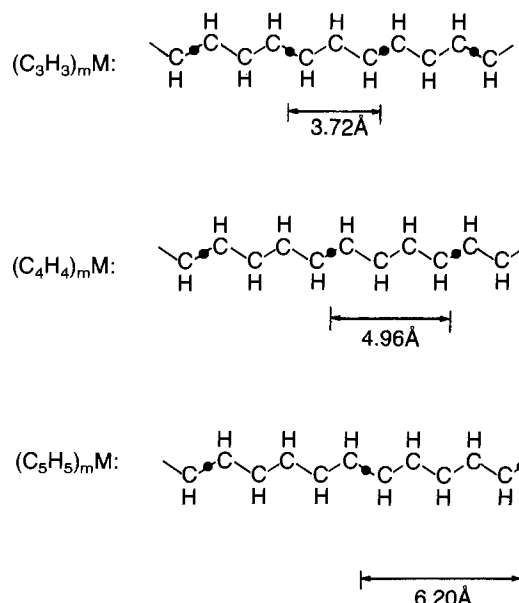


Fig. 7. Possible commensurate phases of reduced polyacetylene. Black dots show the positions of K^+ ions in a given ion column in relation to one of four neighboring PA chains. The spacing of 3.72 Å has been observed for heavily reduced PA.

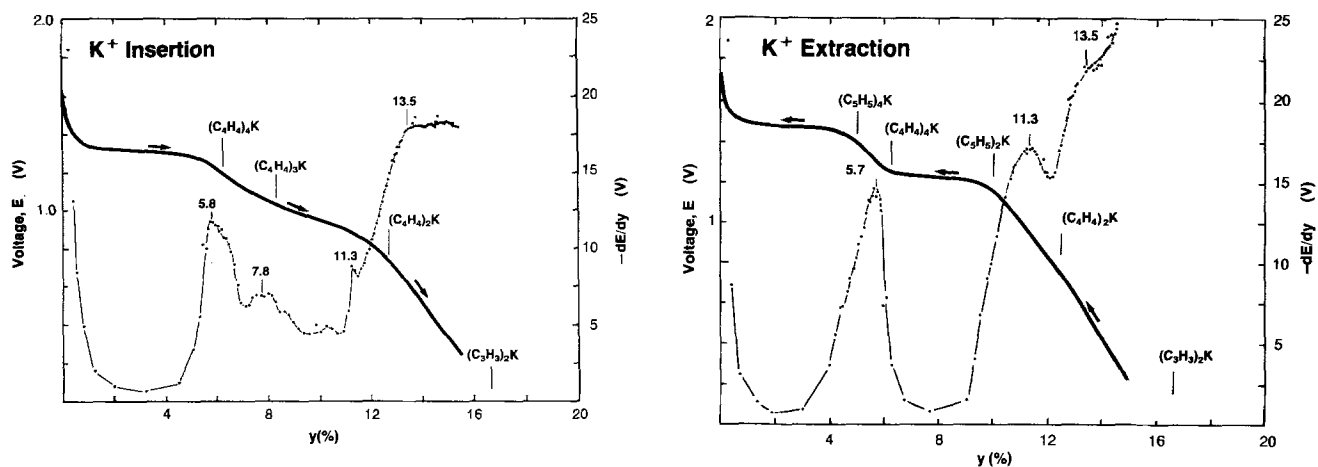


Fig. 8. Immediate open-circuit voltage (solid curve) and its derivative (broken curve) are plotted for K⁺ insertion (a, left) and extraction (b, right). Maxima in $-dE/dy$ indicate probable transition points between the growing of one phase and the next. Possible stoichiometric compositions are also plotted according to their predicted y value.

gions is the appearance of hysteresis in the discharge (ion-insertion) and charge (ion-extraction) curves (Fig. 2, 3, and 4). The disproportionation into two or more separate phases involves first-order phase transformations which proceed with appreciable kinetics only when the reaction takes place some distance from the critical point. Thus, some degree of hysteresis is expected for all systems involving multiple structurally different phases. Hysteresis is best seen with voltammetry measurements. Such measurements are difficult to perform by conventional means on thick nonswollen electrodes. Fortunately, Thompson (9) has developed a stepped-potential technique, called electrochemical potential spectroscopy (ECPS), which is equivalent to linear sweep voltammetry (LSV) at nearly infinitesimal effective sweep rate. Exam-

ples of such scans presented in Fig. 9 and 10 were obtained for Na⁺ and K⁺ insertion (cathodic sweep) and extraction (anodic sweep). Peaks in these voltammograms correspond to the voltages at which plateaus appear in Fig. 3 and 4. In order to have a one-to-one correspondence with LSV, each voltage step should be made at equal time intervals. Then dV/dt is constant for each step and dQ/dV will then be directly proportional to average current per step. In the present case, however, the current was allowed to decay to a fixed low value ($25 \mu A/cm^2$) followed by an open-circuit stand of 1 min; hence, the system was allowed to nearly approach equilibrium at the end of each step rather than being continually perturbed from equilibrium by the imposition of a constant sweep rate. However, very similar curves are in fact obtainable by traditional LSV provided relatively thin films ($< 75 \mu m$) and slow scan rates (0.1 mV/s) are employed (27).

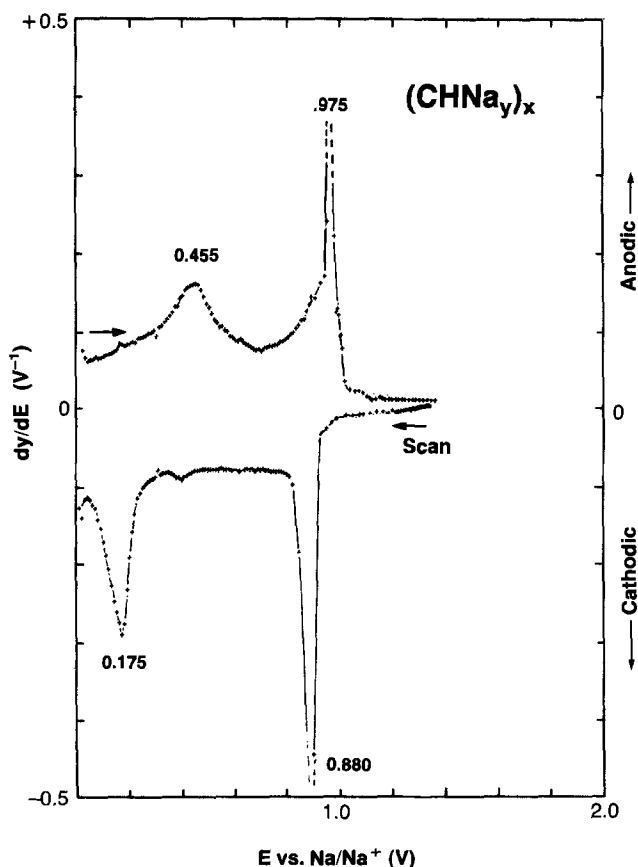


Fig. 9. ECPS data for $[CHNa_y]_x$ in an electrolyte of 1M NaBEt₄ in 2-MTHF. The cathodic sweep corresponds to Na⁺ insertion, the anodic sweep to Na⁺ extraction.

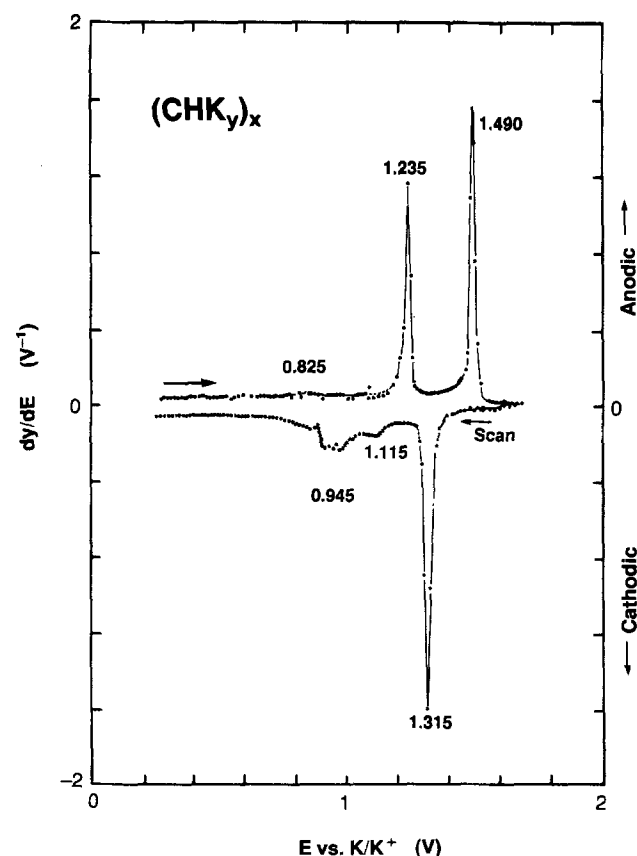


Fig. 10. ECPS data for $[CHK_y]_x$ in an electrolyte of 1M KBBu₃Py in 2-MTHF.

The curves of Fig. 9 and 10 show that ion insertion in PA is not a simple reversible process. Particularly with K^+ ion insertion and extraction, the cathodic and anodic peaks are not well matched. By scanning only in the range 1-1.8V vs. K/K^+ , it can be shown that the reduction at 1.32V is reoxidized at 1.49V. The other two reduction peaks at 1.12 and 0.95V are associated with the reoxidation at 1.24V. Thus, there is not only considerable inherent hysteresis, but also clear evidence for a different sequence of reactions upon ion insertion than appears on ion extraction. This difference is not likely to be the result of solvent coinsertion, since we have observed no tendency for 2-MTHF to be coinserted with K^+ . The explanation lies at least partly with the structural evolution of the polymer during ion insertion and extraction. Figure 8 suggests that the sequence of phases obtained during insertion may be different from that during extraction. This different sequence may be caused by kinetic limitations on transformation from one phase to another. Even though the scan rate is effectively very low, the structural evolution of the sample will tend to proceed along a kinetically favored path. In particular, long spacings between K^+ ions in a given channel [e.g., with $(C_6H_5)_2K$] are most likely to be observed during ion extraction from already established channels. Likewise, one expects that compression into established channels will be kinetically favored over the creation of new channels during ion insertion. Such different pathways on insertion and extraction will cause a large part of the differences observed between cathodic and anodic waves in Fig. 9 and 10. Note that in Fig. 4 there is very little hysteresis in the region above 12% reduction, where x-ray studies indicate that a single structure ("first stage" in Fig. 6) persists over the entire composition range from 12 to 17%. The voltage over this range is rapidly varying because changes in y result in continuous changes in the actual degree of reduction of each chain rather than the growth of a new phase at the expense of an old. The latter process (nucleation and growth) results in a discontinuous change in y and an abrupt change in voltage to a new level, which remains nearly constant while the new phase grows. Other possible influences on hysteresis and reversibility include (i) geometrical relaxation of polymer chains subsequent to insertion (e.g., approach to equalization of bond lengths), (ii) initial insertion of anions rather than removal of cations during reoxidation [the reverse process having been observed for oxidized polypyrrole by microgravimetric measurements (28), and (iii) solvent coinsertion (largely discounted for Na^+ and larger cation insertion with the use of 2-MTHF, but of significant importance with Li^+ or with strongly solvating solvents such as diglyme and DMSO).

Poly(p-phenylene) structure and electrochemistry.—Reduced poly(p-phenylene) also displays many of the characteristics observed with polyacetylene, although reduction takes place at generally lower potentials ($\leq 1V$ vs. Li/Li^+). Reduction of PPP with Li^+ counterions (and with K^+ , not shown) exhibits a series of weak plateaus which are indicative of multiple phases as with PA (Fig. 11). With PPP, both chemical and electrochemical doping techniques give rise to the same approximate limiting reduction level: $y = 0.50$ in Eq. [1] where P is $-C_6H_4-$. The maximum reduction level achieved electrochemically with the use of alkali-metal organoborate salts in an ether is approximately 0.45 for Li^+ , K^+ , and Na^+ (Fig. 12). Thus, the maximum charge storage capacity with Li^+ is 0.15 Ah/g (including weight of Li^+).

As mentioned above, the packing arrangement of pristine polyphenylene is very similar to that of polyacetylene. Likewise, PPP also forms crystalline complexes when inserted by alkali-metal counterions. X-ray diffraction studies on heavily reduced PPP suggest the structure illustrated in Fig. 13, where again alkali-metal atoms are arranged in columns with each column being associated with two polyphenylene chains. If one assumes a commensurate arrangement of ions along each chain (a spacing of K^+ ions in each column matching that of

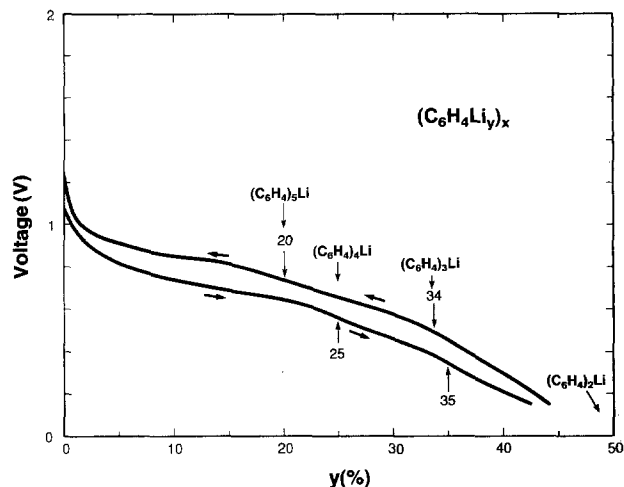


Fig. 11. Li^+ insertion and extraction in poly(p-phenylene), $[C_6H_4Li_y]_{r,r}$, using an electrolyte of lithium tetraphenylborate in THF.

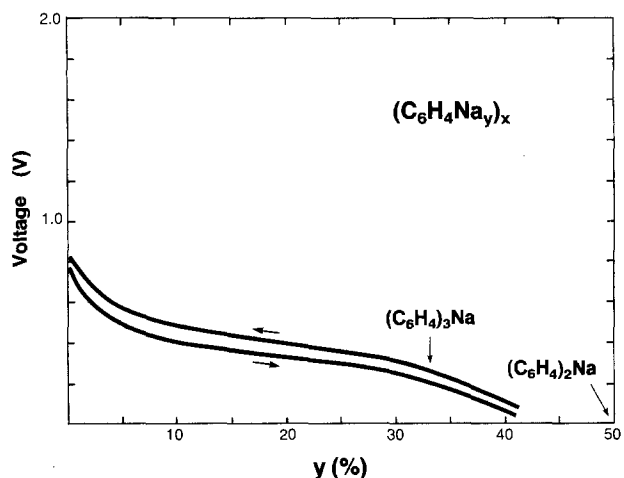


Fig. 12. Na^+ insertion and extraction in poly(p-phenylene), $[C_6H_4Na_y]_{r,r}$, using an electrolyte of sodium tetraphenylborate in THF.

phenyl rings, 4.35Å), then a series of phases may be postulated as described in Table III, where the observed number of chains per column varies from two to four. As this ratio increases, planes containing K^+ columns are presu-

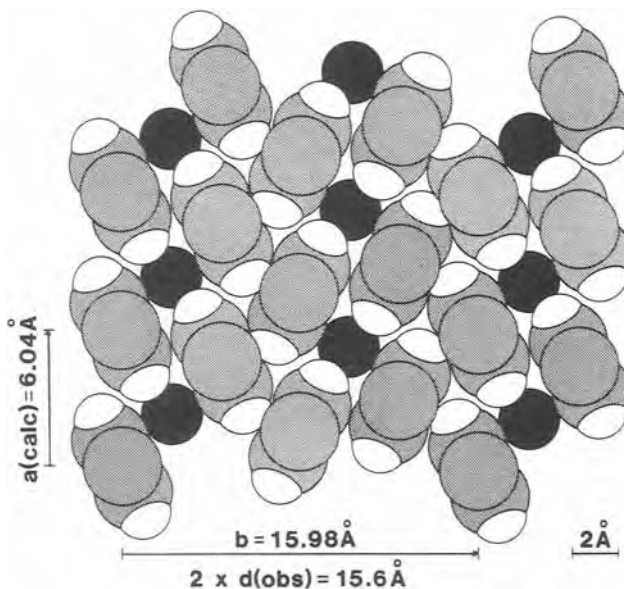


Fig. 13. Proposed structure for PPP inserted by K^+ ions (black circles) to the maximum composition, $y = 0.50$. View is along chain direction. Spacing of ions within each column is assumed to be 4.35Å.

Table III. Possible commensurate phases for alkali-metal-doped poly(p-phenylene)

	Value of y from theory	Value of y from Li ⁺ insertion	Value of y from Li extraction	Value of y from K ⁺ insertion
(C ₆ H ₄) ₁ M	(1.00)		Not observed	
(C ₆ H ₄) ₂ M	0.50	0.48	0.48	0.50
(C ₆ H ₄) ₃ M	0.33	0.35	0.34	0.37
(C ₆ H ₄) ₄ M	0.25	0.25	0.20	0.25

(C₆H₄)_mM denotes m polymer chains per alkali-metal column.

ably separated by increasing numbers of planes containing only PPP chains. Table III illustrates the excellent agreement between the compositions predicted by this model and the inflection points observed for Li⁺ and K⁺ insertion in PPP (25, 26).

Thus as with PA, structural changes during reduction influence electrochemical behavior. PPP, however, does not exhibit plateaus so pronounced as those observed for PA. Hysteresis between insertion and extraction is also significantly less. In addition, although we have not studied it directly, solvent coininsertion does not appear to play as much of a role with PPP, since all three counterions (Li⁺, Na⁺, K⁺) give nearly identical behavior. As we have seen, the behavior of PA with Li⁺ is generally different from its behavior with Na⁺ and K⁺ and is strongly solvent dependent (Fig. 5).

Conclusions

Polyacetylene and polyphenylene have been shown to have competitively high gravimetric charge storage capacity (0.34 Ah/g for PA, 0.15 Ah/g for PPP) when compared with other ion insertion anode materials (e.g., 0.12 Ah/g for Li_xWO₃, 0 < x < 1). Less competitive volumetric charge storage capacities, however, still pose challenges for the practical realization of nonaqueous batteries with electroactive polymeric anodes.

Our electrochemical and x-ray diffraction data demonstrate that alkali-metal insertion in PA and PPP proceeds at least in part via a sequence of stoichiometric phases. The discontinuous transformation from one phase to the next causes the appearance of plateaus in potential vs. composition curves obtained during ion insertion or extraction. Such a process will lead to the nucleation and growth of particular stoichiometric phases and not to a homogeneous distribution of dopant. In other regimes, where plateaus are not evident, continuous evolution of nonstoichiometric phases is suggested.

Since transformations between phases dominate the electrochemistry of reduced polyacetylene and poly(p-phenylene), reduction of these polymers does not proceed by a simple reversible process, although the coulombic efficiency of reduction and reoxidation cycles approaches 100%.

Acknowledgment

We are pleased to thank Dr. J. F. Wolf for the synthesis of various organoborate salts.

Manuscript received Nov. 23, 1984. This was Paper 619 presented at the New Orleans, Louisiana, Meeting of the Society, Oct. 7-12, 1984.

Allied Corporation assisted in meeting the publication costs of this article.

REFERENCES

- D. MacInnes, Jr., M. A. Druy, P. A. Nigrey, D. P. Nairns, A. G. MacDiarmid, and A. J. Heeger, *J. Chem. Soc., Chem. Commun.*, 317 (1981).
- L. W. Shacklette, R. L. Elsenbaumer, R. R. Chance, J. M. Sowa, D. M. Ivory, G. G. Miller, and R. H. Baughman, *ibid.*, 361 (1982).
- L. W. Shacklette, R. L. Elsenbaumer, and R. H. Baughman, *J. Phys. C*, **44**, 559 (1983).
- G. C. Farrington, B. Scrosati, D. Frydrych, and J. Denuzzio, *This Journal*, **131**, 7 (1984).
- A. G. MacDiarmid and A. J. Heeger, *Synth. Met.*, **1**, 101 (1979/80).
- R. B. Kaner and A. G. MacDiarmid, *J. R. Soc. Chem., Faraday Trans 1*, **80**, 2109 (1984).
- L. P. Klemann and G. H. Newman, U.S. Pat. 4,060,674 (1977).
- T. A. Whitney and L. P. Klemann, U.S. Pat. 4,104,450 (1978); G. H. Newman and L. P. Klemann, *This Journal*, **127**, 2097 (1980).
- A. H. Thompson, *Rev. Sci. Instrum.*, **54**, 229 (1983).
- H. Shirakawa and S. Ikeda, *Polym. J.*, **2**, 3 (1971); T. Ito, H. Shirakawa, and S. Ikeda, *J. Polym. Sci. Lett., Polym. Chem. Ed.*, **12**, 11 (1974).
- H. Eckhardt and S. W. Steinhäuser, *Mol. Cryst. Liq. Cryst.*, **105**, 219 (1984).
- P. Kovacic and J. Oziomek, *J. Org. Chem.*, **29**, 100 (1964).
- M. Maxfield, L. W. Shacklette, J. F. Wolf, and S. M. Savner, U.S. Pat. 4,472,489 (1984); M. Maxfield, G. G. Miller, R. H. Baughman, and J. E. Frommer, U.S. Pat. 4,472,487 (1984).
- G. H. Newman, in "Lithium Nonaqueous Battery Electrochemistry" E. B. Yeager, B. Schumm, Jr., G. Blomgren, D. R. Blankenship, V. Leger, and J. Akridge, Editors, p. 149, The Electrochemical Society Softbound Proceedings Series, Pennington, NJ (1981).
- K. M. Abraham, J. L. Goldman, and D. L. Natwig, *This Journal*, **129**, 2404 (1982).
- V. Gutmann, "Donor-Acceptor Approach to Molecular Interactions," Plenum Press, New York (1978); U. Mayer, in "Lithium Nonaqueous Battery Electrochemistry," E. B. Yeager, B. Schumm, G. Blomgren, D. R. Blankenship, V. Leger, and J. Akridge, Editors, pp. 13-33, The Electrochemical Society Softbound Proceedings Series, Princeton, NJ (1980).
- B. Francois and C. Mathis, *J. Phys. C*, **44**, 21 (1983).
- M. Armand and P. Touzain, *Mater. Sci. Eng.*, **31**, 319 (1977).
- J. O. Besenhard and H. P. Fritz, *J. Electroanal. Chem. Interfacial Electrochem.*, **53**, 329 (1974).
- M. S. Whittingham, *Prog. Solid State Chem.*, **12**, 41 (1978), and references therein.
- D. W. Murphy, F. J. Di Salvo, J. N. Carides, and J. V. Waszczak, *Mater. Res. Bull.*, **13**, 1395 (1978).
- L. W. Shacklette, R. R. Chance, D. M. Ivory, G. G. Miller, and R. H. Baughman, *Synth. Met.*, **1**, 307 (1979).
- R. H. Baughman, N. S. Murthy, and G. G. Miller, *J. Chem. Phys.*, **79**, 515 (1983).
- R. H. Baughman, N. S. Murthy, G. G. Miller, and L. W. Shacklette, *J. Chem. Phys.*, **80**, 1065 (1983).
- L. W. Shacklette, N. S. Murthy, and R. H. Baughman, *Molec. Cryst. Liq. Cryst.*, **121**, 201 (1985).
- R. H. Baughman, L. W. Shacklette, N. S. Murthy, G. G. Miller, and R. L. Elsenbaumer, *ibid.*, **118**, 253 (1985).
- T. R. Jow, L. W. Shacklette, and D. Vernick, Unpublished.
- J. H. Kaufman, G. B. Street, and J. C. Scott, *Molec. Cryst. Liq. Cryst.*, To be published.

Optimization of Carbon Cathodes for Li/SO₂Cl₂ Cells

Charles W. Walker, Jr., Michael Binder,* William L. Wade, Jr., and Sol Gilman*

US Army ERADCOM, Power Sources Division, Fort Monmouth, New Jersey 07703-5302

ABSTRACT

Five carbon blacks were evaluated for use as cathode materials in lithium-sulfuryl chloride half-cells. The best overall performance at high discharge rates was obtained with Cabot's CSX-179B. Cathode load voltage and capacity were dramatically increased at 40 mA/cm² current density without resorting to catalysts or additives by chemically treating either Shawinigan acetylene black or CSX-179B powder with acetone prior to cathode fabrication.

The lithium sulfuryl chloride (Li/SO₂Cl₂) primary system employing LiAlCl₄ as conductive electrolyte salt and porous carbon black cathodes has recently evoked considerable interest (1-3) because of its high open-circuit voltage (3.91V). During cell discharge, the lithium anode is oxidized and liquid sulfuryl chloride is reduced at the carbon black cathode. The major conclusions from various studies indicated that the capacity (*i.e.*, life) of the oxyhalide cathodes is determined by the ability of the cathode to accommodate solid LiCl product formed during cell discharge. This is especially prevalent during discharge at high current rates and/or low temperature, where cathode surfaces facing the anode are blocked by deposited LiCl leading to inefficient cathode use. The search for new or improved high performance cathode materials is a major goal in most laboratories.

Although physical and chemical characterizations of carbon blacks, graphites, and activated carbons are known, many aspects of electrochemical interactions of surfaces are not sufficiently understood. Improvements in cathode performance such as increased cathode output voltage and specific cathode capacity are still results of trial and error techniques in cathode fabrication and preparation. Our aim was to increase rate capability and specific room temperature cathode capacity of high rate Li/SO₂Cl₂ cells.

Improved cathode performance is also important from a safety point of view, since, in cathode-limited cells, more efficient cathodes allow less unreacted lithium anode at end of discharge. This implication for greater safety is an important concern for a dense energy package; the energy density of lithium sulfuryl chloride cells (600 Wh/kg) approaches that of dynamite (920 Wh/kg). Although cathodes for lithium thionyl chloride cells formulated with Shawinigan acetylene carbon black (a relatively low surface area carbon black of 60 m²/g) achieve satisfactory performance (4), similarly constructed cathodes in lithium sulfuryl chloride cells produce reduced operating voltages and capacities (1). The explanation for this depends on the nature of sulfuryl chloride itself. Active carbon blacks catalytically induce a decomposition of sulfuryl chloride, SO₂Cl₂, to yield SO₂ and Cl₂, both of which are soluble in SO₂Cl₂. Molecular Cl₂ reduces at higher potentials than does SO₂Cl₂, thereby contributing to increased operating voltages. Gilman and Wade (1) evaluated a number of carbon blacks for use as cathodes in sulfuryl chloride cells and postulated that high surface area carbons increase the SO₂Cl₂ decomposition rate by providing absorption or reaction sites where parent SO₂Cl₂ molecules can absorb and subsequently decompose formation of an adequate supply of chlorine is necessary to maintain high cathode operating voltages.

Gilman and Wade (1) found that highest cathode capacity and operating voltages in lithium sulfuryl chloride cells discharged at medium current densities were obtained using United XC-6310, an experimental, high surface area (1000 m²/g) carbon black. However, the mixability and wettability of this high area carbon black with water are not particularly good; resulting porous cathodes tend to crack and crumble rather easily. Because of these problems, and the fact that United XC-6310

is no longer commercially available, state-of-the-art cathodes for sulfuryl chloride cells have continued to be constructed using lower surface area carbon blacks such as Shawinigan acetylene black.

The need to improve cathode performance in oxyhalide cells when using low surface area carbon blacks has led to a large number of innovative research efforts to consider whether incorporation of expensive additives, modification of TFE levels, or use of various added carbon blacks could improve cathode performance. Additives recently studied in sulfuryl chloride and thionyl chloride systems include Cl₂ (5), metal halides (6), copper metal (7), finely divided expensive precious metal catalysts such as platinum (8), addition of heterogenous and homogeneous macrocyclic electrocatalysts such as cobalt and iron phthalocyanines (9), and tetraazannulenes (10). Lithium anode stability and start-up is expected to be strongly affected by catalytic materials or additives dissolved within the oxyhalide electrolyte, and cathode improvements which do not rely upon external additives are favored.

We felt it was important to extend Gilman and Wade's comparison study to other carbon blacks in order to discover a reasonable substitute for United XC-6310 and also to understand how to improve performance of existing carbon blacks.

Experimental

The porous carbon cathodes were fabricated by slowly adding a 1:3 mixture of isopropyl alcohol:water to carbon black powder and mixing well until the carbon powder was adequately wetted. Typically, 100 cm³ of alcohol:water would wet 18g of carbon black. A 10% TFE-30:water emulsion (1:9 v/v) was slowly added (1 ml/g dry carbon) and mixed well until the resulting carbon paste took on a glossy shine. The resulting paste was spread into both sides of a nickel expanded metal screen and, while sandwiched between absorbing blotting paper, was rolled through a dough sheeter. The cathodes, sandwiched between two dry pieces of blotting paper, were then sandwiched between two flat steel plates, each weighing approximately 8 kg, and placed in a vacuum oven at 100°C for 1h. The cathodes were then removed and placed in an elevated drying oven at 280°C for 1h. Upon cooling, the cathodes were rolled to the desired thickness (1 mm) to give a relatively crack-free cathode surface. Cathodes were then cut to size, and nickel tabs were welded to the ends.

Final cathode dimensions were 0.5 cm on each side for a total geometric area (both sides) of 0.5 cm². Prepared cathode working electrodes were placed in glass half-cells with a large lithium counterelectrode and lithium reference and flooded with excess 1.5M LiAlCl₄-SO₂Cl₂ electrolyte. Our half-cells were clearly cathode limited. Individual cathodes were discharged at constant current and the voltage-time profile was monitored on a strip chart recorder.

Our pretreatment procedure for raw carbon blacks consisted of soaking the carbon black powder in an excess of acetone at room temperature, filtering, washing three times with deionized water, filtering again, and drying overnight at 140°C. We also attempted to oxidize the surface groups of Shawinigan acetylene black by following

* Electrochemical Society Active Member.

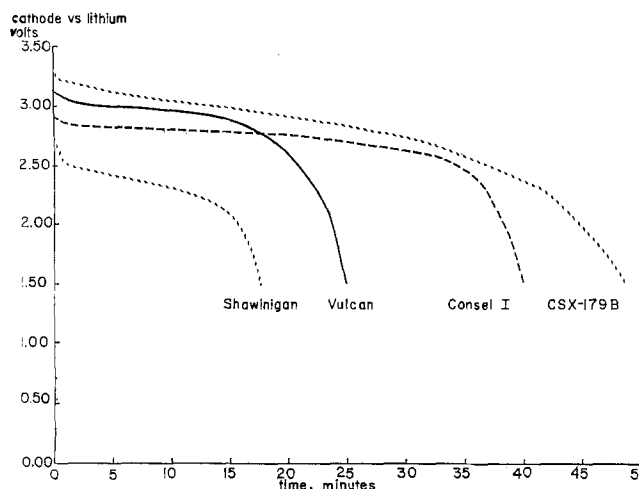


Fig. 1. $\text{Li}/\text{SO}_2\text{Cl}_2$ half-cell capacity curves at $40 \text{ mA}/\text{cm}^2$ constant current discharge for cathodes constructed with various carbon blacks.

an alkaline permanganate oxidation procedure. Approximately 2g of dry acetone treated carbon black was placed in 250 ml of 5% KMnO_4 solution containing 50 ml of 25% KOH solution and allowed to react at 50°C for approximately 1.5h. The carbon was filtered and rinsed with 5% oxalic acid solution and excess distilled water; the carbon was then dried overnight at 140°C . Cathodes were prepared from these carbon blacks in the same manner as cathodes prepared from untreated carbons. The pH's of the carbon blacks were measured at room temperature with a standard combination electrode immersed in enough water to make an aqueous slurry from the various carbon blacks and boiled deionized water.

Results and Discussion

Figure 1 shows typical discharge curves at $40 \text{ mA}/\text{cm}^2$ of geometric cathode area for cathodes constructed with four commercially available carbon blacks and assembled as working electrodes in $\text{Li}/\text{SO}_2\text{Cl}_2$ half-cells. Highest operating voltages and longest operating cathode life (to 1.5V) were obtained with cathodes constructed with CSX-179B. Similar data (within experimental error) were obtained with the commercial product Black Pearls 2000.

Figure 2 compares cathodes constructed with CSX-179B and cathodes constructed with United XC-6310, under both 40 and $80 \text{ mA}/\text{cm}^2$ constant current discharge conditions. Although United XC-6310 has been shown to be the optimum carbon black for $\text{Li}/\text{SO}_2\text{Cl}_2$ cells (1), cathodes constructed from CSX-179B also yield comparable load voltages and capacities. At current drains of $80 \text{ mA}/\text{cm}^2$, cathodes constructed with CSX-179B have even higher operating voltages and capacities than cathodes made from United XC-6310.

Since it was not experimentally possible to maintain constant carbon loadings for the various carbon types, constant current discharge cathode capacities from Fig. 1 and 2 were normalized to both geometric cathode volume and grams of carbon in the cathode (Table I). Untreated CSX-179B and United XC-6310 cathodes yield comparable ampere-hours per gram of carbon, which are about

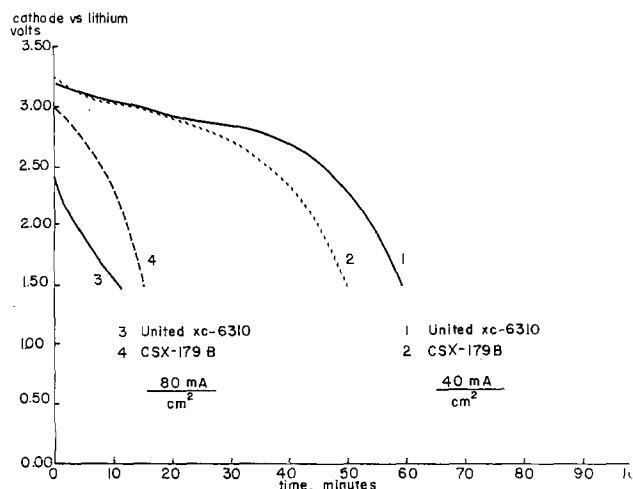


Fig. 2. $\text{Li}/\text{SO}_2\text{Cl}_2$ half-cell capacity curves at 40 and $80 \text{ mA}/\text{cm}^2$ constant current discharge for cathodes constructed with CSX-179B and United XC-6310 carbon black.

twice that of Consel I and about three times that of the commonly used Shawinigan acetylene black. This is an important result; it shows that judicious selection of carbon blacks for cathode applications can yield dramatic improvements in cathode performance without one's resorting to added catalysts or alternate electrolytes. Cathode capacities normalized to cathode volume show that cathodes constructed with CSX-179B yield comparable capacities to cathodes constructed with United XC-6310 and more than three times the capacity of cathodes constructed with Shawinigan acetylene black.

Since Shawinigan acetylene black is one of the most widely used carbon blacks in fabricating cathodes, we first studied effects of solvent pretreatment of Shawinigan acetylene black. Figure 3 shows cathode discharge performance curves for $\text{Li}/\text{SO}_2\text{Cl}_2$ half-cells whose Shawinigan acetylene black cathodes were prepared with acetone-treated carbon black. The dramatic improvement in cathode load voltage and the approximate doubling of cathode capacity are remarkable. Since high surface area carbon blacks should be more susceptible to pretreatment due to larger percentage of exposed surface area, we also compared cathode performance in cathodes prepared from pretreated CSX-179B carbon blacks. Figure 4 clearly shows that acetone treatment of CSX-179B dramatically improves cathode operating voltages and capacities.

In order fully to understand the reasons for dramatic cathode improvements upon acetone treatment, the following experimental avenues were used to explore treated and untreated base line carbon blacks.

Chemical analysis.—There is no clear change in concentration of free radicals present in the carbon black, since ESR spectra of these carbon powders show no difference between treated and untreated samples. Acetone treatment may, however, remove soluble organic impurities. The acetone rinse solution from CSX-179B showed a weak UV fluorescence in the 3900-3500Å region and implies that fluorescing impurities are removed.

Table I. Physical characteristics and cathode capacity for various carbon blacks

Carbon type	Manufacturer	pH	Surface area (m^2/g)	Capacity at $40 \text{ mA}/\text{cm}^2$ (Ah/cm^3)	Capacity at $40 \text{ mA}/\text{cm}^2$ ($\text{Ah}/\text{g carbon}$)
United XC-6310	United Carbon Co.	5.2	1000	0.82	2.27
Vulcan XC72R	Cabot Corp.	6.6	250	0.30	0.63
Consel I	Stonehart Assoc.	8.3	250	0.44	1.10
Shawinigan acetylene black	Gulf	5.2	53.6	0.25	0.73
Shawinigan acetylene black (acetone treated)		—	54.0	0.46	1.47
CSX-179B (Black Pearls 2000)	Cabot Corp.	7.4	1475	0.68	2.31
CSX-179B (Black Pearls 2000) (acetone treated)		4.5	—	0.93	2.94

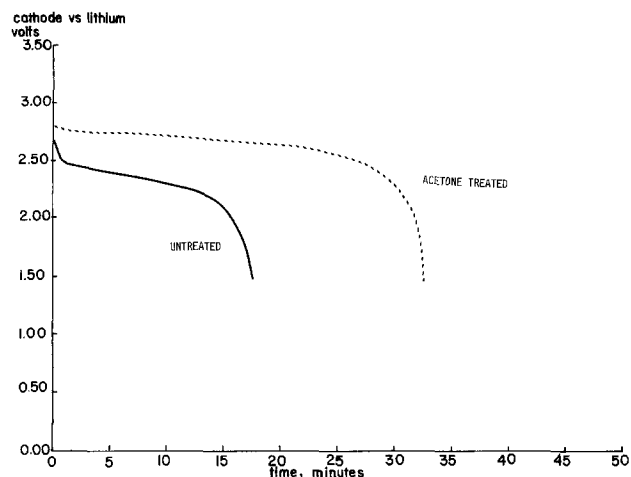


Fig. 3. $\text{Li}/\text{SO}_2\text{Cl}_2$ half-cell capacity curves at $40 \text{ mA}/\text{cm}^2$ constant current discharge for cathodes constructed with treated and base line Shawinigan acetylene black.

From the combined acetone-water rinse solution from CSX-179B, a white fluffy solid was isolated and qualitatively identified by chemical microprobe analysis as containing calcium and sulfur. These impurities could have originated in feedstock or quench water during the carbon manufacturing process, since typical ash analysis by Cabot Corporation shows 2000 ppm of calcium ash present in CSX-179B. No such solid was isolated from the combined acetone-water rinse solutions of Shawinigan acetylene black. Perhaps CSX-179B, because of its higher surface area, absorbs more impurities than does the lower surface-area Shawinigan acetylene black. Acetylene black may also contain fewer impurities. Although calcium impurities are not likely to be soluble in acetone, the acetone rinse may change the water wettability of the carbon black and allow the subsequent water rinse to remove these calcium-based impurities. Soluble calcium ions in the form $\text{Ca}(\text{AlCl}_4)_2$ have been shown to severely reduce cathode capacity and operating voltage in $\text{Li}/\text{LiAlCl}_4/\text{SO}_2\text{Cl}_2$ cells (11). The reason for this decrease is believed to be preferential formation of glassy CaCl_2 at the cathode surface rather than the normally produced crystalline LiCl . Precipitated, glassy CaCl_2 tends to block cathode pores more efficiently than does LiCl , and the pore blockage leads to rapid cathode concentration polarization (12). Since the acetone treatment removes calcium ash from the carbon black starting material, the cathode capacity increases.

It is interesting that, although in lithium battery manufacturing processes extensive care is usually taken in anode and electrolyte preparation, typically no purification

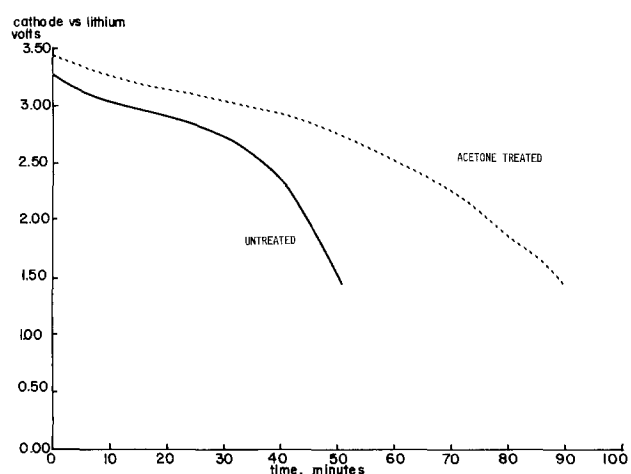


Fig. 4. $\text{Li}/\text{SO}_2\text{Cl}_2$ half-cell capacity curves at $40 \text{ mA}/\text{cm}^2$ constant current discharge for cathodes constructed with treated and base-line CSX-179B carbon blacks.

procedure as such is carried out for carbon black powders. In the strong oxidizing agents such as SO_2Cl_2 , even traces of impurities from carbon black can be readily oxidized and react with the anode. Removal of this impurity from the carbon blacks prior to cathode and cell assembly should diminish anode start-up problems as well.

Treated carbon blacks are expected to show cathode performance improvements primarily at high ($30 \text{ mA}/\text{cm}^2$) cathode discharge rates where electrochemical kinetics considerations and restrictions overshadow mass-transport limitations. Applications would include pulsed power applications where high load voltage and current density are primary considerations and cathode capacity is only of secondary importance.

Cathode capacity improvement at $34 \text{ mA}/\text{cm}^2$, after acetone rinsing, have been recently demonstrated in Li/SO_2 laboratory cells by Reddy and Thurston (14), who found up to 56% improvement in cathode capacity upon treatment of various carbon blends.

We attempted to increase the amount of oxygen containing functional chemical groups on the Shawinigan black carbon surface by using alkaline KMnO_4 as a chemical treatment. Cathode operating voltage and specific cathode capacity of the resulting cathodes were severely decreased. This perhaps indicates that for the cathode reduction process in SO_2Cl_2 , the optimum carbon black would be one containing only a small number of surface oxide groups.

Physical analysis.—Acetone treatment does not change carbon lattice spacings; this is clear because powder x-ray diffraction patterns show that lattice parameters of carbon black powder remain unchanged after acetone treatment. Transmission electron micrographs of CSX-179B carbon black particles before and after acetone treatment also did not show discernable differences in average particle size aggregate morphology of particle shapes. However, a subtle but perhaps subjective change appeared. Particles of treated carbon black under $\sim 1.1 \times 10^6$ magnification appeared to be less dense (*i.e.*, transmitted more light) than the untreated base line carbons. This is fully consistent with our chemical microprobe data, which indicate that calcium and sulfur inorganics or organic species are chemically removed by acetone treatment. Removal of these impurities to give slight surface area enhancement improves interparticle contact and makes a more conductive cathode.

In order to quantify the effects of acetone treatment further, samples of treated and untreated Shawinigan acetylene carbon black were analyzed by Quantachrome, Incorporated (Syosset, New York) for surface area, average pore size, and mercury wetting characteristics. The results are summarized in Table II. This table lists various surface physical measurements using BET techniques on untreated and acetone-treated Shawinigan acetylene carbon black. As expected, the carbon black powder surface area is essentially unchanged after acetone treatment. However, the total pore volume, as well as the calculated average pore diameter (based on surface area and pore volume), more than doubles. This dramatic change is fully consistent with our hypothesis of impurity removal by acetone treatment. As the various impurities are removed, void volume is increased, and, in the finished cathode, more pores are available for deposition of the LiCl cell discharge product. The mercury contact angle is only slightly higher for the treated carbon black sample,

Table II. Comparison of various physical characteristics of acetone-treated and base line Shawinigan acetylene carbon black

	Shawinigan acetylene black	Shawinigan acetylene black (acetone treated)
Surface area (m^2/g)	53.6	54.0
Total pore volume (cm^3/g)	0.186	0.388
Average pore diameter (\AA)	139	287
Mercury contact angle	142.6°	148.5°

which implies less surface roughness. This is also consistent with impurity removal.

Conclusions

Results provided in this study show that substantial improvements in carbon cathode operating voltage and specific cathode capacity at high discharge current densities can be obtained in lithium sulfoxyl chloride cells by simple acetone treatment of the starting carbon black. This inexpensive and rapid treatment may provide a basis of extension to other battery systems which use carbon black in cathode fabrication.

Acknowledgments

We wish to thank the Surface Science Group of the Electronics Research Laboratory at Forth Monmouth and, in particular, Leo Yerkes for the microprobe analysis and Charles Cook for the transmission micrographs. Laura Thorsen greatly assisted in the manuscript preparation.

Manuscript submitted Dec. 3, 1984; revised manuscript received Feb. 15, 1985. This was Paper 135 presented at the New Orleans, Louisiana, Meeting of the Society, Oct. 7-12, 1984.

ERADCOM assisted in meeting the publication costs of this article.

REFERENCES

1. S. Gilman and W. Wade, Jr., *This Journal*, **127**, 1427 (1980).
2. K. A. Klinedinst, *ibid.*, **131**, 492 (1984).
3. W. K. Behl, *ibid.*, **127**, 1444 (1980).
4. A. W. Dey, *ibid.*, **126**, 2052 (1979).
5. (a) C. C. Liang, M. E. Bolster, and R. M. Murphy, *ibid.*, **128**, 1631 (1981); (b) R. M. Murphy and C. C. Liang, *ibid.*, **130**, 1231 (1983); (c) R. M. Murphy and C. C. Liang, *J. Appl. Electrochem.*, **13**, 439 (1983).
6. W. K. Behl, in "Proceedings of the 30th Power Sources Symposium," Atlantic City, NY, June 7-10, 1982, The Electrochemical Society, Inc., p. 163 (1983).
7. W. K. Behl, *This Journal*, **128**, 939 (1981).
8. (a) K. A. Klinedinst, in "Proceedings of the 30th Power Sources Conference," Atlantic City, NJ, June 7-12, 1982, The Electrochemical Society, Inc., p. 157 (1983); (b) K. A. Klinedinst, Abstract 76, p. 190, The Electrochemical Society Extended Abstracts, Vol. 81-2, Denver, CO, Oct. 11-16, 1981; (c) N. Doddapaneni, Abstract 582, p. 1395, The Electrochemical Society Extended Abstracts, Vol. 81-2, Denver, CO, Oct. 11-16, 1981.
9. N. Doddapaneni, Abstract 583, p. 1398, The Electrochemical Society Extended Abstracts, Vol. 81-2, Denver, CO, Oct. 11-16, 1981.
10. (a) F. Walsh and M. Yaniv, DELET-TR-83-0386F, Grant no. DAAK20-83-C-0386; (b) F. Walsh and M. Yaniv, "Proceedings of the 31st Power Sources Symposium," Cherry Hill, NJ, June 11-14, 1984, The Electrochemical Society, Inc. (1985).
11. M. Binder and S. Gilman, Unpublished results.
12. M. Binder, S. Gilman and W. Wade, Jr., *This Journal*, **129**, 897 (1982).
13. T. B. Reddy and E. P. Thurston, "Proceedings of the 31st Power Sources Symposium," June 11-14, 1984, Cherry Hill, NJ, The Electrochemical Society, Inc. (1985).

Sodium Ion Conducting Glasses for the Sodium-Sulfur Battery

Andrew Herczog

Corning Glass Works, Research and Development Division, Corning, New York 14831

ABSTRACT

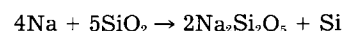
Composition and properties of sodium borate, aluminoborate, and aluminoborosilicate glasses are described. Electrolyte glass degradation by battery environment and chemicals and problems of thermal instability of some glasses are discussed and interpreted on the basis of glass chemistry and structure. A relationship between sodium ion conductivity and composition of the present glasses is established. Constraints on electrolyte glass composition based on its physical and electrical behavior and corrosion stability are tentatively defined, and options allowing various trade-offs between these properties are discussed.

Development of the sodium-sulfur storage battery has been based mostly on the use of β alumina as a solid electrolyte separating anodic and cathodic liquids in the battery operating at 300°C. An alternate approach of development is based on the use of a Na ion conducting glass instead of β alumina for solid electrolyte (1). Because the conductivity of glass is several orders of magnitude lower than β alumina, it has to be used as a large area thin membrane.¹ Glasses used under these conditions have to be stable against corrosion by battery chemicals and should not undergo phase transformation or structural changes; and these characteristics should be coupled with a sufficiently high ionic conductivity, of the order of 10^{-4} - 10^{-5} S, for satisfactory operation of the battery. The object of the present work is to define areas of glass composition best suited for these requirements. Mechanisms of glass corrosion by battery chemicals and structural changes in glasses in the 300°C range are discussed first based on data from the literature. Then, selected composition areas are described and their characteristics compared with the requirements.

Reactivity with metallic sodium.—Reaction between glasses and sodium metal at 300°-500°C has been studied

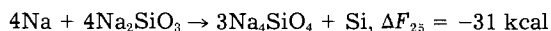
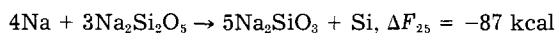
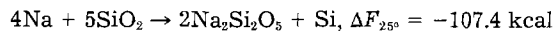
¹The best membrane configuration for mechanical strength is obtained by the use of capillaries or bundles of capillaries (2).

in the past for sodium vapor lamp applications (3). Two effects were observed: a discoloration of the glass due to absorption of sodium, and a surface reaction resulting in the formation of a thin layer of a sodium compound. Resistance to attack decreases in the order aluminates \rightarrow borates \rightarrow silicates \rightarrow phosphates (4). Silicate glasses show a great difference in behavior depending on composition. At high SiO₂ content over 70 mole percent (m/o), there is a strong attack and a black scale is formed, originated by the reaction



The free energy of this reaction at 25°C is -107.4 kcal; that is, the reaction is favored thermodynamically. This is not the case of the direct reduction step $4\text{Na} + \text{SiO}_2 \rightarrow 2\text{Na}_2\text{O} + \text{Si}$, having a low positive free-energy value. With increasing Na₂O content of Na₂O-SiO₂ glasses, scale formation is replaced by discoloration attributed to atomic diffusion of sodium in the glass. This process is at least partially reversible *e.g.* by heating in vacuum, but some residual reaction will take place modifying the transmission spectrum of the glass. At high Na₂O content (45 m/o Na₂O), absorption becomes too low to be detected by simple transmittance measurement. This lack of discoloration, however, does not mean immunity from attack on the surface of the glass by sodium. The explanation is

that diffusivity of neutral sodium atoms is low in the modifier ion-filled silicate glass, but on the glass surface a series of reactions can take place with the formation of silicate crystals in spots or as a thin layer. Later on, atomic diffusion will be replaced by ionic diffusion due to buildup of a large sodium ion concentration gradient. These reactions are



From the standpoint of the Na-S battery operation, both mechanisms, atomic diffusion and surface crystallization, are undesirable. According to Elyard and Rawson (4) discoloration of glass is an early indication of failure in sodium vapor lamps which eventually leads to mechanical embrittlement. Similar processes are likely in battery membrane glass. This assumption is supported by observation of discoloration in β alumina, which has been attributed to battery degradation (5). Structural changes in the glass caused by sodium diffusion can lead to losses of efficiency due to electronic conduction. Besides this bulk effect caused by sodium diffusion, the reaction products formed on the surface, by initiating faults on the glass, are a source of failure by fault propagation under stress. One can also see that, in view of the tendency to surface passivation, immersion tests are unreliable.

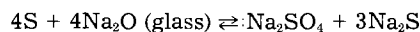
Based on these earlier data (4, 5), one may conclude that high silica glasses are unsatisfactory, whereas borates and aluminoborates are stable, even with a minor percentage of silica in the network. This is important because control of viscosity-temperature characteristics and, therefore, practical usefulness of these glasses depend on their silica content. Below, a method is presented to define the usable silica content in more concrete terms based on kinetics of the reaction between sodium and silica in glass.

Storage of glass prior to use was observed to cause a more severe deterioration in corrosion resistance to sodium for silicate as well as for aluminoborate glasses (4). This question will be discussed later on in relation to corrosion by water vapor.

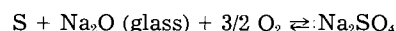
Reactivity with sulfur and sulfides.—No information has been found on corrosion of glasses by sulfur. There are several papers, however, dealing with the solubility of sulfur in glasses. It has been reported (6) that Na_2S can be substituted for Na_2O in all proportions in the $\text{Na}_2\text{O-SiO}_2$ binary at any $\text{Na}_2\text{O/SiO}_2$ ratio; that is, the network remains intact with S^{2-} replacing O^{2-} . Borate glasses behave differently; the amount of sulfur dissolved in the glass increases with the sodium content from zero at zero Na to a maximum for the $\text{Na}_2\text{O} \cdot 2\text{B}_2\text{O}_3$ composition, where up to 100% of the Na_2O can be replaced by Na_2S . The difference in behavior between silicates and borates is attributed to differences in basicity, a concept based on assumption of a Lewis acid-base equilibrium in the glass. Data on basicity have been reported in the literature (7). The main source of basicity is nonbridging oxygen in sites $-\text{O}^- -\text{Na}^+$. In silicate glasses, all the sodium is in such sites and all associated $-\text{O}^-$ ions can be replaced by $-\text{S}^-$ ions. In borate glasses, on the other hand, at first sodium will not break the network by association with nonbridging oxygen. It will, rather, enhance network connectivity by lending oxygen to boron atoms and changing them from three to fourfold coordination ($\text{B}^3 \rightarrow \text{B}^4$). With increasing concentration of B^4 , however, nonbridging oxygen sites will also be formed and the basicity increases. The maximum basicity is reached when the ratio B^4/B^3 reaches its maximum (≈ 1) together with the sulfur solubility. Al atoms in a glass of high Na content all have fourfold coordination and behave like the fourfold coordinated B atoms. In conclusion, sulfur solubility depends on the basicity of the glass, which increases in the order phosphates \rightarrow borates \rightarrow aluminates \rightarrow silicates.

Low concentrations of S in borate glasses give a blue color. These glasses become colorless when irradiated by

x-ray and are used for x-ray dosimetry (8). In silicate glasses of higher S content, the color is red due to polysulfide ions (9). The following mechanisms have been proposed



With high Na^+ activity (basicity) and availability of oxygen, the sulfur is dissolved as sulfate without sulfide formation



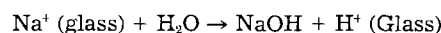
On the other hand, at very low Na^+ activity, the sulfur is oxidized to SO_2 and escapes from the melt. Water dissolved in the glass helps color formation by some synergistic mode.

All the discussion so far was related to the solubility of sulfur in glass melts. From the thermodynamic viewpoint, the processes described above are also allowed at lower temperatures such as 300°C ; because of kinetic limitations, however, the reaction may be limited to random spots or to a thin surface layer. In this respect, consideration has to be given to a reaction mechanism based on interdiffusion between Na_2O and Na_2S resulting in a $\text{O} \leftrightarrow \text{S}$ ion exchange. This process is thermodynamically allowed, and the bond energies Na-O and Na-S are -40 and -37 kcal, respectively. The question is whether the diffusion rates are sufficiently high to cause surface corrosion. The presence of traces of water vapor may be a factor accelerating corrosion by a mechanism to be discussed in the next section.

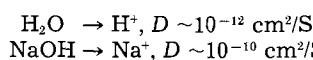
In conclusion, these considerations may provide some guidance for selecting compositions more resistant to attack by sulfur on sodium sulfides. Reactivity is lowered in glass compositions by the following conditions: high boron, or phosphorus, content; alumina content, particularly in association with boron; low soda content; low T/T_g , i.e., low network ion diffusivity; absence of surface water.

Effects of humidity exposure.—Problems from this source are originated from the fiber forming and assembly operations. The room temperature strength of silica fibers of high quality is rapidly degraded by heat-treatment at temperatures above 300°C . This degradation is the result of corrosion of the glass surface by water (10).

Some glasses of high B_2O_3 content are soluble in water. Exposed to humidity, they are gradually converted to crystalline hydrates. For glasses composed with a ratio of $\text{Na/B} : 1/2$, hydration can take place without a change in this ratio, by molecular diffusion of H_2O through the hydrated layer. A more common process applicable to practically all alkali containing glasses is based on the ion exchange mechanism proposed by Doremus (11)



surface: | bulk glass:



This process has been successively verified for soda-lime glass (12) and other glasses and was also used for dating antique glass objects (13). The first step is adsorption of H_2O . This will take place preferentially at defects present on the surface. Later on, an accumulation of NaOH takes place on the same spots forming small protrusions.

Silica glasses are more durable against water, and the durability of borate glasses is improved by silica addition. Durability increases with the SiO_2 content and is higher along the tie-line $\text{Na}_2\text{O} = \text{B}_2\text{O}_3$, near acid-base balance (14). A partial replacement of B_2O_3 by Al_2O_3 can slightly improve durability without changing the general trend.

Initial corrosion by water vapor can cause surface defects, leading to stress-induced fault propagation and mechanical failure. Stresses can be structural or of thermo-mechanical (10) origin. Corrosion by sodium metal is

accelerated by exposure to traces of moisture (4). The same has been reported in the case of sulfur corrosion (9). Such complexities make evaluation of corrosion resistance to sodium or to sulfur particularly difficult.

Stability of glass composition and structure.—Compositional homogeneity and structural stability of electrolyte glass throughout the thermal history of fiber forming, battery assembly, and operational cycling are other key requirements. Glasses known to phase separately should be avoided. An example of such instability is in the well-known Vycor range of sodium borosilicates and the middle range of the $\text{Na}_2\text{O}-\text{B}_2\text{O}_3$ glass system (15). Network former substitutions for boron may extend the range of instability to higher sodium content glasses of interest for electrolyte use. Another instability inherent to all boron containing glasses, in proportion to the boron content relative to other network formers, is the variability of boron coordination with respect to oxygen as a function of alkali content (16) of the glass, temperature, and time (17). Generally, a glass quenched from high temperature has a high B^4/B^3 ratio frozen in. Reheating to, say, 300°-400°C will cause a slow drift toward the low temperature value. This also means a drift in pertinent physical properties such as viscosity, density, electrical conductivity, etc. In aluminoborate glasses of high alkali content, Al is tetrahedrally coordinated, as $[\text{AlO}_4^-]$, while boron remains mostly trigonal (18), so that structural variability as a function of formation conditions and temperature cycling is greatly decreased (17). In sodium borosilicate glasses, on the other hand, the coordination state instability of boron is not affected substantially (17, 19) and these glasses show time dependence of properties.

Devitrification or crystallization of glass is another source of structural instability. Crystalline phases of high sodium content may have increased conductivity if present in concentration sufficient for forming an interconnected dispersion, so that current flow is not limited by the second, low conductivity phase. Grain boundaries, however, are a source of undesired conduction or corrosion processes. Aside from grain boundary effects, structural and corrosion stability is more difficult to obtain in two phases than in one. Crystallization may also be induced by surface reactions, as discussed in the earlier chapters, and proceed from there to the interior, causing current focusing leading to thermomechanical failure.

Other compositional instabilities are related to impurities present in the glass, in the sodium, sulfur, sealants, or electrodes. Most of these instabilities are caused by ion exchange or ion migration phenomena. Mobile ions introduced in the sodium conducting glass, like other alkali, calcium, hydronium, or protons from dissolved water (20), etc., can reduce conductivity due to the mixed alkali effect. Often impurity introduction in or removal from the glass is gradual, resulting in a steady drift in conductivity or other properties. Even anions such as Cl^- or F^- can cause problems. Movement of these ions is very slow compared to sodium, but their displacement can lead to inhomogeneity or accumulation layers at the surfaces. These inhomogeneities may cause resistivity drift, surface stresses, or corrosion.

Composition studies.—Excluded from this study were glasses containing modifiers other than sodium; glasses having network forming ions such as Ge, P, As, Te, easily reduced by sodium; and unstable glasses obtainable by fast cooling only.

Three groups of glasses were studied, all of high sodium content. Glasses of the first group were based on the composition $\text{Na}_2\text{O}-2\text{B}_2\text{O}_3$, and some variations. This work had the objective to improve understanding of the system. The second group included aluminoborate (NABAL) glasses to determine their relative merit compared to the first group. The third group was based on the Al-B-Si network former system. This was investigated systematically to explore any combination of properties of interest for battery use. All glasses were melted in Pt crucibles at 900°-1400°C and formed by pouring on a steel

plate. Afterward, they were annealed sufficiently to allow cutting and grinding necessary for making test samples.

Sodium borate glasses.—The base composition $\text{Na}_2\text{O}-2\text{B}_2\text{O}_3$ can be obtained by melting borax at temperatures sufficiently high for dehydration without significant volatilization. Dissolved water of 0.1% or less has been found to have little effect on electrical properties. The resistivity at 300°C is $6.10^4 \Omega\text{-cm}$ ($\log \rho = 4.8$). Depending on thermal history of the sample, variations of about $\pm 30\%$ in resistivity can be observed, together with variations in viscosity and other properties due to boron coordination changes as discussed earlier.

The composition used in batteries (1) is $\text{Na}_2\text{O}-2\text{B}_2\text{O}_3-0.16\text{NaCl}-0.2\text{SiO}_2$ (21). This has been selected to suit best the requirements for resistivity, formability, and cell performance. This glass has a resistivity of $2.5 \times 10^5 \Omega\text{-cm}$ at 300°C ($\log \rho = 4.4$), or about one-half of the value of the same composition without NaCl addition. Compositions were melted here with variations in the NaCl, SiO_2 , and Na_2O contents. The use of chlorides allows an increase in sodium content, hence the higher conductivity, without making the composition more basic, that is, more reactive with sulfur. The tendency to crystallization is not increased with NaCl addition as much as by the equivalent Na_2O addition. This seems to indicate that in Cl ion containing borate glasses, the equivalent Na^+ is not tied to nonbridging oxygen; it may form, instead, something like a $\text{Na}^+\text{-Cl}^-$ sublattice within the glass network. No such effect is seen in silicate glasses. This may be related to the relatively small ionic size of boron as compared to silicon and to availability of more space in the glass network. In conclusion, conductivity enhancement by chlorides is primarily related to an increase in the number of mobile, dissociable alkali ions and, second, in increased mobility. The use of NaCl addition also has some disadvantages, such as volatility, causing problems in fiber forming by deposition of crystallites by condensation on the fibers. Furthermore, anionic mobility, however slight, may lead to structural drift near the surfaces.

The use of SiO_2 at a low percentage has the purpose of improving glass workability and, very slightly, the humidity sensitivity. Glasses were prepared with combinations of SiO_2 and NaCl at levels up to three times those used in the original composition. At higher chloride levels, particularly if paired with an increase in silica content, crystallization and phase separation became a problem. Benefits were a two to threefold increase in conductivity and 20°-30°C increase in softening point.

Aluminoborate glasses.—Compositions as described before, sodium borate glasses with low SiO_2 content, with and without chlorides, were prepared with varying amounts of boron replaced by aluminum. The structure of aluminoborate (NABAL) glasses is well described in the literature (17, 18). The fraction of tetrahedral boron, $\text{B}^4/(\text{B}^4 + \text{B}^3)$, increases rapidly with the Na/B ratio with no Al in the glass, whereas the increase becomes much less at high Al content. In glasses of high Na content, on the other hand, Al is always tetrahedrally coordinated so that structural connectivity increases with the Al/B ratio. Because of the higher connectivity, higher Na contents are possible without devitrification, and slightly higher conductivities and softening point are obtained. This is well supported by the experimental data in Fig. 1. No advantage has been seen in the use of chlorides at high Al content. Selected compositions and properties are listed in Table I.

In glasses when the Al content is near to or higher than the Na content, there are not enough O ions to form Al-O_4 groups and some Al ions will assume higher coordination. This results in higher viscosities and lower conductivities.

From the standpoint of corrosion behavior, aluminoborate and borate glasses are similar. The stability of aluminoborates with respect to sodium corrosion is equal or better, while stability to sulfur attack is slightly lower be-

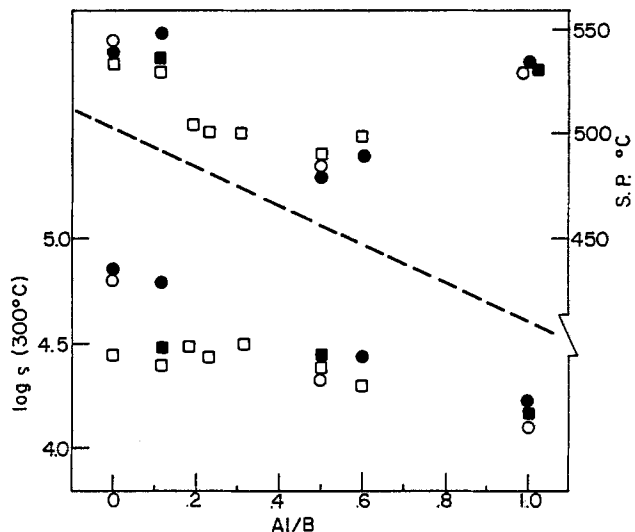


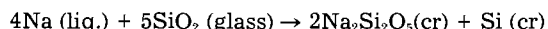
Fig. 1. Resistivity and softening point of sodium-aluminoborate or NABAL glasses. Composition keys: ●, aluminoborate only; ■, 3 ct.% Cl included; ○, 3 ct.% Si included; □, 3 ct.% each Cl and Si.

cause of the decrease in the more acidic trigonal boron content. With respect to sensitivity to water vapor, there is a little improvement with Al content. The use of these glasses for batteries has been proposed by Russian authors (22) and in a U.S. patent (23).

Alumino-borosilicate glasses.—Further search for electrolyte glasses was motivated mainly by the extreme humidity sensitivity of both borates and aluminoborates and by problems in sealing to these somewhat unstable low viscosity glasses. Having excluded phosphate containing systems because of sodium corrosion, the binary aluminosilicate system had to be discarded also because of sodium reactivity due to high silica content. Furthermore, glasses of high soda content, not containing boron, are also likely to fail by sulfur reactivity due to high basicity.

This leaves open for further consideration aluminoborosilicate and binary borosilicate glasses of lower silica content. The question to be addressed is what is the limit of SiO_2 admissible from standpoint of corrosion by sodium. Silica in the range of 3-10%, cation based, has been used without adverse reaction, whereas at more than 50% SiO_2 level reaction with sodium has been observed. In order to define better limits in the 10-50% range, a kinetic model is proposed to explain the reaction with sodium.

The corrosion process has been identified, as discussed earlier, by the reaction



For a polymolecular reaction to proceed at an appreciable rate in the solid state (at 300°-400°C), it is necessary to have the reactants localized in high concentration. For example, liquid sodium and SiO_2 in pure silica glass would satisfy this requirement. On the other hand, a glass network with lower percentage of SiO_2 , such as 10-50% of the network cations, may have the necessary accumulation of Si atoms only at some locations, owing to the randomness of the network. A few spots, however, may be too many if the crack propagation mechanism from point defects on the glass surface is considered. An approach to quantify the problem has been made based on statistical probability calculations.

In a network of tetrahedrally coordinated cations, each network cation shares oxygen with four others. Assuming one cation is silicon (Si) and the other something else (N), one can calculate the probability of finding two Si cations side by side for any given ratio Si/N. Designating

$$R = \text{Si}/N, A = N/(\text{Si} + N), B = \text{Si}/(\text{Si} + N), A + B = 1$$

the probability of finding two Si cations nearby is

$$P_2 = B(1 - A^4)$$

Table I. Selected sodium aluminoborate glasses

Composition	101	102	103	104	105
Weight percent					
Na_2O	28.4	30.3	32.5	27.3	30.9
NaCl	4.3	4.0	—	5.3	—
B_2O_3	53.3	45.9	36.5	27.4	26.0
Al_2O_3	9.7	15.7	26.8	40.0	38.1
SiO_2	4.3	4.1	4.2	—	—
ct. %					
Na	35.5	38.2	38.9	38.3	38.8
B	55.0	48.1	38.9	30.9	29.0
Al	6.9	11.2	19.6	30.8	29.0
Si	2.6	2.5	2.6	—	3.2
(Cl)	(2.6)	(2.5)	—	(3.6)	—
Properties					
$\log(\Omega\text{-cm})$, 300°C	4.4	4.4	4.1	4.2	4.1
Softening point (°C)	528	500	485	530	528
Therm. exp. (ppm/°C)	12.5	13.0	13.1	13.3	13.4

Similarly, the probabilities of finding 3, 4, or 5 silicons close by are respectively, $P_3 = P_2^2$, $P_4 = P_2^3$, and $P_5 = P_2^4$. Values of P_2 , P_3 , P_4 , and P_5 are plotted against R in Fig. 2. The graph shows the probability of finding five SiO_4 groups in proximity as needed for the corrosion reaction. One can see that the probability falls off rapidly at or below the ratio $\text{Si}/N : 1/2$, which has been adopted for the upper limit of silica content in the present compositions. In reality, the probabilities may be lower than indicated by the results obtained by random-distribution-based calculations because (i) there is a degree of ordering in glass melts favoring separation of identical groups, particularly (BO_4) , from each other (17); (ii) the proximity of sodium ions, many linked through nonbridging oxygen to silicon, has been disregarded; and (iii) a single reaction site according to the given equation may not provide a stable nucleus to start the corrosion process, as several events may have to interact locally for that purpose.

The criterion of stabilizing SiO_2 against sodium reduction by sharing oxygen with a cation of higher bond energy can be extended to glasses containing elements like Zr, Ta, lanthanides, etc., as network-formers or modifiers.

The compositions to be discussed are high soda glasses, close to the limit of glass stability in the Si-Al-B network-former ternary. The sodium content of these glasses (Na) is in the range of 36-42 cation-based percent (ct. %). As the effects of variations in sodium content are comparable—

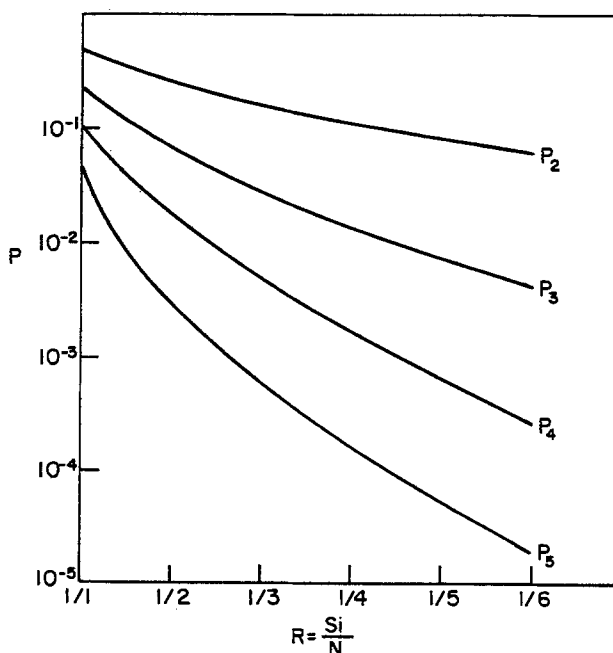


Fig. 2. Probability of silicon clustering in a mixed cation network.

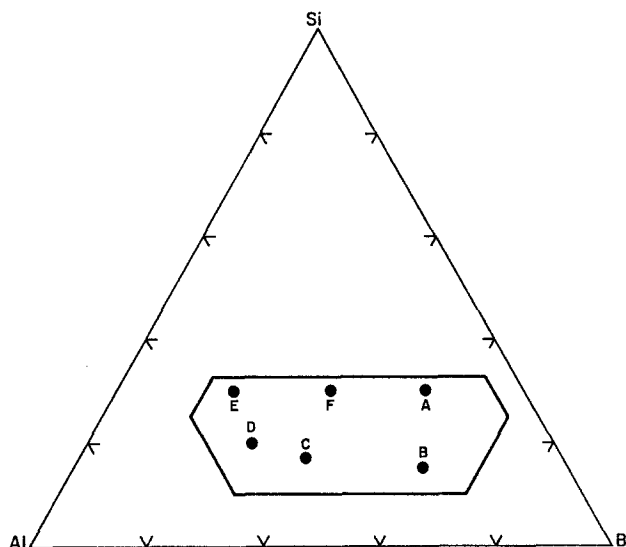


Fig. 3. Range of network forming components in sodium ion conducting glasses for Na-S batteries.

this will be shown below—the present discussion can be based on the network cation ternary system Al-B-Si, remembering that the total network cation content is

100-Na; and therefore, the individual network cation percentages in the compositions are $N(100-Na)/100$ where N is the percentage of Al, Si, or B read from the ternary diagram in Fig. 3. The Si cation content in the network ternary is 10% or more, up to about 33%, as explained above. Compositions below 10% were described earlier as aluminoborates. Al content is below 60% for meltability and above 5% for better structural stability. B content is below 70% to set a limit to humidity sensitivity. The composition and properties of the glasses based on the points shown in the diagram are listed in Table II. The sodium borate glass, no. 112, is included for comparison. All glasses were found to be sodium resistant in static corrosion tests, but glasses of high SiO_2 content were marginal with respect to sulfur corrosion at 350°C ; they were, on the other hand, the best for water durability. These observations are in agreement with the data and interpretations given as background earlier.

Effects related to sodium content.—Table III gives the composition of glasses of different sodium content, all based on point A of the diagram in Fig. 3 as the common network forming system. The change in properties with increasing sodium content illustrated in Fig. 4 is predictable and does not require comments. The main purpose of the series was to determine the maximum sodium content in a glass suitable for fiberdraw or similar forming techniques. The criterion used was devitrification at a

Table II. Composition and properties of the glasses

Network position in Fig. 3	A	B	C	D	E	F	—
Network components							
ct.% Al	17.0	25.4	43.7	51.8	49.8	32.8	—
B	53.0	59.7	39.1	28.1	20.1	37.0	95.2
Si	30.0	14.9	17.2	20.1	30.1	30.1	4.8
Glass composition no.	106	107	108	109	110	111	112
ct.% Na	39.5	38.6	41.2	41.2	41.2	41.1	33.9
Al	10.2	15.6	25.7	30.5	29.3	19.3	—
B	32.0	36.6	23.0	16.5	11.8	21.8	62.9
Si	18.3	9.2	10.1	11.8	17.7	17.7	3.2
w/o Na_2O	30.9	31.4	31.9	31.0	30.1	31.2	(Cl2.5)
Al_2O_3	13.1	20.8	32.8	37.7	35.1	24.1	—
B_2O_3	28.2	33.4	20.1	14.6	9.7	18.6	62.6
SiO_2	27.8	14.4	15.2	17.3	25.1	26.1	5.4
NaCl	—	—	—	—	—	—	4.2
Glass properties							
Log resistivity at 300°C	4.00	4.16	4.00	3.92	3.88	3.90	4.40
Thermal expans. (ppm/ $^\circ\text{C}$)	13.2	13.7	14.6	13.6	14.0	13.8	12.4
Annealing temp. ($^\circ\text{C}$)	457	424	424	550	590	460	456
Softening temp. ($^\circ\text{C}$)	550	514	545	680	720	548	531
Melting temp. at 10 poise	1023	967	1350	1420	1380	1120	840
Estimated stability							
To sodium corrosion	Good	Excellent	Excellent	Excellent	Good	Good	Excellent
To sulfide corrosion	Fair	Excellent	Good	Good	Good	Fair	Excellent
To moisture	Excellent	Poor	Fair	Fair	Good	Excellent	None
To structural change	Good	Fair	Good	Good	Good	Excellent	Poor

Table III. The effect of sodium content on glass properties. Network former composition in ct. %: Al 17.0, B 53.0, Si 30.0, based on point A in Fig. 3

Glass composition no.	113	114	115	116	117	118
ct.% Na	35.0	36.5	38.0	39.5	41.0	42.5
Al	10.0	10.7	10.4	10.2	10.0	9.8
B	34.5	33.6	32.9	32.0	31.3	30.6
Si	19.6	19.2	18.7	18.3	17.7	17.1
w/o Na_2O	27.0	28.3	29.6	30.9	32.3	33.6
Al_2O_3	13.8	13.6	13.4	13.1	12.9	12.7
B_2O_3	29.9	29.3	28.7	28.2	27.7	27.2
SiO_2	29.3	28.8	28.3	27.8	27.1	26.5
Glass properties						
Log resistivity at 300°C	4.98	4.49	4.20	4.00	3.84	3.73
Annealing temp. ($^\circ\text{C}$)	478	471	466	457	449	438
Softening temp. ($^\circ\text{C}$)	562	561	557	550	539	523
Melting temp. at 10 poise	1083	1071	1050	1023	992	955
Thermal expans. (ppm/ $^\circ\text{C}$)	11.5	12.1	12.7	13.2	13.8	14.5
Devitrification at $2^\circ/\text{min}$	—	—	—	—	Trace	Yes

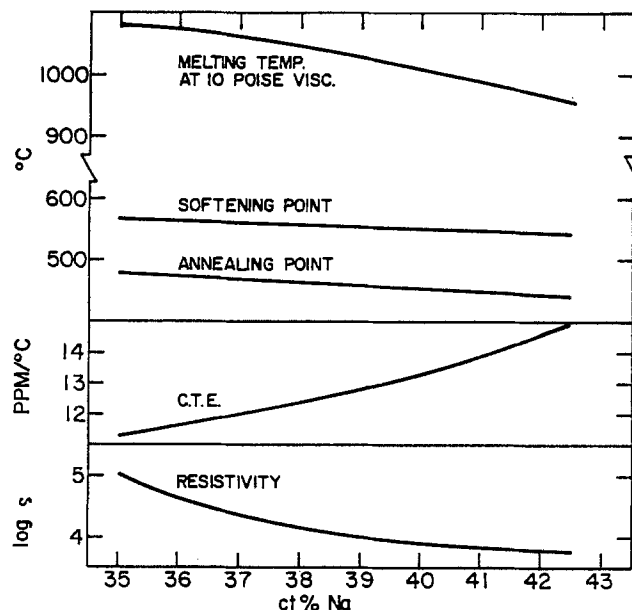


Fig. 4. The effect of sodium content on the properties of glasses with the network Al 17.0, B 53.0, Si 30.0 ct.%.

cooling rate of 2°C/min, a critical value based on past experience. By measuring the viscosity of the glass as a function of temperature at a constant rate of cooling by the rotating cylinder method, any trace of devitrification is readily observed; in the present case, this happened for composition no. 117.

If we assume a critical cooling rate as a constant factor, the associated sodium content, here called sodium threshold, becomes an important characteristic of the network forming system for sodium ion conductor applications. The sodium threshold increases with the coordination number of the network formers. Within the Al-B-Si ternary, it is the highest for silicates, aluminosilicate glasses being a close second, then decreases with increasing borate content. Figure 5 plots log resistivity against the measured or estimated sodium threshold of glasses prepared here or comparable glasses published in the literature. The numbered points of the curve give the resistivity of a particular glass at the sodium threshold. The compositions are identified in Table IV. This figure shows that sodium ion conductivity is determined mainly by the sodium content of these glasses and that differences in resistivity are due to differences in the capability of a network to accept more or less sodium without devitrification.

Ravaine and Souquet (26) demonstrated a linear relationship between sodium ion activity and conductivity in alkali silicate glasses. This is reflected approximately in Fig. 5. Activities are not too far off from the cation-based percentages of sodium ions used here to plot resistivities. Deviation from linearity results from changes in coordination and structure from fourfold coordinated silicates (6) and aluminosilicates (5) to aluminoborosilicates (4), aluminoborates (3), and borates (2, 1) which contain

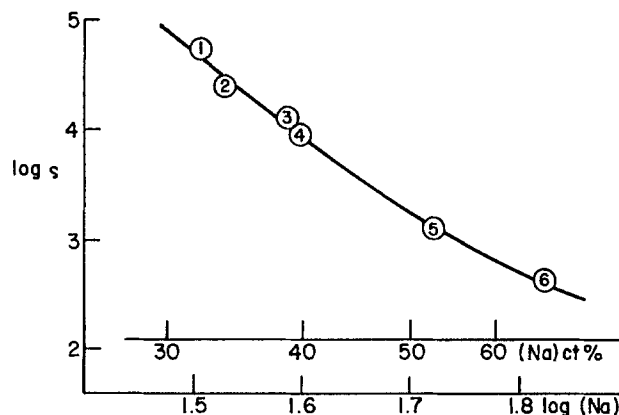


Fig. 5. Resistivity vs. sodium threshold.

increasing amounts of threefold coordinated boron. A more detailed discussion of this relationship in terms of the weak electrolyte theory of glass will be prepared later.

Conclusions

Sodium ion conductivity in glasses based on the Al-B-Si network-former system is mainly determined by the amount of sodium in the glass. This should be maximized without causing devitrification at a preselected cooling rate compatible with the forming method used. This sodium threshold increases with the coordination number of the network forming cations in the glass.

Corrosion by metallic sodium does not affect aluminate and borate glasses. In silicates, because of kinetic limitations, only glasses having silicon in more than one-half of the network forming cation sites are significantly affected. Glasses containing ions more reducible than silicates should not be used. Sodium corrosion is mainly by surface reaction. Reaction below the surface is slight; it is preceded by atomic diffusion of sodium in the glass.

Corrosion by sulfur and sulfides is related to the basicity of the electrolyte glass. Basicity is enhanced by the sodium ion concentration, while it is reduced by the presence of boron and to a lesser extent of aluminum, which form Lewis acid sites in the glass. The mechanism of corrosion is likely to be $O^{2-} \leftrightarrow S^{2-}$ ion exchange. This is a diffusion-controlled process; therefore, the T/T_g ratio is important for the rate of corrosion.

Corrosion of bulk glass exposed to humidity is due to $H^+ \leftrightarrow Na^+$ ion exchange leading to high sodium ion concentration on the surface and a gradient of dissolved OH groups underneath. Sodium accumulation on the surface increases sulfur corrosion, whereas sodium depletion and OH groups under the surface enhance corrosion by sodium metal. Susceptibility to corrosion by humidity is enhanced by boron content and diminished by silicon content for high sodium content glasses.

Phase separation and structural instability is a problem affecting mainly borate and borosilicate glasses.

Summing up the question of glass composition *vs.* corrosion, the requirements for limiting sodium corrosion are less severe than those related to sulfur corrosion. Controlling the latter requires glasses of low sodium and high

Table IV. Composition and resistivity at 300°C of glasses and maximum sodium content

Position in Fig. 5	1	2	3	4	5	6
Composition						
ct.% Na	32.2	33.9	39.1	39.5	52.7	66.6
B	64.6	62.9	39.1	32.0	—	—
Al	—	—	19.4	10.2	15.8	—
Si	3.2	3.2 (2.5 Cl)	2.4	18.3	31.5	33.4
		Resistivity (300°C)				
$\log \rho$ (Ω -cm)	4.75	4.40	4.10	4.00	3.12	2.64
Composition no.	119	112	103	106	123	124
Reference	—	(21)	(23)	—	(24)	(25)

boron content with a sacrifice with respect to conductivity, moisture resistance, and structural stability. Considering these factors, further work may be based on the following options.

1. There must be continued effort on sodium borate glass, avoiding exposure to humidity to preserve fiber strength, and using stress- and water-free sealing and assembly conditions.

2. There must be explorations of the use of compositions of the no. 115 type, barely adequate with respect to sulfur corrosion, good in other respects.

3. There must be use of compositions of the no. 108 type representing a compromise between the first and second options.

4. The perspective of electrolyte glass compositions could be broadened by concentrating on the sulfur corrosion problem and revising the battery system, particularly the anolyte. Reduced sulfur corrosion may be obtained by lowering T/T_g of the glass, for example, with the use of hard, high viscosity glasses. For such glasses, however, new forming techniques would have to be found. The same can be achieved by lowering the battery temperature from 300° to 200°C or below. This would require replacing the Na₂S_x anolyte with a lower melting system, preferably of lower basicity.

Acknowledgments

Summary information on corrosion measurements was obtained from Dr. Tsang and Dr. Gregory of Dow Chemical, D. E. Sempolinski and R. F. Bartholomew of Corning Glass Works. For all glass preparation and property measurements, the work done by the Melting Services and Technical Services group of Corning Glass Works is greatly appreciated.

Manuscript submitted Aug. 27, 1984; revised manuscript received Feb. 20, 1985.

Corning Glass Works assisted in meeting the publication costs of this article.

REFERENCES

1. C. A. Levine and D. Dean, Abstract 95, p. 253, The Electrochemical Society Extended Abstracts, Vol. 78-2, Pittsburgh, PA, Oct. 15-20, 1978.
2. W. E. Brown, U.S. Pat. 3,476,602 (1966).
3. C. J. Brinker and L. C. Klein, *Phys. Chem. Glasses*, **21**, 141 (1980); R. H. Doremus, *J. Non-Cryst. Solids*, **25**, 262 (1977); J. A. Burns, *Glass Technol.*, **6**, 17 (1965).
4. C. A. Elyard and H. Rawson, "Advances in Glass Technology, VI International Congress on Glass," p. 270, Plenum Press, New York (1962).
5. J. R. Rasmussen, G. R. Miller, and R. S. Gordon, Abstract 720, p. 1153, The Electrochemical Society Extended Abstracts, Vol. 82-1, Montreal, Quebec, Canada, May 9-14, 1982; D. S. Park, M. W. Breiter, and R. W. Powers, Abstract 721, p. 1155, The Electrochemical Society Extended Abstracts, Vol. 82-1, Montreal, Quebec, Canada, May 9-14, 1982.
6. T. Hanada, *J. Non-Cryst. Solids*, **21**, 65 (1976).
7. J. A. Duffy, *ibid.*, **21**, 363 (1976).
8. K. O. Otle, *J. Appl. Phys.*, **23**, 499 (1951).
9. A. Paul, *J. Mater. Sci.*, **9**, 1123 (1974).
10. C. R. Kurkijean and J. T. Krause, Paper 45G, presented at the American Ceramic Society Fall Meeting, 1982.
11. R. H. Doremus, *J. Non-Cryst. Solids*, **19**, 137 (1975).
12. W. A. Lanford, *ibid.*, **33**, 249 (1979).
13. W. A. Lanford, *Science*, **196**, 975 (1977).
14. P. B. Adams and D. L. Evans, "Borate Glasses," p. 525, Plenum Press, New York (1978).
15. R. R. Shaw and D. R. Uhlmann, *J. Am. Ceram. Soc.*, **51**, 377 (1968).
16. P. J. Bray and J. G. O'Keefe, *Phys. Chem. Glass*, **4**, 37 (1963).
17. T. Abe, *J. Am. Ceram. Soc.*, **35**, 284 (1952).
18. R. Gresch and W. Muller, *J. Non-Cryst. Solids*, **21**, 31 (1976).
19. W. A. Weil, *Glass Ind.*, **29**, 200 (1948).
20. H. A. Schaffer, *J. Am. Ceram. Soc.*, **62**, 343 (1979).
21. F. L. Tsang, U.S. Pat. 3,829,331 (1974).
22. I. M. Bushueva, *Univ. Leningrad, Vestn. Fiz. I Khim.*, **4**, 122 (1979).
23. C. L. Booth, U.S. Pat. 4,190,500 (1980).
24. K. Von Benda and H. Kistrup, U.S. Pat. 4,230,778 (1980).
25. K. Otto, *Phys. Chem. Glass*, **7**, 29 (1966).
26. D. Ravaine and J. L. Souquet, *ibid.*, **18**, 27 (1977) and *ibid.*, **19**, 115 (1978).

Application of Linear Stability and Bifurcation Analysis to Passivation Models

Jan B. Talbot* and R. A. Oriani**

Corrosion Research Center, Department of Chemical Engineering and Materials Science, University of Minnesota, Minneapolis, Minnesota 55455

Mark J. DiCarlo

3M Company, Industrial Specialties Division, St. Paul, Minnesota 55144

ABSTRACT

Linear stability and bifurcation analysis is applied to two passivation models from the literature. The necessary and sufficient conditions for multiple steady states are determined for one of the models. For the other model, the parameter values for oscillatory solutions of the two-dimensional system of equations are evaluated. The results of these analyses show the power of these mathematical techniques in determining the conditions for multiple steady states and periodic solutions of various nonlinear models

Over the past century, the formation of passive films on metals has been investigated experimentally and mechanisms for their formation have been hypothesized. There still remains much uncertainty about the specific electrochemical steps or the important elements necessary for passivity under particular environmental conditions. Efforts have been made to define the mechanism of passivation by developing models (1-4) to reflect the

special nature of the anodic polarization curves, which show that with increasing anodic potential the oxidation current reaches a maximum and then quickly decreases by several orders of magnitude to the passivation current at the Flade potential. Thus, the models developed have attempted to account for the multiple values of potential for a particular current in the active-passive transition region.

Current oscillations at constant potential or potential oscillations at constant current have often been observed

*Electrochemical Society Student Member.

**Electrochemical Society Active Member.

in the active-passive transition range for a variety of metal-electrolyte systems (5-8). These oscillations can take diverse forms, periodic or aperiodic, and of constant, changing, or even damped amplitude. Although most of the explanations of electrochemical oscillations are phenomenological, there have been some attempts to postulate mechanisms and to mathematically model these oscillations (9-11). However, the only endeavor prior to our own (12, 13) to model the oscillations found in the passivation process is that of Franck and Fitzhugh (10). Their work models iron polarized at a constant potential, focusing on the change of overpotential and of electrode surface coverage.

It may be possible to gain a better insight into the mechanisms of passivation by the investigation of the multiple values of potential characteristic of anodic polarization curves and the oscillatory behavior observed in the active-passive region. By utilizing linear stability and bifurcation analysis, the existence of and conditions for multiplicity of steady states and periodic solutions of the model equations may be determined. The purpose of this paper is to apply these mathematical tools to two models in the literature to show the usefulness of these techniques for evaluating the criteria for multiple steady states (MSS) in one case (4) and oscillations in another (10).

Linear Stability Analysis

Generally, differential equations which represent oscillatory behavior are nonlinear and seldom lend themselves to analytical solutions. There are many texts on the theory of analysis of nonlinear differential equations [for example, Ref. (14-16)], and only a brief discussion of certain fundamental concepts and results is needed here. Linear stability analysis allows qualitative information to be obtained about the solutions of differential equations by examining what a small change in the initial conditions does to the solution by linearizing the original nonlinear equations. Application of bifurcation theory results in information regarding the dynamic behavior of the system of equations as parameters change.

Suppose we have a system of nonlinear autonomous equations

$$\frac{dx}{dt} = F(x) \quad [1]$$

The steady-state solution is defined by

$$\frac{dx}{dt} = F(x_s) = 0 \quad [2]$$

If we expand $F(x)$ in a Taylor series about the steady-state solution, x_s , and truncate at the linear terms, we obtain

$$F(x) = F(x_s) + \frac{\delta F}{\delta x_s} (x - x_s) \quad [3]$$

By letting $u = x - x_s$ and substituting Eq. [3] into Eq. [1], and knowing by Eq. [2] that $F(x_s) = 0$, one obtains

$$\frac{du}{dt} = J u \quad [4]$$

where $J_{ij} = (\delta F_i / \delta x_j)_s$, the linearized Jacobian evaluated at the steady state. Since the solution of Eq. [4] is of the form $u = \exp(Jt)u_0$, the stability of the solution to infinitesimal perturbations depends on the eigenvalues of J . The character of the steady state is determined by the real parts of the eigenvalues (λ) of Eq. [4]: $\text{Re}(\lambda) < 0$ means stable, $\text{Re}(\lambda) > 0$ means unstable, and $\text{Re}(\lambda) = 0$, $\text{Im}(\lambda) \neq 0$ may indicate periodic solutions.

Usually, we are interested in the behavior of a system of equations such as Eq. [1] as parameters (p) vary, that is

$$\frac{dx}{dt} = F(x,p) \quad [5]$$

Bifurcation is the change of stability or changes in the qualitative structure of the solutions for certain values of

the parameters. A static bifurcation occurs when a single eigenvalue passes through the origin of the complex plane as a particular parameter changes, leading to MSS. Hopf bifurcation to periodic solutions occurs when a pair of complex conjugate eigenvalues crosses the imaginary axis of the complex plane. In other words, Hopf bifurcation requires two purely imaginary eigenvalues, with the remaining eigenvalues, if any, having negative real parts and $d \text{Re}(\lambda)/dp \neq 0$ at the imaginary axis.

For a two-dimensional system of differential equations, the eigenvalues are the roots of following equation

$$\lambda^2 - (\text{tr } J)\lambda + \det J = 0 \quad [6]$$

These roots are

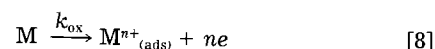
$$\lambda_{\pm} = 1/2 \text{tr } J \pm 1/2 [(\text{tr } J)^2 - 4 \det J]^{1/2} \quad [7]$$

and they can be expressed in terms of the system parameters. The necessary and sufficient conditions for local asymptotic stability are that $\det J > 0$ and $\text{tr } J < 0$. If $\det J < 0$, the two eigenvalues are real and opposite in sign, and this specifies a saddle (an unstable steady state). If $\det J > 0$ and $\text{tr } J > 0$, an unstable steady state (node or focus) is signified. If, under certain parameter conditions, $\det J = 0$ with $\text{tr } J < 0$, then a static bifurcation to MSS would occur. If $\text{tr } J = 0$ with $\det J > 0$ and $d \text{Re}(\lambda)/dp \neq 0$, then Hopf bifurcation to oscillatory solutions would occur.

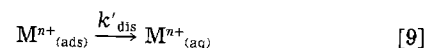
The results of stability analysis can be pictorially represented by phase-plane portraits where the solutions of Eq. [5] are traced as trajectories by plotting one variable *vs.* another. Trajectories can approach or leave the vicinity of a steady state depending on its stability. An isolated closed trajectory is called a limit cycle, such that any trajectory in the neighborhood either approaches it (a stable limit cycle) or leaves it (an unstable limit cycle). A limit cycle represents sustained oscillations independent of initial conditions. A stable limit cycle represents unchanging periodic oscillations, whereas an unstable limit cycle represents either damped or growing oscillations. Bifurcation diagrams trace the Hopf points or limit points (points of static bifurcation) as system parameters change.

Case I — Analysis of Griffin's Model

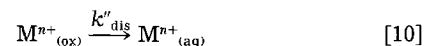
Griffin's simple phase-transition model (4) for metal passivation kinetics consists of only two rate processes: (i) the oxidation of surface metal atoms M to produce adsorbed cations M^{n+} , according to



and (ii) the subsequent dissolution of cations into the electrolyte, either from adsorbed atoms at low coverage on the electrode surface



or from a high coverage adsorbed layer, also called an oxide layer (4)



The rate constant for cation dissolution, whether according to Eq. [9] or [10], is written as

$$k_{\text{dis}} = k^{\circ}_{\text{dis}} \exp(-\beta\theta) \quad [11]$$

where k°_{dis} is the rate constant for the dissolution of an isolated adsorbed cation, θ is the surface coverage by adsorbed cations, and β is a Temkin-type adsorbate-adsorbate interaction parameter. The rate expression for the dissolution current for either Eq. [9] or [10] is given by

$$i_{\text{dis}} = k^{\circ}_{\text{dis}} \theta \exp(-\beta\theta) \quad [12]$$

and the rate of adsorbed cation formation (Eq. [8]) is expressed by the Tafel relation

$$i_{\text{ox}} = k^{\circ}_{\text{ox}} (1 - \theta) \exp(fE) \quad [13]$$

where $f = \alpha F/RT$, E is the potential, and k_{ox}° is the chemical rate constant. By equating Eq. [12] and [13], an expression relating the steady-state potential, E_s , and steady-state coverage, θ_s , is determined

$$E_s = (1/f)[- \beta \theta_s + \ln(k_{dis}^{\circ}/k_{ox}^{\circ}) + \ln(\theta_s/1 - \theta_s)] \quad [14]$$

The solution of Eq. [14] yields MSS for $\theta_s(E_s)$ for $\beta > 4$. Polarization curves for $\beta > 4$ calculated from Eq. [12]-[14] show the multiple-valued active-passive region. The critical value of 4 for the interaction parameter, β , represents the mean field approximation of a phase transition between isolated cations and the continuous oxide layer.

An alternate approach to determine the parameters necessary for multiplicity for Griffin's model is to apply bifurcation analysis. First, we must write a differential equation to express the change of surface coverage with time for the proposed mechanism, as follows

$$\begin{aligned} \Omega \equiv d\theta/dt &= k_{ox}(1 - \theta) - k_{dis}\theta \\ &= k_{ox}(1 - \theta) - k_{dis}^{\circ} \exp(-\beta\theta) \end{aligned} \quad [15]$$

where $k_{ox} = k_{ox}^{\circ} \exp(fE)$. At steady state, $d\theta/dt = 0$. We can graphically show the steady-state solutions by letting

$$\Gamma_1 = (k_{ox}/k_{dis}^{\circ})(1 - \theta_s) \equiv \gamma(1 - \theta_s) \quad [16]$$

$$\Gamma_2 = \theta_s \exp(-\beta\theta_s) \quad [17]$$

where the intersections of the curves Γ_1 and Γ_2 are the steady states. This is illustrated in Fig. 1 for several values of β . The necessary and sufficient conditions for MSS are found by evaluating

$$\left. \frac{\delta\Omega}{\delta\theta} \right|_s = 0 \quad [18]$$

and knowing $\Omega = 0$ at steady state, which indicate the points of stability change. This gives the following expression in terms of θ_s

$$\theta_s^2 - \theta_s + 1/\beta = 0 \quad [19]$$

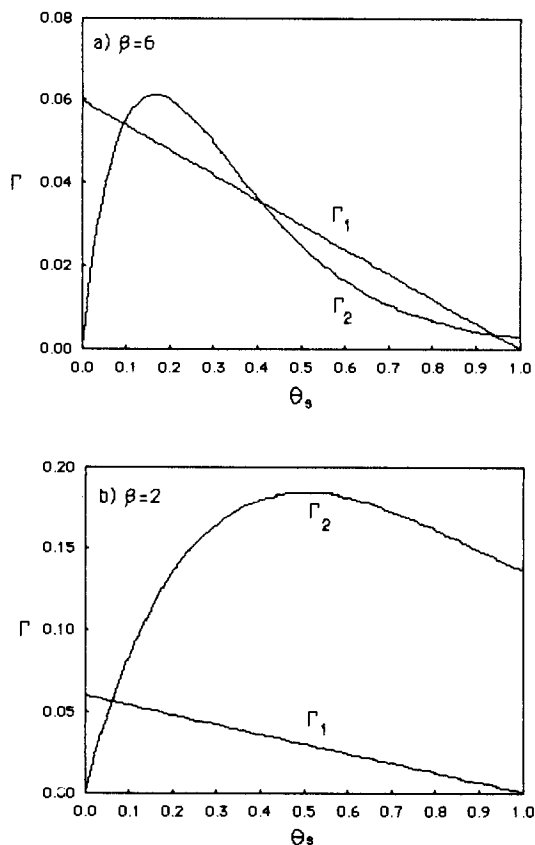


Fig. 1. Steady-state functions Γ_1 and Γ_2 from Eq. [16] and [17]. Intersections of Γ_1 and Γ_2 are the steady-state values. The following parameters were used: (a) $\beta = 6$, $\gamma = 0.06$; (b) $\beta = 2$; $\gamma = 0.06$.

Solving for θ_s yields

$$\theta_s = 0.5 \pm 0.5[1 - 4/\beta]^{1/2} \quad [20]$$

Real roots exist for $\beta \geq 4$. Therefore, the bifurcation point is $\beta = 4$ ($\theta_s = 0.5$) and MSS occur for $\beta > 4$. Also from Eq. [18]

$$\gamma = (\beta\theta_s - 1) \exp(-\beta\theta_s) \quad [21]$$

and at the bifurcation point $\beta = 4$, $\gamma = 0.135$. Therefore, another condition for MSS is that $\gamma < 0.135$ calculated from Eq. [21]. Figure 2 shows the bifurcation set of γ vs. β .

The stability of solutions of Eq. [15] can be determined from the sign of the eigenvalue, which is $\delta\Omega/\delta\theta$ evaluated at the steady state. When three steady states exist, the middle solution is unstable and the outer two are stable. This also can be checked by evaluating the trajectory $d\theta/dt$; the trajectory always moves away from the central steady state. In Fig. 3, the regions of stability are shown for θ_s vs. β at constant γ and θ_s vs. γ at constant β . This one-dimensional model cannot give oscillations, since a pair of purely imaginary eigenvalues is required. In other words, the model must be at least two dimensional for periodic solutions. In Griffin's analysis, the current density-potential curves were calculated for an electrode potential range of about -1230 to -1250 mV for MSS for the fixed parameters: $k_{dis}^{\circ} = 1300$ mA/cm², $k_{ox}^{\circ} = 8 \times 10^{32}$ mA/cm², and $f = 57.6$ V⁻¹. Using these parameters, $\gamma = 6.15 \times 10^{28} \exp(57.6E)$. From bifurcation analysis for $\beta = 6$, $0.0529 < \gamma < 0.0754$ or $-1250 < E < -1235$ mV, which is in agreement with Griffin's results.

The requirement for β for MSS was determined by Griffin for one particular set of rate constant values by solving Eq. [14], and our results agree with those of Griffin. However, our analysis gives much more information. As shown in Fig. 2, the region of multiplicity in parameter space is evaluated; that is, $\gamma = k_{ox}/k_{dis}^{\circ} < 0.135$ and $\beta > 4$. From our analysis, we can determine the range of all parameter values that are important for this model to predict the active-passive transition feature of the polarization curve.

Case II — Analysis of the Franck and Fitzhugh Model

Franck and Fitzhugh (10) formulated a mathematical model of iron polarized at a constant potential and found oscillatory solutions of the two system variables, surface coverage and an overpotential, $E = E_p - E_r$, where E_p is the constant applied potential and E_r is the Flade potential. The Flade potential is defined by them as the electrode potential at which the transition from the active to passive state takes place. The mechanism which was modeled is

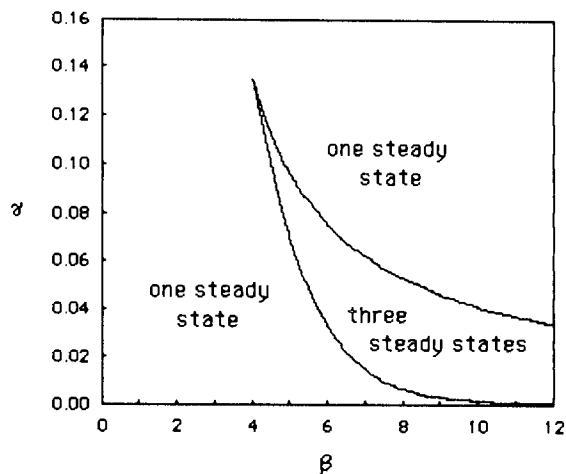
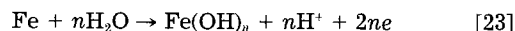


Fig. 2. Bifurcation diagram showing regions of one and three steady states in the parameter space of β vs. γ .

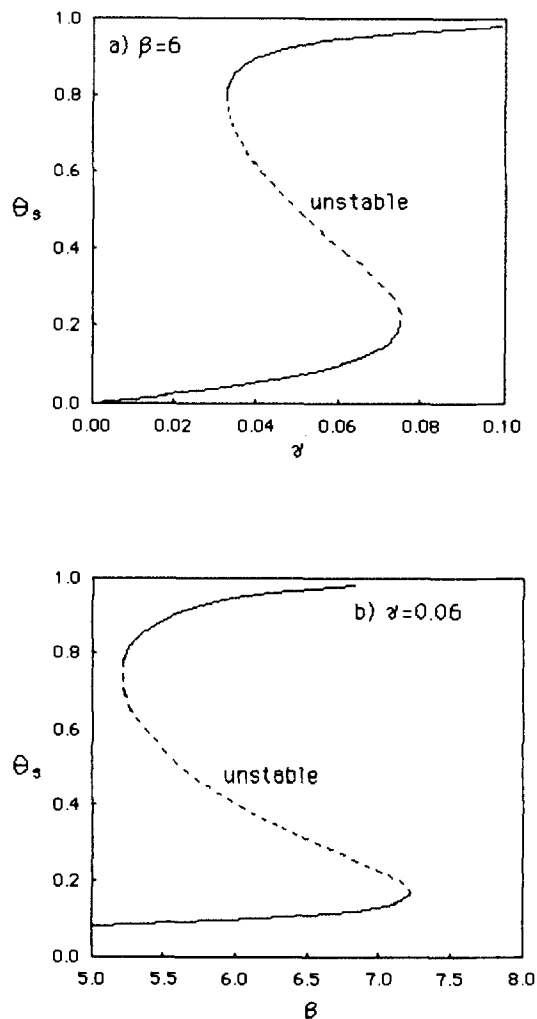


Fig. 3. Stability diagrams for multiple steady states of surface coverage θ_s for (a) γ at $\beta = 6$ and (b) β at $\gamma = 0.06$. Unstable region denoted by a dotted line.

Qualitatively, the model describes the following sequential steps as iron is anodically polarized in H_2SO_4 . First, the iron electrode is in an active state with a local current density of ~ 10 A/cm². Because of the presence of Fe^{2+} , hydrogen ions electromigrate away from the electrode, consequently reducing the H^+ concentration at the electrode. The Flade potential depends upon the H^+ concentration, and it is shifted negatively as the H^+ concentration decreases. The overpotential therefore increases, causing passivation to occur and the current density to decrease to a few microamperes per square centimeter. However, the back-diffusion flux of H^+ is increased, eventually increasing the H^+ concentration at the electrode. Hence, the overpotential decreases and the electrode becomes active again. This cycle of events is said to produce the observed electrochemical oscillations.

The basic features of the model are the assumptions of a discontinuity in the kinetics at the Flade potential ($E = 0$) and the dependence of the Flade potential on H^+ concentration. The model is simplified by linearizing (i) the current-potential curve, (ii) the dependence of Flade potential on the concentration of H^+ , and (iii) the concentration profiles in the electrode diffusion layer. The oxide film is formed on the electrode when $E > 0$ and dissolves when $E < 0$. The rate of film dissolution is proportional to coverage θ , and the rate of film formation is proportional to the active electrode area ($1 - \theta$). At the active sites, metallic dissolution occurs when $E < 0$. The sum of the partial currents of both reactions (Eq. [22] and [23]), each of which depends linearly on potential, may be written as

$$I_p = k_i(1 - \theta) + k_g E \theta^* \quad [24]$$

where

$$\theta^* = \theta \quad \text{for } E < 0$$

$$\theta^* = 1 - \theta \quad \text{for } E > 0$$

k_i is the current density of metallic dissolution (Eq. [22]) at E_p , and k_g is the gradient of the linearized polarization curve for the passivation reaction (Eq. [23]). By linearizing the Nernst equation, an expression for E as a function of H^+ concentration is given by

$$E = k_c(h_0 - h) - (E_i^0 - E_p) \quad [25]$$

where h_0 is the H^+ concentration at a constant standard potential of a given electrolyte, h is the H^+ concentration at the electrode surface, E_i^0 is the Flade potential at h_0 , and $k_c = RT/F$. It is assumed that only the H^+ ions are charge carriers in the electrolyte and that the flux of H^+ is equal to the sum of the diffusional and electromigrational terms. Writing the change of H^+ concentration from the flux equation yields

$$\frac{dh}{dt} = k_d(h_0 - h) - k_m I_p \quad [26]$$

where $k_d = 2D/\delta^2$, $k_m = 2/F\delta$, D is the diffusion coefficient for H^+ , and δ is the diffusion-layer thickness. By differentiating Eq. [25] and then by substitution of Eq. [24] and [26], the result is

$$\frac{dE}{dt} = K_1 - K_2 E - K_3 \theta + K_4 E \theta^* \quad [27]$$

where

$$K_1 = k_d(E_p - E_i^0) + k_m k_c k_i$$

$$K_2 = k_d$$

$$K_3 = k_m k_c k_i$$

$$K_4 = k_m k_c k_g$$

The change in coverage is given by

$$\frac{d\theta}{dt} = K_5 E \theta^* \quad [28]$$

where

$$K_5 = k_r k_g$$

and k_r is equal to the passive layer area, square centimeters per coulomb.

The system of equations (Eq. [27] and [28]) is nonlinear due to the $E\theta$ terms. By means of an analog computer, these equations were integrated by Franck and Fitzhugh and a combination of the five K parameters (or eight individual constants) was found, evidently by a considerable searching effort, to give sinusoidal periodic solutions. A phase-plane portrait was drawn of the solutions for the set of differential equations for three cases: $E > 0$, $E < 0$, and for the discontinuous case of all E not equal to zero. The trajectories indicated an unstable focus for the cases of $E > 0$ and $E < 0$, but a stable limit cycle was found for the discontinuous case for the following set of parameter values: $K_1 = 1250$ mV s⁻¹; $K_2 = 2$ s⁻¹; $K_3 = 2000$ mV s⁻¹; $K_4 = 20$ s⁻¹; and $K_5 = 1$ mV⁻¹ s. Therefore, it was concluded that the discontinuity in E was essential for periodic solutions. Additionally, it was inferred that the assumed linearizations in the model caused it to be invalid, since initial values of E and θ far outside the limit cycle resulted in trajectories tracing toward infinity.

The authors were able to improve their model by assuming a logarithmic dependence of Flade potential on H^+ concentration and including a function for charge transport of SO_4^{-2} and Fe^{2+} ions. However, the charge-transport function was given only graphically and the new parameter values, which resulted in relaxation oscillations, were not stated explicitly. Therefore, this improved model will not be used in the present analysis.

Table I. The determinant and trace of the linearized Jacobian evolved at the steady states of Eq. [27] and [28]

Steady state (E_s, θ_s)	det J	tr J
$E < 0$ ($0, K_1/K_3$) ($K_1/K_2, 0$)	$K_1 K_5$ $-K_1 K_5$	$-K_2 + (K_1 K_4 / K_3)$ $-K_2 + (K_5 K_1 / K_2)$
$E > 0$ ($0, K_1/K_3$) ($[K_1 - K_3]/K_2, 1$)	$K_5(K_3 - K_1)$ $-K_5(K_3 - K_1)$	$-K_2 + K_4 - (K_1 K_4 / K_3)$ $-K_2 + (K_5 / K_2)(K_1 - K_3)$

By applying linear stability and bifurcation analysis to the model of Franck and Fitzhugh, we can gain much information about the steady states and conditions for periodic solutions. By setting both dE/dt and $d\theta/dt$ (Eq. [27] and [28]) equal to zero, the following steady states are determined

$$(E_s, \theta_s) = \{(0, K_1/K_3), (K_1/K_2, 0)\} \quad \text{for } E < 0$$

$$(E_s, \theta_s) = \{(0, K_1/K_3), ([K_1 - K_3]/K_2, 1)\} \quad \text{for } E > 0$$

The model equations may be linearized about the steady state and the determinant and trace of the linearized Jacobian may be evaluated, as shown in Table I, to determine the stability of the steady states and the conditions for bifurcation. Although K_2 through K_5 are always positive, considering the definitions in Eq [27] and [28], K_1 can be positive if $E^{\circ}_i - E_p < K_3/K_2$ or negative if $E^{\circ}_i - E_p > K_3/K_2$. However, since $0 \leq \theta \leq 1$ and $(0, K_1/K_3)$ is a common steady state in both cases of $E \geq 0$, K_1 must be greater than zero.

Franck and Fitzhugh concluded in their paper (10) that a discontinuity in E is necessary for oscillations of the model variables E and θ . However, from our analysis, the steady state $(0, K_1/K_3)$ is a Hopf bifurcation point for the following conditions

$$\text{for } E < 0 \quad K_1 > 0, K_4 = K_2 K_3 / K_1$$

$$\text{for } E > 0 \quad K_3 > K_1, K_4 = K_2 K_3 / (K_3 - K_1) \quad [29]$$

Notice that the conditions are different for the two cases and coincide only when $K_1 = 0.5K_3$. This corresponds to a steady state of $(0, 0.5)$ and a bifurcation parameter $K_4 = 2K_2$ for $E \geq 0$. If we inspect the parameter values found by Franck and Fitzhugh to produce oscillations and thought by them to correspond to a stable limit cycle, we find that a limit cycle occurs not when $K_1/K_3 = 0.5$, but when $K_1/K_3 = 0.625$. The steady state where Hopf bifurcation can occur is at the discontinuity $E = 0$, which is not defined in the model differential equations (Eq. [27] and [28]). This is a weak point of this model.

As shown from the present analysis, conditions for Hopf bifurcation to periodic solutions do exist for the two separate sets of model equations. If we can neglect the development of the model which includes the reasoning for the discontinuity at $E = 0$, then both sets of equations can produce oscillatory behavior for certain parameter values. By using the parameter values given by Franck and Fitzhugh, except for the bifurcation parameter K_4 , which is calculated from Eq. [29], a stable limit cycle is determined around the steady state $(0, 0.625)$ for both sets of model equations with $\theta^* = \theta$ or $\theta^* = 1 - \theta$. In Fig. 4, a stable limit cycle and oscillations are shown for $\theta^* = \theta$ and $K_4 = 3.2$. The frequency of the oscillations is 5.6 Hz, with very small amplitudes of E and θ of 0.88 mV and 0.0016, respectively. Figure 5 shows a stable limit cycle and periodic solution transients for $\theta^* = 1 - \theta$ and $K_4 = 5.33$. The frequency is 4.4 Hz, and the amplitudes of E and θ are somewhat larger than in Fig. 4, 1.68 mV and 0.022, respectively. Thus, both sets of differential equations from Eq. [27] and [28] can give limit cycles and sinusoidal oscillations of E and θ . However, the model development must be reconsidered to give a basis for these equations to represent the active-passive transition region.

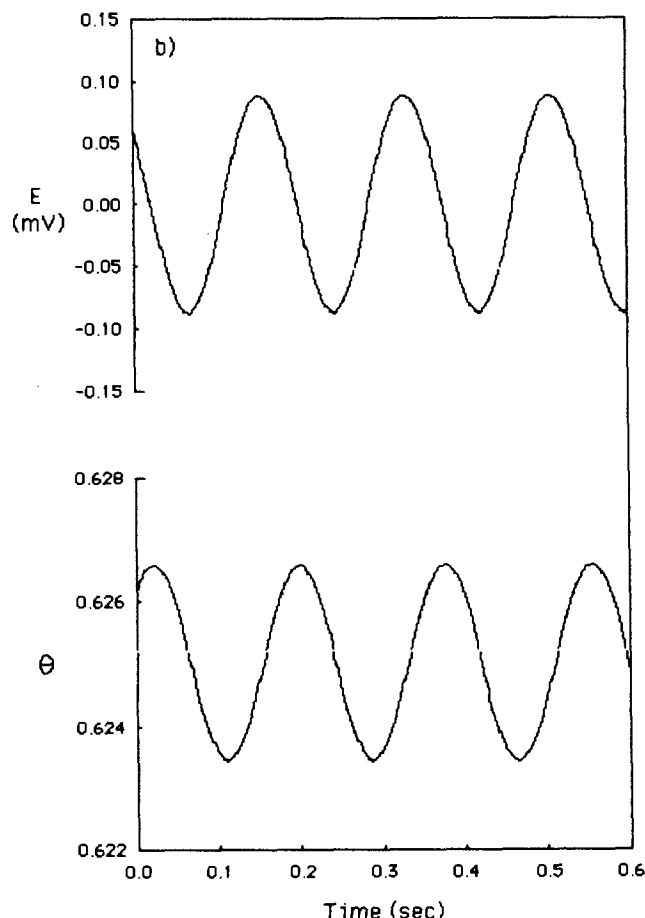
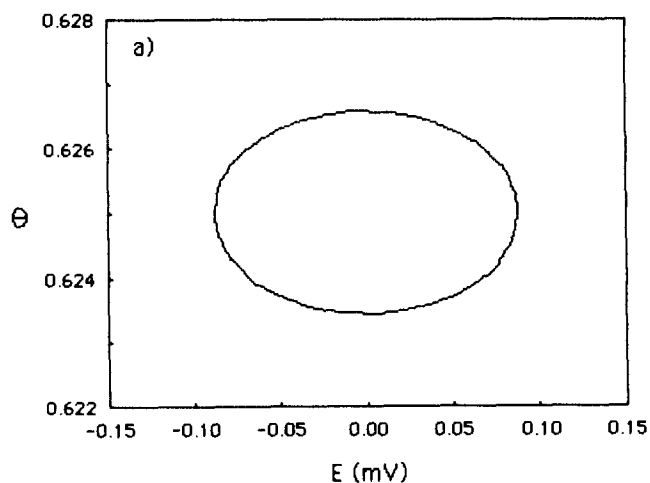


Fig. 4. Limit cycle of E vs. θ around the steady state $(E_s, \theta_s) = (0, 0.625)$ and trajectories of E and θ for the following parameter values: $K_1 = 1250 \text{ mV s}^{-1}$; $K_2 = 2 \text{ s}^{-1}$; $K_3 = 2000 \text{ mV s}^{-1}$; $K_4 = 3.2 \text{ s}^{-1}$; and $K_5 = 1 \text{ mV}^{-1} \text{ s}$.

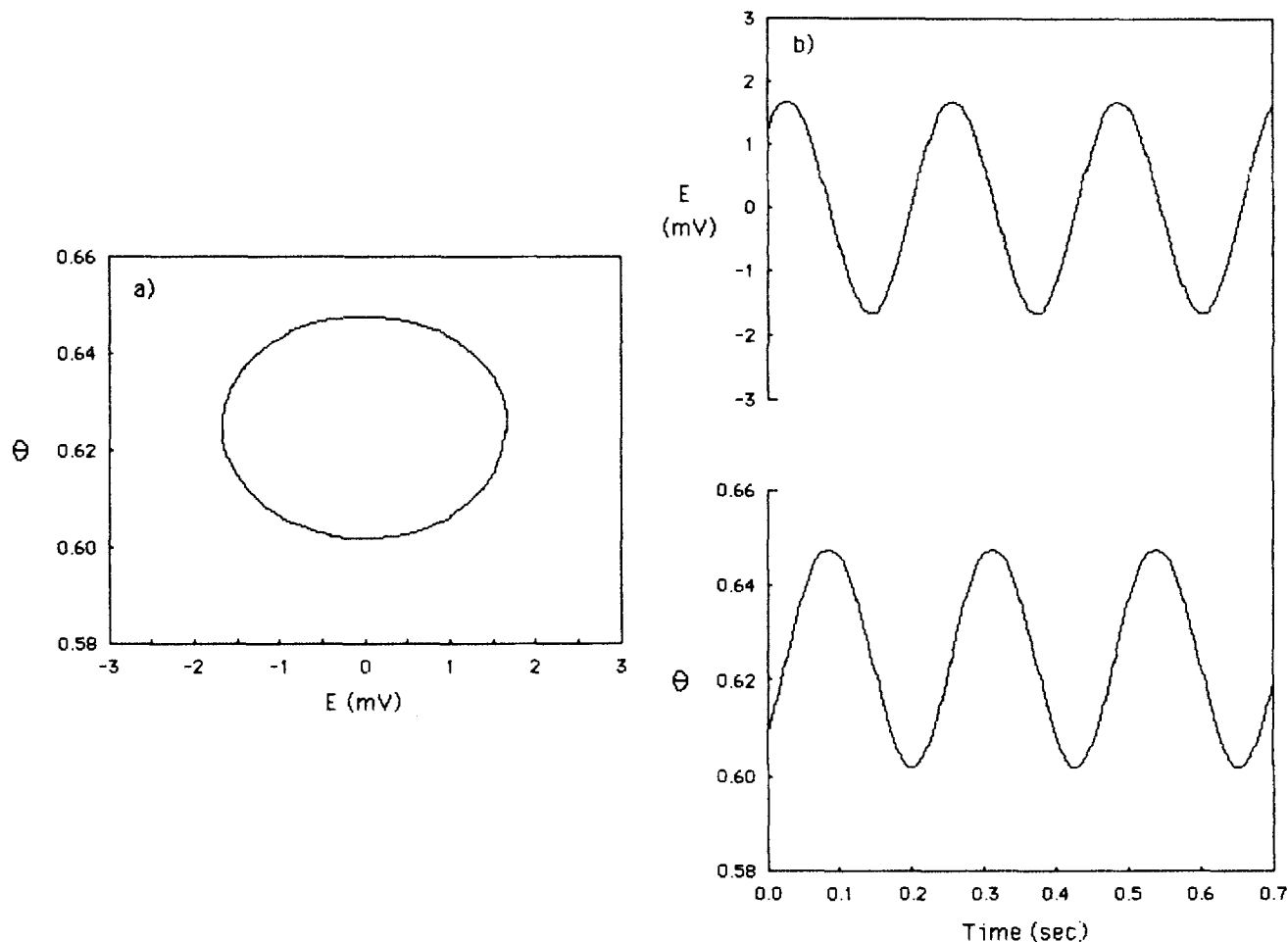


Fig. 5. Limit cycle of E vs. θ around the steady state $(E_s, \theta_s) = (0, 0.625)$ and trajectories of E and θ for the following parameter values: $K_1 = 1250 \text{ mV s}^{-1}$; $K_2 = 2 \text{ s}^{-1}$; $K_3 = 2000 \text{ mV s}^{-1}$; $K_4 = 5.33 \text{ s}^{-1}$; and $K_5 = 1 \text{ mV}^{-1} \text{ s}$.

Another conclusion drawn by Franck and Fitzhugh (10) was that the model did not represent the real system far outside the limit cycle. This is incorrect, for at initial conditions far from the limit cycle trajectories would approach the other steady state. The other steady state in each case is an unstable saddle point, since $\det J < 0$, as displayed in Table I. Actually, these saddle points are each out of the region of consideration of the model. But as a saddle point, the trajectories near them would eventually wind back to the stable steady state.

Summary

The application of stability and bifurcation analysis to two models of passivation from the literature shows the strength of these relatively new mathematical tools. For the one-dimensional model of Griffin (4), the conditions for a static bifurcation to MSS were determined. The two-dimensional model of Franck and Fitzhugh (10) was analyzed for a Hopf bifurcation to periodic solutions. Obviously, MSS does not necessarily imply oscillatory solutions. Indeed, a system of equations of at least two dimensions is required for oscillations to exist. This type of analysis, together with the inherent physical constraints, such as possible positive-valued constants and $0 \leq \theta \leq 1$, for example, gives limits and sometimes exact values of the system parameters for MSS and periodic behavior. Therefore, the search for a set of physically reasonable parameter values which give the desired system dynamics, particularly if there are numerous parameters that could be varied, can be immensely aided by these techniques of analysis. In some cases, the necessary conditions imposed upon the model may prove not to be physically realistic; such an outcome would cast serious doubt on the physical reasonableness of the mechanism itself.

Acknowledgment

This work was sponsored by the Corrosion Research Center of the University of Minnesota, supported by the U.S. Department of Energy under Contract no. DE-FG02-84ER45173.

Manuscript submitted Dec. 18, 1984; revised manuscript received March 5, 1985.

The University of Minnesota assisted in meeting the publication costs of this article.

REFERENCES

1. D. Gilroy and B. E. Conway, *J. Phys. Chem.*, **69**, 1259 (1965).
2. U. Ebersbach, K. Schwabe, and K. Ritter, *Electrochim. Acta.*, **12**, 927 (1967).
3. A. A. El Miligly, D. Geana, and W. J. Lorenz, *ibid.*, **20**, 273 (1975).
4. G. L. Griffin, *This Journal*, **131**, 18 (1984).
5. U. F. Franck, *Z. Phys. Chem. NF*, **3**, 183 (1954).
6. M. C. H. McKubre and D. D. MacDonald, *This Journal*, **128**, 524 (1981).
7. J. J. Podestá, R. C. V. Piatti, and A. J. Arvia, *Electrochim. Acta.*, **24**, 633 (1979); *This Journal*, **126**, 1363 (1979); *Corros. Sci.*, **22**, 193 (1982).
8. S. Hackwood and G. Beni, Paper 90 presented at The Electrochemical Society Meeting, Detroit, MI, Oct. 17-21, 1982.
9. J. Wojtowicz, in "Modern Aspects of Electrochemistry," Vol. 8, J. O'M. Bockris and B. E. Conway, Editors, p. 47, Plenum Press, New York (1972).
10. U. F. Franck and R. Fitzhugh, *Z. Elektrochem.*, **65**, 156 (1961).
11. J. Keizer and D. Scherson, *J. Phys. Chem.*, **84**, 2025 (1980).
12. J. B. Talbot and R. A. Oriani, in "Proceedings of the 9th International Congress on Metallic Corrosion, June 1984," Vol. 3, p. 440, National Research Council, Canada (1984).
13. J. B. Talbot and R. A. Oriani, Paper 271 presented at

The Electrochemical Society Meeting, New Orleans, LA, Oct. 7-12, 1984.
 14. N. Minorsky, "Nonlinear Oscillations," Van Nostrand, Princeton, NJ (1962).

15. J. K. Hale, "Oscillations in Nonlinear Systems," McGraw-Hill, New York (1963).
 16. A. H. Nayfeh and D. T. Mook, "Nonlinear Oscillations," John Wiley and Sons, New York (1979).

Digital Impedance for Faradaic Analysis

I. Introduction to Digital Signal Analysis and Impedance Measurements for Electrochemical and Corrosion Systems

William H. Smyrl^{*1}

Sandia National Laboratories, Albuquerque, New Mexico 87185

ABSTRACT

The faradaic impedance for single reactions on electrodes and for multiple parallel reactions (*e.g.*, corrosion) is discussed for both voltage and concentration perturbations. Concentration perturbations in the presence of convective flow are discussed for the rotating disk. The measurement of impedance by the techniques of digital signal analysis is briefly discussed, and instrumentation to perform the measurements is described.

Previous reports (1, 2) have described preliminary work on the application of digital signal analysis to impedance measurements on corroding systems. The technique of digital impedance for faradaic analysis (DIFA) is to be more fully discussed here. In the following papers, application of DIFA to copper electrodisolution and to copper corrosion in HCl will be discussed in turn. In other papers in the series, DIFA studies of copper corrosion in H₂SO₄ will be described.

An electrochemical cell with two electrodes is characterized by the impedance contributions as shown in Fig. 1. The electrolytic solution has an impedance, Z_s , due only to the resistivity of the solution, except at high frequencies, where the Debye-Falkenhagen effect becomes important (4). Ionic conduction in the solution is transformed to electronic conduction in the metal phase by charge transfer at the interface, which leads to an interfacial impedance Z_i at each electrode. Z_i is composed of a capacitance arising from the departure of the composition from electroneutrality (electrical double layer) and a faradaic impedance associated with the charge-transfer reaction.² In the simplest case of a single electrode reaction on an electrode, the interfacial impedance is a parallel combination of the double-layer capacitance, Z_c , and the faradaic impedance, Z_f , *i.e.*

$$\frac{1}{Z_i} = \frac{1}{Z_c} + \frac{1}{Z_f} \quad [1]$$

The faradaic impedance is determined by the kinetics of the charge-transfer reaction.

The current for a single electrode reaction may be expanded in a Taylor series about steady-state conditions, *i.e.*

$$i = \bar{i} + \left(\frac{\partial i}{\partial V} \right)_{\bar{C}_o} \tilde{V} + \left(\frac{\partial i}{\partial C} \right)_{\bar{V}} \tilde{C}_o \quad [2]$$

The Taylor expansion of the current in Eq. [2] is for small perturbations of the voltage and concentration

$$\begin{aligned} V &= \bar{V} + \tilde{V} \\ C &= \bar{C} + \tilde{C} \end{aligned} \quad [3]$$

where \bar{V} and \bar{C} are steady-state terms and the time varying voltage and concentration are \tilde{V} and \tilde{C} , respectively.

^{*}Electrochemical Society Active Member.

¹Present address: Department of Chemical Engineering and Materials Science, University of Minnesota, Minneapolis, Minnesota 55455.

²A *priori* separation of double-layer impedance and faradaic impedance is assumed here.

The subscript on the concentration in Eq. [2] denotes interfacial conditions. The derivatives in Eq. [2] are determined at steady state, *i.e.*, $V = \bar{V}$, $C = \bar{C}$. With more than one reaction, as in corrosion, a similar expansion may be made for each reaction. Coupling them appropriately will yield the total current as a function of all the perturbations.

Impedance with No Concentration Perturbations

The Butler-Volmer relationship for the current and voltage of a single anodic dissolution reaction is

$$\frac{i}{nF} = k_a \exp \left\{ \frac{\alpha_a F}{RT} V \right\} - k_c C_o \exp \left\{ \frac{-\alpha_c F}{RT} V \right\} \quad [4]$$

where k_a and k_c are heterogeneous rate constants and α_a and α_c are transfer coefficients. V is the voltage with respect to an arbitrary reference electrode, and both k_a and k_c depend on that choice of reference electrode. C_o is the concentration of the metal product ion at the surface. For negligible concentration fluctuations, Eq. [4] and [2] yield a relationship for the faradaic impedance. Since

$$Z_f = \frac{\tilde{V}}{\tilde{i}A} = 1 / \left(\frac{\partial i}{\partial V} \right)_{\bar{C}_o} A \quad [5]$$

the faradaic impedance at zero current density is

$$Z_f = \frac{RT}{i_o n (\alpha_a + \alpha_c) A F} \quad (\text{at } i \rightarrow 0) \quad [6]$$

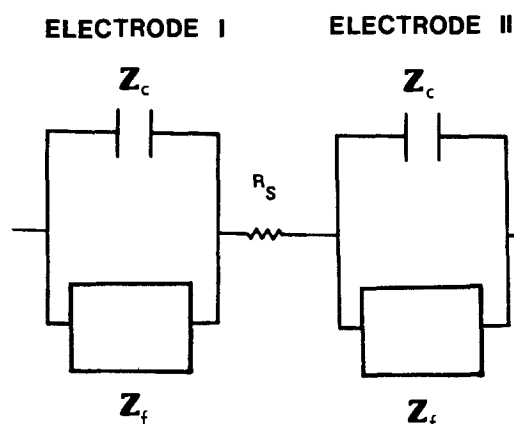


Fig. 1. Equivalent circuit for a simple electrochemical cell consisting of an interfacial impedance on each electrode and a resistor for the electrolytic solution separating the two.

where A is the area of the electrode. The exchange current density for the reaction is related to the heterogeneous rate constants by

$$i_0 = [(k_a^{\alpha_c})(k_c C_0)^{\alpha_a}]^{1/(\alpha_a + \alpha_c)}$$

At large anodic or cathodic current densities, the impedance depends on the current density. In the Tafel limit of large anodic current densities, from Eq. [4] and [2]

$$Z_f = \frac{RT}{\bar{i} \alpha_a A F} \quad [7]$$

A similar expression holds for the cathodic Tafel region.

For situations such as corrosion where several parallel reactions occur simultaneously, the development above may be generalized to

$$\frac{\bar{i}_T}{\bar{V}} = \sum_{\text{anodic}} \left(\frac{\partial i_a}{\partial V} \right) + \sum_{\text{cathodic}} \left(\frac{\partial i_c}{\partial V} \right) \quad [8]$$

or

$$\frac{1}{Z_{f,T}} = \sum_{\text{anodic}} \frac{1}{Z_{f,a}} + \sum_{\text{cathodic}} \frac{1}{Z_{f,c}} \quad [9]$$

The faradaic impedance for a corrosion couple (single anodic reaction 1, single cathodic reaction 2) at the corrosion potential, i.e., $i_T = 0$, is given by

$$Z_{f,T} = \frac{RT}{i_{\text{corr}}(\alpha_{a1} + \alpha_{c2})AF} \quad [10]$$

The corrosion current density is

$$i_{\text{corr}} = \bar{i}_{a1} = -\bar{i}_{c2} \quad [11]$$

The faradaic impedance in Eq. [10] has also been called the linear polarization resistance in the corrosion literature (5).

As an aside, two assumptions were made in developing Eq. [8] and [9]. The first assumption is the principle of superposition of several parallel reactions (6-8). This supposes that each reaction makes an independent contribution (except for electrical coupling) to the total faradaic process. The second assumption is really an approximation that the faradaic process may be treated as a linear system. Electrode processes are inherently nonlinear (see Eq. [4]), but for small perturbations in voltage or concentration, the response may be linear in the limit. This is implied in the use of the Taylor expansions in Eq. [2]. Armstrong *et al.* (9) have also used Taylor expansions for the treatment of impedance of electrochemical systems.

The interfacial impedance for the systems described by Eq. [6]-[10], coupled with the double-layer capacitance, has the well-known semicircular behavior in the complex plane as shown in Fig. 2. The low frequency intercept on the real axis gives the faradaic impedance Z_f . A resistance characterizing the solution resistivity would act in series with the interfacial impedance to shift the entire semicircle in Fig. 2 along the real axis. The low frequency intercept would then be the sum of the faradaic impedance and the solution series resistance. The high frequency intercept on the real axis would be the solution series resistance. Sluyters *et al.* (4, 10) give a complete description of the analysis. More will be said below about the application to the copper corrosion system.

Impedance with both Voltage and Concentration Perturbations

In the presence of concentration effects, the last term of the Taylor expansion in Eq. [3] must be included in the impedance analysis. It is useful to introduce the concentration term for a particular problem, and we choose mass transfer at the rotating disk for further discussion. The classical Warburg treatment (3) of the impedance of diffusion is valid for situations with no convection, and has received adequate treatment in the literature. The impedance for diffusion with superimposed convective flow

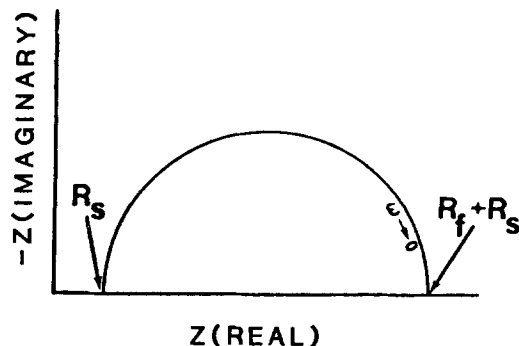


Fig. 2. Complex plane impedance plot of interfacial impedance of an electrode.

has only recently received attention, and will be described here for the purposes of this paper and the succeeding two papers. The concentration of a reactive species C , in the presence of a large excess of supporting electrolyte, obeys the equation

$$\frac{\partial^2 C}{\partial \xi^2} + 3\xi^2 \frac{\partial C}{\partial \xi} - \frac{\partial C}{\partial t^*} = 0 \quad [12]$$

The dimensionless distance normal to the disk surface is

$$\xi = z \left(\frac{\alpha \nu}{3D} \right)^{1/3} \left(\frac{\Omega}{\nu} \right)^{1/2} \quad [13]$$

and the dimensionless time t^* is defined by

$$t^* = t \left(\frac{\alpha \nu}{3D} \right)^{2/3} \left(\frac{\Omega D}{\nu} \right) \quad [14]$$

In the above equations, z is the distance normal to the electrode, α is a constant ($=0.51023$), ν is the kinetic viscosity, D is the diffusion coefficient, and Ω is the rate of rotation of the rotating disk. Homay and Newman (11) and Tribollet and Newman (12) described the concentration fluctuations caused by sinusoidal signal superimposed on a steady-state signal at the limiting current. The time varying current, \bar{i} , and surface concentration, \bar{C}_0 , are related by

$$\frac{\bar{i}}{nF} = -D \left. \frac{\partial C}{\partial y} \right|_{y=0} \quad [15]$$

or

$$\frac{\bar{i}}{nF} = \frac{-D \bar{C}_0}{\delta} \left. \frac{d\theta}{d\xi} \right|_{\xi=0} \quad [16]$$

The last equation was derived by recognizing that C would be given by a separation of variables

$$\bar{C} = B (\exp iKt^*) \theta \quad [17]$$

for a sinusoidal current of frequency ω . The parameter K is a dimensionless frequency given by

$$K = \omega \left(\frac{3D}{\alpha \nu} \right)^{2/3} \left(\frac{\nu}{\Omega D} \right) \quad [18]$$

δ is the steady-state diffusion layer thickness on the rotating disk, i.e.

$$\delta = \left(\frac{3D}{\alpha \nu} \right)^{1/3} \left(\frac{\nu}{\Omega} \right)^{1/2} \Gamma(4/3) \quad [19]$$

The variable θ obeys the equation

$$\frac{d^2 \theta}{d\xi^2} + 3\xi^2 \frac{d\theta}{d\xi} - jK\theta = 0 \quad [20]$$

where $j = \sqrt{-1}$, subject to the boundary conditions

$$\begin{aligned} \theta &= 1 \text{ at } \xi = 0 \\ \theta &= 0 \text{ as } \xi \rightarrow \infty \end{aligned}$$

Tribollet and Newman (12) have solved Eq. [19] for both low and high frequencies, and Levart and Schuhman (13, 14) treated the problem earlier. Analytic results were also obtained for

$$\left. \frac{d\theta}{d\xi} \right|_{\xi=0} = \theta'(0)$$

which is the surface flux and is important for impedance calculations through Eq. [16].

The Taylor expansion, Eq. [3], may now be written

$$\bar{i} = \left(\frac{\partial i}{\partial V} \right)_{\bar{c}_o} \bar{V} + \left(\frac{\partial i}{\partial C_o} \right)_{\bar{V}} \left[- \frac{\bar{i}\delta}{nFD\theta'(0)} \right] \quad [21]$$

or

$$\bar{i} = \left[\left(\frac{\partial i}{\partial V} \right)_{\bar{c}_o} \bar{V} \right] / \left[1 + \frac{\left(\frac{\partial i}{\partial C_o} \right)_{\bar{V}} \delta}{nFD\theta'(0)} \right] \quad [22]$$

The faradaic impedance is given by the formal equation

$$Z_f = \frac{\bar{V}}{\bar{i}A} = \left[1 - \left(\frac{\partial i}{\partial C_o} \right)_{\bar{V}} \left(\frac{\delta}{nFD} \right) \left(- \frac{1}{\theta'(0)} \right) \right] / A \left(\frac{\partial i}{\partial V} \right)_{\bar{c}_o} \quad [23]$$

The concentration-dependent term is the Warburg impedance in the presence of convective flow. The Warburg impedance is dependent on the frequency of the perturbation, becoming negligible at high frequencies, but with a finite value at low frequencies. The latter property should be contrasted with the classical Warburg impedance (no convective flow), which approaches an infinite value as the frequency decreases to zero. Equation [23] will be used in succeeding papers in the analysis of copper dissolution kinetics in HCl, and further discussion will be presented there.

To summarize this section, the departure from steady-state current due to small perturbations of voltage and concentration may be treated by a Taylor series expansion. Equations [6] and [7] give the faradaic impedance for single reactions, and Eq. [8] and [10] give the impedance for coupled, parallel reactions—all in the absence of concentration perturbations. For the reaction of a minor component in an excess of supporting electrolyte, concentration effects lead to a faradaic impedance which is given by Eq. [23] for a rotating disk system.

Digital Impedance for Faradaic Analysis

In the previous section, the relation between the total impedance and the faradaic impedance was briefly described for simple systems. Several equations for the faradaic impedance were developed which gave the dependence on reaction parameters for single and multiple reactions. These results will be used in the following papers for analysis of the impedance of copper dissolution and corrosion in order to determine the kinetics of the reactions. The purpose of the present section is to describe the measurement of the overall interfacial and cell impedance by digital acquisition and processing of voltage and current signals.

Studies of the impedance of electrochemical cells have been carried out for many years for the purpose of determining the kinetics of faradaic processes. Reviews are available on the classical techniques of measurement (4, 10, 15), and in the analysis of results (4), and for corrosion systems as well (16). The present paper will describe the technique of digital impedance for faradaic analysis (DIFA), which was first described elsewhere (1, 2). This represents the first application of fast Fourier transform (FFT) processing of multiple-frequency signals for corrosion studies. It is similar to the studies of Smith *et al.* (17-23) on electroanalytical applications, and Epelboin *et al.* (24) have used similar ideas for frequency-by-frequency impedance analysis in corrosion systems.

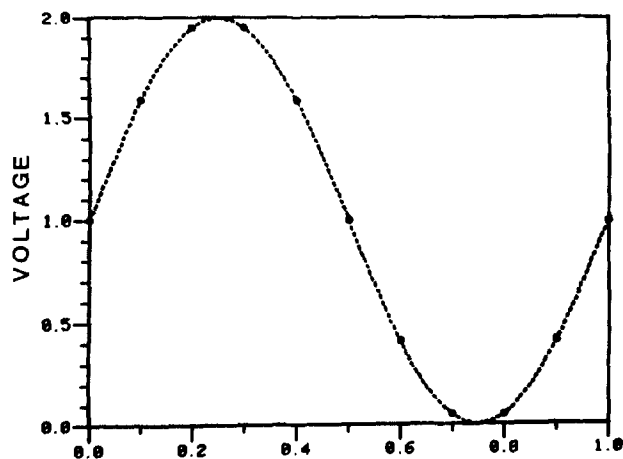


Fig. 3. Continuous signal and the equal interval samples over one period.

The basic ideas of digital signal analysis (1, 25) may be developed by considering the signal in Fig. 3. The signal $f(t)$ is sampled at regular intervals Δt to produce a set (not a series) of samples, $[f_n(t)]$. The total sampling interval is $T = n\Delta t$. The sample $f_n(t)$ is presumed to be the value of the continuous function $f(t)$ at the sampling point. The discrete Fourier transform (DFT) of the sample set is defined by (25)

$$\hat{F}(j\omega) = \sum_{n=-\infty}^{\infty} f_n(t) e^{-jn\omega\Delta t} \quad [24]$$

\hat{F} has both real and imaginary parts, and is periodic over ω with period $2\pi/\Delta t$. In actual practice, one samples over a finite period T , so that Eq. [24] becomes

$$\hat{F}(j\omega) = \sum_{n=0}^{N-1} f_n(t) e^{-jn\omega\Delta t} \quad [25]$$

where there are a total of N samples which begin at $t = 0$. Since there are only N independent samples, there are N independent parts of \hat{F} , to be computed over one of its periods, say $\omega\Delta t = 0$ to 2π . Let

$$\omega = \frac{2\pi m}{N\Delta t} \quad m = 0, 1, \dots, N-1 \quad [26]$$

and Eq. [25] becomes

$$\hat{F}_m = \sum_{n=0}^{N-1} f_n(t) e^{-j(2\pi mn/N)} \quad m = 0, 1, \dots, N-1 \quad [27]$$

Of the $2N$ parts (real and imaginary) of F_m in Eq. [26], only the values from $m = 0$ to $N/2$ need to be computed since

$$\hat{F}_m = \hat{F}_{N-m}^* \quad [28]$$

and the asterisk denotes complex conjugate. We complete the definitions by noting that the inverse DFT is

$$f_n(t) = \frac{1}{N} \sum_{m=0}^{N-1} \hat{F}_m e^{j(2\pi mn/N)} \quad n = 0, 1, \dots, N-1 \quad [29]$$

For each set of samples in the time domain $[f_n(t)]$, there is a set of values in the frequency domain (F_m), and the two sets are related by Eq. [27] and [29]. The frequency ω of an individual member of $[F_m]$ is given by Eq. [26].

For a sinusoidal signal such as in Fig. 3

$$f(t) = \bar{A} e^{j\omega_0 t} \quad f_n(t) = \bar{A} e^{jn\omega_0 \Delta t} \quad [30]$$

all the spectral content is concentrated at ω_0 . Using Eq. [24]

$$\hat{F}(j\omega) = \bar{A} (1 - e^{jN(\omega_0 - \omega)\Delta t}) (1 - e^{j(\omega_0 - \omega)\Delta t}) \quad [31]$$

As $\omega \rightarrow \omega_0$, one obtains

$$\hat{F}(j\omega_0) = \bar{A}N \quad [32]$$

and at multiples of ω_0 , i.e., $\omega = m\omega_0$

$$\hat{F}(j\omega) = 0 \quad [33]$$

This means that at harmonics of the input signal of frequency (ω_0), the DFT gives the correct spectrum if the frequency of a member of the set $[F_m]$ matches ω_0 , i.e.

$$\omega_m = \frac{2\pi m}{N\Delta t} = \omega_0 \quad [34]$$

All other members of the set $[F_m]$ are zero. For specifics, we choose $m = 1$, and see that the product $(N\Delta t)$ must be chosen such that Eq. [34] is obeyed. This constitutes "matching" the frequency of the DFT to that of the input signal to obtain accurate results. Stated another way, the input spectrum should be sampled over an integral number of periods. Failure to do this leads to a "leakage" error, which is discussed elsewhere (25).

The results may be generalized as follows. For an input spectrum which consists of superimposed sinusoids such that the higher frequency members are harmonics of the lowest frequency ω_0 , the DFT gives a spectrum set $[F_m]$ which is accurate at ω_0 and each of the higher harmonics, provided that sampling is over exactly an integral number of periods of the lowest frequency. This requirement automatically ensures that the higher frequency harmonics are sampled over an integral number of periods as well. One other restriction concerns the highest frequency that may be included in the spectrum. For a given sample interval, Δt , the highest frequency that may be accurately sampled is given by the relation

$$\omega_{HI} \leq \frac{1}{2\Delta t} \quad [35]$$

otherwise, "aliasing" will occur (25). Thus, it is seen that the full power of DFT processing is utilized by multiple frequency signals subject to the restrictions of periodicity and aliasing. The use of such an excitation signal (1) is described further below. Smith *et al.* (17-23) and de Levie (26) have used multiple frequency signals for impedance determinations in other applications.

Performing the discrete Fourier transform on a computer is done by the fast Fourier transform (FFT) algorithm (25). The operation gives the spectral content of the processed signal in terms of a set (not a series) of values $[F_m]$. This has a close similarity to the classical method of approximating an arbitrary function by the superposition of sinusoids, i.e., a Fourier series. The set $[F_m]$ has a close correspondence to the coefficients of the Fourier series representation. In the present application, the input signal is not arbitrary, but has known frequency content, which is chosen to match the requirements of the FFT, as discussed above.

The ratio of the voltage excitation spectra $[V_m]$ to the current response $[I_m]$, at each frequency, is the impedance for a linear system, i.e.

$$Z_m = \frac{\hat{V}_m}{\hat{I}_m} \quad [36]$$

The subscript m identifies the frequency of the respective functions, as given in Eq. [26]. The requirement of linearity is met for electrochemical systems for voltage perturbations of < 5 mV as a general rule, and means that the impedance at one frequency is independent of that at other frequencies. A more detailed discussion of the impedance transfer function for linear electrical circuits and networks is given by Stearns (25). As a closing comment, it should be noted that Eq. [36] is valid at the frequency ω_m (see Eq. [26]), independent of the form of the input. Several different voltage excitation signals could be used, but, compared at the same frequency, all would give identical values of the impedance.

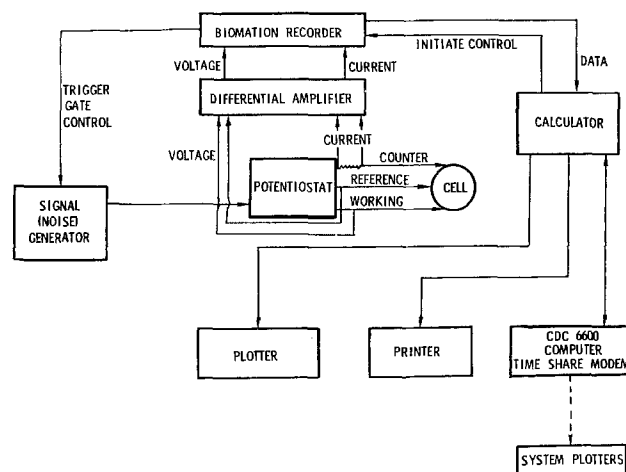


Fig. 4. Block diagram of system used for digital impedance for faradaic analysis measurements.

Measurement System Description

The measurement of impedance by DIFA is reported here and following with a system (1, 2, 27) which consisted of four elements.

1. The first component was the multiple frequency signal generator (Hewlett-Packard Noise Generator) which provided a signal of known frequency content. It consisted of several (in our case, either 51 or 101) sinusoids superimposed to produce the final signal. The lowest frequency of the set was ω_0 , and the higher members were harmonics (both odd and even) up to the cutoff frequency.

2. The second component was the digitizer (Biomation Waveform Recorder Model 1015) and low-pass filter and amplifier (Preston Scientific). The filter eliminated high frequency noise to prevent aliasing. The digitizer had a 1024 word memory per channel, so that a total of 511 frequencies would be analyzed simultaneously. The signal generator cannot be matched with the digitizer for more than 101 frequencies and still avoid leakage and/or aliasing, and the results described below typically used 51 frequencies in the input signal. The digitizer was synchronized exactly with the signal generator so that the total sampling period is equal to the generating sequence period.

3. The third member of the system was the calculator-controller (Hewlett-Packard 9830), which initiated the measurement cycle and stored the data received from the digitizer. Repetitive cycles could be run for time domain averaging of data. No FFT processing was done with the calculator. The data were transmitted via phone line to a large-scale computer (CDC 6600) for FFT processing and plotting. Impedance data could be transmitted back to the calculator for mass storage, but were stored on magnetic tape in the 6600 system more typically.

4. The electrochemical cell and control potentiostat constituted the fourth element of the system. The voltage excitation signal was superimposed on the steady-state control voltage at the input to the potentiostat and was a small perturbation to the control voltage, typically 3-5 mV peak to peak. The data described below were taken at 500 Hz and below, which was quite adequate for analysis of the copper dissolution and corrosion system. The voltage signal between the working electrode and the reference electrode was measured at the electrochemical cell by a voltage follower, and the signal was filtered and input to one channel of the digitizer. Simultaneously, the current response signal was measured as a voltage drop across a precision resistor in series with the electrochemical cell. The current signal was filtered in a duplicate filter and input to a second channel of the digitizer. In this way, the impedance data corresponded to the interfacial impedance plus a solution ohmic drop for that part of

the electrolytic solution between the reference electrode and the working electrode.

The system is capable of application over a wide range of frequencies. The signal generator can generate spectra between 1.5×10^{-4} Hz and 50 kHz. The digitizer can sample signals between 2×10^{-5} Hz and 50 kHz, and the low-pass filters may be used to 100 kHz. The system has been used successfully over the frequency range 10^{-4} to 50,000 Hz with no difficulty. The precision of the results has been limited by the Biomation digitizer which stored the data as 10 bit words, *i.e.*, the precision as 1 part in 1024. Noise pickup over some frequency ranges limited the precision for single runs to about 1%, but multiple run averages significantly improved the results. Typical precision has been found to be 0.5-1%. The accuracy of the system checked with precision resistor-capacitor networks approached 0.1%.

A final word may be said about convenience of DIFA as compared to frequency-by-frequency techniques. At high frequencies, the two are rather comparable in the time involved for data collection. DIFA offers significant savings of time at lower frequency ranges where the data are collected at the higher harmonics in the frequency band at the same time that the fundamental frequency is sampled. The time savings may be crucial for electrochemical systems that change with time, such as corrosion.

Summary

The impedance of several electrochemical processes have been reviewed in general, with use of a Taylor expansion for small amplitude voltage and concentration perturbations. Special attention was given to the Warburg impedance in the presence of convective flow for a rotating disk electrode. The principles of digital signal analysis have been reviewed briefly, and an experimental apparatus for conducting FFT electrochemistry has been described.

Acknowledgment

This work was supported by the U.S. Department of Energy under Contract no. DE-AC04-76DP00789.

Manuscript submitted Feb. 1, 1984; revised manuscript received *ca.* Feb. 8, 1985.

REFERENCES

1. W. H. Smyrl, in "Electrochemical Techniques for Corrosion Testing," F. Mansfeld and U. Bertocci, Eds.,

- tors, ASTM, Philadelphia (1980).
2. W. H. Smyrl, Paper 132 presented at The Electrochemical Society Meeting, Denver, CO, Oct. 11-16, 1981.
3. W. H. Smyrl, Unpublished data.
4. M. Sluyters-Rehbach and J. H. Sluyters, in "Electroanalytical Chemistry," Vol. 4, A. J. Bard, Editor, Marcel Dekker, New York (1970).
5. F. Mansfeld, in "Advances in Corrosion Science and Corrosion Engineering," Vol. 8, M. Fontana and R. Staehle, Editors, Plenum Press, New York (1978).
6. C. Wagner and W. Traud, *Z. Electrochem.*, **44**, 391 (1938).
7. W. H. Smyrl, in "Comprehensive Treatise of Electrochemistry," Vol. 4, J. O'M. Bockris *et al.*, Editors, Plenum Press, New York (1981).
8. H. Kaesche, *Z. Metallk.*, **61**, 94 (1970).
9. R. A. Armstrong, M. F. Bell, and A. A. Metcalfe, "Specialist Periodical Reports — Electrochemistry," Vol. 6, The Chemical Society, London (1978).
10. J. H. Sluyters, *Recl. Trav. Chim. Pays-Bas*, **79**, 1092 (1960).
11. R. V. Homsy and J. Newman, *This Journal*, **121**, 521 (1974).
12. B. Tribollet and J. Newman, *ibid.*, **130**, 822 (1983).
13. E. Levart and D. Schuhmann, *J. Electroanal. Chem. Interfacial Electrochem.*, **53**, 77 (1974).
14. E. Levart and D. Schuhmann, *This Journal*, **122**, 1082 (1975).
15. D. D. MacDonald, "Transient Techniques in Electrochemistry," Plenum Press, New York (1977).
16. D. D. MacDonald and M. C. H. McKubre, in "Electrochemical Techniques of Corrosion Testing," F. Mansfeld and U. Bertocci, Editors, ASTM, Philadelphia (1980).
17. S. C. Creason and D. E. Smith, *J. Electroanal. Chem. Interfacial Electrochem.*, **36**, A1 (1972).
18. S. C. Creason and D. E. Smith, *ibid.*, **40**, 1 (1972).
19. D. E. Smith, *Anal. Chem.*, **48**, 517A (1976).
20. R. J. Schwall, A. M. Bond, and D. E. Smith, *ibid.*, **49**, 1805 (1977).
21. R. J. Schwall, A. M. Bond, and D. E. Smith, *J. Electroanal. Chem. Interfacial Electrochem.*, **85**, 217 (1977).
22. A. M. Bond, R. J. Schwall, and D. E. Smith, *ibid.*, **85**, 231 (1977).
23. D. E. Smith, *Anal. Chem.*, **48**, 221A (1976).
24. I. Epelboin, M. Keddam, and H. Takenouti, *J. Appl. Electrochem.*, **2**, 71 (1972).
25. S. D. Stearns, "Digital Signal Analysis," Hayden, Rochelle Park, NJ (1975).
26. R. de Levie, *J. Electroanal. Chem. Interfacial Electrochem.*, **62**, 111 (1975).
27. W. H. Smyrl and S. L. Pohlman, Paper 5 presented at The Electrochemical Society Meeting, Seattle, WA, May 21-26, 1978.

Digital Impedance for Faradaic Analysis

II. Electrodeposition of Cu in HCl

William H. Smyrl^{*1}

Sandia National Laboratories, Albuquerque, New Mexico 87185

ABSTRACT

The electrodeposition of Cu was studied experimentally by both steady-state and impedance (DIFA) techniques on a rotating disk. The anodic dissolution was found to be largely mass-transfer controlled, but a kinetic contribution could be identified at high rotation rates. The steady-state behavior was satisfactorily modeled, and kinetic parameters α_a , α_c and the exchange current density were determined. The impedance of the system was also modeled; experimental results confirmed the steady-state kinetic parameters and the mass-transfer-kinetic model at all frequencies.

Copper anodically dissolves in acidic chloride solution to form CuCl_2^- (1-14) at low current densities and Cl^- concentrations less than $\sim 1\text{M}$. Higher complexes are formed at other current densities and concentrations (11). The dissolution to form CuCl_2^- has been found to follow Tafel-like behavior with a slope of 60 mV/decade at 25°C (1-14). The current at any potential has been found to be

strongly dependent on stirring conditions, and the dependence is roughly the square root of rotation speed for a rotating disk (7, 8, 10-13). The purpose of the present paper is to extend these measurements on electrodeposition, and to give a more complete analysis for both steady-state and impedance determinations.

Kinetics of Electrodeposition

Copper anodically dissolves in acidic chlorides by the one-electron reaction

^{*}Electrochemical Society Active Member.

¹Present address: Department of Chemical Engineering and Materials Science, University of Minnesota, Minneapolis, Minnesota 55455.



The cuprous species also participates in a complexation reaction, which has the equilibrium constant (15)

$$K_c = \frac{[\text{CuCl}_2^-]}{[\text{Cu}^+][\text{Cl}^-]^2} = 6.96 \times 10^4 \quad [2]$$

The current density for copper dissolution is then (16)

$$\frac{i}{F} = k_a \exp \left\{ \frac{\alpha_a F}{RT} V \right\} - k_c (C_{\text{Cu}^+}^0) \exp \left\{ \frac{-\alpha_c F}{RT} V \right\} \quad [3]$$

or, with Eq. [2]

$$\frac{i}{F} = k_a \exp \left\{ \frac{\alpha_a F}{RT} V \right\} - k_c \frac{C_1}{K_c (C_2^0)^2} \exp \left\{ \frac{-\alpha_c F}{RT} V \right\} \quad [4]$$

In these equations, the first term is the anodic term, the second is cathodic, and both reactions are taken to be fast, *i.e.*, both k_a and k_c , the heterogeneous rate constants, are large. The superscripts on the concentrations in the cathodic term indicate interfacial conditions ($z = 0$). C_1 is the surface concentration of CuCl_2^- , and C_2^0 that for Cl^- . α_a and α_c are the kinetic transfer coefficients for the forward and backward reactions, respectively, and are shown below to be equal to 0.5. F , R , and T have their usual significance. The potential V is the potential of the electrode with respect to the saturated calomel electrode, unless otherwise noted. This choice of a reference of potential is arbitrary, but convenient for electrodisolution measurements in solutions containing none of the product metal ion.

For zero bulk solution concentration of CuCl_2^- , and a large excess of Cl^- in solution, Eq. [4] becomes

$$\frac{i}{F} = k_a \exp \left\{ \frac{\alpha_a F}{RT} V \right\} - \frac{k_c C_1^0}{K_c C_2^2} \exp \left\{ \frac{-\alpha_c F}{RT} V \right\} \quad [5]$$

The surface concentration C_1^0 at steady state is determined by the kinetics of the reactions, subtracting that which is transported into the solution by diffusion and convection. The rotating disk electrode system was chosen for the studies in this and the following paper because the mass transport can be characterized quantitatively under both steady-state and time varying conditions at the surface (17-19).

The steady flux of CuCl_2^- at the surface may be shown to be (for zero CuCl_2^- concentration in the bulk)

$$N_1 = \frac{D_1 C_1^0}{\delta} \quad [6]$$

Equation [6], along with

$$N_1 = \frac{i}{F} \quad [7]$$

may be used to eliminate C_1^0 in Eq. [5], to yield

$$\frac{i}{F} = \frac{k_a \exp \left\{ \frac{\alpha_a F}{RT} V \right\}}{\left[1 + \frac{\bar{k}}{C_2^2 \Omega^{1/2}} \exp \left\{ \frac{-\alpha_c F}{RT} V \right\} \right]} \quad [8]$$

The diffusion-layer thickness for the rotating disk, δ , in Eq. [6] is given by the relationship (17, 18)

$$\delta = 1.6117 D_1^{1/3} \nu^{1/6} \Omega^{-1/2} \quad [9]$$

where ν is the kinematic viscosity of solution, D_1 is the diffusion coefficient of CuCl_2^- , and Ω is the disk rotation rate. In Eq. [8], \bar{k} is

$$\bar{k} = \frac{k_c}{K_c} (1.6117 D_1^{-2/3} \nu^{1/6}) \quad [10]$$

Equation [8] describes the general current-voltage behavior expected for electrodisolution of copper in HCl. In the limit that the second term in the denominator of

Eq. [8] is much larger than the first

$$\frac{i}{F} = \frac{k_a C_2^2 \Omega^{1/2}}{\bar{k}} \exp \left\{ \frac{(\alpha_a + \alpha_c) F}{RT} V \right\} \quad [11]$$

The slope

$$\frac{dV}{d(\log i)} = \frac{2.303 RT}{(\alpha_a + \alpha_c) F} \quad (\text{constant rotation rate}) \quad [12]$$

is 59 mV/decade at 25°C when

$$(\alpha_a + \alpha_c) = 1 \quad [13]$$

The slope given by Eq. [12] and [13] is that found experimentally in all laboratories (1-14), including our own (to be reported below). The slope $dV/d(\log i)$ expected for the general Eq. [8] is a complex function which approaches Eq. [12] as a limiting case.

Equation [11] describes the limiting behavior when the dissolution rate is controlled by the rate at which the product species is removed from the surface by convection and diffusion. The limiting case would be expected for fast kinetics (specifically fast cathodic kinetics) and slow rates of mass transfer. Conversely, as the rotation rate of a rotating disk is increased, the dissolution rate should deviate from Eq. [11] and should follow the more general Eq. [8], where there is mixed mass-transfer-kinetic control. The mixed mass-transfer-kinetic regime for electrodisolution of Cu was investigated in this laboratory, and the results are described further below.

Bockris and Despic (20) were apparently the first to develop a relationship similar to Eq. [8], but not for a rotating disk. The same equation was derived again later (6), for discussion of the electrodisolution of Cu and Cu-Ni alloys, but it was never used. Instead, an equation similar to Eq. [11] was used under conditions of modest rates of mass transfer. Kiss *et al.* (7-8) developed Eq. [11], and, for general complexation reactions, for Cu dissolution studies on a rotating disk. Equation [11] (or an equivalent) for the rotating disk was used by all other investigators for Cu electrodisolution in chloride solutions. No one has previously investigated the mixed mass-transfer-kinetic regime for Cu dissolution.

Nobe *et al.* (11) found the dissolution current density to be proportional to the square of the chloride concentration, in agreement with Eq. [11]. At higher current densities and chloride concentrations, some deviations were observed, but these were found to be due to the formation of higher cuprous complexes or to precipitation of chloride films.

Kiss *et al.* (7, 8), Bonfiglio *et al.* (14), Nobe *et al.* (11), and Moreau (10) all found the Cu dissolution rate to be a function of rotation rate for a rotating disk. The current density was shown to be a linear function of $\Omega^{1/2}$, with $i \rightarrow 0$ as $\Omega^{1/2} \rightarrow 0$, as given by Eq. [11]. In all these studies, the mass-transfer rates were either modest (low rotation rates) or the chloride concentration was high and Eq. [11] would be expected to be a suitable approximation for mass transfer controlled dissolution.

Riddiford (21) has suggested the use of the rotating disk for the study of fast electrode reactions under mixed mass-transfer-kinetic control, but it has not been used for the study of anodic dissolution reactions. For anodic dissolution, a desirable procedure would be to use high rotation rates and zero solution concentration of the product ion. Inverting Eq. [8], one obtains

$$\frac{F}{i} = \frac{1}{k_a} \exp \left\{ \frac{-\alpha_a F}{RT} V \right\} + \frac{\bar{k}}{k_a C_2^2 \Omega^{1/2}} \exp \left\{ \frac{-(\alpha_a + \alpha_c) F}{RT} V \right\} \quad [14]$$

The reciprocal of the current density should be a linear function of $\Omega^{-1/2}$, with a finite intercept at $\Omega \rightarrow \infty$. The intercept is just the anodic contribution to the current density, evaluated in the absence of mass-transfer effects, *i.e.*

$$\lim_{\Omega \rightarrow \infty} \left(\frac{F}{i} \right) = \left(\frac{1}{k_a} \right) \exp \left\{ \frac{-\alpha_a F}{RT} V \right\} \quad [15]$$

and the slope at constant potential is

$$\frac{\partial \left(\frac{F}{i} \right)}{\partial (\Omega^{-1/2})} = \frac{\bar{k}}{k_a C_2^2} \exp \left\{ \frac{-(\alpha_a + \alpha_c) F}{RT} V \right\} \quad [16]$$

The two heterogeneous rate constants

$$k_a \exp \left\{ \frac{\alpha_a F}{RT} V \right\}$$

and

$$k_c \exp \left\{ \frac{-\alpha_c F}{RT} V \right\}$$

may be determined from Eq. [15] and [16]. The present investigation used this analysis technique with high rotation rates and low chloride concentration to enhance the influence of kinetics on the dissolution process. It should be noted that the behavior described in Eq. [15] and [16] is general and should be approached by all "mass-transport-controlled" dissolution reactions as the rotation rate is increased. In this sense, the technique of determining the rate constants by extrapolating to $\Omega \rightarrow \infty$ is general and may be applied to other situations as well. Aside from aqueous systems, the dissolution of Cr in molten $\text{AlCl}_3\text{-NaCl}$ also appears to be described by the formalism given above (22).

The exchange current density for the Cu/CuCl_2^- system is related to the heterogeneous rate constants by

$$\frac{i_0}{F(C_{\text{Cu}^+})^{\alpha_a/(\alpha_a+\alpha_c)}} = (k_a)^{\alpha_c/(\alpha_a+\alpha_c)} (k_c)^{\alpha_a/(\alpha_a+\alpha_c)} \quad [17]$$

Thus, one may obtain the quantities

$$k_a \exp \left\{ \frac{\alpha_a F}{RT} V \right\} \quad \text{and} \quad k_c \exp \left\{ \frac{-\alpha_c F}{RT} V \right\}$$

as described above at any measured potential. The exchange current density, given in Eq. [17], is independent of the choice of the reference electrode, since

$$\left[k_a \exp \left\{ \frac{\alpha_a F}{RT} V \right\} \right]^{\alpha_c/(\alpha_a+\alpha_c)} \times \left[k_c \exp \left\{ \frac{-\alpha_c F}{RT} V \right\} \right]^{\alpha_a/(\alpha_a+\alpha_c)} = k_a^{\alpha_c/(\alpha_a+\alpha_c)} k_c^{\alpha_a/(\alpha_a+\alpha_c)} \quad [18]$$

The measurements to be described below were analyzed to yield the exchange current density for Cu/CuCl_2^- , a fundamental kinetic parameter for the system. A procedure described earlier (6) to determine the exchange current density involved Eq. [11], and this appears to be inappropriate.

DIFA Measurements in Electrodeposition

Time varying measurements on electrodeposition supplemented the steady-state investigations. The digital impedance for faradaic analysis (DIFA) technique was described in the first paper of this series (23) and was used here for the kinetic investigation. The rotating disk was used for the impedance studies, and the time varying current (\bar{i}) and concentration gradient at the electrode surface are related by

$$\frac{\bar{i}}{F} = -D_1 \frac{\partial \bar{C}_1}{\partial z} \Big|_{z=0} \quad [19]$$

As in the previous paper, the concentration of CuCl_2^- has a steady part and a time varying component

$$C_1 = \bar{C}_1 + \tilde{C}_1 \quad [20]$$

where \tilde{C}_1 is of the form [cf. Ref. (19) and (24)]

$$\tilde{C}_1 = B \theta \exp(jt\omega) \quad [21]$$

where B is a constant, $j = \sqrt{-1}$, ω is the excitation frequency, and the function θ contains the spatial dependence of \tilde{C}_1 . Equation [19] becomes

$$\frac{\bar{i}}{F} = \frac{-D_1 \bar{C}_1}{\delta} \frac{\partial \theta}{\partial \xi} \Big|_{\xi=0} \quad [22]$$

the variable ξ is

$$\xi = z\Gamma(4/3)/\delta \quad [23]$$

and δ is given by Eq. [9]. Γ is the gamma function (31).

The faradaic impedance was given formally in the preceding paper, i.e.

$$Z_f = \left[1 + \frac{\left(\frac{\partial i}{\partial \bar{C}_1} \right) \delta}{FD_1 \theta'(0)} \right] / \left(\frac{\partial i}{\partial \bar{V}} \right)_{\bar{C}_1} \quad [24]$$

and

$$\theta'(0) = \frac{\partial \theta}{\partial \xi} \Big|_{\xi=0} \quad [25]$$

The time varying voltage and concentration are small perturbations about steady state, and the derivatives may be evaluated from the previous section. From Eq. [5]

$$\left(\frac{\partial i}{\partial \bar{C}_1} \right)_{\bar{V}} = \frac{k_c F}{K_c C_2^2} \exp \left\{ \frac{-\alpha_c F}{RT} \bar{V} \right\} \quad [26]$$

$$\left(\frac{\partial i}{\partial \bar{V}^c} \right)_{\bar{C}_1} = \frac{F^2 (\alpha_a + \alpha_c) k_a}{RT} \exp \left\{ \frac{\alpha_a F}{RT} \bar{V} \right\} - \frac{\alpha_c F^2}{RT} \left(\frac{\bar{i}}{F} \right) \quad [27]$$

where \bar{V} , \bar{C}_1 , and \bar{i} are steady-state quantities. With Eq. [26] and [27], the equation for the faradaic impedance of copper electrodisolution becomes

$$Z_f = \frac{\left[M \left\{ 1 - \frac{1}{\Gamma(4/3)(-\theta'(0))} \right\} + \frac{1}{\Gamma(4/3)(-\theta'(0))} \right]}{\frac{iA(\alpha_a + \alpha_c)F}{RT} \left[1 - \frac{\alpha_c}{(\alpha_a + \alpha_c)} M \right]} \quad [28]$$

The quantity M is the ratio

$$M = \frac{(\bar{i}/F)}{k_a \exp \left\{ \frac{\alpha_a F}{RT} \bar{V} \right\}} \quad [29]$$

which measures the steady-state current density relative to the current density extrapolated to $\Omega \rightarrow \infty$ (see Eq. [15]), and A is the area of the electrode.

The complex function $\{-1/\theta'(0)\}$ has all the frequency dependence of Z_f . This function has been discussed previously for another impedance situation (17, 24), and has the properties

$$\left. \begin{aligned} \text{Re} \left(-\frac{1}{\theta'(0)} \right) &\rightarrow \Gamma(4/3) \\ \text{Im} \left(-\frac{1}{\theta'(0)} \right) &\rightarrow 0 \end{aligned} \right\} \omega \rightarrow 0 \quad [30]$$

and

$$\left. \begin{aligned} \text{Re} \left(-\frac{1}{\theta'(0)} \right) &\rightarrow 0 \\ \text{Im} \left(-\frac{1}{\theta'(0)} \right) &\rightarrow 0 \end{aligned} \right\} \omega \rightarrow \infty \quad [31]$$

In Eq. [30] and [31], the limits are given for the real and imaginary parts, respectively. Therefore, the impedance from Eq. [28] has the limits

$$Z_f \Big|_{\omega \rightarrow 0} = \frac{RT}{\bar{i}A(\alpha_a + \alpha_c)F} \left[\frac{1}{1 - \frac{\alpha_c}{\alpha_a + \alpha_c} M} \right] \quad [32]$$

$$Z_f \Big|_{\omega \rightarrow \infty} = \frac{RT}{\bar{i}A(\alpha_a + \alpha_c)F} \left[\frac{M}{1 - \frac{\alpha_c}{\alpha_a + \alpha_c} M} \right] \quad [33]$$

In the limit of mass-transfer control, $M \rightarrow 0$, and

$$Z_f = \left(\frac{RT}{\bar{i}A(\alpha_a + \alpha_c)F} \left[\frac{1}{\Gamma(4/3)[- \theta'(0)]} \right] \right)_{M=0} \quad [34]$$

with the limits

$$Z_f \Big|_{\omega \rightarrow 0} = \left(\frac{RT}{\bar{i}A(\alpha_a + \alpha_c)F} \right)_{M=0} \quad [35]$$

$$Z_f \Big|_{\omega \rightarrow \infty} = 0 \quad (M = 0) \quad [36]$$

It will be shown below that Eq. [35] and [36] are good approximations for copper electrodisolution impedance because M is small.

The faradaic impedance of copper electrodisolution should be a function of the level of current, \bar{i} , and the ratio M , both of which are obtained from steady-state measurements. Determinations of the impedance and the steady-state quantities provide an independent check on the consistency of the measurements. The frequency dependence of the faradaic impedance is given by the convective Warburg function $\{-1/\theta'(0)\}$ discussed by Newman *et al.* (17, 24), and arises from the transport of CuCl_2^- away from the surface. At high excitation frequency ω , the magnitude of the real and imaginary parts of $\{-1/\theta'(0)\}$ are equal, in agreement with classical Warburg impedance behavior for diffusion with no convection. Convection becomes important at low excitation frequency, however, and there is deviation from the classical semi-infinite Warburg impedance to give a finite value for the real part of the impedance and zero for the imaginary part at zero frequency (see Eq. [30]). In other words, there is a steady-state flux of the diffusing species with convection because there is a steady diffusion-layer thickness. Without convection, there is no steady-state flux into an infinite medium and the diffusion boundary layer grows as \sqrt{t} .

Experimental

Both steady-state and impedance measurements of Cu electrodisolution were made. The steady measurements were more extensive, and the impedance provided an indication of consistency for the mass-transport-kinetic model derived above.

A rotating disk electrode system was used for all the determinations. The disk assembly was constructed so that the disk could be attached to the rotating shaft by a threaded mount. The shaft and attached disk had an eccentricity that was less than 0.1% of the disk diameter (19). Electrical contact to the rotating shaft was made by a silver ring-silver graphite brush assembly (Graphite Metallizing Corporation). Rotation of the shaft was controlled by a dc servo motor, and the speed was calibrated with a stroboscope. The copper rotating disk was fabricated by attaching a copper button onto a brass rod and inserting the lower end into a Teflon body with a tight press fit. The upper end of the brass shaft was threaded to mount on the rotating shaft. The lower part of the assembled electrode was immersed in the solution through a matched hole in the Teflon cover of a glass vessel in which the experiments were conducted. A Pt mesh counterelectrode was mounted in the bottom of the vessel, facing the Cu rotating disk. A reference electrode capillary was inserted through the cover and positioned just outside (5 mm) the outer Teflon edge of the rotating disk, and in the plane of the disk. Nitrogen gas was

sparged continuously through the solution during the course of the measurements.

Surface preparation of the Cu rotating disk consisted of polishing on a metallography wheel with 0.05 μm alumina in deionized water. The polishing cloth used on the wheel was extensively washed with deionized water before use, and the cloth was replaced after 3-4 h of use. The polished specimen was rinsed in deionized water and soaked in 0.1N HCl for 1-2 min, mounted on the rotating disk shaft, and immersed in the solution for measurement. The preparation technique produced a surface that gave highly reproducible results. Light etching of the Cu with dilute HNO_3 in an ultrasonic bath gave identical electrochemical behavior if the specimen was rinsed carefully in water and HCl after the etch step. Electrode area, A , equals 0.695 cm^2 .

Copper for the rotating disk electrode was OFHC rod of 99.99% purity. HCl solutions (0.1N) were prepared from ampuls available commercially for analytical standards (Baker Analyzed) and diluted to volume with freshly prepared deionized water. The water was 20 M Ω quality produced by cascaded ion-exchange beds in series with activated charcoal. The nitrogen gas used was Ultra High Purity Grade (99.999%) from Matheson.

Steady-state electrochemical measurements were performed under potentiostatic control. Current to the rotating disk was measured after steady state was achieved at each potential (~ 5 min), and the potential was changed in increments of 5 mV between measurements. Current was measured as the potential drop across a precision 10 Ω resistor in series with the electrochemical cell.

Impedance measurements were made as described in the preceding paper and as demonstrated in an earlier paper (26). A multiple frequency voltage signal from a signal generator (Hewlett-Packard 3722A Noise Generator) was superimposed on a constant control voltage at the input of the control amplifier of the potentiostat. The maximum amplitude of the voltage perturbation was 3-5 mV peak to peak, independent of the frequency range used. Each frequency range contained 51 superposed sinusoids consisting of a fundamental frequency and the next 50 harmonics (both even and odd). The voltage signal was measured between the working and reference electrode leads at the cell with a voltage follower, amplified and filtered by a differential amplifier with a low-pass filter, and digitized on one channel of a Biomation Waveform Recorder (Model 1015). The current signal was measured as the voltage drop across a precision resistor in series with the cell. The signal was also passed through a differential amplifier with a low-pass filter, and recorded on a second channel of the digitizer. The voltage and current signals were recorded simultaneously and strobed out of the waveform recorder buffer memory into the calculator-controller (Hewlett-Packard 9830B). The data were stored on a floppy disk for subsequent treatment and analysis. The data were digitized over two periods of the lowest frequency in the spectra. The higher frequencies were also periodic in this sequence length, and the sampling rate was always greater than five times the highest frequency to avoid "aliasing" (26). The total time for data taking was two times the period of fundamental frequency summed over the number of frequency ranges sampled. This was approximately 22s for the data described here. Additional time was required for manually setting up the instrumentation for each frequency range, initiating the data acquisition through software control, and strobing out the data. The total elapsed time for data acquisition was typically 1-2 min for the total of three frequency ranges (153 frequencies). The DIFA apparatus could be used for time domain averaging of multiple determinations (26), but the data reported here were from single runs.

The stored data were transmitted to a CDC 6600 computer for analysis. A fast Fourier transform (FFT) was performed on the voltage and current. The ratio of the voltage to the current at each frequency yielded the dimensionless impedance at that frequency, *i.e.*

$$\bar{Z} = \frac{\bar{V}}{I} \quad [37]$$

The dimensional impedance was calculated by the procedure introduced by Smith (28). This consists of making measurements on a "dummy cell" of precision resistors and capacitors that closely approximate values for the electrochemical cell. All amplifier gains and other instrumentation settings are then identical for the two determinations. From the known values of the "dummy cell," the theoretical impedance at each of the measured frequencies is calculated and compared to the measured dimensionless impedance of the dummy cell, *i.e.*

$$Z_{RD} = Z_{TD}/Z_D \quad [38]$$

The application of Z_{RD} to the dimensionless impedance of the electrochemical system then yields the impedance at each frequency, *i.e.*

$$Z = (\bar{Z}) Z_{RD} \quad [39]$$

The procedure amounts to a calibration of the measurement system at the measured frequencies and automatically corrects for instrumentation gain and phase-shift errors.

Results and Discussion

Results of the steady-state investigation of electrodis-solution of Cu from a rotating disk are given in Fig. 1. Also plotted therein are cathodic H_2 evolution results on the Cu electrode. Identical results in both regions were obtained with either H_2 or N_2 as the cover gas. The Tafel slope for hydrogen evolution was 110 mV/decade, in good agreement with the investigation by Bockris and Pentland (29). At cathodic current densities greater than 10 mA/cm², deviation from Tafel behavior, in large part due to ohmic drop in the solution, was observed.

Anodic current curves are shown for two rotation rates, and additional data were obtained at 2000 rpm. The Tafel-like slope was 60 mV/decade at all three rotation rates, in agreement with Eq. [12] and [13] and earlier results (1-14). This result implies that the anodic dissolution is largely mass-transport controlled at these rotation rates and $(\alpha_a + \alpha_c) = 1$. At higher current densities, ohmic drop caused deviations from the Tafel-like behavior.

To determine the influence of kinetics, the data were plotted as a function of rotation rate, as shown in Fig. 2. The data follow Eq. [14] for mass-transport-kinetic control with a finite intercept on the current axis as $\Omega \rightarrow \infty$. The same behavior was observed over the entire potential range investigated, up to current densities where ohmic drop became significant. The finite intercept in Fig. 2 provides a measurement of the anodic kinetic rate constant according to Eq. [15], and the slope is identified in Eq. [16]. The anodic term determined from the intercept

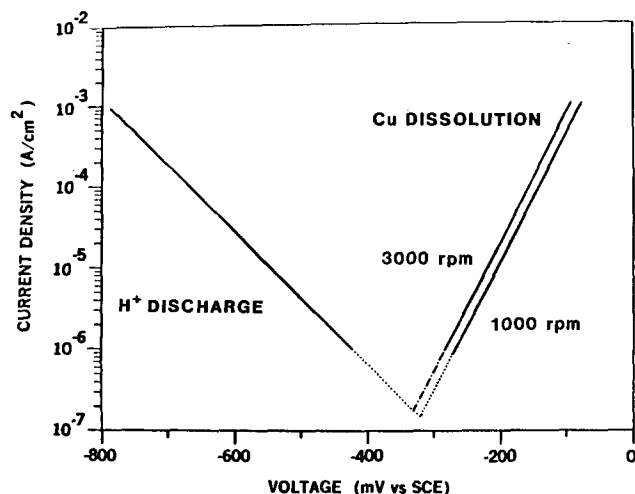


Fig. 1. Electrodissolution kinetics of a copper rotating disk in oxygen-free 0.1N HCl at 25°C.

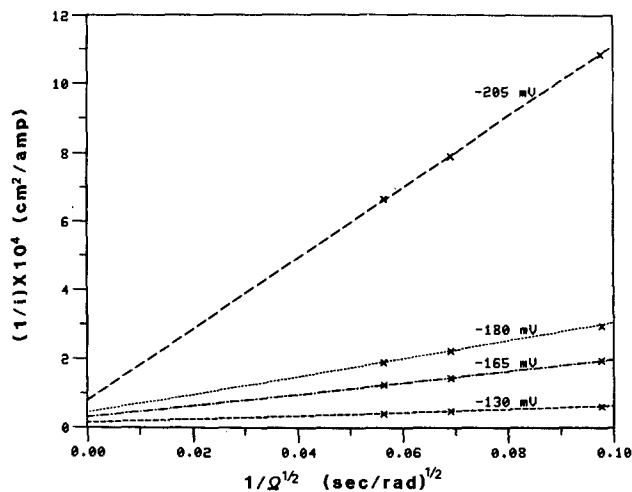


Fig. 2. Reciprocal current density as a function of disk rotation rate

was found to be a function of potential as demonstrated in Fig. 3, where the function

$$\log \left[k_a \exp \left\{ \frac{\alpha_a F}{RT} V \right\} \right]$$

is plotted *vs.* V . The straight line has a slope of 120 mV/decade, and, therefore, $\alpha_a = 0.5$. This leads to the conclusion that $\alpha_c = 0.5$ as well. The quantity $[\partial(F/i)/\partial\Omega^{-1/2}]$ in Eq. [16] was found to be a function of potential, and the data are shown in Fig. 4. The straight line has a slope of 60 mV/decade, in agreement with the finding above that $(\alpha_a + \alpha_c) = 1$.

The anodic and cathodic rate constants

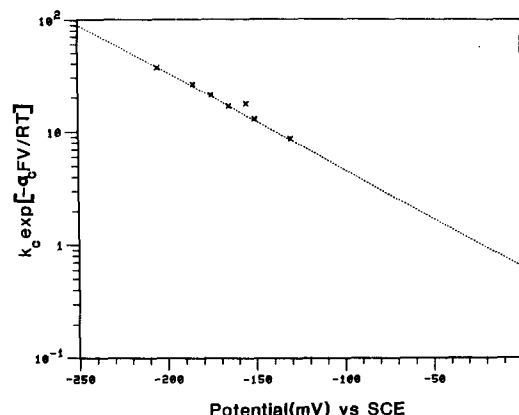
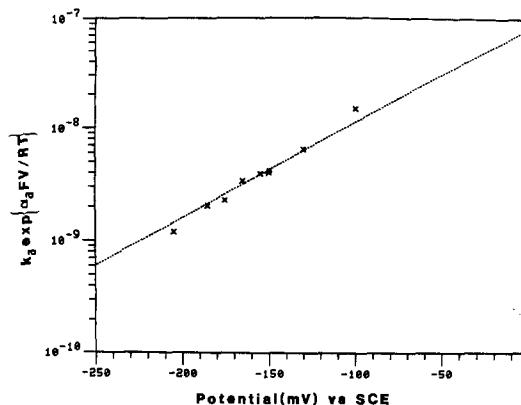


Fig. 3. Anodic and cathodic rate constants as a function of applied potential.

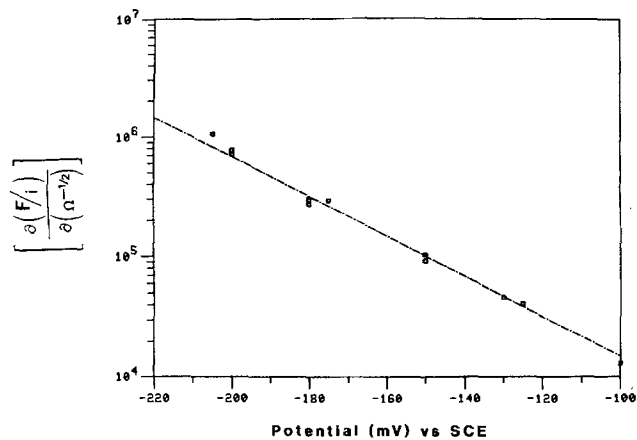


Fig. 4. Dependence of (current-rotation rate) function on applied potential.

$$k_a \exp \left\{ \frac{\alpha_a F}{RT} V \right\} \quad \text{and} \quad k_c \exp \left\{ \frac{-\alpha_c F}{RT} V \right\}$$

respectively, were determined at several potentials from the data above and plotted in Fig. 3. The constants in \bar{k} (see Eq. [10]) were assigned the values

$$\nu = 0.89 \times 10^{-2} \text{ cm}^2/\text{s} \quad [30]$$

$$D_1 = 5.68 \times 10^{-6} \text{ cm}^2/\text{s}$$

$$K_c = 6.96 \times 10^4 \quad [15]$$

$$\Gamma(4/3) = 0.89298 \quad [31]$$

The diffusion coefficient, D_1 , was evaluated from the impedance measurements described below.

The exchange current density divided by the CuCl_2^- concentration, i.e., $i_0/C_1^{1/2}$, was calculated from Eq. [17], [18], and [2]

$$\left(\frac{i_0}{C_1^{1/2}} \right) = \frac{F k_a^{1/2} k_c^{1/2}}{K_c^{1/2} C_2} \quad [40]$$

The quantity $[i_0/C_1^{1/2}]$ was found to be independent of potential, as shown in Table I.

The results reported here are in substantial agreement with previous studies. The major contribution of the present study has been the determination of the kinetic parameters of the dissolution reaction enabled by the use of lower Cl^- concentration and higher rotation rates than used previously. The kinetic contribution, though measurable, was found to be small in the voltage ranges studied here. A measure of the kinetic contribution is given by the ratio M (see Eq. [32]). For complete control by mass transfer, $M = 0$, and departures from this limit increase as kinetics become important for anodic dissolution. The kinetic contribution is dominant as $M = 1$. In the limit of small M , the "Tafel" slope was found to be 60 mV/decade, in agreement with literature values. Even at -150 mV, where M was found to be substantially different from zero (see Table II), the Tafel slope was almost unaffected. Using Eq. [8] and the M values from Table II, the Tafel slope at -150 mV was calculated to be 66 mV/decade. One

Table I. Exchange current density

$i_0/C_1^{1/2}$	V (mV vs. SCE)
0.866	-130
0.841	-150
0.969	-155
0.881	-165
0.793	-175
0.852	-185
0.767	-205

Avg. = 0.853 (± 0.045)

Table II. Values of the ratio M as a function of potential and rotation rate

M	V (mV vs. SCE)	Rotation Rate (rpm)
0.275	-130	1000 rpm
0.357		2000 rpm
0.415		3000 rpm
0.227	-150	1000 rpm
0.301		2000 rpm
0.353		3000 rpm
0.151	-155	1000 rpm
0.234		2000 rpm
		3000 rpm
0.154	-165	1000 rpm
0.203		2000 rpm
0.240		3000 rpm
0.129	-175	1000 rpm
0.203		2000 rpm
0.203		3000 rpm
0.095	-185	1000 rpm
0.135		2000 rpm
0.160		3000 rpm
0.079	-205	1000 rpm
		2000 rpm
0.130		3000 rpm

would expect to achieve full kinetic control at $M = 1$, which is equivalent to the condition

$$\left[\frac{\bar{k}}{C_2^2 \Omega^{1/2}} \right] \exp \left\{ \frac{-\alpha_c F}{RT} V \right\} \ll 1 \quad [41]$$

$$\left(\frac{k_c}{2.33} \right) \exp \left\{ \frac{-\alpha_c F}{RT} V \right\} \ll 1 \quad [42]$$

for 1000 rpm. From Fig. 3, it can be seen that the equality

$$\left(\frac{k_c}{2.33} \right) \exp \left\{ \frac{-\alpha_c F}{RT} V \right\} = 1 \quad [43]$$

should be obeyed at about -65 mV. The inequality would then be observed at potentials more positive than approximately $+45$ mV, where the current density would be approximately 19 mA/cm^2 . The dissolution current density would be independent of rotation rate, and the Tafel slope would be 120 mV/decade. Verification of the prediction was outside the scope of the present study, but it is of interest for future study in this laboratory.

Impedance Results

The digital impedance results were found to confirm the description given above for electrodisolution of copper. The complex impedance at -205 mV is given in Fig. 5 both as a function of frequency and rotation speed. An important quantity to be derived from these measurements is the impedance at zero frequency, Z_f^0 , where the imaginary part goes to zero (Eq. [30]) and the real part becomes proportional to the steady-state dissolution current (see Eq. [32] and [35]).

The determination of the faradaic impedance was accomplished by the following procedure.

1. The ohmic solution concentration, R_s , was determined as the high frequency intercept on the real impedance axis, since R_s acts in series with the interfacial impedance. For the current voltage range studied, R_s was found to be 15Ω , and this agrees with the ohmic drop calculated for the position of the reference electrode and the solution resistivity (24).

2. R_s was vectorially subtracted from the total impedance, and the admittance/frequency, Y/ω , was calculated.

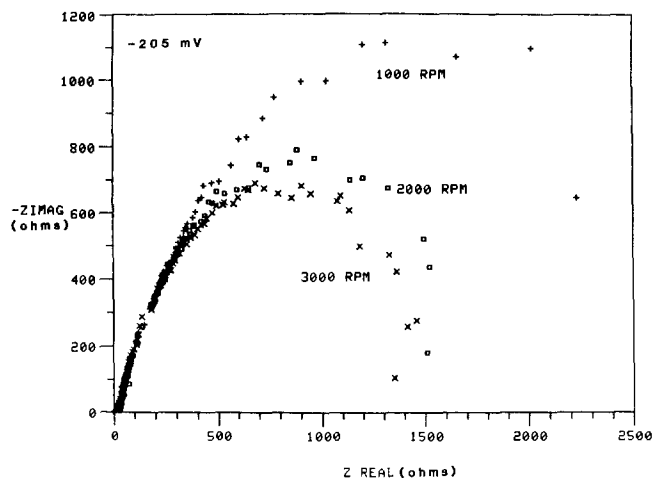


Fig. 5. Impedance of Cu electrodisolution

A plot of $Y(\text{imag.})/\omega$ vs. $Y(\text{real.})/\omega$ yielded the double-layer capacitance, CA , as the intercept on the $Y(\text{imag.})/\omega$ axis as $\omega \rightarrow \infty$. The double-layer capacitance C was calculated from the result by dividing by the area of the disk electrode. C was found to be $40\text{--}46 \times 10^{-6}$ F/cm² for all the tests.

3. Vectorial subtraction of CA from the interfacial impedance yielded the faradaic impedance for the system.

The faradaic impedance calculated as described above is plotted in Fig. 6 as $Z_f(\text{real.})$ vs. $-\omega Z_f(\text{imag.})$. A straight line was fitted to the low frequency data, and extrapolation to zero frequency gave $Z_f(\text{real.})$. The imaginary part of Z_f should be zero at zero frequency (Eq. [30]), and the real part can be related to the steady-state current density by Eq. [32] or [35], depending on the value of M . M was calculated from Eq. [32], and is given in Table III at two potentials and three rotation rates. The results compare favorably with M values determined in the steady-state measurements (Table II).

The experimental faradaic impedance was made dimensionless according to Eq. [28] with the experimental values of the current density and M . The result should be identical to the theoretical convective Warburg function $\{-1/\theta'(0)\}$. The two are compared in Fig. 7. The two agree very well. This was found to be true at all rotation rates and potentials used in the study. The agreement confirms that the faradaic impedance for Cu dissolution in HCl is given by Eq. [28].

It is noted that Eq. [28] gives the general behavior of the faradaic impedance where there is mixed kinetic and mass-transfer control of dissolution. In the limit of mass-transfer control, $M = 0$, the impedance is given by Eq. [34] with the limits given by Eq. [35] and [36]. For $M = 1$, i.e.,

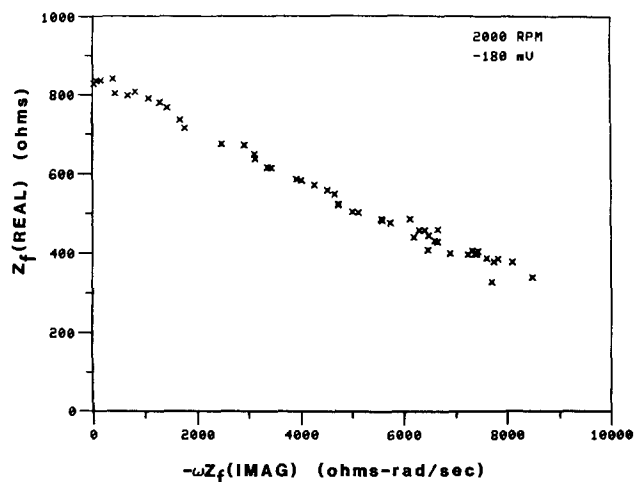


Fig. 6. Faradaic impedance of Cu electrodisolution at low frequencies in 0.1N HCl.

Table III. M values from impedance measurements

M	V (mV vs. SCE)	
0.07	-200	1000 rpm
0.10		2000 rpm
0.11		3000 rpm
0.245	-150	1000 rpm
0.263		2000 rpm
0.300		3000 rpm

kinetic control of anodic dissolution, from Ref. (28)

$$Z_f = \frac{RT}{iA\alpha_a F} \quad [44]$$

as expected.

Finally, a new technique was discovered for determination of the diffusion coefficient of CuCl_2^- from the impedance measurements. The technique involves calculation of the diffusion coefficient from the slope of the linear relationship observed between $Z_f(\text{real.})$ and $[-\omega Z_f(\text{imag.})]$ at low excitation frequencies (see Fig. 6). The linear behavior is expected from the properties of the function $\{-1/\theta'(0)\}$. Theoretical values of the real and imaginary parts of this function taken from the literature (19, 31) yield the relationship valid for Schmidt number $(\nu/D_1) \rightarrow \infty$

$$\frac{d\left[\text{Re}\left\{-\frac{1}{\theta'(0)}\right\}\right]}{d\left[\text{KIm}\left\{-\frac{1}{\theta'(0)}\right\}\right]} = -0.373 \quad [45]$$

where (23)

$$K = \omega\nu\left(\frac{3D_1}{a\nu}\right)^{2/3} (\Omega D_1)^{-1} \quad [46]$$

and a has the value 0.51023 (17, 18, 21). The experimental slope, S , is defined as

$$\frac{dZ_f(\text{real.})}{d[\omega Z_f(\text{imag.})]} = S = -0.373\left(\frac{dK}{d\omega}\right) \quad [47]$$

or

$$D_1^{1/3} = -0.373\left(\frac{3}{a}\right)^{2/3} \nu^{1/3}(S\Omega)^{-1} \quad [48]$$

Equation [48] for the diffusion coefficient is general for $(\nu/D_1) \rightarrow \infty$, and does not require knowledge of the solution

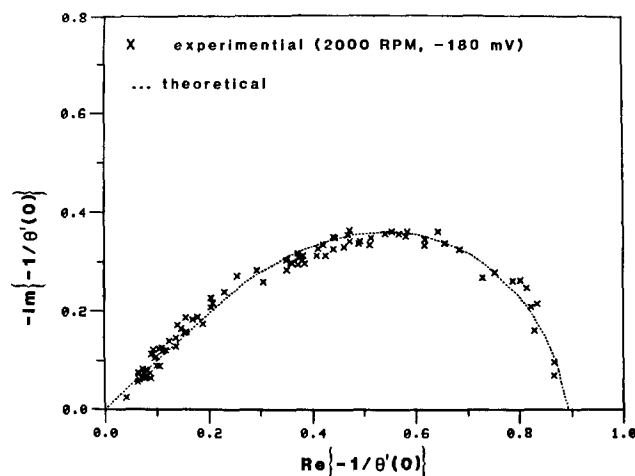


Fig. 7. Dimensionless convective Warburg impedance function compared to experimental data for Cu dissolution.

concentration C° , or the electrode area for calculation of the diffusion coefficient. For finite values of the Schmidt number, Sc , the limiting slope at low frequency is a function of Sc , and may be calculated from the results given in Ref. (19) and elsewhere (33). For example, for $Sc = 1500$, the functional relationship is obeyed

$$\frac{d \left[\operatorname{Re} \left\{ -\frac{1}{\theta'(0)} \right\} \right]}{d \left[\operatorname{KIm} \left\{ -\frac{1}{\theta'(0)} \right\} \right]} = -0.400 \quad [49]$$

Equation [48] for the diffusion coefficient becomes

$$D_1^{1/3} = -0.400(3/\alpha)^{2/3} \nu^{1/3} (S\Omega)^{-1} \quad [50]$$

for $Sc = 1500$.

D_1 was determined for several rotations rates and steady-state currents, and was found to $5.68 \times 10^{-6} \text{ cm}^2/\text{s}$. This compares favorably with values quoted in the literature (3), which were $6.2\text{--}6.6 \times 10^{-6} \text{ cm}^2/\text{s}$. It should be noted again that the calculation of the diffusion coefficient from the low frequency impedance measurements is independent of solution concentration and electrode area. The calculation is based solely on the experimental faradaic impedance and the properties of the convective Warburg impedance function $\{-1/\theta'(0)\}$ which are described in the literature. Further discussion is outside the scope of this paper, but a more detailed description of this technique for diffusion coefficient measurements will be published shortly. Some results have been discussed previously (35).

Conclusions

A theoretical model was developed for electrodisolution of Cu in 0.1N HCl solutions which were copper free. The mass-transfer-kinetic model agreed with steady-state measurements on a rotating disk. The kinetic parameters α_a , α_c , and the product $(k_a^{1/2}k_c^{1/2})$ were determined from the experimental data. The faradaic impedance for the electrodisolution was also developed for the mass-transport-kinetic model. Experimental results agreed with the theoretical development here as well, and gave confirmation to the steady-state model. The experimental impedance results, made dimensionless in an appropriate way, match the theoretical function $\{-1/\theta'(0)\}$, in agreement with the development given in the section on DIFA measurements in electrodisolution. A new technique for determination of diffusion coefficients from impedance measurements at low frequency was used to evaluate the diffusion coefficient of CuCl_2^- . The value was $5.68 \times 10^{-6} \text{ cm}^2/\text{s}$, which compares favorably with literature results.

Acknowledgment

This work was supported by the U.S. Department of Energy under Contract no. DE-AC04-76-DP00789.

Manuscript submitted Feb. 1, 1984; revised manuscript received ca. Feb. 8, 1985.

REFERENCES

- H. Lal and H. R. Thirsk, *J. Chem. Soc.*, 2638 (1953).
- T. Hurlen, *Acta Chem. Scand.*, **15**, 1231 (1961).
- A. LiBacarella and J. C. Griess, *This Journal*, **120**, 459 (1973).
- R. S. Cooper and J. H. Bartlett, *ibid.*, **105**, 109 (1958).
- L. Stephenson and J. H. Bartlett, *ibid.*, **101**, 571 (1954).
- J. O'M. Bockris, B. T. Ruben, A. Despic, and B. Lovrecek, *Electrochim. Acta*, **17**, 973 (1972).
- L. Kiss, J. Farkas, and A. Korosi, *Acta Chim. Hung.*, **67**, 179 (1971).
- L. Kiss, J. Farkas, and A. Korosi, *ibid.*, **68**, 359 (1971).
- R. S. Cooper, *This Journal*, **103**, 307 (1956).
- A. Moreau, *Electrochim. Acta*, **26**, 497 (1981).
- M. Braun and K. Nobe, *This Journal*, **120**, 1666 (1979).
- M. Turner and P. A. Brook, *Corros. Sci.*, **13**, 973 (1973).
- A. H. Taylor, *This Journal*, **118**, 854 (1971).
- C. H. Bonfiglio, H. C. Albaya, and O. A. Cobo, *Corros. Sci.*, **13**, 717 (1973).
- NBS Technical Notes 270-3, 270-4, U. S. Government Printing Office, May 1969.
- W. H. Smyrl, in "Comprehensive Treatise of Electrochemistry," Vol. 4, J. O'M. Bockris et al., Editors, Plenum Press, New York (1981).
- V. G. Levich, "Physicochemical Hydrodynamics," Prentice-Hall, Englewood Cliffs, NJ (1962).
- J. S. Newman, "Electrochemical Systems," Prentice-Hall, Englewood Cliffs, NJ (1973).
- E. Levart and D. Schuhmann, *J. Electroanal. Chem. Interfacial Electrochem.*, **55**, 77 (1974).
- J. O'M. Bockris and A. R. Despic, in "Physical Chemistry, an Advanced Treatise," Vol. IXB, Henry Eyring, Editor, Academic Press, New York (1970).
- A. C. Riddiford, in "Advances in Electrochemistry and Electrochemical Engineering," Vol. 4, P. Delahay and C. W. Tobias, Editors, Interscience, New York (1966).
- W. Smyrl, Unpublished results.
- W. H. Smyrl, *This Journal*, **132**, 1551 (1985).
- R. V. Homsy and J. Newman, *ibid.*, **121**, 521 (1974).
- W. H. Smyrl and J. Newman, *ibid.*, **119**, 208 (1972).
- W. H. Smyrl, in "Electrochemical Corrosion Testing," F. Mansfeld and U. Bertocci, Editors, ASTM Special Technical Publication 727, Philadelphia (1981).
- S. D. Stearns, "Digital Signal Analysis," Hayden, Rochelle Park, NJ (1975).
- R. J. Schwall, A. M. Bond, and D. E. Smith, *Anal. Chem.*, **49**, 1805 (1977).
- J. O'M. Bockris and N. Pentland, *Trans. Faraday Soc.*, **48**, 833 (1952).
- R. A. Robinson and R. H. Stokes, "Electrolyte Solutions," Butterworths, London (1959).
- "Handbook of Mathematical Functions," M. Abramowitz and I. A. Stegun, Editors, NBS Applied Mathematics Series no. 44, USGPO, Washington, DC (1972).
- B. Tribollet and J. J. Newman, *This Journal*, **130**, 822 (1983).
- B. Tribollet and J. Newman, Unpublished results.
- A. Rizenkamp and E. Beltovska, *Sov. Electrochem.*, **11**, 348 (1975).
- W. H. Smyrl, Paper 689 presented at The Electrochemical Society Meeting, Montreal, Que., Canada, May 9-14, 1982.

Digital Impedance for Faradaic Analysis

III. Copper Corrosion in Oxygenated 0.1N HCl

William H. Smyrl* and Larry L. Stephenson

Sandia National Laboratories, Division 1841, Albuquerque, New Mexico 87185

ABSTRACT

Impedance measurements have been made on copper rotating disks corroding in oxygenated 0.1N HCl. A model is developed here for the first time for the faradaic impedance of a corrosion couple consisting of an anodic dissolution reaction dominated by convective diffusion and a cathodic reaction under kinetic control. The model was found to be obeyed for all values of disk rotation rate, oxygen concentration, and voltage excitation frequency. The corrosion rate was found to depend on oxygen concentration to the 2/3 power, and on rotation rate to the 1/6 power.

The corrosion of copper in aqueous acid solutions occurs on an oxide-free surface that makes it an attractive metal for generic studies. Copper corrodes slowly in acids free of oxidizing agents (1, 2), but in the presence of dissolved oxygen or other reactants the corrosion rate increases substantially, depending on the oxidation potential of the reactant, its concentration, and rate of supply to the copper surface (2-4). The acid participates in the process by stabilizing either the cuprous [Cu(I)] or cupric [Cu(II)] product ion.

In HCl solutions, the CuCl_2^- species is dominant at low concentrations of Cl^- (5), with other chloro complexes becoming important at higher chloride concentrations. Miller and Bellavance (6) investigated the corrosion of copper in oxygenated acid chloride solutions by a rotating ring-disk technique. CuCl_2^- was produced at the disk electrode and detected at the outer ring electrode. The corrosion rate was found to depend weakly on the rotation speed (see below), and was controlled by the rate of reduction of dissolved oxygen at only 5-10% of the diffusion limiting current of O_2 . These studies established that the corrosion process obeyed the principle of superposition (7, 8) for the metal dissolution and O_2 reduction. The present investigation confirmed that the system obeys the superposition principle, as described below.

The faradaic impedance of the parallel simultaneous reactions is (9)

$$\frac{1}{Z_{f,T}} = \frac{1}{Z_{f,a}} + \frac{1}{Z_{f,c}} \quad [1]$$

The reduction of oxygen has complex kinetics, and proceeds by an overall two-electron reaction to produce peroxide (10, 11) in chloride solutions. Subsequent reduction of peroxide to hydroxide or water is not important for this discussion [see Miller *et al.* (6)]. The faradaic impedance of the oxygen reduction is assumed to be given by (see below)

$$Z_{f,c} = \frac{-RT}{i_c \alpha_{oc} \text{FA}} \quad [2]$$

The impedance of the Cu dissolution reaction was shown in the preceding paper (5) to be given by

$$Z_{f,a} = \frac{\left[M \left\{ 1 - \frac{1}{\Gamma(4/3)[- \theta'(0)]} \right\} + \frac{1}{\Gamma(4/3)[- \theta'(0)]} \right]}{\frac{i_a(\alpha_{aa} + \alpha_{ac})\text{FA}}{RT} \left[1 - \frac{\alpha_{ac}}{(\alpha_{ac} + \alpha_{cc})} M \right]} \quad [3]$$

where M is the quantity (5)

$$M = \frac{\left(\frac{\bar{i}_a}{\bar{F}} \right)}{k_{aa} \exp \left\{ \frac{\alpha_{aa} \text{F} \bar{V}}{RT} \right\}} \quad [4]$$

From Eq. [1]-[3], one obtains for the corrosion couple

*Electrochemical Society Active Member.

$$\frac{1}{Z_{f,t}} = \frac{i_{\text{corr}} \text{FA}}{RT} \times \left\{ \alpha_{cc} + \frac{(\alpha_{aa} + \alpha_{ac}) \left[1 - \frac{\alpha_{ac} M}{(\alpha_{aa} + \alpha_{ac})} \right]}{\left[M \left\{ 1 - \frac{1}{\Gamma(4/3)[- \theta'(0)]} \right\} + \frac{1}{\Gamma(4/3)[- \theta'(0)]} \right]} \right\} \quad [5]$$

where

$$i_{\text{corr}} = i_a = -i_c \quad [6]$$

when the anodic dissolution reaction is completely mass-transfer controlled (5)

$$M = 0 \quad [7]$$

and Eq. [5] becomes

$$\frac{1}{Z_{f,t}} = \frac{i_{\text{corr}} \text{FA}}{RT} \{ \alpha_{cc} + (\alpha_{aa} + \alpha_{ac}) \Gamma(4/3)[- \theta'(0)] \} \quad [8]$$

Equations [5] and [8] are the fundamental relationships between copper corrosion current density and measured impedance. The oxygen concentration in solution and the copper disk rotation rate influence the corrosion rate and will be discussed below. It should be emphasized that Eq. [5] and [8] are specific to an anodic reaction which is influenced by mass-transport coupled to a cathodic reaction which is kinetically controlled. The treatment here is the first for a corrosion system of this type, but other systems may exhibit the behavior described here as well. One might expect, for example, that the behavior shown here will be obeyed for molten salt systems where many anodic dissolution reactions are known to be mass-transfer-kinetic controlled.

It will be demonstrated in this paper that the corrosion rates measured by weight loss, by prediction from deaerated solution currents at the same potential, and by direct impedance measurement agree very well. The corrosion rate will also be reported as a function of dissolved oxygen concentration and rotation rate of the corroding copper disk. It will be shown that this agrees with the behavior predicted from the kinetics of the reactions. Both steady-state and impedance results will be reported. Preliminary results were published earlier (8, 12).

Experimental

Copper for the rotating disk electrodes was OFHC rod, of 99.99% purity. Copper foil for the weight loss experiments was 99.999% purity. HCl solutions (0.1N) were prepared from ampuls available commercially for analytical standards (Baker Analyzed) and diluted to volume with freshly prepared deionized water. The water was 18-20 MΩ quality produced by cascaded ion exchange beds in series with activated charcoal. Gases used were Ultra High Purity Grade (99.999%) from Matheson.

The analysis of dissolved oxygen concentration was done by a specific oxygen electrode assembly. O_2 concentrations obtained by analysis were in excellent agree-

ment with those calculated from the gaseous O₂ partial pressure with Henry's law (13). Copper concentration in solution from the foil corrosion tests was determined with a specific copper electrode and confirmed by emission spectroscopy.

The rotating disk assembly was described in the preceding paper (5). As before, gas was sparged continuously through the solution during the course of the measurements. The copper disk was prepared as before (5).

Weight loss measurements were conducted on copper foils of 100 cm² surface area. Experiments were performed either at constant-potential (no O₂ in solution) or at open-circuit corrosion conditions (with dissolved O₂). The constant-potential measurements were made at the same potentials as were observed for the corrosion tests. The rectangular-shaped Cu foil was surrounded on both sides with a Pt screen, with a Teflon screen separating the two. Gas was sparged through the solution during the measurements. The experimental arrangement made it possible to conduct the dissolution and corrosion tests under identical conditions of dissolution distribution and solution convection. The solution volume was 295 ml.

The foils were degreased with methyl ethyl ketone and acetone, lightly etched in air-saturated HCl in an ultrasonic bath, rinsed in deionized water and acetone sequentially in the ultrasonic bath, and air dried to constant weight (~10 min). After a dissolution of corrosion experiment, the foil was again rinsed in water and acetone and air dried. Repeated measurements showed the weights to be good to $\pm 1 \times 10^{-3}$ g.

Impedance measurements were made with the apparatus described earlier (5, 9), over the frequency range 0.1-500 Hz. The measurements were performed under potentiostatic conditions at the corrosion potential. The copper disk was immersed in the solution after polishing. The measurements after 10 and 30 min were identical to the 2 min measurements. One set of data in each frequency range (*i.e.*, 0.1-5, 1-50, and 10-500 Hz) was taken in approximately 1 min elapsed time. The actual data collection required 12s, with the remaining time being required to change manual settings on amplifiers, signal generator, and digitizer.

Results and Discussions

The results of the Cu foil experiments are summarized in Table I. The agreement is excellent between the weight loss and solution analysis in O₂-saturated 0.1N HCl, on one hand, and the current density measured in deaerated solution, on the other hand. This agreement confirms that superposition is obeyed for the Cu/O₂ corrosion system in HCl. The rate of corrosion was found to be at ~10% of the O₂ diffusion-limited current density, so we assume that O₂ reduction was under kinetic control. The reduction, when coupled with Cu dissolution, gave a corrosion system which was used as a model for impedance studies.

The impedance measurements on the Cu rotating disk were made in the frequency range 10⁻¹-500 Hz, at disk rotation rates of 700, 1000, 2000, and 3000 rpm, respectively,

Table I. Results of the Cu foil experiments

	Calculated rate Cu dissolution (g/s-cm ²)	Calculated current density (A/cm ²)
100% O ₂ -saturated 0.1N HCl		
Weight loss	$2.29 (\pm 0.04) \times 10^{-7}$	3.49×10^{-4}
Solution analysis	$2.37 (\pm 0.16) \times 10^{-7}$	3.60×10^{-4}
	Potential (vs. SCE) (mV)	Measured current density (A/cm ²)
Deaerated 0.1N HCl	-54	3.5×10^{-4}
	-58	3.1×10^{-4}

and for dissolved oxygen concentrations of from 3.2 to 33.5 ppm. All measurements were made under potentiostatic control at the corrosion potential.

In Fig. 1 are plotted the results of impedance measurements at three different rotation rates and an oxygen concentration of 33.5 ppm. The results at other oxygen concentrations were similar. At low excitation frequencies, the impedance was found to depend strongly on rotation rate as shown, but at high frequency the curves coincide, as expected for a diffusion-dominated process (Cu dissolution). That is, for values of $(\omega/\Omega) > 0.6$, the real and imaginary parts of the impedance are of equal magnitude (this is strictly true only for the convective Warburg part of the interfacial impedance).

The impedance data at each rotation rate and oxygen concentration were analyzed to determine the corrosion rate. As shown above, it is necessary to extrapolate the measured impedance to zero frequency to determine the steady-state corrosion rate. For the present system, the extrapolation was straightforward and unequivocal because the reactions (kinetics) and processes (mass transfer) were successfully modeled and obeyed Eq. [5] (see also Eq. [8]). Accounting for all reactions and processes was necessary before the extrapolation could be performed with any confidence. For systems more complex than copper corrosion in oxygenated solutions, the reactions modeling may not be unequivocal and the impedance information will not give a unique determination of rate parameters. The data treatment is described further below, and will be the subject of work to be reported elsewhere.

In the limit of zero frequency, Eq. [5] yields

$$\frac{1}{Z_{f,t}} \Big|_{\omega \rightarrow 0} = \frac{i_{\text{corr}}FA}{RT} \left\{ \alpha_{\text{cc}} + (\alpha_{\text{aa}} + \alpha_{\text{ac}}) \left[1 - \frac{\alpha_{\text{ac}}M}{(\alpha_{\text{aa}} + \alpha_{\text{ac}})} \right] \right\} \quad [9]$$

For the additional condition, $M = 0$ (see Eq. [8])

$$\frac{1}{Z_{f,t}} \Big|_{\substack{\omega \rightarrow 0 \\ M \rightarrow 0}} = \frac{i_{\text{corr}}FA}{RT} (\alpha_{\text{aa}} + \alpha_{\text{ac}} + \alpha_{\text{cc}}) \quad [10]$$

Thus, some knowledge of the magnitude of M and the values of the kinetic transfer coefficients α_{aa} , α_{ac} , α_{cc} is required in order to determine the corrosion rate from the limiting impedance. For the copper dissolution reaction studies in the previous paper (5), α_{aa} and α_{ac} are both equal to 0.5. For the present paper, the cathodic transfer coefficient for oxygen reduction, α_{cc} , is assumed to be 0.5. It will be shown below that the data are satisfactorily represented by Eq. [10], where $M = 0$.

The extrapolation to zero frequency is performed as in the previous paper (5), *i.e.*, by noting that the total impedance obeys the empirical relationship

$$\frac{dZ_{\tau}(\text{real})}{-d[\omega Z_{\tau}(\text{imag.})]} \Big|_{\omega \rightarrow 0} = \text{const.} \quad [11]$$

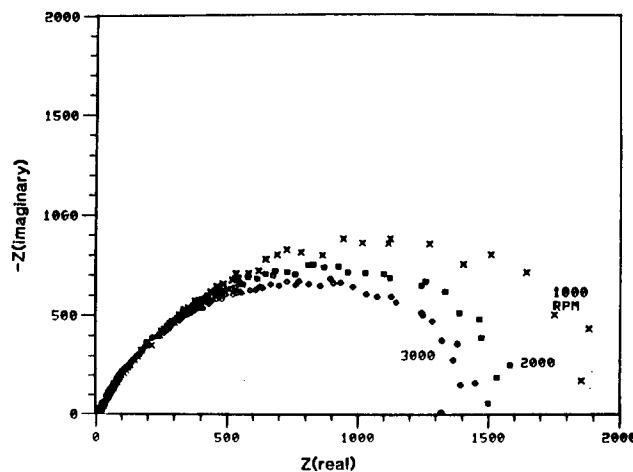


Fig. 1. Impedance of copper rotating disk at three rotation rates and 33.5 ppm dissolved oxygen.

The linear behavior is shown in Fig. 2 for one particular rotation rate and oxygen concentration. A linear relationship would yield

$$\frac{dZ_T(\text{real})}{-d[\omega Z_T(\text{imag.})]} = \frac{dZ_{i,T}(\text{real})}{-d[\omega Z_{i,T}(\text{imag.})]} \quad [12]$$

and the total impedance and the interfacial impedance would be identical except for the (constant) solution resistance, i.e.

$$Z_T = Z_s + Z_{i,T} \quad [13]$$

Further, we have assumed that the interfacial impedance is composed of a double-layer capacitance (CA) in parallel with the faradaic impedance given by Eq. [5] or [8]. Therefore

$$A_{i,T}(\text{real}) = Z'_{i,T} = \frac{([Z_{i,T}(\text{real})]^2 + [Z_{i,T}(\text{imag.})]^2) Z_{i,T}(\text{real})}{[Z_{i,T}(\text{real})]^2 + \{\omega CA([Z_{i,T}(\text{real})]^2 + [Z_{i,T}(\text{imag.})]^2) - Z_{i,T}(\text{imag.})\}^2} \quad [14]$$

$$Z_{i,T}(\text{imag.}) = Z''_{i,T} = \frac{-j[\omega CA\{[Z_{i,T}(\text{real})]^2 + [Z_{i,T}(\text{imag.})]^2\} - Z_{i,T}(\text{imag.})]}{[Z_{i,T}(\text{real})]^2 + \{\omega CA([Z_{i,T}(\text{real})]^2 + [Z_{i,T}(\text{imag.})]^2) - Z_{i,T}(\text{imag.})\}^2} \quad [15]$$

and as $\omega \rightarrow 0$

$$|\omega CA([Z_{i,T}(\text{real})]^2 + [Z_{i,T}(\text{imag.})]^2)| \ll |Z_{i,T}(\text{imag.})| \quad [16]$$

so that

$$\left. \frac{dZ'}{-d(\omega Z'')} \right|_{\omega \rightarrow 0} = \left. \frac{dZ_{i,T}(\text{real})}{-d[\omega Z_{i,T}(\text{imag.})]} \right|_{\omega \rightarrow 0} \quad [17]$$

It may be shown

$$\left. \frac{dZ_{i,T}(\text{real})}{-d[\omega Z_{i,T}(\text{imag.})]} \right|_{\omega \rightarrow 0} = \frac{d\text{Re} \left[-\frac{1}{\theta'(0)} \right]}{-d \left[\omega I_m \left(-\frac{1}{\theta'(0)} \right) \right]} + 0(\omega) \quad [18]$$

and this is the basis for the linear behavior in Fig. 2 at low frequencies. The last term in Eq. [18] denotes the order of magnitude of terms which are negligible compared to the first term at low frequencies. Further discussions of the linear behavior at low frequencies will be given elsewhere.

Both Eq. [9] and [1] were used to determine the corrosion rate from the measured impedance. For the corrosion potentials observed here, the value of $M(5)$ was always of the order of 0.1 or less. The maximum contribution from the last term in Eq. [9] was thus less than or equal to 5% of the dominant contribution, and Eq. [10] was then used to analyze the data since the experimental uncertainty was larger than this.

Table II contains the results of several determinations of the corrosion rate at 1000 rpm and 33.5 ppm O_2 . Also

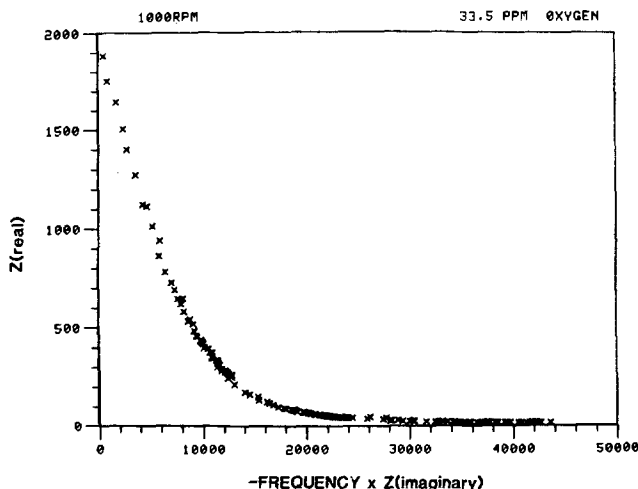


Fig. 2. Faradaic impedance plotted to display the linear behavior low frequency.

Table II. Corrosion rate from DIFA measurement compared to dissolution rate in deaerated 0.1M HCl solutions. 1000 rpm, 33.5 ppm O_2 (100%)

Corrosion potential (mV vs. SCE)	Corrosion rate from DIFA (A/cm ²)	Current density deaerated solution (A/cm ²)
-190	1.64	1.8
-195	1.45-1.48 × 10 ⁻⁵	1.5-1.52 × 10 ⁻⁵
-200	1.39-1.43	1.24-1.25
Avg.	1.45 (±0.06) × 10 ⁻⁵	1.394 (±0.16) × 10 ⁻⁵

given are the corrosion potential of each run and the corrosion current calculated from this potential and the results from the previous paper for deaerated solutions. The corrosion currents show satisfactory agreement, confirming that superposition was obeyed for the kinetics. Results at other oxygen concentrations and rotation rates are plotted in Fig. 3 and 4. The uncertainty bars shown in the figures are the result of different corrosion rates for different runs, even though the rotation rate and oxygen concentration were closely controlled at the values shown. The corrosion potential also varied, but the corrosion current always agreed closely with the deaerated solution results. We conclude that most of the data scatter in Fig. 3 and 4 was caused by variations of the oxygen re-

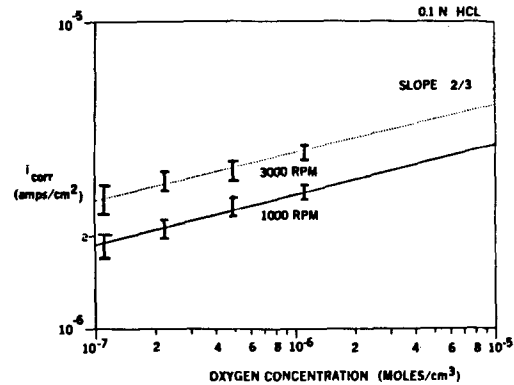


Fig. 3. Corrosion current density of copper in oxygenated 0.1N HCl at several rotation rates, 25°C.

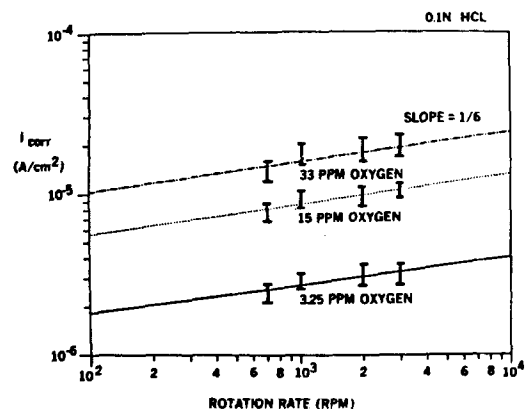


Fig. 4. Corrosion current density of copper in oxygenated 0.1N HCl as a function of disk rotation rate.

duction reaction rate. It was outside the scope of the investigation to pursue the matter further.

In Fig. 3, $\log i_{\text{corr}}$ vs. \log oxygen concentration, C_o^∞ , have a slope of 2/3 for the 1000 and 3000 rpm data, respectively. These curves reflect the assumptions already described above. That is, when oxygen reduction kinetics are irreversible, and first order in oxygen concentration, one has the relationship for the cathodic current

$$\frac{i_{\text{cc}}}{2F} = -k_{\text{cc}}C_o^\infty \exp\left[\frac{-\alpha_{\text{cc}}F}{RT}V\right] \quad [19]$$

Here, C_o^∞ is the dissolved oxygen concentration and k_{cc} is the rate constant for the reduction of oxygen. This may be an oversimplification of the oxygen reduction reaction [see, for example, Ref. (8, 9)], but the data were satisfactorily represented with this assumption. Therefore, Eq. [19] will be adopted for the remainder of the discussion. Equation [19] yields then the expression for the corrosion current density (5)

$$i_{\text{corr}} = \left(\frac{k_{\text{aa}}K_c}{k_{\text{ac}}}\right)\left(\frac{D_1C_{\text{Cl}^{-2}}}{\delta}\right)^{\frac{(\alpha_{\text{aa}} + \alpha_{\text{ac}})}{(\alpha_{\text{aa}} + \alpha_{\text{ac}} + \alpha_{\text{cc}})}} \left\{\frac{2k_{\text{ac}}k_{\text{cc}}C_o^\infty}{k_{\text{aa}}}\left(\frac{\delta}{D_1K_cC_{\text{Cl}^{-2}}}\right)\right\} \quad [20]$$

Since

$$\alpha_{\text{aa}} = \alpha_{\text{ac}} = \alpha_{\text{cc}} = 0.5 \quad [21]$$

i_{corr} is proportional to $(C_o^\infty)^{2/3}$, as is shown by the data in Fig. 3. It is clear that this relationship provides a satisfactory fit to the experimental data. Other powers of C_o^∞ would also fit the data, within some narrow limits, but the simple model adopted above has been preferred here.

Equation [20] was also used to fit the data in Fig. 4 for the dependence of the corrosion current on disk rotation rate. The dependence is quite weak, as was noted earlier by Miller and Bellavance (6). For the assumptions in Eq. [21] and the definition for the diffusion layer thickness from the previous paper (5)

$$i_{\text{corr}} \text{ proportional to } (\Omega)^{1/6} \quad [22]$$

The lines in Fig. 4 were drawn to obey this relationship. Again, the fit to the experimental data is satisfactory. As a final note, it was found that expression [22] also fits the earlier data of the Miller and Bellavance (6) satisfactorily.

One may derive the corrosion potential of the couple as a function of oxygen concentration and disk rotation rate as well. From Eq. [12] of the previous paper (5) and Eq. [20] above (both for $M = 0$), it may be shown that the corrosion potential V^* is given by

$$V^* = \frac{RT}{(\alpha_{\text{aa}} + \alpha_{\text{ac}} + \alpha_{\text{cc}})F} \ln \left\{ \left(\frac{3.2234k_{\text{ac}}k_{\text{cc}}}{k_{\text{aa}}K_c} \right) \left(\frac{C_o^\infty}{\Omega^{1/2}} \right) D^{-2/3}\nu^{1/6}C_{\text{Cl}^{-2}} \right\} \quad [23]$$

In Fig. 5, the quantity $C_o^\infty/\Omega^{1/2}$ is plotted vs. V^* in a semi-logarithmic fashion. The line has a slope of 39.4 mV/decade, i.e.

$$\frac{RT(2.303)}{(\alpha_{\text{aa}} + \alpha_{\text{ac}} + \alpha_{\text{cc}})F} = 39.4 \text{ mV} \quad [24]$$

for 25°C and the α values from Eq. [21]. The line fits the experimental data for all values of C_o^∞ and Ω . C_o^∞ represents the contribution from the dissolved oxygen concentration, and $\Omega^{-1/2}$ comes from the copper dissolution rate dependence on the disk-rotation rate.

Conclusions

It is concluded that impedance measurements by DIFA gave excellent results for the corrosion rates of copper in oxygenated 0.1N HCl. The steady-state corrosion rates were calculated from the straightforward zero frequency

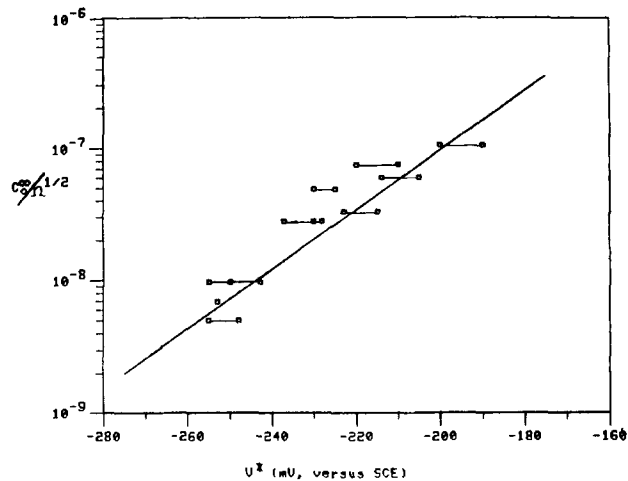


Fig. 5. Dependence of corrosion potential on dissolved oxygen concentration and disk rotation rate.

extrapolation of the impedance, a procedure which was justified by modeling the coupled kinetic processes. The experimental corrosion rate results were consistent with the model, and were found to depend on oxygen concentration and rotation rate as $(C_o^\infty)^{2/3}$ and $(\Omega)^{1/6}$. The observed corrosion potential was also derived and was found to depend on these variables as $\ln C_o^\infty/\Omega^{1/2}$. The model of an anodic dissolution reaction, dominated by convective diffusion, and coupled with a kinetically controlled cathodic reaction, may also be applicable to a wide range of metals in molten salt corrosion systems. The analysis of the impedance will largely follow that described here for the first time, and DIFA measurements will be very useful for these systems as well.

From Eq. [8] and [10]

$$\frac{Z_{f,T}}{\bar{Z}_{f,T}} \left[\frac{\alpha_{\text{aa}} + \alpha_{\text{ac}}}{\alpha_{\text{aa}} + \alpha_{\text{ac}} + \alpha_{\text{cc}}} \right] = \frac{1}{1 - \frac{Z_{f,T}}{\bar{Z}_{f,T}} \left[\frac{\alpha_{\text{cc}}}{\alpha_{\text{aa}} + \alpha_{\text{ac}} + \alpha_{\text{cc}}} \right]} = \frac{1}{\Gamma(4/3)[- \theta'(0)]} \quad [25]$$

where

$$\bar{Z}_{f,T} = Z_{f,t} \Big|_{\substack{\omega \rightarrow 0 \\ M \rightarrow 0}} \quad [26]$$

Thus, the faradaic impedance of the corrosion system when made dimensionless at each frequency by dividing by $\bar{Z}_{f,T}$, and arranged as in Eq. [25], should be identical to the convective Warburg impedance function (5). Further, one single curve, the convection Warburg impedance function curve, should fit the data for all rotation rates and oxygen concentrations. As in the previous paper (5), the solution resistance and double-layer capacitance were subtracted vectorially from the total impedance to yield the faradaic impedance for the corrosion couple. Figure 6 verifies Eq. [25] for the faradaic impedance at one of the rotation rates shown in Fig. 1. All other data were found to fall on the same curve as well at all voltage excitation frequencies. The double-layer capacitance used to fit the data at all frequencies was found to be 40-42 $\mu\text{F}/\text{cm}^2$, as found in the previous paper (5).

The general use of impedance measurements in corrosion systems will be most productive for those cases which resemble the simple system studied here and for the study of transient corrosion processes. In the first case, the ability to extrapolate to zero frequency with confidence and to fit the impedance data at all frequencies enables one to determine all the system properties that are important. The multiple-frequency determination of system properties will be greatly facilitated by experimental equipment such as the array-processor-enhanced DIFA system developed at our laboratory (14). Multiple-frequency modeling by digital signal analysis adaptive

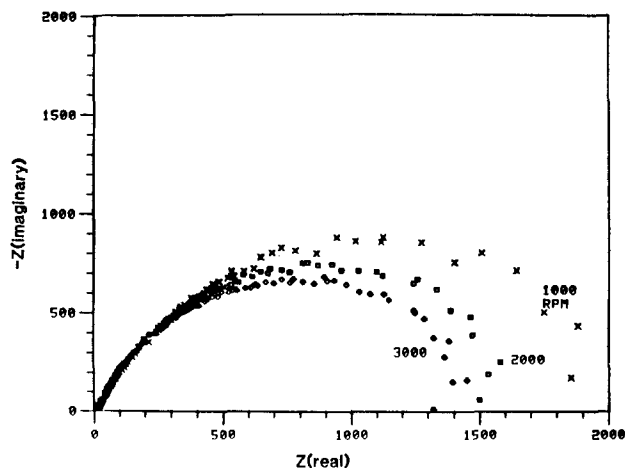


Fig. 6. Impedance of copper rotating disk at three rotation rates and 33.5 ppm dissolved oxygen.

filter procedures have been described in the literature (15, 16) for electrical engineering applications. This procedure improves on the use of "limiting behavior" for characterizing system properties, and gives the best fit to the data at all frequencies.

Acknowledgment

The work on corrosion of copper foils was performed by a summer student, Maureen Lindsay. The work was supported by the Office of Basic Energy Sciences of the Department of Energy under Contract no. DE-AC04-76DP-00789.

Manuscript submitted Feb. 1, 1984; revised manuscript received ca. Feb. 8, 1985.

REFERENCES

1. A. W. Tracy, in "Corrosion Resistance of Metals and Alloys," F. L. LaQue and H. R. Copson, Editors, Reinhold, New York (1963).
2. H. Leidheiser, Jr., "The Corrosion of Copper, Tin, and Their Alloys," John Wiley and Sons, New York (1971).
3. "Corrosion Data Survey," NACE, Houston, TX (1974).
4. U. Bertocci, in "Encyclopedia of Electrochemistry of the Elements" Vol. II, A. J. Bard, Editor, Marcel Dekker, New York (1974).
5. W. H. Smyrl, *This Journal*, **132**, 1555 (1985), and Ref. (1-14) therein.
6. B. Miller and M. I. Bellavance, *ibid.*, **119**, 1510 (1972).
7. C. Wagner and W. Traud, *Z. Electrochem.*, **44**, 391 (1938).
8. W. H. Smyrl, in "Comprehensive Treatise of Electrochemistry," Vol. 4, J. O'M. Bockris, *et al.*, Editors, Plenum Press, New York (1981).
9. W. Smyrl, *This Journal*, **132**, 1551 (1985).
10. J. P. Hoare, "The Electrochemistry of Oxygen," Interscience Publishers, New York (1968).
11. K. J. Vetter, "Electrochemical Kinetics," Academic Press, New York (1967).
12. W. H. Smyrl, in "Electrochemical Techniques for Corrosion Investigations," F. Mansfeld and U. Bertocci, Editors, ASTM, Philadelphia (1980).
13. International Critical Tables.
14. W. H. Smyrl, Paper 132 presented at The Electrochemical Society Meeting, Denver, CO, Oct. 11-16, 1981.
15. S. D. Stearns, "Digital Signal Analysis," Hayden, Rochelle Park, NJ (1975).
16. S. D. Stearns, Paper presented at the Ninth Annual Asilomar Conference on Circuits, Systems, and Computers, Nov. 1975.

Crystalline Anodic Oxide Growth on Aluminum Foil in an Aqueous Ammonium Dihydrogen Phosphate Anodization Electrolyte

C. T. Chen* and G. A. Hutchins

Sprague Electric Company, North Adams, Massachusetts 01247

ABSTRACT

The parameters affecting the growth of small crystallites within the anodic oxide film formed on aluminum during anodization in an 85°C aqueous ammonium dihydrogen phosphate electrolyte have been investigated. The degree of crystallinity of the anodic oxide was observed to increase with decreasing anodization current density and increasing voltage. The more crystalline films had a higher capacitance, were thinner, and contained less phosphorus than largely amorphous films anodized to the same voltage. A short thermal treatment of the aluminum foil at 600°C produced tiny platelets of γ - Al_2O_3 , which acted as effective nucleation sites for the growth of crystalline anodic oxide. Nucleation of crystalline anodic oxide also occurred on electropolished foil; however, the deposition of a thin amorphous oxide film on the electropolished aluminum prevented crystal growth during subsequent anodization. The crystalline anodic oxide has the γ - Al_2O_3 crystal structure and shows a strong preferred orientation related to the orientation of the aluminum substrate. A much smaller number of crystal growth sites was observed in the anodic oxide grown on (100) aluminum grains than in the oxide grown on any other substrate orientation.

The growth of crystalline aluminum oxide on aluminum foil during anodization has been discussed in numerous technical papers. In one commercial process, the aluminum foil is reacted with hot water for several minutes to form a layer of pseudoboehmite (γ' - $\text{Al}(\text{OH})_3$) containing excess water (1, 2). The barrier oxide formed during subsequent anodization is mostly crystalline γ' - Al_2O_3 and results in part from field-assisted dehydration of the hydrous oxide (2-5). The capacitance of the crystalline barrier oxide formed after hydration is greater than that of a largely amorphous oxide formed at the same anodization voltage without the hydration layer. The capacitance increase has been attributed to the greater density and field strength of the crystalline oxide (3, 6), and the practical advantage was recognized long before the structure

of the oxide was fully analyzed (7, 8). The crystalline composite oxide grown by this method exhibits an electrical instability which has been related to the presence of voids (6, 9, 10) and/or trapped oxygen (5, 11). This instability may be corrected by a relaxation or depolarization step followed by reanodization (3, 10).

Since the hydration in hot water smooths the etch structure of capacitor foil, and since the hydrous oxide remaining after anodization has a tendency to plug fine pores, the process described above is suitable only for high voltage foil with a coarse etch structure. It has recently been discovered that an increase in capacitance may also be achieved by a short thermal oxidation prior to anodization (12), and that this capacitance increase is due to the growth of crystalline anodic oxide (13-15). The thermal oxide developed can be very thin (< 10 nm) and

* Electrochemical Society Active Member.

still be effective; this treatment is therefore preferable for low voltage foil with a fine etch structure.

It has been suspected that tiny crystallites of thermal oxide formed during heat-treatment provide effective nucleation sites for crystalline anodic oxide growth (14). The existence of crystalline nuclei in thin thermal films is shown in this paper (Fig. 4); however, it is also found that nucleation of crystalline anodic oxide can occur on electropolished foil without thermal treatment (16). Growth of crystalline anodic oxide on foils with or without thermal treatment occurs most easily in aqueous solutions of organic acids or their salts such as ammonium citrate (15), ammonium pentaborate (13), or boric acid (17). In a phosphate electrolyte, crystalline anodic oxide growth is considerably more sluggish, possibly because the presence of incorporated phosphate inhibits crystallization (15).

We have observed that crystalline oxide grows slowly on electropolished foil and somewhat more rapidly on electropolished foil with thermal treatment during anodization at 85°C in an aqueous electrolyte containing 1 g/liter ammonium dihydrogen phosphate (ADP). Our primary interest has been to investigate the dynamics of crystal growth in anodic oxide. We report here on some of the parameters that effect the extent of crystal growth during anodization in an aqueous phosphate electrolyte. The relationships between degree of crystallinity, capacitance, field strength, oxide uniformity, and phosphate concentration are also explored.

Experimental Procedure

Specimens 100 cm² in area were cut from 100 μm thick, O-temper, 99.99% Al capacitor grade foil from the Aluminum Company of America (Alcoa). This foil exhibited a typical [100] rolling texture, and only approximately 5% of the foil grains were oriented with the (100) plane parallel to the foil surface. In addition to the predominant (110) orientation, (111), (311), and occasionally higher index planes were present parallel to the foil surface. For purpose of comparison, a few experiments were carried out with 100 μm thick, 99.99% Al high cubicity aluminum foil from Showa Aluminum Corporation (Showa). For this foil, approximately 85% of the area was oriented with the (100) plane parallel to the surface. For both foils, the grains were typically 100-400 μm in diameter and extended through the foil thickness. All foil specimens were electropolished in perchloric acid and acetic anhydride at 25°C with a current density of 10 mA/cm². Selected specimens were heated in air at 600°C prior to anodization.

The aluminum specimens were anodized between two 100 cm² platinum counterelectrodes suspended from a Teflon head. The electrolyte contained 1 g/liter ammonium dihydrogen phosphate in water and was held at 85°C during most anodizations. For comparison, a few specimens were anodized in the same electrolyte at 30°C. A constant current was passed until the potential difference between the aluminum and the platinum reached the preset anodization voltage; after this, the current was permitted to decay to a desired value. The anodization current was recorded on a Houston 2000 X-t recorder during the anodization process, and the total charge was obtained by graphical integration. Capacitance values in a 50 Ω-cm aqueous ammonium borate solution were measured at 120 Hz in a Pyrex cell with platinized platinum counterelectrodes using a General Radio 1657 RLC Digibridge. Measurements for repetitive specimens indicate a reproducibility within ±1% for both the charge and the capacitance measurements. All listed values are averages of two or more individual determinations.

Relative concentrations of phosphorus and oxygen were measured with an Applied Research Laboratories SEMQ electron probe microanalyzer equipped with wavelength dispersive spectrometers. During each individual measurement, a 1 μm diam, 10 keV electron beam was rastered over a 25 × 25 μm area on the oxide surface. For all specimens, the electron beam penetrated through the anodic oxide film into the aluminum substrate; x-rays were produced within both the film and the substrate

down to a total depth of approximately 0.6 μm. Since P and O were present only in the film, the P Kα and O Kα intensities increased with the mass thickness (micrograms/square centimeter) of the anodic oxide.

The oxygen intensity can be used as a measurement of the relative mass thickness of the oxide film provided the oxygen concentration of the anodic oxide does not vary greatly with the anodization conditions. This was considered to be a valid assumption even though differences in the amount of phosphate present would cause small changes in the oxygen content. Both P Kα and O Kα measurements were standardized to the intensity measured on a specific foil that was not thermally treated and was anodized to 180V with a current density of 3 mA/cm². The measured values are given here as ratios to facilitate comparison between specimens. All listed P and O values are an average of eight or more measurements at different locations on the specimen and are reproducible within ±0.01.

Specimens for transmission electron microscopy and selected area electron diffraction were prepared by dissolution of the aluminum substrate in a warm solution of bromine in methanol. For the very fragile thermal oxide films, a modified dissolution technique was used which resulted in very small holes in the foil which were bridged on one side by the thermal oxide film. The surrounding aluminum foil acted as a support and allowed the thermal oxide to be examined at high resolution without a carbon support film. All micrographs and diffraction patterns were taken in a Hitachi HU-125 transmission microscope operated at 100 keV.

Results and Interpretation

Effect of current density—thermally treated foils.—Electropolished Alcoa foil specimens which had been heated for 2 min at 600°C were anodized in the aqueous ADP electrolyte. Several different values for the anodization current density were used to study the effect on capacitance and anodization charge. The experimental results are listed in Table I, and they clearly show an increase in capacitance as the current density is decreased. The total anodization charge and the weight of the oxide decrease with decreasing current density. The relative phosphorus values decrease faster than the relative oxygen values, but a considerable phosphorus concentration is present in all of the specimens.

The 180V anodic oxide which grew on (100) grains of the aluminum substrate is thicker than the oxide which grew on other orientations of the same substrate. The (100) substrate areas could be distinguished easily with light microscopy due to their slightly different interference color; they were measured separately during the microprobe measurements, as indicated in Table I. Much smaller differences between the anodic oxides grown on the other substrate orientations were noted, but these small differences were not investigated systematically.

The transmission electron micrographs in Fig. 1 correspond to the isolated oxide films of samples I-1 and I-3. The upper half of each micrograph shows the less crystalline dielectric grown on the (100) substrate orientation; the lower half of each micrograph shows a more crystalline dielectric grown on a different crystallographic orientation of the foil. The relatively large dark areas, prevalent especially in the upper half of Fig. 1A, represent regions of thicker, amorphous oxide. The bright areas contain large numbers of γ'-Al₂O₃ crystallites embedded in amorphous oxide. The crystal structure is more fully developed in the micrograph of Fig. 1B than in that of Fig. 1A. This is fairly obvious in the upper (100) substrate area of the micrographs, but is not as clearly visible in the lower non-(100) substrate areas.

A more quantitative measure of the depth development of the crystal structure in the non-(100) substrate areas may be obtained by a measurement of the remaining film thickness after most of the amorphous oxide has been stripped off in a solution of 5% H₃PO₄ and 2% CrO₃. This solution will remove amorphous oxide at a rapid rate with

Table I. Effect of anodization current density on anodic oxide (electropolished and heat-treated Alcoa foil anodized at 85°C)

Sample no.	Minutes at 600°C	Anodization voltage (V)	Current density (mA/cm ²)	Charge ^a (C/cm ²)	Capacitance (10 ⁻² μF/cm ²)	Relative oxygen ^b	Relative phosphorus ^b
I-1	2	180	3.0	0.361	3.27	0.834 (0.968)	0.789 (0.951)
I-2	2	180	1.2	0.338	3.43	0.768 (0.943)	0.711 (0.888)
I-3	2	180	0.6	0.318	3.68	0.763 (0.874)	0.666 (0.792)
I-4	2	180	0.1	0.314	4.13	0.712 (0.758)	0.549 (0.609)
I-5	2	60	3.0	0.142	9.32	0.323	0.305
I-6	2	60	0.02	0.129	10.89	0.284	0.255

^a Constant current anodization charge to anodization voltage plus charge during current decay from stated current density to 0.1 mA/cm² for 180V and to 0.02 mA/cm² for 60V.

^b Relative to average measured value in non-(100) areas of 180V standard film without thermal treatment. Values in parentheses are for (100) substrate orientation.

essentially no attack of the crystalline oxide (18). For the 180V anodic oxides, most of the amorphous oxide has been removed after a 2 min stripping time in the boiling solution. The average thickness of the remaining film can be determined with the electron probe measurement of the oxygen intensity. Table II gives the weight fraction of the original anodic oxide thickness remaining as a function of stripping time for three of the specimens from Table I. The other specimens follow a similar trend, and it may be concluded that a decrease in the anodization current density produces an increase in the weight fraction of crystalline oxide in the resulting anodic oxide film.

Figure 2 shows an area of the isolated oxide from specimen I-6 grown on a (110) substrate orientation. Crystalline oxide growth decreases markedly with decreasing anodi-

zation voltage and this 60V dielectric shows a much lower degree of crystallinity than the 180V oxides. The structure consists of relatively large amorphous patches (dark gray) and brighter clusters of crystals and voids. The partly crystalline areas of the anodic oxide permit a greater field strength during anodization and are therefore thinner and appear brighter in the image. The small fuzzy black structures are the result of selective diffraction of the transmitted electron beam by specific crystallites. As the plane of the specimen is tilted slightly, different crystallites will show this diffraction contrast effect, which is also visible in Fig. 1.

An electron diffraction pattern of specimen I-6 is shown in Fig. 3. The oxide area selected for the diffraction pattern grew on a (111) grain of the aluminum foil; the six

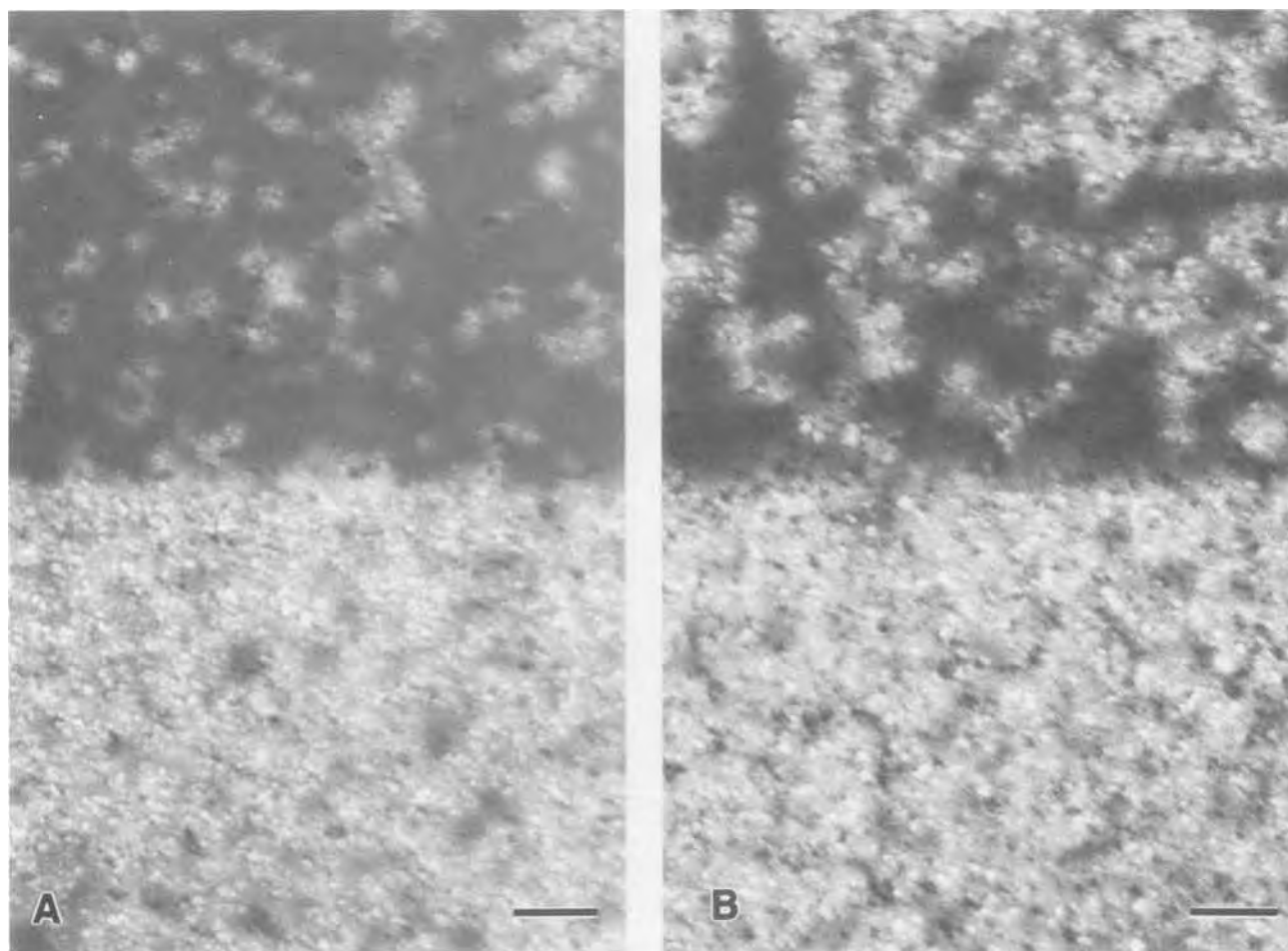


Fig. 1. Transmission electron micrographs of isolated 180V oxide grown on (100) substrate (top) and non-(100) substrate (bottom). A: Specimen I-1; current density = 3 mA/cm². B: Specimen I-3; current density = 0.6 mA/cm². Marker length is 500 nm.

Table II. Weight fraction of anodic oxide remaining after immersion in boiling solution of 5% H_3PO_4 and 2% CrO_3

Sample no.	Anodization current density	30s immersion (%)	60s immersion (%)	120s immersion (%)
I-1	3.0	57	39	25
I-3	0.6	59	45	43
I-4	0.1	68	66	65

strong arcs at the 220 positions are indicative of a pronounced (111) preferred orientation. Diffraction patterns for oxide grown on a (110) substrate show a (110) preferred orientation, while the diffraction patterns for oxide grown on a (100) substrate are weak and fairly random.

The crystal structure of the anodically grown crystalline oxide is a less ordered form of the thermally grown $\gamma-Al_2O_3$ and has been designated as $\gamma'-Al_2O_3$ in the literature (17, 19, 20). Both structures have a close-packed oxygen lattice; the differences lie in the greater or lesser degree of order in the positions of the aluminum atoms. All diffraction patterns examined corresponded to the $\gamma'-Al_2O_3$ structure; no evidence was seen of the additional diffraction lines present in the more highly ordered $\gamma-Al_2O_3$.

Microstructure of thermal oxide films.—During the short thermal treatment at 600°C, tiny crystallites of $\gamma-Al_2O_3$ are formed and grow into the aluminum metal. We believe that these thermal oxide crystallites are the nucleation sites for the anodic oxide crystal clusters seen in Fig. 1 and Fig. 2, and have therefore studied them in some detail. Micrographs of the isolated thermal oxide formed during oxidation times of 1 and 3 min at 600°C are shown in Fig. 4. The continuous film consists of the oxide originally present on the electropolished foil plus the amorphous oxide formed during heating. The overall

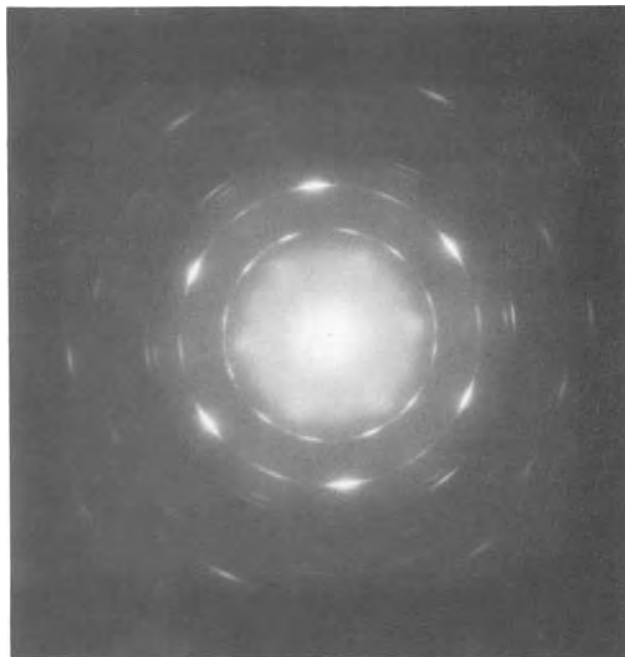


Fig. 3. Selected area transmission electron diffraction pattern of isolated 60V oxide grown on (111) substrate orientation.

“orange peel” structure is related to the topography of the electropolished foil, rather than to differences in oxide thickness (21). The specimens were tilted slightly to maximize topography and thickness contrast. In Fig. 4, a few of the well-developed thermal oxide crystallites are indicated by arrows; they are typically 10 nm wide after 1 min at 600°C and 40 nm wide after 3 min at 600°C. The small spots (circles) may be either crystallites at an early

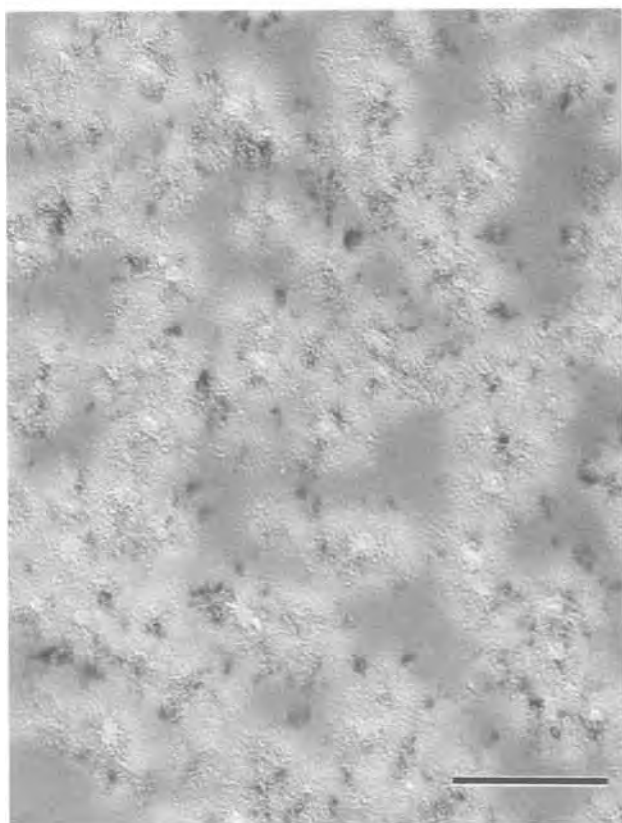


Fig. 2. TEM of isolated 60V oxide from specimen I-6. The area pictured grew on the (110) substrate orientation and shows large amorphous patches (dark gray) and brighter clusters of crystals and voids. Fuzzy black spots correspond to diffracting crystallites. Marker length is 200 nm.

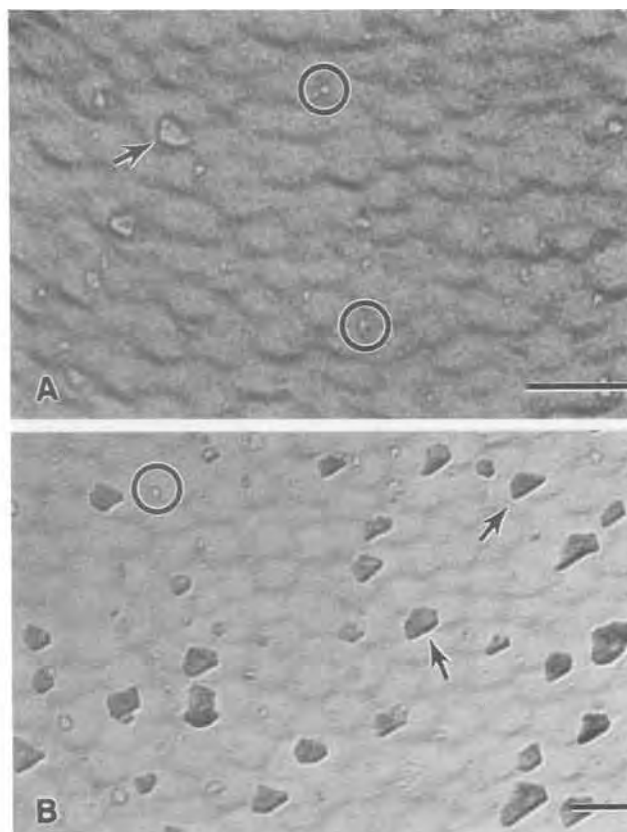


Fig. 4. TEM of isolated thermal oxide formed during heating at 600°C for 1 (A) and 3 min (B). Marker length is 100 nm. Note that B is at lower magnification than A.

stage of growth or flaws in the thermal oxide. Very few of these small structures were observed on foils without thermal treatment. Transmission electron diffraction patterns of specimens similar to that shown in Fig. 4B typically consisted of sharp spots which could be indexed to correspond to the (110), (111), and (311) planes of γ - Al_2O_3 .

These results are in general agreement with studies of crystalline thermal oxide growth reported in the literature. Previous work has been limited to very low oxygen partial pressures (22-24), or to relatively thick oxide films (21, 25-28). However, the morphologies observed for the early stages of the very rapid nonequilibrium growth in the present study were not markedly different from those observed for the very slow growth at low oxygen partial pressure within an electron microscope (22, 23).

Anodization of electropolished foil.—Specimens of electropolished Alcoa foil without thermal treatment were anodized at different values of the anodization current density. The experimental measurements on these anodic oxides are given in Table III. The capacitance of the dielectric films also increased with decreasing anodization current density, although the capacitance values were not as high as those of corresponding thermally treated specimens. Furthermore, the anodization charge, the phosphorus concentration, and the oxide thickness again decreased with decreasing current density. The transmission electron micrographs of these specimens show an increasing number of γ '- Al_2O_3 crystallites in the anodic oxide as the anodization current density is decreased. The principal differences between the micrographs of these specimens and the corresponding thermally treated specimens anodized at the same current density appear to be related to the number of nucleation sites for crystalline anodic oxide formation. For anodizations at relatively high current density, the anodic oxides grown on thermally treated foils tend to be more uniform with more fully developed crystal clusters, while the untreated specimens contain relatively large patches of amorphous oxide.

Electron diffraction patterns of the anodic oxide formed on electropolished foil without thermal treatment also show a preferred orientation related to the crystallographic orientation of the aluminum substrate. However,

the patterns are much weaker than for thermally treated foils and little crystallinity is observed for (100) substrate areas on the untreated Alcoa foils.

Effect of substrate orientation and anodization temperature.—For the Alcoa foils used in this investigation, the (100) grains comprised only approximately 5% of the total surface area. We observed that the difference in thickness and microstructure between the anodic oxide grown on (100) and non-(100) substrate areas was most pronounced near the grain boundaries of relatively small (100) grains which were totally surrounded by non-(100) grains. This led us to the investigation of anodic oxides grown on high cubicity Showa foil for which approximately 85% of the grains were of the (100) orientation and non-(100) grains were in the minority.

The first four entries in Table IV give data for anodic oxides grown under identical conditions on Alcoa and Showa foils with and without a thermal treatment. A comparison of specimens IV-1 and IV-2 is of particular interest because it indicates that the substrate orientation effect of a particular grain may be modified considerably by the orientation of the surrounding grains. The anodic oxide grown on (100) substrate areas is thicker than the anodic oxide grown on non-(100) substrate areas for both foils, but the corresponding measured oxygen intensity values are very different. For each foil, the thickness of the anodic oxide grown on the majority of the grains approaches an average value, while the substrate effect for oxide grown on the differently oriented grains is enhanced. Thus, the "thick" (100) substrate anodic oxide is thicker and less crystalline on the Alcoa foil, where it constitutes only 5% of the area, while the "thin" non-(100) substrate anodic oxide is thinner and more crystalline for the Showa foil, where it constitutes only 15% of the area. As a result of these compensating effects, the capacitance measured for the Showa foil is only slightly lower than that for the Alcoa foil.

Specimens IV-3 and IV-4 are Alcoa and Showa foils without heat-treatment anodized under identical conditions. In this case, the relative oxygen intensities measured for the (100) substrate areas are the same for both foils because very little crystallization occurs during anodization on this substrate orientation unless the foil

Table III. Effect of anodization current density on anodic oxide (electropolished Alcoa foil anodized at 85°C)

Sample no.	Minutes at 600°C	Anodization voltage (V)	Current density (mA/cm ²)	Charge (C/cm ²)	Capacitance (10 ⁻² μ F/cm ²)	Relative oxygen	Relative phosphorus
III-1	0	180	3.0	0.443	3.09	1.000 (1.020)	1.000 (1.022)
III-2	0	180	1.2	0.438	3.17	0.981 (1.027)	0.928 (0.976)
III-3	0	180	0.6	0.407	3.26	0.922 (1.007)	0.833 (0.935)
III-4	0	180	0.1	0.350	3.47	0.775 (0.914)	0.632 (0.787)
III-5	0	60	3.0	0.157	8.47	0.334	0.318
III-6	0	60	0.02	0.147	9.77	0.315	0.254

Table IV. Effects of substrate orientation and anodization temperature (180V anodization; current density = 0.6 mA/cm²)

Sample no.	Foil	Minutes at 600°C	Electrolyte temperature (°C)	Charge (C/cm ²)	Capacitance (10 ⁻² μ F/cm ²)	Relative oxygen	Relative phosphorus
IV-1	Alcoa	2	85	0.318	3.68	0.763 (0.874)	0.666 (0.792)
IV-2	Showa	2	85	0.370	3.51	0.722 (0.787)	0.600 (0.701)
IV-3	Alcoa	0	85	0.407	3.26	0.922 (1.007)	0.833 (0.935)
IV-4	Showa	0	85	0.428	3.07	0.867 (1.014)	0.782 (0.917)
IV-5	Alcoa	2	30	0.436	3.28	0.788 (0.883)	0.566 (0.640)

has been thermally treated. The anodic oxide grown on non-(100) substrate areas is thinner and more crystalline on the Showa foil, where it constitutes only 15% of the surface area.

The typical microstructure of the isolated 180V anodic oxide grown on thermally treated Showa foil is shown in Fig. 5. The area in the micrograph corresponds to the grain boundary region between two (100) grains of the substrate; it is at the same magnification as Fig. 1B, which shows the oxide grown near a (100)/non-(100) grain boundary on the corresponding Alcoa foil. The anodic oxide that grew over the grain boundary in Fig. 5 is highly crystalline. The rest of the microstructure is characteristic of the (100) substrate orientation and consists of crystal clusters separated by amorphous patches. The (100) crystal clusters are more fully developed in this specimen than in the corresponding Alcoa foil.

Crystalline anodic oxide grown during anodization in the ADP electrolyte near room temperature has a different microstructure. The crystals appear to grow primarily by enlargement of the original thermal oxide nuclei rather than by the clusterlike growth observed for 85°C anodizations. A comparison of the microstructures of the isolated anodic oxides from non-(100) substrate areas of thermally treated Alcoa foils anodized at 85°C and 30°C is given in Fig. 6. Without the thermal treatment, only a few isolated small crystals could be seen in the anodic oxide grown at 30°C.

Current efficiency.—The current efficiency is relatively independent of the anodization current density for 85°C formations in the ADP electrolyte. In Fig. 7, the total anodization charge has been plotted against the measured relative oxygen intensity for the data in the three tables. A weighted average between the (100) and non-(100) substrate measurements has been used for the oxygen intensity to take into account the very different substrate orientations of the Alcoa and Showa foils. With the exception of the two labeled data points, the measurements fall in a pattern close to a straight line. The anodization charge values for thermally treated specimens tend to fall slightly below the measurements for untreated specimens. This is as expected, since some amorphous and

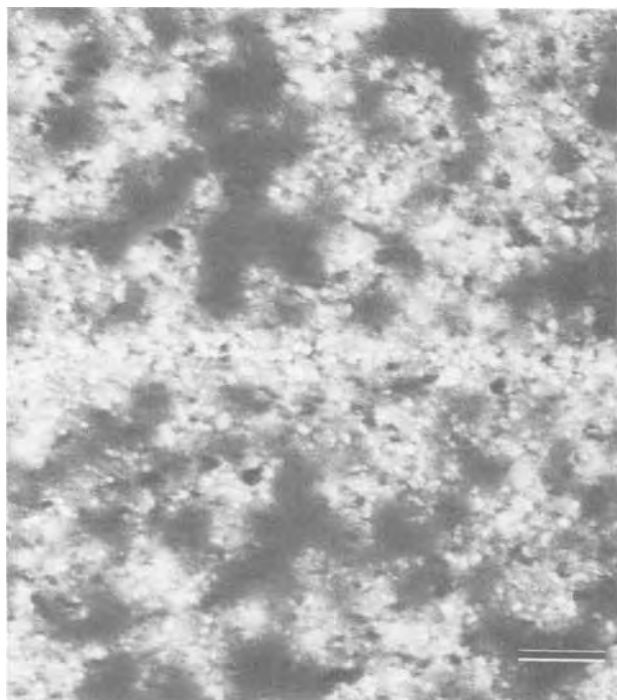


Fig. 5. TEM of isolated 180V anodic oxide grown on (100) substrate area of Showa foil (specimen IV-2). The more crystalline strip across the center corresponds to a substrate grain boundary. Marker length is 500 nm.

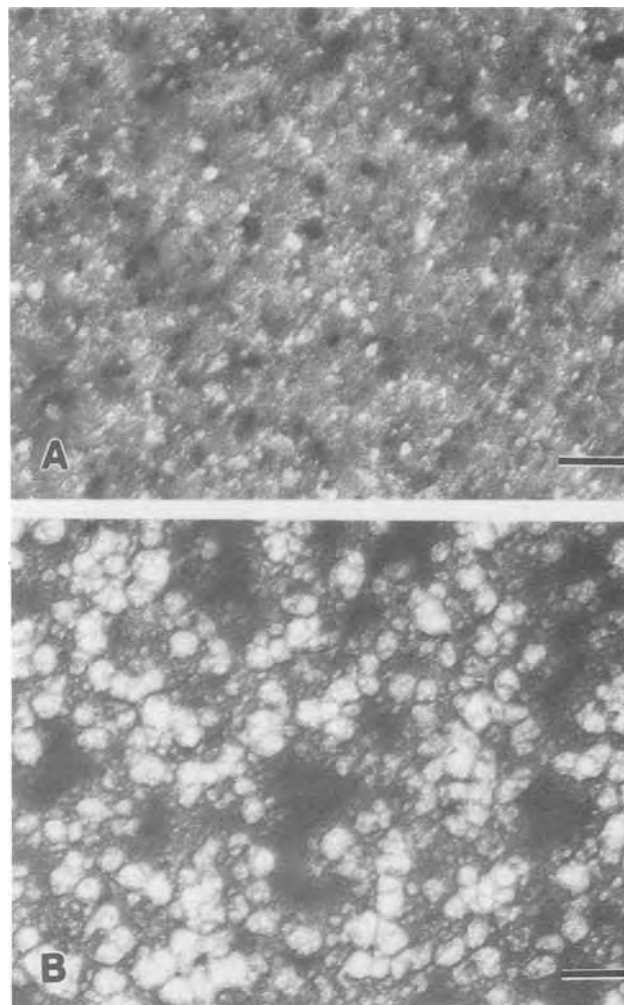


Fig. 6. TEM of isolated 180V anodic oxide grown on non-(100) substrate areas of Alcoa foil. A: 85°C anodization, specimen IV-1. B: 30°C anodization, specimen IV-5. Marker length is 200 nm.

crystalline oxide forms during the thermal treatment without passage of current.

Data points A and B deviate further from the linear relationship than would be expected from measurement error and data spread. Point A corresponds to the 30°C anodization on thermally treated Alcoa foil (specimen IV-5). The apparent current efficiency under those condi-

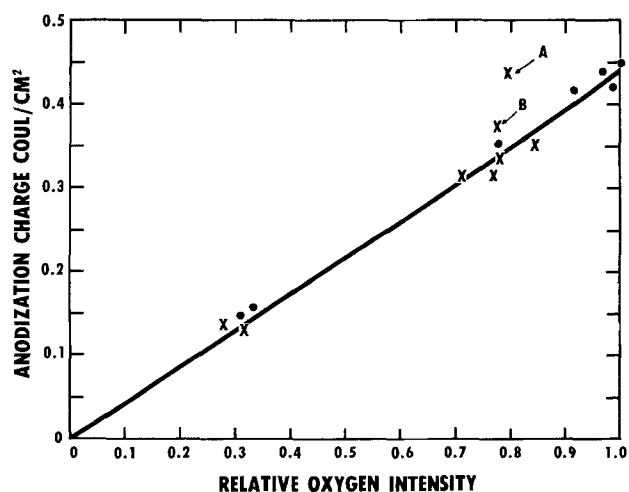


Fig. 7. Total anodization charge vs. measured relative oxygen intensity for data in Tables I, III, and IV. See text for discussion of labeled data points. X: Thermally treated specimens. ●: Not thermally treated prior to anodization.

tions is only 80% of the average for the other specimens. This value is in good agreement with the relative current efficiencies reported by Randall and Bernard (29) for anodization at 25° and 90°C in 0.01M NaH_2PO_4 with a current density of 1 mA/cm². Data point B corresponds to the 85°C anodization on thermally treated Showa foil (specimen IV-2). The apparent current efficiency for this predominantly (100)-oriented foil is 92% of the average for the other specimens.

Effect of surface films on the growth of crystalline anodic oxide.—Electropolished foil dried at room temperature is covered by an amorphous oxide on the order of 2 nm thick. The specimen preparation techniques used in a number of the investigations reported in the literature result in a somewhat different amorphous surface film of aluminum oxide that may modify or inhibit crystal growth within the anodic oxide. For example, Alwitt and Takei (15) chemically polished their specimens in $\text{HNO}_3 + \text{H}_3\text{PO}_4$ followed by cleaning in NaOH and water. They reported that anodization of these specimens in a citrate electrolyte produced an amorphous anodic oxide film unless the specimens were thermally treated prior to anodization. We have observed that this “bright dip” specimen preparation resulted in the growth of amorphous anodic oxide in citrate and phosphate electrolytes, while electropolished specimens anodized under the same conditions were highly crystalline.

The effect of surface films is of interest because the etched capacitor foil surface is typically covered by an amorphous oxide film (30, 31). For this reason, crystalline anodic oxide may not grow on etched foil during anodization at 85°C unless the surface film has been modified or removed by special cleaning steps and/or thermal treatment (32). The surface films may also effect the growth rate of the crystalline thermal oxide.

To simulate the surface condition of etched foil, we have generated a thin surface film on electropolished foil by an electrochemical method. The electrolyte consisted of 0.15M $\text{HNO}_3 + 0.011\text{M H}_3\text{PO}_4 + 400 \text{ ppm H}_2\text{SO}_4$ and was derived from an AC etch solution (33) by omitting the HCl and AlCl_3 , so that pits would not be etched into the electropolished foil. To create the simulated “AC etch film” in this electrolyte, the potential of the aluminum foil was switched at 20 Hz between -0.45 and $-2.25\text{V vs. a saturated calomel electrode}$.

A micrograph of an amorphous, nearly featureless 180V anodic oxide grown on electropolished Alcoa foil with the simulated “etch film” is shown in Fig. 8A. When the substrate containing the etch film was heated at 600°C for 5 min prior to anodization, the microstructure of the anodic oxide changed to that shown in Fig. 8B. The surface film inhibited the growth of crystalline thermal oxide, and a somewhat longer heating time was required to generate the crystalline thermal oxide under the amorphous film. This is indicated in Fig. 9, which shows the isolated thermal oxide formed in 5 min at 600°C on electropolished foil with and without the simulated etch film. The micrograph of Fig. 9A is focused on the fine structure of the residual etch film; the darker irregular shapes are the thermal oxide crystals which are growing into the aluminum metal. The $\gamma\text{-Al}_2\text{O}_3$ crystals in Fig. 9B have grown laterally to cover most of the aluminum surface.

Discussion

The relative phosphorus intensities listed in the tables are proportional to the phosphorus present in the total thickness of the aluminum oxide. Our measurements indicate a trend that the more crystalline films contain less phosphorus, but it is unlikely that the phosphorus concentration is uniform throughout the film. For anodic oxide films that were largely amorphous, Randall and Bernard (29) have determined with radiotracer techniques that the inner third of the oxide film is free of phosphorus. A similar result has been obtained by Thompson *et al.* (34) by direct STEM/EDS analysis of an oxide section prepared by ultramicrotomy. Phosphorus distributions in partly crystalline films may be more complex than in

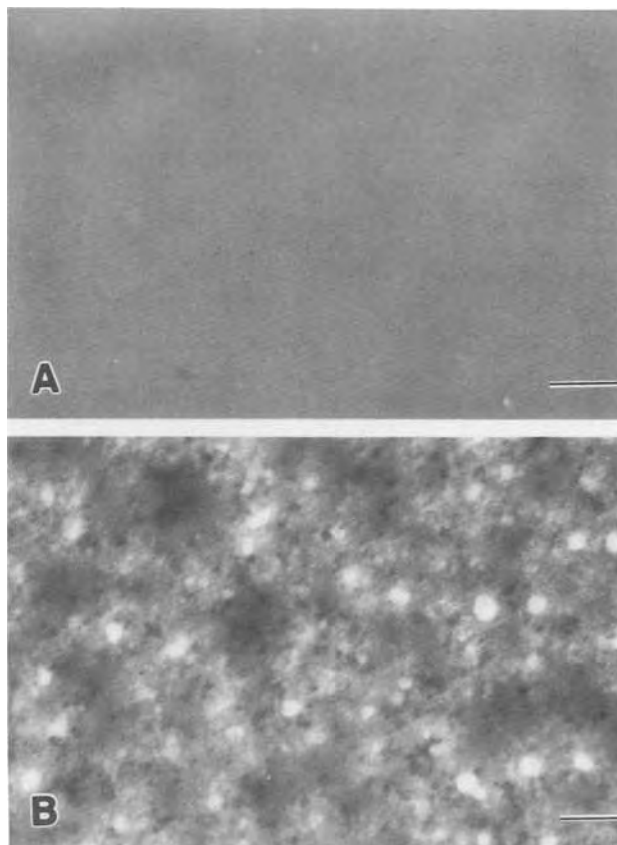


Fig. 8. TEM of isolated 180V anodic oxides grown on non-(100) substrate areas of electropolished Alcoa foil covered by simulated “etch film.” A: 85°C anodization at 1 mA/cm². B: 5 min at 600°C + 85°C anodization at 1 mA/cm². Marker length is 200 nm.

amorphous films, since the $\gamma'\text{-Al}_2\text{O}_3$ crystallites are non-uniformly distributed within the anodic oxide film both laterally and in depth.

The crystalline anodic oxide films have a lower weight per unit area than amorphous oxide films anodized at the same voltage in the ADP electrolyte. The presence of crystalline anodic oxide permits a greater field strength (6); therefore, less oxide is required to sustain the anodization voltage at a specific current. The decrease in oxide thickness with increasing crystallinity qualitatively explains the increase in capacitance measured for the more crystalline oxide films anodized at low current density. For the more nonuniform films, the thickness of the dielectric also varies considerably from one point to another on a submicron scale.

To maximize the crystallinity of the anodic oxide grown in the ADP electrolyte, both the crystal nucleation and the crystal growth conditions need to be optimized. Thermal oxide crystallites formed during heating for a short time at 600°C provide effective growth sites for the crystalline anodic oxide. The substrate-related preferred orientation of the growing $\gamma'\text{-Al}_2\text{O}_3$ anodic oxide crystallites is established by the thermally formed $\gamma\text{-Al}_2\text{O}_3$ platelets that have grown epitaxially on the aluminum substrate during thermal treatment.

Initiation of crystalline oxide growth will also occur on electropolished foil in the ADP electrolyte. The number of crystalline sites increases markedly with electrolyte temperature and is influenced by the crystallographic orientation of the aluminum substrate. On any specimen, the (100) grains have a considerably lower number of crystalline sites than all other substrate orientations. Amorphous films deposited on the electropolished aluminum appear to interfere with the initiation of crystalline growth sites.

Growth of the individual sites is optimized by high electrolyte temperature, low current density, and high anodization voltage. A low current density primarily de-

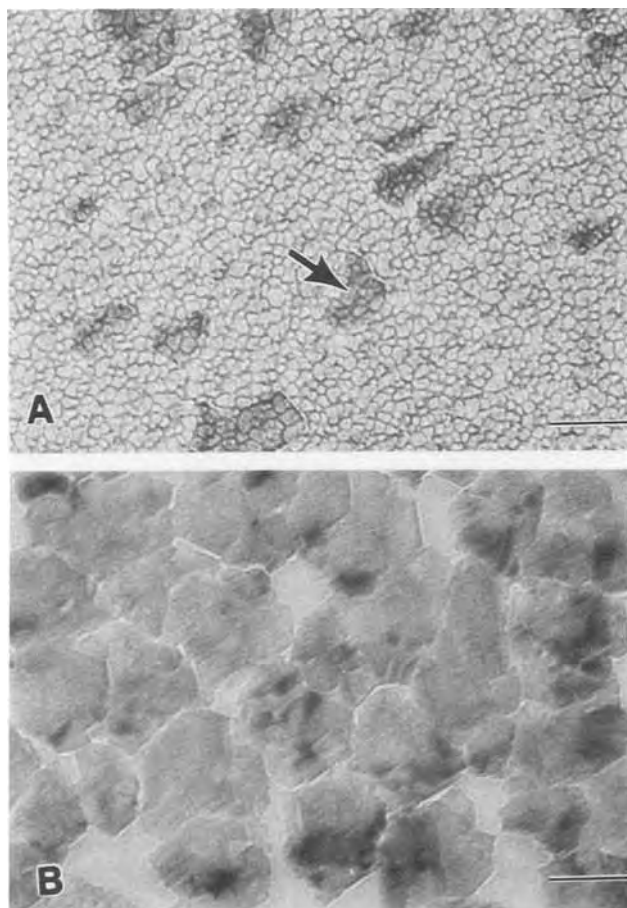


Fig. 9. TEM of isolated thermal oxide grown on non-(100) substrate areas of Alcoa foil during heating for 5 min at 600°C. A: Electropolished foil with simulated "etch film." Arrow indicates a thermal oxide crystallite. B: Electropolished foil. Marker length is 100 nm.

creates the rate of oxide growth and increases the time required for the total anodization; this, apparently, favors crystalline oxide growth. The exact growth process is not known; the crystalline oxide may grow by conversion of amorphous oxide, by direct crystal growth, or by a combination of the two.

The crystal clusters described in the preceding text differ from the flaws containing γ' -Al₂O₃ reported by Shimizu and others (18, 35, 36). The flaws are typically seen in largely amorphous anodic oxide films formed in 25°C aqueous borate electrolytes with current densities greater than 1 mA/cm² and formation voltages greater than 200V. They occur in greater number on as-received and chemically cleaned foil than on electropolished foil. The crystal clusters are smaller and can be seen at much lower anodization voltages than can the flaws reported by Shimizu *et al.* The crystal clusters are much more numerous on electropolished foil than on chemically cleaned foil and are most prevalent in anodic oxide films formed at high anodization temperatures and low current densities in the ADP electrolyte.

Acknowledgment

The authors wish to thank W. J. Bernard, S. M. Florio, S. D. Ross, C. E. Hutchins, and S. E. Summers for numer-

ous helpful discussions during the course of this investigation.

Manuscript submitted Dec. 19, 1984; revised manuscript received March 4, 1985.

Sprague Electric Company assisted in meeting the publication costs of this article.

REFERENCES

1. W. J. Bernard and J. J. Randall, Jr., *This Journal*, **107**, 483 (1960).
2. D. Altenpohl and W. Post, *ibid.*, **108**, 628 (1961).
3. R. S. Alwitt, *ibid.*, **114**, 843 (1967).
4. R. S. Alwitt and W. J. Bernard, *ibid.*, **121**, 1019 (1974).
5. C. Crevecoeur and H. J. de Wit, Paper 174 presented at The Electrochemical Society Meeting, Seattle, WA, May 21-26, 1978.
6. C. K. Dyer and R. S. Alwitt, *Electrochim. Acta*, **23**, 347 (1978).
7. C. F. Coggins, U.S. Pat. 2,396,685 (1946).
8. D. Altenpohl, U.S. Pat. 2,859,148 (1958).
9. R. S. Alwitt, C. K. Dyer, and B. Noble, *This Journal*, **129**, 711 (1982).
10. R. S. Alwitt and C. K. Dyer, *Electrochim. Acta*, **23**, 355 (1978).
11. W. J. Bernard and P. G. Russell, *This Journal*, **127**, 1256 (1980).
12. Republic Foil Inc., Br. Pat. 1,056,609 (1967).
13. C. Crevecoeur and H. J. de Wit, Paper 132 presented at the 27th ISE Meeting, Zurich, Sept. 6-10, 1976.
14. R. S. Alwitt, Paper C-118 presented at the ECIS Meeting, Tokyo, Oct. 15, 1980.
15. R. S. Alwitt and H. Takei, in "Passivity of Metals and Semiconductors," M. Froment, Editor, p. 741, Elsevier Science Publishers, Amsterdam (1983).
16. C. T. Chen and G. A. Hutchins, U.S. Pat. 4,481,084 (1984).
17. D. J. Stirland and R. W. Bicknell, *This Journal*, **106**, 481 (1959).
18. K. Shimizu, S. Tajima, G. E. Thompson, and G. C. Wood, *Electrochim. Acta*, **25**, 1481 (1980).
19. E. J. W. Verwey, *Z. Krist.*, **91**, 317 (1935).
20. E. J. W. Verwey, *J. Chem. Phys.*, **3**, 593 (1935).
21. J. J. Randall and W. J. Bernard, *J. Appl. Phys.*, **35**, 1317 (1964).
22. K. Shinohara, T. Seo, and H. Kyogoku, *Z. Metallkd.*, **73**, 775 (1982).
23. R. K. Hart and J. K. Maurin, *Surf. Sci.*, **20**, 20 (1970).
24. K. Thomas and M. W. Roberts, *J. Appl. Phys.*, **32**, 70 (1961).
25. P. E. Doherty and R. S. Davis, *ibid.*, **34**, 619 (1963).
26. A. F. Beck, M. A. Heine, E. J. Caule, and M. J. Prior, *Corros. Sci.*, **7**, 1 (1967).
27. M. J. Dignam, *This Journal*, **109**, 1884 (1962).
28. M. J. Dignam and W. R. Fawcett, *ibid.*, **113**, 663 (1966).
29. J. J. Randall and W. J. Bernard, *Electrochim. Acta*, **20**, 653 (1975).
30. S. M. Florio, W. M. Moore, G. A. Hutchins, and S. E. Summers, *Corrosion*, **39**, 151 (1983).
31. C. K. Dyer and R. S. Alwitt, *This Journal*, **128**, 300 (1981).
32. W. J. Bernard and S. M. Florio, Unpublished results; C. E. Hutchins, Unpublished results.
33. H. Ngyuen, J. J. Randall, and A. B. McPherson, U.S. Pat. 4,427,506 (1984).
34. G. E. Thompson, G. C. Wood, and K. Shimizu, *Electrochim. Acta*, **26**, 951 (1981).
35. K. Shimizu and S. Tajima, *ibid.*, **25**, 250 (1980).
36. K. Shimizu, G. E. Thompson, and G. C. Wood, *Thin Solid Films*, **92**, 231 (1982).

Frequency Response of Plug-Flow Electrochemical Reactors

Thomas Z. Fahidy*

Department of Chemical Engineering, University of Waterloo, Waterloo, Ontario, Canada N2L 3G1

ABSTRACT

A theoretical analysis of PFER reactor response to sinusoidal perturbations in inlet electrolyte concentration, electrolyte temperature, and electric current is presented, on the basis of transfer functions. The existence of resonance, typical of systems under distributed forcing, is also shown.

The study of the dynamics of a PFER (plug-flow electrochemical reactor) has so far received very little attention in the electrochemical literature, [e.g., Ref. (1, 2)] although its steady-state design and performance have been thoroughly discussed (3, 4). The knowledge of dynamic behavior is important not only for a proper understanding of reactor transients (*i.e.*, transition from one steady state to another), but also for the design of control against deleterious effects of process perturbations (*e.g.*, in current or potential drop, inlet electrolyte flow rate, temperature, and concentration). An important aspect of PFER dynamics and, indeed, of any electrochemical reactor is its response to sinusoidal perturbations in process variables, called the frequency response. In systems such as the CSTER, where process variables, *e.g.*, electrolyte concentration and temperature, are not space dependent, the classical transfer-function approach is a convenient means of studying frequency response in terms of relatively uncomplicated algebraic functions. In distributed-parameter systems such as the PFER, where process variables are time and space dependent, the transfer-function approach is less straightforward, but it remains an inviting method to analyze the resonance phenomenon, characteristic of such systems (5). Resonance occurs when a perturbation is suddenly imposed along the characteristic space coordinate, acting essentially as a spatial amplifier for system response; as a result, the response variables will oscillate with distinctly larger or lower amplitudes at certain frequencies (resonance frequencies) than at neighboring frequencies. The existence of resonance has been amply documented in process equipment, *e.g.*, in heat exchangers (5, 6).

The subject of this paper is the extension of the theory of frequency response and resonance phenomena to a PFER by means of the transfer-function approach applied to both isothermal and nonisothermal operations, but in the absence of any dispersion effect. It illustrates a further application of well-established principles of chemical process dynamics to electrochemical engineering, with results connected directly to the rational design of electrochemical process control.

The general problem of transfer-function representation of the isothermal plug-flow reactor.—The geometry, electrode arrangement, and limitations pertaining to the PFER model have been previously discussed [e.g., Ref. (1-3)] in detail. The substance balance

$$\frac{\partial c}{\partial t} = -v \frac{\partial c}{\partial z} - k_1 i \quad [1]$$

with auxiliary conditions $t = 0$, $c = c^*(z)$, $i = i^*(z)$ and $z = 0$, $c = c^*(0)$, and $i = i^*(0)$ defines the concentration distribution of the electrolyte in time and distance in the reactor. In terms of perturbation variables

$$c(t, z) - c^*(z) \equiv y_1(t, z)$$

and

$$i(t, z) - i^*(z) \equiv x(t, z)$$

Eq. [1] may be replaced by its isomorphic equivalent

$$\frac{\partial y_1}{\partial t} = -v \frac{\partial y_1}{\partial z} - k_1 x \quad [2]$$

*Electrochemical Society Active Member.

with auxiliary conditions $t = 0$, $y = 0$, $x = 0$ and $z = 0$, $y_1 = y_1^0(t)$, $x = 0$. Using the Laplace transforms of y_1 and x with kernel $\exp(-st)$, Eq. [2] is transformed into the ordinary differential equation

$$\frac{dY_1(s, z)}{dz} + \frac{s}{v} Y_1(s, z) = -\frac{k_1}{v} X(s, z) \quad [3]$$

Let $X(s, z)$ represent the product of two mutually independent functions of each independent variable; *i.e.*, $X(s, z) = f(s)g(z)$. Let $F(s, z)$ be a bounded function defined as $F(s, z) \equiv \int g(z) \exp(z/v s) dz$. Then, using appropriate theorems of Laplace transform theory [e.g., Ref. (7)], the expression

$$Y_1(s, z) = Y_0(s) \exp\left(-\frac{z}{v} s\right) - \frac{k_1 f(s)}{v} [F(s, z) - F(s, 0)] \exp\left(-\frac{z}{v} s\right) \quad [4]$$

is obtained; $Y_0(s)$ is the Laplace transform of $y_1^0(t)$. Hence, a transfer-function formulation is formally possible

$$G_c(s, z) \equiv \frac{Y(s, z)}{X(s, z)} = \frac{Y_0(s)}{X(s, z)} \exp\left(-\frac{z}{v} s\right) - \frac{k_1 f(s)[F(s, z) - F(s, 0)]}{v X(s, z)} \exp\left(-\frac{z}{v} s\right) \quad [5]$$

although it is not unique in the sense that to any arbitrary space element z_1 along the coordinate z a transfer function $G(s, z_1)$ can be assigned; for practical purposes only, the exit position $z = L$ is of importance, where

$$G_c(s, L) = \frac{Y(s, L)}{X(s, z)} = \frac{Y_0(s)}{X(s, z)} \exp(-T_d s) - \frac{k_1 f(s)[F(s, L) - F(s, 0)]}{v X(s, z)} \exp(-T_d s) \quad [6]$$

and T_d is the transportation lag (or transportation time delay), *i.e.*, the time required for a flow element to traverse the entire reactor of length L with constant plug-flow velocity v . The following special cases lead to simplified forms of Eq. [6].

1. No change in the inlet concentration occurs: $y_1^0(t) = 0$. Since $Y_0(s) = 0$, the first term in Eq. [6] vanishes and

$$G_c(s, L) = \frac{k_1 f(s)[F(s, 0) - F(s, L)]}{v X(s, z)} \exp(-T_d s) \quad [7]$$

2. No change in the inlet concentration occurs. In addition, $x(t, z) = z^n f(t)$, n being an integer. Since $X(x, z) = z^n f(s)$

$$G_c(s, L) = \frac{k_1 F(s, 0) - F(s, L)}{v z^n} \exp(-T_d s) \quad [8]$$

where

$$F(s, z) = \sum_{r=0}^{n-1} (-1)^r \frac{n! z^{n-r}}{(n-r)! \left(\frac{s}{v}\right)^{r+1}} \exp\left(\frac{z}{v} s\right) + (-1)^n \frac{n!}{\left(\frac{s}{v}\right)^{n+1}} \exp\left(\frac{z}{v} s\right)$$

3. No change in the inlet concentration occurs. In addition, $x(t,z) = f(t)$ (not a function of z). This is a practically important case, representing, e.g., pulse, step, and periodic perturbations of the current in time. The transfer function assumes the relatively simple form

$$G_c(s,L) = k_1 \frac{\exp(-T_d s) - 1}{s} \quad [9]$$

Equation [9] is the starting point for the analysis of frequency response.

The frequency response of an isothermal PFER: resonance effect.—In the case of purely oscillatory perturbations expressible in terms of a sine or cosine function of the angle (ωt), and in view of the classical Euler-deMoivre relationship $\exp(\pm j u) = \cos u \pm j \sin u$, Eq. [9] may be represented by an amplitude function

$$M_c(j\omega, T_d) = \sqrt{2} k_1 \frac{\sqrt{1 - \cos T_d \omega}}{\omega} \quad [10a]$$

and by a phase-angle (or phase-shift) function

$$\phi_c(j\omega, T_d) = -\arctan \frac{1 - \cos T_d \omega}{\sin T_d \omega} \quad [10b]$$

$M(j\omega, T_d)$ is also known as the gain amplitude of the system. If the periodic current perturbation is expressed as $x(t,z) = x^0 \sin \omega t$, the response of the exit electrolyte concentration is given at sufficiently large times by

$$y(t,z) = M_c(j\omega, T_d) x^0 \sin[\omega t + \phi_c(j\omega, T_d)] \quad [11]$$

indicating a frequency-dependent perturbation amplitude and phase shift in the oscillatory concentration, with reference to current perturbation. Introducing $\beta \equiv T_d \omega$, Eq. [10a] and [10b] can be rewritten as

$$\psi_c(\beta) \equiv \frac{M_c(j\omega, T_d)}{\sqrt{2} k_1 T_d} = \frac{\sqrt{1 - \cos \beta}}{\beta} \quad [12a]$$

and

$$\phi_c(\beta) = -\arctan \frac{1 - \cos \beta}{\sin \beta} \quad [12b]$$

Equations [12a] and [12b] indicate the oscillatory nature of the transfer function past a monotonic domain of β : if perturbation in current occurs at frequencies increasing within this domain, the exit electrolyte concentration will oscillate with monotonically decreasing amplitudes until a threshold frequency called the first resonance frequency ω_1 is reached. If current oscillations occur at $\omega > \omega_1$ (i.e., $\beta > \beta_1$), the amplitude of the exit electrolyte concentration will oscillate itself, reaching local maxima and minima at gradually decreasing intervals of frequency. The phase shift will also oscillate in this fashion—this is the resonance phenomenon.

The characteristic resonance frequencies are found by satisfying conditions of local extrema for $\psi_c(\beta)$, defined by $d\psi_c(\beta)/d\beta = 0$, and by finding points of discontinuity for $\phi_c(\beta)$. Differentiation of Eq. [12a] yields the first condition

$$\frac{\sin \beta}{1 - \cos \beta} = \frac{2}{\beta} \quad [13]$$

whereas the second condition is satisfied at $\beta = 2\pi, 4\pi, 6\pi, \dots$, where $\phi_c(\beta)$ suddenly jumps from -180° to 0° upon increasing β at an infinitesimally small distance to the left. By inspection, Eq. [12a] has the value of zero at $\beta = \pi, 3\pi, 5\pi, \dots$, and since $\psi_c(\beta)$ cannot be negative, $\phi_c = 2\pi, 4\pi, 6\pi, \dots$, are the positions of local minima. The local maxima are found from Eq. [13] by an appropriate root finding procedure. The first five local maxima are given in Table I, and Fig. 1 and 2 depict the variation of the magnitude and phase-angle functions with the frequency angle.

Table I. The first five resonance maxima of the magnitude function of a PFER

Position of the maximum, β	Locally maximum value of $\psi_c(\omega)$	$\phi_c(\omega)$, degree
0	$1/\sqrt{2} = 0.7071^a$	0
2.86π	0.1536	-77.43
4.90π	0.09074	-81.18
6.94π	0.06458	-84.81
8.94π	0.05014	-85.00

^a Obtained by the series expansion of the function $\sqrt{(1 - \cos \beta)/\beta^2}$ and taking the limit as $\beta \rightarrow 0$.

Frequency response and resonance effect in the nonisothermal PFER.—The nonisothermal PFER is described by the substance balance Eq. [1] and by the thermal balance (1, 2)

$$\frac{\partial T}{\partial t} = -v \frac{\partial T}{\partial z} - k_2(T - T_a) + k_3 i^2 - k_4 i \quad [14]$$

with auxiliary conditions $t = 0, c = c^*(z), T = T^*(z), i = i^*(z)$ and $z = 0, c = c^*(0), T = T^*(0), i = i^*(0)$. The perturbation variables are defined as $y_1(t,z) \equiv c(t,z) - c^*(z), y_2(t,z) \equiv T(t,z) - T^*(z)$, and $x(t,z) \equiv i(t,z) - i^*(z)$. As in the previous section, it is assumed that there is no change in inlet conditions. If perturbations in current are sufficiently small, the linear approximation

$$i^2(t,z) - [i^*(t,z)]^2 \approx 2i^*(z)x(t,z)$$

may be employed to linearize Eq. [14], which can be rewritten as

$$\frac{\partial y_2}{\partial t} + k_2 y_2 + v \frac{\partial y_2}{\partial z} = f(z)x(t,z) - k_4 x(t,z) \quad [15]$$

where $f(z) \equiv 2k_3 i^*(z)$. In order to obtain transfer-function representations, the current perturbation must be once again space independent, i.e., $X(s,z) = X(s)$. The following cases can be distinguished.

1. $i^*(z) = \text{const}$. The transfer function is

$$G_T(s,L) = k_5 \tau_2 \frac{1 - \exp(-k_2 T_d) \exp(-T_d s)}{\tau_2 s + 1} \quad [16]$$

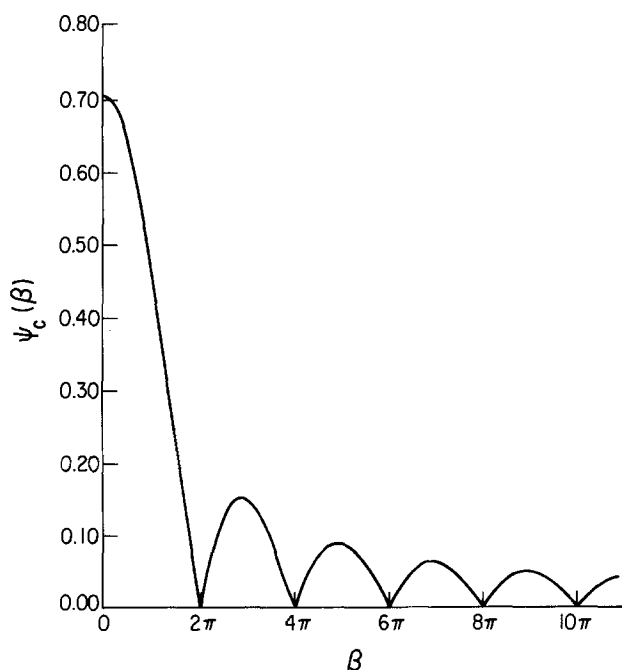


Fig. 1. The variation of the gain amplitude with frequency in an isothermal PFER (Eq. [12a]).

where $k_2\tau_2 = 1$. Equation [9] complements Eq. [16] for a full representation via transfer functions. The frequency response of electrolyte temperature to periodic perturbations in current is given by the gain amplitude

$$M_T(j\omega, T_d) = \frac{T_d}{\tau_2} \sqrt{\frac{1 - \exp(-T_d/\tau_2) - 2 \exp(-T_d/\tau_2) \cos \beta}{(T_d/\tau_2)^2 + \beta^2}} \quad [17a]$$

and phase angle

$$\phi_T(j\omega, T_d) = \arctan \frac{-\tau_2 + \tau_2 \omega \exp(-T_d/\tau_2) \cos \beta + \exp(-T_d/\tau_2) \sin \beta}{1 - \exp(-T_d/\tau_2) \cos \beta + \tau_2 \omega \exp(-T_d/\tau_2) \sin \beta} \quad [17b]$$

Hence, at sufficiently large times

$$y_2(t, z) = M_T(j\omega, T_d) x_2^0 \sin[\omega t + \phi_T(j\omega, T_d)] \quad [18a]$$

and (see Eq. [11])

$$y_1(t, z) = M_c(j\omega, T_d) x^0 \sin[\omega t + \phi_c(j\omega, T_d)] \quad [18b]$$

The resonance frequencies are obtained by setting $dM_T/d\beta = 0$ and solving the resulting equation

$$\frac{\sin \beta}{\cosh(T_d/\tau_2) - \cos \beta} = \frac{2\beta}{(T_d/\tau_2)^2 + \beta^2} \quad [19]$$

2. $f(z) = a_0 z^m$; a_0 and m are (experimental) regression parameters. If m is a noninteger, no closed-form analytical solution of Eq. [15] can be obtained, and hence transfer function representation becomes awkward. If m is an integer, the transfer function may be written, upon cumbersome manipulations, as

$$G_T(s, L) = \left[\frac{a_0 v}{(s + k_2)^2} + \frac{k_4}{s + k_2} \right] \exp(-k_2 T_d) \exp(-T_d s) + a_0 \left[\frac{L^m}{s + k_2} + \sum_{j=1}^m (-1)^j \frac{v^j m(m-1) \dots (m-j+1)}{(s + k_2)^{j+1}} L^{m-j} \right] \quad [20]$$

which degenerates to the simpler form of

$$G_T(s, L) = \frac{a_0 v}{(s + k_2)^2} [\exp(-k_2 T_d) \exp(-T_d s) - 1] + \frac{k_4}{s + k_2} \exp(-k_2 T_d) \exp(-T_d s) + \frac{a_0 L}{s + k_2} \quad [21]$$

in the specific case of $m = 1$. Equations [16], [20], and [21] all indicate the existence of resonance past a certain frequency; the mathematical form of $i^*(z)$ determines, however, the numerical value of the resonance frequencies and the shape of the given amplitude and phase angle curves.

Discussion

The frequency response of the isothermal PFER shows similarity to that of the steam-heated heat exchanger (8) with steam condensing in the outer pipe and a coolant flowing in the inner pipe [compare Fig. 1 and 2 to Fig. 9b and 10, respectively, and Eq. [12] to Eq. [62] in Ref. (8)], but the two responses are not identical. The transfer function analysis becomes much simpler if the perturbation in electrolyte concentration may be approximated as a linear function of the imposed current density

$$c - c^* \cong \alpha(i - i^*) \quad [22]$$

Here, variations in the inlet concentration of the electrolyte can be considered as a perturbation and Eq. [2] takes the rearranged form of

$$\frac{\partial y_1}{\partial t} + v \frac{\partial y_1}{\partial z} + \frac{k_1}{\alpha} y_1 = 0 \quad [23]$$

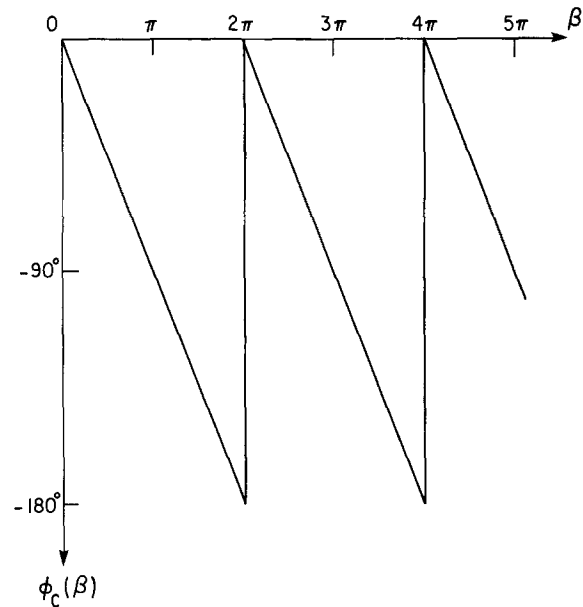


Fig. 2. The variation of the phase angle with frequency in an isothermal PFER (Eq. [12b]).

Then, the transfer function relating electrolyte concentration in the PFER and inlet electrolyte concentration is

$$G'_c(s, z) \equiv \frac{Y_1(s, z)}{Y_0(s)} = \exp\left(-\frac{k_1 z}{\alpha v}\right) \exp\left(-\frac{z}{v} s\right) \quad [24]$$

In the specific case of $z = L$, the transfer function

$$G'_c(s, L) = \exp\left(-\frac{k_1 T_d}{\alpha}\right) \exp(-T_d s) \quad [25]$$

represents a pure time-delay effect with gain magnitude

$$M'_c(\omega) = \exp\left(-\frac{k_1 T_d}{\alpha}\right) \quad [26a]$$

and phase angle

$$\phi'_c(\omega) = -T_d \omega \quad [26b]$$

for the exit electrolyte concentration. The absence of a resonance phenomenon is demonstrated by the independence of the response magnitude of perturbation frequency: the latter affects only the delay of the response.

The analytical construction of the frequency response of the nonisothermal CSTR is rather complicated (Eq. [20]), and can be simplified only by major assumptions [Eq. [16]]. The qualitative course of the gain magnitude and phase-angle curves for the $i^*(z) = \text{const.}$ case is shown in Fig. 3 for τ_2 values of modest size. Further simplifications may be carried out, however, for many practical electrolyzers where τ_2 is very large. Taking a typical electrolyzer tank of 0.1 m² cross-sectional area (assumed to be normal to the direction of flow) and an axial length of 2m, an average electrolyte density of 1200 kg/m³, and an average overall heat-transfer coefficient of 7.5 W/m² · K, the numerical value of $\tau_2 \cong 741$ min is computed. Thus, Eq. [16] degenerates to the form Eq. [9] (except for the coefficients), i.e., the frequency-dependent terms in gain amplitude and phase-angle expressions become identical, respectively, and the plots in Fig. 3 become identical to plots of the form shown in Fig. 1 and 2.

The preceding analysis suggests a semiquantitative means of detecting deviations from PFER behavior via experimentally obtained frequency response by perturbing the current in an electrochemical reactor sinusoidally over a carefully selected frequency band. A strong dissimilarity between experimental and PFER frequency response indicates the existence of considerable dispersion, although its true nature (the relative impor-

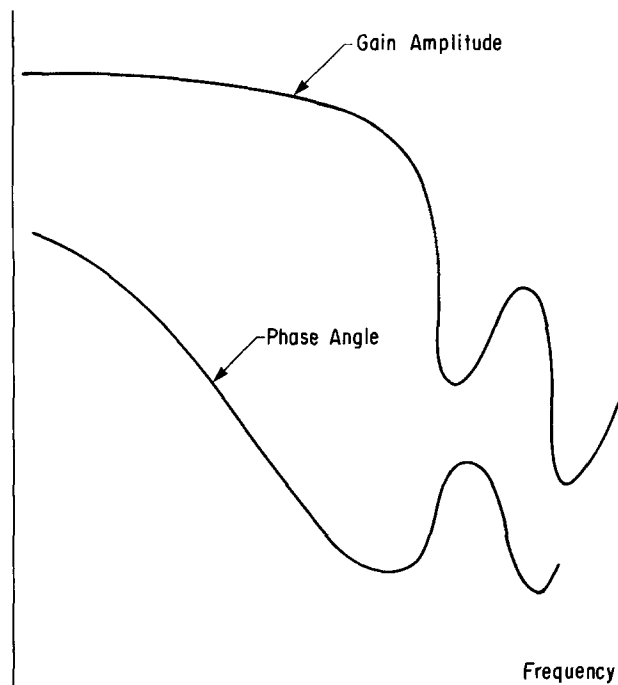


Fig. 3. Qualitative variation of the gain amplitude and phase angle with frequency according to Eq. [16] (only the first resonance peaks are shown).

tance of axial-to-radial dispersion) may not be easily determined; an experimental residence-time distribution study would be more quantitative. Nevertheless, the use of frequency response for this purpose, at least as a relatively fast preliminary investigation, could be attractive due to its experimental simplicity with respect to residence-time distribution. (The experimental investigation of PFER frequency response is beyond the scope of the current paper.)

Concluding Remarks

The major finding of practical importance of the transfer-function-based analysis of frequency response is the prediction of locally high oscillation amplitudes in electrolyte concentration and temperature at large-frequency perturbations in current due to its distributed-forcing effect: this phenomenon is in sharp contrast with continuous flow stirred tank electrochemical reactor (CSTER) response, where system inertia acts essentially as a low-pass filter and, consequently, concentration and temperature fluctuations are gradually smaller with increasing perturbation frequencies. The resonance effect in a PFER is an important factor to consider in the design and implementation of controllers on electrolyzers.

Acknowledgment

This and similar studies by the author's research group have been supported by a Natural Sciences and Engineering Research Council of Canada grant.

Manuscript submitted Oct. 25, 1984; revised manuscript received Feb. 6, 1985.

The University of Waterloo assisted in meeting the publication costs of this article.

LIST OF SYMBOLS

c	electrolyte concentration
$G_c(s,z)$	transfer function for electrolyte concentration
$G_T(s,z)$	transfer function for electrolyte temperature
i	current density
j	$\sqrt{-1}$
k_1	coefficient in the mass balance of a PFER (reciprocal of the product of reactor height, valency, and Faraday's constant) related to electrolysis
k_2	coefficient in the thermal balance (ratio of the overall heat-transfer coefficient to the product of reactor height, density, and specific heat capacity) related to heat losses
k_3	coefficient in the thermal balance (reciprocal of the product of density, specific heat capacity, and electric conductivity) related to the Joule effect
k_4	coefficient in the thermal balance (ratio of the heat of the electrode reaction to the product of reactor height, density, specific heat capacity, valency, and Faraday's constant) related to the heat of reaction
k_5	coefficient in Eq. [16], equal to $2k_3i^*(z) - k_4$ if $i^*(z) = \text{const.}$
L	length of the electrode; characteristic length along the axis
s	Laplace transform variable
T	electrolyte temperature
T_d	transportation lag of the PFER, equal to L/v
t	time
v	electrolyte velocity
x	current perturbation variable
y_1	concentration perturbation variable
y_2	temperature perturbation variable
z	axial space coordinate
β	equal to $T_d\omega$
τ_2	the reciprocal of k_2 ; an apparent time constant
ω	perturbation frequency

REFERENCES

1. T. Z. Fahidy, *Electrochim. Acta*, **29**, 1321 (1984).
2. T. Z. Fahidy, Paper B2-2, p. 533, Extended Abstracts of the Norbert Ibl Memorial Symposium, 35th meeting of the ISE, Berkeley, CA, Aug. 5-10, 1984.
3. D. J. Pickett, "Electrochemical Reactor Design," Chap. 5, Elsevier, Amsterdam (1979).
4. F. Coeuret and A. Storck, "Elements de Génie Electrochimique," Chap. 5, 6, Lavoisier, Paris (1984).
5. J. C. Friedly, "Dynamic Behavior of Processes, Part III," Prentice-Hall, Englewood Cliffs, NJ (1972).
6. P. Harriott, "Process Control," Chap. 11, McGraw Hill, New York (1964).
7. R. V. Churchill, "Operational Mathematics," Chap. 1, 2, McGraw Hill, New York (1972).
8. W.-J. Yang, *J. Heat Transfer*, **86**, 133 (1964).

Photoactive Synthetic Polycrystalline Pyrite (FeS₂)

A. Ennaoui, S. Fiechter, H. Goslowsky, and H. Tributsch

Hahn-Meitner-Institut für Kernforschung Berlin, Bereich Strahlenchemie, D-1000 Berlin 39, Germany

ABSTRACT

Polycrystalline layers of As-doped pyrite (FeS₂) have been produced in bromine atmosphere with the aim of developing this sulfide material for solar energy applications. Its photoelectrochemical behavior in contact with an aqueous I₃⁻/I₂ electrolyte was investigated. It operated as a photoelectrochemical solar cell and showed reasonably stable behavior under illumination. Optical measurements performed on FeS₂ show that visible light is absorbed in an extremely thin layer of 160Å in spite of the apparently indirect gap of this semiconductor ($E_g = 0.95$ eV). This would make this photosensitive material an interesting candidate for thin-layer solar cells. Scanning electron micrographs of the samples reveal well-developed crystallites of about 5-10 μm with distinct boundaries. Scanning laser spot analysis over macroscopic areas (5 mm) showed homogeneous as well as inhomogeneous regions. The photoelectric properties of these first polycrystalline pyrite samples studied are poor, but there is presently no reason to assume that they cannot be developed.

Single crystals of FeS₂ with pyrite structure have recently been considered in publications from our laboratory as a semiconducting material for photoelectrochemical and photovoltaic solar cells (1-3). FeS₂ crystals in contact with an iodide/iodine containing electrolyte have exhibited large quantum efficiency and very high stability against photocorrosion (3). We are still far from understanding the solid-state chemistry of single-crystalline pyrite in all details. Nevertheless, it seems to be appropriate to start the development of polycrystalline pyrite at an early stage, owing to its potential advantage as a cheap material with promising photoelectrochemical properties.

As a material in photoelectrochemical cells, FeS₂ has the advantage of being a d band semiconductor like MoS₂ or WS₂ with photoexcited holes reacting from quasi-nonbinding d states constituting the upper edge of the valence band (3).

Pyrite Preparation and Properties

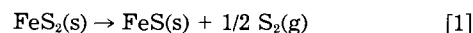
Previous studies on pyrite synthesis.—Although large pyrite deposits have been found in the earth (4) and natural pyrite crystals of considerable size are well known, there has been no success in artificial growth of pyrite crystals in centimeter dimension. Synthesis of pyrite was first described by Wöhler (5) in the last century. Reacting sulfur and Fe₂O₃ in an open system, he succeeded in the preparation of small brass-yellow octahedra. Bouchard (6) reported on the growth of pyrite crystals with 3 mm edge length by chemical vapor transport with chlorine. Transport from hot to cold occurred in a temperature gradient from 715° to 655°C. Our own experiments (3) show that transport with bromine at a gradient from 650° to 550°C yields crystals up to 6 mm edge length, while in the presence of iodine as transporting agent a transport rate two orders in magnitude smaller has been established. Wilke and co-workers (7) did not obtain larger crystals in growing pyrite from the solution with PbCl₂ as solvent.

Up to now, no attempts to prepare polycrystalline layers of photosensitive FeS₂ have been reported. However, FeS₂ formation has been observed during corrosion of carbon steel in the presence of a H₂S gas/water mixture in nuclear power reactions, and the process, which is of electrochemical nature, has been studied (8).

Synthesis of FeS₂ powder.—Stoichiometric amounts of high purity, H₂-reduced iron powder and high purity sulfur lumps were heated up to 650°C in evacuated (10⁻⁵ mbar) and sealed quartz ampuls of 20 mm diam and 200 mm length. In the presence of a small amount of iodine (0.5 mg/cm³), the reaction was terminated within 100h.

Preparation of polycrystalline FeS₂ layers.—2g of yellowish-white shining FeS₂ powder and 5 mg As as dopant were filled in quartz ampuls ($\phi \approx 22$ mm, $l = 300$ mm) and evacuated to 10⁻⁵ mbar. After admittance of 0.5 mg/cm³ bromine, the tubes were sealed. FeS₂ powder was placed in one end of the ampul and, in order to clean the

growth chamber from persisting powder particles, the free end was heated up to 800°C for 6h. Afterward, the temperature was reversed. The FeS₂ powder was heated to 800°C, and the powder-free end was kept at 550°C (Fig. 1, stage I) for 10 days. On account of the high dissociation pressure of FeS₂ at 800°C [$p = 1$ atm (16)], a thermal decomposition of FeS₂ according to the simplified equation



was observed. Sulfur distilled into the cool end of the quartz ampul. The decomposition was accompanied with a strong coalescence (Ostwald ripening) of the produced FeS to large hexagonal pyrrhotite crystals (Fig. 1, stage II) up to 10 mm edge length and 2 mm thickness. By reversing the temperature gradient for 10 days, realized by the opposite position of the growth ampul in the furnace (Fig. 1, stage III), the pyrrhotite crystals were transformed into pyrite under preservation of their hexagonal shape (pseudomorphism). Investigations of the hexagonal surfaces with scanning electron microscopy revealed that the pseudomorphous crystals consisted of small pyrite crystals (5-10 μm edge length) that were grown together forming a reasonably homogeneous surface (Fig. 2). In some areas, larger pyrite crystals (0.5 mm edge length) appeared on the polycrystalline substrate.

Polycrystalline layers were also prepared by transport in a gradient from 650° to 600°C in evacuated and closed quartz ampuls ($l = 110$, $\phi = 22$ mm). The concentration of transporting agent NH₄Br amounted to 0.5 mg/cm³. 0.35 mg As was added to 1.15g FeS₂ feed material. The intergrown pyrite crystals of the layer had dimensions of 10-100 μm.

Solid-State Studies

Concerning the band structure of pyrite FeS₂ (9), two details are particularly interesting because they permit a

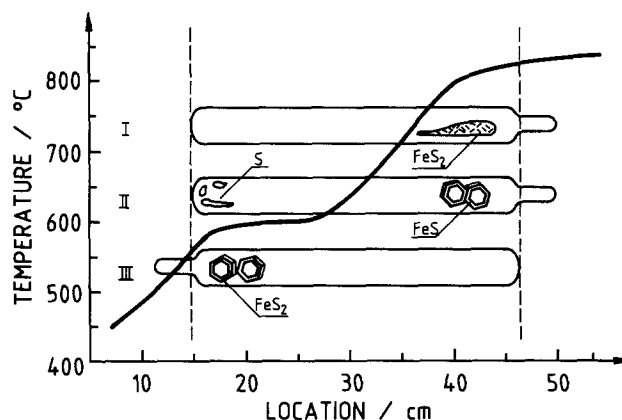


Fig. 1. Position of growth tubes in the temperature gradient of the furnace and growth region of polycrystalline layers.

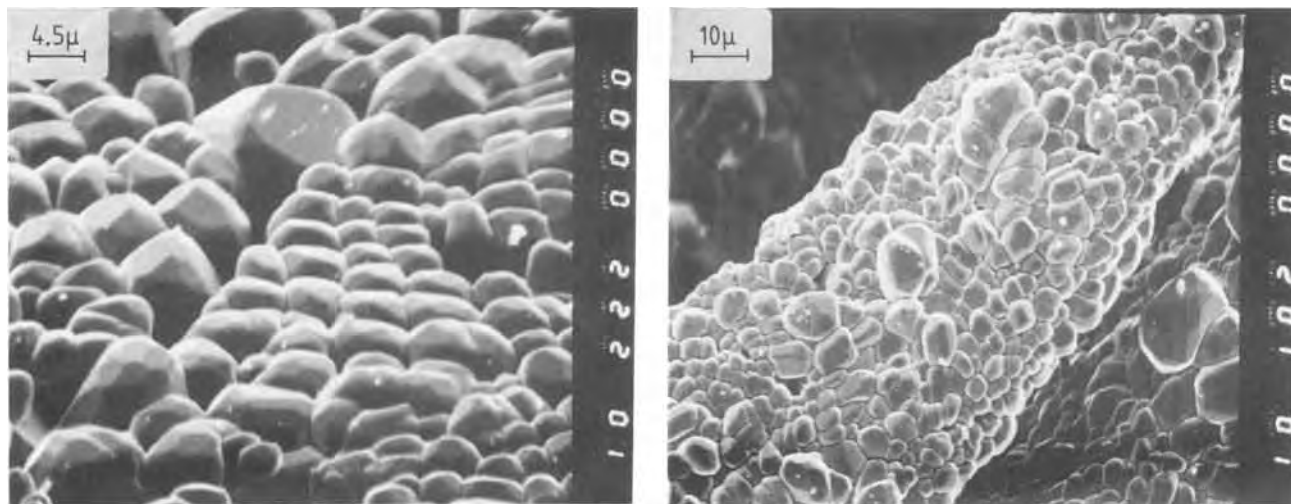


Fig. 2. Scanning electron micrographs of polycrystalline FeS_2 . a(left): Front view of polycrystalline platelet. b(right): Edge side of platelet

better interpretation of the electric, magnetic, and optical properties.

First, the clear separation of a t_{2g} and a e_g energy band in relation with a low-spin t_{2g}^6 system which results in a 0.95 eV t_{2g}/e_g bandgap.

Second, a relatively broad e_g band has been predicted (9) and XPS data confirm a single strong 3d peak of 0.9 eV width arising from a d energy band at the top of the FeS_2 valence band (10). These XPS data have been confirmed and extended in our laboratory (3).

The reported high electron mobility of $230 \text{ cm}^2\text{V}^{-1}\text{s}^{-1}$ in synthetic crystals (11) confirms that the electronic structure of the material is sufficiently favorable for charge transport.

The electrical resistivity of our samples was measured using a four-probe technique. The measurements covered the temperature range from 76 to 500 K, and an exponential temperature dependence between 400 and 500 K according to the relation $l = l_0 \exp \Delta E/KT$ was found. The activation energy $\Delta E = 0.23 \text{ eV}$ of our samples is smaller than $\Delta E = 0.46 \text{ eV}$, previously reported for n-type single crystals of FeS_2 (9). At room temperature, the resistivity of our polycrystalline FeS_2 was $6 \Omega\text{-cm}$; Hall effect measurements gave a carrier concentration of $3 \times 10^{17} \text{ cm}^{-3}$. The Hall mobility in our samples was quite low: $3 \text{ cm}^2\text{V}^{-1}\text{s}^{-1}$. The pyrite layers studied showed n-type behavior in photoelectrochemical measurements.

Optical Experiments

Optical transmission measurements for FeS_2 have up to now only been performed in the infrared toward the bandedge region. Schlegel and Wachter determined the absorption constant of FeS_2 up to a photon energy of $h\nu = 1.1 \text{ eV}$, where it was found to be approximately $\alpha = 8 \times 10^6 \text{ cm}^{-1}$ (12). A crystal of natural pyrite (from Elba) with a cross section of $10 \times 5 \text{ mm}^2$ was polished down to a thickness of $\alpha = 8 \pm 0.5 \mu\text{m}$ while fixed to a glass support. This sample had holes on a surface area much smaller than 1%, so that a background was obtained in transmission. This gave rise to an apparent decrease of the absorption constant in the region of very high absorption coefficients. Since the small fraction of light passing through these holes does not depend on the wavelength, a calibration measurement is needed to adjust the absorption curve to the real values. This was done with the help of a null ellipsometer. In order to get the bulk properties, the surface of FeS_2 was etched using $\text{HF}/\text{CH}_3\text{COOH}/\text{HNO}_3$ (1:1:2), which, according to ESCA studies, yields a FeS_2 surface free of any covering layer (3). During the measurement, the FeS_2 was flushed with dry nitrogen. The complex refractive index determined at $n = 632.8 \text{ nm}$ was $n = 4.032 - 3.245i$.

The real reflective index was checked using the transmission interferences occurring in the range between 1800 and 2500 nm. The result was $\text{Re}(n) = 3.96 \pm 0.25$.

A cross check was made using published data on the reflection properties of pyrite in combination with a calculation based on the Kramers-Kronig relation (12, 9). The values obtained were $n = 3.6 - 3.03i$ [from Ref. (12)] and $n = 3.5 - 3.8i$ [from Ref. (9)]. They only differ by less than 30%, which might be due to surface layers, which were not controlled in these measurements. Such deviations are to be expected according to variations of interface properties (13). Therefore, our measurements have to be considered reliable. The absorption coefficient determined from our data can be calculated to be $\alpha = 6.4 \times 10^5 \text{ cm}^{-1}$ at 632.8 nm.

The relative absorption coefficient in the visible spectral region measurement with a Perkin-Elmer Model 330 would thus be calibrated as shown in Fig. 3. Beyond 1050 nm, a normal absolute measurement was possible.

It can therefore be concluded that FeS_2 is absorbing visible light within a narrow surface layer of approximately 160 \AA . Pyrite is thus absorbing at least one order of magnitude better than GaAs, which has a direct energy gap.

Photoelectrochemical Experiments

The FeS_2 samples were treated with an In-Ga alloy followed by Ag epoxy, making contact to a copper rod, which was then encapsulated with insulating resin (Scotchcast 3MXR 5241). A conventional three-electrode potentiostatic arrangement was applied. For photocurrent measurements, a 250W tungsten iodine lamp, a xenon lamp, or a helium neon laser were used.

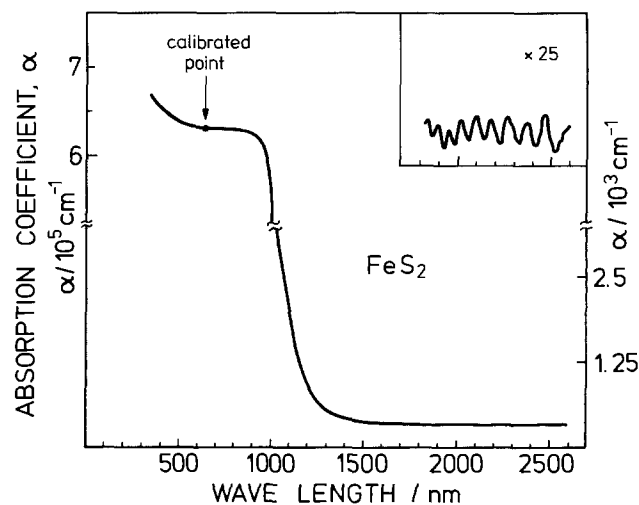


Fig. 3. Adsorption coefficient of FeS_2 measured in transmission using a platelet $8 \mu\text{m}$ thick (exposed area: 50 mm^2). The value of $6.4 \times 10^5 \text{ cm}^{-1}$ at 632.8 nm was calibrated using ellipsometry. The insert shows the interference patterns of transmission.

Results

When an electrode, prepared of a polycrystalline FeS₂ layer, is placed in contact with an aqueous electrolyte containing 0.5M H₂SO₄ and polarized in an electrochemical cell with three electrodes, a much more complicated current voltage behavior is observed than is with single crystals (3). A photocurrent of the order of 10 mA·cm⁻² is measured in concentrated xenon light (~ 1 W·cm⁻²). It is superposed by a dark current, which is rapidly growing as the magnitude of the applied voltage is increased. The shape of the current voltage curve is complicated due to oxide formation, and corrosion to Fe³⁺ and SO₄²⁻ is clearly visible at elevated potentials. No oxygen evolution is observed. In the presence of redox systems such as I⁻/I₃ (E₀ = 0.53V), V²⁺/V³⁺ (E₀ = -0.7V), or S²⁻/S_n (E₀ = -0.51V), a FeS₂/redox electrolyte/carbon configuration operates as solar cell (Fig. 4). Instead of largely different redox potentials, the open-circuit photopotentials are comparable and equally small (0.024-0.08V). Both the poor limiting current behavior of the semiconducting FeS₂ layer and the constancy of the photovoltage indicate high concentrations of surface states and a situation of pinning of energy bands. Similar to single-crystalline FeS₂ (3), etching treatment improves the photoelectrochemical behavior. Since the electrochemistry of FeS₂ has been described using single crystals (3), we will limit ourselves to characterizing the photoeffect which has not yet been described with polycrystalline FeS₂. Figure 5 shows the spectral dependence of photocurrent efficiency (η) of polycrystalline FeS₂. Plots of $(\eta h\nu)^{n/2}$ with $n = 1$ and $n = 4$ are given in Fig. 6.

The plot $(\eta h\nu)^{1/2}$ vs. $h\nu$ gives a straight line, suggesting that the optical transition in FeS₂ is indirect and yields a bandgap of 0.95 eV consistent with theory (14). This is in good agreement with reflection measurements, which indicated an optical bandgap of 0.9 ± 0.1 eV (9), and with our optical results (Fig. 3). Laser spot measurements were made to test the homogeneity of the FeS₂ films produced. A sample of 0.7×0.5 cm was scanned over a distance of 0.5 cm in three distinct positions. Figure 7 shows that homogeneous and heterogeneous regions are present. It is possible that creeklike structures in the polycrystalline film which can be seen in the optical microscope are responsible for some of the variations.

Discussion

Pyrite (FeS₂), an abundant natural product which consists of cheap elements, has recently been proposed as a semiconductor material for solar cells (1-3). First experi-

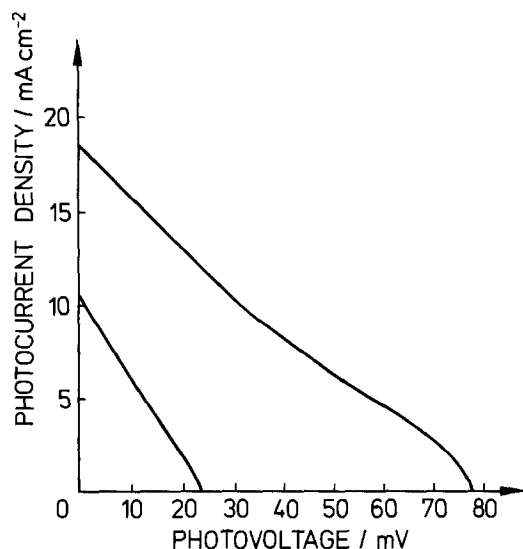


Fig. 4. Power output characteristic of a synthetic polycrystalline FeS₂ liquid junction solar cell. Electrolyte: (a, left curve) 3M KI, 10⁻³M I₂ (pH 2). Layer preparation I (b, right curve) 1M CaI₂, 0.05M. Layer preparation II.

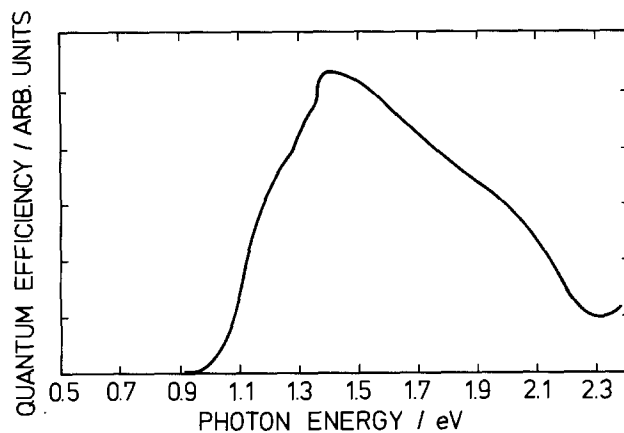


Fig. 5. Relative spectral response of FeS₂ solar cell under short-circuit condition.

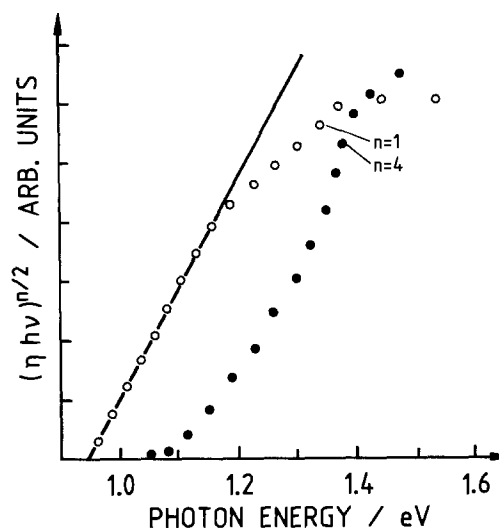


Fig. 6. Plot of $h\nu$ vs. $(\eta h\nu)^{n/2}$, where $n = 1$ and $n = 4$ (FeS₂ in 3M KI, 10⁻³M I₂, aqueous electrolyte).

ments with synthetic single crystals yielded photovoltages of 200 mV and quantum efficiencies for photocurrent generation exceeding 90%, although neither doping nor interfacial properties has been optimized. The lack of knowledge of many solid-state properties makes it, at present, difficult to judge the development possibilities of this material with high reliability. However, information on certain parameters which are decisive for solar energy materials are becoming more transparent.

Our first experiments to produce polycrystalline layers of photosensitive FeS₂ were successful. These layers could even be operated in low efficient solar cells. The choice of As as doping agent was probably not favorable, especially since this additive reduces the mobility (11). The control of doping remains an important task which has to be accomplished for FeS₂, and we feel that the very low photopotential of our polycrystalline samples is due to a Fermi level, which is situated too distant from the conduction band. As shown by the improvement obtained between the sample of curve a and that of curve b in Fig. 4, some systematic progress has already been obtained. We hope to have shown that polycrystalline FeS₂ is an interesting solar material for long-term development, especially since ambient temperature and low temperature processes for FeS₂ synthesis in geological environments have also become known (17).

Our measurement of an indirect energy gap of 0.95 eV in polycrystalline FeS₂ layers (Fig. 6) is in agreement with optical (12) and electrical (9) measurements. Such an energy gap, which is only slightly smaller than those of CuInSe₂ (1 eV) and Si (1.1 eV), still permits a theoretical solar energy conversion efficiency between 14 and 18%

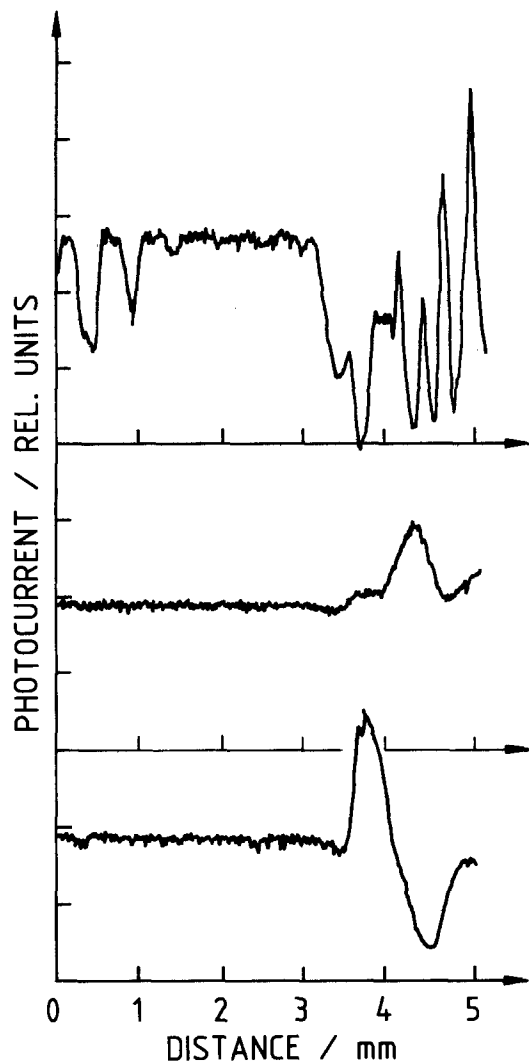


Fig. 7. Scanning laser spot analysis of polycrystalline FeS_2 in I^-/I_2 solution under short-circuit condition. (Three parallel scans on a 7 mm platelet in distinct regions. Scan velocity: $25 \mu\text{m}$ steps in X-direction. Beam width: $20 \mu\text{m}$.)

and a photovoltage output of approximately 0.5V. This, however, will necessitate a careful optimization of bulk and surface properties of FeS_2 . An important parameter is the nature of the electronic transition of FeS_2 . Scientists dealing with solar energy materials usually associate with indirect energy gaps a deep penetration of light which can only be compensated by high diffusion lengths of charge carriers (as in crystallized Si). Such materials cannot be used for light collection as very thin layers. Experience with transition metal sulfides of d band character such as WS_2 or MoS_2 , however, shows that indirect bandgaps can be associated with high absorption constants ($\sim 1 \times 10^5 \text{ cm}^{-1}$) (14). This is also the case for FeS_2 .

With an absorption coefficient of approximately $\alpha = 6.4 \times 10^5 \text{ cm}^{-1}$ in the visible, the photogeneration of electron-hole pairs occurs in a thin surface layer of approximately 160 \AA . The spectral dependence of photocurrents (Fig. 5)

shows a gradual decay from the near infrared toward shorter wavelengths in spite of a reasonably constant absorption coefficient. As many experiments showed, this decay depends on surface treatment (Fig. 4) and is smaller with a more ideal surface without any covering layer (as determined by ESCA measurements).

Further research will be needed to understand how the state of the surface interacts with holes, generated with different photon energy in a comparable distance from the semiconductor of electrolyte interface. Interestingly RuS_2 , which also has an extremely high absorption coefficient ($\alpha = 3 \times 10^5 \text{ cm}^{-1}$), a similar crystal structure, comparable energy gap ($E_g = 1.25 \text{ eV}$), and an analogous electronic structure, does not show a decay of photocurrents towards the UV region (15). This gives rise to the hope that it will be possible to develop solar cells which are only several hundred angstroms thick and extremely flexible and easy to handle.

Acknowledgments

The authors would like to thank Mr. W. Beran for his assistance in SEM measurements and Dr. Jaegermann for interesting discussions. The project was supported by BMFT Grant no. 03E-83 5-A.

Manuscript submitted June 18, 1984; revised manuscript received March 25, 1985.

Hahn-Meitner-Institut für Kernforschung Berlin assisted in meeting the publication costs of this article.

REFERENCES

1. W. Jaegermann and H. Tributsch, *J. Appl. Electrochem.*, **13**, 743 (1983).
2. A. Ennaoui and H. Tributsch, *Solar Cells*, **13**, 197 (1984).
3. A. Ennaoui, S. Fiechter, W. Jaegermann, and H. Tributsch, Submitted to *This Journal*.
4. J. C. Bailar, H. J. Emeléus, R. Nyholm, and A. F. Trotman-Dickenson, "Comprehensive Inorganic Chemistry," Vol. 2, p. 796, Pergamon Press, London (1973).
5. W. Wöhler, *Lieb. Ann.*, **17**, 260 (1836).
6. R. J. Bouchard, *J. Cryst. Growth*, **2**, 40 (1968).
7. K.-Th. Wilke, D. Schultze, and K. Töpfer, *ibid.*, **1**, 41 (1967).
8. D. W. Shoesmith, T. E. Rummery, M. G. Bailey, and D. G. Owen, *This Journal*, **126**, 911 (1979).
9. A. T. Bither, R. J. Bouchard, W. H. Cloud, P. C. Donohue, and W. J. Siemons, *Inorg. Chem.*, **7**, 2208 (1968).
10. H. Van der Heide, R. Hemmel, C. F. van Bruggen, and C. Haas, *J. Solid State Chem.*, **33**, 17 (1980).
11. R. T. Shuey, "Semiconducting Ore Minerals," R. T. Shuey, Editor, pp. 304-318, Elsevier Scientific Publishing Co., Amsterdam (1975).
12. A. Schlegel and P. Wachter, *Solid State Phys.*, **9**, 3363 (1976).
13. D. E. Aspnes and A. A. Studna, *Phys. Rev. B*, **27**, 985 (1983).
14. Ch. Sugiura, *J. Chem. Phys.*, **80**, 3 (1984).
15. H.-M. Kühne and H. Tributsch, *J. Electroanal. Chem.*, To be published.
16. R. Juza and W. Biltz, *Z. Anorg. Allg. Chem.*, **205**, 273 (1932).
17. R. O. Halberg, *N. Jahrbuch F. Mineralogie, Monatshefte*, 481 (1972).

The Effect of Thickness on the Performance of PTFE-Bonded Raney Nickel Hydrogen Electrodes in Relation to the Electrolyte Diffusivity of Catalyst Layers

T. Kenjo

Department of Applied Science for Energy, Muroran Institute of Technology, Mizumoto-cho, Muroran 050, Japan

ABSTRACT

The polarization resistance of Raney nickel hydrogen electrodes decreases with increasing thickness of catalyst layers, but there is a lower limit that can be attained by the thickness effect. The present study aims to prove that this limit depends on the electrolyte diffusivity of catalyst layers. The diffusivity was measured using multilayered electrodes where a ZrO_2 layer separates electronically the test layers from working layers. The theoretical polarization resistance was calculated on the basis of two different assumptions "ohmic potential drop" and "concentration polarization." The former predicts much higher electrolyte resistivity of catalyst layers than the observed value. However, the diffusivity values predicted by the latter agreed well to the experimental data. It has been thus proved that the concentration polarization assumption is valid and the electrolyte diffusivity is an essential factor to determine the lower limit of polarization resistance.

The structure and operating mechanism of Raney nickel hydrogen electrodes have been described by Mund and his co-workers on the basis of a thin film model (1-3). The distinguishing feature of this model is a thin electrolyte film which covers the inside face of macropore while leaving interparticle spaces for hydrogen diffusion. The hydrogen gas dissolves into the electrolyte film at the gas/film interface after diffusing through the macropore. The film is connected with each other by the electrolyte bridge. The electrochemical hydrogen oxidation takes place at the film/catalyst interface distributed in the catalyst layer like a three-dimensional network. The catalyst layer is therefore electrochemically reactive not only at the two-dimensional electrode/electrolyte-bulk interface, but also over a zonal area extending toward the gas-side edge of the electrode. This effective reaction area is a geometrical factor to determine the polarization loss. This viewpoint predicts that the polarization loss decreases with increasing thickness of catalyst layers. The predicted relationship has been found in the Raney nickel hydrogen electrodes (3, 4).

There is, however, a lower limit in the polarization loss attained by the "thickness effect." In load condition, the potential gradient arises in the thickness direction because of the ohmic resistance of the film. Taking the film resistivity ρ_t into account and assuming a linear function between the local polarization and faradaic current density, Mund derived the polarization resistance ω as a function of the thickness of catalyst layers d

$$\omega = \sqrt{\rho_t \rho_i} \coth \sqrt{\frac{\rho_t d^2}{\rho_i}} \quad [1]$$

where ρ_i is the interfacial resistance between the film and catalytic surface. When the catalyst layers are very thick ($\rho_t d^2 \gg \rho_i$), the polarization resistance tends to a limiting value $\sqrt{\rho_t \rho_i}$. This is the explanation for the limiting thickness effect in terms of the ohmic potential drop.

He estimated 10-20 Ω -cm as a ρ_t value at 80°C by parameter matching. The present author treated similarly the data of PTFE-bonded Raney nickel electrodes and obtained a value of the same order (4). However, it is still not certain if the film resistivity is really a limiting factor for the thickness effect, because the ρ_t value predicted has not been confirmed yet experimentally.

When hydrogen oxidation takes place in the electrode pores, the electrolyte film is diluted with the water formed. This concentration drop raises the equilibrium potential for the hydrogen oxidation and lowers the driving potential for the local current generation in the pores, resulting in the same effect as the ohmic potential drop assumed by Mund. The raise in the equilibrium potential can be expressed in terms of the concentration polariza-

tion, which is also a possible factor to limit the thickness effect.

In the present study, by using a multilayered electrode, direct measurements of electrolyte diffusivity and resistivity of the catalyst layers are attempted. The feature of the electrode is an electron insulating but electrolyte-permeable porous zirconia layer which is inserted between the test and working layers, thereby separating the former from latter layer electronically by holding an ionic contact between the two. The concentration polarization occurred in the test layer is measured as a potential difference between the electrodes with and without the test layer. The electrolyte diffusivity coefficient of test layer can be calculated from these polarization data.

Assuming these two types of potential gradient and using the diffusivity and resistivity coefficients thus obtained experimentally, we can calculate theoretical polarization values of electrodes based on the two different assumptions. Which of the two is valid can be tested by the fitting to the experimental polarization data. The goal of the present work is to determine whether the essential factor to limit the thickness effect is the concentration polarization or ohmic potential drop.

Experimental

Preparation of Raney nickel catalyst.—A melt of Ni-Al alloy containing 40% Ni and 60% Al by weight was prepared by using an induction furnace. It was quenched by pouring it into an iron cylinder. The ingot was crushed and powdered in a mill to a particle size smaller than 37 μ m. The Raney alloy powder was treated with 6M KOH solution at 80°C for 16h to leach aluminum. The Raney nickel precipitate thus obtained was washed with water and methyl alcohol alternately.

Preparation of the electrodes.—A weighed amount of a PTFE dispersion (D-1, Daikin Industrial Company) was added to the Raney catalyst. When the mixture was milled under blowing at room temperature, it became a paste, which was then calender-rolled by hand into sheets. The surfactant which had been contained in the dispersion was removed by washing with hot acetone. The PTFE content in the dry sheets was 10% in weight. These sheets were used as catalyst layers.

Gas-side layers were used to block the electrolyte leakage. Nickel black powder prepared from nickel formate was hydrophobized with PTFE and formed into sheets with the same procedure described above. Two sheets of them were attached to a stainless steel screen (used as a current collector) from both sides and pressed at 200 kg/cm². The raw layer obtained was heated in a nitrogen atmosphere at 380°C to sinter the PTFE hydrophobizer and to remove the surfactant contained. The catalyst

layer prepared previously was attached to the gas-side layer by pressing at 420 kg/cm². The double-layered electrode thus obtained was heated at 150°C in a hydrogen atmosphere for 1h to activate the catalyst layer.

Cell arrangement and polarization measurement.—The geometrical working area of the electrodes was a circle with a diameter of 3.5 cm. The electrolyte used was 6M KOH solution and it was circulated at a rate of 5 ml/min. The electrolyte temperature was maintained at 60° ± 1°C with an electric furnace. The ohmic drop was eliminated by the current interruption method (5).

Measurement of the concentration polarization in catalyst layers.—The zirconia layer was prepared similarly by binding a reagent-grade zirconia powder with the PTFE hydrophobizer. The catalyst, zirconia, and gas-side layers were arranged in a structure as illustrated in Fig. 1. The test layer is a Raney nickel layer, the concentration polarization in which is to be measured. The load current is sustained by the working layer which is catalyzed with 0.4% chromium-doped Raney nickel (6). Use of this catalyst not only lowers the polarization loss of the working layer, but also stabilizes its polarization characteristics, thereby providing more accurate and reproducible polarization data for the test layer.

Measurement of the gas diffusivity in the electrodes.—The cell arrangement for measuring the gas diffusivity is illustrated in Fig. 2. Hydrogen gas was supplied through the test electrode set at the gas side of the working electrode. The test electrode used was 0.32 mm thick. The gas diffusivity coefficient was calculated from the polarization difference between the working electrodes with and without the test electrode. Before measurement, the test electrode was wetted with the electrolyte by loading about 100 mA/cm² for 1h. This is a conditioning process to arrange the penetrating electrolyte in the pores to the amount in load condition.

Measurement of electrolyte resistivity in the catalyst layers.—The electrolyte resistivity of catalyst layers was measured by applying the current interruption method to the multilayered electrode illustrated in Fig. 1. The resistivity difference between the electrodes with and without the test layer is its electrolyte resistivity. The bulk electrolyte resistance in the geometry of electrolyte compartment used was calculated to be 13 mΩ, which is negligible in comparison to the total resistance measured.

Results and Discussion

Effect of the thickness on the polarization resistance.—Polarization curves of Raney nickel hydrogen electrodes are shown in Fig. 3 as a function of the thickness of catalyst layers. They are almost linear at low load currents, so that the polarization resistance ω can be calculated from the slopes. The experimental plots of reciprocal polarization resistance ω^{-1} vs. thickness d are given in Fig. 4. The solid line in the figure is the best fit curve calculated from Eq. [1] for $\rho_t = 7.5 \Omega\text{-cm}$ and $\rho_l = 4.0 \times 10^{-3} \Omega\text{-cm}^3$.

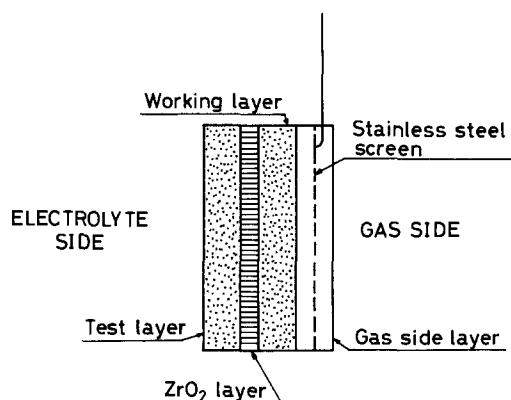


Fig. 1. Structure of multilayered electrodes used for measurement of electrolyte diffusivity.

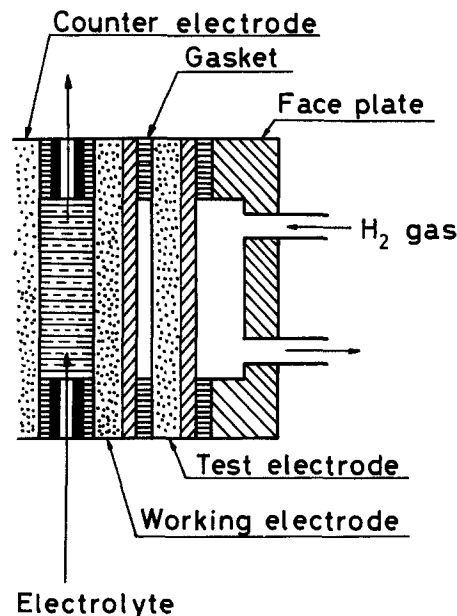


Fig. 2. Cell arrangement for measurement of gas diffusivity

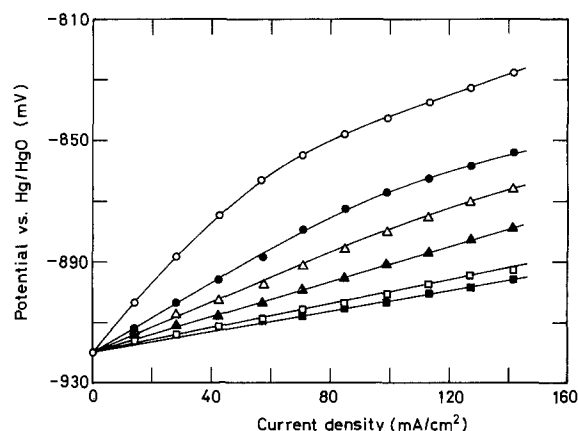


Fig. 3. Polarization curves of PTFE-bonded Raney nickel hydrogen electrodes. Thicknesses of the catalyst layers are as follows. Open circles: 0.045 mm. Closed circles: 0.086 mm. Open triangles: 0.12 mm. Closed triangles: 0.16 mm. Open squares: 0.22 mm. Closed squares: 0.42 mm. Ohmic drop eliminated.

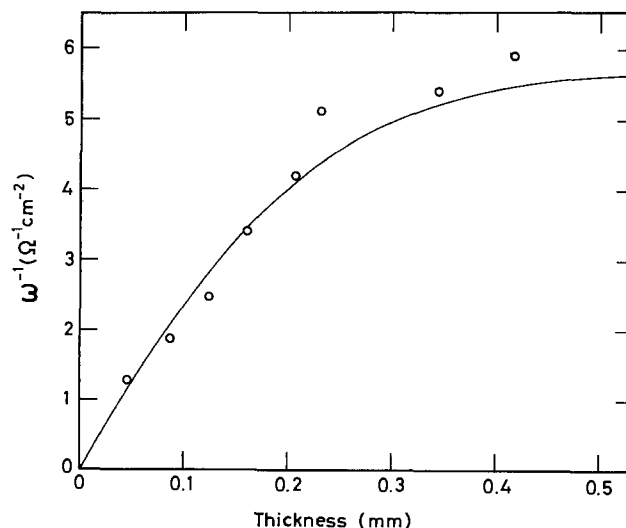


Fig. 4. Reciprocal polarization resistance of Raney nickel electrodes as a function of thickness of catalyst layers. Solid line calculated from Eq. [1] for $\rho_l = 4.0 \times 10^{-3} \Omega\text{-cm}^3$ and $\rho_t = 7.5 \Omega\text{-cm}$.

The electrolyte resistivity in the catalyst layer expected from the ohmic drop assumption thus is 7.5 $\Omega\text{-cm}$.

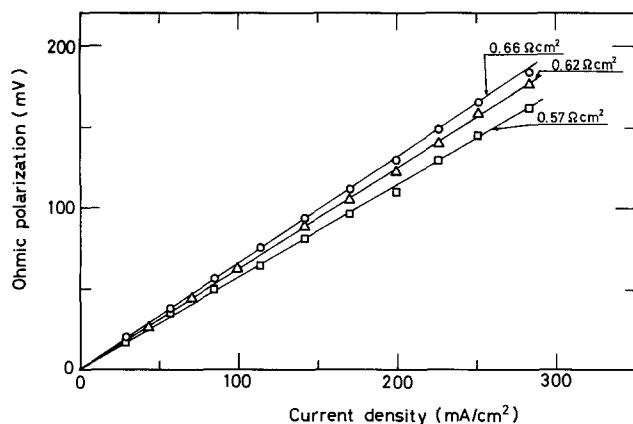


Fig. 5. Ohmic polarizations of multilayered electrodes. Thicknesses of test layers are as follows. Open triangles: without test layers. Open circles: 0.14 mm. Open squares: 0.22 mm. Resistances per square centimeter of electrodes shown in the figure were calculated from the slopes.

Electrolyte resistivity of catalyst layers.—The ohmic polarizations of multilayered electrodes are given in Fig. 5 as they vary with the thickness of catalyst layers. The ohmic resistances per square centimeter of electrode area calculated from the slopes are shown also in the figure. If the test layers possess the expected electrolyte resistivity, resistances of 0.72 and 0.79 $\Omega\text{-cm}^2$ must be observed for thicknesses of 0.14 (circles in the figure) and 0.22 mm (squares), respectively. These expected deviations from the value for zero thickness 0.62 $\Omega\text{-cm}^2$ are detectable by the current interruption method used. Observed resistance values, however, scatter around the value for zero thickness, and no systematic increases are found, suggesting that the electrolyte resistivity is much smaller than that expected theoretically. The assumption of ohmic potential drop therefore is very questionable.

The electrolyte diffusivity in catalyst layers.—The polarization curves of multilayered electrodes with and without a test layer are shown in Fig. 6. The polarization difference between the two electrodes $\Delta\eta_c$ is due to the concentration polarization occurred in the test layer

$$\Delta\eta_c = \frac{RT}{F} \ln \frac{C_{\text{OH}^-}^t}{C_{\text{OH}^-}^c} \quad [2]$$

where superscript t denotes the diffusivity test, $C_{\text{OH}^-}^t$ is

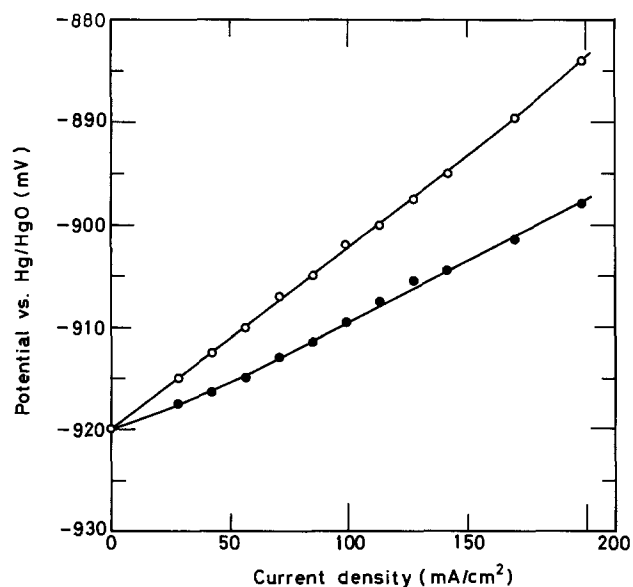


Fig. 6. Polarization curves of multilayered electrodes. Thickness of test layers: closed circles are for without test layers, and open circles are for 0.11 mm. Ohmic drop eliminated.

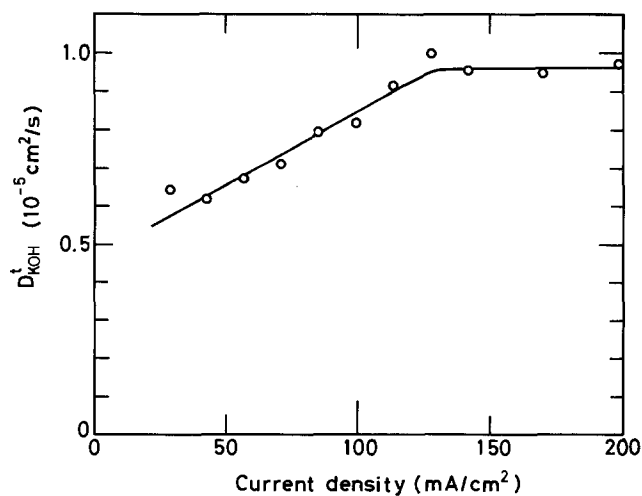


Fig. 7. Electrolyte diffusivity coefficient of Raney nickel catalyst layer as a function of current density. Thickness of catalyst layer: 0.11 mm.

the concentration of OH^- ion at the test and working layer interface, $C_{\text{OH}^-}^c$ is the bulk concentration 6M, and the other symbols have the usual meanings. The electrode current density I^t is proportional to the concentration gradient in the test layer

$$\frac{I^t}{F} = D_{\text{KOH}^t} \frac{C_{\text{OH}^-}^c - C_{\text{OH}^-}^t}{d^t} \quad [3]$$

where D_{KOH^t} is the electrolyte diffusivity coefficient of test layer and d^t is its thickness 0.11 mm. By eliminating $C_{\text{OH}^-}^t$ from Eq. [2] and [3] and inserting the polarization data given in Fig. 6, we obtain D_{KOH^t} values as a function of current density. Figure 7 shows plots of D_{KOH^t} vs. current density. A gradual increase observed in a low current region is probably due to a proceeding in the electrolyte penetration with increasing load. A constant D_{KOH^t} value of $9.57 \times 10^{-6} \text{ cm}^2/\text{s}$ is attained at 100 mA/cm^2 . This value will be used for the calculation of polarization resistance of electrodes.

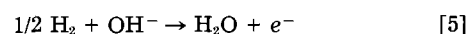
Gas diffusivity of the electrodes.—The gas diffusivity of electrodes was measured in fashion similar to the above case. In the cell construction shown in Fig. 2, the potential difference between the electrodes with and without the test electrode $\Delta\eta_p$ is due to the gas pressure drop that occurred in the test electrode

$$\Delta\eta_p = \frac{RT}{F} \ln \frac{P_{\text{H}_2}^t}{P_{\text{H}_2}^c} \quad [4]$$

where $P_{\text{H}_2}^t$ is the gas pressure at the compartment between the test and working electrodes, and $P_{\text{H}_2}^c$ is the operating pressure 1 atm. Figure 8 shows the polarization curves of electrodes with and without the test electrode. No significant polarization differences can be seen between the two curves. This indicates that the electrodes used in this study are so gas diffusive that the concentration polarization due to the gas pressure drop can be neglected.

Calculation of the polarization resistance with considering concentration polarization.—The geometric model used is a cylinder, the inside face of which is covered with a thin electrolyte film, as shown in Fig. 9. The analysis considers a differential element dx cut from the cylinder. The local current is generated at the film/cylinder-wall interface, and its gathering flows as the pore current in the axial direction.

The Volmer reaction is assumed as a rate-controlling step for the hydrogen oxidation in alkaline solution (7)



In this case the local current density i can be expressed as a function of local potential E (8)

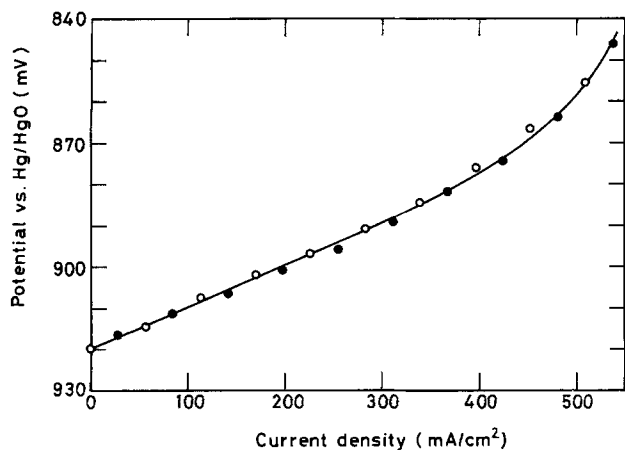


Fig. 8. Gas diffusivity test of a wetted Raney nickel electrode by means of polarization difference. Open circles: without a test electrode. Closed circles: a test electrode of 0.32 mm thickness set at the gas-side of working electrode. Ohmic drop eliminated.

$$i = -F \left\{ k^+ C_{OH^-} \sqrt{P_{H_2}} \exp \left(\frac{\alpha F}{RT} E \right) - k^- C_{H_2O} \exp \left(- \frac{(1-\alpha)F}{RT} E \right) \right\} \quad [6]$$

where k^+ and k^- are the rate constants, C_{OH^-} and C_{H_2O} are the concentrations of OH^- ion and water in the film, respectively, and P_{H_2} the hydrogen pressure. The gas diffusion in the pore is very fast so that $P_{H_2} = \text{const.} = 1 \text{ atm}$ throughout the cylinder. At equilibrium potential $E = E_0$

$$k^+ F C_{OH^-} \exp \left(\frac{\alpha F}{RT} E_0 \right) = k^- F C_{H_2O} \exp \left(- \frac{(1-\alpha)F}{RT} E_0 \right) = i_0 \quad [7]$$

where i_0 is the exchange current density. Substituting Eq. [7] into Eq. [6] yields

$$i = -i_0 \left\{ \exp \left(\frac{\alpha F}{RT} \eta \right) - \exp \left(- \frac{(1-\alpha)F}{RT} \eta \right) \right\} \quad [8]$$

where η is the local polarization and $\eta = E - E_0$. When η is small, the exponential function can be approximated to the linear function

$$i = - \frac{i_0 F}{RT} \eta \quad [9]$$

The exchange current density i_0 can be derived from Eq. [7] in the form

$$i_0 = k^+ F C_{OH^-} \left(\frac{k^-}{k^+} \right)^\alpha \left(\frac{C_{H_2O}}{C_{OH^-}} \right)^\alpha \quad [10]$$

Assuming $\alpha = 1/2$, we obtain

$$i_0 = F \sqrt{k^+ k^-} \sqrt{C_{H_2O} C_{OH^-}} \quad [11]$$

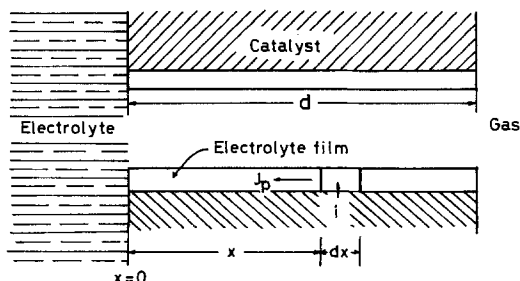


Fig. 9. Thin film model used for the calculation of polarization resistance.

Equation [9] then becomes

$$i = -k \sqrt{C_{OH^-}} (E - E_0) \quad [12]$$

where $k = F \sqrt{k^+ k^-} \sqrt{C_{H_2O}}$. It is essentially constant because the change in C_{H_2O} is negligible in the concentrations around 6M.

The local potential E is assumed to be constant throughout the cylinder from the fact that the electrolyte resistivity in the catalyst layer is very low.

The equilibrium potential E_0 is a function of x owing to the concentration polarization. Applying the Nernst's equation to E_0 , we obtain

$$E_0 = E_0^o - \frac{RT}{F} \ln \frac{C_{OH^-}}{C_{OH^-}^o} \quad [13]$$

where $C_{OH^-}^o$ is the bulk concentration 6M and E_0^o is the equilibrium potential at $C_{OH^-} = C_{OH^-}^o = 6M$.

In load condition, the potential E_0 rises with x due to the lowering of the concentration, while the potential E remains constant throughout the pore. The driving potential $E - E_0$ for the local current generation therefore lowers with x . Hence, an additional improvement in the polarization loss by thickening the layer becomes less as the layer is thick. This is a qualitative explanation for the limit of thickness effect in terms of the concentration polarization.

The local current density is related to the pore current flowing in the axial direction J_p by making a current balance on the differential element

$$i = \frac{1}{2\pi r} \frac{dJ_p}{dx} \quad [14]$$

where r is the mean radius of pores.

The electrolyte used is KOH, and only the OH^- ion is electroactive. For this case, the gradient in the OH^- ion concentration is related to the ionic current J by

$$J = n_{OH^-} \left(1 + \frac{|n_{OH^-}|}{n_{K^+}} \right) D_{OH^-} F \frac{dC_{OH^-}}{dx} \quad [15]$$

where n_{OH^-} and n_{K^+} are ionic valences of OH^- and K^+ ions, respectively, and D_{OH^-} the diffusivity coefficient of OH^- ion (9). The pore current is proportional to the cross-sectional area of the film

$$J_p = 2\pi r \delta J = -2\pi r \delta D_{KOH} F \frac{dC_{OH^-}}{dx} \quad [16]$$

where $D_{KOH} = -n_{OH^-} (1 + |n_{OH^-}/n_{K^+}|) D_{OH^-}$ and δ is the mean thickness of the electrolyte films. Multiplying J_p by the number of pores per unit electrode area $1/\pi r^2$ to convert to the current density per unit electrode area I , we get

$$I = - \frac{2\delta}{r} D_{KOH} F \frac{dC_{OH^-}}{dx} \quad [17]$$

The factor $2\delta/r$ is the structural parameter of the electrode used and is involved in the experimental diffusion coefficient so that the term $2\delta/r D_{KOH}$ can be equalized to d_{KOH}^t , which appears in Eq. [3]

$$\frac{I}{F} = -d_{KOH}^t \frac{dC_{OH^-}}{dx} \quad [18]$$

Combining Eq. [12]-[14] and multiplying J_p by $1/\pi r^2$, we obtain

$$\frac{dI}{dx} = -K \sqrt{C_{OH^-}} \left\{ \eta_0 + \frac{RT}{F} \ln \left(\frac{C_{OH^-}}{C_{OH^-}^o} \right) \right\} \quad [19]$$

where $K = 2k/r$ and $\eta_0 = E - E_0$, which is the electrode polarization.

The electrode current density is obtained as an I value at $x = 0$ by integrating Eq. [18] and [19] simultaneously under the boundary conditions $C_{OH^-} = 6M$ at $x = 0$ and $I = 0$ at $x = d$. The integration was performed numerically using the modified Runge-Kutta method.

The K value is determined by the parameter matching from the slope of the polarization curve for the thin electrode; the linear part in the ω^{-1} vs. thickness plots in Fig. 4 indicates that the effect of concentration polarization is negligible in the thickness region. On fitting to the thin electrode data, $316 \Omega^{-1}\text{-cm}^{-1.5}\text{-mol}^{-1/2}\text{-atm}^{-1/4}$ was obtained as a K value. This value and the experimental D_{KOH}^{\dagger} value $9.57 \times 10^{-6} \text{ cm}^2/\text{s}$ being inserted into Eq. [19] and [18], respectively, the theoretical polarization resistances were calculated as a function of thickness. Figure 10 shows the relationship between ω^{-1} and thickness. The theoretical values (solid line) agree quite well with the experimental data (open circles). The thickness effect has been thus reproduced theoretically by assuming the concentration polarization. We can therefore say that the lower limit attained by the thickness effect in the polarization loss is determined by the electrolyte diffusivity, and not by the electrolyte resistivity in catalyst layers.

As seen in Fig. 6, when a current of, e.g., 200 mA/cm² flows across a test layer 0.1 mm thick, a concentration polarization of 14 mV arises. When Ohm's law is applied mechanically to this potential-current relationship, 7 $\Omega\text{-cm}$ is obtained as an apparent resistivity. This is very close to the ohmic resistivity expected from the parameter matching to Eq. [1], 7.5 $\Omega\text{-cm}$. Experimentally, the concentration polarization is almost a linear function of current density (Fig. 6) and the potential gradient due to the concentration polarization has a sign opposite of that due to the ohmic drop. The concentration polarization, therefore, is theoretically equivalent in effect on the driving potential to the ohmic potential drop brought about by the hypothetical resistivity of 7.5 $\Omega\text{-cm}$. This is why Eq. [1] leads to a theoretical curve fitting to the experimental data in spite of its starting from a different operating mechanism. These two, however, are physically different from each other. The fitness to Eq. [1] is just a coincidence resulting from the linear relationship between the concentration polarization and current density. A resistivity as high as 7.5 $\Omega\text{-cm}$ has not been found from the direct measurement so that the gradient in the driving potential in the pores should be attributed to the concentration polarization.

Chromium-doped Raney nickel catalyst.—The catalytic activity of Raney nickel is enhanced by doping a small amount of chromium (6). Figure 11 shows ω^{-1} vs. thickness plots for the hydrogen electrodes catalyzed with this Raney nickel. By assuming the same D_{KOH}^{\dagger} value, but using $K = 854 \Omega^{-1}\text{-cm}^{-1.5}\text{-mol}^{-1/2}\text{-atm}^{-1/4}$ obtained from the polarization data, the ω^{-1} values were calculated similarly. A solid line in Fig. 11 is theoretical, and open circles denote experimental data. The polarization loss is im-

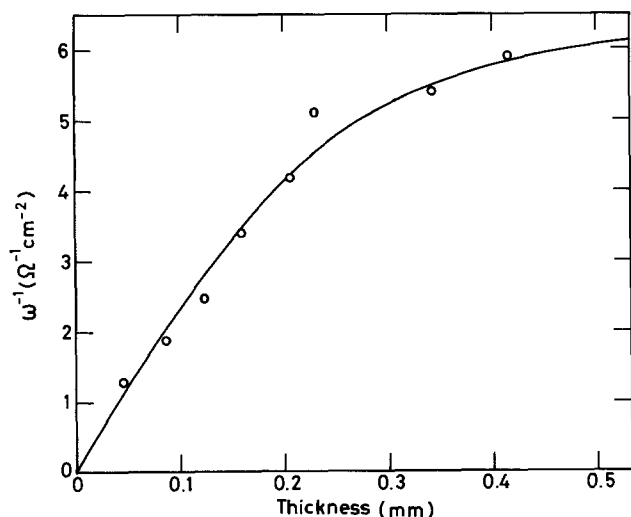


Fig. 10. Reciprocal polarization resistance of Raney nickel electrodes as a function of thickness of catalyst layers. Solid line calculated from Eq. [18] and [19] for the experimental D_{KOH}^{\dagger} value: $9.57 \times 10^{-6} \text{ cm}^2/\text{s}$.

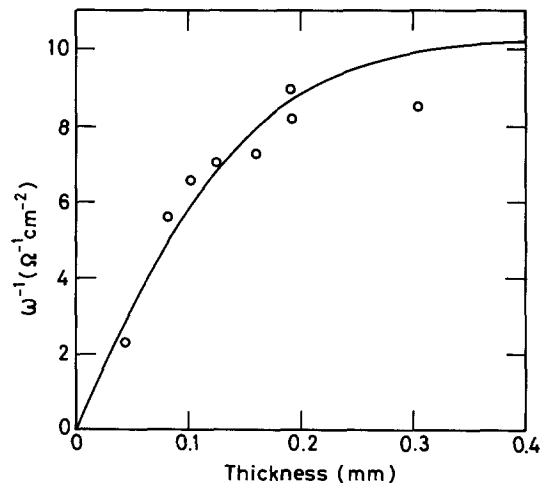


Fig. 11. Reciprocal polarization resistance of chromium-doped Raney nickel electrodes as a function of thickness of catalyst layers. Solid line calculated from Eq. [18] and [19] for the same D_{KOH}^{\dagger} values as in Fig. 10.

proved markedly by using this new catalyst. This indicates that the catalytic activity also is an important factor for the polarization loss and the K factor is its measure.

Depth profile of the local current density.—The local current density and concentration polarization can be calculated as a function of x from Eq. [18] and [19]. Figure 12 shows the depth profile for nondoped Raney nickel electrode polarized to 10 mV. The concentration polarizations η_c are given as differences from E° . The areas surrounded by the curves i and x coordinate correspond to the load current density sustained by the electrode, and the gaps between curves η_c and $\eta_c = -10$ mV to the driving potential. The lower limit in the polarization loss is reached at a limiting thickness not because the driving potential becomes zero at the gas-side edge of pore, but because increasing thickness makes the curve i steeper. As seen in Fig. 4, the polarization loss almost attains its

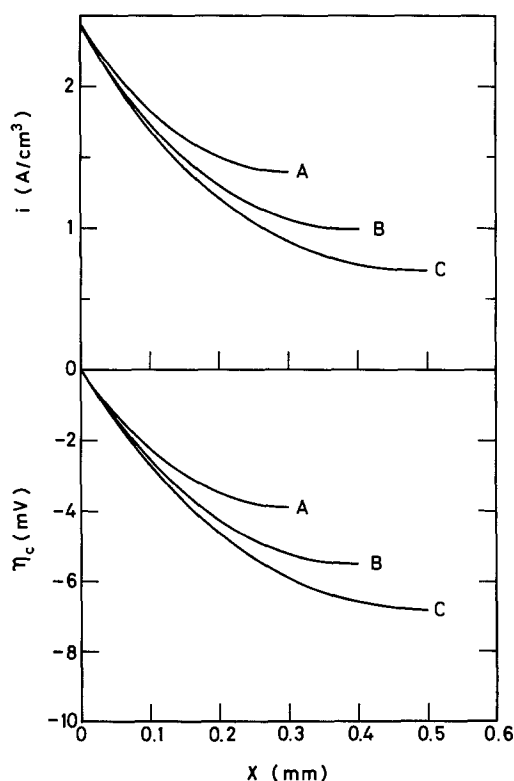


Fig. 12. Depth profiles of local current density (top) and concentration polarization (bottom) for various thicknesses. Thickness: (A) 0.3 mm, (B) 0.4 mm, (C) 0.5 mm.

lower limit at about 0.3 mm thick, where 60% of the full potential is still held as a driving potential at $x = 0.3$ mm (curve A in the bottom of Fig. 12). If more electrolyte-diffusive catalyst layers can be used, the profile becomes flatter and the thickness effect extends over a wider thickness range. From a practical point of view, this means that the performance improvement can be made by enhancing the electrolyte diffusivity as well as catalytic activity.

Conclusion

The polarization loss of Raney nickel hydrogen electrodes can be decreased by thickening the catalyst layers. However, there is a lower limit to the polarization loss that can be attained by the thickness effect. This limiting behavior has been described on the basis of concentration polarization assumption in contrast to the ohmic potential drop mechanism. The electrolyte diffusivity coefficient of catalyst layer required for the theoretical calculation was obtained by using a multilayered electrode installed with a zirconia layer to separate the test layer electronically from the working layer. The theoretical calculation by use of the experimental value reproduced well the experimental limiting behavior in the thickness effects, and the concentration polarization assumption has thus been proved to be valid. The importance of the electrolyte diffusivity in the catalyst layer has been pointed out as a performance controlling factor.

Manuscript submitted Oct. 31, 1984; revised manuscript received March 29, 1985.

Muroran Institute of Technology assisted in meeting the publication costs of this article.

LIST OF SYMBOLS

C_{OH^-}	concentration of OH^- ion in electrolyte film (mol/dm ³)
$C_{OH^-}^0$	bulk concentration of electrolyte (6 mol/dm ³)
$C_{OH^-}^{-1}$	concentration of OH^- ion at test and working layer interface (mol/dm ³)
C_{H_2O}	concentration of water in electrolyte film (mol/dm ³)
d	thickness of catalyst layer (cm)
d^t	thickness of test layer (cm)
D_{OH^-}	diffusivity coefficient of OH^- ion (cm ² /s)
D_{KOH}^-	electrolyte diffusivity coefficient (cm ² /s)
D_{KOH}^+	electrolyte diffusivity coefficient of test layer (cm ² /s)
E	local potential (V)
E^0	equilibrium local potential (V)

E^0	equilibrium local potential at $C_{OH^-} = 6M$ (V)
F	Faraday's constant (96,487 C/eq)
i	local current density (A/cm ²)
i_0	local exchange current density (A/cm ²)
I	electrode current density (A/cm ²)
I^t	electrode current density for diffusion test (A/cm ²)
J	ionic current density (A/cm ²)
J_p	current generated per pore (A)
k	$F\sqrt{k^+k^-}\sqrt{C_{H_2O}}$ ($\Omega^{-1}\text{-cm}^{-1.5}\text{-mol}^{-1/2}\text{-atm}^{-1/4}$)
k^+, k^-	rate constant for electrochemical hydrogen oxidation
K	$2k/\tau$ ($\Omega^{-1}\text{-cm}^{-1.5}\text{-mol}^{-1/2}\text{-atm}^{-1/4}$)
n_{OH^-}	ionic valence of OH^- ion
n_{K^+}	ionic valence of K^+ ion
P_{H_2}	hydrogen pressure in macropore (atm)
$P_{H_2}^0$	operating pressure (1 atm)
$P_{H_2}^i$	hydrogen pressure at compartment between test and working electrode (atm)
τ	mean radius of pores
R	gas constant (8.3176 J/mol-K)
T	temperature (K)
x	axial distance from electrolyte-side edge in pore (cm)

Greek symbols

α	charge-transfer coefficient
δ	thickness of electrolyte film (cm)
η	local polarization (V)
η_0	electrode polarization (V)
η_C	concentration polarization (V)
$\Delta\eta_C$	polarization difference between two multilayered electrodes with and without test layer (V)
$\Delta\eta_P$	polarization difference between two cell arrangements with and without test electrode
ρ_t	resistivity of electrolyte film ($\Omega\text{-cm}$)
ρ_i	interfacial resistance between film and catalytic surface ($\Omega\text{-cm}^2$)
ω	polarization resistance of electrode ($\Omega\text{-cm}^2$)

REFERENCES

1. K. Mund, *Siemens Forsch. Entwickl. Ber.*, **4**, 1 (1975).
2. K. Mund, *ibid.*, **4**, 68 (1975).
3. K. Mund, G. Richter, and F. von Sturm, *This Journal*, **124**, 1 (1977).
4. T. Kenjo, *Bull. Chem. Soc. Jpn.*, **54**, 2553 (1981).
5. K. V. Kordes and A. Marko, *This Journal*, **107**, 480 (1960).
6. T. Kenjo, *ibid.*, **132**, 383 (1985).
7. R. Brown and J. A. Rockett, *ibid.*, **113**, 865 (1966).
8. K. J. Vetter, "Electrochemical Kinetics," p. 518, Academic Press, New York (1967).
9. K. J. Vetter, "Electrochemical Kinetics," p. 170, Academic Press, New York (1967).

Electrochemical Behavior of Water in Immobilized Salt Electrolytes

II. Cyclic Voltammetry

Armand Bettelheim, Federico Broitman, and Uri Mor

Nuclear Research Center-Negev, Beer Sheva 84190, Israel

ABSTRACT

Cyclic voltammetry is used to determine the concentration of water and hydrolysis products in a pelletized LiCl-KCl-MgO mixture. This method, effective at temperatures above the melting point of the electrolyte, completes other electrochemical and thermal methods which have been previously used to investigate the various states of water at lower temperatures.

The determination of water and its reaction products in molten LiCl-KCl eutectic is of interest for the development of primary as well as secondary batteries for load leveling and electric vehicle applications. The presence of water as well as other contaminants formed near the electrodes during exposure to humid air could affect cell performance and accelerate self-discharge (1).

Cyclic voltammetry has been widely applied to liquid electrolytes to study redox reactions. Important param-

eters related to the reactions such as redox potential, rate constant, Tafel slope, and diffusivity of the redox species can be easily obtained (2, 3). This technique, recently used in solid electrolyte systems (4, 5), has not yet been applied to pelletized salt electrolytes. In these systems, a binder (such as MgO or SiO₂) is added in order to gel and immobilize the electrolyte, which would otherwise flow when subjected to the battery operation temperature, some 150°C above the electrolyte melting point. In a pre-

vious study (6), we reported the use of electrical conductivity and thermal measurements to detect water and hydrolysis products in a pelletized LiCl-KCl (64-36 mole percent [m/o])-MgO (50 weight percent [w/o]) mixture. In the present work, cyclic voltammetry is used for the *in situ* determination of water and hydroxyl ions and investigation of their electrochemical behavior.

Experimental

AR-grade LiCl, KCl, and MgO (Merck) are used. Pellets of electrolyte composed of LiCl-KCl (64-36 m/o) in presence of MgO (50 w/o) as binder are prepared as described in a previous publication (6).

A schematic diagram of the apparatus for cyclic voltammetric (CV) measurements of pellets is illustrated in Fig. 1. The platinum working and auxiliary electrodes are spot welded to a 0.5 mm diam platinum wire sheathed in glass. The reference electrode consists of a pure nickel wire inserted into a thin-walled, 2 mm od Pyrex tube containing a $10^{-2}M$ solution of NiCl₂ in LiCl-KCl eutectic. The Ni/Ni(II) ($10^{-2}M$) reference electrode, which has a potential 795 mV more negative than the Pt/Pt(II) ($10^{-2}M$) electrode (7), is allowed to be in contact with the pellet as shown in Fig. 1. The whole set is heated under vacuum at below the melting point and under dry argon after melting. The heating is achieved by means of a programmable device which permits a constant temperature within $\pm 1^\circ C$.

Melts of LiCl-KCl (in the absence of binder) are contained in alumina crucibles and are maintained at 430°C

in an atmosphere of dry argon. Additions of hydroxide and oxide ions are accomplished using KOH and CaO. Lithium chloride with a water content of 1.6% is used to increase H₂O concentration in the melt. The platinum working and auxiliary electrodes, as well as the Ni/Ni(II) ($10^{-2}M$) reference electrodes, are as described for the CV of pellets.

Cyclic voltammetry is performed using a PAR 174 potentiostat coupled with a PAR 175 sweep generator. The voltammograms are recorded on a Type 3078 Yokogawa X-Y recorder.

Results and Discussion

Figure 2 shows a typical cyclic voltammogram obtained at 430°C for a pelletized LiCl-KCl-MgO mixture originally containing 2.5 w/o water. The CV curve shows two cathodic peaks (I and II) at -1.48 and -2.26V. Plots of the peak current (i_p) vs. the square root of the scan rate ($\nu^{1/2}$) are linear, indicating diffusion-controlled processes (Fig. 3).

The addition of solutes to a pellet cannot be accurately accomplished but is relatively simple for a LiCl-KCl melt (in the absence of MgO) of the same eutectic composition and temperature. The CV at 430°C of a LiCl-KCl melt which has not been prepurified to remove water and hydrolysis products (Fig. 4, curve a) shows characteristics very similar to those of the pellet. Peaks I and II are attributed to the reduction of water and hydroxide ions, respectively, and the process occurring in region VII to oxidation of oxide ions. The identification of the various peaks is inferred on the basis of proportionality between known added concentrations of H₂O, OH⁻, and O⁻² ions in the melt and peak height. The relative potential position of various processes is in agreement with other studies conducted with several reference electrodes and various molten salt systems (8-12).

By varying the upper and lower limit of the potential sweep, some of the peaks corresponding to the different reduction peaks can be identified. For example, peak VI is the oxidation peak corresponding to the reduction peak I which increases when H₂O is added to the melt. The potential difference between the cathodic and anodic peaks ($E_{p,c} - E_{p,a}$) is 140 mV, which is similar to the theoretical

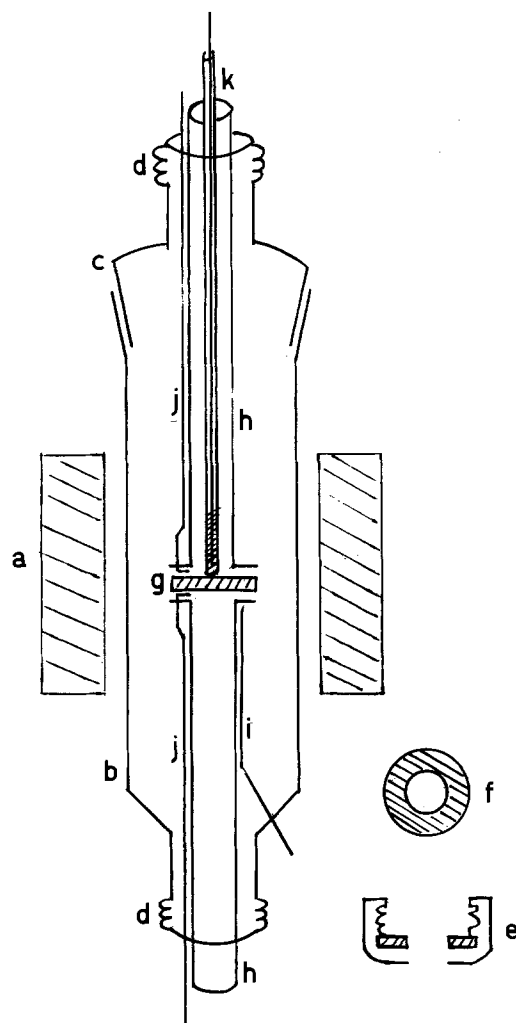


Fig. 1. Cell for CV measurements of a pelletized LiCl-KCl-MgO mixture. a, furnace; b, glass cell; c, glass joint; d, screwthread; e, quickfit plastic screwcap; f, silicone rubber ring; g, pellet; h, glass tubes; i, thermocouple; j, platinum working and auxiliary electrodes; k, Ni/Ni(II) reference electrode.

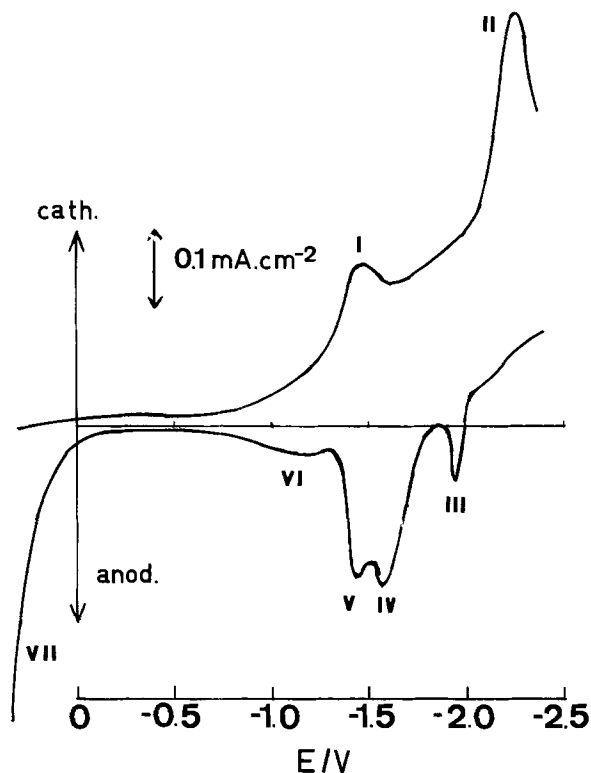


Fig. 2. CV at 20 mV s⁻¹ and 430°C of a pelletized LiCl-KCl-MgO mixture originally containing 2.5% water.

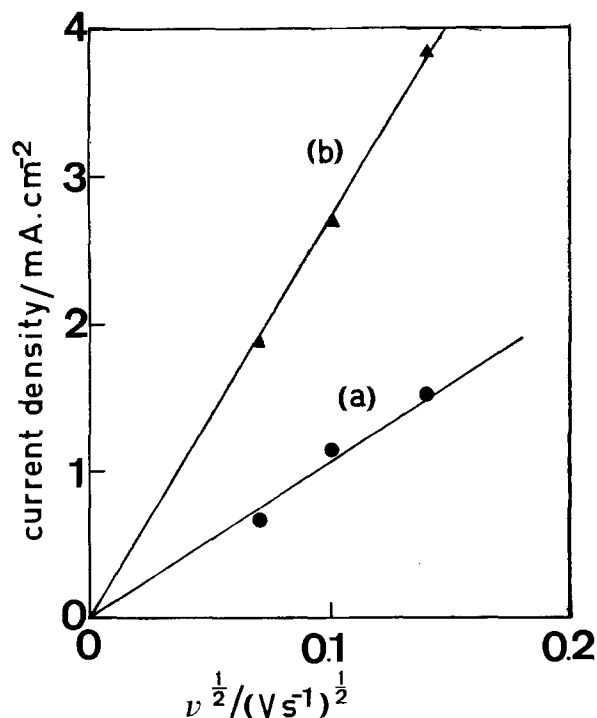


Fig. 3. Current density of peaks I and II (water and hydroxyl ions, curves a and b, respectively) vs. the square root of scan rate for a pelletized LiCl-KCl-MgO mixture at 430°C.

value, i.e., 138 mV for one-electron transfer reaction at 430°C. Moreover, the half-wave potential of the water wave moves cathodically upon addition of KOH or CaO, while an anodic shift is observed when HCl is introduced

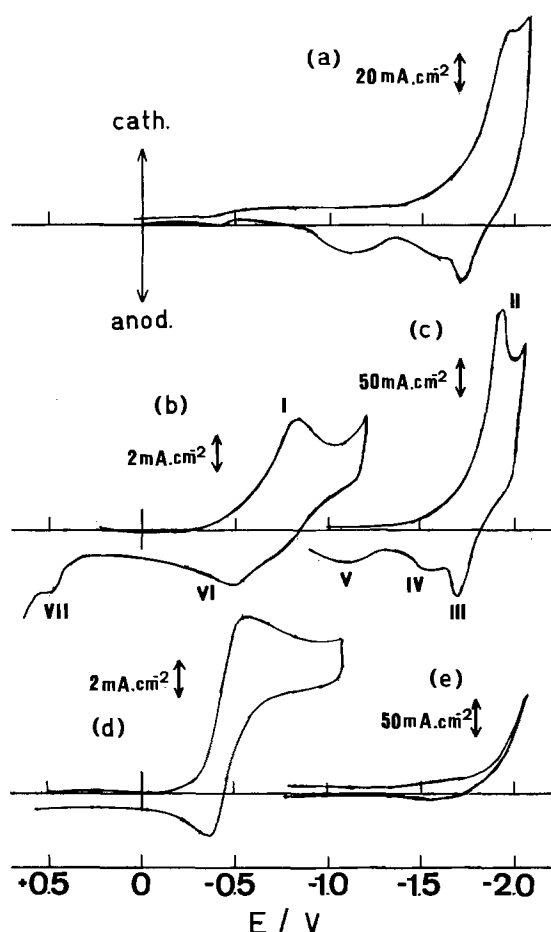


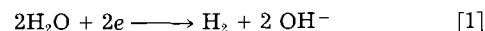
Fig. 4. CV at 50 mV s⁻¹ and 430°C of a LiCl-KCl melt. a: Without any purification treatment. b and c: After addition of 9.6 × 10⁻²M KOH. d and e: After 1h treatment with HCl.

Table I. CV data for a pelletized LiCl-KCl (64-36 m/o)-MgO (50 w/o) mixture and LiCl-KCl (64-36 m/o) melt at 430°C

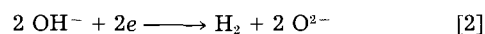
Peak	Pellet	E_p/V	Melt	Electrode reaction
I	-1.48	-0.84		$2H_2O + 2e \rightarrow H_2 + 2 OH^-$
II	-2.26	-1.94		$2 OH^- + 2e \rightarrow H_2 + 2 O^{2-}$
VII	+0.1 ^a	+0.5		$2 O^{2-} \rightarrow O_2 + 4e$

^a Due to the high oxide concentration, a distinct peak is not observed and the potential of the foot wave is reported.

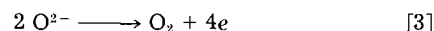
to the melt (Fig. 4, curves b and d). The influence of basicity of the melt on $E_{1/2}$ suggests the involvement of hydroxyl ions in the reduction process. These results are in agreement with the overall reaction scheme (8)



Similarly, peak II is due to the reduction of hydroxyl ions. The presence of the corresponding peaks III, IV, and V indicates a sequence of oxidation reaction steps. No attempt was made to identify the reduction or oxidation products. However, the overall reaction [2] was deduced from the electrochemical measurements of Kan-zaki and Takahashi (8)



Wave VII is due to oxidation of oxide ions according to the reaction (12)



The currents of the OH⁻/H₂ and O²⁻/O₂ couples decrease to very small values when the melt is treated with HCl for a period of 1-2h (compare curves b and c to d and e in Fig. 4). This is probably a consequence of the reaction of OH⁻ and O²⁻ ions with HCl, as reported for LiCl-KCl-MgO pellets in a previous publication (6), and for the LiCl-KCl melt reported in other studies (11, 13)

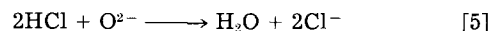
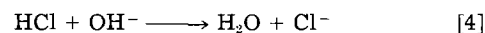


Table I summarizes the CV data. The cathodic shift of peaks I and II for the pellet as compared to the melt is due to the high oxide concentration in the pellet and the expected dependence of redox potential on the p_{OH^-} and the $p_{O^{2-}}$ (8, 12). The large amount of oxide ions in the pellet also accounts for the high current obtained for wave VII. Moreover, the potential shift of this wave for the pellet is opposite in direction to peaks I and II, again in agreement for the proposed identification of the various electrochemical reactions in the melt and the pellet.

The comparison of the CV curves for the melt and the pellet allows not only the identification of the various electrode reactions, but also a quantitative estimation of H₂O and OH⁻ concentrations in the pellet. According to the Randles-Sevcik equation (14), the peak current (i_p) is directly related to the concentration (c) of the electroactive species and to the square root of the scan rate ($\nu^{1/2}$)

$$i_p = kAC(\nu/RT)^{1/2}(FnD)^{3/2} \quad [6]$$

where k is a constant for a given reaction, A is the electrode area, T is the absolute temperature, R is the gas constant, F is Faraday's constant, and ν is the potential sweep rate. In Fig. 5a, the peak current densities for various water concentration increases are plotted against the square root of scan rate. The slope of the straight line recorded before the first addition of water is related to the residual water concentration in the melt at the start of the measurements. If the slope measured for the initial unknown concentration is deduced from the values determined from the added concentrations, one obtains the corrected slopes corresponding to the added concentrations. The corrected values are plotted against the added concentrations of water in Fig. 5b. Assuming the same

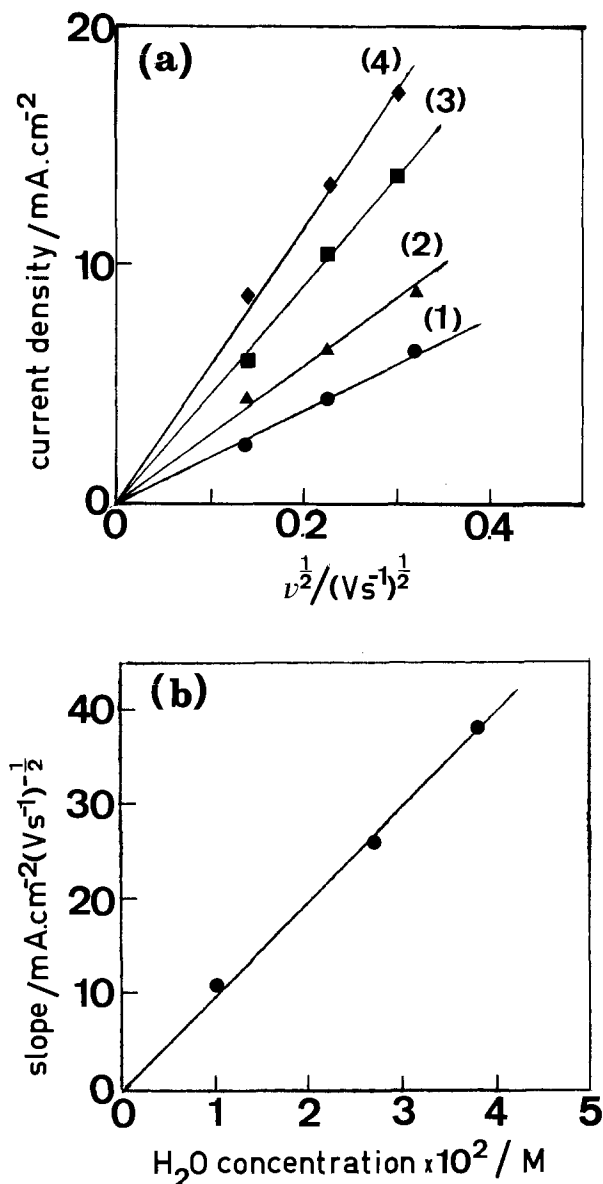


Fig. 5. a: Current density of peak I vs. the square root of scan rate for a LiCl-KCl melt at 430°C. Curve 1 is relative to the initial water concentration, while curves 2-4 are for the addition of 10^{-2} , 2.7×10^{-2} , and 3.8×10^{-2} M H₂O. b: Corrected slopes of curves in Fig. 5a vs. the water concentration in the melt.

diffusion coefficient for H₂O in the pellet and the melt maintained at the same temperature, the water concentra-

tion in the pellet can be estimated using the slope of i_p vs. $v^{1/2}$ for the pellet and the calibration curve shown in Fig. 5b. Using this procedure, an approximate value of 10^{-2} M is obtained for this specific example.

The same calibration technique can be used to determine the hydroxyl ion concentration in the pellet.

Conclusion

It has been shown that cyclic voltammetry can easily be applied to molten pelletized mixtures. The redox potentials for H₂O and different hydrolysis products agree with other published data (8, 12). CV also allows a quantitative determination of H₂O and OH⁻ ions at temperatures above the melting point of the electrolyte ($\geq 370^\circ\text{C}$). This technique completes other methods (ac electrical conductivity, DTA, and TGA) previously employed for the detection and characterization of the different states of water in pelletized specimen at lower temperatures (6).

Manuscript submitted Nov. 16, 1984; revised manuscript received March 5, 1985.

REFERENCES

1. W. Borger, D. Kunze, and H. S. Panesar, *Prog. Batt. Solar Cells*, **3**, 251 (1980).
2. P. Delahay, "New Instrumental Methods in Electrochemistry," Chap. 6, Interscience Publishers, New York (1954).
3. R. S. Nicholson and I. Shain, *Anal. Chem.*, **36**, 706 (1964).
4. P. Fabry and M. Kleitz, *This Journal*, **126**, 2183 (1979).
5. C. Y. Yang and H. S. Isaacs, *J. Electroanal. Chem. Interfacial Electrochem.*, **123**, 411 (1981).
6. R. Parash, F. Broitman, U. Mor, D. Ozer, and A. Bettelheim, *This Journal*, **131**, 2531 (1984).
7. H. A. Laitinen and C. H. Lin, *J. Am. Chem. Soc.*, **80**, 1015 (1958).
8. Y. Kanzaki and M. Takahashi, *J. Electroanal. Chem. Interfacial Electrochem.*, **58**, 349 (1975).
9. P. Tilman, J. P. Wiaux, C. Dauby, J. Glibert, and P. Claes, *ibid.*, **167**, 117 (1984).
10. C. A. Melendores, J. P. Ackerman, and R. K. Steunenberg, in "Molten Salts," J. P. Pemsler, J. Braunstein, D. R. Morris, K. Nobe, and N. E. Richards, Editors, p. 575, The Electrochemical Society Soft-bound Proceedings Series, Princeton, NJ (1976).
11. S. H. White, in "Ionic Liquids," D. Inman and D. G. Lovering, Editors, Chap. 12, Plenum Press, New York (1981).
12. Y. Kanzaki and M. Takahashi, *J. Electroanal. Chem. Interfacial Electrochem.*, **58**, 339 (1975).
13. H. A. Laitinen, W. S. Ferguson, and R. A. Osteryoung, *This Journal*, **104**, 516 (1957).
14. J. E. Randles, *Trans. Faraday Soc.*, **44**, 327 (1948); A. Sevcik, *Collect. Czech. Chem. Commun.*, **13**, 349 (1948).
15. R. Combes, in "Ionic Liquids," D. Inman and D. G. Lovering, Editors, Chap. 15, Plenum Press, New York (1981).

Electrolytic Purification of Aqueous Solutions of Potassium Chloride Containing Manganese Ions

J. Fujioka and H. Riveros

Institute of Physics, National University of Mexico, Coyoacán, Mexico

ABSTRACT

The purification by electrolysis at a mercury electrode of aqueous solutions of potassium chloride containing manganese ions is investigated. The concentration of manganese decreased from 112 to 0.4 ppm after 20 min of electrolysis at -1.85V (vs. SCE).

The procedures reported over the last ten years to purify aqueous solutions of alkali metal chlorides involve the use of precipitating agents, ion-exchange resins, or both types of substances (1-18). Of these procedures, the great majority is focused on the elimination of calcium

and magnesium ions present in the solution (5-9, 11-15, 17, 18).

In this paper, the purification by electrolysis of aqueous solutions of potassium chloride contaminated with manganese is studied. This method of purification and

the impurity chosen are not very common in the field of purification of alkali halides.

The elimination of Mn^{2+} ions from aqueous solutions of KCl could be useful in the electrochemical production of Cl_2 and KOH, which generally involves the use of coated titanium anodes and mercury cathodes. The presence of Mn^{2+} in the aqueous KCl fed to the cells is very detrimental in that MnO_2 deposits on the coated titanium anodes. This causes the cell voltage and power consumption to increase. Furthermore, the removal of MnO_2 from the coated titanium anodes without damaging the coating on the anodes is difficult.

As a method of purification, electrolysis has been used on a small scale. In particular, in the purification of aqueous solutions of alkali halides, its use has been very rare. However, it has been proven that electrolysis is an effective method to remove certain unknown impurities found in high purity KCl, using a graphite electrode as the working electrode (19).

The use of electrolysis in the purification of aqueous solutions renders it possible to employ the same equipment used in the purification to check the decrease in the impurity concentration, and to observe some of the characteristics of the reaction by which the impurity is eliminated. This can be accomplished by applying a triangular potential $E(t)$ to the working electrode, and plotting the current $i(E)$ that flows through the cell (*i.e.*, using the technique known as linear potential sweep chronopotentiometry or linear sweep voltammetry). To interpret these i - E curves (voltammograms), the theory of stationary electrode polarography can be used (20-23). However, it must be remembered that the mercury electrode used in this study is much larger than the tiny drops used in polarography. The results of Reeves *et al.* (24) concerning the reduction of K^+ at a mercury cathode will also be helpful.

Experimental

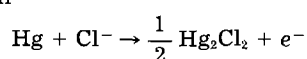
A three-electrode cell (EG&G PAR Model 377A) was used both for the purification and the voltammetric study. The working electrode (Hg) had 12.8 cm^2 in contact with the solution, and the reference electrode was a saturated calomel electrode. The potential of the working electrode was controlled with the EG&G PAR Model 173 potentiostat, and the triangular signal was provided by the EG&G PAR Model 175 programmer. The voltammograms were recorded on the EG&G PAR Model RE 0074 X-Y recorder with the aid of the EG&G PAR Model 176 current-to-voltage converter. The analyses of the solutions were done with the Perkin Elmer Model 403 spectrophotometer. The mass spectrographic analysis of the salt was done by the Northern Analytical Laboratory.

The salt bridges communicating the reference and counterelectrodes with the cell were filled with solutions of pure KCl at the same concentration as that of the KCl contained in the cell.

Each of the voltammograms was obtained using 10 ml of solution. The scan rate utilized in all the voltammograms was 200 mV/s. All potentials are reported *vs.* the saturated calomel electrode.

Results

In order to fully appreciate the effect produced by the impurity, some voltammograms of pure KCl solutions were obtained. Curve A of Fig. 1 shows that the mercury oxidation is already noticeable at 0.02V and the reduction of K^+ is initiated approximately at -1.85V , approximately 0.5V above the value quoted by Bard and Faulkner (20). Curve B shows the response of the solution over a wider potential range. In this figure it can be seen that the anodic reaction



is reversible, while the cathodic reaction is almost irreversible. Reeves *et al.* (24) found that the irreversibility of this reaction is due not to the reduction of K^+

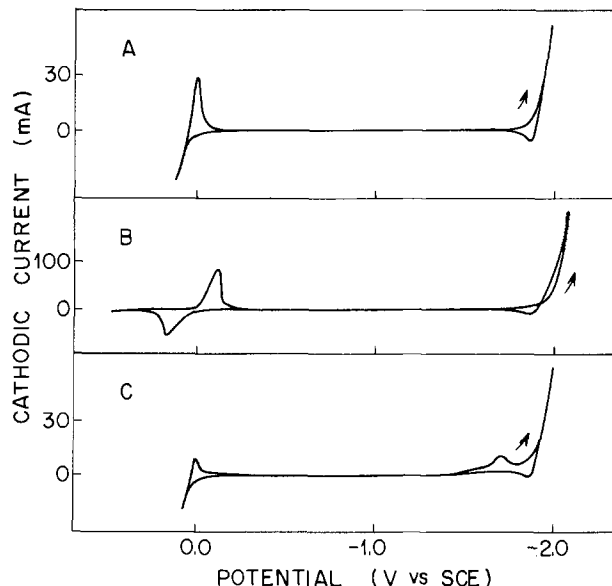
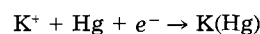
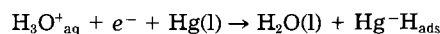


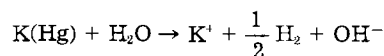
Fig. 1. Voltammograms of solutions containing: 2M KCl (A), 2M KCl (B), 2M KCl with 0.2 mM $MnCl_2$ (C).



which is a reversible reaction, but rather to the evolution of hydrogen



which is a very irreversible reaction. They also found that the reduction of K^+ is accompanied by a second, irreversible reduction process, attributed to the reduction of water



The effect of adding some Mn^{2+} ions to the solution was then studied. Curve C of Fig. 1 shows the voltammogram of a solution containing 2M KCl and 0.2 mM $MnCl_2$. It confirms that Mn^{2+} is reduced at a potential less negative than that of K^+ , as was already known (21), and shows that this reaction is irreversible.

To observe in greater detail the reduction of Mn^{2+} , 4M and 2M KCl solutions were prepared containing different concentrations of manganese. In Fig. 2 and 3, the voltammograms of these solutions are shown. It can be seen that two waves, situated around -1.63 and -1.74V , respectively, are produced. Curve A of Fig. 4 shows that the height i_p^+ of the first of these waves depends linearly on the concentration C_m of manganese and is independent of the concentration C_p of potassium. This behavior indicates that this wave is due to a reaction controlled by diffusion, the type usually found in stationary electrode polarography (20-22). On the other hand, the height i_p^- of the second wave, measured from the potential axis as a

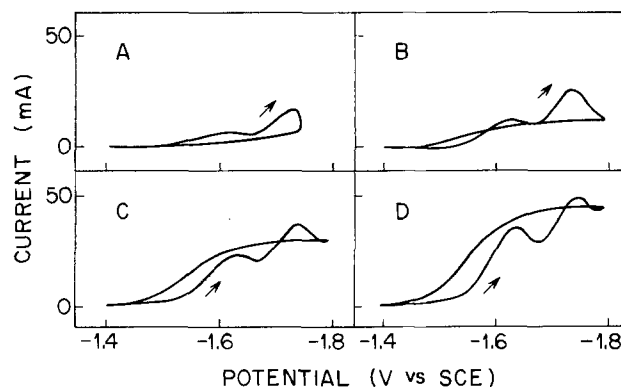


Fig. 2. Voltammograms of 4M KCl solutions containing: 0.4 mM $MnCl_2$ (A), 1 mM $MnCl_2$ (B), 2 mM $MnCl_2$ (C), and 3 mM $MnCl_2$ (D).

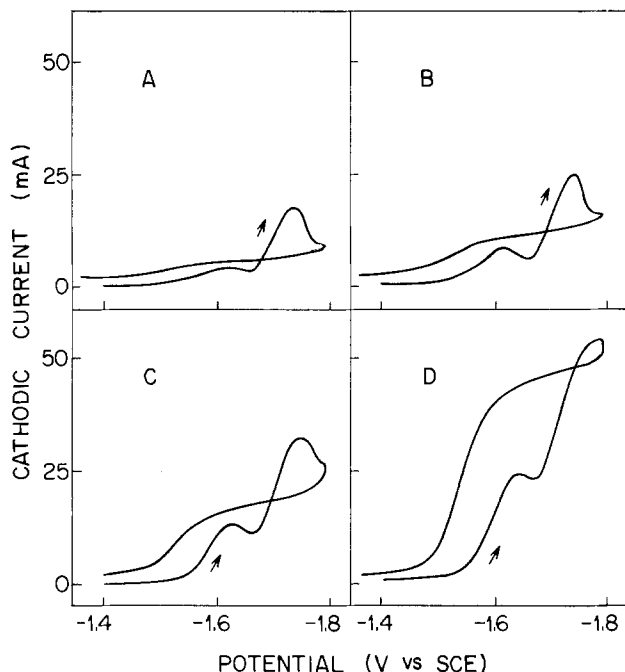


Fig. 3. Voltammograms of 2M KCl solutions containing 0.2 mM MnCl₂ (A), 0.5 mM MnCl₂ (B), 1 mM MnCl₂ (C), and 2 mM MnCl₂ (D).

base line, exhibits a different behavior. The dotted lines of Fig. 4 show that i_p^- follows approximately straight lines as C_m increases, but the slopes of these lines depend on C_p .

The voltammograms of Fig. 2 and 3 also show that the current flowing through the cell in the reverse scan of the potential can be higher than the current produced during the forward scan. The comparison of these voltammograms reveals that this effect is accentuated if the ratio C_m/C_p is increased.

The presence of the second wave, the influence of C_p on the value of i_p^- , and the slow decay of the current during the reverse scan, must be the consequences of a second reaction involving manganese. The mechanism of this reaction will not be investigated in this communication.

Having observed some of the characteristics of the cathodic reaction, the purification of the solution was studied.

In the first place, a cyclic voltammetry of a solution containing 4M KCl and 4 mM MnCl₂ was performed. The potential of the mercury cathode was linearly varied from -1.4 to -1.8V and vice versa, at scan rate of 200 mV/s. The electrolysis was maintained for 90 cycles. In Fig. 5, the voltammograms of some of the cycles can be seen, showing that the amount of manganese gradually decreases.

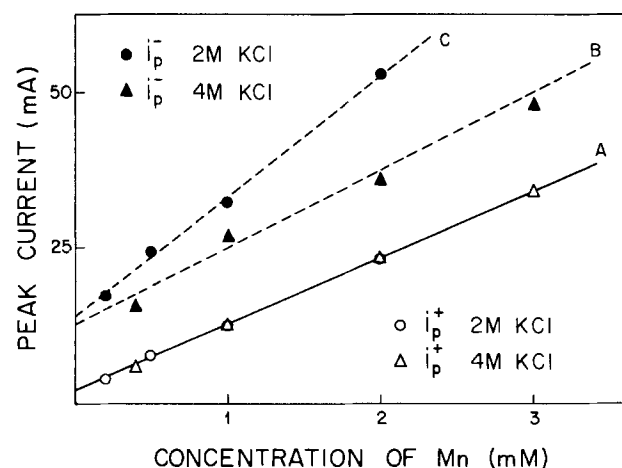


Fig. 4. Variation of i_p^+ and i_p^- with the concentrations of Mn and KCl.

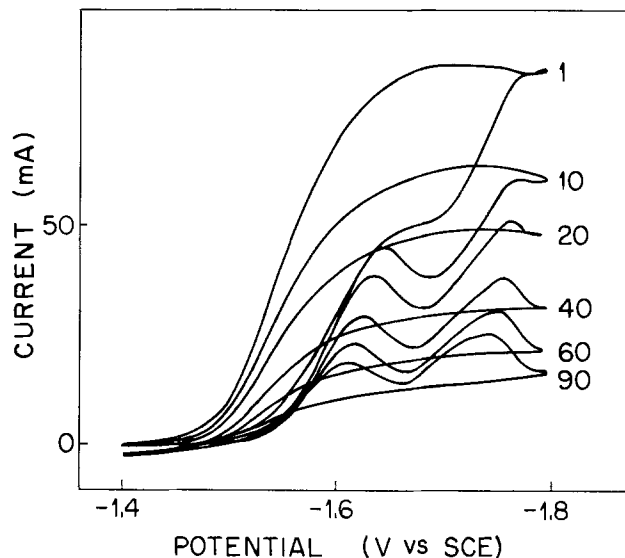


Fig. 5. Cyclic voltammetry of a solution containing 4M KCl and 4 mM MnCl₂. The numbers of the cycles are indicated in each case.

The analysis of the solution before and after the electrolysis indicated that the concentration of manganese decreased from 224 to 77 ppm.

Next, an electrolysis using agitation was performed. The solution contained 2M KCl and 2 mM MnCl₂, and was electrolyzed for 20 min with the potential of mercury fixed at -1.85V. The analysis of the solution indicated that the concentration of manganese decreased from 112.5 to 0.4 ppm. This result proves the feasibility of this method for purifying KCl contaminated with Mn. The net charge transferred during the electrolysis was nearly twice the charge of the manganese ions eliminated from the solution. This indicates that the current efficiency of this purification process is approximately 50%.

Finally, 20 ml of a solution containing 2M KCl and 2 mM MnCl₂ were electrolyzed for 1h. After the electrolysis, the solution was filtered through a 1.2 μ m millipore filter, and the water was evaporated to recover the salt contained in the solution. A mass spectrographic analysis of this salt indicated that the concentration of Mn atoms was 0.02 ppm.

Acknowledgments

The authors wish to thank M. C. Garza for the analysis of the solutions and E. Camarillo for his valuable comments and suggestions.

Manuscript submitted Dec. 17, 1984; revised manuscript received March 2, 1985.

Universidad Nacional Autónoma assisted in meeting the publication costs of this article.

REFERENCES

1. E. J. Botwick and D. B. Smith, C. A., **75** (4), 29399w (1971); Pat. DE 2051725, Germany Offen. (1971).
2. J. T. De Souza, *ibid.*, **82** (20), 127108q (1974); Pat. ZA 7305564, South Africa (1974).
3. I. I. Sirenko, Yu. A. Tarasenko, and Z. A. Krasnova, *Khim. Prom-St. (Moscow)*, **1**, 37 (1975).
4. C.-J. Chia, C. A., **84** (10) 66966k (1975); Pat. DE 2522509, Germany Offen. (1975).
5. M. Seko, H. Ono, and R. Takemura, *ibid.*, **85** (22), 168892w (1976); Pat. JP 7686100, Japan (1976).
6. G. Hoffmann, H. Kaden, and H. Hofmann, *J. Chem. Technol. (Leipzig)*, **28**, 734 (1976).
7. H. Ueshima and T. Kudo, C. A., **88** (26), 200009p (1978); Pat. JP 7805099, Japan (1978).
8. K. Miura and T. Hamano, *ibid.*, **90** (14), 112152r (1978); Pat. JP 78137097, Japan (1978).
9. Sh. Ogawa, T. Nishimori, and T. Kanke, *ibid.*, **90** (16), 124036u (1978); Pat. DE 2816772, Germany Offen. (1978).
10. C. E. Kisilinskaya, Y. A. Sheka, W. A. Trikhleb, I.

- Denisova, and Yu. A. Tarasenko, *Khim. Tekhnol. (Kiev)*, **2**, 9 (1979).
11. H. Ueshima and H. Suzuki, *C. A.*, **91** (2), 11385j (1978); Pat. JP 7902998, Japan (1979).
 12. H. Nakata, and Y. Chiba, *ibid.*, **91**, (6), 46449k (1978); Pat. JP 78149197, Japan (1978).
 13. Y. Kihara, S. Odanaka, and Sh. Miyake, *ibid.*, **91** (14), 114519k (1979); Pat. JP 7980296, Japan (1979).
 14. K. Ikawa, M. Ogai, and M. Kikuchi, *ibid.*, **91** (18), 148548j (1979); Pat. JP 7978398, Japan (1979).
 15. W. B. Darlington, *ibid.*, **92**, (4), 31044w (1979); Pat. DE 2916344, Germany Offen. (1979).
 16. Y. Iwai, A. Ito, and T. Okazaki, *ibid.*, **92** (20), 171629r (1980); Pat. JP 8015926, Japan (1980).
 17. D. Bergner and K. Hannesen, *ibid.*, **93** (8), 83692w (1980); Pat. DE 2854543, Germany Offen. (1980).
 18. J. M. French and I. V. Kadija, *ibid.*, **93** (8), 83697b (1980); Pat. US 4207152, United States (1980).
 19. M. Rosen, H. H. Bauer, and P. Elving, *This Journal*, **117**, 878 (1970).
 20. A. J. Bard and L. R. Faulkner, "Electrochemical Methods," Chap. 1 (p. 6), John Wiley and Sons, New York (1980).
 21. H. Matsuda and Y. Ayabe, *Z. Elektrochem.*, **59**, 494 (1955).
 22. R. S. Nicholson and I. Shain, *Anal. Chem.*, **36**, 706 (1964).
 23. R. H. Wopschall and I. Shain, *ibid.*, **39**, 1514 (1967).
 24. R. M. Reeves, M. Sluyters-Rehback, and J. H. Sluyters, *J. Electroanal. Chem.*, **34**, 55, 69 (1972); *ibid.*, **36**, 101, 287 (1972).

Electrochemical Activation of Prothrombin on Platinum Electrode

H. Durliat, C. Davet, and M. Comtat*

Laboratoire de chimie physique et électrochimie, UA no. 192, Université Paul Sabatier, Toulouse, France

ABSTRACT

When a solution of prothrombin in 0.15M NaCl is put in contact for 10 min with a platinum electrode held at a given potential (between 1.15 and 1.35V *vs.* NHE), it may react with a chromogenic substrate specific to thrombin. A characteristic band of this molecule appears on electrophoresis gel. Moreover, this electrochemically treated solution induces the clotting of a fibrinogen solution in which an immunoenzymatic assay allows the identification of fibrinopeptide A. The results are very dependent on the potential and the surface state of the electrode. For instance, the application of high potentials greater than 1.45V leads to a splitting of the prothrombin molecules into many fragments without any particular biological activity. However, an electrode modified by thrombin adsorption before the application of potential allows the specific splitting of prothrombin to thrombin. Further experiments have shown that it is possible to diminish the enzymatic activity of thrombin solutions under specific conditions of potential (0.35V) without splitting the molecules and that linear sweep voltammetry modifies only the intrinsic pathway of coagulation when carried out on human platelet-free plasma.

Some electrochemical experiments related to the interfaces between metals and plasma or coagulation protein solutions are described in the literature. These studies were carried out to explain facts observed during experiments about blood compatibility with various materials. For example, metals and alloys immersed in circulating blood or in plasma do not induce coagulation when their potential at zero current is negative with respect to a normal hydrogen electrode (NHE) (1, 2). Moreover, metals having a positive potential at zero current *vs.* NHE in blood, but maintained at a negative potential by means of a direct or alternating current, become nonthrombogenic (3, 4). Two examples widely cited are ac polarization of copper, which leads to the occurrence of copper oxides or complexes, and the polarization behavior of titanium alloy (Ti₆Al₄V). The positive spontaneous potentials of these alloys become negative, and thrombosis no longer occurs. Furthermore, the materials chosen to make cardiac valves, sometimes on the basis of the evolution with time of open-circuit potentials, are often cobalt and titanium alloys (5, 6). Physical and chemical justifications of these observations are very difficult because of the complexity of the biological phenomena and the lack of a satisfactory explanation of these experimental results (7, 8).

The electrochemical study of the behavior of coagulation factors in contact with metals may provide an explanation for these phenomena. But although the systems are simpler than the blood-metallic valve interface, the conclusions are not yet clear.

The changes observed in the voltammograms when prothrombin, thrombin, or fibrinogen are present in solution (9-11) are difficult to identify. Indeed, they can be attributed either to adsorption phenomena at lower concentrations or to charge transfer at higher concentrations.

With a fibrinogen solution, optical and electrochemical methods were used (10, 12, 13) to obtain information regarding the charge-transfer reaction of the proteins and to suggest a classification of semiconductor materials according to their thrombogenicity (14).

The electrochemical transformation of bovin prothrombin (9) on a platinum electrode is a hypothesis based only on the modification of the clotting time of a solution of fibrinogen in which electrolyzed prothrombin was added. Coagulation times diminished when the applied potential was greater than 0.45V, and the higher the potential the faster the clotting time. For example, a time of 27h when the potential was 0.95V become 9.5h when the potential was 1.45V.

It should be noted that these molecules did not act as electronic relays in the biological process. Heterogeneous electron transfer with a metal may eventually occur with oxidation of terminal amino acids or the reduction of disulfide bridges. All of the commonly used potential ranges, however (9, 11), appeared to be insufficient to cause this kind of electrochemical reaction which would probably lead to products with no noticeable biological activity.

We tried to work on this problem because the arguments in favor of the electrochemical transformation of prothrombin in thrombin were not satisfactory. New methods to improve the purity of the prothrombin solution, commercialization of chromogenic substrates specific to thrombin, and immunoassay of fibrinopeptide A were very helpful in carrying out all our experiments.

On the basis of the plasmatic coagulation scheme, particularly for the activation of prothrombin and for fibrinofornation (15-19), we were able to define an experimental strategy designed to identify thrombin in electrochemically treated prothrombin solution. Two tests related directly to the solutions in which an electrode, at a given potential, was kept: gel electrophoresis for the identification of the molecular mass of the various molecules present in the sample, and the use of chromogenic substrates specific to thrombin. Two additional tests were designed to measure the coagulation times of fibrinogen solutions mixed with electrochemically treated prothrombin solutions and to identify by an immunoenzymatic assay the fibrinopeptide A released during coagulation. At present, these four methods are all

* Electrochemical Society Active Member.

that exist for the identification of thrombin and the estimation of its biological activity.

Experimental Procedure

Reagents and tests of coagulation.—All the electrochemical experiments were carried out in 0.15M NaCl solution prepared from analytical-grade reagents and doubly distilled water at temperature of 25°C. Fibrinogen was from Kabi Diagnostica. Human prothrombin was from Sigma or was extracted and purified in the laboratory according to the method described in Ref. (20); its purity was checked by gel electrophoresis (21).

The method used to assay prothrombin was the measure of the clotting time at 37°C of a sample to which all the coagulation factors were added except prothrombin.

The results are given in percentage of prothrombin with respect to a test plasma. For each sample, a straight line was obtained, plotting the clotting time against the logarithm of the reciprocal of the dilutions of the samples. The prothrombin concentration of the test plasma, a pool of plasmas from different blood donors assumed to be in good health, was assumed to be equal to 100% (22).

The thrombin from Sigma was not of high purity (three bands on gel electrophoresis), but it was used without further purification; its enzymatic activity was measured either by the clotting time of a 0.2% fibrinogen solution or by the reaction on a chromogenic specific substrate (from Diagnostica Stago) Tos-Gly-Pro-Arg-pNA, where pNA is paranitraniline. The principle of this assay is based on the amidase activity of thrombin to release yellow paranitraniline, which absorbs light at 405 nm (23).

Electrophoresis was carried out in polyacrylamide gel with sodium dodecyl sulfate (21). A mixture of five proteins of molecular weight in the range of 12,000-78,000 allowed calibration of the gel under our experimental conditions.

Reagents necessary to perform all the coagulation tests were from Diagnostica Stago.

For some experiments, platelet-free plasma was used. The Kaolin Cephalin (KC) clotting time detects alteration of factors from the intrinsic system (22). In this test, coagulation was induced by recalcifying a sample in the presence of a platelet substitute and of a suspension of Kaolin, which activated the Hageman factor.

A deficiency in the extrinsic pathway was detected with the Quick time, comparing the coagulation time of the analyzed plasma in the presence of calcium thromboplastin to the coagulation time of a reference plasma (22).

Controlled potential experiments and cyclic voltammetry were performed using a Tacussel Model PRT 20-2X potentiostat and a Tacussel Model GSTP 2 function generator. The voltammograms were recorded using a Sefram X-Y recorder (Model Luxytrace).

A cell with two compartments was used: each compartment received 0.4 cm³ of solution. The working electrode was a platinum minigrad or a platinum disk of 2 mm diam. The reference electrode was a saturated calomel electrode, with a Luggin capillary filled with 0.15M NaCl solution. Both these electrodes were separated from the platinum auxiliary electrode by a low porosity glass frit. All the potentials were expressed *vs.* the normal hydrogen electrode.

All spectrophotometric measurements were carried out with a Beckman spectrophotometer (Model Acta IV).

Cyclic voltammetry experiments did not provide satisfactory results regarding the behavior of thrombin and prothrombin at the metal-solution interface. Voltammograms obtained at a sweep rate of 0.05 V/s between -0.55 and 1.25V with thrombin concentrations of about 4.16 units NIH¹ were identical to those obtained from the 0.15M NaCl solution. The results were the same with physiological concentrations of prothrombin. In this case,

¹Approximately 100 NIH units of thrombin correspond to the amount of thrombin obtained when physiological concentration prothrombin is completely transformed.

however, unlike the results observed with bovine prothrombin (9), changes in the curves were observed only after 5h of sweeping. These results are difficult to explain. They demonstrated particularly a decrease in intensity in the platinum oxide reduction zone, due probably to adsorption phenomena.

Several works have already treated this adsorption process by optical and electrochemical methods (24-25). The protein adsorption process on platinum is especially complex in the environment we used, as it competes with the adsorption of chloride and hydroxyl ions (26). It should be noted that with the potential limits chosen on the voltammograms no oxidation or reduction of the solvent that could modify the pH occurred.

Cyclic voltammetry, conducted on platelet-free plasma, led to a high oxidation current near 0.9V, noninterpreted. What is important is that the intrinsic pathway of the coagulation was altered without affecting the extrinsic pathway (the usual K.C. clotting time of 44s became 52s). Additionally, a very sticky, yellow film appeared on the electrode, confirming the significance of the adsorption phenomena in these systems. This film did not appear with platinum in contact with the plasma when there was no electric field. Controlled potential experiments were carried out from 5 to 20 min in 0.4 cm³ of solution. The potential was maintained at a value in the range of -0.40 to +1.75V, specified for each experiment. The results were always compared with those of a control experiment, which used nonpolarized platinum in contact with the same solution for the same length of time.

Results are presented in Fig. 1. With thrombin, the application of potentials lower than 0.05V for 10 min with 25 NIH units per cubic centimeter solutions produced a solution which, when mixed with chromogenic substrate, no longer led to a release of paranitraniline. Experiments conducted with potentials between 0.00 and 1.30V demonstrated a conservation of the enzymatic activity of thrombin. This activity disappeared completely with potentials greater than 1.35V.

For prothrombin, the use of potentials lower than 1.15V caused no change in detectable molecules using the four tests at our disposal. However, a potential of +1.25V applied for 10 min caused the occurrence of new molecular fragments in the solution. The molecular weights determined by electrophoresis were of about 10,000, 20,000, 40,000, 50,000, and 70,000, respectively (Fig. 2). One band corresponded to the remaining prothrombin; another corresponded to a thrombin-like molecule. From time to time, the solution had a thrombin activity similar to that observed physiologically. The clotting time and chromogenic tests indicated that, at best, 10% of prothrombin was transformed into thrombin.

Potentials higher than 1.35V induced a wild splitting of prothrombin molecules. This phenomenon can have a

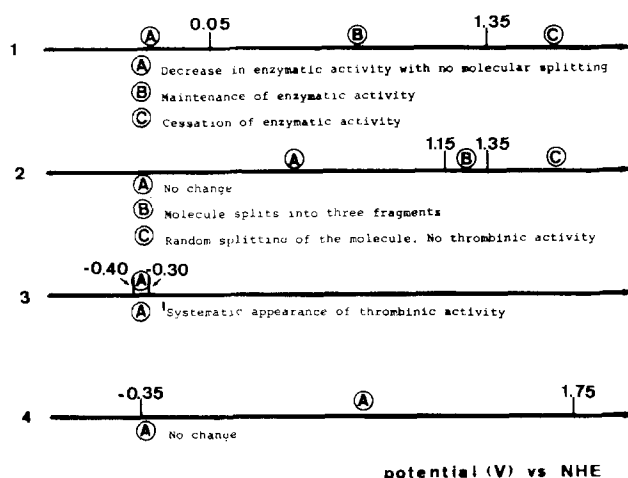


Fig. 1. Summary for various potentials applied for 15 min to different solutions. 1: Thrombin. 2: Prothrombin. 3: Prothrombin, platinum electrode covered with thrombin. 4: Platelet-free plasma.

number of causes (occurrence of chloride complexes of platinum, modification of the pH).

Other experiments were performed with electrodes modified by thrombin adsorption. First, in open circuit, the electrode was dipped for 5 min into a thrombin solution (250 unit/cm³). Then it was thoroughly rinsed in 0.15M NaCl solution until the cleaning solution had no enzymatic activity. A potential of -0.35V was then applied for 10 min to a prothrombin solution. In the previous experiments under the same electrical conditions, no modification of the molecule occurred. Here, however, three bands of molecular weights 52,000, 39,000, and 29,000 appeared on the electrophoresis gel. Moreover, the chromogenic substrate test demonstrated the occurrence of thrombin from the splitting of about 10% of the prothrombin molecules. No transformation occurred if the modified electrode was immersed into a prothrombin solution in an open-circuit experiment.

These experiments are reproducible, and it is possible to assay the fibrinopeptide A in a fibrinogen solution where electrochemically treated prothrombin was added. When the modified electrode was maintained at a potential of -0.35V in a 0.15M NaCl solution for various times before the electrolysis of prothrombin was carried out, it appeared that the higher the time the less the amount of thrombin formed in the electrical field.

With platelet-free plasma, the application of a variety of potentials in the range of -0.35 to +1.75V for 15 min resulted in no modification of the coagulation factors that can be assayed by clotting time tests. Nevertheless, application of potential equal to 1.25V for 3h lowered by 30% the fibrinogen concentration without any decrease in the prothrombin concentration.

Discussion

Depending on the potentials applied to the platinum electrode, it is possible to: (i) inhibit thrombin (a decrease in thrombinic activity was observed, with no break in the molecule, for potentials lower than 0.05V), (ii) split the prothrombin molecule into multiple fragments (potentials greater than 1.45V), and (iii) split the prothrombin molecule (with potentials between 1.5 and 1.35V); the resulting fragments will have molecular weights equal to those of the molecules obtained during enzymatic activation, by Stuart factor, particularly to thrombin. However, the thrombinic activity, deduced from measurements made on chromogenic substrates and immunoenzymatic assays of fibrinopeptide A, does not appear with regularity.

A similar splitting occurred with a potential of -0.35V when the platinum electrode was covered with adsorbed thrombin. In this case, the appearance of thrombinic activity was systematically reproducible.

In every case, the shape of the voltammogram and the range of potentials used (while the latter was too limited to cause the oxidation of amino acids or a reduction of disulfur bridges) demonstrate that the results were not caused by an electronic transfer. At the present stage of our research, we can only hazard some hypothesis to explain these facts.

With thrombin, positively charged at working pH, the molecule is attracted by an electrode with a sufficiently negative charge. It is then subjected to an intense electrical field, which causes structural modifications with a loss of enzymatic activity.

With prothrombin, at high potentials, the appearance on the surface of the electrode of platinum chloride complexes was noticed. These may play some role as catalyst in the hydrolysis of peptidic bonds. With lower potentials, we noticed biomimetic splitting of the molecule in the electric field. This may be due to a variety of causes. It may be the result of the molecules being adsorbed onto the electrode in such a way that some peptidic bonds are weakened and are therefore more sensitive to hydrolysis. This would be an electrocatalytic phenomenon in the hydrolysis of the peptide bond in the electrical field. Such a phenomenon has, to the best of our knowledge, never been described for biological molecules. It is comparable

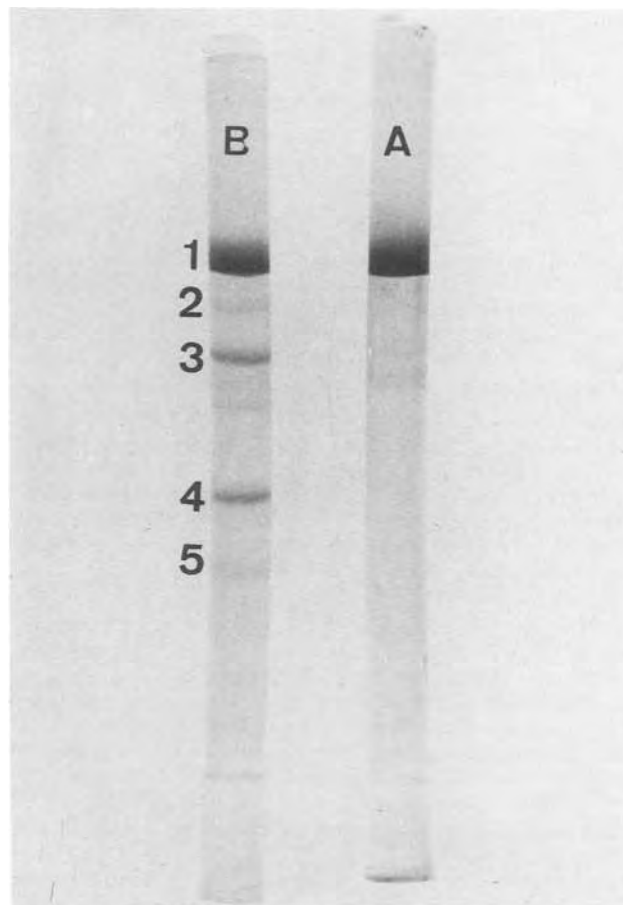


Fig. 2. Electrophoresis in polyacrylamide gel. A: a prothrombin solution. B: a prothrombin solution put in contact with a platinum electrode held at 1.2V during 10 mn. The molecular weights corresponding to the various bands are as follows. 1: 70,000. 2: 50,000. 3: 40,000. 4: 20,000. 5: 10,000.

only to the hydrolysis of ethylacetate (27). It should not come as a surprise that the electrical fields weakened bonds which, in a biological process, are more sensitive to hydrolysis. If a 10% thrombin conversion can be reached, it is clear that this surface process creates nonadsorbed products on the electrodes which remain free for the adsorption of new prothrombin molecules.

The fact that the molecules thus formed are not consistently active leads us to assume a transformation of the structure of most of the prothrombin molecules in the electrical field. We could, of course, imagine that the electrical field activated another coagulation factor present in the prothrombin solution, itself capable of activating the prothrombin (*i.e.*, Stuart factor). In this case, there would be no reason to find a molecule similar to thrombin but having no enzymatic activity.

When the electrode, whose surface was first modified by the adsorption of thrombin, is brought to a potential of -0.35V, the negatively charged prothrombin molecule can reach the electrode because of the electrostatic interactions with thrombin. Under these conditions of potential, the molecule retains its structure, which explains the appearance of enzymatic activity. It is not thrombin which acts to split the molecule in an autocatalytic phenomenon, since without an electrical field there is no reaction.

The role of electrochemistry must also be emphasized in modifying the nature of platelet-free plasma (cyclic voltammetry induces an impairment of the intrinsic pathway, and the application of potentials near 1.25V for 3h caused the fibrinogen level to fall without producing a corresponding decrease in prothrombin).

Our experimental results have not all been satisfactorily explained. It is, however, necessary to emphasize their importance in the field of the fundamental biology of co-

agulation (they may suggest the existence of an electrochemical coagulation pathway). Ultimately, the use of an electrical field may make it possible to inhibit or to activate some factors of coagulation. We should not be too hasty in generalizing or in formulating rules for the choice of hemocompatible materials or for explaining their properties. In fact, it is enough to put physiological concentrations of albumin in contact with an electrode to protect prothrombin from the action of the electrical field.

Acknowledgments

This research was supported in part by the CNRS (ATP Matériaux hémocompatibles). We are deeply grateful to the late Professor F. Josso for the initiation of this work and his encouragement. The authors would like to thank Professor M. Jozefowicz (Paris Nord) and Dr. R. Eloy (Lyon) for helpful discussions, Dr. M. C. Boffa (Paris) for generous gift of prothrombin solutions, Professor B. Boneu and A. Baudras (Toulouse) for help in extraction of prothrombin, and Dr. J. L. Sérès (Lacq) for the fibrinopeptide A analysis.

Manuscript submitted Sept. 12, 1984; revised manuscript received March 4, 1985.

Université Paul Satatier assisted in meeting the publication costs of this article.

REFERENCES

- P. S. Chopra, S. Srinivasan, T. Lucas, and P. N. Sawyer, *Nature*, **215**, 1494 (1967).
- S. D. Bruck, *Biomat. Med. Dev. Art. Org.*, **1**, 79 (1973).
- E. Gileadi, B. Stanczewski, A. Parmiggiani, T. R. Lucas, M. Ranganathan, S. Srinivasan, and P. N. Sawyer, *J. Biomed. Mater. Res.*, **6**, 489 (1972).
- T. R. Lucas, B. Stanczewski, N. Ramasamy, S. Srinivasan, G. W. Kammlott, and P. N. Sawyer, *Biomat. Med. Dev. Art. Org.*, **3**, 215 (1975).
- T. P. Hoar and D. C. Mears, *Proc. R. Soc. London, Ser. A*, **294** 486 (1966).
- N. Ramasamy, B. R. Weiss, B. Stanczewski, and P. N. Sawyer, *This Journal*, **123**, 1662 (1976).
- P. N. Sawyer, "Biophysical Mechanism in Vascular Homeostasis and Intravascular Thrombosis," Appleton Century Crofts (1965).
- E. Findl, in "Modern Aspects of Electrochemistry," Vol. 14, J. O'M. Bockris, B. E. Conway, and R. E. White, Editors, Plenum Press, New York (1982).
- L. Duic, S. Srinivasan, and P. N. Sawyer, *This Journal*, **120**, 348 (1973).
- N. Ramasamy, M. Ranganathan, L. Duic, S. Srinivasan, and P. N. Sawyer, *ibid.*, **120**, 354 (1973).
- S. Srinivasan, L. Duic, N. Ramasamy, P. N. Sawyer, and G. E. Stoner, *Ber. Bunsenges. Gesell.*, **77**, 798 (1973).
- M. Schaldach, *Klin. Wschr.*, 1029 (1975).
- M. Schaldach, R. Thull, P. Baur Schmidt, and R. Blaser, *Ber. Bunsenges. Gesell.*, **77**, 794 (1973).
- P. Baur Schmidt and M. Schaldach, *Med. Biol. Eng. Comput.*, **18**, 496 (1980).
- R. Biggs, "Human Blood Coagulation, Haemostasis and Thrombosis," Blackwell (1976).
- S. S. Shapiro and S. McCord, in "Progress in Haemostasis and Thrombosis," Vol. 4, T. H. Spaeth, Editor, Grune and Stratton (1978).
- J. W. Suttie and C. M. Jackson, *Physiol. Rev.*, **1**, 57 (1977).
- C. M. Jackson, *Br. J. Haemat.*, **1**, 39 (1978).
- G. Murano and R. L. Bick, "Basic Concepts of Haemostasis and Thrombosis," C. R. C. Press, Boca Raton, FL (1980).
- W. Kisiel and D. J. Hanahan, *Biochim. Biophys. Acta*, **304**, 103 (1973).
- W. Kisiel and D. J. Hanahan, *ibid.*, **103**, 304 (1973).
- C. Sultan, G. Priolet, Y. Beuzard, R. Rosa, and F. Josso, "Techniques en Hématologie," Flammarion (1978).
- G. Axelsson, K. Korsan Bengtson, and J. Waldenström, *Thrombos. Haemostas.*, **36**, 517 (1976).
- G. E. Stoner and S. Srinivasan, *J. Phys. Chem.*, **74**, 1088 (1970).
- M. F. Lecompte, J. Clavilier, C. Dode, J. Elion, and I. R. Miller, *J. Electroanal. Chem.*, **163**, 345 (1984).
- D. M. Novack and B. E. Conway, *J. Chem. Soc. Faraday Trans.*, **77**, 2341 (1981).
- A. R. Despic, D. M. Drazic, M. L. Mihailovic, L. L. Lorenc, R. Arzic, and M. Ivic, *J. Electroanal. Chem.*, **100**, 913 (1979).

Doped Polydithienothiophene: A New Cathode-Active Material

Maria Biserni, Annamaria Marinangeli, and Marina Mastragostino

Istituto chimico G. Ciamician, Università degli Studi di Bologna, 40126 Bologna, Italy

ABSTRACT

Films of doped polydithienothiophene, anodically synthesized on Pt or SnO₂-coated Pyrex electrodes in CH₂Cl₂ solution containing the monomer (dithienothiophene) and MX (M⁺ = N(Bu)₄⁺, X⁻ = ClO₄⁻, PF₆⁻) as the supporting salt, are electroactive. These films can be driven repeatedly, in CH₂Cl₂/MX solution, between the doped and the undoped state releasing and storing charges. The coulombs efficiency of the redox process is ca. 100%, and the charge involved is equal to 20% of that involved in the initial electrochemical preparation of the doped polymer. Doped p-DTT/Pt electrodes with high doping level (50%) have a value of V_{oc} of ca. 1V. In the discharge in CH₂Cl₂/MX solution of doped p-DTT/Pt electrodes at constant current density up to 0V, high values of charge are recovered with respect to the stored (40-60% at -2 mA·cm⁻²). All these features of doped p-DTT are attractive and relevant to its application in battery technology. However, doped p-DTT films preserved in CH₂Cl₂/MX solution show the disadvantage of a fast self-discharge (18-100h). This phenomenon is due not to polymer degradation, but to an undoping process, presumably owing to an uncontrolled redox reaction involving the used electrolytic medium.

Recently, much scientific work has been devoted to organic conducting polymers because of the large field of potential applications (as electrode materials of rechargeable batteries or as electro-optic display devices, etc.). The main interest concerns their ability to be switched, by chemical or electrochemical doping, from a neutral (nonconducting) state to an oxidized or reduced conducting state. The electrochemical preparation approach is more attractive than the chemical, because the polymer is produced directly in its conducting oxidized form, a wide selection of counterions being available from the electrolyte. The variety of aromatic compounds which have been found to undergo electrochemical polymeriza-

tion [pyrroles (1), thiophene (2), furan (2), carbazoles (3)] demonstrates the facility of this approach. Diaz *et al.* (4) indicate that the electrosynthesis of the polypyrrole proceeds via the oxidation of pyrrole with a mechanism involving a series of oxidation and deprotonation steps. The electrochemical stoichiometry is 2.2-2.4 electron/pyrrole ring, where 2 electron/pyrrole ring is involved in the polymer formation. The extra charge (0.2-0.4 electrons) accounts for the concurrent oxidation of the polymer which has a lower oxidation potential than the monomer.

In the present paper, we report a few electrochemical properties of doped polydithieno(3,2-b:2',3'-d)thiophene (shown in Fig. 1) relevant to their applications in battery

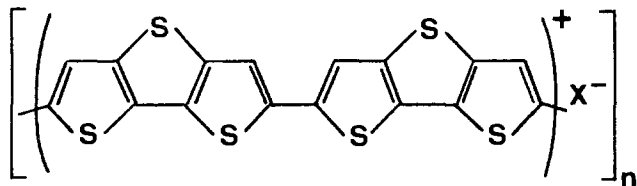


Fig. 1. Doped polydithieno(3,2-b:2',3'-d')thiophene (p-DDT), where $X^- = \text{ClO}_4^-, \text{PF}_6^-$.

technology. This material is a new electrogenerated conducting polymer (5).

Experimental

The monomer dithieno(3,2-b:2',3'-d')thiophene (DDT) was synthesized following the de Jong-Janssen method (6). Doped p-DDT was electrochemically prepared at controlled current and at controlled potential, on Pt and SnO_2 -coated Pyrex electrodes, in degassed and anhydrous ($[\text{H}_2\text{O}] < 0.1 \text{ mM}$) electrolytic medium formed by methylene chloride (CH_2Cl_2), the monomer 2 mM, and the supporting salt:tetrabutylammoniumperchlorate (TBAP) 0.1M. Tetrabutylammoniumhexafluorophosphate (TBAFP) 0.1M was also used as electrolyte. The cell had two separated compartments. Pt and saturated calomel electrode (SCE), with suitable liquid junction, were used as counter and reference electrodes. All the potential data are referred to SCE. The solvent CH_2Cl_2 (RPE, C. Erba) was purified by double distillation and followed by dehydration with activated molecular sieves (4A Pellets, 4 mm, C. Erba) under N_2 . TBAP "purum" Fluka was crystallized from methanol before use. TBAFP was prepared following the method of Lind *et al.* (7). All electrochemical experiments were performed with an Electrochemolab AMEL apparatus at 288 K. The spectroscopical measurements in visible, near IR were made utilizing a Perkin Elmer Model 323 Spectrophotometer.

Results and Discussion

Polydithienothiophene (p-DDT) was generated in its doped state with different anions ($X^- = \text{ClO}_4^-, \text{PF}_6^-$) typically at a constant current of $0.4 \text{ mA}\cdot\text{cm}^{-2}$ (the charge potential value was *ca.* 1.3V). The electrode surface becomes quickly covered by a black, adherent film of doped p-DDT. The thickness of the film was controlled by the electrolysis time and varied between $0.1 \mu\text{m}$ and 1 mm. Films of *ca.* $0.1 \mu\text{m}$ thick were grown by passing $13 \text{ mC}\cdot\text{cm}^{-2}$. The elemental analysis of these polymers indicates that the ratio of DDT units to X^- anions is 2:1; the conductivity measurements of these polymers gave σ values ranging from 3.10^{-3} to $1.10^{-2} \Omega^{-1}\cdot\text{cm}^{-1}$ (5).

Electrochemical reduction of the doped polymers to an undoped state was tested by cyclic voltammetry. Figures 2 and 3 report ten continuous cyclic voltammograms at Pt electrode in a solution of DDT in CH_2Cl_2 with ClO_4^- and PF_6^- , respectively, as anion of electrolyte. These figures show that the monomer oxidation starts at 1.2V with the growth on the electrode surface of the doped polymer. This polymer is reduced and, then, in the following cycle, oxidized at lower potentials than that of monomer oxidation. p-DDT films produced by sweeping continuously were transferred to an electrolytic medium not involving DDT and cycled between -0.5 and $+1.7\text{V}$ at different sweep rates ($20\text{--}200 \text{ mV}\cdot\text{s}^{-1}$). Linear relationships between the anodic and the cathodic peak currents and the sweep rate were found as expected for the reaction of surface localized material. The redox reaction is accompanied by color change, since the reduced film is red and the oxidized is black.

The electroreduction of the doped polymer produces the undoped film, and the electro-oxidation of this latter, in $\text{CH}_2\text{Cl}_2/\text{TBAP}$ solution, regenerates the doped polymer, as demonstrated by the absorption spectra visible near IR recorded during the electrochemical cycle. Figure 4 shows the spectrum of the polymer film electro-synthesized, at $I = 0.3 \text{ mA}\cdot\text{cm}^{-2}$, on SnO_2 -coated Pyrex electrode

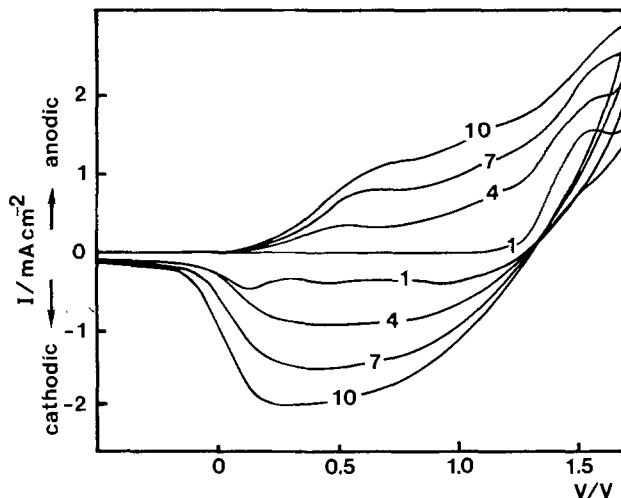


Fig. 2. Continuous cyclic voltammograms ($v = 0.2 \text{ V/s}$, from -0.5 to 1.7V and reverse) on Pt in an electrolytic medium (CH_2Cl_2 , TBAP 0.1M) involving DDT 2 mM.

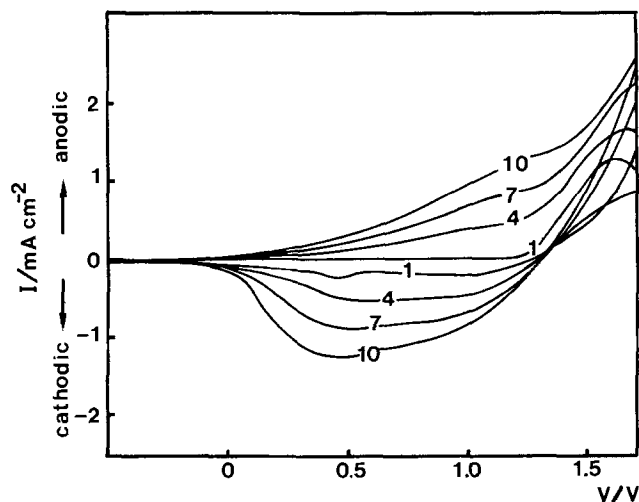


Fig. 3. Continuous cyclic voltammograms ($v = 0.2 \text{ V/s}$, from -0.5 to 1.7V and reverse) on Pt in an electrolytic medium (CH_2Cl_2 , TBAFP 0.1M) involving DDT 2 mM.

with $Q = 47 \text{ mC}\cdot\text{cm}^{-2}$ and the spectrum of the film after its total electrochemical reduction ($Q_{\text{red}} = 9.4 \text{ mC}\cdot\text{cm}^{-2}$ at $I = -0.1 \text{ mA}\cdot\text{cm}^{-2}$). Figure 4 also shows a series of spectra taken during the gradual electrochemical reoxidation of the film in $\text{CH}_2\text{Cl}_2/\text{TBAP}$ solution at $I = 0.1 \text{ mA}\cdot\text{cm}^{-2}$ and

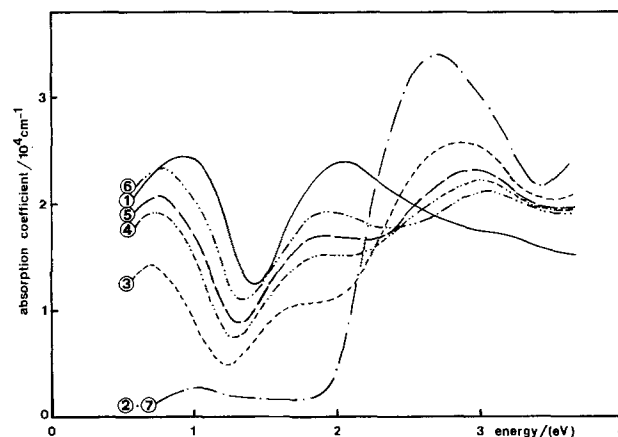


Fig. 4. Series of absorption spectra. 1: Electro-synthesized doped p-DDT (with ClO_4^-). 2: Undoped p-DDT. 3-6: Gradually doped p-DDT (with ClO_4^-) during electrochemical reoxidation. 7: Electrochemically regenerated undoped p-DDT.

the spectrum of the fully rereduced film. The band at higher energy in the visible region is characteristic of the undoped polymer (π - π^* transition), and the two bands at lower energy in the near-IR region are characteristic of the doped polymer. The gradual evolution from the undoped to doped state is evidenced by the intensity variation of the characteristic bands with shift of the absorption peaks toward higher energy. A similar behavior has been observed in polythiophene (8), and the interpretation of the spectra bands is referred to Ref. (8). In our case, however, unlike highly doped polythiophene, the presence of a single broad band in the low energy region, which is characteristic of the free-carrier spectrum of the metallic state, was not observed. The redox process is a regenerative process which does not change the material; in fact, identical spectra were obtained after the first and second total reduction.

Figures 5 and 6 show the first and one-hundredth of the series of continuous cyclic voltammograms of

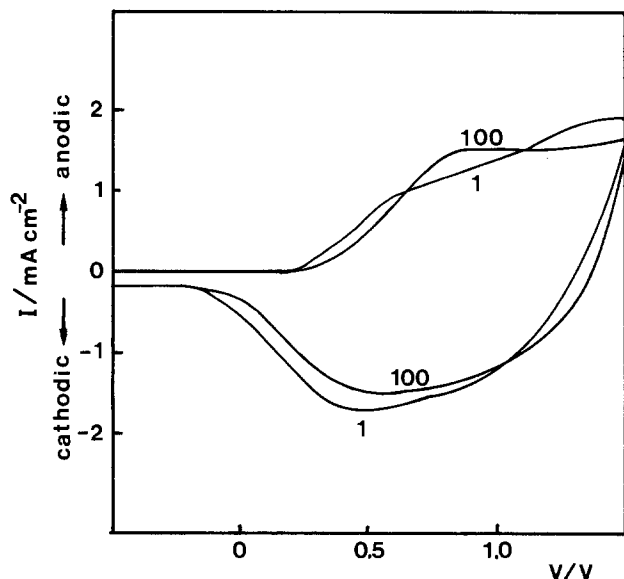


Fig. 5. Cyclic voltammograms of a p-DTT/Pt film in $\text{CH}_2\text{Cl}_2/\text{TBAP}$ 0.1M; the first and the one-hundredth cycles ($\nu = 0.2$ V/s, from -0.5 to 1.5 V and reverse). The p-DTT/Pt film has been produced by sweeping continuously (10 cycles, $\nu = 0.2$ V/s, from -0.5 to $+1.7$ V and reverse) in $\text{CH}_2\text{Cl}_2/\text{TBAP}$ 0.1M with DTT 2 mM.

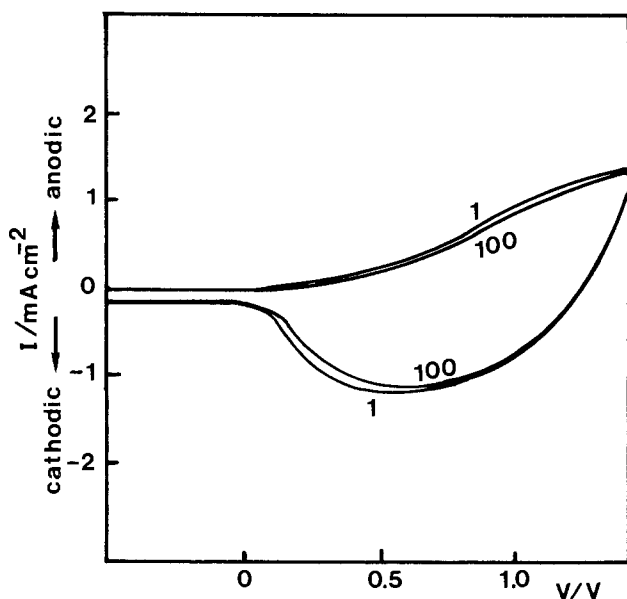


Fig. 6. Cyclic voltammograms of a p-DTT/Pt film in $\text{CH}_2\text{Cl}_2/\text{TBAFB}$ 0.1M; the first and the one-hundredth cycles ($\nu = 0.2$ V/s, from -0.5 to 1.4 V and reverse). The p-DTT/Pt film has been produced by sweeping continuously (10 cycles, $\nu = 0.2$ V/s, from -0.5 to 1.7 V and reverse) in $\text{CH}_2\text{Cl}_2/\text{TBAFB}$ 0.1M with DTT 2 mM.

p-DTT/Pt film in CH_2Cl_2 solution (in absence of DTT). The films are quite stable and can be cycled without evidence of important decomposition over the time range of voltammetric experiments.

The separation and different shape of the oxidation and reduction waves of the polymer show that the redox process is not electrochemically reversible. However, the fact that the film can be repeatedly cycled indicates chemical reversibility of the doping-undoping process. The broadness of the waves suggests that the doping and undoping processes are complex. Presumably, reorganization processes of the polymeric chains are present; similar behavior has been observed with other polymers (9, 10).

Moreover, since the integrated charges under the oxidation and the reduction waves of p-DTT are approximately equal ($Q_{\text{ox}} \approx Q_{\text{red}}$), the coulombic efficiency ($Q_{\text{red}}/Q_{\text{ox}}$) over a cycle of charge-discharge is ca. 100%. These estimates have been made on cyclic voltammograms ($\nu = 20$ mV/s, from 1.4 to -0.5 V and reverse, in $\text{CH}_2\text{Cl}_2/\text{TBAP}$ solution) of several p-DTT films, galvanostatically grown on Pt ($Q = 358$ mC/cm 2). The amount of charge was always ca. 20% of the total charge $Q_{\text{ox}} \approx Q_{\text{red}} \approx 0.2Q$ involved in the preparation of the film. This value is in accord with the charge concentration deducible from the results of elemental analysis of the electrosynthesized polymer, taking into account the fact that, as for polypyrrole (11), 2 electron/DTT unit should be involved in neutral polymer formation.

The same values of doping level of p-DTT (50%) were obtained when the polymer, grown galvanostatically, was exhaustively reduced to the neutral state at controlled potential of 0V in $\text{CH}_2\text{Cl}_2/\text{TBAP}$ solution, as shown in Table I.

The fact that the redox process of the polymer film occurs at a far anodic potential value and that the charge which can be cycled (ca. 20% of that consumed in the initial preparation of the film) is not very diminished after 100 continuous cycles indicates the p-DTT doped as an attractive cathode-active material in battery application.

In order to test the performance of doped p-DTT as cathode-active material, we discharged at different constant currents, in $\text{CH}_2\text{Cl}_2/\text{TPAP}$ solutions, doped p-DTT/Pt films immediately after their electrogeneration.

Figures 7 and 8 show the variation of the electrode potential during electrochemical polymerization, at constant current density ($I = 0.4$ mA/cm 2) (regions A), and during the first discharge of the polymer films at selected constant current densities (regions B).

Table II reports, for two series of experiments with films of different thickness (some of which are shown in Fig. 7 and 8) the charge amounts recovered in the first discharges at different current densities together with the percentage of the charge recovered with respect to that stored in the doped polymer. The point where the discharging potential reached 0V was assumed as the indicator of the discharge completion.

Table III summarizes the coulombic efficiencies of six regenerative cycles of charge-discharge of a p-DTT/Pt electrode at $|I| = 0.4$ mA-cm $^{-2}$ in $\text{CH}_2\text{Cl}_2/\text{TBAP}$ solution. This p-DTT/Pt electrode was obtained by reducing at $I = -0.4$ mA-cm $^{-2}$ with $Q_{\text{red}} = 72$ mC-cm $^{-2}$ a doped film electrosynthesized at $I = 0.4$ mA-cm $^{-2}$ with $Q = 358$ mC-cm $^{-2}$. During the recharge processes up to $Q_{\text{ox}} = 48$ mC-cm $^{-2}$,

Table I. Doping level of electrosynthesized p-DTT

Charge involved in p-DTT synthesis (C/cm 2)	Charge involved in undoping process (C/cm 2)	Percentage doping level
0.358	0.070	48
0.478	0.095	50
0.583	0.124	53
0.750	0.142	47
0.875	0.189	54
3.60	0.780	55
12.1	2.40	47

Table II. Charge recovered, with respect to that stored, in the first discharges at I constant of p-DTT films immediately after preparation

I discharge (mA/cm ²)	$Q = 358$ mC/cm ²		$Q = 717$ mC/cm ²	
	Q_{red} (mC/cm ²)	Percentage charge recovered w.r.t. that stored	Q_{red} (mC/cm ²)	Percentage charge recovered w.r.t. that stored
-0.04	68.1	95		
-0.20	62.3	87	114.5	80
-0.40	56.9	78	111.5	78
-0.80	52.1	73	103.5	72
-2.0	41.2	58	55.7	39
-4.0			39.0	27

Table III. Coulombic efficiency of six charge-discharge regenerative cycles at $I = 0.4$ mA/cm²

Number regenerative cycle	Coulombic efficiency
1	0.75
2	0.66
3	0.72
4	0.68
5	0.63
6	0.68

the electrode potential (under current) increases up to $V_{\text{max}} = 1.15$ V in the same way in all successive cycles. The efficiency values were calculated by assuming the value of 0V of the discharging potential as the indicator of discharge completion (as in Table II). In the present case, however, so as not to accumulate charge in the regenerated active material, the discharge was stopped not at 0V potential, but only when all the stored charge was recovered. The data of Table III show that there are no significant differences of the coulombic efficiencies in the regenerative cycles.

Figure 9 shows the variation of the open-circuit potential *vs.* time of doped p-DTT/Pt electrodes in $\text{CH}_2\text{Cl}_2/\text{TBAP}$ solution. The electrodes, as soon as coated with the polymer film, were removed in air from the electro-synthesis cell and immersed in degassed $\text{CH}_2\text{Cl}_2/\text{TBAP}$ solution. Then the films of the runs in Fig. 9 were discharged at constant current density, at different times after the end of their electro-synthesis. The percentage values of the recovered charge with respect to that stored in the polymers are reported in Table IV.

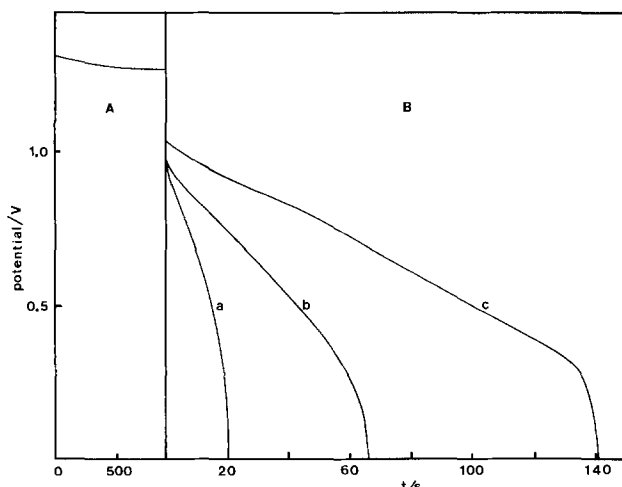


Fig. 7. $V(t)$ during processes at constant current densities. A: Electro-synthesis of doped p-DTT/Pt in $\text{CH}_2\text{Cl}_2/\text{TBAP}$ 0.1M solution with DTT 2 mM, $I = 0.4$ mA/cm², $Q = 358$ mC/cm². B: First discharges of films ($Q = 358$ mC/cm²) in $\text{CH}_2\text{Cl}_2/\text{TBAP}$ 0.1M at $I = -2.0$ (a), -0.8 (b), -0.4 mA/cm² (c).

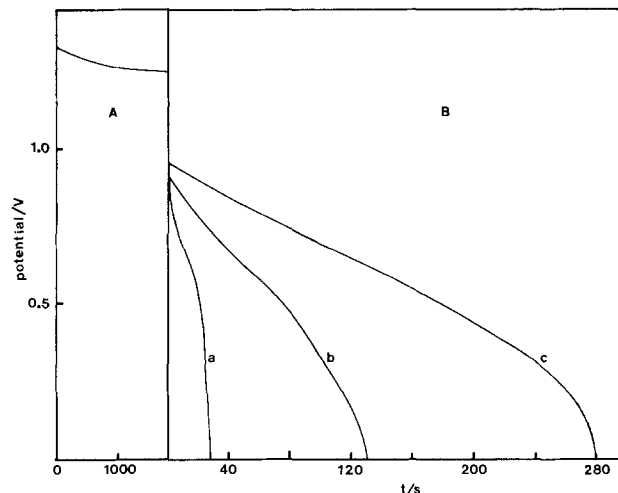


Fig. 8. $V(t)$ during processes at constant current densities. A: Electro-synthesis of doped p-DTT/Pt in $\text{CH}_2\text{Cl}_2/\text{TBAP}$ 0.1M solution with DTT 2 mM, $I = 0.4$ mA/cm², $Q = 717$ mC/cm². B: First discharges of films ($Q = 717$ mC/cm²) in $\text{CH}_2\text{Cl}_2/\text{TBAP}$ 0.1M at $I = -2.0$ (a), -0.8 (b), -0.4 mA/cm² (c).

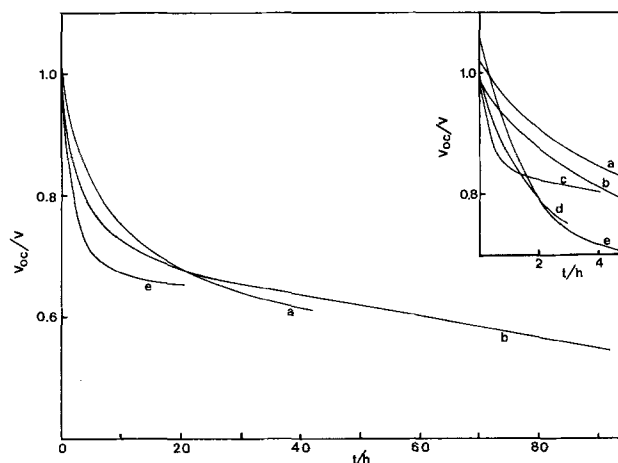


Fig. 9. $V_{\text{oc}}(t)$, in $\text{CH}_2\text{Cl}_2/\text{TBAP}$ 0.1M solution of different films grown with 717 (a), 358 (b), 400 (c), 400 (d), 537 mC/cm² (e).

The comparison (at the same I) of the results in Table IV with those of Table II (concerning films discharged immediately after their preparation) indicates that about one-half of the cyclable charge is lost when the electrode potential is decreased by ca. 0.2V. The loss is not due to an irreversible degradation process of the polymer. In fact, if the films are charged again and immediately discharged, the percentages of the recovered charge are the same as those of Table II. No significant difference was observed (in the range time of 24h) if doped p-DTT/Pt electrodes were preserved in nondegassed solutions in the dark.

A decrease of the open-circuit potential and of the percentage of the charge recovered with respect to that stored (e.g., after 18h, $\Delta V_{\text{oc}} = 0.25$ V and the charge recovered with respect to that stored is 30%, at $I = 0.2$ mA·cm⁻²) was also observed with doped p-DTT grown on SnO_2 -coated Pyrex electrode ($Q = 60$ mC·cm⁻² at $I = 0.4$ mA·cm⁻²) and preserved in $\text{CH}_2\text{Cl}_2/\text{TBAP}$ solution. This spontaneous decrease of V_{oc} with loss of charge over time, accompanied by a color change from black to red, was tested by spectroscopy.

Figure 10 shows the observed modification of the visible and near-IR absorption spectra. The same figure also reports the spectrum of the polymer after its exhaustive electrochemical discharge in $\text{CH}_2\text{Cl}_2/\text{TBAP}$ solution and the spectrum of the polymer electrochemically recharged with $Q_{\text{ox}} = 10$ mC·cm⁻², after its discharge. Taking into

Table IV. Charges recovered with respect to that stored, in discharges at I constant, of p-DTT films preserved in $\text{CH}_2\text{Cl}_2/\text{TBAP}$ solution after different times elapsed from their electro-synthesis

Run	Q Charge involved in p-DTT synthesis (mC/cm ²)	(V _{oc}) _{t=0} (V)	t Time elapsed from p-DTT synthesis (h)	(V _{oc}) _t (V)	I Discharge at t (mA/cm ²)	Q _{red, t} Charge recovered in undoping process (mC/cm ²)	Percentage of charge recovered w.r.t. stored at t time
a	717	1.02	43	0.61	-0.2	38.2	27
b	358	1.00	92	0.54	-0.04	1.2	2
c	400	1.01	4	0.80	-0.4	33.8	42
d	400	1.00	3	0.75	-0.4	29.2	37
e	537	1.05	21	0.65	-0.2	29.1	20

account the spectra of the doped and undoped polymers (Fig. 4), Fig. 10 suggests that in losing the charge, doped p-DTT does not undergo appreciable chemical degradation.

A point worth mentioning is that all the electrochemical results are reasonably reproducible, except the time in which the doped films, preserved in $\text{CH}_2\text{Cl}_2/\text{TBAP}$ solution, lose their charge. Electrochemical and spectroscopic tests showed that the total self-discharge of identically doped p-DTT films occurred in an 18-100h time range. This suggests that film stability is related to some uncontrolled parameters such as, for instance, impurities of the solvent due to its partial decomposition. On the other hand, film of doped p-DTT preserved not in CH_2Cl_2 solution but in air are more stable. In fact, after 240h, the polymer preserved 65% of its charge. It was also observed that the lost charge occurred in the beginning (maximum, ca. 20h). In fact, spectra recorded after this time are practically unchanged.

As a battery application, a simple cell¹ was assembled utilizing oxidized and neutral polymer films, adherent to Pt, as the two terminals and immersed in $\text{CH}_2\text{Cl}_2/\text{TBAP}$ solution. The oxidized form was galvanostatically electro-generated in $\text{CH}_2\text{Cl}_2/\text{TBAP}$ -DTT solution with 717 mC·cm⁻² and the reduced form was obtained fully undoping a doped film of a thickness identical to that of the cathode. This battery yielded a maximum open-circuit voltage of ca. 0.6V and an initial short-circuit current density of 2.7 ± 0.3 mA·cm⁻². These preliminary results were taken from six batteries. The short-circuit current was calculated by utilizing the difference poten-

¹Since we observed that the neutral polymer requires a certain time (ca. 3h after its electrochemical preparation) before assuming a stable potential of ca. 0.3V, the battery was assembled when the neutral polymer was stable.

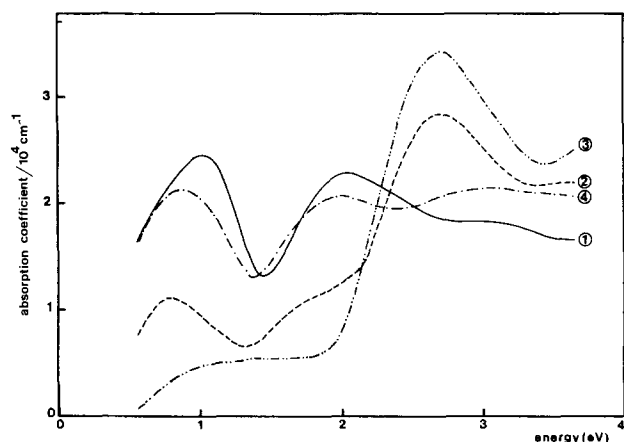


Fig. 10. Series of absorption spectra. 1: Doped p-DTT (with ClO_4^-) immediately after its electro-synthesis. 2: Doped p-DTT preserved for 18h after its electro-synthesis in $\text{CH}_2\text{Cl}_2/\text{TBAP}$. 3: Undoped p-DTT. 4: Electrochemically regenerated doped p-DTT (with ClO_4^-).

tial values measured under different conditions of the external load. The difference potential values were taken 0.5s after a discharge was commenced. During the initial 0.2s, the voltage fell very rapidly from the V_{oc} value and then decreased more slowly.

Conclusions

We observed that anodically synthesized doped p-DTT can release and store charge equal to 20% of the charge involved in its initial electrochemical preparation. Doped p-DTT presents some attractive features relevant to its application in battery technology, e.g., a high doping level which corresponds to a capacity of 54 mAh/g (with ClO_4^- as dopant), an initial value of V_{oc} of ca. 1V, high values of the charge recovered at constant currents up to 0V, with respect to that stored, from a maximum of 95% for $I = -0.04$ mA·cm⁻² to a minimum of 27% for $I = -4$ mA·cm⁻², cyclability with no evidence of appreciable degradation, and an apparent O_2 stability. On the other hand, film of doped p-DTT preserved in $\text{CH}_2\text{Cl}_2/\text{TBAP}$ solution had the disadvantage of a fast self-discharge. This phenomenon is not due to polymer degradation, but to an uncontrolled redox reaction involving the used electrolytic medium.

Work is in progress to investigate the behavior of this material in other nonaqueous solvents and in water.

Acknowledgments

This work was carried out with the financial support of the CNR Progetto Finalizzato Energetica 2, no. 830211759. The technical assistance of Mr. Lino Cludi is acknowledged and appreciated.

Manuscript submitted Oct. 22, 1984; revised manuscript received March 19, 1985.

Universita di Bologna assisted in meeting the publication costs of this article.

REFERENCES

1. A. F. Diaz, K. K. Kanazawa, and P. Gardini, *J. Chem. Soc., Chem. Commun.*, 635 (1979).
2. G. Tourillon and F. Garnier, *J. Electroanal. Chem. Interfacial Electrochem.*, **135**, 173 (1982).
3. J. Bargon, M. Mohmand, and R. J. Waltman, *IBM J. Res. Dev.*, **27**, 330 (1983).
4. A. F. Diaz and K. Kanazawa, in "Extended Linear Chain Compounds," Vol. 3, J. Miller, Editor, p. 417, Plenum Press, New York (1983).
5. P. G. Di Marco, M. Mastragostino, and C. Taliani, Patent N°21430A/84 (Italy), Application 6, 15 (1984); P. G. Di Marco, M. Mastragostino, and C. Taliani, *Mol. Cryst. Liq. Cryst. Conf. Proc. ICSM*, **84**, 118,241 (1985).
6. F. de Jong and M. J. Janssen, *J. Org. Chem.*, **36**, 1645 (1971).
7. J. E. Lind, Jr., H. A. A. Abdel-Rehim, and S. W. Rudich, *J. Phys. Chem.*, **70**, 3610 (1966).
8. T. C. Chung, J. H. Kaufman, A. J. Heeger, and F. Wudl, *Phys. Rev. B*, **30**, 702 (1984).
9. A. F. Diaz and J. A. Logan, *J. Electroanal. Chem. Interfacial Electrochem.*, **111**, 111 (1980).
10. G. Tourillon and F. Garnier, *ibid.*, **161**, 51 (1984).
11. A. F. Diaz, K. K. Kanazawa, J. I. Catillo, and J. A. Logan, *Polym. Sci. Technol.*, **15**, 149 (1981).

Cycling Behavior of Thin Film LiAl Electrodes with Liquid and Solid Electrolytes

W. C. Maskell* and J. R. Owen*

Wolfson Unit for Solid State Ionics, Department of Metallurgy and Materials Science, Imperial College, London, England SW7 2BP

ABSTRACT

An Al foil was partially converted to β -LiAl by electrodeposition onto one side. The remaining unalloyed Al acted as a substrate for the film. Cycling was carried out with the film in contact with either the liquid propylene carbonate/1M LiClO₄ (PC) or the solid (PEO)₈LiCF₃SO₃. After initial substantial capacity losses, coulombic efficiencies were 97 and 99% with the PC and PEO electrolytes, respectively. There was an additional loss with PEO (2 μ A cm⁻²) due to a combination of oxygen and water vapor ingress and Li diffusion into the steel current collector. The loss in PC occurred during active operation, there being negligible loss on standing. Lithium incorporation into the film occurred readily due to the high diffusion coefficient of Li in β -LiAl. Stripping of the Li caused some cracking of the film as a result of the large molar volume change in forming α -Al(Li) from β -LiAl, but adhesion of the film to the Al substrate was strong. Literature values for the diffusion coefficient of Li in α -Al(Li) are low (10⁻¹⁶ and 10⁻²² cm²s⁻¹ at 140° and 25°C, respectively), indicating that the growth of a few monolayers of the α phase on the surface of the β -LiAl could prevent further discharge. A model is proposed whereby the β -LiAl at the interface with the electrolyte becomes "super depleted" on discharge, but not enough to nucleate α -Al(Li). Thus a diffusion gradient is set up in the β -LiAl film, causing the α -Al(Li) to grow from the α/β interface in a needle-like morphology towards the electrolyte. Such a model is compatible with the substantial capacity losses during initial cycles.

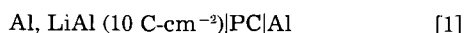
This study represents one aspect of a project to develop a rechargeable solid-state lithium battery for traction applications (1). An electrode of unalloyed lithium tends to display the problems of reaction with the electrolyte, dendrite formation, and shape change. Dey (2) showed that lithium alloys readily with aluminum, and a number of electrochemical studies of this binary combination in either molten salt or liquid organic electrolytes have subsequently been reported (3-13).

In the present study, results are presented for the LiAl electrode in contact with solid polyethylene oxide (PEO). Some work was also carried out using the liquid propylene carbonate/LiClO₄ (PC) as electrolyte for preparation of the LiAl alloy and for comparison with the investigations using PEO.

Experimental

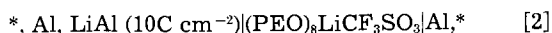
The starting material was 99% pure aluminum foil of 50 μ m thickness. This was degreased with a jet of trichloroethylene, immersed in 7M NaOH for approximately 10s to etch the surface lightly, washed with water, and then dried in a stream of warm air.

Al samples for Li electrodeposition were mounted onto glass slides. All exposed immersed surfaces, apart from the deposition area, were masked with Parafilm (Gallenkemp U.K.), a thermoplastic tissue which adhered well with gentle heat from a hot-air gun. The electrochemical cell was assembled in a dry air box (water content < 5 ppm) with a massive Li strip as counterelectrode, Li wire as reference electrode, and propylene carbonate/1M LiClO₄ (PC) as electrolyte. The counterelectrode was of dimensions similar to those of the Al electrode and was placed parallel to it. Typically, 10 C-cm⁻² Li was deposited by passage of current at 1 mA cm⁻², forming a LiAl layer ~20 μ m thick; the supporting Al substrate was 30-40 μ m thick. For cycling tests in PC, the electroformed film was not removed from the electrolysis cell and the cell was assembled as follows



LiAl samples, for work involving PEO electrolyte, were washed with dry PC followed by acetonitrile and allowed to evaporate naturally prior to storage over Li metal in a dry argon box. Disks of 1 cm diam were cut to fit the cells (Fig. 1), which were semisymmetrical in the sense that after the first half-cycle both electrodes contained LiAl. Cells were assembled as follows

*Electrochemical Society Active Member.



the asterisk representing a steel current collector. The electrodes were of equal geometric area, each being a sample under study. Al foil was freshly etched as described above prior to assembly. The cells each contained four layers of electrolyte film (each layer was 35 \pm 5 μ m thick). The glass cell with steel pistons (Fig. 1) was assembled in a dry argon box, then removed and fitted into a spring holder (pressure 3 bar) for cycling in an oven at 140°C (in air). O-rings used were Viton,¹ which is stable at the operating temperature.

Galvanostatic charge/discharge was monitored and controlled using a Research Machines 380Z computer. Data were stored on a floppy disk.

Propylene carbonate (Koch Light, puriss.) was dried over 4Å molecular sieve before use. Analar LiClO₄ was predried under vacuum at 200°C for 70h. PEO film was prepared at A.E.R.E. Harwell Laboratory according to the method described by Sequeira *et al.* (14).

Scanning electron microscopy was carried out on a JEOL T200 machine. Specimens were prepared for sectional examination by simply tearing the foils to reveal the fracture surfaces.

Results and Discussion

Propylene carbonate electrolyte.—The first charge of an Al electrode at either 1.0 or 0.1 mA-cm⁻² and subsequent charges at 0.1 mA-cm⁻² showed similar characteristics (Fig. 2), in agreement with previous studies. The initial overpotential "spike" has been attributed to a nucleation

¹Vinylidene fluoride/hexafluoro-propylene copolymer.

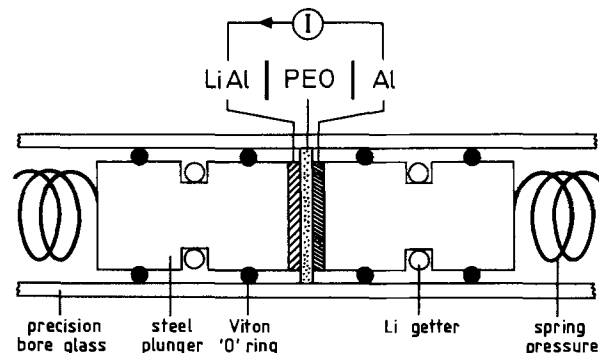


Fig. 1. PEO cell arrangement

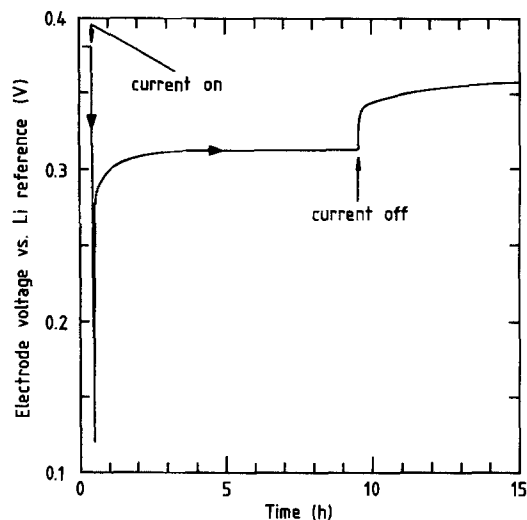


Fig. 2. Cathodic deposition of Li onto Al(Li) in propylene carbonate at 0.1 mA-cm^{-2} .

overvoltage for the initiation of the β -LiAl phase (6, 13). This was followed by a slow decrease in overpotential until the current was discontinued.

A typical discharge at 0.1 mA-cm^{-2} is shown in Fig. 3. There was an initial relatively rapid potential change, followed by an approximately linear increase with time and a rapid increase towards the discharge end point.

The 50 mV potential differential between charge and discharge reported by Epelboin *et al.* (10) and discussed by Baranski and Fawcett (13) was observed in the present study. The phenomenon appears to be associated with Li incorporation (335 mV vs. Li) as the stripping potential (385 mV) is close to the value calculable for the free energy of formation of β -LiAl.

Electrode capacity was determined to a cell voltage end point of 1.0V. Cycling data are shown in Fig. 4 and 5. The latter figure indicates a capacity loss of 6% per cycle. Comparison of the two figures clearly shows that capacity loss is minimal on wet stand, in agreement with the findings of Besenhard (8). Capacity loss only appears to occur during active operation, suggesting that a passivating film protects the surface on standing (8, 10). The amount of capacity loss was proportional to the charge time, *i.e.*, the charge passed, leading to a constant coulombic efficiency of 97% (3% loss per half-cycle) after the initial rapid decrease in the first few cycles (8).

Scanning electron micrographs of the two sides of the metal foil are shown in Fig. 6a and 6b. The Al surface,

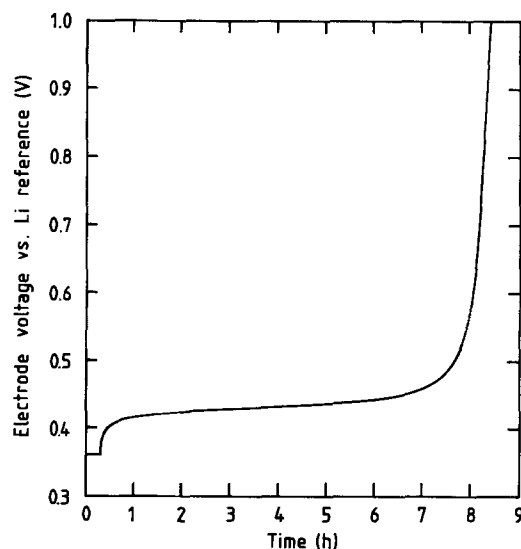


Fig. 3. Anodic stripping of Li from LiAl in propylene carbonate at 0.1 mA-cm^{-2} .

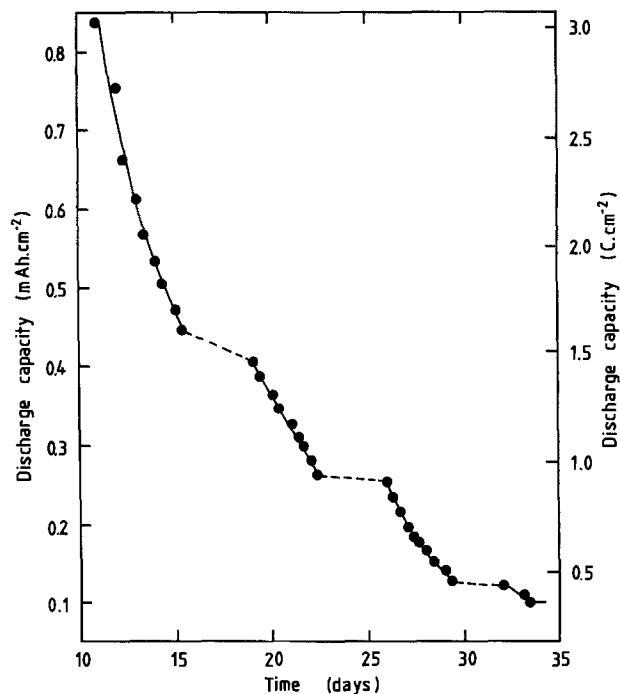


Fig. 4. Cycling data for a symmetrical LiAl/propylene carbonate/ LiClO_4 cell at 0.1 mA-cm^{-2} and ambient temperature.

shown in Fig. 6a, is clearly flat apart from minor features, probably resulting from rolling. The β -LiAl surface is shown in Fig. 6b. The incorporation of Li has added surface features indicative of a nucleation and growth process. A solitary nucleus would be expected to grow three dimensionally and, because of the volume change upon Li incorporation, would protrude approximately spherically from the surface; each protrusion from the surface represents a single nucleation. These overlap and result in the morphology observed. Having merged, the α - β interface tends to become planar as it proceeds into the foil. The edge of the foil, charged to 10 C-cm^{-2} , observed from both the Al and LiAl sides, is shown in Fig. 6c and 6d, respectively. The plane at the interface of the active film and the substrate can clearly be identified indicating thicknesses of $20\text{-}25 \mu\text{m}$ and $35\text{-}40 \mu\text{m}$ for the β -LiAl and α -Al phases, respectively. The cracking of the LiAl layer in Fig. 6d was the result of mechanical damage during sectioning of the specimen and was not present away from the edge. It did demonstrate that the LiAl layer was less ductile than the Al substrate.

Micrographs of a 10 C-cm^{-2} film discharged to a cell voltage of 1.0V (discharge capacity 6.1 C-cm^{-2}) are shown

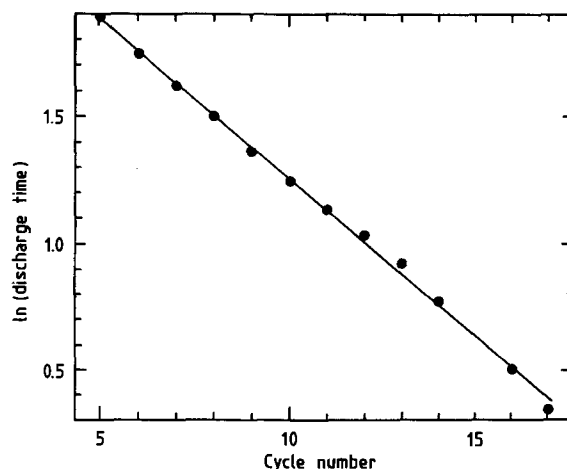


Fig. 5. Logarithm of discharge time vs. cycle number for a symmetrical LiAl/PC cell at 0.1 mA-cm^{-2} and ambient temperature. Data as in Fig. 4.

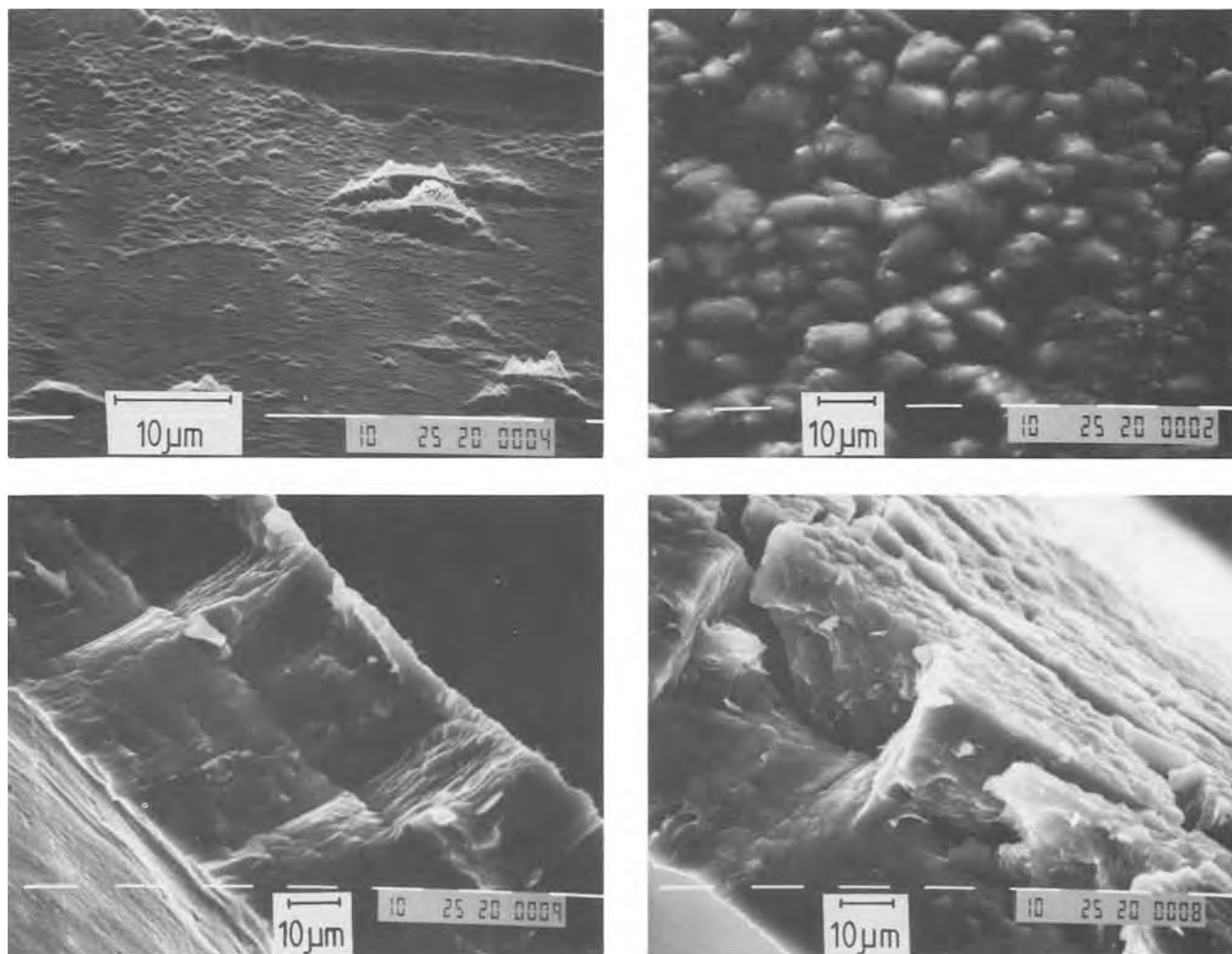


Fig. 6. Scanning electron micrographs. a: Al surface. b: Al surface after Li incorporation (10 C-cm^{-2}). c: Fracture edge of Al, LiAl (10 C-cm^{-2}) duplex foil viewed from Al side. d: As in c, viewed from LiAl side.

in Fig. 7. The surface cracking in Fig. 7a has been reported previously by Garreau *et al.* (11) and is a result of the volume reduction upon extraction of Li from the β -LiAl. Higher magnification micrographs of the cracks meeting the torn edge are shown in Fig. 7b and 7c.

The change in molar volume associated with Li stripping is 49%, which, in this experiment to 61% depth of discharge, should have resulted in a 30% overall volume change of the film. An isotropic contraction would then result in a 10% thickness change and a crack area corresponding to 20% of the film surface. Although the micrographs do not allow an accurate estimate of the thickness change, the fraction of crack area in Fig. 7a can be calculated reasonably well as follows. Average crack width equals $15 \pm 3 \mu\text{m}$. Total crack length in frame equals 0.52 cm. Total micrograph area equals $40 \times 10^{-4} \text{ cm}^2$. Therefore, the fraction of crack area in film surface equals $20 \pm 4\%$. The agreement with the theoretical value indicates that the film has a low porosity, which is important in considerations of the discharge mechanism below.

The final micrograph (Fig. 7d) shows the Al substrate surface after Li stripping observed from a shallow angle (18°). This may be compared with Fig. 6a and shows that, as the Li is stripped, the active film shrinks and the contraction imposes considerable strain on the substrate, causing mechanical deformation. It also shows that the LiAl is bonded strongly onto the substrate.

Polyethylene oxide electrolyte.—Cycling data for duplicate type-2 cells are shown in Fig. 8 and 9. Figure 10 shows a typical voltage-time curve for these cells. Capacities were calculated to a cell end point of 1.0V. On the first discharge, capacities were comparable to that in PC (5.9 and 4.9 C-cm^{-2} for PEO, 6.1 C-cm^{-2} for PC). Com-

parison of Fig. 8 and 9 shows that capacity loss was principally due to aging and not to cycling. It appears that coulombic efficiency of cycling after the initial rapid loss may have been $> 99\%$. This behavior contrasts with that in PC, where the loss occurred principally during cycling.

The linear loss of each cell with time shown in Fig. 8 was equivalent to a current of $1.2 \mu\text{A}$. This loss could be due to ingress of water vapor or oxygen into the cell converting the Li to an oxide or alternatively to diffusion of Li into the steel piston. The possibility of the latter was investigated by setting up a type-2 cell but omitting the Al electrode. The cell was shorted, with a resistor in the circuit (voltage drop across it $< 10 \text{ mV}$) to monitor the current due to Li alloy formation on the surface of the steel and subsequent Li diffusion (Fig. 11, 12).

A straight line passing through the origin is anticipated for semi-infinite diffusion (15) when current is plotted vs. $t^{-1/2}$. Both the long- ($> 1\text{h}$) and short-time ($< 100\text{s}$) data satisfy the semi-infinite theory but with different slopes. At short times, diffusion fronts are parallel to the surface and the surface area is greater than the geometric value by a factor equal to the roughness factor. At long times, diffusion fronts merge to form a planar front proceeding in the direction of the axis of the piston; in this case, the appropriate area is the geometric value. Hence, the ratio of the slopes in Fig. 11 and 12 reveals the reasonable value for the roughness factor of 2.

Clearly, Li loss into the current collector can be high and could rapidly exhaust a 10 C-cm^{-2} LiAl electrode when there is an electrolyte path between the active LiAl surface and the current collector together with electronic contact between the two. It was found that in type-2 cells stored at 140°C , electrolyte did squeeze between these two components.

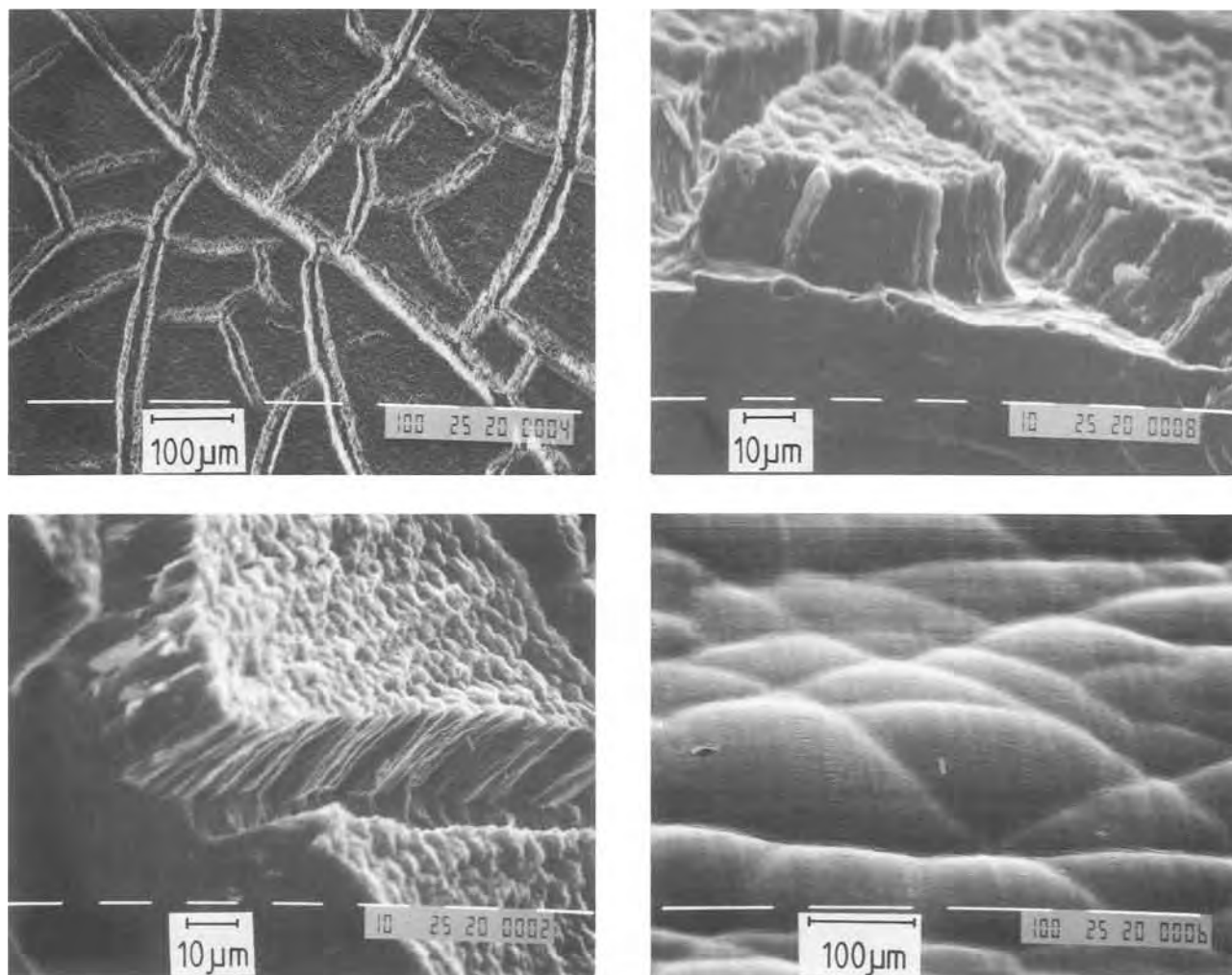


Fig. 7. Scanning electron micrographs of Al foil after Li incorporation ($10 \text{ C}\cdot\text{cm}^{-2}$) and Li stripping (61%). a: Cracking of active layer on continuous Al substrate. b and c: Fracture edges of duplex foil where cracks meet edge. d: Al substrate viewed from a shallow angle (18°) demonstrating distortion due to shrinkage of the active layer on the other side of the foil.

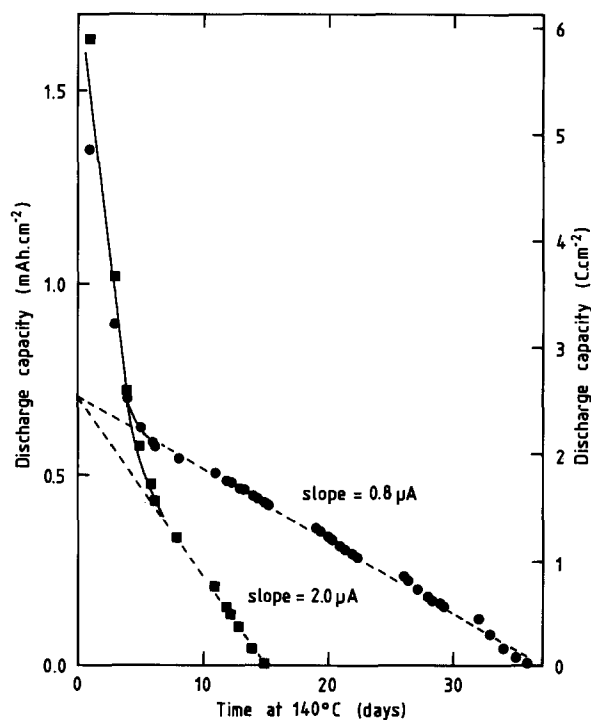


Fig. 8. Initial capacity decrease and subsequent time-dependent loss on cycling of duplicate symmetrical LiAl/PEO cells. Current density: $0.1 \text{ mA}\cdot\text{cm}^{-2}$. Temperature: 140°C .

A further aspect of the data in Fig. 12 is the intercept at $t^{-1/2} = 0$ of $1 \mu\text{A}$, which could be due to ingress of water vapor and/or oxygen and is comparable to the losses noted in Fig. 8. Thus, the capacity losses revealed by cycling may result either from O_2 or H_2O ingress, Li diffusion into the current collector, or any combination of

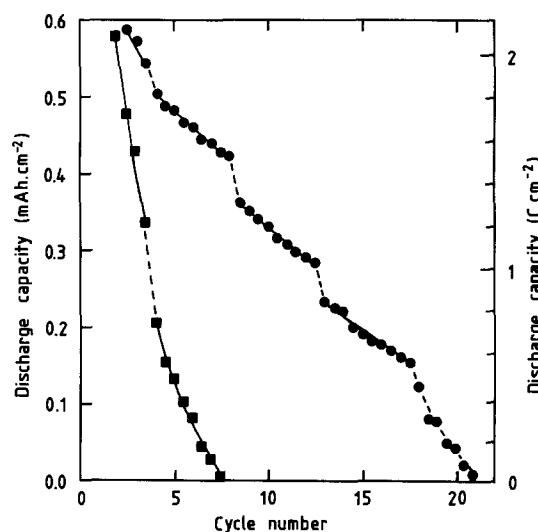


Fig. 9. Capacity decrease of duplicate symmetrical LiAl/PEO cells vs. cycle number. Data as in Fig. 8.

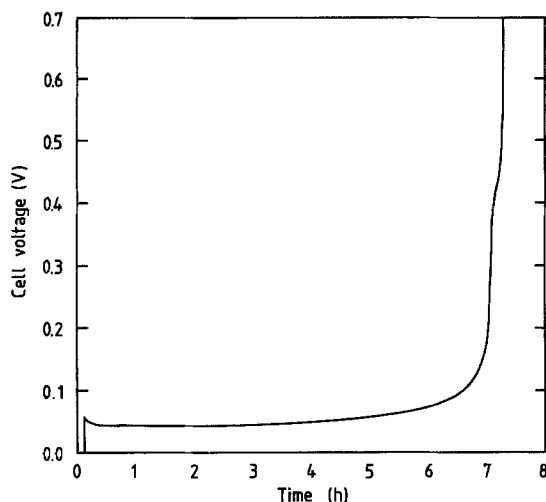


Fig. 10. Voltage vs. time curve of a symmetrical LiAl|PEO cell at $0.1 \text{ mA}\cdot\text{cm}^{-2}$ and 140°C .

these. If residual currents were eliminated by effective sealing, a long-term cycling capacity of $2.5 \text{ C}\cdot\text{cm}^{-2}$ may be achievable for these cells. This is applicable to high depth of discharge under which condition secondary cells such as lead-acid often do not perform well.

Mechanism of charge/discharge.—There seems little doubt concerning the mechanism of Li incorporation as β -LiAl into the electrode. Where the surface is initially α -Al or α -Al(Li) then β -LiAl must nucleate on the surface. This nucleation requires a substantial overvoltage. The nuclei grow three dimensionally, overlap, and then grow into the α -phase approximately on a planar front. Incorporation takes place readily at $1 \text{ mA}\cdot\text{cm}^{-2}$; this can occur because Li has a high diffusion coefficient in β -LiAl (D_β), which is a consequence of the large Li vacancy concentration in this material (17-19). Wen *et al.* (9) carried out an extensive study of LiAl including measurements of D_β in the range $415^\circ\text{--}600^\circ\text{C}$. They found it to be concentration dependent, reaching a maximum value of $10^{-4} \text{ cm}^2\cdot\text{s}^{-1}$ at the lower phase limit. Thus the value of $10^{-8} \text{ cm}^2\cdot\text{s}^{-1}$ determined at 24°C by Jow and Liang (12) seems not unrea-

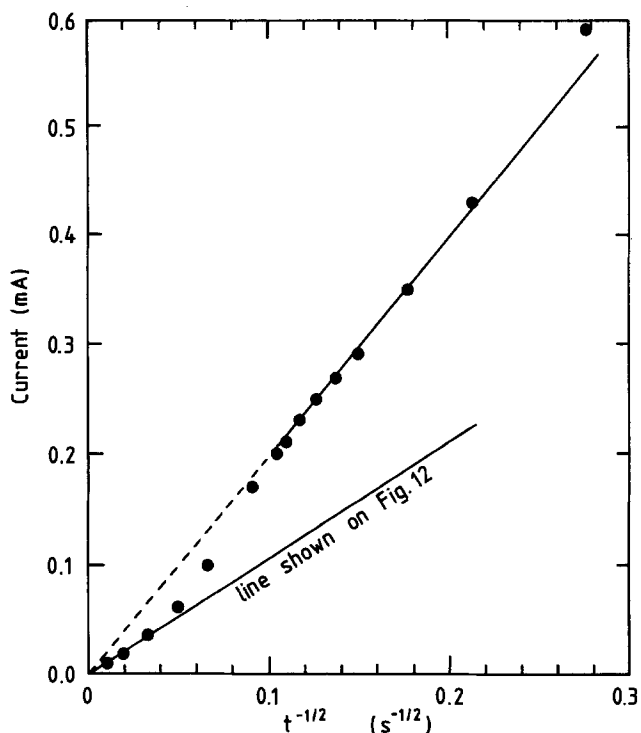


Fig. 11. Current vs. $t^{-1/2}$ for Li incorporation and diffusion into the steel piston showing data for short and long times.

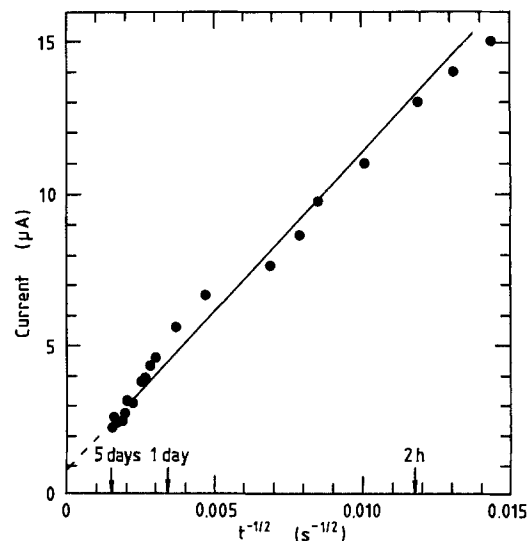


Fig. 12. As Fig. 11 for data at long times only

sonably high. Using this latter value in an equation derivable from Fick's first law, the concentration difference (Δc) across the film may be calculated

$$\Delta c = id/D_\beta F$$

i is the current ($1 \text{ mA}\cdot\text{cm}^{-2}$), d the film thickness ($20 \mu\text{m}$), and F the Faraday constant. This revealed $\Delta c = 2 \times 10^{-3} \text{ mol}\cdot\text{cm}^{-3}$ (i.e., $2M$). The molar volume (V_m) of β -Li_xAl is $20 \text{ cm}^3\cdot\text{mol}^{-1}$ and to a first approximation may be assumed to be independent of x . The Li concentration, c , is given by

$$c = x/V_m$$

Hence

$$\Delta x = V_m \Delta c$$

Substituting in the above values for V_m and Δc leads to $\Delta x = 0.04$. This value of Δx represents a change from the equilibrium stoichiometry of the β phase at the α/β boundary of $\text{Li}_{0.96}\text{Al}$, which is approximately equivalent to 48 atom percent (a/o) Li (12) to LiAl. Therefore, in terms of mole fraction, the surface may reach 50 a/o Li. The low concentration difference required to sustain diffusion under the above charging conditions is important, since the fast diffusing β phase width extends only as far as 56 a/o (12).

A satisfactory mechanism of Li stripping, however, has not been proposed. The difficulty arises from the very low values measured for the diffusion coefficient of Li in α -Al(Li) (D_α). The data of Wen *et al.* (20) determined over the range $400^\circ\text{--}600^\circ\text{C}$ may be extrapolated to give D_α values of $10^{-16} \text{ cm}^2\cdot\text{s}^{-1}$ (140°C) and $10^{-22} \text{ cm}^2\cdot\text{s}^{-1}$ (25°C). This is in good agreement with the data of Williams and Edington (21) giving a D_α value of $10^{-16} \text{ cm}^2\cdot\text{s}^{-1}$ at 140°C . Clearly, at best, $D_\alpha/D_\beta \approx 10^{-8}$ and diffusion of Li will only occur at reasonable rates ($0.1 \text{ mA}\cdot\text{cm}^{-2}$) through very thin layers ($\sim 5\text{\AA}$) taking the molar volume of α -Al (Li) as $10 \text{ cm}^3\cdot\text{mol}^{-1}$ and phase width as 0.5 a/o ($D_\alpha = 10^{-16} \text{ cm}^2\cdot\text{s}^{-1}$). Thus it seems unreasonable to propose a model in which a coherent film of α -Al (Li) grows on the front face of the β -LiAl film. The next proposition to consider is the growth of an incoherent film of α -Al (Li). Such a proposal would suggest that the stripped film might be porous so that electrolyte could enter the pores generated as stripping proceeds. This would be possible for a liquid electrolyte (e.g., PC) but unlikely for PEO, which has a high viscosity and would be slow to enter small pores. In the case of PC, the cycling was carried out at room temperature, where D_α is several orders of magnitude lower than that assumed in the above calculation. Also, it was shown earlier that the stripped film was probably non-porous apart from macroscopic cracks. Thus, the proposi-

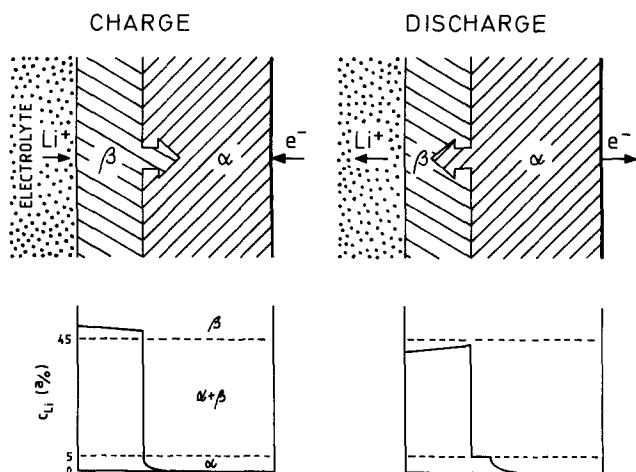


Fig. 13. Model for the charge/discharge processes of a LiAl electrode

tion of a mechanism via an incoherent film also appears untenable both for PC and PEO electrolytes.

A third possibility is that at the commencement of Li stripping α -Al(Li) is not nucleated at the front face. As a result, β -LiAl is driven into a Li-deficient region beyond its phase limit at the electrolyte interface. This is a metastable state which might be termed "superdepletion." Considering a calculation similar to the charging case, the magnitude of depletion can be small as a result of the very large diffusion coefficient, as reported by Wen *et al.* (9). (Very high D_β values can be explained by a thermodynamic enhancement factor or a large point-defect concentration.) Moreover, the critical superdepletion required for α -phase nucleation can be expected to be relatively large due to the severity of the structural rearrangement. Superdepletion sets up a concentration gradient in the β -LiAl film so that α -Al(Li) grows from the α/β phase boundary towards the electrolyte. The α phase might be expected to grow in a needle-like fashion towards the front face as the Li concentration gradient would tend to promote this type of morphology. Upon reaching the front face, lateral growth of α phase would take place until a coherent passivating film of α -Al(Li) covered the active surface, effectively preventing further discharge. This would tend to entrap β -LiAl between the α -Al(Li) needles from which Li could not be stripped. This would be manifested as a coulombic efficiency substantially below 100%. In fact, on the first charge/discharge in PC an efficiency of 61% was recorded. Some evidence in favor of this mechanism may be gleaned from examination of the photographs of the discharged film. The sides of the cracks, induced by volume reduction, and the fracture edges suggest the needle-like growth in the active film predicted above. Such a structure is not apparent in the undischarged film (particularly that shown in Fig. 6d). The model described above is depicted in Fig. 13.

Conclusions

The LiAl electrode shows a coulombic efficiency of 97% in PC and possibly in excess of 99% in combination

with a PEO electrolyte. There were additional losses in the latter case due to ingress of air or water vapor and/or diffusion of Li into the current collectors. Attention to cell design must be undertaken to minimize these additional losses. In all tests performed, there was no indication of shorting due to dendrite formation and no evidence of mass redistribution.

The initial capacity loss on cycling is unfortunate, but it may be acceptable considering the high theoretical energy density of LiAl. LiAl must be considered a promising electrode material for solid-state rechargeable Li cells.

Acknowledgment

The authors thank the Commission of the European Community for financial support.

Manuscript submitted Aug. 15, 1984; revised manuscript received March 5, 1985.

Imperial College assisted in meeting the publication costs of this article.

REFERENCES

1. "Advanced Battery Development, Solid State Rechargeable Batteries," A. Hooper and J. Jensen, Editors, Final Summary Report for Period Sept. 1980-March 1984, Odense University Press, Odense, Denmark (1984).
2. A. N. Dey, *This Journal*, **118**, 1547 (1971).
3. N. P. Yao, L. A. Heredy, and R. C. Saunders, *ibid.*, **118**, 1039 (1971).
4. E. C. Gay, D. R. Vissers, F. J. Martino, and K. E. Anderson, *ibid.*, **123**, 1591 (1976).
5. B. M. L. Rao, R. W. Francis, and H. A. Christopher, *ibid.*, **124**, 1490 (1977).
6. C. A. Melendres, *ibid.*, **124**, 650 (1977).
7. C. A. Melendres and C. C. Sy, *ibid.*, **125**, 727 (1978).
8. J. O. Besenhard, *J. Electroanal. Chem.*, **94**, 77 (1978).
9. C. J. Wen, B. A. Boukamp, R. A. Huggins, and W. Weppner, *This Journal*, **126**, 2258 (1979).
10. I. Epelboin, N. Froment, M. Garreau, J. Thevenin, and D. Warin, *ibid.*, **127**, 2100 (1980).
11. M. Garreau, J. Thevenin, D. Warin, and Ph. Champion, in "Lithium Nonaqueous Battery Electrochemistry," E. B. Yeager, B. Schumm, Jr., G. Blomgren, D. R. Blankenship, V. Leger, and J. Akridge, Editors, p. 158, The Electrochemical Society Soft-bound Proceedings Series, Pennington, NJ (1981).
12. T. R. Jow and C. C. Liang, *This Journal*, **129**, 1429 (1982).
13. A. S. Baranski and W. R. Fawcett, *ibid.*, **129**, 901 (1982).
14. C. A. C. Sequeira, J. M. North, and A. Hooper, *Solid State Ionics*, **13**, 175 (1984).
15. J. Crank, "The Mathematics of Diffusion," 2nd ed., p. 32, Oxford University Press, Oxford, England (1975).
16. J. R. Owen, P. C. Spurdens, J. E. Shemilt, and B. C. H. Steele, Abstract 492, p. 750, The Electrochemical Society Extended Abstracts, Vol. 83-1, San Francisco, CA, May 8-13, 1983.
17. S. Susman and T. O. Brun, *Solid State Ionics*, **1**, 133 (1980).
18. T. O. Brun, J. D. Jorgensen, M. Misawa, F. J. Rotella, and S. Susman, *This Journal*, **129**, 2509 (1982).
19. T. O. Brun, S. Susman, R. Dejus, B. Graneli, and K. Skold, *Solid State Commun.*, **45**, 721 (1983).
20. C. J. Wen, W. Weppner, B. A. Boukamp, and R. A. Huggins, *Metall. Trans. B.*, **11**, 131 (1980).
21. D. B. Williams and J. W. Edington, *Metal Sci.*, **9**, 529 (1975).

Photoelectrochemical Characterization of CdSnP₂ Crystals

J. C. W. Folmer, J. R. Tuttle, J. A. Turner, and B. A. Parkinson*

Solar Energy Research Institute, Photoconversion Research Branch, Golden, Colorado 80401

ABSTRACT

Crystals of the II-IV-V₂ chalcopyrite semiconductor, CdSnP₂, were grown from a tin melt. Photoelectrochemical techniques were used to characterize the properties of this material. Doping level, carrier type, optical transitions, absorption coefficient, and minority carrier diffusion length were determined and compared with values obtained with other techniques. Polysulfide electrolytes were found to be most suitable for the formation of liquid junctions, but did not completely stabilize the material during extended illumination and resulted in the formation of a CdS overlayer.

The recent successes of the use of III-V semiconductors for photoelectrochemical energy conversion have been encouraging from a fundamental scientific viewpoint. A GaAs or GaAs_xP_{1-x} photoelectrochemical cell has been demonstrated to produce electricity at about 12% solar efficiency (1), while InP photocathodes, plated with small islands of noble metal catalysts, are capable of producing hydrogen gas from hydrogen ions at a solar efficiency in excess of 13% or act as the photocathode in a haloacid splitting cell (2). Practical large-scale systems for solar conversion from such materials are limited, mainly because of the relative scarcity and high cost of indium and gallium.

A class of materials exists isoelectronic with the III-V materials, but containing relatively more abundant metals from the groups adjacent to the Group III metals (Zn, Cd, Si, Ge, Sn). These II-IV-V₂ materials crystallize in the chalcopyrite structure (see Fig. 1). There has been considerable work on the optoelectronic properties of these materials (3), but very little on their application to photovoltaic or photoelectrochemical energy conversion. This is somewhat surprising considering that many members of this family have optical bandgaps in the energy range which is optimal for solar energy conversion (1.1-1.7 eV). The optical transitions in these materials are direct or pseudodirect, both of which result in a steeply rising absorption above the bandgap energy. Pseudodirect gaps are a consequence of band folding resulting from the doubled periodicity in the *c* direction of the chalcopyrite unit cell, placing the conduction band states with minimum energy at the gamma point in the Brillouin zone.

As a result, isoelectronic analogs of an indirect III-V material will have much steeper absorption edges (*i.e.*, ZnGeP₂ as compared to the indirect gap material, GaP, CdSnP₂, however, is isoelectronic with a direct gap material, InP). Steeply rising absorption edges are required for the construction of thin film devices.

We earlier reported a preliminary investigation of CdSnP₂ (4), and we now report on a more detailed study of the photoelectrochemical behavior of this compound. We have chosen to study CdSnP₂ (5) because it has a bandgap in the region of interest for solar conversion, it has been shown to have very favorable electronic properties (high absorption coefficients and carrier mobilities) (6), and it is isoelectronic with InP, a material which is used successfully in both photoelectrochemical photovoltaic and photoelectrolysis cells (2). When in contact with aqueous acid solutions, the high efficiency and stability of InP photocathodes has been attributed to the formation of a thin, hydrated, 6-10Å pore-free layer of indium oxide, through which carriers can tunnel freely (7). This oxide layer has been shown to provide stability against oxidative photocorrosion and also to passivate the radiationless recombination of photogenerated electrons and holes (8). Owing to the variety of possible surface oxides that can be formed from the components of a ternary material, the II-IV-V₂ compounds provide an opportunity for more detailed study of the role of surface oxides in the passivation of surface recombination and the protection against photocorrosion. A recent note dealt with the pho-

* Electrochemical Society Active Member.

toelectrochemical characterization of CdGeP₂, another member of the II-IV-V₂ family (9).

Experimental

Crystal growth.—Barlike crystals of CdSnP₂ (maximum dimensions 7 × 3 × 2 mm) were grown from a tin melt as previously described (10). Quartz ampuls were loaded with cadmium (99.999%), red phosphorus (99.999%), and an excess of tin (99.999%) in an inert atmosphere glove box. The ampuls were then evacuated to a pressure of 2 μtorr (0.3 mPa) and sealed. The sealed ampuls were then placed in a furnace with the temperature-time profile dictated by a microprocessor-controlled programmer. The programmer controlled the overall cooling rate and superimposed temperature "spikes" at various intervals to control the nucleation of the crystallites. In some cases, nucleation was controlled by cooling a point on the ampul by contacting it with a copper wire which led out of the furnace (5). The crystals were recovered from the melt by heating in glycerol to melt away the main mass of tin and then dissolving the remaining tin in 1:5 nitric acid/water mixtures or an etchant consisting of 1 part HF, 3 parts nitric acid, and 4 parts water. A final bath of 4M KOH was used to remove white coatings of hydrated tin nitrate precipitate, which sometimes built up on the crystals during the tin dissolution process. The crystals usually occurred as radiating masses of dark gray bars similar to those shown in Ref. (3) and (5). X-ray powder diffraction was used to verify that the crystals had the chalcopyrite structure and lattice parameters identical to those reported in the literature for CdSnP₂ (11). The unintentionally doped materials were n-type.

¹¹⁹Sn Mössbauer spectroscopy showed an average isomer shift, relative to a calcium stannate standard, of 1.601 + 0.002 mm/s. In some samples, a small second Mössbauer peak could be seen at an isomer shift of 2.73 + 0.05 mm/s, consistent with the presence of less than 1% Sn₄P₃ (12). The Sn₄P₃ is assumed to be present as small occlusions in the CdSnP₂ crystals. Macroscopic (2 × 6 × 1 mm) platelike Sn₄P₃ crystals were also identified by x-ray diffraction and Mössbauer spectroscopy in the crystal

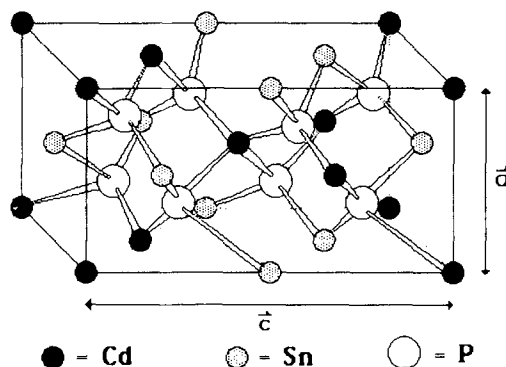


Fig. 1. The structure of cadmium tin phosphide showing the tetrahedral bonding throughout the structure. The *c/a* ratio is a measure of the distortion of the structure from the diamond structure, where this ratio would be 2.0. For cadmium tin phosphide, the *c/a* ratio is 1.95.

masses remaining after acid dissolution of the tin, but could be easily physically separated because of their different crystal habit and color.

Photoelectrochemical characterization.—Mott-Schottky (C^{-2} - V) plots were obtained using an automated computer-controlled capacitance measurement system which has been described elsewhere (13). Photocurrent spectra were also obtained with an automated system which controls the monochromator, collects photocurrent data, and corrects for the lamp response. A 250W tungsten lamp was the source, and the lamp spectral output was measured using a Model 2M thermopile with a quartz window (Dexter Research Center). Photocurrent-voltage response was also obtained with a computer-controlled system using a staircase voltage function and which collected photocurrent data using chopped light and a lock-in amplifier. Redox electrolytes were prepared from reagent-grade chemicals which were used as received with water purified through a Millipore ion exchange system with an organic absorption column and a final UV light treatment.

Electrodes were prepared by first making low resistance contacts to crystals with indium-gallium eutectic and securing them to a small copper plate. The copper plate was then connected to a wire and mounted at the end of a glass tube. Epoxi-Patch[®] epoxy was then used to insulate the copper and all but the desired crystal face(s). Indium-gallium eutectic was found to give consistently good low resistance contacts, but in some cases silver epoxy also proved adequate. Prior to the photoelectrochemical measurements, the crystals were etched in the HF-nitric acid etch described above. Extended stability runs used a 150W tungsten-halogen lamp positioned about 7.5 cm from the sample in a two-electrode cell with a platinum counterelectrode (the resulting light intensity is about 65 mW/cm²).

Results and Discussion

We attempted to determine the relative energy position of the conduction and valence bands and the doping level of the CdSnP₂ samples with capacity measurements. Mott-Schottky measurements (plotting $1/C^2$ vs. potential) were in general complicated by hysteresis between the forward and reverse scans, inversion effects, and potential regions where capacities were independent of potential. If the range of the potential scan was limited between -1.1 and about -0.65V vs SCE on a crystal with a smooth-crystal face, we obtained Mott-Schottky plots for n-type samples in sulfide/polysulfide solutions that showed close to linear behavior with a minimum of hysteresis (Fig. 2). The doping density obtained from the slope of the Mott-Schottky plot is 8.0×10^{17} , which agrees well with values obtained with the Hall technique ($3\text{--}5 \times 10^{17}$).

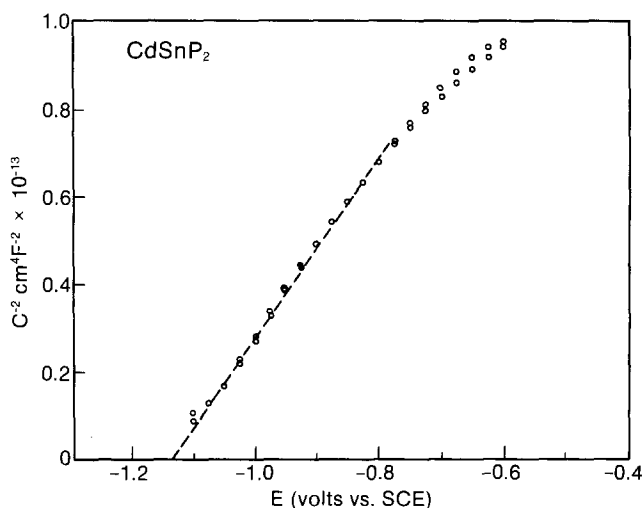


Fig. 2. Mott-Schottky plot of n-CdSnP₂ at 5000 Hz in a 1M Na₂S, 1M NaOH, 1M Na₂S₂ solution.

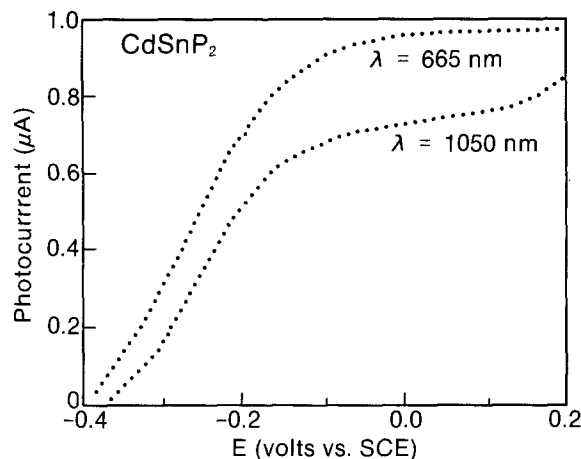


Fig. 3. Monochromatic photocurrent voltage behavior of n-CdSnP₂ in a 1M Na₂S, 1M NaOH, 1M Na₂S₂ solution at two different wavelengths but with identical photon flux.

The slightly higher photoelectrochemical value may be a result of the microscopic surface area of the crystal being larger than the macroscopic surface area which was used to calculate the slope. A rather negative value of the flatband potential is obtained from the analysis of the Mott-Schottky plot (-1.17V vs. SCE). The influence of a possible surface layer of cadmium sulfide on the flatband potential is not clear, since good Mott-Schottky behavior was not obtained in other redox electrolytes or buffers. The influence of the CdS layer on the photo-stability of the system is discussed later in this report.

Photocurrent-voltage curves for an n-type material in an aqueous sulfide/polysulfide solution illuminated at two different wavelengths, but with identical photon fluxes, are shown in Fig. 3. The figure shows that the quantum yield at shorter wavelengths is higher than at longer wavelengths. This can be explained by the fact that the shorter wavelength photons are absorbed in the space-charge region of the semiconductor/electrolyte interface and that the diffusion length of minority carriers (holes) is not long. The plateau region of the photocurrent curve can be analyzed with an equation derived from the Gärtner (14) model to obtain the minority carrier diffusion length for the crystal. A value of about 0.1 μm is obtained for 1050 nm excitation when a dielectric constant of 10.0 is assumed and when the doping density obtained from the Mott-Schottky data and an absorption coefficient of 5.6×10^4 cm⁻¹ are used.

Figure 4a shows the photocurrent spectra for an n-type CdSnP₂ sample in a polysulfide electrolyte. The photocurrent onset is usually at about 1.1 eV, but in some cases a subbandgap response is also observed. If the bandedge of a sample without the low energy response is analyzed for the transition type, by plotting the power dependence of the photocurrent-energy product against the photon energy, the best fit is found for direct transitions (the square of the energy photocurrent product) at 1.17, 1.23, and 1.37 eV (Fig. 4b). These values agree very well with the literature values, obtained with electroreflectance, of 1.16, 1.24, and 1.32 eV (15). The transitions can be identified as excitation from the three spin-orbit split valence band levels of the chalcopyrite structure (3). Such fortuitous results were not obtained on another crystal. Figure 5a shows the spectra of another sample (and perhaps another crystal face) obtained in a D₂O solution of polysulfide. In this case, the lowest lying transition is identified as an indirect transition at 1.11 eV, followed by direct transitions at 1.14 and 1.20 eV (Fig. 5b). D₂O is used to avoid a water absorption band at 1.27 eV or 975 nm (arrow in Fig. 4b), which could affect the interpretation of the highest direct transition in the first crystal. Substantial optical anisotropy in this material (16) and the partially polarized beam from the monochromator may also complicate the photocurrent spectra in CdSnP₂. A complete study of these effects is beyond the scope of this study.

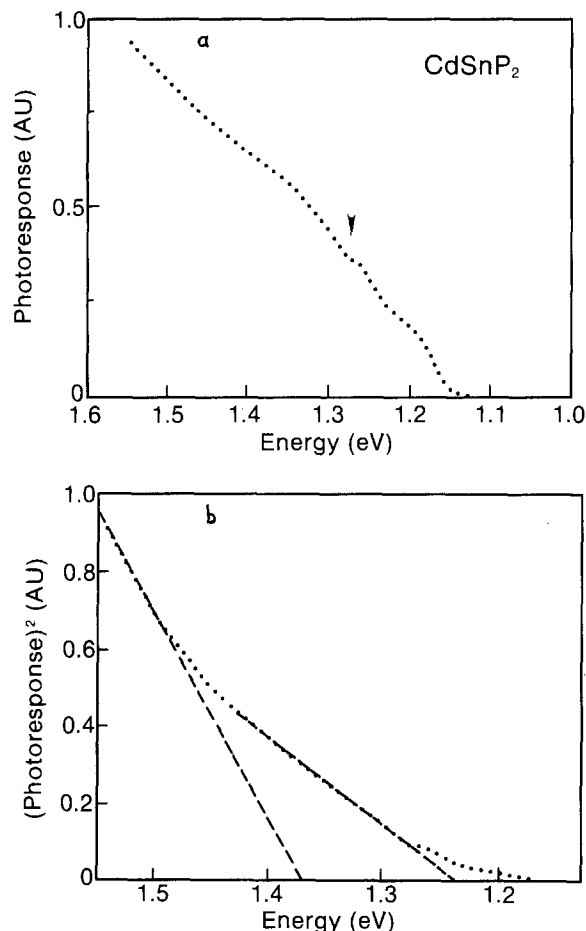
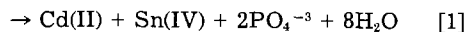
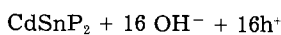


Fig. 4. a: Photocurrent spectra of n-CdSnP₂ in polysulfide solution. b: Analysis of two of the direct transitions from the data in a. The arrow is at the energy of a water absorption band.

The stability of the n-type CdSnP₂ to photocorrosion was tested by continuous illumination of an electrode in polysulfide electrolyte for five days at short circuit. The time response of the current was characterized by an initial rapid decrease in the current followed by a slow rise to the maximum current density of 5 mA/cm², which then began to decay after three days, as seen in Fig. 6. Note that the log time scale greatly exaggerates the initial current variations with respect to the slow long-term degradation. The total charge per unit area passed through the interface was 2350 C/cm². The total charge passed through the electrode (47C) was almost sufficient to totally corrode the sample through the path most demanding of holes (55C) which is written in Eq. [1]. (Note that these products have not been identified as the final corrosion products, but are used only to estimate stability.)



After only several hours of the test, an orange-yellow layer was observed to form on several of the faces of the crystal. The layer was shown, by electron microprobe analysis, to contain both Cd and S but no Sn. Cathodoluminescence confirmed the layer to be CdS. The tin is assumed to dissolve as a sulfide complex or as a stannate.

Initially, the CdS layer did not reduce the current flow through the interface, presumably because the blue light, which would be absorbed by the layer, was already removed by the orange-yellow sulfide/polysulfide electrolyte. The layer was observed to grow thicker with time and eventually grew thick enough to absorb light beyond the short wavelength cutoff of the electrolyte, which resulted in the decay of the short-circuit current. This was

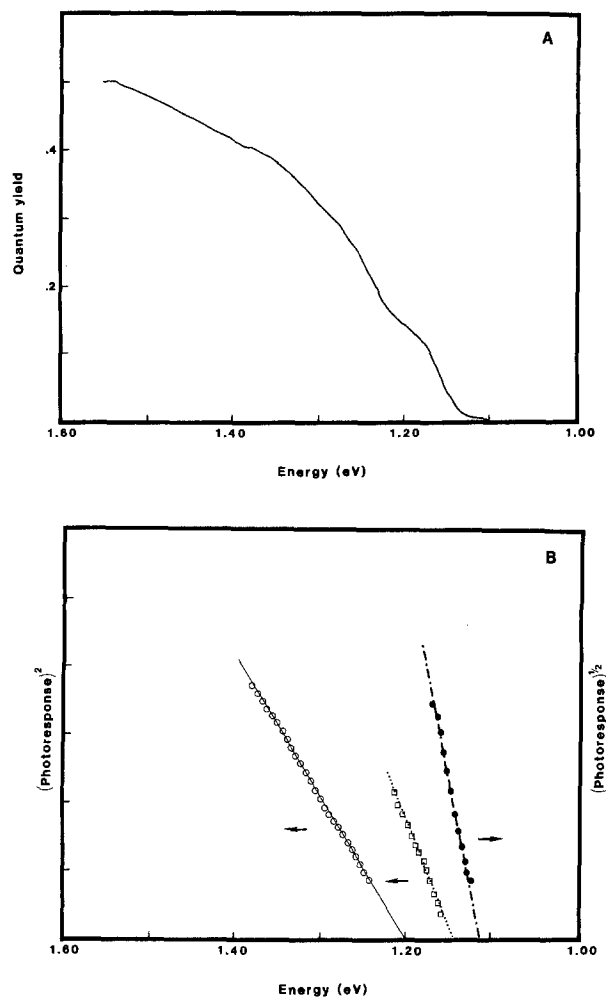


Fig. 5. A: Photocurrent spectra of another n-CdSnP₂ sample in a polysulfide solution in D₂O. B: Analysis of the spectrum in part A showing an indirect transition followed by two direct transitions.

verified by the decrease in the visible light response in the photocurrent spectra of a sample on which a substantial amount of CdS had accumulated. Presumably, the layer does not interfere with the transport of carriers to the electrolyte since the loss of photocurrent could be accounted for totally by absorption losses. If a blocking heterojunction was formed, the current would quickly decay to zero even with the formation of a very thin layer.

The layer forms with a coulombic efficiency of less than 1% because the thickness of the layer was less than 100 μm after the passage of enough charge to dissolve

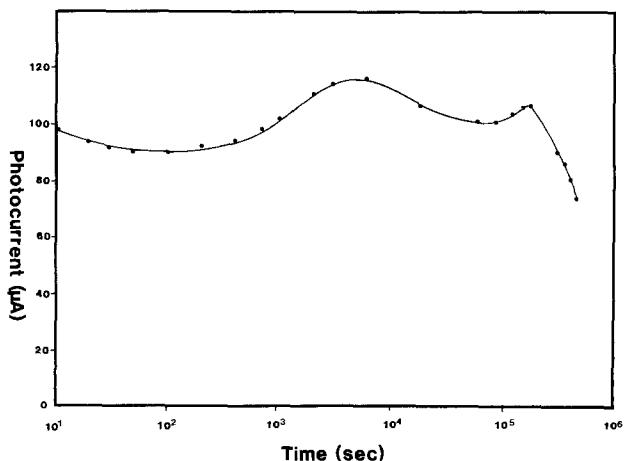


Fig. 6. Short-circuit photocurrent as a function of time for a n-CdSnP₂ sample under continuous illumination in a 2M KOH, 1M Na₂S, 1M Na₂S₂ solution. Note the logarithmic time axis.

Table I. Comparison of photoelectrochemically determined materials parameters of CdSnP₂ with values from other techniques

Parameter	PEC value	Other value(s)	Ref.
Doping level	$8 \times 10^{17} \text{ cm}^{-3}$	$5 \times 10^{17} \text{ cm}^{-3}$	This work
Optical transitions	1.17, 1.23, 1.37 eV 1.11(i), 1.14, 1.20 eV ^a	1.16, 1.24, 1.32 eV	(15)
Diffusion length	0.1-0.35 μm	—	This work
Absorption coefficient	$5.6 \times 10^4 \text{ cm}^{-1}$ (1050 nm)	$1-10 \times 10^4 \text{ cm}^{-1}$	(3)
Electron mobility	290-1100 (Hall)	$2000 \text{ cm}^2\text{V}^{-1}\text{s}^{-1}$	(19)

^a Different sample and perhaps crystal face. The i indicates an indirect transition.

most of the crystal. The exact percentage of photogenerated holes participating in the oxidation of the lattice to CdS is not known, but it is expected that it will be a strong function of the photocurrent density, as is the case with other semiconductor photoelectrodes (such as CdSe) (17).

Conclusion

Table I shows a summary of the materials parameters obtained from photoelectrochemical techniques for an n-type sample of CdSnP₂. It is clear from the table that reliable information about the materials properties of this material can be obtained with the photoelectrochemical techniques described in this communication. The high quantum yields at visible wavelengths (see Fig. 5a) obtained for this system confirm that the electronic properties of the material are favorable and high conversion efficiencies are achievable if the diffusion length of minority carriers can be increased to above 1 μm .

The marginal stability of the system, at least in the sulfide/polysulfide electrolyte, suggests that further work on the n-type material is needed in order to make this material attractive for use in a photoelectrochemical solar cell. The marginal stability of the n-type material in polysulfide solutions mimics the behavior of n-InP in similar solutions. However, p-type InP has been shown to be stable in several redox electrolytes, suggesting that the same may be true for p-CdSnP₂. Attempts to grow the latter material by doping with copper produced a low mobility compensated material with pronounced photoconductivity and subbandgap response (5, 18). A detailed study of this material is underway. Alternate methods for the preparation of p-type materials are also under investigation, as well as crystal growth and photoelectrochemical characterization of other members of the II-IV-V₂ family of semiconductors.

Acknowledgments

This work was supported by the Directors Discretionary Fund of the Solar Energy Research Institute. We are indebted to Satyen Deb for suggesting CdSnP₂ as an interesting material for study, and along with David Cahen for helpful discussions and performing Hall measurements. Don Williamson is acknowledged for Mössbauer measurements. Chuck Herrington and Ben Yacobi provided the electron microprobe analysis. J.A.T. acknowledges support from the U.S. Department of Energy, Office of Energy Sciences, Division of Chemical Sciences.

Manuscript submitted Nov. 12, 1984; revised manuscript received March 18, 1985.

Solar Energy Research Institute assisted in meeting the publication costs of this article.

REFERENCES

1. B. A. Parkinson, A. Heller, and B. Miller, *Appl. Phys. Lett.*, **36** (1978); B. A. Parkinson, A. Heller, and B. Miller, *This Journal*, **126**, 954 (1979); C. M. Gronet and N. S. Lewis, *Appl. Phys. Lett.*, **43**, 115 (1983).
2. E. Aharon-Shalom and A. Heller, *This Journal*, **129**, 2865 (1982); A. Heller, B. Miller, and F. A. Thiel, *Appl. Phys. Lett.*, **38**, 282 (1981); A. Heller, *Acc. Chem. Res.*, **14**, 154 (1981); C. Levy-Clement, A. Heller, W. A. Bonner, and B. A. Parkinson, *This Journal*, **129**, 1701 (1982).
3. J. L. Shay and J. H. Wernick, "Ternary Chalcopyrite Semiconductors: Growth, Electronic Properties and Applications," Pergamon Press, Oxford, England (1975).
4. J. C. W. Folmer, J. A. Turner, S. K. Deb, and D. Cahen, 510 RNP, *This Journal*, **130**, 442C (1983); D. Cahen, J. R. Tuttle, J. A. Turner, D. L. Williamson, S. K. Deb, and B. A. Parkinson, *Prog. Crystal. Growth Character.*, To be published.
5. J. R. Tuttle, M. S. Thesis, Colorado School of Mines, Golden, CO (1984).
6. E. Buehler, J. A. Wernick, and J. L. Shay, *Mater. Res. Bull.*, **6**, 303 (1971).
7. S. Menezes, H. J. Lewerenz, F. A. Thiel, and K. J. Bachmann, *Appl. Phys. Lett.*, **36**, 710 (1981).
8. A. Heller, B. Miller, H. J. Lewerenz, and K. J. Bachmann, *J. Am. Chem. Soc.*, **102**, 6555 (1980).
9. B. Scrosati and L. Fornarini, *This Journal*, **131**, 948 (1984).
10. E. Buehler and J. H. Wernick, *J. Cryst. Growth*, **8**, 324 (1971).
11. JCPDS (Joint Committee on Powder Diffraction Studies): File 20-1294 (Sn₄P₃), File 22-517 (CdSnP₂), International Center for Diffraction Data, Swarthmore, PA (1978).
12. L. Häggström, J. Gullman, T. Ericsson, and R. Wäppling, *J. Solid State Chem.*, **13**, 204 (1975).
13. J. A. Turner, J. Manassen, and A. J. Nozik, *Appl. Phys. Lett.*, **37**, 488 (1980); G. Cooper, J. A. Turner, and A. J. Nozik, *This Journal*, **129**, 1973 (1982).
14. W. W. Gärtner, *Phys. Rev.*, **116**, 84 (1959).
15. G. F. Karavaev, *Phys. Status Solidi A*, **45**, 443 (1971).
16. J. L. Shay and E. Buehler, *Phys. Rev. Lett.*, **26**, 506 (1971).
17. A. Heller, G. P. Schwartz, R. G. Vadimsky, S. Menezes, and B. Miller, *This Journal*, **125**, 1156 (1978).
18. G. A. Medvedkin, Yu. V. Rud, Yu. A. Valov, and V. I. Sokolova, *Phys. Status Solidi A*, **45**, K95 (1978).
19. I. A. Karpovich, *Sov. Phys. Semicond.*, **10**, 594 (1976).

Electrode Kinetics in Nonaqueous Aprotic Solvents

Jacob Jorné*

Department of Chemical Engineering, University of Rochester, Rochester, New York 14627

Purnachandra G. Pai*

Energy Conversion Devices, Inc., Troy, Michigan 48084

ABSTRACT

The electrode kinetics of Na⁺ reduction are studied at dropping mercury electrode in four polar aprotic solvents, propylene carbonate (PC), dimethylformamide (DMF), dimethylsulfoxide (DMSO), and acetonitrile (AN), using the faradaic impedance method. The true rate constants measured for 1M NaClO₄ in PC, DMF, DMSO, and AN are 0.38, 0.21, 0.05, and 0.35 cm·s⁻¹, respectively. The corresponding cathodic transfer coefficients are measured to be 0.62, 0.81, 0.43, and 0.42, respectively. Na⁺ reduction is found to be a simple charge-transfer reaction, based on its conformance to the analysis using the classical Randles circuit. Using relative rate constants (k_{sh}^1)_{rel} for Na⁺ with water as reference solvent, a standard potential scale for Na⁺/Na vs. NHE is developed for all four solvents and compared with standard potential scales for K⁺/K vs. NHE. The surface potentials of all four solvents are calculated to be positive and discussed in terms of solvent dipole orientation. Comparison of rate constants and free energy of Na⁺ solvation is made to determine the effect of solvation on the kinetics of Na⁺ reduction in PC, DME, DMSO, and AN. The trend of standard rate constants follows the trend of sodium ion solvation in the nonaqueous solvents PC ≅ AN < DMF < DMSO.

The developments in electrochemical energy conversion and storage and the need for high energy density have created a growing interest in the electrochemistry of alkali metals in nonaqueous solvents (1, 2). The fact that the rate constant of an electrochemical reaction can vary significantly from one nonaqueous solvent to another raises a very fundamental question: What is the influence of the solvent on the rate of an electrochemical reaction?

The purpose of the present work is to study the electrode kinetics for sodium ion reduction in four popular aprotic solvents and to attempt to correlate the rate constants with the thermodynamics of ion solvation in the four solvents. A comparative study of the electrode kinetics of Na⁺ reduction was therefore conducted in four aprotic solvents: propylene carbonate (PC), dimethyl formamide (DMF), dimethyl sulfoxide (DMSO), and acetonitrile (AN), using dropping mercury electrode (DME) and the faradaic impedance method. These solvents are widely used in electrochemistry due to their high dielectric constants, the unavailability of a proton for reduction, their weak acidic and basic characters, and their relatively low viscosities.

The rate of a simple charge-transfer electrochemical reaction is affected by factors such as electrode kinetics, solvation, double-layer effects and thermodynamics. These aspects are discussed below.

Kinetics and energetics in nonaqueous solvents.—The electrode kinetics and the equilibrium of an electrochemical reaction are greatly affected by the nature of the solvent and the electrolyte employed. There are various reasons, usually difficult to explain in a simplified manner, for such differences in rate constants and equilibrium properties. Factors such as medium effects, solvation of ions, and the free energy, enthalpy, and entropy changes occurring during an electrode reaction, and double layer vary from one solvent to another. Thermodynamic measurements, namely, emf, calorimetric, and solubility measurements, are usually used for the study of free energy, enthalpy, and entropy changes for electrochemical reaction. The rate constants of an electrode reaction in different solvents also aid in the evaluation and comparison of the free energy changes associated with an electrode process.

Consider the electrode reaction at a mercury electrode



where $M_{(s)}^+$ is the solvated cation and M^\ddagger is the activated complex of the metal ion. For this reaction, the true heterogeneous rate constant may be expressed in general terms as

* Electrochemical Society Active Member.

$$k_{sh}^1 = \tau(kT/h) \exp [(-\Delta G_o^\ddagger - \beta nF\phi_{(m)}^0)/RT] \quad [2]$$

where τ is the transmission coefficient (taken approximately as unity), (kT/h) is the universal frequency factor, ΔG_o^\ddagger is the electrochemical standard free energy of activation, defined as the difference in free energy between the solvated ion and the activated complex, $\phi_{(m)}^0$ is the standard electrode potential of the metal, and β is the cathodic transfer coefficient. Equation [2] may also be written in the form

$$k_{sh}^1 = \tau(kT/h) \exp [(\Delta G_s^0(M^+) - \Delta G_s^0(M^\ddagger) - \beta nF\phi_{(m)}^0)/RT] \quad [3]$$

where $\Delta G_s^0(M^+)$ and $\Delta G_s^0(M^\ddagger)$ are the solvation energies of the ion and the activated complex, respectively.

In order to compare the standard electrode potential, $\phi_{(m)}^0$, in different solvents, one must have either a common reference electrode workable in all solvents under consideration or a means to determine the liquid junction potential between the solvents. Both of these conditions are not easily surmountable and hence pose problems in comparison of $\phi_{(m)}^0$. Furthermore, the energetics of the activated complex of M^\ddagger in various solvents is unknown, which makes the comparison of the rate constants in various solvents difficult. This has led to the concept of relative rate constant, $(k_{sh}^1)_r$, defined by

$$(k_{sh}^1)_r = (k_{sh}^1)_1 / (k_{sh}^1)_2 = \exp [(\Delta G_t^0(M^+) - \Delta G_t^0(M^\ddagger) + nF(\beta_2\phi_2^0 - \beta_1\phi_1^0))/RT] \quad (4)$$

where subscripts 1 and 2 refer to solvents 1 and 2, $\Delta G_t^0(M^+)$ and $\Delta G_t^0(M^\ddagger)$ are the standard electrochemical free energy of transfer of M^+ and M^\ddagger from solvent 2 to solvent 1, β is the cathodic transfer coefficient, and ϕ^0 is the standard electrode potential. Equation (4) is helpful in comparison and evaluation of standard electrochemical free energy of transfer of M^+ and M^\ddagger from one solvent to another when the rest of the parameters are known.

Double-layer effects.—The double layer plays a key role in the kinetics, since the electrode reaction occurs within the double layer. This complicates the simple charge-transfer process, and either a prior knowledge of the double-layer capacitance or the elimination of its effects on the reaction rates is essential in our study. At high concentrations of the solute, the effects of the diffuse double layer diminish substantially and one may neglect the variation of the diffuse double-layer potential with the total metal-solution potential difference. Thus, fairly concentrated (1M) solutions of NaClO₄ are used in this investigation.

The structure of the solvent and the solvation of the ion affect the structure of the double layer and the specific

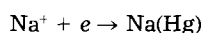
adsorption of an ion on the electrode surface. It has been noted in several double-layer studies (5, 6) that ClO_4^- anion is less specifically adsorbed from various aprotic solvents than halide ions. The solvation in aprotic solvent depends on the polarizability of the anion which increases with the size of the anion (7). Hence it is considered that the choice of NaClO_4 as the solute minimizes the effect of specific adsorption on the kinetics of the electrode reaction.

Scope of the present work.—Since the effects of the medium on the electrode reaction and the role of a solvent in solvating an ion taking part in an electrode reaction are of particular interest to this study, the measurement of kinetic parameters and their comparison in various solvents make up the major part of this study. The investigation concentrates on the determination of the kinetic parameters for the reaction $\text{Na}^+ + e \rightleftharpoons \text{Na}(\text{Hg})$ in NaClO_4 -PC, DMF, DMSO, and AN solutions.

The free energies of transfer of cations from one solvent to another can also be related to the rate constants of those cations in the respective solvents. Using this principle and some extra thermodynamic assumptions, an attempt has been made to determine a relationship between free energies of transfer of Na^+ , from various solvents to water, and the rate constants for Na^+ reduction in various solvents.

Experimental

Faradaic impedance measurements.—Faradaic impedance measurements were conducted in 1M NaClO_4 in PC, DMF, DMSO, and AN to determine kinetic parameters for the reaction



at dropping mercury electrode (DME). Lower concentrations of 0.5 and 0.1M NaClO_4 in PC and 0.1M NaClO_4 in DMF were also employed. To reduce the ohmic resistance at low concentrations of NaClO_4 , tetrabutyl ammonium perchlorate (TBAP) was used as a supporting electrolyte. However, the results with TBAP were not used in the analysis because of a strong evidence of TBAP adsorption even at the potential for sodium reduction.

The DME (Heath Instruments, Benton Harbor, Michigan) was equipped with a Sargent Welch Scientific capillary which was rated for drop times of 2-5s and had an inside diameter of 0.03-0.05 mm. This capillary was further extruded to form an elongated tip to minimize the shading of the tip (8). The bulb at the base of the extruded portion was very small to minimize gas retention (9). The extruded capillary was cut at a right angle to form a smooth edge. The drop time was regulated by the mercury column. Within the potential range employed, the weight of the drops remained the same within 0.5%. A pool of mercury was employed as the counter and reference electrode.

All experiments were conducted in an argon atmosphere glove box. The solvents were purified by storage for 1 week over molecular sieves followed by vacuum distillation (10). The reflux ratio was 1:10. The water content in the purified solvents was measured gas chromatographically to be below 10 ppm in PC, and below 20 ppm in DMF, DMSO, and AN using Karl Fisher titration. Salts were dried at 100°C under vacuum with periodic flushes of argon.

The impedance bridge (Electroscientific Industries, Portland, Oregon, Model 290B) and the ac generator-detector (Model 861A) were used to measure the cell impedance. In all the measurements, the equivalent circuit for the unknown cell was considered to be a capacitance in series with a resistance. Sluyters-Rehbach and Sluyters (11) used a similar bridge circuit. A Model 280 Wenking potentiostat was used for the dc bias potential. The frequency range was 20 Hz-20 kHz. Two different methods were used for measuring the ohmic resistance at DME. The first was made using the impedance bridge in a resistance mode after compensating for the electrode capacitance at constant frequency. The second was conducted

in a capacitance mode, at constant frequency and a potential outside the faradaic region. Both methods gave concurrent results within 1%.

The behavior of 1M NaClO_4 solutions in all four solvents followed the classical Randles circuit. The Warburg's coefficient, σ , charge-transfer resistance, θ , anodic transfer coefficient, α , and the apparent rate constant, k_{sh}^{a} , were evaluated by analysis of the electrode admittance. The measured resistance and capacitance for each solution at constant potential and varying frequency were converted to electrode impedances and then to electrode admittances, after accounting for the ohmic resistance. The frequency dependence of the admittance components determines the Warburg's coefficient, σ , the charge transfer resistance, θ , and the kinetic parameters k_{sh}^{a} and α . In lower concentrations of 0.5 and 0.1M NaClO_4 in PC and DMF and in the presence of TBAP supporting electrolyte, specific adsorption was detected. The adsorption admittance was separated from the total admittance (11) to evaluate the kinetic parameters. The electrode admittance analysis is detailed elsewhere (10, 12, 39). The apparent rate constants were evaluated by approximation, $E_{1/2}^{\text{r}} \approx E_0$, and neglecting the difference in diffusion coefficients. However, the polarographic half-wave potentials obtained from the literature were corrected using the calculated activity coefficients following the Debye-Hückel equation (10). Furthermore, the true rate constant, k_{sh}^{t} , and anodic transfer coefficients, α , were obtained by correcting the apparent parameters for double-layer effect using the differential double-layer capacity curves.

Results and Discussion

Data analysis.—The data for the impedance measurements, after subtraction of the solution resistance, were converted to admittance

$$Y'_{\text{e1}} = \frac{\omega^{1/2}}{\sigma} \frac{p+1}{(p+1)^2 + 1} \quad [5]$$

$$Y''_{\text{e1}} = \frac{\omega^{1/2}}{\sigma} \frac{1}{(p+1)^2 + 1} + \omega C_d \quad [6]$$

where

$$p = \frac{\theta}{\sigma\omega^{-1/2}} = p'\omega^{1/2} \quad [7]$$

and plots of $(Y'_{\text{e1}})^{-1} \omega^{1/2}$ vs. $\omega^{1/2}$ were made, where Y'_{e1} is the real admittance and ω is the frequency. The trends of these plots indicate the presence of specific adsorption and deviation from the Randles circuit. An example is shown in Fig. 1 and 2 for 1M NaClO_4 in PC where no deviation from the classical Randles circuit is observed. Approximate Warburg's coefficients, σ , which can be estimated by extrapolation of $Y'_{\text{e1}})^{-1} \omega^{1/2}$ vs. $\omega^{1/2}$ plot at low frequencies to $\omega = 0$, were very close to the σ values obtained by numerical data fitting. An example of a plot of $\log \sigma$ vs. E for 1M NaClO_4 in PC is shown in Fig. 3. As expected from theory, this plot is a straight line with a slope of -15.74V^{-1} , which closely compares with the theoretical slope of -16.91V^{-1} . The values of $p' = \theta/\sigma$ were obtained by finding a frequency-independent C_d for each potential. The charge-transfer resistance, θ , was obtained at each potential by numerical fitting. A plot of $-\log p'$ vs. E is shown in Fig. 4. The anodic transfer coefficient, α , can be obtained from the slope; in this particular example, $\alpha = 0.38 \pm 0.15$. The apparent rate constant k_{sh}^{a} is obtained by extrapolating Fig. 4 to $E_{1/2}$. In this particular example, $k_{\text{sh}}^{\text{a}} = 0.81 \pm 0.17 \text{ cm s}^{-1}$.

The same analysis has been performed for all the experimental systems in the four various solvents. The details of the analyses are presented elsewhere (10).

Kinetic parameters.—A summary of apparent rate constants and anodic transfer coefficients for Na^+ reduction in the four solvents in presented in Table I.

The standard heterogeneous true rate constants were obtained by double-layer correction (12)

$$k_{\text{sh}}^{\text{a}} = k_{\text{sh}}^{\text{t}} \gamma_0^\alpha \gamma_{\text{R}}^\beta \exp(-anF\phi_s/RT) \quad [8]$$

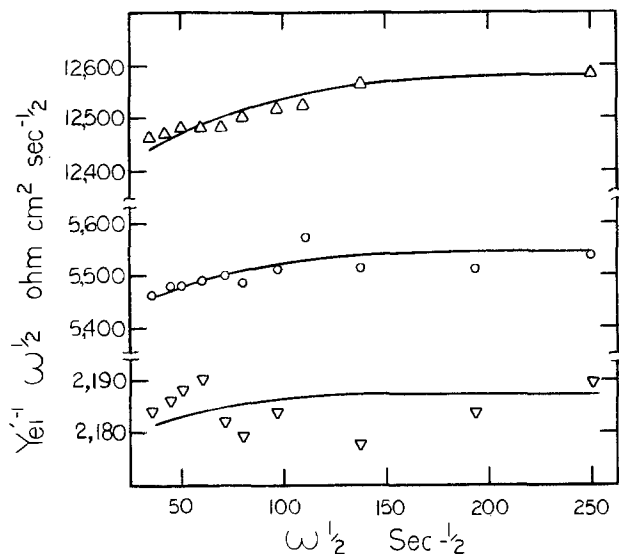


Fig. 1. $(Y'_{ei} \omega^{-1/2})$ vs. $\omega^{1/2}$ plots in 1M NaClO₄-propylene carbonate. E vs. Hg pool: (Δ)-1.85V; (O)-1.875V; (∇)-1.900V (expanded scale).

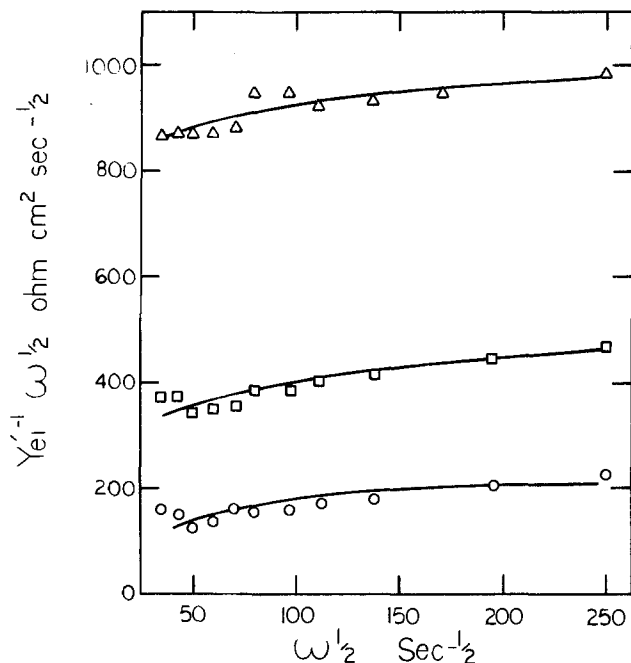


Fig. 2. $(Y'_{ei} \omega^{-1/2})$ vs. $\omega^{1/2}$ plots in 1M NaClO₄-propylene carbonate. E vs. Hg pool: (Δ)-1.925V; (\square)-1.950V; (O)-1.975V.

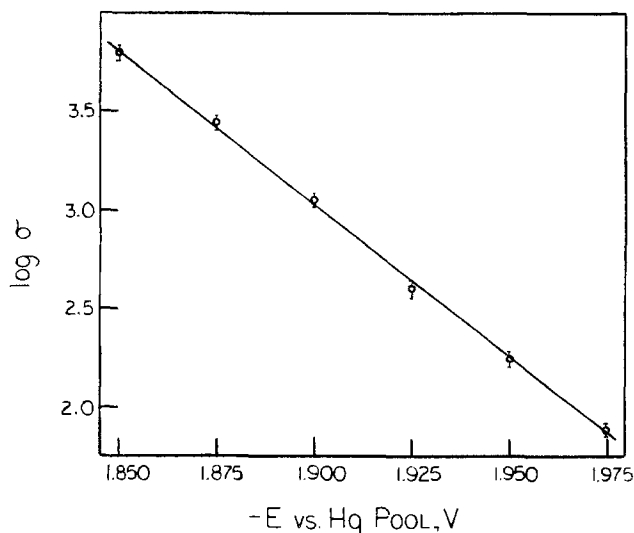


Fig. 3. $\log \sigma$ vs. E plot for 1M NaClO₄ in propylene carbonate

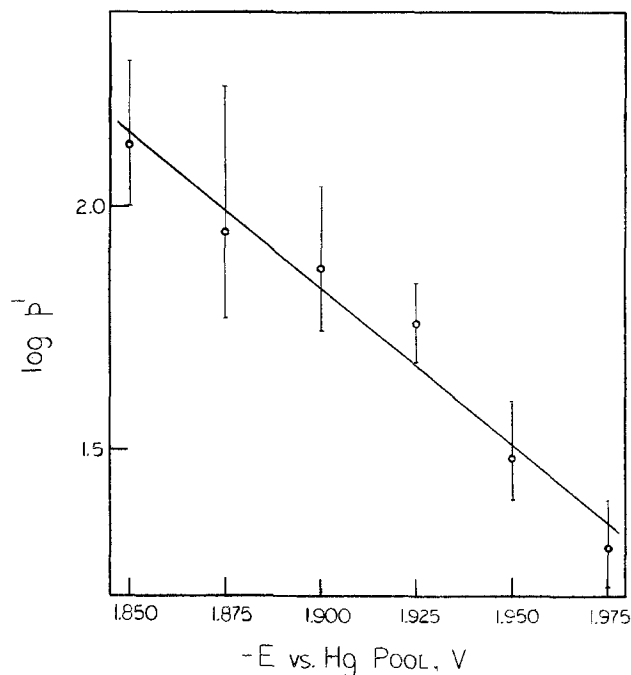


Fig. 4. $-\log p'$ vs. E. plot for 1M NaClO₄ in propylene carbonate

where ϕ_2 is the potential of the outer Helmholtz layer and γ_0 and γ_R are the activity coefficients of the oxidized and reduced species, respectively. The coefficient α is related to the apparent α^a by

$$\alpha^a = \alpha + g$$

where $g = (RT/nF)d(\ln k_{sh}^a)/dE$ is the double-layer correction to the apparent anodic transfer coefficient (13).

The double-layer correction is frequently referred to as the "Frumkin correction." In order to determine ϕ_2 , it is necessary to know the potential dependence of the double-layer capacity. The capacity vs. potential curve can be integrated to give the electrode surface charge density q^M

$$q^M = \int_{E_z}^E C dE \quad [9]$$

where E_z is the potential of zero charge. The surface charge density is related to ϕ_2 according to the Gouy-Chapman theory.

Differential double-layer capacity curves in nonaqueous solvents.—The double-layer capacity studies in nonaqueous solvents are not as abundant as in aqueous systems. The double-layer capacitance curves for the propylene carbonate-NaClO₄ system are given by Biegler and Parsons (16). It may be noted that at far cathodic potentials, $E < -1.5V$ (vs. Ag/Ag⁺), the differential capacity is virtually independent of NaClO₄ concentration in PC. The differential capacitance curve for 0.5M NaClO₄ in dimethylformamide is reported by Doilido *et al.* (17). They studied the effect of deoxygenation of the solution on the ECM in this system. The potential of zero charge is taken as 0.80V vs. NCE. The differential capacity curves for 0.1M NaNO₃ and 0.1M LiClO₄ in DMSO are reported by

Table I. Apparent and true rate constants for Na⁺ reduction in nonaqueous systems

System	k_{sh}^a (cm/s)	k_{sh}^t (cm/s)	α , anodic transfer coefficient
PC-1M NaClO ₄	0.81 ± 0.17	0.38 ± 0.09	0.38 ± 0.15
DMF-1M NaClO ₄	0.35 ± 0.11	0.21 ± 0.07	0.19 ± 0.06
DMSO-1M NaClO ₄	0.90 ± 0.31	0.05 ± 0.03	0.57 ± 0.12
AN-1M NaClO ₄	1.93 ± 0.17	0.35 ± 0.04	0.58 ± 0.22

Payne (18). The 0.1M NaNO₃ curve is used for obtaining q_m . The potential of zero charge of the 0.1M NaNO₃-DMSO system is -0.303V vs. aqueous NCE (18). The differential capacity vs. potential curve for 0.8M NaClO₄ in acetonitrile shows that the ECM occurs at a potential -0.380V vs. SCE (19).

The potential ϕ_2 can be determined by the Gouy-Chapman theory for symmetrical electrolyte

$$q^M = 41.887 \times (DC^*)^{1/2} \sinh(19.46Z\phi_2) \quad [10]$$

where C^* , the bulk concentration, is in moles per cubic centimeter and D is the dielectric constant. The values of q^M are obtained by integration of the differential double-layer capacity curves according to Eq. [9]. The obtained values of q^M and the corresponding values of ϕ_2 , calculated according to Eq. [10], are shown in Table II.

Based on the calculated ϕ_2 , $d\phi_2/dE$ were calculated, assuming a linear relationship, and substituted in a differential form of Eq. [8] in order to obtain $d(\ln k_{sh}^a)/dE$, which was subsequently used to obtain g . In all the cases, the values of g so obtained were smaller than the error limits on α^a and, hence, no correction was applied to the value of α . However, based on values of ϕ_2 , the values of k_{sh}^a were corrected to obtain k_{sh}^t . The true rate constants, k_{sh}^t , along with the apparent rate constants, k_{sh}^a , and anodic transfer coefficient, α , are shown in Table I.

Rate constants in nonaqueous solvents.—The results in Table I show that standard rate constants for Na⁺ reduction in nonaqueous solvents are at least an order of magnitude smaller than the standard rate constant for Na⁺ observed in water (>3.4 cm s⁻¹) using low concentrations of NaI with 1M LiCl supporting electrolyte (13). Qualitatively, the trend of standard rate constants follows the trend of solvation of ions in the nonaqueous solvents.

The relative magnitude of the standard rate constants in the various solvents indicates that Na⁺ ion is solvated in the order PC \approx AN < DMF < DMSO. The relevant discussion of this trend with respect to solvation is given below.

Kinetic parameters in PC.—It is interesting to note that the rate constants for Na⁺ reduction in PC are comparable to those measured by Hills and Peter (20). Using voltammetric measurements at hanging mercury drop electrode (HMDE), they have obtained kinetic parameters for several cations in PC and DMSO. The peak potential separation for Na⁺ reduction remained unchanged at 60 mV at sweep rates of up to 10³ V s⁻¹, hence it was concluded that the k_{sh}^a for Na⁺ is greater than 1.0 cm s⁻¹ and Na⁺ reduction reaction is totally diffusion controlled in PC. Jorné and Tobias (21, 22) also have measured the standard rate constants for the reduction of alkali-metal cations in AlCl₃ (1M)-PC using micropolarization technique. They used stationary pools of alkali-metal amalgams for working and counterelectrodes. The measured apparent rate constant for Na⁺ in AlCl₃ (1M)-PC was 0.0492 cm s⁻¹, which is much lower than the rates measured by Hills and Peter and the current study. The difference may be attributed to the measurement techniques as well as the nature of the working electrode employed. Both the DME and HMDE have advantages over a stationary pool elec-

trode in that DME has a continuously renewed surface concentration which changes with the increasing drop size and HMDE can be extruded to perform the measurements instantaneously. This enables one to avoid the adsorption of reactants, products, and contaminants at the surface of the electrode. Hills and Peter (20) have claimed that adsorption of contaminants was avoided by preparing the Hg drop and conducting the measurements rapidly. Hence, the lower rate constant for Na⁺ in PC measured by Jorné and Tobias (21, 22) may be due to the adsorption of the impurities on the electrode surface. Hills and Peter (20) were unable to measure the cathodic transfer coefficient for Na⁺. However, the cathodic transfer coefficient of 0.61 measured by Jorné and Tobias (21, 22) closely agrees with our cathodic transfer coefficient of 0.62.

Kinetic parameters in DMF.—Baranski and Fawcett (23) have measured the standard rate constant for Na⁺ reduction in DMF and the effect of supporting electrolyte on the measured rate constant. The variation is only observed in apparent rate constants, since true rate constants, which are obtained through double-layer correction, are independent of concentrations of the active and supporting electrolytes. The method of measurement used by Baranski and Fawcett (23) is similar to this method, and their measured apparent rate constant of 0.16 cm s⁻¹ agrees reasonably with our rate constant of 0.21 cm s⁻¹. However, their cathodic transfer coefficient of ~ 0.5 differs from the present value of 0.81 for 1M NaClO₄ in DMF.

Analysis of the electrode admittance showed the presence of specific adsorption for 0.1M NaClO₄ + 0.5M TBAP in DMF for our study. Baranski and Fawcett (23) have noted that, when a supporting electrolyte of a larger ion is used in place of a smaller ion, e.g., TBAP in place of TEAP, there is a marked increase in the apparent transfer coefficient. However, for 0.1M NaClO₄ + 0.5M TBAP in DMF, in our case, there was no significant change in the transfer coefficient compared to 1M NaClO₄ in DMF. Similar specific adsorption was noticed for 0.5M NaClO₄ + 0.375 TBAP in PC and 0.5M NaClO₄ + 0.375 TBAP in PC during the analysis of our admittance data.

Kinetic parameters in DMSO.—In DMSO, the Na⁺ ion is strongly solvated (20), and, consequently, one should expect a lower standard rate constant for Na⁺ reduction. The measured standard rate constant of 0.05 cm s⁻¹ for Na⁺ reduction in DMSO is the lowest of all the four solvents. Hills and Peter (20) measured the apparent rate constant of 0.014 cm s⁻¹ for Na⁺ in DMSO, which is reasonably close to our measurement. However, they did not measure the cathodic transfer coefficient for Na⁺ because of the limitations of their methods. The Na⁺ reduction reaction is considered to be quasi-reversible (0.1 > k_{sh}^a > 0.01) because of the magnitude of the apparent rate constant. It may be noted that this is strictly a qualitative observation.

Kinetic parameters in AN.—AN is supposed to be a weak solvator of Na⁺ (23), and Na⁺ reduction in AN is reversible. A standard rate constant of 0.57 cm s⁻¹, using ac admittance technique, has been measured for Na⁺ in 0.1M TEAP supporting electrolyte in AN (23). The cathodic transfer coefficient measured was 0.55. This compares reasonably with the standard rate constant of 0.35 cm s⁻¹ and cathodic transfer coefficient of 0.42 measured in this study.

Energetics in nonaqueous solvents.—Free energy of transfer and standard potential.—Since the kinetic parameters and free energy of transfer are affected by the nature of the solvent, Eq. [11] may be used to compare $\Delta G_i^o(\text{Na}^+)$, $\Delta G_i^o(\text{Na}^{\#})$, and $\phi^o(\text{Na}^+)$ from water to various solvents

$$(K_{sh}^t)_r = (k_{sh}^t)_r / (k_{sh}^t)_w = \exp \{ [\Delta G_i^o(\text{Na}^+) - \Delta G_i^o(\text{Na}^{\#}) + nF(\beta_2\phi_2^o - \beta_1\phi_1^o)] / RT \} \quad [11]$$

Experimentally determined free energies of transfer for Na⁺ from water to various solvent are listed in Table III.

Table II. Surface charge densities and outer Helmholtz potentials in nonaqueous solvents

Solvent	Electrolyte	E_z (V)	q^M ($\mu\text{C}/\text{cm}^2$)	ϕ_2 (V)
PC	0.9M NaClO ₄	1.0 ^a	12.80	-0.052
PC	0.5M NaClO ₄	1.0	12.35	-0.065
PC	0.1M NaClO ₄	1.0	11.91	-0.102
DMF	0.5M NaClO ₄	0.8 ^b	8.79	-0.063
DMSO	0.1M NaNO ₃	0.303 ^c	17.55	-0.129
AN	0.8M NaClO ₄	0.380 ^d	14.34	-0.075

^a vs. Ag/Ag⁺ electrode from Ref. (16).

^b Estimated from Ref. (17) vs. NCE.

^c vs. NCE from Ref. (18).

^d vs. SCE from Ref. (19).

Table III. Free energy of transfer for Na⁺ from water to various solvents

Solvents	$\Delta G_t^\circ(\text{Na}^+)^a$ (kcal/g-mol)	$\Delta G_t^\circ(\text{Na}^+)$ (kcal/g-mol)
	I	II
PC	+3.6	-0.5 ^b
DMF	-2.5	-2.5 ^a
DMSO	-3.3	-3.3 ^a
AN	+3.3	-2.3 ^c

^a Ref. (24), TATB assumption.

^b Ref. (26, 27).

^c Estimated from Ref. (28, 29).

It is noted that $\Delta G_t^\circ(\text{Na}^+)$ values in column I of Table III are listed by Popovych and Tomkins (24). These values are determined through the TATB extrathermodynamic assumption, which states that the free energy of solvation for tetraphenylarsonium ion (Ph_4As^+) is equal to the free energy of solvation of tetraphenylborate ion (Ph_4B^-) in all the solvents. Krishnan and Friedman (25) have given a brief explanation of this assumption. TATB assumption is one of many in a class of extrathermodynamic assumptions, which are generated through similar arguments. However, when a generalized scale for single free energies ΔG° are prepared through TATB assumption, errors may exist which may be uniform throughout. The values of $\Delta G_t^\circ(\text{Na}^+)$ in column II for PC and AN are derived from independent studies. The references are listed in Table IV. The values of $\Delta G_t^\circ(\text{Na}^+)$ from H₂O to PC and AN are given as +3.6 and +3.3 kcal/g-mol, respectively, in column I, which would indicate that Na⁺ is more solvated in H₂O than in PC and AN, which is not believed to be true. Solomon (26-27) has determined -0.5 kcal/g-mol for Na⁺ transfer through EMF measurements. Jorné and Tobias (30, 31) also have measured $\Delta G_t^\circ(\text{Na}^+)$ for Na⁺ transfer from water to $\text{AlCl}_3(1m)$ -PC to be negative (-4.2 kcal/g-mol). These measurements indicate Na⁺ to be more solvated in PC and $\text{AlCl}_3(1m)$ -PC systems than in water. Hence, the values of $\Delta G_t^\circ(\text{Na}^+)$ in column II of Table III are believed to be more reliable and are used in the determination of $\phi^\circ(\text{Na}^+)$, the standard potential of Na⁺ in various solvents.

In order to determine $\phi^\circ(\text{Na}^+)$ from Eq. [11], one must know $\Delta G_t^\circ(\text{Na}^\ddagger)$, the free energy of transfer of the activated complex. There is no information available regarding $\Delta G_t^\circ(\text{Na}^\ddagger)$. Generally, the activated complex is considered to have the same free energy in all the solvents. Consequently, $\Delta G_t^\circ(\text{Na}^\ddagger)$ may be considered to be zero. Parker (32), in an elaborate review of bimolecular reactions in nonaqueous solvents, has found this to be true. Solomon (27) also has demonstrated, in his study of ion solvation in methanol, that the free energy of transfer of the activated complex from water to an organic solvent to be, effectively, zero. Hence, based on this assumption and using $\Delta G_t^\circ(\text{Na}^+)$ in Table III and Eq. [11], the values of $\phi^\circ(\text{Na}^+)$ were calculated and are shown in Table IV.

Parker and co-workers (33) have determined the transfer properties of several ions in nonaqueous solvents,

using heats of solution and heat of precipitation measurements. With the aid of TATB assumption, they have developed a standard potential scale for K⁺/K vs. NHE, which is presented in Table IV. Comparison of $\phi^\circ(\text{Na}^+/\text{Na})$ and $\phi^\circ(\text{K}^+/\text{K})$ scales shows that Na⁺ is more electropositive than K⁺ in all the solvents under consideration. This observation is consistent with the findings of Jorné and Tobias (21) for $\text{AlCl}_3(1m)$ -PC system and of Solomon (27) for PC. Pleskov (34) has measured the standard potential of Na⁺ in AN to be -2.87V, which is comparable to -2.778 vs. NHE obtained in this study. It must be noted that $\phi^\circ(\text{Na}^+/\text{Na})$ is derived by assuming $\Delta G_t^\circ(\text{Na}^\ddagger)$ to be zero, and hence, any discrepancies in the values of $\phi^\circ(\text{Na}^+/\text{Na})$ obtained may be attributed to this assumption.

Surface potentials in nonaqueous solvents.—With the knowledge of $\phi^\circ(\text{Na}^+/\text{Na})$ in various solvents, the surface potential χ of a solvent may be calculated using the following

$$\Delta\phi^\circ(\text{Na}^+) = \phi^\circ(\text{Na}^+)_1 - \phi^\circ(\text{Na}^+)_2 \\ = \Delta G_t^\circ(\text{Na}^+)/nF + (\chi_1 - \chi_2) \quad [12]$$

where χ_1 and χ_2 are the surface potentials of the solvents under consideration. The calculated surface potentials for all the solvents studied are listed in Table IV. It is noted that all four solvents and water have positive surface potentials.

The surface potential of a solvent indicates the orientation of the solvent dipole at the interface of the solvent and the electrode. As a general rule, it is assumed that for dipolar aprotic solvents the sign of the surface potential indicates the charged end of the dipole pointing toward the electrode surface. Thus, if the surface potential of the solvent is positive, the positive end of the dipole is pointing toward the electrode and vice versa. However, this is an oversimplified view for the analysis of the surface potential of a solvent. There are other interactions occurring at the electrode surface besides the ion-dipole interaction and the specific adsorption of the solvent molecule. There exists considerable experimental evidence that points to the fact that preferred orientation of water dipole in aqueous solution is that with the negative end of the dipole toward the metal. However, it is known that water has positive surface potential (18, 36).

Payne (37), through the capacitance measurements at the mercury electrode, has concluded that the positive end (methyl group) of the PC dipole orients toward the electrode surface. This is in qualitative agreement with the surface potential of +0.179V obtained in this study. The conformational analysis of PC molecules adsorbed at a mercury electrode is presented by Brasseur and Hurwitz (40) and compared to experimental capacitance measurements. Yeager *et al.* (41) studied spectroscopically the ionic solvation in PC. Considerable electron density was found on all PC oxygen atoms, while the positive end was found to be diffuse.

An explanation for the orientation of simple aliphatic molecules at the mercury electrode is given by Payne (18). The two methyl groups, which form the positive end of

Table IV. Standard potentials and surface potentials in nonaqueous solvents^e

Solvent	Relative rate constant ($k_{sh}^{\ddagger})_{rel}^a$	$\phi^\circ(\text{Na}^+/\text{Na})$ vs. NHE (V)	$\Delta\phi^\circ(\text{Na}^+)^d$	$\phi^\circ(\text{K}^+/\text{K})^b$ vs. NHE (V)	χ , Surface potential (V)
PC	0.111	-2.653	+0.057	-2.918	+0.179
DMF	0.062	-2.771	-0.061	-3.028	+0.147
DMSO	0.015	-2.768	-0.058	-3.050	+0.185
AN	0.103	-2.778	-0.068	-2.826	+0.132
H ₂ O	1.000	-2.710	0.000	-2.924	+0.1 ^c

^a ($k_{sh}^{\ddagger})_{H_2O} = 3.4 \text{ cm s}^{-1}$, Ref. (13, 35).

^b TATB assumption, Ref. (33).

^c Ref. (36).

^d $\Delta\phi^\circ(\text{Na}^+) = \phi^\circ(\text{Na}^+)_1 - \phi^\circ(\text{Na}^+)_w$.

^e For 1M NaClO₄ systems.

the DMSO dipole, tend to orient themselves facing the electrode surface. Also, since DMSO has a large dipole moment (4.3D), owing to its sulfoxide group, a positive surface potential is observed at the electrode surface. The crystallographic data for molecular models at low temperature point to the suggestion that the DMSO dipole might be directed away from the normal to the electrode surface by as much as 60°. The obtained value of +0.185V for the surface potential of DMSO concurs with the considerations of Payne (18) and Solomon (27), since the value is positive and any discrepancy in the value itself may be attributed to experimental errors and extrathermodynamic assumption (TATB).

According to Payne (18), DMF molecules also follow the same trend at the electrode surfaces as DMSO. The DMF molecule with its large dipole moment (3.8D), due to the C-O end of the molecule, tends to orient the two methyl groups (the positive end) toward the electrode surface. This orientation of DMF is stronger than DMSO, and hence, reorientation does not occur as in the case of DMSO. A positive surface potential of +0.147V for DMF is consistent with the observations made by Payne (18, 5) through the double-layer capacity studies.

The AN molecule, in comparison, is not as large a molecule as DMSO, but has a comparable dipole moment (3.84D). The nitrogen (N⁻) forms the negative end of the dipole. Solomon (27, 28) has estimated the value for the surface potential of AN in the vicinity of -1.0V. The negative sign indicates that the N⁻ end of the AN dipole is oriented towards the electrode surface. This observation, however, is not consistent with our calculated value of the surface potential of +0.1V for AN. Using similar data for K⁺, $\Delta G_T^\circ(\text{K}^+) = 1.6$ kcal/g-mol (24) and $\phi^\circ(\text{K}^+/\text{K})$ from Table V (33), we can calculate a value of +0.128V for the surface potential of AN. This value is consistent with our findings and, hence, we may qualitatively state that AN dipole has the methyl group oriented toward the electrode.

Free energy of transfer of activated complex Na[‡].—In the foregoing discussion, it was assumed that $\Delta G_T^\circ(\text{Na}^\ddagger)$ in Eq. [11] was equal to zero. It may be noted that there are empirical methods of calculating $\Delta G_T^\circ(\text{M}^\ddagger)$ for an activated complex. However, the information so obtained is of very little use. Solomon (27) has stated that $\Delta G_T^\circ(\text{M}^\ddagger)$, which may be calculated empirically, explains everything but is of no value in predicting anything. Secondly, the extrathermodynamic assumptions made in the determination of single-ion free energies in any solvent result in certain error which may be small as compared to the magnitude of free energy of solvation of the ion [$\Delta \bar{G}^\circ(\text{M}^+)_{\text{solv}}$]. But, when compared to the free energy of transfer [$\Delta G_T^\circ(\text{M}^+)$], this error can be enormous. For example, single-ion solvation free energies in water for various ions are listed from ten different sources (28). For Na⁺, $-\Delta \bar{G}^\circ_{\text{solv}}(\text{Na}^+)$ varies between 72.4 and 107 kcal/g-mol. When $\Delta G_T^\circ(\text{Na}^+)$ is calculated for the transfer of Na⁺ from water to any other solvent, variations in $\Delta G_T^\circ(\text{Na}^+)$ could be as large as ~35 kcal/g-mol. In view of this fact, if one assumes $\Delta G_T^\circ(\text{Na}^\ddagger) = 0$, the error caused by such assumption will be much smaller than those caused through experimental errors and extrathermodynamic assumptions.

Solomon (27) has discussed the effect of the $\Delta G_T^\circ(\text{M}^\ddagger) = 0$ assumption on the proton discharge at Hg cathodes in MeOH and water. He has calculated $\Delta G_T^\circ(\text{H}^\ddagger)$ to be 35 cal/g-mol, which is very small compared to -2.9 kcal/g-mol used for $\Delta G_T^\circ(\text{H}^+)$. Solomon calculated $\Delta G_T^\circ(\text{H}^\ddagger)$ using his own measurements for $\Delta \bar{G}^\circ(\text{H}^+)_{\text{solv}}$ in H₂O of -235 kcal/g-mol and $\Delta \bar{G}^\circ(\text{H}^+)_{\text{solv}}$ in MeOH of -237.9 kcal/g-mol. However, when these values are compared to Izmailov's (38) measurements for $\Delta \bar{G}^\circ(\text{H}^+)_{\text{solv}}$, a $\Delta G_T^\circ(\text{H}^\ddagger)$ of -5 kcal/g-mol is obtained, which is roughly 70% larger than Solomon's value. This example is chosen to show the large inherent discrepancies and errors existing in $\Delta G_T^\circ(\text{M}^\ddagger)$ derived through extrathermodynamic assumptions, and it may be concluded that assuming $\Delta G_T^\circ(\text{M}^\ddagger) = 0$ will not add to the error to a great extent. Moreover, assuming the standard free energy of transfer of activated complex from water to any other solvent to be zero greatly simplifies the evaluation of the parameters such as $\phi^\circ(\text{M}^+)$ and χ . Through this assumption, the $\phi^\circ(\text{Na}^+/\text{Na})$ obtained can establish the trend of $\phi^\circ(\text{Na}^+/\text{Na})$ in various solvents and give a magnitude of $\phi^\circ(\text{Na}^+/\text{Na})$ and χ , which may be compared with $\phi^\circ(\text{Na}^+/\text{Na})$ and χ obtained through other similar assumptions.

Solvation in nonaqueous solvents.—In order to determine the effects of solvation and electrostatic ion-ion interactions in a solvent, the modified Born equation along with the donor numbers (DN) may be used. Tanaka (4) has listed DN for several solvents. Using these, the value of δ , the Latimer, Pitzer, and Slansky parameter, may be derived, which in turn will help derive the electrostatic free energy of transfer, $\Delta G_T^\circ(\text{Na}^+)_{\text{el}}$. Table V shows the calculated free energies of transfer for Na⁺ from water to various solvents. It is seen from Table V that $\Delta G_T^\circ(\text{Na}^+)_{\text{el}}$ is negative for DMF and DMSO and positive for PC and AN. This indicates that transfer of Na⁺ from water to PC or AN is "endergonic" and that from water to DMF or DMS "exergonic" (33).

Among the ion-ion- and ion-solvent-type interactions, the "Born-type" interactions contribute about 80% to the free energy of transfer of ion from vacuum to a dielectric medium. Consequently, the $\Delta G_T^\circ(\text{Na}^+)_{\text{solv}}$ reflects only 20% of the interactions between the ions and the solvent.

The values of $\Delta G_T^\circ(\text{Na}^+)_{\text{solv}}$, the solvation free energy of Na⁺ for transfer from water to all the solvents, are negative, and hence, the "ion-solvent interaction" or solvation free energy is higher in all four solvents than in water. The donor-acceptor interactions, H bonding interactions, and structure making and structure breaking interactions contribute to $\Delta G_T^\circ(\text{Na}^+)_{\text{solv}}$ (32). The dipole moments of the solvents also contribute significantly to $\Delta G_T^\circ(\text{Na}^+)_{\text{solv}}$. Generally, a solvent with a higher dipole moment is a better solvent. The dipole moments of H₂O, PC, DMF, DMSO, and AN are 1.84, 4.94, 3.82, 4.3, and 3.84D, respectively. It is noticed that there is no direct relationship between the dipole moments and $\Delta G_T^\circ(\text{Na}^+)_{\text{solv}}$.

In order to relate the rate constants in nonaqueous solvents to their solvation properties, one may consider the general observation regarding transfer of small cations from water to an organic solvent. $\Delta G_T^\circ(\text{M}^+)$ for such transfer is usually negative and, hence, the rate constants in organic solvents are usually lower than those in water.

Table V. Free energies of transfer for Na⁺ from H₂O to various solvents

Solvent	Relative rate constant $(k_{\text{rel}})_{\text{r}}$	Donor number DN ^b	$\delta(\text{\AA})$	$\Delta G_T^\circ(\text{Na}^+)_{\text{el}}$ (kcal/g-mol)	$\Delta G_T^\circ(\text{Na}^+)_{\text{el}}$ (kcal/g-mol)	$\Delta G_T^\circ(\text{Na}^+)_{\text{solv}}$ (kcal/g-mol)	$\Delta G_T^\circ(\text{Na}^+)_{\text{solv}}^{\text{a}}$ (kcal/g-mol)
PC	0.111	15.1	0.8	-0.5	4.6	-5.5	-1.0
DMF	0.062	26.6	0.68	-2.5	-0.9	-1.6	-1.6
DMSO	0.015	29.8	0.66	-3.3	-2.7	-0.6	-0.6
AN	0.103	14.1	0.81	-2.3	6.3	-8.6	-3.0
H ₂ O	1.000	18.0	0.72	—	—	—	—

^a $\Delta G_T^\circ(\text{Na}^+)$ from column I, Table III, TATB assumption, Ref. (24).

^b Ref. (4).

^c $\Delta G_T^\circ(\text{Na}^+) = \Delta G_T^\circ(\text{Na}^+)_{\text{el}} + \Delta G_T^\circ(\text{Na}^+)_{\text{solv}}$.

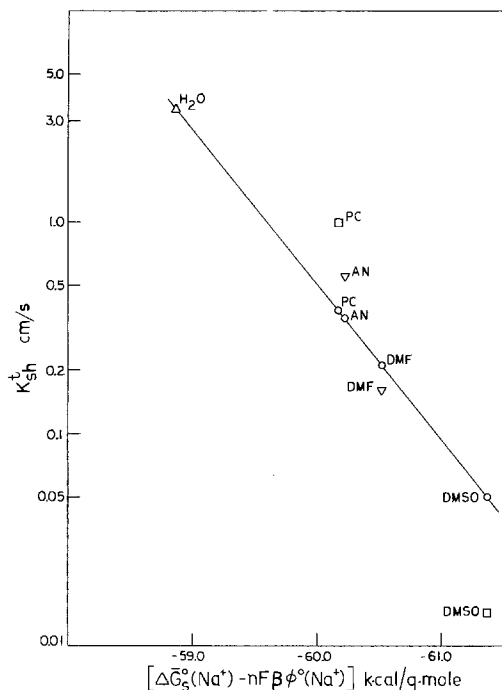


Fig. 5. Plot of true rate constant vs. medium dependent activation energy of (Na^+) in various solvents. (○) current study; (Δ) Reeves *et al.* (13); (□) Hills and Peter (20); (▽) Baranski and Fawcett (23).

Reexamining Eq. [3] and [4], it may be deduced that the rate constant in a medium is exponentially proportional to $\Delta G_s^0(\text{M}^+) - nF\beta\phi^0$, which is the medium-dependent part of the activation energy. In order to illustrate this, $\log k_{sh}^0$ is plotted vs. $\Delta G_s^0(\text{Na}^+) - nF\beta\phi^0$ in Fig. 5. The relevant data for Na^+ reduction obtained from previous studies are also shown in Fig. 5 for comparison. The agreement is reasonable, considering the fact that those rate constants were obtained by different experimental methods and in somewhat different electrolytes. The values of $\Delta G_s^0(\text{Na}^+)$ in any solvent are obtained by adding $\Delta G_s^0(\text{Na}^+)_{\text{H}_2\text{O}} = -97$ kcal/g-mol (28) to $\Delta G_t^0(\text{Na}^+)$ in various solvents. The relationship between $\log k_{sh}^0$ and $\Delta G_s^0(\text{Na}^+) - nF\beta\phi^0$ is linear because the values of ϕ^0 were calculated accordingly. However, this plot can serve in determining the qualitative trend of the rate constants in various solvents. Once the solvation energy and the standard potential in a particular solvent are known, the true rate constant can be estimated from Fig. 5.

It is interesting to note that the trend of rate constants increases in the order $\text{DMSO} < \text{DMF} < \text{AN} \approx \text{PC}$. The same order is observed for free energy of transfer of Na^+ [$\Delta G_t^0(\text{Na}^+)$] from water to various solvents ($\text{DMSO} < \text{DMF} < \text{AN} < \text{PC}$).

In conclusion, $\text{Na}^+ + e \rightleftharpoons \text{Na}(\text{Hg})$ reaction is "fast" and reversible in PC, DMF, and AN and quasi-reversible in DMSO. The standard potential scale for Na^+ in PC, DMF, DMSO, and AN is comparable to the standard potential scale for K^+ in the same solvents. The difference in absolute potential between H_2O and four solvents is considered to be ± 70 mV. The surface potentials of PC, DMF, DMSO, and AN indicate their dipoles are oriented with the positive ends toward the surface. Na^+ ion is strongly solvated by DMSO and weakly by AN and PC; hence, the rate constant for Na^+ reduction in DMSO is the lowest and in PC the highest.

Manuscript submitted Feb. 27, 1984; revised manuscript received Feb. 16, 1985.

The University of Rochester assisted in meeting the publication costs of this article.

LIST OF SYMBOLS

A	Debye-Hückel constant (kg/mol) ^{1/2}
α	D/δ k_{sh}
α	activity coefficient

α	mean ion diameter (cm)
B	Debye-Hückel constant (kg/mol) ^{1/2}
C	concentration at the electrode surface (mol/cm ³)
C_d	double-layer capacitance ($\mu\text{F}/\text{cm}^2$)
D	diffusion coefficient (cm ² /s)
D	medium dielectric constant
E	dc potential (V)
E_0	standard potential (V)
F	Faraday constant (C/eq)
ΔG^0	standard free energy of transfer (kcal/g-mol)
ΔG_t^0	free energy of transfer (kcal/g-mol)
h	Planck's constant
i	current density (A/cm ²)
k	Boltzmann constant
k_{sh}	heterogeneous rate constant (cm/s)
k_{sh}^a	apparent rate constant (cm/s)
k_{sh}^t	true rate constant (cm/s)
k_0^a	standard rate constant (cm/s)
M^\ddagger	activated complex or transition state
M	metal
M	Molarity (mol/liter of solvent)
N_A	Avogadro's number
n	number of electrons transferred
p	$\delta/\sigma\omega^{-1/2}$ (s ^{-1/2})
p'	irreversibility quotient (θ/σ)
q	charge density (C/cm ²)
R	universal gas constant (J/g-mol-K)
R	resistance ($\Omega\text{-cm}^2$)
r	crystallographic radius (Å)
T	temperature (K)
t	time
V	potential (V)
x	distance (cm)
Y	admittance (mho/cm ²)
Y'	real admittance (mho/cm ²)
Y''	imaginary admittance (mho/cm ²)
Z	impedance ($\Omega\text{-cm}^2$)
Z'	real impedance ($\Omega\text{-cm}^2$)
Z''	imaginary impedance ($\Omega\text{-cm}^2$)

Greek letters

α	anodic transfer coefficient
β	cathodic transfer coefficient
γ	activity coefficient
δ	Latimer, Pitzer, and Slansky solvent parameter (Å)
δ	diffusion layer thickness (cm)
ϵ	permittivity of the dielectric medium
η	overpotential (V)
θ	charge transfer resistance ($\Omega\text{-cm}^2$)
σ	Warburg's coefficient ($\Omega\text{-cm}^2 \text{ s}^{1/2}$)
Γ	surface excess (mol/cm ²)
ψ	$nF(E - E_0)/RT$
ϕ_z	phase angle of the faradaic impedance
ϕ_M^0	standard equilibrium potential (V)
ϕ_2	potential of the outer Helmholtz layer (V)
ω	angular frequency (s ⁻¹)
χ	surface potential (V)

Suffixes

a	apparent
ct	charge transfer
el	electrode
el	electrostatic
f	faradaic
f	formal
mt	mass transfer
min	minimum

REFERENCES

- C. K. Mann, in "Electroanalytical Chemistry," Vol. 3, A. J. Bard, Editor, p. 57, Marcel Dekker, New York (1967).
- "Nonaqueous Solvent Systems," T. C. Waddington, Editor, Academic Press, New York (1965).
- W. Latimer, K. Pitzer, and C. Slansky, *J. Chem. Phys.*, **7**, 108 (1939).
- N. Tanaka, *Electrochim. Acta*, **21**, 701 (1976).
- R. Payne, in "Advances in Electrochemistry and Electrochemical Engineering," Vol. 7, P. Delahay, Editor, Interscience, New York (1970).
- R. Payne, in "Physical Chemistry of Organic Solvent Systems," A. K. Covington and T. Dickinson, Editors, p. 733, Plenum Press, New York (1973).
- B. Tremillon, "Chemistry in Nonaqueous Solvents," p. 26, Reidel Pub., Boston (1974).

8. C. W. DeCruick, M. Sluyters-Rehbach, and J. H. Sluyters, *J. Electroanal. Chem.*, **35**, 137 (1972).
9. J. H. Sluyters, Personal communication.
10. P. G. Pai, Ph.D. Thesis, Wayne State University, Detroit, MI (1982).
11. M. Sluyters-Rehbach and J. H. Sluyters, *J. Rec. Trav. Chim.*, **82**, 535 (1963).
12. M. Sluyters-Rehbach and J. H. Sluyters, in "Electroanalytical Chemistry," Vol. 4, A. J. Bard, Editor, Marcel Dekker, New York (1970).
13. R. M. Reeves, M. Sluyters-Rehbach, and J. H. Sluyters, *J. Electroanal. Chem.*, **34**, 69 (1972).
14. C. K. Mann and K. K. Barnes, "Electrochemical Reactions in Nonaqueous Systems" p. 452, Marcel Dekker, New York (1970).
15. V. Gutman and R. Schmid, *Monatsh. Chem.*, **100**, 2113 (1969).
16. T. Biegler and R. Parsons, *J. Electroanal. Chem.*, **21**, App. 4-6 (1969).
17. Y. Doilido, R. V. Ivanova, and B. B. Damaskin, *Elektrokhimiya*, **4**, 567 (1968).
18. R. Payne, *J. Am. Chem. Soc.*, **89**, 489 (1967).
19. P. Champion, *C. R. Acad. Sci. Paris, Ser. C*, **269**, 1159 (1969).
20. G. J. Hills and L. M. Peter, *J. Electroanal. Chem.*, **50**, 175 (1974).
21. J. Jorné and C. W. Tobias, *This Journal*, **121**, 994 (1974).
22. J. Jorné, Ph.D. Thesis, University of California, Berkeley, CA (1972).
23. A. Baranski and W. R. Fawcett, *J. Electroanal. Chem.*, **94**, 237 (1978).
24. O. Popovych and R. P. T. Tomkins, "Nonaqueous Solution Chemistry," p. 188 and references therein, John Wiley and Sons, New York (1981).
25. C. V. Krishnan and H. L. Friedman in "Solute Solvent Interactions," Vol. 2, J. F. Coetzee and C. D. Ritchie, Editors p. 13, Marcel Dekker, New York (1969).
26. M. Solomon, *J. Phys. Chem.*, **74**, 2519 (1970).
27. M. Solomon, *This Journal*, **118**, 1609 (1971).
28. M. Solomon, in "Review in Physical Chemistry of Organic Solvent Systems," A. K. Covington and T. Dickinson, Editors, p. 137, Plenum Press, New York (1973).
29. C. M. Criss and E. Luksha, *J. Phys. Chem.*, **72**, 2966 (1968).
30. J. Jorné and C. W. Tobias, *ibid.*, **78**, 2576 (1974).
31. J. Jorné and C. W. Tobias, *This Journal*, **122**, 624 (1975).
32. A. J. Parker, *Chem. Rev.*, **69**, 1 (1969).
33. A. J. Parker, *Electrochim. Acta*, **21**, 671 (1976).
34. V. A. Pleskov, *Zh. Fiz. Chim.*, **22**, 351 (1948); *Chem. Abstr.*, **42**, 6249.
35. R. M. Reeves, M. Sluyters-Rehbach, and J. H. Sluyters, *J. Electroanal. Chem.*, **34**, 55 (1972).
36. D. J. Schriffrin, *Trans. Faraday Soc.*, **66**, 2464 (1970).
37. R. Payne, *J. Phys. Chem.*, **71**, 1548 (1967).
38. N. A. Izmailov, *Russ. J. Phys. Chem.*, **34**, 1142 (1960).
39. B. Timmer, M. Sluyters-Rehbach, and J. H. Sluyters, *J. Electroanal. Chem.*, **18**, 93 (1968).
40. R. Brasseur and H. D. Hurwitz, *ibid.*, **148**, 249 (1983).
41. H. L. Yeager, J. D. Fedyk, and R. J. Parker, *J. Phys. Chem.*, **77**, 2407 (1973).

Metal Deposition-Dissolution in Molten Halides: On the Question of Measurability of Very Fast Electrode Reaction Rates

J. L. Settle and Z. Nagy*

Argonne National Laboratory, Chemical Technology Division, Argonne, Illinois 60439

ABSTRACT

Metal deposition-dissolution reactions in molten salts are very fast and difficult to investigate, as evidenced by large discrepancies in the reported exchange current densities. An error analysis of the dc relaxation techniques was carried out, and it was determined that the measurement of the exchange current density can have a systematic error if the surface reaction rate is much faster than the diffusion rate. This systematic error will result in measured exchange current densities approximately equal to the largest exchange current density measurable under the given conditions. This systematic error can also result in fortuitously linear $\log i_0$ vs. $\log C$ and $\log i_0$ vs. $1/T$ plots, even when the results are grossly in error. A computer curve fitting data evaluation coupled with a statistical sensitivity analysis is suggested to avoid these problems. The exchange current densities of iron, nickel, and molybdenum were measured in LiCl-KCl eutectic melt at 450°C using an improved double-pulse galvanostatic technique. Only that of iron could be measured reliably (1.7 ± 0.4 A-cm⁻² at 1.3×10^{-6} mol-cm⁻³ Fe²⁺ ion concentration). The nickel reaction is too fast to be measured (at least 5 A-cm⁻² at 1×10^{-6} mol-cm⁻³ Ni²⁺ ion concentration), and the molybdenum results are unreliable because of melt decomposition. The large discrepancies between these results and some results reported by earlier workers can be explained on the basis of the above-described error analysis. It is concluded that past experiments resulting in large exchange current densities should be reexamined with improved measuring and data-evaluation techniques because it is possible that the reported values represent only the applicability limit of the measuring technique rather than the true exchange current density.

Metal deposition-dissolution reactions are a special class of electrode reactions; their atomistic mechanism includes the electrochemical building or breaking of the metallic crystal lattice in addition to the usual series of elementary processes, such as chemical reactions at or near the surface, charge-transfer step(s), adsorption at the surface, material and charge-transport processes, etc. Under some conditions, the crystal building or breaking processes can be rate determining. Therefore, the elementary steps of these processes and the variables affecting these steps have to be elucidated for a full understanding of the overall reaction. These include the type and density of surface dislocations, diffusion of adatoms to and from these sites, incorporation (or exclusion) of adatom into the lattice, charge transfer at dislocation sites or at the smooth surface, two- or three-dimensional nucleation, etc. A good overall understanding of these processes exists

*Electrochemical Society Active Member.

for metal deposition in room temperature aqueous systems (1-7). On the other hand, our understanding of these processes in high temperature molten salts is much less satisfactory, as shown by a brief discussion in a recent review on the electrochemistry in molten salts (8). This is, at least partly, due to the fact that the high temperature electrode kinetics data base, from which the mechanistic conclusions could be drawn, is rather limited, and, as will be shown below, often contradictory. In addition to the obvious scientific importance, these reactions are part of many practical processes, such as metal winning and refining, batteries, and corrosion processes.

The aim of the present work was to investigate the kinetics of deposition-dissolution of transition metals in molten LiCl-KCl eutectic. This solvent has been a popular one among previous investigators, and much thermodynamic data and some electrode kinetic data are available (9). Three metals were investigated in this work: iron,

nickel, and molybdenum. A summary of previously reported exchange current densities of these metals (10-18) is presented in Table I. These data reveal the very large discrepancies among the results reported by different investigators and among the results reported by the same investigators when using different measuring techniques. The reported exchange current densities vary as much as three orders of magnitude. Results on other solid metals in LiCl-KCl eutectic, such as cobalt, chromium, copper, silver, and platinum, also exhibit large discrepancies (10, 12, 14-17, 19-25). These reactions are generally fast, and, therefore, relaxation techniques were used for the determination of their exchange current density. The most-often used techniques were dc relaxation techniques, particularly single- and double-pulse galvanostatic techniques and also voltage and potential step techniques. A comparison of the exchange current densities in Table I to the reported limitations of the measuring techniques (26, 27) revealed that many of the very large values are of the same order of magnitude as the upper limit of the techniques. It was also noteworthy that the potential-step technique gave consistently smaller exchange current densities than the double-pulse galvanostatic technique, indicating that the results may be method dependent. To ensure that our measurements are being performed with a method which can be reliably used for fast reactions, we have performed a detailed, comparative error analysis of all dc relaxation techniques and suggested several modifications to the existing techniques that improve their ability to measure large exchange current densities. Most of this work has been pub-

lished already (28-34) and will only be briefly summarized below.

Error Analysis

The limits of applicability of dc relaxation techniques have been determined in terms of time constants of the electrode system (28-31), and a comparison of all techniques has been published (32). In these studies, a field of applicability was defined for each technique, indicating the combinations of time constants for which the exchange current density is measurable with an error of less than 20%. The two main conclusions of these earlier studies, relating to the present work, were that the galvanostatic double-pulse technique is best suited for the measurement of large exchange current densities, and that the applicability field of every technique can be enlarged to reactions approximately two orders of magnitude faster by two modifications. These modifications are (i) the reduction of the errors of measurements by about an order of magnitude through the use of digital instrumentation (transient recorder) in place of an analog oscilloscope, and (ii) the use of the computer curve-fitting data-evaluation method instead of a graphical method. No attempt was made in these earlier studies to examine whether the large errors occurring outside the field of applicability display any systematic behavior. The error behavior outside the field of applicability is examined in this present investigation.

The method of error calculations was the same as reported earlier (28-32) and will be described here only briefly. Synthetic data were generated by using the basic

Table I. Reported exchange current densities in LiCl-KCl eutectic melt

Metal	Metal ion concentration (mol-cm ⁻³)	Temperature (K)	Exchange current density (A-cm ⁻²)	Method	Ref.
Nickel	1 × 10 ⁻⁶	723	0.6	GDP	(10)
	1 × 10 ⁻⁵	723	4.0		
	5 × 10 ⁻⁵	723	13.0		
	7.7 × 10 ⁻⁶	723	0.19	PS	(11-13)
	9.4 × 10 ⁻⁶	723	0.22		
	2.0 × 10 ⁻⁵	723	0.26		
	3.8 × 10 ⁻⁵	723	0.30		
	6.0 × 10 ⁻⁵	723	0.38		
	7.8 × 10 ⁻⁵	723	0.42		
	3.66 × 10 ⁻⁶	723	85.8		
	7.80 × 10 ⁻⁶	723	103		
	1.56 × 10 ⁻⁵	723	177		
	3.42 × 10 ⁻⁵	723	232		
	6.59 × 10 ⁻⁵	723	376		
	2.9 × 10 ⁻⁶	773	1.18	ACI	(15)
	2.6 × 10 ⁻⁵	773	4.08		
	2.9 × 10 ⁻⁵	773	4.10		
	2.4 × 10 ⁻⁴	773	9.75		
	Iron	5.8 × 10 ⁻⁶	773	4.7	GDP
2.9 × 10 ⁻⁵		773	9.3		
5.8 × 10 ⁻⁵		673	5.2		
5.8 × 10 ⁻⁵		723	9.1		
5.8 × 10 ⁻⁵		773	14.0		
2.1 × 10 ⁻⁶		723	0.028	PS	(12)
7.8 × 10 ⁻⁶		723	0.041		
4.0 × 10 ⁻⁵		723	0.064		
1.1 × 10 ⁻⁴		723	0.077	GDP	(17)
2.9 × 10 ⁻⁶		773	1.5		
5.8 × 10 ⁻⁶		773	1.6		
2.9 × 10 ⁻⁵	673	1.0			
2.9 × 10 ⁻⁵	723	1.4			
2.9 × 10 ⁻⁵	773	3.0			
Molybdenum	5.0 × 10 ⁻⁷	729	0.0025	GSP	(18)
	1.8 × 10 ⁻⁶	729	0.0056		
	8.7 × 10 ⁻⁶	729	0.011		
	8.7 × 10 ⁻⁶	820	0.072		
	8.7 × 10 ⁻⁶	877	0.180		
	1.0 × 10 ⁻⁵	729	0.014		

GDP = Galvanostatic double pulse.
 PS = Potential step.
 ACI = AC impedance.
 GSP = Galvanostatic single pulse.

equations of the particular relaxation technique at a fixed set of electrode reaction parameters and by including random errors in the data. The exchange current density was then calculated from these synthetic data using the data-evaluation method under investigation, and this "measured" exchange current density was compared to the exchange current density used in the synthetic data generation. Calculations were carried out for the following dc relaxation techniques: galvanostatic single- and double-pulse techniques, potential (and voltage) step technique, and coulometric technique. Both graphical and computer curve-fitting data-evaluation methods were examined. Some typical examples of the results are shown in Fig. 1-3.

Figure 1 shows an example of exchange current densities obtained by the potential-step technique. As the true exchange current density increases, the measured exchange current density increases only to around the largest value of the exchange current density measurable under the given conditions and then remains approximately constant while the error of the measurement increases. Similar results were obtained for all relaxation techniques, using both graphical and computer curve-fitting data analysis. Figure 2 shows an example of the $\log i_0$ vs. $\log C$ relationship obtained by the galvanostatic double-pulse technique. The experimental results are quite different from the exchange current densities used to generate the relaxation curves, but the expected linear relationship is still obeyed. This can be explained by two factors: (i) the largest measurable exchange current density is increasing as the concentration increases, and (ii) the type of error behavior indicated on Fig. 1 is followed. Figure 3 indicates that a fortuitously linear $\log i_0$ vs. $1/T$ plot can also be obtained in this example of the galvanostatic single-pulse technique even though the results are grossly in error. The explanation for this behavior is similar to that given for the data shown in Fig. 2. Again, similar behavior can be demonstrated for all techniques.

The error behavior does not always follow the potentially misleading character shown in Fig. 1-3; under certain conditions, the error is random and the measured exchange current density is widely scattered. Because of the potentially large number of calculations needed, no attempt was made to define the conditions under which the error becomes systematic. However, this is really immaterial; what is important, from a practical standpoint, is that such behavior can occur. Furthermore, there is no obvious indication in the experimental data when the system is outside the field of applicability of the experimental technique, but there are several techniques which can be used to extract information about the reliability of the data. Four such techniques are described below.

1. A plot of the experimental data can often reveal possible problems. At short times, a plot of potential vs.

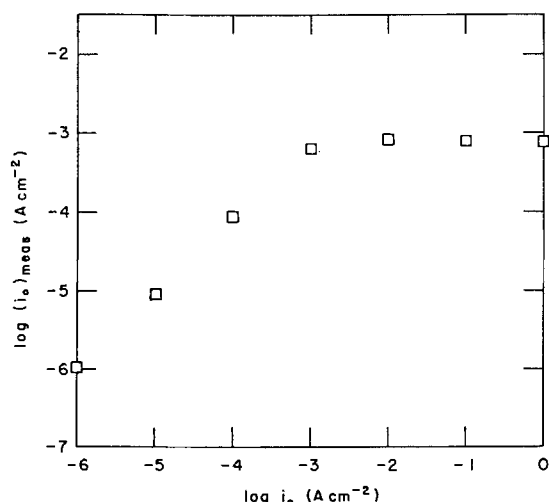


Fig. 1. Comparison of known and measured exchange current densities. Potential-step technique, graphical data evaluation.

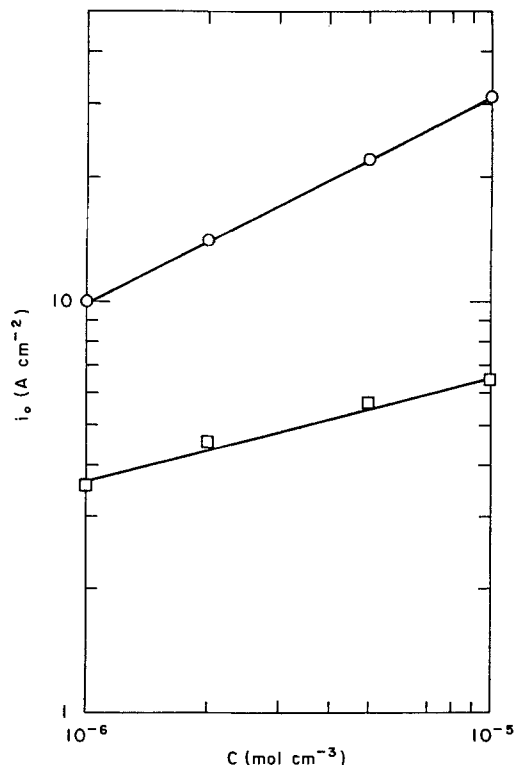


Fig. 2. Concentration dependence of known (circles) and measured (squares) exchange current densities. Double-pulse galvanostatic technique, graphical data evaluation.

square root of time should be concave toward the time axis for the galvanostatic single-pulse technique; a completely linear or convex plot indicates overwhelming diffusion control. Similarly, at short times, a plot of current density vs. square root of time should be convex to the time axis for the potential-step technique. For the coulometric technique, a plot of logarithm of the potential vs. time should be linear for a considerable time after the start of the experiment; the diffusional effects are serious when the plot curves soon after time zero. For the double-pulse galvanostatic technique, a plot of potential at the potential minimum vs. the square root of the prepulse length can be linear even when the results are grossly in

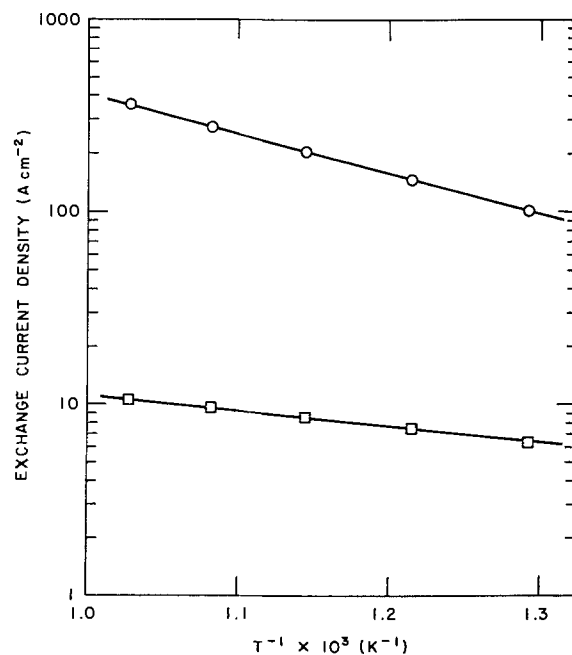


Fig. 3. Temperature dependence of known (circles) and measured (squares) exchange current densities. Single-pulse galvanostatic technique, graphical data evaluation.

error; a very large exchange current density and, consequently, the possibility of large error are indicated when negative intercepts are obtained on the potential axis. Unfortunately, none of these indicators is quantitative and borderline cases are difficult to decide.

2. The measured system parameters can be used to calculate the time constants of the system, and the system can be located on the applicability diagram of the measuring technique. However, as demonstrated above, this method is not reliable when the measured parameters place the system near the border of the applicability field.

3. The generation and evaluation of synthetic data were described in the above error analysis. When used properly, this is a powerful method for indicating the reliability of the parameters calculated from the experimental data. The measurement conditions have to be taken fully into consideration in the data generation (e.g., risetime of pulses, error of all measurements including the IR correction), and several data sets should be generated by varying the assumed exchange current density around the calculated value. The question is not only whether the parameters in question can be used to generate a data set similar to the experimental one, but also whether similar data sets can also be generated using different parameter (e.g., exchange current density) values, thereby indicating the insensitivity of the curve-fitting to that particular parameter. The generation of synthetic data sets requires negligible programming effort and computing time compared to the curve-fitting calculations, and it is worthwhile to make such calculations a routine part of all data evaluations.

4. Finally, a statistical sensitivity analysis can be carried out (33) by determining the covariance matrix of the parameters. This will indicate the information content of the experimental data with respect to the parameters. Results are reliable only if their standard deviation is small compared to the numerical value of the parameter (not more than a few percent). The last two methods, or a combination of them, are useful for very fast reactions, while for slower reactions the first two methods will suffice.

In summary, it was found that if the electrode system falls outside the field of applicability, because the surface reaction is fast compared to the diffusion to and from the surface (i.e., the diffusional time constant is small), the exchange current density measurement can display a systematic error, resulting in a measured exchange current density approximately equal to the largest exchange current density measurable with the measuring technique under the given conditions. This can result in exchange current densities whose values seem to fall within the field of applicability; furthermore, the dependency of the exchange current density on concentration and temperature can have the expected linear form, even though the measurements are grossly in error. There is not always an obvious indication in the experimental data that the exchange current density will be in error. The reliability of the measurement can be best established by a statistical sensitivity analysis of the results of the computer curve-fitting data evaluation. These conclusions are valid for all dc relaxation techniques (potentiostatic, galvanostatic, and coulometric) using both graphical and computer curve-fitting data-evaluation methods.

Experimental

Measuring techniques.—The galvanostatic double-pulse relaxation technique was used for most experiments. Some measurements were also carried out with galvanostatic single-pulse and coulometric (with constant-current pulse charging) relaxation techniques. Both graphical (26, 27) and computer curve-fitting (28, 29, 32) data-evaluation methods were used. A modified double-pulse galvanostatic technique was applied (34). This modification consisted of overcharging the double layer during the prepulse to produce a minimum in the overpotential relaxation during the second pulse; the minimum could be

adjusted to occur after the unavoidable ringing of the signal and, therefore, could be clearly observed. This modification was shown to have smaller error and a larger field of applicability than the unmodified technique (28, 34). Two graphical data-evaluation methods were used for the double-pulse technique based on the following equation (34)

$$\eta_m = \frac{\nu RT i_2}{n F i_0} + \frac{4RT i_2}{3 \sqrt{\pi} n^2 F^2 D^{1/2} C} [q^{3/2} - (q-1)^{3/2}] t_1^{1/2}$$

where η_m is the overpotential minimum after the prepulse, ν is the stoichiometric number of the reaction mechanism, i_2 is the measuring current density (second pulse), D is the diffusion coefficient, C is the concentration of the metal ion, q is the ratio of the time of the potential minimum to the prepulse length (t_m/t_1), and t_1 is the prepulse length; the other symbols have their usual meaning. The two methods are as follows. A series of measurements were made at varying prepulse lengths, with the prepulse current adjusted to keep the ratio q constant; the exchange current density¹ can be calculated from the intercept of a plot of potential at the minimum vs. square root of prepulse length. With this method, a considerable number of trial pulses are needed to achieve a constant q . In an experimentally easier method, the prepulse length was kept constant and the prepulse current was varied, resulting in a series of relaxations where the time of the potential minimum and, consequently, the q values varied from pulse to pulse. The exchange current density can be calculated from the intercept of a plot of potential at the minimum against $[q^{3/2} - (q-1)^{3/2}]$.

The curve-fitting data evaluations were carried out using a multidimensional nonlinear least squares technique based on the Levenberg-Marquardt algorithm (35, 36). More detailed descriptions and tests of the programs have been published before (28, 29, 32). The risetime of the pulses was taken into consideration in the data evaluations using a linear rise approximation; general relaxation equations for nonzero risetime were published previously (37). Two curve-fitting methods were used. A three-parameter curve-fitting was carried out to determine the exchange current density, the double-layer capacitance, and the diffusion coefficient. The experimental data were corrected for the IR drop in the electrolyte which was determined from the initial rise of the potential. The measurement of the IR correction involves a certain error, and this, in the extreme case, could result in a considerable error in the determination of a large exchange current density (31). Therefore, the following modification was used to improve the IR correction. Using the second method, a four-parameter curve-fitting was carried out to calculate, in addition to the above-stated variables, the solution resistance between the two working electrodes. The same IR-corrected input data as for the three-parameter fitting were used; therefore, the resistance calculated by the curve-fitting program was, in effect, the error of the original IR correction. An iterative procedure was then followed: the experimental data were now corrected using the adjusted solution resistance, a new four-parameter curve fit was calculated, and so on. This was continued until none of the calculated parameters changed more than 1%, which usually occurred within a few iterations.

Instrumentation.—A block diagram of the experimental setup is shown in Fig. 4. Two Hewlett-Packard pulse generators (Model 214B) were used to generate fast rising constant-voltage pulses which were converted into constant-current pulses by two large load resistors (R1 and R2). The first H-P pulse generator and the digital recorder were triggered simultaneously from an Instrument Research Company (Santa Barbara, California) Model 910A pulse generator, and the second H-P pulse generator

¹The value determined was actually that of i_0/ν because of the linearization of the current density-overpotential equation. The term "exchange current density" refers to this ratio throughout this communication.

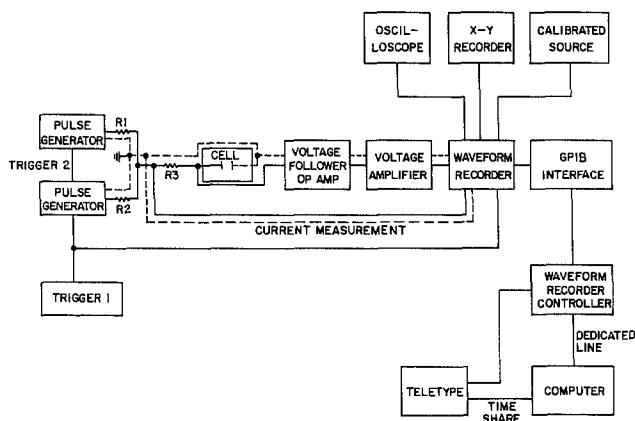


Fig. 4. Block diagram of the experimental setup

was triggered, with adjustable delay, from the first one. To obtain a single-ended current measurement, the sum of the potential drops over R_3 and the cell was measured; the cell introduced only a small error, since its resistance was always at least three orders of magnitude smaller than R_3 . The cell voltage was measured through a Tektronix AM501 voltage follower and an EG&G PAR Model 115 amplifier and was recorded simultaneously with the current using a dual-channel transient waveform recorder having 10 bit amplitude resolution and 10 MHz sampling rate (Physical Data, Incorporated, Beaverton, Oregon, Model 523-A). Calibration of the instrumentation was carried out with an Electronic Development Corporation (Boston, Massachusetts) sine wave amplitude and frequency standard Model 4100. The recorded data could be viewed locally or sent to a VAX 11/780 computer for data evaluation and storage. Some preliminary data were recorded on a Tektronix 7623A storage scope and photographed. It was estimated that the error of measurements was less than 0.5% for the digital measurements and about 5% for the analog measurements.

Cell design.—Certain special requirements had to be fulfilled because of the large expected values of the exchange current densities to be measured. These requirements were, among others, (i) a uniform current distribution on the working electrode, (ii) electrode mounting allowing repeated polishing of the working surface, (iii) small solution IR drop included in the measured potential, and (iv) a small overall inductance to minimize the initial ringing of the signal. A general discussion of cell design requirements for measurement of kinetics of fast electrode reactions has been published previously (38). The cell was a two-electrode, thin-layer design, consisting of two identical working electrodes and no reference electrode. The use of two identical working electrodes, one polarized anodically and the other cathodically, has been shown to extend the range of the linear approximation of the current density-overpotential relation (39, 40), an approximation which is always used in the calculation of the exchange current density from the experimental data. This is especially important for a metal deposition-dissolution reaction; in this case, the linearization error is larger than for a redox reaction because the activity of one species remains unity throughout the reaction (40, 41). The measured potential relaxation included the sum of anodic and cathodic overpotentials and IR drop in the electrolyte; the latter was kept small by the thin-layer design. The large ratio of electrode diameter to interelectrode gap also ensured small edge effects and, consequently, a uniform current distribution. The cell is shown in Fig. 5. The cell body and the electrode holders were made of high purity boron nitride (Union Carbide, Grade HBC, containing less than 1% oxygen) and treated (after fabrication) at 1750°C in nitrogen atmosphere for 18h to remove surface oxide. The two metal rod working electrodes were press fit into the holders and polished. The electrolyte gap was controlled by a 1.25×10^{-2} cm thick

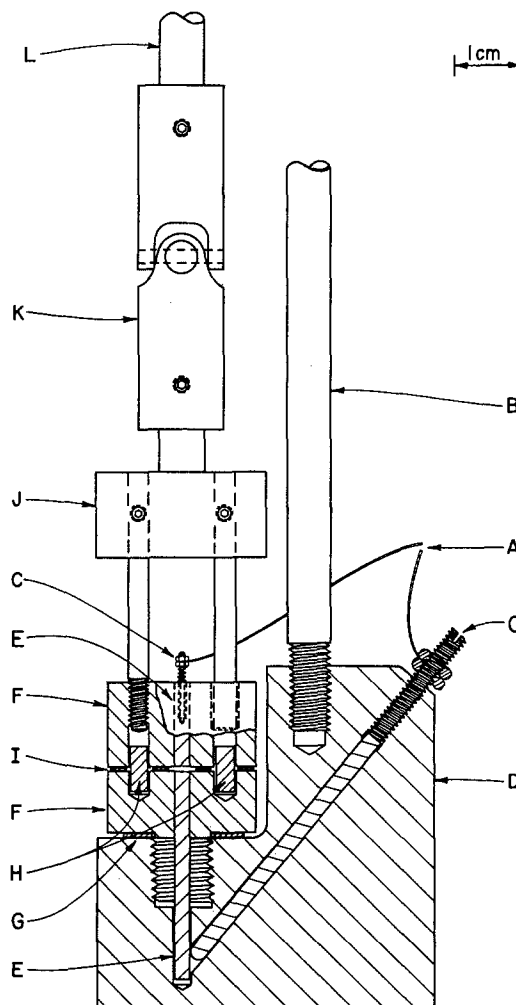


Fig. 5. Cell design. A: to coaxial electrical leads. B: steel support rod. C: metal electrode contacts. D: boron nitride housing. E: metal electrodes. F: boron nitride electrode holders. G: Grafoil gasket. H: metal alignment pins. I: metal spacer. J: steel adapter. K: steel universal joint. L: steel rod connecting to micrometer head.

metal spacer between the electrode holders. The spacer and the alignment pins were fabricated from the same metal as the working electrodes to avoid contaminating the melt.

The overall cell arrangement was like a long micrometer; the top electrode holder was vertically movable to facilitate the introduction of electrolyte into the interelectrode gap. The movement was controlled by a micrometer head through a universal joint in order to avoid misalignments. The cell was immersed into the electrolyte contained in a beaker at the bottom of a furnace well, which was attached to the floor of a glove box. The cell was immersed to a level somewhat above the interelectrode gap; therefore, only boron nitride and the electrode metal were in contact with the melt. Fused quartz or boron nitride beakers were used to contain the melt. The furnace well was open to the helium-filled glove box; the oxygen and moisture contents of the atmosphere were kept below 5 ppm by continuous purification.

Short copper wires were used to connect the electrodes to two high-temperature coaxial cables (one for current and one for the potential measurement) which were made of solid copper wire conductor, glass capillary tube insulator, and copper tubing outer conductor. Such a coaxial arrangement has been shown to reduce the inductive EMF generation during fast galvanostatic transients (42, 43). The instrumentation was connected with regular coaxial cables using coaxial feedthroughs in the wall of the glove box, which was isolated from the circuit.

Electrode preparation.—The electrode materials were electron-beam zone-refined metal rods with a purity bet-

ter than 99.99% from Materials Research Corporation (Orangeburg, New York). They were machined slightly larger than the hole in the holder and were inserted under liquid nitrogen to obtain a tight fit in the boron nitride holder. Oil-based diamond compounds were used in the polishing, finishing with 0.25 μm size. A pair of electrodes, which were to be used together in an experiment, were polished together in a frame. Joint polishing developed a common plane through the boron nitride electrode holders such that, even if the electrodes were not perfectly perpendicular to this plane, the electrodes were parallel to each other in the cell; therefore a uniform interelectrode gap was ensured. The polishing frame rested on four metal feet made of the same material as the electrodes to avoid undercutting the soft boron nitride during polishing. After polishing and ultrasonic cleaning, the electrodes were vacuum dried at 260°C and were reduced in 5% hydrogen/95% helium at 450°C for 2h. The reduction was carried out in a furnace attached to the glove box, immediately before the final assembly of the cell in the box.

Electrolyte.—Most experiments were carried out in LiCl-KCl eutectic (44.2 and 55.8%) at 450°C. Some experiments were carried out at lower temperatures in triple halide melts: LiCl-RbCl-CaCl₂ eutectic (28.7, 67.7, and 3.6%) which melts at 270°C (44) and LiBr-KBr-CsBr eutectic (39.1, 18.2, and 42.7%), melting at 236°C (45). The eutectic salts were polarographic grade material prepared by Anderson Physics Laboratories, Incorporated (Urbana, Illinois). The salts were further purified by pre-electrolysis immediately before the experiment. The pre-electrolysis was carried out with a platinum screen working electrode in a stirred solution. The reference electrode was a metal/metal ion electrode made from the metal to be investigated, and it contained 1×10^{-5} mol-cm⁻³ metal ions. The potential of the working electrode was controlled at -0.8V to the nickel, -0.5V to the iron, and -1.0V to the molybdenum reference electrode. Consequently, the potential was always approximately -1.7V to a molar platinum reference electrode in LiCl-KCl eutectic. The reference electrode and a graphite counterelectrode were contained in fused quartz tubes and were separated from the main body of the melt by fritted disks. The pre-electrolysis was carried out for at least 18h, or until the residual current decreased below 5 $\mu\text{A-cm}^{-2}$. The required amount of metal ion was then introduced by constant current anodic dissolution of a metal wire electrode. Molybdenum could not be introduced into the melt by anodic dissolution because of fast disproportionation; therefore, anhydrous K₃MoCl₆ (Pfaltz & Bauer Incorporated, Stamford, Connecticut) was added to the melt. The wires used for reference electrodes and for metal dissolution were of the same source and quality as the metal electrodes to be investigated.

Results and Discussion

Preliminary experiments.—Early results with iron and nickel in LiCl-KCl eutectic indicated that the exchange current density of the reactions is very high (46). The double-pulse galvanostatic technique was used with analog instrumentation and graphical data evaluation; the results were very scattered, some being in the many tens of amperes per square centimeter, and the intercepts of the plots were often negative. This prompted an effort to make measurements in lower melting salts, with consequently lower exchange current densities, to prove the validity of the experimental approach. A few measurements were made with nickel in LiCl-RbCl-CaCl₂ eutectic melt at 340°C containing 1×10^{-6} mol-cm⁻³ nickel ions. An exchange current density of 0.45 ± 0.1 A-cm⁻² was obtained, but some plots still resulted in negative intercepts. The system was at the very edge of the applicability field (28). Further measurements were carried out with an even lower melting salt and improved experimental and data-evaluation techniques selected on the basis of the above-described error analysis.

Nickel in LiBr-KBr-CsBr.—Measurements were carried out with analog instrumentation and computer curve-fitting data evaluation. Galvanostatic single- and double-pulse and coulometric pulse relaxation techniques were used to compare their performance to the predictions of the error analysis. The temperature was varied from 275° to 331°C while the Ni²⁺ ion concentration was kept at 4×10^{-7} mol-cm⁻³. The temperature dependence of the exchange current density is shown in Fig. 6 for data taken with double-pulse galvanostatic and coulometric techniques; the points show the average of four to fourteen measurements with a spread of approximately ± 0.2 A-cm⁻² for each point. The results for single-pulse galvanostatic technique were widely scattered, and plots of potential vs. square root of time indicated complete diffusion control. The apparent heats of activation, calculated from the slopes of the lines on Fig. 6, are 39.4 and 41.8 kJ-mol⁻¹ for the double-pulse and coulometric techniques, respectively. The double-layer capacitance values were 33 ± 11 $\mu\text{F-cm}^{-2}$ with all three techniques. The diffusion coefficients were rather large, 2.7, 11, and 114×10^{-5} cm²-s⁻¹ at 275°, 303°, and 331°C for the double-pulse technique, 3.0, 4.9, and 29.7×10^{-5} cm²-s⁻¹ for the single-pulse technique, and 1.9, 6.4, and 46×10^{-5} cm²-s⁻¹, respectively, for the coulometric technique. This system has not been investigated by other workers; therefore, no other values are available for comparison. However, indicators discussed in the error analysis section prove that the exchange current densities measured with the double-pulse galvanostatic technique are reliable: the system is within the field of applicability and the standard deviations are low. For the single-pulse galvanostatic and coulometric techniques, the electrode system is on the border of the applicability field for the determination of the exchange current density and, indeed, the single-pulse data were unreliable and the coulometric results were somewhat lower and more scattered than the double pulse results. These findings are in agreement with the applicabilities of the relaxation techniques predicted by our earlier error analysis (32).

Iron in LiCl-KCl.—Experiments were carried out with digital instrumentation coupled with curve-fitting data evaluation. The temperature was controlled at 450°C, and the Fe²⁺ ion concentration was 1.3×10^{-6} mol-cm⁻³. Eight experiments were carried out using the double-pulse

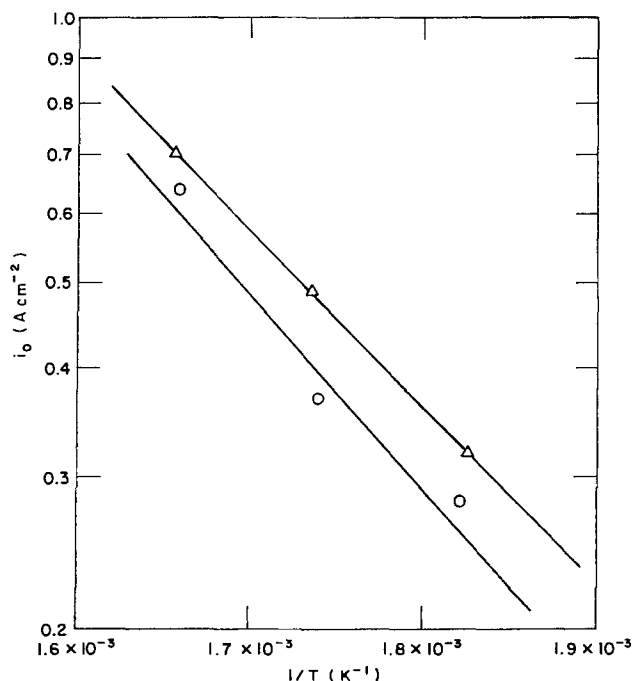


Fig. 6. Exchange current density of nickel in LiBr-KBr-CsBr. Triangles: double-pulse galvanostatic technique. Circles: coulometric technique.

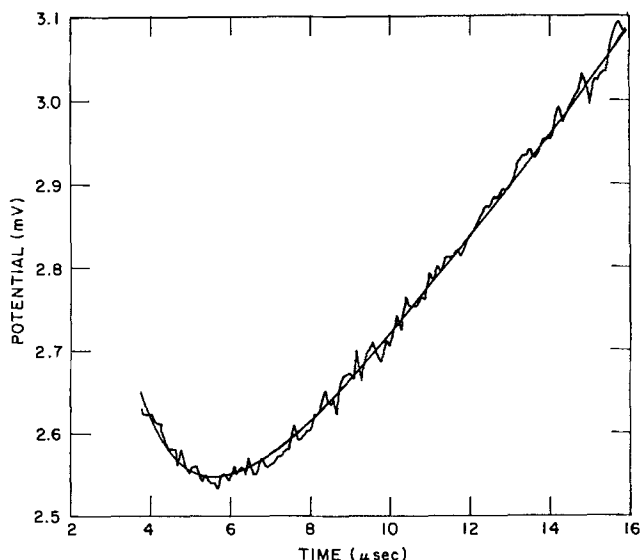


Fig. 7. An example of the galvanostatic double-pulse relaxation curve together with the smooth curve generated by the computer curve-fitting data evaluation.

galvanostatic technique. An example of relaxation curves is given in Fig. 7, showing both the digital data (connected with a continuous line) and the smooth curve generated by the curve-fitting data-evaluation program. The results were an exchange current density of 1.7 ± 0.4 A-cm⁻², a double-layer capacitance of 120 ± 10 μF-cm⁻², and a diffusion coefficient of $10 \pm 1.5 \times 10^{-5}$ cm²-s⁻¹. The exchange current density is higher than any values previously reported for this system (12, 17); this will be discussed in more detail below. The double-layer capacitance is comparable to those reported for iron [191 μF-cm⁻² at 3×10^{-6} mol-cm⁻³ Fe²⁺ concentration, from Ref. (17)] and for other metal electrodes in halide melts containing the corresponding metal halides (10, 16, 17, 20, 47, 48). These large capacitance values are generally explained as a pseudocapacitance caused by the presence of adatoms (adions) on the surface (8, 47, 48), a phenomenon well demonstrated for metal deposition-dissolution in aqueous solutions (2, 3, 7). For solid electrodes, the surface roughness also contributes to the large capacitance. The diffusion coefficient was measured by several workers using chronopotentiometric and chronoamperometric techniques: Poinet and Barbier reported 1×10^{-5} at 450°C (49), Piron *et al.* reported 5.6×10^{-5} at 466°C (50), and Inman *et al.* reported 2.1×10^{-5} at 500°C (51). The discrepancy between our results and those previously reported can be explained as follows. The double-pulse galvanostatic measurements were carried out in a few microseconds time range; therefore, during a considerable portion of the measuring time, the dimension of the surface roughness of the electrode and that of the diffusion layer were comparable, resulting in a nonlinear contribution to the diffusion flux. A direct comparison of diffusion coefficients measured in molten LiCl-KCl eutectic with the double-pulse galvanostatic technique and linear potential sweep technique has indeed shown that the former technique tends to result in diffusion coefficients several times larger than those for the latter (16). A few experiments were also tried with single-pulse galvanostatic and coulometric techniques. The results, not surprisingly, were unreliable: the values calculated for the exchange current density were widely scattered, exhibiting large standard deviation, and appropriate plots of the data indicated complete diffusion control.

Nickel in LiCl-KCl.—Seventy-five runs were made, mostly with the double-pulse galvanostatic technique, using digital instrumentation and curve-fitting data evaluation. The nickel ion concentration ranged from 9×10^{-7} to 1×10^{-5} mol-cm⁻³, and the temperature was 450°C. The exchange current densities were very scattered, ranging from tens to thousands of amperes per square centimeter;

the high standard deviations and the graphical plots of the data indicated that the values were unreliable. A minimum value for the exchange current density was determined by generating synthetic data for the conditions of the experiment at a series of exchange current density values. It was determined that an exchange current density up to 5 A-cm⁻² at 1×10^{-6} mol-cm⁻³ could have been determined; therefore, the true exchange current density of the nickel reaction must be larger than 5 A-cm⁻². The double-layer capacitance ranged between 10 and 40 μF-cm⁻², and the diffusion coefficient was between 0.3 and 3.0×10^{-5} cm²-s⁻¹. Previously reported diffusion coefficients range from 0.73 to 4.14×10^{-5} cm²-s⁻¹ (49, 52-58).

Molybdenum in LiCl-KCl.—A few measurements were attempted at 450°C using digital instrumentation with galvanostatic double-pulse technique and curve-fitting data evaluation. Difficulties were encountered because of the instability of Mo³⁺ ion in the melt; the concentration was continuously decreasing, and a black precipitate appeared in the melt. Similar behavior was observed by Senderoff and Mellors, who attributed it to disproportionation to Mo⁵⁺ and molybdenum metal (59). Because of the close similarity of their observations to ours, further work was not carried out on this phenomenon, even though it would deserve further studies since other workers have found Mo³⁺ to be a stable species in the same melt (18, 60). Exchange current densities on the order of a few amperes per square centimeter were observed at a Mo³⁺ ion concentration of approximately 1×10^{-4} mol-cm⁻³; this exchange current density is much larger than the values of Selis (18), who did not report any melt instability. It is possible that our large exchange current densities are due to a large surface area caused by the precipitated metal powder; this is corroborated by a very large (around 800 μF-cm⁻²) double-layer capacitance.

A comparison of these exchange current densities, measured in the LiCl-KCl melt, to literature values and an evaluation of all reported exchange current densities with respect to the applicability diagrams of the measuring techniques revealed two facts: our exchange current densities were always larger than any previously reported value, and the reported values of the exchange current densities have placed all the electrode systems considered in this work at the edge of the applicability fields of the respective measuring techniques.

For the case of nickel, our minimum exchange current density² of 5 A-cm⁻² at 450°C and at a nickel ion concentration of 1×10^{-6} mol-cm⁻³ can be compared to the results of Bouteillon *et al.* (11-13), who, for similar conditions, report an exchange current density of about 0.1 A-cm⁻² using the potential-step technique. (The different investigators used different temperatures and metal ion concentrations, therefore comparisons are somewhat approximate; see Table I). Laitinen *et al.* (10) obtained approximately 0.5 A-cm⁻² using the double-pulse galvanostatic technique with graphical data evaluation, and Haruyama *et al.* (16, 17) reported values in the low amperes per square centimeter range for the same technique. Bouteillon *et al.* also used the double-pulse galvanostatic technique (14) and reported values near 100 A-cm⁻²; however, these results are so far outside the field of applicability of the technique that they cannot be considered reliable. The error may have been caused by a nonlinear extrapolation technique to correct for the solution IR drop. A similar trend with measuring technique can be demonstrated for iron. Bouteillon (12) found an exchange current density near 0.01 A-cm⁻² with the potential-step technique, while Haruyama *et al.* reported about 1 A-cm⁻² using the double-pulse galvanostatic technique with graphical data evaluation (17). Both of these values are lower than our 1.7 A-cm⁻².³

²Equivalent to a standard apparent rate constant of 0.026 cm-s⁻¹, assuming a transfer coefficient of 0.5 and taking the metal concentration as unity.

³Equivalent to a standard apparent rate constant of 0.008 cm-s⁻¹, assuming a transfer coefficient of 0.5 and taking the metal concentration as unity.

A certain amount of approximation is involved in the comparison of the reported exchange current density values to the applicability diagrams of the experimental techniques. Much information is needed on the details of the experiments which are not reported by the investigators, and estimated values must be used. One needs values for the double-layer capacitance, diffusion coefficient, risetime of pulse generators, accuracy of the measurements, and the size of the uncorrected IR drop. Even with these uncertainties, the trend is clear both for iron and nickel dissolution-deposition reactions: the electrode system always falls near the edge of the applicability field of the respective measuring techniques.

It can be concluded that reported exchange current densities are a strong function of the experimental techniques used for their measurement. The potential-step technique with graphical data evaluation resulted in the lowest exchange current densities for both iron and nickel. The galvanostatic double-pulse technique with graphical data evaluation gave considerably larger exchange current densities; this is in agreement with the fact that the latter technique can be used for much faster reactions than the potentiostatic measurement. Finally, our measurements, which were carried out with an improved double-pulse galvanostatic technique, resulted in even larger exchange current densities. This conclusion is corroborated by the result of the error analysis described above in which it was found that a measured exchange current density may indicate only the limitation of the technique rather than the true exchange current density of the reaction when the latter is outside the field of applicability of the measuring technique. These results suggest that large exchange current densities reported in the literature should be reexamined using improved experimental and data-evaluation techniques to prove their validity.

Acknowledgments

This work was performed under the auspices of the Division of Materials Science, Office of Basic Energy Sciences, U.S. Department of Energy. We are grateful to Dr. V. A. Maroni for his critical reading of the manuscript.

Manuscript submitted Sept. 13, 1984; revised manuscript received March 2, 1985. Parts of this paper were presented as Paper 8 at the Cincinnati, Ohio, Meeting of the Society, May 6-11, 1984.

Argonne National Laboratory assisted in meeting the publication costs of this article.

REFERENCES

- M. Fleischmann and H. R. Thirsk, in "Advances in Electrochemistry and Electrochemical Engineering," Vol. 3, P. Delahay and C. W. Tobias, Editors, p. 123, Interscience, New York (1963).
- J. O'M. Bockris and A. Damjanovic, in "Modern Aspects of Electrochemistry," Vol. 3, J. O'M. Bockris and B. E. Conway, Editors, p. 224, Butterworths, Washington (1964).
- J. O'M. Bockris and A. R. Despic, in "Physical Chemistry," Vol. IXB, H. Eyring, Editor, p. 611, Academic Press, New York (1970).
- J. A. Harrison and H. R. Thirsk, in "Electroanalytical Chemistry," Vol. 5, A. J. Bard, Editor, p. 67, Marcel Dekker, New York (1971).
- A. R. Despic and K. I. Popov, in "Modern Aspects of Electrochemistry," Vol. 7, B. E. Conway and J. O'M. Bockris, Editors, p. 199, Plenum Press, New York (1972).
- E. B.udevski, in "Comprehensive Treatise of Electrochemistry," Vol. 7, B. E. Conway, J. O'M. Bockris, E. Yeager, S. U. M. Khan, and R. E. White, Editors, p. 399, Plenum Press, New York (1983).
- A. R. Despic, in "Comprehensive Treatise of Electrochemistry," Vol. 7, B. E. Conway, J. O'M. Bockris, E. Yeager, S. U. M. Khan, and R. E. White, Editors, p. 451, Plenum Press, New York (1983).
- D. Inman and D. G. Lovering, in "Comprehensive Treatise of Electrochemistry," Vol. 7, B. E. Conway, J. O'M. Bockris, E. Yeager, S. U. M. Khan, and R. E. White, Editors, p. 593, Plenum Press, New York (1983).
- J. A. Plambeck, in "Encyclopedia of Electrochemistry of the Elements," Vol. 10, A. J. Bard, Editor, p. 11, Marcel Dekker, New York (1976).
- H. A. Laitinen, R. P. Tischer, and D. K. Roe, *This Journal*, **107**, 546 (1960).
- J. Amosse, J. Bouteillon, and M. J. Barbier, *C. R. Acad. Sci., (Paris)*, **C267**, 22 (1968).
- J. Bouteillon, Thesis, University of Grenoble, Grenoble, France, (1969).
- J. Bouteillon and M. J. Barbier, *Electrochim. Acta.*, **21**, 817 (1976).
- J. Bouteillon, J. de Lepinay, and M. J. Barbier, *J. Chim. Phys.*, **71**, 346 (1974).
- H. Numata and S. Haruyama, *J. Jpn. Inst. Metals*, **43**, 866 (1979).
- A. Nishikata and S. Haruyama, *ibid.*, **47**, 198 (1983).
- S. Haruyama, H. Numata, and A. Nishikata, in "Proceedings of the First International Symposium on Molten Salt Chemistry and Technology," Abstract I-102, p. 153, Kyoto, Japan, April 20-22, 1983.
- S. M. Selis, *J. Phys. Chem.*, **72**, 1442 (1968).
- J. Bouteillon, J. de Lepinay, and M. J. Barbier, *C. R. Acad. Sci. (Paris)*, **C267**, 801 (1968).
- D. L. Hill, K. W. Fung, S. Hsieh, and H. L. Lee, *J. Electroanal. Chem. Interfacial Electrochem.*, **38**, 57 (1972).
- D. L. Hill, K. W. Fung, and H. L. Lee, *ibid.*, **38**, 67 (1972).
- D. L. Hill, K. W. Fung, and H. L. Lee, *ibid.*, **38**, 75 (1972).
- S. C. Levy and F. W. Reinhardt, *This Journal*, **122**, 200 (1975).
- D. Inman, J. C. L. Legey, and R. Spencer, *J. Electroanal. Chem. Interfacial Electrochem.*, **61**, 289 (1975).
- Y. K. Delimarsky, N. K. Tumanova, A. V. Gorodysky, and M. U. Prikhodko, *Electrochim. Acta.*, **21**, 367 (1976).
- J. Kuta and E. Yeager, in "Techniques of Electrochemistry," Vol. 1, E. Yeager and A. J. Salkind, Editors, p. 141, Wiley-Interscience, New York (1972).
- D. D. Macdonald, "Transient Techniques in Electrochemistry," Plenum Press, New York (1977).
- Z. Nagy, *This Journal*, **128**, 786 (1981).
- Z. Nagy, *Electrochim. Acta.*, **26**, 671 (1981).
- Z. Nagy, *This Journal*, **129**, 1943 (1982).
- Z. Nagy, *Electrochim. Acta.*, **28**, 557 (1983).
- Z. Nagy and J. T. Arden, *This Journal*, **130**, 815 (1983).
- Z. Nagy, *Electrochim. Acta.*, **29**, 917 (1984).
- Z. Nagy, *This Journal*, **126**, 1148 (1979).
- J. J. More, in "Numerical Analysis," G. A. Watson, Editor, p. 105, Lecture Notes in Mathematics 630, Springer-Verlag, New York (1978).
- J. J. More, B. S. Garbow, and K. E. Hillstrom, Argonne National Laboratory Report, ANL-80-74, Argonne, IL (1980).
- Z. Nagy, *This Journal*, **125**, 1809 (1978).
- Z. Nagy and J. L. Settle, in "Molten Salts," M. Blander, D. S. Newman, M. L. Saboungi, G. Mamantov, and K. Johnson, Editors, p. 534, The Electrochemical Society Softbound Proceedings Series, Pennington, NJ (1984).
- D. J. Kooijman, M. Sluyters-Rehbach, and J. H. Sluyters, *Electrochim. Acta.*, **11**, 1197 (1966).
- Z. Nagy, R. H. Land, G. K. Leaf, and M. Minkoff, Submitted to *This Journal*.
- R. L. Birke and D. K. Roe, *Anal. Chem.*, **37**, 450 (1965).
- E. Blomgren, D. Inman, and J. O'M. Bockris, *Rev. Sci. Instrum.*, **32**, 11 (1961).
- W. E. Triaca, C. Solomons, and J. O'M. Bockris, *Electrochim. Acta.*, **13**, 1949 (1968).
- I. I. Ilyasov, M. Davranov, and A. I. Rodionov, *Russ. J. Inorg. Chem.*, **20**, 1115 (1975).
- G. G. Diogenov and V. I. Ermachkov, *ibid.*, **12**, 436 (1967).
- Z. Nagy and J. L. Settle, Abstract 158, p. 408, The Electrochemical Society Extended Abstracts, Vol. 79-2, Los Angeles, California, October 14-19, 1979.
- A. D. Graves, G. J. Hills, and D. Inman, in "Advances in Electrochemistry and Electrochemical Engineering," Vol. 4, P. Delahay and C. W. Tobias, Editors, p. 117, Interscience, New York (1966).
- R. Prange, K. Heusler, and K. Schwerdtfeger, *Metall. Trans. B*, **15**, 281 (1984).
- J. C. Poignet and M. J. Barbier, *Electrochim. Acta.*, **17**, 1227 (1972).
- D. L. Piron, S. Asakura, and K. Nobe, in "Metal-Slag-Gas Reactions and Processes," Z. A. Foroulis and W. W. Smeltzer, Editors, p. 625, The Electrochemical Society Softbound Proceedings Series, Princeton, NJ (1975).
- D. Inman, J. C. Legey, and R. Spencer, *J. Appl. Electrochem.*, **8**, 269 (1978).

52. P. Drossbach and P. Petrick, *Z. Elektrochem.*, **58**, 95 (1954).
 53. E. Schmidt, *Electrochim. Acta.*, **8**, 23 (1963).
 54. W. K. Behl, U.S. Government Report, AD 696430 (1969).
 55. W. K. Behl, *This Journal*, **118**, 889 (1971).
 56. J. Bouteillon and M. J. Barbier, *J. Electroanal. Chem. Interfacial Electrochem.*, **56**, 399 (1974).
 57. D. L. Piron, *Corros. Sci.*, **15**, 377 (1975).
 58. D. L. Piron, S. Asakura, and K. Nobe, *This Journal*, **123**, 503 (1976).
 59. S. Senderoff and G. W. Mellors, *ibid.*, **114**, 556 (1967).
 60. D. Inman and R. Spencer, in "Advances in Extraction Metallurgy and Refining," J. M. Jones, Editor, p. 413, Institute of Mining and Metallurgy, London (1972).

Interferometric Observation of Turbulent Mass Transfer in Channel Flow

F. R. McLarnon*

Applied Science Division, Lawrence Berkeley Laboratory, University of California, Berkeley, California 94720

R. H. Muller* and C. W. Tobias*

Materials and Molecular Research Division, Lawrence Berkeley Laboratory, and Department of Chemical Engineering, University of California, Berkeley, California 94720

ABSTRACT

A traveling, dual-beam laser interferometer has been used to investigate mass-transfer boundary layers on planar electrodes in turbulent channel flow. The effect of secondary flows induced near the electrode/electrolyte interface by small flow obstacles in laminar bulk flow is compared to the effect of turbulent bulk flow produced by high electrolyte flow rates in an obstacle-free flow channel. It is shown that mass-transfer enhancement can be attained more efficiently by the use of small flow obstacles than by the use of high flow velocities.

Turbulent fluid flow can often be successfully employed to increase interfacial transport rates in a variety of industrial unit operations. Many electrochemical processes, such as electrowinning, electrochemical synthesis, and electro dialysis, tend to be rate limited by slow mass transfer. The application of turbulent in place of laminar electrolyte flow in these processes permits higher operating current densities and thereby improves the space-time yield of the electrochemical system. The most direct method to induce turbulent flow in an electrochemical cell is to raise the electrolyte velocity (1), but this technique may result in an unacceptable increase in electrolyte pumping power (2). Other viable methods include insertion of flow obstacles into the electrolyte flow stream (3), moving nets across the electrode surface (4), applying magnetic fields (5) or ultrasonic waves (6), and use of suspended particles (7).

The limiting current technique (8) is a powerful tool that has been used by many investigators (9) to characterize the local distribution of mass-transfer rates at electrode surfaces under conditions of turbulent flow. Of particular relevance to the present study are applications of the limiting current technique (3, 10-18) to evaluate the enhancement of mass-transfer rates by placing flow obstacles in the electrolyte flow stream. These investigations have provided valuable data to guide the optimal section of fluid flow rates, cell geometry, and obstacle shape, size, and spacing.

The purpose of the present work is to employ interferometry (19, 20) to characterize mass-transfer enhancement by turbulent flow, thereby providing data complementary to those obtained by the limiting current technique. In this method, local variations in the phase of transmitted light are measured, and the corresponding variations in refractive index (linearly related to concentration under the conditions of this study) are subsequently derived. The technique provides direct, continuous visualization of the local concentration boundary layer at any level of current density on continuous (unsectioned) electrodes. The interferometric method has been previously applied to study electrochemical mass

transfer under conditions of pure diffusion (21-24), natural convection (25-29), forced convection (30-32), combined forced and natural convection (33), and turbulent flow (32, 34).

Experimental

Flow channel.—Mass-transfer experiments were carried out in a 3m long rectangular-duct flow channel (35-37), the heart of which is depicted in Fig. 1. Gravity feed from a storage tank provides a steady flow of electrolyte. The duct is $w = 1.00$ cm wide and $h = 2.54$ cm high. The $L = 100$ cm long electrodes fully occupy the space between the two parallel, optically-flat glass sidewalls downstream of a 200 cm long (140 hydraulic diameters) entry region. All experiments were performed with the cathode facing down and the anode facing up. This configuration will produce less-dense electrolyte regions above more-dense regions, eliminating the possibility of electrolyte flow induced by natural convection. The primary current density distribution in this cell was calculated (31) to be

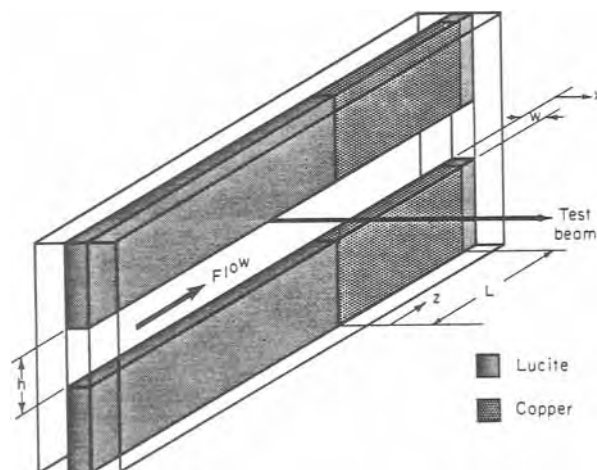


Fig. 1. Semiscale drawing of the flow channel. Channel width $w = 10.0$ mm. Channel height $h = 25.4$ mm. Electrode length $L = 100.0$ cm.

* Electrochemical Society Active Member.

nearly uniform; local current densities deviate from the average current density by no more than 1% for 97% of the electrode surface. The deviations from uniform primary current density occur only within a few centimeters of the coplanar junctions between conductor and insulator, *i.e.*, at the leading and trailing edges of the electrode. When current is passing, the electric field effect (and the associated small nonuniformity of the primary current density distribution) is moderated by the presence of charge-transfer and mass-transfer overpotentials. The resulting tertiary current distribution is even more uniform than the primary distribution. Near the limiting current density, the current distribution reflects local variations in mass-transfer boundary-layer thickness.

Flow obstacles.—Experiments were performed with five different obstacles placed in the flow channel, and the sizes, shapes, and spacings of these obstacles are shown in Fig. 2. The sizes and shapes were chosen to approximate those employed by Leitz and Marincic (3), and the spacings were chosen to be sufficiently large to allow flow disturbances to decay between obstacles. Figure 2 also illustrates the sizes of the obstacles relative to the local mass-transfer boundary layer thickness. The largest obstacle is a 12.7 mm diam, 10.0 mm long glass circular cylinder sandwiched between the two glass sidewalls, midway between the two electrodes. This object occupies 50% of the channel cross section, and it can create turbulence by increasing the local electrolyte flow velocity. The other four obstacles shown in Fig. 2 are a rectangular parallelepiped, a triangular parallelepiped, and two semicircular cylinders. All four of these obstacles, extending across the entire 10.0 mm channel width, were machined from acrylic and were glued to the cathode surface. The three larger obstacles extend 0.76 mm from the cathode surface and occupy 3% of the channel cross section. The smallest obstacle extends 0.28 mm from the cathode surface and occupies only 1% of the channel cross section. The dashed curves in Fig. 2 indicate the edge of the 99% mass-transfer boundary layer¹ predicted (38, 2, 9) for laminar flow conditions ($Re = 500$ and $Re = 1500$). Figure 2 shows that the dimensions of the smaller obstacles are comparable to those of the mass-transfer boundary layers expected under laminar flow conditions.

Electrolyte and electrode preparation.—The 99.999% pure copper electrodes were designed with two goals in

¹ The distance from the electrode surface where the local concentration reaches the sum of the surface concentration plus 99% of the total concentration difference (bulk less surface).

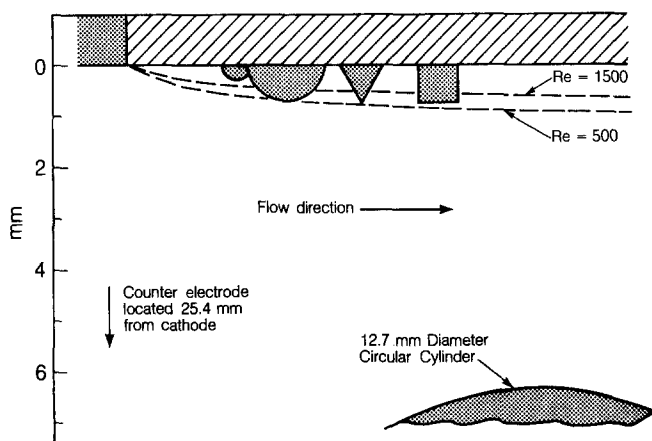


Fig. 2. Placement and sizes of obstacles in the flow channel. Ordinate: distance from cathode surface (mm). Abscissa: distance from cathode leading edge (cm). The 0.28 mm semicircular cylinder is attached to the cathode surface at $z = 22$ cm, the 0.76 mm semicircular cylinder at 32 cm, the 0.76 mm triangular parallelepiped at 47 cm, the 0.76 mm rectangular parallelepiped at 62 cm, and the 12.7 mm diam large circular cylinder is wedged between the two glass sidewalls at $z = 82$ cm. Dotted line: Mass-transfer boundary edge (Eq. [2]), calculated as twice the Nernst boundary-layer thickness (33).

mind: (i) the horizontal electrode surfaces should be flat and smooth, and (ii) the test beam should traverse the cell parallel to the surface. These requirements were met by first polishing a vertical side of each electrode flat and optically smooth. Then, a right-angle polishing jig was used to prepare the electrode working surfaces perpendicular to the reflecting sides. The cell was then aligned so that the test beam was parallel (to within 0.1°) to the electrode working surface by reflecting the beam from the side under exactly normal incidence (the reflected beam retraced its path back to its source). The working surface profile was flat to within $1 \mu\text{m}$ over 80% of its width. However, the edges were very slightly rounded (to about $10 \mu\text{m}$) below the level of the center of the surface.²

The aqueous CuSO_4 electrolyte was prepared by dissolving reagent-grade $\text{CuSO}_4 \cdot 5\text{H}_2\text{O}$ crystals into twice-distilled water in a 25 gal polyethylene container. The dependence of electrolyte refractive index on CuSO_4 concentration was determined with an Abbé critical-angle refractometer, and sample concentrations were determined by gravimetric analysis. Least squares analysis provided a linear correlation for the refractive index at $\lambda = 632.8 \text{ nm}$ (He-Ne laser), $0 \leq C \leq 0.1\text{M CuSO}_4$, 20°C . All electrolysis experiments employed 0.1M CuSO_4 electrolyte and were conducted at 20°C .

Interferometer.—A cross section of the duct and dual-emission laser interferometer is shown in Fig. 3. A He-Ne laser was modified to emit light from each end of the laser cavity, and the interferometer was mounted on the carriage of a lathe bed to permit travel of the instrument along the length of the electrodes (35-37). The plane of focus (optically conjugate to the film plane of the camera) was located at the inside of the glass sidewall farthest from the camera, $x = 0$ (Fig. 1). This is the recommended plane of focus for the observation of cathodic boundary layers in which the refractive index decreases toward the electrode surface (40).

Electrochemical experiments.—Steady-state, constant-current electrodeposition of Cu onto a downward facing cathode was studied at $Re = 500, 1500, 5000$, and $10,000$ ($v_{\text{avg}} = 3.5, 10.5, 35$, and 70 cm/s , respectively). Average current densities ranged from 2.0 to 25.0 mA/cm^2 . Local

² This small deviation from planarity has been shown (39) to result in reflection of the test beam from the rounded electrode edge, which can cause anomalous curvature of the interference fringes in the immediate vicinity of the electrode surface.

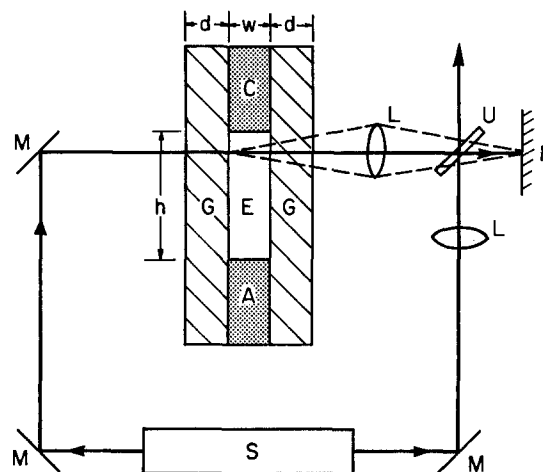


Fig. 3. Schematic diagram of interferometer and electrochemical cell. Solid line: light path. Dotted line: off-axis rays demonstrating point-to-point relationship between plane of focus and film plane. A: Copper anode. C: Copper cathode. E: 0.1M CuSO_4 electrolyte. F: Film plane. G: Glass sidewalls. L: Lens (the test lens, focal length = 87 mm , is 115 mm from the center of the cell. The focal length of the reference lens is 81 mm . M: Mirror. S: Light source (HeNe laser). U: Beam splitter. d : Thickness of glass wall (12.7 mm). h : Electrode separation (2.54 mm). w : Electrode width (10.0 mm).

Table I. Experimental matrix

v_{avg} (cm/s)	Re	i_{avg} (mA/cm ²)	Flow obstacles present
3.5	500	2.0	Yes
3.5	500	5.0	No
10.5	1,500	2.5	Yes
10.5	1,500	5.0	No
35	5,000	15.0	No
35	5,000	25.0	No
70	10,000	25.0	No

limiting current densities under laminar flow conditions at the trailing edge of the cathode surface range from 3.8 mA/cm² at Re = 500 to 5.5 mA/cm² at Re = 1500. Average limiting current densities under turbulent flow conditions ranged from 34 mA/cm² at Re = 5000 to 56 mA/cm² at Re = 10,000. Average applied current densities are listed in Table I. Note that limiting current densities are not approached, except near the trailing edge of the cathode for the single experiment at Re = 500 and $i_{avg} = 5.0$ mA/cm², which was performed for qualitative comparison purposes only.

The five obstacles were placed in the flow channel for some of the laminar flow experiments (Re = 500 and 1500); no flow obstacles were employed for the turbulent-flow experiments (Re = 5000 and 10,000). The four attached flow obstacles together occlude less than 0.3% of the cathode surface area. The current density, calculated by dividing the cell current by the projected cathode area, is therefore a good approximation to the true average current density.

Results and Discussion

The effect of electrolyte flow velocity on the steady-state mass-transfer boundary layer, formed by constant-current electrodeposition of Cu from 0.1M CuSO₄ without obstacles in the flow channel, is illustrated in Fig. 4. The curvature of the interference fringes seen near the electrode surface indicates reduced CuSO₄ concentration in the mass-transfer boundary layer. In this region, the electrolyte refractive index is lower than that in the bulk electrolyte, where the interference fringes are straight and perpendicular to the plane of the electrode surface. To a first approximation, the shape of an interference fringe represents the CuSO₄ concentration profile, with a displacement of one fringe spacing corresponding to a concentration change of 0.0022M CuSO₄. Inspection of Fig. 4 leads to the following observations.

1. Increasing the electrolyte flow velocity from Re = 500 to Re = 10,000 reduces the mass-transfer boundary layer thickness from (approximately) 1 to 0.1 mm.

2. The interfacial concentration gradient appears to be similar in all four experiments, even though the current density varies by a factor of five.

3. The apparent location of the electrode/electrolyte interface shows considerable deviation from its actual location, marked by the "0" ordinate designation, observed in the absence of refractive-index gradients. In the absence of mass-transfer boundary layers, the interference fringes are arranged to be straight and perpendicular to the plane of the electrode surface. There is, however, a very slight curvature of the fringes within 0.2 mm of the electrode surface caused by reflection from the very slightly rounded edge of the electrode surface (39).

4. The decrease of electrolyte concentration at the interface (relative to the bulk solution) appears to be much larger for the laminar-flow experiments than that for the turbulent-flow experiments.

Of the four observations listed above, only the first correctly describes the CuSO₄ concentration profiles. Observations 2-4 are artifacts of light-ray deflection (refraction) in the mass-transfer boundary layer. Simple methods of interpretation of interferograms which neglect light-curvature effects can lead to large errors (40, 41) in derived current densities, concentration changes, and boundary-layer thicknesses. Quantitative reduction of experimental interferograms to concentration profiles requires extensive computations to account for light-ray curvature effects. Correction procedures of varying degrees of complexity have been developed (26-30, 40-49). In general, larger interfacial refractive-index gradients result in greater light-ray deflection, which in turn requires more complex computational procedures. The present study employed a complex iterative procedure (42), which was shown to be accurate for the steep refractive-index (concentration) gradients expected.

Previous studies of the mass-transfer boundary layer formed by constant-current electrodeposition under laminar channel flow conditions have been reported elsewhere (31). Local steady-state concentration profiles were found to be consistent with well-established heat- and mass-transfer correlations (38, 2, 9) and the appropriate solution to the convective-diffusion equation (31), provided that the experimental interferograms were interpreted by the above-mentioned procedure (42) to properly account for light-ray deflection.

Quantitative interpretation of interferograms measured under turbulent flow conditions proved to be very difficult. The interference fringes and the associated de-

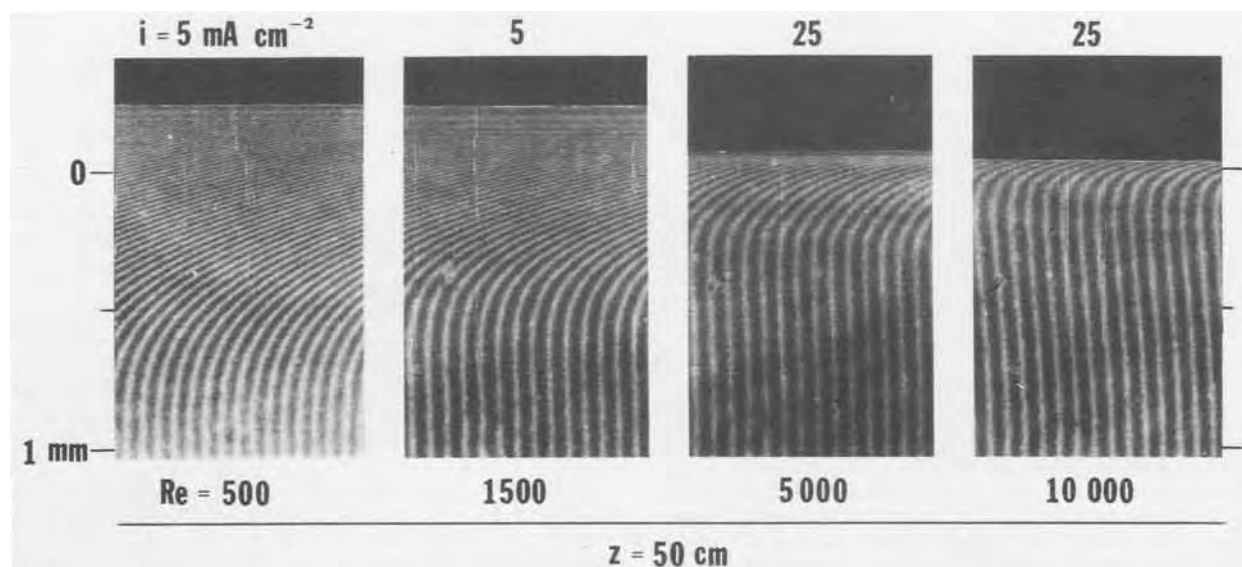


Fig. 4. Experimental interferograms showing the effect of electrolyte flow velocity on steady-state mass-transfer boundary layer thickness. Ordinate: distance from the cathode surface (mm).

rived current densities showed rapid and random fluctuations. Current densities (interfacial concentration gradients) varied between 10 and 100% of the expected values over time intervals of ca. 0.03s, as revealed by analysis of high speed (up to 64 frame/s) motion pictures of the interferograms. Concentration differences (between bulk and interface) showed similar fluctuations, while boundary-layer thicknesses showed somewhat smaller fluctuations. This observation is an indication that the smoothly varying, one-dimensional concentration profiles employed in the computational procedure (42) to interpret the interferograms cannot account for the (expected) random perturbations of local concentrations within the mass-transfer boundary layer, caused by turbulent eddy motion. This result could be expected, because the interferometric measurements produce a two-dimensional representation of a three-dimensional concentration field. Local refractive-index information is averaged along the optical path of the test beam, but the stirring action of the turbulent fluid motion can lead to substantial and random variations along the same optical path, an effect not easily accounted for in the computational procedure to interpret interferograms.

In Fig. 5, the measured Nernst boundary-layer thicknesses³ in the obstacle-free channel are compared with those predicted by the Chilton-Colburn analogy (50)

$$\text{Sh}_{\text{avg}} = \frac{d_e}{\delta_N} = \frac{f}{2} \text{Re Sc}^{1/3} \quad [1]$$

where f is the Fanning friction factor (51), and the other terms are defined in the List of Symbols. The error bars reflect the uncertainty due to the above-mentioned fluctuations in the experimental interferograms. The measured Nernst boundary-layer thicknesses show fair agreement with those predicted by the Chilton-Colburn analogy, with the greatest deviations occurring near the leading edge of the cathode ($z < 5$ cm), as expected, because the mass-transfer boundary layer is not fully developed in that region. Note that the Nernst boundary-layer

³ The Nernst boundary layer thickness is defined by the ordinate location where the extrapolated interfacial concentration gradient intersects with the extrapolated bulk concentration.

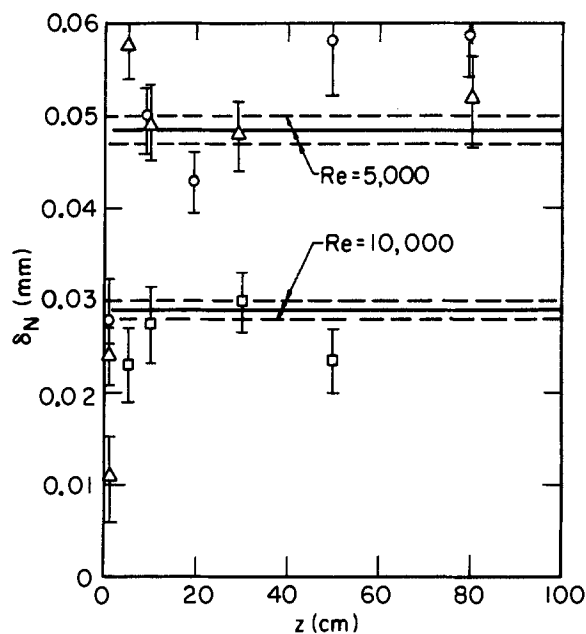


Fig. 5. Turbulent boundary-layer thicknesses. Ordinate: Nernst boundary-layer thickness δ_N (mm). Abscissa: Distance z from cathode leading edge (cm). Solid line: Thickness computed from Eq. [1]. Broken line: Represents uncertainty of computed values due to a 10% uncertainty in diffusion coefficient data. Circles: Derived from experimental interferograms, $\text{Re} = 5000$, $i_{\text{avg}} = 15.0 \text{ mA/cm}^2$. Triangles: $\text{Re} = 5000$, $i_{\text{avg}} = 25.0 \text{ mA/cm}^2$. Squares: $\text{Re} = 10,000$, $i_{\text{avg}} = 25.0 \text{ mA/cm}^2$.

thickness at $\text{Re} = 10,000$ is only about 0.03 mm, whereas the precise location of the electrode/electrolyte interface can only be determined (on the interferogram) with an accuracy of ± 0.005 mm. It is therefore beyond the practical resolution limit of double-beam interferometry to measure boundary-layer thicknesses for Reynolds numbers much larger than 10,000.

Figures 6-9 display interferograms of the concentration field in the immediate vicinity of the four flow obstacles attached to the cathode surface. Note that the presence of a flow obstacle can produce a major effect on the mass-transfer boundary layer downstream of the obstacle. This effect is caused by disruption of the hydrodynamic flow near the obstacle, and it is unrelated to the nonuniform current density distribution expected in the vicinity of the obstacle. The following conclusions can be made by inspecting Fig. 6-9.

1. Significant secondary flows are induced by the three larger obstacles at $\text{Re} = 1500$, and all four obstacles have a relatively small effect on the mass-transfer boundary layer at $\text{Re} = 500$.

2. The smaller semicircular cylinder has little effect at either $\text{Re} = 500$ or $\text{Re} = 1500$.

Consideration of the above observations in light of the sizes of the flow obstacles relative to those of the local mass-transfer boundary-layer thicknesses (see Fig. 2) leads one to the following generalization: the secondary flow induced by small flow obstacles significantly thins the local mass-transfer boundary layer only when the characteristic dimension (*i.e.*, the distance that the obstacle protrudes from the electrode surface into the electrolyte) of the obstacle is comparable to, or exceeds the local mass-transfer boundary-layer thickness.

Figures 10 and 11 illustrate interferograms of the mass-transfer boundary layers just upstream of, and up to 12.5 cm downstream from, the triangular-parallelepiped obstacle attached to the cathode surface. It is seen that the secondary flow induced by the triangular parallelepiped effectively thins the local mass-transfer boundary layer for more than 2.5 cm (33 times the obstacle height) downstream of the obstacle for $\text{Re} = 1500$, and for about 1 cm downstream from the obstacle at $\text{Re} = 500$.

Conversion of the experimental interferograms of the mass-transfer boundary layers in the presence of flow obstacles at $\text{Re} = 500$ and $\text{Re} = 1500$ was performed exactly as described above for $\text{Re} = 5,000$ and $\text{Re} = 10,000$. Difficulties similar to those encountered for interpretation of interferograms under turbulent flow conditions were experienced when interferograms of the wake regions just downstream of the flow obstacles were analyzed. In Fig. 12 and 13, the Nernst boundary-layer thicknesses measured at $\text{Re} = 500$ and $\text{Re} = 1500$ are compared with those predicted by the well-known Norris-Steird correlation (38, 2, 9)

$$\text{Sh}(z) = 1.23 \left(\text{Re Sc} \frac{d_e}{z} \right)^{1/3} \quad [2]$$

for heat and mass transfer under laminar flow conditions. The measured Nernst boundary-layer thicknesses show the expected agreement (31) with the Norris-Steird correlation at locations remote from the vicinity of the flow obstacles. Significant thinning of the local mass-transfer boundary layer is observed only at $\text{Re} = 1500$ for the flow obstacles attached to the cathode surface, which is consistent with the previous qualitative observations of the interferograms. The large cylinder sandwiched midway between the cathode and anode shows the expected reduction of local mass-transfer boundary-layer thickness caused by restriction of the flow channel cross-sectional area.

It is instructive to compare the effective reduction in local mass-transfer boundary-layer thickness caused by placing a flow obstacle on the electrode surface with that obtained by increasing the electrolyte flow rate. For example, Fig. 8, 11, and 13 show that the otherwise laminar mass-transfer boundary layer at $\text{Re} = 1500$ is substantially

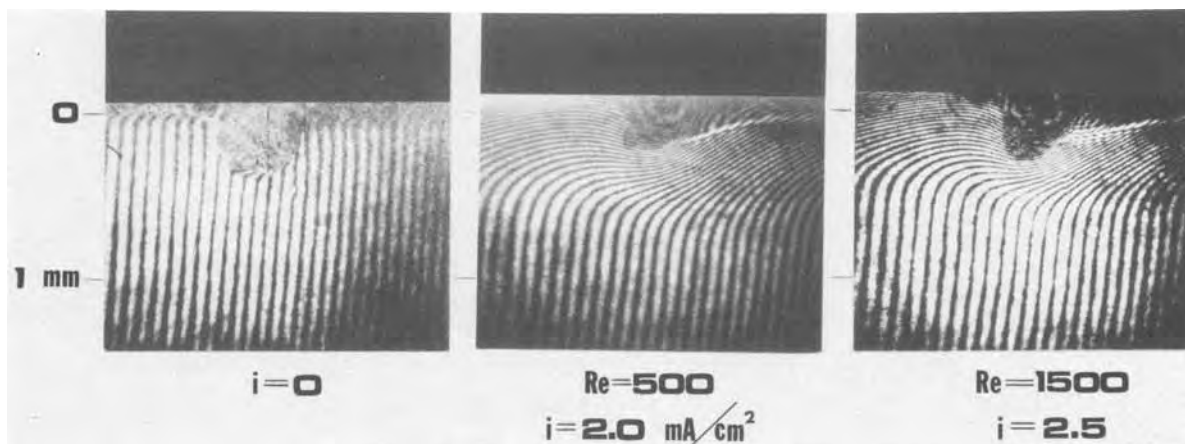


Fig. 6. Experimental interferograms of the 0.28 mm semicircular cylinder. The electrolyte flow is from left to right. Left: $i_{\text{avg}} = 0$. Center: $Re = 500$, $i_{\text{avg}} = 2.0 \text{ mA/cm}^2$. Right: $Re = 1500$, $i_{\text{avg}} = 2.5 \text{ mA/cm}^2$.

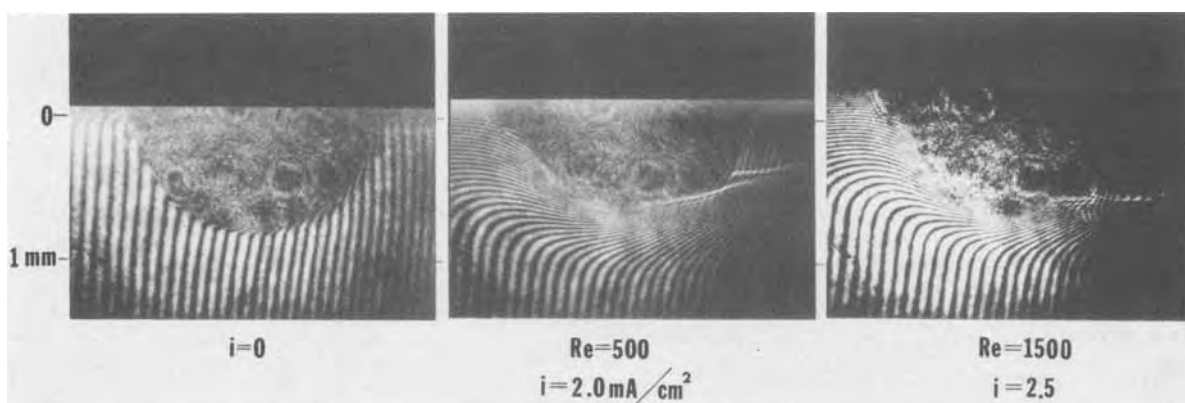


Fig. 7. Experimental interferograms of the 0.76 mm semicircular cylinder. Designations as in Fig. 6

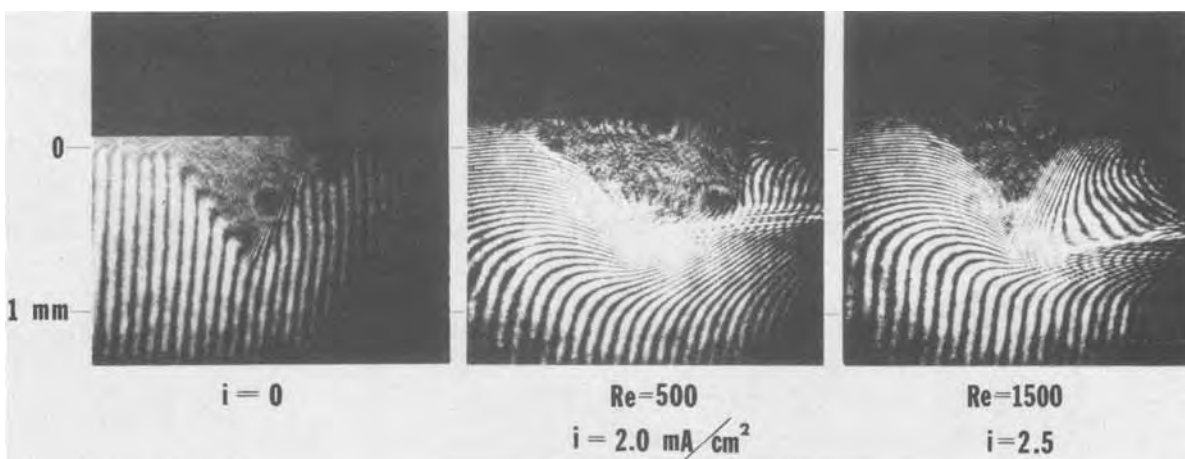


Fig. 8. Experimental interferograms of the 0.76 mm triangular parallelepiped. Designations as in Fig. 6

thinned for at least 2.5 cm downstream from the triangular parallelepiped flow obstacle. The Nernst boundary-layer thickness is reduced from about 0.25 mm just upstream from the obstacle to about 0.08 mm 1.5 cm downstream from the obstacle. The electrolyte flow velocity required to produce a Nernst thickness of 0.08 mm can be computed from Eq. [1] to correspond to $Re = 2790$. The pressure drop (directly related to pumping power and cost) required to maintain a given average flow velocity is given by

$$\frac{dP}{dz} = 2\rho v_{\text{avg}}^2 \frac{f}{d_e} \quad [3]$$

Since the friction factor f varies only slightly (51) from $1500 \leq Re \leq 2790$, and the flow velocity v is proportional to the Reynolds number Re , the ratio of the pressure drop for the two flow velocities considered is approximately

$$\frac{(dP/dz)_{Re=2790}}{(dP/dz)_{Re=1500}} = \left| \frac{2790}{1500} \right|^2 = 3.5$$

Therefore, reduction of the Nernst thickness from 0.25 to 0.08 mm by increasing the electrolyte flow rate from $Re = 1500$ to $Re = 2790$ requires a 3.5-fold increase in pressure drop.

The corresponding increase in pressure drop caused by attachment of triangular-parallelepiped flow obstacles to

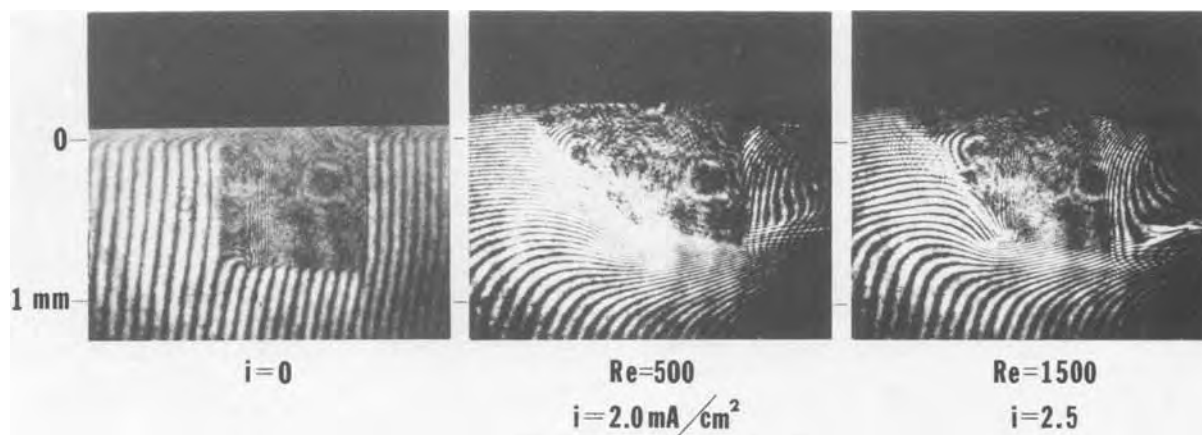


Fig. 9. Experimental interferograms of the 0.76 mm rectangular parallelepiped. Designations as in Fig. 6

the electrode surface can be computed from the correlation presented by Leitz and Marincic (3)

$$f = \frac{\alpha}{Re} + 0.175n_p d_e \frac{1 - \beta^2}{\beta^2} \quad [4]$$

where α is a specific channel dimension parameter, n_p is the number of promoters per centimeter along the length of the channel, and β is the ratio of the open area perpendicular to the flow at the obstacle to the cross-sectional area of the channel without the obstacle. For the triangular obstacle and the given flow-channel dimensions (Fig. 1), the parameters are $\alpha = 16.6$ and $\beta = 0.97$. If triangular-parallelepiped flow obstacles were spaced 2 cm apart along the length of the cathode ($n_p = 0.5 \text{ cm}^{-1}$), the friction factor f computed from Eq. [4] for $Re = 1500$ would increase by a factor of 1.7 over that for a smooth electrode. Therefore, insertion of triangular-parallelepiped

flow obstacles results in a 70% increase in pressure drop at $Re = 1500$.

The electrolyte pumping costs associated with various means to enhance mass-transport rates at the electrode surface are directly related to the power dissipation, which is the pressure gradient multiplied by the average electrolyte velocity. The power dissipation, therefore, varies in direct proportion to the friction factor and as the cube of the average electrolyte velocity. Reduction of the Nernst thickness from 0.25 to 0.08 mm by increasing the electrolyte flow rate therefore requires a 6.4-fold increase in power dissipation, which may be compared to a 1.7-fold increase in power dissipation caused by insertion of triangular-parallelepiped flow obstacles.

Conclusions

Double-beam interferometry has been shown to provide qualitative and quantitative information about mass-

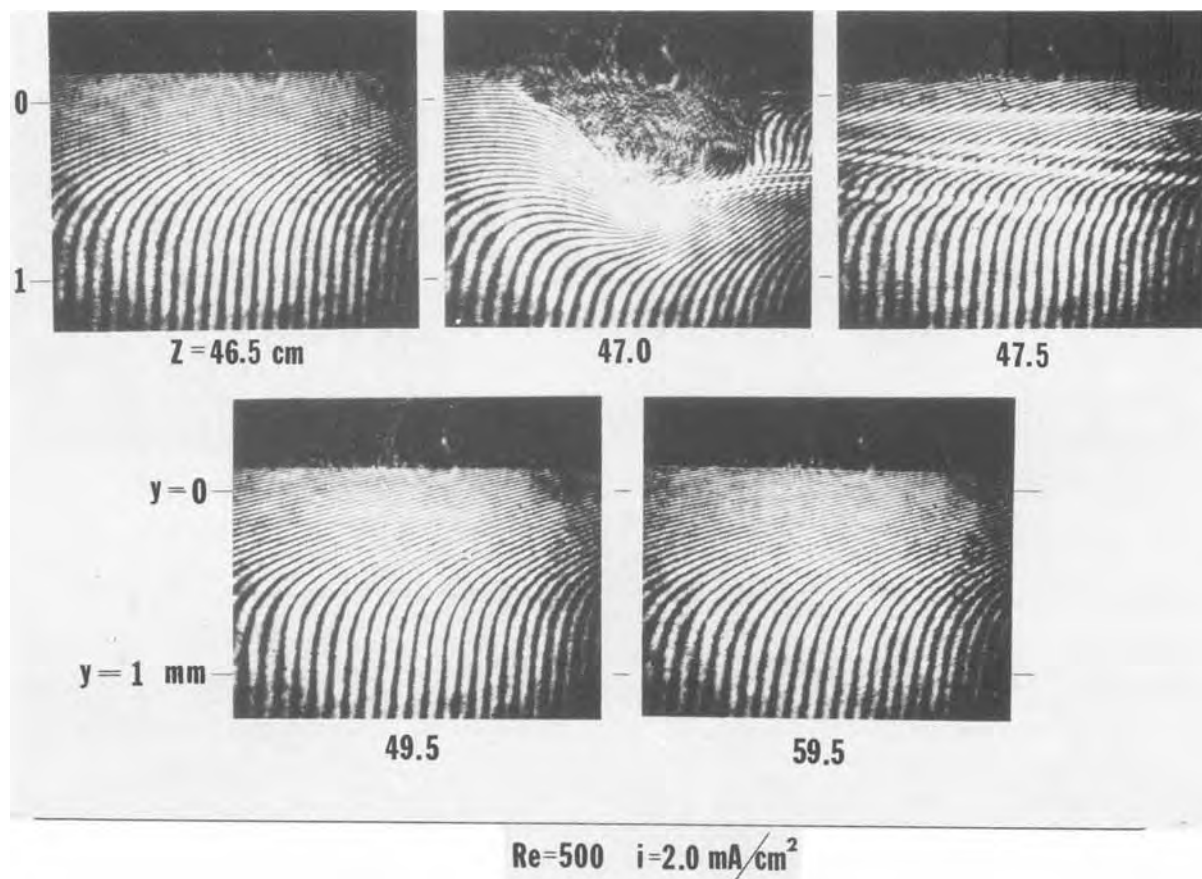


Fig. 10. Experimental interferograms of the region near the 0.76 mm triangular parallelepiped. $Re = 500$, $i_{avg} = 2.0 \text{ mA/cm}^2$. The electrolyte flow is from left to right. a: $z = 46.5 \text{ cm}$. b: $z = 47.0 \text{ cm}$. c: $z = 47.5 \text{ cm}$. d: $z = 49.5 \text{ cm}$. e: $z = 59.5 \text{ cm}$.

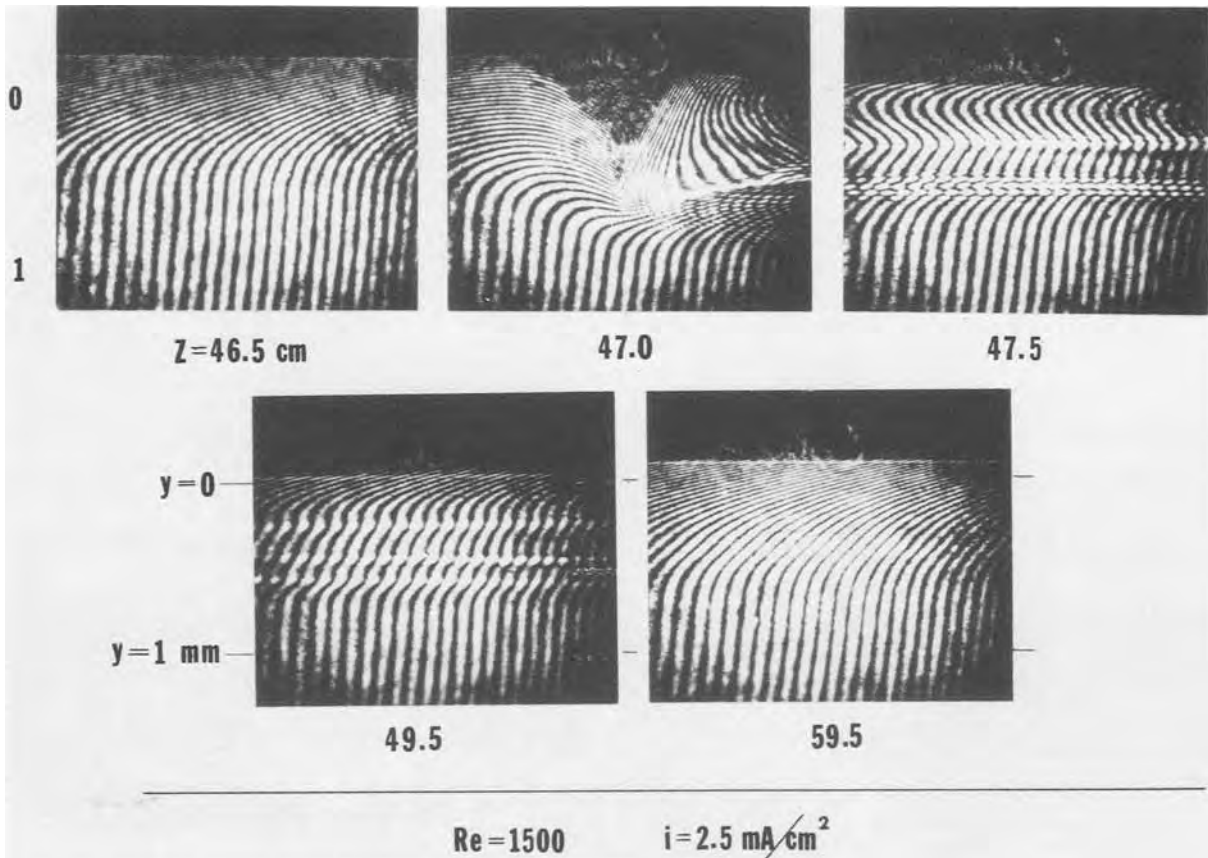


Fig. 11. Experimental interferograms of the region near the 0.76-mm triangular parallelepiped. $Re = 1500, i_{avg} = 2.5 \text{ mA/cm}^2$. Designations as in Fig. 10.

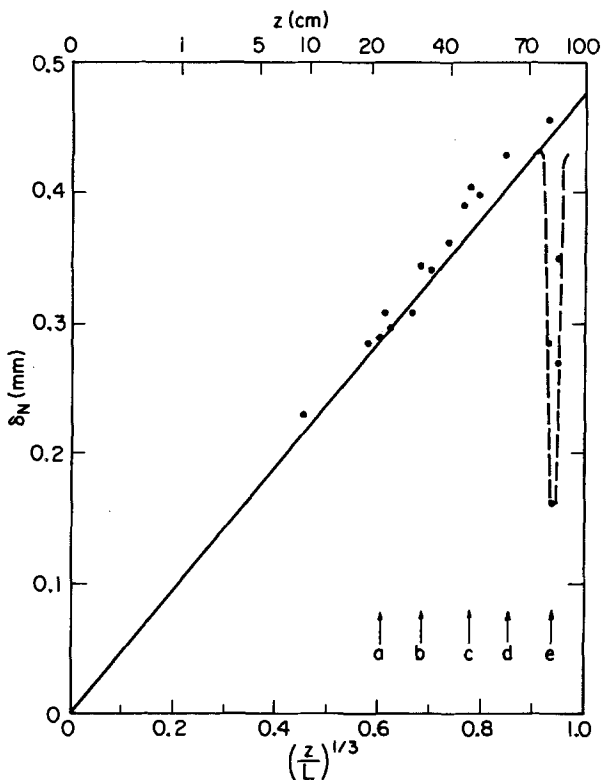


Fig. 12. Nernst boundary-layer thicknesses at $Re = 500$. Ordinate: Nernst-boundary layer thickness (mm). Abscissa: reduced distance z/L from cathode leading edge. Circles: derived from experimental interferograms. Solid line: Norris and Streid correlation (38). Dotted line: boundary-layer thicknesses near obstacles. a: $z = 22 \text{ cm}$, location of smaller semicircular cylinder. b: $z = 32 \text{ cm}$, larger semicircular cylinder. c: $z = 47 \text{ cm}$, triangular parallelepiped. d: $z = 62 \text{ cm}$, rectangular parallelepiped. e: $z = 82 \text{ cm}$, large circular cylinder.

transfer processes under turbulent flow conditions. Derived mass-transfer boundary-layer thicknesses under turbulent flow conditions show the expected agreement with well-established heat- and mass-transfer correlations.

It is shown that the insertion of certain flow obstacles in an otherwise laminar flow stream can result in increased mass-transfer rates. The increased pressure drop and associated pumping power caused by the presence of the flow obstacle are shown to be substantially less than those required to produce the same increase in mass-transfer rates by an increase in flow velocity.

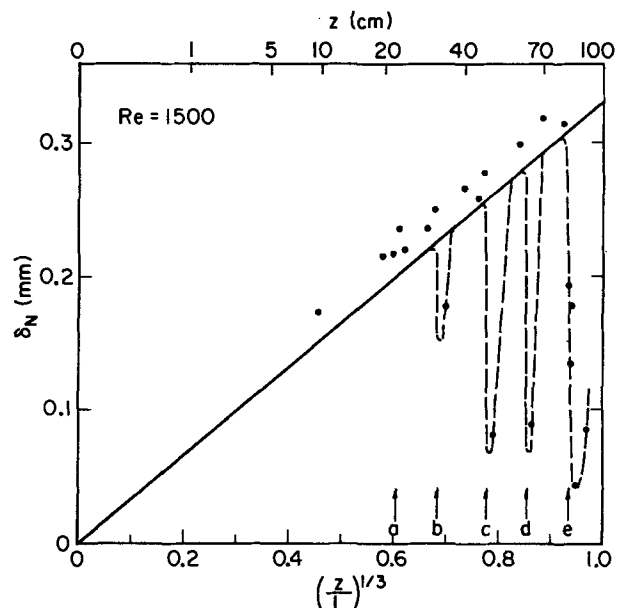


Fig. 13. Nernst boundary layer thicknesses at $Re = 1500$. Designations as in Fig. 12.

Acknowledgment

This work was supported by the Director, Office of Energy Research, Office of Basic Energy Sciences, Materials Sciences Division of the U.S. Department of Energy under Contract no. DE-AC03-76SF00098. We also thank the National Aeronautics and Space Administration for a predoctoral fellowship.

Manuscript submitted Oct. 29, 1984; revised manuscript received March 15, 1985. This was Paper 157 presented at the Pittsburgh, Pennsylvania, Meeting of the Society, Oct. 15-20, 1978.

Lawrence Berkeley Laboratory assisted in meeting the publication costs of this article.

LIST OF SYMBOLS

a	specific channel dimension parameter [see Ref. (3)]
C	CuSO_4 concentration (mol/liter)
d	glass sidewall thickness (cm)
d_e	hydraulic diameter of flow channel (cm)
f	Fanning friction factor [see Ref. (50)]
h	electrode separation (cm)
i_{avg}	average current density (mA/cm^2)
L	electrode length (cm)
n_p	obstacle spacing frequency (cm^{-1})
Re	Reynolds number
Sc	Schmidt number
$Sh(z)$	local Sherwood number
Sh_{avg}	average Sherwood number
v_{avg}	average flow velocity (cm/s)
w	electrode width (cm)
z	coordinate parallel to electrolyte flow, measured from electrode leading edge (cm)
β	flow channel cross-sectional area contraction coefficient
δ_N	Nernst boundary layer thickness (cm)
λ	light wavelength (cm)
ν	kinematic viscosity (cm^2/s)
ρ	density (g/cm^3)

REFERENCES

- W. H. Safranek and C. H. Layer, *Trans. Inst. Metal Finish.*, **53**, 121 (1975).
- R. E. Acosta, Ph.D. Thesis, University of California, Berkeley, CA (1974); *A.I.Ch.E.J.*, To be published.
- F. B. Leitz and L. Marincic, *J. Appl. Electrochem.*, **7**, 473 (1977).
- E. Schalch and N. Ibl, *Electrochim. Acta*, **20**, 435 (1975).
- S. Mohanta and T. Z. Fahidy, *Can. J. Chem. Eng.*, **50**, 248 (1972).
- W. R. Wolfe, H. Chessin, E. Yeager, and F. Hovorka, *This Journal*, **101**, 590 (1954).
- R. H. Muller, D. J. Roha and C. W. Tobias, in "Transport Processes in Electrochemical Systems," R. Yeo, T. Katan, and D. Chin, Editors, pp. 1-5, The Electrochemical Society Softbound Proceedings Series, Pennington, NJ (1982); see also S. Eisner, *Plating*, **58**, 995 (1971).
- J. R. Selman and C. W. Tobias, *J. Electroanal. Chem.*, **65**, 67 (1975).
- J. R. Selman and C. W. Tobias, *Adv. Chem. Eng.*, **10**, 211 (1978).
- J. S. Watson and D. G. Thomas, *A.I.Ch.E. J.*, **13**, 676 (1967).
- G. Belfort and G. A. Guter, *Desalination*, **10**, 221 (1972).
- Y. Winograd, A. Solan, and M. Torren, *ibid.*, **13**, 171 (1973).
- F. B. Leitz, L. Marincic, P. Johnson, and J. Liston, "Effect of Turbulence Promoters on Local Mass Transfer, 3rd Report," Ionics Technical Report, Waltham, MA (1974).
- M. S. Isaacson and A. A. Sonin, *Ind. Eng. Chem. Proc. Res. Dev.*, **15**, 313 (1976).
- A. Storck and F. Coeuret, *Electrochim. Acta*, **22**, 1155 (1977).
- A. Storck and D. Hutin, *Can. J. Chem. Eng.*, **58**, 92 (1980).
- D. H. Kim, I. H. Kim, and H. N. Chang, *Int. J. Heat Mass Transfer*, **26**, 1007 (1983).
- W. W. Focke, *Electrochim. Acta*, **28**, 1137 (1983).
- R. H. Muller, in "Advances in Electrochemistry and Electrochemical Engineering," Vol. 9, R. H. Muller, Editor, pp. 326-353, Wiley-Interscience, New York (1973).
- W. Hauf and U. Grigull, in "Advances in Heat Transfer," Vol. 6, J. P. Hartnett and T. F. Irvine, Editors, pp. 133-366, Academic Press, New York (1970).
- F. R. McLarnon, R. H. Muller, and C. W. Tobias, *Electrochim. Acta*, **21**, 101 (1976).
- R. N. O'Brien, *This Journal*, **113**, 389 (1966).
- A. Tvarusko and L. S. Watkins, *ibid.*, **118**, 248 (1971).
- L. Hsueh and J. S. Newman, *Electrochim. Acta*, **16**, 479 (1971).
- N. Ibl, Y. Barrada, and G. Trumpler, *Helv. Chim. Acta*, **37**, 583 (1954).
- Y. Awakura and Y. Kondo, *This Journal*, **123**, 1184 (1976).
- Y. Awakura, M. Okada, and Y. Kondo, *ibid.*, **124**, 1050 (1977).
- Y. Awakura, Y. Takenaka, and Y. Kondo, *Electrochim. Acta*, **21**, 789 (1976).
- N. Ibl and R. H. Muller, *Z. Elektrochem.*, **59**, 671 (1955).
- M. Clifton and V. Sanchez, *Electrochim. Acta*, **24**, 445 (1979).
- F. R. McLarnon, R. H. Muller, and C. W. Tobias, *Ind. Eng. Chem. Fundam.*, **18**, 97 (1979).
- C. S. Lin, R. W. Moulton, and G. L. Putnam, *Ind. Eng. Chem.*, **45**, 640 (1953).
- F. R. McLarnon, R. H. Muller, and C. W. Tobias, *This Journal*, **129**, 2201 (1982).
- K. J. Hanson, M.S. Thesis, University of California, Berkeley, CA (1979).
- F. R. McLarnon, Ph.D. Thesis, University of California, Berkeley, CA (1975).
- K. W. Beach, Ph.D. Thesis, University of California, Berkeley, CA (1971).
- K. W. Beach, R. H. Muller, and C. W. Tobias, *Rev. Sci. Instrum.*, **40**, 1248 (1969).
- R. H. Norris and D. D. Streid, *Trans. ASME*, **62**, 525 (1940).
- F. R. McLarnon, R. H. Muller, and C. W. Tobias, *Appl. Opt.*, **14**, 2468 (1975).
- K. W. Beach, R. H. Muller, and C. W. Tobias, *J. Opt. Soc. Am.*, **63**, 559 (1973).
- F. R. McLarnon, R. H. Muller, and C. W. Tobias, *This Journal*, **122**, 59 (1975).
- F. R. McLarnon, R. H. Muller, and C. W. Tobias, *J. Opt. Soc. Am.*, **65**, 1011 (1975).
- U. Grigull, *Int. J. Heat Mass Transfer*, **6**, 669 (1963).
- W. L. Howes and D. R. Buchele, *J. Opt. Soc. Am.*, **56**, 1517 (1966).
- E. E. Anderson, W. H. Stevenson, and R. Viskanta, *Appl. Opt.*, **14**, 185 (1975).
- A. M. Hunter and P. W. Schreiber, *ibid.*, **14**, 634 (1975).
- C. M. Vest, *ibid.*, **14**, 1601 (1975).
- C. Forgacs, J. Leibovitz, R. N. O'Brien, and K. S. Spiegler, *Electrochim. Acta*, **20**, 555 (1975).
- R. N. O'Brien and H. Kolny, *Corrosion*, **34**, 262 (1978).
- D. W. Hubbard and E. N. Lightfoot, *Ind. Eng. Chem. Fundam.*, **5**, 370 (1966).
- W. L. McCabe and J. C. Smith, "Unit Operations of Chemical Engineering," p. 102, McGraw-Hill, New York (1967).

Reaction Pathways of the Anodic Oxidation of Formic Acid on Pt Evidenced by ^{18}O Labeling—A DEMS Study

O. Wolter,^{*,1} J. Willsau, and J. Heitbaum

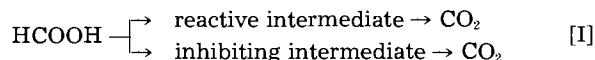
Institute of Physical Chemistry, 5300 Bonn, Germany

ABSTRACT

Using either normal formic acid in H_2^{18}O or ^{18}O -labeled formic acid in H_2^{16}O , the following results were obtained: the oxygen atoms of formic acid are homogeneously exchanged with water; the strongly bound intermediate, however, does not exchange oxygen with water; the ^{18}O -labeled intermediate is oxidized in H_2^{16}O to $\text{C}^{18}\text{O}^{16}\text{O}$ by a three-electron process; direct oxidation of $\text{HC}^{16}\text{O}^{16}\text{OH}$ in H_2^{18}O delivers $\text{C}^{16}\text{O}^{16}\text{O}$.

The anodic oxidation of formic acid has attracted much attention in the last several decades because it was considered to be a possible fuel for direct energy conversion in fuel cells (1-3). In addition, the electrode process was regarded as a simple one which could be taken as a model for organic electrocatalysis (4).

It turned out, however, that the anodic oxidation of formic acid on Pt is by no means a simple process, as the excellent reviews of Capon and Parsons (4-6) show. These authors concluded from the charge obtained in the double-layer region that formic acid is oxidized in a dual path mechanism which is principally written as (5)



Direct oxidation of formic acid is assumed to occur via a so-called "reactive intermediate," described as COOH (5). In parallel, the formation of a strongly bound intermediate takes place which inhibits the direct oxidation and is stable up to at least 0.6V (5, 6). The intermediate is formed especially fast in the hydrogen region on Pt and was assumed to be $\overset{+++}{\text{C}}\text{OH}$ based on the charge consumed to oxidize it as well as on comparison with methanol (6).

While the $\overset{+++}{\text{C}}\text{OH}$ species seemed to be widely accepted in the early seventies, this being supported by radiometric measurements (7), recently vibrational spectroscopy has given strong evidence (8) that the adsorbed species is $\overset{+}{\text{C}}\equiv\text{O}$. This view was corroborated by investigations on single-crystal electrodes (9) and by measuring the number of electrons per site (eps) transferred when the adsorbate is desorbed as CO_2 (10).

In contradiction to these findings, the authors of the present paper were able to measure the number of electrons consumed by the formation of one CO_2 molecule out of the adsorbate. In the case of methanol, it turned out that three electrons are released upon oxidation of the intermediate to CO_2 , and, therefore, CO was excluded to be the inhibiting intermediate (11, 12). Analogous experiments for HCOOH are reported below. In addition, ^{18}O labeling was used to obtain direct evidence for the dual path mechanism mentioned above. This type of measurement is made possible, now, by differential electrochemical mass spectroscopy (DEMS) (13) developed by the authors. This method offers the unique advantages of on-line monitoring the volatile products of an electrochemical process and discriminating between different reaction pathways by isotope labeling.

Experimental

The mass spectroscopic technique (DEMS) applied in the following experiments is described elsewhere (13). In short, it uses a porous Teflon membrane as the inlet system, being directly connected with the ion source of a mass spectrometer. A porous catalyst layer is attached to the membrane on the electrolyte side. It is prepared from

a conducting lacquer (Doduco, Dürrwächter AG) and activated by cycling the electrode between H_2 and O_2 evolution in H_2SO_4 . The surface layer diagram has its usual shape (13), and the catalyst behaves like smooth polycrystalline Pt. This is corroborated by electron microscopy, showing that the catalyst consists of smooth Pt particles of 5 μm mean size. Figure 1 reproduces the respective microphotograph. Therefore, the porous catalyst layer resembles more smooth Pt than a high surface area electrode prepared by platinization.

A minicell containing about 1 ml electrolyte was used, constructed in a way that the solution could be exchanged under potentiostatic control. For example, ^{18}O -labeled formic acid in H_2^{18}O could be adsorbed at a constant potential, and then it was possible to substitute the solution quantitatively by H_2^{16}O . This procedure took about 2-4 min. It should be emphasized that all solutions were carefully deaerated by Ar and that oxygen had no access at any stage of the experiment. Special attention was paid to this point because the experiments with methanol (12) have shown that oxygen or its reduction intermediates react with the adsorbed species. The ion current of the product in the mass spec was recorded in parallel to the current potential curve in the usual way (13). H_2^{18}O was 90% enriched and used as obtained from Ventron GmbH. ^{18}O -labeled formic acid could be prepared from the normal chemical (p.A. grade, Merck) by oxygen exchange with H_2^{18}O as will be shown below. In all cases, the base electrolyte was 0.5M H_2SO_4 (Merck Suprapure) in H_2^{16}O or H_2^{18}O , respectively. Millipore water was used as H_2^{16}O . Solutions were deaerated by

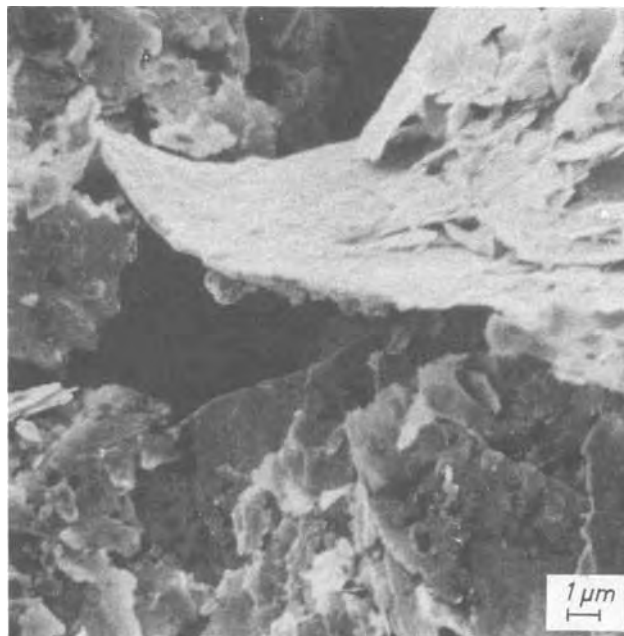


Fig. 1. SEM photograph of the Pt catalyst after electrochemistry

* Electrochemical Society Active Member.

¹ Present address: IBM, GMTC, 7037 Sindelfingen, Germany.

99.999 Ar. All potentials were measured against a hydrogen electrode (RHE) and are reported with respect to this reference.

Results

Homogeneous oxygen exchange between H_2O and $HCOOH$.—Direct experimental evidence for the dual path mechanism (5) of the formic acid oxidation is gained if the origin of the oxygen atoms in the product molecule CO_2 is known. This information can readily be obtained by DEMS using ^{18}O isotope labeling. At first, it has to be found out, however, whether oxygen is exchanged between H_2O and $HCOOH$. It is one advantage of DEMS that a homogeneous isotope exchange reaction can be monitored as well (15).

The experiment was done using the membrane inlet system without the catalyst layer in order to make sure that no heterogeneous exchange reaction takes place. Under these conditions, the acid evaporates through the membrane and the incoming flux into the mass spectrometer is directly proportional to the concentration of the respective species in the solution. The flux is directly related to the measured ion current I_1 which is given in the diagrams below. In previous papers, I_1 was called mass intensity (MI) (11-14).

The cell was filled with $0.5m H_2SO_4$ in H_2O at a ratio of $^{18}O:^{16}O = 9$. At $t = 0$, normal formic acid was added, thereby obtaining a $0.02m$ solution, and the different ^{18}O -labeled formic acid molecules were recorded as a function of time. The fragment spectrum of unlabeled formic acid has the measured intensity distribution for CO_2 (44): HCO_2 (45): H_2CO_2 (46) of 100:12:15,² CO_2 being the base peak. Consequently, the mass numbers 44, 46, and 48 can be identified as $HC^{16}O^{16}OH$, $HC^{16}O^{18}OH$, and $HC^{18}O^{18}OH$, respectively.

Figure 2 shows the result indicating that oxygen is completely exchanged between formic acid and H_2O , since the ion current of the originally added $HC^{16}O^{16}OH$ decreases, whereas that of $HC^{18}O^{18}OH$ increases with time. $HC^{16}O^{18}OH$ appears as an intermediate, having its maximum concentration after 6 min. The reaction obeys pseudo first-order kinetics and probably proceeds via a formate anion as intermediate, which means that both oxygen atoms are equivalent. The fact that formate is present only to a small extent in acidic solutions explains the rather slow oxygen exchange rate.

It should be noted that exactly the same result was obtained with the catalyst layer attached to the membrane when the potential was kept constant at $0.1V$. Therefore, a heterogeneous catalysis of the oxygen exchange reaction between formic acid and water seems not to occur within the limits of error.

Anodic oxidation of $HC^{16}O^{16}OH$ in $H_2^{18}O$.—Since oxygen is homogeneously exchanged between formic acid and water, the anodic oxidation of $HC^{16}O^{16}OH$ in $H_2^{18}O$ was studied in a single potential scan experiment immediately after addition of the acid to the electrolyte at $E = 0.1V$. Figure 3 shows the respective I-E curves together with the production rate of the differently labeled CO_2 species. Note that the ion currents differ by about two orders of magnitude from those in Fig. 2.

The intensity ratios of the different CO_2 species (44, 46, 48) correspond exactly to the homogeneous oxygen exchange reaction throughout the whole potential range, as can be easily deduced by comparing the intensity ratios at different times with those obtained from Fig. 2. This shows that both O atoms originate from formic acid which is directly oxidized to CO_2 . One exception is to be observed, however, namely, in the peak around $0.7V$, where an exceptional high intensity of $C^{16}O^{18}O$ is measured, which considerably exceeds the expected value. Evidently, within the peak around $0.7V$ a different type of mechanism takes place, and, as a whole, the result of Fig. 3 gives evidence of the dual-path mechanism (5) of the formic acid oxidation.

² This distribution differs from that reported in the literature (16) because of the high partial pressure of H_2O in our ionization chamber.

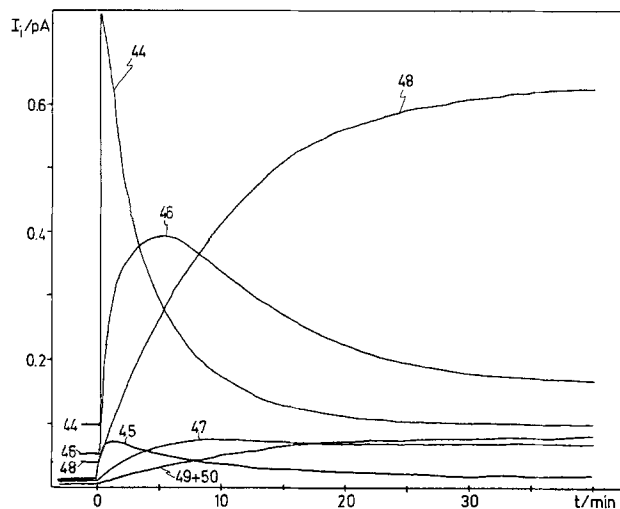


Fig. 2. Ion currents of masses 44-50 as function of time. The signal is due to evaporation of formic acid into the mass spec after adding $HC^{16}O^{16}OH$ to $0.5m H_2SO_4$ in $90\% H_2^{18}O$ at $t = 0$. The obtained solution contained $0.02m HCOOH$.

On the nature of the strongly bound intermediate.—Number of O atoms present in the adsorbate.—Accepting the usual view (5, 6, 8-10) that the extra reaction in the

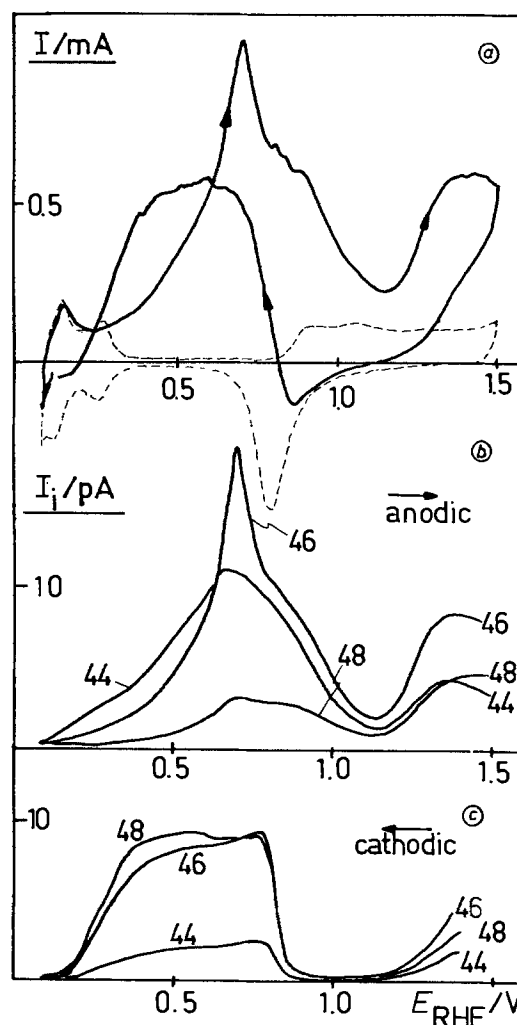


Fig. 3. Electro-oxidation of $0.01m HCOOH$ on a porous Pt electrode. Base electrolyte is $0.5m H_2SO_4$ in $H_2^{18}O$ (90% enriched). First cycle after adding $HC^{16}O^{16}OH$ at an electrode potential of $100 mV_{RHE}$ is shown. Sweep rate is $6.25 mV \cdot s^{-1}$. a: The solid line shows the cyclic voltammogram; the broken line shows the surface layer diagram in base electrolyte. b, c: Corresponding I_1/E curves for the masses 44-48 during the anodic (b) and cathodic (c) scan.

peak at 0.7V originates from a strongly bound intermediate formed within the hydrogen region on Pt, experiments were done to find out how many oxygen atoms this adsorbate contains. Therefore, formic acid was equilibrated with base electrolyte of the isotope ratio $^{16}\text{O}:^{18}\text{O} = 0.84$. It is assumed that HCOOH adjusts itself to the same ratio, due to the homogeneous oxygen exchange reaction. This solution was brought into contact with the electrode at $E = 0.1\text{V}$ for 3 min, thus allowing the adsorbate to form. Then, the solution was quantitatively replaced by $\text{H}_2^{16}\text{O} + 0.5\text{m H}_2\text{SO}_4$, and an anodic scan was recorded, as is shown in Fig. 4. Evidently, the strongly bound intermediate was formed, and it is desorbed in a peak around 0.7V, the product being CO_2 , represented by the mass numbers 44, 46, 48. The intensity ratios between these species in the desorption peak amount to $\text{C}^{16}\text{O}^{16}\text{O}:\text{C}^{16}\text{O}^{18}\text{O}:\text{C}^{18}\text{O}^{18}\text{O} = 84:100:0$. This corresponds exactly to the isotope ratio of the initial solution and shows unambiguously that the adsorbate contains one oxygen atom only. Otherwise, the ratios would have been $\text{C}^{16}\text{O}^{16}\text{O}:\text{C}^{16}\text{O}^{18}\text{O}:\text{C}^{18}\text{O}^{18}\text{O} = 71:168:100$, as can be calculated statistically ($8.4^2:2 \cdot 8, 4 \cdot 10:10^2$).

Reactions between the strongly bound intermediate and the solution.—The results of the preceding section seems to indicate that the strongly bound intermediate does not react with water, *e.g.*, exchanging oxygen. To ensure this, $\text{HC}^{18}\text{O}^{18}\text{OH}$ in ^{18}O -base electrolyte (both containing 90% ^{18}O) was adsorbed at 0.1V for 3 min and afterwards the solution was replaced by ^{16}O -base electrolyte. After 2.5 min waiting at this potential, $\text{HC}^{16}\text{O}^{16}\text{OH}$ was added to yield a 0.005m solution. The potential was kept constant for another 2 min to allow the adsorbate to react with the solution. Finally, an anodic scan was performed and the ion currents of the mass numbers 44, 46, and 48 were recorded. Figure 5 shows the result.

Evidently, only $\text{C}^{16}\text{O}^{16}\text{O}$ is formed by the direct oxidation of bulk $\text{HC}^{16}\text{O}^{16}\text{OH}$. Within the desorption peak, however, $\text{C}^{16}\text{O}^{18}\text{O}$ is predominant. The intensity of $\text{C}^{17}\text{O}^{16}\text{O}$ (45) corresponds to the isotope ratio of ^{17}O in the preadsorbed formic acid,³ whereas the intensity of $\text{C}^{16}\text{O}^{16}\text{O}$ slightly exceeds the ^{16}O ratio. This is explained by the continuous adsorption of $\text{HC}^{16}\text{O}^{16}\text{OH}$.

This experiment shows clearly that the strongly bound intermediate does not exchange oxygen with H_2O . Moreover, it does not react with bulk HCOOH either, at least outside the potential range of desorption.

Number of electrons consumed to oxidize the adsorbate to CO_2 .—Analogous to the experiments with methanol (12), the number of electrons necessary to form the CO_2 molecule out of the adsorbate was measured. This was done using the equation (12, 14)

³ The ^{18}O -labeled water used in our experiments contained 3.5 atom percent ^{17}O .

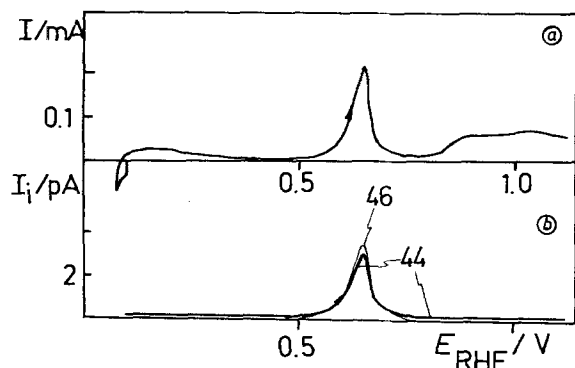


Fig. 4. Electrodesorption of preadsorbed formic acid on a porous Pt electrode in the absence of bulk HCOOH 0.01m HCOOH (equilibrated with base electrolyte of the isotope ratio $^{16}\text{O}:^{18}\text{O} = 8.4:10$) was adsorbed at $E = 100\text{ mV}_{\text{RHE}}$ for 3 min. Then the electrolyte was substituted by base electrolyte in H_2^{16}O (3.5 min). Figure shows first anodic scan after exchange at a sweep rate of $3.125\text{ mV}\cdot\text{s}^{-1}$. a: Cyclic voltammogram. b: Corresponding I_i/E curves for the masses 44-48.

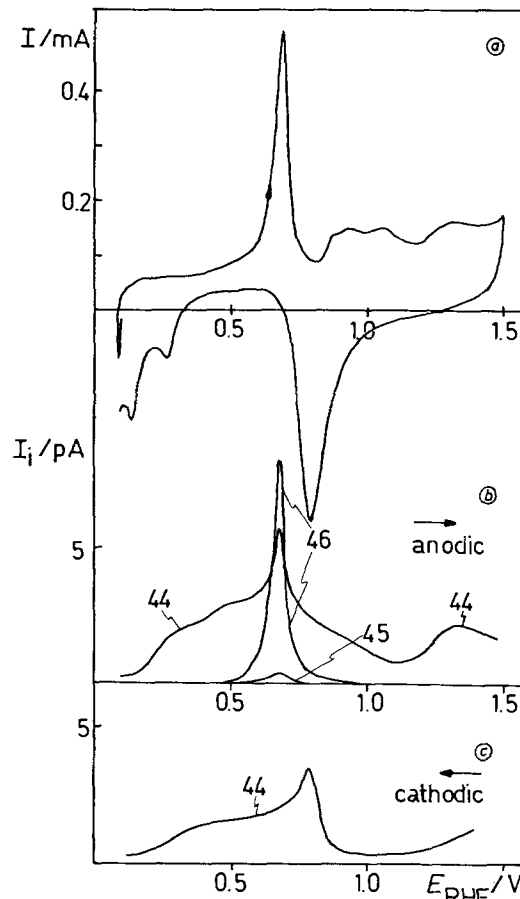


Fig. 5. Electro-oxidation of both adsorbed and bulk HCOOH on a porous Pt electrode in 0.5m H_2SO_4 . 1: Adsorption of $\text{HC}^{18}\text{O}^{18}\text{OH}$ in ^{18}O -base electrolyte (90%) for 3 min at 0.1V_{RHE} . 2: Replacement of the solution by ^{16}O -base electrolyte (2.5 min). 3: Waiting for 2.5 min at $E = 0.1\text{V}$. 4: Adding of $\text{HC}^{16}\text{O}^{16}\text{OH}$ to obtain a 0.005m solution (2 min). 5: Waiting for 2 min at $E = 0.1\text{V}$. Figure shows first cycle after this procedure at a sweep rate of $6.25\text{ mV}\cdot\text{s}^{-1}$. a: Cyclic voltammogram. b, c: Corresponding I_i/E curves for the masses 44-48 during the anodic (b) and cathodic (c) scan.

$$I_i = K^+ \frac{1}{n} AI \quad [1]$$

with I_i being the ion current (A) of species i ; K^+ the proportionality constant, including all factors not specific for a given electrochemical process; n the number of electrons necessary to form one product molecule; A the current efficiency; and I the faradaic current (A).

In order to compare the total charge used within the desorption peak with the corresponding mass signal, one has to integrate Eq. [1]

$$Q_{ii} = K^+ \cdot \frac{1}{n} \cdot A \cdot Q_f \quad [2]$$

with Q_{ii} being the amount of product detected in the mass spec and Q_f the faradaic charge of the desorption process.

The constant K^+ is measured by an adsorption/desorption experiment for which n is known. Thus, CO is adsorbed at constant potential, removed from the solution by Ar flushing and desorbed as CO_2 by an anodic sweep. If the integration is done over a complete potential cycle, starting and ending with the same surface condition, $n = 2$ exactly (12). A is proven to be 1 by recording the second cycle which coincides with the surface layer diagram as well as by showing that no product other than CO_2 is formed.

With HCOOH , the analogous procedure was performed. The strongly bound intermediate was formed at 0.15V, then the solution was substituted by the base electrolyte and the adsorbate desorbed in an anodic scan. Figure 6 shows the $I-E$ curve together with the ion current of CO_2 .

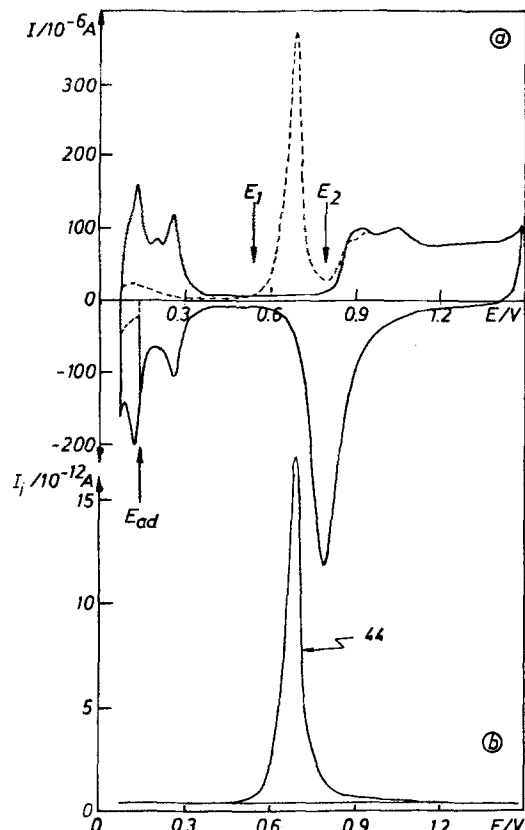
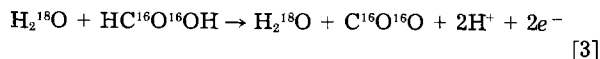


Fig. 6. HCOOH-adsorption-desorption experiment in $0.5m$ H_2SO_4 on a porous Pt electrode. HCOOH was adsorbed at $0.15V$ for 3 min from a $0.01m$ solution. Then, excess fuel was removed by replacing the solution by base electrolyte. a: The solid line shows the surface layer diagram in $0.5m$ H_2SO_4 ; the dashed line shows the first anodic scan at a sweep rate of 6.25 $mV \cdot s^{-1}$ after exchange of the electrolyte. b: Corresponding I_1/E curve for CO_2 (44) during the electrodesorption of the preadsorbed HCOOH.

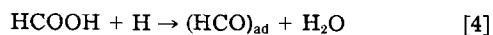
Integration of both curves together with $K^+ = 1.5 \times 10^{-7}$, obtained by the CO-adsorption-desorption experiment, gives $n = 3.0 \pm 0.15$. Therefore, $(CO)_{ad}$ can be ruled out as the strongly bound intermediate, but $(HCO)_{ad}$ is more likely.

Conclusions

Formic acid exchanges oxygen atoms with water. Taking this into account, it could be shown clearly that formic acid is oxidized on Pt in a dual path mechanism. The direct oxidation occurs without loss of oxygen (5)



The second reaction proceeds via a strongly bound intermediate, preferentially formed within the hydrogen region (6) by splitting off an oxygen atom from the acid. The most probable way by which this can occur is the formation of a water molecule as proposed by Parsons (6)



In principle, the analogous process could take place with an intermediate like $(COOH)_{ad}$ (5) to give CO_{ad} . But at $0.15V$, the rate of the direct oxidation of formic acid is

very slow, whereas the formation of the strongly bound intermediate is rather fast (6). Therefore, reaction [4] seems to be more likely. Moreover, the adsorbate $(CHO)_{ad}$ has the correct stoichiometry to be oxidized to CO_2 in a three-electron process, and we were able to prove that the adsorbate contains hydrogen (17). In conclusion, the present paper provides direct evidence for the dual-path mechanism described by scheme [I], where the "reactive intermediate" probably is $COOH_{ad}$ and the "inhibiting intermediate" is HCO_{ad} . Indirect evidence for the dual-path mechanism was recently given by Adzic (18) as well as by Pletcher (19).

Unfortunately, however, the intermediate proposed in Eq. [4] contains a carbon oxygen double bond and therefore does not match with the vibrational spectroscopy data (8). Several reasons could be envisaged for this discrepancy: strong shift of the adsorption band, perhaps due to bridge bonding; high absorption cross section of CO, being formed in a side reaction; oxidation of the initially formed intermediate to CO_{ad} by oxygen impurities in the solution (11, 12).

Acknowledgment

Financial support by the Deutsche Forschungsgemeinschaft (DFG) is gratefully acknowledged.

Manuscript submitted Oct. 10, 1984; revised manuscript received March 19, 1985.

The Institute of Physical Chemistry assisted in meeting the publication costs of this article.

REFERENCES

- P. G. Grimes and H. M. Spengler, in "Hydrocarbon Fuel Cell Technology," B. S. Baker, Editor, p. 221, Academic Press, New York (1965).
- M. W. Breiter, "Electrochemical Processes in Fuel Cells," Springer Verlag, New York (1969).
- W. Vielstich, "Fuel Cells," Revised English ed., Interscience, New York (1970).
- A. Capon and R. Parsons, *J. Electroanal. Chem.*, **44**, 1 (1973).
- A. Capon and M. Parsons, *ibid.*, **44**, 239 (1973).
- A. Capon and M. Parsons, *ibid.*, **45**, 205 (1973).
- V. E. Khazarinov, G. Y. Tsymanaya, and V. N. Andreev, *Elektrokhimiya*, **8**, 396 (1972).
- B. Beden, A. Bewick, and C. Lamy, *J. Electroanal. Chem.*, **148**, 147 (1983).
- C. Lamy, J. M. Leger, J. Clavilier, and R. Parsons, *ibid.*, **150**, 71 (1983).
- J. Clavilier, R. Parsons, and S.-G. Sun, Abstract A7-37, p. 445, 35th ISE Meeting, Berkeley, CA (1984).
- J. Willsau and J. Heitbaum, Abstract A8-20, p. 498, 35th ISE Meeting, Berkeley, CA (1984).
- J. Willsau, O. Wolter, and J. Heitbaum, *J. Electroanal. Chem.*, **185**, 163 (1985).
- O. Wolter and J. Heitbaum, *Ber. Bunsenges. Phys. Chem.*, **88**, 2 (1984).
- O. Wolter and J. Heitbaum, *ibid.*, **88**, 6 (1984).
- J. Willsau, O. Wolter, and J. Heitbaum, *Anal. Chem.*, In press.
- E. Stenhagen, S. Abrahamsson, and F. W. McLafferty, "Registry of Mass Spectral Data," Vol. 1, John Wiley and Sons, New York (1974).
- J. Willsau and J. Heitbaum, *J. Electroanal. Chem.*, **185**, 185 (1985).
- R. R. Adzic, A. V. Tripkovic, and W. O'Grady, in "Electrocatalysis," F. Will, W. O'Grady, and P. Ross, Editors, p. 254, The Electrochemical Society Soft-bound Proceedings Series, Pennington, NJ (1982).
- A. Razaq and D. Pletcher, *This Journal*, **131**, 957 (1984).

Electrochemical and Spectroscopic Studies of Sulfur in Aluminum Chloride-N-(n-Butyl)Pyridinium Chloride

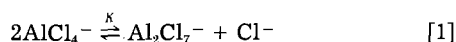
R. Marassi,¹ T. M. Laher, D. S. Trimble, and G. Mamantov*

Department of Chemistry, University of Tennessee, Knoxville, Tennessee 37996-1600

ABSTRACT

The behavior of sulfur in aluminum chloride-N-(n-butyl)pyridinium chloride (AlCl_3 -BPC) was studied using Raman spectroscopy and electrochemical techniques. In basic (BPC-rich) melts, sulfur can be reduced to sulfide, probably in the form of an AlSCl_2 -like species. No oxidation to positive oxidation states of sulfur is observed in basic melts. In acidic (AlCl_3 -rich) melts, sulfur can be oxidized to S(I) and eventually to S(IV), which is only stable in the melt for short periods of time. No reduction to sulfide-like species or formation of low oxidation states is observed in acidic melts.

Mixtures of aluminum chloride and N-(n-butyl)pyridinium chloride (BPC) form melts which are liquid at or near room temperature (1, 2). Raman spectroscopic (3) and potentiometric (4) studies indicate that the acid-base properties of this system can be described by the expression



where $K = 1.2 \times 10^{-13}$ at 40°C (5). Substantial changes in the Lewis acidity of these melts may be made by varying the AlCl_3 /BPC molar ratio. Electrochemical studies of several organic and inorganic species in this system and other related systems indicate that the solute chemistry and electrochemistry of these species are dependent on the melt acidity (6).

Several studies have been published on the electrochemistry of sulfur in alkali metal chloroaluminate melts, partly because of potential use of positive oxidation states of sulfur as cathode-active materials in secondary molten salt batteries (7-10). In basic (NaCl -rich) AlCl_3 - NaCl melts, sulfur can be reduced to sulfide in the form of an AlSCl_2 -like species and oxidized to S(I) (11-13). In acidic (AlCl_3 -rich) AlCl_3 - NaCl melts, sulfur, in addition to being reduced, undergoes successive oxidations through several intermediates leading eventually to S(IV) in the form of SCl_3^+ (14, 15). In contrast to the work on sulfur in the AlCl_3 - NaCl system, only a brief voltammetric study of sulfur in AlCl_3 containing room temperature melts has been reported (16).

Experimental

AlCl_3 -BPC melts were prepared by slowly mixing preweighed amounts of AlCl_3 and BPC while stirring inside a Vacuum Atmospheres dry box with a moisture level less than 3 ppm. The preparation of AlCl_3 (17) and BPC (2) is described elsewhere. Sulfur was obtained from Alfa Products (99.99%); $\text{SCl}_3\text{AlCl}_4$ was prepared according to the method outlined by Mamantov *et al.* (18). Standard procedures were employed to clean aluminum and tungsten (both Alfa Products, 99.999%) wire electrodes. An H-type cell, which was constructed with a center compartment, equipped with a stirring bar, and two outer compartments for the counter and reference electrodes, was employed for electrochemical studies. Fine porosity frits (4.5-5.0 μm) were used to separate the different compartments. Threaded glass joints and Teflon bushings were used to insert the electrodes into the cell, which was held at 60°C by means of a simple glass furnace. Working electrodes were either glassy carbon (GC) (Tokai) or tungsten (W) sealed in glass with the exposed surfaces polished with 0.1 μm alumina. Working electrodes for coulometric studies were fabricated from reticulated vitreous carbon (RVC). Counter and reference electrodes were tungsten and aluminum coils, respectively, dipped in AlCl_3 -BPC (66.7 mole percent [m/o] AlCl_3). All electrochemical experiments were performed inside the dry box.

* Electrochemical Society Active Member.

¹ Present address: University of Camerino, Camerino, Italy.

Cyclic and normal pulse voltammetric measurements were conducted using a PARC Model 174A polarographic analyzer and a PARC Model 175 universal programmer. Coulometric studies were performed utilizing a PARC Model 173 potentiostat equipped with a PARC Model 179 digital coulometer. All current-potential and current-time transients were recorded with a Houston 2000 X-Y recorder.

Samples for Raman spectroscopic studies were loaded into 5 mm pathlength Pyrex cells inside the dry box and then sealed under reduced pressure. Raman spectra of the samples were obtained using a JY-2000M instrument equipped with a LEP (900015) controller and an argon ion laser.

Results and Discussion

Solubility and Raman spectroscopic studies of sulfur and $\text{SCl}_3\text{AlCl}_4$ in AlCl_3 -BPC melts.—Initial experiments were conducted in order to determine the solubility and stability of various sulfur species in basic (BPC-rich) and acidic (AlCl_3 -rich) AlCl_3 -BPC melts. Sodium sulfide (Na_2S) was found to be insoluble in these melts. On the other hand, elemental sulfur is slightly soluble in both acidic and basic AlCl_3 -BPC melts. No quantitative solubility data are, however, available at present. Several attempts were made to determine the nature of the dissolved sulfur by means of Raman spectroscopy. No evidence for Raman bands due to species such as S_8 was found for basic melts, probably because of the rather low solubility of elemental sulfur in these melts. Although the solubility of elemental sulfur was observed visually to be greater in acidic AlCl_3 -BPC melts, no Raman bands were observed. These results contrast with the results reported for AlCl_3 - NaCl melts (19), where bands assigned to S_8 were detected.

Sulfur (IV) in the form of $\text{SCl}_3\text{AlCl}_4$ was found to dissolve in both acidic and basic AlCl_3 -BPC melts. In the latter case, a rapid reaction occurred resulting in a red solution. In acidic melts, the reaction between $\text{SCl}_3\text{AlCl}_4$ and the melt is much slower, as shown by Raman spectra taken at different times. A typical Raman spectrum of a fresh solution of $\text{SCl}_3\text{AlCl}_4$ in AlCl_3 -BPC [60 (m/o) AlCl_3] is shown in Fig. 1A. The bands at 208, 276, 501, and 523 cm^{-1} can be assigned to SCl_3^+ (18). The other bands may be attributed to AlCl_4^- , Al_2Cl_7^- , and the BPC cation (6). The spectrum changes with time, as may be seen in Fig. 1B, obtained using the same sample after six days at 60°C . The bands for SCl_3^+ have almost completely disappeared. In addition, the ratios of the intensities of the $\text{Al}_2\text{Cl}_7^-/\text{AlCl}_4^-$ bands at 310 and 351 cm^{-1} have changed, reflecting an increase in the Al_2Cl_7^- concentration, and hence in melt acidity, at the expense of AlCl_4^- . No other bands attributable to sulfur species may be detected from the spectra. The decomposition produces gases, shown by an increase in pressure inside the sealed sample cell; however, several attempts to collect and identify the gaseous products failed. The results clearly indicate a reaction between tetravalent sulfur and the melt leading to an increase in melt acidity.

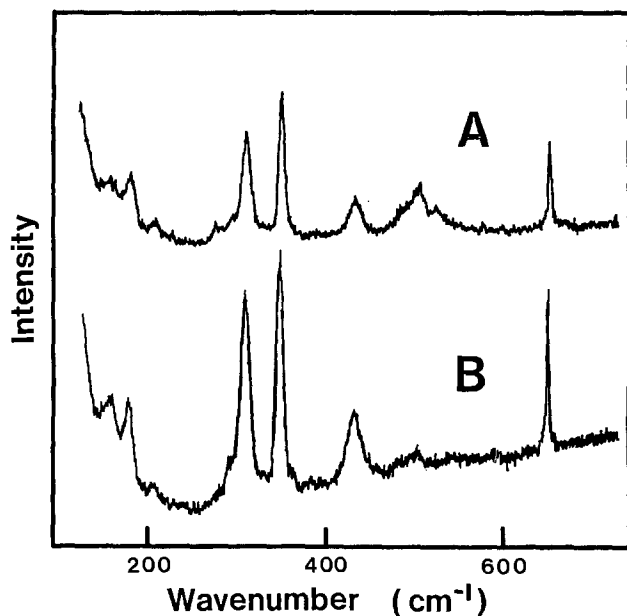


Fig. 1. Raman spectra of $\text{SCl}_3\text{AlCl}_4$ (0.115M) in $\text{AlCl}_3\text{-BPC}$ (60 m/o AlCl_3) at 60°C (photon counting mode, $\tau = 250$ ms): fresh solution (A) and same solution 6 days later (B).

Electrochemistry of sulfur in basic $\text{AlCl}_3\text{-BPC}$ melts.—On the basis of the spectroscopic studies outlined in the previous section, only elemental sulfur has been studied in basic (44.9 m/o AlCl_3) $\text{AlCl}_3\text{-BPC}$ melts. A voltammetric scan over the entire electrochemical window of the basic melt containing elemental sulfur reveals only a single reduction wave at ca. -0.60V vs. Al (2.0:1.0 $\text{AlCl}_3\text{-BPC}$) at both GC and W electrodes (Fig. 2). The reduction process in both cases appears to be totally irreversible. Similar behavior has also been observed in basic $\text{AlCl}_3\text{-MEIC}$ melts (16).

Coulometry was conducted at an RVC electrode held at a potential of -0.75V . The value of n , computed from the amount of charge passed or from $\log i$ vs. t plots, was 2.1 ± 0.1 . This clearly indicates that the reduction process occurring in basic $\text{AlCl}_3\text{-BPC}$ is the reduction of sulfur to a sulfide species.

Plots of $\log(i_a - i)/i$ vs. E , constructed from pulse voltammetric experiments at W electrodes at 60°C , were linear, with slopes in the range 155–180 mV depending on the pulse width. Assuming a two-electron process, this corresponds to a value of ~ 0.2 for the transfer coefficient. Scan rate cyclic voltammetric studies at GC and W electrodes (Tables IA and IB, respectively) show that, while the half-peak width remains rather constant, the peak potentials shift to more negative values with increasing scan rate. Based on the shift of the peak potentials with the

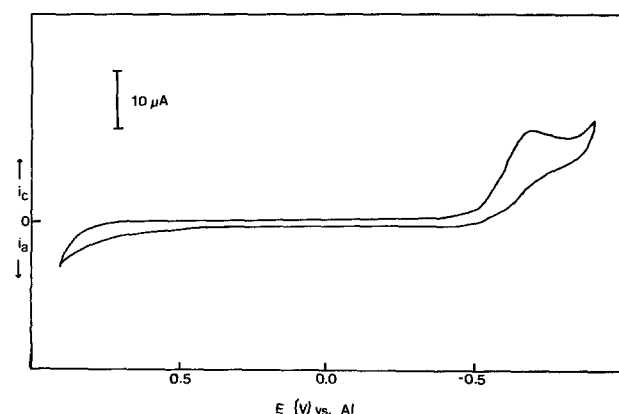


Fig. 2. Cyclic voltammogram for the reduction of sulfur in $\text{AlCl}_3\text{-BPC}$ (44.9 m/o AlCl_3). GC electrode area, 0.0707 cm^2 ; $C_S = 4.4 \times 10^{-3}\text{ M}$; $T = 60^\circ\text{C}$; scan rate = 50 mV/s .

Table I. Cyclic voltammetric data for the reduction of elemental sulfur in $\text{AlCl}_3\text{-BPC}$ (44.9 m/o AlCl_3). $C_S = 4.4\text{ mM}$; $T = 60^\circ\text{C}$

Scan rate (mV·s ⁻¹)	i_p (μA)	$i_p/v^{1/2}$ (μA·V ^{-1/2} ·s ^{-1/2})	E_p (mV)	$E_p - E_{p/2}$ (mV)
A. Glassy carbon electrode (area = 0.0707 cm^2)				
50	11.0	1.55	-690	90
100	15.5	1.55	-700	90
200	21.0	1.50	-720	100
B. Tungsten electrode (area = 0.0176 cm^2)				
50	0.80	0.133	-650	210
100	1.25	0.125	-660	190
200	1.75	0.124	-680	220
500	2.55	0.123	-730	210

scan rate, the transfer coefficients at 60°C are 0.21 and 0.18 at W and GC electrodes, respectively. These calculations should be taken with caution, since the reduction process probably involves prekinetic (bond cleavage if sulfur is present as S_8) and postkinetic (reaction with the melt to form an AlSCl -like species) complications.

Electrochemistry of sulfur in acidic $\text{AlCl}_3\text{-BPC}$ melts.—Electrochemical studies of the behavior of sulfur in acidic $\text{AlCl}_3\text{-BPC}$ over the composition range 66.7–52.2 m/o AlCl_3 indicate that the electrochemistry of sulfur is essentially the same over the entire acidic composition region of the melt. The cyclic voltammograms, shown in Fig. 3a and 3b (W and GC electrodes, respectively) for sulfur solutions in $\text{AlCl}_3\text{-BPC}$ (60 m/o AlCl_3), may be considered representa-

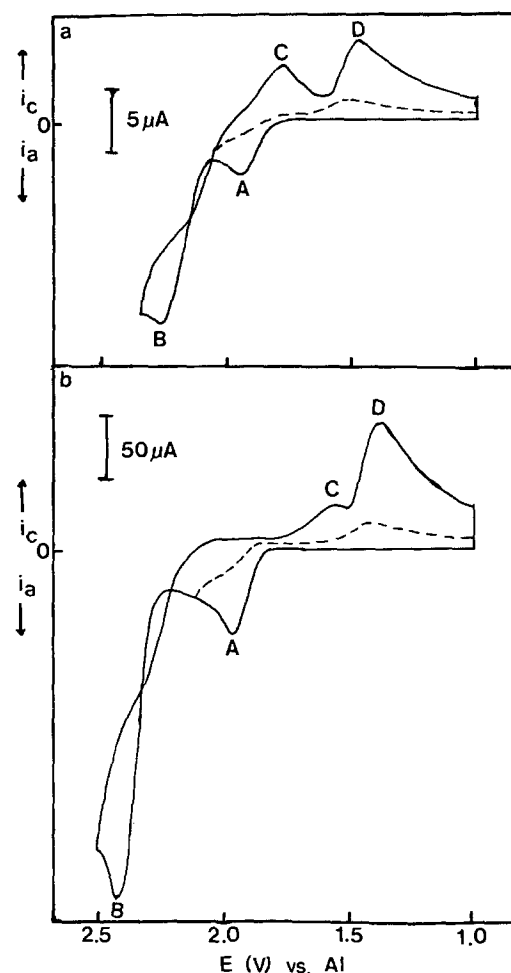


Fig. 3. Cyclic voltammograms for the oxidation of sulfur in $\text{AlCl}_3\text{-BPC}$ (60 m/o AlCl_3) at W (a) and GC electrodes (b), respectively. $C_S = 1.65 \times 10^{-3}\text{ M}$; scan rate = 50 mV/s ; $T = 60^\circ\text{C}$; electrode area = 0.0176 cm^2 (W) and 0.0707 cm^2 (GC). The dashed curves represent in each case the respective cyclic voltammograms obtained for the first oxidation wave only.

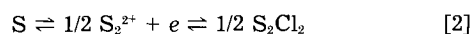
Table II. Cyclic voltammetric results for the first sulfur oxidation process (wave A-D) in AlCl₃-BPC (60 m/o AlCl₃).
C_S = 25.8 mM; GC electrode area = 0.0707 cm²; T = 60°C

Scan rate (mV·s ⁻¹)	<i>i</i> _p ^A (μA)	<i>i</i> _p ^D (μA)	<i>E</i> _p ^A (mV)	<i>E</i> _p ^A - <i>E</i> _{p/2} ^A (mV)	<i>E</i> _p ^D (mV)	<i>E</i> _p ^D - <i>E</i> _{p/2} ^D (mV)	<i>i</i> _p ^D / <i>i</i> _p ^A
A. Before coulometry							
5	22.5 (10.1)	2.5 (1.1)	1940	47	1490	—	0.11
10	30.5 (9.6)	6.3 (1.9)	1950	54	1470	—	0.20
20	41.7 (9.3)	9.0 (2.0)	1960	50	1460	—	0.22
50	63.0 (8.9)	16.0 (2.3)	1970	58	1430	—	0.25
100	85.0 (8.5)	22.5 (2.2)	1980	62	1400	—	0.26
B. Same solution as in A, but after performing coulometry at 2.1V							
10	20.0 (6.3)	21.2 (6.7)	1940	50	1450	92	1.06
20	27.0 (6.0)	26.0 (5.8)	1950	50	1430	100	0.96
50	41.5 (5.8)	40.0 (5.6)	1965	50	1400	105	0.96
100	55.0 (5.5)	50.0 (5.0)	1970	60	1360	120	0.91
200	66.0 (4.6)	68.0 (4.8)	1990	60	1330	140	1.03

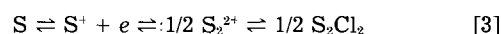
The values in parentheses represent the various current functions (*i*_p^D/*i*_p^A).

tive of the electrochemical behavior of sulfur in acidic melts. Two oxidation processes (waves A and B) and two reduction processes (waves C and D) are observed; no electrochemical activity is observed below 1V, indicating that no reduction of elemental sulfur occurs in acidic melts. The dotted lines in Fig. 3 show the electrochemical behavior observed when the potential scan is reversed after wave A but before wave B. On this basis, two redox pairs may be tentatively assigned to peaks A-D and B-C.

Exhaustive coulometry, conducted on a sulfur solution in AlCl₃-BPC (60 m/o AlCl₃) at an RVC electrode at a potential such that only the oxidation process attributed to wave A occurs, yields an *n* value of 1.19, indicating that the redox pair A-D can be attributed to the couple S(SI). Log *i* vs. *t* plots were concave, suggesting chemical complications. The S(SI) redox couple was also studied using cyclic and normal pulse voltammetric techniques. Tables IIA and IIB show relevant parameters for couple A-D obtained during a scan rate study in a sulfur solution and the same solution, respectively, after exhaustive coulometry at 2.1V [S(I) solution]. This scan rate study and subsequent studies were conducted over a scan rate range of 5-200 mV/s. A brief scan rate study of the ferricinium/ferrocene couple, which is known to be a simple reversible redox couple in AlCl₃-BPC (20), exhibited purely diffusion-controlled behavior in AlCl₃-BPC (60 m/o AlCl₃) at 60°C over the entire scan rate range studied. The data in Table II pertain to cyclic voltammograms where the potential sweep was reversed before wave B. For both waves, the parameters are scan rate dependent. It may be seen from Table II that the data for wave A are quite similar regardless of the scan direction [direct oxidation of sulfur or reduction of S(I)]. The peak potentials move in the positive direction and the current functions decrease with increasing scan rate in both of the cases. At low scan rate, the half-peak width approaches the value expected for an electrochemical process involving dimerization (33 mV at 60°C), while it becomes close to the value expected for a first-order process at the higher scan rates (66 mV at 60°C). The most revealing parameter is, however, the current ratio *i*_p^D/*i*_p^A, which is quite different in sulfur and in S(I) solutions. In the former case, the current ratio is small (increasing moderately with the scan rate), while the same parameter is close to 1 in S(I) solution. If the final product of the oxidation of sulfur is S₂Cl₂, which escapes from the diffusion layer, it is expected that at higher scan rates, less of it can escape (12). In the case of S(I) solutions utilizing a closed cell, some S₂Cl₂ will be in the gas phase and some will be in solution. The electrochemistry of soluble S₂Cl₂ is dependent only on the diffusion of that species in solution, and hence the current ratio is close to 1 and not affected by the scan rate. Thus, a set of equations such as



or



where reaction [2] prevails at low scan rates and reaction [3] at high scan rates, may, at least partially, account for the observed behavior. In reactions [2] and [3], sulfur has been written as a monomer. However, a set of rapid chemical reactions leading to the fragmentation of sulfur rings or chains initiated electrochemically or chemically such as those proposed in basic AlCl₃-NaCl melts (12) does not change the overall picture.

The conclusions for wave A deduced from the cyclic voltammograms are supported by the pulse voltammetric experiments at both W and GC electrodes (Table III). The product *i*_p^C/*i*_p^B is not constant with increasing pulse width, thus indicating a process which is not purely diffusion controlled. The slopes of the logarithmic plots constructed from the pulse polarograms are close to the theoretical value for a simple one-electron process at short pulse widths and approach the value expected for a second-order process at longer times, in agreement with the trend observed in the half-peak width of the cyclic voltammograms.

Results from exhaustive coulometric experiments of sulfur solutions in AlCl₃-BPC (60 m/o AlCl₃) melts, conducted at an RVC electrode held at a potential such that the oxidation process attributed to wave B can occur, indicate that wave B results from the oxidation of S(I) to S(IV). This evidence is supported by the fact that S(IV), as shown by the Raman results, is stable (at least initially) in acidic AlCl₃-BPC melts. However, the log *i* vs. *t* behavior observed for coulometric experiments is rather complex, indicating that the charge-transfer process leading to S(IV) involves chemical complications.

A cyclic voltammetric scan rate study of the overall electrochemical process was conducted at GC and W electrodes on a sulfur solution in AlCl₃-BPC (60 m/o AlCl₃) melt at 60°C (Tables IVA and IVB, respectively). In addition to the scan rate dependence of the various current functions, useful information can be obtained by examining the current ratios. These parameters as a function of the scan rate are shown in Fig. 4 for the GC electrode. The ratios *i*_p^C/*i*_p^B, *i*_p^C/*i*_p^D, and *i*_p^D/*i*_p^A increase until a steady value is reached at the scan rate of about 20 mV/s. At the same time, *i*_p^B/*i*_p^A decreases to a steady value at the same scan

Table III. Pulse voltammetric results for the oxidation of sulfur in AlCl₃-BPC (60 m/o AlCl₃). W electrode area = 0.0176 cm²; C_S = 16.5 mM; scan rate = 1 mV/s; time between pulses = 5s. T = 60°C

Pulse width (ms)	<i>i</i> _a ^A (μA)	<i>E</i> _{1/2} ^A (mV)	<i>i</i> _a ^B (μA)	<i>E</i> _{1/2} ^B (mV)	<i>i</i> _a ^B / <i>i</i> _a ^A	<i>i</i> _a ^C / <i>i</i> _a ^D (μA·ms ^{1/2})	<i>i</i> _a ^D / <i>i</i> _a ^A (μA·ms ^{1/2})
57	19.5	1970	17.5	2245	0.90	147.2	132.1
102	16.0	1930	15.0	2170	0.94	161.6	151.1
192	10.0	1930	10.0	2170	1.00	138.5	138.5
484	6.0	1900	10.4	2200	1.73	132.0	110.0

Table IV. Cyclic voltammometric data for the oxidation of sulfur (first and second steps) in $\text{AlCl}_3\text{-BPC}$ (60 m/o AlCl_3). $C_s = 16.5 \text{ mM}$; $T = 60^\circ\text{C}$; (A), GC electrode area = 0.0707 cm^2 ; (B), W electrode area = 0.0176 cm^2

Scan rate (mV s^{-1})	i_p (μA)				E_p (mV)				i_p^B/i_p^A	i_p^C/i_p^B	i_p^D/i_p^A	i_p^C/i_p^D	
	A	B	C	D	A	B	C	D					
(A)													
5	23 (10.3)	106 (47.4)	2 (0.9)	14 (6.3)	1940	2330	1720	1490	4.61	0.02	0.61	0.14	
10	33 (10.4)	140 (44.3)	10 (3.2)	34 (10.7)	1950	2340	1650	1460	4.24	0.07	1.03	0.29	
20	46 (10.3)	180 (40.2)	20 (4.5)	62 (13.8)	1960	2380	1620	1430	3.91	0.11	1.35	0.32	
50	68 (9.6)	158 (36.5)	30 (4.2)	94 (13.3)	1970	2430	1570	1380	3.79	0.12	1.38	0.32	
100	95 (8.5)	360 (36.0)	50 (5.0)	130 (13.0)	1980	2470	1510	1350	3.78	0.14	1.37	0.38	
(B)													
5	1.6 (0.7)	6.7 (2.9)	5.4 (2.4)	—	1900	2110	1890	1590 ^a	4.18	0.80	—	—	
10	2.1 (0.7)	8.6 (2.7)	6.8 (2.2)	1.9 (0.6)	1910	2140	1860	1560	4.09	0.79	0.90	3.58	
20	2.8 (0.6)	10.4 (2.3)	8.4 (1.9)	3.0 (0.7)	1930	2180	1850	1550	3.71	0.81	1.07	2.80	
50	4.3 (0.6)	13.6 (1.9)	12.0 (1.7)	4.8 (0.7)	1960	2230	1830	1510	3.16	0.88	1.12	2.50	
100	6.0 (0.6)	—	—	—	1950	2280 ^a	1810 ^a	1490	—	—	—	—	

The values in parentheses represent the current functions ($i_p/v^{1/2}$).

^a Estimated values.

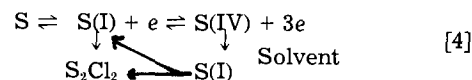
rate. The shapes of the cyclic voltammograms, as well as the relative values of i_p^C/i_p^D , i_p^C/i_p^B , and i_p^D/i_p^A at GC electrodes, suggest that the couple B/C is irreversible and/or that, as evidenced by the Raman results, S(IV) decomposes readily to give a product which is reducible at the potentials of wave D. At W electrodes, the values of i_p^C/i_p^B and i_p^D/i_p^A , both close to one, and the large value of i_p^C/i_p^D suggest a quasi-reversible behavior of both redox couples and/or that the decomposition of S(IV) is less favored having less time to occur because of the increased reversibility of the B/C couple. This is consistent with the fact that wave B occurs at much more positive potentials at GC than at W electrodes resulting in a greater possibility of interaction of S(IV) with the solvent.

In the absence of chemical complications, the ratio i_p^B/i_p^A should be 5.19 (21) if, as indicated by the coulometric results, wave B corresponds to the oxidation of S(I) to S(IV). The results indicate that this value is approached only at low scan rates. The same kind of behavior has been observed for the ratio i_d^B/i_d^A in normal pulse voltammometric experiments performed at different pulse widths. Table III lists the results of a typical run at a W electrode. It may be seen that the ratio i_d^B/i_d^A increases

from about 0.9 to 1.7 over the pulse width range 57-484 ms, compared to a theoretical value of 3. At GC electrodes, wave B is reasonably well defined only at long pulse times (484 ms).

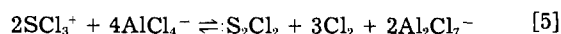
An additional feature was noted in the $i-t$ curves at GC electrodes. When the potential is stepped to the rising part of wave B and, hence, when the oxidation of S(I) to S(IV) occurs at an appreciable rate, after an initial decay the current rises to a maximum before decaying again with a behavior similar to the one observed for a nucleation-type mechanism. The same happens at W electrodes for both waves A and B at much shorter times as reflected by the values of $i_d t^{1/2}$. As may be seen from Table III, this parameter reaches a maximum value at 102 ms.

A reaction sequence that may explain the experimental evidence may be written as follows



where S(I) is regenerated at the electrode by a reaction of S(IV) with the solvent. When a volatile product such as S_2Cl_2 that may escape from the diffusion layer is formed, a rigorous fit of the experimental data with the theory of catalytic processes (22, 23) is not expected. However, at both GC and W electrodes, the current function $i_p^B/v^{1/2}$ decreases with increasing scan rate as expected for a catalytic process. The ratio i_p^C/i_p^B is almost 1 at W, where the couple B/C is quasireversible, and close to 0 at GC, where the same couple appears irreversible. The above considerations and the proposed mechanism hold only if the rate of the chemical reaction regenerating S(I) is lower than the rate at which S(I) is complexed and escapes from the diffusion layer as S_2Cl_2 .

The chemical reaction between S(IV) or SCl_3^+ and the melt leading to regeneration of S(I) or S_2Cl_2 may be written as



which takes into account that, as evidenced by the Raman results, decomposition of SCl_3^+ leads to melts of increased acidity and to the buildup of vapor pressure (Cl_2 and S_2Cl_2) in the sample cell.

Conclusion

It may be seen that the electrochemical behavior of sulfur in $\text{AlCl}_3\text{-BPC}$ melts is quite different from that observed for $\text{AlCl}_3\text{-NaCl}$ melts. In basic $\text{AlCl}_3\text{-BPC}$ melts, sulfur can only be reduced; in $\text{AlCl}_3\text{-NaCl}_{\text{sat}}$ melts, it is possible to reduce sulfur to sulfide and oxidize it to S(I). In acidic $\text{AlCl}_3\text{-BPC}$ melts, no evidence has been found for low oxidation state sulfur species that are important in determining the electrochemistry of sulfur in $\text{AlCl}_3\text{-NaCl}$ melts. In addition, SCl_3^+ is not stable in acidic $\text{AlCl}_3\text{-$

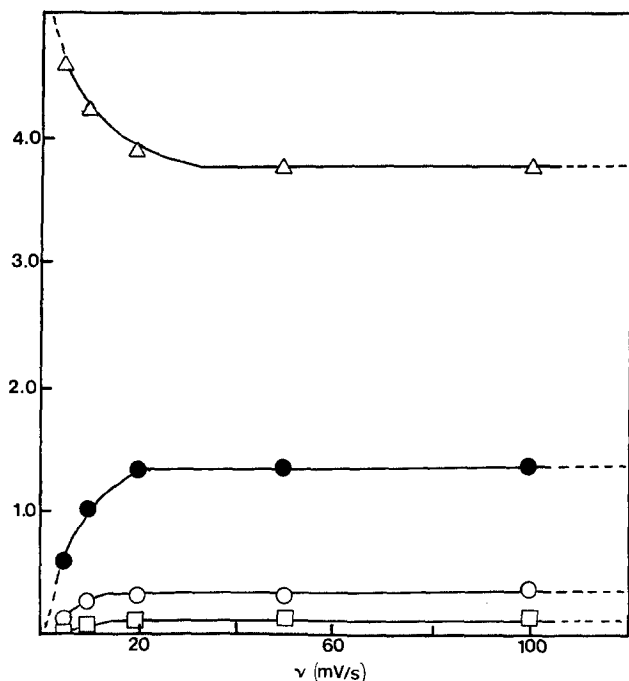


Fig. 4. Current ratio vs. scan rate curves for the oxidation of sulfur in $\text{AlCl}_3\text{-BPC}$ (60 m/o AlCl_3) at 60°C at a GC electrode: i_p^B/i_p^A , (triangles), i_p^D/i_p^A , (dots), i_p^C/i_p^D , (circles), and i_p^C/i_p^B , (squares). Electrode area = 0.0707 cm^2 ; $C_s = 1.65 \times 10^{-2} \text{ M}$.

BPC melts, and it is not possible to reduce sulfur to sulfide. In comparison, in acidic AlCl_3 -NaCl melts, tetravalent sulfur is stable and can be used as active cathode material in long lasting secondary batteries (7-10).

Acknowledgment

This work was supported by the Department of Energy under the University of California Subcontract 4502810.

Manuscript submitted Sept. 24, 1984; revised manuscript received Feb. 22, 1985.

The University of Tennessee assisted in meeting the publication costs of this article.

REFERENCES

1. R. A. Carpio, L. A. King, R. E. Lindstrom, J. C. Nardi, and C. L. Hussey, *This Journal*, **126**, 1644 (1979).
2. J. Robinson and R. A. Osteryoung, *J. Am. Chem. Soc.*, **101**, 323 (1979).
3. R. J. Gale, B. Gilbert, and R. A. Osteryoung, *Inorg. Chem.*, **17**, 2728 (1978).
4. R. J. Gale and R. A. Osteryoung, *ibid.*, **18**, 1603 (1979).
5. J. P. Schoebrechts and B. Gilbert, *This Journal*, **128**, 2679 (1981).
6. C. L. Hussey, in "Advances in Molten Salt Chemistry," Vol. 5, G. Mamantov, Editor, Plenum Press, New York (1983), and references therein, pp. 185-230.
7. G. Mamantov and R. Marassi, U.S. Pat. 4,063,005 (1977).
8. G. Mamantov, R. Marassi, M. Matsunaga, Y. Ogata, J. P. Wiaux, and E. J. Frazer, *This Journal*, **127**, 2319 (1980).
9. G. Mamantov, K. Tanemoto, and Y. Ogata, *ibid.*, **130**, 1528 (1983).
10. G. Mamantov and J. Hvistendahl, *J. Electroanal. Chem.*, **168**, 451 (1984).
11. R. Marassi, G. Mamantov, and J. Q. Chambers, *Inorg. Nucl. Chem. Lett.*, **11**, 245 (1975).
12. R. Marassi, G. Mamantov, and J. Q. Chambers, *This Journal*, **123**, 1128 (1976).
13. K. A. Paulsen and R. A. Osteryoung, *J. Am. Chem. Soc.*, **98**, 6866 (1976).
14. R. Marassi, G. Mamantov, M. Matsunaga, S. E. Springer, and J. P. Wiaux, *This Journal*, **126**, 231 (1979).
15. K. Tanemoto, R. Marassi, C. B. Mamantov, Y. Ogata, M. Matsunaga, J. P. Wiaux, and G. Mamantov, *ibid.*, **129**, 2237 (1982).
16. B. J. Piersma and J. S. Wilkes, USAE Report FJSRL-TR-82-0004 (1982).
17. G. Torsi, K. W. Fung, G. M. Begun, and G. Mamantov, *Inorg. Chem.*, **10**, 2285 (1971).
18. G. Mamantov, R. Marassi, F. W. Poulsen, S. E. Springer, J. P. Wiaux, R. Huglen, and N. R. Smyrl, *J. Inorg. Nucl. Chem.*, **41**, 260 (1979).
19. R. Huglen, F. W. Poulsen, G. Mamantov, R. Marassi, and G. M. Begun, *Inorg. Nucl. Chem. Lett.*, **14**, 167 (1978).
20. Z. J. Karpinski, C. Nanjundiah, and R. A. Osteryoung, *Inorg. Chem.*, **23**, 3358 (1984).
21. J. M. Saveant and E. Vianello, *Electrochim. Acta*, **12**, 1545 (1967).
22. J. M. Saveant and E. Vianello, *ibid.*, **10**, 905 (1965).
23. R. S. Nicholson and I. Shain, *Anal. Chem.*, **36**, 706 (1964).

Electroreflection Measurements on Semiconductor/Electrolyte Interfaces to Determine the Voltage Distribution

G. A. Scholz*¹ and H. Gerischer*

Fritz-Haber-Institut der Max-Planck-Gesellschaft, D-1000 Berlin 33, Germany

ABSTRACT

The electroreflectance signal from a semiconductor electrode surface is sensitive to the magnitude of the space charge. It is used to determine the voltage distribution between the space-charge layer and the Helmholtz double layer at an electrode/electrolyte interface. In this paper, the first of two, we describe the experimental arrangements and measurements of the electroreflectance spectra for n-MoSe₂ and n-WSe₂ under anodic and cathodic bias. Important features in the spectra are found to be in agreement with existing theories. Flatband values inferred from the electroreflectance spectra are in agreement with those from Mott-Schottky plots. The effects of Fermi level pinning on the electroreflectance spectra are demonstrated with n-GaAs.

The Group VI transition metal dichalcogenides have been shown to be promising electrodes in electrochemical photocells (1, 2). The primary reason for their appeal is that the upper valence or lower conduction band of the n- or p-type materials, respectively, consists predominantly of metal d_{z^2} atomic orbitals, which are nonbonding with respect to the chalcogen atoms (3) and are shielded by the chalcogen layers against interaction with the electrolyte. Therefore, holes, which may possibly be created in the valence band of an n-type specimen and swept to the crystal surface by a Schottky barrier, will not necessarily cause the photoanodic destruction of the electrode with the exception of the reactions occurring at defects and steps (4).

One very important parameter in accessing the performance of an electrochemical solar cell can be defined by the photovoltage yield

$$\frac{e_0 V_{OC}}{|U_{FB} - U_{redox}|} < 1 \quad [1]$$

which, for a good cell, should be as close to unity as possible.

*Electrochemical Society Active Member.

¹Present address: Energy Research Institute, Simon Fraser University, Burnaby, British Columbia, Canada V5A 1S6.

In Eq. [1] the open-circuit photovoltage is V_{OC} , U_{FB} is the flatband potential at which a space charge is absent, and U_{redox} corresponds to the potential of the redox couple in solution. Changes in U_{redox} should produce corresponding changes in V_{OC} since the degree of band bending (in the dark) is determined by U_{redox} , providing no change in the Helmholtz double-layer voltage drop (V_H) is produced. If a change in V_H does appear, V_{OC} may be unexpectedly small or, in extreme cases, may even become independent of U_{redox} . Some common situations that will result in large variations of V_H are the pinning of the Fermi level by a sufficiently large density of surface states (5), or the creation of an inversion layer by, for example, the injection of holes into the valence band of an n-type semiconductor (6). In every case, a Helmholtz voltage will appear at the expense of the space-charge voltage (V_{SC}).

Bard *et al.* (7) have pointed out that the concept of Fermi level pinning at semiconductor/electrolyte interfaces is a major cause for the observed discrepancies between V_{OC} and $U_{FB} - U_{redox}$, analogous to the discrepancies between barrier heights and metal work functions in semiconductor/metal interfaces. As examples, they cite their results for n- and p-GaAs (8) and those of Tributsch *et al.* (2) for some of the Group VI dichalcogenides. In this

work, we have investigated n-MoSe₂ and n-WSe₂, via modulation spectroscopy, and determined ΔV_H and ΔV_{SC} across the electrode/electrolyte interface as a function of the applied voltage because this will provide further insight as to whether it is Fermi level pinning or hole injection that is the dominant mechanism responsible for the apparent inconsistencies observed. The optical properties of the above transition metal dichalcogenides have been extensively reviewed (9), and are very suitable for electroreflectance measurements primarily because of their excellent resistance to corrosion. In addition, their highly anisotropic character is also of value because it allows the preparation of high quality surfaces by simply peeling off (using sticky tape) some of the top layers, so that, for example, it is possible to quickly and easily repair electrodes with corroded surfaces. In this paper, we discuss the experimental arrangement and present some general results of electroreflectance measurements on n-MoSe₂, n-WSe₂, and n-GaAs in contact with an electrolyte. These results will serve as a basis for the second paper in this series where detailed results of the changes in V_{SC} and V_H as a function of the applied voltage will be presented for n-MoSe₂ and n-WSe₂ in the presence of various electrolytes.

The electroreflectance technique has already been applied by Tomkiewicz *et al.* to monocrystalline (10) and polycrystalline (11, 12) CdSe electrodes in order to monitor the voltage distribution between the space-charge and Helmholtz layers. They found that the reflectance signal disappears at the flatband potential of the monocrystalline material, as should be expected, and that the amplitude of the signal increased linearly with the modulation voltage, indicating a negligible change of the voltage drop in the Helmholtz layer. A decrease in the amplitude of the electroreflectance signal obtained with the polycrystalline layers as they are biased from flatband to depletion has been interpreted as Fermi level pinning by surface states. Lemasson *et al.* (13) have determined the flatband potential of ZnSe by electroreflectance, and Tomkiewicz *et al.* (14) have applied this technique to CdIn₂Se₄ crystals in order to analyze the influence of photoetching on the position of the flatband potential and the variation of the potential drop in the Helmholtz double layer.

Methods

Modulation spectroscopy has in the past been used as a powerful tool in studying the electronic band structure of semiconductors (15, 16) because one measures a derivative-like signal which considerably enhances features in the ordinary optical structure. The technique essentially consists of inducing changes in the transmission or reflection of a sample by applying a periodic perturbation. Common techniques that have been used include, among others, electromodulation (17), piezomodulation (18), and thermomodulation (19). These induced changes will be large at the fundamental edge and at any critical point for which $\nabla k(E_f - E_i) = 0$, so that one obtains detailed information predominantly on the critical points in the band structure. The theoretical ground work was laid by Franz and Keldysh (20), who calculated the effect of an electric field on the optical absorption associated with interband transitions. A very general theoretical description of the electroreflectance phenomena which can be observed in the low field region has been given by Aspnes (21). The Franz-Keldysh theory does not explicitly include excitonic effects, which can dominate in the region near the fundamental absorption edge, so that subsequent calculations by Blossey, which include excitonic effects (22), are expected to apply to the transition metal dichalcogenides.

Because of the possibility of modulating the very large electric fields associated with space-charge layers (23), electroreflectance (ER) can be an ideal technique in the study of the semiconductor/electrolyte interface. The principles and techniques of electroreflectance have been reviewed by Cardona (15) and Seraphin (16, 24), and,

more recently, the application to semiconductor electrodes has been discussed by Pollak (25).

The electroreflectance signal is defined by

$$\frac{\Delta R}{R_0} = \frac{R(E) - R_0}{R_0} \quad [2]$$

where $R(E)$ is the optical reflectance when an internal electric field E is present, and R_0 is the reflectance in the absence of such a field. The reflectance change depends on both, the real part ϵ , and the imaginary part ϵ_i of the dielectric constant ϵ and their changes $\Delta\epsilon$, $\Delta\epsilon_i$ (27)

$$\Delta R/R_0 = \alpha(\epsilon_r, \epsilon_i)\Delta\epsilon_r + \beta(\epsilon_r, \epsilon_i)\Delta\epsilon_i \quad [3]$$

It turns out that at low photon energies (typically ≤ 3 eV), the factor α can be much larger than β so that the reflectance change is mainly controlled by the change of the real part of ϵ (24, 36).

If an external voltage is applied to a semiconductor/electrolyte interface, it will essentially appear either as V_{SC} across the space-charge layer, or as a combination of V_{SC} and V_H if for some reason a large number of carriers is present on the crystal surface, as will be the case, for example, in the three situations mentioned above. The height of a Schottky barrier is related to the concentration N_0 of ionized donors or acceptors in n- or p-type semiconductors by (28)

$$V_{SC} = e_0 \frac{N_0 x_0^2}{2\epsilon\epsilon_0} \quad [4a]$$

or

$$x_0 = \left(\frac{2\epsilon\epsilon_0}{e_0 N_0} V_{SC} \right)^{1/2} \quad [4b]$$

respectively, where e_0 is the elementary electric charge, ϵ the static dielectric constant, ϵ_0 the permittivity of free space, and x_0 the depletion-layer thickness (Fig. 1). Aspnes has treated electric field modulation in a Schottky barrier (29, 30) by using the relation

$$\Delta R/R_0 = E^2 L(h\nu) \quad [5]$$

where $L(h\nu)$ is the spectral line shape function which is entirely determined by the band structure and contains the influence of the electric field. By combining this with the correlation between the field strength in a depletion layer and the voltage drop V_{SC} , he obtained the reflectance signal when modulating V_{SC} . For a depletion layer, the field strength at the surface E_s can be approximated by (28)

$$E_s^2 = \frac{e_0 N_0}{2\epsilon\epsilon_0} V_{SC} \quad [6]$$

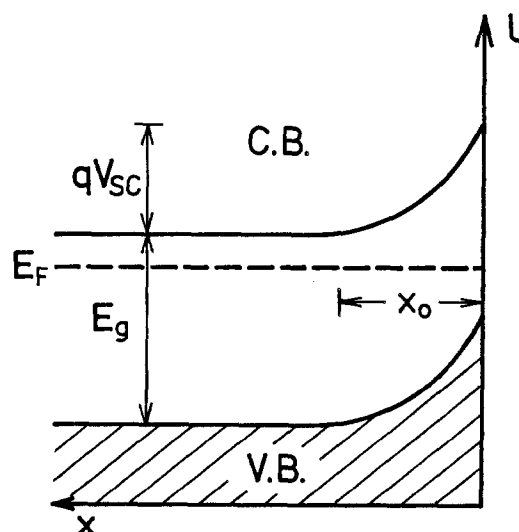


Fig. 1. Simple one-dimensional band schematic of a depletion layer with an effective thickness x_0 . The other symbols have their usual meaning.

while the field strength in the depletion layer, which depends on the distance x from the surface and becomes zero at $x = x_0$, can be approximated by

$$E^2(x) = \frac{e_0 N_0}{2\epsilon\epsilon_0} \left(1 - \frac{x}{x_0}\right)^2 V_{sc} \quad [7]$$

Since x_0 depends on V_{sc} (Eq. [4b]), a modulation of V_{sc} will complicate Eq. [7]. However, within a range of the depletion layer thickness $x \leq 0.2x_0$, one can neglect the variability of x_0 caused by the modulation of V_{sc} and assume that the reflectance change should be proportional to V_{sc}

$$\Delta R/R_0 \propto V_{sc} L(h\nu) \quad [8]$$

The conclusion is that when the space-charge layer extension $x_0 > 1/a$, where a is the absorption coefficient for light of the respective wavelength, the effective field strength modulation is proportional to $V_{sc}^{1/2}$, so that Eq. [8] can be applied. In particular, this means that the doping level must be low enough to fulfill this condition. Note that the applicability of the "low field strength" case of the theory (21, 30) is simultaneously guaranteed.

If a change in the Helmholtz layer voltage drop is produced at a semiconductor/electrolyte interface, ΔV_H will appear at the expense of ΔV_{sc} for a given applied voltage, so that the magnitude of the ER signal will decrease, since it is, of course, not sensitive to ΔV_H . Therefore, if some care is taken that no stray voltages develop, such as, for example, those caused by IR drops in the semiconductor or electrolyte or, even worse, voltage losses due to a surface layer produced by electrochemical reactions, one can write to a good approximation

$$\Delta V_{app} = \Delta V_{sc} + \Delta V_H \quad [9]$$

By comparing the ER signals produced under different situations (such as the presence of a variety of redox systems, different methods for preparing electrode surfaces, etc.) it is possible to infer the magnitude of ΔV_H by monitoring, via ER measurements, the relative changes in ΔV_{sc} .

Experimental

The experimental arrangement for measuring the ER spectra is sketched in Fig. 2. In essence, the Fermi level of the semiconductor electrode is modulated via the standard three-electrode potentiostatic configuration using a saturated calomel electrode (SCE) as reference, and 0.1N H_2SO_4 as support electrolyte. All voltages are reported with respect to the SCE. Modulation was accomplished with a low frequency (16 Hz) variable amplitude square wave voltage from a PAR 175 Universal Programmer externally triggered with a Philips pm 5132 function generator. The modulating voltage could thus be conveniently varied in amplitude, polarity, and frequency. In an at-

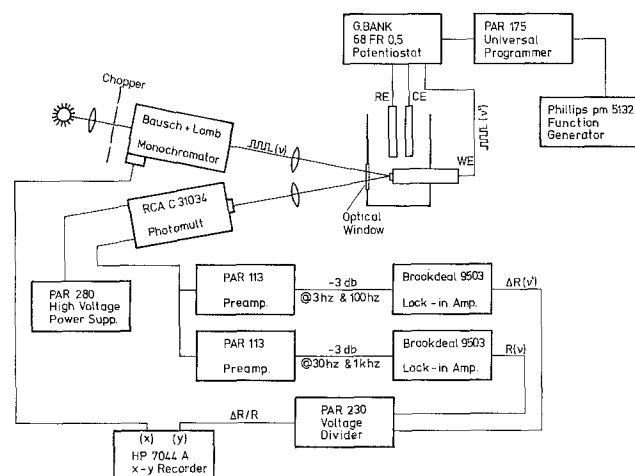


Fig. 2. Experimental arrangement for measuring the electroreflectance spectra of semiconductor electrodes in an electrochemical cell.

tempt to keep corrosion at a minimum, the polarization voltages for the n- and p-type semiconductors were usually set anodic or cathodic, respectively, of their flatband potential, so that high impedance depletion layers, with their negligible current flows, were produced.

Chopped (~ 300 Hz) unpolarized light from a Bausch and Lomb double monochromator was then focused at near normal incidence to the electrode surface, and ΔR (16 Hz), along with R (~ 300 Hz), was measured with an RCA C31034 photomultiplier tube via two EG&G Brookdeal 9503 lock-in amplifiers. The monochromatic light was of very low intensity, and so possible photovoltages were of no concern. Low frequency intermodulation products from the 16 and 300 Hz signals could be minimized by varying the frequency of either the ΔR or R signal slightly, and was necessary for a sufficient reduction of the noise level.

To insure a good quality ER signal and to minimize corrosion problems, great care was taken with the transition metal dichalcogenides so that no steps, or similar corrosion centers, were exposed to the electrolyte. It was possible, due to the anisotropic nature of these dichalcogenides, to prepare surfaces of several square millimeters in area parallel to the basal planes which, even under the microscope (at 50 times magnification), appeared free of steps and other crystal imperfections.

Results and Discussion

To illustrate the basic soundness of using changes in the ER signals magnitude as a measure of changes in V_{sc} , we show in Fig. 3 the room temperature ER spectra of the E_1 and $E_1 + \Delta_1$ transitions (31) of n-GaAs following different surface preparation methods. The ER spectra was first taken after polishing the crystal with 1 μm diamond paste (Fig. 3a) and then, with identical apparatus settings, after subsequent etching in a 2% solution of bromine in methanol (Fig. 3b). Modulation was from 0 mV (found to be $\sim V_{FB}$ from a Mott-Schottky plot) to 600 mV anodic.

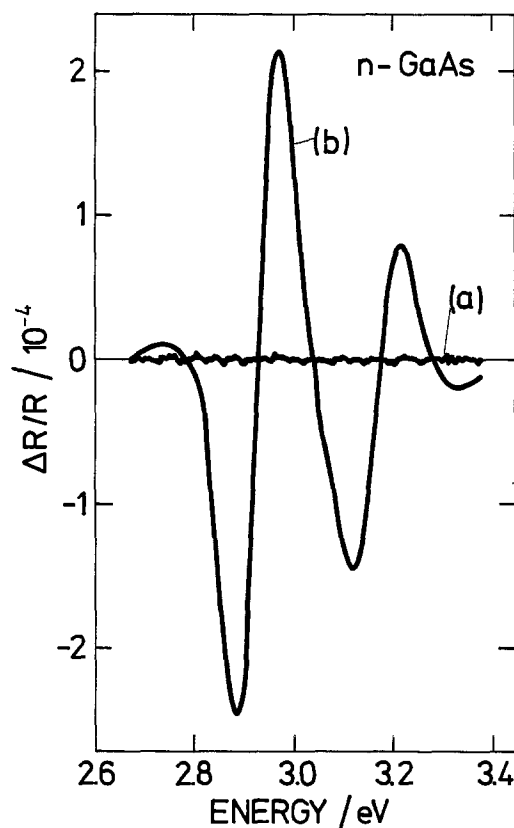


Fig. 3. Electroreflectance spectra under anodic bias of a n-GaAs electrode in 0.1N H_2SO_4 . a: After polishing with 1 μm diamond paste. b: After subsequent etching in a solution of 2% Br_2 in methanol.

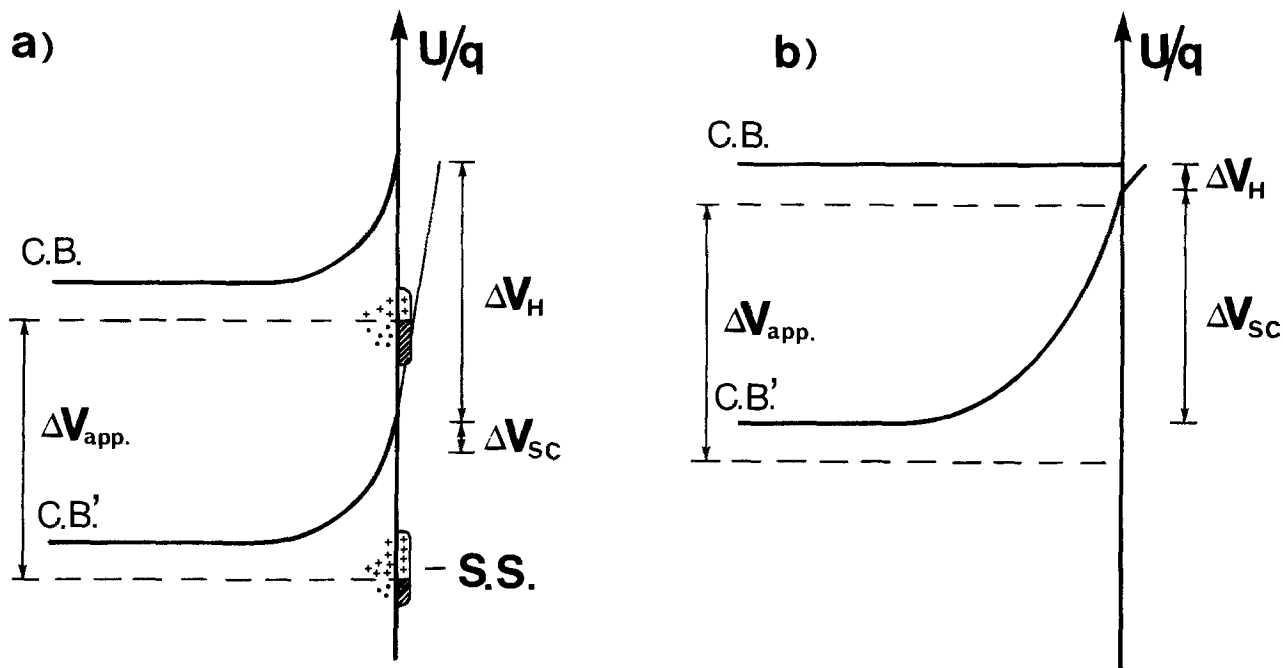


Fig. 4. The voltage distribution across the GaAs/0.1N H₂SO₄ interface, showing only the conduction band. a: After mechanical polishing created surface states or surface near states in the bulk (SS) which will pin the Fermi level so that V_{sc} remains constant and $\Delta V_{app} = \Delta V_H$. b: After subsequent etching removes the surface states so that V_H remains constant and $\Delta V_{app} = \Delta V_{sc}$.

The probable reason for the absence of an ER signal in the former case (Fig. 3a) is the creation of a large number of crystal defects in a layer close to the surface which form traps for electrons, but it is also possible that surface states act as donor/acceptor sites which will screen the electric field from the bulk crystal. In any case, the Fermi level is pinned relative to the surface, so that ΔV_{app} will appear across the double layer as ΔV_H (Fig. 4a), and, as expected, no ER signal is observed (Fig. 3a). Tomkiewicz *et al.* (14) have already described similar effects on the ER signal and interpreted this as pinning of the Fermi level due to an abundance of surface states. It should be mentioned that a decrease of the line shape factor $L(h\nu)$ could also have a similar effect (26), although it appears unlikely that this effect would be so drastic.

After etching the crystal surface and removing this damaged layer, the Fermi level is no longer pinned (Fig. 4b), and V_{sc} can vary with the applied voltage so that an ER signal can be observed (Fig. 3b). Various etches (combinations of acids, H₂O₂, etc.) resulted in ER curves which had the same structure but differed in their magnitudes. The ER curve shown in Fig. 3b, after etching with the bromine in methanol solution, yielded the largest signal and therefore identifies this etching solution as superior for preparing a GaAs surface low in defects.

Typical room temperature ER spectra of n-MoSe₂ and n-WSe₂ near the fundamental gap are shown in Fig. 5 and Fig. 6, respectively. The voltage modulation was performed from close to the flatband potential to anodic or cathodic voltages. Whereas in the anodic case currents were restricted to well below 1 μ A, in the cathodic case larger currents ($\approx 50 \mu$ A) were generated.

Even though MoSe₂ and WSe₂ lose much of their excitonic structure at room temperature, one structure labeled A₁ at 1.53 eV (MoSe₂) and 1.63 eV (WSe₂) (3) remains very well defined. According to the literature (32), A₁ corresponds to the $n = 1$ state of a Wannier-type exciton resulting from a nondegenerate direct transition at the Γ point in the Brillouin zone. By simultaneously monitoring the reflectivity in addition to the ER spectra, we found experimentally² that A₁ is located at 1.55 ± 0.01 and 1.63 ± 0.01 eV for our MoSe₂ and WSe₂ samples, respectively, in good agreement with other work (3, 33). Therefore, by using exciton binding energies of 67 and 50 meV (34), re-

²The largest gradient of the steep negative slope, following the peak in R , is taken as the position of the A₁ excitons.

spectively, we can place the absorption edge at room temperature near 1.62 and 1.68 eV for our MoSe₂ and WSe₂ samples, respectively. By referring to Fig. 5 and 6, we can see that for both dichalcogenides the ER structure appears well to the low energy side of the direct gap, and clearly shows that the ER structure is excitonic in nature.

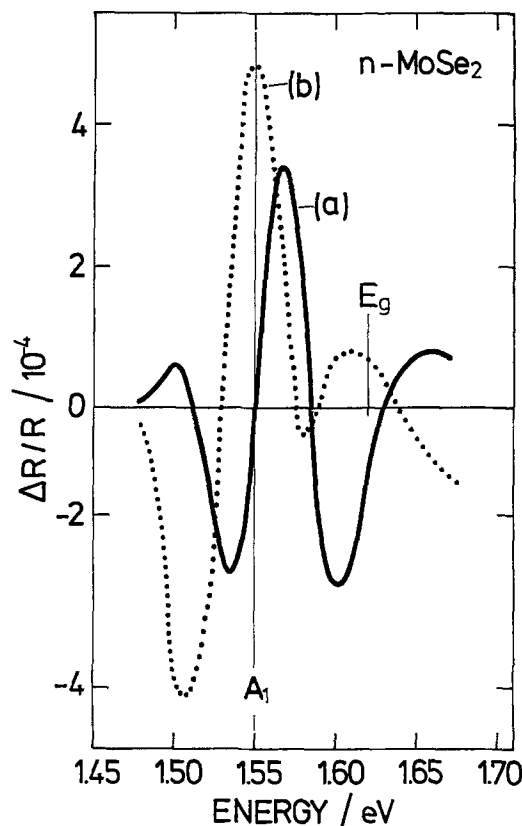


Fig. 5. Room temperature electroreflection spectra from n-MoSe₂ for a 500 mV square wave modulation from V_{FB} when (a) polarizing anodically (depletion layer), and (b) polarizing cathodically (accumulation layer). The edge is indicated by E_g , and the excitons position by A₁.

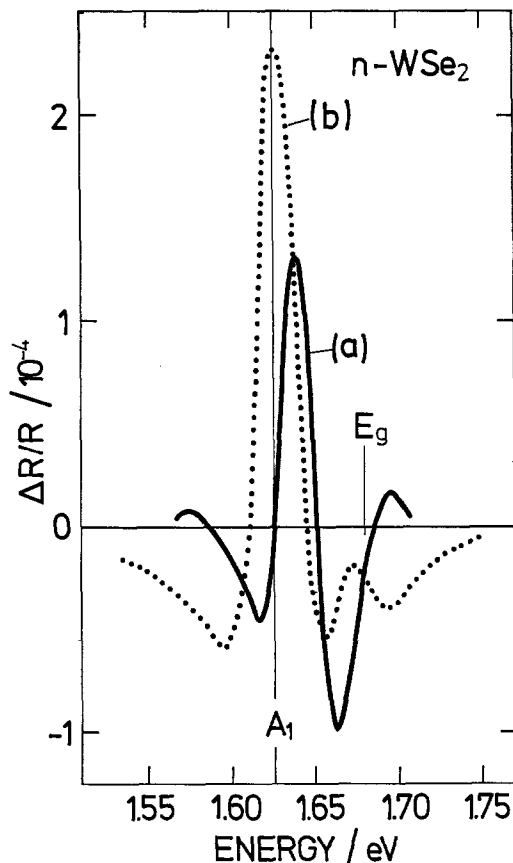


Fig. 6. Room temperature electroreflection spectra from n-WSe₂ for a 500 mV square wave modulation from V_{FB} when (a) polarizing anodically (depletion layer), and (b) polarizing cathodically (accumulation layer). The edge is indicated by E_g , and the excitons position by A_1 .

For clarity, we will discuss the ER spectra from accumulation layers (dotted lines) later, and first discuss those produced from depletion layers (solid lines). Keeping in mind that ER spectra are largely dependent on the real part of the dielectric constant (ϵ_r), we can compare them with the $\Delta\epsilon_r$ curves computed numerically by Blossey (22) for Wannier excitons. Theory predicts that in excitonic $\Delta\epsilon_r$ spectra, the first zero below the edge, corresponding to A_1 , is pinned for fields small compared to the excitonic ionization field (E_i). For somewhat larger fields, about $E \sim E_i/2$, the zero is expected to shift to lower energies because of the second-order Stark effect, and, finally, for $E \geq E_i$, the zero will move rapidly to higher energies. A very rough estimate of E_i for the A_1 state yields $\sim 3 \times 10^5$ V-cm⁻¹ for both dichalcogenides, and is arrived at by dividing the excitons binding energy by its effective Bohr radius. Experimentally, we observe that for low fields ($V_{sc} \leq 1/2V$), the first zero below the edge is consistently at 1.558 ± 0.002 and 1.627 ± 0.002 eV for MoSe₂ and WSe₂, respectively (Fig. 5 and 6). When V_{app} was increased further, the zero crossing shifted toward lower energies (Fig. 7), but an eventual reversal of the zero shift toward higher energies was never observed. The A_1 position is therefore in excellent agreement with Blossey's excitonic ER theory and the zero shifts suggest that the electric fields induced were always below $E_i/2$, that is, below about 10^5 V-cm⁻¹, so that judging from Eq. [4] the doping levels (N_0) should be near or below about 5×10^{17} cm⁻³. The Mott-Schottky plots for these crystals (Fig. 9) confirm this by indicating doping levels of 3×10^{16} and 1×10^{16} cm⁻³ for the n-MoSe₂ and n-WSe₂ samples, respectively.

Knowing the solid-state properties of the semiconductor and using models such as Blossey's, we could, in principle, determine the magnitude of the electric fields from the zero shifts (Fig. 7) in the ER spectra themselves. However, even ignoring the simple facts that the electric

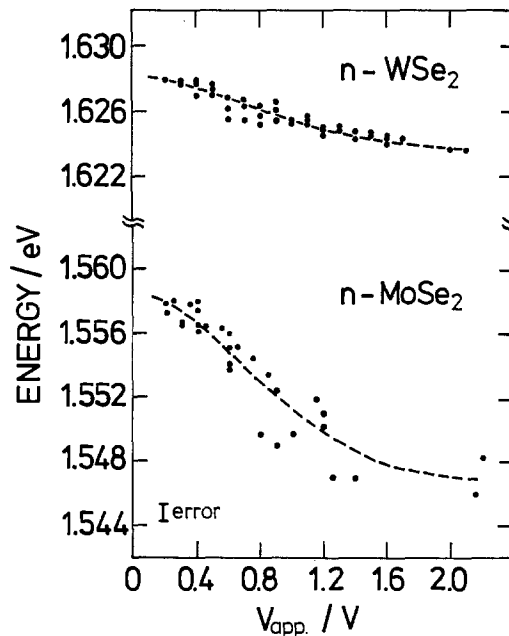


Fig. 7. Shift in the zero crossing (A_1) for increasingly anodic polarization. The data points are collected from several samples of each type.

field in a space-charge layer is not constant and that the dichalcogenides have extremely anisotropic electrical and optical properties, the zero shift is such a small effect that nothing else than the general trend of the shift can be established with any certainty because of the relatively large scatter in the measurements.

If a cathodic bias, relative to the flatband potential, is applied to an n-type semiconductor, an accumulation layer is formed. The ER signals from cathodically biased n-MoSe₂ and n-WSe₂ is shown in Fig. 5b and 6b, respectively, and one can observe marked changes in comparison with the ER spectra produced by depletion layers (Fig. 5a and 6a). In particular, we note that at the A_1 position a peak has developed in place of the zero crossing, and the ER signals now have a striking similarity to the $-\Delta\epsilon_r$ rather than to the $\Delta\epsilon_r$ curves computed by Blossey. This interchange of line shapes is expected and is explained in terms of field inhomogeneities (35). Whereas for an anodic bias (depletion layers) the penetration depth of the electric field is greater than 200 nm and therefore in the order of, or greater than, the penetration depth of light (≤ 200 nm), for cathodic bias (accumulation layers)

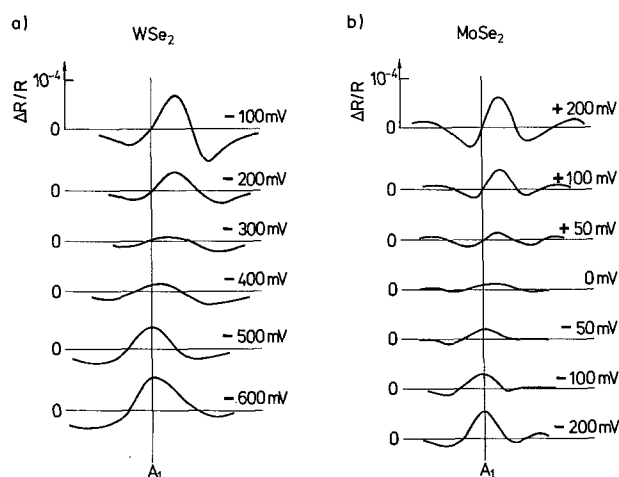


Fig. 8. Room temperature ER spectra taken by modulating at a constant amplitude of 200 mV, but varying the dc bias in 100 mV steps. V_{FB} is located between the bias where the spectra change line shape; e.g., at 0 ± 20 mV and -350 ± 50 mV for n-MoSe₂ and n-WSe₂, respectively.

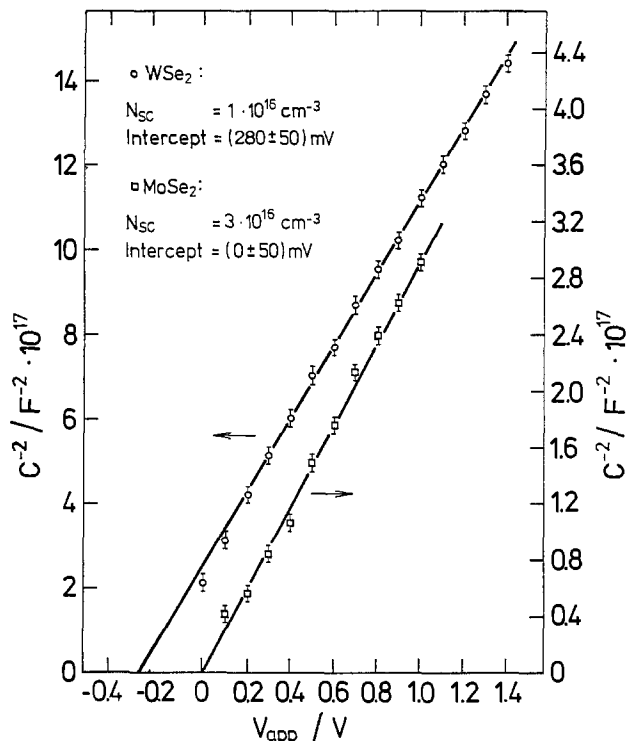


Fig. 9. Mott-Schottky plot of the dichalcogenides in contact with 0.1N H₂SO₄. Frequency: 500 Hz.

the penetration depth is in the order of 10-20 nm and therefore much less than that of the light. Under these conditions, $\Delta\epsilon_r$ and $\Delta\epsilon_i$ are mixed (35) and since $n_o > k_o$ (36), as is often the case in this energy range, an interchange of the line shapes will occur. The additional change in sign, when compared to the calculated $\Delta\epsilon_i$ curves, is not caused by the reversal of the electric field, but comes about because for anodic polarization relative to V_{FB}

$$\Delta R (\text{anodic}) = R(E) - R_o$$

and for cathodic polarization relative to V_{FB}

$$\Delta R (\text{cathodic}) = R_o - R(E) = -\{R(E) - R_o\}$$

The change in the ER spectra when going from an anodic to cathodic bias is therefore a very useful means by which the flatband potential of the dichalcogenides can be determined. In Fig. 8, we show a series of ER spectra produced by keeping the amplitude of the modulating voltage constant but varying its dc bias. The change in amplitude and position of the ER spectra signals the position of V_{FB} so that, judging from Fig. 8, the flatband potentials for our n-MoSe₂ and n-WSe₂ crystals occur at 0 ± 20 and -350 ± 50 mV, respectively. The respective flatband potentials deduced from the Mott-Schottky plots (Fig. 9) are 0 ± 50 and -280 ± 50 mV and are therefore in excellent agreement.

In conclusion, the various ER spectra observed can be understood within the framework of existing theories. In the second paper of this series, the voltage distribution within the n-MoSe₂ and n-WSe₂ electrolyte interface is investigated as a function of the applied voltage, and in the presence of a variety of redox couples.

Acknowledgments

Valuable discussions with Dr. K. Doblhofer and the technical assistance of S. Wasle are gratefully acknowledged. One of us (G.A.S.) would also like to thank the Max-Planck-Gesellschaft for the very generous support received during the stay at the Fritz-Haber-Institut.

Manuscript submitted May 14, 1984; revised manuscript received March 11, 1985.

Fritz-Haber-Institut assisted in meeting the publication costs of this article.

REFERENCES

- H. Tributsch, *Z. Naturforsch., Teil A*, **32**, 972 (1977).
- H. Tributsch, H. Gerischer, C. Clemens, and E. Bucher, *Ber. Bunsenges. Phys. Chem.*, **83**, 655 (1979).
- J. A. Wilson and A. D. Yoffe, *Adv. Phys.*, **18**, 193 (1969).
- W. Kautek, H. Gerischer, and H. Tributsch, *Ber. Bunsenges. Phys. Chem.*, **83**, 1000 (1979).
- K. W. Frese, Jr., and S. R. Morrison, *This Journal*, **126**, 1235 (1979).
- H. Gerischer, D. M. Kolb, and J. K. Sass, *Adv. Phys.*, **27**, 437 (1978).
- A. J. Bard, A. B. Bocarsly, F. F. Fan, E. G. Walton, and M. S. Wrighton, *J. Am. Chem. Soc.*, **102**, 3671 (1980).
- P. A. Kohl and A. J. Bard, *This Journal*, **126**, 59 (1979).
- B. L. Evans, in "Physics and Chemistry of Materials with Layer Structure," Vol. 4, P. A. Lee, Editor, p. 1, D. Reidel Publishing Co., Dordrecht, Holland (1976).
- M. Tomkiewicz, J. K. Lyden, R. P. Silberstein, and F. H. Pollak, in "Photoreflexes at Semiconductor-Electrolyte Interfaces," ACS Symposium Series 146, A. J. Nozik, Editor, p. 267, American Chemical Society, Washington, DC (1980).
- R. P. Silberstein, J. K. Lyden, M. Tomkiewicz, and F. H. Pollak, *J. Vac. Sci. Soc.*, **19**, 406 (1981).
- R. P. Silberstein, F. H. Pollak, J. K. Lyden, and M. Tomkiewicz, *Phys. Rev. B*, **24**, 7397 (1981).
- P. Lemasson, J. Gautron, and J. P. Dalbéra, *Ber. Bunsenges. Phys. Chem.*, **84**, 796 (1980); P. Lemasson, J. P. Dalbéra, and J. Gautron, *J. Appl. Phys.*, **52**, 6296 (1981).
- M. Tomkiewicz, W. Siripala, and R. Tenne, *This Journal*, **131**, 736 (1984).
- M. Cardona, "Modulation Spectroscopy," Solid State Physics Supplement 11, Academic Press, New York (1969).
- B. O. Seraphin, in "Semiconductors and Semimetals," Vol. 9, R. K. Willardson and A. C. Beer, Editors, p. 1, Academic Press, New York (1972).
- B. O. Seraphin and R. B. Hess, *Phys. Rev. Lett.*, **14**, 138 (1965).
- W. E. Engeler, H. Fritzsche, M. Garfinkel, and J. J. Tieman, *ibid.*, **14**, 1069 (1965).
- B. Bantz, *Solid-State Commun.*, **4**, 241 (1965).
- W. Franz, *Z. Naturforsch., Teil A*, **13**, 484 (1958); L. V. Keldysh, *Sov. Phys. JETP (Engl. Trans.)*, **34**, 788 (1958).
- D. E. Aspnes, *Surf. Sci.*, **37**, 418 (1973).
- D. F. Blossey, *Phys. Rev. B*, **3**, 1382 (1971).
- K. L. Shaklee, F. H. Pollak, and M. Cardona, *Phys. Rev. Lett.*, **15**, 883 (1965).
- B. O. Seraphin, in "Optical Properties of Solids," S. Nudelman and S. S. Mitra, Editors, p. 153, Plenum Press, New York (1969).
- F. H. Pollak, in "Photoelectrochemistry: Fundamental Processes and Measurement Techniques," W. L. Wallace, A. J. Nozik, S. K. Deb, and R. H. Wilson, Editors, p. 608, The Electrochemical Society Softbound Proceedings Series, Pennington, NJ (1982).
- D. E. Aspnes, S. M. Kelso, C. G. Olson, and D. W. Lynch, *Phys. Rev. Lett.*, **48**, 1863 (1982).
- B. O. Seraphin and N. Bottka, *Phys. Rev. A*, **193**, 560 (1965).
- See, for instance, S. R. Morrison, "Electrochemistry at Semiconductor and Oxidized Metal Electrodes," Plenum Press, New York (1980).
- D. E. Aspnes and J. E. Rowe, *Solid-State Commun.*, **8**, 1145 (1970).
- D. E. Aspnes, *Phys. Rev. Lett.*, **28**, 913 (1972).
- M. Cardona, K. L. Shaklee, and F. H. Pollak, *Phys. Rev.*, **154**, 696 (1967).
- R. A. Bromley, *Phys. Lett. A*, **33**, 242 (1970).
- P. M. Amirtharaja, F. H. Pollak, and A. Wold, *Solid-State Commun.*, **41**, 581 (1982).
- A. R. Beal, J. C. Knights, and W. Y. Liang, *J. Phys. C*, **5**, 3540 (1972).
- D. E. Aspnes and A. Fropa, *Solid-State Commun.*, **7**, 155 (1969); in "Physics and Chemistry of Material, with Layer Structure," Vol. 4, P. A. Lee, Editor, p. 214, D. Reidel Publishing Co., Dordrecht, Holland (1976).
- S. Antoci, P. Camagni, A. Manara, and A. Stella, *J. Phys. Chem. Solids*, **33**, 1177 (1972).



Photocorrosion of n-CdSe in Sulfide Electrolytes

K. W. Frese, Jr.,* and D. Canfield

SRI International, Menlo Park, California 94025

ABSTRACT

The stabilization efficiency for n-CdSe in polysulfide electrolytes has been determined. Under experimental conditions, the corrosion current was 1 to 500 ppm of the photocurrent. A hole tunneling model was used to provide the link between stabilization efficiency and the photocurrent decay parameter. The surface coverage of sulfide was shown to depend on current density and electrolyte concentration. The stability of the electrode was a function of electrode potential and electrolyte composition. More cathodic potentials and increasing sulfur content of the electrolyte enhanced the stability. The stability of the electrode appears to be controlled by a chemical step involving adsorbed sulfur.

A limiting problem in the application of photoelectrochemical solar cells is stability of the photoelectrode. The n-CdSe-polysulfide system has been of considerable interest in this connection. Detailed studies of the redox properties of the electrolyte are now being conducted, and models for the photocurrent decay are now being investigated. A number of issues need consideration to fully understand this system. These are, first, properties and models for the photocurrent decay; second, models for the stability, including the effect of photocurrent density, concentration (adsorption), electrolyte composition, and electrode potential, and third, use of the results of the first and second items to obtain predictions of the long-term stability from accelerated decay results. The study described here is an attempt to deal with some of these issues.

The model for the stabilization efficiency, S , used here is an extension of our earlier work (1-4). Adsorption of the reducing agent and dissolution of the corrosion product are now considered in the mechanism. The decaying photocurrent is assumed to be controlled by hole tunneling through a corrosion layer. It will be shown that this assumption allows determination of S from the photocurrent decay characteristics. The existing literature (5-8) concerning the polysulfide electrolyte was used to provide a description of the electrolyte composition.

There is a large body of work concerning CdSe and CdS electrodes in sulfide electrolytes that has preceded our efforts. The recent review by Hodes (9) can be consulted for details.

Experimental

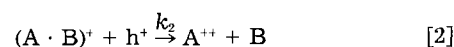
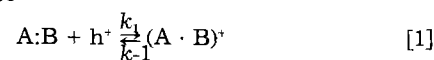
All measurements were made on n-CdSe (11 $\bar{2}$ 0) single-crystal electrodes (Cleveland Crystals) with donor densities of $1 \times 10^{17} \text{ cm}^{-3}$. The surfaces were chemomechanically polished with 1% $\text{Br}_2/\text{CH}_3\text{OH}$ mixed 50/50 (v/v) with 1M HCl. The electrodes were etched before each measurement using a cotton-tip applicator saturated with the etch solution. A Pine analytical rotator and RDE-3 potentiostat were used to control the rotation speed and electrode potential. The electrode was illuminated with a tungsten-halogen lamp. All chemicals were reagent grade. Stock solutions of polysulfide electrolyte were prepared and added to the cell to form the desired composition. High purity N_2 was continuously bubbled through the electrolyte. Voltages are reported vs. the saturated calomel electrode.

*Electrochemical Society Active Member.

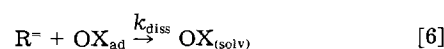
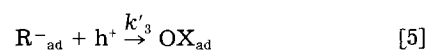
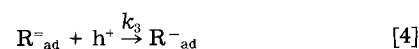
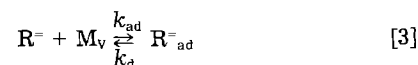
Theory

Kinetics of stabilization with an adsorbing two-equivalent reducing agent.—Consider the following mechanism that is proposed to describe the case when oxidation of adsorbed sulfide species competes with the anodic corrosion of the CdSe electrode.

Equations [1] and [2] were included in the earlier model (1, 2) for weakly interacting one-equivalent reducing agents. They represent bond breaking steps corresponding to removal of an electron pair bond between lattice atoms, A and B. Here we assume both holes are captured by the more electropositive element, e.g., Cd. B represents elemental Se



The reducing agent participates in the following events: adsorption, desorption, electron transfer, and surface dissolution. These steps are



R^- is a two-equivalent reducing agent, e.g., S_n^{2-} ; M_v is a vacant adsorption site, k_3 and k'_3 are rate constants for surface hole capture, and k_{diss} is a rate constant for removal of the oxidized form. The meaning of Eq. [6] is that an electrolyte species, e.g., SH^- , removes the adsorbed oxidized species, e.g., S_{ad} .

Considering steps 1, 2 and 4, 5 (those that contribute to the observed photocurrent density, j) and the steady-state analysis given previously (2, 10), Eq. [7] is obtained

$$j = \frac{2k_1k_2}{k_{-1}} (h^+)^2 + j_3 \quad [7]$$

where j_3 and S , the stabilization efficiency, are defined by

1555

$$j_3 = 2k_3(R^-)_{ad}(h^+) = Sj \quad [8]$$

Equation [8] may be used to eliminate the steady-state hole concentration. Performing this operation on Eq. [7] and rearranging the result yields

$$S = \frac{2}{1 + \left[1 + \frac{2\alpha j}{(\Theta M_T)^2} \right]^{1/2}} \quad [9]$$

where Θ is the steady-state coverage of R^-_{ad} , M_T is the total number of sites, and the composite rate constant $\alpha = k_1 k_2 / k_{-1} k_3^2$. Equation [9] states that S will decrease as j increases or as Θ decreases. These predictions have already been shown (2, 11) to agree with the experiment for the one-equivalent nonadsorbed reducing agent case. In that case, an equation very similar to Eq. [9] was applied, but with ΘM_T replaced by C_{R^-} , the concentration of reducing agent in solution.

Stabilization efficiency and tunnel model.—One of our objectives in the present work is to quantify the instabilities of the CdSe (1120) single-crystal electrode. The photocurrent decay method can be used to measure corrosion rates. By modelistic interpretation of the characteristic photocurrent decay parameter

$$\alpha \equiv \frac{-d \ln(j/j_0)}{d \Sigma q} \quad [10]$$

we can obtain values for the stabilization efficiency, correlate results, and ultimately extrapolate the behavior of electrodes to different conditions of photocurrent density and redox species concentrations. In Eq. [10], j is photocurrent, j_0 is initial photocurrent, and Q is the integrated photocharge.

A model for the decay of photocurrent in the CdSe-alkaline polysulfide system has been suggested (12, 13). The essential assumptions of the model are diagrammed in Fig. 1. The photocorrosion of CdSe in the presence of sulfide species leads to a layer of CdS on the CdSe surface. This occurs because in the corrosion process Cd^{2+} ions are produced along with elemental Se. The selenium is assumed to be rapidly dissolved by the sulfide electrolyte, and the Cd^{2+} ions form CdS by a precipitation mechanism. A key element in this picture is the relative energy level for hole transport, ΔE_{VB} , in the CdS and CdSe.

By consideration of the bandedges CdS and CdSe, it is found that the CdS valence band is about 0.64V below the CdSe valence band. Transport of holes from CdSe to the electrolyte species can occur by tunneling through this potential step at the interface between the two solid phases. This tunnel process was also used to discuss the behavior of the Si/SiO₂ electrode in aqueous electrolytes (14, 15).

With simple arguments we can begin to build a quantitative model. We will adapt the tunneling probability, P_T , for the rectangular barrier as the controlling factor in the decay of the photocurrent. Then we have

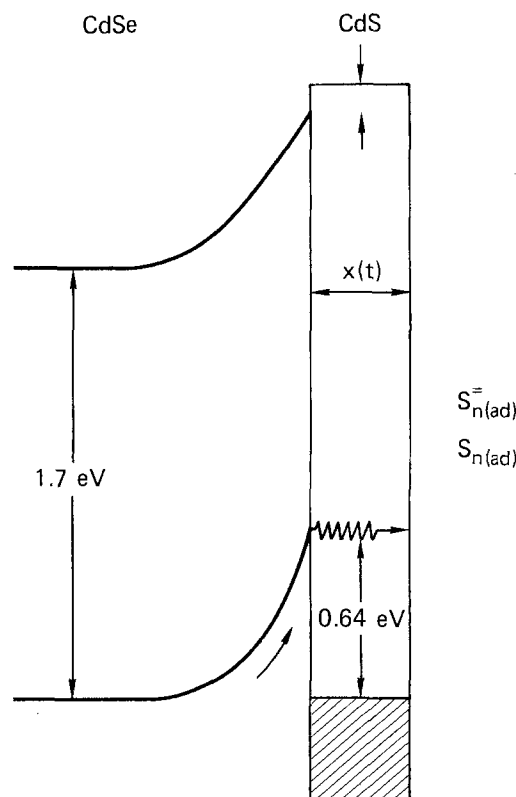
$$P_T = \exp - \left[\frac{2}{\hbar} (2m \Delta E_{VB})^{1/2} x \right] \quad [11]$$

where m is the hole effective mass in CdS, $0.8 m_0$, x is the thickness of the CdS layer, and \hbar is Planck's constant divided by 2π .

Next we formulate an expression for the thickness, x , in terms of the stabilization efficiency, S , the photocurrent, and Faraday's law. The stabilization efficiency (see Eq. [9]) is the fraction of photocurrent that flows to the redox species; so that $(1 - S)j$ is the corrosion current density. Therefore, x may be written

$$x(\text{cm}) = \frac{\bar{V}_m}{nF} \int_0^t (1 - S)j dt \quad [12]$$

The integral represents the corrosion photocharge passed



$$j(t) = j_0 e^{-bx(t)}$$

$$b = \frac{2}{\hbar} (2m \Delta E_{VB})^{1/2}$$

$$x(t) = \frac{V}{nF} (1 - S) Q$$

Fig. 1. Tunnel model for photocurrent decay of CdSe in sulfide electrolyte.

up to time t , \bar{V}_m is the molar volume of CdS (29.97 cm³/mol), F is the Faraday constant, and $n = 2$. The goal of this analysis is to obtain S , which has been modeled in terms of j , concentration, corrosion, and electron-transfer rate constants. If we assume that S is constant during the time domain where the photocurrent is controlled by tunneling, Eq. [12] may be rewritten $x = 1.55 \times 10^{-4} (1 - S)Q$, where Q is the integral photocharge passed. Substitution for x and the physical constants in Eq. [11] leads to Eq. [13]

$$j = j_0 \exp - [\alpha Q] \quad [13]$$

where $\alpha = 1.14 \times 10^4 (1 - S)$. Equation [13] will be used below as the basis for determination of the stabilization efficiency, S . Once S is known, the surface coverage parameter $(M_T/\sqrt{\alpha})\Theta$ can be obtained by means of Eq. [9]. Since total concentration of sites and the rate constants in α are unknown, we cannot obtain absolute values for the coverage. However, the coverage parameter should be simply related to an adsorption isotherm (see below).

Polysulfide electrolyte composition.—The composition of polysulfide electrolytes has been investigated (6, 7) by combining spectroscopic and thermodynamic methods. According to the work of Giggenbach (5, 6), the dominant species are SH^- , S_2^- , S_3^- , S_4^- , and S_5^- . The concentration of the various species is determined by $[OH^-]$ and, more importantly, by the ratio, X_s , of sulfur to sulfide (Na_2S), used in preparing the electrolyte. Solutions rich in sulfur contain increased amounts of higher polymers. As the pH is increased, smaller polymers are favored. The majority of measurements reported here were performed using the $X_s = 1$ electrolyte in 1M NaOH. The effect of X_s on elec-

trode stability was also investigated at constant current density.

It is of interest, therefore, to have some indication of the composition of these electrolytes. The results of our calculations using Fig. 5 of Ref. (6) and Eq. [2] of Ref. (7) are given in Table I. All concentrations are expressed in moles per liter. A common electrolyte mix is described on the first line of Table I. This 1:1 polysulfide mix is actually dominated by the hydrosulfide ion. Since the pK_a of this ion (5) is 17.1, there are virtually no $S^{=}$ ions present. Addition of one sulfur causes large increases in the acidity in moderately basic solution. As expected, larger sulfur/sulfide ratios lead to progressively longer chains. A saturated solution ($X_s = 3.5$) exclusively contains $S_4^{=}$ and $S_5^{=}$ species. These calculations provide a guide concerning the composition of the electrolyte. However, it is not clear (16) that they are exact under our conditions, i.e., ionic strength $>1M$.

Results

Typical photocurrent decay curves are shown in Fig. 2. The CdSe electrode was rotated at 1600 rpm and the electrode potential was 0.0 V (SCE). The insets show plots of $\ln(j/j_0)$ vs. the integrated charge density. These plots were linear after a period of nearly constant photocurrent. The absolute value of the slope of these logarithmic plots is to be identified with the parameter, α , (Eq. [10] and [13]) defined above. A large number of decay curves at various initial current densities and concentration were obtained. In each case, the coverage parameter, $(M_T/\sqrt{\alpha})\theta$, a measure of the steady-state surface coverage, was obtained as described earlier. The dependence of these values on initial photocurrent is shown in Fig. 3. It can be seen that the steady-state coverage dropped as the photocurrent increased. However, the slope of the log plot was practically constant for each concentration. A value of $350 (A/cm^2)^{-1}$ was typical. The plots of Fig. 3 were extrapolated to $j = 0$, yielding values for $(M_T/\sqrt{\alpha})\theta_0$. It was found that a universal curve could be obtained by normalizing the coverage using the zero current value of the coverage parameter at each concentration. These results are shown in Fig. 4.

It was expected that $(M_T/\sqrt{\alpha})\theta_0$ values should vary with concentration in a manner consistent with an adsorption isotherm for the polysulfide species. Figure 5 (solid symbols) shows a plot of the zero current coverage parameter as a function of $\log[S^{=}]$. The data appear to conform to a logarithmic isotherm such as the approximate form of Frumkin's isotherm (17).

The steady-state sulfide coverage at $j = 10 \text{ mA/cm}^2$ is also plotted in Fig. 5. These data behave qualitatively similar to the zero current data. However, no thermodynamic meaning can be attached to these steady-state results. The general isotherm-behavior of the derived coverage parameter is both reasonable and expected.

The stability of the electrode as measured by the photocurrent half-life was investigated as a function of X_s . The results are shown in Fig. 6. A large increase in stability was found for electrolytes rich in sulfur. The half-life of the photocurrent was also determined as a function of electrode potential. These results for $X_s = 1$ are summarized in Fig. 7 for several sulfide concentrations. At a critical potential, V_c , an exponential increase in half-life was observed. The quantity V_0^* is the onset potential for the

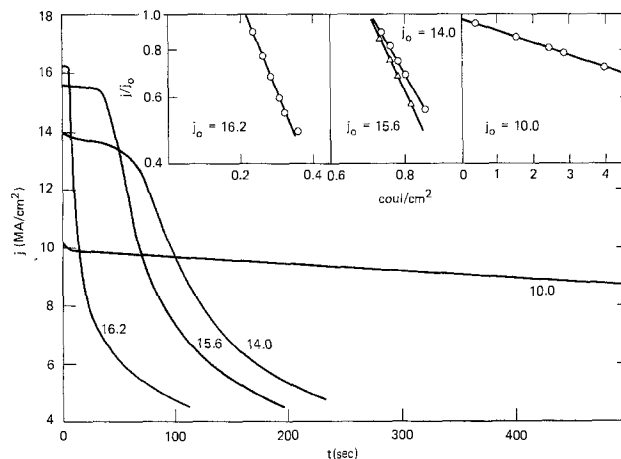


Fig. 2. Photocurrent vs. time and relative photocurrent vs. integral charge for RDE n-CdSe (1120). Electrolyte: 0.3M each $Na_2S/S^{=}$ in 1M NaOH. 1600 rpm, $V_{DISK} = 0.0 \text{ V(SCE)}$.

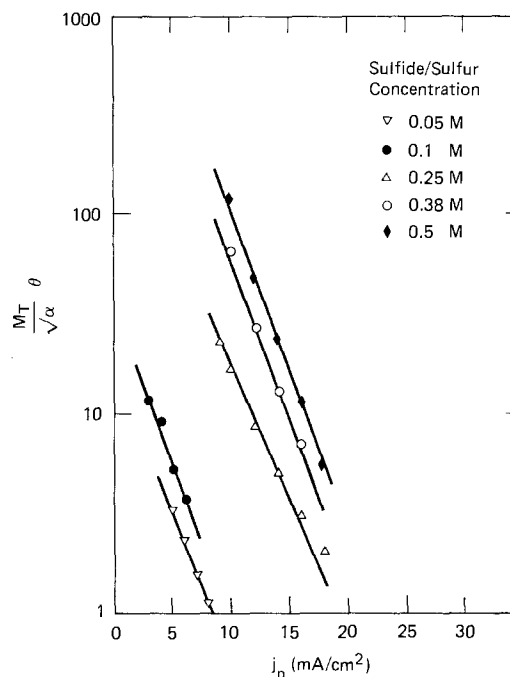


Fig. 3. Derived values of surface coverage parameter with $S_n^{=}$ as a function of initial photocurrent density with concentration of equimolar $S^{=}/S^0$ as a parameter: n-CdSe (1120) RDE, 1600 rpm. $V_{DISK} = 0.0 \text{ V(SCE)}$. 1M OH^- .

anodic photocurrent. The rate of increase of $t_{1/2}$ with voltage was greater for more concentrated electrolytes. It has already been shown (18) that electrode potential affects the stability of CdS in $10^{-3}M Na_2S$ solution. In that case stability decreased sharply for potentials positive of $\sim -0.8V$ (SCE).

Discussion

The decay curves in Fig. 2 show there is a region of nearly constant photocurrent before the decay sets in. Part of the charge passing in this region is due to oxidation of adsorbed sulfide and part is due to oxidation of CdSe (CdS formation). According to our model, the fraction of charge for the latter process is $(1 - S) = a/1.14 \times 10^4$. Table II shows decay characteristics for various conditions. Of particular interest is the $(1 - S)$ value calculated from the decay curve proper using Eq. [10] and [13], and the total charge density, $(1 - S)Q$, that measures the amount of corrosion product that is formed before the decay begins. A typical value of this charge is $\sim 10^{-4} \text{ C/cm}^2$. Note especially the last entry in Table II where the conditions strongly differ from the remaining data. The average for the data in Table II is $2.4 \times 10^{-4} \text{ C/cm}^2$. Formation of a

Table I. Polysulfide electrolyte composition^a

X_s	S	Na_2S	SH^-	$S_2^{=}$	$S_3^{=}$	$S_4^{=}$	$S_5^{=}$
1.0	1	1	0.62	0	0.15	0.23	0
2.0	2	1	0.265	0	0.20	0.53	0.005
3.0	3	1	0.007	0	0.066	0.87	0.057
3.5	3.5	1	0	0	0	0.58	0.43
3.5	8.0	2.3	0	0	0	1.3	1.0
2.5	1.0	2.5	2.15	0	0.075	0.004	0.276
1.33	4	3	0	0	0.60	0.93	0

^a pH = 14.0.

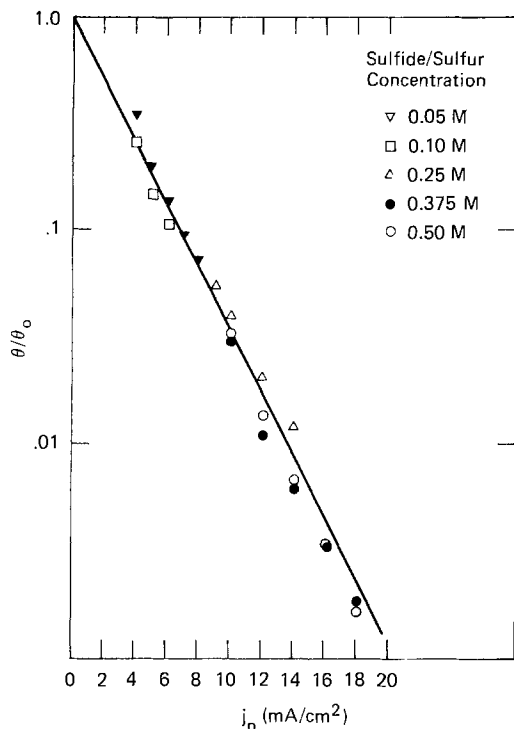


Fig. 4. Derived values of the relative degree of surface coverage of S_n as a function of initial photocurrent density (conditions as in Fig. 3).

monolayer of CdS requires about $1.6 \times 10^{-4} \text{ C/cm}^2$ so that 1.5 layers ($\sim 4\text{\AA}$) of corrosion product are necessary to initiate the decay process. This result is very reasonable and provides an indication of the layer thickness required for the tunnel model to be applicable.

The values of stabilization efficiency reported in Table II are high. The corrosion current ranges from 5 parts per thousand to 1 ppm for the 1M electrolyte at (30 mA/cm^2) . The electronic barrier for holes that results from the formation of CdS makes this system moderately susceptible to photocurrent decay. A similar but more severe problem exists for the Si/SiO₂ system, where the ideal electronic barrier for holes is 4-5 eV.

According to the plots in Fig. 3 and 4, the coverage as a function of initial photocurrent density may be represented by

$$\Theta = \Theta_0 e^{-Bj} \quad [14]$$

where Θ depends on concentration in a manner consistent with the Frumkin isotherm (Fig. 5). The empirical factor B , appears to be independent of concentration.

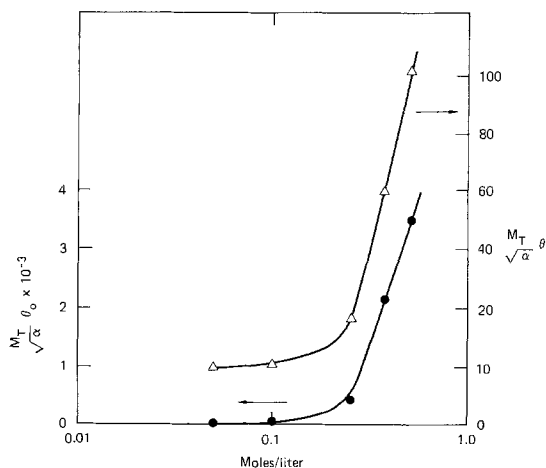


Fig. 5. Coverage parameter vs. log concentration of sulfide for zero photocurrent (lower curve) and 10 mA/cm^2 (upper curve) (conditions as in Fig. 3).

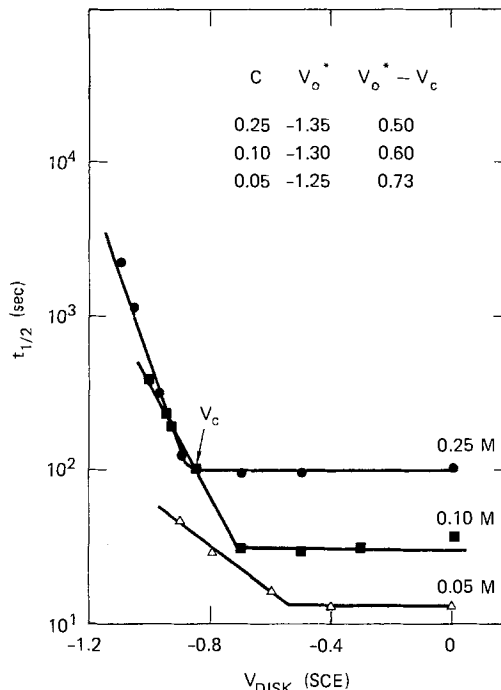


Fig. 6. Photocurrent half-life for n-CdSe (1120) RDE in 0.1M Na₂S, 1M NaOH electrolyte with various amounts of sulfur added. $V_{\text{DISK}} = 0.0 \text{ V (SCE)}$, 1600 rpm. Initial photocurrent, 10 mA/cm^2 .

Since the adsorption step (Eq. [3]) and the dissolution of sulfur oxidation product (Eq. [6]) proceed at a finite rate, it is expected that the coverage should drop as the current density increases. According to the simple sequence of steps, Eq. [3]-[6], the coverage should decrease with j according to

$$\frac{\Theta}{\Theta_0} = 1 - \frac{j}{(k_{\text{ad}} + k_{\text{diss}})} \quad [15]$$

where concentration terms would appear in the k 's.

This relation is not in agreement with the observations (Eq. [14]), and further mechanistic analysis is needed. A difficulty is that the change of coverage with current is independent of Na₂S concentration contrary to the proposed Eq. [6].

Two interesting observations following from our analysis are that the intercepts of the $\log [(M_T/\sqrt{\alpha})\Theta_0]$ plots depend on concentration and that the slopes are independent of concentration. We have already discussed the behavior of the zero current values of $(M_T/\sqrt{\alpha})\Theta_0$ parameter in terms of adsorption properties.

Now we will postulate a different mechanism that gives an improved interpretation of the values of $(M_T/\sqrt{\alpha})\Theta_0$ and

Table II. Decay characteristics of single-crystal n-CdSe in polysulfide electrolyte.^a $X_s = 1$, 1M NaOH

[S ²⁻]	$j_0(\text{mA/cm}^2)$	$a(\text{C/cm}^2)^{-1}$	$-\log(1-S)$	Q	$(1-S)/Q \times 10^4$
0.02	2.54	10.0	3.06	0.23	2.0
0.025	4.0	7.24	3.20	0.10	0.63
0.05	7.1	15.7	2.86	0.076	1.0
0.05	8.9	53.5	2.33	0.046	2.2
0.10	8.4	12.0	2.98	0.87	9.1
0.10	10.2	7.28	3.20	0.20	1.2
0.10	14.7	13.9	2.91	0.045	0.55
0.30	16.2	5.01	3.36	0.70	3.0
0.38	11.0	0.16	4.85	5.4	0.76
1.0 ^b	30	0.0133	5.94	300	3.4

2.4 Avg.

^a Conditions as in Fig. 3, charge in coulombs per square centimeter.

^b From Ref. (12).

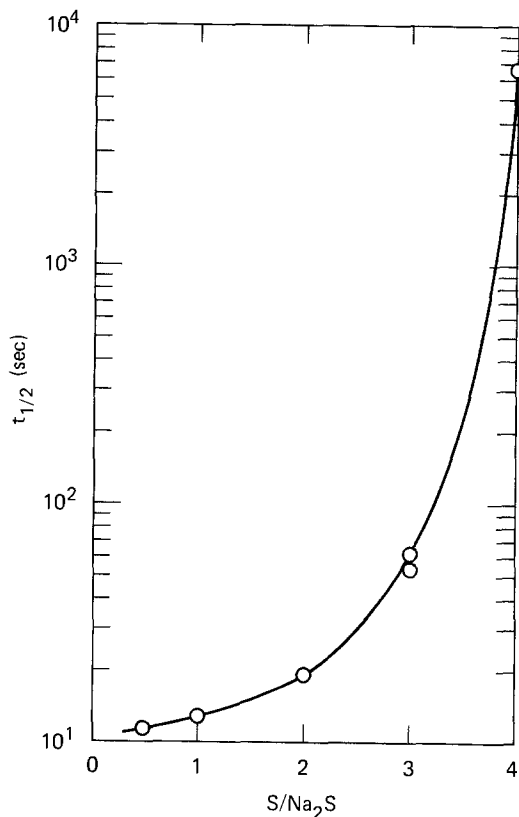
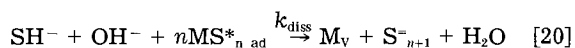
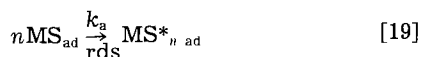
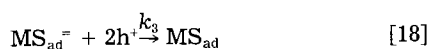
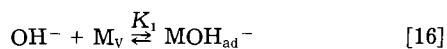


Fig. 7. Photocurrent half-life for n-CdSe (11 $\bar{2}$ 0) RDE as a function of electrode potential. Electrolyte: equimolar S²⁻/S⁰ in 1M NaOH. 1600 rpm. Initial photocurrent, 10 mA/cm².

also rationalizes the concentration independent slopes in Fig. 3 and 4.

In a recent paper (19), we have shown that both OH⁻ and S²⁻ are important coadsorbing species in the basic Na₂S solutions. In 1M OH⁻ the CdSe is saturated with OH_{ad}⁻. As Na₂S is added to the electrolyte, S_{ad}²⁻ replaces OH⁻ until saturation is again obtained. These equilibria are included in the mechanism below. In addition, the dissolution of adsorbed sulfur is written in two steps. The following steps are considered in place of Eq. [3]-[6]. Here M_v stands for a vacant site and the asterisk indicates an activated form of adsorbed sulfur



For convenience, both hole transfer steps are combined in Eq. [18]. In summary, the new mechanism accounts for the competitive adsorption of OH⁻ and S²⁻ and maintains the key feature that S_{ad} has to undergo some type of rearrangement or activation with rate constant, k_a , in order to be desorbed. This rearrangement is postulated to be the rate-limiting step. At this time, we do not know the identity of the activated state of sulfur. The process might be, for example, conversion from a strongly bound to a weakly bound state involving different bonding properties. Another possibility is that the rate-determining step is a chemical combination of adjacent S atoms to form S_{nad} which then could be removed by S²⁻ to form S_{n+1}²⁻. Note that S₂²⁻ is not stable under our conditions according to the data of Gigenbach (5, 6) (Table I). It is plausible that some S_{ad} is desorbed as S₃²⁻ as in the X_s = 1 electrolyte.

The goal of the present analysis is to obtain a relationship for Θ/Θ_0 analogous to Eq. [15]. Conservation of sites requires that

$$1 = \Theta_{\text{OH}^-} + \Theta_{\text{S}^{2-}} + \Theta_{\text{S}} + \Theta_{\text{V}} \quad [21]$$

where we have used Θ_{V} to indicate the fraction of sites that are vacant. In the analysis, Θ_{OH^-} and $\Theta_{\text{S}^{2-}}$ are eliminated by the thermodynamic definitions of K_1 and K_2 , respectively. The high stability of the system (Table II) justifies the approximation that the rate of hole transfer, Eq. [8], equals the photocurrent, j_p . In terms of the rate limiting step, Eq. [19], we have

$$j_p = \frac{k_a}{n} \Theta_{\text{S}}^n \quad [22]$$

where n is the number of S atoms and k_a is the rate constant. The results of combining Eq. [16]-[19], and Eq. [21] and [22] is

$$\frac{\Theta}{\Theta_0} = 1 - \left(\frac{n j_p}{k_a} \right)^{1/n} \quad [23]$$

where Θ_0 is the coverage at zero photocurrent. Its value is given by

$$\Theta_0 = \frac{K_2(\text{SH}^-)(\text{OH}^-)}{1 + K_2(\text{SH}^-)(\text{OH}^-) + K_1(\text{OH}^-)} \quad [24]$$

By suitable algebraic manipulation, Eq. [23] can be written, for low coverage

$$\ln \Theta \cong \ln \Theta_0 - \left(\frac{n}{k_a} j_p \right)^{1/n} \quad [25]$$

Plots of the experimental data according Eq. [25] with $n = 1$ were shown in Fig. 3.

The most important observation is that the constant slopes in Fig. 3 and 4 are rationalized by means of Eq. [25], thereby supporting the rate-determining step in Eq. [19]. In the revised mechanism, a role of OH⁻ concentration is suggested in Eq. [16], [17], and [20]. Equation [24] predicts that Θ_0 will be maximal at a certain [OH⁻] and that electrode stability will depend on pH. The deleterious effect of too-high (OH⁻) would probably be most noticeable when large S_n²⁻ polymers dominate in the electrolyte. Preliminary flatband potential data (20) show that there is less negative charge on the CdSe surface in electrolytes richer in sulfur but with constant OH⁻ composition. This could mean that OH⁻ competes better with larger S_n²⁻ species. It follows that less adsorbed sulfide means lower stability because OH_{ad}⁻ is not efficiently oxidized by illuminated CdSe.

Having presented our data and analysis, it is important to compare our results with those of previous studies. Most notable is the work performed by the groups at the Weizman Institute in Israel. In many ways, our data supports and extends these investigations. Hodes (9) has recently reviewed photoelectrochemistry in polysulfide electrolytes.

The Weizman groups have considered a number of properties, including photocurrent decay under stationary conditions, effects of electrolyte composition, and kinetic modeling (21). Our experiments generally differ in two ways. We used a lower range of sulfide concentration and a rotating electrode. In addition, we tried to obtain more detailed quantitative data relating to corrosion rates and surface coverage.

Our kinetic model follows from the derivations given earlier (1, 4) concerning one-equivalent nonadsorbing reducing agents. We assume that the corrosion current is second order in hole concentration. This was proven by means of the concentration dependence of the stabilization efficiency for the CdSe electrode using the iron cyanide electrolyte. We also assume that the oxidation of adsorbed sulfur is two equivalent. In both of these respects, we differ from Tenne *et al.* (21). The first-order corrosion reaction proposed in Ref. (21) is known to lead to photo-

current-independent stability as long as diffusion control is avoided. In our results and those of Tenne *et al.*, the photocurrent level exerts a strong influence on the stability.

Siberstein and Tomkiewicz (23) found then that both CdS and CdS_xSe_{1-x} are formed as corrosion products on stationary electrodes. These corroded surfaces were formed in 30-day experiments with initial photocurrents of ~ 50 mA/cm². These conditions are quite different from ours. We used much lower photocurrents, short times (< 1h), and rotating electrodes. In addition, according to Ref. (23), electrodes aged in the dark did not show Se/S exchange. While we cannot rule out the CdS_xSe_{1-x} surface composition, the finding of the above authors does not necessarily mean such mixed compounds were formed in our experiments. We can add that the energy level for hole conduction in CdS_xSe_{1-x} will be more closely matched to that of CdS. The stabilization efficiencies reported here would be lowered to the extent that CdSe_xS_{1-x} replaced CdS.

It has been reported that an optimum stability obtains for a sulfur/sulfide ratio of about 1.3 or 2 (9). Our data do not show such a trend. As Fig. 6 indicates, the stability, as measured by the photocurrent half-life, increases and accelerates as X_s approaches 4. Since the value of 1.3 matched the optimum in the known rate of sulfur dissolution, it was concluded previously (9) that removal of elemental sulfur controls the photocurrent decay. This may be true for certain stationary conditions, but this conclusion cannot be made from our results. It is reasonable that the dissolution of adsorbed sulfur occurs at a faster rate at the RDE because of the effective stirring rate. The enhancement of stability by increasing the sulfur content of the electrolyte (Fig. 6) may be related to the dissolution rate of sulfur. The argument is based on the fact that, if the rate of removal of adsorbed sulfur is increased, a greater steady-state coverage of sulfide should result. The effect of X_s on the dissolution rate of sulfur has been reported (24). It was found that sulfur dissolved more rapidly as X_s increased to ~ 4.0 [see Fig. 7, Ref. (24)]. This known behavior explains the results in Fig. 6. Our calculations in Table I, therefore, indicate that larger polymer species such as S₄²⁻ and S₅²⁻ may be most effective in removing dissolved sulfur. Considering the nonpolar character of sulfur, it is not too surprising that increasing the sulfur content of the ions in solution promotes faster dissolution. On the other hand, there may be special stability associated with a certain size polymer which is formed by addition of sulfur from the electrode surface to an existing favorable polysulfide species in the electrolyte.

Since the free energies of formation of the polysulfide species differ by ~ 1 kcal-mol (8), we expect the changes in thermodynamic redox properties for different compositions to be small.

The effect of electrode potential on stability is an interesting one. We have already observed the effect on the n-CdSe/iron cyanide system (26) using the rotating ring-disk corrosion competition method. An effect of voltage on stability of CdSe in sulfide electrolytes was described earlier (22). At negative potentials and constant light intensity, lower photocurrent and, thus, higher stability are obtained. Our effect of voltage is different because we adjusted the light intensity to keep the photocurrent level constant. Therefore, another voltage effect was observed in our results.

Two possible explanations for the present case are the following. It is reasonable to expect that adsorbed sulfur is present on the surface as a reaction product. If the steady-state coverage with sulfur could be lowered, then the stability of the electrode should increase because more sulfide can be adsorbed. If part of the adsorbed sulfur is electrochemically reduced to sulfide and desorbed, by the preceding argument the stability should increase. The extent of the reduction of sulfur should depend on the cathodic voltage in agreement with the observations.

Alternatively, we can explain the data in Fig. 7 by in-

volving a recombination mechanism. It has been suggested (25,26) that if corrosion intermediates such as (A · B)⁺ can function as recombination centers, then their steady-state concentration will depend upon the concentration of electrons, n_s, at the surface. Higher cathodic bias means higher n_s and less (A · B)⁺ and lower corrosion rate. Without additional detailed analysis, we cannot decide which model is correct. But if the recombination mechanism is correct, it appears from the quantity V₀* - V_c that the energy level of the recombination center depends on concentration of sulfide. It is clear that the recombination effect on stability is not unique to systems with adsorbed redox species.

Summary

It has been shown that, by recognizing the electronic properties of substrate and corrosion layer, the photocurrent decay can be used to obtain information about the corrosion properties of semiconductor electrolyte systems. Because of the complexity of the system, detailed models had to be applied. A tunnel model for hole photocurrent was combined with the relation for stabilization efficiency to determine a quantity proportional to sulfide surface coverage. It was shown that such coverage data behaved, with respect to concentration, as expected on the basis of a general adsorption isotherm. The dependence of the coverage on current density was also investigated. The results indicated that the coverage was quite low for the current densities and concentrations used. This is not unexpected, since we designed the experimental conditions so that relatively fast decays would be observed. Our data suggest that one to two monolayers of corrosion product are sufficient to allow application of the tunnel model for hole current. Electrode potential and electrolyte composition have major influences on the electrode stability. Higher sulfur ratios and more cathodic voltages enhance the stability. While detailed modeling has led to the stability data, exact interpretation in terms of a kinetic mechanism has not been done. However, we were able to conclude that the stability of a rotating CdSe electrode is determined by a chemical process probably involving surface adsorbed sulfur.

Acknowledgment

Support by the Solar Energy Research Institute under Contract no. XE-2-02073-1 and XB-3-03106-1 is gratefully acknowledged.

Manuscript submitted Feb. 21, 1984; revised manuscript received Feb. 15, 1984.

SRI International assisted in meeting the publication costs of this article.

REFERENCES

1. K. W. Frese, Jr., M. J. Madou, and S. R. Morrison, *J. Phys. Chem.*, **84**, 3172 (1980).
2. K. W. Frese, Jr., M. J. Madou, and S. R. Morrison, *This Journal*, **128** 1527 (1981).
3. K. W. Frese, Jr., and D. Canfield, "Annual Report: Investigation of Photoelectrochemical Corrosion of Semiconductors," Solar Energy Research Institute, Golden, CO, May 1983.
4. K. W. Frese, Jr., and D. Canfield "Annual Report: Investigation of Photoelectrochemical Corrosion of Semiconductors," Solar Energy Research Institute, Golden, CO, June 1984.
5. W. Gigenbach, *Inorg. Chem.*, **10**, 1333 (1971).
6. W. Gigenbach, *ibid.*, **11**, 1201 (1972).
7. A. Teder, *Acta Chem. Scand.*, **25**, 1722 (1971).
8. M. C. H. McKubre and D. D. Macdonald, "Electrochemical Removal of Dissolved Sulfide from Geothermal Brines," Final Report from SRI International to the Environmental Protection Agency, EPA Contract no. 63-07-2778 (1981).
9. G. Hodes, in "Energy Resources through Photochemistry and Catalysis," M. Gratzel, Editor, Academic Press, New York (1983).
10. S. R. Morrison, in "Photoelectrochemistry: Fundamental Processes and Measurement Techniques," W. L. Wallace, A. J. Nozik, S. K. Deb, and R. H. Wilson, Editors, p. 103, The Electrochemical Society Softbound Proceedings Series, Pennington, NJ (1982).

11. K. W. Frese, in "Photoelectrochemistry: Fundamental Processes and Measurement Techniques," W. L. Wallace, A. J. Nozik, S. K. Deb, and R. H. Wilson, Editors, p. 157, The Electrochemical Society Softbound Proceedings Series, Pennington, NJ (1982).
12. A. Heller, G. P. Schwartz, R. G. Vadimsky, S. Menzies, and B. Miller, *This Journal*, **125**, 1156 (1978).
13. R. N. Noufi, A. A. Kohl, J. W. Rogers, J. M. White, and A. J. Bard, *ibid.*, **126**, 949 (1979).
14. M. J. Madou, K. W. Frese, Jr., and S. R. Morrison, *J. Phys. Chem.*, **84**, 4323 (1980).
15. S. R. Morrison, M. J. Madou, and K. W. Frese, Jr., in "Photo Effects at Semiconductor Electrolyte Interfaces," A. J. Nozik, Editor, ACS Symposium Series, no. 146, Washington, DC (1981).
16. R. J. Remick and E. H. Camara, "L. B. L. Final Report," Project 65911, July 1983.
17. Electrosorption, E. Gileadi, Editor, Plenum Press, New York (1967).
18. B. Miller and A. Heller, in "Electrode Materials and Processes for Energy Conversion and Storage," J. D. E. McIntyre, S. Srinivasan, and F. G. Will, Editors, p. 91, The Electrochemical Society Softbound Proceedings Series, Princeton, NJ (1977).
19. K. W. Frese, Jr., and D. G. Canfield, *This Journal*, **131**, 2614 (1984).
20. K. W. Frese, Jr., and D. Summers, "Investigation of Photoelectrochemical Corrosion of Semiconductors," Quarterly Report no. 2, Solar Energy Research Institute, Golden, CO, January 1985.
21. R. Tenne, N. Muller, Y. Mirovsky, and D. Lando, *This Journal*, **130**, 852 (1983).
22. R. Tenne, D. Lando, Y. Mirovsky, N. Muller, J. Marasen, D. Cohen, and G. Hodes, **143**, 103 (1983).
23. R. P. Silberstein and M. Tomkiewicz, *J. Appl. Phys.*, **54**, 5428 (1983).
24. N. Harlter, J. Libert, and A. Teder, *I&EC Process Design Dev.*, **6**, 398 (1967).
25. D. Vanmaekelbergh, W. P. Gomes, and F. Cardon, *This Journal*, **129**, 546 (1982).
26. K. W. Frese, Jr., and D. G. Canfield, "Investigation of Photoelectrochemical Corrosion," SRI Annual Report, Solar Energy Research Institute, Golden, CO, May 1983.

An Ellipsometric Study of the Electrochemical Surface Modifications of n-InP

Alain Gagnaire and Jacques Joseph

Laboratoire de Physicochimie des Interfaces (U.A. 404), Ecole Centrale de Lyon, 69131 Ecully Cedex, France

Arnaud Etcheberry and Jacques Gautron

Laboratoire d'electrochimie Interfaciale du CNRS, 92190 Meudon/Bellevue, France

ABSTRACT

The cathodic decomposition of InP is studied by cyclic voltammetry and *in situ* ellipsometry. During the hydrogen evolution, an indium-rich film grows on the surface of the semiconductor. Afterward, this film undergoes transformations between oxidized and reduced forms following the electrode polarization. A theoretical model based upon a three: "InP/oxide or indium/electrolyte" or a four: "InP/oxide/indium/electrolyte" medium enables one to correctly interpret the ellipsometric data.

An electrochemical modification of the surface of a semiconductor, say, n-type, can occur just as well during an anodic reaction as a cathodic one. The former reaction, which will lead to the dissolution of the semiconductor or to the formation of an oxide on its surface, has been the most studied. These surface transformations, which can be usable, for instance, in electronics—etching (1) or the preparation of a MOS structure (2)—are, on the other hand, disastrous in a photoelectrochemical cell (3).

The cathodic reaction has mainly been used as a means to activate the semiconductor: for example, hydrogen coming from the reduction of the electrolyte can diffuse into the electrode and modify its properties. Concerning oxides, it is possible to enhance their conductivity (4) or to change their color (5). There have not been many studies published on the cathodic decomposition of semiconductors. In this last case, it seems that the nature of the products of this decomposition depends on the particular bonding of the semiconductor. Thus, for covalent compounds such as Ge and Si, the surface will be covered with hydrides (7), while it will become metallic with II-VI compounds having a strong ionic character (6). A recent study (8) shows that the decomposition of III-V compounds also yields a deposit of the metallic element. It is noteworthy that for InP in an acidic medium the metal (indium) after anodic dissolution forms a passivating film which protects the semiconductor against corrosion. This last point indicates the possibility offered by this kind of reaction to modify in a useful manner the surface of semiconductors. This is particularly interesting for InP, as its use in optoelectronics (9) and in photoelectrochemistry (10) mainly comes from its surface properties. *In situ*

methods are necessary to understand the mechanisms of such reactions. For instance, the ring-disk method can be useful in addition to cyclic voltammetry (8). However, it is necessary that the products of the decomposition go into the solution so as to be detected at the ring. On the other hand, optical methods will be directly sensitive to any surface modification at any potential. Thus, in this way, Kolb *et al.* (11) have studied the decomposition of ZnO and CdS by electroreflectance.

Here we present some results relating to cathodic modifications of InP using ellipsometry coupled with voltammetry. By this optical method we will see in particular that the indium cathodic film transforms into an oxide whose behavior is different from that of the initial oxide. This could be interesting, as we know the nature of the oxide film greatly influences the performance of InP devices.

Experimental Details

The InP single crystals are (100) oriented and have an electron concentration of $2 \times 10^{18} \text{ cm}^{-3}$. The face in contact with the electrolyte has been chemomechanically etched with a 1% bromine-methanol solution, warm methanol rinsed, and argon dried. An ohmic contact on the rear side of the electrode was made by an indium solder at 350°C in a hydrogen stream.

Cyclic voltammetry was done by means of a classical electrochemical setup already described (12). The electrolytes were prepared with "millipore" purified water and chemicals were Merck Suprapur grade. They were purged by argon bubbling. A saturated calomel electrode (SCE) served as a reference for the potential applied to the working electrode.

The optical cell was a Plexiglas cylindrical vessel with quartz windows fixed to give an angle of incidence of 70° at the mounted working electrode. The optical measurements were conducted with an automatic ellipsometer equipped with a He-Ne laser (632.8 nm). Data acquisition was made for 15 rev of the rotating analyzer, which rotates at 15 rev/s, hence averaged over 1s. The time interval between two measurements was 12s.

Just after etching and prior to any polarization, we determined by ellipsometry the thickness (d) and the optical index (n) of an equivalent layer lying on the surface of the samples ($1.6 < n < 2.0$ and $1.5 < d < 4$ nm). These values were calculated with the aid of a one-layer model, by considering this layer as transparent ($k = 0$) and by taking $n = 3.535 - i 0.308$ (13) for the index substrate. With respect to ellipsometry, the equivalent layer takes into account the residual oxide (14), the carbon contamination (15), and all the surface imperfections (16).

Results

For a better understanding of the phenomena concerning the basic electrolyte, electrochemical and ellipsometric results are presented separately.

Electrochemistry.—Figure 1 illustrates the electrochemical behavior of InP at pH 10. Three points are typical of this behavior.

1. There is one domain of potential (Fig. 1a) in which the current is stable and does not present any oxidation or reduction peaks. On the anodic side, this domain is limited by the beginning of oxidation; the corresponding potential is $V_A = -0.1V$. The cathodic limit, $V_C = -1.35V$, located in the domain of the onset of hydrogen evolution,

is such that no peak exists during the following anodic scan.

2. As soon as the electrode polarization reaches potentials more cathodic than V_C , a well-defined oxidation peak appears on the next anodic scan (Fig. 1b). After this peak, the current intensity remains almost constant until V_A . The next forward scan (anodic to cathodic) also becomes marked by a reduction peak (dashed line) located just before strong hydrogen evolution sets in (Fig. 1b).

From this point, I-V voltammograms always keep the same shape on condition that the cathodic limit remains more negative than V_C . An increase in either cathodic or anodic current only takes place after a larger number of scans (Fig. 1c) or if the working electrode is held at a potential less than V_C (Fig. 1d). It should be observed that this rise is more marked when the cathodic potential is more negative. However, the evolution of hydrogen which perturbs the optical measurements restricts the cathodic potential to around $V_{H_2} = -1.50V$.

3. This last point concerns the existence of a quasi-stable cycle (Fig. 1e). As for the one described in point 1 above, it is limited by V_A and V_C , but the current now presents two peaks, one of oxidation and one of reduction.

The stability of this cycle necessitates several potential scans during which the current diminishes. On the other hand, the form and the position of the two peaks remain unchanged.

Ellipsometry.—The surface modifications lead to a variation of the two ellipsometric parameters Ψ and Δ (15). Their evolution, which occurs during the various electrochemical polarizations (Fig. 1), has been drawn in the (Ψ , Δ) plane (Fig. 2).

Along with the electrochemical measurements discussed above, three other types of behavior can be distinguished.

1. During this first cycle, the (Ψ , Δ) variations are small and the corresponding A_0 point stays near the one obtained initially with InP covered with its residual layer.

2. When the potential becomes more negative than V_C , one observes an appreciable change of Δ , A_0 moving towards the B_1 point (solid curve). This rise is especially strong, as the thickness of the equivalent layer is large. The return to the anodic potential V_A brings back the (Ψ , Δ) point to the vicinity of A_0 , slightly above it (A_1). In a more and more distinct manner, this phenomenon happens again during the running scans, the point A_j always being located above the point A_{j-1} . It is noteworthy that now after the first cathodic scan, the major part of the variation of $\Delta(A_{j-1} - B_j)$ occurs with the reduction peak.

Finally, holding at potentials more cathodic than V_C leads not only to a rise of Δ , but also to one of Ψ . In the reverse (anodic) scan, the corresponding point A_{j+1} is located much further on A_j than the one obtained in a non-stop cycle.

3. The quasi-stable electrochemical cycle ($V_A - V_C$) described in Fig. 1e gives ellipsometric results (upper

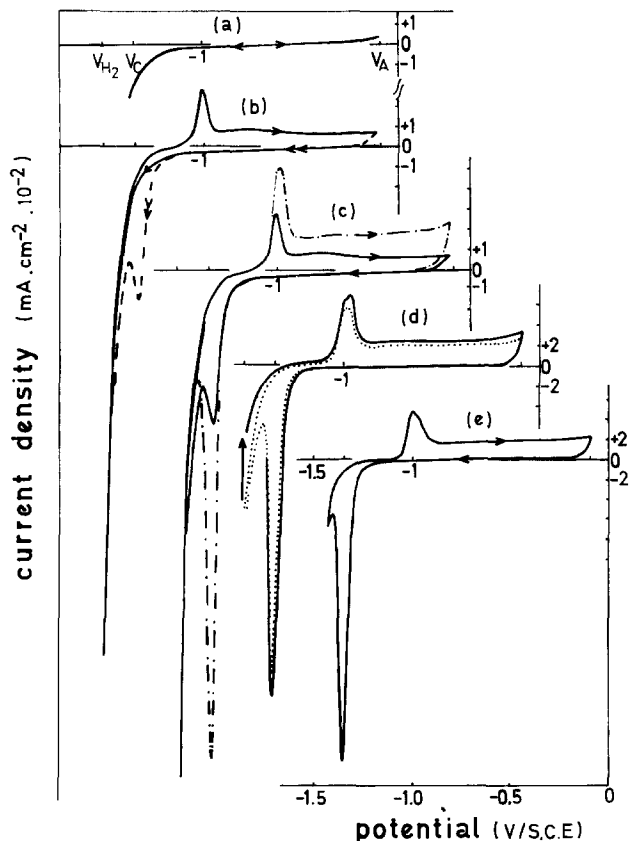


Fig. 1. I-V voltammograms of InP in aqueous medium, pH 10 (buffered solution: H_3BO_3 , KCl, NaOH); voltage sweep: 10 mV s^{-1} . a: Continuous polarization between $V_A = -0.1V$ and $V_C = -1.35V$. b: First potential excursion at $V_{H_2} = -1.50V$ followed by the immediate anodic (solid line) and cathodic (broken line) scans. c: Two " $V_A - V_{H_2}$ " cycles obtained in a time interval of 30 mn; initial (solid line), final (dot-dash) line. d: The electrode potential is kept 2 mn at V_{H_2} ; initial cycle (solid line), final cycle (dotted line). e: Quasi-reversible " $V_A - V_C$ " cycle obtained after c and d and after stabilization (see text).

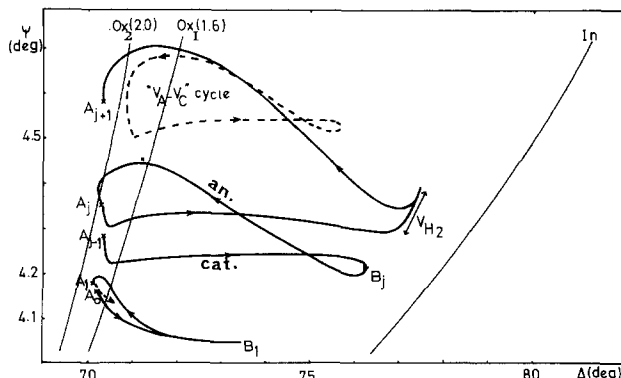
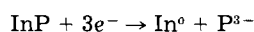


Fig. 2. Observed changes in Ψ and Δ during electrochemical cycles as described in Fig. 1. The points indicated ($A_0, B_1, A_1, \dots, A_j$) label specific steps in the process.

dashed curve, Fig. 2), which also requires a minimum delay of scanning to be stable. Note that the (Ψ , Δ) values of the extremities of the cycle are different from those attained when polarizing beyond V_C .

Discussion

The results as a whole give evidence of a surface transformation of the semiconductor which occurs during the reduction of the solvent. Keeping in mind what was recalled in the introduction, we will suppose that the cathodic decomposition of InP leads to a surface rich in indium. The position of the potential of decomposition, located just below the conduction band, thermodynamically allows (3) the following reaction



with the P^{3-} going into solution as PH_3 (17a). Note that a similar decomposition mechanism was proposed for GaAs (17b).

A primary interpretation of the ellipsometric data can be made through a simple model based upon three media: substrate/layer/electrolyte. Two cases emerge when the layer consists of oxide or of indium. Curves labeled Ox₁ and Ox₂ correspond to a transparent oxide layer for which the refractive indexes are, respectively, equal to 1.6 and 2.0. The curve labeled (In) corresponds to an indium layer on InP having an index value of $n = 1.44 - i 2.8$ (18).

The change from the Ox curve to the In curve necessitates a more complex model, one either the same as above with the intermediate layer composed of a mixture of oxides and indium, or a four-media model: InP/oxide/indium/electrolyte, where the respective part of oxide and indium can be exchanged. These various models, considering the small thickness involved, give similar results. In the following, our analysis uses the last model, which seems the more accurate to describe the surface transformations of InP. The variations of Ψ and Δ calculated from this model are reported in Fig. 3. Curves lying between "Ox" and "In" represent a growth of indium upon oxide films of different thicknesses. Note that the choice of our theoretical model is, *a posteriori*, justified as all the experimental variations of Ψ and Δ remain in an area limited by the "Ox" and "In" curves.

In order to get a better correlation between the ellipsometric and the electrochemical behavior, it is interesting to express the variations of Ψ and Δ in terms of the applied potential V (Fig. 4a and 4b).

In the course of the first scan at potential smaller than V_C , the large ellipsometric variation, which essentially concerns Δ (through a rise), indicates that a surface modification happens at the same time as hydrogen evolves. Our explanation is that the surface grows richer in indium. When returning to positive potentials, the decrease of Δ when the current becomes anodic (peak) shows an oxidation of the "cathodically activated" surface. During the following negative scans, the strong increase of Δ begins with a potential more anodic than the

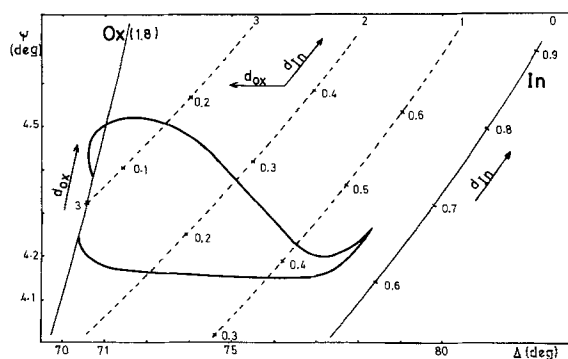


Fig. 3. Ellipsometric models. Solid curves are relative to the three-layer model: oxide or indium of constant index on InP. Dashed curves represent the four-layer model in which indium grows on InP covered with oxide of constant thickness.

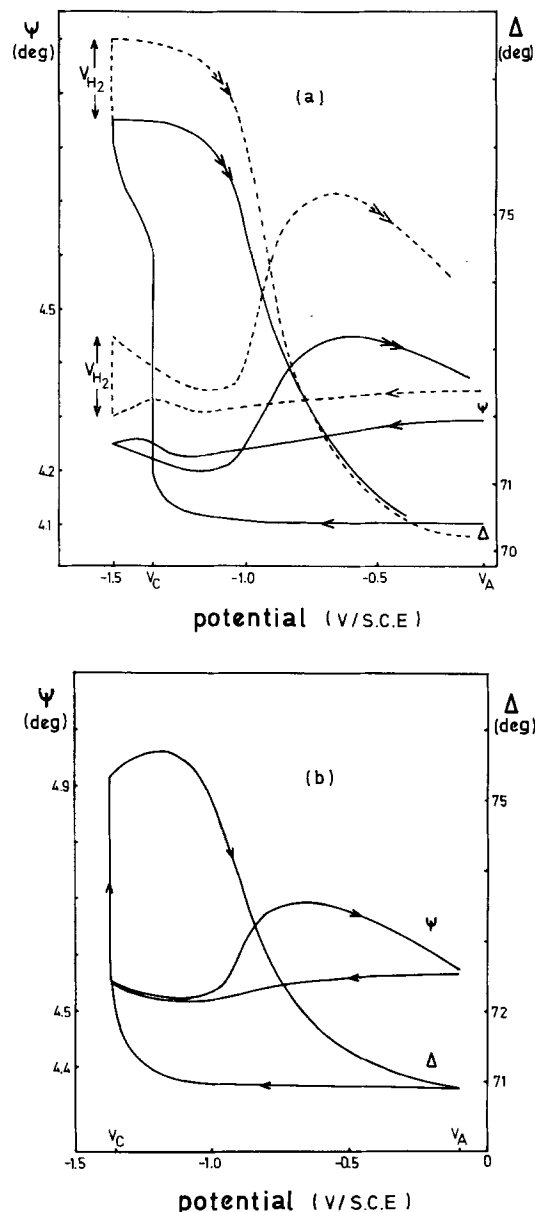


Fig. 4. Variations of Ψ and Δ with the applied potential. Top: During a complete potential sweep (solid line) and after a hold on at V_{H_2} (dashed line). Bottom: During the " $V_A - V_C$ " cycle of Fig. 1.

previous "activation" potential (Fig. 4a). This, added to the existence of a cathodic current peak, shows that indium now is formed from the reduction of the oxide previously fabricated.

If the polarization becomes more negative, a new increase of Δ occurs which is similar to the one observed in the first scan. Here the formation of indium comes from the decomposition at one and the same time of the remaining oxide and of the substrate.

Later on, the amount of indium will increase at each cathodic sweep just as does the oxide at the next anodic scan. An amplification of this phenomenon appears when the electrode is maintained at more cathodic potentials (Fig. 4a).

The quasi-stable cycles (Fig. 4b) obtained after several scans between V_A and V_C , without then reactivating the electrode, are easily explained by an oxidation reduction of the indium film. The quasi equality of the electrical charges required for the reactions, anodic as well as cathodic, indicates that there is no indium dissolution in this basic electrolyte. On the contrary, such a dissolution occurs in an acidic medium (8). The disparity in magnitudes between these cycles and those going to the decomposition implies, on the one hand, a lesser important thickness of indium, in accordance with an unreactivated elec-

trode, and, on the other hand, an oxide layer remaining below the metallic layer. This last remark means the reduction of the oxide due to a potential scan as far as V_A is not fully achieved.

The last point of this discussion concerns the nature of the oxide grown from the cathodic metal film. To answer this question, electronic spectroscopy techniques, unfortunately *ex situ*, such as ESCA, XPS, etc., will be required. However, the following observations already give one some ideas about this oxide.

First, it is different from the oxide which initially exists on the surface of InP after etching and being in contact with electrolyte. This is simply proved by the absence (Fig. 1a) and the presence (Fig. 1b) of one reduction peak. From its electrochemical and ellipsometric behavior, it is also different from the anodic oxide grown in this electrolyte at potentials slightly higher than V_A . In general, these oxides are composed of indium and phosphorus-mixed oxides, especially when thicknesses are smaller than 30Å (19). Here, on the contrary, indium is the predominant element as the oxide is grown from an indium-rich surface.

The composition of this oxide would, therefore, be close to that of In_2O_3 and most likely under a more or less hydrated form as $\text{In}(\text{OH})_3$. This is supported by the dissolution of this oxide in an acidic medium.

Conclusion

For the entire body of results, good agreement is found between ellipsometric and electrochemical measurements. Ellipsometry confirms a cathodic decomposition of InP and follows *in situ*, the oxidation and the reduction of the film coming from this decomposition. Furthermore, this optical technique gives information on the nature of the various films which cover the electrode.

This work once again shows the utility of using electrochemical reactions to modify the surface of semiconductors. Thus, with InP we were able to transform the residual layer into an indium-rich one, this latter being oxidized or reduced according to the applied potential. An extension of this process to other media, especially acidic, would offer the possibility of getting surfaces of various compositions.

Acknowledgments

We would like to thank the GRECO "semiconductor photoelectrodes" (Centre National de la Recherche Scientifique) for partial financial support of this work.

We would also like to thank Professor R. Parsons and Professor P. Clechet for their useful comments.

Manuscript submitted Nov. 8, 1984; revised manuscript received Feb. 18, 1985.

CNRS assisted in meeting the publication costs of this article.

REFERENCES

- (a) L. Hollan, J. C. Tranchard, and R. Memming, *This Journal*, **126**, 855 (1979).
(b) E. Haroutiounian, J. P. Sandino, P. Clechet, D. Lamouche, and J. R. Martin, *ibid.*, **131** 27 (1984).
- B. Schwartz and W. J. Sundberg, *ibid.*, **120**, 576 (1973).
- H. Gerischer, *J. Electroanal. Chem.*, **82**, 133 (1977).
- M. J. Madou, K. W. Frese, and S. R. Morisson, *This Journal*, **126**, 1827 (1979).
- B. W. Faughan, P. S. Crandall, and P. M. Heyman, *RCA Rev.*, **36**, 177 (1975).
- H. Gerischer, in "Physical Chemistry, An Advanced Treatise," Vol. IXA H. Eyring, Editor, Academic Press, New York (1970).
- (a) D. R. Turner, in "Electrochemistry of Semiconductors," P. J. Holmes, Editor, Academic Press, London (1962).
(b) M. F. Ehman, K. Vedam, W. B. White, and J. W. Faust, Jr., *J. Mater. Sci.*, **6**, 969 (1971).
- S. Menezes, B. Miller, and K. J. Bachmann, *J. Vac. Sci. Technol. B*, **1**, 48 (1983).
- D. L. Lile, *ibid.*, **2**, 496 (1984).
- A. Heller, B. Miller, and F. A. Thiel, *Appl. Phys. Lett.*, **38** 282 (1981).
- D. M. Kolb and H. Gerischer, *Electrochim. Acta.*, **18**, 987 (1973).
- J. Gautron, Ph. Lemasson, F. Rabago, and R. Triboulet, *This Journal*, **126**, 1868 (1979).
- D. E. Aspnes and A. A. Studna, *Phys. Rev. B*, **27**, 985 (1983).
- H. Burkhard, H. W. Dinges, and E. Kuphal, *J. Appl. Phys.*, **53**, 655 (1982).
- D. T. Clark, T. F. Fok, G. G. Roberts, and R. W. Sykes, *Thin Solid Films*, **70**, 261 (1980).
- R. M. A. Azzam and N. M. Bashara, in "Ellipsometry and Polarized Light," North Holland, Amsterdam (1977).
- (a) P. H. L. Notten, *This Journal*, **131**, 2641 (1984).
(b) F. W. Ostermayer, Jr., and P. A. Kohl, *Appl. Phys. Lett.*, **39**, 76 (1981).
- J. Bor and C. Bartholomew, *Proc. Phys. Soc. London*, **90**, 1153 (1966).
- J. F. Wager and C. W. Wilsen, *Appl. Phys. Lett.*, **53**, 5789 (1982).

Effects of Corona-Discharge-Induced Oxygen Ion Beams and Electric Fields on Silicon Oxidation Kinetics

II. Electric Field Effects

Douglas N. Modlin*

Department of Electrical Engineering, Stanford University, Stanford, California 94305

William A. Tiller

Department of Materials Science and Engineering, Stanford University, Stanford, California 94305

ABSTRACT

Using an *in situ* corona discharge ion current source directed to the front side of oxidizing silicon wafers, the effect of the electric field induced in the oxide on the back side of the wafers was studied. Oxidation enhancement was found to occur when the surface of the oxide was positive relative to the silicon. No enhancement or a slight retardation occurred for the opposite sign of field. This is exactly opposite to the effect found by Jorgensen (1), which has been traced to his use of platinum electrodes, in that the presence of the platinum dramatically influences the growth rate of the SiO_2 via the formation of an intermediate phase of platinum silicide. The results and analysis presented here support the theory that neutral O_2 is the diffusing species in the thermal oxidation of silicon.

In the early 1960's, Jorgensen (1) described an experiment wherein porous platinum electrodes were applied to a silicon sample which was subsequently oxidized. He found that the oxidation rate could be enhanced or retarded depending upon the sign of dc current flow through the electrodes. When the Si was at a positive potential with respect to the electrode, the oxidation rate was enhanced, and when it was at a negative potential with respect to the electrode, the rate was retarded. Based on this result and the results of a permeation experiment (2) also utilizing Pt electrodes, Jorgensen (1-4) deduced that a negatively charged oxygen species was the oxidant and presumed that O_2 from the gas phase entered the SiO_2 and therein acquired a negative charge. Similar results were observed a few years later by Laverty *et al.* (5), although their conclusions differed from those of Jorgensen. These findings were at variance with the findings of Deal and Grove (6) and Doremus (7), whose work supported a neutral oxidant model. Raleigh (8, 9) also criticized the conclusions of Jorgensen and provided an alternate explanation for the experimental results which was based on the superposition of an electrolytic decomposition reaction at the Si/ SiO_2 interface and the normal oxidation reaction. He also showed that no sustained oxidation was possible without electron flow in an external circuit connecting the silicon and the Pt electrode, since any nonohmically-induced field would be canceled by charge redistribution within the SiO_2 .

An even more striking variance with other oxidation results was that Jorgensen (1) and Laverty *et al.* (5) found the oxidation rate to be parabolic no matter whether the current was positive, negative, or zero; *i.e.*, no linear oxidation region was observed. In recent years, this type of totally parabolic oxidation behavior has been associated with the oxidation of silicon via an intermediate metal silicide layer (10), and theoretical analysis of oxidation under such conditions indicates why this behavior occurs (11). Thus one might suspect that perhaps Jorgensen's Pt electrodes were deposited, in part, on Si without an intervening SiO_2 layer and that his data related to oxidation via an intermediate platinum silicide layer. Since this is such an important issue in the fundamental understanding of silicon oxidation, the old experimental data need to be reexamined and new experimental evidence generated. The purpose of the present paper is to provide such new experimental data so that this issue can be put to rest.

In a companion paper (12), oxidation enhancement via the use of low energy oxygen ion beams in a neutral oxy-

gen ambient was studied for the intermediate temperature range 600°-950°C. With this new technique (13), no Pt electrodes need be placed on the wafer, as a constant-current ion beam is generated via a corona discharge between a Pt needle and a Si wafer located ~0.5 cm from the needle tip. Oxidation on the front side (FSO) of the wafer involves enhancement effects from both oxygen ions and the associated electric field, and this has already been reported on (12). Oxidation on the back side of the wafer (BSO) involves enhancement effects only from the electric field associated with the current flow, and these results will be reported upon here. Since our observations were exactly opposite to those reported by Jorgensen (1-4), we went on to explore the effects of Pt contamination on Si oxidation, and those results are also presented in this paper.

Experimental

Techniques.—The experimental apparatus and protocol used in the present study are identical to those described previously (12, 13). As can be seen in the inset of Fig. 1, the Si wafer rests on a 2.5 in. diam quartz substrate (1.6 mm thick) the bottom of which is coated with a 2 in. diam, 1 μm thick, sputter-deposited layer of Pt. The entire assembly rests on a 0.002 in. Pt sheet which is spot welded to a 0.010 in. Pt lead-in wire. This ensemble provides electrical contact to the Si sample while allowing back-side oxidation to occur. The quartz plate acts as a diffusion barrier between the Pt and the Si, yet the electrical conductivity of the quartz is sufficiently high at 900°C to pass a 10 μA current with a voltage drop of less than 100V (15). This is deemed acceptable because it is small compared to the ~1-3 kV required to generate an oxygen ion beam current of 10 μA .

Electric field effects on BSO.—The oxide thickness on the back sides of the wafers was difficult to measure with high accuracy because the wafers were usually placed on the experimental apparatus with the unpolished sides of the wafers adjacent to the quartz substrate. This was necessary because, if the polished sides were placed against the substrate, it was very difficult to remove the wafers after the corona treatment without breaking them. Apparently, the wafers stuck to the quartz substrate (which was also polished flat) after the corona treatment because (i) the oxygen between the wafers and the substrate was expelled during the corona treatment and (ii) the wafers tended to form a weak bond to the substrate. Although it was less desirable to study the unpolished surfaces, numerous control experiments without the corona showed that the oxide thicknesses measured on the unpolished sides of the wafers agreed with measurements on the pol-

* Electrochemical Society Active Member.

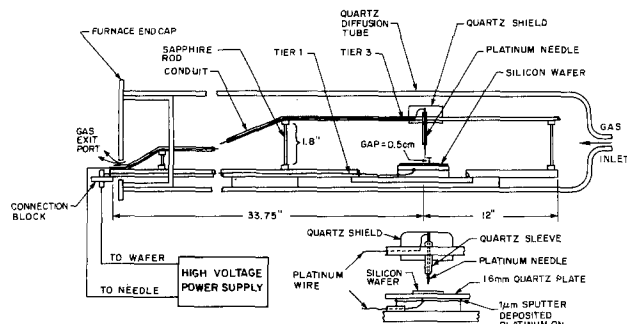


Fig. 1. Illustration of the apparatus used for generating an ion beam. The inset shows a magnified view of the ion beam generator.

ished sides to within about 2-5%. Another problem with back-side oxide thickness measurements taken after the corona treatment was that the wafer surfaces were somewhat disrupted at the points of electrical contact to the quartz substrate; however, it was found that a reasonably good ($\pm 10\%$) measurement could be made by averaging the results of 6-12 ellipsometric measurements taken in between the disrupted areas at 3-6 separate locations on the wafers.

Data obtained for Si(111) at 900°C with $I = -5$ and $-10 \mu\text{A}$ are shown in Fig. 2. Despite the obvious nonlinear effect, these oxidation curves show a significant oxidation enhancement and are seen to be parallel to those for wafers oxidized under the standard conditions. For this sign of current, the oxide surface on the back side of the wafer is positive relative to the Si. In Fig. 3, data are plotted for $I = +5 \mu\text{A}$, where the Si wafer has a positive potential compared to the quartz plate. In this case, the results are found to lie slightly below the standard dry O_2 data for 900°C , although, because of the expected scatter band of the BSO data, a firm conclusion concerning a retardation effect or a null effect does not seem to be justified. We note that these results are opposite in sign to those found by Jorgensen (1).

Platinum effects.—In order to ascertain whether or not the samples oxidized in our apparatus were contaminated with Pt from the needle or from the back-side quartz electrical contact at a level sufficient to affect the oxidation rate in the experiments of Fig. 2 and 3, the front sides and back sides of such samples were analyzed with Auger electron spectroscopy (AES), Rutherford back scattering spectroscopy (RBS), and secondary ion mass spectroscopy (SIMS). Pt presence was not indicated using any of these techniques, and we conclude that possible Pt contamination was at too low a level to have influenced the oxidation rate. This conclusion is supported by the fact that the BSO and FSO proceeded at the normal rate for $I = 0$.

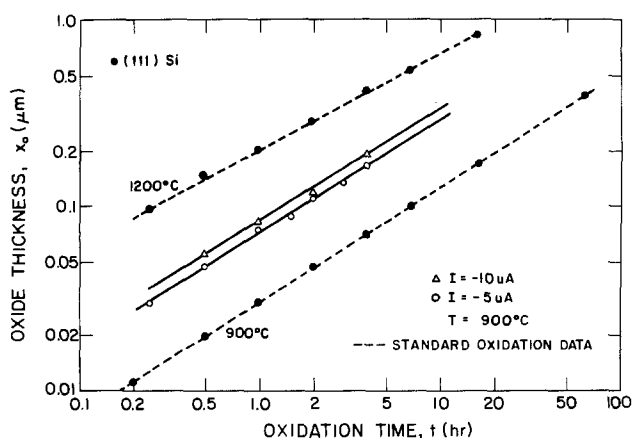


Fig. 2. Comparison of back-side oxidation for $\langle 111 \rangle$ -oriented wafers exposed to -5 and $-10 \mu\text{A}$ at 900°C to data obtained under standard conditions.

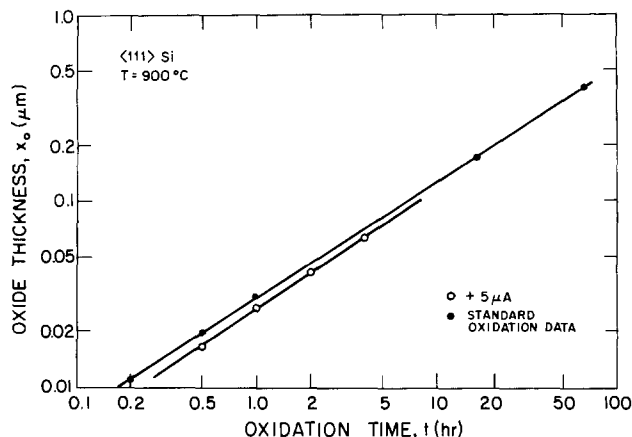


Fig. 3. Comparison of back-side oxidation data for $\langle 111 \rangle$ -oriented wafers exposed to $+5 \mu\text{A}$ at 900°C to data obtained under standard conditions.

To determine the effect on Si oxidation for deposition of Pt on an initial SiO_2 layer, an experiment was performed wherein $\sim 50\text{\AA}$ of Pt was sputter deposited on a Si(111) wafer after $\sim 300\text{\AA}$ of SiO_2 had been thermally grown at 900°C . After oxidation for 0.5h at 900°C , the Pt films were observed to "ball up," to give Pt islands ~ 500 - 1000\AA in diameter, and, after 5h of oxidation, most of the Pt islands disappeared leaving only small spots to register their prior locations. RBS spectra for the 0.5 and 5h states confirmed that a 30% decrease in Pt signal occurred at the surface after the 5h oxidation. Although most of the Pt was lost to the ambient gas as a volatile oxide after 5h, SIMS analysis¹ showed that sufficient Pt had diffused through the oxide to provide a Pt concentration of $\sim 5 \times 10^{17}$ atom/ cm^3 at the Si/SiO₂ interface.

After etching off the surface Pt, the oxide thickness was measured for various oxidation times at 900°C . To account for the original oxide layer thickness, 1h has been added to each of these subsequent oxidation times to arrive at the total oxidation time, and the data are plotted in Fig. 4. From Fig. 4, we see that the Pt does, in fact, dramatically enhance the oxidation rate over what would normally occur at 900°C . Instead of following along the 900°C standard oxidation curve, the Pt-coated samples oxidized at an accelerated rate. The back-side oxides, which were not coated with Pt, grew at the normal rate.

In an additional experiment, $\sim 50\text{\AA}$ of Pt was deposited on a Si(111) substrate containing only a native oxide layer that had been argon sputter etched for 1 min to remove only the surface monolayer. These samples were then oxidized at 850° and 900°C . Apparently, the native oxide layer was thick enough, and the Pt layer thin enough, that the

¹ The SIMS work was carried out by Charles Evans and Associates (San Mateo, California).

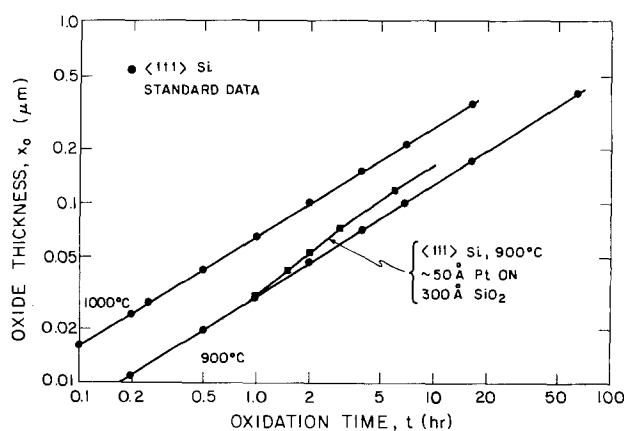


Fig. 4. Data obtained for $\langle 111 \rangle$ -oriented silicon with a 300\AA initial SiO_2 layer that was subsequently coated with $\sim 50\text{\AA}$ of Pt and oxidized at 900°C .

Pt balled up into unreacted Pt islands instead of reacting to form PtSi. It was observed that, for both $T = 850^\circ$ and 900°C , the FSO was enhanced, while the BSO proceeded at the normal rate, indicating that physical contact is needed for the catalytic action of Pt to influence the oxidation rate (see Fig. 5).

SEM studies showed that the Pt balled up on the surface in the same manner as noted for the 300\AA thick oxide. Figure 6 shows depth profiles for Pt and O^{16} obtained using SIMS on a sample oxidized for 10h at 850°C with $\sim 50\text{\AA}$ of Pt deposited on the native oxide. Here, one sees a classically shaped diffusion profile extending from the surface to the Si/SiO₂ interface with the Pt concentration increasing significantly at the Si/SiO₂ interface. Apparently, the Pt balled up into small islands which to some extent connected to PtSi in the early stages of the oxidation, thus producing the interface peak.

To test the hypothesis that the deposited Pt in the Jorgensen (1) and the Laverty *et al.* (5) experiments formed platinum silicide, the following experiment was performed at 850°C in dry O₂. After a standard chemical cleaning (13) and a 5 min sputter etch, $\sim 1200\text{\AA}$ of Pt was sputtered onto the front side of a Si(111) wafer which had previously been cut into eighths and reassembled in the sputtering chamber. The samples were placed side by side in a diffusion furnace, and the eighths were removed for testing after different oxidation times. Just prior to the oxidation step, a 20 min anneal at 850°C in ultrahigh purity argon took place to facilitate the PtSi formation.

In Fig. 7, the results of the sputter-cleaned samples (open triangles) are plotted along with the "zero field" results of Jorgensen (1) and of Laverty *et al.* (5) on a background of standard oxidation data. In addition, data for oxides grown on Si with an intermediate layer of TaSi₂ and NiSi₂ at 850°C have been included (24, 25). We note that our data, the TaSi₂ and NiSi₂ data, the Jorgensen (1) and the Laverty *et al.* (5) data, plus the standard 1200°C data, all exhibit a slope of 1/2. In addition, all the 850°C data fall fairly close to one another. Further, we note that our back-side data fall at the expected location for a standard oxidation.

Discussion

Electric field dependence of oxidation enhancement.—On the back side of the wafer, a negative electric field is developed in the oxide as a consequence of a positive ion beam incident on the front surface. In this case, we find that the oxidation enhancement is either zero or slightly negative. For the opposite situation of a negative ion beam incident on the front surface, the resulting oxide field is positive and the oxidation enhancement is strongly positive.

Since no significant Pt contamination of the Si samples from the experimental apparatus was detected using SIMS, AES, and RBS, and the BSO and FSO proceeded at the normal rate for the $I = 0$ case, we deduce that the observed electric field dependencies were not significantly influenced by Pt contamination.

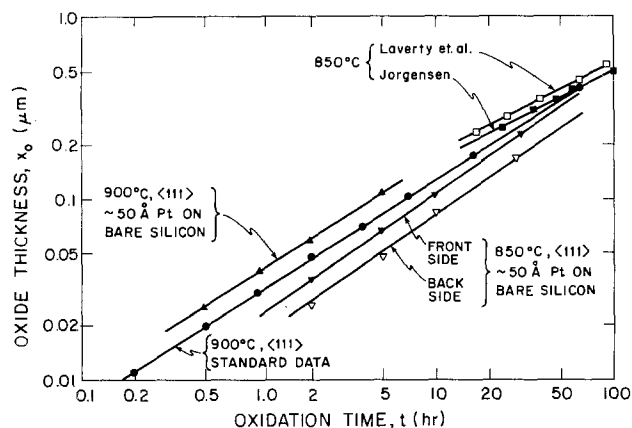


Fig. 5. Data obtained for $\langle 111 \rangle$ -oriented silicon oxidized at 850° and 900°C after an $\sim 50\text{\AA}$ Pt deposition on the native oxide.

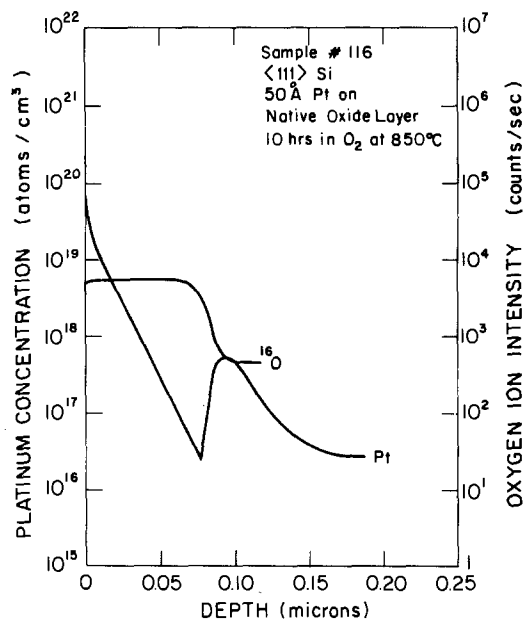


Fig. 6. Concentration profile at platinum in an SiO₂ layer grown at 850°C for 10h with a sputter-deposited layer of platinum $\sim 50\text{\AA}$ thick on the surface. The platinum was deposited onto the native SiO₂ layer.

Interpreting the Jorgensen experiments.—In his early work, Jorgensen stated that "platinum electrodes were sputtered on the silicon to a thickness of approximately 2000\AA and the SiO₂ layer was grown underneath the platinum film" (4). This is an important point, in that Jorgensen's interpretation of his results is based on the assumption that Pt films remain on top of the SiO₂ layer and do not, in any way, affect the oxidation process. However, Jorgensen's experimental protocol outlined in the above quote and much of the experimental data of this paper point to a mechanism involving oxidation via a platinum silicide layer which would have formed as soon as his samples were heated.

In the last decade or so, the reaction of Pt thin films with silicon substrates has been extensively studied due to the importance of PtSi and PtSi₂ as Schottky barriers and metallization interconnect materials in semiconductor technology (17, 18). This reaction is now known to become quite complicated, depending on experimental conditions such as purity of the starting materials, cleaning procedures, thermal history of the sample, etc. In any event, we expect that the Pt would have either reacted with the Si, remained on the surface, or both. The combination of Jorgensen's data with those presented in this paper suggests that the results of Jorgensen's experiment

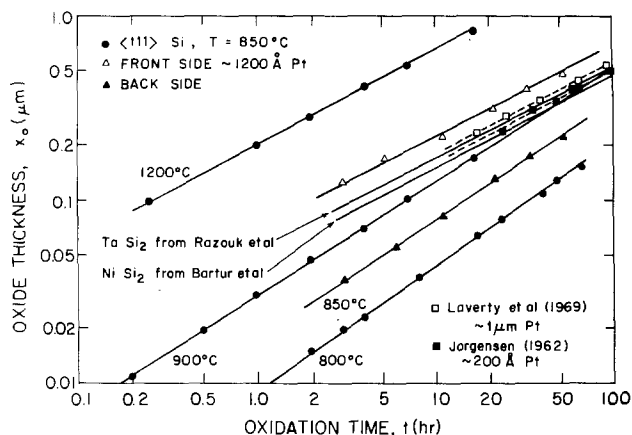


Fig. 7. Comparison of data for oxidation of PtSi obtained in our investigation to the oxidation data presented by Jorgensen and Laverty *et al.* Data for silicon, TaSi₂, and NiSi₂ oxidation under standard conditions are included for reference.

cannot be interpreted so as to deduce the identity of the diffusing species in the thermal oxidation of silicon. Since we have shown that the oxidation rate of silicon is increased via intimate contact with Pt, it is quite clear that the Pt electrodes were not inert, as was assumed by Jorgensen. This point is made rather dramatically by considering the disparity between the currently accepted distinctly "nonparabolic" oxidation at 850°C and Jorgensen's "parabolic" no-field growth rate.

The dominant diffusing species in Si thermal oxidation.—It has been repeatedly shown by radioactive tracer experiments (20-23) that the diffusing species in the thermal oxidation of Si is oxygen and not silicon. One can rule out the possibility of either O^+ or O_2^+ as the dominant form, since the ionization energy of either species is too high (it exceeds the free energy of formation of SiO_2), even though they could explain our BSO results. Hall (26) has suggested that the energy levels for oxygen ions in SiO_2 can be estimated by considering their electron affinities in vacuum. Because the electron is attached by relatively short-range forces, Hall argues that the electron affinity will be only slightly reduced in the SiO_2 lattice. Since the vacuum electron affinities for O and O_2 are ~ 1.7 and ~ 0.4 eV (27), respectively, the energy of an electron bound to either species should lie below the SiO_2 conduction band by an amount roughly equal to the electron affinity.

If Hall's assertion is correct, then the energy levels for both O and O_2 ions would be located at a level considerably above the Fermi level in the Si. The SiO_2 conduction band lies about 4.2 eV (28) above the Si conduction band at room temperature, so the energy levels for O and O_2 would be above the Fermi level in the Si by 1.95 and 3.3 eV, respectively. Hence we can conclude that it is thermodynamically unfavorable to form interstitial O^- and O_2^- species by the transport of electrons or holes across the SiO_2 layer to the SiO_2 /gas interface. Such a process would require the charged carriers to flow against the gradients of their electrochemical potentials. Any effects of the oxidizing temperature on the bandedges or on the electron energies are not expected to meaningfully alter this conclusion.

From experiment, neutral O_2 diffusion through the bulk SiO_2 layer is consistent with the linear pressure dependence of the parabolic rate constant, B , reported in the literature (29, 30). The sublinear pressure dependence reported for the linear rate constant, B/A , is consistent with dissociation, and possibly ionization, of the O_2 very near the Si/ SiO_2 interface (31, 32). Combined, this yields neutral O_2 species diffusing through the bulk SiO_2 (thickness $\approx 1300\text{\AA}$) and subsequent transformation to O or O^- at the edge of the Si/ SiO_2 interface blocking layer (33).

Measured values of the total electrical conductivity, σ_T , of SiO_2 films grown on Si can also be used to support the proposal that neutral O_2 is the dominant diffusing species. Wagner oxidation theory predicts a value for the parabolic rate constant, B , as given by (34)

$$B = \frac{kT}{N_0 q^2} \int_{P_{O_2}^i}^{P_{O_2}^0} \sigma_T t_{ion} t_{el} d(\ln P_{O_2}) \quad [1]$$

where k is Boltzmann's constant, N_0 is the atomic density of oxygen in SiO_2 , q is the electronic charge, $P_{O_2}^i$ and $P_{O_2}^0$ are the O_2 pressures at the Si/ SiO_2 and SiO_2 / O_2 (gas) interfaces, respectively, while t_{ion} and t_{el} are the transference numbers for ions and electrons, respectively. Evaluating this integral under the assumptions that t_{ion} and t_{el} are independent of the oxygen pressure and that O_2^- is the electrically active species (being consistent with the linear pressure dependence for B), one obtains an expression for B of the form

$$B = \frac{kT \sigma_T t_{ion} t_{el}}{N_0 q^2} (P_{O_2}^0 - P_{O_2}^i) \quad [2]$$

Using Wagner's (14) measured values of $\sigma_T \approx 3 \times 10^{-10} \Omega^{-1}\text{-cm}^{-1}$, $t_{ion} \approx 0.9$, $t_{el} \approx 0.1$, and $P_{O_2}^i \ll P_{O_2}^0$ at 900°C, one finds $B(1 \text{ atm}) \approx 1.2 \times 10^{-4} \mu\text{m}^2/\text{h}$, as compared to the measured value of $B(1 \text{ atm}) \approx 3.7 \times 10^{-3} \mu\text{m}^2/\text{h}$ (6, 29, 30).

Since the calculated value of B is a factor of 30 smaller than the measured value, it seems unlikely that oxygen ions could sustain the oxidation reaction at the observed rate.

Srivastava *et al.* (14) have also shown that σ_T for SiO_2 grown on Si varies with the substrate doping for room temperature substrates in the 3.3-22 $\Omega\text{-cm}$ range, whereas the oxidation rate does not, so a portion of the above-used value for σ_T comes from the substrate dopant and our value of $B \approx 1.2 \times 10^{-4} \mu\text{m}^2/\text{h}$ is an overestimate. Thus, the disparity between the measured B and our ion-origin-calculated B may be $\approx 10^2$. This calculation further supports the view that neutral O_2 is the dominant oxidant during thermal oxidation.

Conclusions

1. Electric-field-enhanced oxidation occurs when the surface of the SiO_2 is made positive relative to the silicon. No enhancement or a slight retardation occurs for the opposite sign of field. This is exactly opposite to the effect found by Jorgenson (1-4).

2. The Jorgensen results cannot be used to deduce the identity of the diffusing species in the thermal oxidation of silicon, since the Pt electrodes were not inert as assumed but, rather, dramatically influenced the oxidation kinetics via PtSi formation, etc.

3. A thermodynamic argument shows that it is energetically unfavorable to form interstitial O^- and/or O_2^- species by the transport of electrons or holes across the SiO_2 layer to the SiO_2 /gas interface.

4. Based on 1-3 above, and the fact that the parabolic oxidation rate as calculated from the Wagner oxidation theory is much too low to sustain the observed oxidation rate, it is concluded that the dominant oxidant during the thermal oxidation of Si is neutral O_2 . This conclusion applies strictly to oxides thicker than about 3000 \AA , since the growth mechanisms for thin oxides are complex and, as yet, not fully understood.

Acknowledgments

This work was supported by the Defense Advanced Research Projects Agency, Contract no. MDA 903-79-C-0257. The authors wish to thank John McBryer for his assistance with the RBS work done for this study.

Manuscript submitted May 17, 1984; revised manuscript received Oct. 24, 1985.

Stanford University assisted in meeting the publication costs of this article.

REFERENCES

1. P. J. Jorgensen, *J. Chem. Phys.*, **37**, 874 (1962).
2. P. J. Jorgensen and F. J. Norton, *Proc. Int. Congr. Glass*, **VII**, 310 (1966).
3. P. J. Jorgensen, *This Journal*, **114**, 820 (1967).
4. P. J. Jorgensen, in "Oxidation of Metals and Alloys," pp. 157-176, American Society for Metals, Metals Park, OH (1970).
5. S. J. Laverty and W. D. Ryan, *Int. J. Electron.*, **26**, 519 (1969).
6. B. E. Deal and A. S. Grove, *J. Appl. Phys.*, **36**, 3770 (1965).
7. R. H. Doremus, *J. Phys. Chem.*, **80**, 1773 (1976).
8. D. O. Raleigh, *This Journal*, **113**, 782 (1966).
9. D. O. Raleigh, *ibid.*, **115**, 111 (1968).
10. J. E. E. Baglin, F. M. d'Heurle, and C. S. Peterson, *J. Appl. Phys.*, **53**, 1849 (1983).
11. L. Lie, W. A. Tiller, and K. C. Saraswat, *ibid.*, **56**, 2127 (1984).
12. D. N. Modlin and W. A. Tiller, *This Journal*, **132**, 1163 (1985).
13. D. N. Modlin and W. A. Tiller, *Rev. Sci. Instrum.*, **55**, 1433 (1984).
14. J. K. Srivastava, M. Prasad, and J. B. Wagner, Jr., Abstract 305, p. 478, The Electrochemical Society Extended Abstracts, Vol. 83-2, Washington, DC, Oct. 9-14, 1983.
15. D. N. Modlin, Ph.D. Thesis, Stanford University, Stanford, CA (1983).
16. W. A. Tiller, *This Journal*, **127**, 625 (1980).
17. A. K. Sinha, R. B. Marcus, T. T. Sheng, and S. E. Haszko, *J. Appl. Phys.*, **43**, 3637 (1972).
18. R. Pretorius, W. Strydom, J. W. Mayer, and C. Comrie,

- Phys. Rev. B*, **22**, 1885 (1980).
19. J. D. McBrayer, R. M. Swanson, T. W. Sigmon, and J. Brauman, *Appl. Phys. Lett.*, **43**, 653 (1983).
 20. N. Karube, K. Yamamoto, and M. Kamiyama, *Jpn. J. Appl. Phys.*, **2**, 11 (1963).
 21. E. Rosencher, A. Straboni, S. Rigo, and G. Amsel, *Appl. Phys. Lett.*, **34**, 254 (1979).
 22. S. S. Cristy and J. B. Condon, *This Journal*, **128**, 2170 (1981).
 23. J. W. Rouse, C. R. Helms, and C. J. Han, "Computer-Aided Design of Integrated Circuits Fabrication Processes for VLSI Devices," TR DXG 501-82, pp. 261-276, Stanford Electronics Laboratories, Stanford University, Stanford, CA (1982).
 24. R. R. Razouk, M. E. Thomas, and S. L. Pressacco, *J. Appl. Phys.*, **53**, 342 (1982).
 25. M. Bartur and M. A. Nicolet, *Appl. Phys. Lett.*, **40**, 175 (1982).
 26. R. N. Hall, Unpublished General Electric Corporation Internal Report (1968).
 27. L. B. Loeb, "Electrical Coronas, Their Basic Physical Mechanisms," p. 18, University of California Press, Berkeley-Los Angeles (1965).
 28. R. S. Muller and T. I. Kamins, "Device Electronics for Integrated Circuits," p. 307, John Wiley and Sons, New York (1977).
 29. L. N. Lie, R. R. Razouk, and B. E. Deal, *This Journal*, **129**, 2828 (1982).
 30. H. Z. Massoud, Ph.D. Thesis, Stanford University, Stanford, CA (1983).
 31. Y. J. van der Meulen, *This Journal*, **119**, 530 (1972).
 32. R. Ghez and Y. J. van der Meulen, *ibid.*, **119**, 1100 (1972).
 33. W. A. Tiller, *ibid.*, **130**, 501 (1983).
 34. P. Kofstat, "Nonstoichiometry, Diffusion, and Electrical Conductivity in Binary Metal Oxides," pp. 96-108, Wiley-Interscience, New York (1972).

The Influence of an Electrolyte on Impedance Characteristics in n-GaP Electrodes

G. Nogami, R. Shiratsuchi, H. Nakamura, and H. Taniguchi

Department of Electrical Engineering, Kyushu Institute of Technology, Tobata-ku, Kitakyushu 804, Japan

ABSTRACT

Impedance of n-GaP electrodes was measured by using a microcomputer-aided measuring system. Mott-Schottky plots were quite dispersive. Large frequency dispersion was ascribed to the interface state which was assumed to be formed as a result of corrosion. Charging and discharging of the interface states by ions in the electrolyte were determined by charge transfer at the electrode-electrolyte interface and diffusion in the electrolyte, which could be characterized by charge-transfer resistance R_t and diffusion impedance Z_w . R_t became predominant at low ionic concentration. It is pointed out that the influence of an electrolyte must be taken into consideration in interpreting the impedance data of some kinds of semiconductor electrodes.

In developing suitable semiconductor electrodes for solar energy conversion, GaP electrodes have also been extensively investigated by many workers (1-12). However, the long-term stability of the GaP electrode, especially of the n-GaP electrode to be used at an anodic mode, is rather questionable. In such a system, the kinetic stability has been studied: anodic decomposition of illuminated n-type semiconductor is prevented by means of competing hole reactions with reducing species added to the solution (10). In discussing the kinetic stability, a full characterization of the electrode may be required. Impedance measurements are a useful tool for characterizing the electrode. Impedance measurements on this material have been made by Madou *et al.* (6). They discussed the frequency dispersion of Mott-Schottky plots on the basis of an empirical law, but they did not refer to the role of an electrolyte. Nakato *et al.* (8) have reported that surface intermediates may be formed in an n-GaP electrode by photogenerated holes. If this phenomenon should be commonly observed in this material, impedance characteristics must reflect the detailed characteristics of the electrolyte used because intermediates are formed as a result of an electrode reaction. The flatband potential in an n-GaP electrode is typically about $-1.0V$ vs. SCE. A large band bending results in a weak inversion layer where some holes are present. Surface holes contribute to the formation of the intermediates as photogenerated holes do: even at dark, some kinds of decomposition may proceed, although the rate may be quite slow. Alternatively, the hole injection from redox couples to the GaP electrode plays the same role, as suggested by several workers (1-4). In other words, intermediates may be formed when the electrode is immersed in an aqueous electrolyte.

The objective of the present study is to propose a model which enables us to detect the formation of an interface layer or intermediates by impedance measurements. It is pointed out that if there exist intermediates which can ex-

change charges (electrons) with ions in the electrolyte, the impedance of that system is influenced by a Warburg (diffusion) impedance of the electrolyte and charge-transfer resistance at the electrode-electrolyte interface.

Experimental Results

The $\langle 100 \rangle$ n-GaP wafers were supplied by Sumitomo Electric Industries, Limited. The doping concentration was $5 \sim 7 \times 10^{17} \text{ cm}^{-3}$. The wafers were mirror polished and then etched for ~ 30 s using a mixture (by volume) of six parts nitric acid one part hydrochloric acid, and one part perchloric acid. Ohmic contact was made using a Sn/In alloy which was annealed at 550°C under N_2 for 5 min (12).

A microcomputer-aided measuring system was used to obtain the impedance data. The amplitude of the ac signal across the sample was ~ 3 mV (rms). Outputs of in- and out-of phase of a dual-phase lock-in amplifier (PAR 5204) were converted into digital signals by 12 bit A/D converters (Datel ADC HZ-12BGC). Resultant data were stored and analyzed by an NEC PC 8001 microcomputer. This system permitted a quick measurement and supplied many more data than a usual system did. Capacitance C and resistance R in a series equivalent circuit diagram and capacitance C_p and conductance G in a parallel equivalent circuit diagram, as well as the modulus and phase of impedance, were quickly printed out. About 30 samples were studied. Figure 1 shows the typical current-voltage curve under a chopped light illumination of $\sim 60 \text{ mW/cm}^2$. Light source used was a 150W Xe lamp. The electrolyte was 0.1M KOH solution. All samples studied showed approximately the same J-V characteristics as Fig. 1. Dark current was low, implying that thermal generation rate of holes at the electrode surface was very low. Anodic dark current was also caused by electron transfer from the electrolyte to the semiconductor bulk via intermediates or surface states. Low dark current implies that electron-

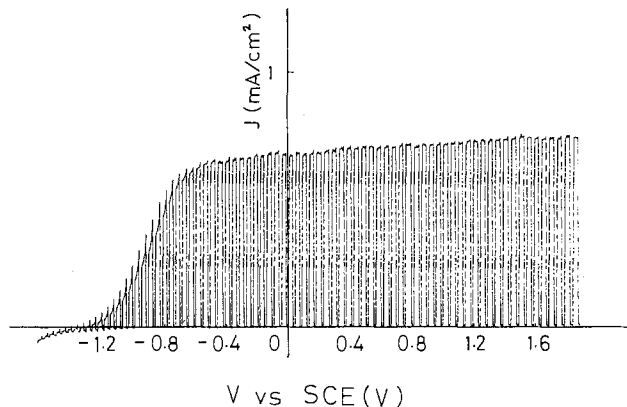


Fig. 1. Current-voltage characteristics for the N-GaP 6, under a chopped light illumination of $\sim 60 \text{ mW/cm}^2$. The electrolyte used was 0.1M KOH solution.

transfer rate is very low. This fact is suggestive in considering the equivalent circuit diagram.

Impedance characteristics differed from sample to sample, even though they were subjected to the same experimental conditions. All samples studied showed, more or less, a large frequency dispersion in Mott-Schottky plots. Figure 2 shows the Mott-Schottky plots for the same sample (N-GaP 6) as in Fig. 1. The slopes are much smaller than that expected from the doping concentration (a dotted line). Each slope gives nominal large doping concentration: the doping concentrations estimated from the slopes were larger than that specified by the supplier ($5 \sim 7 \times 10^{17} \text{ cm}^{-3}$) by a factor of $30 \sim 50$. Moreover, the intersections of the C^{-2} -V plots with the V axis do not converge to a common point on the V axis.

By replotting the data in Fig. 2, we obtain the Bode plots; Fig. 3 shows the modulus and phase of the impedance against frequency with an external bias as a parameter. Figure 4 shows the pH dependence of the Bode plot for a freshly prepared sample. It is clearly seen that impedance is largely influenced by ionic concentration in the electrolyte. There are two characteristic regions at pH 13 and 1. The slope of the $\log |Z|$ vs. f plot is ~ -1 at low

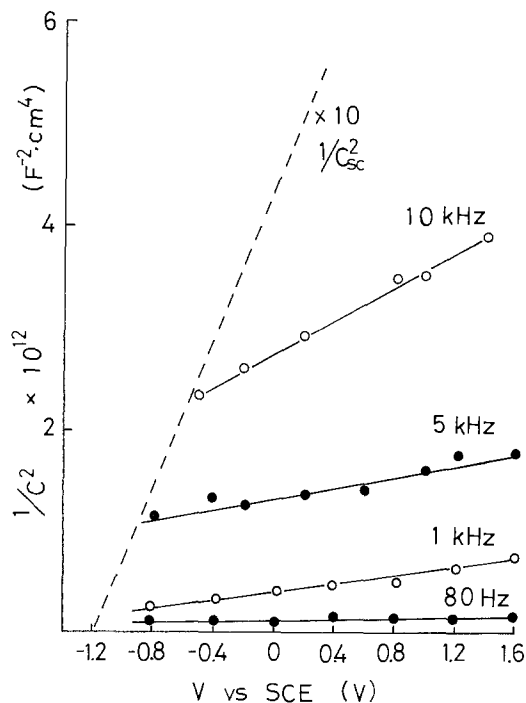


Fig. 2. Mott-Schottky plots for the same sample as in Fig. 1. Series equivalent capacitance C was plotted. The slope of the dotted line reflects the real doping concentration. The flatband potential is estimated from the turn-on potential in the J - V curve (Fig. 1).

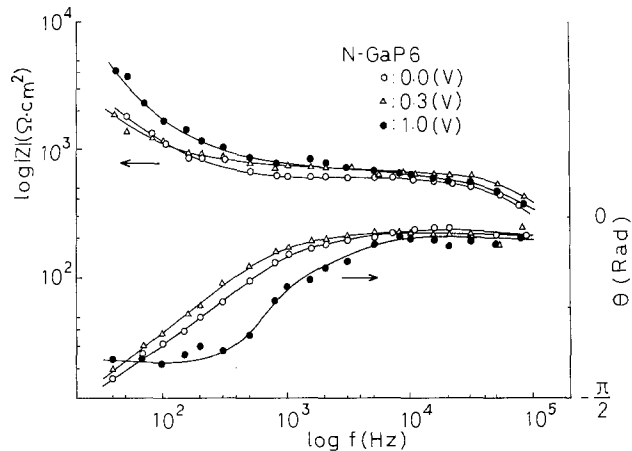


Fig. 3. Bode plots for the N-GaP 6 with an external bias as a parameter.

frequencies where phase angle is ~ 90 , and lower than $-1/2$ at high frequencies where phase angle approaches zero.

Figure 5 depicts the temperature dependence at pH 10.0. After measurements at 70°C , the sample turned deep yellow, implying that the surface structure may change drastically. This fact implies that some sort of decomposition occurs even at dark: elevated temperature promoted the rate of reaction. Figure 5 shows that the Bode plot at 70°C differs from that at low temperatures. As is discussed below, resistance R_s , which characterizes the relaxation time of the interface state, may increase as a result of formation of the surface layer.

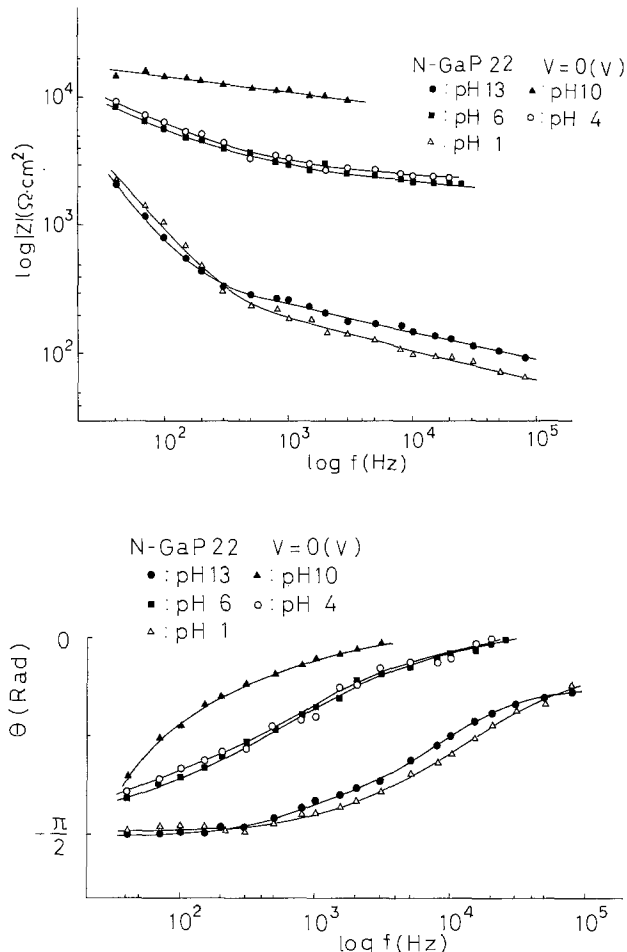


Fig. 4. pH dependence of Bode plots at 0 V vs. SCE for a freshly prepared sample (N-GaP 22).

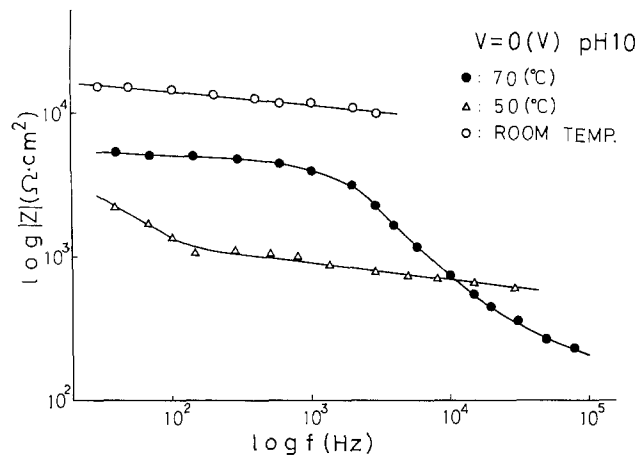


Fig. 5. Temperature dependence at 0 V vs. SCE and pH 10.0 (N-GaP 22).

Discussion

Impedance measurements offer a useful tool for evaluating a semiconductor electrode. However, interpretation for a Mott-Schottky plot in a semiconductor-electrolyte contact is based on the theory applicable to a metal-semiconductor contact. Any type of capacity in the electrolyte is usually neglected in the equivalent circuit because it is so large. The present results suggest that impedance characteristics in a semiconductor-electrolyte contact cannot be explained, at least in an n-GaP electrode, unless the effects of the electrolyte are taken into consideration.

There have been proposed several possible mechanisms which cause large frequency dispersion in $C-V$ characteristics (14, 15): nonuniform current distribution (due to edge effects, surface roughness, etc.), residual faradaic process, surface states, and the frequency dispersion of the dielectric constant. However, these mechanisms cannot explain, in the authors' opinion, the observed large frequency dispersion which gives one or two orders of magnitude larger (nominal) doping concentration.

One of the authors (G.N.) has proposed a new idea which can explain the above-mentioned phenomenon (16, 17): charging and discharging of the interface states, distributing rather deep into the semiconductor bulk, by ions in the electrolyte cause large frequency dispersion in $C-V$ characteristics. The basic idea is that the interface states are in quasi equilibrium with the Fermi levels of the semiconductor and electrolyte. Figure 2 clearly shows that the conventional interpretation for a dispersive Mott-Schottky plot could not be applicable to our system. Hence, we try to apply the model proposed elsewhere (16, 17): the equivalent circuit as shown in Fig. 6 is considered here. In Fig. 6, the deep interface state, the penetration length of which is 300\AA or more, is assumed; the depletion layer width of our system [$N = 6 \times 10^{17} \text{ cm}^{-3}$, $\epsilon = 10.2 \epsilon_0$ (18)] is typically $200 \sim 300\text{\AA}$ with a band bending of $1 \sim 2 \text{ eV}$.

The assumption of the interface state which distributes in the forbidden gap is rather speculative, but it is possible that the surface structure may be drastically altered by corrosion. In fact, as mentioned above, the sample turned deep yellow after measurements at 70°C , implying that the atomic composition at the surface changed drastically. Elimination of atoms, for example, Ga atoms, from the electrode surface may result in a rearrangement of energy levels: the introduction of new levels into the forbidden gap is likely to occur. The energy level of the interface state is also unknown. The fact that $C^{-2}-V$ plots are dispersive at the very vicinity of the flatband potential implies that the energy level of the interface state may be rather shallow: the level seems to lie just below the bulk Fermi level (17, 19).

In Fig. 6, C_w and R_w are diffusion capacitance and resistance, respectively, while R_t is the charge-transfer

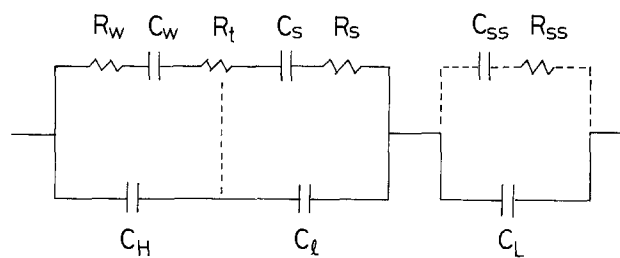


Fig. 6. The equivalent circuit used in the interpretation of the experimental results.

resistance. R_t gives a measure of a rate of charge exchange between the electrolyte and the interface states. Charging and discharging of the interface states by the ions (for example, OH^- or H^+) in the electrolyte can take place as the following reactions: for discharging, electrons must be transferred from the interface state to the electrode surface (R_s), then transferred to the ions (R_t), and finally the reaction products must diffuse away into the bulk of the electrolyte (R_w). The rate-determining step will determine the impedance characteristics.

The product of C_s and R_s shows the relaxation time of charging and discharging of the interface states by ions in the electrolyte. The product of C_{ss} and R_{ss} shows the additional relaxation time of charging and discharging of the interface states by electrons in the semiconductor bulk. This branch becomes effective if the energy level of the interface state is shallow. One may ask if a parallel branch of C_{ss} and R_{ss} might result in large dark current. It is noteworthy here that the interface state has different effects on $C-V$ and $J-V$ characteristics. If we consider the case where anodic dark current is caused by the electron transfer from the electrolyte to the semiconductor bulk via interface states, we must assume a constant and high electron-transfer rate in order to explain large dark current. On the contrary, the limited amount of charges can cause large interface state capacitance C_{ss} , because they only swing to and fro in accordance with the small amplitude ac signal. Relaxation times $R_s C_s$ and $R_{ss} C_{ss}$ are both constant and independent of an external dc bias in the present configuration (19). Observed large frequency dispersion (Fig. 2) implies that both mechanisms might be operative. An equivalent circuit diagram as shown in Fig. 6 predicts quite an interesting phenomenon that the total capacity of that system can exceed the Helmholtz capacity ($50 \mu\text{F}/\text{cm}^2$ or more) if C_w , C_s , and C_{ss} are large. In the present analysis, however, we assume for simplicity that $R_{ss} C_{ss}$ is large enough: electron transfer between the interface state and the semiconductor bulk is assumed to be negligible. This assumption will not alter the following conclusions.

Charge-transfer resistance R_t depends on concentration of electrolyte through the exchange current density i_0 (20)

$$R_t = \nu RT/nF i_0$$

where n and ν are the electrode reaction valence and stoichiometric factor, respectively. R_t is also dependent on temperature because i_0 is determined by a Boltzmann factor. R_t is independent of frequency, if the amplitude of the ac signal is small enough. The diffusion (Warburg) impedance Z_w is typically given by

$$Z_w = R_w (1 - j)$$

where

$$R_w = 1/\omega C_w = RT\nu^2/n^2 F^2 C (2\omega D)^{1/2}$$

with D being the diffusion coefficient. R_w depends on temperature, frequency, concentration, and diffusion coefficient. D is also determined by a Boltzmann factor: D increases and then R_w decreases with temperature. If we assume that $C_H \gg C_L$, then the impedance of our system is given by

$$Z = \frac{1}{j\omega C_L} + \frac{1 + j\omega\tau_{ws}}{j\omega C_{ws} (1 + j\omega\tau_{ws})}$$

where $C_{wsl} = C_1 + C_{ws}$, $C_{ws} = C_w C_s / (C_w + C_s)$, $\tau_{ws} = RC_{ws}$, $\tau_{wsl} = RC_{wsl} / C_{wsl} = \tau_{ws} C_1 / C_{wsl} < \tau_{ws}$, and $R = R_w + R_t + R_s$. Two inflecting points in the Bode plot, f_l and f_h , are given by $1/\tau_{ws}$ and $1/\tau_{wsl}$, respectively.

At low frequencies, $\omega\tau_{wsl} < \omega\tau_{ws} \ll 1$; then we obtain

$$|Z| = \frac{1}{\omega} \left(\frac{1}{C_L} + \frac{1}{C_{wsl}} \right), \quad \theta = -\frac{\pi}{2}$$

If $C_w \gg C_s$, the slope of the $\log |Z|$ vs. f plot will precisely equal -1 . At intermediate frequencies, where $\omega\tau_{wsl} < 1 < \omega\tau_{ws}$, we obtain the following relationships under the assumption of $1/\omega C_L \sim 0$

$$|Z| = \frac{C_{ws}}{C_{ws} + C_1} R; \quad \theta = 0$$

At high frequencies, $1 \ll \omega\tau_{wsl} < \omega\tau_{ws}$,

$$|Z| = \frac{1}{\omega C_1}; \quad \theta = -\frac{\pi}{2}$$

Characteristic features of our system can be found at intermediate frequencies, where $|Z|$ depends on $R = (R_t + R_s) + R_w$; R_t and R_s are independent of frequency, while R_w depends on $\omega^{-1/2}$, and R_t corresponds to a differential resistance. Hence, the assumption that R_t is independent of frequency may be incorrect if the amplitude of the ac signal is large. We assume here that the amplitude of 3 mV rms used is small. Then the slope of a Bode plot at intermediate frequencies may range from 0 to $-1/2$ as typically found in Fig. 4. The inflecting point in Fig. 4 may therefore correspond to f_l ; the higher inflecting point f_h could not be observed in the frequency range used. Considering these situations, we will obtain the schematic Bode plots as shown in Fig. 7. We can see some characteristics in Fig. 7. Charge transfer and diffusion impedance become predominant at low ionic concentrations, so that the resultant Bode plot may show gradual change. At high temperatures or high ionic concentrations, both R_w and R_t become low so that the impedance of the semiconductor electrode becomes comparable with them. The slopes of the Bode plot may range from -0.5 to -1 at low frequencies where R_w and the reactance component of the electrode are comparable (16), and from 0 to -0.5 at intermediate frequencies where R_w and $(R_t + R_s)$ are comparable.

R_s determines the relaxation time of charging and discharging of the interface states. R_s is easily expected to be sensitive to the past history of the electrode. Hence, R_s may differ from sample to sample. Some samples may have large R_s and others small R_s . This may be the reason why the N-GaP 6 (Fig. 3) and N-GaP 22 (Fig. 4) show different impedance characteristics. The inflecting points in

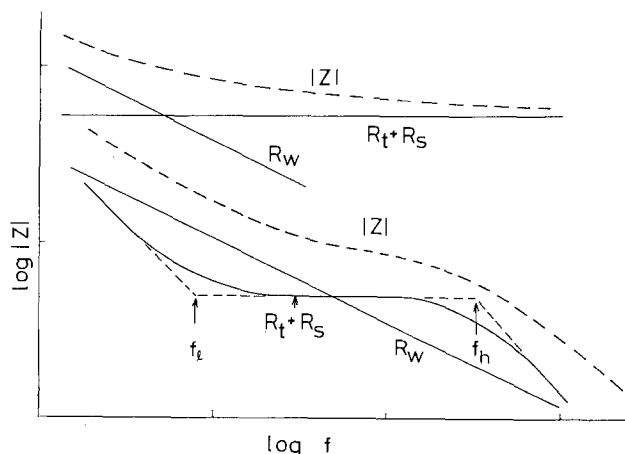


Fig. 7. Schematic Bode plots for the charge-transfer resistance R_t , diffusion resistance R_w , and R_s .

the $\log |Z|$ vs. f plot, f_l and f_h , are also dependent on R_s . Increase in R_s will result in lowering of f_l and f_h . If R_s increases as a result of the formation of the defective surface layer, f_l will disappear and f_h will appear, as typically found in the Bode plot at 70°C (Fig. 5). The surface layer may be formed due to accelerated reaction rate at 70°C.

There are some differences between the present results (for n-GaP) and the preceding ones [n-TiO₂ (16)]. In TiO₂ electrodes, appreciable influences of the charge-transfer resistance R_t on the impedance characteristics could not be found, although the electrolyte used was sufficiently high (1M KOH): the slopes of the Bode plots ranged from -0.5 to -1 , which was explained by considering the diffusion resistance R_w only. The present result suggests that a charge-transfer resistance must also be taken into consideration in interpreting the impedance data, especially at low ionic concentrations.

Conclusions

A computer-aided measuring system enabled us to collect quickly a great number of data. Rather corrosive n-GaP electrodes have shown a variety of interesting C-V characteristics. Temperature and pH dependences of C-V characteristics have clearly shown that the effects of the electrolyte must be taken into consideration in order to explain the impedance characteristics of the electrolyte/n-GaP interface. In the present study, too, we could not find the role of the Helmholtz capacitance. In general, impedance characteristics of the electrolyte-electrode interface are determined by the charge transfer and dielectric response. The latter contributes to the Helmholtz capacitance which is determined by the dielectric constant of the electrolyte. The present result may imply that the impedance characteristics of the electrolyte/n-GaP interface may be controlled by the charge transfer between the electrolyte and intermediates at the electrode surface.

It has been confirmed in some detail that intermediates are certainly formed in the n-GaP electrodes: intermediates are interpreted here as the interface states.

Acknowledgment

We are grateful to Dr. S. Iguchi of Sumitomo Electric Industries, Limited, who has kindly supplied GaP wafers.

Manuscript submitted July 19, 1984; revised manuscript received Feb. 8, 1985.

REFERENCES

1. R. H. Memming and G. Schwandt, *Electrochim. Acta*, **13**, 1299 (1968).
2. K. H. Beckmann and R. Memming, *This Journal*, **116**, 368 (1969).
3. R. Memming, *ibid.*, **116**, 785 (1969).
4. B. Pettinger, H. R. Schoppel, and H. Gerischer, *Ber. Bunsenges Phys. Chem.*, **80**, 849 (1976).
5. L. A. Harris, M. E. Gerstner, and R. H. Wilson, *This Journal*, **124**, 1511 (1977).
6. M. J. Madou, F. Cardon, and W. P. Gomes, *ibid.*, **124**, 1623 (1977).
7. M. A. Butler and D. S. Ginley, *ibid.*, **127**, 1273 (1980).
8. Y. Nakato, A. Tsumura, and T. Tsubomura, *ibid.*, **127**, 1502 (1980); **128**, 1300 (1981).
9. G. Horowitz, *Appl. Phys. Lett.*, **40**, 409 (1982).
10. D. Vanmaekelbergh, W. P. Gomes, and F. Cardon, *This Journal*, **129**, 546 (1982).
11. D. S. Ginley and M. B. Chamberlain, *ibid.*, **129**, 2141 (1982).
12. W. J. Albery and P. N. Bartlett, *ibid.*, **129**, 2254 (1982).
13. S. R. Morrison, "Electrochemistry at Semiconductor and Oxidized Metal Electrodes," Chap. 7, Plenum Press, New York (1980).
14. M. Tomkiewicz, *This Journal*, **126**, 1505, 2220 (1979).
15. S. Schoonman, K. Vos, and G. Blasse, *ibid.*, **128**, 1154 (1981).
16. G. Nogami, *ibid.*, **132**, 76 (1985).
17. G. Nogami, Submitted to *This Journal*.
18. Shionoya, in "Luminescence of Inorganic Solids," P. Goldberg, Editor, p. 205, Academic Press, New York (1966).
19. G. Nogami, *This Journal*, **129**, 2219 (1982).
20. K. J. Vetter, "Electrochemical Kinetics," Academic Press, New York (1967).

Effect of Trace Elements on Etching of Aluminum Electrolytic Capacitor Foil

K. Arai, T. Suzuki, and T. Atsumi

Showa Aluminum Corporation, Research and Development Laboratory, Sakai, Osaka, Japan

ABSTRACT

An investigation was made as to the effect of trace impurities, particularly bismuth and boron, on etching morphology and capacitance of aluminum electrolytic capacitor foil. It was found that as little as 2 wt-ppm bismuth in foil strongly accelerated surface etching, inhibited tunneling, and consequently lowered capacitance. 3 wt-ppm boron also enhanced surface etching, but lowered capacitance less than bismuth. The reason for these results was considered

Etching of aluminum electrolytic capacitor foil is generally performed in hydrochloric acid (1) or sodium chloride solution (2). The capacitance of aluminum electrolytic capacitors is mostly determined by etching. Since impurities contained in aluminum markedly influence etching, it is essential to control them in order to manufacture excellent aluminum electrolytic capacitor foil. A number of studies (3-12) on the effect of impurities or alloying elements contained in aluminum have been reported.

We have found that trace bismuth or boron in aluminum greatly influenced etching morphology. Herein we report the effect of these elements on etching morphology and capacitance.

Experimental

Sample preparation.—The samples used were three kinds of 99.99% aluminum foils, manufactured by conventional semicontinuous casting, 0.1 mm thick annealed at 823 K for 1h in a dry inert gas (Ar) atmosphere. Table I shows the chemical compositions of these samples. Sample A contains iron, silicon, copper, and 2 wt-ppm bismuth. Sample B contains iron, silicon, copper, and 3 wt-ppm boron, and sample C contains only iron, silicon, and copper. Sample C is the standard. Anodic stripping voltammetry, atomic absorption spectrophotometry, and absorption spectrophotometry were used as the methods to analyze these samples.

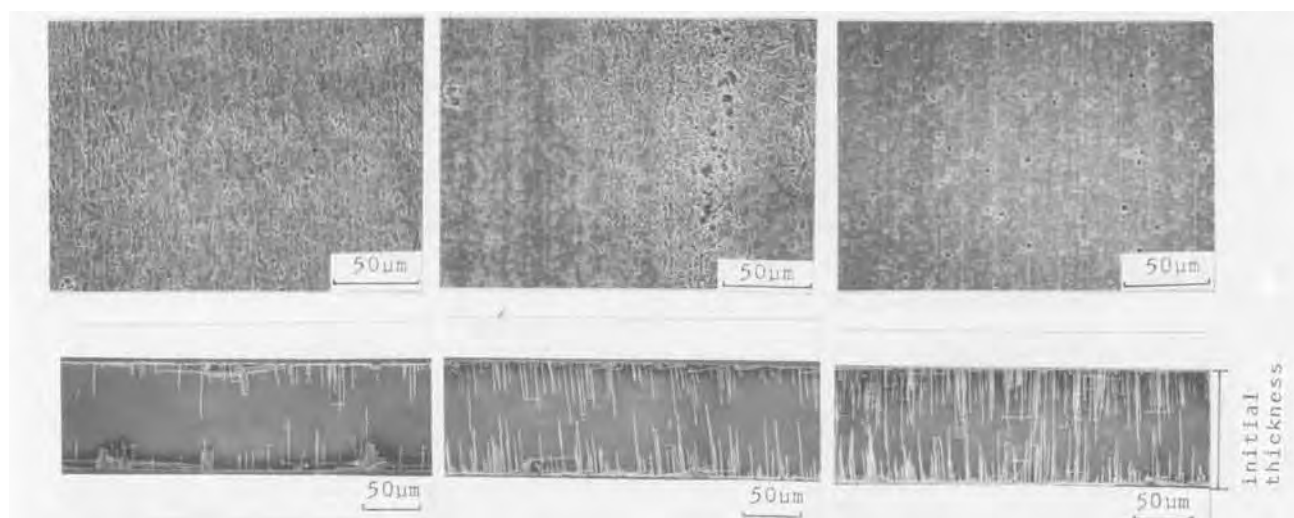


Fig. 1. SEM photographs of surface (top row) and cross section (bottom row) after 30s etching. First column: sample A. Second column: sample B. Third column: sample C.

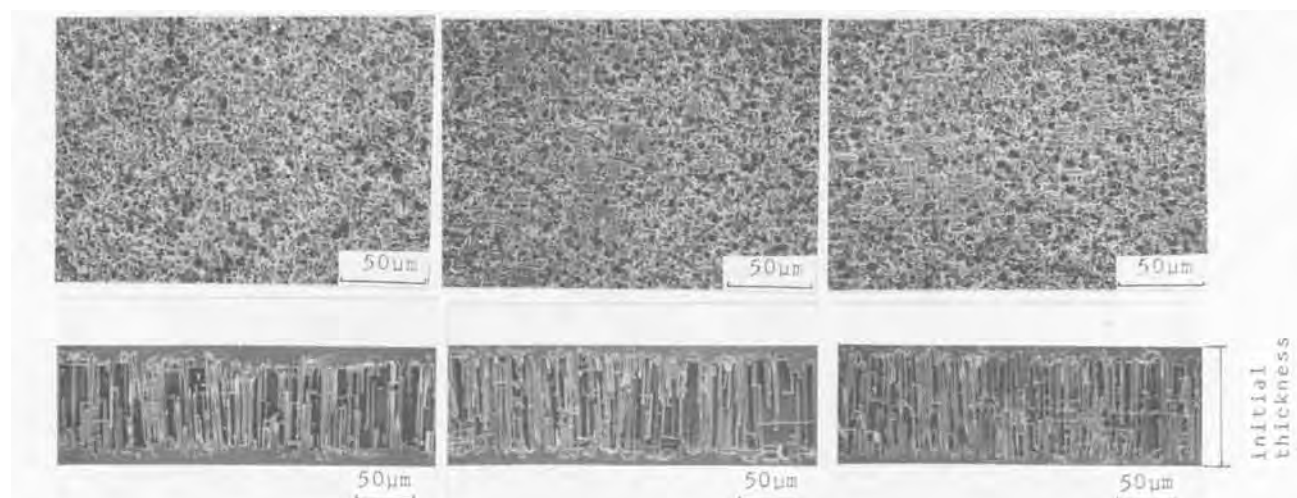


Fig. 2. SEM photographs of surface (top row) and cross section (bottom row) after 630s etching (first and second etching). First column: sample A, capacitance = 1.60 F-V/m². Second column: sample B, capacitance = 1.97 F-V/m². Third column: sample C, capacitance = 2.50 F-V/m².

tion shows, the surface of sample A was dissolved the most, so the foil thickness of sample A was reduced.

At the final etching, these tendencies remained the same. The tunneling density decreased in order from C to B to A. On the other hand, the degree of surface dissolved was decreased in order from A to B to C. Accordingly, the capacitance of sample C was the highest, that of sample B, containing trace boron, was next, and that of sample A, containing trace bismuth, had the lowest capacitance of all samples. In 99.99% Al as electrolytic capacitor material, it was found that trace bismuth and boron in aluminum greatly influenced the etching morphology and capacitance.

Depth profiles by an IMA.—To resolve the existent state of trace bismuth and boron in aluminum, depth profiles were measured by an IMA. Figure 3 shows bismuth depth profiles of sample A containing bismuth and of sample C not containing bismuth addition after annealing at 823 K for 1h. The longitudinal axis in Fig. 2 indicates ion intensity, while the transverse axis indicates sputtering time by Ar ion and the corresponding distance from the oxide-metal interface. The sputtered depth was measured by means of a Talystep instrument (Rand Taylor Hobson Corporation) with maximum resolving power of 0.5 nm. The position of the oxide-metal interface was estimated from the total ion curve because the efficiency of ionization at the oxide layer is much higher than at the aluminum substrate (13). In sample A, the peak of concentrated bismuth is in the aluminum substrate near the oxide layer. However, the peak in sample C was very low. It appears that bismuth atoms are concentrated at the metal-oxide interface by annealing at 823 K for 1h.

Next, bismuth depth profiles at various temperatures were measured to study the behavior of bismuth during annealing. The results are shown in Fig. 4. Reports con-

cerning diffusion of bismuth atoms in aluminum have not appeared, but the study of surface segregation in aluminum-based dilute alloys has been reported (14, 15). It is suggested that solute atoms in a metal are concentrated at the surface by annealing.

Figure 5 shows iron depth profiles of samples A and C. In samples A and C, the iron content is almost the same; the height of the iron peak after annealing at 823 K for 1h is also the same. Iron was concentrated at the metal-oxide interface.

Figure 6 shows magnesium depth profiles of samples A and C. Magnesium was concentrated at the outer surface, unlike iron. This fact agrees with measurements made using Auger spectroscopy (15). In samples A and C, the magnesium content is less than 1 wt-ppm. However, magnesium easily concentrated at the surface by annealing, and there was no difference in the degree of concentration in samples A and C.

Reliable results for the other principal elements, silicon and copper, could not be obtained because of the low sensitivity of the IMA and the existence of interfering elements. The difference of etching morphology between A and C (Fig. 1 and 2) is not due to the concentration of iron and magnesium on the surface.

The grain size of each sample was of about 50-200 μm diam, and there were minimal differences between the samples. The texture of each sample, which affects its capacitance sensitivity, particularly cube texture, developed remarkably. However, the differences of cube texture were minimal.

Therefore, it is thought that the difference in bismuth between samples A and C caused the difference in the etching morphology and capacitance; that is, concentrated bismuth on the surface reacts nobly to aluminum. It was thought that if the surface layer in sample A, which contains much Bi, was removed, then capacitance similar to that of sample C should be obtained. However, we

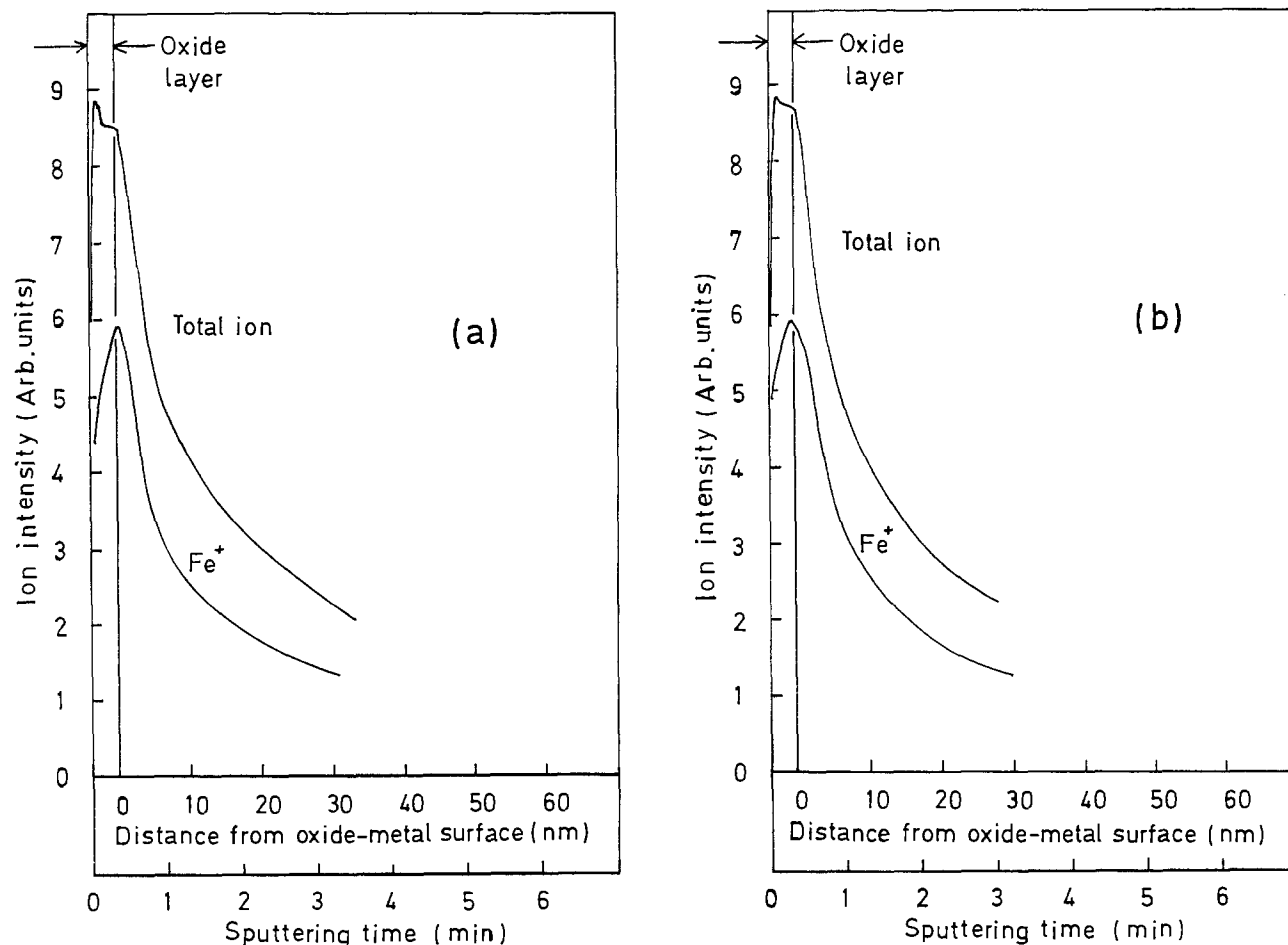


Fig. 5. Iron depth profiles in (a) sample A and (b) sample C after annealing at 823 K for 1h

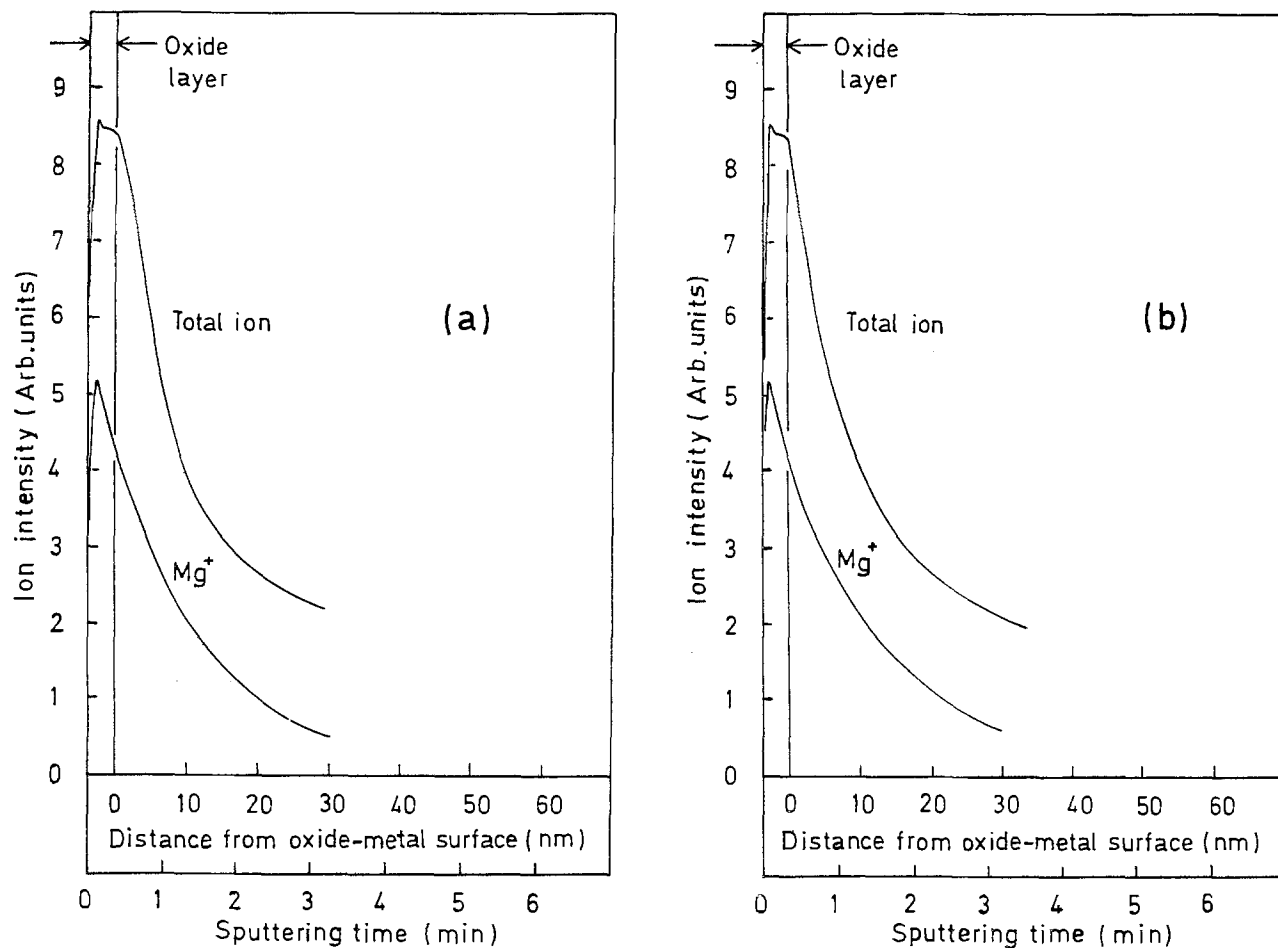


Fig. 6. Magnesium depth profiles in (a) sample A and (b) sample C after annealing at 823 K for 1h

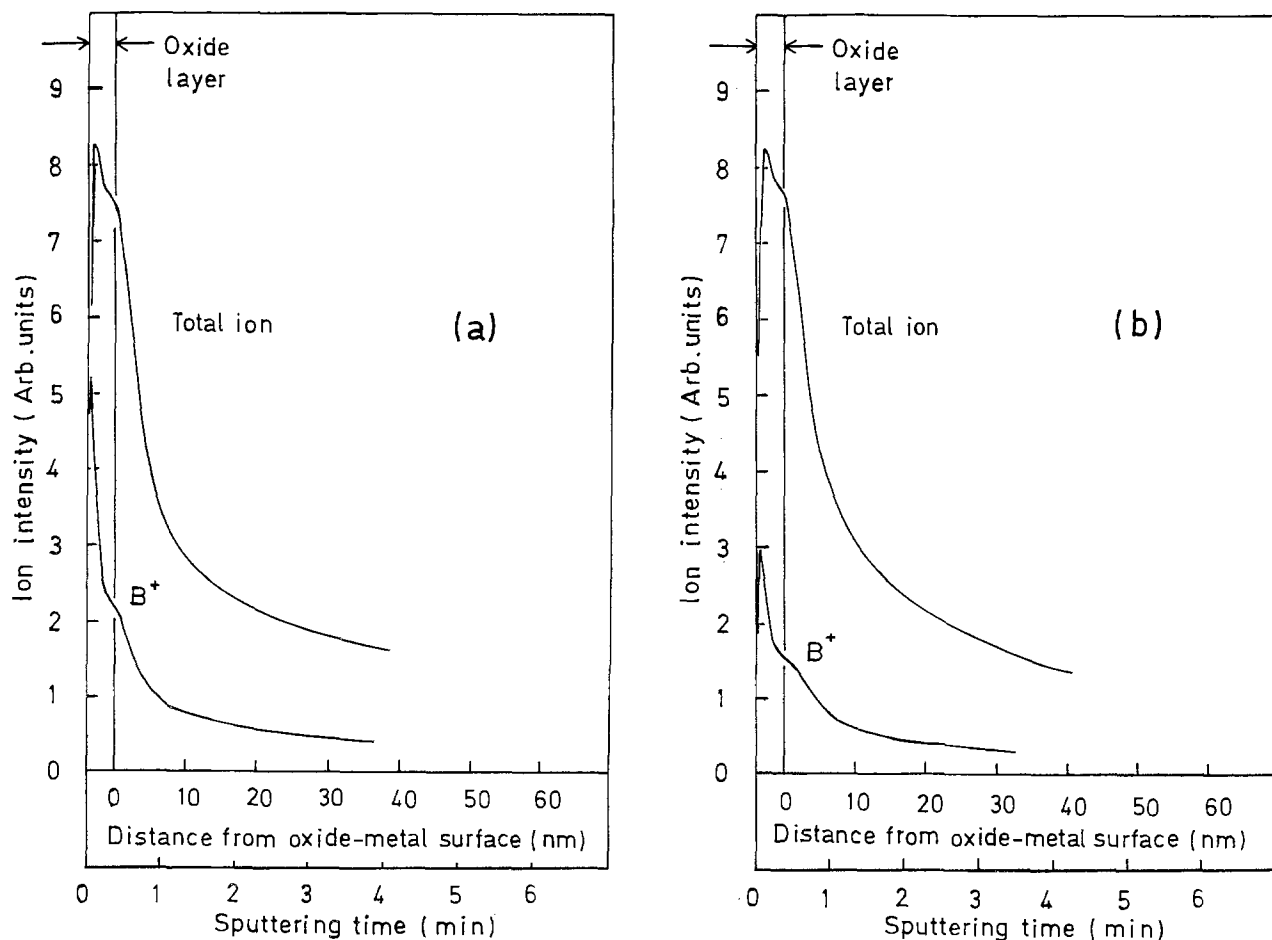


Fig. 7. Boron depth profiles in sample B. a: Strong surface etching part. b: Normal homogeneous part after annealing at 823 K for 1h

could not make such a comparison because the etching morphology of the sample when the surface layer was removed, was not uniform and was unlike either of the original samples.

Figure 7 shows boron depth profiles of both the normal etching and the portion of strong surface etching in sample B containing 3 wt-ppm boron. The concentration peak of the portion with strong surface etching was higher than that of the portion with normal etching, and boron was concentrated at the outer surface in both portions, in a manner similar to the behavior of magnesium in aluminum (Fig. 6). It is thought that the difference in surface boron concentration caused the difference in etching morphology.

Acknowledgment

The authors would like to thank Dr. Robert S. Alwitt at United Chemi-Con, Incorporated, for his valuable advice and assistance.

Manuscript submitted July 16, 1984; revised manuscript received Sept. 17, 1984. This was Paper 95 presented at the Minneapolis, Minnesota, Meeting of the Society, May 10-15, 1981.

Showa Aluminum Company assisted in meeting the publication costs of this article.

REFERENCES

1. S. Tajima and F. Iida, *Denki Kagaku*, **19**, 283 (1951).
2. S. Wernick and R. Pinner, "The Surface Treatment and Finishing of Aluminum and its Alloys," Vol. 1, 4th ed. (1972).
3. N. Kawashima, Y. Nakamura, and M. Nishizaka, *J. Jpn. Inst. Light Met.*, no. 17, 75 (1955).
4. N. Kawashima, Y. Nakamura, and M. Nishizaka, *ibid.*, no. 21, 54 (1956).
5. Y. Nakamura and M. Nishizaka, *ibid.*, no. 20, 58 (1956).
6. Y. Nakamura, *ibid.*, **9**, 67 (1959).
7. F. Erdmann-Jesnitzer, H. Hadamovsky, and W. Schroder, *Aluminium*, **36**, 258 (1960).
8. R. Bakish, R. J. Kornhaas, and E. Z. Borders, *J. Electrochem. Technol.*, **1**, 358 (1963).
9. D. Altenpohl, "Aluminium und Aluminiumlegierungen," Springer, Berlin (1956).
10. R. B. Diegle, *This Journal*, **121**, 583 (1974).
11. T. Lach and Z. Lach, *Pr. Inst. Met. Niezelaz*, **6**, 88 (1977).
12. L. V. Alphen, P. Nauwen, and L. Slakhorst, *Z. Metallkd.*, **70**, 158 (1979).
13. K. Kusao, Y. Yoshioka, and F. Konishi, in "Micro Beam Analysis Committee, the 5th Local Meeting," p. 1 (1977).
14. H. P. Stüwe and I. Jager, *Acta Metall.*, **24**, 605 (1976).
15. J. D. Gruthrie and B. J. Sparr, *Thin Solid Films*, **43**, 303 (1977).

Effect of Powder Characteristics on Microstructure and Properties in Alkoxide-Prepared PZT Ceramics

R. C. Buchanan* and J. Boy

Department of Ceramic Engineering, University of Illinois at Urbana-Champaign, Urbana, Illinois 61801

ABSTRACT

The effects of coprecipitation parameters on agglomerate structure in PZT (53:47) powders prepared from butoxide precursors were studied. Results showed that differences in agglomerate structures developed during coprecipitation persisted throughout subsequent processing steps, and the resulting sintered densities and microstructures to be correlated with the agglomerate structures. Coprecipitation parameters which most significantly affected the powder characteristics included temperature, dilution, pH, and hydrolysis rate (controlled by H₂O concentration). Such processing parameters as powder rinsing, calcination temperature, and spray drying conditions also significantly influenced the developed microstructures. For equivalent processing conditions, the most dense and uniform microstructures were developed with the softer (and smaller) agglomerate structures, achieved from an acid (pH 3.7) medium of low (3-5 volume percent) solids content with rapid hydrolysis (~32 ml H₂O/min) and low temperature rise (10° to 15°C). Measured dielectric constants on the sintered PZT samples were found, generally, to increase with average grain size.

Commercial PZT (lead zirconate titanate) ceramic powders are typically formed from calcined mixtures of oxide or carbonate precursors. Difficulties with mixing often lead to incomplete reactions and localized inhomogeneities in the microstructure of the sintered ceramic. This condition in PZT contributes to a lack of reproducibility in the dielectric properties and aging characteristics and has the effect of limiting PZT use for many critical transducer applications. Consequently, alternate methods for powder preparation aimed at achieving intimate mixing by coprecipitation or by suspension of the oxide precursors in a finely dispersed and highly reactive state have been investigated.

In preparing PZT ceramics, chemical coprecipitation from alkoxide precursors of Zr and Ti has been a widely used technique. Brown and Mazdiyasi (1) used Zr and Ti alkoxide solutions blended with lead isoamyl oxide in distilled water to bring about decomposition and precipitation of the PZT phase. Excess lead oxide in the form of Pb(OR')₂ was added to compensate for Pb loss during sintering. Calcination of the powder at ~500°C for 30-60 min produced the PZT phase.

Haertling and Land (2) prepared high purity PLZT powders from materials consisting of lead oxide (PbO),

* Electrochemical Society Active Member.

lanthanum acetate (La(AC)₃), zirconium tetra-n-butoxide (ZNB), and titanium tetra-n-butoxide (TBT). The procedure consisted of weighing out the proper amounts of PbO and butoxides followed by blending in isopropyl alcohol. Lanthanum acetate solution was then added to the blending mixture which hydrolyzed the butoxides and produced a precipitate of mixed hydroxides, a process which was accelerated by the heat produced in the exothermic reactions.

Modifications to the basic alkoxide process aimed at producing coprecipitated PZT and PLZT with different powder characteristics have been described by many authors (3-6). The coprecipitation process has also been used for adding minor ingredients to PZT compositions, either as sintering aids or for property control. Wittmer and Buchanan (7) achieved significant reduction in the densification temperature of PZT (53:47) by incorporation of up to 1 weight percent (w/o) V₂O₅ during coprecipitation. The as-dried coprecipitated powders were found to be x-ray amorphous, but powders calcined as low as 350°C produced XRD patterns characteristic of tetragonal PZT, with only slight lattice distortion. More recently, Tuttle (8) coprecipitated powders of PSZT + Nb₂O₅ using a process similar to that employed by Wittmer and Buchanan (7). PbO, SnO₂, and Nb₂O₅ were added to the

blending mixture of TBT and ZNB. A 4:1 alcohol:water solution was used as the precipitating agent and superior dielectric properties were reported for the fired coprecipitated powders. Fired densities between 92.4% and 95.6% theoretical were obtained by firing at 1380°C using a standard double-crucible technique.

From the reported work, it is evident that much sensitivity attaches to the alkoxide precipitation process, when such parameters as pH, dilution, dispersion, temperature, and method of hydrolysis of the butoxide mixtures are considered. These parameters greatly affect agglomerate cohesion and size distribution in the precipitated powders (9). The effects of postprecipitation processing—washing, drying, calcination, dispersion, pressing—on powder characteristics and final densification have also been explored and were found to significantly influence the final densities and microstructures achieved (6-8).

The object of this study, therefore, was to investigate the relative influence of the coprecipitation and processing parameters on the powder characteristics, final densification, microstructure, and dielectric properties of sintered PZT ceramics.

Experimental

The PZT composition chosen for this study was $\text{Pb}(\text{Zr}_{0.53}\text{Ti}_{0.47})\text{O}_3$. This composition is near the morphotropic phase boundary for the PbZrO_3 - PbTiO_3 system and is known to give optimum permittivities and coupling coefficients (10, 11). The powders were prepared by coprecipitation from starting high purity materials of electronic-grade PbO (Hammond Lead Products, Incorporated, Hammond, Indiana), tetra-n-butyl titanate (E. I. du Pont de Nemours, Incorporated, Wilmington, Delaware), and zirconium tetra-n-butylate (Dynamite Nobel Company, Norwood, New Jersey).

Initially, a modified version of Wittmer's (7) coprecipitation procedure was used. This procedure had only one blending step during coprecipitation and was termed the "single-step" process. It was modified such that the precipitated slurry was filtered in a Buchner funnel to speed dewatering and washing of the precipitate. The coprecipitation procedure consisted of: (i) mixing the stoichiometric amounts of PbO, TBT, and ZNB (200g batch) in a blender at medium speed for about 15 min, (ii) adding a precipitating solution consisting of deionized water (30-100 volume percent [v/o]) in isopropanol (~250 ml of solution for a 200g batch; pH ~5.0), (iii) blending the thickened mixture for ~15 min until a smooth slurry was obtained, (iv) filtering the slurry using a Buchner funnel with solvent washing as appropriate, and (v) drying the washed powder in a vacuum oven at 150°C for 4h.

With this single-step blending, a significant rise in the temperature (85°-95°C) and viscosity of the mixture occurred, which made it difficult to maintain fluid mixing. To eliminate these problems, the process was further modified by diluting the batch with additional alcohol and using a two-step procedure which separated the coprecipitation and blending processes. This two-step coprecipitation procedure may be detailed as follows. First, to 200 ml of a 50/50 solution of isopropanol and n-butyl alcohol in a polyethylene beaker was added, while magnetically stirring, 85 ml of a mixture of Ti and Zr butoxides and PbO, calculated to give a 50g batch of (53:47) PZT composition. A wetting agent, Darvan C (~5 drops) was also added to aid dispersion. Second, 200 ml of the water/isopropanol solution (to which glacial acetic acid or ammonium hydroxide was added for pH control) was added at 40-60 ml/min to cause precipitation of the mixed oxides. Third, after stirring an additional 10 min, the precipitated mixture was transferred to a high speed blender and blended for 15 min to produce a smooth, relatively stable slurry. Fourth, the blended slurry was then directly spray dried using a laboratory spray drier (Buchi Model 190, Brinkman Instrument Company) or else was washed and vacuum dried as described.

Several parameters in the coprecipitation process for lead zirconate titanate prepared from the butoxide pre-

cursors were investigated. These included the percentage of water, the rate of addition, and the pH of the precipitation solution. Also investigated were the solids content of the PbO and butoxide mixtures, the blending process, the temperature rise during coprecipitation, and the washing of the precipitate with different solvents. In evaluating the above parameters, the following ranges were used: concentration of suspended solids ranged from 2.0 to 7.0 v/o; water content of the precipitating water/alcohol solution varied from 25 to 100 v/o (12.5-49 v/o total liquid content) and was added at the rate of 6 to 60 ml/min. The pH range studied varied from 3.0 to 12.0, while the temperature rise during coprecipitation ranged from 10° to 15°C (two-step blending) to 70°C for the single-step process. Where vacuum drying was used, washing of the filtrate was carried out using deionized water, isopropanol, or a 60 v/o isopropanol mixture of the two solvents.

Calcination of the spray- or vacuum-dried precipitated powders was carried out in open platinum crucibles at 600°-850°C, to develop the PZT phase and promote grain growth. The calcined powder was milled for 5h in polyethylene jars using ZrO_2 grinding media. A 60/40 v/o isopropanol/water solution with Darvan C dispersant was found to be the most effective milling medium. A binder solution consisting of 1.0 w/o polyvinyl alcohol in water was added for the final hour of milling. The milled slurry was spray dried, and pellets ~1.6 cm diam and 0.3 cm thick were uniaxially pressed at 207 MPa. The pressed pellets were sintered on Pt foil supported on ZrO_2 setters at 1280°C/4h using the standard double crucible technique of Okazaki *et al.* (4) or in air at 950°C/1h (for samples containing 0.5 w/o V_2O_5 as flux additive) (7).

The spray-dried, vacuum-dried, and calcined powders as well as crushed sintered samples were analyzed by x-ray diffraction, using a Phillips Norelco diffractometer with filtered Ni K_α radiation at 40 kV and 10 mA filament current, at a scanning rate of 1° 2 θ /min. The powders were also subjected to DTA and TGA analysis using a thermal analysis system (du Pont 1090). Particle size distribution measurements were made using an x-ray sedimentation analyzer (Micromeritics) and surface area measurements by a BET technique. SEM analysis on powders and sintered sections were made using an ISI-DS-130 scanning electron microscope equipped with an energy dispersive x-ray analyzer. Sample densities were measured by water and mercury immersion techniques. Dielectric constant and dissipation factor measurements were made at 1.0 kHz using a capacitance bridge. Poling of the samples proved to be difficult with the smaller average-grain-sized samples.

Results and Discussion

Figure 1 shows SEM photomicrographs for the dried, as-precipitated powders prepared by the one- and two-step blending processes. Both powders were precipitated from acid medium of pH = 5. With the single-step process (Fig. 1a), the morphology of the precipitated powders appeared to consist of hard, nearly dense agglomerates within the size range 2-5 μm . Reed *et al.* (12) differentiated between soft and hard agglomerates (aggregates), the latter being postulated to be held together by chemical or diffusion bonds, compared to soft agglomerates, which are believed to be bonded by van der Waal's bonds or by magnetic forces. In contrast to the single-step process, powders prepared by the two-step blending (Fig. 1b) gave soft agglomerates in the size range 1-4 μm . These powders also showed a distinct subagglomerate structure with cluster sizes of ~0.1 μm . These differences are illustrated in Fig. 2, which shows agglomerate size distributions for the PZT coprecipitated powders as a function of pH and blending process. Significantly larger size distributions were measured with the single-step blending process at equivalent pH (8.5), confirming the trend noted in Fig. 1. Agglomerate size distributions also increased with pH for the same blending process.

The striking difference in morphology between the two powders in Fig. 1 and 2 can be attributed to the more

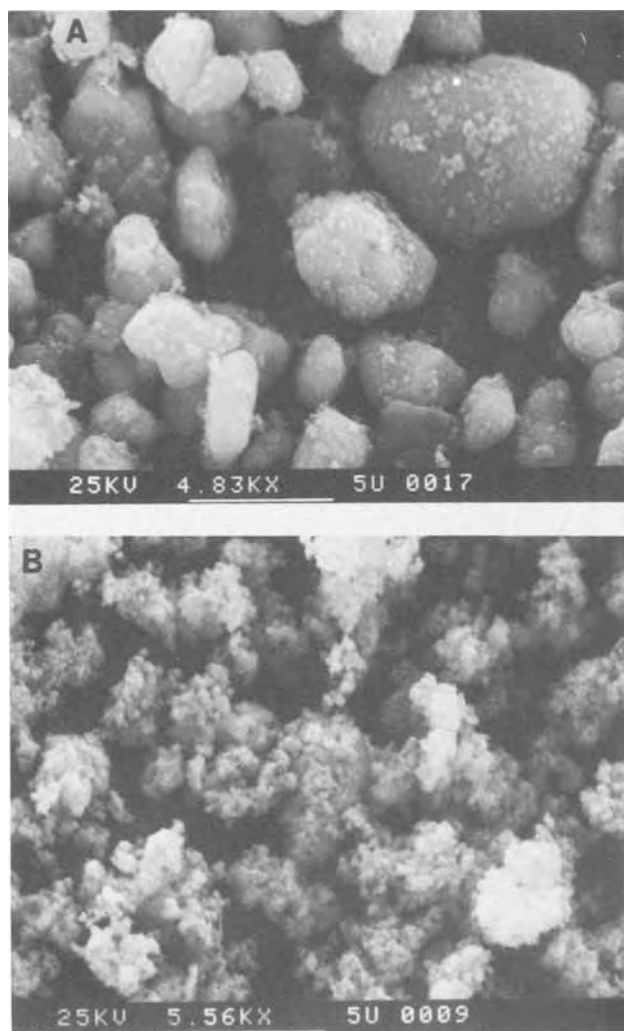


Fig. 1. SEM micrographs of "as-precipitated" powders comparing precipitating procedures: a: One-step. B: Two-step blending processes.

highly dispersed state, greater fluidity, and lower temperature of the two-step blending process. As indicated for the single-step process, there was difficulty in maintaining homogeneous mixing during coprecipitation due to gelation of the mixture and the high temperatures ($\sim 90^\circ\text{C}$) experienced during the hydrolysis reaction. With the diluted mixture used in the two-step process, the maximum temperature experienced was approximately 40°C . This lower temperature would be expected to slow

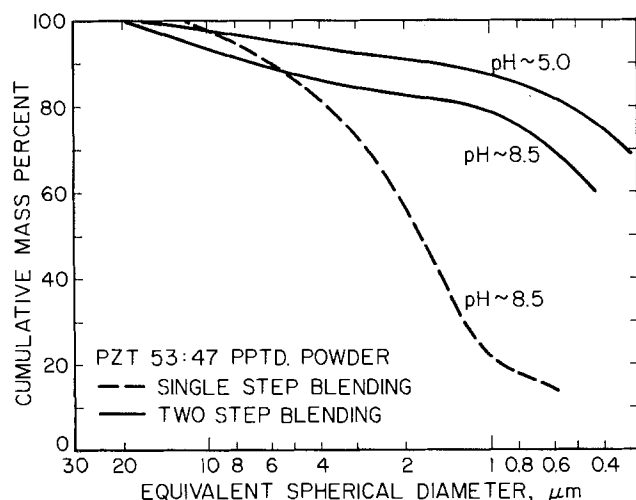


Fig. 2. X-ray sedigraph plot of agglomerate size distribution for coprecipitated PZT powders as a function of pH and blending process.

the hydrolysis reaction (13), and, as pointed out by Yoldas (14), dilution of the reacting species with neutral solvents also slows the reaction rate and enhances the uniformity of the hydrolysis reaction throughout the system. In contrast to the present finding where hard agglomerates were obtained at the higher precipitating temperatures ($85^\circ\text{--}95^\circ\text{C}$), work by van der Graaf *et al.* (15) revealed that ZrO_2 powders precipitated at room temperature yielded harder agglomerates than powders precipitated at higher temperatures ($\sim 100^\circ\text{C}$), which yielded the softer agglomerates.

The effect of water content and rate of addition on the amorphous character of the precipitated powders, as determined by x-ray diffraction analysis, is illustrated in Fig. 3. Water contents of 33 and 67 v/o in the precipitating alcohol/water solutions were equivalent to 16 and 33 v/o of the total liquid content. Rates of water addition, as indicated, varied from 5.5 to 22 ml/min. The x-ray diffraction patterns for the dried precipitated powders were characterized by the presence of an amorphous hump, confirming the very small crystallite size of the powders and the absence of a clearly distinct PZT phase. Superimposed on the amorphous hump were crystalline diffraction peaks of unreacted PbO. The intensities of these peaks decreased with increasing hydrolysis (water content and addition rate), in line with the completely amorphous powders reported by Brown (1), Haertling (16), and Wittmer (7). Calcination of the powders at $800^\circ\text{C}/4\text{h}$ gave only the PZT phase.

Harder and somewhat larger agglomerates were evident in the precipitates formed from low water content solutions due to the higher temperatures experienced. Differences in the precipitated agglomerate structures were also retained throughout subsequent processing. This is illustrated in Fig. 4, where SEM fracture micrographs of calcined ($800^\circ\text{C}/4\text{h}$), pressed (207 MPa) but unfired samples are compared with fired ($950^\circ\text{C}/1\text{h}$), polished, and thermally etched sections for powders precipitated with 25 and 67 v/o H_2O in the precipitating solution. The bimodal cluster and grain size distribution obtained with the 25 v/o H_2O solutions were in sharp contrast to the smaller clusters and uniform grain sizes obtained with the 67 v/o H_2O precipitate. These microstructures would not be predicted from the respective pressed (5.0 vs. 4.4 g/cm^3) and fired (7.5 vs. 7.8 g/cm^3) densities for the two powders (25 vs. 67 v/o H_2O). Coprecipitated powders sintered at $1280^\circ\text{C}/4\text{h}$ (without V_2O_5 additions) showed essentially the same trends.

DTA heating and cooling curves for the water- and/or alcohol-rinsed coprecipitated powders are presented in Fig. 5. The DTA analyses showed exothermic reaction

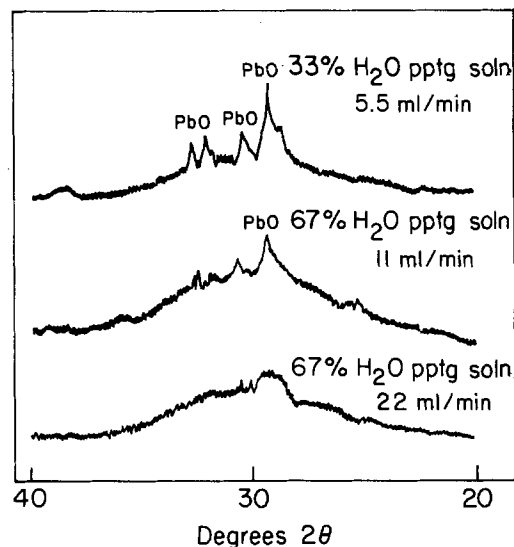


Fig. 3. X-ray diffraction patterns showing decrease in unreacted PbO content of "as-precipitated" PZT powder with increasing H_2O content and faster addition rate of the precipitating solution.

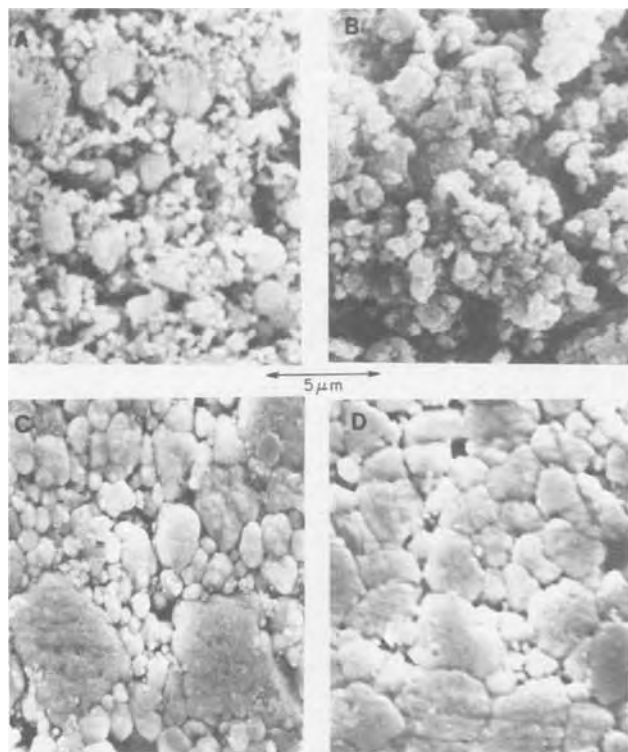


Fig. 4. SEM photomicrographs of fracture surfaces of unfired PZT (single-step process) samples from precipitating solutions containing the following: A: 25 v/o H₂O. B: 67 w/o H₂O (pH 5). C: Fired (950°C/1h), polished, and thermally etched photomicrographs of A and B shown in C and D, respectively.

peaks occurring at approximately 200°, 300°, and 530°C. TGA analysis showed the first two peaks to be associated with weight losses, the maximum losses occurring near 300°C, and all weight loss occurring below ~400°C. The peaks were attributed respectively to loss of residual alcohol, elimination of the butoxide decomposition products, and formation of the PZT phase. Rinsing with H₂O suppressed the exothermic peaks at ~200° and 300°C, in contrast to rinsing with (isopropyl) alcohol, which enhanced the lower peak and shifted the second peak to a higher temperature. With no rinsing of the precipitate, the peak at 300°C was disproportionately larger, consistent with a higher content of organic residues.

In terms of densification, the H₂O-rinsed powders gave significantly lower fired densities (~91% ThD) compared the alcohol/water rinsed with (~96% of ThD), with isopropanol-washed samples intermediate at 95% ThD. The

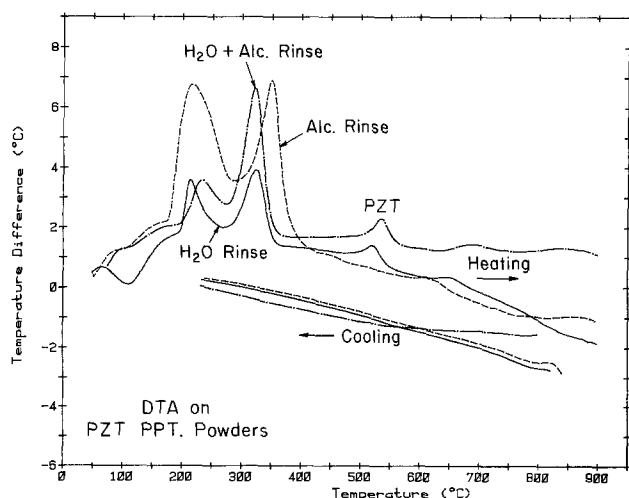


Fig. 5. Differential thermal analysis curves comparing washing media: isopropanol, water, and isopropanol/water solution.

base density for PZT (53:47) was taken as 8.0 g/cm³. These observations are consistent with fired densities obtained by Haberko (17) on water- and alcohol-washed stabilized ZrO₂ powders. The differences were attributed to the weaker bonded agglomerates formed with alcohol-washed powders as a result of reduced surface ionic absorption.

Figure 6 shows the effect of pH on the agglomerate structure of the "as-precipitated" powders following initial spray drying. The acid powder (pH 3.7) had an average agglomerate size of ~5 μm with a well-defined sub-agglomerate structure. In contrast, the basic powder (pH 11) had an average agglomerate size of ~10 μm, appeared harder, and had a less distinct substructure. The increase in the agglomerate size for the basic powders was confirmed by the sedigraph analysis shown in Fig. 7. The powders precipitated by the pH 3 solution had an average agglomerate size of ~0.5 μm, which increased to ~0.9 μm for the pH 10 solution with a narrower size distribution. The difference in average size distribution between the SEM and sedigraph data was due to the partial breakup of the spray-dried agglomerates by addition of a defloculant and by mechanical dispersion during the sedigraph tests.

Figure 8 shows SEM fracture micrographs for sintered (1280°C/4h) samples of the two powders discussed in Fig. 6. The pH 3.7 powders, which had a uniform pressed microstructure, yielded a very dense microstructure and smaller average grain size (~10 μm) than the pH 11 sample (~20 μm avg GS). Both samples were calcined at 800°C/4h, which throughout this study generally resulted

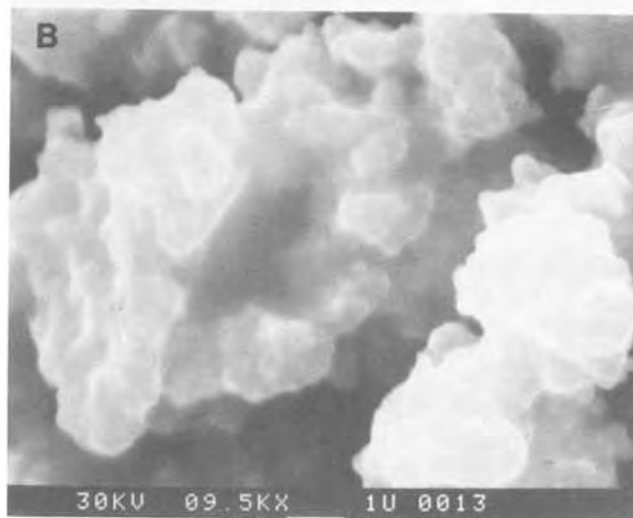
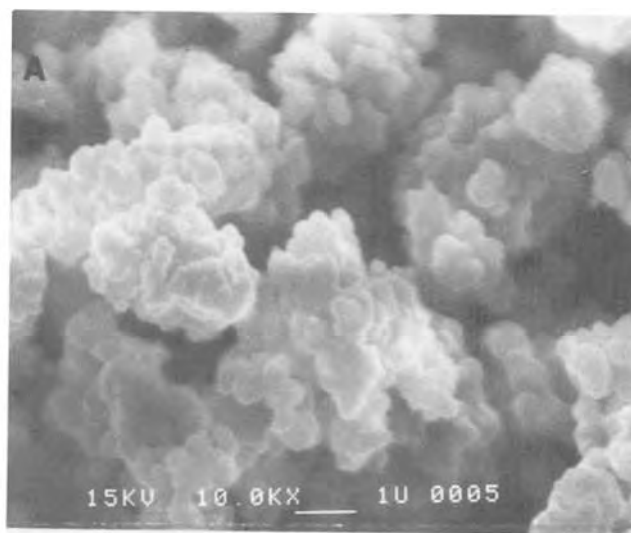


Fig. 6. SEM photomicrographs of precipitated powders following drying for precipitation conditions of pH 3.7 (A) and pH 11 (B).

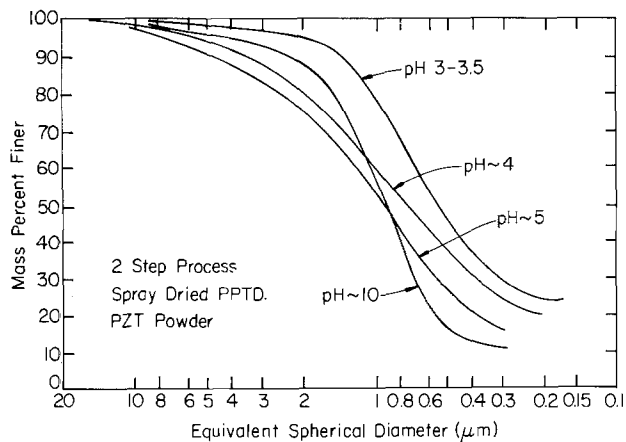


Fig. 7. Agglomerate size distribution of precipitated PZT powders showing effect of pH on equivalent spherical diameters.

in larger grain sizes for the basic powders. The grain-size disparity was in line with the size disparity and hardness of the agglomerated structures formed during coprecipitation of the powders. Transgranular and intergranular cracks were observed, particularly for the larger grain-sized sample due in part to microcracks introduced by quenching to prevent accumulation of liquid phase on the sample surface.

BET surface areas determined for the two powders were $132 \text{ m}^2/\text{g}$ (pH = 3.7) and $128 \text{ m}^2/\text{g}$ (pH = 11) compared to the $26 \text{ m}^2/\text{g}$ reported by Biggers *et al.* (6) for PZT pow-

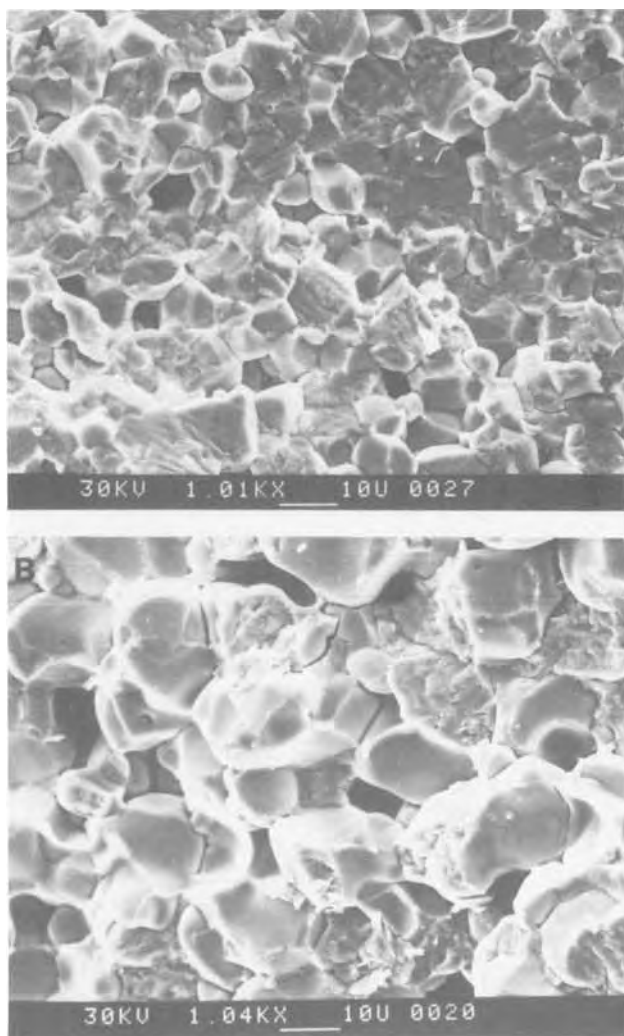


Fig. 8. SEM photomicrographs of fracture surfaces of fired ($1280^\circ\text{C}/4\text{h}$) PZT for precipitation conditions as follows. A: pH 3.7. B: pH 11. Both calcined at $800^\circ\text{C}/4\text{h}$.

ders precipitated from aqueous medium. This difference reflects the more highly dispersed conditions prevailing during the coprecipitation process. The large surface area also reflected the very small crystallite sizes ($\sim 150\text{-}200\text{\AA}$) of the precipitated powders. The pH, therefore, did not greatly affect crystallite size formation; rather, it affected agglomeration tendency and bonding within the structures formed.

This difference in agglomeration tendency caused marked differences in powder morphology on calcination. Figure 9 shows SEM fracture micrographs of calcined powders following spray drying, a second milling, and pressing at 207 MPa. For the powders calcined at $800^\circ\text{C}/4\text{h}$, (Fig. 9a, 9b), the aggregates for the pH 3.7 powders were readily broken up after milling but were solidified or essentially sintered for pH 11 powders, indicating the formation of much harder agglomerates in the basic powder during coprecipitation. In general, powders calcined at $750^\circ\text{C}/4\text{h}$ (Fig. 9c, 9d) gave smaller and more uniform aggregate sizes, but always larger for the basic powders.

Figure 10 shows SEM fracture micrographs of the sintered ($950^\circ\text{C}/4\text{h}$) samples for the pH and calcination conditions detailed in Fig. 9. The effect of pH and calcination conditions on the pressed and fired densities are shown in Fig. 11. Densities obtained for the pH 3.7 and 11 powders were similar for equivalent calcination and sintering conditions, but were lower for other pH values. Powders calcined at $750^\circ\text{C}/4\text{h}$ gave highest densities for both pH conditions.

The existence of density maxima at pH 3.7 and 11.0 in the densification curves coincides with the observed stability maxima, as a function of pH, for colloidal suspensions of oxide materials such as SiO_2 . At the lower pH values (2.5-3.5), the particles have very little ionic charge, and stability is maintained by a hydration layer surrounding each particle rather than by electrostatic repulsion. Dried solutions of such acid pH powders, therefore, tend to be bonded by van der Waals forces and, in consequence, are softer and less agglomerated. In contrast, in the pH range 9-11, electrolyte presence causes develop-

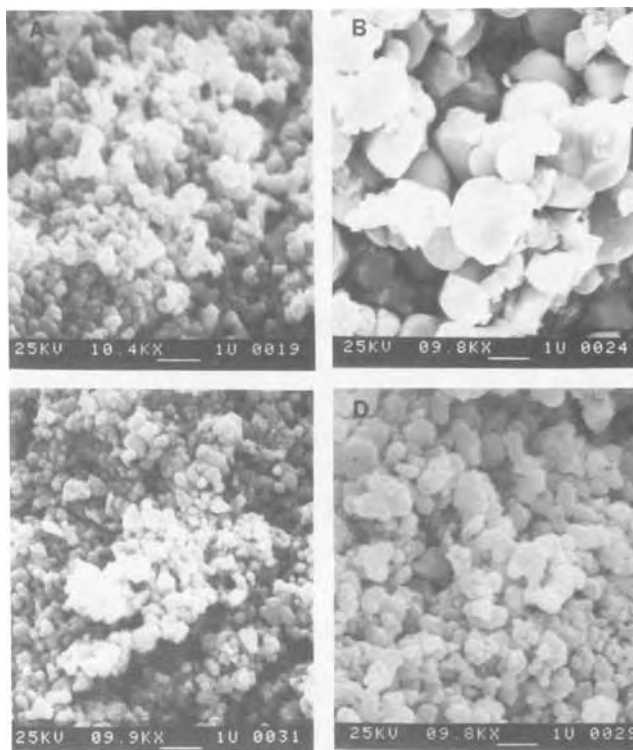


Fig. 9. SEM photomicrographs of fracture surfaces of unfired PZT obtained for precipitation and calcination conditions as follows. A: pH 3.7, calcined $800^\circ\text{C}/4\text{h}$. B: pH 11, calcined $800^\circ\text{C}/4\text{h}$. C: pH 3.7, calcined $750^\circ\text{C}/4\text{h}$. D: pH 11, calcined $750^\circ\text{C}/4\text{h}$.

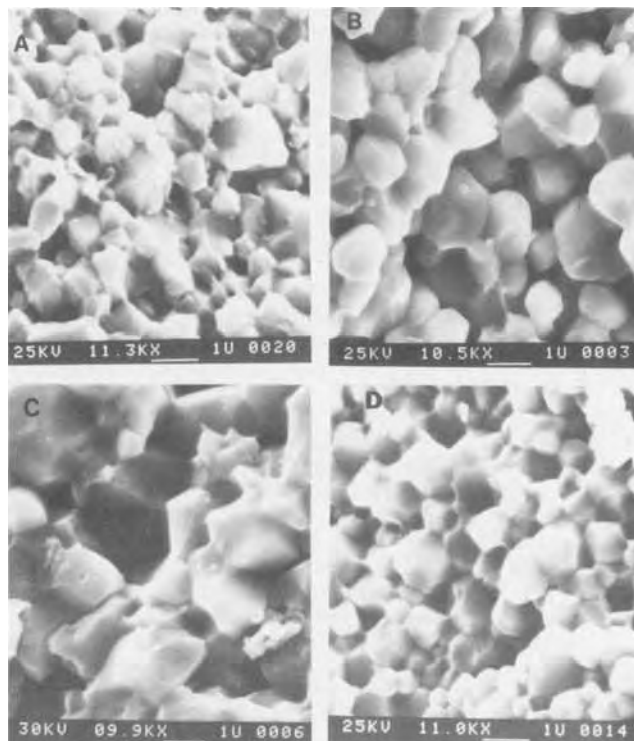


Fig. 10. SEM photomicrographs of fracture surfaces of fired ($950^{\circ}\text{C}/1\text{h}$) PZT + 0.25 w/o V_2O_5 obtained for precipitation and calcination conditions in Fig. 9. A: pH 3.7, calcined $800^{\circ}\text{C}/4\text{h}$. B: pH 11, calcined $800^{\circ}\text{C}/4\text{h}$. C: pH 3.7, calcined $750^{\circ}\text{C}/4\text{h}$. D: pH 11, calcined $750^{\circ}\text{C}/4\text{h}$.

ment of net charges on the particle surfaces and stability is maintained by electrostatic repulsion (19, 20). Dried solutions of high pH, therefore, tend to be more strongly bonded, resulting in larger and harder agglomerate structures. These observations are in keeping with the observed agglomerated states as a function of pH for the precipitated PZT powders, and suggest a state of maximum dispersion for the pH 3.7 and 11 suspensions. This, in turn, would lead to higher packing and sintered densities, and to the marked differences in the grain size and microstructures noted.

The average grain size for the powders calcined at 800°C increased, following sintering at $950^{\circ}\text{C}/1\text{h}$, from 0.3 to 1.9 μm for the pH 3.7 powders (Fig. 9 and 10) and from 1.0 to 2.3 μm for the pH 11 powders. For the powders calcined

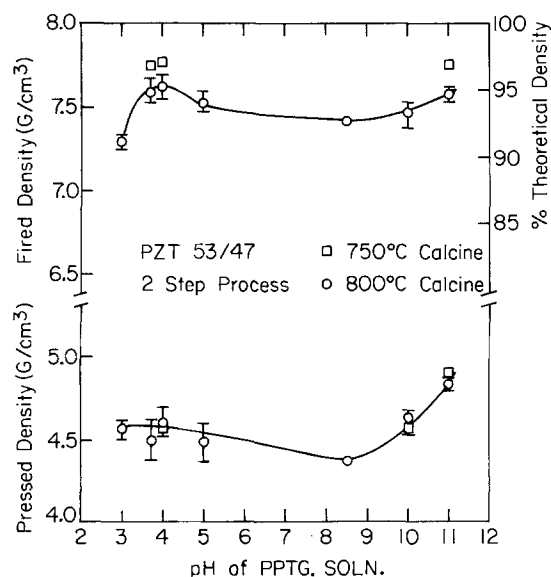


Fig. 11. Effect of pH of precipitating solution on the pressed and fired densities ($950^{\circ}\text{C}/1\text{h}$) of PZT (+0.25 w/o V_2O_5).

at 750°C , the average grain size increased from 0.25 to 3.9 μm for the pH 3.7 powder, and from 0.5 to 1.7 μm for the pH 11 powder. The data show densification and grain growth rates to be significantly enhanced for the lower temperature ($750^{\circ}\text{C}/4\text{h}$ vs. $800^{\circ}\text{C}/4\text{h}$) calcined powders, reflecting the higher driving force for densification with the smaller-sized aggregates with the liquid phase-assisted sintering. Grain sizes and final microstructures developed were much influenced by the calcination conditions, reported also by Venkataramani and Biggers (18), but, significantly, also by the powder morphology developed, as a function of pH, during coprecipitation from the alkoxide precursor mixtures. With close control of the coprecipitation parameters (especially pH) combined with manipulation of the calcination conditions, therefore, controlled microstructures in sintered PZT can be achieved (at least under conditions of low temperature liquid phase-assisted sintering), which would lead to improved reproducibility of dielectric properties and aging characteristics.

Table I gives grain size and dielectric property data for the samples shown in Fig. 10 with sintered densities $\geq 95\%$ theoretical density. Measured dissipation factors were $< 2.0\%$ and dielectric constants were in the range 700-1000 at 25°C , in line with reported values for PZT (21). The increase in dielectric constant noted with grain size is similar to that reported by Okazaki (22) for small grain size ($< 4 \mu\text{m}$) PLZT samples. The observed increase in dielectric constant with grain size can be attributed to a volume decrease in the more insulating boundary phase as well as to a measured increased conduction and ease of polarization of the larger grains. This is further illustrated in Fig. 12, which compares the dielectric constant as a function of temperature for the nonfluxed PZT samples in Fig. 8 (sintered at $1280^{\circ}\text{C}/4\text{h}$) for pH conditions 3.7 and 11.0. These samples showed a marked increase in dielectric constant with average grain size in the range 10-20 μm . This is in contrast to the reported decrease in dielectric constant with grain size by Webster (23) and also by Haertling (16). For both samples in Fig. 12, loss tangents up to $\sim 200^{\circ}\text{C}$ were below 2.0%, but increased sharply on approach to the Curie points ($\sim 394^{\circ}\text{C}$). The dielectric constants also increased almost linearly up to $\sim 250^{\circ}\text{C}$ and attained values $> 10,000$ at the Curie points. The marked differences in dielectric constants between the two powders indicated the sensitivity of the final microstructure and properties to initial powder characteristics.

Conclusions

1. This study has shown that in the coprecipitation of PZT from butoxide precursors, such powder characteristics as amorphous structure, agglomerate cohesion (hardness), and size distribution were established during the coprecipitation process. Differences at this level tended to persist throughout subsequent processing, resulting in significantly different microstructure and properties.

2. The parameters which most sensitively affected coprecipitation were found to be dilution, pH, temperature, and precipitation or hydrolysis rate (controlled by H_2O addition). Low solids constant ($\sim 3\text{-}5$ v/o PbO), low temperature rise ($< 15^{\circ}\text{C}$), acidic pH ($\sim 3\text{-}4$), and high precipitation rates (25-32 ml $\text{H}_2\text{O}/\text{min}$) were found to promote

Table I. Effect of pH and calcination temperature on grain size and dielectric property of PZT

pH	Calcination (temp./t)	Grain size (μm)	Dielectric constant	Percentage disp. factor
3.7	$800^{\circ}\text{C}/4\text{h}$	1.9	760	1.2
11.0	$800^{\circ}\text{C}/4\text{h}$	2.3	880	1.0
3.7	$750^{\circ}\text{C}/4\text{h}$	3.9	930	1.1
11.0	$750^{\circ}\text{C}/4\text{h}$	1.7	700	2.0

Sintering temp: $950^{\circ}\text{C}/1\text{h}$. Dielectric data at 25°C .

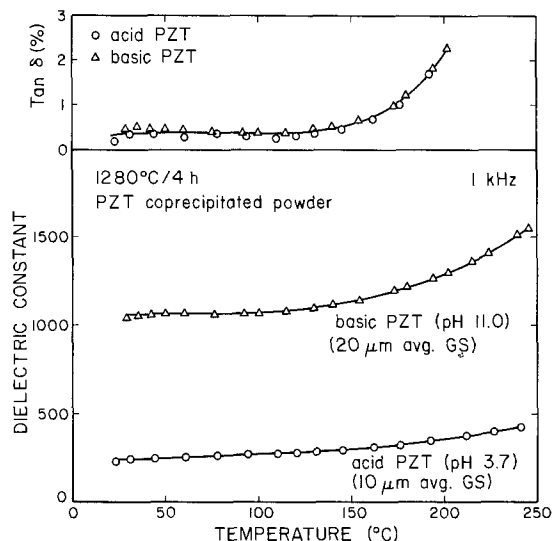


Fig. 12. Plot of dielectric constant and $\tan \delta$ for sintered (1280°C/4h) coprecipitated PZT powders in Fig. 8 showing effect of pH and grain size.

smaller and more uniformly sized agglomerates. These conditions were readily achieved in the two-step blending process described.

3. As both a milling and washing medium, isopropanol/water solution (60/40 v/o) was found to promote higher fired densities and more uniform microstructures.

4. Calcination temperature and spray drying of dispersed powders were found to be important processing variables. Lower calcination temperatures were required with the basic powders to achieve equivalent microstructures.

5. Grain sizes and dielectric constants obtained with the basic (pH 11) powders were generally larger, particularly at the higher (800°C) calcination temperatures.

Acknowledgments

This work was supported by the Office of Naval Research under Contract US Navy N00014-80-K-0969 and in part by the National Science Foundation under MRL Grant no. DMR-80-20250, and is gratefully acknowledged.

Manuscript submitted Dec. 14, 1984; revised manuscript received March 22, 1985.

The University of Illinois assisted in meeting the publication costs of this article.

REFERENCES

1. L. M. Brown and K. S. Mazdiyasi, *J. Am. Ceram. Soc.*, **55**, 541 (1972).
2. G. Haertling and C. Land, *Ferroelectrics*, **3**, 269 (1972).
3. M. Murata, K. Wakino, K. Tanaka, and Y. Hamakawa, *Mater. Res. Bull.*, **11**, 323 (1976).
4. K. Okazaki, *Ferroelectrics*, **41**, 77 (1982).
5. R. Brooks and D. K. Murphy, *ibid.*, **27**, 179 (1980).
6. J. V. Bigger and S. Venkataramani, *Mater. Res. Bull.*, **13**, 717 (1978).
7. D. E. Wittmer and R. C. Buchanan, *J. Am. Ceram. Soc.*, **64**, 485 (1981).
8. B. A. Tuttle, Ph.D. Thesis, University of Illinois, Urbana, IL (1981).
9. T. B. Weston, *J. Can. Ceram. Soc.*, **32**, 100 (1963).
10. L. E. Cross and K. H. Haertl, "Encyclopedia of Chemical Technology," Vol. 10, pp. 1-30, John Wiley and Sons, New York (1980).
11. Ya. S. Bogdanov, A. Ya. Dantsiger, V. F. Zhestkov, E. N. Siderenko, A. V. Turik, and E. G. Fesenko, *Izv. Akad. Nauk. SSSR, Neorg. Mater.*, **16**, 1048 (1980).
12. J. S. Reed, T. Carbone, C. Scott, and S. Kukasiewicz, "Processing of Crystalline Ceramics: Materials Science Research," Vol. 11, pp. 171-180, Plenum Press, New York (1978).
13. T. Yamaguchi, S. H. Cho, M. Hakomori, and H. Kuno, *Ceramurgia Int.*, **2**, 76 (1976).
14. B. E. Yoldas, *J. Am. Ceram. Soc.*, **65**, 387 (1982).
15. M. A. C. G. van der Graaf, K. Keizer, and A. J. Burggraaf, in "Science of Ceramics," Vol. 10, E. Hausner, Editor, pp. 88-92, Deutsche Keramische Gesellschaft, Weiden, FRG (1980).
16. G. H. Haertling, *J. Am. Ceram. Soc.*, **54**, 303 (1971).
17. K. Haberko, *Ceramurgia Int.*, **5**, 148 (1979).
18. S. Venkataramani and J. V. Biggers, *Ceram. Bull.*, **59**, 462 (1980).
19. M. J. Rosen, "Surfactants and Interfacial Phenomena," Chap. 9, John Wiley and Sons, New York (1978).
20. R. E. Mistler, D. J. Shanefield, and R. B. Runk, in "Ceramic Processes Before Firing," G. Onoda and L. Hench, Editors, pp. 411-448, John Wiley and Sons, New York (1978).
21. Z. Wrobel and Cz. Kus, *Ferroelectrics*, **22**, 801 (1978).
22. K. Okazaki and K. Nagata, *Ceram. Int.*, **12**, 173 (1977).
23. A. H. Webster, T. B. Weston, and R. R. Craig, *J. Can. Ceram. Soc.*, **34**, 121 (1965).

Radiation-Induced Reactions of Chloromethylstyrene-Based Resist Materials Analyzed from Radiolysis of Low Molecular Model Compounds

Katsumi Tanigaki, Masayoshi Suzuki,* Yasushi Saotome, and Yoshitake Ohnishi

NEC Corporation, Fundamental Research Laboratories, Miyamae-ku, Kawasaki City 213, Japan

Kazuo Tateishi

NEC Corporation, Resources and Environment Protection Research Laboratories, Miyamae-ku, Kawasaki-City 213, Japan

ABSTRACT

The radiation-induced reactions of chloromethylstyrene-based resist materials are studied by low temperature ESR and gas chromatography-mass spectrometry (GC-MS) analyses using low molecular model compounds. Low temperature ESR analyses indicate that main radiation-induced active species in the initial stage of the reaction are benzyl radicals formed through chlorine removal from chloromethylstyrene units and simultaneously produced active chlorines. The amount of the α radicals formed through α -hydrogen cleavage is less than one-tenth that of the benzyl radicals. GC-MS analyses indicate that large amounts of α radicals are produced through the subsequently occurring hydrogen abstractions by radiation-induced active chlorines. The susceptibilities of individual constituents to hydrogen abstractions are determined as 6.2 for a methylstyrene unit, 2.6 for a styrene unit, and 1 for a chloromethylstyrene unit.

Chloromethylstyrene-based resist materials, such as chloromethylated polystyrene (CMS) (1) and chlorinated poly(vinyltoluene) (CPMS) (2), provide high etch resistance to plasma and ion beams, as well as excellent resolution and high sensitivity to radiation, which are required for electron beam and deep-UV lithographies.

Gokan *et al.* explained etch resistance of metal-free organic materials under ion beam etching conditions in terms of the carbon content in a polymer (3). As for resolution, there is no rule to determine resolution capability, because resolution in cross-linking negative resists is largely influenced by swelling during development process. Recently, the radiation-induced reactions of these resist materials have been studied in order to understand high sensitivity obtained in these resists.

Tagawa *et al.* studied the reaction mechanism for polystyrene, poly(α -methylstyrene), and their chloromethyl derivatives by pulse radiolysis and laser flash photolysis (4). In their study, reactive intermediates in the cross-linking reaction were detected and the reaction mechanism was discussed from the viewpoint of transient phenomena. Harita *et al.* studied the photolysis of benzylchloride in toluene and cummene by deep-UV radiation at 313 nm as a model photochemical reaction for chlorinated poly(vinyltoluene) (5). However, the reactions taking place on individual units of a polymer in these resist materials have not been clarified yet, because they are polymeric systems.

In the present study, the radiation (deep UV and ^{60}Co γ -ray) induced reactions of chloromethylstyrene-based polymers have been studied on the basis of the radiolysis of low molecular model compounds, *i.e.*, isopropylbenzene (IPBZ) for a styrene unit, 4-methylisopropylbenzene (4-MIPBZ) for a vinyltoluene unit, and 4-chloromethylisopropylbenzene (4-CMIPBZ) for a chloromethylstyrene unit, with the intention of clarifying the reactions occurring on individual units of a polymer. Low temperature ESR analyses have been carried out to trap the radiation-induced free radicals and to determine their production yields from individual constituents in the initial stage of the reaction. Gas chromatography-mass spectrometry (GC-MS) analyses have been carried out to detect final products and to determine their relative yields. The susceptibilities of individual constituents to hydrogen abstractions by radiation-induced active species were determined from the relative final product yields. The whole features for the reaction of these resist materials are discussed in detail.

*Electrochemical Society Active Member.

Experimental

Chemicals.—Isopropylbenzene (IPBZ), 4-methylisopropylbenzene (4-MIPBZ) and 4-chloromethylisopropylbenzene (4-CMIPBZ) (*ca.* 15% *ortho*-form) were purchased from Tokyo Kasei Company and purified by distillation under reduced pressure (bp 39°C/11 mm Hg, 67°C/14 mm Hg, and 68°C/3 mm Hg, respectively). These compounds are suitable as low molecular model compounds, although they have no β -hydrogen, because β -hydrogen is not sensitive to radiation as compared with α -hydrogen (4, 6).

Methods.—Electronic absorption measurements were carried out using a Cary Model 14 recording spectrophotometer and 1 cm optical pathlength quartz absorption cells. Spectrograde ethanol was used as a solvent without further purification. The concentration of sample solutions was 10^{-3}M .

For ESR study, a JEOL JES-FE X-band spectrometer (100 kHz modulation) equipped with an ESC-10 NP cavity (Echo Electronics) was used. Irradiation was performed using an Original Hanau D₂ lamp (466 $\mu\text{W}/\text{cm}^2$) for 20 min *in vacuo*. All measurements were carried out at 77 K.

For GC-MS study, a Shimadzu AUTO GC-MS 9020 DF spectrometer equipped with a TIC GC detector and a Silicon GE SE-30 (5% on chromosorb W AW DMCS) (3 \times 2 mm) column was used. Samples (0.1 microliter) were introduced, and the column temperature was retained at 70°C for 4 min and then raised to 230°C at a rate of 8°C/min. Irradiation was carried out with a ^{60}Co γ -ray irradiation machine (4.81 \times 10⁵R) for 80h or with a Canon PLA-521 aligner equipped with a 250 Cold Mirror (40 mW/cm²) for 50 min. The relative product yields were determined by the integrated intensities of signals, assuming that ionization efficiencies are the same for all the compounds studied here.

Results

Electronic absorption spectra.—Electronic absorption spectra of the low molecular model compounds are shown in Fig. 1. Substituents, such as methyl and chloromethyl groups, enhance the optical density in the range of 260–280 nm. The chloromethyl group also enhances the optical density shorter than 260 nm; on the other hand, the methyl group decreases the optical density in these regions. From these electronic absorption spectra, UV light around 250 nm wavelength was used as a deep UV irradiation source.

ESR analyses.—In the initial stage of the reaction, low temperature ESR is an effective method for use in de-

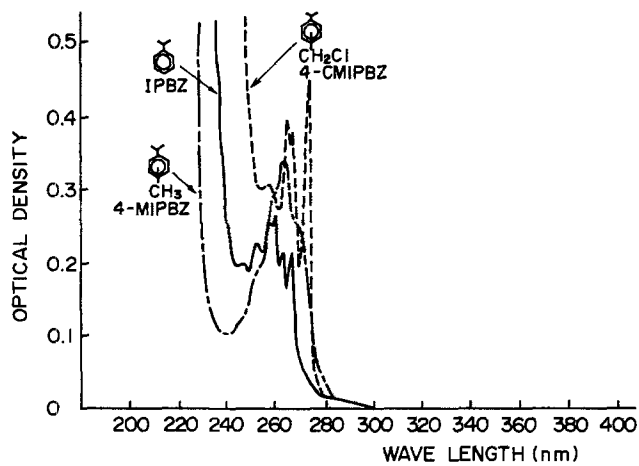


Fig. 1. Electronic absorption spectra of isopropylbenzene IPBZ, 4-methylisopropylbenzene 4-MIPBZ, and 4-chloromethylisopropylbenzene 4-CMIPBZ.

detecting radiation-induced free radicals and in determining their amounts. ESR spectra measured at 77 K after being irradiated with deep UV are shown in Fig. 2. Some comments are given for individual compounds below.

IPBZ and 4-MIPBZ.—Both compounds showed the same featureless singlet signal of 1.7 mT width (Fig. 2c). This signal is assigned to the radical produced on the α position through α -hydrogen removal by radiation (this type radical is hereafter abbreviated as Alpha, see Fig. 3). GC-MS analyses using IPBZ or 4-MIPBZ, where Alpha products were mainly formed, indicate that the assignment of the observed signal is reasonable. However, the signal observed was somewhat different from that of irradiated polystyrene, *i.e.*, it did not show the hyperfine splittings (7). The assignment of the signals observed after being irradiated in the case of polystyrene has not been sufficiently completed and remains in an area of active research.

4-CMIPBZ.—This compound showed the same spectrum as that of CMS films (Fig. 2a and 2b) after being irradiated at 77 K. This fact indicates that 4-CMIPBZ is suitable as a low molecular model compound for a chloromethylstyrene unit.

The observed spectrum of 4-CMIPBZ (Fig. 2b) is not assigned to one radical, because the observed hyperfine splittings are not interpreted as the signal arising from one radical. In order to analyze the observed spectrum, experiments were carried out in mixtures of IPBZ or 4-MIPBZ with carbon tetrachloride. These experiments were conducted to study the interaction between

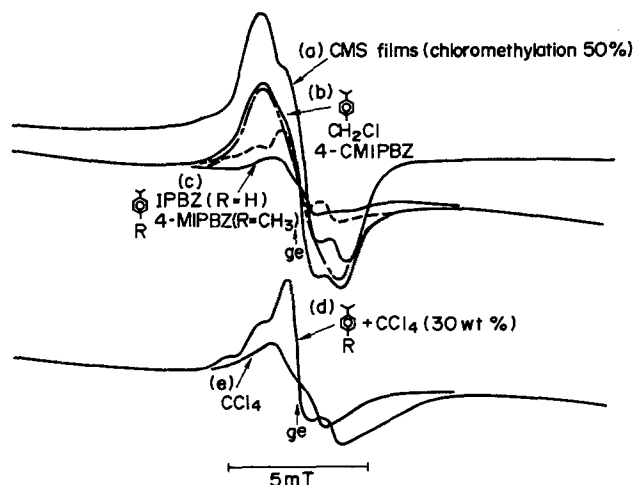


Fig. 2. Low temperature ESR spectra of deep-UV-irradiated samples. Solid line: observed spectra. Dot-dashed and dashed lines: simulated spectra.

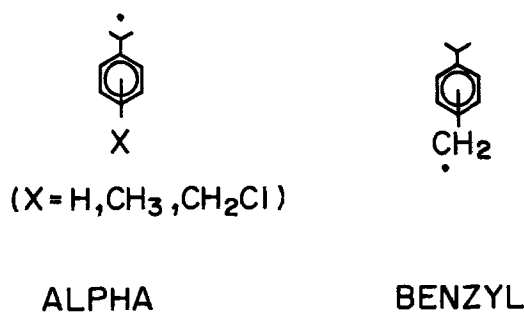


Fig. 3. Formulas for produced radicals

radiation-induced active chlorines and the model compounds. The mixtures showed a 1:4:6:4:1 quintet-featured signal (hyperfine splitting, 1.4 mT) (Fig. 2d), while carbon tetrachloride itself showed a singlet signal of 3.0 mT width (Fig. 2e). Thus, it is concluded that the quintet-featured signal is also formed through the interaction with radiation-induced active chlorines, in addition to the signal of a radiation-induced free radical.

Based on the conducted experiments mentioned above, the observed signal was analyzed using the 1:4:6:4:1 quintet signal and the gaussian-type singlet signal, with varying their signal strength and the singlet signal width so as to simulate the observed spectrum. Consequently, the observed spectrum was explained as a broad singlet signal (dot-dashed line in Fig. 2) of 4.4 mT width and a small quintet signal (dashed line). The deconvoluted main broad signal (dot-dashed line) is assigned to the radical formed through chlorine removal from a chloromethyl group (this type radical is hereafter termed "Benzyl," see Fig. 3). Bridge observed only a broad singlet signal of 4.6 mT width from γ -irradiated toluene at 77 K and assigned it to the benzyl radical (8). The obtained result is in good agreement with his result.

From these ESR analyses, the radicals produced by radiation in the initial stage of the reaction are found to be Benzyl generated from chloromethyl substituted constituents, and Alpha from the other substituents. From the integrated intensities of measured ESR signals (Fig. 2b and 2c), the amount of Benzyl produced through chlorine removal from 4-CMIPBZ is found to be ten times larger than that of Alpha produced through α -hydrogen removal from IPBZ or 4-MIPBZ. As a result, in the initial stage of the reaction, the main active species induced by radiation in chloromethylstyrene-based resists are Benzyl and simultaneously produced active chlorines, while Alpha is negligibly little.

GC-MS analyses.—The reactions of chloromethylstyrene-based resist materials, which take place on individual constituents of a polymer, have not been clarified sufficiently, because they are polymeric systems. GC-MS analyses using low molecular model compounds of which chemical structures are close to the repeating units of polymers can give us the information on the final products and their relative yields to clarify the reactions of individual constituents.

Final products from CMS model compounds.—CMS resist materials are composed of styrene and chloromethylstyrene. Thus, mixtures of IPBZ and 4-CMIPBZ can be used as model systems for them.

Measured GC gas chromatograms for a mixture of IPBZ (1 mol) and 4-CMIPBZ (1 mol) after being irradiated with deep UV are shown in Fig. 4. The signals of the final products formed were assigned by MS analyses.

The measured chromatograms show somewhat complicated features due to the isomers that result from *ortho*-, *meta*-, and *para*-CMIPBZ forms. The final products are classified into three groups. The first group products, [6], [12], and [14], are formed through the recombination of Alpha produced from IPBZ and CMIPBZ. The second group products, [10], [11], are formed through the recombination of Benzyl produced from CMIPBZ. The third

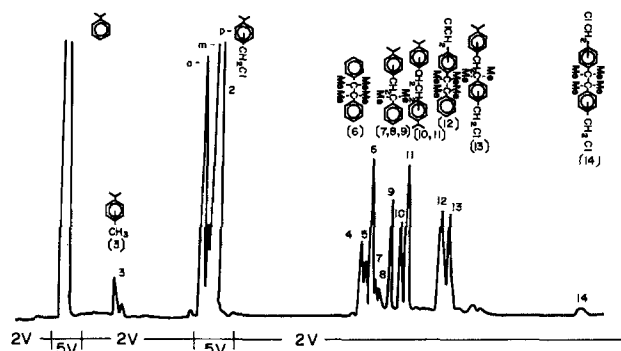


Fig. 4. Gas chromatograms for a deep-UV-irradiated mixture of isopropylbenzene IPBZ (1 mol) and 4-chloromethylisopropylbenzene 4-CMIPBZ (1 mol).

group products, [7, 8, 9] and [13], are formed through the recombination of Alpha and Benzyl. The product [3] is formed through the hydrogen abstractions by Benzyl [Bockrath *et al.* have recently reported in detail on hydrogen abstractions by benzyl radicals (9)].

Figure 5 shows production yields for the mixture (1:1 molar ratio) as a function of deep-UV irradiation time. Nonlinear parts were observed in the products [3] and [7, 8, 9]. This is because these products are formed through a thermally induced reaction, when mixtures were introduced into a GC-MS spectrometer for analyses, as well as through a radiation-induced reaction. In order to understand the thermally induced reaction, experiments were carried out on nonirradiated samples. The products [3] and [7, 8, 9] were produced thermally from nonirradiated mixture samples; on the other hand, the other products were not produced thermally. However, each compound was thermally stable and no change could be observed when it was introduced into a GC-MS spectrometer. An explanation for this phenomenon might be an intermolecular interaction between IPBZ and 4-CMIPBZ. The relative product yields were determined from the linear parts by excluding the parts of the thermally induced products.

The mixtures were also subjected to ^{60}Co γ -ray radiation for 80h. This radiation dose is estimated to be $20 \mu\text{C}/\text{cm}^2$ in electron-beam radiation using the depth-dose function (10). The main spectrum features were almost the same as those observed in deep-UV radiation. This indicates that the γ -ray radiation-induced reaction in this system is almost the same as the deep-UV-induced reaction.

Final products from CPMS model compounds.—A resist material obtained by chlorination of anionically prepared poly(vinyltoluene) (CPMS) has more than four types of units (5, 11). However, the main constituents are vinyltoluene and chloromethylstyrene. Thus, mixtures of 4-MIPBZ and 4-CMIPBZ can be used as model systems for this resist.

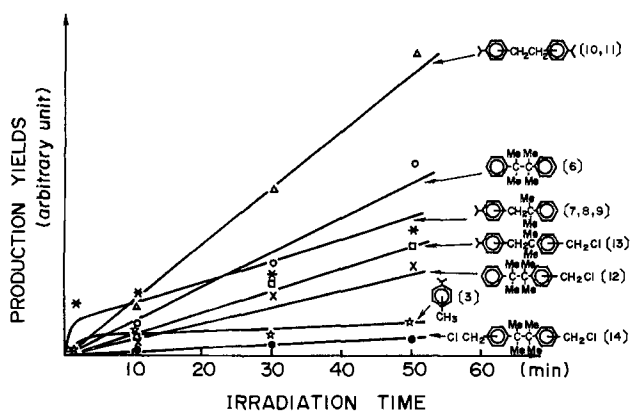


Fig. 5. Irradiation time dependences of production yields in a deep UV-irradiated mixture of isopropylbenzene IPBZ (1 mol) and 4-chloromethylisopropylbenzene 4-CMIPBZ (1 mol).

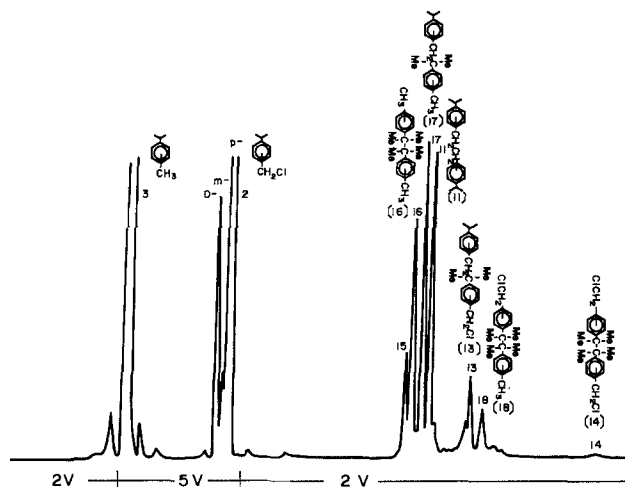


Fig. 6. Gas chromatograms for a deep UV-irradiated mixture of methylisopropylbenzene MIPBZ (1 mol) and 4-chloromethylisopropylbenzene 4-CMIPBZ (1 mol).

Measured GC chromatograms for a mixture of 4-MIPBZ (1 mol) and 4-CMIPBZ (1 mol) after being irradiated with deep UV are shown in Fig. 6. The signals of the final products formed were assigned by MS analyses. The final products are classified into three groups: Alpha-Alpha recombination products [14], [16], and [18], Benzyl-Benzyl recombination product [11], and Alpha-Benzyl recombination products [13] and [17].

In this mixture system, [17] was also produced through the thermally induced reaction; on the other hand, the other products were not formed thermally. The relative yields of final products were determined, taking this phenomenon into account in the same way as the case of CMS model systems.

4-CMIPBZ concentration effects on final product yields.—Sensitivity for chloromethylstyrene-based resist materials is markedly influenced by the component ratio for chloromethylstyrene moieties. Therefore, the effects of the 4-CMIPBZ concentration on final product yields are important factors in these resists. The relationships between relative yields and 4-CMIPBZ concentration are examined (see Fig. 7).

Observed signal intensities of final products produced from irradiated IPBZ and 4-MIPBZ ($x = 0$) were very weak and usually not detected¹; whereas mixtures containing 4-CMIPBZ showed large amounts of signals after being irradiated. This result indicates that chloromethylstyrene units are highly sensitive to radiation and that styrene and vinyltoluene units are rather less sensitive to it. Addition of small amount of 4-CMIPBZ to IPBZ or 4-MIPBZ enhanced the sensitivity of mixtures to radiation remarkably. This is in good agreement with the fact that small amount of chloromethylation enhances sensitivity markedly in chloromethylstyrene-based polymers (1).

It is noted that recombination products related to Alpha are formed largely in mixture samples, although the amount of Alpha in the initial stage of the reaction is negligibly little as indicated by the low temperature ESR analyses. This is because large amounts of Alpha are produced through subsequently occurring hydrogen abstractions by radiation-induced active species. The hydrogen abstractions take place through two types of processes. One is through the hydrogen abstraction by Benzyl, and

¹The observed signal strength from IPBZ or 4-MIPBZ was negligible compared with that from 4-CMIPBZ- or 4-CMIPBZ-containing mixtures. Thus, higher measurement range of a GC-MS spectrometer was employed in order to detect the very weak signals. The results indicated that Alpha-Alpha recombination product from IPBZ or 4-MIPBZ is mainly formed with being irradiated by ^{60}Co γ -ray or deep UV. This reveals that free radicals are formed on the α position of isopropylbenzene derivatives, if the benzene rings are not substituted by highly sensitive chloromethyl groups, and that the assignment of observed ESR signals from IPBZ or 4-MIPBZ is reasonable.

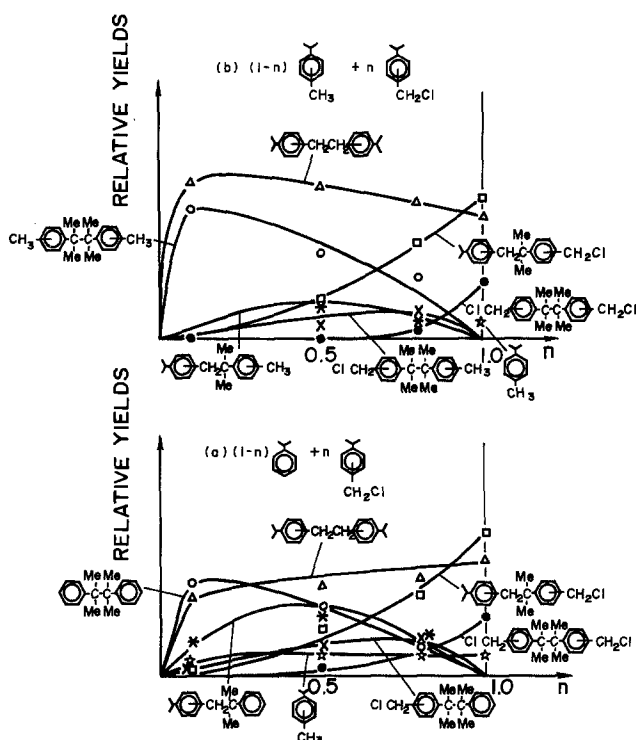


Fig. 7. Relationships between relative yields of final products and concentration of 4-chloromethylisopropylbenzene 4-CMIPBZ: (a) IPBZ-4-CMIPBZ for CMS, and (b) 4-MIPBZ-4-CMIPBZ for CPMS. 4-MIPBZ was detected as a final product from 100% 4-CMIPBZ and its mixtures with IPBZ (a). On the other hand, in the case of 4-CMIPBZ mixtures with 4-MIPBZ (b), the 4-MIPBZ formation as a final product could not be discussed because of the existence 4-MIPBZ as an irradiated component.

the other is through the hydrogen abstraction by active chlorines. Active chlorines are produced equivalently to the amount of Benzyl in the initial stage of the reaction. The amount of the hydrogen abstractions by Benzyl can be calculated with the amount of the final product [3], and its amount was found to be only less than 5% of the amount of the hydrogen abstractions by radiation-induced active chlorines. Thus, it is concluded that Alpha is produced mainly by the hydrogen abstractions by radiation-induced active chlorines.

The difference between the reaction of CMS model compounds (Fig. 7a) and that of CPMS model compounds (Fig. 7b) is the susceptibilities of individual constituents to hydrogen abstractions. Detailed discussions are presented quantitatively in the following section.

Discussion

Susceptibilities of individual constituents to hydrogen abstractions.—Susceptibilities of individual constituents to the hydrogen abstractions by radiation-induced active chlorines can be determined from the final product yields in 1:1 molar ratio mixtures. The relative yields in 1:1 molar ratio mixtures for CMS and CPMS are shown in Table I. Relative yields are expressed as the total amount of recombination products (I-VI) is unity. The amount of the radicals formed from individual moieties can be calculated through relating radical recombinations. For example, the Alpha-Benzyl recombination product VI is formed from Benzyl A and Alpha C.

In the radiation-induced model reaction for CMS, the relative amounts of radicals formed through the radiation-induced and the subsequent hydrogen abstractions are as follows: Benzyl 0.99, Alpha from IPBZ 0.74, and Alpha from 4-CMIPBZ 0.28. Therefore, the ratio of the hydrogen abstraction from IPBZ to that from 4-CMIPBZ is 2.6 to 1.

In the radiation-induced model reaction for CPMS, the amount of radicals formed through the radiation-induced and through subsequent hydrogen abstractions is as follows: Benzyl 1.23, Alpha from 4-MIPBZ 0.60, and Alpha from 4-CMIPBZ 0.17. In this case, Benzyl is considered to be partly produced from 4-MIPBZ through the hydrogen abstraction process by active chlorines, because large amounts of Benzyl, not explained quantitatively, are produced. In the initial stage of the reaction, equivalent amounts of active chlorines to those of Benzyl are produced by radiation, while Alpha produced through α -hydrogen removal is extremely little, as indicated by the low temperature ESR analyses. Furthermore, in the subsequent hydrogen abstraction reactions, the hydrogen abstractions by radiation-induced Benzyl can be negligible (less than 5%), compared with those by radiation-induced active chlorines. Thus, the total amount of the radicals formed through the subsequent hydrogen abstractions by active chlorines is equivalent to that of the radiation-induced Benzyl, assuming that all the radiation-induced active chlorines contribute only to the hydrogen

Table I. Final product relative yields for 1:1 molar ratio model compound systems for CMS and CPMS, and the relative amount of the produced radicals. The relative yields are expressed, taking the total amount of final products responsible for a cross-linking reaction as unity.

Final products		Systems	CMS (R=H)	CPMS (R=CH ₃)
ALPHA - ALPHA	I		0.22 (p ²)	0.23 (p ²)
	II		0.095 (2pq)	0.043 (2pq)
	III		0.015 (q ²)	0.007 (q ²)
BENZYL - BENZYL	IV		0.32	0.51
ALPHA - BENZYL	V		0.20	0.10
	VI		0.15	0.11
Produced radicals		Systems	CMS (R=H)	CPMS (R=CH ₃)
BENZYL	A		0.99	1.23
ALPHA	B		0.74	0.60
ALPHA	C		0.28	0.17

abstractions. The data obtained in the radiation-induced model reaction for CMS confirmed this hypothesis. For example, the amount of Benzyl (0.99) is almost the same as the total amount of Alpha B and C (1.02) in a 1:1 mixture sample. Thus, it is concluded that the extra amounts of Benzyl are formed from the methyl group of 4-MIPBZ, and its amount is the difference (0.46) between the amount of Benzyl A (1.23) and the total amount of Alpha's B and C (0.77). Therefore, the hydrogen abstractions from individual moieties is 6.2 from 4-MIPBZ (3.5 parts from the α position and 2.7 parts from the methyl group) to 1 from 4-CMIPBZ. This high susceptibility of 4-MIPBZ to hydrogen abstractions, in addition to the position of chlorination (11), could give CPMS resists somewhat different characteristics from those for CMS resists.

As a result, the susceptibilities of individual constituents to the hydrogen abstractions by radiation-induced active chlorines are 6.2 for 4-MIPBZ, 2.6 for IPBZ, and 1 for 4-CMIPBZ. These obtained susceptibilities are interpreted in terms of the electron donation of the substituents. The methyl group shows +I effects; on the other hand, the chloromethyl group shows -I effect. +I effect can stabilize the intermediate complex between a benzene ring and a chlorine radical. These results obtained are in good agreement with the photolysis data for substituted toluenes in carbon tetrachloride solution (12).

Radiolysis of model compounds.—The reactions for model compounds are shown in Fig. 8. In the initial stage of the reaction, free radicals and active chlorines are produced by deep UV or high energy radiation, such as ^{60}Co γ -ray and EB. In this stage, the amount of Alpha is less than one-tenth that of Benzyl produced through the chlorine removal. This is confirmed by the low temperature ESR analyses. Thus, Alpha produced is neglected in this stage.

In the next stage of the reaction, the two types of hydrogen abstractions take place by radiation-induced active chlorines and Benzyl. The abstractions by active chlorines take place through the charge-transfer complex between a benzene ring and an active chlorine (3). In this stage, the abstractions by radiation-induced active chlorines are the major process and their amount is 20 times more than that of the abstraction by Benzyl.

In the final stage of the reaction, final products are formed through the radical recombinations among the free radicals produced by radiation and by subsequently occurring hydrogen abstractions. It is noted that relative yields of the final products formed through the Alpha

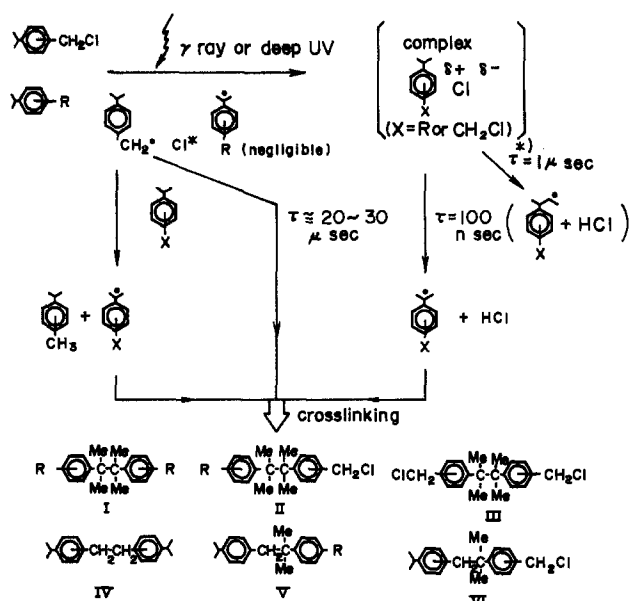


Fig. 8. Radiolysis of low molecular model compounds. R: substituents besides chloromethyl group. Cl^* : radiation-induced chlorine, Cl or Cl^- . *: For lifetime data, see Ref. (4).

cross- or home-recombinations (I, II, and III, see Table I) are nearly the same as the random collision probability for the related Alpha's; that is, the production yields of the product B-C formed through the cross-recombination between radical B and radical C is $2pq$, while the production yield of the home-recombination products B-B and C-C are p^2 and q^2 , respectively, where p and q denote the probabilities for the production of Alpha's B and C. This relationship can be seen in Table I. This fact implies that Alpha-Alpha recombination reactions take place through random collisions among Alpha's produced through hydrogen abstractions, and needs only small activation energy in this stage.

From GC-MS analyses, high energy (^{60}Co γ -ray) radiation and deep-UV radiation gave rise to the same final products with the same quantities. Thus, it was concluded that the high energy radiation-induced reactions are almost the same as the deep-UV radiation-induced reactions. Here, the high energy radiation-induced reactions are discussed in more detail.

In high energy radiation, such as electron beam, x-ray, and ^{60}Co γ -ray, ionization of organic materials is predominant in the initial stage of the reaction; on the other hand, in deep-UV radiation, excitation is predominant. This is the difference in the initial stage of both radiation-induced reactions.

In Fig. 9, high energy-induced reactions of CMIPBZ are shown as an example. Electrons produced through ionization generate Benzyl and chlorine anions through dissociative electron attachment, or generate excited CMIPBZ through geminate ion recombination. Whereas, the excited CMIPBZ generate Benzyl and chlorine radicals through homolytic splitting of covalent bonds. However, in the next stage of the reaction, both active chlorines, a chlorine anion and a chlorine radical, form the same charge-transfer complex to generate Alpha, as reported by time-resolved spectroscopic study (4). Therefore, the same final products are observed between the high energy radiation-induced reactions and the deep-UV radiation-induced reactions, in spite of the difference in the initial stage of the reaction.

Radiation-induced reaction of chloromethylstyrene-based resist materials.—On the basis of the radiolysis of model compounds, radiation-induced reactions of chloromethylstyrene-based resist materials are discussed. There are some differences to be considered between the radiation-induced reactions in polymeric materials and those in low molecular compounds. The differences arise mainly from the lifetimes and the diffusivities of free radicals. Therefore, when the radiation-induced reactions for polymeric materials are discussed compared with those for the model compounds, the lifetimes of free radicals responsible for a cross-linking reaction and the diffusion length of radiation-induced active chlorines have to be taken into account.

Tagawa *et al.* reported the lifetimes of Benzyl and the charge-transfer complex between a polymer unit and a

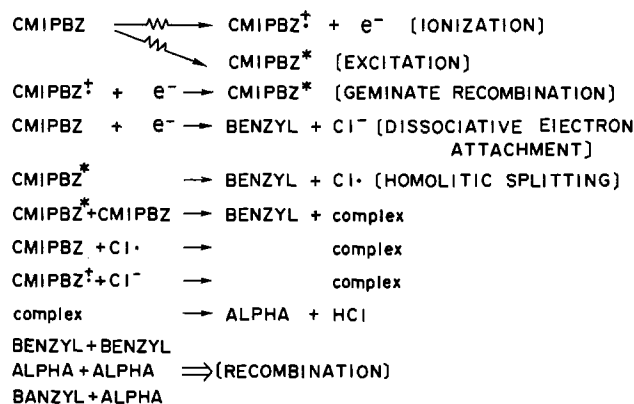


Fig. 9. High energy radiation-induced reactions of chloromethylisopropylbenzene CMIPBZ. Asterisks denote the excited states.

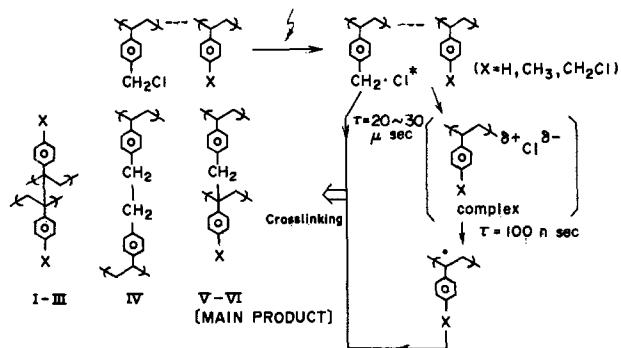


Fig. 10. Radiation-induced reactions of chloromethylstyrene-based resist materials.

radiation-induced active chlorine (4). Using the reported lifetimes, it can be determined which is the predominant reaction, recombination of radiation-induced Benzyl or hydrogen abstraction from polymer units through charge-transfer complexes. From their time-resolved spectroscopic data, the lifetime of Benzyl is about 20 μ s, and that of charge-transfer complexes is about 100 ns. Thus, 99.5% of Benzyl is still remained without recombination, while free radicals are formed through the subsequent hydrogen abstractions. Therefore, it is concluded that recombination of free radicals occurs after hydrogen abstraction reactions.

The other important factor is the diffusion length of radiation-induced active chlorines. This is because it is determined by the active chlorine diffusion length how closely the free radicals responsible for the cross-linking reaction are produced. Diffusion data for gases in polymers have been reported (13). Diffusivity coefficient of chlorines in polystyrene ($D = 9 \times 10^{-8}$ cm²/s at 25°C) was used to estimate the diffusion length [= $(D\tau)^{1/2}$] during hydrogen abstractions, where τ is the lifetime of the charge-transfer complex. The diffusion length is estimated as 9.5×10^{-8} cm. Thus, hydrogen abstractions by radiation-induced active chlorines extend to more than five units of a polymer. On the other hand, one Benzyl is estimated to be formed among 10-100 units of a polymer by radiation in resist materials from Charlesby's gel formation theory (14). Consequently, it is concluded that although Benzyl-Alpha recombinations are predominant in these resist materials, Alpha-Alpha and Benzyl-Benzyl recombinations cannot be neglected even in the polymeric materials, due to the large diffusion length of radiation-induced active chlorines.

Bartlett and McBride reported the disproportionation of 3,4-diphenyl-2,3,4,5-tetramethylhexane, which was formed through decomposition of azobis(2-phenyl-3-methylbutane) (15). According to their report, when large free radicals are put on Alpha, disproportionation (which would not lead to cross-linking) is considered to be important in polymeric materials compared with that in low molecular model compounds. However, in the case of the used model compounds, no ring-substituted α -methylstyrenes produced through the disproportionation of Alpha-Alpha products were observed. Furthermore, Weir and Milkie reported that the formation of C-C double bonds through disproportionation is not so predominant in ring-substituted polystyrenes (6). Therefore, the disproportionations of Alpha-Alpha products might occur, but they are not considered to be predominant in chloromethylstyrene-based polymeric materials.

The radiation-induced reactions of chloromethylstyrene-based resists are shown in Fig. 10. High sensitivity is achieved in these resists due to the hydrogen abstractions by radiation-induced active chlorines, which produce free radicals responsible for a cross-linking reaction, and the

high production yield of Benzyl. It is worthwhile to denote that the determined susceptibilities of individual constituents to hydrogen abstractions using model compounds are valid even in these polymeric materials.

Conclusion

The radiation-induced reactions of chloromethylstyrene-based resist materials have been discussed in detail, from the viewpoint of the radiolysis of low molecular model compounds of which chemical structures are close to the repeating units of the polymers. Low temperature ESR data show that main active species in the initial stage of the reaction are Benzyl radicals from chloromethyl derivatives and simultaneously produced active chlorines, while Alpha radicals induced by radiation through α -hydrogen removal are negligibly little. GC-MS data show that the hydrogen abstractions by radiation-induced active chlorines are the major process in a subsequently occurring reaction. It was found that large electron donating ring substituents increase the susceptibilities of individual constituents to the hydrogen abstractions.

Acknowledgments

The authors thank Professor Y. Hatano, Dr. Y. Shin-saka, and R. Yugeta, of Tokyo Institute of Technology, for their discussions in this study. They also thank Dr. H. Makino for affording them the chance to use the ESR spectrometer and H. Honda for her technical assistance in ESR measurements, and T. Masumoto for affording them the chance to use a Cary recording spectrophotometer.

Manuscript submitted Sept. 27, 1984; revised manuscript received March 22, 1985.

NEC Corporation assisted in meeting the publication costs of this article.

REFERENCES

1. S. Imamura, *This Journal*, **126**, 1628 (1979); E. D. Feit and L. E. Stillwagon, *Polym. Eng. Sci.*, **20**, 1058 (1980); K. Sukegawa and S. Sugawara, *Jpn. J. Appl. Phys.*, **20**, L583 (1981); H. S. Choong and F. J. Kahn, *J. Vac. Sci. Technol.*, **19**, 1121 (1981); S. Imamura, K. Harada, and S. Sugawara, *J. Appl. Polym. Sci.*, **27**, 937 (1982); T. Tamamura, K. Sukegawa, and S. Sugawara, *This Journal*, **129**, 1831 (1982).
2. Y. Kamoshida, M. Koshiba, H. Yoshimoto, Y. Harita, and K. Harada, *J. Vac. Sci. Technol. B*, **1**, 1156 (1983).
3. H. Gokan, S. Esho, and Y. Ohnishi, *This Journal*, **130**, 143 (1983).
4. S. Tagawa, M. Washio, Y. Tabata, and S. Hayashi, *Polym. Prepr., Jpn.*, **31**, 2073 (1983); Y. Tabata, S. Tagawa, M. Washio, and S. Hayashi, *Polym. Prepr. Am. Chem. Soc., Div. Polym. Chem.*, **25**, 289 (1984).
5. Y. Harita, Y. Kamoshida, K. Tsutsumi, M. Koshiba, H. Yamamoto, and K. Harada, Paper 287 presented at The SPSE 22nd Fall Symposium, Washington, DC, 1982.
6. N. A. Weir and T. H. Milkie, *J. Polym. Sci. Polym. Chem. Ed.*, **17**, 3735 (1979).
7. See, for example, R. E. Frorine, L. A. Wall, and D. W. Brown, *J. Polym. Sci., Part A*, **1**, 1521 (1963); S. Ohnishi, T. Tanei, and I. Nitta, *Chem. Phys.*, **37**, 2402 (1962).
8. N. K. Bridge, *Nature*, **185**, 31 (1960).
9. B. Bockrath, E. Bittner, and J. McGrew, *J. Am. Chem. Soc.*, **106**, 135 (1984).
10. J. S. Greeneich, *This Journal*, **122**, 970 (1975).
11. R. Tarascon, M. Hartney, and M. J. Bowden, *Polym. Prepr., Am. Chem. Soc., Div. Polym. Chem.*, **25**, 289 (1984).
12. G. A. Russel, in "Free Radical," Vol. 1, J. K. Kochi, Editor, pp. 275-331, John Wiley and Sons, New York (1973).
13. J. Crank and G. S. Park, "Diffusion in Polymers," Academic Press, New York (1968).
14. A. Charlesby, *Proc. R. Soc. London, Ser. A*, **222**, 542 (1954).
15. P. H. Bartlett and J. M. McBride, *Pure Appl. Chem.*, **15**, 89 (1967).

Diffusivity and Thermal Cracking Rate of Metalorganic Gases by Chromatography

Motoyuki Suzuki* and Michio Sato

Institute of Industrial Science, University of Tokyo, Tokyo 106, Japan

ABSTRACT

Metalorganic gases such as trimethylaluminum (TMA), trimethylgallium (TMG), triethylaluminum (TEA), and triethylgallium (TEG) are often used as metal sources of chemical vapor deposition for producing epitaxial thin films of GaAs or GaAlAs. Film growth kinetics are governed by thermal cracking of those gases in a thermal boundary layer which is expected to develop on the heated substrate and also by diffusion of those gases from bulk stream into the boundary layer. Since there has been poor understanding on physicochemical properties of these gases, such as rate of thermal cracking reaction and molecular diffusion, the present work is aimed to determine these properties by means of a chromatographic technique (pulse-response analysis) developed in the field of chemical engineering. Method of moment was used to analyze chromatographic elution curves and measurements at different temperature ranges provided diffusivities (293-428 K) and thermal cracking rate coefficients (454-580 K) of the four gases in hydrogen stream.

During the last decade, metalorganic chemical vapor deposition (MOCVD) has collected wide attention because of its advantages: ease in controlling an epitaxial layer thickness and adaptability to production in large scale. This technique was first developed by Manasevit for growing GaAs epitaxial film on an insulator substrate (1). Since then, many applications of this technique have been tried to prepare devices of different compositions.

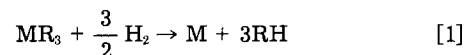
When epitaxial growth of GaAs, for instance, is tried, the growth rate of the film appears proportional to the concentration of metalorganic gas, while it is little influenced by the concentration of arsine or a substrate temperature when the same equipment and the same total gas velocity are used. Also, gas velocity has some influence on the growth rate (2). These facts suggest that supply of metalorganic gas from a bulk stream to the surface of epitaxial layer is one of the significant factors in controlling overall kinetics of the epitaxial growth. Transport phenomena involved in MOCVD have to be studied in more detail in order to determine the precise mechanisms of the growth in this arrangement. Then on the basis of this information, a rational design for the reactor becomes possible, and precise control of product layer thickness, alloy composition, and other resultant electronic characters become controllable. For the above described purpose, it is essential to know such properties of metalorganic gases as diffusivity and thermal cracking rate for an understanding of what happens near the substrate kept at a high temperature.

Trimethylaluminum (TMA), trimethylgallium (TMG), triethylaluminum (TEA), and triethylgallium (TEG) are often employed as the metal-source gases for the growth of GaAs or GaAlAs files by MOCVD method. The present work focuses on determination of the diffusivities and the thermal cracking rate coefficients of these gases in a hydrogen stream which is usually used as a carrier in MOCVD. Those properties are determined by employing chromatographic technique (Fig. 1 outlines the chromatographic experiment) which has been often used for obtaining rate parameters in a complexed system (3). Pulse of metalorganic gas was introduced in a hydrogen stream flowing in a column packed with inert glass beads kept at a constant temperature. The effluent peak from the column was detected by mass spectrometry and analyzed by the method of moment. Measurements at the low temperature ranges where thermal cracking is considered negligible provided diffusibilities of these gases, while thermal cracking rate coefficients were obtained from the higher temperature runs.

Theory of Chromatography

Metalorganic gas in hydrogen is decomposed to metal and hydrocarbon at high temperature. The overall reaction is

*Electrochemical Society Active Member.



When hydrogen exists in large excess, the reaction rate is considered first order regarding concentration of metalorganic gas. Then mass conservation of metalorganic gas in the column packed with inert glass beads leads to an equation which describes a concentration pulse introduced at the inlet of the column

$$Ez \frac{\partial^2 C}{\partial z^2} - u \frac{\partial C}{\partial z} = \epsilon k C + \epsilon \frac{\partial C}{\partial t}$$

$$z = 0 : C = M \delta(t)$$

$$z = \infty : C = 0 \quad [2]$$

where Ez represents the axial dispersion coefficient of metalorganic gas, u is the superficial velocity of a carrier gas based on the cross-sectional area of the column, ϵ is the void fraction of the column, and k is the first-order reaction rate constant. As the boundary conditions, M is the intensity of pulse introduced at the inlet of the column and $\delta(t)$ means the delta function defined as

$$\delta(t) \begin{cases} \delta(0) = \infty \\ \delta(t \neq 0) = 0 \\ \int_{-\infty}^{\infty} \delta(t) dt = 1 \end{cases} \quad [3]$$

Equation [2] can be transformed and solved in the Laplace domain, and the solution in the Laplace domain which contains three parameters (Ez , ϵ , and k) directly gives moments of the effluents peak in the time domain (3). The moments of the effluent peak are defined by the following equations.

The zeroth reduced moment, which is defined as the ratio of the amount of the unreacted sample detected at the outlet of the column and that of the sample introduced at the inlet, is calculated as

$$\mu_0 = \frac{\int_0^{\infty} C dt}{M} \quad [4]$$

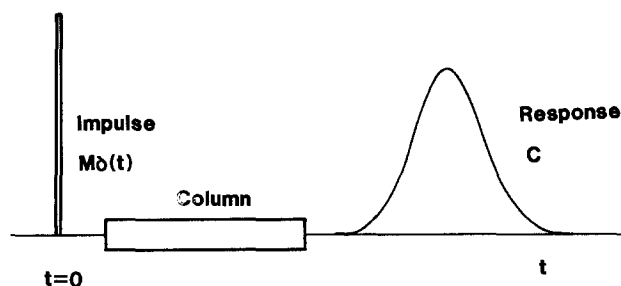


Fig. 1. Chromatographic experiment

The first absolute moment is obtained as

$$\mu_1 = \frac{\int_0^\infty tC dt}{\int_0^\infty C dt} \quad [5]$$

and the second central moment as

$$\mu_2 = \frac{\int_0^\infty (t - \mu_1)^2 C dt}{\int_0^\infty C dt} \quad [6]$$

The moment solutions of the general equations, which describe the mass balance in a fixed bed reactor, have been obtained by Suzuki and Smith (3). Equation [2] is a simplified form of the general equation and the moment solution of Eq. [2] can be obtained from their work by omitting the terms related to adsorption, intraparticle diffusion, and surface reaction in the general moment solutions.

Zeroth-reduced, first-absolute and second-central moments are written as

$$\begin{aligned} \mu_0 &= \exp \left[\frac{uz}{2Ez} (q_0 - 1) \right] \\ &= \exp \left(- \frac{\epsilon z}{u} k \frac{2}{q_0 + 1} \right) \end{aligned} \quad [7]$$

$$\mu_1 = \frac{\epsilon z}{u} \frac{1}{q_0} \quad [8]$$

$$\mu_2 = \frac{2Ez\epsilon^2 z}{u^3} \frac{1}{q_0^3} \quad [9]$$

where

$$q_0 = \sqrt{1 + \frac{4Ez\epsilon k}{u^2}} \quad [10]$$

By comparison among Eq. [7]-[10] and the corresponding moments determined for varieties of conditions, parameters Ez , ϵ , and k can be obtained.

Special cases.—No reaction—diffusivity from the second moment.—If the column is kept at a low temperature, thermal cracking can be neglected. When k can be regarded as zero in Eq. [10], q_0 becomes 1 and then the zeroth moment, which represents the fractional ratio of the uncracked metalorganic gas, becomes unity. Then from the second central moment, the axial dispersion coefficient, Ez , can be obtained as

$$Ez = \frac{\mu_2(2z/u)}{(\epsilon/u)^2} \quad [11]$$

where the void fraction of the column, ϵ , is readily obtained from the first moment

$$\epsilon = \mu_1/(z/u) \quad [12]$$

Axial dispersion coefficient in a packed column may be written as (4)

$$Ez = \eta D + lu \quad [13]$$

The first term in the right side of Eq. [13] means the effect of molecular diffusion, and the second term shows the effect of convective dispersion due to the gas flow. In the case of very low gas velocity, the effect of dispersion becomes small enough and Ez approaches the constant value ηD . Diffusibility η is a parameter specific to the column determined by packing configurations. First, the measurement of η is carried out by using helium pulse in a hydrogen carrier, where molecular diffusivity is known.

Then the diffusivity of each gas is obtained from Ez determined from Eq. [11] by using Eq. [13].

Thermal cracking rate coefficient from the zeroth moment.—If the column temperature is raised, thermal cracking occurs and zeroth reduced moment becomes less than unity. Also, when the cracking rate is not too high, q_0 is calculated from Eq. [10] to be about 1.001. Then the magnitude of $[2/(q_0 + 1)]$ in Eq. [7] can be regarded as approximately 1. Then the thermal cracking rate coefficient can be obtained from semilog plots of the zeroth moments for each temperature *vs.* the residence time ze/u .

Experimental

The schematic diagram of experimental apparatus is shown in Fig. 2. A column was a copper tube 1/4 in. in outer diameter, 2m long, and packed with glass beads (Shiraki Rikagaku Company) whose average diameter was 0.5 mm. Carrier gas was pure hydrogen of research grade. Flow rate of the carrier gas was limited up to 70 cm³/min because of the excessive pressure drop of the column beyond this rate. Metalorganic gas was maintained in a stainless bubbler cooled in a constant-temperature bath and was vaporized by introducing a small amount of pure hydrogen flow. The bubbler temperature was 283 K for TEG and 273 K for TMA, TMG, and TEA. The column temperature was maintained constant by a thermostatic oven. A six-way valve was used to introduce the gas pulse whose volume was 0.30 cm³. Gas flow rate was measured by a soap flow meter situated after the column.

A needle valve splitter just behind the column was used to lead a small amount of the outlet gas into quadrupole mass spectrometer (QMS) (TE-600 Anelva Corporation), which is furnished with multiple ion selector (MIS). About 0.3 cm³/min effluent gas was led into the QMS. The chamber pressure of the QMS was about 10⁻⁶ torr.

A mass spectrometer is suitable for the present chromatographic experiment, since it has very little effective dead volume because of the high vacuum of the chamber and it also has the base line stability brought about from its principle of detection: MS detects the sample dislocated electrically at the ion source. If the amount of introduced gas and the chamber pressure are kept constant during the experimental run, MS is not influenced by the alteration of another parameter (gas velocity or temperature in the column).

In this experiment, mother peaks of metalorganic gases were scarcely detected, so that fragment peaks (CH₃⁺ of 15 amu for TMA and TMG, C₂H₅⁺ of 29 amu for TEA and TEG) were measured for determination of uncracked metalorganic gases.

When carrier gas is hydrogen, hydrocarbon is easily formed by combination of the alkyl ions, which are products of electrical cracking, and the hydrogen in vacuum chamber, and it appears as recombination peaks. Metalorganic gas and the corresponding hydrocarbon gas (CH₄ or C₂H₆) are indistinguishable by QMS only.

In thermal cracking rate measurement, Dry Ice-methanol cold trap was prepared for the purpose of

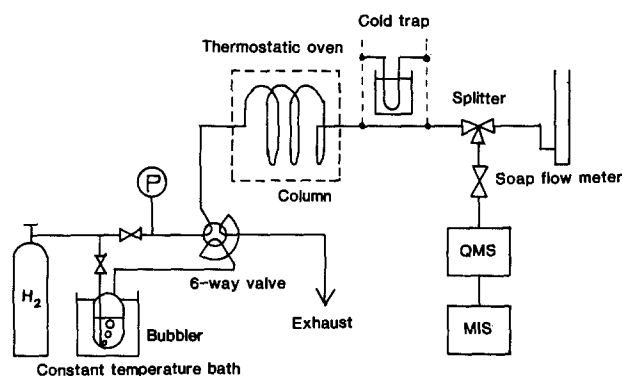


Fig. 2. Schematic diagram of experimental apparatus. Cold trap was used in thermal cracking rate measurement.

removing the uncracked metalorganic gases from the stream. The glass beads packed column (1/8 in. od, 30 cm long) was kept in the Dewar vessel filled with Dry Ice-methanol. Fragment peaks of hydrocarbon were used for quantitative determination of the extent of thermal cracking reaction.

The amount of hydrocarbon was

$$\int_0^{\infty} C dt \text{ (with cold trap)} \quad [14]$$

and the amount of total CH_3 or C_2H_5 , which represents total amount of metalorganic gas and hydrocarbon, was

$$\int_0^{\infty} C dt \text{ (without cold trap)} \quad [15]$$

The zeroth moment was defined as

$$\mu_0 = \frac{\int_0^{\infty} C dt \text{ (without cold trap)} - \int_0^{\infty} C dt \text{ (with cold trap)}}{\int_0^{\infty} C dt \text{ (without cold trap)}} \quad [16]$$

Results and Discussion

Preliminary runs.—First, temperature effects on cracking of the gases were examined from decrease of elution peak area, *i.e.*, zeroth moments. Below 450 K, no appreciable decrease of the peak area was observed, and then the diffusion measurements were performed between room temperature and 450 K. As a consequence, thermal cracking rates were obtained above 450 K until the temperature where no elution peak of metalorganic gas was detected.

Second, for determining column characteristics, helium pulse was introduced into a hydrogen stream flowing in the column and then elution curve analysis gave void fraction, ϵ , and diffusibility, η , in the column which becomes important for correcting the effect of the gas flow in calculating the molecular diffusivities of the metalorganic gases.

From the first moment of the helium peak, the void fraction of the bed was determined in good accuracy to be 0.405. This value is used for the estimation of axial dispersion coefficient of helium from the second moment of helium elution peaks as described earlier. Since molecular

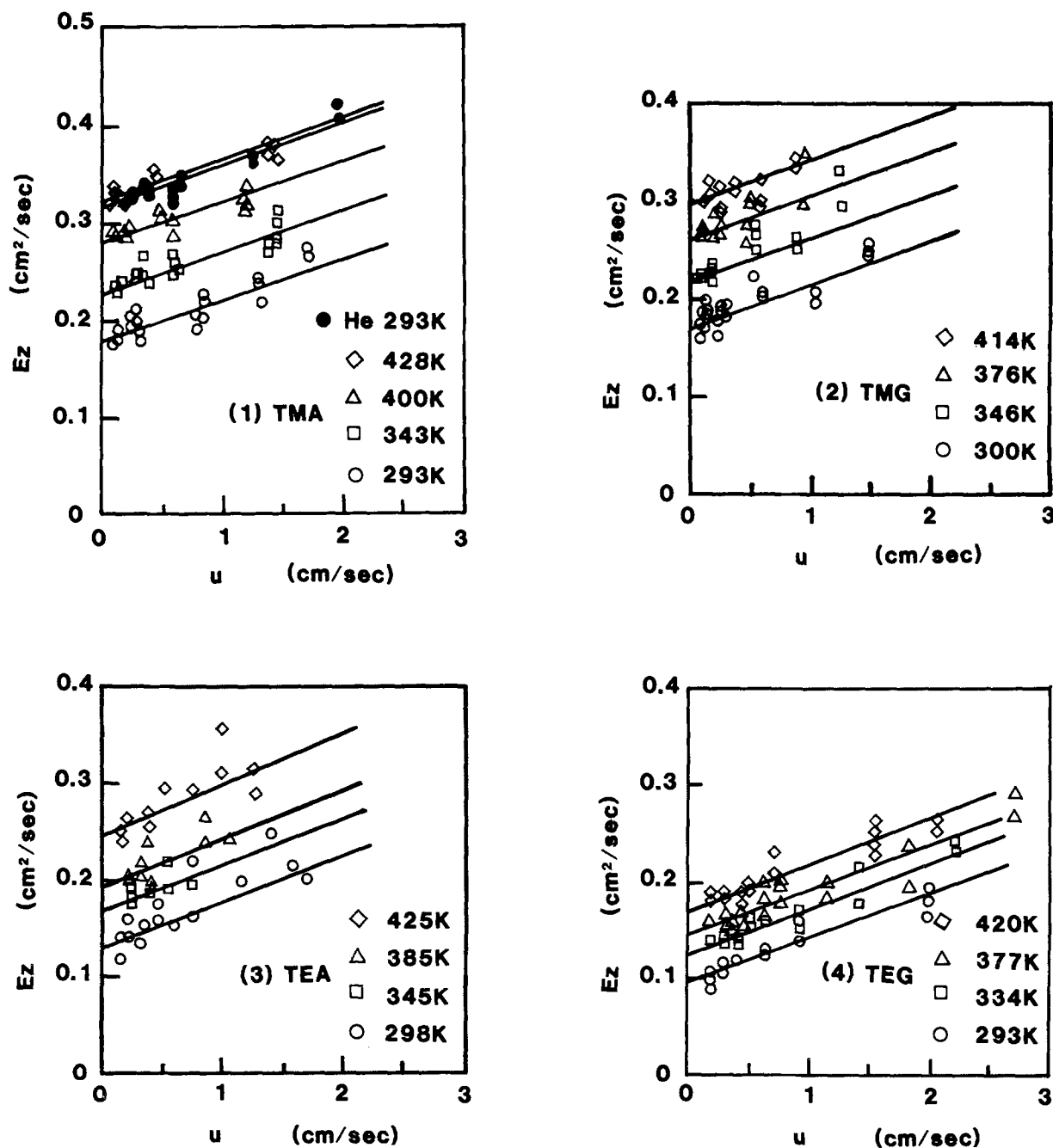


Fig. 3. Relationship between axial dispersion coefficient, E_z , and superficial velocity, u . 1: TMA: $\text{Al}(\text{CH}_3)_3$ and He. 2: TMG: $\text{Ga}(\text{CH}_3)_3$. 3: TEA: $\text{Al}(\text{C}_2\text{H}_5)_3$. 4: TEG: $\text{Ga}(\text{C}_2\text{H}_5)_3$.

diffusivity of helium in hydrogen is given as $D_{He} = 1.132 \text{ cm}^2/\text{s}$ at 298.2 K (5), from the plot shown by solid circles in Fig. 3.1, diffusibility, η , is determined as $\eta = 0.285$. Suzuki and Smith reported $\eta = 0.30$ for a similar glass beads ($d_p = 0.51 \text{ mm}$) packed column (4), which suggests that the figure given here is reasonable.

Diffusivity of metalorganic gases.—Figures 3.1-3.4 show the relationship between axial dispersion coefficient, E_z , of metalorganic gases and superficial velocity, u , at room temperature or at high temperatures to about 420 K.

Though the second moments, from which E_z is calculated, are susceptible to scattering error introduced by experimental difficulties on evaluation of tail part of the elution peaks, the reproducibility of E_z is upgraded by careful experiments at low gas velocities and repeated measurements at similar conditions. From the linear regression lines of slope, l , according to Eq. [13], the intercept at the ordinate in the figures gives diffusivity of the gas from Eq. [13] by using the diffusivity determined in the preliminary runs. Thus obtained molecular diffusivities of the four gases are shown as functions of temperature in Fig. 4. Molecular diffusivities are proportional to the 1.7 power of the absolute temperature. This tendency is quite reasonable when compared with the general equations presented for diffusivity of gas (6). Also, the magnitudes of diffusivities determined here are similar to those of the hydrocarbons whose carbon numbers are the same (propane with TMA and TMG, cyclohexane or hexane with TEA and TEG).

Fuller *et al.* (6) reported that molecular diffusivity is proportional to the value $\sqrt{1/M_1 + 1/M_2}$. Since $1/M_1$ of hydrogen is so large, molecular weight of metalorganic gas has little influence on the diffusivity. Mainly, the diffusion volume or collision diameter in H_2 has a controlling effect on the diffusivity.

In the vapor phase TMA, monomer is considered to exist in an equilibrium state with its dimer and the equilibrium constant of the dissociation is given as 2.83×10^{-3}

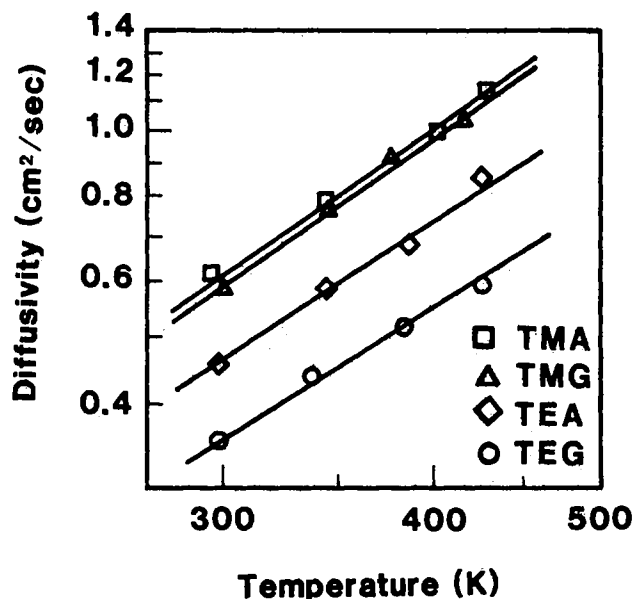


Fig. 4. Temperature dependency of molecular diffusivity. Metalorganic gases in hydrogen.

atm at 373.5 K (7). The TMA bubbler was kept at low temperature, and the gas pulse was steadily spread in the column; the concentration of TMA was estimated to be below $8 \times 10^{-3} \text{ mol/m}^3$ ($2 \times 10^{-3} \text{ atm}$) in the column, which is small enough to assume that dimerization is negligible.

Also, it may be reasonable to assume that the metal atom attracts the alkyl groups and that the molecular shape of metalorganic gas is globular, as the alkyl groups are distributed around the metal atom as a center. Thus, the volume of the metal has little influence on the diffusion volume. Because the bonding energy of aluminum

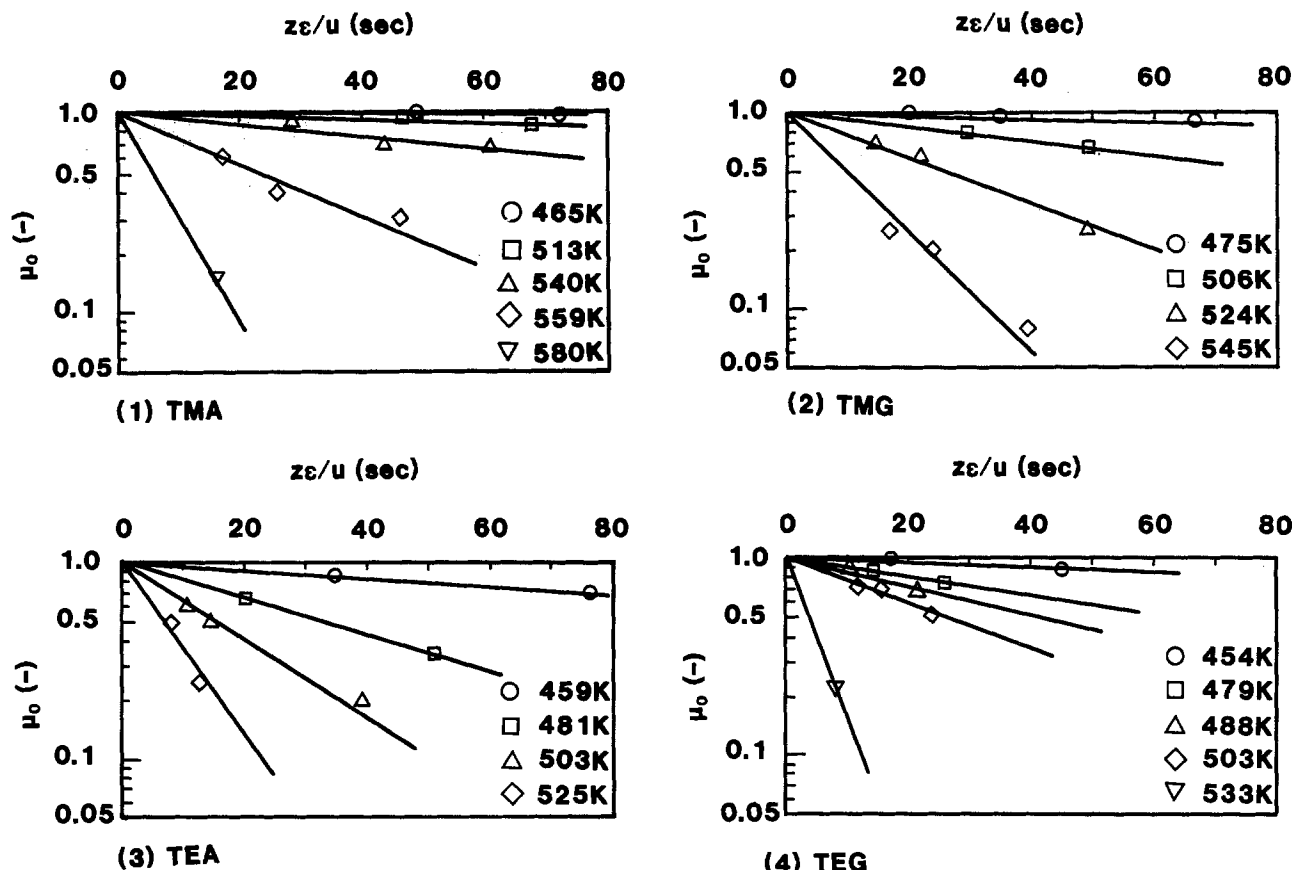


Fig. 5. Relationship between zeroth moment, μ_0 and residence time, $z\epsilon/u$. 1: TMA:Al(CH₃)₃. 2: TMG:Ga(CH₃)₃. 3: TEA:Al(C₂H₅)₃. 4: TEG:Ga(C₂H₅)₃.

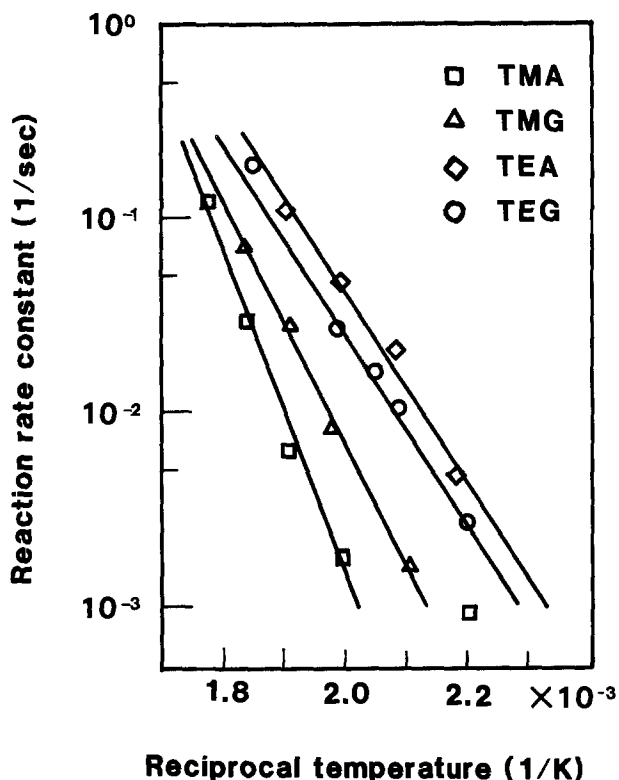


Fig. 6. Arrhenius plots of thermal cracking rate constant of metalorganic gases in hydrogen.

and carbon is stronger than that of gallium (8), the ethyl groups of TEA cannot spread themselves. Thus the diffusion volume of TEA may become smaller than that of TEG, resulting in higher diffusivity of TEA.

Thermal cracking rate coefficient.—Metalorganic gas in hydrogen is decomposed to metal and hydrocarbon at higher temperatures. Hydrogen, the carrier gas of this experiment and also of ordinary MOCVD systems, is also a reactant of the thermal cracking reaction. However, it usually exists in excess enough to make it possible to assume that the reaction is first order regarding the metalorganic gas.

Glass beads are expected to be inert fillers in this experiment. In the thermal cracking experiment, metal of aluminum and gallium deposited in the column and covered the surface of the glass beads, but there was observed no difference between the reaction rate in a new column and that after many repeated runs. Then, it may be reasonable to assume that glass beads or metal surface have no influence on the cracking reaction.

Figures 5.1-5.4 show the relationship between the residence time and μ_0 , the fraction of the uncracked metalorganic gas. The linearities of these plots mean that the assumption of the first-order kinetics is reasonable. From the slope of the line, the cracking rate coefficient, k , at that temperature can be obtained by means of Eq. [7]. Temperature dependencies of the reaction rate coefficient, k , are shown by Arrhenius plot in Fig. 6.

The elementary process of this cracking reaction is not known, and in this experiment intermediate products (MR or MR_2 were expected) could not be detected by QMS. But from the slopes of the plots given in Fig. 6 using Eq. [17], the activation energy for the overall kinetics can be obtained for each reaction, and these are listed in Table I.

$$k = A \exp\left(-\frac{E_{act}}{RT}\right) \quad [17]$$

Heats of the thermal cracking reactions in concern can be calculated from the quoted data by Stone and West (8) and are included for comparison in Table I. Methyl com-

Table I. Activation energy and heat of cracking. Metalorganic gases in hydrogen

	Activation energy (kJ/mol)	Heat of cracking (kJ/mol)
TMA, [Al(CH ₃) ₃]	158.6	90.4
TMG, [Ga(CH ₃) ₃]	119.7	139.3
TEA, [Al(C ₂ H ₅) ₃]	84.5	193.3
TMG, [Ga(C ₂ H ₅) ₃]	91.6	203.3

pounds have larger activation energies and smaller heats of the cracking reaction compared with the corresponding ethyl compounds. This suggests that they are more stable than the ethyl compounds in hydrogen at higher temperatures.

Conclusion

Molecular diffusivities and thermal cracking rate coefficients were obtained by chromatographic experiment for the four metalorganic gases, trimethylaluminum, trimethylgallium, triethylaluminum, and triethylgallium, in hydrogen stream. The chromatographic method is found to be an appropriate method for the objective of those measurements. The diffusivities of these gases are of the same magnitude as the common hydrocarbons with the same carbon number. From the thermal cracking rate data, it was concluded that trimethyl compounds are more stable than the corresponding triethyl compounds. By employing these data, kinetics of growth of thin films in MOCVD reactors can be more precisely described in terms of transport processes and chemical reaction in a boundary layer developed on the thin film, which helps future progress in this field.

Manuscript submitted Nov. 19, 1984; revised manuscript received March 13, 1985.

LIST OF SYMBOLS

A	frequency factor (s^{-1})
C	concentration of metalorganic gas (mol/cm^3)
d_p	particle diameter (mm)
D	molecular diffusivity (cm^2/s)
E_{act}	activation energy of thermal cracking (J/mol)
E_z	axial dispersion coefficient based on cross-sectional area of column (cm^2/s)
k	first-order reaction rate constant (s^{-1})
l	scale of dispersion (cm)
M	amount of pulse (mol)
M_i	molecular weight of i (g/mol)
R	gas constant (J/K-mol)
t	time(s)
T	absolute temperature (K)
u	superficial velocity of gas (cm/s)
z	length of column (cm)

Greek letters

ϵ	void fraction of column (-)
$\delta(t)$	delta function defined in Eq. [3]
η	diffusibility (-)
μ_0	zeroth reduced moment (-)
μ_1	first absolute moment (s)
μ_2	second central moment (s^2)

REFERENCES

- H. M. Manasevit, *Appl. Phys. Lett.*, **12**, 156 (1968).
- M. R. Leys and H. Veenvliet, *J. Cryst. Growth*, **55**, 145 (1981).
- M. Suzuki and J. M. Smith, *Chem. Eng. Sci.*, **26**, 221 (1971).
- M. Suzuki and J. M. Smith, *Chem. Eng. J.*, **3**, 256 (1972).
- "Kagaku-Kogaku Binran," 4th ed., Chap. 1-7, M. Yorimi, S. Saito, and N. Yoshimura, Chapter Editors, Maruzen, Tokyo (1978).
- E. N. Fuller, P. D. Schettler, and J. C. Giddings, *Ind. Eng. Chem.*, **58**, 19 (1966).
- A. W. Laubengayer and W. F. Gilliam, *J. Am. Chem. Soc.*, **63**, 477 (1941).
- S. G. A. Stone and R. West, "Advances in Organometallic Chemistry," Vol. 2, Academic Press, New York (1964).

Reduction of Sodium Ion Density in Molybdenum-Gate MOS Devices with the Addition of Tantalum to Gate Electrodes

Shin-ichi Ohfuji* and Noboru Shiono

Nippon Telegraph and Telephone Public Corporation, Atsugi Electrical Communication Laboratory, 1839 Ono, Atsugi-shi, Kanagawa Prefecture, 243-01 Japan

ABSTRACT

The reduction mechanism of mobile ion contamination in Ta-Mo alloy gate MOS structures has been examined by varying the deposition and annealing conditions of gate metals. Mobile ion density in the gate SiO₂ for the Ta-Mo gate structures decreases drastically after forming gas annealing at 1000°C, whereas the density increases during nitrogen gas annealing. The structure and composition analysis for the Ta-Mo gate observed by x-ray diffraction, SIMS, and AES indicates that nitriding of Ta-Mo films occurs during the forming gas annealing, and the nitride, MoTa₃N (tetragonal, CrNbN-type structure), is stable even at 1000°C during annealing. These facts suggest that MoTa₃N formation at the boundaries of Mo grains, which is similar to the stuffing effect observed in TiN films, is responsible for immobilizing the sodium atoms within the gate electrodes. As a result, the diffusion of sodium from the gate electrode into the SiO₂ layers is suppressed.

With regard to the development of highly conductive and self-aligned gate electrodes and interconnection lines, molybdenum (Mo) is under active investigation as an alternative to the widely used polycrystalline silicon gate in MOS LSI's (1). In the self-aligned gate process, high temperature annealing above 900°C is necessary to activate implanted ions in the source and drain regions following gate electrode formation. This process causes the impurities sodium (Na) and potassium (K), contained in the Mo electrodes and having a concentration less than 1 ppm (2), to diffuse into the gate SiO₂ layers. This alkali ion contamination is known to result in flatband voltage shifts in MOS structures (3). It is essential to prevent this ionic Na and K contamination in the thermally grown SiO₂ layers in order to stabilize the Mo-gate MOS characteristics.

A phosphosilicate glass stabilization process (4) and an oxidation technique for silicon in the presence of chlorine and chlorine compounds (5) have been developed as methods to obtain passivated oxides. Another possible solution, high temperature annealing of Mo gate electrodes in a forming gas, has been reported to be effective in reducing this contamination (6). We have recently shown that the effect of forming gas annealing is enhanced by hydrogen doping and the addition of tantalum to Mo films (2). The Ta addition is intended to increase the amount of doped hydrogen in the films as a result of the fact that Ta has a higher hydrogen absorption property than Mo (7). It has also been shown that the Na diffusion from these specially designed gate electrodes into the gate oxides is almost entirely prevented when high temperature annealing is performed in a forming gas, although the physical origin of this effect remains unclear.

In this work, a reduction mechanism of mobile ion contamination in the Ta-Mo alloy gate MOS structures is examined by varying the deposition and annealing conditions of gate metals. Structural and compositional changes in the Ta-Mo films as a function of process conditions are measured using an x-ray diffractometer, SIMS, and AES, and are compared with the mobile ionic charge density in the gate SiO₂ measured by the triangular voltage sweep method. Metal nitride formation, which is induced by the Ta addition, is discussed as a cause for the reduction of Na ion density in the gate SiO₂.

Experimental

Ta-Mo alloy-gate MOS capacitors were fabricated on p-type (100) Si wafers of 4-6 Ω-cm resistivity. Thin gate SiO₂ was grown on the wafers in a dry O₂ ambient at 950°C to a 400Å thickness. The H-doped Ta-Mo alloy films, 3300Å thick, were co-sputtered using an RF planar magnetron sputtering apparatus with two independent Ta and Mo targets at pressure 1 × 10⁻² torr in a mixed H₂(20%) and Ar(80%) ambient for H doping. The purity of

* Electrochemical Society Active Member.

both the Mo and Ta targets was more than 99.95%. The RF power was divided between the two targets at various ratios so as to control the Ta concentration in the films from 0 to 100 atom percent (a/o).

Gate electrodes of 500 × 500 μm were defined by conventional photolithography and chemical etching using an H₃PO₄-HNO₃ solution. After patterning the gate electrodes, high temperature annealing was carried out at 1000°C in an N₂ ambient and/or a forming gas ambient (H₂:N₂ = 1:9 by volume). This annealing step also serves as an activation of implanted dopant in the source and drain regions in the self-aligned gate process for FET's. A subsequent low temperature annealing in forming gas (H₂:N₂ = 1:2) was performed at 450°C for 30 min for all samples in order to reduce the interface trap density at the Si/SiO₂ interface.

The mobile ionic charge density N_m in the MOS structures was measured by the triangular voltage sweep method (TVS) with a 50 mV/s ramp rate at 270°C. The detection limit of this method was less than 5 × 10⁹ cm⁻². The electrical resistivity of the films were determined by a four-point probe method in conjunction with thickness measurements using a Talystep (Rank Taylor Hobson). Depth distribution profiles for the Na in the MOS structures were measured by SIMS (CAMECA, IMS-3F) with a 15 kV primary O₂⁺ ion beam. The film structure was investigated using an x-ray diffractometer. The average grain size for Mo was determined from the broadening of the diffraction peaks of Mo(110), using Scherrer's equation (8).

Results and Discussion

Reduction of ionic charge density.—Figure 1 shows variations in mobile ionic charge density, N_m , and electrical resistivity of electrode films for H-doped Ta-Mo alloy gate MOS structures (denoted as "H-Ta-Mo"), after annealing in forming gas at 1000°C for 30 min, as a function of Ta concentration in the electrodes. In this case, gate electrodes of 500 × 500 μm were fabricated by depositing H-Ta-Mo films through a metal mask onto SiO₂ layers. The reason for this is that it is difficult to etch H-Ta-Mo films selectively from the SiO₂ layers when the H-Ta-Mo films contain more than 10 a/o Ta. A several atomic percent Ta addition is found to be effective in reducing N_m , whereas more than this is not very effective. Since bulk resistivity of Ta is higher than that of Mo, as shown in Fig. 1b, the electrical resistivity increases with an increase in the Ta concentration. A resistivity of 4.2 × 10⁻⁵ Ω-cm can be obtained even for a sample with as high as 20 a/o Ta. This resistivity is only four times as large as the resistivity for the samples without Ta (denoted as "H-Mo"), and this H-Ta-Mo is applicable to conductive gate electrodes.

Figure 2 shows the N_m for an Mo gate (not doped with hydrogen) and an H-Ta-Mo gate with 7 a/o Ta as a func-

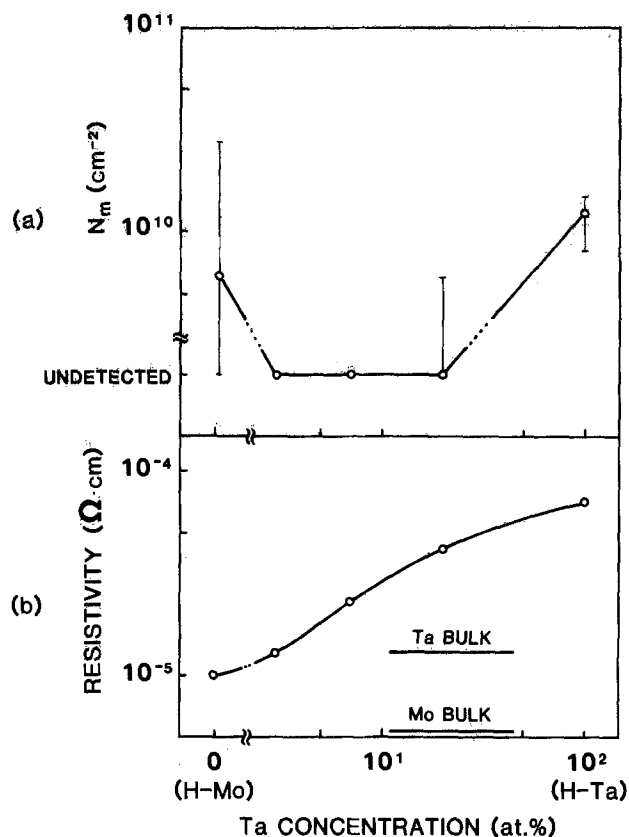


Fig. 1. Mobile ionic charge density N_m (a) and electrical resistivity of electrode films (b) for H-Ta-Mo gate MOS structures after annealing in forming gas at 1000°C for 30 min as a function of Ta concentration in the electrodes.

tion of H₂ gas concentration in the H₂-N₂ annealing ambient at 1000°C for 30 min. More than 3 volume percent (v/o) H₂ is found to be required to reduce N_m in both gate structures. The H-Ta-Mo gate is more influenced by the H₂

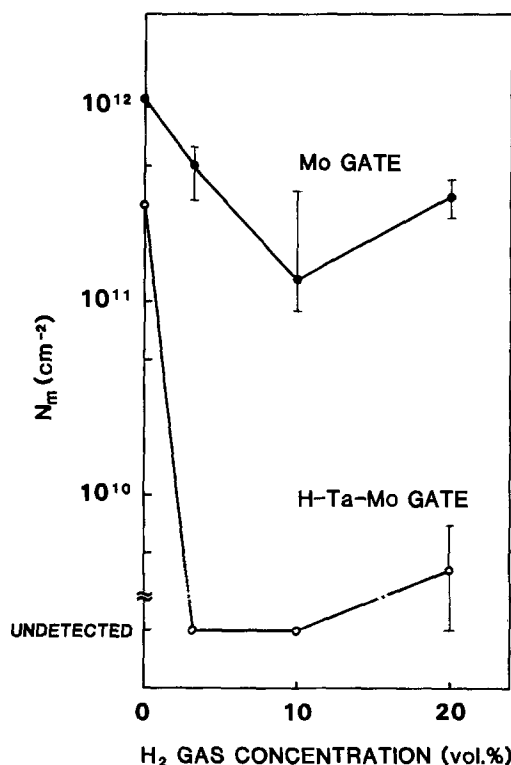


Fig. 2. Mobile ionic charge density N_m for Mo gate and H-Ta-Mo (7 a/o Ta) gate MOS structures as a function of H₂ gas concentration in the annealing ambient at 1000°C for 30 min.

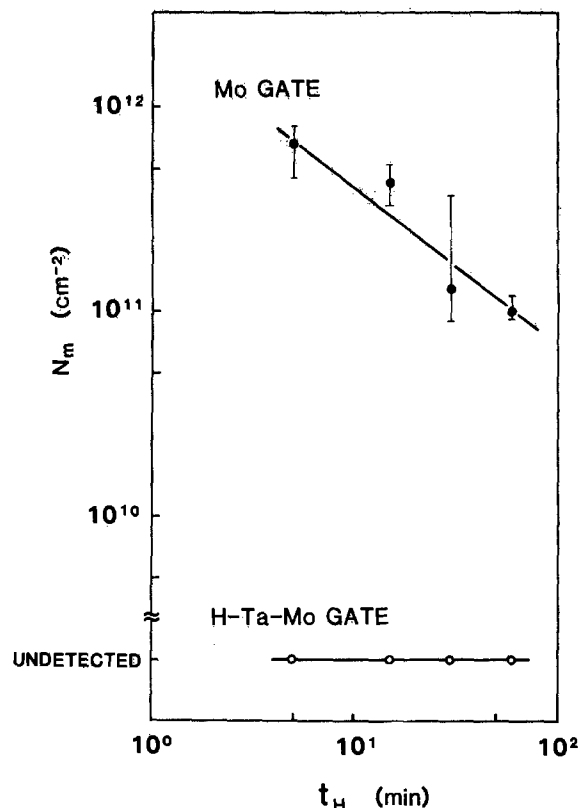


Fig. 3. Variations in mobile ionic charge density N_m for Mo gate and H-Ta-Mo (7 a/o Ta) gate as a function of annealing time t_H in forming gas at 1000°C.

concentration than the Mo gate. This indicates that H doping and Ta addition enhance the reduction effect during forming gas annealing (2).

The effect of the annealing time t_H in the forming gas at 1000°C is shown in Fig. 3 for the Mo gate and H-Ta-Mo gate (7 a/o Ta). Mobile ionic charges are undetected for the H-Ta-Mo gate. For the Mo gate, N_m is as high as 7×10^{11} cm⁻² at $t_H = 5$ min and gradually decreases with an increase in t_H . This result suggests that mobile ionic charges, which are mostly Na ions, are not diffused into the gate oxides in the H-Ta-Mo gate structures, even at the initial stage of the annealing, whereas Na contamination occurs within 5 min and is gradually reduced with an increase in t_H for Mo gate structures. The difference in N_m between the gate structures is caused by the amount of hydrogen absorbed in the films before annealing and by the Ta addition to the electrodes in the deposition process.

The following mechanisms may be proposed for the reduction effect on the mobile ionic charge density: (i) blocking of Na thermal diffusion into the SiO₂ at the metal/SiO₂ interface by an H-Ta-Mo alloy diffusion barrier, (ii) immobilization of Na contained in the gate electrodes, (iii) neutralization of Na ions in the SiO₂ layers, and (iv) gettering of Na from the SiO₂ by H-Ta-Mo films. The appropriateness of these mechanisms is next discussed.

To clarify the blocking effect [mechanism (i)], N_m has been compared for various MOS structures of an H-Ta-Mo(150Å)/Mo(3100Å) double-layered gate, an Mo(3300Å) gate, and an H-Ta-Mo(3300Å) gate after annealing in forming gas at 1000°C for 30 min. The results are shown in Table I. The blocking effect by the thin H-Ta-Mo layer is concluded to be very weak. This is because the N_m for the double-layered gate is as large as that for the Mo gate.

Figure 4 shows a variation in N_m as a function of annealing time t_N in N₂ at 1000°C for the H-Ta-Mo gate (7 a/o Ta). Subsequent annealing was carried out on several samples in forming gas at 1000°C for 30 min. More than 2×10^{11} cm⁻² of N_m , which was measured after annealing in N₂ within 20 min, is found to decrease to undetectable levels

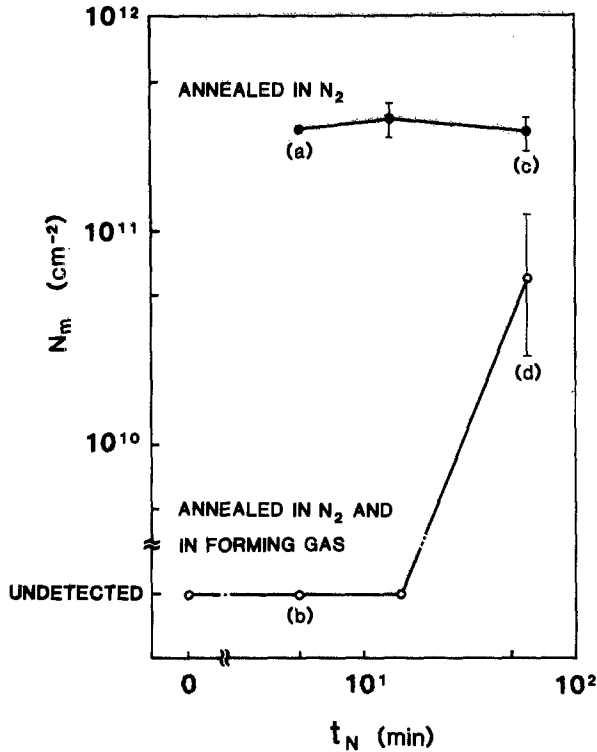


Fig. 4. Mobile ionic charge density N_m as a function of annealing time t_N in N_2 at 1000°C for H-Ta-Mo (7 a/o Ta) gate. Several samples were subsequently annealed in forming gas at 1000°C for 30 min.

Table I. Mobile ionic charge density N_m for three types of MOS capacitors annealed in forming gas at 1000°C for 30 min

Electrode structures	N_m (cm^{-2})
Mo(3100Å) on H-Ta-Mo(150Å)	$> 2 \times 10^{11}$
Mo(3300Å)	1.3×10^{11}
H-Ta-Mo(3300Å)	Undetected ^a

^a The detection limit of N_m measurements is less than $5 \times 10^9 \text{ cm}^{-2}$.

when subsequent annealing is carried out in forming gas. This indicates that mobile ionic charge contamination in the gate oxides can be removed by annealing in forming gas. However, the reduction effect is not so remarkable when t_N is extended to 60 min. The prolonged annealing for 60 min in N_2 may have induced a change in film structures which suppresses the reduction effect. These results suggest the possibility that the removal of the mobile ionic charge contamination in the gate oxide is caused not only by the immobilization of Na in the electrodes [mechanism (ii)] but also by the gettering of Na from the SiO_2 by H-Ta-Mo films [mechanism (iv)].

Depth distribution profiles of Na for the samples examined in Fig. 4 are shown in Fig. 5. $^{23}\text{Na}^+$ intensity peaks are clearly observed in the SiO_2 region for the samples annealed only in N_2 (Fig. 5a, 5c), and are nearly independent of annealing time t_N in N_2 . For samples which were subsequently annealed in forming gas for $t_H = 30$ min, $^{23}\text{Na}^+$ intensity, normalized by $^{28}\text{Si}^+$ intensity in the SiO_2 region, decreases to 1/100 for the sample with $t_N = 5$ min (Fig. 5b) and 1/2 for the sample with $t_N = 60$ min (Fig. 5d). These re-

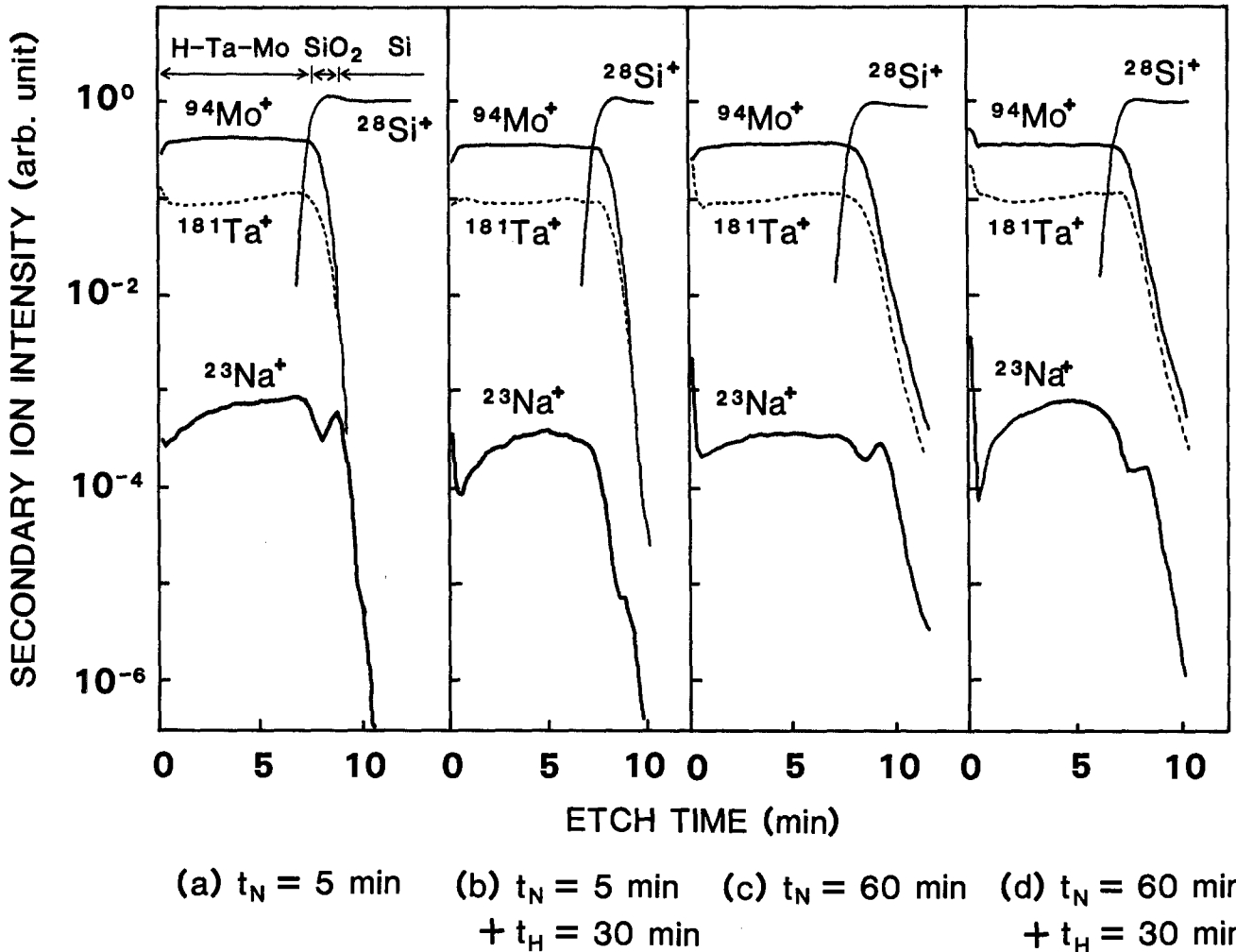


Fig. 5. Depth distribution profiles for $^{23}\text{Na}^+$, $^{28}\text{Si}^+$, $^{94}\text{Mo}^+$, and $^{181}\text{Ta}^+$ ions in H-Ta-Mo(3300Å)/ SiO_2 (400Å)/Si(substrate) structures. Analysis was done after annealing in N_2 at 1000°C for (a) $t_N = 5$ min, and (c) 60 min. Subsequent forming gas annealing was carried out at 1000°C for $t_H = 30$ min (b, d).

sults agree well with the N_m values measured by TVS (shown in Fig. 4), and indicate that very few Na atoms are contained in the SiO_2 when ionic charges are not detected in MOS capacitors. Therefore, the neutralization mechanism of Na ions in the SiO_2 [mechanism (iii)] can be ignored. Immobilization [mechanism (ii)] and gettering [mechanism (iv)] are still consistent with these experimental results.

Structural effects of Ta addition.—Figure 6 shows x-ray diffractometer traces for the H-Ta-Mo films with 0-100 a/o Ta after annealing in forming gas at 1000°C for 30 min. When the Ta concentration is 0 a/o, i.e., H-Mo (Fig. 6a), only Mo can be found. However, with the increase in the Ta concentration to 20 a/o (Fig. 6b and 6c), diffraction peaks for tetragonal MoTaN (CrNbN-type structure, space group $P4/nmm$) (9) appear in addition to the Mo peaks. For the films with 100 a/o Ta, i.e., H-Ta (Fig. 6d), hexagonal TaN is found instead of Ta, which is ordinarily observed after annealing in N_2 . The nitrogen in the H-Ta-Mo films was also analyzed by AES. Figure 7 shows Auger peak-to-peak heights of nitrogen (379 eV, KLL transition) in the middle depth of Mo and H-Ta-Mo films as a function of annealing time t_H in forming gas at 1000°C . The peak heights for H-Ta-Mo films are relatively higher than those for Mo films at any t_H . The nitrogen concentration in the H-Ta-Mo films, evaluated from these peak heights using sensitivity corrections for the constituent elements (10), is more than 5 a/o, whereas the concentration for Mo films is less than 2 a/o. From the results of the diffractometer traces and the AES analysis data, H doping and Ta addition are found to activate nitriding in the matrix Mo films.

Figure 8 shows Auger peak-to-peak heights of nitrogen in the middle depth of H-Ta-Mo gate electrodes as a function of annealing time t_N in N_2 at 1000°C . After annealing in N_2 , some samples were subsequently annealed in forming gas at 1000°C for 30 min. Immediately after an-

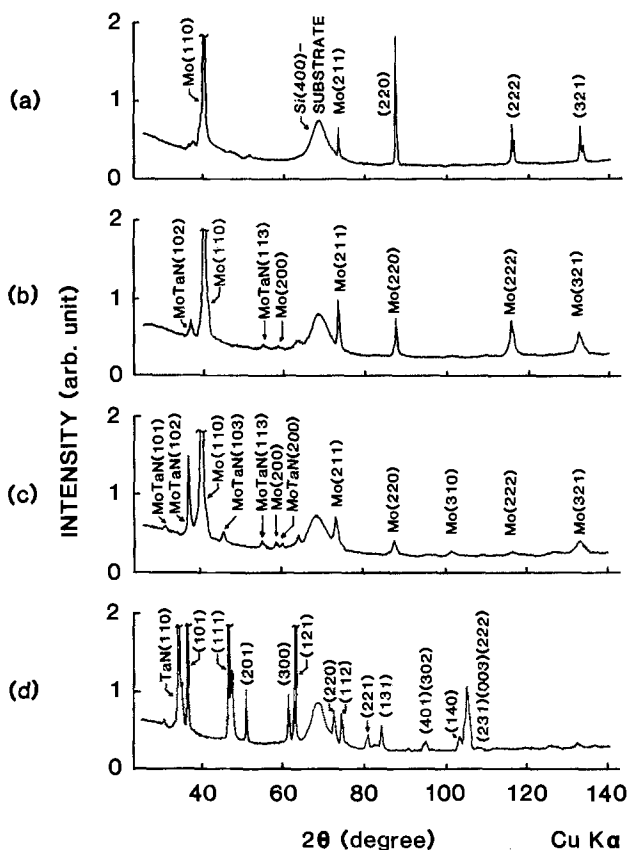


Fig. 6. X-ray diffractometer traces for H-Ta-Mo films with 0-100 a/o Ta after annealing in forming gas at 1000°C for 30 min. a: 0 a/o Ta (H-Mo films). b: 7 a/o Ta. c: 20 a/o Ta. d: 100 a/o Ta (H-Ta films). Some peaks have not been identified. The traces were measured with a θ angle offset by 2° to minimize Si substrate reflections.

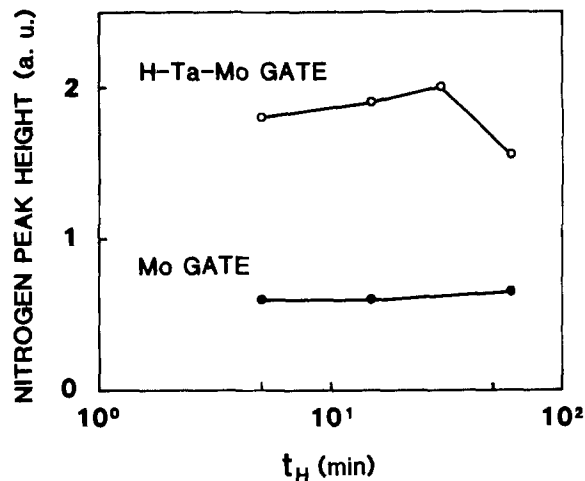


Fig. 7. Auger peak-to-peak heights of nitrogen (379 eV, KLL transition) in the middle depth of Mo and H-Ta-Mo gate electrodes as a function of annealing time t_H in forming gas at 1000°C .

nealing in N_2 , the peak heights are as low as those for Mo gate annealed in forming gas (shown in Fig. 7). However, subsequent annealing in the forming gas results in peak heights as high as those in the H-Ta-Mo gate annealed only in the forming gas (shown in Fig. 7), whereas the peak heights decrease when t_N is increased up to 60 min. This indicates that the nitriding reaction of the films proceeds remarkably when forming gas annealing is combined with Ta addition, and that nitriding occurs even on samples previously annealed in N_2 .

Mo grain growth is shown in Fig. 9, and corresponds to the samples shown in Fig. 8. Subsequent annealing in forming gas is found to increase the Mo grain size even more when the annealing time t_N in N_2 is less than 30 min. However, at $t_N = 60$ min, an increase in the Mo grain size is not observed after the subsequent annealing in forming gas. This phenomenon at $t_N = 60$ min agrees with the relatively low AES peak heights of nitrogen in the same samples shown in Fig. 8 as well as with the increased N_m shown in Fig. 4, sample (d). It is thought that large Mo grains, grown by prolonged annealing for 60 min in N_2 , suppress the nitriding of the samples due to the subsequent annealing in forming gas. This is because amorphous structures, which can be easily converted into nitrides, are almost completely eliminated from the Mo grain boundaries after prolonged annealing.

As described above, the Auger peak heights of nitrogen shown in Fig. 7 and 8 are found to agree with the ionic charge densities N_m , which change with process condi-

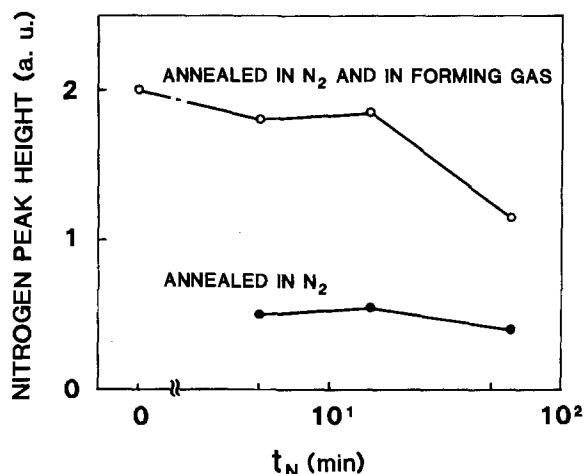


Fig. 8. Auger peak-to-peak heights of nitrogen (379 eV, KLL transition) in the middle depth of H-Ta-Mo gate electrodes as a function of annealing time t_N in N_2 at 1000°C . After annealing in N_2 , some samples were subsequently annealed in forming gas at 1000°C for 30 min.

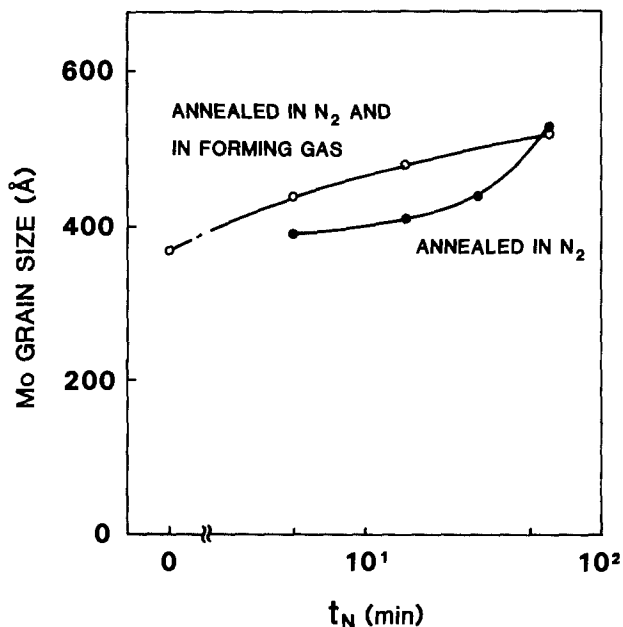


Fig. 9. Average grain sizes of Mo in H-Ta-Mo gate electrodes as a function of annealing time t_N in N_2 at 1000°C . Prior to grain size measurements, same samples were subsequently annealed in forming gas at 1000°C for 30 min.

tions such as annealing time t_H in forming gas (Fig. 3) and annealing time t_N in N_2 (Fig. 4). In these figures, the relatively high N_m of more than $1 \times 10^{11} \text{ cm}^{-2}$ corresponds with the low nitrogen concentration of less than 2 a/o. On the contrary, when ionic charges are not detected in MOS structures, the nitrogen concentration in the gate electrodes reaches more than 5 a/o. These facts suggest that the reduction in N_m is significantly influenced by the structural and compositional changes in gate electrodes, which supports the immobilization mechanism taking place within the electrodes.

Effects of nitride on sodium diffusion.—The nitriding of H-Ta-Mo gate electrodes is found to be closely related to the reduction effect on the Na ion density in the gate oxide. The following effects on Na diffusion from gate electrodes into gate SiO_2 due to the nitride formation are supposed: (i) dramatic decrease in the diffusion coefficient of Na in the electrodes due to nitriding, and (ii) the capture of Na cations in the electrodes as a result of a stable nitride formation due to high electronegativity of nitrogen.

Thin metal nitride films, such as TiN (150Å thick) (11), TaN (12), and Mo-N (13), have been well known to work as diffusion barriers. A stuffing effect in grain boundaries has been proposed (14) as the mechanism for the diffusion-barrier properties of these metal nitrides. This effect is expected to be applicable to the blocking of Na diffusion in the present results, although thermal processing temperatures ($<600^\circ\text{C}$), applicable to these diffusion barriers, are lower than those in the present experiments ($900^\circ\text{--}1000^\circ\text{C}$).

Nitriding of Mo films has been reported for Mo formed by reactive sputtering in a mixture of Ar and N_2 gases (15), and for Mo annealed at $700^\circ\text{--}800^\circ\text{C}$ in an ammonia gas ambient (16) or in a mixture of H_2 and N_2 gases (16, 17). However, nitride does not form when Mo films are annealed in N_2 or in a mixture of H_2 (5%) and Ar (95%) (17) at temperatures up to 1000°C . Since the heat of dissociation of nitrogen molecules to monatoms is very high at these temperatures (113 kcal/mol) (16), the nitriding reaction between monatomic nitrogen and Mo can be ignored thermodynamically. When annealing is carried out in a forming gas, the heat of dissociation has been estimated to be reduced by half (16), which results in nitride formation, mainly $\gamma\text{-Mo}_2\text{N}$, at low temperatures of $700^\circ\text{--}800^\circ\text{C}$. As with Mo, Ta can be nitrided by annealing in forming gas but not in N_2 , as shown in Fig. 6. Therefore, H doping in

the films and/or in the annealing ambients is concluded to be effective in the nitride formation of Mo and Ta.

It has also been reported that the molybdenum nitride, formed in the processes described above, is thermally decomposed into elementary molybdenum by high temperature annealing at more than 900°C in N_2 or in a mixture of H_2 and N_2 (17-19). This agrees with the experimental results shown in Fig. 6a. However, as is shown in Fig. 6d, TaN is stable under annealing up to 1000°C . In addition, the melting point of TaN is as high as 3088°C . The formation and stability of MoTaN have been also confirmed in the samples annealed at 1000°C by x-ray diffraction, as shown in Fig. 6b and 6c. Therefore, the addition of Ta in the appropriate amount to Mo is thought to have a remarkable effect on preventing the decomposition of formed nitrides even after high temperature annealing up to 1000°C .

In molybdenum nitride gate MOS structures formed by reactive sputtering, passivation effects on ionic charge contamination have not been reported (15). This suggests that nitriding of gate electrodes is not required to reduce the contamination. The volume expansion caused by high temperature nitriding processes, which is estimated to reach to 27% in MoN from Mo (16), is thought to increase the density of Mo grain boundaries and to result in blocking Na diffusion at the boundaries.

To clarify the second mechanism in connection with electronegativity, oxygen-doped molybdenum films were examined as the gate electrodes for MOS structures. This is because oxygen has a higher electronegativity (3.5) than nitrogen (3.0) (20). Figure 10 shows N_m in the MOS structures as a function of the oxygen concentration in the electrodes. Here, the oxygen was doped by reactive sputtering of Mo in a mixture of O_2 and Ar gases. After annealing in N_2 at 1000°C for 30 min, the oxygen was converted into stable MoO_2 in the electrodes (21). With an increase in the oxygen concentration, N_m shows a tendency to increase after annealing above 800°C . This indicates that the possibility of capturing Na cations in oxygen-doped Mo films is eliminated. Similarly, the capturing of Na in H-Ta-Mo films may be eliminated.

The decrease in N_m resulting from forming gas annealing after N_2 gas annealing, shown in Fig. 4, can be ex-

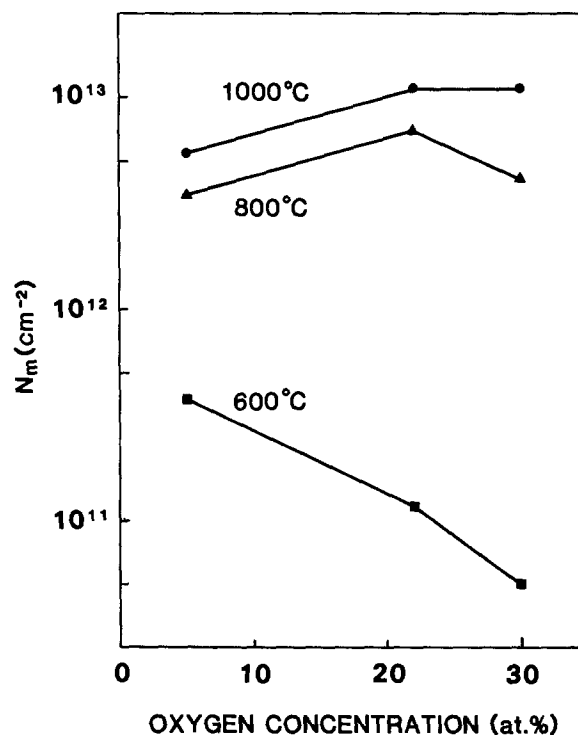


Fig. 10. Mobile ionic charge density N_m for oxygen-doped Mo gate MOS structures after annealing in N_2 at $600^\circ\text{--}1000^\circ\text{C}$ for 30 min as a function of oxygen concentration in the electrodes.

plained by the blocking effect on Na diffusion, discussed above. When t_N is within 15 min, Na in the gate SiO_2 , diffused from gate electrodes by the annealing in N_2 , continues to diffuse toward the Si substrate during subsequent annealing in forming gas. In this case, an additional Na supply from the gate electrodes to the gate SiO_2 is abruptly blocked by the nitriding of the H-Ta-Mo gate. This results in a decrease in Na density in the SiO_2 . When t_N is 60 min, however, the blocking of Na diffusion is not sufficient and a relatively high density of Na remains in the SiO_2 even after the annealing in forming gas.

Conclusion

The reduction mechanism of mobile ion contamination in Ta-Mo alloy gate MOS structures is examined. The formation of tetragonal MoTaN is found in the Ta-Mo alloy gate electrodes during high temperature annealing up to 1000°C in forming gas. A possible explanation for the reduction in Na ion density in the gate SiO_2 is that the incorporated nitrogen changes the amorphous boundary structures of Mo grains to the crystalline MoTaN in the electrodes, and increases the density of the boundaries in the same way as the stuffing effect observed in TiN diffusion barrier films. These changes are believed to immobilize the Na in the electrodes and block Na diffusion from the gate electrodes into the gate SiO_2 .

Acknowledgments

The authors would like to thank T. Matsumoto, E. Arai, and K. Nawata for their advice and encouragement. The authors are also grateful to T. Amazawa for his advice and TVS measurements and to I. Kawashima for his work on SIMS.

Manuscript submitted Aug. 28, 1984; revised manuscript received March 12, 1985. This was Paper 471 presented at the New Orleans, Louisiana, Meeting of the Society, Oct. 7-12, 1984.

Nippon Telegraph and Telephone Corporation assisted in meeting the publication costs of this article.

REFERENCES

1. T. Mano, K. Takeya, T. Watanabe, N. Ieda, K. Kiuchi, E. Arai, T. Ogawa, and K. Hirata, *IEEE J. Solid-State Circuits*, **sc-15**, 865 (1980).
2. S. Ohfuji and N. Shiono, *This Journal*, **131**, 1688 (1984).
3. S. M. Sze, "Physics of Semiconductor Devices," 2nd ed., Chap. 7, John Wiley and Sons, New York (1981).
4. T. Nozaki and H. Okabayashi, *This Journal*, **128**, 175 (1981).
5. R. J. Kriegler, Y. C. Cheng, and D. R. Colton, *ibid.*, **119**, 388 (1972).
6. H. Ishikawa, M. Yamamoto, H. Tokunaga, N. Toyokura, F. Yanagawa, K. Kiuchi, and M. Kondo, *IEEE Trans. Electron Devices*, **ed-27**, 1586 (1980).
7. T. Schober and H. Wenzl, "Hydrogen in Metals II," G. Alefeld and J. Völkl, Editors, p. 11, Springer-Verlag, Berlin (1978).
8. B. D. Cullity, "Elements of X-Ray Diffraction," Chap. 3, Addison-Wesley, Reading, MA (1956).
9. JCPDS Card, No. 32-674; A. Vendl, *Monatsh. Chem.*, **109**, 1001 (1978).
10. P. W. Palmberg, *Anal. Chem.*, **45**, 549A (1973).
11. W. J. Garceau, P. R. Fournier, and G. K. Herb, *Thin Solid Films*, **60**, 237 (1979); H. von Seefeld, N. W. Cheung, M. Mäenpää, and M-A. Nicolet, *IEEE Trans. Electron. Devices*, **ed-27**, 873 (1980).
12. M. Wittmer, *Appl. Phys. Lett.*, **36**, 456 (1980).
13. R. S. Nowicki and I. Wang, *J. Vac. Sci. Technol.*, **15**, 235 (1978).
14. M-A. Nicolet, *Thin Solid Films*, **52**, 415 (1978).
15. H. Okabayashi, K. Higuchi, and T. Nozaki, Abstract 302, p. 753, The Electrochemical Society Extended Abstracts, Vol. 81-1, Minneapolis, MN, May 10-15, 1981.
16. M. J. Kim, D. M. Brown, and W. Katz, *This Journal*, **130**, 1196 (1983); M. J. Kim and D. M. Brown, *IEEE Trans. Electron. Devices*, **ed-30**, 598 (1983).
17. H. Ishikawa, H. Tokunaga, N. Toyokura, and M. Shinoda, Abstract 152, p. 406, The Electrochemical Society Extended Abstracts, Vol. 79-1, Boston, MA, May 6-11, 1979.
18. K. Fujinaga and H. Harada, *Jpn. J. Appl. Phys.*, **21**, 373 (1982).
19. M. J. Kim and D. M. Brown, *This Journal*, **130**, 2104 (1983).
20. L. Pauling, "The Nature of the Chemical Bond," 3rd ed., Cornell University Press, Ithaca, NY (1960).
21. S. Ohfuji, C. Hashimoto, T. Amazawa, and J. Murota, *This Journal*, **131**, 446 (1984).

Dopant Effect of Yttrium and the Growth and Adherence of Alumina on Nickel-Aluminum Alloys

Alfred B. Anderson and S. P. Mehandru¹

Department of Chemistry, Case Western Reserve University, Cleveland, Ohio 44106

J. L. Smialek

NASA-Lewis Research Center, Cleveland, Ohio 44135

ABSTRACT

The atom superposition and electron delocalization molecular orbital theory and large cluster models have been employed to study cation vacancy diffusion in α -Al₂O₃ and the bonding of α -Al₂O₃ to nickel, aluminum, and yttrium surfaces. Al³⁺ diffusion barriers in α -Al₂O₃ by the vacancy mechanism are in reasonable agreement with experiment. The barrier to Y³⁺ diffusion is predicted to be much higher. Since addition of yttrium to transition metal alloys is known to reduce the growth rate and stress convolutions in protective alumina scales, this result suggests the rate-limiting step in scale growth is cation vacancy diffusion. This may partially explain the beneficial effect of yttrium dopants on scale adhesion. The theory also predicts a very strong bonding between alumina and yttrium at the surface of the alloy. This may also be important to the adhesion phenomenon. It is also found that aluminum and yttrium atoms bond very strongly to nickel because of charge transfer from their higher lying valence orbitals to the lower lying nickel s-d band.

The essential requirement for high temperature oxidation resistant alloys is the development and maintenance of a continuous protective oxide scale on their surfaces. However, it is observed that, during cyclic heating and cooling, stresses are developed, leading to the spalling of the protective layer, thus corroding the alloy surface. It is well known that the addition of small amounts of rare-earth elements such as yttrium, zirconium, and hafnium improves the oxidation resistance of the alloy, first by decreasing the growth rate of the oxide, and second by increasing the adherence of the oxide scale to the alloy surface. Various hypotheses have been put forward to explain these beneficial effects of the rare-earth dopants. These mechanisms have been reviewed by Whittle and Stringer (1), Delaunay and Hunz (2), and Hindam and Whittle (3). It may be noted that there is an optimum amount of the rare-earth dopant necessary for obtaining optimal resistance to oxidation and optimal oxide scale adherence. In the case of yttrium, this optimum amount is about 100-300 ppm (2). The yttrium-implanted aluminum containing alloys show behavior similar to that of the cast alloys.

It is known on the basis of platinum marker studies (4) and ¹⁸O tracer studies (5) that the Al₂O₃ grains of the oxide scale grow inward into the alloy. The implication is that oxygen in some form diffuses inward along grain boundaries and aluminum oxidation takes place in the vicinity of the grain-alloy interface. Nothing is known about the details of the oxidation chemical reaction mechanism. That is, if cation vacancy migration is involved, it is not known if the cation vacancies diffuse some distance through the interfacial region prior to reduction at the grain-alloy interfacial region, or if they diffuse down from upper regions of the oxide grain boundaries for some distance prior to reduction, or if they diffuse some distance through the grains to the reduction sites at the grain-alloy interface. If such cation vacancy diffusion is unimportant, then anion vacancies might diffuse to the grain boundary region from the grain-alloy interface either through the Al₂O₃ or through the interfacial region. If the grain-alloy interfacial region is similar to the oxide grain boundary, then oxygen may diffuse all the way to the metal before being reduced. In this case, to continue inward grain growth, anion vacancy diffusion from the base of the grain through the interfacial region will occur and oxidation will take place in the interfacial region at the alloy surface. Alternatively, Al₂O₃ clusters may form in the alloy at the grain boundary-alloy interface and these would

then have to migrate to the center of the grain-alloy interface.

The present theoretical study shows that yttrium present in a nickel-aluminum alloy has the effect of preventing cation vacancy diffusion. This and the observed reduction in grain growth (1-3) implies that the rate-limiting step in the kinetics of Al₂O₃ grain formation has a mechanism involving cation vacancy diffusion.

The reduction in grain growth has the well-known beneficial effect of slowing the consumption of aluminum metal in the alloy due to spalling which occurs during cyclic heating and cooling (1-3). It is commonly hypothesized that an additional effect of reduced grain growth is a significant reduction in stresses in the scale which, when high (i.e., when no rare-earth dopant is present), cause rapid spalling. A cation vacancy migration blocking mechanism such as ours is not inconsistent with this hypothesis.

It has been suggested that the rare-earth dopants reduce interfacial void formation (1-3), although more recent studies cast doubt on the generality of this explanation (6), at least based on initial stages of scale growth. Less often considered is the possibility that void formation is a consequence of growth stresses.

The last general effect sometimes invoked to help explain rare-earth dopant effects on alumina scale adhesion to alloy surfaces centers on chemical bond strengths between the alumina and alloys and how the rare-earth elements may increase these strengths. In the present study, we find some support for this hypothesis. This comes from examining theoretically the binding energies of aluminum and yttrium metal atoms in nickel and the binding of Al₂O₃ to the alloyed surface. The calculated energies are large in each case, suggesting that the alloy is especially strong and that oxide scales should bond more strongly to yttrium on the surface of a Ni-Al-Y alloy than to nickel or aluminum.

Method of Calculation

We use the atom superposition and electron delocalization molecular orbital (ASED-MO) theory (7). This theory is based on separating the electronic charge density of a molecule or solid into a sum of rigid free atom components and a delocalized bond charge component. In a diatomic molecule (the generalization to polyatomics is straightforward), the binding energy E is exactly equal to the energy of integrating the electrostatic force on a nucleus as the two atoms come together forming the molecule (7a). The energy thus obtained for the superposition of rigid atoms, E_R , is equal to the interaction of one nucleus with the nucleus and electronic charge density of

¹ On leave from K. M. College, University of Delhi, Delhi 110007, India.

the other atom and is repulsive. The energy due to the interaction of the nucleus with the charge redistribution density, E_D , is attractive. Thus

$$E = E_R + E_D \quad [1]$$

If the electron redistribution density, which can be viewed as a bond charge density, is assumed to be made up of point charges, then the laplacian of the total energy evaluated at equilibrium is equal to the equilibrium harmonic bond stretching force constant, k_e (7a)

$$k_e = 4\pi Z_a \rho_b(a) \quad [2]$$

where Z_a is the charge of nucleus a, $\rho_b(a)$ is the atomic charge density centered on a and evaluated at nucleus b, and the laplacian is $\nabla_{R_a}^2$ when nucleus b is at the origin and nucleus a is at position R_a . Equation [2] is of the form of a classical electrostatic Poisson equation. Its derivatives contain, to good accuracy, harmonic, cubic and quartic force constants for molecules (8a, 8b) and solids (8c). In ionic molecules and solids such as aluminum and yttrium oxides, the point charge approximation is especially favorable, as shown below. In applying Eq. [1] for the total energy, E_R is easily calculated using atomic charge density functions. The bond charge density function is not available for calculating E_D , but it has been found that the total molecular orbital energy, E_{MO} , from diagonalizing a one-electron hamiltonian similar in form to the extended Hückel hamiltonian, is generally a good approximation to E_D , allowing predictions of molecular structures and reaction energy surfaces using Eq. [1] (7b). Numerous studies of molecular and surface structures and reactions have been published using the ASED-MO theory and Eq. [1]. The present paper is representative of the growing number of studies of solid-state systems using the theory. Past studies include the lattice and harmonic force constants of diamond structure carbon, silicon, germanium, and tin (8c), the lattice constant and optical properties of α -quartz (8d), the optical properties of ferrous and ferric oxides (8e) and bismuth and molybdenum oxides (8f), and the structures of defect clusters in wustite, $Fe_{1-x}O$ (8g).

In the ASED-MO theory, atomic valence orbital parameters are based on standard values,² modified by increasing cation and decreasing anion valence orbital ionization potentials to yield charge transfers in diatomic fragments approximating those from Pauling's ionicity and electronegativities relationship. Cation valence orbital exponents are for +1 charge. Oxygen anion valence orbital exponents are decreased by 0.5 a.u., which allows the theory to produce reasonable diatomic AlO and YO equilibrium bond lengths in this study. Parameters thus chosen are in Table I, and calculated diatomic properties are in Table II. It may be noted from Table II that the classical electrostatic Poisson equation, Eq. [2], does a good job of predicting the force constants of AlO and YO, which is additional support for the choice of oxygen valence orbital exponents.

Oxide and Alloy Model

For modeling cation diffusion in the scale, a 72-atom cluster model of bulk α - Al_2O_3 , shown in Fig. 1, is used. It consists of five nearly close-packed oxygen anion layers and four aluminum cation layers sandwiched between

² Valence orbital ionization potentials from Ref. (9a); valence orbital Slater exponents from Ref. (9b).

Table II. Calculated bond lengths (R_e), harmonic force constants (k_e), and dissociation energies (D_e) for AlO and YO^a

Molecule	R_e (Å)	k_e (mdyn/Å)		D_e (eV)
AlO	1.64 (1.62)	4.67 ^b	5.85 ^c (5.67)	4.95 (5.03)
YO	1.84 (1.79)	5.13 ^b	7.03 ^c (5.80)	8.66 (7.39)

^a Numbers in parentheses are the experimental values taken from Ref. (18).

^b From total energy calculation, Eq. [1].

^c From Poisson equation, Eq. [2].

them. Al³⁺ ions are shown on lines perpendicular to the close-packed planes of oxygen ions. The X's indicate the positions where these lines intersect the oxygen planes. α - Al_2O_3 belongs to the R $\bar{3}c$ space group, and the lattice is rhombohedrally centered hexagonal with $a = 4.763\text{Å}$ and $c = 13.003\text{Å}$ (10). Each aluminum cation is coordinated to six oxygen anions in a distorted octahedron. Three anions are at a distance of 1.93Å from the central cation and form a large triangle with 2.87Å edges, and the other three anions are at a distance of 1.89Å and form a small triangle with 2.52Å edges. Each anion is approximately tetrahedrally coordinated to four cations. In α - Al_2O_3 , two-thirds of the distorted octahedral sites are occupied by aluminum cations and the remainder are unoccupied interstices.

It will be seen that all of our oxide cluster models are charged. This results in proper molecular orbital occupations corresponding to the formal oxidation states of the cations and anions in the clusters. Since electronic structures in the ASED-MO theory depend only on atom valence orbital ionization potentials and orbital symmetries, exponents, and overlap, and not explicitly on electron repulsions, these extra charges do not enter into the calculation of E_R or the E_{MO} approximation to E_D .

We first model the cation vacancy diffusion by a vacancy migration, parallel to the C axis. For this, consider the tube of oxygen triangles shown in Fig. 2, through which the cations diffuse downward from the point marked a to the point marked e. This motion is segmented into three parts: (i) motion from a to b is studied with a cation vacancy at c; (ii) motion from b to c is studied with a cation vacancy at a; and (iii) motion from c to e is studied with a cation vacancy at f. Points a, c, and f represent the normal lattice sites of aluminum cations; points b and d show the centers of the small and large oxygen triangles, respectively; and point e represents an unoccupied octahedral interstice.

Calculations for diffusion along the C axis direction are performed both with and without lattice relaxations about aluminum cation vacancies and yttrium cation substitutions. Additional calculations modeling diffusion perpendicular to the C axis without lattice relaxation are also made using a wider 94-atom cluster. Additional calculations allow an estimate of the vacancy formation energy.

For modeling the binding of the oxide to a metal substrate, we have chosen a two-layer thick cluster of ten nickel atoms, with seven atoms in the top layer, representing the Ni(111) surface (Fig. 3). In alloy models, the top central atom is replaced by Al and Y, whose positions are relaxed. In treating the bonding of small oxide clusters to the metal surface, the oxide cluster is kept rigid and its height is variationally optimized.

Table I. Parameters used in the calculations. Principal quantum number (n). Slater exponents (ζ) in atomic units, coefficients (c), and ionization potentials (IP) in electron volts

Atom	s			p			d					
	n	ζ	IP	n	ζ	IP	n	c_1	ζ_1	c_2	ζ_2	IP
Ni	4	2.0	8.635	4	1.7	4.99	3	0.5600	5.95	0.6200	2.2	11.0
Y	5	1.6601	8.480	5	1.362	6.630	4	0.5547	2.8539	0.5335	1.5985	8.38
Al	3	1.5213	12.62	3	1.5041	7.986						
O	2	1.7458	26.48	2	1.7266	11.62						

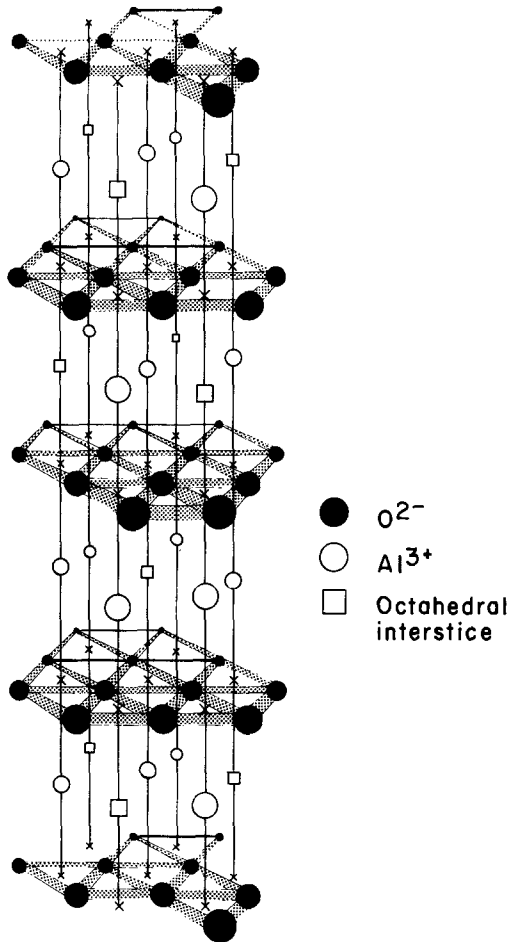


Fig. 1. $Al_{18}O_{54}^{54-}$ cluster model of $\alpha-Al_2O_3$ used in the theoretical calculations.

Our metal atom clusters are high spin, meaning each d band molecular orbital is occupied by at least one electron. Thus, while lower levels are doubly occupied, some upper ones are singly occupied. The result is that the clusters have spin magnetic moments approximating bulk values. It may also be noted that these are initial state calculations and do not include shake-up and relaxation shifts evident in photoemission studies of the electronic structure. Such phenomena are unimportant to chemical bond strengths and molecular structures analyzed in this paper.

Results

Cation vacancy diffusion and oxide grain growth.—We plot the variation of E , E_R , and E_{MO} as a function of the dif-

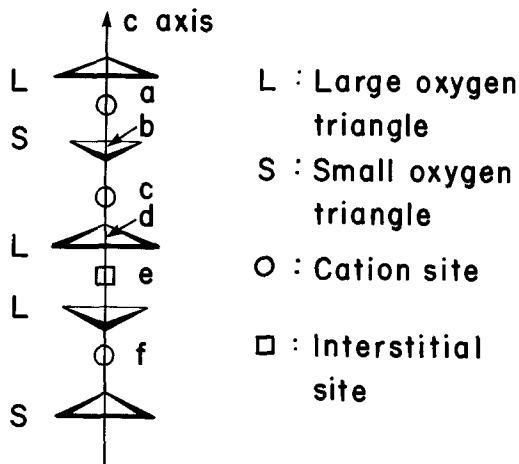


Fig. 2. Sites traversed in the cluster model of Fig. 1 by migrating Al^{3+} and Y^{3+} cations during Al^{3+} cation vacancy migration.

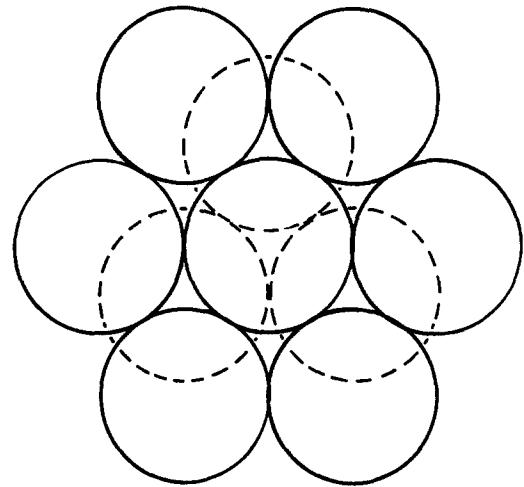


Fig. 3. Cluster model of the Ni(111) surface

fusion distance of Al^{3+} cation through the oxygen network without relaxation of the lattice in Fig. 4. As the cation moves towards the center of the small oxygen triangles (point b), the molecular orbital energy (E_{MO}) decreases but the two-body repulsion energy (E_R) increases much more rapidly, with the result that the total energy (E) is much less stable at point b than that for the lattice site of the cation (point a). The calculated diffusion barrier at point b is 4.6 eV. When the cation is at b, the cation vacancy becomes a split vacancy, one-half at a and one-half at c. As the cation moves down further towards point c, the total energy decreases and becomes minimum on reaching c.

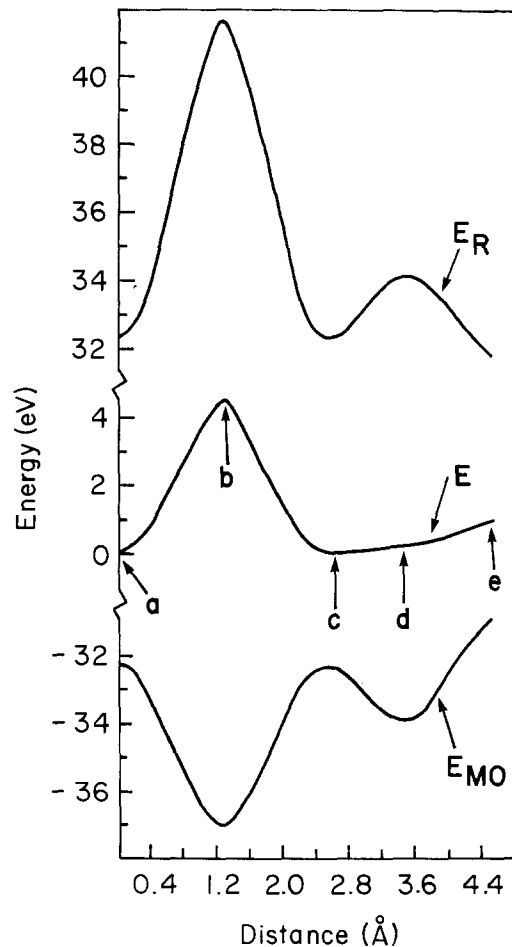


Fig. 4. Dependence of total energy, E , and its components, E_R and E_{MO} , as an Al^{3+} cation moves through the cluster model according to the scheme in Fig. 2. Motion from a to c represents vacancy motion from c to a. Motion from c to e is with the vacancy at f.

During its subsequent motion from c to d, the center of the large oxygen triangle, the stabilization in E_{MO} is only marginally less than the destabilization in E_R . This produces a diffusion barrier of only 0.3 eV at d. As the Al^{3+} cation moves further towards point e, the unoccupied octahedral interstice, the molecular orbital energy becomes more stable, whereas the two-body energy becomes less stable, producing a diffusion barrier of 0.9 eV at point e. Thus the maximum barrier height for the diffusion of the cation during its motion from a to e is 4.6 eV, and this is while passing through the small oxygen triangles. Our calculated diffusion barrier might appear to be consistent with the experimental value of 4.9 eV determined for the diffusion of aluminum cations in polycrystalline Al_2O_3 by Paladino and Kingery (11). However, it must be remembered that this experimental barrier includes the vacancy formation energy, assuming the diffusion is by the vacancy diffusion mechanism. Within the unrelaxed model, we calculate a vacancy formation energy of 4.7 eV and Dienes *et al.* (12) determine a value of 9.1 eV using a pairwise potential method including a polarization energy term and lattice relaxation about the defect. The procedure employed here and also by Dienes *et al.* for determining the Al^{3+} vacancy formation energy takes into account the energy for removing a bulk-coordinated Al^{3+} ion and placing it on the surface. Dienes *et al.* found a vacancy migration barrier along the C axis of 6.6 eV with the lattice relaxed. Thus, the result of adding the formation energies and migration energies is 9.3 eV in our work without lattice relaxation and 15.7 eV in the work of Dienes *et al.* including lattice relaxation. Both overestimate the experimental value of 4.9 eV. It should be remembered that it is unlikely that one will find the results of calculations based on a quantum mechanical model and those based on a parameterized classical model for a solid in agreement. The Dienes *et al.* method appears to severely overestimate the diffusion barrier for Al^{3+} ion. The present result, a bit closer, does not include lattice relaxation. When we allow the oxygen anions making up a small triangle to relax against a fixed surrounding cation environment, then the Al^{3+} vacancy diffusion barrier reduces to 0.6 eV. The relaxation amounts to a 0.2\AA increase in the distance between the center and vertices of the small triangle. When this energy is added to 4.7 eV, the cation vacancy formation energy, the total is 5.3 eV, which compares favorably with the experimental value of 4.9 eV. Vacancy migration in other directions may also be possible. Two pathways perpendicular to the C axis were examined and yielded barriers of 7.0 and 3.8 eV. The 7.0 eV transition state was along a path through an interstitial site. For this pathway, relaxation produced no stabilization. The other pathway takes the cation through an oxygen triangle, which is larger than the small triangle discussed above. No relaxation in this site was made, but because of the larger size of this triangle the relaxation energy is expected to be no more than a few tenths of an electron volt. From these results, it appears that migration along the C axis is favored over the other direction. Let us now consider the diffusion of the Y^{3+} cation along the C axis in the $\alpha-Al_2O_3$ lattice. Consider its motion again from point a to point e, which is the same diffusion pathway used for the Al^{3+} cation. The variations in E , E_R , and E_{MO} are graphed in Fig. 5. For the unrelaxed lattice model, the calculated diffusion barrier for the Y^{3+} ion to pass through the small oxygen triangle is 26.5 eV, that for crossing the large oxygen triangle is 6.4 eV, and that for passing through the octahedral interstice is only 0.3 eV. In a lattice relaxation calculation for Y^{3+} in the center of the small triangle, the Y-O distances increase by 0.3\AA and the barrier to reach this position drops to 7.5 eV. These results show that there is a very large increase in the diffusion barriers for the Y^{3+} ion passing through the lattice along the C axis, compared to the values calculated for Al^{3+} ion diffusion as discussed above. Most of this difference is due to the large ionic radius of the Y^{3+} ion (0.93\AA) as compared to that for the Al^{3+} ion (0.50\AA). In the framework of ASED-MO theory, the large nuclear charge of Y

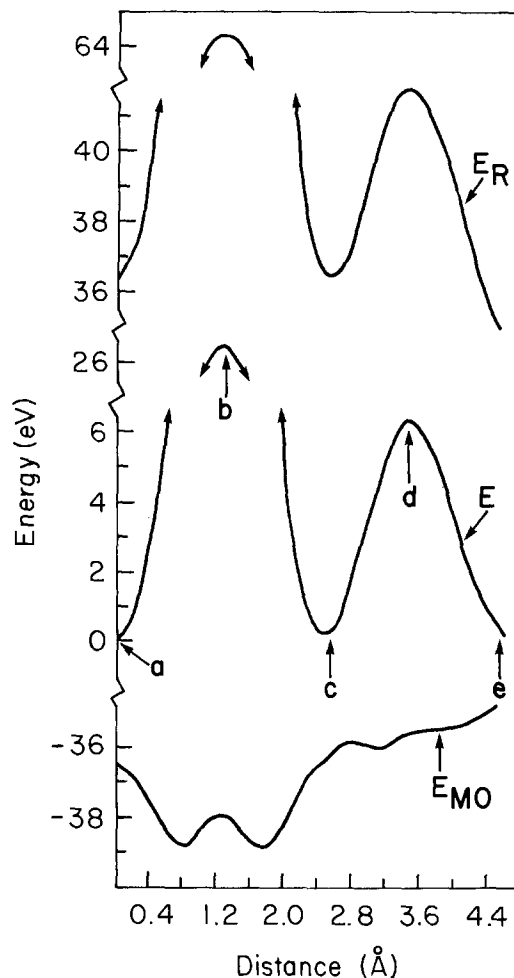


Fig. 5. As in Fig. 4, but for Y^{3+} and Al^{3+} vacancy pair diffusion

(39) compared to Al (13) increases the two-body repulsion energy considerably and this is mainly responsible for the high Y^{3+} diffusion barriers on crossing the oxygen triangles. In the octahedral interstice, however, the two-body repulsion energy is small, which gives rise to lower barrier at this site.

As discussed in the opening of this paper, cation vacancy migration may be, although the mechanistic details have not yet been deduced experimentally, the rate-limiting step in the grain and hence protective-scale growth rate. The mechanism of growth within an individual oxide grain may be illustrated by considering a schematic packing of the metal alloy (M), aluminum (Al), and oxygen (O), as shown in Fig. 6. There will be excess O_2 at the grain surface due to rapid short-circuit diffusion. This will lead to cation vacancies at the grain surface which may be associated with O^{1-} anions or perhaps O_2 mole-

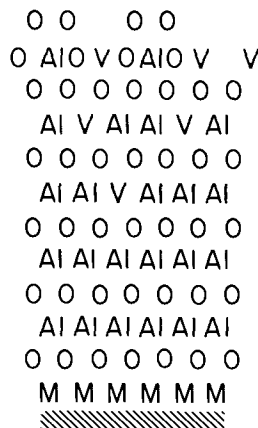


Fig. 6. Schematic view of a cross section of an alumina grain bonded to a metal alloy. Aluminum cation vacancies at the alumina surface are due to excess oxygen.

cules, either of which will be reduced during oxide growth. A cation vacancy may be viewed as carrying a charge of +3, but in the bulk the charges are actually holes in oxygen 2p band. When vacancies with accompanying holes in the O 2p band reach the metal alloy surface, they are reduced and metal atoms fill the vacancies and are themselves oxidized, as shown schematically in Fig. 7 and 8. As the process continues, voids begin to form at the interface, but these can be filled by metallic aluminum and oxide rebonding to the void bottoms as structure and kinetic factors allow, but some voids may never be filled. During this process of reduction of vacancies at the metal-oxide interface, yttrium will be introduced to the interfacial region, but, its diffusion barrier being high compared to aluminum, it will block cation vacancy diffusion through the interface. The consequent reduction in oxide growth within the scale will decrease internal strains which lead to the convoluted grain morphologies associated with poor adhesion as shown by Golightly *et al.* (13, 14).

Bonding of yttrium and aluminum oxide to nickel.—Because of the high diffusion barrier of a Y^{3+} and Al^{3+} vacancy pair in Al_2O_3 , it may be that Y^{3+} never enters the oxide but forms a monolayer of cations sandwiched between the alloy and the first anion layer of the oxide grains. Nevertheless, we have modeled the effects of Y^{3+} when fully coordinated to oxygen anions in the first layer of oxide bonded to the alloy.

Our model consists of $[AlO_6]^{6-}$ and $[YO_6]^{6-}$ binding on the center of the top of Ni_{10} cluster. We obtain comparable binding energies for both (Table III). These oxide clusters are structured to be superimposable in bulk Al_2O_3 , and the triangular face (edge length of 2.52\AA) bonds nearly in registry with the threefold hollow sites of the surface spaced 2.48\AA apart. The difference in energy for $[AlO_6]^{6-}$ bonded to threefold sites with atoms or hollows in the second nickel layer is only 0.02 eV , so the former sites are used throughout this study. The clusters are given charges of -6 , so that the surface is oxidized by three electrons. The binding energies are so close to one another for $[AlO_6]^{6-}$ and $[YO_6]^{6-}$ clusters that we conclude that the oxide adhesion bond to the surface is not affected by the presence of yttrium in the oxide should it penetrate the first layer of anions. When the central Ni atom is removed, representing the metal vacancy site formed when Al or Y enter a vacancy site in the oxide, the respective $[AlO_6]^{6-}$ and $[YO_6]^{6-}$ binding energies to the surface are both increased about the same amount (Table III). While these energies are higher, reflecting the increased bonding ability of partially coordinated Ni atoms surrounding the vacancy, they are again comparable in magnitude.

Bonding of aluminum and yttrium atoms in nickel.—The alloy surface is expected to contain, in addition to Ni, some Al and Y atoms. We calculate binding energies about two and three times larger for Al and Y, respectively, compared to Ni in the center of a Ni_9 cluster. As

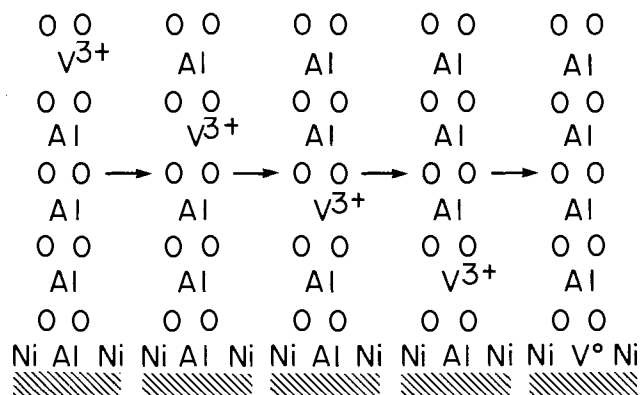


Fig. 7. Schematic view of cation vacancy migration through an alumina grain to the alloy substrate.

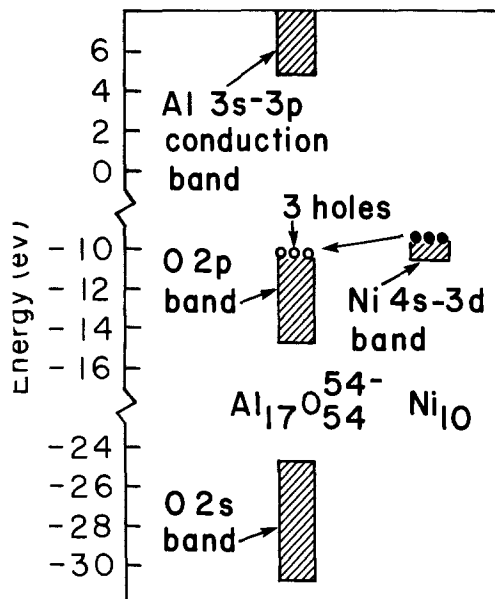


Fig. 8. Electronic structure leading to vacancy reduction at the alumina-alloy interface.

may be seen in Table III, these results are about the same when metal cation parameters are used, and thus are parameter insensitive. The large binding energy of Al is consistent with $\sim 1.75\text{ eV}$ enthalpy of formation of Al-Ni alloys in the limit of low Al concentration (15).

There are two separable contributions to consider for adatom adsorption energies. One, which is quite strong for all three, is the binding stabilization resulting from the adatom s orbital mixing with the Ni_9 cluster s band. The second occurs only for Al and Y adatoms and involves charge transfer to the Ni_9 band. These two effects are clearly visible in Fig. 9. The charge-transfer interaction may be a general feature of tenacious alloys.

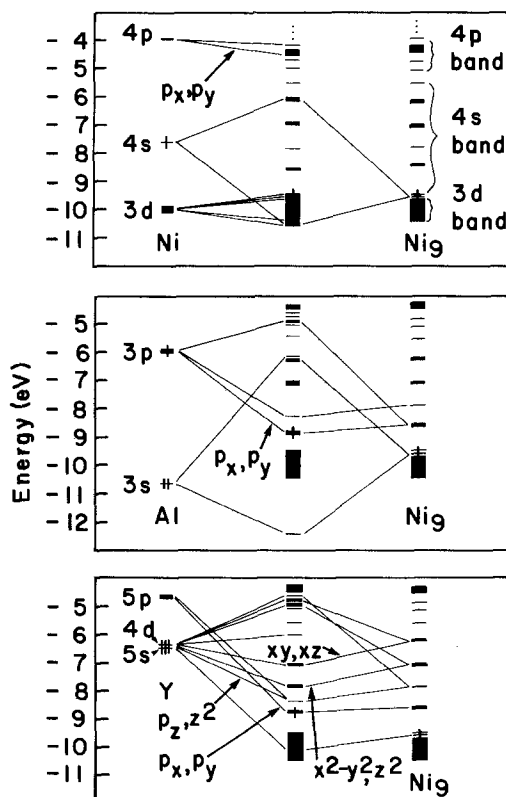


Fig. 9. Molecular orbital energy level correlation diagrams for Ni, Al, and Y atoms binding to the center position of a Ni_9 cluster based on removing the top central atom from the cluster in Fig. 3.

Table III. Number of unpaired electrons (*s*), binding energy (BE) in electron volts, and height (*h*) in angstroms optimized to the nearest 0.05Å

M	MO ₆ ⁶⁻ on Ni ₁₀				MO ₆ ⁶⁻ on Ni ₉		
	<i>s</i>	BE	<i>h</i> (O)	<i>h</i> (Ni)	<i>s</i>	BE	<i>h</i> (O)
Al	5	4.0	1.40	-0.15	5	4.9	1.35
Y	5	3.9	1.45	-0.15	5	4.9	1.40

M	M on Ni ₉			AlO ₆ ⁶⁻ on MNi ₉			
	<i>s</i>	BE	<i>h</i> (M)	<i>s</i>	BE	<i>h</i> (O)	<i>h</i> (M)
Ni	2	3.4 (3.0) ^a	0.00 (0.10) ^a	5	4.0	1.40	-0.15
Al	1	6.3 (6.3) ^a	-0.60 (-0.45) ^a	2	4.0	1.40	-0.74
Y	1	10.4 (9.8) ^a	-0.30 (-0.05) ^a	2	5.8	1.45	0.00

^a Results using free atom parameters. Based on Table I, decrease all IP by 1 eV for Ni; decrease all ζ by 0.3 and all IP by 2 eV for Y; $\zeta_s = 1.3724$, $\zeta_p = 1.352$, and decrease all IP by 2 eV for Al.

Bonding of alumina to the alloy.—We have modeled the bonding of alumina to alloys both low in aluminum and yttrium concentration at the interface and high. For the low concentration case, we find [AlO₆]⁶⁻ binds to Ni₁₀, Ni₉Al, and Ni₉Y with the respective energies 4.0, 4.0, and 5.8 eV (Table III). For the high concentration case, we find [AlO₆]⁶⁻ binds to Al₁₀ and Y₁₀ hexagonally-packed bulk-superimposable clusters with respective energies of 4.8 and 12.8 eV (Table IV). These results imply that the presence of yttrium on the surface of the alloy at monolayer coverage will greatly strengthen the bond between the oxide grain and the alloy. As shown in Fig. 10, the stabilization of the lowest asymmetry orbital of the O 2p band by the lowest asymmetry orbital of the Ni 4s band dominates the interfacial bond. The strong bond in the yttrium case is a result of the mixing of its high lying empty d orbitals with the O 2p band orbitals, stabilizing many of them by a small amount. The strengths of the oxide cluster bonds to Al and Y are consistent with the high standard heats of formation of α -Al₂O₃ and Y₂O₃, 17.5 and 18.2 eV, respectively (15). The standard heat of formation of NiO is only 2.5 eV (16). Thus the combination of strong Al-Ni and Y-Ni bonds and great stability of Al-O and Y-O bonds are likely to be important to the adherence of the oxide to the alloy.

Other models for the interfacial bond strength may also be considered. The [MO₆]⁶⁻ (M = Al,Y) clusters oxidize the surface on bonding to it. It might be thought that a more appropriate model is [MO₆]⁹⁻ representing an oxide layer bonding by means of its nonbonding electrons to the alloy surface. A similar model has been employed to discuss the bonding between [AlO₆]⁹⁻ and Fe, Ni, Cu, and Ag atoms (17). We find that [AlO₆]⁹⁻ binds much more weakly to Ni₁₀ (0.2 eV) and does not bind at all to Ni₉Al and Ni₉Y. This is expected because the [AlO₆]⁹⁻ cluster is closed shell and the metal clusters are nearly d¹⁰, also closed-shell systems. The [AlO₆]⁶⁻ cluster, which serves to oxidize the metal surface, is a more reasonable model and results in strong bond formation. It is likely that this inability of the stoichiometric oxide to bind to the alloy serves to help prevent the closing of voids that form at the oxide-alloy interface. Only short-circuit oxygen diffusion into an interfacial void or cation vacancy migration to the surface of the oxide facing the void or metal flow into the void will allow the void to close.

Table IV. Binding energy (BE) of AlO₆⁶⁻ with Al₁₀ and Y₁₀ cluster models. Heights of oxygens [*h*(O)] and central metal atom [*h*(M)] are optimized to the nearest 0.05Å

Cluster	BE (eV)	<i>h</i> (O)	<i>h</i> (M)
Al ₁₀	4.8	0.70	-0.60
Y ₁₀	12.8	0.45	-0.90

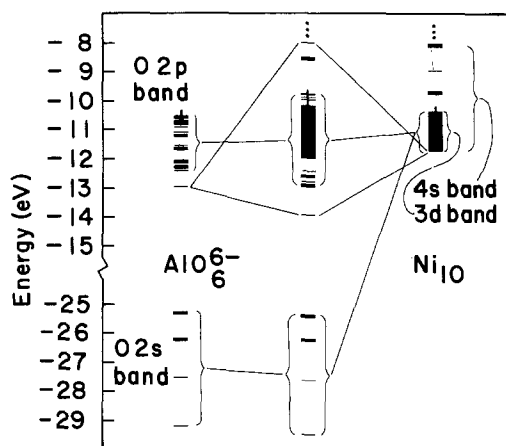


Fig. 10. Molecular orbital energy level correlation diagram showing bonding stabilizations at the alumina-nickel interface.

Conclusion

We find that Y³⁺ cations, once they are incorporated at monolayer levels in the oxide metal interface, cannot diffuse into the oxide and block oxide growth by the cation vacancy diffusion mechanism. If cation diffusion is the rate-limiting growth mechanism, then this may serve to retard void formation at the interface and rapid grain growth, which would lead to convoluted morphologies in response to growth stresses. This conclusion, derived from our theoretical treatment of diffusion, supports suggestions of Golightly *et al.* (13, 14) based on observations of a reduction of interfacial void formation, the development of columnar oxide grain growth on alloys doped with yttrium, and a reduction of scale-growth rate on the yttrium-doped alloy.

We also find that alumina bonds very strongly to yttrium when at the surface of the alloy. If adhesion failures involve rupture of Y-O bonds at the interface, then this may be important to adhesion. Interestingly, we find aluminum and yttrium bind very strongly in nickel as alloying elements. This extra strength is a result of a charge-transfer interaction and is likely to be a general explanation for the high strengths of many alloys.

Acknowledgment

This research has been supported by NASA Grant no. NAG-3-341.

Manuscript received Feb. 1, 1985.

Case Western Reserve University assisted in meeting the publication costs of this article.

REFERENCES

- D. P. Whittle and J. Stringer, *Trans. R. Soc. London, Ser. A*, **295**, 309 (1980).
- D. Delaunay and A. M. Hunz, *J. Mater. Sci.*, **17**, 2027 (1982).
- H. Hindam and D. P. Whittle, *Oxid. Met.*, **18**, 245 (1982).
- a. J. K. Tien and F. S. Pettit, *Met. Trans.*, **3**, 1587 (1972); b. H. M. Hindam and W. W. Smeltzer, *Oxid. Met.*, **14**, 337 (1980).
- K. P. R. Reddy, J. L. Smialek, and A. R. Cooper, *Oxid. Met.*, **17**, 429 (1982).
- J. L. Smialek and R. Gibala, *Metall. Trans.*, **14A**, 2143 (1983).
- (a) A. B. Anderson, *J. Chem. Phys.*, **60**, 2477 (1974); (b) *ibid.*, **62**, 1187 (1975).
- (a) A. B. Anderson and R. G. Parr, *ibid.*, **53**, 3375 (1970); (b) A. B. Anderson, *J. Mol. Spectrosc.*, **44**, 411 (1972); (c) A. B. Anderson, *J. Chem. Phys.*, **63**, 4430 (1975); (d) A. B. Anderson, *Chem. Phys. Lett.*, **76**, 155 (1980); (e) N. C. Debnath and A. B. Anderson, *This Journal*, **129**, 2169 (1982); (f) A. B. Anderson, Y. Kim, D. W. Ewing, R. K. Grasselli, and M. Tenhover, *Surf. Sci.*, **134**, 237 (1983); (g) A. B. Anderson, R. W. Grimes, and A. H. Heuer, *J. Solid State Chem.*, **53**, 353 (1984).
- W. Lotz, *J. Opt. Soc. Am.*, **60**, 206 (1970); C. E. Moore,

- "Atomic Energy Levels," NBS Circ. 467, National Bureau of Standards, U.S. Government Printing Office, Washington, DC (1958); (b) E. Clementi and D. L. Raimondi, *J. Chem. Phys.*, **38**, 2686 (1963); E. Clementi and C. Roetti, "Atomic Data and Nuclear Data Table," Vol. 14, Academic Press, New York (1974); J. W. Richardson, W. C. Nieuwpoort, R. R. Powell, and W. F. Edgell, *J. Chem. Phys.*, **36**, 1057 (1962); H. Basch and H. B. Gray, *Theor. Chim. Acta*, **4**, 367 (1966).
10. H. D. Megaw, "Crystal Structures: A Working Approach," p. 226, W. B. Saunders Company, Philadelphia (1973).
 11. A. E. Paladino and W. D. Kingery, *J. Chem. Phys.*, **37**, 957 (1962).
 12. G. J. Dienes, D. O. Welch, C. R. Fischer, R. D. Hatcher, O. Lazareth, and M. Samberg, *Phys. Rev. B*, **11**, 3060 (1975).
 13. F. A. Golightly, F. H. Stott, and G. C. Wood, *Oxid. Met.*, **10**, 163 (1976).
 14. F. A. Golightly, F. H. Stott, and G. C. Wood, *This Journal*, **126**, 1035 (1979).
 15. R. Hultgren, R. L. Orr, P. D. Anderson, and K. K. Kelley, "Selected Values of Thermodynamic Properties of Metals and Alloys," John Wiley and Sons, New York (1963).
 16. "Handbook of Chemistry and Physics," C. D. Hodgman, Editor, Chemical Rubber, Cleveland, OH (1962).
 17. K. H. Johnson and S. V. Pepper, *J. Appl. Phys.*, **53**, 6634 (1982).
 18. "Spectroscopic Data Relative to Diatomic Molecules," B. Rosen, Editor, Pergamon Press, Oxford, England (1970).

The Effects of Thermal History during Growth on O Precipitation in Czochralski Silicon

G. Fraundorf, P. Fraundorf,* R. A. Craven,* R. A. Frederick, J. W. Moody, and R. W. Shaw

Monsanto Electronic Materials Company, St. Louis, Missouri 63167

ABSTRACT

High oxygen wafers from 100 mm diam Si crystals grown by the Czochralski process, but subjected to three different thermal histories in an experimental puller, were examined by Wright etching, transmission electron microscopy, and Fourier transform infrared spectroscopy after wafer heat-treatments at 775°, 1050°, 775° + 1050°, and 1320° + 775° + 1050°C. Only wafers near the seed end of each ingot were used, thus minimizing differences in parameters other than thermal history. The observations show that defect morphology and O precipitate number density (not total O precipitation) after the one- and two-step heat-treatments depend on thermal history in the puller. In particular, 775°C heated wafers which spent less than an hour in the puller below 1000°C show number densities down by more than a factor of 100 from those which spent longer. On the other hand, the observations indicate that effects of puller thermal history are erased with a short 1320°C anneal, or typical VLSI multistep pretreatments which enhance bulk oxygen precipitation. In addition, the results suggest two possible complications for simple models of oxygen precipitation. These are that 500°C annealing can be much more effective than 775°C annealing for nucleating oxygen precipitates, contrary to model predictions, and that critical sizes for precipitate dissolution at 1050°C can be much larger than predicted by classical calculations.

Oxygen in Czochralski-grown silicon crystals plays an important role in device performance. After certain thermal treatments, it can have such negative effects as the formation of "thermal" (1) and "new" (2) donors, or such positive effects as the formation of bulk defects which act as gettering sites for metallic impurities and native point defects (3).

During crystal growth, the silicon crystal receives not only its specified oxygen allotment, but also its first thermal annealing treatment. This annealing treatment introduces oxygen donors and precipitate nuclei which can determine precipitation behavior during subsequent wafer heat-treatments. Previous investigators have reported precipitation behavior differing with position along the length of a 3 in. diam crystal even in regions with similar oxygen content (4), but the roles of puller thermal history and those of other factors associated with position in the ingot were not separated. In related work, Tsuya *et al.* (5) found that extended annealing in the puller enhanced the rate of precipitation and the number density of defects in the middle of a 35 cm long ingot. Independently, Nakanishi *et al.* (6) have demonstrated that defect density after a 1050°C wafer heat-treatment can be decreased, and the defect radial distribution modified, by rapid cooling of a 3 in. diam ingot after crystallization. However, no detailed study of the effects specifically of puller thermal history after a wide variety of heat-treatments was available.

The goal of this study was to assess (for 100 mm diam crystals) the dependence on puller thermal history of defect type, precipitate number density, and total oxygen

precipitation after a variety of wafer heat-treatments. Instead of using position in the ingot for indirect control of thermal history, position in the ingot was held constant and only thermal history was modified. To be specific, silicon crystals were cooled by three different methods: (i) quenching in air, (ii) shielding the growing crystal from heat radiated by the hot melt, and (iii) gradual cooling of the ingot in direct view of the melt. The results which follow support many of the observations cited above. In addition, they indicate that the strongest effects of puller history involve defect type and precipitate number density, not total precipitation, and that those effects are most obvious after precipitation in a single low temperature step (*e.g.*, 775°C). However, the strong puller effects observed conflict markedly with predictions from a simple semiempirical model for oxygen precipitation. Possible explanations of this are discussed as well.

Experimental

Nine 100 mm diam boron-doped [100] silicon crystals grown in an experimental puller with 18-22 Ω-cm resistivity and different oxygen levels were used. Six of these crystals were grown for about 2h, plucked from the crystal puller, and then allowed to cool to room temperature. These crystals, which will be referred to as Quench crystals, were pulled sequentially from the same melt. Another crystal, which will be referred to here as the Shield crystal, was grown for 10h in a crystal puller fitted with a shroud suspended directly above the melt, which surrounded and shielded the pulled crystal from the hot melt below. For comparison, two unshielded crystals grown for a similar time were also used. These crystals, for con-

*Electrochemical Society Active Member.

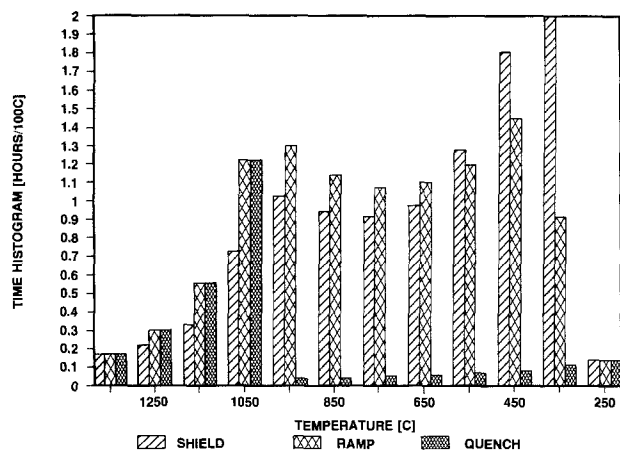


Fig. 1. Thermal profiles in the crystal puller. Estimated time spent in each 100°C temperature interval, based on optical pyrometer measurements, for seed-end material from ingots with three different thermal histories.

venience, will be called Ramp crystals. Figure 1 shows histograms of the time per degree centigrade spent in the crystal puller by seed-end silicon from each process. These profiles were inferred from optical pyrometer measurements on the ingot exterior during crystal growth. Note that the thermal history of the Quench crystals is similar to what one might expect for material from the bottom end of a Ramp ingot.

Slices cut with (110) or (100) orientation from the first 10 cm of each of the nine crystals were subjected to a variety of annealing treatments. The treatments (and their abbreviations) are: 16h at 775°C in N₂ (L), 24h at 1050°C in N₂ (H), and 16h at 775°C followed by 16h at 1050°C (LH) in N₂. To assess the possibility of erasing puller history effects with a high temperature heat-treatment, the LH heat-treatment was also performed after a 3h "dispersing" heat-treatment at 1320°C (DLH) in argon. The two precipitation temperatures in these treatments, 775° and 1050°C, were chosen because the combination of these two is known to facilitate efficient precipitation in Czochralski crystals.

Before and after the annealing treatments, the concentration of oxygen was inferred from FTIR absorption coefficient (α) measurements using the DIN relationship: $O/[cm^3] = 2.45 \times 10^{17} \alpha [cm^{-1}]$. Carbon in all wafers was below FTIR detectability ($< 3 \times 10^{15} [cm^3]$). Optical microscope characterization was done after a 20 min Wright etch to verify defect uniformity. Several 3 mm disks (typically four) from the center of each of the 20 wafers for this study were examined in the TEM. Defect types, precipitate sizes, and precipitate number densities were determined from TEM observations. Although Wright etching did not distinguish precipitates from other defects, in cases where defects were large enough to result in distinct etch pits, the optical observations qualitatively supported TEM density determinations over a larger sampled volume. Finally, some wafers with each puller history were subjected to a denuding treatment (7). This involved a denuding step at 1150°C, a multistep annealing treatment in the 500°-800°C temperature range, and 8h annealing steps at 900° and 1050°C, to allow residual puller effects on denuded zone depth after a lengthy treatment process to be assessed.

Results

Table I summarizes the comparative data on Shield, Ramp, and Quench material which had oxygen concentration near 18 ppma. It includes information on initial carbon and oxygen concentrations and thermal history in the puller as well as interstitial oxygen concentrations, defect types, precipitate number densities, and precipitate sizes after the heat-treatments described above. Figure 2 shows TEM micrographs of some of the defect population types referred to in Table I.

The consistency between IR and TEM observations should be addressed first. Figure 3 shows a log-log plot

Table I. Experimental observations

	Shield	CZ-Std. Ramp	Quench
Puller history			
Initial [O _i /cm ³] ^a	9.0×10^{17}	9.0×10^{17}	9.0×10^{17}
Initial [C/cm ³]	$< 3 \times 10^{15}$	$< 3 \times 10^{15}$	$< 3 \times 10^{15}$
Hours at 1200°-1000°C	1.1	1.8	1.8
Hours at 1000°-700°C	2.9	3.5	0.1
Hours at 700°-400°C	4.1	3.7	0.2
After L (775°C, 16h)			
Final [O _i /cm ³]	8.0×10^{17}	8.0×10^{17}	9.0×10^{17}
Defect types	A--X--	A--X--	A----
Log (precipitate/cm ³) ^b	12.9 ± 0.3	13.0 ± 0.2	10.7 ± 0.3
Precipitate size (μ m)	0.02	0.02	0.01
After LH [(775°C, 16h) + (1050°C, 16h)]			
Final [O _i /cm ³] ^a	2.2×10^{17}	4.0×10^{17}	3.5×10^{17}
Defect types	A--Z	AbcdXyZ	ABCD--Z
Log (precipitate/cm ³) ^b	11.6 ± 0.3	11.9 ± 0.2	10.3 ± 0.1
Precipitate size (μ m)	0.03	0.05	0.2
After H (1050°C, 24h)			
Final [O _i /cm ³] ^a	8.0×10^{17}	8.0×10^{17}	8.0×10^{17}
Defect types	-BCD--	-BCD--	-----
Log (precipitate/cm ³) ^b	9.4 ± 0.4	9.5 ± 0.2	None found
Precipitate size (μ m)	0.2	0.3	NA
After DLH [(1320°C, 3h) + (775°C, 16h) + (1050°C, 16h)]			
Final [O _i /cm ³] ^a	2.2×10^{17}	2.2×10^{17}	2.3×10^{17}
Defect types	-B--Z	-B--Z	-B--Z
Log (precipitate/cm ³) ^b	10.8 ± 0.3	10.0 ± 0.4	10.8 ± 0.3
Precipitate size (μ m)	0.2	0.4	0.2
After denuding heat-treatment			
DZ depth (μ m)	10	9	10
Defect type notation ^c			
Primary defects		Related defects	
A	Tiny precipitates	X	Dislocation dipoles
B	Square platelets	Y	Hexagonal loops
C	Punched-out dislocation loops	Z	Stacking faults
D	Precipitate dislocation complexes		
Other			
-	None found in, typically, 4×10^{-8} cm ³ searched		
NA	Data not available		

^a Interstitial oxygen uncertainties around 5×10^{16} [O/cm³].

^b Errors in mean based on empirical sampling variations.

^c A lower case letter denotes a minor presence only.

of precipitated oxygen (initial minus final) per precipitate vs. precipitate size. These data cluster along a line of slope 2, as expected if precipitates above a few hundred angstroms in size are platelets which grow laterally, but not in thickness, as has been suggested previously (8). If we assume the density of oxygen in the precipitates to be typical of silica minerals (e.g., 5×10^{22} [O/cm³]), then the volume-averaged thickness of these precipitates is around 60Å. Such thicknesses appear consistent with some TEM edge-on precipitate observations (9). Thus we have reason to believe that oxygen precipitation is the primary operating process, and that we can get some idea of the number of oxygen atoms per defect as a function of precipitate size from the above correlation.

Concerning the overall effects of wafer thermal history, we find very little of the total oxygen precipitated after individual 775°C or 1050°C wafer heat-treatments, but a sizeable fraction (e.g., 70%) precipitated after 775° + 1050°C treatments, regardless of prior history. In the specimens with a single wafer heat-treatment, we find a much lower number density of defects after 1050° than after 775°C. This was expected, and probably results because much smaller nuclei are able to survive and grow at 775° than at 1050°C (10). Unexpected, however, was the slight decrease in defect density for Ramp and Shield material in going from 775° to 775° + 1050°C treatments. It is certainly plausible that the 1050°C treatment redissolves some of the precipitates which had not grown large enough during the 775°C treatment to survive higher temperature. However, one might expect (as we show in the discussion) that defects large enough to be detected in the TEM after the 775°C treatment would not dissolve at 1050°C.

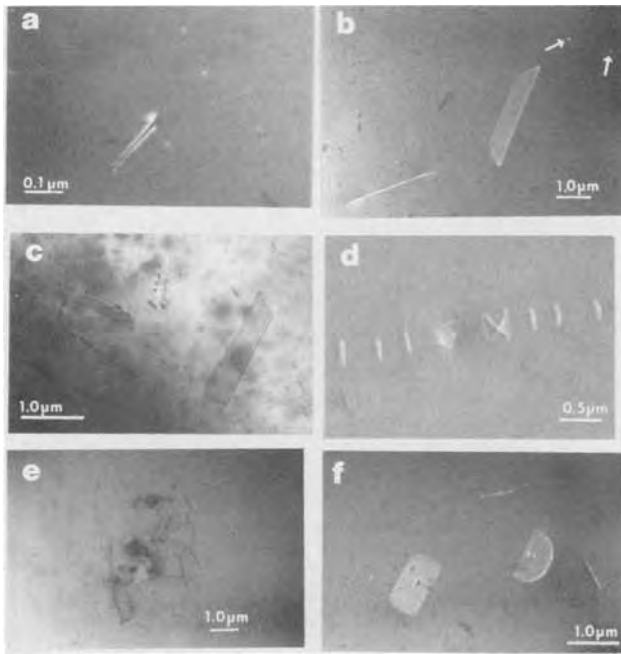


Fig. 2. a: Defects in Ramp crystals after 775°C wafer heat-treatment. Dipoles and tiny precipitates were found in the Ramp as well as in the Shield wafers; only precipitates in Quench material. b: Stacking faults and tiny precipitates (arrowed) in Shield wafers after 775°C + 1050°C treatment. c: Defects in Ramp crystals after 775°C + 1050°C. d: A punched-out dislocation in a Quench wafer after 775°C + 1050°C. e: Precipitate dislocation complex in a 1050°C Shield crystal. This type of defect was also found in 1050°C Ramp wafers. f: Defects in a Shield crystal after the 1320°C + 775°C + 1050°C treatment. Similarly treated Ramp and Quench wafers also contained these defect types.

Concerning different puller histories, the most striking differences in precipitate number density occur after single-wafer heat-treatments. The relative absence of detectable defects in approximately 10^{-7} cm³ of Quench material after the 1050°C treatment is consistent with the observation by Nakanishi *et al.* (6) that densities after such annealing in Quench material can be down from those in Ramp/Shield material by several orders of magnitude. This may be easy to understand, since the 1050°C heat-

treatment is an unlikely source of precipitate nuclei itself. A similar drastic reduction in number density going from Ramp/Shield to Quench wafers (in this case, by nearly two orders of magnitude) is observed after the 775°C treatment, although this time it is unexpected since 775°C is considered to be a very effective nucleation temperature (10). The trend to lower number densities in quench material after the 775°C + 1050°C treatment is also present, although not as large. However, both Ramp and Shield material show number densities similar to that of the Quench material if they have been first put through a 1320°C “dispersing” heat-treatment. This provides evidence that the Quench differences are in fact due to puller thermal history, and are not otherwise intrinsic to the crystals. Differences in precipitate number density of smaller than a factor of 10 between ingots might also result from thermal history differences. However, since such differences exist between ingots after the 3h “dispersing” anneal, intrinsic ingot differences may be responsible as well.

Defect types are in general correlated with the size of precipitates, with few lattice deformation effects (*e.g.*, punched-out loops, dislocation complexes) associated with defects in the 100-200Å size range. But there are also unexplained differences, especially after the two-step heat-treatment. The most drastic is the much larger diversity of defects in Ramp as compared to Shield wafers. That thermal history is the cause, as opposed to subtle intrinsic differences, is this time supported by the similarity of defect types (in all crystals) observed in wafers which have undergone a 1320°C treatment prior to the two-step anneal.

Discussion

The results above confirm that precipitate number density and type (but not necessarily total oxygen precipitation) after one or two wafer heat-treatments can be strongly dependent on prior thermal history in the puller. Along the length of a single ingot, these effects may be offset by axial impurity and point defect profiles (4) which are present as well. The results also confirm that the effects of thermal history can be erased to a large extent by a short wafer heat-treatment at 1320°C, and that puller history may have little effect on denuded zone depths after a multistep denuding treatment which includes temperatures below 800°C.

The results also provided a few surprises. The first concerns the loss of detectable precipitates in 775°C-treated wafers after a subsequent 1050°C anneal. Critical radius calculations (*e.g.*, 11, 12) predict that precipitates with more than 60-100 oxygen atoms should be stable at 1050°C, and yet Fig. 3 suggests that many of the precipitates “lost” after the 1050°C anneal probably contained more than 10^4 atoms of oxygen. Even if they did not, the defects certainly were detectable in the TEM in darkfield images at rather low magnifications (*e.g.*, 50,000 times). Between 10^3 and 10^4 atoms is probably a lower limit for detectability for equidimensional precipitates under the observing conditions, and hence a large discrepancy exists. The problem may lie with the assumption of spheres in critical radius calculations. If many of the defects are very small in one or more directions (*e.g.*, as disks or rods), then their surface area and propensity to dissolve may increase. Of course, their effective size (longest linear dimension) for TEM detection would also increase. The “small dislocation loop contrast” associated with many of the defects in the 775°C material (Fig. 2a) and the observations by Bourret *et al.* (13) and others of rodlike defects which are unstable when too large suggest further that shape effects may be quite important in nucleation models.

A second surprise was the strong effect of puller history on defects after a 16h wafer treatment at 775°C. Figure 4 compares measurements of precipitate number density after the 775°C treatment with predictions of the nucleation model of Inoue *et al.* (10-12). Their model is based on observations after LH-type heat-treatments, which indicate that the number of detectable precipitates is propor-

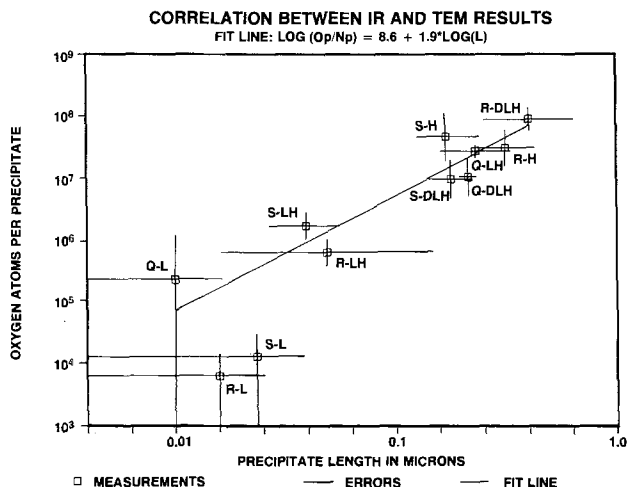


Fig. 3. Oxygen atoms per precipitate (O_p/N_p) vs. mean precipitate size (maximum projected dimension L). Data from Table I are plotted here along with a least squares power law fit (linear on log-log) which suggests two-dimensional growth for precipitates larger than 0.03 μ m in size. Vertical bars reflect IR and precipitate number density uncertainties, and have been considered in the fitting process. The horizontal bars do not represent uncertainties in mean size, but do indicate relative limits on the range of precipitate sizes observed in each specimen type.

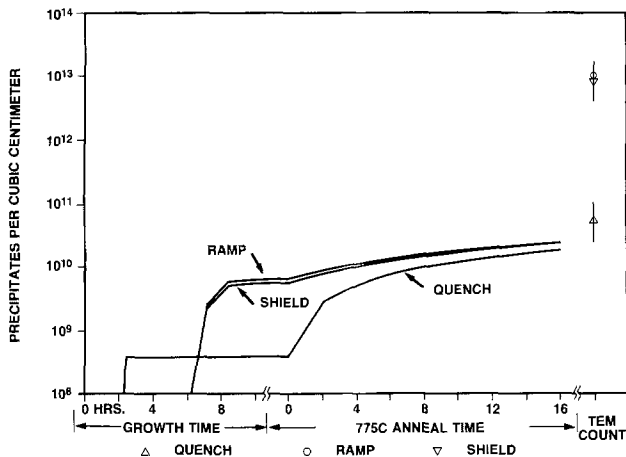


Fig. 4. Theoretical vs. observed number densities after a 16h, 775°C heat-treatment. The curves show precipitates per cubic centimeter as a function of processing time. Nucleation rates were calculated with the algorithm of Inoue *et al.* (10) using numbers recommended by Rogers *et al.* (12). Total number densities were determined by convoluting those rates with the growth thermal history (Fig. 1) followed by a 16h 775°C heat-treatment. Observed number densities are from Table I.

tional (for small changes in interstitial oxygen concentration) to the time spent at various temperatures in the 600°-900°C range. As can be seen, the number of precipitates predicted after the 775°C anneal for all material is near that observed for the Quench crystal. This suggests relatively short puller histories for the material used to calibrate the model. More importantly, the modeled nucleation rate curve [*cf.* Ref. (12)] peaks at 700°C with a full width at half-maximum of 100°C. Thus a 6h thermal history in the puller between 400° and 1000°C (*i.e.*, the Shield/Ramp puller treatments) should have increased the number of observed precipitates by 30%, instead of the observed 18,000%.

Ingot position, initial oxygen concentration, initial carbon concentration, but not thermal history, were the same for the Quench and Ramp/Shield material examined. Since the differences between Quench and Ramp/Shield number densities are removed by a 3h 1320°C "dispersing" treatment, they almost certainly arise from differences in thermal history. In subsequent work (15), this conclusion has been confirmed by TEM/etching observations on Quench wafers which indicate that 3h pretreatments at 500° or 600°C are adequate to bring the 16h, 775°C precipitate number densities in Quench wafers up to those found in Ramp/Shield wafers. Taken in the context of the single-stage nucleation model of Inoue *et al.* (10), this would imply nucleation rates below 700°C that are at least three orders of magnitude higher than rates predicted by the model. Reconciliation of these observations with those of Inoue *et al.*, especially concerning the temperature dependence of nucleation rate, appears to require that the critical-density term in the nucleation equation be dependent on prior history. This problem with a steady-state critical-density term has already been mentioned in the discussion by Osaka *et al.* (11) of an "induction time" for nucleation in quenched materials, and appears to be due to the kinetic stability of clusters with only a few oxygen atoms (14) and the existence of a site in the lattice able to trap its first oxygen only at temperatures below 700°C (15). A precipitation model which considers these issues may be important for modeling low temperature history effects.

Conclusion

A systematic study of the effects of thermal history during the growth of 100 mm Czochralski silicon ingots is reported. It shows that puller thermal history, if separated from other axial effects in the ingot, can play a strong role in the type of defects and number density of precipitates (but not necessarily the total oxygen precipitated) after one- or two-wafer heat-treatments. In particular, the study of precipitate number density differences after a single 775°C heat-treatment provides evidence for a low temperature process enabling precipitate nucleation at rates much higher than predicted from the model of Inoue *et al.* The observations also call into question the relevance of classical critical radius calculations in such models. On the other hand, differences due to puller thermal history from the point of view of device manufacture do not survive intentional low temperature annealing or multistep intrinsic gettering schemes which add additional processing in the 500°-800°C temperature range. Effects of puller thermal history may also be completely erased by a short 1320°C heat-treatment.

Acknowledgment

The authors would like to thank B. Linebaugh, M. Johnson, and J. Collins for technical assistance, and H. Chiou, H. Korb, B. Rogers, and F. Shimura for helpful advice and discussion.

Manuscript submitted Oct. 15, 1984; revised manuscript received March 19, 1985.

Monsanto Electronic Materials Company assisted in meeting the publication costs of this article.

REFERENCES

- W. Kaiser, H. L. Frisch, and H. Reiss, *Phys. Rev.*, **112**, 1546 (1958).
- P. Capper, A. W. Jones, E. J. Wallhouse, and J. G. Wilkes, *J. Appl. Phys.*, **48**, 1646 (1977).
- T. Tan, E. Gardner, and T. Tice, *Appl. Phys. Lett.*, **30**, 175 (1977).
- F. Shimura and H. Tsuya, *This Journal*, **129**, 1062 (1982).
- H. Tsuya, F. Shimura, K. Ogawa, and T. Kawamura, *ibid.*, **129**, 374 (1982).
- H. Nakanishi, H. Kohda, and K. Hoshikawa, *J. Cryst. Growth*, **60**, 80 (1983).
- R. A. Craven, in "Semiconductor Silicon 1981," H. R. Huff, R. J. Kreigler, and Y. Takeishi, Editors, p. 254, The Electrochemical Society Softbound Proceedings Series, Pennington, NJ (1981).
- K. Wada and N. Inoue, *J. Cryst. Growth*, **49**, 749 (1980).
- I. Y. T. Chan, R. W. Carpenter, C. J. Varker, L. Chang, and L. J. Demer, in "Proceedings of the 40th Annual Electron Microscope Society of America Meeting," p. 500, G. W. Bailey, Baton Rouge, LA (1982).
- N. Inoue, J. Osaka, and K. Wada, *This Journal*, **129**, 2780 (1982).
- J. Osaka, N. Inoue, and K. Wada, *Appl. Phys. Lett.*, **34**, 288 (1980).
- B. Rogers, R. B. Fair, W. Dyson, and G. A. Rozgonyi, in "VLSI Science and Technology/1984," K. E. Bean and G. A. Rozgonyi, Editors, p. 74, The Electrochemical Society Softbound Proceedings Series, Pennington, NJ (1984).
- A. Bourett, J. Thibault-Desseaux, and D. N. Seidman, *J. Appl. Phys.*, **55**, 825 (1984).
- See, for example, A. Ourmazd, A. Bourett, and W. Schroter, *J. Appl. Phys.*, **56**, 1670 (1984).
- P. Fraundorf, G. K. Fraundorf, and R. A. Craven, in "VLSI Science and Technology/1985," W. M. Bullis and S. Broydo, Editors, p. 436, The Electrochemical Society Softbound Proceedings Series, Pennington, NJ (1985).

Structural Effects on a Submicron Trench Process

Daeje Chin,* Sang H. Dhong,* and Glenn J. Long

IBM Thomas J. Watson Research Center, Yorktown Heights, New York 10598

ABSTRACT

Recently, silicon trenches have been widely used for device isolation or three-dimensional capacitors in dynamic memories. In this work, trenches with submicron openings have been fabricated and several structure-dependent effects were discovered. A reactive ion etching rate in the vertical direction inside a trench decreases significantly as the aspect ratio (depth/width) becomes larger. A bottle-shaped profile due to undercutting starts to appear with trenches whose openings are smaller than a micrometer and becomes worse as the width decreases. A film thickness on sidewalls for refilling trenches shows no strong dependence on the structural aspect when chemically vapor deposited at low pressure.

Isolation technology using silicon trenches is employed in high-speed bipolar integrated circuits (1, 2) and in latchup-free CMOS devices (3). A high density MOS dynamic RAM cell utilizes trench sidewalls to increase storage capacitance (4). Three steps are involved in a silicon trench process: reactive ion etching of Si substrate, refilling with dielectric materials, and planarization. Technical constraints include: (i) no void remains inside a trench after refilled; (ii) defect density is low at sidewalls and corners; and (iii) a dielectric layer can be deposited uniformly.

As lithographic technology improves, the trench opening width is expected to shrink, while the depth is kept the same or even larger in dynamic memories to maintain a minimum storage capacitance. Currently the minimum feature size definable by lithography, however, is about 1 μm or slightly less by advanced optics and 0.5 μm by an electron beam. By making features smaller than the lithographic limit, this work aims at investigating potential problems in a submicron trench process in the future, particularly the reactive ion etching of silicon substrates with small mask openings and chemical vapor deposition into narrow and deep trenches.

Experiments

On p-type wafers, 100 nm nitride and 600 nm polysilicon layers were sequentially deposited. An optical lithographic step was done to create patterns on the polysilicon layer with different linewidths, as shown in Fig. 1a. After etched vertically by reactive ion etching (RIE) with a photoresist mask, the polysilicon film was oxidized at 1100°C. The film thickness after oxide was grown was 1.1 μm , and the oxide shape was round near the edges, as shown in Fig. 1b. Oxide grown laterally from the polysilicon edges was about 0.4 μm thick, and this shrank the original polysilicon openings by 0.8 μm , creating openings smaller than the lithographic limit. The nitride layer preventing the Si substrate from being oxidized was removed by RIE in CF_4 , and then silicon trenches were formed by reactive ion etching in a mixture of CCl_2F_2 and O_2 using the oxide layer as a mask after a precleaning step using CCl_2F_2 and Ar. The etch rate of silicon was approximately 92 nm/min, and the selectivity to oxide was over 15 in this experiment. In order to study refilling, an oxide layer (75 nm) was deposited into 8 μm deep trenches by a chemical vapor deposition at atmospheric pressure (APCVD), followed by deposition of a polysilicon layer (150 nm) at 400 mtorr (LPCVD).

Results and Discussion

Cross sections of silicon trenches with various etching times are shown in SEM's of Fig. 2. The initial openings measured from Fig. 2a were 2.5, 1.3, 0.9, 0.7, 0.45, 0.3, and 0.2 μm , respectively. These widths, however, slightly decreased as the RIE continued because of deposition of a polymer layer on sidewalls (5), which will be discussed below. The depth of a wide trench, when plotted with respect to etching time in Fig. 3a, linearly increases, while

that of a narrow one increases with a slower rate. The trench depths of 0.2 μm wide line and a square (0.3 \times 0.3 μm), for instance, were shorter by about 1 and 3.2 μm , respectively, than a trench wider than 2 μm by the time it becomes 4.7 μm deep. This two- or three-dimensional phenomenon was more pronounced as the etching pro-

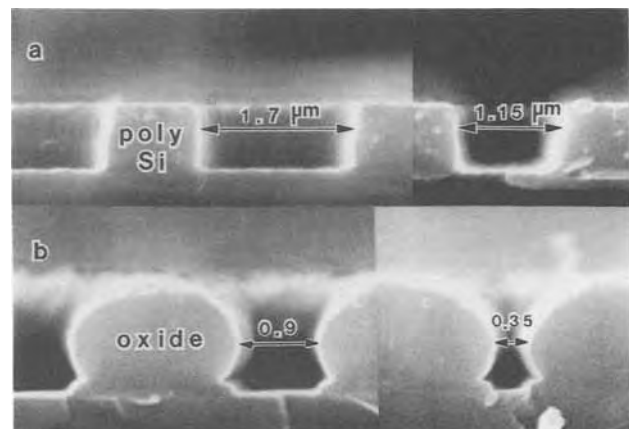


Fig. 1. A technique for creating features smaller than the lithographic limit. a: A polysilicon layer with opening widths of 1.7 and 1.15 μm . b: These openings become 0.9 and 0.35 μm after oxidation.

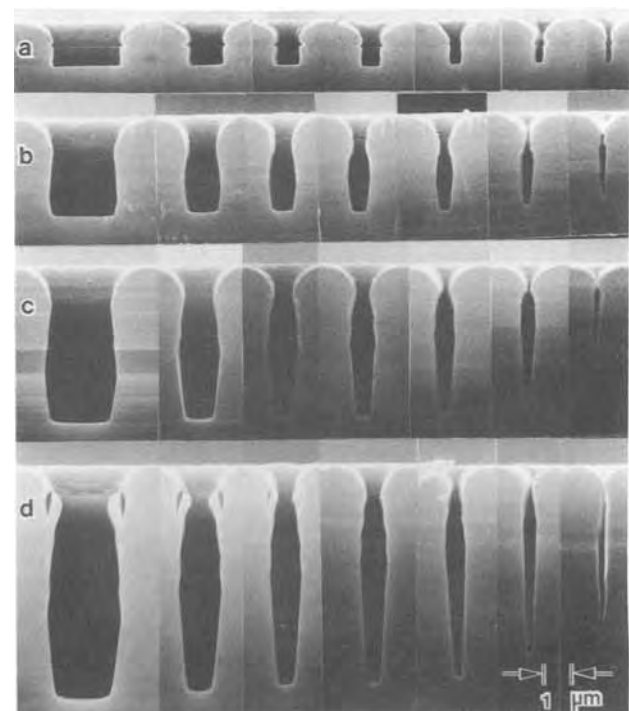


Fig. 2. Silicon trenches with various opening sizes. The etching times are (a) 5, (b) 20, (c) 40, and (d) 60 min, respectively.

* Electrochemical Society Active Member.

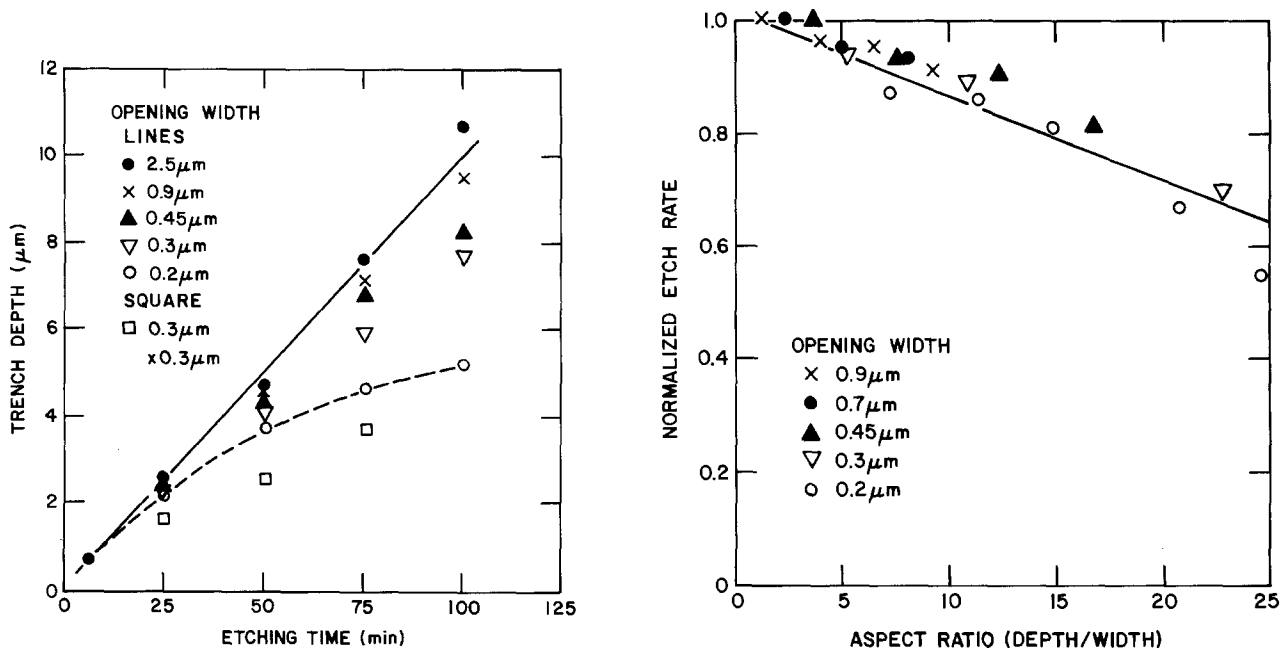


Fig. 3. Structural effects of a silicon RIE. a (left): Trench depth vs. etching time. b (right): Normalized etching rate vs. aspect ratio

ceeded or as the opening was a small square rather than a line. In particular, the depth decrease of the square hole is about twice as large as that of the line trench with the same width.

Figure 3b shows a plot of the silicon etch rate vs. the aspect ratio (width/depth) of the two-dimensional trenches, in which the etch rate decreases almost linearly as the aspect ratio increases and it is solely determined by the aspect ratio regardless of the opening sizes. The etch rate E with width W and depth D was obtained empirically as

$$E(W/L) = \left(1 - 0.16 \frac{W}{L}\right) E_w \quad [1]$$

where E_w represents the etch rate at a trench wide enough not be affected by the two-dimensional effect. It should be noted that the depth and width are changing continuously as etching goes on. In calculating the etch rate and the aspect ratio in Fig. 3b, therefore, the average depth between two consecutive time steps was chosen. However, the initial width measured from Fig. 2b was used because the deposited polymer material reduces the width. This is done to avoid measurement errors of the narrow trench openings, and it also seems more practical in determining trench dimensions on a mask level.

There may be several reasons responsible for the two- and three-dimensional phenomena on the deep-trench RIE. In this paper, a diverging electric field inside a trench is considered to qualitatively explain the two-dimensional effect. The electric field across a sheath near a powered electrode due to a self-bias in an RIE system is mostly perpendicular to a silicon substrate because the sheath width is much smaller than the electrode size. The field within a trench, however, should diverge because the silicon surface is at a constant potential. Some of the ions entering the trench through its opening, consequently, are captured at the sidewalls, and therefore fewer of them can arrive at the trench bottom. In this particular process used involving a mixture of $\text{CCl}_2\text{F}_2 + \text{O}_2$, the polymer material deposited on the trench sidewalls reduces the trench opening significantly. Therefore, this diverging field effect becomes more pronounced. Although no precise relationship between the etch rate and the ion flux has been reported yet, the etch rate is known to be greatly enhanced by the ion bombardment (6). It is, therefore, not difficult to conceive that the etch rate at the trench bottom should be reduced due to the fewer number of ions bombarding the bottom surface. The linear dependence on the aspect ratio may be derived from

this diverging field associated with the two-dimensional structure.

Figure 4 shows some of the trenches in Fig. 2b after all polymer layers (about 80 nm thick) were removed in buffered HF. The thickness of the polymer layer increases initially but saturates as the etching goes on. This phenomenon actually helps tapering the sidewall slope for ease of refilling, as seen in wide trenches. The polymer layer, however, together with the two- or three-dimensional effect described earlier, results in pointed bottoms when the opening is 0.5 μm or smaller. In Fig. 4, significant undercutting was also noticed in trenches with 1 μm or smaller width, which results in a bottle-shaped trench. The length of the narrow bottle neck is approximately equal to the opening width, and clearly depends on the shape of the oxide mask. The narrowest trench in Fig. 4, for an example, has an asymmetric mask whose steeper angle at the right side creates undercutting at a deeper location at the left side. From these observations, it was conjectured that ions deflecting from the oxide-mask edges are responsible for the undercutting. The round shape of oxide edges resulting from lateral oxidation of the polysilicon layer may have enhanced such ion deflection in the present experiment. Since mask edges during RIE are always subjected to a facet effect causing a round shape (5), a layer thicker than the opening width may be desirable to avoid such undercutting. This bottle shape makes it difficult to refill without a void, and sharp corners at the bottoms are prone to defect generation in subsequent hot processing steps. These are major concerns related to reliability in a submicron trench process.

In Fig. 5, the initial opening of a trench before deposition of 75 nm oxide was about 1 μm . Then it shrank to

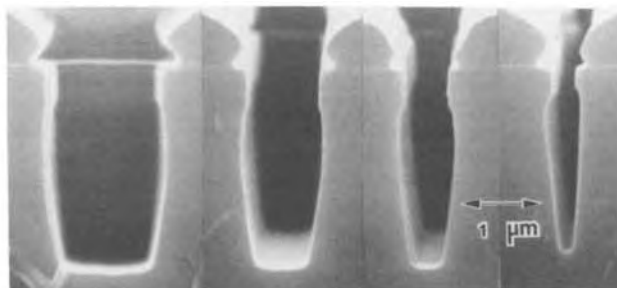


Fig. 4. Trenches after the polymer layer on sidewalls was removed in BHF.

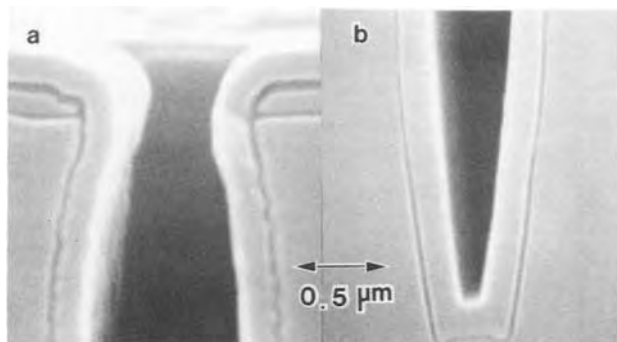


Fig. 5. A trench (1 μm wide and 8 μm deep) after the APCVD oxide and LPCVD polysilicon were deposited. The SEM's show (a) the top and (b) the bottom of the trench.

0.55 μm after 150 nm polysilicon was deposited. The thickness of the polysilicon layer changes very little with depth, even for a trench with an aspect ratio as large as 20, while the oxide thickness becomes less than half at the bottom. This may be attributed to the fact that the mean-free path of a gas molecule, inversely proportional to pressure, is smaller than 1 μm at 1 atm, but larger than 100 μm at 400 mtorr (7). As a result, it is concluded that LPCVD is necessary to deposit dielectric layers uniformly inside trenches with large aspect ratios.

Conclusions

Trenches with openings as small as 0.2 μm have been successfully made by oxidizing a polysilicon layer after its being patterned by optical lithography. Several structure-dependent effects were found. The silicon etch

rate drops significantly as the trench opening becomes smaller. This may cause problems if there are many different trench sizes. Undercutting also appears below 1 μm width, and otherwise on vertical and tapering sidewalls. These technical problems must be considered in optimizing any submicron trench process. Low pressure chemical vapor deposition into trenches, however, is less sensitive to their structures than atmospheric pressure CVD, and it is necessary for successful refilling in a trench process.

Acknowledgment

The authors would like to thank the personnel of the silicon facility for sample preparation and T. Ross and P. A. McFarland for SEM support.

Manuscript submitted Jan. 31, 1985; revised manuscript received March 13, 1985.

IBM Corporation assisted in meeting the publication costs of this article.

REFERENCES

1. D. D. Tang, P. M. Solomon, T. H. Ning, R. D. Isaac, and R. E. Burger, in "ISSCC Digest of Technical Papers," pp. 242-243 (1982).
2. A. Hayasaka, Y. Tamaki, M. Kawamura, K. Ogiue, and S. Ohwaki, *IEDM Tech. Dig.*, 62, (1982).
3. R. D. Rung, H. Momose, and Y. Nagakubo, *ibid.*, 237 (1982).
4. H. Sunami, T. Kure, N. Hashimoto, K. Itoh, T. Toyabe, and S. Asai, *ibid.*, 806 (1982).
5. S. M. Sze, "VLSI Technology," McGraw-Hill, New York (1983).
6. J. W. Coburn and H. F. Winters, *J. Vac. Sci. Technol.*, 16, 391 (1979).
7. L. I. Maissel and R. Glang, "Handbook of Thin Film Technology," McGraw-Hill, New York (1970).

Determination of Conversion Factor for Infrared Measurement of Oxygen in Silicon

T. Iizuka, S. Takasu,* M. Tajima, T. Arai, T. Nozaki, N. Inoue,* and M. Watanabe*

Japan Electronic Industry Development Association, Kikaishinkokaikan, Shibakoen 3-5-8, Minato-ku, Tokyo 105, Japan

ABSTRACT

A reliable conversion factor for the infrared absorptiometry of oxygen in silicon has been determined by round-robin infrared measurement followed by charged particle activation analysis with the $^{16}\text{O}(^3\text{He},p)^{18}\text{F}$ reaction. As for the round-robin samples, 70 dislocation-free CZ silicon wafers with oxygen contents ranging from 3 to 20×10^{17} at.-cm $^{-3}$ and thicknesses of 2, 1, and 0.5 mm were carefully prepared by five organizations. A good linear relationship has been obtained between the absorption coefficient and the oxygen content. The relationship is expressed as [oxygen concentration (at.-cm $^{-3}$)] = $(3.03 \pm 0.02) \times 10^{17} \times$ [absorption coefficient (cm $^{-1}$)].

Oxygen in Czochralski (CZ) grown silicon crystals is known to be an important impurity in connection with defect control and wafer deformation. Oxygen concentration in silicon wafers is determined by infrared absorption at 9 μm due to the localized vibrational mode of the interstitial oxygen. The conversion factor correlating the infrared absorption coefficient to the oxygen content is obtained by the use of some analytical method which gives absolute oxygen concentration, such as vacuum fusion or activation analysis. Since Kaiser and Keck first determined this calibration relationship, several different conversion factors have been reported and used (1-7). Thus, oxygen concentration values for a given silicon wafer reported by different organizations frequently show considerable disagreement. In order to improve this situation, a working committee was organized in the Japan Electronic Industry Development Association (JEIDA) in 1979. The committee decided to determine highly reliable conversion factor using carefully prepared silicon crystals.

*Electrochemical Society Active Member.

This is a report on the newly determined conversion factor obtained by round-robin measurement of infrared absorption at 9 μm followed by activation analysis of the total oxygen in silicon. The work continued from October 1979 to November 1982. The following organizations participated: Electrotechnical Laboratory; Hitachi Limited; Institute of Physical and Chemical Research; Komatsu Electronic Metals; Matsushita Corporation; Mitsubishi Electronic; Nippon Telegraph and Telephone Corporation; Musashino Electrical Communication Laboratory; NEC Corporation; Nippon Silicon; Osaka Titanium; Shin-Etsu Handotai; The University of Tokyo; The University of Tsukuba; Toshiba Corporation; VSLI Cooperative Laboratory; Monsanto Corporation; Nicolet Japan; and Wacker Chemitronic.¹

Experimental

Sample preparation.—Dislocation-free, low carbon (100) CZ silicon crystals of 70-100 mm diam were pre-

¹Monsanto, Nicolet, and Wacker participated from the middle of the round-robin.

pared by Komatsu Electronic Metals, Musashino Electrical Communication Laboratory, Nippon Silicon, Osaka Titanium, and Shin-Etsu Handotai. The oxygen contents of these crystals ranged from 3 to 20×10^{17} at.-cm⁻³, which were obtained using a tentative conversion factor of 3.0×10^{17} at.-cm⁻², and their resistivities were more than 10 Ω-cm. In order to investigate the effect of the wafer thickness on the infrared measurement, a set of wafers 2, 1, and 0.5 mm thick were so taken from an adjacent portion of each ingot so as to assure its containing nearly the same concentration of oxygen. Both sides of the wafers were mirror-polished to a surface flatness of better than 3 μm for the infrared measurement. Thus, 70 wafers (26 of 2 mm, 22 of 1 mm, and 22 of 0.5 mm thickness) with different growth histories were prepared for this investigation. Reference samples with the same thicknesses and surface finish were prepared by float-zone method.

Infrared measurement.—In order to obtain the infrared absorption coefficient of the samples as accurately and reproducibly as possible by the round-robin measurement, the following measurement procedures were recommended by the committee. Each organization was requested to undertake the measurement following the practices shown in Table I and to take into account other recommendations considering the variety of the apparatus used.

Apparatus.—Dispersive, as well as Fourier transformation-type, spectrometers are used. In case of dispersive spectrometers, the double-beam type has an advantage of applying the difference method. Transmittance accuracy is the most important performance in the measurement. The transmittance error must not exceed 1% of the percentage transmission scale, and, therefore, it was decided that the transmittance accuracy of the spectrometer in each organization should be checked by the use of a chopper or specially prepared ND filter. The chopper passes 10-90% (10% interval) of incident beam, while the ND filters pass 72, 61, and 30% of incident beam at 1100 cm⁻¹, respectively. An example of instrumental accuracy is shown in Fig. 1, revealing the error as much as 2% before adjustment but below 0.4% after adjustment, the latter being the best accuracy one can expect for a grating spectrometer.

Procedure.—In case of a dispersive spectrometer, the difference method with the oxygen-free reference specimen in the reference beam is superior to the air reference method for accurate determination of the absorption coefficient. The transmittance mode is recommended because it is more convenient for calculating the absorption coefficient for the specimens with large surface reflection than is the absorbance mode. A Fourier transform spectrometer is substantially a single-beam type. Differential transmittance or absorbance spectra are calculated from reference and sample spectra. All measurements are performed at room temperature. Slight temperature variations do not affect the accuracy. Before the measurement, verification of 0 and 100% transmission must be performed. The holders for sample and reference must prevent any source radiation from bypassing the specimen. Transmittance spectrum is taken from 1300 to 900 cm⁻¹,

Table I. Recommended practices for infrared measurement

Item		Recommended
Spectrometer	Type	Dispersive or FTIR
	Path	Double-path (single-path)
	Accuracy	1% of the percentage T scale
	Mode	Transmittance T (absorbance)
Measurement	Reference	Difference method (air reference)
	Scan range	1300-900 cm ⁻¹
	Blank check	100%; 0%
	Resolution	Good enough to resolve the 9 μm absorption band (FWHM: 38 cm ⁻¹)
	Temperature	Room temperature

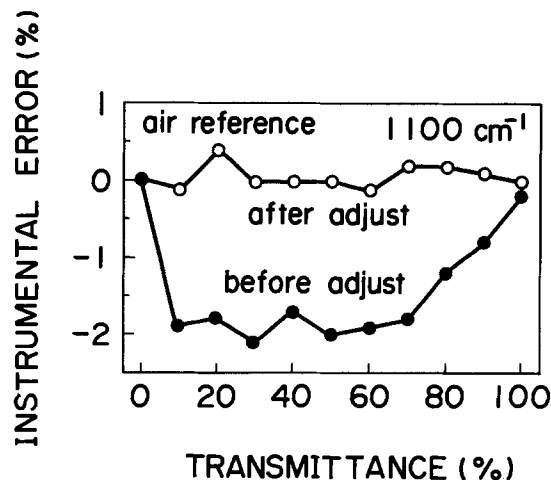


Fig. 1. Example of instrumental accuracy (grating spectrometer, air reference method using a chopper with the transmittance of 10-90%).

which is wide enough to examine the background spectrum. Measurement conditions must be so selected as to assure required resolution; the full width at half maximum (FWHM) of the oxygen absorption band should be no more than 38 cm⁻¹ in transmittance (32 cm⁻¹ in absorbance).

Typical measurement conditions for a grating spectrometer are a resolution of 4 cm⁻¹, a scan rate of less than 1 cm⁻¹/s, a pen response of 2s of time full scale deflection. Repeating measurements (at least two) and taking their average improves the accuracy.

Typical measurement conditions for Fourier transform spectrometer are resolution of 4 cm⁻¹ and accumulation of 100 times.

The size of the measured area (beam size) depends on the respective spectrometer. Typical sizes are 5 × 15 mm² and 15 mm diam.

The round-robin measurement was performed on the 70 samples by 16 organizations. Examples of measured spectra following the recommended practices on 2, 1, and 0.5 mm thick samples are shown in Fig. 2. A 0.5 mm-thick sample shows considerable interference fringes due to multiple internal reflection. The uniqueness of the base line and absorption peak is lost by the interference fringe. The simplest way to eliminate the interference fringe is to reduce the resolution. The FWHM and peak absorbance values of the oxygen absorption band do not show detectable change if the resolution is better than 6 cm⁻¹.

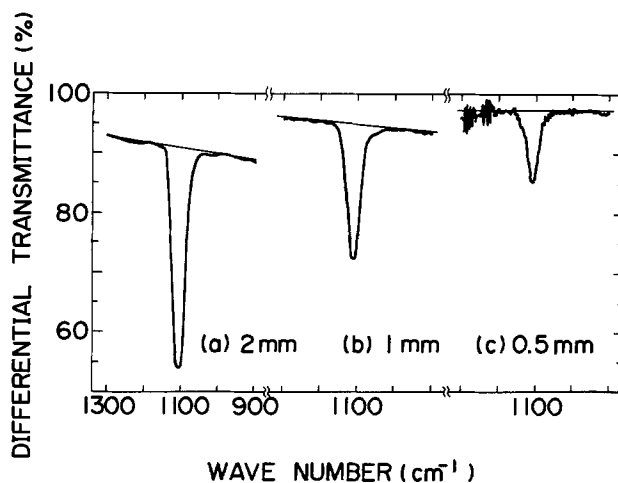


Fig. 2. Examples of measured spectra of differential transmittance for 2, 1, and 0.5 mm thick samples containing 8.2×10^{17} at.-cm⁻³ of oxygen. Measurements were performed following the recommended practices with the resolution of 2 cm⁻¹. Base lines are also shown.

Calculation.—The transmittance measured by the air reference method for normal incidence considering multiple reflection is expressed by

$$T_{\text{air}} = \frac{(1 - R)^2 \exp(-\alpha d)}{1 - R^2 \exp(-2\alpha d)} \quad [1]$$

where R is the reflectivity, α is the absorption coefficient, and d is the sample thickness. Absorption coefficient consists of α_o (due to oxygen), α_f (free carrier), and α_l (lattice vibration). The α_o and α_f terms are negligibly small in FZ reference specimen. Differential transmittance is given as

$$T_{\text{diff}} = \frac{T_{\text{samp,air}}}{T_{\text{ref,air}}} \quad [2]$$

Differential transmittance of the absorption peak and background are

$$T_{\text{diff,peak}} = \frac{T_{\text{samp}}}{T_{\text{ref}}} = \frac{\{1 - R^2 \exp(-2\alpha_1 d)\} \exp\{-(\alpha_f + \alpha_o)d\}}{1 - R^2 \exp\{-2(\alpha_1 + \alpha_f + \alpha_o)d\}} \quad [3]$$

$$T_{\text{diff,bg}} = \frac{\{1 - R^2 \exp(-2\alpha_1 d)\} \exp(-\alpha_f d)}{1 - R^2 \exp\{-2(\alpha_1 + \alpha_f)d\}} \quad [4]$$

respectively, where sample thickness and reference thickness are assumed to be equal. Thickness agreement to within 10 μm does not introduce the error in the absorption coefficient determination. The reflectivity and lattice vibrational absorption coefficient at the oxygen absorption peak, used in the present calculation, are

$$R = 0.30$$

and

$$\alpha_l = 0.85 \text{ cm}^{-1}$$

The base line is used to obtain the differential transmittance of the background (Eq. [4]). The base line is approximated by a straight line on a differential transmittance spectrum between 1300 and 900 cm^{-1} , as shown in Fig. 2. The $\alpha_f + \alpha_o$ and α_f values are separately determined from Eq. [3] and [4], and their difference gives the oxygen absorption coefficient α_o .

For present samples, the effect of free carrier absorption is negligibly small.² Therefore, the relative transmittance of the oxygen absorption band with respect to the base line is expressed as

$$T_{\text{rel}} = \frac{T_{\text{diff,peak}}}{T_{\text{diff,bg}}} = \frac{1 - R^2 \exp(-2\alpha_1 d)}{1 - R^2 \exp\{-2(\alpha_1 + \alpha_o)d\}} \exp(-\alpha_o d) \quad [5]$$

Conventionally, the following equation is used for rough estimation of oxygen concentration

$$T_{\text{rel}} = \exp(-\alpha'_o d) \quad [6]$$

The α'_o term corresponds to the absorption coefficient which does not include the multiple reflection effect. The relationship between T_{rel} and α_o and that between α'_o and α_o are given in Fig. 3 and 4, respectively. These were distributed to each organization in the round-robin measurement, where the relationship between α'_o and α_o is given in a table form with an α_o interval of 0.02 cm^{-1} .

The recommended procedure for obtaining the absorption coefficient of oxygen, α_o , is summarized as follows: (i) measure the differential transmittance (absorbance) spectrum using the FZ reference specimen; (ii) draw base line on the spectrum between 1300 and 900 cm^{-1} ; (iii) cal-

²The value of the free carrier absorption, α_f , is less than 0.1 cm^{-1} for most samples. Two samples show the highest value of 0.4 cm^{-1} . The maximum error of T_{rel} in Eq. [5] caused by this α_f value is only 1%.

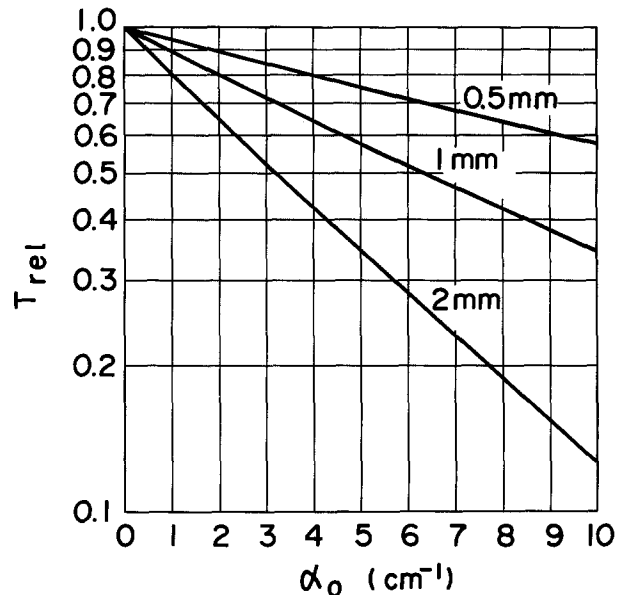


Fig. 3. Relationship between the relative transmittance of the oxygen absorption band, T_{rel} , and the absorption coefficient due to oxygen, α_o . (Refer to Eq. [5].) Curves are plotted for the sample thickness of 0.5, 1, and 2 mm.

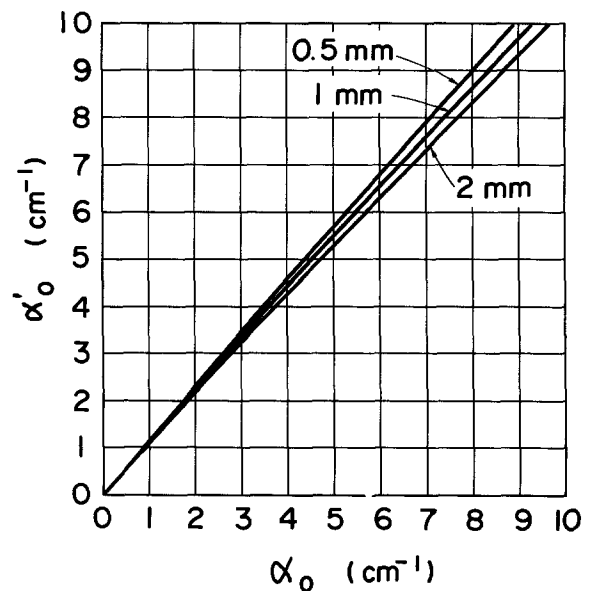


Fig. 4. Relationship between the α'_o value determined by Eq. [6] and the absorption coefficient due to oxygen, α_o . (Refer to Eq. [5] and [6].) Curves are plotted for the sample thickness of 0.5, 1, and 2 mm.

culate T_{rel} (Eq. [5]) or α'_o (Eq. [6]); (iv) obtain α_o using Fig. 3 or 4.

Charged particle activation analysis.—After the infrared measurement, the 22 wafers 1 mm thick were analyzed for oxygen by charged particle activation analysis with the $^{16}\text{O}(^3\text{He,p})^{18}\text{F}$ reaction (^{18}F : 110m, β^+ , no γ). The sample was bombarded with ^3He particles (18 MeV, about 2 μA) for 20 min behind aluminum foil (30 μm thick) in the cyclotron of the Institute of Physical and Chemical Research. The surface layer ($23 \pm 2 \mu\text{m}$) of the bombarded wafer was etched with HF-HNO₃ solution for complete removal of the surface oxygen effect. After 1h from the end of the bombardment, the sample wafer was placed directly on a Ge(Li) detector, and the positron annihilation radiation was measured for 200s. The measurement was repeated several times at about 1h intervals to give the decay curve, which indicated the absence of any notable positron activity other than ^{18}F . As for the activation standard, a quartz plate was used with an aluminum

Table II. Oxygen concentration, IR absorption coefficient, and conversion factor for each sample

Sample no.	Oxygen concentration ($\times 10^{17} \text{ cm}^{-3}$) ^a	Mean adsorption coefficient (cm^{-1})						Mean conversion factor ^e ($\times 10^{17} \text{ cm}^{-2}$)		
		2 mm ^b		1 mm		0.5 mm		2 mm ^b	1 mm	0.5 mm
		Data exclusion No ^d	Yes ^c	Data exclusion No ^d	Yes ^c	Data exclusion No ^d	Yes ^c			
1	2.68	0.783	0.765	0.941	0.930	0.644	0.590	3.500	2.878	4.538
2	3.06	0.963	0.961	0.989	1.017	0.846	0.902	3.186	3.012	3.395
3	4.31	1.384	1.366	1.471	1.503	1.262	1.290	3.159	2.869	3.344
4	4.71	1.498	1.500	1.480	1.476	1.393	1.451	3.138	3.190	3.244
5	5.71	1.803	1.790	1.909	1.893	1.680	1.683	3.192	3.019	3.396
6	7.46	2.339	2.350	2.420	2.390	2.266	2.269	3.176	3.123	3.290
7	8.27	2.663	2.635	2.773	2.761	2.574	2.590	3.138	2.994	3.193
8	11.28	3.754	3.743	3.905	3.903	3.702	3.718	3.013	2.890	3.034
9	21.06	6.579	6.652	6.931	6.677	6.776	6.515	3.166	3.154	3.233
10	7.17	2.411	2.372	2.443	2.353	2.408	2.433	3.012	3.046	2.945
11	7.04	2.355	2.351	2.382	2.324	2.281	2.287	2.996	3.031	3.080
12	9.14	2.843	2.824	3.190	3.114	2.992	3.118	3.238	2.937	2.933
13	9.21	2.951	2.929	3.155	2.953	3.055	3.022	3.143	3.117	3.046
14	5.99	2.137	2.101	1.994	1.993	1.936	1.992	2.849	3.003	3.005
15	8.42	2.742	2.691	2.808	2.750	2.641	2.767	3.128	3.061	3.042
16	8.84	2.838	2.798	2.922	2.833	2.753	2.798	3.159	3.119	3.158
17	9.39	3.257	3.223	3.299	3.241	3.114	3.157	2.913	2.897	2.974
18	15.19	5.095	5.071	5.087	4.992	5.146	5.233	2.996	3.043	2.903
19	6.06	2.277	2.232	1.987	1.953	2.188	2.223	2.717	3.106	2.727
20	7.50	2.574	2.587	2.503	2.342	2.515	2.527	2.898	3.202	2.968
21	8.73	3.342	3.338	2.960	2.783	2.878	2.788	2.616	3.137	3.132
22	9.19	3.733	3.737	3.245	3.252	3.749	3.586	2.458	2.825	2.562
23	—	1.601	1.579	—	—	—	—	—	—	—
24	—	1.779	1.728	—	—	—	—	—	—	—
25	—	1.961	1.939	—	—	—	—	—	—	—
26	—	1.935	1.939	—	—	—	—	—	—	—

^a Oxygen concentration in 1 mm thick samples obtained by activation analysis.

^b 2 mm thick sample, etc.

^c Data deviating more than 10% from the mean values are excluded.

^d Not excluded.

^e Conversion factor obtained by using absorption coefficient with data exclusion.

cover (20 μm), in which the ^3He particle loses its energy equally as in the sample surface removed by the etching. Within each cyclotron machine time period, usually eight such plates were bombarded in order to check the reproducibility. The analysis of each silicon sample was repeated at least twice. Samples for which the results of the two analyses deviated more than 5% from each other were analyzed once again. When the three analyses gave no satisfactory results, a fourth analysis was undertaken. At the same time, one assigned sample was analyzed in every machine times, in order to ascertain the reproducibility of the result.

Since the ^{18}F activity in the infrared reference sample was so weak as to be masked by the radiation of ^{31}Si β -ray, it was measured after chemical separation. The sample was bombarded with a higher beam current for a longer time, and then pulverized and dissolved in a NaOH solution containing F^- carrier (15 mmol). After silicon was removed from the solution by precipitation, the fluorine was collected as $\text{CaF}_2\text{-CaCO}_3$ coprecipitate, distilled, and precipitated as BaSiF_6 . The annihilation radiation from the BaSiF_6 was measured by a NaI detector, and the absence of bremsstrahlung was checked. The carrier recovery was measured by alkali titration.

Results and Discussion

From the results of activation analysis, some values showing considerable deviations were eliminated when the reason of the deviation could be understood. The other values were averaged to give the final results for the total oxygen concentration; they are shown in Table II. The infrared reference wafer was found to contain $(1.3 \pm 0.4) \times 10^{15}$ at.-cm $^{-3}$ oxygen. This value can be legitimately ignored in our succeeding calculations.

Of all the methods for quantitative determination of oxygen in CZ silicon, the nondestructive activation analysis with the $^{16}\text{O}(^3\text{He,p})^{18}\text{F}$ reaction can at present be regarded as the most accurate because of the following three reasons: (i) freedom from the surface oxygen effect and oxygen contamination in the analytical process; (ii) capability of repeated analysis for a single sample and no need of

chemical separation, in which any possible loss of oxygen should be taken into account; and (iii) requirement of only relative measurements of the bombardment data (beam current and time) and the induced ^{18}F activity for the sample and activation standard of quartz, which is of well-defined stoichiometry.

In vacuum fusion, some correction for surface oxygen is indispensable. This introduces a considerable uncertainty in the final result, especially for a sample of relatively low oxygen content. By the ^3He activation analysis with chemical separation of the ^{18}F , we have actually obtained a result of as low as $(2.3 \pm 0.5) \times 10^{14}$ at.-cm $^{-3}$ oxygen for a specially prepared FZ silicon. The surface oxygen effect thus proved to be eliminated completely by etching after bombardment. Modern instrumental methods available for the oxygen analysis (e.g., secondary ion mass spectroscopy) are likely to be interfered with by residual oxygen in the apparatus and have need of some suitable standard, which is difficult to prepare. In photon activation analysis with the $^{16}\text{O}(\gamma,n)^{15}\text{O}$ reaction, the ^{15}O (122s half-life) should usually be separated very quickly after the surface etching (6). It is natural that the result of this analysis inevitably involves more uncertainty than the result of our analysis. Our method, when carried out carefully, can be thought to give the most reliable result with the smallest systematic error of all the methods available for the present analysis.

In the results of our analysis, however, the following two kinds of uncertainty should be taken into account: (i) error in the analytical process, mainly in the measurement of the sample-to-standard ratio for the bombardment data and for the ^{18}F activity; and (ii) uncertainty due to some inhomogeneous distribution of oxygen in the sample. The first kind of uncertainty can be estimated to be about 4%, about 3%, and under 3% for oxygen concentrations of under 5×10^{17} , $5\text{--}10 \times 10^{17}$, and over 10×10^{17} at.-cm $^{-3}$, respectively. As for the sample inhomogeneity, it is easily understood from the excitation function for the $^{16}\text{O}(^3\text{He,p})^{18}\text{F}$ reaction and the range-energy relations of charged particles that oxygen only in the depth region of less than 200 μm from the bombarded surface is sensitive

to our analysis (8). Thus, the most sensitive part in the original sample changed in each analysis due to the surface etching in the preceding analysis and to some fluctuation of the bombarded portion of the sample. Actually, we experienced considerable scatter (5-10%) in the results of repeated analysis for several samples. Most samples, however, gave well reproducible results, as is exemplified by an assigned sample (no. 16 in Table II) analyzed every machine time to give the values of 8.84, 8.74, 8.77, 8.87, and 8.91×10^{17} at.-cm⁻³.

The effect of instrumental error of infrared measurement on the error in determining the absorption coefficient is negligible for the following reasons. Transmittance error of 2% is not unlikely for grating-type spectrometers, as shown in Fig. 1. However, the transmittance error generally changes slowly with transmittance. Maximum transmittance, corresponding to the background transmittance (Eq. [4]), ranges from 53% (0.5 mm thick) to 44% (2 mm thick). The minimum transmittance corresponding to the oxygen absorption band (Eq. [3]) varies from 47% (0.5 mm thick and 3×10^{17} at.-cm⁻³) to 11% (2 mm thick and 20×10^{17} at.-cm⁻³). Within this transmittance range, the differential transmittance error is expected to be within 0.5% if the air reference transmittance error is within 1% for 0-100% transmittance and varies slowly with the transmittance. Therefore, the transmittance error of 1% does not cause a noticeable error in the determination of the absorption coefficient.

The reported absorption coefficients sometimes showed considerable scattering, although the infrared measurement had been expected to be fairly precise and most reported values actually agreed with one another. Mean values over all the reported absorption coefficients were calculated for the individual wafers, together with their standard deviations. The standard deviations were then averaged over all the samples belonging to the same thickness to give the mean standard deviation. The total numbers of the reported data for each sample thickness are shown in Table III together with the numbers and percentages of the data deviating more than 10% from the mean values and also with the mean standard deviation. The mean standard deviation is regarded as the measure of precision in the infrared measurement, and is seen to become better with the sample thickness in the three thicknesses tested. The standard deviation of the 1 mm-thick data is only slightly larger than that of the 2 mm-

Table III. Scattering in the reported absorption coefficient

Sample thickness (mm)		2	1	0.5
Total number of reported values		434	267	263
Values with more than 10% deviation	Number	94	96	123
	Percentage	22	36	47
Mean standard deviation (%)		10	14	32

thick data. The standard deviation of 0.5 mm-thick data is noticeably larger than that for the 1 and 2 mm-thick data, showing that samples of this thickness are not adequate for accurate oxygen-content determination.

The mean absorption coefficients are shown in Table II for the individual samples. Each set of three samples cut from adjacent positions of each ingot but with the different thicknesses was expected to give nearly the same absorption coefficient. Actually, however, the mean absorption coefficient for a 2 mm sample is sometimes found to differ by more than 10% from that for the corresponding 1 mm sample, as shown in Fig. 5. This is probably due to the oxygen inhomogeneity in such samples. In order to keep the 2 mm samples for future use as infrared standard samples, the 1 mm samples were used in the activation analysis. Because of this and the only slightly larger mean standard deviation for the 1 mm samples than for the 2 mm samples, it is thought to be better to calculate the infrared conversion factor from the absorption coefficients for the 1 mm samples than from those of the 2 mm samples.

About half of the organizations used infrared spectrometers of Fourier transformation type and the others of the dispersive type. No significant difference in the round-robin measurement results due to the difference of the spectrometer type was observed (Fig. 6 and 7). In order to get the absorption coefficient more accurately, it can be recommended to exclude some of the data. A few organizations reported values invariably larger or smaller by more than 10% than the mean values. Hereafter, a reported absorption coefficient is expressed as α_{ijk} , where $i = 1, 2, 3$ is for 2, 1, and 0.5 mm thickness, respectively, j is a sample number for each thickness, and k is an organization number. The number of data (absorption coefficients) for a particular sample is n_{ij} , which is a number of organization measuring the sample. The mean absorption

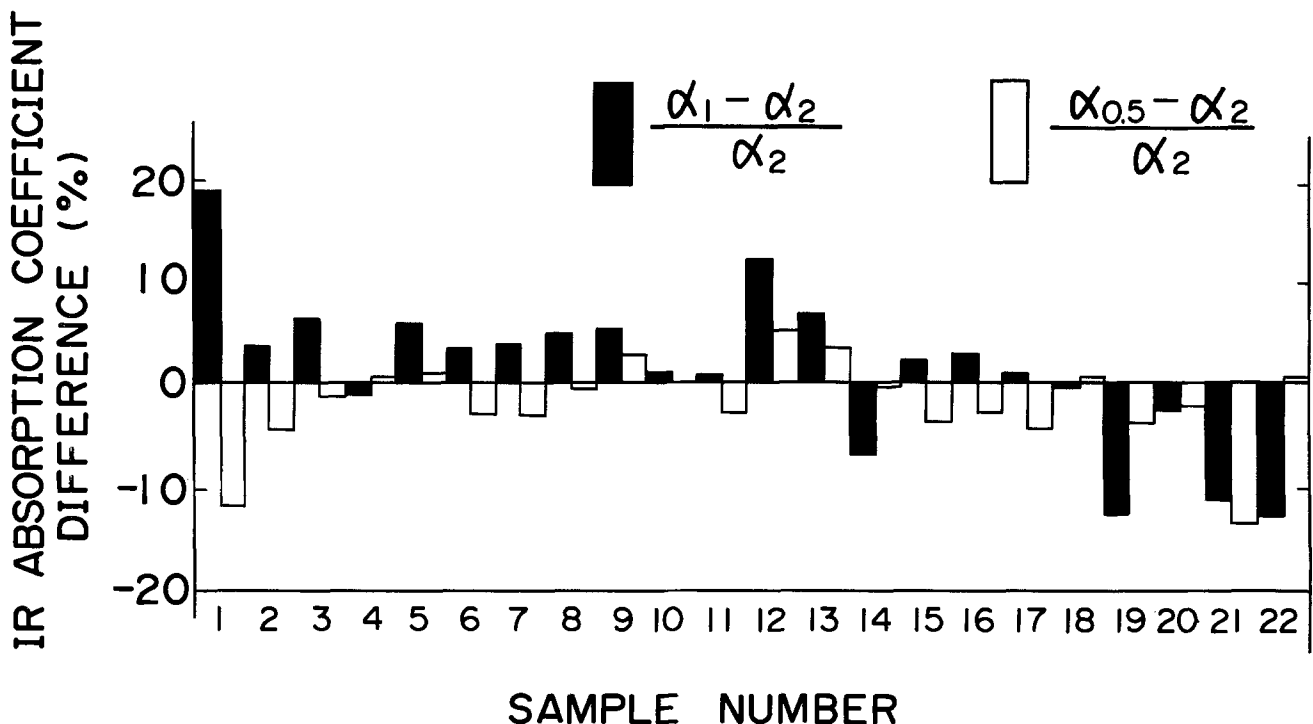


Fig. 5. Difference of infrared absorption coefficient for 2, 1, and 0.5 mm samples

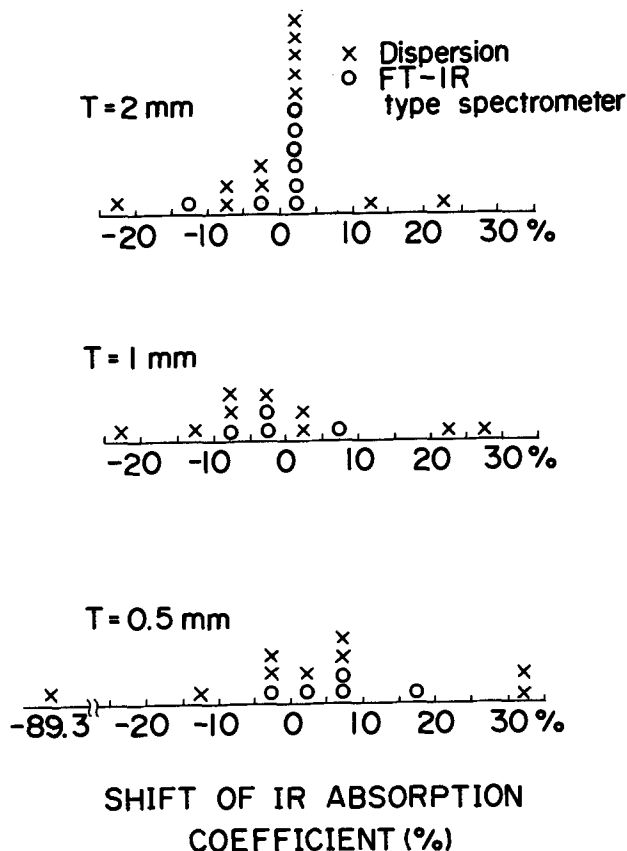


Fig. 6. Shift of mean infrared absorption coefficient of the laboratories.

coefficient for the particular sample is given by

$$\bar{\alpha}_{ij} = \frac{1}{n_{ij}} \sum_k \alpha_{ijk} \quad [7]$$

The absorption coefficients scatter around $\bar{\alpha}_{ij}$, and some of them deviate more than 10%. Table III shows the total number of data, $n_i = \sum_j n_{ij}$ for 2, 1, and 0.5 mm thick samples. It also shows the number of data which deviated more than 10% from $\bar{\alpha}_{ij}$. The percentage of such data decreases with increasing sample thickness. This means the reproducibility of infrared measurement is better for thicker samples. The standard deviation of data for a particular sample, σ_{ij} , is expressed by

$$\sigma_{ij} = \left\{ \frac{1}{n_{ij} - 1} \sum_k \left(\frac{\alpha_{ijk} - \bar{\alpha}_{ij}}{\bar{\alpha}_{ij}} \right)^2 \right\}^{1/2} \quad [8]$$

and then the mean standard deviation is given by

$$\sigma_i = \frac{1}{N_i} \sum_j \sigma_{ij} \quad [9]$$

where N_i is a number of 2, 1, or 0.5 mm-thick samples. The reproducibility of infrared measurements for 1 mm samples is not best, but is not so bad as is a case of 0.5 mm samples, as shown in Table III.

A few organizations reported values invariably larger or smaller by more than 10% than the mean values. The following two kinds of organization-dependent scatterings were considered in the reported absorption coefficients. The first one, X_{ik} , is a shift of the mean absorption coefficient for a particular organization

$$X_{ik} = \frac{1}{n_{ik}} \sum_j \left(\frac{\alpha_{ijk} - \bar{\alpha}_{ij}}{\bar{\alpha}_{ij}} \right) \quad [10]$$

where n_{ik} is the total number of samples with a given thickness, i , measured by the organization in question, k . The second one, Y_{ik} , is the scattering of the data of the particular organizations around the shifted mean

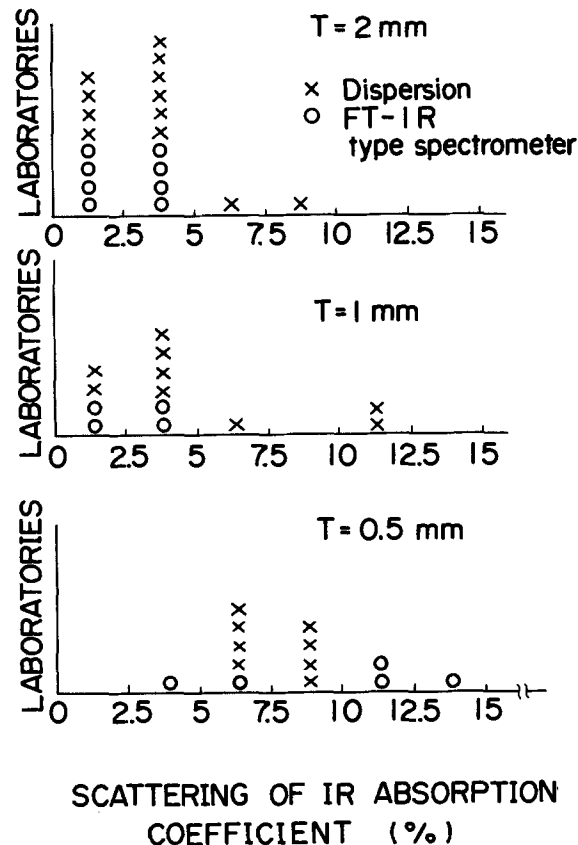


Fig. 7. Scattering of infrared absorption coefficient around the shifted mean absorption coefficient.

$$Y_{ik} = \left\{ \frac{1}{n_{ik}} \sum_j \left(\frac{\alpha_{ijk} - \bar{\alpha}_{ij}}{\bar{\alpha}_{ij}} - X_{ik} \right)^2 \right\}^{1/2} \quad [11]$$

These X_{ik} and Y_{ik} are shown in Fig. 6 and 7, respectively. In the scattering around the shifted mean, no marked difference is found between the data of those few organizations which reported invariably deviated data and those of the other organizations. From this fact, the use of samples with accurately known absorption coefficients as interlaboratory infrared standards is seen to be highly recommendable.

The least squares method is the most conventional way to investigate the correlation between the two groups of data. By this method, the relationship between the absorption coefficient, α , and oxygen concentration, C , is expressed by

$$C = f\alpha + g \quad [12]$$

The f and g values are mathematically determined. According to Beer's law, however, the relationship between α and C should be given by

$$C = f\alpha \quad [13]$$

where f is called conversion factor. If we used the least squares method for the present data, the g term in Eq. [12] does not necessarily go to zero. The physical meaning of the g term is ambiguous. Therefore, the conversion factor for a particular sample with a thickness, i , and sample number, j , is not determined by the least squares method but by the relationship in Eq. [13]

$$f_{ij} = C_{ij}/\alpha_{ij} \quad [14]$$

Since we have assumed $C_{ij} = C_{2j}$, Eq. [14] is rewritten as

$$f_{ij} = C_{2j}/\alpha_{ij} \quad [15]$$

The mean absorption coefficient $\bar{\alpha}_{ij}$ and corresponding conversion factor f_{ij} are shown in Table II. The mean conversion factor f_i , the standard deviation σ_i^f , and the standard error ϵ_i are expressed as

$$f_i = \frac{1}{N_i} \sum_j f_{ij} \quad [16]$$

Table IV. Conversion factor

Sample thickness (mm)	Data exclusion ^a	Conversion factor ($\times 10^{17} \text{ cm}^{-2}$)		
		Mean value (f_i)	Standard deviation ($\sigma_i^{(f)}$)	Standard error (ϵ_i)
2	No	3.015	0.224	0.048
2	Yes	3.036	0.228	0.049
1	No	2.973	0.089	0.019
1	Yes	3.030	0.110	0.023
0.5	No	3.157	0.328	0.070
0.5	Yes	3.143	0.373	0.080

^a Infrared absorption coefficient data deviating more than 10% from the mean values are excluded (yes), are not excluded (no).

$$\sigma_i^{(f)} = \left\{ \frac{1}{N_i - 1} \sum_j (f_{ij} - f_i)^2 \right\}^{1/2} \quad [17]$$

$$\epsilon_i = \sigma_i^{(f)} / N_i \quad [18]$$

These values are summarized in Table IV. As shown in the table, the conversion coefficient depends on a choice of data. The committee members have agreed that the most reliable conversion factor is obtained from the results of 1 mm samples with the data exclusion. Therefore, the conversion factor has been determined to be $(3.03 \pm 0.02) \times 10^{17} \text{ at}\cdot\text{cm}^{-2}$. The value of the conversion factor is believed to be quite reliable because the present value agrees remarkably with recent independent investigations. Yatsurugi *et al.* reported the value of $3.0 \times 10^{17} \text{ at}\cdot\text{cm}^{-2}$ by using charged particle activation (4), Li *et al.* reported $(3.1 \pm 0.05) \times 10^{17} \text{ at}\cdot\text{cm}^{-2}$ by inert gas fusion and $(3.1 \pm 0.2) \times 10^{17} \text{ at}\cdot\text{cm}^{-2}$ by charged particle activation (5), and Rath *et al.* reported $(3.0 \pm 0.2) \times 10^{17} \text{ at}\cdot\text{cm}^{-2}$ by photon activation (6) and $(3.0 \pm 0.25) \times 10^{17} \text{ at}\cdot\text{cm}^{-2}$ by charged particle activation (7).

In Fig. 8, the mean absorption coefficients with their standard deviations for the results of 1 mm samples with the data exclusion are plotted against the oxygen concentration. All of the absorption coefficients lie on the straight line within their standard deviations. It should be noted that the 2 mm-thick sample measurement gives the same conversion factor (3.036) as the 1 mm-thick sample measurement. The measurement on 0.5 mm-thick samples, however, gives a little larger conversion factor than those of 2 and 1 mm-thick samples. In other words, it gives a lower oxygen content. The conversion factor determined here is obtained from the as-grown crystals and as-received wafers. Figure 8 implies that very small portions of oxygen, if any, are precipitated in our samples even at higher oxygen concentration ranges, because no significant deviation of the obtained absorption coefficient from the linear relationship is observed.

The use of the standard samples with accurately known oxygen concentration is quite helpful for improving the accuracy of the infrared absorption analysis. Many sets of standard samples are now under preparation at JEIDA. The oxygen concentrations were determined by infrared measurement using the present 2 mm-thick samples as calibration standards. Each set consists of three samples with high, medium, and low levels of oxygen concentrations and one reference sample. The oxygen concentrations of respective samples are in the range of 10.2-10.7, 7.8-9.1, 5.4-6.3, and $<0.1 \times 10^{17} \text{ at}\cdot\text{cm}^{-2}$. The maximum error in oxygen concentration is estimated to be less than $\pm 5 \times 10^{16} \text{ at}\cdot\text{cm}^{-2}$. Details of the preparation of the standard samples will be reported elsewhere. These samples, we believe, are highly useful also for the re-examination of our conversion factor by various groups in the world with various techniques.

Summary and Conclusion

1. Seventy samples with the oxygen concentration of $2.7\text{-}21 \times 10^{17} \text{ at}\cdot\text{cm}^{-2}$ and 2, 1, and 0.5 mm thick were carefully prepared by five organizations.

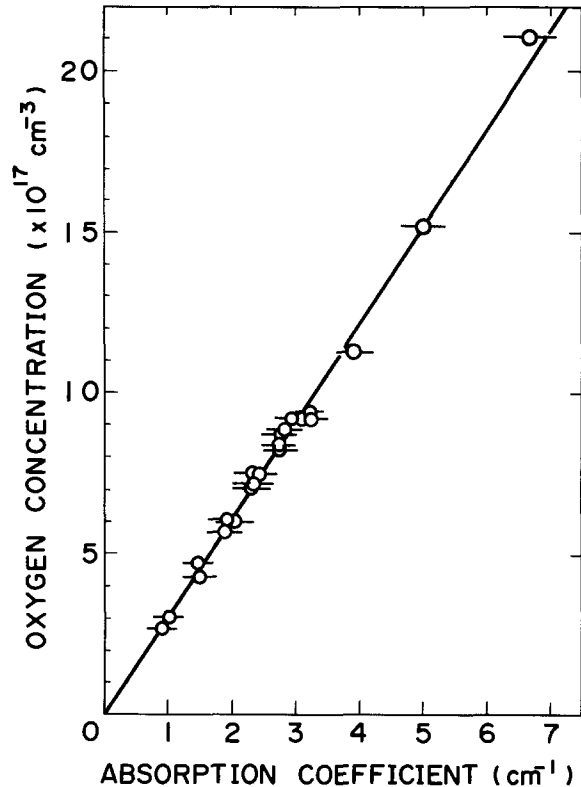


Fig. 8. Oxygen concentration vs. mean infrared absorption coefficient of 1 mm sample after data exclusion. The standard deviation is shown for each infrared data.

2. A round-robin measurement of the infrared absorption due to the interstitial oxygen at room temperature was carried out by 16 organizations with 20 spectrometers. The total oxygen content was determined by charged particle activation analysis.

3. A good linear relationship has been obtained between the infrared absorption coefficient and oxygen content from the results of 22 samples with 1 mm thickness. The relationship is given as: [oxygen concentration ($\text{at}\cdot\text{cm}^{-3}$)] = $(3.03 \pm 0.02) \times 10^{17} \times$ [absorption coefficient (cm^{-1})].

4. There is no essential difference between the results by Fourier transformation-type infrared spectrometers and those by dispersive-type spectrometers.

5. The analysis of the round-robin measurement shows that the use of the standard samples with known oxygen content is quite helpful for determining the oxygen content accurately by the infrared absorption and for suppressing interlaboratory discrepancies.

Acknowledgment

This work was greatly assisted by the continued efforts of Mr. K. Higuchi of JEIDA.

Manuscript submitted July 25, 1984; revised manuscript received March 13, 1985. This was Paper 300 presented at the San Francisco, California, Meeting of the Society, May 8-13, 1983.

The Japan Electronic Industry Development Association assisted in meeting the publication costs of this article.

REFERENCES

1. W. Kaiser and P. H. Keck, *J. Appl. Phys.*, **28**, 882 (1957).
2. J. A. Baker, *Solid-State Electron.*, **13**, 1431 (1970).
3. K. Graff, E. Grallath, S. Ades, G. Goldbach, and G. Tolg, *ibid.*, **16**, 887 (1973).
4. Y. Yatsurugi, N. Akiyama, Y. Endo, and T. Nozaki, *This Journal*, **120**, 975 (1973).
5. Y. Li, H. He, G. Zhao, R. Yan, Q. Lu, and M. Qi, Academy of Science of China, May 1981; *Mater. Lett.*, **101** (1983).
6. H. J. Rath, P. Stallhofer, D. Huber, and B. F. Schmitt, *This Journal*, **131**, 1920 (1984).
7. H. J. Rath, P. Stallhofer, and D. Huber, Private communication.
8. T. Nozaki, M. Iwamoto, and T. Ido, *Int. J. Appl. Radiat. Isotopes*, **25**, 393 (1974).

Interface Charges at the Back Surface of Seeded, Recrystallized Silicon Films

T. I. Kamins*

Hewlett-Packard Laboratories, Palo Alto, California 94304

ABSTRACT

Interface charges at the back of seeded, recrystallized silicon films on insulating oxide layers were investigated and compared to those at the back of unseeded films. Both the fixed charge density and the interface trap density were found to be appreciably lower for the seeded devices than for unseeded devices. A recrystallization technique which melted the silicon film a minimum number of times produced the lowest interface charge densities. The differences between seeded and unseeded structures may be related to the higher charge densities expected for grain orientations other than {100} or to traps located at the grain boundaries near the back surface of the silicon film.

Control of charges at the Si-SiO₂ interfaces in metal-oxide-semiconductor transistors has long been a source of concern for reliable and reproducible device fabrication. In silicon-on-insulator (SOI) structures, an additional Si-SiO₂ interface is present below the thin silicon film. Charges at the underlying interface can influence the behavior of MOS transistors in the film. n-Channel transistors are especially affected because a positive charge can induce an inversion layer near the back interface in parallel with the desired front-channel transistor. For thin films, a space-charge region induced by interface charges at the back surface can influence the characteristics of p-channel transistors also. In more advanced structures, the channel to be controlled by the gate may be located at the back interface. In this case, accurate control of the interface charges there is critical to the basic device performance.

Several recent reports have discussed the interface charges beneath recrystallized silicon films (1-3). In all these cases, however, the recrystallized film was large-grain polycrystalline silicon, rather than single-crystal silicon. The fixed charge density at the back interface was found to be about $1 \times 10^{11} \text{ cm}^{-2}$, under optimum conditions, and considerably higher if the materials and processing were not carefully controlled. This value is much higher than that found for Si-SiO₂ interfaces formed on bulk single-crystal silicon wafers. The difference can be related to two dominant effects. First, the silicon film is composed of grains of several different orientations. The important crystal orientations other than {100} have higher fixed charge densities than do {100}-oriented silicon, so a polycrystalline film is expected to have a higher fixed charge density than does a single-crystal film. Second, grain boundaries in the silicon film near the interface can contribute states which increase the effective interface charge.

The present study investigated the interface charges beneath single-crystal silicon films formed by laterally seeding the recrystallization so that grain-boundary-free, {100}-oriented single-crystal films were obtained. The fixed-charge density Q_f^B and the interface-trap density D_{it}^B were investigated by measuring both the high frequency and quasistatic capacitance-voltage characteristics. These structures were compared to unseeded devices fabricated simultaneously.

Experimental Device Structure

To probe the interface characteristics at the back of the recrystallized silicon film, the present experiment used an inverted capacitor structure in which the "gate" voltage was applied to heavily doped regions of an n-type substrate wafer, and the depletion region extended into a lightly doped, recrystallized silicon film above an oxide thermally grown on the "gate" wafer. Thus, the interface at the back of the recrystallized silicon film was probed.

Because of the limited lateral propagation of high quality, single-crystal recrystallization, a structure containing

a number of parallel stripes of silicon-on-insulator material was used (Fig. 1). The unseeded structures needed for comparison were simultaneously fabricated using the same mask set by omitting the seeding mask. The mask contained 13 parallel SOI stripes, each about 21 μm wide, separated by seed regions about 9 μm wide. Most of the area under the oxide stripes was implanted with phosphorus to act as a heavily doped counterelectrode. However, to avoid dopant migration from the substrate into the film during recrystallization, the heavily doped regions were confined under the SOI stripes and away from the seeding regions.

After recrystallization, the seeding regions were sealed by a thick local oxide so that the major part of the capacitance was contributed by recrystallized regions over the gate oxide and heavily doped regions of the substrate. The final structure contained about $1.6 \times 10^{-3} \text{ cm}^2$ of gate oxide, $9.5 \times 10^{-4} \text{ cm}^2$ of field oxide over the seed, and $6.3 \times 10^{-4} \text{ cm}^2$ of slightly thicker field oxide adjacent to the seed, but outside the buried-layer region.

The seeded wafers were lightly doped, n-type, {100}-oriented wafers with [100]-aligned flats. Some of the unseeded wafers were also lightly doped, while others were heavily doped to allow more direct comparison with previous experiments. Bulk control wafers were also included.

Device Fabrication Details

Phosphorus was first implanted into selected regions of the seeded wafers and the lightly doped unseeded wafers through a thin oxide. After the implant was annealed and the thin oxide was removed, a 200 nm-thick gate oxide was grown at 1000°C in a chlorine containing, dry oxygen ambient. This type of oxide beneath the silicon film was found in our previous experiments to produce the lowest back interface charge density. On the seeded wafers, the seed windows were then opened by etching the oxide between the heavily doped regions, and a 550 nm thick layer of LPCVD polysilicon was deposited at 625°C. This layer was implanted with boron to produce an average dopant concentration of about $2 \times 10^{16} \text{ cm}^{-3}$ after it was redistributed during recrystallization.

Stabilization layers were then formed; a 64 nm thick LPCVD oxide deposited at 900°C was placed over the seed regions, and a 6 nm thermal oxide was grown over

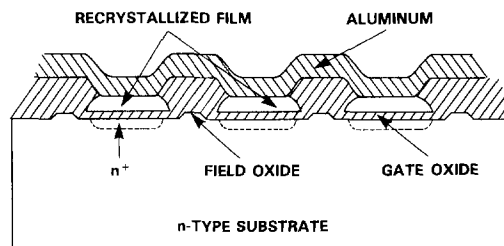


Fig. 1. Schematic cross section of seeded capacitor structure

*Electrochemical Society Active Member.

the SOI regions. Both regions were further covered with 6 nm of LPCVD silicon nitride deposited at 700°C. This patterned stabilization layer allowed more power to be absorbed in the seed regions, which lose energy rapidly to the substrate through the seed windows and, consequently, require more energy to melt the silicon film.

To recrystallize the films, an argon-ion laser was rastered across the wafer while the substrate was externally heated to about 500°C. On some seeded wafers a $20 \times 60 \mu\text{m}$ elliptical beam was swept parallel to the long axis of the beam and stepped by $6 \mu\text{m}$ perpendicular to the long axis between scans ("shuttle beam"). On other seeded wafers the elliptical beam was swept at 45° to its long axis, with a step of $29 \mu\text{m}$ between scans ("slanted beam") (4). In both cases, the scan was parallel to the SOI stripes. The unseeded structures were recrystallized with a circular beam which melted a region about $40 \mu\text{m}$ across, and the beam was stepped by about $20 \mu\text{m}$ between scans. The beam swept across the wafer at $20 \text{ cm}\cdot\text{s}^{-1}$ in all cases.

After the stabilization layers were removed, the silicon in the seed regions and areas outside the device was oxidized through its entire thickness by local oxidation using a nitride mask. Phosphorus was implanted into the back of each wafer to ensure ohmic contact, and several heat cycles simulated a complete transistor fabrication process. Contact to the recrystallized silicon film was made by depositing and defining an Al/2%Si layer, and the device fabrication was completed with a 450°C anneal in a hydrogen ambient for 30 min.

Results

High-frequency C-V characteristics.—High frequency (1 MHz), capacitance-voltage characteristics were measured on all wafers. The flatband voltage was found after a negative bias-temperature stress, and the corresponding fixed charge density was calculated. No measurable mobile ion drift was observed on any of the recrystallized wafers.

The complex structure used to obtain seeded devices in these experiments impeded extraction of a quantitative value of the fixed charge density directly from the high frequency C-V data. Although the contributions to the capacitance from the gate and field oxides and that resulting from the finite doping in the gate (substrate wafer) can be separated, the gradual transition region between gate and field oxide cannot readily be analyzed. Because of the long periphery of the gate-oxide region, the contribution of this transition region to the total capacitance is not negligible, complicating determination of the flatband voltage. However, the relative values of fixed charge density calculated from the flatband voltage allow a semiquantitative comparison between the different structures in this experiment.

To compare seeded and unseeded structures, we assume the back-side fixed charge density of the unseeded structures to have the value of $1 \times 10^{11} \text{ cm}^{-2}$ repeatedly found in this laboratory with a simpler capacitor structure covered with the same stabilization layers during recrystallization. This assumption produces consistent results.

The seeded wafers recrystallized with the slanted beam can be compared most directly with the unseeded wafers containing an n^+ buried layer in a lightly doped substrate. In both cases, the silicon was melted about two times. The primary difference is the presence or absence of seeding windows in the underlying oxide, so that the field-oxide capacitance is very slightly different.

In the seeded devices recrystallized with the slanted beam, the indicated fixed charge density was about $6.6 \times 10^{10} \text{ cm}^{-2}$ lower than for the unseeded wafers, suggesting a fixed charge density of about $3 \times 10^{10} \text{ cm}^{-2}$. The seeded structures recrystallized with the shuttle beam generally indicated a higher fixed charge density than did those recrystallized with the slanted beam. The fixed charge density with the shuttle beam was $6.4 \times 10^{10} \text{ cm}^{-2}$ for the lower laser power, and somewhat higher for the higher power.

The fixed charge density indicated for the bulk wafers was about $1 \times 10^{10} \text{ cm}^{-2}$. This is consistent with the value of $1.6 \times 10^{10} \text{ cm}^{-2}$ obtained on bulk wafers in recent experiments with the simpler capacitor structure, suggesting that this method of interpreting the data is reasonable. These values are consistent with those obtained in normal MOS transistor processing on bulk wafers.

To obtain further semiquantitative information about the differences between seeded and unseeded structures in a manner that minimizes the effect of the device structure, the maximum slope was determined for each C-V characteristic and normalized by the total capacitance change.

The normalized slope for the seeded structures recrystallized with the slanted beam is $0.24 \pm 0.01 \text{ V}^{-1}$, while that for the corresponding unseeded structures is $0.19 \pm 0.02 \text{ V}^{-1}$. The other seeded structures also had greater slopes than did the unseeded structures, indicating that the interface trap density is lower in seeded structures.

The voltage corresponding to the intersection of the tangent to the curve with the maximum capacitance is influenced both by the fixed charge density and the interface trap density. It was $2.03 \pm 0.13 \text{ V}$ for the seeded structures recrystallized with the slanted beam and $2.58 \pm 0.14 \text{ V}$ for the unseeded devices, corresponding to a charge difference of $6 \times 10^{10} \text{ cm}^{-2}$ between the two structures.

After correcting for the field-oxide regions, the effective dopant concentration in the seeded films was calculated to be $2 \times 10^{16} \text{ cm}^{-3}$, in good agreement with the value expected from the amount of implanted dopant. The oxide thicknesses calculated are also consistent with the values measured directly.

The maximum high frequency capacitance appears to be the same for the seeded and unseeded structures, but the minimum capacitance is about 3% greater for the unseeded structure. This could be related to expansion of the depletion region into the film being limited by defect levels in the unseeded structure or by loss of dopant from the seeded film to the substrate during recrystallization. It is unlikely that the defect levels increase the effective carrier concentration.

Quasistatic C-V measurements.—Comparison of quasistatic and high frequency C-V characteristics also shows a significant difference in the interface trap density between seeded and unseeded structures (Fig. 2a and 2b, respectively). As the film is being depleted, no difference can be resolved between the high frequency and quasistatic characteristics for the seeded structure, while a clear difference is seen for the unseeded structure.

Figure 3 shows that the minimum in the quasistatic curve is broader and shallower for the unseeded structure

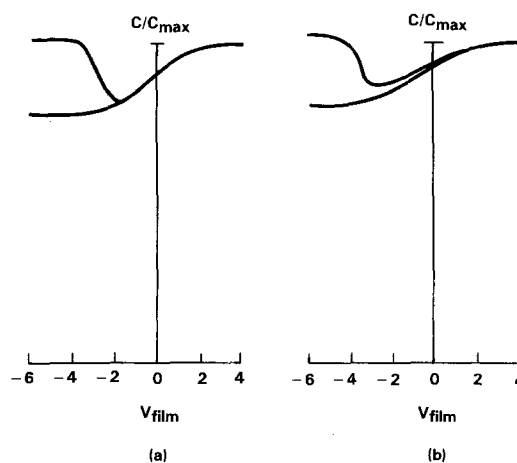


Fig. 2. High frequency and quasistatic capacitance-voltage characteristics of (a) seeded structure recrystallized with the slanted beam and (b) unseeded structure with an n^+ buried layer in a lightly doped substrate. Voltage is that applied to the recrystallized film (i.e., the negative of the "gate" voltage applied to the wafer).

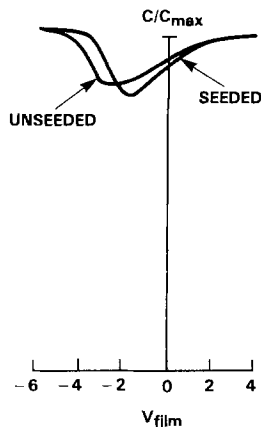


Fig. 3. Quasistatic capacitance-voltage characteristics of seeded and unseeded structures.

than for the seeded structure. This difference is consistent with the different slopes of the high frequency C-V characteristics noted above.

The major difference in the shape of the quasistatic characteristics of the two devices occurs during the transition from the accumulation region to the minimum capacitance. The region from the minimum to inversion is similar in the two cases, with primarily a parallel shift of approximately 0.9V, corresponding to a difference in the integrated number of traps of about $9.5 \times 10^{10} \text{ cm}^{-2}$. If the traps were uniformly distributed across the gap from accumulation to weak inversion (about $30 kT/q = 0.77 \text{ eV}$), the trap density would be about $1.2 \times 10^{11} \text{ cm}^{-2} \text{ eV}^{-1}$ higher in the unseeded structure than in the seeded structure. A nonuniform distribution would lead to a lower minimum trap density.

The width of the quasistatic characteristic was also significantly greater for the unseeded structure than for the seeded structure. The widths of the capacitance minimum (FWHM) are 3.34V for the unseeded structure and 2.86V for the seeded structure, corresponding to a charge difference of about $5 \times 10^{10} \text{ cm}^{-2}$ contained within a 0.6 eV wide region of the bandgap. The width of the calculated C-V characteristic was about 2.76V, close to that in the seeded structure.

The minimum values of the interface trap density computed using the conventional data-reduction program are useful for comparison of the different devices. Although their values may not be accurate because of lateral non-uniformities in the device structure used, the structure should influence all the devices in the same manner, so the differences are related to the seeding and recrystallization conditions. The minimum values indicated by the data-reduction program are used for convenience in this comparison. They are $(1.2 \pm 0.5) \times 10^{10} \text{ cm}^{-2} \text{ eV}^{-1}$ for the seeded devices recrystallized with the slanted beam and $(11.9 \pm 2.5) \times 10^{10} \text{ cm}^{-2} \text{ eV}^{-1}$ for the unseeded wafers with the n^+ buried layer. The minimum value occurs slightly above midgap.

As with the fixed charge density, the shuttle beam produced seeded material with a higher interface trap density than did the slanted beam (although it was still lower than in the unseeded structures). This higher density may be related to the repeated melting and recrystallization caused by the small step size used with the shuttle beam. The effect appears to be significantly more detrimental at the higher laser power. This is consistent with our previous observations on simpler capacitor structures that the interface charge densities were higher with the shuttle beam than with the slanted beam.

Little difference is seen between the unseeded devices with an n^+ buried layer and those on an n^+ wafer, again consistent with the dominant differences being caused by the seeding and consequent single-crystal growth. When different powers were used with the unseeded structures, no significant differences in the interface trap density

were seen; any effect is probably hidden by the defects in the unseeded structure itself.

Discussion

Two effects are expected to cause higher interface charges in an unseeded structure than in a seeded structure. First, the unseeded devices contain a large number of grains with crystal orientations other than {100}; these other orientations are expected to have higher interface charge densities. Second, traps at the grain boundaries can contribute to the measured charges. As the depletion region extends into the unseeded material, the charge state of some of the grain-boundary traps must be changed, so that more voltage is required for formation of an inversion layer. This causes dispersion in the C-V characteristic. In addition, the discrete location of the grain boundaries can cause dispersion because of the resulting lateral nonuniformity; *i.e.*, a higher voltage is required to invert the region near the grain boundary than that away from the grain boundary. These effects cannot readily be separated.

Lateral nonuniformities arising from the device structure with adjacent gate-oxide and field-oxide regions should affect the C-V characteristics similarly for both structures. Therefore, the differences seen between seeded and unseeded devices appear to be related to the different charge densities at or near the back surface of the recrystallized silicon films. The value found for the seeded structures may be limited by the resolution of the measuring system.

Conclusions

Both the fixed charge density and the interface trap density at the back of seeded, recrystallized silicon films on insulating oxide layers are significantly lower than those in unseeded devices. A recrystallization technique which melts the silicon film a minimum number of times produces the lowest interface charge.

From the flatband voltage observed during high-frequency C-V measurements, the difference in fixed charge density between optimum seeded and unseeded structures was found to be about $6 \times 10^{10} \text{ cm}^{-2}$. Differences in the slopes of the high frequency characteristics suggested that the interface trap densities were different also. Quasistatic C-V measurements indicated a minimum interface trap density of about $1.2 \times 10^{10} \text{ cm}^{-2}$ for the seeded structures, and $1.2 \times 10^{11} \text{ cm}^{-2}$ for the unseeded devices. The difference in integrated interface trap densities between seeded and unseeded structures is about $5 \times 10^{10} \text{ cm}^{-2}$ over a 0.6 eV portion of the bandgap and $1.0 \times 10^{11} \text{ cm}^{-2}$ over 0.8 eV.

Seeded films remelted a number of times had higher interface charge densities, but these were still less than in unseeded films. Higher laser powers also appeared to be detrimental.

The differences between seeded and unseeded structures may be related to the higher charge densities expected for grain orientations other than {100} and to traps located at the grain boundaries near the back surface of the silicon film. Quantitative values of the interface charge density distributions could not be confidently determined because of the laterally nonuniform nature of the structure used to obtain seeded material.

Acknowledgment

The author would like to thank Dr. S.-y. Chiang, Dr. C. Drowley, Dr. D. Ilic, and Dr. P. Zorabedian for helpful discussions during this investigation and C. Heimberg, J. Turner, and Dr. C. Drowley for experimental assistance.

Manuscript submitted Nov. 19, 1984; revised manuscript received March 18, 1985.

Hewlett-Packard Laboratories assisted in meeting the publication costs of this article.

REFERENCES

1. H. P. Le and H. W. Lam, *IEEE Electron Device Lett.*,

- edl-3, 161 (1982).
 2. C. I. Drowley and T. I. Kamins, *Mater. Res. Soc. Sym. Proc.*, **13**, 511 (1983).
 3. J. Sturm and J. F. Gibbons, Paper 3.2 presented at the

- IEEE SOS/SOI Workshop, Hilton Head Island, Oct. 2-4, 1984.
 4. P. Zorabedian and T. I. Kamins, *Mater. Res. Soc. Sym. Proc.*, **33**, 81 (1984).

In_xGa_{1-x}As Photodetector for the 1.7-2.0 μm Spectral Region

C. B. Morrison*,¹ and S. M. Bedair

Department of Electrical Engineering, North Carolina State University, Raleigh, North Carolina 27650

K. J. Bachmann*

Department of Chemistry, North Carolina State University, Raleigh, North Carolina 27650

ABSTRACT

InGaAs photodetectors for the 1.7-2.0 μm region have been fabricated by LPE growth of InGaAs layers on intermediate layers of InAsP on an InP substrate. p-n Junctions were formed either by Zn diffusion into an n-type In_xGa_{1-x}As layer or by epitaxial growth of a p-type layer of In_xGa_{1-x}As doped with Mn. The effect of threading dislocations on minority carrier lifetime is analyzed on the basis of minority carrier diffusion length data obtained by fitting a computer model to the experimentally observed quantum efficiency.

In_xGa_{1-x}As_yP_{1-y} lattice matched to InP is currently the preferred materials system for the fabrication of light sources and detectors for optical communications. The maximum wavelength accommodated in this system is 1.65 μm , corresponding to the bandgap of Ga_{0.47}In_{0.53}As, and thus it encompasses the wavelength region of minimum total loss of silica-based fiber optical waveguides (1). Although for such fibers the position of this minimum is not likely to shift much farther into the infrared, small adjustments in the most desirable wavelength of transmission beyond 1.7 μm may become necessary in the future. This paper reports on the fabrication of a photodetector that covers the 1.7-2.0 μm region (2). The detector is fabricated in the In_xGa_{1-x}As ternary system (0.53 < x < 0.70) on InP substrates by liquid phase epitaxy (LPE). To accommodate the lattice mismatch, InAs_yP_{1-y} step-graded layers have been grown between the substrate and the active region. The In-As-P ternary system was chosen because it is easy to step grade and can also act as a window on the active region if the detector is illuminated from the substrate side.

Experimental and Results

The present work was preceded by the determination of the phase diagrams of both the In-Ga-As (3) and the In-As-P (4) ternary systems. The respective solidus and liquidus isotherms for several temperatures were generated by the aid of the regular solution approximation in conjunction with extended data from across the solidus composition of each ternary system. The extended solidus and liquidus data sets were acquired by growing by LPE multiple epitaxial layers using step grading techniques (3). For the present work, saturation temperature for the In-Ga-As melts was 650°C. In-As-P melts were saturated at slightly higher temperatures.

The possibility of growing by LPE an InGaAs layer on intermediate layers of InAsP on an InP substrate is demonstrated in Fig. 1. This pattern shows clearly seven of the eight expected peaks from a single InGaAs epitaxial layer grown on two intermediate, step-graded layers of InAsP on a (111)B InP substrate. The InGaAs layer is approximately 3 μm thick and the InAsP layers are each approximately 5 μm thick. The copper K_{α2} peak of the InGaAs layer is overlapping with the copper K_{α1} peak of the top-most InAsP layer. As indicated in Fig. 1, the compositions

of the InAs_yP_{1-y} layers are y = 0.057 and 0.095 and the composition of the In_xGa_{1-x}As layer is x = 0.62. The overall lattice mismatch between the InP substrate and the InGaAs layer shown in Fig. 1 is calculated to be 0.57%. The lattice mismatch between the top InAsP step-graded layer and the InGaAs layer shown in Fig. 1 is calculated to be 0.27%. In later growth runs, the lattice mismatch between the top two epitaxial layers was successfully decreased to the resolution of our x-ray diffractometer, which is 0.10%.

Etch pit density (EPD) studies were performed on the mismatched InGaAs epitaxial layer by etching for 5-30s in AB etch at room temperature. The revealed defect density in all cases tested exceeded 10⁶ cm⁻². This high EPD is attributed to the large mismatch between adjoining epitaxial layers and to some extent to the (111) orientation of the epitaxial layer.

The In_xGa_{1-x}As undoped n-type epitaxial layer was characterized by Hall data from an epitaxial layer grown on a semi-insulating substrate and C-V measurement data on a junction. These data show consistently a carrier concentration of n = 4 × 10¹⁵ cm⁻³. The Hall data result in a mobility of μ = 9100 cm²/V-s for x = 0.54. Devices were fabricated either by Zn diffusion into an n-type In_xGa_{1-x}As layer or by epitaxial growth of a p-type layer

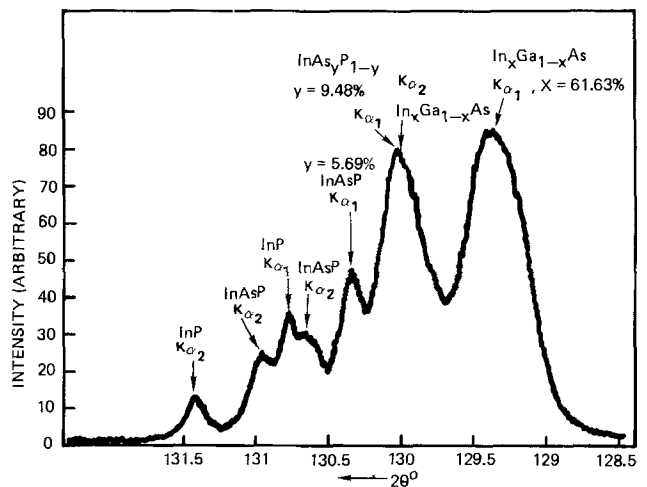


Fig. 1. X-ray diffraction pattern from a simple In_xGa_{1-x}As epitaxial layer grown on two intermediate step-graded layers of InAs_yP_{1-y} on an InP substrate.

* Electrochemical Society Active Member.

¹ Present address: TRW Electro Optics Research Center, Redondo Beach, California 90278.

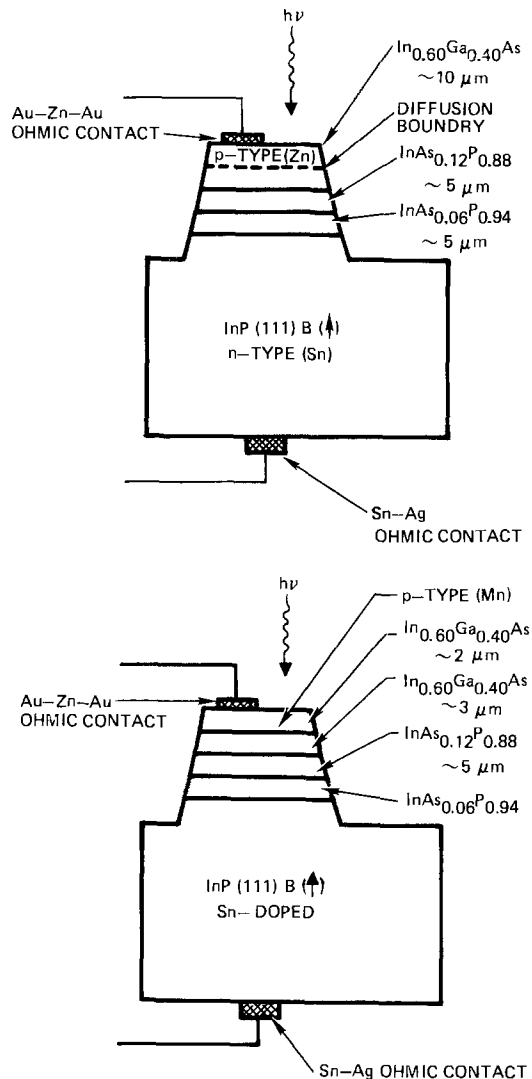


Fig. 2. Sketches of $\text{In}_x\text{Ga}_{1-x}\text{As}$ photodetectors for 1.7-2.0 μm region. Top: Zn diffused. Bottom: Mn doped.

of $\text{In}_x\text{Ga}_{1-x}\text{As}$ doped with Mn, as illustrated in Fig. 2a and 2b, respectively. Zn diffusion was performed either by sealed ampul diffusion or by plating with Zn followed by diffusion on a strip heater. The Zn-diffused material was characterized by Hall data resulting in typically $p = 5 \times 10^{18} \text{ cm}^{-3}$ and $\mu = 73 \text{ cm}^2/\text{V}\cdot\text{s}$. For Mn-doped growth, Mn was added to the melt at the ratio 1.0-1.5 mg/g-In. For a ratio of 1.2 mg/g-In in Mn-doped material, the net hole concentration and Hall mobility were $p = 3 \times 10^{19} \text{ cm}^{-3}$ and $\mu = 17 \text{ cm}^2/\text{V}\cdot\text{s}$.

The devices were characterized by I-V characteristics and spectral response. Representative I-V characteristics are shown in Fig. 3 and 4. For the I-V light and dark currents, reverse bias breakdown became increasingly soft as lattice mismatch increased. For Zn-diffused $\text{In}_x\text{Ga}_{1-x}\text{As}$ junctions of compositions of $x = 0.545, 0.58, \text{ and } 0.625$, open-circuit voltages were 0.21, 0.18, and 0.14V, respectively, and peak quantum efficiencies were 0.662, 0.628, and 0.226, respectively. The quantum efficiency spectra of these three devices are depicted in Fig. 5. Mn-doping $\text{In}_x\text{Ga}_{1-x}\text{As}$ junctions of compositions of $x = 0.54, 0.59, \text{ and } 0.69$ had peak quantum efficiencies of 0.265, 0.202, and 0.059. For the Mn-doped $\text{In}_x\text{Ga}_{1-x}\text{As}$ photodetector of composition $x = 0.69$, the quantum efficiency was fairly flat to 1.9 μm and dissipated thereafter to 2.0 μm as viewed in Fig. 6.

Analysis and Discussion

The difference in the quantum efficiencies between the Zn-doped and the Mn-doped $\text{In}_x\text{Ga}_{1-x}\text{As}$ photodetectors may be attributed to several causes. The order-of-mag-

nitude-higher doping concentration of Mn explains the lower mobility and quantum efficiencies because of a reduction of the minority carrier lifetime due to increased scattering effects. With lower Mn doping, higher quantum efficiencies can be expected. On the other hand, because the electrical p-n junction is separated from the metallurgical junction in the Zn-diffused devices, quantum efficiencies are improved (5, 6). Furthermore, in agreement with the higher mobility of the Zn-diffused epitaxial layers and in view of the fact that the field generated by the doping gradient guides minority carriers toward the collecting junction, the Zn-diffused devices have higher efficiencies.

The density of misfit dislocations depends to a large extent on the lattice misfit strain between adjacent mismatched epitaxial layers or between a mismatched epitaxial layer and the adjacent substrate. Furthermore, these dislocations tend to bend into the epitaxial layers, creating "inclined" or "threading" dislocations that can transmit the impact of the lattice misfit into the bulk of the epitaxial layer and thus contribute to a degradation of the layer properties (7). The direct relationship between an increased lattice mismatch, an increase in misfit dislocation density, and a decrease in device performance has been reported in several lattice-mismatched ternary systems (8-10). In view of these observations, an analysis of the known lattice mismatch and corresponding device

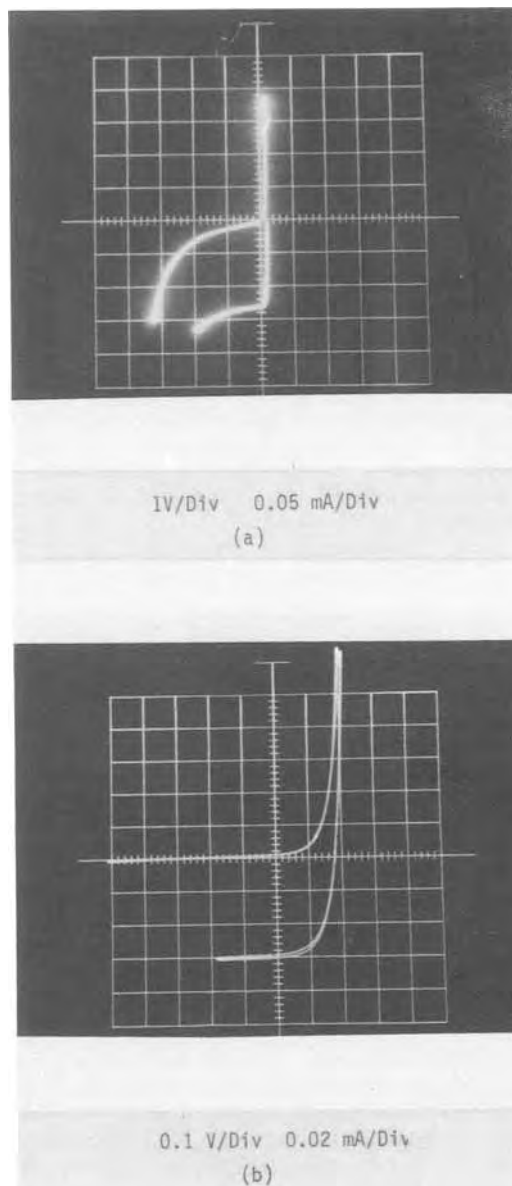


Fig. 3. a: I-V characteristic of a Zn-diffused $\text{In}_{0.58}\text{Ga}_{0.42}\text{As}$ photodetector. b: Alternative view.

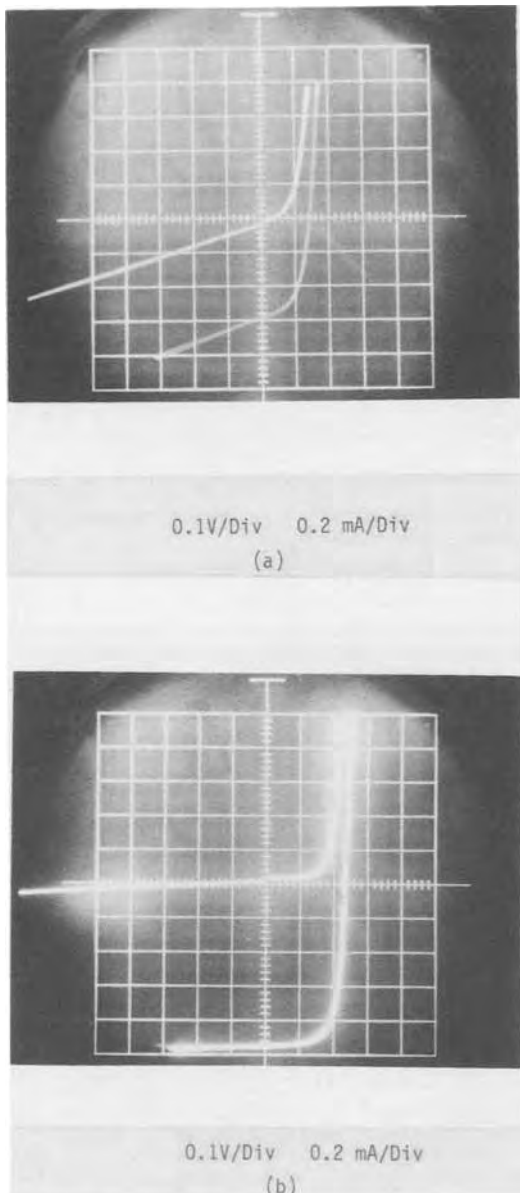


Fig. 4. a: I-V characteristic of a Zn-diffused In_{0.625}Ga_{0.375}As photodetector. b: Lattice-matched Mn-doped photodetector.

quantum efficiencies for the In_xGa_{1-x}As photodetectors described in this paper is appropriate.

The quantum efficiency spectra of the Zn-diffused devices were fitted on the basis of a homojunction model for solar cells (11). A computer algorithm performed the fit by finding optimum values of the diffusion lengths of the minority carriers and junction depth. An example of this fit is shown in Fig. 7 for the Zn-diffused In_{0.58}Ga_{0.42}As detector. The fit is not perfect, since the model itself is meant to be only a first approximation of a diffused junction. Furthermore, the model requires estimated values for wavelength-dependent parameters such as the absorption coefficient and the reflectance. The modeling results indicated that the quantum efficiency spectra were fairly insensitive to the minority carrier hole diffusion length on the n-type side of the electrical junction. This insensitivity can be expected if most of the absorption takes place near the surface of the device.

Under these circumstances, the minority carrier lifetime, τ_n , of the electrons in the p-type side of the electrical junction can be calculated on the basis of the modeling results by the relationship of $\tau_n = L_n^2/D_n$, where D_n is the electron diffusion coefficient and L_n is the electron diffusion length. Also, the threading dislocation density can be calculated from the derived expression (12)

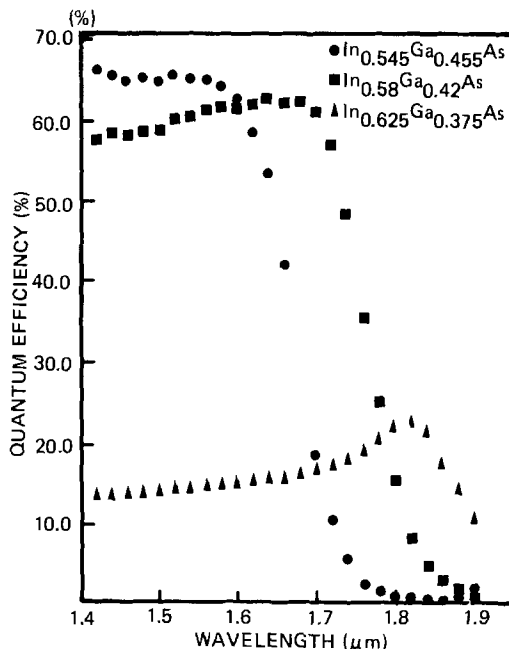


Fig. 5. Quantum efficiency spectra of three Zn-diffused In_xGa_{1-x}As photodetectors.

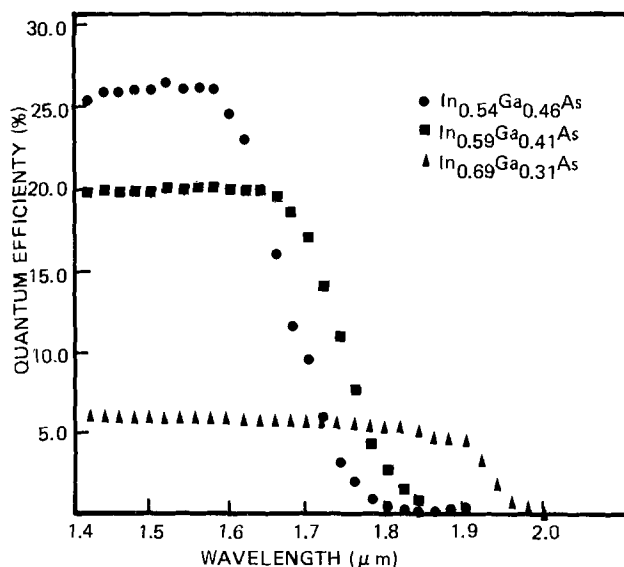


Fig. 6. Quantum efficiency spectra of three Mn-In_xGa_{1-x}As photodetectors.

$$\frac{\eta}{\eta_0} \approx (1 + \Pi^2 L_n^2 \rho_d)^{-1}$$

where ρ_d is the threading dislocation density, η_0 is the peak quantum efficiency in the absence of dislocations, and η is the peak quantum efficiency in the presence of

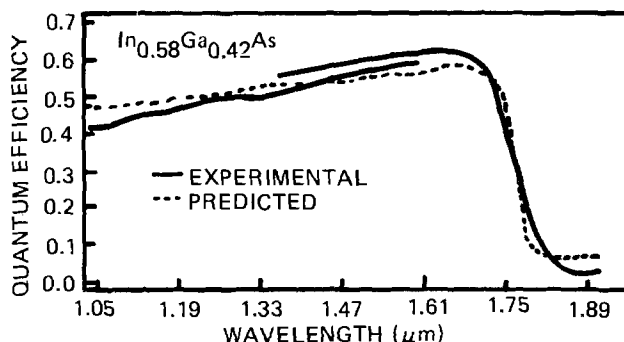


Fig. 7. Quantum efficiency experimental data and the fitted model for a Zn-diffused In_{0.58}Ga_{0.42}As photodetector.

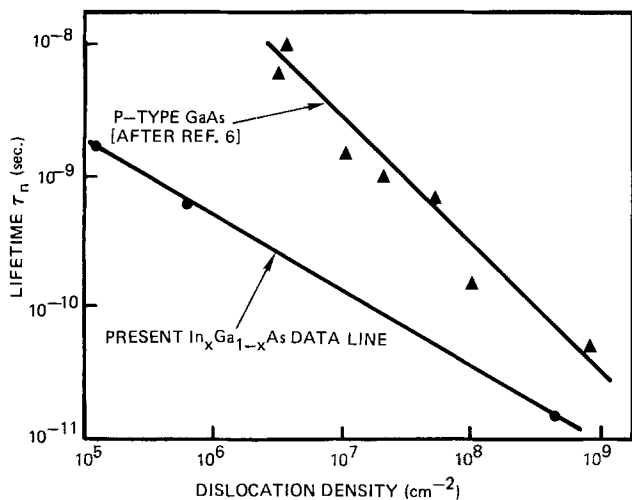


Fig. 8. Minority carrier lifetime vs. misfit dislocation of Zn-diffused $\text{In}_x\text{Ga}_{1-x}\text{As}$ photodetectors.

dislocations. By allowing η_0 to be 70% (13, 14), η to be the peak value for each of the Zn-diffused devices, and L_n to be the corresponding values deduced from the fitting procedures, the threading dislocation density can be estimated for each device. Figure 8 indicates the relationship between the computed minority carrier lifetimes and their corresponding estimated dislocation densities for the Zn-diffused devices of the present work. Figure 8 thus indicates the estimated trend of the effects of threading dislocation density on the minority carrier lifetime. Similar work with p-type GaAs (7) is also presented in Fig. 8 for comparison.

On the basis of the analysis resulting in Fig. 8, the decrease in lifetime due to the increase in misfit dislocations in $\text{In}_x\text{Ga}_{1-x}\text{As}$ appears to be less critical than the decrease in lifetime due to the increase in defect density in GaAs specifically and other materials (Ge, Si, GaP, and AlGaAs) in general (7). This difference in part reflects the fact that devices with short diffusion lengths are less sensitive to a moderate dislocation density than devices with long diffusion lengths. This difference can also be attributed to the differences in the nature of the defects in those other materials and as well to the presence of step-graded layers used in the present study. Improved electrical performance of mismatched material due to the presence of step-graded layers included to relieve mismatch strain has been noted in GaAsSb photodiodes (8) and in $\text{In}_x\text{Ga}_{1-x}\text{As}$ layers grown on GaAs substrates (9). This effect has also been noted in the present work, as can be observed in Fig. 9. This figure shows the responsivities of $\text{In}_{0.58}\text{Ga}_{0.42}\text{As}$ homojunction photodiodes both with and without intermediate step-graded layers of $\text{InAs}_y\text{P}_{1-y}$. Both devices were Zn diffused and otherwise identical except for the presence of the intermediate step-graded layers. The device with the intermediate step-graded layers has more than twice the responsivity of the device with a single mismatched layer. Thus, although increased threading dislocations due to lattice-mismatched material cause a serious decrease in efficiency of the device de-

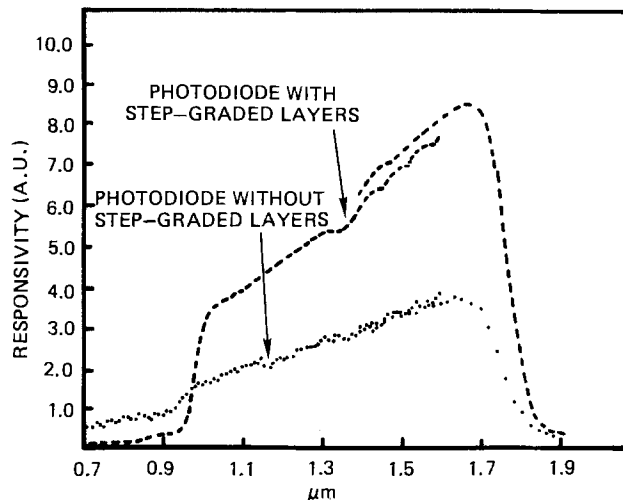


Fig. 9. Responsivity of $\text{In}_{0.58}\text{Ga}_{0.42}\text{As}$ photodetectors with and without step-graded layers of $\text{InAs}_y\text{P}_{1-y}$.

scribed in the present work, the introduction of intermediate step-graded epitaxial layers has made it possible to produce by LPE InGaAs photodetectors for the 1.7-2.0 μm spectral region.

Acknowledgment

This work was supported by the Army Research Office, Research Triangle Park, North Carolina.

Manuscript submitted April 4, 1984; revised manuscript received Jan. 31, 1985.

TRW Electro Optics Research Center assisted in meeting the publication costs of this article.

REFERENCES

1. H. Osonai, T. Shioda, T. Moriyama, S. Araki, M. Horigaki, T. Izawa, and H. Taketa, *Electron. Lett.*, **12**, 550 (1976).
2. C. B. Morrison, S. M. Bedair, and K. J. Bachmann, in "III-V Opto-Electronics Epitaxy and Device Related Processes," V. G. Keramidas and S. Mahajan, Editors, p. 139, The Electrochemical Society Softbound Proceedings Series, Pennington, NJ (1983).
3. S. M. Bedair, C. Morrison, R. Fang, and N. A. El-Masry, *J. Appl. Phys.*, **51**, 5413 (1980).
4. C. B. Morrison and S. M. Bedair, To be published.
5. A. K. Chin, B. V. Dutt, H. Temkin, W. A. Bonner, and D. D. Roccasecca, *Appl. Phys. Lett.*, **36**, 924 (1980).
6. T. P. Lee, C. A. Burrus, Jr., and A. G. Dentai, *IEEE J. Quantum Electron.*, **qe-17**, 232 (1981).
7. H. Kressel, *Semicond. Semimetals*, **16**, 1 (1981).
8. R. L. Moon, *J. Appl. Phys.*, **51**, 556 (1980).
9. M. Ettenberg, C. J. Neuse, J. R. Appert, J. J. Gannon, and R. E. Enstrom, *J. Electron. Mater.*, **4**, 37 (1975).
10. M. L. Timmons and S. M. Bedair, *J. Appl. Phys.*, **52**, 1134 (1981).
11. H. J. Hovel, *Semicond. Semimetals*, **11**, (1975).
12. R. J. Roedel, A. R. Van Neida, R. Caruso, and L. R. Dawson, *This Journal*, **126**, 637 (1979).
13. K. J. Bachmann and J. L. Shay, *Appl. Phys. Lett.*, **32**, 446 (1978).
14. T. P. Pearsall, *IEEE J. Quantum Electron.*, **qe-16**, 709 (1980).

Gettering of Carbon and Oxygen in Silicon Processing

W. E. Bailey,* R. A. Bowling,* and K. E. Bean*

Texas Instruments, Incorporated, Dallas, Texas 75265

ABSTRACT

The control of carbon and oxygen is of great importance in today's silicon materials and device processing, and it will become a critical parameter in the immediate future for VLSI device processing. Although considerable technology and some understanding are available today in the control of oxygen in silicon materials through processing, there is little technology and even less understanding of carbon control in silicon wafer processing. We have determined, for high carbon content silicon, that carbon can be gettered to damage sites such as dislocations, stacking faults, and/or wafer surfaces, thus creating a carbon-denuded zone in epitaxial silicon, as well as in bulk Czochralski silicon substrates. The gettering effects of carbon have been investigated using controlled time, temperature, and ambient gas thermal anneals. The characterization of these materials was carried out using chemical etches, Fourier transform infrared spectroscopy, and scanning Auger microprobe analysis.

The control of oxygen and carbon in Czochralski (CZ) silicon is the subject of a great number of recent studies because of its importance in defect formation and gettering of impurities. Intrinsic gettering can be used to remove unwanted impurities from device active regions (1-5); thus, the control of oxygen and its effects on intrinsic gettering have been particularly examined (1, 2, 5-16). Intrinsic gettering has been found to retard material slip (17-18), reduce slip formation (19), control epitaxial stacking fault formation (20), reduce p-n junction leakage currents, and improve MOS generation lifetimes (21-23). Oxygen donors can significantly alter silicon electrical properties (24). Interstitial oxygen and small oxygen clusters can strengthen wafers to prevent process-induced warpage (25, 26). The effects of carbon on both oxygen precipitation and oxygen donor formation have also been often investigated (1, 3, 24, 27-32), but not with as much success of definitive behavior as for oxygen. Pinizzotto and Marks (5) concluded that both the initial carbon and oxygen concentrations affect the final measured oxygen solubility in silicon, that carbon is involved in precipitate nucleation, but not in precipitate growth, and that carbon content does not strongly affect oxygen precipitation in high oxygen silicon (> 30 ppm), but does control the oxygen precipitation in low oxygen content silicon (< 25 ppm). In this paper, the role of carbon in high carbon-content silicon is examined (32, 33).

Experimental

In these experiments, (100) p-type, 5-20 Ω -cm silicon wafers with various levels of carbon were used to study effects introduced during the processing of VLSI devices and epitaxial silicon deposition. The samples were within an oxygen concentration range of 1.25×10^{18} cm^{-3} (25 ppm) to 1.7×10^{18} cm^{-3} (34 ppm), which is considered to be a useful range to achieve intrinsic gettering effects. A heat-treatment sequence was picked to simulate current VLSI processing and to provide denuded substrates for epitaxial deposition. The heat cycles were three separate anneals of 1100°C, in nitrogen, for 2h to out-diffuse oxygen (anneal 1), of 650°C, in nitrogen, for 20h to begin nucleation (anneal 2), and of 1000°C, in oxygen, for 20h to simulate precipitate growth during processing (anneal 3). Push-pull rates between each cycle were 20 cm/min, with the two high temperature cycles being ramped up from 850°C after the push cycle, and ramped down to 850°C prior to the pull cycle.

CZ Single-Crystal Silicon Wafers

Carbon and oxygen.—Carbon and oxygen measurements were made using a Nicolet MX-ECO FTIR spectrometer. The measurements of substitutional carbon and interstitial oxygen in silicon were based on ASTM Methods F-121-76 and F-123-74 as refined by Vidrine (34). In this work, the materials used were of a production nature obtained from several silicon wafer vendors, each sub-

strate being single-side polished with various types of back-side treatments particular to each vendor. The values of carbon and oxygen are relative to repeated measurements on the same wafer, but are not intended to be absolute in magnitude. Figure 1 shows differences in the FTIR traces due to the various back-side surfaces as produced by four different vendors, A, B, C, and D. Traces A and D are from wafers that have been acid etched to relieve stress caused by sawing and lapping processes during wafer production, while traces B and C are from wafers that received a caustic etch as part of the vendors' standard processes. The differences in the curves are caused by changes in scattering and internal reflection of the infrared beam due to the texture of the back side of the wafers. All four wafers were then back-side polished to remove the texture of the relief etches. Major differences in the background of the FTIR traces were removed, as shown by a superposition of all four back-side polished wafer FTIR traces, A', B', C', D', in Fig. 1.

The plots in Fig. 2 show the behavior of interstitial oxygen for silicon material with low carbon (< 0.2 ppm) as a function of the three-step anneal described in the Experimental section. The initial data points are the interstitial oxygen concentrations of the as-received wafers, after crystal growth and vendor resistivity stabilization anneals, but prior to any further heat-treatments. The other points are after the cumulative anneals to the step designated. The oxygen reduction during the third anneal step is shown to be dependent on the initial oxygen concentration as previously reported by Pinizzotto and Marks (5).

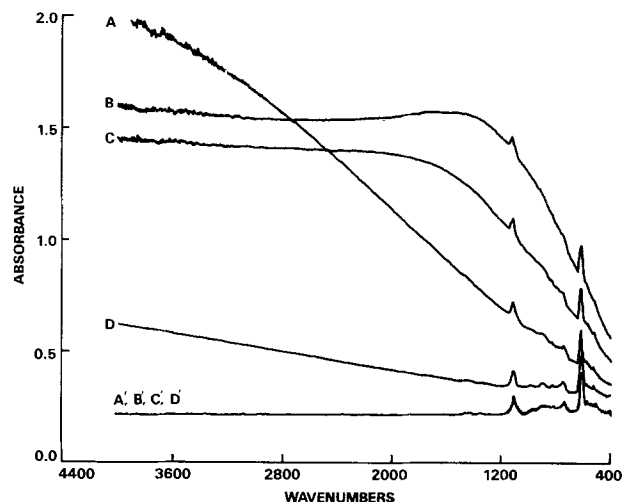


Fig. 1. FTIR traces of silicon wafers from different wafer vendors, A, B, C, and D, with various types of back-side texture. A and B are acid etched by vendors; C and D are caustic etched by vendors. Also shown are FTIR traces of silicon wafers from the same four vendors, but with a back-side polish; all four traces, A', B', C', and D', are superimposed.

*Electrochemical Society Active Member.

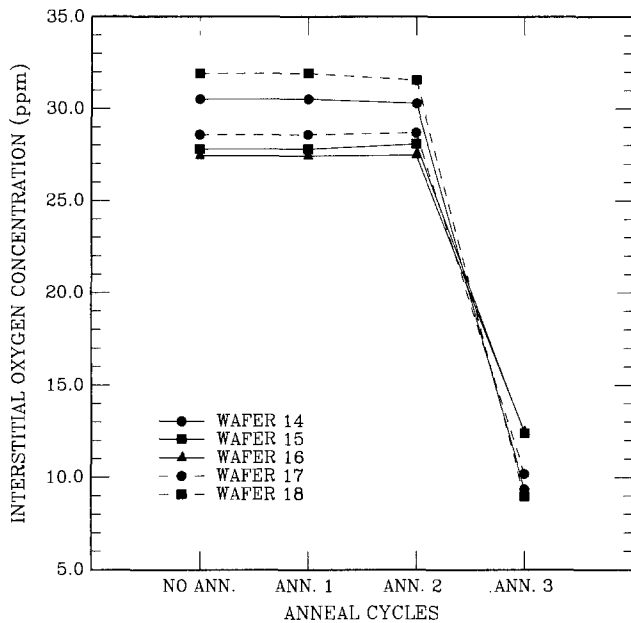


Fig. 2. The change of interstitial oxygen concentration in bulk CZ silicon wafers as a function of the three-step anneal for <0.2 ppm carbon wafers; data from FTIR measurements with carbon below the detection limits in each case.

Figures 3 and 4 give the changes in interstitial oxygen and substitutional carbon, respectively, for high carbon (> 2 ppm) concentration wafers. The change in substitutional carbon, in this case, is linear with respect to the initial concentration of carbon. This is shown in Fig. 5, which is a plot of the differences between the initial carbon and final carbon concentrations shown in Fig. 4 vs. the initial carbon content for those wafers. The points of this plot fit well, within experimental error, to a straight line. This observation of linearity, however, may be oxygen concentration dependent as reported by Pinizzotto and Marks (5). The change in interstitial oxygen with respect to the initial oxygen concentration is similar to the curves in Fig. 2 for low carbon wafers. This change has been previously shown to follow a straight line (2). The main difference between low and high carbon, shown in Fig. 2 and 3, is that the high carbon wafers had approxi-

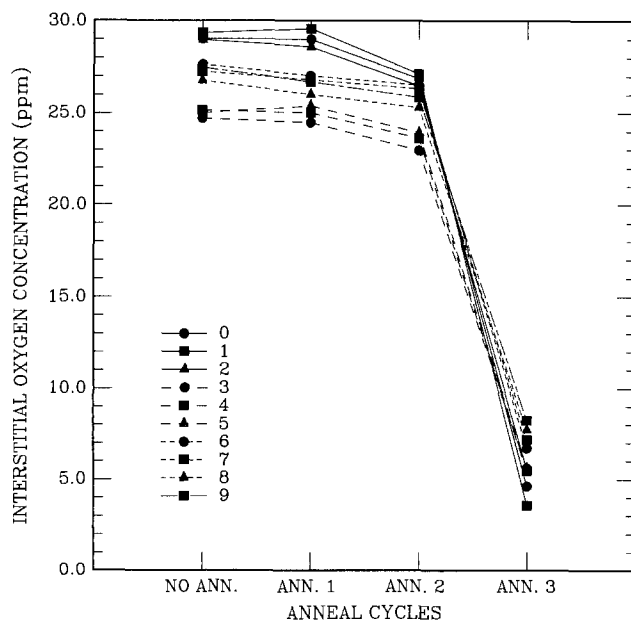


Fig. 3. The change of interstitial oxygen content in >2.0 ppm carbon content silicon wafers as a function of the three-step anneal; data from FTIR measurements. Initial carbon concentrations in ppm for wafers 0 through 9, respectively, were 3.18, 3.09, 3.58, 6.18, 5.41, 5.43, 1.95, 2.75, 2.64, and 2.02.

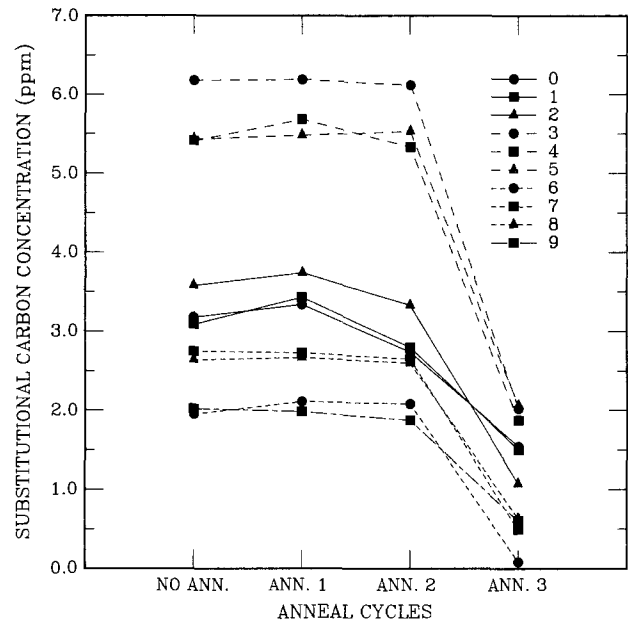


Fig. 4. The change in substitutional carbon content in 24-30 ppm oxygen content silicon wafers as a function of the three-step anneal; data from FTIR measurements. Initial oxygen concentrations in ppm for wafers 0 through 9, respectively, were 29.03, 29.35, 28.97, 24.71, 25.15, 25.02, 27.64, 27.25, 26.76, and 27.47.

mately 5 ppm greater change in interstitial oxygen for a given initial oxygen content than the low carbon material. All materials represented in Fig. 2, 3, and 4 were received from the same vendor, with the higher carbon levels being achieved by intentional doping by the vendor of the molten silicon with carbon.

Dislocation and defect analyses.—The CZ-grown single-crystal wafers intentionally doped with carbon from non-detectable limits to greater than 5 ppm were processed using the three-cycle heat-treatment. The bulk of each wafer was examined using a variation of the groove-and-etch method described by McDonald and Goetzberger (35). A 5 min Wright-Jenkins dislocation etch (36) was used to display precipitated sites within a $35 \mu\text{m}$ deep cylindrical groove. Inspection of the groove using an optical microscope with Nomarski interference contrast revealed a clear denuded area approximately $10\text{-}20 \mu\text{m}$ deep. Standard stacking faults and dislocation loops associated with oxygen precipitation appeared at the bottom of the

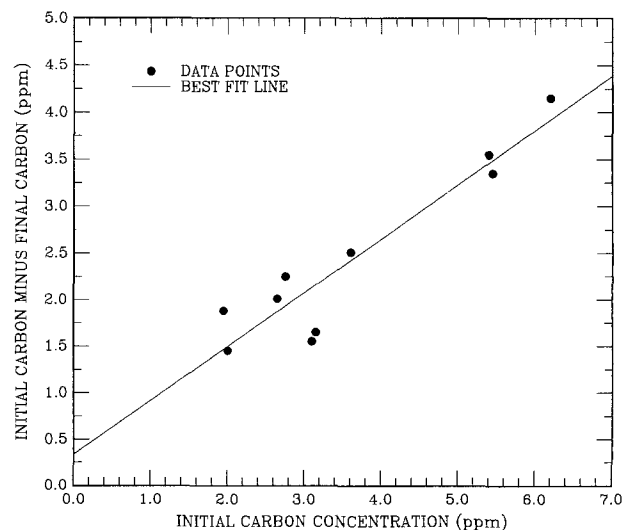


Fig. 5. Plot of the differences between the initial carbon and final carbon concentrations for wafers in Fig. 4 vs. the initial carbon content for those wafers. The correlation coefficient for the least squares best fit line to the data is 0.936.

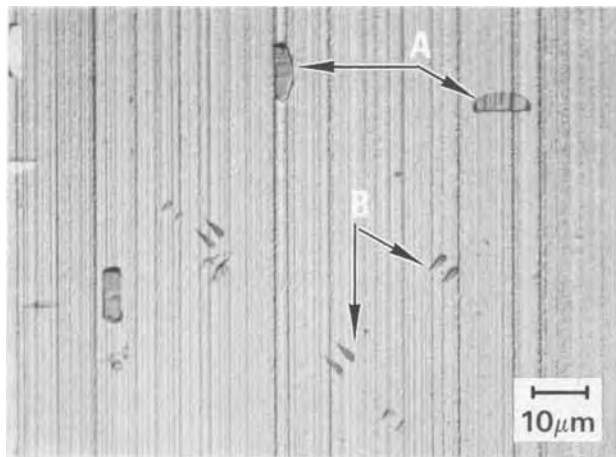


Fig. 6. Optical photograph of (A) normal (100) bulk stacking faults, and (B) c pits as found in high carbon concentration silicon.

groove and were oriented along $\langle 110 \rangle$ directions. In the higher carbon samples, a new defect, which we call "c pits," also appears. Its axis of symmetry is oriented 45° to the $\langle 110 \rangle$ direction defined by the bulk stacking faults. Several such c pits are shown in relationship to bulk stacking faults in Fig. 6. The parallel, vertical lines in the figure are groove artifacts due to the polishing wheel used to prepare the cylindrical groove. This new c pit defect has been found to occur singly or in pairs; the c pits shown in Fig. 6 are all in pairs. Recently, Matlock (4) also noted these new defects in high carbon silicon wafers used for processing 64K DRAM devices. Extended time anneals were performed on the low carbon silicon and have not, in any instance, created the c pit defects observed on the high carbon samples.

Figure 7 is a transmission electron micrograph (TEM) image of an area of a high carbon wafer containing c pits and a bulk stacking fault. The stacking fault, which runs horizontally across the picture, and several of the 45° c pit dislocations are shown in the (100) sample plane. The stacking fault, which lies in the (111) plane, defines the (011) plane. The 45° c pit dislocation can be visualized as

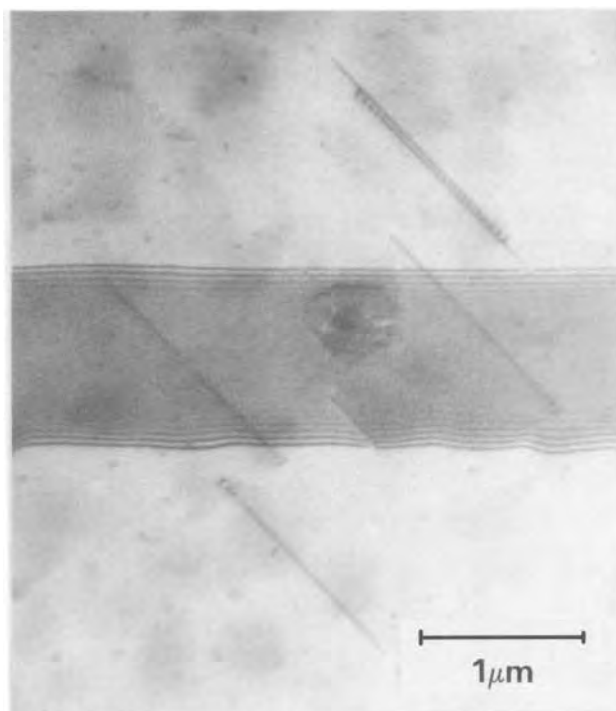


Fig. 7. TEM micrograph from an area of high carbon in silicon after three-step anneal, showing a stacking (horizontal across the micrograph) and several c pits (diagonal across the micrograph).

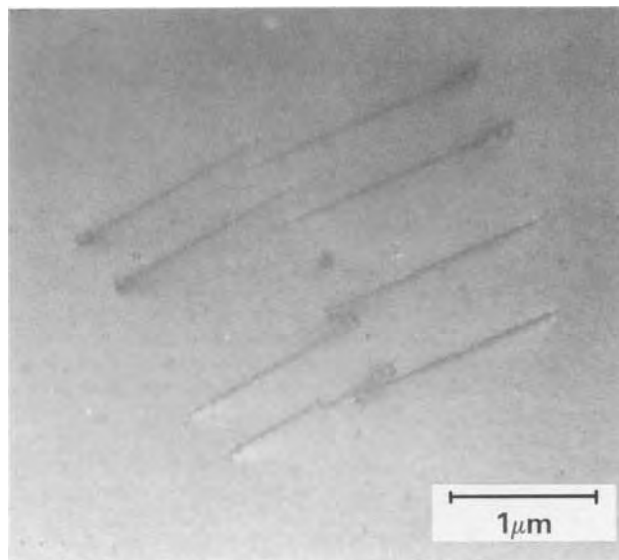


Fig. 8. TEM micrograph of four pairs of c pits in high carbon silicon

lying in the (101) plane and projected onto the (100) plane at 45° with respect to the projection of the stacking fault on the (100) plane. Figure 8 is another TEM image of a high carbon content wafer showing a higher density of these c pits, in this case, four pairs.

Subsequent examination of the heat-treated high carbon grooved samples using a JEOL JAMP-3 scanning Auger electron microscope has revealed low levels of atomic carbon in the upper $10\text{--}20\ \mu\text{m}$ of the groove and in clear areas around the defects in the bottom of the groove. The concentration of carbon at the dislocation sites, both c pits and bulk stacking faults, was found to be from two to six times greater than in the bulk of the wafer. Typical Auger results for one sample are shown in Table I. This gettering of carbon to sinks and nearby wafer surfaces has been previously proposed (27, 37, 38), but not experimentally verified, in CZ single-crystal silicon wafers or in epitaxial silicon films. Standard carbon wafers having the same heat-treatments were not found by Auger analysis to exhibit this difference in carbon levels. In each case, the Auger spectrometer electron beam spot size was focused to approximately $2000\ \text{\AA}$ diam and line rastered on the defect or bulk defect-free area (clear area) over a distance of about $1\ \mu\text{m}$. Argon ion sputtering was used to remove surface contaminants and sputter into the defect or bulk clear area. Analyses were made at 1 min sputter intervals to monitor the progress of the sputtering. The Auger data presented are for depths, given in sputter minutes, at which no significant changes in the carbon, oxygen, or silicon levels were noted over several minutes of sputtering. This typically ranged from 5 to 10 min of sputtering. This was taken to be the point at which most surface contamination, which might be largely carbon, has been removed. 1 min of sputtering has been empiri-

Table I. Scanning Auger data for defects in high carbon silicon (data for each sample are for 6 min sputtered)

Sample	Relative atomic percent		
	Carbon	Oxygen	Silicon
Clear areas			
Area 1	3.3	2.0	93.8
Area 2	6.5	3.6	88.8
45° Dislocations			
C pit 1	20.6	1.4	77.8
C pit 2	25.1	1.6	73.2
C pit 3	25.3	1.9	71.8
90° Dislocations			
Stacking fault 1	26.7	3.2	69.2
Stacking fault 2	18.9	2.1	77.9
Stacking fault 3	29.4	1.4	68.4

cally determined, for our system, to correspond to approximately 150Å depth in the silicon wafer. The Auger system base pressure before sputtering was typically $5-8 \times 10^{-10}$ torr, pressure during argon ion sputtering while using a Kratos Minibeam-II differentially pumped ion sputter gun was about 5×10^{-8} torr, and pressures during Auger analyses were usually from 1×10^{-9} to 5×10^{-9} torr. The tabulated Auger data are given as typical examples of the data obtained from multiple samples of each type.

Gettering of Carbon in Epitaxial Silicon

Chemically vapor deposited epitaxial silicon was grown on (100) silicon substrates with low (< 0.1 ppm), normal (< 0.5 ppm), and high (> 1.0 ppm) carbon concentrations in the bulk crystal. Epitaxy was also grown on normal carbon concentration substrates with known carbon surface contamination (from the substrate holder) in specific areas of the wafer, as well as on high carbon substrates. In all cases of epitaxial silicon over areas of high carbon, defect-denuded regions were observed around stacking faults in the epitaxial film. Figure 9 is a phase contrast photograph of such a region which shows the denuding or gettering effect of damage around the stacking fault in the epitaxial film on a high carbon wafer. This denudation occurs as a result of the epitaxial deposition process only; no further heat-treatments or surface treatments were necessary to observe this phenomenon. Large dislocations, with precipitates, are observed at the corners of the stacking fault. Auger analyses of the corners of the stacking fault, a clear denuded area around the stacking fault, and a clear area away from the stacking fault showed the precipitates to contain a high concentration of carbon, with much less carbon being observable in the clear areas. Heavy metals, which are also expected to be associated with these corner precipitates, and the denuding region were not observed by Auger, probably because of the 0.5% or higher detection limits of scanning Auger spectroscopy for such metals. Slightly higher carbon was observed for a clear area away from the stacking fault as compared to the clear denuded area near the stacking fault. These areas are designated A, B, and C in Fig. 9, and the Auger data for these areas are summarized in Table II. Another example of this gettering process in epitaxial films is shown in Fig. 10. Scanning Auger analysis results for the area of one of the stacking faults in Fig. 10 showed little or no carbon in the zone around the stacking fault as compared to 20% or more carbon in the stacking fault. Auger analyses of the defects around the clear denuded area and clear areas around those defects revealed no measurable differences in carbon levels between these two areas. Figure 11 is an optical phase con-

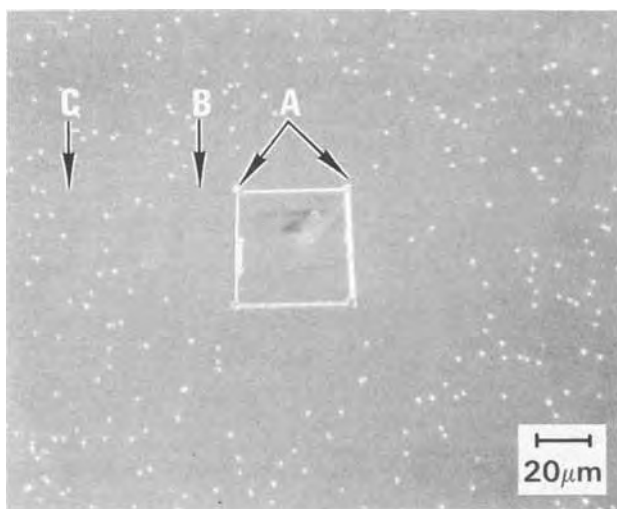


Fig. 9. Epitaxial stacking fault area with (A) dislocation precipitation, (B) denuded area, and (C) high defect area on high carbon silicon due to the epitaxial CVD processing only.

Table II. Scanning Auger data for epitaxial stacking fault areas on high carbon silicon shown in Fig. 9 (data for each sample are for 10 min sputtered)

Sample	Relative atomic percent		
	Carbon	Oxygen	Silicon
Area A			
Corner 1	22.5	0.6	76.7
Corner 2	23.2	2.1	74.7
Area B			
Run 1	3.2	2.4	94.4
Run 2	2.9	1.8	95.5
Area C			
Run 1	9.3	5.7	85.0
Run 2	10.9	3.1	86.0

trast photograph of a cleaved cross section of a heat-treated epitaxial film on a high carbon substrate. The cleaved sample was Wright-Jenkins etched, but was not polished. It clearly shows a typical oxygen precipitation denuded region beneath the junction of the epitaxial layer; the surface itself does show a number of defects. The denuded region in the sample is about 20 μm deep.

Discussion

Interstitial oxygen measurements indicate less than 2 ppm total change in oxygen concentration during the 1100° and 650°C anneal with usually a 15-25 ppm reduc-

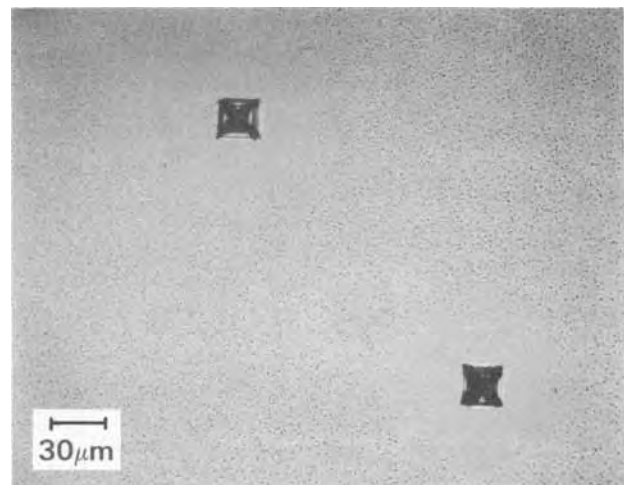


Fig. 10. Epitaxial stacking faults on high carbon silicon showing denuded areas due to the epitaxial CVD processing only.

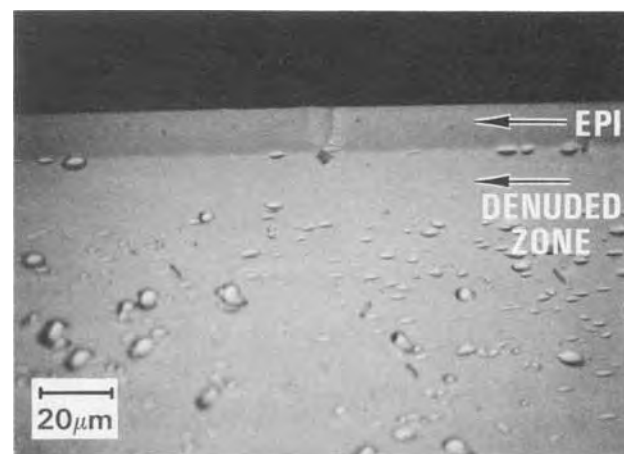
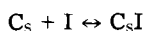


Fig. 11. Cleaved cross section of epitaxial layer on high carbon silicon following the three-step anneal showing the denuded region beneath the epitaxial interface. The denuded zone is approximately 20 μm deep.

tion in oxygen concentration during the final 1000°C anneal. The initial interstitial oxygen concentration of all samples ranged from about 24 to 32 ppm. Significant changes in substitutional carbon levels occurred only during the 1000°C growth cycle.

Gosele and Tan have speculated on the coprecipitation of carbon and self-interstitials to enhance the diffusivity of carbon in silicon (39). They have concluded that carbon either migrates rapidly via a complex involving an intrinsic point defect (I) or has a fast diffusing component via interstitial carbon (C_i). The two methods are illustrated as follows, where C_s is substitutional carbon



and



This association of carbon atoms with self-interstitials leads to nuclei for microdefect formation; hence, the influence of carbon would depend upon the concentration of self-interstitials present. New donors created in CZ silicon at 650°C are considered to be oxygen precipitates with nuclei provided by carbon. Tajima *et al.* (40) have shown that the density of new donors can be affected by either high carbon concentrations or extended 470°C anneal cycles which precede a 650°C anneal. Thus oxygen precipitation is governed by the thermal history of the wafers, and knowledge of the thermal behavior of microdefects at lower temperatures is indispensable if one is to understand the complete system of nucleation and growth of defects (41). Also, the control of carbon concentration in silicon will be necessary to achieve proper control and understanding of oxygen precipitation and gettering.

Acknowledgment

The authors would like to thank G. Keefe-Fraundorf, Electronics Division, Monsanto Company, for skillful experimental assistance in preparation of the transmission electron micrographs.

Manuscript submitted Oct. 1, 1984; revised manuscript received March 25, 1985. This was Paper 287 presented at the San Francisco, California, Meeting of the Society, May 8-13, 1983.

Texas Instruments, Incorporated, assisted in meeting the publication costs of this article.

REFERENCES

- R. A. Craven, in "Semiconductor Silicon/1981," H. R. Huff, J. Kriegler, and Y. Takeishi, Editors, The Electrochemical Society Softbound Proceedings Series, Pennington, NJ (1981).
- H. R. Huff, H. F. Schaake, J. T. Robinson, S. C. Baber, and D. Wong, *This Journal*, **130**, 1551 (1983).
- S. Kishino, Y. Matsushita, M. Kanomori, and T. Iizuka, *Jpn. J. Appl. Phys.*, **21**, 1 (1982).
- J. H. Matlock, in "Defects in Silicon," W. M. Bullis and L. C. Kimerling, Editors, p. 3, The Electrochemical Society Softbound Proceedings Series, Pennington, NJ (1983).
- R. F. Pinizzotto and S. Marks, in "Defects in Semiconductors II," S. Mahajan and J. W. Corbett, Editors, p. 147, Materials Research Society Symposia Proceedings Vol. 14, North-Holland, New York (1983).
- J. M. Andrews, S. Muller, and G. A. Rozgonyi, in "VLSI Science and Technology/1982," C. J. Dell'Oca and M. W. Bullis, Editors, p. 43, The Electrochemical Society Softbound Proceedings Series, Pennington, NJ (1982).
- K. Kugimiya, S. Akiyama, and S. Nakamura, in "Semiconductor Silicon/1981," H. R. Huff, J. Kriegler, and Y. Takeishi, Editors, p. 294, The Electrochemical Society Softbound Proceedings Series, Pennington, NJ (1981).
- K. Nagasawa, Y. Matsushita, and S. Kishino, *Appl. Phys. Lett.*, **37**, 622 (1980).
- M. Ogino, T. Usami, and M. Watanabe, Abstract 435, p. 1097, The Electrochemical Society Extended Abstracts, Vol. 80-2, Hollywood, FL, Oct. 5-10, 1980.
- M. Sasaki, K. Nishi, and S. Ushio, Abstract 393, p. 954, The Electrochemical Society Extended Abstracts, Vol. 81-2, Denver, CO, Oct. 11-16, 1980.
- R. W. Series, K. G. Barraclough, and W. Bardsley, in "Semiconductor Silicon/1981," H. R. Huff, J. Kriegler, and Y. Takeishi, Editors, p. 304, The Electrochemical Society Softbound Proceedings Series, Pennington, NJ (1981).
- H. Shimizu, A. Yoshinaka, and Y. Sugita, *Jpn. J. Appl. Phys.*, **17**, 767 (1978).
- F. Shimura, in "VLSI Science and Technology/1982," C. J. Dell'Oca and M. W. Bullis, Editors, p. 17, The Electrochemical Society Softbound Proceedings Series, Pennington, NJ (1982).
- F. Shimura, H. Tsuya, and T. Kawamura, *This Journal*, **128**, 1579 (1981).
- "Defects in Semiconductors," J. Narayan and T. Y. Tan, Editors, Materials Research Society Symposia Proceedings Vol. 2, North-Holland, New York (1981); "Defects in Semiconductors II," S. Mahajan and J. W. Corbett, Editors, Materials Research Society Symposia Proceedings Vol. 14, North-Holland, New York (1983).
- "Semiconductor Silicon/1981," H. R. Huff, J. Kriegler, and Y. Takeishi, Editors, The Electrochemical Society Softbound Proceedings Series, Pennington, NJ (1981).
- S. M. Hu, *J. Vac. Sci. Technol.*, **14**, 17 (1977).
- K. Yasutake, M. Umeno, and H. Kawabe, *Appl. Phys. Lett.*, **37**, 789 (1980).
- W. Lin and C. W. Pearce, *J. Appl. Phys.*, **51**, 5540 (1980).
- L. E. Katz and D. W. Hill, *This Journal*, **125**, 1151 (1978).
- G. A. Rozgonyi and C. W. Pearce, *Appl. Phys. Lett.*, **32**, 747 (1978).
- T. Y. Tan, E. E. Gardner, and W. K. Tice, *ibid.*, **30**, 175 (1977).
- K. H. Yang, H. F. Kappert, and G. H. Schwuttke, *Phys. Status Solidi A*, **50**, 221 (1978).
- U. Gosele and T. Y. Tan, *Appl. Phys. A*, **28**, 79 (1982).
- S. M. Hu, *Appl. Phys. Lett.*, **31**, 53 (1977).
- S. M. Hu and W. J. Patrick, *J. Appl. Phys.*, **46**, 1869 (1975).
- B. O. Kolbesen and A. Muhlbauer, *Solid State Electron.*, **25**, 759 (1982).
- J. Lerouille, *Phys. Status Solidi A*, **67**, 177 (1981).
- G. S. Oehrlein, D. J. Challou, A. E. Jaworski, and J. W. Corbett, *Phys. Lett. A*, **86**, 117 (1981).
- G. S. Oehrlein, J. L. Lindstrom, and J. W. Corbett, *Appl. Phys. Lett.*, **40**, 241 (1982).
- A. Ohsawa, R. Takizawa, K. Honda, A. Shibatomi, and S. Ohkawa, *J. Appl. Phys.*, **53**, 5733 (1982).
- W. E. Bailey, R. A. Bowling, and K. E. Bean, Abstract 287, p. 444, The Electrochemical Society Extended Abstracts, Vol. 83-1, San Francisco, CA, May 8-13, 1983.
- W. E. Bailey, R. A. Bowling, and K. E. Bean, in "Defects in Silicon," W. M. Bullis and L. C. Kimerling, Editors, p. 204, The Electrochemical Society Softbound Proceedings Series, Pennington, NJ (1983).
- D. W. Vidrine, *Anal. Chem.*, **52**, 92 (1980).
- B. McDonald and A. Goetzberger, *This Journal*, **109**, 141 (1962).
- M. W. Jenkins, *ibid.*, **124**, 757 (1977).
- U. Gosele and W. Frank, in "Defects in Semiconductors," J. Narayan, and T. Y. Tan, Editors, p. 55, Materials Research Society Symposia Proceedings Vol. 2, North-Holland, New York (1981).
- B. O. Kolbesen, in "Aggregation Phenomena of Point Defects in Silicon," E. Sirtl and J. Goorissen, Editors, p. 155, The Electrochemical Society Softbound Proceedings Series, Pennington, NJ (1983).
- U. Gosele and T. Y. Tan, in "Aggregation Phenomena of Point Defects in Silicon," E. Sirtl and J. Goorissen, Editors, p. 17, The Electrochemical Society Softbound Proceedings Series, Pennington, NJ (1983).
- M. Tajima, T. Matsui, T. Abe, and T. Iizuka, in "Semiconductor Silicon/1981," H. R. Huff, J. Kriegler, and Y. Takeishi, Editors, p. 72, The Electrochemical Society Softbound Proceedings Series, Pennington, NJ (1981).
- H. R. Huff, *Solid State Technol.*, **26**, (2), 89 (1983).

An Electrical Test Structure for Proximity Effects Measurement and Correction

D. Yen and L. W. Linholm*

National Bureau of Standards, Semiconductor Devices and Circuits Division, Gaithersburg, MD 20899

W. B. Glendinning

ERADCOM, Electronic Technology and Devices Laboratory, Fort Monmouth, New Jersey 07703-5302

ABSTRACT

This paper describes the design of a proximity effect test structure and electrical test method for estimating the magnitude of proximity effects in electron-beam lithography. The test structure consists of a van der Pauw cross resistor for measuring sheet resistance, a bridge resistor for measuring electrical linewidth, and a second bridge resistor simulating a close line-space environment for measuring electrical linewidth where proximity exposure effects from nearby patterns may be encountered. In this experiment, test structures were delineated in aluminum on silicon wafers using electron-beam exposure and wet chemical etching. Electrical measurements from these test structures are compared to optical measurements to verify the measurement method. In addition, results from the test structures are used to estimate the parameters for the gaussian model commonly used for proximity correction.

Proximity effects in electron-beam (E-beam) lithography are the additional exposure in the resist due to electron scattering in regions not addressed by the electron beam (1-3). This scattering of electrons in the resist and additional patterns in close proximity to that being exposed. In both cases, linewidth control for fine-line patterns with high packing density will deteriorate. The magnitude of proximity effects in the exposed resist depends on the beam voltage, beam diameter, resist material, resist thickness, and substrate material. In general, for linewidth and line-to-line spacings of less than $2 \mu\text{m}$, proximity effects can have significant effect on the resultant linewidths (4, 5).

Theoretical models and Monte Carlo simulations are the basis for much of the understanding of proximity effects and for predicting the magnitude of these effects on linewidth control (6, 7). However, detailed experimental data for comparison to calculated values are limited by time and by the complexity of obtaining accurate linewidth measurements of resist profiles on wafer.

This paper describes an electrical technique for determining the magnitude of proximity exposure on linewidth control. An electrical test structure and a test method were developed for the rapid and precise determination of linewidth of an E-beam-exposed pattern from samples simulating a dense line-space environment. Electrical linewidth measurements were compared to optical linewidth measurements to verify the magnitude of the proximity effects. In addition, a practical application for the measurements from the test structure for proximity correction was investigated.

Proximity Effect Test Structure

The proximity effect test structure (PETS) is an extension of the cross-bridge sheet resistor (8). A PETS, shown in Fig. 1, consists of a van der Pauw cross resistor, an upper bridge resistor, and a lower bridge resistor with proximity inducing bars of width T separated from the bridge resistor at a spacing S . The cross-bridge resistor allows electrical measurements of the linewidth of a conducting layer and is sensitive to small variations in linewidth (9). Hence, the PETS allows for the electrical measurement of linewidth differences between bridge resistors with and without proximity inducing bars. This linewidth difference is the result of proximity effects from electron scattering registered in the resist of the lower bridge.

The PETS can be tested electrically to determine sheet resistance (R_s), top linewidth (W_t), and bottom linewidth (W_b). Sheet resistance of the conducting layer is deter-

mined at the cross resistor connected to probe pads 2, 3, 7, and 8. Current I_c is forced between two probe pads, and voltage drop V_c is measured at the other two probe pads. R_s is calculated by the van der Pauw method (10) where

$$R_s = (\pi/\ln 2)(V_c/I_c) \quad [1]$$

W_t is determined at the upper bridge resistor

$$W_t = R_s L_t (I_o/V_t) \quad [2]$$

where V_t is the voltage drop measured at probe pads 1 and 2 for a current I_o forced between probe pads 9 and 4. L_t is the center-to-center design length of the top bridge resistor. Similarly, W_b is determined at the lower bridge resistor

$$W_b = R_s L_b (I_o/V_b) \quad [3]$$

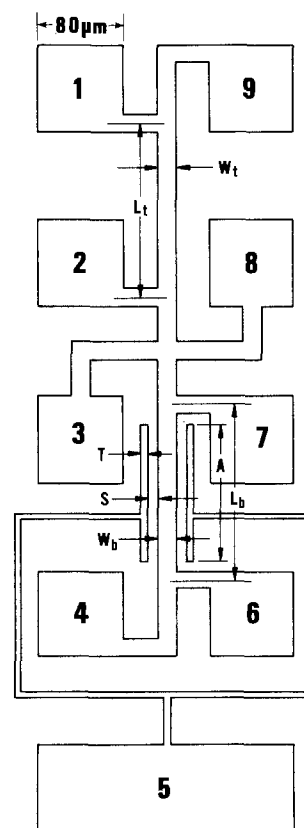


Fig. 1. Proximity effect test structures

*Electrochemical Society Active Member.

where V_b is the voltage drop measured between probe pads 7 and 6 for I_0 forced between probe pads 9 and 4. L_b is the center-to-center design length of the bottom bridge resistor.

To minimize differences in the electrical measurement due to variations in the current supply, V_t and V_b are measured for the same current I_0 forced between probe pads 4 and 9. Assuming that $L_t = L_b$ and that the upper and lower linewidths do not vary over the distance separating the two bridges, W_b is equal to W_t . Differences between the two lines are the result of the presence of the proximity inducing bars. Magnitude of this difference is

$$\Delta W = W_b - W_t \quad [4]$$

For practical test structure design, a small correction to ΔW is necessary because the length of the proximity inducing bars is always less than L_b . As shown in Fig. 2, the length, A , of the right side of the proximity inducing bar must be less than L_b to avoid shorting the taps to the probe pads. To calculate the correct ΔW , let R_b , the resistance of the lower bridge, be

$$R_b = V_b/I_0 = (R_1 + R_2) \quad [5]$$

where the sum $(R_1 + R_2)$ is the total resistance between the midlines of the two voltage taps. In terms of sheet resistance R_s , the resistances R_1 and R_2 are

$$R_1 = R_s A / (W + \Delta W) \quad [6]$$

$$R_2 = R_s (L_b - A) / W \quad [7]$$

where W is the width without proximity effects. Assuming $W = W_t$, combining Eq. [6] and [7] into Eq. [5] and solving for ΔW

$$\Delta W = \frac{A}{\frac{R_b}{R_s} - \frac{L_b - A}{W_t}} - W_t \quad [8]$$

Note that, if $A = L_b$, Eq. [8] is identical to Eq. [4].

As the space S between the bridge resistor and the proximity inducing bars diminishes, proximity effects as well as process variations can lead to the incomplete resolution of these line pairs, resulting in bridging between the bars and the bridge resistor. To identify and exclude these faulty structures, an electrical continuity test between probe pads 5 and 7 is conducted prior to any measurements.

Experiment

An evaluation of the performance of the test structure and test method was conducted with the design, fabrication, and measurements on test samples. A test chip was developed for fabrication by an E-beam system. Six PETS having a single proximity inducing bar (left) with drawn line-to-line spacings (S) of 1, 1.5, 2, 2.5, 3, and 4 μm and five PETS with two proximity bars (one on each side) with spacings of 1, 1.5, 2, 2.5, and 3 μm were included on the test chip. A control structure with no proximity bar was included for establishing the accuracy and precision of the measurement technique. Design dimensions are for $W_t = W_b = 5 \mu\text{m}$, $L_b = L_t = 200 \mu\text{m}$, $T = 2 \mu\text{m}$, and $A = 190 \mu\text{m}$.

A 50 mm diam silicon wafer was thermally oxidized to obtain an oxide thickness of 500 nm. Aluminum was then

evaporated onto the wafer to a thickness of 220 nm. The wafer was then coated with approximately 400 nm of a positive resist, AZ1350J, and baked at 90°C for 30 min. A commercial vector-scan E-beam system exposed a 5×5 array of the test chip on the wafer. Operating conditions with the gaussian beam system were 20 keV beam voltage, 0.2 μm beam diameter, 10 nA beam current, and a varying dwell time depending on the feature sizes.

After exposure, the resist was flood exposed with UV for 30s and then developed. A negative image pattern of the E-beam exposure can be obtained using this technique (11). Final patterns were delineated in the aluminum by wet chemical etching.

Measurements were obtained using a computer-controlled wafer prober and dc parametric test system. The test system included a digital current source with micro-ampere resolution and a digital voltmeter with microvolt resolution. Typical measurement time for each PETS is 4s. Precision of the test system for measuring nominal 5 μm linewidth was determined to be better than 0.002 μm (1σ) based upon 60 repeated measurements of one cross-bridge test structure.

Results

Experimental results are summarized in Table I. Each value is an average of 25 measurements on a wafer. The maximum standard deviation is less than or equal to 0.06 μm . The average sheet resistance and linewidth (without proximity) across the wafer are 0.156 Ω/\square and 3.71 μm , respectively. The magnitude of proximity effects as a function of S for the two-sided PETS and the one-sided PETS are shown in rows 1 and 2, respectively. As expected, the magnitude of proximity effects corresponding to the smallest spacing is largest. These results are in qualitative agreement with that expected from the exposure of photosensitive materials having a finite exposure threshold. Also, the average ΔW as measured from the two-sided PETS is twice that from the single-sided PETS, as would be expected. The average linewidth differences for the "control" structure is zero. This assures that systematic spatial nonuniformities are not responsible for the measured linewidth differences. Similar results have been obtained from other wafers using another E-beam system and process.

In order to verify the magnitude of the electrically measured values, optical linewidth measurements were performed on one chip in the center of the wafer. The optical measurement system used was a bright-field incident-light image scanning optical microscope employing a 1.4W krypton ion laser illumination source at a wavelength of 530 nm (12). This system illuminates a 30-50 μm radius area, which in turn is imaged onto a stationary scanning slit. The upper and lower bridge resistor widths for a set of two-sided PETS with spacings of 1.5, 2, 2.5, and 3 μm were measured optically. The linewidth difference between the upper and lower bridge resistors from optical measurements on each device and the correspond-

Table I. ΔW measured for the proximity effect test structures

	Spacing (μm)			
	1.5	2.0	2.5	3.0
2-bar (μm)	0.58	0.35	0.21	0.11
1-bar (μm)	0.27	0.17	0.11	0.06
Control	0.0 \pm 0.04 μm			$\sigma = 0.06 \mu\text{m}$ N = 25

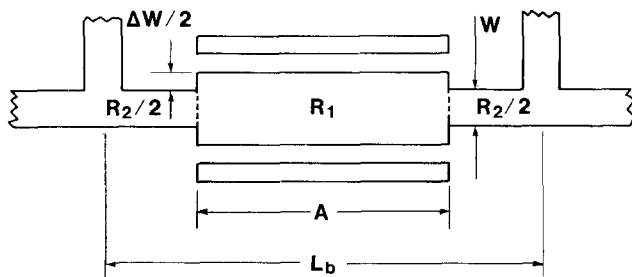


Fig. 2. Correction for ΔW

Table II. Comparison of ΔW between optical and electrical measurements

	Spacing (μm)			
	1.5	2.0	2.5	3.0
Optical (μm)	0.68	0.48	0.22	0.12
Electrical (μm)	0.62	0.41	0.23	0.10

ing electrical linewidth differences are shown in Table II. The results of the comparison are in sufficient quantitative agreement (within one standard deviation of the electrical measurements) to verify the magnitude of the proximity effects measured electrically.

Proximity Correction

An electrical test structure can also serve as a tool for determining inputs to computer programs to correct for proximity effects during E-beam writing. Computer programs have been developed based upon the two-gaussian proximity function (4) defined as

$$f(r) = C_1 \exp(-r^2/S_1^2) + C_2 \exp(-r^2/S_2^2) \quad [9]$$

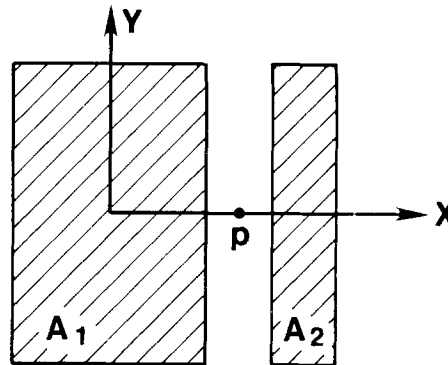
where r is the distance from the center of an electron beam, and C_1 , C_2 , S_1 , and S_2 are gaussian parameters. The first term of the function models the forward-scattered electrons and the second term models the back-scattered electrons. This proximity function represents the exposure intensity distribution in the resist due to a beam of electrons incident at $r = 0$. Monte Carlo simulations of E-beam exposure have shown that the gaussian model serves as a good approximation for the back-scattered electron distribution from the silicon substrate (13). However, the determination of the gaussian parameters for varying process conditions remains a difficulty for this model. A number of techniques for acquiring the gaussian parameters have been proposed (14-16). They require microscopic inspections and an unavoidable degree of subjective judgment regarding exposure and development. An alternative method for determining the gaussian parameters based upon electrical data from the test structures is now described.

The method can be used to obtain an optimum set of gaussian parameters from a least squares search by comparing the calculated results from the model to the measured results from the PETS. First, an initial estimate of the gaussian parameters based upon published data and the knowledge of the materials and process conditions is made. With these parameters and the gaussian model (Eq. [9]), the exposure intensity distribution or dose in the resist at point p due to the area exposure of A_1 and A_2 , as shown in Fig. 3, can be determined. A_1 represents a portion of the bridge resistor and A_2 represents a portion of the proximity bar. The dose at point p is the cumulative effect of exposure of A_1 and A_2 and can be calculated as

$$\text{Dose}(p) = \sum_{i=1}^2 \int f(r) dA_i \quad [10]$$

The integral of $f(r)$ can be approximated by error functions following the approach outlined in Ref. (17). The region of interest is between the bridge and the proximity bar where electron scattering during exposures of the proximity bar will shift the patterned bridge edge. Using Eq. [10], the dose as a function of position along the X axis as well as for different spacings of the proximity bar can be calculated.

Figure 4 shows an example of a plot of the exposure intensity distribution curve for the four spacings of the proximity bar ($S = 1.5, 2, 2.5,$ and $3 \mu\text{m}$). In addition, the



$$\text{Dose}(p) = \sum_{i=1}^2 \int f(r) dA_i$$

Fig. 3 Exposed pattern or geometry

exposure intensity distribution curve corresponding to an isolated line with no proximity bar is also shown. As would be expected, the presence of a proximity bar increases the total exposure received in the bridge resistor. In effect, the bridge edges shift to the right by a small amount for a given exposure level.

Since the measured data were obtained from developed resist and etched wafers, the effect of resist development on this model must be considered. As described earlier, the AZ resist was processed to provide a negative image of the exposed pattern. Thus, following development, resist area not exposed to the electron beam is removed. Using the threshold energy density model (6), the developed image in the resist can be determined given the threshold energy density or critical dose, D_c . The estimation of D_c will be described shortly. Because all the exposed patterns on a wafer were developed at the same time, the value of D_c is the same for different spacings of the proximity bar and can be used to extrapolate the predicted shift in the bridge edge from the exposure intensity distribution curves. Figure 5 is an expansion of Fig. 4 around the bridge edge to illustrate how the bridge edges (X_c) are determined for the different spacings. To briefly summarize, with an initial set of gaussian parameters, the gaussian model was used to calculate the exposure intensity distribution curves for the exposed patterns as a function of the spacing of the proximity bars. From these curves and an estimate of D_c , the magnitude of proximity effects for different spacings of the proximity bars can be determined.

As shown in Fig. 5, D_c is determined as the intersection of the point X_c to the exposure intensity curve with no

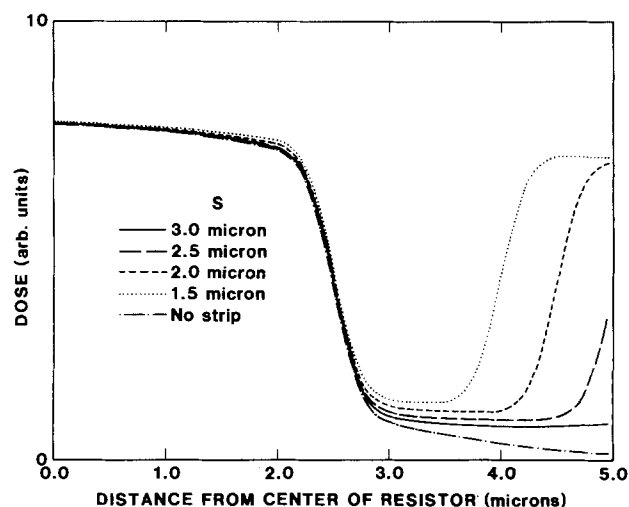


Fig. 4. Exposure intensity distribution curves for different spacings

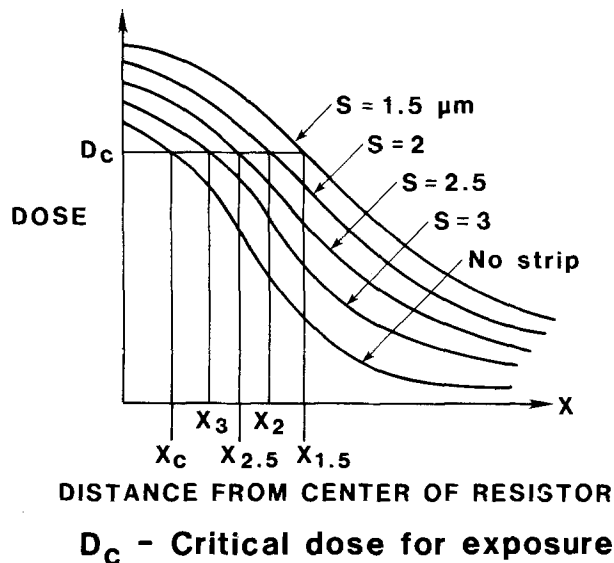


Fig. 5. Electron dose distribution as a function of spacing of proximity strips.

proximity bar. X_s is the location of the right edge of the bridge resistor following resist development. X_c was estimated to be $1.85 \mu\text{m}$ from the center of the bridge resistor based upon the averaged measured electrical linewidth with no proximity bar. Because of the uncertainty introduced by the wafer etching process on this estimate, small variations about this estimate were considered and are described below. Also, since the initial set of gaussian parameters is an estimate, other sets of parameters which are independent small variations of each of the initial parameters are also used to calculate the curves. In this experiment, 625 sets of gaussian parameters were used to determine the values of the X_s for the different spacings.

In the least squares search, the criterion for determining the optimum set of parameters is that set which minimizes the least squares error (LSE). LSE is defined as

$$\text{LSE}(X_c) = \sum_s (\Delta W_s - \Delta X_s)^2 \quad [11]$$

where

$$\begin{aligned} S &= 1.5, 2, 2.5, 3 \mu\text{m} \\ X_c &= 1.85 \pm m(0.05) \mu\text{m} \\ m &= 0, 1, 2 \end{aligned}$$

where ΔW_s is the measured results from the PETS, ΔX_s is the calculated data from the exposure intensity curves and is defined as $(X_s - X_c)$, and S denotes the spacings of the proximity bar. As mentioned earlier, due to the uncertainty introduction by the wet etching process, X_c is varied about the initial value of $1.85 \mu\text{m}$ in $0.05 \mu\text{m}$ steps. Equation [11] thus solves for the LSE values for each of the 625 sets of gaussian parameters and for each of the five values of X_c for each set of gaussian parameters. The set of gaussian parameters that resulted in the minimum least squares error for the exposure and development conditions used in this experiment is $C_1 = 0.637$, $C_2 =$

0.242 , $S_1 = 0.277$, and $S_2 = 2.332$ at $X_c = 1.85 \mu\text{m}$. The value of X_c determined by this method is in agreement with that previously obtained from independent electrical measurements. The average minimum LSE value obtained from these calculations was $0.008 \mu\text{m}$. Both the magnitude of the LSE value and the close agreement between the calculated and measured X_c values indicate that the gaussian parameters extracted from this procedure are sufficient to model the proximity effects for the process described.

Conclusion

The proximity effect test structure provides a rapid and precise method for measuring the magnitude of proximity effects due to electron scattering in the course of direct-write E-beam lithography. This electrical measurement technique provides an alternative to optical measurements for determining effective linewidth in a dense circuit environment and for evaluation of proximity correction algorithms. The results from the test structure can also be used to determine the gaussian parameters for proximity correction.

Acknowledgments

The authors would like to thank J. F. Bass and D. E. Cheville, of the Naval Research Laboratory, Washington, DC, for fabricating sample wafers, and C. F. Cook and J. Kwiatkowski, of the Electronic Technology and Devices Laboratory, Fort Monmouth, New Jersey, for technical support. Thanks are also due to D. Nyyssonen at the National Bureau of Standards for providing the optical measurement data and to P. Roitman for his review of this paper.

Manuscript submitted Aug. 6, 1984; revised manuscript received March 11, 1985.

The National Bureau of Standards assisted in meeting the publication costs of this article.

REFERENCES

1. D. F. Kyser and C. H. Ting, *J. Vac. Sci. Technol.*, **16**, 1759 (1979).
2. J. C. H. Phang and H. Ahmed, *ibid.*, **16**, 1754 (1979).
3. R. J. Hawryluk, H. I. Smith, A. Soares, and A. M. Hawryluk, *J. Appl. Phys.*, **46**, 2528 (1975).
4. T. H. P. Chang, *J. Vac. Sci. Technol.*, **12**, 1271 (1975).
5. M. Parikh, *IBM J. Res. Dev.*, **24**, 438 (1980).
6. R. J. Hawryluk, *J. Vac. Sci. Technol.*, **19**, 1 (1981).
7. J. S. Greeneich and T. Van Duzer, *IEEE Trans. Electron Dev.*, **ed-21**, 286 (1974); *J. Vac. Sci. Technol.*, **10**, 1056 (1973).
8. M. G. Buehler, S. D. Grant, and W. R. Thurber, *This Journal*, **125**, 650 (1978).
9. D. Yen, L. W. Linholm, and M. G. Buehler, *This Journal*, **129**, 2313 (1982).
10. L. J. van der Pauw, *Philips Res. Rep.*, **13**, 1 (1958); *Philips Tech. Rev.*, **20**, 220 (1958).
11. S. Okazaki, F. Mulai, Y. Takeda, K. Mochiji, E. Takeda, H. Kume, and S. Asai, *J. Vac. Sci. Technol.*, **19**, 927 (1981).
12. D. Nyyssonen, *Opt. Eng.*, **21**, 882 (1982).
13. M. Parikh and D. F. Kyser, *J. Appl. Phys.*, **50**, 1104 (1979).
14. C. Shaw, *J. Vac. Sci. Technol.*, **19**, 1286 (1981).
15. W. Grobman and A. Speth, in "Electron and Ion Beam Science and Technology," R. Bakish, Editor, p. 276, The Electrochemical Society Softbound Proceedings Series, Princeton, NJ (1978).
16. N. Aizaki, *J. Vac. Sci. Technol.*, **16**, 1726 (1979).
17. A. Kikuchi, A. Kanamaru, N. Okazaki, Y. Nakane, and T. Tsuboi, *ibid.*, **16**, 1764 (1979).

Phosphorus Diffusion Using Spin-On Phosphosilicate-Glass Source and Halogen Lamps

Juri Kato and Yoshiteru Ono

Suwa Seikosha Company, Limited, Fujimi Plant, 281 Fujimi, Fujimi-Machi, Suwa-Gun, Nagano-Ken 399-02, Japan

ABSTRACT

Formation of phosphorus-diffused layers using spin-on phosphosilicate glass (SOPSG) source and rapid isothermal halogen lamp annealing (HLA) were investigated with respect to sheet resistivities, junction depths, carrier concentrations, and contact resistances. Higher HLA temperature and SOPSG phosphorus weight percent results in lower average resistivities (sheet resistivity \times junction depth). With a 1205°C, 2s HLA using 37.5 w/o SOPSG, a shallow junction (junction depth = 0.23 μm) with low resistivity (37.7 Ω/\square) was achieved. Carrier concentration profiles of phosphorus-diffused layers formed by 1205°C HLA using 37.5 w/o SOPSG have very abrupt shapes and can be expressed by a function of x/\sqrt{t} , where x is the depth and t is the HLA soak time. They have almost the same maximum carrier concentration and the same contact resistance as the phosphorus-doped layer formed by ^{31}P ion implantation and HLA.

We have been studying the application of halogen lamp annealing (HLA) technologies (1-5) to VLSI fabrication processing. The scaling down of electronic device dimensions requires shallower junctions and lower sheet resistivities. In order to achieve these, ion implantation technology and predeposition solid-state diffusion technology have been most frequently employed in the VLSI fabrication processing. Formation of phosphorus-diffused layers using spin-on phosphosilicate glass (SOPSG) source and halogen lamp rapid isothermal processing is a new solid-state diffusion technology (6-8). From a practical viewpoint, this diffusion technology has advantages due to the low cost fabrication equipment and simple cassette-to-cassette single wafer processing. The predeposition solid-state diffusion excludes the enhance diffusion which seems to take place during the initial portion of the rapid heating of ion-implanted silicon yet leaves the matrix free of extended effects (9). This paper describes the basic characteristics of the predeposition solid-state phosphorus diffusion technology using SOPSG and HLA, such as sheet resistivities, junction depths, carrier concentrations, and Al [2 weight percent (w/o)]Si-N-type silicon contact resistances.

Experimental Procedure

Czochralski-grown P-type silicon crystals of (100) orientation, 6-9 $\Omega\text{-cm}$, were used for the experiments. The 4-in.-diam wafers were chemically and mechanically polished on one side. The wafers were dipped in dilute HF solution to remove the native oxide and were 3500 rpm spin coated with 1500Å phosphosilicate glass using OCD.¹ After having baked the wafers at 250°C for 60 min, they were heated for a few seconds using halogen lamps in nitrogen gas at atmospheric pressure. A 1205°C, 6s soak time HLA was carried out using 4.5, 9.0, 16.5, or 37.5 w/o SOPSG. Also, a 1205°C, 2, 6, 15, or 30s soak time HLA was carried out using 37.5 w/o SOPSG. The temperatures of HLA's were measured by a Chromel-Alumel thermocouple attached to the bottom surface of the wafer. The rise times of HLA's were 6s throughout this study. Sheet resistivities were measured by means of the four-probe method. Junction depths and carrier concentration profiles were obtained by the spreading resistance method. Contact resistances were measured by four-terminal test structure (10), which allows a direct kelvin measurement of interfacial contact resistance.

Results and Discussion

Figure 1 shows the junction depths and sheet resistivities of phosphorus-diffused layers which were formed by the new diffusion technology as a function of phosphorus weight percent $[\text{P}_2\text{O}_5/(\text{SiO}_2 + \text{P}_2\text{O}_5)]$ of the spin-on phosphosilicate glass (SOPSG). A 1205°C, 6s halogen

lamp rapid isothermal processing (HLA) was carried out as shown in Fig. 1. To obtain a slip line free mass produced wafer, about 1200°C is the maximum temperature (3) of halogen lamp rapid isothermal processing which can be allowed. The sheet resistivities and junction depths depend much on the phosphorus weight percent of SOPSG. As the phosphorus weight percent increases, the sheet resistivities decrease and junction depths increase. The higher phosphorus weight percent SOPSG also results in a lower average resistivity (sheet resistivity \times junction depth), and a minimum average resistivity of 867 $\mu\Omega\text{-cm}$ is achieved at 37.5 w/o phosphorus.

Figure 2 shows the sheet resistivities and junction depths of the phosphorus-diffused layers as a function of HLA temperature for a soak time of 6s and a phosphorus weight percent SOPSG of 37.5. Figure 2 determines the maximum HLA cycle which causes little diffusion of the phosphorus dopant from SOPSG. A 1000°C, 6s HLA causes a little diffusion from the 37.5 w/o SOPSG. This is almost the same annealing condition that causes phosphorus diffusion from high dose ^{31}P ion-implanted layers (3). The higher HLA temperature results in the lower average resistivity. In order to achieve shallower junctions and lower sheet resistivities, higher phosphorus weight percent SOPSG and higher HLA temperature are preferable. With a 1205°C, 2s HLA using 37.5 w/o SOPSG, phosphorus-diffused layers which had 0.23 μm junction depth and 37.7 Ω/\square sheet resistivity were achieved.

Figure 3 shows the sheet resistivities and junction depth relationships measured for phosphorus-diffused layers formed by 37.5 w/o SOPSG and a 1205°C, 2, 6, 15, or 30s halogen lamp rapid isothermal processing. For constant phosphorus weight percent and HLA temperature,

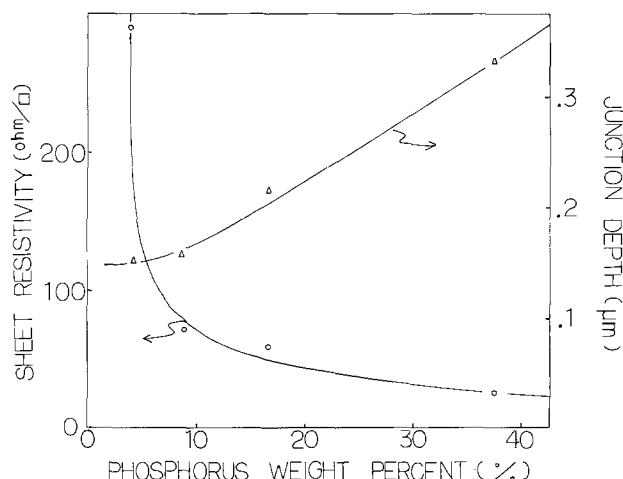


Fig. 1. Sheet resistivities and junction depths of phosphorus-diffused layers as a function of phosphorus weight percent.

¹ OCD is spin-on glass made by Tokyo Ohka Kogyo Company, Limited.

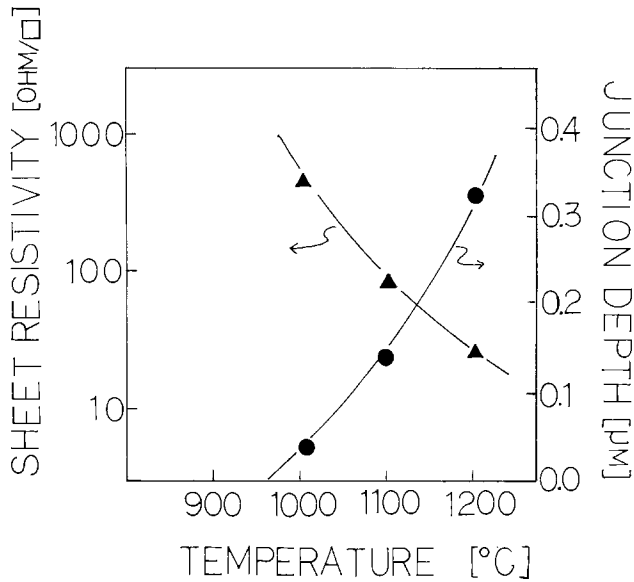


Fig. 2. Sheet resistivities and junction depths of phosphorus-diffused layers as a function of HLA temperature.

the sheet resistivities are inversely proportional to the junction depths. This means that the average resistivity of the phosphorus-diffused layer is constant irrespective of the HLA soak time.

Figure 4 shows the electrical active dopant concentration profiles of phosphorus-diffused layers formed by 37.5 w/o SOPSG and 1205°C HLA as a function of normalized distance x/\sqrt{t} ($\text{\AA}\cdot\text{s}^{-1/2}$), where x is the depth and t is the HLA soak time to 2, 6, 15, or 30s. These profiles are almost coincident with each other. This means that the phosphorus diffusivity in silicon is independent of soak time or depth. This characteristic is the same as that of phosphorus-diffused layers formed by 900°C furnace annealing (10 ~ 240 min) (12). The profiles of Fig. 4 have a flat region near the surface and drop abruptly without any kink. Profiles without kinks are also observed in the phosphorus-diffused layers formed by high temperature (> 1050°C) furnace annealing (13). These results lead to the conclusion that the qualitative profile shaping diffu-

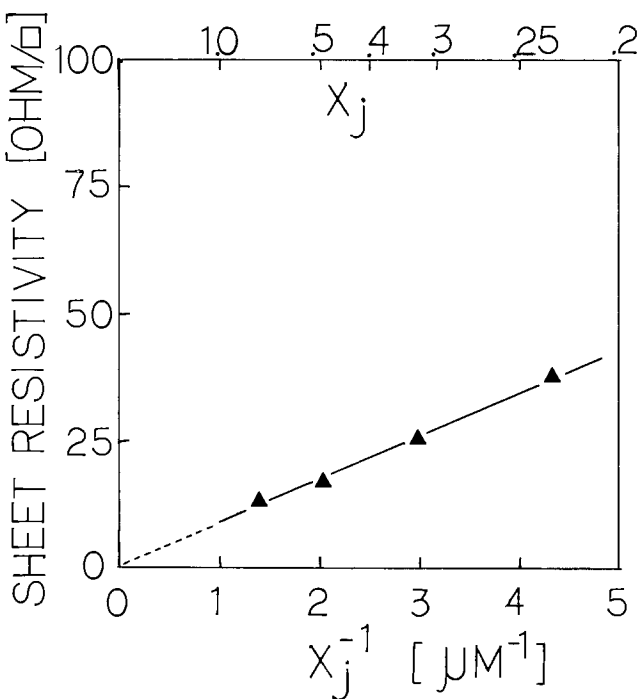


Fig. 3. Sheet resistivities and junction depths relationship measured for phosphorus-diffused layer formed by 1205°C HLA using 37.5 w/o SOPSG.

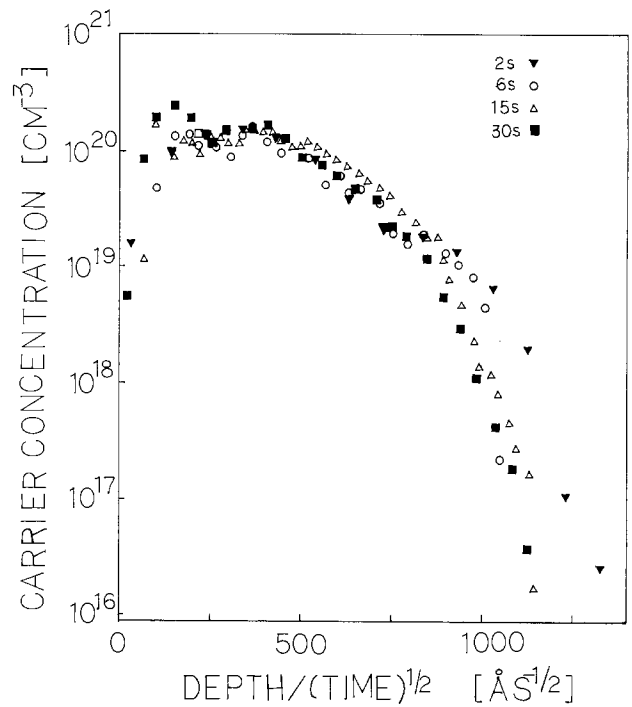


Fig. 4. Electrical active dopant concentration profiles of phosphorus-diffused layers formed by 1205°C HLA using 37.5 w/o SOPSG, as a function of reduced distance $x\sqrt{t}$.

sion mechanisms at high temperature are the same in halogen lamp annealing for a few seconds and in furnace annealing for tens of minutes. The low average resistivity of the phosphorus-diffused layers formed by 1205°C HLA using 37.5 w/o SOPSG is not only due to the absence of a tail but also to the high maximum carrier concentration.

Figure 5 shows the electrical active dopant concentration profiles of phosphorus-diffused layers. The open-square sample was formed by a 1208°C, 2s HLA using 37.5 w/o SOPSG. The open-circle sample was heated with 37.5 w/o SOPSG for 30 min at 800°C in nitrogen gas at atmospheric pressure after the 1208°C, 2s HLA. An 800°C, 30

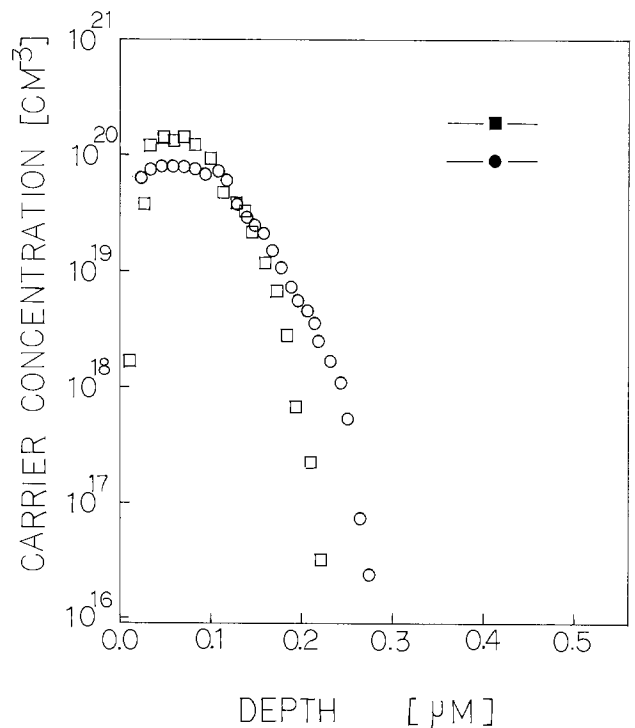


Fig. 5. Electrical active dopant concentration profiles of phosphorus-diffused layers. Those represented by the open squares are formed by 1208°C, 2s HLA using 37.5 w/o SOPSG. Those presented by the open circles are formed by 800°C 30 min FA after 1208°C, 2s HLA using 37.5 w/o SOPSG.

min furnace annealing (FA) reduces the maximum carrier concentration and increases the sheet resistivity. Also, the FA increases the tail of the carrier profile and increases the average resistivity. Figure 5 indicates that the rapid cooling of the silicon wafer is important to get the higher maximum carrier concentration and the absence of kink. The closed square in Fig. 5 indicates the maximum carrier concentration of the phosphorus-diffused layers formed by ^{31}P , 40 keV, $4 \times 10^{15} \text{ cm}^{-2}$ through 400\AA SiO_2 ion implantation followed by HLA (800°C 6s or 1000°C 6s). The closed circle in Fig. 5 indicates the maximum carrier concentration of the phosphorus-diffused layers formed by ^{31}P , 40 keV, $4 \times 10^{15} \text{ cm}^{-2}$ through 400\AA SiO_2 ion implantation followed by FA (900°C 30 min, 1000°C 30 min, or 1050°C 30 min).

While HLA or FA temperature changes, the maximum carrier concentration does not change for both ion-implanted layers, respectively. The difference of the maximum carrier concentration between ^{31}P ion-implanted layers annealed by HLA and by FA is due to the rapid isothermal annealing effect (4, 14, 15). Figure 5 indicates that rapid annealing effect of high maximum carrier concentration exists for both thermal diffusion from SOPSG and ion implantation. The difference of the maximum carrier concentration between HLA sample and FA sample is almost the same for both thermal diffusion from SOPSG and ion implantation, and a 1208°C HLA with 37.5 w/o SOPSG has almost the same maximum carrier concentration as that formed by ^{31}P ion implantation and HLA. This result suggests that the rapid annealing effect at high maximum carrier concentration of both ion-implanted and thermal-diffused layers may be due mainly to the rapid cooling of the wafer.

Relative surface carrier concentrations are assured by measuring contact resistance, too. Figure 6 shows Al(2 w/o)Si/phosphorus-diffused silicon contact resistances as a function of annealing temperature for three types of phosphorus-diffused layers. The sintering was carried out at 450°C for 20 min in H_2 forming gas. The electrical measurements were performed on phosphorus-diffused silicon having contact windows of $4 \times 4 \mu\text{m}$. Contact resistance depends on electrical active phosphorus dopant concentrations (16), and the higher electrical active phosphorus dopant concentration has the lower contact resistance. In Fig. 6, the closed circles represent contact resistance of Al(2 w/o)Si/phosphorus-diffused layer formed by 37.5 w/o SOPSG and a 6s soak time HLA (1065° , 1150° ,

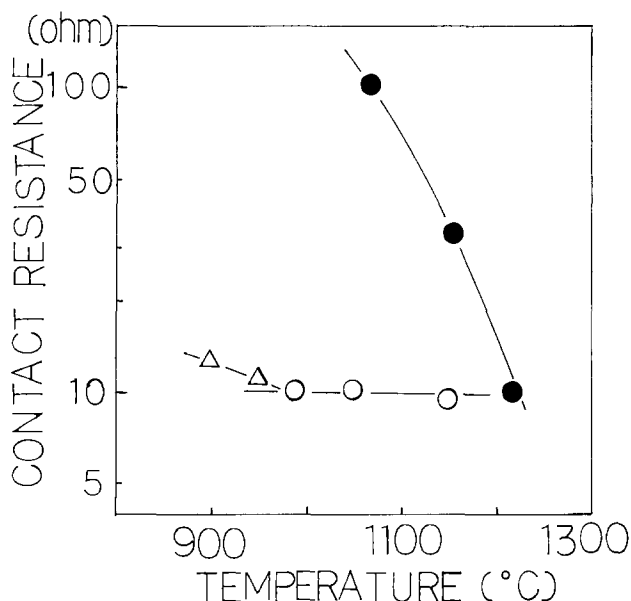


Fig. 6. Contact resistances of three types of phosphorus-diffused layers as a function of isothermal heating temperatures. That represented by the closed circles is formed by HLA using 37.5 w/o SOPSG. That represented by the open circles is formed by ion implantation and HLA. That represented by the open triangles is formed by ion implantation and FA.

1215°C). Before being spin coated with SOPSG, the wafer was implanted with ^{31}P (40 keV, $3 \times 10^{12} \text{ cm}^{-2}$) in order to prevent Al penetration. The open circles represent the contact resistance measurement of phosphorus-diffused layers formed by implanting ^{31}P (40 keV, $4 \times 10^{15} \text{ cm}^{-2}$) through 400\AA SiO_2 followed by a 6s soak time HLA (980° , 1050° , 1150°C). The open triangles stand for implanted ^{31}P (40 keV, $4 \times 10^{15} \text{ cm}^{-2}$) through 400\AA SiO_2 followed by a 30 min FA (900° , 950°C). The contact resistances of the ion-implanted layers followed by HLA are independent of annealing temperatures and have the lowest contact resistances ($< 10\Omega$). The contact resistances of the ion-implanted layers followed by FA are not so much dependent on annealing temperatures and have slightly higher contact resistances compared to HLA samples. The contact resistances of phosphorus-diffused layers formed by SOPSG and HLA depend much on the HLA temperatures. Above 1200°C , halogen lamp rapid isothermal processing with 37.5 w/o SOPSG results in the same contact resistance as for the ^{31}P ion-implanted layers followed by HLA. The measured contact resistances are consistent with the phosphorus carrier concentrations.

Summary

The sheet resistivities and junction depths of phosphorus-diffused layers formed by SOPSG and HLA depend not only on HLA temperature, but also on SOPSG phosphorus weight percent. The highest HLA temperature using the highest phosphorus weight percent SOPSG results in the lowest average resistivity. With a 1205°C , 2s HLA using 37.5 w/o SOPSG, a shallow junction ($x_j = 0.23 \mu\text{m}$) with low resistivity ($37.7 \Omega/\square$) was achieved. The carrier concentration profiles of phosphorus-diffused layers formed by 1205°C HLA using 37.5 w/o SOPSG have very abrupt shapes without kinks and can be expressed by a function of x/\sqrt{t} , where x is the depth and t is the HLA soak time. They have almost the same maximum carrier concentration and the same contact resistance as that formed by ^{31}P ion implantation and HLA.

Acknowledgments

We would like to thank Mr. Mizuno, General Manager, Dr. Iwamatsu, Manager, Mr. Ichikawa, Chief Engineer, Mr. Asahina, Chief Engineer, and Mr. Furuhashi, of Suwa Seikosha Company, Limited, Fujimi Plant, for their helpful discussion and cooperation in this study.

Manuscript submitted June 18, 1984; revised manuscript received Feb. 10, 1985.

Suwa Seikosha Company, Limited, assisted in meeting the publication costs of this article.

REFERENCES

1. J. Narayan, O. W. Holland, R. E. Eby, J. J. Wortman, V. Ozguz, and G. A. Rozgonyi, *Appl. Phys. Lett.*, **43**, 15 (Nov. 1983).
2. T. O. Sedgwick, *This Journal*, **130**, 484 (1983).
3. J. Kato and S. Iwamatsu, *ibid.*, **131**, 1145 (1984).
4. S. Iwamatsu and J. Kato, *J. Vac. Soc. Jpn.*, **25**, 735 (1982).
5. K. Nishiyama, M. Arai, and N. Watanabe, *Jpn. J. Appl. Phys.*, **19**, L563 (1980).
6. V. E. Borisenko and A. Nylandsted Larsen, *Appl. Phys. Lett.*, **43**, 15 (Sept. 1983).
7. M. E. Greiner and J. F. Gibbons, *ibid.*, **44**, 750 (1984).
8. A. N. Larsen, V. E. Borisenko, and L. D. Nielsen, *J. Phys. (Paris)*, **44**, C5 (1983).
9. R. Kalish, T. O. Sedgwick, S. Mader, and S. Shatas, *Appl. Phys. Lett.*, **44**, 1 (Jan. 1984).
10. S. J. Proctor, L. W. Linholm, and J. A. Maze, *IEEE Trans. Electron Devices*, **ed-30**, (1983).
11. S. M. Sze, "Physics of Semiconductor Devices," 2nd ed., p. 32, John Wiley and Sons, New York (1981).
12. M. Yoshida, E. Arai, H. Nakamura, and Y. Terunui, *J. Appl. Phys.*, **45**, 1498 (1974).
13. R. B. Fair and J. C. C. Tsai, *This Journal*, **124**, 1107 (1977).
14. A. Lietoila, R. B. Cold, J. F. Gibbons, and T. W. Sigmon, *J. Appl. Phys.*, **52**, 230 (1981).
15. K. Kugimiya and G. Fuse, *Jpn. J. Appl. Phys.*, **21**, L16 (1982).
16. A. Y. C. Yu, *Solid State Electron.*, **13**, 239 (1970).

Thermodynamic Comparison of InGaAsP Vapor Phase Epitaxy by Chloride, Hydride, and Metalorganic-Chloride Methods

M. Yoshida and H. Watanabe

NEC Corporation, Fundamental Research Laboratories, Miyazaki 4-chome, Miyamae, Kawasaki 213, Japan

ABSTRACT

A thermodynamic comparison of composition controllability is made between three InGaAsP vapor phase epitaxial (VPE) methods: namely, chloride, hydride, and the newly proposed metal organic (MO)-chloride VPE processes for the growth of an alloy lattice matched to InP and emitting at $1.3 \mu\text{m}$. In order to discuss the dynamic aspects of an open-flow system, the calculated model includes a completeness factor, e , for the reaction between a liquid metal source and gas phase, and a saturation factor, s , for the metal source with a Group V element. It is shown that control of the temperatures to within 2.4°C makes it possible to keep the lattice mismatch less than 3×10^{-4} in all three VPE systems. Control of the flow rates to within 1.2% in both chloride and hydride VPE systems and to within 0.3% in the MO-chloride system are sufficient for that purpose. It is found that the alloy composition varies greatly with e and s . A decrease in either e by 0.4% or s by 3.4% produces a lattice mismatch of 3×10^{-4} .

Quaternary alloys of $\text{In}_{1-x}\text{Ga}_x\text{As}_y\text{P}_{1-y}$ have received increasing attention as materials for many semiconductor devices. The alloys lattice matched to InP are important both for microwave devices and for sources and detectors of light in the $1.0\text{--}1.7 \mu\text{m}$ wavelength range. The alloys lattice matched to GaAs are expected to be used for light sources in the visible wavelength range.

These alloys have been grown by liquid phase epitaxy (LPE), chloride transport vapor phase epitaxy (CTVPE), metal organic vapor phase epitaxy (MOVPE), and molecular beam epitaxy (MBE). However, it is difficult to grow InGaAsP with some of these techniques. LPE cannot prevent compositional inhomogeneity (1). With MBE, it is difficult to control the P/As ratio; also, one needs a special pumping system for volatile phosphorus vapor (2). In contrast to these two methods, uniform InGaAsP layers except for the alloys in the miscibility gaps (3-5) can be grown by CTVPE (6) and low pressure MOVPE (7). In MOVPE, the composition of III-V alloys is independent of the growth temperature in some cases (8), and x and y in $\text{In}_{1-x}\text{Ga}_x\text{As}_y\text{P}_{1-y}$ are controlled independently by the $\text{Ga}/(\text{Ga} + \text{In})$ and $\text{As}/(\text{As} + \text{P})$ ratios in the vapor phase, respectively (9). However, one cannot control x and y separately in CTVPE since not only x , but also y varies with the $\text{Ga}/(\text{Ga} + \text{In})$ ratio in the vapor phase (10). Therefore, there is much interest in how the composition of InGaAsP grown by CTVPE varies with the growth parameters. To know these variations in alloy composition is important both for growing a particular alloy of InGaAsP and for controlling the alloy composition to increase a device yield. In this paper, VPE means CTVPE.

There have been chloride and hydride VPE methods since the early years of III-V materials research. In addition to these, a new VPE method using Group III metal organics and Group V trichlorides (MO-chloride VPE) has been proposed (11). The purest compound semiconductor has been grown by chloride VPE. The hydride VPE system has shown its advantage for alloy growth, and the MO-chloride VPE process is of great advantage to the productivity and the safety since it is free from heterogeneous liquid-vapor source reactions and fatally toxic Group V hydrides.

The purpose of this paper is to compare thermodynamic composition controllabilities of the three InGaAsP VPE methods. The comparison is made by calculating the variations in alloy composition with the growth parameters. In order to discuss the dynamic aspects of an open-flow system, a completeness factor for the reaction between a metal source and gas phase (12) and a saturation factor for the metal source with a Group V element are introduced into the thermodynamic model.

VPE Growth Systems

Figures 1a-1c show schematic diagrams of the three InGaAsP VPE systems. Hot-wall reactors are used to

form reactants for growth and to avoid deposition of III-V compounds upstream from the substrate. The reaction rates for the decomposition of AsCl_3 , PCl_3 , AsH_3 , PH_3 , TEG, and TEI may be kinetically limited; however, the decomposition will be considered to be complete.

In the chloride system, a four-barrel reactant formation region is arranged. In each barrel, the Group V trichloride reacts with H_2 to form HCl and the Group V element, which is absorbed into the Group III metal source. Undecomposed AsCl_3 (13) is not considered since it is a problem only when the source temperature is too low and the flow rate is too high. When each source is saturated with

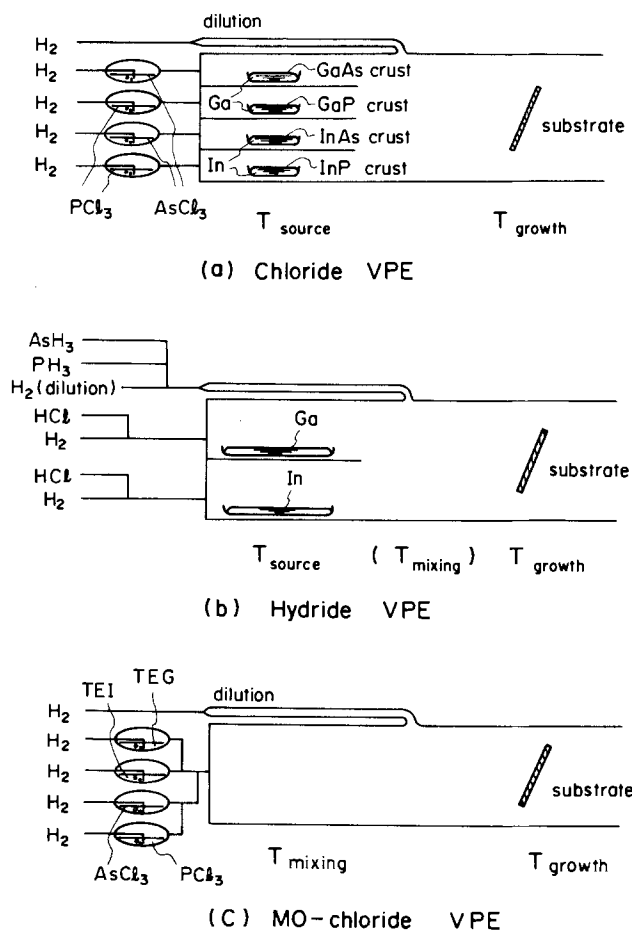


Fig. 1. Schematic diagrams of InGaAsP VPE systems. a: For a chloride VPE system. b: For a hydride VPE system. c: For a MO-chloride VPE system. AsCl_3 , PCl_3 , TEG, and TEI are carried by H_2 flows passing through them. A chloride system has four metal sources covered with III-V crusts. A hydride system has two metal sources. A MO-chloride system has no liquid metal source.

the Group V element and covered with the thin III-V crust, the chloride VPE system is in a steady-state condition for growth (14). There are four sources: the Ga metal saturated with As and covered with a GaAs crust; the Ga metal with P and GaP; the In metal with As and InAs; and the In metal with P and InP. The Group III chloride is formed by the reaction between HCl and the III-V crust in each barrel. A dilution H₂ flow is added between the source region and the growth region. The incompleteness of the reaction between the source and the gas phase due to incomplete mixing in the gas phase, and the unsaturation of the source with the Group V element due to depletion of the Group V element during the heat-up, are problems associated with this VPE system. The kinetic process at the source surface is considered to be complete because an etching reaction in a chloride system is mass-transport limited at the temperature considered. To increase the completeness of mixing in the gas phase, one can make the flow rate in the source region low and enlarge the source region. However, the low flow rate causes the back-diffusion of HCl produced downstream from the substrate, and the large source makes the unsaturation more serious. Therefore, it is impossible to make the source reaction and the source saturation complete simultaneously. The four source temperatures are chosen to be equal in the following calculation for the sake of simplicity.

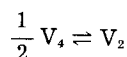
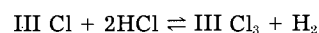
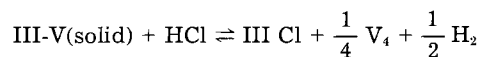
In the hydride system, a two-barrel Group III chloride formation region is arranged. One barrel contains Ga, and the other contains In. HCl in and H₂ carrier flow reacts with the Group III metal source and converts it to the Group III chloride in each barrel. The incompleteness of the source reaction similar to that in the chloride system is a problem associated with this VPE system. The surface of the source can be enlarged to complete the mixing of the gas phase during contact to the source. However, the slow saturation of the In source with InCl (15) presents a serious problem. Therefore, the incomplete source reaction should be considered. The Group V hydrides carried by a dilution H₂ flow are decomposed to form the Group V elements. It is shown that PH₃ does not so readily decompose even in a hot-wall system (16). However, the incomplete decomposition of the Group V hydrides is not considered since the longer residence time for the decomposition reaction is expected to make the decomposition perfect. The two source temperatures are chosen to be equal, again for the sake of simplicity.

In the MO-chloride system, a single-barrel reactant formation region is arranged. The Group III organics [for example, triethylgallium (TEG) and triethylindium (TEI)] are used instead of the Group III metals. It is shown that trimethylgallium (TMG) does not readily pyrolyze (17). However, it decomposes perfectly in H₂ at temperatures above 600°C in a hot-wall open-flow system (18). TEG (18) and TEI (19) also decompose perfectly at temperatures above 500°C. Therefore, the metal organics are like metals in the vapor phase when they are introduced into a hot region. The Group V trichlorides are also decomposed perfectly as is the case in the chloride system. Hence, in the mixing region the Group III chlorides and the Group V elements are formed. An excess of the number of Group III atoms over the number of chlorine atoms causes deposition of III-V compounds in the mixing region. This deposition depletes the Group V elements in the growth region. Contrary to the above, when the number of chlorine atoms greatly exceeds the number of Group III atoms, etching takes place. A III/V ratio sufficient not to deposit III-V compounds in the mixing region and not to etch a substrate is chosen. The temperature of the mixing region is kept high enough to eliminate the wall deposition. The MO-chloride system is defined to be an ideal chloride system with $e = s = 1$ with other AsCl₃ and PCl₃ introduced between the source and the substrate (20).

Thermodynamic Calculation Procedure

Preparation of reactants for growth reaction.—Chloride system.—In each barrel, the species other than III-

V(solid), H₂, HCl, III Cl, III Cl₃, V₄, and V₂ (III = Ga or In, V = As or P) are assumed to be nonexistent since the Group V trichloride, Group V hydride, and chlorine are negligible in a state of equilibrium at temperatures between 600° and 900°C (21, 22). The reactions in each source region are



and proceed under constant atmospheric pressure (1 atm). The numbers of hydrogen and chlorine atoms in the vapor phase are kept at n_{H}^0 and n_{Cl}^0 (n_{H}^0 is the number of supplied H atoms, and n_{Cl}^0 the number of supplied Cl atoms) since there are no other phases containing hydrogen and/or chlorine atoms. The number of Group V atoms in the vapor phase is also kept at n_{V}^0 (the number of supplied Group V atoms), since the Group V element acts as if it passes through this region when the thickness of the crust and the amount of the Group III metal saturated with the Group V element are unchanged. The partial pressures of six species are obtained from three equilibrium equations and three equations for the conservation of total pressure, $c (= n_{\text{Cl}}^0/n_{\text{H}}^0)$, and $b (= n_{\text{V}}^0/n_{\text{H}}^0)$.

A completeness factor for the source reaction, e ($0 < e \leq 1$), is introduced assuming that $1 - e$ of the gas flow passes above the source metal without any reaction with it. A saturation factor for the Group III source, s ($s \leq 1$), is introduced assuming that s of the Group V element passes through the source region. The other $1 - s$ of the Group V element is absorbed into the source; that is, the number of Group V atoms in the vapor phase is kept at sn_{V}^0 (then $b = sn_{\text{V}}^0/n_{\text{H}}^0$). This assumption is valid only when the source is covered with a crust. Therefore, s should not be much smaller than 1.

Since stoichiometric III-V compounds are deposited, the difference between the number of Group III and Group V atoms, $n_{\text{III}} - n_{\text{V}}$, is kept constant throughout the growth process. Hence, we get c and $d [= (n_{\text{III}} - n_{\text{V}})/n_{\text{H}}]$ as constants in the growth region

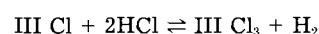
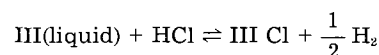
$$c = \frac{3 \sum_{i=1}^4 F_{\text{H}_2(i)} \left(\frac{P_{\text{VCl}_3^0}}{1 - P_{\text{VCl}_3^0}} \right)_i}{2 \sum_{i=1}^5 F_{\text{H}_2(i)}} \quad [1]$$

where F is the flow rate and P^0 vapor pressure (in atmospheres)

$$d = \frac{2 \sum_{i=1}^4 e_i F_{\text{H}_2(i)} \left(\frac{P_{\text{III Cl}} + P_{\text{III Cl}_3}}{2P_{\text{H}_2} + P_{\text{HCl}}} \right)_i - \sum_{h=15}^4 s_h F_{\text{H}_2(i)} \left(\frac{P_{\text{VCl}_3^0}}{1 - P_{\text{VCl}_3^0}} \right)_i}{2 \sum_{i=1}^5 F_{\text{H}_2(i)}} \quad [2]$$

where P is the equilibrium partial pressure in each source region (in atmospheres), and 1-5 denote the relation to the barrels containing Ga-As, Ga-P, In-As, In-P, and the dilution line, respectively.

Hydride system.—The following are reactions in each source region



As in the chloride system, two equilibrium equations and two equations for the conservation of total pressure and c give the partial pressures of four species.

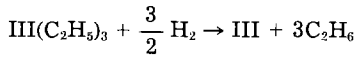
The completeness factor for the source reaction similar to that in the chloride system is introduced. The Group V hydrides are assumed to convert to arsenic and phosphorus perfectly in a state of equilibrium. Hence the constants c and d in the growth region are

$$c = \frac{\sum_{i=1}^2 F_{HCl}(i)}{2 \sum_{i=1}^3 F_{H_2}(i) + \sum_{i=1}^2 F_{HCl}(i) + 3(F_{AsH_3} + F_{PH_3})} \quad [3]$$

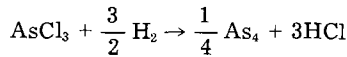
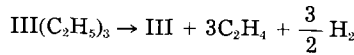
$$d = \frac{\sum_{i=1}^2 e_i [2 F_{H_2}(i) + F_{HCl}(i)] \left(\frac{P_{III Cl} + P_{III Cl_3}}{2P_{H_2} + P_{HCl}} \right)_i - (F_{AsH_3} + F_{PH_3})}{2 \sum_{i=1}^3 F_{H_2}(i) + \sum_{i=1}^2 F_{HCl}(i) + 3(F_{AsH_3} + F_{PH_3})} \quad [4]$$

where 1, 2, and 3 denote the relation to the barrels containing Ga and In, and the dilution line, respectively.

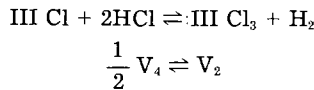
MO-chloride system.—As has been mentioned, the triethyl Group III compounds and the Group V trichlorides are perfectly decomposed in the mixing region



or



The produced hydrocarbons are completely ignored in the equilibrium system since the reverse reactions to form triethyl Group III compounds do not proceed. When no deposition occurs in the mixing region, the reactions are



We get c and d in the growth region only from the input gas flow rate data

$$c = \frac{3 \sum_{i=3}^4 F_{H_2}(i) \left(\frac{P_{VCl_3^0}}{1 - P_{VCl_3^0}} \right)_i}{2 \sum_{i=1}^5 F_{H_2}(i)} \quad [5]$$

$$d = \frac{\sum_{i=1}^2 F_{H_2}(i) \left(\frac{P_{MO^0}}{1 - P_{MO^0}} \right)_i - \sum_{i=3}^4 F_{H_2}(i) \left(\frac{P_{VCl_3^0}}{1 - P_{VCl_3^0}} \right)_i}{2 \sum_{i=1}^5 F_{H_2}(i)} \quad [6]$$

where 1-5 denote the relations to the TEG, TEI, AsCl₃, PCl₃, and dilution lines, respectively.

In_{1-x}Ga_xAs_yP_{1-y} growth.—The growth takes place through the same process in the three VPE systems. In the growth region, the following species are considered: For the surface of grown layer, GaP, GaAs, InAs, and InP in a solid solution, and for the vapor phase, H₂, HCl, GaCl, GaCl₃, InCl, InCl₃, As₄, As₂, P₄, P₂, As₃P, As₂P₂, AsP₃, and AsP. The reactions are reactions [A]-[L] listed in Table I.

According to Koukitu and Seki (23), the activities of the binary III-V components in the In_{1-x}Ga_xAs_yP_{1-y} alloy system, a_{GaAs} , etc., are

$$a_{GaAs} = \gamma_{GaAs} \frac{m + (1 - m)(x + y) - \sqrt{[m + (1 - m)(x + y)]^2 - 4(1 - m)xy}}{2(1 - m)} \quad [7]$$

$$a_{GaP} = \gamma_{GaP} (x - a_{GaAs}/\gamma_{GaAs}) \quad [8]$$

$$a_{InAs} = \gamma_{InAs} (y - a_{GaAs}/\gamma_{GaAs}) \quad [9]$$

$$a_{InP} = \gamma_{InP} (1 - x - y + a_{GaAs}/\gamma_{GaAs}) \quad [10]$$

where

$$m = \frac{K_B K_D}{K_A K_C} \frac{\gamma_{GaAs} \gamma_{InP}}{\gamma_{GaP} \gamma_{InAs}}$$

K_i is the equilibrium constant of the reaction i , and γ_j the activity coefficient of the j component. The activity coefficients are given theoretically (24) as

$$kT \ln \gamma_{GaAs} = \alpha_{InP-GaP} (1 - x)(1 - y)(1 - 2x) + \alpha_{InAs-GaAs} (1 - x)[(1 - x)y + x(1 - y)] + \alpha_{InP-InAs} (1 - x)(1 - y)(1 - 2y) + \alpha_{GaP-GaAs} (1 - y)[(1 - x)y + x(1 - y)]$$

etc., where the α 's are the interaction parameters.

The equations for the conservation of total pressure (1 atm), c , and d are given as follows

$$P_{H_2} + P_{HCl} + P_{GaCl} + P_{GaCl_3} + P_{InCl} + P_{InCl_3} + \sum P_{V_4} + \sum P_{V_2} = 1 \quad [11]$$

$$\frac{P_{HCl} + P_{GaCl} + P_{InCl} + 3(P_{GaCl_3} + P_{InCl_3})}{2P_{H_2} + P_{HCl}} = c \quad [12]$$

$$\frac{P_{GaCl} + P_{GaCl_3} + P_{InCl} + P_{InCl_3} - (4\sum P_{V_4} + 2\sum P_{V_2})}{2P_{H_2} + P_{HCl}} = d \quad [13]$$

where

$$\sum P_{V_4} = P_{As_4} + P_{As_3P} + P_{As_2P_2} + P_{AsP_3} + P_{P_4}$$

$$\sum P_{V_2} = P_{As_2} + P_{AsP} + P_{P_2}$$

From Eq. [7]-[13] and the 11 equilibrium equations for the reactions [A]-[C] and [E]-[L], the partial pressures of 14 species are obtained (see Appendix).

The composition of the grown In_{1-x}Ga_xAs_yP_{1-y} alloy is calculated with an iterative procedure. The differences in both x and y between the assumed alloy balanced with

Table I. Equilibrium constants for reactions

	Reaction	log ₁₀ K	Ref.
[A]	GaP + HCl ⇌ GaCl + 1/4 P ₄ + 1/2 H ₂	5.05 - 6.00 × 10 ³ /T	(25)
[B]	GaAs + HCl ⇌ GaCl + 1/4 As ₄ + 1/2 H ₂	4.75 - 5.50 × 10 ³ /T	(25)
[C]	InAs + HCl ⇌ InCl + 1/4 As ₄ + 1/2 H ₂	5.84 - 5.63 × 10 ³ /T	(26)
[D]	InP + HCl ⇌ InCl + 1/4 P ₄ + 1/2 H ₂	5.81 - 5.04 × 10 ³ /T	(27)
[E]	GaCl + 2HCl ⇌ GaCl ₃ + H ₂	-6.68 + 8.61 × 10 ³ /T	(28)
[F]	InCl + 2HCl ⇌ InCl ₃ + H ₂	-3.42 + 4.84 × 10 ³ /T	(29)
[G]	1/2 As ₄ ⇌ As ₂	3.76 - 6.67 × 10 ³ /T	(26)
[H]	1/2 P ₄ ⇌ P ₂	3.97 - 5.94 × 10 ³ /T	(27)
[I]	3/4 As ₄ + 1/4 P ₄ ⇌ As ₃ P	0	
[J]	1/2 As ₄ + 1/2 P ₄ ⇌ As ₂ P ₂	0	
[K]	1/4 As ₄ + 3/4 P ₄ ⇌ AsP ₃	0	
[L]	1/2 As ₂ + 1/2 P ₂ ⇌ AsP	0	
[M]	Ga + HCl ⇌ GaCl + 1/2 H ₂	2.93 - 1.29 × 10 ³ /T	(27)
[N]	In + HCl ⇌ InCl + 1/2 H ₂	2.36 - 0.42 × 10 ³ /T	(27)

the vapor phase and the deposited alloy from the vapor phase are made smaller than 1×10^{-5} . Note that the composition is independent of the activity of the substrate surface prior to growth. The composition is determined only from the conservation of In, Ga, As, and P. The vapor phase is balanced with the surface just grown from it.

Thermodynamical data.—The equilibrium constants of reactions are listed in Table I (25-29) in the form of $\log_{10} K = A + B/T$. The standard free energies of formation for the As-P complexes are assumed as

$$\Delta G_{\text{As}_4 - m\text{P}_m}^0 = \frac{4 - m}{4} \Delta G_{\text{As}_4}^0 + \frac{m}{4} \Delta G_{\text{P}_4}^0 \quad (m = 1, 2, 3)$$

$$\Delta G_{\text{As}_2\text{P}}^0 = \frac{1}{2} \Delta G_{\text{As}_2}^0 + \frac{1}{2} \Delta G_{\text{P}_2}^0$$

That is, the equilibrium constants for the reactions [I]-[L] are supposed to be 1 at any temperature. The selection of the values for the equilibrium constants A-D (23) and the above assumption for the constants I-L make the calculations best fit to the experimental data (10, 30, 31). The selection of the values for the constants E-H affects the calculations little. [The comparison was made between the data in Ref. (25-29) and (32), the assumption for the constants I-L, and the nonexistence of As-P complexes ($K_{I-L} = 0$).] The interaction parameters are listed in Table II (33).

Data for growth systems.—The vapor pressures of materials in the containers are 0.01 atm for AsCl_3 at 18°C, TEG at 30°C, TEI at 74°C, and 0.05 atm for PCl_3 at 2°C. Tentatively, the imaginary Cl atom gas flow rate in each system is set at 0.03 standard-liter/min. This value corresponds to a flow rate of H_2 passing through AsCl_3 of 0.99 standard-liter/min and an HCl flow rate of 0.03 standard-liter/min. In the MO-chloride system, the III/V ratio is set at 2.9 to avoid deposition in the mixing region. The V/III ratio in the hydride system is set at ~ 1 ($[\text{VH}_3]/[\text{HCl}] = 1$) (30, 34), which differs from the ratio of about 0.4 in the chloride and MO-chloride systems. The effect of V/III ratio on the composition controllability will be discussed below. A source temperature of 800°C and a growth temperature of 700°C are selected. The selected source temperature is $\sim 50^\circ\text{C}$ lower than that temperature in the experimental hydride VPE system so as not to make the unsaturation in the chloride system serious (35).

Table II. Interaction parameters for ternary III-V systems (33)

System	α (cal/mol)
InP-GaP	3500
InAs-GaAs	3000
InP-InAs	400
GaP-GaAs	400

Table III. Input flow rate data for $\text{In}_{0.74}\text{Ga}_{0.26}\text{As}_{0.55}\text{P}_{0.45}$ growth with various dilution flow rates

System	Input data (liter/min)	F_{H_2} (dilution)			
		0	1	10	100
Chloride	$F_{\text{H}_2}(\text{AsCl}_3 \rightarrow \text{Ga})$	0.02277	0.01759	0.01164	0.00669
	$F_{\text{H}_2}(\text{PCl}_3 \rightarrow \text{Ga})$	0.01194	0.01088	0.00954	0.00857
	$F_{\text{H}_2}(\text{AsCl}_3 \rightarrow \text{In})$	0.24247	0.21676	0.17613	0.12230
	$F_{\text{H}_2}(\text{PCl}_3 \rightarrow \text{In})$	0.12716	0.13414	0.14442	0.15667
Hydride	$F_{\text{HCl}}(\text{Ga})$	0.00174	0.00167	0.00145	0.00120
	$F_{\text{HCl}}(\text{In})$	0.02826	0.02833	0.02855	0.02880
	F_{AsH_3}	0.00698	0.00684	0.00632	0.00534
	F_{PH_3}	0.02302	0.02316	0.02368	0.02466
MO-chloride	$F_{\text{H}_2}(\text{TEG})$	0.12472	0.12126	0.10803	0.08954
	$F_{\text{H}_2}(\text{TEI})$	2.74628	2.74974	2.76297	2.78146
	$F_{\text{H}_2}(\text{AsCl}_3)$	0.24167	0.23484	0.20554	0.14781
	$F_{\text{H}_2}(\text{PCl}_3)$	0.14362	0.14493	0.15055	0.16163

Under the conditions above and $e = s = 1$, the flow rates for the growth of $\text{In}_{0.74}\text{Ga}_{0.26}\text{As}_{0.55}\text{P}_{0.45}$, which is lattice matched to InP and emitting at 1.3 μm , were calculated with various dilution flow rates. The flow rate data are listed in Table III. $F_{\text{H}_2}(\text{AsCl}_3 \rightarrow \text{Ga})$ is the flow rate of H_2 passing through AsCl_3 and over a Ga source, $F_{\text{HCl}}(\text{Ga})$ the HCl flow rate over a Ga source, F_{AsH_3} the AsH_3 flow rate, and $F_{\text{H}_2}(\text{TEG})$ the flow rate of H_2 passing through TEG. As the dilution H_2 flow rate increases, the Cl/H ratio in the vapor phase decreases. Figure 2 shows the variation in alloy composition from $\text{In}_{0.74}\text{Ga}_{0.26}\text{As}_{0.55}\text{P}_{0.45}$ with the increase in either flow rate by 3% or temperature by 3°C as a function of the Cl/H ratio in the hydride system. The solid lines denote the variations in x , and the broken lines denote the variations in y . The Cl/H ratio does not greatly affect the variations in x and y caused by the increase in the growth parameters, though it changes the vapor composition for the growth of a particular solid composition. Therefore, the likely dilution flow rate of 1 standard-liter/min is selected as the standard for the comparison of composition controllability. Under this dilution flow rate, the Cl/H ratios and thermodynamic growth rates of $\text{In}_{0.74}\text{Ga}_{0.26}\text{As}_{0.55}\text{P}_{0.45}$ are 1.1×10^{-2} and 6.1×10^{-5} mol/min in the chloride system, 5.0×10^{-3} and 1.4×10^{-4} mol/min in the hydride system, and 3.5×10^{-3} and 6.8×10^{-5} mol/min in the MO-chloride system.

Results

The calculated variations in alloy composition with the increase in the flow rate by 3% and the temperature by 3°C are shown on X-Y planes for $\text{In}_{1-x}\text{Ga}_x\text{As}_y\text{P}_{1-y}$ in Fig. 3a for the chloride VPE system, in Fig. 3b for the hydride VPE system, and in Fig. 3c for the MO-chloride VPE system, where $e = s = 1$. The solid arrows show the variations with the flow rates, and the thin arrows show the variations with the temperatures. Two solid lines and two broken lines parallel to the line lattice matching to InP represent lattice mismatches (without any consideration for the lattice distortion), $|\Delta a/a_0|$, of 1×10^{-3} and 3×10^{-4} , respectively. The notations in Fig. 3 are the same as in Table III. A short arrow is equivalent to good composition controllability. The length of the arrow perpendicular to the line lattice matching to InP and reaching to the line with a lattice mismatch of 3×10^{-4} is 0.004 on the X-Y plane. The variations in the chloride and hydride systems are comparable in the length. However, some of the variations in the MO-chloride system are much larger than the others.

Figure 4 shows the variation in alloy composition with the completeness factor, and Fig. 5 shows the variation with the saturation factor. An incompleteness of 1% pro-

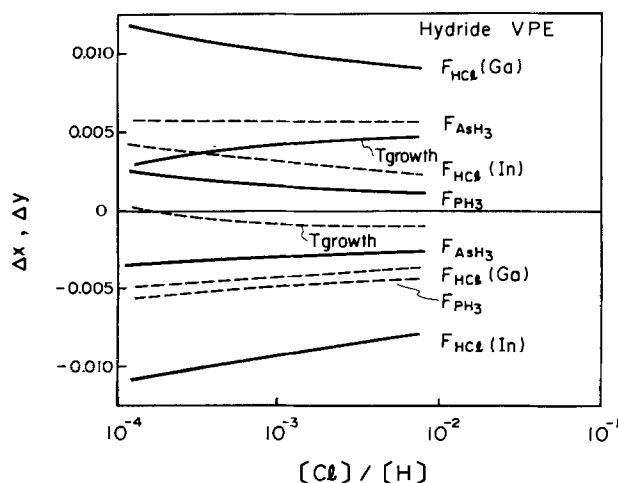
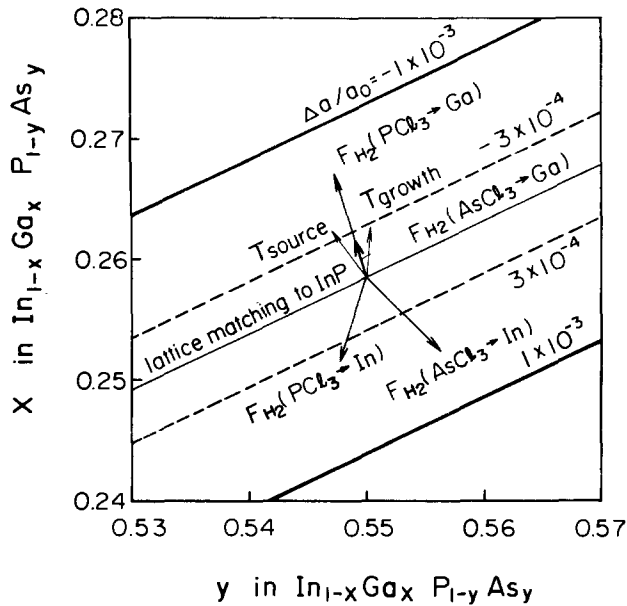
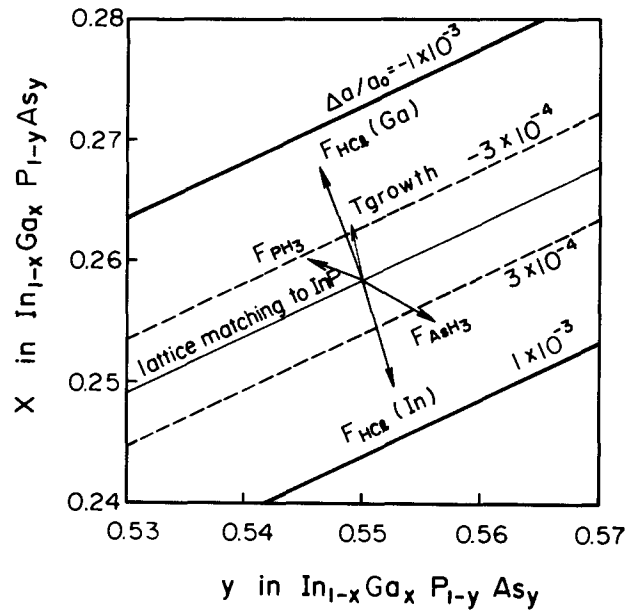


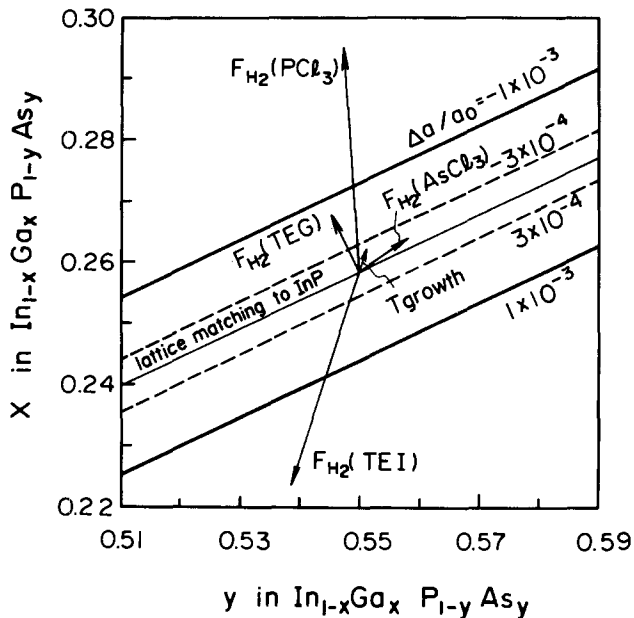
Fig. 2. Variation in alloy composition with the increase in either flow rate by 3% or temperature by 3°C as a function of the Cl/H ratio in a hydride VPE system. Solid lines and broken lines show Δx 's and Δy 's, respectively.



(a) Chloride VPE



(b) Hydride VPE



(c) MO-chloride VPE

duces a lattice mismatch of 8×10^{-4} , and an unsaturation of 5% produces one of 4.4×10^{-4} .

Because the relation between the variation in alloy composition and the change in the growth parameters for $\text{In}_{0.74}\text{Ga}_{0.26}\text{As}_{0.55}\text{P}_{0.45}$ is nearly linear, Fig. 3-5 can be summarized in Table IV, where the lengths of the variations on the X-Y plane and the required accuracies for a length of variation of 0.004 (proportional to the reciprocal of the length of variation) are listed. The required accuracies are greater than 2.4°C in the temperatures in all three VPE systems and greater than 1.2% in the flow rates in both chloride and hydride systems. Precise flow rate control to within 0.3% is needed in the MO-chloride system. The compositional accuracy stated above also requires control of the completeness factor to within 0.3% in the chloride system and 0.4% in the hydride system and of the saturation factor to within 3.4% in the chloride system.

Discussion

The constituent partial pressures (P_{GaCl} , P_{InCl} , P_{As_4} , P_{P_4}) can be changed independently only in the hydride sys-

Fig. 3. Variation from $\text{In}_{0.74}\text{Ga}_{0.26}\text{As}_{0.55}\text{P}_{0.45}$ on an X-Y plane. a: For chloride VPE. b: For hydride VPE. c: For MO-chloride VPE. Flow rates and temperatures increase by 3% and 3°C, respectively. A line lattice matching to InP is shown. Solid lines and broken lines show lattice mismatches of 1×10^{-3} and 3×10^{-4} , respectively.

tem. In the chloride system, the partial pressures of GaCl and As_4 , for example, are changed simultaneously due to the change in $F_{\text{H}_2}(\text{AsCl}_3 \rightarrow \text{Ga})$. In the MO-chloride system, the change in the constituent material flow rates (F_{TEG} , F_{TEI} , F_{AsCl_3} , F_{PCl_3}) causes changes in both the constituent partial pressures and the HCl partial pressure. Therefore, the hydride system is discussed first to see the effect of the GaCl, InCl, As_4 , and P_4 partial pressures on the alloy composition.

Effect of constituent partial pressures.—It is shown in Fig. 3b that the variations in alloy composition with $F_{\text{HCl}}(\text{Ga})$ and F_{PH_3} go in the Ga-P direction and the variations with $F_{\text{HCl}}(\text{In})$ and F_{AsH_3} go in the In-As direction. The calculated solid-vapor composition curves for ternary III-V compounds in the hydride VPE system are shown in Fig. 6a and 6b to explain these directions. The above data were used for the calculation. It is seen that increases in As- and Ga-related partial pressures cause decreases in x and y, respectively. The interaction parameters make the solid-vapor curves S-shaped. However, the selection of the values for the equilibrium constants plays

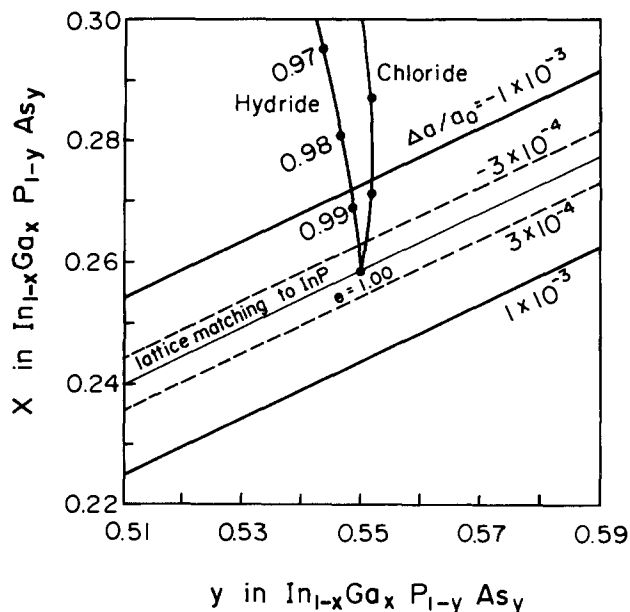


Fig. 4. Variation from $\text{In}_{0.74}\text{Ga}_{0.26}\text{As}_{0.55}\text{P}_{0.45}$ with the completeness factor, e , in chloride and hydride systems.

a more important role in determining the direction of the variation in alloy composition.

Effect of incomplete source reactions.—Figure 4 shows that the incomplete source reactions cause the variations in the Ga-P direction in the hydride system ($V/\text{III} \approx 1$) and in the Ga-As direction in the chloride system ($V/\text{III} \approx 0.4$). Since each source reaction has the same completeness factor, the $\text{Ga}/(\text{Ga} + \text{In})$ ratio in the vapor phase is unchanged. (The total Group III chloride partial pressure decreases to $e\%$.) A decrease in the completeness factor results in a much greater increase in the HCl partial pressure and thus causes a large variation in the alloy composition. Therefore, the incompleteness of the source reaction is analogous to an increase in the HCl partial pressure.

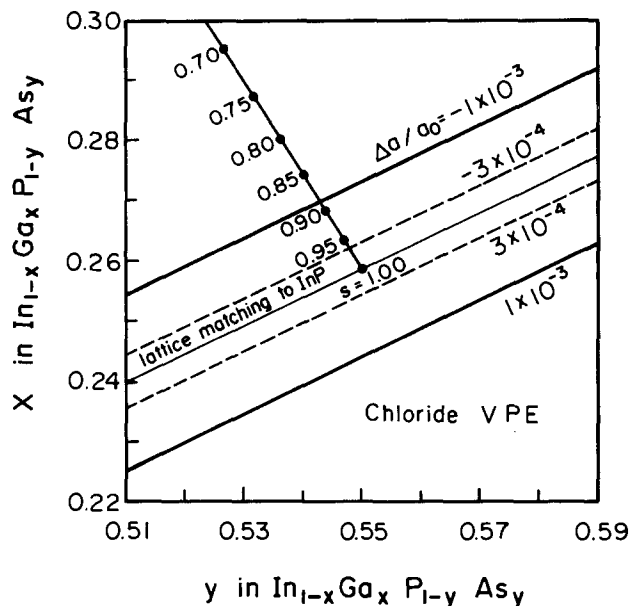
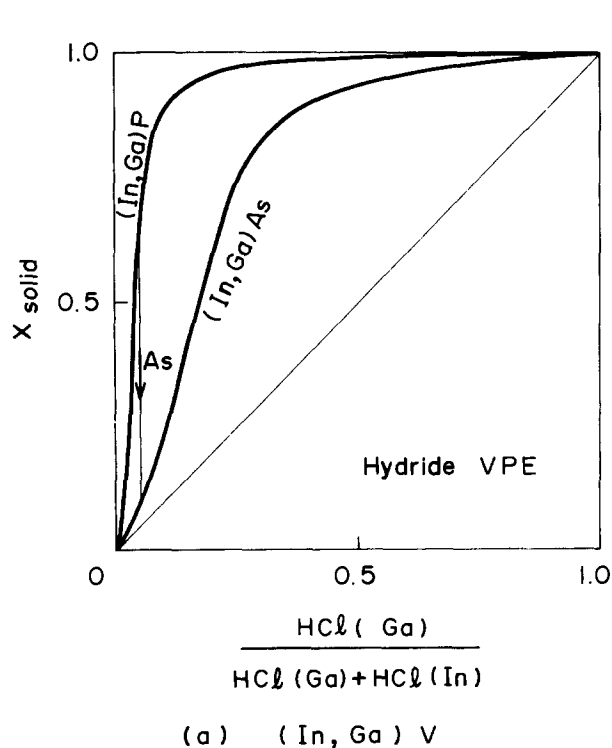


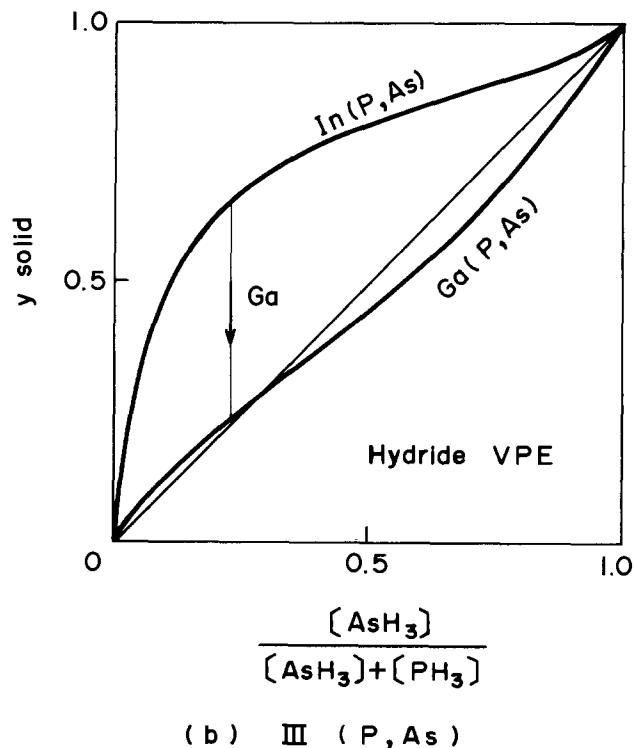
Fig. 5. Variation from $\text{In}_{0.74}\text{Ga}_{0.26}\text{As}_{0.55}\text{P}_{0.45}$ with the saturation factor, s , in a chloride system.

Effect of flow rates in chloride and MO-chloride systems.—The discussion on the direction of the variation in alloy composition in the hydride system can be applied to the chloride and MO-chloride systems. In the chloride system, the alloy composition changes in the III-V-rich side with the VCl_3 flow rate over the group III source, except for $F_{\text{H}_2}(\text{AsCl}_3 \rightarrow \text{Ga})$, whose increase results in the variation going in the Ga-P direction because of the increase in the GaCl partial pressure.

In the MO-chloride system, it is rather complicated to foresee the variation in alloy composition with the flow rates because the partial pressure of HCl greatly changes with the flow rates. The MO-chloride system is more like the chloride system ($V/\text{III} = 0.35$). Therefore, the variation in alloy composition goes in the Ga-As direction with the



(a) $(\text{In}, \text{Ga})\text{V}$



(b) $\text{III}(\text{P}, \text{As})$

Fig. 6. Solid-vapor composition curves for ternary III-V compounds calculated at a growth temperature of 700°C , a Cl/H ratio of 5×10^{-3} , and a V/III ratio of ~ 1 in a hydride VPE system. a: For $(\text{In}, \text{Ga})\text{V}$. b: For $\text{III}(\text{As}, \text{P})$. Arrows represent adding As- and Ga-related species in the vapor phase, respectively.

Table IV. Variations in alloy composition on a X-Y plane and required accuracies of growth parameters for a length of variation of 0.004

Growth parameter	Variation ^a	Required accuracy ^b
Chloride		
Source temp.	0.0050	2.4°C
Growth temp.	0.0041	2.9°C
H ₂ (AsCl ₃ → Ga)	0.0033	3.6%
H ₂ (PCl ₃ → Ga)	0.0091	1.3%
H ₂ (AsCl ₃ → In)	0.0087	1.4%
H ₂ (PCl ₃ → In)	0.0072	1.7%
e	0.0131	0.3%
s	0.0058	3.4%
Hydride		
Source temp.	0	—
Growth temp.	0.0047	2.6°C
HCl (Ga)	0.0101	1.2%
HCl (In)	0.0091	1.3%
AsH ₃	0.0070	1.7%
PH ₃	0.0050	2.4%
e	0.0105	0.4%
MO-chloride		
Growth temp.	0.0040	3.0°C
H ₂ (TEG)	0.0104	1.2%
H ₂ (TEI)	0.0368	0.3%
H ₂ (AsCl ₃)	0.0096	1.3%
H ₂ (PCl ₃)	0.0368	0.3%

^a Length of the variation from In_{0.74}Ga_{0.26}As_{0.55}P_{0.45} on a X-Y plane with the change in the temperature by 3°C, the flow rate by 3%, e by 1%, or s by 5%.

^b Required accuracy for a length of variation of 0.004. This is comparable to a lattice mismatch of 3×10^{-4} when the variation is perpendicular to the line lattice matching to InP.

HCl partial pressure. An increase in either TEG or TEI flow rate decreases the HCl partial pressure. Hence, the increase in the TEI flow rate causes the large variation in the In-P direction as a consequence of the addition of the In-As direction and the In-P direction (opposite to the Ga-As direction). Because the TEG flow rate is much smaller than the VCl₃ flow rate, an increase in the TEG flow rate by 3% decreases the HCl partial pressure little. Therefore, the variation with the TEG flow rate is about the same as that with F_{HCl}(Ga) in the hydride system. The variation in alloy composition with either AsCl₃ or PCl₃ flow rate shows the effect of the increase in the HCl partial pressure. Each variation goes in the Ga direction.

Effect of unsaturation of sources.—The total Group V partial pressure decreases with the unsaturation of the sources. The As/(As + P) ratio in the vapor phase is unchanged since each source has the same saturation factor. The variation in the Ga-P direction with decreasing saturation factor is seen in Fig. 5. In the real chloride VPE system, the saturation factors are different from one another. Probably, an In source covered with an InAs crust has the smallest saturation factor, considering the solubility of III-V compounds in Group III liquids (36).

Effect of source temperature.—The variation in alloy composition with the source temperature goes in the Ga-P direction only in the chloride system. The Ga/Cl and In/Cl ratios increase to a maximum value of 1 as the source temperature increases. Since the In/Cl ratio (> 0.9) is larger than the Ga/Cl ratio (≈ 0.8), the GaCl partial pressure increases more than the InCl partial pressure, which causes the variation in the Ga-P direction. As is well known, the hydride system is less sensitive to the source temperature than the chloride system because the III/Cl ratio in the hydride system is more than 0.98 and fully saturated. Since all of the Group III organics are converted to the Group III chlorides, the III/Cl ratio is independent of the mixing temperature in the MO-chloride system.

Effect of growth temperature.—Because of the similarity of the growth process in the three VPE systems, the variations in alloy composition with the growth temperature are comparable to one another. The difference in the di-

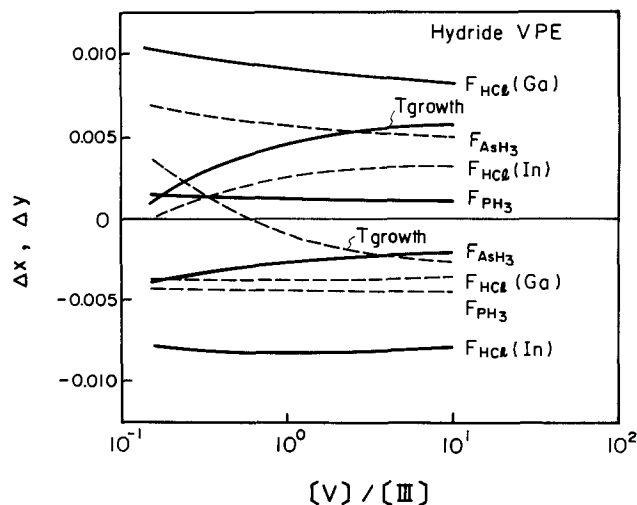


Fig. 7. Variation in alloy composition from In_{0.74}Ga_{0.26}As_{0.55}P_{0.45} with the increase in either flow rate by 3% or temperature by 3°C as a function of the V/III ratio in a hydride VPE system. Solid lines show Δx 's, and broken lines show Δy 's.

rection of the variation between the hydride system and the chloride and MO-chloride systems arises from the difference in the V/III ratio. As shown in Fig. 7, the variation with the growth temperature goes in the Ga-As direction also in the hydride system at a V/III ratio of 0.4. This variation goes in the Ga-P direction at V/III ratios above 0.6. The other variations in alloy composition do not change their direction with the V/III ratio. The values of the variations are affected a little by the V/III ratio.

Summary

A thermodynamic comparison of composition controllability was made between the chloride, hydride, and newly proposed MO-chloride InGaAsP VPE systems for the growth of an alloy lattice matched to InP and emitting at 1.3 μ m. In order to discuss the dynamic aspects of the VPE methods, the calculated model includes a completeness factor for the reaction between a source metal and gas phase and a saturation factor for the metal source with a Group V element.

Control of the temperatures to within 2.4°C in all three VPE systems and of the flow rates to within 1.2% in both chloride and hydride systems are enough to make the length of variation on the X-Y plane less than 0.004 (a length which produces a lattice mismatch of 3×10^{-4} at the maximum). In the MO-chloride system, more precise control of the flow rates to within 0.3% is needed. It is found that the completeness and saturation factors greatly affect the alloy composition. Control of the completeness factor to within 0.3% in the chloride system and to within 0.4% in the hydride system and control of the saturation factor to within 3.4% in the chloride system are also required to keep the alloy composition in a circle with a radius of 0.004 on the X-Y plane.

Acknowledgments

The authors wish to thank D. Shinoda and T. Kawamura for encouragement, and A. Usui and H. Terao for useful discussions.

Manuscript submitted June 8, 1984; revised manuscript received March 8, 1985.

NEC Corporation assisted in meeting the publication costs of this article.

APPENDIX

Equilibrium Eq. [B] and [C] give

$$P_{\text{GaCl}} + P_{\text{InCl}} = h_1 P_{\text{GaCl}} \quad [\text{A-1}]$$

where

$$h_1 = 1 + (K_C/K_B)(a_{\text{InAs}}/a_{\text{GaAs}})$$

Equilibrium Eq. [E] and [F] give

$$P_{\text{GaCl}_3} + P_{\text{InCl}_3} = h_3 P_{\text{GaCl}_3} \quad [\text{A-2}]$$

where

$$h_3 = 1 + (K_{\text{F}}K_{\text{C}}/K_{\text{E}}K_{\text{B}})(a_{\text{InAs}}/a_{\text{GaAs}})$$

Equilibrium Eq. [A], [B], and [I]-[K] give

$$P_{\text{As}_4} + P_{\text{As}_3\text{P}} + P_{\text{As}_2\text{P}_2} + P_{\text{AsP}_3} + P_{\text{P}_4} = h_4 P_{\text{As}_4} \quad [\text{A-3}]$$

where

$$h_4 = 1 + K_{\text{I}}z + K_{\text{J}}z^2 + K_{\text{K}}z^3 + z^4$$

and

$$z = (K_{\text{A}}/K_{\text{B}})(a_{\text{GaP}}/a_{\text{GaAs}})$$

Equilibrium Eq. [G], [H], and [L] give

$$P_{\text{As}_2} + P_{\text{AsP}} + P_{\text{P}_2} = h_2 P_{\text{As}_2} \quad [\text{A-4}]$$

where

$$h_2 = 1 + K_{\text{L}}(K_{\text{H}}/K_{\text{G}})^{1/2}z + (K_{\text{H}}/K_{\text{G}})z^2$$

Substitution of Eq. [A-1]-[A-4] in Eq. [11]-[13] gives

$$P_{\text{H}_2} + P_{\text{HCl}} + h_1 P_{\text{GaCl}} + h_3 P_{\text{GaCl}_3} + h_4 P_{\text{As}_4} + h_2 P_{\text{As}_2} = 1 \quad [\text{A-5}]$$

$$2cP_{\text{H}_2} + (c-1)P_{\text{HCl}} - h_1 P_{\text{GaCl}} - 3h_3 P_{\text{GaCl}_3} = 0 \quad [\text{A-6}]$$

$$2dP_{\text{H}_2} + dP_{\text{HCl}} - h_1 P_{\text{GaCl}} - h_3 P_{\text{GaCl}_3} + 4h_4 P_{\text{As}_4} + 2h_2 P_{\text{As}_2} = 0 \quad [\text{A-7}]$$

Thus Eq. [E] and [A-6] give

$$P_{\text{GaCl}}(1) = \frac{2cP_{\text{H}_2} + (c-1)P_{\text{HCl}}}{h_1 + 3h_3 K_{\text{E}} P_{\text{HCl}}^2 / P_{\text{H}_2}} \quad [\text{A-8}]$$

Equations [G], [A-5], and [A-7] give

$$P_{\text{As}_4}^{1/2} = \frac{-3h_2 K_{\text{G}} + \sqrt{9h_2^2 K_{\text{G}}^2 + 20 h_4 [1 - (2d+1)P_{\text{H}_2} - (d+1)P_{\text{HCl}}]}}{10 h_4} = g(P_{\text{H}_2}, P_{\text{HCl}}) \quad [\text{A-9}]$$

Then substitution of Eq. [G] and [A-9] into Eq. [A-5] gives

$$P_{\text{GaCl}}(2) = \frac{1 - P_{\text{H}_2} - P_{\text{HCl}} - h_4 g^2(P_{\text{H}_2}, P_{\text{HCl}}) - h_2 K_{\text{G}} g(P_{\text{H}_2}, P_{\text{HCl}})}{h_1 + h_3 K_{\text{E}} P_{\text{HCl}}^2 / P_{\text{H}_2}} \quad [\text{A-10}]$$

Equations [B] and [A-9] give

$$P_{\text{GaCl}}(3) = K_{\text{B}} a_{\text{GaAs}} P_{\text{HCl}} / [g(P_{\text{H}_2}, P_{\text{HCl}}) P_{\text{H}_2}]^{1/2} \quad [\text{A-11}]$$

A set of P_{H_2} and P_{HCl} when $P_{\text{GaCl}}(1) = P_{\text{GaCl}}(2) = P_{\text{GaCl}}(3)$ gives a solution.

REFERENCES

- P. E. Brunemeier, T. J. Roth, N. Holonyak, Jr., and G. E. Stillman, *Appl. Phys. Lett.*, **43**, 373 (1983).
- W. T. Tsang, *J. Appl. Phys.*, **52**, 3861 (1981).
- B. de Cremoux, P. Hirtz, and J. Ricciardi, in "GaAs and Related Compounds (Vienna 1980)," p. 115, Institute of Physics, London (1981).
- G. B. Stringfellow, *J. Cryst. Growth*, **58**, 194 (1982).
- K. Onabe, *Jpn. J. Appl. Phys.*, **21**, 797 (1982).
- H. Watanabe and A. Usui, *ibid.*, **22**, 315 (1983).
- J. P. Duchemin, J. P. Hirtz, M. Razeghi, M. Bonnet, and S. D. Hersee, *J. Cryst. Growth*, **55**, 64 (1981).
- G. B. Stringfellow, *ibid.*, **62**, 225 (1983).
- S. Sugou, A. Kameyama, H. Katsuda, Y. Miyamoto, K. Furuya, and Y. Suematsu, *Electron. Lett.*, **19**, 1037 (1983).
- G. H. Olsen and T. J. Zamerowski, *IEEE J. Quantum Electron.*, **qe-17**, 128 (1981).
- M. Yoshida, H. Terao, and H. Watanabe, *This Journal*, To be published.
- K. Morizane and Y. Mori, *J. Cryst. Growth*, **45**, 164 (1978).
- H. Watanabe, *Jpn. J. Appl. Phys.*, **14**, 1451 (1975).
- D. W. Shaw, *J. Cryst. Growth*, **8**, 117 (1971).
- A. G. Sigai, C. J. Nuese, R. E. Enstrom, and T. Zamerowski, *This Journal*, **120**, 947 (1973).
- V. S. Ban, *ibid.*, **118**, 1473 (1971).
- M. G. Jacko and S. J. W. Price, *Can. J. Chem.*, **41**, 1560 (1963).
- M. Yoshida, F. Uesugi, and H. Watanabe, *This Journal*, **132**, 677 (1985).
- M. Yoshida, Unpublished data.
- T. Nozaki and T. Saito, *Jpn. J. Appl. Phys.*, **11**, 110 (1972).
- D. T. J. Hurle and J. B. Mullin, in "Proceedings of the International Conference on Crystal Growth (Boston), 1966," p. 241, Pergamon Press, Oxford, England (1967).
- J. B. Mullin and D. T. J. Hurle, *J. Luminescence*, **7**, 176 (1973).
- A. Koukitsu and H. Seki, *J. Cryst. Growth*, **49**, 325 (1980).
- K. Onabe, *J. Phys. Chem. Solids*, **43**, 1071 (1982).
- D. J. Kirwan, *This Journal*, **117**, 1572 (1970).
- V. S. Ban and M. Ettenberg, in "Chemical Vapor Deposition," G. F. Wakefield and J. M. Blocher, Jr., Editors, p. 30, The Electrochemical Society Softbound Proceedings Series, Princeton, NJ (1973).
- V. S. Ban and M. Ettenberg, *J. Phys. Chem. Solids*, **34**, 1119 (1973).
- R. R. Fergusson and T. Gabor, *This Journal*, **111**, 585 (1964).
- H. Seki and S. Minagawa, *Jpn. J. Appl. Phys.*, **11**, 850 (1972).
- T. Mizutani, M. Yoshida, A. Usui, H. Watanabe, T. Yuasa, and I. Hayashi, *Jpn. J. Appl. Phys.*, **19**, L113 (1980).
- S. Y. Narayan, J. P. Paczkowski, S. T. Jolly, E. P. Bertin, and R. T. Smith, *RCA Rev.*, **42**, 491 (1981).
- O. Mizuno and K. Arai, *Jpn. J. Appl. Phys.*, **13**, 1955 (1974).
- M. B. Panish and M. Ilegems, in "Progress in Solid State Chemistry," Vol. 7, H. Reiss and J. O. McCaldin, Editors, p. 39, Pergamon Press, Oxford, England (1972).
- A. Usui, Y. Matsumoto, T. Inoshita, T. Mizutani, and H. Watanabe, in "GaAs and Related Compounds (Osaka 1981)," p. 137, Institute of Physics, London (1982).
- J. Komeno, M. Takikawa, and M. Ozeki, *Electron. Lett.*, **19**, 473 (1983).
- R. N. Hall, *This Journal*, **110**, 385 (1963).

N-CuInS₂/Sulfide-Polysulfide Electrochemical Photovoltaic Cells

Michael A. Russak and Charles Creter

Grumman Aerospace Corporation, Research and Development Center, Bethpage, New York 11714

ABSTRACT

Large-grained photovoltaic n-CuInS₂ was prepared by directional solidification. The as-grown material had doping levels of $\sim 6 \times 10^{16} \text{ cm}^{-3}$, a minority carrier diffusion length of $\sim 1 \mu\text{m}$, and a maximum efficiency of 6.4% in a sulfide-polysulfide electrolyte under simulated AM2 conditions. CuInS₂ thin films were also made by an elemental vacuum evaporation technique with observed efficiencies of 2%. These electrodes had high doping densities ($\geq 10^{17}$), short diffusion lengths ($\sim 0.05 \mu\text{m}$), and recombination dominated I-V behavior.

Photoelectrochemical conversion systems that utilize narrow bandgap (1.3-1.7 eV) thin film II-VI materials with sulfide/polysulfide (SPS) containing electrolytes have been investigated quite extensively in recent years (1-5). While solar conversion efficiencies in the range of 7-8% have been obtained with these materials, the long-term output stability of the II-VI/SPS systems remains questionable.

Conversely, I-III-VI₂ compounds, which are ternary analogues of the II-VI materials, have received considerably less study in SPS electrolytes, and reported efficiencies are much lower than for the II-VI compounds, especially for thin film electrodes (6-8). However, the most notable feature of these materials is their outstanding output stability (6-8). While high quality materials are more difficult to produce in the ternary system, their potential for very stable cells justifies further investigation of them. It is also interesting to note that when S and Se are combined with Cu and In to form CuInS_{2-x}Se_{2(1-x)} solid solutions, direct bandgap, high absorptivity materials with bandgaps in the range of 1.0-1.5 eV can be obtained (9). This presents optimization possibilities for a given electrode/electrolyte system similar to those found in the CdSe_{1-x}Te_x ternary system (4, 5).

P-CuInS₂ has been successfully used in solid-state thin film photovoltaic cells with CdS or Cd_xZn_{1-x}S to achieve efficiencies greater than 10% with very high current outputs. However, the voltage output of these cells is low (10). This is also the case for CuInS₂ used in concert with a SPS electrolyte (8). This reflects the fact that the bandgap of this material is narrow (*i.e.*, 1.0 eV). In a photoelectrochemical cell, a material with a bandgap closer to 1.5 eV, such as CuInS₂, should provide maximum photovoltaic performance (11).

In this paper, we report results with n-CuInS₂ in the form of directionally solidified, large-grained, polycrystalline material and vacuum-evaporated thin films as photoanodes in a SPS electrolyte.

Experimental

Stoichiometric amounts of high purity (5N⁺ or 6N) Cu, In, and S were reacted in an evacuated quartz tube at $\sim 1100^\circ\text{C}$ for 36h to form CuInS₂. The material was subsequently removed, crushed to ~ 200 mesh, and used as the starting material for directional solidification processing. A boron nitride growth ampul (1 cm diam \times 7.5 cm length) was filled with the CuInS₂ powder and supported within an evacuated ceramic tube. The details of the ampul are shown in Fig. 1. Directional solidification was performed using the Bridgman-Stockbarger method in a high temperature apparatus (12). The apparatus consisted of a three-zone furnace, capable of translating at velocities of from 0.01 to 50 cm/h and had an upper limit temperature of 1600°C . For the solidification of CuInS₂, a hot zone temperature of 1150°C ($\sim 100^\circ\text{C}$ greater than the melting point of CuInS₂) was used and a linear gradient of $\sim 60^\circ\text{C}/\text{cm}$ was employed. The ampul was held stationary and the furnace moved at ~ 0.02 cm/h.

After processing, the ampul was sliced perpendicular to the direction of solidification to form disk-shaped samples for electrode fabrication. Evaporated indium was

used to make an ohmic contact and silver-filled epoxy was used to connect a copper wire to the material.

A triple-source vacuum evaporation system, the construction details of which have been reported previously (5), was used to make the CuInS₂ thin films on titanium substrates. The system had resistive heated elemental sources, a tungsten dimple boat for copper, and Al₂O₃ crucibles for indium and sulfur, arranged in parallel with baffles between them. The power to each source was controlled by a microprocessor-driven feedback controller activated by an oscillating quartz crystal monitor which drove a SCR power supply. The key feature of the evaporation system was a tubular shielding arrangement of the crystal monitors whereby no interference between deposition sources was registered. Substrate heating was supplied by a copper block substrate holder, into which cartridge-type heaters and a thermocouple were inserted. X-ray diffraction analysis was performed using a diffractometer with Cu K α radiation. Quantitative compositional data were obtained using a wavelength dispersive electron microprobe at the Solar Energy Research Institute (SERI, Golden, Colorado).

Photoelectrochemical measurements were made using a standard potentiostatic test setup. I-V traces were obtained in an aqueous 2.5M Na₂S-1M S-1M KOH electrolyte using a platinum counterelectrode and a saturated calomel reference electrode. Electrodes were chemically etched in 25% HNO₃, and when photoetching was done a dilute HCl:HNO₃ etchant was used (13).

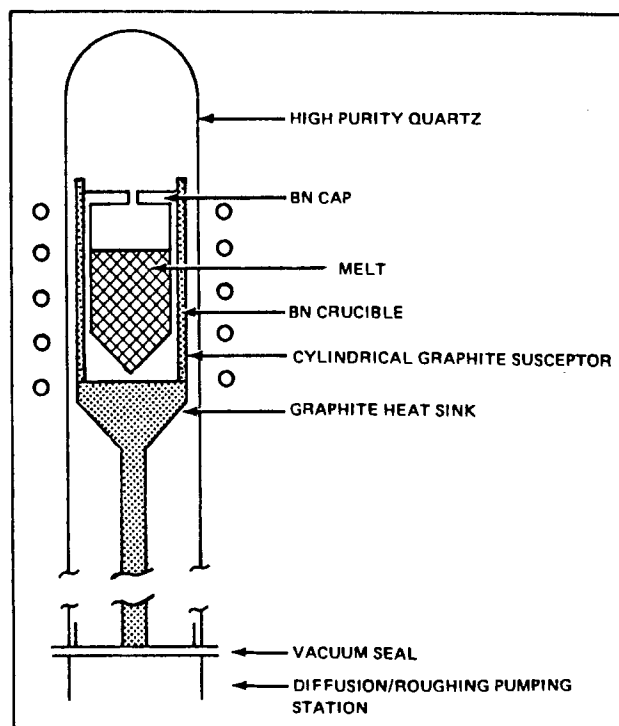


Fig. 1. High temperature schematic ampul for directional solidification.

White light measurements were obtained using a simulated AM2 spectrum provided by a W-I ELH lamp mounted in a dichroic parabolic reflector (14). A 0.25m grating monochromator with 1 kW Xe light source was used with a light chopper and lock-in detection to obtain monochromatic I-V curves and action spectra. All light intensities were measured with a calibrated thermopile detector.

Results and Discussion

The material that was synthesized in the quartz tubes was single-phase CuInS_2 with the chalcopyrite structure as shown in Table I. The resultant directionally solidified material had excellent compositional uniformity over the middle 1.8 cm of the sample, as shown in Fig. 2. The material was n-type as formed and required no further annealing or doping. It was also polycrystalline, with an irregular grain structure having some grains as large as several millimeters in length. X-ray diffraction analysis of the electrode surface indicated the material was single-phase CuInS_2 with a slight 112 growth orientation. Electrodes which had been mounted, polished, chemically etched, and then photoetched were evaluated photoelectrochemically. The best performance was obtained after photoetching, as shown in Fig. 3, for the electrode with the highest output observed. The efficiency of the other electrodes cut from this sample after similar optimization were 2.8, 3.6, and 5.4%. The spectral response (at zero bias) of the electrode from Fig. 3 is shown in Fig. 4. While the quantum yield of the optimized electrode is uniformly high (ϕ external ~ 0.7) across this spectrum (the dropoff at $\lambda < 550$ nm is due to electrolyte absorption), some subbandgap photoresponse is present. As a result, determination of the bandgap of this material by taking the onset of photocurrent to indicate the interband transition energy as well as a plot of the square of the photocurrent vs. the light energy near the bandedge (i.e., J_{ph}^2 vs. $h\nu$) (15, 16) yielded a value of ~ 1.48 eV (see Fig. 5), which is almost 0.5 eV lower than that reported in the literature (9, 17-20). This subbandgap response may be indicative of intrinsic defect states in the material which give rise to optical transitions with less than full bandgap energy light (21, 22).

At the low light intensities used to generate the action spectrum (i.e., $I \leq 1$ mW/cm²), electrode kinetics are not rate limiting and the semiconductor-electrolyte interface may be treated as a Schottky barrier. The Gartner model can then be used to determine optical and electronic parameters of the semiconductor from spectral photocurrent data taken in reverse bias (i.e., at potentials anodic of the dark rest potential in photoelectrochemical systems) (23).

Majority carrier density (N) and minority carrier diffusion length (L_p) can be determined using this model from a plot of $\ln(1 - \phi)$ vs. $(V_{FB} - V_a)^{1/2}$, where ϕ is the monochromatic quantum yield, V_a is the applied reverse bias voltage, and V_{FB} is the flatband potential provided the absorption coefficient (α) is known (23). Using monochro-

Table I. X-ray diffraction data for CuInS_2

Calculated ^a (Cu K _α radiation)			Synthesized powder		Thin film	
<i>d</i> (Å)	hkl	Relative intensity	<i>d</i> (Å)	Relative intensity	<i>d</i> (Å)	Relative intensity
4.87	101	10	4.90	7	^b	^b
3.16	112	100	3.18	100	3.18	100
3.04	103	5	3.06	≤ 5	^b	^b
2.74	200,004	30	2.76	25	2.74	15
2.39	211	5	2.40	≤ 5	^b	^b
2.04	213,105	5	2.05	5	2.07	≤ 5
1.94	220,204	80	1.95	60	1.95	80
1.66	312,116	60	1.67	70	1.66	50
1.59	224	10	1.59	10	1.59	5

^a Data from ASTM File Card 15-681.

^b Peak too weak to be resolved from background.

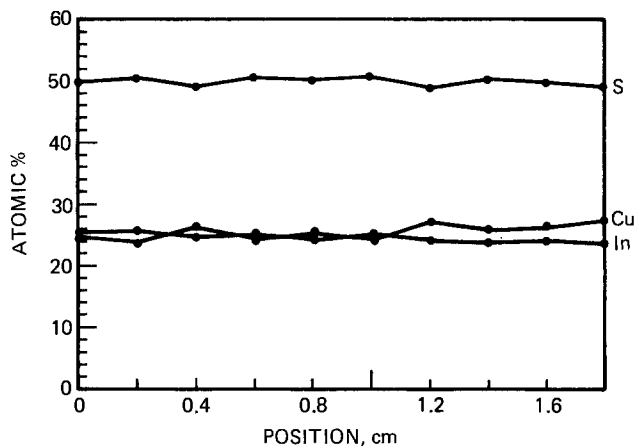


Fig. 2. Compositional uniformity of directionally solidified CuInS_2

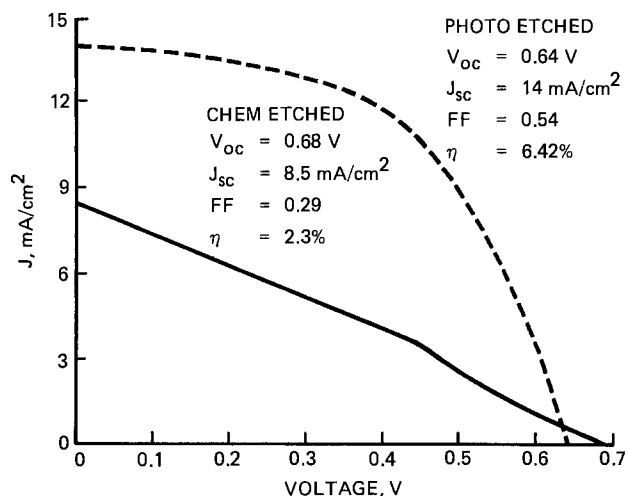


Fig. 3. Photovoltaic performance of directionally solidified CuInS_2 before (solid line) and after (broken line) photoetch/KCN treatment.

matic I-V traces obtained at 800 nm and $\alpha = 4.6 \times 10^4$ cm⁻¹ (20), the above-mentioned analysis yielded the following values: $N = 6.8 \times 10^{16}$ cm⁻³ and $L_p = 0.8$ μm . It is likely that the good L_p value for this material is responsible for its superior I-V performance as compared to the results reported in Ref. (7) for CuInS_2 with $L_p \sim 0.2$ μm . Direct measurement of the resistivity through the thickness of this disk electrode yielded a value of 5 $\Omega\text{-cm}$. Using this value, a majority carrier mobility of ~ 18 cm²/V-s was calculated.

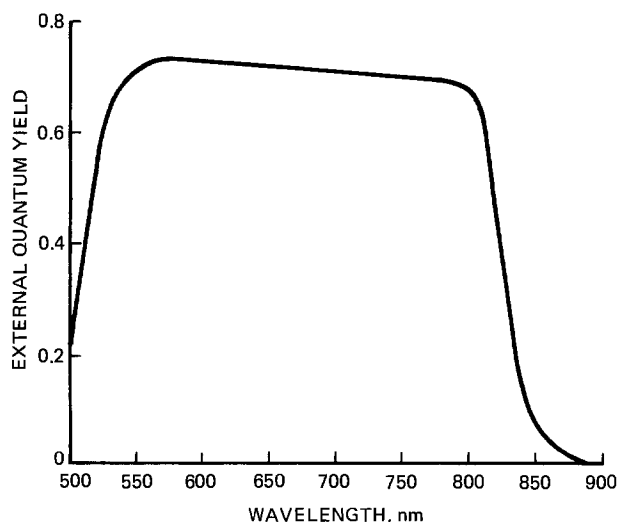


Fig. 4. Action spectrum of photoetched CuInS_2 electrode from Fig. 3

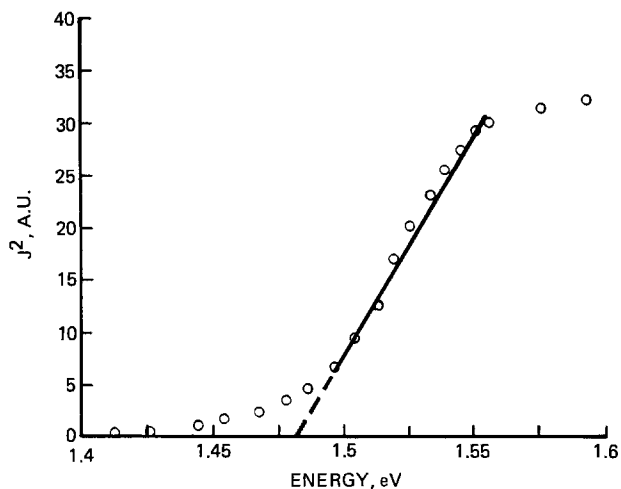


Fig. 5. J^2 vs. $h\nu$ plot for determination of bandgap for directionally solidified CuInS_2 material.

It has been shown by several workers that the Gartner model can be further used to determine V_{FB} , provided certain conditions are satisfied (15, 16, 24). Specifically, if monochromatic I-V data are taken at a wavelength of relatively weak absorption so that $\alpha L_p < 1$ and $\alpha W_0 < 1$, where W_0 is the width of the space-charge layer in the semiconductor, a quadratic relation between Φ (or J) exists such that $J^2 \propto V_a - V_{FB}$. V_{FB} may then be obtained by extrapolation of the J^2 vs. V_a plot to $J = 0$. In the present case (800 nm) for $N = 6.8 \times 10^{16} \text{ cm}^{-3}$, $W_0 = 0.116 \mu\text{m}$, and $\alpha W_0 < 1$, however, because α is large, the product $\alpha L_p > 1$, so the use of this model becomes somewhat questionable. Even so, a plot of J^2 at 800 nm as a function of V_a is linear, as shown in Fig. 6. The V_{FB} value of -1.5 V vs. SCE obtained from this extrapolation was in agreement with the value of -1.52 V vs. SCE obtained by noting the onset of photocurrent with high intensity chopped white light (25). So, while the above-mentioned assumptions are not rigorously met, the J^2 vs. V_a relationship still holds and a good value for V_{FB} can be obtained. This V_{FB} value is slightly lower than that of -1.54 V vs. SCE reported by Mirovsky *et al.* (7), also determined using the Gartner model, but is probably within experimental variability in view of the fact that different SPS electrolytes were used.

Initially, considerable difficulty was encountered in producing good quality CuInS_2 thin films by the elemental evaporation process, because the Cu source tended to overheat the S source, which made the S deposition rate erratic. Placement of a ceramic baffle between these two sources significantly improved the situation.

In CuInS_2 , which is not extrinsically doped, the carrier type is determined by the Cu/In ratio as well as the

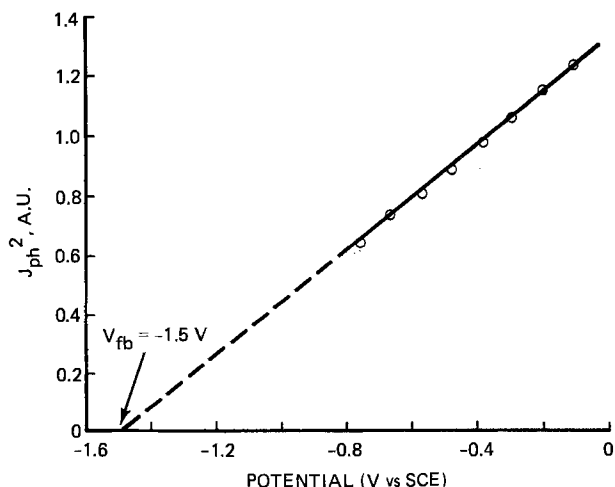


Fig. 6. Monochromatic J^2 vs. reverse bias plot for flatband determination of CuInS_2 in $2.5\text{M Na}_2\text{S}$, 1M S , 1M KOH electrolyte.

S/metal ratio. In producing thin films of CuInS_2 by the elemental evaporation technique, n- and p-type films could be made by adjusting the Cu/In ratio. If $\text{Cu/In} > 1$, p-type films resulted, and if $\text{Cu/In} < 1$, n-type films were made. It should be noted that in all cases the S rate was held at a slight excess over stoichiometry (nominal composition of $\text{CuInS}_{2.1}$), because nonuniform and poorly adhering films resulted if the films were made too sulfur deficient. The p-type films exhibited very little photovoltaic activity in SPS electrolyte, which is consistent with results reported previously with p-type CuInS_2 (7).

The most consistent results in terms of obtaining single-phase n- CuInS_2 films were achieved using substrate temperatures between 350° and 400°C and running the evaporator with a slight excess of In. The x-ray diffraction pattern of a film produced with these processing conditions is presented in the last column of Table I. It is difficult to determine conclusively if the thin film has the chalcopyrite or sphalerite structure, due to the weakness of the 213, 105 reflection, which belongs to the chalcopyrite structure alone. It is interesting to note that while the microstructure of this type of film, shown in Fig. 7, appears columnar, the x-ray diffraction pattern does not indicate a growth texture. This is in contrast to CdSe thin films grown by elemental evaporation in the same temperature regime, where similar microstructures are accompanied by a strong 001 growth texture (26, 27). These results imply that there is a random orientation of crystallites within the columns in Fig. 7. This would provide higher grain boundary recombinations for carriers going through the film than in a textured microstructure. This is probably one factor limiting the performance of the n- CuInS_2 thin films at present.

The compositional uniformity of these films was found to be quite good, as indicated by the EPMA line scan shown in Fig. 8. The excess In in this film is evident in this microprobe scan. The average composition of the film was 23.07% Cu, 26.38% In, and 50.44% S. Although not detected in the film's x-ray diffraction pattern, the formation of some In-S or In-O compound, or CuIn_5S_8 , might have occurred (28, 29).

A 30 min heat-treatment at 200°C in air followed by photoetching and rinsing in 1M KCN was found to optimize the photovoltaic output of this type of thin film. Figure 9 presents the photovoltaic output of a CuInS_2 thin film electrode and demonstrates how postdeposition treatment improves the I-V performance of the heat-treated electrode. Even though the photoetch treatment significantly improves the performance, the I-V curve still has a recombination-dominated shape in forward bias. While the dark current is very low in forward bias, the photocurrent still drops off rapidly (30). The action spectrum of this electrode, which was only somewhat modified by photoetching, shows significant subbandgap response, as seen in Fig. 10. The major effect of photo-

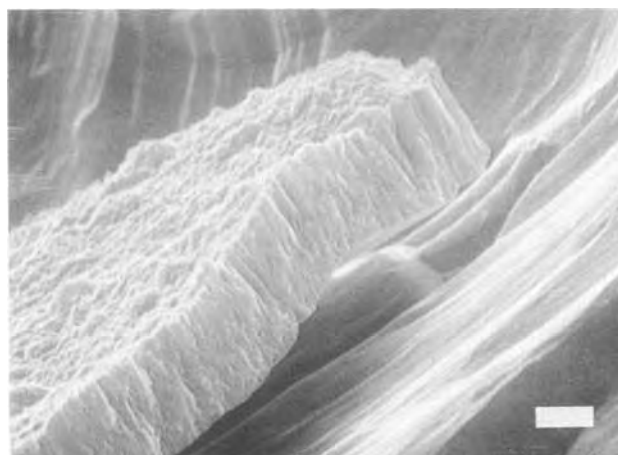


Fig. 7. SEM micrograph showing CuInS_2 thin film deposited at $T_s = 400^\circ\text{C}$. White bar equals $1 \mu\text{m}$.

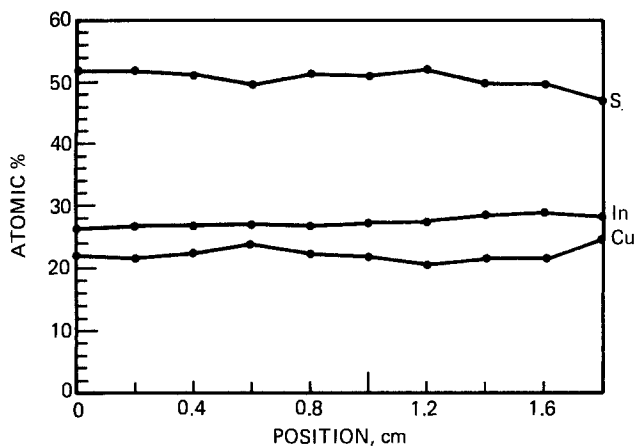


Fig. 8. EPMA line scan of CuInS_2 film shown in Fig. 7

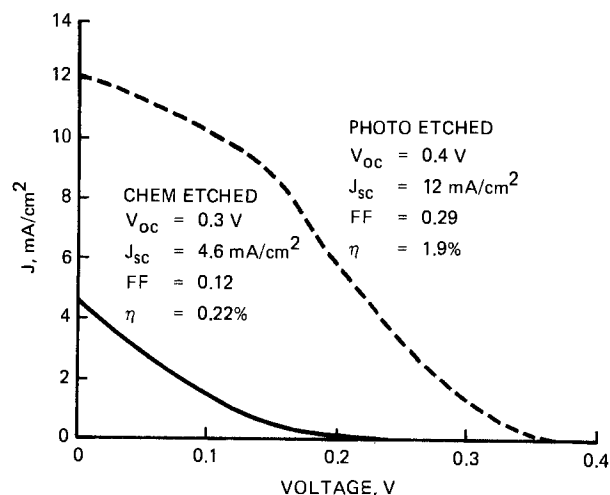


Fig. 9. Photovoltaic performance of CuInS_2 thin film electrode before (solid line) and after (broken line) photoetch/KCN treatment.

etching is seen in the improvement of the red response of the electrode and in the maximum external quantum yield which improves from ~ 15 to $\sim 50\%$. In analyzing these films, it became obvious that they are far from optimized. There are probably several major efficiency limiting mechanisms present, *e.g.*, poor electronic properties, kinetic limitations, surface states, and/or bulk defect states.

Application of the Gartner model analysis to the thin film material indicated $N = 6.2 \times 10^{17} \text{ cm}^{-3}$ and $L_p = 0.05$

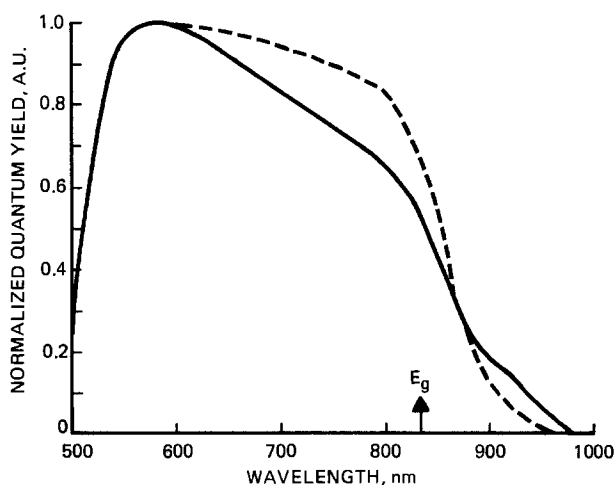


Fig. 10. Action spectrum of CuInS_2 thin film electrode before (solid line) and after (broken line) photoetching showing significant sub-bandgap photoresponse.

Table II. Effect of temperature on photovoltaic output of a CuInS_2 thin film electrode (simulated AM2 conditions)

T (°C)	V_{oc} (V)	J_{sc} (mA/cm ²)	FF	η (%)
20	0.40	12.0	0.29	1.9
60	0.41	12.3	0.32	2.1

μm . Because reliable resistivity measurements could not be made due to contact difficulties, the mobility was not calculated. However, the high N value is not surprising, due to the excess In found in the film. The low L_p value is consistent with poor photovoltaic output. Calculation of the film depletion width (W_0) based on the measured N value and a built-in potential (V_B) of 0.7V from the relation $W_0 = (\epsilon\epsilon_0 V_B / qN)^{1/2}$ where ϵ is the dielectric constant of CuInS_2 which was taken to be 11 (31), $\epsilon_0 = 8.86 \times 10^{-14}$ F/cm, and $q = 1.602 \times 10^{-19}$ C, yields $W_0 = 380\text{\AA}$. Such a thin W_0 should minimize field-assisted collection, especially in forward bias, and bulk collection would be poor due to the low L_p value. This interpretation is supported by the recombination-dominated curve shape seen in forward bias as well as the falloff in collection efficiency found at the red end of the spectrum (Fig. 10), where carriers are generated deeper into the film and must rely on diffusion for collection (27).

In order to evaluate the effect of electrode kinetics on the I-V performance of the thin film material, a series of monochromatic I-V curves (550, 700, and 800 nm) was taken at temperatures between 20° and 60°C using lock-in detection at 30 Hz. Significant effects have been reported in this temperature regime for CuInS_2 (6, 7). Monochromatic I-V data were used so that spectral information could be obtained and dark currents eliminated. Very little temperature dependence was found as a function of wavelength or voltage, indicating that, at least for the light intensities employed ($< 1 \text{ mW/cm}^2$), kinetics are not the major efficiency limiting factor. This contention was further supported by white light measurements at 75 mW/cm^2 in the same temperature range. Here, about a 10% increase in efficiency, due mostly to an improvement to fill factor, was seen in going from 20° to 60°C. The photovoltaic output parameters of the electrode at 20° and 60°C are presented in Table II. It is not surprising that there is little temperature dependence seen at these low efficiency levels, considering the large actual surface area of the electrode (Fig. 7) and small diffusion length of this material.

The output stability of the CuInS_2 materials produced in this work was quite good. The electrode whose I-V trace is shown in Fig. 3 was run at maximum power at a current density of 20 mA/cm^2 (*i.e.*, $2 \times \text{AM2}$ intensity) for a total of 10,000 C/cm², with a slight increase in efficiency from 6.4 to 6.6%. The thin film electrode of Fig. 9 was run at maximum power at 10 mA/cm^2 for a total of 5000 C/cm², with a slight decrease in output of from 1.8 to 1.7%.

Summary

It has been shown that photovoltaically active, large-grained n- CuInS_2 can be prepared by the directional solidification of prereacted CuInS_2 starting material. The best electrode fabricated from the as-grown material had a minority carrier diffusion length of $\sim 1 \mu\text{m}$, excellent output stability in SPS electrolyte, and a simulated AM2 efficiency of 6.4%. CuInS_2 thin films were also produced by elemental vacuum evaporation, and results were more variable. These electrodes, when optimized, exhibited only modest efficiency levels ($\sim 2\%$) and recombination-dominated I-V curve shapes. Analysis of monochromatic I-V data indicated that the films had high doping densities ($N \geq 10^{17}$) and short effective diffusion lengths ($L_p \sim 0.05 \mu\text{m}$).

Acknowledgments

Funding for this work was provided by the Solar Energy Research Institute, Golden, Colorado. The authors

gratefully acknowledge the contributions of Ronald Pirich and William Poit of Grumman in the area of directional solidification of CuInS₂ and Chuck Herrington of SERI for providing quantitative chemical data using electron microprobe analysis.

Manuscript submitted Nov. 15, 1984; revised manuscript received March 1, 1985.

Grumman Aerospace Corporation assisted in meeting the publication costs of this article.

REFERENCES

- G. Hodes, J. Manassen, and D. Cahen, *Nature*, **261**, 406 (1976).
- J. Manassen, G. Hodes, and D. Cahen, *This Journal*, **124**, 532 (1977).
- M. A. Russak, J. Reichman, H. Witzke, S. K. Deb, and S. N. Chen, *ibid.*, **127**, 725 (1980).
- G. Hodes, *Nature*, **285**, 29 (1980).
- M. Russak and C. Creter, *This Journal*, **131**, 556 (1984).
- M. Robbins, K. Bachmann, B. Lambrecht, F. Theil, J. Thompson, Jr., R. Vadimsky, S. Menezes, A. Heller, and B. Miller, *ibid.*, **125**, 831 (1978).
- Y. Mirovsky, D. Cahen, G. Hodes, R. Tenne, and W. Girat, *Sol. Energy Mater.*, **4**, 169 (1981).
- Y. Mirovsky and D. Cahen, *Appl. Phys. Lett.*, **40**, 727 (1982).
- I. V. Bodnar, B. V. Korzun, and A. I. Lukomskii, *Phys. Status Solidi B*, **105**, K143 (1981).
- R. A. Mickelsen and W. S. Chen, in "Proceedings of the 15th IEEE PVSC-1981," p. 800, IEEE, New York (1981).
- J. Loferski, *J. Appl. Phys.*, **27**, 777 (1956).
- R. G. Pirich, Grumman R&D Center Report RE-692, Grumman Corp., Bethpage, NY, December 1984; *Met. Trans. A.*, To be published.
- R. Tenne and G. Hodes, *Appl. Phys. Lett.*, **37**, 428 (1980).
- K. Yaas and H. B. Curtis, NASA Report no. NASA TM-X-3059, Springfield, VA (1968).
- M. A. Butler, *J. Appl. Phys.*, **48**, 1914 (1977).
- Y. Mirovsky, D. Cahen, R. Tenne, and G. Hodes, in "Photoelectrochemistry: Fundamental Processes and Measurement Techniques," W. L. Wallace, A. J. Nozik, S. K. Deb, and R. H. Wilson, Editors, p. 517, The Electrochemical Society Softbound Proceedings Series, Pennington, NJ (1982).
- L. Y. Sun, L. L. Kazmerski, A. H. Clark, P. J. Ireland, and D. W. Morton, *J. Vac. Sci. Technol.*, **15**, 265 (1978).
- J. L. Shay and B. Tell, *Surf. Sci.*, **37**, 748 (1973).
- L. L. Kazmerski and C. C. Shieh, *Thin Solid Films*, **41**, 35 (1977).
- H. Neumann, W. Horig, V. Savelev, J. Lagzdonis, B. Schumann, and G. Kuhn, *ibid.*, **79**, 167 (1981).
- C. Binsma, *ibid.*, **97**, 237 (1982).
- R. Haak, D. Tench, and M. A. Russak, *This Journal*, **131**, 2709 (1984).
- W. W. Gartner, *Phys. Rev.*, **116**, 84 (1959).
- R. Tenne, Y. Mirovsky, Y. Greenstein, and D. Cahen, *This Journal*, **129**, 1506 (1982).
- J. Reichman and M. A. Russak, in "Photoeffects at Semiconductor-Electrolyte Interfaces," A. J. Nozik, Editor, p. 359, ACS Symposium Series 146, American Chemical Society, Washington, DC (1981).
- D. Bonnet and E. Rickus, in "Proceedings of the 14th PV Specialist Conference," p. 629, IEEE, New York (1980).
- J. Reichman and M. Russak, *This Journal*, **128**, 2025 (1981).
- M. L. Hwang, C. L. Cheng, L. M. Liu, Y. C. Liu, and C. Y. Sun, *Thin Solid Films*, **67**, 83 (1980).
- F. A. Theil, *This Journal*, **129**, 1570 (1982).
- J. Gobrecht and H. Gerischer, *Sol. Energy Mater.*, **2**, 131 (1979).
- J. L. Shay, B. Tell, H. M. Kasper, and L. M. Schiavone, *Phys. Rev. B*, **7**, 4485 (1973).

Thermal Oxidation of Silicon in Dry Oxygen

Accurate Determination of the Kinetic Rate Constants

Hisham Z. Massoud*¹ and James D. Plummer*

Integrated Circuits Laboratory, Stanford University, Stanford, California 94305

Eugene A. Irene*²

IBM Thomas J. Watson Research Center, Yorktown Heights, New York 10598

ABSTRACT

Based upon the linear-parabolic growth model of silicon oxidation, accurate kinetic rate constants are determined for (100), (111), and (110) silicon oxidized in dry oxygen in the 800°-1000°C range. The oxide growth was monitored by high temperature automated *in situ* ellipsometry. It is shown that fitting the maximum number of oxidation data points to a linear-parabolic relationship yields accurate oxidation rate constants that are unique to the oxidation process as described in the Deal-Grove model, and not just good empirical fitting parameters. This approach is denoted the "optimum X_i technique." Both linear and parabolic rate constants exhibit a break in their activation energies at 950°C. This behavior is discussed and interpreted in terms of the viscoelastic properties of SiO₂.

The thermal oxidation of silicon in the thin regime (< 500Å) is of vital importance to VLSI device designers because thin layers of SiO₂ are exclusively used as the gate dielectric for high performance MOS devices. In early studies of the growth kinetics of silicon dioxide in dry oxygen, it has been observed that the oxidation rate, in the early stages (< 250Å) of SiO₂ growth, is faster than described by the linear-parabolic growth relationship (1). This observation was later confirmed by a number of investigations [e.g., Ref. (2)]. In a quantitative study of the oxidation-rate enhancement in the thin regime (to be published in forthcoming papers), accurate values of the ox-

idation rate constants were needed in calculating the magnitude of the rate enhancement. Some discrepancies, however, exist in the reported values of the linear and parabolic rate constants (2). In this paper, the techniques commonly used to determine these constants from oxidation data are analyzed, an alternative method is introduced, and all methods are compared. The approach that yields physically meaningful results is then applied to a large body of oxidation data obtained using high temperature *in situ* ellipsometry. The results are then explained in terms of the potentially important role played by the viscoelastic properties of SiO₂ (3) in determining the oxidation rate constants.

The Thermal Oxidation of Silicon

The growth kinetics of thermal layers of silicon dioxide on silicon were successfully modeled by Deal and Grove

*Electrochemical Society Active Member.

¹Present address: Department of Electrical Engineering, Duke University, Durham, North Carolina 27706.

²Present address: Department of Chemistry, University of North Carolina, Chapel Hill, North Carolina 27514.

(1), using a simple linear-parabolic relationship. This model was derived by considering three fluxes of oxidizing species to be in steady state: the flux of oxidant from the gas ambient to the gas-SiO₂ interface, the diffusive flux of oxidant through the SiO₂ film, and the flux representing the consumption of oxidant at the Si-SiO₂ interface by the oxidation reaction. In this description, the oxidation rate was expressed as

$$\frac{dX_{ox}}{dt} = \frac{B}{2X_{ox} + A} \quad [1]$$

where X_{ox} is the oxide thickness, and B and B/A are the parabolic and linear constants, respectively. The parabolic rate constant is directly proportional to the product of the diffusion coefficient and solubility of the oxidizing species in the oxide, whereas the linear rate constant is a function of the solubility of the oxygen species in the SiO₂ and the surface-reaction rate constant. It is important to note that this relation represents a "steady-state" description of the oxidation process wherein B and B/A are both time- and thickness-independent parameters; this corresponds to constant values for the diffusion coefficient and solubility of the oxidizing species in the oxide and for the surface-reaction rate constant. The fit of oxidation data over a wide range of temperatures and growth ambients—with values for the linear and parabolic rate constants which are only temperature dependent—would appear to support these assumptions (1, 4, 5). The relationship between oxide thickness X_{ox} and oxidation time t_{ox} is obtained by integrating Eq. [1] to yield

$$(X_{ox}^2 - X_i^2) + A(X_{ox} - X_i) = Bt_{ox} \quad [2]$$

or

$$X_{ox}^2 + AX_{ox} = B(t_{ox} + \tau) \quad [3]$$

where X_i is the oxide thickness at $t_{ox} = 0$, and τ is a correction parameter for the presence of any initial oxide X_i . From Eq. [2] and [3], the relationship between X_i and τ is

$$\tau = \frac{X_i^2 + AX_i}{B} \quad [4]$$

These parameters have also been used to account for the fast initial oxidation rate observed at the onset of silicon oxidation in dry oxygen (1). In this case, the fit to the oxidation data using the linear-parabolic model is only true for oxides thicker than X_c and oxidation times longer than t_c , as shown in Fig. 1 (1, 2).

Experimental Procedure

The use of automated ellipsometry reduces the time required for a single measurement of the ellipsometric parameters ψ and Δ to, typically, a few tens of milliseconds.

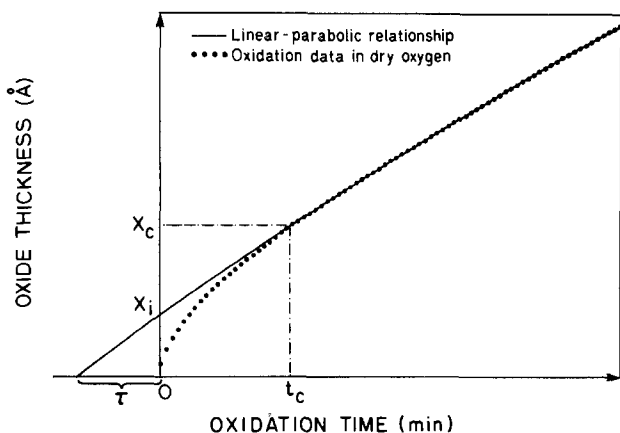


Fig. 1. The fit of the linear-parabolic relationship to oxidation data in dry oxygen. Parameters X_i and τ are defined as the intercepts at $t_{ox} = 0$ and $X_{ox} = 0$, respectively. Data point (X_c, t_c) denotes the onset of linear-parabolic kinetics.

Such a reduction in time makes automated ellipsometry an effective technique for studying the kinetics of physical and chemical processes on the surface of solids and liquids. It is especially suited to the study of oxide-growth kinetics in the initial stages of oxidation in dry oxygen where the growth rate is particularly high (1). The automated ellipsometry system used in this study was adapted to high temperature operation by van der Meulen and Hien (6) from the ellipsometric thickness analyzer (ETA) developed at the IBM Thomas J. Watson Research Center by Hauge and Dill (7). This system permits *in situ* monitoring of oxide growth at high temperatures.

Single-crystal, CZ-pulled, lightly doped with 1×10^{15} cm⁻³ phosphorus or boron, (100), (111), and (110) silicon wafers were used in this study. To investigate doping effects on oxidation, some wafers were doped using POCl₃ predeposition and subsequent drive-in to obtain surface concentrations of 1.8×10^{20} and 3.2×10^{20} cm⁻³. The pre-oxidation cleaning sequence consisted of H₂O₂-based solutions of NH₄OH and HCl with appropriate DI water rinses followed by a dip in dilute HF and a final DI rinse. The wafers were dried using nitrogen and immediately loaded in the oxidation tube in an argon ambient. Details of the operation of the automated ellipsometry system and the optical properties of Si and SiO₂ at high temperatures are described elsewhere (6).

The native-oxide thickness was measured *in situ* at the oxidation temperature at the onset of every oxidation run. Its thickness ranged between 7 (on lightly doped samples) and 22 Å (on heavily doped samples). After the background-intensity measurement, 33 data points were taken for every oxidation experiment over the thickness range of 0-600 Å. Thickness reproducibility from run to run was better than 2%.

Accurate modeling of the oxide growth kinetics, based on an understanding of the physical mechanisms involved, requires a complete characterization of the experimental conditions affecting oxide growth at the onset of oxidation in dry oxygen. As a result, the effects of growth temperature, partial pressure of oxygen in the oxidizing ambient, silicon orientation, and substrate doping on oxidation in the thin regime were investigated. A complete set of silicon-dioxide growth data (X_{ox} vs. t_{ox}) for (100), (111), and (110) silicon doped with phosphorus at 1×10^{15} , 1.8×10^{20} , and 3.2×10^{20} cm⁻³ in dry oxygen-argon mixtures corresponding to oxygen partial pressures of 1.0, 0.1, and 0.01 atm was obtained (8). An example is shown in Fig. 2 for lightly doped (100) silicon oxidized in dry oxygen.

Determination of the Oxidation Rate Constants

Accurate modeling of thermal oxidation in the thin regime necessitates a comprehensive body of experimental data to differentiate between proposed models or define new ones. In any study of the early stages of oxidation, it is important to define the onset of linear-parabolic kinetics.

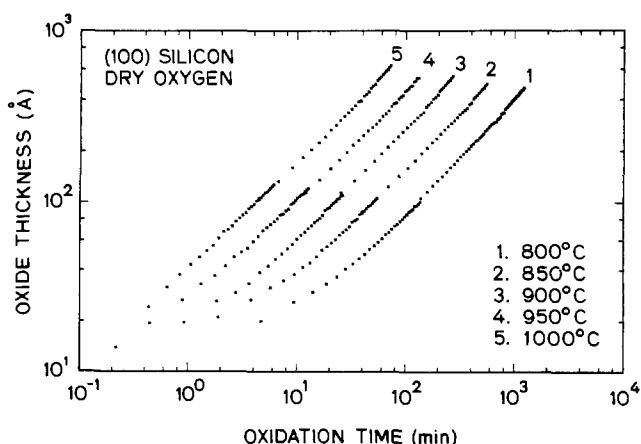


Fig. 2. Oxide thickness vs. oxidation time for (100)-oriented lightly doped silicon oxidized in dry oxygen in the 800°-1000°C range.

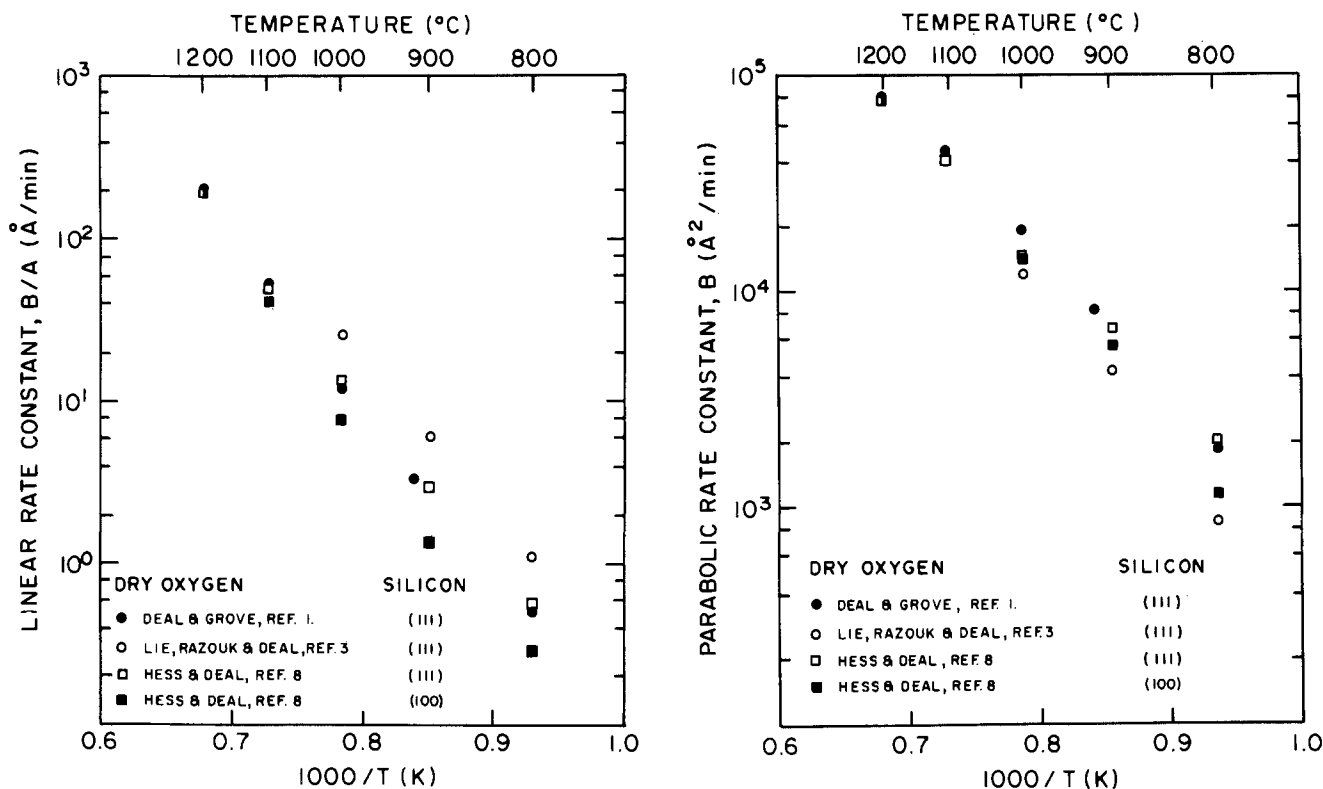


Fig. 3. Differences in some of the reported values of the linear (left), and the parabolic (right) rate constants for the oxidation of silicon in dry oxygen (1, 3, 8).

ics accurately, which, in turn, requires an equally accurate estimation of the oxidation rate constants in the linear and parabolic regimes. Details of the physical, chemical, and electrochemical mechanisms that may affect the oxidation process have not been fully identified. For example, the transport of oxidizing species through the oxide is modeled by the diffusion of neutral molecules of oxygen, using a simple diffusion constant, and the oxidation reaction is expressed in terms of a single rate constant. Little information is available regarding the interaction and influence of point defects, stress, and electric field in the oxide on the transport of oxidant species through it.

In comparison to B and B/A defined in the general oxidation relationship, other rate constants can be determined by fitting the oxidation data to a polynomial expression in the form of

$$t_{\text{ox}} = a_0 + a_1 X_{\text{ox}} + a_2 X_{\text{ox}}^2 + \dots \quad [5]$$

where the constant coefficients, a_0, a_1, a_2, \dots , are fitting parameters obtained when the error in the fit is lower than some allowable limit. It is important to note that, although these constants may result in a good empirical fit to the oxidation data over a limited thickness range, insight into the oxidation process based on such fitting constants could be misleading. In contrast, the linear-parabolic model is based upon physically meaningful constants. To the extent that this model can fit experimental data, it provides insight into the physical mechanisms present during thermal oxidation. Consequently, this analysis is based on the description of silicon oxidation by linear-parabolic kinetics. A survey of the results of oxidation studies, however, would indicate some discrepancies in the reported values of the linear and parabolic rate constants (2). Some of these results (1, 5, 9) are reproduced in Fig. 3, where it can be seen that substantial variations in B and B/A were obtained, particularly at lower temperatures. Such differences stem from variations in the techniques and fitting parameters used in calculating the rate constants, and will be discussed later. These differences in oxidation rate constants introduce large uncertainties in the magnitude of oxidation-rate enhance-

ment in the thin regime. Being interested in the physical mechanisms responsible for the "anomalous" thin-regime kinetics, accurate values of B and B/A were necessary to determine accurately the end of the thin regime and the onset of linear-parabolic kinetics. For these reasons, an evaluation of the methods used to determine B and B/A was undertaken.

In this section, the techniques used to determine the oxidation rate constants are discussed, and a novel method is introduced to obtain constants that are representative of the oxidation process as defined by the linear-parabolic model and not merely empirical fitting parameters.

Determination of the rate constants based on X_1 .—By dividing both sides of Eq. [2] by $(X_{\text{ox}} - X_1)$, the linear-parabolic relationship can be rewritten as

$$(X_{\text{ox}} + X_1) = B \frac{t_{\text{ox}}}{(X_{\text{ox}} - X_1)} - A \quad [6]$$

For thickness-time data that fit the linear-parabolic model, a plot of $(X_{\text{ox}} + X_1)$ vs. $t_{\text{ox}}/(X_{\text{ox}} - X_1)$ should result in a straight line whose slope is B and intercept at $t_{\text{ox}}/(X_{\text{ox}} - X_1) = 0$ is $-A$. The value of X_1 used to generate this plot is obtained by estimating the intersection of the extrapolation of the linear-parabolic relationship with the thickness axis, as seen in Fig. 1 (1).

Determination of the rate constants based on τ .—By dividing both sides of Eq. [3] by X_{ox} , the linear-parabolic relationship can be rewritten as

$$X_{\text{ox}} = B \frac{(t_{\text{ox}} + \tau)}{X_{\text{ox}}} - A \quad [7]$$

A plot of X_{ox} vs. $(t_{\text{ox}} + \tau)/X_{\text{ox}}$ should again result in a straight line whose slope is B and intercept at $(t_{\text{ox}} + \tau)/X_{\text{ox}} = 0$ is $-A$. The value of τ used to generate this plot is also obtained by estimating the intersection of the extrapolation of the linear-parabolic relationship with the time axis, as shown in Fig. 1 (1).

It should be noted that, in the two above equivalent methods, the values of X_1 and τ are estimated approximately and are used as fitting parameters.

Determination of the rate constants based on X_c and t_c .—This approach eliminates the need for a fitting parameter and is based on the assumption that the oxidation data fit a linear-parabolic relationship beyond the fast initial regime. If X_c and t_c are the oxide thickness and oxidation time at or beyond the onset of linear-parabolic kinetics, then

$$(X_{ox}^2 - X_c^2) + A(X_{ox} - X_c) = B(t_{ox} - t_c) \quad [8]$$

for any set of oxide thickness X_{ox} and oxidation time t_{ox} , such that $X_{ox} > X_c$ and $t_{ox} > t_c$. A plot of $(X_{ox} + X_c)$ vs. $(t_{ox} - t_c)/(X_{ox} - X_c)$ should yield a straight line with a slope equal to B and an intercept equal to $-A$. This method is equivalent to shifting the thickness and time axes to a point (X_c, t_c) on the linear-parabolic portion of the data.

The onset of linear-parabolic kinetics can be determined by calculating the error in fitting the oxidation data, starting from a point (X_s, t_s) to the largest data point (X_f, t_f) , to a linear-parabolic expression. If the starting point is smaller than (X_c, t_c) , the error is large, and the values obtained for B and B/A are lower and higher than their true values, respectively. If the starting point, however, is equal to or larger than (X_c, t_c) , the error reaches a minimum and stays at that value, and the oxidation rate constants remain unchanged, as illustrated in Fig. 4. This analysis is based on the assumptions of steady-state and thickness-independent rate constants. This method was first introduced by Irene and van der Meulen (2) in a study of the discrepancies in the reported values of the rate constants for the oxidation of silicon in dry oxygen.

Determination of the rate constants based on $(dX_{ox}/dt)^{-1}$.—In this method, the oxidation rate is obtained numerically or graphically from the growth data. The dependence of the inverse of the oxidation rate on oxide thickness is found by inverting Eq. [1] as

$$\left(\frac{dX_{ox}}{dt}\right)^{-1} = \left(\frac{2}{B}\right) X_{ox} + \left(\frac{A}{B}\right) \quad [9]$$

A plot of $(dX_{ox}/dt)^{-1}$ vs. X_{ox} , therefore, results in a straight line whose slope is $(2/B)$ and intercept at $X_{ox} = 0$ is (A/B) . This method was used by Hopper *et al.* (10) in discussing the results of the oxidation of (111) silicon in the 700°-950°C range in various oxygen partial pressures.

Comparison.—The methods based on X_i or τ depend on an estimate of either parameter which is normally made by examining the oxidation data, such as that shown in Fig. 1. The accuracy with which the rate constants are determined is dependent on the value of X_i or τ , as will be discussed in the following section. No fitting parameter is required in the (X_c, t_c) or the inverse-rate method; in

Table I. Reported values of X_i used to determine the oxidation rate constants (1965-1982)

Workers	$X_i(\text{Å})$
Deal and Grove (1)	230 ± 30
Hess and Deal (8)	160 ± 40
Lie <i>et al.</i> (3)	40 ± 0

both, the rate constants obtained should be unique, provided the data can be described by the linear-parabolic model. The process of differentiation, however, requires a large number of closely spaced data points to avoid errors resulting from interpolation.

Optimum X_i Technique

In a study of the oxidation of (111)-oriented silicon in dry oxygen (1), Deal and Grove used the τ method to calculate the rate constants. Based on the different values of τ obtained in the 700°-1200°C range, corresponding values of X_i were calculated using Eq. [4], and a constant value of 230Å resulted. The value of X_i used in the determination of rate constants, however, has not been the same over the years, as demonstrated in Table I. The trend towards decreasing values of X_i reflects the interest in fitting data covering the growth of thinner oxides.

In this section, it will be demonstrated that values of the linear and parabolic oxidation rate constants determined from oxidation data depend on the value of X_i used in the analysis. An optimum X_i technique is introduced, wherein the value of X_i is obtained by maximizing the number of data points (X_{ox}, t_{ox}) that fit a linear-parabolic expression, and this optimum value is referred to as $X_{i(opt)}$. It will also be shown that the rate constants obtained using $X_{i(opt)}$ are the same as those obtained by the inverse-rate method, which, as discussed earlier, does not require any fitting parameters.

The oxidation data of (100) silicon oxidized in dry oxygen at 1000°C is used, as an example typical of all temperatures and orientations, in plotting $(X_{ox} + X_i)$ vs. $t_{ox}/(X_{ox} - X_i)$ for different values of X_i , as shown in Fig. 5. It can be seen that an optimum value of X_i exists for which the number of data points fitting a straight line (*i.e.*, a linear-parabolic relationship) is maximum. The thickness X_c above which the growth can be modeled as linear-parabolic is a strong function of X_i , and is at minimum in the case of the optimum X_i . For oxides thinner than X_c , the data deviate sharply from a straight line because of the fast initial-oxidation regime. For oxides thicker than X_c , a straight-line plot of $(X_{ox} + X_i)$ vs. $t_{ox}/(X_{ox} - X_i)$ is obtained for a range of values of X_i around the optimum value. The following observations are apparent from the figure.

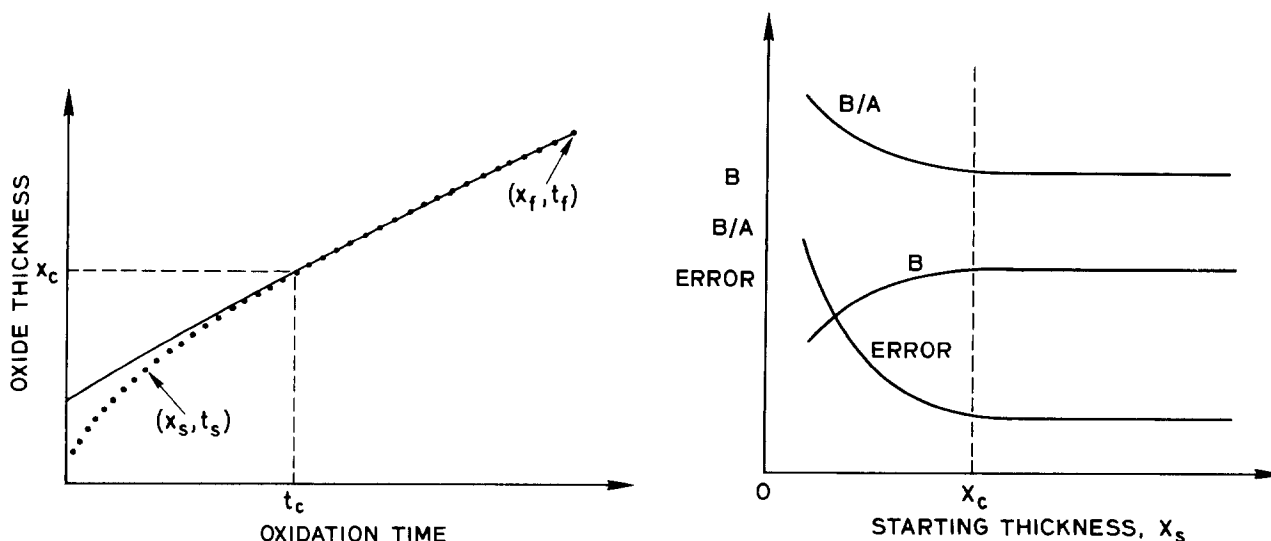


Fig. 4. The (X_c, t_c) method showing dependence of the linear and parabolic rate constants and the error in the fit to oxidation data on the position of the starting point (X_s, t_s) with respect to (X_c, t_c) .

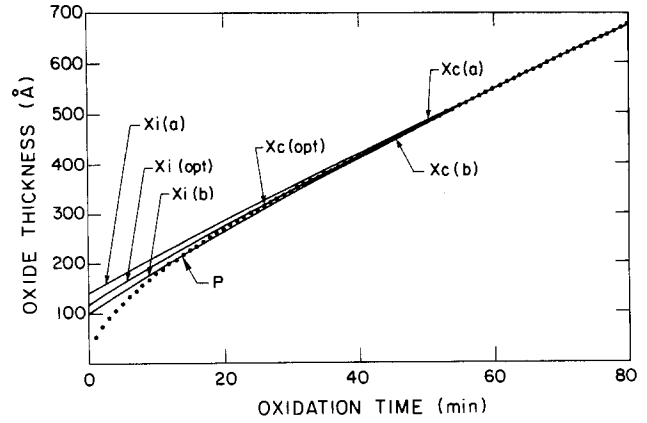
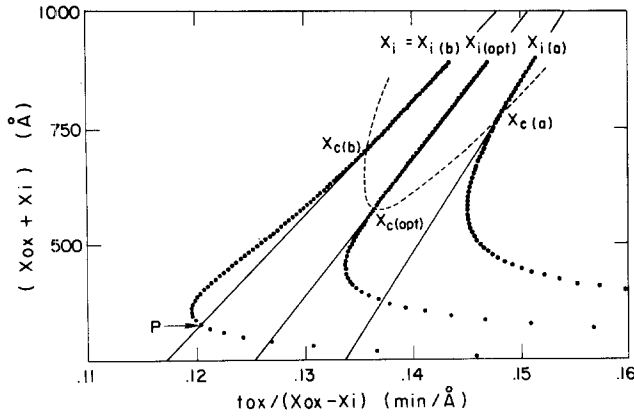


Fig. 5. Effect of the value of X_i on (a, left) the linear and parabolic rate constants as seen from the slope and intercept of the straight-line fit in a $(X_{ox} + X_i)$ vs. $t_{ox}/(X_{ox} - X_i)$ plot, and (b, right) the fit to the oxidation of (100) silicon at 1000°C in dry oxygen.

1. The straight-line plot obtained for $X_i = X_{i(a)} > X_{i(opt)}$ is steeper than that obtained for $X_i = X_{i(opt)}$; therefore, B is larger and B/A is smaller than the rate constants obtained with $X_{i(opt)}$. This is seen from the change in slope and intercept of the two plots. The linear-parabolic relationship fits the data beyond $X_{c(a)}$, where $X_{c(a)} > X_{c(opt)}$, as in Fig. 5b.

2. The straight-line plot obtained for $X_i = X_{i(a)} < X_{i(opt)}$ is less steep than that obtained for $X_i = X_{i(opt)}$ and, as a result, B is smaller and B/A is larger than the rate constants obtained with $X_{i(opt)}$. This is also seen from the change in slope and intercept of the two plots. In this case, the linear-parabolic relationship and the (X_{ox}, t_{ox}) data intersect at point P. The thickness $X_{c(b)}$, beyond which the linear-parabolic expression fits the data, is also larger than $X_{c(opt)}$.

This observed behavior was found to be qualitatively the same for all other orientations and at all temperatures. It should be noted that such results were only made possible because of the closely spaced data points obtained by automated ellipsometry.

Having established that the oxidation rate constants depend on the value of the parameter X_i , it is important to estimate quantitatively the deviation in the rate constants from their optimum values due to different values of X_i . For this purpose, B and B/A are obtained by applying the optimum X_i method to the $X_{ox} - t_{ox}$ data points of (100) silicon oxidized in dry oxygen at 1000°C. This is illustrated in Fig. 6, where plots of $(X_{ox} + X_i)$ vs. $t_{ox}/(X_{ox} - X_i)$ are shown for X_i values in the 100-140Å range in steps of 10Å. It can be observed that the maximum number of data points that fit a straight line corresponds to X_i approximately equal to 120Å. Similar plots were obtained for different values of X_i around 120Å in increments of 2.5Å, and it was found, by comparing plots, that the maximum

number of data points that fit the straight-line portion of the plot corresponds to $X_i = 117.5\text{Å}$. From the slope and intercept of this plot, the optimum rate constants obtained are

$$B = 28,500 \text{ Å}^2/\text{min}$$

and

$$B/A = 8.66 \text{ Å}/\text{min}$$

It can also be observed in Fig. 6 that values of X_i other than the optimum will also result in a straight-line fit for data points corresponding to thicker oxides from which the linear and parabolic rate constants could be determined. Modeling oxide growth with these values of B and B/A would result in small errors in fitting the data. The error in the rate constants themselves, however, can be rather large, and attempts to identify the physical processes involved might also be in error. Table II summarizes the values obtained for the rate constants when using values of X_i other than the optimum value in the example shown in Fig. 5 and 6. It can be seen that, for $X_i = 140\text{Å}$, the deviations in B and B/A from their values determined with $X_{i(opt)}$ are approximately 30 and 10%, respectively; here, X_i is only 22.5Å away from the optimum 117.5Å.

It is, therefore, concluded that variations in the parameter X_i can result in substantial deviations in the obtained oxidation rate constants. It is shown next why this optimum technique should be used.

A plot of the thickness dependence of the inverse of the oxidation rate for (100) silicon oxidized in dry oxygen at 1000°C is shown in Fig. 7. There are the same data shown in Fig. 5 and 6. The oxidation rate was obtained by numerical differentiation of the oxide-growth data points using a five-point parabolic-fit routine (11). It can be seen that the linear-parabolic relationship (corresponding to the straight-line portion) applies beyond the fast initial oxidation regime ($\sim 350\text{Å}$). The rate constants obtained from the slope and intercept of this straight-line fit are

$$B = 28,600 \text{ Å}^2/\text{min}$$

and

$$B/A = 8.65 \text{ Å}/\text{min}$$

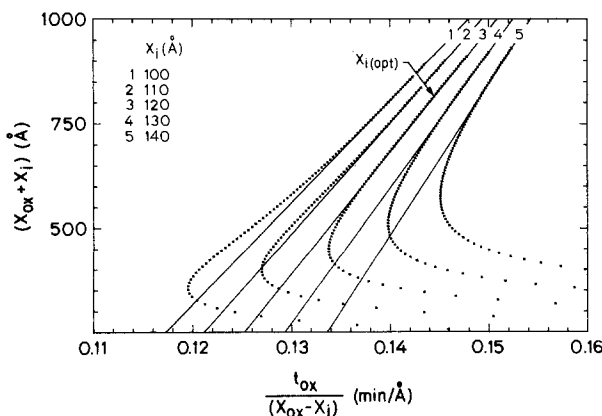


Fig. 6. Effect of the values of X_i on the oxidation rate constants obtained from plots of $(X_{ox} + X_i)$ vs. $t_{ox}/(X_{ox} - X_i)$ for $X_i = 100, 110, 120, 130,$ and 140Å .

Table II. Dependence of B , B/A , and the resulting deviations in B and B/A (from their values obtained using $X_{i(opt)}$) on the parameter X_i

$X_i(\text{Å})$	$B(\text{Å}^2/\text{min})$	$B/A(\text{Å}/\text{min})$	Deviation in B (%)	Deviation in B/A (%)
100	24,400	9.36	-14.60	+7.97
110	26,000	9.01	-8.75	+3.95
120	29,400	8.56	+3.00	-1.17
130	33,000	8.19	+15.60	-5.46
140	36,700	7.88	+28.50	-9.04

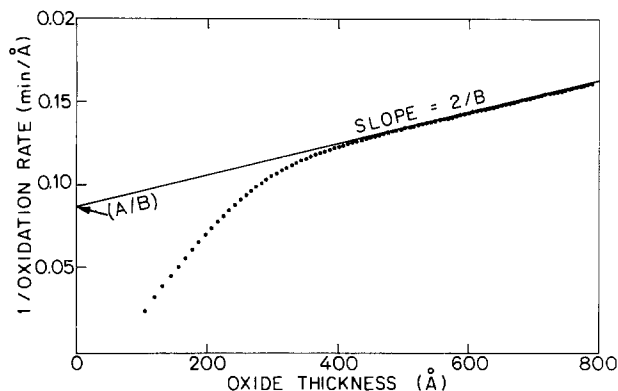


Fig. 7. Determination of the linear and parabolic rate constants based on the inverse-oxidation-rate method. Oxidation data is for (100) silicon oxidized at 1000°C in dry oxygen (same data used in Fig. 5).

the same as those obtained using the optimum X_i technique.

The inverse-oxidation-rate method yields the linear and parabolic rate constants relevant to the description of the oxidation process by the linear-parabolic model, because it does not require any additional fitting parameters. This assumes that the oxidation process is accurately described by this model. It has also been shown that identical results are obtained if the optimum X_i is used in the determination of the oxidation rate constants by plotting $(X_{ox} + X_i)$ vs. $t_{ox}/(X_{ox} - X_i)$ and fitting the maximum number of data points to the straight-line portion of the plot. The added advantage of the optimum X_i method is that no differentiation is required and, therefore, no accuracy is lost as a result of the inherently noisy differentiation process. The accuracy of both of these techniques depends, however, on the availability of a dense data set which can only be provided by *in situ* ellipsometry techniques. These findings confirm the conclusions of Irene and van der Meulen (2) in comparing the methods of analysis of SiO_2 film growth data.

Oxidation Rate Constants of Lightly Doped Silicon

In this investigation, (100)-, (111)-, and (110)-oriented lightly doped silicon wafers were oxidized in dry oxygen up to a thickness of $\sim 600\text{\AA}$. The growth was monitored by a high temperature automated *in situ* ellipsometer. The linear and parabolic rate constants were determined by increasing X_i by 2.5\AA steps until its optimum value, corresponding to the maximum number of data points fitting the linear-parabolic relationship, was reached. Table III summarizes the results obtained at five temperatures in the 800°-1000°C range; the values of $X_{i(\text{opt})}$ are also shown. It can be seen that, for (100) and (111) orientations, $X_{i(\text{opt})}$ decreases with temperature and is nearly constant for (110).

Parabolic rate constant.—The parabolic rate constants of (100)-, (111)-, and (110)-oriented lightly doped silicon oxidized in dry oxygen are plotted in Fig. 8. The values obtained by the $X_{i(\text{opt})}$ technique are plotted at 800°, 850°, 900°, 950°C, and 1000°C. Results plotted at 1100° and 1200°C are obtained by applying the same method to published oxidation data (5). These published data were not obtained using *in situ* ellipsometry and, therefore, larger

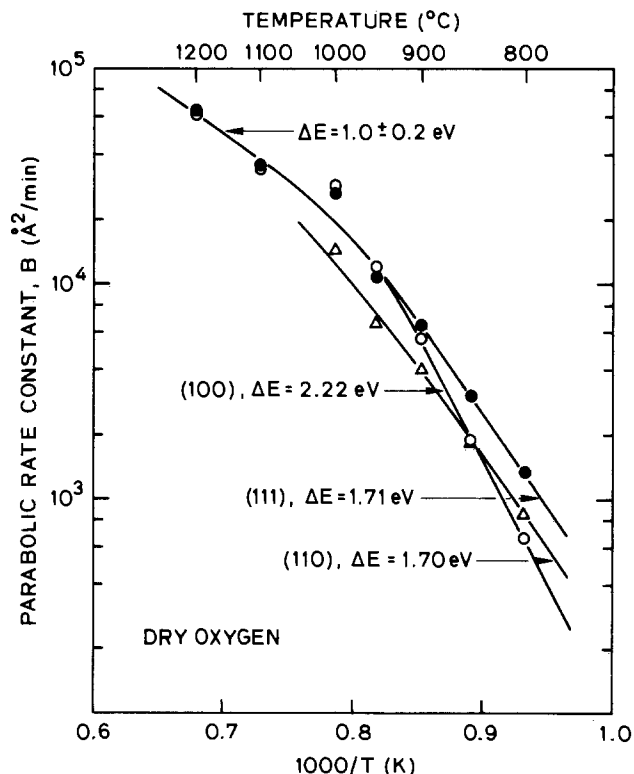


Fig. 8. Parabolic rate constant for the oxidation of (100)-, (111)-, and (110)-oriented lightly doped silicon in dry oxygen in the 800°-1000°C range.

error bars would be expected for the rate constants at 1100° and 1200°C. It can be seen that the parabolic rate constant exhibits a break in its activation energy between 950° and 1000°C. Above this temperature, it is independent of substrate orientation and has an activation energy of 1.0 ± 0.2 eV for both (100) and (111). At lower temperatures, B is dependent on the orientation of the underlying substrate and has low temperature activation energies of 2.22, 1.71, and 1.70 eV for (100), (111), and (110), respectively. These low temperature activation energies are asymptotic values obtained by a least squares fit to the lowest temperature data points to an Arrhenius expression. The dependence of the parabolic rate constant on substrate orientation in the low temperature range was observed by Irene (12) while studying the effects of trace amounts of water on the oxidation of silicon in dry oxygen in the 800°-1000°C range. The orientation dependence of B (12) is the same as observed in this work.

Deal and Grove (1) reported an orientation-independent parabolic rate constant with a single activation energy of 1.23 eV for the oxidation of (100)- and (111)-oriented silicon in dry oxygen in the 700°-1200°C range, which is close to the 1.2 eV activation energy of oxygen diffusion through fused silica. Pliskin (4) also observed the parabolic rate constant to be independent of substrate orientation at temperatures as low as 910°C. Irene and van der Meulen (2) reported a single activation energy of 2.3 eV when oxidizing (100)-oriented silicon in dry oxygen in the 780°-980°C range.

Table III. Linear and parabolic rate constants and the optimum value of X_i for the oxidation of (100)-, (111)-, and (110)-oriented lightly doped silicon in dry oxygen in the 800°-1000°C range

T_{ox} (°C)	(100)			(111)			(110)		
	B ($\text{\AA}^2/\text{min}$)	B/A ($\text{\AA}/\text{min}$)	$X_{i(\text{opt})}$ (\AA)	B ($\text{\AA}^2/\text{min}$)	B/A ($\text{\AA}/\text{min}$)	$X_{i(\text{opt})}$ (\AA)	B ($\text{\AA}^2/\text{min}$)	B/A ($\text{\AA}/\text{min}$)	$X_{i(\text{opt})}$ (\AA)
1000	28,600	8.65	112.5	26,600	16.4	117.5	14,300	25.4	90.0
950	12,100	4.01	105.0	10,800	9.91	105.0	6,590	10.4	97.5
900	5,590	2.08	85.0	6,500	4.60	87.5	4,000	4.61	97.5
850	1,890	0.93	82.5	2,980	2.09	80.0	1,840	1.75	100.0
800	660	0.43	70.0	1,350	0.90	67.5	855	0.72	100.0

In more recent oxidation studies, a break in the activation energy of both the parabolic and linear rate constants was observed and reported. Irene and Dong (13) observed that the activation energy of the parabolic rate constant for the oxidation of (100)-oriented silicon in ultradry oxygen (< 1 ppm H₂O) changed from 1.3 eV in the 980°-1150°C range to 2.1 eV in the 780°-1000°C range. For the oxidation of (100)- and (111)-oriented silicon in dry oxygen in the 800°-1000°C range, these activation energies were found to be 1.40 and 1.78 eV for temperatures higher and lower than 900°C, respectively (5). Values of the parabolic rate constant reported in Ref. (13) at 780°, 893°, and 980°C fall on the solid line in Fig. 8.

The low temperature activation energy of *B* obtained in this study is in agreement with values reported for (100) (2, 13) and (111) (5). The high temperature activation energy is also in agreement with the (100) value (13). As concluded in Ref. (13), disagreements in published values of the parabolic rate constant are, therefore, confirmed here to be the result of studying different temperature ranges where the activation energy is different.

Linear rate constant.—The linear rate constants obtained for (100)-, (111)-, and (110)-oriented lightly doped silicon oxidized in dry oxygen are plotted in Fig. 9. The values obtained using $X_{1(100)}$ are plotted at 800°, 850°, 900°, 950°, and 1000°C. Values plotted at 1100° and 1200°C are the result of applying the same technique to oxidation data in the literature (1, 5). It should be pointed out here that the error margins at 1100° and 1200°C are large ($\pm 20\%$) because the data are sparse, values of the quantity *A* are small, and any slight error in the straight-line fit will result in a small error in the extracted value of *B* and a large error in that of *B/A*. For example, the 1200°C data nearly fit a parabolic growth law, which mathematically corresponds to a linear-parabolic relationship where *A* is very small and, consequently, *B/A* is very large.

The linear rate constant also exhibits a break point in its activation energy at approximately the same temperature as the parabolic rate constant; however, the direction of the break is opposite to that of *B* (the high temperature range has a larger activation energy than does the low

temperature range). At low temperatures, activation energies of 1.76, 1.74, and 2.10 eV were observed for (100), (111), and (110), respectively. As for the parabolic rate constant, these low temperature activation energies are obtained by a least squares fit of the lowest temperature data points to an Arrhenius expression. The (100) and (111) orientations have nearly the same slope, and the average ratio between the linear rate constants of the two orientations $(B/A)_{111}:(B/A)_{100}$ is 2.18. At high temperatures, the activation energy is 2.75 ± 0.22 eV for both (100) and (111).

The activation energy of the linear rate constant was originally reported to be 2.0 eV for the oxidation of (100)- and (111)-oriented silicon in dry oxygen (1). This value is similar to the Si-Si bond breaking energy of 1.83 eV, which supports the suggestion that the rate-limiting step in the linear regime is the reaction of oxygen and silicon at the Si-SiO₂ interface. The ratio between the linear rate constants of the two orientations $(B/A)_{111}:(B/A)_{100}$ was found to be 1.68. Irene and van der Meulen (2) reported an activation energy of 1.5 eV for the oxidation of (100)-oriented silicon in dry oxygen in the 780°-980°C range and concluded that oxygen-oxygen bond breaking is important in linear kinetics.

Breaks in the activation energy of the linear rate constant have also been discussed in the literature. In the oxidation of (100)-oriented silicon, a change from 2.2 eV in the 980°-1150°C range to 1.6 eV in the 780°-1000°C range in the activation energy of *B/A* was reported (13). A break was also observed in the linear rate constant, but it was less pronounced than that observed in the parabolic rate constant (5). The observed activation energy was 1.87-1.89 eV. Values of the linear rate constant reported by Irene and Dong (13) nearly fall on the solid line in Fig. 9.

The low temperature activation energy of *B/A* obtained in this study is similar to the (100) reported value (2, 13); however, at higher temperatures, it is larger than those obtained in earlier studies (5, 13). Here again the discrepancy in published values of the rate constants is the result of studying different temperature ranges with different activation energies.

The temperature dependence of the linear and parabolic rate constants suggests that they could be fitted to expressions of the forms

$$B = 1/[K_1 \exp(+E_1/kT) + K_2 \exp(+E_2/kT)]$$

and

$$B/A = C_1 \exp(-E_1/kT) + C_2 \exp(-E_2/kT)$$

The use of the above expressions, however, resulted in large errors in the fit of the data points in comparison to fitting them to a single activation-energy expression in designated temperature ranges. Minimum errors in the fitting to such single activation-energy expressions were obtained by choosing 1000°C as the break temperature. The results of such fits are as follows

$$B = \begin{cases} 1.70 \text{ E } 13 \exp(-2.22 \text{ eV}/kT) & (100) \\ 1.34 \text{ E } 11 \exp(-1.71 \text{ eV}/kT) & (111) \\ 3.73 \text{ E } 10 \exp(-1.63 \text{ eV}/kT) & (110) \end{cases} \quad T < 1000^\circ\text{C}$$

$$B = \begin{cases} 1.31 \text{ E } 07 \exp(-0.68 \text{ eV}/kT) & (100) \\ 2.56 \text{ E } 07 \exp(-0.76 \text{ eV}/kT) & (111) \end{cases} \quad T > 1000^\circ\text{C}$$

and

$$B/A = \begin{cases} 7.35 \text{ E } 07 \exp(-1.76 \text{ eV}/kT) & (100) \\ 1.33 \text{ E } 08 \exp(-1.74 \text{ eV}/kT) & (111) \\ 4.73 \text{ E } 09 \exp(-2.10 \text{ eV}/kT) & (110) \end{cases} \quad T < 1000^\circ\text{C}$$

$$B/A = \begin{cases} 3.53 \text{ E } 13 \exp(-3.20 \text{ eV}/kT) & (100) \\ 6.50 \text{ E } 12 \exp(-2.95 \text{ eV}/kT) & (111) \end{cases} \quad T > 1000^\circ\text{C}$$

where *B* is in square angstroms per minute and *B/A* is in angstroms per minute. The above expressions were obtained by a least squares fit of the rate constants to an Arrhenius expression for temperatures above and below 1000°C. It should be remembered that such data

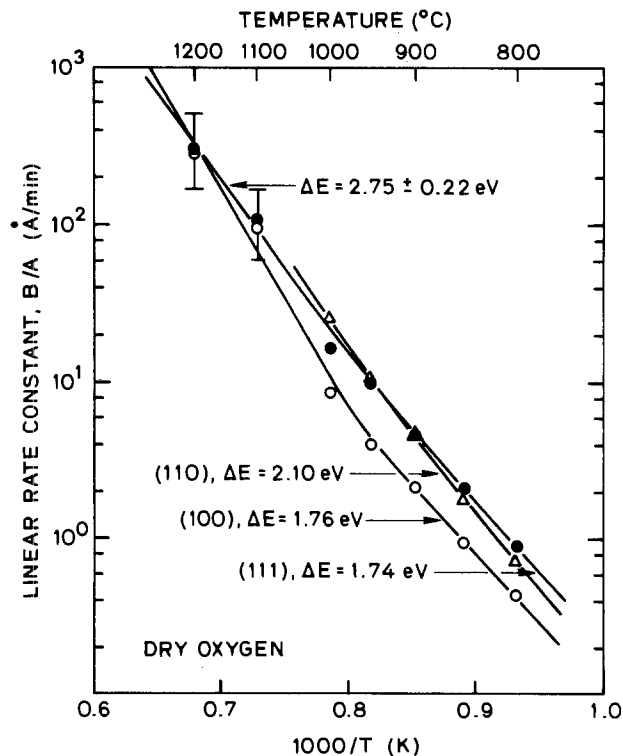


Fig. 9. Linear rate constant for the oxidation of (100)-, (111)-, and (110)-oriented lightly doped silicon in dry oxygen in the 800°-1000°C range.

consisted of a relatively small number of data points, which reflects itself in correspondingly large error bars for the linear and parabolic rate constants at temperatures higher than 1000°C.

When the results of this study are compared with previous studies, as shown in Fig. 3 for example, it is noticed that some differences exist. It should be first pointed out that all of the data obtained in this study were for oxides thinner than 1000Å. The B and B/A values obtained in this study do not all agree with earlier values, which were largely obtained from the analysis of thicker oxides and less dense data sets (1, 5, 9). Such differences could result in errors when predicting the oxide growth for very thick oxides (several thousand angstroms) when using the B and B/A values obtained in this study. The values of B and B/A obtained in this work agree with the results of Irene and van der Meulen (2) and Irene and Dong (13) because of the use of closely spaced data sets and an optimized method for the determination of the rate constants. Of great interest here is that, in Ref. (2) and (13), the oxide growth was studied up to 1100Å. The results of this study should, therefore, be used with caution when modeling oxide growth for oxides thicker than 1100Å. Differences between thin and thick values of the oxidation rate constants, if confirmed by further experiments, may suggest that B and B/A are indeed thickness-dependent rate constants. Such experiments are needed to quantify the differences, which, if true, would be a strong evidence for changes in the properties of the growing oxide affecting the rate constants.

Discussion

Breaks in the activation energies of the parabolic and linear rate constants (Fig. 8 and 9) indicate that B and B/A are composite rate constants rather than kinetically simple single-activated steps. Other interpretations of a temperature-dependent activation energy are possible. A break in the activation energy of a rate constant could be analyzed by assuming that more than one kinetic step is involved. According to the direction of the break, these steps could occur at the same time (in parallel) or one after the other (in series). The direction of the break in the parabolic rate constant is an example of two simple steps occurring in series, while the break in the activation energy of the linear rate constant is an indication of two parallel processes. The direction of the curvature in the Arrhenius plots of the linear rate constant gives strong support for the interface mechanism to be occurring by the reaction of silicon with two oxidant species, molecular and atomic oxygen (14). This description of the interface reaction was proposed by Ghez and van der Meulen (15) to explain the less-than-linear pressure dependence of the linear rate constant. Figure 10 illustrates the temperature behavior of a composite process consisting of two activated steps with different activation energies occurring either in series or in parallel. The resulting process is limited in the series case by the slower mechanism, and dominated in the parallel case by the faster.

Another possible interpretation of the behavior of the linear and parabolic rate constants with temperature is to assume that the same physical mechanism is present at all temperatures but that it is affected by some other temperature-dependent process. In a revised model of thermal oxidation, Irene (3) proposed that high temperature oxidant transport is dominated by the classical mechanism of thermal diffusion through the oxide, while low temperature transport is dominated by a flux of oxidizing species in micropores. The effect of stress in thermal SiO₂ during growth and the influence of the viscoelastic properties of the oxide on the transport and reaction of the oxidant species through the oxide and at the Si-SiO₂ interface are proposed as one such mechanism. A revised expression for the linear rate constant that takes into account the rate of viscous flow in the oxide has been formulated (2). Viscous flow is known to occur in SiO₂ films on silicon at 960°C (16, 17), which is close to where the parabolic rate constant changes from its high

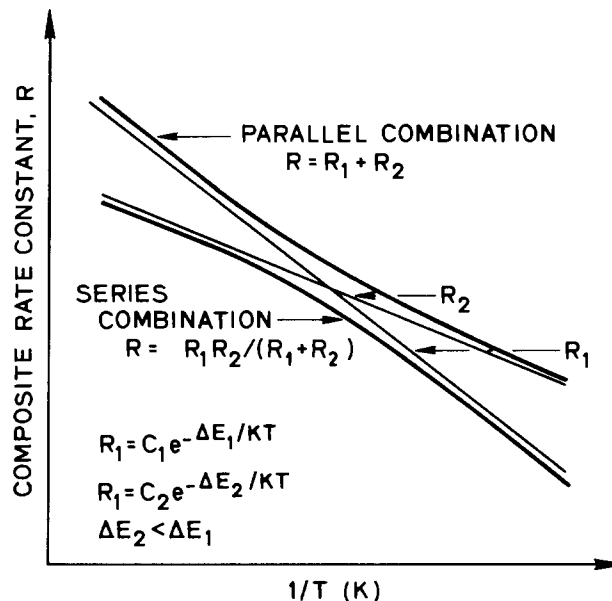


Fig. 10. Example of a composite rate constant consisting of two processes with different activation energies occurring either in series or in parallel.

temperature low activation orientation-independent behavior to its low temperature high activation orientation-dependent behavior in Fig. 8. Below 960°C, the oxide does not experience significant viscous flow and is expected to be in a high state of stress. If the transport process of the oxidant species is stress-dependent, then the magnitude and activation energy of B should reflect the influence of substrate orientation on oxide stress. All three orientations have different values of B in the low temperature range; however, (111) and (110) have similar activation energies, which may indicate that, at low temperatures, the state of stress in the oxide may be similar for these two orientations. Above 960°C, the silicon-dioxide layer experiences viscous flow and the stress is relieved. Transport of the oxidant species then proceeds with a lower activation energy. The oxide then bears no signature of the underlying substrate, and the parabolic rate constant is independent of orientation; its magnitude and activation energy are the same for all orientations.

The behavior of the linear rate constant can also be explained by considering the effect of oxide stress on the oxidation reaction at the Si-SiO₂ interface. In the low temperature range, the Si-Si bond breaking energy is lowered by stress in the silicon-dioxide layer. The activation energies of (100) and (111) indicate that the stress in the oxide is similar for these two orientations. The atomic arrangement of silicon atoms at the Si-SiO₂ interface is different for these orientations, but the resultant activation energy for linear kinetics is the same. The (110) orientation has a higher activation energy, which may again be a combined result of the interaction of oxide stress and the details of the silicon-oxygen reaction at the interface. In the high temperature range, the oxide has experienced viscous flow, stress is accordingly greatly reduced, and the Si-Si bond breaking energy must be supplied thermally. This explains the greater activation energy at high temperatures where, despite the inaccuracy in the extracted rate constants, the values of B/A for (100) and (111) are similar. This suggests that the activation energy for the oxygen-silicon reaction is the same for these orientations and is much higher than values previously reported.

The rather abrupt change in behavior of the rate constants at 960°C may be the result of the large activation energy (5.29-7.68 eV) of the viscosity of vitreous silica (18). This implies essentially that no measurable flow occurs below 960°C and that it is practically complete above 960°C.

The fit of the linear-parabolic model to oxidation data beyond the fast initial regime indicates that B and B/A

can be considered constant, in a first-order analysis, over a wide range of oxide thicknesses. Some of the discrepancies between values of the rate constants obtained in this study and earlier studies may suggest a thickness dependence in B and B/A , as discussed earlier. The thin oxide regime which is not well modeled by constant B and B/A is the subject of forthcoming papers (19, 20) where the same dense oxidation data sets are analyzed to resolve some of the physical mechanisms present in the early stages of oxidation in dry oxygen.

Conclusions

The techniques used to determine the linear and parabolic rate constants have been reviewed and compared. The optimum X_i technique, wherein the maximum number of data points are fitted to a linear-parabolic expression, was shown to result in unique values for these constants as defined in the Deal-Grove model. It has also been shown that such values of the rate constants have physically relevant information about the oxidation process as described by the linear-parabolic model. Applying this technique to the oxidation data obtained in this study and those published in the literature resulted in activation energies of the rate constants that changed with temperature. Viscous flow occurs in SiO_2 at the same temperature where a break appears in the Arrhenius-type plots of the rate constants. The viscoelastic properties of the oxide and possible additional transport mechanisms in the oxide were discussed as possible physical mechanisms in interpreting the results.

Acknowledgments

The authors would like to acknowledge many helpful discussions with Dr. Bruce E. Deal, Dr. C. P. Ho (who suggested stress having a possible effect on the rate con-

stants), and Dr. Reda R. Razouk. This study was sponsored by DARPA Contract no. MDA 903-79-C-0257.

Manuscript received Nov. 30, 1984.

Stanford University assisted in meeting the publication costs of this article.

REFERENCES

1. B. E. Deal and A. S. Grove, *J. Appl. Phys.*, **36**, 3770 (1965).
2. E. A. Irene and Y. J. van der Meulen, *This Journal*, **123**, 1380 (1974).
3. E. A. Irene, *J. Appl. Phys.*, **54**, 5416 (1983).
4. W. A. Pliskin, *IBM J. Res. Dev.*, **10**, 198 (1966).
5. L. N. Lie, R. R. Razouk, and B. E. Deal, *This Journal*, **129**, 2828 (1982).
6. Y. J. van der Meulen and N. C. Hien, *J. Opt. Soc. Am.*, **64**, 804 (1974).
7. P. S. Hauge and F. H. Dill, *IBM J. Res. Dev.*, **17**, 472 (1972).
8. H. Z. Massoud, Ph. D. Thesis, Stanford University, Stanford, CA (1983).
9. D. W. Hess and B. E. Deal, *This Journal*, **124**, 735 (1977).
10. M. A. Hopper, R. A. Clarke, and L. Young, *ibid.*, **122**, 1216 (1975).
11. G. Dahlquist and A. Bjorck, "Numerical Methods," Prentice-Hall, Englewood Cliffs, NJ (1974).
12. E. A. Irene, *This Journal*, **121**, 1613 (1974).
13. E. A. Irene and D. W. Dong, *ibid.*, **125**, 1146 (1978).
14. E. A. Irene, *Appl. Phys. Lett.*, **40**, 74 (1982).
15. R. Ghez and Y. J. van der Meulen, *This Journal*, **119**, 1100 (1972).
16. E. P. EerNisse, *Appl. Phys. Lett.*, **30**, 290 (1977).
17. E. P. EerNisse, *ibid.*, **35**, 8 (1979).
18. G. Hetherington, K. H. Jack, and J. C. Kennedy, *Phys. Chem. Glasses*, **5**, 130 (1964).
19. H. Z. Massoud, J. D. Plummer, and E. A. Irene, Submitted to *This Journal*.
20. H. Z. Massoud, J. D. Plummer, and E. A. Irene, Submitted to *This Journal*.

Isotope Studies of Fe-18Cr-3Mo (100) Oxidation Using Raman Spectroscopy

J. C. Hamilton* and R. J. Anderson

Sandia National Laboratories, Livermore, California 94550

ABSTRACT

Raman spectra have been obtained for chromia and iron-chromium spinels grown on an Fe-18Cr-3Mo (100) surface by exposure to oxygen 16, oxygen 18, and a mixture of the two isotopes, at 700°C and 1.3×10^{-4} Pa total pressure. Raman spectroscopy has been combined with ion bombardment to profile the isotopically tagged compounds produced during sequential oxidation in the two isotopes. We conclude that growth of spinel and chromia on this surface occurs predominantly by cation diffusion. Mixing of isotopes by diffusion within the oxide scale during these oxidations was minimal. Mixing of isotopes during ion sputtering was not an impediment to the Raman analysis.

Many experimental techniques are routinely used to determine the predominant transport mechanisms involved in scale growth during high temperature corrosion. The simplest and oldest technique is the placement of inert markers at the surface before corrosion occurs. By noting the position of the marker within the scale after high temperature exposure, it is possible to determine whether scale growth occurs by cation or anion diffusion. Alternatively, sequential exposure to isotopes such as ^{18}O and ^{16}O allows study of the location of these tagged atoms within the oxide scale. For thick scales, this is commonly done using nuclear reactions (1-3). These techniques provide a qualitative picture of the mechanisms responsible for scale growth.

In the case of thinner scales, an alternate technique is appropriate. Sputter ion mass spectroscopy (SIMS) is used to determine the position of isotopically tagged atoms in a scale. The sample is mounted in a vacuum

*Electrochemical Society Active Member.

chamber, and an ion beam is used to sputter atoms from the surface. A fraction of the sputtered atoms are ionized and are detected using a quadrupole mass analyzer. Using this technique with ^{16}O and ^{18}O , uranium oxidation (4) and anodization of tantalum (5) have been studied. More recently, molecular fragments such as $\text{Cr}^{18}\text{O}_2^-$ have been detected with SIMS in studies of chromium oxidation (6-8).

In this paper, we report a new technique using isotopic tagging of scale constituents in conjunction with ion bombardment and Raman spectroscopy. This approach allows depth profiling of the chemical and isotopic composition of the scale. Raman spectroscopy has previously been demonstrated as a probe of oxide composition providing data at temperatures up to 1000°C (9, 10). Raman spectroscopy has been used with ion bombardment to depth profile oxide scales (11, 12). In this paper, we describe oxidation experiments on an Fe-18Cr-3Mo (100) crystal using ^{16}O and ^{18}O isotopes. Raman spectroscopy

was used to determine whether initial oxidation proceeded by anion or cation diffusion in this system.

Experimental

The Fe-18Cr-3Mo single crystal used in this study was oriented to within $1/2^\circ$ of the (100) face, polished, and mounted in a Varian sample holder on an ultrahigh-vacuum manipulator. Provision for temperature measurement and control during annealing and oxidation was provided by attaching a Chromel-Alumel thermocouple to the front face of the sample and mounting a resistive heater behind the sample. The sample was mounted in a vacuum chamber with a base pressure in the 10^{-8} Pa range. A Kratos Minibeam I ion gun, operated in a dynamic mode, was used for ion sputtering to remove oxides and to clean the sample. The ion gun was used in conjunction with Raman scattering to determine the isotopically tagged compounds present through the scale.

Raman spectra were collected using the 488 nm line from a Spectra Physics Model 165 argon ion laser, a SPEX Triplemate triple spectrograph, and a Tracor Northern diode array. The light from the argon laser was focused to a line approximately $50 \mu\text{m} \times 2 \text{mm}$ on the single-crystal sample, producing an estimated power density of about 1 kW/cm^2 . Since the sample was highly reflecting, only a very small fraction of this incident power was absorbed. An $f/2$ lens was used to collect the light scattered for analysis by the spectrograph and diode array. The spectrum was integrated for 200s and the characteristic background of the diode array subsequently subtracted. Each pixel on the diode array corresponded to about one wave number dispersion. The resolution was limited largely by the diode array intensifier which produced a full width at half-maximum of about 5 pixels. Thus, the resolution of the system was about 5 cm^{-1} .

All oxidations reported in this paper were performed at 700°C in 1.3×10^{-4} Pa oxygen. Prior to oxidation the sample was sputtered until Auger spectroscopy showed the bulk composition at the surface. The sample was then annealed for 20 min at 937°C , cooled to 700°C , and oxidized.

Results

Hamilton and Anderson reported that during oxidation of this alloy, the first oxide to appear on the surface was a spinel (13). Auger measurements indicated the presence of iron and chromium in the spinel. For longer oxidation times, chromia was formed. These oxides grew reproducibly if standardized sample cleaning and annealing procedures were used.

We grew iron-chromium spinel and chromia on the Fe-18Cr-3Mo single crystal using 5 and 20 min oxygen exposures, respectively. Exposures were performed at 1.3×10^{-4} Pa in naturally occurring oxygen (99.76% ^{16}O) and in oxygen 18. Figure 1 shows the Raman spectra of spinels grown in natural oxygen (hereafter referred to as oxygen 16) and in oxygen 18. The major spinel peak which appears at 662 cm^{-1} for oxygen 16 spinel is shifted to 628 cm^{-1} when the compound is grown using oxygen 18. These two spectra clearly demonstrate the isotope effect on the Raman peak position. The position of the peak is approximated by the formula

$$\text{shift}(^{18}\text{O}) = \text{shift}(^{16}\text{O}) (16/18)^{1/2}$$

as would be expected from a simple classical model of the vibrational frequency for an oxygen atom attached to an infinitely massive atom. Using this formula the calculated position of the spinel peak with oxygen 18 is 624 cm^{-1} . If the reduced mass for an oxygen and a chromium atom is used, the calculated position of the spinel peak with oxygen 18 becomes 633 cm^{-1} . We conclude that the normal mode giving rise to this scattering peak involves large displacements of the oxygen atoms relative to those of the chromium and iron atoms.

Isotopically substituted spectra were also obtained for chromia. Figure 2 shows the Raman spectra obtained after 20 min exposures at 1.3×10^{-4} Pa. The largest

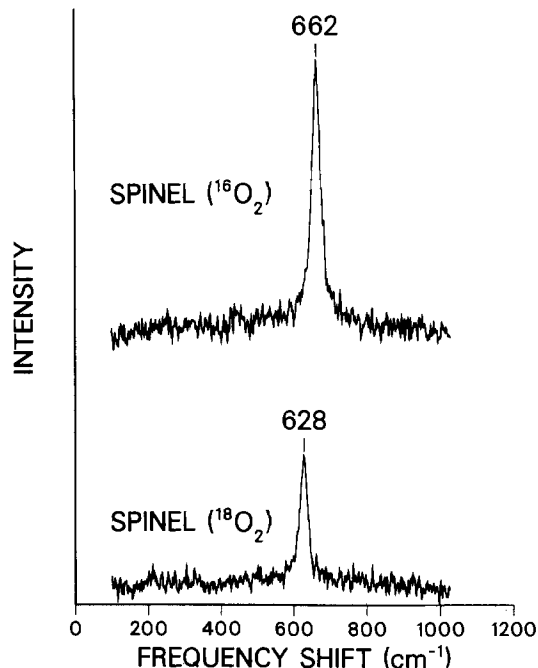


Fig. 1. Raman spectra of iron-chromium spinels grown on Fe-18Cr-3Mo (100) by 5 min exposures to 1.3×10^{-4} Pa oxygen at 700°C . Oxides were grown using oxygen 16 and oxygen 18, respectively.

chromia peak is shifted from 549 to 520 cm^{-1} when oxygen 18 is substituted for oxygen 16. A smaller chromia peak is shifted from 347 to 332 cm^{-1} when oxygen 18 is substituted for oxygen 16. The peak at 302 cm^{-1} is little shifted by isotope substitution. It appears that the modes at 549 cm^{-1} (A_{1g}) and 347 cm^{-1} (E_g) involve large displacements of the oxygen atoms relative to those of chromium, whereas the mode at 302 cm^{-1} (A_{1g}) involves very small displacements of the oxygen atoms.

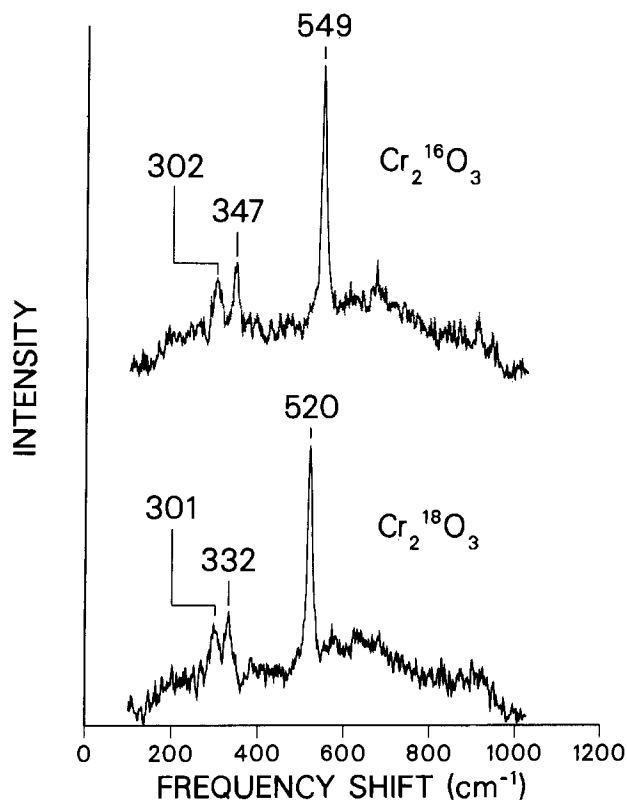


Fig. 2. Raman spectra of chromia grown on Fe-18Cr-3Mo (100) by 20 min exposures to 1.3×10^{-4} Pa oxygen at 700°C . Oxides were grown using oxygen 16 and oxygen 18, respectively.

The spectra shown in Fig. 1 and 2 demonstrate that Raman spectroscopy can easily distinguish chromia and iron-chromium spinels grown using oxygen 16 from those grown using oxygen 18. The Raman spectra of oxides grown in mixed oxygen 16 and oxygen 18 are also of interest. Oxides grown under these conditions should have both oxygen isotopes randomly substituted within the lattice. A randomly substituted oxide could also be produced by sequential exposures to oxygen 18 and oxygen 16 if lattice diffusion or other mixing processes occurred during the experiment. We were particularly interested in the Raman spectrum of the mixed oxide, since knowing this spectrum would allow us to determine if mixing occurred in later experiments involving sequential exposure to two oxygen isotopes.

Exposures to mixed oxygen isotopes were accomplished by admitting oxygen 18 to a partial pressure of 6.7×10^{-5} Pa and then adding oxygen 16 to a total pressure of 1.3×10^{-4} Pa. Gases were admitted using Varian variable leak valves, and the total pressure was monitored with an ion gauge. Since the partial pressures of the two isotopes were not monitored simultaneously, it is not possible to be sure of the resulting isotope ratio, although we believe it was close to 1:1. Figure 3 shows the Raman spectra obtained after 5 and 20 min exposures to this mixture. Table I presents the observed peak positions and full widths at half-maximum for the spinel and chromia grown in single isotopes and in the mixture. The effect of a randomly substituted lattice is to produce a Raman shift intermediate between those of oxides grown with single isotopes of O^{16} and O^{18} . The peaks are also somewhat broadened for the randomly substituted lattice. We conclude that the phonon modes involve significant motions of a number of oxygen atoms.

Our next set of experiments involved sequential exposures to the different oxygen isotopes. Raman spectroscopy

Table I. Peak positions and widths

Compound	^{16}O (cm $^{-1}$)	$^{16}O + ^{18}O$ (cm $^{-1}$)	^{18}O (cm $^{-1}$)
Spinel	662 (26 + 1)	650 (31 + 1)	628 (25 + 1)
Chromia	302 (21 + 3)	302 (23 + 3)	301 (18 + 3)
	347 (11 + 3)	341 (19 + 3)	332 (17 + 3)
	549 (14 + 1)	541 (26 + 1)	520 (14 + 1)

Peak positions and observed full widths at half maxima are given. The FWHM include about 5 cm $^{-1}$ of instrumental broadening attributable largely to the diode array. Estimated error limits are given for the FWHM.

copy was combined with ion bombardment in order to depth profile the oxide layer. This combination of techniques has been described in previous publications (11, 12). The depth probed by Raman spectroscopy varies tremendously depending upon the optical absorption of the sample. For highly absorbing samples, the incident beam penetrates only a short distance and the depth probed is small. For transparent or translucent samples, the depth probed is determined by the overlap of the focusing volumes of the lenses used for incident and scattered light. For such materials, the depth probed may be many microns. Optical absorption data has been published for Fe_2O_3 , Fe_3O_4 , and Cr_2O_3 (14, 15); however, we have been unable to locate absorption data for iron-chromium spinels. For 488 nm light in Fe_2O_3 , the absorption coefficient is about 1.8×10^5 cm $^{-1}$ (14). In Fe_3O_4 , the absorption coefficient is about 2×10^4 cm $^{-1}$ (14), and in Cr_2O_3 , the absorption coefficient is about 2×10^4 cm $^{-1}$ (15). In all cases, these absorption coefficients were interpolated from small published plots with consequent large uncertainties. From these absorption coefficients, we estimate probe depths of 50 nm for Fe_2O_3 and 500 nm for Fe_3O_4 and Cr_2O_3 . Experiments performed on oxidized chromium samples in our laboratory suggest a probe depth of about 100 nm for Cr_2O_3 (16).

Based upon these estimates of depth probed, it would seem likely that Raman spectroscopy would sample the entirety of these thin oxide films. However, we note that the absorption coefficients for Cr_2O_3 and Fe_2O_3 change very rapidly with wavelength in the vicinity of 488 nm. Furthermore, our samples likely contain small quantities of other phases in solution (e.g., some Fe_2O_3 in solution in Cr_2O_3). The electronic structure and thus the absorption coefficients of these solids would be expected to be very sensitive to such impurities. For these reasons, and since the absorption coefficient of the spinel is unknown, we are reluctant to attribute quantitative significance to relative peak heights in the Raman spectra published here.

An advantage of the ion bombardment plus Raman spectroscopy technique is that spectra appear to be little affected by beam effects such as reduction or mixing of oxide layers, presumably because the depth probed by Raman spectroscopy is much larger than that damaged by the ion beam (typically tens of angstroms). This insensitivity to lattice damage is a major advantage for chemical characterization. A spinel layer was grown by exposing the sample to oxygen 18 for 4 min, followed by oxygen 16 for 4 min all at 1.3×10^{-4} Pa and 700°C. A Raman spectrum was obtained for the oxidized sample. The sample was then ion bombarded for 2 min, removing about 2 nm of the oxide, and another Raman spectrum was obtained. Additional spectra were obtained after 4, 6, 10, and 16 min of cumulative bombardment time. These spectra are shown in Fig. 4. The major feature seen in the spectra from the oxidized alloy is a peak characteristic of the oxygen 16 spinel. There is also a smaller peak characteristic of the oxygen 18 spinel. After 2 min of sputtering, the oxygen 16 and oxygen 18 spinel peaks are nearly equal in size. Longer sputtering times remove more of the oxygen 16 spinel, until after 10 min of sputtering little or no oxygen 16 spinel is apparent in the spectrum. We conclude that the oxide as grown consisted of an inner layer of oxygen 18 spinel and an outer layer of oxygen 16 spi-

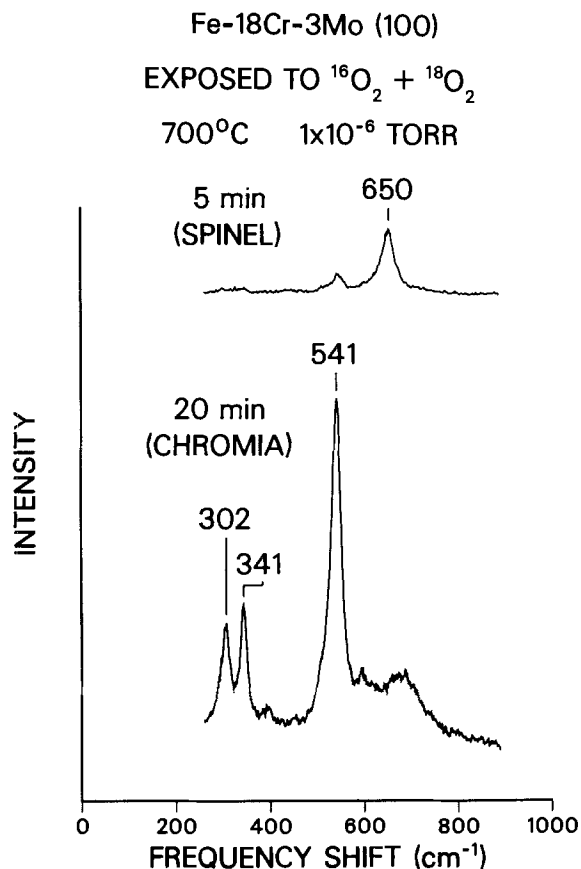


Fig. 3. Raman spectra of iron-chromium spinel and chromia grown on Fe-18Cr-3Mo (100) by 5 and 20 min exposures, respectively, to 1.3×10^{-4} Pa oxygen at 700°C. Oxides were grown in a mixture of oxygen 16 and oxygen 18 with approximately equal proportions of each isotope.

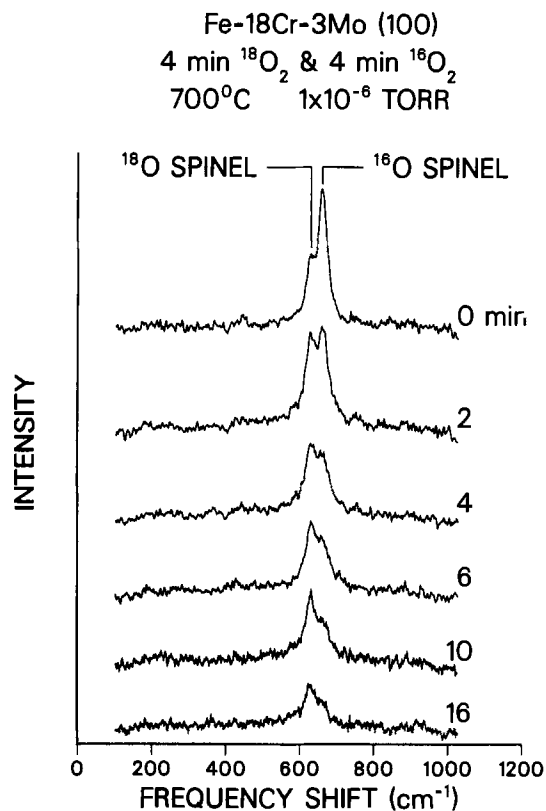


Fig. 4. Raman spectra obtained after various ion bombardment times from an oxide grown on Fe-18Cr-3Mo (100). Oxides were grown by sequential exposure to oxygen 18, then oxygen 16, each for 4 min at 1.3×10^{-4} Pa and 700°C. Spectra are labeled with bombardment time.

nel. The thickness of the outer oxygen 16 spinel is about 4 nm, based on a sputtering rate measured for identical sputtering parameters using an anodized tantalum standard.

In the last exposure reported here, chromia was grown on this alloy by exposing the sample to oxygen 18 for 10 min followed by oxygen 16 for 10 min both at 1.3×10^{-4} Pa and 700°C. Figure 5 shows Raman spectra obtained after 0, 10, 20, and 30 min of cumulative bombardment time. The oxidized alloy shows a Raman spectra with peaks from oxygen 16 chromia and oxygen 18 chromia. The two peaks are comparable in size, although the oxygen 16 chromia peak is a little larger. After 10 min of ion bombardment, only the oxygen 18 chromia peak remains.

Conclusions

The spectra shown in Fig. 1 and 2 clearly demonstrate that oxygen isotope shifts in the Raman scattering from chromia and iron-chromium spinels allow differentiation of oxides grown in oxygen 16 from those grown in oxygen 18. It is also possible to distinguish oxides which are randomly substituted with a mixture of the two isotopes from oxides grown with either isotope alone.

We have combined Raman spectroscopy with ion bombardment to profile the isotopic composition of oxide films grown during sequential exposures to oxygen 18 and oxygen 16 at high temperatures. For both spinels and chromia grown at 700°C in 1.3×10^{-4} Pa oxygen, the predominant mechanism of oxide growth on single crystals of Fe-18Cr-3Mo appears to be cation diffusion of chromium through the oxide. Mixing of the isotopes during ion bombardment appears not to be a problem with Raman analysis, although it complicates SIMS analysis unless molecular ions are detected (7). We see no evidence for interdiffusion of the oxygen isotopes during these exposures. There is no evidence for short-circuit diffusion of oxygen through these films, a result which is perhaps not surprising since the films are quite thin and relatively homogeneous. For such thin films, stresses

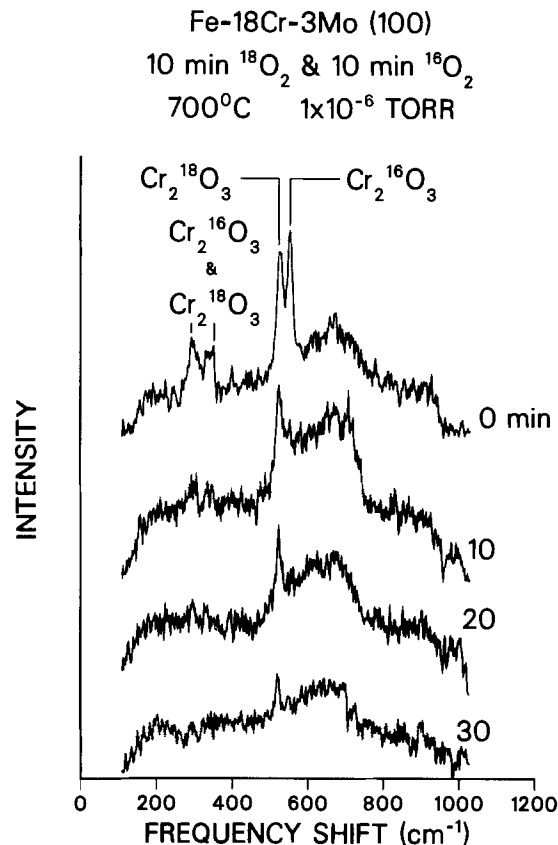


Fig. 5. Raman spectra obtained after various ion bombardment times from an oxide grown on Fe-18Cr-3Mo (100). Oxides were grown by sequential exposure to oxygen 18, then oxygen 16, each for 10 min at 1.3×10^{-4} Pa and 700°C. Spectra are labeled with bombardment time.

occurring during growth probably are not sufficient to produce oxide cracking. Furthermore, the use of single-crystal samples should reduce grain boundary effects resulting in a more homogeneous oxide.

Acknowledgment

This research was supported by the Office of Basic Energy Sciences, U.S. Department of Energy, Division of Materials Sciences.

Manuscript submitted Jan. 14, 1985; revised manuscript received March 21, 1985.

Sandia National Laboratories assisted in meeting the publication costs of this article.

REFERENCES

1. A. Bruckman, R. Emmerich, and S. Mrowec, *Oxid. Met.*, **5**, 137 (1972).
2. D. G. Barnes and J. M. Calvert, *Philos. Mag.*, **28**, 1303 (1973).
3. A. Atkinson, R. I. Taylor, and P. O. Goode, *Oxid. Met.*, **13**, 519 (1979).
4. S. S. Christy and J. B. Condon, in "Proceedings of the Second International Conference on Secondary Ion Mass Spectroscopy (SIMS II)," pp. 151-153, Stanford University Press, Stanford, CA (1979).
5. C. A. Evans, Jr. and J. P. Pemsler, *Anal. Chem.*, **42**, 1060 (1970).
6. M. J. Graham, in "Proceedings 9th International Conference on Metallic Corrosion," pp. 1-4, Toronto (1984).
7. D. F. Mitchell, R. J. Hussey, and M. J. Graham, *J. Vac. Sci. Technol. A*, **1**, 1006 (1983).
8. D. F. Mitchell, R. J. Hussey, and M. J. Graham, in "Proceedings JIMIS-3 (1983): High Temperature Corrosion Transactions of the Japan Institute of Metals," Supplement p. 121-125, Japan Institute of Metals (1983).
9. R. L. Farrow and A. S. Nagelberg, *Appl. Phys. Lett.*, **36**, 945 (1980).
10. R. L. Farrow, P. L. Mattern, and A. S. Nagelberg, *ibid.*, **36**, 212 (1980).

11. J. C. Hamilton, B. E. Mills, and R. E. Benner, *ibid.*, **40**, 449 (1982).
12. J. C. Hamilton, R. E. Benner, and B. E. Mills, *J. Vac. Sci. Technol.*, **20**, 946 (1982).
13. J. C. Hamilton and R. J. Anderson, *High Temp. Sci.*,

- To be published.
14. I. Balberg and H. L. Pinch, *J. Magn. Mater.*, **7**, 12 (1978).
15. D. S. McClure, *J. Chem. Phys.*, **38**, 2289 (1963).
16. J. C. Hamilton, Unpublished results.

Preparation and Properties of Amorphous Boron Nitride Films by Molecular Flow Chemical Vapor Deposition

Katsumitsu Nakamura

Department of Chemistry, College of Humanities and Sciences, Nihon University, Sakurajohsui Setagaya-ku, Tokyo 156, Japan

ABSTRACT

A new chemical vapor deposition method of thin film in molecular flow region (MF-CVD) is proposed, and is applied to the preparation of boron nitride films using ammonia and decaborane reaction gases. It is found that the composition of the films can be closely controlled by regulating the pressure of source gases and stoichiometric boron nitride films deposited at $\text{NH}_3/\text{B}_{10}\text{H}_{14} \geq 20$ at the substrate temperature of 850°C. From the chemical shift of boron $\text{K}\alpha_2$ peak in the x-ray fluorescence spectra, the BN_x films having the composition $x < 0.75$ are mixture of boron and boron nitride. X-ray diffraction study indicates that the films are amorphous. The optical properties of the boron nitride films are also clarified. The energy of the direct allowed transition is estimated to be 5.90 eV.

Boron nitride has properties such as being electrically insulating, chemically inert, thermally stable, resistant to corrosion, and having desirable mechanical properties, and is considered to be one of wide bandgap semiconductors. Potential applications of boron nitride films have been proposed such as high temperature dielectrics (1), heat-dissipation coatings (2), passivation layers (3), diffusion sources of boron (4), and sodium barriers (3). Since boron nitride is highly transparent to x-rays, it can also be used in the fabrication of mask for x-ray lithography (5). Its unique crystal structure and physical properties induce a great deal of scientific and technological interest.

Boron nitride films have been prepared by the reaction of boron trichloride with ammonia at 250° ~ 1200°C (6-9), by the reaction of diborane with ammonia at 250° ~ 1250°C (3, 4, 6, 11), by the reaction of these gases in a plasma (12-14), by pyrolysis of borazine and trichloroborazine at 300° ~ 650° (15) and 1100°C (16), and by sputtering at 250° ~ 900°C (17, 18).

In many reports, boron nitride films deposition have been carried out by the general CVD, which is considered to take place at the thermal equilibrium condition in stagnant layer. Accordingly, boron nitride deposited by the CVD has nearly stoichiometric composition.

Here, we propose a new method in which CVD is carried out at the pressure of molecular flow region ($< 10^{-3}$ torr). We call this method molecular flow chemical vapor deposition (MF-CVD). In this method, the composition of compound films is easily controlled by controlling the component ratio of source gases. Boron nitride films were prepared by MF-CVD using the reaction of decaborane with ammonia. The composition of the films are analyzed by electron probe x-ray microanalysis (EPMA) and electron spectroscopy for chemical analysis (ESCA). Dependences of the gas ratio and substrate temperature on the film composition are investigated. The optical properties of the films are studied in the ultraviolet, visible, and infrared spectral regions.

Experimental

Figure 1 shows a schematic diagram of the apparatus used for the deposition of boron nitride films. The vacuum chamber is evacuated by an oil diffusion pump and a rotary pump system, and ultimate pressure is 2×10^{-7} torr.

Sapphire and silicon were used as the substrates. The substrates were fixed on the tungsten sheet (0.05 mm thick) and were heated from 300° to 1200°C by resistant

heating of the tungsten, as described in the previous paper (19). A tantalum sheet, which was cut into a wedge shape in order to induce the temperature gradient on the substrate, was also used as a substrate. By this method, we obtained the samples of various temperatures between 300° and 800°C using one run. The temperatures of the sapphire and silicon substrates were estimated from that of the tungsten heater, which was determined by an optical pyrometer and thermocouple. The relation between the temperature of the substrate and that of the heater had been obtained. Three points of tantalum substrate temperatures were measured by using thermocouples welded on the substrate surface.

The decaborane was introduced into the growth chamber at 2×10^{-5} torr through the variable leak valve (19), and then the ammonia was introduced at between 2×10^{-5} and 8×10^{-4} torr. The vacuum valve was throttled to maintain the pressure gradient between the growth chamber and the diffusion pump. The pressure was measured by a B-A-type ionization gauge. These pressures were measured as a corresponding nitrogen pressure. We varied the deposition time from 30 to 300 min, depending on the gas pressure and the substrate temperature. The conditions of the film deposition are summarized in Table I.

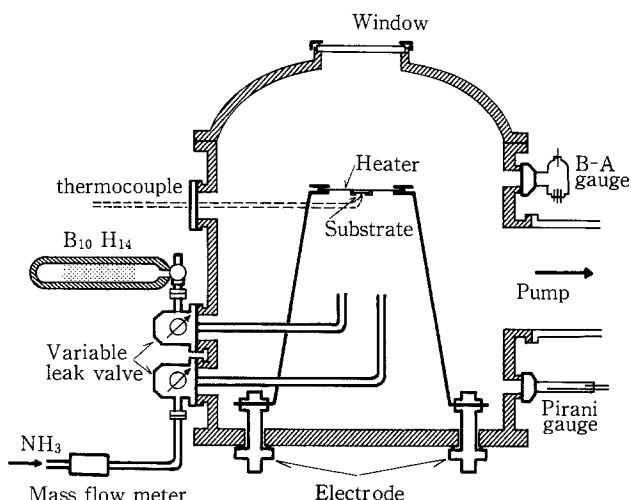


Fig. 1. Schematic diagram of the apparatus for deposition of boron nitride films by MF-CVD.

Table I. Experimental condition data

Decaborane	2×10^{-5} torr
Ammonia	2×10^{-5} - 8×10^{-4} torr
$\text{NH}_3/\text{B}_{10}\text{H}_{14}$	1-40
Temperature	300°-1150°C
Time	30-300 min
Substrate	Sapphire, Ta, Si

The crystal structures of the films obtained were studied by an x-ray diffraction method. The optical transmission and reflection spectra of the films on sapphire were measured in the wavelength range of 200-2500 nm using a spectrophotometer MPS-50 (Shimadzu). In the transmission and reflection measurements, an uncoated sapphire and an evaporated aluminum film were used as the references, respectively. The absorption coefficient of the films were calculated from the measured transmittance and reflectance. Infrared transmission and refraction spectra of the films deposited on the high resistive silicon wafers were measured in the wavelength range of 2.5-50 μm using an infrared spectrophotometer, DS-701G (Jasco).

The composition of the films was estimated from the x-ray fluorescence intensities of boron and nitrogen measured by EPMA using EMX-SE (Shimadzu). Measurements were carried out at 7 kV acceleration voltage, 0.1 μA sample current, and 100 μm beam diameter by using the lead stearate as a spectral crystal. Since the penetration depth of primary electron was about 6000 \AA , the thicknesses of the films used for analysis were less than 6000 \AA . The intensities of the boron and nitrogen x-ray fluorescence were corrected by those of the standard boron nitride sample. As the films deposited were highly resistive, beryllium was deposited on the sample surface to avoid charge up. The wavelength of x-ray fluorescence of boron $\text{K}\alpha_2$ was 67.5-68.5 \AA , and that of nitrogen $\text{K}\alpha_2$ was 32 \AA . The ESCA spectra of boron- and boron nitride-deposited films are measured by an HP5950 ESCA spectrometer (Hewlett-Packard) with Al $\text{K}\alpha$ (1487 eV).

Results and Discussion

Structure and optical properties of the films.—The color of the films change continuously from black-brown to colorless with the increase of the ammonia pressure. The x-ray diffraction analyses indicate that all the films obtained are amorphous.

The absorption coefficients of a colorless and transparent film in the ultraviolet spectral region are shown in Fig. 2 as a function of incident photon energy. The absorption coefficient α near the absorption edge for direct allowed transition is described as a function of photon energy $h\nu$ as,

$$\alpha h\nu \propto (h\nu - E_g)^{1/2} \quad [1]$$

where E_g is the optical bandgap energy. The variation of $(\alpha h\nu)^2$ with incident photon energy for the boron nitride film is shown in Fig. 3. The figure shows that the boron nitride obtained is a semiconductor having a direct energy gap. The energy gap, E_g , is estimated to be 5.90 eV by the extrapolation of the linear part to the horizontal axis in the figure. This value is larger than the value of 5.80 eV reported by Sano (3) and Zunger (18).

Figure 4 shows the infrared transmission spectra of the films deposited on the silicon substrate at 300°, 400°, 500°, and 700°C with the molar ratio of source gases $\text{NH}_3/\text{B}_{10}\text{H}_{14} = 15$. The four absorption bands are seen in the spectrum of the film deposited at 300°C. These correspond to NH stretching (3200 cm^{-1}) (19, 20), BH stretching (2500 cm^{-1}) (20), and antisymmetric and symmetric NH_3 deformation mode (1550 cm^{-1} , 1405 cm^{-1}) (19). Above 500°C, the absorption due to the BN lattice vibration appears at 1380 and 800 cm^{-1} (21), and that due to the BH and NH stretching vibration disappears. Figure 5 shows the infrared transmission and reflection spectra of the film deposited at 1000°C. The characteristic absorption and reflection band of boron nitride are found at 1380 and 800 cm^{-1} and 1565 and 800 cm^{-1} , respectively.

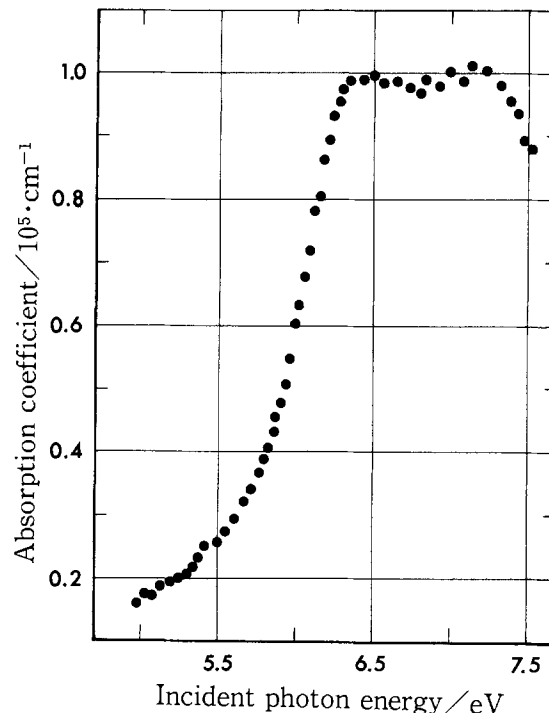


Fig. 2. The adsorption coefficient of the stoichiometric boron nitride film near absorption edge as a function of incident photon energy.

We can conclude from IR spectra the following. The films deposited at 300°C due to the reaction of decaborane with ammonia still contain B—H and N—H bonds. A B—N bond is, remarkably, formed at 400°C. The film deposited at 500°C is substantially boron nitride. The temperature of 700°C is enough to produce boron nitride because the spectrum of the film deposited at 700°C is almost the same as that of the film deposited at 1000°C.

Analysis of the films by EPMA and ESCA.—The composition of the films was determined from the peak area ratio of boron $\text{K}\alpha_2$ and nitrogen $\text{K}\alpha_2$. Typical peak

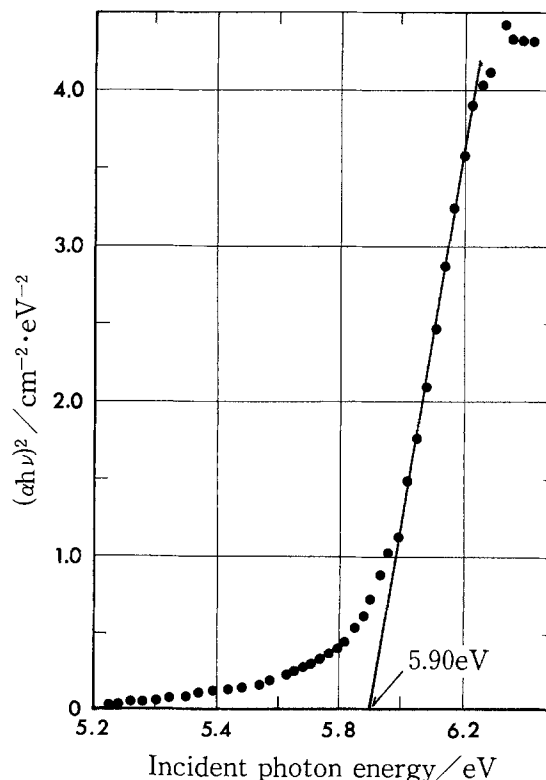


Fig. 3. The absorption edge fitted to direct allowed transition

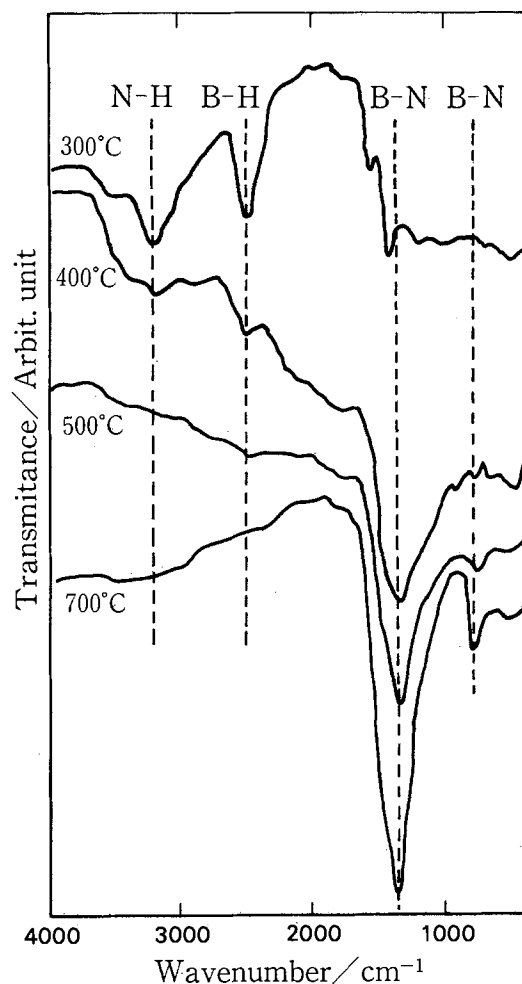


Fig. 4. The effect of substrate temperature on the infrared transmission spectra.

profiles of boron $K\alpha_2$ and nitrogen $K\alpha_2$ of boron and boron nitride films deposited are shown in Fig. 6. The chemical shift of $K\alpha_2$ peak of boron in boron nitride is estimated to be 1.0\AA . The chemical shift of nitrogen $K\alpha_2$ is less than 0.2\AA and is smaller than that of boron.

In Fig. 7 and 8, the dependence of the peak wavelength, the center wavelength at half-maximum and the full width at half maximum (FWHM) of the boron $K\alpha_2$ and nitrogen $K\alpha_2$, on the composition of the films are shown.

The shift of the peak wavelength of boron $K\alpha_2$ from 67.5\AA to 68.5\AA implies the decrease of the gap between the $1s$ and $2p$ energy levels in the boron atom. In order to understand this chemical shift, detailed knowledge of the electronic structure of boron and boron nitride is re-

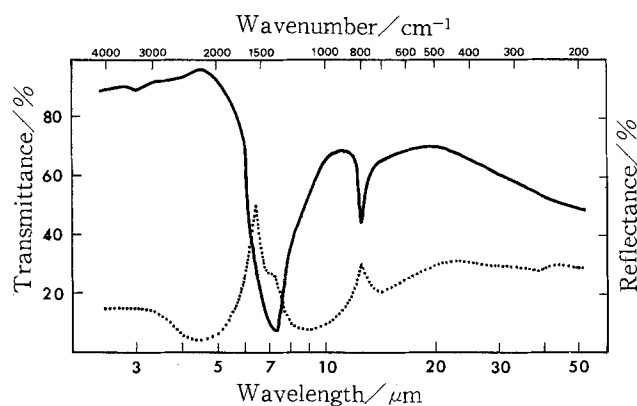


Fig. 5. Infrared transmission and reflection spectra of deposited boron nitride film at 1000°C . Solid and dotted lines represent the transmission and reflection spectra, respectively.

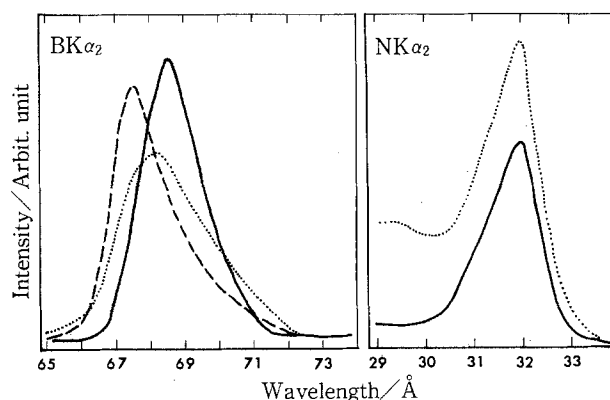


Fig. 6. Typical peak profile of $B K\alpha_2$ and $N K\alpha_2$ on boron and boron nitride analyzed by EPMA. Solid, dotted, and broken lines correspond to B, $BN_{0.5}$, and BN, respectively.

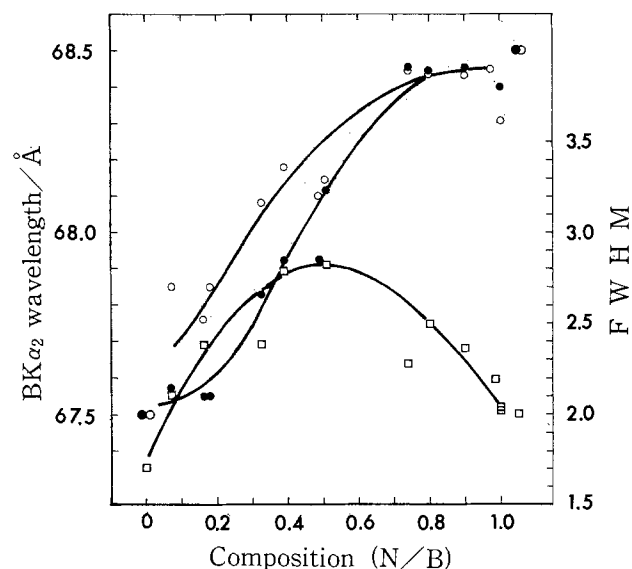


Fig. 7. The dependence of composition ratio of boron nitride film on the wavelength of $B K\alpha_2$. Closed circles show the wavelength of maximum, open circles show the center wavelength at half maximum, and open squares show the FWHM.

quired. These electronic structures have been studied experimentally by ESCA (24, 25), AES (26), x-ray emission measurements (27), and, theoretically, by the band structure calculation for boron (28, 29) and boron nitride (30, 31). By adding the energy of boron $K\alpha_2$ 183.7 eV (67.5\AA) in the boron film to the valence band energy of boron 8.43 eV (25), we can obtain 192 eV for the boron $1s$ energy level in the boron film. We can also obtain 194 eV

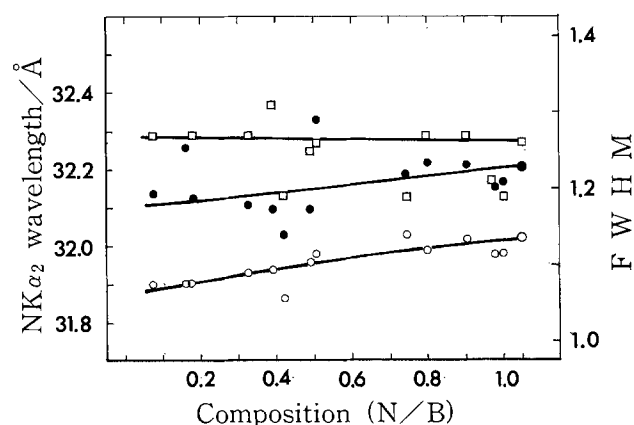


Fig. 8. The effect of composition ratio of boron nitride film on the wavelength of $N K\alpha_2$; symbols correspond to those in Fig. 7.

for the boron 1s and 400.5 eV for nitrogen 1s by adding the energy of boron $K\alpha_2$ 181 eV (68.5Å) and the nitrogen $K\alpha_2$ 387.5 eV (32Å) in the boron nitride films to the valence band energy of boron nitride, 13 eV (28).

The ESCA spectra for the boron film and the stoichiometric boron nitride film are shown in Fig. 9. In the spectrum shown in part a, the peaks at 192 and 285 eV correspond to boron 1s and carbon 1s, respectively. This carbon peak can be due to carbon impurities in the film or absorbed carbon on the surface. In the spectrum shown in part b, the peaks at 193 and 401 eV correspond to boron 1s and nitrogen 1s, respectively. The spectrum shown in part c shows the valence band (0-50 eV) of the boron nitride films. The peak of 23.0 eV corresponds to nitrogen 2s. The broad peak of 12.7 eV marks the 2p electrons of boron and nitrogen. Since these values agree in the value given above 13 eV, an x-ray emission mechanism, we considered, seems reasonable.

The chemical shift of boron $K\alpha_2$ is in agreement with the value reported by Grusserbaure (32), where the chemical shifts of boron $K\alpha_2$ for the several boron compounds (BN, B_2O_3 , B_4C , BP) were measured by EPMA. The shift is explained by the localization of electron due to the difference in electron negativities.

It is found from Fig.7 that the chemical shift of boron $K\alpha_2$ changes continuously in the nonstoichiometry composition region from boron to boron nitride. However, above the composition $N/B = 0.75$, the chemical shift of boron $K\alpha_2$ is not seen. It is considered that the electronic structure of boron nitride film with the composition $N/B = 0.75$ will be nearly the same structure as that of stoichiometric boron nitride. The FWHM of boron $K\alpha_2$ peak increases with an increase of the composition. It has a maximum value of 2.95Å at about $N/B = 0.5$ and then decreases to 2.0Å at $N/B = 1.0$. The increase of the FWHM is considered to be caused by superposition of the boron $K\alpha_2$ of boron and that of boron nitride. The dependences of the composition of the film on the peak wavelength and the FWHM of the nitrogen $K\alpha_2$ are shown in Fig. 8.

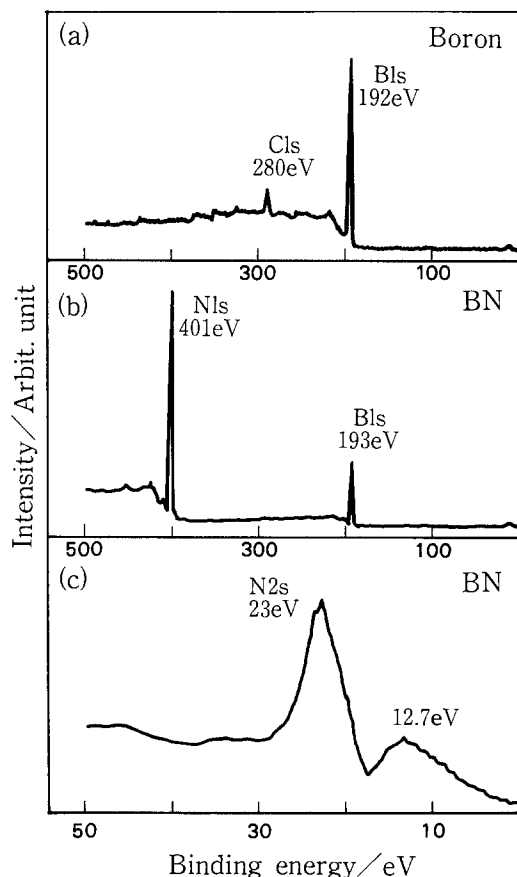


Fig. 9. The ESCA spectra for boron and boron nitride

These dependences are smaller than those of boron $K\alpha_2$. This fact suggests that nitrogen atoms included in the films are always bound with boron atoms. According to these facts, we can conclude that the deposited films are considered to be the mixture of boron and boron nitride in the nonstoichiometric composition region.

The reaction process.—The dependence of the composition of the films on the substrate temperature is shown in Fig. 10 at temperatures between 300° and 1200°C. The temperature dependence of the composition when the pressure ratio of the reaction gases $NH_3/B_{10}H_{14} = 20$ is stronger than that when $NH_3/B_{10}H_{14} = 1$. When $NH_3/B_{10}H_{14} = 20$, the nitrogen content in the films increases with increasing substrate temperature in the temperature range 350°-850°C, and then decreases gently. As the intensity of boron and nitrogen x-ray fluorescence is proportional to the amount of the boron and nitrogen per unit area, the deposition rates of boron and nitrogen are given by dividing the x-ray fluorescence intensity of boron and nitrogen by the deposition time. The temperature dependences of the deposition rate of boron and nitrogen are shown in Fig. 11.

Nitrogen atoms cannot stay on the substrate surface without bonding boron atoms. The dependence of nitrogen deposition rate normalized by the boron deposition rate on the substrate temperature is shown in Fig. 12. The figure shows that the deposition rate is determined by the kinetic process which indicates the increase of nitrogen bound to boron at temperatures between 350° and 850°C. The nitrogen bonding to boron can decrease with an increase of temperature to above 850°C, because the substrate temperature's increasing shortens the residence time of nitrogen on the surface. The reaction of nitrogen with boron requires enough residence time of nitrogen on the deposition surface. The relation between the loga-

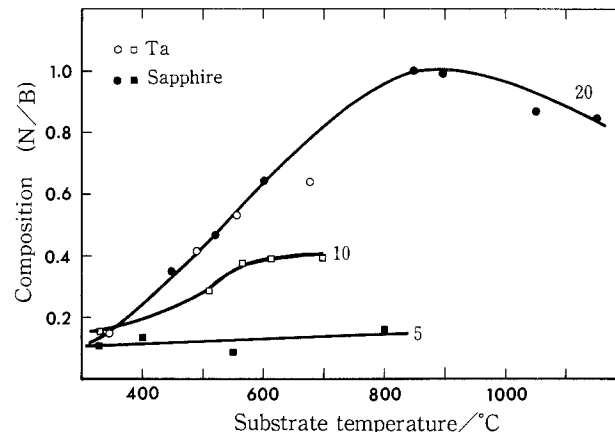


Fig. 10. The composition ratio of boron nitride as a function of substrate temperature.

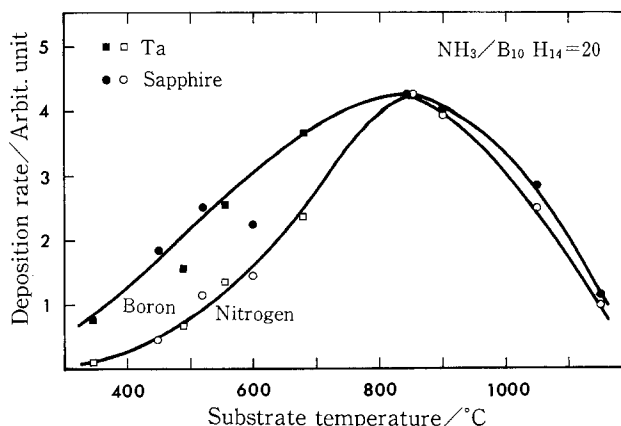


Fig. 11. The deposition rate of boron and nitrogen as a function of substrate temperature.

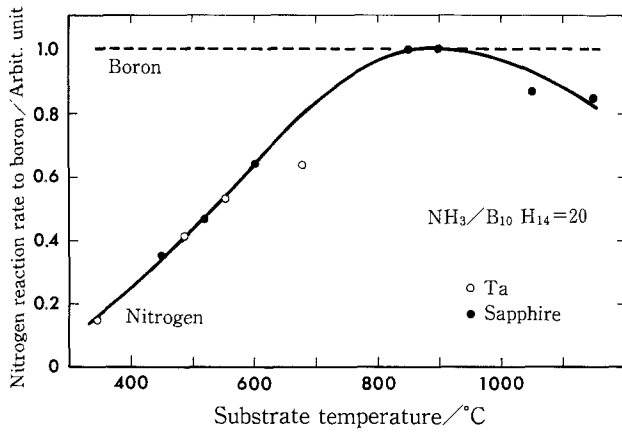


Fig. 12. Normalized deposition rate of nitrogen by deposition rate of boron as a function of substrate temperature.

rithm of nitrogen deposition rate and the reciprocal absolute temperature is shown in Fig. 13. We obtain the activation energy of this reaction 6.3 and 0.4 kcal/mol at temperatures above and below 850°, respectively. The activation energy of 6.3 kcal/mol is based on the reaction of boron with nitrogen atoms. However, detailed information on this small activation energy is unknown.

At constant decaborane pressure of 2×10^{-5} torr and substrate temperature of 850° and 550°C, the dependence of the film composition on the ammonia pressure at the pressure range of $2 \times 10^{-5} - 8 \times 10^{-4}$ torr is shown in Fig. 14. It is found from the figure that, at the substrate temperature of 850°C, the composition increases with the increase of ammonia pressure up to $NH_3/B_{10}H_{14} = 20$ and then saturates at $N/B = 1.0$.

In general, the amount of the decaborane and ammonia molecule impinging onto the substrate surface, S , is given from the gas dynamics as

$$S = P(Mw/2\pi RT_g) = 5.8 \times 10^{-2} P(Mw/T_g)^{1/2} \quad (\text{g/cm}^2) \quad [2]$$

where P is the gas partial pressure in torr, Mw the molecular weight, R the gas constant, and T_g is the gas temperature considered to be at room temperature (*i.e.*, $T_g =$

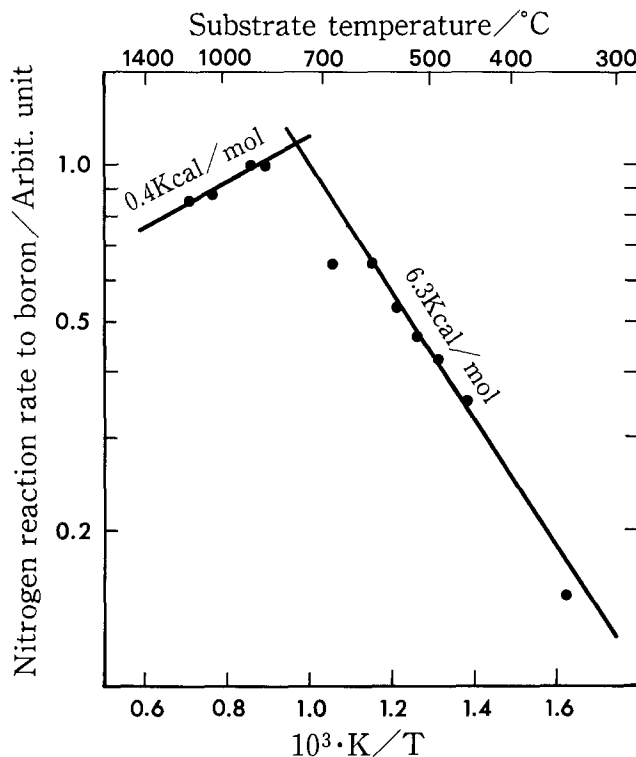


Fig. 13. Logarithm of nitrogen deposition rate as a function of reciprocal absolute temperature.

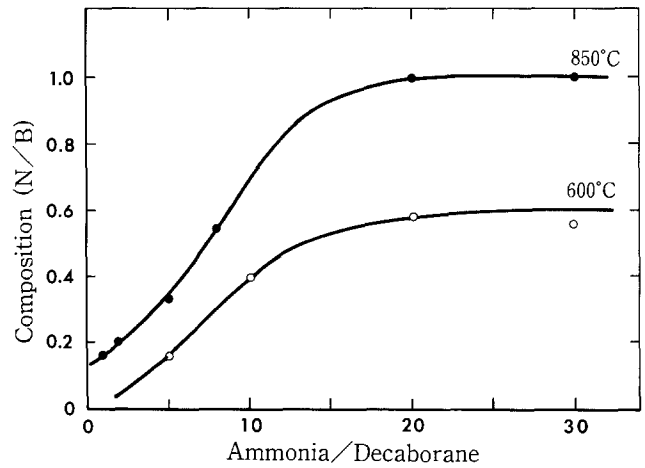


Fig. 14. The effect of ammonia pressure on composition ratio of boron nitride at the constant decaborane pressure 2×10^{-5} torr and substrate temperatures 600° and 850°C.

300 K). By using the Avogadro number, Eq. [2] is rewritten to give the number of impingement molecules, ν , as

$$\nu = 3.5 \times 10^{22} P / (Mw/T)^{1/2} \quad (\text{molecule/cm}^2\text{-s}) \quad [3]$$

When $P = 2 \times 10^{-5}$ torr, $Mw = 122$, and $T_g = 300$ K are substituted in Eq. [3] in the case of decaborane, $\nu_{B_{10}H_{14}} = 3.7 \times 10^{15}$ molecule/cm²-s is obtained. In the case of ammonia, substituting the value of $Mw = 17$ and $T_g = 300$ K in Eq. [3] yields the equation $\nu_{NH_3} = 4.9 \times 10^{20} P$ molecule/cm²-s. The compositions of the films are shown in Fig. 15 as a function of the partial pressure of ammonia together with the ν_{NH_3} at the constant $\nu_{B_{10}H_{14}} = 3.7 \times 10^{15}$ molecule/cm²-s and the substrate temperatures of 600° and 850°C. At the substrate temperature of 850°C, the composition of the films increases with increasing ammonia partial pressure, P_{NH_3} , and the stoichiometric composition is completed above $P_{NH_3} = 4 \times 10^{-4}$ torr, which is $\nu_{NH_3}/\nu_{B_{10}H_{14}} = 54$. In the case of 600°C, the composition at the $P_{NH_3} = 6 \times 10^{-4}$ torr will be essentially much larger than the value of 0.6 obtained in the present study, and stoichiometric composition will be completed at about $P_{NH_3} = 7 \times 10^{-4}$ torr, which is $\nu_{NH_3}/\nu_{B_{10}H_{14}} = 100$. Therefore, it is found that the stoichiometric boron nitride deposits when the ratio of impingement frequency of nitrogen and boron atoms, ν_N/ν_B , is larger than 5.4 and 10 at the substrate temperatures of 850° and 600°C, respectively.

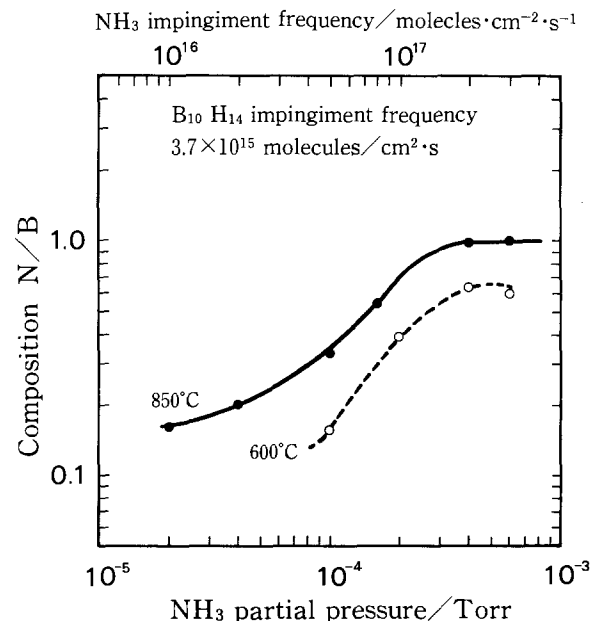


Fig. 15. Composition of boron nitride as a function of ν_{NH_3} at the constant $\nu_{B_{10}H_{14}}$.

The compositions of the films are determined by the impingement frequency ratio of decaborane and ammonia in the nonstoichiometric composition region.

Conclusion

A new CVD method in the molecular flow region is proposed to deposit boron nitride films using the reaction of decaborane with ammonia. At substrate temperatures between 300° and 1200°C, the deposition films are amorphous. Infrared spectra of the films deposited above 700°C shown the characteristic absorption of boron nitride. The optical bandgap is estimated to be 5.90 eV from the optical absorption measurements. It is found from the chemical shift of boron $K\alpha_2$ wavelength that the films of nonstoichiometric composition below the atomic ratio N/B = 0.75 are a mixture of boron and boron nitride. It is also found from the relationship between the pressure ratio of ammonia to decaborane and the film composition that the composition of the films is proportional to the partial pressure ratio at high temperatures. Therefore, the stoichiometric boron nitride films can easily deposit by this method, which is easy to control because composition is determined by the ratio of impingement frequency of source gases onto the substrate surface in all composition regions. This new deposition method must be useful for other compound materials.

Acknowledgments

The author would like to thank Professor K. Yoshimura and A. Itoh for suggesting this study and for their continuous encouragement. He wishes to express his thanks to S. Nakagawa, S. Misawa, and Dr. S. Gonda for helpful contributions and support of this work. Numerous valuable and stimulating discussions with Professor A. Amano, Dr. S. Yoshida, and Dr. F. Shinoki are also acknowledged with many thanks. He is also grateful to T. Asano for a critical reading of the manuscript.

Manuscript received Jan. 21, 1985.

Nihon University assisted in meeting the publication costs of this article.

REFERENCES

1. L. G. Carpenter and P. J. Kirby, *J. Phys. D*, **15**, 1143 (1982).
2. A. Simpson and A. D. Stuckes, *J. Phys. C*, **4**, 1710 (1971).
3. M. J. Rand and J. F. Roberts, *This Journal*, **115**, 423 (1968).
4. M. Hirayama and K. Shono, *ibid.*, **122**, 1671 (1975).
5. D. Maydan, G. A. Coquin, H. J. Levinstein, A. K. Sinha, and D. N. K. Wang, *J. Vac. Sci. Technol.*, **16**, 1959 (1979).
6. S. Motojima, Y. Tamura, and K. Sugiyama, *Thin Solid Films*, **88**, 269 (1982).
7. M. Sano and M. Aoki, *ibid.*, **83**, 247 (1981).
8. W. Baronian, *Mater. Res. Bull.*, **7**, 119 (1972).
9. T. Takahashi, H. Itoh, and M. Kuroda, *J. Cryst. Growth*, **53**, 418 (1981).
10. A. C. Adams and C. D. Chapio, *This Journal*, **127**, 399 (1980).
11. S. P. Murarka, C. C. Chang, D. N. K. Wang, and T. E. Smith, *ibid.*, **126**, 1951 (1979).
12. O. Gafri, A. Grill, D. Itzhak, A. Inspector, and R. Avni, *Thin Solid Films*, **72**, 523 (1980).
13. S. b. Hyder and T. O. Yep, *This Journal*, **123**, 1721 (1976).
14. H. Miyamoto, M. Hirose, and Y. Osaka, *Jpn. J. Appl. Phys.*, **22**, L216 (1983).
15. A. C. Adams, *This Journal*, **128**, 1378 (1981).
16. W. Shmolla and H. L. Hartnagel, *Solid State Electron.*, **26**, 931 (1983).
17. M. D. Wiggins, C. R. Aita, and F. S. Hickernell, *J. Vac. Sci. Technol. A*, **2**, 322 (1984).
18. N. Puychevriev and M. Menoret, *Thin Solid Films*, **36**, 141 (1976).
19. K. Nakamura, *This Journal*, **131**, 2691 (1984).
20. A. Zunger, *Phys. Rev. B*, **13**, 5560 (1976).
21. J. Williams, R. L. Williams, and J. C. Wright, *J. Chem. Soc.*, 5816 (1963).
22. W. C. Price, R. D. B. Fraser, T. S. Robinson, and H. C. Longuet-Higgins, *Discuss. Faraday Soc.*, **9**, 131 (1950).
23. R. Geick and C. H. Perry, *Phys. Rev.*, **146**, 543 (1966).
24. "ESCA Spectrometer System 5950 Manual," Section IV, Hewlett-Packard Co. (1972).
25. D. J. Joyner and D. M. Hercules, *J. Chem. Phys.*, **72**, 1095 (1980).
26. H. E. Bishop and J. C. Riviere, *Appl. Phys. Lett.*, **16**, 21 (1970).
27. V. A. Fomichev, T. M. Zmkina, and I. I. Lyakhovskaya, *Sov. Phys. Solid State*, **12**, 123 (1970).
28. G. Bambakidis and R. P. Wager, *J. Phys. Chem. Solids*, **42**, 1023 (1981).
29. F. Perrot, *Phys. Rev. B*, **23**, 2004 (1981).
30. M. S. Nakhmanson and V. P. Simirnov, *Sov. Phys. Solid State*, **13**, 2763 (1972).
31. F. C. Brown, P. Z. Bachrach, and M. Skibowski, *Phys. Rev. B*, **13**, 2633 (1976).
32. M. Grasserbauer, *Mikrochim. Acta*, **1**, 145 (1975).

A Comparison Between Silicon Nitride Films Made by PCVD of N_2 - SiH_4 /Ar and N_2 - SiH_4 /He

K. Allaert and A. Van Calster

Laboratory of Electronics, Ghent State University, B-9000 Ghent, Belgium

H. Loos and A. Lequesne

Bell Telephone Manufacturing Company (I.T.T.), B-9000 Ghent, Belgium

ABSTRACT

This paper reports on the passivating properties of PCVD silicon nitride obtained from the gas mixtures $N_2 + SiH_4$ diluted in Ar (SiH_4/Ar) and $N_2 + SiH_4$ diluted in He (SiH_4/He). Ellipsometric data, Auger data, IR data, mechanical stress, pinholes, and electrical data are presented. The stability of the hydrogen bonds in the silicon nitride is evaluated by low temperature annealing. By comparison of the properties of nitrides made from $N_2 + SiH_4/He$ and $N_2 + SiH_4/Ar$, it is concluded that the former one yields more uniform films, less critical to deposition temperature, while the latter process behaves better for passivating purposes. On the other hand, it is shown that the carrier gas (He or Ar) has a marked influence on the properties of the films, especially on the hydrogen content. It is found that both PCVD nitrides are best described as $Si_xN_yH_zO_t$.

Undoubtedly, the major advantage of PCVD techniques is the low temperature processing involved. Thus, the most important application of PCVD silicon nitride is the passivation of integrated circuits. In this application, the deposition temperature is at most 350°C. Therefore, we examined silicon nitride films deposited at 150°, 200°, and 300°C. A capacitively coupled parallel plate PCVD reactor, manufactured by L.F.E., Incorporated (Model PND-301), has been used for the depositions. A schematic diagram of this apparatus has been given elsewhere (1).

Among the different possible gas mixtures, we used diluted silane (as a safety precaution) and nitrogen. Nitrogen was preferred to ammonia, because it leads to silicon nitride films with a lower hydrogen content. SiH_4 was diluted up to 1.75% in commonly used Ar (SiH_4/Ar) or in He (SiH_4/He). He was used because it was mentioned in the literature (2) that films deposited with SiH_4/He show more uniform properties.

A review of the literature on PCVD silicon nitrides shows that a major part of the work has been done on nitride films deposited by mixtures of SiH_4 and NH_3 . It is also found that the properties of the nitride films not only depend on the gases, but also on the actual reactor configuration used. This explains why some of the results reported here are not fully comparable to previous work on a L.F.E. reactor reported by Dun *et al.* (3). Dun premixes the gases SiH_4 and N_2 , while our equipment configuration consists of a separated gas inlet system.

We found, for both SiH_4/Ar and SiH_4/He gas mixtures, the resulting nitride films to be Si rich and become even more Si rich as deposition temperature increases. This is in agreement with results obtained by Maeda *et al.* (1) in the same L.F.E. reactor. However, Maeda did not examine the influence of different carrier gases. This Si dependency on deposition temperature will be explained by the fact that PCVD silicon nitrides have no fixed stoichiometry, so that they are best described as $Si_xN_yH_zO_t$. From this formula, a consistent definition for the Si/N ratio will be derived.

As our goal was the investigation of the dependence of the passivation properties of silicon nitride on the deposition parameters, we focused our experiments on pinhole detection, step coverage, and low temperature annealing. The purpose of annealing is to investigate how strongly hydrogen is bonded to Si, because in passivation applications H should not escape from the nitride and penetrate

into the underlying circuits. If this should happen, failure of the circuits might occur.

Experimental Techniques and Results

It is well known that the composition of the nitride films depends on the deposition parameters. Two thicknesses of nitride films were evaluated: thin films of about 100 nm were deposited on 2 in. bare silicon wafers for ellipsometric and Auger measurements, while film thicknesses of 500 nm were used for IR, mechanical stress, pinhole, and electrical measurements. As deposition parameters for all films made, we used an RF power (W) of 100W at a frequency of 13.56 MHz, a total pressure (P) of 2700 mtorr for both gas mixtures SiH_4/Ar and SiH_4/He , a N_2/SiH_4 ratio of 1.55 in the case of SiH_4/Ar or 3.05 in the case of SiH_4/He , and deposition temperatures (T) increasing from 150° to 300°C. We did not examine the influence of W and P , as this was already done by previous authors (1, 3). In this way, we obtained a refractive index (n) of 2.0 for $Si_xN_yH_zO_t$ (Ar) and 2.3 for $Si_xN_yH_zO_t$ (He) at $T = 275^\circ C$. These different refractive indexes could be tolerated, first because the aim of this evaluation was to compare changes of (structural) properties related to deposition temperature for both gas mixtures, SiH_4/Ar and SiH_4/He , and, second, because a refractive index of 2.0 does not mean a stoichiometric film due to the incorporation of oxygen and hydrogen in the film, as will be discussed later. Nevertheless, the measurement of n may be considered as a simple criterion to check the deposition conditions. Ellipsometric measurements with an automatic Gaertner ellipsometer (wavelength 632.8 nm, angle of incidence 70°) also give us an idea of the uniformity of the deposited layers. In Table I, we have summarized the uniformity of n and thickness t of the silicon nitride films. It is seen that both gas systems (SiH_4/Ar and SiH_4/He) produce acceptably uniform films, but SiH_4/He leads to somewhat more uniform films. In Fig. 1, the refractive index n and the growth rate G vs. the deposition temperature T are presented. It is seen that n increases with T , while G nearly becomes independent of T in the case of He but increases with T in the case of Ar.

As mentioned above, an important feature of the assessment of silicon nitride deposits is knowledge of how strongly H is bonded to Si. To investigate this, the H content was measured by infrared transmission spectros-

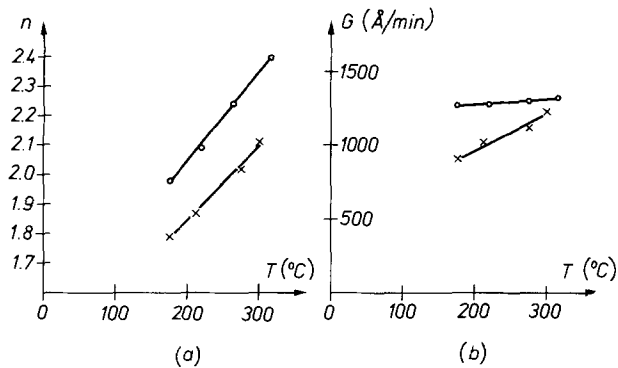


Fig. 1. a: Refractive index as a function of deposition temperature. b: Growth rate as a function of deposition temperature. o: SiH_4/He . x: SiH_4/Ar .

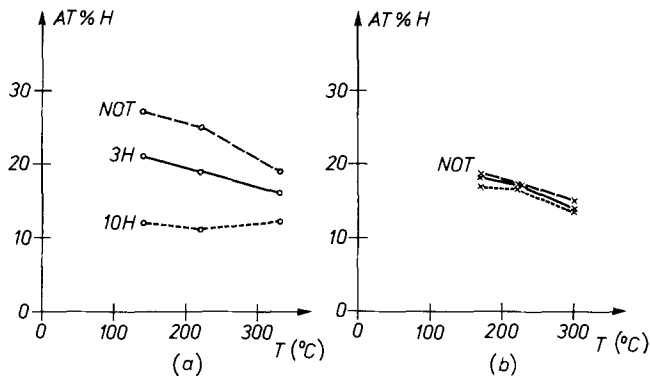


Fig. 2. Atomic percent H as a function of deposition temperature and annealing. a: for SiH_4/He . b: for SiH_4/Ar . NOT = not annealed; 3H = annealed for 3h; 10H = annealed for 10h. o: SiH_4/He . x: SiH_4/Ar .

copy. Measurements were done before and after low temperature annealing at 300°C using an automatic dispersive, double beam ratio, recording IR spectrophotometer (Perkin-Elmer Model 1420). This annealing at 300°C , on the one hand, simulates possible further low temperature processing of devices coated with PCVD silicon nitride and, on the other hand, will accelerate the outdiffusion of H which might occur at lower temperatures. To obtain the total atomic percent of H and the amounts of N-H and Si-H bonds, we used the calibration values of Lanford and Rand (4). Therefore, a realistic value of $2.7 \text{ g}/\text{cm}^3$ for the density of the films has been assumed. In Fig. 2, the total atomic percent H is shown vs. deposition temperature T for different annealing times (3 and 10h). In Fig. 3, the percent N-H bonds are shown vs. T for different annealing times. First it is seen that in the case of unannealed films, the amount of H decreases with increasing T . The amount of H is smaller in the case of Ar (18-15%) than in the case of He (27-19%). Annealing for 3 and 10h reduces this H content, but the effect is far more pronounced for SiH_4/He than for SiH_4/Ar . In the latter case, only minor changes are detected. This probably means that H is less tightly bonded in the case of SiH_4/He and diffuses out of the films more easily. This is in accordance with the fact that these films seem to be more po-

Table I. Nonuniformity of refractive index (n) and thickness (t) over a 3 in. wafer

	n (%)	t (%)
SiH_4/He	≤ 1	≤ 2
SiH_4/Ar	≤ 2	≤ 4

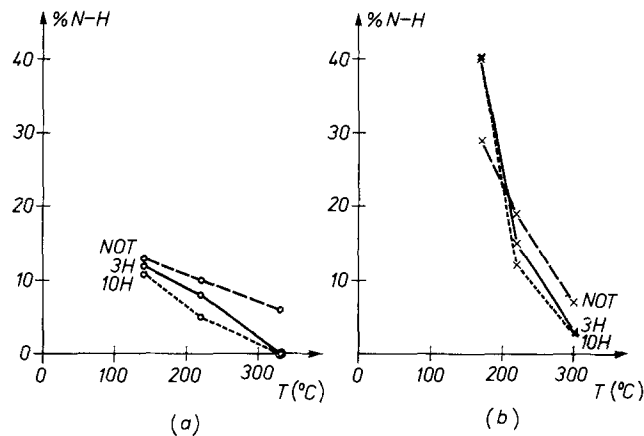


Fig. 3. Percent of N-H bonds as a function of deposition temperature and annealing. a: for SiH_4/He . b: for SiH_4/Ar . o: SiH_4/He . x: SiH_4/Ar . NOT = not annealed; 3H = annealed for 3h; 10H = annealed for 10h.

rous (see AES results). We may conclude that one has to be aware of the fact that H may escape from silicon nitride films, especially in the case of films made by SiH_4/He . Furthermore, it follows from Fig. 3 that there is a remarkable change in the amount of N-H bonds with changes in deposition temperature and annealing. The amount of N-H bonds decreases both with annealing time and with increasing deposition temperature T . By comparing Fig. 2b and 3b, we see that, in the case of SiH_4/Ar , the amount of Si-H bonds increases, due to annealing time and increasing deposition temperature, in such a way that the total amount of hydrogen stays more or less the same (the sum of N-H and Si-H bonds is used to obtain the total H content).

To get some insight into the composition of the deposited films, we used Auger electron spectroscopy (AES). The different atomic percents of Si, N, and O were measured on Physical Electronics 590 AES. The Auger data were corrected with the atomic H content obtained from IR spectroscopy. In Fig. 4, the atomic percents of Si, N, O, and H are plotted vs. the deposition temperature T . The amount of oxygen ($\geq 2\%$) is within the detectability range of Auger analysis and may not be neglected. As reported by Dun *et al.* (3), we believe the large amounts of oxygen (10%) at low temperatures ($\leq 175^{\circ}\text{C}$) are due to the moisture released from the inner wall of the reactor by the plasma.

From the above considerations, it follows that PCVD nitrides have to be described by the formula $\text{Si}_x\text{N}_y\text{H}_z\text{O}$. A possible molecular structure may be as follows

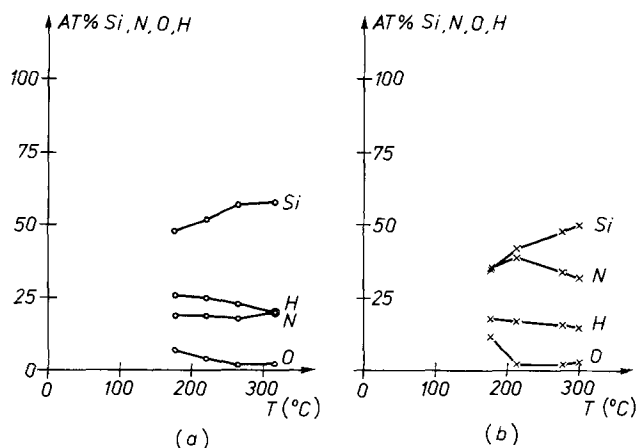
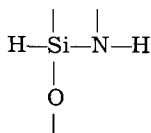


Fig. 4. Atomic percent Si, N, O, H as a function of deposition temperature. a: for SiH_4/He . b: for SiH_4/Ar . o: SiH_4/He . x: SiH_4/Ar .



where we assume that N-N bonds may be neglected and that only Si-N, Si-H, N-H, and Si-O bonds have to be taken into account (N-O bonds were not detected by IR spectroscopy). Therefore, we correct the Si/N ratio used by Dun *et al.* (3) as follows

$$\frac{\text{Si}}{\text{N}} = \frac{[\text{Si a/o}] + 1/4 [\text{H}_\text{N} \text{ a/o}]}{[\text{N a/o}] + 2/3 [\text{O a/o}] + 1/3 [\text{H}_\text{Si} \text{ a/o}]}$$

where the atomic percent (a/o) N-H bonds (H_N) and Si-H bonds (H_Si) are taken into account. For a stoichiometric structure, this ratio always equals 0.75. A value larger than 0.75 must most probably be associated with $\equiv\text{Si}-\text{Si}\equiv$ bonds. In other words, Si/N ratios larger than 0.75 indicate the incorporation of excess Si in the nitrides. In Fig. 5, Si/N vs. deposition temperature is plotted. All films are Si rich, especially in the case of He nitrides, and become even more Si rich as T increases. This is in accordance with the fact that the refractive index n also increases with T (Fig. 1). Indeed, the refractive index may be correlated with the ratio Si/N (1, 5). An increasing Si/N ratio will show an increasing refractive index. However, a refractive index $n = 2.0$ does not necessarily mean stoichiometric silicon nitride Si_3N_4 . As discussed above, we always found films with a composition $\text{Si}_x\text{N}_y\text{H}_z\text{O}_t$ with $x \neq y \neq z \neq t \neq 0$, and, as is seen from Fig. 1, $n = 2.0$ may be obtained.

Another interesting feature is the sputter rate s of the $\text{Si}_x\text{N}_y\text{H}_z\text{O}_t$ films under a 2 keV argon bombardment. This sputter rate s (Table II) gives an idea of the density of the films. As a reference value for s , the measured sputter rate of stoichiometric LPCVD Si_3N_4 is included. It follows from Table II that $\text{Si}_x\text{N}_y\text{H}_z\text{O}_t$ (He) has a high value of s and therefore is porous, while $\text{Si}_x\text{N}_y\text{H}_z\text{O}_t$ (Ar) deposited at 300°C has the lowest value of s and therefore has the largest density.

Pinholes are another important criterion for characterizing silicon nitride films. In order to measure this feature, Si wafers with 500 nm Al on top were coated with 500 nm nitride and afterwards etched in a 5% NaOH solution for 4 min. The measured pinhole density is shown in Table III. As could be expected, the pinhole density decreases as T increases. At 150°C, $\text{Si}_x\text{N}_y\text{H}_z\text{O}_t$ (He) behaves better than $\text{Si}_x\text{N}_y\text{H}_z\text{O}_t$ (Ar), but at 300°C both gas mixtures (SiH_4/He and SiH_4/Ar) produce films of about the same quality. It has to be remarked that, in the case of Ar, a deposition temperature of 300°C is a necessity to obtain good quality films. Although we estimated that the films made with SiH_4/He were more porous, from the point of view of pinholes, both gas systems are about equal.

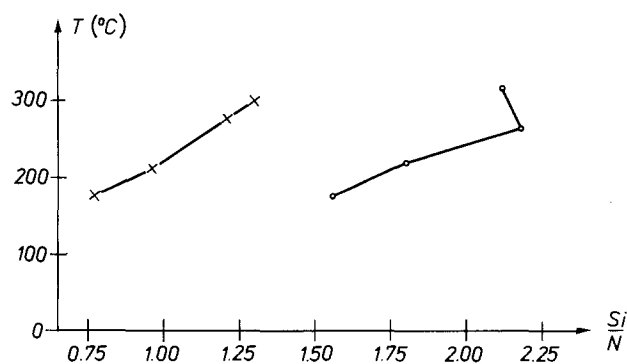


Fig. 5. Si/N ratio as a function of deposition temperature. o: SiH_4/He . x: SiH_4/Ar .

Table II. Sputter rate (s) in $\text{nm}/\text{mC}\cdot\text{cm}^{-2}$ for SiH_4/He and SiH_4/Ar as a function of deposition temperature

T (°C)	150	200	300
SiH_4/He	1.70	1.73	1.71
SiH_4/Ar	1.82	1.38	1.36

LPCVD Si_3N_4 : $s = 1.24 \text{ nm}/\text{mC}\cdot\text{cm}^{-2}$.

Table III. Pinholes per square centimeter for SiH_4/He and SiH_4/Ar as a function of deposition temperature

T (°C)	150	200	300
SiH_4/He	≤ 300	≤ 75	≤ 1
SiH_4/Ar	≤ 1000	≤ 750	≤ 1

To investigate the step coverage, we examined the ability of PCVD silicon nitride to cover entirely a gold wire bond on an Al bonding path of an IC. This may be considered as an extreme test case for step coverage. The samples were etched in a 5% NaOH solution. SEM analysis revealed that in the case of the low temperature nitrides, the Al etchant penetrated under the Au bonding balls and etched the Al away. This effect was far less pronounced for nitrides deposited at 300°C. For both gas systems (SiH_4/Ar and SiH_4/He), a rather good protection of the bonding paths was obtained. Nevertheless, nitrides made out of SiH_4/He behaved somewhat better.

It is established that the stability and the step coverage of films are related to the mechanical stress of the films. We therefore evaluated the mechanical stress of silicon nitride films deposited on bare Si wafers. The stress was determined by an interference technique (6). The results for the nitride films made under different deposition conditions are shown in Fig. 6. It is seen that films made with Ar have a compressive stress and show no clear correlation with the deposition temperature T . The measured value of the compressive stress ($2.5 \times 10^8 \text{ N}/\text{m}^2$) is acceptable (7, 8) from the point of view of mechanical stability. On the other hand, films made with He show a clear dependence on T , going from compressive to slightly tensile at 300°C. Pinhole experiments indicated that films at 300°C have to be preferred, which means that $\text{Si}_x\text{N}_y\text{H}_z\text{O}_t$ made with He should have a somewhat better mechanical stability due to its lower mechanical stress compared to $\text{Si}_x\text{N}_y\text{H}_z\text{O}_t$ deposited with Ar. This is in agreement with the fact that, although both nitrides afforded good protec-

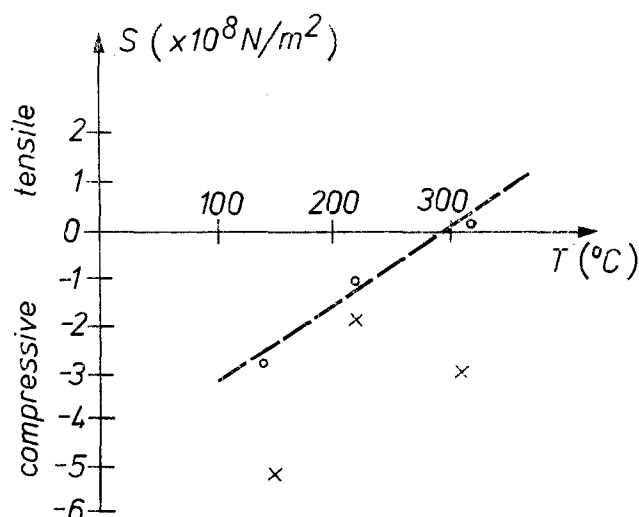


Fig. 6. Stress as a function of deposition temperature. o: SiH_4/He . x: SiH_4/Ar .

tion of the Al bonding paths, fewer failures were detected in the case of He.

Electrical measurements of dielectric constant and of dielectric losses on 500 nm $\text{Si}_x\text{N}_y\text{H}_z\text{O}_w$ capacitors made at 300°C with Al electrodes showed that He nitrides behaved similarly to Ar nitrides. The measurements were performed on a HP 4274A multifrequency LCR meter. Both nitride films have a dielectric constant (ϵ) between 7 and 8 comparable to the bulk value of 7.5. The loss factor ($\tan \delta$) is smaller than 0.2% and nearly constant over the frequency range 100 Hz-100 kHz. The measured breakdown strength (E_b) is 5 MV/cm. This corresponds to the fact that nitrides deposited at 300°C have practically no pinholes, and have a good step coverage, provided the nitrides have a thickness of at least 500 nm. In other words, a thickness of 500 nm for silicon nitride is a necessity. These features, especially the fact of its low loss factor, make PCVD silicon nitride also an attractive isolator for thin film capacitors.

Conclusions

We may conclude from studies of PCVD $\text{Si}_x\text{N}_y\text{H}_z\text{O}_w$ made at different deposition temperatures, using two types of carrier gases (He and Ar) for SiH_4 , that low temperature nitrides (150°-200°C) are less dense and contain more hydrogen than nitrides made at 300°C. SiH_4 diluted in He gives more uniform films and is less critical to deposition temperature, but the release of hydrogen by a low temperature annealing is more pronounced in this case.

As for optimum device protection, a low pinhole density and an acceptably small mechanical stress in the passivation layer are needed; only nitrides made at 300°C are suitable for this purpose. The disadvantage of nitrides made with SiH_4/He is that the hydrogen content is higher

and is easily released by low temperature processing (for instance, an annealing at 300°C), which cannot be tolerated in a number of applications. Apart from this fact, both high deposition temperature nitrides (300°C) have similar and quite acceptable electrical, mechanical, and pinhole performances.

Acknowledgments

Special thanks are expressed to R. Vlaeminck and R. van den Berghe (Bell Telephone, Ghent), who took care of the AES measurements, and to M. Petit (Bell Telephone, Ghent) for his assistance in the IR spectroscopy. The authors also wish to thank F. Vervaeke (Ghent State University) for valuable and helpful discussions.

Manuscript submitted Nov. 21, 1984; revised manuscript received March 8, 1985.

Ghent State University assisted in meeting the publication costs of this article.

REFERENCES

1. M. Maeda and Y. Arita, *J. Appl. Phys.*, **53**, 6852 (1982).
2. V. S. Nguyen, Paper 136 presented at The Electrochemical Society Meeting, San Francisco, CA, May 8-13, 1983.
3. H. Dun, P. Pan, F. White, and R. W. Douse, *This Journal*, **128**, 1555 (1981).
4. W. A. Lanford and M. J. Rand, *J. Appl. Phys.*, **49**, 2476 (1978).
5. W. Claassen, W. Valkenburg, F. Habraken, and Y. Tamminga, *This Journal*, **130**, 2419 (1983).
6. K. L. Chopra, "Thin Film Phenomena," pp. 266-270, McGraw Hill, New York (1969).
7. E. P. G. T. van de Ven, *Solid State Technol.*, **24**, 169 (1981).
8. A. Sherman, *Thin Solid Films*, **29**, 140 (1984).

Complex Plane and ^7Li NMR Studies of Arsenic Sulfide-Based Lithium Glasses

Steven J. Visco, Peter J. Spellane, and John H. Kennedy*

Department of Chemistry, University of California, Santa Barbara, California 93106

ABSTRACT

The glass forming region of the $\text{LiI-Li}_2\text{S-As}_2\text{S}_3$ system was explored as a function of lithium ion concentration. The most conductive base glass attainable was $\text{Li}_2\text{S-2As}_2\text{S}_3$, and with this glass, up to 45 mole percent LiI could be added. Ionic conductivity was measured using complex plane techniques with room temperature conductivity reaching $2.9 \times 10^{-5} \text{ S-cm}^{-1}$ for 0.45-LiI-0.18 Li_2S -0.37 As_2S_3 . NMR linewidth data were fit to the Hendrickson-Bray equation, and activation energies were obtained. All glasses showed a low activation energy process which was attributed to a local motion. Only the more conductive 30-40% LiI glasses showed a second, higher activation energy process which correlated well with activation energies from conductivity measurements.

There has been a substantial amount of research effort devoted to finding suitable lithium electrolytes, but the search for crystalline lithium electrolytes has not been entirely successful. However, there have been recent exciting advances in the development of lithium ion conductive glasses (1-15). Various glasses have been synthesized (such as $\text{LiI-Li}_2\text{S-P}_2\text{S}_5$ and $\text{LiI-Li}_2\text{S-B}_2\text{S}_3$) that have Li^+ conductivities matching the best crystalline electrolytes ($\sigma = 10^{-3} \text{ S-cm}^{-1}$ at 25°C) and stability ranges appropriate for their use in lithium anode batteries (1-5, 10, 15).

In the course of the development of highly conductive vitreous electrolytes, it has been found that the size and polarizability of the anions to which the mobile cations are coordinated are two major factors that govern high ionic mobility. Thus, replacement of oxygen by sulfur in the glass network former and modifier will result in a

higher mobility of the alkali ions, as will doping the glass with LiI as opposed to, say, LiBr. We therefore decided to investigate the glass forming range of the $\text{LiI-Li}_2\text{S-As}_2\text{S}_3$ system. Furthermore, in light of the relatively high Ag^+ conductivities reported for the $\text{AgI-Ag}_2\text{S-As}_2\text{S}_3$ glass system (13), it was anticipated that the lithium analog might exhibit high Li^+ conductivities.

The structures and mechanisms for conduction in glass electrolytes have been studied less often and consequently not understood as well as their crystalline counterparts. We have previously applied the techniques of both solid-state NMR and ac impedance to study the highly conductive $\text{LiI-Li}_2\text{S-P}_2\text{S}_5$ glasses (16) and now report their use in the study of $\text{LiI-Li}_2\text{S-As}_2\text{S}_3$ glasses.

^7Li NMR has been used effectively to study the diffusion of Li^+ in Li_3N , Li^+ movement in the conductive lithium borate glasses (17-19), $\text{Li}_2\text{S-GeS}_2$ glasses (20), and Li^+ movement in the $\text{LiI-Li}_2\text{S-P}_2\text{S}_5$ glasses (16). A predomi-

* Electrochemical Society Active Member.

nant cause of NMR line broadening in solids is the magnetic dipole-dipole interaction between nuclei. Thermal activation of ions with increasing temperature tends to remove the dipole-dipole interaction between nuclei of activated ions, and the corresponding NMR line narrows. This phenomenon is called motional narrowing. From the NMR linewidth *vs.* temperature data, the Hendrickson-Bray (HB) equation can be used to calculate the activation energy for Li⁺ motion in the solid (18, 19).

In the ⁷Li NMR investigation of the LiI-Li₂S-P₂S₅ glass system, it was found (16) that the activation energies for ⁷Li motion (high activation energy process) correlated well with the activation energies determined from ionic conductivity measurements made on the same glass samples. In order to further explore the nature of the ionic conductivity in glasses, we have applied the same NMR techniques to a new vitreous lithium electrolyte system, LiI-Li₂S-As₂S₃.

Experimental

Starting materials were anhydrous LiI, Li₂S, and As₂S₃, and all manipulations were performed inside a helium dry box equipped with a purification train to keep residual H₂O and O₂ to less than 1 ppm. The Li₂S-As₂S₃ and LiI-Li₂S-As₂S₃ glasses were prepared by mixing and grinding the reagents in the appropriate proportions, sealing them into thick-walled quartz tubes, and heating the tubes inside an Inconel alloy pipe explosion shield to approximately 900°C for 1 h. The melts were then cooled to 700°C and quenched into a water bath at room temperature. The quenched glass was ground to a fine powder, and, for the NMR study, a portion of the glass sample was sealed under vacuum into 5 mm NMR tubes. Some of the remaining powder was then uniaxially pressed into 1/4 in. diam rods with TiS₂ electrodes on both faces. The vitreous electrolyte rod was finally isostatically pressed at approximately 40,000 psi prior to ionic conductivity measurements.

The ionic conductivity of the glasses was determined using a Solartron 1174 Frequency Response Analyzer interfaced to a Hewlett-Packard 9845B desktop computer and a General Radio 1435 programmable decade resistance box. A correction program was incorporated to compensate for inductive effects arising from electrode leads observed at high frequency (10⁵-10⁶ Hz). The signal across the sample was 350 mV. Complex impedance measurements were recorded from 10⁻² to 10⁻⁶ Hz over the temperature range of 25° to (T_g - 20)°C.

⁷Li NMR spectra were obtained on a Nicolet NT-300 Spectrometer. A broad-band probe was tuned to 116.6157 MHz on a solution sample of LiCl, and the magnetic field homogeneity was optimized for this sample at room temperature. The lithium glass sample was then placed in the magnet and cooled gradually to -100°C. The sample was not spun, and no further attempt was made to improve field homogeneity. Thermal equilibration time varied from 15 to 60 min, depending on the selected temperature. A 90° pulse was applied, and data from 1000 transients were Fourier transformed to yield one broad resonance and fit to a Lorentzian curve.

Results and Discussion

X-ray diffraction.—The Li₂S-2As₂S₃ support glass was doped with lithium iodide over the range of 0-50 mole percent (m/o) LiI. Owing to the hygroscopic nature of the vitreous electrolytes in this study, the glass samples were ground to a fine powder and sealed in plastic bags in the dry box prior to x-ray analysis. X-ray diffraction patterns showed the extent of glass formation to lie between 0 and 45 m/o LiI; (LiI)_x-(0.33Li₂S-0.67As₂S₃)_{1-x} (0 < x < 0.45). At 45 m/o LiI, x-ray diffraction patterns detected traces of LiI microcrystals dispersed in the glass matrix. At higher LiI concentrations, the amount of crystallized LiI detected in the glass increased sharply.

Thermal analysis.—Powdered glass samples were hermetically sealed in aluminum containers in the dry box and analyzed by differential scanning calorimetry. The

powders were examined over the temperature range of 25°-300°C at a scan rate of 20°C/min. All samples in the range of 0-45 m/o LiI exhibited the characteristic glass transition temperature (T_g). T_g showed a gradual decrease from about 170° to 140°C as the LiI content increased to 40 m/o.

Complex impedance and ionic conductivity.—The complex impedance plots of the LiI-Li₂S-As₂S₃ glasses conformed to a straight line intersecting the real axis at approximately a 45° angle and a semicircle (Fig. 1). The real axis intercept of the straight line portion of the complex impedance plots was taken to represent the total resistance of the glass sample. In some cases, as shown in Fig. 1, there was some evidence of a small semicircle that could indicate an interface effect, most likely at the electrodes since grain boundary effects would not be expected in glasses. If the high frequency intercept were used as the measure of bulk conductivity, the values reported here would be increased by several percent, but the more conservative approach was adopted in this investigation. For all glass compositions, the ionic conductivity was found to follow the Arrhenius law: $\sigma = \sigma^0 \exp(-E_a/kT)$, as shown in Fig. 2. The activation energies determined from the Arrhenius plots were found to decrease linearly with increasing LiI content (Fig. 3). Similarly, the total ionic conductivity was observed to increase with increasing LiI; a plot of log σ *vs.* m/o LiI yielded a straight line (Fig. 4). Accordingly, the glass sample with the highest measured ionic conductivity and lowest activation energy (Table I) was the glass with the highest attainable LiI concentration, that is, 0.45LiI-0.18Li₂S-0.37As₂S₃.

The ionic conductivities observed for the LiI-Li₂S-As₂S₃ glasses are lower than those reported (4) and observed in this laboratory for the LiI-Li₂S-P₂S₅ glasses. For example, the reported ionic conductivity for the 0.45LiI-0.37Li₂S-0.18P₂S₅ glass was about 10⁻³ S-cm⁻¹ at 25°C (4), while the 0.45LiI-0.18Li₂S-0.37As₂S₃ glass electrolyte was about 3 ×

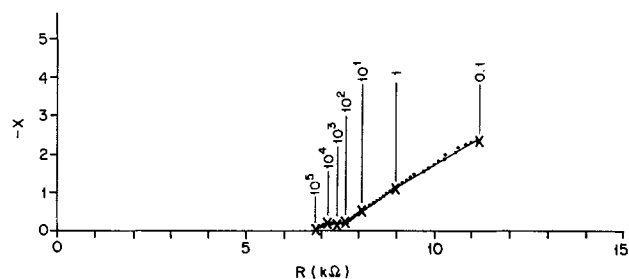


Fig. 1. Complex impedance plot for 0.45LiI-0.18Li₂S-0.37As₂S₃ using TiS₂ electrodes at 89°C.

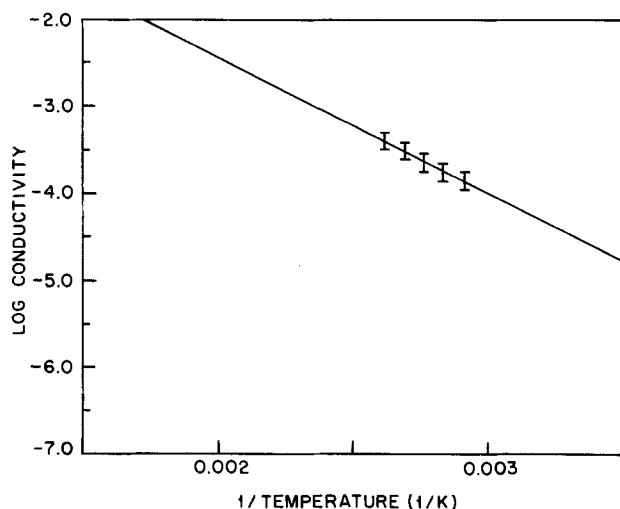


Fig. 2. Arrhenius plot for 0.45LiI-0.18Li₂S-0.37As₂S₃ using TiS₂ electrodes. Activation energy = 7.09 kcal/mol.

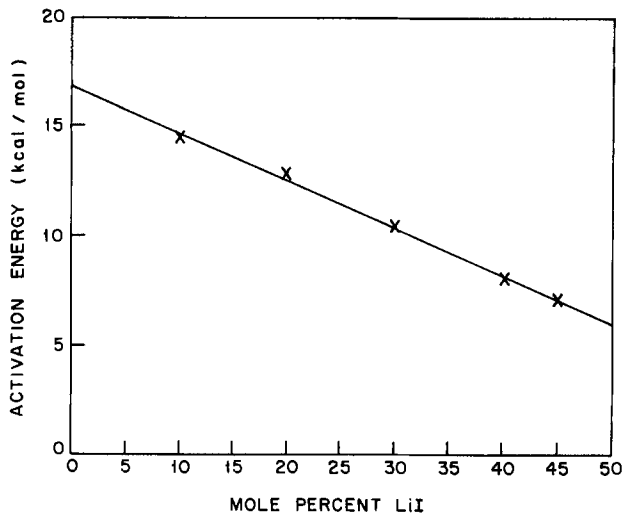


Fig. 3. Activation energy as a function of LiI content in LiI-Li₂S-As₂S₃ glasses.

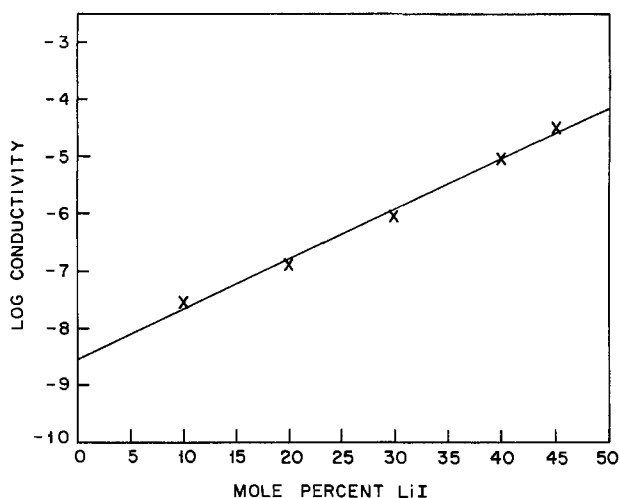


Fig. 4. Conductivity at 25°C as a function of LiI content in LiI-Li₂S-As₂S₃ glasses.

10^{-5} S-cm⁻¹ at 25°C. Both of these glass compositions correspond to the saturation limit of LiI in their respective support glasses 2Li₂S-P₂S₅ and Li₂S-As₂S₃. The smaller glass forming range of the Li₂S-As₂S₃ system limits the Li₂S content of the support glass to Li₂S-2As₂S₃. The conductivity of the 2Li₂S-P₂S₅ base glass is reported to be approximately 10^{-4} S-cm⁻¹ (1), whereas the ionic conductivity of the Li₂S-2As₂S₃ base glass is about 3×10^{-9} S-cm⁻¹. Although the ionic conductivities of the (LiI)_r(0.33Li₂S-0.66As₂S₃)_{1-r} glasses increase quite rapidly with increasing Li concentration (Fig. 4), the maximum conductivity is, unfortunately, not as high as other similar glass systems. This may be due to the lower total lithium content at the LiI saturation limit for the LiI-Li₂S-As₂S₃ system as compared to other glass electrolytes such as LiI-Li₂S-P₂S₅ (4) or LiI-Li₂S-B₂S₃ (10).

⁷Li NMR.—The ⁷Li NMR spectra for the lithium glasses investigated exhibited a single ⁷Li resonance over the

Table I. Conductivities and activation energies for arsenic sulfide glasses

Glass composition	σ (S-cm ⁻¹) at 25°C	E_a (kcal/mol)	E_a (eV)
0.0LiI-0.33Li ₂ S-0.67As ₂ S ₃	3.0×10^{-9}	16.8	0.73
0.10LiI-0.30Li ₂ S-0.60As ₂ S ₃	2.8×10^{-8}	14.4	0.62
0.20LiI-0.27Li ₂ S-0.53As ₂ S ₃	1.3×10^{-7}	12.9	0.56
0.30LiI-0.23Li ₂ S-0.47As ₂ S ₃	9.1×10^{-7}	10.4	0.45
0.40LiI-0.20Li ₂ S-0.40As ₂ S ₃	9.0×10^{-6}	8.1	0.35
0.45LiI-0.18Li ₂ S-0.37As ₂ S ₃	2.9×10^{-5}	7.1	0.31

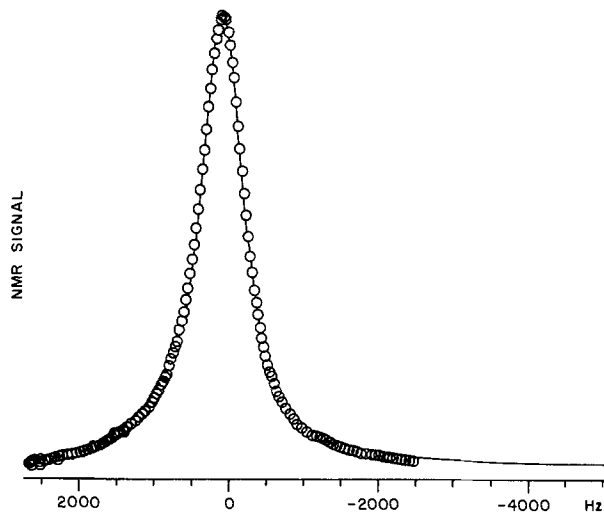


Fig. 5. ⁷Li NMR line for 0.30LiI-0.23Li₂S-0.47As₂S₃ glass at 20°C. Circles are data points; line is fit to Lorentzian line shape.

temperature range of -100° to 20°C that could be fit to a Lorentzian curve as shown in Fig. 5. Hendrickson and Bray (19), have developed the theory for a case where the solid contains a collection of nonexcited ions on their lattice sites with a very short T_2 relaxation time and a collection of excited ions with a long T_2 . One NMR line will be observed with its width given by a weighted average of the two T_2 's involved

$$T_2 = f_A T_{2A} + f_B T_{2B} = 1/W$$

This very simple concept leads to the Hendrickson-Bray equation (HB) for motional narrowing in solids as

$$\ln(1/W - 1/A) = -(E_a/kT) + \ln(1/B - 1/A)$$

where W is the observed NMR linewidth, A is the experimentally determined rigid-lattice linewidth, and B is the high temperature linewidth. The rigid-lattice linewidth A is determined by lowering the sample temperature until the NMR linewidth no longer broadens. A plot of $\ln(1/W - 1/A)$ vs. $1/T$ should produce a straight line with a slope of $-E_a/k$ and y intercept of $\ln(1/B - 1/A)$, as shown in Fig. 6 and 7 for 20% LiI doping. Here is where confusion begins for so many NMR studies of solid electrolytes. The activation energy for 20% LiI-doped glass from NMR was only 4.5 kcal/mol, while it was 12.9 kcal/mol from conductivity measurements as given in Table I.

A possible explanation presents itself when we look at higher LiI concentrations. For 0.30LiI-0.23Li₂S-0.47As₂S₃ glass (30% LiI), the fit to the HB equation is excellent

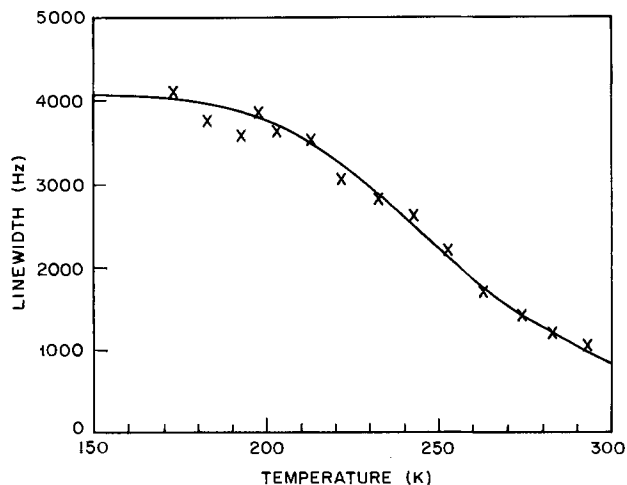


Fig. 6. NMR linewidth as a function of temperature for 0.20LiI-0.27Li₂S-0.53As₂S₃ glass. Line is fit using activation energy obtained from Fig. 7.

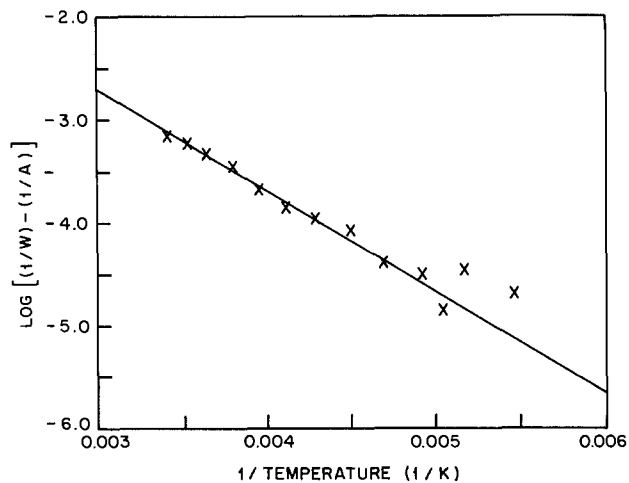


Fig. 7. NMR linewidth data fit to Hendrickson-Bray equation for 0.20LiI-0.27Li₂S-0.53As₂S₃ glass.

(Fig. 8, 9), but the two low temperature points have moved to a new line with a higher activation energy (10.4 kcal/mol). This agrees reasonably well (based on only two points) with the activation energy obtained from conductivity measurements (8.3 kcal/mol).

The picture becomes clearer yet when the NMR data are analyzed for the 40% LiI glass shown in Fig. 10 and 11. The high activation energy line in Fig. 11 gives a value of

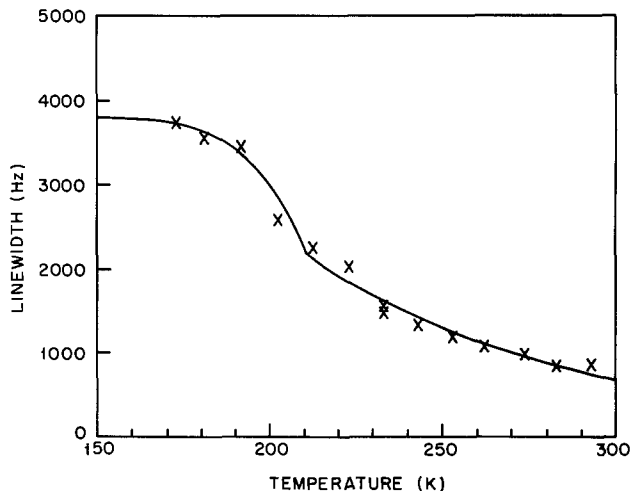


Fig. 10. NMR linewidth as a function of temperature for 0.40LiI-0.20Li₂S-0.40As₂S₃ glass. Line is fit using both activation energies obtained from Fig. 11.

7.1 kcal/mol, which corresponds well with the activation energy of 7.3 kcal/mol determined from conductivity.

Thus, it appears that NMR line narrowing can occur by a low activation energy process involving local motion (rattling in a cage) that does not lead to the long-range motion required for conductivity. At lower temperatures, however, NMR line narrowing is controlled by a high activation energy process involving long-range motion that does correspond to the same process producing ionic conductivity. The values for the parameter *B* in the Hendrickson-Bray equation corroborate this observation. Long-range motion, as in ionic conduction or diffusion, would eliminate the dipole-dipole interaction, whereas a local restricted motion would be far less effective in removing the interaction. Therefore, one would expect the value of *B* corresponding to long-range motion to be considerably smaller than that for short-range motion. From Table II we see, for 40% LiI, that the *B* value for the low temperature region is five orders of magnitude smaller than the high temperature region.

It should be noted that the Hendrickson and Bray approach is only one way to interpret NMR line narrowing. It appears to work satisfactorily, but the experimental fit to theory could be fortuitous. A recent ⁷Li NMR study on conductive glasses, in fact, claims that the activation energy for ⁷Li movement in the glass (which correlates with ionic conductivity) is best obtained from the variation of *T*₁ with temperature (20). Thus, it appears that there is still some confusion as to the interpretation of NMR data, and it will be necessary to follow the evolution of line shape, *T*₂, and *T*₁ with temperature in order to discern

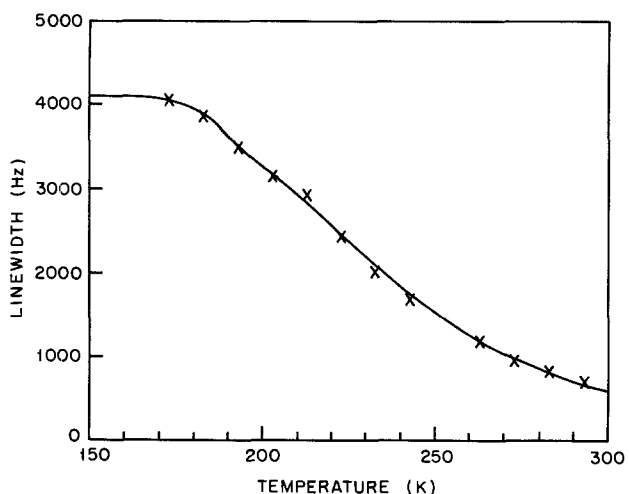


Fig. 8. NMR linewidth as a function of temperature for 0.30LiI-0.23Li₂S-0.47As₂S₃ glass. Line is fit using both activation energies obtained from Fig. 9.

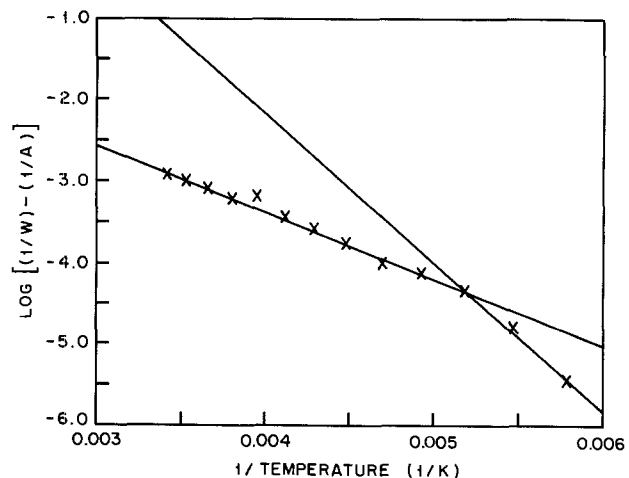


Fig. 9. NMR linewidth data fit to Hendrickson-Bray equation for 0.30LiI-0.23Li₂S-0.47As₂S₃ glass.

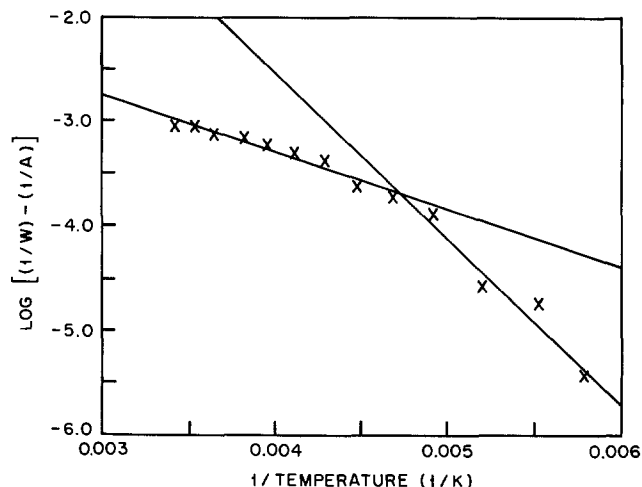


Fig. 11. NMR linewidth data fit to Hendrickson-Bray equation for 0.40LiI-0.20Li₂S-0.40As₂S₃ glass.

Table II. ${}^7\text{Li}$ NMR parameters and E_a 's for arsenic sulfide glasses

Glass composition	E_a (kcal/mol) ^a	B (kHz) ^a
0.10LiI-0.30Li ₂ S-0.60As ₂ S ₃	—	—
0.20LiI-0.27Li ₂ S-0.53As ₂ S ₃	3.4	5.6×10^{-3}
0.30LiI-0.23Li ₂ S-0.47As ₂ S ₃	4.5	5.6×10^{-4}
0.40LiI-0.20Li ₂ S-0.40As ₂ S ₃	8.3	7.6×10^{-9}
	3.7	1.3×10^{-3}
	7.3	1.5×10^{-7}
	2.5	1.3×10^{-2}

^a First listed value is for low temperature; the second value is for high temperature.

which of the various models best describe the observed phenomena. Unfortunately, such an investigation requires instrumentation not readily available, but we plan to undertake this study in the future.

Conclusion

A new vitreous lithium electrolyte system, LiI-Li₂S-As₂S₃, has been synthesized and investigated by both complex plane impedance and ${}^7\text{Li}$ NMR linewidth techniques.

The observed ionic conductivities of the LiI-Li₂S-As₂S₃ glasses increased dramatically with increasing LiI content, and the corresponding activation energies for ionic conductivity decreased linearly with increasing LiI content. The highest measured conductivity in this system was observed for the LiI-saturated 0.45LiI-0.18Li₂S-0.37As₂S₃ glass, which exhibited an ionic conductivity of 3×10^{-5} S-cm⁻¹ at 25°C.

Fitting the NMR data to the Hendrickson-Bray equation showed that, with 10-20% LiI, one line was obtained with activation energies considerably smaller than the activation energies deduced from conductivity measurements. However, with 30-40% LiI, two lines were obtained with the low temperature lines giving activation energies consistent with conductivity activation energies. The higher temperature NMR activation energies are attributed to a local motion that decreases dipole-dipole interaction, while the low temperature NMR activation energies are attributed to a long-range motion that also

reflects ionic conductivity. The fact that long-range motion was not seen from ${}^7\text{Li}$ NMR measurements of 10-20% LiI provides additional evidence that these glass compositions are poor ionic conductors.

Acknowledgments

Financial support is acknowledged from the National Science Foundation (DMR 80-02676) and Union Carbide Corporation.

Manuscript submitted Nov. 30, 1984; revised manuscript received March 7, 1985.

The University of California assisted in meeting the publication costs of this article.

REFERENCES

- J. P. Malugani, R. Mercier, B. Fahys, and G. Robert, Abstract 709, p. 1136, The Electrochemical Society Extended Abstracts, Vol. 82-1, Montreal, Que., Canada, May 9-14, 1982.
- J. P. Malugani and G. Robert, *Solid State Ionics*, **1**, 519 (1980).
- G. Robert, J. P. Malugani, and A. Saida, *ibid.*, **3/4**, 311 (1981).
- R. Mercier, J. P. Malugani, B. Fahys, and G. Robert, *ibid.*, **5**, 663 (1981).
- J. P. Duchange, J. P. Malugani, and G. Robert, *Prog. Batt. Solar Cells*, **4**, 46 (1982).
- J. L. Souquet, *Ann. Rev. Mater. Sci.*, **11**, 211 (1981).
- J. L. Souquet, *Solid State Ionics*, **5**, 77 (1981).
- A. Levasseur, J. C. Brethous, J. M. Reau, and P. Hagenmuller, *ibid.*, **1**, 177 (1980).
- M. Irion, M. Couzi, A. Levasseur, J. M. Reau, and J. C. Brethous, *J. Solid State Chem.*, **31**, 285 (1980).
- H. Wada, M. Menetrier, A. Levasseur, and P. Hagenmuller, *Mater. Res. Bull.*, **18**, 189 (1983).
- A. M. Glass, K. Nassau, and T. J. Negran, *J. Appl. Phys.*, **49**, 4898 (1978).
- A. M. Glass and K. Nassau, *ibid.*, **51**, 3756 (1980).
- K. Nassau, *J. Non-Cryst. Solids*, **42**, 423 (1980).
- K. Nassau, R. J. Cava, and A. M. Glass, *Solid State Ionics*, **2**, 163 (1981).
- M. Menetrier, A. Levasseur, and P. Hagenmuller, *This Journal*, **131**, 1971 (1984).
- S. J. Visco, P. J. Spellane, and J. H. Kennedy, *This Journal*, **132**, 751 (1985).
- S. G. Bishop and P. J. Bray, *J. Chem. Phys.*, **48**, 1709 (1968).
- A. E. Geissberger, F. Bucholtz, and P. J. Bray, *J. Non-Cryst. Solids*, **49**, 117 (1982).
- J. R. Hendrickson and P. J. Bray, *J. Magn. Resonance*, **9**, 341 (1973).
- J. Senegas and J. Olivier-Fourcade, *J. Phys. Chem. Solids*, **44**, 1033 (1983).

High Sensitivity H₂S Gas Sensors

Shinji Kanefusa, Masayoshi Nitta, and Miyoshi Haradome

Physical Science Laboratories, College of Industrial Technology, Nihon University, Narashino-shi, Chiba-ken 275, Japan

ABSTRACT

H₂S gas sensors have been fabricated by the admixture of SnO₂-based powders and alcohol, hydrophobic silica, or trimethylchlorosilane. Their responses to H₂S gas have been investigated. It is found that the resistivity of the sensor whose surface is covered by trimethyl-silyl groups strongly depends on the H₂S gas concentration. A 10 ppm H₂S gas concentration changes its resistivity to a value 1000 times lower than that in air, in spite of there being small changes in the sensor resistivity in other reducing gases. By covering the sensor surface with organic materials, development of sensitivity and selectivity for H₂S gas has been achieved. Also, the mechanism of reaction between the organic materials on the surfaces of sensors and H₂S gas is discussed.

Many methods for detecting harmful gases have been proposed in order to prevent a dangerous environment (1-5). Among these methods, sensors made of semiconductors have been most interesting because of the following attractive features. They are portable, less expensive, and also detect low gas concentration sensitively and reproducibly. Active development of gas sensors using metal oxide semiconductors has been made in this dec-

ade (6-11). It is known that the addition of metal catalysts such as Pd, Pt, and other transition metals to semiconductors increases the detection sensitivity (4, 5, 9, 12) and selectivity (13). Furthermore, the selectivity could be improved by the appropriate choice of sensor operating temperatures (14). By utilizing the above characteristics, sensors made of SnO₂ for C₃H₈, CH₄, CO, or H₂S gases, and of ZnO for petroleum gases, have been reported (4, 8, 9, 15,

16). Because of its harmful nature, H₂S is one of the gases most desired to be detected easily (17). Nevertheless, there are few reports about H₂S gas detection, and the mechanism of reaction between H₂S gas and the surface of semiconductors is not well understood. In general, H₂S gas frequently occurs with reducing gases such as H₂, CO, and CH₄. Therefore, selectivity for H₂S gas against these reducing gases must be high. H₂S gas concentration to be detected for practical use is 10 ppm, corresponding to the tolerable gas concentration. On the other hand, the comparable CO, H₂, and CH₄ gas concentration limits are 50 ppm, 0.4%, and 0.5%, respectively.¹ It is desired that H₂S gas sensors exhibit low sensitivity to CO, H₂, and CH₄ gases in the above gas concentration to prevent the false detection of H₂S gas.

Recently, we discovered a new method for improving the selectivity of CO gas sensors by covering their surface with organic materials (16). With this method, we try here to develop a H₂S gas sensor based on SnO₂. We have achieved a highly sensitive and selective sensor for H₂S gas by using SnO₂ whose surface is covered with trimethyl-silyl groups.

Experimental

SnO₂ was made from SnSO₄ by firing at 600°C for 1h in air. Sensors have been prepared in the following way. SnO₂ powder or SnO₂ powder mixed with PdCl₂ which were previously sintered at 800°C for 1h in air were, respectively, dispersed in alcohol, hydrophobic silica (HP), or trimethylchlorosilane (TM) uniformly to make a paste and were painted between the Au electrodes (distance: 0.1 mm) on a 96% alumina substrate (area: 3.0 × 1.5 mm²). Then the painted samples were fired at 400°C for 1h in air after drying at 80°C for 24h to prevent cracks on the surface of the sensors. On the other side of the substrate, an RuO₂ resistor had been previously printed by use of thick film technology and fired at 780°C for 10 min. It is used as a heater to keep the sensor at an adequate temperature. Hydrophobic silica was made by the reaction between hydrophilic silica and trimethylchlorosilane. It is known that the surface of the sensor mixed with hydrophobic silica is covered with trimethyl-silyl groups (16).

The experimental system and circuit are as already reported (9). A pickup resistor (5-300 kΩ) was connected in series to the sensor, and a dc voltage (10.0V) was applied across the circuit. The resistivity change was calculated from the changes in the detection voltage across the pickup resistor. For practical use, the resistivity changes were measured in gas concentration of 10 ppm, 50 ppm, 0.4%, and 0.5% for H₂S, CO, H₂, and CH₄ gases, respectively. The purity of test gases was higher than 99.9%. The sensor temperatures were measured by an IR thermometer and controlled by the change in the applied voltage to the heater.

Results

In Fig. 1 are shown the dependences of sensitivity to various gases on the concentration of Pd in SnO₂ sensors held at 120°C. The vertical scale is the sensitivity and is expressed by the relative resistivity change. R₀ is the resistivity of the sensor in air and R is that in air containing the test gas. The symbols on the figure are the average values of several measurements, for the response differed slightly between sensors even though they were prepared similarly. The sensitivities for CH₄ and CO gases are very low, though they increase slightly with increasing Pd concentration in SnO₂. On the other hand, SnO₂-based sensors exhibit high sensitivities both to H₂S and H₂ gases. Sensitivities to both gases increase with increase of the concentration of Pd in SnO₂, and the sensors with more than 1 weight percent (w/o) Pd exhibit the same sensitivity to these gases. Thus, selective detection of H₂S gas in an environment containing H₂ gas cannot be done by use

¹The gas concentrations correspond to standard levels decided by the Society of Safety of High Pressure Gas Engineering: 1/10 of the lower explosion limits for combustible gases such as H₂ and CH₄ gases, and tolerable gas concentrations for 8h work days for toxic gases such as H₂S and CO.

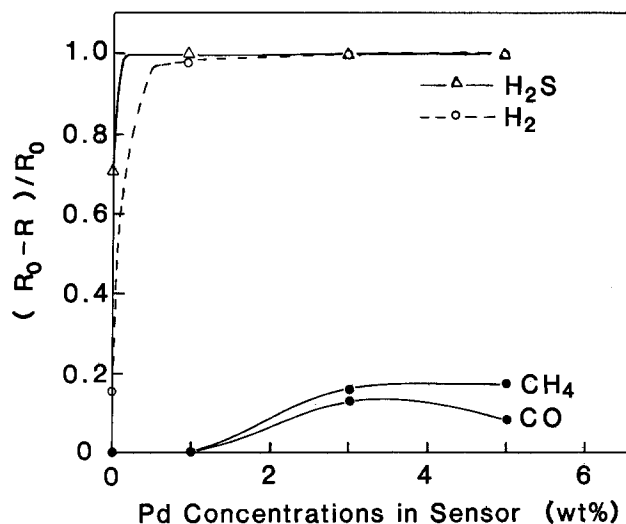


Fig. 1. Relations between the sensitivity and the concentration of Pd in SnO₂ sensors at 120°C.

of these sensors. Therefore, the experiments were done by using sensors having a concentration of less than 1 w/o Pd in SnO₂.

A typical result of sensors having less than 1 w/o Pd at 100°C of sensor temperature is shown in Fig. 2. The result of the sensor mixed with hydrophobic silica (5 w/o) is also shown in the figure. Dotted and solid lines indicate the characteristics of sensors with and without hydrophobic silica, respectively. Triangles and circles denote the characteristics for H₂S gas (10 ppm) and H₂ gas (0.4%), respectively. It is clear that additions of Pd enhance the sensitivity to both H₂S and H₂ gases. Considering selective detection, we find it undesirable for the sensors to have Pd added. On the other hand, Pd-doped SnO₂ with hydrophobic silica exhibits high sensitivities to H₂S gas and shows a remarkable decrease of the sensitivity to H₂ gas. The selectivity is enhanced by the mixture of hydrophobic silica and Pd with the sensors. Furthermore, the most selective sensor for H₂S gas is obtained by SnO₂ with hydrophobic silica.

As shown in Fig. 1 and 2, the sensitivity indicated by $(R_0 - R)/R_0$ is useful for comparing the characteristics of sensors for practical use. However, the value of $(R_0 - R)/R_0$ converges to 1 with increase of the sensitivity. Therefore, the sensitivity is, hereafter, represented by R/R_0 .

Next, the dependences of the sensitivity of SnO₂ containing hydrophobic silica and SnO₂ sensors on the sen-

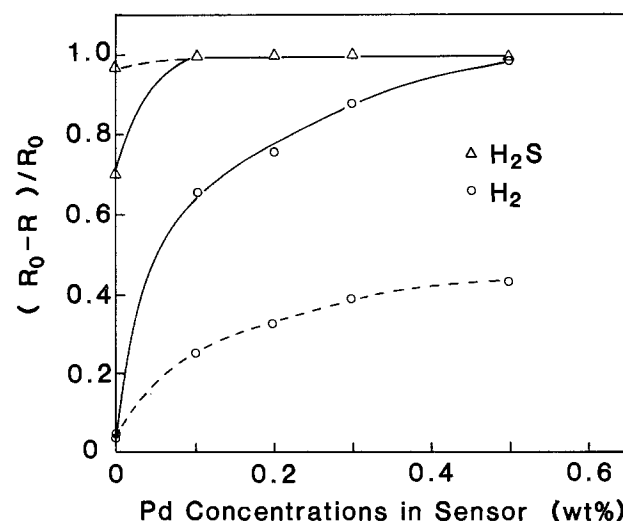


Fig. 2. Relations between the sensitivity and the concentration of Pd in SnO₂ sensors at 100°C.

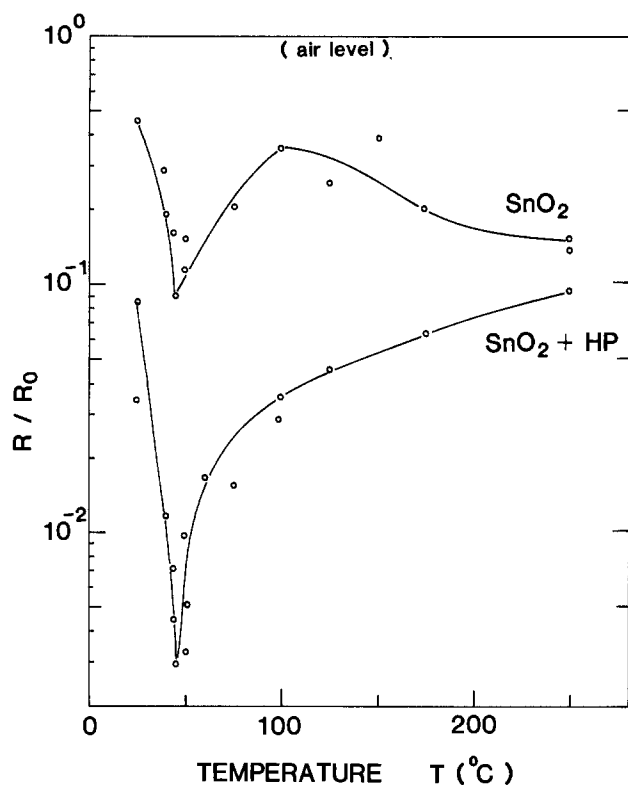


Fig. 3. Relations between the sensitivity and the sensor temperature. H_2S gas concentration is 10 ppm.

sensor temperature were investigated. The results are shown in Fig. 3. The ordinate R/R_0 corresponds to the sensitivity to H_2S gas. In this figure, the lower the numerical value of the R/R_0 , the higher the sensitivity. The sensitivity for each sensor reaches a maximum at 45°C , and it is clear that the hydrophobic silica enhances the sensitivity about 100-fold. The sensitivity of the sensor whose surface is hydrophobic monotonically decreases with increase of sensor temperature above 45°C . On the other hand, the sensitivity of the sensor whose surface is not hydrophobic increases with increase of sensor temperature above 100°C .

Figure 4 shows the response time of sensors as a function of temperature. The response time defines the time taken for the sensitivity to reach 80% of the saturation

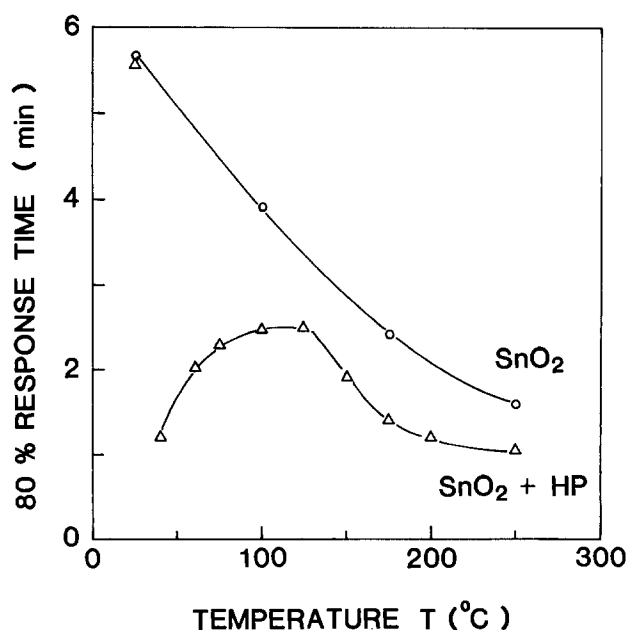


Fig. 4. Relations between the 80% response time and the sensor temperature. H_2S gas concentration is 10 ppm.

values after the contact of the test gas and the surface of the sensors. The response of SnO_2 sensors becomes rapid uniformly with increasing sensor temperature. The curve for SnO_2 with hydrophobic silica has a structure and exhibits a maximum around 120°C . It is, however, clear that the response to gas detection improves by adding the hydrophobic silica to sensors in these temperature regions. Characteristics of recovery time of sensors after the removal of the test gas from the environment surrounding the sensors were also examined. It was found that the higher the sensor temperature, the better the recovery characteristic, for all sensors.

Figure 5 shows the resistivity changes of various sensors as a function of the elapsed time after the injection of H_2S gas (10 ppm) into the chamber at 100°C of sensor temperature. The circles in the figure indicate the response time which was defined above and in Fig. 4. As shown in Fig. 5, the response time of the " $\text{SnO}_2 + \text{TM}$ " sensor is the shortest among these four sensors, and the sensitivities of " $\text{SnO}_2 + \text{TM}$ " and " $\text{SnO}_2 + \text{Pd}$ " are the highest. The " $\text{SnO}_2 + \text{Pd}$ " sensor is, however, poor in selectivity, as shown in Fig. 1 and 2. Therefore, it is clear that the sensitivity and responsiveness of a H_2S gas sensor made of SnO_2 are improved by the mixture of trimethylchlorosilane. From the comparison of the characteristics between the sensors with hydrophobic silica and with trimethylchlorosilane, it is presumed that the silica has no effect on the development of sensitivity and response time in sensors without Pd.

The temperature dependence of the resistivities for those four sensors is shown in Fig. 6. The heating rate of the sensor temperature was $4.4^\circ\text{C}/\text{min}$. The difference of the resistivity in the atmosphere between air and air containing H_2S gas will correspond to the sensitivity to H_2S gas. From Fig. 6, it is small around 400°C and becomes remarkably higher as the sensor temperature decreases. Therefore, it is considered that the response of the sensors to H_2S gas will increase with decrease of sensor temperature.

Discussion

H_2S gas has high reduction activity at room temperature in air containing moisture (19). However, it is known that H_2S gas decomposes to H_2 and S above 400°C (19). Therefore, the sensitivity to H_2S gas will decrease above 400°C of sensor temperature. This explains why the difference of the resistivity in the atmosphere between air and air containing H_2S gas becomes small around 400°C of sensor temperature as shown in Fig. 6. It is expected that

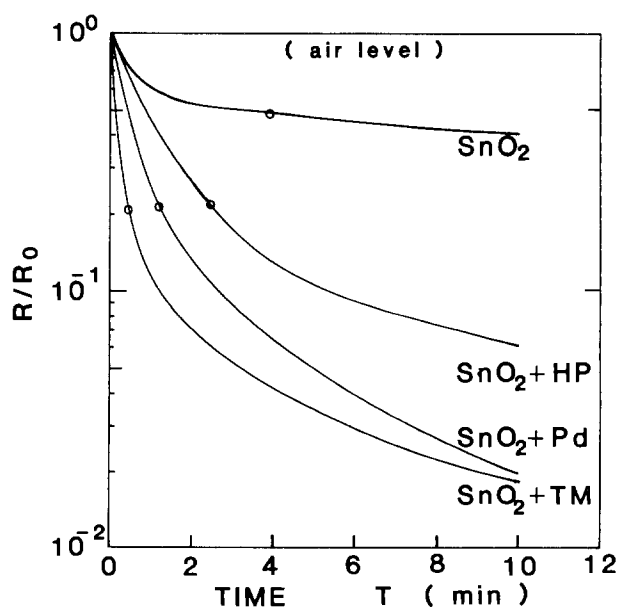


Fig. 5. Decay curves of the resistivity with the elapsed time after the exposure to H_2S gas (10 ppm) at 100°C of the sensor temperature.

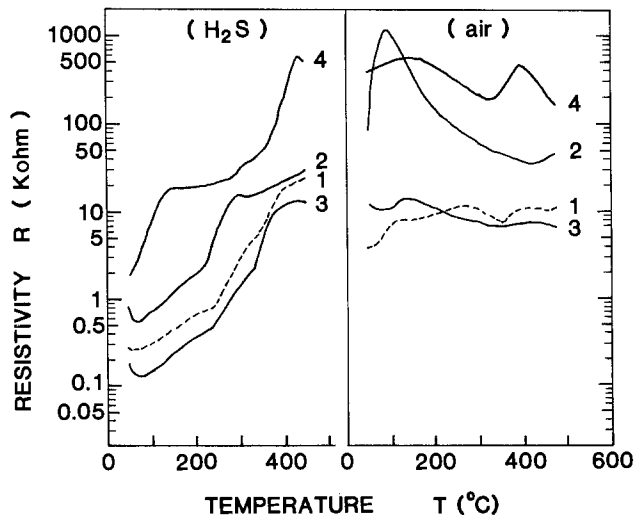


Fig. 6. Temperature dependence of the resistivity in air and in air containing H₂S gas (10 ppm).

the surface of sensors will contain adsorbed oxygen and OH radicals in air. Furthermore, it is well known that the resistivity decreases and increases with the removal of adsorbed oxygen and OH radicals from the surface of SnO₂-based sensors, respectively (20). Therefore, the resistivity of the sensor in air depends on the amount of the adsorbed oxygen and OH radicals. It is presumed that the adsorbed oxygen will desorb from the surface when the H₂S gas reacts with the surface of SnO₂, and the resistivity of sensor thence decreases. H₂S gas will attack the adsorbed OH radicals simultaneously. The changes in the resistivity of sensors will be due to the reaction of H₂S gas with the adsorbed oxygen and with OH radicals. Therefore, the resistivity of sensors whose surface has no OH radicals will decrease noticeably when the sensor is exposed to H₂S gas. In taking account of the results that the trimethyl-silyl groups do not desorb from the surface below 500°C of sensor temperature (18, 21), it is considered that the surface of the sensor mixed with hydrophobic silica or the sensor mixed with trimethylchlorosilane will be hydrophobic in the region of examined temperatures and that there will be few adsorbed OH radicals on the surface of the sensor. This is why their sensitivity to H₂S gas is high. These considerations suggest the results described as follows. As shown in Fig. 3, the sensitivity for H₂S gas of the sensor whose surface is hydrophobic decreases with increase of sensor temperature. On the other hand, the sensitivity of SnO₂ whose surface is not hydrophobic increases with increase of sensor temperature above 100°C, since the amount of OH radicals on the surface of SnO₂ decreases above 100°C of sensor temperature; then the minimum of sensitivity would be observed at 100°C. It is, however, not clear why the highest sensitivity of every

sensor to H₂S gas is obtained around 45°C of sensor temperature. That would be due to other unknown factors. Further experiments about the phenomenon will be carried out in the near future. From the results obtained in this paper, it becomes clear that the condition of the sensor surface would have a large influence on the sensitivity and the selectivity.

Conclusion

The sensitivity of SnO₂ sensors to H₂S gas was enhanced, and that to H₂ gas decreased, by covering the sensor surface with trimethyl-silyl groups. The highest sensitivity and selectivity of the sensors were obtained at 45°C sensor temperature. Taking account of the amount of OH radicals adsorbed on the surface of sensors, we find that almost all of the results in this paper are thereby well explained, except for why the sensitivity of sensors has maximum at 45°C.

Manuscript submitted Nov. 13, 1984; revised manuscript received March 13, 1985.

REFERENCES

1. N. Adams, A. Kaigler, and L. Ingram, *Petroleum Engineer International*, 40 (Jan. 1980).
2. D. W. Hill and T. Powell, "Non-Dispersive Infrared Gas Analysis in Science, Medicine and Industry," Plenum Press, New York (1968).
3. J. D. Bode *et al.*, "Detection of Ambient Pollutants by Chemiluminescence," *Bendix Journal*, Winter (1971).
4. N. Taguchi, *Jpn. Pat.*, S. 45-38200.
5. T. Seiyama, A. Kato, K. Fujishi, and M. Nagatani, *Anal. Chem.*, 34, 1502 (1962).
6. M. Nitta and M. Haradome, *Oyo Buturi*, 48, 977 (1979).
7. B. Bott, T. A. Jones, and B. Mann, *Sensors Actuat.*, 5, 65 (1984).
8. A. Jones, T. A. Jones, B. Mann, and J. G. Firth, *ibid.*, 5, 75 (1984).
9. M. Nitta, Sa. Kanefusa, and M. Haradome, *This Journal*, 125, 1676 (1978).
10. K. Ihokura, The ACS/CST Chemical-Congress at Hawaii, April (1979).
11. Y. Komine, K. Sato, S. Maejima, and T. Takeyama, *IEC Jpn.*, **cpm-84**, 67 (1984).
12. P. J. Shaver, *Appl. Phys. Lett.*, 11, 255 (1967).
13. N. Ichinose and H. Ohkuma, *IEE Jpn.*, **edd-75**, 53 (1975).
14. R. Lalauze and C. Pijolat, *Sensors Actuat.*, 5, 55 (1984).
15. G. Advani and L. Nanis, *ibid.*, 2, 201 (1981/82).
16. M. Nitta and M. Haradome, *J. Electron. Mater.*, 8, 571 (1979).
17. M. Isobe, in "Shin Sensa Handobuku," H. Yanagida, M. Aizawa, and M. Yabe, Editors, p. 423, Saiensu Foulamu, Tokyo (1982).
18. L. H. Little, "Infrared Spectra of Adsorbed Species," p. 259, Kagaku Doujin, Kyoto (1971).
19. "Rikagaku Jiten," B. Tamamushi *et al.*, Editors, p. 1419, Iwanami Shoten, Tokyo (1971).
20. N. Yamazoe, J. Fuchigami, and M. Kishikawa, *Surf. Sci.*, 86, 335 (1979).
21. S. Kanefusa, M. Nitta, and M. Haradome, *Nippon Kagaku Kaishi*, 28, 1591 (1980).



Each issue of the **Journal** will have a section of "Comments." In this section, we provide a means via short pieces, *i.e.*, one column or less, to applaud, dispute, or otherwise discuss the papers published in the **Journal**. Space will be provided for one response by the paper's author(s) to each comment.

Since space available in each issue for the "Comments" section is limited; it is important to be concise.

Comments should be sent to the Editor, Dr. Norman Hackerman, President's Office, Rice University, P.O. Box 1892, Houston, TX 77251.

Norman Hackerman
Editor

The Role of Oxygen in the Redox Chemistry of Lutetium Diphthalocyanine

M. M. Nicholson and T. P. Weismuller
(pp. 2311-2313, Vol. 131, no. 10)

Maurice L'Her:¹ From their observations of the evolution of the UV-visible spectra, the authors conclude that oxygen reversibly binds to lutetium diphthalocyanine dissolved in dimethylformamide (DMF). After dissolution of the lutetium complex, the spectrum is typical of the blue reduced form (maxima at 614 and 693 nm), the compound being reduced by impurities of the solvent, presumably aliphatic amines. When acidified, the solution turns green, the spectrum being the one well-accepted by many authors for the green molecular lutetium diphthalocyanine.^{2,3} If oxygen is removed, the solution slowly goes back to blue, but with a spectrum different from the one observed in unacidified DMF.

These facts are not clear evidences of oxygen addition to the lanthanide diphthalocyanine as stated by the authors. In our opinion, the blue-to-green color change is due to the oxidation of the reduced blue form to the green redox state, oxygen becoming a more powerful oxidizer in the acidified solvent. We observed a very similar behavior in methylene chloride where the blue diphthalocyanine, prepared by electrolysis, is unaffected by air unless an acid is added. Simultaneously, one records the characteristic voltammogram of the green form at a rotating disk electrode instead of the two oxidation waves of the blue complex.⁴ The reverse color change from green to blue in DMF after oxygen removal could be explained by the degradation of the solvent giving back dimethylamine, a known decomposition reaction pro-

moted by acids and bases.⁵ The green-to-blue color change by oxygen removal did not occur in dimethylsulfoxide, nor in acetone. When we prepared solutions of the lutetium diphthalocyanine in various solvents under rigorous exclusion of oxygen, after heating the compound under vacuum, these solutions always exhibited the characteristic spectrum of the green complex, the same as curve a in Fig. 4. Furthermore, the molecular structure obtained from x-ray diffraction analysis of the neodymium diphthalocyanine did not show any evidence of oxygen inclusion in the crystal.⁶ These facts are in favor of a chemical oxidation in acidified DMF instead of a reversible oxygen addition to the lutetium diphthalocyanine.

M. M. Nicholson⁷ and T. P. Weismuller:⁸ We proposed that oxygen adds reversibly to the blue reduction product LuHPC₂, which is present after acidification of the dye solution prepared in DMF that has not been specially purified. Such an addition, forming LuHPC₂⁺O₂⁻, is a chemical oxidation of the blue species to a green one.

The species LuPC₂ and its protonated version LuHPC₂⁺ represent the same oxidation state of the organic complex. Their absorption spectra in solution may be similar, and neither of these forms would be expected to add dioxygen in a pure solvent that contains no reducing agent.

Our paper also pointed out that several apparent anomalies in the chemistry of rare-earth diphthalocyanines may be explained by the existence of an oxygen adduct with a formula analogous to that of the known complex MnPc⁺O₂⁻. Finally, it should be noted that the crystallographic study by Kasuga *et al.*⁶ was made with a dichloromethane solvate of neodymium diphthalocyanine. This is not strictly comparable to the systems discussed here. Further research on the question of oxygen addition is, of course, desirable.

¹C. K. Mann, in "Electroanalytical Chemistry," Vol. 3, A. J. Bard, Editor, p. 78, Marcel Dekker, New York (1969).

¹UA CNRS 322, Faculté des Sciences, 29287 Brest-Cedex, France.

²G. A. Corker, B. Grant, and N. J. Clecak, *This Journal*, **126**, 1339 (1979).

³A. T. Chang and J. C. Marchon, *Inorg. Chim. Acta*, **53**, L241 (1981).

⁴M. L'Her, Y. Cozien, and J. Courtot-Coupez, *J. Electroanal. Chem.*, **157**, 183 (1983).

⁶K. Kasuga, M. Tsutsui, R. C. Petterson, K. Tatsumi, N. Van Opdenbasch, G. Pepe, and E. F. Meyer, Jr., *J. Am. Chem. Soc.*, **102**, 4835 (1980).

⁷Rockwell International Science Center, Anaheim, CA 92803.

⁸Rockwell International Corporation, Defense Electronics Operations, Anaheim, CA 92803.



Electrodeposition of Ruthenium from a LiCl-KCl Melt

A. Bettelheim, F. Broitman, U. Mor, and R. Harth

Nuclear Research Center-Negev, Beer-Sheva 84190, Israel

Electroplating from molten salts seems a promising way of surface finishing, both with respect to protection against corrosion, high temperature oxidation and to the possibility of obtaining very hard surfaces with special mechanical properties (1). The platinum group metals: Pt, Pd, Rh, Ir, Ru and Os can be deposited in aqueous electrolytes (2) only in limited thickness ($<5 \mu\text{m}$). Apparently, it is difficult to eliminate stress cracking from these electrolytes. Better deposits are obtained from fused salt electrolytes, particularly because the deposits show better ductility and a freedom from porosity compared with those obtained in aqueous solutions.

It has been reported that LiCl-KCl eutectic melts at 450°C give deposits which are always dendritic and non adherent (3) while greater success is obtained in molten cyanide systems operated between 450 and 600°C . In the present study, we show that thick, adherent and compact electrodeposits of ruthenium (and other platinum metals, such as Ir, as it will be described in a future publication) are obtained from a LiCl-KCl (45-55 w/o) melt at temperatures as low as 400°C , provided that the melt is saturated with HCl.

An alumina crucible was used to contain the electrolyte. The reference electrode was a nickel wire immersed in a melt containing 10^{-2}M NiCl_2 and separated from the bulk using a thin walled pyrex tube. The cathode and anode were graphite rods, 6 mm in diameter and their pretreatment, before immersion in the melt, was according to procedures described in the

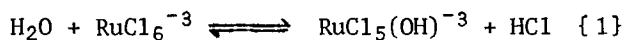
literature (4). Using cyclic voltammetry, the roughness factor was estimated to be between 20 to 30.

Figure 1 shows a voltammetric curve for the reduction of RuCl_3 in an HCl saturated LiCl-KCl melt (curve (a)). The half-wave potential is 0.39 V and the limiting current increases linearly with the Ru(III) ion concentration in the melt. Moreover, a stripping peak with $E_p=0.85$ V, observed when the potential is scanned anodically, indicates that the electrodic process with $E_{1/2}=0.39$ V yields metallic ruthenium. The voltammetric curve (b) is obtained when argon is introduced in the melt to remove all dissolved HCl. From comparison of the limiting currents, it can be concluded that the Ru(III) solubility in the acidic melt is twice higher than found in an argon saturated melt. Moreover, when precautions are not taken to avoid introduction of moisture to the melt, the voltammetric wave is not well shaped and the limiting current decreases as much as fifth as that found in the HCl saturated melt.

Electrodeposition of ruthenium was achieved galvanostatically and the potential of the cathode vs. the reference electrode was followed during the electrolysis. The amount of ruthenium deposited on the surface was estimated by chronopotentiometric stripping curves. On application of a constant anodic current, the electrode potential was nearly constant (0.9 V) until no metallic ruthenium was present on the surface; then it jumped instantly to 1.15 V, which corresponds to that of Cl_2 evolution (5). The electrochemical conditions for electrodeposition and the corresponding calculated thickness of the various coatings are listed in table I. Coatings up to $4.4 \mu\text{m}$ thick with a cathodic current efficiency of 77% were produced in a bath containing a Ru ion

concentration of 0.26 w/o and applying a current density of 5.4 mA cm^{-2} . Increasing twofold this concentration, the current density could be raised to 6.8 mA cm^{-2} and adhesive coatings of $14 \mu\text{m}$ could be obtained with a current efficiency of 70%. Thin but bright deposits were obtained at current densities lower than 2 mA cm^{-2} (fig. 2 (a)). When the current density was increased to higher values, ruthenium electrodeposits were dark but appeared to be tightly adherent to the substrates, with no cracks or large imperfections (fig. 2 (b)). If HCl was continuously supplied to the melt, the deterioration of ruthenium chloride, as verified by voltammetry, was less than 25% after a period of 350 hours.

The different behavior of Ru(III) ions in acidic and basic melts seems to indicate a hydrolysis reaction similar to that suggested for Cr(III) in molten LiCl-KCl (6):



This reaction is expected to be promoted by the presence of water or products of the hydrolytic decomposition of molten LiCl-KCl, i.e. hydroxide and oxide ions, and suppressed by gaseous HCl. This can also account for the successful electrodeposition of Ru in HCl saturated LiCl-KCl melts. The high stability of the baths for large periods of time is probably due to the low melting point of the chloride melt (about 200°C lower than the cyanide melts), allowing operation at temperatures where thermal decomposition of the ruthenium salt is probably slow.

The electrodeposition on metallic substrates was not successful in the acidic LiCl-KCl melt. However, preliminary experiments showed that several metals (as Mo and stainless steel) could be coated with Ru in this melt after applying protective precoatings of Pt or Rh from aqueous solutions.

Table I: Electrodeposition of ruthenium on graphite from a LiCl-KCl melt at 400°C :

Ru/ w/o	I/ mA cm^{-2} (a)	E/ V (b)	η / % (c)	thickness/ μm (d)
0.26	1.35	0.58	87	0.4
0.26	2.70	0.52	88	0.8
0.26	4.05	0.46	88	1.2
0.26	5.40	0.45	88	1.6
0.26	5.40	0.36	77	4.4
0.26	6.75	0.22	64	1.0
0.52	5.40	0.54	70	14.0
0.52	6.75	0.43	82	6.9

(a) based on exposed area of 3.7 cm^2 .

(b) vs. a Ni/Ni(II) (10^{-2}M) reference electrode.

(c) current efficiency of the cathode based on the ratio of applied cathodic charge, to anodic charge calculated from stripping chronopotentiometric curves.

(d) based on geometric area and ruthenium density of 12.2 g cm^{-3} .

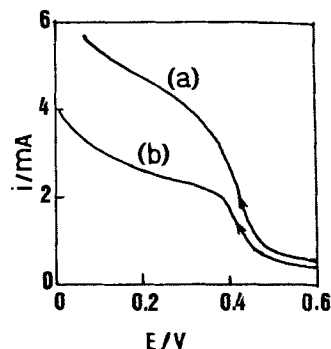


Fig. 1. Voltammograms (2 mV s^{-1}) for a graphite electrode in LiCl-KCl at 400°C containing 0.4 w/o RuCl_3 . Curves (a) and (b) are for the HCl and Ar saturated melt, respectively.

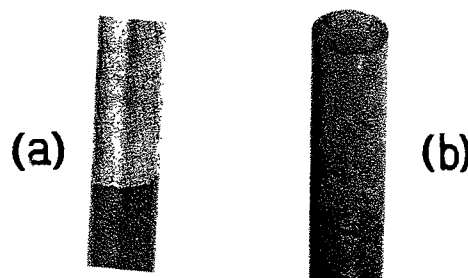


Fig. 2. Ruthenium coatings, (a) 0.5 and (b) $5 \mu\text{m}$ thick, obtained at approximate current densities of 0.4 and 4 mA cm^{-2} , respectively.

References

- W.B Harding, *Plating Surface Finish.*, 64, 48 (1977) and 65, 30 (1978).
- P.C. Hydes, *Platinum Metal Rev.*, 24, 50 (1980).
- J.H.F. Notton, *ibid.*, 22, 98 (1978).
- I. Uchida, J. Nikura and S. Toshima, *J. Electroanal. Chem.*, 107, 115 (1980).
- H.A. Laitinen and C.H. Liu, *This Journal*, 80, 1015 (1958).
- H.A. Laitinen, Y. Yamamura, I. Uchida, *This Journal*, 125, 1450 (1978).

Manuscript received April 2, 1985.



A Mechanism of Electric Potential Generated on the Dissolution and Precipitation of Electrolytes

S. A. Khan, B. N. Tripathi, and T. N. Mishra¹

Department of Chemistry, St. Andrew's College, Gorakhpur 273 001, India

ABSTRACT

A mechanism of electric potential generated on the dissolution and precipitation of electrolytes has been developed. Dissolution potential is found to be equal in magnitude but opposite in sign of precipitation potential. Theoretical values of true dissolution and true precipitation potentials have been calculated and compared with the experimental data. It has been demonstrated that the true dissolution potential does not depend on the concentration of the medium and that true precipitation potential does not depend on undercooling.

The development of electric potential on the dissolution and precipitation of electrolytes has been fairly well established (1-13). Comprehensive studies on these potentials have been reported by Rastogi and co-workers (2-5). These workers have given the operational and conceptual definitions of various types of potentials associated with the crystallization and dissolution processes (5). It has been suggested by these workers (4, 5) that the sign and magnitude of precipitation and dissolution potentials depend on the unequal mobilities of cations and anions. They have postulated that the precipitation potential develops due to a difference in the rate of attachment of cations and anions during crystallization and dissolution potential develops due to a difference in the rate of detachment of cations and anions during dissolution.

Girdhar and co-workers (6-8) have reported their studies on the precipitation and dissolution potentials of electrolytes in aqueous and nonaqueous mediums. Their results are in general agreement with those of Rastogi and co-workers. Ibl and co-workers (9, 10) have also reported careful experiments on crystallization and dissolution potentials using single crystals. They have used "corrosion" model based on the difference in the kinetics of dissolution of cations and anions to explain their results. Vishnu and Khan (11) have also reported their studies on dissolution potential of alkali halides in nonaqueous medium such as D.M.F. Their results are also in general agreement with those of Rastogi *et al.*

These experimental studies show that the precipitation and dissolution potentials depend on (i) nature of the electrolyte, (ii) concentration of the medium, (iii) temperature, (iv) time, and (v) mobilities of cations and anions.

Quite recently, Rastogi and Khan (12, 13) have developed theories of dissolution and precipitation potentials. Although Rastogi and Khan's theory of dissolution potential (12) could explain qualitatively most of the experimental data on the measurement of dissolution potential, they could not make use of this theory for a quantitative calculation of dissolution potential. However, they have given only a semiquantitative treatment of the theory of precipitation potential (13) which is based on an inequality but the results are far from satisfactory. Further studies are necessary in order to have a clear understanding about the mechanism of the development of these potentials.

¹ Present address: Department of Chemistry, Gorakhpur University, Gorakhpur 273 001, India.

In the present communication, an attempt has been made to have a more comprehensive view of the processes responsible for the development of dissolution and precipitation potentials. The potential recorded by the dissolution cell may be split into (i) true dissolution potential, (ii) phase potential, (iii) diffusion potential, (iv) potential due to the establishment of a concentration cell with transference during the course of dissolution, (v) Nernst potential, and (vi) thermodiffusion potential. However, all are not simultaneously applicable. Similar splitting of observed precipitation potential has also been made. Experimental results on the measurement of these potentials are reported in the present communication. An attempt has also been made to get a quantitative check of Rastogi and Khan's thermodynamic theories of dissolution (12) and precipitation (13) potentials. An improvement of the theory of precipitation potential has also been made. True precipitation potential is found to be just the opposite of true dissolution potential.

Theory of Dissolution Potential

The physics of the development of dissolution potential can be understood from the schematic diagram given in Fig. 1. When a platinum electrode loaded with the crystals of an electrolyte (α phase) is introduced in the solvent, dissolution starts immediately, ions detach from the surface of the crystal, and a narrow zone of solute-enriched crystal/solution interface is set up in the vicinity of crystal surface. We may call it the β zone for convenience. From the kinetics of dissolution, it has been found that the process of dissolution is diffusion controlled and the crystal maintains a state of near saturation in the narrow zone adjacent to it (14). The crystal side of this zone maintains a state of supersaturation where the ions are unhydrated or only partially hydrated. The solution side of this zone maintains a state of near saturation. The ions diffuse away from β phase and go into the bulk of the solvent, where a concentration gradient is set up. We will call it a δ phase for convenience.

The process of dissolution of an electrolyte may be visualized to be made up of the following main steps: (i) detachment of unhydrated cations and anions from kink sites and their diffusion toward dissolving crystal surface in α phase; (ii) diffusion of partially solvated cations and anions from a locally solute enriched crystal/solution interface into a zone of near-saturation on the other side of β phase; (iii) complete solvation of cations and anions on

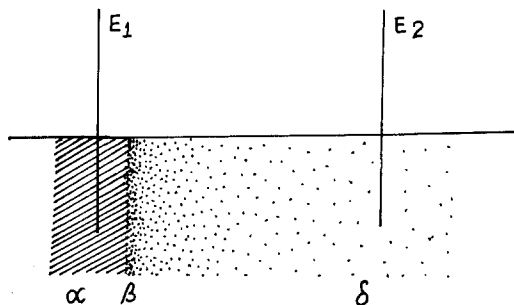


Fig. 1. Schematic diagram for the development of dissolution potential. α = solid phase; β = crystal/solution interface; and δ = solution phase. E_1 and E_2 are the platinum electrodes.

the solution side of β phase, where a state of saturation is maintained throughout the course of the dissolution process; (iv) diffusion of completely solvated ions from saturated zone (solution side of β phase) into the bulk of the solution (δ phase); and (v) adsorption of heat of solvation, which may occur stepwise after each of the solvation steps.

Conditions at a dissolving crystal surface are not completely understood, but it would not be expected that the tendencies (as measured by exchange current density) of the cation and the anion to pass from crystal into solution would be exactly equal because of intrinsic energy barriers. The rates of detachment of cations and anions from the surface of the crystal, step (i), will be different. However, electrostatic coupling in β phase forces the fluxes J_+ and J_- of cations and anions to be equal. Or in other words, electrostatically generated potential $(\Delta\phi)_{\text{diss}}$ hinders the faster process and accelerates the slower process, so that J_+ and J_- tend to be equal. The unequal rates will be directly proportional to the mobilities of respective ions in the β phase. Since the crystal side of β phase is solute enriched, the ions in this phase will be mostly unsolvated or only partially solvated. Therefore, it may be noted that the mobilities of cations and anions in β phase will be quite different from conventional mobilities. Rastogi and Khan (12) have also pointed out such a difference in the two types of mobilities in their thermodynamic theory of dissolution potential.

It is obvious that the true dissolution potential—a term coined by Rastogi *et al.* (4, 5) in 1970—would be generated between the steps (i) and (ii). Because of step (iv), a diffusion potential would also be generated. Since the α phase remains in equilibrium with the β phase till the end of dissolution process, the equilibrium phase potential would also be present at the dissolving crystal/solution interface. Moreover, since the electrodes E_1 and E_2 remain situated in the regions of different concentrations till the completion of dissolution process, and the transfer of ions keeps on taking place from the region around the electrode E_1 towards the region around the electrode E_2 , a potential difference would also be developed on account of the establishment of a concentration cell with transference. The potential difference between the electrodes E_1 and E_2 would also include the Nernst potential and thermodiffusion potential. The latter will be developed on account of enthalpy changes involved in various solvation steps. However, their values are negligible in comparison to other potentials.

The observed dissolution potential would thus be given by the equation

$$(\Delta\phi)_{\text{obs(diss)}} = (\Delta\phi)_{\text{diss}} + (\Delta\phi)_{\text{phase}} + (\Delta\phi)_{\text{diff}} + (\Delta\phi)_{\text{cc}} \quad [1]$$

where the first, second, third, and fourth term on the rhs of the above equation are true dissolution potential, phase potential, diffusion potential, and potential of the concentration cell with transference, respectively.

Thus, in order to evaluate the experimental value of true dissolution potential, we can make use of the following equation

$$(\Delta\phi)_{\text{diss}} = (\Delta\phi)_{\text{obs(diss)}} - [(\Delta\phi)_{\text{phase}} + (\Delta\phi)_{\text{diff}} + (\Delta\phi)_{\text{cc}}] \quad [2]$$

It is, therefore, obvious that the experimental values of all the terms on rhs of Eq. [2] should be known before one can evaluate the experimental value of $(\Delta\phi)_{\text{diss}}$.

Now let us consider each of the four potentials given on the rhs of Eq. [1].

The phase potential (5) is the potential difference arising from an electrical double layer and dipole orientation developed at crystal/liquid interface as a result of the dynamic equilibrium of ion migration from the liquid phase to the crystal phase and vice versa. The algebraic sign of the phase potential is the same as the electrostatic polarity (+ or -) of the end of the dipolar double layer on the crystal side of the interface.

According to Rastogi and Khan's (12) thermodynamic theory of dissolution potential, the values of dissolution and phase potentials are given by the equations

$$(\Delta\phi)_{\text{diss}} = \frac{RT}{F} (t_+^0 - t_-^0) \ln \frac{\alpha^\beta}{\alpha^{\text{sat'd}}} \quad [3]$$

$$(\Delta\phi)_{\text{phase}} = \pm \frac{1}{F} [\mu_{\pm}^{\alpha} - \mu_{\pm}^{\delta} - RT \ln \alpha^{\text{sat'd}}] \quad [4]$$

where t_+^0 and t_-^0 are the transference numbers of unhydrated cations and anions, respectively, and α^β and $\alpha^{\text{sat'd}}$ are the activities of the electrolyte in the α/β interface and saturated solution, respectively. μ_{\pm}^{α} and μ_{\pm}^{δ} are the standard chemical potential of cations (+) and anions (-) in α and δ phases, respectively. R , T , and F are gas constant, temperature, and the Faraday constant, respectively.

Because of the existence of a concentration cell with transference in the experimental setup of dissolution cell, $(\Delta\phi)_{\text{diff}}$ and $(\Delta\phi)_{\text{cc}}$ could also be developed. The total EMF of such a concentration cell can be easily calculated (15) with the help of the equation

$$(\Delta\phi)_t = 2t_- \frac{RT}{F} \ln (\alpha^{\text{sat'd}}/\alpha^\beta) \quad [5]$$

which may also be written as

$$(\Delta\phi)_t = 2 \frac{RT}{F} \ln (\alpha^{\text{sat'd}}/\alpha^\beta) - 2(1 - t_-) \ln (\alpha^{\text{sat'd}}/\alpha^\beta) \quad [6]$$

where the first term gives the contribution of the two electrodes in contact with the solutions of two different mean activities $\alpha^{\text{sat'd}}$ and α^β , and the second term gives liquid junction or diffusion potential. Thus $(\Delta\phi)_{\text{cc}}$ and $(\Delta\phi)_{\text{diff}}$ of Eq. [1] are given as

$$(\Delta\phi)_{\text{cc}} = 2(RT/F) \ln (\alpha^{\text{sat'd}}/\alpha^\beta) \quad [7]$$

and

$$(\Delta\phi)_{\text{diff}} = 2(1 - t_-) (RT/F) \ln (\alpha^{\text{sat'd}}/\alpha^\beta) \quad [8]$$

where t_+ and t_- are the conventional transference numbers of cations and anions, respectively.

An idea about the functional dependence of dissolution potential can easily be obtained from Eq. [3]. It is obvious from this equation that $(\Delta\phi)_{\text{diss}}$ would depend on (i) temperature T , (ii) transport numbers t_+^0 and t_-^0 of unhydrated or partially hydrated cations and anions, and (iii) activities α^β and $\alpha^{\text{sat'd}}$ of the electrolyte in β phase and saturated solution, respectively.

In order to have a quantitative check of Eq. [3], we have to find out appropriate values of t_+^0 , t_-^0 , α^β , and $\alpha^{\text{sat'd}}$. Since the ions are mostly unhydrated or only partially solvated in the β phase, the transport numbers t_+^0 and t_-^0 associated with the migration of cations and anions from crystal lattice to the crystal/solution interface should be different from conventional transport numbers. The region between crystal lattice and β phase is filled up mostly by unsolvated or only partially solvated ions. This is a solute-enriched zone which may be supposed to behave like a sheet of ionic melt. Hence, t_+^0 and t_-^0 will be closer to the transport number of bare ions (12, 13) in comparison to the conventional transport numbers. An idea about the transport number of the bare ions of an electrolyte can easily be obtained from the masses (16) or

the radii (17) of cations and anions from the following equations

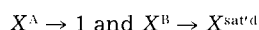
$$t^{\circ} = \frac{M^{-}}{M^{-} + M^{+}}$$

or

$$t^{\circ} = \frac{r^{-}}{r^{-} + r^{+}} \tag{9}$$

where M^{-} and M^{+} are the masses of anions and cations, respectively, in atomic mass units, and r^{-} and r^{+} are the radii of respective ions. Theoretical values of the transport numbers of bare ions calculated from the above equations are found to be in reasonable agreement with the experimental values (18). Thus we can make use of these equations for calculating the values of t° , and t°_{-} .

On the basis of arguments presented in the preceding paragraph it is also evident that the mean activity a^{β} of the electrolyte on the crystal side of the crystal/solution β interface would be approaching unity. Since the mole fraction of the solute is very close to unity in this region, it may be supposed to be present in its standard state. Therefore, a^{β} will be equal to unity. This conclusion can also be made obvious in another way. Let us consider the concentration profile depicted in Fig. 2 about the variation of mole fraction of the solute during the course of dissolution. The curve AB of this diagram represents the change of mole fraction during the detachment of ions from crystal lattice and the establishment of a saturated zone in the crystal/solution interface. As already pointed out by Rastogi and Shukla (4), the true dissolution potential would be generated along the curve AB on account of a difference in the rate of detachment of cations and anions during the course of dissolution. The mole fraction of the solute thus changes from X^{α} to X^{β} and the corresponding mean activity changes from a^{α} to a^{β} during the development of dissolution potential. Since



we shall get

$$a^{\alpha} = a^{\beta} \rightarrow 1 \text{ and } a^{\beta} \rightarrow a^{\text{sat'd}} \tag{10}$$

Thus from Eq. [3] and [10] we shall get

$$(\Delta\phi)_{\text{diss}} = -\frac{RT}{F} (t^{\circ} - t^{\circ}_{-}) \ln a^{\text{sat'd}} \tag{11}$$

since

$$a^{\text{sat'd}} = \gamma_{\pm}^{\text{sat'd}} m^{\text{sat'd}} \tag{12}$$

where $\gamma_{\pm}^{\text{sat'd}}$ is the activity coefficient of the electrolyte in its saturated solution and $m^{\text{sat'd}}$ is its corresponding molality, Eq. [11] may also be written as

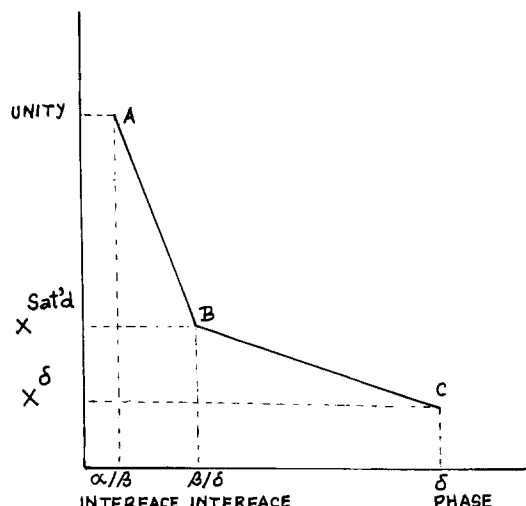


Fig. 2. Concentration profile depicting the variation of mole fraction of the solute during the dissolution of electrolyte.

$$(\Delta\phi)_{\text{diss}} = -\frac{2.303RT}{F} (t^{\circ} - t^{\circ}_{-}) (\log \gamma_{\pm}^{\text{sat'd}} + \log m^{\text{sat'd}}) \tag{13}$$

Equation [13] may now be used for calculating theoretical values of $(\Delta\phi)_{\text{diss}}$. Theoretically calculated values of $(\Delta\phi)_{\text{diss}}$ of some binary alkali-metal salts for which $\gamma_{\pm}^{\text{sat'd}}$ and $m^{\text{sat'd}}$ values were available (19, 20) are presented in Table I. These values were obtained by making use of Eq. [9] and [13].

We may now examine the data presented in Table I. It is evident from the data presented in columns 4 and 5 of this table that the magnitude of $(\Delta\phi)_{\text{diss}}$ is directly proportional to the magnitude of $(t^{\circ} - t^{\circ}_{-})$. This is in accordance with the hypothesis of Rastogi and Shukla (4). On the basis of their experimental observations, they had postulated that the magnitude of true dissolution potential should be directly proportional to the magnitude of $(t_{+} - t_{-})$ where t_{+} and t_{-} are the conventional transport numbers of cations and anions, respectively. However, Rastogi *et al.* (4, 5) could not explain the negative sign of dissolution potential of alkali halides in water on the basis of these transport numbers. Now we can easily explain the negative sign of dissolution potential of alkali halides in water on the basis of present theory. Since the mobility of unsolvated or only partially solvated cations is greater than that of similar anions, the former would detach at a greater speed, leaving behind the latter. Therefore, the electrode on which dissolution occurs would be negative. This is in accordance with the experimental observations of various workers.

In order to get an idea about the functional dependence of $(\Delta\phi)_{\text{diss}}$ on other factors, let us consider Eq. [13] once again. It can easily be predicted from this equation that $(\Delta\phi)_{\text{diss}}$ would be directly proportional to the absolute temperature and it should be independent of concentration of the medium. Since $(\Delta\phi)_{\text{diff}}$ and $(\Delta\phi)_{\text{cc}}$ depend on concentration and these are part of $(\Delta\phi)_{\text{obs(diss)}}$, the latter would also depend on concentration. However, $(\Delta\phi)_{\text{diss}}$ would not depend on concentration since it is a function of $a^{\text{sat'd}}$ only.

In order to verify the predictions made on the basis of Eq. [13], further experimental studies were made. These are reported in the proceeding sections.

Theory of Precipitation Potential

The physics of the development of precipitation potential from a supersaturated solution can be understood from the schematic diagram given in Fig. 3.

The experimental setup for the measurement of precipitation potential is such that the crystallization takes place at only one electrode. The other electrode remains free from crystal during the development of precipitation potential. Various methods have been employed in order to do so. Some of them are given below.

1. One of the electrodes is kept inside the supersaturated solution and the other is kept a little above its surface. The solution is cooled in a controlled manner, and when a tiny crystal appears on the surface of the first

Table I. Theoretically calculated values of $(\Delta\phi)_{\text{diss}}$ of some binary alkali-metal salts. These values are based on 25°C

Electrolyte	$m^{\text{sat'd}}$ [Ref. (19)]	$\log \gamma_{\pm}^{\text{sat'd}}$ [Ref. (20)]	$(t^{\circ} - t^{\circ}_{-})$ calculated on the basis of Eq. [9]	$(\Delta\phi)_{\text{diss}}$ calculated on the basis of Eq. [13] (mV)
KCl	4.68	-0.2322	0.54	-14
NaCl	6.17	-0.0061	0.60	-28
KClO ₃	0.73	-0.2891	0.68	-17
KBrO ₃	0.48	-0.2580	0.76	-26
LiOH	5.30	-0.3442	0.70	-16 ^a
LiNO ₃	5.20	+0.1301	0.80	-41
LiClO ₄	3.50	+0.2682	0.86	-41

^a This value is based on 0°C.

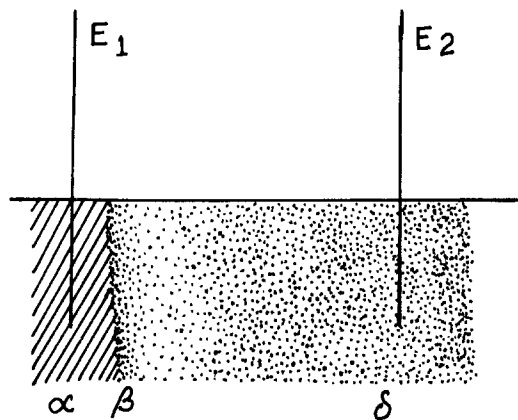


Fig. 3. Schematic diagram for the development of precipitation potential. α = solid phase; β = supersaturated/crystal interface; and δ = supersaturated solution. E_1 and E_2 are the platinum electrodes.

electrode, the other electrode is also inserted into the solution and the development of precipitation potential is recorded potentiometrically (4, 5).

2. Crystal seeds are introduced in the surface of one of the two platinum electrodes and the other is kept bright. Both the electrodes are kept a little above the surface of the supersaturated solution which is gradually cooled. When a desired undercooling is obtained, both the electrodes are simultaneously inserted into the solution. Crystallization takes place at the seeded electrode and the development of precipitation potential is recorded electrostatically (13).

3. Both the electrodes are kept inserted in the saturated solution of the electrolyte. The solution around one electrode is cooled and the crystallization potential is recorded at the desired undercoolings (9).

In all these methods, crystallization takes place at only one electrode and the other remains free from it.

During the course of the crystallization from a supersaturated solution, the ions move from a zone of supersaturation into a zone of saturation, and therefore, a diffusion potential would be developed on account of a difference in the mobilities of cations and anions during this transition. Since the mean activity of the electrolyte changes from $a^{(ss)}$ to $a^{(sat'd)}$ during this diffusion the corresponding potential would be given by the equation

$$(\Delta\phi)_{diff} = \frac{RT}{F} (t_+ - t_-) \ln \frac{a^{(sat'd)}}{a^{(ss)}} \quad [14]$$

where $(\Delta\phi)_{diff}$ is the diffusion potential generated during crystallization from supersaturated solution and t_+ and t_- are the conventional transport numbers of cations and anions, respectively.

The situation at the growing crystal/solution interface is exactly similar to the situation at a dissolving crystal/solution interface. In both the cases, the solution side of the interface is populated by saturated ions and the crystal side of the interface is populated by the bare ions (unsolvated or only partially solvated in the case of dissolution and desolvated in the case of precipitation). Thus, following an argument similar to that presented in the case of true dissolution potential, it can easily be shown that the true precipitation potential would be given by the relation

$$(\Delta\phi)_{pption} = \frac{2.303RT}{F} (t_+ - t_-) \log \frac{a^{(sat'd)}}{a^{(\beta/\alpha)}} \quad [15]$$

where $a^{(sat'd)}$ is the activity of the electrolyte in the saturated δ/β interface, and $a^{(\beta/\alpha)}$ is the activity of the electrolyte in the desolvated β/α interface.

It may be pointed out here that an equation exactly similar to Eq. [15] has been derived by Rastogi and Khan (13) in their thermodynamic theory of precipitation potential. In this theory, they have converted the equation

$$(\Delta\phi)_{pption} = \frac{RT}{F} (t_+ - t_-) \ln \frac{a_1}{a_2} \quad [16]$$

into an inequality

$$(\Delta\phi)_{pption} < - \frac{1}{F} \frac{(\Delta H)(\Delta T)}{T_s} \quad [17]$$

by making use of Clausius-Clapeyron equation

$$\ln \frac{a_1}{a_2} = \frac{(\Delta H)}{R} \left(\frac{T_1 - T_2}{T_1 T_2} \right) \quad [18]$$

and putting

$$(t_+ - t_-) < 1 \quad [19]$$

It has been suggested by Rastogi and Khan (13) that ΔH in Eq. [17] is equivalent to the lattice energy. In fact, ΔH in the Clausius-Clapeyron equation (18), is simply the heat of fusion. It may be called the heat of precipitation in the present case, but there is no thermodynamic justification for substituting lattice energy in place of heat of fusion. As a matter of fact, the values of precipitation potential calculated on the basis of lattice energy are found to be much greater in comparison to the experimental values [Ref. (13), Table II]. On the other hand, the values of precipitation potential calculated on the basis of ordinary heat of precipitation are found to be extremely low. Thus, use of the Clausius-Clapeyron equation is not justified in the present case.

It is a well-known fact that during crystallization the lattice energy is used up in the desolvation of ions. Lattice formation and desolvation are interdependent, and crystallization process will be hampered if lattice energy is used for any other purpose. It is quite possible that the thermal energy of the system may be used in the development of precipitation potential and, consequently, a cooling may be produced around the electrode on which crystallization takes place, as reported by Rastogi and Khan (13). However, the separation of lattice energy from desolvation of ions does not seem plausible.

Now let us consider Eq. [15]. Since the β/α interface is populated mostly by desolvated ions, we shall have

$$a^{\beta/\alpha} = \text{unity} \quad [20]$$

Thus, making use of Eq. [12], [15], and [20], we get

$$(\Delta\phi)_{pption} = \frac{2.303RT}{F} (t_+ - t_-) (\log \gamma_{\pm}^{sat'd} + \log m^{sat'd}) \quad [21]$$

Now, comparing Eq. [13] and [21], we can say that the phenomenon of true precipitation potential is exactly opposite to the phenomenon of true dissolution potential. Their values are equal in magnitude but opposite in sign.

Since the α phase remains in equilibrium with the β phase until the end of crystallization process, equilibrium phase potential given by Eq. [4] would also be present along with the precipitation and diffusion potentials. Ignoring the contribution made by other very small potentials such as Nernst potential, etc., the observed precipitation potential would be given by the equation

$$(\Delta\phi)_{obs(pption)} = (\Delta\phi)_{diff} + (\Delta\phi)_{pption} + (\Delta\phi)_{phase} \quad [22]$$

It follows, therefore, that the experimental values of observed precipitation potential, diffusion potential, and phase potential should be known before one can evaluate the experimental value of $(\Delta\phi)_{pption}$. Its theoretical value would be equal in magnitude but opposite in sign to that of dissolution potential. It is also evident from Eq. [21] that true precipitation potential would be directly proportional to the saturation temperature, but it should remain independent of undercooling. Overall observed precipitation potential would depend on ΔT , owing to the dependence of thermodiffusion potential on it, but true $(\Delta\phi)_{pption}$ would remain constant. Experimental studies have been reported in the following sections in order to corroborate these points.

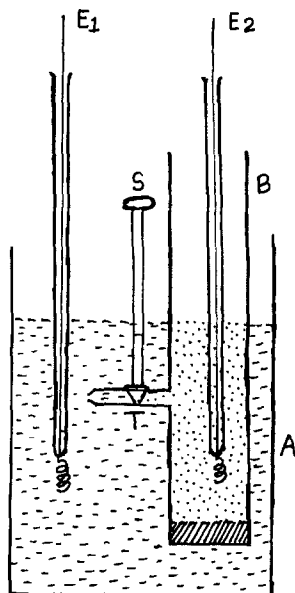


Fig. 4. Schematic diagram of the cell used for the measurement of $(\Delta\phi)_1$.

Experimental

Experimental techniques for the measurement of dissolution, precipitation, phase and thermodiffusion potentials were the same as already reported by Rastogi *et al.* (4, 5). While determining the precipitation potential, crystallization was invoked on only one electrode by adopting the process (ii) described earlier.

The cell used for the measurement of $(\Delta\phi)_1$, the potential associated with the establishment of a concentration cell with transference in the dissolution cell, is shown in Fig. 4. A is a Pyrex glass vessel containing conductivity water. B is another Pyrex glass vessel containing saturated solution of the electrolyte. B has a side tube T which has a stopper S. Conductivity water in vessel A and saturated solution in vessel B are adjusted at the same level. The platinum electrodes E_1 and E_2 are placed in the conductivity water and saturated solution, respectively. Solid electrolyte is kept in equilibrium with the saturated solution by putting a small amount of solid electrolyte at the bottom of vessel B in order to create a situation exactly similar to that present in the dissolution cell. Care is taken that the electrode E_2 does not come in contact with the solid electrolyte. Both the electrodes are connected with the electrometer amplifier. When the stopper S is opened, diffusion starts immediately. The buildup and decay of potential is recorded as a function of time.

A high impedance ($R > 10^{14}$) electrometer (Annadigi, Hyderabad) was used for the measurement of all these potentials. All the measurements were made in air, since it has been reported that observed potential remains almost unaffected even when the measurements are made in nitrogen atmosphere. Platinum electrodes fused in Pyrex glass tubes were welded to copper wire in order to avoid electrical contacts through mercury which might form unsuspected secondary cells. Coaxial cables were used in order to avoid the effect of stray external fields. The platinum electrodes were thoroughly cleaned by boiling in nitric acid and then by heating in a flame before each experiment. Asymmetry potential was minimized as far as possible, and it was always taken into account while evaluating the experimental values.

Results and Discussion

The dissolution, precipitation, phase potentials, and potential associated with the concentration cell with transference were recorded for KCl, KClO_3 , KBrO_3 , LiNO_3 , and LiClO_4 . The values of true dissolution potential and true precipitation potential evaluated on the basis of Eq. [2] and [22], respectively, and their theoretical values calculated from Eq. [13] and [21] are presented in Tables II, III, and IV.

Table II. Comparison of experimental and theoretically calculated values of $(\Delta\phi)_{\text{diss}}$ for some alkali-metal salts. These values are based on 25°C

Electrolyte	Observed dissolution potential (mV)	$(\Delta\phi)_1$ (mV)	$(\Delta\phi)_{\text{phase}}$ (mV)	Experimental dissolution potential evaluated from Eq. [2] (mV)	Theoretically calculated $(\Delta\phi)_{\text{diss}}$ on the basis of Eq. [13] (mV)
KCl	-76	-36	-18	-22 ± 3	-14
KClO_3	-55	-11	-20	-24 ± 3	-17
KBrO_3	-63	-10	-23	-30 ± 3	-26
LiNO_3	-130	-50	-32	-48 ± 3	-41
LiClO_4	-125	-34	-36	-55 ± 3	-41

Table III. Experimental and theoretically calculated values of $(\Delta\phi)_{\text{pptn}}$ for some alkali-metal salts. These values are based on saturation temperature of 25°C and $\Delta T = 15^\circ\text{C}$

Electrolyte	Observed precipitation potential (mV)	$(\Delta\phi)_{\text{phase}}$ (mV)	$(\Delta\phi)_{\text{ppt}}$ (mV)	Experimental $(\Delta\phi)_{\text{pptn}}$ evaluated from Eq. [22] (mV)	Theoretical $(\Delta\phi)_{\text{pptn}}$ calculated on the basis of Eq. [21] (mV)
KCl	-10	-18	-3	$+11 \pm 3$	+14
KClO_3	+3	-20	+3	$+20 \pm 3$	+17
KBrO_3	+9	-23	+4	$+28 \pm 3$	+26
LiNO_3	+15	-32	+5	$+42 \pm 3$	+41
LiClO_4	+18	-36	+5	$+49 \pm 3$	+41

Table IV. Comparison of dissolution potential with precipitation potential

Electrolyte	Experimental $(\Delta\phi)_{\text{diss}}$	Experimental $(\Delta\phi)_{\text{pptn}}$	Theoretically calculated $(\Delta\phi)_{\text{diss}}$	Theoretically calculated $(\Delta\phi)_{\text{pptn}}$
KCl	-22	+11	-14	+14
KClO_3	-34	+30	-17	+17
KBrO_3	-40	+38	-26	+26
LiNO_3	-48	+42	-41	+41
LiClO_4	-55	+49	-41	+41

The dependence of observed dissolution potential, true dissolution potential, and $(\Delta\phi)_1$ of LiNO_3 on concentration of the medium were also studied. The results are presented in Table V. The plot of $(\Delta\phi)_{\text{obs(diss)}}$ vs. $\log C$ of the medium and $(\Delta\phi)_1$ vs. $\log C$ of the medium are given in Fig. 5. Experimental studies on the effect of temperature and undercooling on $(\Delta\phi)_{\text{pptn}}$ of KClO_3 , KBrO_3 , and LiNO_3 are presented in Table VI and VII and Fig. 6.

A perusal of Tables II and III makes it quite clear that the theoretical values of true dissolution and true precipitation potentials calculated on the basis of Eq. [13] and [21], respectively, are in a good agreement with the experimental data. It is also evident from the data presented in Table IV that the precipitation potential is a phenomenon exactly opposite dissolution potential. Their experimental values are approximately equal in magnitude but opposite in sign. These observations are in accordance with the present mechanism of electric potential generated on the dissolution and precipitation of electrolytes. Theoretically

Table V. Dependence of observed dissolution potential, true dissolution potential, and $(\Delta\phi)_1$ of LiNO_3 on the concentration of the medium. All the measurements were made at 25°C

Molarity of LiNO_3 in water	$(\Delta\phi)_{\text{obs(diss)}}$ (mV)	$(\Delta\phi)_1$ (mV)	$(\Delta\phi)_{\text{phase}}$ (mV)	True $(\Delta\phi)_{\text{diss}}$ (mV)
0	-130	-50	-32	-48
2.0	-107	-28	-32	-47
3.0	-94	-17	-32	-45
4.0	-85	-7	-32	-45
4.5	-80	-3	-32	-45

Table VI. Effect of undercooling on $(\Delta\phi)_{\text{Pption}}$ of KClO_3 , KBrO_3 , and LiNO_3 . Saturation temperature of 25°C

Electrolyte	$(\Delta\phi)_{\text{phase}}$	$\Delta T = 10^\circ\text{C}$			$\Delta T = 15^\circ\text{C}$			$\Delta T = 20^\circ\text{C}$		
		$(\Delta\phi)_{\text{obs}}$	$(\Delta\phi)_{\text{TID}}$	$(\Delta\phi)_{\text{Pption}}$	$(\Delta\phi)_{\text{obs}}$	$(\Delta\phi)_{\text{TID}}$	$(\Delta\phi)_{\text{Pption}}$	$(\Delta\phi)_{\text{obs}}$	$(\Delta\phi)_{\text{TID}}$	$(\Delta\phi)_{\text{Pption}}$
KClO_3	-20	+2	+2	+20	+3	+3	+20	+5	+4	+21
KBrO_3	-23	+7	+3	+27	+9	+4	+28	+9	+5	+27
LiNO_3	-32	+14	+4	+42	+15	+5	+42	+16	+6	+43

The data presented in this table are the nearest integer of the average of several observations. Since the magnitude of various potentials were very low and the sensitivity of the instrument was only 1 mV, several observations had to be made in order to ascertain the reliability of an experiment.

cally calculated values of $(\Delta\phi)_{\text{diss}}$ and $(\Delta\phi)_{\text{Pption}}$ and their subsequent experimental verifications are found to be in accordance with the observation made by Ibl *et al.* (9) in their work. Girdhar and co-workers have also reported similar observations in case of ammonium salts (6-8).

Results reported in Table V and plotted in Fig. 5 support the view that the true $(\Delta\phi)_{\text{diss}}$ does not depend on concentration of the medium. Since the plots of $(\Delta\phi)_{\text{obs(diss)}}$ vs. $\log C$ and $(\Delta\phi)_t$ vs. $\log C$ are parallel to each other and since $(\Delta\phi)_{\text{obs(diss)}}$ and $(\Delta\phi)_t$ are related by the equation

$$(\Delta\phi)_{\text{obs(diss)}} = \frac{[(\Delta\phi)_t]}{I} + \frac{[(\Delta\phi)_{\text{diss}} + (\Delta\phi)_{\text{phase}}]}{II} \quad [23]$$

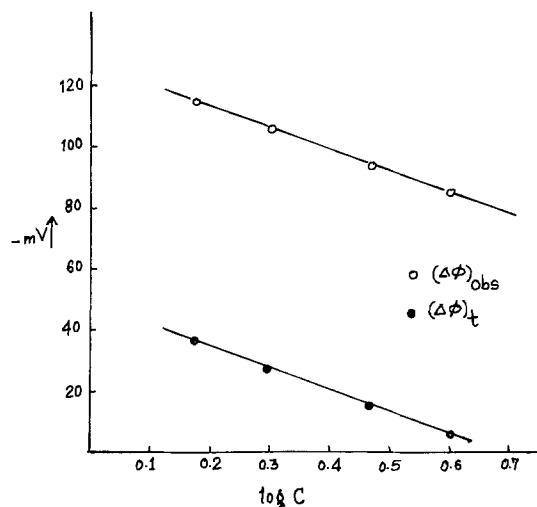


Fig. 5. Dependence of observed dissolution potential and $(\Delta\phi)_t$ on $\log C$ of LiNO_3 .

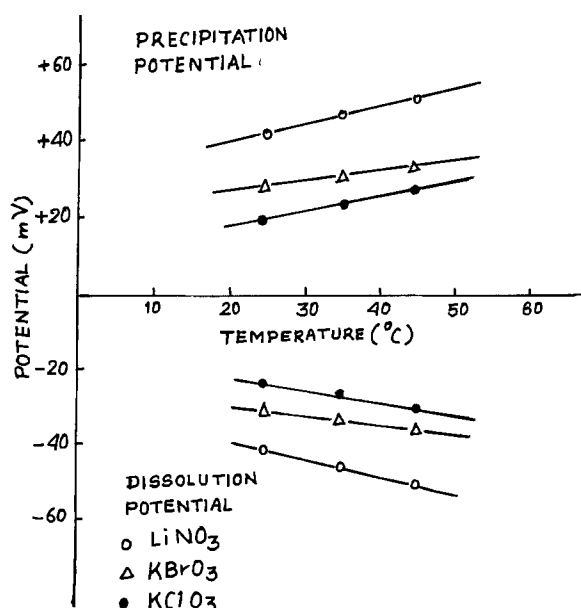


Fig. 6. Effect of temperature on true dissolution and precipitation potentials of KClO_3 , KBrO_3 , and LiNO_3 .

Table VII. Effect of temperature on true dissolution potential and true precipitation potentials of KClO_3 , KBrO_3 , and LiNO_3 . Precipitation potential data are based on $\Delta T = 15^\circ\text{C}$. Equations [2] and [22] were used for the evaluation of respective potentials

Electrolyte	True dissolution potential			True precipitation potential		
	25°C (mV)	35°C (mV)	45°C (mV)	25°C (mV)	30°C (mV)	35°C (mV)
KClO_3	-24	-27	-31	+20	+24	+28
KBrO_3	-30	-33	-36	+28	+30	+33
LiNO_3	-41	-45	-50	+42	+47	+51

it is quite evident that the second term in the rhs of Eq. [23] should be independent of $\log C$. It therefore follows that $(\Delta\phi)_{\text{diss}}$ does not depend on the concentration of the medium.

Experimental observations on the dependence of $(\Delta\phi)_{\text{Pption}}$ on undercooling (columns 5, 8, and 11, Table VI) support our theoretical view that the true precipitation potential does not depend on ΔT . These observations are in accordance with the experimental studies reported by Workmann and Reynolds (21), Parreira and Eydtt (22), Heinmeles (23), Gross (24), and many others about the independence of freezing potential on undercooling. They have reported that ΔT has no particular effect on freezing potential. On the basis of these arguments, it can also be predicted that the phenomenon of true precipitation potential is somewhat similar to the phenomenon of freezing potential. The effects of temperature on dissolution and precipitation potential of KClO_3 , KBrO_3 , and LiNO_3 were also studied. The data are presented in Table VI and VII and plotted in Fig. 6. The true dissolution and precipitation potentials are found to be directly proportional to the temperature. These observations are also in accordance with the theory. The data presented in Table VII once again support the view that the dissolution and precipitation potentials are equal in magnitude but opposite in sign.

Acknowledgment

The authors wish to thank Dr. John Patterson, Principal, St. Andrews' College, Gorakhpur, for providing necessary facilities. Thanks are also due to U.G.C. (India) for financial support.

Manuscript submitted Sept. 6, 1984; revised manuscript received April 1, 1985.

REFERENCES

- W. Jaenicke, *Z. Electrochem.*, **56**, 473 (1952).
- R. P. Rastogi, R. K. Dass, and B. P. Batra, *Nature*, **191**, 765 (1961).
- R. C. Srivastava, L. P. Abrol, and O. P. Khurana, *ibid.*, **216**, 682 (1967).
- R. P. Rastogi and R. D. Shukla, *J. Appl. Phys.*, **41**, 2787 (1970).
- R. P. Rastogi, R. D. Shukla, and S. Bhagat, *This Journal*, **121**, 1564 (1974).
- H. L. Girdhar and R. P. Matta, *Electrochim. Acta*, **22**, 173 (1976).
- H. L. Girdhar and R. P. Matta, *Indian J. Chem.*, **14A**, 160 (1976).

8. H. L. Girdhar and R. P. Matta, *J. Electroanal. Chem.*, **89**, 407 (1978).
9. N. Ibl, W. Richarz, and H. Wiederkher, *Z. Phys. Chem. (Leipzig)*, **988**, 123 (1975).
10. N. Ibl, C. Natsis, W. Richarz, H. Wiederkher, A. M. Frier, H. Arendi, M. Burri-Nonteil, and K. Zahorska, in "Topics in Pure and Applied Electrochemistry," S. K. Rangarajan, Editor, SAEAST, Karaikudi, India (1975).
11. Vishnu, S. A., Khan, and E. Jahan, *Electrochim. Acta*, **24**, 387 (1979).
12. R. P. Rastogi and S. A. Khan, *This Journal*, **127**, 1989 (1980).
13. R. P. Rastogi and S. A. Khan, *ibid.*, **130**, 1327 (1983).
14. C. W. Davies, "Electrochemistry," p. 96 George Newnes Ltd., London (1967).
15. J. Koryta, J. Dvorak, and V. Bohackova, "Electrochemistry," p. 161, Methuen and Co. Ltd., London (1970).
16. B. R. Sundheim, *J. Phys. Chem.*, **60**, 1381 (1956).
17. M. F. R. Mulcahy and E. Heymann, *ibid.*, **47**, 485 (1943).
18. H. Bloom, "The Chemistry of Molten Salts," p. 97, W. A. Benjamin, Inc., New York (1967).
19. J. A. Dean, "Lange's Hand Book of Chemistry," McGraw Hill, New York (1974).
20. K. S. Pitzer and L. Brewer (Revision of Lewis and Randall), "Thermodynamics," pp. 643-657, McGraw Hill, New York (1961).
21. E. J. Workman and S. E. Reynolds, *Phys. Rev.*, **74**, 709 (1948).
22. H. C. Parreira and A. J. Eydt, *Nature*, **33**, 208 (1965).
23. F. Heinmetes, *Trans. Faraday Soc.*, **58**, 788 (1962).
24. G. W. Gross, "Trace Inorganics in Water," Advances in Chemistry Series 73, American Chemical Society, Washington, DC (1968).

Effects of Curing and Other Variables on Deep-Discharge Cycling of Pb-Ca Positive Plates

T. G. Chang* and E. M. Valeriote*

Cominco Ltd., Product Research Centre, Mississauga, Ontario, Canada L5K 1B4

ABSTRACT

Effects of curing temperature and humidity, paste density, plate thickness, soaking time before formation, and electrode support on deep cycling performance of Pb-Ca positive plates were studied. It was found that although improvements could be obtained by adjusting these variables, the capacity retention was still inferior to that of Pb-Sb plates. Examination of the plates revealed that preferential discharge of the corrosion product and the formation of a PbSO₄ barrier around Pb-Ca grid wires might cause the loss of capacity. Means of extending the cycle life of nonantimonial lead positive plates are discussed.

Although lead-calcium (Pb-Ca) alloy grids were introduced for lead-acid storage batteries early in the 1930's by Bell Laboratories (1), before 1970 they were used almost exclusively for float-service applications. In recent years, they have been employed ever increasingly in starting-lighting-ignition batteries. They are also used, although not widely, in batteries for deep-discharge applications. However, it has been known that Pb-Ca batteries do not usually retain their capacities as well as lead-antimony (Pb-Sb) batteries in deep cycling, for reasons which are not clear in spite of considerable research (2-8). Means have been suggested to improve the deep cycling performance of Pb-Ca batteries (2, 5). In this work, effects of curing and other variables on deep cycling of Pb-Ca positive plates were studied. The cycled plates were also examined to determine the causes of failure.

Experimental

The Pb-Ca grids used in the experiments were expanded from Pb-0.09% Ca-0.3% Sn cast strip and measured 102 mm (H) × 52 mm (W). Pastes were prepared from a commercial leady oxide, Grenox, which contained about 25% metallic lead. The variables studied were (i) paste density (wet) of 4.0 and 4.3 g/cm³, (ii) curing temperatures of 85°, 40°, and 22°C, (iii) curing humidity of 100 and 50% RH, (iv) plate thickness of 3.5 and 2.2 mm (the grids were 1.9 and 1.4 mm thick, respectively), (v) soaking time before formation of 1 and 3h, and (vi) plate retention: without any support and with stack pressure on the electrode assembly.

For each set of experimental parameters, three to five replicates were subjected to deep-discharge cycle life testing.

The pastes were prepared by mixing leady oxide, sulfuric acid (1.350 sp gr), and water. The PbO/SO₃ ratio was 6 for pastes of 4.0 g/cm³ density, and 8 for those of 4.3 g/cm³ density. Cured plates, 2.2 and 3.5 mm thick, were formed in 1.10 sp gr H₂SO₄ at 40°C and cycled in an amount of 1.25 sp gr H₂SO₄ well in excess of the stoichiometric requirement. The potential of the positive test plate was

measured against a Hg/Hg₂SO₄ reference electrode (in 1.25 sp gr H₂SO₄) during cycling. When a plate was tested without any support, it was placed in a 600 ml beaker with a negative plate on each side and no separator, but with a wide gap between the plates. When a plate was tested with retainers, it was wrapped in a glass-fiber mat and placed in a Plexiglas cell, 26 (W) × 102 (L) × 165 (H) mm, with a Daramic® (microporous polyethylene) enveloped negative plate on each side. A stack pressure was imposed by inserting polyethylene sheets between the electrode assembly and the cell walls. The test plates were discharged at about the 5h rate to a potential of 900 mV (*i. e.*, 100% depth of discharge). After a rest time of 5 min, they were recharged at a constant potential of 1300 mV with a maximum current of 2A. When the charging current decreased to 250 mA for the 3.5 mm plates, or 185 mA for the 2.2 mm plates, the test plates were recharged at the same respective constant current till 115% (Ah) of the previous discharge was returned. Again, there was a 5 min rest before the next discharge. Cycled plates were washed, dried, and examined by optical and scanning electron microscopy. For comparison, positive plates prepared from Pb-3% Sb book-mold grids (47 × 75 × 1.9 mm) and 4.26 g/cm³ paste were also cycled and examined. These plates were pasted to a thickness of 3.3 mm when dried. They were cured at 40°C and formed and cycled without support, under the same cycling conditions already described for Pb-Ca plates.

To investigate the activity of the active material in failed Pb-Ca plates, a set of Pb-Ca book-mold grids (0.1% Ca, 0.35% Sn) was pasted and cycled in excess amount of 1.25 sp gr H₂SO₄ without support at 30°C. After the plates failed in cycling, the acid concentration was lowered to 1.10 sp gr, and the discharge capacities in the new cycling acid were recorded.

Results and Discussion

Curing temperature (at 100% RH).—X-ray diffractometry indicated that all sulfate in the plates cured at 85°C was in the form of 4PbO · PbSO₄ and that in those cured at 40° and 22°C was in the form of 3PbO · PbSO₄ · H₂O.

*Electrochemical Society Active Member.

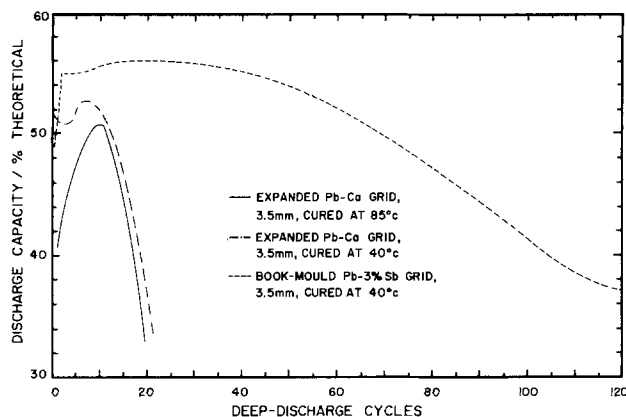


Fig. 1. Deep-discharge performances of unsupported positive plates. All plates were prepared from a paste of 4.3 g/cm^3 density, cured in 100% RH, and cycled in $1.25 \text{ sp gr H}_2\text{SO}_4$ at 30°C .

The mechanical integrity of the cured plates appeared to increase with increased curing temperature. Figure 1 presents capacity-cycle curves for 3.5 mm plates cycled without retainers. Obviously, plates prepared from Pb-Ca grids did not retain deep-discharge capacity as well as those with Pb-Sb grids, and no improvement had been achieved by raising the curing temperature to 85°C . Figure 2 shows how Pb-Ca plates cured at different temperatures performed with retainers under the deep cycling conditions. The 85°C cured plates did not really perform better than the 40°C cured plates. Their cycle life was longer (Fig. 2), but their initial discharge capacity was very low compared with those cured at lower temperatures. It took 10-15 deep cycles for the 85°C cured plates to reach maximum capacity (Fig. 1 and 2), which was lower than that of the 40°C cured plates. Figure 2A also shows that although plates cured at 22°C had poorer integrity, when they were adequately supported and not disturbed in cycling their performance was comparable to that of plates cured at higher temperatures.

Curing humidity.—When plates were subjected to a low humidity (50% RH) environment at the beginning of the curing process, they developed numerous hairline cracks and retained a high metallic lead content in the paste. The resulting plates gave very poor performance. No $4\text{PbO} \cdot \text{PbSO}_4$ was produced in plates cured at low humidity even when the curing temperature was raised over 80°C . When the humidity was held at 50% RH, the higher the curing temperature, the greater was the damage to the plate integrity because of the higher evaporation rate at higher temperatures.

Plate thickness and paste density.—The experimental data, as shown in Fig. 2, demonstrate the well-known fact

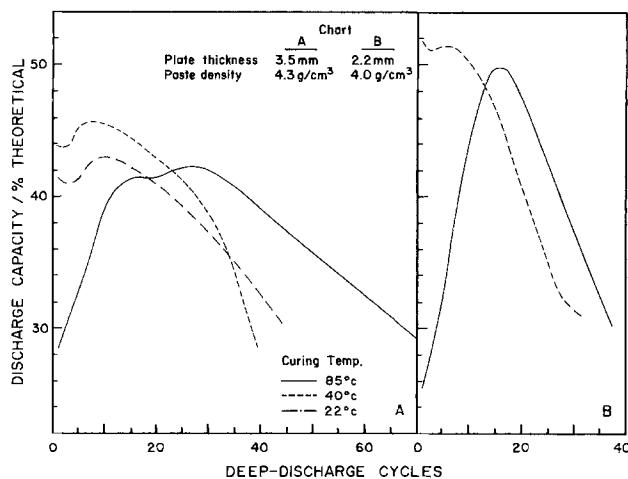


Fig. 2. Deep-discharge performances of Pb-Ca positive plates cured at 85°C , 40°C , and 22°C , and 100% RH, and cycled with retainers in $1.25 \text{ sp gr H}_2\text{SO}_4$ at 30°C .

that when the paste density or plate thickness is reduced the discharge capacity increases and the cycle life decreases (9, 10).

Soaking time.—In general, a soaking time before forming of longer than 1h, in a cell with excess electrolyte, resulted in plates of shorter cycle life. However, plates with poor integrities, e.g., plates subjected to a low humidity environment in the incipient period of the curing process, performed better when they were soaked for 3h before commencement of formation than those soaked for 1h. Perhaps heavier and deeper sulfation due to the long soaking improved the plate integrity.

Retainer.—By comparison of Fig. 1 with Fig. 2, it is apparent that, when the plates were supported, their cycle life was substantially extended with some sacrifice in discharge capacity.

All the results clearly showed that even under the most favorable of the above-mentioned experimental conditions, the deep cycling performance of the Pb-Ca positives did not equal that of Pb-Sb.

Microscopical study.—The test plates were examined by both optical and scanning electron microscopy. Sulfur contents in the plates were measured by EDX microprobe.

Examination of the prematurely failed Pb-Ca plates revealed that the active material close to the plate surface was different from that in the center of the plate. The active material lying closer to the plate surface had either formed or was in the process of consolidating to form a coralloid structure (11-13) depending on the number of cycles the plate had undergone. Figure 3 shows the active material lying close to the surface of plates which failed after fewer than 30 cycles. The coralloid structure can be clearly seen. The center part (which was about one-third of the total plate thickness) of the failed Pb-Ca plates did not contain any coralloid structure. Figure 4a shows active material at the center of a 85°C cured plate (2.2 mm thick) which failed before the twenty-ninth cycle. The large bar-like particles retained the shape of the original $4\text{PbO} \cdot \text{PbSO}_4$ crystals, and their interior remained dense

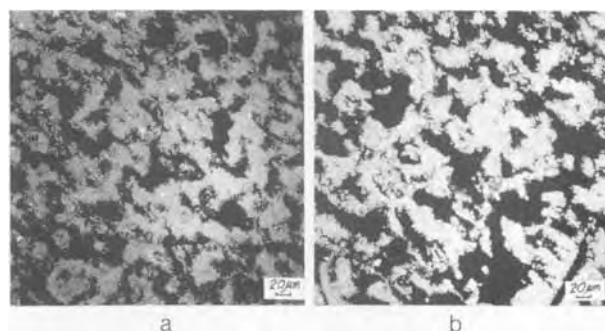


Fig. 3. Active material close to surface of failed Pb-Ca plates which were cured at 40°C and deep cycled in $1.25 \text{ sp gr H}_2\text{SO}_4$ at 30°C . a: 30 cycles, charged. b: 31 cycles, discharged.

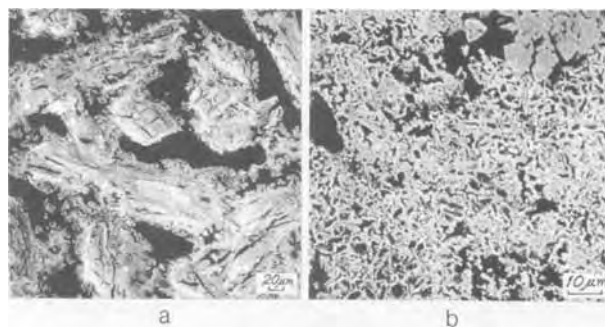


Fig. 4. Active material in the center of Pb-Ca plates which failed in deep cycling in $1.25 \text{ sp gr H}_2\text{SO}_4$ at 30°C . a: Cured at 85°C , 29 cycles, discharged. b: Cured at 40°C , 41 cycles, discharged.

and quite pore-free. This indicates that most of the material had never taken part in the charge-discharge process. The active material shown in Fig. 4b was in the center of a 3.5 mm plate which was cured at 40°C and had undergone 41 cycles. The structure is distinctively cellular and normally occurs when the active material has undergone only a single discharge-charge cycle after formation (13, 14). This structure in fact is optimal for high utilization (13). Microprobe analysis and visual inspection (Fig. 4) indicated that less than 5% of the active material in the center part of a failed Pb-Ca plate was converted to PbSO₄ at the end of discharge.

The book-mold Pb-Ca plates which were cycled to failure in 1.25 sp gr H₂SO₄ were placed in 1.10 sp gr H₂SO₄. It was found that the capacities of the plates increased substantially, ranging from 25 to 55%. This is in agreement with the results obtained by Nakayama *et al.* (6). The evidence suggests that the discharge of the active material was obstructed by sulfation in some parts of the plate, rather than by either reduced electrochemical activity of the active material or poor interparticle contact.

The active material close to the surface of the failed plates was carefully examined for a possible pore-free PbSO₄ layer which could have obstructed the diffusion of sulfuric acid to the interior of the plate. It was not found. On the contrary, in general, the active material close to the plate surface was much more porous than that in the plate center. When a plate was discharged, part of the microporous lead dioxide, as shown in Fig. 3a, was converted to regular nonporous PbSO₄ crystals with a dimension of about 5 μm. As shown in Fig. 3b, although there should be a volume increase of almost 90% in the conversion from PbO₂ to PbSO₄, by elimination of micropores the structure actually appeared to become much more open. It is quite reasonable to assume that, as a consequence, the diffusion of sulfuric acid would not be impeded.

The active material on the Pb-Sb plates which had undergone various lengths of cycling was also inspected. It was found that active material on either Pb-Ca plates or Pb-Sb plates, which were subjected to the same number of cycles with comparable active material utilization, appeared essentially the same, morphologically. Since the active material in the center part of a failed Pb-Ca plate appeared to be healthy and had participated in previous cycling, and since the accessibility of acid was unlikely to be limiting the capacity, the reason for the low dischargeability must be sought elsewhere.

Careful examination was, therefore, made of the grid/active material interfacial region. The corrosion product on the grid usually had two layers, regardless of whether the grid was Pb-Ca or Pb-Sb. One was dense and dark, and was adjacent to the grid; the other was porous and lighter in color. The thickness of the inner layer was about 20 μm, and that of the outer layer varied. When a plate was fully charged, no sulfate was found in either of these layers. No irreversible formation of a PbSO₄ barrier layer surrounding the Pb-Ca grids, as reported by Tudor *et al.* (2) and Perkins (15), has been observed in our laboratory. Indeed, hardly any PbSO₄ was found in a fully charged plate. When a plate was fully discharged (100% DOD), the inner corrosion layer remained unchanged and the microprobe detected no sulfur in it. The state of the outer layer depended, however, on the depth of discharge, its relative location in the plate, and the nearness of the plate to failure. When a plate was being discharged, regardless of whether it was healthy or failed, the part of the outer corrosion layer which was close to the plate surface, *i.e.*, near the bulk electrolyte, was always sulfated at the end of a deep discharge. The sulfation process started from the outside surface of the outer layer and then spread inward. Figure 5a shows that the outside surface of the outer corrosion layer in a discharged plate was covered by PbSO₄ crystals. From the outer surface inward, the sulfur content, as determined by microprobe, decreased to zero at the inner surface, where it met the dense corrosion layer. In a plate which had not yet failed,

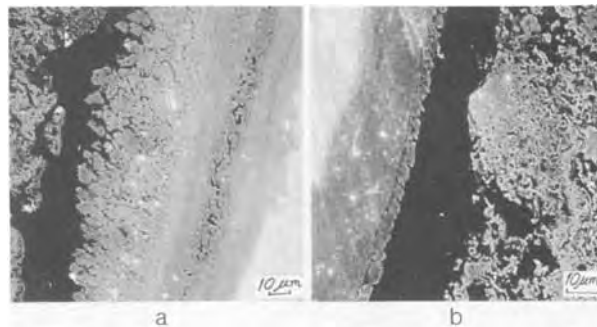


Fig. 5. Corrosion layers on grid in discharged failed Pb-Ca plate at various locations. a: Close to plate surface. b: At the center of the plate.

or which was only shallowly discharged, the part of the corrosion layer farther from the plate surface, *e.g.*, at the center of the plate, was either not at all or only slightly sulfated. But when a failed plate was fully discharged, usually all the outer surface of the corrosion layer, regardless of its position in the plate, was completely covered by PbSO₄ crystals. Figure 5b shows part of the corrosion layers in the center of a failed plate which had undergone 22 deep cycles. The grid metal can be seen in the upper left corner of this photomicrograph. The porous substance on the right-hand side is the active material. As shown in the photomicrograph, the outer surface of the corrosion layer is completely masked by tightly packed PbSO₄ crystals. It is noteworthy that, as shown in Fig. 5, the active material next to the sulfated corrosion layer was almost completely free of sulfur. This phenomenon was found to be quite common in failed Pb-Ca plates. Figure 6 shows a microtomed failed Pb-Ca plate without any mounting material. Thus, looking down into the small interstices between corrosion products and active material, one can see that the outer surface of the corrosion layer, as shown in Fig. 6b, is completely masked by PbSO₄ crystals.

Nakayama *et al.* (6) also observed sulfation of the corrosion product around the Pb-Ca grid. However, in their model, the sulfation process is initiated on the inner surface of the dense corrosion layer contacting the grid, and then proceeds outward until all the corrosion product is sulfated to form a PbSO₄ barrier. The model also implies that the sulfation develops uniformly in every part of the corrosion product around the grid, regardless of the relative position of the part of the corrosion product with respect to the plate surface. As previously described, this model is not in agreement with our findings.

A comparison microscopical study of Pb-Sb plates was also carried out. Failure appeared to follow the same general course. The corrosion product around the grid usually also had a two-layered structure; the layer adjacent to the grid was dense and dark, and the outer layer was porous and lighter in color. As in Pb-Ca plates, no sulfur was found in the inner layer either in the charged or dis-

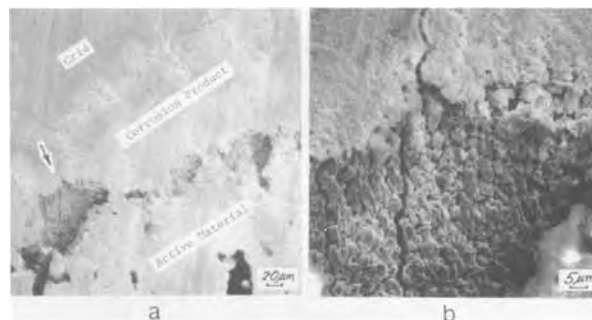


Fig. 6. Interfacial region between grid and active material in a failed Pb-Ca plate which was cured at 40°C and 100% RH, and had undergone 22 deep-discharge cycles. The specimen was microtomed without mounting material. b is an enlargement of the location indicated by an arrow in a.

charged state. After 24 cycles, when the discharge capacity was at about the maximum (see Fig. 1), the outer corrosion layer, at locations close to the plate surface and bulk electrolyte, was already well developed and was heavily sulfated at the end of a deep discharge. In contrast, at locations farther from the plate surface, *e.g.*, at the center of the plate, the second layer was either nonexistent or not well developed. Thus, at the end of discharge the dense corrosion layer at these locations was not completely covered by PbSO_4 crystals, if they were at all present. As cycling proceeded further, the structure of the active material close to the plate surface became more open, because of coralloid structure formation, and the active material farther inside the plate participated increasingly in charge-discharge cycling. However, opening up of the structure also promoted discharge of the corrosion product. Thus the porous outer corrosion layer progressed to locations farther inside the plate; at the end of the discharge period, a larger portion of the grid became enveloped in a layer of sulfate. At the end of cycle life, the coralloid structure dominated in the plate; large pores of greater than $100\ \mu\text{m}$ diam formed even in the center of the plate, as we described previously (13). By this time, at the end of a discharge the grid was completely surrounded by a thick PbSO_4 layer having a dendritic structure, as shown in Fig. 7.

It becomes apparent that it was the formation of a continuous PbSO_4 layer around the grid that effectively prevented the discharging of the active material, thus ending the cycle life of the plate. This occurs for both antimonial and nonantimonial plates. The difference between these two kinds of plates is that it occurs in Pb-Ca plates at a much earlier stage, before the coralloid structure has formed throughout the plate. In contrast, in a Pb-Sb plate, the grid surface deep in the center of the plate is not covered by PbSO_4 until the active material in the same location has been utilized in cycling and transformed to a very open structure, *i.e.*, a well-developed coralloid structure.

Once a plate enters the last stage of its cycle life, if it is subjected to a deep discharge, the outer corrosion layer is discharged in preference to the active material in the interior of the plate. As Fig. 5 and 7 show, the active material in contact with the almost completely discharged outer corrosion layer can be completely undischarged. In other words, the physical change in cycling becomes increasingly concentrated in the corrosion layer. The adhesion of the active material to the corrosion layer (and, thereby, to the grid) is therefore weakened. This could explain partly why apparently healthy active material spalled in big chunks from Pb-Ca plates.

It was also noted that the development of the corrosion layer in Pb-Ca plates was different from that in Pb-Sb plates. Although concentric cracks, which developed parallel to the grid surface, formed in both Pb-Ca and Pb-Sb grids, they started to form earlier and were much more numerous in Pb-Ca plates than those in Pb-Sb plates. The cracks formed in the dense layer adjacent to the grid. In Pb-Ca plates, almost immediately after the cracks were

formed, sulfate crystals started to grow in them, and, consequently, enlarged them. In contrast, cracks in Pb-Sb plates could experience many cycles without any sulfate being formed in them. Thus, the corrosion layer in a Pb-Ca plate, which has been subjected to more than 50 deep cycles, usually had a multilayered structure. Furthermore, if that plate was failing, it was often found that at the end of a discharge, layers closer to the grid were sulfated, but the outer layers were not.

All the evidence suggests that the premature failure of Pb-Ca positive plates is caused by preferential discharge of the corrosion product surrounding the grid. Therefore, design features or additives which limit access of acid to the grid or reduce its activity, or which retard discharge of corrosion product, might extend cycle life. This can be achieved in many ways, for example, by increasing the paste density or the plate thickness (2), or by reducing the quantity of acid (as in "starved" electrolyte batteries) or the concentration of acid (5). According to this model, the tubular form would be preferable for Pb-Ca positive plates, since this configuration eliminates the short cuts for acid to reach the grid surface which exist in a flat plate. The application of pressure on the plates has been shown to beneficially affect cycle life (25, 26). Pressure might function by slowing down the development of macropores as a result of structural changes which occur in the active material during cycling (13). These macropores increase access of acid to the plate interior; thus, prevention of their formation would be expected to result in an increase in cycle life.

Some additives may achieve extended cycle life by retarding the discharge of the corrosion product. Antimony and phosphoric acid have been proven to extend cycle life (2, 4, 16), and both of them have also been shown to inhibit the discharge of PbO_2 (2, 16-21). There is also evidence that antimony and phosphoric acid promote the formation of $\alpha\text{-PbO}_2$ over that of $\beta\text{-PbO}_2$ (18-24). It is usually agreed that $\alpha\text{-PbO}_2$ is more difficult to discharge than $\beta\text{-PbO}_2$. This may be why the presence of antimony and phosphoric acid prevents a PbSO_4 barrier from forming in the corrosion layer.

Conclusions

Retention of the deep-discharge capacity of Pb-Ca plates could not be improved appreciably by modification of curing and forming conditions within the range of those considered to constitute normal practice. A low humidity environment in the initial stage of curing should be avoided; otherwise, substantial loss in capacity and cycle life results.

The premature loss of discharge capacity of Pb-Ca plates was caused by preferential discharge of the corrosion product and the formation of a PbSO_4 barrier around the grid. It followed that the cycle life of the plate might be extended by reduction of access of acid to the corrosion layer on the grid and by additives which retard discharge of the corrosion product around the grid.

Acknowledgments

The plate preparation and cycling were carried out by Mr. M. J. Dewar. Specimen preparation and part of the microscopic study were done by Mr. W. W. Gregory; Mr. K. Cowan also assisted with specimen preparation.

Manuscript received Oct. 13, 1984. This was Paper 7 presented at the New Orleans, Louisiana, Meeting of the Society, Oct. 7-12, 1984.

Cominco Ltd. assisted in meeting the publication costs of this article.

REFERENCES

1. E. E. Schumacher and G. S. Phipps, *Trans. Electrochem. Soc.*, **68**, 309 (1935).
2. S. Tudor, A. Weisstuch, and S. H. Davang, *Electrochem. Technol.*, **3**, 90 (1965); *ibid.*, **4**, 406 (1966); *ibid.*, **5**, 21 (1967).
3. J. Burbank and A. C. Simon, *This Journal*, **100**, 51 (1953).

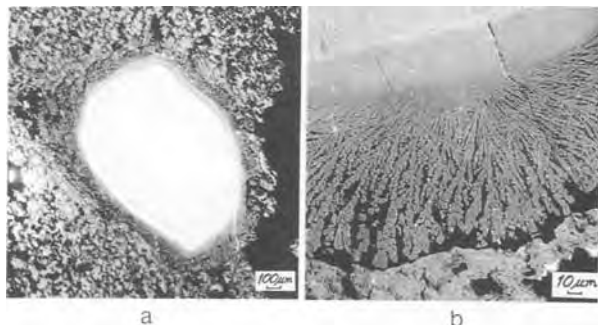


Fig. 7. a: A cross section of a failed Pb-3%Sb plate which had undergone 127 deep cycles without retainers. Note the dendritic growth around the grid. b: Shows the detail of the dendritic structure of the corrosion product.

4. E. J. Ritchie and J. Burbank, *ibid.*, **117**, 299 (1970).
5. H. Nakashima, M. Kono, and S. Hattori, *Yuasa-Jiho*, **51**, 24 (1981).
6. Y. Nakayama, T. Takayama, and M. Kono, *ibid.*, **53**, 56 (1982).
7. B. K. Mahato, *This Journal*, **126**, 365 (1979).
8. S. Osumi, N. Tsujino, and K. Yonezu, *G. S. News*, **41**, 18 (1982).
9. G. W. Vinal, "Storage Batteries," 4th ed., John Wiley and Sons, Inc., New York (1955).
10. H. Bode, "Lead-Acid Batteries," R. J. Brodd and K. V. Kordesch, Translators, John Wiley and Sons, New York (1977).
11. A. C. Simon, S. M. Caulder, and J. T. Stemmlé, *This Journal*, **122**, 461 (1975).
12. A. C. Simon and S. M. Caulder, in "Power Sources 5," D. H. Collins, Editor, p. 109, Academic Press, London (1975).
13. T. G. Chang, *This Journal*, **131**, 1755 (1984).
14. A. C. Simon and S. M. Caulder, *ibid.*, **118**, 659 (1971).
15. J. Perkins, *Mater. Sci. Eng.*, **28**, 167 (1977).
16. K. R. Bullock and D. H. McClelland, *This Journal*, **124**, 1478 (1977).
17. D. Barrett, M. T. Frost, J. A. Hamilton, K. Harris, I. R. Harrowfield, J. F. Moresby, and D. A. J. Rand, *J. Electroanal. Chem.*, **118**, 131 (1981).
18. T. Sharp, *This Journal*, **124**, 168 (1977).
19. H. Tamura, H. Yoneyama, C. Iwakura, and O. Ikeda, "Annual Report for ILZRO Project LE 254," March 10, 1977.
20. G. Kawamura, S. Mochizuki, and A. Komaki, *Denki Kagaku*, **48**, 554 (1980).
21. A. Boggio, M. Maja, and N. Penazzi, *J. Power Sources*, **9**, 221 (1983).
22. T. Rogatchev, G. Papazov, and D. Pavlov, *ibid.*, **10**, 291 (1983).
23. W. Visscher, *ibid.*, **1**, 257 (1976-1977).
24. J. A. Bialacki, N. A. Hampson, and K. Julian, *Surf. Technol.*, **19**, 347 (1983).
25. K. Takahashi, M. Tsubota, K. Yonezu, and K. Ando, *This Journal*, **130**, 2144 (1983).
26. J. Alzieu and J. Robert, *J. Power Sources*, **13**, 93 (1984).

Characterization of the Li/MnO₂ Multistep Discharge

John C. Nardi

Union Carbide Corporation, Battery Products Division, Westlake, Ohio 44145

ABSTRACT

The electrochemical discharge, differential capacity, open-circuit voltage-temperature dependence, and open-circuit relaxation techniques were combined to investigate the cathodic reduction mechanism of the Li/MnO₂ nonaqueous couple. These techniques indicate three different stages of MnO₂ reduction by insertion of lithium ions into the lattice of the cathode. The initial stage of the reduction of the MnO₂ occurs within approximately the first 10% of discharge. It involves the insertion of lithium ions into the lattice of the MnO₂ forming Li_xMnO₂ (0 ≤ x ≤ 0.1). It is typical of a homogeneous reaction. The next step in the discharge involves a heterogeneous or two-phase reaction. It is distinguished by the flat portion of the Li/MnO₂ discharge curve (0.1 ≤ x ≤ 0.4). The final discharge regime is again a homogeneous reaction. This reaction involves insertion of lithium ions into the new structural form of Li_xMnO₂ (x > 0.4) and accounts for the final sloping section of the discharge curve.

Considerable work has been focused on the development of nonaqueous lithium batteries. A promising class of nonaqueous cathode materials appears to be the transition metal oxides, with one of the most studied being MnO₂ (1-4). Still, little is known about the mechanistic aspects of lithium ion incorporation into the MnO₂ structure. This study reports results of investigations into the cathodic reduction process of MnO₂. Electrochemical discharge, differential capacity, and open-circuit relaxation techniques at selected temperatures were used.

Experimental

Two types of electrochemical cell configurations were used in this series of experiments. A flooded experimental cell consisted of an electrically insulated, sealed, stainless steel container that provided good internal electrode contact by means of a stainless steel spring. Such cells were cathode limited in capacity. The other cell configuration was of the anode-limited CR 2016 "coin" type.

The flooded electrochemical cells were assembled in a dry box by placing in the cell holder a MnO₂ cathode pellet, a highly porous separator material, lithium disk, a stainless steel contact plate and spring. The cells were then filled with electrolyte and closed. The electrolyte was 1M LiCF₃SO₃ dissolved in a 50/50 volume percent propylene carbonate (PC)-dimethoxyethane (DME) solution. The PC and DME organic solvents were obtained from the Burdick and Jackson Laboratories, Incorporated, and the Grant Chemical Corporation, respectively. The salt was purchased from the 3M Corporation. Scrupulous drying of the solvents and solute resulted in an electrolyte with a water content below 25 ppm. The organic solvents were stored over 4Å molecular sieves in order to remove any traces of residual water while electrolyte solutes were dried under vacuum. Water analyses were accomplished using a Photovolt Aquatest IV. The

cathode consisted of a pressed powder pellet containing nonheat-treated (NHT) or heat-treated (HT) electrolytic manganese dioxide (EMD), a carbon conductive additive, and a Teflon® binder (5). Heat-treatment consisted of heating the EMD at 350°C for 8h. Before heat-treatment, the adsorbed or 120°C water is typically 3-4% of the MnO₂. After heat-treatment, this was reduced to approximately 0.2%. The x-ray diffraction patterns of these MnO₂'s are comparable to x-ray data already reported in the literature (1). All cathode pellets were dried at 150°C under vacuum for 16h prior to incorporation in the complete cell.

The CR-2016's are similar to commercially available cells and represent state-of-the-art design and manufacture. These cells also contained the 1M LiCF₃SO₃-PC/DME electrolyte (6).

Discharge and open-circuit potentials were continuously monitored using an automatic data acquisition system consisting of an Esterline-Angus PD-2064 datalogger and Hewlett-Packard HP-9835A desktop computer. This system was also used to store, tabulate, correlate, and graph the electrochemical data from all cells tested. A Thermotron S1.2 environmental chamber capable of maintaining a preset temperature within ± 0.5°C was used when evaluating cells at temperatures other than ambient.

Results and Discussion

Differential capacity analysis.—Figure 1 shows discharge curves at 35°C for the flooded experimental cells containing the NHT and HT MnO₂. The cells were discharged to a 2.0V cutoff across a constant resistive load of 30,000Ω. This represents a current density of approximately 0.05 mA/cm² at 3.0V. The NHT MnO₂ has a higher initial discharge plateau than does the heat-treated MnO₂. However, the overall corrected cathode efficiencies for freshly discharged NHT and HT MnO₂ are quite close. To better assess the shape of the Li/MnO₂ discharge profile,

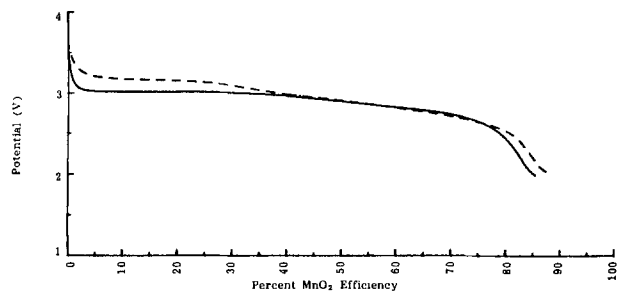


Fig. 1. Discharge curves at 35°C for Li/MnO₂ experimental cell under 30 kΩ background load. Cathodes utilize HT MnO₂ (solid line) or NHT MnO₂ (broken line).

a differential capacity analysis (DCC) was performed on these data (7-9). The sensitivity of the DCC method prevents its use on cells not discharged in strictly controlled temperature environments. The DCC analysis uses the slope of the discharge curve to interpret the data. It involves calculating the change in charge divided by a change in voltage over a specified time interval and plotting such against the average potential for this time increment. If, during the discharge, a very stable potential plateau exists, the DCC curve will indicate it by a sharp peak at the plateau's voltage. The sharpness of the peak also gives an indication of the relative flatness of the discharge plateau it represents. Any slope or voltage step in the discharge curve will be seen as a sharp decrease in the DCC curve. The DCC analysis of the two curves of Fig. 1 are shown in Fig. 2. The NHT MnO₂ has a very sharp peak at 3.2V, while the same relatively sharp peak occurs at 3.0V for the HT MnO₂. An initial, very sloping discharge region is denoted by the flat DCC region prior to the main peak. After the sharp peak, the NHT curve displays a sharp decrease followed by a second, more washed-out peak. This peak is centered at about 2.9V. Note that the HT material has the same washed-out peak at 2.9V. It suggests that the latter halves of the two discharge curves are almost identical and in all likelihood represent the same reaction. Heat-treatment has not affected this part of the MnO₂'s discharge curve. The main effect of the heat-treatment has been to shift the high voltage plateau to a lower average potential. This technique clearly shows the differences and similarities in the discharge of the two types of MnO₂'s. The flatness of the Li/MnO₂ discharge between approximately 10 and 40% depth of discharge (DOD) indicates a reaction that is not entirely homogeneous in nature, contrary to previously published descriptions (3, 4).

Figures 3 and 4 show the discharge and DCC analysis curves of NHT MnO₂ under 15, 7.5, and 4 kΩ loads at 35°C. The discharge of HT MnO₂ under 15, 7.5, and 4 kΩ loads at 35°C with their corresponding DCC curves are shown

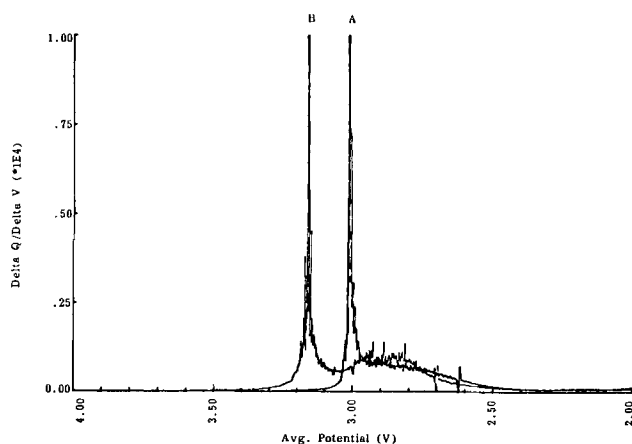


Fig. 2. Differential capacity curves for Li/MnO₂ experimental cells at 35°C under 30 kΩ background load. Cathodes utilize HT MnO₂ (curve A) or NHT MnO₂ (curve B).

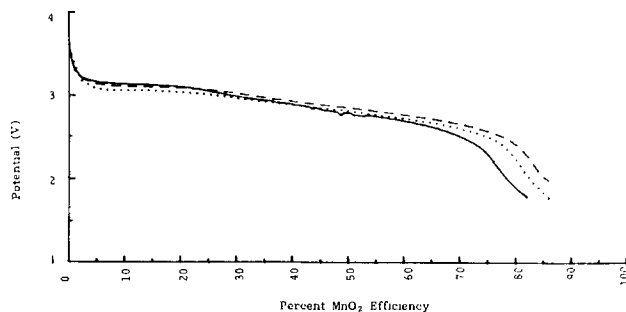


Fig. 3. Discharge curves for Li/MnO₂ (NHT) experimental cells at 35°C under 15 kΩ (solid line), 7.5 kΩ (broken line), or 4.0 kΩ (dotted line) background loads.

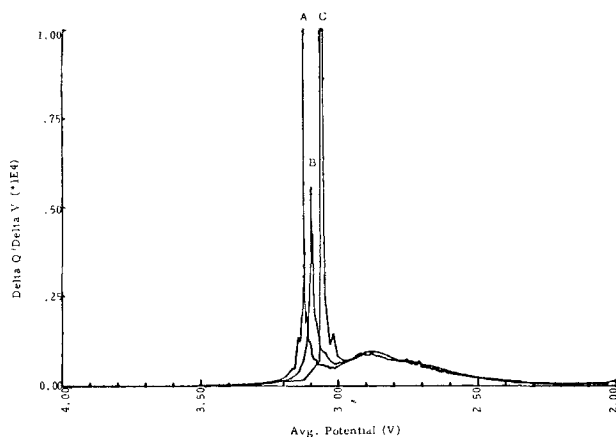


Fig. 4. Differential capacity curves for Li/MnO₂ (NHT) experimental cells at 25°C under 15 kΩ (A), 7.5 kΩ (B), or 4.0 kΩ (C) background loads.

in Fig. 5 and 6, respectively. The DCC analyses (Fig. 4 and 6) show that, as the current density is increased, the sharp peak representing the flat discharge plateau for HT MnO₂ moves to lower and lower potentials, but the second, more washed-out peak remains stationary. The reaction responsible for the voltage plateau is easily polarized as the current density is increased, but still remains very flat, as evidenced by the sharpness of the peaks. The second reaction, while more sloping, can tolerate the increased current density with little or no increased polarization. The same general trend is seen in the DCC analysis of the NHT MnO₂ and is consistent with potential pulse experiments and open-circuit voltage recovery rates.

Another important characteristic of the Li/MnO₂ discharge is the length of the voltage plateau. It appears that the heat-treatment process controls both the discharge potential and length of the voltage plateau. Table I shows the percent capacity delivered to the second inflection point in the discharge curve as calculated from the DCC curves. The percent capacity delivered by the NHT MnO₂ remains relatively constant at 25% until high current den-

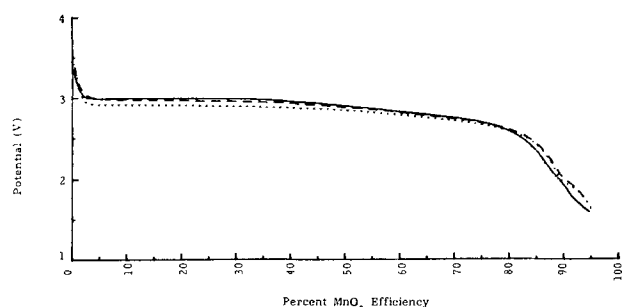


Fig. 5. Discharge curves for Li/MnO₂ (HT) experimental cells at 35°C under 15 kΩ (solid line), 7.5 kΩ (broken line), or 4.0 kΩ (dotted line) background loads.

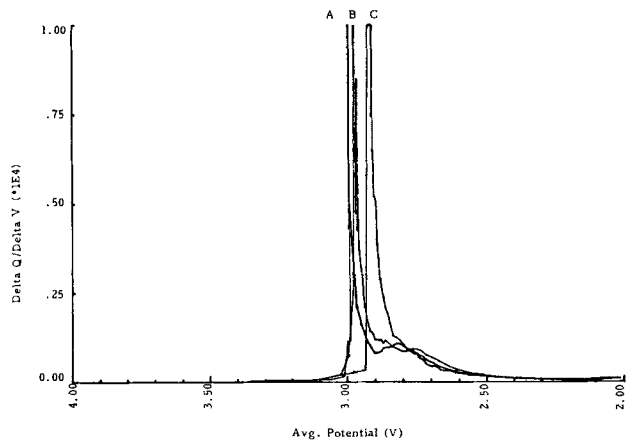


Fig. 6. Differential capacity curves for Li/MnO₂ (HT) experimental cells at 25°C under 15 kΩ (A), 7.5 kΩ (B), or 4.0 Ω (C) background loads.

sities are imposed on the cell. For HT MnO₂, the inflection point at end of flat portion of discharge curve is extended to 40% DOD despite the lower discharge voltage.

Open-circuit voltage.—An important aspect in attempting to establish a discharge mechanism is the equilibrium open-circuit voltage corresponding to various depths of discharge along the discharge curve. In the Li/MnO₂ system, these values cannot be easily obtained by simply removing the load and measuring the open-circuit potentials, since a steady state is attained only after an appreciable length of time. Depending upon the depth of discharge and cell temperature, weeks or even months are required to achieve this steady state. This work represents the first thoroughly equilibrated open-circuit recovery curves for Li/MnO₂ cells at various depths of discharge. Similar work (10, 11) has been done, but it used cells that still had rising OCV's (10 mV/24h), and the EMD was heat-treated for 24h at 350°C. This would produce an MnO₂ with decidedly more beta character. Such differences could have an effect on the discharge and subsequent open-circuit recovery profiles. At selected depths of discharge, CR-2016's discharged at 60°C were taken off load and allowed to reach a steady-state potential. Each open-circuit recovery curve represents an individual cell. Reproducibility between cells discharged to nominally the same DOD was ± 5 mV. Figure 7 shows the first 2000h of open-circuit recovery at room temperature for selected cells. Within the first 200h of open-circuit recovery, all the curves are similar in that they display two different time constants. However, the OCV recovery curves do have different shapes, indicating a different recovery mechanism or structure present during this equilibration period. Even after a period of 2000h, the potentials of the equilibrating CR-2016's are still increasing except for cells discharged past 60% DOD. This is graphically shown in Fig. 8. The open-circuit voltages are plotted at various times in their recovery phase. The most rapid increase in

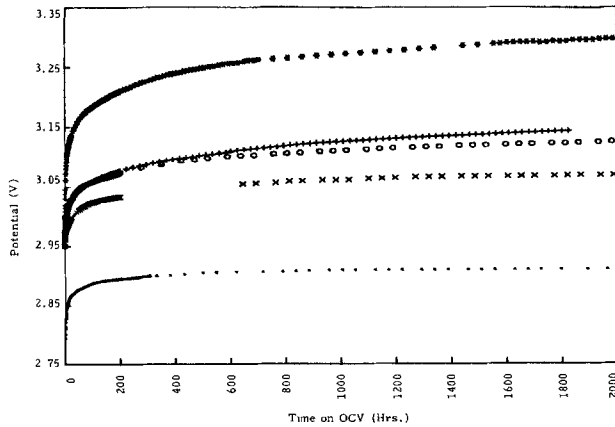


Fig. 7. Long-term, room temperature open-circuit recovery curves for selectively discharged CR2016's: 0.8% (*), 10.1% (+), 25.5% (o), 43.0% (x), and 65.7% (-).

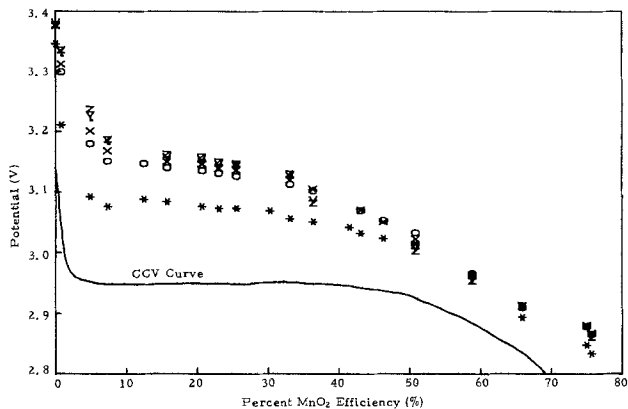
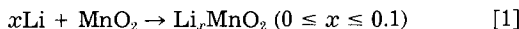
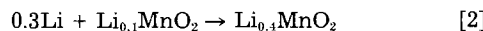


Fig. 8. Comparison of room temperature OCV recovery curves as a function of time on open circuit: 3 weeks (*), 3 months (o), 4 months (x), 5 months (-), 7 months (v), and 8 months (z).

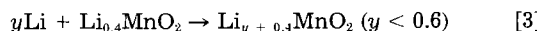
the open-circuit voltages was seen after three months. However, it must be noted that the OCV remained essentially constant after three weeks off load for cells discharged past 70% DOD. Initially, the open-circuit recovery curve was S shaped. However, after approximately eight months, the recovery curve appeared to stabilize. Three distinct regions of recovery became apparent. The first region occurs between 0 and 10% DOD. This sloping recovery profile is indicative of a homogeneous reaction and is most likely the insertion of lithium into the hexagonal close-packed oxygen lattice of the MnO₂ (Eq. [1])



It may also partially reflect contributions of carbon, Teflon, and impurities to the open-circuit voltage. However, a lithium cell with a cathode made solely from the carbon and Teflon used in the MnO₂ cathodes delivered only a negligible capacity at a low current density. The second portion of the MnO₂ discharge occurs between 10 and 40% DOD. This is characterized by the flat open-circuit recovery profile and is representative of a heterogeneous reaction (Eq. [2]).



This indicates the possible occurrence of a two-phase reaction occurring. This can be explained if the MnO₂ is undergoing a slow solid-state transformation as shown by the slow open-circuit recovery. The final discharge region occurs at depths of discharge greater than 40% and might involve the homogeneous insertion of lithium ions into a new structure (Eq. [3])



This new structure and new grain boundaries formed during the solid-state transformation, reaction [2], now al-

Table I. Li/MnO₂ inflection point position as a function of discharge rate

Li/MnO ₂ (Nonheat-treated) 35°C	
Rate (mA/cm ²)	MnO ₂ efficiency (%)
0.05	25
0.10	25
0.20	24
0.375	22
0.75	18
Li/MnO ₂ (Heat-treated) 35°C	
Rate (mA/cm ²)	MnO ₂ efficiency (%)
0.05	40
0.10	40
0.20	40
0.375	39
0.75	18

Table II. CR2016 open-circuit voltages as a function of temperature

MnO ₂ efficiency (%) ^b	Open-circuit voltage ^a								ΔV
	60°C	50°C	40°C	30°C	20°C	10°C	0°C	-10°C	
0.1	3.350	3.353	3.356	3.359	3.362	3.366	3.369	3.371	0.021
1.8	3.300	3.302	3.305	3.307	3.309	3.311	3.313	3.315	0.015
5.1	3.264	3.268	3.269	3.271	3.274	3.278	3.281	3.286	0.024
7.4	3.249	3.251	3.253	3.254	3.257	3.261	3.265	3.270	0.021
23.4	3.226	3.229	3.229	3.228	3.228	3.228	3.229	3.230	0.004
33.7	3.196	3.199	3.198	3.196	3.195	3.195	3.195	3.195	0.003
44.3	3.077	3.078	3.079	3.078	3.078	3.078	3.078	3.079	0.002
51.9	3.006	3.007	3.007	3.006	3.006	3.007	3.007	3.007	0.001
62.1	2.966	2.967	2.967	2.967	2.966	2.966	2.967	2.967	0.001
73.8	2.930	2.931	2.932	2.931	2.931	2.931	2.931	2.932	0.002

^a 24h at temperature prior to reading.

^b Cells on open circuit minimum two months.

lows for the more rapid movement of lithium ions and thus a faster open-circuit recovery is realized for cells discharged past approximately 60% DOD. It was found that the partially discharged MnO₂'s were air and water sensitive. This led to poor and somewhat confusing x-ray diffraction patterns.

A series of CR-2016's were also discharged at 60°C. At various points in the discharge, the cells were taken off load and their recovery closely monitored and recorded. Figure 9 compares the OCV recovery curves for equally discharged cells at 25° and 60°C. The two sets of recovery curves display the same general shape, but the 60°C curves have shorter time constants. Comparisons of the recovery voltages at three weeks for both temperature regimes and seven months at 25°C are made in Fig. 10. Cells discharged past approximately 50% DOD have very similar open-circuit voltages, while cells discharged to less than 50% DOD have very different recovery potentials. The latter part of the Li/MnO₂ discharge appears to be temperature insensitive during open-circuit recovery, while recovery in the early part of the discharge is quite temperature dependent. The differences in recovery voltages at the two different temperatures most likely reflect kinetic rather than temperature effects since the recovery voltages at a selected depth of discharge (Table II) do not significantly differ as a function of temperature. A similar phenomenon was seen in the DCC analysis. The peak centered at 2.9V did not change after heat-treatment of the MnO₂. This again suggests two or more different recovery processes or structures present. Figure 10 shows that three weeks' recovery at 60°C is comparable to seven months' recovery at 25°C. It has revealed that recovery at 60°C can provide a rapid way to equilibrate Li/MnO₂ cells for further study.

Another method to determine if there has been a change in the reaction mechanism during the discharge of the Li/MnO₂ couple is to monitor the change in the system's entropy as a function of depth of discharge. CR-2016's that had been previously discharged to varying degrees and been on open circuit at 60°C for a minimum of two months were cycled in temperature from 60° to -10°C and back. The new open-circuit voltage was recorded for every 10°C change in temperature (Table II). From the slope of the curves generated from these data and the open-circuit voltages, a series of thermodynamic values were calculated (Table III) and plotted as a function of depth of discharge (Fig. 11). The calculated entropies compare favorably with similar data ranging from -28.9 to -13.3 J/mol-K generated for another insertion-type compound, Li_xV₆O₁₃ (11). The abrupt change in the calculated entropies from an average -26.9 to -1.6 J/mol-K after 7.4% DOD suggests that a process change has occurred in the system, which would not be expected for a single-insertion-type mechanism.

Consideration has also been given (4) to the possibility that EMD would be suitable for use in nonaqueous secondary batteries owing to its insertion-type mechanism. However, the solid-state transformation apparent in this work may preclude EMD's use in such a cell system.

Table III. CR-2016 thermodynamic data

MnO ₂ efficiency (%)	ΔG (kcal)	ΔS (e.u.)	ΔH (kcal)
0.1	-77.4	-7.1	-79.5
1.8	-76.2	-5.0	-77.7
5.1	-75.4	-6.8	-77.4
7.4	-75.0	-6.7	-77.0
23.4	-74.3	-0.7	-74.5
33.7	-73.6	-1.0	-73.9
44.3	-70.9	-0.3	-71.0
51.9	-69.2	-0.2	-69.3
62.1	-68.3	-0.1	-68.3
73.8	-67.5	-0.3	-67.6

Other investigators (13, 14) report that discharged Li/MnO₂ exhibits poor cycling for DOD's as low as 25%.

Conclusions

From the results of long-term open-circuit recovery data, differential capacity analysis, and electrochemical discharge, the cathodic reduction process in Li/MnO₂ nonaqueous cells is dependent on the structure and composition of the MnO₂. These two factors establish three distinct stages in the discharge profile. The overall process apparently involves a change in the MnO₂'s structure during discharge. The initial stage of the MnO₂'s reduction occurs within approximately the first 10% of discharge. Insertion of lithium ions into the lattice of MnO₂ forming Li_xMnO₂ (0 ≤ x ≤ 0.1) is proposed for this stage. It is a homogeneous reaction, as evidenced by the sloping nature of the discharge and recovery curves. The next stage in the discharge is consistent with a heterogeneous or two-phase reaction. This occurs between approximately 10 and 40% depth of discharge. It is distinguished by the flat portion of the open-circuit and discharge curves. This may involve a slow, solid-state transforma-

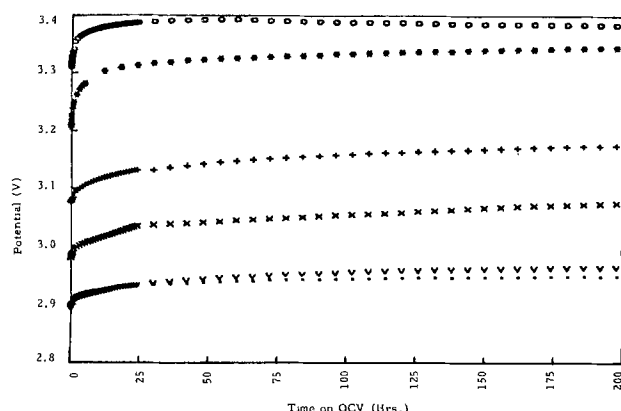


Fig. 9. Comparison of open-circuit recovery curves for selectively discharged CR2016's: 0.1% at 25°C (*), 60°C (o), 25.2% at 25°C (x), 60°C (+), 58.7% at 25°C (v) and 62.1% at 60°C (·).

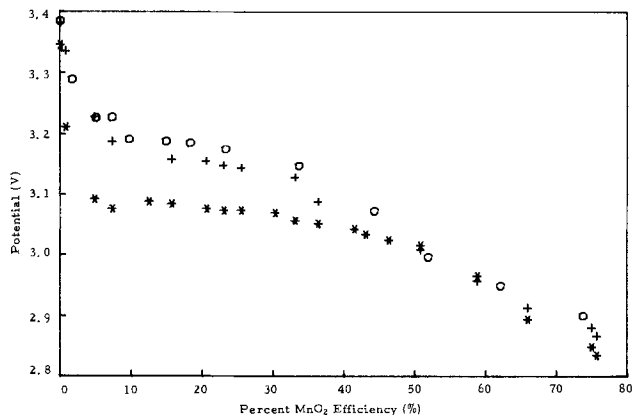


Fig. 10. Open-circuit recovery voltages as a function of percentage of MnO₂ utilization, temperature, and time on open circuit: 3 weeks at 25°C (*), 3 weeks at 60°C (o), and 7 months at 25°C (+).

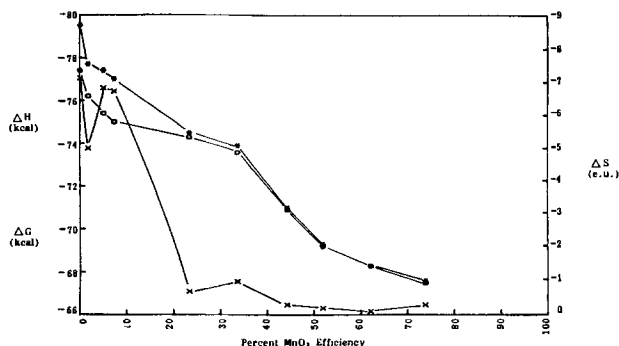


Fig. 11. CR2016 thermodynamic data as a function of percentage of MnO₂ utilization: ΔH (*), ΔG (o), ΔS (x).

tion or structural change in the MnO₂ from its initial hexagonal close-packed configuration to a cubic close-packed structure characteristic of the LiMnO₂ reaction product. This slow structural change would be responsible for the slow open-circuit recovery curves typical of

Li/MnO₂ cells discharged in this region. The final discharge regime is again characteristic of a homogeneous reaction and may involve insertion of lithium ions into the new structural form of Li_xMnO₂ ($x > 0.4$).

Acknowledgments

The author would like to thank Dr. George E. Blomgren and Dr. Richard L. Middaugh for a number of suggestions that were useful in the interpretation of the results.

Manuscript submitted Dec. 19, 1984; revised manuscript received ca. April 22, 1985. This was Paper 75 presented at the New Orleans, Louisiana, Meeting of the Society, Oct. 7-12, 1984.

Union Carbide Corporation assisted in meeting the publication costs of this article.

REFERENCES

1. H. Ikeda, T. Saito, and H. Tamura, in "1st International Symposium on Manganese Dioxide", Cleveland, Ohio, 1975, p. 384.
2. H. Ikeda, M. Hara, and S. Narukawa, in "Proceedings of the 28th Power Sources Symposium," Atlantic City, NJ, June 12-15, 1978, The Electrochemical Society, Inc., p. 210 (1979).
3. H. Ikeda and S. Narukawa, in "Lithium Nonaqueous Battery Electrochemistry," E. B. Yeager, B. Schumm, Jr., G. Blomgren, D. R. Blankenship, V. Leger, and J. Akridge, Editors, p. 110, The Electrochemical Society Softbound Proceedings Series, Princeton, NJ (1980).
4. H. Ikeda and S. Narukawa, *J. Power Sources*, **9**, 329 (1983).
5. H. Ikeda, U.S. Pat. 4,133,856 (1979).
6. V. Leger, U.S. Pat. 4,419,423 (1983).
7. L. Balewski and J. Brenet, *Electrochem. Technol.*, **5**, 517 (1967).
8. J. Nardi, C. Hussey, J. Erbacher, and L. King, FJSRL Technical Report 77-0002, USAF Academy, Colorado Springs, CO (1977).
9. A. Thompson, *This Journal*, **126**, 608 (1979).
10. M. Voinov, *ibid.*, **128**, 1822 (1981).
11. M. Voinov, *Electrochim. Acta*, **26**, 1373 (1981).
12. B.C.H. Steele, *Solid State Ionics*, **9**, 391 (1983).
13. G. Pistoia, *This Journal*, **129**, 1861 (1982).
14. G. Pistoia, *J. Power Sources*, **9**, 307 (1983).

Microscopic Ellipsometric Observation of the Change in Passive Film on 18Cr-8Ni Stainless Steel with the Initiation and Growth of Pit

Katsuhisa Sugimoto,* Shiro Matsuda, Yoshiaki Ogiwara, and Koza Kitamura

Department of Metallurgy, Faculty of Engineering, Tohoku University, Sendai 980, Japan

ABSTRACT

Changes in passive films on 18Cr-8Ni stainless steel with the initiation and growth of pit have been measured in 1 kmol · m⁻³ NaCl using a microscopic ellipsometer which provides a maximum magnification of ca. 600 times. The spatial distribution of film thickness within each grain was observed on the steel before pit initiation. The first pit initiated at a site where there was a small difference of 0.2-0.5 nm in the film thickness. With the growth of the first pit, film thinning first occurred around the pit, and then film thickening started beneath the pit. The second pit broke out on the boundary between the film thinned area and the original film thickness preserved area.

Ellipsometry is one of the promising methods for examining *in situ* the change in films on passivated metals and alloys with the introduction of Cl⁻ ions, which leads to the initiation of pitting. For example, using this method, McBee and Kruger (1, 2) have demonstrated that significant changes occur in the optical properties of the passive film on iron upon introduction of chloride.

* Electrochemical Society Active Member.

Matsuda *et al.* (3) also have reported the changes in the thickness and optical constant of the passive film on commercial 18Cr-8Ni stainless steel as a function of potential in NaCl solution and of the lapse of time after the introduction of Cl⁻ ions into Na₂SO₄ solution. It is impossible, however, to observe a microscopically localized change in the film by conventional ellipsometry which measures an area of more than tens of square millimeters on a specimen.

In order to overcome this limitation of ellipsometry, Sugimoto and Matsuda (4) have developed a microscopic ellipsometer which provides the determination of the thickness and optical constant of a thin film on an area of ca. 10 μm diam. This ellipsometer was first applied to the measurement of passive films on α and γ grains of 22Cr-10Ni austeno-ferritic stainless steel. The results showed that significant differences in film thickness exist between α and γ grains and the film thickness varies even among grains of the same phase (4).

The purpose of the present investigation is to examine the distribution of thickness of the passive film on a microstructure of solution-treated 18Cr-8Ni stainless steel, to reveal the change in this distribution with the initiation and growth of a pit, and to observe the effect of this change on the inducement of a successive pit. To accomplish these objectives, the spatial distributions of film thickness on the steel have been measured by the microscopic ellipsometer before and after pit initiation in NaCl solution.

Experimental

Microscopic ellipsometry.—The same microscopic ellipsometer as that reported in our previous paper (4) was used in the present study. The characteristic of this ellipsometer is that it is equipped with two groups of lenses behind the analyzer for magnifying the polarized reflection image of specimen, in addition to a common polarizer-compensator-sample-analyzer configuration. This combination of lenses can provide a maximum magnification of ca. 600 times and makes it possible to measure a region of ca. 10 μm diam on the specimen surface.

Monochromatic light of wavelength 546.1 nm was used for all measurements. The angle of incidence of the monochromatic light was 59.65°, except for measurements using the technique of multiple-angle-of-incidence ellipsometry. The compensator was fixed at an angle of -45°. Two optical parameters, the relative phase retardation Δ and the relative amplitude reduction Ψ , were obtained from the extinction angles of the polarizer P and the analyzer A for a desired position in the microstructure of specimen. An area of ca. 25 \times 50 μm was subjected to a single determination of Δ and Ψ in the present experiment. The determination of Δ and Ψ was performed every 50 μm in a horizontal direction and also every 25 μm in a vertical direction using a point-by-point scanning technique.

Cell.—A Pyrex glass cell with two optical windows was used. It was also equipped for electrochemical measurements.

Specimen.—A cold-rolled sheet 2 mm thick of high purity 18Cr-8Ni stainless steel with chemical composition given in Table I was used. Coupons 12 \times 28 mm were cut from the sheet, heated at 1050°C under vacuum for 1h, and then water quenched. The surfaces of all the specimens were ground with emery paper up to no. 1500, finished with diamond paste, and degreased in ultrasonic baths of acetone and ethyl alcohol. The degreased specimen was electrochemically etched in 10 weight percent (w/o) oxalic acid to reveal crystallographic microstructure. The area for the measurement of the spatial distribution of film thickness, ca. 500 \times 700 μm , were marked by a Micro-Vickers hardness tester. Then, the etch structure on the surface was erased by polishing slightly with diamond paste. After degreasing again in ultrasonic baths, the specimen was covered by a clear vinyl chloride coating except for the marked area.

Solutions.—In most electrochemical experiments, 1 kmol \cdot m⁻³ NaCl adjusted to pH 6.0 was used. Deaeration was achieved by bubbling purified N₂ through the solution for 4h. All experiments were

carried out in a N₂ atmosphere at 20° \pm 0.5°C under stationary condition.

Electrochemical polarization.—The passivation and pitting of the specimens were accomplished under potentiostatic control. Electrode surfaces of the specimens were set vertically. After keeping a specimen at a given potential for a given time, ellipsometric parameters of the specimen surface were measured. A saturated calomel electrode was used as the reference electrode, and the potentials reported here are referred to this base.

Processing of ellipsometric data.—Drude's exact optical equations were used in the calculation of theoretical Δ vs. Ψ curves for the growth of passive films with given optical constants and also in the determination of thicknesses and optical constants of passive films with multiple-angle-of-incidence ellipsometry. In these calculations, 1.342 for the refractive index of 1 kmol \cdot m⁻³ NaCl and 2.67 - 4.03i for the complex refractive index of the matrix of 18Cr-8Ni stainless steel (5) were used.

Easy method for the determination of film thickness.—In the case of the measurement of a specimen surface before the initiation of pitting, an easy method was employed in order to reduce the time required for the measurement. That is, the change in the angle of P at an extinction condition was only followed at a fixed angle of A.

Figure 1 shows calculated P vs. A, or Δ vs. Ψ , plots for the growth of passive films with varying optical constants of N₂ = n₂ - k₂i, where 2.4 \leq n₂ \leq 2.6 and 0.4 \leq k₂ \leq 0.6, on 18Cr-8Ni stainless steel in 1 kmol \cdot m⁻³ NaCl. The value N₂ = 2.5 - 0.5i has been reported as the optical constant for a passive film on 18Cr-8Ni stainless steel in 1 kmol \cdot m⁻³ Na₂SO₄ (5). As will be mentioned in "Change in film thickness with pit growth" section, almost the same value has been obtained for the passive film before pit initiation in 1 kmol \cdot m⁻³ NaCl in the present study. It can be seen from the figure that the change in A, or Ψ , at a given optical constant N₂ with a unit change in film thickness d is much smaller than that in P, or Δ . The change in P, or Δ , at a given film thickness with changes in n₂ and k₂ is also small. This substantiates the propriety of making use of the easy method.

Relations between d and P for films with three different optical constants around N₂ = 2.5 - 0.5i are derived from Fig. 1 and given in Fig. 2. Linear relations can be seen at least for the films having thicknesses of less than 5.0 nm. Errors in the determination of film thickness due to deviations in n₂ and k₂ such as N₂ = (2.5 \pm 0.1) - (0.5 \pm 0.1)i can be estimated, for example, as \pm 2.5% at d = 2.0 nm, \pm 3.3% at d = 3.0 nm, and \pm 3.6% at d = 5.0 nm.

Multiple-angle-of-incidence ellipsometry.—In the measurement of specimen surface after the initiation of

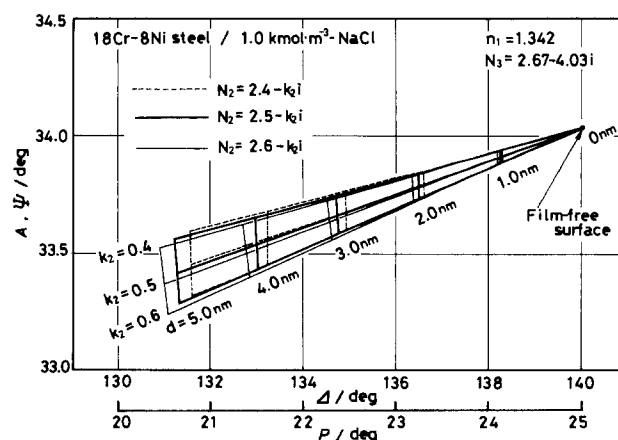


Fig. 1. Calculated P vs. A, or Δ vs. Ψ , plots for the growth of passive films having optical constants N₂ = n₂ - k₂i in the ranges 2.4 \leq n₂ \leq 2.6 and 0.4 \leq k₂ \leq 0.6.

Table I. Composition of 18Cr-8Ni stainless steel (w/o)

Cr	Ni	Mn	C	Si	Mo	Cu	S	Fe
18.8	8.92	0.0017	0.0014	0.026	0.0018	0.0017	0.0083	Balance

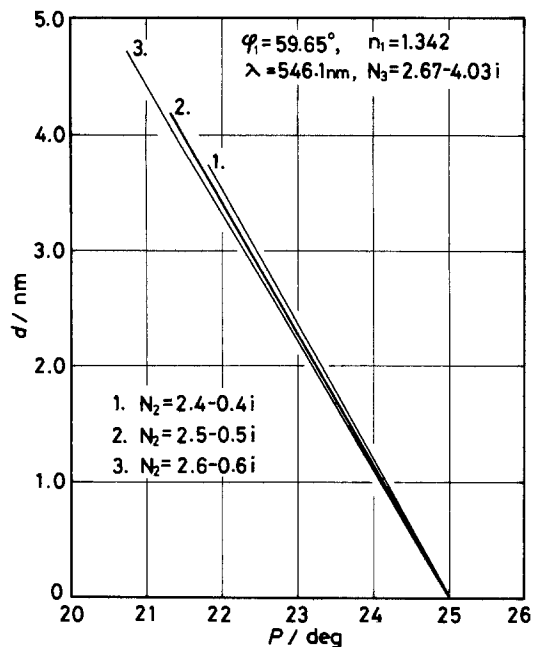


Fig. 2. Relations between d and P for films having three different optical constants.

pitting, multiple-angle-of-incidence ellipsometry (6, 7) was used together with the easy method. First, the optical change in a given area was measured by the easy method and an approximate spatial distribution map of film thickness over the area was immediately made. Then, in order to determine one consistent value of the optical constant in association with compatible value of film thickness, measurements by multiple-angle-of-incidence ellipsometry were performed at several points within each area where a characteristic change in the film thickness was recognized in the map. Three incident angles 50.00° , 55.00° , and 59.65° were used. In the estimation of the most reasonable values of optical constants and thicknesses of films, a computer program, similar to the one used by Johnson and Bashara (7), in which the sum of squares of the residuals was minimized, was employed.

Results and Discussion

Spatial distribution of film thickness before pit initiation.—Figures 3a, 3b, and 3c show the microstructure of an 18Cr-8Ni stainless steel specimen, the spatial distribution of film thickness on the microstructure, and the detailed distribution of film thickness around the site at which the first pit initiated, respectively. The specimen was passivated in $1 \text{ kmol} \cdot \text{m}^{-3}$ NaCl at 0.3V for 5h. No pitting occurred at this potential. After the passivation, $4.44 \text{ kmol} \cdot \text{m}^{-3}$ NaCl was added to the solution in order to start pitting. The site at which the first pit occurred is indicated by a dotted circle in the figures.

As shown in Fig. 3b, the film thickness varies from place to place in the small area of $500 \times 500 \mu\text{m}$ on the specimen. By overlapping Fig. 3a and 3b, the distribution of film thickness within each grain can be seen. Furthermore, we notice that the configuration of the electrode affects the distribution of film thickness; namely, the film on the lower part of electrode, which corresponds to the lower part of Fig. 3b, is slightly thicker than that on the upper part. Concerning the relationship between the distribution of film thickness and the preferable site for pit initiation, as seen from Fig. 3c, it has been frequently experienced that the place where there was a small difference of 0.2-0.5 nm in film thickness tended to offer the site for pit initiation.

Change in film thickness with pit growth.—Pitting was performed in $1 \text{ kmol} \cdot \text{m}^{-3}$ NaCl at 0.8V for a given period after preliminary passivation at 0.3V for 3h. In this solution, the pitting potential obtained with the scanning rate

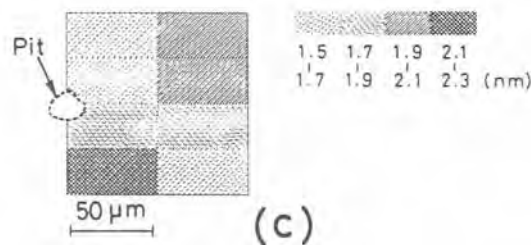
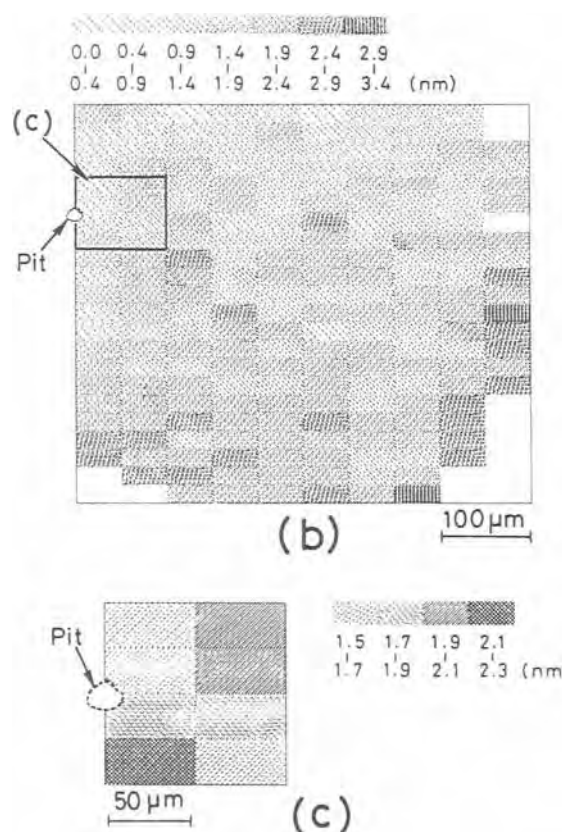
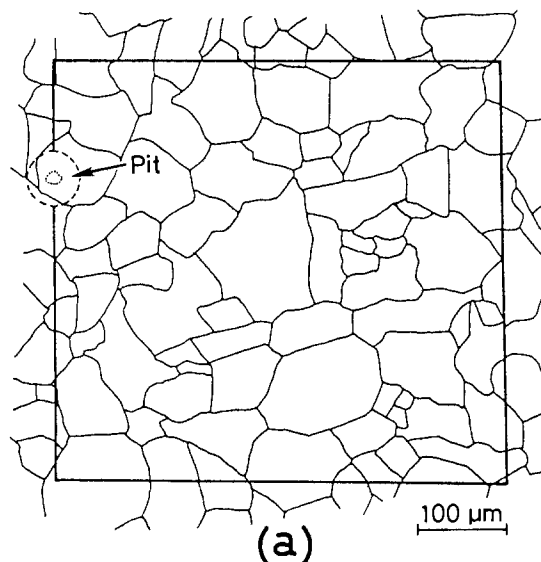


Fig. 3. Microstructure (a), the spatial distribution of film thickness on the microstructure (b), and the detail of the distribution around the initiation site of the first pit (c) on 18Cr-8Ni stainless steel passivated in $1 \text{ kmol} \cdot \text{m}^{-3}$ NaCl at 0.3V for 5h.

of $22 \text{ mV} \cdot \text{min}^{-1}$ was 0.55V . In most cases, pitting started after an average induction time of 230s at 0.8V. Figure 4 shows the increase in film thickness with lapse of time at 0.8V; a film *ca.* 2.6 nm thick is formed before the start of pitting.

After growing the first single pit for given periods the polarization current was stopped and the distribution of film thickness was measured at the corrosion potential of *ca.* -0.01V . The ellipsometric measurement by the easy method at the angle of incidence of 59.65° was first performed over the area of *ca.* $400 \times \text{ca. } 400 \mu\text{m}$ around the pit. On the basis of the result of this measurement, a map showing the approximate spatial distribution of film thickness was made assuming the optical constant of films over the area as $N_2 = 2.5 - 0.5i$. Three characteristic areas—that is, a film thickened area, a film thinned area, and an original film thickness preserved area—were rec-

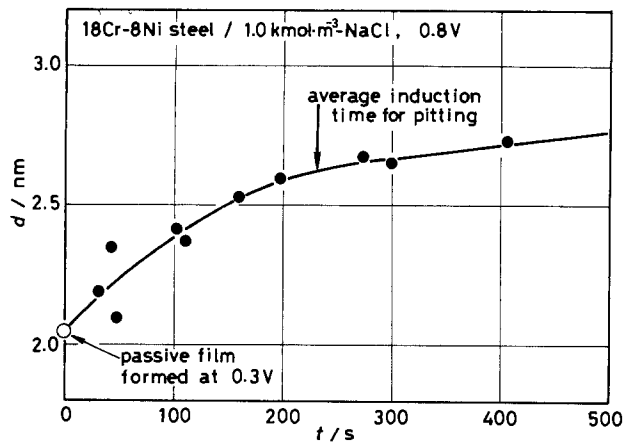


Fig. 4. Relation between d and t for 18Cr-8Ni stainless steel in $1 \text{ kmol} \cdot \text{m}^{-3} \text{ NaCl}$ at 0.8V .

ognized on the map. Then, in order to determine precisely the optical constants and thicknesses of films, the multiple-angles-of-incidence ellipsometry was applied on these areas. From this analysis, it was found that each area has its own optical constant: $N_2 = 2.53 - 0.48i$ for the original film preserved area, $N_2 = 2.32 - 0.27i$ for the film thinned area, and $N_2 = 1.65 - 0.00i$ for the film thickened area. Figure 5 shows d vs. P (or Δ) relations calculated using these optical constants. These relations were used to get the exact spatial distributions of film thickness on the areas.

Figures 6a, 6b, and 6c show the spatial distributions of film thickness around pits grown for 3, 6, and 12s, respectively. The figures on the left-hand side are maps and those on the right-hand side are the bird's-eye views of the distributions.

In the early stage of the growth of a pit, film thinning occurred around a pit (Fig. 6a). Then, after several seconds, film thickening started below the pit in a downward direction, accompanying the area of film thinning (Fig. 6b). With further growth of pit, both the areas of film thinning and film thickening expanded and the distribution of film thickness with high hills and deep valleys was accomplished around the pit (Fig. 6c).

It is thought that the film thinning is due to etching by a low pH solution which is discharged from the inside of

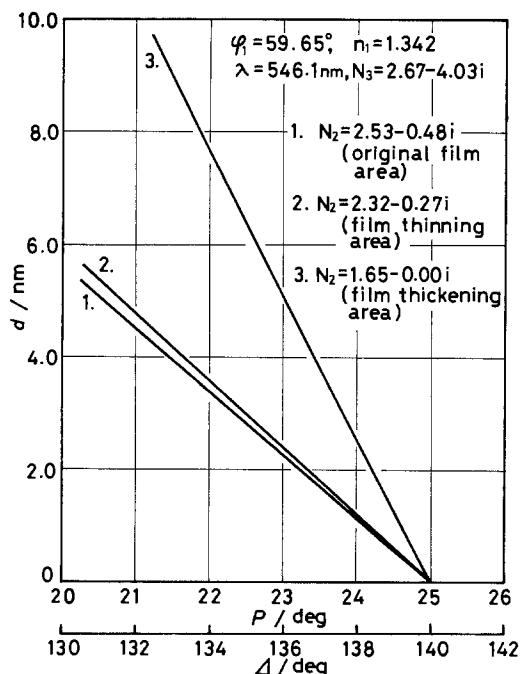


Fig. 5. Relations between d and P , or Δ , for films on three characteristic areas formed around the first pit.

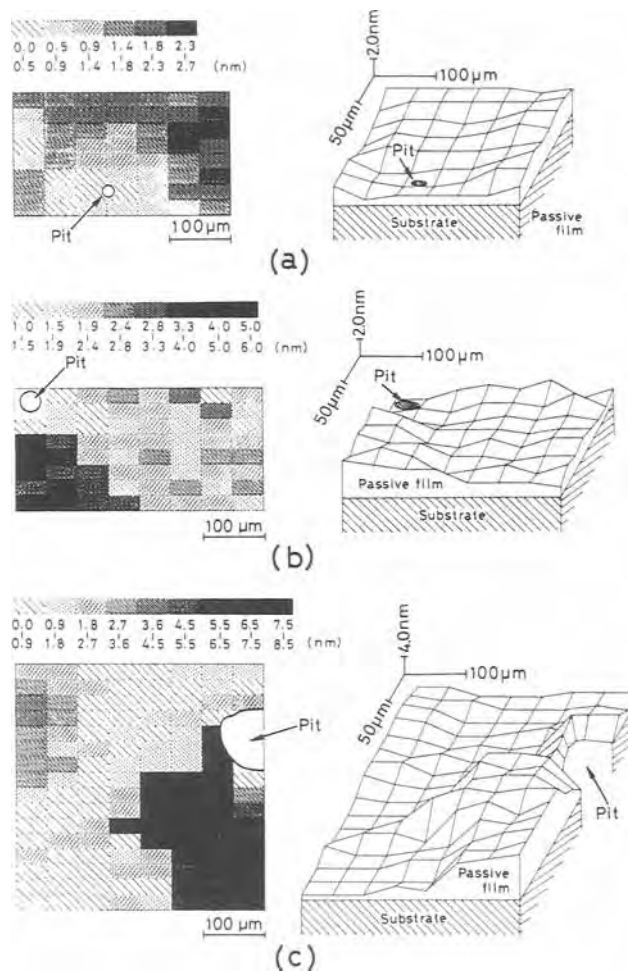


Fig. 6. Spatial distributions (left) and their bird's-eye views (right) of film thickness around pits grown for 3 (a), 6 (b), and 12s (c), respectively, on 18Cr-8Ni stainless steel in $1 \text{ kmol} \cdot \text{m}^{-3} \text{ NaCl}$ at 0.8V .

a growing pit. Suzuki *et al.* (8) have reported that the pH of solutions within active pits of Type 304L is lowered to 0.60-0.80. The film thickening below the pit should be mainly due to the deposition of iron hydroxide by the hydrolysis of Fe^{2+} ions contained in the solution from the inside of pit. The low refractive index value of 1.65 and the value of zero of extinction coefficient of the optical constant for the film on the film thickened area suggest the existence of hydroxide (5). An increase in film thickness around a pit has been reported by Kodama (9, 10) in the case of pitting of iron in a borate-buffer solution containing SO_4^{2-} ions.

Effect of changes in passive film caused by first pit on initiation of second pit.—Figures 7a, 7b, and 7c show the optical micrograph of the first and the second pits, the spatial distribution of film thickness around the first pit and the initiation site of the second pit, and the bird's-eye view of the distribution, respectively. The first pit was grown in $1 \text{ kmol} \cdot \text{m}^{-3} \text{ NaCl}$ at 0.8V for 25s, and then polarization current was stopped. After the measurement of the distribution of film thickness around the first pit, the potential was again set at 0.8V and the second pit was introduced and grown for 3s.

In Fig. 7b, the area of film thinning can be seen above the level of the lower edge of the first pit and the area in the shape of an inverted triangle of film thickening below the level. On both the sides of the inverted triangle area are areas in which the original film thickness is preserved without the effect of the first pit. The second pit occurred on the boundary between the area of film thinning and the area of original film thickness. The difference of ca. 0.5 nm in the film thickness was on this boundary. This result again shows the tendency of pit ini-

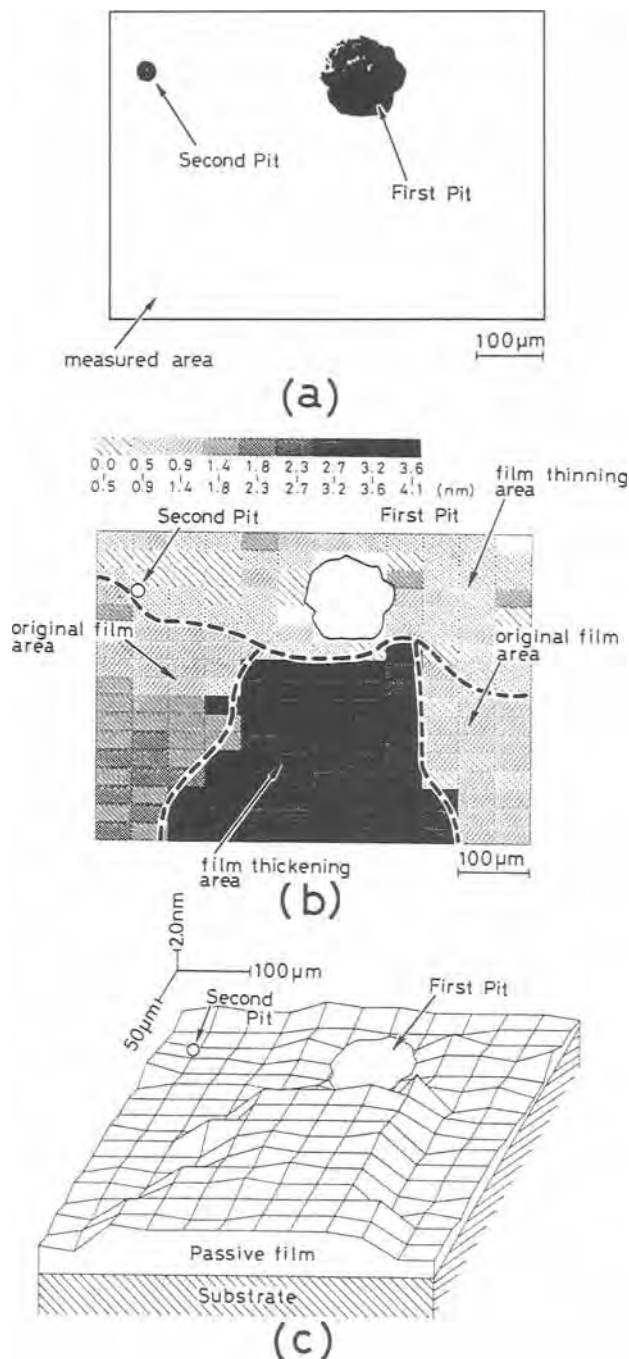


Fig. 7. Optical micrograph of the first and the second pits (a), the spatial distribution of film thickness around the first pit (b), and the bird's-eye view of the distribution (c) on 18Cr-8Ni stainless steel pitted in $1 \text{ kmol} \cdot \text{m}^{-3} \text{ NaCl}$ at 0.8V .

tiation at the place where there is a slight difference in the film thickness.

Although the reason why the second pit initiates preferentially on such a boundary is not clear at present, it is possible to assume that microcracks leading to the nucleation of pits arise on the boundary. That is, stress caused by differences in the volume, chemical composition, hydration, electrostriction pressure, and interfacial tension of films could act concentrically on the boundary and cause the mechanical breakdown of films there. The adsorption of Cl^- ions on the films is reported by Sato (11) to decrease the critical breakdown stress. This should be accelerated by higher chloride concentration caused by discharge from the first pit (8). This atmosphere should accelerate the initiation of pit nuclei at the microcracks thus formed on the boundary in question.

Conclusion

1. There is a spatial distribution of film thickness within each grain of 18Cr-8Ni stainless steel.
2. The first pit tends to occur at the place where there is a small difference of 0.2-0.5 nm in film thickness.
3. With the growth of the first pit, an area of film thinning is first formed around the pit and then an area of film thickening below the pit.
4. The second pit tends to occur on the boundary between the film thinned area and the original film thickness preserved area.

Manuscript submitted Dec. 26, 1984; revised manuscript received April 19, 1985. This was Paper 235 presented at the New Orleans, Louisiana, Meeting of the Society, Oct. 7-12, 1984.

Tohoku University assisted in meeting the publication costs of this article.

REFERENCES

1. C. L. McBee and J. Kruger, *Nature (London)*, **230**, 194 (1971).
2. C. L. McBee and J. Kruger, in "Localized Corrosion," R. W. Staehle, B. F. Brown, J. Kruger, and A. Agrawal, Editors, p. 252, NACE, Houston (1974).
3. S. Matsuda, K. Sugimoto, and Y. Sawada, in "Passivity of Metals," R. P. Frankenthal and J. Kruger, Editors, p. 699, The Electrochemical Society Corrosion Monographs Series, Princeton, NJ (1978).
4. K. Sugimoto and S. Matsuda, *This Journal*, **130**, 2323 (1983).
5. S. Matsuda, K. Sugimoto, and Y. Sawada, *J. Jpn. Inst. Met.*, **39**, 848 (1975), *Trans. Jpn. Inst. Met.*, **18**, 66 (1977).
6. J. Shewchun and E. C. Rowe, *J. Appl. Phys.*, **41**, 4128 (1970).
7. J. A. Johnson and N. M. Bashara, *J. Opt. Soc. Am.*, **61**, 457 (1971).
8. T. Suzuki, M. Yamabe, and Y. Kitamura, *Corrosion*, **29**, 18 (1973).
9. T. Kodama, *Corros. Eng. (Boshoku Gijutsu)*, **23**, 5 (1974).
10. T. Kodama, *Denki Kagaku*, **42**, 344 (1974).
11. N. Sato, *Electrochim. Acta*, **16**, 1683 (1971).

Stochastic Models of Pitting Corrosion of Stainless Steels

I. Modeling of the Initiation and Growth of Pits at Constant Potential

D. E. Williams,* C. Westcott, and M. Fleischmann*

AERE Harwell, Materials Development Division, Oxon, England OX11 0RA

ABSTRACT

A stochastic model for pit initiation is developed, involving as parameters an initiation frequency for pit nuclei, a death probability for unstable pits, and a critical age which defines the transition between a stable and an unstable pit. Emphasis is placed on validating methods for data analysis to recover the parameters of the model from observed current-time series. Such methods are developed and tested using data generated by computer simulation of the process. The expected induction time for stable pit initiation is derived. Results for the statistics of ensembles of current-time transients are given. Methods of analysis of the spectral power density of the current, taking into account the nonstationary process of stable pit propagation, are considered.

Localized corrosion processes of metals such as stainless steels in aqueous environments (1) are interesting and unusual because most of the material is in fact not corroding; it is passive and stable. In general, localized corrosion processes — pitting corrosion, crevice corrosion, stress corrosion cracking, corrosion fatigue, intergranular corrosion — are unpredictable as regards the time of initiation and often also as regards the place of attack. Indeed, localized corrosion is properly considered as a rare event, and a statistical treatment is appropriate for its description (2). Such a treatment is presented in this and the following papers (3, 4). Although the work is concerned with the pitting corrosion of stainless steels in dilute aqueous solutions of sodium chloride, it is believed that the stochastic model developed from the results is of general application. Preliminary reports of the work have appeared elsewhere (5, 6).

Several different mechanisms for the initiation of pitting corrosion have been proposed. These have been reviewed recently (7-9). It is agreed that corrosion pits propagate as a result of the development and maintenance of an elevated local acidity. As far as the nucleation of pits is concerned, authors have variously emphasized, among other phenomena, inhomogeneity in the metal, cracking and slow healing of the passive film (8, 9), development of critical acidity levels in microscopic flaws (7), defect transport in passive films (10), and chloride adsorption or incorporation into localized areas of passive film (11, 12), including the idea of adsorption of a number of halide ions into a "transitional complex" (12) or of local thinning of the oxide under chloride "islands" (13). Local acidification (14) has been related to local adsorption of chloride (15).

Recent literature has been concerned with the definition of critical potentials for pit initiation and repassivation. Simple cyclic polarization experiments to measure these parameters can be determined by the formation of only one pit on the surface of the test specimen, so it is not surprising that the resulting data can be extremely variable. Despite this, relationships have been given for the chloride-concentration dependence of pitting potentials obtained in such an experiment (7-9).

A further feature of pitting corrosion of stainless steels is the observation of an induction time, τ , before pit initiation (12, 15), either following potential change from the inert into the pitting range in a halide solution, or upon the addition of halide into an inert solution. Hoar and Jacob (12), using the second approach, in which the specimen was prepassivated in a slowly flowing solution, with subsequent addition of halide ions, showed that the induction time for initiation of stable pitting on 18Cr 8Ni stainless steel varied as $[X^-]^n$ with $2.5 < n < 4.5$ for $X = Cl^-$ and $4 < n < 4.5$ for $X = Br^-$; the exponent n was different at different electrode potentials E , but did not show an obvious systematic variation with E . It was also shown that the induction time has a very strong temperature de-

pendence and an electrode potential dependence of 250-450 mV/decade for chloride solutions and 30-70 mV/decade for bromide solution.

It has been noted above, however, that localized corrosion is properly considered as a rare event, so that statistical treatments are appropriate for its description (2). A consequence of these rare events is the generation of current fluctuations at constant potential (3, 5, 6, 15, 17), and these fluctuations during the induction period make a definite induction time difficult to define experimentally. Shibata and Takeyama (18, 19) determined τ as the time for the current to exceed an arbitrarily determined (and rather high) value. The induction time thus defined is a statistical variable; the survival probability for steel specimens determined as a function of time showed a Poisson distribution with a potential-dependent nucleation rate. It is evident that the values of the derived parameters must depend on the current level chosen.

More generally, pitting corrosion must be described by potential-dependent and chloride-concentration-dependent pitting probabilities and the values of parameters such as the "critical potential" depend on the threshold values of the probability chosen for the description (20) (as well as on other probabilities such as that of repassivation). One objective of our work is to take some steps towards a more rigorous definition of the parameters of a stochastic model so that the potential and concentration dependences can be modeled. Another objective is to define and validate methods of data analysis for obtaining such parameters from experimental data with some degree of confidence. We shall show that this is not straightforward. The application and limitation of each method needs to be carefully considered, particularly when experimental data are being treated and one wishes to make a distinction between the inadequacies of the model being tested and the inadequacies of the data processing methods.

The general modeling is based on nucleation-type theory in conjunction with the statistical methods used to describe rare-event processes; the evolution of the current at a site following nucleation is assumed to follow a definite rule determined, perhaps, by the shape of the evolving defect. The theory describing the statistics of current-time transients resulting from random nucleation processes followed by a deterministic evolution of the current to the resulting growth centers has already been developed in some detail for electrocrystallization (21-28), and one objective of this present work is to explore to what extent this theory can be applied to pitting corrosion. The experimental approach (3, 5, 6) dictated by this modeling is the determination of ensembles of transients of the corrosion current and the analysis of the changes in the ensemble statistics brought about by changing the alloy, solution conditions, stirring, electrode potential, or other variables. We also show (4) that a new technique, an interrupted potentiodynamic sweep, can be used to evaluate rapidly the potential dependence of pitting probability.

*Electrochemical Society Active Member.

The phenomenological model is developed in this paper and analyzed by simulation and algebraic methods. Methods for data processing are developed and tested using simulated data. In the following paper (3), parameters derived from a comparison with experimental data are related to appropriate microscopic models of pitting corrosion.

Model

We model the pitting process as a series of events which are randomly distributed in time and space over the metal surface. Each event results in a local current which evolves with time according to rules which are the same for every event, and the total current is obtained as the sum of the local currents. This type of model is easily explored by computer-based simulation procedures. Agreement with experiment (3-6) is obtained with a model having the following features: (i) events are nucleated with a frequency λ ($s^{-1} \cdot cm^{-2}$); (ii) events have a probability, μ (s^{-1}), of dying; (iii) events which survive beyond a critical age, τ_c (s), do not die; and (iv) each event has an induction time, τ_1 (s), during which the local current does not increase but during which the event may die.

According to this model, pits are unstable when they are first nucleated. A pit then becomes stable only after it has survived past the critical age.

Simulation Technique

The electrode surface was considered as an array of equal areas, each of which was allowed to support at most one pit. In each cycle of the program, the time increment of the experiment, each area was examined and a random-number generator used to decide whether or not to nucleate a pit there, according to a predetermined probability of birth; each existing pit was examined and eliminated or not according to a predetermined probability of death; the current to each pit was incremented according to a predetermined rule, the same for each pit, and the total current at the end of the time increment obtained by summation of the pit currents. A "pit area" of 1/50 of the total area was normally assumed.

Linear and quadratic rules for the current increase to each pit, the effect of changing probabilities of birth and death, and the effect of circumstances in which pits which had survived beyond some predetermined critical age continued to grow indefinitely were explored. The model is represented schematically in Fig. 1.

The effect of defining a precursor state is also interesting. This was allowed for in the simulation by defining a fixed time period after each nucleation event during which the current remained zero, but in which the event could die [assumption (iv) above]. The effect of the precursor state appeared as an apparent reduction in nuclea-

tion rate, with the apparent nucleation rate being a function of the death probability chosen. This apparent nucleation rate was very sensitive to the values chosen for the precursor time and death probability.

Algebraic Formulation

Statistics of pit formation.—It will be shown that by selecting a first or last passage time of a given current level as defining the formation of a stable pit the statistics of stable pit formation can be defined. Modeling of the birth of stable pits is developed in this section; the modeling of the ensemble statistics of current-time transients is discussed in the following section.

We denote the specimen area by a (cm^2). Then the expected number of events in time t is λat , and the probability of survival of a single event for time τ_c is $\exp(-\mu\tau_c)$. Thus, the rate of birth of stable pits Λ (s^{-1}) is given by

$$\Lambda = a\lambda \exp(-\mu\tau_c) \quad [1]$$

and the probabilities $P(n,t)$ of generating stable pits are governed by the set of simple differential equations (see Appendix A)

$$\frac{dP(n)}{dt} = \Lambda P(n-1) - \Lambda P(n) \quad [2]$$

By defining a probability generating function, the set of equations can be solved. The following results are obtained (see Appendix A for details).

The expected number of stable pits at any time, $t > \tau_c$, is

$$\langle n \rangle = \lambda a(t - \tau_c) \exp(-\mu\tau_c) \quad [3]$$

Evidently, if $t < \tau_c$, $\langle n \rangle = 0$. This is one of the assumptions of the model.

The probability that no stable pit is formed within a time, $t > \tau_c$ is $P(0)$, is given by

$$\ln [P(0)] = -\lambda a(t - \tau_c) \exp(-\mu\tau_c) \quad [4]$$

Again, an assumption of the model is that $P(0) = 1$ if $t < \tau_c$.

Equation [4] gives the probability of a specimen remaining unpitted as a function of the exposure time and of the parameters of the model, λ , μ , and τ_c . An expected value for the induction time before the onset of stable pitting, $\langle \tau \rangle$, can be obtained by substituting $\langle n \rangle = 1$ in Eq. [3]

$$\langle \tau \rangle = \left(\frac{1}{a\lambda} \right) \exp(\mu\tau_c) + \tau_c \quad [5]$$

and Eq. [4] can then be conveniently rewritten

$$\ln [P(0)] = -(t - \tau_c) / (\langle \tau \rangle - \tau_c) \quad [6]$$

Current-time transients: theory of ensemble statistics.—The theory outlined in the previous section refers to the observation of the probability of the formation of a defined number of pits or, more specifically, to the probability of the survival of an unpitted specimen. While these probabilities can be derived under favorable circumstances, the directly measured variable is the current and the processes are therefore more correctly modeled using this as the stochastic variable (21-23). Alternatively, a variable directly related to the current such as the surface area or volume of the pits should be used. Modeling at this level is closely related to the modeling of fluctuations in electrocrystallization processes (21-28), except that we are here considering the birth, growth, and, under certain circumstances, death of two- or three-dimensional holes rather than that of two- or three-dimensional growth centers.

An ensemble of experiments is a set of experiments all starting from the same initial condition, and the ensemble mean value and standard deviation of the current are defined as the mean and standard deviation of the values of current observed in all of the experiments at a given time.

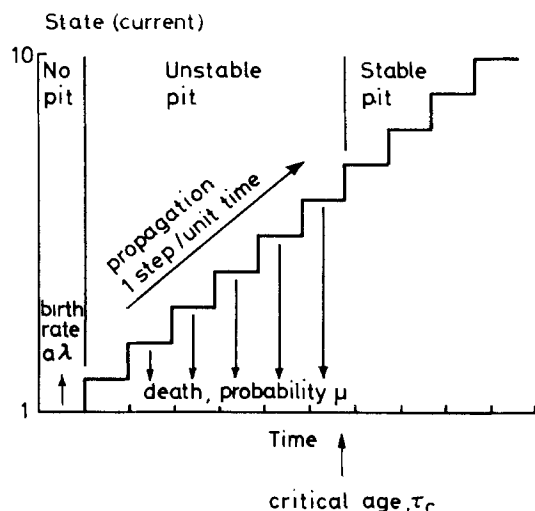


Fig. 1. State diagram illustrating the behavior of an element of surface in the simulation procedure.

It has been shown that it is particularly convenient to interpret the time dependence of the ratio of the ensemble standard deviation, $\sigma(I)$, to the ensemble mean, $\langle I \rangle$ (21-26). Additional information can be obtained from an analysis of the spectral power density of the current, $G_i(\omega)$, and this is discussed in the Spectral power density of the current section below.

The model outlined above can be divided into two time ranges. In the stable pitting limit, at long times ($t > \tau_c$ and $\Lambda t > 1$), the behavior of the system is dominated by the nucleation and growth of stable pits, since the current due to these is assumed to increase without limit.

In the unstable pitting limit, at short times ($t < \tau_c$ or $\Lambda t < 1$), only the nucleation, growth, and death of unstable pits are observed. The theory for these two limits of the model is largely available, and we will confirm its applicability using simulated data in the Discussion section. We also use the simulated data to explore the circumstances under which the behavior of the unstable pits can be distinguished from that of the stable pits and to develop methods of analysis of the data to recover the parameters of the model.

Stable pitting limit.—For the nucleation (rate Λ , Eq. [1]) and unrestricted growth of pits, we obtain, at sufficiently long times (21-23)

$$\sigma(I)/\langle I \rangle = (\Lambda/\Lambda t)^{1/2} \quad [7]$$

irrespective of whether the growth takes place in two (islands) or three (holes) dimensions.

The model described above postulates the nucleation of stable pits subject to a delay time, τ_c (the critical age parameter). This is not a simple delayed-nucleation problem, however, since there is a current due to any given pit before it reaches the critical age.

If the current to a stable pit increases with its age, ν , according to some general rule $i = f(\nu)$, then the ensemble mean current at time t is

$$\langle I \rangle = \int_0^t \Lambda f(\nu) d\nu \quad [8]$$

Given a constant rate parameter, Λ , then the function $f(\nu)$ can be recovered from experimental data by differentiation of $\langle I \rangle$ with respect to t .

For the special case of a linear growth law for pits, the current to a pit of age ν at time t being

$$i = C\nu \quad [9]$$

the effect on the ensemble mean of the introduction of a critical age parameter, τ_c , can be obtained by writing the current as

$$i = C(\nu_1 + \tau_c) \quad [10]$$

The ensemble mean current at time $t > \tau_c$ is, then

$$\langle I \rangle_s = \int_0^{t-\tau_c} \Lambda C(\nu_1 + \tau_c) d\nu_1 = \frac{\Lambda C}{2} (t^2 - \tau_c^2) \quad [11]$$

where the subscript s denotes stable pits.

Unstable pitting limit.—The ensemble mean current in the unstable pitting limit can be obtained by calculating the contribution to the average from each pit, weighted by the probability of observing that pit. If $P(\nu_1)$ denotes the probability of observing a pit dying at age ν_1 , and $Q(\nu_1)$ the charge contributed by that pit, then

$$\langle I \rangle = \frac{1}{t} \int_0^t Q(\nu_1) P(\nu_1) d\nu_1 \quad [12]$$

With the assumption of the Model section of a uniform probability, μ , of death of pits

$$\begin{aligned} P(\nu_1) &= \{\text{probability of observing the birth of a pit} \\ &\quad \text{in the interval } (0, (t - \nu_1))\} \\ &\times \{\text{probability of survival of the pit to age } \nu_1\} \\ &\times \{\text{probability of death of the pits}\} \\ &= \alpha\lambda (t - \nu_1) [\exp(-\mu\nu_1)] \mu \end{aligned} \quad [13]$$

With the special assumption of a linear growth law for pits (Eq. [9]), the charge, $Q(\nu_1)$, contributed by a pit dying at age ν_1 is $C\nu_1^2/2$. Hence, the ensemble mean current is, from Eq. [12] and [13]

$$\begin{aligned} \langle I \rangle_{un} &= \frac{1}{t} \int_0^t (C\nu_1^2/2) \cdot P(\nu_1) d\nu_1 \\ &= \frac{1}{t} \int_0^t \frac{C\nu_1^2}{2} \cdot \mu e^{-\mu\nu_1} \cdot \alpha\lambda (t - \nu_1) d\nu_1 \\ &= \frac{\alpha\lambda C\mu}{2} \left[\frac{te^{-\mu t}}{\mu^2} + \frac{2}{\mu^3} (1 + 2e^{-\mu t}) - \frac{6}{\mu^4 t} \right. \\ &\quad \left. (1 - e^{-\mu t}) \right] \end{aligned} \quad [14]$$

where the subscript, un , denotes unstable pits. In the limit at long enough time

$$\langle I \rangle_{un,z} = \alpha\lambda C/\mu^2 \quad [15]$$

If the birth of stable pits is sufficiently rare in comparison with the birth of unstable pits, then the ensemble mean current for the complete model can be obtained as the sum of Eq. [11] and [14].

The behavior of the variance of the current can be obtained in the limit of short and long times. At short times, the system is dominated by the birth of unstable pits, so (23)

$$\sigma(I)/\langle I \rangle = (1/\alpha\lambda t)^{1/2} \quad [16]$$

while at long times the system reaches an equilibrium distribution of the number and age of unstable pits, and

$$\sigma(I)/\langle I \rangle \sim (\mu/\alpha\lambda)^{1/2} \quad [17]$$

The transition from Eq. [16] to [17] occurs around $t \sim 1/\mu$. Derivations, and some additional results, for the mean and variance of the number and age of pits, are given in Appendix B.

Effects of overlap of pits.—In the limit where one has overlap of two- or three-dimensional holes, pitting corrosion becomes active dissolution or anodic brightening. In these cases, different forms for $\sigma(I)/\langle I \rangle$ are expected, depending on the details of the process (21-26). Pits may also interact over greater distances than their physical diameter by virtue of their associated concentration and potential gradients. Such effects would appear in diagrams of $\sigma(I)/\langle I \rangle$ as effects due to overlap.

Spectral power density of the current.—In the case of a system whose behavior is dominated by the nucleation, growth, and death of unstable pits, analysis of the spectral power density of the resulting current leads directly to the nucleation rate and average lifetime of the pits. Some information about the form of the elementary current-time transient for an individual pit can also be obtained. The process is a "stationary" one,¹ and data processing to yield the estimate of spectral power density from a set of experimental records is straightforward.

A system whose behavior is dominated by the nucleation and growth of stable pits, is "nonstationary": the estimate of spectral power density obtained from a set of experimental records depends both on the observation time and on the details of the method used to process the data. One particular problem is that, in the application of a discrete Fourier transform to a record of limited length, the record is assumed to be cyclic, repeating with period equal to the record length.

In this section, we consider some methods for obtaining spectral power density estimates for systems having both stable and unstable pits. We give some theoretical results, and, in the Discussion section, we compare these results with calculations on simulated data. Our objective is to define and test the methods of data analysis which we will be applying to experimental data.

¹That is, one for which the statistical properties are independent of time.

The theory of the spectral power density of the current resulting from the pitting model outlined above can be developed in a simple fashion with the assumption that each pit, whether stable or unstable, is an independent noise source. The total power can therefore be obtained by summation of the power due to each of the individual sources.

The spectral power density cannot formally be defined for a nonstationary process, such as the unlimited current increase assumed here for stable pits. However, the imposition of a restricted observation time produces a signal for which a discrete Fourier transform, and hence a spectral power density, can be calculated. The difficulty arises in producing an analytical description of the result of such a procedure, given knowledge of the process which gave rise to the nonstationary signal.

Unstable pitting limit.—It is difficult to calculate the spectral power density of the current for the model assumed here of uniform probability of death of an unstable pit. However, the spectral power density has been previously derived for the related case of random nucleation at rate $\alpha\lambda$, of centers of a defined lifetime, ν_1 (23), i.e.

$$i = C(t - u) \quad u < t < \nu_1 + u \quad [18]$$

$$= 0 \quad \text{otherwise} \quad [19]$$

where u is the time of birth of the center. The spectral power density of the current for the process thus defined is

$$G_I(\omega) = \alpha\lambda C^2 \left[\frac{2}{\omega^4} + \frac{\nu_1^2}{\omega^2} - \frac{2\nu_1 \sin(\omega\nu_1)}{\omega^3} - \frac{2 \cos(\omega\nu_1)}{\omega^4} \right] \quad [20]$$

The noise is white at low frequencies

$$G_I(\omega) \sim \alpha\lambda C^2 \nu_1^4 / 4 \quad [21]$$

The level of $G_I(\omega)$ begins to fall at $\omega \sim 1/\nu_1$, and the high frequency asymptote is

$$G_I(\omega) = \alpha\lambda \frac{C^2 \nu_1^2}{\omega^2} \quad [22]$$

The linear current-time relationship (Eq. [18]) has been assumed for simplicity of calculation. Different forms for Eq. [18] change the shape of the high frequency asymptote of $G_I(\omega)$. This is a stationary process, so, given a set of experimental records, each with a limited observation time, T_0 , the best estimate of $G_I(\omega)$ is obtained by stringing the data files end to end and calculating using the resulting extended record (Fig. 2a).

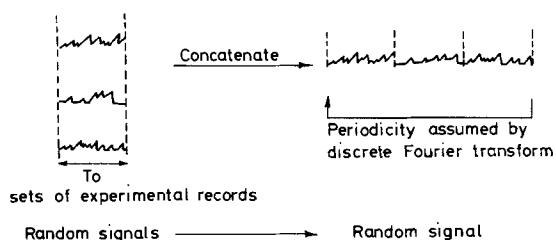
Stable pitting limit.—Consider a stable pit formed at time, u . Again, the linear current-time relationship, Eq. [9], is assumed.

If only stable pits are considered, then an individual experimental record will comprise the sum of a number of current ramps according to Eq. [9], randomly initiated after the start of the experiment, with frequency $\Lambda = \alpha\lambda e^{-\mu\tau}c$, and terminated at $t = T_0$, the observation time. The Fourier transform of the signal can now be defined, as a consequence of the imposition of the artificial constraint $i = 0$ if $t > T_0$. The signal is the same as a set of randomly initiated sawtooth waveforms, constrained such that they all terminate at $t = T_0$.

Two different theoretical results (derivations given in Appendix C) can be given, depending on the value of Λ .

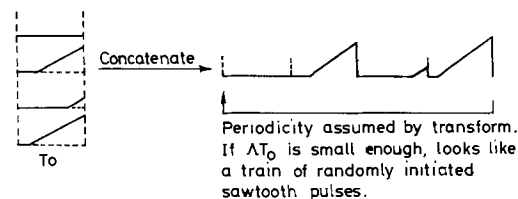
The first result comes about when $\Lambda T_0 < 1$. If $\Lambda T_0 < 1$, then at most one stable pit is expected in each observation interval, and it is likely that many of the intervals will show no stable pit. Stable pits nucleated within the observation interval grow until they reach an age, ν_1 , determined by the observation time, T_0 : $0 \leq \nu_1 \leq T_0$. If the condition $\Lambda T_0 \leq 1$ holds, then the extended record obtained by concatenating the data files from each observation interval (Fig. 2b) can be approximated as a series of randomly initiated triangles, with a uniform distribution of age, ν_1 , in the range $0 \leq \nu_1 \leq T_0$.

(a) Stationary process



(b) Non-stationary process

(I) $\Lambda T_0 < 1$



(II) $\Lambda T_0 \gg 1$

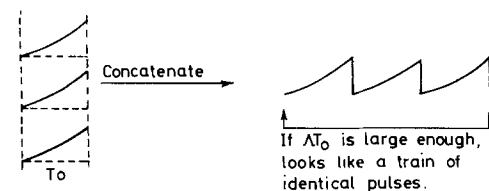


Fig. 2. Processing experimental records to obtain spectral density estimates.

The spectral power density of such a current trace is

$$G_I(\omega) = \frac{\Lambda C^2}{T_0} \left[\frac{2T_0}{\omega^4} + \frac{T_0^3}{3\omega^2} + \frac{2T_0 \cos(\omega T_0)}{\omega^4} - \frac{4 \sin(\omega T_0)}{\omega^5} \right] \quad [23]$$

The noise does not become white at low frequency. The high frequency asymptote is

$$G_I(\omega) \cong \frac{\Lambda C^2 T_0^2}{3\omega^2} \left(\omega > \frac{1}{T_0} \right) \quad [24]$$

and there may be a possibility of determining Λ from the value of the power at $\omega = 1/T_0$

$$G_I\left(\frac{1}{T_0}\right) = 0.048\Lambda C^2 T_0^4 \quad [25]$$

The second result obtains when $\Lambda T_0 \gg 1$. If the density of stable pits is sufficiently high, then the current in each observation period can be approximated as the ensemble mean current, Eq. [11]. Thus, in the concatenated data set, in the r th interval

$$I \cong \frac{1}{2} \Lambda C(t - rT_0)^2 \quad [26]$$

In this case (see Appendix for details)

$$G_I(\omega) = \frac{\Lambda^2 C^2}{4T_0} \left[\frac{T_0^4}{\omega^2} + \frac{4T_0^2}{\omega^4} \cos(\omega T_0) - \frac{8T_0 \sin(\omega T_0)}{\omega^5} - \frac{8}{\omega^6} \cos(\omega T_0) + \frac{8}{\omega^6} \right] \quad [27]$$

and the high frequency asymptote is

$$G_I(\omega) = \Lambda^2 C^2 T_0^3 / 4\omega^2 \quad [28]$$

The power given by Eq. [28] is a factor of $(3/4)\Lambda T_0$ greater than that given by Eq. [24]. Since ΛT_0 is the expected

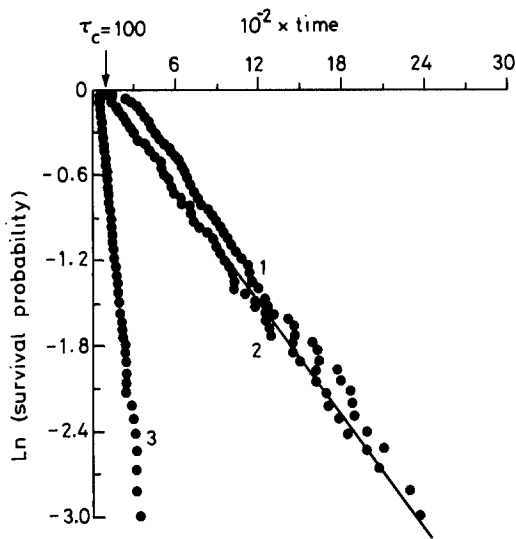


Fig. 3. Survival probability derived from passage times. $\sigma = 5$. $\lambda = 0.05$. $\mu = 0.05$. $\tau_c = 100$. $C = 0.1$. The critical age corresponds to pit current = 10. Passage time assumptions are as follows. 1: First passage through $i = 40$. 2: Last passage through $i = 15$. 3: First passage through $i = 15$.

number of stable pits, $\langle n \rangle$, Eq. [24] and [28] may be rewritten

$$G_1(\omega) = C^2 T_0 \langle n \rangle / 3\omega^2 \quad (\langle n \rangle \leq 1) \quad [29]$$

and

$$G_1(\omega) = C^2 T_0 \langle n \rangle^2 / 4\omega^2 \quad (\langle n \rangle \gg 1) \quad [30]$$

emphasizing how the power level obtained using this method of concatenation of data files increases with the expected number of stable pits formed in each observation interval.

Discussion

The probability of survival of an unpitted specimen.—We have shown above that this probability is given by Eq. [4], but we have noted that there is an ambiguity in the definition of induction time as a time of first passage through some arbitrary current level. The results will be dependent on the choice of level. A better definition is the time of last passage through some lower level of current. This hypothesis has been tested using the ensemble of simulated current-time transients, and Fig. 3 both confirms the validity of Eq. [4] and shows that, with the definition of last passage time, the critical age parameter can be recovered accurately.

Shibata and Takeyama (18, 19) interpreted their data on the induction time distribution for pitting of 18Cr 8Ni stainless steel in terms of three different nucleation frequencies, each applicable to a different time range of the data. Given the uncertainties in the definition of the induction time, Eq. [4] accounts for two of these time ranges, one for $t < \tau_c$ and the other for $t \geq \tau_c$. The data of Shibata and Takeyama and our own data (3) show a deviation at long times from the behavior predicted by Eq. [4]. Specimens which survived for longer than some time seemed less likely to nucleate propagating pits. Shibata and Takeyama postulated the occurrence of a death process, repassivation of active pits, to explain this behavior (29). There are, indeed, a number of possible adaptations of the general model which will account for a deviation like this from the expected behavior. For example, the initiation frequency, λ , could be time dependent or could have a distribution of possible values over the surface, or the critical age, τ_c , could have a distribution of possible values. Another possible phenomenon is the occurrence of a "renewal process," in which nucleation is more likely to occur on the site of a previous unstable pit than elsewhere. It will be a matter of further work to consider the applicability of such adaptations of the model.

Determination of nucleation rate by peak counting.—Since most of the pits nucleated according to the model outlined above are unstable, the rate of death of pits closely matches the rate of nucleation. Since each death results in a sharp reduction in the current, the number of deaths can be obtained simply by counting current peaks. We confirmed, using simulated data, that peak counting gave an accurate determination of the nucleation rate, λ . We shall see subsequently (3), however, that it is not straightforward to apply this technique to real data. Problems arise in the definition of what constitutes a real event and what is merely noise introduced by the measuring instruments.

The statistics of ensembles of current-time transients.—The simulated data, Fig. 4, clearly show the effects described in the Current-time transients section. At short times, Eq. [16] is followed. For only unstable pitting, Eq. [17] is followed at longer time with the transition between the two regimes occurring at $t \sim 1/\mu$. With both stable and unstable pitting, following the transition from Eq. [16] to [17] at $t \sim 1/\mu$, there is a sharp rise in $\sigma(I)/\langle I \rangle$ starting at $t \sim \tau_c$ caused by the delayed nucleation of stable pits; a pronounced maximum is observed in the plot, and Eq. [7] is followed at longer time, when the behavior of the system is dominated by the nucleation of stable pits.

Figure 4c shows that the presence of a small background current changes the time variation of $\sigma(I)/\langle I \rangle$ profoundly at short times, such that information about the nucleation, growth, and death of unstable pits is lost. This is an important consideration in the analysis of experimental data.

Spectral power density analysis.—Figure 5a shows the spectral power density derived from a set of records having only unstable pits. The individual records were concatenated, as illustrated in Fig. 2a.

The simulations assume a uniform probability for the death of centers rather than a defined age as in Eq. [20]–[22]. We have observed empirically that the power level at a frequency

$$\omega = 2\pi\mu \quad [f = \mu \text{ (Hz)}] \quad [31]$$

is 20 dB below the white noise level. The high frequency asymptote of $G(\omega)$ varies as $1/\omega^2$, as in Eq. [22] and as expected from the assumption of a linear current-time relationship for the pits during their lifetime. A comparison of the white noise level observed (Fig. 5a) with that expected theoretically can be made in a semi-empirical fashion. Thus, if the defined lifetime ν_1 in Eq. [21] is replaced by the most probable lifetime, $1/\mu$, the resulting calculated limiting spectral density is close to 40 times less than the observed value, *i.e.*

$$G_1(0) \sim 10\alpha\lambda C^2/\mu^4 \quad [32]$$

We further note that, with the ensemble mean current given by Eq. [15], Eq. [32] gives for the white noise level

$$G_1(0) \sim 10(\langle I \rangle_{un,x})^2/\alpha\lambda \quad [33]$$

Thus, in the case of unstable pits, the spectral density affords a convenient method for determination of both λ and μ . A constant background current shifts the curves parallel to the $G_1(\omega)$ axis. A time varying background would be more difficult to deal with, although if it were small it would not greatly affect the results. Certainly, the spectral density was not as sensitive to small background currents as the ratio $\sigma(I)/\langle I \rangle$ turned out to be (see previous section).

When both stable and unstable pits are present, the power contributed by the stable pits swamps that due to the unstable pits at high values of Λ ; at low enough values of Λ , a separation between the two processes can still be made (Fig. 5b). The stable pits dominate the power at low frequencies. Figure 5c shows how the power changes from that given by Eq. [24] to that given by Eq. [28] as Λ increases.

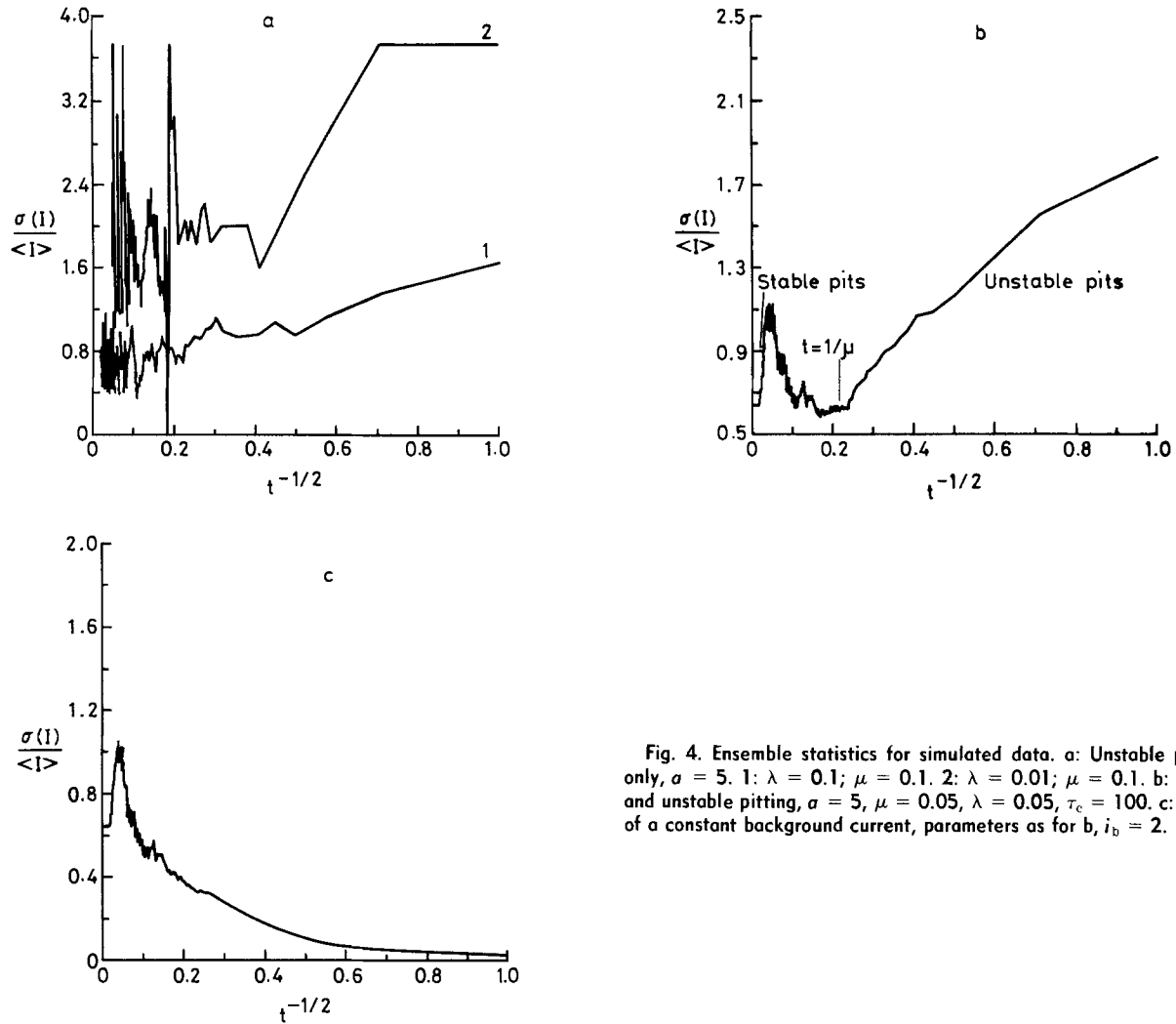


Fig. 4. Ensemble statistics for simulated data. a: Unstable pitting only, $\sigma = 5$. 1: $\lambda = 0.1$; $\mu = 0.1$. 2: $\lambda = 0.01$; $\mu = 0.1$. b: Stable and unstable pitting, $\sigma = 5$, $\mu = 0.05$, $\lambda = 0.05$, $\tau_c = 100$. c: Effect of a constant background current, parameters as for b, $i_b = 2$.

If the power contributed by the unstable pits is not completely swamped by that contributed by the stable pits, then the power due to the stable pits can be estimated and subtracted from the total to give the unstable pit contribution. An induction time is defined as a time of last passage of the current through some level, as in the Probability of survival section. The data for times longer than the induction time are then fitted to a regression polynomial and the data for times shorter than the induction time are set to zero or to some appropriate background level. The resulting set of current-time transients is then assumed to represent the behavior of the stable pits only. Figure 6a shows how the spectral density obtained from a concatenated set of data files processed in this way matches the behavior of the simulation data at low frequency. The differences between the two traces, attributable to the unstable pits, is clearly seen. The parameters, λ and μ , for the unstable pits are recovered.

Even when the power due to stable pits appears to completely swamp that due to the unstable pits, there is still a possibility of recovering information about the unstable pits by using only those sections of data at times earlier than the induction time, or by "detrending" the data. For the first method, the sections of data before the induction time are taken to represent only unstable pitting. These sections are removed and concatenated and the spectral density is calculated. Figure 6b illustrates that λ and μ can be recovered in this way. The assumption that is implicitly made in this procedure is that the sections of data from the different files, where only unstable pits are present, represent different samples of the same stationary, random process. If this assumption is valid, then the data files may be chained and treated as a single record of the process. While this assumption may hold for simulated data, there is no means of being sure of its validity

for experimental data. The success of the method also clearly depends on the use of a reasonable criterion for determining the induction time.

In a process where the resultant current is the sum of the currents from independent events, if the current from any one event can be estimated, it may be subtracted from the record. "Detrending" the data comprises estimating the current due to the stable pits and subtracting it. Clearly, the result can be very dependent on the method used, and the method is only likely to be successful if the fluctuations are not too small in comparison with the trend. Figure 6b illustrates the use of a regression polynomial to detrend data; again, the parameters of the unstable pitting process can be recovered.

Conclusion

The parameters of a general statistical model of pitting corrosion can be recovered by appropriate data analysis. The model includes the phenomena of nucleation, growth, and death of unstable pits and the continued propagation of pits which survive beyond a critical age. Appropriate limiting cases have been derived theoretically and the results confirmed by analysis of simulated data.

Peak counting yields the nucleation rate directly, but the definition of what constitutes a "real" peak as opposed to instrument noise may be difficult in practice. Analysis of passage time distribution yields the critical age and a composite parameter, the nucleation rate of stable pits, but suffers from the difficulty of unambiguous definition of appropriate current levels. Analysis of ensemble statistics yields all the parameters of the model, but is very sensitive to the effects of background currents. Analysis of spectral power density is, in principle, a most useful method, even in the presence of the nonsta-

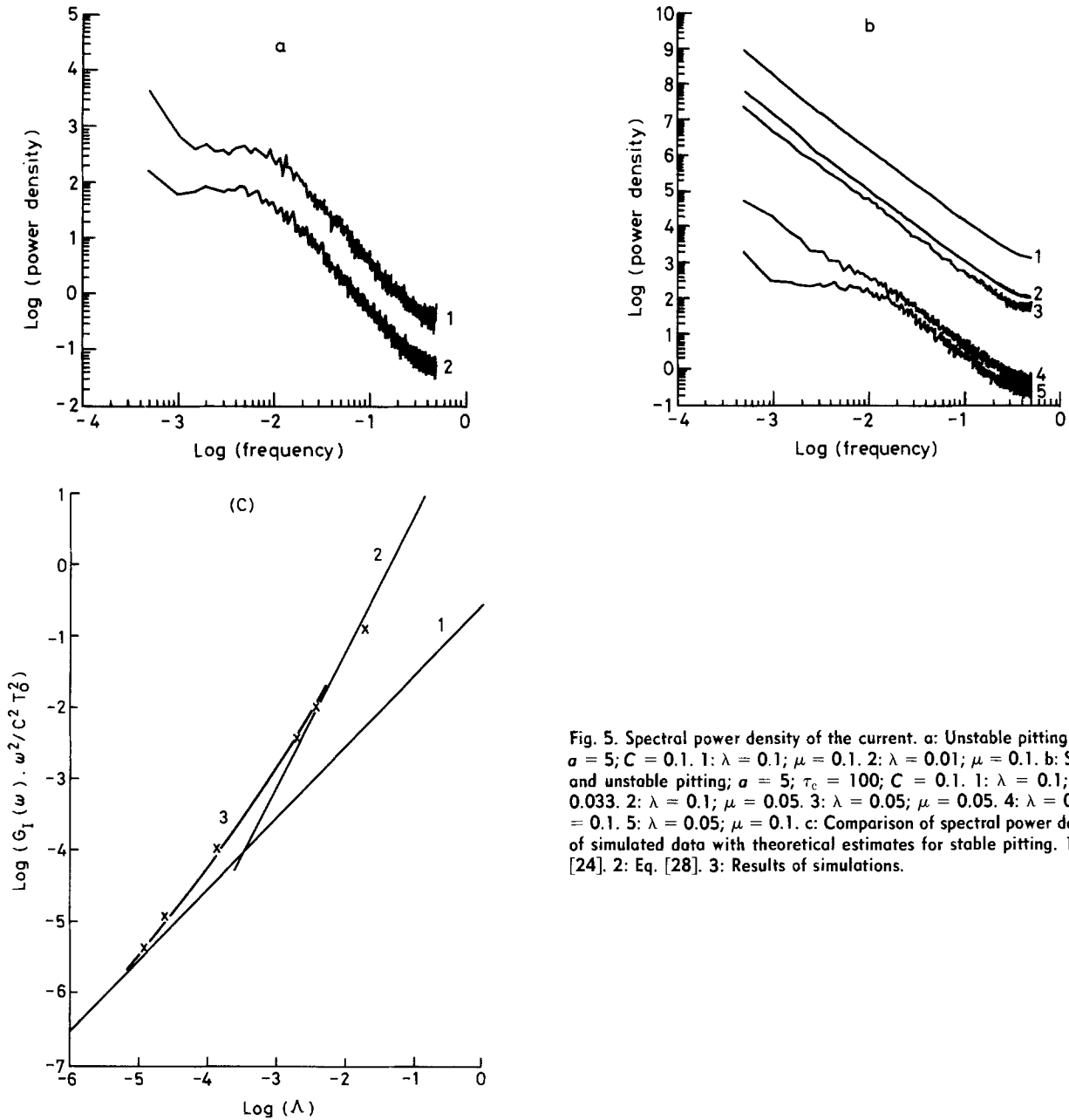


Fig. 5. Spectral power density of the current. a: Unstable pitting only; $\sigma = 5$; $C = 0.1$. 1: $\lambda = 0.1$; $\mu = 0.1$. 2: $\lambda = 0.01$; $\mu = 0.1$. b: Stable and unstable pitting; $\sigma = 5$; $\tau_c = 100$; $C = 0.1$. 1: $\lambda = 0.1$; $\mu = 0.033$. 2: $\lambda = 0.1$; $\mu = 0.05$. 3: $\lambda = 0.05$; $\mu = 0.05$. 4: $\lambda = 0.1$; $\mu = 0.1$. 5: $\lambda = 0.05$; $\mu = 0.1$. c: Comparison of spectral power density of simulated data with theoretical estimates for stable pitting. 1: Eq. [24]. 2: Eq. [28]. 3: Results of simulations.

tionary process of propagation of stable pits. In this case, the results depend on the method used to process the data. The techniques defined here are applied to experimental data in the following paper (3).

Manuscript submitted May 22, 1984; revised manuscript received Feb. 1, 1985. Parts of this article were presented as Paper 10 at the Montreal, Quebec, Canada, Meeting of the Society, May 9-14, 1982.

AERE Harwell assisted in meeting the publication costs of this article.

APPENDIX A Probability of Generation of Stable Pits

We observe that

$$P(n,t) = \left\{ \begin{array}{l} \text{probability that there were } (n-1) \text{ stable pits at} \\ \text{ } (t-\delta t) \text{ and that one pit reached the critical age} \\ \text{ } \text{in the interval } t-\delta t \text{ to } t \\ + \text{ probability that there were } n \text{ stable pits at } t-\delta t \\ \text{ } \text{and that no additional pit reached the critical} \\ \text{ } \text{age in the interval } t-\delta t \text{ to } t \end{array} \right. \quad [\text{A-1}]$$

Then

$$P[n,t] = P[(n-1), (t-\delta t)] \Lambda \delta t + P[n, (t-\delta t)] [1 - \Lambda \delta t] \quad [\text{A-2}]$$

Therefore

$$\left[\frac{P[n,t] - P[n, (t-\delta t)]}{\delta t} \right]_{\delta t \rightarrow 0} = \frac{dP(n)}{dt} = \Lambda P(n-1) - \Lambda P(n) \quad [\text{A-3}]$$

Multiplying the set of equations by s^n where s is a dummy variable and summing

$$\frac{dH(s)}{dt} = \Lambda(s-1) \cdot H(s) \quad [\text{A-4}]$$

where the probability generating function is defined by

$$H(s) = \sum_{n=0}^{\infty} s^n P(n) \quad [\text{A-5}]$$

In practice, the series will be truncated at a finite value of n , but this does not affect the argument.

Since there are no pits at $t \leq \tau_c$, that is $P(n) = 0$ for all nonzero values of n , Eq. [A-5] gives the initial condition

$$H = 1 \text{ at } t = \tau_c \quad [\text{A-6}]$$

Hence

$$H = \exp[\Lambda(s-1)(t-\tau_c)] \quad [\text{A-7}]$$

The mean value of the number of stable pits $\langle n \rangle$ is then

$$\langle n \rangle = \left. \frac{dH}{ds} \right|_{s=1} = \Lambda(t - \tau_c) \quad [\text{A-8}]$$

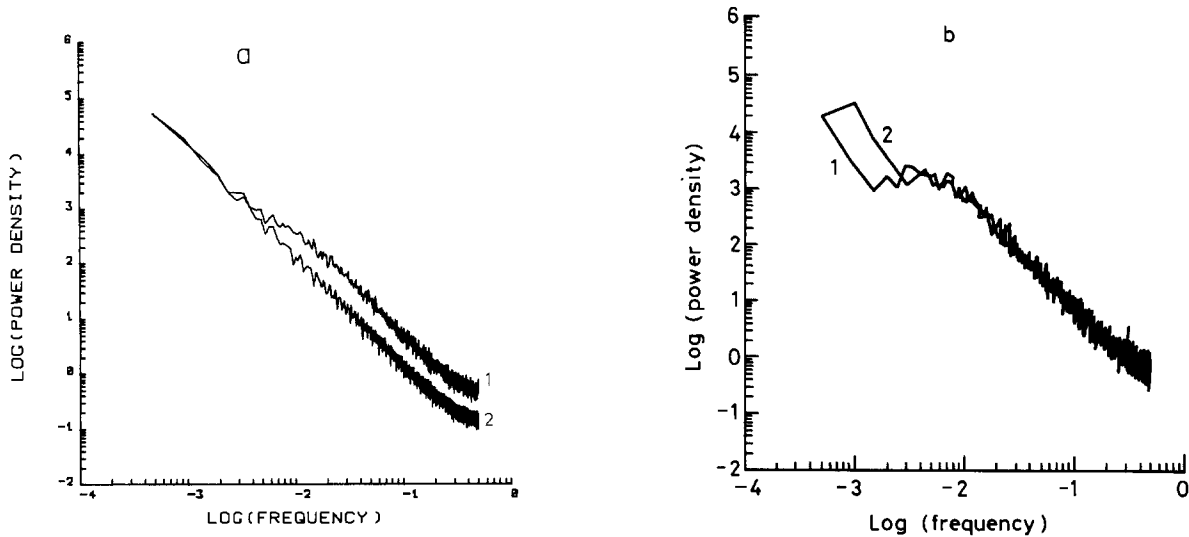


Fig. 6. Recovery of parameters of unstable pitting in the presence of stable pitting. a: Estimation of spectral power density due to stable pitting by use of a regression polynomial. $\lambda = \mu = 0.1$; $\tau_c = 100$; $\sigma = 5$; $C = 0.1$. 1: Unprocessed data. 2: Stable pits only. b: Estimation of spectral power density due to unstable pitting, in the presence of stable pitting. $\lambda = \mu = 0.05$; $\tau_c = 100$; $\sigma = 5$; $C = 0.1$. 1: Spectral density of sections of dots lying within the induction period. 2: Result of detrending using a regression polynomial.

so that

$$\langle n \rangle = \lambda a(t - \tau_c) \exp(-\mu\tau_c) \text{ for } t \geq \tau_c \quad [A-9]$$

Furthermore

$$\sigma^2(n) = H''(1) + H'(1) - [H'(1)]^2 = \Lambda(t - \tau_c) = \langle n \rangle \quad [A-10]$$

we also obtain from Eq. [A-7]

$$P(0) = H|_{s=0} = \exp(-\Lambda(t - \tau_c)) \quad [A-11]$$

and

$$\ln P(0) = -\Lambda(t - \tau_c) \exp(-\mu\tau_c) \quad [A-12]$$

APPENDIX B
Statistics of Unstable Pitting

For the case where unstable pits are nucleated at a rate $a\lambda$, with a probability μ of death, the probability generating function for the number of pits can be written (30)

$$H(s,t) = \exp\left\{\frac{a\lambda}{\mu}(s-1)(1-e^{-\mu t})\right\} \quad [B-1]$$

The mean and variance of the number of unstable pits can then be obtained, as above

$$\langle n \rangle = \sigma^2(n) = \frac{a\lambda}{\mu}(1-e^{-\mu t}) \quad [B-2]$$

The mean, $\langle \nu \rangle$, and variance, $\sigma^2(\nu)$, of the age of unstable pits can be computed

$$\begin{aligned} \langle \nu \rangle &= \frac{1}{a\lambda t} \int_0^t \nu a\lambda t \mu e^{-\mu \nu} d\nu \\ &= \frac{1}{\mu} \{1 - e^{-\mu t} \cdot (\mu t + 1)\} \quad [B-3] \\ &\rightarrow 1/\mu \text{ as } t \text{ increases} \end{aligned}$$

and

$$\begin{aligned} \sigma^2(\nu) &= \frac{1}{a\lambda t} \int_0^t \nu^2 \cdot a\lambda t \mu e^{-\mu \nu} d\nu \\ &= \frac{1}{\mu^2} \{2 - e^{-\mu t} \cdot (t^2 \mu^2 + 2)\} \quad [B-4] \\ &\rightarrow 2/\mu^2 \text{ as } t \text{ increases} \end{aligned}$$

The variance of the current at longer time can be obtained

$$\begin{aligned} \sigma^2(I) &\sim \left(\frac{\partial I}{\partial \langle n \rangle}\right)^2 \cdot \sigma^2(n) \text{ (} t \rightarrow \infty \text{)} \\ &\sim (C \langle \nu \rangle)^2 \cdot \sigma^2(n) = \frac{C^2 a \lambda}{\mu^3} (t \rightarrow \infty) \quad [B-5] \end{aligned}$$

which, together with Eq. [15], gives Eq. [17] in the main text.

APPENDIX C
Spectral Density Estimates for the Stable Pitting Process,
Constrained by a Limited Observation Time

In the following, the linear-growth rule for stable pits, Eq. [9], is assumed.

Random nucleation of stable pits (limiting case, for $\Lambda T_0 < 1$).—We have a uniform probability in time and space of forming pits of any given age, θ , provided $\theta < T_0$. If the age of a pit is ν then

$$F(\omega) = \int_0^\theta f(\nu) \exp(j\omega\nu) d\nu = \int_0^\theta C\nu \exp(j\omega\nu) d\nu \quad [C-1]$$

$$|F(\omega)|^2 = C^2 \left[\frac{2}{\omega^4} + \frac{\theta^2}{\omega^2} - \frac{2\theta \sin \omega\theta}{\omega^3} - \frac{2 \cos \omega\theta}{\omega^4} \right] \quad [C-2]$$

The effective rate of nucleation of pits of age θ is the fraction nucleated in the interval $d\theta$

$$\Lambda' = \frac{\Lambda d\theta}{T_0} \quad [C-3]$$

The contribution of the nucleation of pits of age θ to the total noise is

$$\begin{aligned} dG_1(\omega) &= \Lambda' |F(\omega)|^2 = \frac{\Lambda |F(\omega)|^2}{T_0} d\theta \quad [C-4] \\ G_1(\omega) &= \frac{C^2 \Lambda}{T} \int_0^{T_0} \left[\frac{2}{\omega^4} + \frac{\theta^2}{\omega^2} - \frac{2\theta \sin \omega\theta}{\omega^3} - \frac{2 \cos \omega\theta}{\omega^4} \right] d\theta \\ &= \frac{\Lambda C^2}{T_0} \left[\frac{2T_0}{\omega^4} + \frac{T_0^3}{3\omega^2} + \frac{2T_0 \cos(\omega T_0)}{\omega^4} \right. \\ &\quad \left. - \frac{4 \sin(\omega T_0)}{\omega^5} \right] \quad [C-5] \end{aligned}$$

Ensemble mean current transient in each observation period (limiting case for $\Lambda T_0 \gg 1$).—If ΛT_0 is sufficiently large, the current due to stable pitting in each observation window can be approximated as the ensemble mean current (stable pitting case, $i = C\nu$ for each pit of age ν)

$$i = ACt^{1/2} \quad [C-6]$$

Here

$$F(\omega) = \int_0^{T_0} \frac{AC}{2} t^2 \exp(j\omega t) dt \quad [C-7]$$

and, since the pulse rate in the chain analyzed is $1/T_0$ (one pulse for each observation window)

$$G(\omega) = \frac{|F(\omega)|^2}{T_0} \quad [C-8]$$

$$= \frac{A^2 C^2}{4T_0} \left[\frac{T_0^4}{\omega^2} + \frac{4T_0^2}{\omega^4} \cos(\omega T_0) - \frac{8T_0}{\omega^5} \sin(\omega T_0) - \frac{8}{\omega^6} \cos(\omega T_0) + \frac{8}{\omega^6} \right] \quad [C-9]$$

REFERENCES

1. "Corrosion—Aqueous Processes and Passive Films," Vol. 23, of Treatise on Materials Science and Technology, J. C. Scully, Editor, Academic Press, London (1983).
2. U. R. Evans, "Corrosion and Oxidation of Metals," Chap. 22, Edward Arnold, London (1960).
3. D. E. Williams, C. Westcott, and M. Fleischmann, *This Journal*, **132**, 1804 (1985).
4. D. E. Williams and C. Westcott, in "Proceedings of the 9th International Conference on Metallic Corrosion, Toronto, 1984," Vol. 4, p. 390, National Research Council of Canada, Ottawa, Ont., Canada (1984).
5. D. E. Williams, C. Westcott, and M. Fleischmann, in "Passivity of Metals and Semiconductors," M. Froment, Editor, p. 217, Elsevier, Amsterdam (1983); AERE report R-10832 Oxon, England (1983).
6. D. E. Williams, C. Westcott, and M. Fleischmann, *J. Electroanal. Chem.*, **180**, 549 (1984).
7. J. R. Galvele, in "Corrosion — Aqueous Process and Passive Films," Vol. 23, of "Treatise on Materials Science and Technology," J. C. Scully, Editor, p. 1, Academic Press, London (1983).
8. M. Janik-Czachor, *This Journal*, **128**, 513C (1981).
9. M. Janik-Czachor, G. C. Wood, and G. E. Thompson, *Br. Corros. J.*, **15**, 154 (1980).
10. L. F. Lin, C. Y. Chao, and D. D. MacDonald, *This Journal*, **128**, 1194 (1981).
11. T. P. Hoar, D. Mears, and G. Rothwell, *Corros. Sci.*, **5**, 279 (1965).
12. T. P. Hoar and W. R. Jacob, *Nature*, **216**, 1299 (1967).
13. K. E. Heusler and L. Fischer, *Werkstoff. Korros.*, **27**, 551 (1976).
14. T. P. Hoar, *Discuss. Faraday Soc.*, **1**, 299 (1947).
15. A. A. Seys, A. A. van Haute, and M. J. Brabers, *Werkstoff. Korros.*, **25**, 663 (1974).
16. M. Janik-Czachor, *ibid.*, **30**, 255 (1979).
17. H. Saito, T. Shibata, and G. Okamoto, *Corros. Sci.*, **19**, 693 (1979).
18. T. Shibata and T. Takeyama, *Nature*, **260**, 315 (1976).
19. T. Shibata and T. Takeyama, *Corrosion*, **33**, 243 (1977).
20. B. Baroux, in "Passivity of Metals and Semiconductors," M. Froment, Editor, p. 531, Elsevier, Amsterdam (1983).
21. M. Bayes, Ph.D. Thesis, University of Southampton, Southampton, England (1982).
22. P. Bindra, M. Fleischmann, J. W. Oldfield, and D. Singleton, *Faraday Discuss. Chem. Soc.*, **56**, 180 (1973).
23. M. Fleischmann, C. Gabrielli, M. Labram, and A. Sattar, *Surf. Sci.*, **101**, 583 (1980).
24. E. Budevski, M. Fleischmann, C. Gabrielli, and M. Labram, *Electrochim. Acta*, **28**, 925 (1983).
25. R. L. Deutscher and S. Fletcher, *J. Electroanal. Chem.*, **164**, 1 (1984); S. Fletcher, *ibid.*, **164**, 11 (1984).
26. M. Fleischmann, M. Labram, and C. Gabrielli, *ibid.*, **150**, 111 (1983).
27. S. K. Rangarajan, *J. Electroanal. Chem. Interfacial Electrochem.*, **46**, 119 (1973).
28. S. Fletcher and T. Lwin, *Electrochim. Acta*, **28**, 237 (1983).
29. T. Shibata and T. Takeyama, in "Proceedings of the 8th International Conference on Metallic Corrosion," p. 146, DECHEMA, Frankfurt, Germany (1981).
30. D. R. Cox and H. D. Miller, "The Theory of Stochastic Processes," p. 168, Methuen, London (1965).

Stochastic Models of Pitting Corrosion of Stainless Steels

II. Measurement and Interpretation of Data at Constant Potential

D. E. Williams,* C. Westcott, and M. Fleischmann*

AERE Harwell, Materials Development Division, Didcot, Oxon, England OX11 0RA

ABSTRACT

The experimental evaluation of the parameters of a general stochastic model for the initiation of pitting corrosion on stainless steels is described. The variation of these parameters with experimental conditions is used in the development of a microscopic model. A microscopic model which accords with the observed behavior attributes the initiation of pitting corrosion to the production and persistence of gradients of acidity and electrode potential on the scale of the surface roughness of the metal. The observed fluctuations are related to fluctuations in the hydrodynamic boundary layer thickness. A pit becomes stable when it exceeds a critical depth related to the surface roughness.

It has been pointed out in a preceding paper (1) that, in common with other localized corrosion processes, pitting corrosion is a rare event so that a statistical treatment is necessary for an adequate description [cf. Ref. (2-4)]. An appropriate level of modeling of the processes is suggested by the analogy to electrocrystallization (5, 6) with formation of pits replacing the growth of crystallites: namely, the triggering (nucleation) of events by a suitably filtered Poisson process coupled to growth of pits by an essentially deterministic mechanism. A special model has been examined (1) which has the features that (i) events are nucleated with frequency λ ($s^{-1} cm^{-2}$), (ii) events have a probability μ (s^{-1}) of dying, and (iii) events which survive beyond a critical age, τ_c (s), do not die.

For certain aspects of the modeling, we also assume that all pits evolve according to the deterministic law

$$i = Cu \quad [1]$$

where u (s) is the age of the pit. The model assumes formation of stable pits [step (iii)] following a "prepitting" stage [steps (i), (ii)]. The microscopic model given recently by Okada (7) falls into this general class. The objective of our work is to derive the parameters of the general model from the experimental data, so that their variation with experimental conditions can be examined. A rigorous assessment of microscopic models of this general class can then follow. Two types of predictions have been based on this model. The first is the probability of survival of unpitted specimens (*i.e.*, specimens in the prepitting stage). The second is the ensemble statistics of potentiostatic current-time transients. We have also shown how to analyze the spectral power density of the current. In this paper, we show how the probability distribution function of the slope of the experimental transients can be ob-

* Electrochemical Society Active Member.

tained and used to reduce the time series of the current to time series of the number of pits; statistical analysis of these time series is simpler than analysis of the current. Predictions have been made both by computer simulations and by algebraic methods, and the two approaches have been compared. It has been shown that the last passage time of the current through a chosen low level is especially useful in defining survival probabilities, and a new method for the rapid determination of quantities related to this probability has been described (8). The present paper is concerned with the determination and evaluation of the statistics of ensembles of potentiostatic current-time transients. The derived data are shown, in general, to accord with the predictions of the phenomenological theory (1), with values of the parameters given by the various methods of data analysis being self-consistent. Measurements of the chloride-ion concentration and the potential dependence of the phenomena as well as of the influence of other solution variables (stirring, support electrolyte concentration, buffer capacity) lead to the definition of a microscopic model of pit initiation. The behaviors of a number of stainless steels are compared.

Experimental

Stainless steels used in this investigation were 18Cr 13Ni 1Nb, ANSI 304L, ANSI 316L, and 25Cr 20Ni. Analyses are given in Table I. Disk specimens 5 cm² in area were stamped out from single sheets of each of the steels, set in a cold setting epoxy mounting resin ("Araldite" HY and EY), polished to a 240 grit finish and rinsed with acetone. The electrochemical cell was formed simply by clamping the specimen mount onto a 25 mm diam glass flange joint set vertically. Gas feed, Luggin capillary, Pt secondary electrode, and glass stirring paddle were introduced from the top. The solution contained in the assembly was purged with purified argon for 30 min before each experiment, and a slow flow of argon was maintained during each experiment. Current was measured as a voltage across a 100Ω resistor in the secondary electrode lead, and was logged from a number of cells simultaneously using a reed relay multiplexer and autoranging digital voltmeter (Datron, 1 μV resolution) controlled via the IEEE 488 interface bus by a microcomputer (CBM, PET 4032). The cells were independently controlled by H. B. Thompson "Microstats"; application of the control potential and potential ramp (H.B. Thompson Digital Ramp Generator) were also under the control of the microcomputer. Data were transferred to a minicomputer for analysis. Potentials were measured with respect to a saturated calomel electrode, and solutions were prepared with analytical reagent-grade chemicals and distilled water. The buffer was tris (hydroxymethyl) amino methane, ("tris") adjusted to pH 7.0 with 1M HClO₄ solution.

The potentials at which pitting would start at a given probability were determined from measurements with the interrupted potentiodynamic sweep technique (IPS technique) described elsewhere (8). The potential of the specimens was changed from the rest potential to potentials predetermined in this way, either stepwise or using a ramp of 10 mV·s⁻¹. The current was monitored for 2400s with a resolution of 0.01 μA, truncated subsequently to 0.1 μA, at a sampling frequency of 1 Hz; a typical ensemble comprised 20-30 experiments. We have previously reported (4) that the initial current pulse associated with a step initiation was sufficient to start crevice corrosion at

the joint between the specimen and mounting material in a significant number of experiments. This effect was avoided with the ramp initiation and, unless otherwise stated, this was employed for the work reported here.

Results

The shape of potentiostatic current-time transients.—Figure 1 shows typical current-time transients and illustrates, first, the general form of the fluctuations and, second, the large variation in results from one experiment to another, performed under nominally identical conditions. The transients comprised fluctuations superimposed on a rising background; the fluctuations had a characteristic form of a slow rise and a sharp fall. The charge passed during a fluctuation was typically 10-500 μC, equivalent to the dissolution of 10⁻¹⁰-10⁻⁸ cm³ of metal, a cube of typical linear dimension of ~10 μm. The form of the fluctuations was opposite to the form of current fluctuation observed by Bertocci (9), namely, sharp rise and slow fall, for steels of lower chromium content (Fe9Cr, below the limit of "stainlessness").

In the following sections, we present, first, the analysis of ensemble statistics; second, the determination of the initiation frequency for the events which cause the current fluctuations; third, the analysis of the slope of the current-time transients and the conversion of these into time series of the number of pits; fourth, the determination of the rate of formation of stable pits; and, last, the determination of the average lifetime of the events from the spectral power density of the current. The development and validation of the methods of analysis have been given in the previous paper (1). Effects of stirring, buffering, supporting electrolyte concentration, chloride concentration, alloy type, and electrode potential are shown.

Ensemble statistics: effects of environment and comparison of alloys.—Figure 2 shows ensemble mean transients and the ratio of ensemble standard deviation to ensemble mean, $\sigma_I/\langle I \rangle$. The potentials were chosen from the cumulative distribution of breakdown potentials measured in IPS experiments (8). The lowest potential for each alloy was the 50% point on this distribution. The general form of the ensemble mean current was concave upward; a tendency for the current to start leveling off at high currents was noted. For each alloy, the time evolution of the ratio $\sigma_I/\langle I \rangle$ changed from being virtually flat (at $\sigma_I/\langle I \rangle = 1$) over the time span of the experiment at the lower potential to a sharply peaked form at the higher potential. The behavior of the 25Cr 20Ni alloy was different from that of the others; for this alloy, the current transients fell into one of two classes, of either very low currents with only isolated small fluctuations, or of a sudden, and early, current increase to high values which oscillated violently about a given level. The ensemble mean current transient for 25Cr 20Ni reflected the behavior of the latter class.

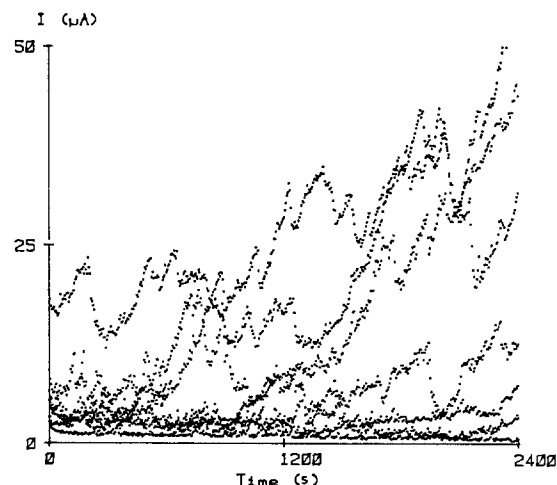


Fig. 1. Ensemble of current-time transients; 18Cr 13Ni 1Nb steel, 5 cm². 0.028M NaCl, + 50 mV SCE, unstirred.

Table I. Composition of stainless steels (major constituents only; weight percent; balance is Fe)

Type	Cr	Ni	Mo	Nb	Mn	C	S
18/13/1	17.6	12.1	—	0.63	1.13	0.06	< 0.01
304L	18.2	9.3	0.38	< 0.01	1.41	0.02	< 0.01
316L	16.8	12.4	2.42	< 0.01	1.66	0.02	< 0.01
25/20	25.4	19.6	0.27	< 0.01	0.79	0.07	< 0.01

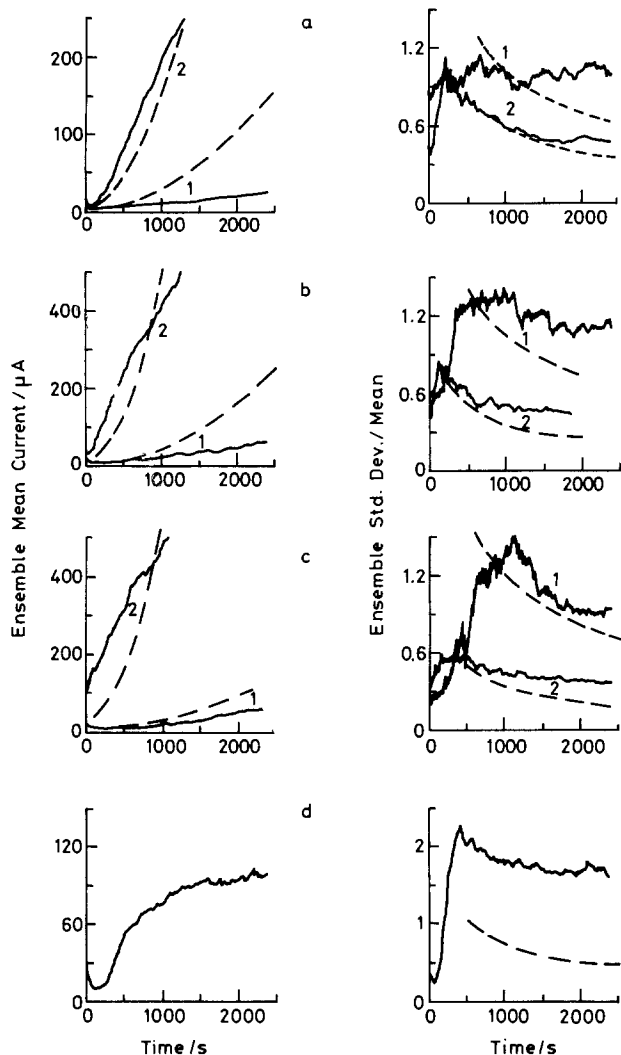


Fig. 2. Ensemble mean current and standard deviation/mean in 0.028M NaCl, unstirred. a: 18Cr 13Ni 1Nb; curve 1 is +50, curve 2 is +200 mV SCE. b: 304L, curve 1 is +200, curve 2 is +300 mV SCE. c: 316L, curve 1 is +300, curve 2 is +400 mV SCE. d: 25Cr 20 Ni, +400 mV SCE. Dashed lines are theoretical results calculated using nucleation rates for stable pitting derived from passage time and slope analysis.

As well as the expected effects of chloride concentration and electrode potential, marked effects of the solution buffer capacity, supporting electrolyte, and stirring were also observed. Figure 3 shows the effects of buffer capacity and supporting electrolyte on ensemble mean transients for the 18Cr 13Ni 1Nb steel. Increasing the buffer capacity decreased the likelihood of pitting corrosion. Adding a sufficient concentration of supporting electrolyte rendered the alloy immune to pitting corrosion. The effect of the presence of 1M NaClO₄ supporting electrolyte persisted up to high potentials (at least +500 mV SCE) in chloride solutions of up to 0.3M for times in excess of 2 days. Addition of the supporting electrolyte into the dilute chloride solution during the propagation of pitting corrosion had the effect of stopping the pits: the current fell immediately to zero (Fig. 5a). Addition of a sufficient concentration of buffer had the same effect (Fig. 5b), although the current fall in this case was in two steps. In both cases, not only was the current reduced but also the fluctuations were eliminated. It is assumed that there would be some depth of pit above which these effects would not be observed.

Vigorous stirring of the solution with a small paddle prevented the initiation of pitting corrosion in dilute chloride solution, and inhibited initiation in more concentrated solutions (Fig. 4). These experiments were designed to illustrate the effects of the hydrodynamics and were not well controlled. We will report separately the results

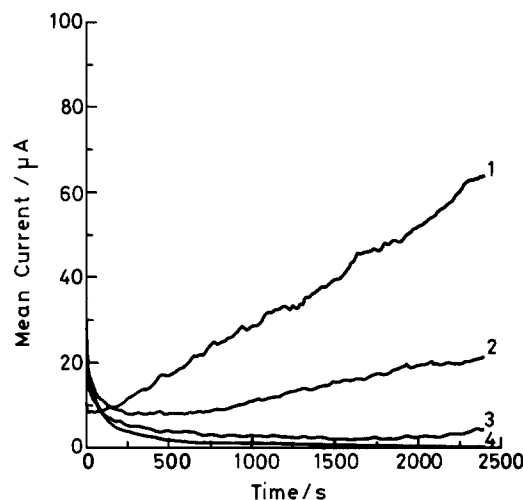


Fig. 3. Effect of buffer capacity, and electrolyte conductivity on ensemble mean current. 18Cr 13Ni 1Nb + 50 mV, potential step initiation, unstirred. 1: 0.028M NaCl. 2: 0.028M NaCl + 0.005M "tris" (pH 7.0). 3: 0.028M NaCl + 0.05M "tris" (pH 7.0). 4: 0.028M NaCl + 1M NaClO₄.

of experiments in which the Reynolds number is systematically varied under conditions of controlled hydrodynamic flow (10).

Initiation frequency of events.—In principle, the initiation frequency of the events which give rise to the current fluctuations can be obtained simply by counting the number of peaks in the current transient. In fact, this gives the number of "deaths" of events, and it is assumed that most events "die" so that the number of "births" is indeed close to the number of deaths. This approach also assumes that the current due to each event increases monotonically with time.

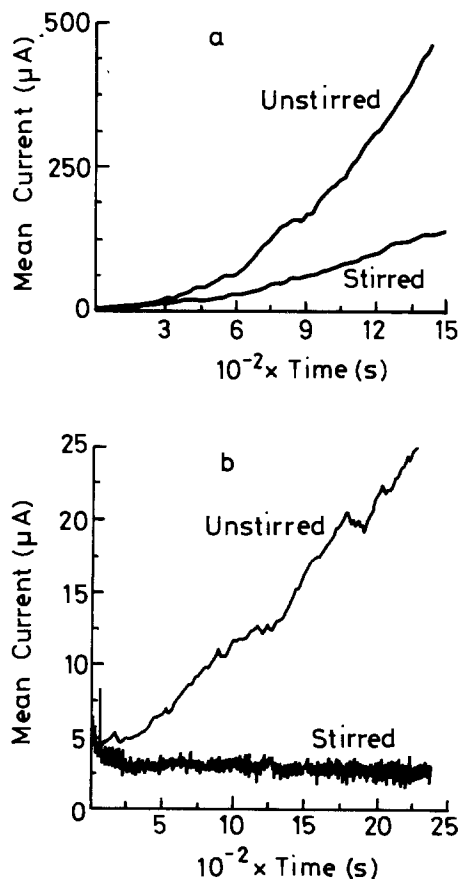


Fig. 4. Effect of stirring on ensemble mean transients. 18Cr 13Ni 1Nb, +50 mV (SCE), 0.28M (a) and 0.028M (b) NaCl.

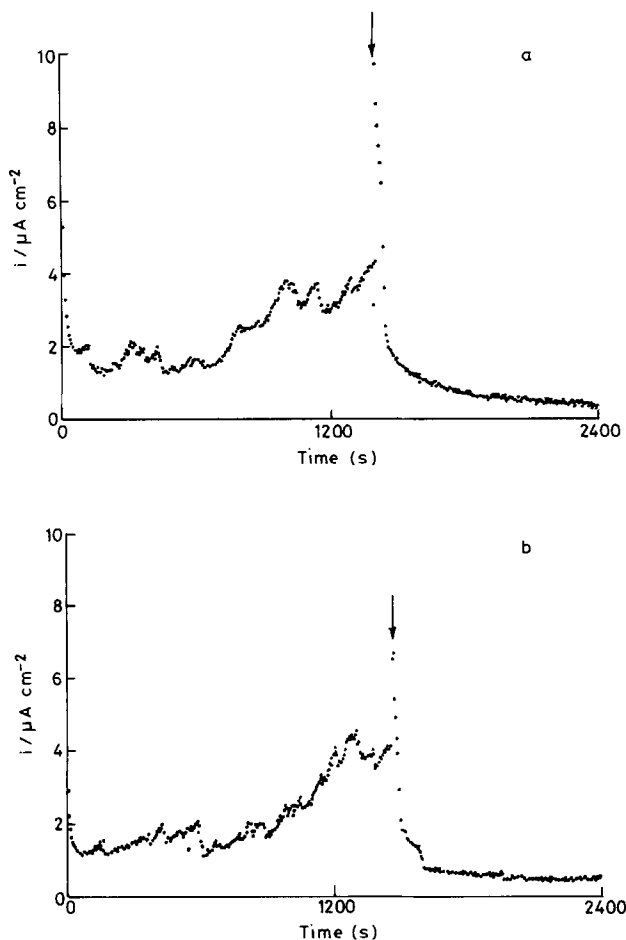


Fig. 5. Effect of addition, in the course of pitting corrosion, of buffer, and supporting electrolyte. a: NaClO_4 added (1M). b: "tris" added (0.05M). Time of addition marked by arrows. 18Cr 13Ni 1Nb, + 50 mV SCE, 0.028M NaCl, unstirred.

The use of any peak counting technique involves some judgment as to what is a significant peak and what is due to mere adventitious noise in the measurement system. In the peak counting procedure that was finally adopted, the experimental data were first smoothed slightly using a short section length (four points) running mean. A second running mean, with a long section length (100 points), was used to smooth out most of the fluctuations, and the difference between the four- and 100-point means calculated to give a trace which oscillated about

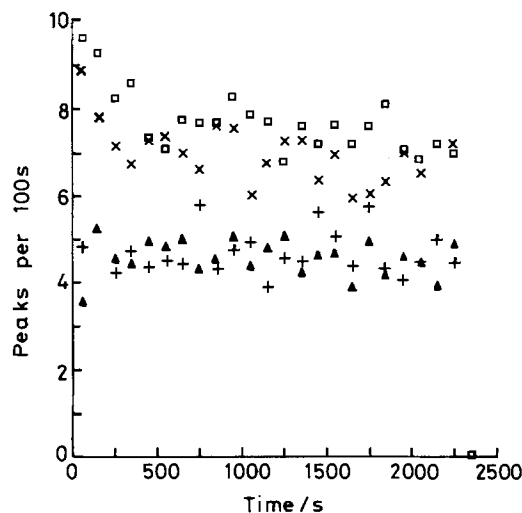


Fig. 6. Initiation frequency, determined by peak counting, as a function of time. Counting on 100s intervals. 0.028M NaCl unstirred. Triangles: 18Cr 13Ni 1Nb, + 50 mV SCE. \times : 18Cr 13Ni 1Nb, + 200 mV SCE. Plus signs: 304L, + 200 mV SCE. Squares: 304L, + 300 mV SCE.

zero. All peaks and troughs outside a noise band ($\pm 0.5 \mu\text{A}$) on the difference trace were counted; division by two yielded the estimate of the initiation rate. The value for the noise band was obtained from measurements made in 1M NaClO_4 , and from measurements made on a dummy cell. Figure 6 illustrates an important result, namely, that the event frequency, or nucleation rate, was effectively constant throughout the current transient. In Table II, nucleation rates for the different steels and environmental conditions are compared. A second important result was obtained, namely, that the nucleation rate was not significantly dependent on the nature of the steel or on the electrode potential. However, at low enough electrode potentials (different for each steel) (8, 10), or in the presence of a sufficient buffer concentration or of a supporting electrolyte, or in the absence of chloride, the nucleation rate was zero.

Slope analysis.—Inspection of the experimental transients (Fig. 1) implied that the current for each event rose linearly with time. If this was the case, then positive values of the slope of the $i-t$ record at any time should be the product of the number of active pits and the slope of the elementary transient, given the assumption that the time evolution of every event is the same. Figure 7 shows the probability density function (PDF) for positive values of the slope obtained over an ensemble of current transients. A running four-point regression, stepping along

Table II. Parameters of the general stochastic model; $A = 5 \text{ cm}^2$; $[\text{NaCl}] = 0.028\text{M}$; asterisk indicates step start; otherwise, ramp start

Steel	E (mV SCE)	Parameter		$10^2 \lambda (\text{s}^{-1}\text{-cm}^{-2})$	$10^2 \mu (\text{s}^{-1})$	10^8 $C (\text{A}\cdot\text{s}^{-1})$	$10^3 \alpha \Lambda (\text{s}^{-1})$	$\tau_c (\text{s})$	$\langle n \rangle$		σ_n		
		Other	Method	Peak counting	Spectral density	Slope analysis	PDF of slope	Passage time	Spectral density	Passage time	Calc.	Slope Analysis	
18/13/1	50*			1.0 ± 0.2	1.6	2	5	0.7 ^a	0	270	2.5	2.5	
	50*	[tris] = 0.005M		0.73 ± 0.2	1.3	3	5				1.2	1.2	
	50*	[tris] = 0.05M		0.29 ± 0.15		2							
	50	[NaClO ₄] = 1M		0.07 ± 0.08									
	0			0.06 ± 0.06									
	50			0.88 ± 0.2	1.6	2.4	5	1.1	0.17	100	240	1.8	1.8
304L	200			1.3 ± 0.3	1.6	1.6	10	3.1	2.8	50	170	4	4
	50	[NaCl] = 0.28M		1.0 ± 0.3	2.3		2			0	200		
	300			0.90 ± 0.2	1.9	2.5	8	1.0	0.35	40	240	1.8	1.8
316L	300			1.5 ± 0.3	2.0	0.8	12	8.8	3.5	50	110	10	8
	400			1.3 ± 0.3	1.2	2.2	5	0.8 ^b	0.5	100	260	3 ^b	2.5
25/20	300			1.5 ± 0.3	1.7	0.9	10	10 ^c	3.5	0	100	8 ^c	7
	400			0.79 ± 0.2	1.3		^d	4.9		10	150	^d	

^a Affected by crevice corrosion.

^b Increase in breakdown rate and number of pits, at longer time.

^c Decrease in breakdown rate and number of pits at longer time.

^d Slope analysis fails (see text).

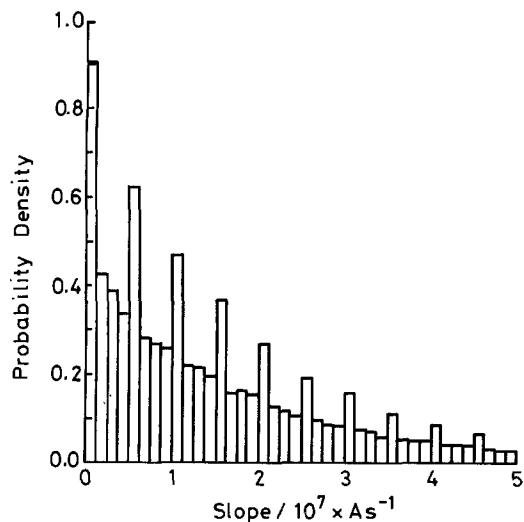


Fig. 7. Probability density function of the slope C of current-time traces. 304L, + 200 mV SCE, 0.028M NaCl, unstirred.

the transient one point at a time, was used to obtain the values of the slope. The PDF shows regularly spaced maxima at values which are multiples of an elementary slope; this result shows that the representation of the current as a sum of identical elementary linear ramps is quite adequate. Values of the elementary slope, C (Eq. [1]), are collected in Table II.

The time series of the current was converted into a time series of the number of pits by dividing the slope at any time by the elementary slope obtained from the PDF and rounding to an integral value. The ensemble mean number and the standard deviation of the number both rose rapidly to constant values (Fig. 8). The values are collected in Table II. The expected values are, for the unstable pits

$$\langle n_u \rangle = \sigma_{nu}^2 = a\lambda/\mu \quad (t \rightarrow \infty) \quad [2]$$

and for the stable pits

$$\langle n_s \rangle = \sigma_{ns}^2 = a\Lambda(t - \tau_c) \quad [3]$$

with the mean and variance for the total number being the sum of the quantities for the stable and unstable pits. It is assumed that, since the experimental records give constant values for $\langle n \rangle$ and σ_n , the unstable pits outnumber

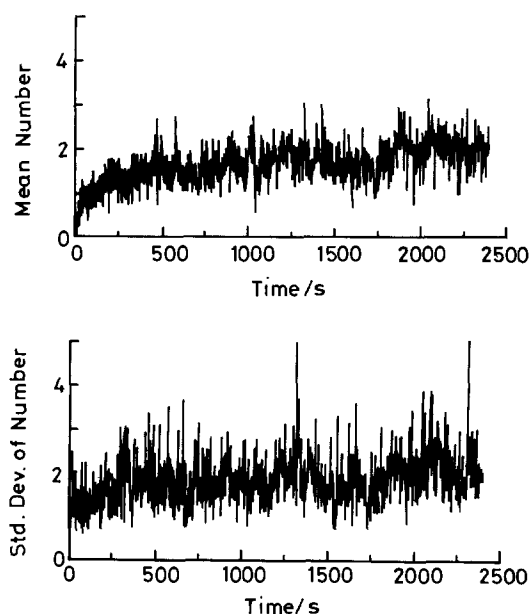


Fig. 8. Ensemble mean, and standard deviation of number of pits, derived from the experimental $i-t$ traces, and the elementary slope, C . 304L, + 200 mV SCE, 0.028M NaCl, unstirred.

ber the stable ones. Hence, given λ from peak counting, μ was calculated from $\langle n \rangle$ using Eq. [2], and values are collected in Table II. The observed σ_n (not σ_n^2 as predicted by Eq. [2] and [3]) were approximately equal to $\langle n \rangle$.

Passage time analysis.—In a previous paper (1), we related the probability of survival of an unpitted specimen to the initiation rate for stable pitting, Λ

$$\ln [P(0)] = -a\Lambda(t - \tau_c) = a(t - \tau_c) \lambda e^{-\mu\tau_c} \quad [4]$$

and showed that the time of onset of stable pitting was best defined as a time of last passage through some predetermined current level. The experimental data were complicated by a time varying charging current induced by the initial transition of the potential (Fig. 1); this introduced an arbitrary element into the definition of the passage current level, which was taken to be just above the minimum value of the ensemble mean current. Figure 9 shows typical plots according to Eq. [4]; values of Λ and τ_c are collected in Table II.

Spectral power density of the current.—Figure 10 illustrates the spectral power density of the current calculated from a chained set of current-time records and from a “detrended” set of records (1). Both traces show a high frequency decay as ω^{-2} , as expected for a linear elementary transient. Comparison of the power levels obtained for the chained set with the simulation and theoretical results given before (1) yielded a value for Λ . Values for μ were obtained from the power spectrum of the detrended records. A check on the consistency of the values for λ , μ , and C (the elementary slope) was obtained by comparing theoretical (1) and observed values for the low frequency white noise (detrended records).

Discussion

The discussion is in two parts. First, we discuss the adequacy of the general model and the self-consistency of the derived parameters, and point out where the general model fails. Second, we discuss the behavior of the derived parameters in terms of microscopic models for the corrosion process.

General model.—For the most part, the general model is adequate for describing the general behavior of the ensemble statistics, the slope distribution, the survival probability, and the power spectrum of the fluctuations. Experimental data and simulated data show the same general form. The values of the parameters C , Λ , λ , and μ derived by the different methods of analysis are self-consistent (Table II). There are, however, a number of deviations of behavior from that predicted by the general model. First, the values of τ_c related to Λ , λ , and μ by the

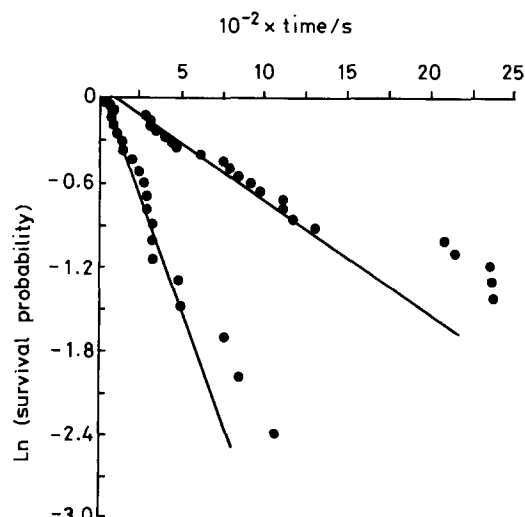


Fig. 9. Survival probability from passage time analysis, of 18Cr 13Ni 1Nb steel specimens, 0.028M NaCl, unstirred. Upper line +50 mV SCE. Lower line: +200 mV SCE.

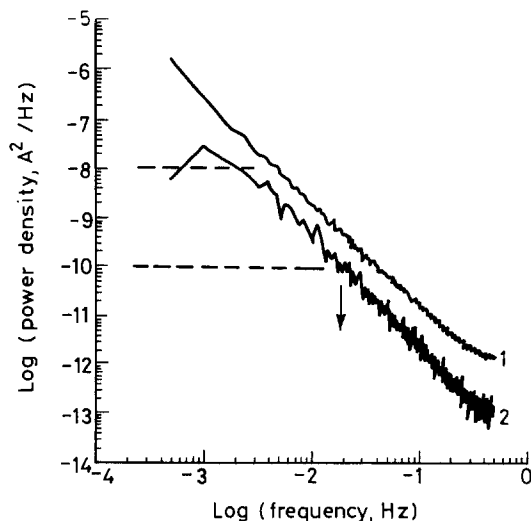


Fig. 10. Spectral power density of the current. 1: Chained records. 2: Detrended records. White noise level and death probability marked. 304L, + 200 mV, 0.028M NaCl, unstirred.

postulates of the model

$$\tau_c = -(1/\mu) \ln (\Lambda/\lambda) \quad [5]$$

are consistently much larger than the value given by passage time analysis. Second (Figure 2), the ensemble statistics show some deviations from the expected behavior for stable pitting (1), calculated using values of Λ (passage time) and C (slope analysis). The agreement between observed and expected behavior is, in general, quite striking, given that the parameters used have come from quite different methods of analysis of the data. However, at longer times, the mean $\langle I \rangle$ falls below, while the standard deviation, σ_I , falls above the value expected: the variability, especially at the lower potential, is greater than predicted. Third, in agreement with the results of Shibata and Takeyama (3), the survival probability at longer times was greater than that predicted by Eq. [4]. It seems that specimens which survive for longer than some given time are less likely to form stable pits than the rest of the ensemble of specimens. This effect is reflected by the values of Λ derived from spectral density analysis being consistently lower than those derived from passage time analysis: the ensemble power spectrum gives an average value of Λ for all specimens.

It would appear (11) that these difficulties with the general model can be resolved by allowing both λ and τ_c to take a distribution of values. Additionally, for both stable and unstable pits, in a development of an earlier idea (12), one could postulate propagation by a succession of growth, death, and renucleation events.

The main conclusions which follow from the application of the general model are as follows.

First, the nucleation frequency of unstable pits, λ , varies from zero to about $0.01 \text{ s}^{-1}\text{-cm}^{-2}$ over a rather narrow range of potential different for each alloy. The limiting value of nucleation rate, λ , does not depend on the nature of the alloy, the chloride concentration, or the electrode potential. This potential dependence is the classical form for a nucleation phenomenon.

Second, the death probability of unstable pits, μ , is also not sensibly dependent on electrode potential, nature of alloy, or chloride concentration.

Third, the critical age for transition of an unstable to a stable pit, τ_c , and elementary slope of the current-time transient, C , depend on the electrode potential.

Additions of buffer, and of supporting electrolyte, reduce the nucleation rate, λ , markedly. Stirring may affect both the nucleation rate and the death probability. We note that the potential at which the nucleation frequency drops to zero provides a rigorous definition of a pitting breakdown potential (8, 10).

These results may be interpreted in terms of a simple microscopic model of local acidification for the initiation of pitting corrosion.

Microscopic model.—We propose that the initiation of pitting corrosion requires the production and persistence of gradients of acidity and electrode potential on the scale of the surface roughness of the specimen. Fluctuations in these gradients, leading to the birth and death of events, could arise because of fluctuations in the boundary layer in the liquid at the metal surface; a pit becomes stable when its depth significantly exceeds the thickness of the solution boundary layer. The solution boundary layer is in two parts, one part defined by the roughness of the surface, the other part being the hydrodynamic boundary layer (Fig. 11). Local acidification would arise as a result of the hydrolysis of metal ions in the solution, formed as a result of the slow dissolution of the passive metal

$$i_p = k_1 f([\text{Cl}^-]_s, [\text{H}^+]_s) \exp\left(\frac{\beta \Delta \phi_{fs} F}{RT}\right) \quad [6]$$

where i_p denotes the passive current density, $\Delta \phi_{fs}$ the potential difference across the film-solution interface, β the transfer coefficient and $[\]_s$ denotes concentrations at the metal surface. In the most general case, the rate constant, k_1 , could be considered to be variable over the surface, for example, because of the presence of inhomogeneities in the alloy composition or of inclusions. The passive dissolution current is, of course, a material-dependent parameter which can, in principle, be measured independently. Its variation with solution composition is susceptible to detailed mechanistic description. One such description, a mechanism for rationalizing the acceleration of oxide dissolution by chloride, is at the heart of the discussion of pitting corrosion given recently by McDonald and co-workers (13).

In their discussion of the initiation of crevice corrosion, Oldfield and Sutton (14) introduced the idea of a critical crevice solution: a solution composition at which the metal could not remain passive, so that, should it be attained, rapid corrosion would commence. We postulate that a critical local solution composition can similarly be defined for the initiation of pitting corrosion. For example (4), if the passive current density has a dependence on $[\text{H}^+]$ of the form

$$i_p = k_2(1 + [\text{H}^+]_s/K_2) \quad [7]$$

then a critical local solution would have $[\text{H}^+]_s \approx K_2$. We derive additional support for this view from the fact that the current pulse associated with potential step initiation of the experiment was sufficient to initiate crevice corrosion around the specimen mount in a significant number of cases (4). This effect was suppressed by buffering the solution and was assumed to be triggered by a momentary local acidification at the edge of the specimen caused by the faradaic component of the charging current.

The parameters of the general model, λ , μ , and τ_c , can now be reconciled with this microscopic model.

Nucleation rate.—The nucleation rate is determined by the time required to establish the critical local pH. Some order-of-magnitude calculations can be given. Thus if δ_r denotes the roughness and δ_h the thickness of the hydrodynamic boundary layer, then the surface acidity attained as a result of the passive dissolution would be at most

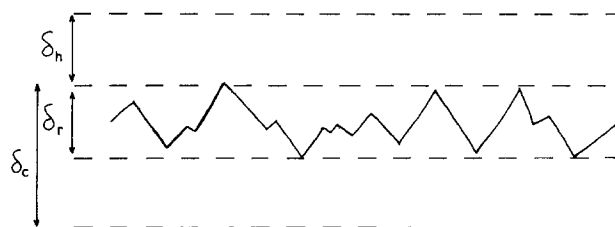


Fig. 11. Representation of boundary layers and critical penetration.

$$[H^+]_s \sim i_p(\delta_r + \delta_h)/FD_H \quad [8]$$

With our specimens, $\delta_r \sim 10^{-2}$ cm, and in an unstirred solution, one expects $\delta_h \sim 10^{-2} \cdot 10^{-1}$ cm, so if $i_p \sim 10^{-7}$ A-cm $^{-2}$, $pH_s \sim 5-6$.

Any change in local potential would result in a local value of i_p which might be substantially larger. In our work (Fig. 1), the ramp of potential at the start of the experiment gave current densities initially in the range 1 to 10 μ A-cm $^{-2}$, while a step change of potential gave local currents momentarily of greater than 100 μ A-cm $^{-2}$; Eq. [8] then implies $pH_s < 2$ if such currents last long enough. Such conditions, if maintained locally for a sufficient time, could certainly lead to a local breakdown.

One consequence of these ideas is that the nucleation rate for unstable pitting should depend upon the passive current density. Since the passive current density decreases steadily with time at constant potential, the probability of observing a pitting breakdown should decrease with time and the survival probability for the specimen should increase. In this respect, these ideas give a natural explanation why the survival probability at longer time was greater than that predicted by Eq. [4] (see Fig. 9, and the General model section above). These ideas also predict that the probability of pitting breakdown in experiments in which the specimen is prepassivated, then chloride introduced, at constant potential, should be less than that observed in experiments in which the potential is changed, provided that the introduction of chloride in the former experiment does not cause a current pulse.

The minimum local pH indicated by Eq. [8] for a passive current density of 10^{-7} A-cm $^{-2}$ ($pH_s \sim 5-6$) is clearly too high to promote a local breakdown, yet pitting events are observed when the current is as low as this. We can achieve some resolution of this difficulty by recognizing that the conditions required to trigger an event might be different from the conditions required to maintain one. Here, we explore qualitatively two ideas concerning the triggering of pitting events; later we discuss the maintenance of the events.

The first idea concerning the triggering of pitting events focuses attention on the transient behavior of the passive current. Any fluctuation of local potential and of local pH would give a local transient in i_p . The transient in i_p would feed back on the local potential and pH. Hence, depending on the coupling between transients in i_p , local potential, and pH, any small local disturbance would either damp out or self-amplify.

The second idea for the triggering of pitting events concerns the nature of the observed passive current density, i_p . It might be argued that the passive current is in reality a stream of rapid current pulses, as could arise from passive film breakage events, filtered by the specimen capacitance to appear as a steady current. As far as the local environment of the surface is concerned, one such pulse could be treated as an instantaneous deposition into the environment of a certain quantity of charge. If the volume of an occluded zone of the solution defined by the surface roughness is taken as 10^{-9} cm 3 , then a local pH 0 could be obtained by a charge pulse of 10^{-7} C—a local current pulse of, say, 100 mA for 1 μ s. Following such a pulse, locally, the resulting pH gradient would begin to disperse by diffusion, and, during a time scale defined by the rate of diffusion, there would be the possibility of a pit initiating in this local environment. If fast current pulses, like the ones which we have just postulated, were to occur all over the surface, then they would be filtered by the specimen capacitance and would only be separately observable if the capacitance was sufficiently low, that is if the area of the specimen was sufficiently small. The interfacial capacitance of the stainless steel in aqueous solution is of the order of 10 μ F-cm $^{-2}$; given this, it might be necessary to use electrodes as small as 10 μ m diam in order to observe noise events on the microsecond time scale.

In the presence of a sufficient concentration of buffer, a critical local pH could not be attained: this would explain why additions of buffer inhibit the nucleation pro-

cess. If i_p were too low, a critical local pH could not be obtained since unreasonably large values of δ_h would be required: a small potential dependence of i_p , different for the different alloys, could thus be the explanation for the fall of the nucleation rate to zero at low enough potential. Low enough chloride concentration at the surface would have the same effect. The effect of stirring would be to inhibit nucleation by reducing δ_h . Specimen orientation would be expected to affect the nucleation rate because of the effects of convection and density gradients in the solution; one might expect pit nucleation to occur more easily on horizontal specimens facing upward, as in our experiments, than on specimens facing downward or mounted vertically.

The effect of a supporting electrolyte is a crucial piece of evidence. In the absence of the supporting electrolyte, electromigration would increase the surface concentrations of chloride. The absence of a supporting electrolyte also increases the solution resistance. Both of these effects mean that, if the local current density was high enough, significant further concentration of chloride, and significant potential gradients on the scale of the surface roughness, could be obtained. However, for these effects to manifest themselves, the local current density would have to be far higher than the passive current density. Of course, once a pit has started, the local current density is much higher: a current of 1 μ A into an area of, say, $10 \times 10 \mu$ m is 1 A-cm $^{-2}$, so that once the critical conditions are established transport by electromigration and local potential gradients become extremely important phenomena (15, 16). Thus, the resistivity of 0.03M NaCl is about 100 Ω -cm, so that, on the scale of the surface roughness, 100 μ m with a local current density of 1 A-cm $^{-2}$ the local potential drop is 100 mV. It is therefore quite conceivable that the pit nucleus could find itself displaced from the passive into the active potential range. However, in the presence of 1M NaClO $_4$, resistivity about 10 Ω -cm, the local potential drop would only be 10 mV, so that the local zone could not get into the active range. One can therefore rationalize the phenomena by saying that a supporting electrolyte would not prevent the attainment of a critical pH, but that even if this was attained in the presence of a supporting electrolyte no pit would develop from it.

This is a more subtle view than the apparently straightforward kinetic idea of a critical pH embodied in Eq. [6]. In the modified view, attainment of the critical pH triggers off a local instability which is maintained by a local potential gradient. The solution resistance and chloride transport are important factors in maintaining this instability. The elementary slope, C , should depend upon the rate of change of the local conditions, upon the alloy composition, and, upon the local potential gradient, determined by the solution resistance. The possibility of the formation of salt films, which then limit the current, has been discussed (16).

Death probability.—Death of an event is supposed to occur as a consequence of a reduction in δ_h , so that the large local concentration excursions, caused by the large local current density, cannot be maintained. The observed event lifetimes, 50-100s in an unstirred solution, are indeed of the magnitude one might expect from fluctuations in a hydrodynamic boundary layer in such an unstirred solution, subject to natural convection. This idea predicts that the lifetime would not depend on anything other than the stirring of the solution, the roughness of the surface, and perhaps the orientation of the specimen.

Critical age.—The critical age can be defined as the ratio critical depth/velocity of propagation. The critical depth is determined by the boundary layers and would be smaller for a rougher specimen. The velocity of propagation is expected to vary strongly with the electrode potential, the chloride concentration, and the nature of the alloy. According to this view, the critical age and elementary slope are related. The elementary slope is a func-

tion of the electrode kinetics and solution resistivity in the local environment. If a simplified view is taken that the pit nuclei propagate at constant area, then the rate of penetration is proportional to the current: $v = \zeta i$. Writing δ_c for the critical penetration, and introducing Eq. [1] and the boundary layer thicknesses δ_r and δ_h , gives

$$\tau_c = [2(\delta_c - \delta_r - \delta_h)/\zeta C]^{1/2} \quad [9]$$

We note that the idea of a critical penetration contains the idea of a critical defect size for pit initiation. A defect could be a crack, for instance, or a microscopic crevice around the edge of an inclusion.

Recently, Okada (7) has given a model for pitting corrosion which postulates the formation of an unstable chloride nucleus as the precursor state. This model falls into the class defined by our general stochastic theory and affords an alternative microscopic interpretation of the values of the parameters. The ideas given (7) imply that the nucleation frequency and death probability should be functions of electrode potential and chloride concentration; effects of buffer capacity and electrolyte conductivity are not predicted. In these respects, Okada's model does not accord with our experimental results.

Conclusion

The application of a stochastic approach to the study of the initiation of pitting corrosion on stainless steels and the development of methods of analysis of data, based on a general phenomenological model, has led to a clarification of which aspects of the process are dependent upon the composition of the steel and which are not. Rigorous definitions of a pitting breakdown potential and of survival probability can be made. Strong effects of buffer capacity, solution conductivity, and stirring at constant chloride concentration have been shown. The results have been interpreted in terms of a simple microscopic model of local acidification for the initiation of pitting corrosion. Production, on the scale of the surface roughness of the specimen, of a gradient of acidity, as a consequence of the small passive dissolution current of the metal, triggers off a local instability, which is maintained by a local potential gradient. Fluctuations in these gradients, leading to the birth and death of events, arise because of fluctuations in the thickness of the solution boundary layer at the metal surface. The concept of a critical penetration or critical defect size for the onset of stable pitting forms a part of this view. It is notable that in emphasizing the importance of boundary layers, roughness, and local transport conditions these ideas eliminate

the need for special postulates to explain why pitting corrosion is localized. It is notable also that, in breaking down a complex phenomenon into much simpler component parts, the stochastic approach and the general model have rendered much more tractable the problem of constructing and testing suitable microscopic models. The use of the stochastic approach has led to the possibility of testing microscopic models much more rigorously than has been possible hitherto.

Manuscript submitted May 22, 1984; revised manuscript received Feb. 1, 1985. Parts of this article were presented as Paper 10 at the Montreal, Quebec, Canada, Meeting of the Society, May 9-14, 1982, and as Paper 238 at the New Orleans, Louisiana, Meeting of the Society, October 7-12, 1984.

AERE Harwell assisted in meeting the publication costs of this article.

REFERENCES

1. D. E. Williams, C. Westcott, and M. Fleischmann, *This Journal*, **132**, 1796 (1985).
2. U. R. Evans, "Corrosion and Oxidation of Metals," Edward Arnold, London (1960).
3. T. Shibata and T. Takeyama, *Corrosion*, **33**, 243 (1977).
4. D. E. Williams, C. Westcott, and M. Fleischmann in "Passivity of Metals and Semiconductors," p. 217, M. Froment, Editor, Elsevier, Amsterdam (1983).
5. M. Fleischmann, M. Labram, C. Gabrielli, and A. Sattar, *Surf. Sci.*, **101**, 583 (1980).
6. E. Budevski, M. Fleischmann, C. Gabrielli, and M. Labram, *Electrochim. Acta*, **28**, 925 (1983).
7. T. Okada, *This Journal*, **131**, 241 (1984).
8. D. E. Williams and C. Westcott, in "Proceedings of the 9th International Conference on Metallic Corrosion, Toronto, 1984," Vol. 4, p. 390, National Research Council of Canada, Ottawa, Ont., Canada (1984).
9. U. Bertocci and Y. Yang-Xiang, *This Journal*, **131**, 1011 (1984); U. Bertocci, Personal communication.
10. D. E. Williams, J. Stewart, and M. Fleischmann, To be published in the Symposium on Electrochemical Methods in Corrosion Research, Toulouse, France, July 9-12, 1985.
11. M. Fleischmann and D. E. Williams, In preparation.
12. T. Shibata and T. Takeyama, in "Metallic Corrosion, Proceedings of the 8th ICMC," p. 146, DEHEMA, Frankfurt, Germany (1981).
13. L. F. Lin, C. Y. Chao, and D. D. MacDonald, *This Journal*, **128**, 1194 (1981).
14. J. W. Oldfield and W. H. Sutton, *Br. Corros. J.*, **15**, 31 (1980).
15. H. W. Pickering and R. P. Frankenthal, *This Journal*, **119**, 1297 (1972).
16. T. R. Beck and R. C. Alkire, *ibid.*, **126**, 1662 (1979).

Cooling Kinetics: Evidence for a Hydrogen Countercell in 304L Stainless Steel Crevices at High Temperatures

D. F. Taylor* and C. A. Caramihas-Foust

General Electric Corporate Research and Development, Schenectady, New York 12301

ABSTRACT

Cell current reversals deep within tubular 304L stainless steel crevices containing 0.2M NaCl electrolyte at 290°C demonstrated H(I) reduction at previously anodic sites. Analysis of transient currents during cooling showed an increase in anodic activity adjacent to the crevice mouth as oxygen reduction at the mouth decreased, a direct indication that molecular hydrogen was diffusing outward and oxidizing in the active/passive transition region. Calculations confirmed that a similar hydrogen counter cell was operating in crevices containing 0.1M Na₂SO₄.

Previous papers in this series on the high temperature aqueous crevice corrosion of Fe-Ni-Cr alloys concluded that the reduction of H₃O⁺ ions or water molecules to molecular hydrogen makes an important contribution to the solution composition and electrode potential in the occluded region (1-3). These experiments examined corro-

* Electrochemical Society Active Member.

sion behavior under conditions where the presence of dissolved oxygen outside a tubular crevice established potential gradients within the system. Since no artificial imposition of potential or current was present to establish a steady state, some rather sudden and dramatic changes in crevice chemistry occurred. In alloys with sufficient nickel content, there was a tendency for the internal crev-

ice electrode potential to attain or exceed the electrode potential of the external surface during acidification (2, 3). Rapid neutralization always followed. In other systems, iron oxidation controlled the anodic corrosion reaction, and the crevice interiors remained acidic until the temperature started to decrease, but those solutions always had attained neutral pH by the time they reached 25°C. Thermodynamic calculations implicated H(I) reduction, but the nature of the neutralization reaction, especially the sink for H⁺, and the extent to which such a cathodic reaction might have been occurring at temperature, prior to the neutralization, were unclear. This paper describes current measurements on active crevices both at 290°C and during cooling that indicate strong opposition to the acid-generating oxygen/metal macrocell by a hydrogen counter-cell.

Experimental

Commercial 304L stainless steel tubing (18.2Cr, 10.9Ni, 0.02C) (3) with an inside diameter of 1 mm was cut into 46 cm lengths, and each of these pieces was subdivided into two parts, either 3, 9, or 15 cm from one end. All components were degreased with trichloroethylene and rinsed first with acetone, then with distilled, deionized water. One end of each longer segment was arc welded closed in an argon atmosphere, and both segments of each pair were attached to autoclave feedthroughs of the same material. The segment pairs were reassembled by inserting electrically insulating 5 mm tubular zirconia spacers with the same inner and outer diameters as the metal tubing and heat shrinking sufficient Teflon® PTFE tubing over the junctions to extend several centimeters on either side. For most experiments, stainless steel tubing unions were modified to fit closely over the Teflon PTFE sleeves. These insulated jackets strengthened the divided crevice fixtures and prevented detrimental amounts of oxygen from reaching the junction.

The tubes were bent into a U shape, filled with deaerated 0.1M Na₂SO₄ or 0.2M NaCl by evacuation, mounted in a 1 liter titanium alloy autoclave, and exposed at 290°C, 10.3 MPa for five days to water which was air saturated at room temperature and pressure (8.5 ppm dissolved O₂) and flowed through the autoclave at 10 cm³ min⁻¹. A PAR Model 173 potentiostat electrically isolated from the autoclave served as a zero resistance ammeter and measured current flow from one section to the other while maintaining both parts of the crevice fixture at the same electrical potential. After cooling, the tubes which had contained Na₂SO₄ solution were immersed in liquid nitrogen, cut into 3 cm segments, and warmed to room temperature for pH measurements on their contents.

Results

Figure 1 illustrates the effect on divided tubular crevices of a protective stainless steel jacket and an electrical connection between open and closed ends. In the absence of an effective barrier, abundant molecular oxygen diffused through the Teflon PTFE coating and established a cathodic region at the open end of the inner segment. Unable to diffuse away easily, excess reaction-product hydroxyl ions accumulated at the junction, and the pH profile at room temperature shows how little mixing occurred during cooling and contraction of the crevice electrolyte. With a protective jacket, but no electrical connection between segments, oxygen eventually passivated the outer portion of the crevice and established a cathodic region at the open end of the inner segment. A comparison of pH profiles shows that this deactivation of the outer segment shifted the acidic region an equivalent distance into the crevice and perhaps slightly reduced the amount of crevice activity, and hence acidity, by restricting oxygen transport.

Figure 2 reproduces the current-time profiles for a set of three divided crevices which contained 0.2M NaCl. The current reversals in the crevices divided at 9 and 15 cm from the mouth show directly the slow development of a net cathodic reaction deep within the crevice. Measure-

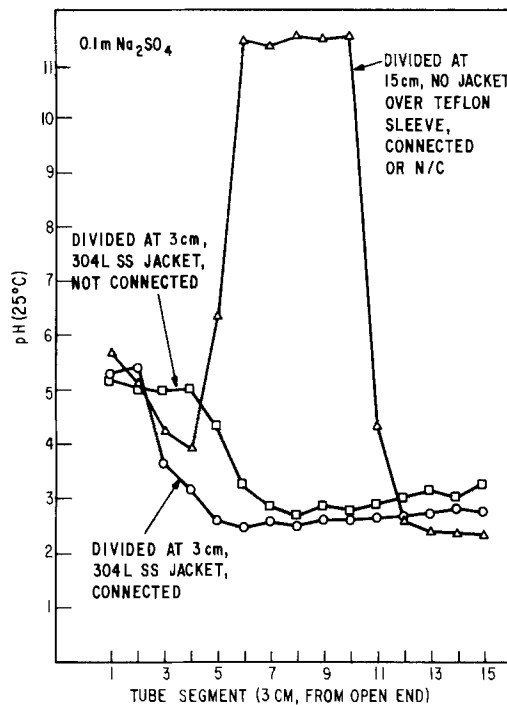


Fig. 1. Room temperature pH profiles in 304L stainless steel crevices after exposure with 0.1M Na₂SO₄ electrolyte to aerated water at 290°C for 5 days. Abscissa units are the number of 3 cm lengths, starting at the open end. "Connected" signifies electronic continuity from one side of the division to the other.

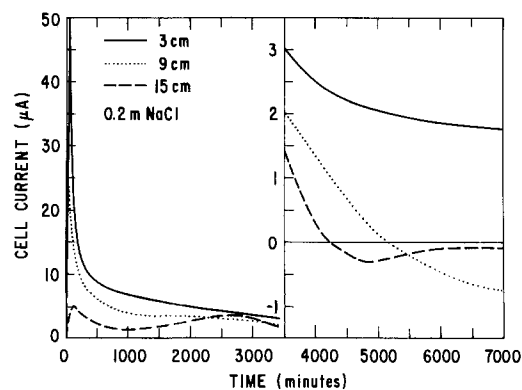


Fig. 2. Cell current in 304L stainless steel crevices during exposure with 0.2M NaCl electrolyte to aerated water at 290°C. Open end cathodic, interior anodic for positive values.

ments on identical crevices containing 0.1M Na₂SO₄ showed no such reversals, but the currents were similar in magnitude.

After the current reversed in chloride containing crevices, cooling the systems increased cathodic current flow within the inner segment. If the location of the dividing insulator was such that no current reversal occurred during exposure at 290°C, cooling induced the anodic to cathodic transition in chloride systems. The dotted curve in Fig. 3 illustrates this latter type of behavior for a sulfate crevice with the junction at 9 cm from the open end. Division of sulfate containing crevices at 3 or 15 cm produced complex cooling-current transients with multiple reversals like those of the dashed curve.

Discussion

Room temperature pH measurements after cooling reveal little about the high temperature behavior of stainless steel crevices containing chloride electrolytes, but Na₂SO₄ solutions produce interesting post-exposure results. Figure 1 shows the characteristic room temperature distribution of acidity in an electrically reconnected divided fixture which macrocell crevice corrosion with Na₂SO₄ always has produced in 46 cm crevice tubes during

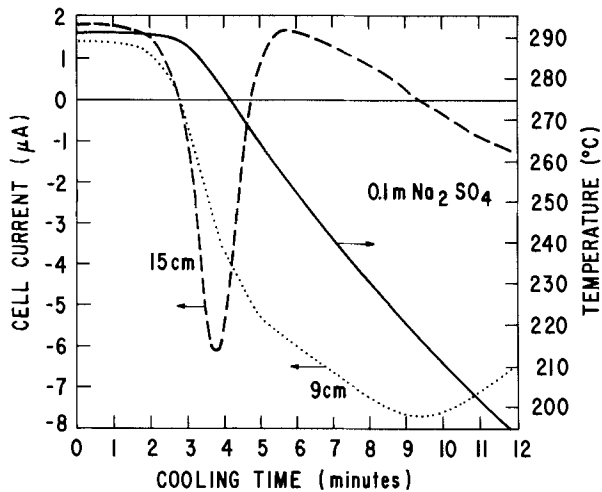


Fig. 3. Cell current in 304L stainless steel crevices during cooling after exposure with 0.1m Na₂SO₄ electrolyte to aerated water at 290°C. Polarity as in Fig. 2.

exposure to aerated water at 290°C (1, 3). The reproducibility of this behavior and the absence of any measurable effect from division provided justification for combining the results from different experiments with the same electrolyte. Positioning the insulators at either 3, 9, or 15 cm limited resolution of the current profiles to the net current between adjacent insulator locations. Thus at any time after the start of an experiment the difference between the current which was flowing into a 9 cm section and that flowing into a 3 cm section should have had its source or sink at the alloy/electrolyte interface between 3 and 9 cm from the crevice mouth. For the 1 mm crevice diameter, an average current of 1×10^{-6} A-cm⁻¹ (linear current density) was equivalent to 3.2×10^{-6} A-cm⁻². Figure 4 shows selected results from this type of reconstructive calculation for crevices containing each electrolyte. Although the cathodic reaction deep in the sulfate crevices never became strong enough at 290°C to reverse the current, it was sufficient to create a locally cathodic region and current profiles quite similar to those in the chloride system.

Oxygen/alloy macrocell corrosion and metal hydrolysis generate hydrogen ions. Thermodynamics dictates that electrochemical reduction of these hydrogen ions must counteract their generation as the pH decreases (4). There is little doubt that the internal cathodic reaction evident between 9 and 15 cm from the crevice mouth was

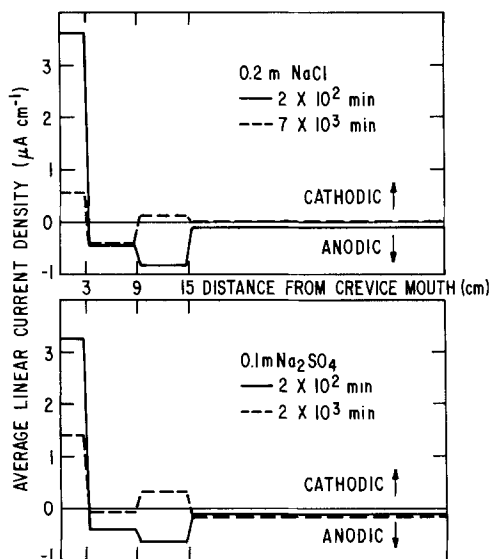
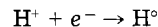


Fig. 4. Calculated average linear current density in 304L stainless steel crevices after 2×10^2 , and 2×10^3 (sulfate), or 7×10^3 min (chloride), at 290°C. Positive values are cathodic.



in both systems, but the isothermal data contained no evidence for a balancing anodic reaction other than metal oxidation. Upon cooling, however, the crevice electrolyte contracted and relatively pure autoclave water entered the crevice mouth. Figure 3 shows how rapidly the separation of conductive electrolyte from the supply of dissolved oxygen external to the crevice allowed an oxidation to take over and dominate the reactions near the opening. Evidently, this anodic reaction was occurring before the temperature started to drop. Figure 5 shows that as the temperature decreased, the current between 0 and 9 cm from the mouth became more anodic, while H⁺ ion reduction increased significantly between 9 and 15 cm. Although some metal may have been oxidizing, the dominating anodic reaction, therefore, must have been the reoxidation of molecular hydrogen, which was diffusing from its source toward the crevice mouth.

The operation of such a hydrogen counter-cell helps to explain the rapid neutralizations, the negligible internal potential drop, and the remarkable uniformity of electrolyte chemistry which are characteristic of these crevice systems (1-3). Once oxygen/alloy macrocell corrosion has lowered the internal pH sufficiently to cause local redox corrosion and establish a flux of molecular hydrogen toward the crevice mouth, reoxidation of that hydrogen reduces the dependency on an internal potential gradient for continued cell operation. Figure 6 summarizes these relationships in a schematic diagram. Thus, in the steady-state limit of a perfect balance with complete hydrolysis,

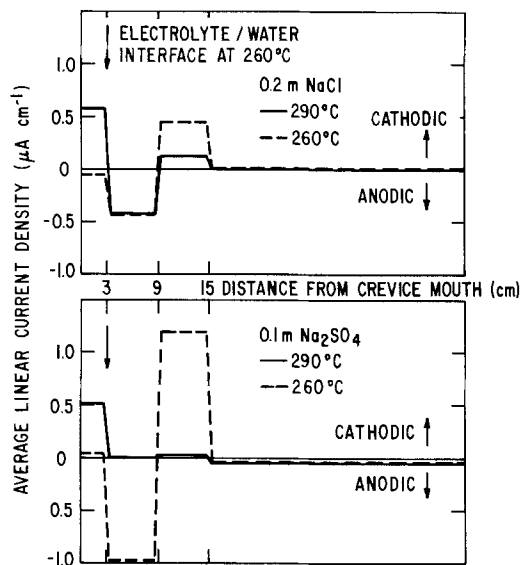


Fig. 5. Calculated average linear current density in 304L stainless steel crevices just before cooling, and at 260°C (electrolyte/water interface at 3 cm). Positive values are cathodic.

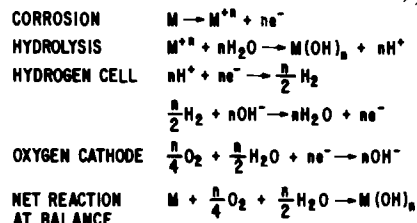
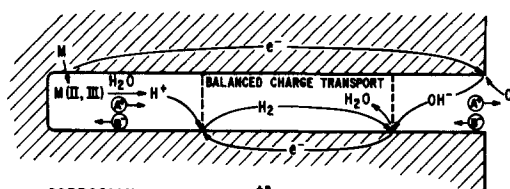


Fig. 6. Schematic representation of crevice corrosion with a balancing hydrogen counter-cell.

diffusion of water and H_2 would replace the transport of charged species between the transition and interior regions, including the movement of electrons in the metal, and corrosion would continue with a constant acidic interior pH. Potential/pH measurements at 290°C on 304L stainless steel crevices containing chloride electrolytes indicated behavior approaching this type of balance (3).

The hydrogen shuttle can reduce, eliminate, or reverse intermediate potential gradients within the crevice, but continuing corrosion still depends on the driving force of an oxygen/alloy macrocell EMF between the crevice mouth and its interior. When this driving force disappears, there are two mechanisms available for crevice neutralization. First, the hydrogen countercell can continue to operate in the absence of oxygen reduction and metal oxidation. This requires an outward flow of negative ionic charge in the crevice electrolyte from the interior to the site of H_2 oxidation, a direction opposite to that required for macrocell acidification, and the cooling-current kinetic curves clearly demonstrated that current reversal. Second, local redox corrosion in the interior could electrochemically reduce excess H^+ ions to H_2 . These experiments showed that hydrogen could diffuse away from the reaction site, but this mechanism also requires that a significant fraction of the metal corrosion products not hydrolyze, *i.e.*, remain as positively charged species or as complexes with anions other than OH^- . The hydrogen countercell offers an attractively simple explanation, but whether one or both mechanisms are opera-

tive, these experiments have revealed directly a substantial and important contribution from the diffusion of molecular hydrogen to the electrochemical conditions in active crevices at high temperatures.

Acknowledgment

The authors are grateful to the Electric Power Research Institute, Incorporated, for financial support of this work under Contract no. RP 2006-6.

Manuscript submitted Dec. 26, 1984; revised manuscript received April 1, 1985. This was Paper 228 presented at the New Orleans, Louisiana, Meeting of the Society, Oct. 7-12, 1984.

General Electric Company assisted in meeting the publication costs of this article.

REFERENCES

1. D. F. Taylor and M. Silverman, *Corrosion*, **36**, 544 (1980).
2. D. F. Taylor and C. A. Caramihas, *This Journal*, **129**, 2458 (1982).
3. D. F. Taylor and C. A. Caramihas, in "Embrittlement by the Localized Crack Environment," R. P. Gangloff, Editor, p. 105, The Metallurgical Society of AIME, Warrendale, PA (1984).
4. M. Pourbaix, Paper presented at the NATO Conference on Atomistics of Fracture, Corsica, May 1981; *Rapports Techniques CEBELCOR* 141, RT. 261 (1981).

A New (W,Mo)C Electrocatalyst Synthesized by a Carbonyl Process

Activity Enhancement Resulting from Water Vapor Treatment in the Synthesizing Process

T. Kudo, A. Ishikawa, G. Kawamura, and H. Okamoto

Hitachi Limited, Central Research Laboratory, Kokubunji, Tokyo 185, Japan

ABSTRACT

It has been revealed that electrocatalytic activity of tungsten and molybdenum mixed carbides formed on a carbon fiber substrate using a process in which metallic film formed by CVD at 450°C from $W(CO)_6$ and $Mo(CO)_6$ is carburized with CO at 820°C is enhanced by exposure to water vapor (~20 torr) at its synthesizing stage before the carburization. Activity tests in relation to electro-oxidation of H_2 and CH_3OH conducted in 1M H_2SO_4 at 50°C show that the potentiostatic current generated by reactants per real surface area of the catalyst thus obtained is 0.27 $A\cdot m^{-2}$ (at 0.2V vs. RHE) and 0.0037 $A\cdot m^{-2}$ (at 0.5V), respectively. The activity enhancement resulting from water vapor treatment is discussed in the light of surface analyses using Auger electron spectroscopy.

Tungsten carbide, often considered to have platinum-like catalytic properties (1), is one of the most promising alternative catalysts for replacing costly platinum for hydrogen electrodes in fuel cells using acidic electrolytes. Ross *et al.* have conducted extensive studies of WC electrocatalyst, especially on the relation between activity and surface compositions, and have demonstrated that only a catalyst having carbon deficient surface composition exhibits high activity (2-4). The most active catalyst reported by them (4) can generate a hydrogen oxidation current as high as 1.05 $A\cdot m^{-2}$ (real or BET surface area of the catalyst) at 177°C, though this value is three or four orders of magnitude lower than that for platinum (5).

In a previous paper (6), the authors disclosed a novel preparation technique whereby WC and (W, Mo)C electrocatalysts are formed on a carbon fiber substrate, in which metallic film formed by CVD at 450°C using $W(CO)_6$ and/or $Mo(CO)_6$ is then carburized with CO at 820°C.

The (W, Mo)C catalyst thus obtained has a hexagonal WC structure (a_0 :2.89Å; c_0 :2.85Å), and there is little contamination by carbon in elemental forms, on its surface, according to observations by Auger electron spectroscopy (AES). Activity tests in relation to electro-oxidation of H_2 , HCHO, and CH_3OH conducted in 1M H_2SO_4 revealed that the potentiostatic current produced by each

reactant per real surface area of the catalyst is 0.12 $A\cdot m^{-2}$ (at 0.2V vs. RHE), 0.04 $A\cdot m^{-2}$ (at 0.3V), and 0.00082 $A\cdot m^{-2}$ (at 0.5V), at 50°C.

Particularly for the oxidation of methanol, Mo is indispensable, as the oxidation current generated by a Mo-free catalyst quickly decays resulting in almost a null current at a steady state. Molybdenum seems, therefore, to act as a center to remove poisonous intermediates from the methanol electro-oxidation, or to lead the reaction to another path in which poisons are not formed.

The (W, Mo)C electrocatalyst obtained by the CVD process is, therefore, expected to provide an economical negative electrode for acid electrolyte-type methanol fuel cells, which would be a most hopeful electrochemical energy conversion device because methanol is a high energy density liquid fuel capable of being easily handled and widespread usage is expected in the near future.

In this report, we show that the activity of (W, Mo)C catalyst is notably improved by a water vapor treatment during its synthesizing process, and this effect is examined by characterizing the catalyst's surface using AES.

Experimental

Catalyst preparation.—A schematic drawing of the apparatus used for catalyst preparation is shown in Fig. 1,

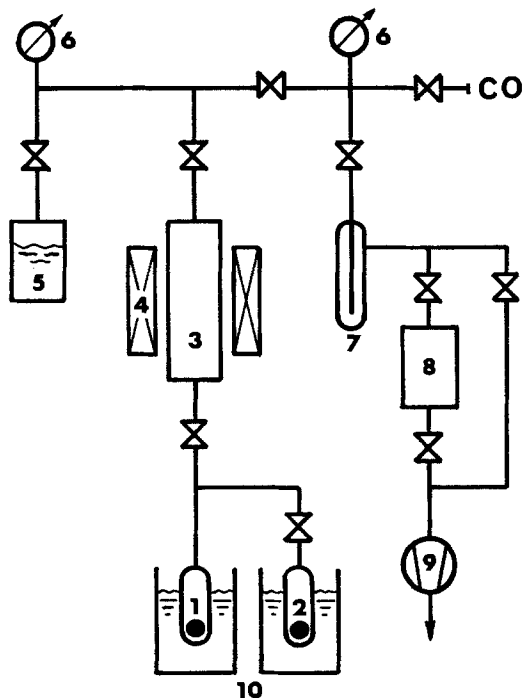


Fig. 1. Schematic drawing of the apparatus to synthesize the catalysts. 1 and 2: CVD sources [$W(CO)_6$ and $Mo(CO)_6$, respectively]. 3: Quartz reaction tube. 4: Image furnace. 5: Water vapor source. 6: Pressure gauges. 7: Liquid N_2 trap. 8: Diffusion pump. 9: Rotary pump. 10: Cald baths.

this being the same in principle as that used in the previous work except that (i) two source vessels for $W(CO)_6$ and $Mo(CO)_6$ are equipped to separately control the evaporations and that (ii) CVD pressure is reduced using a diffusion pump. The CVD rates were controlled by monitoring CO pressure generated by the decomposition of hexacarbonyls. The total pressure employed in this experiment was 1×10^{-3} torr, in which partial pressure from $Mo(CO)_6$ decomposition was 2×10^{-4} torr. The pressure observed when the sources ceased evaporating was 1×10^{-6} torr. In order to induce carbonyls to decompose completely, a porous glassy carbon rod was placed in the downstream side of the reaction tube. However, a considerable part of carbonyls was probably allowed to pass through without decomposition.

The synthesizing procedure and conditions are summarized in Fig. 2. As a substrate, the same carbon paper (E-715, Kureha Chemical Company) was used as in the previous work. The size of the substrate piece was 1.2×3 cm, and its surface area was estimated to be about 50 cm^2 . The sample was stored in 1M sulfuric acid to prevent its coming into direct contact with air.

Electrochemical measurements.—The electrocatalytic activity was investigated by a conventional technique using a potentiogalvanostat (Princeton Applied Research, Model 173), and a three-compartment glass cell, in which the working electrode was connected to the outer circuit through a Au lead wire, as Au proved to be almost inert to the reactants, i.e., H_2 and CH_3OH . The details were reported in the previous paper (6).

The real surface area of the electrode was estimated from its capacitance associated with the double layer and the adsorption-desorption of hydrogen on the electrode. Details about this technique, involving linear sweep voltammetry, are also given in the previous paper.

Surface analyses.—The surface composition in relation to W, Mo, C, and O was determined by AES using an instrument equipped with a thermal field emission-type cathode consisting of titanium-coated tungsten, with a probe diameter of $0.03 \sim 0.5 \mu\text{m}$. This instrument was recently developed at Central Research Laboratory of Hitachi Limited. The details of measuring conditions are given in the caption of Fig. 3.

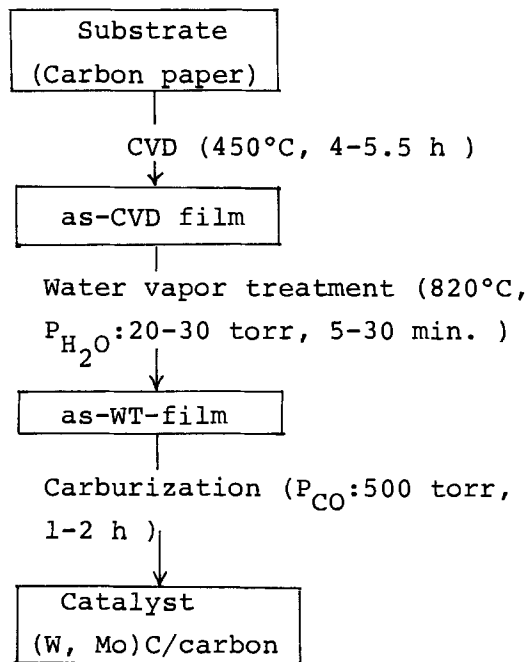


Fig. 2. Catalyst synthesizing procedure

A $5 \times 5 \text{ mm}$ piece of carbon paper coated with catalyst, etc., was used as a specimen for AES analysis. Spots to be analyzed were selected through SEM observations to provide an average. In order to examine distributions of each element as a function of depth from the original surface, sputter etching using Ar ion (5 keV , 5×10^{-5} torr) was conducted. Etching rate was about $10 \text{ \AA} \cdot \text{min}^{-1}$.

A typical Auger spectrum given by (W, Mo)C catalyst with the assignment of each peak is shown in Fig. 3. The concentration of each element was calculated from the peak-to-peak heights of a specific transition on the basis of the following equation

$$C_k = \frac{H_k/S_k}{\sum_i H_i/S_i}$$

where C_k , H_k , and S_k represent atomic concentration, peak-to-peak height, and sensitivity factor, respectively. The values of sensitivity factor (7) corresponding to the transition in the relevant elements used for the analysis with the electron energy at which the peak appears are

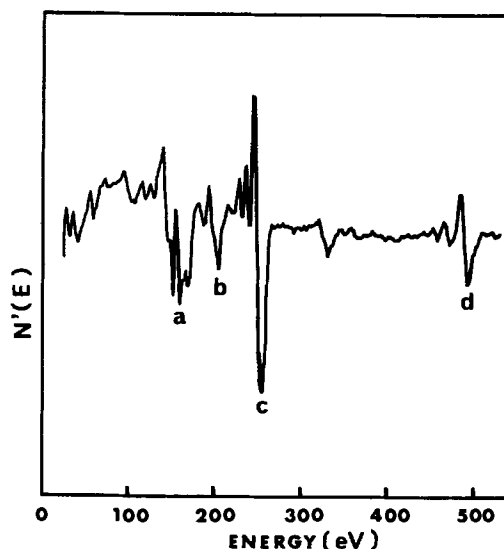


Fig. 3. Auger electron spectrum obtained with (W, Mo)C catalyst (sample C). Peaks a, b, c, and d, assigned to the transitions in W NNN, Mo MNN, C KLL, and O KLL, respectively, are used for quantitative surface analyses. $E_p = 10 \text{ keV}$. $E_m = 4 \text{ eV}$ peak-to-peak. $\tau = 300 \text{ ms}$.

Table I. Peaks of AES and their sensitivity factors used for quantitative surface analyses

Elements	Transition	Energy (eV)	Sensitivity factors
W	N ₅ N ₆ N ₆	180	0.13
Mo	M ₂ N _{4,5} N _{4,5}	221	0.26
C (graphite)	KLL	273	0.11
C (carbide)	KLL	273	0.23
O	KLL	503	0.67

shown in Table I. Although the peak at 188 eV is usually used in a quantitative analysis of Mo, the one at 221 eV was employed in the present study because the former overlaps with the W NNN transition at 180 eV. The factor of this transition is estimated to be 0.26, as compared to peak heights of pure Mo at 188 and 221 eV.

Results

SEM observation and x-ray diffraction.—Scanning electron micrographs of carbon paper substrate, as-CVD film, and catalyst carbide film are shown in Fig. 4a, 4b, and 4c, respectively. The as-CVD film has a smooth surface and shows good coverage. Conversely, there are many fine ripples on the surface of the catalyst film, which may have arisen from a volume increase which accompanied the carburization of the CVD film.

X-ray diffraction showed that the as-CVD film is substantially amorphous, though a weak and broad peak assigned to metallic W or Mo was seen. It was found that all catalysts investigated in the present paper take the hexagonal WC structure with a_0 : 2.84Å and c_0 : 2.90Å, regardless of the differing surface composition in each sample, as shown in a later section.

Enhancement of electrocatalytic activity resulting from water vapor treatment.—Rather accidentally, we have found that the electrocatalytic activity of (W, Mo)C formed on carbon fiber substrate using the CVD process is notably promoted by exposure to water vapor at its synthesizing stage just preceding carburization.

In Table II, electrocatalytic activities, represented by oxidation currents produced by H₂(i_{H_2}) and CH₃OH(i_{CH_3OH}), are shown for several catalysts synthesized under various conditions. The oxidation currents were measured at 50°C in 1M H₂SO₄ containing saturated H₂ or 5M CH₃OH. Data for sample A are taken from the previous report (6).

Activity difference between sample A and B may be attributed to difference of carbonyl pressures at the CVD stage, which has a substantial influence on the amount of carbon inclusion in CVD film, as shown in a later section in this text. The carbon monoxide pressure generated by decomposition of carbonyl compounds in the CVD process was about 1×10^{-3} torr for the apparatus in the present paper, whereas it was around 10^{-2} or more in the previous work.

Sample C, synthesized under essentially the same conditions as for sample B except for having been subjected to the water vapor treatment, shows activity two times

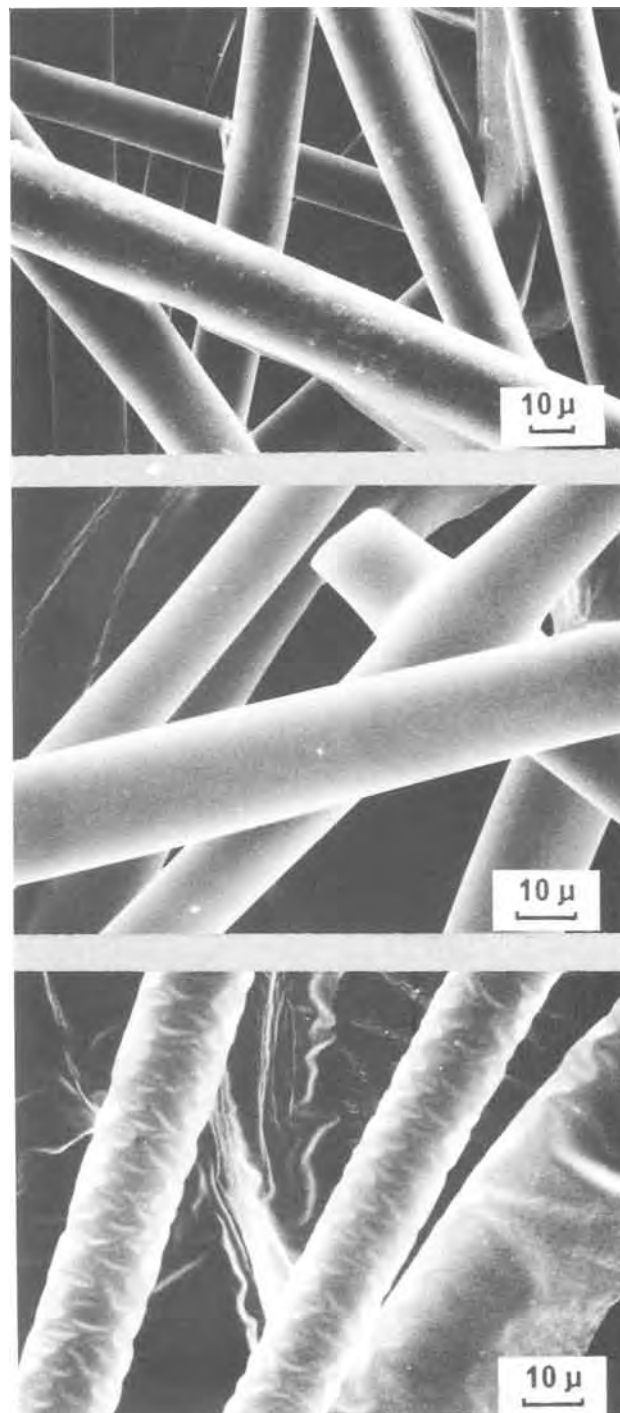


Fig. 4. Scanning electron micrographs of carbon paper substrate (a, top), as-CVD film (b, middle), and catalyst (carbide) film (c, bottom) in the final form. As-CVD film and catalyst are identical to sample D-as-CVD and D in Table III, respectively.

Table II. Activity of catalysts prepared under various conditions

Sample	Pressure at CVD (torr)	H ₂ O treatment	Carburization	Anodic current at 50°C (mA·m ⁻² real surface area)	
				H ₂ ^a	CH ₃ OH ^b
A ^c	10 ⁻²	None	1h, 500 torr	115	0.82
B	1 × 10 ⁻³	None	1h, 500 torr	100	1.5
C	1 × 10 ⁻³	5 min, 20 torr	1h, 500 torr	240	2.9
D	1 × 10 ⁻³	5 min, 20 torr	2h, 500 torr	270	3.7
E	1 × 10 ⁻³	30 min, 30 torr	1h, 500 torr	155	3.0

^a At 0.2V vs. RHE, saturated H₂.

^b At 0.5V vs. RHE, 5M CH₃OH.

^c Identical to sample no. 271 in the previous work (6).

higher than untreated sample B. Sample D, which underwent 2h carburization with CO after water vapor treatment, exhibits still higher activity, in contrast to the fact that, for catalysts without water vapor treatment, prolonged carburization caused deterioration in activity. Sample E, subjected to a water vapor treatment heavier than that for sample C, showed almost the same activity.

The results of potentiostatic current measurements at various potentials conducted at 50°C in 1M H₂SO₄ with H₂ bubbling or 5M CH₃OH are shown in Fig. 5, in which the current is normalized by the real surface area of the electrode. The plot of H₂ oxidation current is nonlinear due to the influence of diffusion control. However, the exchange current for sample D can be estimated to be about 2×10^{-2} A·m⁻² by extrapolation of the quasi-linear part of

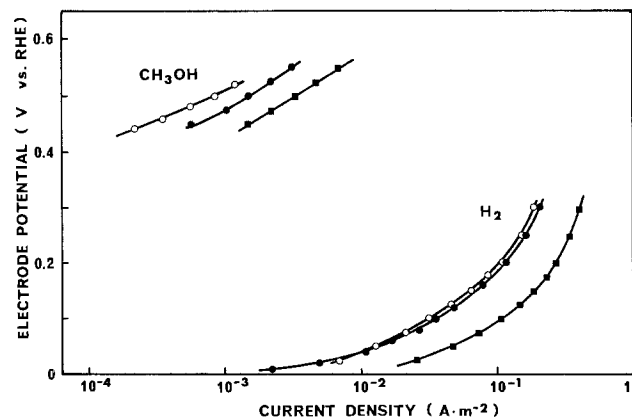
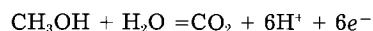


Fig. 5. Potentiostatic currents generated by the oxidation of H_2 and CH_3OH on various catalyst electrodes at $50^\circ C$ in $1M H_2SO_4$. Current densities are based on the real surface area of the electrodes. Concentrations of H_2 and CH_3OH are saturated H_2 and 5 mole/liter. Open circles: Sample A. Solid circles: Sample B. Closed squares: Sample D.

the plot, of which the slope is approximately 65 mV/decade, suggesting the two-electron processes for the relevant H_2 oxidation. The current associated with methanol oxidation, presumably generated by the reaction



is $0.0037 A \cdot m^{-2}$ at $0.5V$ vs. RHE and $50^\circ C$, which is almost the same order of magnitude as the value reported for pure Pt (5).

Surface analyses using AES.—In order to elucidate the promotion of catalytic activities through water vapor treatment, the following analyses were conducted focusing on catalyst surface characterizations.

The surface compositions determined by AES are shown in Table III for the catalysts as well as the films at the intermediate stages of the preparation with three different Ar ion sputtering times before spectra measurements. Sputtering time of 1 min is approximately identical to a depth of 10\AA from the original surface. Samples represented by D-as-CVD and D-as-WT are as-CVD and as-water vapor-treated film, respectively, were taken from the intermediate stage of sample D synthesis for analytical purposes. Samples D, B, and C are identical to those in Table II.

To understand the distributions of component elements in the surface layer and their change according to the synthesizing stage, the ratios of each element's atoms to total metal atoms, i.e., $X/(W + Mo)$, are shown in Fig. 6a-6d as a function of sputtering time, 1 min of which being equal to 10\AA of depth from the original surface.

These results show that as-CVD film includes a significant amount of carbon and that it is distributed

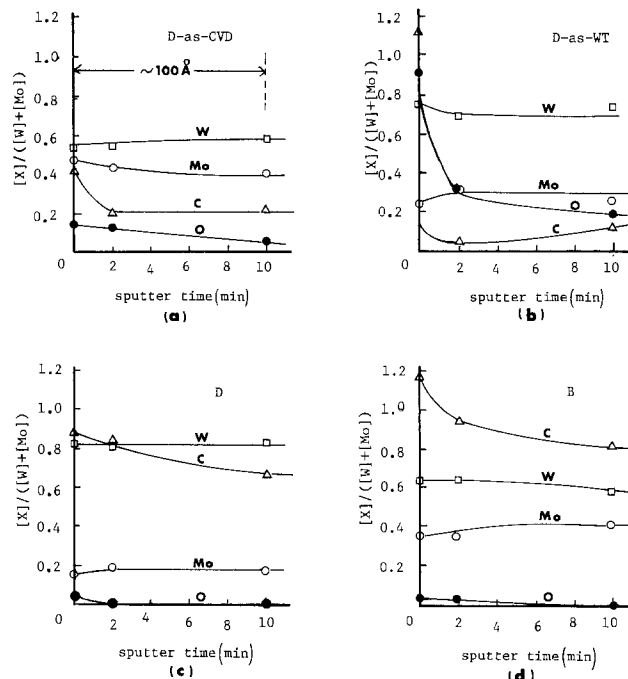


Fig. 6. Variations of the atomic ratio of each element (X) to total metals (W + Mo) in the surface layer with sputtering times for (a) D-as-CVD, (b) D-as-WT, (c) D, and (d) B, each of which is identical to the sample in Table II or III. Sputtering time of 1 min corresponds to a depth of 10\AA .

not solely on the surface but also in the deeper part of the film. A part of surface carbon might be driven into the bulk during Ar ion sputtering, but the amount of carbon thus introduced is so little that it does not affect the bulk concentration. Figures 7a and 7b show patterns of the C KLL transition given by nonsputtered and 2 min sputtered surface of D-as-CVD, respectively. The shapes of Fig. 7b indicate that carbon in the sputtered surface is in a binding state with metal, i.e., W and/or Mo, since the main peak is followed by two smaller but clear subpeaks characteristic of such a binding state.

On the other hand, the spectrum shape in Fig. 7a given by the nonsputtered surface indicates that there are carbons in different states as in graphite or carbonate which may be the contaminants introduced from the storage or handling atmospheres. A much higher carbon concentration at the original surface in Fig. 6a is due to such contaminations. It is, therefore, reasonable to consider that the binding state carbon, probably introduced in the CVD process, is distributed uniformly through the surface layer with its atomic ratio per total metals being about 0.2. A very likely origin of this carbon is carbonyl CVD sources.

The ratio of $Mo/(W + Mo)$ in sample D-as-CVD was determined to be about 0.44 for both sputtered and nonsputtered surfaces, while the CVD process had been controlled so as to give a value of 0.2. This suggests that a significant amount of $W(CO)_6$ passed through the reaction tube without being decomposed, probably because its decomposition rate is considerably slower than $Mo(CO)_6$. X-ray diffraction revealed that the film is almost amorphous, though a very broad peak indicating the onset of metal crystallization was detectable.

Results obtained with sample D-as-WT (Fig. 6b) show that the water vapor treatment at $820^\circ C$ brings about a notable increase in oxygen, which extends more than 100\AA from the original surface, though it decreases as depth increases. Extremely high concentration of C and O at the original surface may be attributed to adsorption species such as CO_2 for the same reason as is given for the as-CVD film. It is interesting to note that the average O/metals ratio between 20 and 100\AA is about 0.3, which coincides with that in compound W_3O_8 or $(W, Mo)_3O_8$, known as β -W, though x-ray diffraction only revealed a pattern

Table III. Surface composition of (W,Mo)C catalysts and films at the intermediate stages in the preparation

Sample	Sputtering time (min)	Composition (atomic percent)			O
		W	Mo	C	
D-as-CVD	0	34	30	27	9
	2	42	33	15	10
	10	46	32	17	5
D-as-WT	0	25	8	37	30
	2	49	23	4	23
	10	56	20	9	15
D	0	44	8	46	2
	2	43	10	45	0
	10	50	10	40	0
B	0	29	16	53	2
	2	33	18	48	2
	10	32	23	45	0
C	0	29	15	51	5
	2	34	15	48	3
	10	36	15	48	1

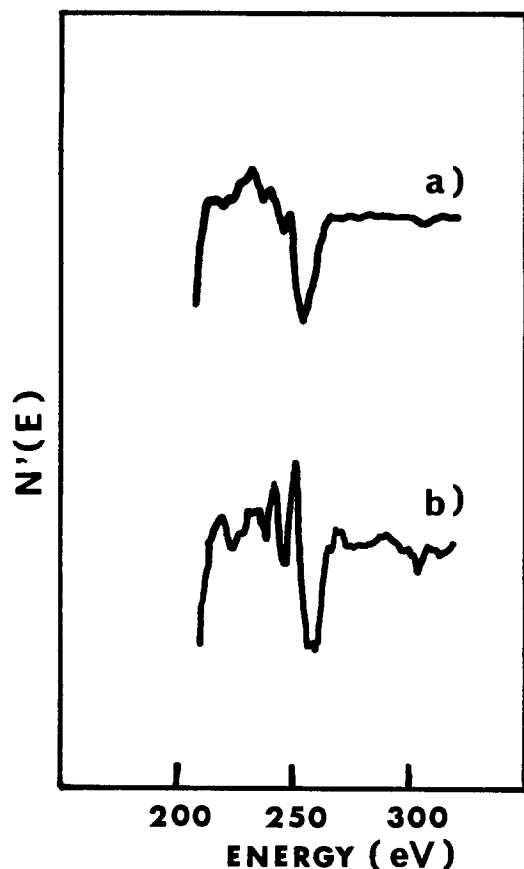


Fig. 7. Change in the AES shape of C KLL transition given by the as-CVD film (sample D-as-CVD) accompanied with sputtering. a: Nonsputtered (original surface). b: 2 min sputtered surface.

identical to W in the bulk of the film. Neugebauer *et al.* (8) stated that β -W can be prepared with less than 0.01 atoms of O per atom of W. It is conceivable, therefore, that the surface layer of water vapor-treated film is a β -W like compound of alloy.

Parallel with the introduction of oxygen, the water vapor treatment gives rise to an elimination of carbon from the surface layer as shown in Fig. 6b. Possibly, carbon escapes from the surface as CO. If this is true, the diffusion of carbon in the surface suboxide layer is considered to be significantly fast.

Another important effect of the water vapor treatment is a significant decrease of Mo in the surface layer. The value of Mo/(W + Mo) in the sputtered surface was found to be reduced from 0.43 in as-CVD film to 0.28. Since MoO₃ has a vapor pressure of 1300 Pa (9) at 820°C, it is likely that Mo evaporated from the surface in this form.

Sample D, given by carburization of as-WT film, is a final form of the catalyst. Figure 6c shows that its surface with a carbon deficient composition provided the stoichiometry of metal to C to be 1:1, and that the ratio of C/(W + Mo) decreases from 0.88 to 0.67 as the depth increases from 0 to 100Å. However, it is not reasonable to assume a monotonic decrease in carbon content in the deeper part of the film, because x-ray diffraction revealed that the film as a whole is in a single phase with a hexagonal WC structure. It was found by the shape of AES spectrum that carbon is in a binding state with metals, not only in the sputtered surface, but also at the original one, suggesting that the original surface of the carbide catalyst is not contaminated with free carbon from the disproportionation of CO or the adsorption of CO₂.

The ratio of Mo/(W + Mo) in the surface layer is about 0.2, suggesting that a Mo loss has occurred during the heating process in vacuum just before the carburization or during the carburization process itself. Although the mechanism is not clear, the former is more likely.

It is worthwhile for these results to be compared with those for sample B, which was prepared in the same way,

except that the water vapor treatment was omitted. As shown in Fig. 6d, the carbon content in sample B is greater than in sample D throughout the surface layer, and, especially in the former's original surface, carbon is excessive for metals. This fact indicates that the non-sputtered surface of sample B is, to some extent, covered with free carbon produced by the disproportionation of CO during the carburization. As a matter of fact, the shape of the C KLL transition showed that a small part of this surface carbon is in elemental forms. In addition, it is observed that the Mo level in sample B is roughly two times greater than that in sample D, confirming that one of the effects of water vapor treatment is to reduce Mo content in the catalyst surface.

Sample C, prepared in the same manner as sample D except that the carburization time was shorter (1h), contains residual oxygen in its surface layer, as shown in Table III. This catalyst exhibits much higher activity than sample B (no water vapor treatment), but less than sample D, in which no oxygen was detected at its sputtered surface. Thus, it seems that oxygen in the surface layer does not play an essential or positive role during electrocatalysis, though there have been many discussions (10, 11) concerning the relation between surface oxygen and activity of WC catalysts for H₂ electro-oxidation.

Discussion

Miles (12) reported that molybdenum-treated WC, synthesized by a carburization of a mixture of ammonium paratungstate and molybdate with CO at 700°C, exhibited catalytic activity for the electro-oxidation of methanol in an acidic solution. However, the oxidation current generated by his catalyst was estimated to be in the order of as little as 10⁻⁷ A·m⁻² (based on real surface area), and a not negligible corrosion current of the catalyst itself was observed even at a potential as low as 0.4V (*vs.* RHE). It was not, therefore, clearly concluded that Mo played an essential role in the electro-oxidation of methanol.

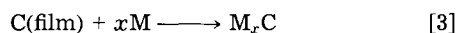
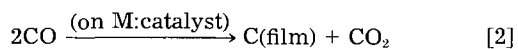
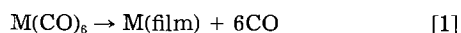
In the previous report (6) the present authors have shown that the oxidation current produced by the pure WC catalyst (Mo free) decays rapidly though it is detectable initially just after methanol is introduced into the electrolyte. We concluded that Mo acts as a cocatalyst to remove poisonous intermediates, or to lead the electrochemical reaction to another path in which poisons are not produced.

Since Mo in the catalyst of the present study plays a role of cocatalyst, there should be an optimum value of x in W_{1-x}Mo_xC, at which the activity is maximized. However, a clear result has not yet been obtained although the present authors have conducted extensive studies to find the optimum composition using not only the CVD technique described above, but also conventional synthesizing methods. It is reasonable to conclude that the results were unsuccessful because the catalytic activity depends more on the microscopic distribution of Mo in the surface layer than it does on the bulk composition.

A typical example showing the importance of a homogeneous distribution of cocatalyst in surface is Pt/Sn electrocatalyst, in which Sn introduced onto Pt surface as adatom is believed to protect it from too strong adsorption of species like CHO, an intermediate of methanol oxidation, by virtue of the microscopic surface geometry consisting of Pt and Sn. For that reason, Pt/Sn has higher activity than pure Pt (13).

As far as the results of x-ray diffraction are concerned, (W, Mo)C catalysts obtained in the present study are in a single-phase and homogeneous substance. This does not always, however, assure that each component element is distributed homogeneously through the film. For example, if Mo is too excessive to form a single-phase compound, the phase separation into WC and Mo₂C might occur in a level so microscopic that it could not be observed by x-ray diffraction. In the present catalyst, however, the likely cause of its possible nonhomogeneity might lie in the CVD process according to the following considerations.

The AES results show that the as-CVD (at 450°C) film contains carbon in a binding state with metal, and its concentration in terms of C/(W + Mo) is about 0.2 for the sputtered surface. It is reasonable to consider that carbon has been introduced into the CVD film according to the following reactions



where M is W and/or Mo. Carbon content in the film may thus be determined by the relation between the rate of reaction [1] and [2]. For example, the higher the CO pressure, the faster reaction [2], and carbon content would increase. Such a tendency has, in fact, been found in the carbonyl pyrolysis process for Mo (14) coating, as the Vickers hardness increases with an increase in CO pressure because of carbon inclusion. Miyake (15) also reported that Mo CVD film prepared under a CO pressure of less than 10^{-4} torr at 400°C exhibits hardness about four times larger than pure Mo, suggesting that an appreciable carbon inclusion occurs at such a low pressure.

At temperatures as low as 450°C, the rate of reaction [2] may depend on the catalytic activity of film itself. Since it has been reported (14) that Mo CVD film from its carbonyl contains much more carbon than W film does, Mo or its carbide is considered to catalyze the reaction better than W. If this stands true for the CVD film of the present study, carbon would be deposited selectively on Mo sites and a fluctuated distribution of carbon would be formed in the film. Suppose reaction [2] proceeds via reaction of two CO's adsorbed on adjacent two Mo's. Then, Mo₂C would readily be formed, and the film would assume a structure in which its clusters are included in metallic W. The fact that the ratio of Mo:C in the as-CVD film is 2:1 suggests such a situation though it is not a direct evidence. In addition, it is worthwhile to note the fact that, according to x-ray diffraction, only the Mo₂C type phase was clearly detected for the film given by annealing the as-CVD film at 820°C for 10 min, though distinguishing between W₂C and Mo₂C was impossible.

Carburizing such a film as it is, the resulting carbide film would have a nonhomogeneous distribution of Mo because diffusion of metals in carbides is very slow at 820°C. Water vapor treatment before the carburization would, conversely, turn the surface into a more homogeneous distribution in the following way. When the as-CVD film is exposed to water vapor, carbide cluster in its surface is decomposed and the surface changes into a suboxide, presumably, such as defective (W, Mo)₃O. Accompanying with this change, the surface Mo distribution would become more homogeneous, because a rather open structure of suboxide would allow Mo to diffuse in the surface layer. Molybdenum would be uniformly distributed also in the carbide film surface obtained from such a suboxide film. It is, therefore, reasonable to conclude that the difference of activity between sample D and B is due to that of the microscopic homogeneity in the surface Mo distribution.

It should be added that the inclusion of Mo₂C gives rise to the degradation of catalytic activity not only through the above manner but also through the surface contamination with free carbon, because Mo₂C catalyzes carbon deposition in the carburization process. The surface of sample B seems to be contaminated with free carbon.

There is no clear answer as to how the Mo loss from the catalyst surface in its synthesizing process influences the

activity. It is, however, presumable that, if Mo in the as-CVD film was too much to form (W, Mo)C in a single hexagonal WC-type phase, a reduction of Mo content would have a positive effect because the catalyst surface would then be prevented from undergoing phase separation, for example, into WC, Mo₂C, and C.

Conclusion

Tungsten and molybdenum mixed carbide [(W, Mo)C] electrocatalysts, synthesized on a carbon substrate using a technique involving CVD from hexacarbonyl compounds, have been investigated. It has been found that the activity is enhanced by exposing the CVD films to water vapor at 820°C just before it is carburized with CO. The catalyst thus obtained generated H₂-oxidation current density of 0.27 A·m⁻² (based on real surface area) in a 1M H₂SO₄ at 0.2V (vs. RHE) and 50°C. An oxidation current of CH₃OH as large as 0.0037 A·m⁻² was also observed with the same catalyst at 0.5V (vs. RHE) at the same temperature.

Surface analyses using Auger electron spectroscopy (AES) revealed that the as-CVD film formed at 450°C contains about 15 atomic percent carbon of which AES spectrum shape is characteristic of one in binding state with metals. This carbon seems to form Mo₂C clusters included in metallic W. Its surface is turned into suboxide like (W, Mo)₃O with water vapor treatment, and carbon content in it is notably reduced, suggesting the decomposition of such clusters. The enhancement of catalytic activity is probably due to the homogenized surface Mo distribution in catalyst carbide brought about during the above process.

Acknowledgment

The authors wish to express their gratitude for the technical contributions and useful advice given by S. Kawase of Hitachi Limited, Central Research Laboratory, Materials Analysis Center.

Manuscript submitted June 12, 1983; revised manuscript received April 4, 1985.

Hitachi Limited assisted in meeting the publication costs of this article.

REFERENCES

1. R. B. Levy and M. Boudart, *Science*, **181**, 547 (1973).
2. P. N. Ross, Jr., J. MacDonald, and P. Stonehart, *J. Electroanal. Chem.*, **63**, 450 (1975).
3. G. Horanyi and E. M. Ryzmayer, *ibid.*, **132**, 119 (1982).
4. P. N. Ross, Jr., in "Proceedings of the Symposium on the Role of Solid State Chemistry in Catalysis," p. 535, Division of Petroleum Chemistry, American Chemical Society, Washington, DC (1977).
5. M. M. P. Janssen and J. Moolhuysen, *Electrochim. Acta*, **21**, 861, 869 (1976).
6. T. Kudo, G. Kawamura, and H. Okamoto, *This Journal*, **130**, 1491 (1983).
7. Adopted from AES catalogue "A data collection of elements," prepared by Anelva Corporation, Tokyo, Japan (1979).
8. J. Neugebauer, A. J. Hegedues, and T. Millner, *Z. Anorg. Chem.*, **293**, 241 (1957).
9. "CRC Handbook of Chemistry and Physics," 58th ed., R. C. Weast, Editor, p. D-185, CRC Press, Inc., Boca Raton, FL (1977).
10. P. N. Ross, Jr., and P. Stonehart, *J. Catal.*, **39**, 298 (1975).
11. P. N. Ross, Jr., and P. Stonehart, *ibid.*, **48**, 42 (1977).
12. R. Miles, *J. Chem. Tech. Biotech.*, **30**, 35 (1980).
13. M. M. P. Janssen and J. Moolhuysen, *J. Catal.*, **46**, 289 (1977).
14. C. F. Powell, in "Vapor Deposition," C. F. Powell, J. F. Oxley, and J. M. Blocher, Jr., Editors, p. 303, John Wiley and Sons, New York (1966).
15. M. Miyake, Y. Hirooka, T. Imoto, and T. Sano, *Thin Solid Films*, **79**, 75 (1981).

Performance Predictions for Solar-Chemical Convertors by Computer Simulation

J. D. Luttmer*

Texas Instruments, Incorporated, Dallas, Texas 75265

Isaac Trachtenberg*

Department of Chemical Engineering, University of Texas, Austin, Texas 78712

ABSTRACT

A computer model which simulates the operation of Texas Instruments solar-chemical convertor (SCC) was developed. The model allows optimization of SCC processes, material, and configuration by facilitating decisions on trade-offs among ease of manufacturing, power conversion efficiency, and cost effectiveness. The model includes various algorithms which define the electrical, electrochemical, and resistance parameters and which describe the operation of the discrete components of the SCC. Results of the model which depict the effect of material and geometric changes on various parameters are presented. The computer-calculated operation is compared with experimentally observed hydrobromic acid electrolysis rates.

The Texas Instruments Solar Energy System (1-14) converts solar energy into chemical energy, stores the chemicals, and on demand converts the chemical energy into electrical energy. The system consists of four major subsystems: solar-chemical convertor (SCC); hydrogen storage; fuel cell/inverter; and heat recovery. This discussion will be limited to the solar-chemical convertor (SCC). The SCC converts solar energy into chemical energy via the electrolysis of hydrobromic acid (HBr) to hydrogen (H_2) and bromine (Br_2). The performance of the SCC is influenced by the electrical characteristics of the spherical solar cells, the electrochemical parameters of the front metal electrodes, the membrane, and the physical arrangement of cells. In operation, the SCC experiences a wide range of operating conditions which include variable electrolyte composition, temperature, and solar insolation.

A computer model was developed which simulates the operation of the SCC and allows characterization and optimization of SCC processes. The model facilitates decisions involving materials selection and design of the SCC to achieve optimum performance and maximum cost effectiveness. By employing the model, the number of actual laboratory experiments needed to begin the design and optimization study was greatly reduced. The computer-modeled SCC processes and comparisons of the calculated and observed SCC performance are outlined below.

Computer Simulation Model

The processes which occur in the SCC are illustrated in Fig. 1. Photons from the sun are absorbed by the spherical n⁺/p and p⁺/n silicon solar cells either directly or by reflection and scattering from the SCC matrix glass. Some photons are lost owing to reflection or absorption by the electrolyte, cover glass, or membrane separator. Photons that are absorbed in the silicon generate electron-hole pairs. The minority carriers diffuse to the junctions. The majority carriers flow to the electrode-electrolyte interfaces. At the electrodes on the n⁺/p cells (cathodes), hydrogen ions are reduced to H_2 . At the electrodes on the p⁺/n cells (anodes), bromide ions are oxidized to bromine. Electroneutrality is maintained by a flow of ions across the separator. The separator functions to minimize backreaction losses by restricting bromine transport to the cathode (n⁺/p) cells.

The computer model incorporates electrical, electrochemical, and resistance parameters which are functions of the SCC panel composition (9, 14). For example, the electrical characteristics of the solar cells are functions of the light incident on the cells, which in turn is dependent

on the incident panel insolation and the optical properties of the panel and electrolyte. The effects of the optical and resistive components of the panel on the electrical characteristics of the solar cells were determined empirically as functions of panel design, electrolyte composition, and insolation. The interdependent relationships among these parameters and functions are outlined in Fig. 2. Algorithms which describe these relationships are included in the computer model.

The model initially assumes a given panel geometry and bulk electrolyte concentration. Various panel designs can be considered in order to maximize the light incident on the solar cells while minimizing the resistance and electrochemical losses. Electrical, electrochemical, and resistance terms are calculated upon selection of insolation, operating temperature, and electrode material. Finally, the algorithms are used with iterative numerical techniques to solve for the electrolysis rate.

The electrical characteristics of the solar cells used in the model are obtained with a semiautomatic probe system. The solar cells of the panel are randomly probed at simulated air-mass 1 insolation using ELH type tungsten-halogen lamps to obtain representative values for the open-circuit voltage (V_{oc}), the short-circuit current (I_{sc}), and the fill factor (FF). When the density of spheres is known, the average maximum power output per sphere can be calculated. Array positioning, lamp power supply switching, and photocurrent-voltage data acquisition are fully automated. A fine tungsten wire probe is positioned manually on each solar cell sphere. Typically, four solar

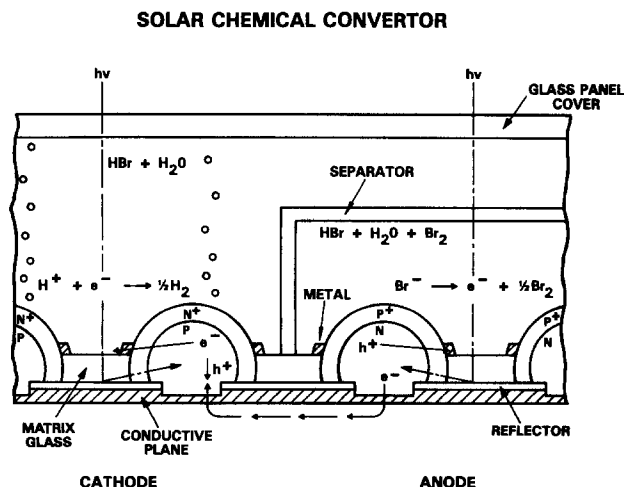


Fig. 1. Cross section of solar-chemical convertor (SCC)

* Electrochemical Society Active Member.

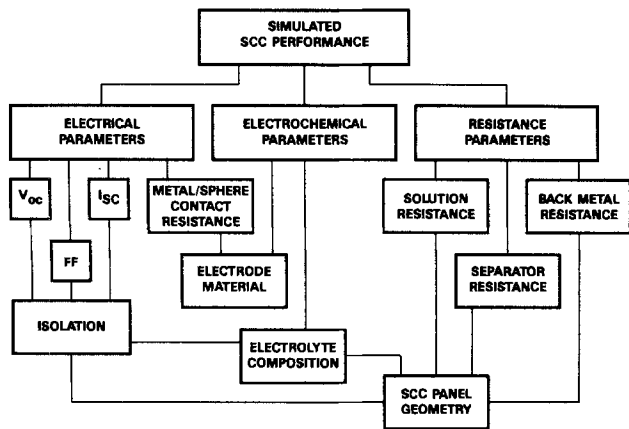


Fig. 2. SCC modeling parameters

cells are probed for each square centimeter of array area for both cell types. The cells sampled correspond to 0.5-0.7% of the total cell population. For the standard size arrays tested, this required probing 160 cells: 80 anodes and 80 cathodes.

The rates for the photoinduced electrochemical oxidation and reduction of hydrobromic acid in the SCC are determined by both the electrical (photovoltaic) characteristics (15) of the individual solar cells and the electrochemical characteristics (16) associated with the front metal electrodes in the HBr electrolyte. During operation, the electrochemical (faradaic) and solar cell currents are equivalent and can be approximated by

$$I_{op} = I_{sc} - I_0[\exp(qV_s/NkT)] = A_e[\exp(\alpha n + \beta)] \quad [1]$$

I_{sc} , I_0 , q , and N are the short-circuit current, reverse bias dark current, absolute value of electronic charge, and quality factor associated with the solar cells, respectively. A_e , α , and β are the electrode area, Tafel slope, and intercept associated with the electrochemistry, respectively. Different values are appropriately used for anode and cathode cells. The solar cell photovoltage V_s and the electrochemical overvoltage are related by

$$\eta = V_s - \sum i_j R_j - V_{ref} \quad [2]$$

where $\sum i_j R_j$ includes all resistance losses associated with the back-side conductor, membrane separator, and electrolyte. The resistance terms can be calculated with simple models of the array geometry using numerical iteration techniques. V_{ref} defines the potential difference between the back-side conductor and the H^+/H_2 and the Br_2/Br^- redox couples. The equations given above define the operation of the anode cells (p^+/n) or the cathode cells (n^+/p). Equations which govern the behavior of anode cells differ from those which govern the behavior of cathode cells only in the sign and magnitude of their coefficients. The values of the electrochemical coefficients are determined experimentally from the electrochemical behavior of thin film electrode materials on n^+ and p^+ silicon substrates in hydrobromic acid-bromine mixtures.

The flow chart for the model is outlined in Fig. 3. The model initially assumes that the operating current of each solar cell is equal to half its short-circuit current and that the potential of the back-side conductor is midway between the two redox couples. The resistance terms are then obtained with a knowledge of the solar cell spacing and SCC panel geometry. iR losses associated with each cell are then calculated from the panel resistance terms and the assumed current flow. The operating currents of the cells are then calculated from Eq. [1] and [2]. On each iteration, the sum of the anode cell currents or cathode cell currents is tested for convergence after the iR loss terms and individual cell operating currents are recalculated. Finally, the back-side conductor potential is varied systematically until the sum of the calculated anode cell currents is equal to the sum of calculated cathode cell currents.

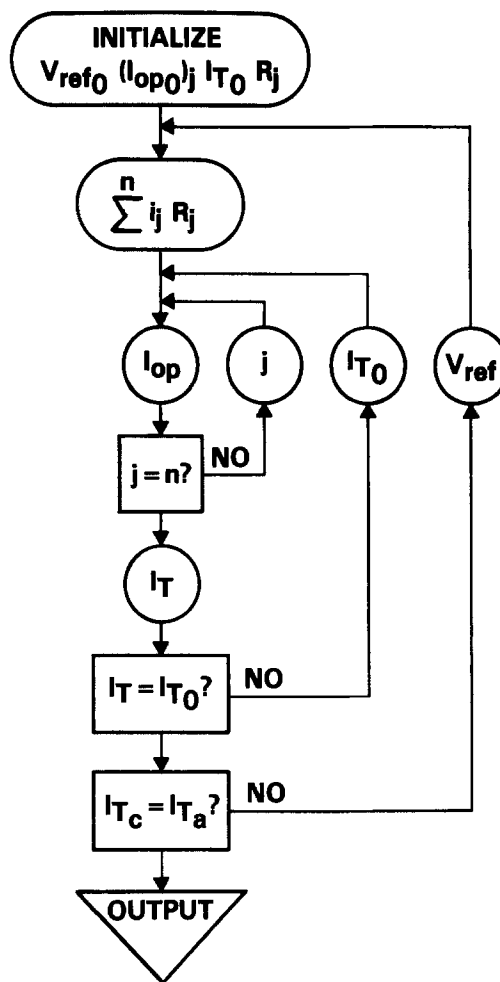


Fig. 3. Computer model flow chart

Figure 4 illustrates the typical interaction between various anode solar cells and a HBr/bromine redox couple. The dashed line represents the electrochemical load imposed on three different solar cells. The operating point for a given solar cell is defined as the point at which solar cell I-V curve intersects the electrochemical load line. The best solar cell anodes produce bromine at a rate approaching the short-circuit current of the solar cell, while the poorest solar cells can consume bromine at the mass-transport-limited rate. Under the conditions given in Fig. 4, two shorted anode cells consume all the bromine produced by three good anode cells. At higher operating bromine concentrations, shorted anode cells have a more detrimental effect. In the cathode compartment, the slight solubility of hydrogen (approximately 0.5 mM) (17) results in negligible losses on the shorted cathode cells.

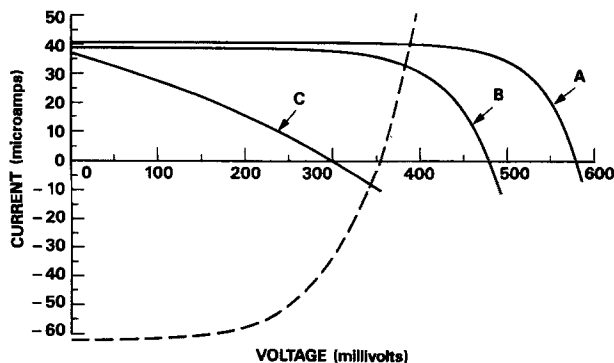


Fig. 4. Simulated electrical and electrochemical behavior of anode section. Dry efficiency of solar cells is 13% (A), 9.33% (B), and 2.44% (C). Operation at 23°C, air-mass 1 insolation, 0.3M bromine + 8.3M hydrobromic acid electrolyte, Pt/Ir electrodes.

Computed SCC Design Performance

Decisions on SCC panel design aided by computer modeling include choice of electrode material, electrode area, solution compartment depth, anode and cathode compartment width, membrane separator, and optimum operating electrolyte concentration. Results of various simulations and optimum SCC operating conditions are listed below.

Calculated solar-chemical conversion efficiencies as a function of anolyte bromine concentration for an ideal SCC panel and for nonideal panels incorporating different electrode materials are depicted in Fig. 5. The efficiency is defined as the product of the operating current density and the difference in the electrochemical potential of the bulk anolyte and the bulk catholyte divided by the incident light power. The simulations assume air-mass 1 insolation, 23°C operation, dry solar cell efficiency of 13%, and fixed anolyte and catholyte bromine-bromide concentrations of 8.9 eq/liter. Simulations in which optical and resistance losses are neglected are given in Fig. 5 (curve A). As the anolyte bromine concentration increases, the solar-chemical efficiency increases from 10% to about 12% before tailing off at the highest concentrations evaluated. The idealized panel simulation includes overvoltage losses associated with the electrochemistry and the mismatch between the electrochemical load and the solar cell electrical output. At low anolyte bromine concentrations, the performance of the panel is limited by the short-circuit current of the solar cells. At high anolyte bromine concentrations, the performance becomes limited by the open-circuit voltage of the solar cells. Coupling the optical and resistance losses into the simulations for typical panels produces results such as those given in Fig. 5, curves B and C. Optical losses are primarily responsible for the decreased solar-chemical conversion efficiency in these examples, especially at high anolyte bromine concentrations. Additional simulations detailing the effect the optical losses have on the SCC performance are outlined below.

The use of less electrochemically active electrode materials results in additional degradation in the solar-chemical conversion efficiency, as illustrated in Fig. 5, curve C. Electrochemical overvoltage losses are minimized by assuming Pt/Ir alloy electrodes in Fig. 5, curves A and B. Iridium electrodes, which are more corrosion resistant but less active electrochemically, were assumed in the simulations depicted in Fig. 5, curve C. Overvoltage losses can be reduced by maximizing the electrode area on the solar cell spheres. This results in attenuation of photons, producing electron-hole pairs in the silicon.

Optical losses caused by light absorption by bromine strongly degrade the solar-chemical conversion efficiency. Figure 6 illustrates the increased optical losses encountered when the anolyte compartment depth is increased. The losses are significant at anolyte depths as

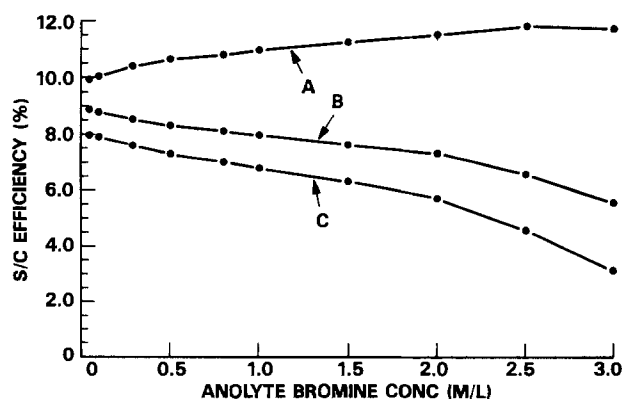


Fig. 5. Simulated SCC array performance Pt/Ir electrodes (A), excluding optical and resistance losses, Pt/Ir electrodes (B), including optical and resistance losses, and Ir electrodes (C), including losses. Dry solar cell efficiency = 13%; 0.32 cm anolyte depth; depth/width ratio = 0.28, temperature = 23°C.

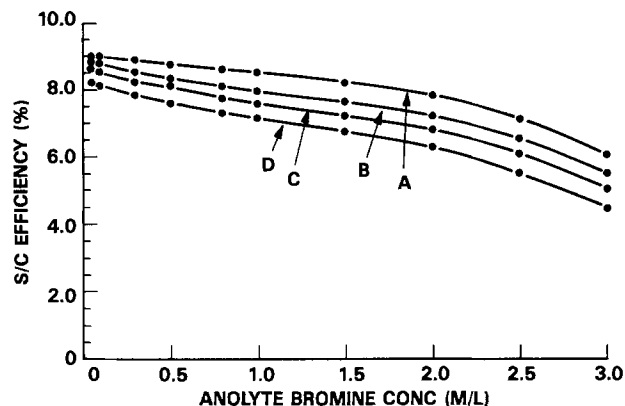


Fig. 6. Effect of anolyte depth on simulated SCC performance. Nafion 115 membrane; dry solar cell efficiency = 13%; depth/width ratio = 0.28; temperature = 23°C; Pt/Ir electrodes. Anolyte depth: 0.15 (A), 0.32 (B), 0.48 (C), 0.64 cm (D).

small as 1.5 mm at high bromine concentrations ($\geq 1.0M$). At low bromine concentrations ($\leq 0.75M$), the major optical losses are caused by the membrane separator over the anolyte compartment and the panel cover glass. Together, these losses reduce the light reaching the solar cells by about 10% and result in lower output.

Characteristics of the membrane separator which affect the operation of the SCC include optical transmittance, resistivity, and bromine diffusivity. The effects of the resistivity and bromine diffusivity parameters on SCC performance are illustrated in Fig. 7. An ideal separator which is transparent and infinitely conductive and which totally restricts bromine transport yields the results depicted in Fig. 7, curve A. The other separators outlined illustrate the trade-offs that can exist between the separator resistance and separator bromine diffusivity. Separators with high resistance and low bromine diffusivity result in low solar-chemical efficiency at low as well as high anolyte bromine concentrations. Separators with low resistance and high bromine diffusivity result in low solar-chemical efficiency only at high anolyte bromine concentrations. These results suggest a requirement for a transparent separator with less than $2 \Omega\text{-cm}^2$ resistance and bromine diffusivity less than $4 \times 10^{-9} \text{ cm}^2/\text{s}$.

SCC panel performance is also influenced by the electrolyte resistance, which is governed almost entirely by the depth/width ratio of the anode and cathode compartments. Figure 8 illustrates the effect that varying the total electrolyte depth has on the SCC panel performance. As the depth increases, the resistance losses associated with the electrolyte become negligible. A modest electrolyte depth/width ratio of ca. 0.2 is suitable for optimal performance in this typical example. Larger resistance values (smaller electrolyte depth/width ratios) are acceptable when the SCC operates at lower rates.

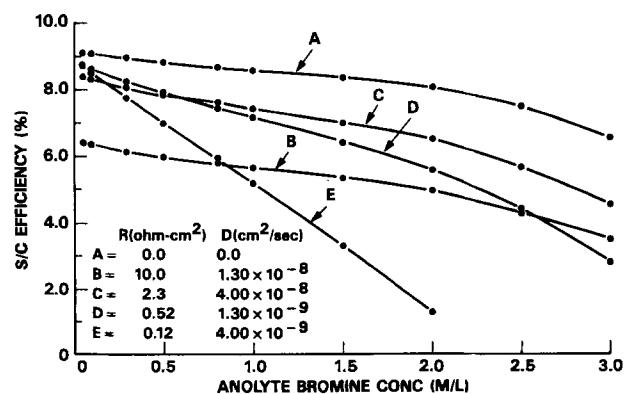


Fig. 7. Effect of membrane separator on simulated SCC performance. Dry solar cell efficiency = 13%; depth/width ratio = 0.28; anolyte depth = 0.32 cm; temperature = 23°C; Pt/Ir electrodes.

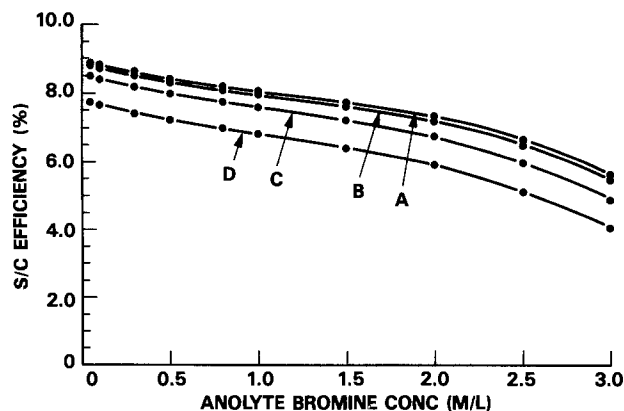


Fig. 8. Effect of solution depth on simulated SCC performance. Dry solar cell efficiency = 13%; anolyte depth = 0.32 cm; temperature = 23°C; Nafion 115 membrane; anode-cathode width = 3.4 cm, Pt/Ir electrodes. Depth: 1.27 (A), 0.95 (B), 0.63 (C), and 0.48 cm (D).

Changes in the operating temperature of the SCC panel most significantly affect the electrical characteristics of the solar cells and the redox potentials required for electrolysis of the acid. Figure 9 depicts the effect of temperature on the performance of a SCC panel. The two temperature effects tend to counteract each other. The required electrolysis voltage decreases by 0.9 mV/°C. The open-circuit voltages of the solar cells decrease by approximately 2 mV/°C. Larger decreases in V_{oc} are obtained at elevated temperature with poor quality solar cells.

Additional electrical energy is obtained from the system if the electrolyte is cooled prior to use in the hydrogen-bromine fuel cell. Cooling the electrolyte increases the potential difference between the anolyte and the catholyte and results in direct thermal-to-electric energy conversion.

Comparison with Experiment

The accuracy of the computer model was determined by comparing the computer-calculated SCC performance with the experimentally observed hydrobromic acid electrolysis rates of various anode-cathode combinations. Hydrobromic acid electrolysis rates of anode-cathode combinations were determined by measuring the hydrogen generation rates of 40 cm² SCC arrays in 48% hydrobromic acid. The SCC sections and arrays were illuminated with multiple tungsten-halogen lamps (ELH) at 1000 W/m².

Excellent agreement is observed between the calculated electrolysis rates and the observed rates for SCC arrays over a wide range of operating conditions. Figure 10 compares the calculated and observed performance of a series of SCC arrays, where the calculated average current efficiency is plotted against the observed average

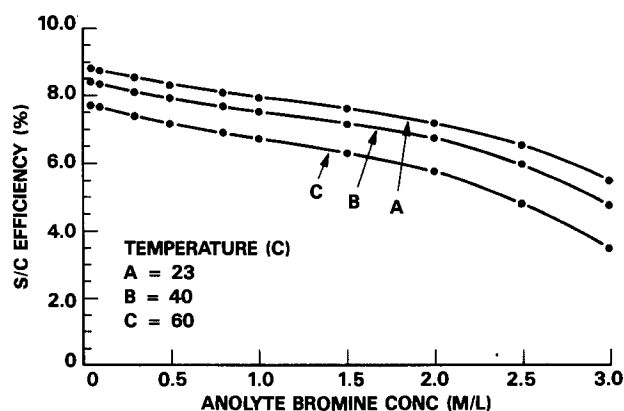


Fig. 9. Effect of operating temperature on simulated SCC performance. Dry solar cell efficiency = 13%; depth/width ratio = 0.28; anolyte depth = 0.32 cm; Nafion 115 membrane; Pt/Ir electrodes. Temperature: 23° (A), 40° (B), and 60°C (C).

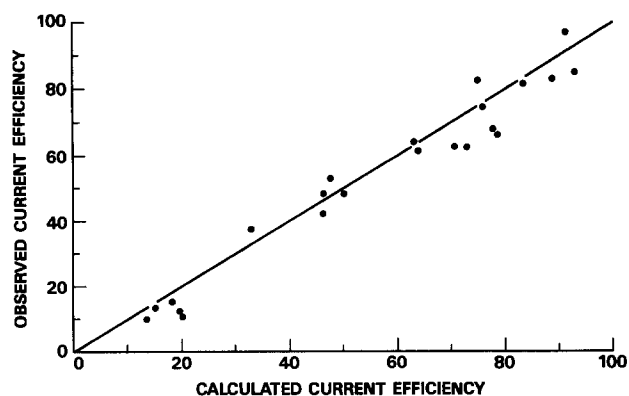


Fig. 10. Comparison of observed and simulated average current efficiency for SCC anode-cathode combinations. Temperature = 23°C; electrolyte = 48% hydrobromic acid.

current efficiency. The average current efficiency is defined as the ratio of the sum of the operating solar cell currents to the sum of the solar cell short-circuit currents

$$\eta_c = \frac{\sum I_{op}}{\sum I_{sc}} \quad [3]$$

Arrays which had low average V_{oc} and FF values were chosen for the series as a more challenging comparison. These arrays consequently operate at rates well below their short-circuit current limitation. Excellent agreement is observed between the calculated rates and the observed rates for SCC arrays constructed of solar cells of widely varying electrical characteristics.

Conclusions

Computer simulation is an accurate technique for predicting the performance and efficiency of a given solar-chemical convertor. Excellent agreement is obtained between the computer-calculated hydrobromic acid electrolysis rates and observed electrolysis rates for a variety of arrays.

Characterization and optimization of SCC processes are readily achieved by computer simulation. The computer model facilitates decisions on trade-offs among ease of manufacturing, power conversion efficiency, design, materials selection, and cost effectiveness. The SCC computer model suggests that solar-chemical efficiencies approaching 10% should be achievable with optimally designed, relatively large area panels.

Acknowledgment

This work was supported in part by a cooperative agreement between the U.S. Department of Energy and Texas Instruments, Incorporated, DE-AC01-79ER10000.

Manuscript submitted Sept. 26, 1983; revised manuscript received April 26, 1985. This was Paper 448 presented at the Montreal, Quebec, Canada, Meeting of the Society, May 9-14, 1982.

Texas Instruments, Incorporated, assisted in meeting the publication costs of this article.

REFERENCES

1. J. S. Kilby, J. W. Lathrop, and W. A. Porter, U.S. Pat. 4,021,323 (1977).
2. J. S. Kilby, J. W. Lathrop, and W. A. Porter, U.S. Pat. 4,100,051 (1978).
3. J. S. Kilby, J. W. Lathrop, and W. A. Porter, U.S. Pat. 4,136,436 (1979).
4. E. L. Johnson, J. S. Kilby, J. W. Lathrop, J. S. McFerren, and D. J. Meyers, U.S. Pat. 4,173,494 (1979).
5. E. L. Johnson, Paper presented at Government Microcircuit Applications Conference, Houston, TX November 1980.
6. E. L. Johnson, in "IEEE Proceedings of the International Electron Devices Meeting," pp. 2-5, IEEE, New York, December 1981.
7. E. L. Johnson, in "Electrochemistry in Industry: New Directions," U. Landau, E. B. Yeager, and T. Kortan,

- Editors, pp. 299-305, Plenum Press, New York (1982).
8. E. L. Johnson and J. S. Kilby, proceedings of the International Photovoltaic Solar Energy Conference," pp. 611-615, Stresa, Italy (1982).
 9. E. L. Johnson, Paper presented at the American Chemical Society Meeting, Kansas City, MO, Sept. 1982.
 10. W. R. McKee, in "IEEE Proceedings of the 32nd Electronic Components Conference," May, 1982, pp. 326-331, IEEE, New York (1982).
 11. I. Trachtenberg, Paper presented at the AS/ISES Conference, Houston, TX, June 1982.
 12. J. D. Luttmner and I. Trachtenberg, Paper 448 presented at the Electrochemical Society Meeting, Montreal, Que., Canada, May 9-14, 1982.
 13. J. D. Luttmner, Paper presented at 5th Annual Photoelectrochemical Cell Contractor's Review Meeting, Denver, CO, June 1982.
 14. W. R. McKee, K. R. Carson, and J. D. Levine, Paper presented at the 16th IEEE Photovoltaic Specialists Conference, San Diego, CA, Sept. 1982.
 15. S. M. Sze, "Physics of Semiconductor Devices," Wiley-Interscience, New York (1969).
 16. A. J. Bard and L. Faulkner, "Electrochemical Methods," Wiley and Sons, New York.
 17. G. G. Barna, S. N. Frank, and T. H. Teherani, *This Journal*, **129**, 2464 (1982).

Photoelectrochemistry of CuIn_5S_8 and HgIn_2S_4

Ralph S. Becker,* Tan Zheng, and John Elton

Department of Chemistry, University of Houston-University Park, Houston, Texas 77004

ABSTRACT

CuIn_5S_8 was prepared by gradient freeze techniques. Doping was done, and annealing was carried out under various sulfur atmosphere vapor pressures and vacuum. HgIn_2S_4 was prepared by chemical vapor phase transport and was annealed under various sulfur vapor pressures. Both materials showed increased photocurrent density with photoetching at short circuit, which was particularly dramatic for HgIn_2S_4 . Purely n-type response was seen for HgIn_2S_4 samples as well as for CuIn_5S_8 , except where phosphorus plus sulfur dopants were used (both n- and p-type responses). Quantum efficiencies of carrier collection were 10-15% at short circuit for CuIn_5S_8 (maximum of 77%) and ~22% for HgIn_2S_4 (maximum of 83%) in a polysulfide couple. Considerable increase in the short-circuit current density and open-circuit photovoltage could be obtained for CuIn_5S_8 in a $\text{Ce}^{4+}/\text{Ce}^{3+}$ couple, but this was offset by substantial photocorrosion. Power efficiencies up to ~0.4% and ~0.2% were obtained for CuIn_5S_8 and HgIn_2S_4 , respectively. Stability in a polysulfide couple was up to ~97% for CuIn_5S_8 and >99% for HgIn_2S_4 .

CuIn_5S_8 appears to be one of two chemical compounds in the $\text{Cu}_2\text{S}-\text{In}_2\text{S}_3$ system (1) (CuIn_2S_4 is the other). CuIn_5S_8 is a cubic spinel with indium found principally on octahedral sites rather than on tetrahedral sites as found in most chalcopyrite structures (2). This material shows an indirect gap near 1.3 eV and a direct gap near 1.5 eV (3).

HgIn_2S_4 appears to have a normal spinel structure (4) and a bandgap of 2.0 eV (4, 5). Its Cd analog, CdIn_2S_4 , also has the spinel structure but with partial inverse character (6), and a bandgap of 2.4 eV (7). Very little information is available for HgIn_2S_4 , although photocurrent-wavelength data indicate a maximum near 615 nm for nonpolished crystals (5). Synthesis employing chemical vapor transport has been reported [see Ref. (4) and (5), for examples]. Only recently have some PEC data been reported in a note for HgIn_2S_4 (8), and more fully for the CdIn_2S_4 analog (7). Also, only very recently has PEC data been reported for CuIn_5S_8 (9).

Experimental

CuIn_5S_8 (1, 3) and HgIn_2S_4 (4, 5, 10) have been previously prepared.

CuIn_5S_8 was prepared by us using gradient freeze techniques employing 99.999% pure elements and dopants. The following technique was developed prior to the appearance of Ref. (3). Table I shows the various samples prepared, conditions of growth, and dopants used.

In particular, the CuIn_5S_8 -2 samples utilized polycrystalline CuIn_5S_8 and In_2S_3 (Sn) ($\sim 1 \times 10^{19}$ at.-cm⁻³ Sn), both of which had been previously prepared and characterized by x-ray diffraction. The In_2S_3 was added to give a dopant level of Sn of $\sim 1 \times 10^{17}$ at.-cm⁻³. The CuIn_5S_8 -3 and CuIn_5S_8 -4 samples were synthesized using polycrystalline CuIn_2S_4 previously prepared by us and In_2S_3 (Cerac, Incorporated). In both cases, 1 atomic percent (a/o) excess S was added in an attempt to obtain p-type material. In addition, for the CuIn_5S_8 -4 sample, phosphorus was added to give a dopant level of $\sim 1 \times 10^{20}$ cm⁻³ of P in an attempt to obtain p-type material.

The starting charges were sealed in 9 mm id quartz tubing which had previously gone through a thorough clean-

ing procedure involving both HF etches and vacuum annealing for ~12h at ~1000°C. Such thorough cleaning is necessary in order to prevent strong adherence of the samples to the quartz walls after synthesis. The ampuls had tapered ends in order to facilitate single-crystal nucleation and growth. Samples were sealed in the quartz tubes at a vacuum of $\sim 10^{-5}$ torr. Those inner ampuls were then placed into an outer protection tube of 13 mm id which had also undergone a cleaning procedure but did not include the vacuum-anneal step. Quartz wool was used to hold the inner ampul rigidly within the outer ampul. The outer quartz tube was then sealed in vacuum at 10^{-5} torr.

The quartz ampul system was next placed into a three-zone Lindberg furnace with independently controlled zones. For the CuIn_5S_8 -2, a mechanical controlling unit was used which could vary the rate of temperature increase or decrease over a range of 0.6°-120°C/h. For the CuIn_5S_8 -3 and CuIn_5S_8 -4 samples, a computerized

Table I. Prepared conditions for various CuIn_5S_8 samples

Sample	Sample temp. (°C)	Sulfur			Dopant
		Low temp. (°C) ^a	Pressure (atm)	Time (h)	
CuIn_5S_8 -2	(Initial growth)	—	—	—	Sn
CuIn_5S_8 -2a	680	325	0.11	24	Sn
CuIn_5S_8 -2b	680	405	0.6	24	Sn
CuIn_5S_8 -2c	645	210	4×10^{-3}	24	Sn
CuIn_5S_8 -2d	645	110	5×10^{-3}	24	Sn
CuIn_5S_8 -2e	645	645	0.15	24	Sn
CuIn_5S_8 -2f	640	645	Vacuum	24	Sn
CuIn_5S_8 -2g	640	640	0.15	19 days	Sn
CuIn_5S_8 -3	(Initial growth)	—	—	—	S
CuIn_5S_8 -3a	645	645	0.15	24	S
CuIn_5S_8 -3b	640	640	0.15	19 days	S
CuIn_5S_8 -4	(Initial growth)	—	—	—	P, + S

^a This is the temperature where the sulfur was located, except for sample 2f (where vacuum annealing was done).

controlling unit was used which had, in principle, no limits to possible rates. The three-zone furnace was positioned in a 45° tilted position with the tapered ends of the inner ampuls at the lowest point. All three samples were taken to above the melting point of CuIn₅S₈ (1085°C) and then slowly cooled at a rate of ~1.25°C/h. Gradients at the melting point were approximately 5°C/cm for the CuIn₅S₈-2, 14°C/cm for CuIn₅S₈-3, and 14°C/cm for CuIn₅S₈-4. The CuIn₅S₈-2 was cooled at the above rate until its temperature was ~800°C and then subsequently cooled to room temperature at a rate of ~10°C/h. The CuIn₅S₈-3 and CuIn₅S₈-4 samples were cooled at the above rate until their temperatures were both ~850°C. At this point, the furnace was turned off and allowed to cool naturally to room temperature. Chromel-Alumel thermocouples were used to monitor temperatures of samples and determine gradients.

Powder x-ray diffraction after synthesis showed single-phase CuIn₅S₈ material in all the cases. The appearance of the samples after synthesis and after polishing of the materials indicated single-crystal material, although this has not been verified by single-crystal x-ray diffraction techniques.

Several different dopants were used and various methods of annealing were carried out, as shown in Table I. Generally, the samples were n-type, except in the case of CuIn₅S₈-4, which was a melt growth with 1% except sulfur and doped with ~10²⁰ cm⁻³ phosphorus which showed both n- and p-type responses.

Samples were polished with diamond paste to a 1 μm finish. All samples were etched in 6-8M HCl for approximately 3 min and then immersed in 0.2M S-1M NaS-1M NaOH solution at 50°C in a sonicator for 1-3 min to remove any surface sulfur. An In-Ga eutectic (25:75) was used to form an ohmic contact. The samples were mounted for study as described previously (7).

The HgIn₂S₄ was prepared using chemical vapor phase transport techniques employing 99.999% pure starting materials (including dopants). The method used represents a notable modification of that given earlier (5, 10). A sample of HgIn₂S₄ was prepared by chemical vapor transport using HgS and In₂S₃ with I₂ as the transport agent as described below. Previously prepared Sn-doped In₂S₃ was also added to give a dopant level of ~1 × 10¹⁹ at.-cm⁻³ Sn in the source material. Iodine was present at a concentration of ~5 mg/cm after ampul sealing. The above starting charge was placed into a 2.2 cm id tube and then placed under a vacuum of ~10⁻⁵ torr. Subsequent sealing of the tube under this vacuum gave a final ampul length of 19 cm.

Since binary compounds (HgS and In₂S₃, and Sn-doped In₂S₃) were used as starting materials, four stages in the synthesis were employed. First, the tube was raised to a temperature of 980°C over a period of 7h and then maintained at this temperature for 16h with a slight reverse gradient to prevent any transport to the other end of the tube. This step was taken in an attempt to presynthesize HgIn₂S₄ before transport. Next, a relatively large reverse gradient of ~10°C/cm was employed for 12h in order to clean the walls at the growth end of the ampul of any material prior to transport. This large reverse gradient was then slowly reduced over a period of 2 days to condition in which no gradient existed, and then a forward gradient was also slowly established over a period of 3 days to give a final forward gradient for transport of 1.5°C/cm. The source and growth ends of the ampul at this point were at ~730° and 700°C, respectively. This condition was maintained for 7 days, and then the ampul was cooled in such a way that the I₂ would condense at the source end of the ampul. The above slow gradient reversal was done because it has been found that this often gives larger crystals than if the final growth conditions are imposed quickly (11).

The crystals so obtained were of moderate size (~3 × 2 × 2 mm) and showed well-developed natural faces. Powder x-ray diffraction of these crystals revealed only single-phase HgIn₂S₄. The appearance of the crystals suggested

their single-crystal nature, but no single-crystal x-ray diffraction methods were performed to verify this.

Polished HgIn₂S₄ samples were subjected to various annealing procedures as shown in Table II. Also, all samples were chemically etched in 6 or 8M HCl for approximately 3 min (sometimes repeated 2-3 times) and finally placed in a polysulfide solution (0.2M S-1.0M Na₂S-1.0M NaOH) at 50°C in a sonicator for 1-3 min to remove any sulfur deposits.

Electrolytes were prepared from analytical-grade materials in deionized water. The polysulfide couple was 0.2M S-1M Na₂S-1M NaOH, the cerium couple was 0.1M Ce(IV) and Ce(III) with 1M H₂SO₄, and the "cyanide" couple was 0.1M [Fe(CN)₆]⁴⁻ and [Fe(CN)₆]³⁻ with 1M Na₂SO₄. All solutions were deaerated with nitrogen or argon prior to PEC experiments.

Electrochemical measurements were carried out as described previously (7). Polychromatic light experiments employed a 150W Xe source with a light intensity of ~100 mW/cm at the plane of the electrode as determined utilizing a calibrated thermopile (Eppley). Monochromatic light was provided as described previously (7) employing a 450W tungsten halogen lamp. Corrections were applied to the photocurrent-wavelength plots for the variation of lamp intensities and monochromator efficiency with wavelength, as determined by a thermopile, to obtain the quantum yield of carrier collection (see Results).

Atomic absorption (AA) analyses were carried out using a Hitachi AA instrument. One standard was a solution of 984 μg In/ml (from InCl₃) in deionized water containing 1.3 volume percent (v/o) HCl (Alfa Products). Analysis of known concentrations of this reference showed a maximum deviation of <0.5% as measured. However, when known concentrations of In were prepared in the polysulfide solution, AA analyses showed the concentration of In to be significantly less than the actual value. The deviation was 50% (too low) at 2 ppm In in polysulfide, and up to 58% (too low) at 100 ppm In in polysulfide. Thus, the reference standard for calculations of In concentration in polysulfide that could result from photocorrosion of CuIn₅S₈ or HgIn₂S₄ (with a polysulfide couple) was that determined in polysulfide. We believe this to be an important observation, and, if it is not recognized, incorrect electrode stability evaluation (too high) could be obtained.

Results

All potentials here and in the discussion are with reference to SCE.

CuIn₅S₈.—With reference to Table I, the resistance of the -2a-type sample was in the 0.25-1 kΩ range; for the -2b sample in the 50-200Ω range, for the -2c, 2e, and -2g samples in the 2 (-2g) to 14 kΩ (-2d) range, for the -3 and -3a samples in the 3-4 kΩ range, and for the CuIn₅S₈-4 sample in the 1 kΩ range.

For the discussion below, reference will be made to a 2a sample unless otherwise noted. Initially, there is considerable dark anodic current positive of -0.2V reaching ~6

Table II. Preparation conditions for HgIn₂S₄ (and annealed) samples

Sample	Sample temp. (°C)	Sulfur			Dopant
		Low temp. (°C) ^a	Pressure (atm)	Time (h) ^b	
HgIn ₂ S ₄ -1	(Initial growth)	—	—	—	Sn
HgIn ₂ S ₄ -1a	690	315	0.1	24	Sn
HgIn ₂ S ₄ -1b	690	400	0.15	24	Sn
HgIn ₂ S ₄ -1c	690	220	0.006	0	Sn
HgIn ₂ S ₄ -1d	690	330	0.1	0	Sn

^a This is the temperature where the sulfur was located.

^b Sample 1a was annealed for 24h with controlled 120°C/h temperature increase to and decrease from 690°C. Sample 1b was annealed as 1a. Sample 1c was annealed by controlled 120°C/h temperature increase to and decrease from 690°C with no time at 690°C. Sample 1d was annealed as 1c.

mA/cm² at +0.2V. Upon multiple dark current scans from -0.8 to +0.8V, this dark current decreases significantly to 0.4 mA/cm² at +0.2V (and 0.8 mA/cm² at +1.0V). A rapid onset of dark cathodic current occurs at -1.5 to -1.6V in initial dark scans. The photocurrent can show up to approximately 150% increase near short circuit with multiple light scans but progressively less with forward bias. A typical current-voltage plot (I-V) in polysulfide after multiple light scans is shown in Fig. 1 for a sample having a resistance of 260Ω using polychromatic light (light chopping not shown). Short-circuit current densities of 4.5 mA/cm² were obtained and up to ~22 mA/cm² at +0.1V.

The onset of photocurrent occurs near -1.08V, and a Mott-Schottky plot of 1/C² (where C is capacitance) vs. applied potential gave an intercept value of -1.14V. This indicates an open-circuit photovoltage of 0.3V.

A typical photocurrent vs. wavelength plot is shown in Fig. 2 at -0.4V. Quantum yields of carrier collection (ϕ_c) were calculated at several applied potentials at 600 nm, which is at slightly shorter wavelength than the maximum attainable (625 nm). For the sample of concern here, ϕ_c at 600 nm is 12% at short circuit (-0.8V), 24% at -0.4V, and 77% at +0.8V after light cycling in polysulfide.

Extrapolation of the long wavelength linear region (840-940 nm) of the wavelength vs. photocurrent plot, Fig. 2, leads to a bandgap of 1.25-1.30 eV. We also analyzed the data using I_{ph}^x vs. $h\nu$ plots, where x is equal to 0.5 or 2 for indirect and direct allowed transitions [see, for example, Ref. (12, 13)]. Using data in the 900-980 nm region, we obtained a linear plot with an extrapolated value of 1.16 eV when $x = 0.5$, indicating an indirect transition. Using data over the 780-860 nm region as well as that over the 820-910 nm region, we obtained separate linear plots extrapolating to 1.36 and 1.31 eV, respectively, when $x = 2$, indicating a direct transition. Appropriate plots of $\log(h\nu I_{ph})$ vs. $\log(h\nu - E_d)$ or $\log(h\nu - E_{ind})$ gave slopes of 0.55 for the direct cases and 2.0 for the indirect case, presumably verifying the assigned nature of the transitions. These data are not in agreement with those of others (3, 9), where an indirect transition was found at 1.3-1.35 eV (vs. direct in our case). Also, no indirect transition was assigned in the 1.16 eV energy region.

The calculated power efficiency, ϕ_p , with 100 mW/cm² white light was calculated to be 0.3% (the fill factor was ~0.22). No corrections were made for light reflection (for ϕ_c or ϕ_p).

A photocurrent vs. time experiment was carried out. At an initial applied potential of -0.8V, the photocurrent first increased ~20% over the first hour and slowly decreased over the next 6h (by ~6%). The potential was then changed to +0.2V, after which there was a gradual increase (~14%) up to 11h. A total photocharge of ~390C/cm² was passed. Following this, atomic absorption analysis of the solution for In was accomplished. Assuming a photocorrosion reaction

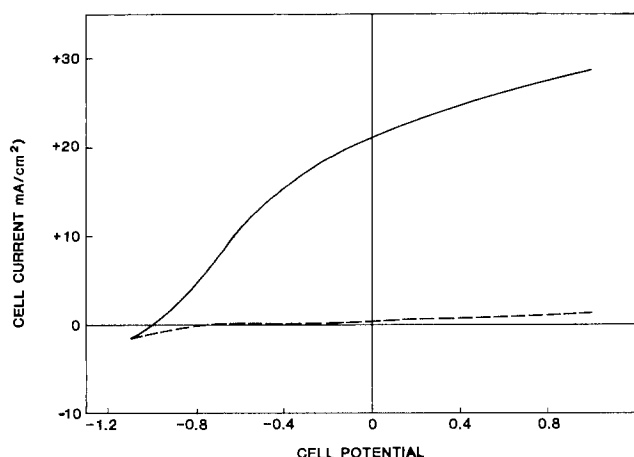


Fig. 1. Photocurrent-potential (vs. SCE) response of CuIn_5S_8 in the polysulfide couple. Dotted line: dark. Solid line: white light.

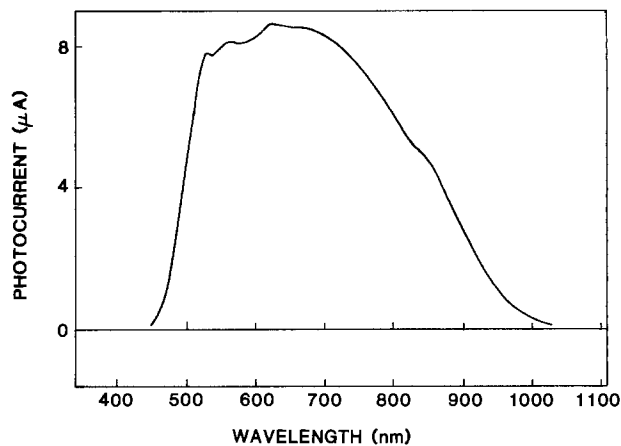
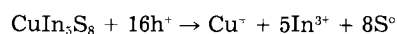


Fig. 2. Photocurrent vs. wavelength response of CuIn_5S_8 in the polysulfide couple. Short wavelength cutoff is due to absorption by the redox couple.



the In analysis showed an approximate 97+% stability of the cell (using In in polysulfide at the standard; see the discussion in the Experimental section concerning the correct standard that should be used).

In addition to the polysulfide couple, a $[\text{Fe}(\text{CN})_6]^{3-}/[\text{Fe}(\text{CN})_6]^{4-}$ couple ($E_{\text{redox}} = +0.25\text{V}$ at pH = 9) and a Ce(IV)/Ce(III) couple ($E_{\text{redox}} = +1.15\text{V}$ at pH = 0) were employed. These were chosen in an attempt to increase the photovoltage. In the cyanide couple, a substantial shift of the photocurrent onset occurred to approximately -0.1V (relative to polysulfide at -1.15V). Also, there was a notable decrease in current at short circuit compared to polysulfide. In the Ce(IV)/Ce(III) couple, the photocurrent onset of 0.0 V was nearly the same as for the cyanide couple. At short circuit, the current density was ~18 mA/cm² (compared to ~4 mA/cm² in polysulfide), and the open-circuit photovoltage was 1V (compared to 0.3V in polysulfide). However, a photocurrent vs. time plot showed a rapid decay of photocurrent at short circuit. After the passage of 20°C/cm² photocharge, the current had decayed by ~95% and yellow sulfur deposits appeared on the surface of the electrode.

Other samples of the CuIn_5S_8 -2 type, such as 2b-2e and 2g, showed lower short-circuit photocurrents in polysulfide; recall that all 2b-2e and 2g samples have resistances higher than that of 2a. In the case of a sample of type 4, where sulfur and phosphorus were used as dopants in the melt growth, both n- and p-type responses were clearly seen. The transition potential (V_{tr}) between n- and p-type response was near -0.9V. The p-type response was weaker than the n-type at the same applied potential by a factor of approximately two.

One sample of the 2 type, 2f, was treated differently than the others in that annealing was done in vacuum instead of a sulfur atmosphere. This sample showed the highest current density at short circuit, approximately 6 mA/cm². It also showed an onset the most negative of any type 2 sample, -1.2V, giving an open-circuit potential of 0.4V. However, the fill factor was only ~0.16 (vs. 0.22 for the 2a sample described above). Nonetheless, the power efficiency was ~0.4%, which was 60% greater than for the 2a sample discussed above. We also found that during photoetching in the polysulfide couple (done by multiple white light scans), the photocurrent of the 2f sample decreased by ~50% in 3h.

n-HgIn₂S₄ (Sn-doped).—Samples 1a and 1b had high resistances of ~110 and 150 kΩ, respectively, 1c of 0.3 kΩ, and 1d of 3 kΩ after etching with HCl followed by sonication in a polysulfide solution.

Both with and without annealing, only n-type material resulted.

The initial unannealed material (HgIn_2S_4 -1) showed poor photoresponse and essentially no photocurrent at

short circuit (in polysulfide). The 1a sample initially showed only 0.15-0.2 mA/cm² photocurrent at short circuit, as did the 1b and 1c samples. The 1d sample was the best and is discussed below.

A typical voltage-current plot for the 1d sample is shown in Fig. 3. Note that, initially, the dark current was essentially absent over the range -1.2 to 1.0V. The photocurrent showed a marked increase with photoetching in the polysulfide couple as shown in Fig. 1, and the fill factor also increased significantly. At short circuit, a current density of ~2.7 mA/cm² was obtained after photoetching, which rapidly increased to a near-maximum value of 6.5 mA/cm² at -0.4V (maximum current density was 7.4 mA/cm²). Accompanying this photocurrent increase was a dark current increase, but only in the -0.8 to -1.1V region. The onset of photocurrent occurred near -1.06V. The calculated fill factor was ~0.22.

Figure 4 shows a wavelength vs. photocurrent plot at -0.2V applied bias. From this and other parallel plots, a bandgap of approximately 1.95 eV was calculated (by extrapolation of the linear rising portion at long wavelength). Analyses of the data for indirect and direct transitions were carried out as previously described for CuIn₅S₈. Data over the 560-600 nm region showed the presence of a direct transition with a value of 2.04 eV. Data over the 570-650 nm region indicated the presence of an indirect transition with a value of 1.78 eV. In addition to these, a plot of $I_{ph}^{1/2}$ vs. $h\nu$ over the 710-760 nm region was linear, extrapolating to 1.19 eV.

Quantum yields of carrier collection (ϕ_c) were calculated at 550 nm and were 22% at short circuit (-0.8V) and ~66% at 0.4V (the maximum obtained was 83%).

Stability studies were carried out in polysulfide. At short circuit, the photocurrent first increased (first 15 min) and then stayed approximately constant for ~2h. After this, the potential was increased to +0.4V, at which time the current increased again over a 3h period (by approximately twofold), followed by a 5% decrease in current over the next hour, and then became constant for the next 6h, at which time the experiment was stopped. A few yellow spots were observed on the crystal after the experiment. Atomic absorption analysis for In showed a >99.5% stability of the electrode.

The power efficiency with 100 mW/cm² white light was calculated to be 0.2%. No corrections were made for light reflections (for either ϕ_c or ϕ_p).

Discussion

CuIn₅S₈.—Sulfur annealing can improve the overall PEC performance of this material. However, this improvement clearly depends on the sulfur vapor pressure and temperature, since the 2a type was definitely the best of the sulfur-annealed samples. It is also clear that dark current cycling in the polysulfide is necessary to

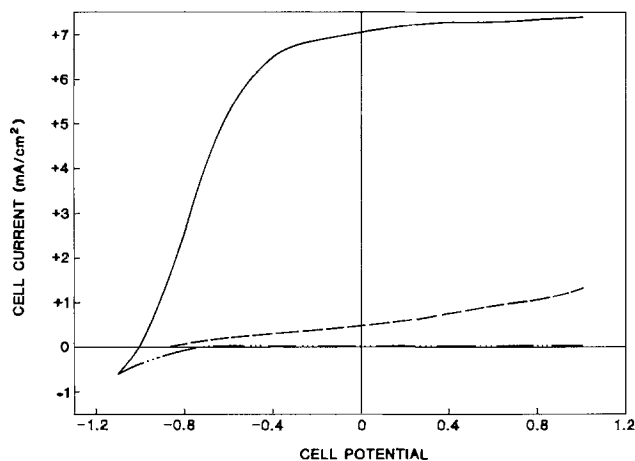


Fig. 3. Photocurrent-potential (vs. SCE) response of HgIn₂S₄ in the polysulfide couple. Dashed line: initial response. Solid line: response after photoetching. Dotted-dashed line: dark current.

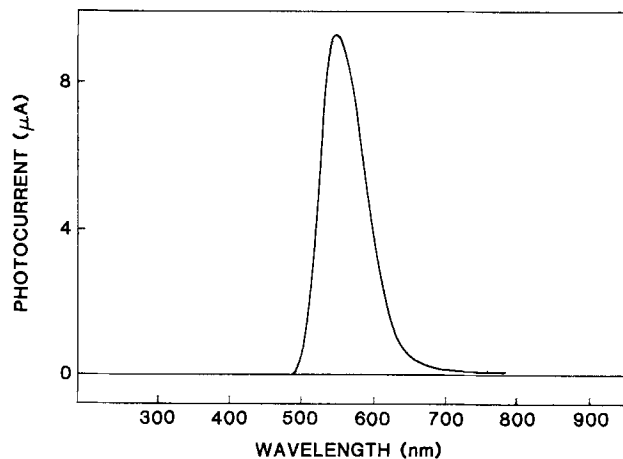


Fig. 4. Photocurrent vs. wavelength response of HgIn₂S₄ in the polysulfide couple. Short wavelength cutoff is due to absorption by the redox couple.

first condition the surface and that photoetching in the couple definitely improves the fill factor. Others have also found that chemical and photoetching improve the PEC performance of this kind of material (9).

Quantum efficiencies of carrier collection using a polysulfide couple were relatively small at short circuit (10%), but they did improve significantly upon photoetching of the electrode. However, significant bias is required to attain >50% efficiency. This indicates substantial (h^+e^-) recombination must be occurring in the vicinity of the depletion layer at short circuit. Nonetheless, the attainment of 77% quantum efficiency for carrier collection indicates that improvement of the crystal quality in general, and particularly near the surface, could result in significant improvement in the PEC results. Also, there is a question of whether the tin dopant is properly distributed as a true dopant, since, if it is not, it could act as a recombination center, at least in part.

Our photocurrent onset of -1.08V and Mott-Schottky plot intercept value of -1.14V are very similar to what was referred to as the flatband values by others (-1.1 and -1.15V respectively, by the two preceding methods). However, in our case, we are not certain if these represent flatband values and have not called them such. If we consider the potential -1.5 to 1.6V, at which cathodic dark current becomes rapidly increasing (nearly exponential) as a measure of the conduction bandedge and if the Fermi level is within 0.1-0.2 eV of this edge because of the doping, then the flatband would really be located near -1.4V. In such a case, the situation would be worse than described above in that even at the photocurrent onset there is already some 0.25-0.35V forward bias and even greater recombination is occurring than indicated in the discussion above. In one of our cases where vacuum annealing was done instead of sulfur annealing, we found the photocurrent onset (-1.2V) to be 0.1-0.15V more negative than the representative 2a sample (sulfur annealed). It is also interesting to note that others found the "flatband" potential moved 0.3V more negative than -1.1V for a freshly etched electrode (9). These latter two results are consistent with our earlier analysis, indicating the possibility that the photocurrent onset and the Mott-Schottky data may not provide true flatband potentials for this material, or that the flatband potential is varying because of variable different composition at the surface.

The foregoing, plus the relatively small fill factor of 0.22, resulted in a poor power efficiency of ~0.25%. However, 0.4% was obtained for a vacuum-annealed sample. Others (9) have reported values of short-circuit current, open-circuit photovoltage, and power efficiencies (~0.5%) similar to ours, although in isolated cases larger values of the first two were found (also, they found quantum efficiencies significantly higher than ours in at least one instance). In one of our cases where sulfur annealing was not done but vacuum annealing was done instead,

larger short-circuit current, open-circuit voltage, and power efficiency were obtained compared to the representative sulfur annealed 2a type. This material did show a reduced fill factor and less stability than the 2a type. It appears as if both the sulfur annealing and vacuum treatment improve the surface quality. This may be due in part to a temperature annealing effect.

The stability results for the 2a (sulfur annealed) type in polysulfide (0.2M S-1M Na₂S-1M NaOH) do not indicate total stability, but indicate a respectably high value (97+%). Others (9) have also reported an initial increase and then a decrease in photocurrent at short circuit, but did not test for the increase again at positive applied potential. Pitting of the surface was noted, but stability was not determined (9) (in a polysulfide couple of twice our concentrations). The greater apparent instability of the vacuum-annealed material may result from removal of sulfur on the surface, although it did not at all affect the open-circuit voltage, short-circuit current, or power efficiency (but did lower the fill factor). There is probably a critical balance required regarding the amount of sulfur present in terms of crystal quality, lattice vacancies, and interstitial sites, all of which affect the PEC results.

The results in the Ce(IV)/Ce(III) couple are interesting from the point of view of the dramatic improvement in PEC results. However, the great instability negates the improvement. The results in the cyanide couple were not as good at short circuit as for polysulfide. Others (9) have noted increased performance in the cyanide couple, and Fe(III)/Fe(II), but the electrodes were also unstable in these couples.

Our data for direct and indirect transition values differ from others. Our absorption over the 900-980 nm region may be the result of states in the gap which happens to plot correctly for an indirect transition. However, it is not apparent why our data in the ~780-910 nm region indicate a direct transition (1.33 ± 0.02 eV) vs. an indirect one for others. A direct comparison may be difficult since the wavelength region over which one group (9) determined their results may not have been the same as ours and the methodology used in the other case (3) was different.

It is clear that substantial improvement in the quality of the crystal matrix (and possibly dopant distribution) needs to be achieved to improve the performance of this kind of material before it approaches that of the ternary CuInS₂ (14, 15). Nonetheless, there seems to be potential for this.

HgIn₂S₄.—In contrast to CuIn₂S₈, dark current cycling was not necessary for the 1d sample to reduce dark currents, since they were already very small (<25 μA/cm). However, there was a significant increase in photocurrent upon photoetching (12-fold at short circuit). This obviously indicates a conditioning of the surface by photoetching was important in improving PEC (ϕ_c) performance. Nonetheless, based on the stability studies, this conditioning did not involve any significant corrosion of bulk HgIn₂S₄; also, very little visual change in the surfaces occurred over a 2h photoetch generally required to obtain maximum PEC performance. Thus, it would appear that excess sulfur (from the annealing procedure) was removed, plus perhaps some surface modification, which provided a surface considerably more free of recombination sites than without photoetching.

Quantum efficiencies for carrier collection are higher at short circuit and with applied bias than for CuIn₂S₈, but the fill factor is almost identical. Nonetheless, the power efficiency is smaller than for CuIn₂S₈ principally because of smaller short-circuit current. Obviously, the considerably higher bandgap contributes to the poorer results compared to CuIn₂S₈.

The open-circuit photovoltage is almost identical to that of CuIn₂S₈. This low value (0.25V) also contributes to a poor power efficiency. Also, as in the case of CuIn₂S₈, a dark photocathodic current becomes rapidly large near -1.6V. Again, if this is considered to be the conduction bandedge and if the Fermi level is within 0.2 eV positive

of this edge, then the flatband potential should be near -1.4V. Therefore, considerable recombination must again be occurring as for CuIn₂S₈, although it is not quite so severe, since ϕ_c at short circuit is about twice that of CuIn₂S₈ (22% vs. 10% for CuIn₂S₈). Nonetheless, it is clear that the quality of the crystal near the surface and/or dopant distribution must be providing significant recombination sites. Despite the foregoing results, it is clear that sulfur annealing produces much better results than those found for the initial material (unannealed).

The stability results indicate very little corrosion (<0.5%) of the electrode in the polysulfide couple.

Our data indicate the presence of a direct transition at 2.04 eV. Others (4, 5) indicate a bandgap of 2.0 eV, but whether it was direct or indirect was not indicated. Also, over the 570-650 nm region, we found indication of an indirect transition with a value of 1.78 eV. Again, whether the latter represents a true indirect transition or is the result of states in the gap depends upon one's estimation of the reliability of the methodology.

Based on the results of others (8) for polycrystalline HgIn₂S₄, our photocurrent onset appears to be more negative (by ~0.2V) where our couple was 0.2M S-1M Na₂S-1M NaOH, while that of the others was 1M Na₂S-1M NaOH. Our photocurrent onset appears not to be significantly different than that of others (8) (~850-900 nm), but our data showed a noticeable tail before a rapid increase in photocurrent began at shorter wavelengths. Also, our photocurrent maximum is at ~550 nm, whereas that of others (8) is near ~725 nm. Although it is not possible to be exact, it would appear that a bandgap calculated from extrapolation of the approximately linear long wavelength edge of the photocurrent vs. wavelength plot of others (8) would give a bandgap value considerably lower (up to 0.5 eV) than that we determined by the same method (1.94 eV); moreover, the latter value is close to that determined from our I_{ph}^2 vs. $h\nu$ plots for a direct transition, 2.04 eV and to the value in other literature (4, 5), 2.0 eV.

Comparison with CdIn₂S₄ results indicate that HgIn₂S₄ has a somewhat smaller photopotential (0.3 vs. 0.4V), a larger short-circuit current density (2.7 vs. 0.5 mA/cm²), and a somewhat higher power efficiency (0.2 vs. 0.1%). The photocurrent onset of CdIn₂S₄ is ~0.15V more negative than with HgIn₂S₄.

Acknowledgment

This research was sponsored by a grant from Phillips Petroleum Corporation.

Manuscript submitted July 30, 1984; revised manuscript received April 2, 1985.

The University of Houston assisted in meeting the publication costs of this article.

REFERENCES

1. J. J. M. Binsma, L. J. Giling, and J. Bloem, *J. Cryst. Growth*, **50**, 429 (1980).
2. M. Robbins and M. A. Milovsky, *Mater. Res. Bull.*, **6**, 359 (1971).
3. A. Usujima, S. Takevuchi, S. Endo, and T. Irie, *J. Appl. Phys.*, **20**, L505 (1981).
4. L. I. Berger and V. D. Prochukhan, "Ternary Diamond-like Semiconductors," pp. 41-46, 80, Consultants Bureau, New York (1969).
5. J. A. Beun, R. Nitsche, and M. Lichtensteiger, *Physica*, **26**, 47 (1960).
6. F. Cerrina, I. Abbatic, L. Braicovitch, F. Levi, and G. Margaritodo, *Solid State Commun.*, **26**, 99 (1978).
7. G. F. Epps and R. S. Becker, *This Journal*, **129**, 2628 (1982), and references therein.
8. F. Mayet, L. Mosoni, M. Roubin, and R. Olier, *C.R. Acad. Sci. Paris, Ser. II*, **294**, 701 (1982).
9. G. Dagan, S. Endo, G. Hodes, G. Sawatzky, and D. Cahen, *Solar Energy Mater.*, **11**, 57 (1984).
10. R. Nitsche, *J. Phys. Chem. Solids*, **17**, 163 (1960).
11. C. Paorici, L. Zanotti, N. Romeo, G. Sberveglieri, and L. Tarricane, *Mater. Res. Bull.*, **12**, 1207 (1977).
12. R. Tenne, Y. Mirovsky, Y. Greenstein, and D. Cahen,

This Journal, **129**, 1506 (1982).

13. Y. Mirovsky, R. Tenne, G. Hodes, and D. Cahen, *Thin Solid Films*, **91**, 349 (1982).
14. M. Robbins, K. J. Bachmann, V. G. Lambrecht, F. A.

- Thiel, J. Thomson, R. G. Vadimsky, S. Menezes, A. Heller, and B. Miller, *This Journal*, **125**, 831 (1978).
15. Y. Mirovsky, D. Cahen, G. Hodes, R. Tenne, and W. Giriat, *Solar Energy Mater.*, **4**, 169 (1981).

Ternary Chalcogenide-Based Photoelectrochemical Cells

VII. Analysis of the Chemical Processes Occurring at the CdIn₂Se₄ Surface during Photoelectrochemical Operation

R. Tenne

Department of Materials Research, The Weizmann Institute of Science, Rehovot 76100, Israel

Y. Mirovsky

Department of Structural Chemistry, The Weizmann Institute of Science, Rehovot 76100, Israel

G. Sawatzky

Laboratory for Physical Chemistry, University of Groningen, Groningen, The Netherlands

W. Giriat

Centro de Fisica, I.V.I.C., Caracas, Venezuela

ABSTRACT

The photoelectrochemical properties of the ternary semiconductor CdIn₂Se₄ is further investigated. Photoelectrochemical etching increases the photocurrent of this material by an order of magnitude in various electrolytes. Cyclic voltammetry, Auger analyses, and thermodynamic calculations suggest that oxide is unlikely to be produced during photoetching. Degradation of the photocurrent with time in polysulfide electrolyte due to photocorrosion is studied with x-ray photoelectron spectroscopy (XPS). Thermodynamic and solid-state data are used for the construction of the band diagram of CdIn₂Se₄/polysulfide system. It is shown that the time behavior of this system resembles that of CdSe/polysulfide photoelectrochemical cell.

Ternary semiconductor compounds have many interesting physical and chemical properties and also show great potential for use in electro-optical devices and solar cells in particular. Much of the research is focused on the CuInX₂ (X = Se, S) group (1-5), but other families of compounds have been investigated as well (6-11).

The mixing of Cu 4d and Se 4p atomic orbitals which leads to a decrease in the optical gap of CuInSe₂ as compared to its binary analog (CdSe) (5), and to the remarkable stability of this material against photocorrosion is of much interest. For CdIn₂X₄ compounds, there is a change in the structure between, say, CdIn₂Se₄ to CdIn₂S₄ with concomitant changes in the optical gaps (6).

CdIn₂Se₄ is material with a "defect" structure material (the space group D_{2d}¹). Each fourth cation site is unoccupied. The energies of the optical bandgaps are 1.73 eV for the direct transition and 1.55 eV for the indirect transition (6, 8). It was recently observed (8) that a short photoelectrochemical etching (photoetching) of this material leads to at least tenfold increase in the short-circuit photocurrent of the CdIn₂Se₄/polysulfide photoelectrochemical cell. Subbandgap photocurrent, which was attributed to a surface state located some 0.3 eV below the conduction band, disappeared after short photoetching. Electrolyte electroreflectance measurements (11) lent further support to this hypothesis. Fermi energy pinning substantially increased after photoetching (11). This result was attributed to yet another type of surface state, the density of which increased while photoetching. Their chemical nature was not fully resolved, although indications that they consist of chemisorbed sulfide ions were found.

The present study is a continuation of our effort to understand the chemical and electrochemical processes

which occur at the CdIn₂Se₄ surface while operating in a photoelectrochemical cell. One important aspect of that chemistry is the Se/S exchange. According to a recent study (12), CuInSe₂ is stable in polysulfide solution, and no evidence for Se/S exchange was found after ~20,000C of charge passed under illumination. Contrarily, CdSe undergoes under most solar conditions slow photodecomposition in polysulfide solution and Se/S exchange (13). Long-term stability tests of CdIn₂Se₄ electrode in polysulfide electrolyte revealed that, although the photoelectrode is stable for appreciable time, slow photocorrosion takes place. Its extent depends on the quality of the electrode material and its surface in a manner similar to Cd-chalcogenide electrodes (14).

Here, we use cyclic voltammetry and Auger spectroscopy for the analysis of the electrochemical processes which occur during photoelectrochemical etching of CdIn₂Se₄, and x-ray photoelectron spectroscopy (XPS) in conjunction with output stability runs were employed for the analysis of the Se/S exchange during the slow photocorrosion which takes place in polysulfide electrolyte.

On the basis of the proposed mechanism for the Se/S exchange and using rough estimates for the free energy of formation of CdIn₂Se₄, we have established the decomposition potential toward oxidation of this material. Taking into account the estimated flatband potential of CdIn₂Se₄, the full band diagram for the CdIn₂Se₄/polysulfide interface has been established. It is concluded that this system is expected to have similar stability as the CdSe/polysulfide photoelectrochemical cell.

Finally, experiments are described in which we have tried to evaluate the role of an In₂O₃ overlayer on the performance and output stability of the above cell. It appears

that, in contrast with CuInX_2 ($X = \text{S}, \text{Se}$) (12), thin over-layers of In_2O_3 have no positive effect on this surface. Other surface treatments are briefly discussed as well.

Experimental

CdIn_2Se_4 crystals (n-type) were grown by one of us (W.G.). Their resistivity was $<5 \Omega\text{-cm}$. Crystallographic faces were not used. The surfaces of the semiconductors were polished down to $0.3 \mu\text{m}$, etched in aqua regia (1:4 v/v HNO_3 : HCl mixture) and immersed in KCN (10% w/w) for a few minutes. Ohmic contact was established by rubbing an In-Ga alloy on the back surface of the crystals. The crystals were then attached to a Ti plate by means of a silver epoxy (Transene 50) and were finally encapsulated with the help of an insulating epoxy, apart from the front surface which was exposed to the electrolyte. Etching procedures included aqua regia etching; Br_2 (2% v/v)-methanol etch and dichromate (4g $\text{K}_2\text{Cr}_2\text{O}_7$, 10 ml HNO_3 ; 20 ml H_2O) etch; the former procedure led to the best results. Photoetching in either five times diluted aqua regia or 4M HClO_4 solution led to at least tenfold increase in the photocurrent (8). Solutions for photoelectrochemical measurements included (2;2;2) polysulfide (S; Na_2S ; KOH , 2M for each component); 1M sulfite (Na_2SO_3), and a solution of potassium ferri/ferrocyanide. A conventional three electrode setup was used for the electrochemical measurements with standard calomel electrode (SCE) as a reference electrode. A home-made programmer (linear scan generator) was used for the cyclic voltammetry measurements together with a Wenking MP 81 potentiostat and Graphtec Model WX 4422 X-Y recorder. A Philips 505 scanning electron microscope (SEM) was used to determine the morphology of the CdIn_2Se_4 surface prior to and after photoetching. A Physical Electronics Model 590A scanning Auger microprobe (SAM) was used for Auger analysis prior to and after photoetching. Se/S exchange was followed by x-ray photoelectron spectroscopy (XPS) on a AEI ES 200B spectrometer, using Mg $K\alpha$ (1253.6 eV) radiation.

Results

Figure 1 shows the I-V curve of CdIn_2Se_4 in three different solutions prior to and after photoetching (the photocurrent of the electrode exhibited in Fig. 1a is not larger than $0.5 \text{ mA}\cdot\text{cm}^{-2}$ before photoetching). In all three solutions, a remarkable increase in the photocurrent was observed after photoetching and dip in KCN solution. No effect of the KCN solution alone was observed. These results show that the improved performance of CdIn_2Se_4 after short photoetching is not limited to a specific solution. Rather, it is a manifestation of the improved state of the semiconductor surface.

The micrographs of Fig. 2 allow one to compare the surface morphology of aqua-regia etched (a), and photoetched (b), CdIn_2Se_4 . The corrugation of the surface after photoetching is obvious. The distribution of etch pits is not nearly the same as in Cd-chalcogenide and Zn-chalcogenide semiconductors (15, 16) although in certain regions of the semiconductor surface they are quite dense and uniformly distributed. This was essentially our first indication for the spatial nonuniformity of the semiconductor, a conclusion that was reinforced by the Auger analysis.

Cyclic voltammetry is a useful tool for the study of decomposition mechanisms of semiconductors. In the case of n-type semiconductors, one can photo-oxidize the semiconductor in the anodic half-cycle and dissolve the oxidation products or reduce the outdiffusing metal ions in the cathodic half-cycle (17).

Figure 3 exhibits such cyclic voltammogram for CdIn_2Se_4 in 0.5M KCl solution. The first cycle is run in the dark. A small reduction peak is observed at -1050 mV vs. SCE. Going back to zero bias, the light source is opened and a second (half) cycle is carried out in the anodic direction which is followed by a third (half) cycle (in the dark) in the cathodic direction. A series of reduction peaks is observed which cannot be easily deconvoluted. A fourth cycle (in the dark) exhibits two reduction peaks only. Referring to previous work with CdSe (17),

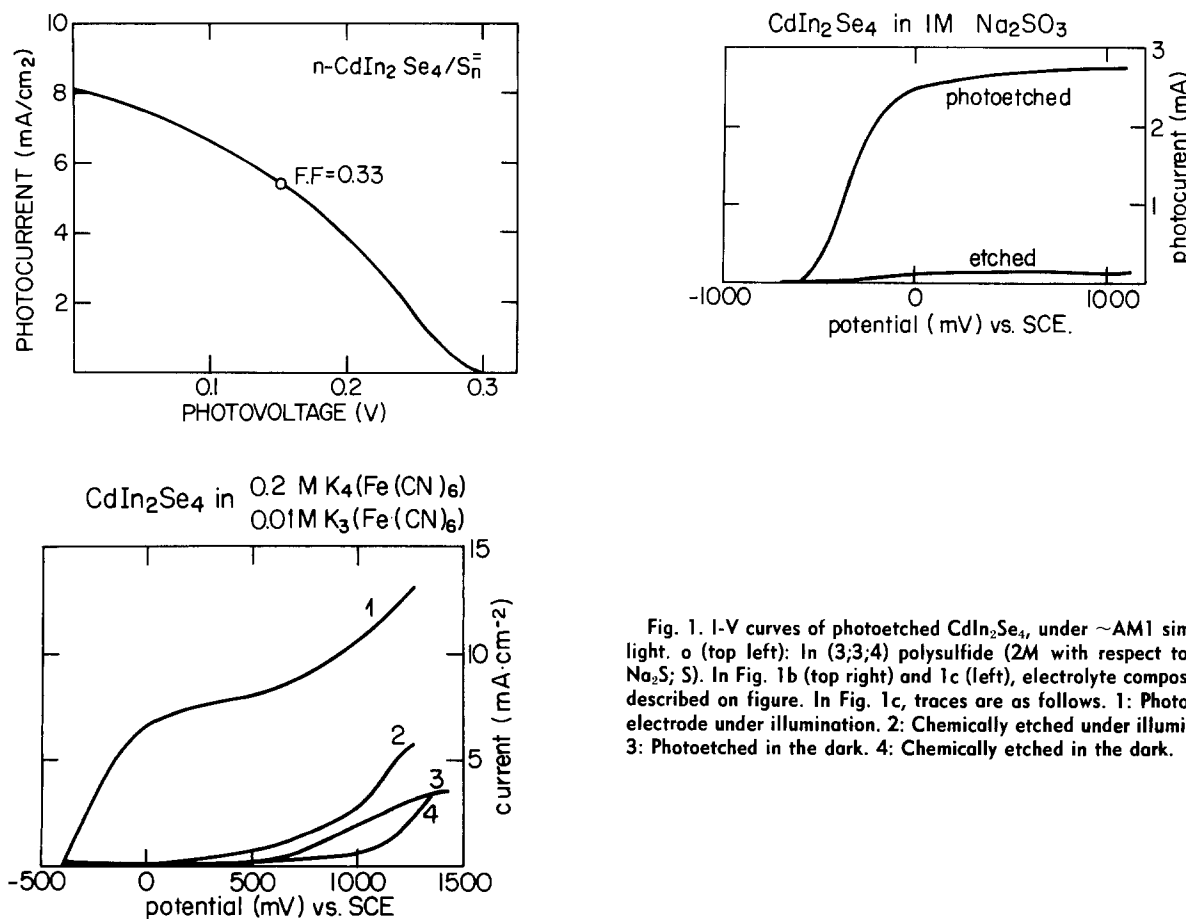


Fig. 1. I-V curves of photoetched CdIn_2Se_4 , under $\sim\text{AM1}$ simulated light. (a) (top left): In (3;3;4) polysulfide (2M with respect to KOH ; Na_2S ; S). In Fig. 1b (top right) and 1c (left), electrolyte composition is described on figure. In Fig. 1c, traces are as follows. 1: Photoetched electrode under illumination. 2: Chemically etched under illumination. 3: Photoetched in the dark. 4: Chemically etched in the dark.

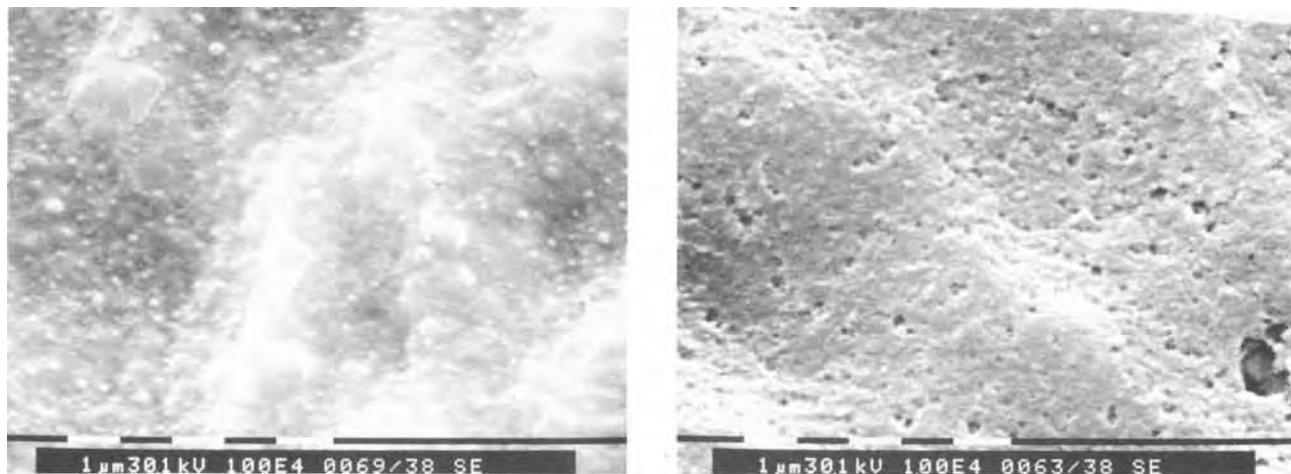


Fig. 2. Scanning electron micrographs for etched (a, left) and photoetched (b, right) CdIn_2Se_4 .

these two peaks can be attributed to reduction of elemental selenium which was produced during the second cycle (photoetching). The third cycle included, in addition to the reduction peaks of selenium, reduction peak(s) of the metal ion(s) which out-diffuse from the semiconductor surface following the anodic half-cycle under illumination. This is further visualized in Fig. 4. Here two experiments were carried out. In the first one (1 + 2), the cathodic part in the dark (2) followed the anodic half-cycle under illumination (1) immediately. Thus, in addition to the Se reduction peaks, some reduction peak of the outdiffusing metal ions(s) is observed at -500 mV vs. SCE. In the second experiment (1 + 3), the cathodic half-cycle (3) is carried out only 1 min after the completion of the photoetching (1). Thus, all metal ions have diffused from the semiconductor surface already and the Se reduction peak is observed under cathodic scan only. The separation between metal ion(s) reduction peak(s) and selenium reduction becomes even more evident when the photoetching (anodic part) is done at higher light intensities. However, the separation between the reduction peaks of indium (3+) and cadmium (2+) ions is not nearly as simple since on a platinum electrode they are only 60 mV apart. In the Discussion section, we propose a mechanism for the light-induced decomposition of CdIn_2Se_4 which is consistent with the results of cyclic voltammetry.

Additional information on the surface chemistry which is involved in the photoetching was obtained from Auger spectroscopy. The results of the Auger analysis are summarized in Table I.

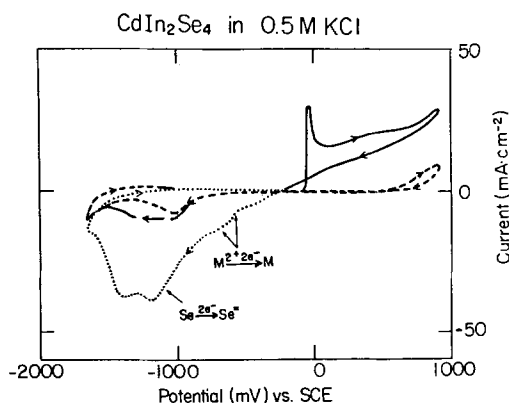


Fig. 3. Cyclic voltammograms of CdIn_2Se_4 ($200 \text{ mV}\cdot\text{s}^{-1}$), in the dark and under illumination. Curve 1 (short dashes) In the dark prior to illumination. Curve 2 (solid line): Anodic half-cycle under illumination (photoetching). Curve 3 (dotted line): In the dark immediately after photoetching. Curve 4 (long dashes): After few cycles (in the dark). Light intensity ca. $5 \times \text{AM1}$.

The sample showed a large heterogeneity on each of the two analyzed surfaces, but it was especially large on the etched surface, which contained appreciable amounts of oxygen in either adsorbed form or more likely as an oxide of indium. Thus, Fig. 5 presents a wide scan of the Auger

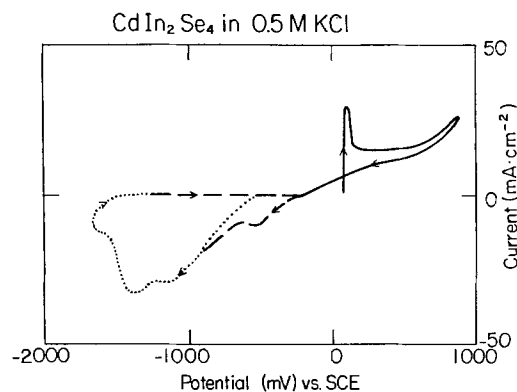


Fig. 4. Cyclic voltammogram of CdIn_2Se_4 ($200 \text{ mV}\cdot\text{s}^{-1}$). Solid line: Under illumination (photoetching). Dashed line: Immediately after photoetching. Metal reduction is seen. Dotted line: Starts 60s after photoetching. Most metal ions outdiffused already. Light intensity ca. $5 \times \text{AM1}$.

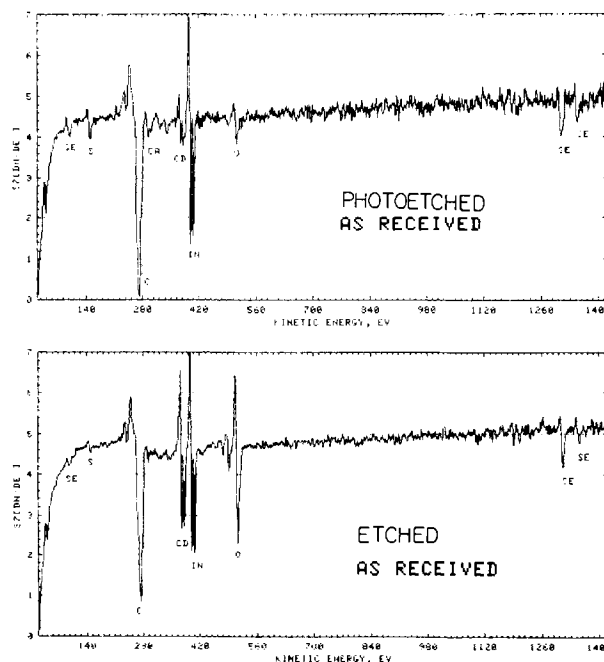


Fig. 5. Wide Auger scan of CdIn_2Se_4 prior to and after photoetching.

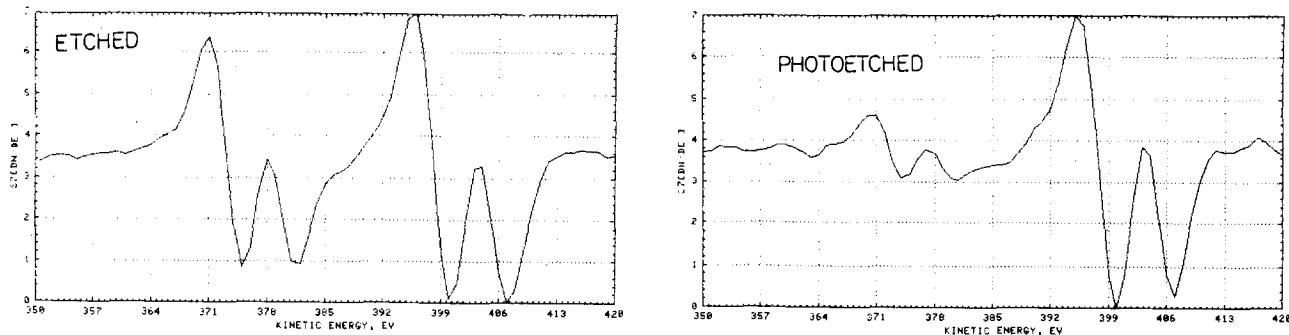


Fig. 6. Narrow Auger scan of cadmium (374, 381 eV) and indium (400, 407 eV) peaks of the sample presented in Fig. 5.

spectrum prior to and after photoetching. Some carbon contamination is obvious, but, nevertheless, the abundance of oxygen on the chromate etched surface is clearly exhibited. The oxygen signal almost disappears after photoetching. Furthermore, comparison of the narrow scans (Fig. 6) indicates that indium oxide is the most likely oxygen containing species. This is indicated from the ratio R between the height of the 407 eV peak of In to the height of the 400 eV peak of In. Thus, R is larger than one for the etched electrode (Fig. 6a). After photoetching (Fig. 6b), this ratio (R) becomes smaller than 1 (18).

Also observed is the relative depletion of cadmium after photoetching. The larger amount of sulfur and selenium after photoetching can be attributed to (i) release of elemental selenium during photoetching (see Eq. [1]-[3]) and to (ii) the post-treatment of the electrode, after photoetching, in polysulfide solution. Although a thorough rinse and immersion in hot KCN solution follows the immersion in polysulfide (which should dissolve all the free selenium generated during photoetching), the high degree of porosity of the photoetched surface inhibits the completion of these two processes and thus both sulfur and selenium are more abundant after photoetching. Generation of some selenium oxide during photoetching cannot be ruled out conclusively, but both thermodynamic calculations (see Table II) and surface analyses of photoetched CdSe (17a) suggest that this reaction is not favorable here.

After sputtering a layer of 285 Å, the oxygen concentration went down appreciably and the composition of the etched part became almost stoichiometric (CdIn_2Se_4). Contrarily, the photoetched surface had much less oxide on it, but cadmium depletion, which increased with the depth, is evident here.

Figures 7 and 8 exhibit a wide and a narrow scan, respectively, of CdIn_2Se_4 after sputtering of a layer of a few hundred angstroms. Figure 7 exhibits much less oxygen

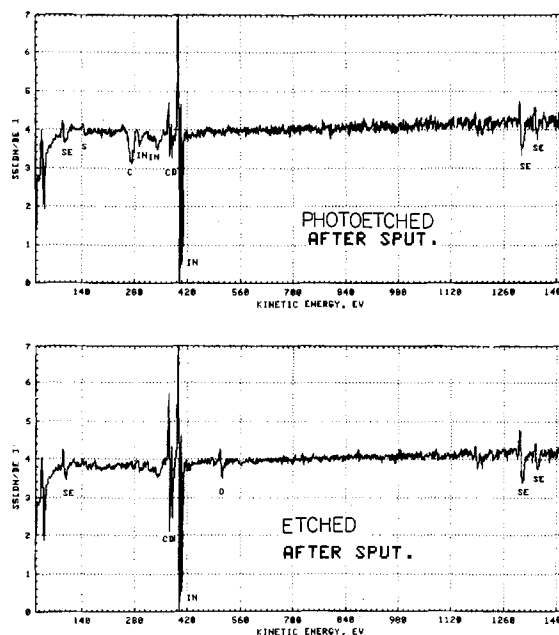


Fig. 7. Wide Auger scan of CdIn_2Se_4 prior to and after photoetching and after ion sputtering of $\sim 300\text{Å}$.

on the etched surface after Ar sputtering. This is further shown in the narrow scan, where the ratio R for the In peaks is smaller than 1 now. Hence the amount of indium oxide went down drastically, on the chromate etched surface, following argon sputtering. Cadmium depletion increases, on the photoetched surface, after sputtering.

The Auger analyses suggest that the oxide layer on the etched surface (probably indium oxide) has an adverse effect on the performance of CdIn_2Se_4 in photoelectrochemical cells in contrast with CuInSe_2 (12, 13). Thermodynamic calculations (see Discussion section) show that the oxide layer is unstable during photoetching.

A second phase of the present study concerns the long-term stability of CdIn_2Se_4 in polysulfide solution under illumination and the Se/S exchange. It was shown previously (8) that CdIn_2Se_4 is remarkably stable in polysulfide electrolyte after photoetching. Figure 9 compares the output stability of photoetched CdIn_2Se_4 to that of CdSe in (2;2;2) polysulfide electrolyte. The CdIn_2Se_4 is very stable at a current density of $80\text{ mA}\cdot\text{cm}^{-2}$, and the sharp drop in the photocurrent occurs upon addition of water, which is lost due to evaporation under intense illumination. At a higher photocurrent ($\sim 100\text{ mA}\cdot\text{cm}^{-2}$), the photocurrent drops somewhat faster in the beginning,

Table I. Relative composition of CdIn_2Se_4 prior to and after photoetching as determined by scanning Auger analysis

	Chromate etched ^b	Photoetched ^b
Surface	$\text{CdIn}_4\text{Se}_{2.74}\text{O}_{3.86}\text{S}_{0.082}$	$\text{CdIn}_{2.42}\text{Se}_{3.46}\text{O}_{1.338}$
160 Å ^a	$\text{CdIn}_{2.46}\text{Se}_{3.98}\text{O}_{1.84}\text{S}_{0.12}$	$\text{CdIn}_{4.46}\text{Se}_{9.55}\text{O}_{0.2}\text{S}_{0.2}$
285 Å ^a	$\text{CdIn}_{2.12}\text{Se}_{4.52}\text{O}_{0.51}\text{S}_{0.05}$	$\text{CdIn}_{3.6}\text{Se}_{11.39}\text{O}_{0.3}\text{S}_{0.3}$

^a Calibrated according to Ta_2O_5 .

^b Immersion in polysulfide and in 10% (w/w) KCN solution for 15 min was done prior to Auger analysis. Immersion in polysulfide leads to the dissolution of elemental selenium, the final cleaning of the surface from elemental sulfur and selenium is done in KCN solution. This procedure was favored over KCN treatment alone since it permitted less frequent disposal of the KCN solution.

Table II. Free energy of formation for chemical species involved in reactions [1]-[3]

	Cd^{2+}	In^{3+}	H_2O	SeO_2	In_2O_3	CdSe	In_2Se_3	$\text{CdIn}_2\text{Se}_4^*$
ΔG° (kcal·mol ⁻¹)	-18.58	-23.41	-56.65	-49.3	-198.5	-33.8	-79.08	-135.2 (-112.88)
Ref.	(21)	(23)	(22)	(22)	(22)	(23)	(23)	

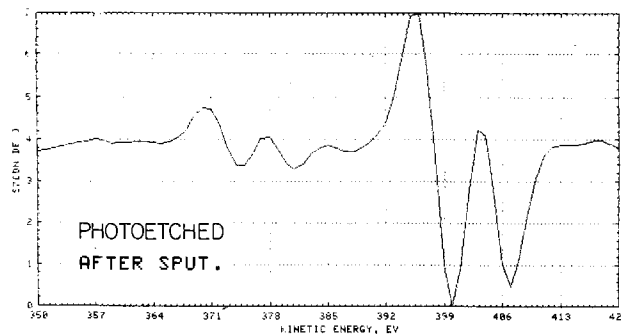
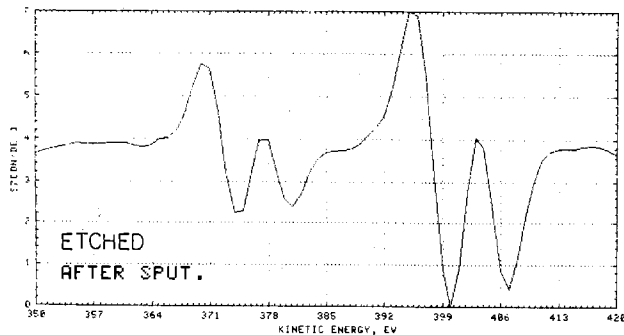


Fig. 8. Narrow Auger scan of cadmium and indium peaks of the sample presented in Fig. 7.

and then it falls off slowly. The output stability of CdSe is somewhat inferior to that of CdIn₂Se₄, as shown in Fig. 9. This is even more important if one takes into account that (i) the photocurrent of CdSe is two times higher than that of CdIn₂Se₄ under the same illumination intensity, so that in order to get the same photocurrent one must utilize at least twice as intense light for CdIn₂Se₄ than for CdSe and (ii) CdIn₂Se₄ is a "defect" structure material, and one would expect that migration of ions through it may facilitate the photocorrosion process.

Figure 10 presents the XPS depth profile of a photoetched CdIn₂Se₄ sample which passed 1200C of photocharge. These results show that the Se/S exchange occurs, and even after 62 min of Ar⁺ sputtering, which can be roughly estimated as 500Å (100 atomic layers), there is some sulfur present. The fact that Se/S exchange occurs to such an extent and that during that period the cell performance went down by 30% could only indicate that the surface is highly nonuniform and that surface corrugations may have a large effect on the XPS results. The Se/S exchange implies that CdIn₂Se₄ is oxidized under illumination in the photoelectrochemical cell to Cd²⁺, In³⁺, and Se, which agrees well with the cyclic voltammetry results (Fig. 3). The Cd²⁺ and In³⁺ ions recombine with excess S⁻ ions to give CdS and In₂S₃, respectively, which precipitate on the surface of the electrode. The results presented in Fig. 7 show that the CdIn₂Se₄ is more akin to the Cd-chalcogenide family than to the CuInX₂ family. The CdS and In₂S₃ become obstructive for hole tunneling if their thickness exceeds, say, 20-30Å, in which case the photocurrent goes down and the rate of photocorrosion increases (19).

It is also important to note that electrodes which were properly prepared (*i.e.*, received optimal surface treatment) show both improved I-V characteristics and better output stability. This observation is not unique to that system (20). Higher rate for the charge transfer (higher photocurrent) leaves a smaller concentration of holes at the semiconductor surface to carry out the photocorrosion reaction (better stability) (19b).

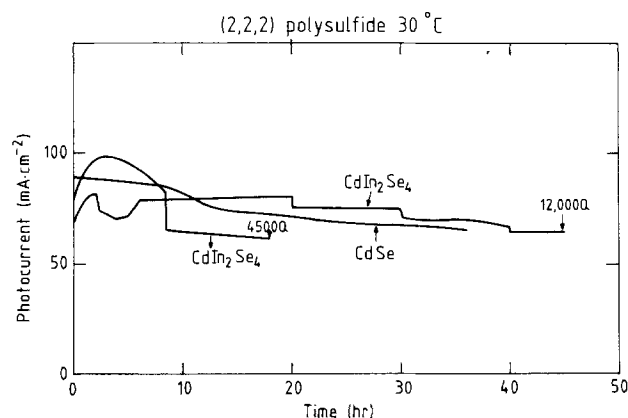
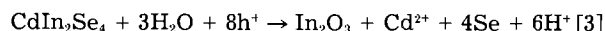
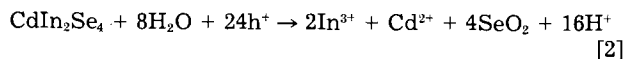
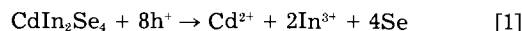


Fig. 9. Comparison of the output stability of photoetched CdIn₂Se₄ under two light intensities and compared also to photoetched CdSe. All experiments carried out in (2;2;2) polysulfide. Potential 0 vs. SCE. Temperature: 30°C.

Discussion

Based on energy of formations for the oxidation products of CdSe, it was recently shown (17a) that the most favorable oxidation product of CdSe in acidic and neutral media is Se, rather than the oxides of selenium (although SeO₂ formation is only slightly less likely). From the many decomposition reactions which may occur during photoetching, we list the following three as representative ones



In the absence of any quantitative data on the free energy of formation of CdIn₂Se₄, we take it as a rough estimate to be four times the free energy of formation of CdSe (-135.2 kcal·mol⁻¹) (14). Another estimate for the free energy of formation of CdIn₂Se₄ can be done from the sum of the free energy of formation of CdSe and In₂Se₃ (-112.88 kcal·mol⁻¹). All the calculations which rely on this latter value are given in parentheses. Table II is a list of the free energy of formation of species involved in Eq. [1]-[3] (21).

Table III summarizes the free energy of decomposition for reactions [1]-[3] and their respective decomposition potentials.

Clearly then, Eq. [1] is the most favorable decomposition reaction for CdIn₂Se₄ under oxidative conditions; the

¹Systematic overestimation of ~20% was obtained by a similar calculation for CuInX₂ compounds for which experimental figures were published recently.

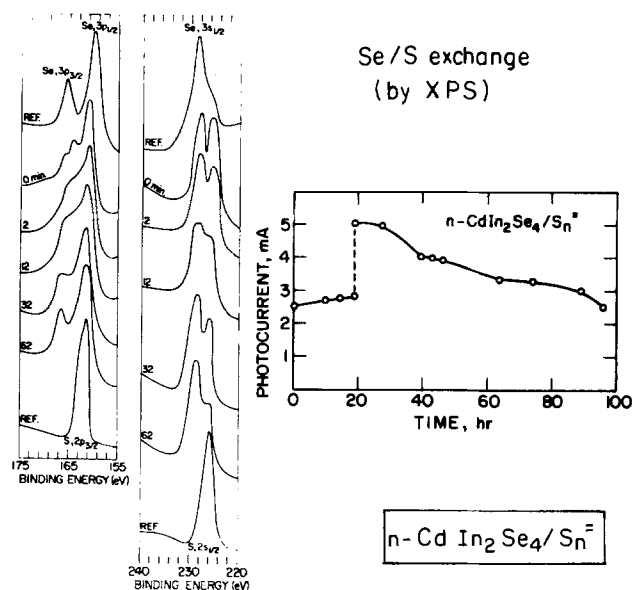


Fig. 10. XPS analysis of a partially deactivated CdIn₂Se₄ which show the Se/S exchange (photocorrosion). Numbers on curves represent the time (min) for argon sputtering. Curve on the right is the photocurrent vs. time (stability) of the examined electrode (0.1 cm²).

Table III. Free energies of decomposition and decomposition potentials for reactions [1]-[3]

Reaction	[1]	[2]	[3]
$P\Delta G_D^\circ$ (kcal-mol ⁻¹)	-64.6(-47.5)	-339.2(-322.06)	-82.87(-65.75)
PE_D° (V vs. SCE)	0.100(0.007)	0.363(0.332)	0.199(0.106)

Table IV. Free energies of formation for species involved in reactions [4] and [5]

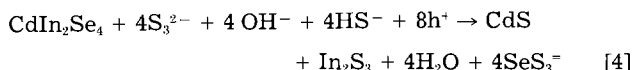
	S_3^{2-}	SeS_3^{2-}	In_2S_3	CdS	OH^-	HS^-
ΔG° (kcal-mol ⁻¹)	17.61	16.48	-98.55	-37.39	-37.56	3.01
Ref.	(22)	(22b)	(22)	(22)	(22)	(21)

Table V. Decomposition potentials for CdSe and CdIn₂Se₄ in aqueous polysulfide solution

	CdSe	CdIn ₂ Se ₄
$P\Delta G_D^\circ$ (kcal-mol ⁻¹)	-26.8	-98.86 (-115.98)
PE_D° (V vs. SCE)	-0.83	-0.78 (-0.88)

differences are even larger than for CdSe. This estimation supports the Auger measurements which have shown little oxide on the semiconductor surface after photoetching. It may also suggest that oxides, and particularly In_2O_3 , which was found to benefit the performance of $CuInX_2$ ($X = S, Se$) electrodes are not stable in the oxidative environment which prevails at the semiconductor surface during illumination (see below for further details on the matter).

The output stability of $CdIn_2Se_4$ in polysulfide electrolyte is more akin to that of CdSe than to that of $CuInX_2$ family (3). A possible overall mechanism for the Se/S exchange in $CdIn_2Se_4$ is (14)



For CdSe, the following mechanism is consistent with the experimental observations

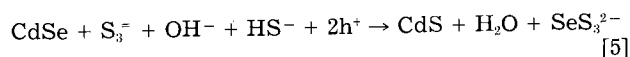


Table IV gives the free energy of formation of the species involved in reactions [4] and [5].

Based on these values and on the values given in Table II, the decomposition potentials for CdSe and $CdIn_2Se_4$ in aqueous polysulfide solution are summarized in Table V.

To establish the full band diagram, one has to know the flatband potential of the semiconductor in the respective electrolyte. For CdSe, this figure is available (-1.54V vs. SCE). For $CdIn_2Se_4$, this number is estimated from the maximum open-circuit potential (under strong illumination). For CdSe, the density of states in the conduction band N_c is calculated from the known (22) effective mass of the electron.

Table VI. Various data relevant for constructing the band diagram and thermodynamic stability diagrams

	N_c (cm ⁻³)	$E_{CB} - E_F$ (eV)	E_F vs. SCE (eV)	E_{CB} vs. SCE (eV)	E_g (eV)	E_{VB} vs. SCE (eV)
CdSe	1.25×10^{18}	0.125	-1.59	-1.72	1.72	0.00
$CdIn_2Se_4$	5.2×10^{18}	(0.15)	(-1.2)	(-1.35)	1.55	+0.20

N_c : density of states in the conduction band.
 E_{CB} : bottom of the conduction band.
 E_F : Fermi level.
 E_{VB} : top of the valence band.
 Numbers in parentheses are best estimates.

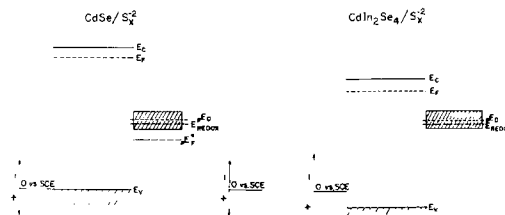
**Fig. 11. Band diagram and decomposition potential (shaded area) for CdSe and CdIn₂Se₄ in polysulfide.**

Figure 11 and Table VI summarize these calculations. The most prominent result here is that the band diagram and the decomposition potential for $CdIn_2Se_4$ /polysulfide interface resembles that of CdSe/polysulfide and hence the output stability of the two systems are expected to be similar if thermodynamic considerations are taken into account only. Thus, the experimental observations in Fig. 5 agree with the model calculations presented herein that similar output stability is obtained for photoetched CdSe and $CdIn_2Se_4$ in (2;2;2) polysulfide electrolyte. However, no consideration of the kinetic factors affecting the photocorrosion processes were used, although, ultimately, they may be of greater relevance to the present problem than the thermodynamic factors.

Some unsuccessful attempts were carried out to improve the performance of the $CdIn_2Se_4$ /polysulfide photoelectrochemically. It was attempted to create a thin In_2O_3 overlayer by several means. Thus, $CdIn_2Se_4$ was heated at 100°-150°C for different periods of time in air atmosphere. Such heating is beneficial for the $CuInX_2$ cells (12). Furthermore, electrochemical deposition of In which was followed by a heat-treatment was not of great help either. Immersion in $InCl_3$ solution (at different temperatures) was not successful either. Finally, $InCl_3$ was dissolved in a concentrated (2;2;2) polysulfide which led to a rapid deactivation of the electrode.

Treatments in solutions of ionic Cu (23) and Zn (24) were attempted, the latter treatment being of little help only. Addition of small quantities of Se did not lead to an improved output stability.

So far, we have not found a surface treatment which has but a marginal effect on the performance or output stability of $CdIn_2Se_4$ in polysulfide electrolyte other than photoetching. Further work is necessary in that direction and also in order to understand the basic physics of that interface.

Very recently, Fornarini *et al.* (25) presented some new observations on the $CdIn_2Se_4$ /polysulfide photoelectrochemical cells. First, the quality of their starting material was superior to the one used during this work. This is borne out by the higher photocurrents produced after photoetching (~ 20 mA-cm⁻²), and also through the lack of Fermi level pinning as observed in our crystals (11) *i.e.*, no breakdown of the Schottky barrier under reverse bias (8). They observe Se/S exchange and discuss the output stability of $CdIn_2Se_4$, which they find also more akin to the CdSe than to $CuInSe_2$.

Acknowledgment

We are indebted to Philips Company and to Dr. Van-Haas of Philips for the assistance with the electron microscopy. We are also grateful to Dr. D. Cahen for his ad-

vice in the interpretation of the surface analyses results. We are also grateful to Mr. Arend Heeres for his assistance in the XPS experiments. R. T. is grateful to Helen and Milton A. Kimmelman for support of his work.

Manuscript submitted Sept. 27, 1984; revised manuscript received April 3, 1985.

REFERENCES

- S. Wagner, J. L. Shay, P. Migliorato, and H. M. Kasper, *Appl. Phys. Lett.*, **25**, 434 (1974).
- R. A. Mickelsen and W. S. Chen, in "Fifteenth IEEE Photovoltaic Specialists Conference 1981," IEEE Publication 81CH 1644-4, p. 800, IEEE, New York (1981).
- Y. Mirovsky and D. Cahen, *Appl. Phys. Lett.*, **40**, 727 (1982).
- M. Robbins, K. J. Bachmann, V. G. Lambrecht, F. A. Thiel, J. Thomson, Jr., R. G. Vadimsky, S. Menezes, A. Heller, and B. Miller, *This Journal*, **125**, 831 (1978).
- J. E. Jaffe and A. Zunger, *Phys. Rev. B.*, **28**, 5822 (1983); *ibid.*, **29**, 1882 (1984).
- L. S. Koval, S. I. Radautsan, and V. V. Sobolev, *Inorg. Mater.*, **8**, 1776 (1972) Translated from Russian.
- H. Fujita and Y. Okada, *Jpn. J. Appl. Phys.*, **13**, 1823 (1974).
- R. Tenne, Y. Mirovsky, Y. Greenstein, and D. Cahen, *This Journal*, **129**, 1506 (1982).
- G. F. Epps and R. S. Becker, *ibid.*, **129**, 2628 (1982).
- T. Hailing, G. A. Saunders, and W. A. Lambson, *Phys. Rev. B.*, **26**, 5786 (1982).
- M. Tomkiewicz, W. Siripala, and R. Tenne, *This Journal*, **131**, 736 (1984).
- Y. Mirovsky, G. Sawatzky, R. Tenne, and D. Cahen, Submitted to *This Journal*.
- (a) D. Cahen, G. Hodes, and J. Manassen, *ibid.*, **125**, 1156 (1978); (b) R. Noufi, P. A. Kohl, and A. J. Bard, *ibid.*, **125**, 376 (1978).
- Y. Mirovsky, Ph.D. Thesis, Weizmann Institute of Science, Rehovot, Israel (1983).
- R. Tenne and G. Hodes, *Surf. Sci.*, **135**, 453 (1983).
- R. Tenne, H. Flaisher, and R. Triboulet, *Phys. Rev. B.*, **29**, 5779 (1984).
- (a) R. Tenne, *J. Electroanal. Chem.*, **186**, 127 (1985); (b) R. Tenne and G. Hodes, *Berl. Bunsenges. Phys. Chem.*, **89**, 74 (1985).
- M. Potak, *Thin Solid Films*, **90**, 345 (1982).
- (a) D. Cahen, J. Manassen, and G. Hodes, *Solar Energy Mater.*, **1**, 343 (1979); (b) H. Flaisher and R. Tenne, *J. Phys. Chem.*, **87**, 3061 (1983).
- R. Tenne, N. Müller, Y. Mirovsky, and D. Lando, *This Journal*, **130**, 852 (1983).
- W. M. Latimer, "Oxidation Potentials," 2nd edition, Prentice-Hall, Inc., New York (1952).
- (a) D. D. Wagman, The NBS Tables of Chemical Thermodynamic Properties, National Bureau of Standards, Washington, DC (1982); (b) D. Cahen and Y. Mirovsky, *J. Phys. Chem.*, To be published.
- K. C. Mills, "Thermodynamic Data for Inorganic Sulfides, Selenides and Tellurides," Butterworth, London (1974).
- Cleveland Crystals, Inc., Information Sheet, Cleveland, OH (1980).
- H. Flaisher, T. Tenne, and G. Hodes, *J. Phys. D.*, **17**, 1055 (1984).
- (a) G. Hodes, D. Cahen, J. Manassen, and M. David, *This Journal*, **127**, 2252 (1980); (b) M. A. Russak and J. Reichman, *ibid.*, **129**, 542 (1982).
- L. Fornarini, F. Stirpe, E. Cardarelli, and B. Scrasati, *Solar Cells*, **11**, 389 (1984).

The Properties of Electrochromic Film Electrodes of Lanthanide Diphthalocyanines in Ethylene Glycol

G. C. S. Collins

IBM (UK) Laboratories, Process Technology, Winchester, Hampshire, England

D. J. Schiffrin*

Wolfson Centre for Electrochemical Science, Department of Chemistry, The University, Southampton, Hampshire, England SO9 5NH

ABSTRACT

The electrochromic properties of film electrodes of lutetium, erbium, gadolinium, and ytterbium diphthalocyanines in contact with ethylene glycol solutions have been studied. The stability of the electrochromic film under electrochemical cycling in this medium is at least three orders of magnitude better than that in neutral aqueous solutions. The stability of the electrochromic is improved if the film is written galvanostatically from the yellow-tan to the green state. A simplified model for the galvanostatic transition is proposed, and some of the problems of this family of electrochromic materials are discussed.

The preparation of the diphthalocyanine complexes of the rare earth elements [Lan(PC)₂]¹ by reaction of their acetates with o-phthalonitrile was first achieved by Kirin *et al.* in 1967 (1). Subsequently, Moskalev and Kirin (2) showed that the absorption spectrum of Lu(PC)₂ changed reversibly with electrode potential and later proved that all the lanthanide diphthalocyanines as well as those of yttrium and scandium were electrochromic (3).

Because these compounds are stable and those of Eu through to Lu can be sublimed (4) onto an electrode surface to form a thin electrochromic film, there has been

* Electrochemical Society Active Member.

¹ Although the stoichiometry Lan(PC)₂ is used in this paper, there is still some discussion regarding the presence of an imino hydrogen in the molecule. In particular, very recent spectroscopic work by Nicholson and Weismuller (32) favors the existence of Lu H(PC)₂ · O₂⁻ as the green form. Further work is required to elucidate the discrepancy between the spectroscopic results and the isotopic mass distribution of the parent ion in the mass spectra, which appears to favor the Lu (PC)₂ stoichiometry (10).

considerable interest in their possible use as visual display units (5-8).

The structure and electrochemistry of the lanthanide diphthalocyanines have been widely studied over the last few years. This work has been recently reviewed by Nicholson (9), who concluded that there was a problem with stability under switching and that the development of practical displays would depend on the achievement of adequate cycle life (10⁶-10⁸ color transitions) and a technique for matrix addressing.

Repeated cycling of Lu(PC)₂ film electrodes in neutral aqueous electrolytes between the green and the red states results in the degradation of the color change after 10⁴ cycles. It has been proposed that this is due to attack of the nitrogen atoms in the phthalocyanine rings by water or by OH⁻ ions (10), when the dye is in its oxidized form, *i.e.*, as a diradical dication (11, 12). In common with many radical cations, the oxidized form appears to be stabilized by strong acid solutions, and Bessonnat *et al.* (13) achieved 5

$\times 10^6$ color changes for a dye electrode in sulfuric acid medium.

The purpose of the present work was to study the electrochemistry of $\text{Lu}(\text{PC})_2$ in a nonaqueous solvent having a lower ionization constant than water, thus reducing the problems of nucleophilic attack by OH^- on the oxidized form of the rare earth complexes.

Experimental

The $\text{Lu}(\text{PC})_2$ and other (Gd, Er, Yb) phthalocyanines were prepared and purified as described previously (10). The remaining chemicals used were either BDH AnalaR grade (ethylene glycol, sodium chloride, potassium chloride, ammonium fluoride) or Fluka "purum" grade (tetraethyl ammonium halides).

Most of the cycling experiments were carried out using purpose-built electrochemical modules with a single array of 28 pels per cell. The working electrodes consisted of evaporated layers of titanium (50 nm) covered with platinum (200 nm), on Rowi glass. The electrode pattern was obtained by a lift-off technique using photoresist leaving 28 square electrode pads of 1.25 mm²/side. The conductor lines to each electrode were protected by a 1.1 μm layer of cured du Pont 5057 polyimide, except at the contact points. The electrochromic film was evaporated over the working electrode surfaces as a continuous film at 10^{-4} torr in an Edwards 6E4 coating unit by resistance heating to $450^\circ \pm 50^\circ\text{C}$. Film thickness measurement was established by relating optical density at λ_{max} (Table I) to the step height of standard films as measured by a profilometer (Tencor Alphastep).

The module was built up by placing a silicone rubber gasket on the glass substrate followed by an acrylic molded spacer with an adhesive-bonded glass top. The acrylic spacer had inlets for a platinum black counterelectrode, a reference electrode, for filling the module, and also for a thermocouple. The various items fitted to the molding were glued in place with 3M 3532 structural adhesive. Silicone rubber gaskets protected the module from copper platens, which were tightened to form a liquid-tight seal. The upper platen had a square opening through which the pels could be viewed. Modules were then filled with electrolyte and the filling tubes sealed. No attempt was made to deoxygenate the electrolyte prior to use.

Solutions of the halide salts in ethylene glycol were used as electrolytes. With chloride electrolytes, an Ag/AgCl reference electrode was used, but with fluorides this was changed to Cu/CuF₂. Prior to use, each reference electrode was anodized to form the salt on the electrode surface. Ethylene glycol was used without further purification. The electrolyte used in most of this work was a saturated solution of NaCl (ca. 1M), which has a conductivity $5 \times 10^{-3} \text{ Scm}^{-1}$ at 20°C and $1 \times 10^{-2} \text{ Scm}^{-1}$ at 40°C .

The modules were driven by a purpose-built microprocessor potentiostat/galvanostat. This instrument had potentiostatic, tensiostatic, and galvanostatic units coupled together to enable writing or erasing from either one or two of the units. The range was $\pm 2\text{V}$ in 10 mV steps on the potentiostatic and tensiostatic units and $\pm 40 \text{ mA}$ in 100 μA steps on the galvanostatic unit. The current and voltage required could be set either manually or by com-

puter, but the time base was computer controlled over a wide range down to 250 μs .

The potentiostat/galvanostat incorporated a Motorola M6800 microprocessor, and was linked to an IBM 5100 computer for input. Control programs were written in a high level language based on APL and compiled to 6800 machine code, which was loaded into the 6800 from the 5100 memory, thus freeing the 5100 for other tasks. Using this system, it was possible to set up and change the write, hold, erase, and off parameters simply and at will. The current and voltage transients were fed from the potentiostat/galvanostat to a Tektronix 7633 storage oscilloscope for observation and evaluation.

Optical density changes on simple pels were measured using a spotmeter (Spectra, Model UBD, 1/4 degree). This precluded obtaining absolute absorption measurements.

In all cycling experiments a four-step cycle will be referred to containing write, off, erase, and off periods. The off periods were used for measuring decay transients and to study fade rates. Because both potential and current steps and varying time were used to write and erase in a cycle, a particular experiment will always be defined in the text.

A Hi-Tek potentiostat, transient recorder, and signal generator were used for the voltammetric measurements, and the results were plotted on a Bryans 26000 X-Y recorder. In these experiments, a tin oxide electrode was used. The film electrodes were prepared as previously described (10).

The x-ray photoelectron spectroscopy (XPS) studies were performed with a VG Scientific ESCA 3 Mark II instrument. The $\text{C}_{(1s)}$ band was used as the internal reference.

The potential limits of the 1M NaCl/ethylene glycol electrolyte on Pt were arbitrarily taken as the potential for which the current density was $10 \mu\text{A}\cdot\text{cm}^{-2}$, and were determined by cyclic voltammetry. The values obtained were +800 and -600 mV, corresponding to glycol oxidation and the hydrogen evolution reaction, respectively. It was found that ammonium fluoride attacked the glass of the module, and for this reason tetraethylammonium fluoride was used for the tests with F^- ion containing solutions. Similar potential limits were found for this electrolyte.

The polarization limits of the electrolytes for a Pt electrode were further confirmed by studying the possible formation of polymeric oxidation films by x-ray photoelectron spectroscopy (XPS). It was found that at 1.2V, a tenfold increase in the $\text{C}_{(1s)}$ and $\text{O}_{(1s)}$ signals was observed after 30 min of polarization, whereas at +0.7V, no detectable change in the XPS spectrum was obtained. Similar results were observed by cycling between the positive and negative limits established from the cyclic voltammetry results. From these results, an anodic limit of +0.7V was chosen for most of the cycling experiments, as no significant solvent decomposition or solvent degradation products were observed.

Stability problems of the base platinum were experienced when writing the electrochromic film galvanostatically to the yellow-tan (0.7V) color from the green state (0 V). The anodic excursion led eventually to Pt dissolution due to inevitable inhomogeneities in the current distribution, which resulted in some parts of the Pt surface becoming sufficiently positive to initiate its anodic dissolution in the chloride containing solutions. This problem was particularly serious when working at high current densities, of over $\sim 250 \text{ mA}\cdot\text{cm}^{-2}$, and for this reason a cycle comprising a galvanostatic write from the yellow-tan to the green state was used for long-term testing experiments. The erase to the yellow-tan state was carried out potentiostatically in order to avoid the problems of substrate instability mentioned above.

Results

Similar to aqueous electrolytes (10), the current-potential response during the first color transition in ethylene glycol differed significantly from the response of a

Table I. Absorption maxima of vacuum-deposited films of various lanthanide diphthalocyanines

Compound	λ_{max} (nm)	
	Blue form	Green form
$\text{Lu}(\text{PC})_2$	630	665
$\text{Er}(\text{PC})_2$	—	665
$\text{Gd}(\text{PC})_2$	644	—
$\text{Yb}(\text{PC})_2$	—	665

The absorbance of the $\text{Lu}(\text{PC})_2$ film was approximately of 1 unit per 100 nm of film.

cycled electrode (Fig. 1 and 2). The cyclic voltammogram of a virgin electrode showed a very irreversible behavior, with the main oxidation wave occurring at +0.8V. The charge required for the first color transition was similar to that required for the cycled electrodes, and the difference in charge between cycled and uncycled electrodes observed for aqueous solutions (10) was not apparent with the organic solvent used. The origin of this difference is not clear at present.

The difference in color stability previously observed with aqueous F^- and Cl^- containing solutions (10) was again apparent. In fluoride solutions, the yellow-tan to green color fade occurred in 2-4 min in the off condition, whereas the films cycled in chloride media retained their color for several hours on open circuit.

Figure 3 shows typical potential-time responses of $Lu(PC)_2$ film electrodes for different current densities of the galvanostatic-potentiostatic cycle. The initial potential step corresponds to the total ohmic drop in the solution and in the film. This potential drop was found to be linearly dependent on the applied current density. The slope of the galvanostatic transient was dependent on the applied current density, and for a given state of charge of the film, a linear dependence was observed, as is shown in Fig. 4.

The fast degradation of the $Lu(PC)_2$ electrochromic film on continuous switching from the green to the yellow-tan state in aqueous electrolytes is shown in Fig. 5a. There is a rapid loss in color over 10^4 cycles allied to a drop in the current flow during switching.

Figure 5b shows a similar experiment when using ethylene glycol as the solvent. There is little visual degrada-

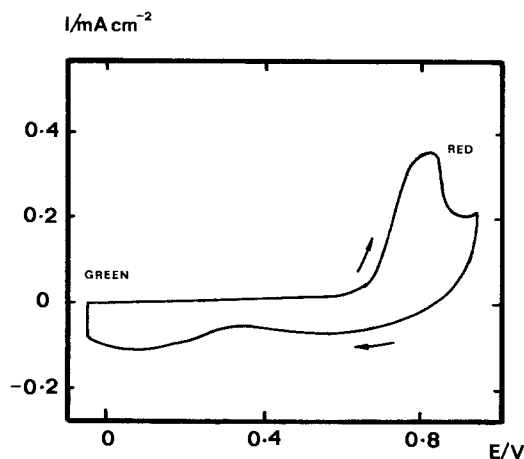


Fig. 1. Cyclic voltammetry of a $Lu(PC)_2$ film electrode supported on conducting tin oxide glass in contact with a 0.7M NaCl/ethylene glycol electrolyte. First sweep; $T = 21^\circ C$, sweep rate = $0.02V \cdot s^{-1}$. The observed colors are indicated in the figure.

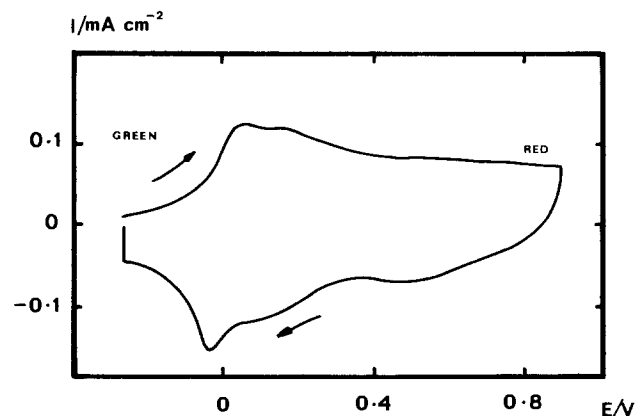


Fig. 2. As in Fig. 1 but after 516,000 red-green potentiostatic cycles (Write 0V/0.5s; Erase 0.9V/0.5s). The electrode was left at $-0.25V$ for 5 min before recording the voltammogram. The observed colors are indicated in the figure.

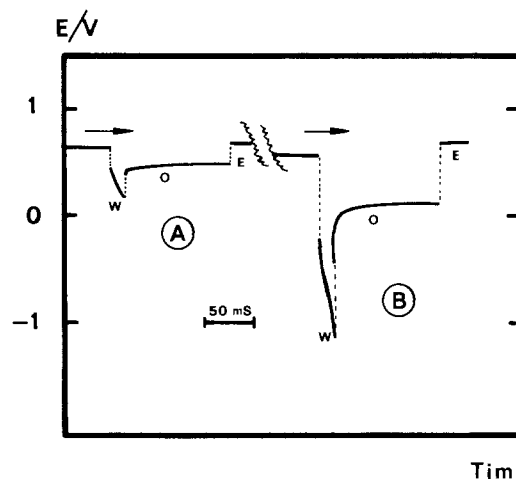


Fig. 3. Galvanostatic-potentiostatic cycling experiment for pel electrodes of $Lu(PC)_2$ in 1M NaCl. The cycle was: Write/10 ms; Off/100 ms; Erase +700 mV/50 ms; Off/50 ms. The writing current was $12.3 mA \cdot cm^{-2}$ for A and $49.2 mA \cdot cm^{-2}$ for B and the film was written from the yellow-tan to the green state. W = Write; O = Off; E = Erase.

tion of the film after 5×10^6 cycles. The use of a variety of electrolytes such as 1M sodium chloride, 3.5M tetra-ethyl ammonium chloride, 3.5M lithium chloride, and 2M tetra-ethyl ammonium fluoride gave similar results. More than 10^6 potentiostatic switching cycles have been obtained with the diphthalocyanines of lutetium, erbium, gadolinium, and ytterbium in the same potential range using these electrolytes in ethylene glycol.

The films did lose some electroactivity with time. The rate of decay of a $Lu(PC)_2$ film on cycling can be seen from the current-time transients measured with a digital transient recorder shown in Fig. 6. These experiments were carried out cycling the electrode into the red color region, where the dye is less stable and solvent decomposition can begin to interfere with the electrochromic behavior of the film. The total loss of charge for 516,000 cycles was $\sim 8\%$, but even under this cycling condition a useful lifetime of over 4×10^6 cycles could be estimated. Figure 7 shows the potential-time dependence in a long-term cycling experiment, using galvanostatic writing conditions from the yellow-tan to the green state. As can be

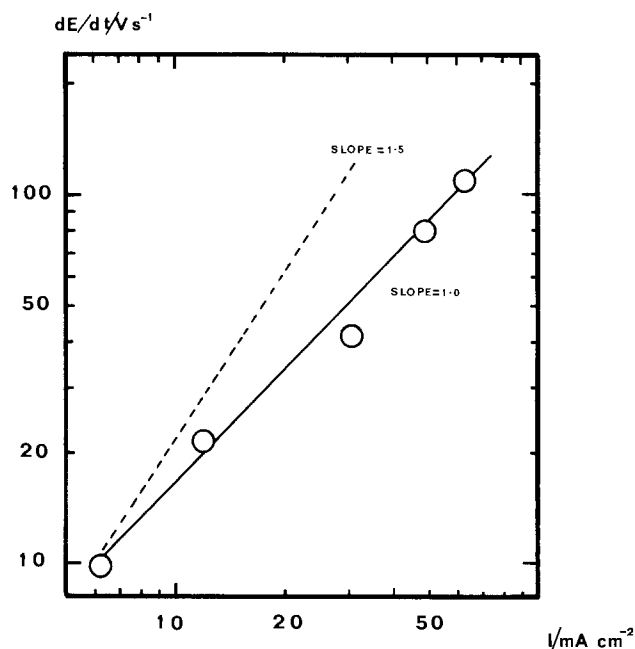
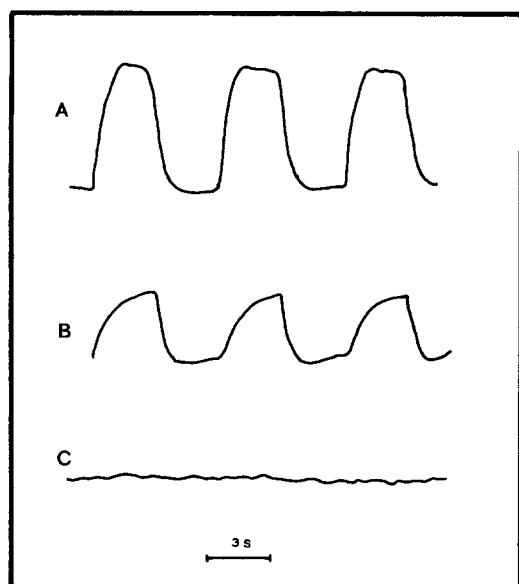


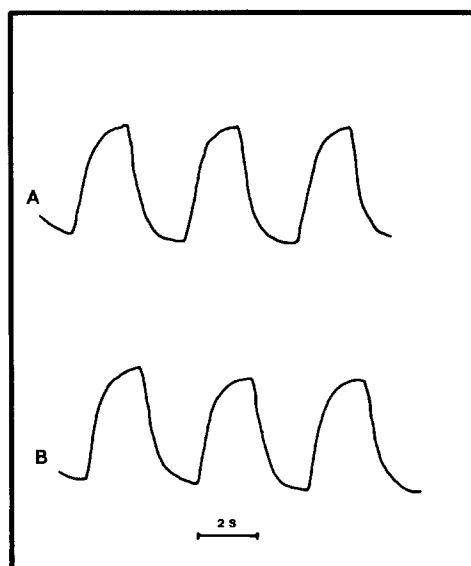
Fig. 4. Dependence of the slope of the galvanostatic transients for $Lu(PC)_2$ pel electrodes on current density. The slope was calculated for an injected charge of $0.27 mC \cdot cm^{-2}$.

Absorbance



Time

Absorbance



Time

Fig. 5. a (left): Absorbance change (in arbitrary units) for a $\text{Lu}(\text{PC})_2$ pel electrode for different degrees of cycling in 1M aqueous NaCl. Writing charge: $1 \text{ mC}\cdot\text{cm}^{-2}$. Potentiostatic erase at 0.15V. Curve A: 100. Curve B: 2200. Curve C: 9200 cycles. b (right): As in Fig. 5a, but in 1M NaCl in ethylene glycol. Curve A: 100. Curve B: 1×10^6 cycles.

seen, aging of the cycled film results in a greater negative potential excursion during the galvanostatic charging process. For 6.4×10^5 cycles, the difference in the negative limit was of $\sim -0.1\text{V}$. From an estimation of the film capacitance in the negative limit, this amounted to a loss of electrochemical film activity of $\sim 10\%$, i.e., of the same order of magnitude as observed for the potentiostatic transients. However, further cycling did not lead to a linear loss of charge with time. Furthermore, the optical density changes observed with the spot meter were independent of cycling time (Fig. 5b), and the small decay observed is probably related to a small change of active area of the dye film. A slight degradation of the Pt substrate was observed with cycling; this reduced the pel area and hence increased the current density.

Discussion

The difference between the first redox transformation of the film and its electrical characteristics after cycling has been observed repeatedly for film and polymer elec-

trodes (10, 14-17). As can be seen in Fig. 1, the first color transition occurs in a well-defined potential range. It is likely that the extension of the potential range in which the solid-state film oxidation occurs is related to the loss in crystallinity on cycling of the vapor phase deposited dye. The x-ray diffraction pattern of a sample of $\text{Lu}(\text{PC})_2$ that had been purified by vacuum sublimation indicated a crystalline structure for the powder.² It is expected that the structure of the film will become rapidly amorphous on cycling and, hence, a wide spread of redox potentials will be observed, related to the different inductive effects of the randomly oriented phthalocyanine rings.

The difference in fade rates of the diradical cation-anion complex responsible for the color change (12) between chloride and fluoride solutions is similar to previous observations in aqueous media (10). The greater stability of the chloride complex is due to the lower solvation energy of Cl^- as compared with the F^- ion, resulting in an enhancement of the thermodynamic stability of the $\text{Lu}(\text{PC})_2^+$, Cl^- complex formed by a $1e^-$ oxida-

² X-ray spectra of vacuum-deposited films were measured by Mr. B. A. Hatt of the Fulmer Research Institute.

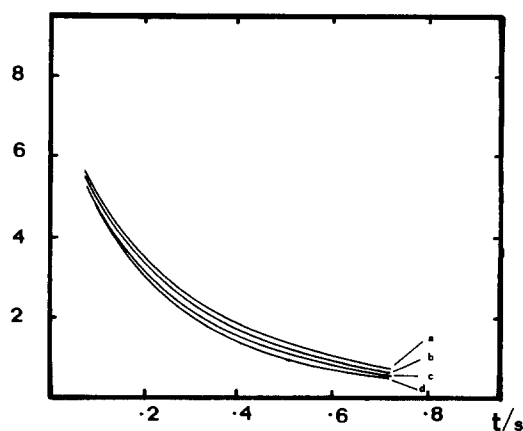
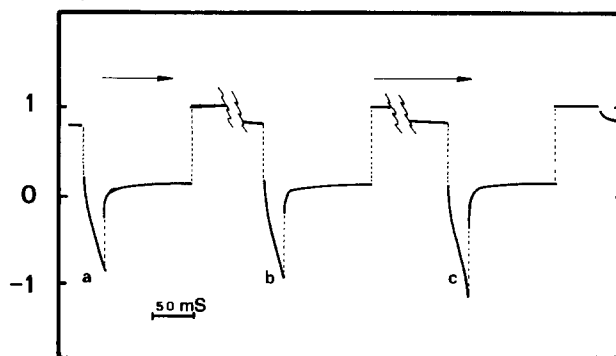
 $I/\text{mA}\cdot\text{cm}^{-2}$ 

Fig. 6. Current-time transient for a $\text{Lu}(\text{PC})_2$ film electrode supported on a SnO_2 conducting glass electrode in contact with 0.7M NaCl in ethylene glycol at 21°C after cycling. Potentiostatic cycle between 0 and 0.9V. Write: 0 V/0.75s. Erase: 0.9V/0.75s. a: 4200 cycles. b: 114,000 cycles. c: 344,000 cycles. d: 516,000 cycles.

E/V



Time

Fig. 7. Influence of cycling on the potential-time response of $\text{Lu}(\text{PC})_2$ film pel electrodes in 1M NaCl in ethylene glycol. Write: $50 \text{ mA}\cdot\text{cm}^{-2}/20 \text{ ms}$. Off: 100 ms. Erase: $+1\text{V}/50 \text{ ms}$. Off: 50 ms. a: 100 cycles. b: 320,000 cycles. c: 640,000 cycles. The erase conditions of this experiment were similar to those in Fig. 6.

tion. This is probably a general feature of electrochromic film electrodes, which can be used as a selection criterion of the anions of the electrolyte to be used to give a long fade rate. It was found that the replacement of Cl^- by Br^- gave very stable compounds and, as expected, the iodide-diradical cation complex is even more stable (18). This compound is so stable that its use has been suggested for decontaminating solutions containing radioactive iodine.

The Kinetics of the Color Transition

Nicholson and Pizzarello (5) proposed a space-charge-limited (SCL) mechanism for the kinetics of the color transition. The model was based on the observation that a moving boundary of the red oxidation product of $\text{Lu}(\text{PC})_2$ was generated when a dye film deposited on an insulating substrate was immersed in an aqueous electrolyte solution, and a current was passed between the dye film and the solution (7). It was observed that the moving boundary contained the anion of the electrolyte (6). Charge neutralization must occur within the film as the net amount of free charge that can be supported by the geometrical capacitance of the film is always orders of magnitude smaller than the requirements of film oxidation or reduction. In the case of $\text{Lu}(\text{PC})_2$, anion incorporation appears to be the charge neutralization mechanism, as has been determined by XPS analysis (10). Similarly, for Fe, Co, Ni, Cu, and Zn monophthalocyanine film electrodes, changes in the redox state of the film results in the corresponding uptake or elimination of the anion of the electrolyte, as determined by Auger electron spectroscopy (19). Similar effects on thionine film electrodes have been observed by Alberty *et al.* (20, 21). Charge neutralization is also a general feature of polymer electrodes displaying redox properties (16, 22), and the understanding of the mechanism of anion incorporation is of general importance.

The SCL mechanism is of interest, as it provides a simple interpretation to the optical transition observed by Nicholson *et al.* (5). There are, however, several features that require some further discussion. Green and Faulkner (19) carried out Auger depth profiles of partially oxidized films of monophthalocyanines, and observed that the distribution of the anion was uniform throughout the film, and no boundary between the oxidized and reduced regions in films of transition metals phthalocyanines could be detected. The technique used for film etching did not result in films reorganization as it was shown in separate experiments with sandwich layers of different metal phthalocyanines (23). The absence of a clearly defined front does not exclude the SCL mechanism. The basic assumption of the SCL equations used by Nicholson *et al.* (5) is that the diffusion of the transported species is unimportant within the time scale of the experiment and the drift of the transported ions accounts entirely for the observed transients. The results of Green and Faulkner (19) perhaps indicate that the film reaches a distribution equilibrium in the time required for the extraction and analysis of the samples, due to diffusion.

The complete formulation of the SCL problem requires taking diffusion into account; in the steady state, the current for the one dimensional case is given by (25, 26)

$$I = Z_j F D_j \frac{dC_j}{dx} + Z_j F \mu_j X C_j \quad [2]$$

where F is the Faraday constant, D_j is the diffusion coefficient of the transported species j , μ_j is its mobility, Z_j is its charge, C_j its concentration, and X is the field.

The integration of Eq. [2] has been discussed several times (25-28) and the diffusional transition time, τ_D , is given by

$$\tau_D = \frac{d^2}{2D_j} \quad [3]$$

where d is the film thickness. In order to assess τ_D across the film, and therefore have an indication of the validity

of using only the second term in Eq. [2] for determining the SCL currents, a value of the diffusion coefficient of the diffusing species is required. Nicholson *et al.* (7) estimated that the mobility of the chloride ion was $4 \times 10^{-6} \text{ cm}^2 \cdot \text{V}^{-1} \cdot \text{s}^{-1}$ in the oxidized $\text{Lu}(\text{PC})_2$. Using the Einstein relationship

$$D_j = \frac{RT\mu_j}{F} \quad [4]$$

a diffusion coefficient $D_{\text{Cl}^-} = 1.1 \times 10^{-7} \text{ cm}^2 \cdot \text{s}^{-1}$ can be estimated for the chloride ion in the film. In the case of the thionine films studied by Alberty *et al.* (20), of a value of D_{Cl^-} of $6.5 \times 10^{-13} \text{ cm}^2 \cdot \text{s}^{-1}$ was estimated. The difference between the thionine and $\text{Lu}(\text{PC})_2$ films may be significant because the former are probably more compact (20) compared with the open structure of the rare earth biphthalocyanines (28). These considerations are particularly relevant to cycled films, where an amorphous structure probably prevails.

Using the value of D_{Cl^-} derived from the electrical mobility, the diffusional characteristic time calculated from Eq. [3] and for $d = 100 \text{ nm}$, is $\tau_D \approx 0.5 \text{ ms}$. This very short diffusional time is lower than the time scale of the galvanostatic transients studied by Nicholson *et al.* (5) and in the present work. This could imply that the film is always at equilibrium with respect to the transported anion and should behave as a homogeneous redox electrode of finite thickness for the time scale of the transients studied.

The observed linear dependence of the slope of the galvanostatic transient (Fig. 4) is characteristic of a capacitance. This is confirmed by the linear response of the current with sweep rate in cyclic voltammetry experiments (10). The capacitance response of the film is potential dependent, and is given by

$$\frac{dE}{dt} = \frac{I}{C(E)} \quad [5]$$

where E is the potential, $C(E)$ is the differential capacitance as a function of potential, and t is the time. The decrease in slope with charge passed, observed in the galvanostatic results (Fig. 3 and 7) is simply a consequence of the potential dependence of the film capacitance indicated also by the cyclic voltammetry results shown in Fig. 2. In fact, the differential capacitance of the film does increase with potential when the film is reduced from the yellow-tan region at $+0.7 \text{ V}$, to the green state, and passes through a maximum at $\sim 0 \text{ V}$.

The results shown in Fig. 4 are for a constant injected charge of $0.27 \text{ mC} \cdot \text{cm}^{-2}$. For a greater degree of reduction, an inflection in the potential time dependence should be observed, and Fig. 8 shows that this is indeed the case. As expected, the potential of the inflection point is very close to the pseudo-capacitance maximum observed for the corresponding cyclic voltammogram (Fig. 2).

The SCL Capacitance

It is interesting to compare the predictions of the simple SCL model used in Ref. (5) with those derived from a simple redox capacitance model. The latter predicts a linear dependence of the slope dE/dt with current density. In the SCL model used by Nicholson *et al.* (5), the potential drop across the moving front is

$$E_2 = \frac{I}{\epsilon_2 \epsilon_0 \mu_2} x_2^3 \quad [6]$$

where E_2 is the potential drop across the product layer [the red form of $\text{Lu}(\text{PC})_2$], x_2 and ϵ_2 are its thickness and dimensionless dielectric constant, respectively, and ϵ_0 is the permittivity of free space ($8.85 \times 10^{-14} \text{ F} \cdot \text{cm}^{-1}$). Since the mobility of the electron in the $\text{Lu}(\text{PC})_2$ lattice is much greater than that of an anion such as Cl^- , the total potential drop predicted by this model will occur only in the red layer. If a well-defined boundary is formed, *i.e.*, when the first term in the steady-state approximation given by

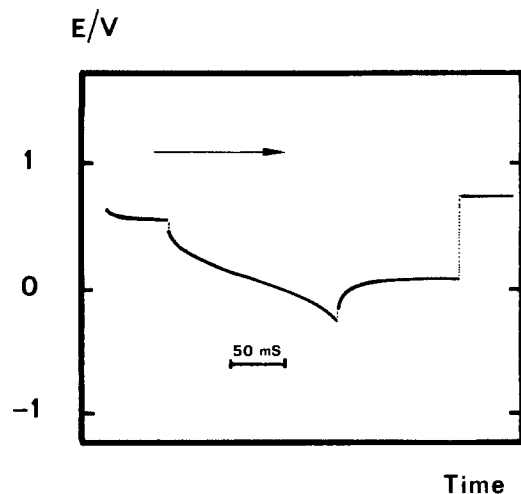


Fig. 8. Potential-time transient for a cycled Lu(PC)₂ film pel electrode in 1M NaCl in ethylene glycol. Charging current during the galvanostatic transient = 6.4 mA·cm⁻². Writing from the yellow-tan to the green state.

Eq. [2] is negligible, the boundary velocity is given by (5)

$$\frac{dx}{dt} = \frac{I}{C_j F} \quad [7]$$

From Eq. [6] and the integrated form of Eq. [7], the current-potential time relationship for the idealized SCL model discussed is obtained

$$E_2 = \left(\frac{1}{\epsilon_2 \epsilon_0 \mu_2} \right)^{1/2} \left(\frac{1}{Z_j C_j F} \right)^{3/2} I^{2/3} t^{3/2} \quad [8]$$

From Eq. [8], and for a given amount of injected charge $Q_{inj} = \text{const.}$, the slope of the galvanostatic transient is given by

$$\left(\frac{\partial E}{\partial t} \right)_{Q_{inj}} = \frac{3}{2} \left(\frac{1}{\epsilon_2 \epsilon_0 \mu_2} \right)^{1/2} \left(\frac{1}{Z_j C_j F} \right)^{3/2} I^{3/2} Q_{inj}^{1/2} \quad [9]$$

A comparison between the SCL (Eq. [9]) and a distributed capacitance model (Eq. [5]) can be made by comparing the current density dependence of the slope $(\partial E/\partial t)_{Q_{inj}}$ predicted from the two models. As shown in Fig. 4, the experimental results are in better agreement with a simple capacitance model, although a distinction between the two models is not easy to make only on the basis of this type of information.

A Reversible Redox Film Electrode Model

The voltammetry of cycled films indicates a fairly reversible redox behavior. However, the response of a reversible redox film electrode should result in a sharp peak centered at the standard potential for the film redox reaction. The peak half-width ($\Delta E_{1/2}$) of this peak is the potential difference between the two conditions in the voltammetric scan for which the current is half the maximum and has a value of 90.46 mV at 25°C (10) for a one-electron process. The voltammetric response observed for the cycled films does not correspond to this model with a single redox species. As discussed by Albery *et al.* (20), a spread in redox potentials of the electroactive species in the film is a more realistic model of a redox film electrode, and some digital simulations of the voltammetric response of film electrodes for discrete redox potentials in the film and considering interaction coefficients between the electroactive species have been carried out by Peerce and Bard (29).

It is very difficult to discriminate between different film models on the basis of voltammetric experiments only. Several parameters can be used simultaneously to match the observed cyclic voltammogram, such as the distribution of standard potentials for the different spe-

cies present in the film, the distribution in concentration of species having different standard potentials, and interaction coefficients (29).

For a discrete centers model, the equilibrium condition of each center i having a standard potential E_i° is

$$P_i = \ln \frac{q_{i(\text{ox})}}{q_{i(\text{red})}} \quad [10]$$

where

$$P_i = (E - E_i^\circ)F/RT \quad [11]$$

and $q_{i(\text{ox})}$ and $q_{i(\text{red})}$ are the equilibrium charges of oxidized and reduced i at the potential E . F is the Faraday constant. Equation [10] assumes equality of the activity coefficients of the different species in the film (20).

For an oxidation reaction, the total charge accumulated at a given potential, $Q_{(\text{ox})}$, is

$$Q_{(\text{ox})} = \sum^N q_{i(\text{ox})} \quad [12]$$

when N is the number of discrete redox centers in the film. From Eq. [10]-[12]

$$\int_0^t i dt = Q_{(\text{ox})} = Q_T \sum \frac{\tau_i G_i}{1 + G_i} \quad [13]$$

where Q_T is the total charge required to oxidize all the centers of the film, τ_i is the fraction of the total charge corresponding to the redox centers i , *i. e.*

$$\tau_i = \frac{q_i(t)}{Q_T} \quad [14]$$

$q_i(T)/F$ is the total number of moles of species having a standard potential E_i° . G_i is defined by

$$G_i = \exp(P_i) \quad [15]$$

Equation [13] can be used for determining the potential-time dependence of the galvanostatic transients. The linear sweep voltammetry response of a film electrode can be derived from Eq. [13] and [11], *i. e.*

$$i = Q_T \frac{\nu F}{RT} \sum^N \frac{\tau_i G_i}{(1 + G_i)^2} \quad [16]$$

where ν is the sweep rate.

Equations [13] and [16] can be converted to the corresponding integral forms when a continuous distribution of redox states is assumed. Albery *et al.* (20) used this approach for the thionine film electrodes and considered that the E_i° values were spread in a gaussian distribution around the average value of the standard potential of the film. The cycled lutetium biphthalocyanine electrodes studied appear to have a much wider spread of redox potentials for the different centers than that encountered in the thionine films (20, 21) or in other polymer electrodes (14-17). The physical basis of a gaussian distribution corresponds to a model where all distinct microscopic states of the assembly are equally probable and independent of each other. As we are attempting to describe a system for which the state of charge is a variable, the *a priori* use of the normal distribution does not necessarily follow. In fact, the loss in crystallinity that appears to occur on cycling will give a fixed range of inductive effects on the phthalocyanine rings and hence on the values of E_i° . Another important consideration is the possible coexistence of several oxidation states of the dye in the film due to the proximity of the values of E_i° corresponding to the different redox centers. The standard potentials of the blue-green and the green-yellow transitions in dichloromethane are -0.45 and 0.03V *vs.* the ferrocene/ferrocinium couple, respectively (30). Although the yellow-red transition was not studied, the results of Corker *et al.* (7) indicate a similar difference in redox potentials between the green and yellow-red states. In the solid state, the ex-

pected spread of redox potentials for the amorphous material will result in the overlap of the $1e^-$ and the $2e^-$ processes, leading thus to a very wide range of possible redox potentials.

For these reasons, an oversimplified cutoff approximation of the redox centers in the film will be used for analyzing the transients. In this approximation, a uniform distribution of species between the two standard potentials E_1° and E_2° is assumed, and it is considered that no sites having potentials outside the range E_1° - E_2° exist. Thus the fraction of sites within the standard potential E_1° and $E_1^\circ + dE^\circ$ is $dE/(E_2^\circ - E_1^\circ)$, and Eq. [16] can be integrated

$$i = \frac{Q_T \nu F}{(E_2^\circ - E_1^\circ) RT} \int_{E_1^\circ}^{E_2^\circ} \frac{G(E^\circ) dE^\circ}{[1 + G(E^\circ)]^2} \quad [17]$$

and

$$i = \frac{Q_T \nu}{(E_2^\circ - E_1^\circ)} \left[\frac{1}{1 + G_2} - \frac{1}{1 + G_1} \right] \quad [18]$$

The voltammetric response will depend on the spread in the range of standard potential values considered, and Fig. 9 shows the behavior expected for different values of $\Delta E^\circ = E_2^\circ - E_1^\circ$. The voltammetric response of the film occurs in a wider potential range as the values of ΔE° are increased, as might be expected. The galvanostatic transients can be analyzed using the same model; from Eq. [18].

$$i = \frac{Q}{\Delta E^\circ} \left[\frac{1}{1 + G_2} - \frac{1}{1 + G_1} \right] \frac{dE}{dt} \quad [19]$$

and the galvanostatic transient is given by

$$\frac{it}{Q_T} = \frac{RT}{\Delta E^\circ F} \ln \left\{ \frac{1 + G_1}{1 + G_2} \right\} \quad [20]$$

Figure 10 shows the expected galvanostatic transients for different values of ΔE° . From Eq. [18], the slope of the galvanostatic transient at any potential is given by

$$\frac{dE}{dt} = \frac{\Delta E^\circ i}{Q_T} \frac{(1 + G_1)(1 + G_2)}{(G_1 - G_2)} \quad [21]$$

and Eq. (20) predicts that an inflection point will occur at a potential E_{inf} given by

$$E_{inf} = \frac{1}{2} (E_1^\circ + E_2^\circ) \quad [22]$$

From Eq. [21] and [22]

$$\left(\frac{dE}{dt} \right)_{E = E_{inf}} = \frac{\Delta E^\circ i}{Q_T} \frac{1 + \cosh \left(\frac{\Delta E^\circ F}{2RT} \right)}{\sinh \left(\frac{\Delta E^\circ F}{2RT} \right)} \quad [23]$$

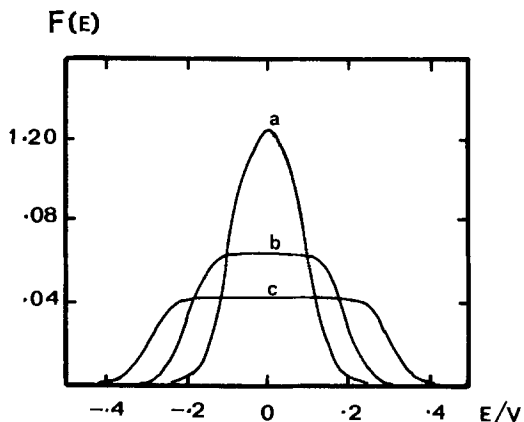


Fig. 9. Linear sweep dependence voltammetry for a distributed redox potential model. Equation [18] for values of ΔE° of: 0.2 (a); 0.4 (b); and 0.6V (c). $F(E) = i \Delta E^\circ / Q_T$; the potential E is referred to the middle point of the redox potential distribution, i.e., with respect to $1/2(E_2^\circ + E_1^\circ)$.

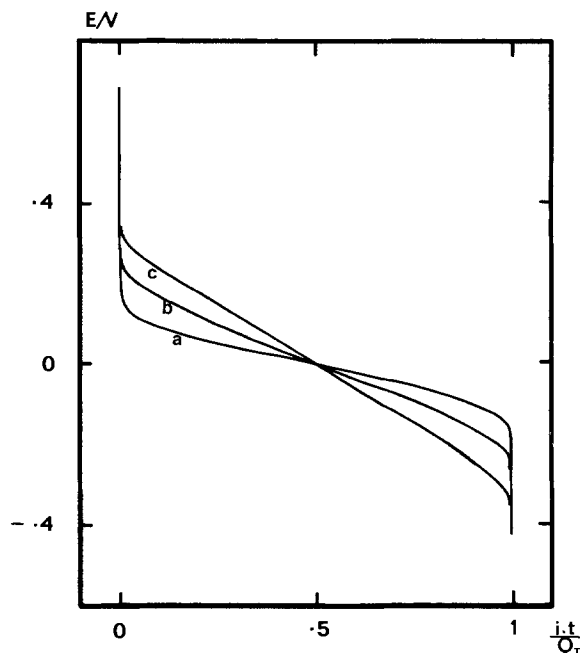


Fig. 10. Potential-fractional charge dependence for a galvanostatic transient predicted for a distributed redox potential model (Eq. [20]) for different values of ΔE° of 0.2 (a); 0.4 (b); and 0.6V (c).

The simple cutoff approximation predicts the correct shape of the galvanostatic transients and a linear dependence of the slope dE/dt with current density, in accordance with the results in Fig. 4. For values of $\Delta E^\circ > 0.20V$, Eq. (22) simplifies to

$$\left(\frac{dE}{dt} \right)_{E = E_{inf}} = \frac{\Delta E^\circ i}{Q_T} \quad [24]$$

and the apparent film capacitance at this potential is simply related to the spread in redox potentials of sites in the film. From the data shown in Fig. 8, an approximate value of $\Delta E^\circ = 0.55V$ can be estimated for the cycled films. This value is consistent with the cyclic voltammetry results, although the latter show a fine structure in the distribution of redox potentials for the electroactive centers in the film, which, as expected, is not apparent under constant current charging conditions. The reason for this is that cyclic voltammetry gives a differential measurement of the electrical properties of the film, whereas chronopotentiometry gives integral quantities.

The main difficulty in the analysis of a film model is in the many different parameters that can be, in principle, used for assigning a response to a particular model, and the purpose of the analysis given above is to show that a very simple cutoff approximation can give a reasonable qualitative description of the switching behavior.

Technological Problems

Although the rare earth biphthalocyanine film electrodes appear very attractive for colored flat display applications, there are still many unresolved problems. The underlying substrate degradation problem is related to fast switching applications, i.e., for transition times of less than ~ 20 ms, where inhomogeneities in current distribution can result in excessive potential excursions at the edges of the pels. The loss in switching charge observed in some of the long-term fast switching experiments is most likely related to problems of cell geometry. Certainly, the optical response does not appear to be degraded on cycling. For switching times greater than approximately 40 ms and using a galvanostatic write procedure to the green state, the lifetime expected is well over 10^7 cycles.

The color contrast of the $\text{Lan}(\text{PC})_2$ is, unfortunately, not very good. The color transitions must be restricted to present to the red-yellow tan-green states, since all at-

Potential

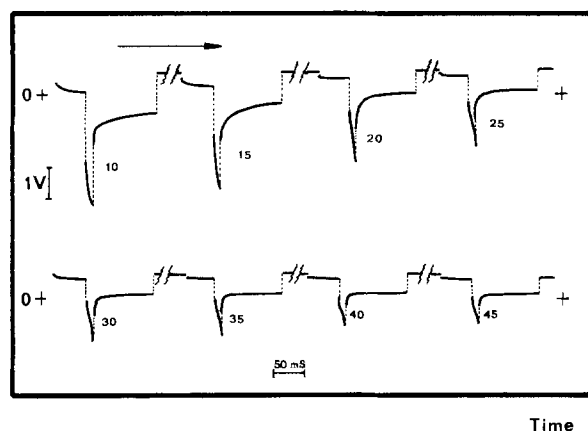


Fig. 11. Effect of temperature on the potential-time dependence for a $\text{Lu}(\text{PC})_2$ film pel electrode. The temperatures in degrees centigrade are indicated in the figure. The cycle was Write $77 \text{ mA-cm}^{-2}/10 \text{ ms}$, Off 100 ms , Erase 0.7V , Off 50 ms .

tempts to drive the film electrodes in the blue region resulted in rapid failure. Part of the problem is that the blue transition occurs at a potential range where water or ethylene glycol are electroactive and the adhesion between the film and the substrate becomes a problem. The origin of these difficulties is not clear at present, but multichromatic displays may be achievable using substituted phthalocyanines.

A general feature of film electrodes, in common with many electronic devices, is the need to have accurate control of the operating conditions as they are not self-healing and any accidental operation outside the stability range results in the irretrievable loss of electrochromic activity. One such operation variable is the temperature and the response of the film electrodes is strongly temperature dependent. The temperature dependence of a $\text{Lu}(\text{PC})_2$ film electrode is shown in Fig. 11 for a cycling condition using a galvanostatic write and a potentiostatic erase. As can be seen, a decrease in operating temperature results in two effects: (i) the ohmic drop in the cell increased substantially, and (ii) the integral capacitance of the film decreases resulting in a wider potential excursion for a given state of charge. However, this limitation reduces the color contrast, which may be a problem in display applications.

A high ohmic drop in the electrolyte is deleterious for the device, as the resulting decrease in throwing power leads to current inhomogeneities which cause rapid deterioration of the substrate and loss of adhesion of the film. The electrochemical parameters of the film are also altered, with the electrochemical reaction becoming increasingly irreversible at low temperatures; an optimum temperature of operation was around $35^\circ\text{--}40^\circ\text{C}$.

Conclusions

The rapid decay of the electrochromic characteristics of rare earth diphthalocyanines film electrodes on cycling in neutral aqueous solutions has been considerably reduced by using ethylene glycol as the solvent, and by limiting the range of colors used to yellow-tan and green. However, this is an unfortunate limitation to the potential use of $\text{Lu}(\text{PC})_2$ displays, as the contrast between these colors is not very good. Further work is necessary, possibly with other electrolytes and solvents, to extend the stable color range.

The number of color reversals possible has been increased from 10^4 to a minimum of 5×10^6 . Under these conditions, the parameters that control the stability of the film electrode are the temperature and switching speed.

The equivalent electrical circuit for the film electrode is a capacitance in series with a resistance and a distributed redox state model can account for the observed galvanostatic transients.

Acknowledgments

The authors would like to thank H. G. Youlton, who prepared the thin film metallurgy, and Dr. V. V. Patel (IBM Thomas J. Watson Research Center, Yorktown Heights, New York), who supplied the sample of $\text{Lu}(\text{PC})_2$. IBM United Kingdom Laboratories are thanked for permission to publish this work.

Manuscript submitted Sept. 21, 1984; revised manuscript received March 12, 1985.

REFERENCES

- I. S. Kirin, P. N. Moskalev, and Y. A. Makashev, *Russ. J. Inorg. Chem.*, **12**, 369 (1967).
- P. N. Moskalev and I. S. Kirin, *Optik. Spektrosk.*, **29**, 414 (1970).
- P. N. Moskalev and I. S. Kirin, *Russ. J. Phys. Chem.*, **46**, 1019 (1972).
- P. N. Moskalev, V. Y. Mishin, E. M. Rubstov, and I. S. Kirin, *ibid.*, **21**, 1243 (1976).
- M. M. Nicholson and F. A. Pizzarello, *This Journal*, **127**, 821 (1980).
- F. A. Pizzarello and M. M. Nicholson, *J. Electron. Mater.*, **9**, 231 (1980).
- M. M. Nicholson and F. A. Pizzarello, *This Journal*, **126**, 1490 (1979).
- H. Yamamoto, M. Noguchi, and M. Tanaka, *Jpn. J. Appl. Phys.*, **23**, 221 (1984).
- M. M. Nicholson, *Ind. Eng. Chem. Prod. Res. Div.*, **21**, 261 (1982).
- G. C. S. Collins and D. J. Schiffrin, *J. Electroanal. Chem.*, **139**, 335 (1982).
- G. A. Corker, B. Grant, and N. J. Clecak, *This Journal*, **126**, 1339 (1979).
- A. T. Chang and J.-C. Marachon, *Inorg. Chim. Acta*, **53**, L241 (1981).
- Y. Bessonnat, G. Gerard, and G. Leroy, in "Proceedings of the First European Display Research Conference, Munich," p. 104, Society for Information Displays (SID), Nachrichte Technische Gesellschaft im Ved (1981).
- F.-R. Fan and L. R. Faulkner, *J. Am. Chem. Soc.*, **101**, 4779 (1979).
- H. Tachikawa and L. R. Faulkner, *ibid.*, **100**, 4379 (1978).
- F. B. Kaufman, A. H. Schroeder, E. M. Engler, S. R. Kramer, and J. Q. Chambers, *ibid.*, **102**, 483 (1980).
- R. W. Day, G. Inzelt, J. F. Kinstle, and J. Q. Chambers, *ibid.*, **104**, 6804 (1982).
- P. N. Moskalev, G. N. Shapkin, and N. I. Alimova, *Russ. J. Inorg. Chem.*, **27**, 794 (1982).
- J. M. Green and L. R. Faulkner, *J. Am. Chem. Soc.*, **105**, 2950 (1983).
- W. J. Albery, M. G. Boutelle, P. J. Colby, and A. R. Hillman, *J. Electroanal. Chem.*, **133**, 135 (1982).
- M. D. Archer, M. I. Ferreira, W. J. Albery, and A. R. Hillman, *ibid.*, **111**, 295 (1980).
- J. Q. Chambers, F. B. Kaufman, and K. H. Nichols, *ibid.*, **142**, 277 (1982).
- R. E. David and L. R. Faulkner, *This Journal*, **128**, 1349 (1981).
- L. Lindmayer, J. Reynolds, and C. Wrigley, *J. Appl. Phys.*, **34**, 809 (1963).
- R. H. Tredgold, "Space Charge Conduction in Solids," Elsevier, Amsterdam (1966).
- G. T. Wright, *Solid State Electron.*, **2**, 165 (1961).
- N. Sinharay and B. Meltzer, *ibid.*, **7**, 125 (1964).
- K. Kasuga, M. Tsutsui, R. C. Petterson, K. Tatsumi, N. Van Opdenbosch, G. Pepe, and E. F. Mayer, Jr., *J. Am. Chem. Soc.*, **102**, 4835 (1980).
- P. J. Pearce and A. J. Bard, *J. Electroanal. Chem.*, **114**, 89 (1980).
- M. L'Her, Y. Cozien, and J. Courtot-Coupez, *ibid.*, **157**, 183 (1983).
- M. M. Nicholson and T. P. Weismuller, *This Journal*, **131**, 2311 (1984).

Mechanism of Oxygen Permeation Through Lime-Stabilized Zirconia

S. Dou and C. R. Masson

National Research Council of Canada, Atlantic Research Laboratory, Halifax, Nova Scotia, Canada B3H 3Z1

P. D. Pacey

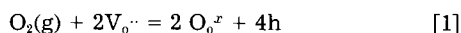
Department of Chemistry, Dalhousie University, Halifax, Nova Scotia, Canada B3H 4J3

ABSTRACT

The isothermal permeation of oxygen through CaO-ZrO₂ was studied at 960°-1450°C and oxygen pressures P'_{O_2} of 10⁻³ to 1 atm on one side of the permeation cell and P''_{O_2} of 10⁻⁶-10⁻⁴ atm on the other. In the steady state, the permeating flux was directly proportional to $(P'_{O_2}{}^{1/n} - P''_{O_2}{}^{1/n})$, where n varied from 2.5 to 4.0. The value of n depended on the microstructure of the sample. For samples without micropores, a value of $n = 4$ was found. These samples also contained a second phase whose composition depended on the nature and extent of impurities. For samples with nonconnected micropores, n varied from 3.6 to 2.5, depending on the thickness, and the results were consistent with a mechanism in which permeation is limited partly by diffusion within the solid and partly by a surface reaction. Both the bulk and surface processes have activation energies of about 200 kJ·mol⁻¹.

The semipermeability of lime-stabilized zirconia (CSZ) to oxygen has received increasing attention in recent years due to the ever more stringent demands on the use of this material as a solid electrolyte at high temperatures. Although electronic conduction and accompanying transport of oxygen are often considered to be negligible in the ionic domain this cannot always be assumed, and drifting EMF's due to oxygen permeability are a common occurrence in unbuffered systems. In addition, oxygen permeability can influence the equilibrium between the electrode microsystem and the surrounding gas, yielding errors far larger than predicted purely on the basis of departure of the ionic transference number from unity (1).

In the present study, the isothermal permeation of oxygen through CSZ tubes was measured at 960°-1450°C and from 10⁻⁶ to 1 atm. It is well established that the permeability in this regime is due to p-type electronic conduction. Electronic defects are considered to arise by the reaction



where, using Kröger's notation, O_o^x is an oxygen ion on a normal lattice site, $V_{O^{\cdot\cdot}}$ is an anion vacancy, and h is a positive hole. The flux, J , of oxygen permeating is then given by (2, 3)

$$J = \frac{\beta}{l} (P'_{O_2}{}^{1/4} - P''_{O_2}{}^{1/4}) \quad [2]$$

where l is the thickness of the electrolyte, P'_{O_2} and P''_{O_2} are the oxygen pressures on opposite sides of the electrolyte, and β is a proportionality factor, which we shall call the bulk permeation coefficient. It should be noted that Eq. [2] is derived on the basis of the following assumptions: (i) only free or untrapped electron holes contribute to the conductivity; (ii) their concentration is directly proportional to $P_{O_2}{}^{1/4}$, as derived (4) from Eq. [1]; and (iii) the transport process is governed entirely by diffusion in the solid.

In spite of numerous studies (3, 5-14) there is no universal agreement on the general validity of Eq. [2]. The expected 1/4 power oxygen pressure dependence of the permeability was observed by Smith *et al.* (7), Fisher (9), Palguev *et al.* (11), and Iwase *et al.* (12). An exponent of 1/3 was reported by Heyne and Beekmans (3), who suggested that the observed deviation from 1/4 might be due to either a different incorporation mechanism for the electronic defects or to partial rate control by a surface reaction. An exponent of 1/2 was reported by Alcock and Chan (8) and one of 1/2-1/4 by Kitazawa and Coble (10).

In the present study, we resolve these apparent discrepancies and show that the value of the exponent depends

on the microstructure of the specimen. This, in turn, is governed by the nature and extent of impurities. For samples with an exponent greater than 1/4, the exponent depends on the thickness of the specimen. For this case, a steady-state treatment is presented which describes the kinetics in terms of combined bulk and surface control.

Experimental

Specimens.—The properties of the CSZ tubes are given in Table I. For the tubes supplied by the Zirconium Corporation of America (Zircoa) and the Nippon Chemical Ceramics Company Limited, the analyses were provided by the manufacturers. Tube G was made in our laboratories by a slip casting technique (15). For analysis, a portion of this tube was fused with anhydrous sodium carbonate and boric oxide, dissolved in water, and the solution examined by inductively coupled plasma atomic emission spectroscopy.

The densities of the specimens, also listed in Table I, were determined by weighing in kerosene and in air.

The microstructure of the specimens was examined by means of a JEOL Type JXA-35 scanning electron microscope, equipped with a Kevex 7000 energy dispersive x-ray analyzer and Quantex software. Figure 1a shows a photomicrograph typical of tubes A to D. Numerous small pores, less than 10⁻⁵m in diameter, can be seen. These pores, about 10% of the total volume, account for the lower densities of these tubes (Table I). The other tubes, exemplified by Fig. 1b, had fewer pores but had a dark second phase between the grains of CSZ. X-ray analysis showed that the second phase consisted largely of impurity elements, which were generally present to a greater extent in tubes E, F, and G.

The tubes were 30 cm long and 1.4-2.0 cm in outside diameter and were closed at one end. The wall thicknesses varied between 1.6 and 2.75 mm. A 3 cm long portion adjacent to the closed end of tube D was milled to a wall thickness of 0.5 mm.

Permeation cell.—The cell assembly used for the permeability measurements is shown in Fig. 2. The specimen tube, B, was mounted centrally within a mullite tube C by an arrangement of water-cooled brass flanges A. Vacuum-tight connections between the ceramic and metal parts were made by silvering the ceramic by chemical deposition, followed by copper electroplating and soldering. A mullite thermocouple sheath F passed through the lower flange and extended upwards to within 0.2 cm of the CSZ tube B. Platinum radiation shields D were used in some experiments.

The diffusion cell was attached to a vacuum system and an electronic manometer (Barocel pressure transducer,

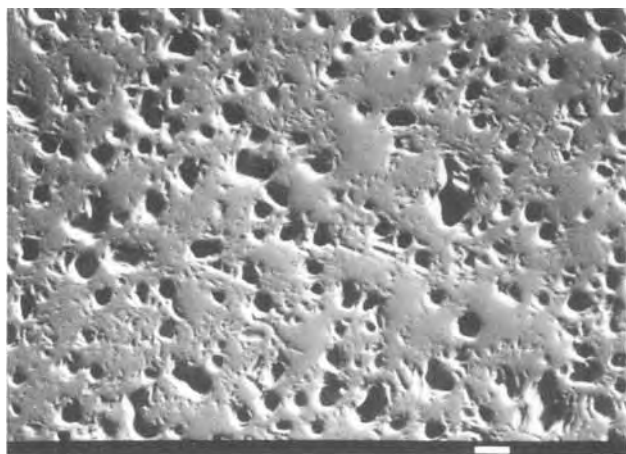
Table I. The chemical composition and density of calcia-stabilized zirconia tubes

Designation of tube	CaO (w/o)	Al ₂ O ₃ (w/o)	SiO ₂ (w/o)	MgO (w/o)	Fe ₂ O ₃ (w/o)	TiO ₂ (w/o)	Density (g-cm ⁻³)	Source
A to D	7.5	0.15	0.40	0.55	0.024	0.10	4.90	Zircoa
E	5.9	0.46-0.71	1.50-1.58	0.67-0.92	0.17-0.20	0.14-0.24	5.39	Nippon
F	3.5	0.20	0.5	0.9	0.14	0.20	5.63	Zircoa
G	7.5	2.0	1.3	0.063	0.90	0.22	5.23	Home made

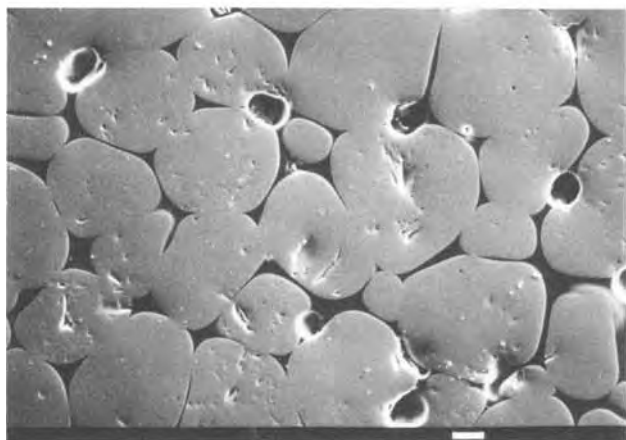
Type 590 A, Datametrix, Incorporated) by means of four flexible, bellows-type metal tubes H, also shown in Fig. 2. The entire cell assembly could be raised or lowered by a scissors-type jack J within a tubular resistance furnace E, wound with platinum-rhodium wire. Stops were attached to the jack to define accurately the upper and lower limits of travel.

Experimental procedure.—The vacuum and measurement system, illustrated in Fig. 3, consisted essentially of a calibrated gas burette, 3, a two-stage mercury diffusion pump, 4, and associated stopcocks and gauges.

For the permeability measurements, a combination of the techniques described by Alcock and Chan (8) and Smith *et al.* (7) was employed. Before each experiment, both sides of the sample tube were evacuated at the temperature of measurement for 12h. An argon-oxygen mixture, dried by passage through a column of Drierite, 8, was introduced to the exterior of the CSZ tube. The oxygen which permeated through the specimen was collected and measured in the gas burette, 3.



(a)



(b)

Fig. 1. Photomicrographs of CSZ. a: Tube A. b: Tube G. The white bar just below each photograph represents a length of 10⁻⁵m.

The temperature profile along the furnace, as measured by means of a Pt/13% RhPt thermocouple, was constant to within $\pm 2^\circ\text{C}$ over a length of 3 cm. The sample tube was located so that its lower end coincided with the lower end of this zone for a series of measurements of the volume collected as a function of time. A second series of measurements was made by raising the sample tube to the upper limit of this zone and repeating. By taking the difference between the two measurements, one could obtain an isothermal permeability through a defined area of the tube. During an experiment, the temperature was controlled with respect to time to within $\pm 1^\circ\text{C}$.

Results

Analysis by mass spectrometer indicated that at least 99.5% of the collected gas was oxygen even when the outside of the tube was flushed with 99.9% argon and 0.1% oxygen.

Figure 4 shows the number of moles of oxygen, Q_t , collected as a function of time for specimen tube C in the upper and lower positions, with thermocouple G2 at 1210°C and with $P'_{\text{O}_2} = 0.21$ atm. Following an induction period, the amount of O₂ collected increased linearly with respect to time. This was also reported in Ref. (11). The difference between the two curves represents the isothermal permeation through a length of tube equal to the displacement. In the steady state, the ratio, f , of the amount collected in

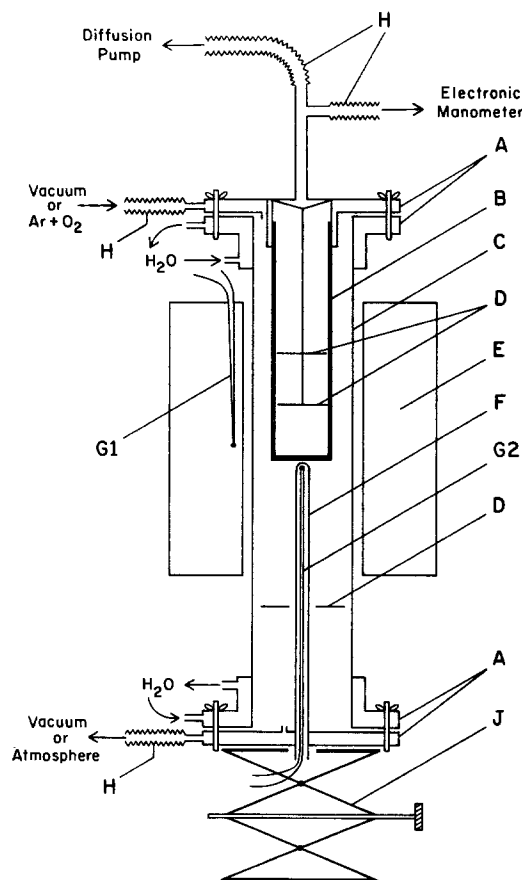


Fig. 2. Diagrammatic representation of the permeation cell. A: Brass flanges. B: CSZ tube. C: Mullite tube. D: Platinum radiation shields. E: Pt-Rh resistance furnace. F: Mullite tube for thermocouple. G: Pt-PtRh thermocouples. H: Flexible metal tubes. J: Jack.

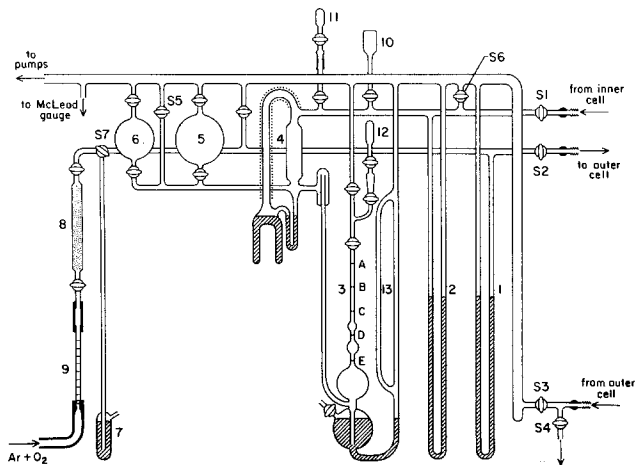


Fig. 3. Vacuum system. 1, 2: Mercury manometers. 3: Gas burette. 4: Diffusion pump. 5, 6: Expansion volumes for collected oxygen. 7: Mercury seal. 8: Drierite. 9: Flowmeter. 10: Ionization gauge. 11: Calibrated bulb. 12: Bulb for mass spectrometer samples. S1-S7: Stopcocks.

the upper position to the amount collected during an equal period in the lower position varied from one tube to another, but, for each tube, this was constant and independent of temperature and oxygen pressure. The gas collection rate, R_1 or R_u , was equal to the slope of line V_1 or V_2 in Fig. 4.

For all tubes and under all conditions of this work, the pressure of O_2 in the chamber inside the CSZ tube, P''_{O_2} , as measured with the electronic manometer, varied in an approximately linear manner with the gas collection rate, as shown in Fig. 5. This observation may be explained simply by Knudsen flow through the tubing and valves between this chamber and the diffusion pump. Figure 5 could be used to estimate P''_{O_2} in cases where this was not measured directly.

Different flow rates of Ar- O_2 mixtures were used. No effect on permeation rate was observed provided the rate of supply of oxygen was kept substantially faster than the collection rates.

The flux, J ($\text{mol}\cdot\text{cm}^{-2}\cdot\text{s}^{-1}$), was calculated from Eq. [3]

$$J = (R_1 - R_u)/A \quad [3]$$

where A is the average circumference of the specimen multiplied by the distance between the upper and lower positions.

Oxygen pressure dependence.—In general, the results did not conform to the theoretical order of $1/4$ as given by Eq. [2], but were consistent with the following equation, where the order, $1/n$, was allowed to vary

$$J = J^0(P''_{O_2})^{1/n} - P''_{O_2}^{1/n} \quad [4]$$

Here J^0 is numerically equal to the flux with 1 atm of O_2

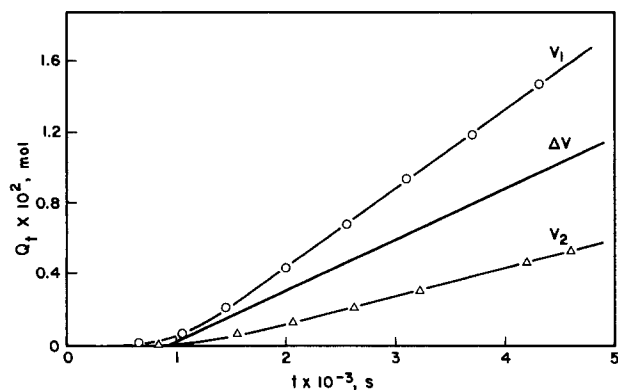


Fig. 4. Numbers of moles of oxygen which permeated specimen tube C with thermocouple G2 at 1210°C with $P''_{O_2} = 0.21$ atm. V_1 : Tube at lower position. V_2 : Tube at upper position. ΔV : Difference between quantities at the two positions.

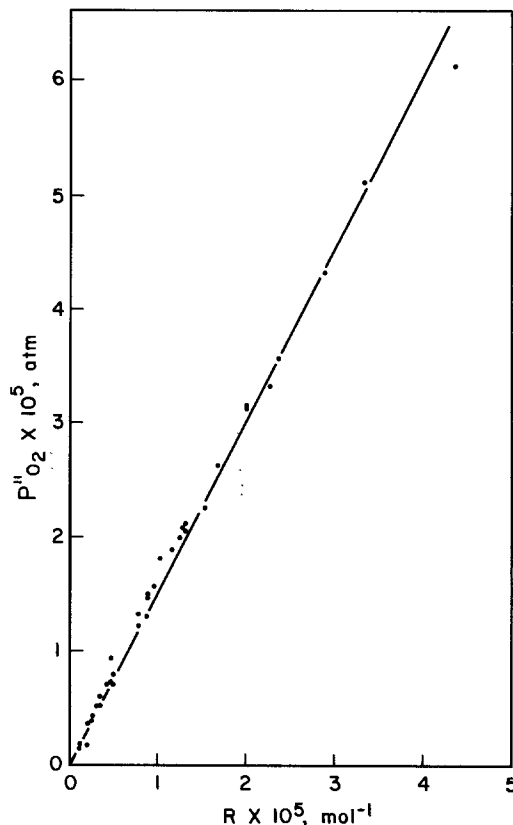


Fig. 5. Relation between the pressure inside the CSZ tube and the gas collection rate, R_1 or R_u . $T = 1100^\circ\text{--}1300^\circ\text{C}$; $P'_{O_2} = 0.005\text{--}1.0$ atm.

on one side and a negligible pressure on the other side. By means of a nonlinear least squares computer program, the parameter J^0 and the order $1/n$ were determined for each tube at the temperature of measurement. Values are listed in Table II. The listed uncertainties are standard deviations. It can be seen that values of n vary from 2.5 to 3.6 for samples A to D, while n is approximately equal to 4 for samples E to G. Examples of fits to Eq. [4] are shown in Fig. 6.

Effect of thickness of specimens.—Figure 7 shows plots of flux against thickness for tubes A to D, which have the same composition. At high pressures of oxygen, the flux decreases with increasing thickness, as expected from Eq. [2]. However, at low P''_{O_2} , flux is approximately independent of thickness.

Figure 8 shows a plot of the order, $1/n$, from Table II as a function of specimen thickness. One can see that the order decreases from 0.4 to 0.28 as the thickness increases from 0.05 to 0.194 cm for samples A to D, and remains constant at 0.25 as the thickness increases from 0.175 to 0.275 cm for samples E to G. The order does not appear to be affected significantly by the temperature.

Discussion

For specimens E to G, in which a second phase was present, the observed order was $1/4$. This is consistent with Eq. [2] and with the hypothesis that permeation is limited by bulk diffusion of electron holes, as is generally favored in the literature.

It is evident from Fig. 8 and from Table II that the order is variable for samples A to D. This indicates that permeation is limited by two or more processes. The relative importance of these processes depends on the experimental conditions.

The order increases with decreasing sample thickness. For thick samples, the order appears to approach $1/4$. Under these circumstances, transport within the solid ceramic is expected to be limiting and the observed order is consistent with the accepted model. For thin samples, transport in the gas phase or on the ceramic surface could participate in limiting the overall transport.

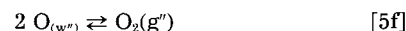
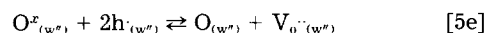
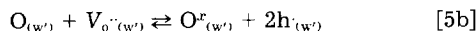
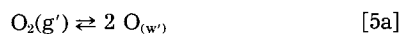
Table II. The dependence of flux on oxygen pressure, from least squares fits to Eq. [4] ($1/n, J^\circ$), Eq. [7] (α, β), and Eq. [13] (γ, δ).
 $P'_{O_2} = 10^{-3}$ -1 atm; $P''_{O_2} = 10^{-6}$ - 10^{-4} atm

Sample	Thickness (cm)	T (°C)	Order, $1/n$	$J^\circ \times 10^{10}$ (mol-cm ⁻² -s ⁻¹ -atm ^{-1/n})	$\alpha \times 10^9$ (mol-cm ⁻² -s ⁻¹ -atm ^{-1/2})	$\beta \times 10^{10}$ (mol-cm ⁻¹ -s ⁻¹ -atm ^{-1/4})	$\gamma \times 10^9$ (mol-cm ⁻² -s ⁻¹ -atm ^{-1/2})	$\delta \times 10^{10}$ (mol-cm ⁻¹ -s ⁻¹ -atm ^{-1/4})
A	0.194	960	0.296 ± 0.010	0.14 ± 0.01	0.12 ± 0.06	0.03 ± 0.02	0.053 ± 0.007	0.026 ± 0.007
		1090	0.292 ± 0.011	0.94 ± 0.03	7.70 ± 6.04	0.19 ± 0.17	0.35 ± 0.08	0.173 ± 0.007
		1230			3.66 ± 3.66	1.04 ± 1.07	1.26 ± 0.41	0.925 ± 0.06
		1239	0.280 ± 0.012	6.13 ± 0.11	4.63 ± 4.53	1.20 ± 1.19	2.38 ± 0.81	1.07 ± 0.06
B	0.165	1228	0.325 ± 0.008	5.46 ± 0.09	3.60 ± 3.01	1.02 ± 0.85	1.68 ± 0.51	0.90 ± 0.07
		1450	0.333 ± 0.009	83 ± 14	25.9 ± 12.3	7.56 ± 3.85	13.4 ± 2.6	6.55 ± 0.30
C	0.165	1230	0.335 ± 0.010	5.65 ± 0.03	3.28 ± 3.44	1.04 ± 1.02	1.45 ± 0.14	0.95 ± 0.03
		1338	0.329 ± 0.009	21.2 ± 1.1	8.34 ± 4.70	4.69 ± 2.56	4.68 ± 0.68	3.77 ± 0.29
D	0.050	1112	0.411 ± 0.016	2.91 ± 0.36			0.54 ± 0.05	0.157 ± 0.011
		1205	0.368 ± 0.005	7.25 ± 0.11	1.48 ± 0.44	0.51 ± 0.23	1.61 ± 0.21	0.39 ± 0.03
		1230			2.84 ± 2.05	0.65 ± 0.49	2.52 ± 0.18	1.91 ± 0.23
E	0.253	1267	0.258 ± 0.005	5.88 ± 0.03	17800 ± 230	1.43 ± 0.18	2.91 ± 0.64	1.39 ± 0.33
		1288	0.254 ± 0.003	6.71 ± 0.05	175 ± 68		4.07 ± 1.10	1.59 ± 0.34
F	0.175	1340	0.257 ± 0.007	15.8 ± 0.8			6.94 ± 1.13	2.45 ± 0.06
		1395	0.256 ± 0.003	22.2 ± 0.8			11.6 ± 1.8	3.52 ± 0.07
G	0.275	1344	0.233 ± 0.006	18.4 ± 0.7	590 ± 6.2	4.78 ± 0.06	2616 ± ~	4.16 ± 1.07

It has been shown in the previous section that the flow rate of the Ar/O₂ mixture had no influence on the overall transport. The resistance of the tubing and stopcock between the CSZ tube and the diffusion pump was such that a measurable P''_{O_2} was obtained. However, we estimate that this pressure reduced the overall rate of transport by only 17% in the worse case. This factor was taken into account by the second term in Eq. [4].

It is necessary then to suggest that a surface reaction participates in limiting the overall transfer. For thin tubes, the order appears to approach 1/2. It is possible that the surface reaction involves adsorbed O atoms, whose concentration would be expected to be proportional to $(P'_{O_2})^{1/2}$.

To incorporate a surface reaction and bulk diffusion, a possible mechanism is as follows



Here g refers to a gas phase species and w to a surface species; single and double primes refer to opposite sides of the CSZ tube. As in a previous treatment (4), we assume that $(V_{O'})$ and $(O_{O'})$ are constant.

This mechanism has been interpreted by supposing that reactions [5a] and [5f] are at equilibrium and by making the steady-state approximation for electron holes. It has not been possible to obtain an analytic expression for the permeability unless one of three additional approximations is made, as described in the next three paragraphs.

If it is assumed that reactions [5b] and [5e] are at equilibrium, an expression of the form of Eq. [2] is obtained, with $\beta = 0.25k_dK_b^{1/2}K_a^{1/4}[(V_{O'})/(O_{O'})]^{1/2}$. Here k_d is the rate coefficient for reaction [5d], and K_a and K_b are equilibrium constants for reactions [5a] and [5b].

If it is supposed that reactions [5b] and [5e] are limiting and that reaction [5d] is rapid and at equilibrium, as for a very thin sample, it is found that

$$J = \frac{1}{4} \alpha (P'_{O_2})^{1/2} - P''_{O_2})^{1/2} \quad [6]$$

Here, the surface parameter, α , equals $k_bK_a^{1/2}(V_{O'})$. The order is predicted to be 1/2 for the case of surface control.

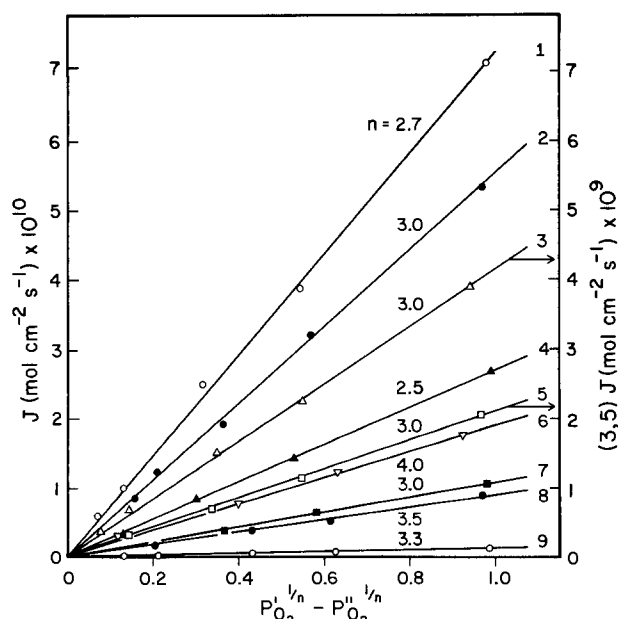


Fig. 6. Examples of fits of flux and pressure data to Eq. [4]. Line 6 is for specimen G; others are for specimens A to D. Values are as follows for the various lines. 1: $l = 0.05$ cm, $T = 1205^\circ\text{C}$. 2: 0.165 cm, 1230°C . 3: 0.165 cm, 1450°C (right scale). 4: 0.5 cm, 1112°C . 5: 0.165 cm, 1338°C (right scale). 6: 0.275 cm, 1344°C . 7: 0.165 cm, 1115°C . 8: 0.194 cm, 1090°C . 9: 0.194 cm, 960°C .

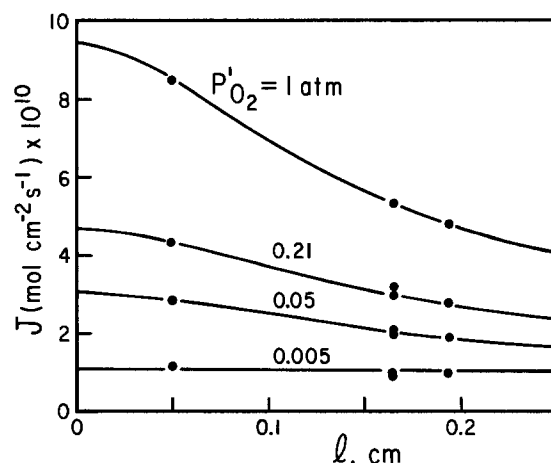


Fig. 7. The effect of the sample thickness on oxygen flux at 1230°C . The points are experimental for specimens A to D. Solid lines are theoretical results calculated from Eq. [7] by nonlinear least squares. The quoted pressures are P'_{O_2} .

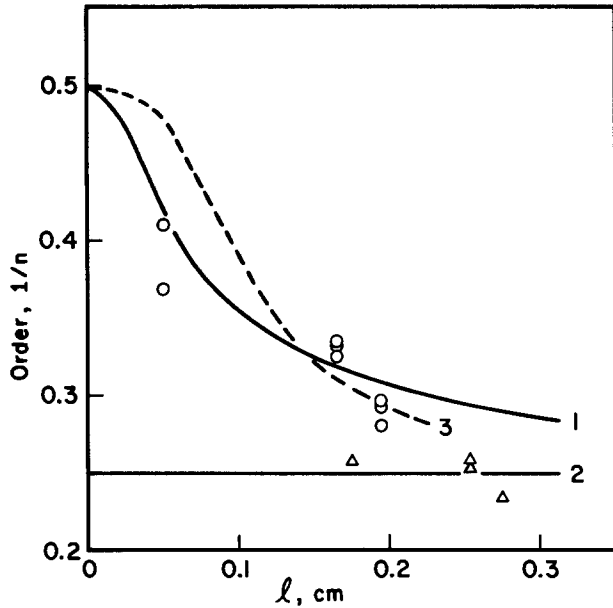


Fig. 8. The effect of sample thickness on the order. Open circles: specimens A-D. Triangles: specimens E-G. Curves 1 and 2 were generated by Eq. [8] for $L = 4.4 \times 10^{-2}$ and 0.0 cm, respectively. Curve 3 was generated by Eq. [14] with $M = 8 \times 10^{-2}$ cm.

If both reactions [5b] and [5d] are limiting, but the inside pressure, P'_{O_2} , is negligible, the following expression is obtained

$$J = \frac{\beta^2}{\alpha l^2} [(1 + \alpha^2 l^2 P'_{O_2} / \beta^2)^{1/2} - 1] \quad [7]$$

As shown earlier, P'_{O_2} makes little difference to permeation, so there is reason to expect that this equation will be a good approximation.

The order, $1/n$, may be determined by differentiating Eq. [7] as follows

$$\begin{aligned} 1/n &= d \ln J / d \ln P'_{O_2} \\ &= 1/4 [(L_2/l^2 + 1)^{1/2} - L/l]^{-1} (L_2/l^2 + 1)^{-1/2} \end{aligned} \quad [8]$$

Here L equals $\beta/[\alpha(P'_{O_2})^{1/4}]$ and is a characteristic thickness at which bulk and surface processes compete about equally.

The observed orders for specimens A to D have been fitted by least squares to Eq. [8], as shown by curve 1 in Fig. 8. The value of the parameter L was found to be $4.4 (\pm 1.4) \times 10^{-2}$ cm. The average value of $(P'_{O_2})^{1/4}$ for these experiments was $0.604 \text{ atm}^{1/4}$, so that $\beta/\alpha = 2.7 (\pm 0.8) \times 10^{-2} \text{ cm-atm}^{1/4}$. This indicates that the transition from bulk control to surface control would occur at 1 atm pressure for a sample thickness of about 2.7×10^{-2} cm.

A nonlinear least squares computer program was used to fit Eq. [7] to the experimental permeabilities at 1230°C . The calculated results at fixed pressures and varied thicknesses are represented by solid lines in Fig. 7. The bulk and surface parameters, β and α , for these fits are listed in Table III. It can be seen that the bulk coefficient is independent of pressure, with an average value of $(1.25 \pm 0.06) \times 10^{-10} \text{ mol-cm}^{-1}\text{-s}^{-1}\text{-atm}^{-1/4}$. The surface coefficient appears to increase slightly as the pressure decreases. The order of this quantity with respect to P'_{O_2}

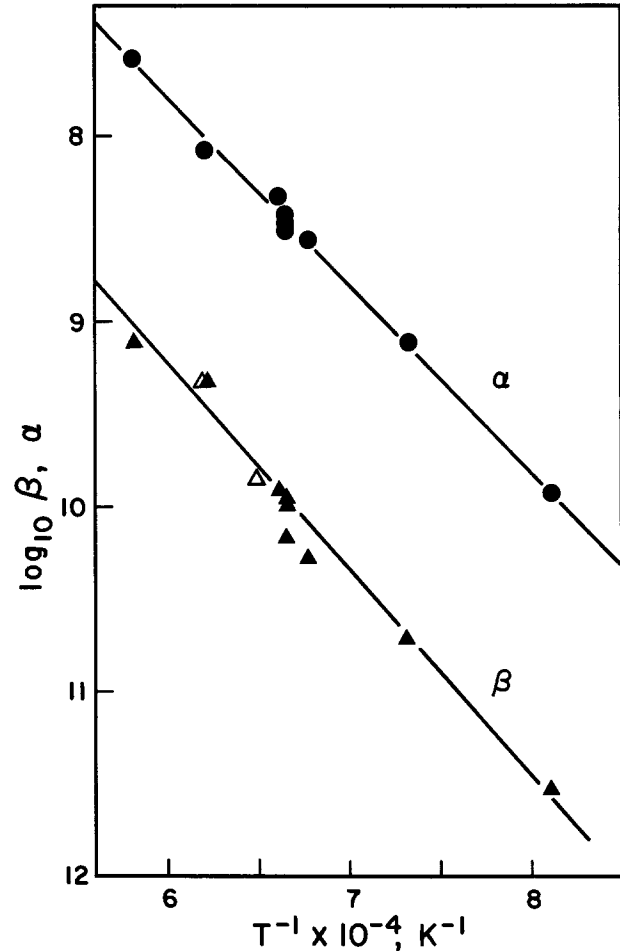


Fig. 9. The temperature dependence of the bulk diffusion and surface reaction parameters. Points on line α : specimens A to D. Closed triangles on line β : specimens A to D. Open triangles on line β : specimens E to G.

is -0.10 ± 0.07 , which is not significantly different from the order of zero assumed in the preceding derivation.

Equation [7] was similarly fitted to permeabilities with fixed l and temperature, but with P'_{O_2} variable. The resulting parameter values are listed in Table II. For samples A to D at 1230°C , it can be seen that both β and α are independent of sample thickness, with the average values being $\beta = (9.38 \pm 1.44) \times 10^{-11} \text{ mol-cm}^{-1}\text{-s}^{-1}\text{-atm}^{-1/4}$ and $\alpha = (3.34 \pm 0.25) \times 10^{-9} \text{ mol-cm}^{-2}\text{-s}^{-1}\text{-atm}^{-1/2}$. The ratio, $\beta/\alpha = 2.7 \times 10^{-2} \text{ cm-atm}^{1/4}$, agrees with the value found from Fig. 8.

It can also be seen from Table II that both β and α increase with increasing temperature. Arrhenius plots are shown in Fig. 9. The straight lines, as determined by least squares, have the following equations

$$\begin{aligned} \ln \alpha \text{ (mol-cm}^{-2}\text{-s}^{-1}\text{-atm}^{-1/2}) \\ = -(0.690 \pm 0.437) - \frac{191 \pm 5 \text{ kJ/mol}}{RT} \end{aligned} \quad [9]$$

$$\begin{aligned} \ln \beta \text{ (mol-cm}^{-1}\text{-s}^{-1}\text{-atm}^{-1/4}) \\ = -(3.08 \pm 0.96) - \frac{206 \pm 11 \text{ kJ/mol}}{RT} \end{aligned} \quad [10]$$

Table III. The surface reaction and bulk diffusion parameters as determined by a nonlinear least squares fit of Eq. [7] or [13] to the data of Fig. 7 at fixed P'_{O_2} and variable thickness ($T = 1230^\circ\text{C}$)

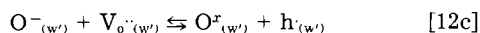
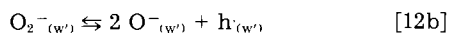
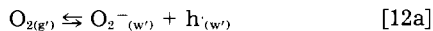
P'_{O_2} (atm)	$\alpha \times 10^9$ (mol-cm ⁻² -s ⁻¹ -atm ^{-1/2})	$\beta \times 10^{10}$ (mol-cm ⁻¹ -s ⁻¹ -atm ^{-1/4})	$\gamma \times 10^9$ (mol-cm ⁻² -s ⁻¹ -atm ^{-1/2})	$\delta \times 10^{10}$ (mol-cm ⁻¹ -s ⁻¹ -atm ^{-1/4})
1.0	1.88 ± 0.19	1.33 ± 0.06	1.21 ± 0.01	1.00 ± 0.01
0.21	2.03 ± 0.04	1.21 ± 0.04	1.34 ± 0.04	0.89 ± 0.03
0.05	2.70 ± 0.05	1.26 ± 0.02	1.81 ± 0.07	0.84 ± 0.04
0.005	3.10 ± 1.33	1.17 ± 0.50	2.14 ± 0.20	0.95 ± 0.25

It is seen that the activation energies for bulk diffusion and for surface reaction are very similar. From the expression for β , the following expression may be obtained (3, 12, 13) for the electronic conductivity σ^o at 1 atm

$$\ln \sigma^o (\Omega^{-1}\text{-cm}^{-1}) = (10.9 \pm 3.4) - \frac{195 \pm 10 \text{ kJ/mol}}{RT} \quad [11]$$

The activation energy may be compared with the following values (in kilojoules per mole) from the literature: 217 (2), 183 (3), 233 (7), 232 (9), 263 (10), 155 (11), and 98 (12).

Reactions [5a]-[5f] are not the only ones which allow a competition between surface and bulk processes of differing order. Setaka and Kwan (16) have observed the species O_2^- on the surface of zirconia. This species could be an intermediate if reactions [5a] and [5b] were replaced by the following



If these reactions are interpreted as before, with reactions [12b] and [5d] limiting, Eq. [7] and [8] are replaced by the following

$$J = \frac{\delta^2}{\gamma l^2} [(1 + \gamma^4 l^4 P'_{\text{O}_2} / \delta^4)^{1/2} - 1]^{1/2} \quad [13]$$

$$1/n = 1/4(M^4/l^4 + 1)^{-1/2} [(M^4/l^4 + 1)^{1/2} - M^2/l^2]^{-1} \quad [14]$$

Here $\gamma = (k_a K_b K_d/2)^{1/2}$, $\delta = 0.25 k_a (K_a K_b)^{1/4} [K_c (V_{\text{O}^{2+}})/(O_{\text{O}^{2+}})]^{1/2}$, and $M = \delta/[\gamma(P'_{\text{O}_2})^{1/4}]$.

Equation [14] was fitted to the experimental orders, as shown by curve 3 in Fig. 8. The average value of M was $(8.0 \pm 2.3) \times 10^{-2}$ cm, so $\delta/\gamma = (4.8 \pm 1.4) \times 10^{-2}$ cm-atm $^{1/4}$. It can be seen that the change in order occurs over a smaller range of thickness for this model.

Equation [13] was fitted to the permeability data. The resulting values of the surface, γ , and bulk, δ , parameters are listed in Tables II and III. The patterns of values for these parameters are similar to those noted earlier for α and β , respectively. The temperature dependences are given by the following equations for specimens A to D

$$\begin{aligned} \ln \gamma (\text{mol}\cdot\text{cm}^{-2}\cdot\text{s}^{-1}\cdot\text{atm}^{-1/2}) \\ = -(4.39 \pm 0.58) - 196 \pm 7 \text{ kJ}\cdot\text{mol}^{-1}/RT \quad [15] \end{aligned}$$

$$\begin{aligned} \ln \delta (\text{mol}\cdot\text{cm}^{-1}\cdot\text{s}^{-1}\cdot\text{atm}^{-1/4}) \\ = -(6.54 \pm 0.78) - 207 \pm 9 \text{ kJ}\cdot\text{mol}^{-1}/RT \quad [16] \end{aligned}$$

In order to distinguish more clearly between these mechanisms, it would be desirable to extend the range of experimental conditions.

Effect of pores.—Figure 1a shows that there are significant numbers of pores in specimens A to D. Pores on the outer and inner surfaces of the specimens will increase the surface area. We estimate the true area of the surface to be 10% greater than calculated in the Results section. The surface coefficients, α and γ , should then be reduced by 10% for an ideal sample without pores.

Most of the pores are in the bulk of the specimen. If the pores served as barriers to solid-state diffusion, they would increase the path of diffusion and decrease the effective volume. The true permeability would then be larger than the measured permeability. Alternatively, diffusion could be sustained by gaseous transport across the pores. This would shortcut the solid-state diffusion, and the true diffusion distance would be shorter than the overall thickness of the tube. Electron holes would have a choice of two paths on passing from one side of a pore to the other. They could diffuse around the pore through the ceramic, traveling a distance $\pi\rho$, where ρ is the radius of the pore, or they could pass across the pore by reactions [5a], [5b], [5e], and [5f] or [12a], [12b], and [12c].

In previous sections of this article, we have considered the competition for dominance between surface and bulk processes. There the competition was between two suc-

cessive processes, and the slower of these processes was found to dominate. In particular, bulk diffusion was predicted to be slower when the diffusion distance was greater than about 4.7×10^{-2} cm at 1 atm. Now we are considering competition for dominance between two parallel processes; the faster of these will dominate. For diffusion around a pore, the average distance is about 10^{-3} cm. Therefore, diffusion should be faster and should dominate transport within the specimens.

For specimens A to D, with 10% pores by volume, the diffusion distance would be increased by 4% and the cross-sectional area of ceramic between pores reduced by 10%, in comparison with an ideal ceramic without pores. For an ideal ceramic, the bulk diffusion parameter would be expected to be 14% greater.

Effect of segregation.—As discussed previously, the surface effect was responsible for the variable order for samples A to D. The order for samples E to G was, however, approximately constant. The surface parameters, α and γ , and the bulk parameters, β and δ , are given in the lower part of Table II for these samples. The bulk parameters are similar to those for samples A to D, as seen in Fig. 9. The surface parameters were larger, indicating that surface processes were not limiting. To account for these observations, the possible effect of a surface phase must be considered.

In Fig. 1, it was seen that there was a second phase in samples E to G but not in samples A to D. The second phase consisted of a mixture of metal silicates with an approximate composition of 40% SiO_2 , 40% CaO , and 20% Al_2O_3 . This composition is similar to that of a SiO_2 - Al_2O_3 - CaO eutectic with melting point at about 1250°C . Permeation of oxygen through this liquid was studied by Sasabe *et al.* (17). The order with respect to oxygen pressure was found to be 1/4. For similar conditions, permeation was an order of magnitude faster than for CSZ. There was no indication of limitation by a surface process, indicating that surface processes on this eutectic are faster than bulk processes, and hence much faster than bulk processes in CSZ. It is possible that a very thin layer of this second phase may be present on the surface of specimens E to G in the present work. Surface processes on this phase would be very rapid, and permeation would be controlled by bulk diffusion.

It is suggested that discrepancies in the orders quoted in the literature are also due to surface effects.

General.—The conclusion that both surface and bulk effects are important in describing the kinetics of oxygen permeation through stabilized zirconia is supported by the results of other studies. It is well known, for example, that the conductivity of CSZ and other oxide electrolytes depends markedly on their microstructure and that the response of grain boundaries or a second phase to an applied electric field is not the same as that of the bulk material (18-23). Chu and Seitz (19) showed that, although the resistivities differed by several orders of magnitude, the resistance values for the bulk and grain boundaries in several CSZ specimens were comparable. Beekmans and Heyne (20) attributed high grain boundary resistivities in CSZ to the presence of a second phase.

Studies of oxygen surface exchange reactions, including electrode kinetics, have also been used to distinguish between bulk and interface effects. Fouletier *et al.* (1) showed that, for cells with Y_2O_3 - ZrO_2 electrolytes of large surface area, considerable time was required for equilibrium to be attained between the surface and the surrounding gas phase, particularly at low partial pressures of oxygen. This effect, coupled with the flux of oxygen through the ceramic, could lead to errors in the EMF even if the flux were not large enough to alter the oxygen pressure in the gas being measured (24). In their studies of electrode phenomena at the Pt/CSZ interface, Kroger *et al.* (25, 26) suggested that oxygen could be absorbed directly on the electrolyte from the gas phase and that the electrons required for the incorporation of oxygen atoms in the lattice were obtained by diffusion from the

electrode-electrolyte interface. Other mechanisms have been discussed by Subbarao and Maiti (22). In studies of polarization phenomena in cells with CSZ electrolytes, Gur *et al.* (27) showed that bulk and interface effects could be separated and analyzed individually.

Summary and Conclusions

The isothermal permeability of oxygen through CSZ tubes was found to be proportional to $(P'_{O_2}{}^{1/n} - P''_{O_2}{}^{1/n})$, where n varied from 2.5 to 4.

The experimental results of this work raised two major questions. First, why is the order variable? Second, why do samples A to D behave differently than samples E to G? To answer the first question, we have proposed mechanisms involving competition between surface processes and bulk diffusion. There are two differences between samples A to D and E to G which could be invoked to explain their differing behavior—the presence of pores in samples A to D and the presence of a second phase in samples E to G. We have shown that diffusion around the pores will dominate over transport through the pores; therefore, the pores cannot explain the variable order for samples A to D. We have also shown that surface exchange on the second phase is likely to be very rapid. This accounts for the lack of a variable order with samples E to G.

The steady-state approach was used to investigate the mechanisms. On the assumption that the bulk process was of order 1/4 and the surface process of order 1/2, rate parameters for the bulk and surface processes were calculated.

Acknowledgments

We thank Dr. M. Iwase, Kyoto University, who kindly supplied one of the ceramic tubes used in this investigation. S. D. thanks the Dorothy J. Killam Trust for the award of a scholarship. P. D. P. thanks the Natural Sciences and Engineering Research Council of Canada for a grant in support of this research. Thanks are given to J. Uher and B. Marple for experimental assistance, to G. W. Caines for chemical analyses, and C. Collings and E. Dyer for SEM analyses.

Manuscript submitted July 27, 1984; revised manuscript received March 18, 1985. This was Paper 423 presented at the Cincinnati, Ohio, Meeting of the Society, May 6-11, 1984.

The National Research Council of Canada assisted in meeting the publication costs of this article.

REFERENCES

1. J. Fouletier, P. Fabry, and M. Kleitz, *This Journal*, **123**, 204 (1976).
2. R. Hartung and H. H. Möbius, *Z. Phys. Chem.*, **243**, 133 (1970).
3. L. Heyne and N. M. Beekmans, *Proc. Br. Ceram. Soc.*, **19**, 229 (1971).
4. K. Kiukkola and C. Wagner, *This Journal*, **104**, 379 (1957).
5. H. H. Möbius and R. Hartung, *Silikattechnik*, **16**, 276 (1965).
6. H. Ullmann, *Z. Phys. Chem.*, **237**, 71 (1968).
7. A. W. Smith, F. W. Meszaros, and C. D. Amata, *J. Am. Ceram. Soc.*, **49**, 240 (1966).
8. C. B. Alcock and J. C. Chan, *Can. Metall. Quart.*, **11**, 559 (1972).
9. W. A. Fischer, in "Fast Ion Transport in Solids," W. van Gool, Editor, p. 503, Elsevier, New York (1973).
10. K. Kitazawa and R. L. Coble, *J. Am. Ceram. Soc.*, **57**, 360 (1974).
11. S. F. Palguyev, V. K. Gilderman, and A. D. Neujmin, *This Journal*, **122**, 745 (1975).
12. M. Iwase and T. Mori, *Met. Trans. B*, **9**, 365 (1978).
13. M. Kleitz, E. Fernandez, J. Fouletier, and P. Fabry, in "Science and Technology of Zirconia, Advances in Ceramics," Vol. 3, A. H. Heuer and L. W. Hobbs, Editors, p. 349, American Ceramic Society, Washington, DC (1981).
14. B. Cales and J. F. Baumard, *J. Mater. Sci.*, **17**, 3243 (1982).
15. C. R. Masson, S. G. Whiteway, and C. A. Collings, *J. Am. Ceram. Soc.*, **42**, 745 (1963).
16. M. Setaka and T. Kwan, *Bull. Chem. Soc. Jpn.*, **43**, 2727 (1970).
17. M. Sasabe and Y. Kinoshita, *Trans. ISIJ*, **20**, 801 (1980).
18. J. E. Bauerle, *J. Phys. Chem. Solids*, **30**, 2657 (1969).
19. S. H. Chu and M. A. Seitz, *J. Solid State Chem.*, **23**, 297 (1978).
20. N. M. Beekmans and L. Heyne, *Electrochim. Acta*, **21**, 303 (1976).
21. M. J. Ververk, B. J. Middeelhuis, and A. J. Burggraaf, *Solid State Ionics*, **6**, 159 (1982).
22. E. C. Subbarao and H. S. Maiti, *ibid.*, **11**, 317 (1984).
23. M. Miyayama and H. Yanagida, *J. Am. Ceram. Soc.*, **67**, C194 (1984).
24. J. Fouletier, H. Seinera, and M. Kleitz, *J. Appl. Electrochem.*, **5**, 177 (1975).
25. H. Yanagida, R. J. Brook, and F. A. Kröger, *This Journal*, **117**, 593 (1970).
26. R. J. Brook, W. L. Pelzmann, and F. A. Kröger, *ibid.*, **118**, 185 (1971).
27. T. M. Gur, I. D. Raistrick, and R. A. Huggins, *Solid State Ionics*, **1**, 251 (1980).

Flow Reactor Studies of the Paired Electro-Oxidation and Electroreduction of Glucose

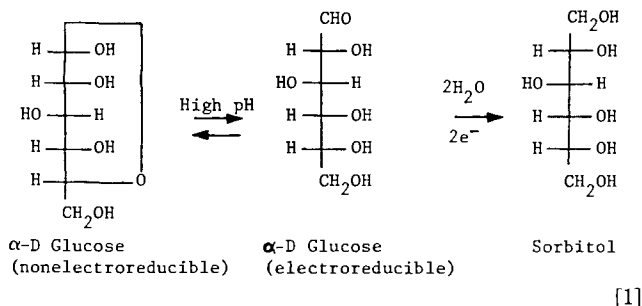
K. Park,* P. N. Pintauro,* M. M. Baizer,* and K. Nobe*

Department of Chemical Engineering, University of California, Los Angeles, California 90024

ABSTRACT

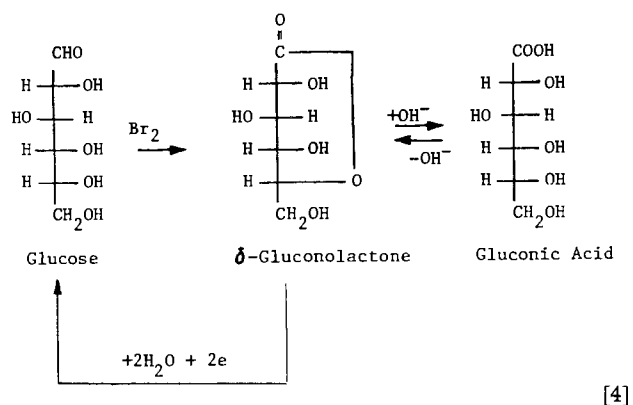
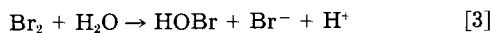
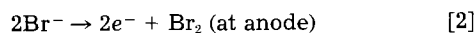
The electrochemical oxidation of glucose to gluconic acid and reduction of glucose to sorbitol have been paired in an undivided packed-bed electrode flow reactor. A Raney Ni powder electrocatalyst significantly improved the current efficiency for sorbitol production, as compared to a high hydrogen overpotential Zn(Hg) cathode. The optimum operating conditions for the paired syntheses are activity W-2 Raney Ni powder cathode, graphite chip anode, a 1.6M glucose and 0.4M CaBr₂ initial solution composition, pH 5-7, 60°C solution temperature, an applied current of 250-500 mA per 10g of nickel powder cathode and a solution volumetric flow rate of 100 ml·min⁻¹. Under these conditions, the sorbitol current efficiencies are 80-100%, the gluconic acid efficiencies are 100%, and the product yields are very high.

The paired syntheses of sorbitol and gluconate from glucose, a biomass-derived aldehyde, in undivided flow reactors have been investigated. There are a number of comprehensive articles on the chemistry of the individual electrode reactions (1-7). The separate oxidation and reduction reactions of glucose have been and are commercial processes (8-10). The commercial production of sorbitol by electrochemical reduction of glucose on high hydrogen overpotential cathodes, such as Pb(Hg) or Zn(Hg)



has been replaced by a high temperature and high pressure catalytic hydrogenation process.

At a graphite anode, glucose can be indirectly oxidized to gluconic acid with electrogenerated HOBr. As shown in Eq. [2]-[4], the oxidation proceeds via an electroreducible δ -gluconolactone intermediate



Our initial investigation of the paired syntheses showed that at 25°C a 0.8M glucose-0.8M NaBr solution can be electrolyzed in an undivided flow reactor to produce both sorbitol and sodium gluconate (4). Optimum results for a flow-through packed-bed reactor were obtained with a Zn(Hg) shot cathode, a graphite chip anode, a constant cathode potential of -2.1V vs. SCE, a solution pH of 7, and an electrolyte flow rate of 0.8 liter/min. Although

Electrochemical Society Active Member.

the sorbitol and gluconate yields were high, current efficiencies for sorbitol and sodium gluconate were low. Current losses at the cathode were primarily due to H₂ evolution; subsequently, it was found that some of the current loss at the cathode and all of the current loss at the anode were due to a parasitic δ -gluconolactone/glucose redox couple (cf. Eq. [4]).

The results presented in this paper are based on more recent experiments to (i) examine the use of CaBr₂ instead of NaBr as the supporting electrolyte because separation of the oxidation product would be facilitated due to the low solubility of calcium gluconate, (ii) increase the gluconate current efficiency at pH 7 by minimizing the transport of δ -gluconolactone from the anode to the cathode, and (iii) increase the sorbitol current efficiency by using low hydrogen overpotential Raney Ni in place of the high hydrogen overpotential Zn(Hg) cathode.

Experimental

Preliminary electrolysis experiments on each half of the glucose oxidation-reduction "pair" were carried out in a standard glass H-cell containing a medium porosity glass frit. Electrode potentials were measured relative to a saturated calomel electrode, and mixing was provided by magnetic stirring bars.

The paired syntheses were studied using flow-through packed-bed flow reactors. One was made of Plexiglas and is shown in Fig. 1. The reactor diameter was 3.2 cm; the anode and cathode packed beds were both 1.2 cm long. The cathode consisted of reagent-grade zinc shot (0.5 cm shot diam with a surface area/volume ratio of 6.6 cm²/cm³) amalgamated with Hg; the anode consisted of cylindrical graphite chips (Poco Graphite, Incorporated) with an area/volume ratio of 8.5 cm²/cm³. External electrical contact was made by a graphite rod in the anode compartment and a zinc amalgam rod in the cathode. 5 mm diam glass beads above and below the electrodes were used to ensure a uniform flow distribution in the packed beds. The anode and cathode were separated from one another by a perforated polypropylene disk sandwiched between two nylon mesh screens. Reference electrode probes were inserted between the anode and the cathode.

A second packed-bed parallel current/electrolyte flow reactor (Fig. 2) was constructed to accommodate a Raney Ni powder cathode. The cylindrical flow reactor (6.7 cm diam) was made of glass with a fine porosity glass frit separating a 2.5 cm thick graphite chip anode from a 3 mm thick Raney Ni powder cathode. The electrolyte flow was in the downward direction to press the nickel powder against the glass frit. A spiral wound nickel sheet (3 mm high) was embedded in the Raney Ni and electrical contact to the sheet was made by a nickel-plated aluminum rod.

The flow reactors were operated in a batch recycle mode by inserting them into a circulation loop (Fig. 3) which normally consisted of a pump, flowmeter, throttle

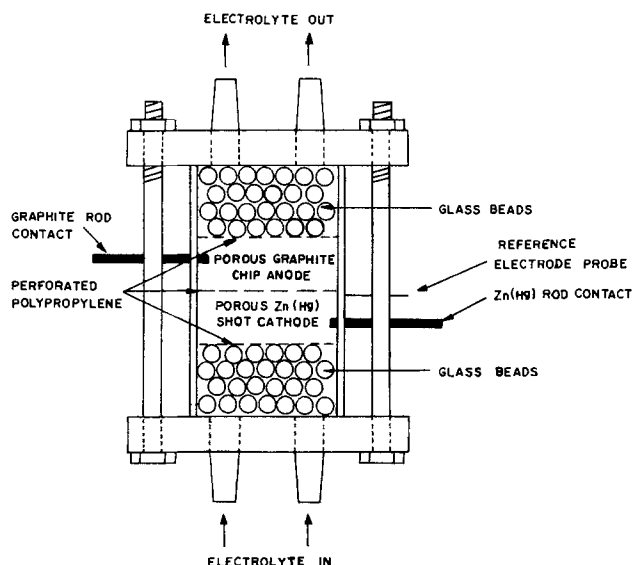


Fig. 1. The packed-bed, undivided flow reactor with a Zn(Hg) cathode and graphite chip anode.

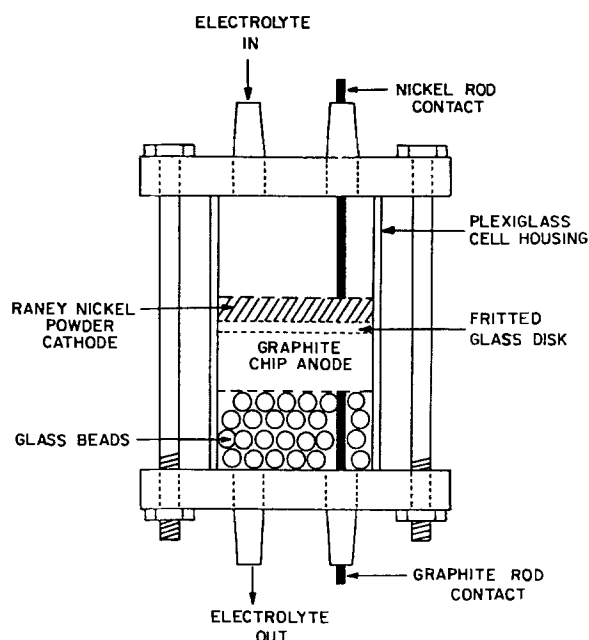


Fig. 2. The packed-bed flow reactor with a Raney Ni powder cathode.

valve, hydrocyclone gas disengager, and a holding tank (500-1000 ml) immersed in a constant temperature water bath. The individual elements of the reaction loop were connected by silicone tubing.

Constant cathode potential experiments were performed with either a Magna Research Model 4700M or a Wenking ST72 potentiostat. A Sorensen DCR80-60B or a Hewlett-Packard Harrison 61D/B dc power supply was used in constant-current electrolyses. Currents were measured with a Simpson ultrahigh sensitivity microammeter; potentials were measured with a Keithley 610B Electrometer and a Keithley 168 digital multimeter; and the total charge passed during an electrolysis was measured using a Model 541 Koslow Scientific Company coulometer.

All chemicals were of analytic reagent grade, and the water was deionized and doubly distilled. The zinc metal shot and flat sheet zinc electrode (for H-cell experiments) were amalgamated using the procedures described by Creighton (11).

The active Raney Ni cathode was prepared from Raney Ni alloy powder (Alfa Products, 50/50 Ni/Al content) by adding the alloy powder to a 17 weight percent NaOH solution. On addition, an exothermic reaction occurred,

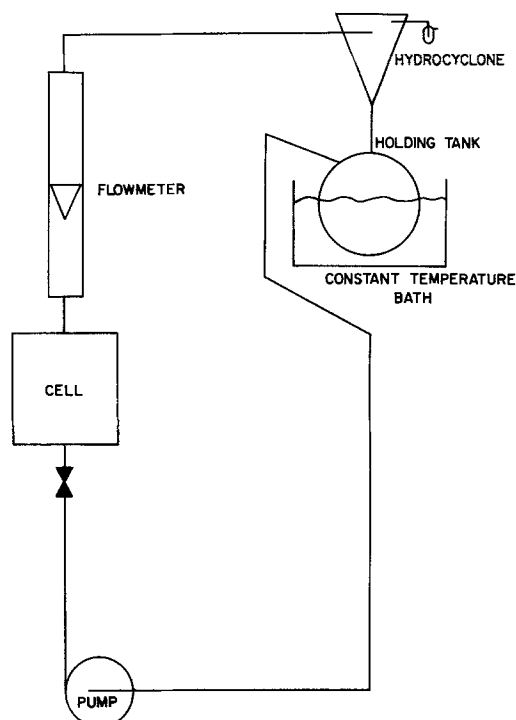


Fig. 3. The batch recycle reaction loop for the paired syntheses of sorbitol and gluconic acid.

with vigorous hydrogen evolution. After the evolution of hydrogen slowed, the metal powder/caustic suspension was heated to 60°C for ca. 1h. The solution was occasionally stirred, then allowed to cool to room temperature. The alkaline solution was then decanted, and the nickel powder washed several times with distilled water until the rinse water pH was neutral. Raney Ni powder catalyst obtained in this way has an activity comparable to that of W-2 (12). Before H-cell and flow reactor electrolysis, adsorbed hydrogen atoms formed on the nickel powder during the activation process were removed by immersion of the catalyst in a 1.0M glucose solution for ca. 20h.

Current efficiencies and product yields were obtained by HPLC analyses of glucose and the reaction product. For glucose and its reduction products, a Bio-Rad Laboratories HPX-87C cation exchange resin column in its calcium ion form was used with a refractive index detector. A cation exchange column in its hydrogen form (Bio-Rad Laboratories HPX-89H) with a UV detector (216 nm wavelength) was used for oxidation product analyses. Products were identified by comparing retention times with those of known commercial samples. Calibration of peak areas with standard solutions indicated that sorbitol concentrations can be determined within $\pm 5\%$, while glucose and gluconate concentrations are within $\pm 10\%$.

Results and Discussion

The δ -gluconolactone/glucose parasitic redox couple.—The electro-oxidation of glucose to gluconic acid proceeds via a gluconolactone intermediate (13), as shown in Eq. [4]. Fedoronko (1) has reported that lactones can be reduced to the corresponding aldoses at a Hg cathode. Since the hydrolysis of δ -gluconolactone is acid-base catalyzed (14), the low gluconic acid current efficiencies and some of the current loss at the cathode for the pH 7 paired electrolysis are attributed to δ -gluconolactone exiting the anode, circulating through the external reaction loop of the experimental apparatus and re-entering the cathode compartment, where it is reduced to glucose; hence, there is no loss in product yields based on glucose consumed.

A series of divided H-cell cathodic polarization experiments were performed to determine the electroreducibility of δ -gluconolactone. Figure 4 shows the i-E curves for the reduction of a 0.15M δ -gluconolactone-0.8M NaBr solution at pH 4.5, 6, and 9 using a Zn(Hg) cathode. These

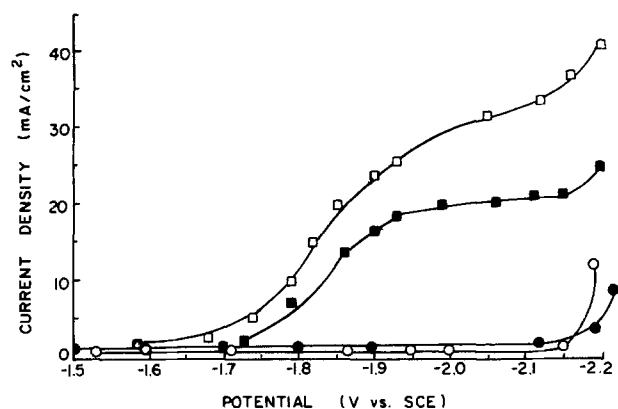


Fig. 4. The effect of pH on the electrochemical reduction of δ -gluconolactone (divided H-cell; Zn(Hg) cathode; $T = 26^\circ\text{C}$). Open circles: 0.8M NaBr , $\text{pH} = 7$. Filled circles: 0.8M NaBr and 0.15M δ -gluconolactone, $\text{pH} = 9$; Filled squares: 0.8M NaBr and 0.15M δ -gluconolactone, $\text{pH} = 6$; Open squares: 0.8M NaBr and 0.15M δ -gluconolactone, $\text{pH} = 4.5$.

results indicate that: (i) at the normal cathodic operating potential in the packed-bed flow reactor (-2.1V vs. SCE), the current densities for lactone reduction (30 mA/cm^2 at $\text{pH} 4.5$ and 20 mA/cm^2 at $\text{pH} 6$) are considerably higher than the current densities for glucose reduction (10 mA/cm^2 at $\text{pH} 6$) and H_2 evolution ($\text{ca. } 2.5\text{ mA/cm}^2$) and (ii) at $\text{pH} 9$, there is no measurable reduction current for the lactone, presumably because at this pH the hydrolysis to gluconic acid is fast and gluconic acid is nonelectroreducible [as established previously (4)].

The rate of δ -gluconolactone hydrolysis to gluconic acid can be increased by increasing the solution temperature. At 25°C and $\text{pH} 7$, $\text{ca. } 3.5\text{h}$ are required to fully hydrolyze the lactone. To determine the rate of hydrolysis at elevated solution temperatures a series of H-cell experiments were performed in which a 0.15M δ -gluconolactone and 0.8M NaBr solution ($\text{pH } 6.7 \pm 0.4$) was maintained at either 45° or 55°C for $\text{ca. } 30\text{ min}$. The Zn(Hg) cathode was periodically polarized to -2.1V vs. SCE and the current measured; these current density values are plotted vs. the hydrolysis time (at 55°C) in Fig. 5. After 8–10 min, the current density decreased from an initial value of 55 mA/cm^2 to the normal background (H_2 evolution) current density of $\text{ca. } 2.5\text{ mA/cm}^2$. The decreasing currents correspond to the decreasing concentration of lactone. At 45°C , 20 min were required to convert the lactone to gluconic acid. Thus, the parasitic lactone/glucose redox couple can be

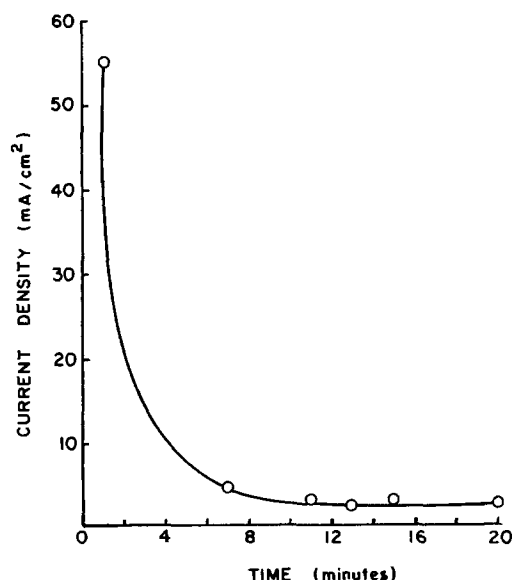


Fig. 5. The current density-time decay curve for the hydrolysis of δ -gluconolactone at 55°C (divided H-cell; Zn(Hg) cathode; $\text{pH} = 6.7$).

Table I. The effect of solution temperature and residence time in holding tank on current efficiencies

Undivided packed-bed flow reactor. Anode: graphite chips. Cathode: Zn(Hg) shot. Initial electrolyte composition: 0.8M glucose and 0.8M NaBr . $\text{pH} = 6.8 \pm 0.3$.

Temperature ($^\circ\text{C}$)	Residence time (s)	Charge passed (F/mol)	Glucose conversion (%)	Current efficiency Gluconic acid %	Sorbitol (%)
58	600	0.084	9	100	58
58	600	0.202	16	100	48
58	600	0.290	26	99	47
58	600	0.309	26	99	44
25	10	0.061	—	100	40
25	10	0.115	6	82	32
25	10	0.179	6	70	25
25	10	0.257	9	71	26

eliminated by performing the paired syntheses at elevated temperatures.

To ensure the absence of δ -gluconolactone in the cathode compartment of the packed bed flow reactor, the electrolyte exiting the anode was kept in a constant temperature ($\text{ca. } 58^\circ\text{C}$) holding tank for approximately 10 min. The size of the holding tank was dictated by the volume (1.5 liter) and volumetric flow rate (0.15 liter/min) of electrolyte in the circulation loop. The packed bed flow reactor operated at a temperature of 58°C with the solution residence time of 10 min outside the reactor. The initial electrolyte composition was 0.8M glucose and 0.8M NaBr . The solution pH was continuously monitored and maintained at 6.8 ± 0.3 by addition of NaHCO_3 during constant cathode potential (-2.1V vs. SCE) electrolysis.

Typical results of sorbitol and gluconic acid current efficiencies are given in Table I. For comparison purposes, current efficiencies of a 25°C , 10s residence time experiment (the holding tank and temperature bath were removed from the recycle loop) are also shown in Table I. The magnitudes of the increase in the sorbitol and gluconic acid current efficiencies for the elevated temperature electrolysis indicate that the parasitic δ -gluconolactone/glucose redox couple had been eliminated. Sorbitol and gluconic acid product yields were very high. Cathodic current losses are ascribed to hydrogen evolution.

CaBr₂ supporting electrolyte.—In order to evaluate CaBr_2 as a supporting electrolyte at $\text{pH} 7$ and 55°C , a series of i-E potentiostatic polarization measurements and constant potential reduction experiments were performed in a divided H-cell using a Zn(Hg) cathode. The H-cell was immersed in a 55°C constant temperature water bath, and the catholyte pH was maintained at 7.2 ± 0.5 by addition of HBr . The i-E curves as well as cathodic polarization data for NaBr supporting electrolyte are shown in Fig. 6.

The initial i-E polarization experiments compare the rate of hydrogen evolution in NaBr and CaBr_2 solutions. Curves A and B in Fig. 6 show a decrease of $\text{ca. } 80\text{ mV}$ in the hydrogen overpotential for 0.4M CaBr_2 as compared to 0.8M NaBr . Upon addition of glucose to the 0.4M CaBr_2 solution, a large increase in current was observed (curve C). The apparent current efficiencies for glucose reduction, based on curves B and C, was 96% at -1.7V vs. SCE . However, the sorbitol current efficiency at 0.2 F/mol was only 32% for a constant potential electrolysis performed at -1.7V vs. SCE (55°C , $\text{pH} 7$, initial glucose concentration of 0.8M). The calculation of the 96% current efficiency did not take into account the increase in hydrogen evolution due to the presence of both glucose and sorbitol. Previous H-cell experiments had shown that glucose caused an anodic shift in the potential for the visual onset of H_2 evolution of Zn(Hg) (4); sorbitol, which is not electroreducible (4), also increases the rate of H_2 evolution (curve D, Fig. 6).

CaBr_2 was also examined as a supporting electrolyte in the undivided packed bed flow reactor (cf. Fig. 1) with a

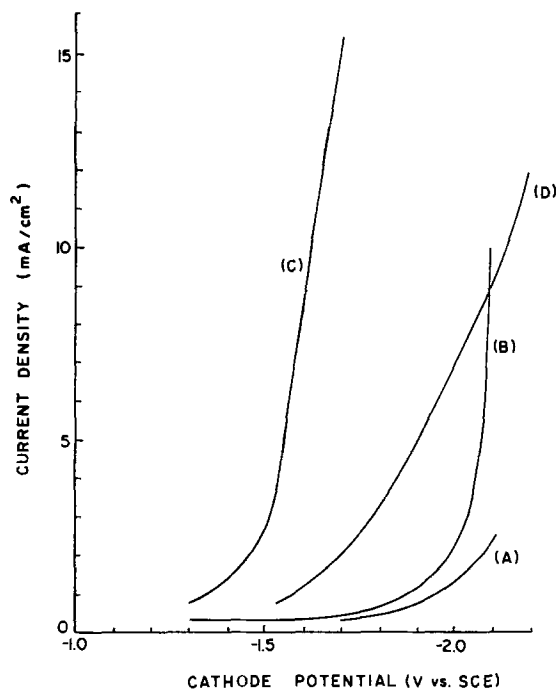


Fig. 6. The effect of catholyte composition on hydrogen evolution and glucose reduction (divided H-cell, Zn(Hg) cathode; pH = 7; $T = 55^{\circ}\text{C}$). A: 0.8M NaBr. B: 0.4M CaBr_2 . C: 0.4M CaBr_2 and 0.8M glucose. D: 0.4M CaBr_2 and 0.5M sorbitol.

Zn(Hg) shot cathode and graphite chip anode. The initial electrolyte composition was 0.8M glucose and 0.4M CaBr_2 , the electrolyte temperature was 55°C , and the solution pH (≈ 7) was maintained constant by periodically adding $\text{Ca}(\text{OH})_2$. The volumetric flow rate (0.2 liter/min) and electrolyte volume in the batch recycle reaction loop (600 ml) were chosen to ensure a 3 min residence time in the holding tank (it was determined in separate H-cell experiments that only 3 min were required to hydrolyze δ -gluconolactone at 55°C when CaBr_2 is the supporting electrolyte).

The results of three constant cathode potential electrolyses are shown in Table II. High gluconic acid current efficiencies at both -1.70 and -1.95V vs. SCE indicate that the lactone oxidation intermediate is completely hydrolyzed in the holding tank. The low sorbitol current efficiencies (compared with the 40-60% efficiencies with NaBr) were not unexpected because of the results obtained in the H-cell experiments. The results of the H-cell and flow reactor experiments show that, while the use of CaBr_2 may simplify and reduce the cost of the separation scheme, there are significant losses in the energy efficiency of the paired syntheses with the Zn(Hg) cathode.

The electrohydrogenation of glucose on Raney nickel.—Sorbitol is currently manufactured by hydrogenation of glucose on Raney Ni and Raney Ni-Mo alloy catalysts at elevated temperatures and pressures (15). Previous work

has shown that low hydrogen overpotential electrocatalysts, such as Raney Ni, and platinum and rhodium black, can effectively hydrogenate organic compounds (16-21). For example, Miller and Christensen (20) obtained high product yields and current efficiencies for electrohydrogenation of phenol to cyclohexanol on rhodium black cathodes in H_2SO_4 ; Kirilyus *et al.* (19) report that Raney Ni is highly active and selective for electrohydrogenation of pyridine to piperidine in alkaline solution, while Belenkaya and Belozersky (16) obtained relatively high current efficiencies for electrohydrogenation of glucose on a Ni-Al alloy cathode. These results indicate that Raney Ni may be an effective electrocatalyst for the hydrogenation of glucose. [Note: according to Chiba *et al.* (21), electrohydrogenation of aliphatic aldehydes would not be expected; however, no data were provided to support this opinion.] Therefore, in order to improve the sorbitol current efficiencies with CaBr_2 as supporting electrolyte, the use of a Raney Ni powder cathode was investigated.

H-cell experiments were performed with the anode and cathode compartments each charged with 50 ml of a 0.4M CaBr_2 solution; the anode was a graphite rod and the cathode consisted of a nickel plate current collector (3.5 cm diam) covered with 2g of activity W-2 Raney Ni powder. The electrolyte temperature and bulk catholyte pH were maintained constant at 60°C and ca. 7.0 (by addition of HBr), respectively.

At first, a constant current of 100 mA was applied for 95 min and then stepped up to 200 mA for 20 min before the current was terminated. While the Raney Ni cathode was set at open circuit, glucose powder (14.4g) was added to the catholyte to make a 1.6M solution. After 3h of continuous stirring of the solution, HPLC analysis indicated the formation of 0.0019 mol sorbitol; this amount required 0.0038 g-atom of adsorbed hydrogen atoms. The latter value provides the basis for the estimate of 56.4 m^2/g for the Raney Ni surface.

Next, a series of experiments was performed in which glucose was present in solution during current passage; the anode and cathode compartments of the H-cell were initially charged with 50 ml of a 1.6M glucose-0.4M CaBr_2 solution. The results are given in Table III. The sorbitol current efficiencies are significantly higher than those obtained for glucose reduction on Zn(Hg) cathodes [Table II and Ref. (4)]. For the 200 mA experiments (Table III), the potential of the Raney Ni bed was -1.10V vs. SCE , which is a considerably lower overpotential than that found for high hydrogen overpotential cathodes, such as Pb, Zn, and Zn(Hg) (-1.7 to -2.2V vs. SCE), as shown in Fig. 6 and Ref. (4). The open-circuit experiment and the lower reduction potentials indicate an electrohydrogenation mechanism for glucose reduction on Raney Ni in which glucose reacts with adsorbed hydrogen atoms to form sorbitol.

Current losses for glucose reduction on Raney Ni at 0.2 F/mol are primarily due to the formation of 2-deoxysorbitol with some current (5-10%) consumed by hydrogen evolution. The selectivities in Table III are the relative amounts of product and by-product(s) detected in the

Table II. Performance of glucose paired reactions in CaBr_2 solutions

Undivided packed-bed flow reactor. Anode: graphite chips. Cathode: Zn(Hg) shot. Initial electrolyte composition: 0.8M glucose and 0.4M CaBr_2 . Temperature: 55°C . Flow rate: 200 ml/min.							
Experiment no.	Cathode potential (V vs. SCE)	Cell potential (V)	pH	Charge passed (F/mol)	Glucose conversion (%)	Current efficiency Gluconic acid %	Sorbitol (%)
1	-1.95	3.5	6.8 ± 0.3	0.076	—	95	—
				0.15	10	100	7
				0.22	17	100	9
				0.30	18	91	9
2	-1.70	3.0	7.0 ± 0.5	0.1	7	96	22
				0.2	11	89	20
				0.3	21	100	16
3	-1.70	3.0	7.0 ± 0.5	0.3	—	100	20

Table III. Electrohydrogenation of glucose on Raney Ni (2g)

Divided H-cell. Initial catholyte: 50 ml of 1.6M glucose and 0.4M CaBr₂. T = 60°C. pH = 7.0 ± 0.5.

	Experiment no.			4 ^a
	1	2	3	
Applied current (mA)	200	300	200	200
Charge passed (F/mol)	0.2, 0.4	0.2	0.2	0.2
Selectivity (%)				
Fructose	24, 29	14	29	39
2-deoxysorbitol	9, 13	8	12	—
Sorbitol	67, 58	78	59	61
Sorbitol current efficiency (%)	83, 61	76	70	60

^a Supporting electrolyte: saturated NaHCO₃ solution, pH = 8.5.

electrolytic solution after the passage of either 0.2 or 0.4 F/mol of glucose. Fructose is formed during an electrolysis by the base-catalyzed isomerization of glucose. 2-deoxysorbitol is formed by the subsequent reduction of fructose on Raney Ni. The pH excursions and fructose formation can be minimized by performing the reduction in a flow reactor, where the residence time in the nickel powder bed is short.

A series of constant current glucose paired syntheses experiments were performed using a Raney Ni powder cathode (10g), a graphite chip anode, and the flow-through packed-bed reactor shown in Fig. 2. In all electrolyses, the initial glucose concentration was 1.6M, the supporting electrolyte was 0.4M CaBr₂, and the electrolyte temperature was maintained constant at ca. 60°C. The solution pH was maintained between 5 and 7 during an electrolysis by addition of Ca(OH)₂. The electrolyte volume in the batch recycle reaction loop and the flow rate were chosen to ensure an adequate solution residence time outside the electrochemical flow reactor for complete hydrolysis of δ -gluconolactone to gluconic acid. Fresh Raney Ni was used in each flow reactor experiment. During an electrolysis, solution samples were periodically removed and analyzed for glucose, sorbitol, gluconic acid, and by-products by HPLC.

The results of the paired syntheses experiments are presented in Table IV. Finely divided Raney Ni powder was used as the cathode material in experiments 1-7. In experiments 8 and 9, the cathode was an industrial grade granular Raney Ni catalyst (kindly provided by S. R. Montgomery of the Davison Chemical Division, W. R. Grace and Company). Linear velocities through the Raney Ni bed, which are also given in Table IV, were determined from the cathode reactor diameter (6.7 cm) and the porosity of the Raney Ni powder (0.74).

The gluconic acid current efficiencies from the paired syntheses experiments are ca. 100% when the electrolyte flow rate was maintained at or above 35 ml/min. In experiments 1 and 2, the high currents and low flow rates

led to anodic current losses by back-diffusion and subsequent reduction of electrogenerated HOBr or oxidation of HOBr to HBrO₃ (bromate does not oxidize glucose, but, rather it circulates through the recycle loop and is reduced to Br⁻ at the cathode). Product yields for gluconic acid were very high.

The sorbitol current efficiencies in Table IV are significantly higher than those obtained when glucose is reduced on Zn(Hg) in a paired reaction using either CaBr₂ (20%; cf. Table II) or NaBr (40-60%, cf. Fig. 3) as supporting electrolyte. The sorbitol yields in all Raney Ni paired syntheses experiments were very high. Cathodic current losses in experiments for electrolyte flow rates \geq 100 ml·min⁻¹ are ascribed to hydrogen evolution. Cathodic current losses in \leq 35 ml·min⁻¹ flow rate experiments were due to hydrogen evolution and either the reduction of anodically generated Br₂, which back-diffused into the cathode compartment or the reduction of BrO₃⁻. The results in Table IV suggest that 100% reduction and oxidation current efficiencies may be obtained at applied currents higher than 250 mA per 10g of Raney Ni by increasing electrolyte flow rate and/or glucose concentration. The overall cell potential in experiment 4 (250 mA, 100 ml/min) was 2.2V, which is 0.8-1.3V less than those given in Table II for the paired syntheses with a Zn(Hg) cathode. The lower cell potential is attributed to the lower operating cathode potential of Raney Ni, as observed in divided H-cell experiments and discussed above.

High sorbitol and gluconic acid current efficiencies were also obtained when granular Raney Ni particles were used as the cathode material. The pressure drop through such a cathode bed is less than that for Raney Ni powder since the glass frit, which is used to trap the nickel powder, is not required for the granular catalyst.

Conclusions

The oxidation and reduction of glucose have been successfully paired in undivided flow-through electrochemical reactors with a graphite chip anode and either a Zn(Hg) shot or Raney Ni powder (activity W-2) cathode. Higher reduction current efficiencies and lower operating potentials have been obtained with the Raney Ni cathode. 100% current efficiencies and very high product yields at 0.2 F/mol for sorbitol (reduction) and gluconate (oxidation) were obtained with a Raney Ni cathode flow reactor under the following operating conditions: 1.6M glucose-0.4M CaBr₂ initial electrolyte composition; solution pH between 5 and 7; 60°C solution temperature; a constant applied current of 250 mA/10g of Raney Ni powder; and a solution flow rate of 100 ml·min⁻¹ (0.064 cm/s linear velocity). Current efficiencies for sorbitol formation in undivided flow reactor experiments with a Zn(Hg) shot cathode were only 9-20% at 0.2 F/mol.

When the flow reactor (Zn(Hg) or Raney Ni cathode) was operated in a batch recycle mode, current losses from a δ -gluconolactone/glucose parasitic redox couple were eliminated when the solution was kept in a holding tank

Table IV. Performance of glucose paired reactions with a Raney Ni cathode

Undivided packed-bed flow reactor. Anode: graphite chips. Cathode: 10g Raney Ni powder. Initial electrolyte composition: 1.6M glucose and 0.4M CaBr₂. Temperature = 60°C. pH = 5-7.

Experiment no.	I (mA)	Flow rate (ml/min)	Linear velocity (cm/s)	Charge passed (F/mol)	Glucose conversion (%)	Current efficiencies	
						Reduction (%)	Oxidation (%)
1	1000	29	0.019	0.2	17	88	85
2	500	20	0.013	0.2	15	64	86
3	250	35	0.023	0.2	17	73	98
4	250	100	0.064	0.2	22	100	100
5	250	100	0.064	0.2	20	100	100
6	500	100	0.064	0.3	28	79	96
7	750	100	0.064	0.3	28	75	100
8 ^a	100	125	0.079	0.15	14	85	100
9 ^b	100	125	0.079	0.1	12	100	79

^a Cathode: 20g of granular Raney Ni (particle diameter = 3 mm).

^b Cathode: 50g of granular Raney Ni (particle diameter = 5 mm).

for ca. 10 min (NaBr supporting electrolyte at 58°C) or 3 min (CaBr₂ at 60°C).

Lower cathode potentials for glucose reduction on Raney Ni as compared to Zn(Hg) were observed in both divided H-cell and flow reactor experiments. In a divided H-cell, sorbitol was produced on a Raney Ni cathode at -1.1V vs. SCE (200 mA applied current), whereas the reduction potential for glucose on Zn(Hg) was between -1.7 and -2.2V vs. SCE. In the flow reactor experiments, the overall cell potential was reduced from 3.0-3.5V to 2.2V when the Zn(Hg) cathode was replaced with Raney Ni powder.

Acknowledgment

This work was supported by the U.S. Department of Energy, Office of Energy Systems Research, Energy Storage Division contract no. DE-AC03-76SF00098 and Office of Basic Energy Sciences, Advanced Energy Projects Division grant no. DE-FG03-84ER13258 and by the University of California's Universitywide Energy Research Group.

Manuscript submitted Aug. 27, 1984; revised manuscript received April 18, 1985.

The University of California assisted in meeting the publication costs of this article.

REFERENCES

1. M. Fedoronko, *Adv. Carbohydrate Chem. Biochem.*, **29**, 107 (1974).
2. A. Bin Kassim, C. L. Rice, and A. T. Kuhn, *J. Appl. Electrochem.*, **11**, 261 (1981).
3. H. Chum, "Review of Electrochemistry of Sugars," SERI Report, TR-332-417, Solar Energy Research

- Institute, Golden, CO (1981).
4. P. N. Pintauro, D. K. Johnson, K. Park, M. M. Baizer, and K. Nobe, *J. Appl. Electrochem.*, **14**, 109 (1984).
5. H. S. Isbell and H. L. Frush, *J. Res. Natl. Bur. Stnds.*, **6**, 1145 (1931).
6. H. S. Isbell, H. L. Frush, and F. J. Bates, *ibid.*, **8**, 571 (1932).
7. C. G. Fink and D. B. Summers, *Trans. Electrochem. Soc.*, **74**, 625 (1938).
8. M. T. Sanders and R. A. Hales, *ibid.*, **96**, 241 (1949).
9. T. R. Beck, R. T. Ruggeri, R. C. Alkire, M. A. Stadtherr, and N. L. Weinberg, "A Survey of Organic Electrolytic Processes," ANL-OEPM-79-5, Argonne National Laboratory, Argonne, IL (1979).
10. H. V. K. Udupa, in "Electroorganic Synthesis Technology," M. Krumpelt, E. Y. Weissman, and R. C. Alkire, Editors, p. 26, AIChE Symposium Series 75, American Institute of Chemical Engineers, New York (1979).
11. H. J. Creighton, *Trans. Electrochem.*, **75**, 289 (1939).
12. H. R. Billica and H. Adkins, *Org. Synth.*, Coll. Vol. III, 272 (1964).
13. H. S. Isbell and W. Pigman, *J. Res. Natl. Bur. Stnds.*, **10**, 337 (1933).
14. Y. Pocker and E. Green, *J. Am. Chem. Soc.*, **95**, 113 (1973).
15. M. A. Phillips, *Br. Chem. Eng.*, **8**, 767 (1963).
16. N. G. Belenkaya and N. A. Belozersky, *Zh. Obshch. Khim.*, **19**, 1664 (1949).
17. B. Sakurai and T. Arai, *Bull. Chem. Soc. Jpn.*, **28**, 93 (1955).
18. I. V. Kirilyus and M. A. Zhuk, *Sov. Electrochem.*, **8**, 967 (1972).
19. I. V. Kirilyus, G. K. Murzatova, and D. V. Sokol'skii, *Sov. Electrochem.*, **15**, 1330 (1979).
20. L. L. Miller and L. Christensen, *J. Org. Chem.*, **43**, 2059 (1978).
21. T. Chiba, M. Okimoto, H. Nagai, and Y. Takata, *Bull. Chem. Soc. Jpn.*, **56**, 719 (1983).

Anodic Oxidation Mechanism of Hypochlorite Ion on Platinum Electrode in Alkaline Solution

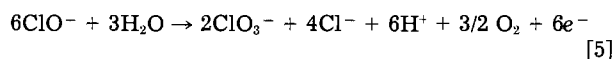
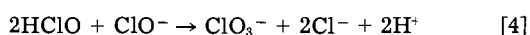
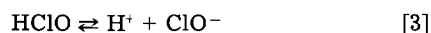
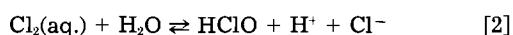
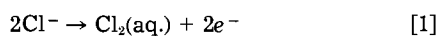
A. Tasaka and T. Tojo

Department of Applied Chemistry, Faculty of Engineering, Doshisha University, Imadegawa-Karasuma, Kamigyo-ku, Kyoto 602, Japan

ABSTRACT

The anodic oxidation of hypochlorite ion (ClO⁻) or chlorite ion (ClO₂⁻) on platinum (Pt) electrode was carried out at 30°C in 1.0M NaOH solution. A plateau was observed on the anodic polarization curve of ClO⁻ in the potential range of 0.90-1.20V and, in the case of ClO₂⁻, a plateau was observed in the potential range of 1.10-1.50V. When alkaline solutions with various concentration ratios of NaClO₂ to NaClO were electrolyzed at 1.20V over 50h, the Raman intensity ratio of ClO₂⁻ to ClO⁻ in the anolyte was found to be constant at a value of ca. 0.12 in every case. From the calibration curves obtained in ClO₂⁻-ClO⁻ system, the concentration ratio of ClO₂⁻ to ClO⁻ was estimated to be ca. 0.08, which is in good agreement with the theoretical value according to a first-order consecutive reaction. Based on these results, it is suggested that the mechanism of the anodic oxidation of ClO⁻ is ClO⁻ → ClO₂⁻ → ClO₃⁻.

The reactions involved in the synthesis of ClO₃⁻ were studied by various workers (1-4). Above all, the mechanism which was formulated by Foerster and Müller at the beginning of this century was fundamental (1). It is as follows



This mechanism well explains the total reaction in the electrolysis of ClO₃⁻. However, it does not pay attention to the elementary process. Especially, the question remains that ClO₂⁻ is neglected, since ClO₂⁻ was produced

industrially as a bleaching agent and the binding energy of Cl-O bond in ClO₂⁻ is larger than that in ClO⁻.

In order to detect the species which would exist in the process of the formation of ClO₃⁻, laser Raman spectroscopy was used. The quantitative analysis of ClO⁻-ClO₂⁻-ClO₃⁻ system in an alkaline solution was carried out, since ClO⁻ and ClO₂⁻ are stable in an alkaline solution (5). In this condition, the reaction of Eq. [4] does not proceed, so only the reaction of Eq. [5] can be investigated. The kinetics of anodic oxidation of ClO⁻ on Pt electrode in 1.0M NaOH was investigated using calibration line obtained by laser Raman spectroscopy.

Experimental

Mixed solutions of ClO⁻-ClO₃⁻ and ClO₂⁻-ClO₃⁻ were prepared in various concentration ratios by dissolving sodium hypochlorite (NaClO), sodium chlorite (NaClO₂), or sodium chlorate (NaClO₃) in 1.0M NaOH. All chemicals used were reagent grade and from Nakarai Chemicals

Limited. Raman spectra of these solutions were taken to determine the relationship between Raman intensity ratios of ClO^- to ClO_2^- or ClO_2^- to ClO_3^- and concentration ratios of those. Concentration of ClO^- was determined by iodometry. A calibration curve of ClO_2^- - ClO^- system was obtained by calculating from those of ClO^- - ClO_3^- and ClO_2^- - ClO_3^- systems. Raman spectra were taken on a 488 nm Ar-ion laser in a JEOL Limited Model JLG-A-04 spectrophotometer. Sample cells were about 2 cm³ of Pyrex tubing. Slit widths for all spectra were 14 cm⁻¹ at 488 nm, and laser output power was 70-100 mW.

The electrochemical cell made by Pyrex glass has a diaphragm of porous glass frits. Smooth Pt plate with a surface area of 2 or 12 cm² was used as an anode, and Pt plate with large surface area as the cathode. Before electrolysis, the working electrode was cleaned in nitric acid, washed with distilled water, and preelectrolyzed anodically at 10 mA·cm⁻² in 1.0M NaOH and cathodically at 100 mA·cm⁻² in another solution of 1.0M NaOH for 30 min. All potentials were measured against a mercury (II) oxide electrode (Hg/HgO, 1.0M NaOH) at 30° ± 0.5°C.

The electrical circuit of the electrochemical cell is shown in Fig. 1. With this circuit, the stationary anodic polarization curves of ClO^- and ClO_2^- in 1.0M NaOH were obtained. The electrolytic solutions were prepared from NaClO, NaClO₂, and 1.0M NaOH solution which was previously deaerated with nitrogen. Solutions of ClO_2^- - ClO^- system at various concentration ratios were electrolyzed at a constant potential, and the variation of concentration ratio of $C_{\text{ClO}_2^-}$ to C_{ClO^-} with time was measured by taking the Raman spectrum of anolyte samples at different times.

Potentiostatic experiments were performed with a Hokuto Denko Limited Model HA-201 potentiostat and a Toa Denpa Kogyo Limited Model CDR-11 recorder.

Results and Discussion

Laser Raman spectra of ClO^- , ClO_2^- , and ClO_3^- .—The Raman spectrum of a solution of commercial NaClO (Fig. 2a) shows six bands at 479, 613, 713, 786, 932, and 1063 cm⁻¹. The band at 713 cm⁻¹ was assigned to the Cl-O stretching vibration of ClO^- (6). In order to assign the other five bands, the Raman spectra of solutions containing 1.0M NaClO₂ + 1.0M NaOH and 1.0M NaClO₃ + 1.0M NaOH were observed. Two bands were observed in NaClO₂ solutions (see Fig. 2b) at 402 and 786 cm⁻¹. The band at 402 cm⁻¹ was assigned to the O-Cl-O symmetric deformation vibration, and the one at 786 cm⁻¹ was as-

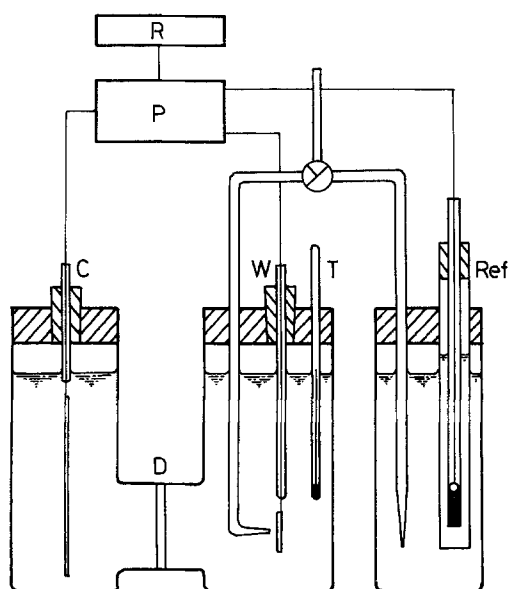


Fig. 1. Experimental apparatus. W: Working electrode (Pt plate). C: Counterelectrode (Pt plate). Ref: Reference electrode (Hg/HgO, 1.0M NaOH). D: Diaphragm of porous glass frits. T: Thermometer. P: Potentiostat. R: Recorder.

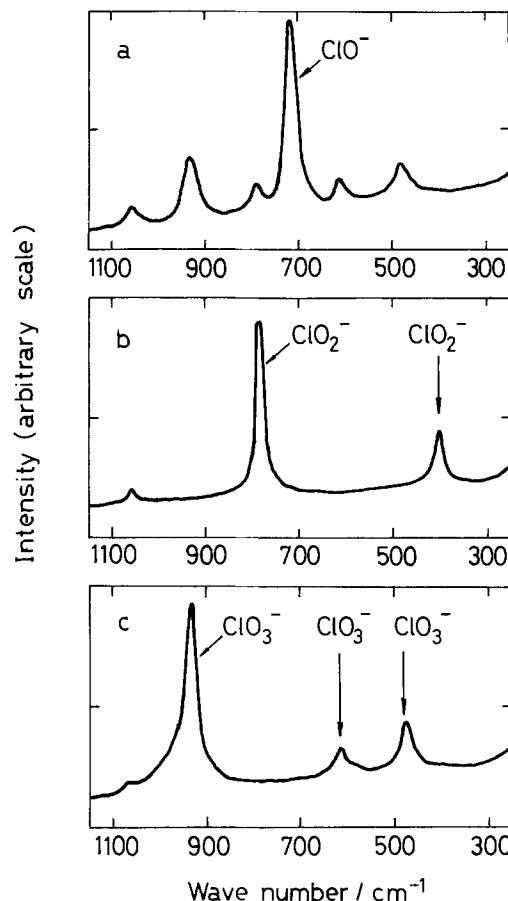
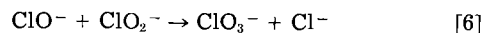


Fig. 2. Laser Raman spectra of solutions of (a) commercial NaClO, (b) 1.0M NaClO₂ + 1.0M NaOH, and (c) 1.0M NaClO₃ + 1.0M NaOH. Excitation: 488 nm argon ion laser line. Slit: 14 cm⁻¹ · 10 mm. Sensitivity: 80 · 250 pulses per second (pps).

signed to the O-Cl-O symmetric stretching vibration of ClO_2^- (6). Three bands were noticed in NaClO₃ solutions (Fig. 2c) at 479, 613, and 932 cm⁻¹. The band at 479 cm⁻¹ was assigned to doubly generated deformation vibration; that at 613 cm⁻¹ was assigned to the symmetric deformation vibration; and that at 932 cm⁻¹ was assigned to the symmetric stretching vibration of ClO_3^- (6). Thus, the band at 786 cm⁻¹ was assigned to ClO_2^- , and those at 479, 613, and 932 cm⁻¹ were assigned to ClO_3^- . In addition, the band at 1063 cm⁻¹ was assigned to the symmetric stretching vibration of carbonate ion which formed by the dissolving carbon dioxide in alkaline solution from air (6, 7).

These results show that commercial solutions of NaClO contain ClO_2^- and ClO_3^- and suggest the formation of ClO_2^- intermediate during the oxidation of ClO^- to ClO_3^- .

Calibration curve of alkaline solution containing ClO_2^- - ClO^- system.—Raman intensity is proportional to the concentration of a given species, if temperature of the solution and intensity of incident laser beam is kept constant. During the course of the experiment, ClO^- is decomposed gradually by the irradiating laser beam. In addition, chemical reaction between ClO^- and ClO_2^- proceeds in alkaline solutions according to Eq. [6]



These factors would reduce the accuracy of the analytical data based on the spectrum of alkaline solution of ClO_2^- - ClO^- system taken directly. Hence, the calibration line for ClO_2^- - ClO^- system was calculated from the data of ClO^- - ClO_3^- and ClO_2^- - ClO_3^- systems. In both cases, the concentration of ClO_3^- was 0.50, 0.75, and 1.00M. Since the ratio of Raman intensity decreased with time in case of ClO^- - ClO_3^- system, the initial ratio of the Raman intensity was estimated by extrapolation to time zero (8).

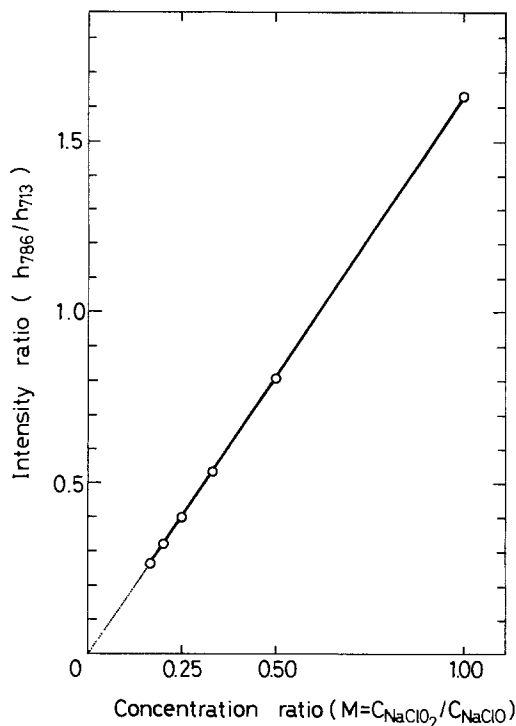


Fig. 3. Calculated relationship between concentration ratio (NaClO_2 to NaClO) and intensity ratio (786 to 713 cm^{-1}).

The slopes for the obtained calibration lines of the ClO^- - ClO_3^- system and the ClO_2^- - ClO_3^- system were 0.60 and 0.97, respectively. Figure 3 shows the calculated calibration graph for the ClO_2^- - ClO^- , from which the concentration ratio of ClO_2^- to ClO^- was evaluated from the Raman intensity data. The slope of the calibration line for the ClO_2^- - ClO^- system was 1.63. Thus, it would be possible to decide the concentration of each ion from these three standardized curves if the total concentration of each ion in the system is known.

Potentiostatic oxidation.—Potentiostatic polarization curves in alkaline ClO^- and ClO_2^- solutions on a Pt anode

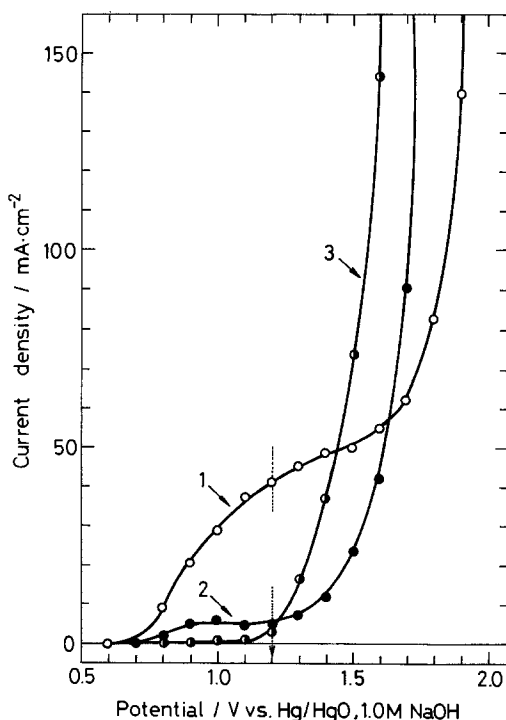


Fig. 4. Potentiostatic polarization curves of Pt anode at 30°C . Curve 1: $0.25\text{M NaClO}_2 + 1.0\text{M NaOH}$. Curve 2: $0.25\text{M NaClO} + 1.0\text{M NaOH}$. Curve 3: 1.0M NaOH .

at 30°C were shown in Fig. 4, where curves 1, 2, and 3 refer to the anodic polarization curves of $0.25\text{M NaClO}_2 + 1.0\text{M NaOH}$, $0.25\text{M NaClO} + 1.0\text{M NaOH}$, and 1.0M NaOH , respectively. A plateau was observed with NaClO_2 solutions in the potential range of 1.10 - 1.50V , and in case of NaClO solution a plateau was observed in the potential range of 0.90 - 1.20V . However, with 1.0M NaOH solutions (curve 3), the current increased beyond 1.10V because of the discharge of O_2 . This potential was less noble compared with those observed with solution containing ClO^- and ClO_2^- .

The anode potential during electrolysis of sodium chloride in industrial operation is about 1.308V vs. NHE , i.e., 1.210V vs. Hg/HgO , 1.0M NaOH (9). Hence, electrolysis of ClO^- or ClO_2^- in alkaline solutions was conducted at 1.20V vs. Hg/HgO , 1.0M NaOH at 30°C for 24h using Pt anode. Figure 5 depicts the Raman spectrum of the anolyte (curve a), along with the Raman spectrum of a synthetic NaClO solution (curve b). In these spectra, the bands were noticed at 713 cm^{-1} (ClO^-), at 786 cm^{-1} (ClO_2^-), and at 479 , 613 , and 932 cm^{-1} (ClO_3^-). Comparison of curves a and b shows that the intensity of the band at 932 cm^{-1} (ClO_3^-) was increased slightly in the spectrum of an electrolyzed solution, whereas the band at 786 cm^{-1} (ClO_2^-) was unaltered. Figure 6 shows the spectrum of a solution containing $0.25\text{M NaClO}_2 + 1.0\text{M NaOH}$ which was electrolyzed at 1.20V on Pt anode for 24h and that of a synthetic NaClO_2 solution (b). In spectrum a, new bands were observed at 479 , 613 , and 932 cm^{-1} which were all assigned to ClO_3^- . These results show that ClO_2^- was easily oxidized to ClO_3^- , and, hence, the concentration of ClO_2^- in the anolyte should approach zero during electrolysis. However, the concentration of ClO_2^- in the anolyte remained unaltered during electrolysis, as shown in Fig. 5.

Concentration dependence on a current density.—Plateaus were observed on the anodic polarization curves of ClO^- and ClO_2^- in alkaline solutions in the potential range of ca. 1.00 - 1.20V . Figure 7 shows the relationship between the concentration of ClO^- or ClO_2^- and the current at 1.20V , where straight lines 1 and 2 refer to ClO^- and ClO_2^- , respectively. In both cases, the current at 1.20V is proportional to the concentration of ClO^- or ClO_2^- . In case of ClO^- , the straight line extrapolated to zero ClO^- concentration did not pass through the origin owing to interference from oxygen evolution reaction. However, in case of ClO_2^- , the extrapolated straight line passed through the origin.

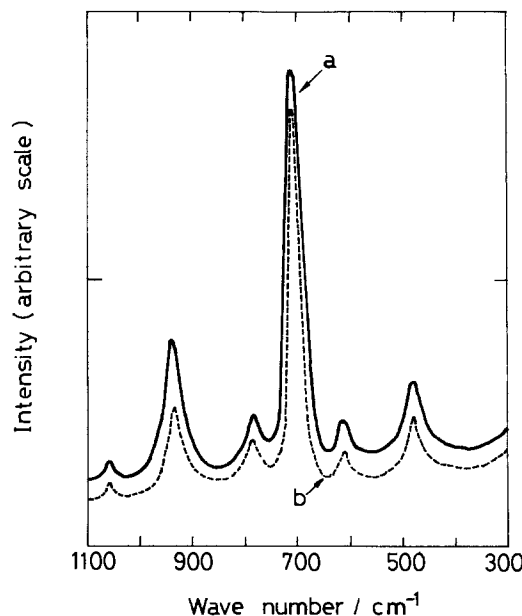


Fig. 5. Laser Raman spectra of 0.25M NaClO before and after electrolysis at 30°C . Curve a: after electrolysis at 1.20V vs. Hg/HgO , 1.0M NaOH . Curve b: before electrolysis. Laser excitation: 488 nm (argon). Slit: $14 \text{ cm}^{-1} \cdot 10 \text{ mm}$. Sensitivity: $40 \cdot 250 \text{ pps}$.

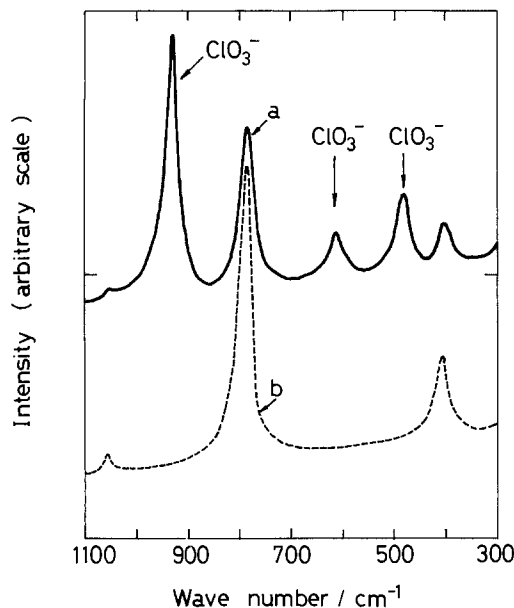
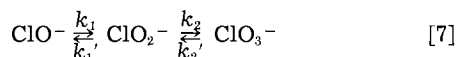


Fig. 6. Laser Raman spectra of 0.25M NaClO₂ before and after electrolysis at 30°C. Curve a: after electrolysis at 1.20V vs. Hg/HgO, 1.0M NaOH. Curve b: before electrolysis. Laser excitation: 488 nm (argon). Slit: 14 cm⁻¹ · 10 mm. Sensitivity: 40 · 250 pps.

Potentiostatic oxidation of an alkaline solution of ClO₂⁻-ClO⁻ system.—Analytical results employing laser Raman spectroscopy show the existence of ClO₂⁻ during the anodic oxidation of ClO⁻ to ClO₃⁻. Hence, the anodic oxidation of ClO⁻ can be described as



where k_1 and k_2 are the rate constants for the forward processes and k_1' and k_2' are those for the backward processes. Since ClO₂⁻ was oxidized anodically only to ClO₃⁻ and ClO₃⁻ cannot be reduced electrochemically (10), the rate constant for the backward processes can be neglected. Hence, the concentration variation of ClO⁻ and ClO₂⁻ with time can be written as

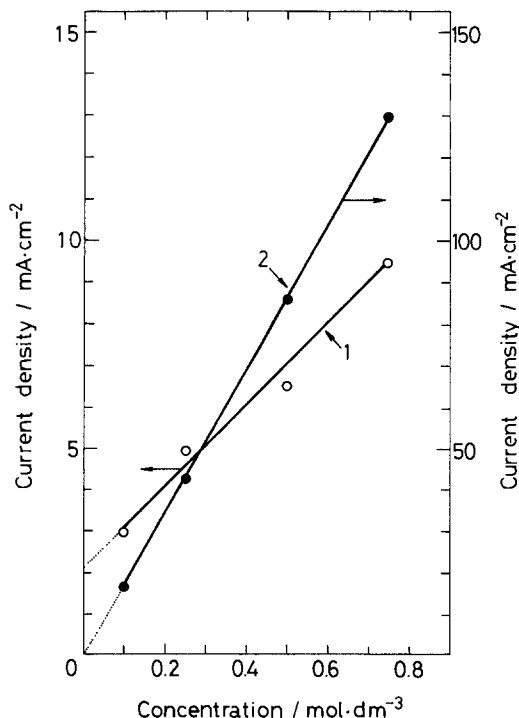


Fig. 7. Relationship between NaClO or NaClO₂ concentration and current density at 1.20V vs. Hg/HgO, 1.0M NaOH. Line 1: NaClO + 1.0M NaOH. Line 2: NaClO₂ + 1.0M NaOH.

$$-dC_{\text{ClO}^-}/dt = k_1 C_{\text{ClO}^-} \quad [8]$$

$$dC_{\text{ClO}_2^-}/dt = k_1 C_{\text{ClO}^-} - k_2 C_{\text{ClO}_2^-} \quad [9]$$

Solving Eq. [8] and [9], the concentrations of ClO⁻ and ClO₂⁻ at time t may be expressed as

$$C_{\text{ClO}^-} = C_{\text{ClO}^-}^{\circ} \exp(-k_1 t) \quad [10]$$

$$C_{\text{ClO}_2^-} = \{k_1/(k_2 - k_1)\} C_{\text{ClO}^-}^{\circ} \{\exp(-k_1 t) - \exp(-k_2 t)\} + C_{\text{ClO}_2^-}^{\circ} \exp(-k_2 t) \quad [11]$$

where $C_{\text{ClO}^-}^{\circ}$ and $C_{\text{ClO}_2^-}^{\circ}$ are initial concentrations of ClO⁻ and ClO₂⁻, respectively. From Eq. [10] and [11], the concentration ratio of ClO₂⁻ to ClO⁻ at time t is obtained as

$$C_{\text{ClO}_2^-}/C_{\text{ClO}^-} = k_1/(k_2 - k_1) - \{k_1/(k_2 - k_1) - C_{\text{ClO}_2^-}^{\circ}/C_{\text{ClO}^-}^{\circ}\} \exp\{-(k_2 - k_1)t\} \quad [12]$$

Since $k_2 > k_1$ (see Fig. 4) $C_{\text{ClO}_2^-}/C_{\text{ClO}^-}$ approaches $k_1/(k_2 - k_1)$ for $t \rightarrow \infty$. Thus, the ratio of $C_{\text{ClO}_2^-}/C_{\text{ClO}^-}$ in the anolyte would approach a constant value, when alkaline solutions of various concentration ratios of ClO₂⁻ to ClO⁻ are electrolyzed potentiostatically.

Alkaline solutions of various concentration ratios of ClO₂⁻ to ClO⁻ were electrolyzed at 1.20V and 30°C. Results illustrating the variation of the Raman intensity ratios of ClO₂⁻ to ClO⁻ (h_{786}/h_{713})¹ with time during electrolysis were shown in Fig. 8. In case of curves c and d, the solution of 0.70 and 0.50M NaClO were prepared and no ClO₂⁻ was added. The concentrations of ClO₂⁻ containing in the commercial solutions of NaClO were different; hence, the initial concentration ratios of ClO₂⁻ to ClO⁻ were different. In case of curves a and b, initial concentration ratios of ClO₂⁻ to ClO⁻ were 0.51 (0.34M/0.67M) and 0.33 (0.25M/0.75M), respectively. As seen in Fig. 8, the Raman intensity ratio (h_{786}/h_{713}) became constant at ca. 0.12, corresponding to a $C_{\text{ClO}_2^-}/C_{\text{ClO}^-}$ ratio of 0.08, after 50h. Since the electrochemical oxidation of ClO⁻ and ClO₂⁻ on Pt electrode is diffusion controlled and the number of electrons involved in both reaction are equal,² $k_1/(k_2 - k_1) = i_{d1}/(i_{d2} - i_{d1})$, where i_{d1} and i_{d2} are limiting current densities of ClO⁻ and ClO₂⁻ at the same concentration. The value of $i_{d1}/(i_{d2} - i_{d1})$ calculated from the value of limiting current density on the anodic polarization curves of 0.25M NaClO and 0.25M NaClO₂ at 1.20V (Fig. 4) was found to be ca. 0.12. Correcting for the O₂ evolution reaction during ClO⁻ oxidation by taking the value of i_{d1} at 1.20V on the anodic polarization curve of 0.25M NaClO + 1.0M NaOH and subtracting the value of the current density at zero ClO⁻ concentration from that at 0.25M NaClO

¹The notations h_{713} and h_{786} mean the height of the band at 713 cm⁻¹ (ClO⁻) and 786 cm⁻¹ (ClO₂⁻).

²The electrochemical oxidation of ClO⁻ and ClO₂⁻ in an alkaline solution are as

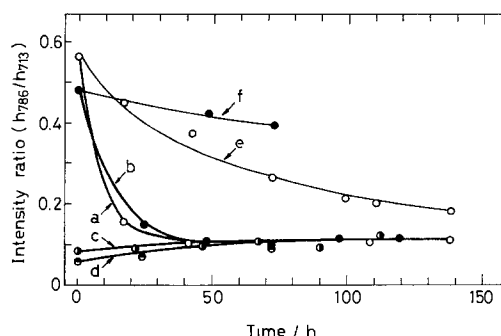
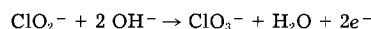
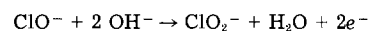


Fig. 8. Relationship between time and intensity ratio (786 to 713 cm⁻¹) in the mixed solution of NaClO₂ and NaClO. Initial concentration ratios ($C_{\text{NaClO}_2}^{\circ}/C_{\text{NaClO}}^{\circ} = M^{\circ}$). Curves a and e: $M^{\circ} = 0.51$. Curves b and f: $M^{\circ} = 0.33$. Curve c (no NaClO₂ added): $M^{\circ} = 0.08$. Curve d (no NaClO₂ added): $M^{\circ} = 0.06$. Curves a, b, c, and d: electrolyzed at 1.20V vs. Hg/HgO, 1.0M NaOH and 30°C. Curves e and f: without electrolysis.

(in Fig. 7), the value of $i_{a1}/(i_{a2} - i_{a1})$ was estimated at ca. 0.08. This value was in good agreement with the value of concentration ratio of ClO_2^- to ClO^- obtained from Raman intensity data. Curves e and f in Fig. 8 show the variation of the Raman intensity ratios of h_{786}/h_{713} with time at 30°C without electrolysis. Since the degree of the decrement of the Raman intensity ratios was obviously different from the results in curves a and b, the reaction of Eq. [6] did not interfere during the present electrochemical studies.

From these results, it is suggested that the anodic oxidation of ClO^- proceeds under the consecutive first-order reaction $\text{ClO}^- \rightarrow \text{ClO}_2^- \rightarrow \text{ClO}_3^-$.

Acknowledgment

Special thanks are due to Professor K. Shimizu, Professor of Doshisha University, for his fruitful discussions.

Manuscript submitted July 30, 1984; revised manuscript received April 18, 1985.

Doshisha University assisted in meeting the publication costs of this article.

REFERENCES

1. F. Foerster and E. Müller, *Z. Elektrochem.*, **8**, 8, 515, 633, 921 (1902).
2. N. Ibl and D. Landolt, *This Journal*, **115**, 713 (1968).
3. D. Landolt and N. Ibl, *Electrochim. Acta*, **15**, 1165 (1970).
4. L. Hammer and G. Wranglen, *ibid.*, **9**, 1 (1964).
5. A. Tasaka, T. Tojo, A. Shimosaka, and M. Yamashita, *Denki Kagaku*, **50**, 241 (1982).
6. H. Siebert, "Anwendungen der Schwingungsspektroskopie in der anorganischen Chemie," pp. 40, 48, 53, 57, Springer-Verlag, Berlin (1966).
7. A. Tasaka, T. Tojo, M. Kubokawa, and K. Shimizu, *Denki Kagaku*, **48**, 123 (1980).
8. A. Tasaka, H. Shibata, M. Kawata, and M. Kubokawa, *ibid.*, **43**, 475 (1975).
9. S. Yoshizawa, H. Jinno, and F. Hine, "Muki Kogyo Kagaku," p. 19, Asakura Press, Tokyo (1976).
10. F. Hine and M. Yasuda, *This Journal*, **118**, 182 (1971).

Photoelectrochemical Measurements on Thermally Grown Platinum Containing Iron Oxide Photoanodes

Michael R. St. John^{*,1} and Anthony J. Tiller

Institute of Gas Technology, Chicago, Illinois 60616

Ronald L. Cook^{*} and Anthony F. Sammells^{*}

Eltron Research Incorporated, Aurora, Illinois 60505

ABSTRACT

Experimental conditions are discussed for the thermal growth of iron oxide photoanodes which promote $\alpha\text{-Fe}_2\text{O}_3$ formation. The photoelectrochemical (PEC) performance of iron oxide electrodes is compared as a function of surface modification procedure. Platinum was found to be an effective electrocatalyst when incorporated into the bulk of the thermally grown iron oxide during the latter's preparation. This procedure was found to increase the carrier density and to give a more negative flatband potential.

Photoanodes based upon iron oxide are potentially useful materials for the photodecomposition of alkaline aqueous solutions into hydrogen and oxygen (1-3). The nominal bandgap for $\alpha\text{-Fe}_2\text{O}_3$ of ≈ 2.2 eV allows, in principle, utilization of up to 40% of the incident solar radiation for the generation of excited carriers. Iron oxides are also relatively inexpensive and possess good stability in alkaline electrolytes. These materials do, in general, have low quantum yields (e.g., single crystals of $\alpha\text{-Fe}_2\text{O}_3$ at high anodic polarization only exhibit quantum yields of 20%) (4), and have poorly positioned flatband potentials relative to that desirable for hydrogen evolution in the absence of an externally applied bias (4-6). However, when n- and p-doped iron oxides are used to form the corresponding photochemical diode particle, the resulting two-photon process may eliminate the need for an externally applied bias. For such particles, the photogeneration of hydrogen and oxygen was achieved in the absence of an external bias (2).

The photoelectrochemical (PEC) characteristics of iron oxide photoanodes have been found to be highly dependent upon the method used for their preparation. Such preparation techniques have included spray pyrolysis of a methanolic solution of ferric oxalate (7), chemical vapor deposition of iron acetylacetonate (1), anodization of a previously reduced iron electrode (5), thermal oxidation (5, 8-10), and sintering of pressed $\alpha\text{-Fe}_2\text{O}_3$ powders (2, 3, 6, 10, 11). The majority of the literature dealing with iron ox-

ide photoelectrodes has involved the use of the latter two preparation methods. Although the thermal growth of oxides on iron has systematically been investigated in connection with the problem of corrosion (12-23), use of this information in the preparation of $\alpha\text{-Fe}_2\text{O}_3$ photoanodes has been overlooked.

Results presented in the corrosion literature relating to the thermal growth of iron oxides on iron substrates has shown that the formation of a single iron oxide phase may be somewhat difficult to obtain (12-23). From the iron-oxygen phase diagram (12, 17), three oxide phases are present: FeO (wustite), Fe_3O_4 (magnetite), and $\alpha\text{-Fe}_2\text{O}_3$ (hematite), with the FeO phase being thermodynamically unstable below 570°C. For iron heated in the atmosphere below 570°C, oxide growth typically consists of inner Fe_3O_4 and outer $\alpha\text{-Fe}_2\text{O}_3$ layers. Hence, it can be concluded that PEC measurements made on " $\alpha\text{-Fe}_2\text{O}_3$ " are undoubtedly being performed on mixed iron oxides. Since $\alpha\text{-Fe}_2\text{O}_3$ is the photoactive component in such iron oxides, there would be a strong incentive to delineate preparative procedures which maximize its presence. An extensive investigation has been performed on the dependency of thermally grown iron oxide composition on various experimental oxidation parameters and will be discussed in a future paper.

In addition to identifying reproducible methods for the preparation of $\alpha\text{-Fe}_2\text{O}_3$ electrodes, their modification with electrocatalysts was also investigated as an approach to improving PEC performance. Previous work has shown that both Pd (24) and Pt (25) can increase photocurrents realized from $\alpha\text{-Fe}_2\text{O}_3$ electrodes.

^{*} Electrochemical Society Active Member.

¹ Present address: Nalco Chemical Company, Naperville, Illinois 60540.

We wish to report here on PEC performance characteristics for thermally grown α -Fe₂O₃ photoanodes both with and without photoelectrocatalytic effects from platinum introduced during the growth procedure.

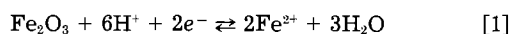
Experimental

Iron foil (0.25 mm thick) (Alfa 99.999%) was used for photoanode preparation. Samples were furnace oxidized in an atmosphere of ultrapure oxygen, which was slowly passed (≈ 25 cm³/min) through an appropriate bubbler to maintain a positive pressure of oxygen inside the alumina furnace tube. Most samples were brought to temperature under high purity argon or helium before the introduction of oxygen. The oxygen atmosphere was maintained during cool-down as well. Although several procedures were followed for the preparation of iron oxide, the greatest photocurrents (and thickest α -Fe₂O₃ layer) were obtained on those samples initially reduced under hydrogen at 600°C for 1/2h. Following this, the general oxidation procedures discussed above were followed.

Current-potential curves were recorded with and without illumination. The most frequently used voltage scan rate was 10 mV/s, which was expected to give current densities differing only slightly from steady-state values. Curves were also recorded under manually chopped illumination to detect transient currents, which have been frequently observed with iron oxide photoanodes. A single-compartment cell was used for all measurements, using a platinum foil counterelectrode and a SCE reference electrode connected via a saturated KCl/agar salt bridge. Illumination of the photoanodes was provided by a General Electric ELH quartz-halogen lamp with light intensity being measured with an Eppley 8-48 pyranometer. Current-voltage measurements were made at light intensities between 0 and 300 mW/cm² using a Stonehart BC 1200 potentiostat connected to a Linear Instruments 8036 X-Y recorder. A Commodore 64 PC interfaced to a HP 7470A plotter was used to reduce the light intensity/exchange current density data. Exchange current densities were obtained from the linear portion of the Tafel plot. Capacitance data for Mott-Schottky plots were obtained at 1000 and 10,000 Hz in 6N KOH electrolyte in a three-electrode cell using a platinum counterelectrode and a SCE reference electrode. A HP-4276A LCZ meter was used to apply a dc bias and to measure the resistance and the phase angle (θ). $1/C$ was then calculated from the relationship: $\theta = \tan^{-1} 1/\omega RC$.

The oxidized iron foil samples were analyzed by reflective powder x-ray diffraction (XRD) using a Phillips vertical powder x-ray diffractometer. The diffraction patterns were matched to ASTM file spectra as well as to spectra obtained from standards.

A cathodic stripping method was used to quantitatively determine the amount of α -Fe₂O₃ present in the thermally grown thin oxide layers. Fe₂O₃ is the most easily reduced Fe oxide, and the application of a cathodic current to an Fe oxide electrode causes the following dissolution reaction to occur



As current is passed, the electrode potential *vs.* a reference is maintained roughly constant until the Fe₂O₃ is consumed, at which time the potential rises to a value required to carry out the next most favorable reduction. This is similar to battery charge/discharge curves, where a potential plateau is generated which specifies the amount of charge utilized in carrying out a given reaction. In this case, the charge passed can then be related to the amount of Fe₂O₃ in the electrode via Eq. [1]

Experimentally, a 50 μ A constant cathodic current was applied to the 0.25 cm² Fe oxide electrodes using either a PAR 173 potentiostat/galvanostat on a Stonehart BC-1200 potentiostat/galvanostat. The iron oxide electrode's potential *vs.* SCE was then monitored as a function of time. The stripping was performed in a single-compartment cell with a Pt counterelectrode, and the cell was thoroughly deaerated with high purity Ar to eliminate the

possibility of the reduction of any dissolved O₂. 0.1M NH₄Cl was used as the electrolyte. The presence of Fe²⁺ was identified by the formation of a bright red complex with 1,10-phenanthroline.

Results and Discussion

From PEC current-voltage curves for α -Fe₂O₃ prepared by thermal oxidation at temperatures between 300° and 800°C under oxygen, it was found that experimental conditions conducive to optimizing α -Fe₂O₃ content required (i) oxidation of iron substrates below 570°C so as to avoid FeO formation, (ii) the maintenance of a high oxygen partial pressure, and (iii) the initial reductive (H₂) pretreatment of the iron substrate prior to its oxidation.

The largest photocurrents were obtained by initially reducing iron substrates under hydrogen at 600°C for 30 min followed by a helium flush prior to the introduction of pure oxygen. Substrate oxidation was typically performed over 6h at 500°C. Somewhat smaller photocurrents were obtained when the hydrogen pretreatment step was omitted (Table I). The growth of the α -Fe₂O₃ layer and the corresponding measured photocurrents correlated well with oxidation time. The samples pretreated with hydrogen and later oxidized for 3h gave higher photocurrents than samples oxidized for 8h with no pretreatment. Thus an increase in the amount of α -Fe₂O₃ (as shown by both the intensity of the α -Fe₂O₃ peaks in the XRD spectra and by cathodic stripping data) (Table II) leads to an increase in the PEC performance of the α -Fe₂O₃ electrodes prepared by controlled thermal oxidation.

Comparison of PEC characteristics for these photoelectrodes with the procedures used for their preparation was performed at three applied anodic potentials, *i.e.*, -300, 0, and +300 mV *vs.* SCE. These results are summarized in Table I. At the slow scan rates used, the light and dark

Table I. Photocurrent and dark current for thermally oxidized iron foil photoanodes at three potentials (2)

Sample no.	Photocurrent/dark current (μ A/cm ²), voltage given <i>vs.</i> SCE		
	At -300 mV	At 0 mV	At +300 mV
1. 500°C (1h)	50/30	110/40	290/50
2. 500°C (3h)	50/30	80/30	450/50
3. 500°C (8h)	30/20	120/30	560/30
4. 500°C ^b (3h)	20/10	140/20	600/20

^a Experimental conditions: 1.0M KOH electrolyte; 100 mW/cm² ELH light intensity; 10 mV/s scan rate; 0.25 cm² anode geometric area.

^b Sample pretreated with hydrogen at 600°C for 30 min.

Table II. Results of Fe₂O₃ determination in thermally oxidized Fe foil photoanodes by cathodic stripping

Heating temperature (°C)	Heating time (h)	Fe ₂ O ₃ mass (μ g) ^a	Fe ₂ O ₃ thickness (μ m) ^b
300	1	109	0.42
300	8	144	0.55
500	3	353(132) ^c	1.35
500	8	504	1.92
500 ^f	3	455(80) ^d	1.74
600	3	372	1.42
Flamed foil	—	66(5) ^e	0.25

^a Equivalent mass based on Eq. [1] and the number of electrons passed during the first potential plateau.

^b Calculated from the mass based on Fe₂O₃ density and an electrode area.

^c Average of eight different electrodes with the standard deviation in parentheses.

^d Average of five different electrodes with the standard deviation in parentheses.

^e Average of four different electrodes with the standard deviation in parentheses.

^f Pretreated hydrogen reduction at 600°C for 30 min.

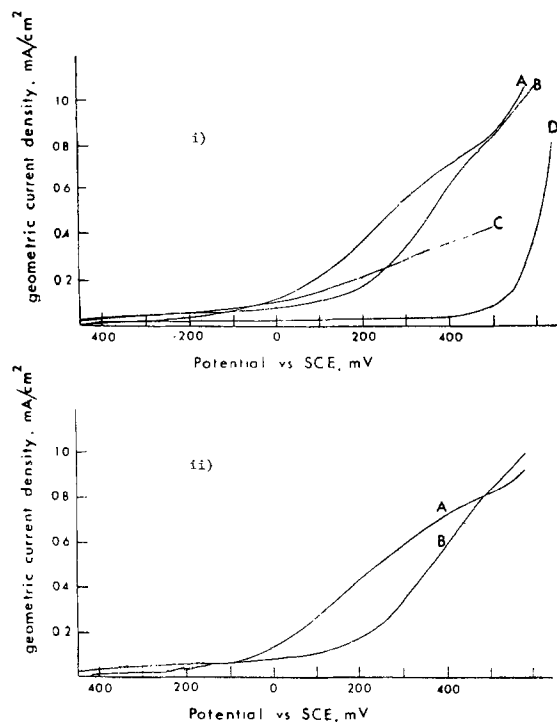


Fig. 1. Comparison of photocurrent-voltage curves for iron oxide photoanodes using various preparation procedures. Electrolyte: 1.0M KOH. Illumination ELH intensity: 100 mW/cm^2 . Scan rate: 10 mV/s . Geometric electrode area: 0.25 cm^2 . i: Furnace oxidized iron foil heated at 500°C for 8h (curve A), 3h (curve B), and 1h (curve C).

current densities were assumed to be steady-state values. A summary of current-voltage curves for iron oxides prepared following varying procedures is shown in Fig. 1.

Figure 1, part i shows the effect of increased oxidation time at 500°C on the photoresponse of the resulting iron oxides. As can be seen, extended oxidation times always gave an improved photoresponse corresponding to the increased presence of $\alpha\text{-Fe}_2\text{O}_3$. The largest photoresponses were observed from iron substrates which were initially reduced under hydrogen prior to furnace oxidation. Comparisons of photoresponse data obtained from an oxidized iron electrode both with and without this initial reduction treatment are shown in Fig. 1, part ii, curves A and B, respectively. The electrode subjected to initial reduction possessed approximately twice the photocurrent density at 200 mV vs. SCE than did the untreated substrate. XRD data indicated a particularly well-defined $\alpha\text{-Fe}_2\text{O}_3$ layer in the former sample. It thus appears that initial surface reduction of the iron substrate with hydrogen enhances the later growth of $\alpha\text{-Fe}_2\text{O}_3$, giving improved PEC performance.

From previously reported literature, flatband potential (3, 4, 26) measurements on $\alpha\text{-Fe}_2\text{O}_3$ photocurrents might be anticipated for electrode potentials up to -300 mV vs. SCE . But, as Table I shows, negligible values were observed in this potential region for all samples prepared. Thermally oxidized iron foils have shown the need for larger bias voltages to attain significant photocurrents when compared to sintered samples (5, 9, 10, 27).

For photoanodes subjected to chopped illumination, significant transient currents were observed. Figure 2 demonstrates this typical behavior for an iron substrate electrode oxidized for 8h at 500°C . Such current transients seem to be a common feature of thermally grown iron oxide films (5, 9, 10). These transients have been attributed to either recombination or cathodic back-reaction of the photogenerated species (10). If the observed transients are due to a cathodic back-reaction and the kinetics of the cathodic back-reaction could be reduced, improvement in overall PEC performance might be realized.

Another explanation for these transient signals is that the thermally grown oxides consist of a mixture of two or more oxides. Fe_3O_4 is reported to be a p-type semicon-

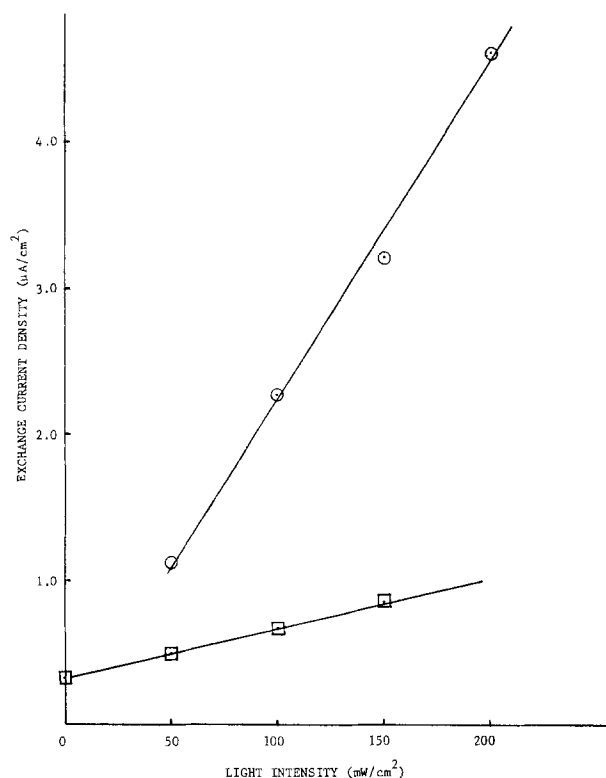


Fig. 2. Plot of exchange current density vs. light intensity for $\alpha\text{-Fe}_2\text{O}_3$ (squares) and platinum-modified $\alpha\text{-Fe}_2\text{O}_3$ (circles) in 6N KOH.

ductor (18, 21), and in all the oxide films investigated it was present along with $\alpha\text{-Fe}_2\text{O}_3$. Therefore, p-n junctions between Fe_3O_4 and $\alpha\text{-Fe}_2\text{O}_3$ may be present. Photo-produced electrons in the $\alpha\text{-Fe}_2\text{O}_3$ that are transferred to a Fe_3O_4 interface may cause an increase in the p-n potential barrier. Thus, the anodic transient currents observed may be sufficient to charge the p-n barrier before a significant photocurrent is obtained under steady illumination. Upon removal of illumination, the cathodic transients observed may be a result of discharging the potential barrier generated under illumination. It is significant that sintered $\alpha\text{-Fe}_2\text{O}_3$ photoanodes, where Fe_3O_4 is absent (1, 10), do not possess current transients proportional to light intensity as observed with thermally grown materials (10).

It has been previously shown that the presence of electrocatalysts of the platinum group metals can significantly improve the PEC performance of III-V photoelectrodes (28, 29). Surface modification of $\alpha\text{-Fe}_2\text{O}_3$ with palladium (24) or platinum (25) has also led to improvements in photoanode performance. In work performed here, the electrochemical deposition of platinum onto an iron substrate prior to the subsequent formation of $\alpha\text{-Fe}_2\text{O}_3$ was found to reduce these transient cathodic currents. Here electrode preparation involved the initial electrochemical deposition of $\approx 100\text{\AA}$ platinum from a 0.1M chloroplatinic acid solution followed by thermal oxidation. As previously discussed, the influence of incorporating platinum in this manner can be seen by reference to the current voltage curves in Fig. 3A and 3B for modified and unmodified electrodes, respectively.

To gain some insight into the electrocatalytic effect of platinum incorporated into the bulk of thermally grown iron oxide electrodes, current-voltage curves were obtained in 6N KOH. Figure 4 shows Tafel plots for $\alpha\text{-Fe}_2\text{O}_3$ (curve a) in the dark and (curve b) under 100 mW/cm^2 illumination. Under illumination, the equilibrium potential was shifted -70 mV cathodic of that in the dark. The electrode was initially potentiostated in the region of its illuminated open-circuit potential. The electrode potential was then adjusted until no current passed.

The hole exchange current densities are summarized in Table III and are shown in Fig. 5. For photoanodes

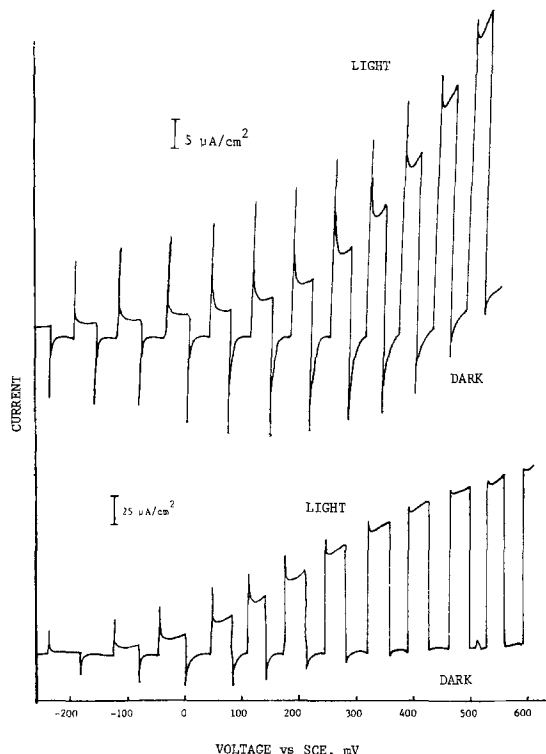


Fig. 3. A: Current-voltage curve for Fe_2O_3 flag in 6N KOH. B: Current-voltage curve for Fe_2O_3 with platinum in 6N KOH. (Platinum deposited on iron foil prior to oxidation.)

modified by platinum, larger hole exchange current densities were found. For both of these electrodes, a linear relationship was observed between light intensity and hole exchange currents. For photoanodes, the relationship between the hole exchange current density and corresponding overpotential is given by relationship [2] (30)

$$i_p = i_{p0} \left[\frac{p_s^*}{p_s} \exp\left(\frac{\alpha_v \rho_e \eta}{kT}\right) - \exp\left(-\frac{\alpha_v \rho_e \eta}{kT}\right) \right] \quad [2]$$

where i_{p0} is the valence-band exchange current, and ρ_s^* and ρ_s are the hole concentrations at the surface of the semiconductor at equilibrium and nonequilibrium, respectively.

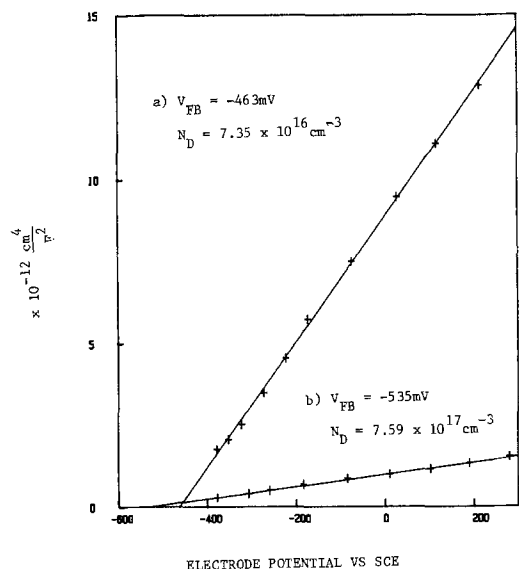


Fig. 4. Mott-Schottky plot for (curve a) iron oxide photoanode prepared by initially depositing 200Å Pt onto Fe substrate followed by furnace oxidation at 500°C for 6h under oxygen and (curve b) iron oxide photoanode prepared by furnace oxidation of iron substrate at 500°C for 6h under oxygen without platinum pretreatment.

Table III. Exchange current densities as a function of light intensity for $\alpha\text{-Fe}_2\text{O}_3$ and platinum-modified $\alpha\text{-Fe}_2\text{O}_3$ electrodes

Electrode	Intensity (mW/cm ²)	i_0 (μA/cm ²)
$\alpha\text{-Fe}_2\text{O}_3$	0	0.313
	50	0.492
	100	0.663
	150	0.843
	200	—
Pt electrochemically deposited onto $\alpha\text{-Fe}_2\text{O}_3$	0	—
	50	1.12
	100	2.27
	150	3.2
	200	4.61
Pt incorporated into $\alpha\text{-Fe}_2\text{O}_3$	0	3.42
	50	5.45
	100	8.15
	150	64.77
	200	44.96
	250	75.21

ρ is the IR overpotential associated with the electrolyte. From this relationship it is clear that an increase in the ratio ρ_s^*/ρ_s (via illumination) will result in an apparent increase in i_{p0} value. Thus, the linear relationship observed in Fig. 5 would be expected. The enhanced hole exchange currents seen for platinum-modified $\alpha\text{-Fe}_2\text{O}_3$ photoanodes are, therefore, expected to be due in part to the electrocatalytic effect of the incorporated platinum. It is not clear, however, why the slope of the hole exchange current line for the platinum-modified $\alpha\text{-Fe}_2\text{O}_3$ electrode is greater than that for the unmodified $\alpha\text{-Fe}_2\text{O}_3$ electrode. Thus, the question remains as to whether the role of the platinum introduced onto the iron oxide is mainly an electrocatalytic effect promoting the oxygen evolution reaction or whether such photoanode modifications also effect changes in their solid-state properties.

To gain some insight into this question, Mott-Schottky plots were performed on platinum-modified and unmodified $\alpha\text{-Fe}_2\text{O}_3$ electrodes. For platinum incorporated into the iron oxide lattice during the thermal growth procedure, it might be expected that the platinum would

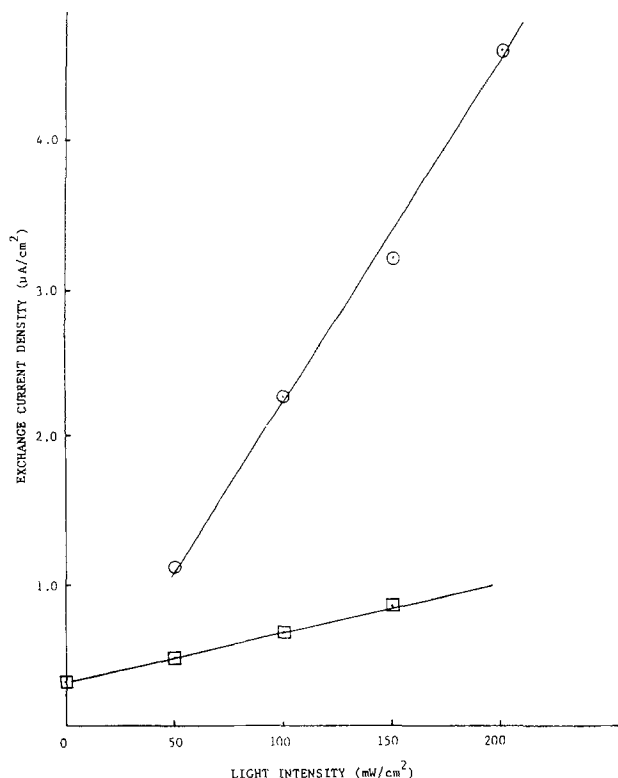


Fig. 5. Plot of the hole exchange current density vs. light intensity for $\alpha\text{-Fe}_2\text{O}_3$ (squares) and platinum surface-modified $\alpha\text{-Fe}_2\text{O}_3$ (circles) in 6N KOH.

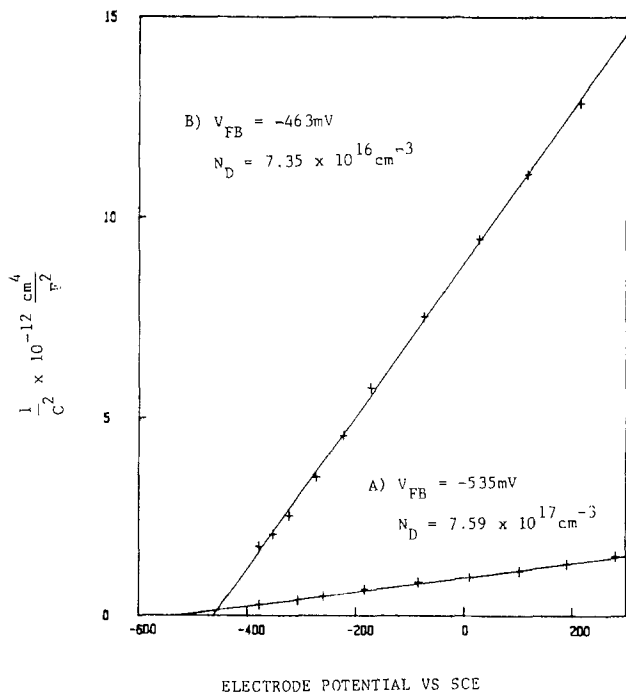


Fig. 6. Mott-Schottky plot for (curve A) iron oxide photoanode prepared by initially depositing 200Å Pt onto Fe substrate followed by furnace oxidation at 500°C for 6h under oxygen, and (curve B) iron oxide photoanode prepared by furnace oxidation of iron substrate at 500°C for 6h under oxygen without platinum pretreatment. Both electrodes measured at 1000 Hz in 6N KOH.

be in the +4 oxidation state. Under such circumstances, the number of carriers would be expected to increase. Mott-Schottky plots for the platinum-modified and -unmodified α -Fe₂O₃ photoanodes are compared in Fig. 6. Little frequency dispersion was observed for measurements taken between 100 and 10,000 Hz. In contrast to Mott-Schottky plots obtained by others (5, 11), the curves obtained here are linear over a relatively large voltage range and do not exhibit deviations ca. \approx 0.3V anodic of the flatband potential. It has been suggested that the observed curvature in polycrystalline α -Fe₂O₃ Mott-Schottky plots may be due to inhomogeneous doping concentration (2). It may be that, in the results discussed here, hydrogen pretreatment and subsequent controlled thermal oxidation may result in more homogeneous intrinsic doping, thus giving the observed linear Mott-Schottky plots.

Comparing the iron oxide-modified (Fig. 6A) and -unmodified (Fig. 6B) electrodes, we see an increase in the carrier density from 7.35×10^{16} to $7.59 \times 10^{17}/\text{cm}^2$ after incorporation of platinum. This is probably a consequence, as discussed earlier, of the Pt⁴⁺ acting as a donor when incorporated into a Fe⁺³ site. The flatband potential was also shifted to more negative values for platinum-modified electrodes. From current-voltage curves performed on this electrode, significantly higher exchange current densities were obtained (see Table III) than, for example, with iron oxide electrodes surface modified by the electrochemical deposition of platinum after thermal growth of the oxide. Of course, the predominant phenomenon here may still be electrocatalytic in nature, but certainly the incorporation of platinum within the bulk of the thermally grown iron oxide phase appears to give improved PEC performance over the surface-deposited catalyst.

Comparison of the α -Fe₂O₃ electrode current densities prepared by hydrogen pretreatment followed by controlled thermal oxidation under O₂ between 500° and 600°C with previous work by others is, however, somewhat difficult to achieve due to the disparity under which photocurrents are measured (i.e., different electrolytes, lack of light intensity data, noninclusion of current densities, etc.). However, Table IV compares photocur-

Table IV. Comparison of photocurrent densities for α -Fe₂O₃ photoanodes prepared under various conditions^a

Conditions	Photocurrent densities ($\mu\text{A}/\text{cm}^2$)
300°C/8h	100
500°C/1h	290
500°C/3h	450
500°C/8h	560
500°C/3h ^b	600
Flamed foils ^c	190

^a Experimental measurement of current densities were carried out in 1.0M KOH at 100 mW/cm² ELH intensity. Scan rate = 10 mV/s; electrode area = 0.25 cm².

^b Initial reduction under Hz at 600°C for 30 min prior to oxidation.

^c Foils were heated with a neutral gas/air torch until bright red for 5 min and then quenched in air.

rent densities for photoanodes prepared under various conditions during this work. From these results, it is clear that hydrogen pretreatment of the electrode at 600°C followed by oxidation at 500°C produces the highest current densities for thermally grown α -Fe₂O₃ electrodes. In addition, bulk modification of the thermally grown iron oxide with platinum during oxide growth seems to result in significant improvement in PEC performance. The incorporated platinum appears to act as a donor species, resulting in an increase in carrier density and a shift of the flatband potential to more negative values.

Acknowledgment

Funding by the Gas Research Institute under Contract no. 5082-260-0671 is gratefully acknowledged.

Manuscript submitted Nov. 16, 1984; revised manuscript received March 1, 1985.

Eltron Research Incorporated assisted in meeting the publication costs of this article.

REFERENCES

- K. L. Hardee and A. J. Bard, *This Journal*, **123**, 1024 (1976).
- J. E. Turner, M. Hendewerk, J. Parmeter, D. Neiman, and C. A. Somorjai, *ibid.*, **131**, 1777 (1984).
- J. H. Kennedy and K. W. Frese, Jr., *ibid.*, **125**, 709 (1978).
- R. K. Quinn, R. D. Nasby, and R. J. Banghman, *Mater. Res. Bull.*, **11**, 1011 (1976).
- S. M. Wilhelm, K. S. Yun, L. W. Ballenger, and N. Hackerman, *This Journal*, **126**, 419 (1979).
- C. Leygraf, M. Hendewerk, and G. A. Somorjai, *J. Catal.*, **78**, 341 (1982).
- A. S. N. Murthy and K. S. Reddy, *Mater. Res. Bull.*, **19**, 241 (1984).
- P. Iwanski, J. S. Curran, W. Gissler, and R. Memming, *This Journal*, **128**, 2128 (1981).
- L. S. R. Yeh and N. Hackerman, *ibid.*, **124**, 833 (1977).
- J. S. Curran and W. Gissler, *ibid.*, **126**, 56 (1979).
- J. H. Kennedy, R. Shinar, and J. P. Ziegler, *ibid.*, **127**, 2307 (1980).
- F. Hauffe, "Oxidation of Metals," Plenum Press, New York (1965).
- O. Kubaschewski and B. E. Hopkins, "Oxidation of Metals and Alloys," Butterworths Scientific Publications, London (1953).
- D. Caplan and M. Cohen, *Corros. Sci.*, **6**, 321 (1966).
- G. P. Huffman and H. H. Polgurski, *Oxid. Met.*, **15**, 323 (1981).
- R. J. Hussey and M. Cohen, *Corros. Sci.*, **11**, 713 (1971).
- M. H. Davies, M. T. Simnad, and C. E. Birchenall, *J. Metals*, **3**, 889 (1951).
- W. E. Boggs, R. H. Kachik, and G. E. Pellissier, *This Journal*, **112**, 539 (1965).
- R. J. Hussey, D. Caplan, and M. J. Graham, *Oxid. Met.*, **15**, 241 (1981).
- R. J. Hussey, C. I. Sproule, D. Caplan, and M. J. Graham, *ibid.*, **11**, 65 (1977).
- W. E. Boggs, R. H. Kachik, and G. E. Pellissier, *This Journal*, **114**, 32 (1967).
- M. J. Graham and M. Cohen, *ibid.*, **116**, 1430 (1969).
- D. E. Davies, U. R. Evans, and J. N. Agar, *Proc. R. Soc.*

London, Ser. A, **225**, 443 (1954).

24. T. Osaka, K. Ejiri, and N. Hirota, *This Journal*, **131**, 1571 (1984).
 25. A. F. Sammells and P. G. P. Ang, *ibid.*, **126**, 1831 (1979).
 26. J. H. Kennedy and R. W. Frese, Jr., *ibid.*, **125**, 723 (1978).
 27. R. M. Candea, *Electrochim. Acta*, **26**, 1803 (1981).
 28. A. Heller, *Acc. Chem. Res.*, **14**, 154 (1981).
 29. P. G. P. Ang and A. F. Sammells, *This Journal*, **131**, 1462 (1984).
 30. W. L. Ahlgren, *ibid.*, **128**, 2123 (1981).

Raman Spectroscopy of Anodic Oxide Films on HgTe

Masao Sakashita,¹ Toshiaki Ohtsuka, and Norio Sato*

Faculty of Engineering, Hokkaido University, Sapporo, Japan

ABSTRACT

Laser Raman spectroscopic measurements of the anodic oxide film formed on HgTe in aqueous solutions reveal the characteristic Raman bands that appear at 422 and 684 cm^{-1} . These bands, which are different from those of crystalline HgTeO₃ and TeO₂ powders, may be attributed to a complex oxide of HgTe₂O₅ or an amorphous oxide of TeO₂ that might be formed in anodic oxidation. The heating effect on the anodic oxide film due to a focused laser beam is also discussed.

Surface passivation of compound semiconductors Cd_xHg_{1-x}Te (CMT) is of considerable importance in their utilization as photoconductive devices. One of the most common methods for surface passivation is anodic oxidation (1). In previous papers, the electrochemical reaction and the anodic oxide films of CMT and HgTe have been investigated by using x-ray photoelectron spectroscopy (XPS) and rotating ring-disk electrode (2-4). Furthermore, there have been a few papers dealing with composition of the anodic oxide (5-7). In recent years, laser Raman scattering spectroscopy has proved useful in studying the structure and composition of surface oxide films on metals. The Raman scattering spectra of bulk powder of HgTeO₃, CdTeO₃, and TeO₂ have been measured by Rhiger and Kvaas (8). In this work, a laser Raman backscattering technique is applied to the measurement of the anodic oxide films on HgTe.

Raman scattering measurements were made with a JASCO 800-T triple monochromator, and an Ar ion laser beam of 514.5 nm wavelength was used for excitation. All measurements were made in the backscattering geometry with an incidence angle of 70°. In order to minimize the effect of sample heating, a slightly defocused laser beam with an incidence power level of 25 mW was used for spectrum measurements. An attempt was, however, made to examine the heating effect on the spectra upon exposure of a focused beam with an incident power level of 50 mW.

The material studied was single crystal of HgTe with the surface of (100) plane. After electrochemical reduction of the mechanically polished surface, the material was anodically oxidized at a given electrode potential. The anodization was carried out in solution of sodium acetate-acetic acid, sodium borate-boric acid, and 0.1M KOH in 90% ethylene glycol-10% water. The procedure for cathodic reduction and anodic oxidation has been described in detail in a previous paper (2).

Figures 1 and 2 show the Raman scattering spectra of HgTe surfaces reduced at -0.6V vs. SHE (spectrum a) and oxidized at 3.0V (spectrum b) in a sodium acetate-acetic aqueous solution of pH 4.9. The thickness of the oxide film formed at 3.0V was found to be about 200 nm from electrochemical coulometric measurements. Spectrum a shows no characteristic bands, revealing that the reduced surface is free from any oxides and that HgTe is a weak scatterer for Raman effects. From spectrum b in Fig. 1 and 2, the Raman bands of the oxidized surface are found at the position of 422 and 684 cm^{-1} . These positions of the bands are not identical to those for TeO₂ shown in spectrum c. Furthermore, the characteristic band at 326 cm^{-1}

for HgO is not observed in spectrum b for the anodic oxide. The Raman bands at 422 and 684 cm^{-1} cannot be used to clearly identify the composition of the anodic oxide. It is, however, likely that the anodic oxide, which has previously been represented by TeO₂-0.5HgO (2), is not a mixture of TeO₂ and HgO, but is a complex oxide such as HgTe₂O₅. Such a complex oxide has been suggested from the results by XPS and ring-disk electrode measurements (2). One may also explain the Raman bands at 422 and 684 cm^{-1} to correspond to those of amorphous TeO₂, because the amorphous oxide may exhibit the Raman band different from that of the crystallized oxide.

The spectrum with the same Raman bands as those of spectrum b in Fig 1 and 2 was obtained for the anodic oxide films with the composition of TeO₂-0.7HgO formed in the sodium borate-boric acid aqueous solution of pH 8.4 and also for the film with the composition of TeO₂-1.0HgO formed in the basic ethylene glycol solution. It appears, therefore, that the Raman scattering spectrum is

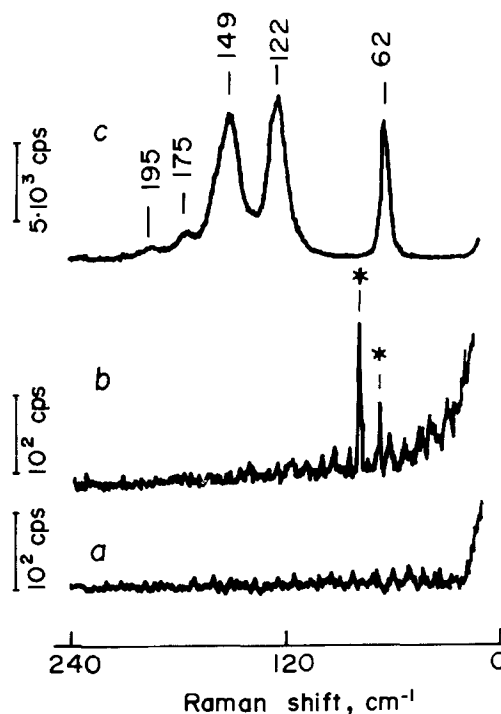


Fig. 1. Raman spectra (10-240 cm^{-1}) for HgTe surfaces reduced at -0.6V vs. SHE (a) and oxidized at 3.0V (b) in pH 4.9, and for TeO₂ powder (c). The monochromator bandpass was 1.1 cm^{-1} . The peaks marked by asterisks are emission lines of Ar ion laser.

*Electrochemical Society Active Member.

¹Present address: Nippon Steel Corporation, Research and Development Laboratories I, 1618 Ida, Nakahara-ku, Kawasaki, Japan.

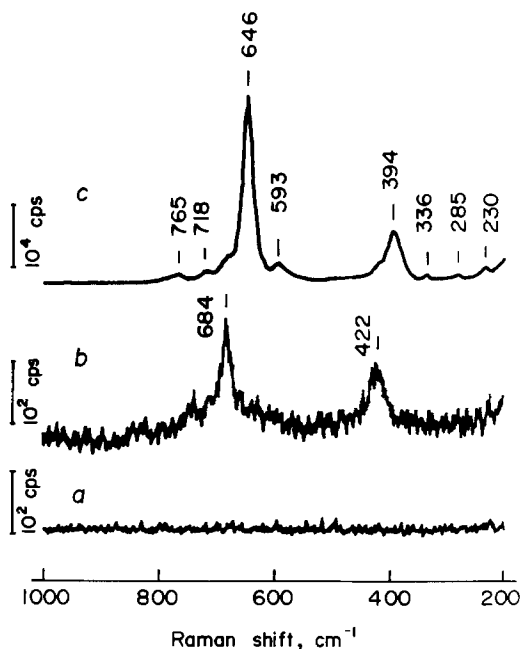
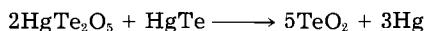


Fig. 2. Raman spectra (200-1000 cm^{-1}) for HgTe surfaces and TeO_2 powder. The monochromator bandpass was 4 cm^{-1} . Notation a, b, and c are those shown in Fig. 1.

incapable of distinguishing the composition difference in the anodic oxide films on HgTe. The characteristic positions of bands, however are markedly different from those reported for bulk powder of HgTeO_3 : 41, 59, 642, and 703 cm^{-1} (8). It is thus likely that the anodic oxide film on HgTe possesses a characteristic structure different from that of the thermally produced bulk oxide. Such a discrepancy of the Raman scattering spectrum was also observed between the oxide film on CdTe (9) and the bulk oxide CdTeO_3 (8).

Figure 3 shows the Raman scattering spectra of $\text{TeO}_2 \cdot 0.5\text{HgO}$ (or HgTe_2O_5) on HgTe measured after exposure of a focused laser beam of 50 mW. In addition to weak bands for the anodic oxide, the Raman scattering bands corresponding to TeO_2 are observed, indicating that TeO_2 is formed by the focused laser beam. This formation of TeO_2 may be represented by the following disproportionation reaction in analogy with the reaction between HgTeO_3 and HgTe



This thermal instability of HgTe_2O_5 and HgTeO_3 requires careful precaution in conducting the Raman spectroscopic studies of the oxide film on HgTe and CMT to eliminate the heating effects due to incident beam.

In summary, the characteristic Raman bands for the anodic oxide films on HgTe are found to be 68, 79, 422, and 684 cm^{-1} from determination by using a defocused laser beam with an incidence power level of 25 mW.

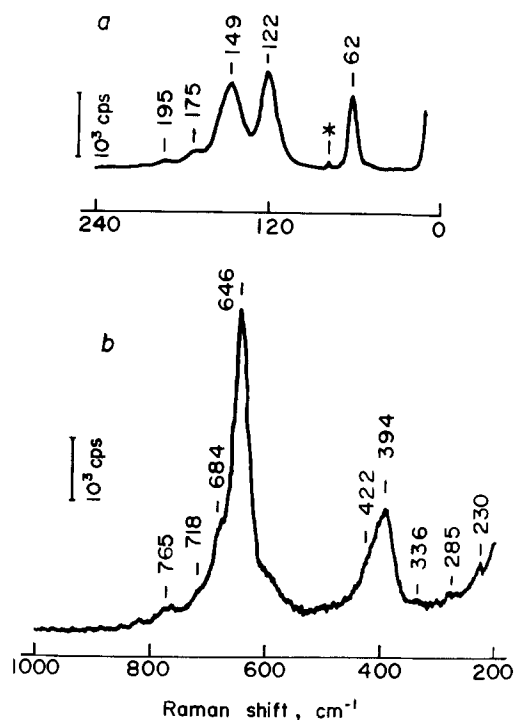


Fig. 3. Raman spectra of the anodic oxide on a HgTe surface after irradiation of a focused laser beam of 50 mW. Raman spectra were measured by using a defocused laser beam of 25 mW with the monochromator bandpass 1.1 cm^{-1} (a) and 4.0 cm^{-1} (b).

Acknowledgments

The authors wish to thank Dr. K. Uosaki and Mr. N. Goto for their assistance. This work was supported by the Japanese Ministry of Education and Culture under Grant in Aid for Scientific Research (Project no. 57430015).

Manuscript submitted Dec. 3, 1984; revised manuscript received March 6, 1985.

Hokkaido University assisted in meeting the publication costs of this article.

REFERENCES

1. P. C. Catagnus and C. T. Baker, U.S. Pat. 3,977,618.
2. M. Sakashita, H.-H. Strehblow, and M. Bettini, *This Journal*, **129**, 1710 (1982).
3. M. Sakashita, H.-H. Strehblow, and M. Bettini, *ibid.*, **129**, 739 (1982).
4. M. Sakashita, B. Lochel, and H.-H. Strehblow, *J. Electroanal. Chem.*, **140**, 75 (1981).
5. G. D. Davis, T. S. Sun, S. P. Buchner, and N. B. Byer, *J. Vac. Sci. Technol.*, **19**, 75 (1981).
6. P. Morgan, J. A. Siberman, I. Lindau, and W. E. Spicer, *ibid.*, **21**, 161 (1982).
7. D. R. Rhiger and R. E. Kvaas, *ibid.*, **21**, 168 (1982).
8. D. R. Rhiger and R. E. Kvaas, *J. Vac. Sci. Technol. A*, **1**, 1712 (1983).
9. K. Uosaki, Private communication.

pH Measurements of High Temperature Aqueous Environments with Stabilized-Zirconia Membranes

S. Hettiarachchi,¹ P. Kedzierzawski,² and D. D. Macdonald*¹

Department of Metallurgical Engineering, The Ohio State University, Columbus, Ohio 43210

ABSTRACT

A pH sensor has been developed for precise pH measurements of high temperature aqueous solutions based on a yttria-stabilized zirconia (9% Y_2O_3) membrane electrode with a Hg/HgO solid-state internal element. In these investigations, the use of calculated pH values in evaluating the performance of the sensor has been eliminated. The excellent one-to-one correlation obtained between the potential of the sensor and a hydrogen reference electrode measured against a Ag/AgCl, 0.1M KCl reference electrode confirms that the pH sensor behaves in a Nernstian manner. The sensor is capable of withstanding high temperatures and pressures and is unaffected by hydrogen and oxygen gases and chloride ion concentration. The electrode remains stable over long periods of time, thus showing its potential use in monitoring the pH of waters in nuclear reactors, geothermal brines, and other high temperature aqueous systems.

A considerable amount of research has been carried out during the past decade to develop electrodes to measure the pH ($= -\log a_{H^+}$) of high temperature aqueous systems (1-12). The failure of the glass electrode to operate at temperatures as high as 250°-300°C necessitated the development of pH sensors for use at elevated temperatures. Such a sensor, if developed, would have a tremendous practical impact in its applications, particularly in geothermal brines and nuclear and fossil-fueled power reactors.

Recently, Niedrach (13, 14) and Macdonald and Tsuruta (15) described the use of a yttria-stabilized zirconia (YSZ) membrane for the measurement of pH of aqueous solutions at temperatures as high as 300°C. In these studies, membrane electrodes with both aqueous and Cu/Cu₂O internal reference elements have been used. These membrane electrodes have been found to exhibit a Nernstian pH response at elevated temperatures, and appear to be ideally suited for the measurement of the pH of a wide variety of systems, including those containing other redox and/or easily reduced species.

Although the preliminary studies demonstrated the potential use of YSZ membranes as pH sensors, their apparent lack of high precision as demanded by many research and control applications of high temperature technology led us to investigate the possible use of Ag/Ag₂O and Hg/HgO as internal references in addition to Cu/Cu₂O. We have also attempted to eliminate the use of calculated pH values based on dissociation constant data to evaluate the performance of these membrane electrodes. In order to achieve this second objective, the potential of the sensor and the potential of a hydrogen reference electrode were measured against an external pressure balanced Ag/AgCl, 0.1M KCl reference electrode (RE) in systems containing known amounts of dissolved hydrogen. The one-to-one correlation obtained between these measurements (16) proves that the zirconia 9% Y_2O_3 pH sensors constructed by us follow a Nernstian behavior, as does the hydrogen electrode with respect to the hydrogen ion activity.

Experimental

Electrode system.—The electrode system (15) used in these studies consists of an external pressure-balanced Ag/AgCl, 0.1M KCl RE (17) a bright platinum electrode, and a pH-sensitive ZrO₂ (9% Y_2O_3) membrane electrode, all fitted to the autoclave containing the buffer solution. The solution was saturated with H₂ gas at 25°C before its entry into the autoclave. Thus the platinum electrode in equilibrium with H₂ served as an internal hydrogen electrode. A bright platinum electrode was used in these stud-

ies instead of a platinum black electrode because they both gave the same potential response with respect to RE.

The upper part of the reference electrode, where the Ag/AgCl active element is located, was cooled by air in order to avoid the thermal degradation of AgCl.

The zirconia membrane electrodes were constructed by filling about 1 in. of the zirconia tube (4 in. long, 1/4 in. od, and 5/32 in. id) with a metal/metal oxide mixture (Cu/Cu₂O, Ag/Ag₂O, or Hg/HgO). This acted as the internal reference junction of the sensor. A mild steel conducting wire embedded in this mixture served as the contact lead from the sensor. The upper part of the sensor was sealed with a Teflon insert and the sensor electrode was then introduced into a tightly fitting Teflon tube, leaving the bottom 1 in. of the sensor (active region) exposed. The sensor was then fitted to a Conax Type EG-125 Gland with a Teflon seal, followed by a steel ferrule. Care was taken to isolate the sensor from the Conax Gland to prevent any form of shunting.

A schematic of the autoclave test cell used in these studies appears elsewhere (15).

Test solutions.—Test solutions were prepared by mixing various amounts of boric acid and lithium hydroxide solutions of varying concentrations. Experiments were also performed with 0.01M H₃PO₄, 5×10^{-3} M and 5×10^{-4} M H₂SO₄, and 0.01M H₃PO₄ + 0.001M NaOH. Doubly distilled water and reagent-grade chemicals were used for the preparation of all solutions.

Before each test run, deaeration was accomplished by purging the solution in the reservoir with purified nitrogen gas for 2h. In experiments where a platinum electrode was used as a hydrogen reference, purified hydrogen gas was used for deaeration of the solution instead of nitrogen.

Experimental procedure.—All potentials were measured using a Keithley 614 electrometer having an input impedance of $5 \times 10^{13}\Omega$. Measurements were made on both the pH sensor electrode and the hydrogen electrode with respect to the same RE. Measured potentials were corrected for isothermal liquid junction potentials using the Planck-Henderson theory (18), and the data reported by Macdonald *et al.* (1). The correction terms varied between -5 and +25 mV. No corrections were made for the thermal diffusion potentials at this stage as this would not alter the slopes of the experimental plots reported in this paper.

Experiments were performed in the temperature range 125°-275°C at 25°C intervals. At each temperature, the potential was allowed to attain a stable value to within ± 2 mV at temperatures $>175^\circ\text{C}$ and ± 3 mV at temperatures $<175^\circ\text{C}$ about a mean value. At higher temperatures ($>175^\circ\text{C}$), this required less than a minute while at lower temperatures the stability was achieved within 5 min.

Since the system was found to be sensitive to static charge, all measuring cables and electrode assemblies were placed in a Faraday cage.

*Electrochemical Society Active Member.

¹Present address: SRI International, Chemistry Laboratory, Menlo Park, California 94025.

²Permanent address: Institute of Physical Chemistry, Polish Academy of Sciences, 01-224 Warsaw, Poland.

Results and Discussion

Figures 1 and 2 illustrate two of the typical potential pH (calculated) variations observed for sensors measured against RE for temperatures from 125° to 275°C. The calculated pH values used in these experiments were obtained from both published (1, 19) and unpublished data (20). It must be noted that these values have been calculated using dissociation constants for acids and bases and the mean activity coefficients for various ions (1, 5, 19-22).

The pH sensors used in the present studies contained either Ag/Ag₂O or Hg/HgO as internal references. Sensors with the Cu/Cu₂O internal reference showed irreproducible results. This is attributed to the poor electrical contact obtained with this mixture, as well as to the relative instability of Cu₂O when compared with Ag₂O and HgO. The stability of the Cu/Cu₂O and the Ag/Ag₂O mixtures was tested by using them as internal references inside the membranes under experimental conditions for ten test runs, and thereafter examining the resulting mixtures by x-ray diffraction and comparing these data with the x-ray diffraction data of Cu/Cu₂O and Ag/Ag₂O mixtures heated in a furnace at 275°C for 12h. These studies confirmed that Cu₂O underwent gradual thermal oxidation to CuO inside the membrane, while Ag₂O underwent gradual thermal decomposition to Ag. Hence, even though the sensors with Ag/Ag₂O internals performed well, all studies reported in this paper, unless otherwise stated, were conducted with sensors having Hg/HgO internal reference electrodes, because of the thermodynamic stability of HgO at temperatures below 500°C (23).

As is clearly seen from Fig. 1 and 2, the largest scatter in the results was observed in weakly acidic solutions (pH = 2.5-5.5): namely, for 5 × 10⁻⁴M H₂SO₄, 0.01M H₃PO₄, and 0.01M H₃PO₄ + 0.001M NaOH. It must be emphasized that, for these solutions, the available thermodynamic data are not sufficient to estimate their pH values to an accuracy better than ±0.5 of a pH unit. Even in the case of the LiOH-B(OH)₃ systems, recent work (1) indicates that the calculated pH values at elevated temperatures may also be in error due to uncertainties in the dissociation constant for boric acid. The 5 × 10⁻⁴M H₂SO₄ solution, in turn, suffers from the disadvantage that, being a poor buffer, corrosion processes occurring inside the autoclave could offset the pH of the system considerably. These two

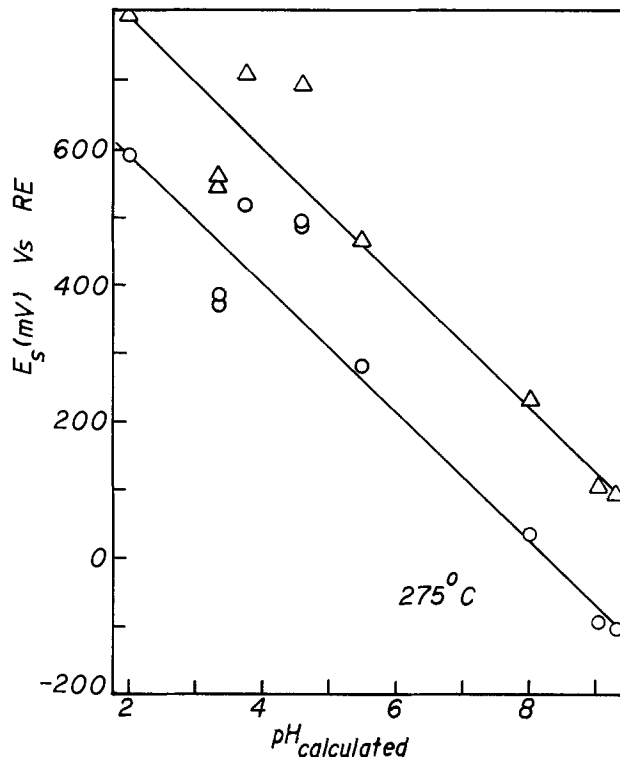


Fig. 2. Variation of E_{sensor} with calculated pH at 275°C. Triangles: Ag/Ag₂O internal. Circles: Hg/HgO internal.

reasons possibly explain the observed deviation from the linear behavior in the $E_{\text{sensor}}/\text{pH}$ (calculated) diagrams for the above solutions.

The experimental slopes of the $E_{\text{sensor}}/\text{pH}$ plots over the temperature range 125°-275°C, calculated by linear regression analysis, are listed in Table I together with the theoretical values ($-2.303RT/F$). The linearity of this variation was established by the near-unity regression coefficients obtained. The experimental slopes with the Hg/HgO internal reference deviate from the theoretical slopes by about 11% at lower temperatures (e. g., 125°C), and gradually decrease to less than 5% at higher temperatures (e.g., > 225°C), the theoretical slopes being always greater than the experimental slopes.

The scatter observed in the $E_{\text{sensor}}/\text{pH}$ plots (Fig. 1 and 2) and the observed deviation in the experimental slopes of these plots are attributed to the uncertainty of the calculated pH values, rather than to the nature and the performance of the electrodes.

In order to test this hypothesis and to avoid uncertainties associated with the calculated pH values, experiments were repeated in which the potential of the sensor and the potential of an internal hydrogen reference electrode (H₂, Pt/H⁺_{ac}) were simultaneously monitored with respect to Ag/AgCl, 0.1M KCl RE. When these potential values were plotted one against the other, an excellent one-to-one correlation over the temperature range 125°-275°C was obtained. Figure 3 illustrates an example of

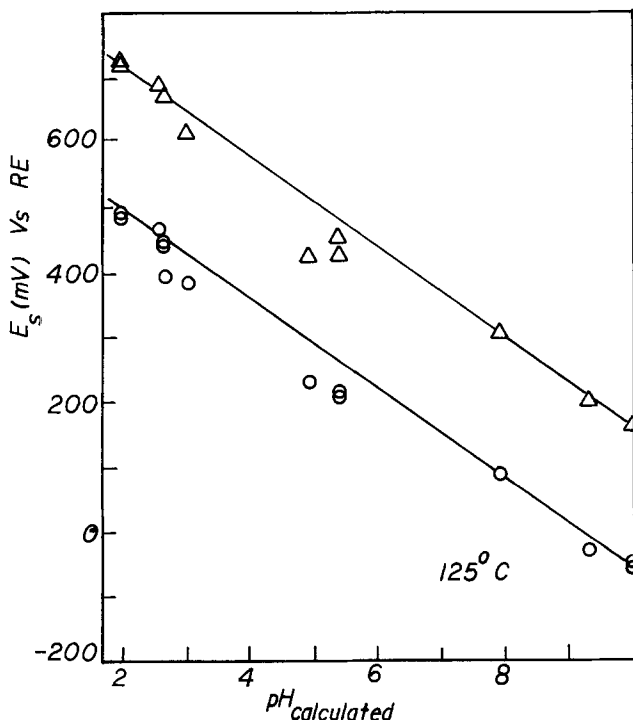


Fig. 1. Variation of E_{sensor} with calculated pH at 125°C. Triangles Ag/Ag₂O internal. Circles: Hg/HgO internal.

Table I. Comparison of experimental and theoretical slopes of E_{sensor} vs. pH (calculated) plots at various temperatures with Ag/Ag₂O and Hg/HgO as internal reference electrodes

Temperature (°C)	Theoretical slope (mV/pH)	Experimental slope (mV/pH)	
		Ag/Ag ₂ O	Hg/HgO
125	- 79	- 71.4	- 70.1
150	- 84	- 77.8	- 75.8
175	- 89	- 81.7	- 82.2
200	- 94	- 87.4	- 87.0
225	- 99	- 95.8	- 94.0
250	-104	- 97.4	-100.4
275	-109	-102.7	-107.9

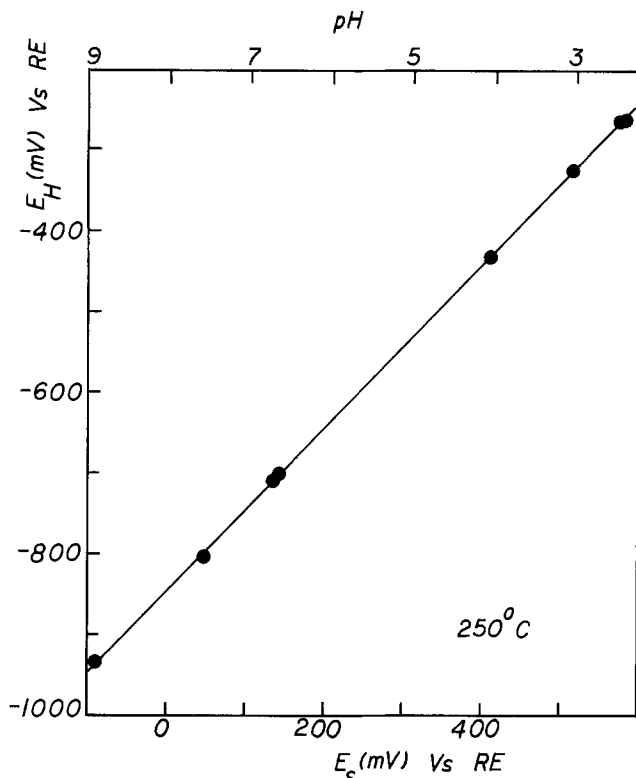
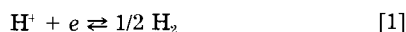


Fig. 3. A typical example of a one-to-one correlation observed between the hydrogen electrode potential (E_H) and E_{sensor} at 250°C along with the actual pH of the system.

such a typical plot at 250°C. The one-to-one correlation obtained, resulting in a regression coefficient of almost unity (Table II), proves that the pH sensor behaves in a Nernstian manner, as does the hydrogen electrode with respect to hydrogen ion activity, thus enabling us to estimate the pH of high temperature aqueous solutions to an accuracy of ± 0.02 of a pH unit. Furthermore these findings also show that the lack of such accuracy apparent in Fig. 1 and 2 and Table I, is not due to a fault of the pH sensor, but can be traced to uncertainty in the calculated pH values of the buffer solutions used for the calibration.

In the present study, the pH value is evaluated using the internal reference hydrogen electrode potential in the following manner. For the hydrogen electrode, the electrode reaction is



The Nernst equation for this reaction can be written as

$$E_T = E_T^0 - \frac{2.303RT}{2F} \log P_{\text{H}_2, T} - \frac{2.303RT}{F} \text{pH}_T \quad [2]$$

where the subscript T refers to the temperature.

At 25°C, if the dissolved H_2 concentration in water is m mol-kg $^{-1}$, then, according to Henry's law, the effective partial pressure of H_2 is

Table II. Slopes of the plots of E_{sensor} vs. Ag/AgCl, 0.1M KCl against Pt, $\text{H}_2/\text{H}_{\text{aq}}^+$ vs. Ag/AgCl, 0.1M KCl

Temperature (°C)	Slope	γ^2
125	1.004	0.9984
150	0.983	0.9981
175	1.018	0.9993
200	1.012	0.9990
225	1.002	0.9999
250	1.002	0.9985
275	0.997	0.9997

N.B.: γ^2 is the regression coefficient.

$$P_{\text{H}_2, T} = m/K_T \quad [3]$$

where K_T is the Henry's law constant for H_2 at temperature T . Since the partial pressure of H_2 corrected for the vapor pressure of water at 25°C is 0.97 atm, from Eq. [3]

$$m = 0.97K_{25} \quad [4]$$

Thus from Eq. [3] and [4], the partial pressure of H_2 at any other temperature T is

$$P_{\text{H}_2, T} = 0.97K_{25}/K_T \quad [5]$$

From Eq. [2] and [5]

$$E_T = E_T^0 - \frac{2.303RT}{2F} \log [0.97K_{25}/K_T] - \frac{2.303RT}{F} \text{pH}_T \quad [6]$$

The potentials have been measured with respect to Ag/AgCl, 0.1M KCl, at elevated temperatures. Thus, a correction has to be carried out to convert the observed potential values (E_{obs}) to hydrogen scale (E_{SHE}) incorporating a correction for thermal junction potentials. These correction factors for various temperatures appear elsewhere (1). Thus

$$E_T = E_{\text{SHE}} = (E_{\text{obs}} + E_{\text{correct}}) \quad [7]$$

The term E_{correct} contains the thermal junction potential correction, while the term E_{obs} has been corrected for the isothermal liquid junction potential according to the procedure outlined in Ref. (1) and (18). The Eq. [6] now yields

$$\text{pH}_T = -\frac{F}{2.303RT} \cdot E_{\text{SHE}} - \frac{1}{2} \log (0.97K_{25}/K_T) \quad [8]$$

which can be used to calculate the pH at any temperature, knowing E_{SHE} and Henry's law constant for the hydrogen/water system at the required temperature (22). These pH values have been used to calibrate the pH sensor at various temperatures as appearing in Fig. 3, thus enabling a completely unambiguous measurement of pH by using an approach which has hitherto not been published elsewhere. The actual pH values thus evaluated for solution systems used in the present study are listed in Table III for temperatures up to 275°C.

The ability to measure pH to an accuracy of ± 0.02 of a pH unit in aqueous systems at elevated temperatures opens up a whole new area of solution chemistry, since we are now in a position to study hydrolysis reactions and activity coefficients of ions more accurately at these temperatures.

The influence of oxygen and hydrogen on the electrode potential of the sensor was investigated by either purging air or hydrogen, respectively, through the solution, and then monitoring the potential with respect to the Ag/AgCl, 0.1M KCl electrode. The results showed no influence of oxygen or hydrogen gases on the sensor potentials. Similarly, the pressure of the system showed no influence on the electrode potential of the sensor over the pressure range 200-1000 psi.

Figure 4 depicts the influence of chloride ion and its concentration on the sensor potential in 0.01M B(OH) $_3$ + 0.001M LiOH at 200°C. This was examined by introducing a known amount of NaCl into the solution tank. It is evi-

Table III. pH values for experimental solution systems as a function of temperature

Solution system	pH						
	398 K	423 K	448 K	473 K	498 K	523 K	548 K
$5 \times 10^{-3} \text{M H}_2\text{SO}_4$	2.59	2.28	2.50	2.34	2.40	2.43	2.64
0.01M H_3PO_4	3.06	2.50	2.92	2.82	2.95	3.05	3.23
0.1M B(OH) $_3$	4.53	4.03	4.36	4.05	4.15	4.07	4.14
0.01M B(OH) $_3$	6.19	6.03	6.53	6.61	6.55	6.69	6.80
+ 0.0001M LiOH							
0.01M B(OH) $_3$	7.84	7.28	7.42	7.45	7.38	7.55	7.73
+ 0.001M LiOH							
0.01M LiOH	9.75	9.20	9.25	9.00	8.90	8.88	8.90

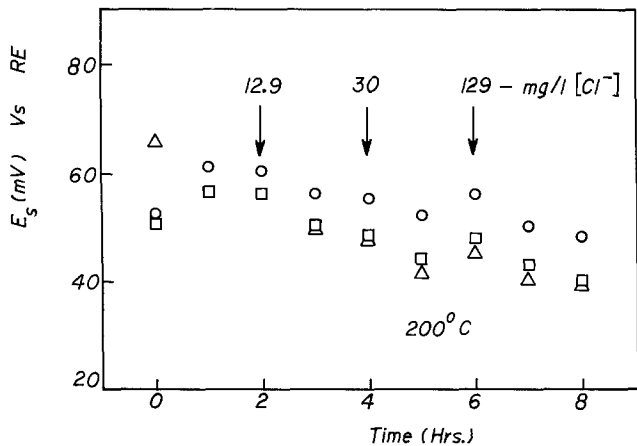


Fig. 4. The influence of chloride ion concentration on E_{sensor} for three different sensors in $0.01M B(OH)_3 + 0.001M LiOH$ at $200^\circ C$.

dent from Fig. 4 that the chloride ion has very little effect on the sensor potential at these concentrations. We attribute the general negative shift in potential to the increasing pH of the system due to the consumption of hydrogen ions by the all-metal loop. A similar shift is also evident in long-term stability tests, as shown in Fig. 5. Subsequent experiments with these membranes confirmed that their pH response is not affected by chloride ion concentrations up to 12 weight percent Cl^- and sulfide ion concentrations up to 780 ppm S^{2-} (24).

The results of long-term stability tests for three sensors with an Hg/HgO internal reference, performed in $0.01M LiOH$ solution at $200^\circ C$, are shown in Fig. 5. A gradual decrease of the potential of the sensor by 7-12 mV from the initial value occurs over a period of 27h. From Fig. 5, it is clearly seen that the electrodes show good reproducibility, in that the potentials obtained for each electrode did not deviate by more than ± 5 mV about a mean value. Thus, the small drift observed in these tests most likely arises from changes in the pH of the test solution stemming from the consumption of hydrogen ions by corrosion processes involving the all-metal loop and the random electrical noise pickup at these high impedances.

We previously surmised that the somewhat sluggish response exhibited by some membranes at low tempera-

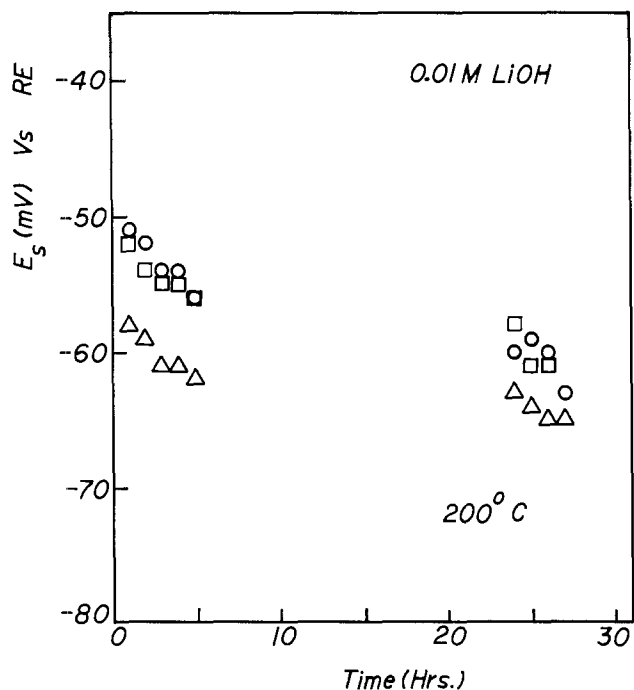


Fig. 5. Time stability of E_{sensor} for three different sensors in $0.01M LiOH$ at $200^\circ C$.

Table IV. Electrical resistance of the exposed area of the $ZrO_2-9\% Y_2O_3$ membrane at various temperatures with Ag/Ag₂O and Hg/HgO internal elements

Temperature ($^\circ C$)	Electrical resistance ($M\Omega$)	
	Ag/Ag ₂ O	Hg/HgO
125	44.90	61.90
150	9.90	11.30
175	2.50	—
200	0.70	0.75
225	0.23	0.24
250	0.10	0.088

tures ($<150^\circ C$) might be due to their very high electrical resistance. For example, silica is sometimes added to the $ZrO_2-Y_2O_3$ mixture to "improve sinterability." It appears that this additive aids bonding by forming a glassy phase of very high electrical resistivity at the grain surfaces, thereby giving rise to very high matrix electrical resistance. If this hypothesis is correct, then a correlation should exist between the response of a membrane and its electrical properties, as reflected by the dc resistance.

The electrical resistance of the membrane was evaluated by measuring the EMF of the cell consisting of the sensor and the Ag/AgCl, $0.1M KCl$ electrode with and without a shunt connected across them. The resistance of the membrane wall was calculated according to the procedure outline by Niedrach (13). These results (Table IV) show that, with the Hg/HgO internal reference, the membrane resistance decreased from 61.9 $M\Omega$ at $125^\circ C$ to 0.088 $M\Omega$ at $250^\circ C$, thus showing that the membrane resistance is strongly temperature dependent. It is likely that the membrane is undergoing a reversible modification (change) during heating and cooling cycles, which is responsible for these drastic changes in membrane resistance. This factor probably explains the sluggish behavior of the membranes at lower temperatures (e.g., $T \leq 150^\circ C$), which disappears at higher temperatures owing to the high conductivity, that imparts a greater stability on the membrane potentials.

The membrane resistance data, plotted as the logarithm of specific conductivity (σ) of the membrane vs. the inverse of the absolute temperature, showed a linear re-

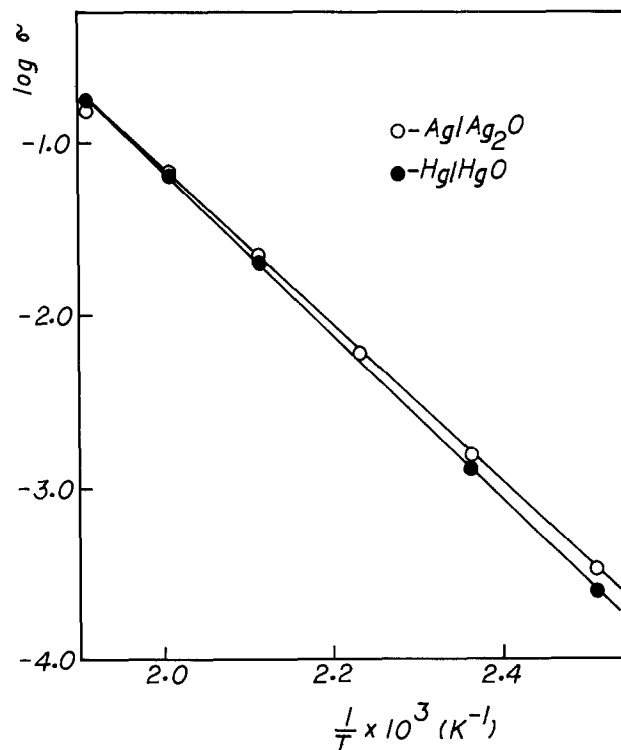


Fig. 6. Arrhenius plots for the specific conductivity (σ) of pH sensors with Ag/Ag₂O and Hg/HgO internal reference electrodes.

sponse with both Ag/Ag₂O and Hg/HgO internal references, as shown in Fig. 6. The activation energies of 20.7 kcal·mol⁻¹ with the Ag/Ag₂O internal, and 21.7 kcal·mol⁻¹ with the Hg/HgO internal, obtained from the above plot are in excellent agreement with those reported in the literature (25). These higher activation energies show that the sensors, in fact, behave as true membranes.

Conclusions

1. The yttria-stabilized zirconia membranes (9% Y₂O₃) with the Hg/HgO internal reference electrode used in these studies behave in a nernstian manner. Hence, they can be used for pH measurements of high temperature aqueous solutions.

2. A unique method, which has hitherto not been published elsewhere, is outlined for evaluating the pH of high temperature aqueous solutions from the sensor response.

3. Oxygen and hydrogen gases, chloride ion concentration, sulfide ion concentration, and pressure of the system have no influence on the sensor potential, and hence on the measured pH.

4. Experiments show that these pH sensors are capable of withstanding high temperatures and pressures over long periods.

Acknowledgment

The authors gratefully acknowledge the financial support from the Standard Oil Company of Ohio under the Contract no. 00196-4634-AB.

Manuscript submitted Dec. 26, 1984; revised manuscript received ca. March 19, 1985.

SRI International assisted in meeting the publication costs of this article.

REFERENCES

1. D. D. Macdonald, P. R. Wentreck, and A. C. Scott, *This Journal*, **127**, 1745 (1980).
2. R. E. Mesmer, C. F. Baes, and F. H. Sweeton *J. Phys. Chem.* **74**, 1937 (1970).
3. R. E. Mesmer, C. F. Baes, and F. H. Sweeton, *Inorg. Chem.*, **10**, 537 (1972).
4. R. E. Mesmer and C. F. Baes, *ibid.*, **10**, 2290 (1971).
5. R. E. Mesmer and C. F. Baes, *J. Soln. Chem.*, **3**, 307 (1974).
6. D. D. Macdonald, P. Butler, and D. Owen, *J. Phys. Chem.*, **77**, 2474 (1973).
7. D. D. Macdonald and D. Owen, *Can. J. Chem.*, **51**, 2747 (1973).
8. D. D. Macdonald, *Corrosion*, **34**, 75 (1978).
9. J. V. Dobson, M. N. Dagless, and H. R. Thirsk, *J. Chem. Soc. Faraday Trans. 1*, **68**, 749 (1972).
10. J. V. Dobson, M. N. Dagless, and H. R. Thirsk, *ibid.*, **68**, 764 (1972).
11. J. V. Dobson, B. R. Chapman and H. R. Thirsk, in "High Temperature High Pressure Electrochemistry in Aqueous Solutions," R. W. Staehle, D. de G. Jones, and J. E. Slater, Editors, p. 341, NACE, Houston, TX (1976).
12. J. V. Dobson, *J. Electroanal. Chem. Interfacial Electrochem.*, **35**, 129 (1972).
13. L. W. Niedrach, *This Journal*, **127**, 2122 (1980).
14. L. W. Niedrach, *ibid.*, **129**, 1446 (1982).
15. T. Tsuruta and D. D. Macdonald, *ibid.*, **129**, 1221 (1982).
16. S. Hettiarachchi and D. D. Macdonald, *ibid.*, **131**, 2206 (1984).
17. D. D. Macdonald, A. C. Scott, and P. R. Wentreck, *ibid.*, **126**, 908 (1979).
18. P. Henderson, *Z. Phys. Chem.*, **59**, 118 (1907); *ibid.*, **63**, 325 (1908).
19. K. Kinoshita, A. C. Scott, S. C. Leach, D. D. Macdonald, and M. C. H. McKubre, Annual Report to Electric Power Research Institute under Contract no. RP 11687-1, April (1981).
20. D. D. Macdonald, Unpublished data (1981).
21. W. L. Marshall and E. V. Jones, *J. Phys. Chem.*, **70**, 4028 (1966).
22. G. B. Naumov, B. N. Ryzhenko, and I. L. Khodakovskiy, "Handbook of Thermodynamics Data," USGS Transl., USGS-WRD-74-001 Washington, DC, (1974).
23. "Handbook of Chemistry and Physics," 57th ed., R. C. Weast, Editor, B-132, CRC Press, Cleveland, OH (1976).
24. S. Hettiarachchi and D. D. Macdonald, In preparation.
25. T. H. Etsell and S. N. Flengas, *Chem. Rev.*, **70**, 339 (1970).

The Influence of Supporting Electrolyte on Kinetics of Electroreduction Process of Poly(methylviologen), Poly(methylviologen)-Nafion Complex, and Poly(methylviologen)-Poly(p-styrenesulfonate) Complex Coated on Electrodes

Takeo Ohsaka and Noboru Oyama*

Department of Applied Chemistry for Resources, Tokyo University of Agriculture and Technology, Koganei, Tokyo 184, Japan

Keiichi Sato and Hiroaki Matsuda*

Department of Electronic Chemistry, Graduate School at Nagatsuta, Tokyo Institute of Technology, Nagatsuta, Midori-ku, Yokohama 227, Japan

ABSTRACT

The influence of supporting electrolytes upon the "heterogeneous" electron-transfer rate of the $MV^{2+/+}$ redox couple ($MV^{2+/+}$ and MV^+ are the dication and monocation of viologen sites, respectively, in polymer coatings) as poly(methylviologen) (PMV), poly(methylviologen)-Nafion complex (PMV-Nafion), and poly(methylviologen)-poly(p-styrenesulfonate) complex (PMV-PSS), which were attached to basal-plane pyrolytic graphite electrodes, as well as upon the "homogeneous" charge-transport rate within these polymer films was examined by the normal pulse voltammetry. The values of standard rate constant (k^0) and cathodic transfer coefficient (α) of the heterogeneous electron-transfer process changed with the supporting electrolytes used. The values of the apparent diffusion coefficient (D_{app}) for the homogeneous charge transport also changed with the supporting electrolytes. The relationship between the size of the counterion and D_{app} was found not to be simple. The D_{app} , k^0 , and α tended to decrease, though not monotonously, with an increase in $\Gamma_{Nafion}/\Gamma_{MV^{2+}^{obs}}$ or $\Gamma_{PSS}/\Gamma_{MV^{2+}^{obs}}$, irrespective of the kind of supporting electrolyte, where $\Gamma_{MV^{2+}^{obs}}$, Γ_{Nafion} , and Γ_{PSS} are the concentration of the electroactive viologen site as PMV and the concentrations of the sulfonyl group as Nafion and PSS, respectively. For a given supporting electrolyte and under the conditions of the same ratio of $\Gamma_{Nafion}/\Gamma_{MV^{2+}^{obs}}$ and $\Gamma_{PSS}/\Gamma_{MV^{2+}^{obs}}$, the D_{app} , k^0 , and α obtained with the PMV-Nafion system were different from those obtained with the PMV-PSS system. Furthermore, a linear correlation between $\log D_{app}$ and $\log k^0$ was observed. On the basis of the results obtained, the influence of the supporting electrolytes and the polymer morphology upon the heterogeneous electron transfer and the homogeneous charge transport is discussed.

The "poly(viologen)"-coated electrodes prepared by the various types of immobilization of polymeric viologen materials on the surfaces of conductors and semiconductors have been getting considerable interest as electron-transfer mediators or catalysts (1-4), as promising electrochromic materials (5), as a potential means of solar energy conversion via the photoelectrochemical reduction of viologen itself (6, 7, 9-11), and as electrode materials for electrochemical deionization (8). The immobilization of polymeric viologen materials on electrodes can be achieved by the formation of insoluble films of the reduced viologen on electrodes (12-15), the formation of the intermolecular polymer complexes (e.g., Nafion®-poly(methylviologen) (PXV) and poly(p-styrenesulfonate) (PSS) (1, 2, 16), the incorporation of monomeric methylviologen into anionic polyelectrolytes (such as Nafion and PSS) coated on electrode surfaces (1, 2, 16, 17), the physical adsorption of viologen polymer itself (3, 4, 11, 16), the chemical bonding of polymeric films of organosilane derivatives by metal -O-Si- linkages to electrode surfaces (9, 10, 18), and the formation of polymeric viologens prepared by electropolymerization of monomeric viologen derivatives possessing vinyl groups (e.g., Vinyldiquat®) (19). From the previous data (3, 4, 16) concerning the "homogeneous" charge transport within the poly(viologen) coatings on electrodes in these various cases, it is obvious that the apparent diffusion coefficients (D_{app}) characterizing the charge transport, actually described as a diffusion process, are functions of the polymer, solvent, electrolyte, concentration of viologen site in coatings, the conditions of coating preparation, temperature, etc. However, quantitative data are still relatively uncommon.

Recently, we (16) have reported that D_{app} as well as the kinetic parameters (i.e., standard rate constant [k^0] and transfer coefficient [α]) of "heterogeneous" electron-transfer reaction of the $MV^{2+/+}$ redox couple (MV^{2+} is the

dication of viologen site in polymer coatings) can vary substantially as the overall morphology of the polymers confining the viologen sites and the concentration of the viologen site are changed and that the empirical linear relationship between $\log D_{app}$ and $\log k^0$, which has been found in some redox complexes (20-23) incorporated electrostatically into the polyelectrolytes on electrodes, also holds for the monomeric methylviologen trapped in a perfluorinated ion-exchange polymer, Nafion. The more detailed examination of both the "homogeneous" charge-transport process through the poly(viologen) films on electrodes and the heterogeneous electron-transfer reactions at the electrode/poly(viologen) film interfaces is thus expected to lead to further insight into the homogeneous and heterogeneous charge-transport processes involved in the electrochromic process, electron-transfer mediation or catalysis, photoassisted hydrogen evolution, etc., when using poly(viologen)-coated electrodes.

Electron hopping between the neighboring redox sites in a polymer matrix, i.e., self-exchange electron-transfer process, has been proposed as the mechanism for transporting electrons through redox polymers (41, 42), since the redox sites are affixed to the polymer film matrix and all of these sites cannot directly contact with the underlying electrode. However, the rate-determining step of the electron transport is not always the intrinsic electron-transfer reaction between the neighboring redox sites. In many cases (3, 4, 16, 20-27, 41-49, 51-53), ion-transport processes such as the diffusion of the redox site itself, the motion of the charge compensating counterion, and the polymer chain motion have been considered to limit this electron-transport process. With the polymeric viologens, such fundamental data for the understanding of the mechanism of homogeneous charge transport are presently limited (3, 4, 16, 19). The influence of the electrolyte and the polymer morphology on the electrochemistry of the viologen polymer films attached to electrode surfaces

* Electrochemical Society Active Member.

should be examined in detail to elucidate the factors controlling homogeneous charge-transport kinetics in viologen polymer films as well as heterogeneous electron-transfer kinetics at electrode/viologen-polymer-film interfaces.

In this paper, the dependence of the D_{app} characterizing the homogeneous charge transport within poly(methylviologen) (PMV) (Fig. 1) and the kinetic parameters (k^0 and α) of heterogeneous electron-transfer reaction of the $MV^{2+/•}$ redox couple as PMV coated on a basal-plane pyrolytic graphite (BPG) electrode upon the supporting electrolytes will be examined by a normal pulse voltammetric procedure. This technique has successfully been applied to the determination of D_{app} , k^0 , and α for "electroactive polymer-coated electrodes" (16, 20-23). In addition, the results will be compared with those obtained with the PMV-Nafion and PMV-PSS intermolecular complexes coated on BPG electrodes under the various ratios of $\Gamma_{MV^{2+}^{obs}}$ to Γ_{Nafion} or Γ_{PSS} in various supporting electrolytic solutions, where $\Gamma_{MV^{2+}^{obs}}$, Γ_{Nafion} , and Γ_{PSS} are the surface concentration of the electroactive viologen site as PMV and the concentrations of the sulfonyl group as Nafion and PSS, respectively. The modification of electrode surfaces by coating the polymeric intermolecular complexes, which were produced by mixing two kinds of polymers having the opposite charges of each other, is a new useful means in the preparation of "polymer-coated electrodes," and the resulting electrodes could be expected to possess many potential applications [e.g., catalytic O_2 reduction at BPG electrodes coated with PXV-PSS or PXV-Nafion (1) and electrochromism of transparent electrode coated with PXV-PSS (5)]. Thus, a more detailed examination of the heterogeneous electron-transfer reaction between the electrode and the redox site confined in the blended-polymer coatings and homogeneous charge-transport process through these polymer coatings was undertaken in order to understand the electrochemical behavior of these intermolecular complex-coated electrodes.

Experimental

Materials.—The poly(methylviologen) (PMV), with average molecular weight of 9.8×10^3 , shown in Fig. 1, was prepared as described elsewhere (1, 6, 7, 16, 17). Nafion membrane 125® was obtained from E. I. du Pont de Nemours and Company (Wilmington, Delaware). According to a previous procedure (1, 6, 7, 17), the stock solution of Nafion was prepared from the membrane in order to facilitate the electrode coating, where ethanol-dimethylsulfoxide mixture (50:50 volume percent) was used as a solvent, and the concentration of Nafion was 2.55 mg·ml⁻¹. Poly(p-styrenesulfonate sodium salt) (PSS) used as an electrode coating film of polyelectrolyte was obtained from Polyscience, Incorporated (Warrington, Pennsylvania), and the average molecular weight was 6×10^6 . The water-soluble PSS used as a supporting electrolyte was prepared by the same procedure as described previously (1). Its average molecular weight was 1.2×10^6 .

The basal-plane pyrolytic graphite (BPG) (Union Carbide Company) disk electrodes (area of 0.17 cm²) were prepared and mounted into glass tube with heat-shrinkable polyolefin tube (24, 25). Fresh electrode surfaces were produced by cleaving the disk with a scalpel.

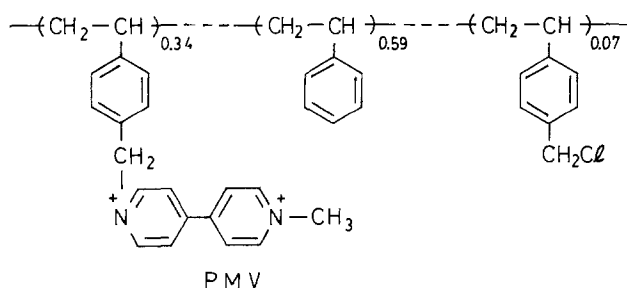


Fig. 1. Structure of the poly(methylviologen) used

Sodium chloride, sodium perchlorate, cesium chloride, sodium p-toluenesulfonate (NaPTS), and tetraphenylphosphonium chloride (TPPCl), which were reagent grade, were obtained from Wako Pure Chemical Industries, Limited (Osaka, Japan) and were used as supporting electrolytes without further purification. In each supporting electrolytic solution, the concentration of supporting electrolyte was 0.2M and the pH value was adjusted to 3.0 by an addition of an acid, which is composed of the same anion as that of the supporting electrolyte used, to the solution. In this process, no buffer solutions were used to avoid the complication of the interpretation (concerning the influence of supporting electrolyte on kinetics of electroreduction process of polymeric viologens) of the data obtained.

Electrode coating procedures.—The polymer film-coated electrodes were prepared by almost the same procedures as described previously (1). The PMV film and the polymer film obtained by mixing of the PMV and Nafion solutions on the electrode surface appeared homogeneous to the naked eye, while the polymer film obtained by mixing of the PMV and PSS solutions appeared less homogeneous.

PMV film coating.—Aliquots (1-10 μ liter) of methanolic stock solution containing 3 mg/ml methylviologen as PMV were spread by a microsyringe on the freshly cleaved electrode surface of BPG, and then the solvent was evaporated at room temperature.

PMV-Nafion film coating.—Aliquots of the stock solutions of PMV and Nafion were pipetted and mixed directly on the freshly cleaved surface and then air-dried to remove the solvent before use.

PMV-PSS film coating.—Aliquots of the stock solutions of PMV and PSS were mixed on the BPG electrode surfaces and dried.

Apparatus and procedures.—Normal pulse voltammograms and cyclic voltammograms were obtained with homemade instruments and were recorded with an X-Y recorder (Watanabe Corporation). Positive feedback circuitry was employed to compensate the resistances associated with the polymer coatings (these were typically ca. 20-50 Ω) as much as possible. In normal pulse voltammetric experiments, the pulse width of 10-100 ms and the interval of 30-60s between successive pulses were employed. Thus it can be safely considered that the depletion layer of reactants produced during the preceding pulse completely disappears before the following pulse starts. Normal pulse voltammetric measurements were confined to times (typically 1-10 ms) sufficiently short to ensure that semi-infinite linear diffusion prevailed (16, 20-23, 26).

The thicknesses of the coating films of PMV, PMV-Nafion, and PMV-PSS were measured as follows. Aliquots of the stock solutions of PMV, PMV and Nafion, or PMV and PSS were cast and then spread by a microsyringe on a glass slide in such a way that the area of the spread coating is equal to that (0.17 cm²) of BPG electrode used. They were then air dried. The resulting dry coatings were soaked for 30 min in the same aqueous solutions as those used in further electrochemical experiments (i.e., the concentration of supporting electrolyte = 0.2M, pH = 3.0), and the "wet" thicknesses were measured with a Surfcom 550A (Surface Texture Measuring Instrument, Tokyo Seimitsu Company). The wet thicknesses of the coating films were almost independent of the kind of the supporting electrolytic solutions used.

The quantities ($\Gamma_{MV^{2+}^{obs}}$ in units of moles per square centimeter) of the electroactive viologen site in electrode coatings were determined coulometrically (25) by integrating the current that passed when the electrode potential was stepped from a value where no current was flowing to a value where the dicationic viologen sites (MV^{2+}) were reduced to the corresponding radical monocations ($MV^{•+}$). The values of $\Gamma_{MV^{2+}^{obs}}$ were also determined by measuring the area of cyclic voltammograms (for the

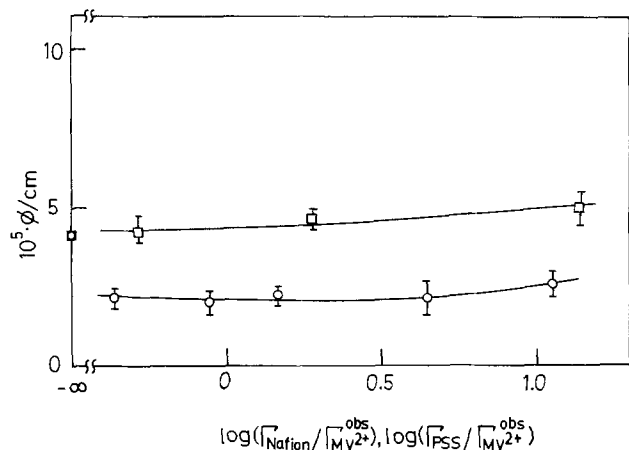


Fig. 2. Variation of the thickness of the coating films with $\Gamma_{\text{Nafion}}/\Gamma_{\text{MV}^{2+}}^{\text{obs}}$ or $\Gamma_{\text{PSS}}/\Gamma_{\text{MV}^{2+}}^{\text{obs}}$. The constant quantity (6.2×10^{-8} mol-cm $^{-2}$) of PMV and the arbitrary quantities (2.0×10^{-8} – 2.0×10^{-7} mol-cm $^{-2}$) of Nafion or PSS were coated on glass slides (area of 0.17 cm 2) and then air dried. The resulting coating films were soaked in 0.2M NaClO $_4$ solution (pH 3.0) for 30 min, and then their thicknesses (ϕ) were measured. Circles: PMV-Nafion system. Squares: PMV-PSS system. Widths of error bars indicate uncertainties in thickness measurements.

oxidation-reduction of the MV $^{2+/+}$ redox couple) obtained at slow potential scan rates of 1–2 mV-s $^{-1}$. The $\Gamma_{\text{MV}^{2+}}^{\text{obs}}$ values estimated by these two procedures were the same within experimental error. The molar volume concentrations of the electroactive viologen site in electrode coatings were calculated by using the $\Gamma_{\text{MV}^{2+}}^{\text{obs}}$ values so obtained and the thicknesses of the coatings (Fig. 2).

Solutions were freed of air by using prepurified nitrogen. Potentials were measured and are reported with respect to a sodium chloride saturated calomel electrode (SSCE). Experiments were conducted at ambient laboratory temperature (25 $^{\circ}$ \pm 2 $^{\circ}$ C).

Results and Discussion

Electrochemical response of poly(methylviologen) (PMV)-coated electrodes.—The typical cyclic voltammetric response for a PMV-coated BPG electrode is shown in Fig. 3A. After several cyclings of the electrode potential, a steady-state cyclic voltammogram was obtained, indicating that the PMV coating becomes swelled relatively quickly. When the potential of this electrode was cycled in the range from 0 to –0.65V vs. SSCE, both anodic and cathodic peak currents of the cyclic voltammogram remained substantially unchanged even after 20h, showing that the PMV was stable and strongly attached to BPG electrode surface so long as the potential of the electrode is cycled within the range where the val-

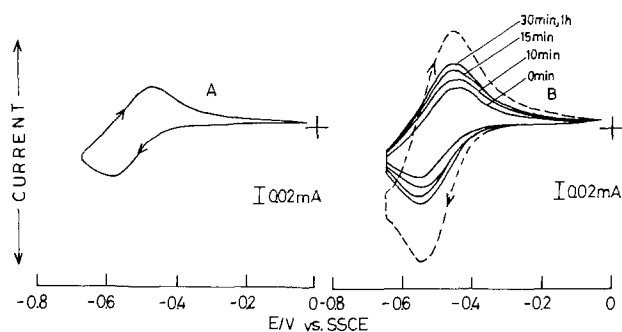


Fig. 3. Panel A: Cyclic voltammogram for a PMV-coated BPG electrode in a 0.2M NaClO $_4$ solution (pH 3.0). Panel B: Cyclic voltammograms obtained when the electrode used in Panel A was washed with water and replaced in a 0.2M CsCl solution (pH 3.0). In both cases, the potential was scanned between 0 and –0.65V vs. SSCE at 200 mV-s $^{-1}$. The arrow indicates the direction of scan. The quantity ($\Gamma_{\text{MV}^{2+}}^{\text{T}}$) of the PMV coating coated originally on BPG electrode surfaces was 6.2×10^{-8} mol-cm $^{-2}$, and in this case the quantity ($\Gamma_{\text{MV}^{2+}}^{\text{obs}}$) of the viologen site detected electrochemically was 1.9×10^{-8} mol-cm $^{-2}$.

ence of the viologen site as PMV is changed between dication and monocation. However, when the potential scanning was extended to the region from 0 to –1.2V vs. SSCE, where the valence of viologen site changes from +2 to 0 (not shown in Fig. 3), the peak currents decreased gradually with the cycling. Such a loss of the electroactivity of the PMV film may be ascribed to the formation of the electroinactive materials via the dimerization reaction among the reduced viologen sites (28, 29) or any interaction between the reduced viologen sites and the original ones (30). Unless otherwise stated, the potential of the electrode was thus scanned only over the first wave (i.e., the reduction wave of the viologen dication as PMV to the radical cation) of the two reduction waves.

The above-mentioned decrease in electroactivity of PMV film with the cycling of the potential between 0 and –1.2V vs. SSCE seems to be different from that observed with the PXV-PSS or PXV-Nafion complex coated on electrodes (1). The PMV itself is water insoluble even in the dication state of viologen site, and thus this insolubility is not thought to decrease when the charge of the viologen sites of PMV is reduced to zero. However, in the case of the PXV-PSS and PXV-Nafion complexes, the PXV itself is water soluble, but the complex salt of PXV with PSS or Nafion is insoluble in water and when the charge of the viologen was reduced to zero the salts of both complexes again become water soluble, probably because of the loss in electrostatic interaction between PXV and PSS or Nafion. The same behavior as in the PXV-PSS or PXV-Nafion complex has been observed in the case of the monomeric dimethylviologen incorporated into Nafion film coated on electrodes (16).

After a steady-state voltammogram was obtained at the PMV-coated BPG electrode in a 0.2M NaClO $_4$ solution (Fig. 3A), this electrode was removed, washed, and transferred to a 0.2M CsCl solution and then the potential of the electrode was cycled between 0 and –0.65V vs. SSCE (Fig. 3B). In this case, the peak currents increased with the cycling of the electrode potential and after about 30 min another steady-state voltammogram was obtained (Fig. 3B), although the anodic and cathodic peak currents were smaller than those (represented by dashed line) obtained with the freshly prepared PMV-coated BPG electrode in a CsCl solution. It was also observed that the redox potential (estimated as the arithmetical mean of anodic and cathodic peak potentials) of the MV $^{2+/+}$ redox couple varied with the supporting electrolyte used. For example, in the case of NaClO $_4$ and CsCl solutions the potential difference was ca. 20 mV. This may reflect the difference in ion association interactions between the MV $^{2+/+}$ redox couple and these supporting electrolytes. Furthermore, the significant difference between the values of peak currents of the voltammograms obtained in the two kinds of electrolytes should be noted. Such a difference can be ascribed to the difference in rates of homogeneous charge transport through the PMV coating and/or heterogeneous electron-transfer reaction of the MV $^{2+/+}$ redox couple as PMV in the two electrolytes (16, 20–23). The details will be described below.

Figure 4 shows the correlation between the quantity ($\Gamma_{\text{MV}^{2+}}^{\text{obs}}$) of the viologen site detected electrochemically and the quantity ($\Gamma_{\text{MV}^{2+}}^{\text{T}}$) of PMV coated originally on BPG electrode surfaces. It is apparent from this figure that the fraction of the material that is electroactive varies with the film thickness, i.e., $\Gamma_{\text{MV}^{2+}}^{\text{obs}}$ decreases slightly with increasing $\Gamma_{\text{MV}^{2+}}^{\text{T}}$ and that the fraction of electroactive viologen site is about 30% of the quantity of the polymer originally deposited on BPG electrodes in the region examined of $\Gamma_{\text{MV}^{2+}}^{\text{T}}$ (3.1×10^{-8} – 3.1×10^{-7} mol-cm $^{-2}$). It can be surmised that about 70% of the quantity of viologen site was located in unswollen portions of the polymer, where it remained inaccessible to the supporting electrolytes and was thus electroinactive. Similar behavior has been observed with the PXV-coated BPG electrode in an aqueous NaClO $_4$ solution by Martigny and Anson (3). It has been sometimes observed (3, 7, 31) that all of the quantity of redox sites in the coating originally deposited

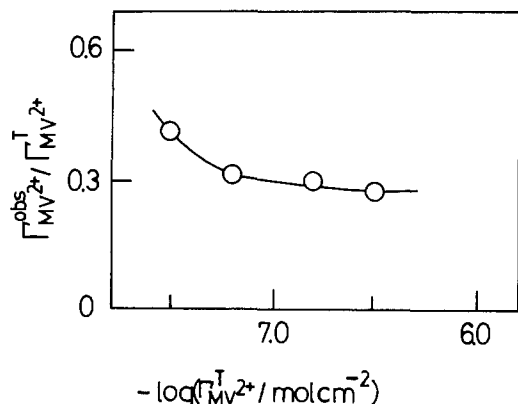


Fig. 4. Correlation between $\Gamma_{MV^{2+}}^{obs}$ and $\Gamma_{MV^{2+}}^T$. Supporting electrolyte was 0.2M NaClO₄ (pH 3.0). The values of $\Gamma_{MV^{2+}}^{obs}$ were measured as described in the Experimental section.

on electrodes is not usually electroactive, especially when an electroactive polymer itself was directly deposited on electrodes.

Effect of supporting electrolyte on effective diffusion coefficient for homogeneous charge-transport process within PMV coatings.—It has been shown that the rate of the charge-transport process through the polymer coating governs the rate of electrochemical and catalytic processes at polymer-coated electrodes (16, 19-27, 32-40). It has been demonstrated experimentally (4, 5, 16, 19-26, 32, 34-40, 43, 45) and theoretically (33, 46) that the charge transport can be treated as a diffusion of "electrons" which follows Fick's diffusion laws. Charge can be transported through the coating by the electron transfer between electroactive sites confined in polymer matrices [i.e., electron self-exchange reaction (41-44)] and/or the physical diffusion of the electroactive species itself (20-23,

45). Both processes will be followed, for charge neutrality, by concurrent uptake of counterions into the polymer matrix or expulsion of coions initially present in the film, and, in addition, the segmental motion of the polymer lattice. Thus the relative contribution of these effects to the overall charge transport is probably different for different kinds of polymer coatings. The apparent diffusion coefficient (D_{app}) for an electron-transfer process within the coatings has been considered as one of the parameters which characterize the charge-transport process through polymers and the evaluation of D_{app} has been mainly carried out by the use of transient chronoamperometry (27, 47), chronocoulometry and chronopotentiometry (25, 27), cyclic voltammetry (26, 48, 49), and normal pulse voltammetry (NPV) (16, 20-23), etc. In this study, NPV is employed for the determination of D_{app} . The D_{app} can be estimated from the dependence of the limiting current of the normal pulse voltammograms upon sampling time (16, 20-23).

In Fig. 5 are shown the typical normal pulse voltammograms for the reduction of the viologen dication (MV^{2+}) (to the corresponding radical monocation, $MV^{\cdot+}$) as PMV coated on BPG electrodes at various sampling times in various supporting electrolytes. In these cases, the concentrations of the electroactive viologen site were almost the same ($\Gamma_{MV^{2+}}^{obs} = 2 \times 10^{-8}$ mol-cm⁻²). Thus the difference in the values of the limiting current in different supporting electrolytes may reflect the difference in the rates of the charge-transport process within the PMV coatings. Plots of the cathodic limiting current (i_{lim}) of these normal pulse voltammograms against the inverse square root of the sampling time (τ) were found to be linear in the range used of τ (1 to ca. 10 ms) (Fig. 6), indicating that in these cases the limiting currents were diffusion controlled. Thus the values of the apparent diffusion coefficients, D_{app} , for the charge-transport process within the coatings were obtained from the slopes of the i_{lim} vs. $\tau^{-1/2}$ plots by using the Cottrell equation (50)

$$(i_d)_{Cott}^c = nFAC^o_p \sqrt{D_{app}/\pi\tau} \quad [1]$$

where $(i_d)_{Cott}^c$ denotes the cathodic limiting diffusion current for the cathodic electrode process, n the number of electrons involved in the heterogeneous electron-transfer reaction, F the Faraday constant, A the electrode area, and C^o_p the volume concentration of the electroactive site (i.e., the viologen dication) in PMV coatings.

The obtained values of D_{app} are summarized in Table I, together with the $\Gamma_{MV^{2+}}^{obs}$ values and the values of the kinetic parameters of heterogeneous electron-transfer reac-

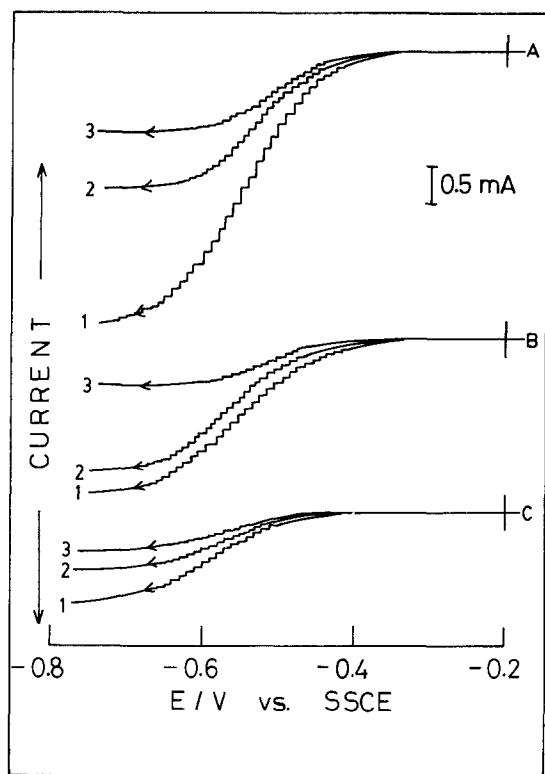


Fig. 5. Typical normal pulse voltammograms for the one-electron reduction of viologen dication as PMV coated on BPG electrodes at various sampling times in aqueous solutions (pH 3.0) of 0.2M NaCl (A), TPPCl (B), and NaClO₄ (C). In all cases, $\Gamma_{MV^{2+}}^T = 6.2 \times 10^{-8}$ mol-cm⁻². $\Gamma_{MV^{2+}}^{obs}$, 2.2×10^{-8} (A) and 1.9×10^{-8} (B and C) mol-cm⁻². Sampling time (τ): (1) 2, (2) 4, and (3) 10 ms. The arrow indicates the direction of normal pulse voltammetric potential step.

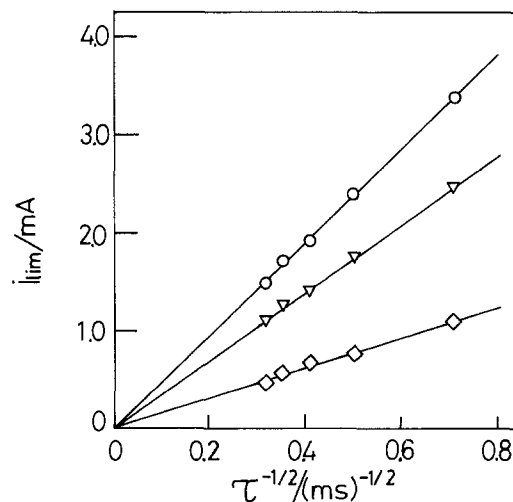


Fig. 6. Normal pulse voltammetric Cottrell plots of limiting current (i_{lim}) vs. (sampling time)^{-1/2} for the one-electron reduction of viologen dication as PMV coated on BPG electrodes. Supporting electrolyte: NaCl (circles), TPPCl (dels), and NaClO₄ (diamonds). Other experimental conditions are the same as in Fig. 5.

Table I. Dependence of the standard rate constant, k° , and the cathodic transfer coefficient, α , of the electron transfer at electrode/film interface and the apparent diffusion coefficient, D_{app} , for the process of charge transport within the film upon the kind of supporting electrolyte in which the PMV-coated BPG electrode is soaked

Supporting electrolyte	$\Gamma_{MV^{2+}}^{obs}$ (mol-cm ⁻²)	$\Gamma_{MV^{2+}}^{obs}/\Gamma_{MV^{2+}}^T$	D_{app} (cm ² -s ⁻¹)	k° (cm-s ⁻¹)	α
NaCl	$(2.2 \pm 0.2) \times 10^{-8}$	0.35	$(9.5 \pm 1.5) \times 10^{-10}$	$(1.7 \pm 0.3) \times 10^{-4}$	0.40 \pm 0.02
NaClO ₄	$(1.9 \pm 0.2) \times 10^{-8}$	0.31	$(1.3 \pm 0.2) \times 10^{-10}$	$(3.1 \pm 0.6) \times 10^{-5}$	0.46 \pm 0.02
H ₃ C-⊖-SO ₃ Na	$(2.0 \pm 0.2) \times 10^{-8}$	0.32	$(1.0 \pm 0.2) \times 10^{-9}$	$(6.7 \pm 1.3) \times 10^{-5}$	0.39 \pm 0.02
CsCl	$(1.7 \pm 0.2) \times 10^{-8}$	0.28	$(1.5 \pm 0.3) \times 10^{-9}$	$(2.2 \pm 0.4) \times 10^{-4}$	0.44 \pm 0.02
(⊖) ₄ PCl	$(1.9 \pm 0.2) \times 10^{-8}$	0.30	$(6.8 \pm 1.3) \times 10^{-10}$	$(9.5 \pm 1.5) \times 10^{-5}$	0.43 \pm 0.02
PSSNa ^a	$(2.3 \pm 0.2) \times 10^{-8}$	0.37	$(1.3 \pm 0.2) \times 10^{-10}$	$(1.4 \pm 0.3) \times 10^{-5}$	0.18 \pm 0.02

All measurements were performed in 0.2M supporting electrolytes adjusted to pH = 3.0.

All electrodes were coated with PMV of $\Gamma_{MV^{2+}}^T = 6.2 \times 10^{-8}$ mol-cm⁻².

^a Poly(p-styrenesulfonate) sodium salt.

tion at the PMV-coated BPG electrodes in various supporting electrolytes. The $\Gamma_{MV^{2+}}^{obs}$ seemed to be almost independent of the kind of the supporting electrolyte used here. With any supporting electrolyte, about 30% of the total quantity of viologen dication in PMV coating originally deposited on electrodes was electroactive. However, it seems that D_{app} varies with the supporting electrolytes. That is, when the sodium salts [e.g., NaCl, NaClO₄, sodium p-toluenesulfonate (NaPTS) and poly(styrenesulfonate) sodium salt (NaPSS)] were used as supporting electrolytes, the values of D_{app} decreased in the order NaPTS ~ NaCl > NaClO₄ ~ NaPSS. Furthermore, when the counterions of the chloride salts as the supporting electrolytes were changed, the values of D_{app} seemed to decrease slightly in the order CsCl > NaCl > tetraphenylphosphonium chloride (TPPCl).

Previous studies (42, 51-53) have shown marked electrolyte effects on the electrochemistry of polymer films deposited on electrode surfaces. The rate limiting process of the charge transport through the swollen polymer films undergoing electrolysis (i.e., oxidation or reduction of electroactive polymer itself or electroactive species confined in electroinactive polymer) is the transport of counterions through the polymer phase. For example, in the case of tetrathiafulvalene polymer (42, 52) and poly(vinylferrocene) films (51) the oxidation of these films can be viewed as being "anion controlled." However, there is no clear relationship between the size of the counterion and the electrochemical oxidation-reduction rate of films. In the case of the PMV film, it is also of interest to examine whether or not there is some relationship between the size of the counterion and the charge-transfer rate, i.e., D_{app} . The actual size of the individual counterions used here is unknown. Thus, Stokes radii (γ_s) of these ions will be used for the discussion about a correlation between the obtained values of D_{app} and the size of the counterions. When the counterions of the chloride salts as supporting electrolytes were changed, the values of D_{app} seemed to decrease slightly in the order Cs⁺ > Na⁺ > tetraphenylphosphonium ion (TPP⁺). In this case, Stokes radii (γ_s) of these cations and Cl⁻ are in the order (54) $\gamma_s(\text{TPP}^+) > \gamma_s(\text{Na}^+) > \gamma_s(\text{Cs}^+) > 2\gamma_s(\text{Cl}^-)$. From this correlation between D_{app} and γ_s , it seems likely that D_{app} increases with a decrease in γ_s . Thus the reduction of PMV film may be considered to be "cation controlled."

However, when the sodium salts were used as supporting electrolytes, the values of D_{app} decreased in the order PTS⁻ \geq Cl⁻ > ClO₄⁻ ~ PSS⁻. Stokes radii of the corresponding anions and sodium ion decrease in the order (54) $\gamma_s(\text{Na}^+) \sim \gamma_s(\text{PTS}^-) > 2\gamma_s(\text{Cl}^-) \sim 2\gamma_s(\text{ClO}_4^-)$, where $\gamma_s(\text{PTS}^-)$ was assumed to be equal to γ_s (benzoic anion) or γ_s (picrate anion) [both are ca. 2.4 times larger than $\gamma_s(\text{Cl}^-)$] (54)]. In this case, the above-mentioned cation-controlled behavior and the correlation between D_{app} and γ_s (for anions) are not observed. The $\gamma_s(\text{Cl}^-)$ and $\gamma_s(\text{ClO}_4^-)$ are almost the same and are half smaller than γ_s of Na⁺. If the

$\gamma_s(\text{TPP}^+)$ is unknown, but is intuitively considered to be larger than γ_s (trimethyl-phenyl ammonium ion), which is ca. 1.4 times larger than $\gamma_s(\text{Na}^+)$ (54).

reduction of PMV film were cation controlled in aqueous NaCl and NaClO₄ solutions, then one could expect that the values of D_{app} are almost the same in both electrolytic solutions on the basis of size alone. However, the difference in D_{app} was observed in NaCl and NaClO₄ solutions. Thus, the difference in D_{app} cannot be only explained by the difference in Stokes radii. As can be seen from the comparison of $D_{app}(\text{PTS}^-)$ and $D_{app}(\text{PSS}^-)$, $D_{app}(\text{PTS}^-)$ is about ten times larger than $D_{app}(\text{PSS}^-)$. This may suggest the difference in the rates of the diffusion of PTS⁻ and PSS⁻ (which can be considered as the polymeric form of PTS⁻) through the swollen PMV film.

While the apparent diffusion coefficients obtained in various supporting electrolytes suggest a dependence on the size of the counterion, it is apparent from the above-mentioned discussion that a simple size relationship is not operative. Further, it should be noted that the rate-determining process of the charge-transport process within PMV coatings is not the intrinsic electron-transfer process between adjacent viologen sites confined in polymer matrix, but the process of charge compensating counterion motion which is necessarily coupled to electron transfer and/or the segmental motions of the polymer lattice.

Effect of supporting electrolyte on rate of heterogeneous electron-transfer reaction between electrode and viologen site.—As mentioned previously (16, 20-23), an analysis of the rising part of the current-potential curves shown in Fig. 5. allows us to estimate the kinetic parameters [i.e., standard rate constant (k°) and cathodic transfer coefficient (α)] of the heterogeneous electron-transfer reaction of the MV^{2+/+} redox couple as PMV. The relevant current-potential relationship for normal pulse voltammograms for the simple electrode process, Ox + ne \rightleftharpoons Red, has already been derived (55) and is given for the reduction by

$$E = E_{1/2}^r + \frac{RT}{\alpha nF} \ln \left\{ \frac{4}{\sqrt{3}} \frac{k^\circ \sqrt{\tau}}{\sqrt{D}} \right\} - \frac{RT}{\alpha nF} \ln \left\{ x \left[\frac{1.75 + x^2 [1 + \exp(\zeta)]^2}{1 - x [1 + \exp(\zeta)]} \right]^{1/2} \right\} \quad [2]$$

where E is the electrode potential, $E_{1/2}^r$ the reversible half-wave potential of the MV^{2+/+} redox couple, α the cathodic transfer coefficient, k° the standard rate constant, τ the sampling time, R the gas constant, T the absolute temperature, ζ the dimensionless parameter expressed as $\{(nF/RT)(E - E_{1/2}^r)\}$, D the diffusion coefficient expressed as $\{[D_{app}(\text{for cathodic process})]^2 [D_{app}(\text{for anodic process})]^{-1-\alpha}\}$,² and x the ratio of the current (i) at potential (E) to the cathodic limiting diffusion current [$(i_a)_{cat}$] expressed by Eq. [1].

Figure 7 shows the typical examples of the modified log plots of normal pulse voltammograms in which the logarithm of the third term on rhs of Eq. [2] is plotted

²It was assumed that $D \approx D_{app}$ (for cathodic process) $\approx D_{app}$ (for anodic process).

against E for the reduction of viologen dication to the corresponding radical monocations in polymer coatings. These plots gave the straight lines the slopes of which were constant at the different sampling times from 1 to 10 ms in each case. Thus, from the slopes $[(RT/\alpha nF)^{-1}]$ of the straight lines shown in Fig. 7 and the intercepts $(E_{1/2}^{\circ} + (RT/\alpha nF) \ln \{(4/\sqrt{3})(k^{\circ}\sqrt{\tau}/\sqrt{D})\})$ of these lines with the axis, the values of k° and α were estimated by using the known values of $E_{1/2}^{\circ}$, D_{app} , and τ . In this case, the values of $E_{1/2}^{\circ}$ were estimated as the average of the anodic and cathodic peak potentials of the cyclic voltammogram for the oxidation-reduction of the $MV^{2+/+}$ redox couple as PMV on BPG electrodes in a solution containing only supporting electrolyte. The results obtained are summarized in Table I. It is clear from this table that the kinetic parameters (k° and α) of heterogeneous electron-transfer reactions of the $MV^{2+/+}$ redox couple vary with the supporting electrolyte. The values of k° in the presence of NaCl or CsCl are $\sim 2 \times 10^{-4} \text{ cm}\cdot\text{s}^{-1}$ and those in the presence of TPPCl, PTSNa, NaClO_4 , or PSSNa are $(1 \sim 9) \times 10^{-5} \text{ cm}\cdot\text{s}^{-1}$. Particularly, one notice that k° in the presence of CsCl is *ca.* one order of magnitude larger than that in the presence of PSSNa. Thus, it is worth noting that the reduction of viologen dication to the corresponding radical monocation is markedly affected by the nature of the supporting electrolyte ions, although at the present stage it is impossible to find out a reasonable explanation for these results.

The effect of supporting electrolytes on the kinetics of heterogeneous electron-transfer reactions at a conventional "bare" electrode has been observed before, for example, for hydrogen ion reduction in the presence of halide ions (56, 57) and anion reduction in the presence of alkali metal cations at a negatively charged mercury electrode (58). In general, such an influence of supporting electrolytes on heterogeneous electron-transfer processes has been ascribed to a variation in the potential distribution in the double layer, usually termed the "double-layer effect" (59), and/or specific interaction between the reacting species and supporting electrolytic ions in the double layer (60, 61). Both of these effects should be taken into account in order to explain the above mentioned supporting electrolyte dependence of the kinetic parameters of heterogeneous electron-transfer reaction at the PMV-coated electrode. At the present stage, however, the related data are still rare. Thus we did not attempt to distinguish these two possibilities.

From Table 1, it is also clear that the values of α change with the supporting electrolyte. Especially, the α value (0.18) in the presence of PSSNa is significantly smaller than those (0.39 ~ 0.46) in the presence of other monomeric supporting electrolytes (*i.e.*, NaCl, NaClO_4 , PTSNa, CsCl, or TPPCl). Recently, we (16) have measured the kinetic parameters (k° and α) for the reduction of the viologen dication to radical monocation in various

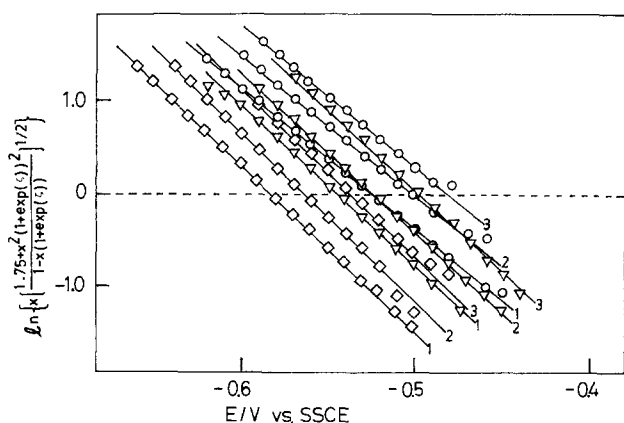


Fig. 7. Modified log plots of normal pulse voltammograms for the one-electron reduction of viologen dication as PMV on BPG electrodes. Sampling time (τ): (1) 2, (2) 4, and (3) 10 ms. Other experimental conditions and the symbols used are the same as in Fig. 5 and 6.

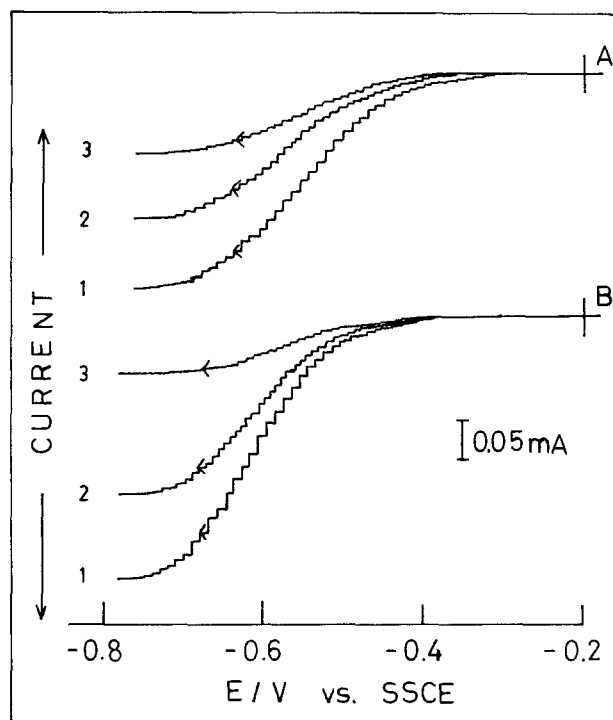


Fig. 8. Typical normal pulse voltammograms for the one-electron reduction of viologen dication as PMV-Nafion (curve A) and PMV-PSS (curve B) intermolecular complexes on BPG electrodes at various sampling times. A: $\Gamma_{MV^{2+}}^{obs} = 6.8 \times 10^{-9} \text{ mol}\cdot\text{cm}^{-2}$ and $\Gamma_{Nafion} = 8.8 \times 10^{-8} \text{ mol}\cdot\text{cm}^{-2}$. B: $\Gamma_{MV^{2+}}^{obs} = 6.1 \times 10^{-9} \text{ mol}\cdot\text{cm}^{-2}$ and $\Gamma_{PSS} = 8.8 \times 10^{-8} \text{ mol}\cdot\text{cm}^{-2}$. In both cases, $\Gamma_{MV^{2+}}^T = 6.2 \times 10^{-8} \text{ mol}\cdot\text{cm}^{-2}$. Supporting electrolyte: 0.2M NaCl (pH 3.0). Sampling time (τ): (1) 2, (2) 4, and (3) 10 ms. The arrow indicates the direction of normal pulse voltammetric potential step.

polymer coatings of PMV, N, N'-dimethyl-4,4'-bipyridinium (MV)-Nafion and PXV-PSS-coated BPG electrodes in 0.2M NaClO_4 solution (pH 3.4). The values of α obtained with PMV, MV-Nafion, and PXV-PSS-coated BPG electrodes were 0.56, 0.58, and 0.20, respectively. These results demonstrate that the values of α vary with not only supporting electrolytes, but also the structure of the polymer coating. Further, note that the α value obtained with PMV-coated electrode in the presence of PSSNa as supporting electrolyte is almost the same as that obtained with PXV-PSS-coated electrode in the presence of NaClO_4 (16) and that these values are considerably smaller than those in the other systems.

Kinetics of electron-transfer processes at electrodes coated with PMV-Nafion or PMV-PSS intermolecular complex.—Figure 8 shows the typical normal pulse voltammograms for the one-electron reduction of the viologen dication (MV^{2+}) as PMV-Nafion and PMV-PSS intermolecular complexes on BPG electrodes at various sampling times. The reduction half-wave potentials of the normal pulse voltammograms shifted in the negative direction as the sampling time was reduced (Fig. 8), and their limiting currents were found to be diffusion-controlled from the Cottrell plots of (cathodic limiting current) *vs.* (sampling time) $^{-1/2}$. The kinetic parameters of the heterogeneous electron-transfer reaction of the $MV^{2+/+}$ redox couple as PMV-Nafion and PMV-PSS and the apparent diffusion coefficients for the charge transport process within polymeric coatings of these intermolecular complexes were evaluated by the same method as described in the previous section. The obtained values of D_{app} , k° , and α at the various ratios of $\Gamma_{MV^{2+}}^{obs}$ to Γ_{Nafion} and Γ_{PSS} under a constant amount ($\Gamma_{MV^{2+}}^T$) of the PMV originally deposited on electrodes are shown in Fig. 9, where Γ_{Nafion} and Γ_{PSS} are the concentrations of the sulfonyl group as Nafion and PSS, respectively.

Some correlations between D_{app} , k° , or α and the ratio $\Gamma_{Nafion}/\Gamma_{MV^{2+}}^{obs}$ or $\Gamma_{PSS}/\Gamma_{MV^{2+}}^{obs}$ can be drawn on the basis of

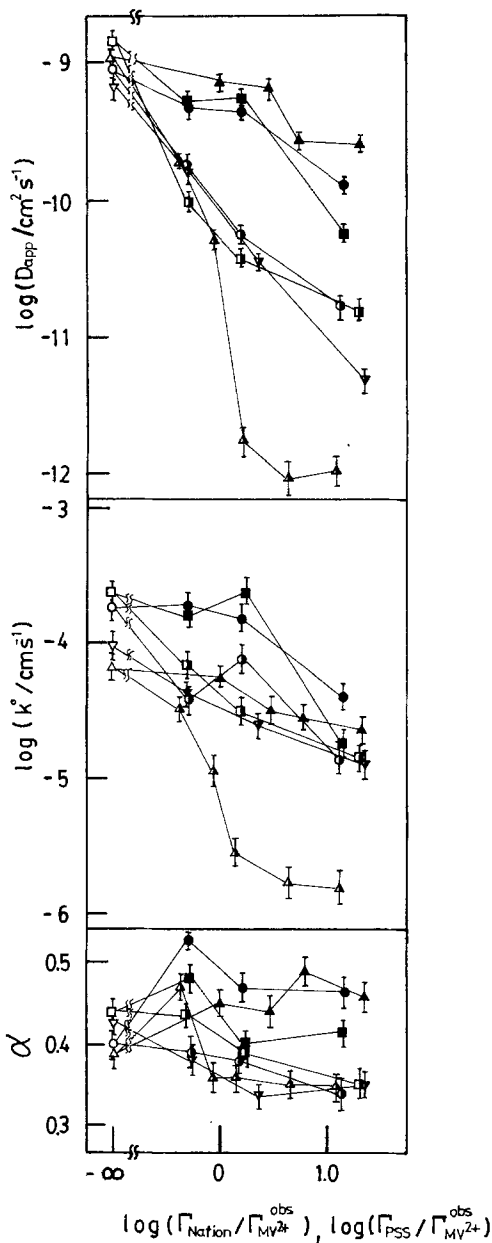


Fig. 9. Dependence of D_{app} , k^o , and α on $\Gamma_{NaFion}/\Gamma_{MV^{2+}}^{obs}$ or $\Gamma_{PSS}/\Gamma_{MV^{2+}}^{obs}$. Supporting electrolyte (0.2M): NaCl (circles), CsCl (squares), NaPTS (deltae), TPPCl (dels). Open, solid, and half-solid symbols represent the data obtained for the PMV, PMV-PSS, and PMV-Nafion systems, respectively. $\Gamma_{MV^{2+}}^T = 6.2 \times 10^{-8} \text{ mol}\cdot\text{cm}^{-2}$. Widths of error bars indicate uncertainties in the measurements of D_{app} , k^o , and α .

the data shown in Fig. 9. (i) The D_{app} , k^o , and α tend to decrease, though not monotonously, with an increase in $\Gamma_{NaFion}/\Gamma_{MV^{2+}}^{obs}$ or $\Gamma_{PSS}/\Gamma_{MV^{2+}}^{obs}$, irrespective of the kind of supporting electrolytes. (ii) At a given ratio of $\Gamma_{NaFion}/\Gamma_{MV^{2+}}^{obs}$ or $\Gamma_{PSS}/\Gamma_{MV^{2+}}^{obs}$, D_{app} , k^o , and α change with the supporting electrolyte used. (iii) For a given supporting electrolyte and under the conditions of the same ratio of $\Gamma_{NaFion}/\Gamma_{MV^{2+}}^{obs}$ and $\Gamma_{PSS}/\Gamma_{MV^{2+}}^{obs}$, D_{app} , k^o , and α obtained with the PMV-Nafion system are different from those obtained with the PMV-PSS system.

It is of considerable interest to compare the above-mentioned results [especially (i)] with those (16) obtained with N, N'-dimethyl-4, 4'-bipyridinium (MV) incorporated into Nafion coatings (abbreviated as MV-Nafion) on electrodes, since the dependence of D_{app} and k^o on the concentration of viologen site in coatings is different in the MV-Nafion system and the PMV-Nafion or PMV-PSS system. In the latter system, D_{app} and k^o can be considered to increase with an increase in the volume concentration ($C_{MV^{2+}}$ in units of moles per cubic centimeter) of viologen dication site in polymer matrices, since $C_{MV^{2+}}$ increases

with decreasing the ratio $\Gamma_{NaFion}/\Gamma_{MV^{2+}}^{obs}$ or $\Gamma_{PSS}/\Gamma_{MV^{2+}}^{obs}$ under the conditions of constant $\Gamma_{MV^{2+}}$. However, in the case of the MV-Nafion system, as reported previously (16), D_{app} and k^o decreased with an increase in $C_{MV^{2+}}$. These different concentration dependences of D_{app} (and k^o) are considered to be associated with the different polymer morphology caused by the different interactions between the viologen sites and their surroundings (i.e., cationic polymer-anionic polyelectrolyte interaction in the PMV-Nafion or PMV-PSS system and cationic monomer-anionic polyelectrolyte interaction in the MV-Nafion system). In the case of the monomeric redox ions confined electrostatically in polyelectrolytes carrying the opposite charge [e.g., the $\text{Fe}(\text{CN})_6^{4-/3-}$ (22), $\text{Mo}(\text{CN})_8^{4-/3-}$ (20, 21), and $\text{IrCl}_6^{3-/2-}$ (23) incorporated into protonated poly(4-vinylpyridine), the $\text{MV}^{2+/+}$ (16), $\text{Co}(\text{bpy})_3^{3+/2+}$ (43) and $\text{Ru}(\text{bpy})_3^{3+/2+}$ (31, 41, 49) incorporated into Nafion], the degree of the electrostatic cross-linking of the polymer films by multiple ion pairing of redox ions with the surrounding sites having the opposite charge is thought to increase with increasing the concentration of the redox ion in polymer films. The increasing electrostatic cross-linking of the films causes the decrease in the rates of the diffusion of the redox ion itself, the charge compensating counterion motion which is necessarily coupled to the intrinsic electron transfer between the redox ions and/or the segmental motions of the polymer film. As a result, the decrease of D_{app} with increasing the concentration of the redox ion is observed. On the other hand, in the case of the PMV-Nafion and PMV-PSS systems, the electrostatic cross-linking between the cationic polymer (i.e., PMV) and the anionic polyelectrolytes (i.e., Nafion and PSS) is thought to be restricted to some extent by the constrained motion of the polymer backbones, which is attributed to the essential structure of the polymer itself. When the ratios of $\Gamma_{NaFion}/\Gamma_{MV^{2+}}^{obs}$ for the MV-Nafion and PMV-Nafion systems and $\Gamma_{PSS}/\Gamma_{MV^{2+}}^{obs}$ for the PMV-PSS system are the same, the degree of the electrostatic cross-linking in the PMV-Nafion or PMV-PSS system can be considered to be much smaller than that in the MV-Nafion system. As a result, the charge transport through the coatings of the PMV-Nafion and PMV-PSS intermolecular complexes seems to be controlled not only by the charge compensating counterion motion and the segmental motions of the polymers, but also by the electron hopping reaction between adjacent viologen sites, as can be demonstrated by the dependence of D_{app} on the kinds of the supporting electrolyte and the electroinactive polyelectrolyte blended with PMV at a constant $C_{MV^{2+}}$ and the increasing values of D_{app} with an increase in $C_{MV^{2+}}$.

A typical example of the charge-transport controlled by the rate of the intrinsic electron-transfer reaction between adjacent pairs of oxidized and reduced forms has been reported by Buttry and Anson with respect to effective diffusion coefficients of $\text{Co}(\text{bpy})_3^{2+}$ in the presence of $\text{Co}(\text{bpy})_3^+$ in Nafion coatings on BPG electrodes (43). Compared with this $\text{Co}(\text{bpy})_3^{2+/+}$ system, the charge transport for the PMV-Nafion and PMV-PSS systems seems to be more complicated and to be controlled by some other factors as mentioned above.

The result (ii) indicates that one of the factors controlling the charge transport is the diffusion of the supporting electrolyte which is necessarily coupled to the intrinsic electron-transfer reaction between the adjacent viologen sites. Note that the effect of the supporting electrolytes on the D_{app} values is larger in the PMV-Nafion and PMV-PSS intermolecular complexes than in the PMV alone. For example, at $\Gamma_{NaFion}/\Gamma_{MV^{2+}}^{obs} = 0$, $D_{app}(\text{NaCl})/D_{app}(\text{PTSNa}) = 0.95$, while at $\Gamma_{NaFion}/\Gamma_{MV^{2+}}^{obs} = 1.6$, $D_{app}(\text{NaCl})/D_{app}(\text{PTSNa}) = 32$. The different, swollen polymer morphology of the PMV-Nafion or PMV-PSS intermolecular complex and the PMV can be considered to cause the significant difference in the rates of the diffusion of supporting electrolytes and thus the difference in the D_{app} values.

For a given supporting electrolyte and at a given ratio of $\Gamma_{NaFion}/\Gamma_{MV^{2+}}^{obs}$ and $\Gamma_{PSS}/\Gamma_{MV^{2+}}^{obs}$, the values of D_{app} are dif-

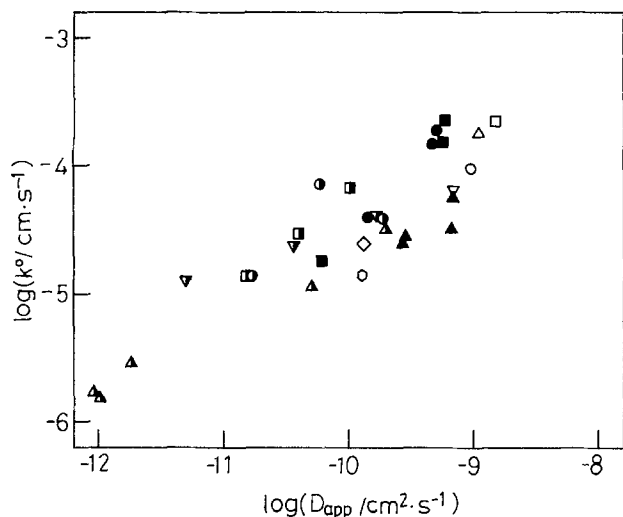


Fig. 10. Correlation between $\log k^\circ$ and $\log D_{app}$. Supporting electrolyte (0.2M): NaClO_4 (diamond), water-soluble poly (p-styrenesulfonate) (sodium salt) (hexagon). The other symbols used are the same as in Fig. 9.

ferent in the PMV-Nafion and PMV-PSS systems. At the higher ratio of $\Gamma_{\text{Nafion}}/\Gamma_{\text{MV}^{2+}^{\text{obs}}}$ and $\Gamma_{\text{PSS}}/\Gamma_{\text{MV}^{2+}^{\text{obs}}}$, the difference in the D_{app} values becomes larger. Such a difference may be due to changes in overall swollen morphology of both intermolecular complexes. The differences in the diffusional behavior of ions in Nafion and sodium poly-(p-styrene sulfonate) (PSSNa) have been recently reported (62-64) to be due to the different structure of both polymers; i.e., Nafion is a polymer with an ion-cluster morphology, while PSSNa is a conventional cross-linked sulfonated ion-exchange resin.

The explanation for the dependence of the kinetic parameters of heterogeneous electron-transfer reaction of the $\text{MV}^{2+/+}$ redox couple upon the supporting electrolytes, the ratio of $\Gamma_{\text{Nafion}}/\Gamma_{\text{MV}^{2+}^{\text{obs}}}$ or $\Gamma_{\text{PSS}}/\Gamma_{\text{MV}^{2+}^{\text{obs}}}$ and the polyelectrolytes blended with PMV seems to be much more difficult compared with that for D_{app} values. However, it should be noted that there is a linear relationship between $\log k^\circ$ and $\log D_{app}$ (Fig. 10). Similar relationships have been obtained for the $\text{Mo}(\text{CN})_8^{4-\beta-}$, $\text{Fe}(\text{CN})_6^{4-\beta-}$, and IrCl_6^{3-2-} incorporated into the protonated PVP, the $\text{Fe}(\text{CN})_5^{3-2-}$ coordinated to PVP and the $\text{MV}^{2+/+}$ incorporated into Nafion (16, 23). The empirical relationship obtained suggests that the factors caused by changing the concentration of the viologen site in polymers, the supporting electrolytes, the polymer structure, etc., contribute in a similar manner to both the rate-determining process of the heterogeneous electron-transfer reaction at the electrode/film interface and the physical diffusion process of the electrochemical charge through the polymer films.

Acknowledgments

The present work was partially supported by a Grant of the Nissan Science Foundation.

Manuscript submitted May 23, 1984; revised manuscript received April 12, 1985.

Tokyo University of Agriculture and Technology assisted in meeting the publication costs of this article.

REFERENCES

- N. Oyama, N. Oki, H. Ohno, Y. Ohnuki, H. Matsuda, and E. Tsuchida, *J. Phys. Chem.*, **87**, 3642 (1983).
- N. Oyama, N. Ohta, Y. Ohnuki, K. Sato, and H. Matsuda, *Nippon Kagaku Kaishi*, 940 (1983).
- P. Martigny and F. C. Anson, *J. Electroanal. Chem.*, **139**, 383 (1982).
- R. J. Mortimer and F. C. Anson, *ibid.*, **138**, 325 (1982).
- H. Akahoshi, S. Toshima, and K. Itaya, *J. Phys. Chem.*, **85**, 818 (1981).
- N. Oyama, S. Yamaguchi, M. Kaneko, and A. Yamada, *J. Electroanal. Chem.*, **139**, 215 (1982).
- M. Kaneko, S. Moriya, A. Yamada, H. Yamamoto, and N. Oyama, *Electrochim. Acta*, **29**, 115 (1984).
- A. Factor and T. O. Rouse, *This Journal*, **127**, 1313 (1980).
- D. C. Bookbinder and M. S. Wrighton, *J. Am. Chem. Soc.*, **102**, 5123 (1980).
- D. C. Bookbinder, J. A. Bruce, R. N. Dominey, N. S. Lewis, and M. S. Wrighton, *Proc. Natl. Acad. Sci. (U.S.)*, **77**, 6280 (1980).
- H. D. Abruna and A. J. Bard, *J. Am. Chem. Soc.*, **103**, 6898 (1981).
- R. J. Jasinski, *This Journal*, **125**, 1619 (1978).
- J. Bruinink and C. G. A. Kregting, *ibid.*, **125**, 1397 (1978).
- S. Fletcher, L. Duff, and R. G. Barradas, *J. Electroanal. Chem.*, **100**, 759 (1979).
- R. C. Cieslinski and N. R. Armstrong, *This Journal*, **127**, 2605 (1980).
- T. Ohsaka, H. Yamamoto, M. Kaneko, A. Yamada, M. Nakamura, S. Nakamura, and N. Oyama, *Bull. Chem. Soc. Jpn.*, **57**, 1844 (1984).
- N. Oyama, T. Ohsaka, K. Sato, and H. Yamamoto, *Anal. Chem.*, **55**, 1429 (1983).
- N. S. Lewis and M. S. Wrighton, *Science*, **211**, 944 (1981).
- K. W. Willman and R. W. Murray, *J. Electroanal. Chem.*, **133**, 211 (1982).
- N. Oyama, K. Sato, S. Yamaguchi, and H. Matsuda, *Denki Kagaku*, **51**, 91 (1983).
- K. Sato, S. Yamaguchi, H. Matsuda, T. Ohsaka, and N. Oyama, *Bull. Chem. Soc. Jpn.*, **56**, 2004 (1983).
- N. Oyama, T. Ohsaka, M. Kaneko, K. Sato, and H. Matsuda, *J. Am. Chem. Soc.*, **105**, 6003 (1983).
- N. Oyama, T. Ohsaka, and T. Ushirogouchi, *J. Phys. Chem.*, **88**, 5274 (1984).
- N. Oyama and F. C. Anson, *Anal. Chem.*, **52**, 1192 (1980).
- N. Oyama and F. C. Anson, *This Journal*, **127**, 640 (1980).
- I. Rubinstein and A. J. Bard, *J. Am. Chem. Soc.*, **103**, 5007 (1981).
- N. Oyama, S. Yamaguchi, Y. Nishiki, K. Tokuda, H. Matsuda, and F. C. Anson, *J. Electroanal. Chem.*, **139**, 371 (1982).
- M. Furue and S. Nozakura, *Chem. Lett.*, **1980**, 821.
- C. L. Bird and A. T. Kuhn, *Chem. Soc. Rev.*, **10**, 49 (1981).
- E. Laviron, *J. Electroanal. Chem.*, **122**, 37 (1981).
- C. R. Martin, I. Rubinstein, and A. J. Bard, *J. Am. Chem. Soc.*, **104**, 4817 (1982).
- K.-N. Kuo and R. W. Murray, *J. Electroanal. Chem.*, **131**, 37 (1982).
- E. Laviron, *ibid.*, **112**, 1 (1980).
- C. P. Andrieux and J. M. Savéant, *ibid.*, **142**, 1 (1982).
- C. P. Andrieux, J. M. Dumas-Bouchiat, and J. M. Savéant, *ibid.*, **131**, 1 (1982).
- C. P. Andrieux and J. M. Savéant, *ibid.*, **134**, 163 (1982).
- F. C. Anson, *J. Phys. Chem.*, **84**, 3336 (1980).
- F. C. Anson, J. M. Savéant, and K. Shigehara, *ibid.*, **87**, 214 (1983).
- F. C. Anson, T. Ohsaka, and J. M. Savéant, *J. Am. Chem. Soc.*, **105**, 4883 (1983).
- N. Oyama, Y. Ohnuki, T. Ohsaka, and H. Matsuda, *Nippon Kagaku Kaishi*, 949 (1983).
- F. B. Kaufman and E. M. Engler, *J. Am. Chem. Soc.*, **101**, 547 (1979).
- F. B. Kaufman, A. H. Schroeder, E. M. Engler, S. R. Kramer, and J. Q. Chambers, *ibid.*, **102**, 483 (1980).
- D. A. Buttry and F. C. Anson, *ibid.*, **105**, 685 (1983).
- D. A. Buttry and F. C. Anson, *J. Electroanal. Chem.*, **130**, 333 (1981).
- F. C. Anson, T. Ohsaka, and J. M. Savéant, *J. Phys. Chem.*, **87**, 640 (1980).
- C. P. Andrieux and J. M. Savéant, *J. Electroanal. Chem.*, **112**, 377 (1980).
- P. Daum, J. R. Lenhard, D. R. Rolison, and R. W. Murray, *J. Am. Chem. Soc.*, **102**, 4649 (1980).
- C. R. Martin, I. Rubinstein, and A. J. Bard, *ibid.*, **104**, 4817 (1982).
- H. S. White, J. Leddy, and A. J. Bard, *ibid.*, **104**, 4811 (1982).
- F. G. Cottrell, *Z. Phys. Chem.*, **42**, 385 (1903).
- P. Daum and R. W. Murray, *J. Phys. Chem.*, **85**, 389 (1981).
- A. H. Schroeder and F. B. Kaufman, *J. Electroanal. Chem.*, **113**, 109 (1980).
- J. Q. Chambers, F. B. Kaufman, and K. Nichols, *ibid.*, **142**, 277 (1982).
- R. A. Robinson and R. H. Stokes, "Electrolyte Solutions," Butterworth, London (1959).
- H. Matsuda, *Bull. Chem. Soc. Jpn.*, **53**, 3439 (1980).
- W. R. Fawcett and S. Levine, *J. Electroanal. Chem.*, **65**,

- 505 (1975).
57. Tsa Chuang-Hsiu and Z. A. Iofa, *Dokl. Akad. Nauk SSSR*, **126**, 1308 (1959).
58. A. N. Frumkin, *Z. Elektrochem.*, **59**, 807 (1955).
59. A. N. Frumkin, *Adv. Electrochem. Electrochem. Eng.*, **1**, 65 (1961).
60. A. N. Frumkin, O. A. Petry, and N. V. Nikolaeva-Fedorovich, *Electrochim. Acta*, **8**, 177 (1963).
61. L. Gierst, L. Vandenberg, E. Nicolas, and A. Fraboni, *This Journal*, **113**, 1025 (1966).
62. R. S. Yeo and A. Eisenberg, *J. Appl. Polym. Sci.*, **21**, 875 (1977).
63. M. Lopez, B. Kipling, and H. L. Yeager, *Anal. Chem.*, **49**, 629 (1977).
64. H. L. Yeager and B. Kipling, *J. Phys. Chem.*, **83**, 1836 (1979).

Incorporation of Complex Reaction Sequences in Engineering Models of Electrolytic Cells

I. Paired Synthesis of Propylene Oxide in an Undivided Cell

Richard C. Alkire* and James D. Lisius**

Department of Chemical Engineering, University of Illinois, Urbana, Illinois 61801

ABSTRACT

A reaction sequence involving 11 chemical species was incorporated into a mathematical model of an electrolytic cell consisting of an undivided parallel-plate reactor operating under steady, continuous flow conditions. The set of coupled, nonlinear, stiff differential equations was solved numerically by dynamic simulation. The technique was applied to the paired synthesis of propylene oxide from propylene-saturated bromide electrolyte. For this system, the eigenvalues associated with the jacobian ranged over ten orders of magnitude. The effect of pH, $[\text{Br}^-]$, mass transfer, space time, and current density were explored to understand their influence on yield, selectivity, conversion, current efficiency, and cell voltage.

Establishment of new electrochemical technologies requires engineering evaluation during early stages of development. The design of electrochemical cells, however, is intimately coupled to chemical transformations which occur within the cell. Robust engineering procedures are needed to evaluate cell design by utilizing scientific understanding of reaction mechanisms to predict cell performance.

Mathematical tools for simulating cell and process behavior are increasingly used in conjunction with experimental programs at the bench scale. Such tools, however, have to date incorporated relatively simple examples of process chemistry. The purpose of the present investigation was to model an electrochemical cell in which a complex sequence of reactions occurs. The method was used to study the paired electrosynthesis of propylene oxide in an undivided parallel-plate cell in which 11 chemical species appear as reactants, intermediates, product, and by-products. In this work, the space-time yield, power consumption, and current efficiency, and their dependence upon cell geometry, flow rate, reactant concentration, and pH, were obtained with use of a mathematical model of the reactor and chemical reaction sequence (1).

Pickett (2) reviewed chemical engineering reactor design concepts used for analysis of electrolytic reactors in terms of simple batch and continuous units. Such cell units can be interconnected to other units to form a process flowsheet. Cera (3) has recently described use of a computer-aided flowsheet simulator for design and optimization of electrochemical processes. In such treatments, the electrochemical reactor is simulated as a process unit which obeys mass, voltage, and thermal balances, but generally without specifying in detail the process chemistry which occurs within the cell.

Detailed models of the interior region of electrolytic cells have taken on a wide range of mathematical complexity (4, 5). Various electrochemical reactor configurations have been analyzed in order to clarify behavior in the presence of coupled mass-transport, potential field, and interfacial processes. Such configurations include, for example, parallel-plate cells (2, 6) and porous electrodes (7, 8), among others. Relatively few such studies,

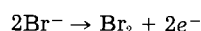
however, include complex reaction sequences beyond a main electrode reaction plus a parasitic side reaction. Notable exceptions are surveyed in Ref. (6) and include treatment of coupled reactions in a laminar boundary layer and multiple homogeneous and heterogeneous reactions in a flow-through porous electrode.

The modeling of chemical reaction sequences by combination of reaction rate and equilibrium equations can be difficult when intermediate species react quickly or are present in very small concentration. In such cases the jacobian matrix of the model equations may exhibit eigenvalues which can be different by many orders of magnitude, and the equations are called "stiff." Because many engineering and scientific disciplines encounter stiffness in modeling, an extensive mathematical literature exists, and special algorithms have been developed for numerical integration of such equations (9, 10). In the present study, stiffness was encountered and efficient algorithms were identified for solving model equations describing the electrosynthesis of propylene oxide.

Baizer recently described advances in scientific understanding of reaction mechanism in the field of electro-organic chemistry (11). Swann and Alkire have indexed several thousand organic compounds which may be synthesized by electrolysis (12). Beck *et al.* discussed evaluation of several electro-organic process candidates (13). Propylene oxide was chosen for the present study because the reaction chemistry has been widely studied, and rate and equilibrium constants are known. Present chemical routes to propylene oxide include chlorohydrin and hydroperoxide processes; electrochemical routes have also been explored (14, 15). Several bench-scale investigations have been conducted with the bromohydrin route in undivided parallel-plate cells (16-19). The propylene oxide reaction, therefore, represents a convenient system for model studies.

System Chemistry

Desired reactions.—Consider an aqueous solution of sodium bromide saturated with dissolved propylene and contained in an undivided electrochemical cell. Bromine is formed by electrolysis at the anode

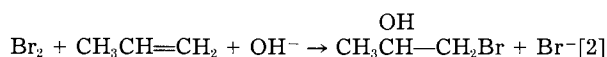


[1]

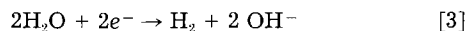
*Electrochemical Society Active Member.

**Electrochemical Society Student Member.

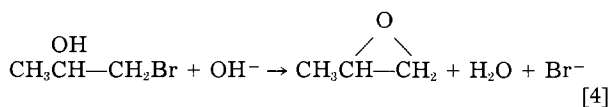
Because in saturated propylene solution the rate for addition of bromine to propylene is over 200 times larger than that for bromine hydrolysis (19, 20), the reaction of dissolved propylene was assumed to occur exclusively with molecular bromine to form propylene bromohydrin (20-24)



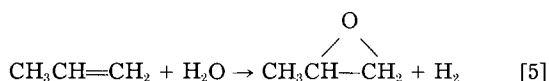
Electrolysis of water occurs at the cathode



Propylene oxide is formed by base-promoted dehydrohalogenation of the vicinal bromohydrin (25-28)



The desired overall cell reaction is



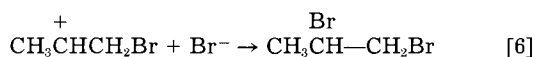
The desired cell reaction utilizes intermediate products from both anode and cathode, and therefore is called a "paired" synthesis. The halogen species does not appear in the overall reaction. Other halogens could be used. However, iodine reaction with propylene is slower and is reversible (28); also, reaction of bromohydrin to propylene oxide is more rapid than that of chlorohydrin, and is of comparable magnitude to that of iodohydrin (26).

Side reactions.—A detailed discussion of side reactions is available elsewhere (1) and will be summarized here. The following paragraphs include reactions of bromine species having higher oxidation states, and reactions involving organic propylene compounds.

Bromine may form polybromides and may also hydrolyze to form hypobromous acid (29). Hypobromous acid can hydrolyze to form the anion which can disproportionate to form bromate (30). Bromate ion can hydrolyze to form the corresponding acid. Electrochemical reactions can also interconvert the different bromine species (31, 32).

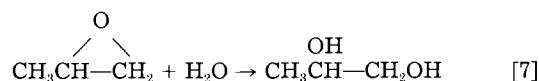
All bromine in valence states of 0 and above (positive) possess strong oxidizing capability and may oxidize organic species. High bromide ion concentrations are known to catalyze addition of molecular bromine to olefins (28). The sole kinetic study of bromine addition to propylene (20) shows no hypobromous acid addition. The speed of the bromine-propylene reaction in comparison to bromate ion formation (20, 33) suggests that essentially all bromine reacts with propylene to form bromohydrin. Reactions of bromine in valence states of 0 and above have thus been neglected in model presented below.

Side reactions involving organic propylene compounds also occur since the carbonium ion intermediate is available for nucleophiles other than water. The major by-product is propylene dibromide (dibromopropane) which is formed by nucleophilic (Br^-) attack on the carbonium ion intermediate formed from reaction of propylene with bromine



The relative proportion of propylene bromohydrin to propylene dibromide depends in a nonlinear manner upon the concentration of bromide ion (20). To an insignificant extent, based upon reactant concentrations, bromohydrin may serve as the nucleophile to yield dibromo-isopropyl ether. Hydrolysis of bromohydrin may occur to form propylene glycol (34, 35), but the rate is slow in comparison with attack of hydroxide ion on bromohydrin to form propylene oxide.

Propylene oxide is susceptible to attack by water since the epoxide ring is readily attacked even by weak nucleophiles. In basic solutions, the $\text{S}_{\text{N}}1$ uncatalyzed and $\text{S}_{\text{N}}2$ hydroxide ion-catalyzed reactions are the dominant mechanisms of glycol formation (36-39)



The foregoing summary indicates clearly that the chemistry of the system has been extensively studied by others. The purpose of the next section is to embody this knowledge in a mathematical model of an electrolytic cell.

Theoretical Formulation

Electrolytic cell and process chemistry.—The electrolytic cell is illustrated in Fig. 1. The cell is an undivided parallel-plate continuous flow unit having a well-mixed core region of uniform composition described by the space-time variable τ . The cell operates with a current of I_{app} . Convective mass-transfer processes are characterized by a diffusion layer at each electrode, represented by the length δ , of equal value at both electrodes. The cell is assumed to operate under isothermal conditions at 25°C and atmospheric pressure. The cell model corresponds to turbulent flow with negligible conversion per pass.

The feed is sodium bromide electrolyte saturated with propylene. The reaction chemistry within the cell is summarized in Fig. 2. The desired reactions are indicated by the heavy arrows. The side reactions are indicated by the light arrows, and account for all unwanted product yields in excess of 1%. The reaction sequence includes 11 chemical species; in addition, the potential is included as a variable. The reaction sequence does not include bromine species of higher oxidation states (+1, +3, and +5).

Rate equations.—Values of thermodynamic data and rate constants which appear in the following equations are tabulated in Table I. Equilibrium constants were calculated from free energies of formation of the reacting species. The standard free energies of formation of all species have been compiled (1).

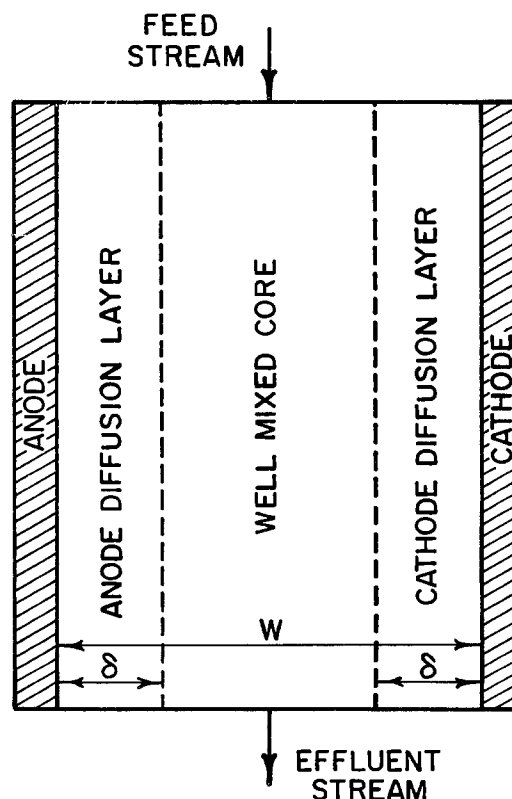


Fig. 1. Schematic diagram of electrolytic cell

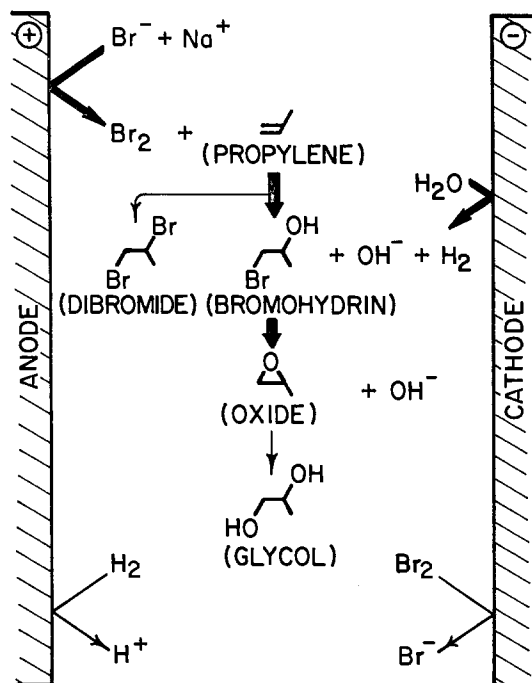


Fig. 2. Model reaction sequence

The electrochemical reaction of the Br^-/Br_2 couple follows a modified Butler-Volmer rate equation (40, 42) which was found to fit experimental data

$$j_1 = i^\circ_{\text{cathodic}} \exp \left[-\frac{anF}{RT} (E - E_{\text{eq}}) \right] - i^\circ_{\text{anodic}} \exp \left[\frac{bnF}{RT} (E - E_{\text{eq}}) \right] \quad [8]$$

where

$$E_{\text{eq}} = E_1^\circ + \frac{RT}{nF} \ln \left[\frac{C_2^*}{(C_1^*)^2} \right]$$

Br_2 which contacts the anode was assumed to reduce back to Br^- and thus lower cathode current efficiency.

The reduction of water at the cathode was expressed by

$$j_2 = \left\{ i^\circ \exp \left[-\frac{anF}{RT} (E - E_{\text{eq}}) \right] - \exp \left[\frac{bnF}{RT} (E - E_{\text{eq}}) \right] \right\} \quad [9]$$

where

$$E_{\text{eq}} = E_2^\circ - \frac{RT}{nF} \ln \{C_8^*\}$$

At each electrode the magnitude of the cell current was equal to the sum of the electrochemical reactions j_1 and j_2 . Hydrogen gas was assumed to be carried out of the cell by convective action and to be present at its saturation value in the bulk solution. The back reaction of dissolved hydrogen occurs at the anode, and serves thus to lower anode current efficiency.

The reaction of bromine with propylene was expressed by a rate equation based on experimental data (20), which were fit by second-degree polynomial regression to the form

$$R_{3,4} = fk_{3,4} \left[C_2C_3 - \frac{C_4C_1}{K_{3,4}C_8} \right] \quad [10]$$

where

$$f = 0.967178 - 0.583315C_1 - 0.367902C_1^2$$

and where

$$k_{3,4} = \frac{k'_{3,4} + k''_{3,4}K'_{3,4}C_1}{1 + K'_{3,4}C_1}$$

Reaction of propylene to propylene dibromide was, in a similar manner, expressed by a rate equation based on experimental data (20) fit by second degree polynomial regression

$$R_{3,5} = (1 - f)k_{3,4} \left[C_2C_3 - \frac{C_5}{K_{3,5}} \right] \quad [11]$$

and f and $k_{3,4}$ are defined as above.

The reaction of propylene bromohydrin to propylene oxide obeys the rate equation (26)

$$R_{4,6} = k_{4,6}C_4C_8 - k_{6,4}C_1C_6 \quad [12]$$

Reaction of propylene oxide to propylene glycol obeys the rate equation (38, 39, 44)

$$R_{6,7} = k'_{6,7} \left[C_6 - \frac{C_7}{K_{6,7}} \right] + k''_{6,7}C_8 \left[C_6 - \frac{C_7}{K_{6,7}} \right] \quad [13]$$

Conservation equations and voltage balance.—This section presents equations for conservation of 11 chemical species plus a voltage balance. The conservation equations were based on the dilute solution approximation (45); while more rigorous expressions could be used in principle, it is unlikely that such refinements would be either cost effective or appropriate to the present level of analysis. In addition, migration terms have been ignored for charged species on the basis that they introduce significant mathematical complexity by coupling the potential and concentration variables, while introducing only modest gains in the expected accuracy of analysis. Finally, the transport coefficients have been assumed to remain constant throughout the concentration fields under study. Table II lists the transport coefficients used in the calculations carried out below; the "calculated" diffusion coefficients were estimated by the correlation of Wilke and Chang (50) with use of the LeBas molar volume correlation (51).

The conservation of species equations are summarized in Table III. The conservation equations were applied in both anolyte and catholyte boundary regions and represent transport by diffusion with simultaneous homogeneous chemical reaction. The central well-mixed core region

Table I. Kinetic parameters

Parameter	Value	Ref.
Bromine/bromide ion couple		
E_1°	1.087V vs. NHE	(41)
n	2	(41)
i°_{anodic}	2.755×10^{-3} A/cm ²	(42)
$i^\circ_{\text{cathodic}}$	8.90×10^{-4} A/cm ²	(42)
a	0.166	(42)
b	0.171	(42)
Water/hydroxide ion couple		
E_2°	-0.828V vs. NHE	(41)
n	2	(41)
i°	2.512×10^{-3} A/cm ²	(43)
a	0.92	(43)
b	0.50	Assumed
Homogeneous kinetic equation constants		
$k'_{3,4}$	4.5×10^6	(20)
$k''_{3,4}$	3.2×10^6	(20)
$K_{3,4}$	1.23×10^{17}	Calculated
$K'_{3,4}$	16	(20)
$K_{3,5}$	3.77×10^{16}	Calculated
$k_{4,6}$	4.56	(26)
$k_{6,4}$	3.09×10^{-4}	(26)
$k'_{6,7}$	1.0×10^{-8}	(38)
$k''_{6,7}$	1.0×10^{-4}	(38)
$K_{6,7}$	8.34×10^{10}	Calculated

All rate constants have units of moles/liters and seconds.

Table II. Transport coefficients

Compound	Diffusion coefficient $\times 10^5$ (cm ² /s)	Ref.
Bromide ion	2.08	(46)
Bromine	1.3	(47)
Propylene	1.44	(48)
Propylene bromohydrin	0.987	Calculated
Propylene dibromide	0.901	Calculated
Propylene glycol	1.01	Calculated
Propylene oxide	1.18	Calculated
Hydrogen	5.85	(46)
Hydrogen ion	9.34	(46)
Hydroxide ion	5.23	(47)
Sodium ion	1.35	(46)
Compound	Mobility (m ² -mol ⁻¹ -s ⁻¹)	Ref.
Bromide ion	78.17	(49)
Hydrogen ion	349.85	(49)
Hydroxide ion	197.6	(49)
Sodium ion	50.15	(49)

is of uniform concentration throughout and therefore enters only as a boundary condition upon the two sets of ordinary differential equations. The boundary conditions of the electroactive species are governed by the sum of the two electrode reactions, where the parasitic reaction occurs at the mass-transfer-limited current. The nonelectroactive species have zero-flux conditions at the electrode and mass balance boundary conditions at the edge of the boundary layer.

The voltage balance across the cell was expressed by Ohm's law based on mobilities and concentrations of ionic species in solution. The effect of hydrogen gas bubbles was ignored. The potential field in the well-mixed core region was therefore

$$\frac{dE}{dx} = - \frac{I_{app}}{F^2 \{u_1 C_1 + u_8 C_8 + u_{10} C_{10} + u_{11} C_{11}\}} \quad [14]$$

The cathode potential was set arbitrarily at zero

$$E = 0 \quad [15]$$

The anodic boundary layer and cathodic boundary layer conditions were

$$E_{abl} = E_{cbl} + \frac{I_{app}}{F^2 \{u_1 C_1 + u_8 C_8 + u_{10} C_{10} + u_{11} C_{11}\}_{cbl}} \quad [16]$$

Method of solution.—The model equations were solved by first isolating those equations which could be solved independently of the remaining set, *i.e.*, for H⁺, H₂, Na⁺, and E. The central problem thus was obtaining a solution for the remaining equations, which were stiff.

In this investigation, the method for converging to the steady-state solution of the boundary value system was to introduce time derivatives and convert the ordinary differential equations (ODE's) into partial differential equations, which were integrated in time until the time derivatives became negligible (52, 53). That is, the problem was solved by dynamic simulation.

The Forsim VI numerical code was used for integration of model equations (53). This package consists of a set of subroutines which contain general procedures for integration of systems of initial value differential equations. Detailed discussion of computation details is available (1).

Two difficulties were encountered in the solution of the equations. The first problem resulted from the range of variables over the spatial interval. The Forsim VI package uses a modified Newton method for convergence of boundary conditions which required scaling of variables. The unscaled problem had a range of variables over ten orders of magnitude with use of reference concentrations presented in Table IV. The variables were scaled such that the range of values between the smallest and largest was reduced three orders of magnitude. The large range

of variable values was the result of fast reaction kinetics. The rapid bromine-propylene reaction, for example, caused sharp gradients at the reaction interface within the anode diffusion layer. The propylene and bromine concentrations exhibited large values on one side of the reaction zone, while values on the opposite side were approximately seven orders of magnitude smaller.

The second problem concerned slow convergence to steady state arising from stiffness of the differing transport time scales. That is, the relaxation time of the diffusion layers was significantly smaller than the space time of the central core. Integration typically proceeded to the stage where all time derivatives across the diffusion layers were essentially zero, while the time derivatives associated with the central region were still significant. The problem was remedied by choosing improved initial guesses for the central core concentrations, which accelerated convergence to steady state. The new initial guesses were determined through a Newton-Raphson technique. The jacobian was assumed to be diagonal, which allowed easy calculation of improved central core concentration estimates.

The set of dependent ODE's were scaled, cast into partial differential equation form, and then solved with use of the Forsim VI package on a CDC Cyber 175 computer. Typical execution times were 150s per case, excluding preliminary evaluation of initial guesses. The local truncation error was set at 1.0×10^{-5} . Five node points were used per diffusion layer. The solution was assumed to have converged when the time derivatives at every point within the spatial interval satisfied the criterion

$$\frac{dC_i}{dt} \leq 5.0 \times 10^{-3} \frac{C_i}{C_i} \quad [17]$$

Decreasing the convergence criteria to 5.0×10^{-5} resulted in a solution different by less than 1% for every variable. The uncoupled variables were then calculated from the coupled variable solutions.

The potential profile was found by solving the finite difference form of Eq. [14] at the discretized points across the diffusion layer. The kinetic overpotentials of each electrode were found by solving nonlinear equations and using a bisection technique. The convergence criterion for the overpotential determination was that the difference of the current predicted from the overpotential equation and the ODE solution agree within 1.0×10^{-4} (A/cm²).

Results and Discussion

The model was used to calculate yield, product selectivities, potential field, and concentration profiles across the cell. A series of test calculations summarized in Table IV was used to explore the response of the system to variation in reactor design parameters and chemical concentration variables.

The following definitions were used. "Conversion" was the fraction of the key limiting reactant which was consumed. "Yield" was the moles of a particular product generated per mole of key reactant consumed. "Selectivity" was the moles of a particular product generated per mole of another coproduct.

The results of one calculation are discussed in order to describe the general features which influence behavior of the electrolytic cell. The example situation had $\tau = 10$ s, $Sh = 2000$, $w = 1.0$ cm, and a feed stream composition of 0.500M NaBr at pH 14, saturated with propylene. The Sherwood number is defined by the ratio of diffusion layer thickness to the equivalent diameter, which for infinite parallel plates is twice the plate spacing $Sh = (2W/\delta) = (2i_s W/mFC_i D_i)$. Experimental measurement of the Sherwood number would be defined using the bromide ion diffusion coefficient. The spatial distributions of all variables except H⁺, OH⁻, and Na⁺ are presented in Fig. 3.

A listing of the reference quantities for scaling of variables appears in Table IV. The reference concentrations for the organic species is the saturation concentration of

Table III. Conservation of species equations

Species	Number	Conservation equation	Anode B.C.	Anolyte B.C.	Catholyte B.C.	Cathode B.C.
Bromide ion	1	$0 = D_1 \frac{d^2 C_1}{dx^2} + R_{3,4} + R_{4,6}$	$\frac{dC_1}{dx} = \frac{1000(I_{app} - j)}{FD_1}$	$0 = \frac{D_1}{W} \left[\frac{dC_1}{dx} \right]_{ab1} - \frac{dC_1}{dx} \Big _{cb1} + \frac{C_1^{in} - C_1}{\tau} + R_{3,4} + R_{4,6}$	$C_1 _{cb1} = C_1 _{lab1}$	$\frac{dC_1}{dx} = -2 \frac{D_2}{D_1} \frac{dC_2}{dx} \Big _{cathode}$
Bromine	2	$0 = D_2 \frac{d^2 C_2}{dx^2} - R_{3,4} - R_{5,5}$	$\frac{dC_2}{dx} = \frac{5000(I_{app} - j)}{FD_2}$	$0 = \frac{D_2}{W} \left[\frac{dC_2}{dx} \right]_{ab1} - \frac{dC_2}{dx} \Big _{cb1} - \frac{C_2}{\tau} - R_{3,4} - R_{5,5}$	$C_2 _{cb1} = C_2 _{lab1}$	$C_2 = 0$
Propylene	3	$0 = D_3 \frac{d^2 C_3}{dx^2} - R_{4,4} - R_{6,5}$	$\frac{dC_3}{dx} = 0$	$0 = \frac{D_3}{W} \left[\frac{dC_3}{dx} \right]_{ab1} - \frac{dC_3}{dx} \Big _{cb1} + \frac{C_3^{in} - C_3}{\tau} - R_{3,4} - R_{5,5}$	$C_3 _{cb1} = C_3 _{lab1}$	$\frac{dC_3}{dx} = 0$
Propylene bromohydrin	4	$0 = D_4 \frac{d^2 C_4}{dx^2} + R_{3,4} - R_{4,6}$	$\frac{dC_4}{dx} = 0$	$0 = \frac{D_4}{W} \left[\frac{dC_4}{dx} \right]_{ab1} - \frac{dC_4}{dx} \Big _{cb1} - \frac{C_4}{\tau} + R_{3,4} - R_{4,6}$	$C_4 _{cb1} = C_4 _{lab1}$	$\frac{dC_4}{dx} = 0$
Propylene dibromide	5	$0 = D_5 \frac{d^2 C_5}{dx^2} + R_{3,5}$	$\frac{dC_5}{dx} = 0$	$0 = \frac{D_5}{W} \left[\frac{dC_5}{dx} \right]_{ab1} - \frac{dC_5}{dx} \Big _{cb1} - \frac{C_5}{\tau} + R_{3,5}$	$C_5 _{cb1} = C_5 _{lab1}$	$\frac{dC_5}{dx} = 0$
Propylene oxide	6	$0 = D_6 \frac{d^2 C_6}{dx^2} + R_{4,6} - R_{6,7}$	$\frac{dC_6}{dx} = 0$	$0 = \frac{D_6}{W} \left[\frac{dC_6}{dx} \right]_{ab1} - \frac{dC_6}{dx} \Big _{cb1} - \frac{C_6}{\tau} + R_{4,6} - R_{6,7}$	$C_6 _{cb1} = C_6 _{lab1}$	$\frac{dC_6}{dx} = 0$
Propylene glycol	7	$0 = D_7 \frac{d^2 C_7}{dx^2} + R_{6,7}$	$\frac{dC_7}{dx} = 0$	$0 = \frac{D_7}{W} \left[\frac{dC_7}{dx} \right]_{ab1} - \frac{dC_7}{dx} \Big _{cb1} - \frac{C_7}{\tau} + R_{6,7}$	$C_7 _{cb1} = C_7 _{lab1}$	$\frac{dC_7}{dx} = 0$
Hydroxide ion	8	$0 = D_8 \frac{d^2 C_8}{dx^2} - R_{3,4} - R_{4,6}$	$\frac{dC_8}{dx} = 2 \frac{D_6}{D_8} \frac{dC_4}{dx} \Big _{anode}$	$0 = \frac{D_8}{W} \left[\frac{dC_8}{dx} \right]_{ab1} - \frac{dC_8}{dx} \Big _{cb1} + \frac{C_8^{in} - C_8}{\tau} - R_{3,4} - R_{4,6}$	$C_8 _{cb1} = C_8 _{lab1}$	$\frac{dC_8}{dx} = \frac{1000(I_{app} - j)}{FD_8}$
Hydrogen	9	$0 = D_9 \frac{d^2 C_9}{dx^2}$	$C_9 = 0$	$C_9 = C_9^s$	$C_9 _{cb1} = C_9 _{lab1}$	$\frac{dC_9}{dx} = \frac{5000(I_{app} - j)}{FD_9}$
Hydrogen ion	10	$C_{10} = \frac{K_a}{C_8}$	—	—	—	—
Sodium ion	11	$C_{11} = C_1 + C_8 - C_{10}$	—	—	—	—

Table IV. List of concentration variable calculations and parameter values

Calculation	Constant parameters	Parameter variation
Feed pH	Sh = 2000 $\tau = 10$ s W = 1.0 cm $I_{app} = 0.100$ A/cm ² $Br^{-in} = 0.500$ Propylene/Br ₂ = 1.46	10 < pH ⁱⁿ < 14
Feed bromide ion	Sh = 2000 $\tau = 10$ s W = 1.0 cm $I_{app} = 0.100$ A/cm ² pH ⁱⁿ = 14 Propylene/Br ₂ = 1.46	0.100 < Br ⁻ⁱⁿ < 0.500
Mass-transport rate	$\tau = 10$ s $I_{app} = 0.100$ A/cm ² W = 1.0 cm $Br^{-in} = 0.500$ pH ⁱⁿ = 14 Propylene/Br ₂ = 1.46	200 < Sh < 2000
Space time	Sh = 2000 $Br^{-in} = 0.500$ W = 1.0 cm pH ⁱⁿ = 14 Propylene/Br ₂ = 1.46	2.00 < τ < 10.0 0.500 < I_{app} < 0.100
Space time	Sh = 2000 $Br^{-in} = 0.500$ W = 1.0 cm pH ⁱⁿ = 14 $I_{app} = 0.100$ A/cm ²	5.00 < τ < 10.0 2.92 > Propylene/Br ₂ > 1.46
Compound	Reference quantities for variable scaling Value	Ref.
Bromide ion	1	
Bromine	0.213	(54)
Propylene	7.56×10^{-3}	(55)
Propylene bromohydrin	7.56×10^{-3}	(55)
Propylene dibromide	7.56×10^{-3}	(55)
Propylene glycol	7.56×10^{-3}	(55)
Propylene oxide	7.56×10^{-3}	(55)
Hydrogen	100*	(56)
Hydrogen ion	1	
Hydroxide ion	1	
Sodium ion	1	

propylene in aqueous solution at 25°C and 1 atm pressure. The reference concentration for bromine is the saturation concentration, and for hydrogen is 100 times the saturation concentration in aqueous solution at 25°C and 1 atm pressure.

The reaction pathway represents, in essence, an indirect oxidation via electrochemically generated reactants.

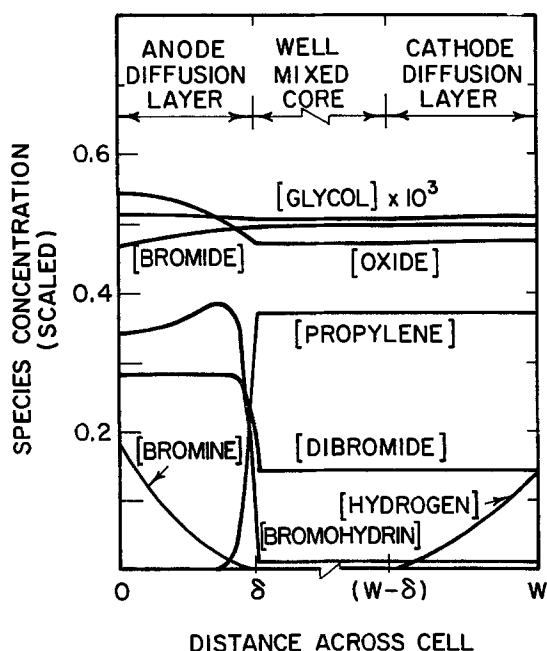


Fig. 3. Spatial variation of chemical species

That is, the electrochemically active species transfer the driving force, via bromine and hydroxide ion, to the propylene species.

Bromide ion entered the cell in the feed stream at a concentration of 0.500M. Bromide ion diffused to the anode, where it was oxidized to form bromine according to Eq. [1]. The Br₂ concentration at the anode surface had a value of 0.157 with respect to its saturation concentration. Within the anode mass-transfer boundary layer, Br₂ reacted with propylene to form propylene bromohydrin by Eq. [2]. The major cathodic reaction was electrolysis of water to form H₂ and OH⁻ ions according to Eq. [3]. Hydrogen concentrations, which were scaled against 100 times the saturation concentration, indicated values of 13 times the saturation concentration, indicated values of 13 times saturation at the cathode surface. The reaction of dissolved H₂ at the anode was found to cause an 8% loss of current efficiency under the conditions shown.

The propylene enters the cell in the feed stream at a dimensionless concentration of 1.0 and was reduced to a value of 0.371 by homogeneous reaction with Br₂. The largest rate of bromine-propylene reaction occurred where propylene contacted Br₂ within the anode diffusion layer. The propylene concentration decreased to essentially zero at the anode.

Bromohydrin and dibromide were formed at the reaction interface of propylene and Br₂. Both species exhibited maximum formation rates in the anodic diffusion layer at the bromine-propylene interface. In contrast to the sharp reaction zone formed by the bromine-propylene reaction, propylene oxide formation occurred over the entire reactor volume. Dibromide was formed in the anodic diffusion layer.

Propylene oxide had a spatial distribution with maximum concentrations near each electrode because the maximum rates of the oxide formation Eq. [4], occurred

near each electrode. The maximum near the anode was from the presence of high concentrations of bromohydrin; the maximum rate near the cathode was from the high concentrations of OH^- .

Glycol had behavior similar to that of propylene oxide, though it was less extreme since the reaction rate of oxide to glycol is four orders of magnitude slower than propylene oxide formation. The maximum near each electrode was caused by a different mechanism in the two-pathway route from oxide to glycol. The maximum rate of glycol formation near the anode was caused by uncatalyzed hydrolysis of oxide and thus exhibited a maximum rate in the regions of high oxide concentration. The cathodic glycol peak was from the base-catalyzed reaction pathway of glycol formation, and occurred from the high concentrations of OH^- within the cathodic diffusion layer.

For the particular case under discussion, the variation of potential across the cell is shown in Fig. 4. The potential drop was the result of IR drop across the cell, reversible electromotive force of the electrode reactions, and the overpotential of each electrode reaction. The example results show that the anodic overvoltage and the IR loss in solution were comparable and that the cathodic overvoltage was small. The conductivity used for this calculation was that which corresponds to dilute solution theory. The actual conductivity of a 0.500M NaBr solution is 32% less than the value predicted by dilute solution theory. Therefore, the IR drop is also in error by this amount.

The foregoing model was also used to investigate the response of the parallel-plate electrochemical cell to design variables. The most sensitive variables in the chemistry were $[\text{Br}^-]$ and pH. $[\text{Br}^-]$ controlled the yield of propylene oxide by determining the fraction of propylene converted to the bromohydrin. pH controlled the rate of propylene oxide generation.

Effect of pH.—The effects of feed-stream pH are summarized for three cases in Fig. 5. Additional data are provided in Table V as well as in the original reference (1). The effect of hydroxide ion concentration was chiefly upon the bromohydrin-oxide reaction, Eq. [4], and, to a lesser degree, on the oxide-glycol reaction, Eq. [7]. The decrease in the feed-stream pH caused the bromohydrin not to be converted to propylene oxide owing both to thermodynamics and also to pH dependence of the reaction rate. At lower feed-stream pH, the hydroxide ions re-

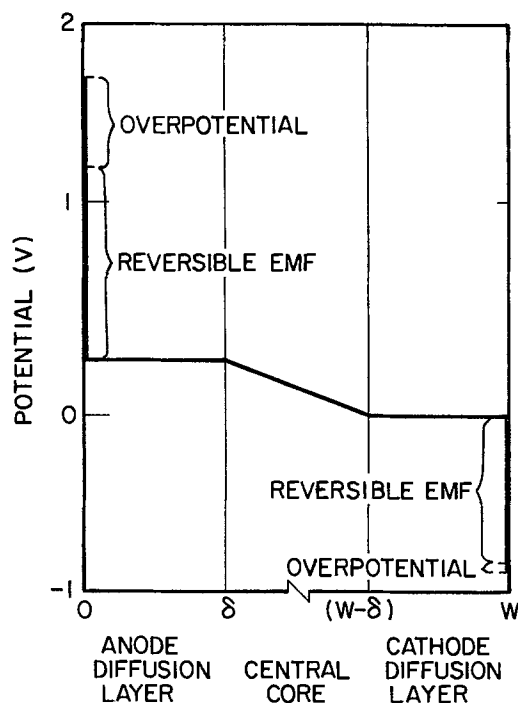


Fig. 4. Spatial variation of potential

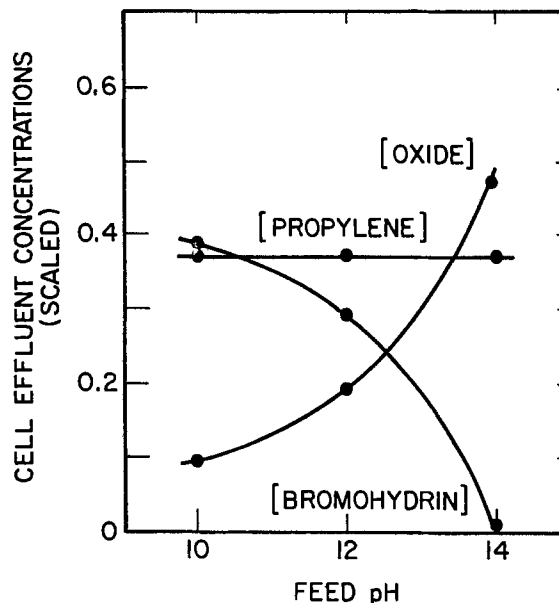


Fig. 5. Effect of feed-stream pH

mained unreacted and served to increase sizably the central region pH above that of the feed. The selectivity of oxide-glycol was decreased through the increase in basicity; glycol formation was not significant at any pH considered. The decrease in hydroxide ion concentration also influenced the cathodic overpotential and decreased the solution conductivity, resulting in increased cell voltage.

Efficient conversion of bromohydrin to oxide was dependent on the pH in the electrolyzer. The equilibrium constant for the oxide formation reaction is 1.03×10^9 at unit concentrations and pH 14, but only 1.01×10^{-5} at pH 1. One method of accomplishing bromohydrin conversion was to force the reaction to completion with large hydroxide ion concentrations; 98% of the bromohydrin was converted to oxide at pH 14.

The operation of the cell at extremely high pH conditions may cause other reactions, not included in the model, to influence the reaction sequence. The hydrolysis of bromine to form $\text{Br}(+1)$ species, and further reaction to $\text{Br}(+5)$, may influence the rate of the propylene-bromine reaction. $\text{Br}(+1)$ formation would cause a decrease in the yield of propylene oxide with increasing pH. Increased basicity may cause other electrode reactions to occur in addition to bromine formation at the anode and water electrolysis at the cathode.

Effect of bromide ion concentration.—The effects of variation in the feed-stream bromide ion concentration are presented in Fig. 6; additional data are given in Table V. Decreasing $[\text{Br}^-]$ did not affect the rate of propylene consumption by bromine, but changed the ratio of bromohydrin to dibromide produced. Higher fractions of bromohydrin are formed when the bromine-propylene reaction occurs at low $[\text{Br}^-]$. Dilute bromide solution allows greater likelihood of hydroxide ion attacking the cation intermediate vs. the bromide ion which forms propylene dibromide. Decreased $[\text{Br}^-]$ thus resulted in increased selectivity of oxide/dibromide. High pH conditions allow the additional bromohydrin to be reacted further to form propylene oxide. The maximum yield observed was 90.4% at 0.100M $[\text{Br}^-]$. Higher yields could be achieved by decreasing $[\text{Br}^-]$ further. The decrease in bromide and sodium ion concentrations increased the cell voltage through IR resistance and the slightly larger anodic overpotential; the possibility of adding inert supporting electrolyte was not explored.

Greatest yields of propylene oxide are formed when low concentrations of Br^- were present at the propylene-bromine reaction interface. Decreased $[\text{Br}^-]$ also minimized formation of dibromide by-product.

Effect of mass transfer.—The effect of mass transfer is shown in Fig. 7 and in Table V. The variation of mass-

transfer conditions was done while holding all other parameters constant. Mass-transfer variation by this procedure corresponds experimentally to modification of turbulence promoters within the flow channel; changing the flow rate would influence reactor space time.

The decrease in mass-transfer rates caused higher conversion of propylene by 4%. The decreased transport of H₂ to the anode reduced the rate of side reaction, Eq. [3], and thus increased the current efficiency, generating more bromine for reaction. Slight increase in the oxide/dibromide selectivity with decreasing mass-transfer rates came about because the bromine-propylene reaction interface was shifted to regions having lower bromide ion concentrations.

Decreasing mass-transfer slightly increased the selectivity of oxide over dibromide, and also increased the cell

Table V. Effect of operating conditions

Conditions			
Sh = 2000	$\tau = 10$ s	Propylene/Br ₂ = 1.46	
$I_{app} = 0.100$ A/cm ²	Br ^{- in} = 0.50	W = 1.0 cm	
$pH_{in} =$	10	12	14
Scaled concentrations and cell potentials			
Bromide ion	0.496	0.496	0.497
Bromine	1.18×10^{-5}	1.17×10^{-5}	1.18×10^{-5}
Hydroxide ion	5.22×10^{-3}	1.41×10^{-2}	1.03
Propylene	0.371	0.372	0.371
Oxide	0.0959	0.192	0.472
Cell voltage	3.69	3.66	2.58
IR resistance	1.55	1.50	0.314
Anode overpotential	0.500	0.500	0.499
Cathode overpotential	-0.076	-0.067	-0.057
Selectivity and yield			
Oxide/bromohydrin	0.247	0.649	48.9
Oxide/dibromide	0.660	1.32	3.21
Oxide/glycol	180,000	72,100	926
Yield	15.2%	30.6%	75.0%
Illustrated in figure	5	5	3-5
Effect of feed-stream bromide ion concentration			
Conditions			
Sh = 2000	$\tau = 10$ s	Propylene/Br ₂ = 1.46	
$I_{app} = 0.100$ A/cm ²	$pH_{in} = 14$	W = 1.0 cm	
Br ^{- in} =	0.100	0.300	0.500
Scaled concentrations and cell potentials			
Bromide ion	0.0971	0.298	0.497
Bromine	1.05×10^{-5}	1.15×10^{-7}	1.18×10^{-7}
Hydroxide ion	1.01	1.02	1.03
Propylene	0.372	0.371	0.371
Oxide	0.567	0.505	0.472
Cell voltage	2.71	2.63	2.58
IR resistance	0.382	0.345	0.314
Anode overpotential	0.523	0.503	0.499
Cathode overpotential	-0.057	-0.057	-0.057
Selectivity and yield			
Oxide/bromohydrin	48.4	48.1	48.9
Oxide/dibromide	11.1	4.50	3.21
Oxide/glycol	968	970	926
Yield	90.4%	80.3%	75.0%
Illustrated in figure	6	6	3, 4, 6
Effect of mass transfer			
Conditions			
t = 10s	$I_{app} = 0.100$ A/cm ²	Propylene/Br ₂ = 1.46	
Br ^{- in} = 0.500	$pH_{in} = 14$	W = 1.0 cm	
Sh =	200	1000	2000
Scaled concentrations and cell potentials			
Bromide ion	0.498	0.497	0.497
Bromine	1.80×10^{-7}	2.03×10^{-7}	1.18×10^{-5}
Hydroxide ion	1.00	1.01	1.03
Propylene	0.327	0.349	0.371
Oxide	0.507	0.489	0.472
Cell voltage	2.85	2.61	2.58
IR resistance	0.340	0.322	0.314
Anode overpotential	0.729	0.513	0.499
Cathode overpotential	-0.071	-0.060	-0.057
Selectivity and yield			
Oxide/bromohydrin	46.8	47.8	48.9
Oxide/dibromide	3.27	3.25	3.21
Oxide/glycol	992	981	926
Yield	75.3%	75.1%	75.1%
Illustrated in figure	7	7	3, 4, 7

Table V (continued). Effect of operating conditions

Effect of space time at constant stoichiometric ratio			
Conditions			
Sh = 2000	Propylene/Br ₂ = 1.46 W = 1.0 cm		
Br ^{- in} = 0.500	$pH_{in} = 14$		
$\tau =$	2.00	5.00	10.0
$I_{app} =$	0.500	0.200	0.100
Scaled concentrations and cell potentials			
Bromide ion	0.497	0.497	0.497
Bromine	1.33×10^{-6}	4.13×10^{-7}	1.18×10^{-3}
Hydroxide ion	1.00	1.00	1.03
Propylene	0.326	0.345	0.371
Oxide	0.467	0.483	0.472
Cell voltage	3.93	2.92	2.58
IR resistance	1.61	0.644	0.314
Anode overpotential	0.513	0.490	0.499
Cathode overpotential	-0.077	-0.065	-0.057
Selectivity and yield			
Oxide/bromohydrin	9.21	23.2	48.9
Oxide/dibromide	3.01	3.20	3.21
Oxide/glycol	4980	2000	926
Yield	69.3%	73.7%	75.0%
Illustrated in figure	8	8	3, 4, 8
Effect of space time at constant current			
Conditions			
Sh = 2000	$I_{app} = 0.100$ A/cm ²	W = 1.0 cm	
Br ^{- in} = 0.500	$pH_{in} = 14$		
$\tau =$	5.00	10.0	
Propylene/Br ₂	2.92	1.64	
Scaled concentrations and cell potentials			
Bromide ion	0.499	0.497	
Bromine	9.62×10^{-8}	1.18×10^{-5}	
Hydroxide ion	1.00	1.03	
Propylene	0.688	0.371	
Oxide	0.231	0.472	
Cell voltage	2.64	2.58	
IR resistance	0.322	0.314	
Anode overpotential	0.590	0.499	
Cathode overpotential	-0.057	-0.057	
Selectivity and yield			
Oxide/bromohydrin	24.4	48.9	
Oxide/dibromide	3.28	3.21	
Oxide/glycol	1960	926	
Yield	74.0%	75.0%	
Illustrated in figure	—	3, 4	

voltage. The yield of propylene oxide was not sensitive to mass transfer over the range of conditions studied.

Effect of space time.—The results of reactor space-time variation under conditions of constant stoichiometry are presented in Fig. 8 and in Table V. The propylene/Br₂ stoichiometric ratio was kept constant by increasing the current with decreasing space time to achieve the same theoretical conversion of propylene; therefore, the decrease in space time caused increased potential drop from IR and overpotential losses owing to the increased current. Decreased space time promoted propylene conversion by increasing anodic current efficiency. The variation in space time affected the conversion of bromohydrin to propylene oxide; the incomplete conversion was from the slowness of the bromohydrin-oxide reaction, Eq. [4], which decreased the oxide/bromohydrin selectivity. The conversion of bromohydrin to propylene oxide decreased with decreasing space time.

The dominant region for the bromohydrin to oxide and oxide to glycol reactions was in the central stirred core, and both reactions were affected by the variation in space time. The faster propylene-bromine reaction was unaffected since the reaction zone was within the anode diffusion layer.

The results of the reactor space-time variation with constant current are also presented in Table V. The decrease in space time with constant cell current decreased the theoretical conversion of propylene. Although the yield of propylene oxide was not significantly influenced, the decreased conversion of propylene gave better selectivity of oxide to dibromide and oxide to glycol. The potential field across the cell was virtually unaffected.

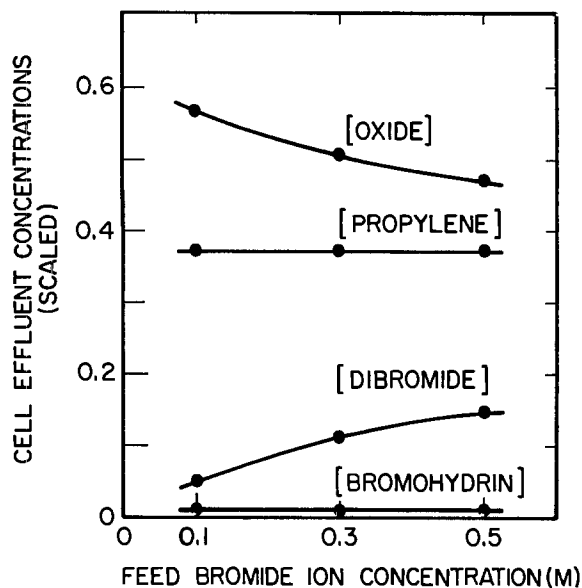


Fig. 6. Effect of feed-stream bromide ion concentration

The synthesis for propylene oxide was found to be more efficient by producing less dibromide under lower conversions of propylene. Additional advantages would be gained in the oxide/dibromide selectivity by operating the reactor at lower conversions and increased propylene concentration (pressure).

Conclusions

This work demonstrates procedures for incorporating realistic reaction mechanisms into models of electrolytic cells. Limitations on computational feasibility were encountered owing to stiffness of the differential equation describing the reactor. It was found that dynamic simulation with the Forsim VI algorithm gave good results. By this procedure, the dependence of space-time yield, conversion efficiency, and power consumption upon variation of design variables were predicted for paired synthesis of propylene oxide in an undivided cell.

The example of propylene oxide synthesis has been useful for the purpose of illustrating the general procedures involved in this study, but the central contribution of this work should be recognized to be applicable to many other specific process candidates, including inorganic syntheses. For the propylene oxide system, the effect of an increase in pH is to facilitate the in-cell conversion of bromohydrin to propylene oxide owing both to

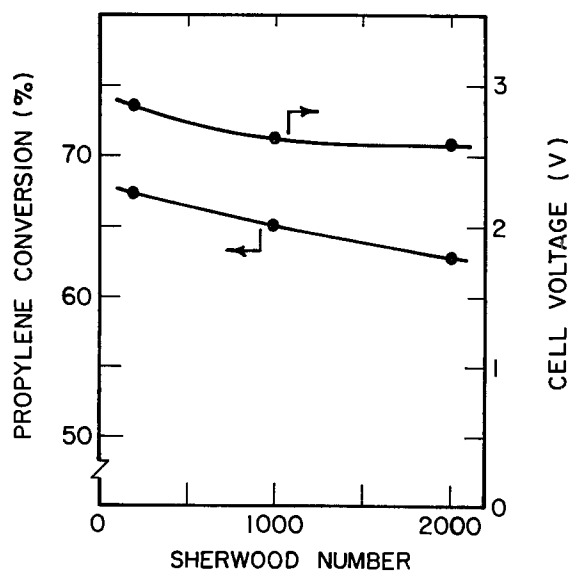
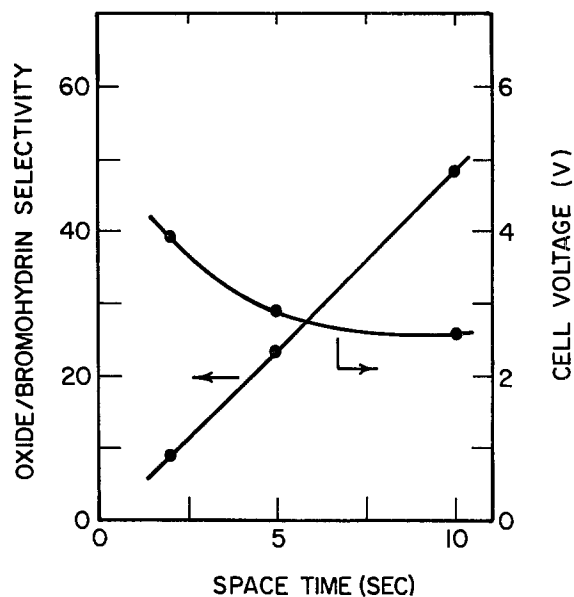


Fig. 7. Effect of mass transfer

Fig. 8. Effect of space time of constant Br_2 /propylene stoichiometric ratio.

the appearance of OH^- in the reaction and also to the pH dependence of the rate constant. The bromide ion concentration influences reaction of bromine and propylene in the anodic diffusion layer, giving dibromide at high concentrations and bromohydrin at low concentrations. The variation of mass-transfer coefficient was found not to influence selectivity or yield significantly. An increase in space time, however, was found to enhance the in cell conversion of bromohydrin to propylene oxide which occurs throughout the cell volume. Variation in space time had an insignificant effect on the dibromide/bromohydrin ratio, which is determined by conditions in the anodic diffusion layer.

As the level of sophistication of mathematical simulation increases, the accuracy of supporting knowledge of mechanism and of data base must also increase. In the present study, it was necessary to have specific rate equations, rate constants, thermodynamic equilibrium constants, transport properties, reaction stoichiometry, knowledge of reaction intermediates, and mass-transfer coefficient. Models of electrolytic cells can also be extended to include economic balances in order to identify reactor designs and operating conditions which optimize economic objectives. The extent to which such auxiliary data are available will determine, to a large degree, the accuracy with which model predictions can simulate realistic cell behavior.

Acknowledgment

This work was supported by the National Science Foundation (Grants ENG 76-83379 and CPE 80-08947).

Manuscript submitted Oct. 13, 1983; revised manuscript received ca. June 15, 1984.

The University of Illinois assisted in meeting the publication costs of this article.

LIST OF SYMBOLS

- a cathodic charge transfer coefficient (dimensionless)
- b anodic charge transfer coefficient (dimensionless)
- C_i concentration of species i ($\text{mol}\cdot\text{liter}^{-1}$)
- D_i diffusion coefficient of species i ($\text{cm}^2\cdot\text{s}^{-1}$)
- E potential (V)
- f fraction of bromine-propylene reaction forming bromohydrin (dimensionless)
- F Faraday's constant ($96,500 \text{ C}/\text{eq}$)
- i^0 exchange current density (A/cm^2)
- I_{app} cell applied current (A)
- j_i current density of electrochemical reaction i (A/cm^2)
- k forward homogeneous reaction rate constant ($\text{mol}\cdot\text{liter}^{-1}$ and s)

K	thermodynamics equilibrium constant (dimensionless)
K_w	water hydrolysis constant (1.0×10^{-14})
n	number of electrons in electrochemical reaction
ODE	ordinary differential equation
Propylene/Br ₂	stoichiometric ratio of propylene to bromine at exit of reactor (dimensionless)
R	universal gas constant ($8.314 \text{ J}\cdot\text{mol}^{-1}\cdot\text{deg}^{-1}$)
$R_{i,j}$	reaction rate of i to j ($\text{mol}\cdot\text{liter}^{-1}\cdot\text{s}^{-1}$)
Sh	Sherwood number (dimensionless)
t	time (s)
T	absolute temperature (K)
u_i	ionic mobility of species i ($\text{cm}^2\cdot\text{mol}^{-1}\cdot\text{s}^{-1}$)
V	V vs. NHE
W	electrochemical cell width (cm)
x	spatial coordinate across electrochemical cell (cm)

Greek Characters

δ	diffusion layer thickness (cm)
τ	reactor space time (s)

Superscripts

in	feed stream value
^o	reference value
s	saturation value
*	central core value
'	value for elementary step or different mechanism
"	value for elementary step or different mechanism

Subscripts

anodic	value for anodic reaction
cathodic	value for cathodic reaction
eq	equilibrium potential for electrochemical reaction
i	species i
j	species j
ij	value for reaction of species i to species j
abl	value at stirred core edge of anodic diffusion layer
cb1	value at stirred core edge of cathodic diffusion layer

REFERENCES

- J. D. Lisius, M. S. Thesis, University of Illinois, Urbana, IL (1982).
- D. J. Pickett, "Electrochemical Reactor Design," Elsevier Scientific Publishing Co., Amsterdam (1979).
- G. D. Cera, Ph.D. Thesis, University of Illinois, Urbana, IL (1983).
- R. C. Alkire, *AICHE Symp. Ser.*, **77**, 121 (1981).
- G. A. Prentice and C. W. Tobias, *This Journal*, **129**, 72 (1982).
- J. Lee and J. R. Selman, *ibid.*, **129**, 1670 (1982).
- J. S. Newman and W. Tiedeman, *Av. Electrochem. Electrochem. Engr.*, **11**, 353 (1978).
- R. C. Alkire and R. M. Gould, *This Journal*, **127**, 605 (1980).
- L. Lapidus, in "Numerical Solution of Boundary Value Problems for Ordinary Differential Equations," A. K. Aziz, Editor, Academic Press, Inc., New York (1975).
- R. A. Willoughby, Editor, "Stiff Differential Systems," Plenum Publishing Co., New York (1974).
- M. M. Baizer, Editor, "Organic Electrochemistry," Marcel Dekker, Inc., New York (1973).
- S. Swann and R. Alkire, "Bibliography of Electro-Organic Syntheses, 1801-1975," The Electrochemical Society, Princeton, NJ (1980).
- T. Beck, R. Alkire, N. L. Weinberg, R. Ruggeri, and M. Stadtherr, in "Technique of Electroorganic Synthesis," Part III, N. L. Weinberg and B. V. Tilak, Editors, p. 423, Wiley Interscience, New York (1982).
- J. A. M. LeDuc, U.S. Pat. 3,288,692 (1966); U.S. Pat. 3,342,717 (1967); U.S. Pat. 3,379,627 (1968); U.S. Pat. 3,723,264 (1973).
- K. H. Simmrock, *AICHE Symp. Ser.*, **75**, 89 (1979).
- P. Robertson, P. Cetton, D. Matic, A. Schwager, and N. Ibl, *AICHE Symp. Ser.*, **75**, 115 (1979).
- F. Beck, in "XXIV International Congress of Pure and Applied Chemistry," Vol. 5, p. 111, Butterworths, London (1973).
- J. Ghoroghchian, R. E. W. Jansson, and D. Jones, *J. Appl. Electrochem.*, **7**, 437 (1977).
- M. Eigen and K. Kustin, *J. Am. Chem. Soc.*, **84**, 1355 (1962).
- J. R. Atkinson and R. P. Bell, *J. Chem. Soc.*, 3260 (1963).
- R. Bolton, in "Comprehensive Chemical Kinetics," Vol. 9, C. H. Bamford and C. F. H. Tipper, Editors, p. 26, Elsevier Scientific Publishing Co., Amsterdam (1973).
- L. S. Boguslavskaya, *Russ. Chem. Rev.*, **41**, 740 (1972).
- J. Hine, "Physical Organic Chemistry," 2nd ed., McGraw-Hill, New York (1962).
- P. D. Bartlett and D. S. Tarbell, *J. Am. Chem. Soc.*, **58**, 466 (1936).
- G. Berti, in "Topics in Stereochemistry," Vol. 7, N. L. Allinger and E. L. Eliel, Editors, Interscience, New York (1973).
- B. L. Vorob'ev and A. L. Shapiro, *Reakts. Sposobnost. Org. Soedin.*, **10**, 1111 (1973).
- A. Rosowsky in "The Chemistry of Heterocyclic Compounds," Vol. 19, Part 1, A. Weissberger, Editor, p. 95, Interscience, New York (1964).
- E. P. White and P. W. Robertson, *J. Chem. Soc.*, 1509 (1939).
- R. O. Griffith, A. McKwoen, and A. G. Winn, *Trans. Faraday Soc.*, **28**, 101 (1932).
- A. G. Sharpe, in "Inorganic and Theoretical Chemistry," Vol. 2, Suppl. 1, John Wiley and Sons, New York (1962).
- A. J. Bard, in "Encyclopedia of Electrochemistry of the Elements," Vol. 1, A. J. Bard, Editor, p. 57, Marcel-Dekker Inc., New York (1973).
- A. J. deBethune and N. A. Swendeman Loud, "Standard Aqueous Electrode Potentials and Temperature Coefficients at 25°C," Hampel Publishing Co., Skokie, IL (1964).
- B. Perlmutter-Hayman and G. Stein, *J. Phys. Chem.*, **63**, 734 (1959).
- G. Forsberg, *Acta Chem. Scand.*, **8**, 135 (1954).
- P. M. Loughton and R. E. Robertson, *Can. J. Chem.*, **39**, 2155 (1961).
- R. A. Wohl, *Chimia*, **28**, 1 (1974).
- A. Rosowsky, in "The Chemistry of Heterocyclic Compounds," Vol. 19, Part 1, A. Weissberger, Editor, p. 270, Interscience, New York (1964).
- F. A. Long and J. G. Pritchard, *J. Am. Chem. Soc.*, **78**, 2663 (1956).
- J. G. Pritchard and F. A. Long, *ibid.*, **78**, 2667 (1956).
- K. J. Vetter, "Electrochemical Kinetics," p. 470, Academic Press, New York (1967).
- W. M. Latimer, "The Oxidation States and Their Potentials in Aqueous Solution," 2nd ed., Prentice-Hall, Inc., New York (1952).
- G. Faita, G. Fiori, and T. Mussini, *Electrochim. Acta*, **13**, 1765 (1968).
- R. Parsons, "Handbook of Electrochemical Constants," p. 97, Butterworths Scientific Publications, London (1959).
- M. J. Blandamer, H. S. Golinkin, and R. E. Robertson, *J. Am. Chem. Soc.*, **91**, 2678 (1969).
- J. S. Newman, "Electrochemical Systems," p. 217, Prentice-Hall, Inc., Englewood Cliffs, NJ (1973).
- R. Parsons, "Handbook of Electrochemical Constants," p. 79, Butterworths Scientific Publishing, London (1959).
- R. H. Perry and C. H. Chilton, Editors, "Chemical Engineer's Handbook," 5th ed., pp. 3-224, McGraw-Hill, New York (1973).
- J. E. Vivian and C. J. King, *AICHE J.*, **10**, 220 (1964).
- R. Parsons, "Handbook of Electrochemical Constants," p. 85, Butterworths Scientific Publishing, London (1959).
- R. C. Reid, J. M. Prausnitz, and T. K. Sherwood, "The Properties of Gases and Liquids," 3rd ed., p. 567, McGraw-Hill, New York (1977).
- R. C. Reid, J. M. Prausnitz, and T. K. Sherwood, "The Properties of Gases and Liquids," 3rd ed., p. 57, McGraw-Hill, New York (1977).
- M. B. Carver, in "Numerical Methods for Differential Systems," L. Lapidus and W. E. Schiesser, Editors, Academic Press, Inc., New York (1976).
- M. B. Carver, D. G. Stewart, J. M. Blair, and W. N. Selander, "The Forsim VI Simulation Package for the Automated Solution of Arbitrarily Defined Partial and/or Ordinary Differential Equation Systems," p. 112, AECL-5821, Atomic Energy of Canada Ltd., Chalk River, Ont., Canada (1978).
- W. F. Linke, Editor, "Solubilities of Inorganic and Organic Compounds," 4th ed., Vol. 1, p. 440, Van Nostrand, Princeton, NJ (1958).
- A. Azarnoosh and J. J. McKetta, *J. Chem. Eng. Data*, **4**, 211 (1959).
- J. A. Dean, Editor, "Lange's Handbook of Chemistry" 12th ed., p. 10-3, McGraw-Hill, New York (1979).

The Wetting Behavior of Dialkylimidazolium Chloroaluminate, a Room Temperature Molten Salt

J. G. Eberhart¹

The Frank J. Seiler Research Laboratory, U.S. Air Force Academy, Colorado Springs, Colorado 80840

The wetting behavior of a battery electrolyte can have a dramatic effect on the internal resistance of the battery as well as its cycle life (1). Good wetting of battery separators by electrolyte is essential for the easy passage of ions through the separator pores during charge and discharge. Porous, gas diffusion electrodes require, on the other hand, a lesser degree of electrolyte wetting, so that the line of contact of the three phases (reactive gas/liquid electrolyte/porous electrode or current collector) can be maintained within the porous electrode through a balance of capillary and hydrostatic pressures.

For several years, a room temperature molten salt system composed of 1-methyl-3-ethylimidazolium chloride ($C_6N_2H_{11}Cl$ or MeEtImCl) plus aluminum chloride has been under study at the Frank J. Seiler Research Laboratory (2-5). The most promising application of this novel liquid solution is as a battery electrolyte. Analysis of available physical and electrochemical data suggests that cells with a chlorine positive electrode reactant and a magnesium, aluminum, or zinc negative electrode material are likely candidates (6).

To assess wetting behavior in this electrochemical system, a study was undertaken of the contact angles of various room temperature molten salts on candidate battery separator and porous electrode materials. The factors examined in the study were the effects on wettability of (i) the melt composition, (ii) chemical constitution of the solid, (iii) chlorination of the organic component of the melt, (iv) replacement of the $AlCl_3$ component by other inorganic compounds, and (v) cleaning procedure for the solid.

Theory

The wettability of a solid surface is defined in terms of the contact angle, θ , made by a liquid drop resting on the solid surface (7); see Fig. 1. The angle θ can take on values ranging from 0° to 180° . The contact angle made by a liquid on a solid can have either one value or a range of possible values, depending on the nature of the solid surface.

If the solid surface is idealized as smooth, chemically homogeneous, isotropic, and nondeformable, and there is no mutual solubility or chemical reaction between the two phases, then there is only one stable, equilibrium contact angle which is given by Young's equation (7)

$$\gamma_{LV} \cos \theta = \gamma_{SV} - \gamma_{SL} \quad [1]$$

where γ_{LV} is the liquid surface tension, γ_{SV} is the solid surface tension, and γ_{SL} is the interfacial tension between the solid and liquid phases.

A real solid surface, on the other hand, may be rough, chemically heterogeneous, and anisotropic and the contacting liquid will have a range of allowed contact angles rather than a single value (7). The maximum angle is called the advancing contact angle, θ_A , while the minimum angle is called the receding contact angle, θ_R . The difference $\theta_A - \theta_R$ is the contact-angle hysteresis. The

¹Permanent address: Department of Chemistry, University of Colorado, Colorado Springs, Colorado 80933-7150

range of contact angles in these systems leads to three categories of wetting behavior (8). If $\theta_R < \theta_A < 90^\circ$, then the solid is easy to wet by the liquid and the liquid will spontaneously penetrate pores of the same solid. If $\theta_R < 90^\circ < \theta_A$, then the solid is difficult to wet by the liquid and the liquid will not spontaneously penetrate pores of the same solid. However, if the liquid is forced into these pores by the application of a hydrostatic pressure, it will remain in the pores after the pressure is removed. Finally, if $90^\circ < \theta_R < \theta_A$, then the solid is impossible to wet by the liquid and the liquid will not spontaneously penetrate pores of the same solid. If the liquid is forced into these pores, it will spontaneously leave the pores when the force is removed.

The advancing and receding contact angles were determined from observations of a tilting sessile drop (7). If the angle of tilt of the substrate is increased, then the upper and lower contact angles of the drop, θ_U and θ_L , will approach their limiting or extreme values of θ_R and θ_A , respectively; see Fig. 2.

Experimental Methods

The 1-methyl-3-ethylimidazolium chloride and aluminum chloride are reactive with moisture, so the preparation of their solutions at various compositions and the determination of contact angles on various solid surfaces was carried out entirely within a helium glove box having moisture and oxygen concentrations of less than 10 ppm (3). The MeEtImCl was prepared from vacuum-distilled 1-methylimidazole (obtained from Aldrich Chemical Company) as previously described (3). The $AlCl_3$ (obtained from Fluka Chemical Corporation) was sublimed (9) before mixing with the MeEtImCl. The salt solutions were prepared at $AlCl_3$ mole fractions, N , of 0.333, 0.500, 0.600, and 0.667. This choice covers the range of basic ($N < 0.5$), neutral ($N = 0.5$), and acidic ($N > 0.5$) behavior and was selected to show the effect of melt composition on wetting behavior.

Solutions were also prepared using the chlorinated imidazolium salt, 4,5-dichloro-1-methyl-3-ethylimidazolium chloride ($C_6N_2H_9Cl_2$), with $AlCl_3$ mole fractions of 0.375, 0.600, and 0.650, to determine the effect of chlorination on wetting behavior.

A solution of the imidazolium salt with lithium chloride was also prepared with a $LiCl$ mole fraction of 0.376 to examine the effect of the $AlCl_3$ on wetting behavior.

A simple tilting stage was fabricated in order to observe upper and lower contact angles as a function of the substrate tilt angle. The stage can hold substrates of interest



Fig. 1. The contact angle of a liquid on a solid surface

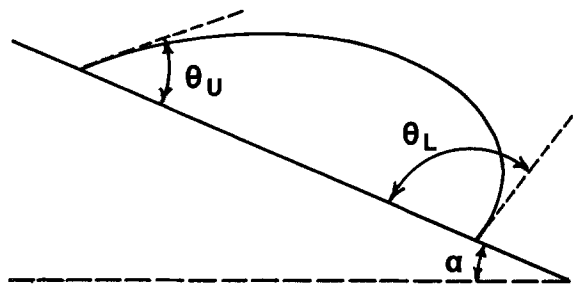


Fig. 2. The upper and lower contact angles of a liquid drop on an inclined solid surface.

(whether rigid or film) in any orientation from horizontal to vertical. The contact angles and tilt angles were observed through the glove box window with a Gaertner telemicroscope equipped with a goniometer and two X-Y positioning micrometers.

The substrates examined were soda-lime glass microscope slides, Teflon (Berghof/America, Incorporated), Celgard 2500 and 3501 polypropylene film (Celanese Corporation) with 45% porosity and 0.04 μm pore size, and reticulated vitreous carbon or RVC (Energy Research and Generation, Incorporated) with a 97% porosity and 70-90 pores per inch.

The substrates were cleaned in various ways. The soda-lime glass was washed either with Alconox solution (Alconox, Incorporated) or with Chromerge chromic-sulfuric acid solution (Manostat), and then rinsed with water and with ethanol. Residual ethanol and water were removed from the samples by evacuation while they were transferred into the glove box. The Celgard films and the RVC were washed in ethanol. Although the two Celgard films have the same mechanical properties and pore structure, the Celgard 3501 is hydrophilic because of treatment with proprietary surfactant. As a result, the Celgard 3501 is more wettable by aqueous systems than the hydrophobic Celgard 2500. This difference could be observed during cleaning of the two films with ethanol. The films are white and opaque, but when the 3501 was cleaned with ethanol it became momentarily transparent. A Celanese technical representative attributed this behavior to the pore filling of the 3501 film and the resultant change in optical properties.

Experimental Results

The advancing and receding contact angles for a number of different room temperature, dialkylimidazolium chloroaluminate molten salts were determined on the substrates described above using the tilting drop technique at temperatures in the range of 27°-28°C. The results of these measurements are summarized in Table I.

The advancing and receding contact angles for the 1-methyl-3-ethylimidazolium chloride plus aluminum chloride melts on glass, Teflon, polypropylene, and RVC surfaces are shown in the first portion of Table I. All of the substrates except the RVC are easy to wet by the melt with spreading observed for several acidic melts on glass. RVC is difficult to wet by basic and neutral melts.

The contact angles for chlorinated melts of 1-methyl-3-ethylimidazolium chloride plus aluminum chloride on glass surfaces are shown in the second part of Table I. As with the nonchlorinated melts, glass is easy to wet by the chlorinated melt.

The last portion of Table I shows the results of replacing AlCl_3 by LiCl in the 1-methyl-3-ethylimidazolium chloride melts. Glass and Celgard 2500 substrates were difficult to wet by a basic melt of this system.

Conclusions

An examination of the data presented suggests the following. 1. The 1-methyl-3-ethylimidazolium chloride plus aluminum chloride melts show easy-to-wet behavior on all substrates tested except RVC. The RVC is difficult to wet by basic or neutral melts and easy to wet by acidic

Table I. Advancing and receding contact angles for various imidazolium containing molten salts on several substrates

Melt	Substrate/cleaning	N^a	θ_a (deg)	θ_r (deg)
$\text{C}_6\text{N}_2\text{H}_7\text{Cl} + \text{AlCl}_3$	Glass/Alconox	0.333	65	13
		0.500	59	15
		0.600	0	0
		0.667	0	0
	Glass/Chromerge	0.333	33	8
		0.500	32	7
		0.600	17	6
		0.667	0	0
	Teflon/ethanol	0.333	77	48
		0.500	77	48
		0.600	60	23
		0.667	0	0
Celgard 2500/ ethanol	0.333	74	32	
	0.500	69	—	
	0.600	58	19	
	0.667	51	8	
Celgard 3501/ ethanol	0.333	74	25	
	0.500	73	39	
	0.600	51	0	
	0.667	63	0	
RVC/ethanol	0.333	108	32	
	0.500	100	41	
	0.600	Penetrated pores		
	0.667	Penetrated pores		
$\text{C}_6\text{N}_2\text{H}_9\text{Cl}_3 + \text{AlCl}_3$	Glass/Chromerge	0.375	50	15
		0.600	16	4
		0.650	0	0
$\text{C}_6\text{N}_2\text{H}_7\text{Cl} + \text{LiCl}$	Glass/Chromerge	0.376	115	9
	Celgard 2500/ ethanol	0.376	112	52

^a N is the mole fraction of the inorganic melt component.

melts. 2. With only one exception (Celgard 3501), wetting behavior improves as the mole fraction of AlCl_3 increases. 3. On glass surfaces, the chlorination of the 1-methyl-3-ethylimidazolium chloride has relatively little effect on the melt's wetting behavior. 4. When aluminum chloride is replaced by lithium chloride the easy-to-wet behavior changes to difficult-to-wet behavior on the surfaces tested. 5. The treatment of polypropylene film with a surfactant to change the surface from a hydrophobic to a hydrophilic nature has little effect on the wettability of the surface by the molten salts studied here. 6. The way in which a surface is cleaned can have a dramatic effect on its wettability.

These results indicate that AlCl_3 plays a key role in the good wetting of these molten salt solutions. This view is supported by the previously reported effectiveness of LiAlCl_4 as a battery-separator wetting promoter for LiCl-KCl molten salt solutions (1, 10).

Based on the above observations, a number of conclusions can be drawn regarding the wetting behavior of battery electrolyte containing AlCl_3 and dialkylimidazolium chloride. 1. It is not expected that any serious problems will be encountered with the wetting of battery separators and porous electrodes, especially in the acidic range of concentrations. 2. It is possible that electrolyte wetting may be better than desired in the case of gaseous electrode reactants. If such problems should occur, it is likely they could be remedied by a decrease in the AlCl_3 mole fraction without serious impairment of separator and current-collector wettability. 3. If chlorinated melts are used in original cell designs or produced as a result of a chlorine gas positive electrode, their wetting behavior is likely to be about the same as that of the nonchlorinated melts. 4. If electrolytes are considered without AlCl_3 as the inorganic component, then the generally favorable wetting picture presented here could change dramatically for the worse.

Acknowledgments

The author would like to thank the Air Force Systems Command, the Air Force Office of Scientific Research, and the Southeastern Center for Electrical Engineering

Education for providing the opportunity to carry out this research. He would also like to acknowledge the support of and helpful technical discussions with Lt. Col. Chester J. Dymek, Jr., Lt. Col. Armand A. Fannin, Jr., and Dr. John S. Wilkes of the Frank J. Seiler Research Laboratory.

Manuscript submitted Oct. 22, 1984; revised manuscript received March 19, 1985.

The U.S. Air Force Academy assisted in meeting the publication costs of this article.

REFERENCES

1. J. G. Eberhart, Argonne National Laboratory Report, ANL-79-34 (1979).
2. J. S. Wilkes, J. A. Levisky, C. L. Hussey, and M. L. Druelinger, Paper 648 presented at the 158th Electrochemical Society Meeting, Hollywood, FL, Oct. 5-10, 1980.
3. J. S. Wilkes, J. A. Levisky, R. A. Wilson, and C. L. Hussey, *Inorg. Chem.*, **21**, 1263 (1982).
4. A. A. Fannin, Jr., L. A. King, J. A. Levisky, and J. S. Wilkes, *J. Phys. Chem.*, **88**, 2609 (1984).
5. A. A. Fannin, Jr., D. A. Floreani, L. A. King, J. S. Landers, B. J. Piersma, D. J. Stech, R. L. Vaughn, J. S. Wilkes, and J. L. Williams, *ibid.*, **88**, 2614 (1984).
6. F. M. Donahue, Private communication, 1984.
7. R. E. Johnson, Jr. and R. H. Dettre, "Wettability and Contact Angles," Vol. 2 of "Surface and Colloid Science," E. Matijevic, Editor, pp. 85-153, Wiley-Interscience, New York (1969).
8. A. M. Schwartz, *Ind. Eng. Chem.*, **61**, 10 (1968).
9. D. W. Seegmiller, G. W. Rhodes, and L. A. King, *Inorg. Nucl. Chem. Lett.*, **6**, 885 (1970).
10. J. G. Eberhart and J. E. Battles, U.S. Pat. 4,189,827 (1980).

Electroplating of Tungsten Carbide from Molten Fluorides

Kurt H. Stern* and M. L. Deanhardt*,¹

Naval Research Laboratory, Chemistry Division, Washington, DC 20375-5000

In previous work (1), it was shown that adherent coatings of tungsten carbide could be deposited on nickel substrates from the molten ternary fluoride eutectic (Li,Na,K)F (FLINAK) containing several weight percent

* Electrochemical Society Active Member.

¹Present address: Department of Science and Mathematics, Lander College, Greenwood, South Carolina 29646.

(w/o) each of Na_2WO_4 and K_2CO_3 . In these preliminary studies, the plating was carried out between a tungsten anode and the nickel cathode at an applied voltage of 1.5V, and solute concentrations of 1-10 w/o. It was found that the coating composition (W_2C , WC), current efficiency (c.e.), and structure of the deposit depends both on the concentration of each solute as well as the so-

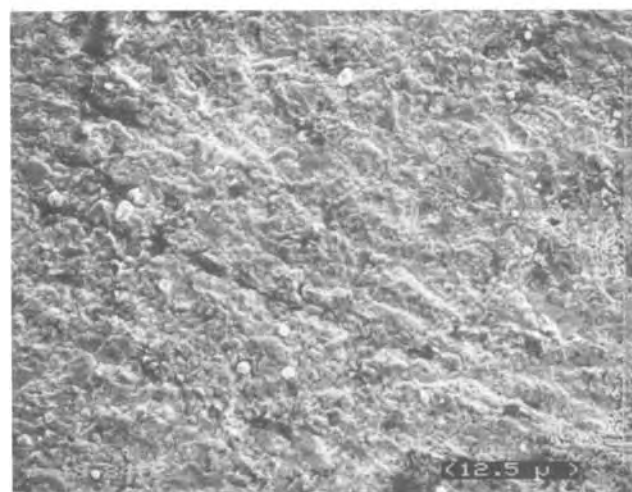
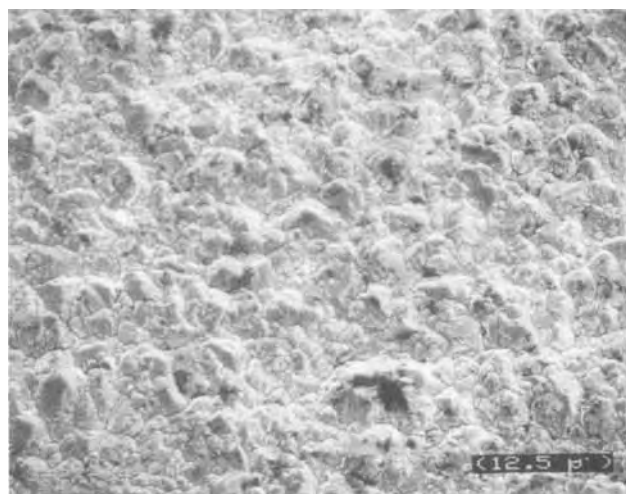
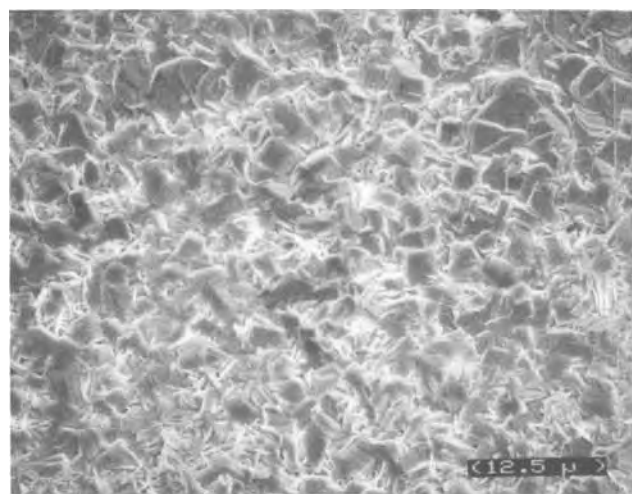


Fig. 1. Electrodeposited W_2C coatings. 3 w/o Na_2WO_4 , 1 w/o K_2CO_3 ; 500°C. a(top left): -1.0V. b(top right): -1.5V. c(left): -2.2V.

lute concentration ratio. For example, at higher C:W ratios (> 2), if the concentrations are also high, the coating is WC, the c.e. is low and the coating structure is unsuitable for a wear coating.

Subsequent to these studies, voltammograms and chronopotentiograms for tungstate reduction were obtained (2). These and the work described above were used to refine and improve the deposition process, using a three-electrode rather than a two-electrode cell arrangement. With this arrangement, the potential of the nickel cathode is controlled relative to a separate platinum quasi-reference electrode. Since essentially no current passes through the quasi-reference electrode, its potential will remain constant, and the potential of the nickel cathode can be accurately controlled. This was not possible in

the previously used two-electrode arrangement since the potential of the nickel cathode varies with the magnitude of current. Since voltammetric studies of WO_4^{2-} reduction (2) had shown that no tungsten deposition occurred more positive than -0.7V , and that below -2V the reduction probably occurred indirectly through the prior reduction of Li^+ , most of the experiments were carried out in the range -1.0 to -1.5V . Furthermore, based on the previous deposition study (1), the concentrations were restricted to 3 w/o Na_2WO_4 and 1-3 w/o K_2CO_3 .

Experimental

The general procedure used has been described previously (3). It was modified in this study by being carried out in a O_2 - and H_2O -free (a few parts per million of each)

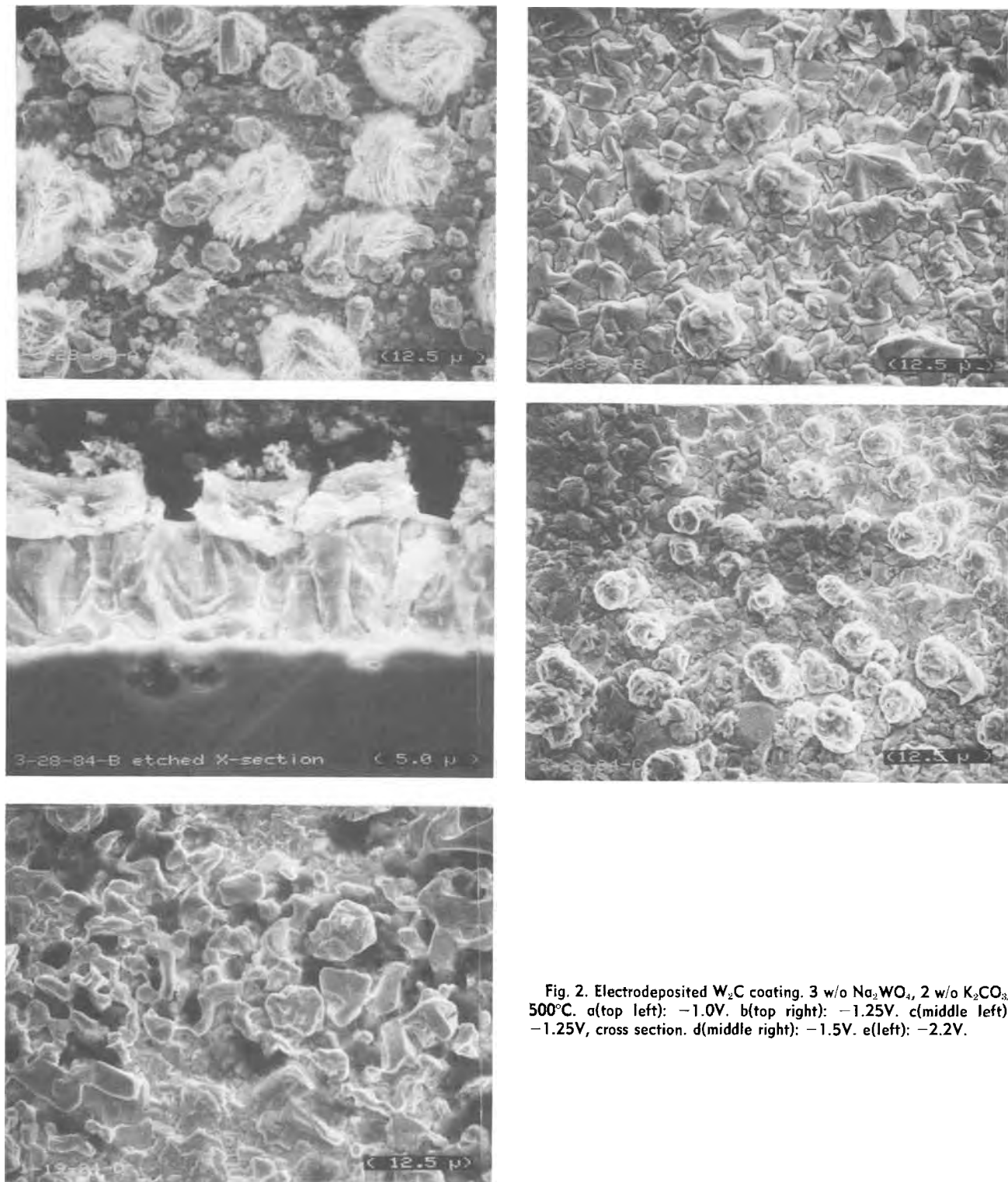


Fig. 2. Electrodeposited W_2C coating. 3 w/o Na_2WO_4 , 2 w/o K_2CO_3 ; 500°C . a(top left): -1.0V . b(top right): -1.25V . c(middle left): -1.25V , cross section. d(middle right): -1.5V . e(left): -2.2V .

glove box with recirculating purification system (Vacuum Atmospheres Corporation) and using 100-200g of melt. After pre-electrolysis, the melt was filtered through a silver gauze into a nickel reaction vessel. Electrodes were positioned in the melt through holes in a lava block. The solutes were added (Na_2WO_4 was prepared by vacuum dehydration of its dihydrate at 200°C), and electrolyses carried out at 750°C using a potentiostat (PAR Model 173), and the amount of charge followed with an electronic coulometer (PAR Model 179). At the end of each run, the nickel electrodes were quickly withdrawn from the reaction vessel, freed of adherent melt and loose deposit by ultrasonic cleaning in water, and examined by scanning electron microscopy (SEM) and x-ray diffraction. In some cases the cross sections were examined also.

Results

Figures 1-3 show the surface structures of deposits, all of which were found to be W_2C by x-ray diffraction, obtained at different voltages and K_2CO_3 concentrations at a constant Na_2WO_4 concentration of 3 w/o. The total amount of charge passed in each case was 500C to plate an area of $\sim 2\text{ cm}^2$.

Figures 1a-1c show the surface of the coating obtained at 1 w/o K_2CO_3 and three different voltages. All voltages are given with respect to the platinum reference electrode. At -1.0V , the surfaces of the individual crystallites are nearly flat and densely packed, whereas with increasing voltage the individual crystals are irregularly shaped and the overall surface becomes increasingly rough.

At 2 w/o K_2CO_3 , the surface structure appears highly dependent on relatively small changes in voltage. At -1.0V (Fig. 2a), the W_2C surface is densely covered with crystal-

lites of varying shapes and sizes. However, beneath this debris the surface appears to consist of a uniform distribution of very small ($<1\ \mu\text{m}$), densely packed crystallites. A change of voltage to -1.25V produces a more uniform surface of densely packed, irregularly shaped crystals (Fig. 2b). A cross-sectional view of this coating (Fig. 2c) indicates that it is dense and columnar (the coating was lightly etched with a $\text{KMnO}_4\text{-NaOH}$ solution to bring out the carbide structure) and that the surface view is probably dominated by the arrangement of crystals on the surface. As was also found previously (1), there appears to be no interdiffusion zone at the coating-substrate boundary. In contrast, an extensive interdiffusion zone was evident for coatings of tantalum carbide (3). However, the adherence of W_2C appears to be excellent, although no tests were carried out to test the adherence of the coating. At -1.5V (Fig. 2d), the crystals are rounded, indicative of nuclei which may grow together on further plating. The structure again changes markedly at -2.2V (Fig. 2e), consisting of an interconnected, serpentine network with a rather smooth overall surface.

A further increase in K_2CO_3 concentration to 3 w/o produces a new set of structures. At -1.0V (Fig. 3a), the underlying surface is quite smooth, with a few large angular crystals and many smaller ones at the surface. At -1.25V (Fig. 3b), the structure of the coating strongly resembles that obtained at 1 w/o and -1.0V (Fig. 1a), whereas at -2.2V (Fig. 3c) there are no distinct crystallites at all, but a fairly smooth, almost glassy looking surface.

The ability of the coating to follow complex surfaces is illustrated, at a much lower magnification, by a comparison of coated and uncoated engravings (Fig. 4). Figure 4a shows some details of an unplated, engraved nickel plate. The lines of the grid are $\sim 60\ \mu\text{m}$ wide and $25\ \mu\text{m}$ deep;

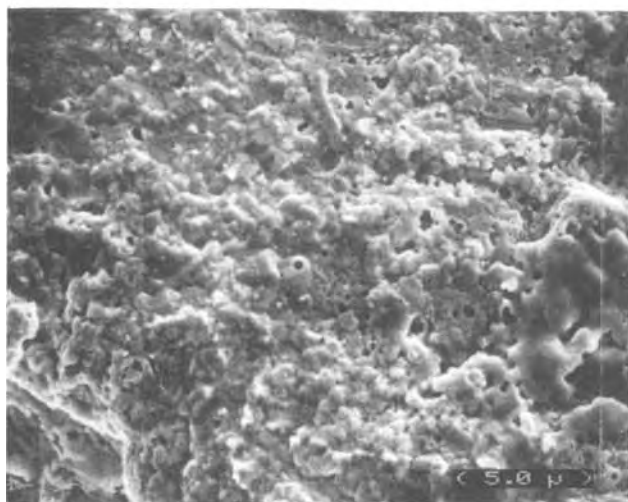
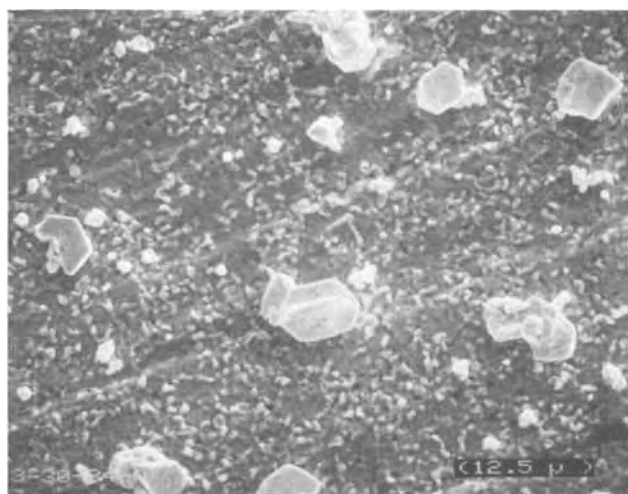


Fig. 3. Electrodeposited W_2C coating. 3 w/o Na_2WO_4 , 3 w/o K_2CO_3 , 500°C . a(top left): -1.0V . b(top right): -1.25V . c(left): -2.2V .

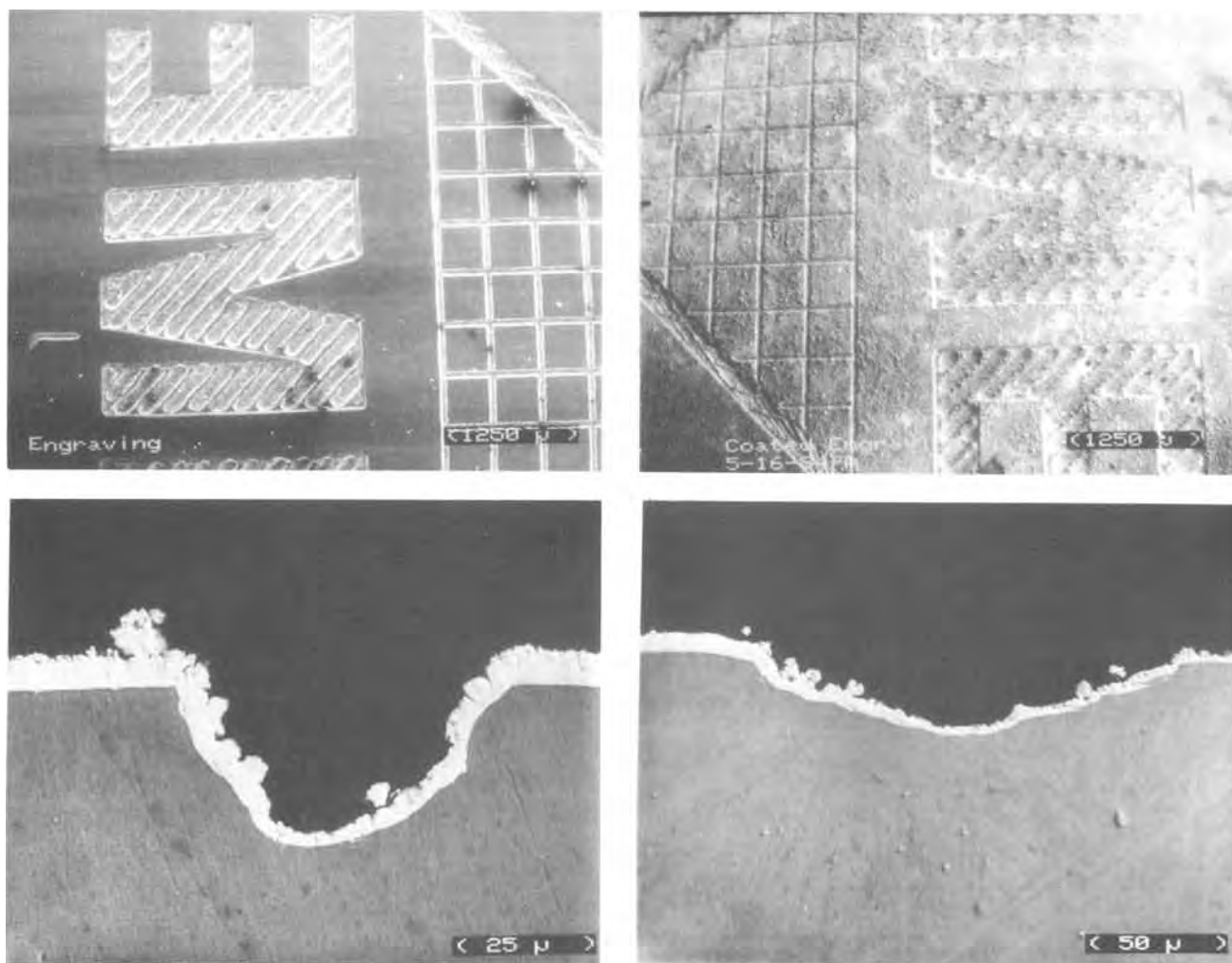


Fig. 4. Engraving plated with W_2C . 3 w/o Na_2WO_4 , 3 w/o K_2CO_3 , $1000^\circ C$. a(top left): Unplated. b(top right): Plated. c(bottom left): Cross sections of plated, engraved line. d(bottom right): Cross section of plated, engraved letter.

the grooves of the letters are $\sim 150 \mu m$ wide and $30 \mu m$ deep. After plating with W_2C (Fig. 4b), the engraved lines and letters are still clearly visible, though somewhat narrowed and fuzzy. The cross sections of both lines and letters show that the coating conforms very well to the metal surface but the coating surface shows some unevenness (Fig. 4c and 4d).

Discussion

The modification of the plating process from two-electrode (1) to three-electrode appears to have improved the coating structure considerably with respect to density, surface smoothness, and conformity to substrate. Presumably, control of the potential of the nickel electrode results in plating conditions such that better coating structure is obtained. In addition, better atmospheric control and melt pre-electrolysis may also have contributed to the improvement.

The optimal voltage range for W_2C deposition, -1.0 to $-1.5V$, is consistent with the reduction of $W(VI)$ to $W(0)$ (2). It is very noticeable, however, that whereas the coating structure of metallic tungsten obtained in this range is quite poor and the current efficiency is $\sim 10\%$, the addition of 1-3 w/o K_2CO_3 and plating in the same voltage range gives very good coatings with current efficiencies of 50%. We do not know how the coreduction of CO_3^{2-} and the subsequent chemical reaction between tungsten and carbon affect the overall deposition; neither of these processes has been studied yet. It does seem that Senderoff and Mellors (4) are correct and oxyanions are detrimental to the metal plating process (current efficiency is poor, and the deposit does not adhere to the substrate).

As is obvious from Fig. 1-3, and also from earlier work (1, 5), the surface structure of the coating is markedly dependent on plating conditions: melt composition, voltage, and even total charge passed (5). However, as can be seen from the cross sections (e.g., Fig. 2c), the coating structure overall is dense and no porosity is visible, even when the surface structure appears to have holes or irregularities. Since the surface is just the coating being formed at the time the plating stops, it follows that the coating being formed undergoes further regrowth and densification as surface becomes bulk. Thus, if a coating were to be polished, one would expect to obtain a smooth, continuous layer of W_2C . From a practical point of view, e.g., for producing wear coatings, one would need to consider whether the cost of such a procedure was justified or whether further research should be done to improve the "as-grown" surface structure.

Acknowledgment

We would like to thank Michael McCollum for the x-ray analyses and SEM photographs.

Manuscript submitted Nov. 16, 1984; revised manuscript received March 18, 1985. This was Paper 438 presented at the New Orleans, Louisiana, Meeting of the Society, Oct. 7-12, 1984.

The Naval Research Laboratory assisted in meeting the publication costs of this article.

REFERENCES

1. K. H. Stern and S. T. Gadomski, in "Fourth International Symposium on Molten Salts," M. Blander, D. S. Newman, M-L. Saboungi, G. Mamantov, and K.

- Johnson, Editors, p. 611, The Electrochemical Society Softbound Proceedings Series, Pennington, NJ (1984).
2. M. L. Deanhardt and K. H. Stern, Submitted to *This Journal*.

3. K. H. Stern and S. T. Gadomski, *ibid.*, **130**, 300 (1983).
4. S. Senderoff and G. W. Mellors, Can. Pat. 688,546 (1964).
5. K. H. Stern, I. L. Singer, C. M. Wu, and R. A. Jeffries, *Thin Solid Films*, **108**, 9 (1983).

Field Test of Platinized Titanium Anodes for Hypochlorite Cells

Tomoyoshi Asaki and Yoichi Kamegaya*

Ishifuku Metal Industry Company, Limited, Department of Research and Development, 1080 Aoyagi-cho, Soka, Saitama 340, Japan

Kiyoteru Takayasu

Showa Company, Limited, 2443-1 Kita Tahara-cho, Ikoma, Nara 630-01, Japan

The demand for chlorine for water and waste treatment is increasing because of the increase of water consumption, a large amount of waste water discharge, and governmental regulations. Transportation and handling of chlorine cylinders and containers are strictly controlled to avoid hazard. As a result, on-site electrolytic production of hypochlorite becomes important for disinfection of drinking water, oxidation of sewage, chlorination of cooling water in process plants, and other uses. There are now a number of publications and patents on hypochlorite cells and the electrodes to be used (1-13).

A hypochlorite cell must be simple in operation with minimum maintenance for a year or more. The energy consumption is also an important factor.

In an electric power station located by the sea, saline water containing some 3% NaCl is fed to the hypochlorite cell and is chlorinated prior to being sent to the heat exchangers in the plant. Because of the low salt concentration, oxygen evolution occurs, and this reduces chlorine current efficiency. Also, sea water contains Mg and Ca ions, which deposit at the cathode, resulting in high cell voltage. Periodic acid cleaning removes the scale, but affects the electrodes, especially the anode coating, and in some cases the electrode activity is not restored.

Pretreatment of sea water prior to electrolysis is preferable, but it is expensive and complicated. Therefore, durable anodes having such characteristics as low chlorine overvoltage and high oxygen overvoltage in sea water must be developed to improve the operating performance of hypochlorite cells.

Experimental Procedure

Two types of the platinized Ti anodes were used as controls. One was Pt-plated Ti sheet prepared by conventional electroplating (hereafter referred to as "regular Pt/Ti"). The other was also a Pt-plated Ti sheet and had a large surface area ("modified Pt/Ti") (14). The average thickness of the Pt coating was 3 μm .

The modified Pt/Ti sheet was painted with a solution containing a metal chloride, such as RuCl_3 or IrCl_3 , depending on the oxide catalyst proposed, dried in air, and then fired at 500°C for few minutes to deposit the oxide on the Pt layer (MODE®). In this work, the Ir oxide-loaded material was used mostly.

Full-scale experiments were conducted in an electric power plant located at Tokyo Bay. The flowsheet is illustrated in Fig. 1. Eight cells were operated in series and parallel connections; the sea water was fed to the top end of the cell series, electrolyzed, and mixed together at the outlet. The chlorinated sea water was sent to the heat exchangers in the plant. Each hypochlorite cell employed was equipped with five anodes and six cathodes (carbon steel plate) in parallel. There were no separators. The design capacity of the cell is as follows. The effective area of

electrode was 80 cm wide and 45 cm high each. The anode-to-cathode gap was 5 mm. The current density was 15 A/dm² at 5.4 kA total current load. The cell voltage was 5.5 \pm 0.5V. The solution flow rate was 60 m³/h. The chlorine generation was 5 kg/h. The conditions of the sea water varied with season in the following ranges: for temperature, 9°-28°C; for electrical conductivity, 42-50 mmhos/cm; for Cl⁻ concentration, 15.5-18.5 g/liter; for pH, 7.6-8.4; for suspended solids, 9.0-22.0 ppm; and for chemical oxygen demand (COD), 0.2-3.2 ppm. Since the COD level was low in winter, the electrolytic current was lowered to avoid residual chlorine in the discharged water.

A small cylinder cell was also operated with various anodes as reference. The nameplate capacity was 150A, producing 160 g-Cl₂/h at 80% current efficiency.

Results and Discussion

Life test of the modified Pt/Ti anode were conducted for 3 years. The thickness and condition of the Pt layer were measured several times. The consumption rate of Pt was large at the beginning, and became smaller with time. Warren *et al.* reported similar behavior for platinized Ti anodes in copper electrowinning cells (15). Since the water hardness in the first cell was high, heavy scales deposited and affected the Pt coating.

The Ti substrate was also attacked by oxygen evolution, affecting the Pt to Ti bond. The service life of the regular Pt/Ti was estimated to be ca. 3 years. However, a tight oxide film just under the Pt layer of the modified Pt/Ti anode (the MODE), prevented further oxidation of the Ti substrate. This resulted in long life for these anode materials.

From the results of the field tests together with practical operations for 6 years, the average consumption of the Pt layer of the modified Pt/Ti anode was estimated to be ca. 0.4 $\mu\text{m}/\text{yr}$ in thickness under normal conditions.

The field test of the MODE was started at the end of November 1982, and is being continued without serious trouble.

Brine flow rate, current, cell voltage, chlorine current efficiency, solution temperature, salinity, COD, electrical conductivity of saline water, and other factors were measured intermittently at intervals of about one month.

The cell was operated at the rated amperage (5.4-5.5 kA) in summer, and at lower currents in other seasons, to

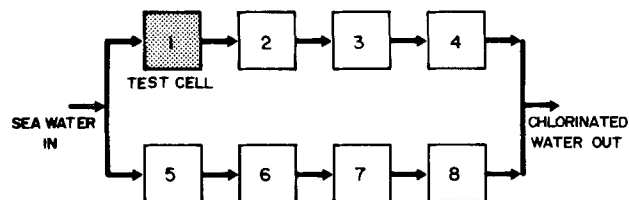


Fig. 1. Flowsheet of the field test with large scale hypochlorite cells in an electric power station.

* Electrochemical Society Active Member.

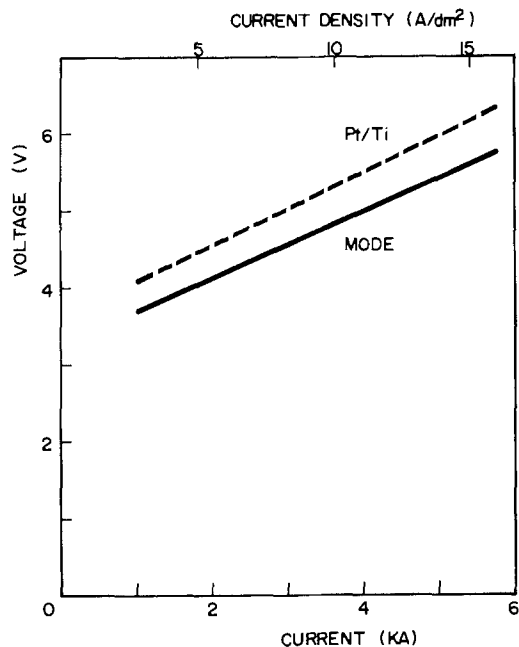


Fig. 2. Terminal voltage of a large scale hypochlorite cell

meet the COD level in the sea water. The cell voltage varied with the season, mainly because of the solution temperature and hence the electrical conductivity. Heavy scaling and fouling on the working electrodes were also factors.

175 data points obtained from the field test for 10 months were processed by desk computer. The variations of the electrical conductivity of sea water with temperature was calculated. The cell voltage with the MODE was about 0.4-0.5V lower than that with the modified Pt/Ti anode, depending on the amperage, as shown in Fig. 2.

The chlorine current efficiency on the MODE was in the range 85-90% compared to less than 80% with the Pt/Ti anodes. The chlorine current efficiency decreased slightly with increase of current density.

Table I shows the breakdown of the terminal voltage of a cylindrical cell with different anode materials at 150A or 8.9 A/dm² in current density. The decomposition voltage is an extrapolation of the volt-ampere curve to zero current. The solution IR drop is the largest factor because the electrical conductivity of sea water is low and the electrode gap is relatively large (ca. 20 mm). This factor may be reduced by adequate design of the cell configuration. The cathode overvoltages for the two cells are equal, so that the cell voltages reflect the anode overvoltage in both cases.

Figure 3 illustrates the polarization curves of various anode materials in 300 g/liter NaCl solution saturated with chlorine at 30°C. The overvoltage of the MODE increased by 150 mV at 10 A/dm² after 4 months of electrolysis with a cylindrical cell in comparison with the virgin sample. Even so, the overvoltage of the MODE was still lower than that of the platinized anodes. The polarization measurements were also conducted in dilute solution (30 g/liter NaCl), and the overvoltage was almost the same as in the concentrated solution. Some oxygen is generated.

The saving in energy consumption by using a low overvoltage anode is represented as follows

Table I. Breakdown of the cell voltages at 150A

	With MODE	With modified Pt/Ti
Decomposition voltage (V)	2.42	2.42
Anode overvoltage (V)	0.60	1.21
Cathode overvoltage (V)	0.61	0.61
Solution IR drop (V)	4.30	4.30
Terminal voltage (V)	7.93	8.54

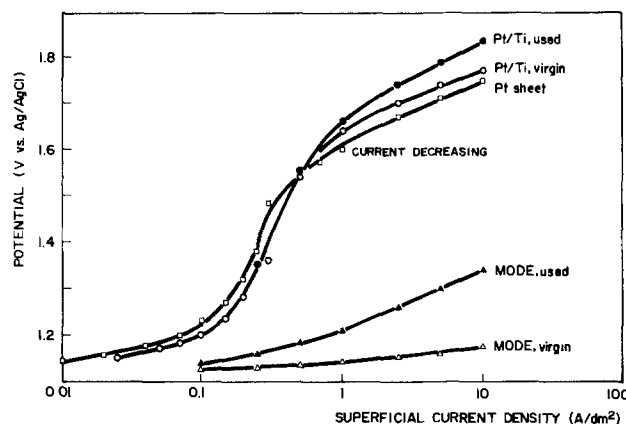


Fig. 3. Polarization curves of the platinized titanium anodes in 300 g/liter NaCl saturated with chlorine at 30°C.

$$\Delta W = \frac{W - W_1}{V\xi_1} = 1 - \frac{V_1\xi}{W\xi_1} \quad [1]$$

where V is the cell voltage in volts, W the energy consumption in kWh/kg-Cl₂, and ξ is the current efficiency. The subscript 1 indicates the test cell.

For a current of 15 A/dm², $V = 6V$, $V_1 = 5.5V$, $\xi = 70\%$, $\xi_1 = 80\%$, and the energy saving is about 20%, which agrees with the data of the field tests.

In conclusion, since physical degradation of the platinized Ti anode was troublesome in the hypochlorite cells, a modified Pt/Ti anode was developed. This was treated further to improve the overvoltage characteristics by coating with iridium oxide by thermal decomposition of an Ir compound. The chlorine overvoltage for this material, MODE, was low, and the chlorine current efficiency was high compared to uncoated platinized titanium. A 10 month field test at an electric power station gave energy saving of ca. 20%.

Acknowledgments

The authors wish to thank N. Koyanagi, Y. Sasaki, and Y. Arai of Ishifuku Metal Industry Company for their collaboration; the Isogo Power Station of the Electric Power Development Company, and Yokohama Denko Company, providing for the field test; Professor F. Hine, Nagoya Institute of Technology, for valuable suggestions and preparing the paper. Permission for publication of the paper was granted by Ishifuku Metal Industry Company and Showa Company.

Manuscript submitted April 2, 1984; revised manuscript received Dec. 10, 1984. This was Paper 216 presented at the Cincinnati, Ohio, Meeting of the Society, May 6-11, 1984.

Ishifuku Metal Industry Company assisted in meeting the publication costs of this article.

REFERENCES

- S. A. Michalek and F. B. Leitz, *J. Water Production Control*, **44**, 1697 (1972).
- J. S. Booth, H. Hamzah, and A. T. Kuhn, *Electrochim. Acta*, **25**, 1347 (1980).
- International Conference on Local Generation and Use of Chlorine and Hypochlorite, Society for Chemical Industry, London, Oct. 14-16, 1980.
- D. W. Kirk and A. E. Ledas, *Int. J. Hydrogen Energy*, **7**, 925 (1982).
- P. M. Robertson, W. Gnehm, and L. Ponto, *J. Appl. Electrochem.*, **13**, 307 (1983).
- "Production of Hypochlorite by Electrolysis of Brine or Sea Water," a brochure of Krebskosmo, Berlin.
- E. Hausmann, "Electrochemical On-Site Production of Chemicals Required in Power Plants," Krebskosmo, Berlin.
- F. Scoville, U.S. Pat. 4,329,215 (1982).
- E. Hausmann, H. Will, and K. Klein, German Pat. 2,919,527 (1980).
- W. C. Conkling, U.S. Pat. 4,248,690 (1981).
- H. Kanai, R. Itai, and T. Yamazaki, Japanese Pat.

- Kokai Sho-55-18503 (1980).
 12. H. Kanai, A. Shinagawa, T. Yamazaki, and R. Itai, Japanese Pat. Kokai Sho-56-146887 (1981).
 13. C. R. Franks, B. A. Schenker, and J. M. Kolb, German Pat. 2,418,739 (1974).
 14. N. Koyanagi, T. Asaki, and Y. Arai, Japanese Pat. 1,170,779 (1983).
 15. I. H. Warren, G. E. Olsen, and K. Seto, Paper pre-

- sented at the Fourth Joint Chemical Engineering Conference of CSChE/AIChE, Vancouver, BC, Canada, Sept. 1973.
 16. J. P. Hoare, "The Electrochemistry of Oxygen," p. 91, Interscience, New York (1968).
 17. J. F. Llopis and F. Colom, in "Encyclopedia of Electrochemistry of the Elements," Vol. 6, A. J. Bard, Editor, p. 208, Marcel Dekker, New York (1976).

Chiral Polypyrroles from Optically Active Pyrrole Monomers

Manuel Salmón*

Instituto de Química de la Universidad Nacional Autónoma de México, Circuito Exterior, Ciudad Universitaria, Coyoacán 04510, México

Gerard Bidan

Laboratoire d'Electrochimie Organique et Analytique, Laboratoires de Chimie, Département de Recherche Fondamentale, Centre d'Etudes Nucleaires de Grenoble, F-38041 Grenoble Cedex, France

Previous reports have shown that the use of electrochemically prepared polypyrrole-coated electrodes further coated with polyaminoacids by the dipping method introduces asymmetry to the electrode surface (1).

Electrodes modified with chiral groups have shown potential as asymmetric inductors in electro-organic synthesis (2). However, in spite of the stability improvements in this class of chiral electrodes, the loss of the asymmetry inducing power is a major problem (3).

Recently, we have shown that N-alkyl- and N-phenyl-substituted pyrroles produced by anodic oxidation result in stable electroactive polymer films which can be used as modified electrodes (4). From among these compounds, we have selected the hydroxy derivatives I and II (5) to synthesize optically active pyrrole monomers (6) III [$\alpha]_D^{18} + 25.4$ and IV [$\alpha]_D^{18} + 11.4$ (Fig. 1) which contain the (+) camphor-10-sulfonate ester as a chiral group.¹ The chiral pyrrole monomers used were ester derivatives of camphorsulfonic acid. This last compound was chosen as the asymmetric chromophore because it is well known that it exhibits circular dichroism.² The results of an electrochemical study have shown that chiral centers can be easily incorporated into polymeric materials.

Cyclic voltammetry of the monomeric pyrrole units III and IV showed one irreversible peak at 0.93 and 1.02V (*vs.* Ag/10⁻²M Ag⁺), while thin polymer films derived from the monomers using a total charge of 2.0 and 3.0 mC/cm² gave a reversible redox system with defined E_{pa} and E_{pc} peaks as shown in Fig. 2. The electrochemical properties of these polymeric materials are not affected by exposure to air and a color change is observed when the oxidized form is driven (brown) to the neutral (yellow) state resembling the polypyrrole matrix (4).

The films are smooth and adhere strongly to the Pt electrode in spite of the large substituent which had very little effect on the redox values (Table I) when compared with other N-alkyl pyrrole polymers (4).

Thin polymer films were obtained from the environmentally stable monomers III and IV on Pt (3×10^{-2} cm²) and on indium-oxide-glass (1 cm²) electrodes by controlled potential at 0.80V *vs.* Ag/10⁻²M Ag⁺ reference electrode. Argon purged acetonitrile solutions containing 0.1 or 0.7M anhydrous LiClO₄ and 3×10^{-2} M optically active pyrrole monomer derivatives were used to grow the films on the electrode surface in a one compartment cell. Pt wire and Ag/10⁻²M Ag⁺ were the counter and reference electrodes, respectively.

*Electrochemical Society Active Member.

¹All new compounds gave correct spectroscopic and combustion data.

²D-(+) camphor 10-sulfonic acid contains a carbonyl chromophore absorbing at $\lambda_{max} = 290$ nm; the keto group is located in a dissymmetric surrounding and so is optically active.

Table I. Summary of data for monomers and polymers *vs.* Ag/10⁻²M Ag⁺

		E_{pa}		E_{pa}	E_{pc}	E_n
Monomer	III	0.93	Polymer	0.28	0.24	0.27
	IV	1.02		0.16	0.26	0.21

Thin polypyrrole films from the optically active monomers were easily prepared in spite of the large camphor-sulfonate ester substituent and were stable when cycled from -0.4 to 0.6V *vs.* Ag/10⁻²M Ag⁺ (Fig. 2) in dry and oxygen-free electrolyte.

The optical activity of the chiral monomers and polymers was evaluated by circular dichroism (CD) measurements using a Dichrographe III Roussell-Jouan instrument. The instrument was calibrated before each measurement using (+)-camphor-10-sulfonic acid solutions, as was suggested by Krueger and Pshigoda (7).

The c.d. study was performed with different quantities of chiral polypyrrole deposits in their oxidized or reduced state. The total charge applied to form these films was in the range of 50 to ca. 90 mC/cm² (Fig. 4a-4f). The stability of the chiral polypyrrole materials as coated electrodes can be compared with those of N-alkyl or N-phenylpolypyrroles (4), which are far more stable than those asymmetric poly(amino acid)-coated electrodes prepared by the dipping method (1).

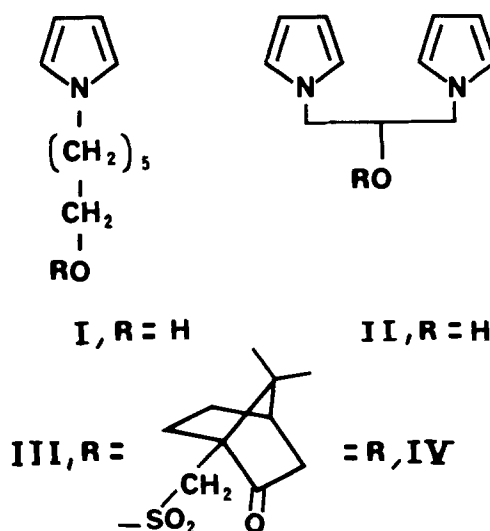


Fig. 1. N-alkylpyrrole (+) camphor-10-sulfonate ester derivatives

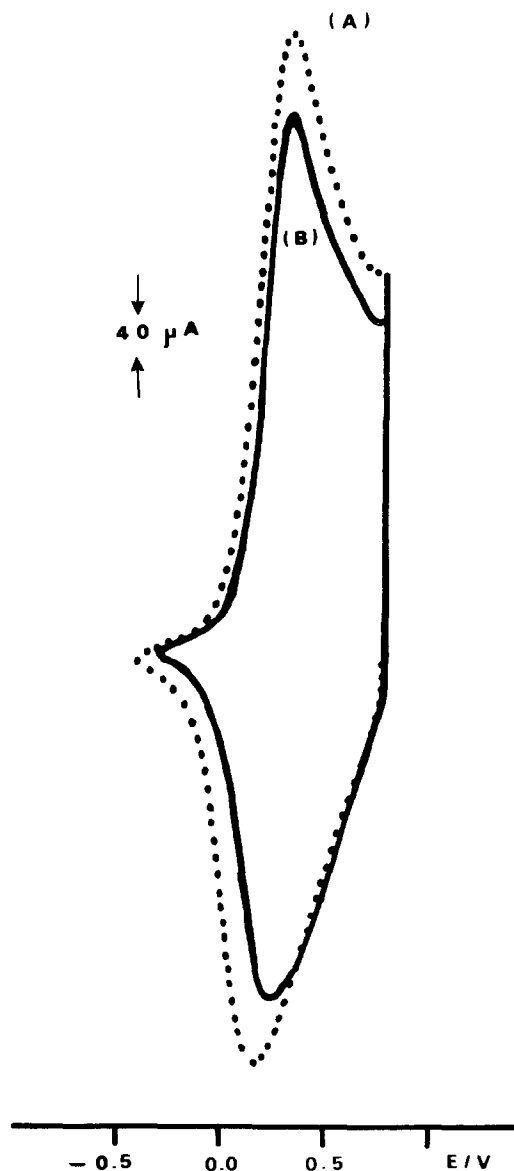


Fig. 2. Cyclic voltammograms with 2 and 3 mC/0.3 cm²/Pt films of chiral polypyrroles derived from monomers III (curve b) and IV (curve a) at 100 mV/s in CH₃CN containing 0.1M LiClO₄.

Figure 3 shows the gaussian-type c.d. curves of the pyrrole monomers compared with dc curves of camphorsulfonic acid and its sulfonyl chloride.³ Positive Cotton ef-

³(+)-Camphor-10-sulfonyl chloride, puriss. from Fluka.

⁴The Cotton effect exhibited by a molecule is associated with the presence of a chromophore (light absorbing group), which is either chiral or in which the dissymmetric vicinity makes the transition optically active (8).

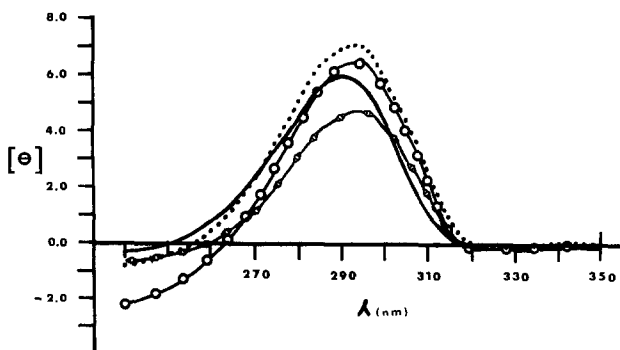


Fig. 3. The circular dichroism curves of (+) camphor-10-sulfonyl chloride (diamond-shaped point), (+) camphor-10-sulfonic acid (solid line), pyrrole monomer derivatives III (dotted line), and (IV) (open circles) reveal positive Cotton effect.

fect⁴ was observed in all samples at $\lambda_{\max} = 290$ nm for (+)-camphor-10-sulfonic acid, $\lambda_{\max} = 293$ nm for (+)-camphor-10-sulfonyl chloride and pyrrole camphorsulfonate IV, and the $\lambda_{\max} = 294$ nm band for the pyrrole monomer camphorsulfonate III.

The c.d. measure was also employed to identify the asymmetric material deposited as a film onto an indium-oxide-glass electrode. No c.d. effects were observed with either a bare indium-oxide-glass electrode or unsubstituted polypyrrole perchlorate film (51 mC/cm²) deposited in the same electrode (Fig. 4a-4b).

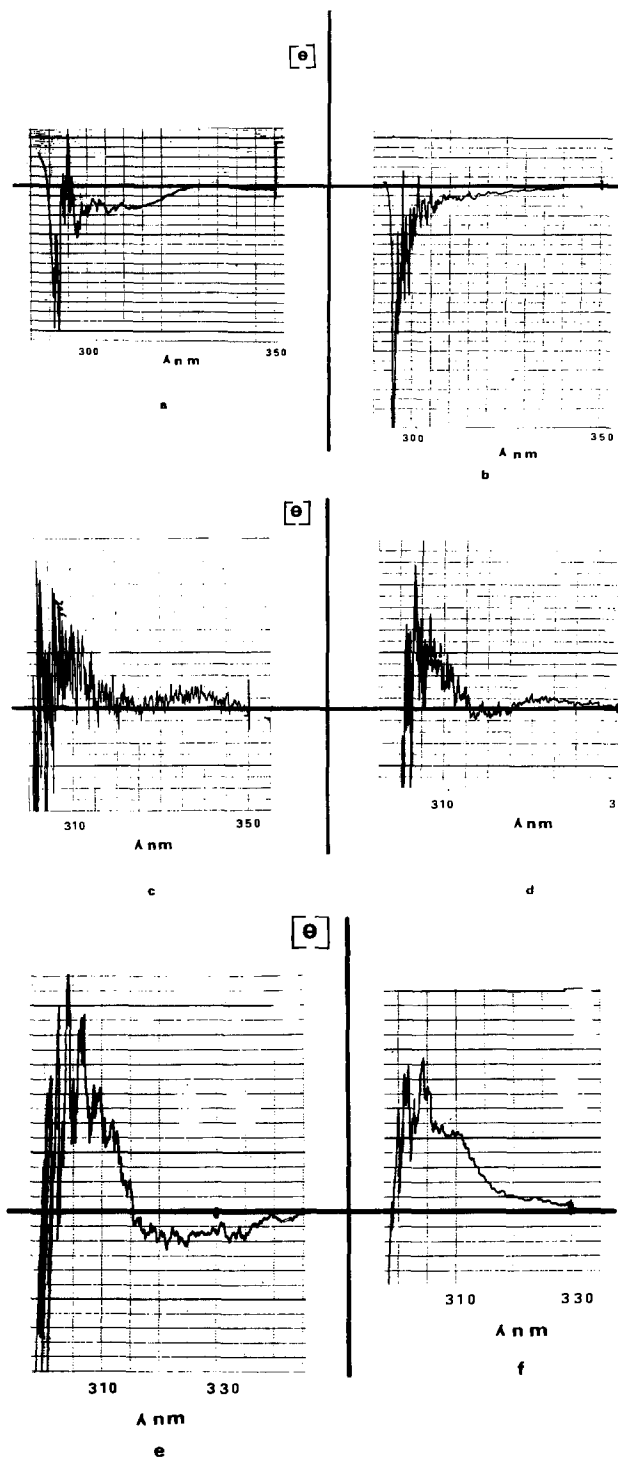


Fig. 4. Circular dichroism curves of bare indium-oxide-electrode (a) and polypyrrole/CIO₄ film-coated electrode 51 mC/cm² (b). Circular dichroism curves of indium-oxide-electrode coated with chiral polymer obtained by oxidation of monomer IV in its oxidized (c) (66 mC/cm²) and reduced state (d) (87 mC/cm²). Circular dichroism curves of indium-oxide-electrode coated with chiral polymer obtained with pyrrole monomer III in its oxidized (e) (70 mC/cm²) and reduced form (f) (50 mC/cm²).

The experience (9) in polymerizing pyrrole monomers substituted with functional electroactive groups showed that the electroactive properties of these groups are not affected by polymerization. Moreover, the polypyrrole matrix also remains stable when cycled from negative to positive potentials. Consequently, the c.d. study of the optically active polymer prepared here shows that the oxidation and the reduction of the polypyrrole matrix do not affect the chiral center of the camphorsulfonate substituent.

As shown in Fig. 4c-4f, the asymmetric polymers give a positive Cotton effect in either the oxidized or the reduced state. These measurements were made on polymer films deposited on the indium-oxide electrode; the films were copiously rinsed with spectroscopic grade acetone and methanol to eliminate any monomeric or electrolyte salt residue.

The c.d. wavelength absorption of these polymers at ca. 305 nm showed a bathochromic shift in comparison with the c.d. absorption maximum of monomers. This variation should be attributed exclusively to the change of solvent, since there is no other obvious reason to be considered.

The electrosynthesis of other chiral polypyrrole derivatives and their use as electrodes is in progress, and the results will be published elsewhere.

Acknowledgments

One of us (M.S.) thanks the French Atomic Energy Commission for financial support during six month's stay in the Laboratoire d'Electrochimie Organique et Analytique, Laboratoire de Chimie. Acknowledgment is made to the Consejo Nacional de Ciencia y Tecnología

(CONACYT) for partial support of this research (Grant 0000-840534). The authors would like to thank M. Rosales Hoz for many clarifying discussions.

Manuscript submitted Dec. 7, 1984; revised manuscript received April 2, 1985.

Universidad Nacional Autónoma de México assisted in meeting the publication costs of this article.

REFERENCES

1. T. Komori and T. Nonaka, *J. Am. Chem. Soc.*, **105**, 5691 (1983).
2. T. Komiry and T. Nonaka, *ibid.*, **106**, 2656 (1984); B. E. Firth, L. L. Miller, M. Mitani, T. Rogers, J. Lennox, and R. W. Murray, *ibid.*, **98**, 8271 (1976).
3. B. E. Firth and L. L. Miller, *ibid.*, **98**, 8272 (1976); S. Abe, T. Nonaka, and T. Fuchigami, *ibid.*, **105**, 3630 (1983).
4. M. Salmón, Ma. E. Carbajal, J. C. Juárez, A. Díaz, and M. C. Rock, *This Journal*, **131**, 1802 (1984); A. F. Díaz, J. Castillo, K. I. Kanazawa, J. A. Logan, M. Salmón, and O. Fajardo, *J. Electroanal. Chem.*, **133**, 233 (1982).
5. G. Bidan, *Tetrahedron Lett.*, 735 (1985).
6. M. Salmón and G. Bidan, *Synth. Commun.*, To be published.
7. W. C. Krueger and Pshigoda, *Anal. Chem.*, **43**, 675 (1971); D. F. Detar, *ibid.*, **41**, 1406 (1969).
8. P. Crabbé, in "An Introduction to the Chiropractical Methods in Chemistry," Universidad Nacional Autónoma de México and Universidad Iberoamericana, Editors, Sintex, Chap. 1, p. 4, S. A. México, D.F. (1971).
9. M. Velazquez Rosenthal, T. A. Skotheim, C. Linkous, M. I. Florit, and M. Salmón, *Polym. Preprints*, **25**, 258 (1984); G. Bidan, A. Deronzier, and J. C. Moutet, *J. Chem. Soc. Chem. Commun.*, 1185 (1984); M. Salmón, Ma. E. Carbajal, J. C. Juárez, A. Díaz, and M. C. Rock, *This Journal*, **131**, 1802 (1984).



A Two-Step Oxidation Process to Improve the Electrical Breakdown Properties of Thin Oxides

Anjan Bhattacharyya* and Charles Vorst

Philips Research Laboratories Sunnyvale, Signetics Corporation, Sunnyvale, California 94086

Altaf H. Carim*

Department of Materials Science and Engineering, Stanford University, Stanford, California 94305

ABSTRACT

We have developed a technique for growth of thin oxides (80-90Å) with an intermediate annealing step. The oxides exhibit a tight distribution in breakdown voltage measurements leading to defect density less than $5/\text{cm}^2$, intrinsic breakdown field of 12 MV/cm, and a value of less than $1 \times 10^{10}/\text{cm}^2\text{-eV}$ for interface trap density in midgap. The inferior electrical properties of thin oxides grown by conventional methods in dry oxygen with Ar dilution have been correlated with Si-SiO₂ interface roughness using high resolution transmission electron microscopy. The intermediate annealing process may be used to improve the endurance and retention properties of EEPROM devices and alleviate the degradation of thin oxides in short-channel MOS devices.

This study investigated the use of an intermediate annealing step to eliminate the failure causing defects that develop in thin oxides during the oxidation process. The principal failure causing mechanism for thin oxides has been attributed to the presence of conducting channels arising from various defects (1) or local crystalline regions (2) in the amorphous oxide. The method of growth and the thickness of the film greatly influence the electrical properties of an oxide film. High defect densities in an oxide film lower the median breakdown field and lead to reliability problems which are associated with time-dependent breakdown phenomenon (3).

There have been detailed reports in the literature on the composition of the very thin interfacial region between the oxide and silicon. The thin interfacial region of maximum thickness less than 30Å has been investigated extensively by ellipsometry, infrared spectroscopy, Auger electron spectroscopy, and etch-rate determination (4, 5). It has been suggested that the near-interface oxide has a silicon-rich composition SiO_x where $x < 2$. Recent work (6) has shown that the interfacial layer is stoichiometric SiO₂ to within one monolayer of the substrate. It has also been demonstrated that compressive stresses (7) exist in thermal oxides depending on the oxidation temperature and growth conditions.

We have characterized the electrical properties of thin oxides ($\approx 80\text{Å}$) grown under various processing conditions by performing oxide breakdown voltage measurements, current vs. voltage measurements, and both high and low frequency capacitance vs. voltage measurements. The nature of the Si-SiO₂ interface has been studied for each processing condition using high resolution transmission electron microscopy.

Sample Preparation

For electrical measurements on the properties of thin oxides, polysilicon gate capacitors were fabricated using the LOCOS process (8). The capacitors had three different areas (0.002, 0.008, and 0.032 cm²) and two different geometries (circular and rectangular). This device variety al-

*Electrochemical Society Active Member.

lowed the effect of area and geometry on the electrical properties of thin oxides to be studied. We did not observe any geometry dependence on the oxide breakdown voltage characteristics for capacitors of the same area. In all cases, electrical contact was made on a pad over the field oxide to avoid any mechanical damage of the thin oxide layer.

The starting material was 4-6 Ω-cm p-type <100> Si wafers. The wafers were subjected to a standard cleaning process consisting of H₂SO₄/H₂O₂ clean followed by a 1:10 HF dip to remove any native oxide. The wafers were loaded immediately in the furnace with argon flowing only. The thin oxides were grown by the following processes.

The first was a standard process: growth of thin oxides of thickness between 80 and 90Å in a single oxidation step at 900° or 950°C.

The second was a two-step oxidation process: growth of $\approx 30\text{-}40\text{Å}$ of oxide at 900° or 950°C followed by an annealing treatment in Ar at 1050°C for 1h and then followed by the growth of additional oxide at 900° or 950°C to a final thickness between 80 and 90Å.

The third and last was the postoxidation anneal process: growth of thin oxides of thickness between 80 and 90Å in a single oxidation step at 900° or 950°C followed by an annealing step at 1050°C for 1h. After metallization, the wafers were annealed in forming gas at 450°C for 30 min.

Structural analysis of the thin oxide interfaces that resulted from the different processing sequences was performed by high resolution transmission electron microscopy (HREM). The instrument used was a Philips 400ST, operated at 120 keV. Cross-sectional specimens were prepared using a standard technique (9), and viewing the samples along <110>-type directions in many-beam conditions allowed structure images to be obtained. Point-to-point resolution was on the order of 3.3Å.

Results and Observations

Oxide thickness measurements.—The thickness of the thin oxides grown by the different processes was measured by three different techniques: (i) by a Rudolph

Auto El II Ellipsometer, (ii) by TEM cross-sectional studies, and (iii) by high frequency capacitance vs. voltage measurements. The oxide thickness measured by the three different techniques agreed within 5%.

Oxide breakdown voltage measurements.—To compare the electrical properties of the thin oxides, we performed breakdown voltage measurements using an automatic prober stepper and a Keithley test system. The test program used a ramp rate of 10 V/s and detected breakdown voltage by measuring the voltage at which a threshold current of 10 μ A occurred. The dielectric breakdown measurements yield the defect density (10). One can also estimate the high field capability of thin oxides as required in EEPROM devices (11).

For each wafer, we collected 110 data points for each type of capacitor. The data was collected for three wafers (330 data points) of similar processing conditions before any statistical analysis was performed. The results of the breakdown voltage measurements were analyzed using the extreme value statistics (3). The cumulative probability of failure $P(E)$ at a field E is given by

$$\ln(\ln[1 - P(E)]^{-1}) \propto E \quad [1]$$

Figure 1 shows a plot of the cumulative probability of failures (corresponding to the left term of Eq. [1]) vs. electric field for the 84Å thin oxide grown under standard process at 900°C. We note that each of the curves has three distinct regions.

In the first region, from 0 to 4 MV/cm, the breakdown can be due to possible contamination control related to the cleanliness of the wafers, furnace, etc. In this region, the cumulative probability of failures is low (less than 2% for the 0.002 cm² capacitors).

In the second region, from 4 to 10.5 MV/cm, the probability of failures increases with the electric field. In this region, the breakdown phenomenon is related to defects in the oxide incorporated during the growth process. In this region, one can calculate the defect density/area (10) from the relation

$$\rho = (-\ln[1 - P])/A \quad [2]$$

where ρ is the defect density per unit area, P is the cumulative probability of failures, and A is the area of the capacitor.

In the third region, at ≈ 10.5 MV-cm, the probability of failures increases sharply as it is related to the intrinsic breakdown characteristics.

For electric fields between 0 and 10.5 MV/cm, the probability of failures increased with the area of the capacitor, as expected from the extreme value statistics (3).

Figure 2 shows a similar plot for circular capacitors for thin oxides of thickness 85Å that underwent two-step oxidation at 900°C with intermediate anneal at 1050°C for 1h in Ar.

Comparing Fig. 1 (standard process) to Fig. 2 (two-step oxidation process), we observe some noticeable differences.

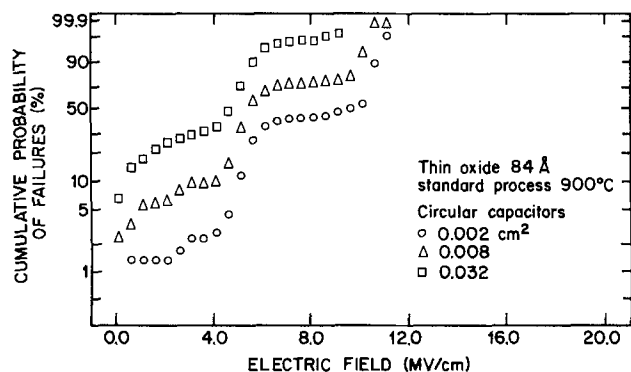


Fig. 1. Plot of cumulative probability of failures (percent) vs. electric field for thin oxides grown under a standard process at 900°C.

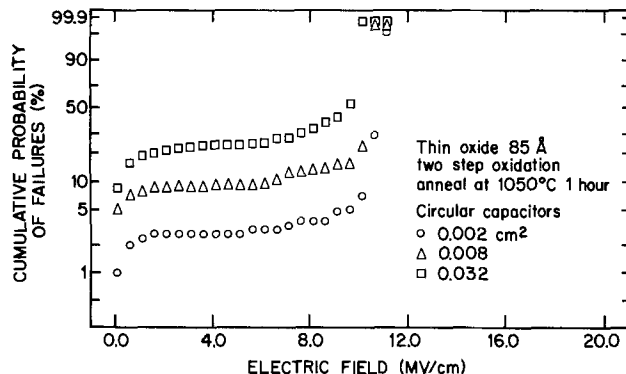


Fig. 2. Plot similar to Fig. 1 for thin oxides grown under a two-step oxidation process.

For the two-step oxidation process, the cumulative probability of failures remains fairly constant for electric field between 0 and 10 MV/cm, independent of capacitor area. This is a marked improvement from the condition observed with the standard process, where, in the range 0-10 MV/cm, the probability of failures increases steadily with electric field. Since the probability of failures is related to defect density, one can deduce that the two-step oxidation process leads to oxides with much lower defect density than those from the standard process (see Table I).

At the intrinsic breakdown field, the cumulative probability of failure does not depend on the area of the capacitor. The defect density per unit area is calculated from the probability of failure at the onset of intrinsic breakdown and thus gives an upper limit value.

We have also observed (Fig. 3) that the postoxidation annealing treatment does improve the electrical breakdown properties of thin oxides somewhat. However, as shown in Fig. 2 for the two-step oxidation process, the intermediate annealing step produces thin oxides with the best electrical breakdown voltage characteristics.

We also note from Fig. 4 that the breakdown characteristics of thin oxides grown at 950°C are better than those grown at 900°C (Fig. 1) for circular capacitors of area 0.002 cm². Also, the two-step oxidation process is more effective in reducing the defect density of thin oxides grown at 950° than 900°C (compare Fig. 4 with Fig. 2).

Table I summarizes the various parameters of thin oxides such as defect density and intrinsic breakdown field as a function of the oxide growth conditions for circular capacitors of area 0.002 cm². Similar tables can be obtained for the other areas.

We have performed high frequency and quasi-static capacitance vs. voltage measurements to determine the oxide thickness, fixed oxide charge density, and the density of interface traps. Figure 5 shows a plot of the density of interface traps (D_{it}) as a function of bandgap position for thin oxides grown at 950°C with an intermediate annealing at 1050°C for 1h. The value of D_{it} at midgap is $8 \times$

Table I. Summary of the oxide breakdown voltage characteristics

Process variable	Oxide thickness (Å)	Defect density (ρ/cm^2)	Breakdown field (MV/cm)
Standard 900°C	84	300	10.5
Two-step oxidation Anneal at 1050°C for 1 h (900°C process)	85	20	11.5
Postoxidation Annealing at 1050°C for 1 h (900°C process)	85	255	10.5
Standard 950°C	82	50	10.5
Two-step oxidation Anneal at 1050°C for 1 h (950°C process)	86	4	12.0

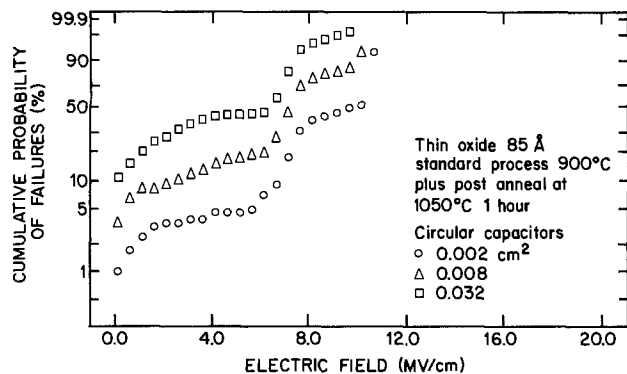


Fig. 3. Plot similar to Fig. 1 for thin oxides grown under a postoxidation anneal process.

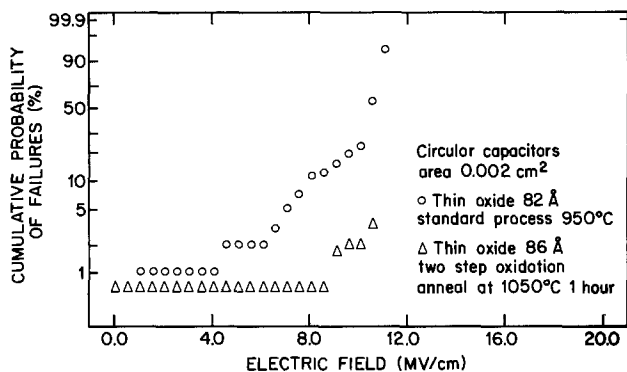


Fig. 4. Plot of cumulative probability of failures (percent) vs. electric field for thin oxides grown under a standard process at 950°C and a two-step oxidation process.

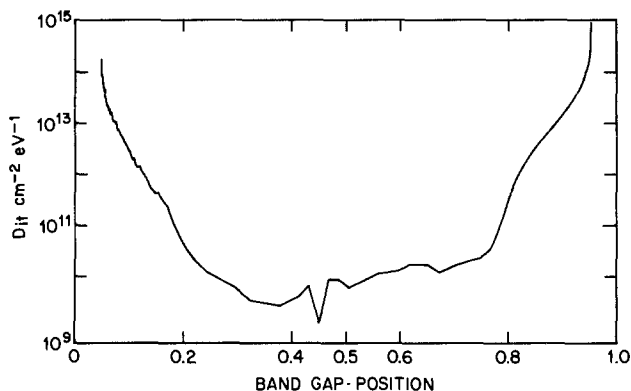


Fig. 5. Interface trap density vs. bandgap position for thin oxides grown at 950°C with a two-step oxidation process.

$10^9/\text{cm}^2\text{-eV}$, compared to a value of $2 \times 10^{10}/\text{cm}^2\text{-eV}$ for oxides grown by the standard process at 950°C.

The intermediate annealing step reduces not only the defect density in the oxides, but also the density of interface traps.

HREM Structural Observations

Figure 6a illustrates the thin oxide interface morphology for the sample that had undergone the standard process. It is evident that considerable atomic-scale roughness exists at the interface between the substrate and the oxide. The height of the individual crystalline protrusions above the single-crystal region may be as much as 20Å or more. The irregular, mottled pattern in the oxide is typical of the appearance of amorphous materials when viewed at high magnification using HREM (12).

The results for the sample which had undergone the intermediate annealing at 1050°C for 1h are quite different. As illustrated in Fig. 6b, both interfaces in this sample are found to be atomically smooth. No sizable silicon protrusions

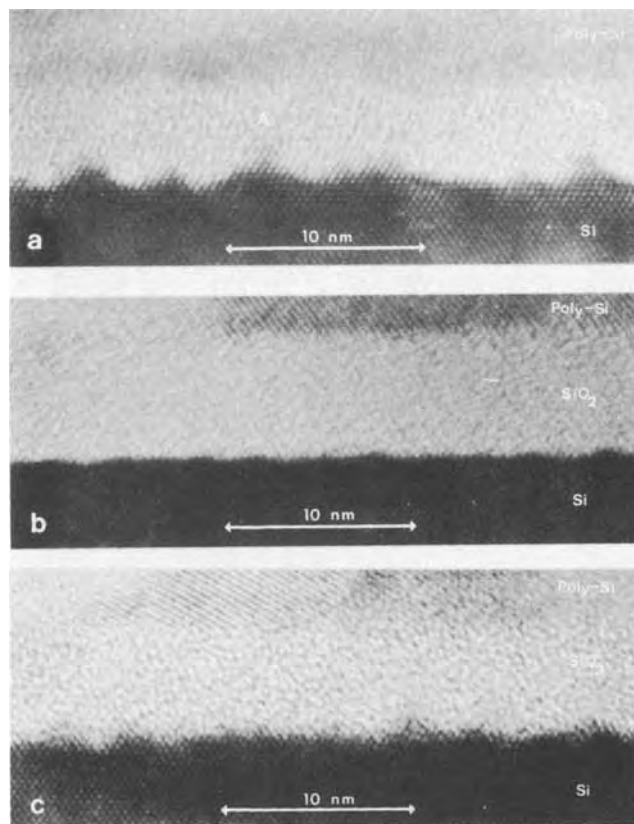


Fig. 6. High resolution electron micrographs illustrating the thin oxide interface morphologies for samples that had undergone: the standard process (a), the two-step oxidation process (b), and the post-oxidation anneal process (c).

are observed, and the degree of interface roughness never exceeds the width of a single monolayer.

Material which received a postoxidation anneal only (Fig. 6c) shows a morphology that is intermediate between those observed in the other two cases. Si/SiO₂ interface roughness existed, but not nearly on the scale of that encountered in the standard process specimen.

Discussion and Conclusion

As seen from the results of the electrical breakdown voltage measurements, the intermediate annealing step is more effective than the postoxidation annealing step in reducing the defect density in thin oxides. Moreover, thin oxides grown at 950° compared to 900°C produce reduced defect density. There seems to be a definite correlation between the electrical properties of thin oxides and the nature of the Si-SiO₂ interface as observed by HREM. The smoothest interface is obtained with the intermediate annealing step, which gives the best electrical properties for the thin oxides.

Stress at the Si-SiO₂ interface is caused by the mismatch between silicon lattice spacings and the restricted range of interatomic separations and bond angles in the amorphous thermal oxide. This molecular mismatch is expressed (13) by the thermodynamic "free volume supply condition," and the release of stress requires the operation of viscous flow in the oxide film. It has also been firmly established, through *in situ* wafer curvature measurements (7), that the viscous flow point of thermally grown SiO₂ on Si is between 950° and 975°C. The dominant free energy term in the initial growth regime is expected to be that associated with defects and strain (13, 14). In the absence of viscous flow (as in our samples oxidized at 900°C), strains that accumulate in the oxide are not easily relieved. Thus, the additional energy required to create strained oxide near any small interface perturbation slows down the oxidation reaction locally and leads to continued growth of the asperity.

With the increase in strain energy as the oxidation continued (15), these protrusions grew to considerable size. Postoxidation annealing at 1050°C allowed viscous flow and relaxation to take place, resulting in a reduction of the interface roughness. Intermediate annealing at 1050°C was even more effective. Its effectiveness is gained by stopping the process before considerable roughness has had time to develop and annealing out the oxide strain before completing the oxidation. Both lower temperature steps (900° or 950°C) were kept short enough to prevent appreciable interfacial asperities from forming. Since the viscous flow point of SiO₂ is between 950° and 975°C (7), the thin oxides grown at 950°C showed a smoother interface than that grown at 900°C.

Substantial interface roughness for the standard process at 900°C leads to a local intensification of the electric field. This leads to a lower value of the oxide breakdown electric field, leading to a higher value of the defect density as observed from the electrical data.

Acknowledgments

It is a pleasure to acknowledge Juanita Sneed and Gerard DeGroot for help with processing the wafers, and W. T. Stacy, S. W. Mylroie, J. C. Bravman, and R. Sinclair for helpful discussions and suggestions.

Manuscript submitted Nov. 7, 1984; revised manuscript received April 4, 1985. This was Paper 208 presented at the Toronto, Ontario, Canada, Meeting of the Society, May 12-17, 1983.

Philips Research Laboratories assisted in meeting the publication costs of this article.

REFERENCES

1. C. M. Osburn and D. W. Ormond, *This Journal*, **119**, 591 (1972).
2. A. C. Adams, T. E. Smith, and C. C. Chang, *ibid.*, **127**, 1787 (1980).
3. D. R. Wolters, T. Hoogestyn, and H. Kraaij, "Physics of MOS Insulators," p. 349, Pergamon Press (1980).
4. C. C. Chang, in "Semiconductor Characterization Techniques," P. A. Barnes and G. A. Rozgonyi, Editors, p. 106, The Electrochemical Society Softbound Proceedings Series, Princeton, NJ (1978).
5. J. F. Wagner and C. W. Wilmsen, *J. Appl. Phys.*, **50**, 874 (1979).
6. F. J. Grunthaler, P. J. Grunthaler, R. P. Vasquez, B. F. Lewis, J. Maserjian, and A. Madhuker, *J. Vac. Sci. Technol.*, **16**, j1443 (1979).
7. E. P. EerNisse, *Appl. Phys. Lett.*, **35**, 8 (1979).
8. J. A. Appels, E. Kooi, M. M. Paffen, J. J. H. Schatorje, and W. H. C. G. Verkuylen, *Philips Res. Rep.*, **25**, 118 (1970).
9. J. C. Bravman and R. Sinclair, *J. Electron. Microsc. Technol.*, **1**, 53 (1984).
10. N. J. Chou and J. M. Eldridge, *This Journal*, **120**, 1139 (1973).
11. W. S. Johnson, G. L. Kuhn, A. L. Renninger, and G. Perlegos, *Electronics*, 113 (Feb., 1980).
12. O. L. Krivanek, P. H. Gaskell, and A. Howie, *Nature*, **262**, 454 (1976).
13. W. A. Tiller, *This Journal*, **127**, 65 (1980).
14. W. A. Tiller, *ibid.*, **127**, 619 (1980).
15. W. A. Tiller, *ibid.*, **128**, 689 (1981).

Acceleration Factors for Thin Oxide Breakdown

J. W. McPherson and D. A. Baglee

Texas Instruments, Incorporated, Houston, Texas 77001

ABSTRACT

Time-dependent dielectric breakdown (TDDB) data for 100Å of thermally grown SiO₂ have been analyzed using an Eyring model. The model has been found to describe the general features of the data: (i) an apparent activation energy which is a function of the stressing electric field, and (ii) a field acceleration parameter that is a function of temperature. Quantitatively, the model suggests the proper field dependence for the activation energy and the observed temperature dependence of the field acceleration in the 100Å oxide material. Because of a decrease (with increasing stress) in the spread (σ) of the time to fail data, acceleration factors derived from $t_{10\%}$ and $t_{50\%}$ are quite different. In the case of $t_{50\%}$, the apparent activation energy is found to decrease from > 1 eV at low field stressing [Eb(50%) - Es > 5 MV/cm] to < 0.3 eV at higher fields [Eb(50%) - Es < 3 MV/cm]. Also, the field acceleration was found to be approximately 5 decades/MV/cm at room temperature, but it reduces to 2 decades/MV/cm at 150°C.

When insulators such as SiO₂, commonly used in VLSI circuits, are stored at a fixed voltage and temperature, they are observed to breakdown with time. This time-dependent dielectric breakdown (TDDB) is judged to be a potential failure mode for MOS integrated circuits and has captured the attention of many investigators. Early investigations centered around the effects of mobile ions (particularly Na⁺) on enhanced conduction via ionic drift to the Si-SiO₂ interface (1-3), or around the effects of radiation damage on dielectric breakdown (4, 5). More recently, with improved processing, oxides have become relatively free from both Na contamination and radiation damage; thus, TDDB attention has turned to intrinsic breakdown (6, 7).

While general agreement seems to exist in that the TDDB data for intrinsic breakdown (6-10) is lognormal in nature, the reported activation energy seems to vary greatly; e.g., Crook (6) reported 0.3 eV, while Anolick (7) gave a value of 2 eV. More recently, TDDB data by Hokari (8) for thin oxides (100Å) suggested an activation energy of 1 eV, while Baglee (9) reported 0.3 eV. Also, the electric field acceleration factors for thin oxides were reported to be < 2 decades/MV/cm (8,9), while the values for thicker oxides (> 400Å) are given (6, 10) to be > 6 decades/MV/cm.

Based on the recent TDDB results reported here for thin oxides, it would seem that many of the above differences are virtual and can be explained by an apparent activation energy which is electric field dependent and a field acceleration factor which depends on temperature. In the next section, we describe the specifics of thin oxide growth and the characterization techniques used in our study. This is followed by a description of the Eyring model used to analyze the results. Acceleration factors for thin oxide stressing are determined with special emphasis given to the impact that the spread (σ) in the time to fail can have on the acceleration factor. The paper is concluded with a discussion and summary of the results.

Oxide Growth and Characterization

Sample preparation.—The basic test structure used to model oxide reliability is the MOS capacitor. However, care must be taken in ensuring that this structure accurately represents the state of oxide in an actual VLSI circuit. For this reason, the test structures reported in this paper were fabricated using a full double-level polysilicon and advanced VLSI process flow and were subjected to all of the standard implants, sputtering, and etch sequences to which typical devices would be subjected.

After initial cleaning of the p-type ($N_A = 10^{15}/\text{cm}^3$) silicon, a pad oxide of 35 nm was grown and a nitride layer of 120 nm was deposited. The thick field oxide was grown using local oxidation of silicon (LOCOS) techniques to a thickness of 600 nm. After removal of the nitride layer, a 40 nm sacrificial oxide was grown in steam and then immediately stripped. The purpose of this is to reduce the Kooi or "white ribbon" effect (11). The pregate oxidation cleanup was a RCA-type cleanup (12). Following the spin-rinse and drying cycle, the slices were immediately loaded into the gate oxidation furnace. The 100Å oxide was grown at 900°C in dry O_2 with 4% HCl and annealed for 20 min in nitrogen. 450 nm LPCVD polysilicon was then deposited and doped from a POCl_3 source. The test capacitors were then patterned and etched.

Following removal of the photoresist, the slices were subjected to a second gate oxidation, a second level of polysilicon deposition and etch, arsenic source-drain implant, deposition and etching of interlayer oxide, deposition and etching of aluminum and compressive silicon nitride was used for the protective overcoat. The samples were then scribed and bonded into ceramic packages.

Initial characteristics.—Before proceeding with a discussion of our initial characterization results, a brief explanation of breakdown in oxides and our measurement techniques will be given.

Care must be exercised in the collection of breakdown data on very thin oxides due to their ability at high electric fields to pass large current densities without actually shorting. In this paper, when we talk about oxide failure we are not referring to the self-healing type of events that can often occur and may cause "soft" errors in memories, but rather to the hard failure due to rupturing of the oxide causing a conducting filament between the anode and cathode. It is beyond the scope of this paper to discuss the actual breakdown mechanisms in silicon dioxide, but there have been many papers written on this subject which provide excellent insight into this phenomenon (*e.g.*, 13-16).

In measuring the breakdown voltage of an oxide, the usual technique is to choose a high current level (say 10 μA) and ramp the voltage until the current through the capacitor reaches this level. Thick oxides (400Å) are always shorted at this point, but this is not necessarily the case for thin oxides, due to the reasons mentioned above. After each stress voltage is applied, the capacitor is subjected to a low reference voltage, V_{ref} (approx 1V). If the capacitor has become shorted, then a large current flows even at the low V_{ref} voltage. This ensures that only shorted devices are monitored.

Using the above technique, we measured the initial breakdown distribution of our oxides after processing was completed. A typical distribution for these 100Å oxides is shown in Fig. 1. There are a few points that should be made about these results. There are two apparent breakdown distributions: those devices which breakdown at approximately 11V and those that are shorted even at 0 V. The breakdowns at 11V are due to intrinsic breakdown, while those seen at 0 V are attributed to pinholes or particulate contamination during processing. It is interesting to note that in this case there is no intermediate distribution between the two. This distinctive distribution for 100Å SiO_2 allows one to investigate very high (8 MV/cm) electric field stressing and still obtain well-behaved TDDB results over a relatively long period of time.

In Fig. 1, the low voltage breakdowns are shaded. This part of the distribution is screened out at multiprobe and would not form part of the actual distribution seen in a real device. The I-V and C-V curves for these thin dielectrics have been reported previously (9).

TDDB testing.—This section will briefly discuss the details of the life testing performed on the packaged capacitors. The polysilicon capacitors (area = 0.01 cm^2) were bonded out, with eight per ceramic package. Each package was then inserted into a life-test board containing 200

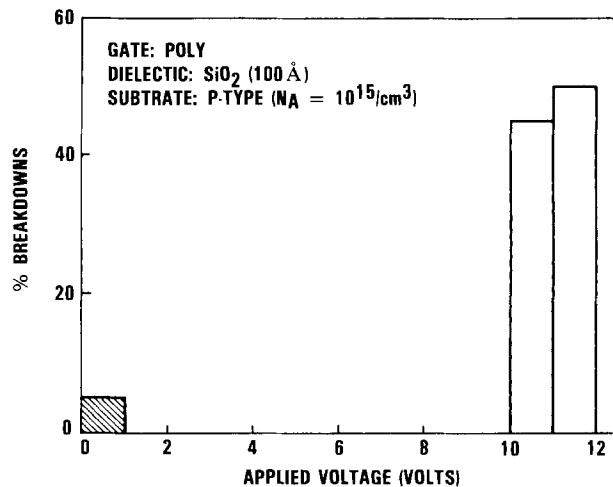


Fig. 1. Bimodal distribution typically seen in 100Å oxides. After a low voltage screen (to eliminate defects causing 0 V breakdowns), the remaining distribution shows $E_b(10\%) = 10 \text{ MV/cm}$ and $E_b(50\%) = 11 \text{ MV/cm}$. Capacitor area is 0.01 cm^2 .

such packages. A 200Ω resistor was placed in series with each capacitor in order to limit the current drawn by each device upon failing and to indicate failed devices (a voltage is dropped across the resistor if the capacitor is shorted). Before beginning the life test, all devices were checked for shorts and continuity. Bad capacitors were removed from the sample population. Four voltages were applied to each package (8, 7, 6, and 5V). The units were then monitored periodically to look for failing devices. This test was repeated at three temperatures: 150°, 85°, and 25°C. Data obtained from these tests will be given in the TDDB Results for Thin Oxide Stressing section.

Eyring Model for Oxide Stressing

The thin oxide TDDB results reported in this investigation seem to be described well by a simplified Eyring model.

Eyring model.—The Eyring model is a theoretical model based on exponential reaction rate theory and free energy considerations (17, 18). The model for TDDB has been written in the form (see Appendix)

$$TF(f\%) = A \exp\left(\frac{\Delta H}{K_B T}\right) \exp[\gamma(T) \mathcal{S}] \quad [1]$$

where $TF(f\%)$ is the time to failure for $f\%$ of the units, ΔH is the enthalpy associated with the activated dielectric breakdown, $\gamma(T)$ is the field acceleration parameter, and \mathcal{S} is the electric field stress function given by

$$\mathcal{S} = E_B(f\%) - E_S \quad [2]$$

Here $E_B(f\%)$ represents the field at which $f\%$ of the capacitors are expected to "instantaneously" break down at room temperature; E_S is the constant electric field applied across the dielectric during TDDB data collection, and the expected temperature variation of $\gamma(T)$ is of the form

$$\gamma(T) = B + \frac{C}{T} \quad [3]$$

where B and C are constants.

Effective activation energy and electric field acceleration parameter.—The "effective" activation energy $(\Delta H)_{\text{eff}}$ is a useful parameter which allows one to relate the time-to-fail data taken at temperature T_1 to data taken at T_2 (with the assumption that the electric field stress function is held fixed). Mathematically, this is expressed as

$$(\Delta H)_{\text{eff}} = K_B \left(\frac{\partial \ln TF(f\%)}{\partial (1/T)} \right)_{\mathcal{S}} = \Delta H + K_B C \mathcal{S} \quad [4]$$

Similar to the activation energy, the electric field acceleration parameter γ allows one to relate the time to failure data taken at one stressing field, \mathcal{S}_1 , to the data taken at another, \mathcal{S}_2 (with the assumption being that the temperature is fixed)

$$\gamma = \left(\frac{\partial \ln TF(f\%)}{\partial \mathcal{S}} \right)_T = - \left(\frac{\partial \ln TF(f\%)}{\partial E_s} \right)_T \quad [5]$$

Acceleration factors for thin oxide stressing.—For reliability estimations, the acceleration factor, AF , is of primary importance. The AF allows one to project the time-to-failure data taken under a given set of stress conditions (ST_2) to some other set of conditions (ST_1), i.e.

$$[TF(f\%)]_{ST_1} = AF * [TF(f\%)]_{ST_2} \quad [6]$$

Normally, it is assumed that the dispersion [$\sigma = \ln(t50/t16) = \ln(t84/t50)$] in the lognormal time-to-fail data is independent of the stress conditions. Under the assumption of a constant σ , any arbitrary $f\%$ of failures may be used for the determination of a unique value of AF .

However, if σ does show a dependence on stress conditions, then the value determined for AF will no longer be unique, but will depend on the $f\%$ of failures used for the AF determination. The impact of σ can be illustrated by comparing AF based on $f = 10\%$ and $f = 50\%$

$$(AF)_{10\%} = (AF)_{50\%} \exp [1.28(\sigma_{ST_2} - \sigma_{ST_1})] \quad [7]$$

This last equation shows that the acceleration factors AF based on 10% and 50% are identical only if σ is independent of stressing conditions.

TDDB Results for Thin Oxide Stressing

Observed time to failure.—Details of the lognormal TDDB data for these 100Å SiO₂ films have been shown elsewhere (9). The TDDB results are summarized here in Table I. One will note that σ is rather sensitive to the stress conditions, decreasing with increasing electric field stress or increasing temperature. This would imply, according to Eq. [7], that the determined value of AF will depend on the failure percent ($f\%$) used for its determination. Therefore, in Fig. 2-4, we show the time-to-failure data as a function of the stressing electric field in two forms: one based on $f = 10\%$ and the other based on $f = 50\%$.

Field acceleration parameter.—The determination of γ is based on the slope of the linear fits to the data shown in Fig. 2-4. The results are shown in Fig. 5. We note that the fit for the data is quite good at $f = 10\%$ and reasonably good for the $f = 50\%$ data. The equations for the lines are

$$(\gamma_e)_{f=10\%} = -3.0 + \frac{0.21}{K_B T} (\text{mV/cm})^{-1} \quad [8]$$

and

Table I. Summary of time-to-failure results for 100Å SiO₂. The values for $t_{50\%}$ and σ were obtained from best lognormal fits to each data set.

TEMP	FIELD (MV/cm)	t _{50%} (HRS)	t _{10%} (HRS)	σ
25 DEG C	6	4x10 ¹¹ *	2.0x10 ⁴	13.1
	7	1.1x10 ⁶ *	2.5x10 ²	6.6
	8	90	1.5	3.2
85 DEG C	6	—	—	—
	7	1.7x10 ⁴	25	5.1
	8	12	.66	2.3
150 DEG C	6	7x10 ⁵ *	50	7.5
	7	2.7x10 ²	5	3.1
	8	2.5	.4*	1.4

* AN EXTRAPOLATION OF MORE THAN ONE DECADE REQUIRED

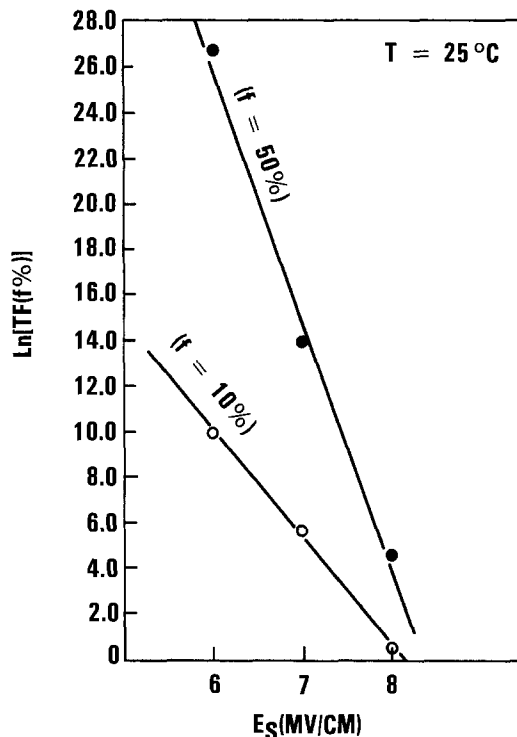


Fig. 2. Room temperature time-to-failure data vs. the stressing electric field. Two data sets are shown: one using $f = 10\%$ and the other using $f = 50\%$.

$$(\gamma_e)_{f=50\%} = -6.0 + \frac{0.43}{K_B T} (\text{mV/cm})^{-1} \quad [9]$$

The electric field acceleration parameters shown in Eq. [8] and [9] are subscripted with an "e" as a reminder to the reader that natural logarithms and exponentials have been used in this work, e.g.

$$TF \propto \exp (\gamma_e \mathcal{S}) \quad [10]$$

However, many authors prefer to express γ in decades/MV/cm, which we will represent as γ_{10} , e.g.

$$TF \propto 10^{\gamma_{10} \mathcal{S}} \quad [11]$$

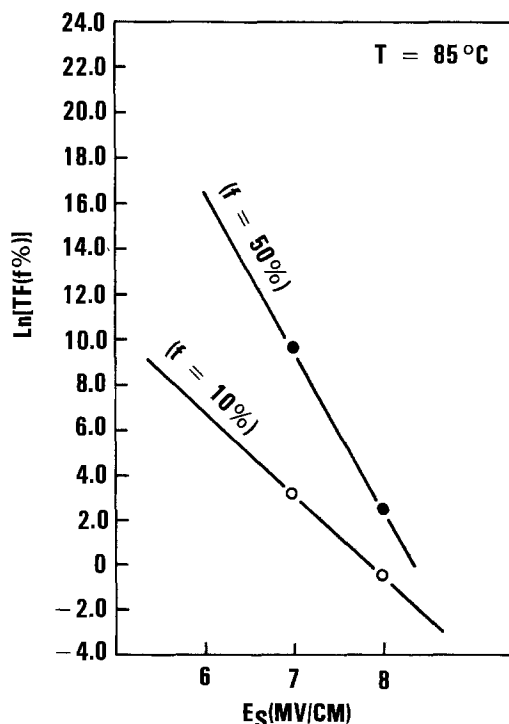


Fig. 3. 85°C time-to-failure data vs. stressing electric field

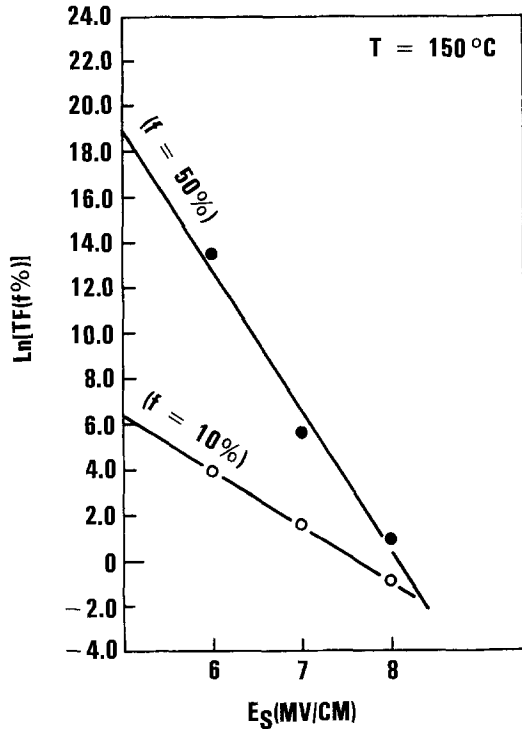


Fig. 4. 150°C time-to-failure data vs. stressing electric field

The relationship between Eq. [10] and [11] is straightforward

$$\gamma_{10} = \gamma_e / \ln_e(10) \quad [12]$$

Effective activation energy.—The effective activation energy $(\Delta H)_{\text{eff}}$ can be determined, according to Eq. [4], from the slope of the Arrhenius plots of the time-to-fail data. These are shown in Fig. 6. The determined activation energy is shown in Fig. 7 and Fig. 8. The equations for the best linear fit to the data become

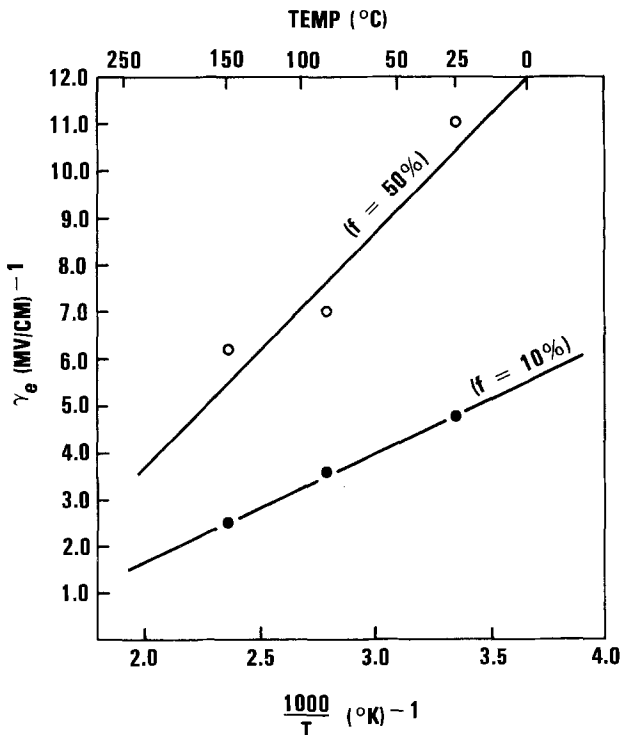


Fig. 5. Observed temperature dependence of the electric field acceleration parameter. Data for two characteristic failure percentages are shown.

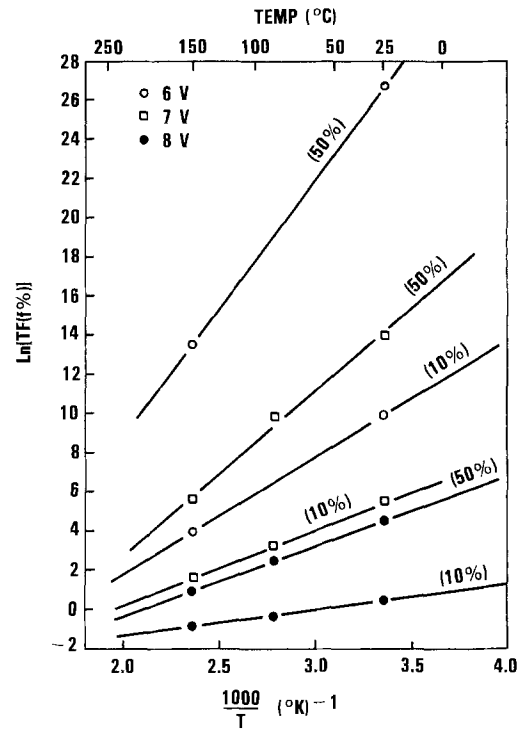


Fig. 6. Arrhenius plot of time to failure data. Results for 6, 7, and 8V are shown for two characteristic failure percentages.

$$(\Delta H)_{\text{eff},10\%} = -0.30 + 0.20\mathcal{F} \text{ (eV)} \quad [13]$$

and

$$(\Delta H)_{\text{eff},50\%} = -0.71 + 0.35\mathcal{F} \text{ (eV)} \quad [14]$$

Note that, in accordance with the observed breakdown distribution (Fig. 1) for the 100Å oxide tested, $E_b(10\%) = 10 \text{ MV/cm}$ and $E_b(50\%) = 11 \text{ MV/cm}$ were used in Eq. [13] and [14], respectively.

Discussion of Results

Before the simplified Eyring model can be used to properly model TDDB data, two basic requirements for the data must first be satisfied: (i) the observed activation energy $(\Delta H)_{\text{eff}}$ should be a linear function of the electric field stress $\mathcal{F} = E_b(f\%) - E_s$ and (ii) the observed electric field acceleration parameter should be a linear function of reciprocal temperature. The results reported here for 100Å oxides suggest that both requirements are met for Eyring model use.

The electric field acceleration factor determined in this study

$$(\gamma_{10})_{f=50\%} = -2.6 + \frac{0.19}{K_b T} \text{ (decades/MV/cm)} \quad [15]$$

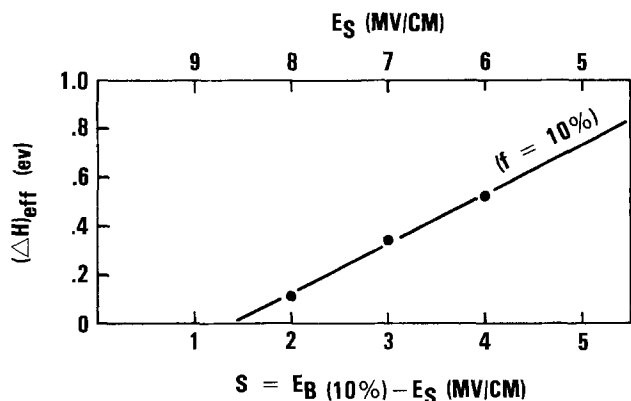


Fig. 7. Observed electric field dependence of the activation energy. $E_b(10\%) = 10 \text{ MV/cm}$ for the SiO_2 material under investigation. $f = 10\%$ was used as the characteristic failure percentage.

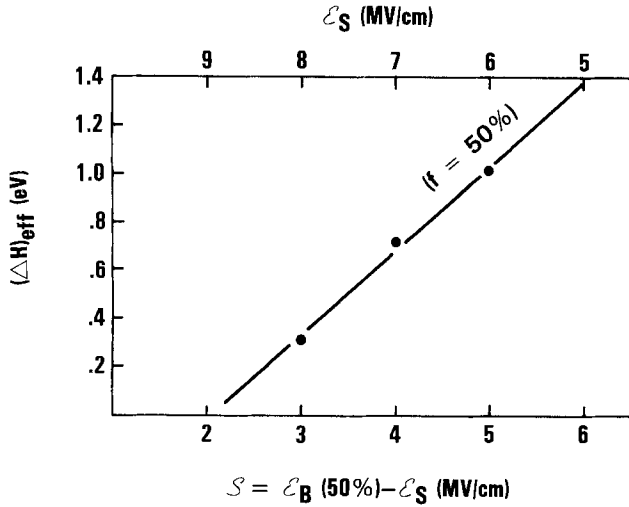


Fig. 8. Observed electric field dependence of the activation energy. $E_b(50\%) = 11$ MV/cm for the SiO_2 material tested. $f = 50\%$ was used as the characteristic failure percentage.

is consistent with the 1.7 decades/MV/cm result reported by Hokari at 250°C for thin oxides. While a slight divergence of the two data sets seems to exist at room temperature (see Fig. 9), at normal operating temperature (55°C and above), good agreement seems to exist with Berman's data (10) for thicker oxides ($\geq 400\text{\AA}$). Also, the functional form of γ is consistent with that suggested by Anolick for thick oxides.

As for the observed activation energy $(\Delta H)_{\text{eff}}$ being a function of the electric field stress function \mathcal{S} (Eq. [13] and [14]), this seems to be required for a unified explanation of the results reported here, in addition to the results of Crook, Anolick, and Hokari. Crook reports an activation energy of 0.3 eV for gate oxides stressed at 3-5 MV/cm and $f = 10\%$. Assuming that $E_b(f = 10\%) = 7$ MV/cm for his oxide tested, then the stress function \mathcal{S} would have ranged from 2-4 MV/cm. Equation [13] would predict an average observed activation energy of 0.3 eV.

Anolick's reported activation energy was based on $f = 50\%$ and low field stressing ($E_s = 1-3$ MV/cm). Assuming that $E_b(f = 50\%)$ was about 9 MV/cm for his material

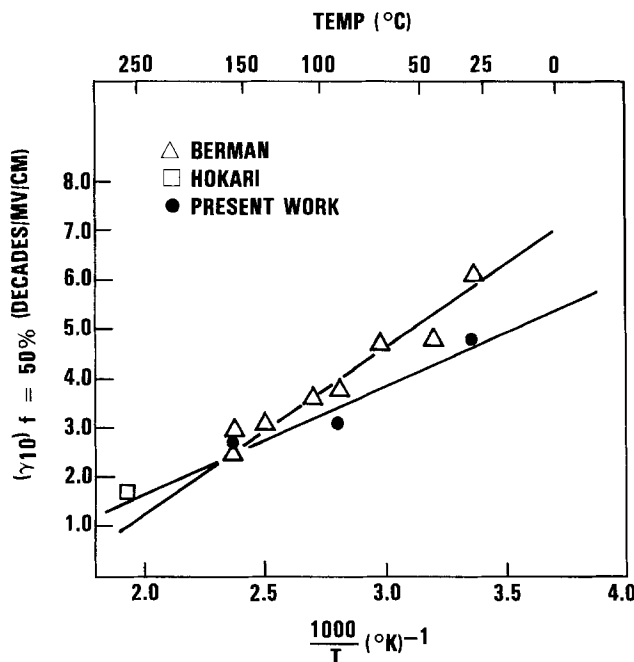


Fig. 9. Observed temperature dependence of the electric field acceleration parameter. Data shown represent (i) the 100\AA SiO_2 results obtained in this work plus the single datum of Hokari (also for 100\AA SiO_2), and (ii) the data of Berman for much thicker SiO_2 ($\geq 400\text{\AA}$).

tested, then \mathcal{S} would have ranged from 6-8 MV/cm during stressing. Equation [14] predicts an average value of 1.8 eV over this stress range and seems to agree with Anolick's reported value at 2 eV.

Also, Hokari's data for thin (100\AA) SiO_2 suggest an activation energy of 1 eV with the stressing field at $E_s = 6$ MV/cm and $f = 50\%$. This again is quite consistent with the results shown in Fig. 8.

Conclusions

In this paper, we have presented TDDB data for 100\AA silicon dioxide films. These data have been found to be fit well by a simplified Eyring model. We have found that the activation energy measured depends upon the electric field stress and that the field acceleration factor is temperature dependent. Both results are in good agreement with the proposed model. We have shown that the acceleration factors derived from $t_{50\%}$ and $t_{10\%}$ can be quite different and that care must be taken with the manipulation of TDDB data in order to get meaningful results. Finally, we have shown that other published data on oxide wearout can be fit with our model, thus removing many of the apparent discrepancies between the results of the various workers.

Acknowledgments

The authors would like to thank George Punter for preparing some of the samples and Ron Parker for much of the data collection.

Manuscript submitted Oct. 26, 1984; revised manuscript submitted April 11, 1985.

Texas Instruments, Incorporated, assisted in meeting the publication costs of this article.

APPENDIX

Thermodynamic Model for Dielectric Breakdown

Thermodynamics of dielectrics.—The internal energy ϵ for a dielectric material under the influence of an external electric field E will be a function of the system entropy S , volume V , mole number N , and polarization P (19)

$$\epsilon = \epsilon(S, V, N, P) \tag{A-1}$$

The polarization P represents the total dipole moment produced (either induced or oriented) by the applied electric field E . The Gibbs free energy as a function of the intensive parameters temperature T , electric field E , chemical potential μ , and pressure p , can be obtained through the Legendre transformation of ϵ giving

$$G(T, E, \mu) = H_0 - TS - \mu N - EP \tag{A-2}$$

where H_0 is the enthalpy. Since the pressure p is constant during dielectric stressing, its impact on the free energy G will not be shown explicitly. We attempt to write the last three terms of the free energy as

$$-TS - EP - \mu N = K_b T f(T) g(E) h(\mu) \tag{A-3}$$

where f , g , and h are functions only of T , E , and μ , respectively. Using the standard thermodynamic relationships

$$S = -\left(\frac{\partial G}{\partial T}\right)_{E, \mu} = -K_b g h \left[f + T \frac{df}{dT} \right] \tag{A-4}$$

$$P = -\left(\frac{\partial G}{\partial E}\right)_{T, \mu} = -K_b T f h \frac{dg}{dE} \tag{A-5}$$

$$N = -\left(\frac{\partial G}{\partial \mu}\right)_{T, E} = -K_b T f g \frac{dh}{d\mu} \tag{A-6}$$

and insertion into Eq. [A-3], we obtain the defining ordinary differential equation

$$\frac{T}{dT} \frac{df}{f} + \frac{E}{dE} \frac{dg}{g} + \frac{\mu}{d\mu} \frac{dh}{h} \tag{A-7}$$

The solution to Eq. [A-7] gives for the free energy

$$G(T, E, \mu) = H_0 + K_b T \sum_m \sum_n C_{mn} \frac{E^m \mu^n}{T^m} \tag{A-8}$$

At breakdown, the dielectric undergoes an irreversible phase transition in which the material is transformed from an insulating phase to a conductive phase. While the driving force for this change is a free energy difference between the two phases, the rate at which the change takes place is controlled by the free energy of activation associated with the conductive poly filament growth shorting the gate to substrate. Equation [A-8] suggests that the free energy of activation ΔG^* associated with dielectric breakdown can be written as

$$\Delta G^* = \Delta H_o^* + K_B T \sum_m \sum_n C_{mn} \frac{(E_B^n - E_s^n) \mu^{m-n}}{T^m} \quad [\text{A-9}]$$

Where H_o^* is the free enthalpy of activation, E_s is the electric field applied during stress, and E_B represents the "time-zero" breakdown strength of the dielectric.

Simplified Eyring model for breakdown reaction rate.—The assumption is made that the time-dependent dielectric breakdown is an activated process obeying standard chemical reaction rate theory (17, 18), with the reaction rate constant given by

$$k \propto \exp \left(- \frac{\Delta G^*}{K_B T} \right) \quad [\text{A-10}]$$

In order to simplify the theory for dielectric breakdown, we keep only the linear terms in Eq. [A-9], giving

$$\Delta G^* = \Delta H_o^* + K_B T \left[B + \frac{C}{T} \right] \mathcal{S} \quad [\text{A-11}]$$

where $\mathcal{S} = E_B - E_s$ and B and C are constants. For capacitors with identical breakdown strengths, the characteristic time-to-failure can be expressed as

$$TF = A \exp \left(\frac{\Delta G^*}{K_B T} \right) \quad [\text{A-12}]$$

where A is a constant. However, in practice, the breakdown strengths of individual capacitors will not be identical (dispersion in breakdown strength). The dispersion in breakdown strength can be taken into account by writing

$$TF(f\%) = A \exp \left(\frac{\Delta H_o^*}{K_B T} \right) \exp [\gamma(T)\mathcal{S}] \quad [\text{A-13}]$$

where

$$\gamma(T) = B + \frac{C}{T} \text{ and } \mathcal{S} = E_B(f\%) - E_s$$

Please note that the model predicts an electric field-dependent activation energy

$$K_B \left(\frac{\partial \ln TF}{\partial(1/T)} \right)_{\mathcal{S}} = \Delta H_o^* + K_B C \mathcal{S} \quad [\text{A-14}]$$

and a temperature-dependent field acceleration parameter

$$\left(\frac{\partial \ln TF}{\partial \mathcal{S}} \right)_{\tau} = - \left(\frac{\partial \ln TF}{\partial E_s} \right)_{\tau} = \gamma(T) \quad [\text{A-15}]$$

Also, note that, according to Eq. [A-13], the observed dispersion σ in the time to failure data should have a temperature dependence given by

$$\sigma = \ln \left[\frac{TF(50\%)}{TF(16\%)} \right] = \gamma(T)[E_B(50\%) - E_B(16\%)] \quad [\text{A-16}]$$

REFERENCES

1. S. I. Raider, *Appl. Phys. Lett.*, **23**, 34 (1973).
2. C. M. Osburn and D. W. Ormond, *This Journal*, **121**, 1195 (1974).
3. S. P. Li and J. Maserjian, *Solid-State Electron.*, **19**, 235 (1976).
4. S. P. Li and J. Maserjian, *ibid.*, **18**, 287 (1975).
5. S. P. Li, *J. Appl. Phys.*, **46**, 4888 (1975).
6. D. L. Crook, in "Proceedings of the 17th Annual IEEE Reliability Physics Symposium," p. 1, IEEE, New York (1979).
7. E. S. Anolick and G. R. Nelson, in "Proceedings of the 17th Annual IEEE Reliability Physics Symposium," p. 8, IEEE, New York (1979).
8. Y. Hokari, T. Baba, and N. Kawamura, *IEDM Tech. Dig.*, 46 (1982).
9. D. A. Baglee, in "Proceedings of the 22nd IEEE Reliability Physics Symposium," IEEE, New York (1984).
10. A. Berman, in "Proceedings of the 19th IEEE Reliability Physics Symposium," p. 204, IEEE, New York (1981).
11. E. Kooi, J. G. Van Lierop, and J. A. Appels, *This Journal*, **123**, 1117 (1976).
12. W. Kern and D. A. Puotinen, *RCA Rev.*, **31**, 187 (1970).
13. C. M. Osburn and D. W. Ormond, *This Journal*, **119**, 592 (1972).
14. T. H. Distefano and M. Shatzkes, *J. Vac. Sci. Technol.*, **13**, 50 (1976).
15. N. Klein, *Adv. Phys.*, **21**, 605 (1972).
16. S. Holland, I. C. Chen, T. P. Ma, and C. Hu, *IEEE Electron Device Lett.*, **ed1-5**, 302 (1984).
17. S. Glasstone, K. Laidler, and H. Eyring, "The Theory of Rate Processes," McGraw-Hill, New York (1941).
18. H. Eyring, D. Henderson, B. Stover, and E. Eyring, "Statistical Mechanics and Dynamics," John Wiley and Sons, New York (1964).
19. E. Desloge, "Thermal Physics," Holt, Rinehart, and Winston, New York (1968).
20. C. M. Osburn and S. I. Raider, *This Journal*, **120**, 1369 (1974).
21. C. M. Osburn and E. Bassous, *ibid.*, **122**, 89 (1975).

A Simplified Viscoelastic Model for the Thermal Growth of Thin SiO₂ Films

G. Camera Roda, F. Santarelli, and G. C. Sarti

Istituto di Impianti Chimici, Università di Bologna, I-40136 Bologna, Italy

ABSTRACT

Recently, thermal dry oxidation of silicon was quantitatively described by the present authors in a model accounting for the relaxation phenomena occurring in the oxide film. Clarity about the underlying physical mechanisms and satisfactory matching with existing data both make the model rather appealing; also, the well-known anomalous behavior encountered in the thin film region appears to be adequately predicted. The resulting numerical problem is rather complex when compared with other existing models. A simplified mathematical formulation of the mentioned model is proposed here. The viscoelastic relaxations occurring in the oxide layer are lumped into a time-dependent effective diffusivity for which an explicit expression was found in terms of the parent model parameters. A deviation of, at most, 2.3% in the oxidation rate was obtained by comparing the results from rigorous and simplified approach. The simplified model proposed requires numerical procedures as simple as for some previously existing models; it has the additional advantage of being written in terms of quantities which all have precise physical meanings and can be measured independently of the oxidation process.

Modern microelectronic technology for LSI and VLSI demands highly reliable although very thin passivating layers. A widely used passivating agent is found in thermally grown silicon dioxide. In the present work, we will only refer to SiO₂ layers grown in dry atmospheres.

The operating conditions at which SiO₂ layers are grown involve a temperature range usually between 800° and 1100°C. The film thickness of practical interest typically does not exceed a few hundred angstroms. In this case, all experimental data (1-9) show marked deviations from the behavior predicted by the so-called linear-parabolic equation (10). The latter equation, however, successfully describes the thermal growth of SiO₂ layers for higher temperatures and/or for oxide thickness larger than 200-300Å. The physical picture underlying the linear-parabolic theory can be summarized as follows (10): (i) molecular oxygen dissolves into the SiO₂ phase and diffuses through the SiO₂ layer; (ii) the oxygen concentration in the SiO₂ layer at the gas-solid interface obeys the thermodynamic phase equilibria requirements; (iii) diffusion of molecular oxygen occurs according to Fick's law, with constant diffusivity, and convective contributions are completely neglected and the diffusion process is assumed to occur under pseudosteady-state conditions; (iv) chemical reaction takes place at the oxide-silicon interface, according to a first-order kinetics with respect to the molar oxygen concentration.

In spite of the crude simplicity embodied by the above assumptions, it is nevertheless apparent that a rather wide variety of physical phenomena simultaneously takes place during the oxidation process.

The crude simplicity embodied by the above assumptions is paralleled by the rather wide variety of physical phenomena which have been found experimentally to occur during the oxidation process.

The mentioned failure of the linear-parabolic theory to predict the experimental behavior and the increasing demand for a satisfactory quantitative description both are the origins of the wide research interest devoted to this field.

Indeed, several different merely mathematical models have been proposed recently which adequately describe experimental data (1, 3, 11-13); owing to their pure phenomenological origin, however, the intervening parameters are just data fitting variables, with no particular meaning. Important questions such as (i) what the main physical and chemical phenomena which govern the observed growth rate are, and (ii) what their suitable mathematical description is, are left unanswered by the purely empirical models.

Thus, the need of quantitative models obtained through a suitable physical schematization of the process is self-evident.

Only very recently Fargeix *et al.* (14-16) proposed a physical based mathematical model of the oxidation pro-

cess suitable also to represent the behavior for thin oxide layers. Their basic assumptions are related to the stress dependence of the oxygen diffusivity and to the viscoelastic behavior of the newly formed oxide film.

The aim of the present work is to develop another physically based mathematical model for the dry oxidation process adequate to represent both thin and thick oxide film formation. To that extent, it is convenient to first recall some relevant features to the experimental observations.

Some experimental evidence (3, 11) suggests that the oxygen transport through the SiO₂ layer occurs through molecular oxygen diffusion at higher temperatures, while at significantly lower temperatures diffusion of atomic oxygen seems to be more plausible. The existence of different parallel paths for O₂ transport was also claimed due to spatial nonuniformities [*viz.*, channeling (17)] in the very early stages of SiO₂ formation.

A significant role seems to be played by the mechanical stresses originated during the process, which can be schematically understood as follows.

Indeed, the oxidation which occurs at the oxide-silicon interface causes a significant increase in the Si-Si interatomic distance, or, in other words, the silicon atomic concentration is higher in the Si single crystal than in the SiO₂ phase. However, adhesion and material continuity at the Si/SiO₂ interface prevent any slipping motion along the interfacial surface. As a consequence, strain and stresses are built in both phases during the oxidation process. The oxide layer is under compression in the directions parallel to the interface; unconstrained displacements can take place only in the oxidation direction, *i.e.*, perpendicularly to the Si/SiO₂ interface; correspondingly, the underlying silicon is under tension in the directions parallel to the oxidation plane (13, 20).

The stress and strain levels in both phases decrease with the distance from the Si/SiO₂ interface according to the mechanical properties of both phases. In this respect, it is worth noting that Si single crystals behave as elastic materials with Young moduli of about 1.7×10^{12} dyn/cm² (18), while the oxide properties show peculiar behavior. Dilatometric measurements (19) indicate that at temperatures lower than about 960°C density is a time-dependent quantity which eventually relaxes toward a final value; at temperatures higher than 960°C, however, the relaxation rate is so high that no relaxation response was observed. An analogous conclusion was drawn on the basis of direct mechanical measurements of the relaxation times (20). Apparently, the value of 960°C plays the role of a transition temperature separating regions of practically instantaneous response, at higher temperatures, from regions of viscoelastic response at lower values.

Undoubtedly, the stress or strain level will influence the overall process kinetics. As a matter of fact, the diffusion through the compressed oxide layers is expected to

be slower than through an unstrained film. However, the oxidation reaction will occur with a pure Si concentration which is altered by the deformation (13); moreover, the rate constant is increased by the strain, as can be qualitatively expected from Eyring kinetic theory (21).

A comprehensive description of the oxidation process thus appears rather complex since the strain, stress, and concentration fields as well as oxide thickness should be simultaneous unknowns of the problem. Additional complexity derives also from the viscoelastic behavior of the SiO₂ phase, whose physical properties must be regarded as time dependent.

As a matter of fact, a detailed analysis of the oxide region, based on the relative intensity of the binding energy (26, 27), showed that there is a SiO₂ layer, about 40Å thick, adjacent to the oxide-silicon interface, with a structure different from the oxide core. More precisely, the amorphous SiO₂ phase is mainly formed by six Si atom rings, with small fractions of four Si atom rings, while close to the Si-SiO₂ interface the oxide is mainly formed by four Si atom rings. As a consequence, during its lifetime the oxide phase experiences significant morphological changes, moving from a lower free volume to a higher free volume state; in other words, the phenomenon can be viewed as a relaxation from a high free energy towards a lower free energy state. Such a relaxation certainly involves stress relaxation, although it does not simply coincide with such.

In spite of the discouraging complexity we are faced with, not all the above mechanisms seem to be equally effective on the oxidation kinetics. Indeed, the existing deformations will be typically in the order of a few percent in the single-crystal phase, so that the pure silicon concentration change induced by the stress presence can be disregarded. Moreover, the strain energy is three orders of magnitude smaller than the activation energy of the reaction so that the influence produced on the kinetic constant is also actually negligible.

More significantly, decoupling the mass transfer from the mechanical stress distribution problem seems to be a reasonable approximation. In fact, parallel to what is currently recognized in polymer physics, e.g., Ref. (22), all mechanical and transport properties are directly related to the free volume associated to a given structure. Thus, as a first approximation, diffusivity does not depend on the stress *per se*; it rather depends on the free volume associated to the existing structure. The free volume relaxes in time toward a final equilibrium value, typically according to an exponential decay (22).

Based on the above observations, a shorthand though satisfactory quantitative description of the oxidation process was recently proposed by the present authors (23). The resulting mathematical formulation will be briefly summarized in the next section for the sake of clarity.

The resulting computational model appears rather cumbersome to be easily used for simulation purposes. The aim of this work is to analyze a simplified formulation of the model proposed in Ref. (23). This simplified model involves lower computational requirements than the parent one without any significant loss of accuracy in representing experimental data.

The Viscoelastic Kinetic Model

The mathematical model developed in Ref. (23) is given by a two moving boundaries diffusion problem since oxygen diffusion takes place within the oxide layer whose interfaces are both moving with respect to the silicon core. The oxygen concentration at the oxide-vapor phase is assumed to obey the equilibrium conditions.

The crucial assumption of the model is related to the constitutive equation for the diffusive flux across the oxide phase. Instead of the usual Fick's law, a viscoelastic-like linear constitutive equation was assumed, given by (24)

$$J_{O_2}(t, \mathbf{x}) = - \rho \int_0^t \mu(t-t') \nabla \omega(t', \mathbf{x}) dt' \quad [1]$$

where ρ is the oxide density and ω the oxygen mass fraction. The memory function $\mu(s)$ was given the following expression

$$\mu(s) = D_1 \delta(s) + \frac{D_x - D_1}{\tau} e^{-s/\tau} \quad [2]$$

where δ is the Dirac function

Equations [1] and [2] were first studied to represent the mass-transfer behavior in relaxing polymers. Qualitatively, they represent a time-dependent diffusive flux: for oxide lifetimes very short with respect to the relaxation time τ , the diffusive flux is roughly equivalent to Fick's law with constant diffusivity D_1 , while at lifetimes much larger than τ it is equivalent to a fickian diffusion with the "relaxed" constant diffusivity D_x . At intermediate lifetimes, we can say that apparent diffusivity relaxes from the value D_1 to the value D_x , according to the relaxation time τ .

Since it can be easily shown that the convective contributions can be disregarded, the mathematical formulation of the problem can finally be written as follows. The distribution of the oxygen mass fraction ω , as a function of time t and of the distance y from the vapor-solid interface, is governed by

$$\frac{\partial \omega}{\partial t} = D_1 \frac{\partial^2 \omega}{\partial y^2} + \frac{D_x - D_1}{\tau} \int_0^t e^{-\frac{t-t'}{\tau}} \frac{\partial^2 \omega}{\partial y^2} dt' \quad [3]$$

with the associated initial and boundary conditions

$$t = 0 \quad \omega = 0 \quad [4]$$

$$t > 0, y = 0 \quad \omega = \omega_e \quad [5]$$

$$t > 0, y = \delta(t) \quad -D_1 \frac{\partial \omega}{\partial y} = k_r \omega \quad [6]$$

The problem must be solved for $y \in (0, \delta(t))$, where $\delta(t)$ represents the thickness of the oxide layer, ω_e is the equilibrium oxygen concentration, while k_r is the kinetic constant of the oxidation reaction.

As shown in Ref. (23), the oxide thickness is governed by the following equation

$$\frac{d\delta}{dt} = \frac{J_{O_2}(t, 0)}{\rho(1 - \omega_e)} + k_r \frac{M_{Si}}{M_{O_2}} \omega(t, \delta(t)) \quad [7]$$

to be solved with the proper initial condition.

It is worth noting, in passing, that Eq. [7] properly reduces to the usual equation reported by Deal and Grove (10) in the special case of fickian diffusion with constant diffusivity.

In Ref. (23), the problem represented by Eq. [1]-[7] was solved in dimensionless terms by using $t_0 = D_1/k_r^2$ and $l_0 = D_1/k_r$ as characteristic time and length, respectively. The dimensionless time, t^* , and the dimensionless relaxation time, τ^* , were consequently defined as

$$t^* = tk_r^2/D_1 \quad [8]$$

$$\tau^* = \tau k_r^2/D_1$$

The comparison with several existing experimental data has shown the satisfactory ability of the model to represent the observed behavior.

The Simplified Viscoelastic Model

The complete model outlined in the previous section is adequate to describe the thermal oxidation of silicon also in the range of relatively low temperatures and of very thin oxide thickness. However, one disadvantage of the model may be represented by the computational requirements involved in its solution. The question then arises of what simplified calculation schemes could be followed to reach in a more straightforward way thickness vs. time relationships which are essentially the same as those resulting from the original model.

First of all, it was observed that the pseudosteady-state approximation, obtained by setting the lhs of Eq. [3] equal to zero, is very reasonable. Actually, for the cases of practical interest, the oxide thickness obtained under this approximation differs from the value given by the original problem at most in the seventh significant digit.

Within the pseudosteady-state approximation, the introduction of a suitable time-dependent effective diffusivity allows, on the one hand, bypassing the solution of the boundary value problem for the oxygen concentration and, on the other hand, accounting for the linear viscoelastic relaxation of the diffusive properties.

The time-dependent effective diffusion coefficient, $D_e(t)$, is defined as

$$J_{O_2}(t) = -\rho D_e(t) \frac{\omega_\delta - \omega_e}{\delta} \quad [9]$$

where J_{O_2} is the time-dependent flux, which is independent of the spatial position in view of the pseudosteady-state approximation, and ω_δ is the oxygen mass fraction at the oxide-silicon interface $y = \delta$.

In view of Eq. [9], Eq. [7] for the thickness growth rate becomes

$$\frac{d\delta}{dt} = \frac{k_r D_e(t)}{D_e(t) + \delta k_r} \omega_e \left(\frac{M_{Si}}{M_{O_2}} + \frac{1}{1 - \omega_e} \right) \quad [10]$$

A suitable expression for the effective diffusivity was found to be

$$D_e(t) = D_x + (D_i - D_x) \exp \left[-a \frac{t^*}{\tau^{*n}} \right] \quad [11]$$

with $a = 0.16$ and $n = 0.9$.

The procedure followed to obtain Eq. [11] is outlined in the Appendix.

Confidence in the use of Eq. [10] and [11] was gained through the comparison of the results from the simplified model with those from the complete one: for the parameters of practical interest, the value of the oxide thickness obtained under the two situations differs typically less than 1%. A maximum deviation of 2.3% was found in the case of $\tau^* = 10^8$.

It is important to notice that Eq. [10] can be reduced to an expression which is formally very similar to the one resulting from the linear parabolic theory.

This is not surprising, since when transport through the layer and chemical reaction at the interface are considered as the significant steps of the process, it is easy to prove that in pseudosteady state the equation

$$\frac{dt}{d\delta} = \frac{1}{K_{L,e}} + \frac{2\delta}{K_{P,e}} \quad [12]$$

formally holds, when both the linear and the parabolic coefficients assume different expressions as the result of the physical assumptions made on the material behavior.

In the present case the effective parabolic coefficient $K_{P,e}$ is then given by

$$K_{P,e} = K_{P,e}(t) = 2D_e(t) \phi \quad [13]$$

where, for the sake of simplicity, use has been made of the following position

$$\phi = \omega_e \left(\frac{M_{Si}}{M_{O_2}} + \frac{1}{1 - \omega_e} \right) \approx \omega_e \frac{M_{SiO_2}}{M_{O_2}} \quad [14]$$

The effective linear coefficient, $K_{L,e}$, is defined as

$$K_{L,e} = k_r \phi \quad [15]$$

and it has the same physical meaning as in the linear-parabolic theory.

Thus, according to the simplified model presented here the slope in the Hopper diagram ($dt/d\delta$ vs. δ) is related to reciprocal effective diffusivity, which changes during oxidation from the value D_i to the value D_x .

From Eq. [12] and [15], it is apparent that the reaction rate constant k_r is related to the reciprocal of the actual intercept, for $\delta = 0$, in the Hopper diagram. In this respect, it can be noticed that the usual practice, e.g. Ref. (3), to evaluate k_r appears to be misleading, insofar as the intercept is not obtained by the true $dt/d\delta$ curve but rather on the straight line which extrapolates down to small thickness the linear behavior observed in the thick oxide region.

In the simplified model proposed so far, use is made of five physical properties, i.e., D_i , D_x , τ , k_r , and ω_e , all of which have a precise physical meaning and can be measured independently of each other as well as independently of the oxidation process.

The same model, however, could also be simply regarded as a mathematical correlation between oxide thickness and oxidation rate. In the latter case, only four independent parameters enter the model. Indeed, in view of Eq. [11] and [8], Eq. [13] can be rewritten as

$$K_{P,e}(t) = 2 \phi D_x \left\{ 1 + \left(\frac{D_i}{D_x} - 1 \right) \exp \left[-\frac{at}{\tau^n} \left(\frac{D_i}{k_r^2} \right)^{n-1} \right] \right\} \quad [16]$$

Therefore, the resulting model parameters turn out to be

$$K_{L,e} = k_r \phi; \quad K_{P,x} = 2 \phi D_x$$

$$A = D_x/D_i; \quad \bar{\tau} = \frac{\tau^n}{a} \left(\frac{k_r^2}{D_i} \right)^{n-1} \quad [17]$$

Accordingly, the model equation for the oxidation rate, Eq. [12], can be rewritten as

$$\frac{dt}{d\delta} = \frac{2\delta}{K_{P,x} \left\{ 1 + \left(\frac{1}{A} - 1 \right) \exp \left(-\frac{t}{\bar{\tau}} \right) \right\}} + \frac{1}{K_{L,e}} \quad [18]$$

In view of the presentation of the results, it may be convenient to solve Eq. [18] in its dimensionless form obtained by using the characteristic time and length defined previously.

Results and Discussion

The dimensionless form of Eq. [18] has been solved for different sets of the relevant variables in order both to assess the role of the significant parameters and to fit some of the published oxidation rate data.

It must be noted that, in all the runs, $\omega_e = 10^{-6}$ has been assumed as a plausible value for the equilibrium oxygen concentration in the silicon dioxide at the gas-solid interface (25).

The effect of the diffusivity ratio $A = D_x/D_i$ is shown in Fig. 1 for a typical value of the relaxation time τ^* . The $A = 1$ case properly coincides with the linear parabolic theory, while increasing values of the diffusivity ratio lead to more pronounced slope changes in the Hopper diagram. At different A values, the slope changes all occur at almost the same time for a given value of the relaxation time.

The role played by the relaxation time τ^* can be grasped from Fig. 2, where curves at different values of this parameter are given for a typical diffusivity ratio. As expected, for higher relaxation times, the slope change occurs at higher oxide thicknesses, as due for the physical meaning of τ^* . Noteworthy is the fact that the two limiting cases of infinite and negligible relaxation time coincide with the classical linear parabolic theory. Indeed, when $\tau \rightarrow \infty$, the effective diffusivity is always unrelaxed at the initial value, i.e., $D_e(t) \approx D_i$. For very small relaxation times ($\tau \rightarrow 0$), on the contrary, the effective diffusivity is always given by its relaxed value, i.e., $D_e(t) \approx D_x$.

On the other hand, experimental data show that the linear-parabolic model does not hold for intermediate temperatures while at higher temperature, say above 1000°C, and at lower temperatures, say below 750°C, much smaller deviations from it are observed.

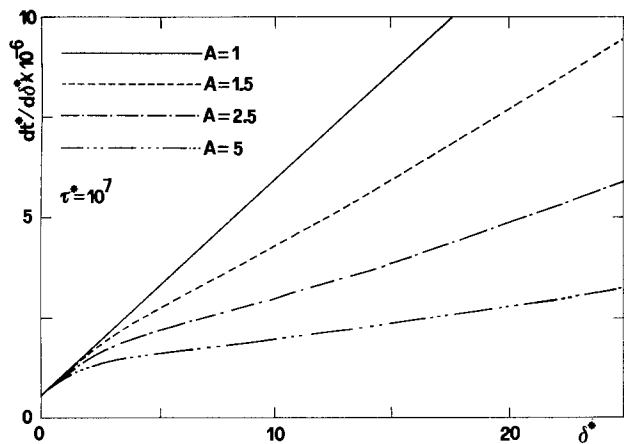


Fig. 1. The reciprocal of the growth rate vs. oxide thickness for $\tau^* = 10^7$ and different values of the diffusivity ratio.

Therefore, the two limiting cases discussed above for the model behavior appear consistent with the trends shown by experimental data, especially if one remembers that relaxation time is a quantity which is strongly dependent on temperature, being rather high at low temperature and quite small at higher temperature values.

The ability of the proposed simplified model to represent experimental data is apparent from Fig. 3, in which a comparison is made between the model behavior and the experimental data reported in Ref. (1, 6, 14): the curves' matching is self-evident and definitely satisfactory.

However, since other existing models (phenomenological and physically based ones) also give a satisfactory representation of the observed behavior, some comments and comparisons are now in order.

As a purely mathematical correlation between oxide thickness and oxidation rate, the present model appears very similar, in many respects, to the phenomenological models presented in Ref. (3) and (12).

Actually, in the Supreme III model (3), two exponential terms and six model parameters enter the complete formulation. However, one exponential term can be neglected since it contributes to the solution for no more than 5%. The resulting four parameters model is usually written as

$$\frac{d\delta}{dt} = \frac{B}{2\delta + A} + C_2 \exp\left(-\frac{\delta}{L_2}\right) \quad [19]$$

The coefficients used merely obey a data-fitting requirement; no precise physical meaning is associated with them. The ability to represent experimental data is known, and the set of parameter values was given for several different temperatures (3).

The model proposed by Ellis *et al.* in Ref. (12) can be reduced to Eq. [12] with

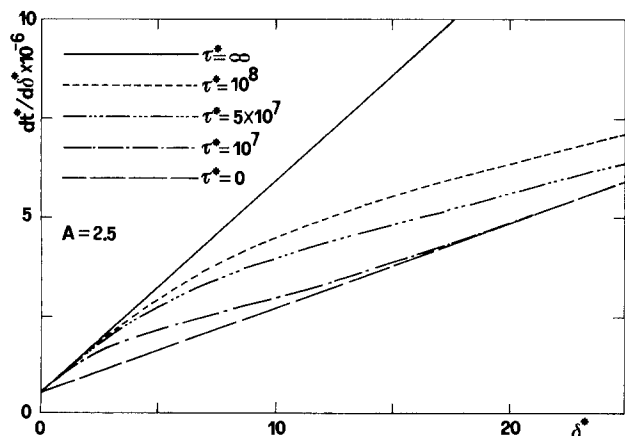


Fig. 2. The reciprocal of the growth rate vs. oxide thickness for $A = 2.5$ and different values of the relaxation time.

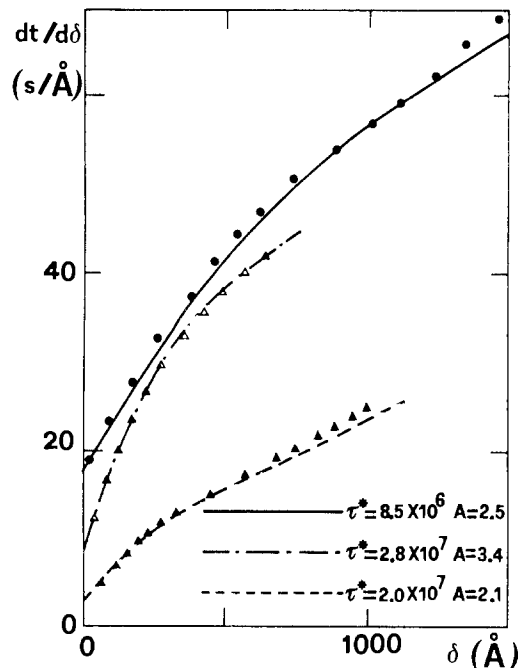


Fig. 3. Comparison of the model results to published experimental data from Ref. (14).

$$K_{L,e} = K_L \left[1 + \delta_r \exp\left(-\frac{\delta}{\delta_r}\right) \right]; K_{p,e} = \text{const.} \quad [20]$$

Apparently, this associates an exponential variation to the linear coefficient. Roughly speaking, such is equivalent to considering an exponential decay in the chemical reaction rate, although, in this case too, the purely phenomenological nature of the model does not attribute a precise physical meaning to all the coefficients. For this model too, a satisfactory agreement between model results and experimental data has been reported (12).

The mathematical relationships between oxide growth rate and oxide thickness given by Supreme III, by Eq. [20], and by the present simplified model, Eq. [10] and [11], have some common features. As a matter of fact, all of them have four adjustable parameters, all of them show comparable complexity of the required numerical solutions, and, finally, all of them can represent experimental data with satisfactory accuracy.

The physically based models, on the contrary, have the advantage of being the mathematical representation of a clearly defined set of assumptions on the basic physical mechanisms. Different models of this type will thus present, in addition to intrinsic differences, several analogies as far as the gross physical picture is concerned.

Both our approach and the one followed by Fargeix *et al.* consider oxygen transport through the oxide and the oxidation reaction localized the Si/SiO₂ interface; in view of what was observed in the previous section, Eq. [12] formally holds true in either theory. Furthermore, in both cases, the origin of the deviations from the linear-parabolic theory is associated to the existence of a very narrow SiO₂ layer in the proximity of the pure silicon phase, endowed with properties very different from those encountered in the bulk SiO₂ phase. In that layer, a non-equilibrium structure is observed, which relaxes towards an equilibrium state; the relaxation process ultimately results in an increase in the effective oxygen diffusivity.

In Ref. (15, 16), the mass flux is given by a fickian constitutive equation in which the diffusion coefficient is changing only as a consequence of a change in the deviatoric stress level. The latter is calculated via a maxwellian fluid constitutive equation in which the deformation rate term is neglected. In our model, on the contrary, the diffusive flux is described by a nonfickian integral type constitutive equation, Eq. [1], [2], the nature of which parallels exactly that of the momentum flux equation in linear viscoelasticity. The viscoelastic response is thus asso-

ciated to the relaxation of the newly formed oxide structure, which may or may not be described by the deviatoric stress. Although it appears useless at the present stage to argue in favor of either approach, we want only to point out that the simplified version of our model, as presented above, results in a quite different mathematical expression for the oxide growth rate which is rather simpler than the one obtained in Ref. (15, 16), while the ability to represent the experimental data is the same for both models.

Conclusions

A simplified viscoelastic model for the thermal dry oxidation of silicon was formulated which accounts for the anomalous behavior observed for the very thin oxide region. The basic assumption of the model is related to the constitutive equation for the oxygen diffusive flux which is represented by a viscoelastic-type equation instead of the usual Fick's law. Qualitatively, the proposed equation can be viewed as an exponential relaxation from an initial fickian behavior with a lower diffusivity D_1 toward a final fickian behavior with a higher diffusivity D_x .

The model was found to provide a satisfactory description of several available experimental data. Furthermore, the model, while it does not require a mathematical formulation more complex than other currently used models, has the important feature that all the intervening parameters have a physical meaning.

Acknowledgments

This work was partially supported by the Italian Ministry of Education (MPI, 60%). Fruitful discussions with Dr. M. Severi, CNR Lamel Laboratories, Bologna, Italy are gratefully acknowledged.

Manuscript submitted Nov. 8, 1984; revised manuscript received March 26, 1985.

Università di Bologna (MPI 60%) assisted in meeting the publication costs of this article.

APPENDIX

For any set of the relevant parameters the effective diffusivity $D_e(t)$ can be calculated through its definition, Eq. [9], once all the other quantities entering Eq. [9] itself have been calculated from the solution of the complete model recalled in the viscoelastic kinetic model section.

The time dependence of $D_e(t)$ has therefore been obtained for several sets of the two most significant parameters, namely, the dimensionless relaxation time $\tau^* = \tau k_1^2/D_1$ and the diffusivity ratio $A = D_x/D_1$ which were allowed to range between 10^5 and 10^8 and between 1 and 10, respectively.

For each of the cases examined the resulting values of the $D_e(t)$ distribution have then been fitted with the analytical exponential form

$$\frac{D_e}{D_1} = \frac{D_x}{D_1} + \left(1 - \frac{D_x}{D_1}\right) \exp(-\beta t^*) \quad [\text{A-1}]$$

where t^* is the dimensionless time and D_x and D_1 maintain the same physical meaning and numerical values as

in the complete original model. The dimensionless time constant β was calculated through a least mean squares procedure.

A set of β values was originated through successive application of Eq. [A-1] to all the cases considered; the resulting values showed a very weak dependence on A , which has thus been neglected, while a significant dependence on τ^* was apparent. The calculated β values were, therefore, required to satisfy a τ^* dependence given by

$$\beta = a (\tau^*)^{-n} \quad [\text{A-2}]$$

The two numerical constants which appear in Eq. [A-2] were then evaluated through a least mean squares procedure and turned out to be $a = 0.16$, $n = 0.9$.

REFERENCES

1. E. A. Irene and Y. J. van der Meulen, *This Journal*, **123**, 1380 (1976).
2. Y. J. van der Meulen, *ibid.*, **119**, 530 (1972).
3. H. Z. Massoud, C. P. Ho, and J. D. Plummer, in "Computer Aided Design of Integrated Circuit Fabrication Processes for VLSI Devices," J. D. Plummer, Editor, p. 194, Stanford University Technical Reports, Stanford, CA (1982).
4. T. Smith and A. J. Carlan, *J. Appl. Phys.*, **43**, 2455 (1972).
5. A. G. Revesz and R. J. Evans, *J. Phys. Chem. Solids*, **30**, 551 (1969).
6. M. A. Hopper, R. A. Clarke, and L. Young, *This Journal*, **122**, 1216 (1975).
7. E. Rosencher, A. Straboni, S. Rigo, and G. Amsel, *Appl. Phys. Lett.*, **34**, 254 (1979).
8. E. A. Irene, *This Journal*, **129**, 413 (1982).
9. E. A. Irene, *ibid.*, **125**, 1708 (1978).
10. B. E. Deal and A. S. Grove, *J. Appl. Phys.*, **36**, 3770 (1965).
11. J. Blanc, *Appl. Phys. Lett.*, **33**, 424 (1978).
12. A. I. Ellis, K. M. Gardiner, and T. E. Cyr, *This Journal*, **130**, 1970 (1983).
13. E. A. Irene, *J. Appl. Phys.*, **54**, 5416 (1983).
14. A. Fargeix, G. Ghibaudo, and G. Kamarinos, *ibid.*, **54**, 2878 (1983).
15. A. Fargeix and G. Ghibaudo, *ibid.*, **54**, 7153 (1983).
16. A. Fargeix and G. Ghibaudo, *ibid.*, **56**, 589 (1984).
17. J. M. Gibson and D. Dong, *This Journal*, **127**, 2722 (1980).
18. R. J. Jaccardine and W. A. Schlegel, *J. Appl. Phys.*, **37**, 2429 (1966).
19. E. A. Irene, E. Tierney, and J. Angilello, *This Journal*, **129**, 2594 (1982).
20. E. P. EerNisse, *Appl. Phys. Lett.*, **30**, 290 (1977).
21. H. Eyring, *J. Chem. Phys.*, **4**, 283 (1936).
22. J. D. Ferry, "Viscoelastic Properties of Polymers," 2nd ed., John Wiley and Sons, New York (1970).
23. G. C. Sarti, F. Santarelli, and G. Camera Roda, in "Proceedings of the 4th Chemical Engineering Conference, Grado 1984," P. Alessi and I. Kikic, Editors, p. 638, Cozzi, Trieste, Italy (1984).
24. P. Neogi, *A.I.Ch.E. J.*, **29**, 833 (1983).
25. F. J. Norton, *Nature*, **171**, 701 (1961).
26. F. J. Grunthaner, P. J. Grunthaner, R. R. Vasquez, B. F. Lewis, J. Maserjian, and A. Madhukar, *J. Vac. Sci. Technol.*, **16**, 1443 (1979).
27. R. N. Nucho and A. Madhukar, *Phys. Rev., B*, **21**, 1576 (1980).

Titanium Silicide Formation on Boron-Implanted Silicon

T. P. Chow,* W. Katz, R. Goehner, and G. Smith

General Electric Company, Corporate Research and Development, Schenectady, New York 12301

ABSTRACT

Thin film interaction between Ti and boron-implanted silicon substrates at 650°-900°C was investigated. The compositional properties were examined with Rutherford backscattering spectrometry and secondary ion mass spectrometry, the structural properties with x-ray diffraction, and the electrical properties with sheet resistance measurements. At 650°C, incomplete Ti/Si reaction led to significant amounts of intermediate silicide phases (Ti_5Si_3 and $TiSi$) and hence higher sheet resistance. Annealing at 700°C or higher resulted in conversion of the titanium film into predominantly $TiSi_2$ and a lower sheet resistance. Boron was found to redistribute into the silicide layer during annealing, leading to an accumulation on the surface and a depletion at the silicide/silicon interface. The diffusion kinetics of boron through titanium silicide are compared with those of other p- and n-type dopants.

Refractory metal silicides have recently attracted much attention as MOS gates and interconnects in silicon integrated circuits because of their low resistivities and MOS process compatibility (1, 2). Among the disilicides studied, $TiSi_2$ has the lowest resistivity ($\sim 15 \mu\Omega\text{-cm}$) (3). Usually, the silicide is formed by cosputtering, coevaporation, or sintering titanium on silicon. For self-aligned silicide structures, the last technique is used. Also, the silicide formation is performed after the source/drain regions are heavily doped by implantation (4, 5). Thin film interaction of Ti with various n-doped silicon substrates, as well as on heavily phosphorus- and boron-doped poly-Si films, has been studied (7-12). However, the reaction with p-doped substrates has not been investigated in detail. We have recently studied titanium silicide formation and boron and fluorine redistribution on BF_2^+ -implanted silicon (13). In this paper, the Ti/Si reaction on boron-implanted, (100) silicon substrates is reported. The compositional, structural, and electrical properties of the silicide layer formed as well as the kinetics of boron redistribution are discussed. Furthermore, the redistribution behavior of boron is compared with those of n-type dopants such as phosphorus and arsenic.

Experimental Procedure

Various doses (5×10^{14} - $6 \times 10^{15} \text{ cm}^{-2}$) of boron ($^{11}B^+$) were implanted at 25 keV ($R_p = 820\text{\AA}$ and $\Delta R_p = 330\text{\AA}$) into (100), 300-500 $\Omega\text{-cm}$, boron-doped silicon substrates and then activated at 900°C in N_2 for 30 min. Low implantation energy and minimum heat-treatment were used to keep

* Electrochemical Society Active Member.

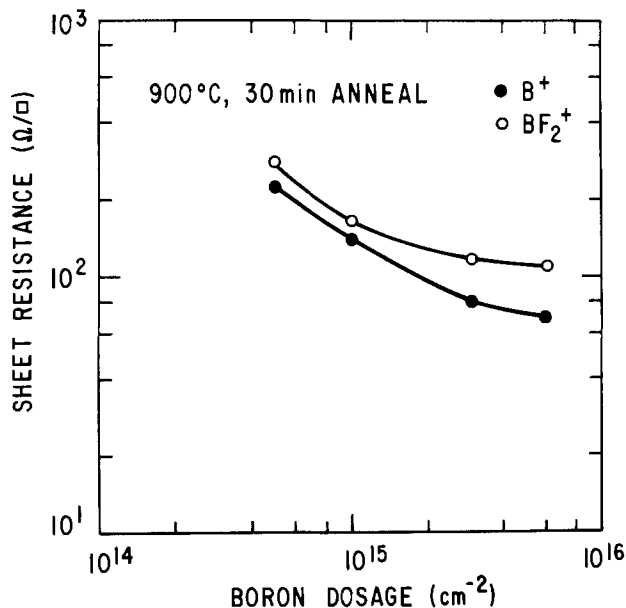


Fig. 1. Sheet resistance of the boron- and BF_2^+ -implanted layers vs. dose after annealing at 900°C for 30 min.

the implanted layer shallow so as to represent typical source/drain junction of short-channel MOS devices. The sheet resistance measured after activation, shown in Fig. 1, varies between 70 and 225 Ω/\square . For comparison, BF_2^+ was also implanted at 40 keV and the same dose range and then similarly activated. Its resistance ranged between 110 and 270 Ω/\square (13). Then, after a dip in 10% HF to remove the surface native oxide, nominally 1000 \AA thick titanium films were electron-beam evaporated onto the silicon substrates at room temperature. The background pressure before evaporation was always 1×10^{-6} torr or lower. The heat-treatment was performed in UHP H_2 at 650°-900°C for 30 min. To minimize the contamination from the ambient, a clean silicon wafer was always used as a cover during annealing.

The compositional and structural properties were studied with Rutherford backscattering spectrometry (RBS), secondary ion mass spectrometry (SIMS), and x-ray diffraction, while the sheet resistance was monitored with a four-point probe. RBS was performed with a 2 MeV $^4He^+$ beam from a linear accelerator. SIMS was done with a Cameca IMS 3-f ion microscope. The in-depth profiles of various negative ion species (namely, $^{11}B^-$, $^{16}O^-$, $^{19}F^{2-}$, $^{30}Si^-$, and $^{48}Ti^-$) were obtained using a mass-analyzed beam of Cs^+ primary ions with an impact energy of 10.5 keV. The concentrations of various ion species in silicon were calibrated with implanted standards. X-ray diffrac-

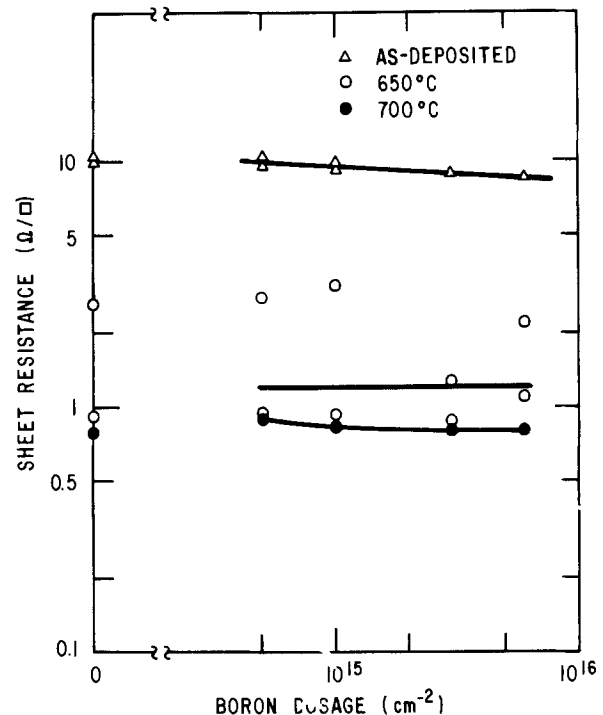


Fig. 2. Sheet resistance of Ti/Si films as a function of boron dosage after annealing at 650° and 700°C for 30 min.

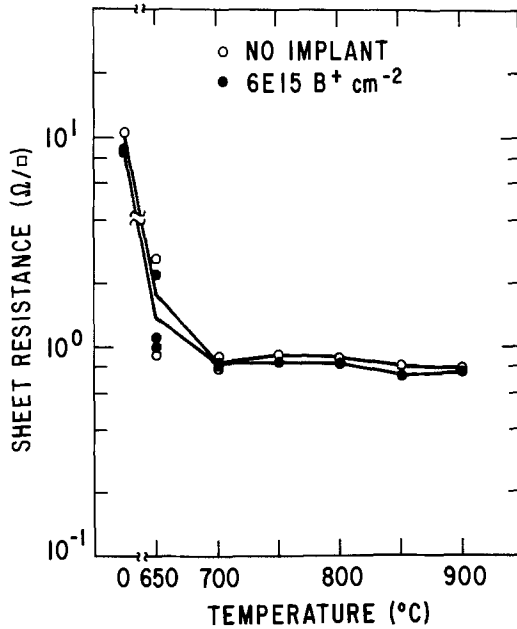


Fig. 3. Sheet resistance of Ti/Si samples with and without a boron implant ($6 \times 10^{15} \text{ cm}^{-2}$) vs. annealing temperature for time period of 30 min.

tion was done in a Rigaku horizontal diffractometer equipped with a Cr tube and a receiving beam graphite crystal monochromator and also checked with a REED thin film camera using Cr $K\alpha$ radiation and a glancing angle of 15° .

Results and Discussions

Sheet resistance.—As deposited, the sheet resistance was about $10 \Omega/\square$ for the unimplanted sample and ranged from 8 to $10 \Omega/\square$ for the boron-implanted ones (Fig. 2). After annealing at 650°C for 30 min, the sheet resistance dropped to $0.9\text{-}3 \Omega/\square$, as shown in Fig. 2. The scatter in the resistance values can be attributed to the difference in silicide content (see below) and appears to relate to the varying presence of native oxide and not to the boron dosage. The effect of a thin native oxide layer on titanium silicide formation has been previously studied in an UHV system (14). After a 700°C anneal for 30 min, the sheet resistance ranged between $0.8\text{-}0.9 \Omega/\square$ for all cases. Annealing at higher temperatures up to 900°C changed the sheet resistance only slightly. For example, in Fig. 3, the sheet resistance of Ti on unimplanted and $6 \times 10^{15} \text{ B}^+ \text{ cm}^{-2}$ -implanted silicon substrates is shown as a function of annealing temperature for a period of 30 min. It is clear from the figure that the presence of boron has little influence on the sheet resistance and the major reduction

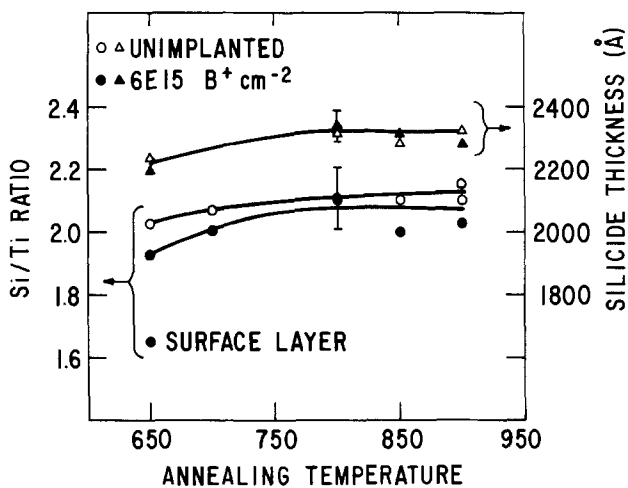


Fig. 4 Si/Ti ratio and silicide thickness, as determined from RBS, as a function of annealing temperature for unimplanted and $6 \times 10^{15} \text{ B}^+ \text{ cm}^{-2}$ -implanted samples.

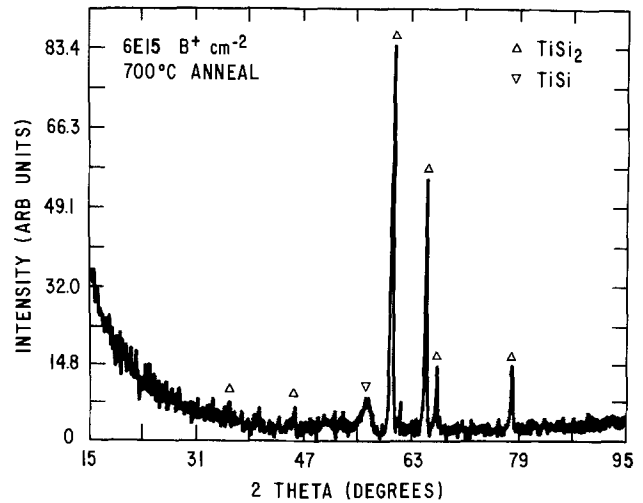
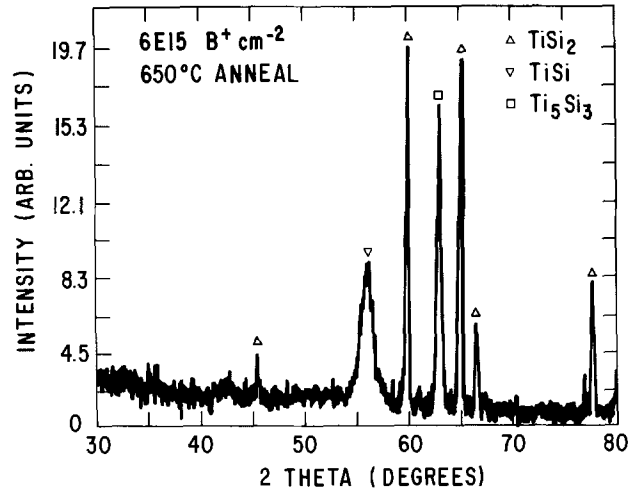


Fig. 5. X-ray diffraction spectra of a Ti/Si sample ($6 \times 10^{15} \text{ B}^+ \text{ cm}^{-2}$) after annealing at (a, top) 650°C and (b, bottom) 700°C for 30 min

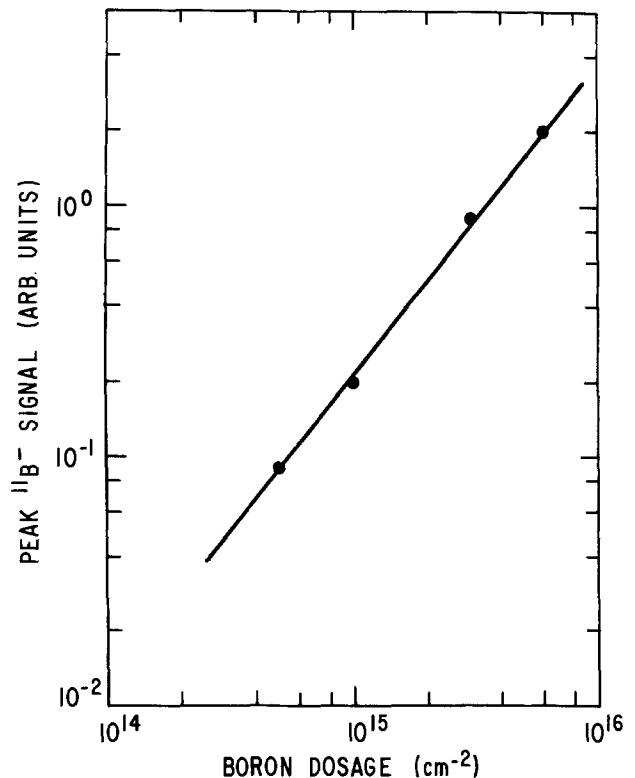


Fig. 6. Peak boron ($^{11}\text{B}^-$) concentration in silicon after titanium deposition but before Ti/Si reaction as determined from SIMS.

in sheet resistance occurs in the temperature range of 650°-700°C. Furthermore, the BF_2^+ -implanted samples yielded very similar values of sheet resistance (13). For example, values of 0.75-2.5 Ω/\square were measured after annealing at 650°C for 30 min and 0.70-0.86 Ω/\square after a 700°C anneal.

Film composition.—From RBS spectra, both the Si/Ti ratio and silicide thickness are obtained. The Si/Ti ratio for unimplanted and $6 \times 10^{15} \text{ cm}^{-2}$ samples are shown in Fig. 4 as a function of annealing temperature. When the Ti/Si films were annealed at 700°C or higher, a Si/Ti ratio between 2.0 and 2.1 was measured. The resulting TiSi_2 thickness after high temperature annealing was 2200-2300Å (close to the theoretical estimate of 2.27 times the

original Ti thickness) and insensitive to the boron doping. For the samples annealed at 650°C, a thin (~650Å) surface region of titanium-rich silicide (Si-Ti ~1.8) was detected together with a near-stoichiometric disilicide underneath. This indicates incomplete conversion of titanium into the end phase of TiSi_2 . As will be pointed out in the next section, the titanium-rich surface layer has been found to contain significant amounts of intermediate silicide phases (Ti_5Si_3 and TiSi).

Film structure.—X-ray diffraction revealed that only the (002) peak (at 2.34Å) of β -titanium (15) was detected in as-deposited films. After annealing at 650°C or higher temperatures for 30 min, no titanium peak was left. These results are similar to those reported for Ti on heavily

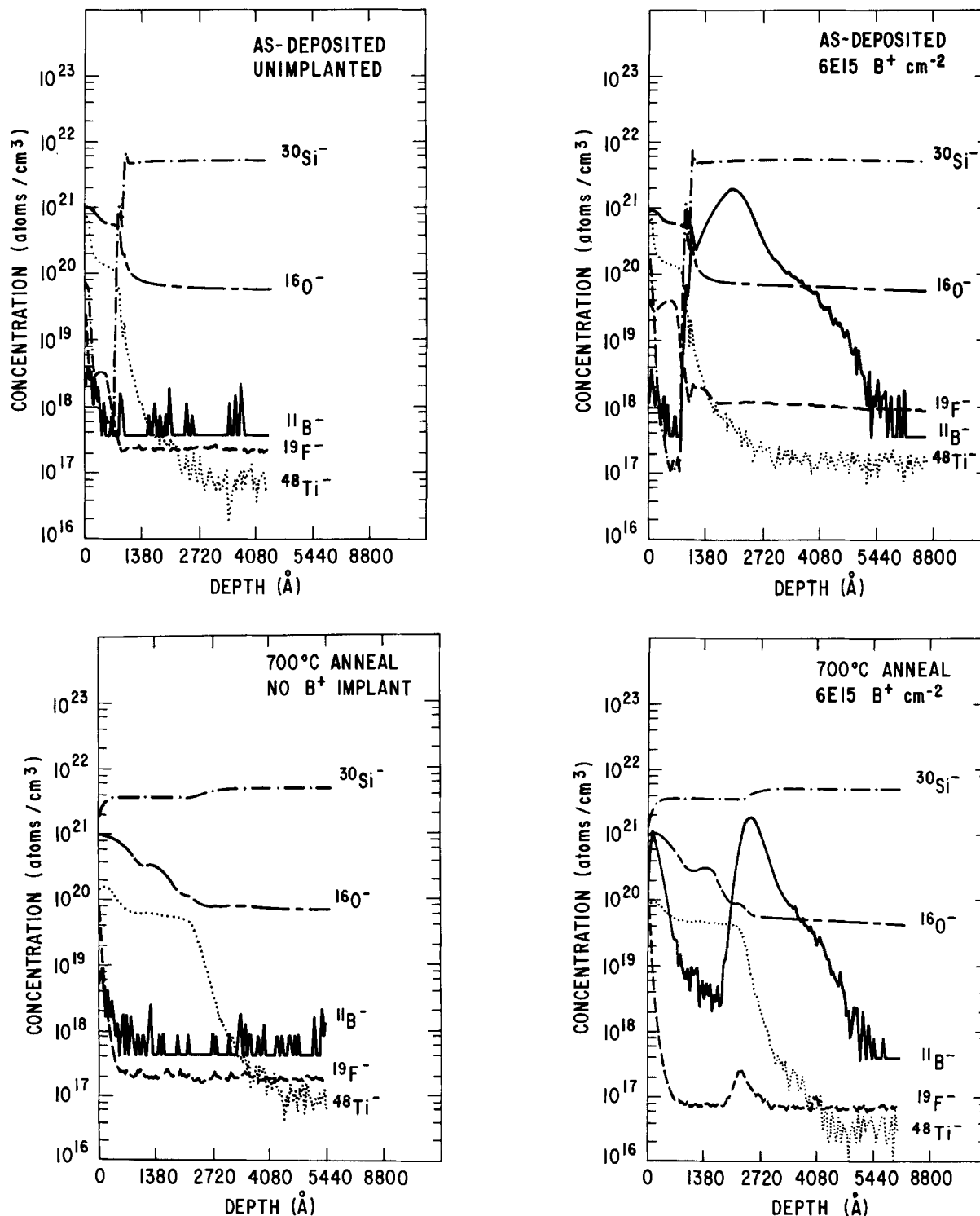


Fig. 7. SIMS depth profiles for two Ti/Si samples (unimplanted and implanted with boron at $6 \times 10^{15} \text{ cm}^{-2}$) before [a (top left) and b (top right)] and after [c (bottom left) and d (bottom right)] annealing at 700°C for 30 min.

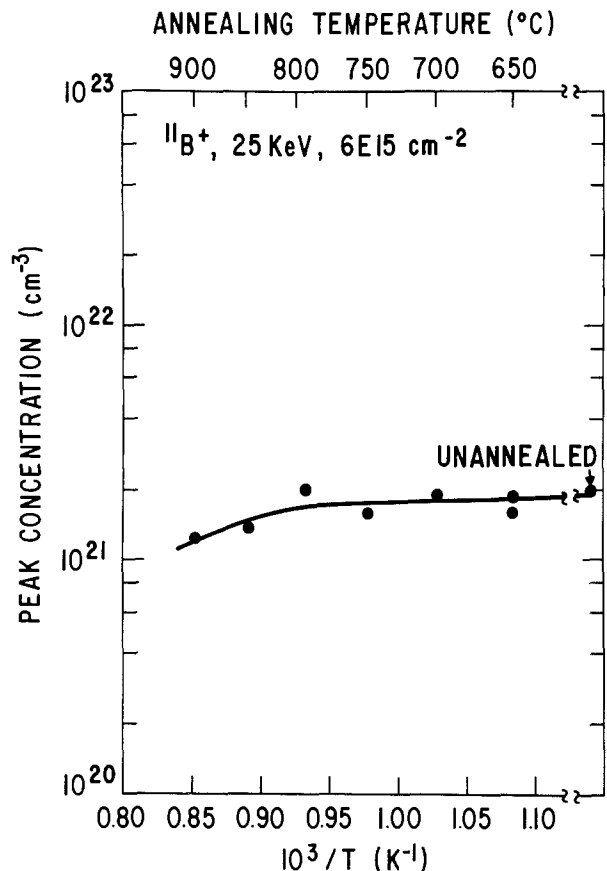


Fig. 8. Peak concentration of boron ($^{11}\text{B}^-$), as determined from SIMS, for Ti/Si samples with a $6 \times 10^{15} \text{ B}^+ \text{ cm}^{-2}$ implant as a function of annealing temperature.

phosphorus-doped (from PBr_3) poly-Si (7). The films annealed at 650°C exhibited three titanium silicide phases. Figures 5a and 5b show the x-ray diffraction spectra of a Ti/Si sample with $6 \times 10^{15} \text{ B}^+ \text{ cm}^{-2}$ after annealing at 650° and 700°C , respectively. Face-centered-orthorhombic TiSi_2 (16) is the major phase formed, with several peaks observed. The main ones were at 2.30, 2.14, 2.09, and 1.83\AA , corresponding to the (311), (004), (022), and (313) peaks, respectively. From the (311) line broadening, a grain size of 550\AA was calculated. Also, for the films with higher sheet resistance, three other peaks (not attributable to TiSi_2) at 2.72, 2.44, and 2.20\AA were enhanced. While the first one can be assigned to the (201) peak of TiSi (17), the last two can be, respectively, from either the (210) and (211) peaks of TiSi or the (120) and (121) peaks of Ti_5Si_3 (18). Since the peak at 2.20\AA has a sharper profile and is narrower than those of the 2.72 and 2.44\AA peaks, it was assigned to Ti_5Si_3 , whereas the latter two to TiSi . (To index all the three peaks to TiSi would require the TiSi grains to have a peculiar orientation.) Grain sizes of 500 and 100\AA were estimated for Ti_5Si_3 and TiSi from breadths of the 2.20 (2θ of 63.0°) and 2.44\AA (2θ of 56.0°) lines, respectively. Similar diffraction spectra (not shown) were also obtained for the unimplanted sample. It was found that a stronger intensity of the intermediate silicide peaks was usually detected on films with a higher sheet resistance. This is consistent with the higher resistivity (two times or higher than that of TiSi_2 , $36\text{--}63 \mu\Omega\text{-cm}$ for TiSi and $55\text{--}350 \mu\Omega\text{-cm}$ for Ti_5Si_3) of these intermediate phases (3). Furthermore, no diffraction peak traceable to any Si-O, Ti-O, or Ti-B phase was found.

After annealing at 700°C or higher, there is no substantial structural difference among the unimplanted (control) and boron-implanted samples. TiSi_2 was the major phase formed with a small amount of TiSi also detected.

Boron diffusion—Boron diffusion after heat-treatment was monitored with SIMS depth profiling. To check the accuracy of boron concentration from SIMS, besides the routine calibration with implanted standards as mentioned earlier, the ion intensity of $^{11}\text{B}^-$ in the Ti/Si

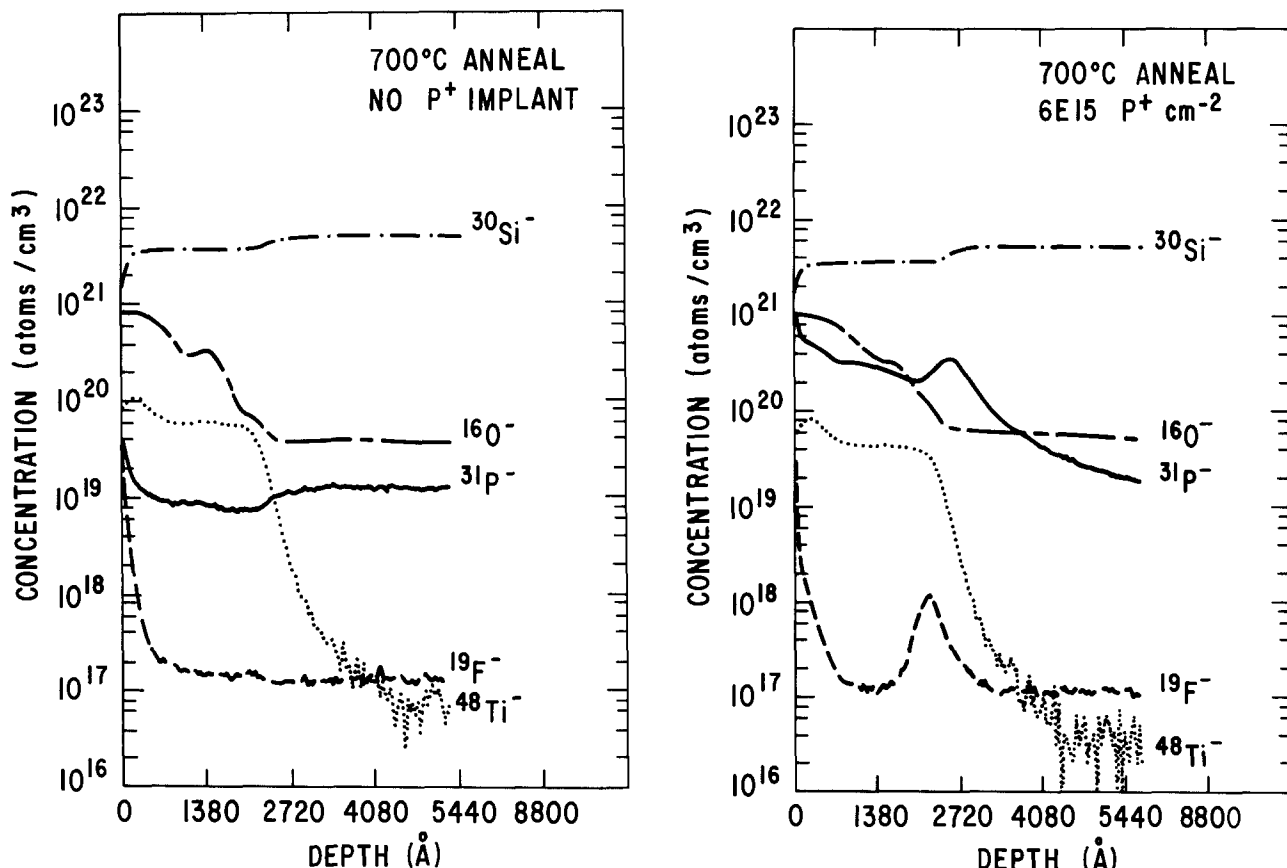


Fig. 9. SIMS depth profiles for Ti/Si films without (a, left) before and with (b, right) $6 \times 10^{15} \text{ P}^+ \text{ cm}^{-2}$ after annealing at 700°C for 30 min

samples after titanium deposition but before thermal annealing was measured and is plotted as function of the implantation dosage in Fig. 6. A linear relationship can be readily seen, confirming that the boron concentration is proportional to the $^{11}\text{B}^-$ signal intensity within the dosage range studied. In Fig. 7, the boron profiles for two Ti/Si samples—one unimplanted and one implanted (at $6 \times 10^{15} \text{ cm}^{-2}$)—before and after annealing at 700°C for 30 min are shown. After Ti deposition, the boron ($^{11}\text{B}^-$) level in the silicide was very low. Then, after annealing at 650°C or higher, the redistribution of boron into the silicide was very significant. At 700°C , it can be seen from comparing Fig. 7b and 7d that about half of the initial boron layer has outdiffused into the silicide layer formed and accumulated on the outer surface of the silicide layer and eventually was lost into the ambient. When the annealing temperature was raised, the decrease of boron concentration in silicon was enhanced, as indicated in Fig. 8, where the boron peak concentration of the $6 \times 10^{15} \text{ B}^+ \text{ cm}^{-2}$ sample was shown against annealing temperature up to 900°C . A 40% decrease in peak concentration (from 2×10^{21} to $1.2 \times 10^{21} \text{ cm}^{-3}$) can be observed. Such a dopant redistribution during silicide growth has been reported for high dosage BF_3^+ (13) and for antimony (8) (but not for arsenic) in TiSi_2 . However, unlike boron and arsenic in PtSi and Pd_2Si (19, 20), no significant snowplow effect is apparent. The absence of the snowplow effect has also been observed earlier for higher dosage arsenic in TiSi (21). Such a characteristic is particularly undesirable for shallow junctions like those studied here because of the significant loss of dopants.

To compare the boron diffusion with n-type dopants in TiSi_2 , we have also annealed titanium on phosphorus- and arsenic-implanted silicon substrates. Phosphorus was found to diffuse like boron while arsenic apparently reacted with titanium or silicon during silicide formation. The SIMS depth profiles of Ti/Si films with and without phosphorus (at the dosage of $6 \times 10^{15} \text{ cm}^{-2}$) after annealing at 700°C for 30 min are shown in Fig. 9. It can be seen that only a small amount (<50%) of the implanted phosphorus was left in the silicon with peak concentration still at the silicide/silicon interface. On the other hand, for arsenic (its SIMS depth profile not shown here), its concentration was constant in the silicide, and, still, a large percentage was retained in the silicon. More on arsenic diffusion during titanium silicide formation will be published later (22).

Summary

Thin film interaction between titanium and boron-implanted, (100) silicon substrates was investigated. X-ray diffraction indicated that the (002)-oriented Ti films was converted into mainly TiSi_2 after annealing at 650°C – 900°C , with intermediate silicide phases (TiSi , Ti_5Si_3) significantly present at 650°C . A higher intermediate silicide content was correlated with a higher sheet resistance. Boron redistributes into the silicide layer during annealing, leading to an accumulation on the surface. Then it was lost into the ambient. Phosphorus, but not arsenic, was found to outdiffuse through the silicide like boron.

Acknowledgment

We would like to thank G. Gidley for technical assistance and Center for Integrated Electronics of Rensselaer Polytechnic Institute for the use of the annealing facilities.

Manuscript submitted Nov. 16, 1984; revised manuscript received March 22, 1985.

General Electric Company assisted in meeting the publication costs of this article.

REFERENCES

1. S. P. Murarka, "Silicides for VLSI Applications," Academic Press, New York (1983).
2. T. P. Chow and A. J. Steckl, *IEEE Trans. Electron Devices*, **ed-30**, 1480 (1983).
3. M.-A. Nicolet and S. S. Lau, in "VLSI Electronics: Microstructure Science," Vol. 6, N. G. Einspruch and G. B. Larrabee Editors, Chap. 6, p. 329, Academic Press, New York (1983).
4. T. Shibata, K. Heida, M. Sato, M. Konaka, D. L. M. Dang, and H. Iizuka, *IEEE Trans. Electron Devices*, **ed-29**, 531 (1982).
5. C. M. Osburn, M. Y. Tsai, S. Roberts, C. J. Lucchese, and C. Y. Ting, in "VLSI Science and Technology/1982," C. J. Dell'Oca and W. M. Bullis, Editors, p. 213, The Electrochemical Society Softbound Proceeding Series, Pennington, NJ (1982).
6. S. P. Murarka and D. B. Fraser, *J. Appl. Phys.*, **51**, 342 (1980).
7. P. Resevz, J. Gyimesi, and E. Zsoldos, *ibid.*, **54**, 1860 (1983).
8. C. Y. Ting, S. S. Iyer, C. M. Osburn, G. J. Hu, and A. M. Schweighart, in "VLSI Science and Technology/1982," C. J. Dell'Oca and W. M. Bullis, Editors, p. 224, The Electrochemical Society Softbound Proceedings Series, Pennington, NJ (1982).
9. J.-R. Chen, Y.-C. Liu, and S.-D. Chu, *J. Electron. Mater.*, **11**, 355 (1982).
10. H. K. Park, J. Sachitano, M. McPherson, T. Yamaguchi, and G. Lehman, *J. Vac. Sci. Technol. A*, **2**, 264 (1984).
11. J. Amano and P. Merchant, *Appl. Phys. Lett.*, **44**, 744 (1984).
12. Y. Mura, S. Mihara, M. Kikuchi, R. Sase, and T. Furuhashi, in "IEEE International Electron Devices Meeting Technical Digest," p. 518, IEEE, New York (1983).
13. T. P. Chow, W. Katz, and G. Smith, *Appl. Phys. Lett.*, **46**, 41 (1985).
14. M. A. Taubenblatt and C. R. Helms, *J. Appl. Phys.*, **53**, 6308 (1982).
15. Standard Powder Diffraction Pattern 5-0682.
16. Standard Powder Diffraction Pattern 33-1384.
17. Standard Powder Diffraction Pattern 17-424.
18. Standard Powder Diffraction Pattern 29-1362.
19. C. Y. Wei, W. Katz, and G. Smith, *Thin Solid Films*, **104**, 215 (1983).
20. M. Wittmer and T. E. Seidel, *J. Appl. Phys.*, **49**, 5827 (1978).
21. C. Y. Ting, M. Wittmer, and K. N. Tu, in VLSI Science and Technology/1982," C. J. Dell'Oca and W. M. Bullis, Editors, p. 242, The Electrochemical Society Softbound Proceeding Series, Pennington, NJ (1982).
22. T. P. Chow, W. Katz, and G. Smith, To be published.

Characterization of the Dual E-Beam Technique for Recrystallizing Polysilicon Films

J. R. Davis,¹ R. A. McMahon, and H. Ahmed

Department of Engineering, Cambridge University, Cambridge, England IP5 7RE

ABSTRACT

Detailed materials properties of silicon on insulator films produced by dual electron-beam recrystallization of polysilicon films are reported. By scanning a line electron beam parallel to the edges of an array of narrow seeding windows, large areas (several square centimeters) of precisely oriented single-crystal silicon have been formed. The optimum beam conditions and substrate geometry to achieve the best recrystallization have been investigated, and it has been found that using a fast scan speed (~ 35 cm/s) allows seeded regrowth without melting the substrate below the isolating oxide. Using these conditions, complete wafers may be recrystallized in around 30s without introducing strain or wafer warping. Remaining crystallographic defects include dislocations midway between seeding windows and an occasional twinning of the regrowth when the windows are aligned along $\langle 110 \rangle$.

There is now considerable interest in the production of single-crystal silicon films on amorphous insulators (SOI), in which advanced electronic devices may be fabricated (1). One of the most promising methods is the recrystallization of deposited polysilicon films by moving a localized molten zone across the specimen surface. Many heat sources have been used to produce this zone, including graphite strip heaters (2), radiant lamps (3), lasers (4), and electron beams (5). The use of a dual E-beam technique capable of producing single-crystal silicon films has been reported previously (6-8). In this paper, recent improvements to the technique and the detailed materials properties of the resulting recrystallized films are described. Also, the dependencies of these properties on the specimen preparation conditions and geometry, and on electron-beam parameters such as speed, power, and scan direction, are investigated. The characterization techniques employed include defect etching, TEM and SEM, x-ray topography, and RBS and ion channeling. Electrical properties of CMOS transistors and circuits fabricated in the films are reported elsewhere (9).

The dual E-beam technique has several desirable features, particularly when the films are required for VLSI applications. One important requirement is that when the substrate is in the form of an oxide-covered wafer the recrystallization technique does not cause any damage to it, either microscopically in the form of slip dislocations or macroscopically as wafer warpage. Production of stacked-layer or three-dimensional circuits calls for a technique in which the silicon beneath the isolating oxide is not melted. For production of more conventional devices, however, limited melting of the underlying silicon is permissible as long as the oxide remains intact and flat and the silicon film on top of it maintains a uniform thickness and smooth surface. To be commercially acceptable, the recrystallization system should have a high throughput, and it must have a large window of recrystallization conditions, thus ensuring that the process is controllable and the yield is high. Finally, the positions in which active devices may be placed must not present unreasonable constraints to the circuit designer. No recrystallization technique, or any other SOI method, has yet fully achieved all these objectives, but the progress with the dual E-beam technique reported here allows most of them to be met.

Method

The dual E-beam system has been described previously (10). The wafer is supported in thermal isolation so that both its surfaces are accessible to the beams. The lower column produces a background temperature of around 1000°C by the multiple-raster-scanned, isothermal heating technique. This uniform temperature is achieved in a few seconds, and is maintained during recrystallization.

¹Present address: British Telecom Research Laboratories, Ipswich, England IP5 7RE.

The upper column images a line beam on the specimen surface, producing a localized molten zone in the polysilicon film which is swept across the wafer. In the present version of the machine, this line beam is synthesized by scanning a 60 μm focused spot with a 100 kHz triangular signal applied to the X-direction electromagnetic deflection coils. This frequency is sufficient to prevent the polysilicon from solidifying between passes of the beam because of the high background temperature and the large amount of energy stored as latent heat. The length of the line in these experiments was typically 2 mm, and was limited only by the power available from the high voltage supply (60W at 20 keV). Recrystallization was performed by scanning the line beam across the wafer at speeds in the range 3-300 cm/s by means of the Y-deflection coils, producing a 2 mm wide recrystallized stripe. Larger areas were recrystallized by stepping the wafer, together with the area scanned by the bottom beam, between sweeps, and with the line blanked. Complete wafers can be recrystallized in around 30s using this technique with a typical scan speed of 35 cm/s. This time is virtually independent of the wafer size, being determined principally by the background heating time constant.

The choice of accelerating voltage for the line beam is a compromise between a low value to maximize the power deposition in the polysilicon, rather than in the substrate, and a high value for ease of producing a high power density. Only 3.3% of the beam power penetrates to the substrate with a 20 keV beam for a structure in which the underlying oxide, the polysilicon, and the capping layer are each 1 μm thick (7).

Previous work (7, 8) has shown that for line-scan speeds of > 10 cm/s, which are used to control the depth of melting, seeding of the regrowth from a single-crystal substrate through holes ("seeding windows") cut in the isolating oxide is necessary to achieve an (001) surface. There is a choice of two obvious directions for the scan relative to the orientation of the seed windows. These have been termed "perpendicular scanning" and "parallel scanning" and are illustrated in Fig. 1. The relative advantages of the two schemes originate from the fact that the seed windows fulfill two roles; not only do they select the crystal orientation of the regrown layer, but they also control the flow of heat during resolidification. Perpendicular scanning, which we originally used (6, 8), produces a slightly wider defect-free zone, but we have recently obtained improved surface flatness and control of the process by using parallel scanning; all the results described in this paper employed parallel scanning.

Specimens for recrystallization were prepared by growing a thermal oxide of between 0.5 and 2.0 μm on (001) silicon wafers. Seeding windows were normally produced by wet etching, giving an oxide edge slope of $\sim 70^\circ$, but some specimens were prepared with an approximately coplanar surface by a LOCOS process. The seed

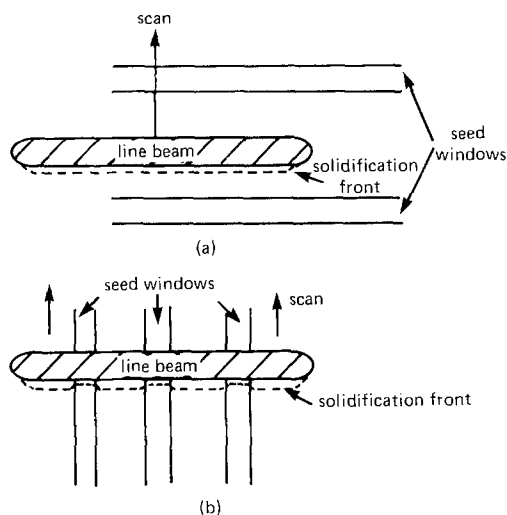


Fig. 1. Schematic diagram of two possible seeding strategies. a: Perpendicular scanning. b: Parallel scanning.

windows were aligned either with the $\langle 110 \rangle$ direction (parallel to the wafer flat and the normal processing orientation), or with the $\langle 100 \rangle$ direction, at 45° to the flat. A 10s dip in dilute HF immediately prior to the low pressure deposition of the 0.5 or 1.0 μm thick polysilicon layer ensured good contact with the substrate in the seeding windows. A capping layer of 1 μm of deposited oxide and 50 nm of silicon nitride was employed.

Results and Discussion

General.—Figure 2 is a set of Nomarski micrographs of several regions taken from a typical recrystallized stripe after removal of the capping layers and Secco etching to reveal any crystallographic defects. Recrystallization in this instance was achieved with a background temperature of 985°C and a scan speed of 35 cm/s. In the central region, the recrystallized film is free of any line features, indicating perfect regrowth. At the start of the scan, the unmelted polysilicon has been removed by the etch, and this is followed by a short region of unseeded growth, with associated grain boundaries, until the polysilicon in the seed windows melts. The contraction of the polysilicon as it initially melts gives rise to a row of small holes, penetrating the film, when the beam first hits the specimen, but once the sweep is underway there are no discontinuities in the mass flow to cause any further loss of surface flatness. This is in contrast to the perpendicular scanning case, where the oxide steps present periodic constrictions to the flow, and the heat sinking effect of

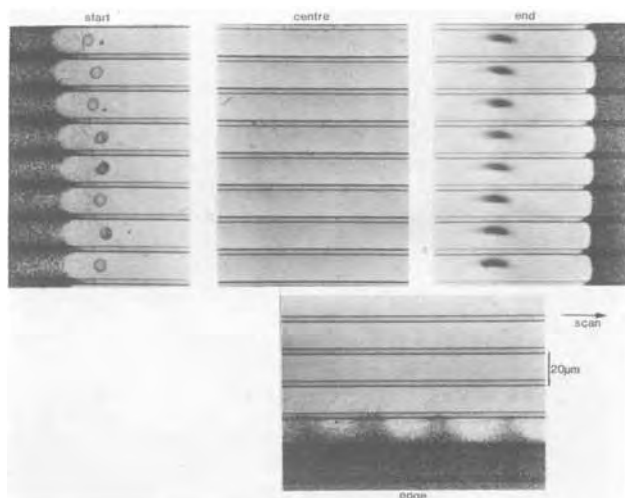


Fig. 2. Secco-etched regions from a 2×8 mm recrystallized stripe, with an $\langle 001 \rangle$ substrate and the seed windows aligned along $\langle 110 \rangle$. The narrow lines are the 4 μm wide seeding windows.

the exposed substrate lowers the temperature and increases the viscosity of the molten silicon, producing the ripples observed in our earlier results (8). At the end of the scan, expansion of the silicon leads to a row of small mounds as the now stationary molten pool solidifies. The extent of the recrystallization beyond these mounds gives an indication of the instantaneous size of the molten zone, with typical values being in the range 50-150 μm , depending on the beam power; that is, they are comparable with the width of the line beam. In a production recrystallization system, the beginning and end of the scan would be arranged to occur either off the wafer or in the scribe lanes between chips, thus removing all evidence of mass flow from the device areas. At the extreme edge of the stripe, the beam power is insufficient to cause melting in the seed windows, leaving a narrow zone of large-grained material. Once again, this zone would be placed outside the active device region.

Figure 3 is a series of SEM micrographs of specimens Secco-etched after cross sectioning, and in which recrystallization was produced by increasing beam powers. The unrecrystallized polysilicon has a columnar grain structure, with grains $\sim 0.1 \times 1 \mu\text{m}$ (Fig. 3a). After recrystallization at the lowest beam power (Fig. 3b) the polysilicon on the oxide shows a dramatic increase in grain size, but the extra heat sinking in the seed window has prevented complete melting there and the regrowth is unseeded. A small increase in the beam power (Fig. 3c) causes the melt to penetrate into the substrate at the sides of the seed window, even though melting in the center is incomplete. This effect, which arises from the lateral heat

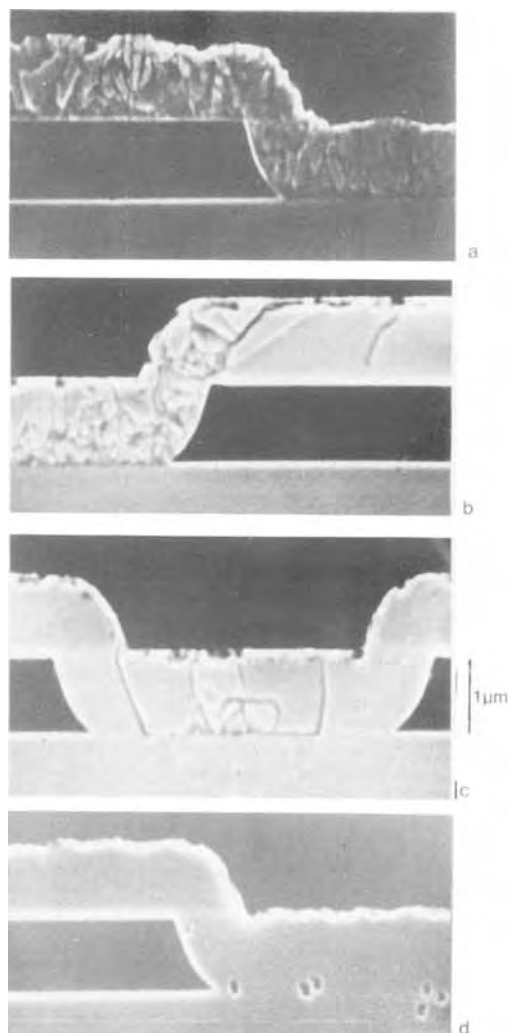


Fig. 3. SEM cross sections of recrystallized films after Secco etching. Pictures a to d are at increasing beam powers. Scan direction is into the plane of the paper.

flow from the oxide-isolated region into the seed area, means that proper seeding can be achieved from windows of submicron widths at powers only very slightly above those needed to melt unseeded films. In Fig. 3d, complete epitaxial growth has occurred in the seed regions, and only a few etch pits at the original polysilicon/substrate interface remain, probably caused by the breakup of the thin native oxide present before polysilicon deposition; these defects do not propagate into the oxide-isolated regions. The difference in beam power between Fig. 3b and 3d is about 15%.

The orientation of the regrown films has been investigated with a variety of techniques. For example, Fig. 4 shows an array of anisotropically etched pits (11) which, by their square shape, show the surface to be (001) oriented. The sides of these squares are accurately aligned parallel to the $\langle 110 \rangle$ seeding window direction, which is to be expected of a pit defined by the intersection of the [111] planes with the (001) surface. Correct orientation of much larger regions is shown by the electron channeling picture of Fig. 5. Two separate recrystallized stripes show the standard (001) channeling pattern, and this pattern is continuous across the vertical scribe lane where the polysilicon is in direct contact with the substrate and has regrown epitaxially. No patterns are seen in the nonrecrystallized regions.

Macroscopic wafer flatness and the possibility of internal stresses in the substrate created by the recrystallization procedure were investigated by means of x-ray topography. The wafer shown in the topographs of Fig. 6 was unseeded and was recrystallized over its entire area by a number of sweeps of the line beam parallel to the wafer flat. After recrystallization, the wafer underwent a full CMOS processing schedule, in the course of which the recrystallized film was etched into small islands. It can be seen that there are no slip dislocations in the substrate, and the evenness of the image intensity indicates that there is no appreciable stress. This is in contrast to graphite strip heater-recrystallized wafers, where the slow

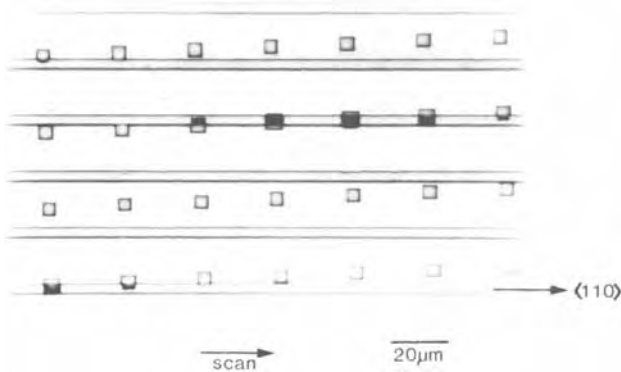


Fig. 4. Square anisotropic etch pits in a recrystallized film seeded from an (001) substrate with the seed windows aligned along $\langle 110 \rangle$.

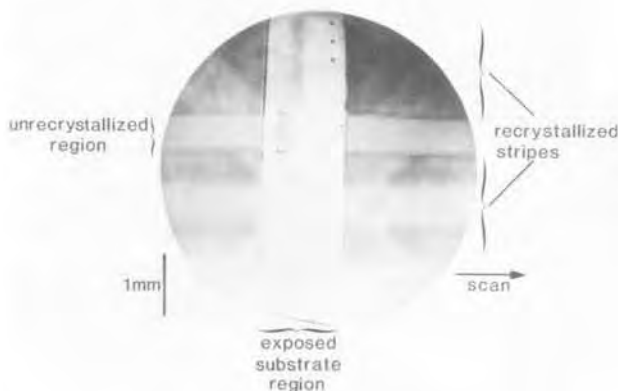


Fig. 5. SEM channeling contrast picture of two recrystallized stripes crossing an epitaxially regrown area on a (001) substrate.

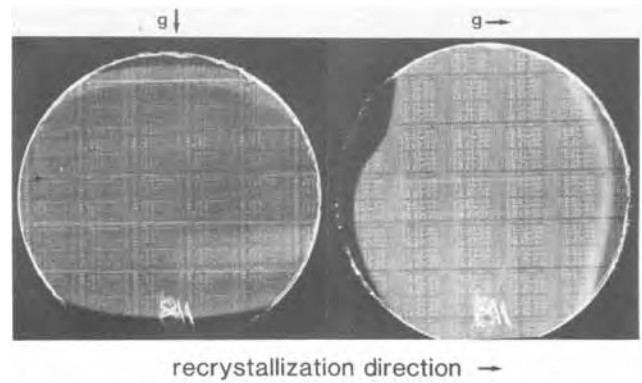


Fig. 6. X-ray transmission topographs (Mo $K\alpha$ radiation) of a wafer recrystallized by a number of 2 mm wide stripes, taken after a full CMOS device process. The fine detail is due to the presence of aluminum bonding pads and device structure. The pictures were taken on the same wafer with the $\langle 220 \rangle$ reflection, for two different beam directions.

movement of a much larger molten zone may cause complex two-dimensional stresses (12). The introduction of seed windows does not produce significant changes to the temperature profile in the substrate, and hence it is expected that seeded wafers will also be stress free.

Crystal defects.—Dual E-beam recrystallized films, although essentially single-crystal sheets, at present show three main types of crystallographic defects. First, with parallel scanning, there is a defect in the center of each oxide bar where the growth fronts from the two seeding windows meet. This defect was not usually revealed by Secco etching, but transmission electron microscopy (Fig. 7) shows the presence of a number of threading dislocations. These dislocations were almost always confined to within $1 \mu\text{m}$ of the geometrical center of the oxide bar by the symmetry of the heat flow, and so could be avoided by the active region of devices fabricated in the films. It is worth noting that no dislocations were found at other positions.

The second form of defect observed was an occasional twinning of the regrowth which, once initiated, could propagate for hundreds of microns in the scan direction. This twinning is shown by the anisotropic etch pits in Fig. 8, where the pits along one half of the central oxide bar are hexagonal. X-ray texture camera studies showed that these regions have a $(2\bar{2}\bar{1})$ surface, resulting from twinning on a (111) plane. Twinning was usually observed on specimens with the seed windows aligned along the $\langle 110 \rangle$ direction. In this case, the {111} twin planes lie along the seed direction, which is also the direction of the maximum temperature gradient produced by the line beam.

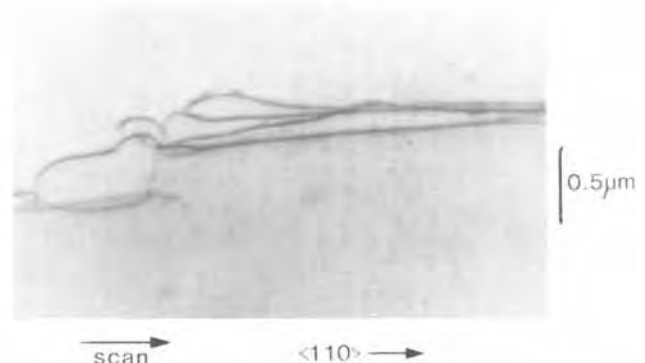


Fig. 7. TEM of dislocations running along the center of a recrystallized stripe.

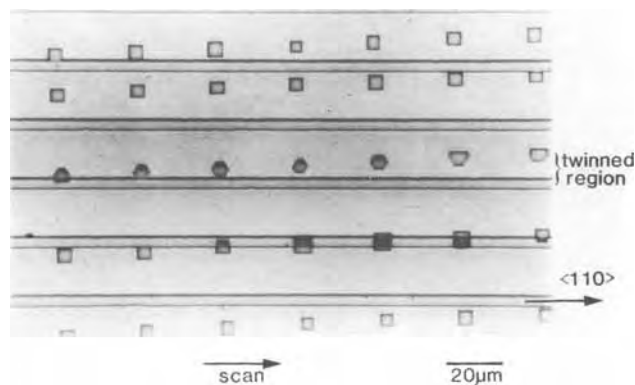


Fig. 8. Anisotropic etch pits in a recrystallized film with the seed windows aligned along $\langle 110 \rangle$, showing hexagonal pits along half of the middle bar indicating twinning and a $(2\bar{2}1)$ surface.

The final form of crystal defect observed was stacking faults, which are shown in the optical and TEM micrographs of Fig. 9. The most common faults were found in twinned regions with $\langle 110 \rangle$ -aligned seed windows. These faults, which again lie on (111) planes, originate at the seed window edge and grow at 56° in towards the center of the oxide bar. In untwinned regions, the traces of the (111) planes make an angle of 90° to the seed edge, and these faults were observed far less frequently, with about one fault per centimeter of seed edge. For seed windows aligned along $\langle 100 \rangle$, where the traces of the (111) planes are at 45° to the seed edge, the stacking fault density was typically two faults per millimeter. Stacking faults on higher-order planes, particularly $(\bar{2}11)$, (311) , and (221) , were sometimes observed in regions where poor photolithography had led to very rough edges to the seed windows. In general, the larger the angle a fault made with the seed edge, the less frequently it was observed, confirming that the driving force for the propagation of the defect is the stress produced by the temperature gradient behind the beam. A more detailed investigation of the defects will be published elsewhere.

Overall crystal quality.—The effects of the various crystal defects described above on the overall perfection of the film have been investigated by Rutherford backscat-

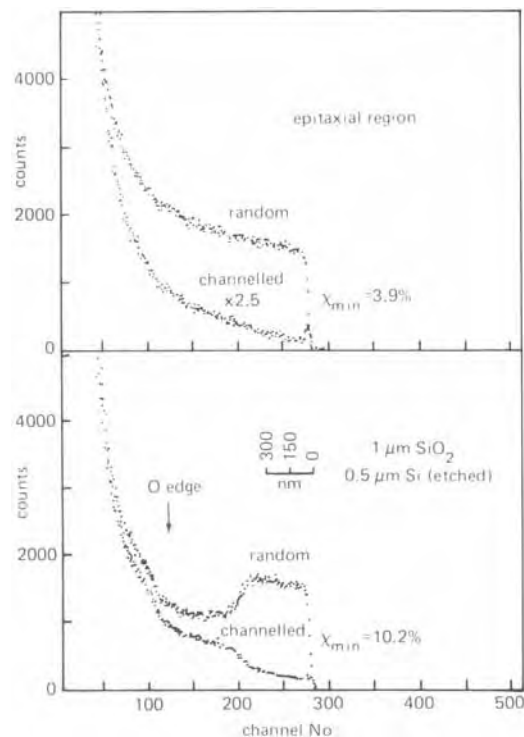


Fig. 10 $^4\text{He}^+$ ion backscattering spectra from recrystallized films. a: Direct contact between the polysilicon and the substrate (equivalent to the seeding region). b: 82% of the recrystallized film separated from the substrate by $1 \mu\text{m}$ of oxide.

tering and ion channeling studies. Figure 10a shows the random and $[001]$ -channeled spectra obtained from an epitaxially regrown polysilicon layer deposited directly onto an (001) substrate, corresponding to the seed area of an SOI specimen. A value of 3.9% is obtained for the minimum channeling yield χ_{min} , approaching that of bulk silicon and indicating good quality regrowth. There is no sign in the channeled spectrum of the original polysilicon/substrate interface, showing that good mixing has occurred. The beam power in this experiment had been optimized for the regrowth of the SOI area, and so even

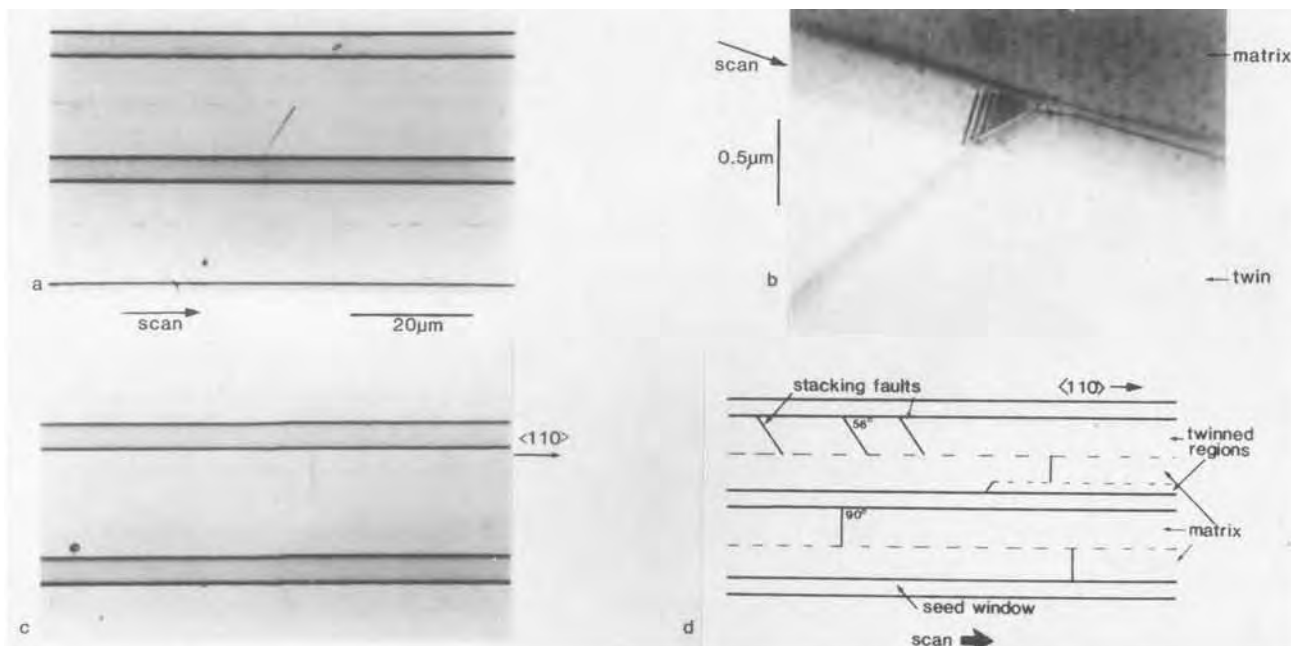


Fig. 9. Stacking faults in a film recrystallized on an (001) substrate with seed windows aligned along $\langle 110 \rangle$. Pictures a and c are Nomarski micrographs of Secco-etched regions in which the recrystallization is twinned and untwinned, respectively. Picture b is a TEM of a single stacking fault. The various types of common faults are shown schematically in d.

better results could be expected for slightly higher powers.

The spectra of Fig. 10b were obtained on the same specimen as used for Fig. 10a without changing its orientation, but in a region where a repetitive array of oxide bars 18 μm wide and spaced 4 μm apart isolated 82% of the silicon film from the substrate. The 1.5 MeV $^4\text{He}^+$ beam used in this study had a diameter of 1 mm, so these spectra represent averages over many separately seeded regions. The specimen, which had $\langle 110 \rangle$ -oriented seed windows, had been lightly Secco etched to reduce the silicon film thickness and to allow the degree of twinning to be estimated optically at around 15% of the total area. This twinning, and the associated stacking faults, have increased the value of χ_{min} to 10.2%, which is similar to values often observed for silicon on sapphire films (13). The increase in the channeled signal with increasing depth is much smaller here than in the case of SOS, however, as the density of defects is largely independent of depth for the recrystallized films, whereas for SOS many microtwins are nucleated at the back interface, giving rise to a gradually increasing defect density with depth. That the recrystallized silicon has good crystal qualities throughout its thickness is confirmed by the electron and hole mobilities at the back interface, which have values comparable to bulk silicon (9). Thus for specimens in which the twinning is reduced, for example by the $\langle 100 \rangle$ alignment of the seed windows, much improved crystal quality should result. Also, it will be possible to provide thinner films, required for small-geometry devices, without degrading the crystal quality.

Choice of regrowth parameters.—Optimum regrowth with the dual E-beam technique depends on the correct choice of the beam conditions and the thicknesses of the various layers. The relationship between the power required in the line beam and the scan speed for a typical experiment is shown in Fig. 11. Along the line marked "partial melting," the beam power raises the polysilicon temperature to the melting point but is insufficient to provide the latent heat requirement of the whole film, resulting in a slush of mixed solid and liquid. For beam powers above the value required for complete melting, there is a window in which good recrystallization occurs, until eventually the liquid silicon is raised to a temperature at which damage is caused. This damage takes the form of dewetting and agglomeration of the silicon into islands ("beading up") at low speeds and a cracking of the cap at high speeds. The increasing window of satisfactory conditions with scan speed makes it attractive to work with as fast a scan as possible, especially as the reduced diffusion of heat into the specimen with the short dwell times minimizes the possibility of substrate melting. The upper limit to the speed is set by the necessity to provide adequate beam power, and by the ability of the seed windows to keep the position of the solidification front under control, preventing random nucleation of grains. This latter effect is also a function of the substrate or background temperature. It is desirable to work with a

high background temperature in order to minimize (i) the difference in power densities required to melt the polysilicon on the thermally insulating oxide and that on the substrate, (ii) the stress produced by the high temperature gradients, and (iii) the total line beam power. The window of beam powers allowing seeded recrystallization (i.e., the minimum power required to melt the polysilicon in the seed window without causing melting under the isolating oxide) is shown in Fig. 12 for a fixed scan speed. As expected, the two lines converge towards the melting point, where the whole specimen is melted without any power input from the line beam. For temperatures above $\sim 1270^\circ\text{C}$, the seed windows, which were widely separated in this experiment, are unable to keep the solidification front close to the line beam and random solidification proceeds vertically from the underlying oxide in small ($\sim 50 \mu\text{m}$ diam) regions, leading to a $\{111\}$ -textured film. Thicker polysilicon or oxide layers or more closely spaced seed windows all result in the polysilicon being in better lateral thermal contact with the substrate, and hence allow seeded regrowth to be maintained to higher scan speeds or substrate temperatures.

Seeded regrowth naturally requires melting to penetrate into the substrate in the seed window, but it is desirable for the substrate below the isolating oxide to remain solid. The depth of melting has been investigated by observing the motion of an As marker implant (1.0^{16} cm^{-2} at 40 keV) positioned in the substrate prior to the low temperature growth of the oxide. Bevel-and-stain and cross-sectional SEM techniques have both been used. The depth of melting, both under the center of an oxide stripe and at the edge of a seed window, is shown in Fig. 13 as a function of the line beam power. There is a window of beam power between 24 and 26 W/mm, or 8%, for seeded regrowth without substrate melting. The size of this window is expected to increase with increasing sweep speed. Increases in the beam power above the melting threshold give a linear increase in the melt depth. The slope of the line indicates that, to a first approximation, there is no change in the amount of heat lost from the sur-

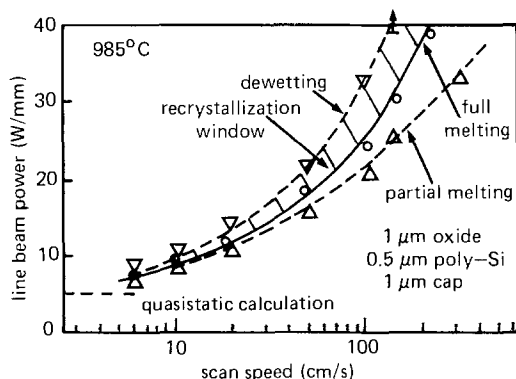


Fig. 11. Power required in the line electron beam as a function of speed, for dual-beam recrystallization.

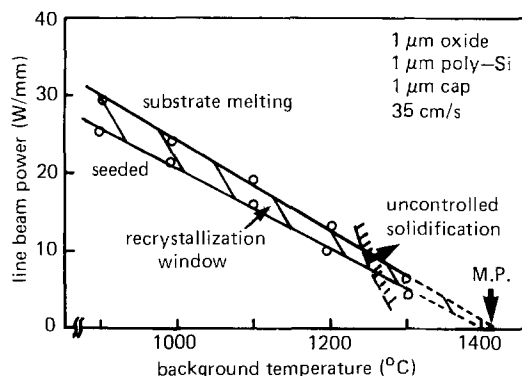


Fig. 12. Dependence of the window of line beam powers for seeded recrystallization on the background temperature.

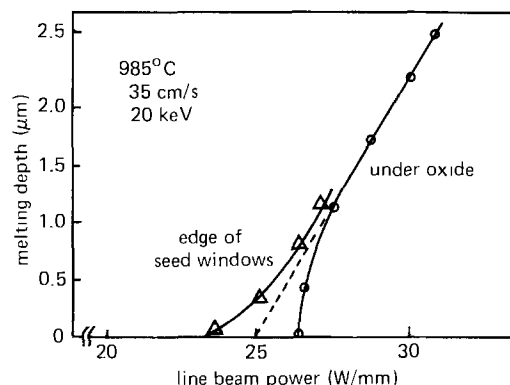


Fig. 13. Dependence of the depth of substrate melting, both under the isolating oxide and in the seed windows, on the line beam power.

face region and that the extra power above threshold is simply absorbed as latent heat. The substrate under the oxide can be melted to a depth of several microns without loss of surface flatness or damage to the oxide stripes, and hence substrate melting should not necessarily be regarded as catastrophic, except, of course, for the case of recrystallization of partially processed wafers. Finally, for beam powers substantially above the melting threshold, molten silicon flows over the oxide stripes which remain intact but sink into the substrate.

The thicknesses of the various layers determine the heat flow in the system and hence the process window. Increasing the thickness of the underlying oxide increases the thermal isolation of the polysilicon film, making it easier to melt it without substrate melting. This means, however, that when the beam power is sufficient to cause melting in the seed window the polysilicon on oxide has been heated well above the melting point and hence it exerts a large stress on the capping layer, sometimes causing it to fracture. Although no problems were experienced in obtaining seeded regrowth up oxide edges 2 μm high, optimum results were usually achieved with 1 μm oxides.

SOI films intended for VLSI applications will probably have thicknesses of 0.5 μm or less. The dual E-beam technique was found to be successful for polysilicon thicknesses down to 0.2 μm , below which dewetting occurred. The uniformity of the crystal structure throughout the film allows it to be thinned after recrystallization (by etching, or by growing and stripping off an oxide, for example) without any loss in crystal quality, and hence a thicker film than is finally required can be chosen for recrystallization. Increasing the polysilicon thickness increases the lateral component of the heat flow compared to the vertical one through the oxide, providing better control of the solidification front. Thus thicker polysilicon layers show a reduced tendency to random nucleation at high scan speeds and also allow a wider spacing of the seed windows without allowing the solidification front to facet and produce sub-boundaries. The maximum window spacing which still produced boundary-free recrystallization with parallel scanning was 50 μm for 0.5 μm films and 70-100 μm for 1 μm thick films. As the spacing was increased towards these maximum values, the severity of the defect above the center of the oxide bar (that is, the number of individual dislocations required to accommodate the mismatch between the two sides) increased.

Conclusions

It has been demonstrated that the dual electron-beam recrystallization technique is capable of producing precisely oriented films of single-crystal silicon on oxide. The films are essentially free of major defects, except for an occasional twinning of the growth on {111} planes which occurs particularly when the seed windows are aligned in the $\langle 110 \rangle$ direction. By arranging for the scan direction of the line beam to be parallel to the seed windows, there are no discontinuities in the mass flow of molten silicon, and so the recrystallized films remain flat.

The optimum beam and specimen parameters for achieving a wide process window have been investigated. Oxide and polysilicon films $\sim 1 \mu\text{m}$ thick produce the best recrystallization, particularly when recrystallized with a background temperature of 1000°C and a scan speed of $> 30 \text{ cm/s}$. Under these conditions, there is a process window of $\sim 8\%$ in beam power between achieving proper seeded regrowth and the onset of substrate melting beneath the isolating oxide. Substrate melting of several microns can be tolerated without degrading the SOI film as long as there are no device structures present, giving a much larger window.

Future work will concentrate on a scaling up of the E-beam equipment and on methods of eliminating the problems of twinning. The speed with which the technique can recrystallize a wafer and the quality of the films that it produces will make it a strong contender for producing SOI substrates for VLSI device fabrication.

Acknowledgments

We would like to thank Dr. G. F. Hopper (GEC Hirst Research Centre) for the supply of the polysilicon specimens. The x-ray topographs were produced by Mrs. M. Halliwell (British Telecom Research Laboratories). Dr. C. Jaynes (University of Surrey) is thanked for his help with the RBS spectra. J. Davis and R. McMahon acknowledge a Research Scholarship and a Research Fellowship, respectively, from British Telecom Research Laboratories.

Manuscript submitted Jan. 14, 1985; revised manuscript received May 2, 1985.

British Telecom Research Laboratories assisted in meeting the publication costs of this article.

REFERENCES

1. *J. Cryst. Growth*, **63**, (1983).
2. M. W. Geis, H. I. Smith, B-Y. Tsaur, J. C. Fan, D. J. Silversmith, and R. W. Mountain, *This Journal*, **129**, 2812 (1982).
3. A. Kamgar and E. Labate, *Mater. Lett.*, **1**, 91 (1982).
4. J. F. Gibbons, K. F. Lee, T. J. Magee, J. Pheng, and R. Ormond, *Appl. Phys. Lett.*, **34**, 831 (1979).
5. T. I. Kamins and B. P. von Herzen, *IEEE Electron Devices Lett.*, **ed1-2**, 313 (1981).
6. J. R. Davis, R. A. McMahon, and H. Ahmed, *Electron. Lett.*, **18**, 163 (1982).
7. J. R. Davis, R. A. McMahon, and H. Ahmed, *J. Phys. C*, **44**, 337 (1983).
8. J. R. Davis, R. A. McMahon, and H. Ahmed, in "Laser-Solid Interactions and Transient Thermal Processing of Materials," J. Narayan, W. Brown, and R. Lemons, Editors, p. 563, North Holland, Amsterdam (1983).
9. G. F. Hopper, J. R. Davis, R. A. McMahon, and H. Ahmed, *Electron. Lett.*, **20**, 500 (1984).
10. R. A. McMahon, J. R. Davis, and H. Ahmed, in "Laser and Electron-Beam Interactions with Solids," B. Appleton and G. Cellar, Editors, p. 783, Elsevier, London (1982).
11. K. A. Bezjian, H. I. Smith, J. M. Carter, and M. W. Smith, *This Journal*, **129**, 1848 (1980).
12. R. F. Pinizzotto, *J. Cryst. Growth*, **63**, 559 (1983).
13. S. T. Picraux and P. Rai-Choudhury, in "Semiconductor Characterization Techniques," P. A. Barnes and G. Rozgonyi, Editors, p. 447, The Electrochemical Society Softbound Proceedings Series, Princeton, NJ (1978).

Plasma Organosilicon Polymers

Deposition, Characterization, and Application in Multilayer Resist

V. S. Nguyen, J. Underhill, S. Fridmann, and P. Pan

IBM General Technology Division, Essex Junction, Vermont 05452

ABSTRACT

Divinyl tetramethyl disiloxane (DVS), hexamethyl disilazane (HMDS), and methyl trimethoxysilane (MTS) polymer films were deposited on p-type silicon substrates using plasma-enhanced chemical vapor deposition (PECVD) processing. The deposition process was implemented in a parallel-plate, capacitively coupled plasma deposition system. Excellent film thickness and refractive index uniformity (std dev = 2-3%) were obtained. The deposition kinetics were studied as a function of process parameters such as pressure, power, density, and substrate temperature. The polymer film's physical properties were characterized by Fourier transformed infrared (FTIR), electron spectroscopy for chemical analysis (ESCA), Auger spectroscopy, electron spin resonance (ESR), and plasma etching. These polymer films were used as an intermediate oxygen etch resistance layer in trilevel resist lithography to produce submicron image patterns ($\approx 0.7 \mu\text{m}$ lines and spaces) using step and repeat photolithography.

The formation of polymeric organosilicon compounds by radio frequency (RF) glow discharge as a thin dielectric film for optics (1-2) and other microelectronic applications (3-9) has been reported widely in several recent publications. Plasma polymer films with unique physical and chemical characteristics can be produced by the passage of organosilicon monomers through low pressure plasma. The polymers are usually amorphous and highly cross-linked with stoichiometric ratios which typically do not relate to those of the starting monomers in a simple way. In microelectronic applications, siloxane, silazane, and silane monomers are the most frequently used compounds for plasma polymerization because of their low toxicity (10) and compatibility with both organic resists and silicon materials. Furthermore, low temperature dry processing in a vacuum minimizes exposure to contamination and is a low cost and attractive technique for VLSI fabrication.

It is well known that properties of plasma-deposited polymers are influenced by process parameters, including power density, pressure, substrate temperature, position of substrate, and type of plasma reactor coupling (capacitive or inductive) (11-13). The complexity of the plasma polymerization mechanism has also been discussed by Haller and others (11, 14-17). Organosilicon polymer tends to have lower internal stress and greater freedom from pinholes, as compared to thermally grown or deposited silicon films, due to the low deposition temperature, highly cross-linked structure, and better thermal matching and compatibility with organic resist. Therefore, the organosilicon polymer films can be used as an intermediate plasma oxygen etch barrier, in place of thin oxide or nitride films, in trilevel resist photolithography.

Recently, Sachdev *et al.* (4) studied some physical properties of organosilicon polymers deposited in a barrel-type inductively coupled plasma system. In this paper, we report the deposition, characterization, and application of divinyl tetramethyl disiloxane (DVS), hexamethyl disilazane (HMDS), and methyl trimethoxysilane (MTS) polymers in a parallel-plate, capacitively coupled, plasma system.

The deposition kinetics were investigated by studying the variation in film deposition rates as a function of process parameters such as power, system pressure, and substrate temperature. The physical properties of deposited polymers were characterized by Fourier transformed infrared (FTIR) spectroscopy, electron spectroscopy for chemical analysis (ESCA), Auger analysis, and electron spin resonance (ESR) techniques. Film properties were studied as deposited, after thermal annealing up to 300°C, and after surface treatment with oxygen or nitrogen plasma. The etch rates of these polymers in CF_4 plasma and in O_2 plasma in reactive ion etching modes were also investigated. The deposited polymers were used as intermediate plasma oxygen etch barriers in trilevel resist

photolithography (18-20). Submicron images with vertical profiles ($\approx 0.7 \mu\text{m}$) were obtained from this multilayer resist technique using step and repeat photolithography.

Experimental

The plasma polymerization and deposition processes were implemented in a high frequency (13.56 MHz), parallel-plate, capacitively coupled, plasma deposition system. The monomers DVS, HMDS, and MTS were purchased from Petrarch Chemical, Limited, and used without further purification. The chemical structure, molecular weight, and boiling point of the monomers are shown in Table I. Polymer films were deposited on bare p-type silicon wafers for process and physical characterization. The monomer liquids were heated to a constant 70°C during the deposition process. The reactor chamber pressure was controlled by gas input and vacuum pump throttle valves. The radius of the electrode is about 31 cm. The volume of the system is about 45 dm³. Since the gas input is controlled by monomer evaporation, exact flow rate calculation is not possible. Approximate flow rates for all monomers is in the range of 300-500 sccm. The centerline process parameters for the best film thickness and refractive index uniformities (std dev = 2-3%) are given in Table II. We also studied the variation

Table I. Structure and properties of organosilicon monomers

Chemical Name	Structure	Molecular Weight (gr/mole)	Boiling Point (°C)
Hexamethyl Disilazane (HMDS)	$\begin{array}{c} \text{CH}_3 \quad \text{CH}_3 \\ \quad \\ \text{H}_3\text{C}-\text{Si}-\text{N}-\text{Si}-\text{CH}_3 \\ \quad \\ \text{CH}_3 \quad \text{CH}_3 \end{array}$	164	127
1,3-Divinyl Tetramethyl Disiloxane (DVS)	$\begin{array}{c} {}_2\text{HC}=\text{CH} \quad \text{HC}=\text{CH}_2 \\ \quad \\ \text{H}_3\text{C}-\text{Si}-\text{O}-\text{Si}-\text{CH}_3 \\ \quad \\ \text{H}_3\text{C} \quad \text{CH}_3 \end{array}$	186	139
Methyl Trimethoxysilane (MTS)	$\begin{array}{c} \text{OCH}_3 \\ \\ \text{CH}_3-\text{Si}-\text{OCH}_3 \\ \\ \text{OCH}_3 \end{array}$	136	103

Table II. Deposition conditions for polymer

Type of Monomer	Power (Watts)	Pressure (mTorr)	Substrate Temperature (°C)	Deposition Rate (nm/min.)	Refractive Index
HMDS	300	110	100	15	1.50 ± 0.01
DVS	300	110	100	27	1.49 ± 0.01
MTS	300	1000	100	6	1.48 ± 0.01

Batch Thickness Uniformity $3\sigma = 6 - 10\%$

of deposition rates as functions of substrate temperature (25°-300°C), power density (0.08-0.24 W/cm²), and reactor pressure (110-1000 mtorr).

Film thickness and refractive index were measured using a He-Ne laser ellipsometer (wavelength = 632.8 nm) and a Talystep.

FTIR studies were performed with 500 nm polymer films deposited on a bare silicon substrate. Background absorption of the substrate was subtracted from the spectra to obtain bulk film spectra. The maximum resolution of the spectrometer was 0.5 cm⁻¹ wave number. FTIR studies of liquid monomers were also performed to detect Si-H and Si-OH bonds which may result from water vapor contamination. However, none of these bonds was detected in the liquid monomer adsorption spectra.

Auger analysis for compositional depth profiles was performed with 100 nm films on a silicon substrate surface. The films were sputtered by 1 keV Ar⁺ ion to determine the composition as a function of depth. The detection limit of the Auger tool was 0.5 atomic percent (a/o). The polymer films were examined as deposited and after annealing in a nitrogen atmosphere for 30 min at 300°C.

The ESCA technique was used to analyze the film surface composition as-deposited, and after either nitrogen or oxygen plasma surface treatment. The surface compositions were also analyzed as a function of RF power. Surface analysis was performed on a Hewlett-Packard HP 5950B photoemission spectrometer. Scans were made in both survey and high resolution modes: survey to detect the possible presence of unexpected elements on the surface, and high resolution to quantify the known elements and help establish their bonding environments.

ESR analysis for unpaired electrons (spin density) in the polymer films was performed with 2 μm films deposited on a bare silicon substrate surface. The measurements were performed both at room and near liquid helium temperatures (≈ 8-9 K). Double integrals were computed for all observed resonance and compared with standardized thin Si₃N₄ film samples with known spin density. The reproducibility of the integrals is about ±15-20%, and, within this limit, integrals can be compared from one sample to another. Bare Si substrates were subjected to similar plasma deposition, and the deposited films were then removed by wet etching in a buffered HF solution. The substrates were measured for any spin resonance that might have arisen from plasma irradiation. The detection limit of the ESR tool is about 1 × 10¹¹ spin-cm⁻³.

The plasma etching experiments were carried out in a parallel-plate, radial flow, etching reactor in a reactive ion etching (RIE) mode. The reactor has a radio fre-

quency of 13.56 MHz. The grounded substrate electrode of the reactor was maintained at 40°C during the etching process. The conditions for RIE were 0.55 W/cm² RF power density, 25 mtorr pressure, and 22 sccm CF₄ flow rate. Etch rates of deposited polymers were studied as deposited and after annealing at 200°C in a nitrogen atmosphere. Etch rates were calculated using laser interferometer end-point traces. (Etch rate $R = \lambda/2nt$, where λ is the wavelength of the laser, n is the film's refractive index, and t is the etch time that changes reflected intensity by one cycle.)

Trilayer resist structures were fabricated using the PECVD organosilicon films for the midlayer oxygen etch barrier (see Fig. 12). The bottom layer was a novalak-based photoresist, 1-2 μm thick, baked to 200°C. The top imaging resist was a positive photoresist approximately 0.5 μm thick. The image resist was exposed using a 0.3 NA lens and 405 nm exposing wavelength and developed in the normal manner. The image was transferred by RIE, first through the organosilicon with CF₄, then through the base polymer with O₂.

Scanning electron microscopy (SEM) was used to study the resulting profiles in multilayer resist structures.

Results and Discussion

Film deposition.—Table II shows the process parameters, deposition rates, and refractive indexes of DVS, HMDS, and MTS polymers. The film thickness and refractive index uniformity is good (std dev = 2-3%). The refractive indexes of all three polymers varied from 1.48 to 1.51 within each batch, and had average deposition rates of 15, 27, and 6 nm/min for HMDS, DVS, and MTS polymers, respectively. It appears that DVS has a higher deposition rate than HMDS under the same process conditions. Since both monomers have comparable molecular weight and boiling points (Table I), the higher deposition rate of the DVS polymer is attributed to the double bond structure of DVS monomer vinyl groups.

Increased substrate temperature substantially reduced the deposition rate of all three polymers (Fig. 1). From this data, we obtain the reversed activation energies (E_{ra}) of 0.55, 0.49, and 0.41 kcal·mol⁻¹ for DVS, HMDS, and MTS, respectively. Here, the reversed activation energy (E_{ra}) is defined as the energy difference between the activated (reactive) species and film product. In general the plasma deposition of polymer primarily involves the bonding and energy transfer deactivation of reactive species A* with a substrate surface to form a polymer film. When the substrate temperature increases, it becomes more difficult for reactive species A* to transfer its energies to, and bond with, the substrate surface due to the process exothermic reaction pathways. This results in lower deposition rates with increased substrate temperature.

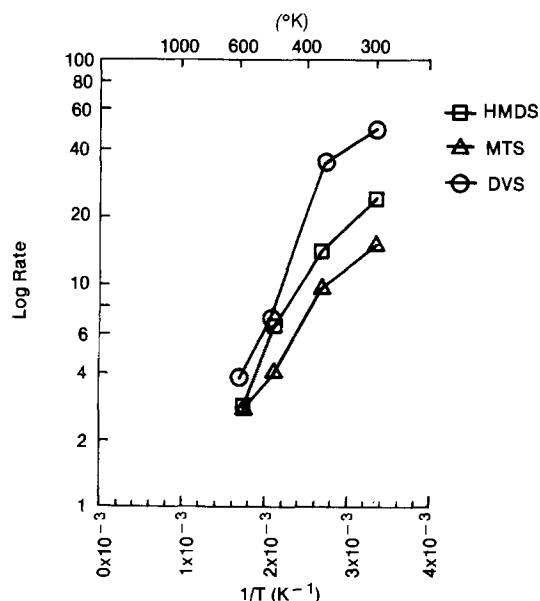


Fig. 1. Variation of deposition rate vs. temperature

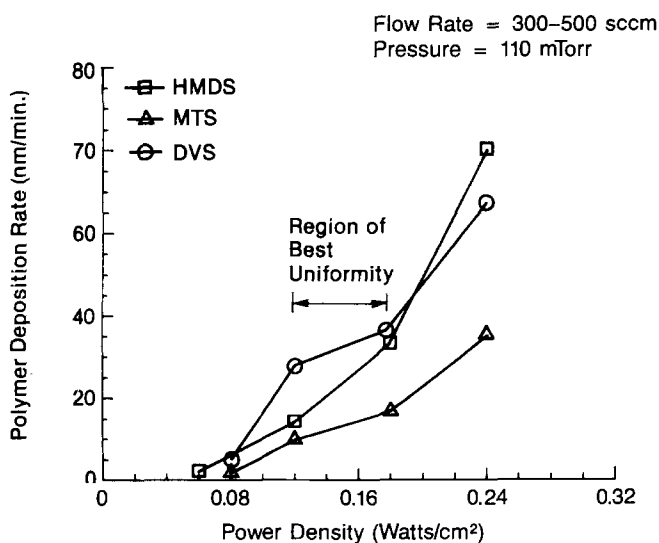


Fig. 2. Variation of deposition rate with power density

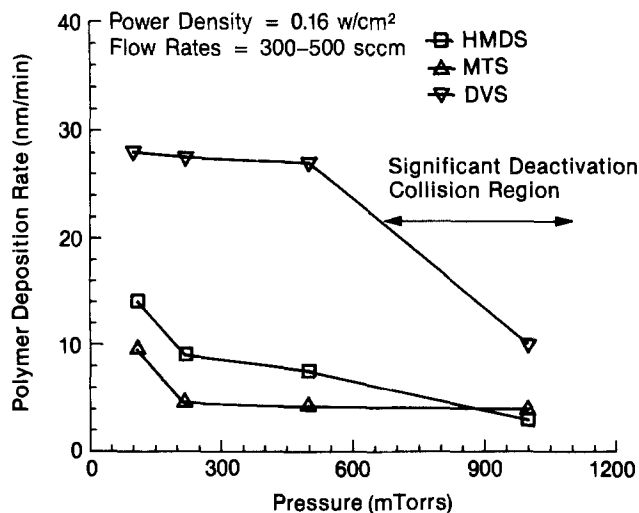
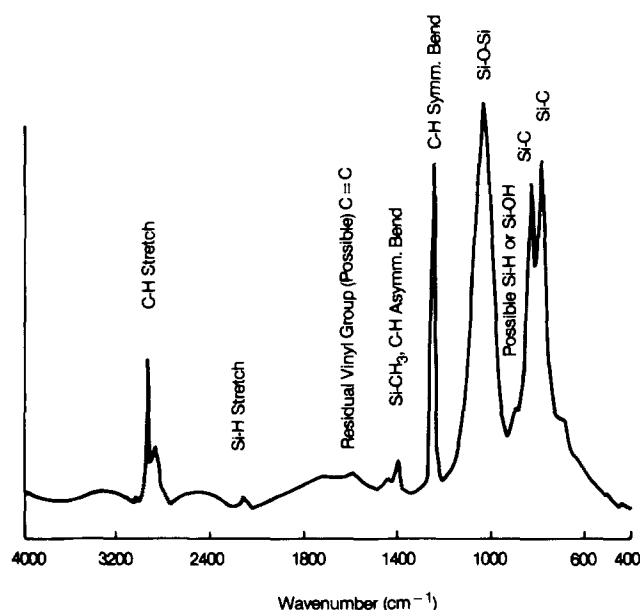


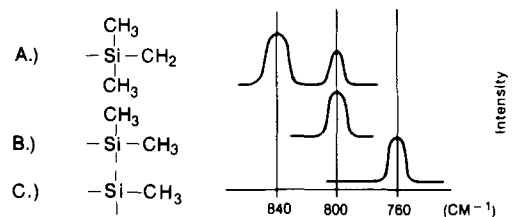
Fig. 3. Variation of deposition rate vs. pressure

Figure 2 shows the variation in deposition rates with power density. A minimum power density of 0.08 W/cm^2 is required to initiate significant polymerization and deposition for all three polymers under the indicated process conditions. Optimum film thickness and refractive index uniformity was observed in the $0.12\text{--}0.18 \text{ W/cm}^2$ ($300\text{--}450\text{W}$) power density range. This indicates that the plasma glow discharge to form a polymer is relatively stable, *i.e.*, the distribution of reactive species is more uniform in the $0.12\text{--}0.18 \text{ W/cm}^2$ ($300\text{--}450\text{W}$) power density range. The significant increase in deposition rate with increased power beyond 450W is attributed to increased reactive species concentration in the glow discharge. When the pressure was increased, the deposition rate dropped sharply for all three polymers (Fig. 3). However, the deposition rate of DVS does not drop significantly until the pressure reaches 1 torr. This reduction may cause more frequent deactivation collisions between reactive species and monomers when the pressure is increased. The results also indicate that these deactivation collisions become significant when system pressure is above 500 mtorr.

Physical characterization of polymer films.—The infrared transmission spectra of as-deposited DVS, HMDS, and MTS polymers are shown in Fig. 4-6. The spectra indicate normal bonding characteristics of organosilicon polymers. The spectrum for the DVS polymer contains the following bonding characteristics.

Table III. Positions and intensity of various Si-CH₃ vibrational bands

- Finding:
- Reduction of C=C vinyl Band (1600 cm^{-1}) → Opening Double Bond for Formation of Repeating Polymer Unit.
 - Siloxane Structure (Si-O-Si at 1050 cm^{-1}) Still Exists.
 - Si-H and Possible Si-OH Groups (2130 cm^{-1} and 900 cm^{-1}) Still Exists.
 - Si-CH₃ Group Exists in Two Different Forms A.) and B.) (840 cm^{-1} , 800 cm^{-1}).

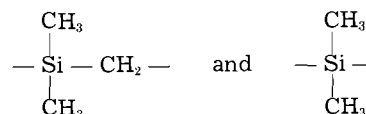


- Reference Data:
- *R. C. Weast, CRC Handbook, 62nd Edition, CRC Press, Boca Raton, Florida.
 - *J. Haslam and H. A. Willis; "Identification and Analysis of Plastic," pages 257-263. Published by D. Van Nostrand Co. Inc., New Jersey, Second Edition, 1967.
 - *Our IR measurement of silicone monomer.

1. Only small amounts of residual vinyl groups (C=C) at $\approx 1600 \text{ cm}^{-1}$ wave number remain in the polymer structure. This indicates that most of the double bonds in the vinyl group of the DVS monomer were opened during the polymerization and deposition process.

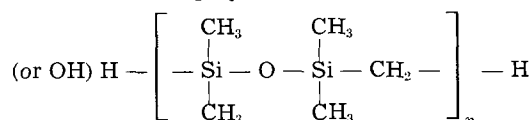
2. The siloxane backbone band structure (Si-O-Si at 1050 cm^{-1}) for DVS remains almost the same after the deposition. This indicates that the siloxane group (Si-O-Si) is also the backbone structure of the DVS polymer.

3. The vibrational bands of Si-CH₃ are located at 840 and 800 cm^{-1} . As shown in Table III, the Si-CH₃ groups in DVS polymers must exist in two forms



4. Si-H (2130 cm^{-1}) and Si-OH (800 cm^{-1}) are present in the DVS polymer.

From the combination of the above bonding characteristics, band position and intensity, the most probable structure of the DVS polymer is



Bond Type	Wavenumber (cm ⁻¹)
C-H Stretch	2960
Si-H	2130
-C=C<	~ 1600
Si-CH ₃	1410
C-H Antisymmetrical Bend	
C-H Symmetrical Bend	1250
Si-CH ₃	1360-1410
Si-O-Si (Siloxane gp.)	1050
Si-C	800
(2 groups)	840
Possible Si-OH	900
Si-H	

Fig. 4. FTIR of plasma-deposited DVS polymer.

Fig. 5. FTIR of plasma-deposited HMDS polymer.

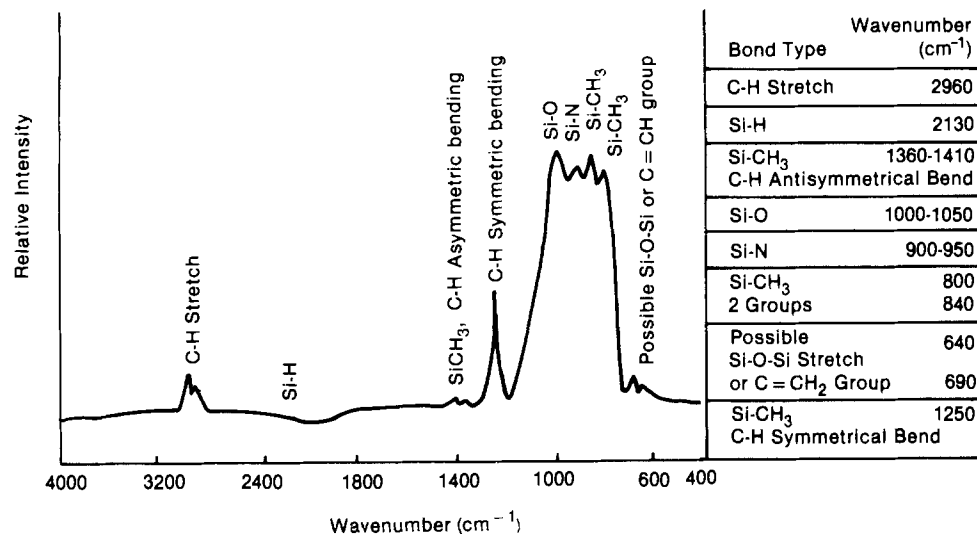
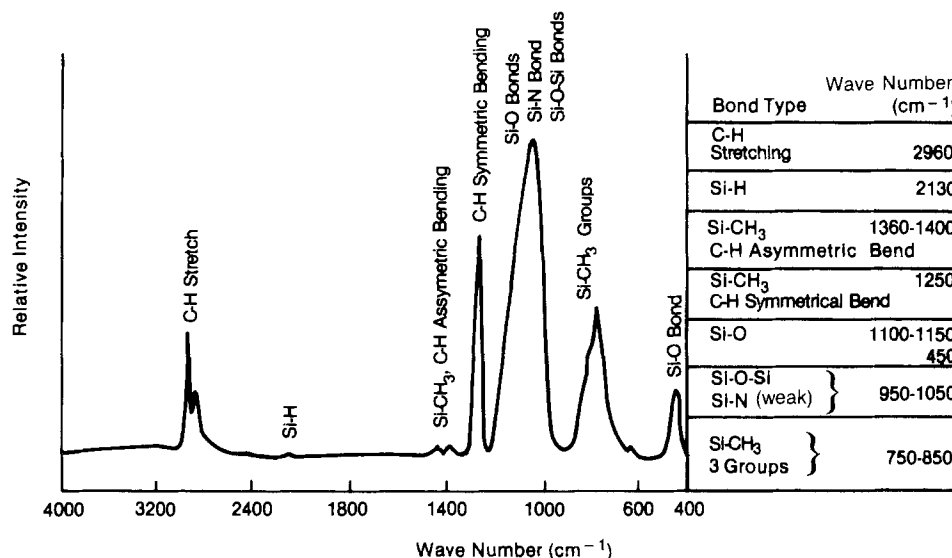
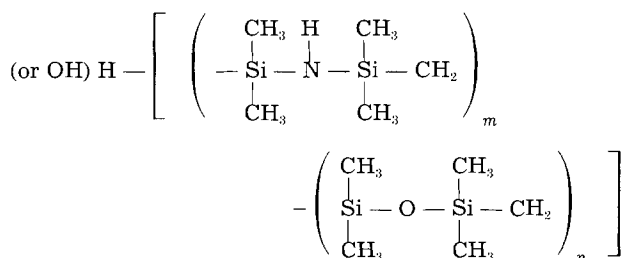


Fig. 6. FTIR of MTS polymer



where n is an integer.

The spectrum of the HMDS polymer is shown in Fig. 5. The presence of strong Si-O bands ($1000-1050\text{ cm}^{-1}$) indicates oxygen contamination in the film's bulk structure. This oxygen probably came from the desorption of water vapor from the cool-wall reactor during the deposition process. The infrared transmission spectrum of the HMDS polymer also showed the presence of Si-CH₃ (800 , 840 , and 1250 cm^{-1}), Si-N ($900-950\text{ cm}^{-1}$), and other bending and stretching bands (2960 , $1360-1400$, 1250 cm^{-1}). The oxygen contamination makes the determination of the exact HMDS polymer structure more difficult. However, the most probable structure of the HMDS polymer, which corresponds well with the band positions and intensity is



where m and n are integers.

The spectrum of the MTS polymer with its band structures is shown in Fig. 6. The presence of a strong and a small overlap (at $900-1050\text{ cm}^{-1}$) range, together with a small amount of nitrogen ($\sim 2\text{ a/o}$) detected by Auger in

the film bulk, leads us to assign this band as an overlap of Si-O-Si and possibly Si-N bonds. The existence of nitrogen indicates that some air contamination may have occurred during the deposition process. From the spectrum band structure, it appears that the MTS polymer was formed from various fragments of the monomer. No clear structure of the MTS monomer can be identified from the spectrum. In summary, FTIR results revealed that most of the DVS polymer and a large portion of the HMDS polymer were made up primarily of their monomer units, while the MTS polymer was formed mostly from its monomer reactive fragments. Although we could not identify cross-linking bonds in these polymers, they may still exist in substantial quantities in all three polymers. The identified polymer structures are only the most probable structures derived from our FTIR results.

Auger depth profiles through $\sim 0.1\text{ }\mu\text{m}$ of polymer films deposited on p-type silicon wafers showed good compositional uniformity with depth for all three polymers (Fig. 7-9). A small amount of oxygen contamination has also been observed in all three polymer surfaces and polymer-silicon interfaces. The oxygen contamination in polymer-silicon interfaces is attributed to the initial desorption of water vapor from the reactor sidewalls. The oxygen in the polymer surfaces is due to oxidation after the polymer was exposed to air.

ESCA results for all three plasma-deposited polymers showed a general trend of increased surface composition for all elements relative to carbon and to monomer compositions (Table IV). It was found that oxygen was incorporated into the polymer surfaces, even when it was not present in the monomer, as in the case of HMDS. This is

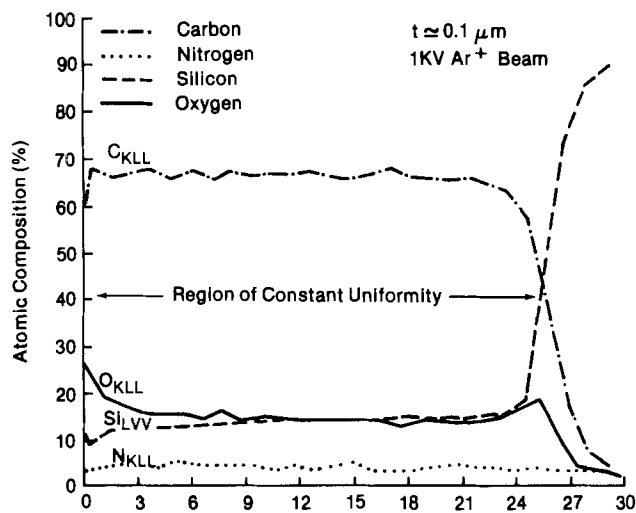


Fig. 7. Auger depth profile of DVS polymer

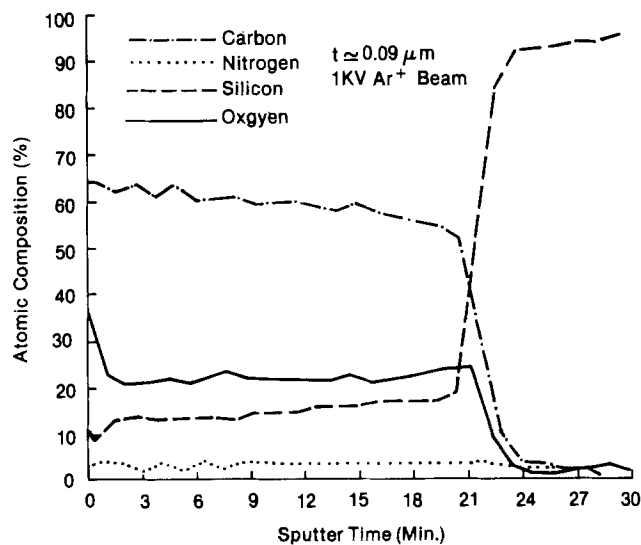


Fig. 9. Auger depth profile of MTS polymer

consistent with the Auger, infrared data, and other published results (21). The variation of substrate temperature produces notable changes in composition. For HMDS and MTS polymers, an increase in substrate temperature from 100° to 300°C further enhanced the silicon and oxygen surface concentration, especially for the MTS polymer. Conversely, for the DVS polymer, the most notable changes were slight reductions in silicon and oxygen. This suggests that the DVS polymer surface may be less sensitive to air oxidation. Although nitrogen was found in the film bulk (2-3% a/o) of MTS polymer, less than 1 a/o of nitrogen was observed in its surface. This must be due to the substitution of oxygen for nitrogen in the film surface as observed by Auger depth profile data.

In marked contrast to their sensitivities to substrate temperature, all three polymer film surface compositions remain about the same with increased power density (Table V). Since the deposition rate increased almost fourfold with increased power under the same process conditions (Fig. 2), the above results suggest that the deposition rate is limited by the concentration of radical reactive species in the glow discharge.

For postdeposition plasma treatment, there is no difference in the effect of using oxygen *vs.* nitrogen plasma among polymer systems: all plasma-treated polymer surfaces become like SiO₂ (Table VI). The similarity between nitrogen and oxygen plasma treatment may be due to (i) the presence of background oxygen in nitrogen plasma with induced surface oxidation, and/or (ii) the generation of an "activated" surface by nitrogen plasma treatment which immediately oxidized upon exposure to air.

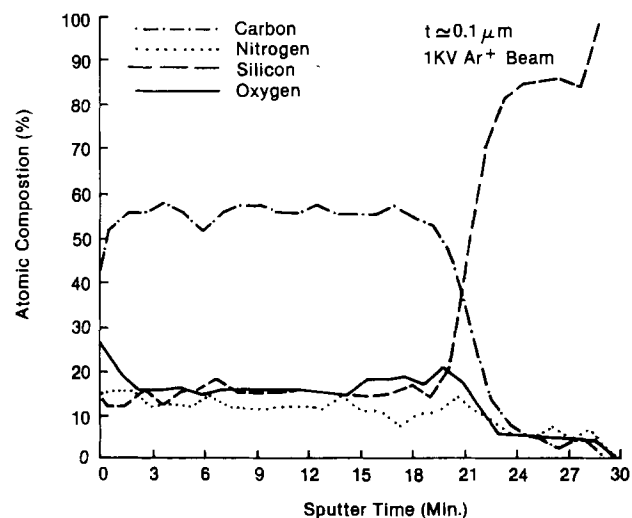


Fig. 8. Auger depth profile of HMDS polymer

Finally, bonding features discernable from high resolution scans show (i) the presence of pronounced carbon-oxygen single bonds in MTS polymer as in the methoxy groups of monomer structures (Fig. 10), and (ii) the presence of low but measurable levels of carbon-carbon double bonds in the DVS polymer. (These were determined by reanalyzing by ESCA after bromination of the surface with a bromine solution.) This is consistent with FTIR data and suggests that some vinyl groups still existed in the DVS polymer.

ESR studies revealed that all polymer films have very low spin density (few unpaired electrons and dangling bonds) except for the as-deposited DVS polymers at 100°C. This DVS film showed a signal 8G wide ($g = 2.0065$) at a magnetic field of 3360G (Fig. 11). As compared to reference thin Si₃N₄ film samples ($\approx 3 \times 10^{16}$ spin/cm³), the integrated spin density of the DVS polymer is 2×10^{17} spin/cm³. The broad signal of the DVS polymer corresponds to the carbon dangling bonds in the polymer structures. This appears to be consistent with the open double bond of DVS monomer vinyl groups during the deposition process. After annealing at 300°C in nitrogen for 30 min, the spin signals disappeared. This is due to the recombination of carbon dangling bonds by thermal excitation. It should be noted that the bare Si substrate subjected to the described plasma deposition and removal of deposited films shows only a small amount of spin density (1×10^{13} spin/cm³). The effect of plasma radiation on the generation in the silicon substrate is therefore minimal.

Reactive ion etching of three polymer films with CF₄ gas at 400W, 22 sccm flow rate, and 25 mtorr pressure yielded etch rates of 41-48 nm/min (Table VII). No significant differences in the etch rate of the polymer film were

Table IV. Distribution of elements in plasma-deposited film surfaces

Polymer Deposition Condition	Atom Distribution				Atom Ratios: Polymer/Monomer			
	C	Si	O	N	C	Si	O	N
HMDS Monomer	6	2	—	1				
HMDS Polymer:								
100 C, 300 W	6	3.9	1.4	1.7	1.0	2.0	—	1.7
100 C, 600 W	6	3.6	1.2	1.5	1.0	1.8	—	1.5
300 C, 300 W	6	5.0	1.8	1.8	1.0	2.5	—	1.8
DVS Monomer	8	2	1	—				
DVS Polymer:								
100 C, 300 W	8	3.6	2.4	—	1.0	1.8	2.4	—
100 C, 600 W	8	3.5	2.0	—	1.0	1.8	2.0	—
300 C, 300 W	8	3.1	1.8	—	1.0	1.6	1.8	—
MTS Monomer	4	1	3	—				
MTS Polymer:								
100 C, 300 W	4	4.6	5.7	—	1.0	4.6	1.9	—
100 C, 600 W	4	4.1	5.7	—	1.0	4.1	1.9	—
300 C, 300 W	4	7.8	10.	—	1.0	7.8	3.3	—

Deposition Conditions:

- 100 m Torr
- 100 °C

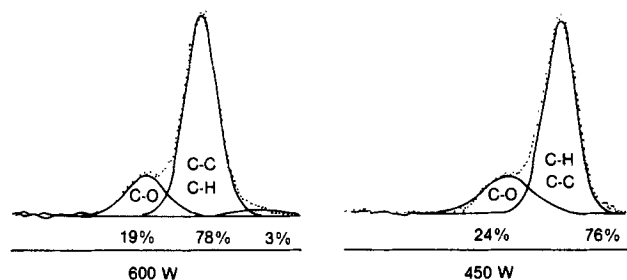
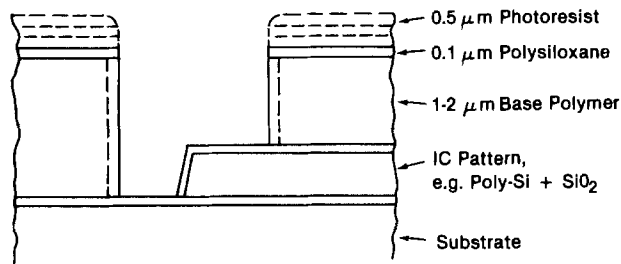


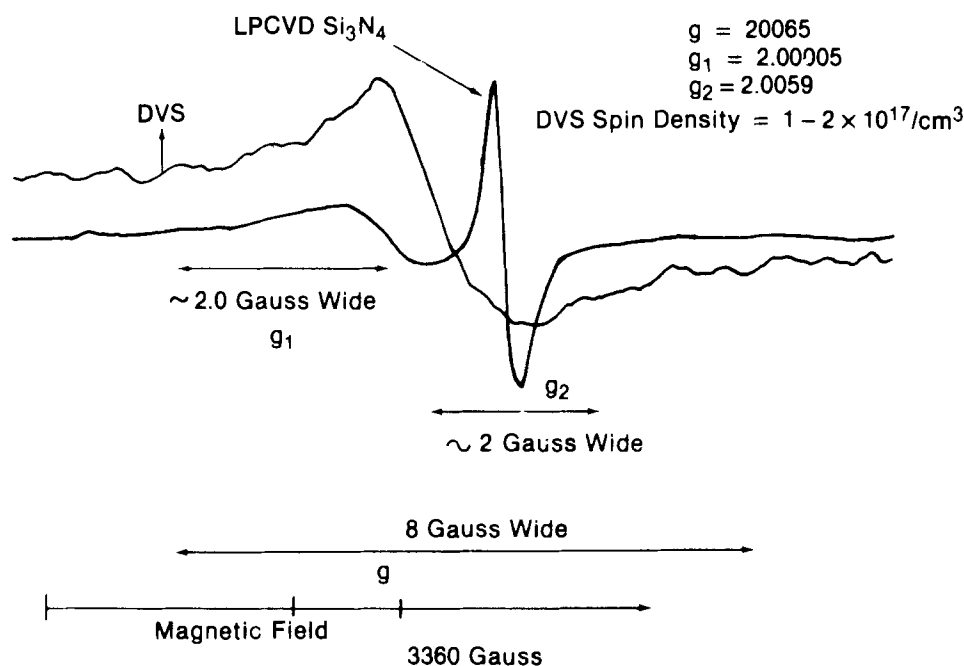
Fig. 10. Carbon 1S spectra for typical MTS polymer



Steps:

1. Pattern Photoresist in Usual Manner
2. Transfer Image Into Polysiloxane by RIE with CF_4 .
3. Transfer Image Into Base Polymer by RIE with O_2 . (Image Resist is Removed At This Time.)
4. For Lift Off Continue Etch of Base Resist in O_2 Plasma to Obtain Under-cut (Dashed Vertical Lines).

Fig. 12. Three-layer resist process using the PECVD organosilicon films.

Fig. 11. ESR of DVS and LPCVD Si_3N_4 films.

observed between the as-deposited and postanneal (30 min, 200°C in a nitrogen atmosphere) films. These results, together with the small variation range of RIE etch rate (41-48 nm/min) suggested that the as-deposited polymers may have a stable cross-linking structure that has not been detected by our analytical method. When all three polymer films were exposed in oxygen plasma, their surface compositions became silicon dioxide-like

and any further etching, after about 5 nm of the surface was oxidized, stopped.

Application to multilayer resist (MLR).—The process steps for MLR are shown in Fig. 12. The actual scanning electron micrographs of submicron patterns are shown in Fig. 13. These structures result after O_2 RIE of the base polymer. The organosilicon film remains, but the top

Table V. Effect of deposition power on surface composition of organosilane plasma-deposited films. Summary of surface composition (a/o)

As Deposited	O	Si	C	F	N
HMDS					
300 W	10.6	30.3	45.9	0.6	12.6
450 W	9.4	29.3	49.7	0.3	11.3
600 W	9.4	29.2	48.3	1.2	11.9
DVS					
300 W	16.8	25.8	57.1	0.3	-
450 W	14.5	26.4	58.8	0.3	-
600 W	14.7	26.3	58.7	0.3	-
MTS					
300 W	40.0	32.2	27.8	0.1	-
450 W	40.5	31.3	28.1	0.2	-
600 W	40.8	30.0	29.0	0.3	-

(-) = Not Detected = 0.1

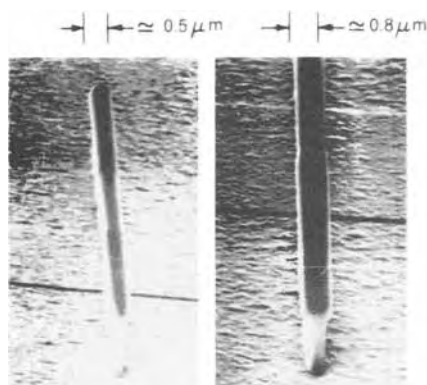
No Change in Surface Compositions with Increased Power Density.

Table VI. Effect of oxygen or nitrogen plasma treatment on surface composition of organosilane plasma-deposited films. Summary of surface composition (a/o)

As Deposited	O	Si	C	F	N
(300 W)					
HMDS	10.6	30.3	45.9	0.6	12.6
DVS	16.8	25.8	57.1	0.3	-
MTS	40.0	32.2	27.8	0.1	-
After N_2 Ash					
HMDS	58.5	33.9	5.1	2.5	0.6
DVS	59.8	33.0	5.2	2.3	0.4
MTS	60.5	33.7	3.6	2.4	0.3
AFTER O_2 Ash					
HMDS	59.5	34.2	4.3	2.0	-
DVS	60.4	34.6	2.8	2.3	-
MTS	59.6	35.0	3.1	2.3	-

(-) = Not Detected = 0.1

The Surface Composition Become Silicon Dioxide Like After Oxygen or Nitrogen Plasma Treatment.



Isolate Resist Lines After RIE Image Transfer

—Dyed Resist Base
 —HMDS O₂ Barrier
 —Substrate: Polysilicon and Polycide Over 0.32 μm High Polysilicon & Oxide Pattern

Fig. 13. Submicron structure of resist over topography.



Vertical Resist Profiles

—After RIE Image Transfer
 1 μm Lines/2 μm Space
 —Undyed Resist Base
 —MTS Barrier Layer
 —Polysilicon Plus Polycide Substrate

Fig. 14. Micron structure of resist over topography.

layer imaging photoresist was removed by the O₂ plasma. The rough surface in Fig. 14 (1 μm line and spaces) is a polysilicon silicide and the 0.8 and 0.5 μm wide lines span 0.35 μm high steps in the oxide pattern under the polysilicon. The uniformly thin imaging resist has resulted in replicating patterns with smaller dimensions than could be obtained with single-layer resist and with the same optics. The stand-alone 0.5 μm line and the vertical profiles in the line/space pattern indicate MLR process extendability to replication of 0.5 μm minimum dimensions.

Conclusion

HMDS, DVS, and MTS polymer films with excellent uniformity have been deposited on p-type silicon substrates using PECVD processing in a parallel-plate reactor. The backbone structure of DVS and HMDS polymers was made up primarily of their monomer units. The polymer film compositions have good depth thickness uniformity. However, the polymer film surfaces and interfaces are slightly contaminated by oxygen. ESCA showed that surface compositional changes are less sensitive to deposition power density as compared to substrate temperature variation. ESR studies revealed that all polymer

films have low spin density, except for as-deposited DVS polymer. Both ESCA and ESR data appear to be consistent with open double bond of the vinyl group's monomer polymerization for the DVS polymer.

Reactive ion etching of these polymer films with CF₄ gas yielded etch rates of 41-48 nm/min for all polymers. When these polymer films are exposed to oxygen (or nitrogen) plasma, their surface composition becomes silicon dioxide-like and ceases etching. Utilizing these properties, the polymer films were implemented as an intermediate oxygen etch resistance layer in trilevel resist lithography to produce submicron image patterns using step and repeat photolithography.

Acknowledgments

The authors acknowledge the assistance of D. Dobuzinsky and D. Sundling for process support, and M. Gibson for FTIR spectra analysis.

Manuscript submitted Nov. 27, 1984; revised manuscript received March 22, 1985.

IBM Corporation assisted in meeting the publication costs of this article.

REFERENCES

1. G. Smolinsky, P. K. Tien, S. Riva-Seuseverion, and R. J. Martin, *Appl. Phys. Lett.*, **24**, 547 (1974).
2. G. Smolinsky, P. K. Tien, S. Riva-Seuseverion, and R. J. Martin, *Appl. Opt.*, **11**, 637 (1972).
3. M. Maisonneuve, Y. Segui, and A. Bui, *Thin Solid Films*, **33**, 35 (1976).
4. K. G. Sachdev and H. S. Sachdev, *ibid.*, **107**, 245 (1983).
5. A. R. Reinbergh, Paper presented at the IUPAC 3rd International Congress on Plasma Chemistry, Limoges, France, July 1977.
6. M. Akik, Y. Segui, and A. Bui, *J. Appl. Phys.*, **51**, 5055 (1980).
7. M. Kryszewski, A. M. Wrobel, and J. Tyczkowski, in "Plasma Polymerization," M. Shen and A. T. Bell, Editors, American Chemical Society Symposium Series, Vol. 108, pp. 219-236, American Chemical Society, Washington, DC (1979).
8. D. Brosset, A. Bui, and Y. Segui, *Appl. Phys. Lett.*, **33**, 87 (1978).
9. Y. Segui and A. Bui, *Thin Solid Films*, **50**, 321 (1978).
10. H. Yasuda, M. O. Bumgarner, H. C. Marsch, and N.

Table VII. Reactive ion etching of organosilicon polymer in parallel-plate plasma reactor

Etching Condition:	
• Gas Flow Rate CF ₄ (sccm)	22
• Pressure (mTorr)	25
• Power Density (watts/cm ²)	0.55 W/cm ²
Etch Rates:	
MTS	41 nm/min.
HMDS	45 nm/min.
DVS	48 nm/min.

- Morosoff, *J. Polym. Sci., Polym. Chem. Ed.*, **14**, 145 (1976).
11. "Plasma Polymerization," M. Shen and A. T. Bell, Editors, American Chemical Society Symposium Series, Vol. 108, American Chemical Society, Washington, DC (1979).
 12. G. Akovali and M. Y. Boluk, *Polym. Eng. Sci.*, **21**, 658 (1981).
 13. W. Kern and R. S. Rosler, *J. Vac. Sci. Technol.*, **14**, 1082 (1977).
 14. I. Haller, *Appl. Phys. Lett.*, **37**, 282 (1980).
 15. I. Haller, *This Journal*, **129**, 180 (1981).
 16. A. K. Hays, *Thin Solid Films*, **84**, 401 (1980).
 17. H. K. Yasuda and T. Hsu, *J. Polym. Sci.*, **15**, 81 (1977).
 18. L. Fried, *IBM J. Res. Dev.*, **26**, 362 (1982).
 19. S. Lyman, *J. Vac. Sci. Technol.*, **19**, 1325 (1981).
 20. J. R. Frankel, *et al.*, U.S. Pat. 4,004,044 (1977).
 21. T. Hirotsu, *J. Appl. Polym. Sci.*, **24**, 1957 (1979).

The Sensitivity of CVD Calculations to Physical Property Values

Helen Rebenne* and Richard Pollard**

Department of Chemical Engineering, University of Houston, Houston, Texas 77004

ABSTRACT

A mathematical model that describes chemical vapor deposition in an impinging jet reactor has been used to assess the sensitivity of theoretical predictions to physical property values for intermediate species. Uncertainties in thermochemical data for a species have greatest impact on predicted deposition rates when the composition level of that species near the surface is comparable to the local compositions of the reactants. Under these circumstances, relatively small changes in the values of thermodynamic quantities used for the species can produce significant differences in deposition rates calculated under equilibrium conditions. Also, with the modified property values, different values of the kinetic parameters may be required to fit available experimental data, and this can lead to different interpretations of the rate-limiting steps in the process. Quantitative information for chemical vapor deposition of boron from boron trichloride and hydrogen is presented.

Chemical vapor deposition (CVD) is a processing technique that is widely used in the manufacture of electronic materials and in the formation of surface coatings for high temperature applications. Several theoretical models of CVD have been proposed (1-12). Each analysis requires physical property values for the species taken into consideration. This information is usually obtained from one or more data compilations (13-28). However, there is often considerable uncertainty in the reported values, particularly for less common species such as intermediates in CVD reactions. In some cases, the tabulated results are estimated using information for similar compounds or are calculated using other physical quantities and statistical thermodynamics, group contribution theory, or empirical rules. Even when experimental data are available, different interpretations or treatments of the measurements can lead to a range of possible values for the property studied. Also, discrepancies between sets of experimental results can exist. The sensitivity of CVD model predictions to these uncertainties in property values has not yet been assessed.

In this paper, a previously developed model (11, 12) which describes CVD in an impinging jet apparatus is used to investigate quantitatively the relationship between theoretical results and values used for thermodynamic and transport properties. The model includes hydrodynamics, multicomponent heat and mass transfer, simultaneous homogeneous and heterogeneous reactions, and variable physical properties. Chemical vapor deposition of boron from BCl_3 and H_2 is treated as an example because sufficient experimental data are available to evaluate the impact of changes in physical property values on both equilibrium calculations and results obtained for actual, nonequilibrium conditions. Specifically, changes in compositions, fluxes, and deposition rates are examined for conditions under which reaction rates are so fast that the system is locally at equilibrium and the deposition rate is limited only by the mass-transfer rate to the surface. Additional sensitivity studies are made for conditions under which rate constants are finite, and new sets of kinetic parameters which give agreement between experimental and predicted deposition rates are determined for different sets of physical property values. Furthermore, the effects of

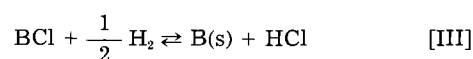
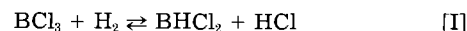
the changes on rate-limiting reactions for the process are evaluated.

The subject of sensitivity analyses for chemically reacting systems has been considered previously (29-36), but has been restricted to sets of homogeneous reactions. The governing equations treated in these studies are highly simplified material balances; this facilitates the use of numerical techniques that are designed for situations where the reaction mechanism or the magnitudes of uncertainties in parameter values are not known. For example, sensitivity coefficients can be determined which indicate the relative effects of arbitrary changes in inlet concentrations and rate constants on species concentrations. This approach is not suitable for CVD of boron because (i) the complexity of the governing equations precludes the evaluation of sensitivity coefficient, (ii) it is not necessary to generate sensitivity coefficients since only specific uncertainties in physical property values need to be considered and the validity of the reaction mechanism has already been established (11), and (iii) sensitivity coefficients do not yield any information on the new sets of kinetic parameters required to match theoretical and experimental results.

Model Description

The details of the mathematical model used to describe CVD in an impinging jet reactor have been presented previously (11) and are not repeated here. However, to explain the sensitivity of model calculations to physical property values, it is necessary to know how the values are incorporated into the model and to understand the significance of the kinetic parameters. These aspects of the model are described below.

For CVD of boron from a mixture of boron trichloride and hydrogen, the elementary reaction steps are taken to be



where reactions [I] and [II] can occur in the gas phase as well as at the deposition surface.

The net rate of each reaction is given by

*Electrochemical Society Student Member.

**Electrochemical Society Active Member.

$$\tau_1 = \left[k_{1f} \prod_{i \atop \nu_{i1} > 0} x_i^{\nu_{i1}} - k_{1b} \prod_{i \atop \nu_{i1} < 0} x_i^{-\nu_{i1}} \right] (\theta_{v1})^{\nu_1} \quad [1]$$

The parameters k_{1f} and k_{1b} are rate constants for forward and backward reactions, respectively. An Arrhenius temperature dependence is assumed for k_{1b}

$$k_{1b} = A_1 e^{-E_{a,1}/T} \quad [2]$$

For elementary reactions, the forward rate constant k_{1f} is related to k_{1b} by

$$K_1 = \frac{k_{1f}}{k_{1b}} \quad [3]$$

where K_1 is the equilibrium constant for reaction 1. The coefficients θ_{v1} in Eq. [1] represent the interactions between gas phase molecules and the surface; they are unity for homogeneous reactions. For surface processes, θ_{v1} may be regarded as the fraction of active surface sites that is available for adsorption of reactants. It can be related to compositions in the gas phase immediately adjacent to the surface by an expression of the form (37)

$$\theta_{v1} = \frac{1}{1 + \sum_i K_{s,i,1} (x_i)^{\nu_{i,1}}} \quad [4]$$

where

$$K_{s,i,1} = A_{s,i,1} e^{-E_{s,i,1}/T_s} \quad [5]$$

Values for the parameters $\nu_{i,1}$, $q_{i,1}$, $A_{s,i,1}$, A_1 , $E_{s,i,1}$, and $E_{a,1}$ in Eq. [1]-[5] can, in principle, be obtained by matching experimental and theoretical results. For a system with five gas phase species, two homogeneous reactions, and three heterogeneous reactions, this treatment would give 58 adjustable kinetic parameters. However, only a few of these parameters have a significant effect on the deposition process. To obtain a physical understanding of CVD systems from model predictions, it is advantageous to use the smallest number of kinetic constants necessary to fit the experimental data.

For CVD of boron from BCl_3 and H_2 , a single expression for $(\theta_{v1})^{\nu_1}$

$$(\theta_{v1})^{\nu_1} = \frac{1}{K_{s,j}(x_j)^{q_j}} \quad ; \quad j = \text{BCl}_3 \quad [6]$$

for all three heterogeneous reactions is sufficient to match theoretical predictions and experimental data (11). As a result, only one activation energy, E_s , is required for adsorption (see Eq. [5]). A physical explanation is that reaction [II] is the dominant heterogeneous reaction; reaction [I] occurs primarily in the gas phase, and reaction [III] is essentially at equilibrium (11). Also, reaction [I] is the only important homogeneous step and, therefore, one activation energy E_a in Eq. [2] is adequate. With the above simplifications, the system can be described by the independent parameters E_a , E_s , q_{BCl_3} , and θ_1 to θ_5 where (11)

$$\theta_1 = \frac{k_{2b}}{k_{1b}} = \frac{A_2}{A_1} \quad [7]$$

$$\theta_2 = \frac{k_{3b}}{k_{1b}} = \frac{A_3}{A_1} \quad [8]$$

$$\theta_3 = \frac{k'_{2b}}{k'_{1b}} = \frac{A'_2}{A'_1} \quad [9]$$

$$\theta_4 = \frac{k_{1b}^2 e^{-(2E_s - E_a)/T_s}}{c_{\infty} \nu_{\infty} k'_{1b} (K_{s,\text{BCl}_3})^2} = \frac{A_1^2}{A'_1 c_{\infty} \nu_{\infty}} \quad [10]$$

$$\theta_5 = \frac{c_{\infty} a e^{-E_a/T_s}}{k'_{2b}} = \frac{c_{\infty} a}{A'_2} \quad [11]$$

The dimensionless ratios θ_1 and θ_2 describe the relative rates of the surface reactions, and θ_3 is a ratio of rate con-

stants for the homogeneous reactions. The dimensionless quantity θ_4 represents the relative rates of homogeneous and heterogeneous reactions and includes the adsorption term from Eq. [6]. The quantity θ_5 can be regarded as the absolute rate of homogeneous BCl production relative to the mass transfer rate in the process because the hydrodynamic parameter a in Eq. [11] is proportional to the mass flow rate of the jet stream that enters the CVD reactor (38). With this formulation of the kinetic parameters, all are independent of inlet gas composition and surface temperature, and all except θ_5 are independent of jet mass flow rate.

The previous analysis (11) provided some insight into the relative importance of the kinetic parameters described above. It was found that any value for θ_3 may be used because, under typical operating conditions, the extent of homogeneous BCl production is unimportant. Also, any value for θ_2 was acceptable provided it was large enough to ensure that reaction [III] remained essentially at equilibrium under all operating conditions. Without this restriction, the correct dependence of deposition rate on the hydrodynamic parameter a could not be obtained. Consequently, it was only necessary to choose specific values for the remaining six kinetic parameters in order to match theoretical and experimental results.

In the model, thermochemical properties are used to calculate the equilibrium constant K_1 defined by Eq. [3]. For ideal gases, K_1 is related to a pressure-independent equilibrium constant K_{p1} by

$$K_{p1} = p^{m_1} K_1 = p^{m_1} \prod_i x_{i,e}^{-\nu_{i1}} \quad [12]$$

Here, the activity of any solid phase is taken to be unity, and m_1 represents the net number of moles produced by reaction 1. Values for K_{p1} are obtained from the relation

$$\left[\frac{\partial \ln K_{p1}}{\partial (1/T)} \right]_p = - \frac{\Delta H_{r1}(T)}{R} \quad [13]$$

The temperature dependence of each heat of reaction $\Delta H_{r1}(T)$ is estimated using specific heats for the reactants and products

$$\tilde{C}_{p1} = \left[\frac{\partial \tilde{H}_1}{\partial T} \right]_p = d_1 + e_1 T + f_1 T^2 \quad [14]$$

Integration of Eq. [13] gives (39)

$$\ln K_{p1} = \alpha_1 + \beta_1/T + \gamma_1 \ln T + \delta_1 T + \epsilon_1 T^2 \quad [15]$$

The standard changes in enthalpy and entropy for each reaction, which are required to evaluate the constants of integration, are obtained from $\Delta H_{f,298}^\circ$ and S_{298}° . Table I lists these properties for the species involved in CVD of boron. Values from a compiled data source (26, 27) are included for all the species. For BCl_3 and BHCl_2 , results based on experimentally determined heats of reaction are also given. These results are calculated using compiled $\Delta H_{f,298}^\circ$ and S_{298}° information (26) for the other reactants and products involved in each experiment. No experimentally determined properties for BCl are available and, hence, only calculated values are given. Since the thermodynamic properties of H_2 and HCl are well known, only values from the compiled source are listed. All the entries in Table I are based on the same reference state.

In this paper, four cases are considered (see Table I). The thermodynamic properties for case A were used previously (11) and, therefore, this example may be regarded as a base case. Case B uses the lowest reported standard heat of formation for BHCl_2 . This value represents a 3% reduction from the base case. Case C uses an independent set of properties for BHCl_2 . The changes correspond to a 5% increase in $\Delta H_{f,298}^\circ$ and a 4% decrease in S_{298}° compared to case A. In case D, $\Delta H_{f,298}^\circ$ for BCl is 33% larger than in case A.

The effect of these variations on the coefficients for the equilibrium constants (see Eq. [15]) is illustrated in Table

Table I. Standard enthalpies of formation and entropies at 298 K. Methods: 1, definition; 2, average of several values determined by calorimetry; 3, calorimetry; 4, average of several values calculated from experimentally determined equilibrium constants; 5, bond energy calculation using spectroscopic data; 6, calculated from molecular constant data. Reactions: [a] $B(\text{amor}) + 3/2 \text{Cl}_2(\text{g}) \rightleftharpoons \text{BCl}_3(\text{g})$; [b] $\text{BCl}_3(\text{l}) + 2403 \text{H}_2\text{O}(\text{l}) \rightleftharpoons \text{H}_3\text{BO}_3(\text{l}) + 3\text{HCl}(\text{l}) + 2400 \text{H}_2\text{O}(\text{l})$; [c] $6\text{BHCl}_2(\text{g}) \rightleftharpoons 4\text{BCl}_3(\text{l}, \text{g}) + \text{B}_2\text{H}_6(\text{g})$; [d] $\text{BCl}_3(\text{g}) + \text{H}_2(\text{g}) \rightleftharpoons \text{BHCl}_2(\text{g}) + \text{HCl}(\text{g})$.

Species	$\Delta H_{f, 298}^\circ$ (kJ/mol)		S_{298}° (J/mol-K)		Ref.	Case(s) (used in Fig. 1-5)
	Value	Method	Value	Method		
H ₂	0.0	1	130.7	5	(27)	A, B, C, D
HCl	-92.4	2	186.9	5	(26)	A, B, C, D
BCl ₃	-403.2	2	290.3	5	(26)	A, B, C, D
	-403.2	3a	—	—	(40)	—
	-402.8	3a	—	—	(41)	—
	-403.2	3b	—	—	(42)	—
BHCl ₂	-248.3	4c, 4d	268.3	5	(26)	A, D
	-248.7	4c	268.3	4c	(43)	—
	-241.0 ^a	4d	268.3	5	(44, 26)	B
	-261.1	4d	258.2	4d	(45)	C
BCl	141.5	5	213.2	5	(26)	A, B, C
	188.7	6	213.2	6	(17)	D

^a This represents a lower bound obtained from a recalculation of $\Delta H_{f, 298}^\circ$ from previously reported experimental data.

II. Only the coefficient α_i is altered by changes in S_{298}° while changes in $\Delta H_{f, 298}^\circ$ affect only β_j . The coefficients γ_i , δ_i , and ϵ_i are determined from d_i , e_i , and f_i , respectively, in Eq. [14]. Values for d_i , e_i , and f_i have been reported previously (11).

Analysis of the momentum, heat, and mass transport phenomena requires a knowledge of viscosity, thermal conductivity, and binary diffusion coefficients as a function of temperature and composition. These properties may be evaluated using the Chapman-Enskog kinetic theory of gases (46). This theory yields expressions for the transport coefficients μ_i , and \mathcal{D}_{ij} in terms of Lennard-Jones force constants and temperature. The thermal conductivity k_i is obtained from the Eucken equation (47). Force constants are generally determined from experimental viscosity or second virial coefficient data. Methods of calculation based on corresponding states theory are also available (48), but these require critical constants and vapor pressure or boiling point data. Force constants for the species used in the analysis of CVD of boron are presented in Table III.

Results and Discussion

The sensitivity of model calculations to standard thermodynamic quantities and Lennard-Jones force constants for the intermediate species BHCl₂ and BCl has been analyzed. The investigation was restricted to these compounds because, in contrast to BCl₃, there are significant uncertainties in the values of their properties.

The effects of altering thermodynamic properties for the intermediates on predicted composition profiles are presented in Fig. 1. These profiles are for the region close to the deposition surface and were obtained for the limiting condition of equilibrium in the gas phase.

Table II. Values of coefficients in Eq. [15]

Case	Coefficient	Reaction		
		[I]	[II]	[III]
A	α	17.51	-0.11	-1.76
	$10^{-3}\beta$ (K)	-8.06	-35.19	27.81
B	α	17.51	-0.11	-1.76
	$10^{-3}\beta$ (K)	-8.94	-34.42	27.81
C	α	16.59	0.81	-1.76
	$10^{-3}\beta$ (K)	-6.53	-36.73	27.81
D	α	17.51	-0.11	-1.76
	$10^{-3}\beta$ (K)	-8.06	-40.86	33.48
A, B, C, D	γ	-2.08	2.61	-1.39
	$10^8 \delta$ (K ⁻¹)	9.37	-26.91	13.83
	$10^7 \epsilon$ (K ⁻²)	-0.70	3.51	-1.31

Table III. Force constants used in evaluation of viscosity, thermal conductivity, and diffusivity. Method 1 calculated by fitting experimental viscosity data at several temperatures.

Method 2 calculated using empirical mixing rules (46), viz.: $\sigma_{ij} = 1/2(\sigma_i + \sigma_j)$ and $(\epsilon/k)_{ij} = \sqrt{(\epsilon/k)_i(\epsilon/k)_j}$; (2a) $i = \text{BCl}$, $j = \text{HCl}$; (2b) $i = \text{B}_2$, $j = \text{Cl}_2$.

Species	$10^8 \sigma$ (cm)	ϵ/k (K)	Ref.	Method
H ₂	2.915	38.0	(46)	1
HCl	3.339	344.7	(16)	1
BCl ₃	5.127	337.7	(16)	1
BHCl ₂	3.329	594.7	—	2a
BCl	3.318	1026.0	(16)	2b

A change in either $\Delta H_{f, 298}^\circ$ or S_{298}° for a species alters the equilibrium constants for the reactions in which that species participates. Hence, equilibrium compositions are modified. For example, when $\Delta H_{f, 298}^\circ$ is made less negative or more positive, the species becomes less stable and its equilibrium mole fraction is reduced (compare cases A and B or A and D in Fig. 1). A change in the properties for one species has a direct effect on the composition of that species. There is also an effect on the compositions of the other species, in accordance with the equilibrium constant relationships in Eq. [12] and the requirement that the mole fractions sum to unity. In case C, $\Delta H_{f, 298}^\circ$ for BHCl₂ differs from the case A value by a larger amount than in case B. On this basis, a larger change in x_{BHCl_2} from the case A result might be anticipated. However, the reduction of S_{298}° in case C lowers the stability of BHCl₂. This offsets the increase in stability caused by the change in $\Delta H_{f, 298}^\circ$ and attenuates the increase in x_{BHCl_2} . Figure 1 also shows that the mole fraction for BCl is always much smaller than the compositions of the other compounds.

In the analysis, the multicomponent diffusion equations link compositions and composition gradients to the species fluxes. For the mechanism given by reactions [I]-[III], the sum of the dimensionless surface fluxes N_m for the boron compounds gives the dimensionless deposition rate

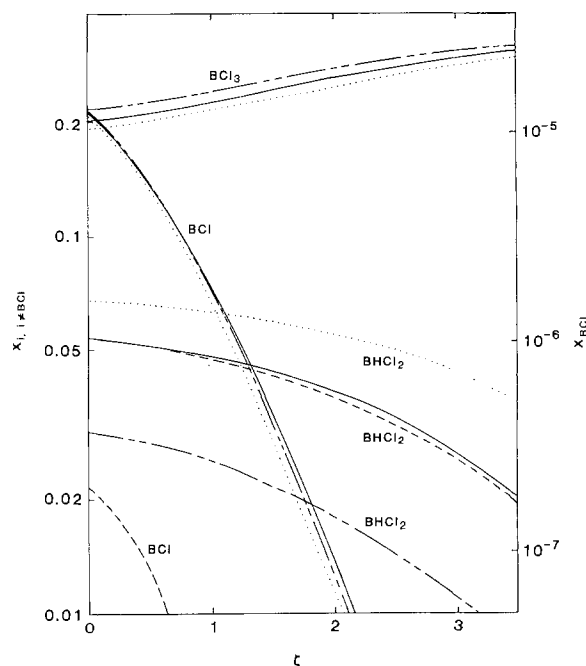


Fig. 1. Gas phase composition profiles in region adjacent to reaction surface. Values are calculated at the thermodynamic mass transfer limit. The outer edge of the diffusion layer occurs at $\zeta \approx 9$. Solid line: case A. Long-short dashed line: case B. Dotted line: case C. Dashed line: case D. Curves A to D are obtained with different values of $\Delta H_{f, 298}^\circ$ and S_{298}° for BHCl₂ and BCl (see Table I). Deposition conditions: $T_s = 1373$ K, $T_x = 298$ K, $p_x = 1.013 \times 10^5$ N/m², $x_{\text{BCl}_3}^0 = 0.4$. Curves A and D coincide for BCl₃.

$$S = -\sum_m N_m \quad [16]$$

Changes in physical property values that alter composition profiles near the surface, and hence surface fluxes, also alter the deposition rate. Figure 2 shows the dependence of dimensionless deposition rate on inlet gas composition for the four cases considered in Fig. 1. Each curve in Fig. 2 is a locus of maximum deposition rates predicted when all kinetic restraints are removed. In the model, this is achieved by increasing the rate constants until the forward and backward rates of each reaction are essentially equal and all compositions are locally at equilibrium. A deposition rate calculated under these conditions is controlled by mass transfer rates between the surface and the inlet and, hence, may be regarded as a thermodynamic mass transfer limit (3).

A substantial change in $\Delta H_{f,298}^0$ for BCl (compare cases A and D) does not influence the predicted deposition rate. This can be attributed directly to the low mole fraction for BCl which ensures that the BCl flux is several orders of magnitude lower than N_{BCl_3} or N_{BHCl_2} . Therefore, a change in x_{BCl} or N_{BCl} has a negligible effect on S . In contrast, cases B and C lead to significantly different predictions for the deposition rate, particularly at high inlet compositions of BCl_3 . At $x_{\text{BCl}_3}^0 = 0.6$, the deposition rate for case B is 19% larger than for case A, while the case C result is 12% smaller than the case A result. Changes in deposition rate are caused by changes in both N_{BCl_3} and N_{BHCl_2} , though N_{BCl_3} is larger in magnitude for the $x_{\text{BCl}_3}^0$ values shown in Fig. 2. At low inlet compositions, changes in N_{BCl_3} and N_{BHCl_2} counteract each other, and this reduces the dependence of deposition rate on physical property values. The results presented in Fig. 1 and 2 are for a surface temperature of 1373 K. If T_s is changed, the deposition rate predicted in the thermodynamic mass transfer limit changes in response to the temperature dependences of the binary diffusion coefficients. However, the differences between cases A, B, C, and D are not altered significantly.

The results presented above demonstrate that, at equilibrium, the sensitivity of deposition rate to the thermodynamic properties of a species is directly associated with

the species composition. A compound with a composition level that is much lower than the other species is expected to have a negligible effect on the deposition rate in the thermodynamic mass transfer limit. This result, shown here for CVD of boron, has also been obtained for CVD of silicon from SiCl_4 in excess hydrogen (49).

The dimensionless deposition rates predicted in Fig. 2 exceed experimental results (50-52) because they do not consider the finite rates of the chemical reactions. In a previous study (11), rate-limiting reactions were identified and a set of kinetic parameters that gave a match between theory and experiment was obtained. Curve A in Fig. 3 shows the agreement between predicted and actual deposition rates obtained with the base-case thermodynamic properties. When the kinetic parameters for case A are used and thermodynamic properties are varied, predicted deposition rates no longer agree with experimental results. Curves B, C, and D in Fig. 3 indicate that the effects of the property changes are not the same as those obtained in the thermodynamic mass transfer limit. This is because the compositions are determined by material balance relationships that include local production terms from the chemical reactions and they are not related directly by the equilibrium constants. One consequence of the more complex interactions obtained with finite kinetic parameters is that a given change in properties can reduce the predicted deposition rate under some circumstances but can increase it under others (see curves A, B, and C).

In contrast to results obtained in the thermodynamic mass transfer limit, the heat of formation of BCl has a marked effect on the deposition rate calculated with finite kinetic parameters (see curve D). This can be attributed to an order of magnitude decrease in N_{BHCl_2} which, under the conditions in Fig. 3, is the dominant surface flux in Eq. [16]. This change can be related to the reduction in stability of BCl, which makes decomposition of BHCl_2 to BCl less favorable and changes the surface composition gradient of BHCl_2 .

Figure 4 shows the dependence of dimensionless deposition rate on surface temperature at two different mass flow rates. Changes in the thermodynamic properties al-

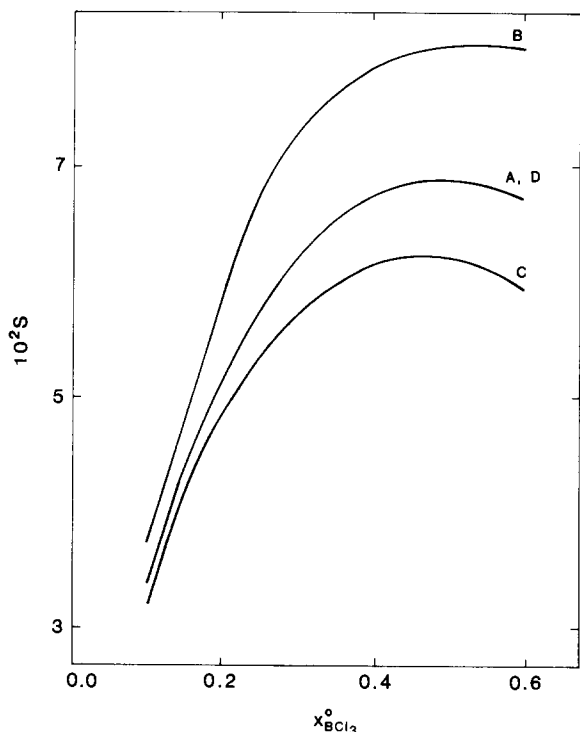


Fig. 2. Influence of inlet gas composition on the dimensionless rate of boron deposition calculated at the thermodynamic mass transfer limit. $S = \text{actual deposition rate}/c_{\infty} \sqrt{\nu_{\infty} a}$. Physical property values and deposition conditions are as in Fig. 1.

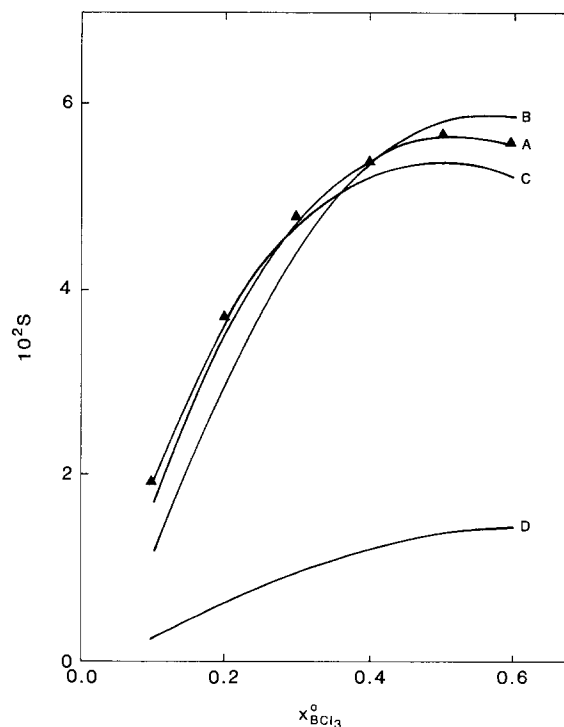


Fig. 3. Influence of inlet gas composition on the dimensionless rate of boron deposition. Experimental data (51): triangles $\sim a = 102 \text{ s}^{-1}$ at $x_{\text{BCl}_3}^0 = 0.4$, $L/d = 0.375$. Curves are theoretical predictions with the case A kinetic parameters (see Table IV). Physical property values and deposition conditions are as in Fig. 1.

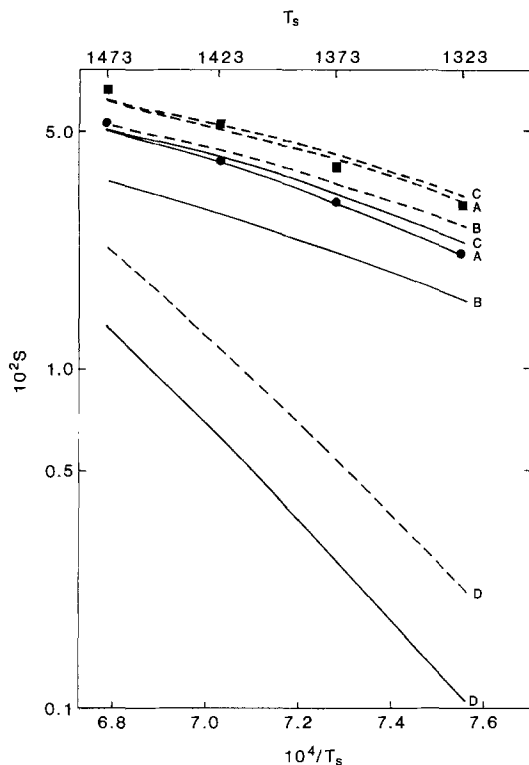


Fig. 4. Influence of substrate temperature on the dimensionless rate of boron deposition. Experimental data (51): $x_{\text{BCl}_3}^0 = 0.4$, squares $\sim a = 310 \text{ s}^{-1}$, dots $\sim a = 626 \text{ s}^{-1}$, $L/d = 0.375$. Curves are theoretical predictions with kinetic parameters as in Fig. 3, except for θ_5 . Dotted line: $a = 310 \text{ s}^{-1}$, therefore $\theta_5 = 3.3 \times 10^{-7}$. Solid line: $a = 626 \text{ s}^{-1}$, therefore $\theta_5 = 6.6 \times 10^{-7}$. Deposition conditions: $T_x = 298 \text{ K}$, $p_x = 1.013 \times 10^5 \text{ N/m}^2$.

ter the theoretical predictions in each case. The results presented in Fig. 3 and 4 indicate that when different values for $\Delta H_{f,298}^0$ or S_{298}^0 are used, it becomes necessary to obtain a new set of kinetic parameters to fit the experimental data.

The sensitivity of kinetic parameters to thermochemical properties is illustrated in Table IV. The set of parameters for each case was obtained by matching the experimentally observed dependence of deposition rate on inlet gas composition, jet mass flow rate, and surface temperature. The original set, used in case A, was changed as little as possible to refit the data in cases B and D. It should be noted that, with the exception of θ_5 and θ_3 (see above), small variations of the parameter values listed for each case would lead to a noticeably poorer fit of the data.

A comparison of cases A and D shows the effect of a 33% increase in $\Delta H_{f,298}^0$ for BCl. A small adjustment in E_s is required to give the correct dependence of deposition rate on surface temperature. This adjustment is needed to offset the changes in the temperature dependences of the equilibrium constants (see β_i values in Table II), since effective activation energies for heterogeneous forward rate constants are $E_s - E_a + \beta_i$. However, a change in the value of $E_s - E_a + \beta_i$ does not produce an identical change in the

Table IV. Values of kinetic parameters used to match experimental data. Superscripts: $a \sim$ values are for $x_{\text{BCl}_3}^0 = 0.4$; $b \sim$ value is for $a = 102 \text{ s}^{-1}$; $c \sim$ based on $n = 1$.

Case	A	D	B
θ_1	2.3×10^5	1.2×10^7	7.7×10^3
θ_2	8.0×10^1	8.0×10^1	8.0×10^1
θ_3	8.0×10^4	8.0×10^4	8.0×10^4
θ_4^a	5.9×10^{-11}	4.7×10^{-10}	1.5×10^{-13}
$\theta_5^{a,b}$	1.1×10^{-7}	1.1×10^{-7}	3.2×10^{-6}
E_s	1.5×10^4	1.4×10^4	2.0×10^4
E_a	3.0×10^3	3.0×10^3	3.0×10^3
$q_{\text{BCl}_3}^c$	0.50	0.50	0.75

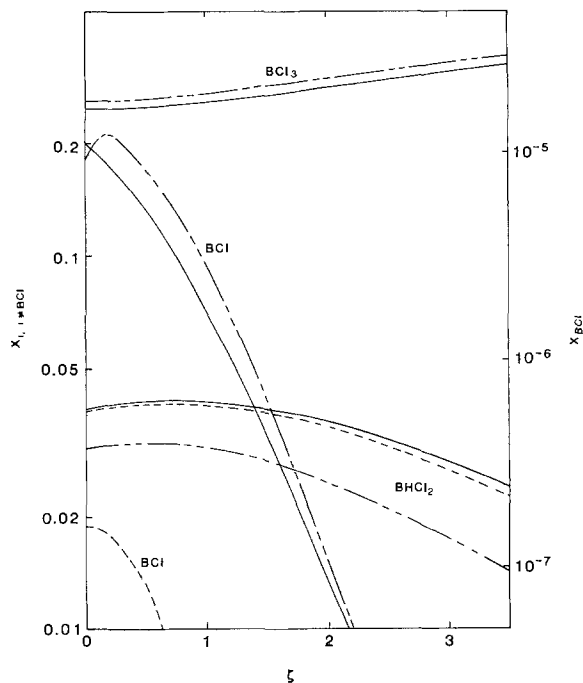


Fig. 5. Gas phase composition profiles in region adjacent to reaction surface. Solid line: case A. Long-short dashed line: case B. Dashed line: case D. Curves A, B, and D are obtained with the kinetic parameters listed in Table V. Deposition conditions: $T_s = 1373 \text{ K}$, $T_x = 298 \text{ K}$, $p_x = 1.013 \times 10^5 \text{ N/m}^2$, $x_{\text{BCl}_3}^0 = 0.4$, $a = 102 \text{ s}^{-1}$. Curves A and D coincide for BCl_3 .

magnitude of the slope in Fig. 4. This is because variations in local compositions with T_s also influence the slope and the compositions are dependent on thermochemical property values (see Fig. 5).

The parameter θ_4 in Table IV influences the relative importance of the parallel heterogeneous and homogeneous pathways for reaction [I]. This quantity must be altered to counteract the change in E_s . The change required for θ_4 cannot be determined exactly from Eq. [10] due to the effects of local compositions on the slope in Fig. 4.

The most noticeable difference between cases A and D is the value of θ_1 . This parameter relates the rates of heterogeneous reactions [I] and [II], in accordance with Eq. [7]. Combination of Eq. [1] and [7] gives

$$\frac{r_{\text{II}}}{r_{\text{I}}} = \theta_1 \frac{x_{\text{BCl}}}{x_{\text{BHCl}_2}} \left(\frac{1 - r_{\text{IB}}/r_{\text{IF}}}{1 - r_{\text{IB}}/r_{\text{IF}}} \right) \frac{r_{\text{IB}}/r_{\text{IF}}}{r_{\text{IB}}/r_{\text{IF}}} \quad [17]$$

where r_{IF} and r_{IB} are the forward and backward rates for surface reaction I. Values for $r_{\text{IB}}/r_{\text{IF}}$ obtained with refitted kinetic parameters are presented in Table V. A small value of $r_{\text{IB}}/r_{\text{IF}}$ indicates that the reaction is far from equilibrium. Table V shows that the magnitudes of $r_{\text{IB}}/r_{\text{IF}}$ are almost identical in cases A and D. In contrast, Fig. 5 shows that the surface compositions of BCl in the two cases differ by nearly two orders of magnitude. The change in the value for θ_1 more than compensates for this difference and gives similar values for the ratios $(r_{\text{II}}/r_{\text{I}})_A$ and $(r_{\text{II}}/r_{\text{I}})_D$.

Overall, the large change in $\Delta H_{f,298}^0$ for BCl results in relatively small changes in the rates of the reactions. There is a slight shift in the importance of heterogeneous reaction [I] (compare values for r_{I} in Table V). Nevertheless, the departures from equilibrium, as indicated by the ratios $r_{\text{IB}}/r_{\text{IF}}$ and $(r'_{\text{int},i})_{\text{B}}/(r'_{\text{int},i})_{\text{I}}$ for all the reactions are essentially unchanged. The homogeneous reaction rates given in Table V are integrals over the diffusion layer. Therefore, values for the homogeneous and heterogeneous reaction rates (r_{I} and $r'_{\text{int},i}$) may be compared directly. However, it should be noted that not all the BHCl_2 produced homogeneously is able to reach the deposition surface. Table V shows quantitatively that, in both cases A and D, reaction [I] occurs predominantly in the gas phase, whereas reaction [II] takes place at the solid surface. The

Table V. Theoretical reaction rates and departures from equilibrium calculated using $T_s = 1373$ K, $T_x = 298$ K, $p_x = 1.013 \times 10^5$ N/m², $a = 102$ s⁻¹, $x_{\text{BCl}_3}^0 = 0.4$. Kinetic parameters for each case are listed in Table IV. Note that $S = r_{\text{III}}/c_x \sqrt{\nu_x a}$.

Case	Reaction	$\frac{r_1}{c_x \sqrt{\nu_x a}}$	$\frac{r_{\text{Ib}}}{r_{\text{I}}}$	$\frac{r'_{\text{int.1}}}{c_x \sqrt{\nu_x a}}$	$\frac{(r'_{\text{int.1b}})}{(r'_{\text{int.1}})}$
A	[I]	0.78×10^{-2}	0.45	0.88×10^{-1}	0.64
	[II]	0.54×10^{-1}	0.87	-0.74×10^{-3}	1.00
	[III]	0.54×10^{-1}	1.00	0.0	—
D	[I]	0.11×10^{-1}	0.45	0.85×10^{-1}	0.64
	[II]	0.55×10^{-1}	0.89	-0.18×10^{-5}	1.00
	[III]	0.55×10^{-1}	1.00	0.0	—
B	[I]	0.16×10^{-1}	0.61	0.61×10^{-1}	0.86
	[II]	0.54×10^{-1}	0.53	0.17×10^{-3}	1.00
	[III]	0.54×10^{-1}	1.00	0.0	—

values for $r'_{\text{int.1}}$ indicate that a small amount of conversion of BCl to BHCl₂ can take place in the gas phase. This is due to the large decrease in the magnitude of K_{II} that occurs at small distances from the surface. Finally, it is emphasized that the small difference in deposition rate in the two cases is insignificant in terms of the overall fit of the data.

A comparison of cases A and B (see Tables IV and V) indicates the influence of a 3% decrease in $\Delta H_{f,298}^0$ for BHCl₂ on the model predictions. Although this percentage change is significantly smaller than the one for the A/D comparison, it has a larger effect on the reactions. As in case D, the values of θ_1 , θ_4 , and E_s had to be altered to refit the data. In addition, changes were required for θ_5 and q_{BCl_3} . The empirical parameter q_{BCl_3} determines the relationship between deposition rate and inlet gas composition, and its value is chosen to give the correct shape of the curves in Fig. 3. If the change in q_{BCl_3} in case B were interpreted physically, it might imply that a different mechanism is involved in adsorption and desorption of species at the surface. The parameter θ_5 links the absolute magnitudes of the chemical reactions to the gas phase hydrodynamics. The change in θ_5 needed to match the data cannot be related to a single factor: variations in local compositions, equilibrium constants, and the other kinetic parameters are involved.

In order to interpret the results presented in Table V from the standpoint of rate-determining steps, it is necessary to consider the reaction pathways in the system. The homogeneous and heterogeneous pathways for reaction [I] are in parallel. Consequently, the magnitudes of r_1 and $r'_{\text{int.1}}$ rather than the extents to which the reactions depart from equilibrium, should be compared to assess the relative importance of the parallel routes. Reactions [II] and [III] may be regarded as consecutive steps, since reaction [II] does not occur to an appreciable extent in the gas phase and reaction [III] is restricted to the surface. Hence, the departures from equilibrium (i.e., $r_{\text{Ib}}/r_{\text{I}}$) for these two heterogeneous reactions can be used to indicate which step is more rate determining. With the parallel pathways for reaction [I], it is difficult to specify the relative importance of reactions [I] and [II]. One approach that could be used to provide an indication of the rate-limiting step is to neglect heterogeneous reaction [I] and to compare departures from equilibrium for the two most important reactions, homogeneous reaction [I] and heterogeneous reaction [II]. On this basis, homogeneous reaction [I] would be the rate-determining step in case A, but heterogeneous reaction [II] would be the limiting step in case B. An additional change in case B is the shift in the relative importance of the pathways for reaction [I]: the heterogeneous rate r_1 is increased and gas phase conversion to BHCl₂ is reduced. This can be attributed, at least in part, to the stronger temperature dependence of the equilibrium constant K_1 (see Table II).

It is emphasized that the results in Table V are for one set of process conditions. If the mass flow rate is increased or the surface temperature is decreased, the reactions are shifted further from equilibrium: i.e., the values

of $r_{\text{Ib}}/r_{\text{I}}$ and $(r'_{\text{int.1b}})/(r'_{\text{int.1}})$ are reduced. These changes tend to make the deposition process more kinetically controlled. However, for the range of operating conditions considered, changes caused by varying thermochemical properties are essentially the same as those described above.

The sensitivity of model predictions to independent variations in S_{298}^0 was also studied. When the value of S_{298}^0 for BHCl₂ was arbitrarily reduced by 3%, results similar to curves B in Fig. 2-4 were obtained. These results emphasize that the system behavior is influenced by changes in equilibrium constants. The origin of the changes, i.e., uncertainties in either $\Delta H_{f,298}^0$ or S_{298}^0 , is not in itself important.

The effects of changes in transport properties on model predictions were tested by varying the Lennard-Jones force constants for BHCl₂ and BCl. Each force constant was independently varied by $\pm 10\%$. At $T_s = 1473$ K, a 10% increase in σ_{BHCl_2} reduced the viscosity and thermal conductivity for BHCl₂ by 17% and lowered the binary diffusion coefficients by 7-10%. However, the corresponding changes in deposition rate are small. For example, at $a = 102$ s⁻¹, and with the case A thermodynamic properties and kinetic parameters, the increase in σ_{BHCl_2} does not alter S at $x_{\text{BCl}_3}^0 = 0.1$ and only increases it by 1.4% at $x_{\text{BCl}_3}^0 = 0.6$. Similar results are obtained for changes in ϵ_{BHCl_2} . Also, the deposition rate showed no sensitivity to σ and ϵ for BCl over the range of inlet compositions used in this work.

Conclusions

A model that describes the coupled multicomponent transport phenomena and reaction kinetics for CVD in an impinging jet reactor has been used to assess the sensitivity of theoretical predictions to uncertainties in physical property values. Results for intermediate species involved in CVD of boron from BCl₃ and H₂ illustrate the trends in behavior that can be expected in general.

An intermediate species with a composition level near the surface that is much lower than the local compositions of the reactants will generally have a small surface flux and, hence, will make a negligible contribution to the deposition rate. Consequently, uncertainties in property values for a species of this kind will not have a significant effect on the deposition rate in the thermodynamic mass transfer limit and can only change the interpretation of rate-limiting steps if the reactions in which the species participates are far removed from equilibrium. For an intermediate species with a gas phase mole fraction comparable to the reactant compositions, small changes in physical properties such as $\Delta H_{f,298}^0$ and S_{298}^0 can lead to noticeable changes in the deposition rates calculated under equilibrium conditions. These changes are more significant when concentrated inlet gas mixtures are used. Also, with modified property values, different values for the kinetic parameters may be required to fit available experimental data and this can lead to different interpretations of the rate-limiting steps in the process. Changes in Lennard-Jones force constants give relatively small variations in the transport properties and these generally have a negligible effect on predicted deposition rates.

Acknowledgment

This work was supported by the National Science Foundation (Grant no. CPE-8203554).

Manuscript submitted Nov. 5, 1984; revised manuscript received April 7, 1985.

LIST OF SYMBOLS

a	hydrodynamic parameter, proportional to mass flow rate of jet stream (s ⁻¹)
A_1	pre-exponential factor for backward rate constant for heterogeneous reaction 1 (mol/cm ² -s)
A'_1	pre-exponential factor for backward rate constant for homogeneous reaction 1 (mol/cm ² -s)
$A_{s,1}$	pre-exponential factor for adsorption/desorption equilibrium constant for species i in reaction 1 (see Eq. [5])

C	total concentration (mol/cm ³)
C_{pi}	molar heat capacity of species i (J/mol-K)
d	nozzle diameter (cm)
d_i	coefficient in Eq. [14] (J/mol-K)
\mathcal{D}_{ij}	diffusion coefficient for binary interactions (cm ² /s)
e_i	coefficient in Eq. [14] (J/mol-K ²)
$E_{a,i}$	activation energy for backward reaction i (see Eq. [2]) (K)
E_a	kinetic parameter representing activation energy for rate-limiting step (K)
$E_{s,i,l}$	activation energy for adsorption/desorption of species i in reaction l (see Eq. [5]) (K)
E_s	kinetic parameter representing activation energy for adsorption/desorption of BCl ₃ (K)
f_i	coefficient in Eq. [14] (J/mol-K ³)
H_i	enthalpy of species i (J/mol)
ΔH_{r1}	enthalpy change of reaction l (J/mol)
$\Delta H_{f,298}^{\circ}$	standard enthalpy of formation at 298 K (J/mol)
k	Boltzmann constant (1.3806×10^{-23} J/K)
k_i	thermal conductivity of species i (W/m-K)
k_l	rate constant for heterogeneous reaction l (mol/cm ² -s)
k'_l	rate constant for homogeneous reaction l (mol/cm ³ -s)
K_l	equilibrium constant for reaction l
K_{pi}	equilibrium constant defined by Eq. [12]
$K_{s,i,l}$	equilibrium constant for adsorption/desorption of species i in reaction l
$K_{s,l}$	equilibrium constant for adsorption/desorption of BCl ₃ (see Eq. [6])
L	distance between end of nozzle and substrate surface (cm)
m_l	net number of molecules produced by reaction l
n_l	exponent in Eq. [1]
N_m	= flux/ $c_s \sqrt{\nu_x a}$, dimensionless surface flux for species m
p	gas pressure (N/m ²)
$q_{i,l}$	exponent in Eq. [4]
r_l	= $r'_{lf} - r'_{lb}$, net rate of heterogeneous reaction l (mol/cm ² -s)
r'_l	= $r'_{lf} - r'_{lb}$, net rate of homogeneous reaction l (mol/cm ³ -s)
$r'_{int,l}$	net rate of homogeneous reaction l , integrated across diffusion layer (mol/cm ² -s)
R	universal gas constant (8.3143 J/mol-K)
S	= deposition rate/ $c_s \sqrt{\nu_x a}$, dimensionless boron deposition rate
S_{298}°	standard entropy at 298 K (J/mol-K)
T	temperature (K)
$x_{BCl_3}^0$	inlet mole fraction of BCl ₃
x_i	mole fraction of species i
z	axial distance from deposition surface (cm)

Greek symbols

$\alpha, \beta, \gamma, \delta, \epsilon$	coefficients in Eq. [15]
ϵ	energy of interaction for Lennard-Jones potential (J)
ζ	= $z\sqrt{a/\nu_x}$, dimensionless axial distance coordinate
θ_{v1}	parameter defined by Eq. [4]
θ_k	dimensionless kinetic parameter ($k = 1-5$) defined in Eq. [7]-[11]
μ_i	viscosity of species i (g/cm-s)
ν_{ii}	stoichiometric coefficient for species i in reaction l (positive for reactants)
ν_x	bulk kinematic viscosity (cm ² /s)
σ	collision diameter for Lennard-Jones potential (cm)

Subscripts

A	case A
b	backward reaction
D	case D
e	at equilibrium
f	forward reaction
i	species i
l	reaction l
m	boron compounds
s	at surface
∞	in bulk

- R. Pollard and J. Newman, *This Journal*, **127**, 744 (1980).
- J. Subrahmanyam, A. K. Lahiri, and K. P. Abraham, *ibid.*, **127**, 1394 (1980).
- M. L. Hitchman and B. Curtiss, *J. Cryst. Growth*, **60**, 43 (1982).
- J. Korec and M. Heyen, *ibid.*, **60**, 286 (1982).
- J. Jüza and J. Čermak, *This Journal*, **129**, 1627 (1982).
- K. F. Jensen and D. B. Graves, *ibid.*, **130**, 1950 (1983).
- J. Korec, *J. Cryst. Growth*, **61**, 32 (1983).
- M. E. Coltrin, R. J. Kee, and J. A. Miller, *This Journal*, **131**, 425 (1984).
- M. Michaelidis and R. Pollard, *ibid.*, **131**, 860 (1984).
- J. Jenkinson and R. Pollard, *ibid.*, **131**, 2911 (1984).
- K. K. Kelley, *U.S. Bur. Mines Bull.*, 584 (1960).
- K. K. Kelley and E. G. King, *ibid.*, 592 (1961).
- K. K. Kelley, *ibid.*, 601 (1962).
- R. A. Svehla, NASA Technical Report R-132, Lewis Research Center, Cleveland, OH (1962).
- B. J. McBride, S. Heimel, J. G. Ehlers, and S. Gordon, NASA Special Project SP-3001, Lewis Research Center, Cleveland, OH (1963).
- C. E. Wicks and F. F. Black, *U.S. Bur. Mines Bull.*, 605, (1963).
- D. D. Wagman, W. H. Evans, I. Halow, V. B. Parker, S. M. Bailey, and R. H. Schumm, *Natl. Bur. Stand. (U.S.), Tech. Note*, 270-1 (1965).
- D. D. Wagman, W. H. Evans, I. Halow, V. B. Parker, S. M. Bailey, and R. H. Schumm, *ibid.*, 270-2 (1966).
- B. J. Zwolinski, "Selected Values of Properties of Chemical Compounds," Texas A&M Research Foundation, College Station, TX (1966).
- O. Kubaschewski, E. L. Evans, and C. B. Alcock, "Metallurgical Thermochemistry," Pergamon Press, New York (1967).
- D. D. Wagman, W. H. Evans, I. Halow, V. B. Parker, S. M. Bailey, and R. H. Schumm, *Natl. Bur. Stand. (U.S.), Tech. Note*, 270-3 (1968).
- "Thermophysical Properties of Gases and Liquids," V. A. Rabinovich, Editor, Government Document no. TT-69-55091 (1970).
- T. B. Reed, "Free Energy of Formation of Binary Compounds," MIT Press, Cambridge, MA (1971).
- "JANAF Thermochemical Tables," 2nd ed., D. R. Stull and H. Prophet, Editors, NSRDS-NBS37 (1971).
- M. W. Chase, Jr., J. L. Curnutt, J. R. Downey, Jr., R. A. McDonald, A. N. Syverud, and E. A. Valenzuela, *J. Phys. Chem. Ref. Data.*, **11**, 695 (1982).
- I. Barin, O. Knacke, and O. Kubaschewski, "Thermochemical Properties of Inorganic Substances," Springer-Verlag, Berlin (1977).
- J. H. Schaibly and K. E. Shuler, *J. Chem. Phys.*, **59**, 3879 (1973).
- E. P. Dougherty, J.-T. Hwang, and H. Rabitz, *ibid.*, **71**, 1794 (1979).
- A. H. Falls, G. J. McRae, and J. H. Seinfeld, *Int. J. Chem. Kinet.*, **11**, 1137 (1979).
- M. Koda, G. J. McRae, and J. H. Seinfeld, *ibid.*, **11**, 427 (1979).
- D. Edelson and V. M. Thomas, *J. Phys. Chem.*, **85**, 1555 (1981).
- M. Koda, A. H. Dogru, and J. H. Seinfeld, *J. Comput. Phys.*, **30**, 259 (1979).
- J. W. Tilden and J. H. Seinfeld, *Atmos. Environ.*, **16**, 1357 (1982).
- D. Edelson, *J. Phys. Chem.*, **87**, 1204 (1983).
- C. G. Hill, Jr., "Chemical Engineering Kinetics and Reactor Design," John Wiley and Sons, Inc., New York (1977).
- D.-T. Chin and C.-H. Tsang, *This Journal*, **125**, 1461 (1978).
- K. G. Denbigh, "The Principles of Chemical Equilibrium," Cambridge University Press, London (1966).
- W. H. Johnson, R. G. Miller, and E. J. Prosen, *J. Res. Natl. Bur. Std.*, **62**, 213 (1959).
- G. L. Gal'chenko, B. I. Timofeev, and S. M. Skuratov, *Russ. J. Inorg. Chem.*, **5**, 1279 (1960).
- S. R. Gunn and L. G. Green, *J. Phys. Chem.*, **65**, 779 (1961).
- L. Lynds and C. D. Bass, *Inorg. Chem.*, **3**, 1147 (1964).
- J. H. Murib, D. Horvitz, and C. A. Bonecutter, *Ind. Eng. Chem., Prod. Res. Dev.*, **4**, 273 (1965).
- B. Attwood and R. A. J. Shelton, *J. Less Common Met.*, **20**, 131 (1970).
- J. O. Hirschfelder, C. F. Curtiss, and R. B. Bird, "Molecular Theory of Gases and Liquids," John Wiley and Sons, New York (1954).
- R. B. Bird, W. E. Stewart, and E. N. Lightfoot, "Transport Phenomena," John Wiley and Sons, New York (1960).

REFERENCES

- C. W. Manke and L. F. Donaghey, *This Journal*, **124**, 561 (1977).
- G. Wahl, *Thin Solid Films*, **40**, 13 (1977).

48. L. S. Tee, S. Gotoh, and W. E. Stewart, *Ind. Eng. Chem. Fundam.*, **5**, 356 (1966).
 49. R. Abber, M.S. Thesis, University of Houston, Houston, TX (1984).
 50. G. E. Vuillard, A. Luque, and L. Vandenbulcke, *J. Less-Common Met.*, **47**, 235 (1976).
 51. L. Vandenbulcke and G. Vuillard, *This Journal*, **123**, 278 (1976).
 52. L. Vandenbulcke and G. Vuillard, *ibid.*, **124**, 1931 (1977).

Photoexcitation Effects on the Growth Rate in the Vapor Phase Epitaxial Growth of GaAs

J. Nishizawa* and Y. Kokubun

Research Development Corporation of Japan, Exploratory Research for Advanced Technology, Nishizawa Perfect Crystal Project, Semiconductor Research Institute, Kawauchi, Sendai 980, Japan

H. Shimawaki

Research Institute of Electrical Communication, Tohoku University, Katahira, Sendai 980, Japan

M. Koike

Semiconductor Research Institute, Kawauchi, Sendai 980, Japan

ABSTRACT

The photoexcitation effects on the growth rate have been demonstrated in the vapor phase epitaxial growth of GaAs. The growth rate is enhanced by irradiating the substrate zone with a 249 nm (KrF) excimer laser over the whole of temperature range 480° ~ 700°C and increases in proportion to the incident power. However, the growth rate is reduced by irradiating the source zone with a 249 or 222 nm (KrCl) excimer laser at low temperatures below 650°C. These effects have been concluded to be caused not by thermal-induced reactions but, rather, by photoinduced reactions because of sharp wavelength dependence. Infrared absorption analyses have shown that the reduction of AsCl₃ by H₂ is promoted by irradiation with a 249 or 222 nm laser. This photodissociation of AsCl₃ causes the growth rate reduction in the case of source zone irradiation.

The development of low temperature processing techniques is increasingly required in the manufacture of semiconductor devices. This requirement comes about because defect generation and propagation, thermal warpage, and impurity redistribution occur at high temperatures. Photoexcited technique has been receiving increasing attention as low temperature processing. One of the authors (J. N.) first proposed the photoexcited process in 1961 (1), and applied this technique to the vapor phase epitaxial growth of Si (2). High quality Si epitaxial layers were grown at low temperatures by irradiating the substrates with UV light.

In photoexcited processes, reactions are less complex and fewer defects are generated due to excess energies, unlike plasma excitation, because a sort of specific radical or ion can be selectively formed by selecting the photon energy. Moreover, photoexcited processes have the possibility that each elementary process can be individually controlled among the competitive processes by using monochromatic light whose wavelength is suited to activate the process. Photoexcited processes can be carried out at low temperatures and are expected to be easily monitored and controlled. Therefore, photoexcited processes are more promising techniques for achieving precise control. Another advantage of photoexcited processes is the ability to localize spatially the reaction region by using a tightly focused laser beam. This paper describes the initial results of an application of photoexcited technique to the vapor phase epitaxial growth of GaAs.

Experimental

The growth of GaAs epitaxial layers was carried out by using a conventional AsCl₃-Ga-H₂ system. A schematic diagram of the growth apparatus is shown in Fig. 1. The apparatus consists of a controlled two-zone furnace, a quartz reactor tube, a Ga source boat, a substrate holder, and an

AsCl₃ bubbler. The furnace has two window ports to introduce light beam into the reactor tube, and the ports are closed with evacuated quartz plugs to keep the thermal condition. The reactor tube has an inside diameter of 34 mm. The hydrogen carrier gas was passed through an absorption-type purifier. The temperature of the AsCl₃ bubbler was kept at 0°C, and the flow rate of hydrogen through the AsCl₃ bubbler was kept at 100 cm³/min by a mass flow controller. The substrates were Cr-O doped semi-insulating GaAs crystals, oriented 4° off (100) toward (110). The substrates were cut in 1 × 1 cm² rectangles and were first etched by 4H₂SO₄:1H₂O₂:1H₂O solution followed by dipping into concentrated HF solution, then slight etching by 10H₂SO₄:1H₂O₂:1H₂O, and finally another concentrated HF dipping prior to epitaxial growth. An excimer laser was mainly used as a light source for irradi-

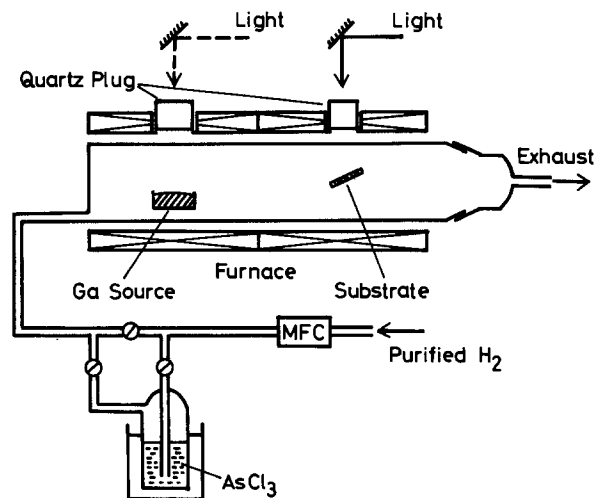


Fig. 1. Schematic diagram of the growth apparatus

* Electrochemical Society Active Member.

ation during crystal growth. The excimer laser which emits $10 \times 20 \text{ mm}^2$ sheet beam was operated with KrCl (222 nm), KrF (249 nm), XeCl (308 nm), or XeF (350 nm) line at repetition rate of 5 ~ 70 pps. The light was introduced into the substrate zone or the Ga source zone without any focusing. The growth rate was derived from the growth time, and the thickness of the grown layer was measured by the cleavage and stain technique on the assumption that it is a linear function of time.

The gas analysis by infrared absorption spectroscopy was carried out in order to clarify the photoexcitation effect on the reduction of AsCl_3 by H_2 . There are two methods for infrared spectroscopy measurements (3); they are sampling and direct (*in situ*) observation methods. Although the sampling method was used in the present experiment, the direct observation method could have also been used. The measurement system is nearly similar to that used in a previous paper (4). A capillary is introduced into the reactor tube to lead reactants into a gas cell for analyzing by an infrared spectrometer. Hydrogen gas was introduced into the reactor tube after passing through the AsCl_3 bubbler and then irradiated with an excimer laser.

Experimental Results

Substrate zone irradiation.—Figure 2 shows the growth rate as a function of incident excimer laser wavelength for an incident average power of $\sim 1.7 \text{ W}$ in the case of substrate zone irradiation. The source temperature and substrate temperature were 720° and 600°C , respectively. The growth rate was increased by the 249 nm laser irradiation but scarcely changed by other wavelength irradiation. Moreover, no enhancement of growth rate was obtained by irradiation with a visible argon-ion laser.

The growth rates are plotted in Fig. 3 as a function of the reciprocal substrate temperature. In this experiment, the temperature difference between the source and the substrate zone was kept to 50°C . In the absence of irradiation shown by curve a, the growth rate monotonically decreased with lowering the substrate temperature to 600°C and then slightly increased, followed by decreasing below 550°C with further temperature decrease. No crystal growth was obtained below 500°C . In the case of substrate zone irradiation with the 249 nm laser shown by curve b, the growth rate slightly decreased with lowering the substrate temperature to 500°C and then rapidly decreased to a small value at 480°C . The growth rate was found to be enhanced over the whole of temperature range of $480^\circ \sim 700^\circ\text{C}$ by the substrate zone irradiation with the 249 nm laser.

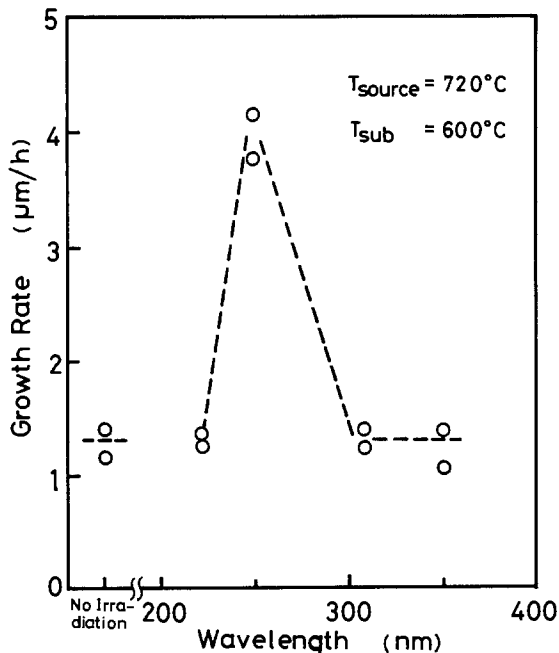


Fig. 2. Wavelength dependence of growth rate for GaAs epitaxial layers grown by the substrate zone irradiation with an excimer laser.

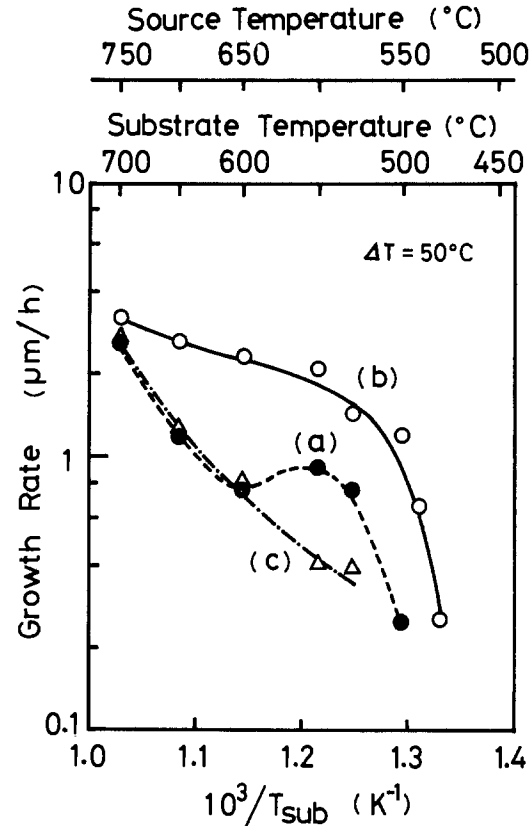


Fig. 3. Temperature dependence of growth rate for GaAs epitaxial layers. Curves a, b, and c show no irradiation, substrate zone irradiation, and source-zone irradiation, respectively.

Figure 4 shows the incident laser power dependence of growth rate in the case of substrate zone irradiation with the 249 nm laser. Since the growth rate increases in proportion to the incident power, the growth rate can be controlled by changing the incident laser power.

Source zone irradiation.—Figure 5 shows the growth rate as a function of incident excimer laser wavelength in the case of Ga source zone irradiation. The source temperature and substrate temperature were 600° and 550°C ,

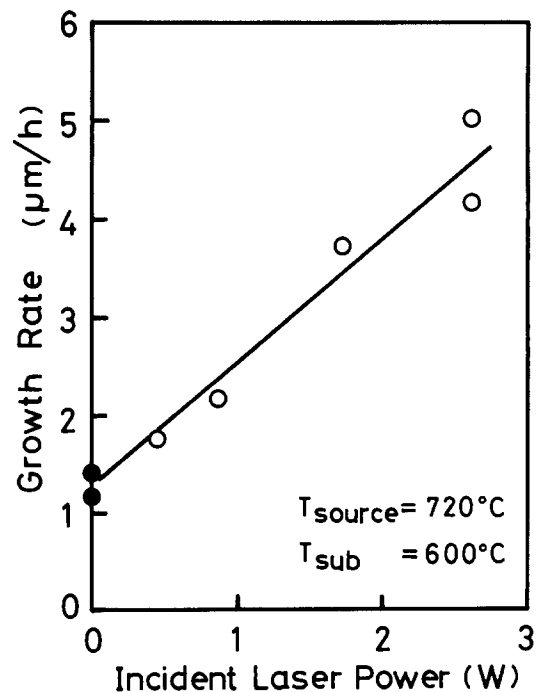


Fig. 4. Incident 249 nm laser power dependence of growth rate for GaAs epitaxial layers.

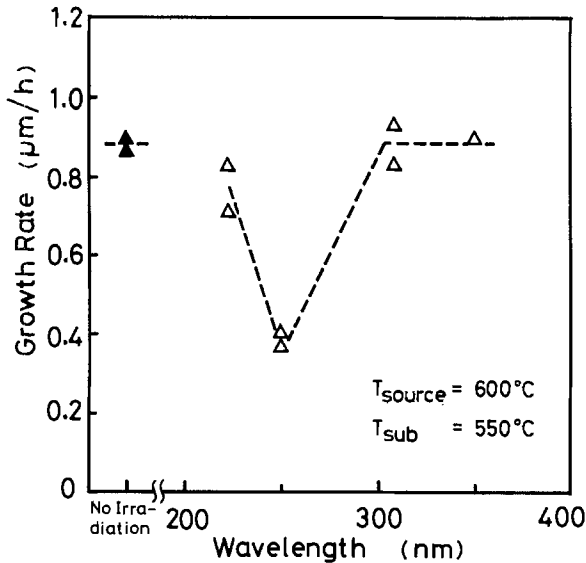


Fig. 5. Wavelength dependence of growth rate for GaAs epitaxial layers grown by the source zone irradiation with an excimer laser.

respectively. The growth rate was markedly reduced by irradiation with the 249 nm laser irradiation and with the 222 nm irradiation but scarcely changed by other wavelength irradiation.

The growth rate in the case of source zone irradiation with the 249 nm laser was comparable to the value without irradiation at the source temperature above 650°C but was smaller than that without irradiation below 650°C, as shown by the curve c in Fig. 3.

Photodissociation of AsCl₃.—Figure 6 shows the temperature dependence of AsCl₃ decomposition measured by infrared absorption spectroscopy. In order to estimate the

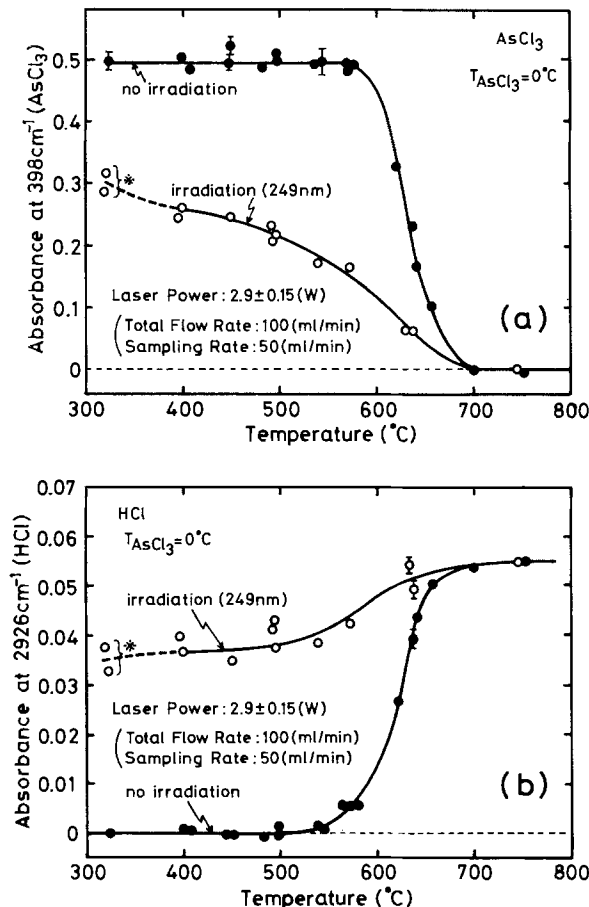


Fig. 6. Temperature dependence of the reduction of AsCl₃ by H₂. *Arsenic was deposited on the irradiated region at low temperatures below 325°C.

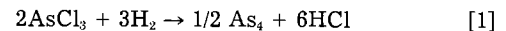
concentration of reactants, we used the absorbance at 398 and 2926 cm⁻¹ for AsCl₃ and HCl, respectively. In the absence of irradiation, AsCl₃ is completely reduced by H₂ and HCl is produced at high temperatures above 700°C, but AsCl₃ is scarcely reduced by H₂ at low temperatures below 600°C. In the case of irradiation with the 249 nm laser, on the other hand, AsCl₃ is reduced by H₂ even at low temperatures below 600°C. The activation energies for reduction reaction of AsCl₃ are 49 and 2.2 kcal/mol without and with irradiation, respectively. The activation energy decreased dramatically with irradiation. However, the activation energy does not necessarily show the energy for the individual process step because there is the possibility that the reaction involves multistep processes.

Figure 7 shows the wavelength dependence of AsCl₃ reduction by irradiation with an excimer laser. The reduction of AsCl₃ is promoted by irradiation with the 222 and 249 nm laser.

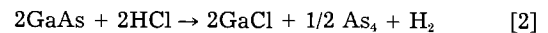
Discussion

Although the detailed mechanism of GaAs epitaxial growth by the chloride method has not been clarified, the following processes are generally considered for the reactions (5).

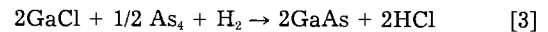
At high source temperatures above 700°C where the growth is usually carried out, introduced AsCl₃ is reduced by H₂ and HCl is produced by



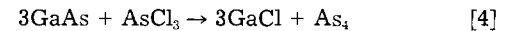
HCl produced by reaction [1] reacts with the GaAs crust formed on the surface of the Ga melt at the source to form GaCl and As₄ by



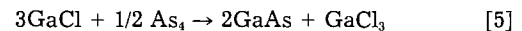
These gases are carried by H₂ onto the substrate at a low temperature, where GaAs is deposited by



At low source temperatures below 600°C, on the other hand, AsCl₃ is not efficiently reduced by H₂ and the source reacts directly with AsCl₃ by reaction [4] and not with HCl (6)



In the deposition region, reaction [3] or reaction [5] should take place



By taking account of the above-mentioned mechanism, we discuss the irradiation effects on the growth rate. In the case of substrate zone irradiation, the sharp wavelength dependence of growth rate enhancement indicates

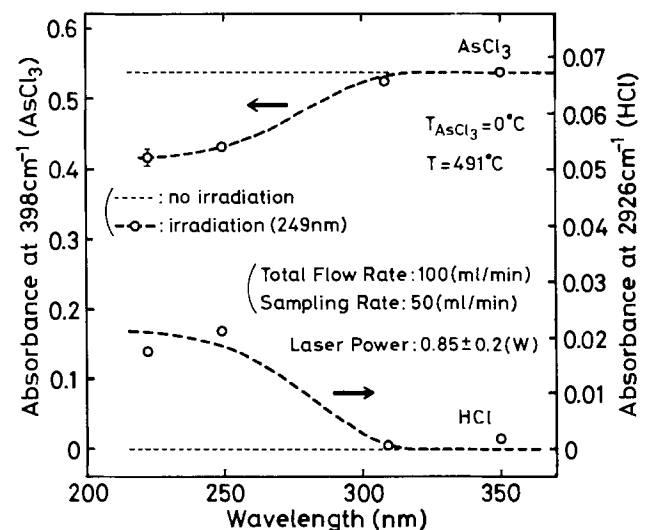


Fig. 7. Wavelength dependence of the reduction of AsCl₃ by irradiation with an excimer laser.

that it is caused not by thermal-induced reactions but by photoinduced reactions. GaCl has an absorption band at around 248 nm (7). The mechanism of the growth-rate enhancement by the substrate zone irradiation is not clear yet, but it is presumably associated with excitation or decomposition of a sort of gallium chlorides by the 249 nm laser irradiation.¹

The temperature dependence of growth rate in the absence of irradiation seems to be related with the degree of AsCl₃ decomposition. At $T_{\text{source}} < 700^{\circ}\text{C}$, AsCl₃ is not completely decomposed, and the Ga source reacts not only with HCl but also directly with AsCl₃ with lowering of the source temperature below 700°C. Therefore, the growth rate behavior as shown by curve a in Fig. 3 is based on the difference of the source reaction mechanism.

Infrared absorption analysis indicates that the AsCl₃ reduction by H₂ can be caused even at low temperatures below 700°C by irradiation. Therefore, the growth rate reduction by the source zone irradiation at low temperatures must be associated with the photodissociation of AsCl₃. At high temperatures above 650°C, AsCl₃ is thermally reduced and then the Ga source reacts with HCl regardless of irradiation. At low temperatures below 650°C, on the other hand, the Ga source reacts directly with AsCl₃ in the absence of irradiation, whereas the Ga source reacts with HCl in the presence of irradiation because of the photodissociation of AsCl₃. The reaction velocity of direct reaction with AsCl₃ is larger than that of the reaction with HCl at low temperatures (6). Therefore, the growth rate is decreased by the source zone irradiation at low temperatures.

Conclusion

We have demonstrated the photoexcitation effects on the growth rate in the vapor phase epitaxial growth of

¹Results will be reported in the next paper.

GaAs. The growth rate can be enhanced by irradiating the substrate zone with the 249 nm laser over the whole of temperature range of 480° ~ 700°C, whereas it is reduced by irradiating the source zone with the 249 or 222 nm laser at low temperatures below 650°C. Infrared absorption analysis showed that the reduction of AsCl₃ by H₂ is promoted by irradiation with the 249 or 222 nm laser. This photodissociation of AsCl₃ causes the growth-rate reduction in the case of source zone irradiation. Further investigations are extended to clarify the detailed mechanism of photoexcitation effects. In future, the crystal growth will be performed by identifying the radicals or ions which participate in the reactions by infrared absorption spectroscopy and then by forming selectively the radicals and ions with photoexcitation.

Manuscript submitted Sept. 21, 1984; revised manuscript received March 19, 1985.

Semiconductor Research Institute assisted in meeting the publication costs of this article.

REFERENCES

1. J. Nishizawa, *J. Jpn. Inst. Metals*, **25**, 149 (1961); *ibid.*, **25**, 177 (1961).
2. M. Kumagawa, H. Sunami, T. Terasaki, and J. Nishizawa, *Jpn. J. Appl. Phys.*, **7**, 1332 (1968).
3. J. Nishizawa and H. Nihira, *J. Cryst. Growth*, **45**, 82 (1978).
4. J. Nishizawa and T. Kurabayashi, *This Journal*, **130**, 413 (1983).
5. T. Arizumi, "Current Topics in Materials Science," Vol. 1, E. Kaldis, Editor, p. 365, North-Holland, Amsterdam (1978).
6. H. Watanabe, *Jpn. J. Appl. Phys.*, **14**, 1451 (1975).
7. Y. Kuniya and M. Hosaka, *J. Cryst. Growth*, **28**, 385 (1975).

Antimony, Arsenic, Phosphorus, and Boron Autodoping in Silicon Epitaxy

M. W. M. Graef* and B. J. H. Leunissen

Philips Research Laboratories, 5600 JA Eindhoven, The Netherlands

H. H. C. de Moor

Research Institute of Materials, Department of Solid State Physics, University of Nijmegen, Toernooiveld, 6525 ED Nijmegen, The Netherlands

ABSTRACT

Lateral autodoping is encountered if silicon wafers with heavily doped areas are subjected to silicon epitaxy. The characteristics of the autodoping profile are determined by the pre-epitaxial bake conditions and by the identity of the impurities. Lateral autodoping originating from arsenic- or antimony-implanted silicon substrates can be suppressed by reduction of the total pressure during the epitaxial process. In contrast, autodoping is enhanced at reduced pressure if boron-doped buried layers are employed. These phenomena can be accounted for if chemical processes in the gas phase, which involve the dopant, are considered. Thermodynamic computations have been carried out in order to explain the influence of process conditions such as temperature, total pressure, and the presence of chlorine on the autodoping behavior or antimony, arsenic, phosphorus, and boron. Evaporated dopant atoms are converted to stable gaseous compounds such as SbCl for antimony, AsH and As₂ for arsenic, PH₃, PH₂, and P₂ for phosphorus, and BHCl₂ for boron. The reincorporation of the dopant in the epitaxial layer is governed by the partial pressure of monoatomic species in the gas phase. Mass action law describes the influence of total pressure on the efficiency of the autodoping process.

During epitaxial deposition of silicon, impurities present in the substrates are redistributed in the epitaxial layer. Transport of dopant atoms can take place by means of solid-state diffusion (1) or according to a two-step mechanism involving impurity evaporation from the substrate and reincorporation into the growing layer (2, 3). The latter phenomenon is usually referred to as autodoping. The result of autodoping is an unintended impurity profile in the epitaxial layer. This may give rise to unwanted device characteristics in schemes where wafers with buried layers or heavily doped substrates are used.

A considerable amount of work on the topic of autodoping has been done in recent years. Most authors pay attention in particular to the physical aspects of the process, such as gas phase diffusion (4), the retainment of impurities in the boundary layer (5, 6), and the adsorption of impurities at the surface (7). Quantitative treatments of gas flow effects have been published (8, 9).

The characteristics of the autodoping profile are determined to a large extent by the pre-epitaxial bake conditions, such as temperature, bake time, and total pressure (10). An important observation is the fact that, in the case

of arsenic, autodoping can be suppressed by low pressure epitaxy (11, 12), which is in agreement with theoretical expectations. However, in the case of boron, enhancement of autodoping at reduced pressure has been reported (13). It seems that in order to explain this and other anomalies, the influence of chemical processes on the autodoping mechanism should be taken into account. This approach has been successfully pursued for the description of intentional doping during epitaxial deposition of silicon, especially for arsenic (14) and phosphorus (15), for epitaxy at both atmospheric and reduced pressure (16). At present, physicochemical models for the incorporation of dopants in epilayers are available (17).

The purpose of this paper is to compare the autodoping behavior of Sb, As, P, and B buried layers and to study the influence of chemical processes in the gas phase on the reincorporation of these dopants.

Experimental Procedure

Epitaxial silicon layers were grown in an AMC7800 radiant-heated barrel reactor. Silicon sources used were dichlorosilane, trichlorosilane, and tetrachlorosilane. The silicon growth rate amounted to $0.43 \mu\text{m}/\text{min}$ during most experiments. Diborane and phosphine were used as dopant gases. Hydrogen was used as a carrier gas; the total gas flow was about 170 standard liter/min. The deposition temperature was varied within the range 1050°C – 1200°C .

The samples for the investigation of autodoping profiles were prepared as follows. Heavily doped substrates were used in order to facilitate CV measurements.

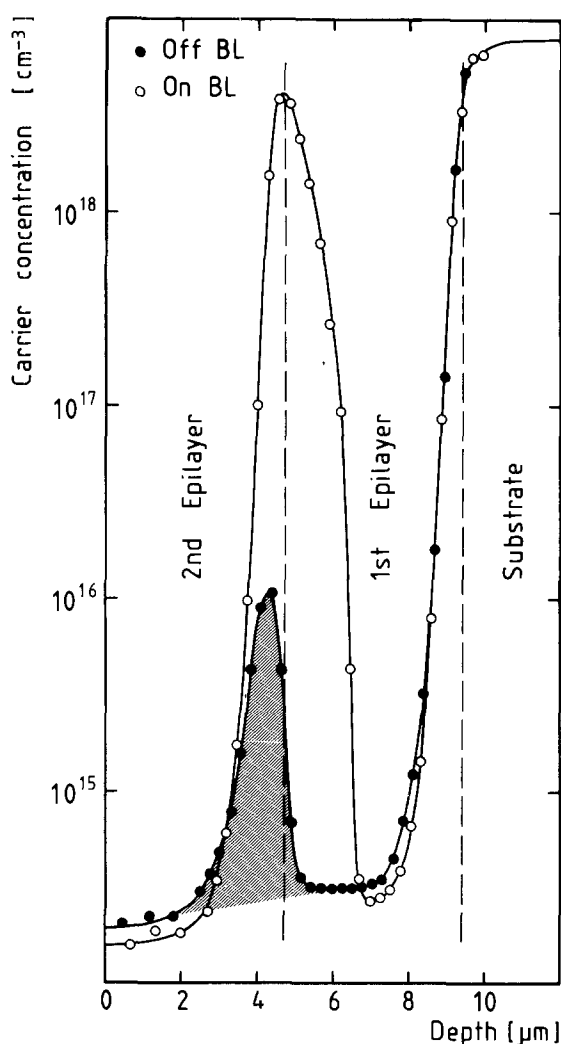


Fig. 1. Doping profiles in epilayer on a substrate with P buried layer. The figure shows the heavily doped substrate, the buried layer (open circles), and the autodoping profile (darkened circles). Shaded area: autodoping peak.

Antimony-doped silicon wafers (resistivity $0.02 \Omega\text{-cm}$) were used as N^+ substrates, and boron-doped wafers ($0.02 \Omega\text{-cm}$) were used as P^+ substrates. The slices were (100) oriented and of 3 in. diam; they were supplied by Wacker. The P^+ substrates were backsealed with $2 \mu\text{m}$ of undoped silicon. The N^+ and P^+ slices were coated on the front side with N^- or P^- epitaxial layers, respectively (carrier concentration of 10^{14}cm^{-3} ; thickness of $5 \mu\text{m}$), in order to separate the buried layers from the substrate doping. Next, the wafers were subjected to ion implantation (dose $3 \times 10^{15} \text{cm}^{-2}$; energy 50 keV) in order to create buried layers doped with antimony, arsenic, phosphorus, or boron. The buried layers were rectangular with dimensions of $6.6 \times 8.8 \text{mm}^2$; the active region was 52% of the total surface area.

Subsequently, a 100 min diffusion drive was performed at 1200°C for Sb and As, and at 1100°C for B and P. Due to differences in the diffusivities of these elements in silicon, this resulted in approximately equal doping profiles in these four types of substrates prior to the epitaxy step. A second epilayer was deposited onto the substrates, doped intentionally to about 10^{14}cm^{-3} n- or p-type.

The autodoping phenomena caused by the presence of the buried layers during epitaxy were investigated with the aid of spreading resistance (SR) measurements on beveled samples. To this end, an SSM two-probe measuring system, Type ASR-100, was used. The uncorrected SR profiles were compared with impurity profiles obtained with an MSI 894 capacitance-voltage (C-V) profiler provided with a mercury probe. Qualitative agreement was observed. The SR data were converted to carrier concentrations with the aid of a series of values of four-point probe resistivities obtained on calibration samples.

Experimental Results

The redistribution of dopant atoms originating from the buried layers was investigated by measuring the spreading resistance profile in between two buried layer (BL) regions. A comparison of the doping profile obtained in this way and a doping profile determined over a buried layer is shown in Fig. 1. The extent of autodoping is indicated by the magnitude of a concentration maximum in the second epilayer, formed during the initial stage of epitaxial growth. The variation of the lateral autodoping peak as a function of distance from the BL edge is shown in Fig. 2. It is seen that the maximum is only slightly dependent on distance in the region within several millimeters from the BL edge. The repetitious pattern of buried layers causes an averaging effect on the off-BL profiles. In investigations where only a single

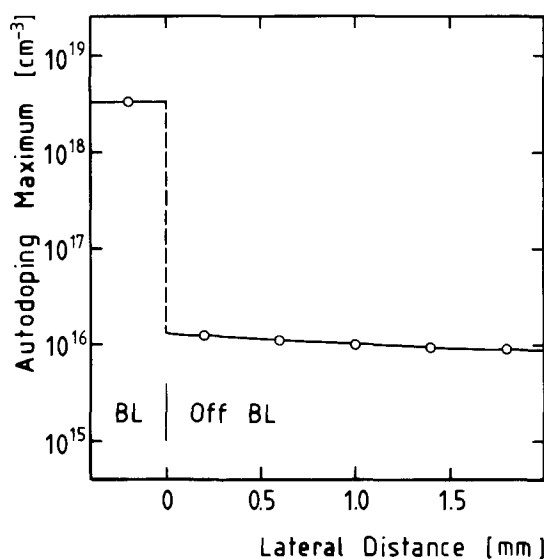


Fig. 2. Lateral autodoping of phosphorus. Autodoping peak height as a function of lateral distance to the BL edge. Background doping is $2 \times 10^{14} \text{cm}^{-3}$.

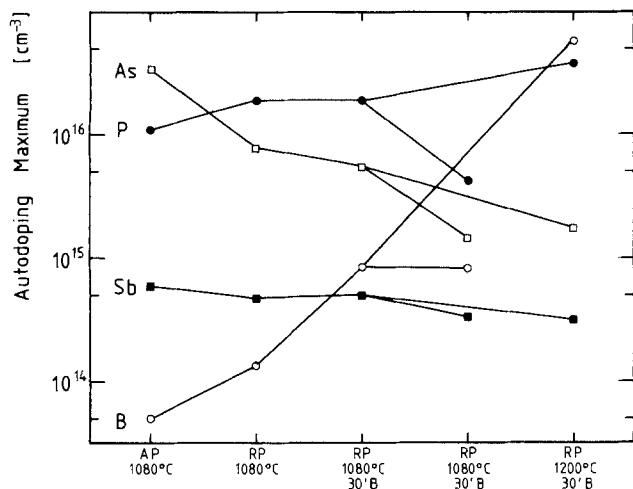


Fig. 3. Influence of pre-epitaxial bake time and temperature, total pressure, and HCl on lateral autodoping peak height (corrected for background doping).

buried layer on an entire wafer was used, the direction of the gas flow affected autodoping (8).

The off-BL profiles presented below were always determined at 2.2 mm from the BL edge, *i.e.*, in the middle between two buried layers. Minor deviations in distance do not affect the profile significantly.

Influence of pre-epitaxial bake conditions on lateral autodoping.—Native oxide, present on the silicon surface, is removed by the action of hydrogen during the pre-epitaxial bake step. Simultaneously, dopant atoms are released from the buried layer, to be reincorporated during the deposition step. The lateral autodoping maximum is affected by the conditions of the pre-epitaxial stage. The following experimental parameters were studied.

Total pressure.—Experiments were done at atmospheric pressure (AP) or at reduced pressure (RP, *i.e.*, 65 torr).

Pre-epitaxial bake temperature.—Pre-epitaxial bake was performed at 1080° and 1200°C. The temperature during growth was the same as the pre-epitaxial temperature.

Pre-epitaxial bake time.—The time required for attaining the set-point temperature was about 3 min. This was des-

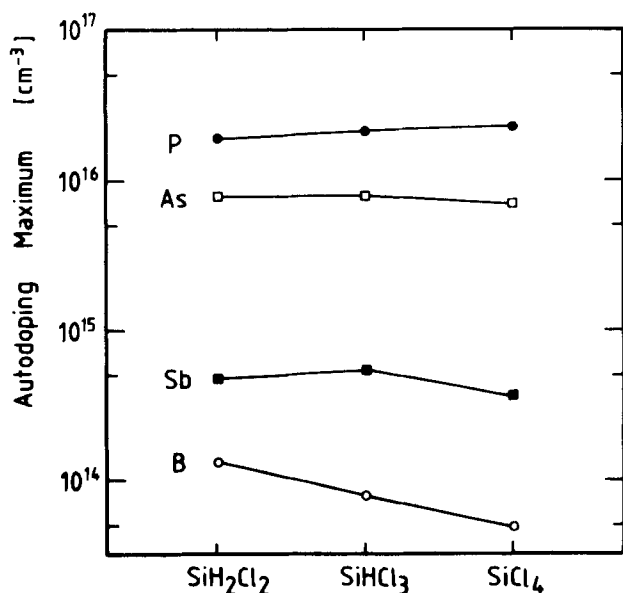


Fig. 4. Influence of silicon source gas on lateral autodoping peak height. Deposition conditions: reduced pressure (65 torr); temperature of 1080°C; growth rate of 0.41 $\mu\text{m}/\text{min}$. (Corrected for background doping.)

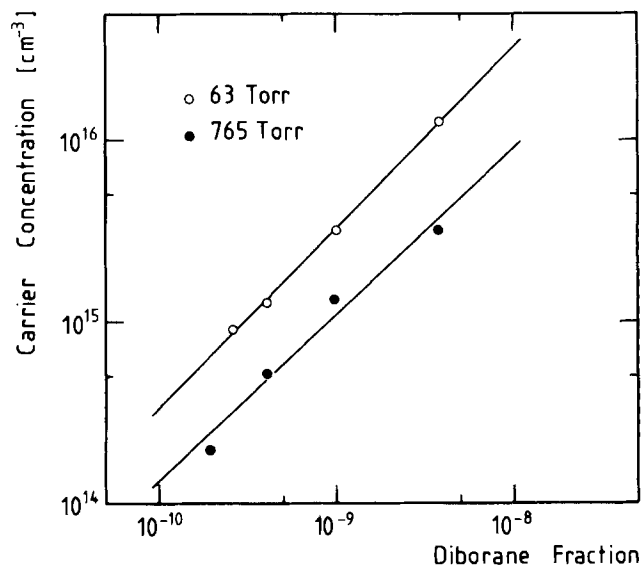


Fig. 5. Boron incorporation from the gas phase at atmospheric and reduced total pressure. Epitaxy conditions: 1.4% SiHCl_3 , 1080°C.

ignated as "No Bake." Alternatively, and additional pre-epitaxial bake (B) was allowed for the duration of 30 min.

The influence of these conditions on the autodoping profile was studied for epitaxial layers deposited onto wafers implanted with Sb, As, P, and B, respectively. The lateral autodoping profiles which result for different conditions for each of the dopant types were published elsewhere (18). The results can be summarized as follows.

For antimony, the Sb lateral autodoping peak was found always below 10^{15} cm^{-3} . The maximum decreased with (i) reduction of the total pressure, (ii) extension of the pre-epitaxial bake time, and (iii) increase of temperature.

For arsenic, the As lateral autodoping peak was strongly affected by the experimental conditions. The highest maximum was found at low temperature and atmospheric pressure. The maximum decreased with (i) reduction of the total pressure, (ii) extension of the pre-epitaxial bake time, and (iii) increase of temperature.

For phosphorus, the P lateral autodoping peak was always larger than 10^{16} cm^{-3} . The maximum decreased with (i) increase of the total pressure, and (ii) decrease of temperature. The maximum was not notably affected by the duration of the pre-epitaxial bake time.

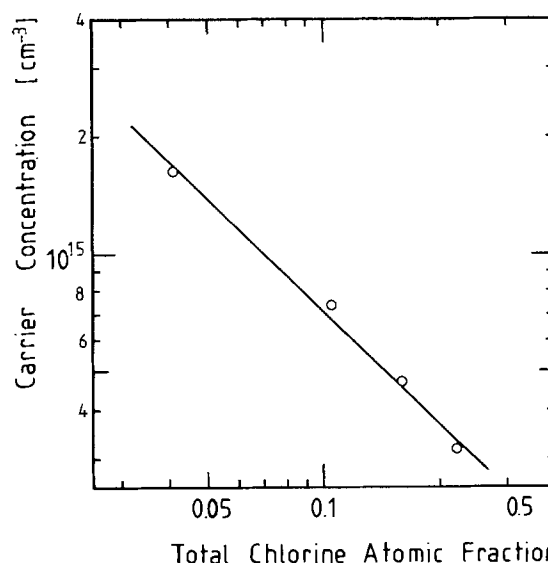


Fig. 6. Boron incorporation from the gas phase. Influence of chlorine on doping efficiency. Epitaxy with SiH_2Cl_2 and 1 ppb B_2H_6 at 1080°C.

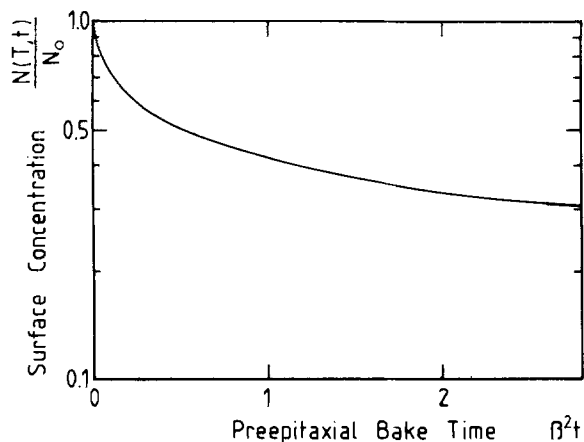


Fig. 7. Dimensionless diagram showing the effect of pre-epitaxial bake time on autodoping.

For boron, the B lateral autodoping peak was found within a large range from 10^{14} to 10^{17} cm^{-3} . The maximum decreased with (i) increase of the total pressure, (ii) shortening of the pre-epitaxial bake time, and (iii) decrease of temperature.

A graphic representation of these results is given in Fig. 3. In addition to the pre-epitaxial conditions mentioned above, the effect of the presence of HCl (1 volume percent) during the pre-epitaxial stage was studied. This resulted in the removal of the top layer (about $0.5 \mu\text{m}$) of the substrate, including part of the implanted region. This caused a reduction of the autodoping maximum for As and P by a factor of four, and by somewhat less for Sb. Etching during the pre-epitaxial bake did not influence the magnitude of the autodoping peak of boron.

Influence of the silicon source on lateral autodoping.—In addition to the experimental conditions prior to the epitaxial process, the identity of the silicon source gas present during deposition appeared to be of importance. In order to avoid possible interpretation difficulties introduced by surface kinetics, the same growth rate ($0.41 \mu\text{m}/\text{min}$) was imposed for the preparation of all samples. This was attained by the choice of appropriate growth gas partial pressure: 0.4% SiH_2Cl_2 , 2.4% SiHCl_3 , and 4% SiCl_4 , respectively, for epitaxial deposition under reduced pressure at 1080°C . The influence of the silicon source on the lateral autodoping peak height is depicted in Fig. 4. For arsenic and phosphorus, the variations of the autodoping maximum were within the uncertainty of the measurement, which was about 15%. This indicates that P and As autodoping is not affected by the identity of the silicon source. The effect on antimony autodoping is

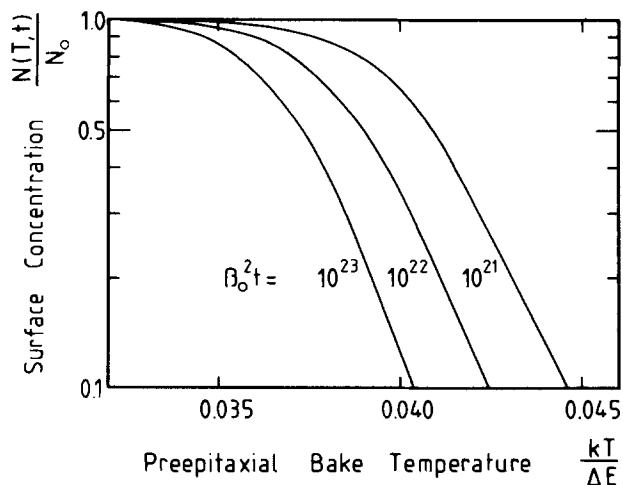


Fig. 8. Dimensionless diagram showing the effect of pre-epitaxial bake temperature on autodoping.

somewhat ambiguous; a decline of the peak height by 25% was observed if tetrachlorosilane was used instead of dichlorosilane. For boron, a clear reduction of the autodoping efficiency was found. If SiH_2Cl_2 was replaced by SiCl_4 , the autodoping maximum decreased with a factor of more than two.

Doping with diborane.—In order to study the influence of the experimental conditions on the mechanism of dopant incorporation from the gas phase, a number of experiments were executed in which the epitaxial layers were intentionally doped with boron. This is the more interesting dopant because of its divergent behavior. The incorporation of arsenic and phosphorus has been described in several publications (14, 15).

When diborane was used as a dopant source, the relationship between the boron concentration in the epilayer N_B and the diborane fraction in the gas $X_{\text{B}_2\text{H}_6}$ during deposition could be expressed by a straight line with slope ϕ

$$\phi = \frac{d(\log N_B)}{d(\log X_{\text{B}_2\text{H}_6})} \quad [1]$$

Experimentally, the following values for ϕ were found (cf. Fig. 5). At atmospheric pressure and 1080°C , $\phi = 0.95$ for 0.4% SiH_2Cl_2 (growth rate $0.43 \mu\text{m}/\text{min}$), and $\phi = 0.98$ for 1.4% SiHCl_3 (growth rate $0.36 \mu\text{m}/\text{min}$). At reduced pressure, similar results were obtained: $\phi = 0.98$ for SiCl_4 at 50 torr, $\phi = 1.01$ for SiCl_4 at 370 torr, and $\phi = 1.00$ for SiHCl_3 at 60 torr.

The influence of the total pressure on the doping process can be studied by comparing these results. The dependence of the impurity concentration in the epitaxial layer on the total pressure P_{tot} (for a constant diborane fraction in the gas phase and hydrogen as a carrier gas) is expressed by

$$\psi = \frac{d(\log N_B)}{d(\log P_{\text{tot}})} \quad [2]$$

The value $\psi = -0.52 \pm 0.07$ was found when SiCl_4 was used as a silicon source. For the case of SiH_2Cl_2 , $\psi = -0.43 \pm 0.10$ was measured. Clearly, the efficiency of the boron incorporation process is enhanced by reduction of the total pressure. In spite of the fact that the total concentration of boron in the gas phase is reduced, the concentration of boron in the solid increases!

In view of the observation that boron autodoping was influenced by the chlorine content of the silicon source (preceding section), the effect of the amount of chlorine present in the gas phase on the boron doping process was also studied. The chlorine fraction was varied by adjustment of the dichlorosilane and trichlorosilane partial pressures. The relationship between the boron concentra-

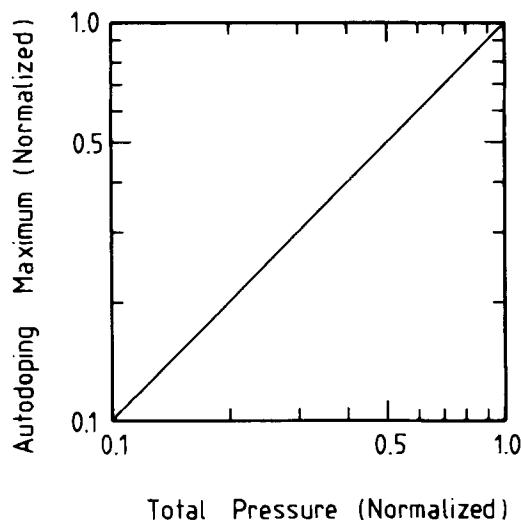


Fig. 9. Dimensionless diagram showing the relationship between autodoping and total pressure.

tion in the epitaxial layer and the chlorine fraction in the gas phase X_{Cl} is given by the equation

$$\xi = \frac{d(\log N_B)}{d(\log X_{Cl})} \quad [3]$$

For SiHCl_3 at atmospheric pressure, $\xi = -0.96$ was found, whereas for SiH_2Cl_2 at 65 torr the value $\xi = -0.86$ was obtained (cf. Fig. 6). It can be shown that the decrease of the boron concentration in the solid with increasing SiH_2Cl_2 and SiHCl_3 partial pressure is not caused by kinetic limitations. If the incorporation of impurities during deposition of silicon is governed by quasi-equilibrium conditions, the number of boron atoms incorporated in silicon is less than the amount of boron atoms arriving at the surface. Essentially, this implies that the effective segregation coefficient, defined at

$$k_{\text{eff}} = \frac{N_B/N_{Si}}{X_B/X_{Si}} \quad [4]$$

must be smaller than unity (19). In Eq. [4], N_{Si} is the concentration of silicon atoms in the solid, X_B is the total boron fraction in the gas phase, and X_{Si} is the total silicon fraction in the gas phase. The theoretical upper limit of k_{eff} (which points to an incorporation process governed by kinetic laws) may be even larger than unity if chlorine is present in the gas phase, since not all silicon arriving at the surface is used for crystal growth in this case. Table I gives a number of values for k_{eff} calculated from the experimental results for trichlorosilane. The figures show that the doping experiments were done well within the regime where equilibrium conditions may be assumed to be present.

Finally, the temperature dependence of boron doping was studied in the range 1050°–1200°C for 0.4% SiH_2Cl_2 and 1 ppb B_2H_6 at atmospheric pressure. For a constant diborane partial pressure, the doping level tended to increase with increasing temperature. An activation energy $E'_{\text{act}} = 0.84$ eV was found.

Discussion

Lateral autodoping is caused by evaporation of impurities from the buried layer area during the pre-epitaxial bake stage. Srinivasan (20) showed that the surface concentration of the dopant source at the end of the pre-epitaxial bake stage can be described by the expression

$$N(T, t)/N_0 = \exp(\beta^2 t) \operatorname{erfc}(\beta t^{1/2}) \quad [5]$$

where $N(T, t)$ is the surface concentration after a bake process with duration t at temperature T , and N_0 is the initial surface concentration. The parameter β contains the mass transfer coefficient for evaporation K , expressed in centimeters per second and the dopant diffusivity in the solid D , expressed in square centimeters per second

$$\beta(T) = K(T) \{D(T)\}^{-1/2} \quad [6]$$

The Arrhenius behavior for β is described by

$$\beta(T) = \beta_0 \exp(-\Delta E/kT) \quad [7]$$

where ΔE represents the activation energies for impurity diffusion and evaporation. The most important experimental parameters influencing the evaporation process are the pre-epitaxial bake time and temperature. These

Table I. Effective segregation coefficient k_{eff} for the incorporation of boron with constant diborane partial pressure and variable trichlorosilane partial pressure. Experimental conditions: $T = 1080^\circ\text{C}$, $X_B = 10^{-9}$, $P_{\text{tot}} = 1$ atm.

X_{Si}	N_B (cm^{-3})	k_{eff}
0.0144	1.6×10^{15}	0.47
0.0396	7.4×10^{14}	0.59
0.0652	4.7×10^{14}	0.61
0.0990	3.2×10^{14}	0.63

relationships are presented graphically in Fig. 7 and 8. As expected, the surface concentration decreases with increasing bake time and temperature, due to enhancement of the evaporation rate. Since the lateral autodoping level is directly proportional to the surface concentration of the dopant source (20), the magnitude of the lateral autodoping peak is influenced in an analogous way. According to this model, lateral autodoping can be suppressed by extension of the pre-epitaxial bake time or by an increase of the bake temperature.

A third experimental parameter that influences the lateral autodoping process is the total pressure. The surface concentration at the end of the pre-epitaxial stage determines the dopant concentration in the gas phase, and this quantity, in turn, governs the dopant reincorporation during epitaxial growth. For dilute solid solutions, the concentration of impurities in the solid phase N_i is directly proportional to the partial pressure P_i of impurities in the gas phase, as given by Henry's law (14)

$$N_i = K_i P_i \quad [8]$$

where K_i is the equilibrium constant. A part of the total amount of evaporated impurities will not be used for reincorporation, but is removed to the main gas stream. This fraction is determined by the magnitude of the diffusion coefficient D_i of species i in the gas phase. The diffusion coefficient is related to the total pressure according to

$$D_i = D_{0,i} P_{\text{tot}}^{-1} \quad [9]$$

where $D_{0,i}$ is the diffusion coefficient at atmospheric pressure. Thus, it can be shown that the effective partial pressure P_i is inversely proportional to the diffusion coefficient and directly proportional to the total pressure.

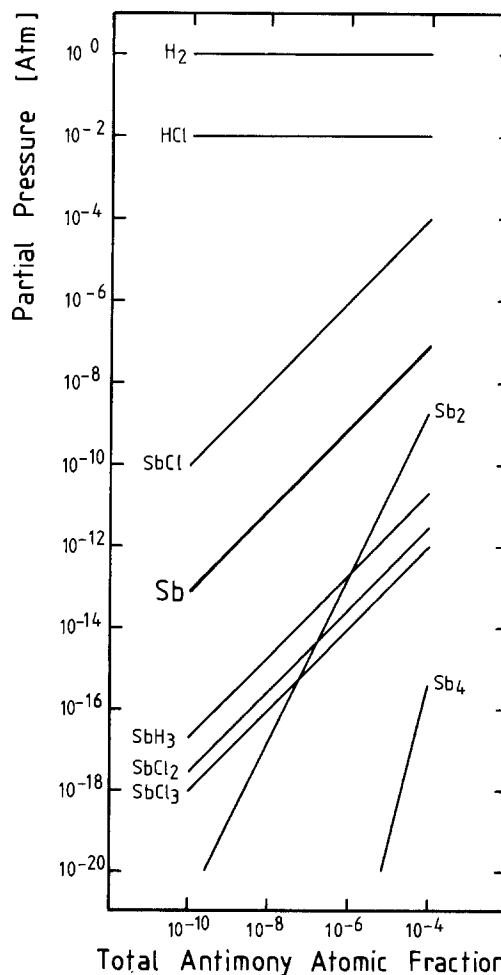


Fig. 10. Equilibrium composition of the Sb-Si-H-Cl system as a function of the Sb atomic fraction. Mass balance: 1% Cl. Total pressure: 1 atm. Temperature: 1350 K.

Table II. Sources of thermodynamic data for chemical species used in equilibrium calculations

Species	Ref.	Species	Ref.
Sb (liquid)	(29)	B (solid)	(38)
Sb	(29)	B	(38)
Sb ₂	(29)	B ₂	(38)
Sb ₄	(29)	BH	(38)
SbH ₃	(31, 32)	BH ₂	(38)
SbCl	(31, 32)	BH ₃	(38)
SbCl ₂	(31, 32)	B ₂ H ₆	(38)
SbCl ₃	(29)	BCl	(38)
SbCl ₅	(31, 32)	BCl ₂	(39)
		BCl ₃	(38)
As (solid)	(30)	B ₂ Cl ₄	(38)
As	(30)	BHCl ₂	(38)
As ₂	(30)	BH ₂ Cl	(32, 42)
As ₃	(30)	BO	(38)
As ₄	(30)	BO ₂	(38)
AsH	(33)	BOH	(40)
AsH ₂	(33, 34)	BO ₂ H	(38)
AsH ₃	(31, 35)	BO ₂ H ₂	(38)
AsCl	(36)	BO ₃ H ₃	(38)
AsCl ₂	(36)	BOCl	(38)
AsCl ₃	(31, 37)	B ₂ O	(38)
		B ₂ O ₃	(39)
P	(38)	B ₃ O ₃ H ₃	(38)
P ₂	(38)	B ₃ O ₃ Cl ₃	(38)
P ₄	(38)		
PH	(38)	Si (solid)	(38)
PH ₂	(38)	Si	(38)
PH ₃	(38)	Si ₂	(38)
PCl	(38)	Si ₃	(38)
PCl ₃	(38)	SiH	(41)
PCl ₅	(38)	SiH ₄	(40)
PO	(39)	Si ₂ H ₆	(32)
PO ₂	(38)	SiCl	(41)
POCl ₃	(38)		
		SiCl ₂	(41)
		SiCl ₃	(41)
		SiCl ₄	(39)
		SiHCl ₃	(41)
		SiH ₂ Cl ₂	(41)
		SiH ₃ Cl	(41)
		SiO	(38)
		SiO ₂ (solid)	(38)
		SiO ₂	(38)
		Cl	(39)
		Cl ₂	(35, 38)
		HCl	(38)
		ClO	(38)
		ClOH	(38)
		Cl ₂ O	(38)
		O	(41)
		HO	(41)
		HO ₂	(38)
		H ₂ O	(38)
		H ₂ O ₂	(38)
		O ₂	(38)
		H	(41)
		H ₂	(34, 41)

Consequently, the magnitude of the lateral autodoping maximum is directly proportional to the total pressure. This is depicted schematically in Fig. 9.

In summary, the lateral autodoping model based on the concept of successive evaporation, diffusion, and reincorporation implies that the pre-epitaxial bake conditions influence the autodoping process in the following way: (i) lateral autodoping is reduced by extension of the pre-epitaxial bake time, (ii) lateral autodoping is reduced by elevation of the pre-epitaxial bake temperature, and (iii) lateral autodoping is reduced by reduction of the total pressure.

In the foregoing, it was assumed implicitly that the evaporated impurity is always present in the gas phase as a monoatomic gas. This appears not to be in the case in every instance. In order to obtain a detailed view of the gas phase composition, it was necessary to perform a number of thermodynamic computations, based on data reported in the literature. A survey of the chemical species used in these calculations is given in Table II. The computer program was based on the minimization of the Gibbs energy for each set of input values. The standard conditions chosen for the calculation were an input com-

position of 1% Cl, 1 ppm O₂, and 10 ppb dopant in a hydrogen ambient, in equilibrium with a condensed silicon phase. The standard temperature was 1350 K. Equilibrium compositions were calculated for several sets of input values of the parameters dopant concentration, total pressure, chlorine concentration, and temperature. The results are presented in a series of diagrams, Fig. 10 to 23. In equilibrium, most chlorine is present in the form of HCl and most oxygen is converted to SiO. Some silicon compounds were included in the calculations, but were omitted in the plots for the sake of clarity. The influence of the partial pressure of hydrogen chloride on the equilibrium composition of the silicon-hydrogen-chlorine system has been reported by several authors (21, 22).

Antimony autodoping.—Autodoping originating from antimony buried layers (cf. Fig. 3) is roughly in agreement with the expected behavior. The influence of the pre-epitaxial bake conditions on autodoping is relatively small, which may be explained by the low evaporation rate of antimony. In order to determine whether the chemical composition of the reaction mixture has any effect on the autodoping mechanism, the results of the equilibrium calculations are considered. Figure 10 gives the gas phase composition as a function of the total amount of antimony present in the reaction mixture. It

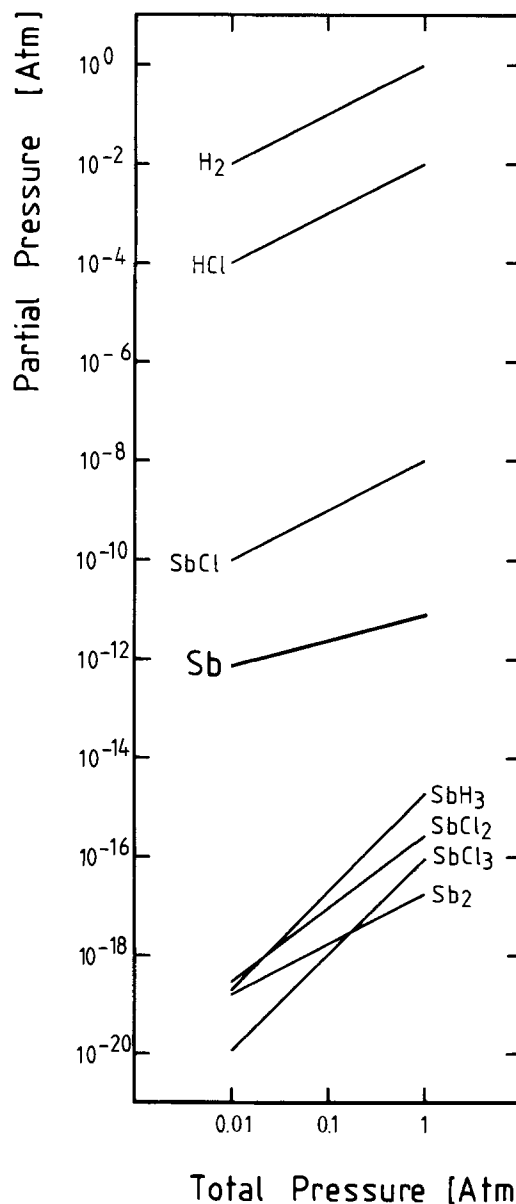
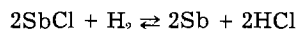


Fig. 11. Equilibrium composition of the Sb-Si-H-Cl system as a function of the total pressure. Mass balance: 1% Cl; 10 ppb Sb. Temperature: 1350 K.

appears that, in the presence of HCl, or, which is equivalent, in the presence of a chlorine containing silicon source, virtually all evaporated antimony is converted to antimony monochloride, SbCl. This is the case within a wide concentration range of evaporated antimony. The influence of the total pressure on the composition is shown in Fig. 11. The dependence of the monoatomic Sb partial pressure on the total pressure is governed by the equilibrium



The mass action law implies that a plot of $\log P_{\text{Sb}}$ vs. $\log P_{\text{tot}}$ yields a straight line with slope equal to 1/2. From the experimental data, it follows that

$$\frac{\Delta(\log N_{\text{Sb,max}})}{\Delta(\log P_{\text{tot}})} = 0.08$$

If all antimony were present in the gas phase as monoatomic Sb, the expected slope would be equal to unity. Clearly, the observed figure is more in agreement with the supposition that the stability of monoatomic Sb is affected by the occurrence of chemical reactions in the gas phase.

The influence of the total amount of chlorine on the gas phase composition is shown in Fig. 12. An increase of the chlorine content tends to reduce the stability of

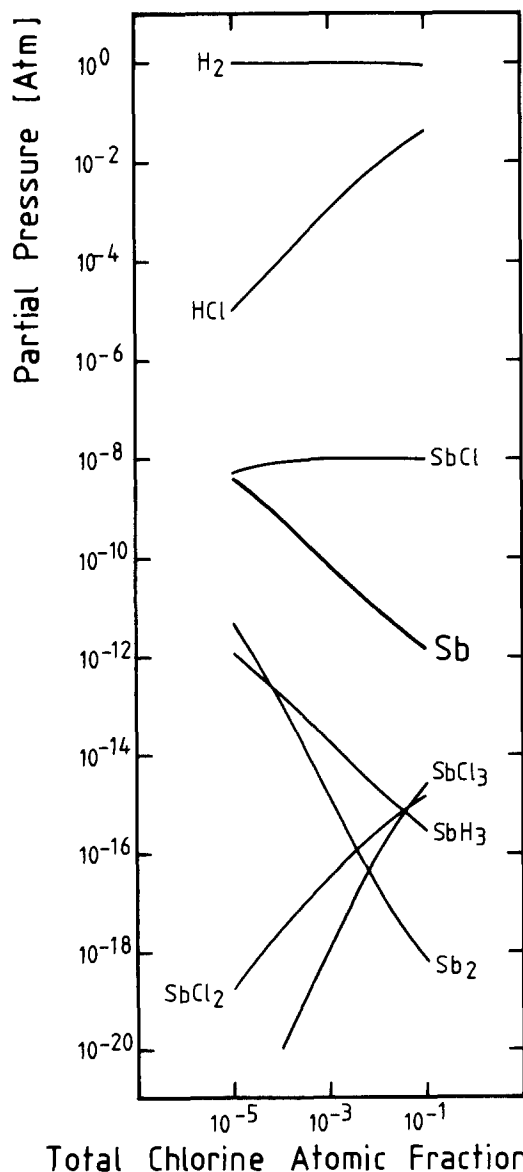


Fig. 12. Equilibrium composition of the Sb-Si-H-Cl system as a function of the Cl atomic fraction. Mass balance: 10 ppb Sb. Total pressure: 1 atm. Temperature: 1350 K.

monoatomic Sb. However, the effect of the Cl concentration on the autodoping maximum cannot be deduced unequivocally from the empirical data (Fig. 4). The fact that an increase of the Cl concentration does not significantly reduce the autodoping maximum seems to indicate that, in the case of antimony, surface kinetics of the incorporation process should be taken into account if a comprehensive description of the antimony autodoping mechanism is to be given.

The temperature dependence of the equilibrium composition is given in Fig. 13. It is seen that the stability of the monoatomic Sb increases slightly with increasing temperature. The activation energy, defined as

$$E''_{\text{act}} = - \frac{d(\ln P_1)}{d(1/kT)} \quad [10]$$

is approximately +2.01 eV. The apparent activation energy for the autodoping process, defined as

$$E'_{\text{act}} = \frac{d(\ln N_{1,\text{max}})}{d(1/kT)} \quad [11]$$

is equal to -0.66 eV. Hence, a net value for the activation energy E_{act} is found equal to -2.67 eV.

Arsenic autodoping.—Autodoping due to arsenic buried layers and heavily doped substrates has been studied extensively by a number of authors (5, 10, 11, 23, 24). The experimental results presented here are in agreement with most of these publications and are consistent with the autodoping model described in the preceding section.

A computation of the equilibrium gas phase composition as a function of the total amount of arsenic present (Fig. 14) shows that either AsH or As₂ is the dominant spe-

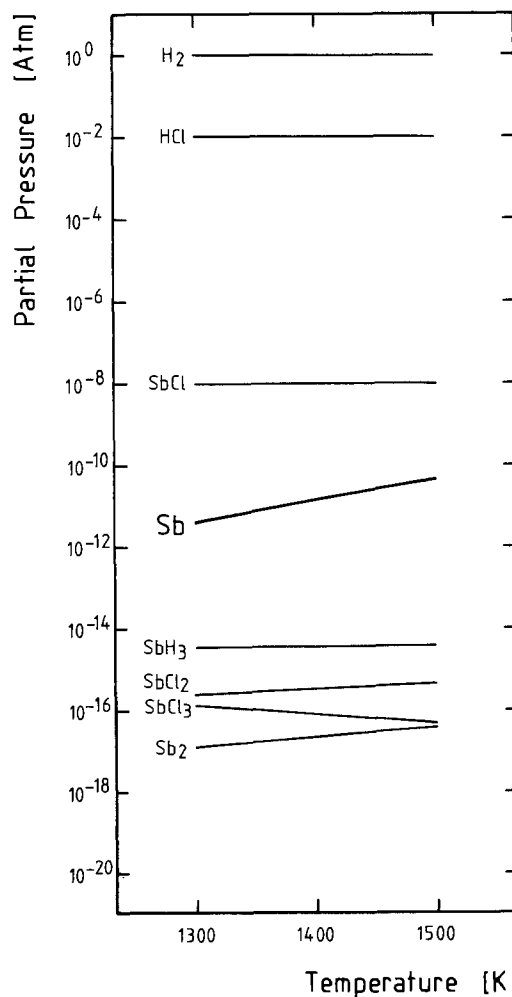


Fig. 13. Equilibrium composition of the Sb-Si-H-Cl system as a function of temperature. Mass balance: 1% Cl; 10 ppb Sb. Total pressure: 1 atm.

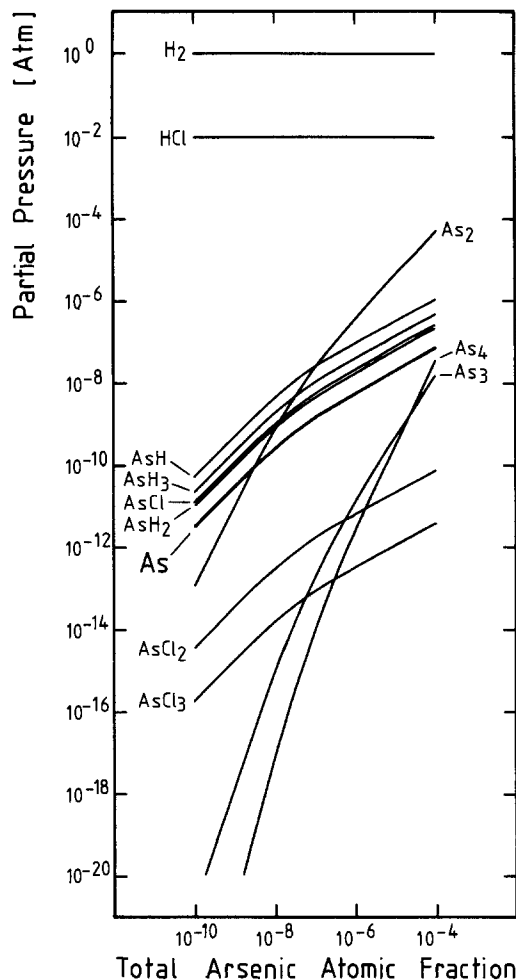
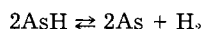


Fig. 14. Equilibrium composition of the As-Si-H-Cl system as a function of the As atomic fraction. Mass balance: 1% Cl. Total pressure: 1 atm. Temperature: 1350 K.

cies. If the arsenic atomic fraction due to evaporation is relatively low, most of the arsenic is converted to AsH. For a higher evaporation rate, virtually all As is converted to As₂. The species AsCl appears to be relatively unimportant. The graphic representation of the relationship between the chemical composition and the total pressure (Fig. 15) shows that the monoatomic As partial pressure is governed by a rather complicated equilibrium, which may be simplified, however, to the equation



The slope of $\log P_{\text{As}}$ vs. $\log P_{\text{tot}}$ is equal to +1/2. (If As₂ is assumed to be the prevailing species, the same result is obtained.) Experimentally, the following relationship between the autodoping maximum and the total pressure was found

$$\frac{\Delta(\log N_{\text{As,max}})}{\Delta(\log P_{\text{tot}})} = +0.62$$

This is in good agreement with the behavior that is predicted according to the thermodynamic analysis. The fact that the empirical slope is larger than 0.5 could be explained by the assumption that the partial pressure of monoatomic As is larger than the value that follows from the equilibrium calculations (24).

In Fig. 16, it can be seen that the stability of monoatomic As increases only to a small extent with temperature. The activation energy E'_{act} amounts to +1.06 eV. The apparent activation energy for autodoping E'_{act} is -1.65 eV, resulting in a net value for E_{act} equal to -2.71 eV.

Phosphorus autodoping.—Whereas arsenic autodoping can be described at least qualitatively with the evapora-

tion-diffusion-reincorporation model without invoking chemical details, the case is more complicated for phosphorus. In particular, the increase of the autodoping maximum if the total pressure is reduced and of the enhancement of autodoping at higher temperature are remarkable.

The results of the equilibrium calculations, presented in Fig. 17, show that the gas phase is governed by the species PH₃, PH₂, and, for high phosphorus concentration, P₂. The presence of chlorine does not affect the equilibrium composition, owing to the poor stability of chlorine containing gaseous phosphorus compounds. Also, no phosphorus oxides are sufficiently stable to play a role of importance in the chemical balance.

The equilibrium composition is influenced, however, by the total pressure of the gas mixture (Fig. 18). The stability of monoatomic phosphorus is enhanced by reduction of the total pressure. The slope of $\log P_p$ vs. $\log P_{\text{tot}}$ changes from -1/2 if PH₃ is the prevailing phosphorus compound to zero if PH₂ is dominant. This phenomenon is reflected in the influence of the total pressure on the lateral autodoping maximum (Fig. 3). The empirical relationship between the autodoping and the total pressure is given as

$$\frac{\Delta(\log N_{p,\text{max}})}{\Delta(\log P_{\text{tot}})} = -0.22$$

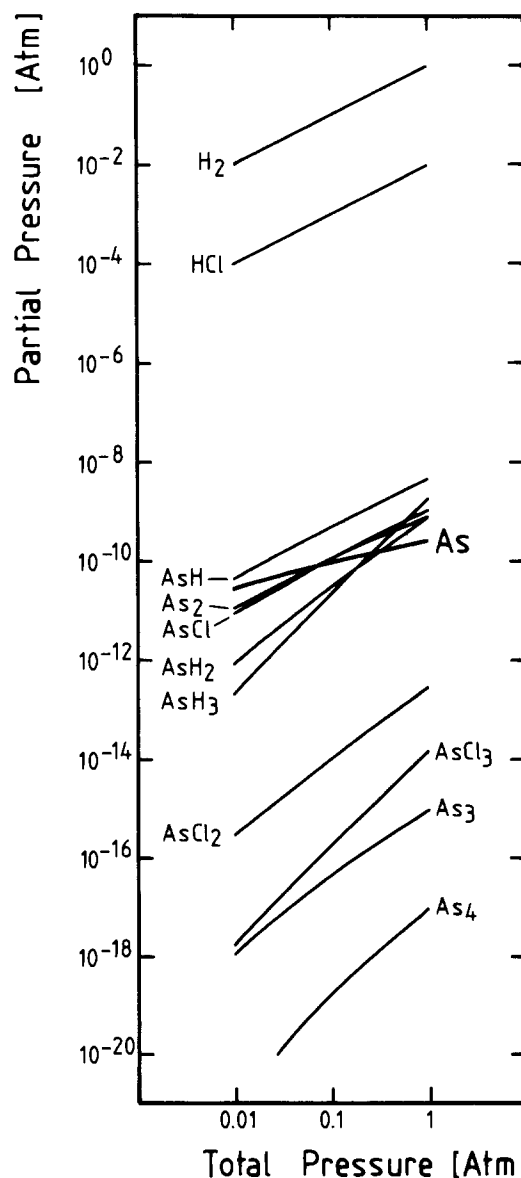


Fig. 15. Equilibrium composition of the As-Si-H-Cl system as a function of the total pressure. Mass balance: 1% Cl; 10 ppb As. Temperature: 1350 K.

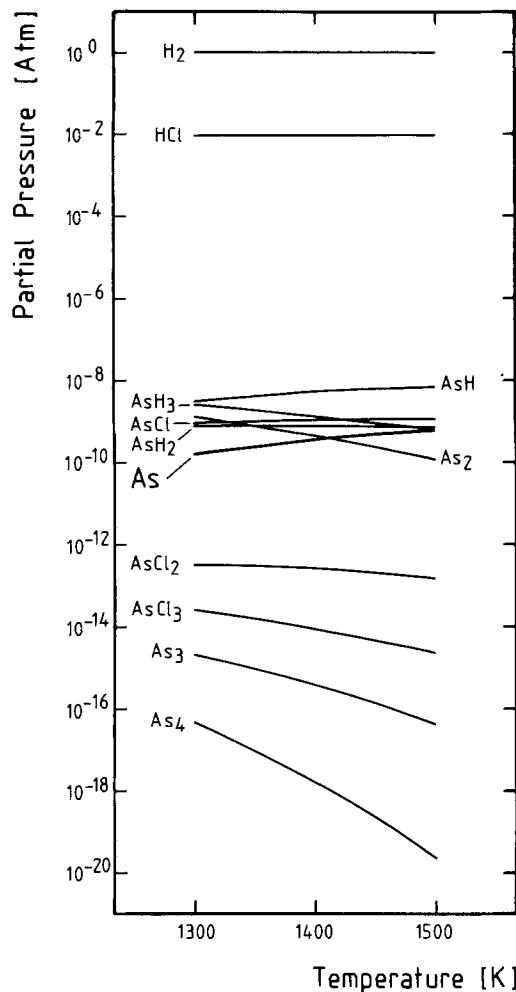


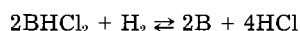
Fig. 16. Equilibrium composition of the As-Si-H-Cl system as a function of temperature. Mass balance: 1% Cl; 10 ppb As. Total pressure: 1 atm.

Thus, the thermodynamic data are consistent with the observations.

The temperature dependence of the chemical equilibrium shows that the relative amount of monoatomic P in the gas phase is enhanced at higher temperatures, with $E'_{\text{act}} = +2.84$ eV (cf. Fig. 19). If this is taken into account in a consideration of the temperature dependence of the autodoping process (Fig. 3), with $E'_{\text{act}} = +0.99$ eV, it can be shown that the actual activation energy for autodoping has a negative sign, viz., $E_{\text{act}} = -1.85$ eV.

Boron autodoping.—The observation that boron lateral autodoping is enhanced by reduction of the total pressure has made it difficult to solve the autodoping problems encountered with the employment of P⁺ substrates (13, 25, 26). Boron autodoping is also increased with increased pre-epitaxial bake time and temperature (cf. Fig. 3).

If chlorine is present in the gas phase, the reaction mixture is dominated by chlorine containing species such as dichloroborane, BHCl_2 (Fig. 20). The gaseous reaction preceding the incorporation of boron can be expressed as



The mass action law implies that reduction of the total pressure enhances the stability of monoatomic boron. This is shown in Fig. 21. The slope of $\log P_{\text{B}}$ vs. $\log P_{\text{tot}}$ is equal to $-1/2$. (It should be remarked that the same value is found if the predominant boron species are assumed to be BCl_3 , BH_2Cl , or BH_3). The autodoping maximum (cf. Fig. 3) is reduced by total pressure reduction according to

$$\frac{\Delta(\log N_{\text{B,max}})}{\Delta(\log P_{\text{tot}})} = -0.49$$

It appears that the reincorporation of boron is indeed governed by the thermodynamic characteristics of the chemical processes in the gas phase. This is further substantiated by the results of experiments in which epilayers were intentionally doped (Fig. 5). The boron doping level vs. the total pressure gave slopes with values of -0.43 and -0.52 for dichlorosilane and tetrachlorosilane, respectively (cf. Experimental section).

The influence of the presence of chlorine on the chemical equilibrium is depicted in Fig. 22. If the total partial pressure of chlorine is relatively small, the predominant species are BH_2 and BH_3 , or, if traces of oxygen or water are present, BOH . For larger chlorine partial pressures, the stabilities of BHCl_2 , BH_2Cl , and BCl_3 are enhanced. In the intermediate range the slope of $\log P_{\text{B}}$ vs. $\log X_{\text{Cl}}$ changes from 0 to -2 . For intentional boron doping, the experimentally found value for ξ was about -1 (cf. Experimental section, Eq. [3]). This indicates that chlorine containing boron compounds indeed play an important role in the gas phase. The observation that the addition of hydrogen chloride to the gas phase during epitaxy causes a decrease of the efficiency of the boron incorporation process has been reported by Bloem (27). A similar phenomenon occurs if water vapor is present in the gas mixture (27, 28). As for lateral autodoping, a significant reduction of the lateral autodoping was observed if a chlorine-rich silicon source was used (Fig. 4).

The influence of temperature on the equilibrium composition is shown in Fig. 23. The strong enhancement of the stability of monoatomic boron with an increase of temperature is clearly visible. The activation energy E'_{act} is $+6.14$ eV. An enhancement of the incorporation efficiency at higher temperatures was indeed observed in the intentional doping experiments (cf. Experimental sec-

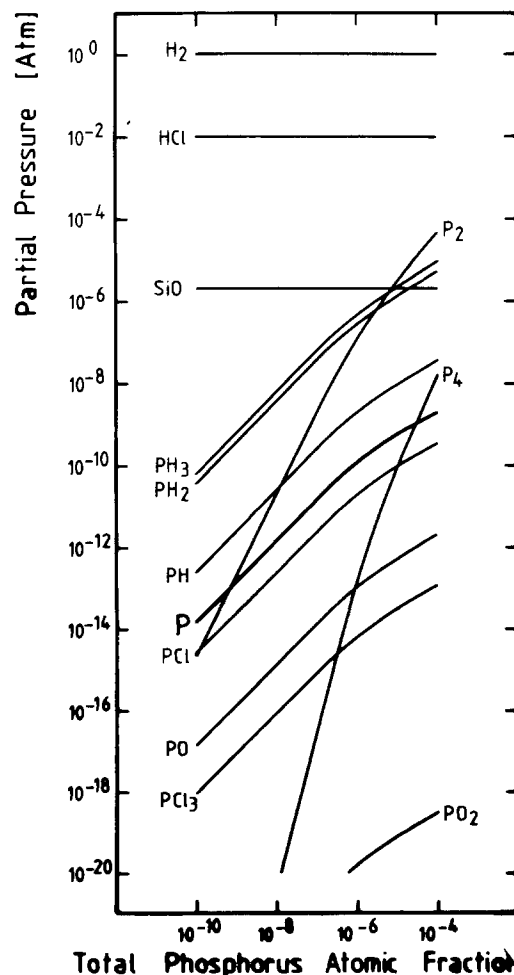


Fig. 17. Equilibrium composition of the P-Si-H-Cl-O system as a function of the P atomic fraction. Mass balance: 1% Cl; 1 ppm O_2 . Total pressure: 1 atm. Temperature: 1350 K.

tion). The increase of the lateral autodoping peak with temperature (Fig. 3) is a remarkable feature of the boron autodoping phenomenon ($E'_{act} = +6.07$ eV). The thermodynamic analysis shows that this increase can be accounted for completely by the temperature dependence of the monoatomic boron stability. The corrected value for the activation energy for autodoping of boron is $E_{act} = -0.07$ eV.

Conclusion

Essentially, the lateral autodoping caused by anti-mony-, arsenic-, phosphorus-, and boron-implanted layers can be described by a mechanism which explains the process in terms of evaporation, gas phase diffusion, and reincorporation. In order to explain the influence of process conditions on autodoping phenomena, this model has to be extended with a description of chemical reactions in the gas phase in which the evaporated dopant is involved. The autodoping level in the epilayer is related to the partial pressure of monoatomic dopant in the gas mixture according to Henry's law, which is valid if surface limitations to the incorporation process are absent. This was shown to be the case for boron doping. Diffusion-controlled incorporation has also been reported for phosphorus (15) and arsenic (14) for low growth rates. On the other hand, evidence for kinetic control of arsenic

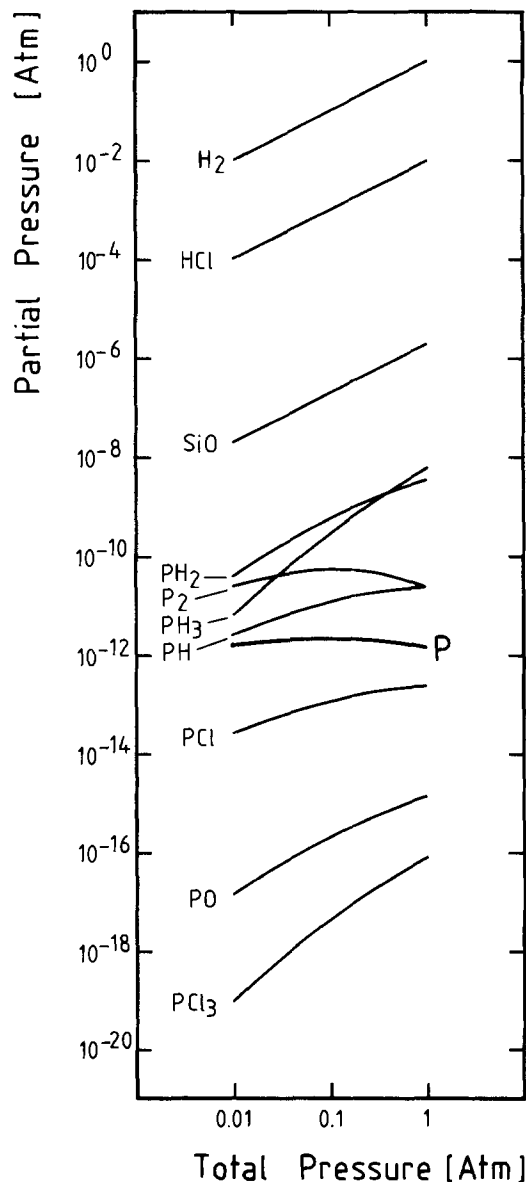


Fig. 18. Equilibrium composition of the P-Si-H-Cl-O system as a function of the total pressure. Mass balance: 1% Cl; 1 ppm O₂; 10 ppb P. Temperature: 1350 K.

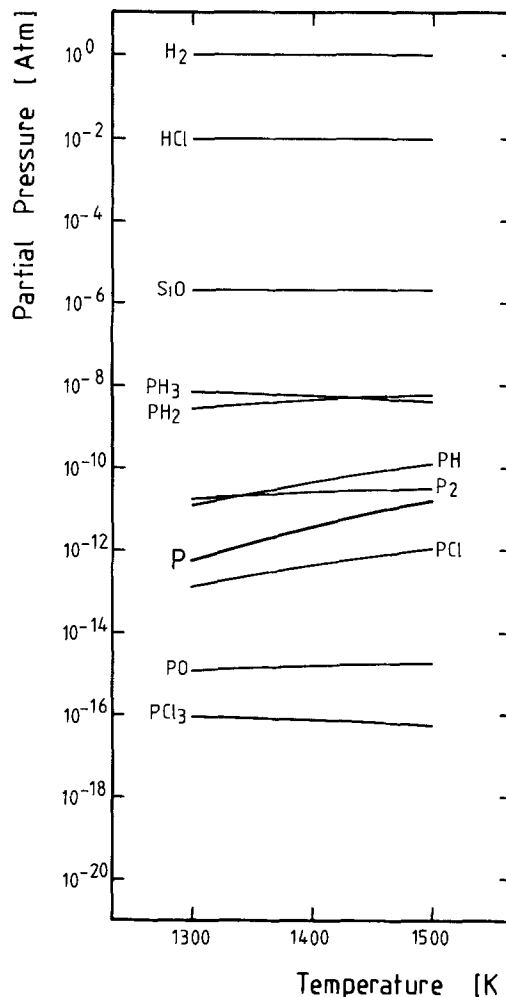
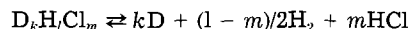


Fig. 19. Equilibrium composition of the P-Si-H-Cl-O system as a function of temperature. Mass balance: 1% Cl; 1 ppm O₂; 10 ppb P. Total pressure: 1 atm.

doping has been published (20), which may explain deviations from the expected behavior.

In general, the partial pressure of a dopant D is governed by the presence of a stable gaseous compound $D_kH_lCl_m$ according to the chemical equilibrium



The mass action law gives the relationship between the monoatomic dopant gas and the experimental conditions and, consequently, between the autodoping level and the process conditions.

For intentional doping

$$\frac{d(\log P_{D,eq})}{d(\log X_D)} = \frac{1}{k} \tag{12}$$

where $P_{D,eq}$ is the equilibrium pressure of monoatomic dopant D and X_D is the total atomic fraction of D in the gas phase.

The influence of the total pressure on lateral autodoping is analogous to the effect of the total pressure on the monoatomic dopant partial pressure

$$\frac{d(\log P_{D,eq})}{d(\log P_{tot})} = \frac{2 - l - m}{2k} \tag{13}$$

It should be noted that for $k = 1$ and $l = m = 0$ the chemistry becomes trivial and the equations reduce to the forms which are in agreement with the implications of the "physical" evaporation-diffusion-reincorporation model.

The presence of chlorine in the reaction gas mixture, introduced via either a chlorine containing silicon source or addition of hydrogen chloride, may affect the autodoping level according to the expression

$$\frac{d(\log P_{D,eq})}{d(\log X_{Cl})} = -\frac{m}{k} \quad [14]$$

which implies that the possible presence of stable dopant chlorides reduces the efficiency of the autodoping process. Hence, if the prevailing dopant species are hydrogen and chlorine containing compounds, the stability of monoatomic dopant gas is enhanced at reduced pressure, resulting in increased autodoping.

If the experimentally observed autodoping behavior of antimony, arsenic, phosphorus, and boron is considered, it appears that arsenic and antimony display a behavior that is qualitatively in agreement with the "physical" model; *viz.*, the autodoping level is reduced by reduction of the total pressure, an extension of the pre-epitaxial bake time, and a rise of temperature. As a matter of fact, an analysis of the chemistry of these systems makes it clear that chemical reactions in the gas phase do not affect the autodoping mechanism qualitatively. In contrast, for phosphorus and boron a different pattern is observed: the autodoping level is enhanced by reduction of total pressure, extension of the pre-epitaxial bake time, and increase of temperature. The increased autodoping at low pressure can be explained by the statement, deduced from the thermodynamic analyses, that in the case of phosphorus and boron the stability of the monoatomic dopant gas is enhanced by reduction of the total pressure. Analogously, the stability of monoatomic phosphorus and boron is considerably enhanced at higher temperatures. The effect of the duration of the pre-epitaxial bake time on boron autodoping remains as yet unexplained. It may be assumed that either accumulation of evaporated impurities at the substrate surface during the pre-epitaxial

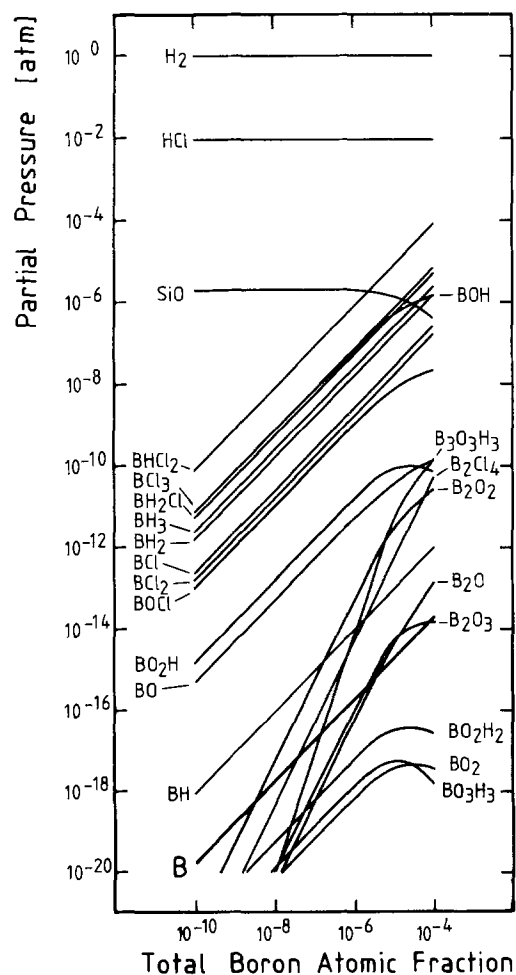


Fig. 20. Equilibrium composition of the B-Si-H-Cl-O system as a function of the B atomic fraction. Mass balance: 1% Cl; 1 ppm O₂. Total pressure: 1 atm. Temperature: 1350 K.

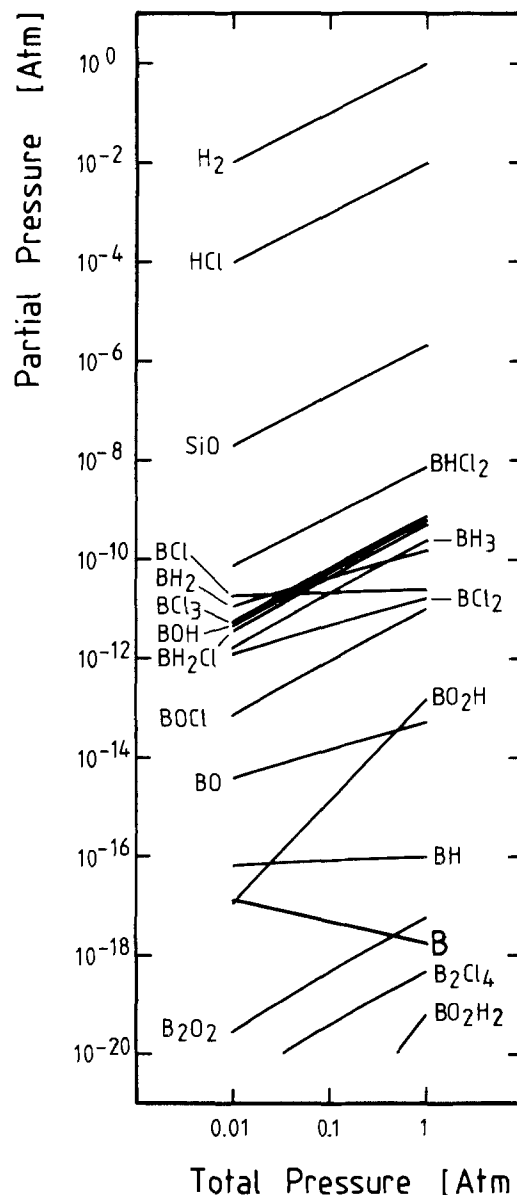


Fig. 21. Equilibrium composition of the B-Si-H-Cl-O system as a function of the total pressure. Mass balance: 1% Cl; 1 ppm O₂; 10 ppb B. Temperature: 1350 K.

bake or departure from pure equilibrium conditions due to kinetic limitations are responsible for these observations. Finally, it has been shown that, in agreement with the considerations given above, the presence of chlorine causes a notable reduction of the autodoping maximum in the case of boron, whereas in the cases of arsenic and phosphorus no effect was observed. This is explained by the assumption that stable boron chlorides can be formed, whereas according to the thermodynamic analyses no stable chlorides of arsenic and phosphorus are present.

Acknowledgments

The authors gratefully acknowledge the helpful discussions with Professor Dr. J. Bloem. They would also like to thank Dr. W. J. M. J. Josquin and his assistants for conducting the implantations.

Manuscript submitted Sept. 27, 1984; revised manuscript received April 11, 1985. This was Paper 456 presented at the New Orleans, Louisiana, Meeting of the Society, Oct. 7-12, 1984.

Philips Research Laboratories assisted in meeting the publication costs of this article.

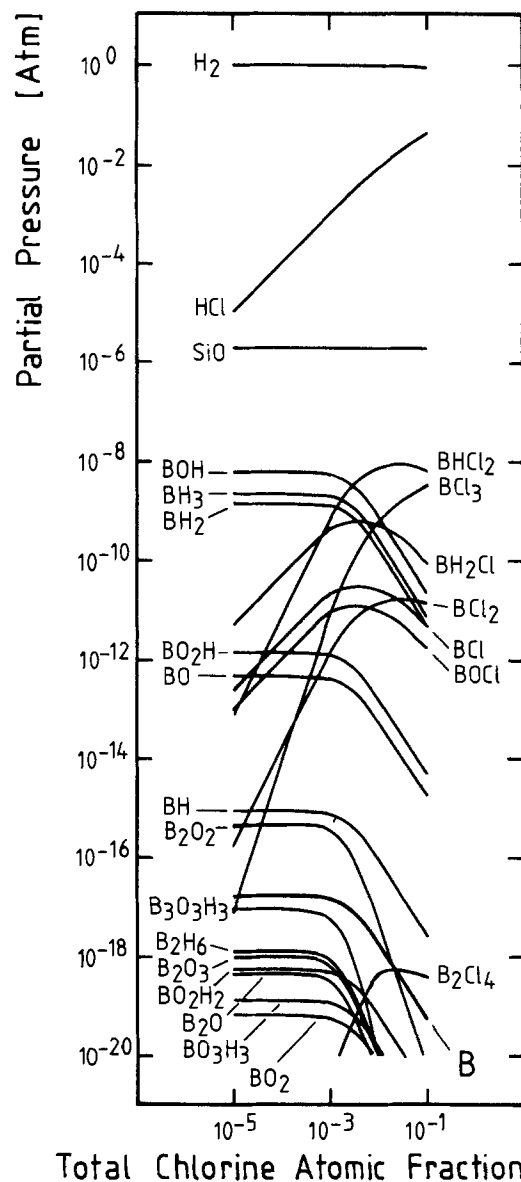


Fig. 22. Equilibrium composition of the B-Si-H-Cl-O system as a function of the Cl atomic fraction. Mass balance: 1 ppm O₂; 10 ppb B. Total pressure: 1 atm. Temperature: 1350 K.

REFERENCES

- A. S. Grove, A. Roder, and C. T. Sah, *J. Appl. Phys.*, **36**, 1065 (1963).
- C. O. Thomas, D. Kahng, and R. C. Manz, *This Journal*, **109**, 1055 (1962).
- J. J. Grossman, *ibid.*, **110**, 1065 (1963).
- P. H. Langer and J. I. Goldstein, *ibid.*, **124**, 591 (1977).
- H. B. Pogge, D. W. Boss, and E. Ebert, in "Chemical Vapor Deposition," J. M. Blocher, Jr., and J. C. Withers, Editors, p. 767, The Electrochemical Society Softbound Proceeding Series, Princeton, NJ (1974).
- M. Onuki and A. Nishikawa, *J. Phys. C*, **43**, 93 (1982).
- M. Tabe and H. Nakamura, *This Journal*, **126**, 822 (1979).
- G. R. Srinivasan, *J. Appl. Phys.*, **51**, 4824 (1980).
- G. R. Srinivasan, *IEEE Trans. Electron Devices*, **ed-27**, 1493 (1980).
- G. R. Srinivasan, *This Journal*, **127**, 1334 (1980).
- N. Ogirima, *ibid.*, **124**, 903 (1977).
- R. B. Herring, *Solid State Technol.*, **22** (11), 75 (Nov. 1979).
- S. B. Kulkarni and A. A. Kozul, Abstract 540, p. 1351, The Electrochemical Society Extended Abstracts, Vol. 80-2, Hollywood, FL, Oct. 5-10, 1980.
- P. Rai-Choudhury and E. I. Salkovitz, *J. Cryst. Growth*, **7**, 353 (1970).
- J. Bloem, L. J. Giling, and M. W. M. Graef, *This Journal*, **121**, 1354 (1974).
- H. Kuhne, *Cryst. Res. Technol.*, **17**, 181 (1982).
- R. Reif, T. I. Kamins, and K. C. Saraswat, *This Journal*, **126**, 644 (1979).
- M. W. M. Graef and B. J. H. Leunissen, Abstract 456, p. 655, The Electrochemical Society Extended Abstract, Vol. 84-2, New Orleans, LA, Oct. 7-12, 1984.
- L. J. Giling and J. Bloem, *J. Cryst. Growth*, **31**, 317 (1975).
- G. R. Srinivasan, *This Journal*, **125**, 146 (1978), and references therein.
- P. van der Putte, L. J. Giling, and J. Bloem, *J. Cryst. Growth*, **31**, 299 (1975).
- E. Sirtl, L. P. Hunt, and D. H. Saywer, *This Journal*, **121**, 919 (1974).
- H.-R. Chang, Abstract 342, p. 548, The Electrochemical Society Extended Abstracts, Vol. 83-2, Washington, DC, Oct. 9-14, 1983.
- J. O. Carlsson and M. Boman, Abstract 158, p. 241, The Electrochemical Society Extended Abstracts, Vol. 84-1, Cincinnati, OH, May 6-11, 1984.
- H.-R. Chang, Abstract 118, p. 177, The Electrochemical Society Extended Abstracts, Vol. 84-1, Cincinnati, OH, May 6-11, 1984.
- W. C. Metz, Abstract 209, p. 305, The Electrochemical Society Extended Abstracts, Vol. 84-1, Cincinnati, OH, May 6-11, 1984.
- J. Bloem, *This Journal*, **118**, 1837 (1971).
- H. T. J. M. Hintzen, J. Bloem, and L. J. Giling, *ibid.*, **131**, 1900 (1984).
- I. Barin and O. Knacke, "Thermodynamical Properties of Inorganic Substances," Springer, Berlin (1973).
- I. Barin, O. Knacke, and O. Kubaschewski, "Thermodynamical Properties of Inorganic Substances," Supplement, Springer, Berlin (1977).
- "Selected Values of Chemical Thermodynamic Properties," NBS Technical Note 270-3, National Bureau of Standards, Washington, DC (1968).
- M. W. Richardson and B. I. Nolang, Private communication.
- A. A. Saaman, Private communication.

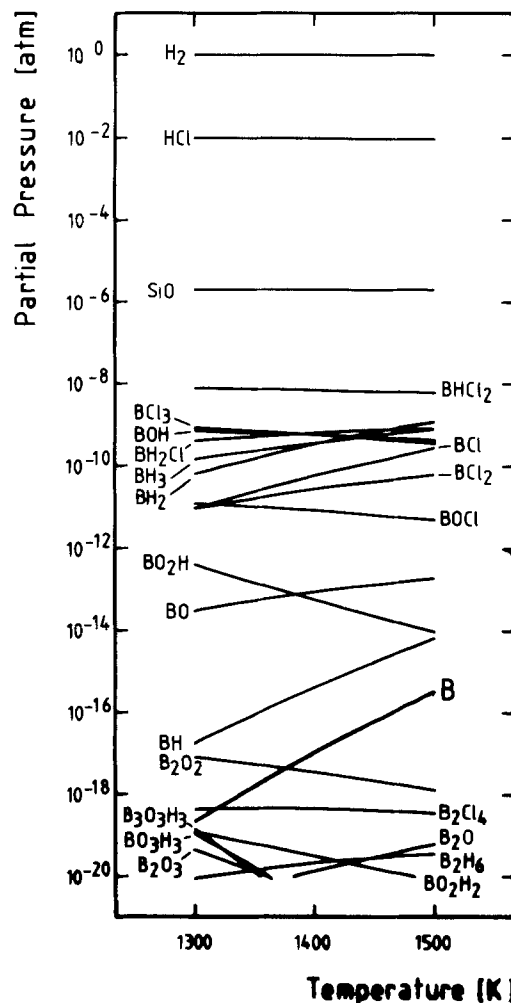


Fig. 23. Equilibrium composition of the B-Si-H-Cl-O system as a function of temperature. Mass balance: 1% Cl; 1 ppm O₂; 10 ppb B. Total pressure: 1 atm.

34. J. L. Gentner, Ph.D. Thesis, University of Clermont II, Clermont, France (1981).
35. D. W. Shaw, *J. Phys. Chem. Solids*, **36**, 111 (1975).
36. P. Klima, J. Silhavy, V. Rerabek, I. Braun, C. Cerny, P. Vonka, and R. Holub, *J. Cryst. Growth*, **32**, 279 (1976).
37. O. Kubaschewski, E. Evans, and C. B. Alcock, "Metallurgical Thermochemistry," 4th ed., Pergamon Press, Oxford (1967).
38. JANAF Thermochemical Tables, 2nd ed., NSRDS-NBS 37, National Bureau of Standards, Washington, DC (1971).
39. JANAF Thermochemical Tables, 1974 Suppl., *J. Phys. Chem. Ref. Data*, **3**, 311 (1974).
40. JANAF Thermochemical Tables, 1978 Suppl., *ibid.*, **7**, 793 (1978).
41. JANAF Thermochemical Tables, 1982 Suppl., *ibid.*, **11**, 695 (1982).
42. J. O. Carlsson, *J. Less-Common Metals*, **71**, 15 (1980).

Dry Etching of Tapered Contact Holes Using Multilayer Resist

R. J. Saia* and B. Gorowitz*

General Electric Corporate Research and Development Center, Schenectady, New York 12301

ABSTRACT

Optimum coverage of contact holes by sputtered metals typically requires sloping of the sidewalls. A number of different types of photoresists and dry etch techniques have been examined for this purpose. Two processes which will be discussed include (i) replication of a presloped single-layer AZ-type photoresist profile by anisotropically etching the resist and the silicon dioxide at comparable rates, and (ii) controlled lateral etching of a vertical-walled poly (methyl methacrylate) (PMMA) layer of a two-layer resist, while etching silicon dioxide in the vertical direction. The latter process preserves the inherent accurate resolution of the vertical PMMA profile, while providing an opportunity for tailored and reproducible sidewall angles. The results of mass and emission spectroscopy suggest that atomic oxygen plays an important role in the lateral etching of the PMMA resist.

With continuously decreasing microcircuit element dimensions, the ability to accurately etch small contact holes or vias in the 1.0-2.0 μm range with controlled sidewall angles provides an opportunity for improved coverage of the sidewalls by the deposited metallizations.

The most widely used method of producing sloped sidewalls is to replicate a presloped single-layer AZ-type photoresist profile by anisotropically etching the resist and silicon dioxide at approximately the same rate. This process is difficult to control and has a number of other disadvantages (to be discussed below) that make it particularly unreliable when used with holes in the 1 μm range.

A new technique for reliably producing tapered contact holes or vias in the 1 μm range will be described. This technique utilizes poly(methyl methacrylate) (PMMA), the lower remaining layer of a two-layer resist, to define holes with initially vertical walls in the mask. The plasma gas chemistry and the process conditions were selected so that the resist is etched laterally at a controlled rate relative to the vertical etch rate of the silicon dioxide. The process has been demonstrated in both a batch-loaded low pressure reactive ion etcher, and a high pressure single-wafer plasma system. The contact sidewall angles could be controlled and varied from 35° to 90°. This process makes use of the inherent accurate resolution and vertical wall profile of the multilayered resist, while providing the ability to taper contact holes or vias as small as 1 μm diam or any other dimension which can be resolved by lithographic techniques.

Experimental

Two types of plasma etchers were used in this study: a batch-loaded reactive ion etcher and a single-wafer high pressure plasma system. The former was an Anelva Model 503. This system is manually loaded, with a capability for etching eight 75 mm diam wafers per run or a lesser number of larger wafers. It is equipped with a cryopumped high vacuum system capable of reducing background pressures to the 10⁻⁶ torr range between runs. The gases are introduced into the chamber circumferentially, and their flows are maintained by electronic mass flow controllers. A roots blower backed by a mechanical pump is used to evacuate the etchant gases and volatile products.

RF power, at a frequency of 13.56 MHz, is provided to the lower of two parallel plate electrodes in a stainless

steel chamber having a volume of about 60 liter. The wafers being etched are placed in holes in a graphite disk which covers the 42 cm diam water-cooled cathode.

The high pressure plasma etcher (Tegal Model 703) was a single-wafer, cassette-to-cassette system. The reactant gases and the reaction products enter and exit, respectively, through arrays of holes in the upper electrode. The upper and lower electrodes are fabricated from aluminum and are separated by a gap of 6 mm. Both electrodes are water cooled. Excitation energy to the lower electrode, which holds the wafer, is provided by a 1000W solid-state RF generator operating at 13.56 MHz.

Analysis of the plasma was performed with an Inficon IQ200 quadrupole mass spectrometer, and a P.T. analytical PSS100 optical emission spectrometer. Both systems were attached to ports in the chamber of the batch reactive ion etching systems.

The silicon dioxide films that were etched were deposited on 75 mm diam silicon wafers by low pressure chemical vapor deposition (LPCVD) using dichlorosilane and nitrous oxide at 900°C. The wafers were then cleaned by standard techniques and coated with the photoresist systems described below.

Etch rates of photoresist and silicon dioxide were determined using a Sloan Dektak II profilometer and a Nanometrics Nanospec film thickness measuring system. Sidewall angles and the amount of lateral etching were measured using scanning electron microscopy.

Profile Control Using Preshaped Photoresist

One method of achieving sloped or tapered silicon dioxide contact hole sidewalls involves controlled photoresist erosion (1, 2). If the photoresist is preshaped to have a sloped profile before etching, the etch rate of photoresist with respect to silicon dioxide can be adjusted so that anisotropic etching of both will increase the photoresist hole diameter as the silicon dioxide is being etched in a vertical direction. This results in the formation of a slope in the oxide sidewall.

In this experiment, the LPCVD oxide films were masked with 10,000Å of Shipley AZ1470 positive photoresist. The photoresist profile was preshaped by reflow baking in a vacuum oven (100 mtorr) at 135°C for 30 min. Figure 1 shows the typical photoresist profile after standard projection lithography, after preshaping the photoresist, and after etching the silicon dioxide at 1:1 and 1.5:1 resist-to-oxide etch-rate ratios. Mixtures of NF₃

* Electrochemical Society Active Member.

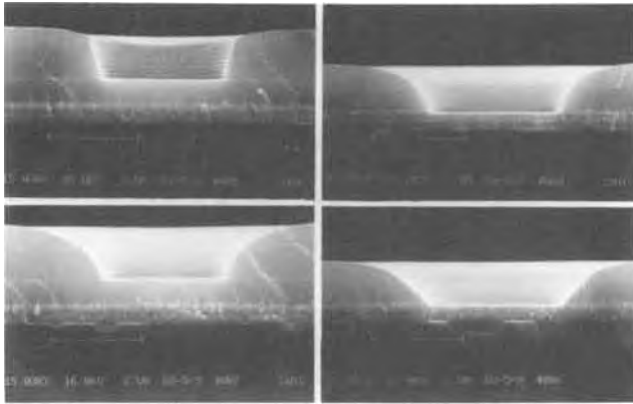


Fig. 1. SEM photos of profile control in 2.5 μm contact holes using preshaped photoresist. A (top left): After exposure and development. B (bottom left): After photoresist has been preshaped at 140°C for 30 min. C (top right): After etching sample shown in B with 20% NF_3 in Ar, photoresist not removed. D (bottom right): After etching sample in B with 50% NF_3 in Ar, photoresist not removed.

and Ar were used in the batch reactive ion etcher to vary the relative etch rates and, consequently, the incline angle of the contact hole sidewall. For example, as can be seen in Fig. 2, approximately equal etch rates of photoresist and silicon dioxide were obtained on planar topography using 20% NF_3 in Ar.

This process for forming sloped sidewalls can be employed reliably for contact holes in the 2 μm or larger range if precise control of the slope and bottom hole dimensions are not required. The photoresist profile depends on the initial lithographic exposure conditions, the surface topography of the wafer, and contact hole size. The resist reflow process is also sensitive to such factors as moisture, white light, temperature, and pressure, if reflowing is done in a vacuum oven. Figure 3 shows the effects of attempts to use the reflow method to produce tapered holes in the 1 μm range. A vacuum bake at 135°C for 15 min only round the top half of the resist profile, while longer oven exposures only decrease the hole diameter until finally it closes completely at the oxide interface. Under some conditions, it has been possible to avoid resist reflow by using the slope inherent to a particular lithographic tool or process. However, the range of conditions for successful use of the sloped resist profile to

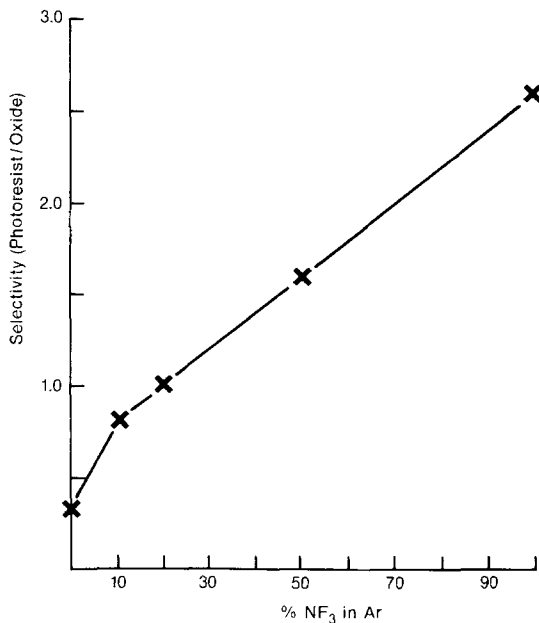


Fig. 2. Selectivity of resist to silicon dioxide vs. NF_3/Ar composition. Etching parameters: flow = 50 sccm; pressure = 100 mtorr; power = 300W.

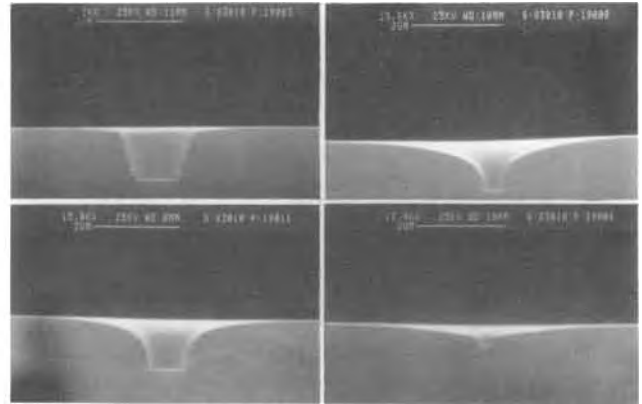


Fig. 3. SEM photos of attempts to preshape photoresist sidewalls of 1 μm diam holes. A (top left): After exposure and development. B (bottom left): After 140°C for 15 min. C (top right): After 140°C for 30 min. D (bottom right): After 140°C for 45 min.

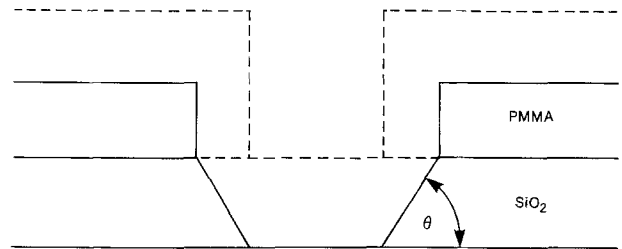


Fig. 4. Sloped sidewall formed by lateral erosion of PMMA, where θ is the sidewall incline angle.

make tapered oxide holes in the 1 μm range is obviously quite narrow, and precise control is difficult.

Tapered Contact Holes Using Multilayer Resist

To avoid the problem of variable photoresist profile and to avoid the need for a resist reflow process, it is desirable to use a high resolution photoresist patterning method that can produce vertical resist sidewalls which offer the best opportunity for precise control of contact hole dimensions. The production of sloped contact sidewalls without sloped photoresist, however, requires

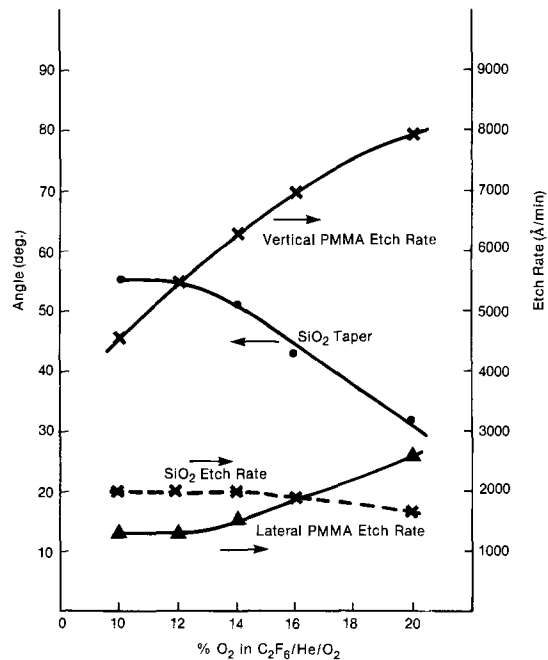


Fig. 5. Contact sidewall angle and etch rate of silicon dioxide and PMMA vs. percentage O_2 in $\text{C}_2\text{F}_6/\text{He}/\text{O}_2$. Etching parameters: flow = 50 sccm, 20% C_2F_6 ; pressure = 2.0 torr; power = 400W.

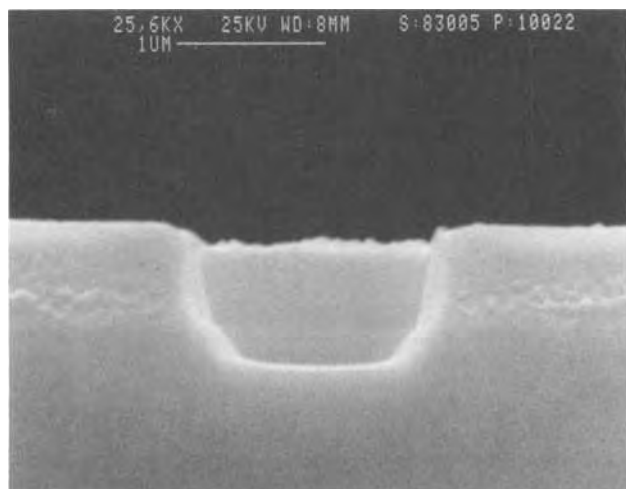


Fig. 6. SEM photo of contact hole etched using PMMA lateral erosion. PMMA has not been removed from oxide.

that the photoresist mask be laterally etched as the silicon dioxide is vertically etched.

The basic steps in pattern formation, using one method of two-layer resist lithography are described in detail elsewhere (3-5). A thick (e.g., 1.5-2.5 μm) planarizing layer of PMMA (avg. Mw \sim 496,000) is applied to the wafer and baked at 200°C for 30 min in a nitrogen atmosphere. The PMMA is then coated with a 3000Å layer of AZ-type photoresist. After exposing and developing the top layer in a conventional manner, the lower PMMA layer is exposed with UV radiation (220-250 nm) using the upper layer as a mask. The PMMA is then developed and the AZ resist layer is removed. The resulting vertical-walled PMMA mask apertures must then be laterally etched at the same time as the silicon dioxide is being vertically etched. Theoretically, the tangent of the incline angle (shown in Fig. 4) produced by this method is equal to the quotient of the vertical etch rate of silicon dioxide and the lateral etch rate of PMMA.

The incline angle θ could be varied in the high pressure etcher from about 55° to 35° by adding oxygen to a $\text{C}_2\text{F}_6/\text{He}$ mixture (see Fig. 5). It can be seen from Fig. 5 that the vertical etch rates of PMMA are relatively high, but with typical interlevel dielectric thicknesses of 4000-5000Å, the loss of resist is not a problem. Figure 6 is a scanning electron microscopy (SEM) photo of a contact hole that was etched using this method. The remaining PMMA is still fairly vertical although the slope of the contact hole is about 60°.

The incline angle could also be controlled from 90° to 35° by adding oxygen to a mixture of CHF_3/Ar in the batch reactive ion etcher (see Fig. 7). To obtain a higher selectivity ratio of silicon dioxide to silicon, a two-step etch can be used in which oxygen is removed from the gas mixture in the second step.

Using an AZ- or Novolak-type resist, tapered contact holes could not be produced with the above conditions because this material did not etch laterally in the range of conditions investigated. What appears to be true lateral etching of photoresist has been observed by others using different etch conditions and gas compositions (6).

PMMA is known to have relatively poor plasma-etch resistance (7). In the case described here, this can be used to advantage. Novolak or AZ resists, conversely, tend to have a higher etch resistance, because they are condensation-type aromatic polymers. With condensation polymers, chain scissioning events during exposure to the plasma might not propagate sufficiently to produce large numbers of fragments that are small enough to be volatile. Acrylates such as PMMA, however, are addition-type polymers that can readily "unzip" via radical intermediates into low molecular weight volatile species.

Two of the species that are known to degrade and etch organic photoresist are atomic oxygen and fluorine.

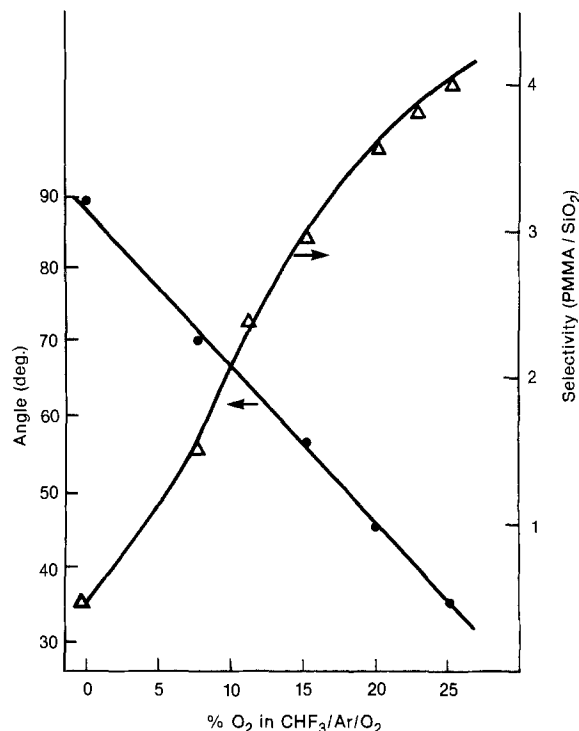


Fig. 7. Contact hole sidewall angles and selectivity of PMMA to silicon dioxide vs. percentage of O_2 in $\text{CHF}_3/\text{Ar}/\text{O}_2$. Etching parameters: flow = 40 sccm, 38% CHF_3 in Ar; pressure = 30 mtorr; power = 225W.

Atoms or radicals are not affected by the sheath electric field of the plasma and therefore can etch in the lateral as well as the vertical directions if the sidewalls are not protected. Oxygen atoms influence the durability of PMMA (8, 9) since they are excellent radical initiators, and can therefore contribute to or enhance the lateral etch rate of PMMA.

Fluorine atoms that are generated in a plasma discharge can also abstract hydrogen from organic polymers providing unsaturated or radical sites. Compared to a normal saturated polymer chain, these sites are highly reactive

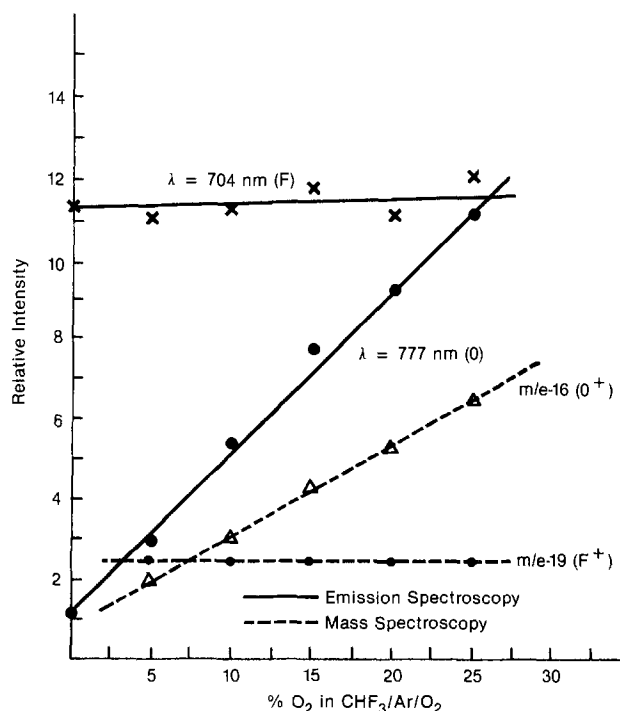


Fig. 8. Relative intensity of F and O atom signals vs. percentage of O_2 in $\text{CHF}_3/\text{Ar}/\text{O}_2$ using both emission and mass spectroscopy.

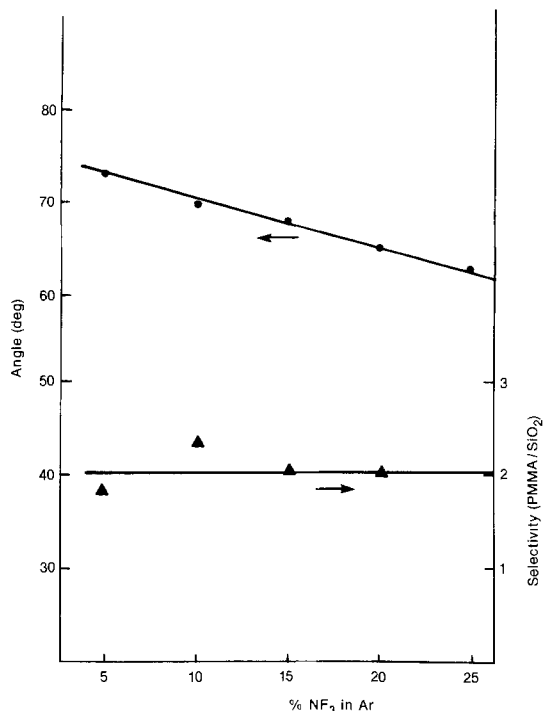


Fig. 9. Contact hole sidewall angle and selectivity of PMMA to silicon dioxide vs. percentage of NF_3 in Ar. Etching parameters: flow = 50 sccm; pressure = 100 mtorr; power = 300W.

and easily combined with oxygen (10). The exothermic nature of hydrogen abstraction by fluorine can itself be enough to cleave carbon-carbon bonds (11).

Figure 8 shows the relative intensity of both F and O atom signals, using both emission and mass spectroscopy, as functions of oxygen addition to CHF_3/Ar . It can be seen that the population of atomic oxygen increases, while atomic fluorine is relatively constant as oxygen is added. This suggests that atomic O plays more of a role than does atomic F in the lateral etching of PMMA, because its presence correlates with the degree of slope produced.

While etching with a gas mixture that does not contain oxygen (for example, NF_3 and Ar), the incline angle could only be controlled from 60° to 73° (see Fig. 9). The corresponding percentages of NF_3 in Ar resulted in large differences in the amount of atomic fluorine present (see Fig. 10). The fact that the incline angles could only be controlled over a small range, in spite of a large difference in the amount of atomic F present, further demonstrates that atomic oxygen has a larger effect. Similar results were also observed for the etching of polyimide in CF_4/O_2 and SF_6/O_2 (12).

Summary

Tapered contact holes or vias were produced using a high resolution two-level resist, without preshaping the vertical-walled resist mask with a reflow method. Contact hole sidewalls were sloped by the controlled lateral etching of a PMMA mask while etching silicon dioxide in the vertical direction.

This process was demonstrated in both a high pressure plasma etcher and a low pressure reactive ion etcher. Mass and emission spectroscopy data suggest that atomic

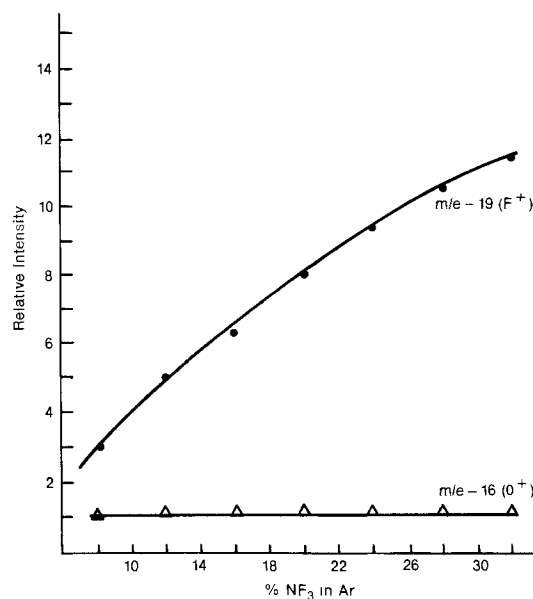


Fig. 10. Relative intensity of F and O atom signals vs. percentage of NF_3 in Ar using mass spectroscopy.

oxygen plays a more important role in the lateral etching of PMMA than does atomic fluorine.

Acknowledgment

The authors would like to thank J. Schermerhorn for his technical assistance, D. Skelly and P. Frank for providing PMMA patterning, and J. Norton for SEM photos.

Manuscript submitted Dec. 26, 1984; revised manuscript received April 18, 1985. This was Paper 707 RNP presented at the New Orleans, Louisiana, Meeting of the Society, Oct. 7-12, 1984.

General Electric Company assisted in meeting the publication costs of this article.

REFERENCES

1. E. Crabbe and E. R. Sirkin, in "Plasma Processing," G. S. Mathad, G. C. Schwartz, and G. Smolinsky, Editors, p. 261, The Electrochemical Society Softbound Proceedings Series, Pennington, NJ (1983).
2. J. A. Bondur and R. G. Freiser, in "Plasma Processing," R. G. Frieser and C. J. Mogab, Editors, p. 180, The Electrochemical Society Softbound Proceedings Series, Pennington, NJ (1981).
3. B. F. Griffing, in "Proceedings of the IEDM," p. 562 IEEE, New York (1981).
4. B. F. Griffing, *J. Vac. Sci. Technol.*, **19**, 1423 (1981).
5. B. J. Lin, E. Bassous, V. W. Chao, and K. E. Petrillo, *ibid.*, **19**, 1313 (1981).
6. M. T. Duffy, R. A. Soltis, and A. Day, Abstract 165, p. 265, The Electrochemical Society Extended Abstracts, Vol. 83-1, San Francisco, CA, May 8-13, 1983.
7. M. P. C. Watts, *Microelectron. Manuf. Testing*, **40** (June 1984).
8. K. Harada, *J. Appl. Polym. Sci.*, **26**, 1961 (1981).
9. B. J. Wu, D. W. Hess, D. S. Soong, and A. T. Bell, *J. Appl. Phys.*, **54**, 1725 (1983).
10. D. L. Flamm, V. W. Donnelly, and D. E. Ibbotson, "VLSI Electronics Microstructure Science," Vol. 8, Chap. 8, p. 231, Academic Press, New York (1984).
11. L. A. Pederson, *This Journal*, **129**, 205 (1982).
12. F. Emmi, F. Equito, V. Vukanovic, and R. Horwath, Abstract 373, p. 525, The Electrochemical Society Extended Abstracts, Vol. 84-2, New Orleans, LA, Oct. 7-12, 1984.

A Study of Silicon Incorporation in GaAs MOCVD Layers

E. Veuhoff, T. F. Kuech,* and B. S. Meyerson*

IBM Thomas J. Watson Research Center, Yorktown Heights, New York 10598

ABSTRACT

The incorporation of silicon in GaAs layers grown by metal-organic chemical vapor deposition has been studied using two different doping sources, silane and disilane. Epitaxial layers were grown on $\langle 100 \rangle$, $\langle 111 \rangle_A$, and $\langle 111 \rangle_B$ surfaces over a wide range of growth temperature and gas phase stoichiometry. When using silane, an influence of the substrate orientation on silicon incorporation was found. This behavior can be described by a qualitative model involving both the surface specific adsorption sites and possible surface chemical reactions. In the case of disilane, the incorporation process appears to be independent of substrate orientation and growth temperature. This temperature independence results in improved uniformity of the electron concentration over large substrate areas when disilane is used as the doping gas.

Silicon is commonly used as a dopant for the growth of n-type GaAs and $\text{Al}_x\text{Ga}_{1-x}\text{As}$ layers in metal-organic chemical vapor deposition (MOCVD) (1-3) and in molecular beam epitaxy (MBE) (4). The low volatility and low diffusion coefficient of silicon in GaAs are properties which make this dopant especially useful for the deposition of layers for device structures requiring abrupt dopant profiles (2). Perhaps a more important requirement for the fabrication of digital devices is the uniformity of the dopant concentration across large substrate areas. Doping with silicon in the MOCVD growth of GaAs and $\text{Al}_x\text{Ga}_{1-x}\text{As}$ is most commonly achieved by the addition of small amounts of silane (SiH_4) to the growth ambient. The silicon concentration exhibits a strong dependence on growth temperature when using silane (1-3). A strong temperature dependence of incorporation can lead to problems in obtaining uniform and reproducible doping levels over large substrate areas (3). We have recently shown that by using disilane (Si_2H_6) as the doping gas, the incorporation of silicon is made independent of growth temperature (5). Owing to this unique behavior of disilane, we expect an improvement in uniformity and reproducibility of the carrier concentration.

Only limited information is available in the literature on the incorporation process of silicon in GaAs MOCVD layers. Generally, the strong temperature dependence of silane as a doping source has been attributed to the stability of the SiH_4 molecule. It is assumed that the incorporation process is rate limited by the decomposition of the SiH_4 molecule (6). If this is the case, the growth temperature would be the major influence on silicon incorporation. The relative importance of the gas phase chemistry between the pyrolysis of SiH_4 and Si_2H_6 can in part be estimated by calculations based on the homogeneous decomposition kinetics of Si_2H_6 and SiH_4 using the available kinetic rate constants (7, 8). These calculations indicate that under our experimental conditions Si_2H_6 reaches gas phase equilibrium with its decomposition products (SiH_2 , SiH_3 , Si_2H_5 , Si_3H_{10} , etc.) on a time scale several orders of magnitude faster than SiH_4 (9), which indicates that SiH_4 is substantially more stable than Si_2H_6 in the gas phase. As a consequence, silicon doping by means of silane decomposition is expected to be more sensitive to reactions at the growing surface than to the gas phase chemistry present in the MOCVD growth ambient.

In the present study, we have investigated the influence of growth parameters, particularly the influence of adsorption sites at the surface, on silicon incorporation when using SiH_4 and Si_2H_6 as doping gases. Substrates of differing orientation were used to alter the number and nature of the adsorption sites present. Growth temperature and gas phase stoichiometry [$\text{AsH}_3:\text{Ga}(\text{CH}_3)_3$ ratio] were also varied over a wide range. To our knowledge, the effect of substrate orientation on the incorporation of Si has previously been studied only for layers grown by liquid phase epitaxy (LPE) (10). In the present study, the same saturation value of the electron concentration of $n \approx$

$5 \times 10^{18} \text{ cm}^{-3}$ is reached, for both SiH_4 and Si_2H_6 . This saturation value has also been reported for MBE (4) and other MOCVD layers (11). The amphoteric nature of silicon in GaAs which is well known for LPE material (12, 13) has been investigated here, particularly at high silicon concentrations. When SiH_4 is used as the dopant source the incorporation behavior of silicon appears similar to that of carbon (14). A correlation between the incorporation of silicon and carbon due to possible surface reactions between their adsorbed species is discussed below. The uniformity of dopant concentration across large substrate areas is compared for the two doping gases.

Growth and Characterization

The layers were grown in a horizontal MOCVD system at a reactor pressure of 77 torr on Cr-doped semi-insulating GaAs substrates. Starting materials were $\text{Ga}(\text{CH}_3)_3$ (TMG) and AsH_3 in a hydrogen carrier gas. SiH_4 and Si_2H_6 were used as doping gases, supplied in the form of dopant/ H_2 mixtures. Three different substrate orientations were used simultaneously during the runs for the study of the influence of adsorption sites on doping: $\langle 100 \rangle$, $\langle 111 \rangle_A$ ($\langle 111 \rangle_{\text{Ga}}$), and $\langle 111 \rangle_B$ ($\langle 111 \rangle_{\text{As}}$). The substrates were cleaned according to a standard procedure (14). The growth rate was held constant in all experiments at $0.05 \mu\text{m}/\text{min}$. The V:III [$\text{AsH}_3:\text{Ga}(\text{CH}_3)_3$] ratio was varied between 20 and 80, although most of the layers were deposited at a V:III ratio of 40. The linear gas velocity was approximately 30 cm/s in the 75 mm diam reactor. The substrates were placed on a RF-heated graphite susceptor during growth. Further experimental details are described in Ref. (15).

The silicon concentration in the layers was determined by secondary ion mass spectrometry (SIMS). The layers were characterized by electrical measurements using capacitance profiling and the van der Pauw-Hall method (16). Photoluminescence measurements were performed at room temperature. The luminescence was excited by the 4880 Å line of an argon laser and detected by a cooled S-1 photomultiplier tube.

In order to measure the uniformity of the carrier concentration across large substrate areas, growths of large area $\langle 100 \rangle$ substrates ($\sim 30 \text{ cm}^2$) were undertaken. Two growths under identical conditions were made. Silane was used as the doping source for one growth, and disilane was used in the second. The growths were carried out at a substrate temperature of 650°C. The carrier concentration was measured across the substrate surface by capacitance profiling, which has a measurement accuracy of approximately 5%.

Experimental Results

The influence of substrate orientation on silicon incorporation is shown in Fig. 1 and 2. Doping with SiH_4 was investigated over the range of the growth temperature 600°-900°C (Fig. 1). The well-known temperature dependence of the electron concentration determined by Hall measurements can be observed on all three surfaces. Over

* Electrochemical Society Active Member.

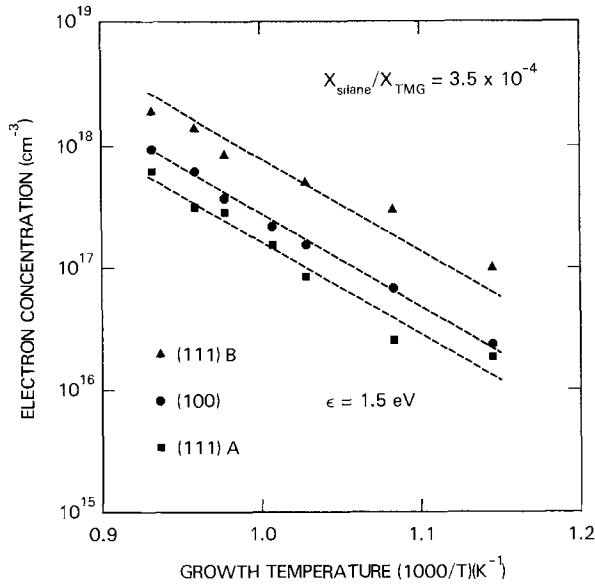


Fig. 1. Influence of growth temperature on electron concentration for the $\langle 100 \rangle$, $\langle 111 \rangle$ A, and $\langle 111 \rangle$ B surfaces when using SiH_4 as doping gas.

the entire temperature range, the carrier concentration in layers grown on the $\langle 111 \rangle$ B surface is systematically the highest; on the $\langle 111 \rangle$ A it is the lowest. The slope of the curves are the same within the accuracy of measurement for the three surfaces which corresponds to an activation energy (ϵ) of 1.5 eV. This activation energy is in agreement with former studies for the $\langle 100 \rangle$ surface (1-3). The surface morphology of the layers grown on the $\langle 111 \rangle$ substrates exhibited hillocks that are characteristic for the particular surface, as described in Ref. (17). The $\langle 100 \rangle$ surfaces always gave a smooth specular surface morphology. Experiments were carried out in the range of 650°-800°C with Si_2H_6 as doping gas (Fig. 2). The accuracy of measurement was 5% for the $\langle 100 \rangle$ and 15% for the $\langle 111 \rangle$ samples. The latter is indicated by error bars in Fig. 2. A primary source of measurement uncertainty is attributed to fluctuations in the film thickness due to the rough morphology of the $\langle 111 \rangle$ surfaces. There is no influence of substrate orientation at the lower growth temperatures, while at higher temperatures above 760°C an influence can be recognized. A comparison of these figures shows that doping with Si_2H_6 is much more efficient than with SiH_4 , as discussed earlier (15). The electron concentration was inversely proportional to the growth rate for both silane and disilane doping. The mole

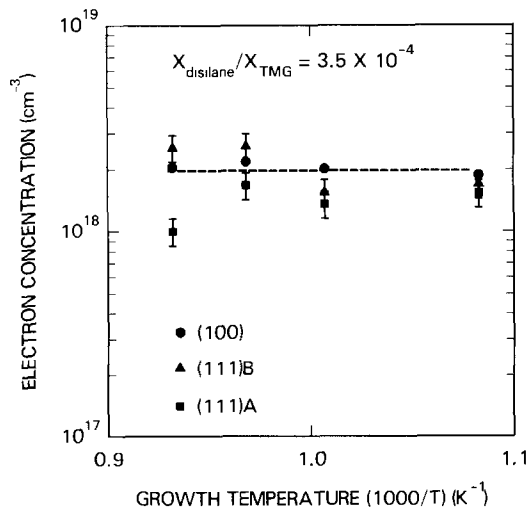


Fig. 2. Electron concentration as a function of growth temperature for the $\langle 100 \rangle$, $\langle 111 \rangle$ A, and $\langle 111 \rangle$ B surfaces when using Si_2H_6 as a doping gas.

fractions of the doping gas were therefore normalized with respect to the growth rate. Both sets of experiments in Fig. 1 and 2 were obtained at a V:III ratio of 40. The V:III ratio had only a weak influence on the electron concentration. For Si_2H_6 a slight increase and for SiH_4 a slight decrease of carrier concentration was observed as this ratio was increased from 20 to 80. The systematic change in carrier concentration was of ~15% in both cases.

The electron concentration in the layers increases linearly with the silicon concentration in the gas phase and saturates at a level of $n \approx 5 \times 10^{18} \text{ cm}^{-3}$. The SIMS measurements show that the silicon concentration equals the electron concentration for the $\langle 100 \rangle$ and $\langle 111 \rangle$ surfaces up to an electron concentration in the low 10^{18} range. At electron concentrations in the saturation region, silicon concentrations up to 10^{20} cm^{-3} were detected.

In the uniformity study previously described, the silane samples showed a fluctuation in carrier concentration of $\Delta n/n \sim \pm 0.15$ over each sample area; the lowest concentrations were obtained at the edges of the graphite susceptor. For the disilane samples we found $\Delta n/n \sim \pm 0.05$ for each sample, with the fluctuation occurring randomly over the substrate surface.

The Hall mobilities measured at room temperature for the silicon-doped samples are plotted as a function of electron concentration in Fig. 3. The solid line represents a fit to the experimental data from layers grown by different techniques [i.e., MBE, LPE, MOCVD, and inorganic vapor phase epitaxy (VPE)] under different experimental conditions (18, 19). In the range of $n = 10^{16}$ - 10^{18} cm^{-3} , the mobilities depend only on the carrier concentration. Both SiH_4 and Si_2H_6 yielded mobility values which are in agreement with this empirical curve.

The results of the photoluminescence measurements on the silicon-doped samples are shown in Fig. 4. The full width at half maximum (FWHM) of the band-edge luminescence is plotted vs. the electron concentration over the range of $n = 1 \times 10^{16}$ to $5 \times 10^{18} \text{ cm}^{-3}$. At low electron concentrations, the FWHM is almost independent of n , whereas above $n \approx 3 \times 10^{17} \text{ cm}^{-3}$ it exhibits a distinct increase with carrier concentration. The same spectra were obtained for both doping gases.

Discussion

Silicon doping during the growth of GaAs can be divided into the process of the physical incorporation of the Si and the electrical activation of the incorporated Si. The first process consists of the transport of the Si source molecule to the growth front, possible adsorption, its decomposition at or near the surface, and the removal of any reaction by-products. In order to become activated as a shallow electrically active impurity, the incorporated Si must reside on specific substitutional lattice sites in the GaAs. The electrical activation of the Si occurs subsequent to its incorporation. These two processes are not necessary correlated.

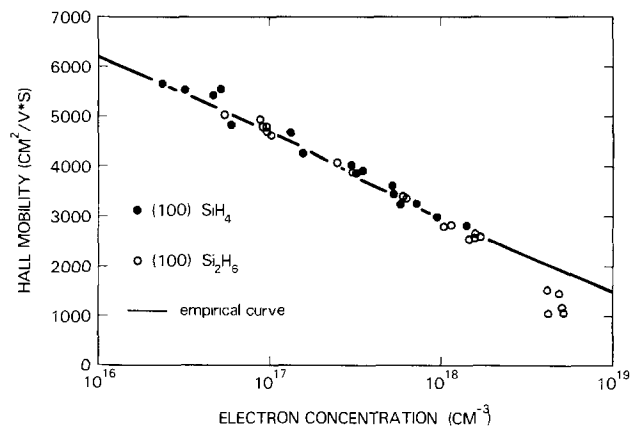


Fig. 3. Dependence of Hall mobilities 300 K on electron concentration. Doping gas: SiH_4 and Si_2H_6 . The solid line is the empirical curve from Ref. (19).

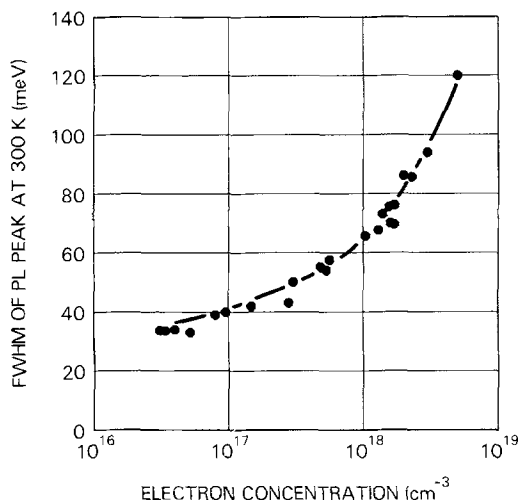


Fig. 4. Full width at half maximum (FWHM) of photoluminescence spectra at room temperature as a function of electron concentration.

The physical incorporation of Si is dependent on both the mass transport of the Si source specie and its subsequent reaction with the crystal surface and growth ambient. The growth conditions during LPE are close to thermal equilibrium, where both the incorporation and activation of the Si can be predicted from equilibrium thermodynamic considerations. In VPE and MOCVD growth of GaAs, the process of Si incorporation can be dominated by surface chemical reactions at the growth front.

The dopant activation, particularly in the case of an amphoteric dopant such as Si, is dependent on the stoichiometry of the crystal which is determined by the exact growth conditions (*e.g.*, temperature and As activity). The nature of the incorporated Si as either a donor or acceptor impurity will depend on the thermodynamic state specific to the growth technique and conditions. Calculations for the site selection predict an incorporation of silicon both on gallium and on arsenic sites under LPE growth conditions, whereas in VPE and MOCVD GaAs layers silicon should be incorporated only as a donor (13). This difference in electrical behavior is expected, because LPE is carried out under gallium-rich conditions, but MOCVD and VPE under arsenic-rich conditions. Photoluminescence data reported in the literature are in agreement with the theoretical thermodynamical site predictions mentioned above (13, 20), *i.e.*, silicon is a donor in layers grown by the MOCVD technique (20). A comparison of our SIMS data with our Hall data supports the conclusion that up to concentrations in the low 10^{18} region silicon is predominately incorporated on gallium sites.

At electron concentrations in the saturation region, the silicon incorporation continues with increasing silicon concentration in the gas phase. This difference between electron concentration and silicon concentration can be caused by compensation due to the amphoteric nature of silicon, by precipitations, or by complex formation. Data which are similar to our results were reported for diffusion of silicon into GaAs (21), where a maximum electron concentration of $5.6 \times 10^{18} \text{ cm}^{-3}$ and a maximum silicon concentration (SIMS) of $2 \times 10^{20} \text{ cm}^{-3}$ were achieved. In that study, the authors concluded that silicon is almost completely compensated due to its amphoteric character (21). Compensation at high doping levels is not unique to the potentially amphoteric Group IV dopants in GaAs. Behavior similar to that of silicon has also been observed in the case of sulfur doping of GaAs in the hydride system (22). In the case of sulfur, SIMS data indicated that beyond the saturation level of the electron concentration the sulfur incorporation still continues. Sulfur, as a Group VI element, is a substitutional impurity residing on arsenic sites and should act only as a donor. It was proposed that at high concentrations sulfur is incorporated as a complex, *e.g.*, a sulfur atom on an arsenic site com-

plexed with a vacancy. Alternatively, precipitations might appear at these high concentrations. When the silicon concentration is high, the incorporation behavior certainly is analogous, with most of the silicon no longer being a simple donor; *e.g.*, complexes between silicon on a gallium site and a vacancy or between silicon on a gallium site and silicon on an arsenic site may be formed. The Hall mobilities drop steeply in the saturation region of the electron concentration for silicon doping (Fig. 3) as well as with sulfur doping (22), indicating a strong compensation for both dopants. Studies of transmission electron microscopy and Rutherford backscattering channeling measurements on high dose silicon- and sulfur-implanted GaAs yield low precipitation (5 and 4%, respectively) and high substitutionality (70 and 85-90%, respectively) (23). The high substitutionality found for the dopants indicates that for both sulfur and silicon the formation of defect complexes at high doping levels is likely despite the substantial difference in the chemical nature of these two species.

Our results in Fig. 1 and our SIMS measurements indicate that for SiH_4 as the doping source more silicon is incorporated in layers grown on the $\langle 111 \rangle \text{B}$ surface than the $\langle 100 \rangle$ and $\langle 111 \rangle \text{A}$ surfaces. In LPE layers, the opposite behavior was found (10). However, the direct comparison between LPE and MOCVD layers is difficult, because of the difference in growth conditions as mentioned above. Our results show the importance of the adsorption site for silicon incorporation. The arsenic surface ($\langle 111 \rangle \text{B}$) seems to be the most active surface. This result is not unexpected, if one takes into account the nature of the ideal GaAs surfaces. The ideal gallium surface ($\langle 111 \rangle \text{A}$) has no free electron pair per surface atom, whereas the arsenic surface has one pair per atom, which would probably lead to enhanced adsorption of SiH_4 molecules on this surface. An analogous behavior was found for doping with sulfur in the hydride system, where the highest incorporation rate was obtained for the $\langle 111 \rangle \text{B}$ surface and the lowest for the $\langle 111 \rangle \text{A}$ surface (22).

There are instructive parallels between our observations of Si incorporation and the previous results on carbon incorporation in MOCVD GaAs (14). It was concluded that on the $\langle 111 \rangle \text{B}$ surface more hydrocarbons are adsorbed than on the $\langle 100 \rangle$ and $\langle 111 \rangle \text{A}$ surfaces. This leads to the highest carbon concentration in $\langle 111 \rangle \text{B}$ layers and the lowest in $\langle 111 \rangle \text{A}$. For decreasing growth temperature and increasing V:III ratio a decrease in carbon incorporation was found. The analogous behavior of silicon incorporation to carbon incorporation might be expected from the similar chemistry of the methane and the silane molecule. If we assume that the thermally stable SiH_4 molecule is adsorbed at the growth surface, it has to decompose by a specific surface reaction. The SiH_4 molecule is probably decomposed through a hydrogen transfer reaction. In such a reaction, the SiH_4 molecule is broken down by the transfer of hydrogen to either the GaAs surface or to other adsorbed species such as CH_3 . In the latter case, an increased density of adsorbed hydrocarbons at the surface might lead to an enhanced decomposition of SiH_4 molecules, thus explaining the increased silicon incorporation observed on $\langle 111 \rangle \text{B}$ layers. The exact nature of these surface chemical reactions is a subject of continuing research.

Using Si_2H_6 as the doping source, we do not expect this influence on substrate orientation, since Si_2H_6 is readily decomposed at the growth temperature (7, 24). If Si_2H_6 decomposes rapidly at or below the typical GaAs growth temperatures, the incorporation of silicon would be limited by the gas phase mass transport of Si_2H_6 to the growth front rather than by surface reaction kinetics. This would result in a weak or negligible temperature dependence to the silicon incorporation. Our experimental results follow these expected trends (Fig. 2). Assuming equal diffusivity of Si_2H_6 and $\text{Ga}(\text{CH}_3)_3$ in hydrogen, one might estimate a doping efficiency of 0.3 from Fig. 2. The interpretation of the numerical value is doubtful as the exact mole fractions of Si_2H_6 and $\text{Ga}(\text{CH}_3)_3$ at the sub-

strate surface cannot be determined without a direct *in situ* measurement. Additionally, since the actual species responsible for Si incorporation from Si_2H_6 is unknown, we cannot determine whether each Si_2H_6 molecule contributes one or two Si atoms to the crystal. The independence of temperature has important consequences for the uniformity of dopant incorporation across large substrate areas. The temperature distribution at the substrate holder will not always be completely uniform in a susceptor system. Due to the strong dependence of silicon incorporation on growth temperature for SiH_4 (Fig. 1), variations in the carrier concentrations are expected. A change in the substrate temperature (ΔT) of 1° at 650°C leads to a variation in carrier concentration ($\Delta n/n$) of 2% according to the following equation, where k is the Boltzmann constant

$$\frac{\Delta n}{n} = \frac{\epsilon \Delta T}{kT^2}$$

Another complicating factor in obtaining uniformity is the thermalization of the gas stream. In a typical MOCVD reactor, the substrate is the only directly heated area. Therefore, the doping gas heats up in the flow direction so that the molecules probably decompose more efficiently downstream than upstream. This effect leads to an increased silicon incorporation in the flow direction for SiH_4 . This effect has already been observed (3). The exact nature of the decomposition process of SiH_4 is yet unknown. Only *in situ* measurements which can distinguish the actual Si species present might clarify whether the rate-limiting processes take place in the gas phase or on the surface. In our silane samples, the decrease of carrier concentration at the edges of the substrate holder indicates a lower growth temperature in these regions, as expected for RF-heated graphite susceptors. In the disilane samples, the variation of the carrier concentration is not systematic across the substrate surface. This improvement of the uniformity across large substrate areas can be realized because of the absence of a temperature dependence of the incorporation process for disilane.

Our mobility data (Fig. 3) show that with Si_2H_6 the same high values can be reached as with other dopant materials at concentrations below the saturation of the electron concentration. It may be concluded that for both SiH_4 and Si_2H_6 the final electrical state of silicon in the crystal lattice appears to be the same. For Si_2H_6 , no additional compensation, for example due to additional carbon in the layers, could be detected. The results of our photoluminescence measurements support this conclusion (Fig. 4). Our data lie in the range of the curve reported for tellurium-doped melt-grown GaAs (25), which were obtained by cathodoluminescence. Additional broadening of the luminescence peaks, reflected in an increased peak width at half maximum, is expected for compensated material. This was not observed for our samples. However, our results disagree with data previously reported for silicon-doped MOCVD grown layers, where larger peak width values and an anomalous luminescence behavior were reported (11). Furthermore, our luminescence data demonstrate that the peak width depends strongly on the carrier concentration at levels higher than $3 \times 10^{17} \text{ cm}^{-3}$. Consequently, room temperature luminescence can be used in order to estimate the carrier concentration, as proposed in Ref. (25). This has the advantages of being a simple, fast, and nondestructive technique.

Summary

A study of silicon incorporation in MOCVD GaAs layers has been presented. Silane and disilane were used as doping sources. With both doping gases, electron concentrations up to a saturation value of $5 \times 10^{18} \text{ cm}^{-3}$ can be

reached. Below this saturation value, the silicon concentration in the layers equals the electron concentration, with silicon incorporated only as a donor. Above the electron concentration saturation value, silicon concentrations up to 10^{20} cm^{-3} have been measured. The incorporation of silicon using silane as the doping source depends on the substrate orientation. This orientational dependence is absent for disilane over the main growth temperature range. It appears that the decomposition of the stable silane molecules is determined by a surface reaction, possibly one with adsorbed hydrocarbons. The use of disilane instead of silane as the doping source leads to an improvement of the uniformity of carrier concentration across large substrate areas.

Acknowledgments

We would like to thank V. Deline for performing the SIMS measurements and H. Hovel for reviewing the manuscript. R. Potemski and J. Van-Leeuwen aided in the uniformity studies.

Manuscript submitted Nov. 5, 1984; revised manuscript received March 4, 1985.

IBM Corporation assisted in meeting the publication costs of this article.

REFERENCES

1. L. Hollan, J. P. Hallais, and J. C. Brice, in "Current Topics In Materials Science," Vol. 5, E. Kaldis, Editor, p. 1, North-Holland Publishing Co., Amsterdam (1980).
2. J. P. Duchemin, M. Bonnet, F. Koelsch, and D. Huyghe, *This Journal*, **126**, 1134 (1979).
3. S. J. Bass, *J. Cryst. Growth*, **47**, 613 (1979).
4. Y. G. Chai, R. Chow, and C. E. C. Wood, *Appl. Phys. Lett.*, **30**, 800 (1981).
5. T. F. Kuech, B. S. Meyerson, and E. Veuhoff, *ibid.*, **44**, 986 (1984).
6. S. D. Hersee, and J. P. Duchemin, *Ann. Rev. Mater. Sci.*, **12**, 65 (1982).
7. J. H. Purnell and R. Walsh, *Proc. R. Soc. London Ser. A*, **293**, 543 (1966).
8. P. John and J. H. Purnell, *J. Chem. Soc., Faraday Trans. 1*, **69**, 1455 (1973).
9. B. S. Meyerson and B. A. Scott, Unpublished data.
10. B. H. Ahn, R. R. Shurtz, and C. W. Trussel, *J. Appl. Phys.*, **42**, 4512 (1971).
11. M. Druminski, H.-D. Wolf, and K.-H. Zschauer, *J. Cryst. Growth*, **57**, 318 (1982).
12. H. Rupprecht, J. M. Woodall, K. Konnerth, and D. G. Pettit, *Appl. Phys. Lett.*, **9**, 221 (1966).
13. D. J. Ashen, P. J. Dean, D. T. J. Hurlle, J. B. Mullin, and A. M. White, *J. Phys. Chem. Solids*, **36**, 1041 (1975).
14. T. F. Kuech, and E. Veuhoff, *J. Cryst. Growth*, **68**, 148 (1984).
15. T. F. Kuech, E. Veuhoff, and B. S. Meyerson, *ibid.*, **68**, 48 (1984).
16. L. H. van der Pauw, *Philips Res. Rep.*, **13**, 1 (1958).
17. D. H. Reep and S. K. Ghandi, *J. Cryst. Growth*, **61**, 449 (1983).
18. H. Poth, H. Bruch, M. Heyen, and P. Balk, *J. Appl. Phys.*, **49**, 285 (1978).
19. G. B. Stringfellow, *ibid.*, **50**, 4178 (1979).
20. T. S. Low, B. J. Skromme, and G. E. Stillman, in "Gallium Arsenide and Related Compounds," G. E. Stillman, Editor, p. 515, The Institute of Physics, London (1983).
21. M. E. Greiner and J. F. Gibbons, *Appl. Phys. Lett.*, **44**, 750 (1984).
22. E. Veuhoff, M. Maier, K.-H. Bachem, and P. Balk, *J. Cryst. Growth*, **53**, 598 (1981).
23. A. K. Ray, R. S. Bhattacharya, and P. P. Pronko, *Appl. Phys. Lett.*, **41**, 1086 (1982).
24. M. Bowrey and J. H. Purnell, *Proc. R. Soc. London, Ser. A*, **321**, 341 (1971).
25. H. C. Casey, Jr., and R. H. Kaiser, *This Journal*, **114**, 149 (1967).

Transient-Enhanced Diffusion during Furnace and Rapid Thermal Annealing of Ion-Implanted Silicon

S. J. Pennycook, J. Narayan,^{*,1} and O. W. Holland²

Oak Ridge National Laboratory, Solid State Division, Oak Ridge, Tennessee 37831

ABSTRACT

A transient-enhanced diffusion has been observed during the furnace or rapid thermal annealing of ion-implanted silicon. We have studied this transient in detail and show that, for doses of Group V dopants sufficient to amorphize the silicon, it arises from the trapping of interstitials by dopant atoms during implantation. These are retained during solid-phase-epitaxial (SPE) growth, but can be released by additional thermal processing to cause the observed transient and the formation of a band of extended defects. We have measured the enhanced diffusion coefficients and the duration of the transient for Sb-implanted Si by careful furnace annealing experiments. We obtain general expressions which predict the effects of the transient during any thermal processing based on SPE growth (furnace, CW laser, or rapid thermal annealing). We show that there is no analogous mechanism of vacancy trapping by Group III elements.

There have been many reports of transient-enhanced diffusion during furnace (1) or rapid thermal (2-5) annealing of ion-implanted silicon. The origin of these effects has, however, been the subject of considerable speculation. In this paper, we study the large transient diffusion which arises from the annealing of high concentrations of trapped point defects as they return to equilibrium concentrations. The transient will be large, since the activation energy corresponds to only the migration enthalpy of the point defects, but will only last until their concentration reduces to normal values. We distinguish between two possible origins of such nonequilibrium point-defect distributions. The first is ion-implantation damage resulting from the implantation of light atoms or low doses of heavy atoms. The silicon is damaged but not amorphized, and subsequent thermal processing to anneal the damage will cause transient-enhanced diffusion of the dopant. This mechanism is referred to as radiation-enhanced diffusion. A second mechanism, which is the principal subject of this paper, can occur when the silicon is turned amorphous before or during implantation. We show that large numbers of Si atoms are trapped by Group V dopant atoms in the amorphous material during implantation. These are retained during solid-phase-epitaxial (SPE) growth, but can be released later during thermal processing to give the transient-enhanced diffusion. We characterize the effect by careful study of Si-Sb alloys and their behavior during furnace annealing and arrive at a model which can predict the transient effects for any concentration of Sb or Bi dopants sufficient to amorphize the silicon, and any thermal processing technology which relies on SPE growth (furnace, CW laser, or rapid thermal annealing). Reasonable agreement is also obtained for the enhanced As diffusion seen during rapid thermal annealing. We show that there is no analogous effect for Group III elements. Finally, we discuss the various mechanisms for enhanced diffusion and their resulting dopant and defect distributions.

Experimental

To measure the enhanced diffusion coefficients during the transient, supersaturated alloys were produced by $^{121}\text{Sb}^+$ or $^{209}\text{Bi}^+$ ion implantation into {100} Si followed by SPE growth in a furnace under flowing dry N_2 gas, typically at 575°C for 40 min. Special implantation schemes were employed so as to produce a high concentration band of dopant well removed from the amorphous/crystalline interface, where radiation-enhanced diffusion would occur. Transient diffusion coefficients were then measured within the band of high, uniform concentration

* Electrochemical Society Active Member.

¹ On leave of absence at the Microelectronics Center of North Carolina, Research Triangle Park, North Carolina 27709 and the Materials Engineering Department, North Carolina State University, Raleigh, North Carolina 27650.

² Present address: Microelectronics Center of North Carolina, Research Triangle Park, North Carolina 27709.

by precipitating out a small fraction of the dopant and measuring the precipitate size distribution by transmission electron microscopy (TEM) (1). Figure 1 shows a Rutherford backscattering spectroscopy (RBS) analysis for one Si-Sb alloy. By scaling the implant doses, various concentrations could be achieved within the uniform band. Figure 2 shows the effect of additional furnace annealing. A band of precipitates formed within the region of uniform concentration, well removed from the damage layer marking the original amorphous/crystalline interface. The uniform dopant concentration allowed an accurate measure of diffusion coefficients as a function of concentration and temperature and ensured that no electric fields were present to affect the diffusion. Both float-zone and Czochralski silicon gave identical results. Transient diffusion coefficients were also measured in a Si-Bi alloy by the same technique.

To study possible point-defect trapping in Si-B alloys, float-zone silicon was first amorphized by $^{30}\text{Si}^+$ implantation (175 keV, $1.5 \times 10^{16} \text{ cm}^{-2}$) at liquid nitrogen temperature, followed by $^{11}\text{B}^+$ (35 keV, 1×10^{16} or $1.5 \times 10^{16} \text{ cm}^{-2}$) implantation. The low energy B implantation produced a broad profile with a large region of fairly uniform concentration. These samples were then SPE grown by furnace annealing at 575°C/1.5h, and diffusion coefficients were measured as before.

Some samples of the $^{121}\text{Sb}^+$ -implanted Si and of $^{75}\text{As}^+$ -implanted (100 keV , $1.0 \times 10^{16} \text{ cm}^{-2}$) Si were rapid thermally annealed using a graphite strip heater under flowing dry nitrogen gas, and the resulting precipitate and loop size distribution studied by TEM and RBS.

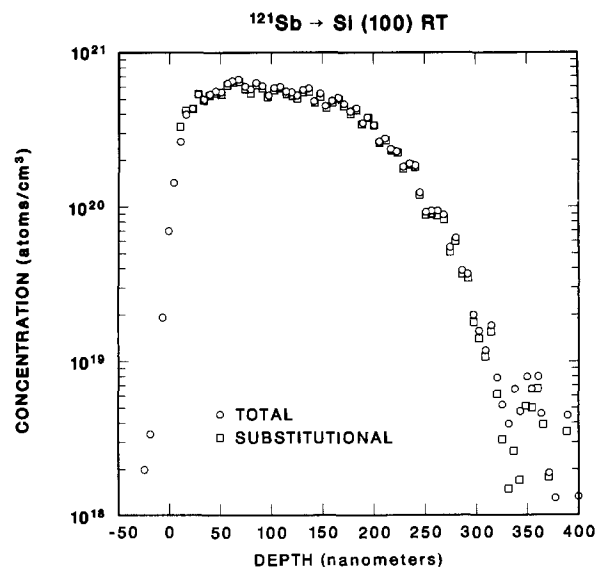


Fig. 1. RBS analysis of Sb ($5.9 \times 10^{20} \text{ cm}^{-3}$)-implanted Si, SPE grown at 575°C for 40 min.

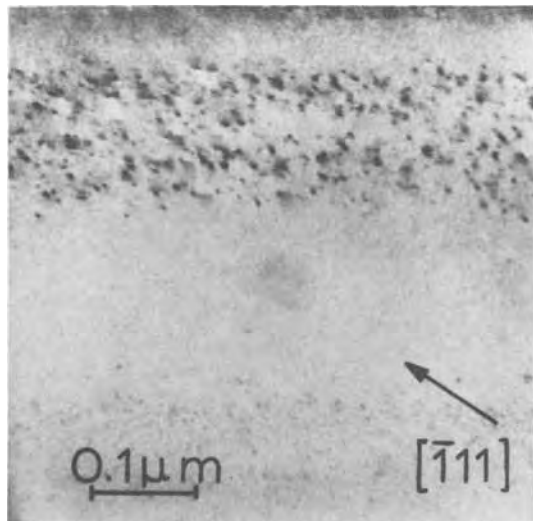


Fig. 2. TEM cross-sectional image of Sb ($8.8 \times 10^{20} \text{ cm}^{-3}$)-implanted Si, SPE grown and furnace annealed at 680°C for 20 min.

Determination of transient diffusion coefficients.—Transient diffusion coefficients D^* were determined for Si-Sb and Si-Bi alloys by furnace annealing for suitable times and temperatures so as to precipitate out a small amount of dopant. The precipitate size distribution observed by TEM allowed the measurement of D^* as a function of temperature and dopant concentration. Typical results are shown in Fig. 3. With high dopant concentrations, it was possible to precipitate some of the dopant with very few loops being generated (Fig. 3a). With continued annealing, loops nucleated at existing precipitates (Fig. 3b) and grew, finally achieving a constant size and number density. This marked the end of the transient; no further precipitation occurred at these low temperatures. Since only a small fraction of dopant had been precipitated, the concentration of dopant in solution was little changed, but the diffusion coefficients dropped by or-

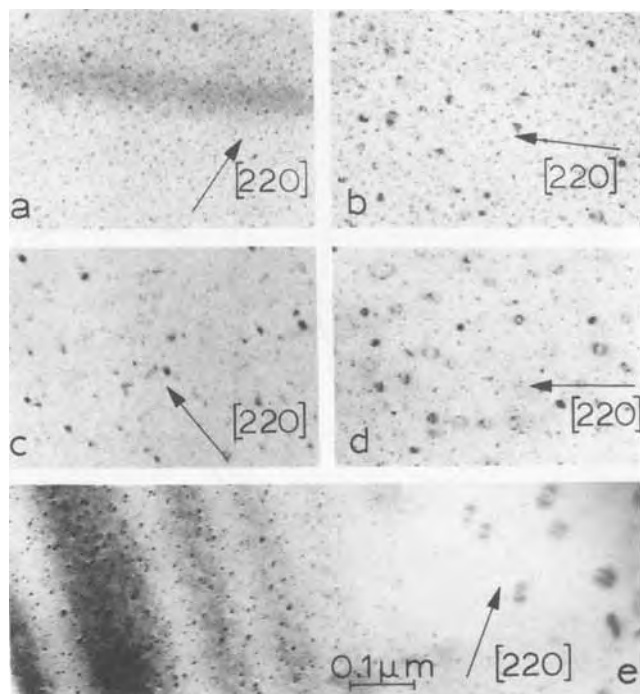


Fig. 3. Results of furnace annealing of Si-Sb alloys of various concentrations. $9.3 \times 10^{20} \text{ cm}^{-3}$ at $700^\circ\text{C}/20 \text{ min}$ (a) and at $720^\circ\text{C}/20 \text{ min}$ (b). $5.0 \times 10^{20} \text{ cm}^{-3}$ at $740^\circ\text{C}/20 \text{ min}$ (c), $780^\circ\text{C}/20 \text{ min}$ (d), and $2.8 \times 10^{20} \text{ cm}^{-3}$ at $850^\circ\text{C}/20 \text{ min}$ (e). Shown are the underlying bands of loops in thick regions.

ders of magnitude. This transient cannot be explained by concentration-enhanced diffusion (6). It is clearly caused by trapped point defects which are released by the anneal, and result in transient-enhanced dopant diffusion before finally condensing into loops. The nature of the loops, therefore, indicates the nature of the trapped point defects. We have determined them to be interstitial in nature, in agreement with other workers (7) and to be faulted, lying on $\{111\}$ planes, and with Burger's vectors of $a/3 \langle 111 \rangle$ (1). This is a clear demonstration of the interstitialcy mechanism of diffusion, whereby substitutional dopant atoms are displaced from site to site by passing interstitials.

At lower dopant concentrations, higher temperatures were needed to cause Sb precipitation, and fewer measurements of diffusion coefficients could be obtained before the concentration of interstitials was significantly reduced by condensation into loops (Fig. 3c, 3d). At even lower concentrations, no loops at all were observed within the band of precipitates (Fig. 3e). Clearly, the interstitials are now being removed by other means, either to the surface, to the underlying damage band, or by recombination with thermally generated vacancies.

The diffusion coefficients determined before significant loop formation are shown on an Arrhenius plot in Fig. 4. They are greatly enhanced over tracer values (8) and show an activation energy of $1.8 \pm 0.2 \text{ eV}$. The low activation energy compared to the tracer value of 3.96 eV again rules out the possibility of concentration-enhanced diffusion effects (6), and corresponds simply to the migration enthalpy of the Sb by the interstitialcy mechanism. However, the enhancement is indeed a strong function of concentration. Figure 5 shows the Sb diffusion coefficient D^* measured or extrapolated to 680°C as a function of Sb concentration C_0 and ion-implantation conditions. It is clear that D^* is proportional to C_0 , although it is higher for room temperature implants than liquid nitrogen implants. This shows that the interstitials are trapped by Sb atoms, since then their concentration $C_i = \alpha C_0$, where α is the fraction of Sb atoms which trap an interstitial, and $D^* = C_i D^{\text{Sb}} = \alpha C_0 D^{\text{Sb}}$, where D^{Sb} is the diffusivity of Sb by the interstitialcy mechanism (9). In the case of the high concentration samples, the loop size and number density following the transient was proportional to C_0 , again showing that $C_i = \alpha C_0$ and allowing an estimate to be made of α . We found $\alpha \approx 0.02$ for room temperature implantation, and $\alpha \approx 0.01$ for liquid nitrogen implantation (10).

Also shown in Fig. 4 and 5 are points for a Sb sample which was recrystallized by ion-beam annealing using a high flux Si beam (11). Although the original Sb implantation was done at liquid nitrogen temperature, the diffusion coefficients are higher than expected for that con-

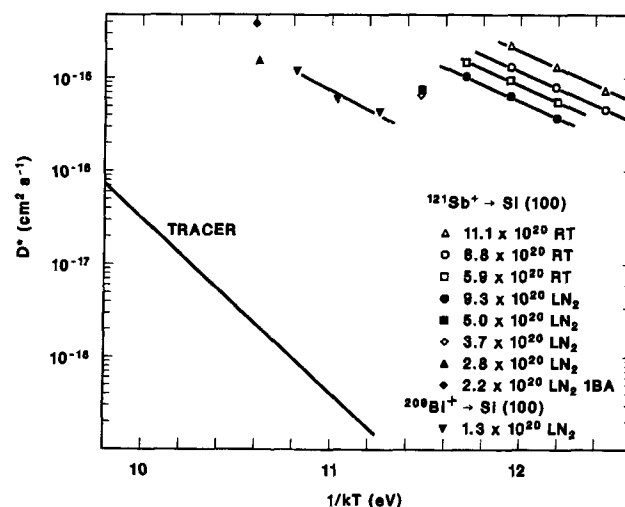


Fig. 4. Arrhenius plot of Sb and Bi transient diffusion coefficients for various concentrations and implant conditions.

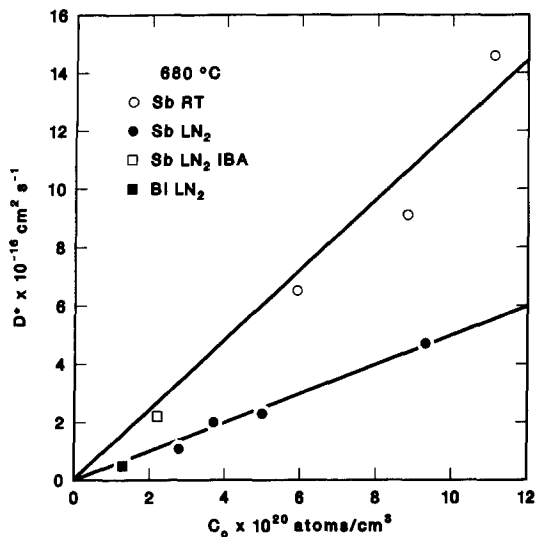


Fig. 5. Plot of transient diffusion coefficients at 680°C against dopant concentration.

centration. Possibly, annealing by Si ion irradiation allowed more Sb atoms to trap interstitials before the SPE growth took place, giving a larger enhancement. Alternatively, some of the damage induced by the continued irradiation of the recrystallized silicon was not removed, and the diffusion transient is due to the combined effects of point-defect trapping and radiation-enhanced diffusion.

Using the data of Fig. 4 and 5, we can arrive at a single, concentration-dependent, transient diffusion coefficient D^* , given by

$$D^* = 0.0083\alpha C_0 e^{-1.8/kT} (\text{cm}^2\text{-s}^{-1}) \quad [1]$$

where $\alpha = 0.01$ for LN_2 implants and $= 0.02$ for RT implants and $C_0 =$ atomic fraction of dopant. Although strictly determined for Sb, it is interesting to note that the Bi points in Fig. 4 are close to those for Sb, and the extrapolation to 680°C (Fig. 5) is even closer to the expected value for liquid nitrogen Sb implants (the activation energy for Bi was measured as 2.0 ± 0.2 eV) (12). This suggests that the trapping ratio α may be very similar for many Group V dopants, and limited only by the availabil-

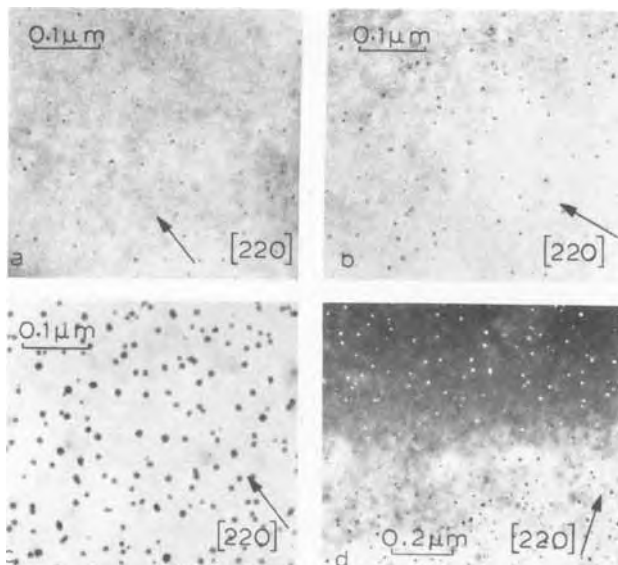


Fig. 6. TEM micrographs of precipitates in Si-B alloys under dynamical diffraction conditions. a: B ($1 \times 10^{16} \text{ cm}^{-2}$) annealed 875°C/20 min. b: B ($1.5 \times 10^{16} \text{ cm}^{-2}$) annealed 875°C/20 min. c: B ($1.5 \times 10^{16} \text{ cm}^{-2}$) annealed 1000°C/60 min. d: low magnification of c showing structure factor contrast.

ity of interstitials during implantation. We show later that this expression for D^* also gives fair agreement with the observed enhanced diffusion of As.

This very high transient diffusivity only lasts until the supply of interstitials is exhausted. We observe experimentally that for room temperature implantations, the end of the transient occurs roughly at $D^*t^* \approx 4 \times 10^{-12} \text{ cm}^2$ independent of dopant concentration, where t^* is the length of the transient in seconds, and at half this value for low temperature implantations. The fraction of dopant precipitated during the transient is approximately 7α , or 15% for room temperature implants. Although the loss of electrically active dopant is fairly small, in the high concentration samples significant effects may arise from the formation of the band of dislocation loops. Another serious effect of the transient-enhanced diffusion may be broadening of the dopant profile. Although not seen with the present Sb^+ or Bi^- implants, where the dopant simply precipitates out, profile broadening may occur with implantations below the solubility limit or perhaps with As^+ or P^+ implants. We will discuss the prediction of such effects in the next section.

We have also looked for transient-enhanced diffusion in $^{11}\text{B}^+$ -implanted silicon, which had been preamorphized by $^{30}\text{Si}^+$ implantation in order to exclude the effects of radiation-enhanced diffusion. Figure 6 shows TEM micrographs of the precipitates obtained. No extra spots were observed in the selected area diffraction patterns, and there was no evidence of coherency strains surrounding the precipitates. Either the precipitates had an identical crystal structure to the silicon or they were amorphous but of insufficient volume fraction to produce rings in the diffraction pattern. The density of boron in the precipitates was determined by completely precipitating out the boron in excess of the solubility limit and measuring the volume fraction of precipitates. Diffusion coefficients were then determined as before and are shown on an Arrhenius plot in Fig. 7. The points fall very close to the tracer values (8), are independent of B concentration, and show the usual activation energy. From these results, we conclude that there is no significant trapping mechanism for Group III elements.

Prediction of transient effects.—The transient diffusion coefficient together with the duration of the transient determined in the last section allow us to predict the transient effects for any processing technology based on the SPE growth of amorphous, ion-implanted layers. Taking the duration of the transient determined previously as $D^*t^* \approx 4 \times 10^{-12}$ or 2×10^{-12} for room or liquid nitrogen temperature implants, respectively, we obtain from Eq. [1]

$$t^* \sim \frac{2.5 \times 10^{-8}}{C_0} e^{1.8/kT} (\text{s}) \quad [2]$$

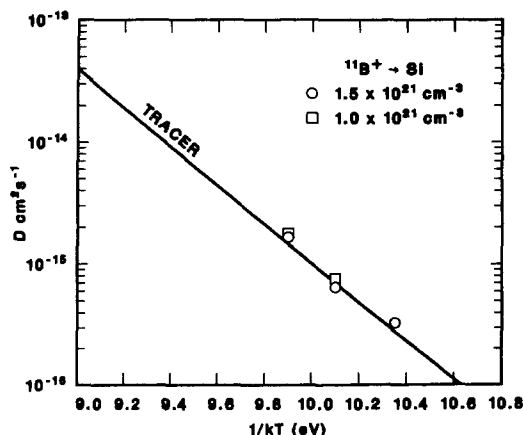


Fig. 7. Arrhenius plot of B diffusion coefficients in preamorphized, SPE-grown Si.

For process times $t < t^*$, we will see enhanced diffusion given by D^* (Eq. [1]). For process times $t > t^*$, we will observe the full transient effect D^*t^* and concomitant effects of precipitation and loop formation, and in addition may see the effects of normal diffusion for the remaining time, characterized by $D(t - t^*)$. The significance of this normal diffusion depends primarily on the temperature. At low temperatures D^* is many orders of magnitude greater than the normal diffusion coefficient D , and, therefore, t would need to exceed t^* by the same factor for the effects of normal diffusion to be observable. However, the situation changes at high temperature, since the tracer diffusion has a much larger activation energy. In fact, at a sufficiently high temperature T^* , D will exceed the transient diffusivity D^* , even for times less than t^* . The extrapolation of the tracer and transient diffusion coefficients in Fig. 4 cross at

$$T^* = 2.5 \times 10^{-5} [\ln(675/kC_0)]^{-1} \quad [3]$$

Here, the diffusion caused by thermally generated point defects equals the diffusion caused by the release of the fixed number of trapped interstitials. In Fig. 8, we summarize these predictions, plotting t^* against $1/kT$ for various dopant concentrations. The bold dotted line marks the temperature T^* above which normal diffusion exceeds the transient for all times. The duration of the transient is difficult to define precisely, and the values of t^* predicted by Fig. 8 are probably only accurate to within a factor of two. Figure 9 shows D^* as a function of $1/kT$ and C_0 , the bold line again marking the division between normal and enhanced diffusion.

To test the prediction of these transient effects we have taken the Sb-implanted Si ($C_0 = 9.31 \times 10^{20} \text{ cm}^{-3}$, implanted at liquid nitrogen temperature) and compared the effects of furnace and rapid thermal annealing (RTA). At typical RTA temperatures, the SPE growth process is completed in a few milliseconds, so that the annealing time can be taken as equal to the processing time. The sample for furnace annealing was first regrown at 575°C for 40 min and then annealed at 700°C for 90 min, at which temperature $t^* \sim 50$ min. The sample for RTA was annealed at 1050°C for a nominal time of 15s, where $t^* \approx 10$ s. Both treatments should therefore take the material to the end of the transient. From Fig. 10, we see that this is indeed the case. Figures 10a and 10b show that the precipitate size distribution is very similar, and the weak beam micrographs in Fig. 10b and 10c show that the loop size and number density are also very similar. These observa-

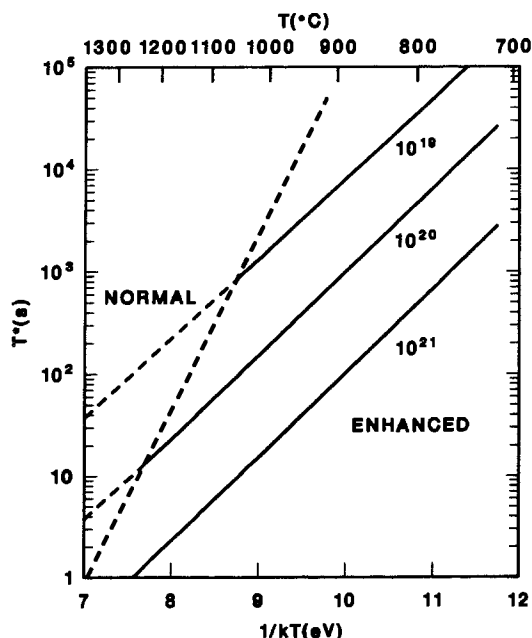


Fig. 8. Predicted duration of the transient as a function of dopant concentration and temperature.

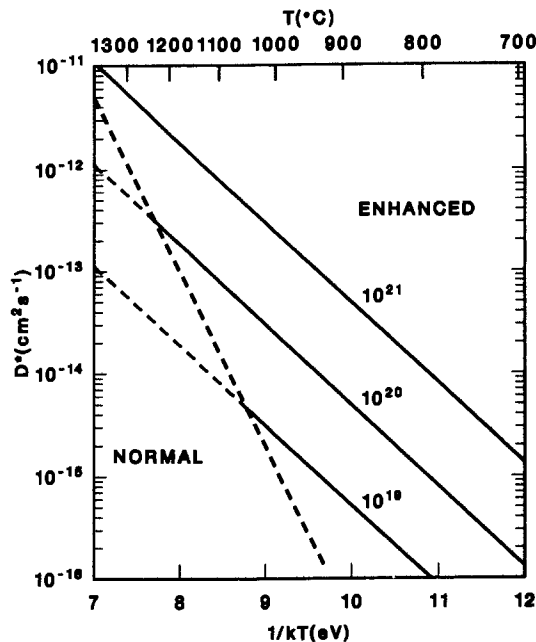


Fig. 9. Predicted enhanced diffusion coefficient as a function of dopant concentration and temperature.

tions reflect the fact that the same numbers of interstitials have condensed with the two thermal processing treatments and have caused the same amount of dopant diffusion. The transient effects with Bi-implanted samples can also be predicted, simply by replacing the 1.8 eV activation energy in Eq. [1] and [2] with 2.0 eV. This increases t^* by a factor of 5 or 6 at typical temperatures of RTA, although we have not yet checked these predictions experimentally.

Transient effects with As-implanted samples have also been shown to have a 1.8 eV activation energy (3). If we assume the same trapping efficiency α for As as for Sb and Bi, the transient effects should again be predictable from Eq. [1] and [2]. Figure 11 shows the profile broadening after 1100°C/5s and 1150°C/10s annealing (nominal times) of As-implanted Si having a concentration of $1.2 \times 10^{21} \text{ cm}^{-3}$. From Fig. 7, we predict the duration of the transient to be ~ 4 s at 1100°C and only 2.5s at 1150°C. We can estimate the total expected profile broadening by combining the effect of the transient with the effect of steady-state concentration-enhanced diffusion (6) D^c to give $x \approx \sqrt{(2D^*t^* + 2D^c t)}$. Taking an average $D^c = 20D$, we predict the profile broadening at the lower temperature to be $\approx 350\text{\AA}$, very close to the observed 380Å, and at the higher temperature to be 470Å, somewhat lower than the measured 650Å. The broadening due to the transient dif-

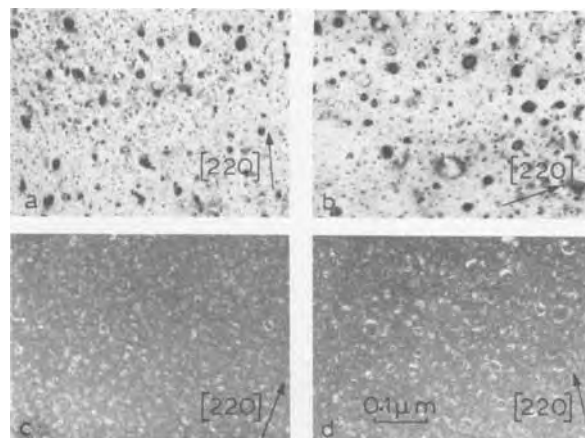


Fig. 10. Comparison of Si-Sb alloy ($9.3 \times 10^{20} \text{ cm}^{-3}$) after furnace annealing at 700°C/90 min (a and c), and after rapid thermal annealing at 1050°C/15s (b and d).

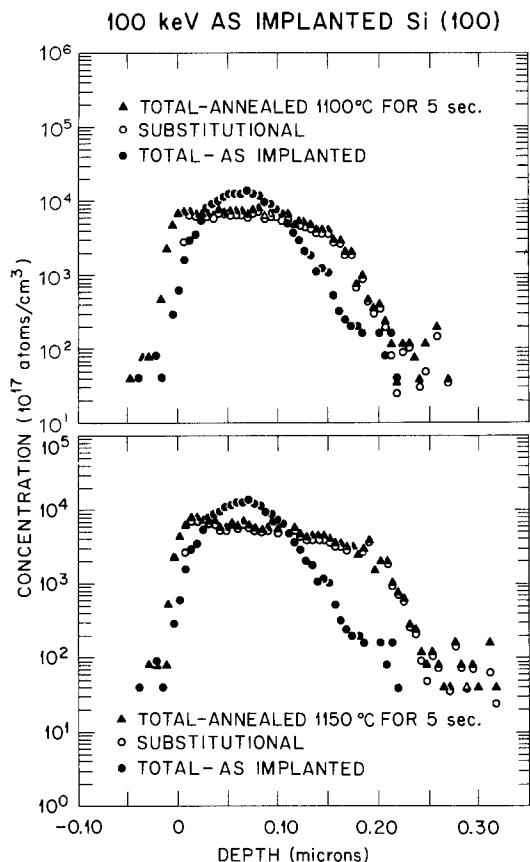


Fig. 11. Profile broadening during rapid thermal annealing of As (100 keV, $1 \times 10^{16} \text{ cm}^{-2}$)-implanted Si.

fusion alone would be given by $x \approx 2D^*t^* = 280\text{\AA}$, and thermally activated diffusion is clearly significant at these high temperatures. The enhancement of the transient diffusion over tracer diffusion increases as the temperature is reduced. Kalish *et al.* (3) report enhancement by 170 times for 1010°C/10s RTA and 50 times for 1118°C/10s RTA. These times are both less than t^* , and we predict enhancements of 63 and 15 times, roughly three times lower than their results. Considering the probable errors in t^* and the experimental values for annealing time and temperature, the model predicts the observed effects very well. It should be noted that other mechanisms such as radiation-enhanced diffusion or pipe diffusion may well be contributing to the observed effects, since for the results shown in Fig. 11 the original amorphous/crystalline interface was at a depth of only $\sim 1400\text{\AA}$. We discuss these possibilities further in the next section.

No enhanced diffusion was reported by Hodgson *et al.* (13) during the RTA of As-implanted ($8 \times 10^{19} \text{ cm}^{-3}$) Si at 1200°C/1s. This is also predicted by the model, since from Fig. 7 we see that these experimental conditions lie very close to the point at which normal diffusion becomes dominant. We predict only a 20% enhancement, whereas they report a factor of two. In general, our model seems able to predict transient effects even in As-implanted Si to within a factor of two or three and explains why some experimental conditions result in no observed enhancement.

Discussion

Interstitial trapping mechanism.—We have clearly identified and characterized the mechanism of the transient-enhanced diffusion observed during thermal processing of Group V ion-implanted Si which has been amorphized. The transient is due to the release of interstitials trapped by the dopant atoms, and ends when they condense into loops or are otherwise removed. The concentration of trapped interstitials is dependent on ion-implantation conditions, but independent of subsequent thermal treatments which can only cause their release.

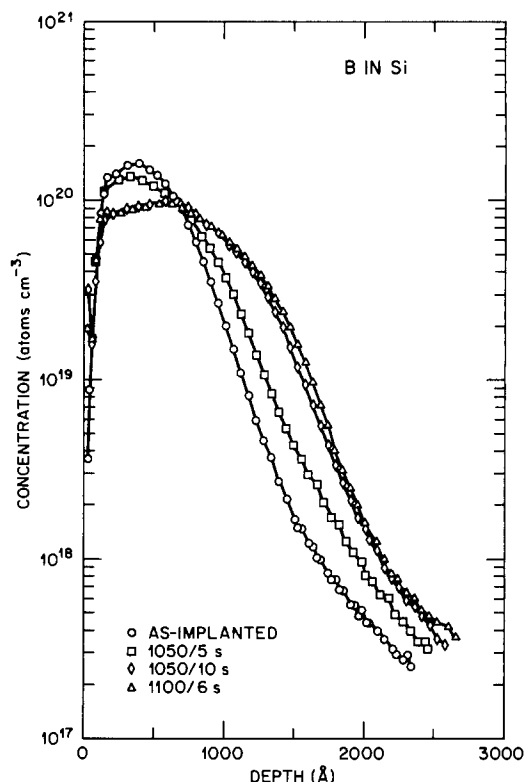


Fig. 12. Profile broadening during rapid thermal annealing of BF_2 (50 keV, $1 \times 10^{15} \text{ cm}^{-2}$)-implanted Si.

The trapping, therefore, occurs during implantation, most likely by the capture of mobile Si atoms by the dopant atoms in order to saturate their valence bands. Following recrystallization by SPE growth, these extra Si neighbors become trapped interstitials. They are not retained during recrystallization from the liquid phase by pulsed laser annealing (1).

There is no analogous effect with Group III dopants. This is not surprising since to reject the fifth Si neighbor from a Group V atom requires that a bond be broken, a process requiring considerable energy. Since SPE growth proceeds with an activation energy of 2.4 eV in the Sb case (14) while the Si-Sb bond energy is likely to be around 3 eV (the Sb-Sb bond energy), the chance of rejecting the fifth Si neighbor as the crystallization interface passes is roughly $e^{0.6/kT}$. Even at the high temperatures involved with RTA, there is less than a 1% chance of breaking the bond. This explains why the transient effects during RTA and furnace annealing are fundamentally similar. With Group III elements, even if many are only threefold coordinated in the amorphous state, to incorporate them substitutionally into the silicon lattice requires no bond breaking. Only an extra Si neighbor must be brought up to the dopant atom, a process probably requiring considerably less energy than the activation energy for SPE growth. It is not surprising, therefore, that no vacancy trapping occurs with Group III dopants during SPE growth, and no enhanced diffusion is observed.

Radiation-enhanced diffusion.—Transient-enhanced diffusion is also observed in silicon which has been damaged by implantation but not amorphized. Thermal processing which anneals the point defects comprising the damage will cause transient diffusion, which ends, as before, when they condense into loops. This mechanism will be effective for both Group III and Group V dopants. It is responsible for the enhanced diffusion reported during RTA of B-implanted Si (which does not amorphize the Si) (4). It may also be significant in situations where the Si is amorphized by the implantation to a depth not much greater than the projected range of the implanted ion. The amorphous/crystalline interface will intersect the dopant profile at a concentration near its peak, and

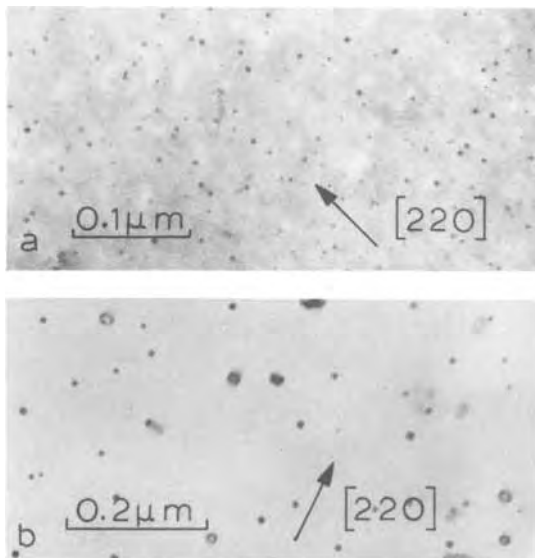


Fig. 13. Precipitates observed in Ga (100 keV , $1 \times 10^{15} \text{ cm}^{-2}$)-implanted Si after SPE growth followed by $720^\circ\text{C}/20 \text{ min}$ anneal (a), and $900^\circ\text{C}/20 \text{ min}$ anneal (b).

radiation-enhanced diffusion may then cause dopant redistribution or precipitation. We have investigated this possibility through the RTA of BF_2 (50 keV , $1 \times 10^{15} \text{ cm}^{-2}$)-implanted Si. The implantation produced an amorphous layer 550\AA thick, so that the damaged layer was located close to the peak in the B profile (15). After $1050^\circ\text{C}/10\text{s}$ RTA, the profile broadened by 400\AA corresponding to a diffusion coefficient of $\sim 8 \times 10^{-13} \text{ cm}^2\text{s}^{-1}$, which is close to the tracer value of $1.9 \times 10^{-12} \text{ cm}^2\text{s}^{-1}$. It would appear that radiation-enhanced diffusion gives much less enhancement over tracer diffusion, at typical temperatures of RTA, than the interstitial trapping mechanism. Increasing the dose may give more enhancement, although the damage layer will then move deeper into the silicon and be further from the peak in the concentration profile.

As with the interstitial trapping mechanism, radiation-enhanced diffusion will show increasing enhancement as the temperature is reduced, owing to the low activation energy involved. We have studied the effect of the transient in Ga (100 keV , $1 \times 10^{15} \text{ cm}^{-2}$)-implanted Si by fur-

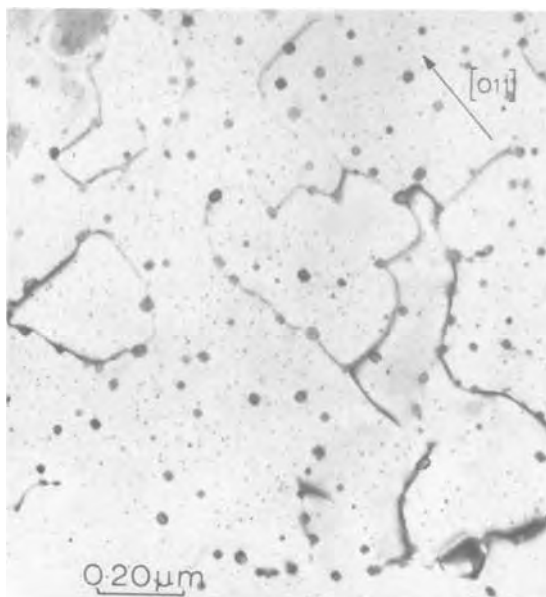


Fig. 14. TEM micrograph of dislocation network formed in Sb (200 keV , $5 \times 10^{15} \text{ cm}^{-2}$)-implanted Si after SPE growth followed by $900^\circ\text{C}/30 \text{ min}$ anneal.

nance annealing. As with the BF_2 implant, a shallow amorphous layer was produced, only 1100\AA deep, close to the peak Ga concentration at 800\AA (14). The sample was SPE grown at $550^\circ\text{C}/40 \text{ min}$ and given furnace annealing treatments to precipitate out some of the Ga. The effects seen were similar to the Sb samples, in that precipitates and loops were observed (Fig. 13). The diffusion coefficient estimated from Fig. 13a is $D^* \approx 1 \times 10^{-14} \text{ cm}^2\text{s}^{-1}$; the tracer value is 5×10^{-18} . It is interesting to note that preliminary measurements again indicate an activation energy of 1.8 eV , suggesting that interstitials may be primarily responsible for the effect. The enhancement of 2000 times is less than the 6000 times seen with the same concentration of Sb from the interstitial trapping mechanism. More significantly, the high concentration of point defects only exists over a fairly narrow depth range in the crystal, whereas with the interstitial trapping mechanism, the concentration of interstitials follows the dopant profile. This may be the reason that radiation-enhanced diffusion appears to give less severe transient effects during RTA than the interstitial trapping mechanism.

Pipe diffusion.—Following either transient, the point defects involved usually condense into dislocation loops, and further annealing will cause these loops to grow and coalesce. Even at this stage, enhanced diffusion may still be observed due to fast pipe diffusion down dislocation cores, and this will not be of a transient nature. The effects of pipe diffusion will become greater than normal bulk diffusion when the dislocations are spaced closer than 1000\AA or so. With Sb, the loops generated as a result of the interstitial trapping mechanism do not produce serious dopant redistribution, since they occur primarily at the peak of the concentration profile and do not extend toward the junction. If of a sufficiently high density they may coalesce and form a planar dislocation network, as shown in Fig. 14. The effect of fast pipe diffusion is to allow precipitates lying on dislocations to grow at a much faster rate than those in the matrix. As the dislocation network anneals, segments are lost and large precipitates are left in the matrix.

The implantation damage around the original amorphous/crystalline interface will also condense into loops during annealing. With continued annealing, they also may grow and coalesce to produce a dislocation network. In the case of the Sb sample shown in Fig. 14, these two networks were clearly separated in depth, as can be seen in the cross-sectional TEM micrographs of Fig. 15. For the loops resulting from the interstitial trapping mechanism to coalesce into a network, they must have a high number density, which requires a high concentration of trapped interstitials and therefore a high dopant concentration. Experimentally, an Sb concentration C_0^* above $3 \times 10^{20} \text{ cm}^{-3}$ leads to a planar network, whereas the threshold for amorphization is only about $1 \times 10^{19} \text{ cm}^{-3}$. From the RBS profile in Fig. 16, we see that the Sb concentration reduces below C_0^* at a depth of 1200\AA , but does not reach 10^{19} cm^{-3} until a depth of 1800\AA . The two defect bands are, therefore, clearly separated, and there are no fast diffusion paths connecting the high concentration Sb region with the underlying crystal.

This is not the case for As^+ -implanted Si since the threshold for amorphization is roughly $2 \times 10^{20} \text{ cm}^{-3}$, which is very close to C_0^* . Therefore, the defect bands re-

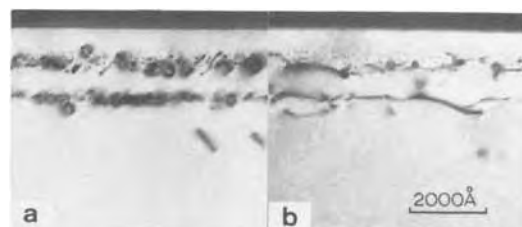


Fig. 15. Cross-sectional TEM micrographs of Sb (200 keV , $5 \times 10^{15} \text{ cm}^{-2}$)-implanted Si, SPE grown, and annealed $900^\circ\text{C}/10 \text{ min}$ (a) and $900^\circ\text{C}/30 \text{ min}$ (b).

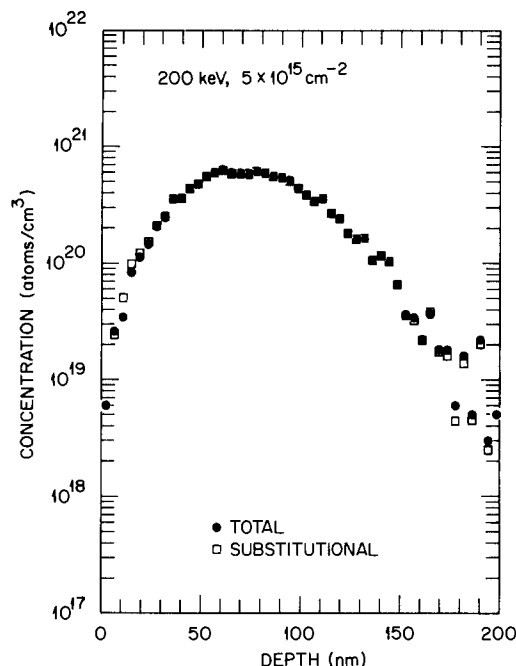


Fig. 16. RBS analysis of Sb (200 keV , $5 \times 10^{15} \text{ cm}^{-2}$)-implanted Si SPE grown at $550^\circ\text{C}/30 \text{ min}$.



Fig. 17. Cross-sectional TEM micrograph of As (100 keV , $1 \times 10^{16} \text{ cm}^{-2}$)-implanted silicon after rapid thermal annealing at $1050^\circ\text{C}/10\text{s}$.

sulting from the interstitial trapping and the underlying damage are very close and will coalesce to produce a single band of defects, as can be seen in the cross-sectional TEM micrograph of Fig. 17. This band is situated just deeper than the peak As concentration, and the dislocation density is clearly high enough for pipe diffusion to be significant. Part of the profile broadening shown in Fig. 10 may, therefore, be due to this mechanism, since the dislocation band extends from 1100 to 1700\AA in depth, well within the broadened profile.

Conclusions

We have studied in detail the transient-enhanced diffusion observed during furnace and rapid thermal annealing of ion-implanted silicon, resulting from the trapping

of interstitials by dopant atoms during implantation. We have measured the transient diffusion coefficients D^* and duration of the transient t^* for Sb- and Bi-implanted silicon and arrive at a model which can predict the transient effects during any thermal processing based on SPE growth. We compare the predictions with experimental results, and we give a temperature T^* above which the transient effects will not be significant. We show that above a certain dopant concentration C_0^* the dislocation loops resulting from the transient will coalesce into a network. We show that radiation-enhanced diffusion and pipe diffusion may also be significant in some experimental circumstances.

Acknowledgment

This work was supported by the Division of Materials Sciences, U. S. Department of Energy, under Contract no. DE-AC05-84OR21400 with Martin Marietta Energy Systems, Incorporated.

Manuscript received Dec. 10, 1984.

Oak Ridge National Laboratory assisted in meeting the publication costs of this article.

REFERENCES

1. S. J. Pennycook, J. Narayan, and O. W. Holland, *J. Appl. Phys.*, **55**, 837 (1984).
2. J. Narayan, O. W. Holland, R. E. Eby, J. J. Wortman, V. Ozguz, and G. A. Rozgonyi, *Appl. Phys. Lett.*, **43**, 957 (1983).
3. R. Kalish, T. O. Sedgwick, S. Mader, and S. Shatas, *ibid.*, **44**, 107 (1984).
4. J. B. Lasky, *J. Appl. Phys.*, **54**, 6009 (1983).
5. T. E. Seidel, *IEEE Electron Device Lett.*, **edl-4**, 353 (1983).
6. R. B. Fair and G. R. Weber, *J. Appl. Phys.*, **44**, 273 (1973).
7. A. P. Pogany, T. Preuss, K. T. Short, H. K. Wagenfeld, and J. S. Williams, *Nucl. Instrum. Meth.*, **209/210**, 731 (1983).
8. H. Reiss and C. S. Fuller, in "Semiconductors," N. B. Hannay, Editor, p. 222, Reinhold, New York (1959).
9. T. Y. Tan, U. Goesele, and F. F. Morehead, *Appl. Phys. A*, **31**, 97 (1983).
10. S. J. Pennycook, J. Narayan, and O. W. Holland, *J. Cryst. Growth*, **70**, 597 (1984).
11. O. W. Holland, J. Narayan, and D. Fathy, *Nucl. Instrum. Meth.*, **B7/8**, 243 (1985).
12. S. J. Pennycook, J. Narayan, and O. W. Holland, in "Ion Implantation and Ion Beam Processing of Materials," G. K. Huble, O. W. Holland, C. R. Clayton, and C. W. White, Editors, p. 293, Vol. 27 in Proceedings of the Materials Research Society, Elsevier, New York (1984).
13. R. T. Hodgson, V. Deline, S. M. Mader, F. F. Morehead, and J. Gelpy, in "Energy Beam-Solid Interactions and Transient Thermal Processing," J. C. C. Fan and N. M. Johnson, Editors, p. 253, Vol. 23 in Proceedings of the Materials Research Society, Elsevier, New York (1984).
14. J. Narayan, O. W. Holland, and B. R. Appleton, *J. Vac. Sci. Technol. B*, **1**, 874 (1983).
15. J. Narayan, O. W. Holland, W. H. Christie, and J. J. Wortman, *J. Appl. Phys.*, **57**, 2709 (1985).

Reactive Ion Etching of Silicon and Silicides in SF₆ or NF₃/CCl₄ or HCl Mixtures

T. P. Chow* and G. M. Fanelli

General Electric Company, Corporate Research and Development, Schenectady, New York 12301

ABSTRACT

Reactive ion etching of silicon (poly- and monocrystalline) and silicides (MoSi₂ and NbSi₂) in SF₆ or NF₃ and CCl₄ or HCl mixtures was investigated. Optical actinometry revealed that as the chlorine-based gas percentage increases, the fluorine atom density decreases most rapidly for SF₆/CCl₄ and most slowly for NF₃/HCl. Generally, both silicon and silicide etch rates exhibited a monotonic increase as the fluorine-based gas content increases. The dc self-bias increased with increasing HCl or NF₃ percentage but decreased with increasing CCl₄ or SF₆ percentage. Cross-sectional SEM of MoSi₂ polycide edge profiles showed, in SF₆/HCl mixtures, the most severe undercutting of the poly-Si layer occurred at 50% HCl.

Plasma etching of mono- and polycrystalline silicon (henceforth denoted by mono- and poly-Si) and various refractory metal silicides (such as MoSi₂ and WSi₂) in either fluorine- or chlorine-based gases have been extensively studied (1-10). Recently, a combination of these fluorine- and chlorine-based gases have been tried to achieve the optimum etching characteristics for silicon (11, 12) and refractory metal silicides (10). The main applications for these processes in silicon integrated circuit fabrication include formation of vertical silicon trenches for dielectric isolation and anisotropic etching of bilayer silicide/poly-Si stack (polycide) for MOS gate electrodes. Usually, both of these applications require highly selective and directional etching of silicon or silicide over photoresist and SiO₂. Basically, there are two ways of introducing two or more halide components into the etching reactions. The first is direct mixing of different halide gases at the inlet of the reaction chamber. Since the ratio of each component is controlled by the gas flow, it can be adjusted at will. The second is to use a molecule containing all of the halide components, such as fluorochloromethane (CF_{1-x}Cl_x). In this paper, a comparative study of reactive ion etching (RIE) of mono- and poly-Si and two metal silicides (MoSi₂ and NbSi₂) in SF₆ or NF₃/CCl₄ or HCl mixtures is reported.

Experimental Procedure

The RIE was performed in a commercial, parallel-plate-type reactor (Plasmatherm PK 1241) with an excitation frequency of 13.56 MHz. The conditions used for the RIE were total reactant gas flow rate of 20 sccm, substrate temperature of 30°C, RF power of 100 or 300W (0.20 and 0.59 W/cm², respectively), and electrode spacing of ~5 cm. The chamber pressure before plasma ignition was 45-50 mtorr with the difference attributed to the variations in pumping speed of various gases. During etching, the change in pressure as well as the dc self-bias on the substrate electrode was monitored and the plasma composition was probed through a quartz window with an automated optical spectrometer scanning between 200 and 800 nm. Also, there are always four 3 in. wafers, one oxide, two silicon, and one silicide, in the chamber. A few percent (2% usually) of argon was added to calibrate the emission intensity of atomic fluorine (13). Molybdenum and niobium silicide films were deposited by dc magnetron sputtering from cold-pressed alloy targets (both with a Si/metal ratio of ~2.3) onto oxidized silicon substrates in a batch system (Varian 3140). Poly-Si was deposited in an LPCVD system at 630°C and subsequently doped in POCl₃ at 1000°C for 15 min to yield a sheet resistance of 15 Ω/□ for a 1 μm thick film. Single-crystal, p-type silicon substrates, with (100) orientation and a resistivity of 1-10 Ω-cm, were used. Thermal oxide was grown in steam at 1000°C. Positive photoresist (Shipley 1470) was used to produce a step for etch-rate determination. The etch

*Electrochemical Society Active Member.

depth of all these films was measured with a stylus (Dektak).

Results and Discussion

Optical emission spectroscopy.—From optical emission spectra, actinometry was performed with argon to determine the fluorine atom density in these plasmas as the composition varies. In Fig. 1, the ratio between atomic fluorine intensity at 703.7 nm and argon intensity at 750.4 nm, normalized to its peak value, is plotted as a function of gas composition for SF₆ or NF₃/HCl or CCl₄ mixtures. (The intensity ratio reached a maximum at 100% SF₆ or NF₃ for all of the four plasmas mentioned here.) The fluorine intensity was found to drop off most rapidly for SF₆/CCl₄ and most slowly for NF₃/HCl. Specifically, the percentage of fluorine-based gas at which I_F/I_{Ar} fell to zero was 40% for NF₃/HCl and 80% for SF₆/CCl₄. Since the fluorine emission intensity can be directly related to the atomic fluorine density (13, 14), the latter follows the same trend. Besides fluorine, the change in chlorine concentration when the gas composition varies is also of interest. Unfortunately, argon actinometry on chlorine has

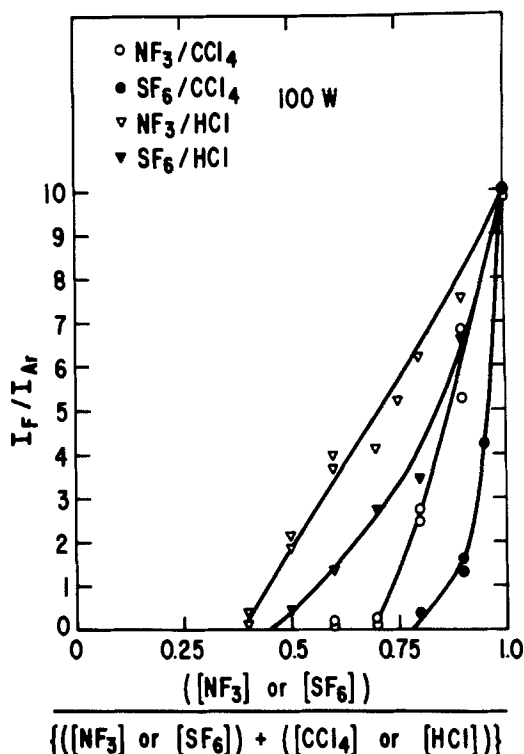


Fig. 1. The ratio between atomic fluorine emission intensity (at 703.7 nm) and argon intensity (at 750.4 nm), normalized to its peak value, as a function of gas composition for various SF₆ or NF₃/CCl₄ or HCl mixtures.

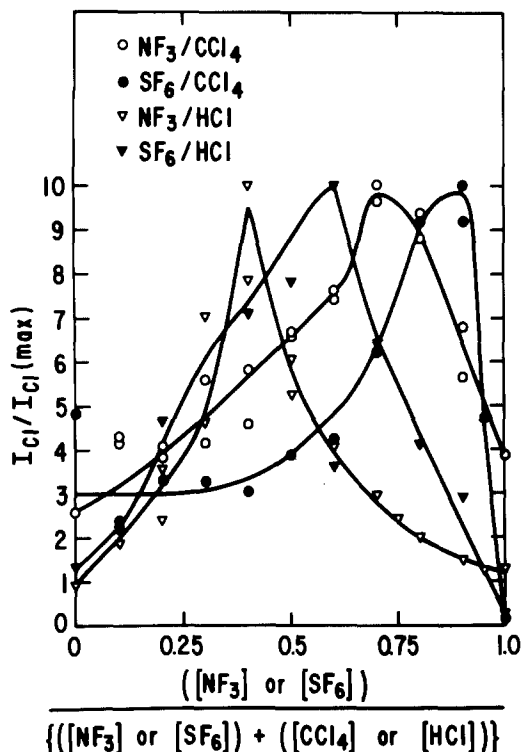


Fig. 2. Atomic chlorine emission intensity (at 725.6 nm), normalized to its own peak intensity, as a function of gas composition for various SF_6 or NF_3/CCl_4 or HCl mixtures.

been established only under certain sampling conditions (14, 15), and we did not try it here. Nevertheless, we monitored the variation in chlorine intensity at 725.6 nm. Its intensity, normalized to its own peak intensity, vs. gas composition is shown in Fig. 2. It can be noted that the composition at which the chlorine intensity reached a maximum was about the same as the one that the fluorine intensity vanished for all the four plasmas studied here.

Etching characteristics.—In general, the etch rate was highest for poly-Si and lowest for SiO_2 . Also, the silicon

etch rate increased monotonically with increasing fluorine content. In Fig. 3, the etch rates of poly- and mono-Si, SiO_2 , photoresist, $MoSi_2$, and $NbSi_2$ are shown as a function of gas composition at a RF power of 100W in NF_3/HCl mixtures. With pure NF_3 , both mono- and poly-Si were etched rapidly ($> 3000 \text{ \AA}/\text{min}$) and very selectively over oxide (30:1) and resist (5:1). As the HCl percentage increased, silicon etch rates as well as silicon-to-oxide and silicon-to-resist etch-rate ratios decreased. It can be seen that while the N+ poly-Si etch rate decreased monotonically with increasing HCl percentage, the mono-Si etch rate first increased slightly and then decreased. Apparently, even though there was an almost 50% decrease in atomic fluorine concentration when 25% HCl was added (Fig. 1), the increase in self-bias (shown later in Fig. 8) has apparently more than offset it, leading to a net gain in etch rate. Also, the etch rate of $MoSi_2$ followed the same trend as poly-Si, but that of $NbSi_2$ did not. For example, $NbSi_2$ was etched slower in 100% NF_3 than 75:25 $NF_3:HCl$. The reason for this could be the difference in vapor pressures among the chlorides and fluorides of molybdenum and niobium (10). MoF_6 is much more volatile than $MoCl_5$ and hence higher $MoSi_2$ etch rate can be obtained at higher fluorinated gas concentration. However, NbF_5 and $NbCl_5$ have about the same vapor pressure and the $NbSi_2$ etch rate decrease with increasing fluorine may be due to the lower dc self-bias. Since there may be other factors that contribute to this, more work is needed to understand this difference in sili- cide etch rate.

Increasing the RF power increases the silicon and sili- cide etch rate but also decreases the etch selectivity over oxide and resist. For example, the etch rate ratio between poly-Si and oxide at 50:50 $NF_3:HCl$ was 25 at 100W and decreased to only 10 at 300W (Fig. 4).

Similar etch rate dependence on fluorine/chlorine gas composition was observed for SF_6/HCl mixtures, as shown in Fig. 5. However, the poly- and mono-Si etch rates were lower. For example, the poly-Si was etched twice as fast at 50:50 $NF_3:HCl$ when compared to 50:50 $SF_6:HCl$. This can be explained by the higher atomic fluorine density in NF_3/HCl as shown in Fig. 1. At 50:50, a factor of 4 higher in fluorine concentration was seen from optical emission spectroscopy for NF_3/HCl vs. SF_6/HCl . This more efficient generation of fluorine from NF_3 is possibly because molecular nitrogen, created by

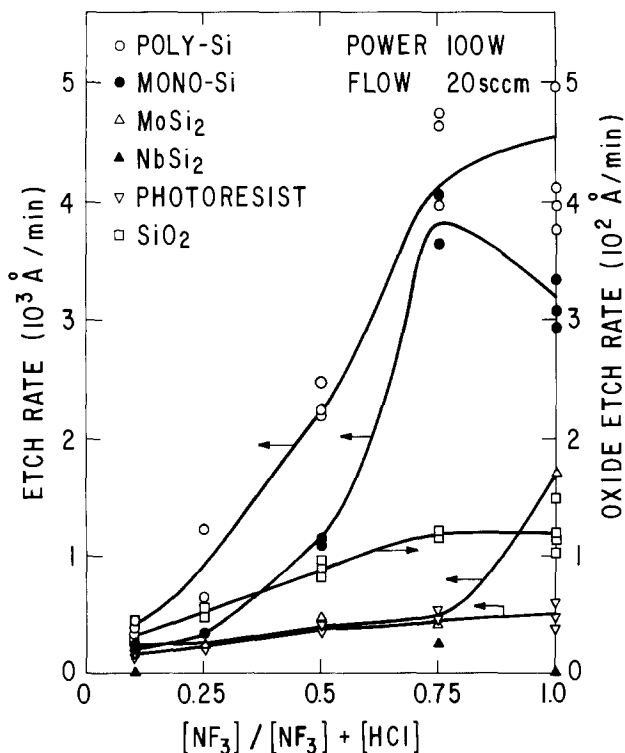


Fig. 3. Etch rates of poly-Si, mono-Si, $MoSi_2$, $NbSi_2$, SiO_2 , and positive photoresist (Shipley AZ 1470) in NF_3/HCl plasmas at 100W.

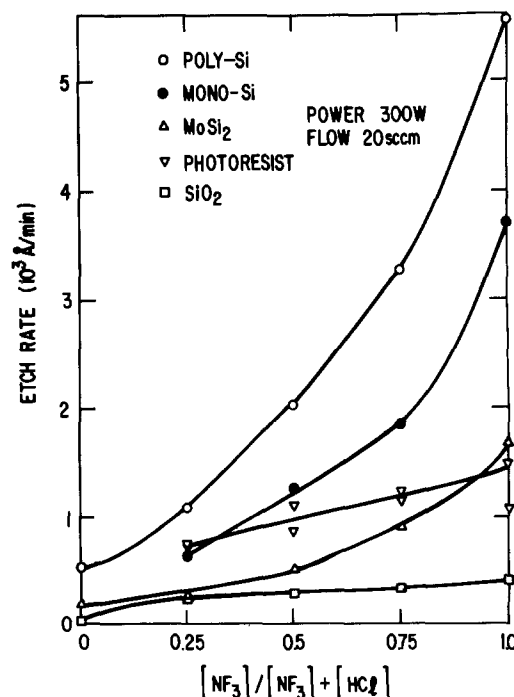


Fig. 4. Etch rates of poly-Si, mono-Si, $MoSi_2$, SiO_2 , and positive photoresist (Shipley AZ 1470) in NF_3/HCl plasmas at 300W.

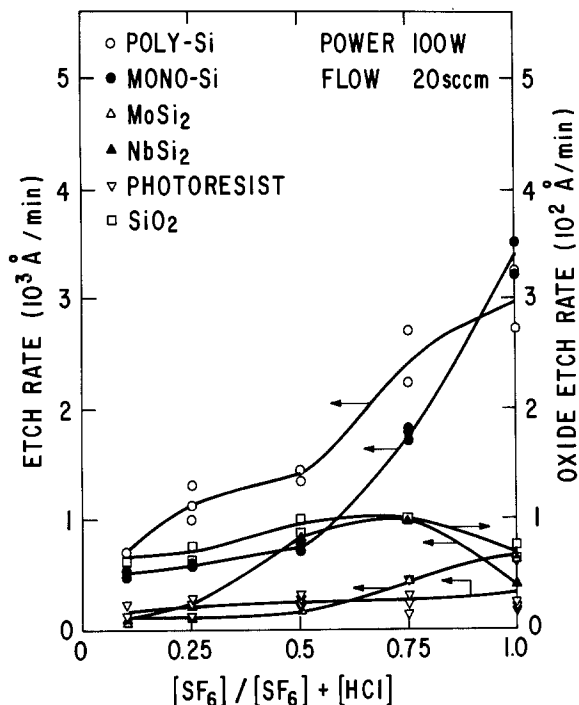


Fig. 5. Etch rates of poly-Si, mono-Si, MoSi₂, NbSi₂, SiO₂, and positive photoresist (Shipley AZ 1470) in SF₆/HCl plasmas at 100W.

the dissociation of NF₃ molecules in such reactions as $2NF_3 \rightarrow N_2 + 2F$, does not react with fluorine atoms. However, sulfur and SF_x ($x < 6$), which are products in the dissociation of SF₆, apparently react with fluorine and hence the steady-state level of [F] will be lower in SF₆ plasmas than in NF₃. This hypothesis is plausible from optical emission spectra data in which significant peaks from N₂ bands were clearly visible, while no sulfur peaks were detectable. Similar observations on more efficient fluorine generation has been reported in an etching comparison between NF₃/Ar and CF₄/O₂ plasmas (20).

When CCl₄ was used instead of HCl, similar etch-rate dependence on gas composition was obtained as shown in Fig. 6 where an RF power of 300W was applied. Nevertheless, the etch rate of all the materials studied were

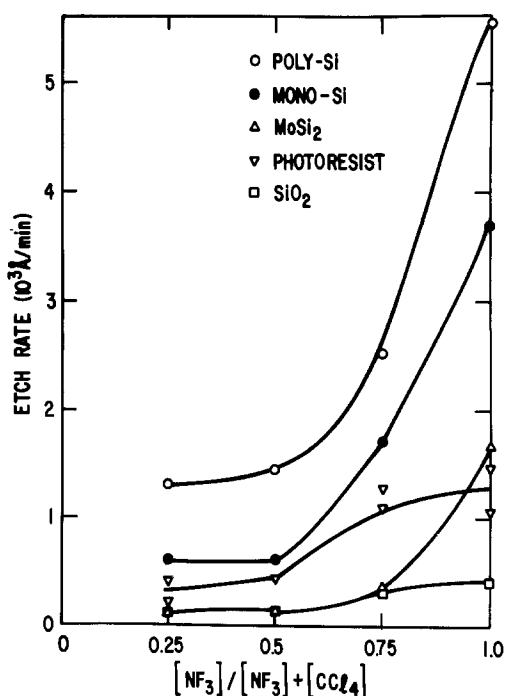


Fig. 6. Etch rates of poly-Si, mono-Si, MoSi₂, SiO₂, and positive photoresist (Shipley AZ 1470) in NF₃/CCl₄ plasmas at 300W.

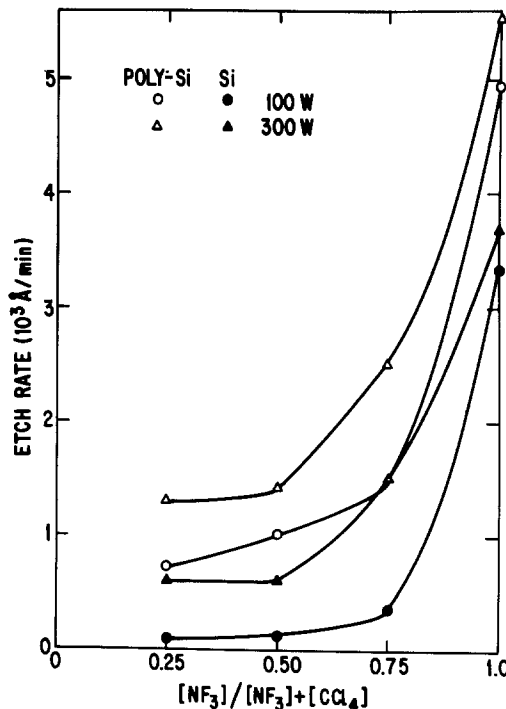


Fig. 7. Mono- and poly-Si etch rates vs. gas composition in NF₃/CCl₄ at two different RF power levels (100 and 300W).

lower in the CCl₄ plasmas. The etch rate difference was most notable at 50:50 where, for example, the photoresist etch rate was halved and poly-Si was lower by over 30% (Fig. 4 vs. Fig. 6). When the applied RF power was lowered, the etch rate was also decreased as in the NF₃/HCl case mentioned earlier. In Fig. 7, a comparison of the poly- and mono-Si etch rates at two RF power levels, 100 and 300W, is shown. While the trend of increasing etch rate with increasing fluorine content is the same, the etch rates were significantly higher at the higher power level, particularly at low fluorine content. This is again consistent with the fact that ion bombardment enhances silicon etch rate more in chlorine-based plasmas (1, 5).

DC self-bias and pressure variations.—The degree of ion bombardment can be inferred from dc self-bias measurements and pressure variations. In Fig. 8, these two parameters are plotted vs. gas composition for NF₃/HCl and NF₃/CCl₄ plasmas. The self-bias of the cathode in HCl plasmas with NF₃ as additive decreased rapidly with increasing NF₃ percentage (from -120V for pure HCl to -30V for pure NF₃). However, when CCl₄ was used in place of HCl, the bias showed an opposite trend and increased from just over -10V for pure CCl₄ to -30V. Similar trends were also observed when SF₆ was substituted for NF₃, as shown in Fig. 9. In fact, even when inert gases like argon and nitrogen were used as additives, the same trends have been seen (8).

Since the pumping speed was held constant (with the throttle valve wide open) throughout the etching cycle, there was a pressure change when the plasma was ignited. Usually this pressure change was positive. It is worth noting that for pure NF₃, such a ΔP was 20 mtorr, and it decreased gradually as either HCl or CCl₄ was added. However, while in a pure CCl₄ plasma the pressure increase was 8 mtorr, in a HCl plasma there was a pressure decrease up to 7 mtorr (Fig. 8). Interestingly, quite different variations in pressure were measured for SF₆-based plasmas as evident from Fig. 9. The pressure change reached a maximum of 12 mtorr at 70:30 SF₆:HCl and 10 mtorr at 50:50 SF₆:CCl₄.

This change in self-bias and pressure may be related to the dissociation reactions of these molecules and apparently are distinct features of these plasmas. However, more work is needed to identify the basic reactions that lead to these variations.

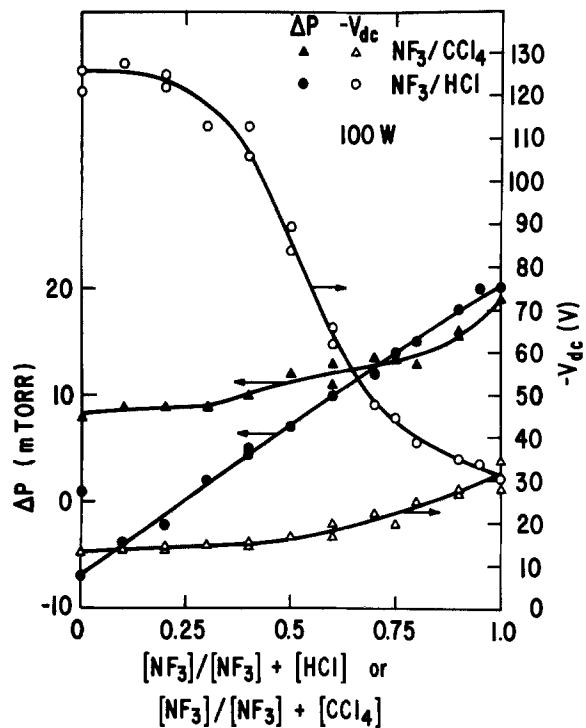


Fig. 8. DC self-bias (V_{dc}) and change in pressure (ΔP) as a function of gas composition for NF_3/HCl and NF_3/CCl_4 plasmas.

Polycide edge profiles.—To study the effect of gas composition on polycide etching, a $MoSi_2$ /poly-Si stack, 3000 and 2000 Å thick, respectively, was etched in various percentages of SF_6/HCl plasmas. Figure 10 shows schematic drawings of the edge profiles before and after etching. The etch cycle is terminated just after the poly-Si layer has been etched so that no intentional overetching is performed. Since both the poly-Si and silicide etch rates decreased with decreasing SF_6 content, the total time needed to etch the polycide stack increased from 7 min

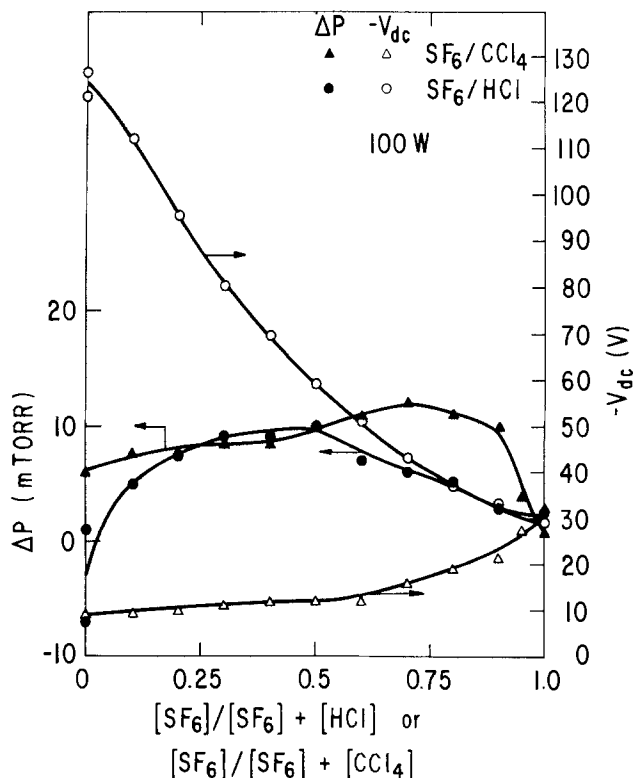


Fig. 9. DC self-bias (V_{dc}) and change in pressure (ΔP) as a function of gas composition for SF_6/HCl and SF_6/CCl_4 plasmas.

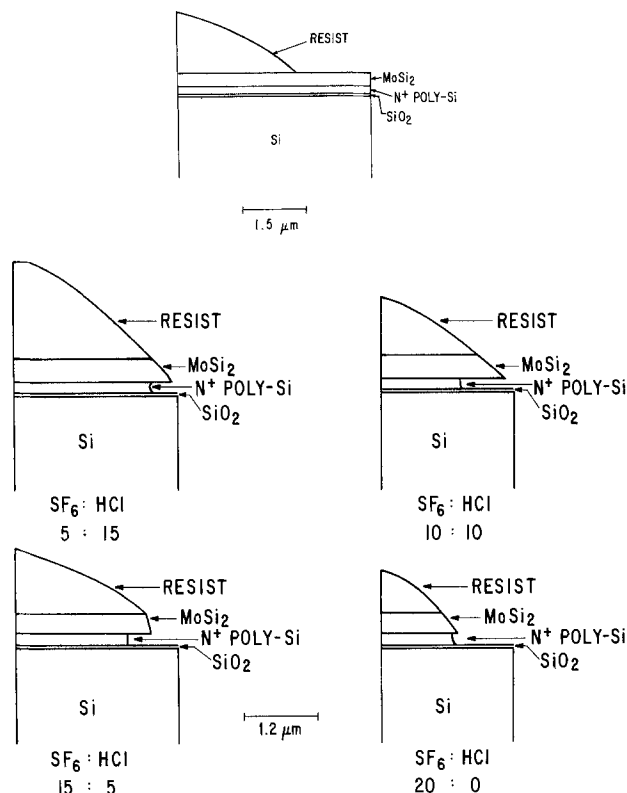


Fig. 10. Edge profiles of $MoSi_2$ /poly-Si stack in various compositions of SF_6/HCl plasmas at 100W.

for pure SF_6 to 32 min for 5:15 $SF_6:HCl$. Furthermore, the poly-Si/ $MoSi_2$ etch rate ratio increases with decreasing SF_6 content, from 4.6 with pure SF_6 to 10 with 5:15 $SF_6:HCl$ as calculated from Fig. 5. As is evident from these profiles, the maximum poly-Si undercut occurred at 10:10 $SF_6:HCl$ were $\sim 1 \mu m$ was observed. While it is difficult to explain the exact cause that results in these edge profiles, it is interesting to point out that chlorine emission peaked at the same composition (Fig. 2) while the fluorine concentration was essentially zero (Fig. 1). Hence, it is possible that the undercut is mainly caused by chlorine species. By contrast, in previous works (9, 16, 17), chlorine was reported to help passivate poly-Si sidewalls to enhance anisotropy. However, in those studies, fluorocarbons (such as C_2F_6) or fluorochlorocarbons (such as $CFCl_3$) were usually added and the etching was performed in relatively high pressure (0.3-0.4 torr) planar plasma reactors. Indeed, when only chlorine was used in conjunction with argon, undercutting of poly-Si was observed (9).

Etching of polycide using mixed fluorine/chlorine plasmas has been reported previously (18, 19). However, because of the difference in reactor configuration, reactants, and silicides used, it is not possible to compare those results with ours.

Summary

In summary, reactive ion etching of silicon and silicides in SF_6 or NF_3/HCl or CCl_4 mixtures is reported for the first time. It was found from optical argon actinometry that, as the percentage of chlorine component increases, the atomic fluorine density decreases most rapidly for SF_6/CCl_4 and most slowly for NF_3/HCl mixtures. The silicon and silicide etch rates generally showed a monotonic increase when more fluorinated gas is added. The self-bias increases with higher HCl or NF_3 percentage but decreases with higher CCl_4 or SF_6 percentage. Cross-sectional edge profiles of $MoSi_2$ /poly-Si stack etched in SF_6/HCl mixtures showed the most severe poly-Si undercut occurred at 50% HCl.

Manuscript submitted Nov. 15, 1984; revised manuscript received March 21, 1985.

General Electric Company assisted in meeting the publication costs of this article.

REFERENCES

1. J. W. Coburn, *Plasma Chem. Plasma Proc.*, **2**, 1 (1982).
2. C. J. Mogab, *This Journal*, **124**, 1262 (1977).
3. R. A. Gdula, Abstract 608, p. 1524, The Electrochemical Society Extended Abstracts, Vol. 79-2, Los Angeles, CA Oct. 14-19, 1979.
4. G. C. Schwartz and P. M. Schaible, *J. Vac. Sci. Technol.*, **16**, 410 (1979).
5. V. M. Donnelly and D. L. Flamm, *Solid-State Technol.*, **24**, (4), 161 (1981).
6. H. B. Pogge, J. A. Bondur, and P. J. Burkhardt, *This Journal*, **130**, 1592 (1983).
7. G. C. Schwartz and P. M. Schaible, *ibid.*, **130**, 1898 (1983).
8. T. P. Chow and P. A. Maciel, in "Proceedings of the 6th International Symposium on Plasma Chemistry" (ISPC-6), M. I. Boulos and R. J. Munz, Editors, p. 583 (1983).
9. C. J. Mogab and J. H. Levinstein, *J. Vac. Sci. Technol.*, **17**, 721 (1980).
10. T. P. Chow and A. J. Steckl, *This Journal*, **131**, 2325 (1984), and references therein.
11. D. L. Flamm, D. N. K. Wang, and D. Maydan, *ibid.*, **129**, 2755 (1982).
12. L. M. Ephrath and R. S. Bennett, in "VLSI Science and Technology," C. J. Dell'Oca and W. M. Bullis, Editors, p. 103, The Electrochemical Society Soft-bound Proceedings Series, Pennington, NJ (1982).
13. J. W. Coburn and M. Chen, *J. Appl. Phys.*, **51**, 3134 (1980).
14. R. A. Gottscho and T. A. Miller, *Pure Appl. Chem.*, **56**, 189 (1984).
15. R. A. Gottscho and V. M. Donnelly, *J. Appl. Phys.*, **56**, 245 (1984).
16. A. C. Adams and C. D. Capio, *This Journal*, **128**, 366 (1981).
17. M. Mieth and R. A. Barker, *J. Vac. Sci. Technol. A*, **1**, 629 (1983).
18. H. J. Mattausch, B. Hasler, and W. Beinvoogl, *J. Vac. Sci. Technol. B*, **1**, 15 (1983).
19. S. E. Clark, J.-K. Tsang, and J. W. Marolf, *Solid State Technol.*, **27**, (4), 235 (1984).
20. V. M. Donnelly, D. L. Flamm, W. C. Dautremont-Smith, and D. J. Werder, *J. Appl. Phys.*, **55**, 242 (1984).

Epitaxial Growth of Silicon by CVD in a Hot-Wall Furnace

J. Bloem,* Y. S. Oei, H. H. C. de Moor, J. H. L. Hanssen, and L. J. Giling

Faculty of Science, R.I.M. Department of Solid State III, Catholic University, Toernooiveld, 6525 ED Nijmegen, The Netherlands

ABSTRACT

A theoretical and experimental study has been performed for the feasibility of epitaxial growth in a furnace. In this study, it is proven that growth in a hot-wall furnace in principle is possible — without deposition of silicon on the quartz ware of the cell — when the growth is carried out at near equilibrium conditions. For supersaturations larger than 10%, deposition also occurs on the quartz of the wafer boat or cell. A constant supersaturation, *i.e.*, a constant growth rate at all slices along the reactor tube can be achieved by imposing a temperature gradient over the cell. The best results are obtained for growth with SiHCl_3 , low Cl/H ratio, and high temperatures. Growth rates amount to 0.1-0.3 $\mu\text{m}/\text{min}$ for these conditions.

The epitaxial growth of silicon has become an inherent part of the silicon device technology since in 1960 the first transistor with epitaxial base was described (1). Recently, silicon solar cells with epitaxial layers on metallurgical-grade silicon substrates showed the feasibility of chemical vapor deposition in this rapidly growing technology (2). The growth of device quality epitaxial material is performed in cold-wall reactors operating at atmospheric pressure and at temperatures well above 1000°C. In this temperature range, the surface reactions leading to growth are relatively rapid and the growth rate is determined by the supply of reactant via gas phase diffusion. The concept of the stagnant boundary layer has been successfully applied to describe and to monitor the growth rate and the growth rate uniformity in production-type reactors (3).

A rather low packing density of substrates can be used in the epitaxial cold-wall reactors and the numbers produced per batch are restricted to, say, 20 slices of 4 in. diam. The epitaxial growth, therefore, is among the most expensive steps in the silicon device technology, and reactors with a high packing density of substrates in a resistance-heated hot-wall diffusion-type furnace should be very welcome.

The hot-wall reactor came into use when polycrystalline silicon had to be grown in thin layers on existing device structures acting as gate material in the self-aligned MOS technique. It appeared that poly-Si could be deposited on slices stacked in a diffusion furnace to give an extremely uniform polycrystalline silicon layer over the whole batch (4).

This method only works at the low temperatures where poly-Si is grown and where the efficiency of the growth

reaction is so low that depletion effects are of minor importance. Growth also occurs on the hot quartz walls and substrate holders. The method is therefore restricted to the deposition of thin polycrystalline layers at relatively low temperatures.

Studies to grow monocrystalline silicon in a hot-wall furnace have been performed since 1960. Deal (5), Lombos and Somogyi (6), and Nishizawa (7) showed the main problems to be the strong depletion and the rapid deposition on the quartz ware of the reactor. Ban (8) introduced a mechanically complex system in which a great number of slices can be processed simultaneously and rotating nozzles are used to direct the gas flow. Recently, Langlais *et al.* (9) gave an analysis of the thermodynamics of silicon deposition in a hot-wall reactor. Depletion effects were not studied specifically, but a growth at reduced pressure is recommended. Indeed, Ogirima and Takahashi (10) showed that SiH_2Cl_2 plus H_2 at a total pressure of 2 torr could give a reasonable growth rate distribution in a LPCVD reactor around 1000°C, with a special nozzle to introduce the reactant. A similar observation has been published by Duchemin *et al.* (11). In all the work cited above, high supersaturations were needed to come to an acceptable growth rate. Deposition of silicon on the hot tube wall and depletion in the direction of the gas stream does restrict the usefulness of the method. Another approach to the epitaxial growth of silicon has been pursued for a number of years in our laboratory (12). Details of the underlying concepts and of some results will be given in the following sections.

Equilibrium calculations.—Thermodynamic calculations of the Si-Cl-H system have been performed with increasing accuracy. Steinmaier (13) was the first to calculate the silicon growth rate as a function of the gas phase

*Electrochemical Society Active Member.

composition. Lever (14), Hunt and Sirtl (15, 16), van der Putte *et al.* (17), and Langlais *et al.* (9) showed the potentials of the computer calculations.

Experimental evidence has been obtained by Sedgwick (18), Ban (19), and Duchemin (20) showing that equilibrium between the gas phase and solid silicon is rapidly established at temperatures well above 1000°C, leading to gas-phase concentrations of SiCl_4 , SiH_2Cl_2 , and HCl close to the ones calculated from thermodynamic data.

In the present study, interest is focused on near-equilibrium situations in which only a small supersaturation is available; the equilibrium calculations, therefore, are even more interesting than in the cases discussed before where large supersaturations are involved.

Using literature data together with an iterative computer program based on minimalization of the Gibbs energy, the equilibrium composition of several Si-H-Cl gas mixtures in contact with solid silicon was calculated. This was performed for several Cl/H ratios, temperatures, and total pressures. Figure 1 gives an example of the equilibrium composition as a function of temperature of a gas mixture for Cl/H = 0.162 and $p_{\text{tot}} = 1$ bar. The total amount of silicon which is present in the gas phase can be deduced for each p , T , and H/Cl ratio by taking the sum total of all the partial pressures of gaseous compounds containing silicon. This total sum is equal to the solubility L of silicon in the gas phase for the given conditions of p , T , and H/Cl under the condition of complete equilibrium between solid and gas.

$$\sum p_{\text{Si}} = L = \sum_j x_j p_j (\text{Si}_x \text{H}_y \text{Cl}_z)_j \quad (x \neq 0) \quad [1]$$

The relative supersaturation percentage for an input pressure p_i follows from

$$\gamma = \frac{p_i - L}{L} 100 \quad [2]$$

The difference in chemical potential ($\Delta\mu$) between input and equilibrium mixtures is given by

$$\Delta\mu = kT \ln p_i/p_{\text{eq}} \quad [3]$$

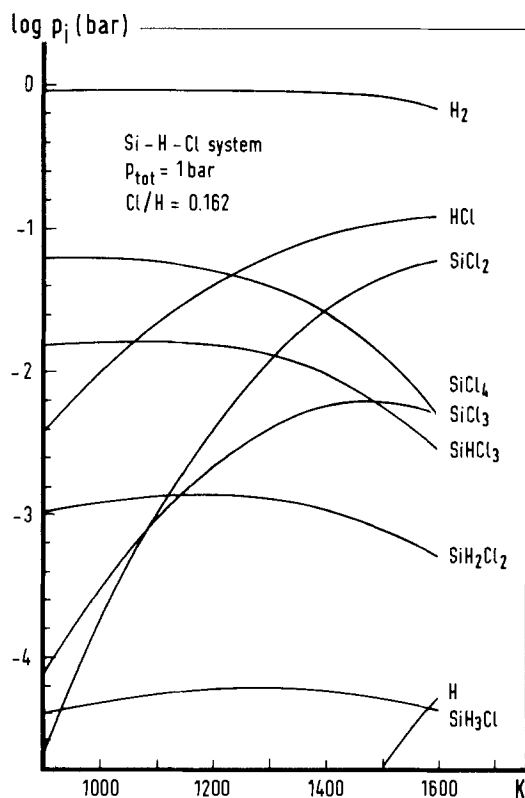


Fig. 1. Calculated values of gas phase species in equilibrium with solid silicon as a function of temperature for Cl/H = 0.162 at 1 bar total pressure.

For small supersaturations and with $p_i = p_{\text{eq}} + \Delta p$, we can put

$$\ln \left(1 + \frac{\Delta p}{p_{\text{eq}}} \right) \cong \frac{\Delta p}{p_{\text{eq}}}$$

so that

$$\frac{\Delta\mu}{kT} = \ln \left(1 + \frac{\Delta p}{p_{\text{eq}}} \right) \cong \frac{\Delta p}{p_{\text{eq}}} \quad [4]$$

In this way, the relative supersaturation γ and $\Delta\mu/kT$ are equal for small supersaturations.

In cases where the chemical reactions in the gas phase give rise to volume changes (nonequal number of reactants and reaction products), it is advisable to use a relative solubility L_{rel} given by the ratio of the number of moles of silicon in the gas phase and the total number of reacting atoms

$$L_{\text{rel}} = \frac{n_{\text{Si}}}{n_{\text{tot}}} = \frac{\sum p_{\text{Si}}}{\sum p_{\text{Si}} + \sum p_{\text{Cl}} + \sum p_{\text{H}}} \quad [5]$$

where $\sum p_{\text{Cl}}$ and $\sum p_{\text{H}}$ are defined in the same way as $\sum p_{\text{Si}}$ in Eq. [1].

In Fig. 1, it is seen that at the lower temperatures SiCl_4 is the main gas phase component in equilibrium with solid silicon; at the higher temperatures the SiCl_4 content decreases, and SiCl_2 becomes the most important gaseous silicon compound. This situation leads to a minimum in the silicon solubility (L) as a function of temperature for a specific Cl/H ratio. Figures 2 and 3 give examples for different Cl/H ratios and total pressures. For lower values of Cl/H, the absolute value of L decreases and the minimum shifts to higher temperatures. For reduced pressures (or a replacement of H_2 by an inert gas), the minimum shifts to lower temperatures. For input partial pressures of SiCl_4 , SiHCl_3 , or SiH_2Cl_2 , the appropriate Cl/H curve can be selected and growth is expected for input values greater than the value of L , for $p_i < L$ etching of solid silicon will occur.

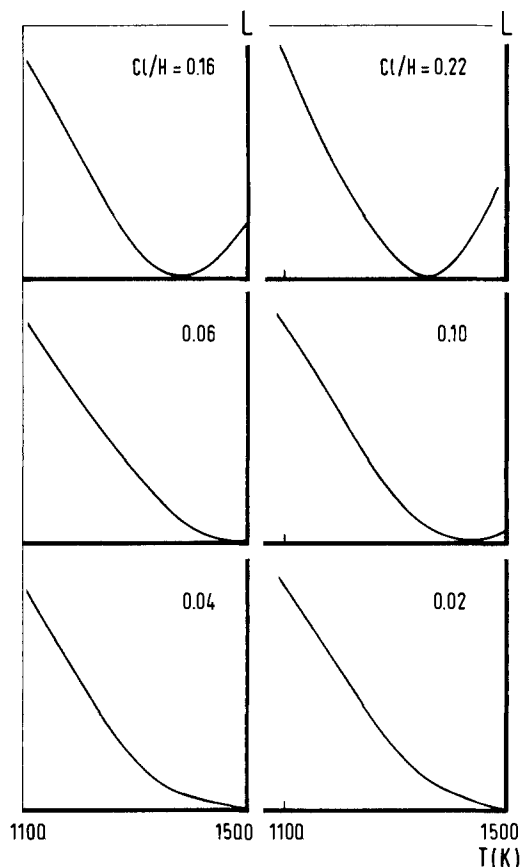


Fig. 2. The silicon solubility L , constructed from calculations as given in Fig. 1 for different values of Cl/H ratio at atmospheric total pressure. The minimum in L shifts to lower temperatures for increasing chlorine content. The preferred epitaxial temperature is around 1350 K.

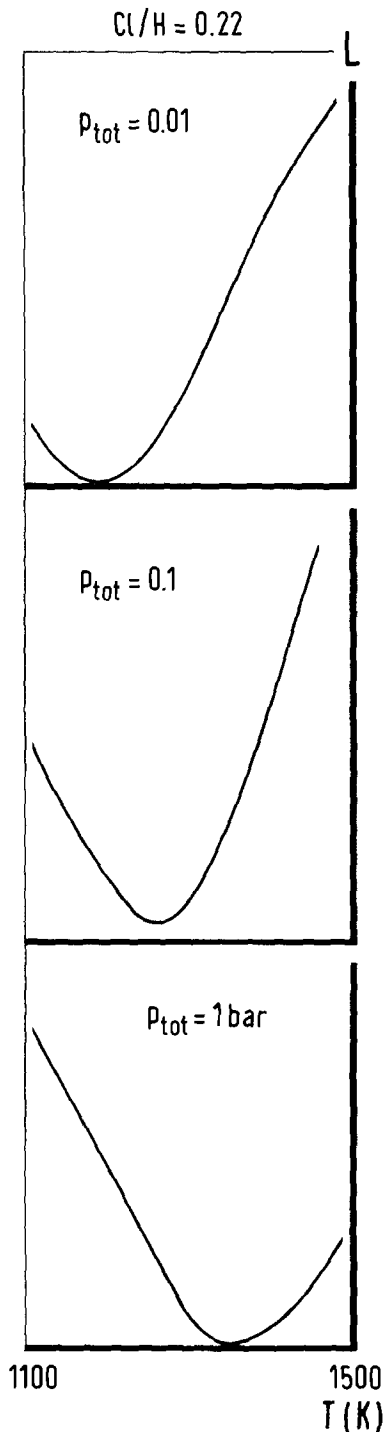


Fig. 3. The silicon solubility L as a function of temperature at a constant Cl/H ratio at various total pressures in the Si-Cl-H system. Replacement of hydrogen by an inert gas as helium has the same thermodynamic consequences.

In Fig. 4, three experimental situations are depicted. Point A corresponds to an experiment where the input of $SiCl_4$, $SiHCl_3$ or SiH_2Cl_2 , and HCl in H_2 is such that for $T = 1000$ K the input mixture contains less silicon than the corresponding equilibrium value. So once this mixture comes into contact with the solid silicon crystals, the system will strive toward an equilibrium situation and the crystals will be etched. This applies for every situation where the combination of input concentration and temperature is lying below the solubility curves. Growth will occur when the input values exceed the solubility line. For mixture A, this is achieved at T larger than 1100 K. So for input concentration A below 1100 K, etching will take place; above 1100 K, the crystal will grow. Starting with an input composition at B directly will give growth be-

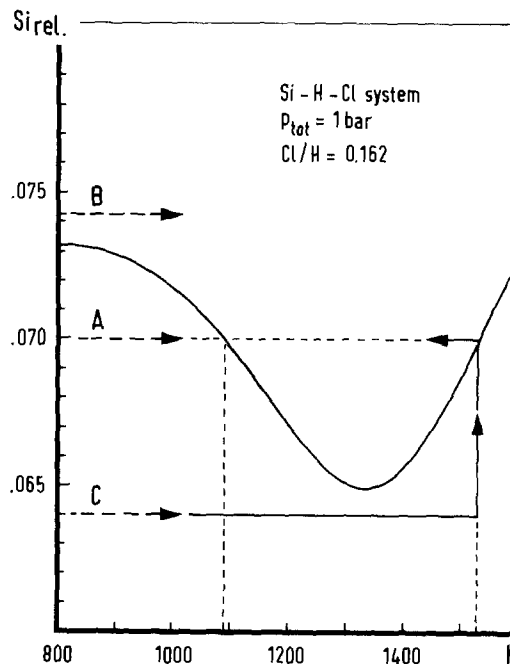


Fig. 4. The silicon solubility as a function of temperature in relation to various input conditions. Input mixtures with a Si/Cl ratio higher than the equilibrium value (L) give rise to growth at all temperatures (B). Lower input concentrations of silicon (A and C) lead to etching or growth dependent on temperature (see text).

cause the silicon content exceeds the solubility of silicon. To prevent deposition of silicon in colder parts of the reactor, conditions have to be chosen such that deposition does not start below a specified temperature (situation A). It has also to be realized that an input mixture of say $SiHCl_3$ in H_2 can have the required Si/Cl and Cl/H ratio; the gas phase species, however, still have to be adjusted to the equilibrium concentrations of $SiCl_4$, SiH_2Cl_2 , $SiCl_2$, etc. This process may take some time.

For a real growth experiment in a hot-wall reactor, a supersaturation has to be introduced in order to come to growth. The small supersaturations envisaged in the present experiments then will lead to a rapid reduction in growth rate in the direction of the gas stream. This depletion can be overcome in two ways. First, it is possible to introduce additional reactant via an inlet tube with carefully designed holes; in this way the Si/H or Cl/H ratio can be altered as a function of position in the reactor. Second, the temperature in the tube can be changed. In the latter case, we work in a temperature gradient and the solubility curve can be followed until the minimum in the solubility is reached. This idea is followed in the present study. All along the temperature gradient the gas phase is brought out of equilibrium and comes to equilibrium again by the deposition of silicon on the substrates.

The growth of silicon under a small supersaturation as can be realized by the gradual change of temperature described above has the additional advantage that growth of silicon on silicon is readily possible; growth of silicon on a foreign substrate, however, meets with nucleation difficulties and needs a higher supersaturation (21). This bears the possibility that growth on tube walls and quartz boats can be prevented and also gives the possibility of selective growth in windows of oxide layers present on a large number of silicon substrates in the reactor.

Growth rate.—For growth at a constant temperature, the growth rate (G) can be calculated for a constant flow rate V liter/min, an initial silicon partial pressure p_i bar, and a solubility L of silicon in the gas phase in bar at the temperature T from

$$G = \frac{(p_i - L)VM}{RTAp} 10^7 \mu\text{m/min} \quad [6]$$

where R is the gas constant ($82.06 \text{ cm}^3 \text{ bar/K-mol}$). M is

the molecular weight of silicon (28.086g), ρ is the density of silicon (2.3 g/cm³), and A is the silicon substrate surface area (cm²).

The flow V depends on temperature and total pressure (p_{tot}) present in the reactor cell

$$V = \frac{V_0 T p_0}{T_0 p_{\text{tot}}} \quad [7]$$

where V_0 is the gas flow at normal p and T ($p_0 = 1$ bar, $T_0 = 298$ K). For growth on a greater number of slices, each wafer has to be in contact with a gas phase with the same supersaturation. This can be realized as discussed before in a temperature gradient in which the gas phase is constantly brought out of equilibrium. In that case the equation for the growth rate becomes

$$G = \left(- \frac{dL}{dT} \right)_T \left(\frac{dT}{dx} \right)_x \frac{l V_0 M}{RT_0 A(x) \rho} \frac{p_0}{p_{\text{tot}}} 10^7 \mu\text{m/min} \quad [8]$$

where $(dL/dT)_T$ is the gradient of the solubility curve at temperature T for the Cl/H ratio and total pressure in question, $(dT/dx)_x$ the gradient of the temperature at position X , l the distance between two slices, and $A(x)$ the substrate surface area at position X . Growth has to be expected for a positive product $(-dL/dT)(dT/dx)$, i.e., at the low temperature side of the minimum of the solubility curve ($dL/dT < 0$) a positive temperature gradient must be applied, whereas a temperature drop in the direction of the flow ($dT/dx < 0$) is needed when one works at the high temperature side of this minimum, where (dL/dT) is positive (Fig. 2-4).

For constant growth rate all along the reactor tube, it is sufficient that the product $(dL/dT)(dT/dx) l$ is constant. In practice, a constant value of dT/dx combined with a constant wafer spacing is preferred. In this case, constant growth rate requires a linear change in the solubility curve. This optimal thermodynamic working point directly will follow from the solubility curves by calculating dL/dT for each T . No real constant value for dL/dT is present; however, a more or less flat region — where the deviations are smaller than 10% — is present around each inflection point in the L vs. T plot, allowing crystal growth in a temperature region with a width of about 100-200 K around 1200 K for each Cl/H ratio.

In principle, it is possible to work at the high temperature side of the minimum in L vs. T . A disadvantage will be that the gas mixture has to enter from the hottest side of the furnace. During the heating up from room temperature, the gas will pass a temperature region where, already, a state of supersaturation will be obtained and spontaneous nucleation in the gas phase may occur. This problem can be solved by following route C as indicated in Fig. 4, where in principle the gas mixture at high T is prepared *in situ* from an unsaturated silicon mixture in contact with a solid silicon source.

This disadvantage does not exist for growing in a positive temperature gradient, i.e., at the low temperature side of the solubility curve. Low temperatures are preferred in hot-wall reactors, especially when lower total pressures are of advantage, in order to prevent damage of the tube and attack of the quartz ware.

Equipment and procedures.—Basically, the system is a normal CVD system equipped with a furnace instead of a RF generator. A schematic presentation including the gas mixing system is depicted in Fig. 5.

The complete system is home-built and consists of a four-zone furnace with a total heated length of 135 cm. The inner diameter of the reactor tube was 45 mm, with a total length of 260 cm, including the necessary load-lock provision. With four independent controllers, any desired temperature profile can easily be adjusted.

Mass flow controllers and mass flowmeters controlled the flow of the hydrogen carrier gas, the dichlorosilane, or trichlorosilane and additional HCl. For the present experiments, the silicon samples [one side polished, low resistivity, Sb doped, (100) orientation, with a diameter of 5

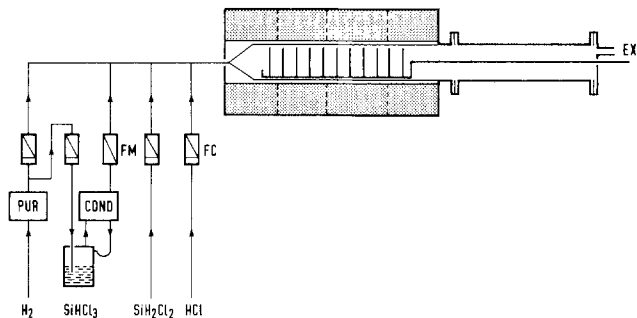


Fig. 5. The apparatus used in the growth experiments consists of a four-zone furnace in which is a long quartz tube such that the load can be flushed at room temperature before introduction into the furnace. All gases can be directed to the vent when needed (not shown in the figure). The slices can be positioned parallel to or perpendicular to the gas stream, the experimental results being comparable.

cm], were cut into two parts and placed parallel to the long axis of the furnace. This has the advantage of giving a small disturbance on the flow characteristics; it has the disadvantage that because of the high heat conductivity of the silicon, the upstream part of the crystal is somewhat higher and the downstream part is somewhat lower in temperature than would correspond with its position in the furnace (for positive T -gradient in the flow direction).

In additional experiments, it has been shown that the slices can be placed parallel to or perpendicular to the main gas stream without significant differences in growth rate and crystallographic quality.

The moisture and oxygen content of the H_2 carrier gas was always below 1 ppm. The total flow (NTP) was always 3.5 liter/min, giving a gas velocity of about 15 cm/s at the growth temperature.

The sample holder loaded with up to 20 slices is introduced into the cold part of the quartz tube, purged with N_2 and H_2 , then slowly moved into the hot furnace. Just before the start of the growth experiments, an *in situ* HCl etch was performed with 0.5% HCl for 5 min. The etch rate of silicon by HCl is rather independent of temperature between 900° and 1200°C and amounts to 0.02 $\mu\text{m/min}$ (21) for the given HCl content.

Results

Experiments were performed with $SiHCl_3$ as well as with SiH_2Cl_2 as silicon sources. $SiHCl_3$ was taken to study (i) the effect of the input concentration on the growth rate (this gives indication about the practical usable concentration for growth and gives information indicating whether the equilibrium situation is achieved) and (ii) the influence of the temperature gradient on the growth rate.

With SiH_2Cl_2 it is possible to check whether a similar growth will be observed for a given Si/H and Cl/H ratio as obtained with $SiHCl_3$. This directly gives proof that equilibrium situations are attained in both situations.

$SiHCl_3/HCl/H_2$ mixtures.—In order to obtain homogeneous epitaxial layers with good crystalline qualities at reasonable growth rates, a number of initial requirements have to be fulfilled when growth is to be performed in an oven.

1. For optimal crystalline quality, the temperature range should be as high as possible (> 1200 K)
2. The adsorption of, e.g., chlorine should be as low as possible, which is favored by high temperatures and low chlorine content.
3. The solubility of silicon preferably should change linearly with T in order to achieve constant growth rates in the temperature gradient of the furnace.
4. The slope of the solubility curve should be as steep as possible to obtain high growth rates and high yields.
5. Deposition on furnace wall and quartz boats has to be prevented.

From the solubility curves as presented in Fig. 2 and 3, it can be seen that the requirements can best be met for Cl/H = 0.06 and $p = 1$ bar. For this ratio, a reasonable

value for dL/dT is obtained at high temperatures. In addition, the chlorine content of the gas mixture is relatively low, which favors a small coverage of the surface with chlorine. A temperature region around 1200 K should be preferred to guarantee constant growth rates. Since it can be expected that the crystalline perfection for $T < 1200$ K is not optimal, the temperature region above $T = 1220$ K was chosen, accepting beforehand that the growth rate theoretically should decrease at higher temperatures (smaller absolute values of dL/dT). For an equilibrium mixture ($\gamma = 0$) at the entrance of the furnace, it is expected that the growth rate starts at zero; as soon as the mixture comes out of equilibrium because of the temperature gradient, a constant growth rate should result. With the gradients used, every centimeter in the furnace gives a change in equilibrium concentration corresponding to $\gamma = 0.1\%$. Several growth experiments have been performed; some results are presented in Fig. 6 and 7. For $Cl/H = 0.0604$, various mixtures with a silicon content above and below the equilibrium value at the temperature at the entrance of the furnace (1220 K) were used. From the figures, it is apparent that etching occurs over the temperature range where the γ of the first wafer is negative (Fig. 6, $\gamma = -5.0$). Etching turns into growth almost at the point which theoretically was calculated. In this respect, the experiment is in agreement with theory. For low initial supersaturations, no growth is observed on the first slices, whereas the growth rate increases on the following slices. Above $x = 70$ cm, the growth rate drops drastically because of the decrease in $(dL/dT)_T$. In Fig. 6, every value of x represents a specific temperature, replotting Fig. 6 as $\log G$ vs. $1/T$ (Fig. 7, $\gamma = 10\%$, $dT/dx = 2$ K/cm) shows that only above 1000°C a constant plateau is reached. Even with a value of γ independent of x , the growth rate is limited by slow surface reactions at the lower temperatures. Higher initial supersaturations increase the growth rate at lower temperatures as long as the gas mixture is not yet in equilibrium. For $\gamma = 6.4$ and 4.8%, no silicon deposit was observed on the quartz ware of the reactor cell or on the wafer boat. For $\gamma \sim 10\%$, a slight deposit on the wafer boat in between the first four slices was observed. For higher initial supersaturations, the first part of the boat up to the fourth slice was covered with silicon; beyond this fourth slice, only the rim of the boat was slightly covered.

By comparing the equivalent experiments at different dT/dx , the highest growth rate is observed for the highest temperature gradient (Fig. 8). A general trend observed in all experiments is that for a given dT/dx all growth curves converge to the same growth rate 40-50 cm from the entrance. This may be an indication that equilibrium has been attained from that place.

The surface morphology of the grown layer strongly depends on the growth temperature and on the Cl/H ratio.

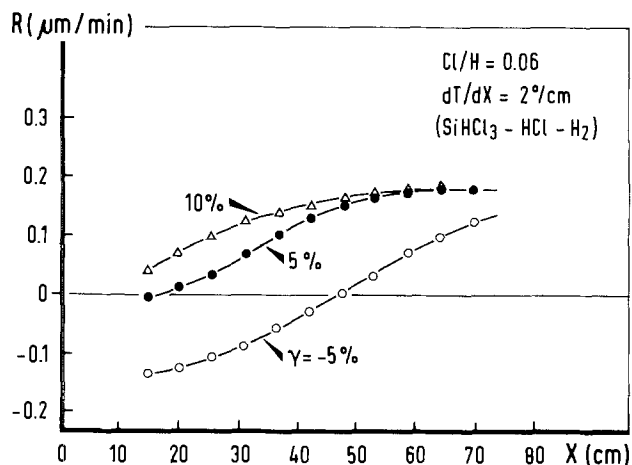


Fig. 6. The silicon growth rate as a function of position in the furnace for $Cl/H = 0.06$, a temperature gradient of 2 K/cm between 1220 and 1340 K in the $SiHCl_3-HCl-H_2$ system for different initial supersaturations.

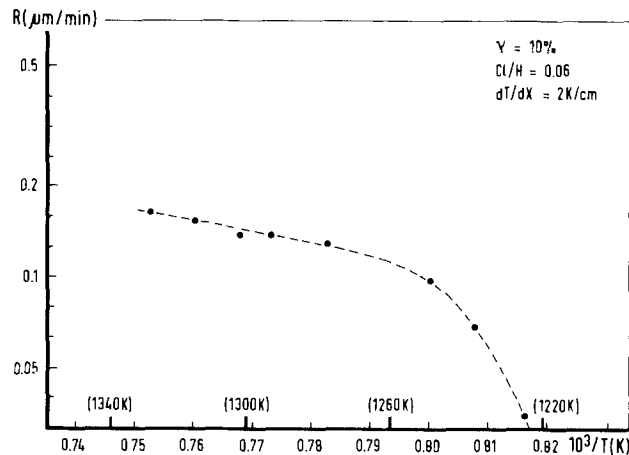


Fig. 7. The silicon growth rate in the furnace system plotted as a function of reciprocal temperature for $Cl/H = 0.06$ in a mixture of $SiHCl_3-HCl$ and H_2 , a temperature gradient of 2 K/cm and an initial supersaturation of 10%. The curve shows the same character as in a cold-wall system at much lower chlorine content.

At low temperatures, the surface contains many growth hillocks; at temperatures between 1050° and 1080°C, the number of large growth pyramids is reduced, but many small bunches which have grown out almost isotropically are observed, whereas at high temperatures ($T > 1080^\circ C$), the surface is almost free of defects (Fig. 9). For the surface morphology, the temperature is more important than the degree of supersaturation. It must be remembered that, although the initial supersaturations may change, a constant Cl/H ratio is always present, so that most probably the same chlorine surface coverage is also present for experiments at the same temperature. For the highest growth rates (high temperature gradient, high γ initial) and low temperatures, locally polycrystalline growth could be observed on the first slices in the wafer boat. Except for these cases, all epilayers were monocrystalline. It has to be stressed that selective growth is nearly perfect for small supersaturations, below $\gamma = 10\%$. Growth on silicon is possible then without deposition on the quartz tube or boat.

SiH₂Cl₂-HCl-H₂ mixtures.—The experiments with SiH_2Cl_2 were performed to check the validity of the principle. For the same Cl/H ratio, temperature gradient, and initial supersaturation, one would expect the same growth curves as obtained in the equivalent $SiHCl_3$ experiment. Figure 10 gives the result for such a series of experiments, which have to be compared with those collected in Fig. 6. Apart from a higher growth rate, the

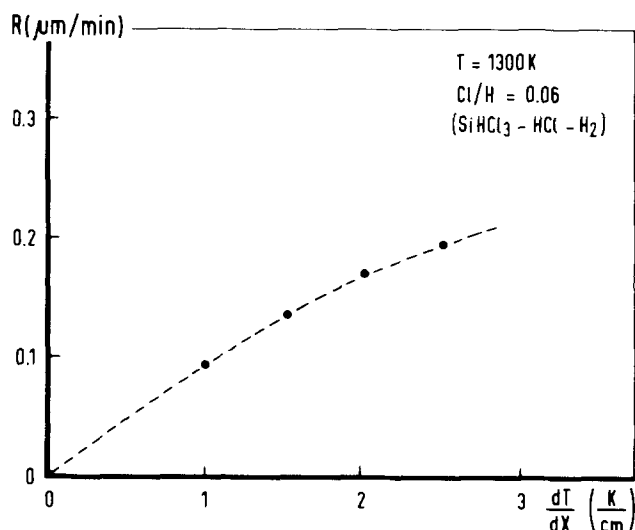


Fig. 8. The silicon growth rate as a function of the temperature gradient in the furnace, measured at 1300 K, for $Cl/H = 0.06$ in the $SiHCl_3-HCl-H_2$ system.

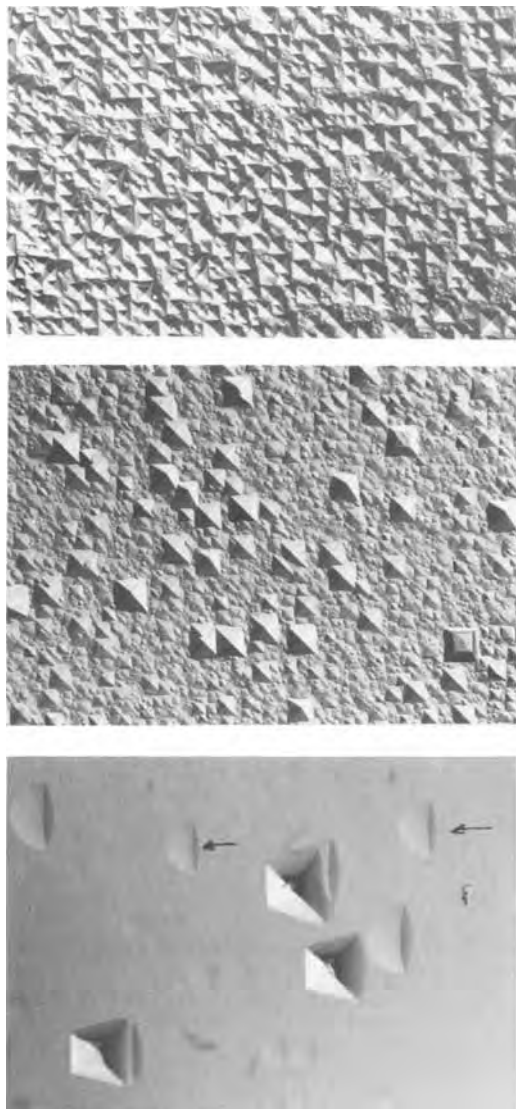


Fig. 9. Surface structures obtained at different temperatures for $Cl/H = 0.06$ and a layer thickness of about $20 \mu\text{m}$. At the higher temperatures, smooth surfaces are obtained, sometimes with characteristic "half-moon terraces" and full-size hillocks. Top, 1000°C ; middle, 1050°C ; bottom, 1080°C . The half-moon terraces are indicated with an arrow. Magnification $100\times$ before reproduction.

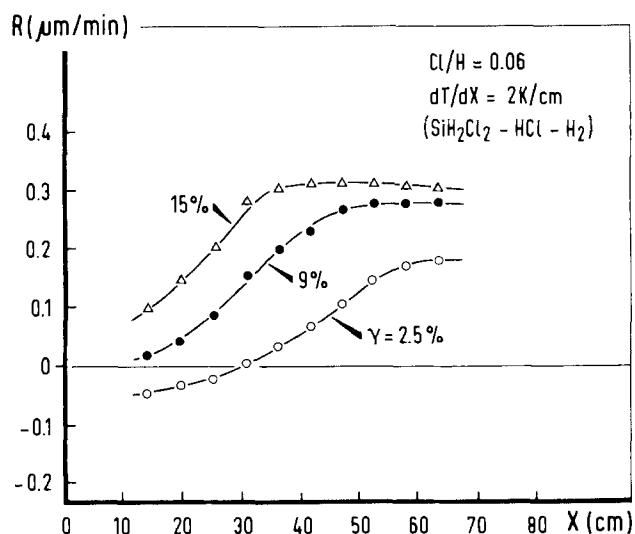


Fig. 10. Silicon growth rates as a function of position in the furnace for $Cl/H = 0.06$ and $dT/dx = 2 \text{ K/cm}$ in the $\text{SiH}_2\text{Cl}_2\text{-HCl-H}_2$ system at different initial supersaturations.

growth curves are very similar, including a complete absence of silicon growth on the boat. On the other hand, the surface morphology for SiH_2Cl_2 -grown layers is not as good as for SiHCl_3 -grown layers under identical conditions. The epilayer is monocrystalline, but many small hillocks are present at these temperatures and growth rates, where the SiHCl_3 grown layers are nearly defect free. This unexpected feature will be discussed below.

Experiments were also performed at higher Cl/H ratios, using mixtures of $\text{SiH}_2\text{Cl}_2\text{-HCl}$ and H_2 . Equilibrium concentrations were calculated for $Cl/H = 0.16$ and 0.35 . The latter case already represents a concentrated mixture of 17% SiH_2Cl_2 and 26% HCl in hydrogen. In all cases, the temperature gradient in the furnace gave rise to silicon growth as expected, indicating the quality of the thermodynamic data. The growth rates, in the order of $0.1\text{-}0.2 \mu\text{m/min}$, are plotted in Fig. 11; the relatively high growth rate at lower temperatures is obvious for the more concentrated systems. The quality of the grown layers was poor compared to growth at $Cl/H = 0.06$; even polycrystalline growth was observed at the lower temperature end of the furnace. Again, silicon deposit on quartz ware was observed for supersaturations exceeding 10%.

Discussion

It has been demonstrated, *e.g.*, by Sirtl *et al.* (22), Arizumi (23), and Claassen (24), and mathematically founded by Bollen *et al.* (25) that by using the mechanism of selective nucleation, growth of silicon is possible on surfaces with low nucleation barriers, *i.e.*, on silicon itself, whereas no growth will occur on foreign surfaces. The present work demonstrates that this principle can be extended to all SiO_2 surfaces within a furnace system; thus, epitaxial growth of silicon is made possible in a hot-wall reactor. Contamination of walls and boats can be prevented provided a low supersaturation can be maintained in the entire system. The experiments have to be guided by a thorough knowledge of the thermodynamics of the system. This point is illustrated in experiments with high Cl/H ratios, *e.g.*, $Cl/H = 0.16$ with 7.9% SiH_2Cl_2 and 14% HCl , and $Cl/H = 0.3482$ with 17.1% SiH_2Cl_2 and 26.4% HCl . Experiments with these mixtures demonstrate the reliability of the thermodynamic data on the Si-Cl-H system as selective growth sets in at $\gamma = 0$ and is restricted to a narrow range of initial supersaturations up to 10%. In the following, the etch and growth behavior and the crystallographic quality of the layers will be sketched in order to come to some conclusions on the feasibility of the system.

Etch and growth behavior.—As pointed out before, an equilibrium mixture entering the furnace will ideally

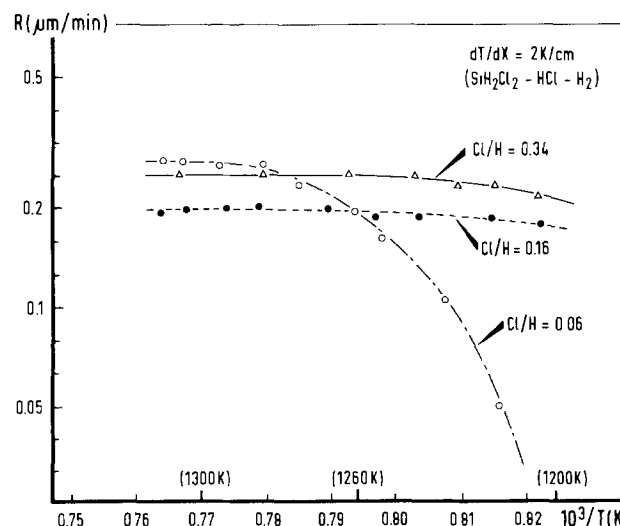
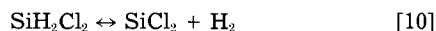


Fig. 11. The silicon growth rate as a function of reciprocal temperature in $\text{SiH}_2\text{Cl}_2\text{-HCl-H}_2$ system at $dT/dx = 2 \text{ K/cm}$ and three Cl/H ratios. The surface reactions appear to be much faster in the more concentrated mixtures (higher Cl/H ratio).

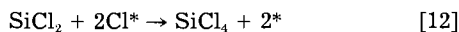
show no growth or etching. In the temperature gradient imposed on the system, a supersaturation is then building up of the order of 0.1% per degree. Figure 6 shows that with a gradient of 2 K/cm, about 40-50 cm are needed to bring the gas phase into equilibrium. This can be interpreted as a supersaturation of 10% being needed to come to continuous growth, this being improbably high; still, it is found that a steeper temperature gradient leads to a somewhat shorter pre-equilibrium zone.

Another possibility, however, points to the time needed to come to complete equilibrium. For the chosen gas velocity of about 15 cm/s, the results given in Fig. 6 point to a preliminary stage of about 3s. This view is further illustrated in the series of experiments with SiH_2Cl_2 in which the temperature gradient is kept constant; the Cl/H ratio, however, is changed from 0.06 to 0.16 and 0.35. Very clearly, the time needed to come to constant growth is much shorter at the higher Cl/H ratios.

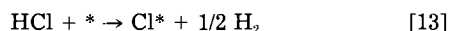
This behavior can be explained from the known characteristics of the SiH_2Cl_2 , SiHCl_3 , and SiCl_4 systems (26, 27), in which two easy gas phase reactions are present



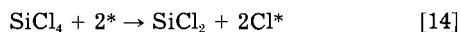
The SiCl_4 concentration, however, can only be brought to the required equilibrium level via a surface reaction



where Cl^* stands for an adsorbed chlorine atom on a reactive silicon site (*) given by



There is a slow reverse reaction



This reaction is the cause of surface controlled kinetics already at 1100°C for SiCl_4 as the initial reactant (27). In the SiH_2Cl_2 -HCl input mixture, therefore, SiCl_2 , SiHCl_3 , and SiH_2Cl_2 can be present in near equilibrium concentrations via the rapid gas phase reactions [10] and [11]. The formation of SiCl_4 , however, lags behind. As long as SiCl_4 is missing, an excess of HCl is present. It is known (21) that HCl etching proceeds at a constant rate rather independent of temperature down to about 900°C (dependent only on the purity, *i.e.*, oxygen content, of the gas). At 900°C, 1% HCl gives an etch rate of 0.1 $\mu\text{m}/\text{min}$; 1.5% HCl already 0.25 $\mu\text{m}/\text{min}$. In this way, the excess HCl can counteract the growth in situations where the complete equilibrium has not yet been established. Changes in SiCl_4 concentration occur via reactions [12] and [14]; a decrease in SiCl_4 content will take place slowly, rather independent of HCl content (27). The reverse reaction, formation of SiCl_4 , will be faster for higher HCl contents. From Eq. [12], the rate of formation of SiCl_4 and thus the rate of "equilibration" can be given as

$$\begin{aligned} R_{\text{SiCl}_4} &= K p_{\text{SiCl}_2} [\text{Cl}^*]^2 = K' p_{\text{SiCl}_2} p_{\text{HCl}^2/p_{\text{H}_2}} \\ &= K'' p_{\text{SiH}_2\text{Cl}_2} p_{\text{HCl}^2/p_{\text{H}_2}^2} \quad [15] \end{aligned}$$

When we now compare the situation for Cl/H 0.06, 0.16, and 0.35, the rate of SiCl_4 formation is calculated to increase from 1:16:105. This may explain the short introduction time as a kinetic factor needed to conform the mixture to a quasi-equilibrium one. The temperature dependence of the growth rate in the SiH_2Cl_2 /HCl system has been given in Fig. 11. The diffusion-limited region of crystal growth is extended to much lower temperatures, presumably because of the enhanced surface reaction rate discussed before. It has been postulated that for a diffusion-limited growth the surface quality will be superior to growth in a surface-limited region. This supposition is not confirmed here; this point will be discussed in the next section. It can be further mentioned that, in the region of constant growth, the growth rates found are not too far from, but always lower than, the calculated values and constant over the diameter of the substrates $\pm 40\%$.

According to Eq. [8], we expect a typical growth rate of 0.41 $\mu\text{m}/\text{min}$, to be compared with the measured rates of 0.1-0.3 $\mu\text{m}/\text{min}$. The calculated growth rate could apply to polycrystalline growth (9); for monocrystalline growth also, the density and velocity of atomic steps on the surface will play a part.

Crystallographic quality.—Growth and etching in the Si-Cl-H system leads to smooth and perfect surfaces only at higher temperatures and relatively low etch and growth rates. For the growth of silicon, Burmeister (28) and Revesz *et al.* (29) showed hillock formation and faceting to occur as a function of growth rate and temperature. A comparable change from monocrystalline to polycrystalline growth habit was observed by Bloem (30). Van der Putte *et al.* performed an extensive study on the silicon surface structure after etching with gaseous HCl (31).

Figure 12 combines these experimental results, indicating regions in which good quality epitaxial layers can be grown, as well as regions with bunched or even polycrystalline growth, all on good quality substrates in the Si-Cl-H system at atmospheric pressure. Trapping of impurities or growth units has to be considered as the main reason for the occurrence of growth defects. The experiments in the near-equilibrium growth in a furnace are reasonably in line with the data in Fig. 12; some additional influence of higher Cl ratios seems to be present. At Cl/H = 0.16 and 0.35, a diffusion-controlled growth regime appears to be present even at low temperatures. The layer quality, however, is by no means superior to layer growth at the same temperature and growth rate in the Cl/H = 0.06 system. This can be caused by the increased adsorption of chlorine containing species. Another point can be important too, *i.e.*, the quality of the HCl gas used in the experiments. The water content of the HCl may be adequate for normal CVD use; in the concentrated mixtures (26% HCl at Cl/H = 0.35) a small impurity content already counts heavily.

At 1000°C the formation of solid SiO_2 is possible for a water content exceeding 1 ppm. More than 4 ppm in the HCl cylinder thus already may be sufficient to deteriorate the crystalline quality because of blocking of moving steps on the growing surface.

Good quality epitaxial growth at still lower temperatures than given in Fig. 12 are possible under UHV condi-

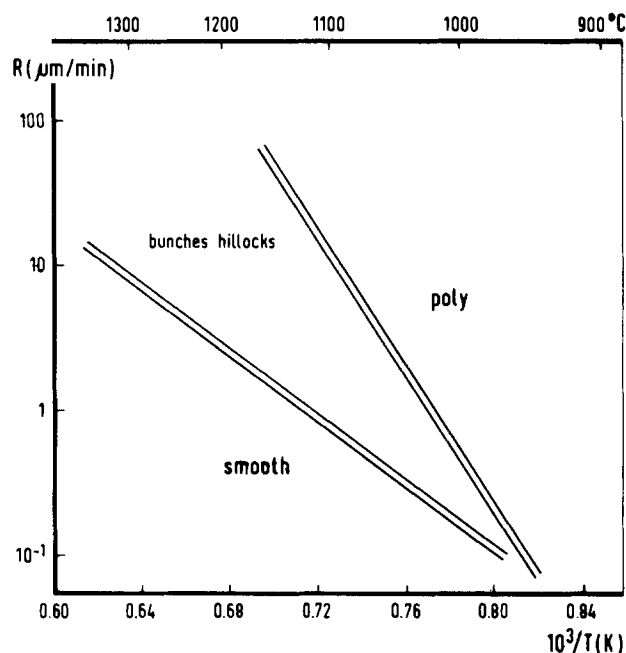


Fig. 12. The experimental growth morphology in the Si-Cl-H system at atmospheric pressure as it depends on growth rate and growth temperature. Trapping of defects and impurities plays an important part in the determination of the resulting structure; low growth rates and high growth temperatures are favorable there.

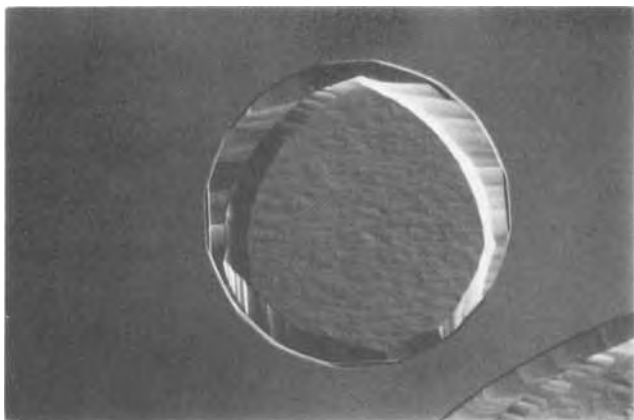


Fig. 13. Example of selective growth of silicon inside a window etched into an oxide layer on top of a silicon wafer.

tions (molecular beam epitaxy), where disturbing effects of undesired impurities are minimized. In this respect, the conclusion comes forward that impurities have a stronger effect on the layer quality than the trapping of silicon containing growth units as such. At the lower temperatures the surface is heavily textured; going to higher growth temperatures, the (100) surface becomes smooth with isolated growth hillocks (Fig. 9). Each hillock has a dislocation in its center; often, hollow cores are observed. Sometimes, however, a typical flat top is present. Tsukamoto and van der Hoek (34) found the same type of defect, called half-moon terraces, on garnets and explained them as growth hillocks that have become inactive and obtained a flat top. On further growth they develop into the half-moon terraces.

The hillocks have a mean deviation of 2.56° from (100), with a variation from 0.5° to 3° . On the edges of growth regions facets form on prolonged growth (Fig. 13), mostly (111) faces are exposed, and some (113) and (115) facets are also found. A closer study of the faceting is underway. A further point in favor of the furnace system is the absence of steep temperature gradients that can be the origin of stress and slip in the substrates (35).

Feasibility of the system.—In CVD intended for growth of silicon on metallurgical silicon substrates for the production of solar cells the crystalline quality obtained in the present setup can be quite satisfactory when the specifications for surface planarity can be relaxed, an increased surface area could even have some advantage.

Another attractive feature is the batch-wise selective deposition of silicon in windows opened in SiO_2 layers on silicon substrates; in this application, thin layers are envisaged.

For other silicon device processes, the CVD in a furnace can be achieved satisfactorily only well above 1000°C . The furnace process will gain when the surface quality at the low temperature side can be improved. Working at lower oxygen impurity levels is one approach.

Introduction of SiCl_4 in the main gas stream reduces the amount of HCl needed and will help in bringing down the impurity content.

The growth rates obtained are in the order of $0.1\text{--}0.3 \mu\text{m}/\text{min}$; in order to obtain thick layers ($< 10 \mu\text{m}$), this rate is too low. Therefore the selective deposition of silicon in oxide windows appears to be the most attractive proposition for practical use of the near-equilibrium system in the furnace.

Conclusion

Chemical vapor deposition in a hot-wall reactor is possible without deposition of silicon on the quartz ware of the cell or the wafer boat. In terms of crystalline quality, the best results are obtained, for growth with SiHCl_3 , low Cl/H ratio, and high temperatures.

An important conclusion is the discovery of fast surface

reactions at high Cl/H ratios, such that a gas phase diffusion-controlled growth rate extends down to nearly 900°C in the furnace system. In order to profit in the sense of improved layer quality, the water content has to be reduced to very low levels.

In general, it can be stated that quite a number of questions are still present, but in principle a new and interesting method to produce epitaxial silicon has become available.

Acknowledgments

The authors like to thank Mr. H. v.d. Linden and Mr. J. van Oyen for skillful technical assistance and Mr. C. Dominguez for his contributions during his stay in Nijmegen. This work was partly supported by the Commission of the European Communities via Contract no. ESC-R-045-NL.

Manuscript submitted Aug. 6, 1984; revised manuscript received March 20, 1985.

Catholic University assisted in meeting the publication costs of this article.

REFERENCES

- H. C. Theuerer, J. J. Kleinack, H. H. Roar, and H. Christensen, *Proc. IRE*, **48**, 1642 (1960).
- R. V. Daiello, P. H. Robinson, and H. Kressel, *Appl. Phys. Lett.*, **28**, 231 (1976).
- F. C. Eversteyn and H. L. Peek, *Philips Res. Rep.*, **25**, 472 (1970).
- R. S. Rosler, *Solid State Technol.*, **20**, 63 (1977).
- B. E. Deal, *This Journal*, **109**, 514 (1962).
- B. A. Lombos and T. R. Somogyi, *ibid.*, **111**, 1097 (1964).
- J. I. Nishizawa, *J. Cryst. Growth*, **56**, 273 (1982).
- V. S. Ban, *ibid.*, **45**, 97 (1978).
- F. Langlais, F. Hottier, and R. Cadoret, *ibid.*, **56**, 659 (1982).
- M. Ogirima, H. Saida, M. Suzuki, and M. Maki, *This Journal*, **124**, 903 (1977).
- J. P. Duchemin, M. Bonnet, and F. Koelsch, *ibid.*, **125**, 637 (1978).
- J. Bloem, Y. S. Oei, J. H. L. Hanssen, and L. J. Giling, in "3rd European Conference on Photo-Voltaic Solar Energy," p. 574, Cannes 1980, Reidel Publishers, Dordrecht, Holland.
- W. Steinmaier, *Philips Res. Rep.*, **18**, 75 (1963).
- JANAF Thermochemical Tables, 2nd ed., NSRDS-NBS 37, National Bureau of Standards, Washington, DC (1971).
- L. P. Hunt and E. Sirtl, *This Journal*, **119**, 1741 (1972).
- L. P. Hunt and E. Sirtl, *ibid.*, **120**, 806 (1973).
- P. van der Putte, L. J. Giling, and J. Bloem, *J. Cryst. Growth*, **31**, 299 (1975).
- T. O. Sedgwick, J. E. Smith, R. Ghez, and M. E. Cowher, *ibid.*, **31**, 264 (1975).
- V. S. Ban and S. L. Gilbert, *ibid.*, **31**, 284 (1975).
- J. P. Duchemin, Thesis, University of Caen, France (1976).
- J. Bloem and W. A. P. Claassen, *J. Cryst. Growth*, **49**, 435 (1980).
- E. Sirtl and H. Seiter, in "Semiconductor Silicon," R. R. Haberecht and E. L. Kern, Editors, p. 189, The Electrochemical Society Softbound Proceedings Series, New York, NY (1969).
- T. Arizumi, in "Current Topics in Material Science," Vol. I, E. Kaldis, Editor, Chap. 5, North Holland, Amsterdam (1978).
- W. A. P. Claassen and J. Bloem, *This Journal*, **127**, 1836 (1980).
- L. J. M. Bollen, C. H. J. van den Brekel, and J. Kuiken, *J. Cryst. Growth*, **51**, 581 (1981).
- W. A. P. Claassen and J. Bloem, *ibid.*, **50**, 807 (1980).
- J. Bloem, W. A. P. Claassen, and W. G. J. N. Valkenburg, *ibid.*, **57**, 177 (1982).
- J. Burmeister, *ibid.*, **11**, 131 (1971).
- A. G. Revesz and R. J. Evans, *Trans. Metall. Soc. AIME*, **230**, 58 (1964).
- J. Bloem, *J. Cryst. Growth*, **18**, 70 (1973).
- P. van der Putte, L. J. Giling, and J. Bloem, *ibid.*, **41**, 133 (1977); **43**, 659 (1978); **47**, 437 (1979).
- W. W. Webb, *J. Appl. Phys.*, **33**, 1961 (1962).
- L. J. Giling, *Mat. Chem. Phys.*, **9**, 117 (1983).
- K. Tsukamoto and B. van der Hoek, *J. Cryst. Growth*, **57**, 131 (1982).
- J. Bloem and A. H. Goemans, *J. Appl. Phys.*, **43**, 1281 (1972).

A Multiresponse Factorial Study of Reactor Parameters in Plasma-Enhanced CVD Growth of Amorphous Silicon Nitride

P. W. Bohn¹ and R. C. Manz

AT&T Bell Laboratories, Murray Hill, New Jersey 07974

ABSTRACT

A 2⁴ factorial design in the growth parameters has been implemented for plasma-enhanced CVD deposition of a-SiNH thin films. A variety of chemical and physical properties were used as responses to measure the strength of interactions between and among the factors studied. Statistically significant interactions of the primary factors (*i.e.*, reactant gas ratio, pressure, temperature, and RF power) were found for almost all responses measured. SiH₄/NH₃ ratio and RF power were found to have the most and largest effects on all responses. Changes in these variables resulted in changes in the film stoichiometry which have far reaching implications for the refractive index and buffered HF etch rate of these films. In each response, the trends observed support conclusions of previous single-variable experiments. The current experiments extend those studies by quantitating the various factor-factor interactions.

The formation of dielectric coatings for passivation and electrical insulation of GaAs has been a long-standing problem to those interested in high speed devices. Although silicon dioxide has been used almost exclusively in the development of silicon technology, its permeability to moisture and alkali ion diffusion eliminate it from consideration for use with GaAs. As an alternative, amorphous silicon nitride has been found to be useful, owing in part to its stability to etching reagents, mechanical robustness, and high resistivity (1). As an insulator it is attractive due to its reasonably large high frequency dielectric constant and breakdown potential (2) and compatibility with current processing techniques.

One method of growing silicon nitride thin films involves the chemical deposition of silane and ammonia at atmospheric pressure with temperatures between 700° and 900°C. However, when this material is used for passivation of GaAs, temperature limitations are imposed. To circumvent this problem with high temperatures, reactive plasmas have been employed to impart sufficient energy to the precursor species to generate the highly reactive intermediates needed for actual film growth (3, 4). This plasma-enhanced CVD process then permits growth of an amorphous hydrogenated silicon nitride (a-SiNH) at temperatures well below 400°C. At these lower temperatures, it is possible to deposit plasma-enhanced a-SiNH films directly on aluminum or gold metallizations on GaAs. Doing so then provides a barrier to chemical or mechanical damage and creates a film with the appropriate electrical characteristics for high quality electrical insulation. Interest also exists in using a-SiNH as a selective mask for further oxidations or doping procedures when deposited at low temperatures.

It is well known from a variety of experiments that, although values usually fall in specific ranges, the exact physical, chemical, and electrical properties of plasma-enhanced a-SiNH films depend strongly on the method and conditions of film growth (5-10). In the plasma-enhanced deposition process, many species are present which have sufficient energy to initiate bond cleavage processes. As a result, a panoply of reaction pathways is possible, and the most thermodynamically favorable products are not necessarily predominant. Thus stoichiometry and related properties can and do vary widely with changes in the deposition conditions. This aspect of the plasma-enhanced growth process is both an advantage and a disadvantage. The wide variation with reactor parameters means that considerable latitude exists to tailor the materials properties of the deposited film. However, very careful attention must be paid to the control of reaction conditions in order to produce films with reproducible properties.

Earlier experiments have addressed the dependence of film properties on plasma reaction conditions (2, 6). How-

ever, those studied have all taken the approach of varying one variable at a time and observing the effect as measured by one or more specific film properties. This approach can at best only examine two-dimensional projections of the *n*-dimensional response surface (11, 13). In addition, this approach is incapable of measuring the extent of interactions between the various growth parameters in determining the chemical and physical properties of a-SiNH. In a system as mechanistically complex as the plasma-enhanced CVD reactor, it is highly likely that several significant interactions will play a role in the growth chemistry. Thus, recognizing the complexity of the film growth process and wishing to understand interactions between system parameters in terms of each of several different responses, a 2⁴ factorial study with center point was planned and implemented. Of the many possible factors which could have been studied, some were eliminated for practical reasons (*e.g.*, changing the electrode spacing) and others were eliminated to leave only the four factors, which from one variable at a time studies, appeared to be most likely to have a statistically significant effect on one of the chosen responses. The experiment examined the effects and interactions of SiH₄/NH₃ molar flow ratio, total gas pressure [*i.e.*, $P(\text{SiH}_4) + P(\text{NH}_3) + P(\text{buffer})$], substrate (GaAs) temperature, and radio frequency power density on the Si/N ratio, refractive index, buffered HF etch rate, growth rate, concentrations of H bound to Si, and concentrations of H bound to N in the grown a-SiNH films.

Experimental

All samples were prepared in a Plasma-Therm radial flow, capacitatively coupled, 13.56 MHz reactor of the general Reinberg design (Fig. 1) (14). This reactor is equipped with automatic power sensing and tuning circuitry to maintain constant power levels during deposition. It also possesses a capacitance manometer-controlled throttle valve for maintenance of constant pressure and a set of temperature sensors which feed back to the pallet heaters to keep the substrate temperature constant. Calibrated mass flow controllers were used to obtain constant known gas flow rates into the reaction chamber. SiH₄ flow rate, NH₃ flow rate, total pressure, and temperature were all controlled to $\pm 1\%$ deviation. For these experiments, the electrode spacing was held constant at 1.9 cm.

The levels of the variables examined in this study are tabulated in Table I. SiH₄ was obtained as 2% SiH₄ in Ar, and NH₃ was obtained as 5% NH₃ in Ar. In each experiment, an auxiliary Ar flow was used to keep the total flow rate of all gases constant in addition to having the preset pressure constant. All gases were delivered from remote safety cabinets through precleaned 316 stainless steel tubing. The centerpoint or zero level of each factor was determined from previously established standard values for production growth of a-SiNH passivation layers in GaAs FET's.

¹ Current address: Department of Chemistry, University of Illinois, Urbana, Illinois 61801.

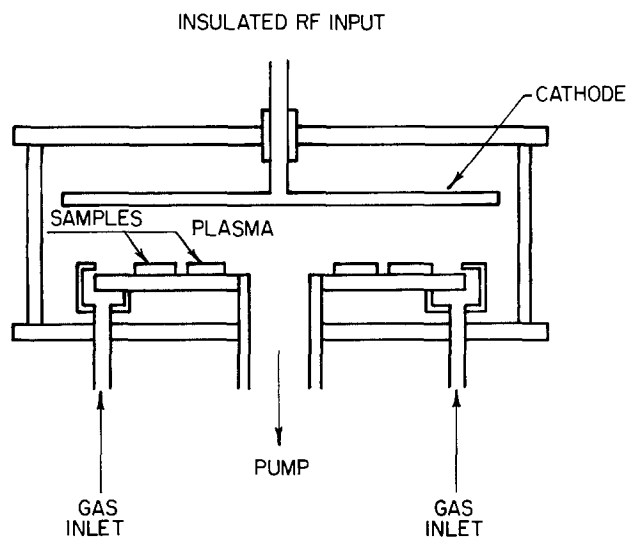


Fig. 1. Cross-sectional diagram of the electrodes and gas flow pattern in the reactor used in these experiments.

Within the design, great care was taken to randomize possible sources of bias which would not be included in the design. Since two experimental runs, at most, could be made in any one day, the time order of the experimental growth runs was randomized. In addition, the positions of each of the test substrates in the reaction chamber were randomized. Each experimental run generated five separate samples for growth rate measurement, bonded hydrogen content, Si/N ratio and refractive index, etch rate measurement, and film stress.

Growth rate measurements were made by monitoring total thickness of material deposited on glass substrates with a pressure-sensitive stylus instrument for each of the 30 min growth runs. Growth rates varied from 76.9 to 210.8 Å/min. Film stress measurements were performed by examining the distortion of an elongated GaAs bar, before and after sample growth, with a laser deflection measuring instrument (Canon wafer flatness monitor). However, several samples had sufficiently low surface reflectivity after a-SiNH growth that reliable signals could not be obtained. Thus film stress was not included in the final response data. In general, however, values of the stress induced by film growth were in the 1×10^8 to 2×10^9 dyn/cm² range with both tensile and compressive values being observed. Measurements of the etch rate of GaAs supported samples were made in NH₄F buffered HF by measuring the difference in thickness between an etched region and a masked region after a standard etching time. Variation from 48 to 434 Å/min was observed.

Information about the total content of Si-H and N-H bonds was obtained by direct quantitative infrared absorption spectrometry of layers deposited on semi-insulating GaAs. Absorber concentrations were obtained by measuring the absorbances near 3350 (N-H) and 2150 cm⁻¹ (Si-H). The absorbances were then combined with bond cross sections calculated from a reanalysis of the nuclear reaction profiling data of Lanford and Rand (8). This new analysis took the physical nature of the system into account by constraining the linear data fit to pass through the origin and yielded cross-sectional values of 5.7×10^{-20} cm² for Si-H and 4.5×10^{-20} cm² for N-H.

Both refractive index and Si/N atomic ratios were obtained from the samples grown on silicon. Bulk Si and N

amounts were inferred from ESCA measurements in the near surface region. Ar⁺ sputtering was used to remove the surface contaminated layer prior to measurements. Tabulated sensitivity factors for the Si_{2p} and N_{1s} peaks were used to calculate the atomic ratios from relative peak areas (15). Refractive index measurements were obtained at 6328 Å with an automated ellipsometer using a He-Ne laser source.

Results and Discussion

The raw data from the experiment along with the design matrix are shown in Table II. In addition to the responses listed above, the total hydrogen content, being the sum of Si-H and N-H concentrations, is included in the last column. The bottom four rows of the table represent the center-point replicates run to establish an estimate of the true run-to-run variability inherent in the experiment. These raw data were reduced using the contrast coefficients algorithm (16) to yield the table of effects for each main factor and interaction. These are shown in Table III. The bottom two figures in each column are the standard error for the measurement of an effect and the size of the 95% confidence interval for the hypothesis that the effect in question is due only to statistical fluctuation and is not statistically significant. The results for each response will be discussed separately. In addition, the present results will be compared directly with the results of careful single-variable variation studies performed previously (17).

The refractive index data show a total of four significant effects. Since the interaction between reactant gas ratio and RF power is also significant, neither of these will be discussed as main effects. Increases in total pressure are found to cause a marginally significant decrease in the refractive index. This observation agrees with the single variable study, but over a much wider pressure range than investigated previously (17). Although both SiH₄/NH₃ ratio and RF power display significant effects alone, their two-way interaction is also significant. Both main effects agree in sign with the single variable results, and examination of the four-way contrast table (Table IVa) shows roughly equivalent averages except for the case of high SiH₄/NH₃ and low power. This combination yields a much higher value for refractive index. At either level of SiH₄/NH₃, decreasing the plasma power increases the index, while at either level of power, increasing the SiH₄/NH₃ ratio increases the observed index. The simplest view of the mechanism behind the statistically significant interaction must involve the separate steps of radical and ion generation, surface adsorption and incorporation into the growing film, and rearrangement of surface species. Generally, increases in the amount of Si incorporated have been associated with higher refractive index values. The differences in dissociation energies as measured by the bond energies of SiH₄ and NH₃ is small (~19 kcal/mol), so the ratio of active silicon containing species to active nitrogen containing species should remain fairly constant with changes in the electron temperature (18). Thus the origin of the interaction is probably not in the gas phase dissociation. However, it has been noted (6) that increases in the amount of incorporated Si can still lead to a decrease in the refractive index, if there exists a large proportion of Si-H vs. Si-Si bonds (*i.e.*, more Si terminations). Thus, the refractive index data must be interpreted in light of the Si/N ratios and [Si-H] concentrations.

The ESCA measurements of Si/N ratio show that the films are nitrogen deficient with respect to the stoichiometric compound, as expected. Also as expected, the SiH₄/NH₃ ratio has a significant effect on the Si/N ratio incorporated, such that increasing the relative proportion of SiH₄ increases the Si/N ratio. In addition, changes in RF power are significant, with decreases in the power leading to increases in the amount of silicon incorporated. These data are consistent with both the refractive index measurements just discussed and the Lorentz-Lorenz correlations observed in a-SiNH (19). The Lorentz-Lorenz

Table I. Levels of the four factors chosen for study. The - and + designations are arbitrary

Variable	Levels		
1 = SiH ₄ /NH ₃ flow ratio	0 = 1.70	- = 1.50	+ = 2.00
2 = Total pressure (torr)	0 = 1.50	- = 1.00	+ = 2.00
3 = Substrate temperature (°C)	0 = 275	- = 250	+ = 300
4 = RF power (W)	0 = 15	- = 10	+ = 20

Table II. Raw data for each of seven responses in the 2¹³ design matrix. Symbols on the left side of the table correspond to the level of the factor at the head of the column (labeled as in Table I) for that experimental run. Each experimental run is represented by a single row in the matrix. Levels for two-, three-, and four-way interactions are obtained by multiplying the signs for the main effects in that row [e.g., sign(12) = sign(1) × sign(2)]. The last four rows represent the center-point replicates, and the final column is derived from the first two data columns

No.	Mean	1	2	3	4	12	13	14	23	24	34	123	124	134	234	1234	[N-H] (× 10 ²² cm ⁻³)	[Si-H] (× 10 ²² cm ⁻³)	Si/N	n	Etch rate (Å/min)	Thick- ness (Å)	[H] _{tot} (× 10 ²² cm ⁻³)
1	+	+	+	+	+	+	+	+	+	+	+	+	+	+	+	+	1.055	0.494	0.99	1.883	230	5685	1.549
2	+	+	+	+	-	+	+	-	+	-	-	+	-	-	-	-	0.250	2.831	1.20	2.391	98	2665	3.081
3	+	+	+	-	+	+	-	+	-	+	-	-	+	-	-	-	1.064	0.570	0.99	1.826	410	5850	1.634
4	+	+	+	-	-	+	-	-	-	+	-	-	+	+	+	+	0.395	2.433	1.11	2.258	192	2307	2.828
5	+	+	-	+	+	-	+	+	-	-	+	-	+	+	+	+	0.317	1.250	0.99	2.112	112	6315	1.567
6	+	+	-	+	-	-	+	-	-	+	-	-	+	-	+	+	0.329	2.225	1.30	2.378	48	4730	2.554
7	+	+	-	-	+	-	+	+	-	+	-	+	-	-	+	+	0.555	1.607	1.05	2.048	182	6005	2.162
8	+	+	-	-	-	-	-	+	+	+	+	+	+	+	+	+	0	2.370	1.13	2.308	125	4885	2.370
9	+	-	+	+	+	-	-	-	+	+	+	-	-	-	+	-	2.321	0	0.97	1.800	412	4405	2.321
10	+	-	+	+	-	-	+	+	-	-	-	-	+	+	-	+	1.065	1.081	1.07	1.870	434	4380	2.146
11	+	-	+	-	+	-	+	-	-	+	-	+	+	-	-	+	1.945	0	0.95	1.781	210	4570	1.945
12	+	-	+	-	-	-	+	+	-	-	+	+	+	-	-	-	0.670	1.958	1.08	1.977	328	3315	2.628
13	+	-	-	+	+	+	-	-	+	+	+	+	+	-	-	+	0.932	0.911	0.99	2.016	87	5005	1.843
14	+	-	-	+	-	+	-	+	-	+	-	+	-	+	-	+	0.407	1.971	0.99	2.019	122	4095	2.378
15	+	-	-	-	+	+	+	-	+	-	-	-	+	+	+	+	1.111	1.053	1.04	1.934	198	5000	2.164
16	+	-	-	-	-	+	+	+	+	+	+	-	-	-	-	+	0.771	1.665	1.07	1.984	313	4320	2.436
17	0	0	0	0	0	0	0	0	0	0	0	0	0	0	0	0	0.738	1.359	1.09	1.909	256	6325	2.097
18	0	0	0	0	0	0	0	0	0	0	0	0	0	0	0	0	1.114	1.314	1.05	1.922	220	6140	2.508
19	0	0	0	0	0	0	0	0	0	0	0	0	0	0	0	0	0.693	1.247	0.99	1.697	141	5720	1.940
20	0	0	0	0	0	0	0	0	0	0	0	0	0	0	0	0	0.989	1.388	0.97	1.909	232	6065	2.377

correlation embodies the observation that for a particular film density the refractive index decreases with decreasing silicon content. Increasing the RF power is observed to decrease both the index and the Si/N ratio. In fact, the sign of the measured effect for all four main factors is the same for both the Si/N ratio and the refractive index, confirming a correlation between the two properties observed previously (17).

The buffered HF etch rate is also expected to be somewhat correlated with the Si/N ratio and refractive index of the films. An examination of the significant effects for the etch rate shows that SiH₄/NH₃ ratio, total pressure, the SiH₄/NH₃-RF power interaction, the pressure-temperature interaction, and the three-way interaction among the SiH₄/NH₃ ratio, pressure, and temperature are all statistically significant. The observation of a statistically significant three-way interaction precludes the discussion of more fundamental effects involving these factors. However, it is consistent with the previous observations that etch rate depends on several film properties including Si-N stoichiometry, H content, and density (6, 17). Because each of these is likely to be affected in a fundamental way by one of the factors studied, it is not surprising that the aggregate effect on etch rate includes a significant three-way interaction.

The growth rate is another response which includes significant three-way interactions, among pressure, temperature, and RF power and among SiH₄/NH₃ ratio, pressure, and RF power. Again, this observation is not surprising, based on the complex series of events (i.e., dissociation, adsorption, rearrangement) which determines the rate of incorporation of new moieties into the nascent epitaxial film. Increasing RF power or decreasing the pressure should act to increase the electron temperature and consequently the frequency of dissociative reactions of the active gases. An increase in the frequency of these dissociative reactions would naturally tend to increase the growth rate. The surface temperature is likely to play a role in the efficiency of adsorption and adatom rearrangement. Lower substrate temperatures would favor the sticking of highly reactive radical and ion species. However, a higher surface temperature would yield a higher surface mobility and enable newly adsorbed species to move to stable growth sites more quickly. Thus, a clear picture of the manner in which substrate temperature enters the growth rate picture is not forthcoming from the present data. This is especially true when it is considered that a sizable number of the species undergoing surface collisions are ionic rather than neutral. For the ions, the surface temperature would be expected to

Table III. Size of the effect for each main factor, two-, three-, and four-way interaction. Each column contains data for a specific response, while each row contains data for a specific effect or interaction. The effects and interaction values are obtained by combining the data in Table II according to the signs in the column for that effect or interaction. The S_i value at the bottom of each column is an estimate of the standard error for that response. The number just below it is the size of the 95% confidence level for the hypothesis that the effect is due to random fluctuation only. Effects which are statistically significant at the 95% level are italicized

	[N-H] (× 10 ²² cm ⁻³)	[Si-H] (× 10 ²² cm ⁻³)	Si/N	n	Etch rate (Å/min)	Thickness (Å)	[H] _{total} (× 10 ²² cm ⁻³)
Mean	0.824	1.401	1.058	2.037	218.8	4596	2.225
1	-0.657	0.643	0.075	0.228	-88.4	419	-0.015
2	0.543	-0.461	-0.025	-0.127	140.9	-897	0.082
3	0.021	-0.112	0.010	0.044	-51.9	129	-0.091
4	0.677	-1.331	-0.123	0.223	22.6	1517	-0.655
12	-0.152	0.180	-0.020	0.005	-25.1	-460	0.028
13	-0.036	0.067	0.040	0.037	-53.4	-41	0.030
14	-0.172	-0.153	-0.058	-0.143	95.1	373	-0.326
23	0.134	-0.027	0.015	-0.019	60.4	145	0.107
24	0.325	-0.479	-0.018	-0.078	29.9	443	-0.154
34	-0.033	-0.032	-0.033	0.011	12.1	-132	-0.065
123	-0.195	0.233	-0.020	0.033	-92.1	-135	0.038
124	-0.092	-0.137	0.033	-0.025	27.4	521	-0.229
134	-0.075	-0.139	-0.048	-0.032	-31.9	118	-0.214
234	0.062	0.133	0.018	0.001	-9.6	-306	0.195
1234	0.113	-0.198	0.018	-0.019	-38.6	59	-0.085
S _i	0.233	0.061	0.055	0.108	49.8	253	0.259
±1.15 S _i	0.269	0.070	0.063	0.125	57.4	292	0.299

Table IV. Contrast tables for various two-way interactions. a: Two-way interaction diagram for the gas ratio-RF power interactive effect on refractive index. The first symbol is factor 1 (gas ratio), and the second symbol is factor 4 (RF power). The values at each lattice point were obtained by averaging the four runs with that specific combination of SiH₄/NH₃ ratio and RF power. b: Two-way interaction diagram for the pressure-RF power interactive effect on [N-H] per cubic centimeter. The first symbol is factor 2 (pressure), and the second is factor 4 (RF power). c: Two-way interaction diagram for the gas ratio-RF power interactive effect on [H]_{total} per cubic centimeter. The symbols are as in a.

(+, +)	(+, -)	(+, +)	(+, -)	(+, +)	(+, -)
1.967	2.334	1.596	0.595	1.728	2.708
(-, +)	(-, -)	(-, +)	(-, -)	(-, +)	(-, -)
1.883	1.963	0.729	0.377	2.068	2.397
(a)		(b)		(c)	

play only a minor role in comparison to other factors such as the surface dc bias arising from differences in ion and electron mobilities. Thus, the most important conclusion from the growth rate data comes from the presence of three-way interactions, which are indicative of a highly complex overall mechanism in which changes in any of the machine parameters can have different implications for various processes in the overall mechanism.

The remaining responses are all measures of the hydrogen content of the film. Examining first the [Si-H] measurements, it is seen that nearly all of the factors affect the amount of hydrogen bonded to silicon. There are two interesting observations. First there is a statistically significant interaction among all four factors studied. This points to an extremely complex mechanism for passivation of Si open valencies by hydrogen. The second concerns the magnitude of the various effects. Far and away the largest effect is that of RF power, which, in the absence of higher order interactions, would suggest that increasing the RF power decreases the concentration of Si-H linkages, presumably by increasing the concentration of Si-Si and Si-N bonds. Concentrations of these latter species could not be measured quantitatively due to overlap of the Si-N stretching band with broad Si-H and N-H bending modes in the mid-IR. The next largest effect is the main effect due to SiH₄/NH₃ ratio. As expected, increasing the SiH₄/NH₃ ratio tends to increase the [Si-H] concentration in the solid.

The [N-H] concentration response shows far fewer statistically significant effects. Increasing the SiH₄/NH₃ ratio decreases the [N-H], while increasing the RF power and pressure together increases the [N-H]. An examination of the four-way contrast table (Table IVb) for the RF power-pressure interaction effect on [N-H] shows that both factors are working in the same direction. Decreasing the pressure at constant RF power acts to decrease [N-H], while decreasing the RF power at constant pressure does the same. Combining observations, the total hydrogen content (i.e., [H]_{total} = [Si-H] + [N-H]) shows a significant SiH₄/NH₃-RF power interaction which can be attributed primarily to the influence of the RF power. Again constructing the table of contrasts (Table IVc) shows that decreasing the RF power while keeping the SiH₄/NH₃ ratio constant increases the total hydrogen content, while the SiH₄/NH₃ ratio has no clear impact from the table.

Note that these results for hydrogen content are consistent with the picture emerging from the refractive index and Si/N data. The main effect of RF power on the refractive index (a decrease in *n* with increasing power) correlates with a decrease in Si/N, a decrease in [Si-H], an increase in [N-H], and a decrease in total hydrogen content. Thus it appears that changing the plasma conditions, by changing its energy, drastically affects film properties through alterations in the stoichiometry. Increasing the power results in relatively less Si and more N incorporation, a loss of bound hydrogen, and an increase

in the amount of hydrogen bound to N atoms. These changes result in a lower refractive index and a higher growth rate but have relatively little effect on the buffered HF etch rate.

Examining only the number of significant main effects summed over all responses shows RF power and SiH₄/NH₃ flow ratio are the most important factors, being statistically significant for six of the seven responses studied. Pressure is somewhat less important, and substrate temperature by itself is relatively unimportant for the specific set of responses measured. In addition, a surprisingly large number of interactions were found to be statistically significant. As would be expected from the main effect observations, these were primarily those which involved RF power and/or the SiH₄/NH₃ ratio.

In summary, a multivariate factorial design experiment has been implemented to examine the hypergeometric response surface for reactor parameters on a-SiNH film properties. This study was performed primarily to examine the interactions of various reactor parameters on film properties, information which could not be gleaned from previous single-variable experiments. The results of the design have led to three major conclusions. First, there are statistically significant interactions of the primary factors for nearly all responses. The large number of these preclude quick conclusions about the effect of changing the level of one of the machine parameters while keeping all others constant. Second, the RF power level and SiH₄/NH₃ ratio are the most important factors for the set of responses studied here. Third, changes in power, reactant gas ratio, or pressure are amplified through changes in the film stoichiometry. Changes in the refractive index, for example, are symptomatic of changes in the Si/N ratio and the amount and placement of bound hydrogen. In each response, the general trends tend to support the directions observed in previous single-variable experiments and extend those conclusions by actually measuring the strength of factor-factor interactions.

Manuscript submitted Jan. 8, 1985; revised manuscript received March 20, 1985.

AT&T Bell Laboratories assisted in meeting the publication costs of this article.

REFERENCES

1. A. K. Sinha, H. J. Levinstein, and T. E. Smith, *J. Appl. Phys.*, **49**, 2423 (1978).
2. H. J. Stein, V. A. Wells, and R. E. Hampy, *This Journal*, **126**, 1750 (1979).
3. M. J. Rand, *J. Vac. Sci. Technol.*, **16**, 420 (1979).
4. A. Reinberg, *J. Electron. Mater.*, **8**, 345 (1979).
5. J. T. Milek, "Handbook for Electronics Materials," Vol. 3,IFI/Plenum Press, New York (1971).
6. H. Dun, P. Pan, F. R. White, and R. W. Douse, *This Journal*, **128**, 1555 (1981).
7. M. J. Rand and D. R. Wonsidler, *ibid.*, **125**, 99 (1978).
8. W. A. Lanford and M. J. Rand, *J. Appl. Phys.*, **49**, 2473 (1978).
9. P. S. Peercy, H. J. Stein, B. L. Doyle, and S. T. Picroux, *J. Electron. Mater.*, **18**, 11 (1979).
10. T. F. Retajczyk, Jr., and A. K. Sinha, *Thin Solid Films*, **70**, 241 (1980).
11. G. E. P. Box and K. B. Wilson, *J. Royal Stat. Soc. B*, **13**, 1 (1951).
12. G. E. P. Box, *Biometrics*, **10**, 16 (1954).
13. G. E. P. Box, *ibid.*, **11**, 287 (1955).
14. A. Reinberg, *Ann. Rev. Mater. Sci.*, **9**, 341 (1979).
15. C. D. Wagner, *Anal. Chem.*, **44**, 1050 (1972).
16. G. E. P. Box, W. G. Hunter, and J. S. Hunter, "Statistics for Experimenters," Chap. 10, John Wiley and Sons, New York (1978).
17. A. K. Sinha, H. J. Levinstein, T. E. Smith, G. Quintana, and S. E. Haszko, *This Journal*, **125**, 601 (1978).
18. M. A. Ring, M. J. Puentes, and H. W. O'Neal, *J. Am. Chem. Soc.*, **92**, 4845 (1970).
19. A. K. Sinha and E. Lugujo, *Appl. Phys. Lett.*, **32**, 245 (1978).

Interference Photovoltage Spectroscopy. Probing of the Silicon-Sapphire Interface of SOS Films

J. Lagowski

Massachusetts Institute of Technology, Cambridge, Massachusetts 02139

L. Jastrzebski,* M. T. Duffy,* and G. W. Cullen*

RCA Laboratories, Princeton, New Jersey 08540

ABSTRACT

The photovoltage spectra of heteroepitaxial silicon on sapphire (SOS) exhibit an oscillatory pattern (thin film interference effects). The amplitudes of the oscillations increase with decreasing film thickness. We attribute this amplitude increase to anomalous optical behavior of the silicon-sapphire interface region, and we propose the use of "interference photovoltage spectroscopy" as a practical means for probing the silicon-sapphire interface.

The optical properties of silicon-on-sapphire in the ultraviolet and in the visible spectral range are known to be dependent on the crystalline quality of the film (1). This dependence is commonly believed to originate from crystallographic disorder (large density of {221} twins and associated defects) which is especially severe in the silicon near the interface between the silicon film and the sapphire substrate. Practical methods have been formulated for the assessment of SOS film quality by visual inspection of the films [haze determination (2)] and by quantitative UV-reflectivity measurements (3). Recently, we proposed using the reflectivity in the near infrared and visible spectral range for an optical probing of the quality of the silicon near the silicon-sapphire interface (4). This approach was based on measurements of reflectivity spectra, and especially on the analysis of the amplitude of reflectivity oscillation vs. photon energy. The method appears to be sufficiently sensitive to distinguish between as-grown SOS films of different crystalline quality. Furthermore, it makes it possible to observe changes induced by the film processing steps (such as thermal annealing or hydrogenation) which are not in all cases resolvable in the UV-reflectivity method and in the haze evaluation.

In this paper, we discuss a simplified version of the method based on photovoltage measurements (5, 6) in which the film itself is a detector of the optical phenomena involved.

SOS films utilized in this study were intentionally thinned by plasma etching from an original thickness of about 6000Å to the desired thickness ranging from 1000 to 3000Å. No significant increase in epilayer roughness was observed after etching, as measured by an α -step and an interference contrast microscopy. Photovoltage spectra of thinned films are shown in Fig. 1. (The spectra are as measured, i.e., they are not normalized to a constant photon flux.) The photovoltage was generated by monochromatic chopped light and detected using lock-in detection previously described (5). Measurements were carried out using a metal-semiconductor (M-S) configuration (5). Semitransparent Au-electrodes were simultaneously evaporated on all films under study. Prior to evaporation, the film surfaces were cleaned by 15s etching in buffered HF.

The photovoltage spectra in Fig. 1. exhibit a characteristic interference pattern, i.e., series of maxima and minima, which are due to interference of the light reflected from the front silicon-Au interface and from the Si-sapphire interface. For the analysis of the magnitude of the oscillations, it is convenient to introduce the parameter Δ defined as

$$\Delta = (V_{\max}/V_{\min})^{1/p} - 1 \quad [1]$$

where V_{\max} and V_{\min} are defined in Fig. 1a, and p is the

parameter describing the power dependence of the photovoltage, V , on the illumination intensity, I , i.e., $V \sim I^p$. The effects of nonlinearity ($p \neq 1$) are significant at low temperature, where trapping effects become more significant. For example, at 220 K [this temperature corresponds to the maximum magnitude of photovoltage (5)] the amplitude of photovoltage oscillations V_{\max}/V_{\min} is smaller by a factor of two than at room temperature; this effect is associated with a reduction of the p value from $p = 1$ at

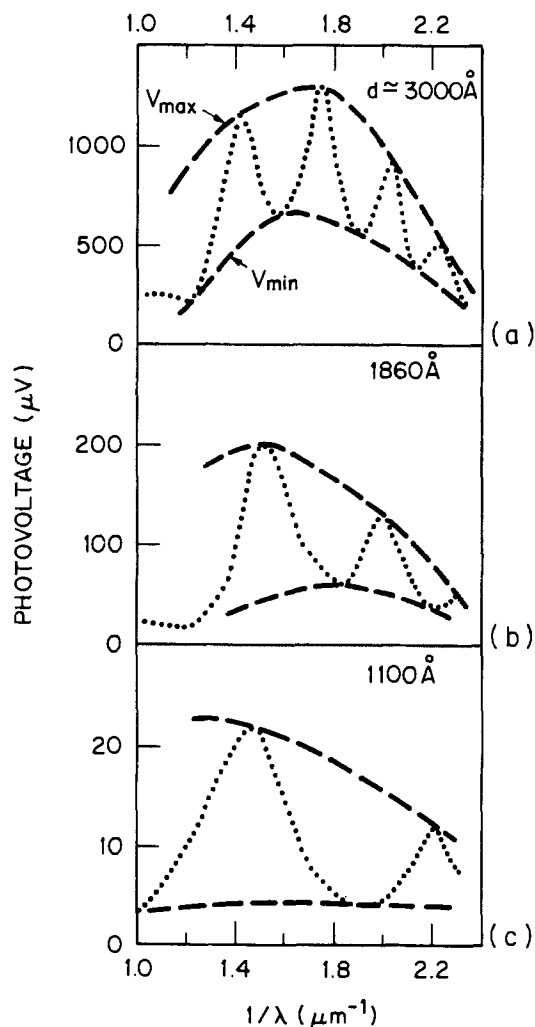


Fig. 1. Photovoltage spectra of "A" category (density of {221} twins less than 4%) SOS film measured at 300 K. (a), (b), and (c) correspond to film thicknesses of about 3000, 1860, and 1100Å, respectively.

*Electrochemical Society Active Member.

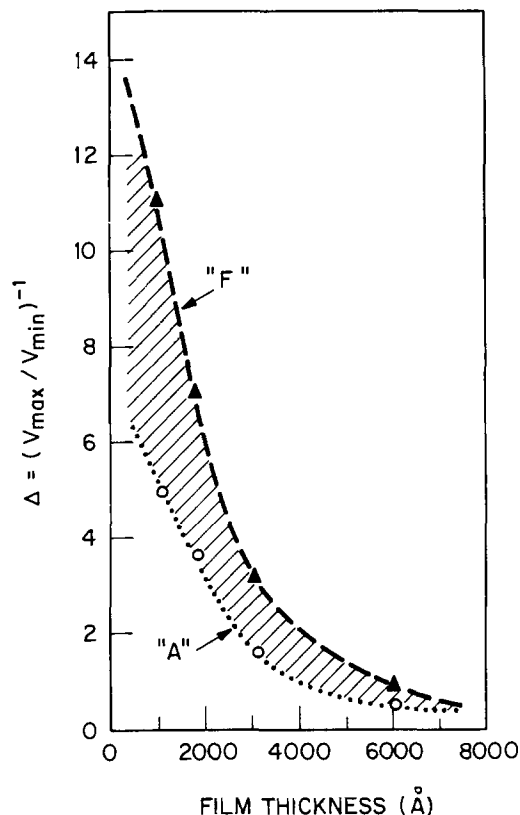


Fig. 2. Interfacial disorder parameter, Δ (see text), measured vs. film thickness for films of "A" and "F" categories. Density of {221} twins less than 4% and about 14%, respectively; Δ is obtained with about 10% error.

room temperature to $p = 0.7$ at 220 K. The results of Fig. 1 illustrate two tendencies: (i) separation of minima-maxima on the energy scale increases with decreasing film thickness, and (ii) in the region of negligible absorption of SOS films (when $\alpha d < 1$), the amplitude of oscillations increases with decreasing film thickness.¹ The first result is an obvious consequence of decreasing the optical path, dn (where d is the film thickness and n is the refractive index). The observation that V_{\max}/V_{\min} increases

with decreasing film thickness is of primary importance, since it demonstrates that V_{\max}/V_{\min} is affected by the Si-sapphire interface region.

The dependence of Δ (measured at $1/\lambda = 1.4 \mu\text{m}^{-1}$, i.e., in a region of negligible optical absorption of the film) on film thickness is shown in Fig. 2 for two films: "A" category film of good crystalline quality (density of {221} twins less than 4%) and "F" category film of the inferior quality ({221} twin density about 14%). The results show that not only does Δ increase with decreasing film thickness, but also the difference between the two films becomes more pronounced for smaller film thickness. The shaded area between the two curves defines a range of values of the parameter expected in SOS films of different thicknesses and crystalline quality. The optical phenomena responsible for the observed differences are not well understood at present. The empirical relation, however, seems to be strong enough to be used as a practical means for probing, on a relative basis, the interface quality. The results in Fig. 2 can be used to compare different films using relatively simple interference photovoltage spectroscopy measurements.

Manuscript submitted Dec. 10, 1984; revised manuscript received March 20, 1985.

RCA Laboratories assisted in meeting the publication costs of this article.

¹The observed reduction in the magnitude of the photovoltage at the short wavelengths is related to the reduction of light intensity (the photovoltage is not normalized to the light level). The observed reduction in the amplitude of oscillations (difference between V_{\max} and V_{\min}) at the short wavelengths is caused by light absorption at the film surface away from sapphire interface.

REFERENCES

1. M. T. Duffy, P. J. Zanzucchi, W. E. Horn, J. F. Corboy, G. W. Cullen, and R. T. Smith, *J. Cryst. Growth*, **58**, 19 (1982).
2. D. E. Passoja, D. McLeod, L. G. Dowell, H. F. Hillery, J. E. A. Maurits, and L. R. Rothrock, *ibid.*, **58**, 44 (1982).
3. M. T. Duffy, J. F. Corboy, G. W. Cullen, R. T. Smith, R. A. Soltis, G. Harbeck, J. R. Sandercock, and M. Blumenfeld, *ibid.*, **58**, 10 (1982).
4. J. Lagowski, L. Jastrzebski, and G. W. Cullen, *This Journal*, **130**, 1744 (1983).
5. J. Lagowski, L. Jastrzebski, and G. W. Cullen, *ibid.*, **128**, 2665 (1981).
6. L. Jastrzebski, M. T. Duffy, J. F. Corboy, G. W. Cullen, and J. Lagowski, *ibid.*, **58**, 37 (1982).

Argon Entrapment and Evolution in Sputtered TaSi₂ Films

R. A. Levy* and P. K. Gallagher

AT&T Bell Laboratories, Murray Hill, New Jersey 07974

ABSTRACT

The use of tantalum disilicide over doped polycrystalline silicon (poly-Si) for gate and interconnect metallization is becoming an integral part of the design and processing of VLSI devices. Under certain sputtering and/or processing conditions, the silicide surface has been seen to exhibit sporadically blisters and voids during high temperature processing. In this study, we shall demonstrate that the occurrence of these defects in TaSi₂ is related to the entrapment of argon during deposition and the evolution of that gas during subsequent processing. This conclusion will be deduced by ascertaining, through a series of controlled experiments, the contributory effect of a wide range of processing parameters, by proposing a phenomenological model to explain the governing mechanism of blister and void formation, and by providing analytical evidence to verify this model.

The use of tantalum disilicide over doped polycrystalline silicon (poly-Si) for gate and interconnect metallization has been implemented in devices designed and processed in accordance with the 2.5 μm Twin-Tub CMOS technology (1). This polycide structure has the advantage of preserving the MOS interfacial stability of poly-Si while reducing, due to the lower resistivity of the silicide

*Electrochemical Society Active Member.

($\sim 50 \mu\Omega\text{-cm}$), IR drops and RC delay times in the circuit (2-4). Although several techniques are available for formation of the disilicide, cosputtering from separate Si and Ta targets in an inert ambient is generally preferred because it produces smoother surfaces and affords better control on the desired stoichiometry of the films (5, 6). Following deposition, the amorphous silicide films typically undergo several high temperature processing steps.

Generally, these include sintering to crystallize the structure and minimize the sheet resistance, passivation to restore the gate oxide thickness uniformity eroded during reactive ion etching, and flow as well as reflow to smooth the phosphosilicate glass (PSG) topography and drive in the junctions (7). Under certain sputtering and/or processing conditions, the silicide surface has been seen to sporadically exhibit blisters and voids after flow. In this study, we shall demonstrate that the occurrence of blisters and voids in TaSi_2 is related to the entrapment of argon during deposition and the evolution of that gas during subsequent high temperature processing. We shall proceed to accomplish this task by ascertaining through a series of controlled experiments, the contributory effect of a wide range of processing parameters, by proposing a phenomenological model to explain the governing mechanism of blister and void formation, and by providing analytical evidence to verify this model. We shall then conclude this investigation by offering recommendations which should prove successful in eliminating the occurrence of these potentially fatal defects.

Processing Variables

If not otherwise specified, the silicide films investigated in this study were deposited at a rate of $\sim 100\text{\AA}/\text{min}$ in a magnetron unit with capabilities for cosputtering from a tantalum target and two boron-doped silicon ($\sim 0.14\ \Omega\text{-cm}$) targets. All wafers were held at ground potential and rotated in a planetary station to enhance deposition uniformity. The sputtering chamber was evacuated to $< 1 \times 10^{-6}$ torr, with the combined aid of a roughing and an oil diffusion pump, and was backfilled with pure Ar (99.995%) at a pressure of 2×10^{-3} torr. Following silicide deposition, device wafers were patterned, reactive sputter etched, sintered, passivated, and implanted (P, B). LPCVD films of undoped oxide ($\sim 1000\text{\AA}$) and PSG ($\sim 16\ \text{k}\text{\AA}$) were then deposited and the wafers subjected, during flow, to the highest thermal treatment of the process. In the case where experiments were conducted on monitor wafers, several steps of the process were purposely deleted to exclude extraneous effects.

The characteristic morphology of blisters and voids, associated with the high temperature processing of cosputtered TaSi_2 , is illustrated in Fig. 1 with SEM micrographs taken both on monitor and device wafers. Blisters in these $\sim 2500\text{\AA}$ thick films are generally seen to be uniform in shape (dome-like) and vary extensively in size, with some stretching in large areas as much as $50\ \mu\text{m}$ across. The distribution of blisters on the silicide surface appears random with some being close enough for PSG to form a partially resolved envelope over the agglomerated units. In some cases, the damage produced by these defects is so severe that parts of the PSG film are literally blown out. Voids, on the other hand, appear to be irregular in size and shape but still randomly distributed across the silicide surface.

One of our initial considerations as the cause of this blistering problem included the possibility that it was instrument-related. Thus, experiments were initially conducted to evaluate possible effect of instrumental variation and then to ascertain effects of other processing variables.

Effect of instrumental variation.—Starting with a group of oxidized ($\sim 610\text{\AA}$) n-type silicon ($1.5\text{-}3\ \Omega\text{-cm}$) substrates, LPCVD polysilicon ($\sim 4000\text{\AA}$) was deposited and doped in a PBr_3/O_2 (1000°C) ambient. Following an oxide clean, TaSi_2 ($\sim 2500\text{\AA}$) was cosputtered at a rate of $\sim 95\ \text{\AA}/\text{min}$ in a sputtering unit using a symmetric two-gun arrangement. The sputtering chamber was pumped to $< 5 \times 10^{-7}$ torr with the combined use of a Vac-Ion and turbomolecular pump prior to backfilling with Ar (99.9%) at a pressure of 4×10^{-3} torr. All wafers were then sintered at 950°C for 30 min in Ar. A wafer selected from this group was introduced, with no additional processing, into a furnace at 1100°C for 20 min in a 99% N_2 -1% O_2 ambient. In Fig. 2a, an optical micrograph of that sample prominently exhibits the presence of blisters confirming, despite character-

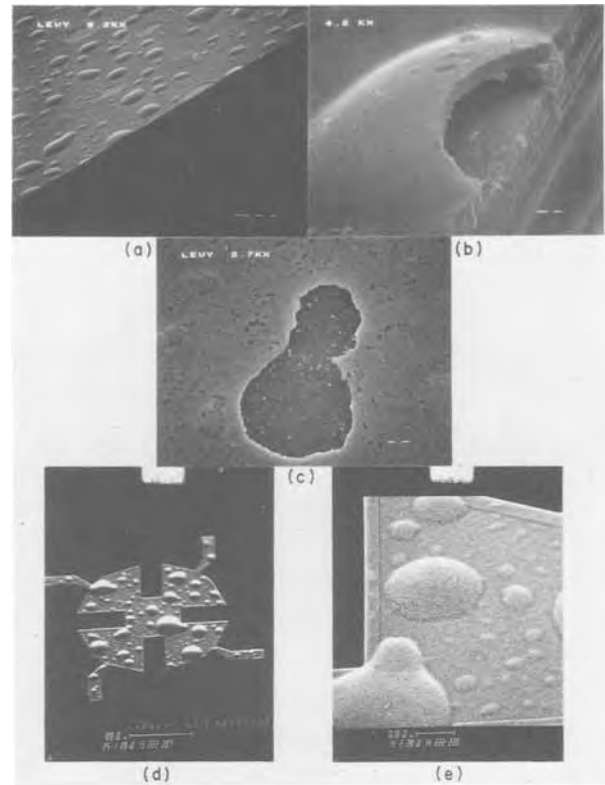


Fig. 1. SEM micrographs illustrating the characteristic morphology of blisters and voids on both monitor and device wafers.

istic differences in the geometries of the sputtering units, the occurrence of the effect. Another result, worthwhile noting at this point, is the fact that blisters and voids are seen here despite the absence of an implant step or the use of an overlaying PSG film.

Effect of PSG deposition and flow.—Another wafer selected from the above group received sequentially $\sim 1000\text{\AA}$ LPCVD undoped oxide and $\sim 16\ \text{k}\text{\AA}$ PSG. Optical examination of the wafer at that stage (Fig. 2b) indicated a surface devoid of relevant morphological structures. How-

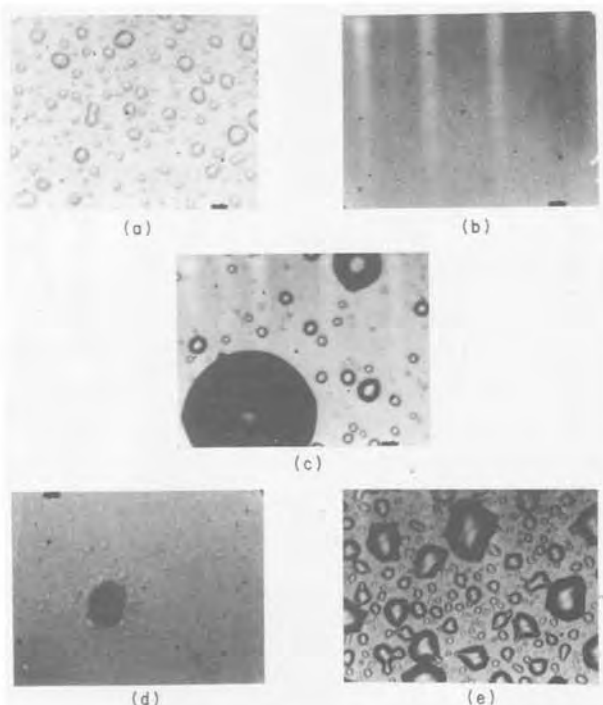


Fig. 2. Optical micrographs of TaSi_2 subjected to various process treatments.

ever, after an 1100°C/20 min/99% N₂-1% O₂ flow, the emergence of large blisters (Fig. 2c) was evident at 400× throughout the surface of the wafer. A comparison of Fig. 2a and c emphasizes the magnification effect produced by the added presence of PSG. Presumably, as the TaSi₂ swells at high temperatures due to an internal gas pressure buildup, evolution of some of this gas from burst bubbles coupled with the high temperature softening characteristic of PSG has a "ballooning" effect on the glass surface. At high enough pressures, the glass itself cracks allowing for the gas to escape.

Effect of thermal flow cycle.—Two of the wafers also withdrawn from the above group with combined ~1000Å LPCVD undoped oxide and 16 kÅ PSG were subjected to a flow cycle of 1000°C/90 min/N₂. Microscopic examination of both wafers after that step revealed, as shown in Fig. 2d, the localized presence of small blisters (~2 μm) and occasional areas devoid of PSG. Consistent with the kinetic theory of gases, there appears to be, here, less of a pressure buildup, which in conjunction with the higher rigidity of PSG at this lower flow temperature further masks the effect. However, reflowing one of the wafers at 1100°C/20 min/99% N₂-1% O₂ readily triggers blistering, as shown in Fig. 2e. Thus flow temperature appears to be a major contributing factor to blister formation.

Effect of oxide passivation.—In an attempt to investigate the effect of oxide passivation on blister formation, a set of n-type silicon monitors was precleaned prior to deposition of ~2500Å TaSi₂. All wafers were then sintered at 900°C for 30 min in Ar and passivated at 900°C for 80 min in dry O₂. One of the wafers from this group, identified as (I), was split into halves (IA, IB). A half of that wafer (IA) had its passivating oxide stripped off, while the other half (IB) was kept untreated for control purposes. Each of these halves was then split forming now four quadrants (IA1, IA2, IB1, IB2) which all received ~1000Å LPCVD oxide for purposes of magnifying the blistering effect. Quadrants IA1 and IB1 were subjected to a 1000°C/90 min/N₂ flow, while quadrants IA2 and IB2 received a 1100°C/20 min/99% N₂-1% O₂ flow treatment. The four quadrants were pieced together to reconstruct the original wafer layout and examined with an optical microscope. Figures 3a and b offer a comparative look at samples IA1 vs. IA2 and IB1 vs. IB2, respectively. It is evident from these photographs that no blistering was apparent, in this case, on both quadrants flowed at 1000°C for 90 min in N₂ regardless of the presence or absence of the passivating oxide, while the 1100°C/20 min/99% N₂-1% O₂ flow treatment triggered blistering in both quadrants. Controlled experiments run in parallel with 1 kÅ PSG and no glass yielded similar results thus ruling out the effect of oxide passivation on blister formation.

The effect of passivation time was also examined with TaSi₂ (~2500Å) deposited directly, after a preclean, onto five p-type Si monitors. The wafers were all sintered at 900°C/30 min/Ar then each passivated at 900°C in O₂ for periods of 1.33, 2, 4, 8, and 16h, respectively. Microscopic examination revealed a brownish silicide surface on the two wafers passivated for 8 and 16h pointing to the presence of an oxide. X-ray fluorescence analysis of the silicide films indicated the presence of a significant amount of entrapped Ar which was observed to gradually de-

crease by a factor of ~3 after 16h of oxidation time. Thus, it appears from this data that SiO₂ formation on the surface, as a result of Si transport from the underlying substrate through the silicide grain boundary, has the effect of also sweeping forward the Ar gas. Following deposition of ~1000Å of LPCVD oxide and flow at 1100°C/20 min/99% N₂-1% O₂, all wafers passivated up to 4h exhibited progressively increasing signs of blisters and voids for shorter oxidation times. Furthermore, the absence of these defects observed in samples passivated for 8 and 16h is believed here to be directly related to the measured decrease in the concentration of entrapped Ar.

Effect of sintering cycle.—The effect of sintering ambient was investigated using a group of wafers with TaSi₂/N⁺ poly Si/SiO₂/Si structure. The polysilicon (~3000Å) was first deposited on oxidized (~600Å) monitors and then doped in a PBr₃/O₂ ambient (1000°C). Following a surface oxide strip and a preclean, the silicide was co-sputtered (~2500Å) and the wafers subsequently submitted for Auger analysis to determine their stoichiometry. A wafer selected with a characteristic composition of TaSi_{2.4} was split into halves with one half sintered at 900°C/30 min/H₂, while the control half received a 900°C/30 min/Ar treatment. Both sections were coated with a ~1000Å LPCVD undoped oxide and subjected to an 1100°C/20 min/99% N₂-1% O₂ flow treatment. Microscopic examination of both sections revealed a similar blistering formation across the surface. However, an interesting observation, noted in the context of this particular investigation, was that the positioning of wafers on the LPCVD sled had the effect of masking parts of the surface from deposition. Microscopic examination of blistering across the bordering areas clearly revealed (Fig. 4) the magnification resulting from the presence of the overlying oxide. That is, again, consistent with previously stated conclusions that blistering does indeed occur in the absence of an overlying oxide and that the visual effect is simply enhanced by the "ballooning" action of the softened glass at high temperatures.

To evaluate the effect of sintering time on blister formation, monitor wafers similar in structure (TaSi₂/N⁺ poly Si/SiO₂/Si) to those described in the previous paragraph were sintered at 900°C in Ar for periods of 0.5, 2, 4, 8, or 16h. X-ray fluorescence analysis of all sintered samples indicated the presence of Ar which was seen to be persistently retained in all cases. The addition of ~1000Å LPCVD oxide on these samples followed by the 1100°C/20 min/99% N₂-1% O₂ flow exhibited, with no exceptions, blisters. Altering the sintering temperature to 1000°C on samples from the same group yielded a significant roughening of the silicide surface and a tendency toward random formation of small blisters (≥1 μm) at that heat-treating stage, *i.e.*, even prior to flow.

Effect of film stress.—In view of the possibility that blister formation could be the result of intrinsic and/or thermal stresses generated during deposition and/or high temperature treatments, a systematic investigation of

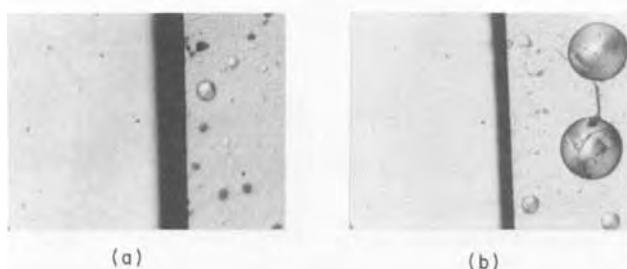


Fig. 3. Comparative optical micrographs of samples (a) IA1 vs. IA2 and (b) IB1 vs. IB2.

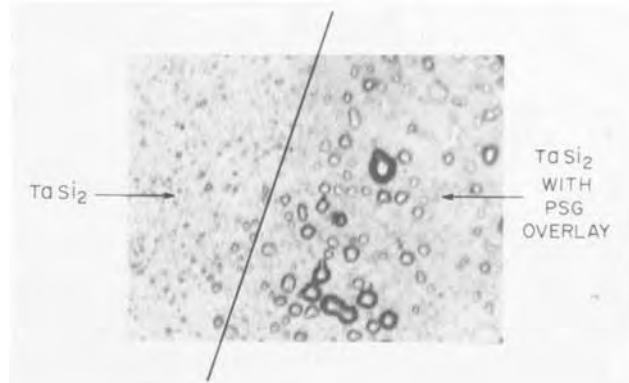


Fig. 4. Optical micrograph revealing the magnification effect resulting from the presence of the overlying oxide.

these stresses at relevant processing steps was undertaken. Starting with five oxidized ($\sim 600\text{\AA}$) n-type silicon monitors (10–20 $\Omega\text{-cm}$), LPCVD polysilicon ($\sim 3000\text{\AA}$) was deposited and doped in a PBr_3/O_2 ambient (1000°C). After stripping the surface oxide, the curvature of all five wafers was measured using a laser leverage technique. Following deposition of $\sim 2500\text{\AA}$ TaSi_2 , the radius of curvature on each of the wafers was remeasured, and the stress due to silicide deposition calculated. Results of those measurements yielded average values of $-1.8 (\pm 2.3) \times 10^9$ dyn/cm², thus revealing at this step a trend toward a compressive state of stress. Two wafers from this group (S1 and S25) were sintered at $900^\circ\text{C}/30$ min/Ar, two others (S5 and S15) at $1000^\circ\text{C}/30$ min/Ar, while the fifth wafer (S20) received a $900^\circ\text{C}/30$ min/Ar sinter followed by a $900^\circ\text{C}/80$ min/ O_2 passivation. Measurement of the radius of curvature, after these steps, registered a change on all five wafers, from a compressive trend to a definite tensile stress with a recorded average value of $1.7(\pm 0.3) \times 10^{10}$ dyn/cm². Following LPCVD deposition of $\sim 1000\text{\AA}$ undoped oxide (wafers placed back to back in the reactor) and ~ 14 kÅ PSG on both sides of each of the wafers, stress measurements revealed little change from the previously recorded average value. Wafers S1 and S5 were then selected for an $1100^\circ\text{C}/20$ min/99% N_2 -1% O_2 flow, while S15, S20, and S25 were subjected to a $1000^\circ\text{C}/90$ min/ N_2 flow. Stress measurement taken, after that stage, yielded insignificant changes, regardless of the type of flow, from the average values observed after the silicide sintering step. There is the possibility that during the high temperature flow cycle the stress becomes compressive. Extrapolation of the stress-temperature data of Retajczyk and Sinha (8), however, does not indicate the onset of compressive stress in TaSi_2 until $\sim 1200^\circ\text{C}$. In view of those results, the characteristic tensile stress of the sintered silicide film as well as that of the composite film structure cannot be reconciled with the high temperature generation of blisters since a compressive, rather than the measured tensile stress, would be expected to generate these defects.

Effect of compositional variation.—In an effort to examine possible trends between compositional variations in the silicide and blister formation, wafers with Si/Ta ratios close to 2.2, 2.4, and 2.7, as determined by Auger analysis, were deposited directly on precleaned p-type Si substrates. Following a $900^\circ\text{C}/30$ min/Ar sinter, the sheet resistance measured across each of the wafers yielded average values of 2.1, 2.2, and 2.4 Ω/\square for $\text{TaSi}_{2.2}$, $\text{TaSi}_{2.4}$, and $\text{TaSi}_{2.7}$, respectively. X-ray fluorescence analysis of the Ar concentration in the silicide showed negligible differences among those three investigated compositions. Addition of $\sim 1000\text{\AA}$ LPCVD oxide followed by flow at 1100°C for 20 min in 99% N_2 -1% O_2 revealed, under microscopic examination, blister formation regardless of the degree of deviation from the stoichiometric composition. An important point to note with regard to this particular experiment is that, just as described above in the section on Effect of oxide passivation; blistering was observed in silicide deposited directly on p-type Si. In view of the total absence of phosphorus in the underlying substrate as well as the overlying oxide there is certainly no plausible argument here for support of any essential role of phosphorus in blister formation.

Effect of poly-Si substrate doping.—In the course of investigating the mechanism of blister formation, the possible role of the phosphorus dopant in the underlying polysilicon was considered. To resolve this question, several experiments were conducted on device wafers (with TaSi_2). Following LPCVD poly-Si deposition ($\sim 3000\text{\AA}$), groups of these device wafers were doped in a PBr_3/O_2 ambient at temperatures of 900° , 950° , and 1000°C yielding variable values for sheet resistance of ~ 112 , 27, and 21 Ω/\square , respectively. Further variations in the doping of poly-Si was achieved by using an LPCVD *in situ* phosphorus doping technique ($R_s \approx 408 \Omega/\square$ for a thickness of $\sim 3200\text{\AA}$ at $\sim 700^\circ\text{C}$ deposition) and an As implant (50 keV, $1\text{E}16 \text{ cm}^{-2}$). Regardless of the doping technique used,

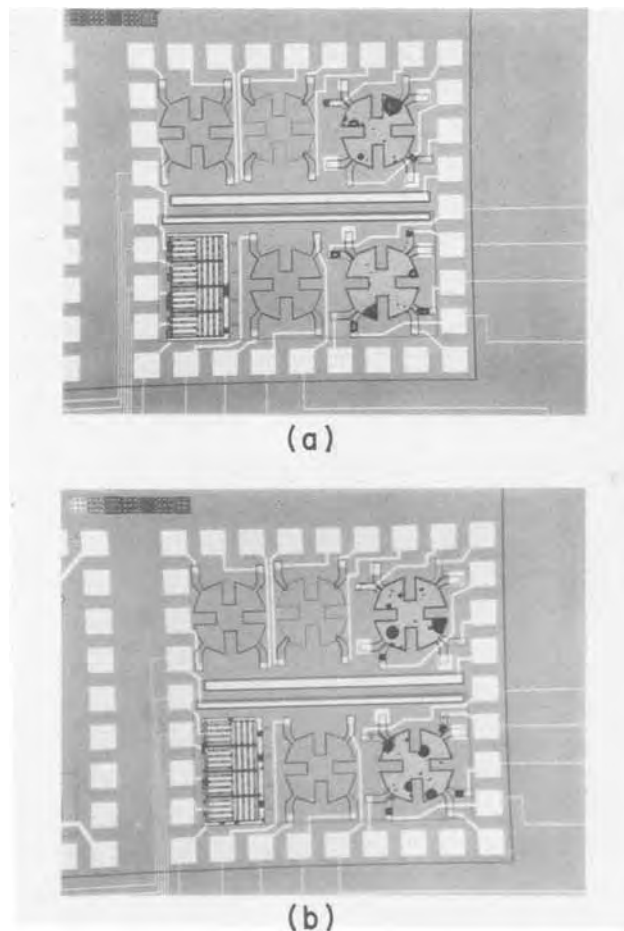


Fig. 5. Optical micrographs of van der Pauw patterns with (a) poly-Si doped at 950°C in PBr_3/O_2 and (b) poly-Si implanted with As (50 keV, $1\text{E}16 \text{ cm}^{-2}$).

processing of all device wafers proceeded with TaSi_2 deposition, sintering ($900^\circ\text{C}/30$ min/Ar), patterning, source/drain implants, PSG deposition and flow ($1100^\circ\text{C}/20$ min/99% N_2 -1% O_2). Microscopic examination after the latter step revealed the presence of blisters of various sizes randomly distributed across wafers from each of these groups. Typical photographs of device wafers with poly-Si doped at 950°C and As implanted are shown, respectively, in Fig. 5a and b. The fact that lowering the phosphorus concentration in the poly-Si or replacing it by arsenic showed no improvement reaffirms our contention, stated in the section on Effect of compositional variation, that blistering can occur even in $\text{TaSi}_2/\text{p-type Si}$, after capping with LPCVD undoped oxide and flowing at 1100°C , despite the total absence of phosphorus. It is important to point out that both the N^+ ($1\text{E}15 \text{ cm}^{-2}$ B, $4\text{E}15 \text{ cm}^{-2}$ P) and P^+ ($1\text{E}15 \text{ cm}^{-2}$ B) van der Pauw patterns of Fig. 5a and b have exhibited blistering after the $1100^\circ\text{C}/20$ min/99% N_2 -1% O_2 flow. That is indeed significant in view of the fact that P^+ van der Pauw patterns have shown, as shall be discussed in the next section, a significant tendency to be less prone to blister formation with a lower temperature flow cycle ($1000^\circ\text{C}/90$ min/ N_2).

Effect of P and B implants.—Following silicide deposition, sintering, and passivation, areas exposed during source/drain definition to double implants of P (100 keV, $4\text{E}15 \text{ cm}^{-2}$) and B (30 keV, $1\text{E}15 \text{ cm}^{-2}$) have reproducibly shown a tendency toward blister formation as opposed to areas implanted solely with B (30 keV, $1\text{E}15 \text{ cm}^{-2}$). A comparative examination of N^+ and P^+ van der Pauw patterns, shown in Fig. 6, clearly illustrates the harmful effect of that double implant. Wafers with the standard TaSi_2/N^+ poly-Si/ SiO_2/Si structure subjected to double P implants (100 keV, $4\text{E}15 \text{ cm}^{-2}$) were observed to blister

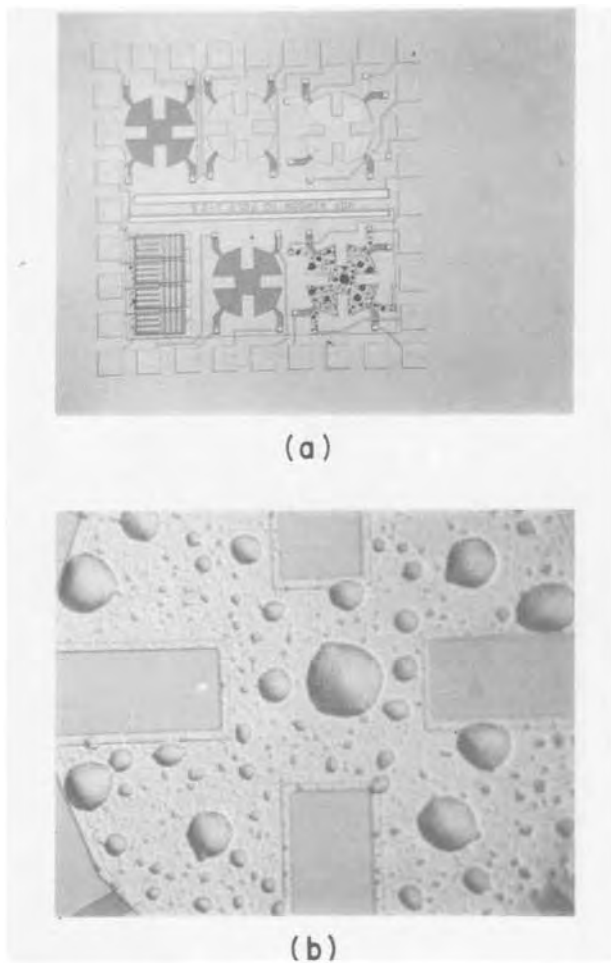


Fig. 6. (a) Comparative examination of N⁺ and P⁺ van der Pauw patterns; (b) magnified portion of N⁺ van der Pauw pattern.

reproducibly after PSG flow (1000°C/90 min/N₂), compared to the marginal situation encountered with single implants. In view of these results, it appears evident that the damage associated with high energy high dose implants and not necessarily the implant species plays a contributory role in the mechanism of blister formation.

Effect of gas ambient during sputtering.—The effect of Ar pressure during deposition on blister and void formation was investigated using a group of monitor wafers with the standard TaSi₂/N⁺ poly-Si/SiO₂/Si structure. The LPCVD polysilicon (~3000Å) was first deposited on oxidized Si (~600Å) then doped in PBr₃/O₂ ambient (1000°C). Following oxide removal, TaSi₂ was cosputtered at varying Ar pressures of 2, 3, 4, 6, or 8 μm (Hg) on these wafers which were subsequently all sintered at 900°C/30 min/Ar. X-ray fluorescence and Rutherford backscattering (RBS) measurements were then conducted on various samples to evaluate the concentration of argon entrapped in the silicide films. The results, shown in Fig. 7 and 8, indicate a monotonic decrease in the entrapped argon concentration as a function of higher Ar pressures. Sections of these wafers, with no additional processing (*i.e.*, no overlaying LPCVD oxide), were subjected to a flow treatment of 1100°C/20 min/99% N₂-1% O₂. Figure 9 illustrates the surface morphology of the silicide after that treatment as a function of Ar pressure. Blistering was observed at this magnification (660×) to emerge in films deposited at Ar pressures of 2, 3, and 4 μm. At higher pressures, no blistering was detected but silicide delamination from the underlying polysilicon was evident. Examination of these photographs also reveals a gradual smoothing of the surface with higher Ar sputter pressures reflecting a dramatic decrease in void density. Sections of these wafers flowed at 1000°C/90 min/N₂ indicated a similar behavior as shown in the SEM photographs of Fig. 10. The high

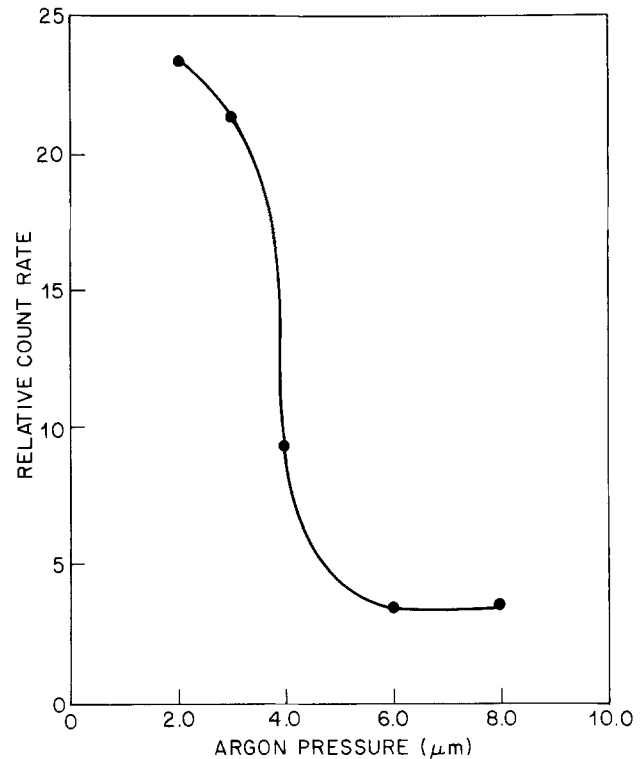


Fig. 7. X-ray fluorescence (XRF) measurements of the argon concentration in TaSi₂ films sintered at 900°C/30 min/Ar as a function of sputtering Ar pressure.

density of voids observed on the sample sputtered at 2 μm gradually gives way to the pore-free surface of the silicide cosputtered at 8 μm. We believe both these observations to be consistent with an Ar entrapment and release

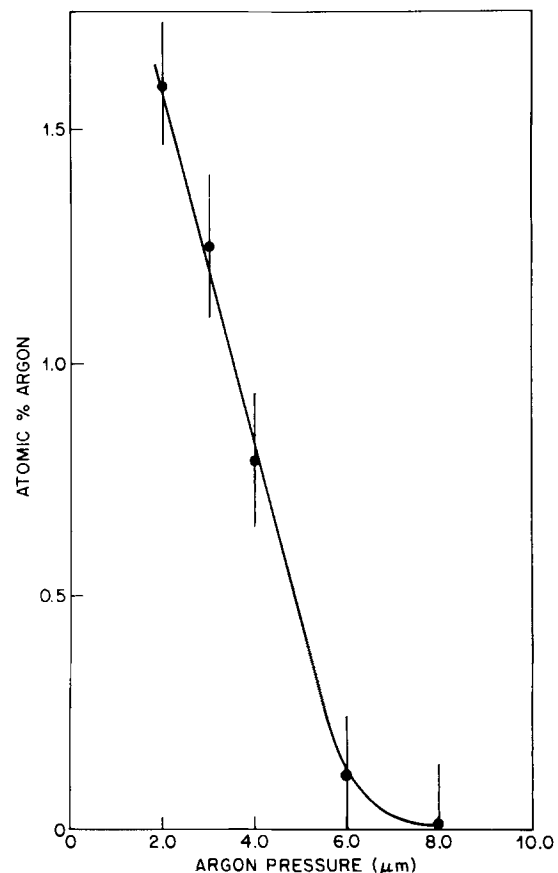


Fig. 8. Rutherford backscattering (RBS) measurements of the argon concentration in TaSi₂ films sintered at 900°C/30 min/Ar as a function of sputtering Ar pressure.

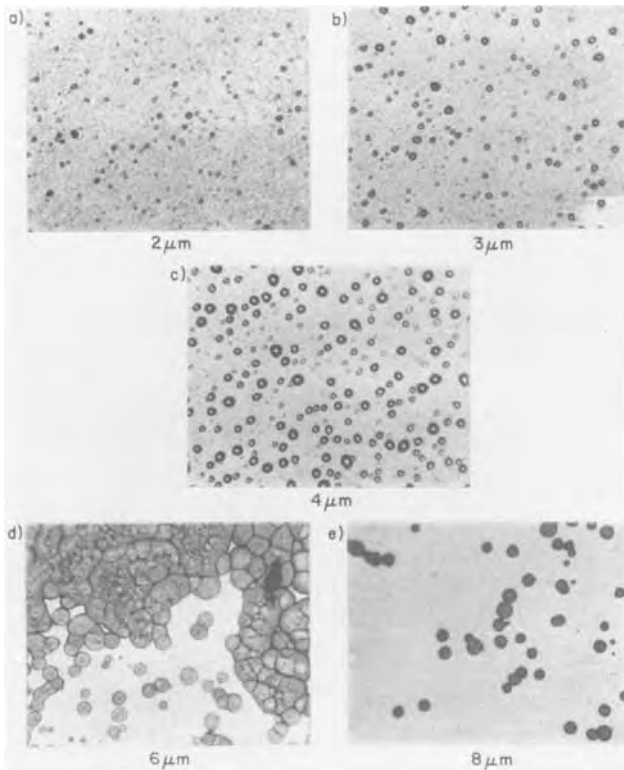


Fig. 9. Optical micrographs of the surface morphology of TaSi₂ films sputtered at an Ar pressure of (a) 2 μm, (b) 3 μm, (c) 4 μm, (d) 6 μm, and (e) 8 μm after a flow treatment (with PSG) of 1100°C/20 min/99% N₂-1% O₂.

mechanism which shall be described in the next section. It is worth noting at this point that the choice of an optimum Ar sputtering pressure should take into consideration not only the minimization of the Ar content in the film but also that of O₂ which often increases at the higher sputtering pressures and is possibly the source of the observed delamination problem.

The idea of sputtering with Xe at a 2 μm pressure rather than Ar has also been considered during the course of this investigation. Split lot experiments have reproducibly shown no evidence of blistering on the Xe-sputtered silicide, after flow at 1000°C/90 min/N₂, despite widespread occurrence of the problem on control wafers. Furthermore, comparative examination of gate interconnects, after P-glass removal, clearly indicate, as shown in

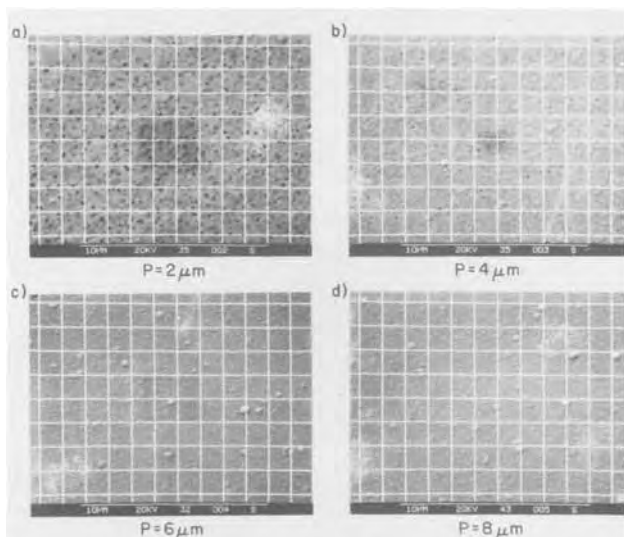


Fig. 10. SEM micrographs of the surface morphology of TaSi₂ films sputtered at an Ar pressure of (a) 2 μm, (b) 4 μm, (c) 6 μm, and (d) 8 μm after a flow treatment (with no PSG) of 1000°C/90 min/N₂.

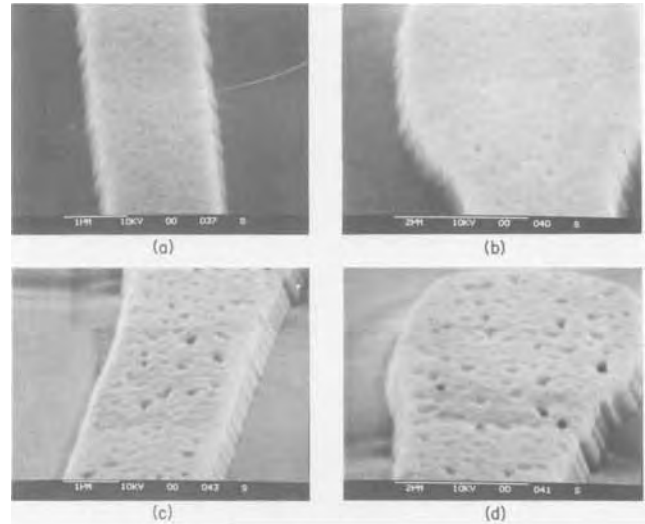


Fig. 11. Comparative examination of TaSi₂ gate interconnects sputtered in Xe (top) and Ar (bottom).

Fig. 11, a decrease both in void density and void depths at the surface of the silicides sputtered in Xe. These results point to the fact that the nature of the gas used for sputtering affects its entrapped concentration, thereby influencing blister and void formation. Based on the above results, we shall now propose a phenomenological model to explain the high temperature blister and void formation mechanism in co-sputtered TaSi₂.

Phenomenological Model

Results from the present investigation as well as other reported studies have shown the formation of blisters and voids in TaSi₂ to be primarily dependent on the concentration of entrapped Ar, the processing temperature, and the extent of implant damage. Quantitative determination of the Ar content, by combined vacuum fusion and mass spectrometric analysis,¹ have indicated the presence of 1.8 a/o of the gas in TaSi₂ films sputtered at a pressure of 2 μm. Generally, the fraction (f), of Ar trapped during sputtering in a film is given by (9)

$$f = \frac{\alpha N}{\alpha N + R}$$

where N is the number of Ar atoms bombarding a unit area of film per unit time during deposition, α is the effective sticking coefficient of the Ar during deposition, and R is the deposition rate of the TaSi₂ film. Clearly, there are three possible ways of reducing f ; these include increasing the deposition rate which is rather difficult to achieve in sputtering, and decreasing N and/or α . Decreasing N may be accomplished by operating in a getter sputtering mode or by depositing at high sputtering pressures provided that does not of itself lead to the incorporation of other contaminants (*i.e.*, H₂O, O₂, ...). Decreasing α may be achieved by operating in a bias or ac sputtering mode, or by increasing the substrate temperature.

For TaSi₂ films sputtered at a pressure of 2 μm, differential thermal analysis measurements have determined, as shown in Fig. 12, the onset of crystallization to be at ~330°C. At that transition temperature, evolved gas analysis has indicated, as seen in Fig. 13, release of most of the entrapped gases including H₂, N₂, O₂, and H₂O but only a small fraction of the Ar. We postulate that this remnant Ar is the source of both blisters and voids formed during high temperature processing of TaSi₂. Upon deposition, the films, as shown in the TEM micrograph of Fig. 14a, are amorphous with the Ar presumed to be distributed randomly throughout the silicide. During the sintering process, the Ar is believed to be swept along by grain boundary formation and occasionally trapped, in its diffu-

¹Gollob Analytical Service, Berkeley Heights, New Jersey 07922.

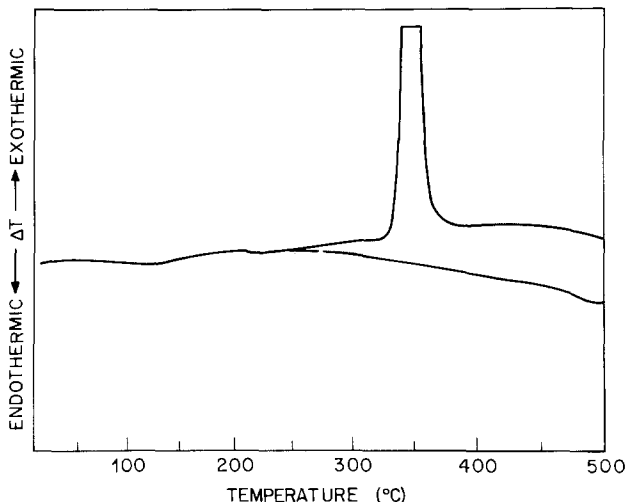


Fig. 12. Differential thermal analysis of TaSi₂ indicating the onset of crystallization at ~ 330°C.

sion path, at random defect sites (*i.e.*, dislocations stacking faults, . . .). The TEM micrograph of Fig. 14b provides evidence that bubbles, typically 60Å in diameter, are indeed present at grain boundaries as well as at random intragranular sites in the sintered silicide (900°C/30 min/Ar). During the diffusion of He in Cu, Barnes and Mazey (10) have reported the velocity of He bubbles to be inversely proportional to the bubble radius. Furthermore, the faster migration of small bubbles at 800°C was observed, by hot stage transmission electron microscopy, to result in coalescence with the larger but slower bubbles. A similar situation appears to have occurred in TaSi₂ during the 1000°C flow cycle. Small bubbles merged, as shown in Fig. 14c, into larger bubbles (~150Å) which seem now to be pinned at triple points of grain boundaries. Thus, due to this thermal migration and coalescence, the density of bubbles has decreased but the volume occupied by individual bubbles has increased causing lo-

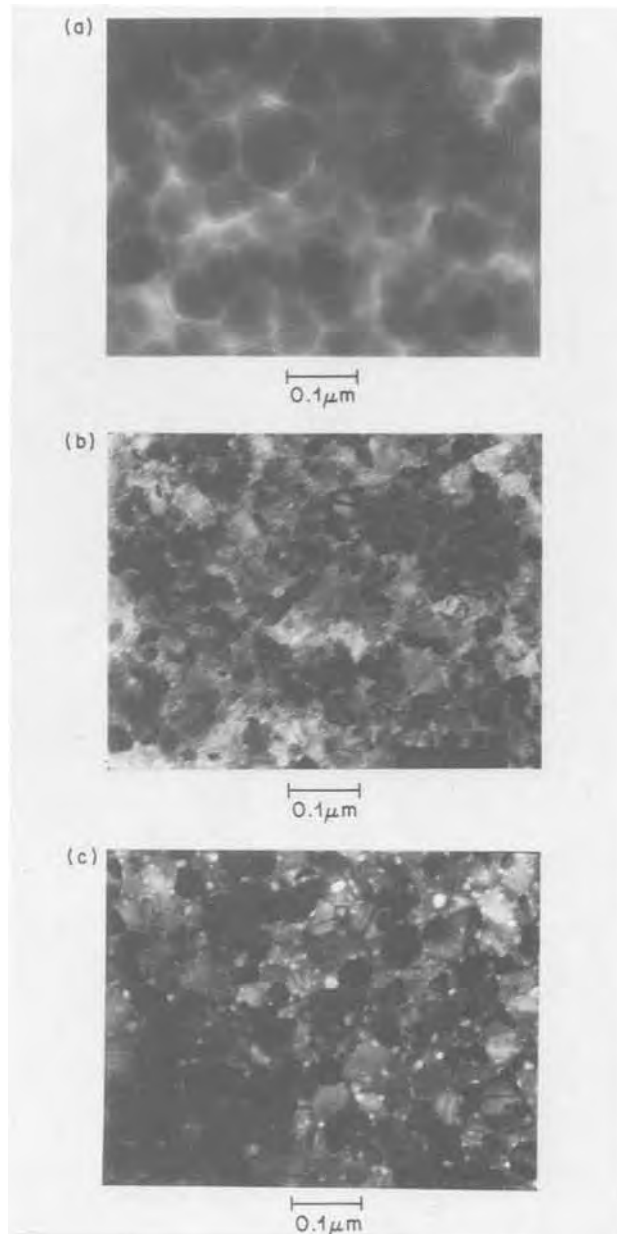


Fig. 14. TEM horizontal cross sections of TaSi₂ (a) in the amorphous state, (b) after a 900°C/30 min/Ar sinter, (c) after sinter and a flow treatment (with no PSG) of 1000°C/90 min/N₂.

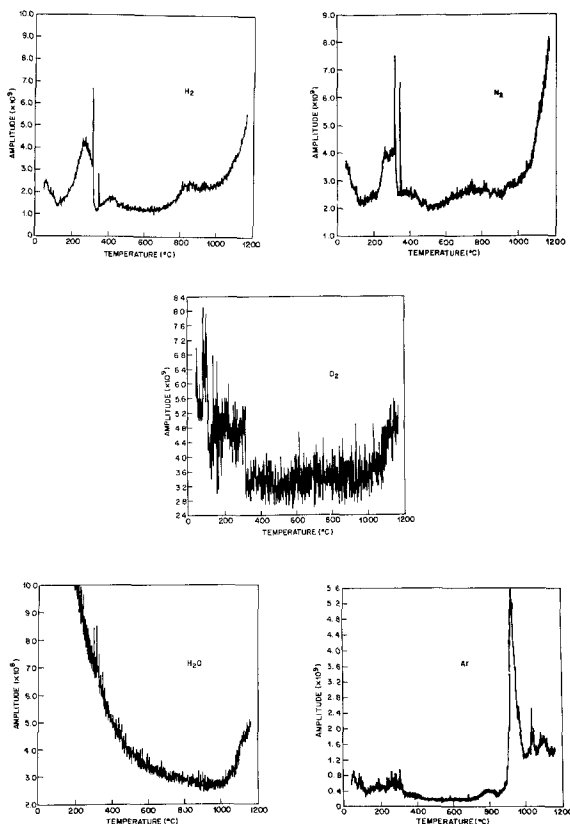


Fig. 13. Evolved gas analysis of entrapped (a) H₂, (b) N₂, (c) O₂, (d) H₂O, and (e) Ar in TaSi₂.

cal silicide swelling. In a thermodynamic equilibrium, the gas pressure within a bubble is balanced by the surface tension force between gas atoms and lattice. For a bubble of radius r , the surface tension force is $2\gamma/r$ where γ is the surface energy and is generally of the order of 10^3 erg/cm² (11). Assuming ideal gas behavior, one obtains for a bubble of radius r

$$\left(\frac{2\gamma}{r}\right) \left(\frac{4}{3} m^3\right) = mkT$$

OR

$$\frac{8}{3} \pi \gamma r^2 = mkT$$

where m is the number of atoms in the bubble, k is Boltzmann's constant, and T the absolute temperature. At a temperature of 1000°C where a bubble diameter is typically 150Å, the calculated value of m amounts to 2.68×10^4 atoms and the corresponding pressure within such a bubble is estimated to be 2.67×10^3 atm. However, these high pressures appear to be still within the order of magnitude of typical values reported for fracture strength of thin

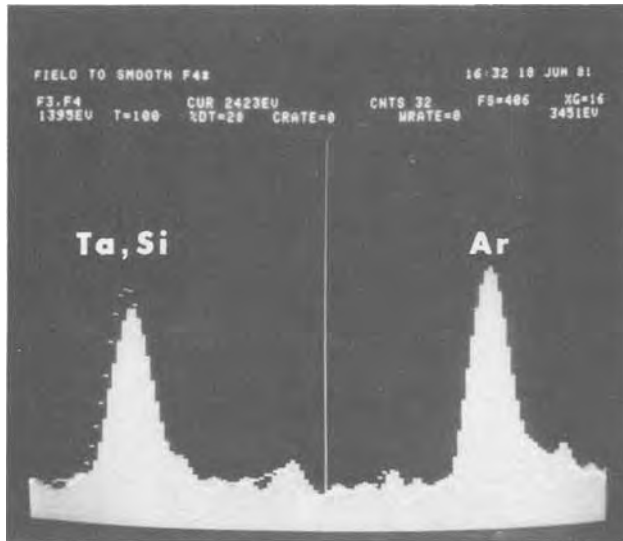


Fig. 15. Superposed x-ray fluorescence spectra of TaSi_2 as deposited (solid line) and after a flow treatment (with no PSG) of $1100^\circ\text{C}/90 \text{ min}/99\% \text{ N}_2\text{-}1\% \text{ O}_2$.

films (12). A quick check on the validity of the above calculations is provided by considering the fact that the observed density of bubbles n , as determined from examination of Fig. 14c, is of the order of $6 \times 10^{15} \text{ cm}^{-3}$ for 2500\AA thick TaSi_2 films. From the product nm , the total number of solute atoms per cubic centimeter is estimated at $\sim 1.6 \times 10^{20}$. Since the density of TaSi_2 (atomic weight $\sim 240\text{g}$) is 9 g/cm^3 , the total number of solvent atoms per cubic centimeters is $\sim 6.7 \times 10^{22}$. Thus, the calculated fraction of Ar atoms in the film is within the order of magnitude of the measured concentration.

For large enough bubbles and high enough temperatures ($\geq 1000^\circ\text{C}$), an equilibrium breakdown resulting from loss of surface tension under such conditions triggers explosions of these bubbles. Such outbursts close to the free surface contribute to formation of the observed surface voids. Gases emerging close to the bottom surface could possibly get trapped at the silicide polysilicon interface, contributing to potential loss of film adherence. Gases bursting from within the silicide cause catastrophic damage to the film integrity. In the presence of a PSG film, the Ar gas evolving from the silicide in turn pressurizes that coating. At adequate flow temperatures where the glass can be plastically deformed, various size blisters readily form reflecting the wide range in pressure outbursts. In extreme pressure conditions, the PSG film itself cracks releasing the gas trapped at the glass-silicide interface.

Because of the considerable vacancy production during high energy high dose implants, and because the strain energy associated with trapped atom-vacancy clusters is expected to be less than that for Ar atoms trapped at defect sites, one can predict, in such cases, significant enhancement of the migration and coalescence process leading to aggravated blistering. That is, indeed, consistent with our reported observations. Analytical evidence to support this proposed model will now be presented.

Analytical Evidence

Several analytical methods have been used to confirm the entrapment of argon in sputtered TaSi_2 and the subsequent evolution of the gas during high temperature processing. These techniques have included x-ray fluorescence (XRF), energy and wavelength dispersive spectroscopy (EDS and WDS), evolved gas analysis (EGA), and transmission electron microscopy (TEM).

The fluorescence data were gathered in an x-ray Milliprobe unit interfaced to a Li-drifted Si detector and a PGT-3 analyzing system. A Cr target operating at 50 kV and 9 mA provided the source of radiation. The sample was placed in a chamber flushed with N_2 to eliminate

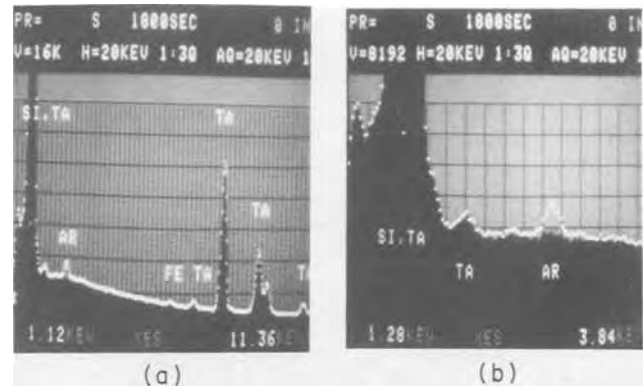


Fig. 16. (a) Superposed energy dispersive spectra (EDS) of a blistered area (white dots) and an undisturbed region (dark background) on the sample; (b) EDS data shown on an expanded scale over a range of 1.28-3.84 keV.

peaks resulting from Ar absorption in air. This is normally done using He, but N_2 is preferred in this case because it suppresses the large Si peak which would otherwise overload the x-ray counting system. A 0.75 mm aperture and 4.8 mm beam stop were used for enhancing count rate efficiency. In cases where extraneous diffraction peaks were observed, the sample was reoriented to lessen their interference effect. Figure 15 exhibits superposed x-ray fluorescence spectra of TaSi_2 as deposited (solid line) and after a 1100°C flow cycle with no glass on (dotted line). The $\sim 2500\text{\AA}$ thick silicide was cosputtered, in this case, at an Ar pressure of $2 \mu\text{m}$ onto a $\sim 3000\text{\AA}$ thick PBr_3 -doped (1000°C) polysilicon substrate. The as-deposited silicide appeared under microscopic examination to be specular while the heat-treated silicide revealed an abundant formation of fine blisters throughout the sample. From a comparison of the spectra of Fig. 15, it is evident that entrapped Ar is indeed present in the as-deposited TaSi_2 film and not in the heat-treated sample confirming total evolution of the gas after the 1100°C thermal cycle. Furthermore, the insignificant change in the magnitude and shape of the overlapped Ta/Si peaks between both spectra reflect, here, the lack of stoichiometric variation in the film after heat-treatment. It is worthwhile noting, at this point, that, although the x-ray fluorescence technique is not quantitative due to the absence of proper standards, it is quite practical and has been extensively used within the context of this investigation in monitoring changes in the Ar content as a function of processing variables.

The x-ray microanalysis data were gathered in conjunction with an SEM by focusing the 20 kV electron beam on the blistered regions of the sample surface or on the flat undisturbed TaSi_2 areas of a device wafer flowed at 1000°C for 90 min in N_2 . Special precautions, in this case, were taken to etch back the P-glass down to the 1000\AA undoped SiO_2 layer to insure minimum absorption of the

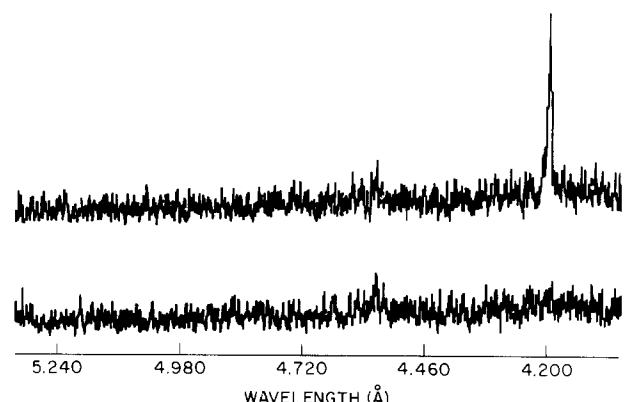


Fig. 17. Wavelength dispersive spectra (WDS) of a blistered area (upper curve) and a undisturbed region (lower curve) on the sample.

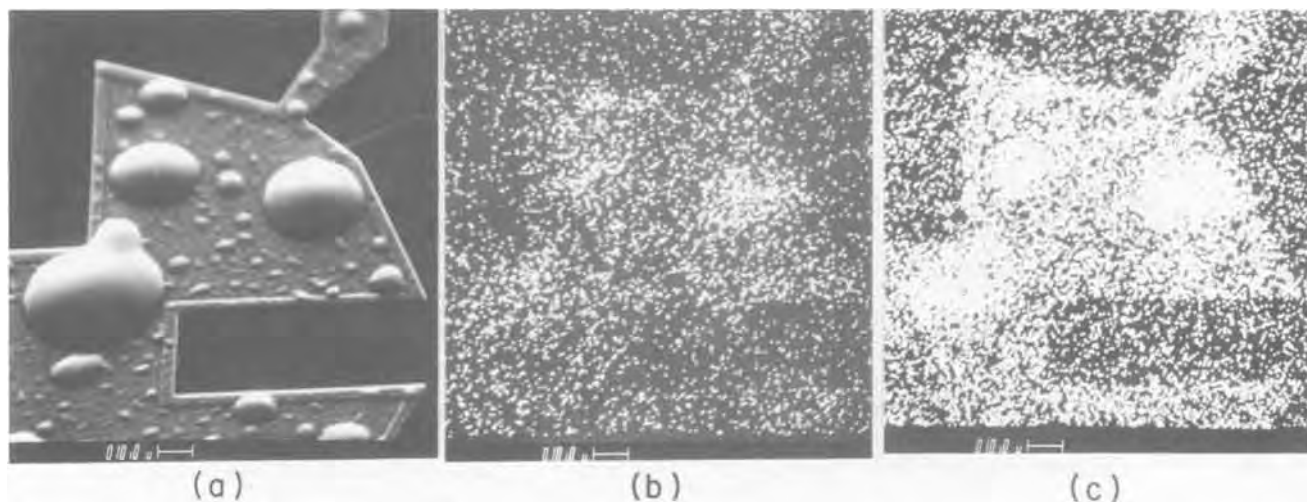


Fig. 18. (a) SEM secondary electron image of a leaf of a van der Pauw pattern; (b) multiple scan Ar x-ray images exposed for 5 min, and (c) 15 min.

electron beam with no disturbance of the underlying trapped gas. Both energy dispersive (EDS) and wavelength dispersive (WDS) x-ray systems were used.

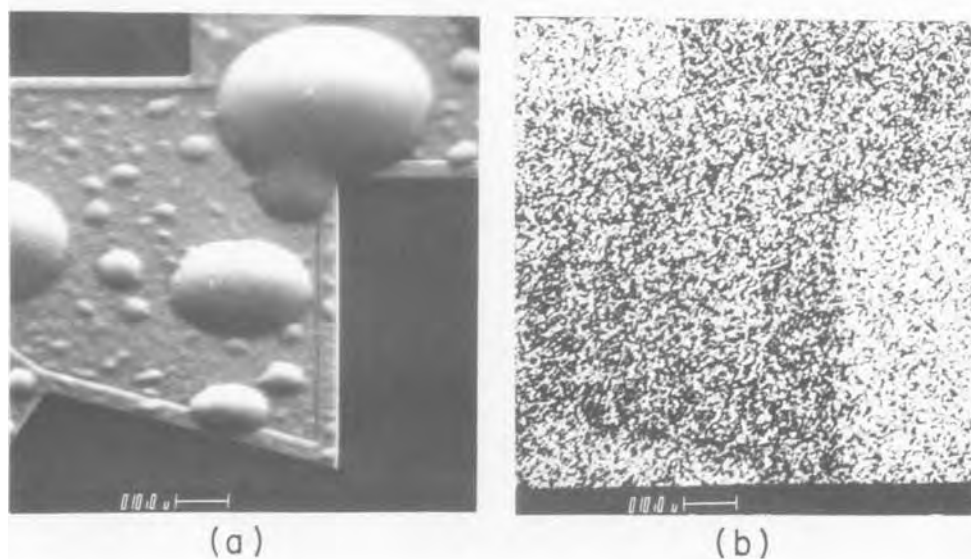
Full EDS spectra of both these regions are shown in Fig. 16a in an overlay fashion. Outlined in white dots is the elemental spectrum from the surface of a blister while the dark background represents an elemental spectrum of a spot in the undisturbed region of the sample. It is evident from examination of this photograph that both spectra exhibit identical intensities for the Si, Ta, and Fe peaks, but only the spectrum of the blistered area shows the presence of an Ar $K\alpha$ peak at 2.96 keV. This may be seen more clearly in Fig. 16b, where the 1.28-3.84 keV range is shown on an expanded scale. This result unequivocally associates the presence of Ar with the blistered areas.

The gathering of the WDS data required an adjusted beam current of ~ 50 mA. Because of the absence of available Ar standards, sample positioning was optimized using the $L\alpha 1$ peak (4.154\AA) of a silver standard. Representative WDS spectra are shown in Fig. 17, where the upper curve denotes the results of the analysis of a blister and the lower curve from the same undisturbed area where the EDS measurements were taken. Both spectra show a weak third order Ta $L\alpha$ line (4.559\AA) but only the upper curve shows the presence of an Ar $K\alpha$ line at 4.193\AA . That again reconfirms the correlation between local presence of blisters and local presence of argon. The WDS Ar $K\alpha$ peak was used in turn to generate x-ray area

maps shown in Fig. 18. Figure 18a is a secondary electron image of one leaf of a van der Pauw pattern. Figures 18b and c are multiple scan Ar x-ray images exposed for 5 and 15 min, respectively. Although the image clarity is partially obscured by background signals over the whole area due to the relatively low Ar peak to noise ratio, one can obviously see a direct correspondence between local Ar agglomeration and the formation of blisters across the sample. Although a single pass WDS spectrum (Fig. 17, lower curve) indicates that the concentration of Ar is below the detection limit, an improved peak to noise ratio at longer exposure time (Fig. 18c) shows that a very low concentration of Ar is present over the whole cloverleaf area. A similar x-ray map of P showed only a uniform distribution of noise, thus ruling out, as previously noted, the role of P in the blistering formation mechanism. X-ray mapping of Si in the same general area is shown in Fig. 19 where a uniform distribution is now seen both within the $TaSi_2$ van der Pauw pattern and the delineated oxide area with signal intensities simply reflecting the difference in the Si concentration. Similarly, an x-ray map for Ta (Fig. 20) shows as expected, a uniform distribution of that element only over the $TaSi_2$ van der Pauw pattern.

The evolved gas analysis (EGA) measurements were gathered from an assembled apparatus comprised primarily of a small Mo furnace with provisions for temperature monitoring and control, a quadrupole mass spectrometer and a turbomolecular pump capable of achieving pressures down to $\leq 1 \times 10^{-8}$ torr. The output of the spec-

Fig. 19. X-ray mapping of Si on a leaf of a van der Pauw pattern.



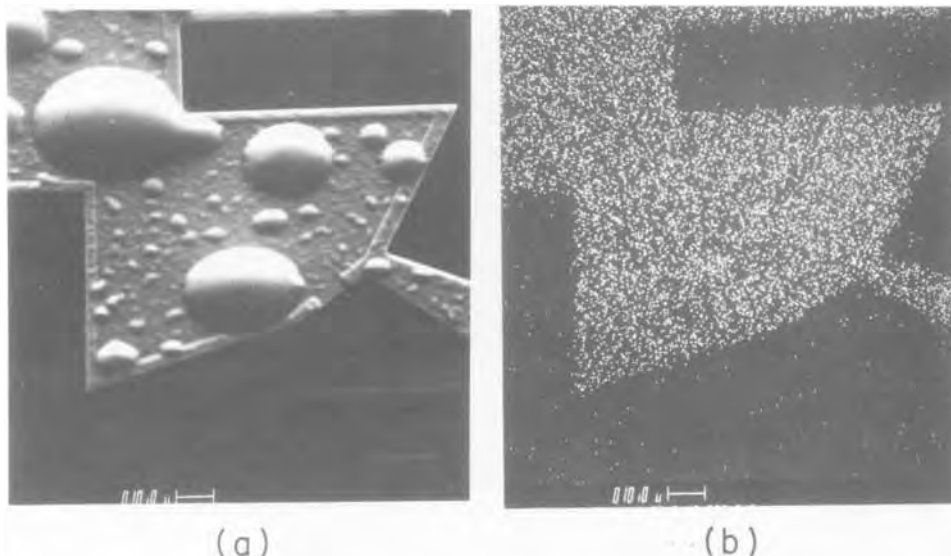


Fig. 20. X-ray mapping of Ta on a leaf of a van der Pauw pattern.

trometer was fed into a data acquisition unit in turn interfaced to a Fluke 1720 microcomputer used for processing and plotting of the data. The temperature was typically stepped up at a rate of $10^{\circ}\text{C min}^{-1}$ up to $\sim 1150^{\circ}\text{C}$. The TaSi_2 samples, under present consideration, were deposited at an Ar pressure of $2 \mu\text{m}$ on Teflon substrates in order to flake off the film and eliminate substrate contributions. It is evident from examination of Fig. 13 that significant evolution of the Ar gas occurs over the temperature range of $900^{\circ}\text{--}1100^{\circ}\text{C}$ in coincidence with the temperature range where blister formation is most evident. EGA measurements of other gases such as H_2 , N_2 , O_2 , and H_2O on similar samples indicated, as shown in Fig. 13, gas evolution only at the $\sim 330^{\circ}\text{C}$ crystallization temperature of TaSi_2 .

A representative vertical TEM micrograph taken on sample with a $\text{Si/SiO}_2/\text{N}^+$ poly-Si/ TaSi_2 structure annealed at 1000°C is shown in Fig. 21. It appears that voids reflecting the gas presence are located at various levels throughout the TaSi_2 film with the voids at the bottom interface presumably accounting for potential poor adherence, those at the center for potential local delamination, and those on top for the surface porosity.



Fig. 21. TEM vertical cross section illustrating presence of voids at various levels of TaSi_2 film.

Concluding Remarks

It is apparent from the present investigation that both blister and void formation result from argon entrapment during sputter deposition and subsequent evolution of that gas during high temperature processing of TaSi_2 . Although other argon-free deposition techniques (evaporation, LPCVD, . . .) may be tried to circumvent the problem, it is evident that with sputter deposition the process must be tailor-fit to minimize the argon concentration in the film. Our results have shown that good quality TaSi_2 films could, indeed, be achieved by optimizing the Ar sputtering pressure, minimizing the implant damage, and reducing the high temperature flow cycle.

Acknowledgments

The authors wish to thank R. V. Knoell for the TEM work, S. M. Vincent for the x-ray fluorescence measurements, F. Ermanis for the EDS, WDS, and x-ray mapping results, T. E. McGahan for the SEM micrographs, R. J. Schutz for the RBS data, B. E. Wilcomb for deposition of the silicide films, L. J. Lecheler for assisting in various tasks of this project, and S. P. Murarka, A. Maury, G. Perez, D. B. Fraser, K. J. Orlowsky, J. C. Desko, L. C. Parrillo, and J. T. Clemens for many fruitful interactions.

Manuscript submitted Jan. 10, 1985; revised manuscript received March 25, 1985.

AT&T Bell Laboratories assisted in meeting the publication costs of this article.

REFERENCES

1. L. C. Parrillo, L. K. Wang, R. D. Swenumson, R. L. Field, R. C. Melin, and R. A. Levy, *IEEE Tech. Dig., Int. Electron Device Meet.*, p. 706 (1982).
2. A. K. Sinha, W. S. Lindenberger, D. B. Fraser, S. P. Murarka, and E. N. Fuls, *IEEE Trans. Electron Devices*, **ed-27**, 1425 (1980).
3. A. K. Sinha, D. B. Fraser, and S. P. Murarka, *Proc. of the 18th Rel. Phys. Symp. IEEE*, 159 (1980).
4. S. P. Murarka, D. B. Fraser, A. K. Sinha, and H. J. Levinstein, *IEEE Trans. Electron Devices*, **ed-27**, 1409 (1980).
5. S. P. Murarka and D. B. Fraser, *J. Appl. Phys.*, **51**, 1593 (1980).
6. S. P. Murarka, *J. Vac. Sci. Technol.*, **17**, 775 (1980).
7. R. A. Levy, S. M. Vincent, and T. E. McGahan, *This Journal*, **132**, 1492 (1985).
8. T. F. Retajczyk, Jr., and A. K. Sinha, *Thin Solid Films*, **70**, 241 (1980).
9. L. I. Maissel and R. Glang, "Handbook of Thin Film Technology," pp. 4-20, McGraw-Hill, Inc., New York (1970).
10. R. S. Barnes and D. J. Mazey, *Proc. Roy. Soc.*, **274**, 47 (1963).
11. G. Carter and J. S. Collington, "Ion Bombardment of Solids," p. 417, American Elsevier Publishing, Inc., New York (1968).
12. D. D'Antonio, J. Hirshhorn, and L. Tarshis, *Trans. AIME*, **227**, 1346 (1963).

A New Fabrication Technique for Optoelectronic Integrated Circuits (OEIC's) — The Graded-Step Process — Applied to the Fabrication of AlGaAs/GaAs PIN/FET and PIN/Amplifier Photoreceivers

O. Wada, S. Miura, H. Machida, K. Nakai, and T. Sakurai

Fujitsu Limited, 1677, Ono, Atsugi 243-01, Japan

ABSTRACT

Process of forming graded steps on a GaAs substrate, which are as deep as 7-8 μm and have an arbitrarily small slope angle down to 13° has been developed by using the rounded edge profile of photoresist layer as a protective mask for Ar ion-beam etching of the substrate. Mask preparation and ion-beam etching have been optimized in terms of both controlling the slope angle and achieving smooth etched surface. The use of a large ion incident angle near 70° has been found to be most advantageous for smoothing an etched surface. Graded steps thus formed have been found to be significantly useful for improving the reproducibility and yield of delineating fine geometries on the substrate by contact lithography, primarily owing to the allowance of using a thin photoresist layer. By using this process, a new optoelectronic integrated circuit (OEIC) fabrication technique has been proposed and applied to the fabrication of AlGaAs/GaAs monolithic photoreceiver circuits, namely, an integrated PIN photodiode/field effect transistor (FET) front end as well as an integrated PIN/amplifier. It has been demonstrated that this technique eliminates previous problems of photolithography and interconnection processes in OEIC fabrication and improved the overall process stability. The circuits fabricated in this study exhibited subnanosecond responses, confirming that the parasitic capacitances have been successfully reduced in the present integrated structure.

Applications of fiber-optic transmission and data processing systems have been widely spread in this decade with the association of a marked improvement in performance and reliability of optoelectronic devices such as lasers and photodetectors. The system's needs for higher bit rate or greater information capacity is the motivation for further improvement in device characteristics. These needs include high performance, high reliability, compactness, ease of interface to electrical circuits, and lower cost. The optoelectronic integrated circuit (OEIC) is a monolithic circuit in which optoelectronic devices and electronic circuits are integrated together on a single semiconductor substrate. This new class of device is regarded as most capable of meeting most of the above-mentioned requirements (1-4). In particular, monolithic integrations of a laser with its driver circuit (5-11) and of a photodetector with an amplifier (12-16) and other electronic signal processing circuits have a capability of increasing the speed and noise performances due to the reduction of parasitic reactances which have been responsible for the performance degradation experienced in previous equipment composed of discrete elements. Development of such OEIC's has been energetically carried out for these several years on both AlGaAs-GaAs (1) and InGaAs(P)-InP (2) systems aimed at wavelength ranges near 0.8 μm and 1.3-1.5 μm , respectively. The high electron mobility in these crystals facilitates high speed electronic circuits. The fabrication technologies of both discrete optoelectronic and electronic devices have been greatly advanced in recent years.

In integrating these elements, however, considerable difficulty in processing has been introduced primarily because of the structural difference between the constituent elements. The optoelectronic devices usually possess multilayer epitaxial structure with a thickness of more than several microns, where the electronic devices such as the field effect transistors (FET's) and bipolar transistors have active layers as thin as 1 μm . Such a structural difference causes, almost inevitably, the appearance of steep mesa steps on the OEIC substrate. These steps degrade the reproducibility of every photolithographic process involved in the series of OEIC fabrication steps, and the overall fabrication yield can be significantly lowered. In order to minimize such effects of steps, a few remedies have been examined so far. A method to etch a well in the substrate before growing the epitaxial heterostructure for the optoelectronic devices has been employed in most of previous studies. It was found to be very effective for ad-

justing the surface level between the optoelectronic and electronic regions so that the fine pattern definition can be carried out in both regions. Kolbas and his co-workers have proposed a method to polish and etch the epitaxial AlGaAs/GaAs structure overgrown in the GaAs substrate region outside the wells, so that the substrate can be planarized (12). Liao and his co-workers have used selective epitaxy to fill a well in the InP substrate by growing InGaAs layer with the aid of silicon nitride mask and then etching the overgrown ridge of InGaAs at the mask periphery (17). Shibata and his co-workers have introduced the use of PIQ to refill and planarize an isolation well generated between the laser and the bipolar transistor areas in their laser/driver structure (8). Although these proposed methods have appreciably improved photolithographic reproducibility, the success of these processes requires a high controllability of the etch and refill procedure and the uniformity of the wafer, which are not easy to achieve primarily because of the complicated cross-sectional structure of the refilled epitaxial layer particularly at the well periphery.

The purpose of this paper is to describe a new OEIC fabrication technique, in which the mesa steps are degraded in a well-controlled fashion and the reproducibility of fine pattern lithography is significantly improved (18). The present technique uses Ar ion-beam etching to produce graded steps so that good control of the etch depth and therefore of the step slope, and also a high uniformity of these parameters over the wafer, can be facilitated. A small slope angle achieved by this technique prevents complicated overgrowth, such as ridges at the substrate well periphery, and simplifies the subsequent photolithographic steps. The use of Ar ion-beam etching to control the slope angle is essentially based on our previous success of fabricating InP microspherical lenses on InGaAsP/InP double heterostructure light emitting diode wafers (19, 20). This method has been now extended to OEIC fabrication in AlGaAs/GaAs system (18). Optimization of two fundamental procedures to form graded steps on the OEIC substrate, namely, the preparation of photoresist mask and the Ar ion-beam etching, has been performed in this study and applied to fabricate AlGaAs/GaAs monolithic photoreceivers.

In the next section, we report the method of obtaining graded steps on a GaAs substrate. The effect of grading on photolithography will be discussed in the third section. The Application section describes the application of the present technique to fabricate OEIC's, in which a

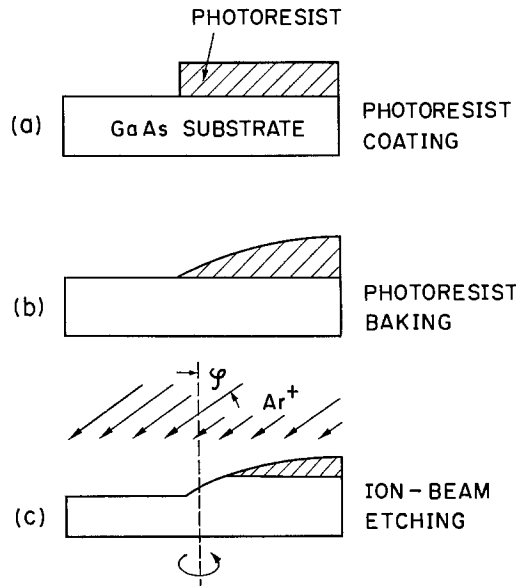


Fig. 1. Fundamental sequence of graded-step process. A mask for Ar ion-beam etching is produced by deforming a photoresist layer at high temperature, and the edge profile of the mask is transferred to the substrate surface.

monolithic AlGaAs/GaAs PIN/FET and also a PIN/amplifier are demonstrated.

Graded-Step Process

The essential procedure for forming graded steps on a substrate is shown in Fig. 1. Photoresist masks for ion-beam etching are first prepared on the GaAs substrate surface Fig. 1a. A commercially available positive acting photoresist, Shipley AZ-4620, has been used in our study. The photoresist patterns with the width appropriate to the device design are delineated by conventional photolithographic technique. They are subsequently baked at a temperature higher than the glass-transition point of photoresist so that rounded contours are generated by the effect of surface tension on the photoresist surface (20). Then the substrate is subjected to Ar ion-beam etching Fig. 1b using, in this experiment, Veeco Microetch system in which Ar⁺ ions are generated by a Kaufman ion gun, neutralized, and then fed to bombard a rotating target. During the etching, the rounded mask contour is transferred to the substrate surface. The shape of the step is dependent on the initial photoresist thickness and the photoresist to substrate ion-beam etch rate ratio which is a function of etching parameters such as the ion incident angle ϕ . The morphology of the etched surface is of the

greatest importance in device applications, and it has to be optimized by choosing suitable etching conditions, as will be described later. By terminating the ion-beam etching when the substrate is etched down to appropriate depth, a graded step can be obtained (Fig. 1c).

In order to obtain a sufficient controllability of the step geometry, it is important to know the deformation behavior of photoresist baked at an elevated temperature. Figure 2 shows the height (h) of the photoresist stripe pattern measured at the center of the stripe width (W) as a function of the baking temperature. The initial resist thickness used was approximately 6.5 μm . The baking was carried out under nitrogen gas flow for 10 min. When the temperature was below 100°C, a concave resist cross section appeared to exhibit a height smaller than the initial value. As the temperature increases, a convex cross section is achieved, as is shown in Fig. 2. The convex shape has been confirmed from stylus measurement to be precisely a part of a cylinder, which is consistent with the fact that the surface tension dominates, stabilizing the resist geometry (20). The temperature for cylindrical deformation is observed to increase with the increase of the pattern width. It is also found that the height variation with the temperature becomes weaker as the pattern width increases. Strong height decreases observed near 200°C, particularly for narrow patterns, would suggest the occurrence of resist decomposition and/or evaporation. It is shown from the present result that the resist geometry can be readily controlled within the accuracy of a few tenths of a micron by using the width of 80-100 μm baking near 200°C. When it is necessary to protect an area of the substrate wider than the stripe, one can use an additional resist layer overlying partly the stripe pattern.

Another important parameter for controlling the step geometry is the ion-beam etch rate ratio between the resist and the substrate. We measured the etch rates of AZ-4620 resist and GaAs as a function of the ion incident angle. The result is shown in Fig. 3 together with their ratio. The ion energy and the current density were kept constant at 500 eV and 0.57 mA/cm², respectively, in this experiment. The etch rate ratio is found to vary monotonically in a wide range from 0.22 to 0.7 by increasing the incident angle from 0° to 70°.

In principle, by combining the resist deformation characteristic and the etch rate ratio variation with the incident angle, one can produce steps with arbitrary geometries on the GaAs substrate. However, the etched surface morphology is known to be affected by the ion-beam etching conditions, particularly by the ion incident angle. This effect has been actually found in our previous study of InP etching (19-21), but no data are available for GaAs,

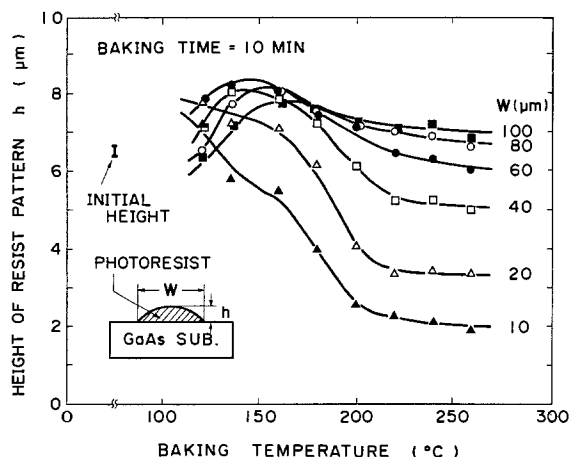


Fig. 2. Photoresist height measured at pattern center as a function of baking temperature for a variety of pattern widths. The initial pattern height is 6.4 μm in this case.

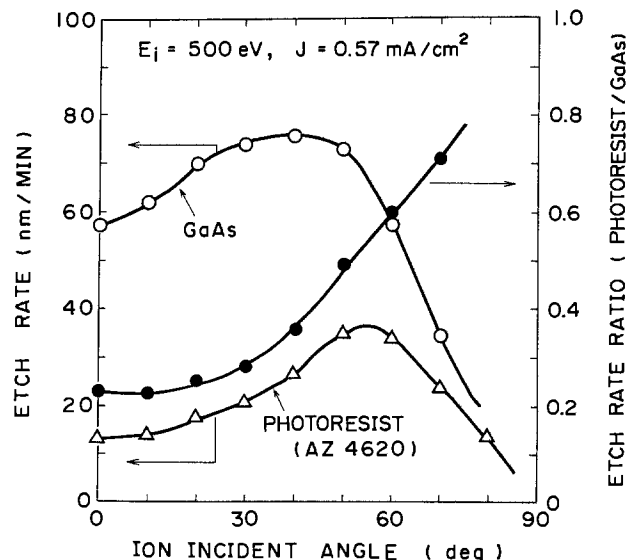


Fig. 3. Ar ion-beam etching rates of GaAs and photoresist and their ratio vs. ion incident angle.

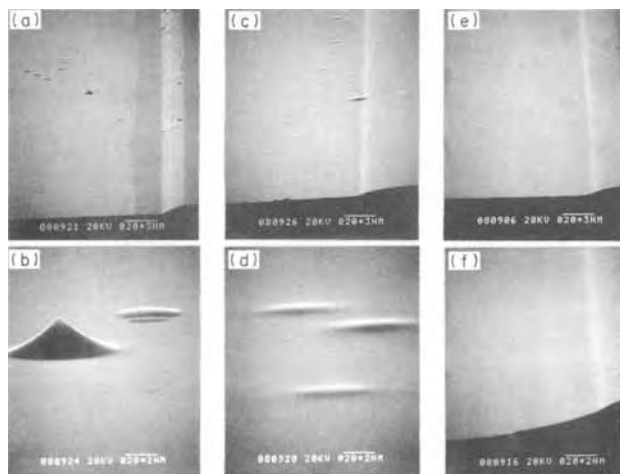


Fig. 4. Scanning electron micrographs showing ion-beam etched surfaces of GaAs. The ion incident angles used are 50° (a, b), 60° (c, d), and 70° (e, f). The ion energy and the current density are 500 eV and 0.57 mA/cm^2 , respectively. The etched depth is approximately $7\text{ }\mu\text{m}$ throughout. The bars in a, c, and e indicate $2\text{ }\mu\text{m}$ scale and in b, d, and f $0.2\text{ }\mu\text{m}$ scale. Note that the etched surface becomes defect free at the incident angle of 70° .

particularly for large etching depth, as would be required in OEIC applications. We attempted to correlate the etched surface morphology with the ion incident angle for a fixed etching depth of $7\text{ }\mu\text{m}$ using the ion energy of 500 eV and the current density of 0.57 mA/cm^2 . In this measurement, we used a substrate holder, as shown in the inset of Fig. 5, which lifts up the substrate to prevent it from being exposed to foreign material atoms sputtered during etching (20, 22). Figure 4 gives a set of scanning electron micrographs showing the GaAs surfaces etched at the ion incident angle of 50° (Fig. 4a, 4b), 60° (Fig. 4c, 4d), and 70° (Fig. 4e, 4f). At the incident angle of 50° , numerous low bumps with the diameter around a few microns are found on the etched surface, some of which form cones, as seen in Fig. 4b. The generation of bumps and cones is presumed to be attributed to the local masking effect (23) brought about by either the residual contamination existing on the surface prior to etching or foreign materials such as sputtered materials redepositing on the surface being etched (20). Column III atoms, Ga in

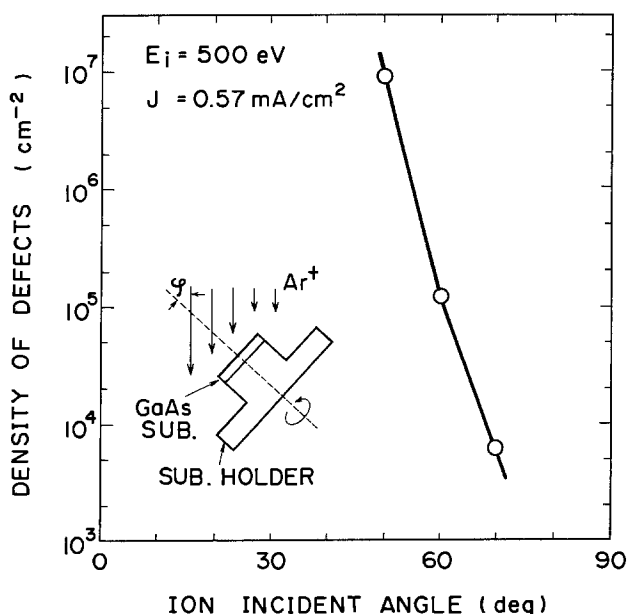


Fig. 5. Density of surface defects observed under microscope plotted vs. ion incident angle. The etching parameters used are same as in Fig. 4. The inset shows schematically the substrate holder used which can lift up the substrate surface for preventing the redeposition effect.

this case, accumulate at the etched surface of III-V semiconductors (27) to eventually form Ga droplets on the surface during prolonged etching. These may contribute to generate a strong masking effect to form bumps and cones as observed here. However, surface defects observed here have very small heights, differing from the feature found for high energy (40 keV) Ar ion bombardment at normal incidence (25). The nature of defect formation during ion-beam etching seems quite complicated, and further studies are required for fully understanding mechanisms of their formation. In practical view, however, glancing ion-beam incidence as has been used here is presumed to be significantly effective for smoothing the surface bumps. The mechanism of surface smoothing during ion bombardment has been discussed previously (25). The surface for the incident angle of 60° exhibits smoother morphology. Although some bumps are observed to remain, their contours are much rounded, as shown in Fig. 4d. By further increasing the incident angle to 70° , the surface smoothness is significantly improved. The number of such surface defects counted under microscope is plotted as a function of the ion incident angle in Fig. 5. The defect density is reduced down to 5000 cm^{-2} at 70° . This is close to the etch pit density of standard boat-grown GaAs crystals, and no additional effect of these ion-beam-generated defects on the device processing is anticipated. Moreover, these residual defects can be removed by carrying out solution etching of the substrate after ion-beam etching. Taking these into account, we have used in the following experiments the ion incident angle of 70° - 75° and short-time etching by $\text{H}_2\text{SO}_4 \cdot \text{H}_2\text{O}_2 \cdot \text{H}_2\text{O}$ system after the ion bombardment. The depth of surface damage production by ion-beam bombardment is expected to be less than 200 nm for GaAs at the ion energy of 500 eV (26). It has also been shown on III-V semiconductors ion-beam etched that the surface composition is modulated by the occurrence of column V atom dissociation and column III atom accumulation (20, 21, 27, 28). The solution etching employed after the ion-beam etching is effective for both smoothing the surface and removing damages.

Effect of Grading Steps in Photolithography

When photoresist technique is applied to the substrate having steps on its surface, the thickness of the photoresist varies at these steps and this causes the degradation of pattern defined by conventional contact lithographic apparatus. Photomicrographs showing such thickness variation at the step are given in Fig. 6. The step shown in Fig. 6a was formed by etching with a solution of $8\text{H}_2\text{O}_2 + 1\text{H}_2\text{SO}_4 + 1\text{H}_2\text{O}$, and the step in Fig. 6b was by the present graded-step process. The step height (d_s) is $7\text{ }\mu\text{m}$ for each, and the slope angles (θ) generated are approximately 45° and 13° for Fig. 6a and 6b, respectively. The photoresist (Microposit 1300-31) spin coated has a thickness of $2\text{ }\mu\text{m}$ when measured on the planar surface. The resist depletion at the top and the resist accumulation at the bottom of the slope are shown in Fig. 6a, and these effects are markedly reduced in Fig. 6b. The resist thicknesses, d_1 at the upper and d_2 at the lower surface, measured as a function of θ are plotted in Fig. 7 for two different values of the resist thickness on the planar surface. When a thicker ($d_0 = 3.4\text{ }\mu\text{m}$) resist is used, the step coverage is realized, but the resist thickness difference between above and below the step is more than $3\text{ }\mu\text{m}$ for every θ value examined. However, the thinner ($d_0 = 2\text{ }\mu\text{m}$) resist cannot cover the step edge for θ larger than 40° . However, the resist thickness difference $d_2 - d_1$ of only $1.4\text{ }\mu\text{m}$ is obtained by decreasing θ to 13° . In previous OEIC structures often having steep and high mesa steps on the substrate, it has been inevitable to thicken the resist layer for complete coverage. It has been shown from the present result that the use of a thin resist is allowed and the thickness variation at steps is reduced by grading steps.

Figure 8 shows scanning electron micrographs showing resist patterns delineated across steps with a height of $7\text{ }\mu\text{m}$ formed by solution etching (Fig. 8a) and the present

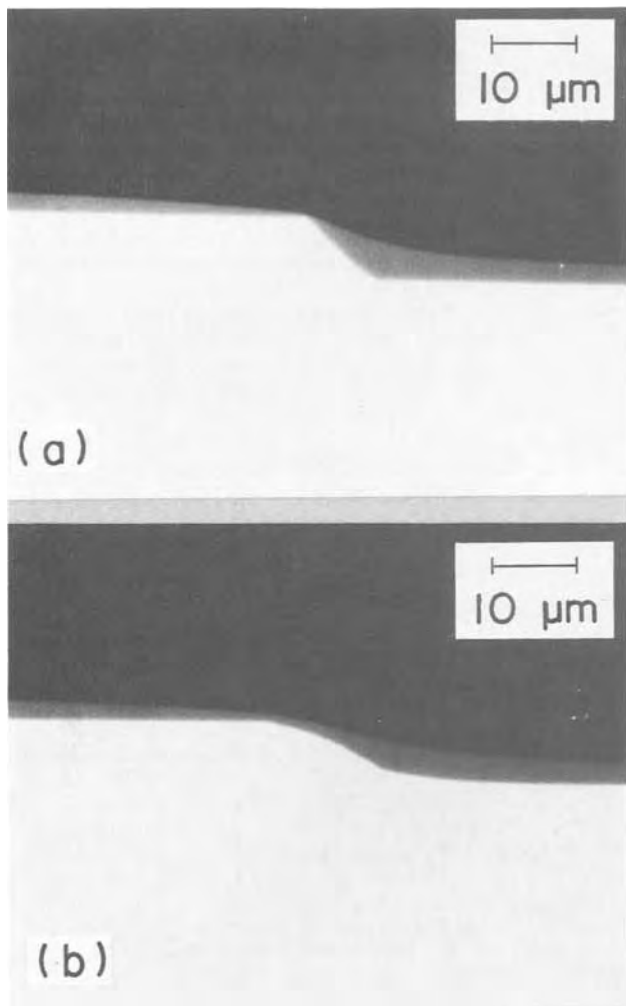


Fig. 6. Photomicrographs showing photoresist thicknesses on substrate steps having slope angle of 45° (a) and approximately 13° (b). It is clearly shown that the thickness uniformity is significantly improved by grading steps.

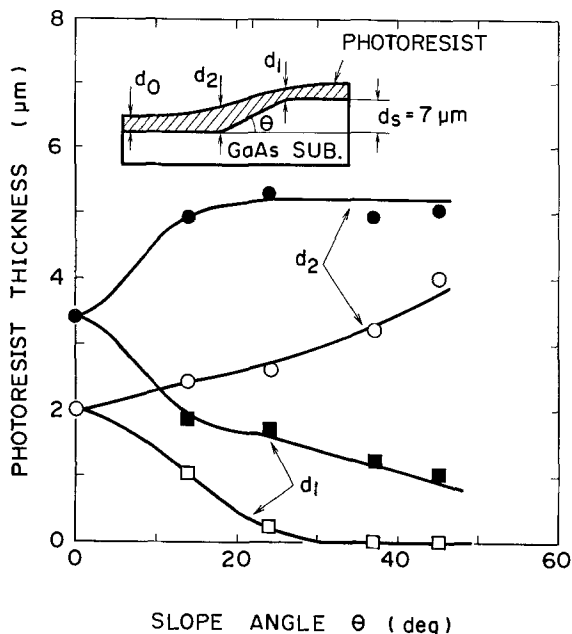


Fig. 7. Dependence of photoresist thicknesses at slope top (d_1) and bottom (d_2) on slope angle θ for two different levels of thickness measured in planar region (d_0). The difference, $d_2 - d_1$, is observed to be greatly reduced by using a graded step and a thin resist layer.

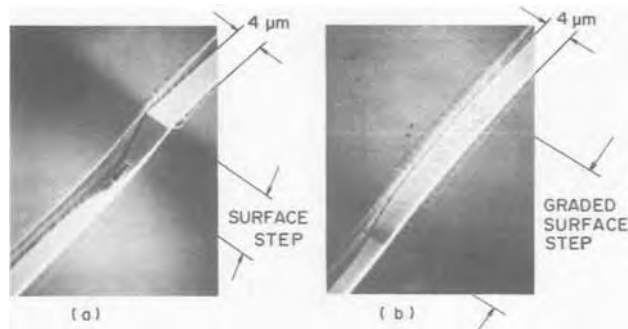


Fig. 8. Scanning electron micrographs showing resist patterns defined across substrate steps having slope angle of 45° (a) and 13° (b), respectively. A resist residue at the slope bottom in a indicates the difficulty of patterning process. The graded step in b is free from this problem.

graded-step process (Fig. 8b), respectively, corresponding to Fig. 6a and 6b. The resist thicknesses used are 3.4 and 2 μm , respectively. It is seen in Fig. 8a that resist residue exists at the slope bottom. Prolonged exposure has been observed to remove the resist residue but simultaneously cause a severe pattern widening at the slope top. The pattern defined across the graded step (Fig. 8b) shows no such problems. Figure 9 summarizes the result of pattern size deviations with respect to the mask pattern width, ΔW_0 on the planar part of the substrate, ΔW_1 at the slope top, and ΔW_2 at the slope bottom, measured as a function of the slope angle for two different resist thickness (d_0) values. In this measurement, the exposure time was adjusted for pattern improvement with the development time kept nearly constant. As shown in Fig. 9, the pattern width difference between the top and the bottom of the slope is in excess of 3.5 μm at θ larger than 40°, and it is reduced well below 0.5 μm by using the resist thickness of 2 μm and the value of θ of 13°. Thus the results shown in Fig. 8 and 9 demonstrate the superiority of graded steps for fine pattern lithography.

The quality of photoresist pattern when defined by contact lithography is sensitive to both the resist thickness and the mask to resist surface separation primarily

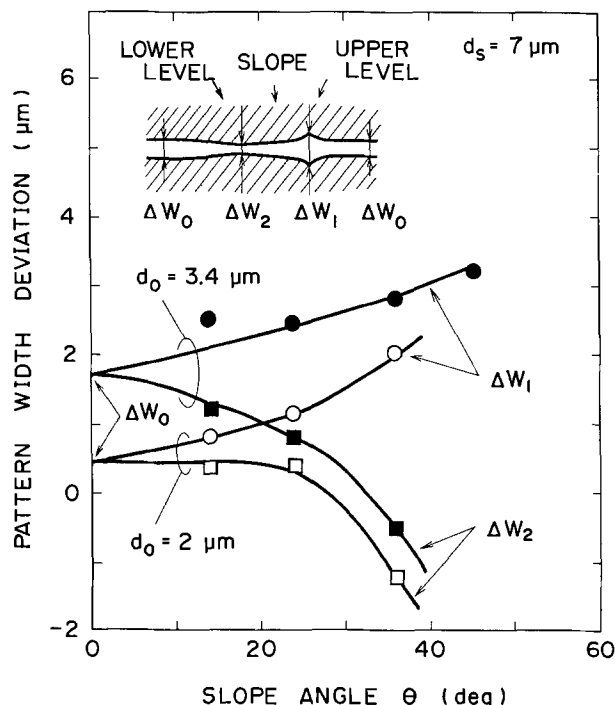


Fig. 9. Relation of deviations of resist pattern widths at slope top (ΔW_1) and slope bottom (ΔW_2) with respect to mask width as a function of slope angle for two different resist thicknesses. The effect of grading steps in improving the width fidelity is obvious. d_0 is defined to be the photoresist thickness measured in the planar region.

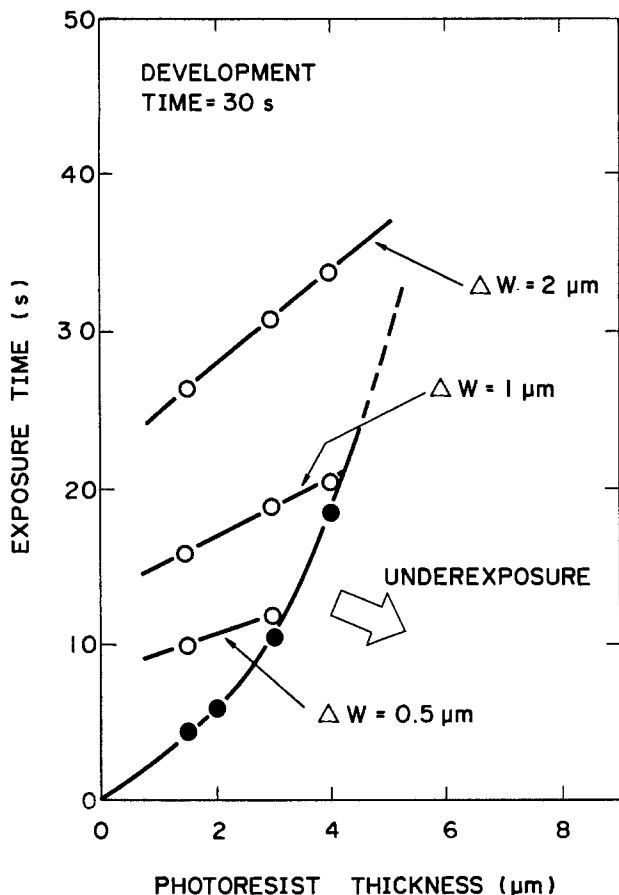


Fig. 10. Relation of exposure time with photoresist thickness at fixed development time. Closed circles show minimum exposure for pattern delineation, and open circles indicate overexposure which exhibit deviations of pattern widths with respect to the mask width as indicated by ΔW . The graded-step process examined here enables the use of exposure time at 8s, whereas the conventional 45° step needs the exposure time near 30s.

due to light diffraction. In view of the results of resist pattern definition described above, we attempted to correlate the pattern size difference observed at the top and the bottom of the step with the resist processing conditions. Figure 10 shows the exposure time required for pattern definition as a function of the thickness of the resist coated on a planar substrate for a constant resist development time of 30s. The minimum exposure time increases sharply as the resist thickness increases, reflecting an exponential decrease of light intensity along the resist depth. Additional plots and lines shown in the figure represent how large deviation (ΔW) of pattern width is produced by overexposure. It is only when the resist thickness of below $2 \mu\text{m}$ is used with minimum exposure time that no pattern width deviation is detected. At the resist thickness of $4 \mu\text{m}$, for example, even the minimum exposure for 20s produces width deviation of $1 \mu\text{m}$. We can estimate by using this characteristic together with Fig. 7 the pattern width deviation to be generated for a variety of slope angles. For the solution-etched step with $\theta = 45^\circ$, the resist layer of thickness $3.4 \mu\text{m}$ in the planar region is needed for obtaining usable step coverage. This causes a resist accumulation of $5 \mu\text{m}$ at the bottom and a thickness reduction to $1 \mu\text{m}$ at the top of the mesa slope, as shown in Fig. 7. The thickness of $5 \mu\text{m}$ is found from Fig. 10 to require the minimum exposure time of approximately 30s. However, this causes a significant overexposure to produce a pattern width deviation from the mask size at the top of the mesa slope. The amount of this is expected to be more than $2 \mu\text{m}$ as indicated in Fig. 10. However, actual pattern width deviation observed between the top and bottom surfaces is much more than $4 \mu\text{m}$, as shown in Fig. 9. For the graded step with $\theta = 13^\circ$, the same proce-

dures for a $2 \mu\text{m}$ thick resist gives the minimum exposure time of 8s and the pattern width deviation becomes smaller than $0.5 \mu\text{m}$, which agrees fairly well with the result shown in Fig. 9. Thus when the step is well graded so that the resist thickness is minimized, the pattern size deviation is reduced and its value can be expected directly from the exposure conditions. On the contrary, when the step becomes steep and the resist is thickened, the deviation becomes significantly more than expected from the thickness effect. This is presumed to be attributed to the second-order effects such as the light diffraction enhancement due to the mask to resist gap increase at the slope bottom and the overdevelopment effect at the slope top. The discussion made above confirms the usefulness of graded steps in fine pattern definition; they reduce the pattern width deviation less than $0.5 \mu\text{m}$ for the step height of $7 \mu\text{m}$.

Application to OEIC Fabrication

The graded-step process enables the use of thin photoresist layers for a series of photolithographic processes involved in OEIC fabrication so that sufficiently fine device geometries can be produced for both optical and electronic elements. This is particularly significant in OEIC's such that mesa step formation for epitaxial structure isolation is carried out in early stages of the fabrication procedure. This advantage of the present process has been used in fabricating monolithic PIN/FET and PIN/amplifier circuits on GaAs substrates. In the present fabrication, a horizontally integrated structure has been adopted, in which the photodiode and the FET's are all prepared on the semi-insulating (SI) GaAs substrate surface. This structure is advantageous in eliminating parasitic reactances which degrade the circuit performances such as the response time, as has been often experienced in assembling discrete elements.

Figure 11 illustrates the sequence of fabrication procedure. A channel was formed on a (100) orientated surface of SI-GaAs substrate using the graded-step process. The step height produced is typically $7\text{--}8 \mu\text{m}$. Then the growth of the photodiode structure consisting of a $2.5 \mu\text{m}$ thick n^+ -GaAs contact layer (Se-doped, $n = 10^{18} \text{cm}^{-3}$), a $2.5 \mu\text{m}$ thick n^- -GaAs photoabsorption layer (undoped, $n \leq 10^{15} \text{cm}^{-3}$) and a $0.5 \mu\text{m}$ thick high resistivity (HR) $\text{Al}_{0.3}\text{Ga}_{0.7}\text{As}$ window layer was performed over the whole surface of the substrate by metal-organic chemical vapor deposition (MO-CVD) as in our previous studies (29). The PIN photodiode mesa structure was delineated within the channel by removing the unwanted parts of the epitaxial structure using the graded-step process. Then the FET layers consisting of a $0.7 \mu\text{m}$ thick undoped-GaAs buffer layer and a $0.35 \mu\text{m}$ thick n -GaAs (Se-doped, $n = 1 \times 10^{17} \text{cm}^{-3}$) channel layer were prepared by MOCVD. The channel mesas were delineated again by the graded-step process. Subsequently, the PIN photodiode and the

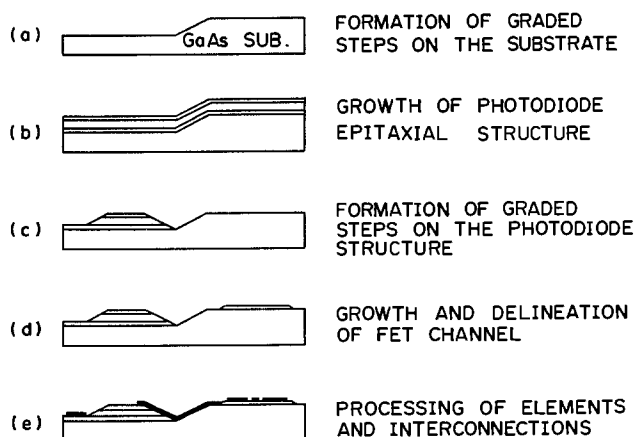


Fig. 11. Fabrication sequence of PIN/FET and PIN/amplifier circuits. The graded-step process is used in every step (except b).

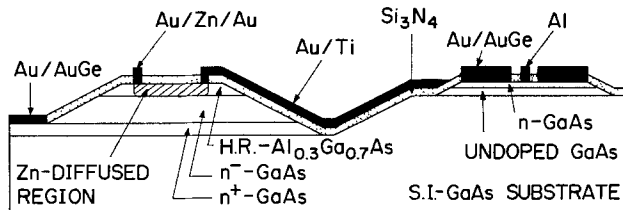


Fig. 12. Schematic cross section of AlGaAs/GaAs monolithic photoreceiver. The graded-step process has been extensively used in constructing this structure. The PIN photodiode and the FET are both formed horizontally and directly on a Si-GaAs substrate, and this configuration eliminates parasitic capacitances.

FET's were processed and the interconnections between the PIN photodiode and the front-end FET as well as among FET's were formed.

The detailed cross section of the monolithic photoreceiver is shown Fig. 12. The p-type region was formed by diffusing Zn into the HR AlGaAs layer to reach the AlGaAs-GaAs interface. Lifting off and subsequent alloying of Au/AuGe and Au/Zn/Au composite films were carried out for forming n- and p-type ohmic contacts, and the Schottky barriers were made by lifting off Al films. The FET's formed in this circuit had recessed-gate structures with the recess depth of approximately $0.15 \mu\text{m}$. The interconnections between the photodiode and the FET and within the amplifier were all formed by lifting off Au/Ti. Silicon nitride films were used for both forming antireflection coating of the photodiode and passivating FET channels. Figure 13 shows scanning electron micrograph of the processed PIN/FET chip. The PIN photodiode has the photosensitive area of $100 \mu\text{m}$ diam, and the FET channel width is $80 \mu\text{m}$. It is demonstrated in this figure that the PIN-FET interconnection and the FET gate contact are successfully formed over the mesa steps, respectively, having widths of 8 and $2 \mu\text{m}$. Figure 13b shows the interconnection exhibiting no pattern size degradation.

The performance of the fabricated PIN/FET was analyzed with the circuit shown in Fig. 14 under dc bias application of $V_1 = 10\text{V}$ and $V_2 = 4\text{V}$. The dark current of the PIN photodiode was less than 10 nA , and a high quantum efficiency of approximately 70% was observed. The pinch-off voltage was -2.5V , and the transconductance of 80 mS/mm were achieved in the present FET owing to the application of the recessed-gate structure. The current amplification characteristic was measured and the current amplification ratio of 1.4 was determined, which is consistent with the PIN load resistance of 200Ω multiplied by the FET transconductance of 6.5 mS . The pulse response measurement was carried out using a $0.85 \mu\text{m}$ wavelength AlGaAs/GaAs laser diode. The upper trace in Fig. 15 shows the driving current of the laser, and the lower one the FET drain current. The rise and fall time

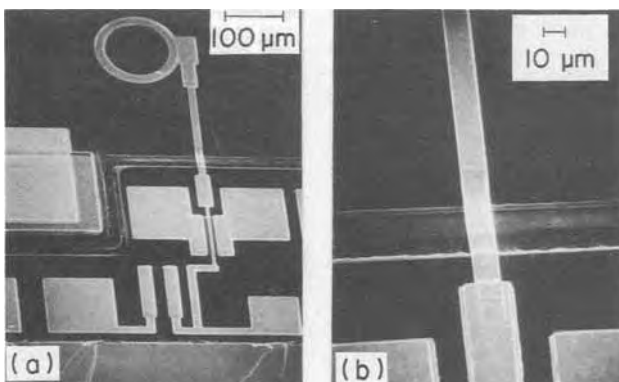


Fig. 13. Scanning electron micrographs showing PIN/FET chip fabricated by the present technique. The PIN-FET interconnection has been successfully formed across $8 \mu\text{m}$ deep steps. Also a $2 \mu\text{m}$ long FET gate has been facilitated.

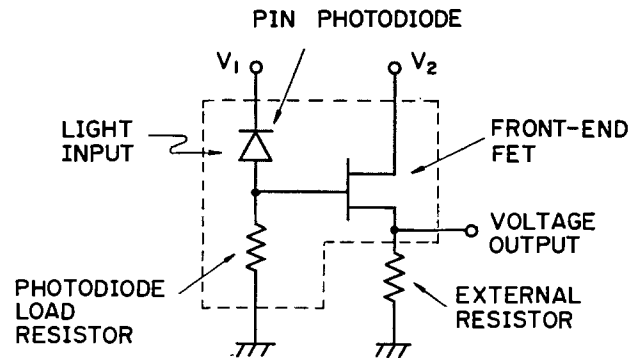


Fig. 14. Diagram of measurement circuit for monolithic PIN/FET. The dotted line indicates the part of monolithic integration.

can be determined to be as small as 0.6 ns from the lower trace. These compare well with the calculation, 0.57 ns , which was made by the sum of the capacitances of the photodiode (1.0 pF) and the FET gate (0.3 pF) and the load resistance.

We previously integrated similar PIN/FET in a form of vertical structure in which the FET layers are positioned above the PIN epitaxial structure with an intermediate high resistivity layer to isolate them (29). The response time of such vertical PIN/FET was observed to be degraded appreciably when the isolation layer becomes thinner than $5 \mu\text{m}$, due to the parasitic capacitance induced between the upper FET layer and the lower conductive (n^+) layer in the PIN structure. No such parasitic capacitance is expected in the present horizontal structure, and the result described above is considered to have demonstrated this advantage of the horizontal structure.

Figure 16 shows the photomicrograph and the circuit diagram of the PIN/amplifier photoreceiver chip. The chip size is $1.6 \times 1.0 \text{ mm}$. In this circuit design, a feedback amplifier including a monolithic resistor and an output buffer to ECL has been adopted. The circuit response analyzed under the application of laser light revealed the rise and fall time to be approximately 1.0 ns , which is consistent with the expectation made by the total capacitance of the PIN photodiode and FET gate (1.35 pF) and the feedback resistor ($1.3 \text{ k}\Omega$). This has again confirmed the elimination of parasitic capacitances in the present integrated structure. The details of the performance analysis are reported in a separate paper (30).

Summary

A new OEIC fabrication technique incorporating a graded-step process has been developed. This process has enabled the formation of steps on the semiconductor sub-

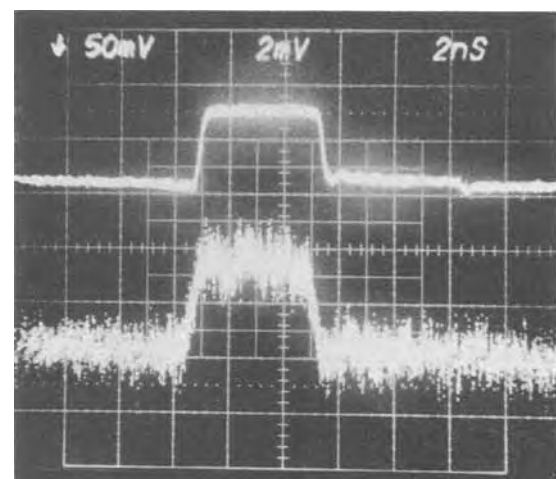


Fig. 15. Oscilloscope traces of current for source laser (upper trace) and output current of PIN/FET (lower trace), indicating fast rise and fall time of 0.6 ns of the present PIN/FET.

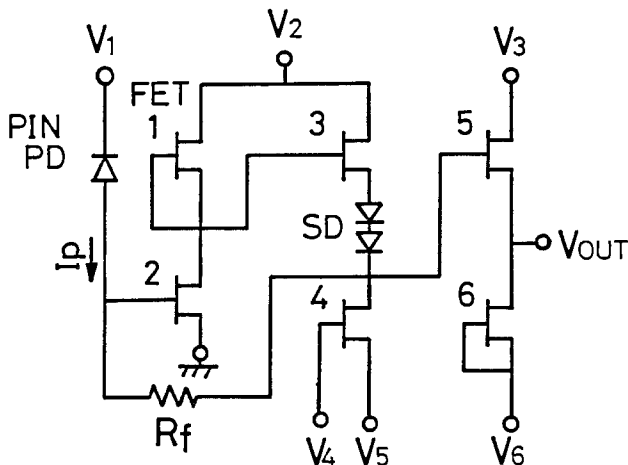
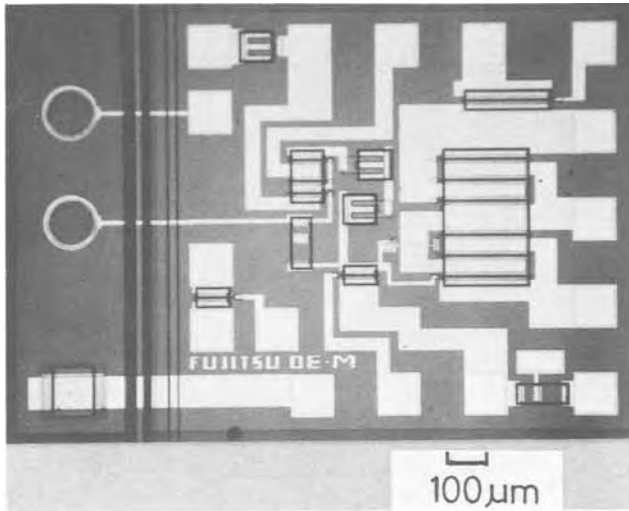


Fig. 16. Photomicrograph (a) and circuit diagram (b) of monolithic PIN/amplifier photoreceiver fabricated by using the present graded-step process.

strate with their slopes much graded, down to the slope angle of 13° , which has not been possible by conventional solution etching. The mask formation and the subsequent Ar ion-beam etching procedures have been optimized for the application to OEIC fabrication. Significant effects of grading substrate steps have been demonstrated in defining fine patterns on the substrate using contact lithography. The graded steps have enabled one to use a thin resist layer, and therefore the pattern size deviation has been markedly reduced. The application of this process to fabricating AlGaAs/GaAs PIN/FET and PIN/amplifier circuits has confirmed a successful and reproducible operation of this process to generate fine device geometries such as $8\ \mu\text{m}$ interconnections and $2\ \mu\text{m}$ gate contacts, regardless of the existence of PIN photodiode mesa as high as $8\ \mu\text{m}$.

The present result has demonstrated the usefulness of this process in OEIC fabrication. When the mesa steps are formed at early stage in the fabrication process sequence, as in most cases of OEIC fabrication, the improvement of photolithographic reproducibility by the present process can contribute enormously to increase in overall fabrication reproducibility and yield. Such an advantage of the present process could play an increasingly important role in extending the integration scale of OEIC's.

Acknowledgments

The authors are grateful to H. Hamaguchi, M. Makiuchi, and T. Touge for useful discussions and to T. Nakagami and K. Dazai for encouragement. The present research effort is part of a major research and development project on optical measurement and control systems conducted under a program set up by the Ministry of International

Trade and Industry's Agency of Industrial Science and Technology.

Manuscript submitted Jan. 2, 1985; revised manuscript received April 23, 1985.

Fujitsu Laboratories assisted in meeting the publication costs of this article.

REFERENCES

1. N. Bar-Chaim, S. Margalit, A. Yariv, and I. Ury, *IEEE Trans. Electron Devices*, **ed-29**, 1372 (1982).
2. U. Koren, S. Margalit, T. R. Chen, K. L. Yu, A. Yariv, N. Bar-Chaim, K. Y. Lau, and I. Ury, *IEEE J. Quantum Electron*, **qe-18**, 1653 (1982).
3. I. Hayashi, in "Technical Digest of the Fourth International Conference on Integrated Optics and Optical Fiber Communication 1983," p. 170, The Institute of Electronics and Communications Engineers of Japan, Tokyo (1983).
4. O. Wada, T. Sanada, H. Hamaguchi, T. Fujii, and T. Sakurai, *Appl. Phys. Lett.*, **43**, 345 (1983).
5. H. Matsuuda, S. Sasaki, and M. Nakamura, *IEEE J. Lightwave Technol.*, **lt-1**, 261 (1983).
6. H. Matsuuda and M. Nakamura, *Appl. Opt.*, **23**, 779 (1984).
7. T. Sanada, S. Yamakoshi, O. Wada, T. Fujii, T. Sakurai, and M. Sasaki, *Appl. Phys. Lett.*, **44**, 325 (1984).
8. J. Shibata, I. Nakao, Y. Sasai, S. Kimura, N. Hase, and H. Serizawa, *ibid.*, **45**, 191 (1984).
9. J. K. Carney, M. J. Helix, and R. M. Kolbas, in "GaAs IC Symposium 1983, Phoenix," Technical Digest, p. 48, IEEE, Piscataway, NJ (1983).
10. M. E. Kim, C. S. Hong, D. Kasemset, and R. A. Milano, in "GaAs IC Symposium 1983, Phoenix," Technical Digest, p. 44 (1983).
11. K. Kasahara, J. Hayashi, and H. Nomura, *Electron. Lett.*, **20**, 619 (1984).
12. R. M. Kolbas, J. Abrokwhah, J. K. Carney, D. H. Bradshaw, B. R. Elmer, and J. R. Biard, *Appl. Phys. Lett.*, **43**, 821 (1983).
13. O. Wada, S. Miura, M. Ito, T. Fujii, T. Sakurai, and S. Hiyamizu, *ibid.*, **42**, 380 (1983).
14. R. F. Leheny, R. E. Nahory, M. A. Pollack, A. A. Ballman, E. D. Beebe, J. C. Dewinter, and R. L. Martin, *Electron. Lett.*, **16**, 353 (1980).
15. K. Kasahara, J. Hayashi, K. Makita, K. Taguchi, A. Suzuki, H. Nomura, and S. Matsushita, *ibid.*, **20**, 315 (1984).
16. K. Inoue, K. Ohnaka, T. Uno, N. Hase, and H. Serizawa, in "Fourth International Conference on Integrated Optics and Optical Fiber Communication 1983, Tokyo, Technical Digest," p. 186, The Institute of Electronics and Communications Engineers of Japan, Tokyo (1983).
17. A. S. H. Liao, T. J. Bridges, E. G. Burkhardt, B. Tell, R. F. Leheny, and E. D. Beebe, p. 479, Technical Digest of the International Electron Devices Meeting 1983, Washington, DC, IEEE, Piscataway, NJ (1983).
18. O. Wada, T. Sanada, H. Machida, S. Yamakoshi, H. Hamaguchi, T. Fujii, T. Horimatsu, and T. Sakurai, Late News Abstract, p. 16, Abstracts of the 16th (1984 International) Conference on Solid State Devices and Materials, Kobe, Japan, Japanese Society of Applied Physics, Aug. 30-Sept. 1, 1984.
19. O. Wada, S. Yamakoshi, M. Abe, Y. Nishitani, and T. Sakurai, *IEEE J. Quantum Electron*, **qe-17**, 174 (1981).
20. O. Wada, *This Journal*, **131**, 2373 (1984).
21. O. Wada, *J. Phys. D*, **17**, 2429 (1984).
22. R. S. Williams, R. J. Nelson, and A. R. Schlier, *Appl. Phys. Lett.*, **36**, 827 (1980).
23. I. H. Wilson and M. W. Kidd, *J. Mater. Sci.*, **6**, 1362 (1971).
24. I. Ishitani, M. Kato, and R. Shimizu, *ibid.*, **9**, 505 (1974).
25. I. H. Wilson, *Rad. Eff.*, **18**, 95 (1973).
26. M. Kawabe, N. Kanzaki, K. Masuda, and S. Namba, *Appl. Opt.*, **17** (1978).
27. R. S. Williams, *Solid State Commun.*, **41**, 153 (1982).
28. P. Rabinzohn, G. Gautherin, B. Agins, and C. Cohen, *This Journal*, **131**, 905 (1984).
29. S. Miura, O. Wada, H. Hamaguchi, M. Ito, M. Makiuchi, K. Nakai, and T. Sakurai, *IEEE Electron Device Lett.* **edl-4**, 375 (1983).
30. O. Wada, H. Hamaguchi, S. Miura, M. Makiuchi, K. Nakai, H. Horimatsu, and T. Sakurai, *Appl. Phys. Lett.*, **46**, 981 (1985).



Reports on the Energy Research Summer Fellowship Awards



Cathryn Goodman



Gary A. Reitz



Holly-Dee Rubin



Hal Van Ryswyk

For the summer of 1984, the following students were awarded Energy Research Summer Fellowships. Each award carried with it a grant of \$2000.

Ms. Cathryn Goodman, of Northwestern University, Evanston, Illinois.

Mr. G. A. Reitz, of the University of Texas, Austin, Texas.

Ms. Holly-Dee Rubin, of Princeton University, Princeton, New Jersey.

Mr. Hal Van Ryswyk, of the University of Wisconsin, Madison, Wisconsin.

The Energy Research Summer Fellowship Awards are made "without regard to sex, citizenship, race, or financial need. They are made to graduate students pursuing work between the degrees of B.S. and Ph.D., in a college or university in the United States or Canada." The recipients' projects are in fields relating to energy research or of interest to The Electrochemical Society. The Awards are sponsored by the Department of Energy and made by the Summer Fellowship Committee of The Electrochemical Society.

Cathryn Goodman received her B.S. degree in Ceramic Engineering from the University of Illinois, Champaign-Urbana in 1981. Following graduation, she worked as a process engineer in the hybrid circuit development laboratory of Motorola, Incorporated, in Franklin Park, Illinois. She is currently a Ph.D. candidate at Northwestern University in Evanston, Illinois. Her thesis topic concerns the characterization of surface states at the semiconductor/electrolyte interface.

Ms. Goodman's report is given below.

Characterization of Surface States at the InP/Liquid Interface

Photoelectrochemical (PEC) cells offer one of the most promising methods for converting solar energy into useful chemical fuels. The primary components of a PEC cell are a semiconductor photoelectrode, an electrolytic solution, and a metal counterelectrode. The energy difference between the redox potential of the redox couples in the electrolyte and the Fermi level in the semiconductor produces a depletion region in the semiconductor at the electrode/electrolyte interface. The depletion region separates charge carriers that are photogenerated near the semiconductor surface before they can recombine. Minority carriers are swept to the interface, where they can take part in a redox reaction. Conversely, majority carriers are swept to the counterelectrode through the external circuit, where they can take part in a different reaction. The net result is the conversion of light energy to chemical free energy. Because of their potential for practical applications, many studies have been conducted to optimize the efficiency of PEC cells (1-7). One particularly promising system involves the production of hydrogen using a p-InP photocathode.

Several properties of p-InP make it a good choice for use as a photocathode in PEC cells. First, the bandgap of the semiconductor used as a photocathode must be small enough to allow for a significant portion of the solar spectrum to generate electron-hole pairs and yet be large enough to straddle the appropriate redox energy levels (H^+/H_2 and O_2/H_2O for photohydrolysis). The efficiency of the cell is optimized when the bandgap of the semiconductor is 1.3 eV (8). Therefore, the bandgap of InP, 1.35 eV, makes it an ideal choice for this purpose. Second, the stability of the electrode is an important factor in determining cell performance. The use of a p-type material is advantageous because the electrons that are swept to the surface of the electrode cathodically protect it against oxidation. Since the products of reductive corrosion reactions are thermodynamically less stable than oxidation products (5), photoelectrodes made of p-type materials are inherently less subject to corrosion than n-type photoelectrodes.

Indeed, several PEC cells with p-InP photoelectrodes have been developed with efficiencies as high as 16% (3, 4, 6, 7). The key factor in obtaining these high efficiencies was the development of surface treatments for the semiconductor electrode. The surface treatment of the semiconductor photoelectrode is important to cell efficiency because of the role that surface states perform in PEC cell operation. The presence of surface states associated, for example, with native defects or adsorbed species can act as charge carrier traps, recombination centers, or intermediate states for charge transfer.

It was previously concluded that the InP surface treatments increased the efficiency of the PEC cells by altering the surface states (5). This suggests that the efficiency of a PEC cell can be maximized only if these surface states are understood and controlled. In order to develop an accurate model for recombination and charge transfer via surface states, quantitative data of surface-state energy levels, den-

sities, and capture cross sections are required. This study utilizes steady-state photocapacitance spectroscopy (9, 10) to characterize the semiconductor electrode/electrolyte interface states, to determine the effect of various surface modifications on these states, and to correlate these results to cell performance.

Steady-state photocapacitance (Phcap) spectroscopy of liquid junction cells involves the measurement of the capacitance of a reverse biased semiconductor electrode as a function of the wavelength of incident sub-bandgap light. For a p-type semiconductor in the dark, the positive charge in the Helmholtz layer is compensated by the fixed negative charge associated with ionized acceptors in the semiconductor. The space-charge layer in the semiconductor has a capacitance that can be described by the equation for a parallel plate capacitor

$$C = Ak \epsilon_r / W$$

where A is the area of the plates, k is the dielectric constant, ϵ_r is the permittivity of free space, and W is the distance between plates. A change in the concentration of fixed charge in the depletion layer will change the depletion layer width, W , and will be detected as a change in the capacitance. In photocapacitance experiments, the fixed charge is altered when defect levels are optically populated or depopulated. When the incident monochromatic light is of the energy required for a particular transition, a normally occupied (unoccupied) state can be depopulated (populated). The change in the trap occupation will alter the space-charge layer width and will be detected as a discontinuity in the measured capacitance. The energy level of the transition can therefore be determined from the threshold energy of a capacitance discontinuity. The density of the states can be calculated from the magnitude of the capacitance change.

The photocapacitance technique also allows for the discrimination between surface and bulk states by two methods. First, if the bias applied a p-type semiconductor photoelectrode is made more cathodic, the depletion width will increase, thereby increasing the number of bulk traps contributing to the Phcap signal. An increase in the magnitude of signals due to bulk traps will then be observed. If only bulk states contribute to the measured capacitance of the electrode when it is exposed to incident light of a particular energy, the capacitance is related to applied voltage by the Mott-Schottky equation (11)

$$\frac{1}{C^2} = \frac{2}{q\epsilon\epsilon_0 N} (V - V_{FB})$$

where q is the electronic charge, ϵ is the dielectric constant of the photoelectrode, N is the total density of fixed charge, V is the applied voltage, and V_{FB} is the flatband voltage. Therefore, if a plot of $1/C^2$ vs. V is linear when C is the capacitance measured with incident light of sufficient energy to promote a particular transition, it can be concluded that the transition is related to a bulk defect state. The second method for distinguishing surface and bulk states is to change the electrolyte. A change in the composition of the solution would be expected to affect only surface-related features.

The work in this laboratory to date has involved the investigation of p-InP photoelectrodes subjected to surface treatments that have been shown to increase PEC cell efficiency. Single-crystal liquid-encapsulated Czochralski InP substrates with net acceptor concentrations of $1-5 \times 10^{16}$ per cubic centimeter were used as the photocathodes. The crystals had a (100) or (111) orientation and were chemically-mechanically polished prior to use. The electrodes were illuminated with monochromatic light from a Zeiss MM12 double prism monochromator equipped with a 250W quartz-halogen lamp. Photocapacitance measurements were performed over the spectral range of 0.5-1.5 eV with a Boonton 72B capacitance meter. The photocapacitance experiments were conducted with a 6M KOH (pH = 14), a 1M KCl + 0.05M CH₃COOH + 0.05M CH₃COONa (pH = 4.8), or a 1M KCl + 0.01M HCl (pH = 2.1) electrolyte. Pt served as the counterelectrode, and a standard calomel electrode served as the reference electrode. The applied bias was controlled with a BAS CV-1B cyclic voltammetry unit. The surface modifications included a 10s concentrated HCl etch and a Co/Pt treatment (7).

A previous study has shown that the Co and Pt treatment has a dramatic effect on the Phcap spectra of an InP electrode (10). The spectra for a sample subjected to an HCl etch exhibited only a single photocapacitance threshold, which occurred at 1.25 eV. The capacitance decrease at 1.25 eV was attributed to the promotion of electrons in a defect state 1.25 eV below the conduction band to the conduction band. After the Co and Pt treatment, the transition at 1.25 eV diminished and an increase in capacitance appeared at 1.20 eV. It was concluded that the Co and Pt treatment introduced a surface state 1.20 eV above the valence band into which electrons were promoted.

The reason for the enhanced efficiency following a Co and Pt treatment appears to be twofold (10). First, the efficiency increased due to a reduction in the number of recombination states near the valence band. Second, the introduction of a state at $E_v + 1.20$ eV presumably allowed for more efficient charge transfer from the semiconductor to the redox couple via the surface state.

These results indicate that photocapacitance spectroscopy is sensitive to semiconductor surface modifications. This information, along with a knowledge of cell efficiencies, allowed a model to be developed for the role of surface states in PEC cell operation. It is desirable, however, to obtain direct quantitative evidence that will allow for the discrimination between surface- and bulk-related states and permit the calculation of defect-state concentrations.

The time period covered by this Fellowship was devoted to studying PEC cell photocapacitance response as a function of bias and electrolyte composition in order to characterize surface and bulk states. The equations developed by Haak and Tench (9) were employed to calculate surface-state densities.

Figure 1 gives a typical Phcap scan for an as-received p-InP photocathode in KOH with no external bias. The spectrum indicates that a transition occurred to a state 1.17 eV above the valence band and that another transition occurred from a state 1.27 eV below the conduction band to the conduction band. Defect states at approximately $E_v + 1.2$ eV and $E_c - 1.3$ eV were consistently observed in a number of electrodes. An analysis of the photocapacitance signals indicates concentrations of $1.1 \times 10^{11}/\text{cm}^2$ and $1.7 \times 10^{11}/\text{cm}^2$ for the $E_v + 1.2$ eV and $E_c - 1.3$ eV transitions, respectively. It should be noted that these measurements were made with a light intensity which may not have been sufficient to saturate the defect states. Therefore, the actual concentrations may have been higher.

To determine if the transitions involved surface or bulk traps, a series of spectra as a function of reverse bias were obtained. The results are shown in Fig. 2. The contribution to the photocapacitance signal due to the $E_v + 1.2$ eV transition can be seen to increase with reverse bias. However, in this case, a plot of $1/C^2$ as a function of applied potential for the capacitance values measured when the electrode was subjected to 1.2 eV light did not reveal the nature of the 1.2 eV transition. The scatter in the data was too great to allow for a conclusion to be made as to whether or not the trap obeyed the Mott-Schottky equation. More precise measure-

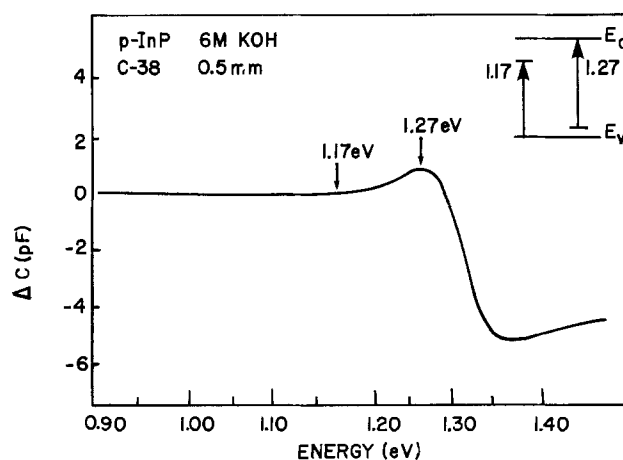


Figure 1

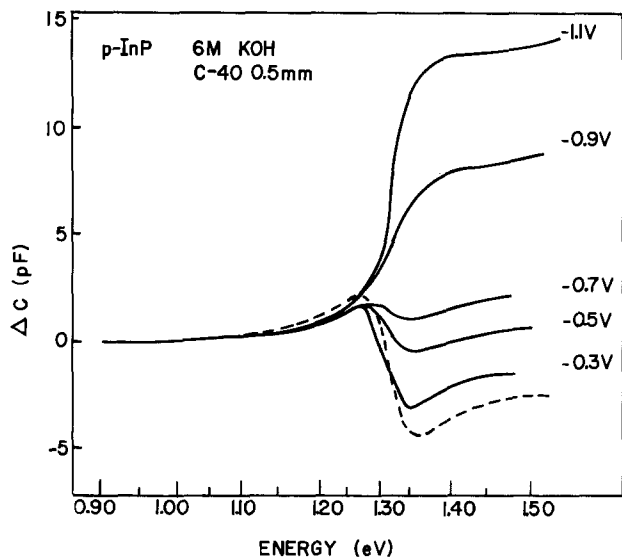


Figure 2

ments are needed to determine if the 1.2 eV transition is bulk related. In contrast, the $E_c - 1.3$ eV Phcap signal decreased as the cathodic bias increased. This indicates that the transition is surface related.

To verify the surface sensitivity of the Phcap measurements, experiments were conducted using several other electrolyte solutions. The photocapacitance response for an as-received sample in solutions with pH = 2 and pH = 5 are shown in Fig. 3. Curve (a), pH = 5, shows the same capacitance transitions that were observed in Fig. 1 (pH = 14). Curve (b), pH = 2, however, differs significantly, owing to a large capacitance increase at approximately 1.25 eV. In ad-

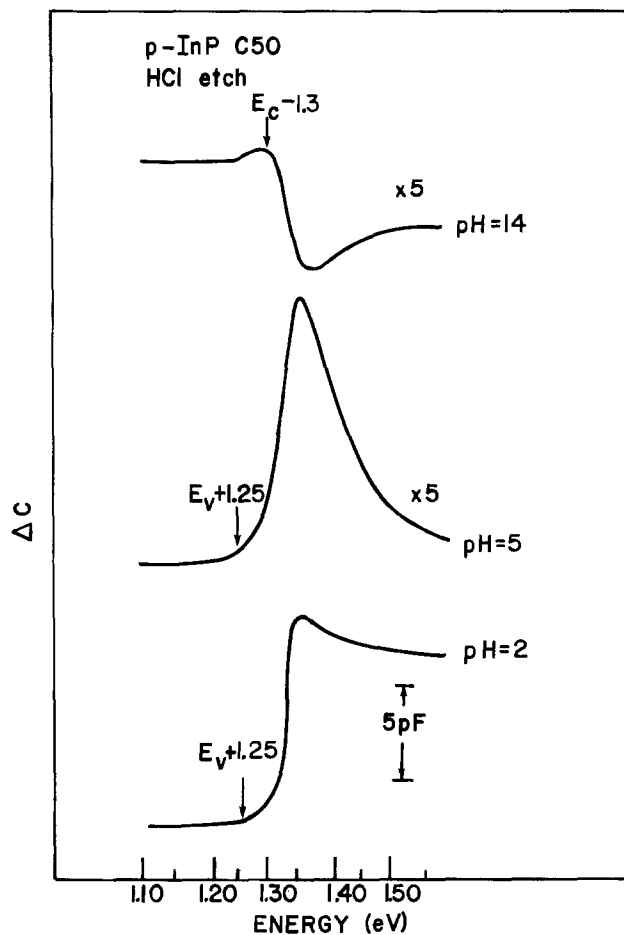


Figure 4

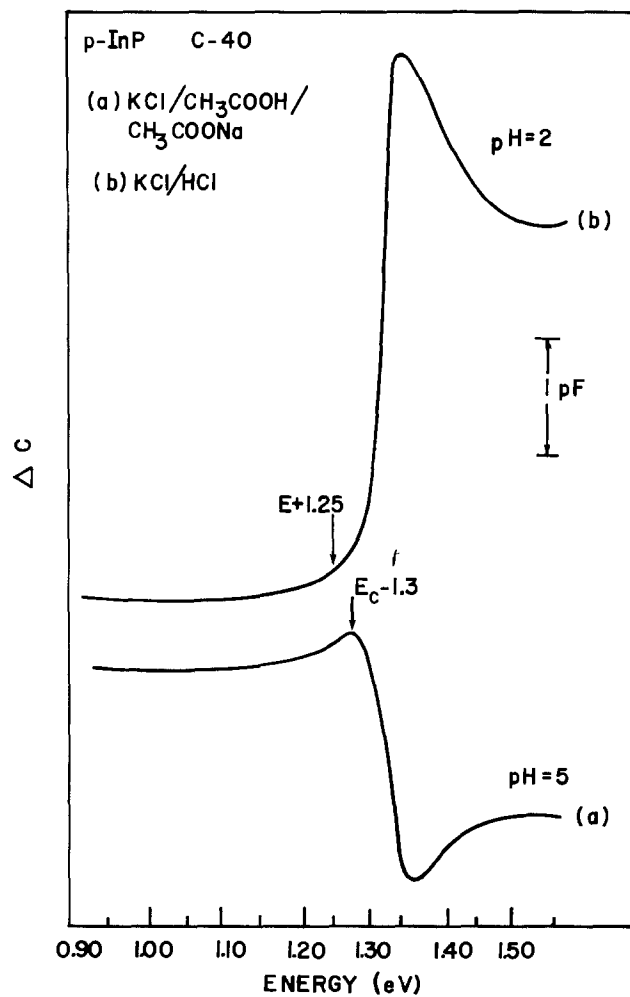


Figure 3

dition, the decrease in capacitance at 1.3 eV is not present in this spectrum. Figure 4 shows the photocapacitance spectra in the three solutions for an electrode subjected to an HCl etch. Again, a transition at 1.25 eV appears, and the 1.3 eV transition disappears in the spectra corresponding to acidic solutions. The dependence of the Phcap spectra on the composition of the electrolyte solution confirms that photocapacitance is sensitive to interface states at the semiconductor/electrolyte interface.

It is interesting to note the similarity between the photocapacitance spectra from the Co- and Pt-treated sample (10) and the as-received and etched samples in an acidic electrolyte (Fig. 3 and 4). The reason for the similarity is not understood, but the capacitance discontinuities may be associated with the same defect states. Work will continue to determine the mechanisms responsible for the photocapacitance results.

In summary, the work to date has shown that steady-state photocapacitance spectroscopy is a powerful tool for obtaining valuable information about the semiconductor/electrolyte interface in a photoelectrochemical cell. The technique allows for the detection and characterization of both bulk and interface charge-carrier traps. Additional information concerning the nature of these states can be obtained by varying the applied bias and the electrolyte. In particular, the work with InP looks promising for detailed kinetic studies, and work will continue to correlate the observed surface states and efficiencies.

The author would like to thank The Electrochemical Society for its support through the Summer Fellowship and Professor B. W. Wessels for helpful consultations. The author is grateful for the continued support of the Gas Research Institute and Eltron Research Incorporated. Optical measurements were performed in the facilities of the Materials Research Center at Northwestern University supported in part by the National Science Foundation.

REFERENCES

1. H. Minoura, T. Oki, and M. Tsuiki, *Chem. Lett.*, 1279 (1976).

2. M. Tomkiewicz, *This Journal*, **127**, 1518 (1980).
3. A. Heller, B. Miller, and F. A. Thiel, *Appl. Phys. Lett.*, **38**, 282 (1981).
4. A. Heller and R. Vandinsky, *Phys. Rev. Lett.*, **46**, 1153 (1981).
5. A. Heller, *Solar Energy*, **29**, 153 (1982).
6. C. J. Liu, P. G. Ang, and A. F. Sammells, *This Journal*, **129**, 1387 (1982).
7. P. G. P. Ang and A. F. Sammells, *ibid.*, **131**, 1462 (1984).
8. C. H. Henry, *J. Appl. Phys.*, **51**, 4494 (1980).
9. R. Haak and D. Tench, *This Journal*, **129**, 891 (1982).
10. C. E. Goodman and B. W. Wessels, *Appl. Phys. Lett.*, **45**, 442 (1984).
11. S. Morrison, "Electrochemistry at Semiconductor and Oxidized Metal Electrodes," Plenum Press, New York (1980).

Gary A. Reitz was born in Gettysburg, Pennsylvania in 1960. He received his B.A. in 1982 from Western Maryland College, located in his home town of Westminster, Maryland.

Currently, Mr. Reitz is pursuing his Ph.D. degree at the University of Texas at Austin.

Mr. Reitz's report is given below.

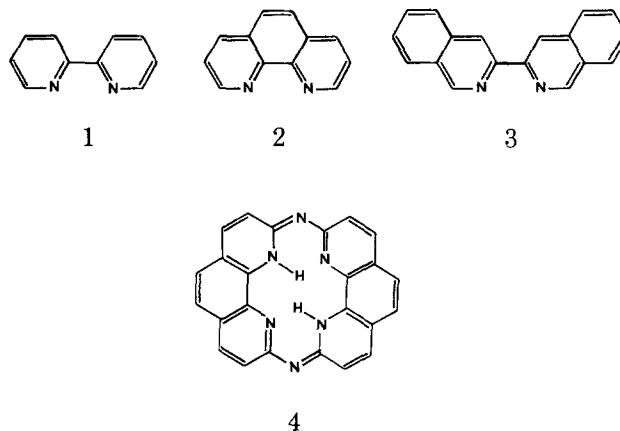
Electrochemical Reduction of Olefins Catalyzed by Nickel Complexes

A recent significant development in catalysis is the discovery of redox transformations mediated by altered oxidation levels of metal complexes or organometallic reagents. We report here our investigation of the catalytic reduction of olefins mediated by controlled reduction of nickel complexes of varying structure and reduction potential.

The physical properties of nickel complexes with bipyridine and related dinitrogen-containing ligands have been extensively studied, both in aqueous and nonaqueous solution, by spectrophotometry (1-4), electrochemical techniques (5-8), ESR (5), and circular dichroism (9), yielding information about their magnetic moments and conductivities (10-12), stability constants (13-15), and heats (16) and kinetics (17) of formation. These nickel complexes have been reported to catalyze a variety of homogeneous reactions, including *cis* addition of deuterium cyanide to olefins (18), insertion of CO into nickel-ligand bonds to yield ketones and tertiary alcohols (19), Michael additions (20), and polymerization of olefins (21-24). Nickel complexes have also been electrochemically generated *in situ* to catalyze the formation of substituted olefins (25).

Both nickel complexes NiL_mX_n and their parent compounds NiX_n form complexes with vinyl monomers such as acrylonitrile (21-24). Under certain conditions, Ni complexation with the vinyl monomer initiates polymerization of the monomer. Kern (21) has noted that anhydrous $NiCl_2$ is unreactive toward acrylonitrile in the absence of Zn metal. Barton *et al.* (22) have determined that free radical polymerization of several vinyl monomers was initiated by the $NiCl_2$ -N,N-dimethylaniline complex. Several aryl (bipyridine) nickel halide complexes, which themselves exhibit no catalytic activity for the polymerization of vinyl monomers, have been prepared by Uchino and co-workers (23). However, in combination with Lewis acids, these nickel complexes catalyzed the polymerization of several vinyl monomers.

The purpose of the work reported herein was to examine whether electrochemical generation of radical ions of several nickel dinitrogen containing complexes would initiate polymerization of the vinyl monomer acrylonitrile. The complexes examined were NiL_2Cl_2 complexes, where L = bipyridine, 1, and substituted bipyridines, phenanthroline, 2, and substituted phenanthrolines, and biquinoline, 3, and substituted biquinolines. One NiL complex was also examined, where L = hexa-aza-macrocycle, 4.



Experimental

Materials.—Anhydrous nickel (II) chloride was obtained by the method of Pray (26). Green $NiCl_2 \cdot 6H_2O$ (MCB, reagent grade) was refluxed with freshly distilled thionyl chloride ($SOCl_2$) (MCB, reagent grade) for 2.5h in a reflux apparatus equipped with a drying tube. Excess $SOCl_2$ was removed by distillation. The flask containing orange anhydrous $NiCl_2$ was then transferred to a vacuum desiccator containing NaOH and allowed to stand for several days to remove any remaining traces of $SOCl_2$.

N,N-dimethylformamide (DMF) (MCB, glass-distilled) was purified by predrying over anhydrous magnesium sulfate (Fisher, Certified grade) or anhydrous barium oxide (Fisher, technical grade) followed by vacuum distillation (bp:78°C at 39 torr). Chloroform (MCB, reagent grade) and methanol (VWR Scientific, reagent grade) was used as received. Tetrahydrofuran (THF) (MCB, reagent grade) was refluxed over calcium hydride and distilled prior to use. Acrylonitrile (MCB, reagent grade) was purified by washing with successive portions of dilute H_2SO_4 , dilute Na_2CO_3 , and water, and drying over molecular sieves (MCB, 4A), followed by simple distillation. This afforded acrylonitrile (bp:77°C), greater than 95% purity by NMR. Anhydrous tetrabutylammonium perchlorate (TBAP) (Southwestern Analytical Chemicals, electrometric grade) was recrystallized from Skelly B: ethyl acetate and dried at 50°C *in vacuo* for 4-6h. Ferrocene (Aldrich) was purified by sublimation prior to use.

Ligands obtained from Aldrich (2,2'-bipyridine, 1,10-phenanthroline [gold label], 4,7-diphenyl-1,10-phenanthroline) and Alfa (4,4'-dimethyl-2,2'-bipyridine, 2,9-dimethyl-1,10-phenanthroline, 2,2'-biquinoline, 4,4'-dicarboxy-2,2'-biquinoline) were all reagent grade unless specified and were used without further purification. All other ligands (2-chloro-1,10-phenanthroline, 2,9-dichloro-1,10-phenanthroline, 2,9-diamino-1,10-phenanthroline, and hexa-aza-macrocycle) were synthesized (27, 28).

The $Ni(bpy)_2Cl_2$ complex was prepared by dissolving anhydrous $NiCl_2$ in methanol, adding excess bipyridine, stripping off the solvent under vacuum, and subliming the excess bipyridine out of the solid mixture. All other nickel complexes were prepared by a variation of the method of Inskeep (1). Stoichiometric amounts of anhydrous $NiCl_2$ and the ligand were dissolved in methanol, warmed to effect complete solution, and the solvent then removed under vacuum. Because of limited solubility in methanol, stoichiometric amounts of both of the biquinoline complexes, the 2,9-dichlorophenanthroline complex, and the hexa-aza-macrocycle complex were refluxed with anhydrous $NiCl_2$ in THF for 6h. The THF was then removed under vacuum.

Instrumentation and equipment.—Cyclic voltammetry was performed using a Bioanalytical Systems BAS-100 Electrochemical Analyzer and a Houston Instruments Hiplot DMP-40 digital plotter. The cell used was a one-compartment cell equipped with a 3 mm² platinum disk working electrode, a platinum wire counterelectrode, and a silver/0.1M silver nitrate in acetonitrile reference electrode. Tetra-n-butyl ammonium perchlorate (TBAP) was used as the supporting electrolyte (0.1M in DMF). All solutions were deaerated with argon for at least 10 min prior to obtaining the voltammograms. Positive IR compensation for

solution resistance was utilized in all experiments. The scan rate in all experiments was 100 mV/s.

Preparative electrolyses were performed using a Princeton Applied Research (PAR) Model 173 potentiostat, a Model 179 digital coulometer, and a Model 175 universal programmer. The cell used was a two-compartment cell with a fine glass frit separating the working and counterelectrode compartments. Solutions of 0.2M TBAP in DMF were used as the electrolyte. A platinum wire coil electrode and a platinum gauze electrode were used as the working and counterelectrodes, respectively, while Ag/AgNO₃ was used as the reference electrode. Typically, 75-100 mg of acrylonitrile and a few milligrams of anhydrous Ni(bpy)₃Cl₂ were dissolved in 5 ml of the electrolyte solution, placed in the working electrode compartment, and deaerated with argon prior to electrolysis. Controlled-potential electrolyses were performed at -2.2V.

All potentials reported herein are referenced to the Ag/AgNO₃ reference electrode. The ferrocene/ferrocenium couple displays a one-electron reversible wave centered at +0.02V vs. Ag/AgNO₃, as compared with +0.307V vs. an aqueous saturated calomel electrode (SCE) (29).

Low resolution mass spectra were obtained on a du Pont 21-491 mass spectrometer with INCOS data system. Proton nuclear magnetic resonance spectra were obtained on a Varian EM-390 spectrometer.

Results and Discussion

The electrochemical reduction of olefins using nickel complexes as catalysts was studied, and acrylonitrile was chosen as a model substrate. Acrylonitrile displayed no electrochemical activity over the DMF solvent window +0.50 to -2.50V vs. Ag/AgNO₃. Addition of acrylonitrile, however, to solutions of the nickel complex caused, in all cases, disappearance of reversibility of the voltammetric waves associated with reduction of the nickel complex and concomitant formation of other waves attributed to association of acrylonitrile with the nickel complex. Peak potentials obtained by cyclic voltammetry of the NiL₃Cl₂ and NiL complexes in DMF are tabulated in Table I. Also included in Table I are the peak potentials seen upon addition of a small amount of acrylonitrile to the NiL_nX₂ solutions.

Cyclic voltammograms of the nickel (tris)bipyridine complex prior to and following addition of acrylonitrile are shown in Fig. 1. The Ni(bpy)₃Cl₂ complex itself displays a nearly reversible wave centered at -1.57V vs. Ag/AgNO₃ and a second irreversible reduction wave at E_{p,c} = -2.40V. These waves are replaced, on addition of acrylonitrile, by a quasireversible wave centered at -2.07V and two other irreversible reduction waves at -1.57 and -1.71V. Since acrylonitrile itself does not undergo cathodic reduction at potentials less negative than -2.50V, the appearance of new waves for the Ni(bpy)₃Cl₂-acrylonitrile complex indicates that electrocatalytic reduction of acrylonitrile by the Ni(bpy)₃Cl₂ complex is occurring. Preliminary examination by mass spectrometry of the products obtained by

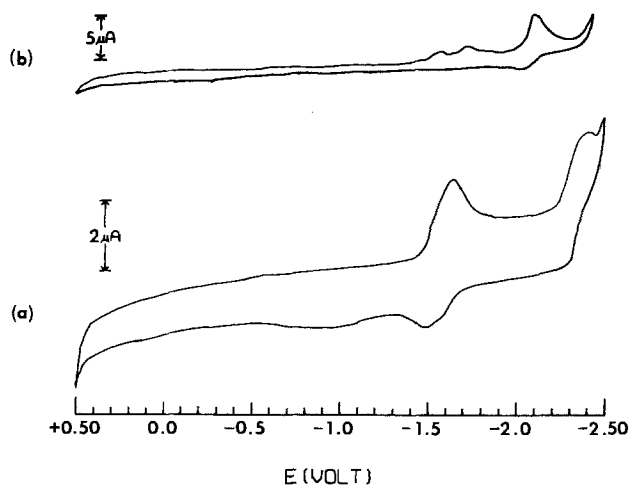


Fig. 1. Cyclic voltammograms of 5×10^{-3} M Ni(bpy)₃Cl₂ in 0.1M TBAP/DMF (a) prior to addition of acrylonitrile and (b) after addition of acrylonitrile. Platinum working electrode area: 3 mm². Scan rate: 100 mV/s. Reference electrode: silver/silver nitrate (0.1M) in acetonitrile.

constant-potential coulometry of a solution of acrylonitrile and Ni(bpy)₃Cl₂ in 0.2M TBAP/DMF reveals the major product of the electrolysis to be a polymer of acrylonitrile. Ni(bpy)₃Cl₂, then, acts as a catalyst for the cathodic polymerization of acrylonitrile.

Similar catalytic behavior is observed for most of the related nickel complexes, as shown in Table I. The parent NiCl₂-acrylonitrile complex is reduced at a potential substantially less negative than that of the Ni(bpy)₃Cl₂ analog; however, the nonreversibility of the NiCl₂-acrylonitrile system makes NiCl₂ a poor choice for a catalyst. Except for the Ni(2-Cl(phen))₃Cl₂-acrylonitrile complex, the largest cathodic peak in all of the NiL_mCl₂-acrylonitrile voltammograms is the most negative of the observed peaks. Focusing on the largest cathodic peak, all of the complexes show catalytic activity toward reduction of acrylonitrile, though with varying reduction potentials depending on the structure of the ligand.

Within each series of related ligands, substituent effects on the reduction potential of the NiL_mCl₂-acrylonitrile complex are observed for the largest cathodic peaks in the voltammograms. For the 2,2'-bipyridine series, substituting the slightly electron-donating methyl groups on the 4,4' positions results in a small negative shift in reduction potential, as would be expected. The parent complex of the phenanthroline series, Ni(phen)₃Cl₂-acrylonitrile complex, shows a quasireversible wave centered at -2.07V. The 4,7-diphenyl substituted phenanthroline complex is much easier to reduce (-1.95V) than the unsubstituted complex. As anticipated, the electron donating methyl and amino groups both shift the reduction potential of the acrylonitrile complex to more negative potentials (-2.16 and -2.33V, re-

Table I. Cyclic voltammetric data for nickel complexes and their interaction with acrylonitrile

Complex ^a	Color	E _{p,c} (complex) ^b	E _{p,a} (complex) ^c	E _{p,c} (complex + AN) ^d	E _{p,a} (complex + AN)
NiCl ₂ (anhydrous)	Yellow-orange	-1.62	-0.40	-1.76	-0.55
Ni(bpy) ₃ Cl ₂	Light pink	-1.63(q) ^e , -2.40	-0.96, -1.51(q)	-1.57, -1.71, -2.11(q)	-2.04(q)
Ni[4,4'-diMe(bpy)] ₃ Cl ₂	Dark orange	-1.78(q), -2.45	-1.05, -1.74(q)	-1.71, -1.86, -2.21(q)	-0.25, -2.10(q)
Ni(phen) ₃ Cl ₂	Dark pink	-1.72(q), -2.35	-1.66(q)	-1.63, -2.10(q)	-2.05(q)
Ni[4,7-diPh(phen)] ₃ Cl ₂	Light orange	-1.59(q), -1.93,	-1.58(q), +0.20	-1.55, -1.68, -1.99(q)	-1.90(q), +0.13
Ni[2-Cl(phen)] ₃ Cl ₂	Dark green	-1.42, -1.85	None	-1.38, -1.91	None
Ni[2,9-diCl(phen)] ₃ Cl ₂	Tan	-1.72, -2.17, -2.32(q)	-2.28(q)	-1.65, -2.19	None
Ni[2,9-diMe(phen)] ₃ Cl ₂	Blue-green	-1.25(q), -1.55(q), -2.10(q)	-1.03(q), -1.49(q), -2.02(q)	-1.27, -1.54, -2.16	-0.83, -1.48, -2.06
Ni[2,9-diNH ₂ (phen)] ₃ Cl ₂	Green	-1.41(q), -1.99	-1.10(q), -1.29	-1.47, -1.98, -2.33	None
Ni(2,2'-biqn) ₃ Cl ₂	Yellow	-1.56, -2.21(q)	-0.49, -0.98, -1.94, -2.11(q)	-1.67, -2.22	None
Ni[4,4'-diCO ₂ H(biqn)] ₃ -Cl ₂	Tan	-1.38	-0.96	-1.43	None
Ni(HAM)	Brown	None	None	-1.43, -2.18	None

^a bpy = 2,2'-bipyridine; phen = 1,10-phenanthroline; biqn = 2,2'-biquinoline; diMe = dimethyl; diPh = diphenyl; Cl = chloro; diCl = dichloro; DiNH₂ = diamino; diCO₂H = dicarboxy; HAM = hexa-aza-macrocyclic.

^b Cathode peak potentials.

^c Anodic peak potentials.

^d AN = acrylonitrile.

^e (q) = Quasireversible.

spectively). Anomalous results are obtained from the Ni(2,9-diCl(phen))₃Cl₂-acrylonitrile complex, though. With two electron withdrawing groups on the ring, the reduction potential would be predicted to be shifted anodically. However, a cathodic shift of 90 mV is obtained for this complex, compared to the parent Ni(phen)₃Cl₂-acrylonitrile complex. The biquinoline series behaves as expected, though. The parent Ni(biqn)₃Cl₂-acrylonitrile complex possesses a reduction potential of -1.67V, while the 4,4'-dicarboxy analog reduces at -1.43V, which exhibits the predicted substantial negative anodic shift.

Between the series of complexes, especially the bipyridine and biquinoline series, there is a large difference in reduction potential between the NiL_mCl₂-acrylonitrile complexes ($\Delta E_p = 0.19V$ for the parent complexes). This difference in reduction potential is probably because the more conjugated biquinoline ring system is easier to reduce than the less conjugated bipyridine ring system, and that difference parallels the change in reduction potential from biquinoline itself to bipyridine (about 0.50V) (30).

It has been demonstrated that nickel complexes with various ligands can catalyze the cathodic reduction of acrylonitrile. Electrochemical stability of the catalyst is also necessary for any practical system. Toward this end, only the Ni(bpy)₃Cl₂, Ni(4,4'-diMe(bpy))₃Cl₂, Ni(phen)₃Cl₂, and Ni(4,7-diPh(phen))₃Cl₂ complexes have demonstrated sufficient reversibility to be potentially useful on a large scale.

Acknowledgments

Synthesis of several ligands (2-chlorophenanthroline, 2,9-dichlorophenanthroline, 2,9-diaminophenanthroline, and hexa-aza-macrocyclic) by Martin Johnson is greatly appreciated. G. A. R. is grateful for support as an Electrochemical Society Energy Research Summer Fellow. A special thanks goes to Professor Marye Anne Fox for her guidance and support. This work was supported by the U. S. Department of Energy, Fundamental Interactions Branch.

REFERENCES

1. R. G. Inskeep, *J. Inorg. Nuc. Chem.*, **24**, 763 (1962).
2. K. Sone, P. Krumholz, and H. Stammreich, *J. Am. Chem. Soc.*, **77**, 777 (1955).
3. V. K. Yamasaki, *Bull. Chem. Soc. Jpn.*, **12**, 390 (1937).
4. K. Nakamoto, *J. Phys. Chem.*, **64**, 1420 (1960).
5. N. Tanaka, T. Ogata, and S. Niizuma, *Inorg. Nuc. Chem. Lett.*, **8**, 965 (1972).
6. H. Sawamoto and T. Fujinaga, *Nippon Kagaku Kaishi*, **5**, 607 (1979).
7. L. Pospisil and J. Kuta, *J. Electroanal. Chem.*, **101**, 391 (1979).
8. R. Prasad and D. B. Scaife, *ibid.*, **84**, 373 (1977).
9. S. F. Mason, B. J. Peart, and R. E. Waddell, *J. Chem. Soc. Dalton Trans.*, **9**, 944 (1973).
10. R. H. Lee, E. Griswald, and J. Kleinberg, *Inorg. Chem.*, **3**, 1283 (1964).
11. C. M. Harris and E. D. McKenzie, *J. Inorg. Nuc. Chem.*, **29**, 1047 (1967).
12. C. M. Harris and E. D. McKenzie, *ibid.*, **19**, 372 (1961).
13. C. D. Hubbard, *Inorg. Nuc. Chem. Lett.*, **7**, 139 (1971).
14. S. Cabani and M. Landucci, *J. Chem. Soc.*, 278 (1962).
15. H. Irving and D. H. Mellor, *ibid.*, 5222 (1962).
16. R. L. Davies and K. W. Dunning, *ibid.*, 4168 (1965).
17. C. D. Hubbard, *J. Inorg. Nuc. Chem.*, **36**, 1177 (1974).
18. J.-E. Backvall and O. S. Andell, *J. Chem. Soc. Chem. Commun.*, **4**, 260 (1984).
19. T. Yamamoto, T. Kohara, and A. Yamamoto, *Chem. Lett.*, 1217 (1976).
20. K. Watanabe, M. Miyazu, and K. Irie, *Bull. Chem. Soc. Jpn.*, **55**, 3212 (1982).
21. R. J. Kern, *J. Inorg. Nuc. Chem.*, **25**, 5 (1963).
22. J. Barton, I. Lebec, and I. Capek, *Makromol. Chem.*, **179**, 2747 (1978).
23. M. Uchino, K. Asagi, A. Yamamoto, and S. Ikeda, *J. Organomet. Chem.*, **84**, 93 (1975).
24. B. Bogdanovic, B. Henc, H. G. Karmann, H. G. Nussel, D. Walter, and G. Wilke, *Ind. Eng. Chem.*, **62**, 34 (1970).
25. Y. Rollin, G. Meyer, M. Troupel, J.-F. Fauvarque, and J. Perichon, *J. Chem. Soc. Chem. Commun.*, **15**, 793 (1983).
26. A. R. Pray, *Inorg. Syn.*, **5**, 153 (1957).
27. B. E. Halcrow and W. O. Kermack, *J. Chem. Soc.*, 155 (1946).
28. S. Ogawa, T. Yamaguchi, and N. Gotoh, *J. Chem. Soc. Perkin Trans. 1*, **9**, 976 (1974).
29. A. J. Bard and L. R. Faulkner, "Electrochemical Methods," p. 701, John Wiley and Sons, New York (1980).

30. L. Meites and P. Zuman, "CRC Handbook Series in Organic Electrochemistry," Vol. 1, CRC press, Cleveland, Ohio (1976).

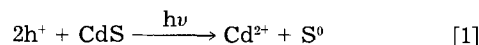
Holly-Dee Rubin was born in Belleville, New Jersey in 1959. She received her B.A. degree from Douglass College, New Brunswick, New Jersey, in May 1981, and her M.A. degree from Princeton University, Princeton, New Jersey, in 1982.

Ms. Rubin is currently working toward her Ph.D. degree at Princeton.

Ms. Rubin's report is given below.

Cation and Wavelength Effects on the CdSe/Fe(CN)₆⁴⁻ Photoelectrochemical Solar Cell

The major obstacles in the utilization of semiconductor liquid junction cells for solar energy conversion have been photocorrosion of the semiconductor material and the rather low energy conversion efficiencies of these devices. As previously reported (1), the photodecomposition of n-CdS in a Fe(CN)₆^{4-/3-} electrolyte is dramatically decreased in the presence of a mixture of K⁺ and Cs⁺ ions. Not only is stability improved, but monochromatic (488 nm) conversion efficiencies in excess of 20% have been observed. Gerischer (2) had previously demonstrated that addition of a K₄Fe(CN)₆/K₃Fe(CN)₆ mixture to the aqueous CdS photocell slightly decreased the photo-oxidation reaction



The slower decomposition has been attributed to a competition between oxidation of solution Fe(CN)₆⁴⁻ and the oxidation of the electrode surface (3). However, we have shown (1) through diffuse reflectance FTIR spectroscopy that there is actually a layer of K_xCs_y[Cd^{II}Fe^{II}(CN)₆] on the surface of the electrode under the conditions employed. This layer is produced when photochemically generated Cd²⁺ ions react with solution Fe(CN)₆⁴⁻. Layers of this type have already been shown to enhance charge transfer and inhibit corrosion at metal electrodes (4). For the case of the semiconductor, we believe that the enhanced stability and efficiency are associated with good orbital overlap between the semiconductor bandedges and the redox active surface layer orbitals. Once reduced, the surface material is then capable of facile charge transfer to solution Fe(CN)₆⁴⁻.

Because of the smaller bandgap of CdSe, and owing to reports (5) of stabilized photocurrents of n-CdSe in aqueous alkaline Fe(CN)₆^{3-/4-}, this system was found to be of interest. The results of this investigation are reported below. Experiments were conducted using both single-crystal and polycrystalline n-CdSe electrodes. Samples were irradiated using either an argon ion or helium-neon laser. The electrolyte was composed of 0.2M K₄Fe(CN)₆ and 0.01M K₃Fe(CN)₆ with 0.1M KOH as supporting electrolyte. A standard potentiostated three-electrode configuration was employed using a platinum counterelectrode and a SCE reference electrode. Analogously to n-CdS, bandgap irradiation leads to the formation of an insoluble K_x[Cd^{II}Fe(CN)₆] surface layer. The n-CdSe/Fe(CN)₆^{4-/3-}/KOH system is stable for periods in excess of several hours when irradiated with 488 nm light (current density ~ 1 mA/cm²). Addition of Cs⁺ leads immediately to a precipitous decay in photocurrent ($t^{1/2} \sim 30$ min), in contrast to the stability effects of Cs⁺ on the n-CdS system.

These results can be explained using the model previously described (1). The incorporation of Cs⁺ cations into the surface layer is expected to cause the redox potential of the surface species to become more positive (6). In the case of the n-CdS, this shift could lead to increased overlap between the semiconductor valence band states and the oxidizable cadmium ferrocyanide surface layer. n-CdSe, though, is expected to have a valence bandedge which is already at a more negative potential than that of n-CdS by ~

700 mV (5a). Therefore, any positive shift in the redox potential of the surface layer may shift these levels significantly positive of the valence band edge, actually decreasing the degree of overlap, and thus slowing interfacial charge-transfer kinetics and enhancing electrode decomposition processes.

A most unusual result was discovered in the course of these studies. The n-CdSe cell photocurrent stability was found to be dependent on the wavelength of incident irradiation. When irradiated with 488 nm light, stable photocurrent output was achieved in excess of several hours. However, when excitation is at 633 nm, the photocurrent decays rapidly ($t^{1/2} \sim 30$ min). Furthermore, preirradiation at 488 nm induces photostability upon subsequent irradiation at 633 nm. To our knowledge, such a wavelength dependent photoelectrochemical decomposition reaction has never before been reported. As will be discussed in a forthcoming communication (7), we attribute the wavelength dependence to the photochemical properties of the surface species, *i.e.*, the surface species undergoes a purely photoinduced reaction, possibly CN^- loss, which modifies the surface layer in such a way so as to enhance charge-transfer rates at the semiconductor electrolyte interface.

REFERENCES

1. H.-D. Rubin, B. D. Humphrey, and A. B. Bocarsly, *Nature*, **308**, 339 (1984).
2. H. Gerischer and J. Gobrecht, *Ber. Bunsenges. Phys. Chem.*, **80**, 327 (1976).
- 3a. A. J. Bard and M. S. Wrighton, *This Journal*, **124**, 1706 (1977).
- b. H. Gerischer, *J. Electroanal. Chem.*, **82**, 133 (1977).
4. S. Sinha, B. D. Humphrey, and A. B. Bocarsly, *Inorg. Chem.*, **23**, 203 (1984).
- 5a. R. A. L. Vanden Berghe, W. P. Gomes, and F. Cardon, *Z. Phys. Chem. N. F.*, **92**, 91 (1974).
- b. K. W. Frese, Jr., *Appl. Phys. Lett.*, **40**, 275 (1982).
6. A. B. Bocarsly and S. Sinha, *J. Electroanal. Chem.*, **140**, 167 (1982).
7. H.-D. Rubin, D. Arent, and A. B. Bocarsly, Submitted to *Appl. Phys. Lett.*

Hal Van Ryswyk is a native of Iowa. He received his B.A. degree in chemistry from Carleton College, Northfield, Minnesota, in 1982.

Mr. Van Ryswyk is now working toward his Ph.D. degree at the University of Wisconsin, Madison, Wisconsin.

Mr. Van Ryswyk's report is given below.

Luminescent Properties of a Surface-Modified Cadmium Selenide Electrode

We have used photoluminescence (PL) and electroluminescence (EL) to characterize electric fields in a variety of semiconductor electrodes. Samples of n-CdSe have been the focus of several such studies (1-4) and reflect the importance of this small bandgap material in the design of efficient photoelectrochemical cells (PEC's).

Modified semiconductor surfaces are now being intensely investigated with regard to device applications. A novel system recently reported by Bocarsly *et al.* is based on the modification of n-CdS and n-CdSe electrodes using a ferri/ferrocyanide electrolyte; for n-CdS, the modified electrode leads, for specific cations, to an appreciable increase in optical-to-electrical energy conversion efficiency obtainable in a PEC (5).

In this report, we examine PL and EL properties of a ferri/ferrocyanide-modified n-CdSe electrode. We show that PL intensity from the modified electrode is in good accord with a dead-layer model found applicable to naked, homogeneous electrodes (4, 7, 8), and that EL properties of

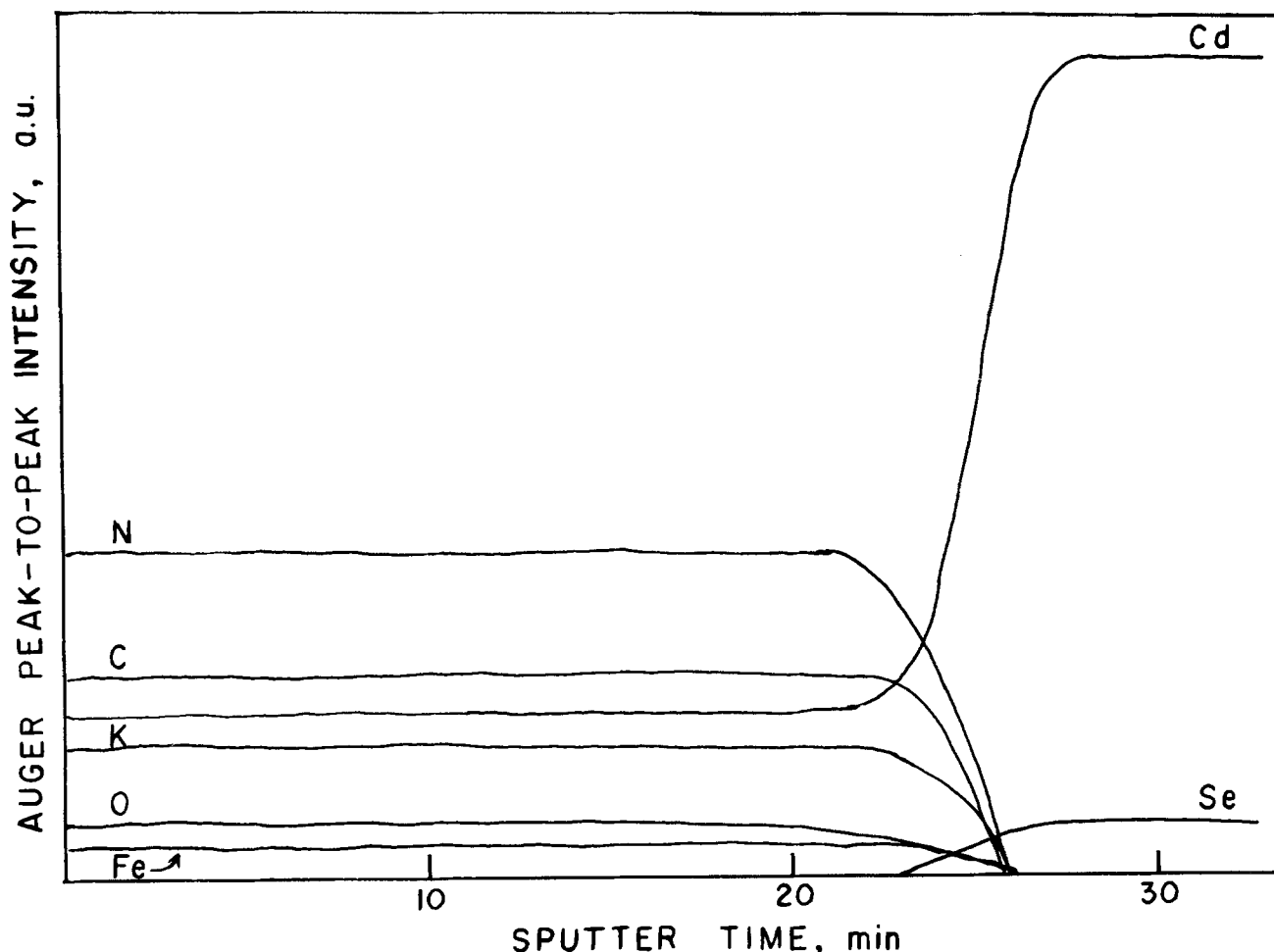


Fig. 1. Auger spectrum of the surface layer of a ferri/ferrocyanide-modified CdSe electrode as a function of sputter time. Conditions are listed in the experimental section. Relative peak-to-peak sensitivities are: K, 0.80; Cd, 1.0; Fe, 0.21; C, 0.20; N, 0.33; Se, 0.06; O, 0.50.

the modified CdSe electrode are comparable to those of the naked electrode.

Experimental

Samples of n-CdSe c-plates were purchased from Cleveland Crystals, Incorporated. The crystals were mounted with the (0001) (Cd-rich) face outwards, then etched in Br₂-methanol (1:10 v/v), rinsed with water, and dipped in conc HCl for 10s. The electrodes were irradiated at open circuit with 50 mW cm⁻² of 488 nm light from an Ar⁺ laser in an electrolyte of 0.2M K₄Fe(CN)₆/0.01M K₃Fe(CN)₆/1M KOH for 25 min before being brought into circuit in the same electrolyte at +0.1V vs. SCE for 10 min. The stability of this modified electrode was tested by operation in a PEC employing fresh ferri/ferrocyanide electrolyte and 633 nm excitation (HeNe laser), a wavelength which did not promote film growth. Only those electrodes showing a steady photocurrent with time were used in succeeding experiments. Unless otherwise noted, the cation used in all electrolytes was K⁺, which was found to stabilize the surface layer on CdSe (6).

The experimental setups for the dead-layer measurements and EL efficiencies are described elsewhere (1, 7). EL experiments were performed using a 0.5M OH⁻/0.1M S₂O₈²⁻ electrolyte with either K⁺ or Na⁺ counterions. Peroxydisulfate concentrations were determined by iodometric titration.

Auger electron spectroscopy (AES) was performed on a modified electrode using a Physical Electronics Model 548 instrument operating with a 3 keV, 25 μA primary electron beam approximately of 200 μm diam. Sputter etching was conducted using a 2 mm diam beam of 5 keV, 25 mA Ar ions with the chamber backfilled to 5 × 10⁻³ torr of Ar.

Results and Discussion

Modification of the shiny CdSe electrode as described above yields a dull black matte surface. An Auger spectrum of the surface layer shows it to consist of K, Cd, Fe, C, N, and O in a ratio of 1.0:1.0:1.0:6.1:6.0:0.70. A sputter etching experiment, illustrated in Fig. 1, shows the surface layer composition to be relatively independent of depth, eventually giving way to the CdSe substrate. Species with related compositions, such as K₂CdFe(CN)₆ and KCdFe(CN)₆, have zeolite-like channels (9). If the modified electrode has a similar structure, the presence of oxygen may signify trapped water.

When the modified electrode is used as a photoanode in a PEC, its PL intensity can be quenched by applied potential. Figure 2 presents photocurrent-μ PL intensity-voltage data (iLV curves); the potential-independent spectral distribution permits PL to be monitored at 720 nm. Quenching of PL in PEC's has been described using a dead-layer model originally applied to semiconductor-metal, Schottky barrier systems: e⁻-h⁺ pairs formed within a distance on the order of the depletion width do not contribute to PL; this model thus relates PL intensity to the thickness of the electric field in the electrode. The quantitative form of the model is given by Eq. [1]

$$\phi_r/\phi_{rFB} = \exp(-\alpha'D) \quad [1]$$

where ϕ_r and ϕ_{rFB} are radiative efficiencies in circuit and at flatband potential (assumed to be open circuit), respectively; D is the dead-layer thickness; and $\alpha' = \alpha + \beta$, with α and β the solid's absorptivities for the exciting and emitted light. For the Fig. 2 data, D is calculated to be approximately 3000 Å at short circuit, which is roughly equal to the depletion width for this sample with N_D of $\sim 1 \times 10^{16}$ cm⁻³. When the experimental curves are compared to curves calculated by assuming that all of the applied potential appears in the semiconductor (7), good accord is found, indicating that applied potential appears predominantly in the semiconductor, and not in the Helmholtz layer or the surface layer.

An additional probe of the surface layer is to use the modified electrode to generate EL in basic S₂O₈²⁻ electrolyte. This can be done with an efficiency equal to that of the naked electrode in the same electrolyte; lower-limit, integrated efficiencies of $\sim 6 \times 10^{-4}$ are reproducibly obtained when pulsing to -1.2V vs. SCE. The spectral distribution of

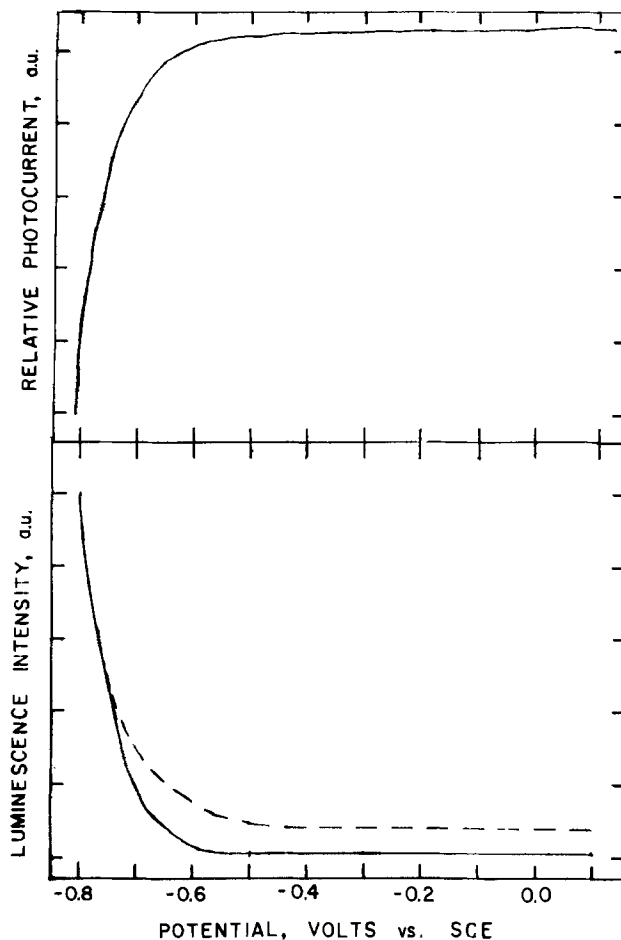


Fig. 2 Relative photocurrent (top panel) and PL intensity (bottom panel) for a modified CdSe electrode with excitation at 514.5 nm (solid line) and 620 nm (dashed line). Values for α' of 1.5×10^5 and 8.4×10^4 cm⁻¹ were used in the dead-layer analysis at 514.5 and 620 nm, respectively (10). The iLV curves for each excitation wavelength were swept simultaneously at 20 mV/s. The electrolyte redox potential is +0.17V vs. SCE.

the EL is also identical with that of the naked electrode. Subsequent stable operation as a PEC with 633 nm irradiation in the ferri/ferrocyanide electrolyte indicates that no drastic change in the surface layer has occurred.

The EL efficiency may be varied by changing the cation present in solution; the use of NaOH/Na₂S₂O₈ electrolyte brought about a two-fold drop in EL efficiency, which could be recovered upon allowing the electrode to stand for 20 min in the original KOH/K₂S₂O₈ electrolyte.

Peroxydisulfate will spontaneously oxidize ferrocyanide, so we attempted to generate EL by dipping the derivatized electrode in a concentrated S₂O₈²⁻ solution to oxidize the surface layer, rinsing with water, then pulsing to -1.2V vs. SCE in a concentrated KCl electrolyte. Although large reduction currents flowed, no EL was detected. This experiment argues against a charge hopping mechanism whereby holes are injected by the electrolyte into the surface layer for transfer to the semiconductor. Nonetheless, the cation specificity of the EL suggests that the surface layer plays some role in the injection process. The mechanism of charge injection is under investigation at this time.

Conclusion

Photoluminescence and electroluminescence from a ferri/ferrocyanide-modified CdSe electrode has been studied. Potential applied to the modified electrode appears primarily in the semiconductor and not in the surface layer, based on an analysis of PL quenching using the dead-layer model. EL can be generated in basic S₂O₈²⁻ electrolyte with an efficiency and spectral distribution which match those of the naked electrode; EL efficiency can be modestly varied by choice of sodium or potassium cation.

Acknowledgments

We wish to thank The Electrochemical Society for an Energy Research Summer Fellowship sponsored by the Department of Energy. Generous support by the Office of Naval Research is also acknowledged. Dr. Ngoc Tran is thanked for his assistance with the AES measurements. Gratitude is expressed to Professor A. B. Ellis for his guidance and assistance throughout this project.

REFERENCES

1. H. H. Streckert, J. Tong, and A. B. Ellis, *J. Am. Chem. Soc.*, **104**, 581 (1982).
2. H. H. Streckert, J. Tong, M. K. Carpenter, and A. B. Ellis, *This Journal*, **129**, 772 (1982).
3. H. H. Streckert, H. Van Ryswyk, R. N. Biagioni, and A. B. Ellis, *J. Phys. Chem.*, **88**, 1544 (1984).
4. R. Garuthara, M. Tomkiewicz, and R. P. Silberstein, *J. Appl. Phys.*, **54**, 6787 (1983).
5. H.-D. Rubin, B. D. Humphrey, and A. B. Bocarsly, *Nature*, **308**, 339 (1984).
6. A. B. Bocarsly, Private communication.
7. W. S. Hobson and A. B. Ellis, *J. Appl. Phys.*, **54**, 5956 (1983).
8. P. M. Smiley, R. N. Biagioni, and A. B. Ellis, *This Journal*, **131**, 1068 (1984).
9. J. B. Ayers and W. H. Waggoner, *J. Inorg. Nucl. Chem.*, **33**, 721 (1971).
10. R. B. Parsons, W. Wardzynski, and A. D. Yoffe, *Proc. R. Soc. A*, **262**, 120 (1961).



Alkaline Water Electrolysis Anode Materials

D. E. Hall*

American Cyanamid Company, Chemical Research Laboratories, Stamford, Connecticut 06904

ABSTRACT

In recent years, considerable progress has been made in developing alkaline water electrolysis anodes. Several laboratories have reported oxygen evolution overpotential reductions of 100-150 mV or more, relative to uncatalyzed nickel. Some candidate anode materials have shown stable operation for thousands of hours under typical commercial electrolysis conditions. Preferred electrocatalysts have been the mixed metal oxides, especially the AB_2O_4 spinels and ABO_3 perovskites. Other metal oxides, alloys, and high surface-area forms of nickel have also been studied. This review summarizes recent work in developing practical alkaline water electrolysis anodes.

Anode overpotential is a major source of inefficiency in alkaline water electrolysis. In commercial electrolysis, the commonly used unactivated nickel anode has an oxygen evolution overpotential, η_{O_2} , of about 400 mV, representing ~20% of the total cell voltage. As a result, higher anode efficiency is an important goal in current electrolyzer development programs.

There are three practical approaches to improving anode efficiency. First, the electrolysis temperature can be increased. In the context of this review, higher temperatures introduce the possibility of increased anode corrosion. Second, the conventional nickel anode can be made more efficient, primarily by increasing its electrochemically active surface area. Third, new anode electrocatalysts, particularly those based on mixed metal oxides, show great promise.

This review summarizes recent progress in improving alkaline water electrolysis anodes. Experimental results from typical commercial electrolysis conditions and advances in practical anode development are emphasized. Other recent reviews (1-3), which also cover subjects outside the scope of this paper, should be consulted for further information.

Practical Considerations

Four main factors must be considered in developing a commercially practical anode for alkaline water electrolysis: electrochemical efficiency, stability, scale-up, and cost.

Efficiency is the initial screening criterion in any anode development program. As shown later in this review, the best electrocatalysts to date provide oxygen evolution overpotentials more than 150 mV lower than η_{O_2} on uncatalyzed nickel. This represents a voltage savings of about 8-9% in modern, high-efficiency electrolysis equipment. Coupled with the need for high electrocatalytic activity is the requirement of low internal anode resistance. This resistance depends on both the anode materials and structure.

Once high efficiency has been demonstrated, the anode must be tested for stability. As a rough goal, physical and chemical degradation should be minimal during several, even as many as ten or more (4), years of operation. The anode must not only be stable at oxygen evolving potentials, but must resist open-circuit corrosion as well. With the recent advent of highly efficient cathode catalysts, the anode corrosion products, however limited, must not foul the cathode surface. In addition to chemical and physical stability, the anode should provide a constant

*Electrochemical Society Active Member.

potential after an initial break-in period, rather than the time-dependent potential increase which occurs at nickel anodes (5-7).

Manufacturing scale-up is a necessary but difficult part of commercial anode development, involving a move from the laboratory to a pilot processing facility. A way must be found to manufacture anodes on the order of 1 m² in area. The process must be under sufficient control to assure constant anode quality. Because of cost constraints, an automated or semiautomated manufacturing process is necessary.

The maximum practical anode cost depends on the capital cost constraints for the entire electrolysis system. This, in turn, depends not only on competing electrolysis systems, but on nonelectrolytic hydrogen production alternatives as well. The permissible cost of any anode improvement will be based on the power savings realized from it and the anticipated anode lifetime.

Nickel Anode Structures

Nickel has traditionally been used as the anode material in alkaline water electrolysis. It is relatively inexpensive and highly corrosion-resistant at positive potentials in alkaline electrolytes. The oxygen evolution efficiency of nickel is among the highest for elemental metals (8). As a result, the nickel anode is the benchmark against which improved anodes are compared. Table I gives some current *vs.* potential data reported for various conventional nickel anodes.

Nickel anode efficiency has been improved by developing high surface-area anode structures. For example, porous, high surface-area anodes have been made by sintering fine nickel powders prepared by nickel tetracarbonyl decomposition. These anodes, although generally less porous, are essentially similar to the positive plaques used in nickel-cadmium batteries. In high-pressure (30 atm) electrolysis at 200°C, the oxygen evolution overpotential, η_{O_2} , on sintered, porous nickel anodes was about 100 mV lower than on smooth nickel anodes, at current densities of 500-1500 mA/cm² in 35% KOH electrolyte (9). However, sintered, porous nickel anodes were only marginally more efficient than nickel cloth anodes in atmospheric pressure electrolysis, over the temperature range 25°-90°C (10). This was attributed to poor inner surface utilization in the porous anode at atmospheric pressure, presumably due to gas blockage. Similar results were obtained in 5N KOH at 25°C, *i.e.*, 100 mesh nickel screen and sintered, porous nickel anodes produced approximately equal current densities when compared potentiostatically at 1.64 V/DHE (11). However, because

Table I. Conventional Ni anodes

Anode	Test conditions	i , mA/cm ²	Potential	Ref.
Solid Ni	30% KOH, 70-80°C	200	$\eta_{O_2} = 415$ mV	(9)
Ni-plated steel	28% KOH, 70°C, initial	75	$\eta_{O_2} = \sim 320$ mV	(6)
Ni-plated steel	28% KOH, 70°C, 160 days	75	$\eta_{O_2} = \sim 400$ mV	(6)
Smooth Ni	29% KOH, 70°C, after 2h	1000	$E_{an} = 0.66$ V/NHE	(56)
Sandblasted Ni	29% KOH, 70°C, after 2h	1000	$E_{an} = 0.64$ V/NHE	(56)
Nickel plated steel	29% KOH, 70°C, after 2h	1000	$E_{an} = 0.64$ V/NHE	(56)
Nickel screen, 100 mesh	5N KOH, 60°C	500	$E_{an} = 1.66$ DHE	(32)
Smooth Ni	34% KOH, 90°C	100	$E_{an} = 1.45$ HE	(10)
Polished Ni	50% KOH 80°C	100	$E_{an} = 1.67$ DHE	(62)
Polished Ni	50% KOH 150°C	100	$E_{an} = 1.55$ DHE	(62)
Polished Ni	50% KOH 208°C	100	$E_{an} = 1.37$ DHE	(62)
Polished Ni	50% KOH 264°C	100	$E_{an} = 1.24$ DHE	(62)
Sandblasted Ni	50% KOH 30°C	100	$E_{an} = 0.70$ V/Hg/HgO	(24)
Sandblasted Ni	50% KOH 70°C	100	$E_{an} = 0.60$ V/Hg/HgO	(24)
Sandblasted Ni	50% KOH 110°C	100	$E_{an} = 0.53$ V/Hg/HgO	(24)
Sandblasted Ni	50% KOH 130°C	100	$E_{an} = 0.50$ V/Hg/HgO	(24)

the sintered, porous anodes degraded less with time, they were superior after about 60h of electrolysis. In contrast, another study (12) showed that 50% and 80% porous nickel anodes were initially superior to massive nickel anode forms in 30% KOH at 80°C, but showed greater overpotential increases with time.

Anodes with thin, sintered, porous nickel coatings were made by applying nickel powders, in polysilicate-based slurries, to nickel and steel substrates (13). The coatings were sintered under a reducing atmosphere. The nickel coating morphology depended on the sintering temperature and, to a lesser extent, the sintering time. Decreasing the sintering temperature through the range 980°-760°C and the sintering time through the range 30-5 min progressively preserved more of the fine structure in the coatings. A corresponding η_{O_2} decrease of about 70 mV was observed in electrolysis at 200 mA/cm² in 30% KOH electrolyte at 80°C. Although the interior coating surfaces participated in the oxygen evolution reaction to some extent, the η_{O_2} reduction obtained by increasing the coating thickness was small. In a subsequent study (14), the porous nickel-coated mild steel anodes were operated for 1200h at 100 mA/cm² in 30% KOH at 80°C. After an initial rise, the anode potential was essentially constant. Nickel-iron alloy formation in the steel surface region, during the high temperature sintering treatment used to bond the coating to the substrate, greatly increased its corrosion resistance.

Nickel coatings made by slurry coating and sintering nickel powder have also been applied to foamed nickel anode supports (15). The resulting anodes were operated at 500 mA/cm² in 40% KOH electrolyte at 90°C. The voltages of cells with porous nickel/foamed nickel anodes and cathodes were about 50-100 mV lower than those of cells with uncoated foamed nickel electrodes. Cells equipped with the coated electrodes maintained a stable 1.68V operating voltage at 200 mA/cm² in 100h electrolyses at 118°C.

The results cited above show that coatings made by sintering fine nickel powder prepared by Ni carbonyl decomposition reduce oxygen overpotential. Avoiding the high temperatures used for nickel sintering, which produce a concomitant loss in surface area, would appear to offer the advantage of maximized anode surface area. However, Balajka found that TFE-bonded nickel powder applied to 100 mesh nickel screen was ineffective (16). Such anodes were actually about 60 mV less efficient than similar screens with electroplated nickel coatings, at a current density of 370 mA/cm² in 30% KOH electrolyte at 80°C. This poor performance was ascribed to possible oxidation of the metal surface during electrode preparation.

Nickel whisker anodes (17, 18) were made from polycrystalline nickel whiskers grown by chemical vapor deposition of Ni(CO)₄ gas in an electromagnetic field. Whiskers, with diameters from 0.1 to 50 μ m and lengths from

one-tenth to several centimeters, were sintered at 800°-1000°C into continuous, fibrous networks on 200 mesh nickel screen. The resulting anodes were up to 90% porous, with specific surface areas of up to 5×10^3 cm²/g. The anodes were tested in 30% KOH electrolyte, at current densities from 100 to 1000 mA/cm², based on apparent anode surface area. Oxygen evolution overpotentials were about 100 mV lower on whisker anodes than on multilayer, 200 mesh nickel screens. There was no loss of structural integrity during 48h of electrolysis at 1000 mA/cm².

Raney Alloy Anodes

Raney nickel is made by alloying nickel with metals such as aluminum or zinc. When the Raney alloy is leached in alkaline electrolyte, a high surface-area structure with high electrochemical activity is produced. Several approaches to making Raney nickel anodes for alkaline water electrolysis have been reported.

Raney Ni-Zn alloy was prepared by electrodeposition from chloride electrolyte (19). The electrodeposition conditions affected both the composition and structure of the alloy. A maximum BET specific surface area, greater than 25 m²/g, for the leached anodes was obtained at a deposition potential of 1.07 V/SCE. Correspondingly, electrolysis cells containing Raney nickel anodes and cathodes had minimum voltages using alloy electroplated at -1.07 V/SCE. Analysis of the experimental data indicated that the improved performance of Raney nickel-coated anodes was due solely to greater anode surface area (20). An electrolysis cell containing Raney nickel-activated iron anodes and cathodes was stable for 3000h at a current density of 200 mA/cm² and a temperature of 110°C.

Electrodeposition of Ni-Zn alloy onto nickel or stainless mesh has also been used to make Raney-type porous electrodes by plating for as much as 24h (21). These electrodes differed from the usual sintered powder porous anodes in their pore structure, which was channel-like and full of very fine hairline cracks. Porosities ranged from 65% to 75%, average pore sizes from 1 to 3 μ m. Electrochemical measurements in 6N KOH showed that the electrodeposited porous anodes were generally inferior to sintered ones.

A plasma-sprayed Ni-Al anode coating produced an initial overpotential reduction of 200 mV in electrolyses at 160° and 200°C (22). After 100h, the η_{O_2} improvement was still 180 mV at 160°C, whereas at 200°C, the improvement decreased to 150 mV after 350h. In contrast, Raney nickel prepared by plasma spraying Ni-Al alloy particles was found to be a poor oxygen evolution catalyst in another study (23). This was attributed to rapid oxidation of the anode surface. The Raney nickel structure was found, however, to be useful as a support for other catalysts, as discussed later in this review.

Raney nickel deposited on foamed nickel anode supports behaved similarly to sintered, porous nickel coat-

ings on foamed nickel, i.e., cell voltages were 50-100 mV lower when Raney nickel-coated anodes, and cathodes were used instead of uncoated foamed nickel electrodes (15). In 40% KOH electrolyte at 118°C, Raney nickel was initially superior to sintered, porous nickel, but the advantage declined to only 20 mV within 100h.

Various Raney alloy anodes tested at 90°C were about 60 mV more efficient than conventional, low surface-area nickel anodes (24). At a current density of 100 mA/cm², η_{O_2} was 240 mV for Raney nickel, 240 mV for Raney nickel-cobalt (30 atom percent (a/o) Co), and 230-240 mV for Raney cobalt. These values compared with 300 mV for steel-blasted nickel and 280 mV for electrodeposited nickel.

Several methods of doping Raney nickel anodes with lithium were studied by Martin *et al.* (25). In almost all cases, anode activity declined greatly during 24h of electrolysis at 80°C, at a current density of 1000 mA/cm². Best results were obtained by preoxidizing the anodes in H₂O₂ + LiOH or thermally in air. In the same study, better results were obtained when Raney nickel anodes were impregnated with cobalt oxide. Overpotential reductions of more than 130 mV were measured after 24h of electrolysis at 80°C, at a current density of 1000 mA/cm². Impregnating Raney nickel with mixed cobalt-nickel oxides was no more effective than using cobalt alone.

Ion-Implanted Nickel Anodes

In an unusual approach to nickel anode activation, the unique characteristics of ion implantation were investigated (26). Ion implantation offers the advantage of controlled additions of dopants to only the near surface region, an important factor when expensive dopants are used. In addition, the maximum surface concentrations of the implanted materials are not limited by solid solubilities.

Various doses of 50 keV Ag⁺, Li⁺, He⁺, and Kr⁺ ions were implanted. Electrochemical measurements in 30% KOH electrolyte at 80°C showed that implantation of 0.3-4.0 × 10¹⁶/cm² Ag⁺ ions reduced η_{O_2} by 20%-40%, with best results in the range 0.3-1.3 × 10¹⁶/cm². After 24h of electrolysis, the Ag⁺ implanted anodes showed a well-defined open-circuit discharge plateau. The discharge corresponded to about two electrons per implanted Ag atom, suggesting formation, during electrolysis, of an intermediate complex containing one oxygen per implanted Ag atom. Unimplanted Ni anodes showed no well-defined discharge plateau.

Inert gas (He⁺ and Kr⁺) implants produced no η_{O_2} reductions, indicating that the improvement caused by Ag⁺ was not due to radiation damage effects. Li⁺ ions were implanted to increase the electronic conductivity of the nickel oxide anode surface layer. As discussed elsewhere in this review, lithium additions by other techniques have increased the oxide film conductivity and produced a corresponding η_{O_2} decrease. Unexpectedly, no η_{O_2} reduction was produced by Li⁺ implants.

High-Temperature Degradation of Nickel Anodes

Nickel anode degradation during high temperature service has been investigated, primarily in conjunction with the French high-temperature electrolysis programs. Giles (27) analyzed the physical and electrical characteristics of roll-compacted, sintered, porous nickel anodes before and after pilot plant operation at CEM. Electrolysis was carried out at 1000 mA/cm², in 35% KOH at 200°C, under 30 atm pressure. During 250h of electrolysis, anode porosity decreased from about 45% to about 20% as corrosion products accumulated within the anode. As the finely porous corrosion products filled the larger anode pores, the mean pore diameter fell from 1.9 to 0.3 μ m after 23h and to 0.1 μ m after 83h. X-ray diffraction showed both Ni(OH)₂ and NiO, but no +3 nickel species, in the corrosion product. Anode tensile strength dropped from 50 to 20 N/mm² after 83h of electrolysis. The electrical resistivity increased from about 27 × 10⁻⁶ Ω -cm to about 46 × 10⁻⁶ Ω -cm during the same period. Despite the slowing of

the nickel corrosion rate with time because of the partly protective nature of the corrosion layer, Giles concluded that using sintered, porous nickel anodes in high-pressure, high-temperature service was questionable.

A joint GDF/EDF study (28) addressed nickel corrosion in the temperature range 130°-180°C. While positive potentials were not imposed on the nickel specimens, the corrosion tests were carried out in an oxygenated environment in 40% KOH. Specimens of Ni 200 and Ni 201 industrial castings, a powder metallurgy compact (Ni 270), and high-purity, zone-refined nickel were studied. In the oxygenated electrolyte, the porous corrosion products were NiO and Ni(OH)₂ at 130°C, while only NiO was observed at 180°C. Corrosion rates at 180°C were 10-15 μ m/yr for high-purity nickel, and 30-45 μ m/yr for Ni 200, 201, and 270. Restricting the sulfur content of the nickel was found to retard corrosion.

Ni(OH)₂-Catalyzed Nickel Anodes

Perhaps the most straightforward approach to catalyzing the nickel anode is to add Ni(OH)₂ to its surface. Under anodic polarization, the Ni²⁺ species can be converted to Ni³⁺. Electrochemical and ellipsometric studies (7) demonstrated that trivalent nickel was the desired species for efficient oxygen evolution. Thus, Ni(OH)₂ may be regarded as the electrocatalyst precursor.

Attempts to catalyze nickel anodes with Ni(OH)₂ have benefited from the extensive work on nickel electrodes for alkaline storage batteries (29). Sintered, porous nickel anodes impregnated with Ni(OH)₂, essentially nickel battery positives, were considerably more efficient for oxygen evolution than similar unimpregnated anodes (10). Electrolysis was carried out at 90°C in 34% KOH electrolyte. At a current density of 400 mA/cm², η_{O_2} was only about 100 mV on the impregnated anodes, while the unimpregnated anodes were, as discussed earlier, no more efficient than nickel cloth anodes. This enhanced activity was attributed to higher superficial surface area rather than improved utilization of the inner anode surfaces. Anodes impregnated with 1.91g of Ni(OH)₂ per cm³ of void volume, a characteristic nickel battery positive loading, showed rapid disintegration under continuous charging at 80°C. This was presumably due to high internal stresses. Anodes with a lower Ni(OH)₂ loading of 1.15 g/cm³ of void volume were dimensionally and structurally stable during more than 100 days of operation at 400 mA/cm².

In a study of nickel battery positive plates, the oxygen evolution reaction was observed at an earlier stage of charging when the plates were impregnated electrochemically rather than chemically (30). Water electrolysis anodes in sheet and woven screen form, with sintered, porous nickel coatings, were electrochemically impregnated with Ni(OH)₂ (31). In a one-step impregnation process, the amount of Ni(OH)₂ precipitated varied linearly with the charge passed. This allowed the catalyst loading to be controlled accurately. On Ni(OH)₂-impregnated anodes, η_{O_2} at 200 mA/cm² was 45-60 mV lower than on similar uncatalyzed anodes, in 30% KOH electrolyte at 80°C. Optimum Ni(OH)₂ loadings were about 1-4 mg/cm² of apparent anode surface area. At higher loadings, overpotentials rose as the outer pores of the nickel coatings became plugged with Ni(OH)₂, resulting in a loss of effective anode surface area.

Lithiated NiO electrocatalyst was prepared by vacuum decomposition of a mixed slurry of Ni(OH)₂ and LiOH (32). Lithium, present at 1 a/o in the finished catalyst, greatly reduced the electronic resistivity from the undoped value (>10⁸ Ω -cm) to 100 Ω -cm. The BET specific surface area of the catalyst was 100 m²/g. Anodes were made by mixing the catalyst with TFE binder and sintering onto 100 mesh nickel screen. In 5N KOH electrolyte at 60°C, the catalyzed anodes were about 55 mV more efficient than uncatalyzed nickel screens and were comparable to NiCo₂O₄-catalyzed anodes, which are discussed in the following section.

NiCo₂O₄

The oxygen evolution characteristics of the mixed oxide spinel, NiCo₂O₄, have been reported extensively, most notably by Tseung and co-workers (11, 32-36). In strongly alkaline electrolytes at high positive potentials, *i.e.*, conditions typical of commercial electrolysis, oxygen evolution proceeds by decomposition of species with tetravalent cations (35, 37).

NiCo₂O₄ has been made in several ways. Freeze-drying mixed Ni and Co nitrates, followed by vacuum decomposition at 250°C and a final heat-treatment for 10h at 400°C in air, is preferred. The resulting catalyst has a high specific surface area (70 m²/g by BET) and a moderate electrical resistivity (10 Ω-cm) (32). Anodes made with freeze-dried NiCo₂O₄ were more efficient than similar anodes catalyzed with NiCo₂O₄ made by mixed nitrate coprecipitation (34). It was proposed that the freeze-dried product was more homogeneous, *i.e.*, there was less separation of Ni and Co oxides. NiCo₂O₄ has also been made by direct thermal decomposition of the mixed nitrate salts on anode substrates (32). However, the anodes were less efficient than those made with freeze-dried NiCo₂O₄.

Highest anode efficiencies have been obtained with the freeze-dried NiCo₂O₄ incorporated into a TFE-bonded coating (32). Optimum efficiency was obtained using 15%-30% TFE binder. For example, at 60°C in 5N KOH, a catalyst loading of 13 mg/cm² produced a current density of 1000 mA/cm² at 1.6 V/DHE. However, oxygen bubbles were observed to cling to the hydrophobic anode surface. Applying a thin, hydrophilic nickel cobalt oxide layer to the anode surface improved bubble release. This reduced the anode potential by about 20 mV at 1000 mA/cm² in 5N KOH at 25°C. In another study (16), TFE-bonded NiCo₂O₄ anodes were about 150 mV more efficient than nickel-plated nickel screen when operated at a current density of 370 mA/cm² in 30% KOH electrolyte at 80°C.

Doping NiCo₂O₄ with varying amounts of Sr and La was effective in reducing η_{O_2} (25). Best results were obtained when 0.5 atoms of (2/3 Sr + 1/3 La) per atom of cobalt were added. The resulting material, with nominal composition NiCo₂Sr_{0.66}La_{0.33}O_{5.17}, produced a 300 mV overpotential at a current density of 1000 mA/cm².

NiCo₂O₄-catalyzed anodes have shown high oxygen evolution efficiency in several laboratories. Long-term anode stability, however, is open to some question. At a current density of 330 mA/cm², an overpotential decrease of 150 mV relative to nickel anodes was reported (5). However, poor stability was noted at temperatures above 100°C and current densities greater than 200 mA/cm². In contrast, thermally decomposed NiCo₂O₄ anodes were stable for 2000h of electrolysis at 1000 mA/cm² at a temperature of 120°C. In another study, NiCo₂O₄ anodes were stable for over 1000h of electrolysis at 1000 mA/cm², at temperatures from 120°C to 200°C (38). However, the catalyst was very sensitive to corrosion at open circuit.

In tests of about 150 days duration at low current density (75 mA/cm²) and temperature (70°C) in 28% KOH, a TFE-bonded, freeze-dried NiCo₂O₄ anode was initially about 60 mV more efficient than a nickel-plated steel anode (6). After 150 days, due to a lower η_{O_2} increase with time, the NiCo₂O₄ anode advantage was over 100 mV. Similarly, in 18 days of electrolysis at 330 mA/cm², η_{O_2} was about 100 mV lower on NiCo₂O₄ anodes than on uncatalyzed Ni screen in 30% KOH at 90°C (39).

Co₃O₄

The spinel Co₃O₄ has shown promising efficiency and long-term performance. Thermally decomposed Co₃O₄ was deposited on electroformed nickel plates with conic holes (40) and was tested in atmospheric pressure electrolysis at 120°C. After 6000h of electrolysis at 1000 mA/cm² in 40% NaOH electrolyte, the anode potential was about 0.59V *vs.* Hg/HgO reference (containing the bulk electrolyte composition). After an initial break-in period, the rate of η_{O_2} rise with time was only 4 mV/1000h.

Co₃O₄ anodes containing 0, 4, 7, and 10 a/o Li dopant were prepared by freeze drying and vacuum decompos-

ing the mixed Li and Co nitrates (33, 37). This was followed by heat-treatment at 600°C for 10h to produce the Li-doped spinels. The electrical resistivities of the catalyst powders varied greatly with the extent of Li doping, from 10⁴ Ω-cm at 0% Li to 10 Ω-cm at 4% Li, and 1 Ω-cm at both 7% and 10% Li. TFE-bonded anodes were made using 10/3 weight ratios of the catalyst powders to TFE. These anodes were operated at 1000 mA/cm² in 5M KOH at 70°C. The anode potential dropped markedly with increasing Li doping, *i.e.*, 1.69V with no Li dopant, and 1.56, 1.535, and 1.52V, respectively, at 4, 7, and 10 a/o doping. The enhanced O₂ evolution activity with increased Li doping was attributed to the increased fraction of Co³⁺ ions which could form if all the Li entered tetrahedral lattice sites (37).

An electrolysis cell equipped with a TFE-bonded, 10% Li-doped Co₃O₄ anode was operated for about 6000h at 1000 mA/cm² (33). The cell contained 45% KOH electrolyte at 85°C. An anode half-cell measurement after approximately 5600h indicated an η_{O_2} increase of about 50 mV during operation. The Li content of the anode was unchanged. A TFE-bonded, Li-doped Co₃O₄ coating was applied to a porous nickel anode substrate (9). In 30% KOH electrolyte at 70°C, at a current density of 1000 mA/cm², η_{O_2} was 300 mV at the beginning of electrolysis and 290 mV after 1000h of operation.

Other AB₂O₄ Mixed Oxides

A variety of AB₂O₄ spinel compounds (B = Al, Cr, Mn, Fe, or Co) were used to prepare TFE-bonded anodes (15). The anodes were tested in 30% KOH at 80°C. At a current density of 1000 mA/cm², the spinel anode overvoltages were 30-70 mV lower than the overvoltage of uncatalyzed nickel.

The mixed oxides NiLa₂O₄, NiPr₂O₄, and NiNd₂O₄ were prepared by thermal decomposition on platinum supports (41). In potentiostatic experiments conducted in 30% KOH at 50°C, the three catalysts showed similar current *vs.* potential characteristics. A low Tafel slope (approximately 40 mV/decade) was observed at current densities of up to 100 mA/cm². At higher current densities, the Tafel slope was about 120 mV/decade. The anode potentials were approximately 1.6 V/RHE at 1000 mA/cm². The oxygen evolution overpotentials on the mixed oxide anodes were observed to be essentially stable for several hundred hours, at current densities as high as 1000 mA/cm².

The NiLa₂O₄ anode electrocatalyst has been doped with Li, Mg, and Fe, replacing some of the Ni, and with partial substitution of sulfur for oxygen (12). The surface properties of the Li-doped materials were claimed to be slightly superior to undoped NiLa₂O₄. However, Li doping produced an increase in bulk catalyst resistivity as x in Ni_{1-x}Li_xLa₂O₄ was increased from 0 to 0.24, in contrast to the lower resistivity produced by doping Co₃O₄ with Li, as discussed in the preceding section. The net effect on η_{O_2} was negligible. Mg doping also increased the electrical resistivity of the catalyst. Similarly, high levels of Fe doping, *e.g.*, $x = 0.06$ in Ni_{1-x}Fe_{2x/3}La₂O₄, increased electrical resistivity. Lower Fe doping (*e.g.*, $x = 0.03$) produced a resistivity decrease, but failed to improve η_{O_2} for the NiLa₂O₄ anode. Cobalt substitution, while effective in reducing η_{O_2} , produced a nonstoichiometric oxide of nominal formula Ni_{1.8}Co_{0.2}LaO₃. Its anodic polarization was about 25 mV lower than that of NiLa₂O₄ in 30% KOH electrolyte at 85°C, over the current-density range 100-1000 mA/cm². At the current density of 500 mA/cm², the Co containing anode also showed superior time behavior during 300h of electrolysis, producing a ~100 mV lower anode potential during the last 150h. However, raising the electrolysis temperature to 110°C produced a significant deterioration in performance, so that the Co containing anode became inferior to NiLa₂O₄. Treatment of NiLa₂O₄ with H₂S to incorporate sulfur into the catalyst worsened the anode polarization behavior. This was attributed to the higher resistance of the sulfur containing anodes.

La-Sr-Co-Oxides and Variants

Perovskite anode catalysts of the La_{1-x}Sr_xCoO₃ type, and substitutional variants, have been studied more extensively than any other mixed oxides, with the possible exception of NiCo₂O₄. Their high activities for oxygen evolution are similar to that of NiCo₂O₄, with the relative superiority of the two types of catalyst still open to question. For example, in 30% KOH electrolyte at 145°C, La_{0.5}Sr_{0.5}CoO₃ was about 120 mV superior to NiCo₂O₄ at 1000 mA/cm² (38). However, under similar conditions (120°C, 1000 mA/cm²), cells with La_{0.5}Sr_{0.5}CoO₃ anodes showed 0.1V higher voltages than similar cells with NiCo₂O₄ anodes (42). A mixed La-Sr-Co oxide of unspecified composition, deposited on a Raney nickel substrate, was 180 mV more efficient than an unactivated nickel mesh anode at a current density of 1000 mA/cm² in 40% KOH electrolyte at 160°C (23). The anode was stable for more than 1000h.

It is generally agreed that the La-Sr-Co perovskite composition has a significant effect on oxygen evolution overpotential. The relationship between η_{O_2} and x in the formula La_{1-x}Sr_xCoO₃ is not completely clear, but an overall trend toward higher catalytic activity in the compositional midrange has been determined. When 5-10 mg/cm² La_{1-x}Sr_xCoO₃ coatings were applied by spray pyrolysis, a broad η_{O_2} minimum, centered at about $x = 0.5$, was observed at a current density of 10 mA/cm² (43). At a current density of 500 mA/cm², optimum overpotentials of about 330 mV were measured over the approximate range $0.5 < x < 1.0$. These results were obtained in 6N KOH electrolyte at 80°C. In a later study with more data points reported, the variation in η_{O_2} with x was refined (25). At current densities of 100, 500, and 1000 mA/cm², an overpotential minimum was found at about $x = 0.75$, while $x \approx 0.15$ produced an overpotential maximum. At low current densities in 45% KOH at 25°C, La_{0.5}Sr_{0.5}CoO₃ and La_{0.8}Sr_{0.2}CoO₃ had approximately equal potentials, while both were superior to LaCoO₃ (44).

The variation in electrical resistivity, ρ , vs. x for several perovskite families Ln_{1-x}Sr_xCoO₃ is roughly similar to that described above for η_{O_2} vs. x (45). This suggests that electrical resistivity is an important factor in the efficiency of perovskite anode catalysts. For most of the lanthanides studied, ρ was 0.1-10 Ω -cm at $x = 0$, decreasing to about $10^{-3.5}$ Ω -cm at $x = 0.5$. The minimum ρ composition interval for La containing perovskites was quite broad, from about $x = 0.2$ through $x = 0.6$, the highest value investigated. The ρ decrease as Sr was substituted for La has been attributed to more Co⁺³/Co⁺⁴ couples in the doped perovskite (44).

La_{0.5}Sr_{0.5}CoO₃ coatings have been prepared by a number of methods. Spray pyrolysis was used to deposit 7 mg/cm² coatings in a study of the effects of final calcination temperature (22). Best results were obtained by calcining the coatings at 600°-700°C. In 8N KOH at 80°C, η_{O_2} was about 380 mV at 1000 mA/cm². Raising the coating loading to about 15 mg/cm² further reduced η_{O_2} to about 340 mV at 1000 mA/cm². Thermally decomposed coatings, containing 1.2 mg/cm² La_{0.5}Sr_{0.5}CoO₃, were also studied (24). At 90°C, these coatings gave η_{O_2} approximately 250 mV at 100 mA/cm² and 330 mV at 1000 mA/cm². From η_{O_2} at 90°C and the rate of overpotential change with temperature, $d\eta_{O_2}/dT$, an overpotential of 220 mV was estimated for 1000 mA/cm² electrolysis at 160°C. TFE-bonded anodes (36% TFE, 14 mg/cm² loading) were nearly as active as anodes without TFE at low current densities, in 6N KOH at 80°C (43). However, η_{O_2} increased rapidly at current densities above 10 mA/cm² due to resistance losses between catalyst particles in the coating. Changes in TFE content and preparation method did not overcome this problem.

The effects of electrolysis temperature on the activity of La_{1-x}Sr_xCoO₃ are unclear. It is generally agreed that, at temperatures up to 160°C, an increase in electrolysis temperature produces an increase in catalyst activity. Because $d\eta_{O_2}/dT$ for the perovskite catalysts is greater than for other anodes (e.g., Raney nickel, unactivated nickel)

their relative improvement is greater with increasing temperature (24). Continuous improvement up to 200°C was reported for electrolysis in 36% KOH at 22 atm pressure (43). The η_{O_2} improvement at 1000 mA/cm² relative to unactivated nickel anodes was 260 mV at 160°C and 280 mV at 200°C. However, a subsequent publication from the same laboratories (22) reported a decrease in activity between 160° and 200°C, at 1000 mA/cm² in 8N KOH. The experimental evidence indicated that this was an intrinsic property of the catalyst.

The stability of La-Sr-Co oxides under anodic polarization has been good. In 36% KOH at 160°C, La_{0.5}Sr_{0.5}CoO₃ was stable during 500h of electrolysis at 1000 mA/cm², producing a 150 mV η_{O_2} reduction (22). A series of La_{1-x}Sr_xCoO₃ compounds, prepared by freeze drying, were corrosion resistant at 220°C in 75% KOH electrolyte (44). No activity loss was observed during 1000h of continuous operation, and 2600h of operation with periodic interruption, at 1000 mA/cm² in the temperature range 120°-200°C (38). However, La-Sr-Co oxides were reported to be very sensitive to passive corrosion.

Several anode electrocatalysts have been made by substituting nickel or iron for some or all of the cobalt in La_{1-x}Sr_xCoO₃. The oxygen evolution activity in the family of compounds La_{1-x}Sr_xFe_{1-y}Co_yO₃ increased with increasing x and y (46). SrCoO₃ itself could not be synthesized as a perovskite. As a result, the most efficient anode catalyst prepared was La_{0.2}Sr_{0.8}Fe_{0.2}Co_{0.8}O₃. In 1M KOH electrolyte at 25°C, that catalyst produced a steady potential of 0.90V vs. Hg/HgO at 100 mA/cm², after an initial potential rise during the first 40h of electrolysis.

Nickel substitution for cobalt, in the series of compounds La_{0.5}Sr_{0.5}Ni_{1-y}Co_yO₃, has also been investigated (22). Coatings with 10 mg/cm² of the perovskites were prepared by spray pyrolysis and tested in 8N KOH at 80°C. At a current density of 1000 mA/cm², a minimum η_{O_2} of about 310 mV was obtained at about $y = 0.6$. The compound LaNi_{0.2}Co_{0.8}O₃ was plasma sprayed to produce 8 mg/cm² coatings (24). At 90°C, η_{O_2} was 270 mV at 100 mA/cm² and 330 mV at 1000 mA/cm². The 90°C data and $d\eta_{O_2}/dT$ were used to estimate an overpotential of 240 mV at 160°C, at a current density of 1000 mA/cm². An anode catalyzed with La_{0.2}Sr_{0.3}Ni_{0.4}Co_{0.6}O₃ produced an initial 140 mV overpotential reduction at 200°C, but lost activity after 1h of electrolysis (25). Surface analysis showed an increase in the Sr/La ratio.

The perovskite electrocatalyst LaNiO₃ was prepared by coprecipitation of La and Ni nitrates, followed by an oxidizing heat-treatment at 800°C (47). Anodes were made by pressing the LaNiO₃ powder into pellets and sintering at 750°C. In approximately 1M hydroxide electrolytes at 25°C, the rate of O₂ evolution on LaNiO₃ was about 10⁵ times faster than on Pt and about 10² times faster than on NiCo₂O₄. At a current density of 100 mA/cm², η_{O_2} was about 310 mV. The Tafel slope was 40 mV/decade. The LaNiO₃ surface was nonstoichiometric, with almost all the nickel in the +2 state. It was proposed that the high activity of LaNiO₃ was due to its high surface carrier density (approximately 10²⁰/cm²).

Recently, Bockris and co-workers suggested a course for future perovskite electrocatalyst development (48). Their XPS examinations indicated a nonstoichiometric surface, in which charge is mainly compensated by oxygen vacancies. Because of the strong affinity of oxygen-deficient surfaces toward oxygen in the form of OH, an increase in electrocatalytic activity would be expected with increasing M²⁺-OH bond strength, where M²⁺ is a surface transition metal ion. As a result, it was proposed that perovskite electrocatalyst research should focus on finding a bonding sequence which produces low intermediate radical coverage. In an experimental study covering 18 perovskite compositions, carried out by the same group, the electrochemical desorption of OH was found to be rate determining in every case (49). Very recently, the study of perovskite electrocatalysis was extended (50). It was shown that reaction rates increase with decreases of magnetic moment, stability of the perovskite lattice, and

enthalpy of transition metal hydroxide formation, and with increased number of d-electrons in the transition metal ion. The latter correlation is consistent with the earlier proposal that rate-determining steps involve OH desorption.

ABO₂ Metal Oxides

Thin films of ABO₂ metal oxides were prepared by RF-sputtering the parent alloys under various O₂ partial pressures, followed by annealing in air (51). Metal A was Pt or Pd, and B was Co, Rh, or Cr. The oxides exhibited the delafossite structure, *i.e.*, for PtCoO₂, alternating layers of Pt linearly coordinated with two oxygen atoms and Co octahedrally coordinated with oxygen. Oxygen evolution activity depended strongly on the transition metal, in the order Co > Rh > Cr, but was nearly independent of the noble metal. It was suggested that this was due to coverage of the noble metal with a poorly conducting oxide. The Co containing oxides produced oxygen evolution potentials more than 100 mV lower than a Pt anode in 1M NaOH at 23°C.

In electrolysis at 120°C, NiCoO₂ anodes prepared by thermal decomposition showed oxygen evolution potentials similar to those of NiCo₂O₄ and La_{0.5}Sr_{0.5}CoO₃ anodes at a current density of 1000 mA/cm² (42, 43). At lower current densities (100-200 mA/cm²), NiCoO₂ was superior to the other anode materials.

Base Metal Alloys, Intermetallics and Non-Oxide Catalysts

It has been known for some time that nickel-iron alloys show relatively low oxygen evolution overpotentials (52, 53). However, the variation of η_{O_2} with alloy composition was not clearly defined, because results vary depending on alloy history and pretreatment.

Recently, Ni-Fe alloy anodes have been re-examined. Gras and Pernet (54) studied the anodic behavior of alloys containing 9, 28, and 50 w/o nickel, in comparison to two forms of nickel. They found that the 9% Ni alloy was unstable, in agreement with earlier results (53), while the catalytic activity of the 28% nickel alloy was lower than that of pure nickel. The corrosion-resistant 50% nickel alloy was about 70 mV more efficient than nickel after 100-200h of electrolysis, in the current-density range 100-1000 mA/cm². Anode composition *vs.* depth profiling, by secondary ion mass spectrometry, showed that the surface was enriched with potassium and oxygen after electrolysis. It was proposed that *in situ* formation of a Ni_xFe_yO_zK_w complex oxide increased the catalytic activity of the anode.

In another study (55), high surface-area nickel-iron alloy anodes were prepared with a 37% nickel powder prepared by codecomposition of nickel and iron carbonyl. The powder was applied to anode substrates as a sintered, porous coating. In 30% KOH electrolyte at current densities up to 400 mA/cm², the alloy anodes evolved oxygen as efficiently as similar anodes prepared with pure nickel powder.

Non-noble metal catalysts were made by plasma spraying coatings of >90 w/o Ni and/or Co plus <10 w/o stainless steel onto preheated iron or nickel-coated iron substrates (56). Anode overpotentials were 60-80 mV lower than on smooth nickel, at 1000 mA/cm², in 29% KOH at 70°C. At current densities <500 mA/cm², there was no variation of anode potential *vs.* time for 1000h of operation. At 1000 mA/cm², the anode potential increased from 1.54 to 1.60 V/NHE during the first 300h of electrolysis, then remained constant up to 1000h.

Ni-W alloys and the intermetallic compounds Ni₃Ti, NiTi, and NiTi₂ were investigated by Lu and Srinivasan (57). Titanium was alloyed with nickel to increase the number of d-band vacancies and, thus, electrocatalytic activity (58). However, as discussed in the following section, such a correlation was not found at the oxide-covered electrodes. Best results were obtained with Ni₃Ti, for which η_{O_2} was 20 mV lower than on nickel, in 30% KOH electrolyte at 80°C.

While the last-cited study found no correlation of oxygen evolution activity to electronic properties, Osaka *et al.* (59) did find a correlation to magnetic properties, which strongly connected, in turn, to electronic properties, for cobalt borides and composite cobalt borides. For cobalt borides, the O₂ evolution activity depended significantly on the Co/B ratio, as well as the sintering temperature used to make the catalyst. Optimum preparations produced higher electrocatalytic activity than nickel or cobalt. These best conditions included a 3:1 ratio of cobalt to boron, and a sintering temperature of 400°-500°C, at which the saturation magnetization showed a maximum. Among the composite cobalt borides, cobalt iron boride (Co:Fe:B = 1:2:1) sintered at 450°C had the greatest catalytic activity. At 100 mA/cm² in 6M KOH at 25°C, cobalt iron boride produced a potential of about 0.65V *vs.* Hg/HgO. It was found that those catalysts which formed thicker and more-stable oxide films in higher oxidation states had higher activities for oxygen evolution.

Precious Metal Catalysis

Available experimental evidence strongly indicates that individual precious metals and their oxides have little or no superiority to nickel in their electrocatalytic activity (10, 11, 15, 60). The exception is ruthenium oxide, which is a highly efficient oxygen evolution electrocatalyst (24) but is unstable in alkaline electrolyte.

Oxygen evolution on smooth platinum and iridium electrodes was examined by Appleby *et al.* (10) and compared to O₂ evolution on nickel. In 25% KOH electrolyte, Ir was markedly superior to Pt in the temperature range 25°-90°C. In 34% KOH, the relative superiority of Ir was somewhat less. Tafel slopes were about 2RT/3F, with evidence of a change to a higher slope at current densities above 10 mA/cm². However, neither Ir nor Pt was as effective an electrocatalyst as pure nickel. Another study (11), in which Ni and Pt screen anodes were compared, produced the same result.

Pt, Pd, Rh, and Ni coatings were electrodeposited onto foamed Ni anode supports and tested at a current density of 200 mA/cm², in 30% KOH electrolyte at 90°C (15). The rhodium coating performed best, providing a cell voltage of 1.72V, followed by Pd (1.74V), Ni (1.75V), and Pt (1.80V).

Ir and Ru alloys with 25, 50, and 75 a/o nickel were investigated as oxygen evolution anodes in 30% KOH electrolyte at 80°C (57). The Ni-Ru alloys with 50 and 75 a/o Ru dissolved anodically. The maximum overpotential reduction was produced by the 50Ni-50Ir alloy, which was 40 mV more efficient than pure nickel at a current density of 20 mA/cm². The electrokinetic parameters for the alloys were similar to those for nickel. Correspondingly, cyclic voltammetry showed that the surface of the alloy anodes was predominantly composed of nickel oxide species. Because of coverage by oxide films, there was no dependence of electrocatalytic activity on alloy electronic structure.

Outstanding oxygen evolution activity was obtained at pyrochlore structure oxide anodes (61). The catalysts are described by the general formula A₂[B_{2-x}A_x]O_{7-y}, where A = Pb or Bi, B = Ru or Ir, 0 < x < 1, and 0 < y < 0.5. In 3M KOH at 75°C, a typical Pb₂[Ru_{2-x}Pb_x]⁴⁺O_{6.5} catalyst evolved oxygen at an overpotential of about 120 mV at a current density of 100 mA/cm². In comparative potential sweep experiments, pyrochlore anodes were >100 mV more efficient than Pt black, RuO₂, or NiCo₂O₄. A supported Pb₂[Ru_{1.49}Pb_{0.51}]⁴⁺O_{6.5} anode was life-tested at a current density of 200 mA/cm² for more than 1000h, in 3M KOH at 75°C. After the first 200h, the rise in anode potential *vs.* time slowed noticeably, reaching a potential of about 1.5 V/RHE, about 50 mV higher than the potential measured at the beginning of the test. X-ray diffraction of the used anode did not reveal chemical degradation. Attempts to maximize anode efficiency using high (62 mg/cm²) catalyst loading TFE-bonded structures produced stability problems as the catalyst layer separated from the support during 504h of operation.

Summary

A number of approaches have been taken to improve the oxygen evolution anode. To date, results using metal oxide electrocatalysis have generally shown more promise than those obtained with modifications of the nickel electrode structure. Catalysts such as NiCo₂O₄, Li-doped Co₃O₄, and the La-Sr-Co oxides have been tested extensively. Work on these systems makes up a large share of the recent literature. It is encouraging that this work has been extended to address the question of what material and surface properties are responsible for electrocatalytic activity. Further research of this type may lead to important catalyst modifications or the development of entirely new catalyst systems.

Less-studied metal oxide catalysts, such as LaNiO₃ and the pyrochlore oxides, have also produced excellent results. More research is needed, however, to determine the full potential of these catalysts.

With the exception of the relatively inexpensive ruthenium, as used in the pyrochlore oxides, it is unlikely that practical oxygen evolution anodes will be based on precious metals. Overpotential reductions obtained with Pt, Ir, or Pd, for example, have been modest. In addition, the promising results obtained with far cheaper materials mitigates on economic grounds against the use of precious metals.

Acknowledgments

The author thanks the International Nickel Company and American Cyanamid Company for assistance in preparing this review. Parts of this review were presented as Paper No. 402 at the Electrochemical Society Meeting in Washington, DC, Oct. 9-14, 1983.

Manuscript submitted May 21, 1984; revised manuscript received Aug. 8, 1984.

American Cyanamid Company assisted in meeting the publication costs of this article.

REFERENCES

- F. Gutmann and O. J. Murphy, in "Modern Aspects of Electrochemistry," Vol. 15, R. White, J. O'M. Bockris, and B. Conway, Editors, Plenum Press, New York (1983).
- C. T. Bowen, R. L. LeRoy, and R. Renaud, Internat. Energy Agency Contract Rep. 06SX.31155-8-6606, September 1979.
- A. Daggetti, G. Lodi, and S. Trasatti, *Mater. Chem. and Phys.*, **8**, 1 (1983).
- C. Bailleux, A. Damien, and A. Montet, *Int. J. Hydrogen Energy*, **8**, 529 (1983).
- P. W. T. Lu and S. Srinivasan, *J. Appl. Electrochem.*, **9**, 269 (1979).
- R. L. LeRoy, M. B. I. Janjua, R. Renaud, and U. Leuenberger, *This Journal*, **126**, 1674 (1979).
- P. W. T. Lu and S. Srinivasan, *ibid.*, **125**, 1416 (1978).
- M. H. Miles, *Electroanal. Chem. Interfacial Electrochem.*, **60**, 89 (1975).
- H. C. Angus, D. E. Hall, and R. D. Giles, in "Proceedings of the 4th World Hydrogen Energy Conference," Pasadena, CA (1982).
- A. J. Appleby, G. Crepy, and J. Jacquelin, *Int. J. Hydrogen Energy*, **3**, 21 (1978).
- A. C. C. Tseung and S. Jasem, *Electrochim. Acta*, **22**, 31 (1977).
- G. Fiori, C. M. Mari, B. Perra, L. Vago, and P. Vitali, in "Proc. Hydrogen as an Energy Vector, Comm. Eur. Communities," p. 223, (1980).
- D. E. Hall, *This Journal*, **128**, 740 (1981).
- D. E. Hall, *ibid.*, **129**, 310 (1982).
- N. Wakabayashi, E. Torikai, Y. Kawami, and H. Takenaka, *Adv. Hydrogen Energy 2, Hydrogen Energy Progress I*, 59 (1981).
- J. Balajka, *Int. J. Hydrogen Energy*, **8**, 755 (1983).
- G. E. Stoner and P. J. Moran, in "Proceedings of the Symposium on Industrial Water Electrolysis," S. Srinivasan, F. J. Salzano, and A. R. Landgrebe, Editors, p. 169, The Electrochemical Society Softbound Proceedings Series, Princeton, NJ (1978).
- G. L. Cahen, Jr., P. J. Moran, L. L. Scribner, and G. E. Stoner, *This Journal*, **128**, 1877 (1981).
- J. Divisek, J. Mergel, and H. Schmitz, in "Proceedings of the 3rd World Hydrogen Energy Conference," Tokyo, Japan (1980).
- J. Divisek and H. Schmitz, *Int. J. Hydrogen Energy*, **7**, 703 (1982).
- P. Ragunathan, S. K. Mitra, and M. G. Nayar, *ibid.*, **6**, 487 (1981).
- M. Bernard, L. Mas, M. Prigent, and J. C. Sohm, in "Proc. Hydrogen as an Energy Vector, Comm. Eur. Communities," p. 283 (1980).
- M. Prigent and T. Nenner, *Adv. Hydrogen Energy 3, Hydrogen Energy Progress IV*, 299 (1982).
- H. Wendt and V. Plzak, *Electrochim. Acta*, **28**, 27 (1983).
- L. Martin, J. Diette, M. Prigent, M. Bernard, J. Demarsy, and C. Sellier, Comm. Eur. Communities Final Report 502-78-1-EHF (1981).
- U. Akano, J. A. Davies, W. W. Smeltzer, I. S. Tashlykov, and D. A. Thompson, *Nucl. Instrum. Methods*, **182**, 985 (1981).
- R. D. Giles, *Adv. Hydrogen Energy 3, Hydrogen Energy Progress IV*, 279 (1982).
- A. Garat and J. Gras, *Int. J. Hydrogen Energy*, **8**, 681 (1983).
- A. J. Salkind and U. Falk, "Alkaline Storage Batteries," John Wiley, New York (1969).
- T. Shirogami, K. Murata, and M. Ueno, Abstract 27, The Electrochemical Society Extended Abstracts, Vol. 81-2, Denver, Colorado, Oct. 11-16, 1981.
- D. E. Hall, *This Journal*, **130**, 317 (1983).
- A. C. C. Tseung, S. Jasem, and M. N. Mahmood, in "Proceedings of the Symposium on Industrial Water Electrolysis," S. Srinivasan, F. J. Salzano, and A. R. Landgrebe, Editors, p. 161, The Electrochemical Society Softbound Proceedings Series, Pennington, NJ (1978).
- P. Rasiyah and A. C. C. Tseung, *Adv. Hydrogen Energy 3, Hydrogen Energy Progress IV*, 383 (1982).
- M. C. M. Man, S. Jasem, K. L. K. Yeung, and A. C. C. Tseung, "Sem. Hydrogen as an Energy Vector, Comm. Eur. Communities," p. 255 (1978).
- P. Rasiyah, A. C. C. Tseung, and D. B. Hibbert, *This Journal*, **129**, 1724 (1982).
- P. Rasiyah and A. C. C. Tseung, *ibid.*, **130**, 2384 (1983).
- P. Rasiyah and A. C. C. Tseung, *ibid.*, **130**, 365 (1983).
- J. Fischer, H. Hofmann, G. Luft, and H. Wendt, *AIChE J.*, **26**, 794 (1980).
- G. Kissel, F. Kulesa, C. R. Davidson, and S. Srinivasan, in "Proceedings of the Symposium on Industrial Water Electrolysis," S. Srinivasan, F. J. Salzano, and A. R. Landgrebe, Editors, p. 216, The Electrochemical Society Softbound Proceedings Series, Pennington, NJ (1978).
- H. Vandenborre, R. Leysen, H. Nackaerts, and Ph. VanAsbroeck, *Adv. Hydrogen Energy 3, Hydrogen Energy Progress IV*, 107 (1982).
- G. Fiori, C. Mandelli, C. M. Mari, and P. V. Scolari, *Adv. Hydrogen Energy 1, Hydrogen Energy Systems I*, 193 (1979).
- H. Vandenborre, R. Leysen, and H. Nackaerts, *Int. J. Hydrogen Energy*, **8**, 81 (1983).
- M. Prigent, L. J. Mas, and F. C. Verillon, in "Proceedings of the Symposium on Industrial Water Electrolysis," S. Srinivasan, F. J. Salzano, and A. R. Landgrebe, Editors, p. 234, The Electrochemical Society Softbound Proceedings Series, Pennington, NJ (1978).
- A. C. C. Tseung, *This Journal*, **125**, 1660 (1978).
- H. Obayashi and T. Kudo, *Mater. Res. Bull.*, **13**, 1409 (1978).
- Y. Matsumoto, S. Yamada, T. Hishida, and E. Sato, *This Journal*, **127**, 2360 (1980).
- T. Otagawa and J. O'M. Bockris, *ibid.*, **129**, 2391 (1982).
- J. O'M. Bockris, T. Otagawa, and V. Young, *J. Phys. Chem.*, **150**, 633 (1983).
- J. O'M. Bockris and T. Otagawa, *ibid.*, **87**, 2960 (1983).
- J. O'M. Bockris and T. Otagawa, *This Journal*, **131**, 290 (1984).
- P. F. Carcia, R. D. Shannon, P. E. Bierstedt, and R. B. Flippen, *ibid.*, **127**, 1974 (1980).
- M. DeKay Thompson and A. L. Kaye, *Trans. Electrochem. Soc.*, **60**, 229 (1931).
- G. Grube and W. Gaupp, *Z. Elektrochem.*, **45**, 290 (1939).
- J. M. Gras and M. Pernot, in "Proceedings of the Symposium on Electrode Materials and Processes for Energy Conversion and Storage," J. D. E. McIntyre, S. Srinivasan, and F. G. Will, Editors, p. 424, The Electrochemical Society Softbound Proceedings Series, Pennington, NJ (1977).
- D. E. Hall, U.S. Pat. 4,240,887, 1980.
- A. Nidola, P. M. Spaziante, and L. Giuffre, in "Proceedings of the Symposium on Industrial Water Electrolysis," S. Srinivasan, F. J. Salzano, and A. R. Landgrebe, Editors, p. 102, The Electrochemical Society Softbound Proceedings Series, Pennington, NJ (1978).

57. P. W. T. Lu and S. Srinivasan, Abstract 328, The Electrochemical Society Extended Abstracts, Vol. 76-1, Washington, DC, May 2-7, 1976.
58. "Hydrogen Storage and Production in Utility Systems," F. J. Salzano, Editor, Brookhaven Nat'l Lab. Report 50472, 1975.
59. T. Osaka, Y. Iwase, H. Kitayama, and T. Tchino, *Bull. Chem. Soc. Jpn.* **56**, 2106 (1983).
60. M. H. Miles, Y. H. Huang, and S. Srinivasan, *This Journal*, **125**, 1931 (1978).
61. H. S. Horowitz, J. M. Longo, and H. H. Horowitz, *ibid.*, **130**, 1851 (1983).
62. M. H. Miles, G. Kissel, P. W. T. Lu, and S. Srinivasan, *ibid.*, **123**, 332 (1976).



Reports on Electrochemical Society Summer Fellowship Awards

During the summer of 1984, the following students received grants of \$2000.00 for use in electrochemical research, as part of the three Summer Fellowship Awards of The Electrochemical Society, Inc.

Mr. Paul M. Kovach, Indiana University, Bloomington, Indiana, received the Edward G. Weston Fellowship.

Ms. E. Tracy Turner Jones, University of Illinois, Urbana, Illinois, was the winner of the Colin Garfield Fink Fellowship.

Mr. Neal T. Sleszynski, State University of New York, Buffalo, New York, was awarded the Joseph W. Richards Fellowship.

The Summer Fellowship Awards are made "without regard to sex, citizenship, race, or financial need, to a fellow or teaching assistant pursuing work between the degrees of B.S. and Ph.D. on a subject in a field of interest to The Electrochemical Society." They are intended to cover a period during which the recipient has no financial support for the continuance of his or her work.

The Edward G. Weston Summer Fellowship Report

Voltammetry of Some Metal Complexes at Electrochemically Treated Electrodes

Paul M. Kovach

Many types of carbon electrodes are widely used in electroanalytical chemistry. The attractive properties of carbon electrodes are their large potential ranges in aqueous solution and low residual current. However, few molecules display diffusion-controlled electrochemical behavior in aqueous solutions because of the various factors that control charge-transfer processes at these electrodes. In addition to the inherent electron-transfer rates of the species being considered, it is also necessary to recognize that the surface of carbon has a rich chemistry that may well affect the observed electrochemistry (1-5). Graphitic carbon has a heterogeneous surface which contains many carbon-oxygen functionalities, such as carbonyls, carboxylates, and phenolic hydroxyls (6), which are located on the edge plane. Attempts have been made to characterize and modify the nature of these functional groups on the carbon surface to influence the observed electrochemistry (7-14).

Many treatments have been developed to improve the electrochemical properties of carbon electrodes (15-25). These treatments are important since many compounds, such as ascorbic acid, display poor electrochemistry at carbon electrodes. This can lead to complicated and often uninterpretable voltammograms, due to the overlap of voltammetric waves. Therefore, it would be desirable to know what types of carbon surfaces contain which types of functionalities, how they affect the electrochemistry, and how to modify the functionalities on the surface to obtain an electrode with predictable electrochemical properties.

Carbon fibers allow the fabrication of electrodes of very small dimensions (26, 27), and their small size gives them several unique electrochemical properties (28). As with other carbon electrodes, carbon fiber electrodes frequently are treated to improve their electrochemical reversibility (29-31). One electrode treatment, which we are examining in detail, involves the electrochemical oxidation of the surface of a single carbon fiber (29). Voltammograms obtained with this electrode exhibit a large shift in half-wave potential for many species relative to untreated electrodes; in particular, the overpotential for the oxidation of ascorbic acid is greatly reduced. This allows the voltammetric resolution of ascorbate from the catecholamine neurotransmitters and their metabolites

(32, 33). However, further investigation has revealed significant changes in the voltammetry of many species at this electrode and severe adsorption of several classes of compounds (34).

In this communication, we report the voltammetry of a series of highly charged metal complexes at an electrochemically treated cylindrical carbon fiber electrode. The voltammetric behavior is explained in part by the interaction of solution species with surface functional groups formed during the oxidative electrochemical treatment of the carbon fiber electrode.

Experimental

Reagents.—The inorganic compounds $\text{Ru}(\text{NH}_3)_6\text{Cl}_3$, $\text{Co}(\text{NH}_3)_6\text{Cl}_3$, and $\text{K}_3\text{Fe}(\text{CN})_6$ were used as received. $\text{K}_4\text{Mo}(\text{CN})_8 \cdot 2\text{H}_2\text{O}$ was synthesized as reported in the literature (35). All other chemicals were reagent grade and used as received. All species were studied in phosphate buffer solution (0.1M total phosphate) adjusted to the proper pH with phosphoric acid. Solutions (1.0 mM) were prepared with doubly distilled water and purged thoroughly with nitrogen before use.

Electrodes.—Cylindrical electrodes were constructed from carbon fibers (Thornel VSB-32, Union Carbide). Individual fibers (radius = $5\mu\text{m}$) were aspirated into glass capillaries which were then pulled to a fine taper with a pipette puller (David Kopf Instruments, Model 700C). The fiber was sealed in the pulled glass capillary by carefully placing a drop of epoxy (EPON 828, Miller-Stephenson) at the end of the glass with another pulled capillary so that the epoxy enters the capillary without coating the carbon fiber that extends beyond the glass. The electrodes were trimmed with a scalpel so that approximately $500\mu\text{m}$ of carbon fiber extended beyond the end of the capillary. The exact length of the protruding fiber was measured with an optical microscope. Electrical contact to the fiber was made by filling the capillary with mercury and inserting a short wire into the capillary.

Apparatus.—Potentiostatic control for cyclic voltammetry (CV) was maintained with a polarographic analyzer (Princeton Applied Research Corporation, Princeton, New Jersey, Model 174A). Potential waveforms for electrochemical treatment of the carbon fiber electrodes were applied through the polarographic analyzer by a function generator (Krohn-Hite, Avon, Massachusetts, Model 1200A). A 25 ml vial served as the electrochemical cell. Potentials are reported *vs.* a saturated calomel electrode.

Electrochemical treatment.—The electrochemical treatment of the cylindrical carbon fiber electrodes was a two-step process (29). The electrochemical treatment was applied to the electrode in phosphate buffer (pH 7.4) and consisted of a triangular wave (70 Hz, 0 to +3.0V *vs.* SCE

reference) for 20s, followed by a constant potential of +1.5V for 20s. The current-potential curves for the triangular wave treatment were monitored with an X-Y oscilloscope. The electrode was then potentiostated at -0.2V vs. SCE for a period of 40-60 min in buffer solution. Previous work in this laboratory has shown that the electrode undergoes some type of equilibration process after electrochemical treatment. The equilibration period allows for a more stable response. Background voltammograms were then obtained.

Results and Discussion

Properties of electrochemically treated electrodes.—Background scans obtained in pH 7.4 solution at 100 mV·s⁻¹ every 60s with an untreated electrode exhibit little background current. In contrast, voltammograms obtained in the same manner after electrochemical treatment show a significant increase in background current, and this current does not change significantly with time. An estimate of the capacitance (*C*) of the carbon fiber surface can be obtained as $C = i/v$, where *i* is the observed current at a particular potential and *v* is the scan rate, from voltammograms recorded in buffer solution. The capacitance of an untreated electrode at pH 7.4 is approximately 30 μF/cm², and that of an electrochemically treated electrode is approximately 270 μF/cm². This appears to indicate a change in the surface roughness of the electrode. This is apparent from observations of the fiber with electron microscopy. The appearance of the fiber after electrochemical treatment is similar to that observed after air oxidation at 680°C (36). The increase in surface roughness of the fiber is caused by the oxidation of the carbon fiber and is known to increase the amount of carbon-oxygen functionalities on the surface (11). The change in capacitance correlates with the change in surface roughness, but may also result in part from a change in carbon-oxygen surface functionality. Indeed, a severe oxidation process at carbon fibers has been shown to double the O:C ratio relative to the control specimen and produce a surface that contains carbon-oxygen functionalities in the ratio 54% carboxyl, 22% carbonyl, and 24% hydroxyl, as determined by x-ray photoelectron spectroscopy (XPS) (12).

Voltammetry of metal complexes.—A series of electroactive metal complexes was used to probe the chemical nature of these functional groups at the oxidized surface. Voltammetry of metal complexes at untreated cylindrical carbon fiber electrodes is generally characterized by poor electrochemical reversibility, due to the character of the carbon fiber surface. The voltammograms of Ru(NH₃)₆³⁺ at untreated electrodes appear to be the most reversible of the compounds examined. Therefore, the electrochemically active area of an untreated carbon fiber electrode was determined from voltammograms of Ru(NH₃)₆³⁺. The length of the fiber was then calculated from the observed current from the equation for the current at a cylindrical electrode

$$i = 4\pi nFDCl / \ln(4Dt/r^2)$$

where *l* is the length of the electrode, *r* is the radius of the fiber, *D* is the diffusion coefficient, and *t* was taken as the time required to reach the limiting current in the voltammogram where steady-state behavior is approximated (37). The length calculated in this manner is typically 60% of the length measured by optical microscopy. The calculated length was used to quantitate changes in voltammetric behavior after electrochemical treatment.

At electrochemically treated carbon fiber electrodes, voltammograms of highly charged inorganic anions are roughly sigmoidal with small amounts of peak-shaped character (Fig. 1). The magnitude of the peak voltammetric current obtained for Fe(CN)₆³⁻ and Mo(CN)₆⁴⁻ at these electrodes at pH 7.4 is less than would be predicted (Table I). When the electrodes were removed from solution containing the electroactive species, washed with distilled water, and transferred to buffer solution, no

Table I. Voltammetric analysis at electrochemically treated cylindrical electrodes

Species	Length calc. ^a	Current ratio ^b	$E_{1/2}$ (V)	ΔE_p (mV)
Fe(CN) ₆ ³⁻	480	0.48	+0.210	205
Mo(CN) ₆ ⁴⁻	370	0.86	+0.550	—
Co(NH ₃) ₆ ³⁺	390	1.3	-0.380	—
Ru(NH ₃) ₆ ³⁺	350	11.8	-0.250	100 ^c

^a Length calculated from voltammograms of Ru(NH₃)₆³⁺.

^b Ratio of observed to calculated current.

^c Obtained from voltammogram which was not first scan.

voltammetric waves were observed which would indicate the adsorption of these species to the electrode.

Voltammograms of highly charged inorganic cations exhibit significant changes in behavior (Fig. 2). The current that is observed in initial voltammograms of Ru(NH₃)₆³⁺ or Co(NH₃)₆³⁺ is significantly larger than expected for diffusion control. The observed current densities for Ru(NH₃)₆³⁺ and Co(NH₃)₆³⁺ at an electrochemically treated electrode are 11.8 and 1.4 times greater, respectively, than those calculated for an untreated electrode (Table I). The increase in current is observed for the reductive scan only. The adsorption of highly charged

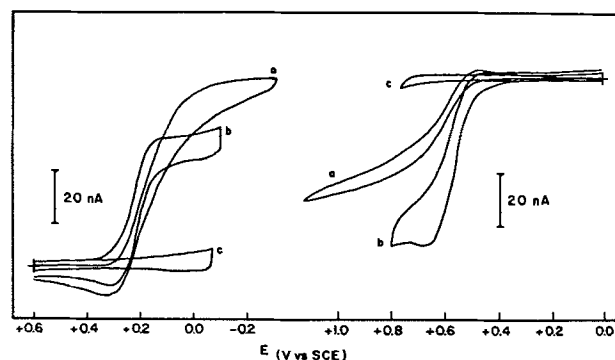


Fig. 1. Voltammetry of Fe(CN)₆³⁻ (left) and Mo(CN)₆⁴⁻ (right) at cylindrical carbon fiber electrode. a: Before treatment. b: First scan after treatment. c: First scan in buffer solution after 25 scans in b. Conditions: C = 1.0 mM Fe(CN)₆³⁻ and 1.0 mM Mo(CN)₆⁴⁻ in 0.1M phosphate buffer pH 7.4; scan rate = 100 mV·s⁻¹.

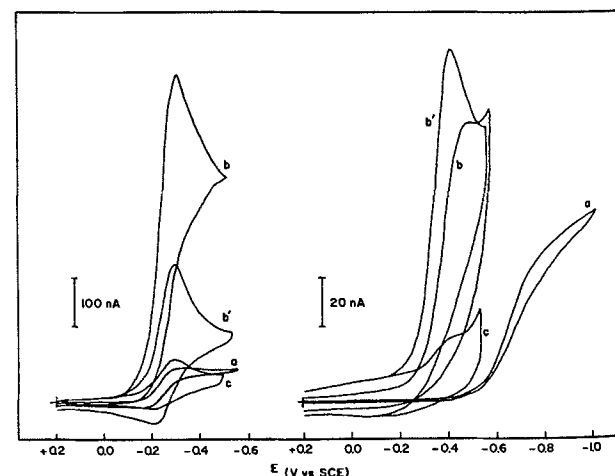


Fig. 2. Voltammetry of Ru(NH₃)₆³⁺ (left) and Co(NH₃)₆³⁺ (right) at cylindrical carbon fiber electrode. a: Before treatment. b: First scan after treatment. b': Twenty-fifth scan after treatment. c: First scan in buffer solution after b'. Conditions: C = 1.2 mM Ru(NH₃)₆³⁺ and 1.1 mM Co(NH₃)₆³⁺ in 0.1M phosphate buffer pH 7.4; scan rate = 100 mV·s⁻¹.

cationic species at the electrochemically treated electrode is responsible for the increased current density. The initial voltammetric scan in a solution of $\text{Ru}(\text{NH}_3)_6^{3+}$ exhibits a very large current, much greater than predicted for diffusion-controlled conditions. Voltammetry in buffer solution, after voltammetry in solution containing $\text{Ru}(\text{NH}_3)_6^{3+}$ and rinse, shows a voltammetric wave presumably due to adsorbed $\text{Ru}(\text{NH}_3)_6^{3+}$. The magnitude of this wave decreases with successive voltammetric scans in buffer solution.

The reduction of $\text{Co}(\text{NH}_3)_6^{3+}$ has a shift in peak potential from -0.65V (*vs.* SCE) at untreated electrodes to -0.38V at treated electrodes. The shift in wave position is indicative of a surface which increases the rate of ligand substitution for the complex or the rate of electrochemical kinetics. It is known that the $\text{Co}(\text{II})$ complex is labile and decomposes in aqueous media without the presence of free ligand (38, 39).

The $\text{Ru}(\text{NH}_3)_6^{3+/2+}$ redox couple exhibits a reverse wave at other types of carbon electrodes. However, no reverse wave is observed on the scale at which the voltammogram is recorded due to the large magnitude of the cathodic current. Voltammograms recorded at more sensitive scales on the first scan do indicate the presence of a reverse wave. Successive scans in a solution of $\text{Ru}(\text{NH}_3)_6^{3+}$ show an exponentially decaying current magnitude that approaches a constant value. The current magnitude, observed when steady-state conditions are reached, is dependent on the length of time between scans (*e.g.*, 30, 60, or 90s). A longer period between scans results in a larger peak current for the voltammogram. If the electrode is allowed then to rest for a long time in solution containing $\text{Ru}(\text{NH}_3)_6^{3+}$ and a voltammogram is then taken, a very large peak current is again observed.

When reduced, the adsorbed ruthenium complex appears to be labile to substitution, and may substitute in a manner similar to that for $\text{Co}(\text{NH}_3)_6^{2+}$. The substituted ruthenium-ammine complex is nonelectroactive and may be adsorbed to the electrode. In this manner, it hinders adsorption of more $\text{Ru}(\text{NH}_3)_6^{3+}$ from solution. The desorption of the substituted ammine appears to occur on a long time scale; therefore, increasing the period between scans results in greater observed current.

Electrochemically treated cylindrical carbon fiber electrodes display significant changes in the observed electrochemical characteristics. Most notable is the improved electrochemical reversibility of a wide number of compounds at these electrodes. Other features, however, such as the susceptibility to adsorption, complicate the use of these electrodes for voltammetric analysis. The primary reason for the change in voltammetric behavior with electrochemical treatment appears to be a change in the nature of the carbon fiber surface due to electrochemical oxidation. The results of the investigations reported here are consistent with the voltammetric behavior expected at a surface containing many carbon-oxygen functionalities. These functionalities appear to be anionic in nature at pH 7.4 and suggest the presence of carboxyl groups. A more detailed account of the characterization of the electrochemically treated carbon fiber electrode will appear in the literature.

Acknowledgments

This work was supported by the Edward G. Weston Fellowship of The Electrochemical Society and is gratefully acknowledged. The careful direction and support of R. Mark Wightman is greatly appreciated.

REFERENCES

- J. P. Randin, in "Comprehensive Treatise of Electrochemistry," Vol. 4, J. O'M. Bockris, B. E. Conway, E. Yeager, and R. E. White, Editors, Plenum Press, New York (1981).
- R. E. Panzer and P. J. Elving, *Electrochim. Acta*, **20**, 635 (1975).
- R. E. Panzer and P. J. Elving, *This Journal*, **119**, 864 (1972).
- E. Yeager, J. A. Molla, and S. Gupta, in "The Electrochemistry of Carbon," S. Sarangapani, J. R. Akridge, and B. Schumm, Editors, p. 123, The Electrochemical Society Softbound Proceedings Series, Pennington, NJ (1984).
- P. A. Throver, in "The Electrochemistry of Carbon," S. Sarangapani, J. R. Akridge, and B. Schumm, Editors, p. 40, The Electrochemical Society Softbound Proceedings Series, Pennington, NJ (1984).
- J. S. Mattson and H. B. Mark, Jr., "Activated Carbon: Surface Chemistry and Adsorption from Solution," Marcel Dekker, New York (1971).
- J. B. Donnet, *Carbon*, **6**, 161 (1968).
- B. D. Epstein, E. Dalle-Molle, and J. S. Mattson, *ibid.*, **9**, 609 (1971).
- K. F. Blurton, *Electrochim. Acta*, **18**, 869 (1973).
- N. L. Weinberg and T. B. Reddy, *J. Appl. Electrochem.*, **3**, 73 (1973).
- A. Proctor and P. M. A. Sherwood, *Carbon*, **21**, 53 (1983).
- T. Takahagi and A. Ishitani, *ibid.*, **22**, 43 (1984).
- J. O. Besenhard and H. P. Fritz, *Angew. Chem. Int. Ed. Engl.*, **22**, 950 (1983).
- H. P. Boehm and H. Knozinger in "Catalysis: Science and Technology," Vol. 4, J. R. Anderson and M. Boudart, Editors, Springer-Verlag, Berlin (1983).
- J. F. Evans, T. Kuwana, M. T. Henne, and G. P. Royer, *J. Electroanal. Chem.*, **80**, 409 (1977).
- J. F. Evans and T. Kuwana, *Anal. Chem.*, **49**, 1632 (1977).
- D. C.-S. Tse and T. Kuwana, *ibid.*, **50**, 1315 (1978).
- J. F. Evans and T. Kuwana, *ibid.*, **51**, 358 (1979).
- C. Degrand and L. L. Miller, *J. Am. Chem. Soc.*, **102**, 5728 (1980).
- L. Bjelica, R. Parsons, and R. M. Reeves, in "Electrode Processes 1979," S. Bruckenstein, B. Miller, J. D. E. McIntyre, and E. Yeager, Editors, p. 190, The Electrochemical Society Softbound Proceedings Series, Princeton, NJ (1980).
- E. Theodoridou, J. O. Besenhard, and H. P. Fritz, *J. Electroanal. Chem.*, **122**, 67 (1981).
- E. Theodoridou, J. O. Besenhard, and H. P. Fritz, *ibid.*, **124**, 87 (1981).
- L. Falat and H.-Y. Cheng, *ibid.*, **157**, 393 (1983).
- K. J. Stutts and R. M. Wightman, *Anal. Chem.*, **55**, 1576 (1983).
- R. M. Wightman, M. R. Deakin, P. M. Kovach, W. G. Kuhr, and K. J. Stutts, *This Journal*, **131**, 1578 (1984).
- J.-L. Ponchon, R. Cespuoglio, F. Gonon, M. Jouvét, and J.-F. Pujol, *Anal. Chem.*, **51**, 1483 (1979).
- M. A. Dayton, J. C. Brown, K. J. Stutts, and R. M. Wightman, *ibid.*, **52**, 946 (1980).
- R. M. Wightman, *ibid.*, **53**, 1125A (1981).
- F. Gonon, C. M. Fombarlet, M. J. Buda, and J.-F. Pujol, *ibid.*, **53**, 1386 (1981).
- A. G. Ewing, M. A. Dayton, and R. M. Wightman, *ibid.*, **53**, 1842 (1981).
- M. Armstrong-James, K. Fox, and J. Millar, *J. Neurosci. Meth.*, **2**, 431 (1980).
- F. Gonon, M. Buda, R. Cespuoglio, M. Jouvét, and J.-F. Pujol, *Brain Res.*, **223**, 69 (1981).
- W. G. Kuhr, A. G. Ewing, W. L. Caudill, and R. M. Wightman, *J. Neurochem.*, **43**, 560 (1984).
- P. M. Kovach, A. G. Ewing, R. L. Wilson, and R. M. Wightman, *J. Neurosci. Meth.*, **10**, 215 (1984).
- J. van de Poel and H. M. Neumann, *Inorg. Synth.*, **11**, 53 (1968).
- E. V. Murphy and B. F. Jones, *Carbon*, **9**, 91 (1971).
- P. M. Kovach, W. L. Caudill, D. G. Peters, and R. M. Wightman, *J. Electroanal. Chem.*, **185**, 285 (1985).
- H. A. Laitiner, A. J. Frank, and P. Kivalo, *J. Am. Chem. Soc.*, **75**, 2865 (1953).
- R. H. Wopschall and I. Schain, *Anal. Chem.*, **39**, 1514 (1967).

The Colin Garfield Fink Summer Fellowship Report

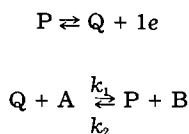
Mediated Oxidation at a Polymer-Modified Electrode. Savéant-Andrieux Treatment of the Kinetics

E. Tracy Turner Jones

In electrocatalysis at a modified electrode, an immobilized reversible redox center acts as a fast electron-

transfer mediator for a solution species that is oxidized or reduced slowly or not at all at the bare electrode. The primary aim is to diminish the overpotential required for direct oxidation or reduction of the substrate. A secondary, related aim is to achieve good catalytic efficiency. While a monolayer of catalyst can indeed reduce the overpotential, the catalytic efficiency will often be poor. If catalyst is instead distributed throughout a polymer film, the catalytic efficiency can, under the right conditions, increase in proportion to the number of equivalent monolayers of catalyst present (1). Such a polymer-modified electrode takes advantage of the three-dimensional distribution of catalyst found in homogeneous electrocatalysis. In addition, the arrangement facilitates separation of product and catalyst and conserves the often expensive catalyst while providing for its high local concentration (2).

In a series of papers published in 1982 (3-5) Andrieux and co-workers presented a kinetic model for the following system



where P and Q make up a mediator redox couple immobilized in a polymer film, and A and B are the reduced and oxidized forms of the substrate. Mediated oxidation is given here; transposition to reduction is straightforward. The model, which was developed for stationary voltammetric techniques such as rotating disk electrode voltammetry, encompasses four factors that determine the magnitude of the mediated current: diffusion of substrate from the bulk solution to the film-solution interface, further diffusion of substrate through the film toward the electrode surface, electron "diffusion" within the film (the sum of the electron propagation processes by mediator self-exchange or physical diffusion), and the rate of the electron cross-exchange reaction between mediator and substrate.

Four redox situations of practical interest were identified and treated under three different case designations: A, B, C (5). In case A, the equilibrium constant for the cross-exchange reaction ($K = k_1/k_2$) may take any value, and the $A \rightleftharpoons B$ electrode reaction is irreversible. Where K is greater than or equal to unity, case A has catalytic possibilities. Case B has limited utility. While not catalytic itself, case C is useful for modeling catalytic systems. The cross-exchange reaction equilibrium constant in case C is greater than or equal to unity, and the $A \rightleftharpoons B$ electrode reaction is fast enough that it occurs at more negative potentials than does oxidation of P. When K is large, two distinct plateau currents may be obtained at a polymer-modified rotating disk electrode. The separation of direct oxidation of substrate from mediated oxidation of substrate facilitates diagnosis of the parameters that limit the currents.

The kinetic behavior of each case above is thoroughly defined by a set of differential equations derived from Fick's laws of linear diffusion and by a set of boundary conditions. Simple closed-form equations defining a few types of characteristic limiting behavior are used in the analysis of experimental data. Andrieux and Savéant (5) have presented these closed-form equations in terms of K and four component currents: i_A , i_S , i_E , i_k . Each current is related to one of the four rate-limiting factors described above. The component current i_A is simply the limiting current that would be observed at the bare electrode rotating in the substrate solution. It is a measure of the maximum deliverance of substrate by diffusion to the film-solution interface of the modified electrode. The magnitude of i_S depends upon the diffusion coefficient of substrate in the film. The diffusion-like transport of electrons among the mediating centers of the film determines i_E . And i_k is the largest current that could be deliv-

ered by the cross-exchange reaction. These currents are described in more detail elsewhere (4).

The closed-form equations for case C in the limit of large K are given in Fig. 1. The type of limiting behavior for each pair of plateau current expressions is given by an ESR designation. In these limiting situations, one or two of the rate-limiting factors predominate over the others. The ESR designation is a general guide to the nature of the limiting processes; the first two letters point to the electron (E) and substrate (S) diffusion processes within the film, and R indicates the influence of the cross-exchange reaction rate. A cycle of concentration profiles taken for a potential at which P is oxidized at the mass-transfer-limited rate is a useful tool for understanding the transitions among limiting behaviors (Fig. 2).

The strategy for analyzing a given polymer-mediator-substrate system involves evaluating i_A , i_S , and i_E , and constructing Koutecky-Levich plots [i^{-1} vs. (rotation rate) $^{-1/2}$] from the sum of the oxidation plateau currents. Much of the experimental validation of the theory to date has been provided by Anson's group in association with Savéant (6, 7).

We have investigated the use of poly(styrene sulfonate) (PSS) as a matrix for the mediated oxidation of ferrocene-1,1'-disulfonate [$Fe(CpS)_2^{2-}$] in CH_3CN by electrostatically bound tris(2,2'-bipyridine)osmium(III) [$Os(bpy)_3^{3+}$], a case C system.

Experimental

Poly(styrene sulfonate, sodium salt) (Polysciences, Incorporated, $M_w = 6 \times 10^6$) was purified through dialysis and filtration. A 1.00% (w/v) PSS, 0.038% (w/v) Zonyl FSN (du Pont) spin coating solution was prepared in 3:2 methanol:water. The FSN, a fluorosurfactant, made it possible to spin coat films of uniform thickness on Teflon-shrouded glassy carbon electrodes. The osmium salt, $Os(bpy)_3(ClO_4)_2$, was synthesized according to a method outlined by Burstall *et al.* (8). The solution used to load films had the following composition: 0.50 mM $Os(bpy)_3^{2+}$, 10 mM dicyclohexyl-18-crown-6 (Aldrich), 0.020M tetra-n-butylammonium tetrafluoroborate (TBABF₄), and 4.0% (v/v) water in distilled-in-glass acetonitrile (Burdick and Jackson). The crown ether was included to force dissociation of the sodium sulfonate moieties (9). The volume of water added was judged to promote swelling of the polymer film without causing its dissolution. Both components were important for achieving rapid exchange of $Os(bpy)_3^{2+}$ into the PSS films. Another loading solution as prepared in the same manner but for the substitution of $Ru(bpy)_3^{2+}$ for $Os(bpy)_3^{2+}$. The perchlorate salt of the ruthenium complex was prepared as described by Glass and Faulkner (10). The acid form of $Fe(CpS)_2^{2-}$ was synthesized according to a method by Knox and Pauson (11) and then titrated with an aqueous

R + S	$\frac{1}{i_1} = \frac{1}{i_A} + \frac{1}{i_S}$ $\frac{1}{i_1 + i_2} = \frac{1}{i_A} + \frac{\tanh(k_f/k_s)^{1/2}}{(k_f k_s)^{1/2}}$	$\frac{1}{i_1} = \frac{1}{i_A} + \frac{1}{i_E}$ $i_2 = 0$	R R + E ER ER + S
SR	$\frac{1}{i_1} = \frac{1}{i_A} + \frac{1}{i_S}$ $\frac{1}{i_1 + i_2} = \frac{1}{i_A} + \frac{1}{(k_f k_s)^{1/2}}$	$i_1 = i_S$ $i_2 = 0$	S
SR + E	$\frac{1}{i_1} = \frac{1}{i_A} + \frac{1}{i_S}$ $\frac{1}{i_1 + i_2} = \frac{1}{i_A} + \frac{i_E^{1/2}}{(k_f k_s)^{1/2} (i_E - (i_1 + i_2))^{1/2}}$	$i_1 = i_S$ $i_2 = i_E$	S + E E

Fig. 1. Closed-form equations for case C in the limit of large K

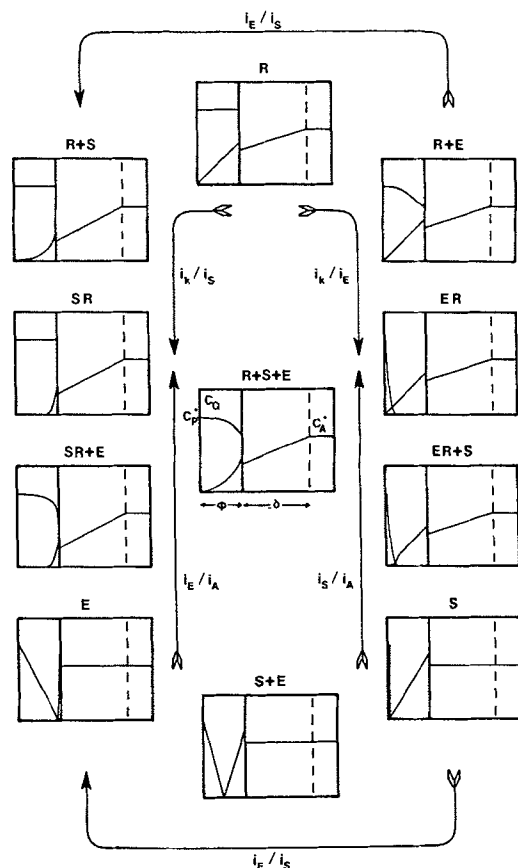


Fig. 2. Cross sections of redox polymer film (thickness ϕ) in substrate solution (diffusion-layer thickness δ) illustrating concentration profiles of Q and A s as a function of ratios of the component currents. Arrowheads indicate ratios $\rightarrow \infty$; arrow tails, ratios $\rightarrow 0$. $R + S + E$ is the general case.

solution of tetra-*n*-butylammonium hydroxide (Aldrich). Tetra-*n*-butylammonium ferrocene-1,1'-disulfonate was recovered in a rotary evaporator and recrystallized twice from ethanol/diethylether. The electrolyte, TBABF₄, was part of a batch for which the preparation has been described (9).

An AFMSR Rotator System fitted with a glassy carbon rotating disk electrode (RDE) (Pine Instrument Company) was used in conjunction with a Z-80 microprocessor based cybernetic-potentiostat (12) to obtain all electrochemical data. Two Teflon-shrouded (12 mm od) 6 mm diam glassy carbon disks were polished with 0.25 μm grit diamond compound then 0.05 μm grit alumina slurry (Buehler Limited). In order to improve the adsorption of PSS films on the glassy carbon, the polished electrodes were treated with 25% ClSO₃H in CH₂Cl₂ (v/v) for several minutes. Apparently, sulfonation of aromatic rings in the glassy carbon structure made the electrode surfaces more polar. Spin coating was accomplished by locking the RDE's onto a shaft driven by a controlled speed motor (Electro-craft Corporation). A special cell was built for the rotation experiments (Fig. 3). The design minimizes convective turbulence and uncompensated resistance. It features a removable platinum auxiliary electrode separated from the spherical working electrode chamber by a glass frit. The Ag/Ag⁺ reference electrode (0.01M, CH₃CN) is sequestered in an adjustable side arm that draws into a Luggin capillary.

Results and Discussion

Spin coating at 4000 rpm consistently produced films that gave an even blue interference color. Loading was accomplished in approximately 12 min by cycling freshly

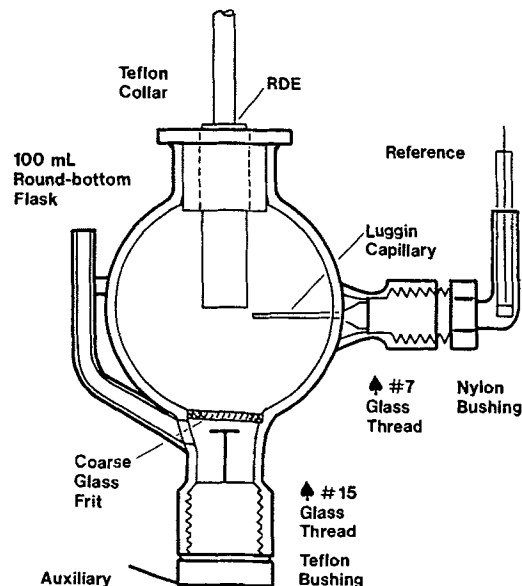


Fig. 3. Diagram of the electrochemical cell built for rotation experiments.

spin-coated electrodes between -0.2 and $+0.8\text{V}$ in the 0.5 mM Os(bpy)₃²⁺ solution (Fig. 4). A dry-loaded film gave a yellow interference color.

Once a film was loaded, the electrode surface was rinsed with CH₃CN and the electrode was transferred to a solution of 0.020M TBABF₄ and 0.50% (v/v) H₂O in CH₃CN. The electrode was cycled in this solution (Fig. 5) until the Os(bpy)₃^{2+/3+} sites within the film reached stable configurations. This process, which took approximately 30 min, was marked by a 200 mV negative shift of the formal redox potential of the PSS-Os(bpy)₃^{2+/3+} couple. Similar behavior was observed by Majda and Faulkner for the PSS-Ru(bpy)₃^{2+/3+} system (9). The Os(bpy)₃^{2+/3+} sites had converted from "weakly bound" configurations, in which the individual osmium center may have interacted with two sulfonate groups, to "strongly bound" configurations, in which each osmium center may have interacted with three sulfonate groups. The formation of

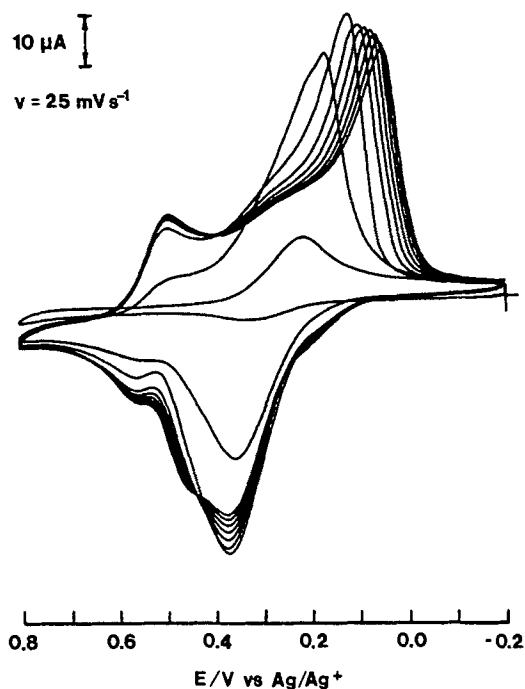


Fig. 4. Growth of voltammetric signal for Os(bpy)₃^{2+/3+} exchanging into a PSS film. Initial and final potentials were -0.2V .

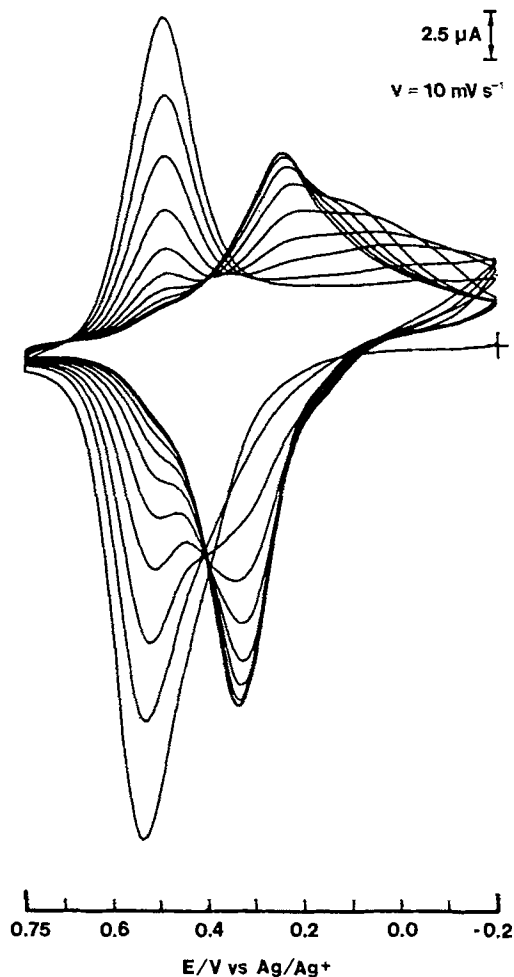


Fig. 5. Conversion of redox polymer film of Fig. 4 to a dehydrated strongly-bound state. Initial and final potentials were $-0.2V$.

tight strongly bound centers and the loss of film fluidity that accompanies dehydration could combine to produce electroinactive domains of mediator sites. This film lockup, as well as leaching, could account for the smaller peak amplitudes of the dehydrated film (Fig. 5).

In order to obtain an effective loading value for a dehydrated $\text{Os}(\text{bpy})_3^{2+/3+}$ -exchanged film, the electrode was poised at $-0.2V$ for 5 min prior to a single cycle between -0.2 and $+0.775V$. The area under the oxidation peak was integrated to determine the effective loading value in microcoulombs. An average of $370 \pm 16 \mu\text{C}$ was calculated for the ten films that form the basis of this study. Ideally, once the loading value for a film was measured, a series of experiments would have been conducted to determine i_E , i_S , and the mediated substrate oxidation current. In practice, the loaded films were not robust enough to survive such a regimen. So the work done with each film was limited, and every effort was made to generate reproducible film systems.

One of the most appealing features of the kinetic model developed by Andrieux and co-workers is that knowledge of the *in situ* film thickness is not required for determining i_E . In addition to a film's loading value in coulombs, all that is necessary is the Anson slope from a chronocoulometric experiment

$$i_E = \frac{\pi}{4} \frac{(\text{slope})^2}{\text{loading value}}$$

In general, potential steps were made from -0.1 to $+0.85V$ for pulse widths ranging from 100 to 1000 ms. The component current i_E was determined to be $250 \pm 20 \mu\text{A}$. Given the high local concentration of the osmium com-

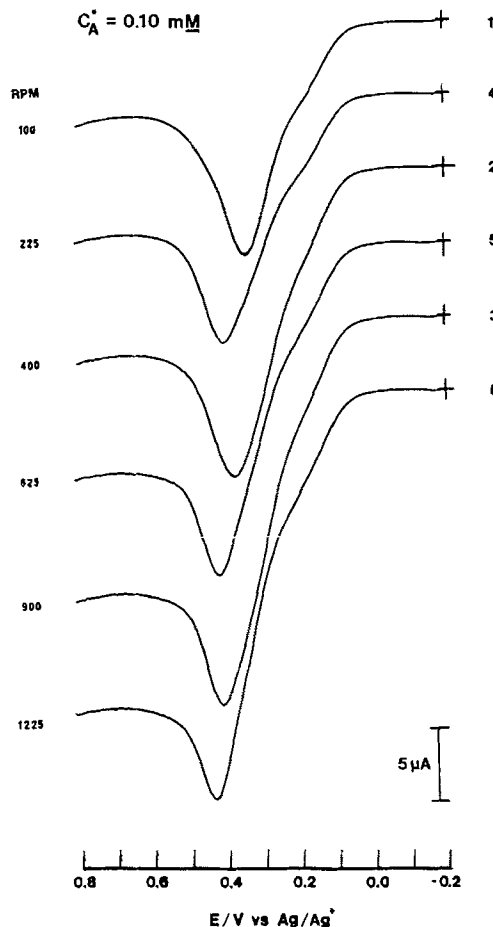


Fig. 6. Current-potential curves for oxidation of $0.10 \text{ mM Fe}(\text{CpS})_2^{2-}$ at a rotating glassy carbon electrode coated with PSS- $\text{Os}(\text{bpy})_3^{2+/3+}$. Order in which rotation rates were selected is given on right. Scan rate = $5 \text{ mV}\cdot\text{s}^{-1}$.

plex in the films (estimated to be $0.3\text{--}0.5M$) relative to the concentration of supporting electrolyte, migration effect were probably present.

Three substrate solutions were used in the mediation experiments: 0.10 , 0.25 , and $0.40 \text{ mM Fe}(\text{CpS})_2^{2-}$ in 0.50% (v/v) H_2O , $0.020M$ TBABF₄ acetonitrile solutions. Rotation rates ranged from 100 to 1225 rpm. Attempts to use higher concentrations or rotation rates failed, apparently because of the accelerated fouling that accompanied the increased substrate flux. Three loaded films were run at each substrate concentration. Two of the nine trials were eventually discounted because the film loading values were too low. Rotation rates were selected in a different order with each trial so that intruding effects could be identified without putting the short-lived films through repeat runs. The suspected fouling process had no discernible impact upon the magnitude of the combined plateau current ($i_1 + i_2$) as long as there was not a total film failure. The fouling did, however, affect the shape and location of the superimposed $\text{Os}(\text{bpy})_3^{2+}$ oxidation peak. In a successful trial shown in Fig. 6, the shrinking peak flattened and shifted to more positive potentials as the film became fouled, reflecting the increasing difficulty with which the mediator sites were oxidized.

The Koutecky-Levich plots for $i_1 + i_2$ are linear and intercept the origin (Fig. 7). The slopes are inversely proportional to substrate concentration. It is not clear from any of the voltammograms whether the shoulder that precedes each mediator peak is an artifact or is actually the first plateau current and a measure of i_S . In any event, another means of measuring i_S was chosen.

The formal redox potential of the polymer-bound $\text{Ru}(\text{bpy})_3^{2+/3+}$ couple is approximately $+0.85V$, well removed from the onset of $\text{Fe}(\text{CpS})_2^{2-}$ oxidation. For i_S

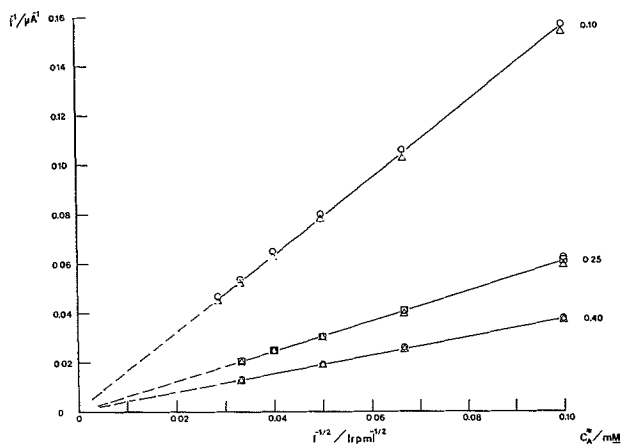


Fig. 7. Koutecky-Levich plots of $(i_1 + i_2)^{-1}$ vs. $(\text{rpm})^{-1/2}$ for the PSS-Os(bpy) $_3^{2+/3+}$ film in Fe(CpS) $_2^{2-}$ solutions.

determinations, then, the ruthenium complex is a natural choice as a surrogate for the closely related osmium bipyridine complex. Freshly spin-coated electrodes were loaded with the ruthenium complex to the level of the osmium complex and then dehydrated using the standard procedure. Care was taken to avoid oxidation of water in the films. Voltammetric data were obtained for three substrate concentrations (Fig. 8). Table I contains the i_s component currents determined from the intercepts of the Koutecky-Levich plots of the plateau currents. The i_s values are roughly proportional to substrate concentration, as expected. They are also very small, less than $1 \mu\text{A}$, indicating slow substrate diffusion through the film.

The Levich constant for oxidation of Fe(CpS) $_2^{2-}$ at a bare electrode had been determined in earlier experiments that employed a wide range of substrate concentrations and rotation rates. Table II gives the i_A values calculated from the Levich constant for the rotation rates and substrate concentrations ultimately used in the mediation experiments.

All the evidence points to SR characteristic limiting behavior (see Fig. 1 and 2). There are two current plateaus, and the i_E/i_S ratio is very large so the R, R + E, ER, ER + S, S, and S + E characteristic behaviors are ruled out. The i_E component current is also larger than the i_A values; the E characteristic behavior is out. Koutecky-Levich plots of $i_1 + i_2$ are linear, which narrows the field to R + S and SR. And finally, the cross-exchange reaction between Os(bpy) $_3^{3+}$ and Fe(CpS) $_2^{2-}$ is likely to be very fast so that i_E/i_S will be large. The SR characteristic limiting behavior becomes the best candidate.

In the SR situation, a rapid cross-exchange reaction and slow substrate diffusion through the film unite to confine the substrate within the film to a thin reaction layer

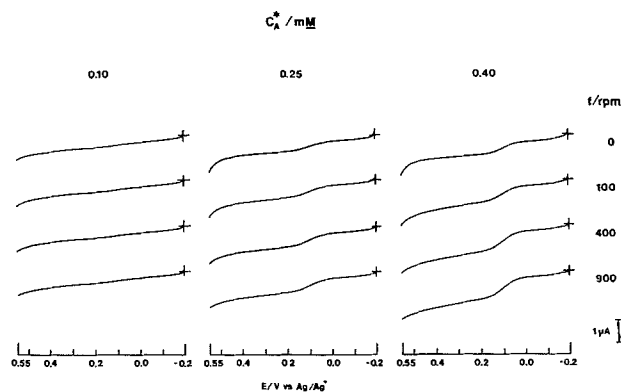


Fig. 8. Current potential curves for direct oxidation of Fe(CpS) $_2^{2-}$ at a rotating glassy carbon electrode coated with PSS-Ru(bpy) $_3^{2+/3+}$. Scan rate = $5 \text{ mV}\cdot\text{s}^{-1}$.

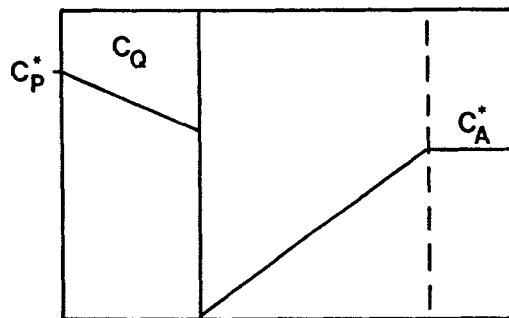


Fig. 9. Cross section of PSS-Os(bpy) $_3^{2+/3+}$ film in Fe(CpS) $_2^{2-}$ solution illustrating proposed concentration profiles of mediator and substrate.

adjacent to the film-solution interface. The mediator concentration profile is generally flat and at the maximum value. We believe that our system represents an extreme of the SR case. The zero intercept of the Koutecky-Levich plots of Fig. 7 means that the modified electrode was able to oxidize the entire Levich flux. Therefore, the concentration of the substrate in the solution was drawn down to zero at the film-solution interface. Substrate did not penetrate the film; the cross-exchange reaction occurred at the interface. And since i_E can be no more than three times as large as i_A , the mediator concentration profile would have sloped down toward the film solution interface to some degree. These features are shown in Fig. 9.

Work is underway to explore the extent to which the parameters that govern the kinetics of the polymer-mediator-substrate system can be tuned. The goal is to use the mediator more efficiently. That is, the entire volume of the film should be involved in the cross-exchange reaction. Toward that end, the water content of the substrate solutions will be increased to further swell the film and the mediator concentration within the film will be lowered.

Acknowledgments

The author is grateful to the Electrochemical Society for the Colin Garfield Fink Summer Fellowship Award and to Professor L. R. Faulkner for his steady support.

REFERENCES

- C. P. Andrieux, J. M. Dumas-Bouchiat, and J. M. Savéant, *J. Electroanal. Chem.*, **114**, 159 (1980).
- J. M. Savéant, Paper presented at the UNESCO/NSF Workshop on Photoelectrochemical Processes and Modified Electrodes, 1984.
- C. P. Andrieux, J. M. Dumas-Bouchiat, and J. M. Savéant, *J. Electroanal. Chem.*, **131**, 1 (1982).
- C. P. Andrieux and J. M. Savéant, *ibid.*, **134**, 163 (1982).
- C. P. Andrieux and J. M. Savéant, *ibid.*, **142**, 1 (1982).
- F. C. Anson, T. Ohsaka, and J. M. Savéant, *J. Am. Chem. Soc.*, **105**, 4883 (1983).

Table I. Dependence of i_s on Fe(CpS) $_2^{2-}$ concentration

C_A^* (mM)	i_s (μA)
0.10	0.10
0.25	0.42
0.40	0.76

Table II. Calculation of i_A values from Levich constant

C_A^* (mM)	$i_A/f^{1/2}C_A^* = 6.2$					
	i_A (μA)					
(f/min^{-1})	100	225	400	625	900	1225
0.10	6.2	9.3	12	16	19	22
0.25	16	23	31	39	46	54
0.40	25	37	50	62	74	87

7. F. C. Anson, Y. M. Tsoy, and J. M. Savéant, *J. Electroanal. Chem.*, **178**, 113 (1984).
8. F. H. Burstall, F. P. Dwyer, and E. C. Gyrfas, *J. Chem. Soc.*, 953 (1950).
9. M. Majda and L. R. Faulkner, *J. Electroanal. Chem.*, **169**, 77 (1984).
10. R. S. Glass and L. R. Faulkner, *J. Phys. Chem.*, **85**, 1160 (1981).
11. G. R. Knox and P. L. Pauson, *J. Chem. Soc.*, 692 (1958).
12. P. He, J. P. Avery, and L. R. Faulkner, *Anal. Chem.*, **54**, 1313A (1982).

The Joseph W. Richards Summer Fellowship Report Analysis of Square Wave Voltammetric Results at a Tin Oxide Semiconductor Microelectrode

Neal T. Sleszynski

Microelectrodes have been used by biochemists and neurophysiologists for several decades to study cell biochemistry and nerve cell communications (1, 2). Although usually used in potentiometry, in a small number of cases these microelectrodes have been used as voltammetric sensors (usually in the amperometric mode) to identify electroactive species such as neurotransmitters (3, 4). Only recently have electrochemists recognized the potential of microelectrodes for classical electrochemical problems. Wightman has published a useful review of microelectrode applications in analytical chemistry as well as biochemistry (5).

The major attraction of microelectrodes for the analytical chemist is the improved signal-to-noise ratio, which arises from the increase in current density associated with nonplanar diffusion. When overall small dimensions are not required, the use of arrays of microelectrodes can be advantageous. Microelectrode arrays offer higher, more easily measurable currents while retaining the desirable features of the individual microelectrodes in the array. Although arrays have been constructed manually (22, 23), certain types of microelectrode arrays may be constructed using semiconductor fabrication technology (6, 7, 24-26) if appropriate materials for the electrode and insulating layer are successfully identified.

In conjunction with the National Research and Resource Facility for Submicron Structure at Cornell University, we have constructed a number of microelectrode arrays from SnO₂, a commonly used semiconductor in the electronics industry, with the goal of testing the recently developed theory of square wave voltammetry at microelectrodes for reversible processes (8). Electrodes constructed of SnO₂ have been examined by a number of experimenters (9-18). Initial work in the area focused on the use of these electrodes in spectroelectrochemistry (10-12). The area of optically transparent electrodes has been reviewed by Kuwana and Winograd (19), and a summary of the uses of SnO₂ for this purpose is given there. A paper by Osa and Kuwana (12) reviews the use of tin oxide and other optically transparent electrodes in non-aqueous solutions.

A number of other studies examined the problem of electron transfer kinetics on these electrodes. Kuwana's review notes that the reversibility of ferrocyanide at these electrodes depends on pH and chloride ion concentration. In a paper with Strojek (11), Kuwana shows cyclic voltammograms which indicate that the maximum reversibility for ferrocyanide on tin oxide electrodes is seen at pH = 1.5, although from their figure it appears that even at this pH the electron transfer is only quasi reversible. Laitinen and co-workers (13) have also noted an effect of chloride ion, which appears to be specifically adsorbed. The peak shape for a cyclic voltammogram indicates ei-

ther a charging process or an exhaustive surface electrolysis. Experiments showed that an electrode removed from a chloride containing electrolyte and placed in a chloride-free environment retained adsorbed chloride for several hours. Access to cathode potentials was found to be limited by reduction of tin oxide to metallic tin. Further studies by this group on the surface properties of these electrodes have included the study of bromide (15) and iodide (16).

Armstrong and co-workers (18) have conducted extensive surface studies of SnO₂ and In₂O₃ semiconductor electrodes using ESCA and Auger spectroscopy. Although a comparison of surface properties with capacitance behavior and accessible potential range was made, no information was provided which would shed light on either the strong adsorption of halides or variations in electrode kinetics.

Albertson and co-workers (17) have determined the electron-transfer rate constant for the reduction of ferrocyanide at SnO₂ using both electrochemical and spectrophotometric means. Unfortunately, the experimental conditions were such that the electron-transfer rate was determined under conditions which other workers had already noted as yielding quasi-reversible behavior (pH 7). The electron-transfer rates determined by the two methods agreed closely, with an average of $4.3 (\pm 0.2) \times 10^{-4}$ cm/s. No measurements were made at lower pH values, where the couple is known to exhibit more reversible behavior.

Laitinen's group has used almost exclusively electrodes constructed in their own lab. They have examined the electrical and electrochemical properties of SnO₂ films with varying amounts of antimony as a dopant (14). Their studies showed the sensitivity of the electrode kinetics to semiconductor composition, in particular the dopant level. In the same study, they measured electron-transfer rates at the best of these electrodes for a number of compounds. They found that for compounds with quasi-reversible electron-transfer rates electron transfer rates are uniformly faster at Pt electrodes. Reversible behavior was seen under certain conditions for Fe(o-phen)₃²⁺ and Fe(CN)₆⁴⁻. Work has also been done on modifying the electrode surface with submonolayers of adsorbed Pt (20). This modified electrode surface showed greater activity for the reduction of oxygen than a bulk Pt electrode.

In order to test the square wave at microelectrode theory, it is necessary to identify a species which is reversible on the commercial SnO₂ material, Nesla Glass, which was used to construct the electrode. For convenience, cyclic voltammetry was used to initially screen compounds, using the peak-to-peak separation criteria of Nicholson and Shain (21). Species examined included ferrocyanide, ferrous oxalate, Ru(bpy)₂²⁺ in aqueous media, and Ru(bpy)₃²⁺ and ferrocene in acetonitrile. All were found to exhibit quasi-reversible behavior under the conditions used, at scan rates as slow as 100 mV/s. These results indicate that commercially available SnO₂ may be an unreliable material for applications in which reversible electron-transfer behavior is necessary. It is apparent from the results reported by Laitinen and co-workers (14), however, that carefully fabricated semiconductor surfaces, or electrode surfaces which have been modified with adsorbed Pt (20), are capable of yielding the desired behavior.

The most reversible of the species tested, ferrocyanide, was used for square wave experiments which compared experimental behavior with that predicted by theory. Figure 1 shows the comparison of the experimental results and the theoretical fit, as calculated using simplex optimization techniques, for an array of 100 disks each 30 μm in radius. The effect of the slow electron transfer can be seen in the quality of the fit, especially at higher overpotentials. Despite this problem, the calculated fit yields a radius of 28 μm, in good agreement with the radius of 30 μm measured using a microscope.

In conclusion, it can be said that the recently developed theory of square wave voltammetry at microelectrodes is

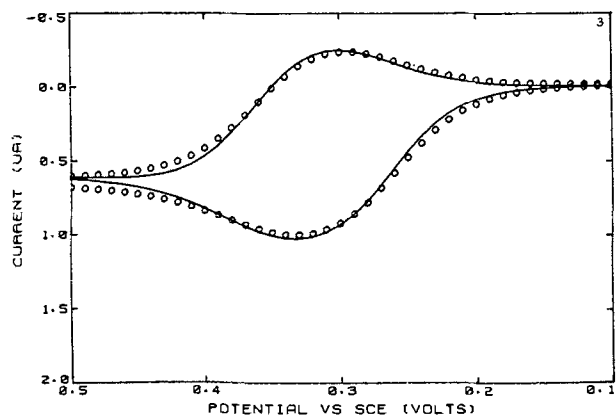


Fig. 1. Square wave voltammogram of 0.5 mM ferrocyanide on a SnO_2 microelectrode array (100 disks of radius $30 \mu\text{m}$). Square wave frequency: 10 Hz. 50 mV step amplitude.

capable of describing the experimental behavior seen at these arrays, even in the absence of a completely reversible electron transfer.

Acknowledgment

In addition to acknowledging The Electrochemical Society for a generous summer fellowship, the author would like to thank Richard Tiberio at Cornell University for electrode construction and the Office of Naval Research for project support.

REFERENCES

1. "Medical and Biological Applications of Electrochemical Devices," J. Koryta, Editor, Wiley-Interscience, New York (1980).

2. R. S. Pickard, *J. Neurosci. Meth.*, **1**, 301 (1979).
3. R. N. Adams, *Anal. Chem.*, **48**, 1126A (1976).
4. F. Gonon, M. Buda, R. Cespeglio, M. Jouvet, and J. P. Pujol, *Nature*, **286**, 902 (1980).
5. R. A. Wightman, *Anal. Chem.*, **53**, 1125A (1981).
6. R. S. Pickard, *Trends Neurosci.*, 259 (Oct. 1979).
7. W. Siu and R. S. C. Cobbold, *Med. Biol. Eng.*, **14**, 109 (1976).
8. K. Aoki, J. Osteryoung, and J. J. Odea, Unpublished results.
9. W. N. Hansen, T. Kuwana, and R. A. Osteryoung, *Anal. Chem.*, **38**, 1810 (1966).
10. N. Winograd, H. N. Blount, and T. Kuwana, *J. Phys. Chem.*, **73**, 3456 (1969).
11. J. W. Strojek and T. Kuwana, *J. Electroanal. Chem.*, **16**, 471 (1968).
12. T. Osa and T. Kuwana, *ibid.*, **22**, 389 (1969).
13. H. A. Laitinen, C. A. Vincent, and T. M. Bednarski, *This Journal*, **115**, 1024 (1968).
14. D. Elliott, D. L. Zellmer, and H. A. Laitinen, *ibid.*, **117**, 1343 (1970).
15. H. Yoneyama and H. A. Laitinen, *J. Electroanal. Chem.*, **75**, 647 (1977).
16. H. Yoneyama and H. A. Laitinen, *ibid.*, **79**, 129 (1977).
17. D. E. Albertson, H. N. Blount, and F. M. Hawkrige, *Anal. Chem.*, **51**, 556 (1979).
18. N. R. Armstrong, A. W. C. Lin, M. Fujihira, and T. Kuwana, *ibid.*, **48**, 741 (1976).
19. T. Kuwana and N. Winograd, in "Electroanalytical Chemistry," Vol. 7, A. J. Bard, Editor, pp. 1-78.
20. M. Watanabe, S. Venkatesan, and H. A. Laitinen, *This Journal*, **130**, 59 (1983).
21. R. S. Nicholson and I. Shain, *Anal. Chem.*, **36**, 706 (1964).
22. W. L. Caudhill, J. O. Howell, and R. M. Wightman, *ibid.*, **54**, 2532 (1982).
23. D. E. Weisshaar, D. E. Tallman, and J. L. Anderson, *ibid.*, **53**, 1809 (1981).
24. K. Aoki and J. Osteryoung, *J. Electroanal. Chem.*, **122**, 19 (1981).
25. K. Aoki and J. Osteryoung, *ibid.*, **125**, 315 (1981).
26. K. Aoki and J. Osteryoung, *ibid.*, **160**, 335 (1984).

Report of the Electrolytic Industries for the Year 1984¹

Dale E. Hall*

American Cyanamid Company, Stamford, Connecticut 06904

Everette Spore*

Kerr-McGee Chemical Corporation, Henderson, Nevada 89015

Chlorine-Caustic Soda

Production and capacity.—Domestic.—Major U.S. chlor-alkali producers are listed in Table I (1). The major end-use markets for chlorine and caustic are summarized in Table II (2).

As Table III shows, the production of chlorine and caustic rebounded from 1983 levels. The average operating rate for 1983 was 68.7% of capacity; in 1984, it was 75.6% of capacity. (3-9).

Returns on caustic soda and chlorine generally increased throughout the year as the general economy recovered. Prices for caustic soda range from \$195 to \$265/ton, 50% caustic, location dependent. Chlorine tabs have gone from \$150 to \$170/ton levels to \$195-200/ton (56-61).

Occidental and PPG have taken an optimistic view of the future, as evidenced by their modernization plans. Occidental is installing a \$30 million, 400 ton/day chlorine, 440 ton/day caustic soda plant at its Taft, Louisiana, facility. The new plant will be Eltech's membrane cell technology. This is reportedly the largest plant in the U.S. The new plant is expected to be on stream in early 1986. PPG is replacing its graphite electrode technology at its Natrium, West Virginia, plant with monopore diaphragm equipment. The trend is to make the plant more energy efficient. The new equipment, at a cost of \$105-\$110 million, is expected to be on line the first quarter of 1985 (10).

By April, Occidental Chemical boosted its chlor-alkali capacity at Taft, Louisiana, to more than 1000 ton/day. This was the result of starting up a 230 ton/day chlor-alkali plant idled more than a year ago at the facility (11, 12).

SRI International has released a report which indicates the problem of excess chlor-alkali production is likely to continue. Year to year fluctuations in demand have been 2% greater since 1975, as compared with the period from 1965 to 1974. Overcapacity generally exists around the world, so the industry cannot expect much help from exports. Western Europe ran at 75% in 1982, and Japan at 76% in 1982. Growth is predicted at 2%/yr in 1982. Growth is predicted at 2% in Western Europe, and 1.1% in Japan. New chlor-alkali capacity is coming on stream in the Middle East and Asia (13).

Pennwalt Corporation announced plans to convert the Tacoma, Washington, 250 ton/day plant to the ICI FM 21 membrane technology, which will be the largest such facility in North America. This will be the second facility to employ coated cathodes. Start-up of the plant is expected in the second half of 1985 (14, 15).

ICI's FM 21 technology is said to be energy efficient due to coated anodes and cathodes and the use of Du Pont's Nafion membrane. The technology was proven in

* Electrochemical Society Active Member.

¹This report is sponsored by the Industrial Electrolytic Division of The Electrochemical Society. It represents a summary of the published information on production, plant capacities, consumption, markets and trends, prices, raw materials, new developments, and health and environmental aspects in the electrolytic and related industries.

The material presented herein has been obtained from many sources, as noted in the list of references, and does not necessarily represent the opinions of the authors.

The Industrial Electrolytic Division is grateful for the support received from the Vittorio de Nora-Diamond Shamrock Fund, which assisted in meeting the publication costs of this article.

three European plants and six other installations will be commissioned in 1984 (15-18).

PPG Industries has received an award from Research and Development magazine (IR-100 award) for its "Bizec" membrane chlor-alkali electrolyzer technology. The cell technology reduces energy by more than 25% as compared to diaphragm cell technology. A demonstration-scale plant is operating at the Lake Charles, Louisiana, complex. This is PPG's first cell technology to use permionic membrane technology (19, 20).

In a bid for further integration, Occidental Chemical Corporation will reopen the 500 million lb ethylene facility at Lake Charles, Louisiana, formerly owned by Cities Service. This move will further integrate the company's chlorine and natural gas liquids (21).

Eltech Systems Corporation, Occidental Chemical Corporation and its subsidiary, Anode Products Incorporated, have settled pending litigation related to Eltech's patents for chlor-alkali diaphragm cells (22).

Japan.—Kashima Chlorine and Alkali Company has converted from mercury cell chlor-alkali technology to ion-exchange membrane technology at its Kashima works. Mercury cells must be replaced in Japan by June of 1986 (23).

Three Japanese companies—Asahi Chemical, Asahi Glass, and Tokugama Soda—are perfecting the ion-exchange membrane processes (24).

Table I. Major U.S. chlor-alkali producers (thousands of tons)

Producer	1984	
	Chlorine	Caustic soda
Dow Chemical	3,360	3,690
PPG Industries	1,363	1,499
Diamond Shamrock	1,234	1,356
Olin	808	889
Occidental ^a	750	828
Vulcan Materials	575	635
du Pont	517	485
LCP Chemicals and Plastics	505	462
Georgia Gulf	438	482
BF Goodrich	414	457
Stauffer Chemical	367	404
Pennwalt	299	378
FMC	290	318
Others	1,072	904
Total	11,992	12,787

^a An additional 300,000 tons back on stream in 1986 (1).

Table II (2). Chlorine-caustic soda 1984 markets

Chlorine	Per-cent	Caustic soda	Per-cent
PVC	20	Organic chemicals	38
Pulp and paper	14	Pulp and paper	20
Chlorinated ethanes	14	Inorganic chemicals	11
Chlorinated methanes	12	Soaps and detergents	5
Inorganics	12	Textiles	5
Propylene oxide	8	Petroleum	5
Other organics	7	Alumina	4
Water treatment	4	Miscellaneous	12
Miscellaneous	9		

Table XVII (106). U.S. aluminum ingot capacity

Company/Location	Jan. 1, 1984 Annual capacity (short tons)	Operating rate (short tons)
Alumax, Incorporated		
Ferndale, WA (Intalco)	280,000	277,000
Frederick, MD (Eastalco)	176,000	153,000
Mt. Holly, SC	200,000	186,000
Total	656,000	616,000
Aluminum Company of America		
Alcoa, TN	220,000	192,500
Anderson County, TX	16,000	0
Badin, NC	127,000	95,300
Massena, NY	226,000	226,000
Rockdale, TX	342,000	304,500
Vancouver, WA	121,000	96,800
Warrick, IN	298,000	275,400
Wenatchee, WA	226,000	226,000
Total	1,576,000	1,416,500
ARCO Aluminum Company		
Columbia Falls, MT	180,000	180,000
Sebree, KY	180,000	180,000
Total	360,000	360,000
Consolidated Aluminum Corporation		
New Johnsonville, TN	144,000	18,000
Kaiser Aluminum and Chemical Corporation		
Chalmette, LA	260,000	0
Mead, WA	220,000	110,000
Ravenswood, WV	163,000	122,250
Tacoma, WA	81,000	81,000
Total	724,000	313,250
Martin Marietta Aluminum		
The Dalles, OR	90,000	0
Goldendale, WA	185,000	185,000
Total	275,000	185,000
National-Southwire Aluminum Company		
Hawesville, KY	190,000	190,000
Noranda Aluminum Company		
New Madrid, MO	230,000	230,000
Ormet Corporation (Revere-Consolidated)		
Hannibal, OH	270,000	270,000
Revere Copper and Brass Incorporated		
Scottsboro, AL	117,000	0
Reynolds Metals Company		
Arkadelphia, AR	68,000	68,000
Jones Mill, AR	125,000	50,000
Lake Charles, LA	36,000	0
Listerhill, AL	202,000	88,000
Longview, WA	210,000	210,000
Massena, NY	126,000	126,000
Troutdale, OR	130,000	80,000
Total	897,000	622,000
Total U.S.	5,439,000	4,220,750
Percent operating		77.6

consumers other than the aluminum producers. Since 1979, prices for producing a pound of aluminum have gone from \$0.024 to \$0.18 (108).

The Tennessee Valley Authority service area has increased rates from 24.8 mill in 1979 to 37 mill this year. Several producers in the TVA area have closed or markedly reduced capacity. The TVA area has become the "swing" area for primary aluminum production. These energy policies will likely send primary aluminum production off shore and to areas with incentive energy policies for smelters (108).

Alcoa announced that it will phase out some of its high cost domestic capacity and will be buying more primary aluminum ingot on the open market (109, 110).

The Bonneville Power Administration made an agreement with six Northwest aluminum producer plants. Eleven Direct Service Industries (DSI's) have agreed to buy 2,640 MW of BPA power at 22.7 mill/kWh. BPA disclosed that over a 6 month period the agency will gain \$1.48 billion in total revenues (111).

Alcoa and Reynolds adjusted their output with respect to BPA's incentive power (112-114).

Kaiser announced that two additional potlines will be closed on September 9 at its Mead, Washington, facility. The domestic aluminum smelting rate will drop a full percentage point with the closing (115-118).

Reynolds Metals Company shutdown its 23,000 ton/year potline at Jones Mill, Arkansas primary smelter. Alcoa announced that it will restart its 25,000 ton/year potline at Alcoa, Tennessee, as the Tennessee Valley Authority decided to provide additional "limited interruptible power." Alcoa shutdown a 34,000 ton/year potline at Rockdale, Texas, a net shutdown of 9,000 ton/year. Martin Marietta Aluminum, Incorporated, announced it would close its 82,000 ton/yr smelter at The Dalles, Oregon, if no buyers were found by December 1. Martin Marietta has decided to divest of all aluminum operations (119-121).

Alcan reached agreement with Arco to acquire Arco's interest and a primary aluminum smelter in Sebree, Kentucky, and rolling mills in Indiana and Kentucky and Arco's alumina interests in Ireland (122-125).

Reynolds Metals Company announced it will temporarily idle its 25,000 ton/yr production lines at its Troutdale, Oregon, facility (126-127).

Vertical integration in the aluminum industry seems to have paid off, with companies integrating smelting of primary aluminum capacity with sources of alumina and bauxite (128, 129).

Martin Marietta, in its withdrawal from the world aluminum production arena, will sell four of its six operating facilities to Comalco Limited, of Melbourne, Australia (130-134).

Alcoa reportedly scrapped plans for a 200,000 metric ton/yr smelter in Manitoba, Canada (135, 136).

Reynolds Metals announced that it revised its primary aluminum capacity downward from 1,150,000 to 1,036,000 ton as a result of the permanent closure of its San Patricio, Texas, aluminum reduction plant near Corpus Christi, Texas (137).

Aluminum consumption is projected to reach new record for the second consecutive year. Total aluminum consumption is projected to exceed 16 billion lb for the first time (138).

Alumax, Incorporated, announced a 40,000 ton cutback as the aluminum market weakened. The Intalco plant at Ferndale, Washington, was cut 3,000 tons, and further reductions were likely when the six month Bonneville Power Administration's power rate reductions expire (139).

Aluminum took one step closer to becoming a commodity as trading in futures contracts began on the New York Commodity Exchange. Fears that volatility of primary aluminum prices would increase seem to have been mollified, and North American producers have been more supportive of COMEX than originally expected (105).

Canada.—Canadian aluminum capacity is tabulated in Table XVIII.

Table XVIII (106). Canadian aluminum ingot capacity

Company/Location	Jan. 1, 1984 Annual capacity (short tons)	Operating rate (short tons)
Alcan Aluminum Limited		
Arvida, Quebec	426,000	411,200
Beauharnois, Quebec	51,800	51,800
Grand Baie, Quebec	188,500	188,500
Isle Maligne, Quebec	80,500	80,500
Kitimat, British Columbia	295,400	295,400
Shawinigan Falls, Quebec	92,600	92,600
Total	1,185,000	1,120,000
Canadian Reynolds Metals Company		
Baie Comeau, Quebec	175,000	175,000
Total Canadian	1,360,000	1,295,000
Percent operating		95.2

Alcan Smelters and Chemical Limited, the main operating unit of Alcan, will begin construction of an \$85 million anode baking facility at its Arvida works in Jonquiere, Quebec. The facility will have an annual capacity of 92,000 metric tons and will replace an older plant at the site (140).

Alcan and ICI have filed suit against the state of California's unitary tax law. Alcan and ICI contend that they should be taxed only on their U.S. earnings, and not on their worldwide earnings. Both Alcan and ICI have interests in California (141).

Alcan Aluminum Limited announced that it was withdrawing its benchmark price for aluminum, the standard which had been in effect for more than 20 years. Aluminum is now traded on the London Metals Exchange (LME) and was the reason cited for the withdrawal (142).

Alcan will build a \$770 million smelter in the Laterriere region near Chicoutimi, Quebec. The first phase of the smelter will have a capacity of 80,000 metric ton/yr and a final production capacity of 250,000 metric ton/yr by the end of 1991. Once completed, this smelter will replace the works at Alcan's Arvida complex (143-149).

Pechiney Corporation, Alumax, and Societe Generale de Financement will construct a new smelter at Becancour, Quebec. Aluminerie de Becancour, Incorporated, (ABI) will be responsible for the construction and operation. The ABI will use Pechiney Aluminum's smelting technology (150-159).

Alcan, citing poor market conditions and uncertain exports, postponed its plans to construct two primary aluminum smelters and a hydroelectric generating facility in British Columbia (160-164).

Alcan reduced its output of aluminum ingot by 37,500 metric tons at its Arvida, Quebec, smelter (165).

Japan.—Japan's aluminum supply and demand and imports are summarized in Tables XIX and XX.

The Ministry of International Trade and Industry (MITI) is restructuring the Japanese aluminum smelting and semifabricating industry. The plan will reduce primary aluminum capacity to 300,000 ton from the present 710,000 ton, although current production is only 350,000 ton. Predicted primary aluminum demand will increase about 3%/yr to 2.1 million metric ton/yr by 1988, compared to 1.8 million metric ton/yr now. The difference will be made up of imports, primarily from Japanese invested smelters overseas (167-169).

Kobe Steel Limited, will supply two Japanese aluminum smelters with 100,000 ton of alumina/yr for four years. The alumina will be supplied from the Worsley alumina project in Western Australia. Nippon Light Metal Company, Limited will receive 20,000 ton and Sumitomo Aluminum Smelting Company, Limited will receive 80,000 ton; all to be processed into primary aluminum for Kobe (170, 171).

New Zealand.—The proposed Aramoana aluminum smelter is still under consideration despite earlier indications that the consortium (Pechiney, CSR Limited, and Fletcher Challenge) had abandoned the project because of increased power costs. New Zealand's energy minister says the government wishes to expand aluminum smelting on the South Island, but that to do so would involve major changes in current power planning including

Table XX (166). Imports of primary aluminum and alloy to Japan (metric tons)

Country	1984 (first half)	1983 (first half)	Percentage change
Canada	40,502	50,213	-19.3
U.S.	87,947	145,524	-39.6
Australia	79,452	46,292	+71.6
New Zealand	66,122	77,903	-15.1
U.S.S.R.	3,674	6,373	-42.4
South Africa	6,600	11,187	-41.0
Norway	42	2,013	-97.9
France	—	—	—
Britain	—	—	—
Federal Republic of Germany	—	501	—
Austria	227	1,347	-83.2
Total	284,566	341,353	-16.6

speeding up some hydropower projects to meet the 1988 "first potline" for Aramoana (172).

Australia.—A confirmed site for the much delayed aluminum smelter in Western Australia was announced in December. The site, at Kemerton, 60 miles south of Perth, was the one originally chosen. The consortium project, comprised of South Korean Kukji-ICC Group (50%), the U.S. Reynolds Group (25%), and the Australian Girffiths Group (25%) is expected to make a development announcement during the first quarter of 1985 (173, 174).

Alcan Australia Limited announced that it is postponing a new third potline at its Kurri Kurri aluminum smelter in New South Wales because of low prices for primary aluminum ingot (175, 176).

Alcoa of Australia Limited's Wagerup alumina refining started up in April. The 500,000 metric ton/yr facility is near Perth and was completed in June 1982, but was mothballed due to low world alumina demand (177, 178).

Australia is emerging as a significant world producer of primary aluminum in contrast to its traditional role as a supplier of bauxite and alumina. Australia has abundant coal resources to supply large quantities of competitively priced electricity. Worldwide decline in capacity was traceable to the oil price rise in the 1970's. By the end of 1986, the total annual rated capacity of all Australian smelters will exceed 1 million metric tons. The Portland smelter, being built by Alcoa of Australia Limited will cost \$1.15 billion and produce 300,000 metric ton/yr by November 1986, all to be exported (179-183).

The Tomago aluminum smelter near Newcastle has been operating the first two 115,000 metric ton/yr potlines at full capacity. The plant is scheduled to reach full capacity of 230,000 metric ton/yr in September 1984. The plant uses 180,000 Ampere technology developed by Pechiney Aluminum (184-186).

Europe.—The European aluminum industry predicts marginal growth for aluminum, only in the transportation sector. The North American market is projecting growth in the transportation, building and construction, and foil and beverage can markets (187).

England.—The Commodities Research Unit in London published a study indicating the importance of the six major producers will decline and that there will be a strengthening trend toward free-market pricing. Cheap energy will continue to be the major influencing factor in plant location selection (188, 189).

Deeside Aluminum Limited is operating a secondary aluminum plant in Wrexham, North Wales, which will toll convert scrap ingot into high quality extrusion ingot. It is said to be the only plant of this type in the world (190).

Italy.—Elfim, the Italian state holding group, has announced plans to shut down two aluminum plants in the next two years. Citing losses of \$105 million in 1980, and \$189 million in 1983, Elfim has asked for \$342 million in aid over the next two years from the Italian government (191).

Table XIX (166). Japan's primary aluminum supply and demand

	1984 (metric tons)
Demand	1,889
Supply from overseas projects	600
From long-term contracts	457
From others (domestic production and spot imports)	835
Total	1,892
Stocks	607

Egypt.—Egypt is to export 110,000 tons of primary metal in 1984. The Aluminum Company of Egypt expanded its capacity from 133,000 tons per year to 166,000 tons per year with Soviet aid (243).

Greece.—The Hellenic Industrial Development Bank (ETVA) has selected Kaiser Engineers and Constructors of Oakland, California, as technical consultants for the planning phase of a 600,000 metric ton/yr alumina refinery to be built in Greece with Russian technology and equipment. Construction is scheduled to begin in 1985 at an estimated cost of \$450 million. The U.S.S.R. would purchase 380,000 metric ton/yr of sandy alumina for 10 years; Bulgaria may buy another 200,000 metric ton/yr, but no agreement has been signed yet (192, 193).

Hungary.—Alumina production was 425,000 ton, while bauxite was 1.47 million metric ton, a 1.7 and 3.1% increase, respectively (194, 195).

Norway.—Ardal Og Sunndal Verk (ASV), Norway's largest aluminum producer, may be taken over by Norsk Hydro AS, currently the third largest Norwegian producer, by year's end (196).

A 50,000 metric ton capacity expansion is being studied by Norsk Hydro for its Karmoe aluminum smelter (197).

Brazil.—Hanna Mining Company plans to sell its minority interest in Alcoa Aluminco SA to Alcoa for \$55 million, if Alcoa negotiates an investment by Grupo Camargo Correa, Brazil's largest construction company. Alcoa and Hanna are joint owners of Alcoa Aluminco, which operates a bauxite mine, an alumina refinery, and a 90,000 metric ton/yr smelter in Southern Brazil (198).

Construction has been completed on 40% of the first 80,000 metric ton/yr potline at Albras, Brazil, the 360,000 metric ton/yr. Japanese-Brazilian aluminum project. Because work was suspended on the 800,000 metric ton/yr Alunorte project, Albras will have to buy alumina from outside sources. The second half of the Albras' phase-one project is due for start-up in June 1986 (199).

The Companhia Vale do Rio Doce (CVRD) has discovered another bauxite deposit in the northern state of Maranhao. The new reserves are estimated at 50 million metric tons, with a mineral content of 66.6%. 90% of the world's bauxite reserves with this mineral content are in Brazil (200).

The \$1.4 billion Alumar alumina-aluminum project was scheduled to start up in February. Alcoa and Shell are partners. Eventually the smelter will produce 300,000 ton/yr of primary aluminum and 500,000 metric ton/yr of alumina (201-203).

Venezuela.—Venezuela's Aluminio del Caroni SA (Alcasa) expects to earn an estimated \$29 million profit in 1984 due to abundant hydroelectricity and extensive alumina supplies from the 1 million ton/yr Interalumina plant (204).

Jamaica.—Bauxite shipments for the first nine months of 1984 amounted to 7,084,999 metric tons, including 3,952,725 tons of crude bauxite and 3,132,274 tons of refined bauxite (alumina). The totals included a GSA shipment of 879,316 tons of bauxite. The final bauxite shipment of Reynolds Metals Company of 1,031,699 tons was also included. Reynolds closed its Jamaican bauxite operations this year. The alumina exports declined mainly because of lack of electric power and labor disputes (205-207).

The Jamaican and Columbian governments have entered into an agreement to build an aluminum smelter in Columbia which will provide another outlet for Jamaican bauxite. The smelter will use abundant Columbian coal. No private or foreign investors are involved (208-210).

Indonesia.—The Aschar aluminum smelter in Indonesia has been completed bringing the rated capacity to 225,000 metric ton/yr of primary aluminum. The smelter is the largest in Asia and the largest source of supply for Japan (211).

Taiwan.—A collapse of negotiations between Taiwan Aluminum Corporation and Aluminum Company of America will cancel a Taiwanese smelter project. The \$50 million project was canceled because the Taiwanese government could not meet Alcoa's terms, for what Alcoa felt was necessary to meet minimum profitability and investment requirements (212).

Advancements in Technology.—The aluminum industry could be threatened in the aerospace market by composites. Sikorsky Aircraft's all composite-airframe helicopter, which made its maiden flight in August, will be turned over to the Army for further testing and evaluation in early 1985. The helicopter is made primarily from graphite and du Pont's Kevlar with small amounts of fiberglass (213). However, since aerospace and aircraft industries account for only about 6% of the total aluminum consumption, the impact will not be that great (214). Aircraft building is expected to increase in 1985 by 25% in the private sector and about 10% in the military (215).

Ford Motor Company announced that it expects 90-95% of the radiators it uses to be made of aluminum, rather than copper and brass, by 1988. About 20% of Ford's radiators are presently made of aluminum (216).

Engineers expect the superplastic forming of aluminum to make rapid inroads into the production of aircraft parts in the U.S. in the next 3-4 years (217).

Bethlehem Steel Corporation introduced a primarily aluminum coal hopper car prototype. The prototype will be tested by Southern Companies Services, Incorporated (218).

Trail King Industries, using a new line of bottom dump trailers, has realized a payload saving which will lead to increased use of aluminum in the future. A weight savings of 43% is realized by using aluminum to replace steel (219).

Carbochlorination for aluminum recovery from Italian leucitites has been studied. Much research work appears necessary for industrial use of chlorination in extractive polymetallic oxide material such as aluminous ores (220).

Alcoa announced that it is selling its ring-furnace technology for producing prebaked carbon anodes. Furnaces using this technology have been operating for up to 15 yr at the company's smelters in Rockdale, Texas, and Warrick, Indiana (221).

Alcoa entered into an agreement with DWA Composites to acquire special metal matrix technology for the development of high strength metal matrix composites using wrought aluminum powder technology aluminum alloys (222).

Toth Aluminum has recently opened an \$8.5 million plant in Vacherie, Louisiana, for producing aluminum, silicon, and titanium chlorides from kaolin clay (223, 224).

Aluminum-lithium alloys, in development for some years, will shortly become a commercial reality, as plans are announced for production by three of the world's major aluminum producers. Alcan, Alcoa, and Pechiney all announced plans to produce the alloy. Alcoa will market under the trade name Alithalite, Alcan will market Lital, and Reynolds Metals Company, which is still doing substantial research to develop its own line, will market under the tradenames Reyalite and Reyalith (225-235). Lithium decreases the density of aluminum-lithium alloys by 3% for every 1% lithium. Alcoa shows 10% more stiffness of the alloy for weight in these alloys (236).

Novamet Aluminum, a unit of Inco U.S. Incorporated, is taking orders for aluminum lithium billet. Novamet is the first company in the U.S. to market the new alloy commercially (237).

Comalco has developed a new aluminum alloy that can withstand 200°C. The key to the unique properties of the alloy seems to be small amounts of strontium and silicon (238).

An aluminum alloy which decomposes in water was marketed by Tafa, a firm in Bow, New Hampshire (239, 240).

Environmental.—Primary aluminum was excluded from Superfund taxing, although aluminum compounds, copper, and zinc were not (241).

Potlinings containing carbon, metal salts, and cyanide compounds are disposal problems to the aluminum industry. Alternatives for waste disposal are being developed by the Aluminum Association, the EPA, and the Bonneville Power Administration. One method uses controlled temperatures of 1500°F, which burns carbon and destroys cyanide, but only partially destroys the fluorides by the addition of limestone to produce calcium fluoride. The second method, pyrosulfolysis, was developed by Martin Marietta Aluminum, Incorporated, and uses direct injection of steam and sulfur dioxide into the combustor which combines with the salts to form sulfates, releasing the fluoride for recycle to the smelter (242).

Beryllium.—Production and price.—Beryllium production and consumption statistics for 1984 are given in Tables XXI and XXII (244).

The sole producer of metallic beryllium in the western world is Brush Wellman, Incorporated (245). Beryllium hydroxide concentrate is produced in Delta, Utah, from both local bertrandite ore and imported beryl ore.

Brush Wellman attributed record second quarter sales and earnings to continuing strong demand for beryllium products in the electronics industry (246). Sales of beryllium and specialty materials increased over 43% to \$68.3 million during the quarter. Chairman Henry Piper noted that the sales upsurge which began in the third quarter of 1983 continued through the first half of 1984 and showed no signs of slackening.

In June, Brush Wellman announced a \$57 million expansion of beryllium copper strip capacity at Elmora, Ohio, and Reading, Pennsylvania (247, 248). The investment will roughly double the company's strip capacity by late 1985, alleviating recent long production lead times. Cabot Corporation's Wrought Products Division invested \$16 million in wide strip rolling mill equipment, which went into operation in June in Elkhart, Indiana.

The General Services Administration awarded a \$13,467,000 contract to Brush Wellman for delivery of 60,000 pounds of beryllium metal (249). The beryllium will be delivered to GSA during the 12 months of calendar year 1985. The purchase is the second in a series un-

der an agreement that provides for future deliveries at prices to be negotiated.

In July, beryllium oxide powder sold for \$25.50/lb, while beryllium containing alloys were selling for \$130-\$140/lb beryllium content (250). The alloy price rose slightly, to \$140-\$144/lb by the close of the year (251). Beryllium 5 in. rod listed for \$241.39 in May (252). At the end of the year, 5 in. beryllium rod was listed at \$313/lb, delivered (253).

There are few notable sources of beryllium minerals. The U.S. Bureau of Mines assesses total world reserves of beryl and bertrandite at about 419,000 tons of contained beryllium (254).

Significant beryllium was found during drilling at Highwood Resources Limited's Thor Lake property, in the Canadian Northwest Territories (255). Two bulk samples assayed 0.93 and 1.6% of BeO. A later report (251) claimed that 2.33% BeO had been assayed. Plans exist for a feasibility study at the find.

Bearcat Explorations Limited and Colt Exploration Limited have acquired mineral claims to a beryllium prospect near Kimberley, British Columbia (256). A surface exploration program indicated that the prospect contained 500,000 tons of ore averaging 0.1% beryllium oxide. The prospect could be developed by open-pit mining. Evaluation work was scheduled to start in the spring of 1984.

Highwood Resources is optimistic about the beryllium prospect it has been exploring near Thor Lake in the Northwest Territories (257). Total reserves have been estimated at 1.61 million tons of ore with an average grade of 0.75% BeO. Development of a commercial operation will require three years of work if results of feasibility studies are positive.

Demand and market.—Beryllium oxide has excellent properties as a heat conductive, dielectric material (258). It is used in sintered form as a heat sink. Its primary uses are in high technology industries such as electronics, aerospace, and national defense (259). Applications have been made in optical components for large spaceborne telescopes in the space shuttle navigation system, and in stereophonic cartridge stylus cantilevers (254).

Brush Wellman, Incorporated, has developed a new alloy for the electrical and electronics industries (245). The new alloy, Brush Alloy 174, contains 0.15-0.50% beryllium and will cost only about half as much as Brush Wellman's beryllium copper, which contains up to 2% beryllium. It has about four times the electrical conductivity of phosphor bronzes, with comparable yield strength, and will be sold primarily to manufacturers of connectors, relays, and switches.

The future of beryllium in the electronics industry appears secure (247). Beryllium copper strip now accounts for 12-15% of the alloy strip market. Double digit growth in use is expected to continue through the decade. Imports are not a major concern; the sole Japanese beryllium copper producer is mainly concerned with internal consumption.

Chromium.—U.S. Chromium production and consumption statistics are given in Table XXIII (260). World mine production and reserve base on chromite are given in Table XXIV (261).

Chromium ore was imported (1980-1983) as chromium contained in chromite and ferrochrome as follows: from Republic of South Africa, 55%; from Zimbabwe, 8%; from U.S.S.R., 7%; from Philippines, 6%; and from other sources, 24% (260).

World resources total about 36 billion tons of shipping-grade chromite, sufficient to meet conceivable demand for centuries (261).

Major South African ferrochrome producers operated at capacity for most of the year without building inventories, while U.S. production of 50-55% charge chrome was reduced to one company, Macalloy, which is in Chapter 11 bankruptcy. Ferrochrome imports into the U.S. totaled 332,537 tons according to the Bureau of Mines. South Af-

Table XXI. U.S. beryllium production and consumption

	1982	1983	1984
Mine production	W ^a	W	W
Imports for consumption (ton)	115	97	70
Apparent consumption (ton)	150	279	330
Price (\$)			
Domestic metal, per pound	194	206	213
Imported ore, per s.t.u. (20 lb BeO)	121	126	90

^a Withheld to avoid disclosing proprietary data.

Table XXII. World mine production of beryllium

Country	Mine production (tons)	
	1983	1984 (est.)
United States	W ^a	W
Brazil	35	35
Republic of South Africa	1	1
Rwanda	3	3
Other market economy countries	5	5
China	NA	NA
Other centrally planned economies	84	85
World total	128	129

^aWithheld to avoid disclosing proprietary data.

Table XXIII. U.S. chromium production and consumption
(data in thousand short tons contained chromium)

	1983	1984 (est.)
Production: chromite	—	—
Imports for consumption	231	389
Exports	13	9
Consumption:		
Reported	301	390
Apparent (total demand)	329	466
Consumer stock at year's end	175	151

Table XXIV. World chromite mine production and reserve base
(data in thousand short tons of contained chromium)

Country	Mine production		Reserve base
	1983	1984	
United States	—	—	—
Brazil	310	350	10,000
Finland	375	400	32,000
India	400	450	66,000
Philippines	365	400	32,000
Republic of South Africa	2,460	2,500	6,300,000
Turkey	440	450	80,000
Zimbabwe	475	500	830,000
Other market economies	351	400	25,000
Albania	990	1,000	25,000
U.S.S.R.	2,700	2,700	142,000
Other centrally planned economies	55	60	4,000
World total (rounded)	8,921	9,210	7,540,000

rican producers accounted for 205,579 tons of the import figure (262, 263).

A new stainless steel, Type 409, a 12% chrome content steel for primary use in automobile catalytic converters and tubular manifolds could amount to 150,000 ton/yr of stainless steel—about 10% of total stainless production (264).

NASA licensed its iron-chromium battery technology to Sohio. Sohio estimated that 15 lb of each metal will be required per kilowatt hour of power generated. Sohio is investigating the technology for large batteries (265).

A new copper-chrome alloy was marketed by Battelle Memorial Institute's Columbus Laboratories. By using rapid solidification or solid state microblending normally immiscible materials can be combined. The copper-chrome alloy is not a solid solution, but a microcomposite material with excellent electrical conductivity (266).

Ferrochrome refining using plasma technology was announced by SKF Steel, Bofors, Sweden (267).

A membrane system to remove chromium from wastewater was announced by Bethlehem Steel, Consep Membranes, and Bend Research (268).

Turkey announced a new chrome chemicals complex. After exporting chromite for 136 years, they will produce 22,000 ton/yr sodium dichromate, 8,500 ton/yr of sodium sulfate, and 3,200 ton/yr of chromium sulfate. Turkey plans to export 75% of the production (269). American Chrome an Chemical announced a chromic acid plant in Corpus Christi, Texas (270). The plant uses proprietary technology (271). Ferrochrome capacity will be doubled at Outokumpu Oy's Tornio works to 120,000 metric ton/yr using process lump concentrate from Outokumpu's Kemi mine (272).

The GSA awarded an upgrading contract to Macalloy Corporation for converting 141,601 tons of chromite into high carbon ferrochrome during 1985. Macalloy contracted to convert 121,753 tons of chrome ore during 1984 (273). Meanwhile, the FEMA (Federal Emergency Management Agency) and GSA evaluated the ferrochrome and chromium metal stockpile for National Defense. High purity chrome (99.5%) was recommended to be purchased (274). The GSA issued a tender for 1,000 tons of electrolytic chrome metal for stockpile which now contains 3763

tons with a goal of 20,000 tons. The GSA apparently designed its specifications around Elkem Metal's specifications, the major U.S. producer of chrome metal (275).

The Bureau of Mines reported that chemical usage of chromium from January to October was 351,649 tons. Consumption for all of 1983 was 188,580 tons (276). Production and consumption in the U.S. are tabulated in Table XXIII. Table XXIV shows world production and reserves of chromium.

A Chromium Association was formed for interested miners, alloy producers, consumers, and traders (278). Chromium mine and plant expansions are summarized in Table XXV.

Copper.—Production.—Copper production and consumption statistics for 1984 are given in Tables XXVI and XXVII (279).

Domestic.—Early in the year, skidding copper prices led to production cutbacks at U.S. mines (280). Kennecott announced a 13% production cut at its Utah Copper Division plant in Bingham Canyon on January 18. Also affected were the division's 200,000 short ton/yr smelter and refinery. At Amoco Minerals' Cyprus Bagdad mine in Arizona, with a capacity of 81,000 short ton/yr, production was reduced by 25% on January 16. All mining and milling activities were later halted (281). Amoco's Cyprus Pima mine, with a capacity of 52,000 short ton/yr, was mothballed on January 1.

Faced with continuing depressed copper prices, Kennecott notified unions representing its copper workers that it wished to reopen all labor agreements as soon as possible (282). A Kennecott spokesman said that the agreements reached in 1983 were based on expectations that the U.S. economic upturn would also benefit the copper industry.

The United Steel Workers of America, the copper industry's principal labor organization, turned down an industry appeal for labor contract concessions (283). The

Table XXV (277). Chromium mine and plant expansions

Company	Capacity (metric ton/yr)	Product	Start-up
Outokumpu Oy	60 M	FeCr	1986
Hellenic Ferroalloys	400	Ore	1985
Swedechrome	78 M	FeCr	1986
Government (Malagasy Rep.)	60 M	FeCr	—
Indian Metals and Ferroalloys	50 M	Chg. Cr	1985
Etibank	106 M	Chg. Cr	1985
Donskoy (U.S.S.R.)	1.2 MM	Ore	—
Acoje Mines	500	Ore	—
Benguet/CMI	400 M	Conc.	1985

Table XXVI. U.S. copper production and consumption
(thousand metric tons copper content)

	1983	1984 (est.)
Production		
Mine	1,038	1,050
Refinery, primary	1,182	1,220
Refinery, secondary	401	310
From scrap, all sources	455	450
Imports for consumption		
Ores and concentrates	91	9
Refined	460	440
All imports	654	540
Exports		
Ores and concentrates	50	53
Refined	81	87
All exports	239	286
Consumption		
Refined, reported	1,767	2,110
Apparent, total	2,020	2,100
Refined stocks, year's end	672	590

Table XXVII. World copper mine production and reserve base (thousand metric tons copper content)

Country	Mine production		Reserve base
	1983	1984 (est.)	
United States	1,038	1,050	90,000
Australia	256	250	16,000
Canada	625	625	32,000
Chile	1,257	1,250	97,000
Peru	322	370	32,000
Philippines	273	250	18,000
Zaire	535	525	30,000
Zambia	543	540	34,000
Other market economy countries	1,228	1,300	101,000
Poland	380	380	15,000
U.S.S.R. (est.)	1,000	1,000	36,000
Other centrally planned economies	587	580	9,000
World total	8,044	8,120	510,000

appeal was made by Kennecott, Inspiration Consolidated, and two divisions of Newmont Mining. A union spokesman said that the union believes that industry guarantees, especially in the area of job security, would be needed before any concessions could be made.

Asarco Incorporated will close one of its three smelting facilities within a year because they cannot meet environmental regulations (284). The closing of the Tacoma, Washington, plant will cost \$38 million. During 1983, the plant accounted for about 30% of Asarco's 213,400 ton output of blister copper. The closing was to be scheduled depending on extension of a federal pollution variance effective until the end of 1984.

Asarco also announced that it would suspend open-pit mining operations at its Silver Bell copper mine on August 15 (285). A leaching operation was to continue producing copper at about one quarter of the mine's normal 21,000 ton/yr rate. Asarco was to reconsider opening the mine at the end of the year. The Silver Bell mine had been closed earlier in 1981, and was reopened in September 1983. An Asarco executive said that Silver Bell was "one of those mines . . . hanging on a thread between continued operations and shutdown at the prices we have seen so far in 1984" (286).

According to the president of Asarco, Richard Osborne, the present plight of the domestic copper industry has resulted in the loss of 18,000 jobs by copper workers, as well as shutdown or curtailment of 40% of U.S. copper production capacity (287). Osborne claimed that, if competitive pressure could be eased, some U.S. operations could be reopened and upgraded (286).

Phelps Dodge closed its 40,000 ton/yr mine and concentrator at Ajo indefinitely in mid-August (289). Previously, the facility had been operating at full capacity. The Ajo smelter will continue to operate, handling material from PD's other mines at Morenci, Arizona, and Tyrone, New Mexico.

Copper refining operations at Copper Range Company's White Pine, Michigan, complex were halted until the price of copper improved or until the facility could be sold (290). The decision to halt operations was based in part on an inability to reduce costs further.

Asarco, Incorporated announced suspension of operations at its Haywood, Arizona, copper smelter for 8-11 weeks beginning November 26 (291). The shutdown was scheduled to allow rebricking of the flash smelting furnace due to recent premature failures in the year-old facility. The furnace has been building to its full capacity of 175,000 short tons, and had supplied about one-third of Asarco's domestic copper output.

Material swapping within the copper industry has increased, as producers and merchants attempt to cut freight and inventory costs to the lowest levels possible (292). Most swapping takes place at the cathode level, where brands are indistinguishable, a factor important to some brand-conscious producers.

Import relief for domestic producers.—Eleven U.S. copper producers, representing 85% of the domestic industry, asked the International Trade Commission for import relief, in the form of a quota limiting foreign imports to 350,000 tons in each of the next five years (293, 294). The domestic industry, in return, pledged to continue modernization programs to insure its economic viability. The January petition, filed by producers including Asarco, Anaconda, and Phelps Dodge, asserted that total imports of refined and blister copper increased 140% since 1979, and about 54% between 1982 and 1983, resulting in the loss of 18,000 jobs (295, 296).

However, opinion was divided on the merits of temporary protection for the copper producers. Representative S. Boehlert, whose district includes copper manufacturing companies, claimed that such relief would harm the employment of nearly 200,000 people in downstream copper manufacturing. Protectionist sentiments were criticized by domestic as well as foreign sources (297). During a Copper Roundtable at the National Association of Recycling Industries, it was claimed that American brass mills would be hurt unless protection was extended to semifabricated and finished goods manufacturers as well as to primary producers.

A joint lobbying effort in Washington was launched by the Copper and Brass Fabricators Council and the National Electrical Manufacturers' Association, against quotas or tariffs on copper imports (298). NEMA claimed that an import quota of 415,000 ton/yr would reduce employment by domestic fabricators by 5,712 jobs, while creating a temporary gain of only 2,594 jobs in mining, smelting, and refining. A \$0.05 tariff would cost 2,117 jobs in the fabricating industry, according to NEMA.

At an International Trade Commission hearing in May, foreign copper producers testified that the domestic copper industry's troubles are due to technologies that have decreased their copper needs by substitution and miniaturization (295). According to a spokesman from Peru's Minpeco mining company, U.S. copper consumption fell 15% relative to other market economies between 1974 and 1983. The foreign producers also faulted U.S. producers for a nonaggressive marketing approach. U.S. producers and legislators testified that Chilean imports of refined and blister copper are the most serious problems, having increased 240% since 1979 and accounting for about 55% of 1983 imports.

Citing a need to address "the issue of fair competition," Representative J. F. McNulty, Jr. urged a national copper policy (299). McNulty criticized multilateral development banks for assisting less developed nations in increasing copper production when the worldwide copper surplus was estimated at 750,000 tons. In February, McNulty and 23 other legislators urged Treasury Secretary Donald Regan to register U.S. opposition to a \$70 million loan application from Zambia to the World Bank. McNulty also continued efforts to pass an environmental equalization tariff to account for the estimated \$0.10-\$0.15/lb that domestic producers spend to comply with environmental laws (300).

Import protection for the copper industry would cost consumers \$602 million, according to the Federal Trade Commission (301). The FTC also told the International Trade Commission that adjustments or tariffs would be more cost-effective methods of relief for the copper industry than import quotas.

Exxon Minerals Company joined the National Electrical Manufacturers Association in opposition to the petition (302). Foreign opposition was nearly universal, with Canadian, Australian, Mexican, Chilean, and Zambian producers, and the Philippine government, all against the U.S. producers' petition. Responding to the U.S. producers' import quota request, a spokesman for the Intergovernmental Council of Copper Exporting Countries (CIPEC) claimed that such a move would damage all copper producers by depressing international copper markets (303).

The International Trade Commission noted, in a formal report sent to the White House in July, that declining domestic ore grades were a major factor affecting U.S. market supplies of copper (304). Ore grades have declined from 2% in the 1920's to about 0.65% and projections suggest 0.45% ore in 2000. Because U.S. copper ore is 35% less rich, on average, than in foreign countries, milling costs are 55% above the foreign average. The commission did note, however, that productivity increases could offset higher wages and lower ore quality enough to hold domestic mining cost increases in line with those in foreign countries.

The report also cited outdated smelting facilities as a problem troubling the domestic industry. Each major copper producer was asked what specific steps it would take to become more competitive if import relief was granted. Asarco outlined plans to invest in mining and milling operations, including technological improvements. Magma Copper, Phelps Dodge, Duval, and Inspiration Consolidated Copper also revealed investment plans predicated on import relief.

On June 14, the ITC voted unanimously that the domestic copper industry had suffered substantial injury from imports of refined and blister copper from nations such as Chile, Zambia, and Zaire (305). ITC Chairman Alfred Eckes stated that "the issues are clearly defined and the evidence is compelling." In addition to the overall quota of about 350,000 ton/yr, the domestic producers requested a 114,000 metric ton/yr quota for Chile, less than half of the 282,000 tons imported in 1983 (306). A 97,000 metric ton/yr limit was recommended for Canada.

However, while recognizing the damage caused by imports, the ITC was split over how to apply remedies (307, 308). While two commissioners recommended that the President impose a 425,000 short ton/yr quota, two others recommended boosting the import duty by \$0.05/lb. One commissioner said that neither would be sufficient to solve the industry's problem (309). Supporting the latter view, Interior Secretary William Clark called for negotiating orderly marketing agreements with foreign producers (310, 311). According to Clark, only a recovery of world copper prices could bring relief, as domestic producers must now sell at a loss.

In September, the President rejected proposals to impose either import quotas or tariffs on foreign copper (312, 313). U.S. Trade Representative William Brock stated that "the argument against quotas and tariffs was abundantly clear, in that they would have raised the cost to our fabricators, placing at risk four jobs for every one saved."

Canada.—In Canada, a government report painted a bleak picture for the future of the copper industry (314). The industry was called more vulnerable than at any time in history. Among the disadvantages of the Canadian industry, the report noted high labor, materials, and handling costs. Also cited was the use of more modern technology at many foreign smelters. William Rompkey, Minister of Mines, also pointed out marketing and financial difficulties (315). The study estimated that plant modernization and pollution abatement measures over the short term would require about C\$1.1 billion.

Harold Fargey, president of the Mining Association of Canada, cited government-imposed costs which erode the ability of Canada's mining industry to compete (316). Because 80% of Canada's mineral output is exported, the industry must be able to compete worldwide or lose much of the \$13 billion/yr in export income and put many of Canada's 650,000 mining jobs in jeopardy.

According to M. N. Anderson, chairman of Cominco, Canada is losing its position as a great mineral producer because of high costs (317). While Canadian copper production costs are about \$0.90/lb, the figure for Peru and Chile is about \$0.50/lb. While Alfred Powis, chairman of Noranda Mines, cited the role of third world governments, a member of the Canadian parliament laid some of the blame on the Canadian government. Michael Wilson

cited regulatory and tax measures enacted in the 1970's when international competition was becoming severe.

The Quebec government reported that it will order Noranda to reduce SO₂ emissions from its Rouyn smelter by 40% (318). The smelter was claimed to be responsible for about one-half of total Quebec SO₂ emissions. Quebec indicated willingness to help Noranda pay the estimated \$100 million cleanup cost. Noranda's Horne copper smelter would have to cut SO₂ emissions by 50%, while a 65% cut would be required at the Gaspé smelter (319).

The Quebec government granted Falconbridge Copper Corporation C\$25 million to encourage development of the Ansil copper deposit near Noranda, Quebec (320). The company had suspended work on the project because of low copper prices. The latest phase of development is expected to be completed by early 1987.

Expecting a stronger copper market, Sherritt Gordon Mines authorized continued operations and development at its Ruttan mine in Manitoba (321). The May decision was a reversal of earlier plans to terminate operations at Ruttan by June 15.

Noranda Mines announced that it would lay off up to 400 workers at its Horne smelter and its Montreal refinery (322). The layoffs were needed because of the continuing copper market slump.

Kidd Creek Mines announced that it would spend C\$54 million to increase the annual capacity of its copper operation from the current level of 59,000 to 90,000 metric tons by 1988 (323). The expansion is expected to reduce the unit cost of copper production.

Brenda Mines of Peachland, British Columbia, indefinitely suspended operations at its copper mine on December 14 (324). Reopening was said to require copper prices of \$0.75-\$0.80/lb. The mine can produce up to 30 million pounds of copper/yr.

Foreign.—In February, Chile's Codelco declined to curtail copper output (326). Copper exports account for 36 percent of the dollar value of all Chilean exports. Severe mid-year storms, which battered Chile with 140 mph winds and avalanches, forced Codelco to close its El Teniente Division (319). The storm damaged water, energy, and ore transport systems at the 350,000 metric ton/yr facility. Also closed was the 100,000 metric ton/yr Andina Division.

At Codelco's Chuquicamata Mine in Chile, the world's largest open-pit copper mine, ore grades were reported to be declining from the present 1.68%, with 1% copper expected by the end of the century (325). A similar level was predicted for El Teniente, the second largest mine, with the 1% level maintainable for 100 years. To counter declining ore grades, Codelco has installed an electrowinning and leaching plant to recover copper from tailings, at a cost of \$0.42/lb. Overall, Chilean production costs were pegged at \$0.50/lb by Hans Feddersen, of Codelco's El Teniente Division. Included was a \$0.05/lb increase due to earlier pollution abatement measures.

A three-year plan issued by Chile's Economic Ministry anticipated a 4% annual increase in copper production and a \$2.5 billion investment in the nation's mining industry (326). The plan calls for copper output to rise from 1,257,000 tons in 1983 to 1,410,000 tons in 1986. Export earnings in 1986 would total \$28.5 million at an average copper price of \$0.70/lb.

Because of a critical shortage of foreign exchange for machinery and parts, Zambia Consolidated Copper Mines experienced operational difficulties (327). World and African Bank loans of \$120 million were expected to be used, in part, to rehabilitate the mines and boost copper output by up to 50,000 metric ton/yr.

Pasar, the Philippine copper concern, lifted force majeure and began supplying customers with 50% of their contracted tonnage on August 1 (328). Following an accident-related shutdown on May 13, its smelter was back at full capacity. The \$122 million smelter is 34.3% owned by the state-controlled National Development Company.

Peru's copper production will rise by 60,000 metric ton/yr to 400,000 metric ton/yr in 1985, with the opening of new mines at Tintaya (329). Peru exported 292,000 of the 322,000 ton of copper it produced in 1983.

Price.—Despite increased demand early in the year, copper prices fell (330). The price decline, as much as \$0.05/lb in only a few days, was blamed on technical factors triggered by the Commodities Exchange, as well as falling precious metal prices. Inspiration Consolidated Copper Company of Phoenix lowered its price for copper cathode to \$0.64/lb on January 9 (331). This was the lowest domestic price quote since October 1982.

Citing increased competition in the marketplace, both Inco and Noranda, announced on January 1, reduced premiums over the Commodities Exchange copper price (332). A wider range of purchasing options was also introduced.

In the second quarter, a healthy demand resulted in a drop in copper stockpiles (333). This was particularly true of the London Metal Exchange, where stocks declined from 436,000 metric tons at the end of 1983 to 252,000 metric tons by mid-May. A short-lived rally pushed U.S. producer prices to \$0.70-\$0.705/lb (334). However, copper prices slid in a market governed by financial factors (333). Rising interest rates in the second quarter, coupled with a strong dollar, were cited as the Comex price dropped from over \$0.70/lb at the beginning of April to \$0.623/lb by mid-May.

Despite the downturn in copper prices, Morton Schultz of Harold Sacks and Company predicted that copper prices would move higher as long as overall business continued to improve (335). Good first quarter earnings and a move away from a situation of copper oversupply were cited as positive factors.

In little more than three weeks in July, the low end of the domestic producer copper price sagged three times to new 26 month lows (336). Kennecott dropped its price by \$0.03 to \$0.62/lb. At the same time, Comex prices rose by more than half a cent, to \$0.5815/lb. and then to \$0.5955/lb. Meanwhile, Merrill Lynch analyst, David Moison, characterized the supply-demand balance as good, primarily due to production losses in Chile, Peru, Brazil, and among domestic producers such as Kennecott, which pared production at its Utah division by two-thirds on July 1.

Codelco purchased 30,000 metric tons of copper on the London Metal exchange in July (319). The purchase was made partly to compensate for storm-related production losses, but also because Codelco considered the price of around \$0.60/lb to be unrealistic (337). Codelco's market actions, according to a company spokesman, were short term and not aimed at supporting prices over a long period. As prices recovered somewhat, Codelco halted copper purchases on the London Metal Exchange in August (338). Company sources, however, acknowledged that Codelco will periodically enter the market in the future to act as a buffer when prices fall, or to add momentum when prices rise. A second factor in Codelco's move was slackened Far East demand, making it unnecessary to buy copper off the LME to supply European customers as copper production was diverted to Japan.

Demand.—A shortage of higher grade copper cathode developed early in the year (339), as Chilean refined copper was diverted from the U.S. East Coast to Japan, where copper producers earlier cut output by 10-15%. Supply problems were also reported in the European market.

Early in the year, commodity specialists were bullish on copper futures despite the depressed markets (340). The building industry, which accounts for 30 percent of U.S. consumption, experienced a 15% jump in housing starts as the year began. Futures traders were hoping for a repeat of 1982, when copper prices leaped by more than \$0.25/lb on the spot market.

During the first half, copper demand improved and inventories declined (341). It was estimated that total nonsocialist world inventories would shrink by 100,000-200,000 short tons in 1984, followed by a larger reduction

of about 400,000 short tons in 1985. Part of the inventory draw down was attributed to demand from European fabricators who had cut stocks to very low levels.

An English study predicted that world copper consumption would grow at 1.5%/yr throughout the 1980's, resulting in a 1985 usage equaling or exceeding the previous 10 million metric ton record of 1979 (342). The relative importance of copper as a pure metal was seen to decline, owing to slackening use in communications wire, while use of copper engineering alloys was expected to grow. Despite the overall growth of copper demand, it was predicted that further North American mine closings would occur as production became more concentrated in mines under government control. The report also predicted that copper prices would continue to be subject to wide fluctuations.

A British report predicted that there would be no substantial short-term copper demand increase in Europe (343). Imports of refined copper by the United Kingdom, according to official import statistics, were lower in 1983 than at any other time in the postwar period.

The Senate approved an amendment to increase national defense stockpile funds by \$250 million in fiscal 1985, with indications that a significant portion would be used to purchase copper (344). The copper inventory goal is 1 million short tons, while only 29,048 short tons are now stockpiled. In addition to taking advantage of favorable copper prices, the measure was seen as a way of aiding the ailing domestic copper industry.

Markets.—The International Copper Research and Development Association (INCRA) proposed strategies for defending current copper markets and developing new applications at its annual meeting in June (345). The focus will be on three areas: improving copper-brass radiators, defining agricultural benefits of copper as a micronutrient in plant growth, and promoting copper-nickel sheathing of off-shore oil rigs and ship hulls.

Two copper executives called for increased research and promotional efforts to expand copper markets (346). Although certain copper markets, such as power transmission lines and automobile radiators, are determined by large companies according to long-term economic analyses, other uses such as plumbing and heating can be increased.

Lithium.—Domestic lithium production and consumption are given in Table XXVIII (347). World mine production and reserve base statistics are given in Table XXIX (348).

Lithium chemical and metal consumption increased by 11% to the equivalent of 60 million pounds of lithium carbonate in the western world (349).

Footo Mineral and the Government of Chile began a joint venture (Sociedad de Litho) production facility, rated at 14 MM lb/yr, in the Salar de Atacama Basin. The lithium content of the salt brine ranges from 1400 to 1500 ppm. The large magnesium ratio extended Footo's research to the better part of a decade. The project reportedly cost \$48 MM (350, 352, 355).

The indicated reserves in the Atacama Basin represent 40% of the world's lithium supply (350).

Table XXVIII. U.S. production and consumption (short tons)

	1983	1984 (est.)
Production	a	a
Imports for consumption	35	40
Exports	2600	2900
Consumption:		
Apparent	a	a
Estimated (assumes 15% lithium loss during conversion)	2200	2600
Producer stocks, year's end	a	a

^a Withheld to avoid disclosing company proprietary data (347).

Table XXIX. World mine production and reserve base
(short tons)

Country	Mine production		Reserve base
	1983	1984	
United States	^a	^a	450,000
Argentina (est.)	5	5	NA
Australia (est.)	75	100	350,000
Bolivia	—	—	6,000,000
Brazil	60	60	NA
Canada	—	—	400,000
Chile	—	560	1,500,000
Namibia	20	20	NA
Portugal	10	10	NA
Zaire	—	—	350,000
Zimbabwe	150	150	30,000
China	350	350	NA
(order of magnitude est.)			
U.S.S.R.	1,400	1,400	NA
(order of magnitude)			
World total (excluding U.S.)	2,100	2,700	9,100,000

^a Withheld to avoid disclosing company proprietary data.
Identified lithium resources total 8.06 million tons (348).

The Bolivian government signed an agreement with the United Nations to carry out a geothermal feasibility study for eventual recovery of the lithium salts of the Salar de Uyuni (356, 357).

Amax, Corfo, and Molibdeno began a development program for a mine plant rated at 12 MM lb/yr of lithium carbonate. Estimated costs are \$210 MM; targeted production is 1988 (358).

A majority of the lithium carbonate from Chile will go to the aluminum industry (355).

The lithium industry overcapacity will be largely dependent upon the aluminum industry. A 10-12% increase in demand is projected. The 2-3% lithium content for aluminum alloys continues to create interest in the aircraft industry. Lithium decreases the density of Al-Li alloys by 3% for every 1% Li content (351). The alloy and lithium batteries will be the major growth areas (352-354).

Several companies are working on lithium metal sulfide batteries for electric vehicles among other applications. This battery system is also promising for utility load leveling (359).

At year's end, lithium carbonate was priced at \$1.54/lb and lithium hydroxide was \$1.93/lb. The lithium metal price was about \$22.70/lb (347).

The EPA notified the Department of Defense that lithium-sulfur dioxide batteries exhibit a characteristic of "radioactivity" and are thus subjected to Resource Conservation and Recovery Act rules when they are discarded (360).

Magnesium.—Magnesium continued the rebound begun in 1983. Early in the year, prices were hiked, and projections for growth in new and existing markets were good.

Production and price.—Western world magnesium production totaled 173,000 metric tons in 1975, and increased each year to a peak of 236,000 tons in 1980 (362). During the recession, production plunged to 156,000 tons in 1982 before rebounding sharply in 1983 and 1984. Production and consumption figures are given in Tables XXX and XXXI (362).

Magnesium price hikes were posted by major producers at the beginning of the year (363). Dow Chemical Company increased the base price for 99.3% Mg ingots and grinding slab by \$0.05, to \$1.43/lb. Die-cast alloys AZ91B and AZ91XD were offered at \$1.28/lb. The price increase for ingot and grinding slab followed a similar price increase posted by Amax, Incorporated.

Dow and Amax increased their prices for die casting magnesium in early April (364). Dow's price for AZ91XD was \$1.30, while the Amax price for AZ91HP was \$1.26/lb.

Table XXX. U.S. magnesium production and consumption

	1983	1984 (est.)
	(thousands of short tons)	
Production		
Primary	115	130
Secondary	46	45
Imports for consumption	6	7
Exports	47	50
Consumption		
Primary, reported	82	90
Apparent	117	100
Consumer stocks, year's end	28	40

Table XXXI. World magnesium production

Country	1983	1984 (est.)
	(thousands of short tons)	
United States	115	130
Canada	9	9
France	10	10
Italy	8	9
Japan	7	7
Norway	39	40
Yugoslavia	4	4
China	8	8
U.S.S.R.	91	91
World total	291	308

The lower Amax quote was viewed as part of a plan to be the leading supplier to the Detroit market.

Increased magnesium earnings were a major factor in the return of Amax to profitability in the first quarter, after eight consecutive quarterly losses (365, 366). Due to both higher margins and shipments, the magnesium business was in the black after losses in 1983.

Under a restructuring of its metals groups, Amax announced that magnesium production at Salt Lake City, Utah, would become part of the new specialty product unit (367, 368). Integrating management and reducing administrative costs were expected to produce cost savings in a continuing austerity program.

According to a Dow spokesman, the company was studying an increase in operating rate at its Freeport, Texas, plant (363). In the third quarter of 1983, the plant output had been raised from about 50% to about 70% of capacity.

Dow Chemical announced that a new, high purity, corrosion-resistant magnesium sand casting alloy had been developed at its Freeport, Texas, facility (369). The new alloy, designated AZ91C/HP, is intended for use in military aircraft exposed to highly corrosive salt water environments. The new alloy contains reduced levels of iron, nickel, and copper contaminants, making the alloy less susceptible to corrosion. The new alloy was initially marketed at \$1.43/lb, the same price as the standard AZ91C alloy it replaced.

Demand and Markets.—Overall magnesium use is expected to increase 5-7% in 1985 (362), as the industry rebounds from the recession. As the lightest structural metal, and with its corrosion resistance properties, magnesium is being used increasingly in the hand tool and military market. Greater use of magnesium sand castings is expected in the aerospace industry, especially for helicopter parts. It is also being used to desulfurize iron during steel production, and to produce titanium and zirconium.

The outlook for magnesium die castings is brighter than it has been for some time (370). New applications are expanding opportunities for magnesium in key areas such as the automotive and electronics industries, high purity alloys, and improved die casting technology. The magnesium die casting market may have increased as much as 75% over 1983 levels. While magnesium's light

weight has always been recognized, its other properties, such as high strength and stiffness, excellent heat dissipation, and improved corrosion resistance, are now being used to advantage.

These properties and others, plus the need to boost fuel economy by building lightweight vehicles, have improved the prospects for magnesium use in new car designs. A survey of producers and die casters indicated that magnesium continued to penetrate the automotive markets held by aluminum (362). Projected growth from 1984 to 1985 was as much as 10-15% in the automotive market. According to a Dow spokesman, growth will result not only from an increase in the number of vehicles built, but also because of increased usage per unit. With one-third of the weight of aluminum, and comparable strength and fracture resistance, magnesium is a serious contender to reduce auto body weight and fuel consumption. Magnesium is about twice the price of secondary aluminum ingot. However, magnesium parts are often easier and more economical to produce than aluminum parts.

There is now about 1 lb of Mg used per domestic auto produced, and as much as a tenfold increase may occur by 1990. Ford's Ranger and Bronco II trucks have magnesium brake and clutch pedal support brackets and clutch housings. The clutch housings are directly exposed to road splash, but do not require special protective coatings. At a weight of 6 lb, the housings have met Ford's weight reduction goal without increased cost. The clutch and brake pedal support was traditionally made from stamped steel, and more recently, from lighter aluminum die castings. The magnesium bracket, with a 20% thinner wall, weighs less than 1.5 lb, vs. 3 lb for the aluminum bracket. Ford is also planning to use magnesium clutch housings in new compact-sized Aerostar vans (370).

General Motors has used magnesium in several new applications, including headlamp assemblies and grill covers on the Pontiac Fiero. In the headlamp assembly, with very thin walls, magnesium outperformed aluminum in wind pressure tests for distortion and cracking. The grill cover, directly above the engine, requires dimensional stability, heat dissipation, and surface finish properties. Magnesium engine valve covers may be used on the Calisto, a new luxury car planned for introduction by Cadillac in the 1987 model year (371). In addition to light weight and rigidity, magnesium offers good sound damping characteristics in the valve covers. GM is also considering new applications for magnesium in engines, transmissions, and interiors. Chevrolet has produced a 3 lb magnesium bracket that may be used on two million cars (362).

Amax Specialty Metals held three seminars in the Detroit area to spur automotive use (371). Major U.S. automakers and their suppliers of cast magnesium components were invited.

Die casters predict a 15-25% increase in magnesium use for computer parts (362). Valuable properties for computer applications are lightness, sound deadening, and tolerances which can be closer than when aluminum is used. The magnesium die casting process is about 40-50% faster than aluminum die casting.

A portable computer by Grid Systems Incorporated, uses several Mg die castings (362). Other computer manufacturers use magnesium in internal parts such as heat sinks and disk drive actuator arms.

Manganese.—Domestic manganese production and consumption statistics are given in Table XXXII (372). World production and reserve base data are given in Table XXXIII (373).

The U.S.S.R. and Republic of South Africa account for more than 80% of the world's identified manganese resources (373).

On a 1983 base, U.S. demand for manganese is expected to follow raw steel production trends and increase at an average annual rate of about 3% through 1990. It is estimated that 1985 U.S. mine production will be zero, based

Table XXXII. U.S. manganese production and consumption

	1983	1984 (est.) (thousands of short tons)
Production	None	None
Imports for consumption		
Manganese ore (35-54% Mn)	368	410
Ferromanganese (74-95% Mn)	342	500
Government stockpile excesses (shipments)		
Manganese ore	74	55
Exports		
Manganese ore	19	140
Ferromanganese	8	6
Reported consumption		
Manganese ore	531	510
Ferromanganese	446	510
Apparent consumption		
Manganese	668	740
Producer-consumer stocks (year's end)		
Manganese ore	617	550
Ferromanganese	195	150

No manganese ore containing 35% or more manganese was domestically produced in 1984 (372).

Table XXXIII. World mine production and reserve base (thousand short tons)

Country	1983	1984 (est.)	Reserve base
United States	—	—	—
Australia	1,491	1,800	540,000
Brazil	2,300	2,300	180,000
Gabon	2,047	2,300	440,000
India	1,455	1,400	120,000
Republic of South Africa	3,181	2,700	8,500,000
Other market economies	860	860	73,000
China	1,760	1,800	110,000
U.S.S.R.	11,500	11,600	2,500,000
Other centrally planned economies	145	140	25,000
World total (rounded)	24,700	24,900	12,000,000

on 35% manganese content ore, and U.S. apparent consumption of manganese will be 750,000 tons, content basis (373).

Tennessee Eastman Company announced that in 1986 it will end a process which requires manganese ore for the production of hydroquinone, owing to cost and efficiency. This change could reduce U.S. capacity considerably for the production of manganese sulfate, a by-product of Tennessee Eastman's process. Manganese sulfate is an important intermediate in other manganese chemicals, synthetic manganese dioxide, fertilizers, and animal feed (375-378). Meanwhile, Sedema, SA increased its capacity because of uncertainty of manganese sulfate supplies (379).

The ITC terminated its countervailing duty investigation of ferroalloys from Spain. The Ferroalloys Association notified the ITC that it wished to cancel its countervailing duty imposition request (380).

The GSA announced that Elkem Metals was awarded a \$17.8 MM contract for upgrading 80,000 tons of manganese ore into high carbon ferromanganese during 1985. Elkem will do the conversion at the Marietta, Ohio, facility (381-383).

During the year, an oversupply situation cut prices and tonnages of the South African producers, with Gabon being the one country which raised production at its Moanda operation, exporting to the U.S.S.R., Japan, Norway, and the U.S. Ghana will make further investment in its manganese mine at Nsuta. The U.S. Fuller Company constructed a calcining kiln to process fine manganese carbonate to manganese oxide at Nsuta. The \$25 MM plant has yet to perform, but is expected to be in full production in 1986 (384, 385).

A Norwegian ferroalloy producer, Elkem AS, will increase production of medium carbon ferromanganese by 40,000 metric ton/yr to 115,000 metric ton/yr (386).

Broken Hill Proprietary, Limited, announced a 3 yr capacity expansion in its manganese alloy operations at Bell Bay, Tasmania, from 135,000 to 190,000 metric ton/yr primarily for the export market (387, 388).

The takeover of Union Carbide's silicon and manganese operations in Quebec by Elkem Metals was completed (389, 390).

Large-scale field tests to remove manganese and silver from ore were successful. Haber, Incorporated, and Houston Mining and Resources have completed tests of Haber's alpha process to extract silver and manganese economically. The process recovers 95% of the manganese and virtually all of the silver (392).

The Exclusive Economic Zone (EEZ) off U.S. and Territorial coasts contain extensive deposits of ferromanganese, says the U.S. Geological Survey. Manganese nodules are most promising off the Hawaiian and Pacific Island Territories EEZ. Recent findings show high concentrations of cobalt in a ferromanganese crust (395).

Imports of manganese dioxide in 1984 surpassed all of 1983 in the first nine months (380).

Foote Mineral announced that it is spending \$17.4 MM to convert part of its electrolytic manganese metal plant to electrolytic manganese dioxide. Electrolytic manganese dioxide capacity is slated for 10,200 ton/yr on stream by late 1985 (380, 391, 393, 394).

Australia's BHP Limited intends to capture a significant slice of the natural manganese dioxide market for dry-cell batteries using the Groote Eylandt deposits in the Northern Territory. Natural manganese dioxide sells for \$200-\$240/metric ton, compared to \$70/metric ton for metallurgical grade ore. Shelf life and leakage tests take 6-12 months before results are known (388, 395).

Companhia Vale do Rio Doce (CVRD), the Brazilian manganese ore producer, is now making 10,000 ton/yr of electrolytic manganese dioxide, 4,000 tons of which were consumed by Brazilian battery makers. CVRD is supplying the U.S., Japan, Germany, France, Norway, and Denmark with test quantities of its electrolytic manganese dioxide (397).

New mining investments in manganese and ferromanganese are listed in Table XXXIV.

Nickel.—Domestic primary nickel consumption increased 17% over 1983 (see Table XXXV) (398).

The low point of 1982 remains, with 1984 being the second consecutive year of increase in primary nickel consumption. On the 1983 base, nickel demand is expected to increase at 2.5% per year through 1990 (398).

1984 mine production increased over 1983, because the sole U.S. nickel mine at Riddle, Oregon, was reopened this past year. Principal impediments to domestic mining and production were low-grade ore, poor market conditions, and energy costs (398).

Identified world resources in deposits averaging 1% nickel or greater contain 143 million tons of nickel. Eighty percent of the nickel is in laterites and 20% is in sulfide deposits (398).

World production and reserves of nickel are tabulated in Table XXXVI.

Nickel consumption by noncommunist nations is shown in Table XXXVII.

Table XXXV. U.S. production and consumption (short tons)

	1983	1984 (est.)
Production		
Mine	—	7,500
Plant	—	8,000
Refined matte	33,400	34,000
Secondary	51,000	50,000
Imports	152,333	200,000
Exports	23,359	29,000
Consumption		
Reported (no secondary)	127,845	150,000
Apparent (includes secondary)	204,000	225,000
Consumer stocks, year's end	20,448	26,000
Producer stocks, year's end	36,000	34,000

Table XXXVI. World mine production and reserve base (short tons)

Country	Mine production		Reserve base
	1983	1984 (est.)	
United States	—	7,500	2,800,000
Australia	99,200	110,000	5,300,000
Botswana	19,300	20,000	500,000
Canada	134,300	148,000	14,800,000
Indonesia	51,400	52,000	5,800,000
New Caledonia	69,400	45,000	17,000,000
Philippines	20,900	10,000	5,100,000
South Africa	22,600	23,000	2,900,000
Other market economy countries	80,972	85,000	19,900,000
Cuba	41,470	42,000	25,000,000
U.S.S.R.	187,000	190,000	8,100,000
Other centrally planned economies	33,100	35,000	4,000,000
World total (rounded)	759,342	768,000	111,000,000

Table XXXVII. 1984 World (noncommunist) nickel consumption

	Consumption (million lb)
United States	330
Europe	451
Japan	344
Other	115
Total	1,240

Canada, as the Western bloc's largest producer of nickel, must improve productivity and at the same time reduce SO₂ emissions by 50% to 2.3 million metric ton/yr (401).

Falconbridge Limited, Toronto, is negotiating with BCL Limited, Botswana, and Amax to acquire BCL's nickel copper ore, currently reserved for Amax in a 15 yr contract, set to expire in 1989 (402).

For Inco Limited the only road to profitability appears to be cost cutting moves, although the market could speed the recovery. Inco is predicting market stability at about 1.25 billion lb for next year. Inco is trying to join the ranks of producers with \$2/lb or below production costs (403-405).

The Nickel Development Institute, an international organization to develop new markets for nickel and to pro-

Table XXXIV (374). New manganese/ferromanganese mining investment

Company	Location	Type	Start	Capacity
CVRD	Carajas, Brazil	Ore	1986	825M
Mineracao	Maraba, Brazil	Mn	1986	400M
Mineroperu	Berenguela, Peru	Ore	—	3M
Sinai Manganese	Sinai, Egypt	FeMn	—	—
Somitam	Tambao, Upper Volta	Ore	—	500M
Broken Hill Pty. Limited	Bell Bay, Australia	Mn alloy	—	135M-190M
Government	Nsuta, Ghana	Mn	—	300M-450M

Table XXXVIII (399). New mine/plant expansions—nickel

Company	Location	Capacity	Type	Start
Falconbridge	Sudbury, Ont., Canada	700 M ton/yr	Ni ore	1987
Falconbridge	Sudbury, Ont., Canada	275 M ton/yr	Ore	Late 1980's
Inco	Thompson, Manit., Canada	3.5 M ton/yr	Ore	1986
California Nickel Corporation	Gasquet Mtn., CA	4 M ton/day	Ore	1987
Government	Punta Gorda, Cuba	66 M lb/yr	Ni	1985
Outokumpu Oy	Enonkoski, Finland	400 M metric ton/yr	Ni-Cu	1986
Lkab	Raana Field, Norway	600 M metric ton/yr	Ore	—
Western Platinum	Rustenberg, South Africa	4 MM lb/yr	Ni	1986
Arabian Shield Developers	Wadi Qatan, Saudi Arabia	32 M metric ton/yr	Fe-Ni	1990
Inco, Taiwan	Kaoh Siung, Taiwan	7 M metric ton/yr	Ni conc.	—
Government	Pomalla, Suawesi, Indonesia	75 M ton/yr	Fe-Ni	1985
Nord Resources/Mim	Ramu River, Papua, New Guinea	55 MM lb/yr	Ni	—
New Zealand Nickel Smelters	South Island, New Zealand	40 M metric ton/yr	Fe-Ni	1987

mote nickel containing products, was formed. The institute was formed because of the significant drop in the growth of nickel consumption (406).

World nickel mine production increases are shown in Table XXXVIII.

The Falconbridge nickel copper mine, scheduled to close in 1989, will be closed by its owner after 55 years of operation. A rockburst in June that killed four miners and registered 3.9 on the Richter scale finalized the decision. Rockbursts are not unknown in the Sudbury nickel deposits, but nothing of this intensity has ever been recorded (407).

Inco, Limited will use a dredge to take the overburden off its crown pillar underground Thompson mine as a first step in developing a new mine in the Thompson nickel belt of northern Manitoba. Only two of the original Thompson mines are now operating, the Pipe and the Thompson. Birchtree, Soab North, Soab South, and Pipe 1 have temporarily suspended operations (408).

Inco announced that a recently completed \$10 million improvement program will allow it to produce 25 ton ingot using ESR, electroslag remelting technology. The ingots will be 43 in. diam, some 30% larger than previous capacity sizes. Inco also installed a 15 ton vacuum induction melting furnace. Inco is responding to what it feels will be increased demand for the oil and gas industry's problems of drilling deeper to find reserves (407).

Hanna Mining Company reopened its Riddle, Oregon, facility after an 18 month closure. The company is not sure how long the mine and plant will remain open. The Bonneville Power Administration made an agreement with Hanna to use reduced cost off-peak power, 12h/day during the week, 15h on Saturday, and 24h on Sunday (410, 411).

The Department of Defense is opposing an amendment to a pending military authorization bill which would require the Pentagon to certify that "all" specialty metals purchased contain no Russian or Cuban nickel (412, 413).

Nickel stainless is finding increasing use in the chemical processing industry due to its corrosion resistance. Ammonia plants overseas also appear to be big consumers (414).

The threat of auto industry strikes helped keep demand and prices depressed for nickel. The strength of the dollar also helped keep prices depressed (415).

Nickel supplies in the Western World are expected to be in line with increase in demand, since the U.S.S.R. is no longer attempting to increase its market share (416).

Raznoimport wants to increase its exports to Japan and reduce its sales to Japan through international traders. In 1983, Japanese traders purchased 5000 tons from Raznoimport, the equivalent of 20% of total Japanese imports (417).

The Cuban government announced that it plans to raise nickel production from 40,000 ton/yr to 100,000 ton/yr within 10 years. The new Punta Gorda 30,000 ton/yr nickel plant will start up late next year and the Camariocas plant, now being built, will increase the total to 100,000 ton/yr in the mid-1990's (418).

Demand for nickel has strengthened mainly as a result of an economic upturn, especially due to the steel industry. The U.S embargo on Cuban nickel has also aided the demand cycle (419).

During 1984, prices were at \$2.08/lb in mid-March, and by year's end, the prices were in the \$2.10-\$2.20 range. The year was largely flat, with the London Metals Exchange unloading metal and producers minimizing inventories (420, 421).

Operation resumed at Marinduque Mining and Industrial Corporation's Nonoc Island nickel refinery, but not at normal production levels. Lack of working capital and supplies have been cited as the major constraints (422).

A typhoon inflicted heavy damage on the Surigao nickel refinery. Operations were suspended for at least one month. The refinery was actually down for two months for typhoon related damage (423, 424).

The refinery and the Marinduque nickel mines are owned by two Philippines banks, which formed the Nonoc Mining and Industrial Corporation. Marinduque's nickel mine has an estimated daily output of 10,000 dry tons of ore/day (424).

Outokumpu Oy will undertake immediate development of a new nickel mine at Enonkoski in eastern Finland. Proven reserves total 3.8 million tons grading 1.2% nickel and 0.3% copper. First year plans are for 400,000 metric ton/yr of ore (425).

Cabot Corporation announced the development of two new nickel alloys designated C-214 and C-22. C-214 is undergoing testing for replacement of ceramic materials in kilns. C-22 will be used for high temperature applications involving acids and offering corrosion resistance over that of previous nickel chromium alloys (426).

Marko Materials, Incorporated, entered a partnership to produce and market amorphous powder alloys based on nickel, iron, copper, and cobalt. The "Markomet" alloys will be used for electronics, carbide tools, and specialty machine tools (427).

Peugeot, the French automaker, announced development of a prototype electric vehicle. The car is powered by twelve 6V batteries of nickel-iron, which drive a 17.5 kW motor. It has a range of 124 miles, with a top speed of 62 mph. The batteries are reportedly good for 125,000 miles and 1500 recharge cycles (427).

MINPRO in Sweden has now successfully completed a nickel segregation process using calcium chloride and coke as additions to the calcining process. The process is kept below 950°C compared to over 1600°C for smelting (428).

Ni-Cal Developments, Vancouver, established Ni-Cal Technology to market its proprietary Acid Leach Process to offshore customers. The technology is presently used at the Gasquet Mountain, California, nickel-cobalt mine. The Ni-Cal Process is based on the commercial pressure acid leach process developed by Freeport Minerals (429, 430).

SKF Engineering has begun the first commercial use of plasma technology for production of nickel and other metals for the dusts of steel smelters. The plant at Sala,

Sweden, is expected to process 70,000 metric tons per year of metal (431).

Ni-Cal Technology Limited announced that it received a letter of interest from Marinduque Mining and Industrial Company for a retrofit of the Surigao nickel refinery with Ni-Cal's pressure leach technology. This would be the first commercial application of Ni-Cal's technology and is expected to significantly reduce energy cost at the Philippine refinery (432, 433).

A hydrometallurgical high pressure sulfuric acid leach process for treating a variety of oxidized nickel bearing ores is ready for commercial application. COFREMME, a joint venture between France's BRGM and Amax (Greenwich, Connecticut) have been testing the process at Golden, Colorado. The process shows wide utility and high nickel and cobalt recoveries combined with low energy and operating costs (434).

Sodium.—There are three domestic producers of sodium. Their estimated production capacities are given in Table XXXIX (435, 436). Because of the high demand for antiknock agents for gasoline, which require sodium for their manufacture, U.S. production has been 70-85% of world production for many years. Estimated foreign production capacity is also given in Table XXXIX (435). Domestic sodium production figures are summarized in Table XL (437).

The major use for metallic sodium is in the manufacture of tetra ethyl lead and other organometallic compounds. Because gasoline additives are being phased out in the U.S., sodium consumption for that market has declined steadily from a high of over 120,000 ton/yr in the late 1960's and early 1970's to less than 80,000 ton/yr in 1980 (435).

Sodium is also used in manufacturing refractory metals by sodium reduction of their halides. It is used as a reducing agent in dye, herbicide, and pharmaceutical manufacture. Some polymerization processes require sodium catalyst. Other uses include hydrocarbon desulfurization and heat-transfer in the primary and secondary loops of liquid metal fast breeder reactors (435).

Titanium.—Production and prices.—Production and consumption statistics for titanium are given in Tables XLI and XLII (438).

After several years of increased worldwide production capacity, 1984 was marked by some important changes among major firms in the industry. At a time when titanium prices were low and production capacity was well in excess of demand, the two largest domestic titanium producers were for sale (439). The owners of both RMI and the Timet division of Titanium Metals Corporation of America either publicly announced or intimated their willingness to sell. Titanium buyers expressed confidence that the companies would continue operating and that product focus would not be changed.

Timet, the largest integrated domestic producer of titanium, was sold to a group of investors including its top management (440). The former owners, Allegheny International and NL Industries, each retained a 5% share. Timet has the capacity to produce about 30 million lb of

Table XL. Domestic sodium production, 1984

Month	Production (short tons)
January	7,607
February	7,347
March	7,923
April	7,666
May	7,647
June	7,635
July	7,476
August	7,236
September	7,721
October	7,736
November	8,086
December	7,676
Total	91,756

Table XLI. U.S. titanium production and consumption

	1983 (short ton)	1984 (est.) (short ton)
Production	13,966	23,000
Imports for consumption, sponge	1,199	2,800
Exports, mainly scrap	7,830	7,300
Sponge consumption, reported	16,072	24,000
Industry sponge stocks, year's end	3,136	3,500

Table XLII. World titanium sponge production and capacity

Country	Production		Capacity
	1983 (short ton)	1984 (est.) (short ton)	1984 (short ton)
United States	13,966	23,000	33,500
Japan	11,600	18,000	37,500
United Kingdom	2,000	3,000	5,500
China	2,000	2,000	3,000
U.S.S.R.	45,000	46,000	52,000
World total (rounded)	74,000	92,000	131,500

sponge and 34 million lb of ingot per year at its Henderson, Nevada, plant.

The joint venture between Kobe Steel and RMI Company, which called for Kobe to convert semifinished titanium products supplied by RMI into mill products, failed to reach expected levels of shipments (441). Weak markets and high transportation costs have hindered progress in the February 1983 agreement. RMI's strategy, including the deal with Kobe, is to increase sales in industrial and commercial markets as the growth in aerospace demand slows. At present, commercial and industrial markets account for about 20% of RMI sales. According to RMI president, Frederick Gieg, the plan is to increase this to about 50% by 1990.

Some companies announced plans to expand production or explore new processing routes. Wyman-Gordon Company constructed a \$13.5 million titanium melting facility in Millbury, Massachusetts (442). The facility, scheduled to become fully operational at the end of 1984, will melt titanium ingot under computer control to improve process repeatability. Also planned is a \$13 million open die forging facility at Grafton, Massachusetts, to be used mainly for converting titanium ingots to forging billets.

Tiline, Incorporated, began commercial production on a new titanium investment casting facility (443). The Albany, Oregon, firm will use a computer-controlled, \$250,000 furnace to penetrate the market for precision medical and aerospace parts. Tiline anticipates \$1 million in additional sales in the first year of the facility's operation.

Albany Titanium, Incorporated, is using a \$4 million grant from the Defense Department to build two pilot plants (444). The plants will use a newly patented process to produce titanium sponge and powder from domestic il-

Table XXXIX. U.S. and foreign sodium production capacity (435)

Country	Company	Capacity (1000 tons/yr)
United States	du Pont	63 (57) ^a
	Ethyl Corporation	63 (45) ^a
	RMI, Incorporated	30 (37) ^a
Federal Republic of Germany	Degussa	9
United Kingdom	ICI	15
	Associated Octel	18
France	Ugine Kuhlmann	9
Japan	Nippon Soda	8
U.S.S.R.	Toyo Soda	13
		9

^aFrom Ref. (399).

menite. According to Fred Mullins of Wright Patterson's Aeronautical/Materials Laboratories, the process could "revitalize the industry." The Air Force will receive 10,000 lb of sponge and 2,000 lb of powder for analysis and evaluation. Pilot plant production startup was scheduled to begin between October and February. A production facility with an annual production capacity of 10 million lb of sponge or powder was planned for 1985. The Albany Titanium process is not expected to have a significant effect on the plentiful supply of ilmenite, or on its low price, currently \$40-\$45/ton.

Howmet, one of the largest nonintegrated producers of titanium ingot, announced that it was seeking to develop a position in titanium sponge production (445). The company did not plan to install in-house facilities, but was expected to seek equity in an existing producer or a long-term supply contract.

As nonintegrated melters sought sources of sponge, marketing executives at Oremet and RMI said they would be able to supply independent melters who had been buying Japanese material (446). Oremet announced that it was only operating at about 60% of its 9 million lb capacity to meet its mill product needs (447). Oremet expressed willingness to sell sponge to nonintegrated producers, with the ability to add 3 million lb production in six months. RMI, with a 9,500 short ton/yr estimated capacity, was soliciting sponge customers. The announcement came as nonintegrated melters claimed they had no alternative to Japanese sponge, with RMI and Timet both operating at or near 100% capacity.

Frankel Metal Company, a newly created, employee-owned firm, announced that it will specialize in recycling titanium scrap and doing toll processing in high temperature alloys (448).

Titanium producers also moved to improve distribution networks and to form joint ventures that would improve their production and marketing positions. As a response to maturing of industrial titanium products, ALS Metal Company announced that it would expand distribution of sheet, strip, plate, and welded tubing products through Metal Goods, Incorporated service centers (448). ALS followed a similar move by RMI Company, who will distribute titanium products through A. M. Castle and Company. Oremet, following the trend of domestic producers to establish national distribution networks, announced that five companies had been lined up as distributors of its titanium products (450). The service centers will sell Oremet titanium bar and billet to small customers. This movement is a departure from the earlier policies of integrated titanium producers involving captive warehouses and direct sales. The most likely distributor customers will be chemical processors, including the chlor-alkali industry.

Martin Marietta Corporation and Nippon Kokkan KK signed an agreement to establish a joint venture for production and worldwide marketing of titanium and aluminum fabricated products (451). Sixty percent of the venture will be held by Martin Marietta. Dynamet, Incorporated, of Washington, Pennsylvania, and Sumitomo Metal Industries have signed an agreement under which Sumitomo will help market Dynamet's titanium mill products in Japan (452). The two companies will work together to develop new materials and processes. Dynamet converts titanium billet into finished products at its Washington, Pennsylvania, and Clearwater, Florida, plants, which have a total estimated annual capacity of 7 million lb per year.

Foreign producers continue to press for greater market share, and to seek new markets for their products in the U.S. Billiton BV entered the titanium business by acquiring a 62.5 percent interest in Deeside Titanium, Limited in Deeside, Wales (453). British Aerospace will substantially increase commercial production of a superplastic and diffusion bonding titanium alloy in the next three years, under a \$10.3 million development program (454, 455). The material may eventually account for 8-10% of the average aircraft's structural weight.

Some of Japan's major commercial pure Ti producers have begun gearing up to produce Ti alloys (456). Long-term targets are the aerospace industries in Japan, the U.S., and Europe. Japan's alloy output is small, amounting to 130-200 metric tons in 1983, or only 2-3% of Japanese titanium mill products. Overseas markets are viewed as difficult to capture, with U.S. and European tariffs on Ti imports at 16.5 and 7%, respectively. A Sumitomo Metal Industries spokesman claimed that new Ti alloy products would be used in both aerospace and automotive applications.

The Chinese government has given high priority to developing titanium refining and processing technology (457). China, rich in ilmenite, rutile, and other rare earth minerals, is building an integrated metals industry around them. Estimated titanium sponge production capacity has grown from 1,000-2,000 ton/yr in 1980 to a current level of 3000 ton/yr. China's main export market is the United States. However, China's major interest in developing its titanium resources is to provide material for domestic consumption (458).

Demand.—Defense-related consumption of Ti sponge in 1984 was estimated at 7,933 tons (459). This is roughly the same as 1982 consumption, and 1,000 tons more than in 1983. Demand will increase at about 1,000 ton/yr through 1986, and will then level off through 1988.

Most of the defense demand arises from aircraft production. In each of the five years covered by the Pentagon prediction, more than 60% of all defense-related demand is accounted for by airframe parts. Aircraft engines and engine parts account for an additional 30%. Engine-related Ti use is spread among all aircraft programs, while airframe needs are limited to high performance bombers and fighters.

Production of the B-1B bomber, begun this year by Rockwell International, plays a major role in the growth of Ti sponge demand by the military. The first bomber was funded in fiscal 1982, followed by seven in 1983 and ten in 1984. Thirty-four have been requested by the Pentagon for 1985.

Titanium industry executives view the military demand as the most stable of their markets. Douglas Blair, Oremet's vice president of marketing, stated, "if it wasn't for the defense business, the titanium industry would be in a sad state of affairs." In nonmilitary areas, major program changes in the past have hurt the titanium industry. A prime example is the SST program, where expected demand never materialized.

An increase in titanium buying was expected toward the end of the year, as commercial airframe makers began work on orders received in the spring (460). Sustained demand into 1985 was expected as engine builders begin to produce new engines which are exiting the development stage. According to a Wyman Gordon Company spokesman, projected shipments of U.S. mill products were expected to reach 50 million lb in 1985, up from the estimated 43 million lb in 1984 (461). In the low year of 1983, only 32 million lb were shipped. It was predicted that titanium sponge would be in ample supply through 1988, leading to price stability. Peak demand of titanium sponge in the 1985-1988 period was expected to be about 58 million lb/yr. Positive factors in the turnaround are increases in the industrial and commercial aircraft markets.

At a Metal Bulletin conference, titanium industry executives expressed optimism for the future, while stressing that growth depends heavily on Washington (462). Increased orders arising from military aircraft and government antipollution efforts were seen as the key to slow but steady growth for the rest of the decade. Frank Caputo, president of Oremet, estimated industry production at 43.7 million lb in 1984, with shipments of 40.8 million lb. The difference between shipment and production figures comes from customer inventories built up several years ago when reports of shortages led to panic buying. Caputo predicted that titanium consumption will reach 50 million lb/yr by 1990, with major increases coming

from new industrial applications and less from the aerospace industry.

After the worst sales year since 1979, Western European producers of semifinished titanium mill products predicted some increased demand as inventories were replenished, but noted that real consumption had not improved (463). Production remained depressed as low price products from the U.S. and Japan were imported. It was estimated that Western Europe's demand for semifinished titanium would be a maximum of 5,000 metric tons in 1984. About half of the demand was being met by U.S. and Japanese producers. A number of factors were cited as preventing an increase in real demand over the next few years. The civil aircraft industry is very slow. Airbus Industrie, a European consortium, will use between 5 and 10 tons of titanium for each passenger aircraft it builds. However, production rates are now running at about 30 plane/yr, well below original expectations of 50-100 plane/yr. Military aircraft construction is also low, and recent cutbacks in capital spending have reduced demand in nonaerospace applications.

Japan's two leading titanium sponge producers reported significantly higher sales in the six months ended September 30, 1984, compared to the same period in 1983 (464). Spurred by the general economic recovery, Osaka Titanium reported a 59.8% jump in titanium sales. Titanium accounted for 75% of Toho Titanium's total sales, compared to 69% a year earlier.

A critical review and evaluation of future prospects for the worldwide titanium industry was announced by Gorham International (465). The study will forecast titanium demand, industry capacities, and price levels for the next ten years, as well as provide information on new technologies and competitive materials.

Markets.—The Titanium Development Association, formed in 1983, is looking for ways to smooth the cyclical nature of the titanium business (466). The titanium industry has followed trends in the aerospace industry, which accounts for about 90% of Ti consumption. The association, open to North American producers only, lists new market development as its number one priority. Several industries have been identified in which titanium could make significant inroads including pulp and paper, chemicals, power generation, and oil production. Association officials say they must convince potential users that the metal is cost effective and that adequate supplies exist, so that new users will not be squeezed short during aerospace industry upswings. The Titanium Industries Association had some 50 members registered by May and 25-30 more were expected by the end of the year.

In the mature pulp and paper industry, which is operating at 90-95% capacity, titanium usage jumped about 6% in 1984 (467). A growth rate of about 2.5% is expected through this decade. The chemical industry usage of titanium is expected to grow about 5%. The advent of membrane cell chlor-alkali technology, which reduces titanium requirements, may slow growth somewhat. The nuclear industry is stagnant, but titanium usage could increase by 2.5%. Other markets include the agricultural chemicals industry, electrowinning of metals, air conditioning systems, flue gas desulfurization units, and deep oil and gas well applications.

Titanium has lost markets to substitutes because of user fears of another titanium shortage similar to the one in the late 1970's. In some cases, substitutions were made even though titanium was preferred on the basis of its properties. Expanded titanium melting capacity will help titanium to reach its potential as a structural metal. Current worldwide sponge capacity appears to be adequate to handle anticipated market growth through the end of the decade (468). However, new alloys and composite materials continue to be developed as titanium replacements for the aerospace industry (469). Advanced nonmetallic composites consisting of high strength fibers in an epoxy base offer modulus or stiffness usually superior to metals. Yields are also high, and investments in tooling and dies are lower. Composites also make inroads on aluminum in

flat surfaces on aircraft. Here, aluminum replacement often increases the demand for titanium fasteners.

Within the commercial aircraft industry, the amount of titanium used in airliners may continue to increase, despite the threat of new material substitutes (460). Aluminum-lithium alloys and composites were both viewed as more of a threat to aluminum than to titanium. According to a Boeing official, "with each succeeding generation of aircraft, there will be a greater percentage of titanium used. The curve started with the 707 and has been moving up since the 1950's."

In aircraft engines, some substitutions for titanium are being made in the latter stages of compression, where temperatures reach 1050°F. However, this will not lead to an overall drop in titanium usage. Pratt and Whitney engineers, for example, anticipate that their jet engines will continue to contain 20-25% by weight.

In recent years, titanium has gained market share in the electric utility condenser market. The titanium condenser tube business, however, has been hurt by the decline in nuclear power plant construction.

If testing confirms, as RMI Company officials suspect, that titanium is technically superior to steel in automotive valve trains, Ti valve trains may be introduced in the near future (470). Bruce Bannon of RMI estimated that the new market would require more than 1 million pounds of titanium/yr. RMI has strengthened its research and development group to find new applications for titanium. In the future, use of titanium in small structural components and in other motor segments may be considered.

Dumping actions.—In October 1983, the General Services Administration purchased 4,500 tons of titanium sponge for the national defense stockpile. All but 1,000 tons of the purchase went to producers from Japan and the United Kingdom. The purchase provoked dumping complaints from domestic producers. As a result, the Department of Commerce issued a preliminary finding that the foreign sponge was bought at prices ranging from 16 to 94% below fair value (471-472).

Lobbying was intense before the final decision was rendered (467). The chairman of the Senate Armed Services Committee took the position that critical and strategic materials were exempt from antidumping and countervailing duties. Nonintegrated producers maintained that integrated producers pushed the dumping charge to gain a competitive edge in the sale of ingot and mill products by driving up raw materials costs. There was widespread concern over a possible price squeeze (473). RMI Company, the primary dumping petitioner, claimed that "exemption from duties does not mean exemption from unfair trade practice."

In its final decision, the Commerce Department found high dumping margins, but also ruled to exclude the 1983 purchases from any requirements to post bonds or duties (474). Both domestic producers and sponge importers claimed a measure of victory in the decision (475).

Subsequent to the Commerce ruling, the International Trade Commission held injury hearings. RMI maintained that, although operating at a 100% rate, it suffered from a low return on investment because of artificially low pricing (474). According to RMI president, Frederick Gieg, additional profits were needed to invest in capital equipment and remain technologically competitive (473, 476).

Confirming the Commerce Department preliminary findings, the ITC ruled in October that Japanese sponge imports had caused material injury to domestic producers, clearing the way for assessment of dumping duties (477). British imports, however, were not found to have been injurious. Following the ITC decision, titanium prices rose as a major U.S. melter relying on Japanese sponge hiked prices (478). The move by Teledyne Allvac was expected to be followed by other major producers.

A formal investigation into alleged dumping of titanium mill products from the U.S. and Japan was opened by the European Economic Community (479). According to EEC estimates, U.S. and Japanese imports climbed from 48 to 61% of the market in the last two years, resulting in a 35%

drop in European capacity utilization. The investigation concerned titanium plate, sheet, strip, bars, and rods, but tubing was excepted. Sponge prices climbed from about \$3.50/lb in 1983 to over \$4/lb (480), while there was no corresponding price rise in mill products in the European market. U.S. producers named in the complaint included RMI, Timet, Oremet, Teledyne Allvac, Martin Marietta, and NF&M. In November, a team of EEC investigators was scheduled to travel to Japan on a fact finding investigation, followed by a similar investigation in the U.S. (481).

Zinc.—Zinc was among the major gainers in the non-ferrous metal industry as the general business recovery begun in 1983 continued (482). The upturn in the automotive industry was a large factor in the strength of zinc markets.

Production and prices.—The 1984 production and consumption statistics for zinc are given in Tables XLIII and XLIV (483).

St. Joe Minerals Corporation, of Clayton, Missouri, acquired the National Zinc Company from its parent company in mid-August (464, 465). Under the agreement, St. Joe paid approximately \$16.5 million for National's fixed assets, and also bought National's inventories and accounts receivable. The total purchase price exceeded \$30 million. Prior to the acquisition, St. Joe's production capacity was about 100,000 ton/yr at its Monaca, Pennsylvania, electrothermic zinc smelter. National operated a 55,000 ton/yr electrolytic zinc refinery in Bartlesville, Oklahoma. The combined production capacity of 155,000 ton/yr results in the largest U.S. zinc producing company. Other major domestic producers include Asarco (107,000 ton/yr capacity), Amax (80,000 ton/yr), Jersey Miniere Zinc (90,000 ton/yr), and Huron Valley Steel (35,000 ton/yr). The purchase of National, which can produce High Grade and Special High Grade material, broadens St. Joe's product line, which was primarily prime western and continuous galvanizing grades, as well as zinc oxide and dust. It was announced that all future St. Joe list prices would reflect zinc products available from both the Monaca and Bartlesville plants (486). In a related development, St. Joe announced that some of its excess zinc concentrates will be refined at the Bartlesville facility (464). Previously, the concentrates, which could not be treated at the Monaca refinery, were sold on the open market and to Amax under a long-term contract.

Sherritt Gordon Mines decided to continue operations at its Ruttan mine, which has a current output of about 30 million lb of zinc/yr (487).

North Broken Hill Holdings of Australia gained majority control of EZ Industries (488). EZ has 210,000 ton/yr of zinc smelting capacity, and has treated nearly all of North Broken Hill's zinc concentrates for almost 25 years.

Gulf and Western sold its 60% interest in Jersey Miniere to its Belgian partner, Union Zinc (489). The acquired company owns a 90,000 ton/yr zinc refinery in Clarksville, Tennessee, as well as mines in Elmwood and Gordonsville, Tennessee. In July, Union Zinc announced

Table XLIV. World zinc mine production and reserve base (thousand metric ton)

Country	Mine production		Reserve base
	1983	1984 (est.)	
United States	275	265	53,000
Australia	695	645	39,000
Canada	1,070	1,185	56,000
Mexico	257	280	8,000
Peru	553	565	12,000
Other market economy countries	1,934	1,950	90,000
Centrally planned economies	1,462	1,460	32,000
World total	6,246	6,350	290,000

a production cutback of 25% of its 90,000 ton/yr capacity (490).

Kidd Creek mines will spend C\$6 million to increase the size of its zinc plant, raising annual capacity by 7,000 metric tons to 127,000 tons by 1986 (491). The expansions will primarily concern upgrading the cellhouse.

Reacting to an oversupply of zinc near year's end, Cominco and its 63% owned Vestgron Mines subsidiary announced one month suspensions of certain zinc operations (492, 493). Cominco suspended operations at its Polaris mine, which produces about 16,000 metric tons of zinc per month. Vestgron shut down its Black Angel zinc-lead concentrator, which produces about 10,000 tons of zinc concentrates per month.

LTV Steel Company and Sumitomo Metal Industries announced a partnership to build a 500,000 ton/yr electrogalvanizing line in Cleveland (494). The jointly managed operation is 60% owned by LTV and 40% by Sumitomo. The \$125 million electrogalvanizing line, scheduled to start up in 1986, will handle widths up to 72 in. Also under discussion was the possibility of Sumitomo providing electrogalvanizing technology to LTV (495). Domestic producers also announced four other electrogalvanizing lines. These include a 400,000 ton/yr line at Great Lakes Steel, a 600,000 ton/yr line owned jointly by U.S. Steel and Rouge Steel, a 400,000 ton/yr line at Armco (494, 496), and a 400,000 ton/yr line jointly owned by Inland Steel, Bethlehem Steel, and Pre-Finished Metals. The latter companies announced that the line would cost \$40 million (497). Product will be available in 1986, in time for the manufacture of 1987 cars.

Outokumpu Metals (U.S.A.), Incorporated, announced that it would begin marketing zinc for Outokumpu Oy, Finland, in January 1985 (498). The company was formed in 1982 to market Outokumpu Oy's products in the U.S. As a result, a 15 year sales agreement between Outokumpu Oy and Afrimet Indussa was ended, eliminating about 35,000 tons of zinc from Afrimet's sales. Afrimet, however, had gained nearly 85,000 tons from its agreement to become the sole sales agent for Union Zinc, Incorporated, of Clarksville, Tennessee.

A plan to cut Zn production capacity by up to 200,000 metric tons was dropped by the European Economic Community (499). In 1982, EEC producers had proposed the capacity reduction as a result of slack demand and excess capacity.

Exxon's Crandon project in Wisconsin is the largest domestic zinc prospect under active investigation, according to a Metals Economics Group publication (500). A production decision was expected during 1984.

Aberfoyle Limited said that zinc and lead reserves at its Hellyer prospect in northwest Tasmania could total ten million metric tons (501). The prospect was said to have a substantial impact on the company's future.

An American Mining Congress spokesman told the Internal Revenue Service in a hearing that Congress should decide to exempt zinc, as well as copper and lead, from the Superfund tax to prevent further serious adverse economic impacts (502). The Washington Conference for Zinc, a group of zinc industry executives, attempted to eliminate the \$14.94/ton cleanup tax in pending Superfund legislation (503).

Table XLIII. U.S. zinc production and consumption (thousand metric tons)

	1983	1984 (est.)
Production		
Mine	275	265
Primary slab zinc	236	260
Secondary redistilled slab	69	70
Imports for consumption		
Ore and concentrates	63	55
Slab	618	630
Exports		
Zinc metal, including scrap	21	35
Ore and concentrates	60	30
Consumption		
Reported, slab zinc	806	890
Apparent, all forms	1,005	1,030

The Lead and Zinc Producers Committee withdrew its petition for the imposition of countervailing duties on Spanish zinc imports (504). The petition, originally filed in 1976, had declined in importance as Spanish zinc imports dropped to 20,643 tons in 1983, representing only about 3% of total imports. Much of the approximately 650,000 ton/yr of imported zinc currently is supplied by Canada, Europe, and Asia, according to an industry consultant.

As worldwide supplies of all zinc grades tightened and LME prices firmed, domestic producer prices of zinc reached an all-time high at the beginning of 1984 (505). Three producers, St. Joe, Asarco, and National Zinc all raised their prices for High Grade Zn by \$0.02, to \$0.51/lb. The price move was quickly followed by EZ America, for slab zinc produced by Electrolytic Zinc Company of Australasia, and by Noranda (506), as well as other producers (507).

The price of zinc dust also jumped by \$0.02/lb to \$0.64/lb (506), in a move by Gulf Metals and its Southern Zinc affiliate. Pointing to the strength of Zn on the LME, industry executives agreed that the price increase was overdue. About two-thirds of zinc dust production is used for anti-corrosion coatings, principally in the auto industry.

Zinc price declines in the spring were not due to consumption, which remained steady, but to production and stock increases (508). According to the International Lead and Zinc Study Group, world production rose from 402,000 tons in April to 417,000 tons in May, a 4.8% increase over May, 1983 production. World consumption was 393,000 tons in April, while producer stocks of refined zinc increased by 23,000 tons, to 407,000 tons in May.

Benchmark High Grade zinc prices plunged to their lowest levels in ten months in August, as Amax and Cominco decreased their prices to \$0.48/lb (509). Price drops were attributed to weak markets resulting from slow-downs in hot dip galvanizing and electrogalvanizing. The move was followed by similar cut backs by European producers (510).

To modernize zinc contracts, the London Metal Exchange board and committee voted in July to initiate trading in High Grade Zinc contracts (511). This reflects the fact that High Grade zinc currently accounts for about 80% of total world zinc production. The existing standard contract for GOB zinc is to be phased out in November 1985. LME participants expressed concern that High Grade stocks would build sufficiently to support trading. At mid year, only 3,700 tons of the LME's 60,125 metric tons of zinc stock were High Grade zinc.

Demand.—The zinc market was predicted to remain fairly strong, with an average price of \$0.46 in 1984 and \$0.48 in 1985 (512).

As total world metal consumption increased by an estimated 5% between the last quarter of 1983 and the first quarter of 1984, a prospect of "supply line bottlenecks" was seen for zinc (513, 514). Zinc stocks were predicted to fall to six-weeks consumption, with prices averaging at least \$0.10/lb higher than a year earlier.

During July, domestic zinc buyers were purchasing zinc on a "hand-to-mouth" basis and drawing on inventories, banking on further decreases in zinc prices (515). Many in the industry agreed that the domestic price had risen too quickly to the \$0.53 level, and expected prices to fall to \$0.47 or \$0.48/lb by summer's end, bringing producer prices in line with prevailing merchant prices. A return to the \$0.53 peak price was not expected for the remainder of the year.

Despite a favorable long-term outlook, short-term zinc fortunes were seen as "iffy" pending the outcome of labor negotiations in the auto industry and the bids offered by zinc suppliers in Bureau of Mint Tenders (516). Although actual zinc consumption had not slowed during the summer, demand decreased as consumers worked off inventories.

The Bureau of the Mint solicited bids for purchases of Special High Grade zinc (517). The offer was for 27 million pounds of zinc, with 18 million pounds for delivery in October and November, followed by an option for 9 million pounds in December. The zinc was to be delivered to Ball Corporation's Zinc Products Division at a rate of 2,250,000 lb/week, beginning the week of October 8 (518).

A 4-5% boost in copper-plated zinc coins was predicted by the U.S. Treasury Department (519). A total of 150 million lb of zinc has been used for the coins since the U.S. Mint began striking the coin in 1981.

Domestic consumption for zinc die casting, in the first upward year-to-year move since 1979, reached 296,863 tons in 1983 (520). Greatest gains in both tonnage and market share were registered in the automotive industry, which accounted for 34% of the overall zinc die casting market.

A Zinc Institute survey showed that the U.S. Big Four car makers used 11.9% more one-sided galvanized steel in 1984 than in 1983, as the average use per car rose to 66 lb (521). Two-sided galvanized growth was even greater, rising from 121 to 136 lb.

Chinese zinc imports jumped 112% between 1982 and 1983, according to Chinese customs figures (522). Expansion in crucial areas requiring intensive metal consumption was expected to keep 1984 demand high.

Markets.—A push for passenger cars with ten year service without rusting through will significantly increase the use of galvanized steel by 1988 (523). Chrysler anticipates that its 1988 cars will employ galvanized steel in almost all of the exterior, exposed body panels. An 850 lb car body will contain about 300 lb of electrogalvanized steel and about 500 lb of hot-dipped galvanized and galvanized steels. A Chrysler spokesman estimated that the steel industry must increase its galvanized capacity by 1.5-2 million ton/yr by 1987, with most of the expansion in electrogalvanizing. The high quality electrogalvanized surface finish is important in exposed body panels.

After-fabrication hot-dip galvanizers anticipated increased business arising from increased highway, bridge, and transit construction and repair (524). As much as one-third of the galvanizers said that they would invest in new equipment if business improves, with capital investments as high as \$550,000/plant. In 1983, about 3 million tons of steel were hot-dip galvanized, with sales of \$750 million. About 180,000 tons of zinc were consumed.

Strong growth for Galvalume™ aluminum-zinc alloy sheet led to projections that the product could grow to 40% of the 40 million ton global market for coated sheet by the end of the century (525). Bethlehem Steel, which developed Galvalume 12 years ago, said facilities already licensed are scheduled to grow to 3 million tons capacity in 1986, up from the present 2 million tons capacity. Galvalume, which contains about 44% zinc, does not compete directly with electrogalvanizing, and is not expected to be used in visible automobile parts because of the surface quality limitations. Strongest growth to date has been in construction and metal building markets, with about 40% of sheet sales going into roofing and sidewall applications.

Increased business was expected for hot-dip galvanizers, leading to possible investment in expansion and modernization projects (524). Highway, bridge, and transit system construction and repair expenditures were expected to benefit from the new \$0.05 Federal Gasoline Tax.

The Electric Utility Industry

In 1984, the electric utility industry continued to rebound from the trough year of 1982, as shown in Table XLV (526, 527). The 2095.2 billion kWh generated in 1984 represented an increase of 8.4% over 1982, and a 3% increase over the peak year of 1981. Nuclear, coal, and gas fueled plants all registered increases; only oil powered plants showed a decline, continuing a trend begun in 1978, when oil powered plants produced 364.2 billion kWh

Table XLV. Electricity generated, by type of fuel (billion kWh)

Year	Nuclear	Coal	Oil	Gas	Total	(Hydro)
1980	251.1	1162.0	245.6	346.2	2010.4	—
1981	272.7	1203.2	206.1	345.8	2034.1	—
1982	282.8	1192.0	146.8	305.3	1932.0	309.2
1983	293.7	1259.4	144.5	274.1	1978.2	332.1
1984	327.6	1341.7	119.8	297.4	2095.2	—

Table XLVI. Fossil fuel consumption, by type

Year	Coal (millions of tons)	Oil (millions of bbl)	Gas (millions of ft ³)
1974	391.2	539.1	3443.4
1975	405.9	506.6	3157.7
1976	448.3	556.5	3080.9
1977	477.0	624.2	3191.2
1978	481.6	635.8	3188.4
1979	527.1	523.3	3490.4
1980	569.5	420.2	3681.6
1981	596.8	351.1	3640.2
1982	593.7	249.8	3225.5
1983	625.2	245.5	2910.8
1984	664.4	204.5	3111.0

(527). These trends are also shown in Table XLVI (526, 527) which shows the industry's fossil fuel consumption.

U.S. electrical generating capacity increased by more than 15,000 MW in 1984, to a total of 673,689.9 MW, as shown in Table XLVII (526, 527). Much of the increase was accounted for by steam plants, while significant gains were also made by nuclear plants and hydro-powered plants. Capital spending by the industry was only about 93.5% of the 1983 level, as shown in Table XLVIII (526, 527). The drop was shared proportionately by investor-owned utilities and other systems. While expenditures on generation equipment declined markedly, the industry increased outlays for both transmission and distribution systems.

Electric Utility Industry Forecast (528).—The September 1984 issue of *Electrical World* presented its forty-fifth annual electric utility forecast. The U.S. economy's upsurge during the latter half of 1983, and its continued strong showing in the first half of 1984, caused short-term projections to be revised upward from those made a year earlier. In general, however long-term projections varied only slightly from those made last year (529, 530).

Important points from the *Electrical World* forecast are summarized below.

Industrial usage.—The sharpest growth in electrical usage during the 1983-1984 economic recovery was registered in the industrial sector. Despite the gradual transition of the U.S. economy toward the service sector, a

growing and vital industrial sector is expected. Although the industrial mix will change, the forecast assumes that industrial sales will continue to account for 35-40% of total electrical utility sales, as shown in Table XLIX. Industrial usage was estimated to be 838.1 billion kWh in 1984, up 4.6% from the 801.1 billion kWh used in 1983. Total U.S. usage was estimated at 2,259.8 billion kWh in 1984, up 4.2% from the 1983 value of 2,163.4 billion kWh. In 2000, industrial and total electricity usage were forecast as 1,320.1 billion and 3,451.6 billion kWh, respectively. An industrial usage breakdown is given in Table L.

Fuel substitution is expected to play an important part in the growth of industrial electric usage, as electricity is substituted for direct use of fossil fuels. In recent years, the country's basic industries have begun to make such a shift.

A number of factors have caused a sharp drop to be made in uranium-enrichment services, compared to last year's forecast. The unsettled state of the enrichment market, a slowdown in nuclear plant construction, and market loss to foreign sources all contributed to lower expectations extending through the end of the century.

The forecast included a pessimistic view for long-term growth prospects of the domestic aluminum industry as shown in Table L. However, some plant capacity additions in the late 1990's were assumed. The actual electric power consumption forecast for the aluminum industry in the long term was no different from last year's forecast.

Recently, industrial customers have taken steps to generate some of their own electricity, for in-house use or resale to electric utilities. However, the forecast assumes that the electric utilities, and those customers that have historically generated electric power, will continue to have favorable electric production economics.

Residential Usage.—This year's residential electric sales forecast was changed only slightly compared to last year's forecast. A downward revision of 2 million in the number of customers anticipated in 2000 reduced the residential sales forecast for that year by 20 billion kWh. In the near term, those factors which will have the biggest influence on residential electricity use are weather-related sales and the higher than expected number of housing starts.

Higher energy efficiency of electric appliances has become increasingly important in recent years. However this has resulted in only minor adjustments to the forecast over the next five years. It is expected that consumers will try to control their utility bills without serious disruption to their lifestyles. The national "Power of Choice" marketing program carried out by investor-owned utilities will also contribute to demand.

In the electric heat housing market, it is projected that the heat pump will come to dominate. Electric heating continues to be the preferred method in new construction. Continuing a pattern in existence for more than a

Table XLVII. U.S. installed generation capacity by plant type (MW)

Year	Total	Hydro	Steam	Nuclear	Gas turbine	Combustion
1982	650,105.0	78,128.3	452,011.3	63,042.0	51,972.3	5131.1
1983	658,172.6	78,967.6	455,507.7	67,073.4	51,627.9	4996.0
1984	673,687.9	80,589.6	464,742.6	71,720.0	51,794.8	4840.9

Table XLVIII. Total U.S. electric power system capital expenditures (millions of dollars)

Year	Generation		Transmission		Distribution		Miscellaneous		Total	
	Total industry	Investor owned	Total industry	Investor owned	Total industry	Investor owned	Total industry	Investor owned	Total industry	Investor owned
1980	25,688	17,875	3,200	2,279	5,307	4,365	1,650	1,297	35,925	25,816
1981	25,823	19,217	3,168	2,326	4,950	4,169	1,882	1,543	35,823	27,254
1982	29,836	22,287	3,497	2,595	5,228	4,432	1,654	1,347	40,216	31,161
1983	29,922	23,741	3,200	2,463	5,381	4,698	1,600	1,332	40,103	32,234
1984 (est.)	24,500	19,800	3,700	2,200	6,700	5,900	2,500	2,200	37,500	30,100

Table XLIX. Electric utility sales forecast

Year	Residential (billion kWh)	Change (%)	Industrial (billion kWh)	Change (%)	Commercial (billion kWh)	Change (%)	Other (billion kWh)	Change (%)	Total (billion kWh)	Change (%)
1973	554.2	8.4	687.2	7.5	396.9	9.7	64.9	-0.1	1,703.2	8.0
1974	555.0	0.1	689.4	0.3	392.7	-1.1	63.7	-1.9	1,700.8	-0.1
1975	586.1	5.6	661.6	-4.0	418.1	6.5	67.2	5.6	1,733.0	1.9
1976	613.1	4.6	725.2	9.6	440.6	5.4	70.8	5.2	1,849.6	6.7
1977	652.3	6.4	757.2	4.4	469.2	6.5	72.1	1.8	1,950.8	5.5
1978	679.2	4.1	782.1	3.3	480.7	2.5	75.8	5.2	2,017.8	3.4
1979	696.0	2.5	817.6	4.5	494.7	2.9	76.1	0.4	2,084.4	3.3
1980	734.4	5.5	793.8	-2.9	524.1	5.9	73.7	-3.0	2,126.1	2.0
1981	730.5	-1.7 ^r	819.6	3.3	521.7	-0.5	78.9	6.9	2,150.7	1.2
1982	731.8 ^r	0.2	769.3 ^r	-6.1 ^r	516.3 ^r	-1.0 ^r	79.7 ^r	1.0 ^r	2,097.1 ^r	-2.5 ^r
1983	751.4	2.7	801.1	4.1	533.0	3.2	77.8	-2.4	2,163.4	3.1
Forecast										
1984	779.7	3.8	838.1	4.6	556.1	4.3	80.9	4.0	2,254.8	4.2
1985	792.2	1.6	861.7	2.8	575.5	3.5	82.6	2.1	2,312.0	2.5
1986	812.7	2.6	887.1	2.9	594.5	3.3	84.3	2.0	2,378.6	2.9
1987	836.2	2.9	918.4	3.5	613.5	3.2	85.9	1.9	2,454.0	3.2
1988	863.3	3.2	952.3	3.7	631.9	3.0	87.5	1.9	2,535.0	3.3
1989	890.3	3.1	990.8	4.0	650.9	3.0	89.2	1.9	2,621.2	3.4
1990	916.9	3.0	1,028.1	3.8	669.8	2.9	90.9	1.9	2,705.7	3.2
1995	1,038.2	2.3	1,166.7	2.2	763.0	2.5	99.8	1.9	3,067.7	2.3
2000	1,161.5	2.1	1,320.1	2.4	860.0	2.4	110.0	2.0	3,451.6	2.3

^r Revised data.

decade, electric heating was installed in more than 50% of new housing units completed last year. It is projected that gas deregulation and the resulting price rise will improve the future market share for electric heat.

A pessimistic view was taken of the growth of the electric vehicle industry. The EV projection was dropped to about one-half of last year's level. The forecast was based on the premise that the EV market had passed a "window of opportunity" without making substantial gains, and that similar opportunities would not arise for the remainder of the century. Fewer than 100,000 electric vehicles, using less than 500 million kWh of electricity, were projected to be in service at the end of the century.

A breakdown of residential use statistics is given in Table LI. Overall, as Table LI shows, residential electricity consumption was expected to be 779.7 billion kWh in 1984, a 3.8% increase over 1983. By the end of the century, the forecast was an annual residential consumption of 1161.5 billion kWh, a 49% increase over the 1984 level.

Commercial usage.—Commercial electricity usage in 1984 was estimated at 556.1 billion kWh, a 4.3% increase

over the 533.0 billion kWh consumed in 1983. As shown in Table XLIX, commercial use of electricity was predicted to rise to 860.0 billion kWh by 2000, for a total growth of nearly 55% over present consumption. No basic changes in the commercial market were evident since the 1983 projection was made. Conservation and energy management were viewed as significant factors in reducing energy use. However increased use of communications and data processing equipment, as well as other developments contributing to greater office use, were expected to produce an overall increase in commercial electricity use.

Generating capacity.—A compound average growth in electrical generating capacity of about 3% has been forecasted through the end of this decade, with growth gradually tapering off through the 1990's, as shown in Table LII. Total electricity output (Table LIII) will climb from 2457.7 billion kWh in 1984 to 3727.7 billion kWh in 2000, an overall increase of nearly 52%. The forecast is predicated on the assumption that smokestack industries are not dying, but are making a transition to more efficient

Table L. Industrial uses of electricity

Year	Billions of kWh							Industrial production index (1967 = 100)	Primary aluminum production (thousand tons)
	Manufacturing	Primary aluminum production	DOE	Total industrial	Generation by industrial plants	Utility industrial sales			
1973	668.1	81.5	33.4	783.0	95.8	687.2	129.7 ^r	4,529	
1974	660.8	88.2	35.4	784.4	95.0	689.4	129.3	4,903	
1975	635.8	68.5	36.6	740.9	79.3	661.6	117.8	3,879	
1976	692.5	73.2	41.8	807.6	82.4	725.2	130.4 ^r	4,251	
1977	723.8	76.0	41.0 ^r	840.7	83.5	757.2	138.1 ^r	4,539	
1978	740.4	79.8	34.3	854.4	72.3	782.1	146.1	4,804	
1979	767.9	82.4	32.7	883.0	65.3	817.6	152.5	5,023	
1980	746.6	82.8	24.8 ^r	854.2	60.4 ^r	793.8	147.0	5,130	
1981	775.9	77.2	22.6	875.7	56.0 ^r	819.6	150.9 ^r	4,948	
1982	742.3 ^r	54.9	22.8 ^r	819.9 ^r	50.6 ^r	769.3 ^r	138.6	3,609	
1983	766.3	55.4	24.0	845.7	44.6 ^r	801.1	147.6	3,696	
Forecast									
1984	747.2	65.3	25.6	882.0	43.9	838.1	164.6	4,410	
1985	771.5	67.2	23.0	905.9	44.1	861.7	169.9	4,600	
1986	798.0	70.1	19.0	931.7	44.6	887.1	176.1	4,800	
1987	826.9	72.5	19.1	963.7	45.3	918.4	183.9	5,000	
1988	858.5	72.5	21.3	998.2	45.9	952.3	192.7	5,000	
1989	889.3	72.0	29.4	1,037.6	46.8	990.8	200.4	5,000	
1990	919.3	72.0	36.8	1,075.9	47.8	1,028.1	207.1	5,000	
1995	1,073.0	74.2	19.5	1,220.5	53.8	1,166.7	240.0	5,300	
2000	1,225.2	75.9	19.5	1,382.6	62.1	1,320.6	278.0	5,500	

^r Estimated.^r Revised data.

Table LI. Residential average annual use, sales, and revenue (1984 dollars)

Year	Midyear customers (million)	Housing starts, private (thousand)	Use per customer (kWh)	Revenue/kWh (cents)	Average annual bill (dollars)	Residential sales (billion kWh)	Heating sales ^a (billion kWh)	Residential revenue (million dollars)
1973	68.6	2,044	8,079	5.04	407.63	554.2	97.2	27,963
1974	70.2	1,332	7,907	5.51	435.41	555.0	100.2	30,560
1975	71.7	1,160	8,176	5.72	467.35	586.1	103.1	33,507
1976	73.3	1,535	8,360	5.84	488.28	613.1	115.7	35,810
1977	75.0	1,962	8,693	6.05	526.38	652.3	126.0	39,501
1978	76.8	2,001	8,849	6.00	531.31	679.2	132.8	40,780
1979	78.7	1,717	8,843	6.07	536.42	696.0	143.1	42,221
1980	81.4	1,300	9,025	6.43	579.85	734.4	140.4	47,187
1981	83.0	1,096	8,825	6.71	592.51	730.5	155.1	49,042
1982	83.8 ^r	1,056	8,733 ^r	6.96	607.33	731.8 ^r	157.5	50,895
1983	85.1	1,704	8,826	7.09	625.06	751.4	164.9	53,219
Forecast								
1984	86.6	1,700	9,000	7.40	666.36	779.7	172.4	57,731
1985	88.2	1,600	8,978	7.73	693.98	792.2	179.7	61,239
1986	88.8	1,700	9,051	8.05	729.01	812.7	187.7	65,457
1987	91.3	1,700	9,160	8.38	767.30	836.2	195.7	70,043
1988	92.8	1,600	9,299	8.67	806.21	863.3	203.5	74,849
1989	94.4	1,400	9,427	8.96	844.27	890.3	210.4	79,735
1990	96.0	1,300	9,547	9.22	880.67	916.9	216.5	84,580
1995	102.4	1,300	10,140	10.23	1,037.75	1,038.2	242.4	106,252
2000	108.8	1,300	10,671	10.61	1,131.97	1,161.5	263.2	123,209

^a Includes residential space heating.^r Revised data.

production from a shrunken labor force, arising from increased energy intensity.

In the next several years, a number of very costly nuclear and fossil fuel plants will come into service. In some cases, as with LILCO's Shoreham nuclear plant, this raises the possibility of 50% electric rate increases. The forecast, however assumes that rate hikes of this magnitude will not be permitted in the short term. Rather, regulatory agencies will phase in cost increases gradually to cushion their impact. This should keep electricity costs competitive with those of other energy forms.

One of the most obvious trends in Table LIII is that the capacity margin in the utility industry will shrink. The capacity margin is defined as the excess of available capac-

ity over peak demand. In 2000, the 14.7% predicted margin will be slightly more than half of what it is today.

Those who run utilities now feel that improved financial health will result from leaving the phase of major capital projects, now that demand for new units is declining. In addition, regulators have begun to demand conclusive demonstrations that such projects are necessary. Another factor influencing future construction is the concept, currently gaining momentum, that existing plants can be updated for much less than the cost of new construction. According to one study, raising the availability of all current plants to the level of the best units would add as much as 12-15% to peak capability, at a cost of about \$200/kW. As a result of these factors, new plant additions

Table LII. Generating capacity additions (MW). (Based on date of commercial operation)

Year	Hydro	Fossil steam ^a	Nuclear steam	Combustion turbines, I.C.	Upgrade ^b	Other ^c	Total
1974	1,807	18,874	9,196	6,236	—	—	36,113
1975	2,369	21,726	7,281	3,523	—	—	34,900
1976	535	11,908	4,457	2,600	—	—	19,500
1977	1,923	16,506	6,530	1,647	—	—	26,609
1978	5,106	14,454	2,162	2,214	—	—	23,935
1979	3,832	10,999	1,874	370	—	—	17,075
1980	1,335	14,214	2,887	446	—	—	18,882
1981	540	6,506	4,286	624	—	—	11,955
1982	2,089	9,125	3,126	600	—	—	14,940
1983	644	5,256	4,210	0	—	—	10,289
Forecast							
1984	800	5,685	5,680	78	0	210	12,451
1985	186	9,345	15,804	0	0	955	26,290
1986	335	2,129	10,760	0	0	565	13,789
1987	1,980	6,865	10,566	216	0	265	19,893
1988	456	2,613	0	6	200	110	3,385
1989	1,079	2,534	3,606	732	750	290	8,991
1990	220	1,825	1,240	50	1,350	597	5,282
1991	695	1,050	2,232	107	1,500	560	6,144
1992	100	2,900	0	396	1,800	330	5,526
1993	—	7,000	0	108	2,100	210	9,419
1994	—	7,993	0	50	2,100	117	10,260
1995	—	18,824	0	50	1,300	118	20,291
1996	—	15,304	0	0	1,300	160	19,764
1997	—	18,226	0	50	1,300	125	19,701
1998	—	16,769	0	136	800	160	17,864
1999	—	21,496	0	187	800	160	22,643
2000	—	24,700	0	188	800	160	25,849

^a Includes geothermal capacity.^b Effective gain in capability due to plant availability and life extension programs.^c Includes wind, solar, biomass, cogeneration, etc.

Table LIII. Total sales, output, peak load, capability, and margin

Year	Total sales (billion kWh)	Total output (billion kWh)	Capability at peak (million kW)	Gross peak margin (%)	Capacity margin (%)	Peak growth (%)
1973	1,703.2	1,875.6	416.8	20.8	—	7.7
1974	1,700.8	1,879.0	444.4	27.2	—	1.3
1975	1,733.0	1,929.8	479.3	34.4	—	2.1
1976	1,849.6	2,051.0	498.8	34.5	—	4.0
1977	1,950.8	2,145.6	517.1	31.0	—	6.5
1978	2,017.8	2,232.3	545.7	34.0	—	3.3
1979	2,084.4	2,273.7	557.5	36.3	—	0.3
1980	2,126.1	2,314.9	570.2	30.7	—	4.8
1981	2,150.7	2,336.8	595.0	35.8	—	0.5
1982	2,097.1 [†]	2,282.4	593.0	39.9	—	-3.5
Forecast						
1984	2,254.8	2,457.7	624.6	35.7	27.0	2.0
1985	2,312.0	2,520.1	650.9	34.8	26.3	5.1
1986	2,378.6	2,587.9	664.7	34.8	25.8	2.8
1987	2,454.0	2,670.0	684.6	31.4	25.8	3.0
1988	2,535.0	2,755.5	687.9	29.2	23.9	3.0
1989	2,621.2	2,849.2	696.9	26.4	22.6	3.0
1990	2,705.7	2,935.7	702.2	23.9	20.9	3.0
1995	3,067.7	3,313.1	756.8	18.2	15.4	2.8
2000	3,451.6	3,727.7	854.1	17.2	14.7	2.6

[†] Revised data.

in the years following those already under construction will decline. Availability improvement and life-extension programs will become more important in the 1990's.

The net mix of generating capacity by fuel type will not change drastically in this century. Nuclear steam capacity, which has grown significantly in the last ten years, will reach a maximum in the early 1990's as units under construction are brought on stream. Thereafter, their percentage contribution will decline, with the slack being taken up by fossil-fueled steam generators, which will contribute about 70% of total capacity in 2000. Combustion turbine and internal combustion plants will continue to supply less than 10% of capacity. Hydropower plants will decline slightly in the overall mix. These overall trends are reflected in the generating capacity additions shown in Table LII.

Nuclear power continues to command great attention, despite indications that construction is waning. Although new types of reactors may be proposed in the future, it is expected that the next wave of nuclear reactors will be those now abandoned in advanced stages of construction. The units will probably have to be relicensed and modified. In any case, there will be little effect on capital spending until late in the century.

Capital spending.—As a result of present plant upgrading, capital budget outlays will be reduced in the late 1980's and early 1990's. The cost of output increases from existing plants, on the order of \$200/kW, is considerably cheaper than that of new plant construction, which is in the \$800-\$1,200/kW range for coal-fired units. Some capacity increase from unconventional technologies such as wind, solar, biomass, and cogeneration will also reduce capital outlays for conventional capacity. Much of this capacity will be built by nonutility companies which sell energy to utilities. As a result, the energy bought is absorbed as an operating cost, and little is added to capital budgets. A summary of forecasted capital expenditures is given in Table LIV.

Distribution and transmission.—The future for distribution expenditures appears strong. Expenditures for 1984 and 1985, shown in Table LIV, are the highest since 1976, in constant dollars. A recent upsurge in housing starts and the general strength of the economy contribute to the general optimism.

Transmission budgets, roughly tied to spending on generating capacity, will not fare as well. Environmental opposition to high voltage transmission lines also has a depressing effect on proposed new lines. In the mid-1990's, transmission spending will increase as generating capacity does. It is expected, too, that transmission net-

works will be strengthened at that time, because of the low reserve power levels which will exist on many systems.

Nuclear.—The year began on a sour note for the nuclear industry, as the Department of Energy's Energy Information Administration released a report showing that final construction costs for 77% of the Nation's operating nuclear plants were at least double the original estimates (531). For 23% of the plants, the final cost was more than four times the preconstruction estimate. The EIA, an independent agency within DOE, attributed the cost overruns to inflation, soaring interest rates and construction costs, and long building delays. In 1971, the estimated construction time for a nuclear plant was four years. However, the average construction time has now ballooned to 14 years.

The report, coming amid a wave of nuclear plant cancellations, cast doubt on the fate of 48 reactors now under construction around the country. Citing quality-control failures, the NRC refused to grant an operating permit for

Table LIV. Annual capital expenditures (millions of 1984 dollars)

Year	Genera- tion	Trans- mission	Distribution	Miscel- laneous	Total
1974	24,339	4,770	8,909	1,994	40,012
1975	22,597	4,225	7,228	1,742	35,792
1976	28,059	4,973	7,682	1,831	42,545
1977	30,478	4,957	7,221	1,577	44,233
1978	32,868	4,098	6,509	1,822	45,297
1979	34,141	4,644	7,315	1,830	47,930
1980	32,250	4,110	6,625	2,031	45,016
1981	34,415	3,525	7,528	1,822	47,290
1982	35,321	3,866	7,002	1,829	48,018
1983	32,813	3,762	7,357	2,059	45,991
Forecast					
1984	27,600	4,200	7,580	1,772	41,152
1985	24,300	3,800	7,600	1,606	37,306
1986	17,500	2,900	7,400	1,251	29,051
1987	12,600	2,200	7,800	1,017	23,617
1988	8,500	1,800	8,100	828	19,228
1989	8,000	1,800	8,250	812	18,862
1990	9,200	2,000	8,400	877	20,377
1991	21,000	2,900	8,300	1,449	33,649
1992	20,000	3,000	8,400	1,412	32,813
1993	26,000	3,900	8,500	1,728	40,128
1994	34,000	5,300	8,600	2,155	50,055
1995	38,000	6,000	8,750	2,373	55,123
1996	40,000	6,000	9,300	2,488	57,788
1997	44,000	6,400	9,530	2,696	62,626
1998	44,000	6,400	9,720	2,705	62,825
1999	46,000	6,500	10,100	2,817	65,417
2000	46,000	6,500	10,200	2,821	65,521

Commonwealth Edison's nearly completed, \$3.35 billion twin-reactor Byron Plant in Illinois (532, 533). The decision marked the first time in the history of the nuclear industry that the government flatly rejected an atomic power license.

Public Service Company of Indiana, bowing to pressure from state officials, abandoned efforts to complete its twin-reactor Marble Hill plant after spending \$2.5 billion. At the time of cancellation, the first unit was 59% completed and the second unit was 37% completed. Previously, the industry had scrapped no plants more than 27% finished. The Marble Hill decisions brought the total number of reactor cancellations to 100 since 1974.

The cost estimate of the troubled Nine Mile Point 2 nuclear power plant in New York State was raised to \$5.1 billion by major partner Niagara Mohawk Power Corporation (533). The new estimate was \$900 million higher than a projection made 14 months earlier. A consortium of utilities financing the plant has begun a study to determine whether further funding is warranted. The bad news followed on the heels of a Nuclear Regulatory Commission's reporting poor management and inadequate quality control (534), and the pullout of the Long Island Lighting Company, an 18% partner (535). LILCO's departure halted its \$180 million annual payment toward the project (536). The New York Public Service Commission put a \$5.4 billion cap on expenditures, ruling that the utilities involved in the project will have to carry 100% of all spending in excess of that amount (537).

Fifteen years after construction was begun, the first reactor at Pacific Gas and Electric's Diablo Canyon site was started up (538). The \$4.9 billion power plant was originally scheduled for completion in 1976, at a cost of about \$400 million. Elsewhere, work was halted on the Seabrook reactor in New Hampshire (539). However, Seabrook's project manager projected that the plant would be completed on schedule, with the first reactor operational by 1986. The estimated cost was revised down to \$6.9 billion from an earlier \$9 billion (540). The original cost estimate in 1968 was \$850 million.

Because of the uncertainty about completing and licensing the project, three utilities announced that the Zimmer nuclear power plant near Cincinnati would be converted to coal (541). The plant, about 97% finished, had been under construction since 1972. While the original cost estimate was \$240 million, the utilities had already spent \$1.6 billion, and the final cost was estimated in September 1983 at \$2.8-\$3.5 billion. In 1982, a licensing board had conditionally rejected an operating permit for the Zimmer plant, citing inadequate evacuation contingency plans.

According to an EPRI official, preserving and upgrading nuclear plants to extend their life expectancy is under consideration as an option to plant retirement and new plant construction (542). Retirement of old plants carries an ever-increasing decommissioning cost, and the high cost of capital makes new construction expensive.

A Senate-House panel agreed on a tax break to help utilities shut down worn-out nuclear power plants (543). The provisions, worth an estimated \$250 million to the industry through 1987, would allow utilities to avoid taxes on money earmarked for plant decommissioning.

A report by the U.S. Office of Technology Assessment says that, without major reforms, commercial atomic power is unlikely to grow in this century (544). As a result of uncertainties in electric demand growth, very high capital costs, operating problems, increased regulatory requirements, and growing public opposition, nuclear power plants currently involve too many financial risks. According to OTA, only one-third of the public supports nuclear plant construction, while more than half are opposed. However, worldwide, the Uranium Institute projects that installed nuclear capacity will increase from 115 GW in 1980 to 315 GW in 1995. The projection includes only operating and committed nuclear generating capacity, with no new orders.

In New York State, the Court of Appeals upheld a Public Service Commission decision that four utilities could recover about \$80 million invested in a nuclear power plant project which the state first approved and later ordered scrapped (545). The PSC found that Rochester Gas and Electric, Niagara Mohawk, Orange and Rockland, and Central Hudson Gas and Electric had acted prudently and were entitled to recover costs from their customers.

A world record for continuous operation was established by the 582 MW Connecticut Yankee plant, which reached 401 days operation without a halt on July 16 (546). The previous world record of 400 days was set by Tokyo Electric's Fukushima units in 1983. The previous U.S. record of 392 days was held by Maine Yankee.

On behalf of nuclear utilities, Kidder-Peabody will form a group called For Responsible Energy Action (547). The organization will lobby for federal aid to utilities struggling with nuclear construction projects.

A joint effort between Israel's Tel Aviv and Ben Gurion Universities is developing thorium-powered light water reactors (548). Thorium is three to four times more plentiful than uranium. The new reactor design should be complete in two years and may be used to produce power within a decade. The reactor uses small quantities of uranium and produces no plutonium by-product.

Uranium oxide prices dropped from about \$24/lb in the fall of 1983 to \$17.50/lb in March, approaching the recent low of \$17/lb in late 1982 (549). The drop was not expected by speculators who predicted the price would remain in the \$20-\$25/lb range because most of the bad news about nuclear plants was known and utilities had reduced stocks.

Conventional fossil fuels.—Coal's future in the utility industry appears secure, as nuclear power plant costs and public acceptance problems have become prohibitive, and economic recovery has restored a growth of electrical demand (550). The American Coal Investment Company president, Zachariah Allen, claimed that coal generation was "the most secure and cost-effective option available to meet this increasing demand." However, indecision on coal purchasing strategies among utilities has led to a mix of long-term coal contracts and spot purchasing.

U.S. demand for bituminous and lignite coal in 1984 was estimated at 740 million tons, up 3.7% from 1983. Electric utilities, which consume about 75% of U.S. coal output, were expected to use about 560 million tons, up 7.2 million tons from 1983 (551). A National Coal Association forecast showed that electric utilities will continue to be the major market for coal, and will also be the highest growth sector (552). With moderate economic growth, it is forecasted that utilities will consume 811 million tons, or 82% of domestic consumption, in 1995 (553).

Mobil Coal Producing, Incorporated, signed a 25 yr contract, valued at \$100 million, to provide 1-2 million ton/yr of coal to Grand River Dam Authority (554). The coal will be shipped to GRDA's 520 MW number 2 generating station near Chouteau, Oklahoma.

A Virginia legislative committee approved a \$1 billion proposal to build a coal slurry pipeline across the state (555). The 450 mile pipeline will connect Western Virginia coal fields with Tidewater electric plants.

EPRI selected New York State E&G's Somerset Station for an \$11 million, advanced high sulfur test center (556). A ten-year research program will be carried out to improve SO₂ removal when burning high sulfur eastern coal. Tests at the center will range up to pilot-plant scale.

DOE and EPRI have agreed to spend about \$4 million in 1985 and 1986 to test coal cleaning techniques (557, 558). New methods to reduce the level of sulfur and other impurities before the coal is burned in utility boilers will be evaluated. The work will be done at EPRI's \$15 million testing site at Pennsylvania Electric's Homer City, Pennsylvania, plant.

The Environmental Protection Agency signed an agreement with Babcock and Wilcox to help fund a test demonstration of B&W's limestone injection technology in a multistage burner (559). The test will be conducted in a

100 MW burner at Ohio Edison's Edgewater generating station.

After eight years of research, TRW planned to conduct 4000h of tests of its atmospheric coal combustion in a 50 million Btu/h unit (560). In small tests, the combustor removed 80-90% of solid coal particulates as well as high percentages of nitrogen and sulfur oxides.

In the Department of Energy's FY-1985 budget, coal-related research and development was scheduled for more than \$327 million in funding (561). Projects within the office of fossil energy account for almost \$253 million of the total. A total of \$750 million was earmarked for a clean coal technology program, designed to fill the gap between small- and large-scale research, with intermediate size facilities using advanced clean coal concepts.

Electrophoresis is being tested at Indiana University to help remove organic sulfur and pyrite from Indiana coals (562). Coal will be inserted into a conductive fluid to see if sulfur-rich particles can be collected at one electrode and coal at the other, by manipulating the chemistry of the particle surfaces and the suspension medium.

Synthetic fuels.—The U.S. synthetic fuels effort lost much support in 1984. Criticism of existing programs, as well as an easing in the fuel-supply picture, combined to cloud the future of synfuels development.

Energy Secretary Donald Hodel called on Congress to reach a consensus on the direction of the federal synfuels program, and supported proposed bills which would slash SFC spending by \$9 billion (563). According to Hodel, "developing a commercial synthetic fuels industry at the pace envisioned by the Energy Security Act of 1980 would require enormous direct budget outlays that would not be offset by economic benefits." The spending cuts, proposed by the President and sponsored by Representative Silvio Conte of Massachusetts, proposed cutting SFC spending to \$5.1 billion (564).

A statement by the President, which accompanied the bill, noted that the energy outlook had improved dramatically since the Synthetic Fuels Corporation was established in 1980 with a budget of \$19 billion (565). Crude oil prices have dropped by 25%, oil imports are down by 33%, and the Strategic Petroleum Reserve contains nearly 400 million barrels of oil.

A spending freeze on the Nation's synfuels program was urged by a bipartisan group of 12 House and Senate members (560). The group, calling the program "highly questionable and very costly," asked the President to hold \$14.8 billion that the Synthetic Fuels Corporation had at its disposal, until Congress can review and approve the company's long-term strategies.

The General Accounting Office, claiming that the SFC will fall far short of production goals, said that it will be relatively ineffective in encouraging private investment, improving the Nation's balance of payments, and providing greater energy security (567).

Similar criticism came from the Office of Technology and Assessment, which found that, as a result of long lead times required to construct coal and oil shale conversion projects, synfuels would not help in the first five years of a prolonged oil supply disruption (568).

SFC Chairman Edward Noble pursued congressional support. According to Noble, in testimony before the House Science and Technology subcommittee, U.S. taxpayers will make \$6 billion from SFC projects if oil prices increase at higher than inflationary rates and the projects come onstream efficiently (569).

The House Appropriations Committee narrowly voted down the administration's synfuels spending cuts, as well as a compromise \$5 billion spending cut (570). However, the House later voted to allow further amendments which would rescind up to \$10 billion from the Energy Security Reserve (571). Intense lobbying resulted in an amendment which would rescind \$5 billion (572), leaving SFC with a budget of \$8.25 billion. In December, the Synfuels Corporation was put back into business as appointments were made to its board of directors, which had lacked a quorum for seven months (573).

Eighteen proposals for financial assistance were received by the Synthetic Fuels Corporation under its fourth solicitation in June (574). Seven proposals were for coal gasification, three were for indirect liquefaction, four for tar sands, and four for oil shale. Only six of the proposals were for new projects.

Coal Gasification.—The \$300 million Cool Water Coal Gasification Project at Daggett, California, began producing electricity from synthetic gas in May (575). According to Southern California Edison, the unit ran for five hours at from 10 to 32 MW using 100% synthetic gas. The project combines two existing technologies for the first time—Texaco's coal gasification process and General Electric's combined-cycle power plant technology—to produce an integrated coal gasification combined-cycle plant (576). The 100 MW project is a commercial-size module which will be used to provide a technological and economic basis for 500 MW or larger facilities. If successful, a new breed of power plants without the pollution problems of coal may be in commercial operation by the 1990's. An EPRI study found that such plants have the potential to be as much as 10% more efficient than conventional coal-fired steam plants with competitive capital costs (577). Both NO_x and SO_x emissions could be substantially reduced. Power will be produced from 1,000 ton/day of coal, the equivalent of 4,000 bbl/day of oil, and will serve 50,000 customers of Southern California Edison (576).

Allis Chalmers planned to modify its KILnGAS coal gasification plant by adding cogeneration equipment, at a cost of \$30 million, depending on Synfuels Corporation aid (578). The existing plant can deliver 409 Btu/h of gas from 600 ton/day of high sulfur coal. With cogeneration, 89% of the input coal energy will be converted into product gas energy.

Site development and construction was set to begin in November at Dow Chemical Company's coal gasification plant near Plaquemine, Louisiana (579). Start-up of the \$139 million project is expected in 1987. The plant will process 2,900 ton/day of Texas lignite into 30 million Btu of gas.

DOE awarded a \$33.7 million development contract, to be cost-shared with KRW Energy Systems, to conduct technical, economic, and environmental risk assessments of commercial introduction of advanced coal gasification technology (580). The project will focus on linking the gasifier to an advanced hot gas cleanup system. The goal is to develop a system for cleaning impurities from coal gas without the energy robbing necessity of cooling the gases.

Encouraged by a feasibility study that the government could save about \$1.4 million per launch in the first year of operation, NASA is considering building a coal gasification plant at Kennedy Space Center to provide fuel and electricity for the space shuttle program (581). The proposed facility would cost about \$151 million, and would process 635 tons of coal/day.

Coal liquids and slurries.—Northern States Power Company awarded a \$20 million contract to Foster Wheeler Energy Corporation to design and build a fluidized bed combustion retrofit (582). The unit, to be completed in 1986, will be the largest FBC boiler in the world. At a cost of about \$50 million, Northern States Power will install an atmospheric fluidized bed boiler in its coal fired 85 MW plant at Burnsville, Minnesota (583). SO₂ and NO_x emissions will be reduced, and electrical output will increase to 125 MW. Start-up is scheduled for 1986.

Occidental Petroleum Corporation and Combustion Engineering will jointly conduct research and development on coal slurry fuels (584).

Shale oil and tar sands.—A continuing world oil surplus reshaped once-ambitious U.S. oil shale production plans (585). However, a number of projects remained active. Geokinetics' shale oil project in northeast Utah has produced more than 90,000 bbl of oil since 1976, and the latest two retorts are producing 250-300 bbl/day. Ameri-

can Syncrude and Stone and Webster Engineering announced formation of the Indiana Shale Oil Project (586). The project will produce 2,011 bbl/day of shale oil.

Chevron Oil Shale and Conoco Shale announced that a \$130 million mining and oil shale retorting operation would begin producing oil early in the spring (587). The Utah plant will produce about 200 bbl/day of oil from 318 tons of Colorado shale using Chevron's staged turbulent-bed retorting process.

Reassessing its timetable for oil shale development, Sohio Shale Oil Company announced that it had withdrawn from the Paraho-Ute oil shale partnership (588). At issue was the interest of other partners in developing technology for licensing rather than commercial production.

Alberta Oil Sands Technology and Research Authority believes new technology can unlock about 95% of an estimated 1 trillion bbl of tar sands oil reserves in Alberta (589). AOSTRA plans to begin construction of a \$100 million project next year to begin production in 1987. By 1990, production should reach 5000 bbl/day.

Fuel cells.—The House Appropriations Committee approved a large boost in spending on fuel cells (590). Fuel cell spending of \$39.9 million was approved, a \$26.2 million increase over the administration request. Of the total, \$27.8 million was earmarked for phosphoric acid cells, and molten carbonate technology was awarded a \$9 million budget. The committee approved \$3.1 million for solid oxide fuel cell work. It also recommended development of an integrated gasified/phosphoric acid fuel cell system of at least 7 MW output. Concern was expressed that "other countries will manufacture fuel cells . . . for our commercial markets before such cells are manufactured in the United States."

Westinghouse Electric Corporation received a contract from Southern California Edison to begin designing a 7.5 MW prototype fuel cell plant for use in the utility's transmission and distribution system (591). The system will include air-cooled, phosphoric acid cells and an advanced steam methane reforming process to convert natural gas to hydrogen for use in the cells. The prototype plant is expected to come on stream no earlier than 1988.

A Consumers Power Company 40 kW fuel cell plant in Jackson, Michigan, has operated for more than 1,500h. The fuel cell ran so smoothly that a scheduled shutdown for routine maintenance after 2,000h of operation was canceled. The project is part of the Onsite Fuel Cell Energy System being developed by the Gas Research Institute, DOE, and a group of gas and electric utilities. About 30 utilities plan to conduct similar experiments across the country.

The Electric Power Research Institute (EPRI) announced that it would not run the Consolidated Edison fuel cell demonstration plant without completely refurbishing the stacks (593, 594). According to an EPRI official, the job could require an additional investment of \$20 million. The present stacks are too old and pose too much of a hazard to continue. They were built before United Technologies Corporation had solved the problem of electrolyte and water leakage. Con Ed and UTC have petitioned Congress for a \$15 million supplement to DOE's budget to refurbish the plant, which would keep the \$80 million project alive.

Meanwhile, a similar demonstration plant in Japan, using newer technology, has been running since April, 1983. Tokyo Electric Power Company's 4.5 MW fuel cell plant has operated for more than 196h.

Magnetohydrodynamics.—In a letter to Congress, DOE requested an additional \$12 million for its magnetohydrodynamics program (595). The additional funds would be used for a multiyear proof-of-concept program which would lead to design, construction, and operation of an integrated, coal-fired MHD retrofit.

A \$33 million budget for fiscal year 1985 was approved by the House Appropriations Committee (596). This represented a 10% increase over FY 1984. The bulk of the funding would go toward preparing a utility-scale MHD

retrofit and testing topping and bottoming systems. The committee also called for significant cost sharing by the private sector.

Solar energy.—Alabama Power and Chronar Corporation formed a joint venture to build a photovoltaic manufacturing plant in Alabama (597). Pending stockholders' approval of the venture, Chronar would supply technology and would buy plant output for the first four years.

Solarex Corporation, a division of Standard Oil Company of Indiana, is constructing a second photovoltaic generating station in Adelanto, California (598). The station is expected to provide 2 MW of power, about 25% more than Atlantic Richfield's Hesperia plant. The Solarex plant will use semicrystalline cells with up to 18% efficiency.

The Solar Energy Research Institute (SERI) estimates that almost 300 MW of windfarm capacity has been installed in the U.S. as of December 1983 (599). About 295 MW of this total is in California. SERI estimated the ultimate planned U.S. windfarm capacity at 687 MW, with 683 MW in California. The SERI figures do not include prototype units or those on government test sites.

California's lead in windpower is partially due to the state's Public Utility Commission, which has ordered investor owned utilities to buy power from qualified small producers and cogenerators. Special tax treatment is also provided.

There are currently more than 50 windfarm developers in the U.S. Some windfarms are being developed by windpower equipment manufacturers such as Boeing, U.S. Wind Power, Incorporated, and Hamilton Standard.

Standard Oil Company and Energy Conversion Devices plan to build two facilities to begin production of photovoltaic cells under their Sovonics Solar Systems partnership (600). The two facilities, costing \$6 million, were expected to be operational in October. The cells, made from silicon alloy deposited on stainless steel, will be made by the proprietary Ovonic roll-to-roll mass production process.

Geothermal.—The northern California geysers area is the most active area in the world for geothermal electricity production (601). Twenty units are now in operation, providing a total generating capacity of 1,379 MW, or enough to meet the needs of 1.3 million people. This is roughly the capacity of one large nuclear plant.

Electric vehicles.—The Lead Industries Association noted that the electric car is making progress, despite a lack of penetration into the market place (602). The Energy Department has continued to fund electric car research, and utility companies are working to promote electric vehicles. Hope Automobil Industri of Denmark planned to begin mass producing the Whisper, a small electric car, by the end of 1984. The car will be marketed in the U.S.

Peugeot unveiled an electric drive version of its Model 205 super mini (603). The car was developed using the same body and interior configurations of the conventional gasoline or diesel powered Model 205. The prototype contains 12 nickel-iron batteries with a life of 200,000 km and a range of up to 140 km. The batteries, developed with SAFT, produce twice as much power as lead-acid batteries having the same size and weight.

Sinclair Vehicle Project and Hoover were reportedly negotiating to build an electric car (604). The new car was planned to be unveiled by early 1985. A novel feature is the minimized weight, achieved by building a battery as the car frame. Reportedly, the car can reach speeds of 30 mph and will cost less than \$3,000.

Environmental issues.—Despite pressure from environmental groups, no clear consensus emerged on what actions should be taken to reduce acid rain and CO₂ emissions. Indeed, disagreement remained over both the causes and the seriousness of the problem.

The degree of concern over the acid rain problem varies considerably (606). Despite the threat of damage to forests, the American Paper Institute and the National Forest Products Association believe the situation is not criti-

cal, concluding that "at the present time, there is no . . . need to reduce acidic deposition . . . to protect the timberlands of North America." Similar conclusions resulted from studies by EPA and the National Acid Precipitation Assessment Plan.

A U.S. Geological Survey review of published reports on acid rain research found that the acidity of precipitation in the Northeast, where the acid rain problem is most acute, has changed little in recent years (606). The review found that acidification increased primarily before the mid-1950's and has been roughly stable since the mid-1960's.

EPA Administrator, William Ruckelshaus told the Senate Committee on Environment and Public Works that the country was not yet ready to adopt an acid rain control program (606). Ruckelshaus said that "before launching the country on an expensive and potentially divisive control program, we feel we need more scientific information." However, Ruckelshaus did say that EPA was taking preliminary steps to prepare for a possible national acid rain control program (607). EPA will work with states to strengthen data bases and reduce implementation time of a control program, when required.

Following the theme for more acid rain research, the President announced, in the State of the Union message, a commitment to double acid rain research funding to \$55.5 million in 1985 (606). As part of the expanded effort, EPA will launch a 12 month, \$6.5 million study of water chemistry in up to 3,000 lakes.

William Karis of Consolidation Coal Company told the Senate Environment and Public Works committee that the costs of major acid rain control legislation have been underestimated by billions of dollars (608). He noted that more than 100,000 jobs could be lost in high sulfur coal producing areas, and that the potential impact on the coal industry could be up to \$10 billion.

Testifying before the Senate Committee on Environmental and Public Works, the chairman of the National Association of Manufacturers electricity task force claimed that proposed acid rain legislation could cost the utility industry up to \$40 billion by 1995, result in major job losses, and still not solve the acid rain problem (609). The NAM endorsed EPA Director William Ruckelshaus' proposal to increase acid rain research funding, and called for a closer look at the effect of electricity rate increases on industries which are heavy electricity users.

According to John Wooten, research director for Peabody Coal's parent firm, legislative proposals calling for 50% cuts in SO₂ emissions from midwestern utilities will actually reduce their contributions to acid deposits by only 10% (610). The finding resulted from a computer simulation of atmospheric chemistry processes, and refutes opinions in a report of the National Academy of Science. Further, according to Wooten, one current bill would cost electricity users more than \$100 billion.

However, the use of air-quality models has been challenged by Ralph Perhac, director EPRI's Environmental Assessment Department (605). According to Perhac, who cites a similar conclusion by the National Academy of Sciences, "present air quality models have an uncertainty factor that is too large to be useful for designing control strategies."

By a 24 to 10 vote, the National Governors Association called for a 5 million ton/yr cut in SO₂ emissions in the 31 states east of the Mississippi River (611). Under the plan, the reduction would be phased in during a six year period.

An EPA report showed that total U.S. SO₂ emissions were actually reduced by 26% between 1973 and 1982 (612). During the same period, utilities SO₂ emissions dropped by nearly 15%, while coal use rose almost 53%. The reductions were attributed to use of lower sulfur coal and compliance with new regulations.

Electric utility spending on pollution control topped all other industries in 1984 (613). A total of \$2.8 billion in expenditures was planned, down 22% from 1983's record \$3.6 billion. In 1985, pollution control spending of \$2.1 bil-

lion is planned. Air pollution control will account for nearly \$1.3 billion in 1984, while water pollution control equipment and solid waste control will consume \$700 million and \$314 million, respectively. Since 1967, the electric utilities have spent about \$33 billion on pollution control, including planned 1985 outlays.

During the period 1975-1982, U.S. air became significantly cleaner (614). According to Joseph Cannon of EPA, the improvement figures included 33% for SO₂, 31% for carbon monoxide, and 15% for particulate matter.

The Tennessee Valley Authority staff recommended approval of a \$35 million contract to Combustion Engineering, Incorporated, for development of boiler technology regarded as a potential solution for acid rain and other power-generation problems (615). The boiler uses fluidized-bed combustion of coal with limestone injection to help remove sulfur during combustion. Currently, more-expensive scrubbers are used to remove sulfur from smoke. The boiler also operates at lower temperatures than conventional boilers, so that nitrous oxide emissions are reduced.

In September, a similar contract was awarded to Pyropower Corporation of San Diego by the Colorado-Ute Electric Association. The project is also being supported by EPRI and the coal industry. A 30 year old coal unit is being converted to fluidized bed combustion by Northern States Power Company, in Minneapolis, in a project with Foster-Wheeler.

Representatives John Serberling and Dennis Eckart of Ohio announced a bill that would attempt to fashion a political consensus on acid rain (614). The bill calls for a 10 million ton annual reduction of SO₂ emissions by no later than 1996. Also, there would be Federal controls on the 50 largest electrical power plant emitters. A trust fund for emission controls would be financed by an indexed 1.5 mill/kWh fee of electricity from nonnuclear power plants and nondomestic sources.

New York State lawmakers approved a bill which, if signed by the governor, would make the state the first in the nation to take anti-acid rain measures at the state level (616). The bill, contingent on the absence of a Federal enactment, would reduce New York's emissions by 12%, or 100,000 ton/yr, by 1988, and by an additional 18% in the early 1990's.

The "Acid Rain Panel Report," a study sponsored by the White House, was criticized by both proponents and foes of increased acid rain control measures (617). The report was written by a panel of U.S. and Canadian scientists and engineers. Both the Edison Electric Institute and the EPA charged that the panel exceeded its mandate by commenting, speculating, and drawing conclusions. Concluding that the Federal government's acid rain research program has been a disappointment, the report called for measures to reduce SO₂ and NO_x emissions. The report also recommended that funding should be increased and that future research should be shifted to nonfederal laboratories. Creative, innovative, and potentially low cost approaches to acid rain control were given a high priority.

Canada doubled its commitment to reducing the acid rain problem, pledging to reduce sulfur dioxide emissions by 50%, instead of the earlier-announced 25%, by 1994 (618). Individual provinces will decide how best to implement controls in their regions. Companies most affected will be Inco, whose Sudbury plant is the largest SO₂ emitter in North America, Noranda Mines, and Ontario Hydro, Ontario's electric utility.

A strong diplomatic protest was delivered by the Canadian government to the State Department against U.S. failure to seek air pollution measures (619). Canada's ambassador stated that the intent was to convince Washington that acid rain was the most important issue between the two countries, threatening to raise "high level concerns" among Canadians.

A recent book, "The Secret Alliance," provoked considerable reaction by accusing Canadian officials of lobbying for U.S. acid rain legislation to allow Canada to increase electricity exports (620). The U.S. and Canada have

exchanged electricity since 1901, although the amount exchanged was small. In 1968, the U.S. was a net exporter of electricity to Canada. However, the exchange balance shifted heavily in the 1970's, as U.S. imports of Canadian electricity burgeoned. Between 1976 and 1982, net U.S. imports rose by 240% from 9,214 to 31,371 GWH.

REFERENCES

1. *Chemical Week*, p. 8, Mar. 13, 1985.
2. *Ibid.*, p. 8, Mar. 13, 1985.
3. Pamphlet no. 10, Chlorine Institute, Inc.; Personal communication.
4. *Chemical and Engineering News*, p. 18, Apr. 2, 1984.
5. *Chemical Week*, p. 34, Jan. 23, 1985.
6. *Ibid.*, p. 65, Dec. 12, 1984.
7. *Ibid.*, p. 36, Oct. 3, 1984.
8. *Ibid.*, p. 28, Oct. 17, 1984.
9. *Ibid.*, p. 40, Nov. 21, 1984.
10. *Chemical Marketing Report*, p. 3, June 4, 1984.
11. *Journal of Commerce*, p. 22B, Apr. 17, 1984.
12. *Chemical Marketing Reporter*, p. 7, Apr. 23, 1984.
13. *Ibid.*, p. 5, Aug. 27, 1984.
14. *Ibid.*, p. 45, July 30, 1984.
15. *Chemical Engineering*, p. 27, Sept. 3, 1984.
16. *Chemical Week*, p. 46, Sept. 5, 1984.
17. *Chemistry and Industry*, p. 397, June 4, 1984.
18. *Ibid.*, p. 315, May 7, 1984.
19. *Modern Paint and Coatings*, p. 68, Nov. 1984.
20. *Chemical Marketing Reporter*, p. 7, Oct. 1, 1984.
21. *Ibid.*, p. 3, Oct. 8, 1984.
22. *Chemical Engineering*, p. 36, June 25, 1984.
23. *Japan Economics Journal*, p. 16, July 17, 1984.
24. *Japan Chemical Week*, p. 4, May 24, 1984.
25. *Ibid.*, p. 5, Mar. 29, 1984.
26. *Chemical Engineering*, p. 25, Apr. 30, 1984.
27. *Chemical Business*, p. 23, Sept. 1984.
28. *Chemical Marketing Reporter*, p. 3, Apr. 2, 1984.
29. *Journal of Commerce*, p. 22B, June 20, 1984.
30. *Ibid.*, p. 22B, Apr. 2, 1984.
31. *Japan Chemical Week*, p. 8, Jan. 24, 1985.
32. *Asian Wall St. Journal*, p. 13, Aug. 21, 1984.
33. *Industrial Mineralogy*, p. 11, Dec. 1984.
34. *Chemistry and Industry*, p. 315, May 7, 1984.
35. *Chemistry Week*, p. 20, Feb. 22, 1984.
36. *Chemistry and Industry*, p. 50, Jan. 16, 1984.
37. *Chemical Marketing Reporter*, p. 7, June 11, 1984.
38. *Journal of Commerce*, p. 22B, June 27, 1984.
39. *Japan Chemical Week*, p. 3, Aug. 16, 1984.
40. *Chemical Weekly*, p. 40, July 24, 1984.
41. *Chemical Marketing Reporter*, p. 5, Sept. 3, 1984.
42. *Japan Economic Journal*, p. 16, Dec. 18, 1984.
43. *Chemical Week*, p. 20, Oct. 31, 1984.
44. *Ibid.*, p. 29, Nov. 14, 1984.
45. *Chemical Engineering*, p. 46, Oct. 29, 1984.
46. *Japan Chemical Week*, p. 2, May 24, 1984.
47. *Chemical Marketing Reporter*, p. 5, Apr. 30, 1984.
48. *Chemical Engineering*, p. 19, May 14, 1984.
49. *Industrial Mineralogy*, p. 70, Aug. 1984.
50. *Chemical Week*, p. 18, Nov. 14, 1984.
51. *Chemical Business*, p. 38, Feb. 1984.
52. *Chemical Marketing Reporter*, p. 5, Jan. 16, 1984.
53. *Chemical and Engineering News*, p. 20, Jan. 16, 1984.
54. *Ibid.*, p. 14, May 28, 1984.
55. *Chemical Marketing Reporter*, p. 54, May 28, 1984.
56. *Ibid.*, p. 5, Feb. 27, 1984.
57. *Ibid.*, p. 7, May 28, 1984.
58. *Chemical Week*, p. 65, Dec. 12, 1984.
59. *Ibid.*, p. 59, Jan. 30, 1985.
60. *Chemical Marketing Reporter*, p. 36, Dec. 3, 1984.
61. *Chemical Week*, p. 24, May 30, 1984.
62. *Ibid.*, p. 14, Aug. 15, 1984.
63. *Chemical Marketing Reporter*, p. 3, Aug. 6, 1984.
64. *Ibid.*, "Chemical Profile," May 21, 1984.
65. *Ibid.*, p. 5, May 21, 1984.
66. *Ibid.*, p. 45, Oct. 22, 1984.
67. *Ibid.*, p. 23, Oct. 29, 1984.
68. "Mineral Commodity Summaries," Soda Ash, p. 142, U.S. Bureau of Mines, Washington DC (1985).
69. "Mineral Commodity Summaries," Soda Ash, p. 143, U.S. Bureau of Mines, Washington, DC (1985).
70. *Chemical and Engineering News*, p. 21, Apr. 2, 1984.
71. *Chemical Marketing Reporter*, p. 3, Aug. 20, 1984.
72. *Engineering and Mining Journal*, p. 25, Jan. 1985.
73. *Chemical Marketing Reporter*, p. 31, July 16, 1984.
74. *Ibid.*, p. 31, June 25, 1984.
75. *Ibid.*, p. 27, Feb. 6, 1984.
76. *Ibid.*, p. 27, Mar. 5, 1984.
77. *Engineering and Mining Journal*, p. 114, Mar. 1985.
78. *Chemical Marketing Reporter*, p. 70, June 18, 1984.
79. *Ibid.*, p. 39, Jan. 2, 1984.
80. *Ibid.*, p. 3, Dec. 24, 1984.
81. *Chemical Week*, p. 61 Jan. 2-9, 1985.
82. *Chemical Marketing Reporter*, p. 2, Dec. 3, 1984.
83. *Ibid.*, p. 5, June 4, 1984.
84. *Chemical Week*, p. 18, Feb. 15, 1984.
85. *Chemical Marketing Reporter*, p. 3, June 18, 1984.
86. *Ibid.*, p. 61, Jan. 7, 1985.
87. *Ibid.*, p. 4, Apr. 23, 1984.
88. *Chemical Engineering*, p. 22, May 14, 1984.
89. *Mining Journal*, Dec. 21, 1984.
90. *American Metal Market*, p. 1, Dec. 11, 1984.
91. *Energy and Mineral Resources*, Feb. 20, 1984.
92. *Metals Week*, Feb. 27, 1984.
93. *Mining Engineering*, p. 420, May 1984.
94. *Energy and Mineral Resources*, Mar. 5, 1984.
95. "Mineral Commodity Summaries," p. 6, U.S. Bureau of Mines, Washington, DC (1985).
96. "Mineral Commodity Summaries," p. 7, U.S. Bureau of Mines, Washington, DC (1985).
97. "Mineral Commodity Summaries," p. 7, U.S. Bureau of Mines, Washington, DC (1985).
98. *Chemical Engineering*, p. 42, Feb. 18, 1985.
99. *American Metal Market*, p. 4, Oct. 11, 1984.
100. *Chemical Week*, p. 18, Jan. 16, 1985.
101. *Business Week*, p. 35, Aug. 27, 1984.
102. *Ibid.*, p. 78, July 23, 1984.
103. *American Metal Market*, p. 8, Jan. 15, 1984.
104. *Engineering and Mining Journal*, p. 26, Jan. 1985.
105. *Ibid.*, p. 23, Jan. 1984.
106. *American Metal Market*, p. 6, Dec. 7, 1984.
107. *Ibid.*, p. 2, Oct. 10, 1984.
108. *Ibid.*, p. 1, Dec. 19, 1984.
109. *Ibid.*, p. 1, Nov. 15, 1984.
110. *Ibid.*, p. 5, Nov. 30, 1984.
111. *Ibid.*, p. 4, Sept. 5, 1984.
112. *Ibid.*, p. 1, Aug. 30, 1984.
113. *Ibid.*, p. 2, Oct. 30, 1984.
114. *Engineering and Mining Journal*, p. 23, Dec. 1984.
115. *American Metal Market*, p. 6, Aug. 28, 1984.
116. *Engineering and Mining Journal*, p. 33, Sept. 1984.
117. *Ibid.*, p. 25, July 1984.
118. *Chemical Marketing Reporter*, p. 7, Aug. 27, 1984.
119. "Mineral Industry Surveys," p. 1, U.S. Bureau of Mines, Washington, DC (1984).
120. *Chemical Marketing Reporter*, p. 4, Nov. 5, 1984.
121. *Ibid.*, p. 4, Sept. 3, 1984.
122. *Chemical Engineering*, p. 48, Aug. 20, 1984.
123. *Journal of Metals*, p. 10, Mar. 1984.
124. *Engineering and Mining Journal*, p. 35, Nov. 1984.
125. *Ibid.*, p. 67, Feb. 1984.
126. *Chemical Marketing Reporter*, p. 5, July 30, 1984.
127. *Journal of Metals*, p. 12, Sept. 1984.
128. *Ibid.*, p. 47, Sept. 1984.
129. *Mining Journal*, p. 89, Feb. 8, 1984.
130. *American Metal Market*, p. 1, Oct. 17, 1984.
131. *Chemical Week*, p. 43, Oct. 24, 1984.
132. *Business Week*, p. 43, Oct. 29, 1984.
133. *Mining Journal*, p. 282, Oct. 19, 1984.
134. *Chemical Marketing Reporter*, p. 7, Oct. 22, 1984.
135. *Ibid.*, p. 7, Dec. 31, 1984.
136. *Ibid.*, p. 5, Apr. 30, 1984.
137. *Ibid.*, p. 48, Feb. 20, 1984.
138. *Ibid.*, p. 4, Dec. 31, 1984.
139. *American Metal Market*, p. 2, Sept. 21, 1984.
140. *Ibid.*, p. 2, Oct. 13, 1984.
141. *Ibid.*, p. 3, Dec. 4, 1984.
142. *Ibid.*, p. 2, Oct. 30, 1984.
143. *Ibid.*, p. 2, Sept. 26, 1984.
144. *Ibid.*, p. 2, June 13, 1984.
145. *Journal of Metals*, p. 12, Sept. 1984.
146. *Chemical Engineering*, p. 34, May 14, 1984.
147. *Ibid.*, p. 10, Apr. 16, 1984.
148. *Engineering and Mining Journal*, p. 125, Nov. 1984.
149. *Chemical Marketing Reporter*, p. 17, Apr. 23, 1984.
150. *American Metal Market*, p. 6, Oct. 23, 1984.
151. *Chemical Engineering*, p. 37, Oct. 29, 1984.
152. *Engineering and Mining Journal*, p. 19, Nov. 1984.
153. *Ibid.*, p. 29, Apr. 1984.
154. *Ibid.*, p. 21, Apr. 1984.
155. *Ibid.*, p. 134, Mar. 1984.
156. *Chemical Marketing Reporter*, p. 31, Nov. 5, 1984.

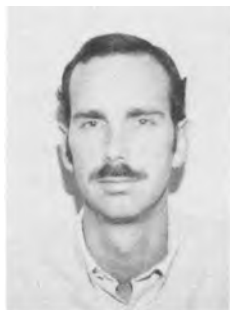
157. *Ibid.*, p. 5, Oct. 1, 1984.
158. *Ibid.*, p. 7, Mar. 14, 1984.
159. *Ibid.*, p. 9, Feb. 27, 1984.
160. *American Metal Market*, p. 1, Oct. 30, 1984.
161. *Engineering and Mining Journal*, p. 77, Dec. 1984.
162. *Ibid.*, p. 15, Jan. 1984.
163. *Chemical Week*, p. 30, Nov. 7, 1984.
164. *Chemical Marketing Reporter*, p. 7, Jan. 23, 1984.
165. *Ibid.*, p. 7, Oct. 29, 1984.
166. *American Metal Market*, p. 16A, Nov. 13, 1984.
167. *Ibid.*, p. 1, Dec. 14, 1984.
168. *Ibid.*, p. 1, Dec. 12, 1984.
169. *Ibid.*, p. 1, Dec. 11, 1984.
170. *Ibid.*, p. 12, Aug. 28, 1984.
171. *Engineering and Mining Journal*, p. 114, June 1984.
172. *Ibid.*, p. 81, Jan. 1984.
173. *Ibid.*, p. 88, Oct. 1984.
174. *Ibid.*, p. 72, Jan. 1984.
175. *Chemical Engineering*, p. 37, Oct. 29, 1984.
176. *Chemical Marketing Reporter*, p. 4, Oct. 8, 1984.
177. *Journal of Metals*, p. 12, June 1984.
178. *Chemical Marketing Reporter*, p. 43, Feb. 27, 1984.
179. *Mining Journal*, p. 186, Sept. 14, 1984.
180. *Journal of Metals*, p. 10, Dec. 1984.
181. *American Metal Market*, p. 2, Aug. 1, 1984.
182. *Engineering and Mining Journal*, p. 25, Sept. 1984.
183. *Chemical Marketing Reporter*, p. 4, Aug. 6, 1984.
184. *Engineering and Mining Journal*, p. 23, Apr. 1984.
185. *Ibid.*, p. 71, Feb. 1984.
186. *Chemical Marketing Reporter*, p. 4, Mar. 12, 1984.
187. *American Metal Marketing*, p. 6, Nov. 9, 1984.
188. *Journal of Metals*, p. 11, Nov. 1984.
189. *American Metal Market*, p. 4, July 25, 1984.
190. *Ibid.*, p. 2, Nov. 29, 1984.
191. *Ibid.*, p. 4, Dec. 13, 1984.
192. *Engineering and Mining Journal*, p. 23, Jan. 1985.
193. *Ibid.*, p. 13, Aug. 1984.
194. *American Metal Market*, p. 20, Aug. 28, 1984.
195. *Engineering and Mining Journal*, p. 112, Apr. 1984.
196. *American Metal Market*, p. 6, July 13, 1984.
197. *Engineering and Mining Journal*, p. 140, Mar. 1984.
198. *Ibid.*, p. 135, Mar. 1984.
199. *Ibid.*, p. 103, Aug. 1984.
200. *American Metal Market*, p. 6, Nov. 7, 1984.
201. *Ibid.*, p. 1, Jan. 11, 1984.
202. *Engineering and Mining Journal*, p. 17, Sept. 1984.
203. *Chemical Marketing Reporter*, p. 5, Aug. 20, 1984.
204. *American Metal Market*, p. 3, Jan. 12, 1984.
205. *Ibid.*, p. 6, Oct. 23, 1984.
206. *Journal of Metals*, p. 12, June 1984.
207. *Chemical Marketing Reporter*, p. 7, Mar. 5, 1984.
208. *American Metal Market*, p. 1, Sept. 18, 1984.
209. *Ibid.*, p. 5, Oct. 11, 1984.
210. *Ibid.*, p. 1, Oct. 11, 1984.
211. *Ibid.*, p. 6, Nov. 9, 1984.
212. *Ibid.*, p. 5, Oct. 16, 1984.
213. *Ibid.*, p. 28, Sept. 3, 1984.
214. *Ibid.*, p. 1, Oct. 16, 1984.
215. *Ibid.*, p. 7, Aug. 13, 1984.
216. *Ibid.*, p. 1, July 30, 1984.
217. *Ibid.*, p. 20, Nov. 26, 1984.
218. *Ibid.*, p. 18, Dec. 3, 1984.
219. *Ibid.*, p. 5, Dec. 6, 1984.
220. *Journal of Metals*, p. 74, Jan. 1984.
221. *Ibid.*, p. 10, Mar. 1984.
222. *Ibid.*, p. 8, Mar. 1984.
223. *Chemical Engineering*, p. 149, June. 25, 1984.
224. *Chemical Marketing Reporter*, p. 4, Feb. 6, 1984.
225. *American Metal Market*, p. 1, Oct. 17, 1984.
226. *Ibid.*, p. 27, Sept. 10, 1984.
227. *Ibid.*, p. 10, Sept. 6, 1984.
228. *Ibid.*, p. 12, July 30, 1984.
229. *Ibid.*, p. 104, Nov. 13, 1984.
230. *Journal of Metals*, p. 25, Jan. 1984.
231. *Ibid.*, p. 9, July 1984.
232. *Ibid.*, p. 10, Nov. 1984.
233. *Chemical Week*, p. 66, Sept. 19, 1984.
234. *Mining Journal*, p. 186, Sept. 14, 1984.
235. *Chemical Marketing Reporter*, p. 4, Sept. 10, 1984.
236. *Welding Design and Fabrication*, p. 53, Mar. 1985.
237. *American Metal Market*, p. 1, Dec. 4, 1984.
238. *Chemical Week*, p. 33, Jan. 16, 1985.
239. *Chemical and Engineering News*, p. 28, Mar. 5, 1984.
240. *Chemical Marketing Reporter*, p. 23, Jan. 2, 1984.
241. *American Metal Market*, p. 19, Aug. 13, 1984.
242. *Chemical Engineering*, p. 33, Apr. 2, 1984.
243. *Mining Journal*, p. 213, Mar. 30, 1984.
244. "Mining Commodity Summaries," p. 18-19, U.S. Bureau of Mines, Washington, DC (1985).
245. *American Metal Market*, p. 6, Sept. 21, 1984.
246. *Ibid.*, p. 5, July 25, 1984.
247. *Ibid.*, p. 5A, Sept. 24, 1984.
248. *Mining Engineering*, p. 1269, Sept. 1984.
249. *American Metal Market*, p. 2, Oct. 24, 1984.
250. *Ibid.*, p. 8, July 24, 1984.
251. *Ibid.*, p. 7, Jan. 8, 1985.
252. *Engineering and Mining Journal*, p. 27, May 1984.
253. *Ibid.*, p. 11, Jan. 1985.
254. *Mining Magazine*, p. 166, Sept. 1984.
255. *Ibid.*, Feb. 1984.
256. *Ibid.*, p. 198, Mar. 1984.
257. *Industrial Minerals*, p. 17, Sept. 1984.
258. *Adhesive Age*, p. 19, June 1984.
259. *American Metal Market*, p. 6, Sept. 21, 1984.
260. "Mineral Commodity Summaries," Chromium, p. 2, U.S. Bureau of Mines, Washington, DC (1985).
261. "Mineral Commodity Summaries," Chromium, p. 33, U.S. Bureau of Mines, Washington, DC (1985).
262. *American Metal Market*, p. 8, Dec. 14, 1984.
263. *Mining Journal*, p. 3, Jan. 6, 1984.
264. *American Metal Market*, p. 12, Dec. 14, 1984.
265. *Ibid.*, p. 17, Aug. 20, 1984.
266. *Ibid.*, p. 19, Nov. 19, 1984.
267. *Chemical Engineering*, p. 19, June 25, 1984.
268. *Chemical Week*, p. 69, Jan. 30, 1985.
269. *Ibid.*, p. 20, Oct. 31, 1984.
270. *Chemical Marketing Reporter*, p. 25, Jan. 30, 1984.
271. *Ibid.*, p. 31, Apr. 16, 1984.
272. *Engineering and Mining Journal*, p. 70, Feb. 1984.
273. *American Metal Market*, p. 1, Nov. 7, 1984.
274. *Ibid.*, p. 7, Aug. 17, 1984.
275. *Ibid.*, p. 1, Aug. 9, 1984.
276. *Journal of Commerce*, Jan. 16, 1984.
277. *Engineering and Mining Journal*, p. 31, Jan. 1985.
278. *Mining Journal*, p. 321, May 11, 1984.
279. "Mineral Commodity Summaries," 1985, pp. 40-41, U.S. Bureau of Mines, Washington, DC (1985).
280. *Engineering and Mining Journal*, Feb. 1984.
281. *Mining Engineering*, p. 234, Mar. 1984.
282. Reuter News Service, May 18, 1984.
283. *American Metal Market*, p. 2, July 17, 1984.
284. *Wall Street Journal*, June 28, 1984.
285. *New York Times*, Aug. 2, 1984.
286. *American Metal Market*, p. 2, Aug. 3, 1984.
287. *New York Times*, June 11, 1984.
288. *Wall Street Journal*, June 11, 1984.
289. *American Metal Market*, p. 2, Aug. 7, 1984.
290. *Ibid.*, p. 2, Sept. 11, 1984.
291. *Ibid.*, p. 25, Nov. 12, 1984.
292. *Ibid.*, p. 9, July 17, 1984.
293. *Ibid.*, May 16, 1984.
294. *New York Times*, July 27, 1984.
295. *Energy and Mineral Resources*, May 21, 1984.
296. *Engineering and Mining Journal*, Mar. 1984.
297. *Iron Age*, Feb. 20, 1984.
298. *American Metal Market*, p. 1, Aug. 2, 1984.
299. *American Mining Congress Journal*, Feb. 8, 1984.
300. *Energy and Mineral Resources*, Mar. 19, 1984.
301. *American Metal Market*, May 15, 1984.
302. *Metals Week*, May, 14, 1984.
303. Reuter News Service, Apr. 9, 1984.
304. *American Metal Market*, p. 5, July 31, 1984.
305. *Ibid.*, p. 1, June 15, 1984.
306. *Ibid.*, June 22, 1984.
307. *Journal of Commerce*, June 28, 1984.
308. *Energy and Mineral Resources*, July 2, 1984.
309. *American Metal Market*, July 31, 1984.
310. *Ibid.*, p. 16, Aug. 17, 1984.
311. *Metals Week*, Aug. 20, 1984.
312. *Wall Street Journal*, Sept. 7, 1984.
313. *American Metal Market*, p. 1, Sept. 10, 1984.
314. *Ibid.*, May 22, 1984.
315. *Ibid.*, May 14, 1984.
316. *CIM Bulletin*, p. 48, Feb. 1984.
317. Reuter News Service, Mar. 14, 1984.
318. *Ibid.*, Mar. 21, 1984.
319. *Metals Week*, July 16, 1984.
320. *American Metal Market*, May 17, 1984.
321. Reuter News Service, May 18, 1984.
322. *Ibid.*, June 1, 1984.
323. *American Metal Market*, p. 1, July 19, 1984.
324. *Ibid.*, p. 2, Oct. 23, 1984.

325. *Ibid.*, Feb. 22, 1984.
326. *Ibid.*, p. 4, Aug. 2, 1984.
327. *Metals Week*, Feb. 27, 1984.
328. *American Metal Market*, p. 16, July 25, 1984.
329. *Ibid.*, p. 4, July 26, 1984.
330. *Ibid.*, Jan. 10, 1984.
331. *Ibid.*, Jan. 11, 1984.
332. *Ibid.*, Jan. 6, 1984.
333. *Ibid.*, May 16, 1984.
334. *Ibid.*, Mar. 6, 1984.
335. *Ibid.*, May 21, 1984.
336. *Ibid.*, p. 1, July 31, 1984.
337. *Reuter News Service*, July 16, 1984.
338. *American Metal Market*, p. 2, Aug. 24, 1984.
339. *Metals Week*, Mar. 19, 1984.
340. *Fortune*, Apr. 2, 1984.
341. *Journal of Commerce*, Apr. 25, 1984.
342. *American Metal Market*, Mar. 21, 1984.
343. *Ibid.*, p. 9, July 24, 1984.
344. *Ibid.*, p. 1, July 26, 1984.
345. *Engineering and Mining Journal*, p. 17, July 1984.
346. *Metal Bulletin*, Apr. 13, 1984.
347. "Mineral Commodity Summaries," Lithium, p. 90, U.S. Bureau of Mines, Washington, DC (1985).
348. "Mineral Commodity Summaries," Lithium, p. 90, U.S. Bureau of Mines, Washington, DC (1985).
349. *Engineering and Mining Journal*, Mar. 1985.
350. *Mining Journal*, p. 372, Nov. 30, 1984.
351. *Welding Design and Fabrication*, p. 53, Mar. 1985.
352. *Chemical Week*, p. 15, July 18, 1984.
353. *Ibid.*, p. 12, Nov. 28, 1984.
354. *New Scientist*, p. 34, Mar. 29, 1984.
355. *Chemical Marketing Reporter*, p. 3, July 9, 1984.
356. *Mining Journal*, p. 435, Dec. 21, 1984.
357. *Ibid.*, p. 295, Oct. 26, 1984.
358. *Engineering and Mining Journal*, p. 36, Jan. 1985.
359. *Chemical Week*, p. 98, Nov. 28, 1984.
360. *The Federal Register*, Mar. 1984.
361. *American Metal Market*, p. 20, Jan. 7, 1985.
362. "Mineral Commodity Summaries," pp. 92-93, U.S. Bureau of Mines, Washington, DC (1985).
363. "Mineral Commodity Summaries," p. 21, U.S. Bureau of Mines, Washington, DC (1985).
364. *Engineering and Mining Journal*, p. 29, Apr. 1984.
365. *American Metal Market*, Apr. 25, 1984.
366. *Metal Bulletin*, Apr. 27, 1984.
367. *Wall Street Journal*, June 25, 1984.
368. *Mining Journal*, Aug. 10, 1984.
369. *American Metal Market*, p. 5, Dec. 5, 1984.
370. *Ibid.*, p. 12, Sept. 18, 1984.
371. *Ibid.*, p. 18, Nov. 5, 1984.
372. "Mineral Commodity Summaries," Manganese, p. 96, U.S. Bureau of Mines, Washington, DC (1985).
373. "Mineral Commodity Summaries," Manganese, p. 97, U.S. Bureau of Mines, Washington, DC (1985).
374. *Engineering and Mining Journal*, p. 25, Jan. 1985.
375. *Mineral Industry Surveys*, p. 1, U.S. Bureau of Mines (June 1984).
376. *Chemical Marketing Reporter*, p. 58, Apr. 23, 1984.
377. *Ibid.*, p. 5, Sept. 24, 1984.
378. *Ibid.*, p. 30, Dec. 10, 1984.
379. *Ibid.*, p. 3, Jan. 7, 1985.
380. *Mineral Industry Surveys*, p. 1, U.S. Bureau of Mines (Oct. 1984).
381. *Ibid.*, p. 1, U.S. Bureau of Mines (Nov. 1984).
382. *Mining Journal*, p. 363, Nov. 23, 1984.
383. *American Metal Market*, p. 1, Nov. 13, 1984.
384. *Mining Journal*, p. 433, June 29, 1984.
385. *Ibid.*, p. 371, Nov. 30, 1984.
386. *American Metal Market*, p. 2, July 24, 1984.
387. *Engineering and Mining Journal*, p. 72, Jan. 1985.
388. *Ibid.*, p. 57, Jan. 1984.
389. *Chemical Marketing Reporter*, p. 9, Aug. 6, 1984.
390. *Chemical Engineering*, p. 33, Sept. 3, 1984.
391. *Chemical Week*, p. 9, Oct. 31, 1984.
392. *Chemical and Engineering News*, p. 24, Sept. 17, 1984.
393. *Chemical Marketing Reporter*, p. 4, June 4, 1984.
394. *Ibid.*, p. 3, Oct. 29, 1984.
395. *Chemical Week*, p. 63, Aug. 22, 1984.
396. *Journal of Metals*, p. 10, Dec. 1984.
397. *American Metal Market*, "Manganese," p. 5A, Dec. 11, 1984.
398. "Mineral Commodity Summaries," p. 106, U.S. Bureau of Mines, Washington, DC (1985).
399. *Engineering and Mining Journal*, p. 67, Mar. 1985.
400. *Ibid.*, p. 32, Jan. 1985.
401. *Ibid.*, p. 23, July 1984.
402. *American Metal Market*, p. 1, Dec. 14, 1984.
403. *Engineering and Mining Journal*, p. 18, Jan. 1984.
404. *American Metal Market*, p. 9, Dec. 11, 1984.
405. *Ibid.*, p. 5, Dec. 13, 1984.
406. *Journal of Metals*, p. 11, Aug. 1984.
407. *Engineering and Mining Journal*, p. 106, Aug. 1984.
408. *Ibid.*, p. 42, Feb. 1984.
409. *American Metal Market*, p. 3, Oct. 3, 1984.
410. *Mining Engineering*, p. 426, May 1984.
411. *Metal Bulletin*, p. 3, May 1984.
412. *American Metal Market*, p. 1, Aug. 15, 1984.
413. *Ibid.*, p. 17, Aug. 20, 1984.
414. *Ibid.*, p. 9A, Nov. 28, 1984.
415. *Ibid.*, p. 7, Sept. 7, 1984.
416. *Mining Journal*, p. 353, Nov. 23, 1984.
417. *Ibid.*, p. 435, Dec. 21, 1984.
418. *Ibid.*, p. 330, Nov. 5, 1984.
419. *Ibid.*, p. 241, Apr. 13, 1984.
420. *Engineering and Mining Journal*, p. 67, Mar. 1985.
421. *American Metal Market*, p. 6, July 19, 1984.
422. *Engineering and Mining Journal*, p. 103, Aug. 1984.
423. *American Metal Market*, p. 7, Nov. 27, 1984.
424. *Ibid.*, p. 7, Sept. 18, 1984.
425. *Engineering and Mining Journal*, p. 21, July 1984.
426. *Journal of Metals*, p. 58, Sept. 1984.
427. *Mineral Industry Surveys, Nickel*, U.S. Bureau of Mines (Nov. 1984).
428. *Journal of Metals*, p. 42, Sept. 1984.
429. *Mining Journal*, p. 289, Oct. 26, 1984.
430. *Chemical Engineering*, p. 18, Feb. 20, 1984.
431. *American Metal Market*, p. 23, Oct. 15, 1984.
432. *Ibid.*, p. 1, Oct. 23, 1984.
433. *Engineering and Mining Journal*, p. 74, Dec. 1984.
434. *Chemical Week*, p. 69, Jan. 30, 1985.
435. "Kirk-Othmer Encyclopedia of Chemical Technology," Vol. 21, 3rd ed., pp. 181-200, John Wiley and Sons, New York (1983).
436. R. D. Varjian and D. E. Hall, *This Journal*, **131**, 374C (1984).
437. "Current Industrial Reports—Inorganic Chemicals," U.S. Department of Commerce, Washington, DC (Jan.-Dec. 1984).
438. "Mineral Commodity Summaries," pp. 166-167, U.S. Bureau of Mines, Washington, DC (1985).
439. *American Metal Market*, p. 10A, June 15, 1984.
440. *Ibid.*, Jan. 3, 1985.
441. *Ibid.*, p. 1, July 26, 1984.
442. *Ibid.*, p. 23A, June 15, 1984.
443. *Ibid.*, p. 15, Aug. 20, 1984.
444. *Ibid.*, p. 1, Aug. 31, 1984.
445. *Ibid.*, p. 6, Sept. 19, 1984.
446. *Ibid.*, p. 1, Dec. 13, 1984.
447. *Ibid.*, p. 2, Nov. 8, 1984.
448. *Ibid.*, p. 9, Aug. 10, 1984.
449. *Ibid.*, p. 1, Aug. 1, 1984.
450. *Ibid.*, p. 2, Dec. 21, 1984.
451. *Ibid.*, p. 1, Aug. 20, 1984.
452. *Ibid.*, p. 1, Dec. 20, 1984.
453. *Ibid.*, June 11, 1984.
454. *Ibid.*, p. 1, Nov. 16, 1984.
455. *Ibid.*, p. 19, Nov. 19, 1984.
456. *Ibid.*, p. 14A, June 15, 1984.
457. *Ibid.*, p. 16A, June 15, 1984.
458. *Ibid.*, p. 1, Oct. 16, 1984.
459. *Ibid.*, p. 4A, June 15, 1984.
460. *Ibid.*, p. 6A, June 15, 1984.
461. *Ibid.*, p. 7, Oct. 19, 1984.
462. *Ibid.*, Apr. 5, 1984.
463. *Ibid.*, p. 12A, June 15, 1984.
464. *Ibid.*, p. 8, Dec. 18, 1984.
465. *High Tech Materials Alert*, p. 8, Sept. 1984.
466. *American Metal Market*, p. 20A, June 15, 1984.
467. *Ibid.*, p. 6, Nov. 21, 1984.
468. *Ibid.*, p. 19A, June 15, 1984.
469. *Ibid.*, p. 17A, June 15, 1984.
470. *Ibid.*, p. 21, Aug. 6, 1984.
471. *Ibid.*, p. 1, Aug. 22, 1984.
472. *Engineering and Mining Journal*, p. 33, June 1984.
473. *American Metal Market*, p. 1, Oct. 11, 1984.
474. *Ibid.*, p. 1, Sept. 27, 1984.
475. *Ibid.*, p. 1, Sept. 28, 1984.
476. *Ibid.*, p. 31, Nov. 15, 1984.
477. *Ibid.*, p. 1, Oct. 30, 1984.
478. *Ibid.*, p. 5, Nov. 5, 1984.
479. *Ibid.*, p. 1, Sept. 11, 1984.

480. *Ibid.*, p. 1, Sept. 20, 1984.
481. *Ibid.*, p. 7, Nov. 2, 1984.
482. *Iron Age*, May 21, 1984.
483. "Mineral Commodity Summaries," pp. 176-177, U.S. Bureau of Mines, Washington, DC (1985).
484. *American Metal Market*, p. 1, Aug. 16, 1984.
485. *American Mining Congress Journal*, p. 13, Aug. 29, 1984.
486. *American Metal Market*, p. 17, Aug. 27, 1984.
487. *Ibid.*, p. 3, Dec. 4, 1984.
488. *Ibid.*, p. 1, Aug. 10, 1984.
489. *American Mining Congress Journal*, p. 13, May 23, 1984.
490. *American Metal Market*, p. 1, Sept. 7, 1984.
491. *Ibid.*, p. 1, July 19, 1984.
492. *Ibid.*, p. 2, Nov. 9, 1984.
493. *Ibid.*, p. 2, Nov. 15, 1984.
494. *Ibid.*, p. 1, Jan. 9, 1985.
495. *Ibid.*, p. 1, Nov. 19, 1984.
496. *Ibid.*, p. 2, Oct. 3, 1984.
497. *Ibid.*, p. 1, Sept. 25, 1984.
498. *Ibid.*, p. 2, Sept. 12, 1984.
499. *Ibid.*, Jan. 11, 1984.
500. *Mining and Engineering Journal*, p. 13, Jan. 1984.
501. *American Metal Market*, p. 6, Aug. 1, 1984.
502. *Mining Engineering*, p. 322, Aug. 1984.
503. *American Metal Market*, p. 1, Aug. 10, 1984.
504. *Ibid.*, p. 8, Aug. 24, 1984.
505. *Ibid.*, Jan. 9, 1984.
506. *Ibid.*, Jan. 10, 1984.
507. *Ibid.*, Jan. 11, 1984.
508. *Ibid.*, p. 17, July 17, 1984.
509. *Ibid.*, p. 1, Aug. 8, 1984.
510. *Ibid.*, p. 25, Sept. 10, 1984.
511. *Ibid.*, p. 1, July 25, 1984.
512. *Financial Times*, May 15, 1984.
513. *Journal of Commerce*, June 1, 1984.
514. *Iron Age*, Apr. 2, 1984.
515. *American Metal Market*, p. 1, July 20, 1984.
516. *Ibid.*, p. 1, Sept. 7, 1984.
517. *Ibid.*, p. 2, Aug. 24, 1984.
518. *Ibid.*, p. 2, Aug. 3, 1984.
519. *Mining Engineering*, Mar. 1984.
520. *American Metal Market*, p. 1, Nov. 20, 1984.
521. *Ibid.*, p. 10, Dec. 21, 1984.
522. Reuters News Service, May 22, 1984.
523. *American Metal Market*, p. 14, Dec. 21, 1984.
524. *Ibid.*, Jan. 9, 1984.
525. *Ibid.*, p. 3, Sept. 11, 1984.
526. *Electrical World*, "1984 Annual Statistical Report," (Apr. 1984); data through 1983.
527. H. Cavanaugh, Electrical World Editorial Staff, Personal communication; *Electrical World*, 1984 data to appear in future issues.
528. *Electrical World*, pp. 49-56, Sept. 1984.
529. R. D. Varjian and D. E. Hall, *This Journal*, **131**, 374C (1984).
530. *Electrical World*, pp. 55-62, Sept. 1983.
531. Associated Press, Jan. 18, 1984.
532. *Ibid.*, Jan. 14, 1984.
533. *Ibid.*, Mar. 31, 1984.
534. *Ibid.*, Feb. 15, 1984.
535. *Ibid.*, Feb. 14, 1984.
536. *Ibid.*, Feb. 11, 1984.
537. *Electrical World*, p. 16, June 1984.
538. Associated Press, Apr. 29, 1984.
539. *Ibid.*, Apr. 19, 1984.
540. *Electrical World*, p. 15, Apr. 1984.
541. Associated Press, Jan. 22, 1984.
542. *Electrical World*, p. 9, July 1984.
543. Associated Press, June 9, 1984.
544. *Mining Engineering*, p. 321, Apr. 1984.
545. Associated Press, Jan. 13, 1984.
546. *Electrical World*, p. 9, Aug. 1984.
547. *Ibid.*, p. 8, Oct. 1984.
548. *Chemical Week*, p. 33, Mar. 28, 1984.
549. *Ibid.*, p. 42, Mar. 28, 1984.
550. *Coal Mining and Processing*, p. 19, Mar. 1984.
551. *Mining Engineering*, p. 13, Apr. 1984.
552. *Coal Mining*, **21**, (4), 16 (1984).
553. *Electrical World*, p. 13, Apr. 1984.
554. *Coal Mining*, p. 13, Apr. 1984.
555. *Ibid.*, p. 13, Feb. 1984.
556. *Electrical World*, p. 14, Aug. 1984.
557. *Coal Mining*, p. 10, Oct. 1984.
558. *American Mining Congress Journal*, p. 12, Nov. 28, 1984.
559. *Coal Technology Report*, p. 1, Oct. 15, 1984.
560. *Ibid.*, p. 1, Oct. 29, 1984.
561. *Ibid.*, p. 1, Dec. 10, 1984.
562. *Ibid.*, p. 2, Sept. 17, 1984.
563. *Synfuels Week*, p. 1, June 11, 1984.
564. *Ibid.*, p. 2, June 11, 1984.
565. *Ibid.*, p. 3, June 11, 1984.
566. Associated Press, Feb. 15, 1984.
567. *Synfuels Week*, p. 3, Aug. 27, 1984.
568. *Ibid.*, p. 2, Sept. 10, 1984.
569. *Ibid.*, p. 4, June 11, 1984.
570. *Ibid.*, p. 1, July 2, 1984.
571. *Ibid.*, p. 1, July 30, 1984.
572. *Ibid.*, p. 1, Aug. 6, 1984.
573. *Ibid.*, p. 1, Dec. 13, 1984.
574. *Ibid.*, p. 3, July 16, 1984.
575. *Electrical World*, p. 16, June 1984.
576. *Mining Magazine*, p. 427, May 1984.
577. *Synfuels Week*, p. 3, June 4, 1984.
578. *Ibid.*, p. 1, July 23, 1984.
579. *Ibid.*, p. 1, Nov. 5, 1984.
580. *American Mining Congress Journal*, p. 11, Nov. 28, 1984.
581. *Mining Engineering*, Apr. 1984.
582. *Coal Technology Report*, p. 1, Aug. 20, 1984.
583. *Electrical World*, p. 16, June 1984.
584. *Coal Mining and Processing*, p. 13, Mar. 1984.
585. *Engineering and Mining Journal*, p. 23, Apr. 1984.
586. *Synfuels Week*, p. 2, July 23, 1984.
587. *Mining Engineering*, p. 124, Feb. 1984.
588. *Ibid.*, p. 327, Apr. 1984.
589. *Ibid.*, p. 122, Feb. 1984.
590. *Coal Technology Report*, p. 2, July 23, 1984.
591. *Ibid.*, p. 3, Aug. 6, 1984.
592. *Ibid.*, p. 4, Sept. 3, 1984.
593. *Ibid.*, p. 1, Aug. 6, 1984.
594. *Electrical World*, p. 8, Sept. 1984.
595. *Coal Technology Report*, June 25, 1984.
596. *Ibid.*, p. 3, July 23, 1984.
597. *Electrical World*, p. 16, May 1984.
598. *Ibid.*, p. 13, Apr. 1984.
599. *Ibid.*, p. 20, Apr. 1984.
600. Associated Press, Jan. 9, 1984.
601. *Mining Magazine*, p. 560, Dec. 1984.
602. *American Metal Market*, p. 34, Sept. 3, 1984.
603. *Financial Times*, July 26, 1984.
604. *Wall Street Journal*, Feb. 28, 1984.
605. *American Mining Congress Journal*, p. 2, May 23, 1984.
606. *Ibid.*, Feb. 8, 1984.
607. *Coal Mining*, Apr. 1984.
608. *American Mining Congress Journal*, Mar. 7, 1984.
609. *Mining Engineering*, p. 322, Apr. 1984.
610. *Journal of Commerce*, July 2, 1984.
611. *Electrical World*, p. 91, Apr. 1984.
612. *Ibid.*, p. 13, May 1984.
613. *Ibid.*, p. 27, July 1984.
614. *American Mining Congress Journal*, p. 5, May 23, 1984.
615. *Wall Street Journal*, Oct. 30, 1984.
616. *Journal of Commerce*, July 2, 1984.
617. *Electrical World*, p. 17, Oct. 1984.
618. *Wall Street Journal*, Mar. 8, 1984.
619. *New York Times*, Feb. 23, 1984.
620. *Electrical World*, p. 25, Oct. 1984.



Reports on the Energy Research Summer Fellowship Awards



Mark R. Deakin



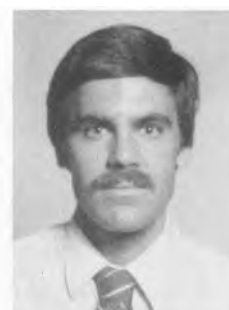
Phelps B. Johnson



Debbie A. LaHurd



Susan E. Morris



David P. Wilkinson

The following students were awarded Energy Research Summer Fellowships for the summer of 1985. Each Award carried with it a grant of \$2000.

Mr. Mark R. Deakin, of Indiana University, Bloomington, Indiana.

Mr. Phelps B. Johnson, of the University of Wisconsin, Madison, Wisconsin.

Ms. Debbie A. LaHurd, of the University of Akron, Akron, Ohio.

Ms. Susan E. Morris, of the University of Illinois, Urbana, Illinois.

Mr. David P. Wilkinson, of the University of Ottawa, Ottawa, Ontario, Canada.

The Energy Research Summer Fellowship Awards are made "without regard to sex, citizenship, race, or financial need. They are made to graduate students pursuing work between the degrees of B.S. and Ph.D., in a college or university in the United States or Canada." The recipients' projects are in fields relating to energy research or of interest to The Electrochemical Society. The Awards are sponsored by the U.S. Department of Energy and are made by the Summer Fellowship Committee of The Electrochemical Society.

Mark R. Deakin was born in Painesville, Ohio, and he received B.S. degrees in Geology and in Chemistry from Florida State University, Tallahassee, Florida, in 1977 and 1982, respectively. He is currently working toward receiving his Ph.D. degree in analytical chemistry at Indiana University.

Deakin's research background includes work on electron transfer at microelectrodes, electrochemical kinetics at carbon electrodes, surface-enhanced Raman spectroscopy, and the electrochemistry of ligated metalloporphyrins. He has published his work in *Analytical Chemistry*, *Journal of Electroanalytical Chemistry*, *Inorganic Chemistry*, and other leading journals.

Mr. Deakin's report appears below.

Quasi-Reversible Electron Transfer at Microcylinder Electrodes

Over the last few years, the availability of very thin conductive fibers, wires, and films (thicknesses on the micron and submicron scale) along with improvements in amplifiers necessary for low current measurement, has led to the development of ultramicroelectrodes (1). These electrodes have been employed in such diverse areas as neurochemistry (2-4), liquid chromatography (5), and stripping voltammetry (6).

The small size of these structures separates them in several respects from conventional electrodes. Microdisk electrodes, for example, are characterized by extremely

small currents. The result is a very small RC time constant for the electrochemical cell and the near elimination of uncompensated voltage drop between the reference and working electrodes (7, 8). Another difference relates to diffusion to these small structures. During a conventional electrochemical experiment in a stagnant solution, the diffusion layer thickness is expected to exceed the width of the electrode. Nonlinear diffusion profiles result (9, 10). Since this leads to higher current densities than observed at conventional planar electrodes, the opportunity exists for near-steady-state measurements of electrochemical kinetics without forced solution convection. Indeed, several authors have explored this possibility at microdisk electrodes (11-13). However, only the case of reversible electron transfer has been treated at microcylinder electrodes (14).

Experimental

All compounds were reagent grade and used as received. Tetraethylammonium perchlorate (TEAP) was obtained from GFS Chemicals (Columbus, Ohio). Solutions were prepared from doubly distilled water and degassed with ultrahigh purity nitrogen before use. A platinum button electrode (Bioanalytical Systems, Purdue, Indiana) with an area of 0.0258 cm² was employed as a conventional planar electrode. A platinum wire electrode [construction described in Ref. (10)] with a radius of 5 μm and a length of 510 μm was employed as a microcylinder electrode. Cyclic voltammetry was performed with a Princeton Applied Research Model 174A potentiostat. A three-electrode cell with a platinum auxiliary and SSCE reference was used. All potentials are reported vs. SSCE.

Digital simulations of cyclic voltammograms at cylinders were performed on an IBM PC equipped with a 8087

numeric coprocessor. The algorithm employed is most fully discussed in Ref. (15).

Theory

The diffusion equation for a cylinder of radius r_0 , ignoring the ends of the cylinder, is

$$\frac{\partial C_A}{\partial t} = D \left[\frac{\partial^2 C_A}{\partial r^2} + \frac{1}{r} \frac{\partial C_A}{\partial r} \right] \quad [1]$$

Assuming the reaction $A + e^- \rightarrow B$ and the equality of the diffusion coefficients for A and B, the boundary conditions are

$$t = 0, r \geq r_0 : C_A = C^0 \quad [2]$$

$$t > 0, r \rightarrow \infty : C_A \rightarrow C^0 \quad [3]$$

$$t > 0, r = r_0 : i = nFAD(\partial C_A / \partial r)_{r_0} \quad [4]$$

where

$$i = nFA[k^0 \exp(\alpha\xi)] \{ C_A^{r_0} - C_B^{r_0} \exp(-\xi) \} \quad [5]$$

$$\xi = [(-nF)/(RT)](E - E^0) \quad [6]$$

The use of dimensionless variables simplifies the solution of Eq. [1] considerably. As is shown elsewhere (15), the diffusion equation can be reduced to the following form with the proper selection of variables

$$\frac{\partial a}{\partial \tau} = [\exp(-\beta y)] \frac{\partial^2 a}{\partial y^2} \quad [7]$$

where the dimensionless variables are defined as

$$a = C_A / C_A^0 \quad [8]$$

$$\tau = (nFvt)/(RT) \quad [9]$$

$$y = [(nFvr_0^2)/(DRT)]^{1/2} \ln(r/r_0) \quad [10]$$

$$\psi = i[(DRT)/(nFv)]^{1/2} / (nFAC_A^0 D) \quad [11]$$

$$\Lambda = k^0[(RT)/(nFvD)]^{1/2} \quad [12]$$

$$\beta = 2[(DRT)/(nFvr_0^2)]^{1/2} \quad [13]$$

Where β is a dimensionless cylindrical factor which is a function of both the electrode radius and time. Thus, the new boundary conditions are

$$\tau = 0, y > 0 : a = 1 \quad [14]$$

$$\tau > 0, y \rightarrow \infty : a \rightarrow 1 \quad [15]$$

$$\tau > 0, y = 0 : \left[\frac{\partial a}{\partial y} \right]_0 = \Lambda [\exp(\alpha\xi)] \{ 1 - (1 - a_0)[1 + \exp(-\xi)] \} \quad [16]$$

For large values of β , it is possible to solve Eq. [7], for cyclic voltammetry, in the Laplace plane. For the electrochemically reversible case, the solution is given by Aoki *et al.* (14). For the more general case, with quasi-reversible or irreversible charge transfer, the following solution by Amatore *et al.* (15) is applicable

$$\frac{i}{i_{lim}} = \left\{ 1 + \exp(-\xi) + \frac{1}{\Lambda^*} \exp(-\alpha\xi) \right\}^{-1} \quad [17]$$

$$\Lambda^* = \frac{2\Lambda \ln \beta}{\beta - 1.1(\beta/\ln \beta)} \quad [18]$$

where i_{lim} is given in Ref. (10).

As β decreases toward zero, the problem reduces to the case of linear diffusion. The region intermediate between linear diffusion and the solution of Amatore is best resolved by digital simulation. For this reason, a finite difference approach was applied to Eq. [7].

Results

A finite difference method with an exponentially expanding grid, as described in Eq. [10], was employed. Hopscotch, an algorithm described by Gourlay (16) and previously employed by Shoup and Szabo (17), was used

to decrease memory requirements and to lower computation time. This method is fully explicit and unconditionally stable. The quantity $\Delta\tau/(\Delta y)^2$ may increase beyond the conventional limit of 0.5 and take any value. This combination of an exponential grid and a Hopscotch algorithm allowed the calculation of voltammograms on a microcomputer (IBM PC), with less than 0.01% error, in less than 10 min. The current was calculated from the concentration profile at the electrode surface using a three-point approximation of $\partial a/\partial y$

$$\psi_1 = \{(-3/2)a_0 + 2a_1 - a_2/2\}(\Delta y)^{-1} \quad [19]$$

The validity of the simulation was tested both by comparison of reversible simulations with the result of Aoki (14) and by comparison of quasi-reversible simulations with the limiting case described in Eq. [17]-[18]. Less than 0.01% error was found with a $\Delta\tau$ value of 0.005.

The simulation shows that, as β approaches infinity, the cyclic voltammogram tends to the sigmoidal shape described in Eq. [17]. Thus, a quasi-steady state is achieved at electrodes of small radius and at long times. Under these conditions, a measurement of the peak potential is difficult, especially if the background current varies with potential. Thus, the traditional measurement of ΔE_{peak} is not a reliable indication of the rate of electron transfer. A better parameter is the shift of the half-peak potential, $E_{p/2}$, away from E^0 . The variation of the dimensionless half-peak potential, $\xi_{p/2}$, with the dimensionless kinetic parameter, Λ^* , is shown in Fig. 1. At small radii cyl-

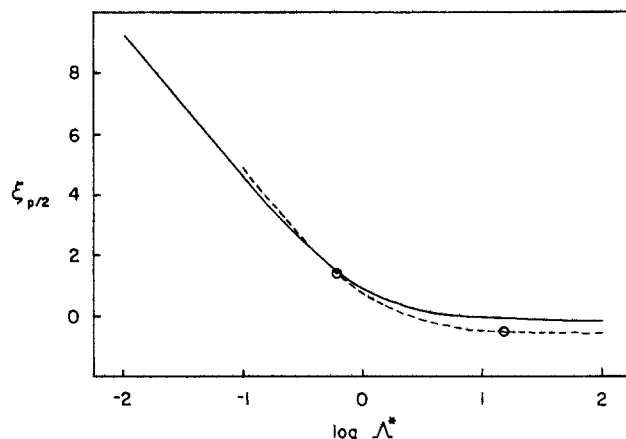


Fig. 1. Variation of the dimensionless half-peak potential with the kinetic parameter, Λ^* . Values taken from simulated voltammograms with $\beta > 100$ (solid line) and $\beta = 10$ (broken line). The circles represent points taken from experimental voltammograms in Fig. 2.

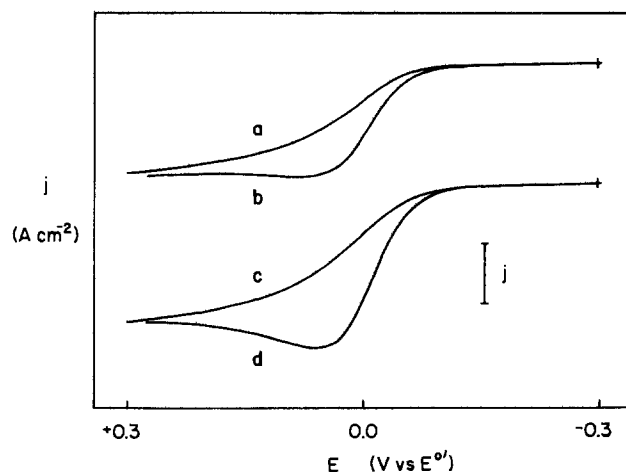


Fig. 2. Experimental voltammograms obtained at a platinum microcylinder with a radius of $5 \mu\text{m}$. Scan speeds of $0.01 \text{ V}\cdot\text{s}^{-1}$ (a, b) and $0.10 \text{ V}\cdot\text{s}^{-1}$ (c, d). Supporting electrolytes: 0.1M TEAP (a, c) and 1.0M NaCl (b, d). Current density bar equals $2 \times 10^{-4} \text{ A}\cdot\text{cm}^{-2}$.

Table I. Comparison of the apparent rates of heterogeneous electron transfer determined by cyclic voltammetry at a planar electrode and quasi-steady-state voltammetry at a microcylinder electrode

Supporting electrolyte	E^0 (V vs. SSCE)	k^0_{planar} ($\text{cm}\cdot\text{s}^{-1}$)	k^0_{cyl} ($\text{cm}\cdot\text{s}^{-1}$)
1.0M NaCl	0.224	$\sim 5 \times 10^{-2}$	^a
0.1M TEAP	0.118	3.0×10^{-3}	3.6×10^{-3}

^a Measurement not possible; see text.

inders and at long times ($\beta > 100$), the curve coincides with the theory presented in Eq. [17]. When β takes an intermediate value there is some deviation from theory, but the overall trend is preserved.

Experimental voltammograms recorded at a platinum microcylinder with a radius of $5 \mu\text{m}$ are shown in Fig. 2. The oxidation of $\text{Fe}(\text{CN})_6^{4-}$ is depicted at two scan rates and with two different supporting electrolytes. The rate constant for this oxidation is known to depend on the type and concentration of the supporting electrolyte employed (18).

At planar electrodes, conventional voltammetric curves are observed. From measurements of the peak potentials, the values for the formal potential and the apparent rate constant shown in Table I are obtained. At microcylinder electrodes, peak potential measurements become unreliable as the system tends toward polarographic behavior. Therefore, for the microcylinder, the half-peak potential and the curve in Fig. 1 were used to obtain values for the apparent rate constant. The results are shown in Fig. 1 and Table I.

It is apparent from Fig. 1 that the lack of variation in $\xi_{p/2}$ at larger values of Λ^* limits the quasi-steady-state measurement of k^0 to relatively slow rates of electron transfer. Quantitation of the rate for ferrocyanide oxidation in 1.0M NaCl is not possible with a $5 \mu\text{m}$ electrode using the quasi-steady-state method. Theoretically, this rate could be measured with a thinner electrode. Construction of a cylinder electrode with a $1 \mu\text{m}$ radius may be possible, but that is probably the experimental limit. Cylinders of smaller radius will not support themselves in solution.

Assuming that an electrode with a radius of $1 \mu\text{m}$ could be constructed, and taking a lower limit of $0.02 \text{ V}\cdot\text{s}^{-1}$ for the scan speed, a diffusion coefficient of 1×10^{-5} gives an upper limit on β of 72. Thus, if a 0.01 V shift in $E_{p/2}$ is sufficient for a rate measurement, then the maximum rate that can be quantified is about $3.5 \times 10^{-2} \text{ cm}\cdot\text{s}^{-1}$. Unfortunately, this analysis shows that the quasi-steady state at cylinders is only useful for measuring rates which are already easily obtained at conventional planar electrodes. For the quasi-steady-state method to become useful, the radius of the effective cylinder must be significantly reduced. This is possible with construction of thin line electrodes (19). Thin films of metals have already been used for this purpose. Using this technique, the effective radius of the electrode can be decreased by at least two orders of magnitude (19). This should allow quasi-steady-state measurement of significantly faster rates. The theory for diffusion to these microline structures is a more complex problem than the microcylinder discussed above. However, simulation of the problem is possible and is now under study.

Acknowledgment

The support of The Electrochemical Society and the U.S. Department of Energy is gratefully acknowledged.

REFERENCES

1. R. M. Wightman, *Anal. Chem.*, **53**, 1125A (1981).
2. J. L. Ponchon, R. Cesapuglio, F. Gonon, M. Jouvot, and J. F. Pojol, *ibid.*, **51**, 1483 (1979).
3. A. G. Ewing, R. M. Wightman, and M. A. Dayton, *Brain Res.*, **249**, 361 (1982).
4. A. G. Ewing, J. C. Bigelow, and R. M. Wightman, *Science*, **221**, 169 (1983).
5. L. A. Knecht, E. J. Guthrie, and J. W. Jorgenson, *Anal. Chem.*, **56**, 479 (1984).

6. K. R. Wehmeyer and R. M. Wightman, *ibid.*, **57**, 1989 (1985).
7. J. O. Howell and R. M. Wightman, *ibid.*, **56**, 524 (1984).
8. A. M. Bond, M. Fleischmann, and J. Robinson, *J. Electroanal. Chem.*, **172**, 11 (1984).
9. Y. Saito, *Rev. Polargr.*, **15**, 177 (1968).
10. P. M. Kovach, W. L. Caudill, D. G. Peters, and R. M. Wightman, *J. Electroanal. Chem.*, **185**, 285 (1985).
11. M. Fleischmann, F. Lasserre, J. Robinson, and D. Swan, *ibid.*, **177**, 97 (1984).
12. R. S. Robinson and R. L. McCreery, *ibid.*, **182**, 61 (1985).
13. M. A. Dayton, A. G. Ewing, and R. M. Wightman, *Anal. Chem.*, **52**, 2392 (1980).
14. K. Aoki, K. Honda, K. Tokuda, and H. Matsuda, *J. Electroanal. Chem.*, **186**, 79 (1985).
15. C. A. Amatore, M. R. Deakin, and R. M. Wightman, Submitted to *J. Electroanal. Chem.*
16. A. R. Gourlay, *J. Inst. Math. Appl.*, **6**, 375 (1970).
17. D. Shoup and A. Szabo, *J. Electroanal. Chem.*, **160**, 1 (1984).
18. J. Kuta and E. Yeager, *ibid.*, **59**, 110 (1975).
19. K. R. Wehmeyer, M. R. Deakin, and R. M. Wightman, *Anal. Chem.*, **57**, 1913 (1985).

Phelps B. Johnson was graduated with a B.A. degree by Gustavus Adolphus College, St. Peter, Minnesota, in 1982. He is now working toward a Ph.D. degree in chemistry at the University of Wisconsin.

Johnson is a winner of the McElvain Scholar Award, and his work has been published in *Applied Physics Letters*.

Mr. Johnson's report appears below.

Stabilization and Photoluminescent Characterization of n-GaP/n- GaAs_{0.4}P_{0.6} Strained-Layer Superlattice Electrodes

The variety of electronic materials amenable to photoelectrochemical characterization is increasing owing to developments in semiconductor growth and device technology. Strained-layer superlattices (SLS's) are a class of materials of potential interest to photoelectrochemists (1, 2). Created by the deposition of alternating thin (40-300Å) layers of two lattice-mismatched semiconductors, SLS's afford the opportunity to study carrier quantization effects, produced by variations in the conduction and valence band offsets (3), and the influence of the terminating (surface) layer composition on electrodes with identical bulk properties.

In this report, we discuss the stabilization against photoanodic corrosion, photoelectrochemical cell (PEC) properties, and photoluminescence (PL) of n-GaP/n-GaAs_{0.4}P_{0.6} SLS electrodes. In particular, we demonstrate that thin (0.37-0.75 μm) SLS structures can be stabilized in PEC's employing aqueous ditelluride electrolyte to yield monochromatic optical-to-electrical energy conversion efficiencies of a few percent. Also, field-induced PL quenching studies on the SLS electrodes are in approximate accord with a dead-layer model (4) previously applied to homogeneous and isotype heterojunction electrodes (5, 6). Some of these results are detailed in a recent publication (2).

The SLS's were grown at Sandia National Laboratories by the metalorganic chemical vapor deposition technique (7-9). Prior to the deposition of the SLS layers, a $1.2 \mu\text{m}$ thick ($1.5 \mu\text{m}$ for SLS-957) graded buffer layer, terminating in a composition of GaAs_{0.2}P_{0.8}, was grown on a GaP substrate. This was followed by alternating layers of

GaP and $\text{GaAs}_{0.4}\text{P}_{1-x}$, terminating in the alloy layer. Four samples were studied, one with $x = 0.39$ and fifty 150Å thick layers (SLS-957), another with $x = 0.43$ and thirty 125Å thick layers (SLS-471), a third with $x = 0.41$ and thirty 200Å thick layers (SLS-472), and the fourth with $x = 0.39$ and thirty 140Å thick layers (SLS-473). Samples were nominally undoped and were not etched prior to use. Telluride electrolyte, synthesized as described previously, had a composition of 7.5M KOH/0.2M ($\text{Te}^{2-} + \text{Te}_2^{2-}$) (10). Potentiostatic experiments were conducted with a standard three-electrode setup, and samples were mounted as previously described (11). The instrumentation and techniques used in PEC and PL quenching experiments have also been described (2, 12).

A 5.5h stability experiment was conducted on SLS-472 at -1.0V vs. SCE with 458 nm excitation. The $\sim 0.8\text{C}$ passed through the $\sim 0.06\text{ cm}^2$, $0.6\text{ }\mu\text{m}$ thick illuminated area was several times the amount required for total SLS decomposition, assuming a photoanodic decomposition stoichiometry of six moles of holes per mole of crystal. Adequate stability was indicated by a modest 7% decline in the initial current density of 0.7 mA/cm^2 , and the unchanged PL quenching behavior of the SLS (*vide infra*). An upper limit to photocurrent density was not firmly established, although $\sim 5\text{ mA/cm}^2$ resulted in the decomposition of SLS-473, as evidenced by loss of the SLS PL and visible damage to the illuminated portion of the electrode.

The bottom panel of Fig. 1 shows a current-voltage (*i-V*) curve for SLS-957, obtained with 488 nm excitation. Such *i-V* curves indicate that SLS-based electrodes have fairly modest optical-to-electrical energy conversion efficiencies. A summary of *i-V* results on SLS-471 and SLS-472 is given in Table I. Sample-to-sample variations in maximum energy conversion efficiency with 473 nm excitation ranged from 2 to 4%. The sharp decline in photocurrent quantum efficiency and maximum energy conversion efficiency with increasing optical penetration depth is attributed to the presence of hole barriers in the valence band perpendicular to the surface of the SLS, limiting the contribution of excess carriers generated in the neutral region to the photocurrent. Small hole diffusion lengths ($\sim 0.1\text{ }\mu\text{m}$) have been reported for GaP/GaAs_{0.2}P_{0.8} SLS's (13).

A photoaction spectrum is shown in Fig. 2 for SLS-957 in telluride electrolyte. Photoaction spectra were studied

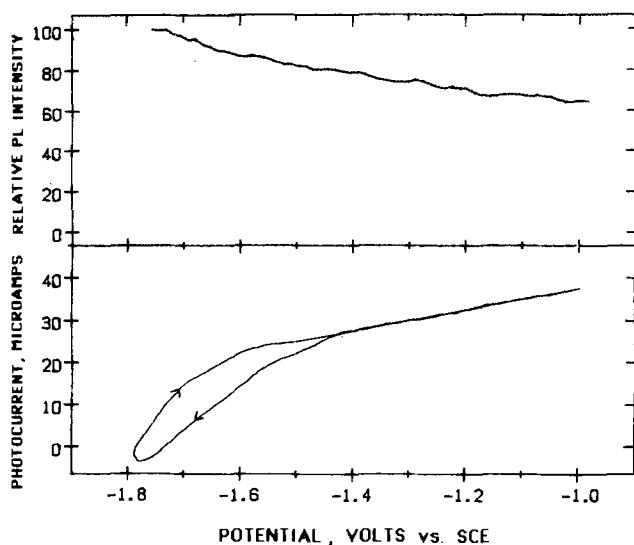


Fig. 1. Photocurrent (bottom panel) and PL intensity (top panel) for the SLS-957 electrode as a function of potential in a PEC employing 7.5M KOH/0.2M ($\text{Te}_2^{2-} + \text{Te}^{2-}$) electrolyte; PL intensity was monitored at 610 nm for two consecutive cycles, averaged, and smoothed. The electrode ($\sim 0.10\text{-cm}^2$ illuminated area) was excited with 488 nm light from a beam-expanded Ar⁺ laser. Both curves were swept simultaneously at 5 mV/s. The electrolyte redox potential, -1.18V vs. SCE , defines the short-circuit potential.

Table I. Optical-to-electrical energy conversion by GaAs_{0.4}P_{0.6}/GaP SLS photoelectrodes in (di) telluride electrolyte^a

SLS	Excitation (nm) ^b	$1/\alpha$ (Å) ^c	ϕ_x ^d	ϕ_x at η_{max} ^{at}	ff ^e	V_o ^f	η_{max} (%) ^g
471	457.9	1000	0.30	0.23	0.44	0.41	3.2
	472.7	1400	0.22	0.15	0.43	0.43	2.3
	488.0	1800	0.18	0.12	0.42	0.44	1.9
	501.7	2400	0.17	0.11	0.43	0.41	1.7
	514.5	3700	0.12	0.09	0.43	0.42	1.4
472	457.9	1000	0.28	0.17	0.37	0.37	2.2
	472.7	1400	0.18	0.13	0.39	0.37	1.6
	488.0	1800	0.15	0.10	0.39	0.36	1.3
	501.7	2400	0.13	0.08	0.39	0.38	1.2
	514.5	3700	0.09	0.06	0.39	0.38	0.9

^aThe results for 457.9, 472.7, and 501.7 nm were published in Ref. (2). Experiments were run under N₂ in stirred solutions of composition 7.5M KOH/0.20-0.23M Te ($\text{Te}^{2-} + \text{Te}_2^{2-}$); redox potential were -1.21 and -1.23V vs. SCE for the SLS-471 and SLS-472 experiments, respectively.

^bExcitation was performed with a beam-expanded Ar⁺ laser. Incident powers ranged from 3-10 mW/cm², adjusted to produce roughly constant open-circuit voltage.

^cApproximate measure of optical penetration depth, based on absorptivities in Ref. (14).

^dShort-circuit photocurrent quantum efficiency.

^eFill factors for *i-V* curves.

^fOutput voltage at η_{max} .

^g(Maximum electrical power out divided by input optical power) $\times 100$. This, along with fill factor and ϕ_x at η_{max} , was calculated on the inner, cathodic-going portion of the *i-V* curve.

in both selenide and telluride electrolyte, and were found to be insensitive to the different redox potentials of the solutions. Spectra exhibit a potential dependence, with the relative response to near-bandgap excitation enhanced by biasing the electrode further into depletion. The photocurrent onset at $\sim 620\text{ nm}$ is slightly potential dependent, but corresponds approximately to the bandgap of the SLS, 2.04 eV from uncorrected 295 K PL.

A study of the weak 295 K PL of these SLS electrodes has shown that, at low resolution, only the PL intensity, and not the spectral distribution, is perturbed by applied potential. The top panel of Fig. 1 shows the PL quenching behavior of SLS-957 excited with 488 nm light. The observed PL quenching of SLS electrodes is in rough accord with the dead-layer model. The quantitative form of this model is given by Eq. [1], where D is the change in dead-layer thickness over the experimental voltage thickness

$$D = (-1/\alpha) \ln(\text{PL}/\text{PL}_{oc}) \quad [1]$$

where α is the absorptivity of the SLS for the excitation

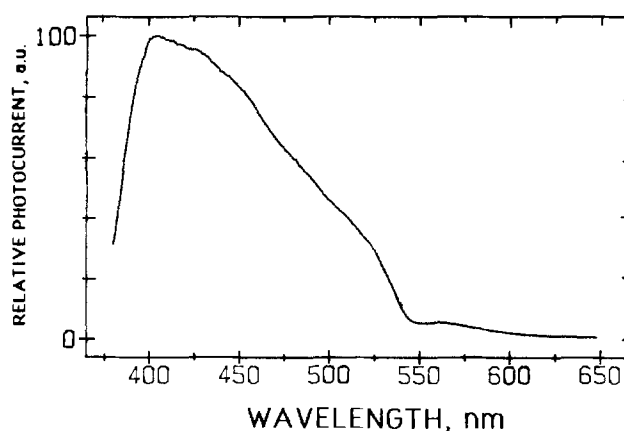


Fig. 2. Relative photocurrent quantum efficiency for SLS-957 in telluride electrolyte at -1.0V vs. SCE . The excitation was chopped, and lock-in techniques used to monitor the photocurrent. The spectrum is corrected for the wavelength dependence of the lamp/monochromator excitation source and is uncorrected for sample reflectivity.

wavelength¹ and PL and PL_{oc} are the in-circuit and open-circuit PL intensities, respectively. Consistent *D* values were obtained for SLS-472 at -1.0V vs. SCE: 260, 290, and 280Å, corresponding to 413, 458, and 473 nm excitation, respectively. Luminescence from an unassigned deep level (uncorrected λ_{max} ~ 780 nm) did not exhibit quenching.

In summary, n-GaP/n-GaAs_{0.4}P_{0.6} SLS electrodes have been stabilized in aqueous telluride electrolyte. Energy conversion efficiencies of these electrodes are modest, because, in part, of small hole diffusion lengths perpendicular to the SLS layers. Studies of SLS structure and surface composition influences (*i.e.*, GaP or alloy terminating layer) upon cell photovoltage and conversion efficiency are currently in progress.

Acknowledgments

The author would like to thank The Electrochemical Society for its support through the Summer Energy Research Fellowship program, and Professor Arthur B. Ellis for his advice and unfailing support. The author is also deeply indebted to Dr. R. M. Biefeld for many helpful discussions and his expert growth of the superlattices, and to Dr. W. S. Hobson for creative suggestions. Thanks also go to Dr. D. S. Ginley and Dr. P. L. Gourley for helpful discussions. Additional support from the U.S. Army Research Office, the University of Wisconsin-Madison University-Industry Research Program, and the U.S. Department of Energy under contract no. DEHAC04-76DP00789 is gratefully acknowledged.

¹To estimate α , we used the absorption curve in Ref. (14), Fig. 4. We shifted this curve (presented for a n-GaP/n-GaAs_{0.44}P_{0.56} SLS with 30 alternating 180Å thick layers and $E_g = 1.92$ eV) 0.07 eV to correspond to our observed PL peak at 1.99 eV. This yields α of 2.7×10^4 , 4.1×10^4 , 4.9×10^4 , 7.4×10^4 , and 1.0×10^5 cm⁻¹ for 514, 502, 488, 473, and 458 nm excitation, respectively. An α value of 1.8×10^5 at 413 nm was estimated by extrapolating the SLS curve parallel to the GaAs absorption curve, which has been shifted to the SLS bandgap in the above-mentioned figure.

REFERENCES

1. A. J. Nozik, B. R. Thacker, and J. M. Olson, *Nature*, **316**, 51 (1985).
2. P. B. Johnson, A. B. Ellis, R. M. Biefeld, and D. S. Ginley, *Appl. Phys. Lett.*, **47**, 877 (1985).
3. G. C. Osbourn, *J. Vac. Sci. Technol.*, **21**, 469 (1982).
4. R. E. Hollingsworth and J. R. Sites, *J. Appl. Phys.*, **53**, 5357 (1982), and references therein.
5. W. S. Hobson and A. B. Ellis, *ibid.*, **54**, 5956 (1983).
6. W. S. Hobson, P. B. Johnson, A. B. Ellis, and R. M. Biefeld, *Appl. Phys. Lett.*, **45**, 150 (1984).
7. R. M. Biefeld, G. C. Osbourn, P. L. Gourley, and I. J. Fritz, *J. Electron. Mater.*, **12**, 903 (1983).
8. R. M. Biefeld, *J. Cryst. Growth*, **56**, 382 (1982).
9. P. L. Gourley and R. M. Biefeld, *J. Vac. Sci. Technol.*, **21**, 473 (1982).
10. W. S. Hobson and A. B. Ellis, *Appl. Phys. Lett.*, **41**, 891 (1982).
11. B. R. Karas and A. B. Ellis, *J. Am. Chem. Soc.*, **102**, 968 (1980).
12. H. H. Streckert, J. Tong, M. K. Carpenter, and A. B. Ellis, *This Journal*, **129**, 772 (1982).
13. P. L. Gourley, R. M. Biefeld, T. E. Zipperian, and J. J. Wiczor, *Appl. Phys. Lett.*, **44**, 983 (1984).
14. P. L. Gourley, R. M. Biefeld, G. C. Osbourn, and I. J. Fritz, in "GaAs and Related Compounds," G. E. Stillman, Editor, p. 249, Institute of Physics, London (1983).

Debbie A. LaHurd was born in Wheeling, West Virginia. The University of Akron granted her a B.S. degree in 1981. She obtained an M.S. degree from the University of Akron in 1984, and is currently working toward a Ph.D. degree there.

LaHurd has been a NASA Fellow and is interested in energy storage devices, electrochemical engineering, transport processes, and applied mathematics.

Ms. LaHurd's report follows.

Simplified Models for Use in Electrochemical Reactor Scale-Up and System Studies

Electrochemical reactor design is, at best, an empirical art owing to the large number of design parameters and their complex interactions. The scale-up from laboratory designs could be expedited by the use of an appropriate mathematical model. Such models use assumptions to simplify the phenomena into a workable set of equations which can predict the relative importance of the kinetics, mass transfer, and ohmic contributions. Numerous mathematical models are available in the literature (1-4), but many of these are cumbersome and expensive to use because their specific nature requires the use of time-consuming complex numerical procedures to obtain a solution. The goal of this research is to develop a simplified model which may be applied to a large number of electrochemical reactors to predict their performance. The verification of this model begins by comparing its predictions with more rigorous model predictions.

Flow electrochemical reactors often utilize two or more redox couples, and some include a membrane separator. The following represents an example of redox reactions occurring at the electrodes of an electrochemical reactor



A general model must be able to incorporate side reactions which occur at an electrode surface. Reaction [3] of the above example can be considered to be a side reaction occurring at the cathode. Many systems require membranes to separate the species by discouraging a chemical discharge reaction. Additionally, many flow electrochemical reactors use high surface area porous electrodes to reduce kinetic and mass-transfer limitations. The porous electrodes can generate up to half of the total cell pressure drop (5), thus reducing the electrical efficiency. Furthermore, porous electrodes are often nonuniform, which causes uneven flow distribution in multiple cell stacks. This modeling effort is uniquely suited to evaluate different types of uniform turbulence promoters which increase mass transfer while effecting a small hydraulic pressure drop. For the purposes of comparison, the model is evaluated by applying it to the iron-chrome energy storage system developed by the NASA-Lewis Research Center (6).

The VOLBAL model has been developed for a single cell and is a one-dimensional simulation easily modified for different flow characteristics (*i.e.*, planar electrode flow or porous electrode flow) by way of the mass-transfer coefficient. The model can be verified experimentally for different flow configurations and different cell sizes or by comparison with a more rigorous model. The purpose of this paper is to present the results of comparing VOLBAL with a more rigorous two-dimensional model developed by White and others at Texas A&M University (1, 7). The White model was developed for channel flow and has been modified for membrane separation of the half-cells (7). Their model also accounts for the effects of migration and multiple reactions.

Model Development

The VOLBAL model.—The VOLBAL model is based upon the overall local voltage balance across a single cell. The mathematical model is simplified by allowing the concentration and current density to vary in only one direction. This model takes into account mass-transfer effects by introducing a correlation for the mass-transfer coefficient such as the Leveque approximation (8). The

assumptions used in the development of the VOLBAL model are: (i) isothermal conditions exist; (ii) there exists one-dimensional variation in concentration and current density; (iii) gas generation effects are ignored; (iv) physical and transport properties are constant; (v) there is a well-developed laminar flow; (vi) a mass-transfer coefficient was used to predict the mass-transfer effects of planar electrodes; (vii) no heterogeneous or homogeneous chemical reactions occur; (viii) steady-state conditions exist; and (ix) for each half-cell, the reference electrode reaction is the same reaction as the main reaction at the electrode and the reference electrode concentrations are the same as the reference concentrations.

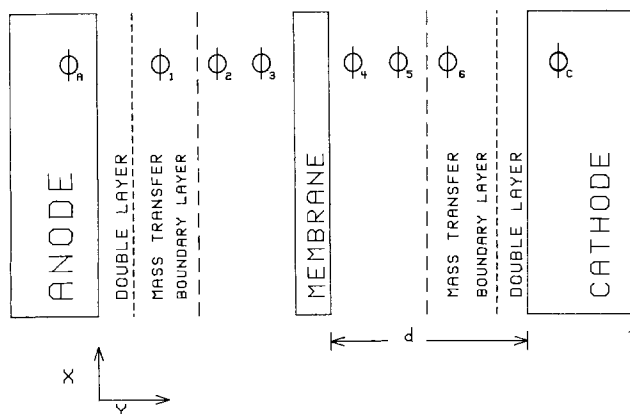
The overall cell potential is the difference between the anode potential and the cathode potential. A schematic of the cell is shown in Fig. 1. Imaginary reference electrodes are placed across the cell in order to divide the overall cell potential into components due to concentration gradients, reaction kinetics, and contributions due to resistances associated with electrolytes in the cell cavities and the membrane. The difference in potential due to concentration gradients and ohmic resistances can be expressed in terms of the concentration overpotential

$$\begin{aligned} \nu_c &= \Delta\phi - \Delta\phi_{IR} \\ &= \frac{RT}{nF} \sum_i S_i \ln \left[\frac{C_{i,bulk}}{C_{i,s}} \right] \end{aligned}$$

where η_c is the concentration overpotential, $\Delta\phi_{IR}$ is the ohmic potential drop, and $\Delta\phi$ is the potential difference between two reference electrodes. The concentrations $C_{i,bulk}$ and $C_{i,s}$ are the bulk and surface concentrations of species i , respectively. Substituting these expressions into the overall cell voltage balance, the following function of bulk and surface concentrations is obtained

$$\begin{aligned} U &= \phi_a - \phi_1 + \frac{2RT}{F} \ln \left[\frac{C_{Fe^{2+},bulk} C_{Cr^{3+},bulk}}{C_{Fe^{3+},bulk} C_{Cr^{2+},bulk}} \right] \\ &+ \frac{RT}{F} \ln \left[\frac{C_{Fe^{3+},s} C_{Cr^{2+},s}}{C_{Fe^{2+},s} C_{Cr^{3+},s}} \right] + \Delta\phi_{IR} \\ &+ V_{formal} + \frac{RT}{F} \ln \left[\frac{C_{Cr^{2+},ref} C_{Fe^{3+},ref}}{C_{Cr^{3+},ref} C_{Fe^{2+},ref}} \right] + \phi_6 - \phi_c \end{aligned}$$

The above equation, in dimensionless form, forms the basis of the VOLBAL model. Full Butler-Volmer kinetic expressions are used to evaluate the potential contributions ($\phi_a - \phi_1$) and ($\phi_6 - \phi_c$). The species concentrations are determined using material balances and reaction stoichiometry. The solution technique requires the assumption of an initial current-density distribution to calculate the



$$\begin{aligned} U &= \phi_A - \phi_C = \\ &\phi_A - \phi_1 + \phi_1 - \phi_2 + \phi_2 - \phi_3 + \phi_3 - \phi_4 + \\ &\phi_4 - \phi_5 + \phi_5 - \phi_6 + \phi_6 - \phi_C \end{aligned}$$

Fig. 1. Schematic of reactor used in the development of the VOLBAL model.

bulk and surface concentrations along the electrode. The calculated concentrations are used to estimate a new current-density distribution. Iterations continue until the new current distribution agrees with the previous values to within three decimal places.

Rigorous model.—The more rigorous model formulated by White is based upon a steady-state material balance for each species [See Ref. (1) for a full development]

$$\nabla \cdot \text{Ni} = 0$$

The model also assumes a small aspect ratio (ratio of the cell gap between the electrodes to the cell length). The resulting system of partial differential equations can be solved for the values of the concentration of species and the potential. The solution technique involves using Newman's technique (BAND) (8) in the normal direction (y) and employing an implicit finite difference technique in the direction parallel to the electrode length. This method yields a two-dimensional field of concentration and potential. The model incorporates a membrane separator through the use of the MacMullin number, which is the ratio of the membrane resistance to the resistance of an equal area of electrolyte. Perhaps the most important difference between the White model and the VOLBAL model is that the former considers well-developed laminar flow and cannot account for other types of mass transfer, such as entrance effects and use of turbulence promoters.

Both models incorporated the hydrogen side reaction into the Butler-Volmer kinetic expression for the cathode. The general kinetic expression as given by White *et al.* (9) can be written as

$$\begin{aligned} i &= i_0 \left\{ \exp \left[\frac{\alpha a F}{RT} \eta_{sj} \right] - \exp \left[\frac{-\alpha c F}{RT} \eta_{sj} \right] \right\} \\ \eta_{s,j} &= V - \phi_0 - U_{j,0} \end{aligned}$$

The final form of the kinetic expression for the side reaction becomes

$$\begin{aligned} i_{H^+} &= i_0 \left\{ \exp \left[\frac{\alpha a F}{RT} (\phi_c - \phi_6 - U_{j,ref}) \right] \right. \\ &\left. - \exp \left[\frac{\alpha c F}{RT} (\phi_c - \phi_6 - U_{j,ref}) \right] \right\} \end{aligned}$$

where

$$\begin{aligned} U_{j,ref} &= U_j^\theta - \frac{RT}{n_j F} \sum_i S_{ij} \ln \left[\frac{C_{i,ref}}{\rho^\circ} \right] - U_{RE}^\theta \\ &+ \frac{RT}{n_{RE} F} \sum_i S_{i,RE} \ln \left[\frac{C_{i,RE}}{\rho^\circ} \right] \end{aligned}$$

This is the same form for the hydrogen reaction as was used by Trainham and Newman (10).

Parameter values.—The predictions of the two mathematical models were compared by applying them to the NASA redox cell. During charge, in the positive half-cell, ferrous ion is oxidized to ferric ion. In the negative half-cell, chromic ion is reduced to chromous ion with some inefficiencies due to proton reduction. The values of the parameters used in calculations with both models are shown in Table I. A membrane resistance of $0.6 \Omega\text{-cm}^2$ is equivalent to a MacMullin number of 3. The simulations appear to incorporate different values for the open-circuit potentials of the electrode with respect to the reference electrode, $U_{j,ref}$. The White model assumes a common reference electrode in both half-cells: the hydrogen reference electrode. VOLBAL assumes that the reference electrode in each half-cell is based on the same reaction as the main reaction occurring at the electrode. This was done to simplify the overall cell voltage expression. The values of $U_{j,ref}$ for VOLBAL are zero for reactions [1] and [2], while the hydrogen side reaction value is given with respect to a chrome reference electrode. The exchange cur-

Table I. Parameter values

Reaction kinetics ^a					
Reaction	α_a	α_c	$i_{0,ref}$ (A-cm ⁻²)	VOLBAL ^b $U_{j,ref}$ (V)	White $U_{j,ref}$ (V)
[1]	0.5	0.5	5.0×10^{-2}	0(0)	0.627 (0.72)
[2]	0.65	0.35	7.5×10^{-3}	0(0)	-0.272 (-0.33)
[3]	0.5	0.5	5.0×10^{-8}	0.272(0.348)	0(0)
Properties					
Species	z	D_i (cm-s ⁻¹)	$C_{ref,i} \times 10^3$ (mol-cm ⁻³)		
Fe ⁺²	+2	6×10^{-6}	0.95 (0.5)		
Fe ⁺³	+3	6×10^{-6}	0.05 (0.5)		
Cr ⁺²	+2	6×10^{-6}	0.05 (0.5)		
Cr ⁺³	+3	6×10^{-6}	0.95 (0.5)		
H ⁺	+	9.31×10^{-5}	1.0 (1.0)		
Cl ⁻	-	2.03×10^{-5}	6.0 (6.0)		
Electrolyte resistivity = 2.0 Ω -cm					
Membrane resistivity = 0.6 Ω -cm ² (ca. $N_{mac} = 3.0$)					
Cell voltage = 1.3V					
Geometry					
Length = 5.31 cm		Width = 4.31 cm			
$d = 0.1$ cm		$V_{avg} = 1.6 - 3.0$ cm/s			

^a α_a , α_c , and $i_{0,ref}$ are from Ref. (11).

^b Terms in parentheses are at 50% state of charge.

rent densities are considered valid for solutions containing 0.45M chrome species and 0.55M iron species at 25°C (11).

Results and Discussion

The predictions of the White and VOLBAL models are compared. In these studies, the VOLBAL model required about nine to ten times less cpu time (IBM 3033U Operating System) than the more rigorous two-dimensional model for three significant digit accuracy. The time savings make the simplified model more attractive for incorporation into multicellular stacks and for optimization studies.

The models have been compared for their predictions of performance after cell scale-up, specifically varying the length of the electrode. The effects of electrolyte velocity as well as the predictions at different states of charge were also compared.

In the comparison of the VOLBAL model and the rigorous White model, the following quantities and their method of calculation should be clarified. The current density calculations are based upon Butler-Volmer kinetics, which allows the current densities predicted by each model to be compared. The bulk concentration predicted by the White model is a "mixing cup" concentration in that the predicted concentrations across the cell are weighed by the velocity and are integrated to generate the average bulk concentration. This effect is similar to the bulk concentration achieved by collecting the electrolyte flowing from a cell and then mixing it well. The VOLBAL model assumes two distinct regions across the gap: the bulk solution and diffusion layers where the concentration variation occurs. Since the diffusion layers are assumed to be very thin, the bulk concentrations of the White model should be comparable to the bulk concentrations calculated by the VOLBAL model. The surface concentrations predicted by VOLBAL depend on the value of the mass-transfer coefficient, whereas the White model solution technique yields concentrations across the cell, including the surface concentration. The reactant species considered in the interpretation of the results is the ferrous ion. The convergence per pass (CPP) of the ferrous species is a measure of the amount of this reactant consumed during one pass through the cell. Through Faraday's law, it is proportional to the total current delivered to the cell. The CPP is obtained by subtracting the di-

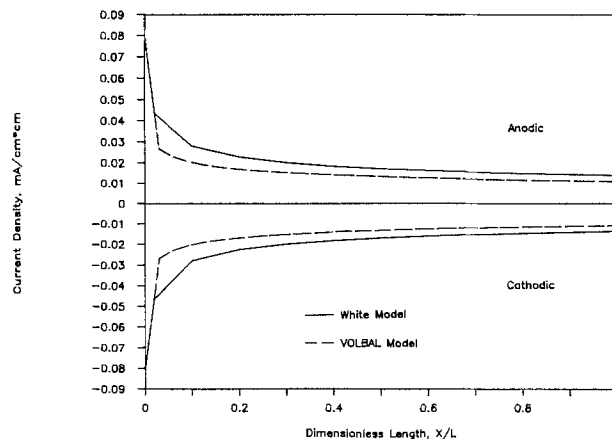


Fig. 2. Calculated anodic and cathodic (main reaction only) current densities at 50% state of charge and $L = 31$ cm.

mensionless bulk concentration at the cell outlet from the dimensionless feed concentration.

Figure 2 shows the predicted current density distribution along the length of the electrode. In this comparison, the electrode length was 31 cm and the solution velocity was 3.0 cm/s. The electrolyte composition corresponds to a 50% state of charge. We found that better agreement in predictions of current density between the two models occurs with larger systems. In this instance, the White model predicts a 23% larger average current density compared to the VOLBAL model. The CPP for the VOLBAL model was 3.2%, and the White model calculated a value of 4.2%. This reflects the differences in the predicted total charging current between the two models.

In order to adjust the VOLBAL model to predict the same average current density as the White model, the mass-transfer coefficient was multiplied by a factor of 1.4. The increased mass-transfer coefficient predicts a current density distribution identical to the White model. The bulk concentrations along the electrode predicted under the three modeling conditions are compared in Fig. 3. The bulk concentration distributions simulated by the VOLBAL model with a modified mass-transfer coefficient closely approaches the White model predictions. In this case, the CPP of the VOLBAL is 4.1%.

The coulombic efficiency predicted by the mathematical models reflects the occurrence of the hydrogen side reaction. Under the conditions reported above, the VOLBAL model calculated a 99.16% coulombic efficiency, while the White model predicted a coulombic efficiency of 99.2%. The calculations using the VOLBAL model with the adjusted mass-transfer coefficient predict a coulombic efficiency of 99.4%. The efficiency increased because of the larger mass-transfer coefficient, which represents an increase in the transport of the chromic reactant to the surface. The larger surface concentration of chrome

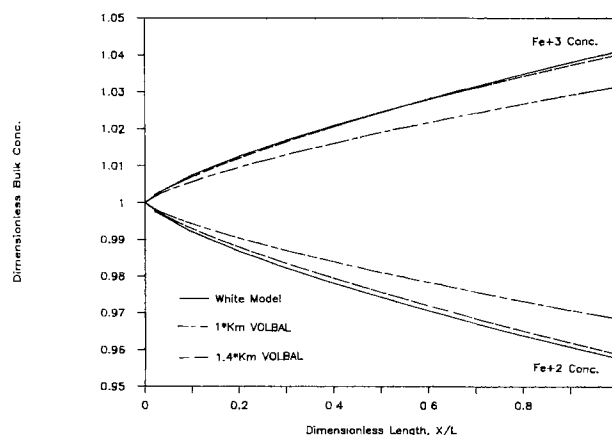


Fig. 3. Simulated bulk concentration profiles of iron species at 50% state of charge and $L = 31$ cm.

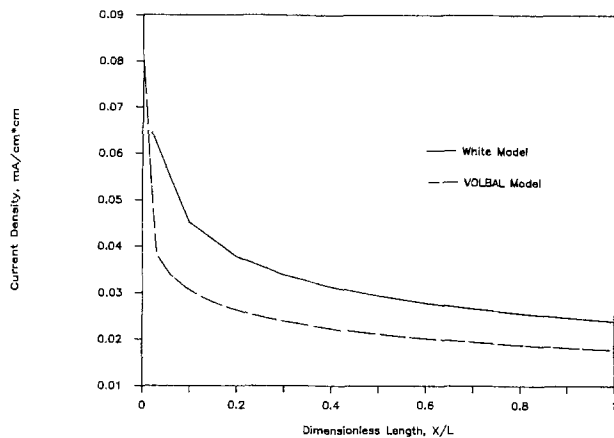


Fig. 4. Anodic current density predictions for 50% state of charge and $L = 5$ cm.

reactant produces a larger overall current density, while the side reaction contribution remains the same.

A cell with an electrode length of 5 cm at 50% state of charge (still with 3.0 cm/s average electrolyte velocity) was simulated next. Figure 4 shows the predicted current density distributions along the length of the electrode. The model predictions for average current density differ by 28% for the small cell. This was expected, since larger gradients will occur in shorter cells. The coulombic efficiencies are identical for both models, at 99.5%. Although the current densities are generally larger for smaller cells, the shorter electrodes mean less area available for reaction and thus a decrease in CPP. The VOLBAL model calculates a CPP value of 0.79%, while the White model prediction is 1.13%.

Lowering the flow rate to 1.6 cm/s while keeping the other conditions constant results in an increase in CPP because more reactant can be consumed at the electrode surface before leaving the cell. The CPP value calculated by the VOLBAL model is 1.3% and by the White model is 1.8%. A lower flow rate also results in a small decrease in coulombic efficiency, 99.4%. Figure 5 shows the bulk concentration distributions simulated by the two models under these conditions.

In general, the more rigorous model predictions of current density are larger than those predicted by the VOLBAL model. The rigorous model accounts for effects of migration while VOLBAL does not, but migration in redox systems generally would cause an effect of only 10% or less (8). In comparing the calculations of the two models, the surface concentrations of the reacting species predicted by the rigorous model are less than those predicted by the VOLBAL model. However, the surface overpotential values calculated by the rigorous model are greater than those of the VOLBAL model. In the Butler-

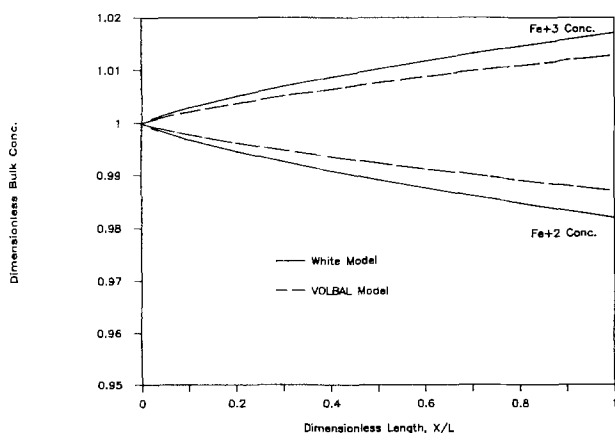


Fig. 5. Model predictions of bulk solution concentration for iron species at 5% state of charge, $L = 5$ cm and average velocity 1.6 cm/s.

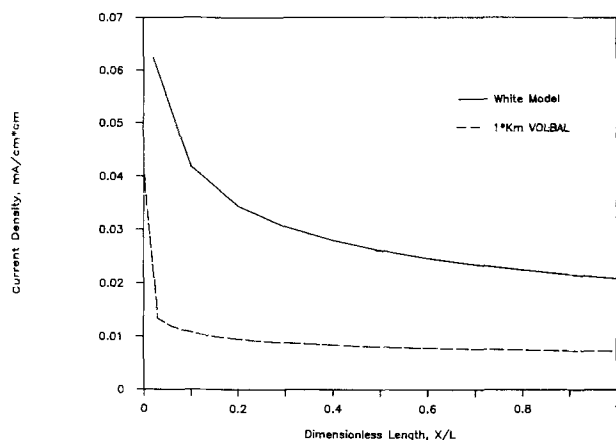


Fig. 6. Anodic current density predicted for 5% state of charge, $L = 31$ cm and average velocity 1.6 cm/s.

Volmer expression, the two effects tend to cancel, allowing for moderate agreement between the two models in predicting current density and bulk concentration distributions. An increase in mass-transfer coefficient in the VOLBAL model causes an increase in surface concentration and surface overpotential, thus resulting in a calculated increase in the current density.

The predictions of the models were compared for the 5% state of charge condition. In this case, the larger cell with 31 cm electrodes having a velocity of 1.6 cm/s was considered. The model predictions of current density distributions are shown in Fig. 6. For the 50% state of charge, the surface overpotential dominated. At 5% state of charge, the concentration overpotential is dominant. The differences in calculated surface concentrations between the two models cause this great disparity. There appears to be a significant boundary-layer effect under these conditions which we cannot explain at this time. Better agreement could probably be achieved if the position dependency of the local mass-transfer coefficient was further investigated.

Conclusions

The predictions of cell performance using the simplified VOLBAL model and a more rigorous model were compared. The VOLBAL model uses about nine to ten times less cpu time than the rigorous model on an IBM 3033U operating system. Comparisons show that the rigorous model generally predicts a higher current density. The model predictions are in closer agreement for large cells. Agreement between model predictions at extreme conditions (i.e., 5% state of charge) is poor, which can be attributed to disagreement between the calculated surface concentrations. Both models need rigorous testing against experimental observations.

Acknowledgments

The generous support of The Electrochemical Society through an Energy Research Summer Fellowship sponsored by the U.S. Department of Energy is gratefully acknowledged. I am grateful to Dr. R. E. White and Mike Mader of Texas A&M University for their modeling code. The help, support, and good-natured guidance provided by my advisor, Dr. Savinell, is deeply appreciated.

LIST OF SYMBOLS

$C_{i,bulk}$	bulk concentration of species i (mol/cm ³)
$C_{i,ref}$	reference concentration of species i (mol/cm ³)
$C_{i,RE}$	concentration of species i in reference electrode solution (mol/cm ³)
$C_{i,s}$	local surface concentration of species i (mol/cm ³)
d	the distance between the electrode and the membrane separator (cm)
D_i	diffusion coefficient of species i (cm ² /s)
F	Faraday's constant (96,487 C/mol)
i	current density (A/cm ²)
i_0	exchange current density (A/cm ²)

$i_{o,ref}$	exchange current density at reference concentrations (A/cm ²)
K_m	mass transfer coefficient (cm/s)
L	electrode length (cm)
n_j	number of electrons transferred in reaction j
R	universal gas constant (8.3143 J/mol-K)
s_{ij}	stoichiometric coefficient of species i in reaction j.
T	absolute temperature (K)
U	overall cell potential (V)
$U_{j,o}$	theoretical open-circuit potential for reaction j at the surface concentrations of species i which participate in reaction j (V)
$U_{j,ref}$	theoretical open-circuit potential evaluated at reference concentrations (V)
U_j^θ	standard electrode potential of reaction j (V)
V_{avg}	average velocity (cm/s)
z	charge number of species

Greek Symbols

α_a	anodic transfer coefficient
α_c	cathodic transfer coefficient
θ_o	solution potential adjacent to the electrode surface (V)
θ_i	reference electrodes; i = 1, 6.
θ_a	anode potential (V)
θ_c	cathode potential (V)

REFERENCES

1. R. E. White, M. Bain, and M. Raible, *This Journal*, **130**, 1037 (1983).
2. W. R. Parrish and J. S. Newman, *ibid.*, **117**, 43 (1970).
3. R. Caban and T. W. Chapman, *ibid.*, **123**, 1036 (1976).
4. J. Lee and J. R. Selman, *ibid.*, **129**, 1670 (1982).
5. M. A. Hobercht, NASA TM-82598.
6. L. H. Thaller, U. S. Pat. 3,996,064 (1976).
7. Modifications by L. G. Kleine and M. Mader.
8. J. Newman, "Electrochemical Systems," Prentice-Hall, Englewood Cliffs, NJ (1973).
9. R. E. White, S. E. Lorimer, and R. Darby, *This Journal*, **130**, 1123 (1983).
10. J. A. Trainham and J. Newman, *ibid.*, **124**, 1528 (1977).
11. P. S. Fedkiw and R. W. Watts, *ibid.*, **131**, 701 (1984).

Susan E. Morris was born in Durham, North Carolina, in 1960. She received her B. S. degree in chemistry from Western Carolina University, Cullowhee, North Carolina, in 1981.

Morris is studying to gain a Ph.D. degree from the University of Illinois at Urbana-Champaign, and has been a Kodak Graduate Scholar.

Ms. Morris' report appears below.

O₂ Diffusion as a Probe of Fluidity in Polymer Films

Polymer films on electrodes provide a convenient narrowly defined spatial region in which redox centers may be immobilized for electrocatalysis or sensing of electrochemically inaccessible analytes. One of the considerations in the use of films is that three-dimensional dispersion within a polymer increases the amount of catalyst, by comparison with monolayer coverage of the electrode, increasing catalytic efficiency (or increasing signal, in the case of a sensor). Within the film, availability of substrate for reaction with the catalyst depends on both the ability of the substrate to partition into the film and to freely diffuse to catalyst centers. Most studies of charge and mass transport in films have focused on the electrochemical response of the catalyst, relying on its adherence to simple diffusion laws which were formulated for systems resembling dilute solutions. Enhancement of mass transport by charge transfer reactions is commonly evaluated using the Dahms-Ruff equation (1, 2)

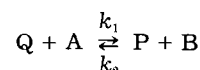
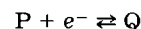
$$D_{eff} = D_m + D_{ex} = D_m + (\pi/4) \delta^2 k C^*$$

where D_{eff} is the observed diffusion coefficient, D_m is the diffusion coefficient observed in the absence of charge

transfer, δ is the intersite charge transfer distance, and k is the charge transfer rate constant.

Difficulty in evaluation of these processes from the electrochemical response of the catalyst within the film using the Dahms-Ruff expression is twofold; both problems stem ultimately from the use of the catalyst as a probe which is inextricably involved with both transport processes and structure of the film. First, the catalyst is present in very high local concentration (catalyst loadings of 10^{-9} - 10^{-8} mol-cm⁻² in films of a few hundred angstroms thickness are common), often rivaling the electrolyte concentration in solution and certainly that within the film. Unavoidable convolution of diffusion and migration contributions to catalyst charge and mass transport result, ensuring that purely diffusional behavior in the film will not be observed. Perhaps more important is the problem created by the inclusion of the catalyst as an integral structural component of the film: stimuli (large amplitude potential steps, for example) which result in observable electrochemical responses should be reasonably expected to simultaneously affect film structure. The result will be time-dependent changes in film physical characteristics such as viscosity or film thickness, both of which will affect apparent diffusional behavior within the film.

A kinetic model for the processes occurring in or at catalyst-loaded films on electrodes has been developed by Andrieux *et al.* (3-5). Catalyst (or mediator) couple in film and oxidized and reduced forms of substrate are represented below



In the model, which was developed for steady-state techniques such as rotating disk voltammetry, the catalytic current may be studied via the use of closed-form equations which represent the catalytic current in terms of characteristic currents which are related to kinetic and mass transport limiting behaviors. Where $K (= k_1/k_2)$ is allowed to take any value, four cases have been identified; the present study utilizes a system of catalyst/substrate which corresponds to the true catalytic situation (Fig. 1). The component currents in which we are interested are i_A and i_s . It is the substrate mass transport as a function of film control by the catalyst, and not the mass or charge transport of the catalyst, with which we are concerned

$$i_A = nFAC^*_o D_o / \delta = 0.62nFAC^*_o D_o \omega^{1/2} \nu^{-1/6}$$

$$i_{R,S} = nFAk_t \kappa C^*_o D_s / \phi$$

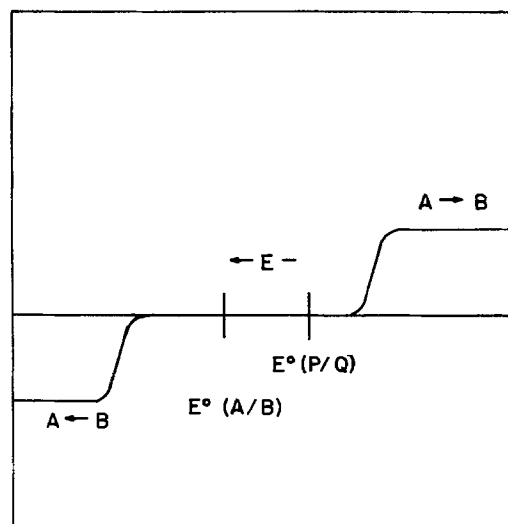


Fig. 1. Relationship of reversible catalyst couple and irreversible substrate couple on potential scale.

where n is the number of electrons transferred, A is the electrode area, C^* is the bulk concentration of substrate in solution, D_s is the solution diffusion coefficient of substrate, ω is the electrode rotation rate, ν is the kinematic viscosity of the supporting electrolyte solution, κ is the partition coefficient of the substrate between the film and solution, D_f is the diffusion coefficient of the substrate in the film, and ϕ is the film thickness. Standard electrochemical units are used.

Transient experiments are performed by applying a large amplitude potential step ($\geq 1.0V$) to the loaded film in the presence and absence of substrate in the solution. Substrate diffusion information is extracted by subtraction of curves generated in the absence of substrate from those generated in substrate-saturated films. Differential charge is plotted against time (ΔQ vs. t or ΔQ vs. $t^{1/2}$) in order to determine the functional time dependence of substrate transport in the film.

We are investigating the physical nature of poly(4-vinylpyridine) (PVP) films loaded at pH 3 with ferricyanide (catalyst) in an ion exchange process. Molecular oxygen (substrate) has been chosen as a structurally independent probe of mass transport in films, having the advantages of electroactivity, neutral charge, and nearly universal solubility. Very small k_f allows simple study of O_2 without complication of catalytic currents. Films are applied to a rotating disk electrode, allowing comparison of steady-state (hydrodynamic) and transient behavior.

All reagents except PVP were reagent grade and were used as received. Loading and ferricyanide-free supporting electrolyte solutions had the following composition: 0.065M potassium nitrate, 0.035M potassium biphthalate, and 0.015M nitric acid in ultrapure water (Continental Millipore Water Systems). Poly(4-vinylpyridine) (Mw = 300,000) received as a sample (Reilly Tar and Chemical Company, Indianapolis, Indiana) was cross-linked using 1,4-dibromobutane in methanol solution, to the extent that 2% of pyridine moieties are involved in cross-links. PVP solution (5% w/v) was dispensed as a drop to completely cover the surface of a static glassy carbon electrode (0.28 cm²) which was then accelerated to 4500 rpm under a methanol-saturated atmosphere to spin coat a thin uniform film. Films were dried 20 min at 80°C in air to complete solvent evaporation and cross-linking. Initially, the dry film has an interference color of blue or deep purple; after loading in 0.1 mM ferricyanide at pH 3 to 2×10^{-8} mol-cm⁻², the dry film is yellow or yellow-green in color.

Potentiostatic control was maintained using a Z-80 microprocessor-controlled cybernetic potentiostat (6) modified for performance of chronocoulometry on a time scale up to 12.5s. All experiments were performed in a specially built hydrodynamic voltammetry cell (7) with Pt wire counter and Ag/AgCl reference electrodes. A variable speed rotator and controller were used to set rotation speed (Pine Instrument Company).

A film of PVP spin coated at 4500 rpm from a dilute MeOH solution of lightly cross-linked PVP leads to a quasi-steady state from 0.1 mM ferricyanide in around 5 min, cycling at 50 mV/s, in an ion exchange-like process (Fig. 2) (8). The electrode is transferred to O_2 -saturated electrolyte solution after shaking away excess loading solution. In Fig. 3, the small peak separation ($\Delta E_p = 39$ mV) and narrow symmetrical peaks of the ferricyanide redox process at +0.25V are indicative of a surface response. The irreversible wave for O_2 reduction observed at $E_{1/2}$ of -0.7V is well separated from the ferricyanide response, and is at the same potential where it is observed on the bare GC electrode.

For longer time experiments ($\tau = 2000$ ms) at varying rotation rates, the limiting penetration current $i_{k,s}$ can be evaluated. The slopes of linear ΔQ vs. t plots are the limiting currents observed at the given rotation rates. When these currents are plotted in the Koutecky-Levich format (i^{-1} vs. $\omega^{-1/2}$) the intercept reflects the rotation-independent substrate penetration current, $i_{k,s}$. For the films studied, this current was found to be $1.2 \times 10^{-3}A$.

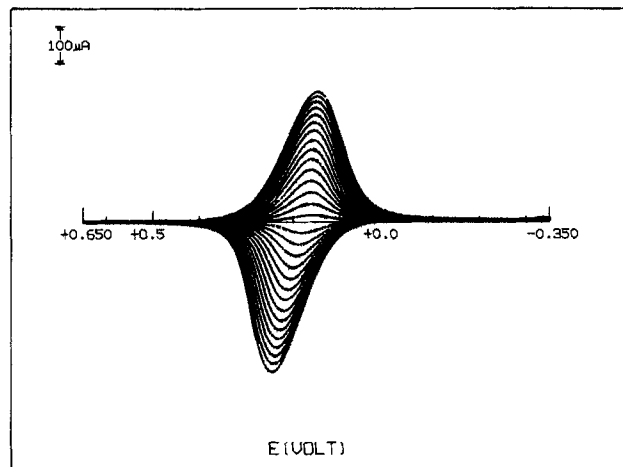


Fig. 2. Cyclic voltammetric scans of loading PVP film in 0.1 mM ferricyanide (pH 3 buffered supporting electrolyte). Scan rate = 50 mV/s. Solution stirred by nitrogen bubbler.

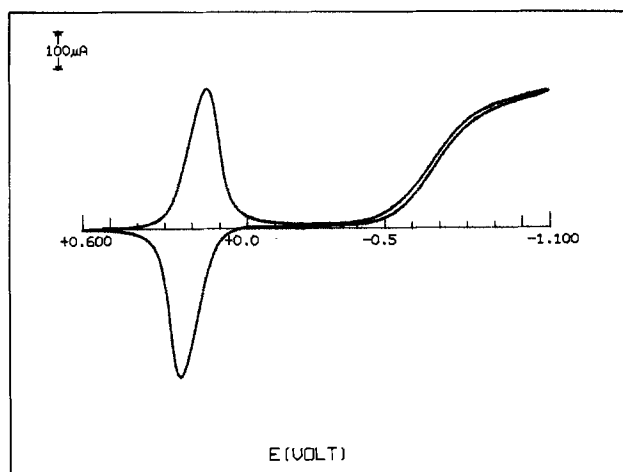


Fig. 3. Cyclic voltammetric scan of a ferricyanide-loaded film in O_2 -saturated ferricyanide pH 3 buffered electrolyte solution. Scan rate = 75 mV/s. Rotation rate = 500 rpm. Electrode area = 0.28 cm².

The corresponding current measured (using i_A^{-1} vs. $\omega^{-1/2}$) for the bare GC electrode is i_k (i_k arises because the oxygen reduction is completely irreversible: the rate constant k_f is also included in $i_{k,s}$). i_k was found to be $8.3 \times 10^{-3}A$. If the expressions for $i_{k,s}$ and i_k are ratioed, the resulting relation is derived

$$\kappa D_s / \phi = 0.145$$

$$i_k = nFAk_f C^*$$

Using reasonable hypothetical values for κD_s and ϕ , ($\kappa D_s = 5 \times 10^{-6}$ cm²-s⁻¹, $\phi = 3000\text{\AA}$), an estimate of $\kappa D_s / \phi$ of 0.17 was reached. These values agree fairly closely, indicating that the method is returning results which agree with the expected behavior.

For diffusion within the film, short time transients ($\tau < 30$ ms) were observed; such short times were necessary to ensure that the initial oxidation state of the film was fundamentally preserved on the experimental time scale (in the case of the initially oxidized film). Differential charge-time plots for O_2 diffusion in an initially oxidized and reduced film (Fig. 4 and 5) show that the diffusion behavior is markedly different depending on the initial state of the film. Slopes of plots are shown in Table I. A $t^{1/2}$ dependence for the oxidized film is similar to the diffusion seen in solution at the bare GC electrode. The ability of the electrode to draw down the concentration of O_2 at a rate faster than it can be diffusively replenished is seen. By contrast, in the initially reduced film a linear charge-time response indicates that the surface concentration of O_2 (at the GC) is not drawn down, indicating that the environment of the reduced film is less viscous than in the oxidized form. If it is assumed that the

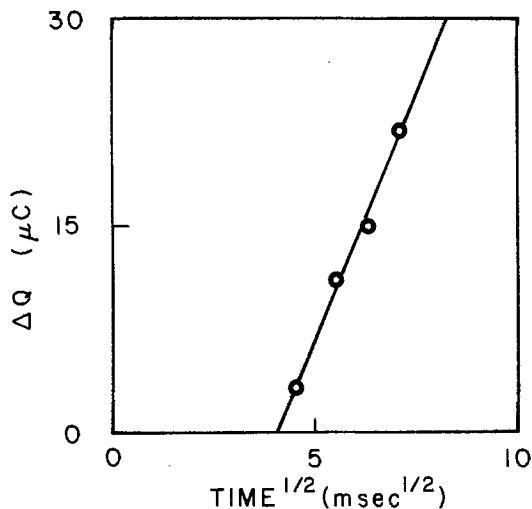


Fig. 4. Transient (ΔQ vs. $t^{1/2}$) plot generated at a rotating disk electrode for an initially oxidized film in O_2 -saturated solution. Rotation rate = 1000 rpm.

oxygen concentration in the film is the same in both states of the film, the diffusion coefficient of oxygen in the reduced film appears greater, allowing diffusive replacement of oxygen faster than it can be replaced. That this phenomenon is occurring within the film, and not homogenizing the oxygen concentration to the film boundary on the time scale of the experiment, is evidenced by the insensitivity of these transients to electrode rotation rate.

A possible explanation for the apparent lower viscosity of the reduced film, where the loading is the same as in the oxidized form, lies in the relative amounts of charge incorporated by both. The negative charge associated with the reduced form, ferrocyanide, is 25% greater than that for the oxidized, ferricyanide. This requires uptake by the film of compensating positive charge: K^+ or H^+ , possibly solvated. For a film which is cross-linked, the polymer structure is limited in its capacity to accommodate excess volume, while it is also under the structural control imposed by the incorporated catalyst. Since cycling the electrode potential over the ferricyanide reduction potential drastically speeds the exchange process, it is likely that the film resists the uptake of electrolyte species, excepting those with large formation constants for complexation within the film (protons and ferricyanide). The excess charge density and volume due to reduction and compensating charges may account for a polymer structure so "stretched" that it acts rigid and porous, allowing very rapid diffusion of O_2 . Indeed, these films have been observed to change interference color upon ox-

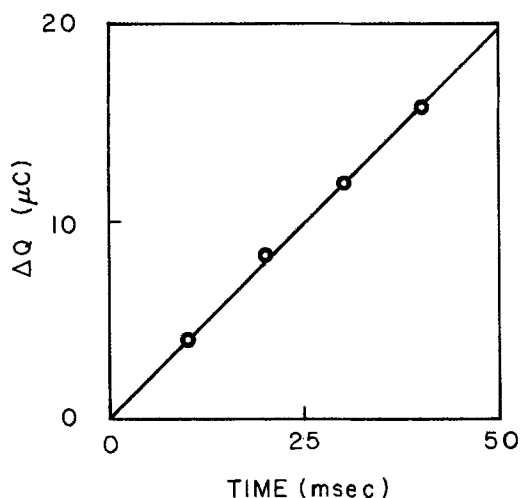


Fig. 5. Transient (ΔQ vs. t) plot generated at a rotating disk electrode for an initially reduced film in O_2 -saturated solution. Rotation rate = 1000 rpm.

Table I. Summary of slope values from differential charge-time plots

Initial potential (V)	Linearity	Slope ^a
-0.100	t	$5.3 (+ 1.1) \times 10^{-4} \text{ C-s}^{-1/2}$
+0.500	$t^{1/2}$	$1.6 (+ 0.65) \times 10^{-4} \text{ C-s}^{-1/2}$

^aAverage of results for three films; $\Gamma_0 = 2 \times 10^{-8} \text{ mol-cm}^{-2}$.

idation or reduction, indicating a change in film thickness. Alternatively, it could be supposed that a rearrangement of the film to allow increased association of protonated pyridine groups with the ferrocyanide, expelling excess negative charge as anions, would occur. This would also change the film thickness by thinning and tightening the film, but since it should lead to an apparent increase in viscosity this mechanism does not seem to correlate with the results. In addition, if the film does not contain a large excess of counterions to begin with, then compensating charge must be drawn from solution rather than expelled from the film.

Continuing work in this project is directed toward determination of the diffusion coefficient of O_2 in PVP films by a spectroscopic technique utilizing fluorescence quenching of an immobilized fluorophore in the film. The results of the electrochemical and spectroscopic experiments will be compared to prove the validity of these methods for study of physical characteristics of polymer films on electrodes.

Acknowledgments

The author is grateful for the support of The Electrochemical Society through a Summer Energy Research Fellowship. Professor L. R. Faulkner deserves many thanks for the support and direction which he has provided.

REFERENCES

1. I. Ruff and V. J. Friedrich, *J. Phys. Chem.*, **75**, 3297 (1971).
2. H. Dahms, *ibid.*, **72**, 362 (1968).
3. C. P. Andrieux, J. M. Dumas-Bouchiat, and J. M. Saveant, *J. Electroanal. Chem.*, **131**, 1 (1982).
4. C. P. Andrieux, J. M. Dumas-Bouchiat, and J. M. Saveant, *ibid.*, **134**, 163 (1982).
5. C. P. Andrieux and J. M. Saveant, *ibid.*, **142**, 1 (1982).
6. P. He, J. P. Avery, and L. R. Faulkner, *Anal. Chem.*, **54**, 1313A (1982).
7. E. T. T. Jones, *This Journal*, **132**, 245C (1985).
8. N. Oyama and F. C. Anson, *ibid.*, **127**, 247 (1980).

David P. Wilkinson was born in Duncan, British Columbia, Canada. In 1978, he received a B.A.Sc. degree in chemical engineering from the University of British Columbia, Vancouver, British Columbia, Canada.

After being graduated, Wilkinson worked as a research engineer for Ballard Research, Incorporated, Vancouver, on primary and secondary lithium battery systems, particularly with the Li/SO_2 system. Currently, he is working for a Ph.D. degree at the University of Ottawa, Ottawa, Ontario, Canada.

Mr. Wilkinson's report follows.

Comparison of "True" Kinetic Parameters for H_2 Evolution from Various Proton Donors in Water, Acetonitrile, and N,N -Dimethylformamide

The electrochemical hydrogen evolution reaction (HER) has often been regarded as a useful model for the

kinetic study of simple and other complex multistep electrode reactions. The mechanism of the activation process in such a coupled atom/electron-transfer process is not yet well understood, despite many papers on HER kinetics published in earlier years.

Study of the temperature and potential dependence of the HER from different proton sources in different solvent media allows the determination of the individual enthalpic and entropic components of the free energy of activation. These quantities for the activation process of proton transfer and neutralization at Hg should lead to a substantially improved understanding of the nature of activation in the elementary act of complex electron and atom transfer. The HER can be studied at a Hg electrode without the complication of a potential-dependent coverage of the electrode by adsorbed H such as arises at Pt or Ni.

Several investigators (1, 2) have studied the HER at Hg from methanolic HCl, but aside from these contributions very little work has been conducted in nonaqueous media. Conway and Tessier (3) have made a comparative study of the kinetics of the HER at Hg from the unhydrated H_3O^+ ion in pure $\text{CF}_3\text{SO}_3\text{-H}_3\text{O}^+$ and the hydrated H^+ aq ion in 1M aqueous $\text{CF}_3\text{SO}_3\text{H}$. Significantly different "apparent" activation parameters (constant overpotential) are found for the HER from different media. Krishtalik and co-workers (4-7) have examined the question of medium and bond stretching activation effects in proton discharge. They emphasized the proton discharge theory of Dogonadze *et al.* (8), the most developed of the continuum solvent reorganization models. In this approach, emphasis is placed on the role of the solution medium in bringing the proton donor into a state from which proton tunneling to a state of equal energy can occur. The observation of equal "apparent" activation energies for CH_3CNH^+ and H_3O^+ in acetonitrile solution at Hg (5) and the significantly different "apparent" activation energies for H_3O^+ in water and acetonitrile was taken to indicate that the activation energy is completely determined by reorganization of the solvent. However, Khan (9) has pointed out that, according to the bond stretching and activation models, one would expect a different free energy of activation on the basis of force constants alone, since the stretching frequencies of CH_3CNH^+ and H_2OH^+ bonds are different. Also, on the basis of a continuum solvent reorganization model, different free energies of activation should be expected because of the unequal radii of the H_3O^+ (0.14 nm) and CH_3CNH^+ (0.25 nm) ions. All of the above studies involved a comparison of "apparent" activation parameters in which the reference electrode metal-solution potential difference, $\phi_{\text{M-S}}^{\text{R}}$ is reversible to the proton source and varies with temperature and solution environment. Under these conditions, a quantitatively meaningful comparison of the proton donor discharge kinetics is difficult.

In view of the criticized but promising line of investigation of the above investigators, "true" activation parameters were investigated for proton donors in the aprotic solvents, acetonitrile (AN) and N,N-dimethylformamide (DMF) and in the protic solvent water. "True" activation parameters correspond to the condition of constant electrode potential (or field) rather than constant overpotential, that is, measurements are made with respect to a reference electrode potential $\phi_{\text{M-S}}^{\text{R}}$ invariant with temperature and solution composition at the working electrode. It is a well-known problem (10) that only "apparent" activation parameters are accessible from experimental electrode-kinetic measurements, but this problem can be circumvented by reasonable extra-thermodynamic assumptions. Temkin (10) first treated the problem of the relation between the "apparent" and "true" heats of activation, but a more direct analysis was given by Conway (11).

The reference electrode potential can be maintained constant with varying temperature by conducting polarization measurements with a reference electrode at the same but varied temperature of the working electrode

(isothermal measurement) and then correcting the potential scale used with a separately measured nonisothermal reference cell potential under conditions, as used in the work reported here, where the thermal junction potential is minimized. This approach was adopted by Weaver and co-workers (12) in their studies of complex ion redox reactions. The reference electrode potential can be fixed for different proton donors and solvents by using appropriate reference electrode cells and correcting polarization data to a common potential scale. For all reference cell corrections, the extrathermodynamic assumption is made that the unknown irreversible liquid-junction potential can be made negligible compared to the difference of the metal-solution potential difference at the two single electrode interfaces. "True" kinetic parameters are then obtained from the relation between $\ln i_v$ and T^{-1} at a fixed electrode potential following previously employed procedures (13) in the analysis of kinetics from Arrhenius plots.

Experimental

Steady-state polarization measurements were made potentiostatically over a range of temperatures for the HER at liquid Hg, from 0.1M aq HCl, 0.1M aq $\text{C}_2\text{H}_5\text{NH}_3\text{Cl}$, 0.1M aq $(\text{C}_2\text{H}_5)_3\text{NHCl}$, 0.1M $\text{CF}_3\text{SO}_3\text{H}$ in DMF, 0.1M $(\text{C}_2\text{H}_5)_3\text{NHCF}_3\text{SO}_3$ in DMF, 0.1M $(\text{C}_2\text{H}_5)_3\text{NHCF}_3\text{SO}_3$ in CH_3CN , and 0.1M $\text{CF}_3\text{SO}_3\text{-H}_3\text{O}^+$ in CH_3CN . No supporting electrolyte was used, as all the acids and salts are strongly dissociated in the respective solvents employed at the concentrations used (14, 15). The Ag/AgCl reference electrode was used in the aqueous systems, and the 0.01M AgClO_4/Ag reference electrode was used in the aprotic solvents. These reference electrodes were referred to the reference half-cell H_2/H^+ 0.1M HCl (H_2O)|KCl sat. (H_2O)| so that all the potential scales could be adjusted to one fixed reference electrode potential.

Pure liquid Hg (Aldrich Gold Label, 99.99999%) was contained in a silanized Pyrex glass cup giving an electrode area of ca. 0.393 cm^2 . The glass cup was resilanized regularly to prevent solvent creep, and the Hg was replaced regularly to minimize any accumulation of impurities at the Hg surface.

Triply distilled water and Burdick and Jackson spectroscopically pure DMF and AN (0.008% and 0.006% H_2O by Karl Fischer titration, respectively) were used directly. High purity $\text{CF}_3\text{SO}_3\text{H}$ (3M Company) was prepared by double distillation (16), and the monohydrate, $\text{CF}_3\text{SO}_3\text{-H}_3\text{O}^+$, was prepared and purified as described previously (3). For the $\text{CF}_3\text{SO}_3\text{H}$ in DMF system, a small amount ($\approx 0.01\text{M}$) of the anhydride $(\text{CF}_3\text{SO}_2)_2\text{O}$ was added to react with any residual H_2O as a "getter" to attain "ultra-dry" conditions. The salt $(\text{C}_2\text{H}_5)_3\text{NHCF}_3\text{SO}_3$ was prepared by adding $\text{CF}_3\text{SO}_3\text{H}$ slowly to a large excess of $(\text{C}_2\text{H}_5)_3\text{N}$ at 233 K. The salt was recrystallized several times from diethyl ether and then vacuum dried at room temperature for several days. For the aqueous systems, high purity Aristar HCl was used directly and the Fluka salts $(\text{C}_2\text{H}_5)_3\text{NHCl}$ and $(\text{C}_2\text{H}_5)_3\text{NH}_3\text{Cl}$ were recrystallized twice from methanol and vacuum dried at 333 K for several days. The melting points of the salts were used as criteria of purity.

Results

Table I shows the "true" activation energies and frequency factors for the different proton donors in their respective solvents. The "true" entropies of activation ΔS^{\ddagger} (proportional to $\ln [A]$, where A is the frequency factor) have also been included. These entropies were derived from the intercepts, $\ln A$, of the electrochemical Arrhenius plots at constant metal-solution potential difference according to the relation

$$\Delta S^{\ddagger} = R\{\ln A - \ln(zFAC(1 - \theta)KT/h)\} \quad [1]$$

where c is the bulk concentration in moles per cubic centimeter and θ is the coverage by H assumed $\ll 1$ for Hg so that $(1 - \theta) \approx 1$.

In the context of a particular rate theory, the magnitude and sign of the entropy of activation are determined by

Table I. "True" kinetic parameters for the HER from different proton donors in H₂O, DMF, and AN

Proton donor	ΔH^\ddagger (kJ·mol ⁻¹)	ΔS^\ddagger (J·K ⁻¹ ·mol ⁻¹)	log [A]	i_0 (A·cm ⁻²) (298 K)	pK _a
H ₃ O ⁺ (H ₂ O)	91.2	-202	3.9	9.1×10^{-13}	-3
C ₂ H ₅ NH ₃ ⁺ (H ₂ O)	101.3	+15	14.9	4.9×10^{-15}	10.81
(C ₂ H ₅) ₃ NH ⁺ (H ₂ O)	181.5	-203	3.4	1.1×10^{-17}	11.01
DMFH ⁺ (DMF)	71.8	-163	5.6	9.3×10^{-8}	-1.5
(C ₂ H ₅) ₃ NH ⁺ (DMF)	95.5	-180	4.7	8.5×10^{-13}	9.25
H ₃ O ⁺ (AN)	68.3	-206	3.3	2.4×10^{-9}	—
(C ₂ H ₅) ₃ NH ⁺ (AN)	116.7	-128	7.4	9.0×10^{-14}	18.46

the choice of standard state for reactant and activated complex as well as by chemically significant factors such as structural or electrostrictive changes. Useful conclusions can be drawn from the relative ordering of frequency factors and entropies of activation, but caution has to be exercised in rationalizing or interpreting the sign and magnitude of entropies of activation. The rates of proton discharge at 298 K for the different systems are all compared at the same metal-solution potential of the hydrogen electrode in 0.1M aqueous HCl. The rates are related to the standard chemical free energy by

$$i = B \exp[-\Delta G^\ddagger/RT] \quad [2]$$

where B is a combination of constants. Double-layer effects at Hg for the systems studied here are expected to be similar except for specific adsorption of the alkyl ammonium ions.

It is evident from a comparison of the kinetic parameters that there are appreciable differences for the same proton donor in different solvent media and for different proton donors in the same solvent. The similar size and bond length where the charge is centered of the proton donors implies a similar electrostatic interaction with the same medium, but the significant activation energy differences indicate that the nature of the ruptured bond and specific solvational and solvent-structure aspects are important in addition to the influence of the medium. An electrochemical Brønsted relation (17) between the rates of proton discharge and the state of solvation of the proton donor is indicated. From the results obtained, it is found that specific as well as general medium effects have to be included in any interpretation of electrode reaction rates involving cathodic H₂ evolution and, probably, in other electrode processes.

The results described briefly above, together with other work related to the HER, will be presented in detail in a forthcoming publication.

Acknowledgments

The author would like to thank The Electrochemical Society for its support through the Energy Research Summer Fellowship and Professor B.E. Conway for helpful consultations.

REFERENCES

1. J. O'M. Bockris and R. Parsons, *Trans. Faraday Soc.*, **45**, 916 (1949).
2. M. Salomon and B. E. Conway, *Discuss. Faraday Soc.*, **39**, 223 (1965).
3. B. E. Conway and D. F. Tessier, *Int. J. Chem. Kinet.*, **13**, 925 (1981).
4. L. I. Krishtalik, V. M. Tsionsky, and G. E. Titova, *J. Res. Inst. Catal., Hokkaido Univ.*, **22**, 101 (1974).
5. G. E. Titova and L. I. Krishtalik, *Elektrokhimiya*, **13**, 897 (1977).
6. L. I. Krishtalik and G. E. Titova, *ibid.*, **13**, 1118 (1977).
7. L. I. Krishtalik, *Faraday Discuss., Chem. Soc.*, **74**, 205 (1982).
8. R. R. Dogonadze, A. M. Kuznetsov, and V. G. Levich, *Electrochim. Acta*, **13**, 1025 (1968).
9. S. U. M. Khan, in "Modern Aspects of Electrochemistry," Vol. 15, R. E. White, J. O'M. Bockris, and B. E. Conway, Editors, Plenum Press, New York (1983).
10. M. I. Temkin, *Zh. Fiz. Khim.*, **22**, 1081 (1948).
11. B. E. Conway, "Theory and Principles of Electrode Processes," Ronald Press Co., New York (1964).
12. E. L. Yee, R. J. Cave, K. L. Guyer, P. D. Tyma, and M. J. Weaver, *J. Am. Chem. Soc.*, **101**, 1131 (1979).
13. M. J. Weaver, *J. Phys. Chem.*, **83**, 1748 (1979).
14. T. Fujinaga and I. Sakamoto, *Pure Appl. Chem.*, **52**, 1387 (1980).
15. T. Fujinaga and I. Sakamoto, *J. Electroanal. Chem.*, **73**, 235 (1976).
16. R. Corkum and J. Milne, *Can. J. Chem.*, **56**, 1832 (1978).
17. B. E. Conway, in "Progress in Reaction Kinetics," G. Porter, Editor, Chap. 10, p. 399, Pergamon Press, Oxford, England (1967).